

1 JUNE 1998
PART 2

VOLUME 83 NUMBER 11

JOURNAL OF APPLIED PHYSICS

Proceedings of the Seventh Joint Magnetism and Magnetic
Materials-Intermag Conference

DISTRIBUTION STATEMENT A

Approved for public release;
Distribution Unlimited

AVAILABLE ONLINE—See www.aip.org

AMERICAN
INSTITUTE
OF PHYSICS

JOURNAL OF APPLIED PHYSICS

CODEN: JAPIAU

ISSN: 0021-8979

URL: <http://www.aip.org/journals/jap/jap.html>

Editor

Steven J. Rothman
Argonne National Laboratory
Argonne, IL

Associate Editors

Roy Benedek	Mitio Inokuti
Robert C. Birtcher	John N. Mundy
Gian P. Felcher	Simon R. Phillot

Editorial Board

Term ending 31 December 1998

Dieter M. Gruen (Argonne Nat'l Lab., Argonne, IL)
James S. Williams (The Australian Nat'l Univ., Canberra)
Patricia M. Mooney (IBM Corp., Yorktown Heights, NY)

Term ending 31 December 1999

David B. Geohegan (Oak Ridge Nat'l Lab., Oak Ridge, TN)
Andreas Mandelis (Univ. of Toronto, Toronto, Canada)
Teh Y. Tan (Duke Univ., Durham, NC)
Akira Tonomura (Hitachi, Ltd., Saitama, Japan)

Term ending 31 December 2000

Robert Hull (Univ. of Virginia, Charlottesville, VA)
Georges Martin (Commissariat à l'Energie Atomique,
Saclay, France)
Jerry R. Meyer (Naval Research Lab., Washington, DC)

Editorial Office Staff

Diane M. Kurtz, *Editorial Supervisor*
Catherine M. Dial, *Editorial Assistant*
Lucila Morales, Lori A. Randolph, Leslie A. Weltmeyer,
Arlene E. Niemann, and Bonnie S. Peters,
Editorial Support

Information for Authors

Submissions: Submit manuscripts (3 copies) to Editor, *Journal of Applied Physics*, Argonne National Laboratory, Bldg. 203, Room R-127, 9700 South Cass Avenue, P.O. Box 8296, Argonne, IL 60439-8296 (E-mail: jap@anl.gov). Submission implies that the manuscript has not been published previously, and is not currently submitted for publication elsewhere. For detailed information for contributors, visit the above URL.

Publication Charge: To support the cost of wide dissemination of research results through publication of journal pages and production of a database of articles, the author's institution is requested to pay a *page charge* of \$60 per page (with a one-page minimum) and an *article charge* of \$20 per article. For any regular, published article that exceeds 10 journal pages, a mandatory \$150 page charge will be added for each page in excess of 10 pages. For Errata the minimum page charge is \$10, with no article charge.

Reprints: Authors may order reprints with or without covers only in multiples of 50 (with a minimum of 100 in each category) from AIP, Circulation & Fulfillment/Reprints, 500 Sunnyside Blvd., Woodbury, NY 11797-2999; Fax: 516-349-9704; Telephone: 800-344-6909 (U.S. and Canada), or 516-576-2234.

Physics Auxiliary Publication Service (PAPS/E-PAPS): For a nominal fee, authors may deposit material that is supplemental to their published papers. Materials may be on paper or electronic media; examples of appropriate items include data tables, graphs, images, and computer codes. Retrieval instructions are noted in the related published paper. Direct requests to the journal Editor; for additional information, see <http://www.aip.org/epaps/epaps.html>.

Comments: Authors may direct comments to Martin Burke, Director of Editorial Operations, AIP, 500 Sunnyside Blvd., Woodbury, NY 11797-2999. Telephone: 516-576-2406; Fax: 516-576-2223; E-mail: mburke@aip.org.

The *Journal of Applied Physics* is the American Institute of Physics' (AIP) archival journal for significant new results in applied physics. The journal publishes articles that emphasize understanding of the physics underlying modern technology, but distinguished from technology on the one side and pure physics on the other. There are two issues per month. *Applied Physics Reviews* is a series of occasional review articles on similar subjects. The Proceedings of the Annual Conference on Magnetism and Magnetic Materials is a regular feature.

AIP Production: Deborah McHone, *Editorial Supervisor*; Margaret Reilly, *Journal Coordinator*; Janet Panarelli, *Chief Production Editor*; Marilyn Schrage, *Senior Production Editor*; Diane Brzozowski, *Production Editor*

Prices

1998 Subscriptions

	U.S.A. & Poss.	Can., Mex., Central & S. Amer. & Caribbean	Foreign Surface Mail	Air Freight	Optional Air Freight
				Europe, Asia, Africa & Oceania	
Members*					
Print + online	\$240 [†]	\$325	\$325	—	\$510
CD-ROM only	\$205	\$205	\$205	—	\$205
CD-ROM + online	\$240	\$240	\$240	—	\$240
Print + CD-ROM + online	\$290	\$375	\$375	—	\$560
Nonmembers					
Print + online	\$2400 [†]	\$2485	\$2485	\$2670	—
CD-ROM only	\$2040	\$2040	\$2040	\$2040	—
CD-ROM + online	\$2400	\$2400	\$2400	\$2400	—
Print + CD-ROM + online	\$2575	\$2660	\$2660	\$2845	—

*AIP Member and Affiliated Societies.

[†]Rate also applies to Microfiche, to all destinations.

Back Issues: 1998 single copies: \$110. Prior to 1998 single copies: \$28 for members; \$110 for nonmembers.

Additional Availability

Online Access: The *Journal of Applied Physics* is available online to print subscribers at no additional charge; for details, please see <http://www.aip.org/ojs/entry.html>. Abstracts of journal articles are available from AIP's SPIN Database, via AIP's PINET Plus Service (<http://www.aip.org/pinet>).

Microform: The *Journal of Applied Physics* is available on microfiche issued at the same frequency as the printed journal, and annually on microfilm. A microform catalog is available from AIP, Circulation & Fulfillment/Single Copy Sales, 500 Sunnyside Blvd., Woodbury, NY 11797-2999; Fax: 516-349-9704; Telephone: 800-344-6908 (U.S. and Canada) or 516-576-2277.

Document Delivery: Copies of journal articles can be ordered for online delivery from the new Articles in Physics online document delivery service (URL: <http://www.aip.org/articles.html>).

Customer Service

Subscription Orders, Renewals, and Address Changes should be addressed to AIP Circulation & Fulfillment Division, 500 Sunnyside Blvd., Woodbury, NY 11797-2999. Allow at least six weeks advance notice. For address changes, please send both old and new addresses and, if possible, include the mailing label from a recent issue.

Claims, Single Copy Replacements, and Back Volumes: Missing issue requests will be honored only if received within six months of publication date (nine months for Australia and Asia). Single copies of a journal may be ordered and back volumes are available in print or microform. Contact AIP Customer Services at 800-344-6902 (U.S. and Canada) or 516-576-2270; Fax: 516-349-9704; E-mail: subs@aip.org.

Reprint Billing: Contact AIP Publication Charge and Reprints/CFD, 500 Sunnyside Blvd., Woodbury, NY 11797-2999; Telephone: 516-576-2230 (800-344-6909); E-mail: pcr@aip.org.

Rights and Permissions

Copying: Single copies of individual articles may be made for private use or research. Authorization is given (as indicated by the Item Fee Code for this publication) to copy articles beyond the use permitted by Sections 107 and 108 of the U.S. Copyright Law, provided the copying fee of \$15 per copy per article is paid to the Copyright Clearance Center, 222 Rosewood Drive, Danvers, MA 01923, USA. Persons desiring to photocopy materials for classroom use should contact the CCC Academic Permissions Service. The Item Fee Code for this publication is 0021-8979/98 \$15.00.

Authorization does not extend to systematic or multiple reproduction, to copying for promotional purposes, to electronic storage or distribution, or to republication in any form. In all such cases, specific written permission from AIP must be obtained.

Other Use: Permission is granted to quote from the journal with the customary acknowledgment of the source. To reprint a figure, table, or other excerpt requires the consent of one of the authors and notification to AIP.

Requests for Permission: Address requests to AIP Office of Rights and Permissions, 500 Sunnyside Blvd., Woodbury, NY 11797-2999; Fax: 516-576-2327; Telephone: 516-576-2268; E-mail: rights@aip.org.

The *Journal of Applied Physics* (ISSN: 0021-8979) is published semimonthly by the American Institute of Physics. Periodicals postage paid at Woodbury, NY 11797, and additional mailing offices. POSTMASTER: Send address changes to *Journal of Applied Physics*, AIP, 500 Sunnyside Blvd., Woodbury, NY 11797-2999.

Copyright © 1998 American Institute of Physics. All rights reserved.

**PROCEEDINGS OF THE SEVENTH JOINT
MAGNETISM AND MAGNETIC
MATERIALS-INTERMAG
CONFERENCE
6-9 JANUARY 1998
San Francisco, California**

Sponsored by

The American Institute of Physics
The IEEE Magnetics Society

In cooperation with

TMS
The Office of Naval Research
The American Society for Testing and Materials
The American Ceramic Society

19980604 034

AIP

DTIC QUALITY INSPECTED 1

**Journal of Applied Physics
Volume 83, Number 11, Part 2, 1998**

International Standard Book Number: 1-56396-801-0
CONF-980102

Copyright © 1998 by the American Institute of Physics
Published by the American Institute of Physics
500 Sunnyside Blvd., Woodbury, New York 11797-2999
Printed in the United States of America

All papers in this volume, and in previous Proceedings of Joint Conferences of the MMM-Intermag, as well as in previous Proceedings of the Conference on Magnetism and Magnetic Materials, published in this series, have been reviewed for technical content. The selection of referees, review guidelines, and all other editorial procedures are in accordance with standards prescribed by the American Institute of Physics.

Conference Organization
Management Committee of the
Seventh Joint Magnetism and Magnetic
Materials-Intermag
Conference

Chairman

W. D. Doyle

Chairman Elect

G. Prinz

Past Chairman

R. E. Fontana, Jr.

Treasurer

W. Yelon

Program Co-Chairmen

A. Chaiken and T. Jagielinski

Members

M. Alex
J. Borchers
F. Cadieu
T. Carr
Z. Celinski
R. Coehoorn
S. Dey
A. Edelstein
G. Fish
H. Fujiwara

B. Gallagher
P. George
R. Gerber
H. How
Y. Idzerda
R. Indeck
R. R. Katti
A. Kim
Y. Kim
K. Klaassen

B. Lairson
M. Lederman
J. MacLaren
M. Mallary
R. Malmhall
I. Mayergoyz
M. McHenry
Y. Miura
B. Pratt
A. Pohm

R. Ramesh
D. Sellmyer
N. Smith
J. Tang
S. Ueno
R. Walser
S. Wang
D. Weller
W. Yelon

Publications Committee

R. R. Katti and J. M. MacLaren, *Co-Chairmen*

Editors

M. Alex
J. Fernandez de Castro
P. George
Y. K. Kim

B. M. Lairson
M. E. McHenry
J. Tang
S. Wang

Local Chairman

H. Gill

Publicity Chairman

J. Nyenhuis

Exhibits Coordinators

J. Teter and R. Dopkin

Industrial Support

M. Sharrock

Student Travel Coordinator

S. Gangopadhyay

IEEE Representative

E. Fontana, Jr.

AIP Representative

J. T. Scott

Editor, J. Appl. Phys.

S. Rothman

Editor, IEEE Trans. Mag.

R. Goldfarb

Conference Management

D. Suiters

D. Arnold

R. Dopkin

Courtesy Associates

AIP Coordinator

J. Bennett

MMM Advisory Committee

R. E. Fontana, Jr., *Chairman*

R. O'Handley, *Secretary*

Term Expires January 1998

E. Della Torre
G. Felcher
P. M. Levy
J. E. Opfer
C. M. Perlov
D. Sellmyer
D. D. Stancil
T. Suzuki
S. von Molnar
W. Yelon

Term Expires November 1998

D. E. Dahlberg
W. D. Doyle
J. Fidler
G. E. Fish
K. Hathaway
R. R. Katti
J. W. Lynn
R. O'Handley
M. Pardavi-Horvath
G. A. Prinz

Term Expires November 1999

A. Chaiken
S. H. Charap
C. L. Chien
Y. Idzerda
T. M. Jagielinski
M. H. Kryder
J. M. MacLaren
J. Nyenhuis
K. O'Grady
R. H. Victora

IEEE Magnetics Society 1998

Officers

D. D. Stancil
President

E. Della Torre
Vice President

R. E. Fontana, Jr.
Secretary-Treasurer

J. E. Opfer
Past President

Administrative Committee

Term Expires 12/31/98

A. Chaiken
F. J. Friedlaender
R. F. Hoyt
D. C. Jiles
J. H. Judy
D. N. Lambeth
M. Pardavi-Horvath
P. E. Wigen

Term Expires 12/31/99

G. E. Fish
T. Jagielinski
F. E. Luborsky
I. Mayergoyz
E. Murdock
J. A. Nyenhuis
K. O'Grady
J. G. Zhu

Term Expires 12/31/00

G. Bertotti
S. H. Charap
E. D. Dahlberg
R. Gerber
R. S. Indeck
R. R. Katti
Y. Miura
S. X. Wang

Sponsoring Society Representatives

American Institute of Physics

J. T. Scott

IEEE Magnetics Society

R. E. Fontana, Jr.

Cooperating Society Representatives

TMS

ASTM Comm. A-6

C. D. Graham, Jr.

Office of Naval Research

K. B. Hathaway

American Ceramic Society

CONTRIBUTORS TO THE SEVENTH JOINT MAGNETISM AND MAGNETIC MATERIALS-INTERMAG CONFERENCE

The Conference expresses its appreciation to the following organizations for their generous support.

\$2500 and above

Motorola

\$2000 and above

EMTEC Magnetix GmbH, formerly BASF Magnetix GmbH

IBM

TDK Corporation

\$1000 and above

Fuji Photo Film Co., Ltd.

Hewlett-Packard

Hitachi, Ltd. Central Research Laboratory

Imation

Quantum Corporation

Sony Corporation

Toda Kogyo Corp.

\$500-\$999

3M

Applied Magnetix Corporation

Komag

\$250-\$499

Digital Measurement Systems Division of ADE Technologies, Inc.

Eastman Kodak Company

Hyundai Electronics America,

MaxMedia Division

Other Contributions

F. G. Jones Associates, Ltd.

Innovative Instrumentation

PREFACE

The Seventh Joint MMM-Intermag Conference was held 6–9 January 1998, in San Francisco, California at the Hyatt Embarcadero Hotel. The Conference was attended by more than 1,800 registrants, and represents the largest conference on magnetic materials and devices held to date. The high attendance indicates the worldwide research in magnetism and expanding applications for new magnetic materials, particularly in the field of magnetic storage.

An exciting program of 1,143 papers included six invited symposia on Present and Future Tape Systems, Layered Manganites, Electrodeposited Magnetic Nanostructures, Exchange Biasing, High Speed Magnetic Recording, and Advances in Magnetic Imaging. Additional highlights included a panel discussion on the history and future of magnetic storage data and a tutorial session on magnetic imaging sponsored by the IEEE Magnetics Society Education Committee. In the IEEE Awards Session, Dr. Jean-Pierre Lazzari was honored as the recipient of the Johnson Storage Medal, and Professor Stanley Charap was the recipient of the Magnetic Society Achievement Award.

The number of abstract submissions representing 45 countries was an astounding 1,940; which was 50% more than at any previous MMM, Intermag, or Joint MMM-Intermag Conference. The size of the program, however, was limited by hotel space and page allotments in the *Journal of Applied Physics* and the *IEEE Transactions on Magnetics*. By creatively using poster space, up to six parallel oral and six parallel poster sessions were accommodated, and, at times, the meeting rooms were crowded. Publication constraints helped limit the allowed number of accepted abstracts at 1,143, resulting in a rejection rate for contributed abstracts of 41% versus a historical figure of approximately 30–35%. This was a painful, but unavoidable process for everyone. It is difficult to make narrow distinctions between hundreds of diverse abstracts and it emphasizes the importance of carefully written submissions.

The conferences historically have had difficulty with social events, largely as a result of the contrary demands within our community of high expectations and low cost. This year, after considerable soul searching, a nearby restaurant-brewery was selected which happily provided an enjoyable, sudsy evening.

This year, as the Conference took shape, I was impressed with our community's ever-increasing use of electronic document processing and handling. This contrasts with processes used in the "early" days. In 1963, for example, the MMM Program Committee met at IBM-Yorktown Heights, New York. After the Program Committee met, the Program Chairman took the accepted abstracts, drove to a rest stop halfway down the Garden State Parkway, and turned the accepted abstracts over to the Local Chairman who then raced back to Philadelphia to have all the abstracts re-typed manually in a common font. Each abstract was then cut-and-pasted one-by-one to fit into the Program Book before going to the printer! Although technology has changed significantly in 35 years, both conferences were very successful.

Questions have been raised about the usefulness of the Joint Conference. The first Joint MMM-Intermag Conference was held in 1976, and, Dr. Emerson Pugh, the General Chairman, summarized the results as follows: "The real success lies in the opportunity afforded scientists, technologists, and engineers from all over the world to discuss topics of mutual interest, to learn to understand each other better, and thus to return to their own laboratories invigorated and better prepared to contribute to this rapidly evolving field of modern technology." I believe this is still a compelling reason to continue having the Joint Conference, which is supported by attendees surveyed at this Joint Conference by a margin of two to one.

A unique feature of our field is the extent to which its history is documented in the familiar, annual printed issues of two journals. Economic realities combined with technological innovation may lead to changes in our traditions. Future Chairmen will be forced to confront these changes, hopefully with the same wisdom shown by the organizers of the first MMM (1955) and the first Intermag (1963) Conferences. Somehow, a conference held solely on the World Wide Web would seem to be a poor substitute for direct contact and interchange in a beautiful city.

Finally, I extend my sincerest thanks to all the members of the organizing committees who worked continually and diligently for more than a year to make this Joint Conference a success.

Bill Doyle
General Chairman
Seventh Joint MMM-International Magnetics Conference
University of Alabama
Tuscaloosa, Alabama

This issue of the *Journal of Applied Physics* contains 389 papers presented at the Seventh Joint MMM-Intermag Conference. This issue also contains the Table of Contents for the papers which are being published in the *IEEE Transactions on Magnetics*.

xxix Table of Contents for the Papers Appearing in the *IEEE Transactions on Magnetism*

Magnetic Microscopy and Imaging I

- 6217 Time-resolved scanning Kerr microscopy of ferromagnetic structures (invited)
- 6223 Magnetic force microscopy image restoration technique for removing tip dependence
- 6226 Quantification of magnetic force microscopy images using combined electrostatic and magnetostatic imaging
- 6229 Magnetic force microscopy using nonoptical piezoelectric quartz tuning fork detection design with applications to magnetic recording studies
- 6232 Kerr effect enhancement by photon tunneling and possible application to a new scanning probe magnetic microscope
- 6235 Design and construction of a sensitive nuclear magnetic resonance force microscope

M. R. Freeman, W. K. Hiebert, A. Stankiewicz

Jian-Gang Zhu, Xiangdong Lin, Rick C. Shi, Yansheng Luo

R. D. Gomez, A. O. Pak, A. J. Anderson, E. R. Burke, A. J. Leyendecker, I. D. Mayergoz

M. Todorovic, S. Schultz

A. Kikitsu, C. M. Falco, M. Mansuripur

T. A. Barrett, C. R. Miers, H. A. Sommer, K. Mochizuki, J. T. Markert

Nanocomposite and Film Hard Magnets

- 6238 Exchange-spring behavior in epitaxial hard/soft magnetic bilayer films
- 6241 Magnetization reversal of Nd(Dy)-Fe-B thin films on Si(111) or Ta/Si(111)
- 6244 Phase formation and magnetic properties of Co-rare earth magnetic films
- 6247 High coercivity SmCo based films made by pulsed laser deposition
- 6250 Mechanism of composition change in sputter deposition of barium ferrite films with sputtering gas pressure
- 6253 Magnetic and structural properties of high coercivity Sm(Co, Ni, Cu) sputtered thin films
- 6256 Mechanically alloyed nanocomposite magnets (invited)
- 6262 Micromagnetic simulation of magnetizability of nanocomposite Nd-Fe-B magnets
- 6265 Thick Fe₃B/Nd₂Fe₁₄B nanocomposite permanent magnet flakes prepared by slow quenching
- 6268 Analysis of magnetic behavior of exchange-enhanced SmFeCo magnets
- 6271 The effect of boron and rare earth contents on the magnetic properties of La and Cr substituted α -Fe/R₂Fe₁₄B-type nanocomposites
- 6274 Anomalous high-temperature coercivities in hard nanocomposite alloys
- 6277 Magnetic interactions in Fe-Ba hexaferrite nanocomposite materials

J. S. Jiang, Eric E. Fullerton, M. Grimsditch, C. H. Sowers, S. D. Bader

J. L. Tsai, T. S. Chin, E. Y. Huang, S. K. Chen

Y. Liu, Richard A. Thomas, S. S. Malhotra, Z. S. Shan, S. H. Liou, D. J. Sellmyer

F. J. Cadieu, R. Rani, X. R. Qian, Li Chen

E. Suzuki, Y. Hoshi, M. Naoe

C. Prados, G. C. Hadjipanayis

P. G. McCormick, W. F. Miao, P. A. I. Smith, J. Ding, R. Street
Thomas Schrefl, Josef Fidler

H. Kanekiyo, S. Hirosawa

M. Dahlgren, R. Grössinger, D. R. Cornejo, F. P. Missell

W. C. Chang, D. Y. Chiou, S. H. Wu, B. M. Ma, Q. Chen, C. O. Bounds

L. H. Lewis, J.-Y. Wang, D. O. Welch, V. Panchanathan

M. I. Montero, F. Cebollada, M. P. Morales, J. M. González, A. Hernando

Surface and Interface Effects

- 6280 Infrared studies of magnetic surface modes on antiferromagnets (invited)

R. E. Camley, M. R. F. Jensen, S. A. Feiven, T. J. Parker

(Continued)

- 6284 Strain induced alteration of the gadolinium surface state
- 6287 Effect of surface roughness on magnetization reversal of Co films on plasma-etched Si(100) substrates
- 6290 Exploring magnetic roughness in CoFe thin films
- 6293 Soft x-ray resonant magnetic reflectivity study of thin films and multilayers
- 6296 Dependence of anti-Stokes/Stokes intensity ratios on substrate optical properties for Brillouin light scattering from ultrathin iron films

Critical Phenomena, Spin Glasses, and Frustration

- 6299 Magnetic phase diagrams of holmium determined from magnetoresistance measurements
- 6302 Magnetostatic critical point phenomena of ErGa garnet
- 6305 Monte Carlo investigation of the eight-state Potts model on quasiperiodic tilings
- 6308 Exact renormalization group equation for systems of arbitrary symmetry free of redundant operators
- 6311 Random-exchange and random-field Ising model-like behaviors in $\text{Fe}_{0.48}\text{Zn}_{0.52}\text{F}_2$
- 6314 Magnetic structures of the triangular lattice magnets $\text{AFe}(\text{SO}_4)_2$ (A=K, Rb, Cs)
- 6317 Phase transition and phase diagram of the J_1-J_2 Heisenberg model on a simple cubic lattice
- 6320 Spin fluctuations and thermal expansion of $\text{La}(\text{Ni}_x\text{Al}_{1-x})_{13}$ amorphous alloys
- 6323 Magnetic relaxation in $\text{Ga}_{0.6}\text{Mo}_2\text{S}_4$ spinel

Nanocrystalline and Amorphous Soft Materials

- 6326 New bulk amorphous Fe-(Co,Ni)-M-B (M=Zr,Hf,Nb,Ta,Mo,W) alloys with good soft magnetic properties
- 6329 Influence of Si addition on thermal stability and soft magnetic properties for Fe-Al-Ga-P-C-B glassy alloys
- 6332 Application of nanocrystalline soft magnetic Fe-M-B (M=Zr, Nb) alloys to choke coils
- 6335 Soft magnetic properties and structures of nanocrystalline Fe-Al-Si-B-Cu-Nb alloy ribbons
- 6338 Compositional dependence of the effective magnetic anisotropy in nanocrystalline Fe-Zr-B-(Cu) alloys
- 6341 Approach to the magnetic saturation in nanocrystalline ferromagnets in the random anisotropy model

Numerical Methods

- 6344 Multigrid methods for computation of magnetostatic fields in magnetic recording problems

- C. Waldfried, D. N. McIlroy, T. McAvoy, D. Welipitiya, P. A. Dowben, E. Vescovo
- M. Li, Y.-P. Zhao, G.-C. Wang, H.-G. Min
- J. W. Freeland, V. Chakarian, K. Bussmann, Y. U. Idzerda, H. Wende, C.-C. Kao
- J. M. Tonnerre, L. Sève, A. Barbara-Dechelette, F. Bartolomé, D. Raoux, V. Chakarian, C. C. Kao, H. Fischer, S. Andrieu, O. Fruchart
- J. F. Cochran, M. From, B. Heinrich

Jeffrey R. Gebhardt, Naushad Ali

Toshiro Tanaka, Kazuo Miyatani
D. Ledue, D. P. Landau, J. Teillet

A. A. Lisyansky, D. Nicolaides

E. P. Raposo, M. D. Coutinho-Filho

H. Serrano-González, S. T. Bramwell, K. D. M. Harris, B. M. Kariuki, L. Nixon, I. P. Parkin, C. Ritter

C. Pinettes, H. T. Diep

A. Fujita, K. Fukamichi

T. Taniyama, I. Nakatani

Akihisa Inoue, Tao Zhang, Hisato Koshiba, Akihiro Makino

T. Mizushima, A. Makino, A. Inoue

Y. Naitoh, T. Bitoh, T. Hatanai, A. Makino, A. Inoue

B. J. Tate, B. S. Parmar, I. Todd, H. A. Davies, M. R. J. Gibbs, R. V. Major

P. García Tello, J. M. Blanco, N. Murillo, J. González, R. Zuberek, A. Slawska-Waniewska, J. M. González

G. R. Aranda, J. González, K. Kulakowski

Igor Tsukerman, Alexander Plaks, H. Neal Bertram

- 6347 Modified scalar potential solution for three-dimensional magnetostatic problems
- 6350 Numerical simulation of the magnetization structures in thin polycrystalline films with the random anisotropy and intergrain exchange
- 6353 Finite element analysis of the influence of a fatigue crack on magnetic properties of steel
- 6356 Magnetohydrodynamic calculation for free surfaces
- 6359 Differential Preisach model for the description of dynamic magnetization processes
- 6362 Influence of the permanent magnet overhang on the performance of the brushless dc motor
- 6365 Optimization of coils for detecting initial rotor position in permanent magnet synchronous motor
- 6368 Temperature analysis of induction motors using a hybrid thermal model with distributed heat sources
- 6371 Bifurcation phenomena and chaotic attractors in a six-dimensional nonlinear system

Symposium on Layered Manganites

- 6374 Two-dimensional ferromagnetic correlations above T_C in the naturally layered CMR manganite $\text{La}_{2-2x}\text{Sr}_{1+2x}\text{Mn}_2\text{O}_7$ ($x=0.3-0.4$) (invited)
- 6379 Chemistry of naturally layered manganites (invited)
- 6385 Role of intergrowths in the properties of naturally layered manganite single crystals (invited)

Rare Earth and Boride Hard Magnets

- 6390 The development of high performance Nd-Fe-Co-Ga-B die upset magnets
- 6393 Plastic deformation modeling of die-upset process for magnequench NdFeB magnets
- 6396 Microstructural analysis of strip cast Nd-Fe-B alloys for high $(\text{BH})_{\text{max}}$ magnets
- 6399 Extension of the primary solidification region of $\text{Nd}_2\text{Fe}_{14}\text{B}$ by levitation of undercooled melts
- 6402 High performance Nd-Fe-B sintered magnets made by the wet process
- 6405 Hydrogen absorption and desorption behavior in Pr-Fe-B type alloys
- 6408 Coercivity of sintered $\text{Nd}(\text{Fe}_{0.92-x}\text{Ga}_xB_{0.08})_{5.5}$ permanent magnets
- 6411 The origin and interpretation of fine scale magnetic contrast in magnetic force microscopy: A study using single-crystal NdFeB and a range of magnetic force microscopy tips
- 6414 Off-axis electron holographic mapping of magnetic domains in $\text{Nd}_2\text{Fe}_{14}\text{B}$
- 6417 Improvement of protective coating on Nd-Fe-B magnet by pulse nickel plating
- 6420 A pump with flat-ring-shaped magnets

K. Sivasubramaniam, S. Salon,
M. V. K. Chari, I. D. Mayergoyz
D. V. Berkov, N. L. Gorn

Y. Shi, D. C. Jiles

Keisuke Fujisaki, Takatsugu
Ueyama

P. Andrei, Al. Stancu, O. Caltun

J. P. Wang, D. K. Lieu, W. L.
Lorimer, A. Hartman

S. Wakao, T. Onuki, K. Tatematsu,
T. Iraha

S. C. Mukhopadhyay, S. K. Pal

T. Sutani, T. Czaszejko, A. Nafalski

D. N. Argyriou, T. M. Kelley, J. F.
Mitchell, R. A. Robinson, R.
Osborn, S. Rosenkranz, R. I.
Sheldon, J. D. Jorgensen

P. D. Battle, N. Kasmir, J. E.
Millburn, M. J. Rosseinsky, R. T.
Patel, L. E. Spring, J. F. Vente,
S. J. Blundell, W. Hayes, A. K.
Klehe, A. Mihut, J. Singleton

S. D. Bader, R. M. Osgood III,
D. J. Miller, J. F. Mitchell, J. S.
Jiang

T. Saito, M. Fujita, T. Kuji, K.
Fukuoka, Y. Syono

S. Guruswamy, Y. R. Wang, V.
Panchanathan

J. Bernardi, J. Fidler, M. Sagawa,
Y. Hirose

R. Hermann, W. Löser

M. Takahashi, K. Uchida, F.
Taniguchi, T. Mikamoto

Yoon B. Kim, W. Y. Jeung

X. C. Kou, F. R. de Boer, H.
Kronmüller

M. Al-Khafaji, W. M. Rainforth,
M. R. J. Gibbs, J. E. L. Bishop,
H. A. Davies

M. R. McCartney, Yimei Zhu

C. W. Cheng, F. T. Cheng, H. C.
Man

H. Saotome, T. Hagiwara, Y. Sato

Heavy Fermions

- 6423 New phase boundary between magnetic and non-Fermi-liquid in $\text{Ce}(\text{Rh}_{1-x}\text{Ru}_x)_3\text{B}_2$, for $0 \leq x \leq 0.4$
- 6426 Magnetic ordering of Ce in the heavy-fermion compound Ce_3Al
- 6429 Size and dimensionality effect in single-impurity Anderson model
- 6432 *f*-Electron delocalization/localization and the abrupt disappearance of uranium magnetic ordering with dilution alloying
- 6435 Evidence for an extended critical region near the metamagnetic transition of UCoAl
- 6438 Electronic structure and magnetic properties of URhSi

E. Bauer, R. Hauser, A. Galatanu, A. Lindbaum, G. Hilscher, H. Sassik, H. Kirchmayr, J. G. Sereni, P. Rogl

W.-H. Li, J. C. Peng, Y.-C. Lin, K. C. Lee, J. W. Lynn, Y. Y. Chen

Feng Chen, Nicholas Kioussis

B. R. Cooper, Y.-L. Lin

A. V. Kolomiets, L. Havela, V. Sechovský, L. E. DeLong, D. B. Watkins, A. V. Andreev

M. Galli, F. Marabelli, A. Continenza, P. Monachesi, F. Canepa, M. L. Fornasini

Biomagnetism and Magnetochemistry

- 6441 Weighted minimum-norm source estimation of magnetoencephalography utilizing the temporal information of the measured data
- 6444 A comparative study of the magnetic separation characteristics of magnetotactic and sulphate reducing bacteria
- 6447 Magneto-electrolysis of copper
- 6450 Impedance magnetic resonance imaging: A method for imaging of impedance distributions based on magnetic resonance imaging
- 6453 Polymerization and dissolution of fibrin under homogeneous magnetic fields
- 6456 Bioluminescence under static magnetic fields
- 6459 Structure of water molecules under 14 T magnetic field
- 6462 Estimation of multiple sources using a three-dimensional vector measurement of a magnetoencephalogram
- 6465 Measurements of biomagnetic fields using a high-resolution dc superconducting quantum interference device magnetometer

Sunao Iwaki, Shoogo Ueno

A. S. Bahaj, P. A. B. James, F. D. Moeschler

G. Hinds, J. M. D. Coey, M. E. G. Lyons

S. Ueno, N. Iriguchi

M. Iwasaka, M. Takeuchi, S. Ueno, H. Tsuda

M. Iwasaka, S. Ueno

M. Iwasaka, S. Ueno

Koichiro Kobayashi, Yoshinori Uchikawa

K. Iramina, B. Hong, S. Uchida, K. Goto, S. Ueno, S. Nakayama

Crystalline Soft Magnetic Materials

- 6468 Magnetic properties and ordering in C-coated $\text{Fe}_x\text{Co}_{1-x}$ alloy nanocrystals
- 6471 Soft magnetic properties of LaCo_{13} and $\text{La}(\text{Co}, \text{Fe})_{13}$ alloys
- 6474 Effects of heat treatment on the magnetic properties of polymer-bound iron particle cores
- 6477 Alternating current magnetic properties of cores made from pressed acicular steel particles
- 6480 Magnetic induction and surface segregation in thin-gauged 3% Si steel
- 6483 New method to predict the magnetic properties of thin gauged Si-Fe sheets
- 6486 Local distribution on magnetic properties in grain-oriented silicon steel sheet

Z. Turgut, J. H. Scott, M. Q. Huang, S. A. Majetich, M. E. McHenry

M. Q. Huang, W. E. Wallace, M. E. McHenry, Q. Chen, B. M. Ma

M. Namkung, B. Wincheski, R. G. Bryant, A. Buchman

R. F. Krause, J. H. Bularzik, H. R. Kokal

N. H. Heo, K. H. Chai, J. G. Na, J. S. Woo

J. G. Na, C. H. Park, J. Kim, N. H. Heo, S. R. Lee, C. S. Lee, J. S. Woo

Masato Enokizono, Ikuo Tanabe, Takeshi Kubota

Computational Micromagnetics

- 6489 Anisotropy design in magnetic media: A micromagnetics study
- 6491 A variational approach to exchange energy calculations in micromagnetics

J. H. Kaufman, T. Koehler, A. Moser, D. Weller, B. Jones

M. J. Donahue

- 6494 Hysteresis loop areas in kinetic Ising models: Effects of the switching mechanism
- 6497 Domain-wall motion in random potential and hysteresis modeling
- 6500 The field-space perspective on hysteresis in uniaxial ferromagnets
- 6503 Micromagnetic localization
- 6506 Computational micromagnetic investigation of magnetization reversal in Nd-Fe-B nanocomposite magnets
- 6509 Influence of the system parameters on the non-Arrhenius magnetic relaxation of systems having distributed properties

Spin-Dependent Tunneling I

- 6512 Voltage dependence of magnetoresistance in spin dependent tunneling junctions
- 6515 Bias voltage and temperature dependence of magnetotunneling effect
- 6518 Finite bias spin dependent tunneling: A nonequilibrium Green's function approach
- 6521 Spin-dependent tunneling in epitaxial systems: Band dependence of conductance
- 6524 Anomalous behavior of temperature and bias-voltage dependence of tunnel-type giant magnetoresistance in insulating granular systems

New Materials and Magnetic Semiconductors

- 6527 High perpendicular anisotropy and magneto-optical activities in ordered Co₃Pt alloy films
- 6530 Thermopower studies of percolating magnetic metallic nanostructures
- 6533 Structural and magnetic properties of Fe_xSe_y thin films during their selenization process
- 6536 Magnetic behavior of the new low- T_c phase of SrRuO₃
- 6539 Growth and characterization of epitaxial thin films of conductive ferromagnetic oxide SrRuO₃
- 6542 A field induced ferromagnetic-like transition below 2.8 K in Li₂CuO₂: An experimental and theoretical study
- 6545 Magneto-optic study of Ni-based diluted magnetic semiconductors
- 6548 Magneto-optic effect of the ferromagnetic diluted magnetic semiconductor Ga_{1-x}Mn_xAs
- 6551 Hall effect and magnetic properties of III-V based (Ga_{1-x}Mn_x)As/AlAs magnetic semiconductor superlattices
- 6554 Long-range antiferromagnetic couplings in [ZnTe|MnTe] superlattices
- 6557 Magnetic measurements on the III-VI diluted magnetic semiconductor Ga_{1-x}Mn_xSe
- 6560 Second harmonic spectroscopy and control of domain size in antiferromagnetic YMnO₃

S. W. Sides, P. A. Rikvold, M. A. Novotny
 M. Pasquale, V. Basso, G. Bertotti, D. C. Jiles, Y. Bi
 Y. T. Millev, J. R. Cullen, H. P. Oepen
 Ralph Skomski
 S. David, B. Kevorkian, J. C. Toussaint, D. Givord
 R. Smirnov-Rueda, O. A. Chubykalo, J. M. González, J. González

J. Zhang, R. M. White

Yu Lu, X. W. Li, Gang Xiao, R. A. Altman, W. J. Gallagher, A. Marley, K. Roche, S. Parkin
 Xindong Wang

J. M. MacLaren, W. H. Butler, X.-G. Zhang

S. Mitani, K. Takanashi, K. Yakushiji, H. Fujimori

Y. Yamada, W. P. Van Drent, E. N. Abarra, T. Suzuki

X. N. Jing, X. Yan

T. Takahashi, S. Kuno, N. Honda, Y. Takemura, K. Kakuno, K. Saito

P. A. Joy, S. K. Date, P. S. Anil Kumar

C. B. Eom, R. A. Rao, Q. Gan, D. B. Kacedon

R. J. Ortega, P. J. Jensen, K. V. Rao, F. Sapiña, D. Beltrán, Z. Iqbal, J. C. Cooley, J. L. Smith

K. Ando, A. Chiba, H. Tanoue

K. Ando, T. Hayashi, M. Tanaka, A. Twardowski

T. Hayashi, M. Tanaka, K. Seto, T. Nishinaga, H. Shimada, K. Ando

J. Lin, J. J. Rhyne, J. K. Furdyna, T. M. Giebutowicz

T. M. Pekarek, B. C. Crooker, I. Miotkowski, A. K. Ramdas

M. Fiebig, D. Fröhlich, S. Leute, R. V. Pisarev

Giant Magnetoimpedance

- 6563 High frequency behavior of soft magnetic wires using the giant magnetoimpedance effect
- 6566 Modeling of domain structure and anisotropy in glass-covered amorphous wires
- 6569 Phenomenological model for magnetoimpedance in soft ferromagnets
- 6572 Field and stress dependence of the irreversible magnetization changes in pure iron
- 6575 Temperature dependence of magnetoimpedance effect in amorphous $\text{Co}_{66}\text{Fe}_4\text{Ni}_{14}\text{Si}_{15}$ ribbon
- 6578 Magneto-impedance effect in high permeability NiFeMo permalloy wires
- 6581 The influence of field- and stress-induced magnetic anisotropy on the magnetoimpedance in nanocrystalline FeCuNbSiB alloys
- 6584 Giant magneto-impedance effect in nanocrystalline glass-covered wires
- 6587 High frequency properties of glass-coated microwire

P. Ciureanu, M. Britel, D. Ménard, A. Yelon, C. Akyel, M. Rouabhi, R. W. Cochrane, P. Rudkowski, J. O. Ström-Olsen

D. Ménard, D. Frankland, P. Ciureanu, A. Yelon, M. Rouabhi, R. W. Cochrane, H. Chiriac, T. A. Óvári

D. Atkinson, P. T. Squire

J. Pearson, P. T. Squire

Y. K. Kim, W. S. Cho, T. K. Kim, C. O. Kim, Heebok Lee

M. Vázquez, J. M. García-Beneytez, J. P. Sinnecker, Lin Li

G. V. Kuryandskaya, J. M. García-Beneytez, M. Vázquez, J. P. Sinnecker, V. A. Lukshina, A. P. Potapov

H. Chiriac, T. A. Óvári, C. S. Marinescu

A. N. Antonenko, E. Sorkine, A. Rubshtein, V. S. Larin, V. Manov

Spin Dynamics

- 6590 Frequency versus Lyapunov exponent map: A new approach to investigate dynamics of nonlinear magnetic systems
- 6593 Coupling of reversal modes for an infinite ferromagnetic cylinder
- 6596 Magnetism and Jahn-Teller effect in LaMnO_3
- 6599 Application of spin-dynamics methods to a study of magnetization tunneling in many-spin systems
- 6602 Spin dynamics in $S=1/2$ chains and ladders from NMR and susceptibility measurements in $\text{Sr}_{14-x}\text{Na}_x\text{Cu}_{24}\text{O}_{41}$
- 6605 Magnetic properties and spin dynamics in hole-doped $S=1$ AF chain: ^{89}Y NMR and susceptibility in $\text{Y}_{2-x}\text{Ca}_x\text{BaNiO}_5$

N. Y. Piskun, P. E. Wigen

Ching-Ray Chang, Ching-Ming Lee

M. Z. Li, Liang-Jian Zou, Q. Q. Zheng

V. V. Dobrovitski, B. N. Harmon

P. Carretta, M. Corti, P. Ghigna, A. Lascialfari

F. Tedoldi, A. Rigamonti, C. Brugna, M. Corti, A. Lascialfari, D. Capsoni, V. Massarotti

Exchange and Film Hard Magnets

- 6608 Coercivity and exchange coupling in PrCo:Co nanocomposite films
- 6611 Nanostructured NdFeB films processed by rapid thermal annealing
- 6614 Magnetic and structural properties of $(\text{Co}_{1-x}\text{Fe}_x)\text{Pt}$ thin films
- 6617 Magnetocrystalline anisotropy in (111) CoPt_3 thin film with growth-induced chemical anisotropy investigated by x-ray magnetic circular dichroism
- 6620 Magnetic properties of NdFeB thin films synthesized via laser ablation processing
- 6623 Maximum energy product of isotropic Nd-Fe-B-based nanocomposite magnets
- 6626 Remanence enhancement in mechanically alloyed isotropic $\text{Nd}(\text{Fe}, \text{Mo})_{12}\text{N}_x$ compounds

J. P. Liu, Y. Liu, D. J. Sellmyer

M. Yu, Y. Liu, S. H. Liou, D. J. Sellmyer

P. W. Jang, D. W. Kim, C. H. Park, J. G. Na, S. R. Lee

W. Grange, J.-P. Kappler, M. Maret, J. Vogel, A. Fontaine, F. Pétrouff, G. Krill, A. Rogalev, J. Goulon, M. Finazzi, N. B. Brookes

ChoongJin Yang, SangWon Kim, Jong Seog Kang

J. Kuma, N. Kitajima, Y. Kanai, H. Fukunaga

Yiaofu Xiao, Qi Zeng, Shengzhi Dong, Run Wang

- 6628 Magnetic properties of $\text{Nd}_8\text{Fe}_{77}\text{Co}_5\text{B}_6\text{CuNb}_3$ melt-spun ribbons
- 6631 Effect of TiC additions to the microstructure and magnetic properties of $\text{Nd}_{9.5}\text{Fe}_{84.5}\text{B}_6$ melt-spun ribbons
- 6634 Application of the shock compaction technique for consolidation of hard magnetic powders
- 6637 Reversible processes and magnetic viscosity of nanocrystalline permanent magnets
- 6640 Magnetic properties of $\text{RFe}_{10.5}\text{Mo}_{1.5}\text{C}_x$ and their nitrides

Soft Thin Films

- 6643 Microstructure and magnetic properties of FeCoN thin films
- 6646 Structure and magnetic properties of a Fe–Zr–N thin film
- 6649 An effect of nitrogen on magnetic properties and microstructure of Fe–Nb–B–N nanocrystalline thin films
- 6652 Soft magnetic properties of as-deposited Fe–Hf–C–N and Fe–Hf–N nanocrystalline thin films
- 6655 Microstructure and soft magnetic properties of FeSiAl(Ti/Ta)(O)N
- 6658 New applications of nanocrystalline Fe(Co–Fe)–Hf–O magnetic films to micromagnetic devices
- 6661 Study on the in-plane uniaxial anisotropy of high permeability granular films
- 6664 Soft magnetic properties of Co–Cr–O granular films
- 6667 Magnetic properties of Fe films deposited by Ar, Kr, and Xe ion beam sputtering
- 6670 Effects of plasma and bias power on magnetic properties of sendust films
- 6673 Preparation of soft magnetic films of nanocrystalline Fe–Cu–Nb–Si–B alloy by facing targets sputtering
- 6676 Measurement of the magnetostriction constants of amorphous thin films on kapton substrates
- 6679 Longitudinal-transverse resonance and localization related to the random anisotropy in a-CoTbZr films

Spin-Dependent Tunneling II

- 6682 Influence of barrier impurities on the magnetoresistance in ferromagnetic tunnel junctions
- 6685 Spin-dependent tunneling junctions with hard magnetic layer pinning
- 6688 Picotesla field sensor design using spin-dependent tunneling devices
- 6691 Ferromagnetic tunnel junctions with plasma-oxidized Al barriers and their annealing effects

H. Chiriac, M. Marinescu

M. J. Kramer, C. P. Li, K. W. Dennis, R. W. McCallum, C. H. Sellers, D. J. Branagan, L. H. Lewis, J. Y. Wang

M. Leonowicz, W. Kaszuwara, E. Jezierska, D. Januszewski, G. Mendoza, H. A. Davies, J. Paszula, D. R. Cornejo, V. Villas-Boas, F. P. Missell

Weihua Mao, Jinbo Yang, Benpei Cheng, Yingchang Yang

P. C. Kuo, S. S. Chang, C. M. Kuo, Y. D. Yao, H. L. Huang

Jong-Sung Baek, Seong-Cho Yu, Woo-Young Lim, Chul-Sung Kim, Taek-Soo Kim, Chong-Oh Kim

J. Y. Park, S. J. Suh, T. H. Noh, K. Y. Kim, H. J. Kim

J. Y. Song, J. J. Lee, S. H. Han, H. J. Kim, J. Kim

M. Hiramoto, N. Matsukawa, H. Sakakima, Y. Ichikawa, K. Ijima

T. Sato, Y. Miura, S. Matsumura, K. Yamasawa, S. Morita, Y. Sasaki, T. Hatanai, A. Makino

W. D. Li, O. Kitakami, Y. Shimada

Takeshi Morikawa, Motofumi Suzuki, Yasunori Taga

S. Iwatsubo, T. Takahashi, M. Naoe

M. S. Araghi, R. E. Hurley, H. S. Gamble, P. M. Dodd, R. Atkinson

Masahiko Naoe, Hiroaki Matsumiya, Takayuki Ichihara, Shigeki Nakagawa

C. Ouyang, T. W. Kim, R. J. Gambino, C. Jahnes

G. Suran, E. Boumaiz

R. Jansen, J. S. Moodera

J. F. Bobo, F. B. Mancoff, K. Bessho, M. Sharma, K. Sin, D. Guarisco, S. X. Wang, B. M. Clemens

Mark Tondra, James M. Daughton, Dexin Wang, Russell S. Beech, Anita Fink, John A. Taylor

M. Sato, H. Kikuchi, K. Kobayashi

- 6694 Tunneling magnetoresistance and current distribution effect in spin-dependent tunnel junctions
- 6697 High conductance magnetoresistive tunnel junctions with multiply oxidized barrier
- 6700 Area scaling of planar ferromagnetic tunnel junctions: From shadow evaporation to lithographic microfabrication
- 6703 Nanometric cartography of tunnel current in metal-oxide junctions

Hard Magnets I

- 6706 $\text{Sm}_2(\text{Co}, \text{Fe}, \text{Cu}, \text{Zr})_{17}$ magnets for use at temperature $\geq 400^\circ\text{C}$
- 6709 Phase transformation and magnetic properties of $\text{Sm}(\text{Co}_{0.91-x}\text{Fe}_x\text{Cu}_{0.07}\text{Zr}_{0.02})_z$ powders for bonded magnet applications
- 6712 The effect of particle size and consolidating pressure on the magnetic properties of $\text{Sm}(\text{Co}, \text{Fe}, \text{Cu}, \text{Zr})_z$ bonded magnets
- 6715 High temperature stability of SmTM magnets
- 6718 Structure and magnetic properties of $\text{SmCo}_{7-x}\text{Zr}_x$ alloys ($x=0-0.8$)
- 6721 Coercivity calculation of $\text{Sm}_2(\text{Co}, \text{Fe}, \text{Cu}, \text{Zr})_{17}$ magnets
- 6724 Finite-temperature behavior of anisotropic two-sublattice magnets
- 6727 Magnetic properties of $\text{DyCo}_{10}\text{V}_2$
- 6730 Investigation of the magnetic properties of $\text{ErFe}_{11}\text{Ti}$ and $\text{ErFe}_{11}\text{TiH}$ in high magnetic field
- 6733 Magnetic properties of TbCo_3B_2 studied by neutron diffraction, magnetization, and ac-susceptibility measurements
- 6736 A Mössbauer spectral study of $\text{Tb}_2\text{Fe}_{17}$ and the $\text{Tb}_2\text{Fe}_{17-x}\text{Si}_x$ solid solutions

Magneto-Optic Materials

- 6739 Asymmetric nonlinear magneto-optic effects in PtMnSb thin films
- 6742 Anisotropic third-order magneto-optical Kerr effect
- 6745 Magneto-optical properties of MnPt_3 : LDA+ U calculations
- 6747 Thickness dependence of interfacial magneto-optic effects in Pt/Co multilayers
- 6750 Optical and magneto-optical properties of Co/Pt/AlN multilayers
- 6753 Effect of Pt in TbFeCo on magnetic and magneto-optical properties
- 6756 Magneto-optical properties of Sc-substituted erbium-iron-garnet single crystals
- 6759 Crystal ion slicing of single-crystal magnetic garnet films
- 6762 Faraday rotation and magnetic properties of erbium gallium gallate under high magnetic field
- 6765 On the origin of the magneto-optical effects in Li, Mg, Ni, and Co ferrite

J. J. Sun, R. C. Sousa, T. T. P. Galvão, V. Soares, T. S. Plaskett, P. P. Freitas

P. K. Wong, J. E. Evetts, M. G. Blamire

H. Boeve, R. J. M. van de Veerdonk, B. Dutta, J. De Boeck, J. S. Moodera, G. Borghs

V. Da Costa, F. Bardou, C. Béal, Y. Henry, J. P. Bucher, K. Ounadjela

C. H. Chen, M. S. Walmer, M. H. Walmer, S. Liu, E. Kuhl, G. Simon W. Gong, B. M. Ma, C. O. Bounds

B. M. Ma, W. Gong, C. O. Bounds, C. H. Chen, M. S. Walmer

A. S. Kim

M. Q. Huang, W. E. Wallace, M. McHenry, Q. Chen, B. M. Ma

M. Katter

Ralph Skomski

C. Zhang, X. C. Kou, Z. G. Zhao, E. Brück, K. H. J. Buschow, F. R. de Boer

O. Isnard, M. Guillot

El'ad N. Caspi, Haim Pinto, Moshe Kuznietz, Hanania Etteedgui, Mordechai Melamud, Israel Felner, Hagai Shaked

Dimitri Hautot, Gary J. Long, P. C. Ezekwenna, F. Grandjean, D. P. Middleton, K. H. J. Buschow

R. Carey, D. M. Newman, M. L. Wears

A. V. Petukhov, Th. Rasing, T. Katayama, N. Nakajima, Y. Suzuki

R. F. Sabiryanov, S. S. Jaswal

Xiang Gao, Michael J. DeVries, Daniel W. Thompson, John A. Woollam

R. Atkinson, P. M. Dodd, I. W. Salter, P. J. Grundy, C. J. Tatnall

Y. Itoh, W. P. Van Drent, T. Suzuki

J. Ostoréro, M. Guillot

M. Levy, R. M. Osgood, Jr., A. Kumar, H. Bakhru

M. Guillot, T. Schmiedel, You Xu

W. F. J. Fontijn, P. J. van der Zaag, R. Metselaar

- 6768 Magneto-optical properties of one-dimensional photonic crystals composed of magnetic and dielectric layers
- 6771 Magneto-chromatic effects of tunable magnetic fluid grating

Mitsuteru Inoue, Ken'ichi Arai,
Toshitaka Fujii, Masanori Abe

Chin-Yih Hong, H. E. Horng, I. J.
Jang, J. M. Wu, S. L. Lee,
Wai Bong Yeung, H. C. Yang

Superconductivity I

- 6774 Suppression of superconductivity by injection of spin-polarized current
- 6777 Magnetoquenched superconducting valve
- 6780 Novel high- T_c transistors with manganite oxides
- 6783 Extended x-ray absorption fine structure measurements of nonsuperconducting $\text{PrBa}_2\text{Cu}_3\text{O}_{6.9}$: Evidence against Ba site Pr substitution
- 6786 Anisotropic thermal conductivity of c -axis aligned $\text{Bi}_2\text{Sr}_2\text{CaCu}_2\text{O}_x$ superconductor in high magnetic fields
- 6789 Superconductivity in the new quaternary ruthenium borocarbide Y-Ru-B-C system
- 6792 Electron correlation in antiferromagnet and superconductor thiospinel Cu-Co-S_4
- 6795 Plausible d -wave cuprate superconductivity: Muon-spin-relaxation studies of $\text{RBa}_2\text{Cu}_3\text{O}_{7-\delta}$ vortex states
- 6798 Flux patterns of multifilamentary Ag-sheathed $(\text{Pb,Bi})_2\text{Sr}_2\text{Ca}_2\text{Cu}_3\text{O}_{10+\delta}$ tapes
- 6801 Depth-dependent magnetism of layered superconductors: Nb/Si
- 6804 Computation of the nonlinear magnetic response of a three dimensional anisotropic superconductor

Daniel Koller, M. S. Osofsky, D. B.
Chrisey, J. S. Horwitz, R. J.
Soulen, Jr., R. M. Stroud, C. R.
Eddy, J. Kim, R. C. Y. Auyeung,
J. M. Byers, B. F. Woodfield, G. M.
Daly, T. W. Clinton, Mark Johnson

T. W. Clinton, Mark Johnson
Z. W. Dong, S. P. Pai, R. Ramesh,
T. Venkatesan, Mark Johnson,
Z. Y. Chen, A. Cavanaugh, Y. G.
Zhao, X. L. Jiang, R. P. Sharma, S.
Ogale, R. L. Greene

V. G. Harris, D. J. Fatemi, V. M.
Browning, M. S. Osofsky, T. A.
Vanderah

S. C. Nakamae, J. Crow, J. Sarrao,
J. Schwartz

Y. Y. Hsu, H. C. Chiang, H. C. Ku

Kazuo Miyatani, Toshiro Tanaka,
Masayasu Ishikawa

C. Boekema, E. J. Ruiz, Z. C.
Pobre, S. R. Punjabi, F. Kong, O.
Vera, D. W. Cooke

M. R. Koblishka, T. H. Johansen,
H. Bratsberg, L. Püst, A. Galkin, P.
Nálevka, M. Maryško, M. Jirsa, M.
Bentzon, P. Bodin, P. Vase, T.
Freltoft

S. M. Yusuf, E. E. Fullerton, R. M.
Osgood II, G. P. Felcher

Igor Žutić, Oriol T. Valls

Exchange Biasing I

- 6807 Temperature dependence of giant magnetoresistance properties of NiMn pinned spin valves
- 6810 Exchange biasing of permalloy films by $\text{Mn}_x\text{Pt}_{1-x}$: Role of composition and microstructure
- 6813 Exchange coupling of NiFe/FeRh-Ir thin films
- 6816 Exchange anisotropy in $\text{Ni}_{82}\text{Fe}_{18}\text{O}\{100\}/\text{Ni}_{80}\text{Fe}_{20}$ bilayers
- 6819 Temperature dependence of ferromagnetic resonance as induced by NiO pinning layers
- 6822 Dependence of exchange coupling on antiferromagnetic layer thickness in NiFe/CoO bilayers
- 6825 Magnetic behavior of NiFe/NiO bilayers

Sining Mao, Nurul Amin, Ed
Murdock

Kannan M. Krishnan, C. Nelson,
C. J. Echer, R. F. C. Farrow, R. F.
Marks, A. J. Kellock

S. Yuasa, M. Nývlt, T. Katayama,
Y. Suzuki

Chih-Huang Lai, Robert L. White,
Connie P. Wang, Thomas C.
Anthony

P. Lubitz, J. J. Krebs, M. M. Miller,
Shufan Cheng

T. Ambrose, C. L. Chien

Zhenghong Qian, John M.
Sivertsen, Jack H. Judy

- 6828 Direct experimental study of the magnetization reversal process in epitaxial and polycrystalline films with unidirectional anisotropy

Magnetic Microscopy and Imaging II

- 6831 Spin-polarized tunneling by spin-polarized scanning tunneling microscopy
- 6834 Imaging of magnetic domains with scanning tunneling optical microscopy
- 6837 Induction mapping of magnetostrictive materials
- 6840 Influence of current density on the magnetization process in active spin-valve elements
- 6843 Magnetic domains of single-crystal $\text{Nd}_2\text{Fe}_{14}\text{B}$ imaged by unmodified scanning electron microscopy
- 6846 A flexible two-dimensional phase correction for interleaved echo-planar imaging reconstruction
- 6849 Metallic needle artifacts in magnetic resonance imaging

Magnetic Ferrites

- 6852 Magnetic properties of MnZnTi and NiZn ferrite films deposited by laser ablation
- 6855 Structure and soft magnetic properties of sputter deposited MnZn -ferrite films
- 6858 Emission studies of Ba-hexaferrite plume produced by a KrF excimer laser
- 6861 Fine grained Mn-Zn ferrite for high frequency driving
- 6864 Particle size dependence of rotational responses in Ni-Zn ferrite
- 6867 Processing and cation redistribution of MnZn ferrites via high-energy ball milling
- 6870 The effect of intragranular domain walls in MgMnZn -ferrite
- 6873 Line width of manganese-zinc ferrite polycrystals with oxygen partial pressure
- 6876 The diffusion of tracer oxygen atoms in Ni ferrites
- 6879 Conversion electron Mössbauer studies on strontium ferrite films with in-plane and perpendicular anisotropies

Symposium on Exchange Biasing

- 6882 Role of the antiferromagnet in exchange-biased $\text{Fe}_3\text{O}_4/\text{CoO}$ superlattices (invited)
- 6888 Role of interfacial uncompensated antiferromagnetic spins in unidirectional anisotropy in $\text{Ni}_{81}\text{Fe}_{19}/\text{CoO}$ bilayers (invited)
- 6893 Measurements of the ferromagnetic/antiferromagnetic interfacial exchange energy in Co/CoO and Fe/FeF_2 layers (invited)

V. I. Nikitenko, V. S. Gornakov, L. M. Dedukh, Yu. P. Kabanov, A. F. Khapikov, A. J. Shapiro, R. D. Shull, A. Chaiken, R. P. Michel

Hiroyoshi Kodama, Takuya Uzumaki, Mitsumasa Oshiki, Kazuhisa Sueoka, Kōichi Mukasa

P. Bertrand, L. Conin, C. Hermann, G. Lampel, J. Peretti, V. I. Safarov

Jennifer Dooley, Marc De Graef, Michael E. McHenry

X. Portier, A. K. Petford-Long, T. C. Anthony, J. A. Brug

L. H. Lewis, J.-Y. Wang, P. Canfield

Haiping Liu

Haiping Liu

M. M. Amado, M. S. Rogalski, L. Guimarães, J. B. Sousa, I. Bibicu, R. G. Welch, S. B. Palmer

M. F. Gillies, R. Coehoorn, J. B. A. van Zon, D. Alders

P. Papakonstantinou, M. C. O'Neill, R. Atkinson, R. Al-Wazzan, T. Morrow, I. W. Salter

K. Takadate, Y. Yamamoto, A. Makino, T. Yamaguchi, I. Sasada

P. S. Anil Kumar, S. R. Sainkar, J. J. Shrotri, S. D. Kulkarni, C. E. Deshpande, S. K. Date

D. J. Fatemi, V. G. Harris, V. M. Browning, J. P. Kirkland

P. J. van der Zaag, M. Kolenbrander, M. Th. Rekvelde

Soon Cheon Byeon, Kug Sun Hong, In-Tae Kim

V. B. Fetisov, G. A. Kozhina, A. Ya. Fishman, T. E. Kurennykh, V. B. Vykhodets

Antony Ajan, B. Ramamurthy Acharya, Shiva Prasad, S. N. Shringi, N. Venkataramani

Y. Ijiri, J. A. Borchers, R. W. Erwin, S.-H. Lee, P. J. van der Zaag, R. M. Wolf

Kentaro Takano, R. H. Kodama, A. E. Berkowitz, W. Cao, G. Thomas

E. Dan Dahlberg, Brad Miller, Bradford Hill, B. J. Jonsson, Valter Strom, K. V. Rao, Josep Nogues, Ivan K. Schuller

Rare Earth Nitride and Carbide Hard Magnets

- 6896 Immobilization diffusion in R_2Fe_{17} nitrides
- 6899 Magnetic anisotropy of $R_2Fe_{17}N_x$ compounds
- 6902 Coercive $Sm_2Fe_{17}N_3$: A model pinning system created by heavy ion irradiation
- 6905 Hydrogenation and disproportionation of $Sm_2Fe_{17-x}Ga_x$ at high hydrogen pressures
- 6908 Electron microscopy studies of high coercive melt-spun $Sm_{2+\delta}Fe_{15}Ga_2C_2$ permanent magnets
- 6911 Pressure induced reversal of the volume expansion caused by interstitial nitrogen in $Nd_2Fe_{17}N_3$
- 6914 A neutron diffraction structural study of $R_2Fe_{17-x}Al_x(C)$ ($R=Tb, Ho$) alloys
- 6917 High remanence $(Sm, Zr)Fe_7N_x + \alpha$ -Fe nanocomposite magnets through exchange coupling
- 6920 Effect of Al substitution on the local environments and magnetic properties of partially nitrogenated $(Er_{0.5}Pr_{0.5})_2Fe_{17}$ permanent magnets
- 6923 ^{57}Fe Mössbauer study of the interstitial nitrogen atom effects of $NdFe_{10.5}V_{1.5}N_x$
- 6926 A study of nitrogenation of a $NdFe_{12-x}Mo_x$ compound by *in situ* neutron powder diffraction
- 6929 Crystallization and Mössbauer studies of melt-spun $NdFe_{10.7}TiB_{0.3}N_\delta$ alloys
- 6932 A Mössbauer study of plasma nitrided iron

- R. Skomski, S. Wirth
- X. C. Kou, F. R. de Boer, G. Chouteau
- N. M. Dempsey, X. L. Rao, J. M. D. Coey, J. P. Nozières, M. Ghidini, B. Gervais
- M. Kubis, K.-H. Müller L., Schutz O. Gutfleisch, I. R. Harris
- J. van Lier, A. Zern, H. Labitzke, J. Thomas, M. Seeger, H. Kronmüller
- G. K. Marasinghe, W. J. James, P. C. Ezekwenna, H. Luo, W. B. Yelon, Y. Zhao, R. B. Von Dreele, M. Ellouze, Ph. l'Héritier
- W. B. Yelon, H. Luo, M. Chen, W. C. Chang, S. H. Tsai
- T. Hidaka, T. Yamamoto, H. Nakamura, A. Fukuno
- V. G. Harris, D. J. Fatemi, K. G. Suresh, K. V. S. Rama Rao
- Jinbo Yang, Weihua Mao, Yingchang Yang, Zhenjie Zhao, Fashen Li
- C.-K. Loong, S. M. Short, J. Lin, Y. Ding
- Chul Sung Kim, Sung Yong An, Young Rang Uhm, Seung Wha Lee, Y. B. Kim, C. S. Kim
- F. A. O. Cabral, J. H. de Araujo, R. C. Araujo, S. Gama

Macroscopic Quantum Tunneling and Spin Dynamics

- 6934 Experimental evidence of macroscopic resonant tunneling of magnetization in antiferromagnetic ferritin
- 6937 Field-tuned quantum tunneling of the magnetization
- 6940 Resonant magnetic quantum tunneling through thermally activated states
- 6943 Unusual properties of the molecular nanomagnet $Mn_{12}ac$
- 6946 Comparison of the spin dynamics in different types of molecular magnetic rings from 1H NMR
- 6949 Analysis of electron paramagnetic resonance experiments in colossal magnetoresistance materials
- 6952 A novel method for quantitative study of domain reversal behavior
- 6955 Surface spin waves in metamagnets with nonuniaxial single-ion anisotropy

- E. del Barco, F. Luis, J. Tejada, X. X. Zhang, J. Bartolomé, J. M. Hernandez, E. M. Chudnovsky
- D. García-Pablos, N. García, H. De Raedt
- J. F. Fernández, J. Bartolomé, F. Luis
- M. A. Novak, A. M. Gomes, R. E. Rapp
- A. Lascialfari, Z. H. Jang, F. Borsa, D. Gatteschi, A. Cornia
- D. L. Huber
- Sug-Bong Choe, Sung-Chul Shin
- D. H. A. L. Anselmo, E. L. Albuquerque, M. G. Cottam

Itinerant Magnetism

- 6958 Exchange narrowing effects in the EPR linewidth of Gd diluted in Ce compounds

- Pablo A. Venegas, Paulo R. S. Netto

- 6961 High field magnetic properties in single crystal Nd_3Co
 Izuru Umehara, Ying Lu, Qing Feng Lu, Yoshiya Adachi, Masato Endo, Kiyoo Sato, Michael Bartashevich, Tsuneaki Goto
- 6964 Evolution of magnetism in $\text{Nd}(\text{Co}_{1-x}\text{Si}_x)_2$ and $\text{Ho}(\text{Co}_{1-x}\text{Si}_x)_2$
 T. D. Cuong, L. Havela, V. Sechovský, Z. Arnold, J. Kamarád
- 6967 On the nature of the magnetic phase transition of the HoCo_2 intermetallic
- 6969 Recovery of ErCo_2 Fermi level by substitution of Co by Ni and Fe
 P. J. von Ranke, N. A. de Oliveira
- 6971 Theoretical study of hyperfine fields at impurity nuclei in GdX ($X=\text{Zn}, \text{Cd}$) compounds: A two-center model
 F. Garcia, H. dos Santos, M. R. Soares, A. Y. Takeuchi, S. F. da Cunha
- 6974 Magnetic transitions in $\text{Tb}_{0.7}\text{Nd}_{0.3}\text{Mn}_2\text{Ge}_2$ compound
 A. L. de Oliveira, V. P. Ramunni, M. V. Tovar Costa, N. A. de Oliveira, A. Troper
- 6977 Magnetic moment, thermal and electrical transport in the inverse Mott systems $\text{BaCo}_{0.9}\text{Ni}_{0.1}\text{S}_{2-y}$ and CuIr_2S_4
 Shibaji Saha, Naushad Ali, Sunil Labroo, Dale Zych
- 6980 Magnetocrystalline anisotropy of $(\text{Fe}_{1-x}\text{Co}_x)_3\text{P}$
 H. Kang, P. Mandal, I. V. Medvedeva, J. Liebe, G. H. Rao, K. Bärner, A. Poddar, E. Gmelin
- 6983 Magnetic moment and hyperfine field on Fe sites in RFe_6Sn_6 compounds
 A. Broddefalk, P. Granberg, P. Nordblad, Hui-ping Liu, Y. Andersson
- 6986 Hydrogen-induced changes in TbNiAl
 Xiao-lei Rao, J. Cullen, V. Skumryev, J. M. D. Coey
- 6989 Thermal transport in $\text{Sr}_{1-x}\text{Ca}_x\text{RuO}_3$
 H. N. Bordallo, H. Nakotte, J. Eckert, A. V. Kolomiets, L. Havela, A. V. Andreev, H. Drulis, W. Iwasieczko
- 6992 Magnetic transitions and oxygen content of $\text{Ca}_3\text{Ru}_2\text{O}_7$
 M. Shepard, P. F. Henning, G. Cao, J. E. Crow
- Anisotropic Magnetoresistance and Granular GMR**
- 6995 Anisotropic magnetotransport properties of epitaxial thin films of conductive ferromagnetic oxide SrRuO_3
 S. McCall, G. Cao, J. E. Crow, R. P. Guertin
- 6998 Giant spontaneous Hall effect and magnetoresistance in $\text{La}_{1-x}\text{Ca}_x\text{CoO}_3$ ($0.1 \leq x \leq 0.5$)
 R. A. Rao, D. B. Kacedon, C. B. Eom
- 7001 Giant magnetoresistance in granular CuFeNi alloys
 A. V. Samoilov, G. Beach, C. C. Fu, N.-C. Yeh, R. P. Vasquez
- 7004 Microstructure and giant magnetoresistance of Co-Cu granular films fabricated under the extremely clean sputtering process
 C. S. Martins, H. R. Rechenberg, F. P. Missell
- 7007 Giant magnetoresistance and remanence in granular CoCu codeposited films
 Masakiyo Tsunoda, Kentaro Okuyama, Makoto Ooba, Migaku Takahashi
- Thin Films: Structure and Magnetism**
- 7010 Structural and magnetic properties of "expanded" Mn
 A. D. C. Viegas, J. Geshev, J. E. Schmidt, E. F. Ferrari
- 7013 Growth and magnetism of one Mn monolayer on $\text{Ag}(100)$
 Ilya L. Grigorov, J. C. Walker, M. E. Hawley, G. W. Brown, M. Lütt, M. R. Fitzsimmons
- 7016 Structural stability, magnetism, and surface magneto-optic Kerr effect spectra of $\text{MnAg}(001)$ surface alloys
 O. Elmouhssine, G. Moraitis, J. C. Parlebas, C. Demangeat, P. Schieffer, M. C. Hanf, C. Krembel, G. Gewinner
- 7019 Artificial $\text{FeCu}(100)$ epitaxial ordered alloy films: Element-selective magnetic properties
 Soon C. Hong, Miyoung Kim, A. J. Freeman
- W. Kuch, M. Salvietti, Xingyu Gao, M. Klaua, J. Barthel, Ch. V. Mohan, J. Kirschner

- 7022 Orbital magnetic moment enhancement at surfaces and interfaces within the framework of the local density approximation+ U method
- 7025 Magnetic extended x-ray absorption fine structure at the $L_{3,2}$ edges of Fe and Co on Cu(001)
- 7028 Probing local magnetic disorder by investigating spin dependent photoelectron scattering
- 7031 Magnetoresistance in single Fe(001) ultrathin films
- 7034 Magnetic properties of very thin single and multilayer NiFeCo and CoFe films deposited by sputtering
- 7037 Ferromagnetic resonance linewidth in thin films coupled to NiO
- 7040 Magnetic ordering in Co films on stepped Cu(100) surfaces
- 7043 Overpotential driven perpendicular magnetization of electrodeposited ultrathin cobalt films
- 7046 Magnetic and structural characterizations of HCP permalloy films grown by molecular beam epitaxy

CMR Materials and Their Properties

- 7049 Transport and magnetic properties of epitaxial and polycrystalline magnetite thin films
- 7052 Observation of spin-dependent transport and large magnetoresistance in $\text{La}_{0.7}\text{Sr}_{0.3}\text{MnO}_3/\text{SrTiO}_3/\text{La}_{0.7}\text{Sr}_{0.3}\text{MnO}_3$ ramp-edge junctions
- 7055 Grain boundary effects on transport in metalorganic chemical vapor deposition-grown, Ca-doped lanthanum manganites
- 7058 Magnetic anisotropy and spin diffusion through spin disordered interfaces in magnetoresistive manganites
- 7061 Scanning magnetoresistance microscopy of $\text{La}_{0.67}\text{Sr}_{0.33}\text{MnO}_3$ films
- 7064 Magnetic anisotropy of doped manganite thin films and crystals
- 7067 Investigation of granular films composed of interdispersed $\text{La}_{1/3}\text{Ca}_{2/3}\text{MnO}_3$ particles and metallic Au particles
- 7070 Magnetic and transport properties of radiation damaged $\text{La}_{0.7}\text{Ca}_{0.3}\text{MnO}_{3.0}$ thin films
- 7073 Evolution of strain-dependent transport properties in ultrathin $\text{La}_{0.67}\text{Sr}_{0.33}\text{MnO}_3$ films
- 7076 Contrasting magnetic and structural properties of two La manganites with the same doping levels
- 7079 Magnetoresistance effects of $\text{La}_{0.7}\text{M}_{0.3}\text{MnO}_{3-\delta}$ far below the Curie temperature ($M=\text{Ca}, \text{Pb}$)

- A. B. Shick, A. J. Freeman, A. I. Liechtenstein
- P. Srivastava, L. Lemke, H. Wende, R. Chauvistré, N. Haack, K. Baberschke, J. Hunter-Dunn, D. Arvanitis, N. Mårtensson, A. Ankudinov, J. J. Rehr
- H. Wende, J. W. Freeland, V. Chakarian, Y. U. Idzerda, L. Lemke, K. Baberschke
- S. Yuasa, T. Katayama, M. Nývlt, Y. Suzuki, T. Yori
- D. Wang, J. M. Daughton, K. Bussmann, G. A. Prinz
- R. D. McMichael, M. D. Stiles, P. J. Chen, W. F. Egelhoff, Jr.
- S. T. Coyle, M. R. Scheinfein
- J. L. Bubendorff, E. Beaurepaire, C. Mény, J. P. Bucher
- J. C. A. Huang, Y. M. Hu, C. C. Yu
- X. W. Li, A. Gupta, Gang Xiao, G. Q. Gong
- C. Kwon, Q. X. Jia, Y. Fan, M. F. Hundley, D. W. Reagor
- J. J. Heremans, S. Watts, S. Wirth, X. Yu, E. S. Gillman, K. H. Dahmen, S. von Molnár
- B. Martínez, Ll. Balcells, J. Fontcuberta, X. Obradors, C. H. Cohenca, R. F. Jardim
- D. K. Petrov, A. Gupta, J. R. Kirtley, L. Krusin-Elbaum, H. S. Gill
- Y. Suzuki, H. Y. Hwang, S-W. Cheong, T. Siegrist, R. B. van Dover, A. Asamitsu, Y. Tokura
- Mark Rubinstein, P. R. Broussard, L. H. Allen, Kristl B. Hathaway, Michael M. Miller, Jonathan Z. Sun
- V. M. Browning, R. M. Stroud, W. W. Fuller-Mora, J. M. Byers, M. S. Osofsky, D. L. Knies, K. S. Grabowski, D. Koller, J. Kim, D. B. Chrisey, J. S. Horwitz
- H. L. Ju, Kannan M. Krishnan, D. Lederman
- T. R. McGuire, P. R. Duncombe, G. Q. Gong, A. Gupta, X. W. Li, S. J. Pickart, M. L. Crow
- K. Dörr, K.-H. Müller, E. S. Vlachov, R. A. Chakalov, R. I. Chakalova, K. A. Nenkov, A. Handstein, B. Holzapfel, L. Schultz

Electronic Structure

- 7082 Fully relativistic theory for the magnetic extended x-ray absorption fine structure
- 7085 Spin-dependent extended x-ray absorption fine structure in magnetic oxides
- 7088 Probing the magnetic microstructure of an amorphous GdFe system with magnetic anomalous small angle x-ray scattering
- 7091 Magnetic x-ray investigation at the $L_{2,3}$ edges of Nd in $\text{Nd}_2\text{Fe}_{14}\text{B}$
- 7094 Epitaxial $\text{Fe}_{100-x}\text{Co}_x/\text{Ag}(001)$ alloy films: Structure and element-specific magnetic moments from magnetic linear dichroism
- 7097 Magnetic anisotropies of Ni-Pt and Co-Pt alloys
- 7100 Ground state properties of a high-spin $\text{Mn}_{12}\text{O}_{12}$ molecule in an organic compound

Hard Magnets II

- 7103 A comparison between a two-material and three-material magnetic current limiter
- 7106 Reversible and irreversible components of tensor magnetization and magnetostriction
- 7109 Fundamental study for rosary-shaped magnetic actuators
- 7112 The design and analysis of axial field multipole impulse magnetizing fixtures
- 7115 Fabrication of a micromotor driven by electromagnetic vibration
- 7118 New permanent magnet couplings for screwing devices
- 7121 A comparative analysis of permanent magnet-type bearingless synchronous motors for fully magnetically levitated rotors
- 7124 Spin reorientation in $(\text{Pr},\text{RE})-(\text{Co},\text{TM})-\text{B}$ magnets ($\text{RE}=\text{Tb}$, $\text{TM}=\text{Fe},\text{Cr},\text{Mn}$)
- 7127 Magnetization processes in hybrid magnets
- 7130 Mechanical strength of the solid-HDDR treated Nd-Fe-B-type materials
- 7133 Thermal expansion of compounds $\text{R}_{n+1}\text{Co}_{3n+5}\text{B}_{2n}$ ($\text{R}=\text{Y}$ and Gd ; $n=1, 2, 3$, and ∞)
- 7136 Specific-heat studies of RCu_4Al_8 compounds ($\text{R}=\text{Er},\text{Y}$)
- 7139 Magnetic and structural properties of commercial $\text{Sm}_2(\text{Co},\text{Fe},\text{Cu},\text{Zr})_{17}$ -based magnets
- 7142 The magnetization study of melt-spun ribbons of B containing TbFe_2 alloys
- 7145 Alternating current susceptibility study of $\text{Dy}_2\text{Fe}_{17-x}\text{Ga}_x$ compounds

D. Ahlers, G. Schütz, V. Popescu, H. Ebert

D. Ahlers, K. Attenkofer, G. Schütz

P. Fischer, R. Zeller, G. Schütz, G. Goerigk, H.-G. Haubold, K. Pruegl, G. Bayreuther

F. Bartolomé, J. M. Tonnerre, L. Sève, D. Raoux, J. E. Lorenzo, J. Chaboy, L. M. García, J. Bartolomé, M. Krisch, A. Rogalev, R. Serimaa, C-C. Kao, G. Cibin, A. Marcelli

E. Kisker, A. Faust, R. Schellenberg, A. Fanelisa, F. U. Hillebrecht

S. S. A. Razee, J. B. Staunton, F. J. Pinski, B. Ginatempo, E. Bruno

S. Y. Wang, Liang-Jian Zou, X. G. Gong, Q. Q. Zheng, H. Q. Lin

S. Young, F. P. Dawson, M. Iwahara, S. Yamada

F. Liorzou, Y. Yu, D. L. Atherton

H. Saotome, K. Sakaguchi

C. D. Riley, G. W. Jewell, D. Howe

T. Honda, J. Yamasaki

L. Quellec, V. Lemarquand, G. Lemarquand

J. F. Charpentier, G. Lemarquand

D. H. Kim, G. Hadjipanayis

M. Emura, A. C. Neiva, F. P. Missell, K. L. Babcock, J. Ormerod, S. Constantinides

H. W. Kwon, S. J. Kang

H. Ido, Y. Suzuki, T. Suzuki

I. H. Hagmusa, F. E. Kayzel, E. Brück, K. H. J. Buschow

X. Chen, J. F. Liu, C. Ni, G. Hadjipanayis, A. Kim

K. S. Kim, S. C. Yu, S. R. Kim, S. H. Lim

V. Skumryev, Xiao-lei Rao, J. M. D. Coey, N. Sheludko

Colossal Magnetoresistance

- 7148 Heat diffusivity of $\text{Nd}_{1-x}\text{Sr}_x\text{MnO}_{3-\delta}$ and $\text{La}_{1-x}\text{Ca}_x\text{MnO}_{3-\delta}$ compounds
J. Liebe, H. Kang, L. Haupt, P. Mandal, I. V. Medvedeva, G. H. Rao, K. Bärner, A. Poddar, P. Muruguraj, R. Fischer, E. Gmelin, E. Gommert, R. v. Helmolt, J. Wecker
- 7151 Magnetic properties of $(\text{Pr}(\text{Ca}, \text{Sr}))\text{MnO}_3$ studied by nuclear magnetic resonance
G. J. Tomka, P. C. Riedi, Cz. Kapusta, G. Balakrishnan, D. McK. Paul, M. R. Lees, J. Barratt
- 7154 Anomalous low-field magnetization in $\text{La}_{2/3}\text{Ca}_{1/3}\text{MnO}_3$ near the critical point: Stable clusters?
V. S. Amaral, J. P. Araújo, Yu. G. Pogorelov, J. B. Sousa, P. B. Tavares, J. M. Vieira, J. M. B. Lopes dos Santos, A. A. C. S. Lourenço, P. A. Algarabel
- 7157 Low field magnetotransport in $\text{La}_{0.7}\text{Sr}_{0.3}\text{MnO}_3$ films
B. S. Teo, N. D. Mathur, S. P. Isaac, J. E. Evetts, M. G. Blamire
- 7160 Magnetostriction and field induced transitions in $\text{La}_{1-x}\text{Sr}_x\text{MnO}_3$ in pulsed magnetic fields
Yu. F. Popov, A. M. Kadomtseva, G. P. Vorob'ev, V. Yu. Ivanov, A. A. Mukhin, A. K. Zvezdin, A. M. Balbashov
- 7163 Magnetic properties, resistivity, and heat capacity of EuMnO_3 and $\text{Eu}_{0.7}\text{A}_{0.3}\text{MnO}_3$ (A=Ca, Sr) compounds
Y. M. Mukovskii, G. Hilscher, H. Michor, A. M. Ionov
- 7166 Evidence for a gap in the excitation spectrum of CrO_2
A. Barry, J. M. D. Coey, L. Ranno, K. Ounadjela
- 7169 Effect of low Fe doping in $\text{La}_{0.8}\text{Sr}_{0.2}\text{MnO}_3$
Antony Ajan, N. Venkataramani, Shiva Prasad, S. N. Shringi, A. K. Nigam, R. Pinto
- 7171 Magnetic and transport properties of Pb perovskites and Fe containing giant magnetoresistance perovskites
J. Gutiérrez, J. M. Barandiarán, M. Insausti, L. Lezama, A. Peña, J. J. Blanco, T. Rojo
- 7174 90 MeV ^{16}O ion irradiation effects on transport and magnetization in epitaxial thin films of $\text{La}_{0.75}\text{Ca}_{0.25}\text{MnO}_3$
Ravi Bathe, S. K. Date, S. R. Shinde, L. V. Saraf, S. B. Ogale, S. I. Patil, Ravi Kumar, S. K. Arora, G. K. Mehta
- 7177 Colossal magnetoresistance in $\text{La}_{1-x}\text{Li}_x\text{MnO}_3$
X. L. Wang, S. J. Kennedy, Peter Gehringer, Wolfgang Lang, H. K. Liu, S. X. Dou
- 7180 Magnetic, dielectric, and transport properties of $\text{La}_{1-x}\text{Sr}_x\text{MnO}_3$ at submillimeter wavelengths
V. Yu. Ivanov, V. D. Travkin, A. A. Mukhin, S. P. Lebedev, A. A. Volkov, A. Pimenov, A. Loidl, A. M. Balbashov, A. V. Mozhaev
- 7183 Unusual substitutional properties of Ru in the $\text{La}_{0.7}\text{Sr}_{0.3}\text{Mn}_{1-x}\text{Ru}_x\text{O}_3$ system
S. Sundar Manoharan, H. L. Ju, Kannan M. Krishnan
- 7186 Angle-resolved magnetic and transport properties of $\text{Pr}_{0.7}\text{Sr}_{0.3}\text{MnO}_3$ thin films
J. Wolfman, W. Prellier, Ch. Simon, B. Mercey
- 7189 Fabrication of $\text{YBa}_2\text{Cu}_3\text{O}_{7-\delta}/\text{SrTiO}_3/\text{La}_{0.7}\text{Sr}_{0.3}\text{MnO}_{3-\delta}$ junctions for the control of supercurrent by spin-polarized quasiparticle current injection
R. M. Stroud, J. Kim, C. R. Eddy, D. B. Chrissey, J. S. Horwitz, D. Koller, M. S. Osofsky, R. J. Soulen, Jr., R. C. Y. Auyeung
- 7192 Magnetism and colossal magnetoresistance in the compound $\text{Sr}_{14}\text{MnSb}_{11}$
D. J. Webb, R. Cohen, P. Klavins, R. N. Shelton, J. Y. Chan, S. M. Kauzlarich
- 7195 Polycrystalline and laminated $\text{La}_{0.7}\text{Sr}_{0.3}\text{MnO}_3$ films made by pulsed laser deposition
F. J. Cadieu, R. Rani, X. R. Qian, C. F. Cadieu, Li Chen, W. Mendoza, S. A. Shaheen
- 7198 Colossal magnetoresistance and Mössbauer studies of the manganites $\text{La}_{1-x}\text{Sn}_x\text{Mn}_{0.985}\text{Fe}_{0.015}\text{O}_{3+\delta}$
Z. W. Li, A. H. Morrish, X. Z. Zhou, S. Dai

(Continued)

- 7201 Electron spin resonance and magnetization in perovskite and pyrochlore manganites

- 7204 Thermal conductivity and magnetic transitions in Mn^{3+}/Mn^{4+} manganites

Exchange Biasing II

- 7207 Influences on relaxation of exchange biasing in $NiO/Ni_{66}Co_{18}Fe_{16}$ bilayers

- 7210 Thermal fluctuation aftereffect of exchange coupled films for spin valve devices

- 7213 Effect of buffer layer on antiferromagnetic grain size and exchange-coupling field of $Cr_{70}Al_{30}/Fe_{19}Ni_{81}$ bilayers

- 7216 Magnetic, temperature, and corrosion properties of the $NiFe/IrMn$ exchange couple

- 7219 Spin-flop tendencies in exchange-biased Co/CoO thin films

- 7222 Dependence of exchange field and coercivity on cooling field in $NiFe/CoO$ bilayers

- 7225 First-principles exchange interactions between ferromagnetic and antiferromagnetic films: Co on $NiMn$, a case study

Critical Phenomena and Phase Transitions

- 7228 Local and global demagnetization process: Is there any self-organized critical behavior?

- 7231 Non-Heisenberg couplings and ferromagnetic instability in a random antiferromagnetic spin-1 chain

- 7234 Universal magnetic fluctuations in the two-dimensional XY model

- 7237 Semiquantitative analysis of magnetic phase transitions in the $MnFeP_{1-x}As_x$ series of compounds

- 7240 Magnetic behavior of the low-dimensional compounds $Ba_2Cu_3O_4Cl_2$ and $Ba_3Cu_2O_4Cl_2$

- 7243 Magnetic, electrical, and structural studies on the metal-insulator transition in $CuIr_2S_{4-x}Se_x$ ($0 \leq x \leq 4$)

- 7246 Finite size scaling in the thin film limit

- 7249 Phase diagram of a highly diluted, disordered Ising system: The Al-rich, Al-Fe system

Magnetoelastic Materials

- 7252 Processing effects on the magnetostrictive and physical properties of $SmFe_2$ /metal composites

- 7255 Magnetomechanical coupling and elastic moduli of polymer-bonded Terfenol composites

M. Tovar, M. T. Causa, G. Ibañez, C. A. Ramos, A. Butera, F. Rivadulla, B. Alascio, S. B. Oseroff, S.-W. Cheong, X. Obradors, S. Piñol

J. Hejtmánek, Z. Jiráček, Z. Arnold, M. Maryško, S. Krupička, C. Martin, F. Damay

P. A. A. van der Heijden, T. F. M. M. Maas, J. C. S. Kools, F. Roozeboom, P. J. van der Zaag, W. J. M. de Jonge

Junichi Fujikata, Kazuhiko Hayashi, Hidefumi Yamamoto, Masafumi Nakada

K. Ikarashi, Y. Otani, K. Fukamichi, O. Kitakami, Y. Shimada, J. Echigoya, H. Uyama, A. Makino

A. J. Devasahayam, P. J. Sides, M. H. Kryder

J. A. Borchers, Y. Ijiri, S.-H. Lee, C. F. Majkrzak, G. P. Felcher, K. Takano, R. H. Kodama, A. E. Berkowitz

T. Ambrose, C. L. Chien

T. C. Schulthess, W. H. Butler

O. A. Chubykalo, J. M. González

R. N. Bhatt, Kun Yang

P. Archambault, S. T. Bramwell, J.-Y. Fortin, P. C. W. Holdsworth, S. Peysson, J.-F. Pinton

R. Zach, M. Guillot, J. Toboła

D. Eckert, K. Ruck, M. Wolf, G. Krabbes, K.-H. Müller

P. Somasundaram, D. Kim, J. M. Honig, T. M. Pekarek, T. Gu, A. I. Goldman

C. Waldfried, D. Welipitiya, T. McAvoy, P. A. Dowben, E. Vescovo

J. Restrepo, G. A. Pérez Alcázar, J. M. González

F. E. Pinkerton, T. W. Capehart, J. F. Herbst, E. G. Brewer, C. B. Murphy

J. Hudson, S. C. Busbridge, A. R. Piercy

- 7258 First-principles theory of magnetoelastic coupling and magnetic anisotropy strain dependence in ultrathin Co films on Cu(001)
- 7261 Effects of heteroepitaxial strain on Laves phases TbFe_2 and DyFe_2
- 7264 Magnetomechanical instability in FeTb/Fe multilayers
- 7267 Magnetic properties and microstructure of giant magnetostrictive TbFe/FeCo multilayers
- 7270 Magnetic properties of amorphous Sm-Fe and Sm-Fe-B thin films fabricated by radio-frequency magnetron sputtering
- 7273 Application of the ratio $\Delta\lambda/\Delta M$ to giant magnetostrictive materials in the $\langle 110 \rangle$ easy regime
- 7276 Magnetostriction and susceptibilities of twinned single crystals of Terfenol-D
- 7279 Magnetization and magnetostriction of dendritic $[112] \text{Tb}_x\text{Dy}_y\text{Ho}_z\text{Fe}_{1.95}$ ($x+y+z=1$) rods under compressive stress
- 7282 Development of Terfenol-D transducer material
- 7285 Magnetostrictive properties of polymer-bonded amorphous Tb-Fe-B composites
- 7288 Piezomagnetic properties, saturation magnetostriction, and ΔE effect in DyZn at 77 K
- 7291 Experimental evidence of pressure-induced magnetic phase transition in $\text{Fe}_{72}\text{Pt}_{28}$ Invar alloy
- 7294 Electrochemical deposition of amorphous FeB films with soft magnetic properties
- 7297 Field-induced strain under load in Ni-Mn-Ga magnetic shape memory materials
- 7300 Magnetoelastic behavior of the Heusler Ni_2MnGa alloy
- 7303 Trial on-silicon micromagnetoelastic devices
- 7306 Nonlinear self-localized magnetoelastic surface waves in antiferromagnetic media
- Superconductivity II**
- 7309 The Re-doped high T_c superconductor $\text{HgBa}_2\text{Ca}_2\text{Cu}_3\text{O}_x$: Magnetic irreversibility versus anisotropy
- 7312 Structural and magnetic properties of $\text{RSr}_2\text{Fe}_3\text{O}_9$ ($\text{R}=\text{La, Y, Pr, and Gd}$)
- 7315 Magnetic and superconducting properties of Pr in $\text{La}_{1-x}\text{Pr}_x\text{BaCaCu}_3\text{O}_7$ system with $0.0 \leq x \leq 1.0$
- 7318 Magnetic properties of $\text{Pb}_2\text{Sr}_2\text{PrCu}_3\text{O}_8$ studied by ac susceptibility
- 7321 Specific heat, magnetization and C-isotope effect of $\text{Y}_2\text{C}_2(\text{Br, I})_2$ superconductors
- A. B. Shick, D. L. Novikov, A. J. Freeman
- M. Huth, C. P. Flynn
- Manfred Wuttig, Quanmin Su, Fabrice Masson, Eckhard Quandt, Alfred Ludwig
- E. Quandt, A. Ludwig, D. G. Lord, C. A. Faunce
- Y. S. Choi, S. R. Lee, S. H. Han, H. J. Kim, S. H. Lim
- S. C. Busbridge, A. R. Piercy
- X. G. Zhao, D. G. Lord
- M. Wun-Fogle, J. B. Restorff, A. E. Clark, J. F. Lindberg
- E. A. Lindgren, S. Haroush, J. C. Poret, A. D. Mazzatesta, M. Rosen, M. Wun-Fogle, J. B. Restorff, A. E. Clark, J. F. Lindberg
- S. R. Kim, S. Y. Kang, J. K. Park, J. T. Nam, Derac Son, S. H. Lim
- J. B. Restorff, M. Wun-Fogle, A. E. Clark
- S. Odin, F. Baudalet, J. P. Itié, A. Polian, S. Pizzini, A. Fontaine, Ch. Giorgetti, E. Dartyge, J. P. Kappler
- Naoyuki Fujita, Mitsuteru Inoue, Ken'ichi Arai, Pang Boey Lim, Toshitaka Fujii
- S. J. Murray, M. Farinelli, C. Kantner, J. K. Huang, S. M. Allen, R. C. O'Handley
- Eduard Obradó, Alfons González-Comas, Lluís Mañosa, Antoni Planes
- M. Takezawa, M. Yamaguchi, K. Ishiyama, K. I. Arai
- Igor E. Dikshtein, Sung-Ho Suck Salk
- L. Fàbrega, B. Martínez, J. Fontcuberta, A. Sin, S. Piñol, X. Obradors
- V. P. S. Awana, S. X. Dou, I. Felner, I. Nowik, S. K. Malik, Apurva Mehta, Rajvir Singh, A. V. Narlikar, W. B. Yelon
- V. P. S. Awana, S. X. Dou, Rajvir Singh, A. V. Narlikar, S. K. Malik, W. B. Yelon
- S. Y. Wu, Y. C. Chang, K. C. Lee, W.-H. Li
- W. Schnelle, R. W. Henn, Th. Gulden, R. K. Kremer, A. Simon

- 7324 H - T phase diagram for the giant magnetic flux jumps in low temperature superconductors and high temperature superconductors
- 7327 Magnetic memory effect in $\text{YBa}_2\text{Cu}_3\text{O}_{7-x}/(\text{BiDy})_3(\text{FeGa})_5\text{O}_{12}$ heterostructures
- 7330 Spin wave scattering and intermode transitions induced by the magnetic vortex lattice in the ferrite-high-temperature superconductor film structure

Advances in Magnetic Force Microscopy

- 7333 Magnetic dissipation force microscopy studies of magnetic materials (invited)

Fundamental Aspects of CMR Materials

- 7339 Long wavelength spin dynamics in $\text{La}_{0.53}\text{Ca}_{0.47}\text{MnO}_3$
- 7342 Spin dynamics of strongly doped $\text{La}_{1-x}\text{Sr}_x\text{MnO}_3$
- 7345 Tilted antiferromagnetic ordering of Mn in $\text{Nd}_{0.62}\text{Ca}_{0.38}\text{MnO}_3$
- 7348 Magnetic correlations in the bilayer manganite $\text{La}_{1.2}\text{Sr}_{1.8}\text{Mn}_2\text{O}_7$
- 7351 The complex magnetic behavior and the role of dynamic structural fluctuations in $\text{La}_{1.2}\text{Sr}_{1.8}\text{Mn}_2\text{O}_7$ crystals
- 7354 Lattice effects in ferromagnetic manganite perovskites
- 7357 Isotope effect and T_c in manganites and high T_c oxides
- 7360 A mean field theory of magnets with competing double exchange and superexchange interactions
- 7363 Composite polaron mechanism for colossal magnetoresistance in perovskite manganites
- 7366 Tunneling evidence of half-metallicity in epitaxial films of ferromagnetic perovskite manganites and ferrimagnetic magnetite
- 7369 Metal-insulator transition induced by ^{16}O - ^{18}O oxygen isotope exchange in colossal negative magnetoresistance manganites

Spin Glasses and Frustrated Systems

- 7372 Magnetic susceptibility of Fe/Cu multilayers: Ferromagnetic, antiferromagnetic, and spin-glass phases
- 7375 Origin of magnetic anomalies in the spin glass system, $\text{La}_{0.85}\text{Sr}_{0.15}\text{CoO}_3$
- 7378 Canted antiferromagnetism and spin glasslike behavior in a family of two-dimensional organic/inorganic nanocomposites
- 7381 Magnetic and structural properties of $\text{PrCo}_{3-x}\text{Si}_x$ compounds
- 7384 Frustration in the paramagnetic phase of spin-density-wave CrFeV alloys
- 7387 A new paradigm for two-dimensional spin liquids
- 7390 Calculation of the energy barriers in strongly interacting many-particle systems

V. V. Chabanenko, A. I. D'yachenko, A. V. Chabanenko, H. Szymczak, S. Piechota, A. Nabialek, N. D. Dung

D. Mou, A. M. Grishin, K. V. Rao

L. V. Lutsev, S. V. Yakovlev

Y. Liu, P. Grütter

J. J. Rhyne, H. Kaiser, H. Luo, Gang Xiao, M. L. Gardel

L. Vasiliu-Doloc, J. W. Lynn, Y. M. Mukovskii, A. A. Arsenov, D. A. Shulyatev

S. Y. Wu, W.-H. Li, K. C. Lee, J. W. Lynn, R. S. Liu, J. B. Wu, C. Y. Huang

S. Rosenkranz, R. Osborn, J. F. Mitchell, L. Vasiliu-Doloc, J. W. Lynn, S. K. Sinha, D. N. Argyriou

R. P. Sharma, P. Fournier, R. L. Greene, T. Venkatesan, J. F. Mitchell, D. Miller

D. J. Singh, W. E. Pickett

Vladimir Z. Kresin, Stuart A. Wolf

D. I. Golosov, M. R. Norman, K. Levin

Liang-Jian Zou, H. Q. Lin, Q.-Q. Zheng

J. Y. T. Wei, N.-C. Yeh, R. P. Vasquez, A. Gupta

N. A. Babushkina, L. M. Belova, V. I. Ozhogin, O. Yu. Gorbenko, A. R. Kaul, A. A. Bosak, D. I. Khomskii, K. I. Kugel

A. J. A. de Oliveira, W. A. Ortiz, D. H. Mosca, N. Mattoso, W. H. Schreiner, S. R. Teixeira

P. S. Anil Kumar, P. A. Joy, S. K. Date

M. A. Gîrțu, C. M. Wynn, W. Fujita, K. Awaga, A. J. Epstein

T. Matsui, R. D. Stevenson, R. D. Kirby, D. J. Sellmyer

V. Yu. Galkin, W. A. Ortiz, E. Fawcett

R. R. P. Singh, O. A. Starykh, P. J. Freitas

D. V. Berkov

7393 Influence of the configurational degeneracy on the hysteretic behavior of a system of magnetostatically coupled magnetic moments

J. M. González, O. A. Chubykalo,
A. Hernando, M. Vázquez

7396 Domain models for aging in spin glasses

Derek Walton

7399 **AUTHOR INDEX**



IEEE TRANSACTIONS ON

MAGNETICS

A PUBLICATION OF THE IEEE MAGNETICS SOCIETY

JULY 1998

VOLUME 34

NUMBER 4

IEMGAQ

(ISSN 0018-9464)

THE SEVENTH JOINT MAGNETISM AND MAGNETIC MATERIALS-INTERNATIONAL MAGNETICS CONFERENCE

Hyatt Regency Embarcadero Hotel, San Francisco, California, January 6-9, 1998

Cover Photograph Credit	
Sponsoring Organizations	
Conference Organization	
Preface	
Contributors	
Exhibitors	
Introduction	
Editors	

PART I

MAGNETIC MULTILAYERS

Determination of the Copper Layer Thickness in Spin Valves by Grazing Incidence X-Ray Fluorescence — <i>T. P. A. Hase, B. K. Tanner, P. Ryan, C. H. Marrows, and B. J. Hickey</i>	
Influence of the Top and Bottom Interface on Perpendicular Magnetic Anisotropy in Tb-Fe-Ag Multilayers — <i>O. Marks, T. Ruckert, J. Tappert, W. Keune, W.-S. Kim, W. Kleemann, and J. Voiron</i>	
NiO/ α -Fe ₂ O ₃ Multilayers Prepared by PLD: A Model System for Magnetic Study of Interdiffusion — <i>N. Keller, M. Guyot, A. Das, M. Porte, and R. Krishnan</i>	
Correlation Between Evolving Magnetic and Morphological Properties in Magnetic Multilayers — <i>S. A. Doherty, J.-G. Zhu, M. Dugas, S. Anderson, and J. Tersteeg</i>	
Spin Valve Structures on NiO Pinning Layers — <i>C. Cowache, B. Dieny, S. Auffret, M. Cartier, R. H. Taylor, R. O'Barr, and S. Y. Yamamoto</i>	
FMR and Magnetization Study of NiFe/Ag/CoNi Trilayer Film — <i>A. R. Koymen, L. R. Tagirov, R. T. Gilmutdinov, C. Topaci, C. Birlikseven, H. Z. Durusoy, and B. Aktas</i>	
Highly Localized Surface Modes in Epitaxial W/Ni/W Films — <i>G. Suran, J. Rothman, and C. Meyer</i>	
Iron and Nickel Surface and Interface Anisotropies — <i>R. Skomski, D. Sander, C. Schmidhals, A. Enders, and J. Kirschner</i>	
Second Harmonic Generation Study of Quantum Well States and Interdiffusion in a Co/Rh Multilayer — <i>F. Manders, K. J. Veenstra, A. Kirilyuk, T. Rasing, H. A. M. van den Berg, and N. Persat</i>	
Role of Magnetoelastic Anisotropy in Ni/Pt Multilayer Films — <i>Y.-S. Kim and S.-C. Shin</i>	

- Strong Anti-Ferromagnetic Coupling in τ MnAl/Co Perpendicular Magnetic Superlattices on GaAs — C. Bruynseraede, G. Lauhoff, J. A. C. Bland, G. Strijkers, J. De Boeck, and G. Borghs
- Competition Between Direct Exchange and Indirect RKKY Coupling in Fe/V(001) Superlattices — G. R. Harp, M. M. Schwickert, M. A. Tomaz, T. Lin, D. Lederman, E. Mayo, and W. L. O'Brien
- Growth of Giant Magnetoresistive Spin Valves with Strong Exchange Bias Field — G. Choe, A. Tsoukatos, and S. Gupta
- Preferred Crystal Orientation of NiFe Underlayers and its Effect on Magnetostriction of Co/Cu/Co Thin Films — T. Yeh, J. M. Sivertsen, and C.-L. Lin
- Magnetic Anisotropies of Fe_nV_m(001) Superlattices Determined by Ferromagnetic Resonance — A. N. Anisimov, W. Platow, P. Pouloupoulos, M. Farle, K. Baberschke, P. Isberg, P. Granberg, and R. Wäppling
- Magnetic Anisotropy and Reorientation in Co/Rh Superlattices — X. Ying, K. V. Rao, P. J. Jensen, and J. J. Xu
- Magnetic and Transport Properties of Sputter Deposited Ni/Co Multilayers — R. J. Pollard, S. E. McCartney, and R. Atkinson
- Thin Soft Sendust Film Laminated CoPt Hard Films — S. S. Xue, J. F. Dolejsi, and P. J. Ryan
- Spin Waves and Interlayer Coupling in CoFe/Mn/CoFe Structures — M. Chirita, G. Robins, R. L. Stamps, R. Sooryakumar, M. E. Filipkowski, C. J. Gutierrez, and G. A. Prinz
- First Principles Calculations of the Energetics of Co/Cu(111) Multilayers — X. Wang and C. L. Fu
- Superlattices of III-V Semiconductor and Heterogeneous Magnetic Layers for CPP Magnetotransport — J. De Boeck, H. Akinaga, C. Bruynseraede, H. Bender, and G. Borghs

GIANT MAGNETORESISTANCE AND TRANSPORT

- Stress Effects on the Magnetic Properties of FeMn and NiMn Spin Valves — E. Linville, D. Han, J. Judy, J. Sivertson, and S. Mao
- Time and Temperature Dependence of High Thermal Stability in NiO/Co/Cu/Co/M Spin Valves — R. D. McMichael, P. J. Chen, and W. F. Egelhoff, Jr.
- Magnetoresistance Due to Domain Walls in Micron Scale Fe Wires with Stripe Domains — A. D. Kent, U. Ruediger, J. Yu, S. Zhang, P. M. Levy, Y. Zhong, and S. S. P. Parkin
- Anisotropic Magnetoresistance as a Probe of Magnetization Reversal in Individual Nano-sized Nickel Wires — J.-E. Wegrowe, S. E. Gilbert, D. Kelly, B. Doudin, and J.-P. Ansermet
- Temperature Dependence of Interlayer Coupling in Fe/Si Superlattices — Y. Endo, O. Kitakami, and Y. Shimada
- Mossbauer Studies of Fe-Pb-O Granular Films with Enhanced Tunneling Magnetoresistance Effect — J.-H. Hsu, Y.H. Huang, P. K. Tseng, and D. E. Chen
- Magnetic Microstructures from Magnetic Force Microscopy and Monte Carlo Simulation in CoFe-Ag-Cu Granular Films — V. Franco, X. Batlle, A. Valencia, A. Labarta, K. O'Grady, and M.L. Watson
- GMR in DC Magnetron Sputtered Ni₈₁Fe₁₉/Cu Multilayers — M. Mao, C. Cerjan, M. Gibbons, B. Law, F. Grabner, S. P. Vernon, and M. Wall
- Highly Field Sensitive and Thermally Stable DC Magnetron Sputtered Soft Ni₈₁Fe₁₉/Cu Multilayers — Y. Huai, M. Tan, and R. Rottmayer
- Improvement of GMR Characteristics in [Ni₈₁Fe₁₉/Cu] Multilayers by Interfacial Modulation Technique using Kr Ions — Y. Miyamoto, K. Watanabe, K. Nishimura, S. Nakagawa, and M. Naoe
- CPP Giant Magnetoresistance of NiFeCo/Cu/CoFe/Cu Multilayers — K. Bussmann, S. F. Cheng, G. A. Prinz, Y. Hu, R. Gutmann, D. Wang, R. Beech, and J. Zhu
- First-Principles Based Semi-Classical Model for Transport in Magnetic Layered Structures — W. H. Butler, X.-G. Zhang, and J. M. MacLaren
- GMR in Magnetic Multilayers from a First Principles Band Structure Kubo-Greenwood Approach — F. Rao and A. J. Freeman
- A Superlattice Effect in the Resistivity of Multilayers — T.-S. Choy, J. Chen, and S. Hershfield
- Influence of Impurity Gas in the Sputtering Atmosphere on the Microstructure and the GMR in Co/Cu Multilayers — S. Miura, D. Takahashi, M. Tsunoda, and M. Takahashi
- Giant Magnetoresistance of Current-Perpendicular Exchange-Biased Spin Valves of Co/Cu — A. C. Reilly, W.-C. Chiang, W. Park, S. Y. Hsu, R. Loloee, S. Steenwyk, W. P. Pratt, Jr., and J. Bass
- Comparison of Computed Amplitudes of Magnetoresistance in Spin-Valve Structures with Wafer Probe Measurements — B. Dieny, L. G. Peireira, R. H. Taylor, and S. Y. Yamamoto
- Process Monitoring of Spin-Valve GMR Deposition — J. C. S. Kools, A. P. Paranjpe, P. V. Schwartz, R. Bubber, B. Bergner, W. Kula, and T. G. S. M. Rijks
- Specular Reflection in Spin Valves Bounded by NiO Layers — H. J. M. Swagten, G. J. Strijkers, R. H. J. N. Bitter, W. J. M. de Jonge, and J. C. S. Kools
- Thermal Stability of Spin Valve with NiO/a-Fe₂O₃ Bilayer Antiferromagnets — J. Fujikata, K. Hayashi, M. Saito, and M. Nakada

- Effect of Microstructure on Resistivity and GMR Ratio in Ion Beam Deposited Spin Valves — *W. E. Bailey, D. Guarisco, and S. X. Wang*
- CoFe/IrMn Spin-Valves Prepared on Cu Islands — *T. Umemoto, A. Maeda, S. Oikawa, K. Yoshioka, S. Takahashi, T. Tanuma, M. Kume, and K. Shibata*

MAGNETIC NANOSTRUCTURES

- Reversible Electrodeposition of Ultrathin Magnetic Co and Films — *W. Schindler, T. Koop, D. Hofmann, and J. Kirschner*
- Magnetic and Transport Properties of Electrodeposited Nanostructured Nanowires — *B. Doudin, J. E. Wegrowe, S. E. Gilbert, V. Scarani, D. Kelly, J. P. Meier, and J.-P. Ansermet*
- Magnetization Reversal in Individual Nanoparticles Macroscopic Quantum Tunneling of Magnetization — *W. Wernsdorfer, E. B. Orozco, B. Barbara, A. Benoit, D. Mailly, N. Demoncey, H. Pascard, O. Kubo, and H. Nakano*
- Single Particle Measurement Showing Agreement with the Model of Uniform Rotation — *E. B. Orozco, W. Wernsdorfer, B. Barbara, K. Hasselbach, A. Benoit, and D. Mailly*
- The Magnetic Properties of Annealed Graphite-Coated Ni and Co Nanocrystals — *J. A. Block, K. Parvin, J. L. Alpers, T. Sezen, R. LaDuca, J. J. Host, and V. P. Dravid*
- Size and Interaction Effects in the Magnetization Reversal in SmCo₅ Nanoparticles — *S. A. Majetich, K. M. Chowdary, and E. M. Kirkpatrick*
- Organizing Nanometer-Scale Magnets with Bacterial Threads — *C. J. Smith, M. Field, C. J. Coakley, D. D. Awschalom, N. H. Mendelson, E. L. Mayes, S. A. Davis, and S. Mann*
- Magnetic Aftereffect in Quasi-1D Amorphous Ferromagnetic Nanocolumns — *J.-P. Nozières, D. Givord, J. C. Toussaint, B. Kevorkian, M. Ghidini, and B. Gervais*
- Magnetic Properties of Au_{1-x}Fe_x Nanowires — *J. Jorritsma and J. A. Mydosh*
- End Domain States and Magnetization Reversal in Submicron Magnetic Structures — *J. Shi, T. Zhu, M. Durlam, E. Chen, S. Tehrani, Y. F. Zheng, and J.-G. Zhu*
- Shape Dependence of the Switching Field in Small Structures — *S. T. Chui*
- Dynamics of Magnetization Reversal in a 20x4 mm Permalloy Microstructure — *A. Stankiewicz, W. K. Hiebert, G. E. Ballentine, K. W. Marsh, and M. R. Freeman*
- Reversal Mechanism of Submicron Patterned CoNi/Pt Multilayers — *M. A. M. Haast, J. R. Schuurhuis, L. Abelmann, J. C. Lodder, and T. J. Popma*
- Magnetization Reversal in Nanostructured Co/Pt Multilayer Dots and Films — *M. Thielen, S. Kirsch, H. Weinforth, A. Carl, and E. F. Wassermann*
- Domain Structures Supported by Micron-Sized Patterned Co/Cu Multilayers with AF and FM Coupling — *P. R. Aitchison, J. N. Chapman, K. J. Kirk, D. B. Jardine, and J. E. Evetts*
- The Relationship Between Structure and Magnetic Properties in Nanostructured FePd Ferromagnets — *H. Okumura, W. A. Soffa, T. J. Klemmer, and J. A. Barnard*
- Chemical Synthesis of Nanostructured Cobalt at Elevated Temperatures — *D. L. Leslie-Pelecky, M. Bonder, T. Martin, E. M. Kirkpatrick, X. Q. Zhang, S.-H. Kim, and R. D. Rieke*
- Magnetic and Magneto-transport Properties of Novel Nanostructured Networks — *K. Liu and C. L. Chien*
- Temperature Dependence of the Coercivity of Fe Films Sputtered On Nanochannel Alumina — *A. Butera, J. L. Weston, and J. A. Barnard*
- Magnetization Reversal in (CoNi/Pt)₆ Dots Connected to a Large Area through Submicron Wide Channels — *F. Fournel, Y. Chen, F. Carcenac, N. Essaidi, H. Launois, V. Kottler, and C. Chappert*
- Paramagnetic-Superparamagnetic Transition in Molecular Sieve Supported Antiferromagnetic Particles — *F. J. Lazaro, A. Lopez, A. Larrea, Q. A. Pankhurst, J. M. Lopez Nieto, and A. Corma*
- Modifications of the Effective Surface and Crystalline Anisotropies of Ag/Fe/Ag-(001)-Layers by Ion Implantation — *D. Kurowski, J. Pflaum, K. Brand, J. Pelzl, and P. Grünberg*
- Temperature Dependence of the Interface Interactions on Fe/Cr Studied by Ferromagnetic Resonance and SQUID — *J. Pflaum, J. Pelzl, P. Bödeker, H. Zabel, Z. Frait, and M. Marysko*
- Evidence for Domain-Condensation near the Ferromagnetic to Paramagnetic Transition in Perpendicularly Magnetized, Ultrathin Fe/2 ML Ni/W(110) Films — *C. S. Arnold and D. Venus*
- Electric Field Effects on Magnetic and Optical Properties of MnAs/GaAs(001) Thin Films — *T. Shin, M. C. Park, Y. Park, G. M. Rothberg, M. Tanaka, and J. P. Harbison*
- NMR Studies of Sputtered CoFe Alloy Thin Films — *T. Thomson, P. C. Riedi, C. L. Platt, and A. E. Berkowitz*
- Magnetic Dipole Model of Magnetization-Induced Surface Second Harmonic Generation — *V. L. Brudny, W. L. Mochán, B. S. Mendoza, A. V. Petukhov, and T. Rasing*
- Effect of Dipolar Interactions in Magnetic Thin Films — *C. Santamaria and H. T. Diep*
- Hybrid Ferromagnet-Semiconductor Nonvolatile Gate — *M. Johnson, B. R. Bennet, M. J. Yang, M. M. Miller, and B. V. Shanabrook*

- Pseudo Spin Valve MRAM Cells with Sub-Micrometer Critical Dimension — *B. A. Everitt, A. V. Pohm, R. S. Beech, A. Fink, and J. M. Daughton*
- Characteristics of AP Bias in Spin Valve Memory Elements — *J.-G. Zhu and Y. Zheng*
- The Effect of End Edge Shape on the Performance of Pseudo-Spin Valve Memories — *J. Gadbois, J.-G. Zhu, W. Vavra, and A. Hurst*
- A New Multilayered Structure for Multilevel Magnetoresistive Random Access Memory (MRAM) Cell — *W.-C. Jeong, B.-I. Lee, and S.-K. Joo*
- Nucleation of Periodic Domain Structure in Micro-Fabricated Spin valve Strip Pattern — *K. Matsuyama, H. Asada, Y. Hosokawa, and K. Taniguchi*
- Generation, Gyroscopic Dynamics and Collisions of the Vertical Bloch Lines in the Orthoferrites — *M. V. Chetkin and Yu. N. Kurbatova*
- Memory Element Based on a Layered Galvanomagnetic Structure — *Y. V. Timoshkov, A. L. Danilyuk, I. S. Molchan, T. I. Orechovskaya, and V. I. Kurmashev*

PATTERNED AND HYBRID MAGNETIC MATERIALS

- Magnetic Coupling in Self-Organized Narrow-Spaced Fe Nanowire Arrays — *A. Sugawara, D. Streblechenko, M. McCartney, and M. R. Scheinfein*
- Magnetic Singularities in Self-Organized Epitaxial Cobalt Structures — *M. Demand, M. Hehn, S. Cherifi, K. Cherifi, K. Ounadjela, and R. L. Stamps*
- Fabrication of Large Area Nanostructured Magnets by Interferometric Lithography — *M. Farhoud, M. Hwang, H. I. Smith, M. L. Schattenburg, J. M. Bae, K. Youcef-Toumi, and C. A. Ross*
- Magnetization Reversal in Submicron Ferromagnetic Dots and Antidots Arrays — *Y. Otani, S. G. Kim, T. Kohda, K. Fukamichi, O. Kitakami, and Y. Shimada*
- Giant Positive Magnetoresistance in Arrays of Semi-metallic Bismuth Nanowires — *K. Liu, C. L. Chien, P. C. Searson, K. Yu-Zhang*
- Magnetic and Transport Properties of Sub-Micron Ferromagnetic Wires — *Y. Otani, S. G. Kim, K. Fukamichi, O. Kitakami, and Y. Shimada*
- Size Dependence of the Magnetization Vector Reversal Processes in Epitaxial Fe(001) Microstripes — *E. Ahmad, J. A. C. Bland, and E. Gu*
- Magnetization Switching Behavior in Nanostructured Nife/Co/Cu/Co Spin-Valve — *H. Asada, K. Matsuyama, Y. Hosokawa, and K. Taniguchi*
- Magnetic Anisotropy in Arrays of Nanometer-Scale Iron Particles — *S. Wirth, J. J. Heremans, S. Von Molnár, M. Field, K. L. Chapman, A. C. Gossard, and D. D. Awschalom*
- Highly Homogeneous Nanoparticulate Fe Films Prepared by Laser Ablation — *J. M. González, M. I. Montero, L. Vásquez, J. A. Martín Gago, D. Givord, C. De Julián, and K. O'Grady*
- Magnetic Properties of a Series of Ferrite Nanoparticles Synthesized in Reverse Micelles — *C. T. Seip, E. E. Carpenter, C. J. O'Connor, V. T. John, and S. Li*
- High Coercivity in Heterogeneous Co-Rich Co-Ag Very Thin Films — *A. Butera, T. J. Klemmer, K. Minor, H. S. Cho, and J. A. Barnard*
- Superparamagnetism of Granular Fe-MgF₂ Films — *T. Furubayashi and I. Nakatani*
- Magnetization and Coercivity of Antiferromagnetic Particles — *K. N. Trohidou, X. Zianni, and J. A. Blackman*
- Magnetotransport and Magnetism in Granular EuS-Co and EuS-Ag Nanocomposites Prepared by Mechanical Alloying — *C. E. O'Connor, L. Feng, C. T. Seip, and J. Tang*
- Magnetization Curve for Iron-Nitride Fine Particles System with Random Anisotropy — *H. Mamiya and I. Nakatani*
- Magnetic Properties of Ball Milled Fe-40Al at .% Alloys — *X. Amils, J. Nogués, S. Suriñach, M. D. Baró, and J. S. Muñoz*
- Structural, Electrical, and Magnetic Properties of Co_xC_{1-x} Granular Films — *H. Weinforth, C. Somsen, B. Rellinghaus, A. Carl, E. F. Wassermann, and D. Weller*
- Magnetic and Magneto-Transport Properties of Metastable Gd_xNb_{1-x} Alloys — *R. L. Sommer, J. Q. Xiao, and C. L. Chien*
- Algorithm for the Computation of the FC and ZFC Magnetization Curves for Nanoparticle Systems — *C. Papusoi, Jr., A. Stancu, C. Papusoi, J.L. Dormann, M. Nogués, and E. Tronc*
- Preparation of Iron Nanoparticles by Reduction of Acicular β -FeOOH Particles — *M. Chen, B. Tang, and D. E. Nikles*
- Fabrication and Properties of Microforged Ferromagnetic Nanoflakes — *R. M Walser and W. Kang*

SOFT MAGNETIC MATERIALS AND DOMAINS

- Domain Walls and Magnetic Properties of Very Thin Permalloy Films for Magnetoresistive Sensors — *M. A. Akhter, D. J. Mapps, Y. Q. Ma, A. K. Petford-Long, and R. Doole*
- Characteristics of Stripe Domains in FeTaN Films Observed by Magnetic Force Microscopy — *H. S. Cho, V. R. Inturi, J. A. Barnard, and H. Fujiwara*

- Magnetic Domains and Transverse Induced Anisotropy in Magnetically Soft CoFeB Amorphous Thin Films — *D. García, J. L. Muñoz, G. Kuryandskaya, M. Vázquez, M. Ali, and M. R. J. Gibbs*
- Incoherent Magnetization Reversal Process in Discontinuous Fe₅₀Co₅₀/Ag Multilayer Thin Films — *P. C. Kuo, Y. D. Yao, J. W. Chen, and H. C. Chiu*
- Giant Magnetoimpedance in CoFeBSi Wires and Polycrystalline Ferrites — *E. Carrasco, K. L. García, and R. Valenzuela*
- The Effects of Axial DC Field on Magnetoimpedance: Circumferential Domain Wall Damping — *K. L. García and R. Valenzuela*
- Surface Magnetic Domain Observation on Thin-Gauged 3% Si-Fe Sheets by using Scanning Electron Microscopy with Polarization Analysis (SEMPA) — *Y. Lee, A. R. Koymen, N. H. Heo, J. G. Na, and J. S. Woo*
- Dynamic Preisach Model and Energy Dissipation in Soft Magnetic Materials — *L. R. Dupré, G. Bertotti, and J. A. A. Melkebeek*
- Determination of Barkhausen Signal Scaling from Higher Order Spectral Analysis — *J. R. Petta, M. B. Weissman, and G. Durin*
- Identification of Microstructure Effects in Magnetic Loss Behaviour of 3.2% SiFe N.O. Electrical Steels by Means of Statistical Power Loss Model — *G. Bán, P. E. Di Nunzio, S. Cicalè, and T. Belgrand*
- Dynamic Effects Driven by Thermal Activation in the Magnetization of Nanocrystalline Soft Magnetic Materials — *V. Basso, M. LoBue, C. Beatrice, P. Tiberto, and G. Bertotti*
- Influence of Surface Roughness on Magnetic Properties of Fe-Si-B Amorphous Alloys — *K. Matsuki, F. Kogiku, and N. Morito*
- Magnetic Properties of 6.5% Silicon Steel Sheets Under PWM Voltage Excitation — *M. Namikawa, H. Ninomiya, Y. Tanaka, and Y. Takada*
- Comparison of Transformer Loss Prediction from Computed and Measured Flux Density Distribution — *A. J. Moses* ...
- Apparent Core Losses and Core Losses in Five-Limb Amorphous Transformer of 160 kVA — *S. Sieradzki, R. Rygal, and M. Soinski*
- Reduction of Inrush Current in Single-Phase Transformer using Virtual Air Gap Technique — *V. Molcrette, J.-L. Kotny, J.-P. Swan, and J.-F. Brudny*

MAGNETIC EFFECTS AND MODELING

- Shifted Magnetization Curves in Ultrathin Co Films on Stepped Cu(100) — *A. Rettori, L. Trallori, M. G. Pini, C. Stamm, C. Wüsch, S. Egger, and D. Pescia*
- Effect of Au Underlayer on Perpendicular Magnetic Anisotropy in Au/Co/Au(111) Sandwiched Films — *A. Murayama, K. Hyomi, J. Eickmann, and C. M. Falco*
- Interface Orbital Moment Anisotropy in CoPd Multilayers — *H. A. Dürr, G. Van Der Laan, J. Vogel, M. Finazzi, and J. B. Goedkoop*
- Magnetic Anisotropy and its Microstructural Origin in Epitaxially Grown SmCo Thin Films — *M. Benaissa, K. M. Krishnan, E. E. Fullerton, and J. S. Jiang*
- Magnetoelectric Néel Anisotropies — *R. Skomski*
- Spin-Reorientation Transitions in Ultrathin Ferromagnetic Films Under Applied Field — *Y. T. Millev, H. P. Oepen, and J. Kirschner*
- Symmetry-Induced Magnetic Anisotropy in Ultrathin Planar Striped Co Films with and without Cu Decoration — *L. Zhong, X. Wang, and A. J. Freeman*
- Changes of Morphology, Structure, and Magnetism of Fe on Stepped Cu(111) — *M. Klaua, J. Shen, P. Ohresser, H. Jenniches, J. Barthel, C. V. Mohan, and J. Kirschner*
- The Effect of Interfacial Steps on the Ferromagnetic/Antiferromagnetic Interface of Thin Fe Films on Cr(001) — *E. J. Escorcia-Aparicio, H. J. Choi, W. L. Ling, R. K. Kawakami, and Z. Q. Qiu*
- Magnetic Easy Axis Engineering in Ultrathin Cu/Co/Cu(110) Structures — *B.-C. Choi, S. Hope, E. Gu, and J. A. C. Bland*
- First Principles Calculations of Interlayer Exchange Coupling in bcc Fe/Cu/Fe Structures — *M. Kowalewski, B. Heinrich, T. C. Schulthess, and W. H. Butler*
- On Rotational Eddy Current Losses in Steel Laminations — *I. D. Mayergoyz*
- Dynamic Preisach Modelling of Ferromagnetic Laminations Under Distorted Flux Excitations — *L. R. Dupré, O. Bottauscio, M. Chiampi, F. Fiorillo, M. L. Bue, J. Melkebeek, M. Repetto, and M. Von Rauch*
- Eddy Current Analysis for the Pipe Welding — *H. Tsuboi, K. Ikeda, M. Kurata, K. Kainuma, and K. Nakamura*
- Analysis of Eddy-Current Brake for High-Speed Railway — *P. J. Wang and S. J. Chiueh*
- Loss Separation Analysis in Ferromagnetic Sheets Under PWM Inverter Supply — *A. Boglietti, M. Chiampi, M. Repetto, O. Bottauscio, and D. Chiarabaglio*
- Current Flow in Long Conductors with a Step Conductivity Change — *K. V. Namjoshi, J. D. Lavers, and P. P. Biringer*

- A Model for Impedance of Planar RF Inductors Based on Magnetic Films — *A. Gromov, V. Korenivski, K. V. Rao, R. B. van Dover, and P. M. Mankiewich*
- Numerical Study of Electric Diffusion Effect Due to Imperfect Electrical Contacts — *B.-K. Kim and K.-T. Hsieh*
- Crack Size and Shape Determination by Moving Magnetic Field Type Sensor — *M. Enokizono, Y. Tsuchida, and T. Chady*
- Ohmic Losses Calculation in SMPS Transformers: Numerical Study of Dowell's Approach Accuracy — *F. Robert, P. Mathys, and J.-P. Schauwers*
- Analysis of Isotropic Materials with Vector Hysteresis — *O. Bottauscio, D. Chiarabaglio, C. Ragusa, M. Chiampi, and M. Repetto*
- Eddy Current Hysteresis and the Preisach Model — *I. D. Mayergoyz*
- Simulation of Field-Temperature Effects in Magnetic Media using Anisotropic Preisach Models — *A. A. Adly and I. D. Mayergoyz*
- Eddy Current and Hysteresis Losses in Ferromagnetic Media — *V. Maló Machado and A. Lopes Ribeiro*
- Hysteretic Energy Losses in Media Described by Vector Preisach Model — *G. Friedman and I. D. Mayergoyz*
- On the Role of the Statistics in the Applicability of the Preisach Transformation — *K. Metlov, I. Tomáš, G. Vértessy, and M. Pardavi-Horváth*
- A Preisach Model for Aftereffect — *E. Della Torre and L. H. Bennett*
- Identification of the Preisach Parameters of a Three Quadrant Medium — *J. Lou, L. H. Bennett, and E. Della Torre*
- Interaction Effects in CrO₂ Audio Tape: AC Versus Thermal Demagnetization — *P. D. Mitchler, R. M. Roshko, and E. D. Dahlberg*
- A New Algorithm for Thermal Decay Simulations — *I. Klik and Y. D. Yao*
- 1/f Nyquist Magnetic Noise, Magnetic Viscosity and Hysteresis — *A. Maraner, S. Vitale, and G. Bertotti*
- Modeling of Magnetic Properties of Heat Treated Dy-Doped NdFeB Particles Bonded in Isotropic and Anisotropic Arrangements — *X. Fang, Y. Shi, and D. C. Jiles*
- Modeling of Hysteresis Loops of Ferrite Cores Excited by a Transient Magnetic Field — *N. L. Mi, R. Oruganti, and S. X. Chen*

MAGNETIC SENSORS AND COMPONENTS

- Increased Field Sensitivity in Co/Cu Multilayers with Soft Adjacent Layers — *D. B. Jardine, N. D. Mathur, M. G. Blamire, and J. E. Evetts*
- InAs/(Al,Ga)Sb Quantum Well Structures for Magnetic Sensors — *M. Behet, J. Das, J. De Boeck, and G. Borghs*
- Fluxgate: Tuned vs. Untuned Output — *P. Ripka and S. W. Billingsley*
- Pyro Photosensor Utilizing Thermally-Sensitive Magnetic Thin Film — *T. Yoshida, Y. Ajishi, H. Osada, S. Chiba, N. Tayama, K. Seki, and H. Matsuki*
- Development of a Moving Magnetic Flux Type Sensor using Shading Coils for ECT — *Y. Tsuchida, T. Chady, and M. Enokizono*
- Effect of Stress on the Bamboo Domains and Magnetization Process of CoSiB Amorphous Wire — *J. N. Nderu, M. Takajo, J. Yamasaki, and F. B. Humphrey*
- A Remotely Interrogatable Sensor for Chemical Monitoring — *P. G. Stoyanov, S. A. Doherty, C. A. Grimes, and W. R. Seitz*
- Dependence of Large Barkhausen Jump on Length of a Vicalloy Fine Wire with Torsion Stress — *S. Abe, A. Matsushita, and M. Naoe*
- High Frequency Carrier Type Bridge-Connected Magnetic Field Sensor — *M. Takezawa, H. Kikuchi, K. Suezawa, M. Yamaguchi, K. Ishiyama, and K. I. Arai*
- Preparation and Properties of Elastically Coupled Electro-Magnetic Elements with a Bonding Structure — *K. H. Shin, M. Inoue, and K. I. Arai*
- Geometry Effects on Low Frequency Noise in Giant Magnetoresistance (GMR) Sensors — *A. F. Md. Nor, E. W. Hill, and M. R. Parker*
- Thermal Activation of Spin Wave Modes in Co Based Multilayers — *M. A. Wongsam and R. W. Chantrell*
- A New Bi-Directional Inductive Force Sensor — *V. Lemaquand*
- Hard-Soft GMR Sensors with Co-Rh based Artificial Antiferromagnetic Subsystem — *H. A. M. van den Berg, G. Rupp, W. Clemens, G. Gieres, M. Vieth, J. Wecker, and S. Zoll*
- A New Giant Magneto-Impedance Head using Magnetic Microstrip Lines — *N. Jiang, K. Yamakawa, N. Honda, and K. Ouchi*
- New Multi-Chambered Power Magnetics Concepts — *G. E. Bloom*
- Application and Analysis of Adjustable Profile High Frequency Switchmode Transformer Having a U-Shaped Winding Structure — *J. Lu, F. P. Dawson, and S. Yamada*
- Analysis of Frequency Characteristics of Small-Sized Wide-Band Compound Transformers — *N. Nishizuka, M. Sato, and Y. Li*

- Design and Analysis of Noise-Reduction Transformer Based on Equivalent Circuit — *T. Yanada, S. Minowa, O. Ichinokura, and S. Kikuchi*
- An Analytical Method of a Planar Parametric Transformer Based on the Magnetic Circuit Model — *Y. Sakamoto, M. Ohta, M. Natsusaka, and K. Murakami*
- Design and Simulation of Film Transformer on Flexible Polyamide Film in Very High Frequency Range — *H. Tsujimoto*
- 2D and 3D Simulation of Toroidal Type Thin Film Inductors — *H. J. Ryu, S. D. Kim, J. Kim, J. J. Lee, J. Kim, S. H. Han, H. J. Kim, and C. H. Ahn*
- The Characteristics of Low Temperature Co-Fired Multilayer Chip LC Filters — *H. M. Sung, C.-J. Chen, L.-J. Wang, and W.-S. Ko*
- Packaging-Compatible Microinductors and Microtransformers with Screen-Printed Ferrite using Low Temperature Processes — *J. Y. Park and M. G. Allen*
- A Microfabricated Transformer for High-Frequency Power or Signal Conversion — *M. Xu, T. M. Liakopoulos, C. H. Ahn, S. H. Han, and H. J. Kim*
- The Effect of Magnetic Film Structure on the Inductance of a Planar Inductor — *T. Inoue, K. Nishijima, S. Yatabe, T. Mizoguchi, and T. Sato*
- Design of High Frequency Inductors Based on Magnetic Films — *V. Korenivski and R. B. van Dover*
- Inductive Microtransformer Exploiting the Magnetoelastic Effect — *L. H. Rissing, S. A. Zielke, and H. H. Gatzert*

MICROWAVE MAGNETICS

- Mode Beating of Spin Wave Beams in Ferrimagnetic $\text{Lu}_{2.04}\text{Bi}_{0.96}\text{Fe}_5\text{O}_{12}$ Films — *O. Büttner, M. Bauer, C. Mathieu, S. O. Demokritov, B. Hillebrands, P. A. Kolodin, M. P. Kostylev, S. Sure, H. Dötsch, V. Grimalsky, Y. Rapoport, and A. N. Slavin*
- Ferromagnetic Resonance Damping in Garnets: Comparison Between Saturated and Unsaturated States — *T. Taffary, D. Autissier, F. Boust, and H. Pascard*
- Enhanced Microwave Magnetic Properties in Nonstoichiometric Yttrium Iron Garnets for High Power Applications — *Y. S. Cho, V. L. Burdick, and V. R. W. Amarakoon*
- Shape-Optimized Ferromagnetic Particles with Maximum Theoretical Microwave Susceptibility — *R. M. Walser, W. Win, and P. M. Valanju*
- Parametric Frequency Conversion with Amplification of a Weak Spin Wave in a Ferrite Film — *B. A. Kalinikos, N. G. Kovshikov, M. P. Kostylev, and H. Benner*
- Theory of MSFVW Excitation in a YIG Film by a Finite-Length Microstrip Transducer — *L. P. Peng, J. P. Parekh, and H. S. Tuan*
- Experimental Investigation of the Nonlinear Interaction Between Optical Guided Waves and Magnetostatic Forward Volume Waves in a Bi-YIG Film — *J. Kurumida and N. S. Chang*
- Design Procedure for Ferrite Microstrip DC Blocks — *M. R. M. L. Albuquerque and A. G. d'Assunção*
- Axially Polarized Wiggler Radiation from a Toroidal Electron Beam Source — *H. A. Leupold, A. S. Tilak, and M. M. Visosky*
- Technical Characteristics of a Novel Helical-Groove Traveling-Wave Tube Structure — *T. M. Walleit, K. R. Vaden, J. Freeman, and A. Haq Qureshi*

MAGNETIC RECORDING HEADS

- Anisotropy Control in Fabrication Process for NiMn Spin-Valve Dual Element Heads — *T. Ishi, T. Suzuki, N. Ishiwata, M. Nakada, K. Yamada, K. Shimabayashi, and H. Urai*
- Effect of Seed Layer on the Magnetoresistance Characteristics in a-CoNbZr-Based Spin Valves — *H. S. Cho, F. Ueda, C. Hou, and H. Fujiwara*
- Thermal Stability of CoFe, Co and NiFe/Co Spin Valves — *A. M. Zeltser, K. Péntek, and M. Menyhárd, and A. Sulyok*
- Activation Energy of Interdiffusion and Interface Structure for CoFe/Cu Spin-Valves — *A. T. Saito, H. Iwasaki, Y. Kamiguchi, H. N. Fuke, and M. Sahashi*
- Enhancement of Magnetoresistance Characteristics in Spin Valve Structures by Two-Step Sputter Deposition — *C.-M. Park and K. H. Shin*
- The Distribution of Blocking Temperature in NiFe-Ru_xRh_yMn Bilayers — *S. Araki, M. Sano, M. Ohta, Y. Tsuchiya, K. Noguchi, H. Morita, and M. Matsuzaki*
- Thermal and Magnetic Stability of Unidirectional Anisotropy in Spin-Valve Magnetoresistive Heads — *N. Ohshima, M. Nakada, and Y. Tsukamoto*
- New Soft Magnetic CoNiFe Plated Films with High $B_s = 2.0\text{--}2.1\text{ T}$ — *T. Osaka, M. Takai, K. Hayashi, Y. Sogawa, K. Ohashi, Y. Yasue, M. Saito, and K. Yamada*
- Improved Magnetic Anisotropy and Magnetostriction by Laminating FeAl(N) with Permalloy to Multilayers — *W. Maass and H. Rohrmann*
- High Frequency Initial Permeability of NiFe and FeAlN — *W. P. Jayasekara, J. A. Bain, and M. H. Kryder*

- Magnetostriction Constants of (110) Oriented Epitaxially Grown FeTaN Thin Films — *L. Varga, H. Jiang, T. J. Klemmer, and W. D. Doyle*
- Texture and Magnetic Properties of FeTaN Films Bias-Sputtered on Sloping Surfaces — *J. Hong, S. X. Wang, and K. Rook*
- Control of Asymmetry of Spin-valve Heads Based on Micromagnetic Analysis — *K.-I. Yamada, H. Kanai, Y. Uehara, and J. Toda*
- A Study of Voltage Fluctuation, Noise and Magnetic Instability in Spin Valve GMR Recording Heads — *A. Wallash*
- Magnetic Domain Instability in MR Heads Due to Overlaid Structure of Permanent Magnet Film — *C. Mitsumata, K. Kikuchi, and T. Kobayashi*
- Crossfeed Response of DMR vs. SAL Multi-Track Heads — *F. Z. Wang, L. N. He, D. J. Mapps, D. T. Wilton, W. W. Clegg, and P. Robinson*
- Multitrack Thin Film Heads for the Digimax™ Tape Storage System — *J. J. M. Ruigrok, H. W. van Kesteren, S. R. Cumpson, D. J. Adelerhof, S. B. Luitjens, E. A. Draaisma, and A. Hoogendoorn*
- Newly Developed Inductive Write Head with Electroplated CoNiFe Film — *K. Ohashi, Y. Yasue, M. Saito, K. Yamada, T. Osaka, M. Takai, and K. Hayashi*
- Two Dimensional Model of Eddy Currents and Saturation in Thin Film Write Heads — *A. F. Torabi, M. L. Mallary, R. Perry, and G. Kimball*
- Off-track Performance of Thin Film Single Pole Head for Perpendicular Double-Layered Media — *H. Yamada, H. Muraoka, Y. Sugita, and Y. Nakamura*
- A New Write Head Trimmed at Wafer Level by Focused Ion Beam — *T. Koshikawa, A. Nagai, Y. Yokoyama, T. Hoshino, and Y. Ishizuki*
- Extremely Low Inductance Thin-Film Single-Pole Head on Flying Slider — *H. Muraoka, K. Sato, Y. Nakamura, T. Katakura, and K. Yazawa*
- Active Cancellation of Mutual Inductance in Split-Coil Thin-Film Heads — *S. E. Stupp and G. R. Lovelace*
- Writer Performance Improvement in MR Head with Over-Sized Trailing Poles Technique — *E. Leung, M. Hayashi, R. Leung, K. Ino, N. Matono, S. Takahashi, and M. Fujita*
- GMR-DMR Read-Element Characterization and Projections of Head Performance on High Areal Density Rigid Media — *I. G. Trindade, M. H. Kryder, P. P. Freitas, and N. Smith*
- Two Leg, Side by Side, 0.6 to 1.0 Micron Wide, High Output, Vertical, GMR, Head Sensors — *A. V. Pohm, J. M. Anderson, R. S. Beech, and J. M. Daughton*
- Three-Dimensional Analysis of Dual Track Complementary Type of Heads for Perpendicular Magnetic Recording — *T. Ichihara, S. Nakagawa, H. Matsumiya, and M. Naoe*
- High-Density Recording using MR Heads in Helical-Scan Tape Systems — *T. Ozue, T. Shirai, T. Saito, T. Ikegami, H. Kano, and S. Onodera*
- Fabrication and Characterization of Contiguous Permanent Magnet Junctions — *M. Xiao, A. J. Devasahayam, and M. H. Kryder*
- Spin-Valves with Bias Compensation Layer — *H. Kanai, K. Yamada, M. Kanamine, and J. Toda*
- A Self-Biased Spin Valve Sensor with a Longitudinally Pinned Layer — *T. Suzuki and H. Matsutera*
- Characteristics of NiFe/CuNi Multilayer GMR Sensors For Vertical GMR Heads — *T. Mizuguchi, S. Terada, T. Miyauchi, and A. Matsuzono*
- Planar, Contact, Yoke GMR Head vs. Conventional, Flying, Shielded GMR Head: A Comparative Study — *Y. Yoshida, K. Araki, S. Sugano, and Y. Kaneta*
- Micromagnetic Analysis and Current Biasing of Dual-Stripe GMR and Dual-GMR Sensors for High Density Recording — *P. P. Freitas, S. Cardoso, and N. J. Oliveira*
- A New Method of Calculating the Medium Field and the Demagnetizing Field for MR Heads — *Y. Suzuki and C. Ishikawa*
- Read Sensitivity in Abutted-Junction Type Spin-Valve Head — *K.-I. Takano, N. Yamanaka, and M. Matsuzaki*
- Magnetic Changes in GMR Heads Caused by Electrostatic Discharge — *A. Wallash and Y. K. Kim*
- ESD Induced Pinned Layer Reversal in Spin-Valve GMR Heads — *M. Takahashi, T. Maeda, K. Inage, M. Sakai, H. Morita, and M. Matsuzaki*
- Amplitude and Asymmetry Correlation Study Between Quasi-Static and Dynamic Electrical Testing of MR Sensors — *J. Zhu and M. Loera*

MAGNETIC RECORDING MEDIA

- Thermal Aftereffects in Thin Film Magnetic Recording Media — *Y. Hosoe, T. Kanbe, K. Tanahashi, I. Tamai, S. Matsunuma, and Y. Takahashi*
- Thermal Stability and Nanostructure of CoCrPt Longitudinal Recording Media — *M. Yu, M. F. Doerner, and D. J. Sellmyer*
- Effects of Thin Cr Interlayer on Time Decay of Magnetization and Magnetization Reversal for CoCrTaPt Thin Film Media — *J.-P. Wang, L.-P. Tan, T. F. Liew, E. Teng and P.-W. Wang*

- Dynamic Coercivity Effects in Thin Film Media — *H. J. Richter, S. Z. Wu, and R. Malmhäll*
- Numerical Simulations of the Effect of Record Field Pulse Length On Medium Coercivity at Finite Temperatures —
H. N. Bertram and Q. Peng
- Coercivity and Frequency Dependence of Track Widths and Erase Bands in Thin Film Media — *L. Mei, M. E. Schabes, and N. H. Yeh*
- Quantitative MFM Study of the Global and Local Magnetic Roughness of the DC-Demagnetized State of Thin Film Media — *X. Song, Q. Chen, C. Leu, and R. Ranjan*
- Under-Keeped Media with MR Heads — *M. Nichols, B. M. Lairson, T. M. Coughlin, B. Gooch, J. Kehl, and J. Perez*
- Recording Physics of Keeped Inductive Media — *E. T. Yen, H. J. Richter, G.-L. Chen, G. Rauch, and T. M. Coughlin*
- Temperature Dependence of Magnetocrystalline Anisotropy Energy Determined using Co-Cr-Ta Single Crystal Thin Films — *N. Inaba, M. Futamoto, and A. Nakamura*
- CrMn Underlayers for CoCrPt Thin Film Media — *L.-L. Lee, D. E. Laughlin, and D. N. Lambeth*
- Chromium Segregation in CoCrTa/Cr and CoCrPt/Cr Thin Films for Longitudinal Recording Media — *J. E. Wittig, T. P. Nolan, C. A. Ross, M. E. Schabes, K. Tang, R. Sinclair, and J. Bentley*
- The Effect of Carbon Overcoat Diffusion on CoCrTa/Cr Thin-Film Media — *J. J.-K. Chang, K. E. Johnson, H. Kawayoshi, P. Ling, and M. Strathman*
- Cr-Ta₂O₅ Seedlayer for Recording Media on Alternative Substrates — *W. Xiong and H.-L. Hoo*
- The Dependence of Media Noise on the Magnetic Cluster Size for Co Based Thin Film Media Fabricated under Ultra Clean Sputtering Process — *M. Takahashi, A. Kikuchi, H. Hara, and H. Shoji*
- Effects of Ultra-High Vacuum on Crystallographic, Recording and Magnetic Properties of Thin Film Media —
C. Gao, S. Wu, J.-P. Chen, R. Malmhall, C. Habermeier, R. Sinclair, H. Laidler, and K. O'Grady
- The Effect of fcc Grains on the Magnetic and Recording Properties of Thin Film Media — *K. O'Grady, N. S. Walmsley, C. F. Wood, and R. W. Chantrell*
- CoCrTa Intermediate Layers on NiAl Underlayers for CoCrPt Longitudinal Thin Film Magnetic Media — *J. Zhou, D. E. Laughlin, and D. N. Lambeth*
- Orientation Ratio Reduction Through Pre-Deposition Substrate Annealing — *B. Y. Wong, J. Ying, and H. Tran*
- Recording Performance of Thin Film Media with Various Crystallographic Preferred Orientations on Glass Substrates —
M. Mirzamaani, X. Bian, M. F. Doerner, J. Li, and M. Parker
- Magnetic and R/W Properties of CoPt-SiO₂ Granular Media — *I. Kaitsu, A. Inomata, I. Okamoto, and M. Shinohara* ...
- Fabrication, Micromagnetic and Recording Properties of CoCrPt on Plastic Disks — *B. R. Acharya, E. N. Abarra, G. N. Phillips, T. Suzuki, K. Adachi, N. Kitagaki and M. Aihara*
- Magnetic Interaction in Co-Cr-Pt-Ta-Nb Media: Utilization of Micromagnetic Simulation — *H. Akimoto, I. Okamoto, and M. Shinohara*
- Small $-dH_c/dT$ Characteristics of CoPt Granular and Thin Film Recording Media — *A. Kikitsu, K. Yusu, K. Ichihara, and T. Tanaka*
- High-Density Recording Capability of Granular Media Composed of Co-Pt Grains and SiO₂ Matrix — *K. Ichihara, A. Kikitsu, K. Yusu, F. Nakamura, and H. Ogiwara*
- Time Decay of the Remanent Magnetization in Longitudinal Thin Film Recording Media as a Function of Distributions of Grain-Size and Easy-Axis Orientation — *C. Yang, J. M. Sivertsen, and J. H. Judy*
- Micromagnetic Study of Network Media — *J.-G. Zhu and H. Fang*
- Thermal Stability of Ultra-Thin Co Recording Media — *H. Gong, W. Yang, D. N. Lambeth, M. Rao, and D. E. Laughlin*
- Effects of ECR Ion Shower Treatment on the Magnetic and Recording Properties of CoCrTaPt Thin Film Media —
Y. Okumura, M. Yasui, T. Akita, M. Maeda, and X. B. Yang
- Effect of Grain Size Dispersion on Read/Write Properties in Thin Film Recording Media Affected by Thermal Fluctuation — *Y. Nakatani, N. Hayashi, Y. Uesaka, and H. Fukushima*
- DC Erasure and Demagnetizing Fields on Written Bits in High Density Longitudinal Media — *E. N. Abarra, G. N. Phillips, I. Okamoto, and T. Suzuki*
- Comparison of Time-Decay of Read-Back Signals in Keeped and Non-Keeped Media — *J. Chen, J. H. Judy, and T. Coughlin*
- Effects of Pt addition on the magnetic and microstructural properties of CoC granular films — *J.-J. Delaunay, T. Hayashi, M. Tomita, and S. Hirono*
- Read Write Characteristics of Hexagonal Barium Ferrite Sputtered Films Prepared by Post Deposition Annealing —
A. Morisako, M. Matsumoto, and M. Naoe
- Microscopic Magnetization Structures and Noise in Single-Layer Perpendicular Thin Film Media — *Y. Honda, Y. Hirayama, K. Ito, and M. Futamoto*
- Effect of Medium Thickness on the Signal-to-Noise Ratio of Perpendicular Media — *Y. Ikeda, Y. Sonobe, and H. Uchida*

- Preparation and Characteristics of Co-Zn Ferrite Rigid Disks without Protective Layers for High Density Recording — *N. Matsushita, M. Ichinose, S. Nakagawa, and M. Naoe*
- Nano-size Magnetic Crystallite Formation in Co-Cr Thin Films For Perpendicular Recording Media — *S. Kadokura, M. Naoe, S. Nakagawa, and Y. Maeda*
- Thermal Relaxation in Perpendicular Double-Layered Media — *W. H. Jiang, H. Muraoka, Y. Sugita, and Y. Nakamura*
- Barium Ferrite Thin Films Without a Dead-Layer — *Y. Chen, M. Rao, D. E. Laughlin, and M. H. Kryder*
- Low Noise Co-Cr-Nb Perpendicular Recording Media with High Squareness — *N. Honda, J. Ariake, K. Ouchi, and S.-I. Iwasaki*
- Barium Ferrite Films Grown by Laser Ablation — *A. Lisfi, J. C. Lodder, P. de Haan, M. A. Smithers, and F. J. G. Roesthuis*
- MFM Observation of Localized Demagnetization in Magnetic Recordings — *A. Jander, P. Dhagat, R. S. Indeck, and M. W. Muller*
- A Comparison between Different Methods for Evaluating the Particle Interactions in Magnetic Recording Systems — *G. Bottoni, D. Candolfo, and A. Cecchetti*
- Analytical Determination of the LLG Zero-Damping Critical Switching Field — *D. G. Porter*
- Development of an Advanced Metal Particulate Tape — *H. Inaba, K. Ejiri, K. Masaki, and T. Kitahara*
- Influence of Magnetic Interaction and Particle Length on MP Tape Noise — *N. Nagai and M. Inoue*
- Measurement of Vector Minor Loops — *F. Vajda and E. D. Torre*
- Epitaxial Growth of NiZn Ferrite on Barium Ferrite Particles — *H.-S. Jung and Y.-K. Hong*
- Non-Arrhenius Behavior in Single Domain Particles — *E. D. Boerner and H. N. Bertram*
- The Effect of Particle Size on the Thermal Switching Characteristics of Metal Particle Tapes — *S. M. Stinnett and W. D. Doyle*
- Mechanical Orientation of Advanced Metal Particle Dispersions — *L. S. Prichard, K. O'Grady, and P. I. Mayo*
- Self-Assembly in Model Magnetic Inks — *P. B. Visscher and Y. Günel*

HEADS AND MEDIA INTERFACES IN MAGNETIC RECORDING

- A New Sub-Femto Slider for Mass Production Planar Silicon Heads — *J.-P. Lazzari, C. Pisella, and L. Tosi*
- Take Off Measurement of Pico Sliders on Laser Zone Textured Media — *D. Harris, S. Venkatesan and K. O'Brien*
- A new Laser Interferometer System for Investigation of the Dynamics at the Head/Disk Interface — *M. Staudenmann, M. J. Donovan, and D. B. Bogy*
- Head-Disk Dynamics of Low Resonance Laser Textures - A Spectrogram Analysis — *W. H. Yao, D. Kuo, R. Ku, B. Marchon, and R. Sundaram*
- Dual Stripe Sensor on a Picoslider for In-Contact Thermal Asperity Testing — *H. H. Gatzen and M. K. Schwabe*
- Variation of the Heat Flux Between a Slider and Air Bearing when the Slider Flies Over an Asperity — *S. Zhang and D. B. Bogy*
- Effect of Lubricant Thickness and Viscosity and Rest Time on Long-Term Stiction in Magnetic Thin-Film Rigid Disks — *Z. Zhao and B. Bhushan*
- Potential Data Loss Due to Head/Disk Contacts During Dynamic Load/Unload — *M. Suk and D. Jen*
- Assessment of Surface Damage Mechanisms of Head/Disk Interface using CSS and Drag Tests — *K.-H. Chung, S.-C. Lee, and D.-E. Kim*
- Ultrathin Protective Overcoats on Hard Magnetic Disks — *E. V. Anoikin, G. S. Ng, M. M. Yang, J. L. Chao, J. R. Elings, and D. W. Brown*
- Nanomechanical Properties of CN_x Overcoats and Cathodic Arc Carbon (CAC) Films — *R. C. Hsiao, D. B. Bogy, and C. S. Bhatia*
- Study of Clock Head/Disk Interface Failure Mechanism in Servo-Writing Process — *B. Liu, G. Sheng, Q. Chen, Q. Leng, C. T. Yeo, and S. G. Lu*
- Measurement of Non-elastic Asperity Compliance of Magnetic Tapes — *S. Tan, E. Baugh, and F. E. Talke*
- High Wear Durability of ECR-Sputtered Carbon Films — *S. Hirono, S. Umemura, Y. Andoh, T. Hayashi, and R. Kaneko*
- Tribological Properties and Environmental Effects of Nano and Pico Sliders on Laser Textured Media — *B. Knigge, Q. Zhao, F. E. Talke, and P. Baumgart*
- Tribological and Mechanical Properties of CN Ultra-Thin Overcoat Films — *R. D. Ott, T. W. Scharf, D. Yang, and J. A. Barnard*
- The Structure of Nitrogenated Carbon and its Interaction with Lubricant Molecules — *P. Dai and C. Gao*
- Material and Tribological Properties of a-C:H Film by Plasma CVD for a Disk Overcoat — *T. Toyoguchi and T. Yamamoto*
- Investigation of Phosphazene Additive for Magnetic Recording Lubrication — *C. M. Mate, P. H. Kasai, G. W. Tyndall, C. H. Lee, V. Raman, D. J. Pocker, and R. J. Waltman*

- Tribology of a Solid Fluorocarbon Film on Magnetic Recording Media — *T. E. Karis, G. W. Tyndall, and M. S. Crowder*
- Deposition of High-Durability Protective Layers with a Composite Structure of DLC and GLC by Facing-Targets Sputtering — *K. Noda, T. Kawanabe, and M. Naoe*
- Stiction Free Slider for Lightly Textured Disks — *T. Yamamoto, T. Yokohata, and Y. Kasamatsu*
- Vibration of Head Suspensions for Proximity Recording — *H. Takahashi, D. B. Bogy, and M. Matsumoto*
- An Investigation of Wireless Suspensions — *T. Ohwe, T. Watanabe, and S. Yoneoka*
- Sensitive Magnetic Readback Head-Disk Spacing Measurements in Recording Drives — *V. J. Novotny and M.-J. Hsiao*
- Flying Height Measurement while Seeking in Hard Disk Drives — *B. C. Schardt, E. Schreck, R. Sonnenfeld, Q. Haddock, and J. R. Haggis*
- A Double-Sideband and Transmitted Carrier Amplitude Modulation Method for Laser Texture Characterization — *Y. Li*
- In-Situ Alumina Recession and Protrusion Measurement on a Magnetic Head — *Y. Li and G. Wang*
- Calibrating ESCA and Ellipsometry Measurements of Perfluoropolyether Lubricant Thickness — *M. F. Toney, C. M. Mate, and D. Pocker*
- Magnetic Readback Microscopy Applied to Laser-Texture Characterization in Standard Desktop Disk Drives — *E. Schreck, R. Kimball, and R. Sonnenfeld*
- Measurement of the Head-to-Disk Stiction Force in an Unmodified Hard Drive using External Hall-Effect Sensors — *R. Milby, E. Schreck, and R. Sonnenfeld*
- Finite Element Based Head-Tape Interface Simulation Including Head-Tape Surface Asperity Contacts — *Y. Wu and F. E. Talke*
- Bump Formation and Growth by Multiple Laser Pulses on Ni-P Disk Substrate — *T. C. Strand, A. C. Tam, P. Baumgart, and J. Colonia*
- A Study of Pulsed-Laser Bump Formation on Smooth Glass Substrates — *J. Brannon, R. White, A. C. Tam, and P. Baumgart*
- Manufacturability of Advanced Laser Texture Designs — *J. J. Liu, W. Li, and K. E. Johnson*
- Design of Sombrero and Donut Shaped Bumps for Optimum Tribological Performance — *S. Chilamakuri and B. Bhushan*
- Formation and CSS Performance of NiP Surface Textured by Argon Ion Laser — *W. J. Wang, Y. F. Lu, T. Liew, A. Ravikiran, M.C. Chai, T.S. Low*
- Inertia Effects on Static Friction Measurements of Laser Textured Media — *M. Sullivan and J. Chao*
- Fly/Stiction: Mechanical Instability of a Head-Disc Interface — **-J. Gui and B. Marchon*
- Issues on High-Speed Laser Zone Texturing of Magnetic Disk Substrates with Improved Quality — **-H. K. Park, P. J. M. Kerstens, P. Baumgart, and A. C. Tam*
- An Investigation of a Slider Air Bearing with a Asperity Contact by a Three-Dimensional Direct Simulation Monte Carlo Method — **-W. Huang and D. B. Bogy*
- Acoustic Emission of Laser Textured Disks Influenced by Bump Excitation — *S. Wang, K.V. Viswanathan, and H.-L. Liu*
- Biquadratic Models for Slider Airbearing Surfaces — *E. Baugh, S. Weissner, and F. E. Talke*
- Identification of Slider/Disk Contacts using the Energy of the Acoustic Emission Signal — **-T. C. McMillan, F. E. Talke, and J. C. Harrison*

MAGNETIC RECORDING

- High Speed Magnetic Recording — *K. B. Klaassen, R. G. Hirko, and J. T. Contreras*
- High Speed Switching Measurements in Thin Film Disk Media — *S. M. Stinnett, W. D. Doyle, P. J. Flanders, and C. Dawson*
- Theory of the Magnetic Damping Constant — *H. Suhl*
- Computational Approaches to Thermally Activated Fast Relaxation — *R. W. Chantrell, J. D. Hannay, M. Wongsam, T. Schrefl, and H. J. Richter*
- Signal to Noise Ratio Scaling and Density Limit Estimates in Longitudinal Magnetic Recording — *H. N. Bertram, H. Zhou, and R. Gustafson*
- Detection and Capacity Limits in Magnetic Media Noise — *R. Wood*
- Bit Cell Aspect Ratio: an SNR and Detection Perspective — *T. C. Arnoldussen*
- Recording at 300 KFCI with Perpendicular Co-Alloy Multilayers — *K. Ho, B. M. Lairson, Y. K. Kim, G. I. Noyes, and S.-Y. Sun*
- Thermal Relaxation in the Strong-Demagnetizing Limit — *N. D. Rizzo and T. J. Silva*
- Resonance Interaction of Grains as a Mechanism of Thermal Stability of Longitudinal Magnetic Medium — *V. L. Safonov and T. Suzuki*

Identification of Magnetic Aftereffect Model Parameters: Temperature Dependence — <i>P. Rugkwamsook and C. E. Korman</i>	
Advanced MR Read/Inductive Write Heads for High Performance, High Density Tape Applications — <i>R. H. Dee and J. C. Cates</i>	
Timing-Based Track-Following Servo for Linear Tape Systems — <i>R. C. Barrett, E. H. Klaassen, T. R. Albrecht, G. A. Jaquette, and J. H. Eaton</i>	
Key Issues in the Design of Magnetic Tapes for Linear Systems of High Track Density — <i>D. B. Richards and M. P. Sharrock</i>	
Tribology in Ultra-High Density Tape Drive Systems: State of the Art and Future Challenges — <i>B. Bhushan and S. T. Patton</i>	
Servo Loop Gain Identification and Compensation in Hard Disk Head-Positioning Servo — <i>C.-I. Kang and M. Abed</i>	
A Novel Disturbance Observer Design for Magnetic Hard Drive Servo System with a Rotary Actuator — <i>Y. Huang and W. Messner</i>	
A Novel Add-On Compensator for Cancellation of Pivot Nonlinearities In Hard Disk Drives — <i>J. Ishikawa and M. Tomizuka</i>	
Optimal Multirate Control Design for Hard Disk Drive Servo Systems — <i>R. Chen, G. Guo, T. Huang, T.-S. Low, and S. Weerasooriya</i>	
A Novel Method for Reduction of the Cross Track Profile Asymmetry of MR Head During Self-Servo-Writing — <i>B. Liu, S.-B. Hu, and Q.-S. Chen</i>	
Multi-Tapped Magnetoresistive Heads for Magnetic Tape Tracking Servo — <i>J. H. Steele, II, W. C. Messner, J. A. Bain, T. A. Schwarz, W. J. O'Kane, and M. P. Connolly</i>	
A High Bandwidth Piezoelectric Suspension for High Track Density Magnetic Data Storage Devices — <i>W. Guo, Z. Wang, X. Yao, T. Huang, and C. Bi</i>	
Shear Mode Piezoelectric Microactuator for Magnetic Disk Drives — <i>S. Koganezawa, Y. Uematsu, T. Yamada, H. Nakano, J. Inoue, and T. Suzuki</i>	
Experimental Investigation of Shock Responses of Cantilever-shaft Design Hydrodynamic Bearing Spindle Motors — <i>C.-P. Roger Ku and M. Shumway</i>	
Patterned Media Recording: Noise and Channel Equalization — <i>S. K. Nair and R. M. H. New</i>	
Performance Comparison of a Class of (1,7) DFE Detectors — <i>G. Mathew, K. C. Indukumar, Y. X. Lee, and R. W. Wood</i>	
Byte Synchronization System and Method using an Error-Tolerant Synchronization Pattern for the PR IV Channel — <i>T. Yasuda, M. Blaum, and D. D. Tang</i>	
High Speed Implementation of Signal Space Detectors — <i>T. Jeon and J. Moon</i>	
Low Complexity Signal Space Detector for (1,7)-Coded Partial Response Channels — <i>Y. Kim and J. Moon</i>	
Digital Detection with Asynchronous Sampling using Amplitude Error Prediction — <i>T. Oenning and J. Moon</i>	
A New Nonlinear Multi-Filter Detection Concept for the High Density Magnetic Recording Channel — <i>F. Obernosterer, A. Kratzert, and W. F. Oehme</i>	
An Error Rate Improvement of Decision Feedback Equalization by Extraordinary Level Detection — <i>M. Umemoto</i>	
An Analysis of Frame Formats for Digital Tape Recording — <i>A. D. Weathers</i>	
Performance of an 8/9 Rate Matched Spectral Null Code on the PR4 Magnetic Recording Channel — <i>S. She, W. G. Bliss, and D. E. Reed</i>	
A High-Rate Matched Spectral Null Code — <i>M. Noda</i>	
Two-Dimensional Coding for a Multi-Track Recording System to Combat Inter-Track Interference — <i>P. J. Davey, T. Donnelly, D. J. Mapps, and N. Darragh</i>	
Sensor Saturation Effects on NLTS Measurements — <i>J. S. Feng</i>	
A Theoretical Study of Nonlinear Transition Shift — <i>Y. Zhang and H. N. Bertram</i>	
TMR Window Measurements with Thin Film Write/MR Read Heads on Metal Particle Tape Including Erase Bands — <i>K. D. McKinstry and R. H. Dee</i>	
An Off-Track Capability Model Including Noise — <i>R. S. Beach and P. I. Bonyhard</i>	
A Description of the Complete Off-track Capability Curve and its Special Application — <i>T.-C. Yu</i>	
Empirical Determination of Areal Density Capability — <i>D. Saunders, T. Madsen, R. Machelski, M. Roe, N. Curland, and P. Bonyhard</i>	
Optimal Track-Width Design of AMR/GMR Heads for High-Track-Density Disk Drives — <i>F. Tomiyama, H. Ide, T. Hamaguchi, H. Takano, T. Yamaguchi, and N. Kodama</i>	
Quantitative MFM Study on Partial Erasure Behavior of Longitudinal Recording — <i>T. K. Taguchi, A. Takeo, and Y. Tanaka</i>	
Finite Element Simulation of Digital Recording on ME Tape and Comparison with Experimental Data — <i>A. Werling, F. Ossart, J.-B. Albertini, and M. Aïd</i>	
A Comparison of Longitudinal and Transverse Recording — <i>J. Miles, P. Sivasamy, M. Wdowin, B. Middleton, and S. Casey</i>	

- Keeped Media Reproduction with Dual MR Heads — *F. Z. Wang, L. N. He, D. J. Mapps, D. T. Wilton, W. W. Clegg, and P. Robinson*
- A New Equalizing Experiment Applying to Perpendicular Digital VCR using FFT Analysis — *K. Kamijo, R. Taguchi, E. Miyashita, and J. Numazawa*
- Gd/Fe Multilayers with an Anisotropy Changing from In-plane to Perpendicular for MSR Applications — *E. Stavrou, H. Rohrmann, and K. Röhl*
- Magnetic and Magneto-Optic Study of a Layered Co/Pt – Dysprosium-Iron-Garnet System — *J. M. Meldrim, R. D. Kirby, M. J. DeVries, J. A. Woollam, and D. J. Sellmyer*
- The Creation of Nanometer Magnetic Domain Structure in Artificially Pinning Hole of Magneto-optical Recording Material — *T.-H. Wu, J. C. Wu, B.-M. Chen, and H.-P. D. Shieh*
- New MSR Method for High Density Read Only Memory Disks — *M. Birukawa, T. Suzuki, and N. Miyatake*
- Estimation of the Resolution by Mammos Read-Out — *N. Takagi, A. Yamaguchi, Y. Uchihara, S. Sumi, H. Awano, H. Shirai, H. Watanabe, and N. Ohta*
- Signal Enhancement of 0.2 μm Packed Domain in Magnetic Domain Expansion Readout Disk with Gating Layer — *H. Awano, H. Shirai, H. Watanabe, K. Shimazaki, N. Ohta, Y. Xiao, and K. V. Rao*
- A Novel Flying Magnetic Readout Head Based on Magneto-optic Transfer — *T. Terada, T. Nomura, R. Tsuchiya, K. Honda, M. Tomita, T. Furuoya, T. Kakezawa, and S. Kato*
- New Magnetic Domain Expansion MO Phenomena using an In-Plane Magnetizing Layer — *K. Shimazaki, H. Watanabe, M. Yoshihiro, H. Takao, H. Awano, S. Ohnuki, N. Ohta, Y. Xiao, and K. V. Rao*
- Imaging of Magnetic Domains in Thin Co/Pt and CoNi/Pt Multilayers by Near-Field Magneto-Optical Circular Dichroism — *V. Kottler, C. Chappert, N. Essaidi, and Y. Chen*

MAGNETIC MEASUREMENT AND IMAGING

- Magnetization, Magnetostriction and Film Stress of Fe Monolayers on W(100) — *D. Sander, A. Enders, and J. Kirschner*
- A Bipolar Pulse-Type Hysteresis Loop Tracer for Rare Earth Based Permanent Magnets — *J. R. Rhee, Y. H. Lee, M. Y. Kim, J. M. Lee, M. Y. Oh, D. G. Hwang, S. S. Lee, and C. M. Park*
- Dependence of Magnetic Properties on Crack Size in Steels — *Y. Bi and D. C. Jiles*
- Measurement of Oxygen Pressure Increase in Magnetic Field — *J. Nakagawa, N. Hirota, K. Kitazawa, H. Yokoi, Y. Kakudate, and S. Fujiwara*
- A Digital Sampling Technique for Amplitude and Pulse Width Measurement — *J. Zhu, T. Carr, and D. Varsanofiev* ...
- MFM Quantification of Magnetic Fields Generated by Ultra-Small Single Pole Perpendicular Heads — *S. K. Khizroev, W. Jayasekara, J. A. Bain, R. E. Jones, Jr., and M. H. Kryder*
- Thermal Wave Interactions in Magnetic Materials — *R. Carey, D. M. Newman, and J. Wiggins*
- Changes in Magnetic Properties of Neutron Irradiated RPV Steel — *D.-G. Park, J.-H. Hong, C.-I. Ok, J.-W. Kim, H. C. Kim*

MAGNETICS APPLICATIONS

- A Vector Oriented Control for a Magnetically Levitated Shaft — *J. De Miras and A. Charara*
- Prototype Microactuators Driven by Magnetostrictive Thin Films — *S. H. Lim, S. H. Han, H. J. Kim, Y. S. Choi, J. W. Choi, and C. H. Ahn*
- Thrust Characteristics of a Linear Oscillatory Actuator at a Low Temperature — *A. Aoki, M. Watada, S. Torii, K. Yamane, and D. Ebihara*
- A Novel Numerical Method for Analyzing of Passive Fault Current Limiter Considering Hysteresis — *A. Mukherjee, S. C. Mukhopadhyay, M. Iwahara, and S. Yamada*
- Planar Integrated Magnetic Component with Transformer and Inductor using Multilayer Printed Wiring Board — *T. Fujiwara*
- Performance Characteristics of a New Type of Linear Parametric Motor with Double Driving Surfaces — *K. Ishikawa, M. Ishizuka, and S. Kikuchi*
- A Magnetic Coupled Charger with No-Load Protection — *H. Sakamoto, K. Harada, H. Abe, and S. Tokuomi*
- The Application of Halbach Cylinders to Brushless AC Servo Motors — *K. Atallah and D. Howe*
- Analysis of Linear Electromagnetic Motion Devices by Multiple-Reference Frame Theory — *C.-T. Liu and S.-C. Hsu* ...
- Development of 3-Phase 100kVa Orthogonal-Core Type Variable Inductor with Sinusoidal Output — *O. Ichinokura, M. Maeda, M. Sakamoto, K. Mitamura, T. Ito, and T. Saito*
- A New Meander Type Contactless Power Transmission System-Active Excitation with a Characteristics of Coil Shape — *F. Sato, H. Matsuki, S. Kikuchi, T. Seto, T. Satoh, H. Osada, and K. Seki*
- Measuring System of Magnetostriction of Silicon Steel Sheet Under AC Excitation using Optical Methods — *T. Nakase, M. Nakano, K. Fujiwara, and N. Takahashi*
- Cogging Torque Reduction of a Single-Phase Brushless DC Motor — *D.-R. Huang, T.-F. Ying, S.-J. Wang, C. Zhou, Y.-K. Lin, K.-W. Su, and C.-I G. Hsu*

- A Novel Spherical Permanent Magnet Actuator with Three Degrees-Of-Freedom — *J. Wang, W. Wang, G. W. Jewell, and D. Howe*
- Magnetostrictive Linear Motor Development — *J. P. Teter, M. H. Sendaula, J. Vranish, and E. J. Crawford*
- A 42-Tesla Pulse Transformer with a Mechanically High Resistant Field Former — *E. Steingroever and G. Ross*
- Fabrication of a Magnetic Drive Unit for that Moves in the Same Direction of the Exciting Magnetic Field —
M. Enokizono, T. Tadoka, and K. Goto
- Electromagnetic Optimization of EMS-MAGLEV Systems — *M. Andriollo, G. Martinelli, A. Morini, and A. Tortella* ..
- A Novel Combined Lift and Propulsion System for a Steel Plate Conveyance by Electromagnets — *H. Hayashiya, D. Iizuka, H. Ohsaki, and E. Masada*
- A Theory for Analyzing the Flap Motion of Wings of Small Flying Elements Driven by a Magnetic Torque —
K. Shimasaki, M. Inoue, K. I. Arai, and T. Honda
- Superconducting Permanent Magnets from Bulk $\text{YBa}_2\text{Cu}_3\text{O}_{7-d}$ Samples — *S. Gruss, G. Fuchs, G. Krabbes, P. Schätzle, J. Fink, K. H. Müller, and L. Schultz*
- Fabrication and Testing of a Small Pump Composed of a Magnet and An Elastic Plate — *T. Honda, J. Yamasaki, and K. I. Arai*
- Design of an Actuator Being Both a Permanent Magnet Synchronous Motor and a Magnetic Suspension — *C. Barthod and G. Lemarquand*
- Optimal Design of Rotor Circuits in Induction Type Bearingless Motors — *A. Chiba and T. Fukao*
- A Method to Compute the Shielding of a 3-D Conductor Array by a Semi-Infinite Permeable Layer — *M. Sharifi, J. D. Lavers, and M. Gyimesi*
- Magnetization Reversal Mechanisms in Colloidal Dispersions of Magnetite Particles — *J. M. González, M. I. Montero, J. A. López-Pérez, J. Mira, M. A. López-Quintela, J. Rivas, X. Batllé, and A. Labarta*
- Inter-Particle Interactions in Biocompatible Magnetic Fluids — *Q.-T. Bui, Q. A. Pankhurst, and K. Zulqarnain*
- Magnetohydrodynamic Calculation for Electromagnetic Stirring of Molten Metal — *K. Fujisaki, T. Ueyama, T. Toh, M. Uehara, and S. Kobayashi*
- Magnetic Separation of Nanoparticles — *D. R. Kelland*
- High Gradient Magnetic Separation of a Biologically Produced FeS Adsorbent using Sulphate Reducing Bacteria —
B. T. Coe, R. Gerber and D. Witts
- Optical Measurements of Magnetophoresis of Macromolecules — *M. Iwasaka and S. Ueno*
- Three-Dimensional Field and Side-Force Design Analyses of a Transverse Flux Linear Switched-Reluctance Machine —
C.-T. Liu, K.-S. Su, and M.-H. Lee
- The Robust Design Approach for Reducing Cogging Torque in Permanent Magnet Motors — *S. X. Chen, T. S. Low, and B. Bruhl*
- Optimization of a Magnetic Actuator with Taguchi Method and Multivariate Analysis Method — *H. Fusayasu, Y. Yokota, Y. Iwata, and H. Inoue*
- A Design Technique for Magnetostrictive Actuators with Laminated Active Material — *F. Stillesjö, G. Engdahl, and A. Bergqvist*
- A Novel Design Approach for Grasping Broad Characteristics of Magnetic Shield Problem — *S. Wakao, T. Onuki, J. W. Im, and T. Yamamura*
- Analysis of Dynamic Characteristics of Switched Reluctance Motor Based on SPICE — *O. Ichinokura, T. Onda, M. Kimura, T. Watanabe, T. Yanada, and H. J. Guo*
- Investigation of the Performances of a Permanent Magnet Biased Fault Current Limiting Reactor with a Steel Core —
S. C. Mukhopadhyay, M. Iwahara, S. Yamada, and F. P. Dawson
- Use of a Conductor Screen to Magnetize NdFeB Magnets — *R. R. Wallace, V. D. Fierro, L. A. Morán, and T. A. Lipo* ..
- Finite Element Modeling of Creep Damage Effects on a Magnetic Detector Signal for a Seam Weld/HAZ-Region in a Steel Pipe — *M. J. Sablik, D. C. Jiles, and M. R. Govindaraju*
- Design Optimization of Stimulation Coil System for Nerve Stimulation — *T. Onuki, S. Wakao, T. Miyokawa, Y. Nishimura, N. Ishikawa, and H. Hosaka*
- Finite Size Bi-Planar Gradient Coil for MRI — *H. Liu*

CONFERENCE AUTHOR INDEX

Magnetic Microscopy and Imaging I

R. D. Gomez, Chairman

Time-resolved scanning Kerr microscopy of ferromagnetic structures (invited)

M. R. Freeman, W. K. Hiebert, and A. Stankiewicz

Department of Physics, University of Alberta, Edmonton T6G 2J1, Canada

Time-resolved microscopy enables valuable new measurements of the dynamics of resonance and relaxation in a range of magnetic systems. An overview of the scope of applications to ferromagnetic microstructures is presented. These include observations of ferromagnetic resonance and spatially nonuniform modes of oscillation, studies of magnetization reversal, and characterizations of the speed of magnetic recording devices. © 1998 American Institute of Physics. [S0021-8979(98)36511-1]

I. INTRODUCTION

Recently, novel experimental information concerning the dynamics of a variety of magnetic systems has been obtained using picosecond time-resolved laser techniques combined with diffraction-limited optical microscopy. Ultrafast optical methods have been in use for some time in the extraction of relaxation and resonance information from magnetic systems.¹⁻⁴ The addition of microscopic spatial resolution powerfully extends the approach to much smaller specimens, enabling measurements of relaxation in micrometer-scale structures, as well as some imaging of spatially nonuniform dynamics.^{5,6} In this paper we describe the study of ferromagnetic dynamics in small permalloy structures using this technique. A similar procedure applies to the time-domain characterization of devices such as high-speed magnetic recording heads.

In addition to the good spatial and temporal resolution achieved using an optical technique, another key aspect is the ability to perform vector measurements of the magnetization. The component of magnetization parallel to the wave vector of the incident light is resolved in the experiments. A vector measurement is not crucial to paramagnetic relaxation measurements, but is essential in order to perform magnetic resonance and ferromagnetic relaxation studies. Controlling the optical configuration, we are able to track dynamical excursions of the magnetization in three dimensions through polar and longitudinal Kerr effect measurements.

II. EXPERIMENTAL DETAILS

An example of an experimental geometry for spatially resolved time-domain ferromagnetic resonance measurements is shown in Fig. 1.⁶ The single turn lithographic coil is patterned from a gold film with a titanium adhesion layer. A fast electrical pulse generated using a photoconductive switch propagates around the coil, inducing a transient magnetic field at the sample, perpendicular to the substrate (the tipping pulse). The rise time of this pulse at the sample is limited to ~ 20 ps by dispersion of the coil leads, and the

decay time constant is ~ 500 ps. Peak tipping field amplitudes are limited to ~ 30 Oe with this coil. The static magnetic field is applied in the plane of the sample, and the polar Kerr effect is used to record the out-of-plane component of the magnetization. Resonant precession of the magnetization (about the static field) induced by the tipping pulse is reflected in oscillations of the polar Kerr signal.

The permalloy films used in this work are sputter deposited in a load-locked ultrahigh vacuum chamber pumped to a base pressure of $\sim 5 \times 10^{-8}$ Torr. A permanent magnet assembly is used to apply an *in situ* static field of approximately 150 Oe in the plane of the substrate to establish an easy axis. The resulting films have low coercivity (< 2 Oe in the easy direction), and low resistivity ($\sim 20 \mu\Omega$ cm) indicating very little oxidation. SIMS analysis of the films show the composition to be 83% Ni 17% Fe (by weight), fairly close to the 81/19 proportion of the target. Patterning of the films is accomplished through photolithography and wet chemical etching, yielding the very smooth edges with a slight undercut profile as seen in Fig. 1(b).

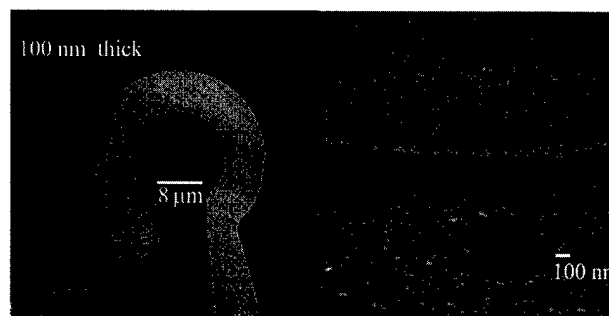


FIG. 1. Electron micrographs of the $8 \mu\text{m}$ diameter permalloy disk sample. Left panel: plan view, showing the surrounding lithographic gold coil. Right panel: tilted close-up view, clearly showing the clean edge of the disk.

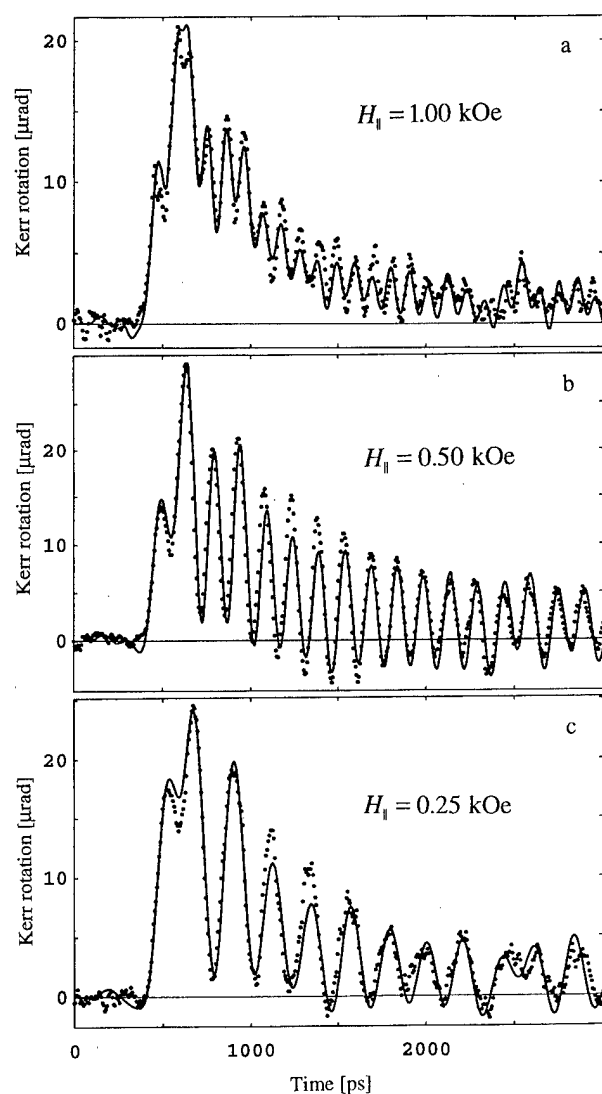


FIG. 2. Examples of the response to the pulsed field of the out-of-plane component of magnetization, measured at the center of the disk by the polar Kerr effect. The solid lines are fits to the data using the Landau-Lifshitz-Gilbert equation, using the same parameters for each value of the static field.

III. RESULTS

A. Resonance

The modal resonance frequencies are determined by the maxima in the power spectra of Fourier transformed time-domain data. The in-plane magnetic field dependence of the characteristic frequency is well described by the Kittel relation for an infinite plane, as may be expected for such a large (on the scale of the domain wall width) disk. Modeling the time-domain data in more detail through numerical integration of the Landau-Lifshitz-Gilbert equation, we find very good agreement.⁶ Data are shown in Fig. 2 for a range of values of the in-plane field. The measurements (shown by the dotted lines in the figure) were made with the $0.7\ \mu\text{m}$ laser spot focused at the center of the particle. The $t=0$ position is arbitrary, corresponding to the initial position of the delay line at a location yielding a reasonable baseline determination before onset of the signal. Using a pulse shape determined from higher field data by the procedure established in Ref. 7, the curves are all fit using the same set of

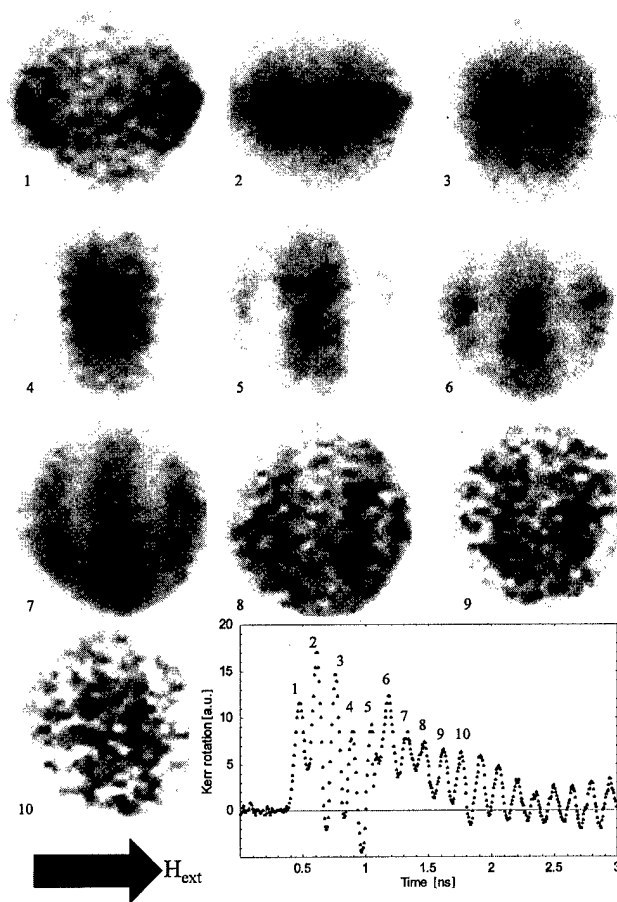


FIG. 3. A collection of full spatial images of the polar Kerr signal at times corresponding to the successive peaks in the signal at the center of the disk in a static field of 500 Oe.

parameters. The results of the fit are shown by the solid lines. Only the dimensionless Gilbert damping parameter is adjustable, and we find $\alpha=0.008$, in reasonable agreement with earlier careful microwave measurements of Patton and co-workers.⁸ Note that these results represent the response of the magnetization to a very broad-band excitation. The high frequency components associated with the rising edge of the pulse excite the resonant oscillations, which then ring-down according to their intrinsic damping rate. Meanwhile the magnetization vector parametrically follows the slowly decaying tail of the field pulse (consisting of that part of the spectrum of the broad-band excitation below the resonance frequency), giving rise to the offset of the centerline through the envelope of the oscillations.

Time-resolved images of the magnetization across the whole disk clearly show the presence of nonuniform modes of oscillation, however. At these dimensions we are in an intermediate size regime, where the modal frequencies are not yet strongly influenced by size effects but the spatial response definitely is.⁶ Figure 3 shows a set of time-resolved magnetic images of the particle. With the static bias field at 500 Oe (horizontal), an image was taken for a series of time delays corresponding to successive peaks in the oscillations measured at the disk's center. Strikingly apparent are the enhanced initial responses at the edges (dark corresponds to

higher signal), that subsequently seem to propagate toward the center as a kind of shock wave. The effective velocity is on the order of 10^4 m/s, much faster than a domain wall velocity, for example. The observation of enhanced response at the edges along the field direction is qualitatively consistent with the fact that in static equilibrium these edges are already demagnetized, and should be able to respond to the tipping field more easily. In contrast, no such effects are seen at the edges one-quarter of a rotation around the disk from these points, where there are no free poles in the initial magnetic configuration. In these data, a reflection in the electrical pulse induces a bit of additional structure after the fifth peak. At long time delays, the spatial mode of oscillation becomes more uniform again. To highlight the nonuniformity, the gray scale in each image is adjusted to span between the minimum and maximum levels of the signal. In the later frames (8,9,10) the signal becomes quite uniform across the disk, with variations not much greater than the noise level in the measurement. The scaling procedure then mainly highlights the noise, which appears as graininess.

From these images we can conclude that we should in fact expect discrepancies between the Landau-Lifshitz-Gilbert model and the time domain data for this sample. Consistently poorer agreement is found between the data and the model in Fig. 2 over a time interval that begins coincident with the arrival of the nonuniform response at the center of the structure. A more detailed numerical model taking into account the initial magnetic configuration of the disk seems essential to further quantitative progress.

B. Reversal

In-plane dynamics of the magnetization, and most specifically those aspects related to magnetization reversal, are also of great interest at the present time.⁹⁻¹³ In order to address these questions using time-resolved microscopy, it is only necessary to reconfigure the "vector geometry." We measure the in-plane components of the magnetization (parallel and perpendicular to the static magnetic field) using the longitudinal Kerr effect implemented in the traditional manner by masking half of the beam. While this is the simplest approach, one must beware that a mix of polar and longitudinal signals is observed when there is also an out-of-plane magnetization present. In addition the effective numerical aperture in the masking direction is halved, resulting in an elongated focus and some loss of spatial resolution.

The other important geometric change is to place the transient magnetic field in the plane of the sample. Placing the sample directly on top of a current carrying transmission line straightforwardly does this. A cross-sectional schematic of the arrangement used in this work is illustrated in Fig. 4. The transmission line is 300 nm by 40 μ m gold, relatively thick for high current carrying capacity, and broad for magnetic field uniformity at the sample. The current pulses in this case are generated by an avalanche transistor pulser (Picosecond Pulse Labs Model 2000D). An insulating spacer (25 nm SiO_2) on top of the gold electrically insulates the permalloy from the transmission line, and optimally positions the magnetic sample in the in-plane field. The calcu-

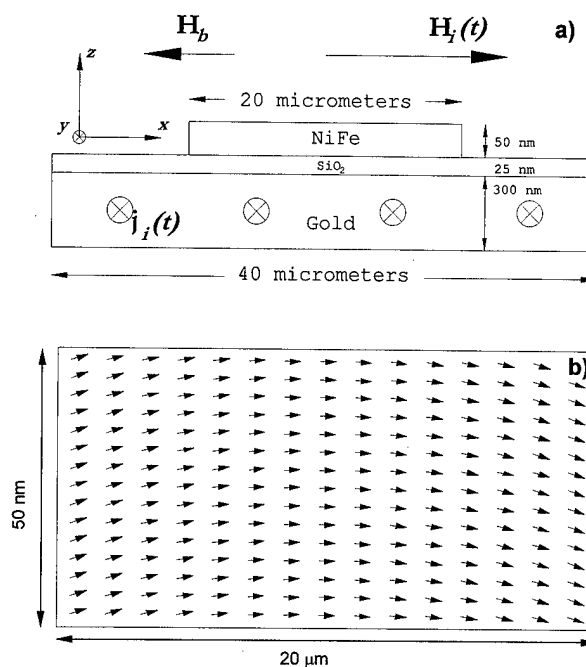


FIG. 4. (a) Cross-sectional geometry showing the configuration for applying transient fields in the plane of the sample. (b) Calculated cross-sectional transient field profile for the volume occupied by the samples.

lated field distribution above the transmission line is shown in Fig. 4(b).

The permalloy samples for this study are rectangular bars, again produced by sputtering in the UHV system followed by optical lithography and wet chemical etching. Initial magnetic characterizations are performed optically, using a small electromagnet to apply in-plane field to the sample. Spot measurements of the hysteresis are performed, with the laser focused at specific locations. As these results are strongly position dependent (the bars are much easier to saturate near the center than near the ends) we also use an imaging method to characterize the static magnetic properties of the samples. The synchronous response to low frequency (280 Hz) ac fields is measured, yielding a signal representing the difference of the magnetization between positive and negative fields. Magnetic images taken for different field amplitudes show how the hysteresis varies as a function of position. A typical result is shown in Fig. 5. This is the longi-



FIG. 5. A longitudinal Kerr image showing the signal change due to magnetization reversal of the 10×4 μ m bar in a ± 30 Oe field switching at 280 Hz.

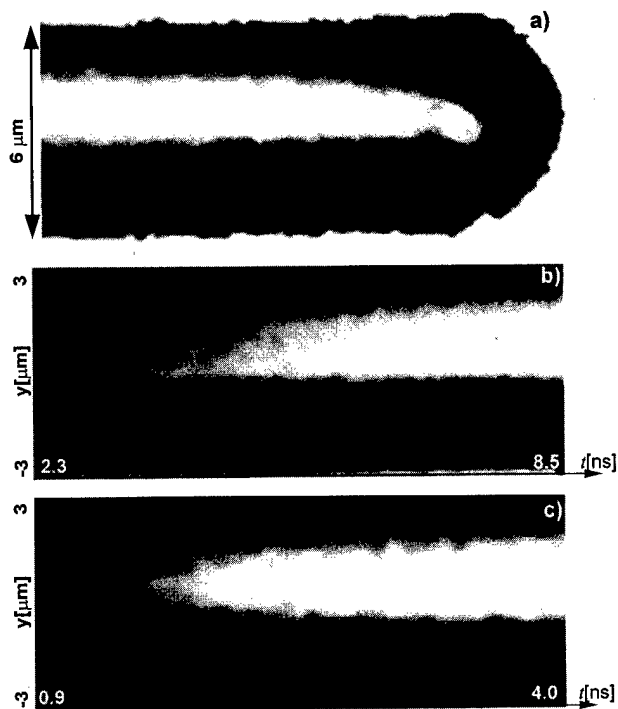


FIG. 6. Changes of the x component of magnetization (larger signals shown brighter) for a $20 \times 6 \mu\text{m}$ bar in a -5 Oe static biasing field. (a) Shift of the domain wall after 5.5 ns in a small tipping field. (b) and (c) are typical y - t diagrams for small and large tipping fields, respectively, where a linear vertical spatial scan across the center of the bar is repeated for increasing delay times. Note the change in time scale between (b) and (c).

tudinal Kerr signal (x component of the magnetization, parallel to the static field) from a $4 \times 10 \mu\text{m}$ particle for a ± 30 Oe square-wave field modulation, showing a uniformly magnetized and saturated central region. Recording the different Kerr components reveals information about the magnetic anisotropy at the ends (due mainly to demagnetizing effects). Such static images provide a direct point of comparison for the dynamical studies. A very detailed portrait of static reversal in permalloy bars was developed much earlier through Bitter pattern images, which have higher spatial resolution than the present optical experiments.¹⁴

A first glimpse at the dynamical information accessible in time-resolved studies of magnetization reversal is seen in the following data of the response of a nonuniformly magnetized permalloy rectangle to a pulsed field in the plane of the particle. We examine a $20 \mu\text{m} \times 6 \mu\text{m}$ rectangle (50 nm thick) with the static bias magnetic field parallel to the long direction. This bar is oriented transverse to the current flow direction of the transmission line so that the transient magnetic field is parallel (or antiparallel) to the bias field. In a field of -5 Oe, the static configuration of the particle corresponds to two antialigned domains along most of the length of the bar, with the domain wall near the center, and some closure domains at the ends. Time-resolved measurements are then performed to study the approach to saturation induced by the (0.4 ns rise time, 1.5 ns fall time, 10 ns duration, opposite polarity to the static field) pulsed magnetic fields, starting from this simple demagnetized state.

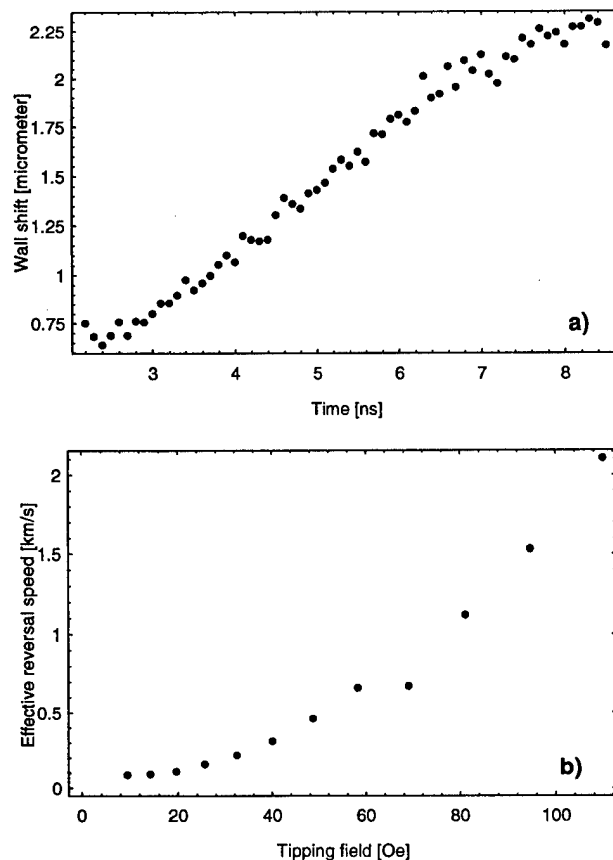


FIG. 7. (a) Wall shift as a function of time determined by integrating the reversed component along y in data as shown in Fig. 6(b). (b) The effective reversal speed as a function of tipping field amplitude, determined from the linear slope of curves as in (a).

As a function of the amplitude of the pulsed field, two distinct regimes are observed in the reversal dynamics of the initially antialigned domain. At smaller pulse amplitudes (less than ~ 60 Oe) the reversal proceeds via uniform motion of the central domain wall towards the edge of the bar. Characteristic data are shown in Fig. 6. Panel (a) is a snapshot of the magnetization change 5.5 ns after the onset of the pulse. The light area is the region that has been swept out by the moving domain wall. To see the progression in detail, the change in the longitudinal Kerr signal is shown in two dimensional images in Figs. 6(b) and 6(c) where the vertical axis corresponds to position along a line section through the center of the bar (in the short direction, y), while the horizontal axis is time. The signal growing with time in Fig. 6(b) for a small tipping field arises from motion of the domain wall with nearly constant velocity. The initial displacements of the wall are well below the spatial resolution of the microscope, so the rate of reversal is extracted by integrating the Kerr signal across the particle and plotting the integral as a function of time, as in Fig. 7(a). Normalizing the curve by the saturation signal divided by the width of the bar, the slope can be converted to a wall velocity.

Reversal rates as a function of pulsed field amplitude are shown in Fig. 7(b). A couple of points are of particular note. First, we do not observe a linear region at low fields, indicating that the motion cannot properly be described using a wall mobility. This may be indicating that we cannot ignore

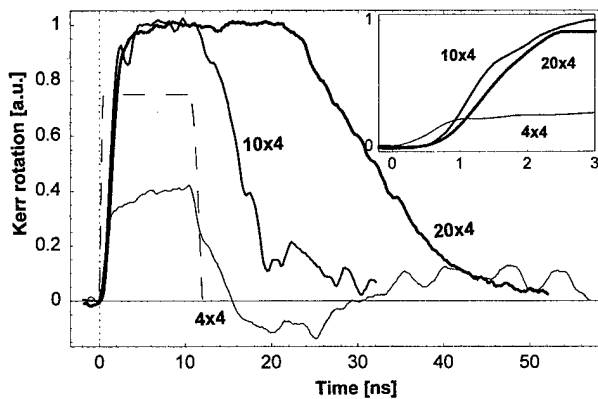


FIG. 8. Time dependence of the x component of magnetization measured at sample center for three different structures, 4×4 , 10×4 , and $20 \times 4 \mu\text{m}$ (light, medium, heavy line, respectively). -35 Oe static field, tipping field amplitude $+140$ Oe. The dashed line shows the shape of the pulse, and the inset shows the rising edge response in more detail.

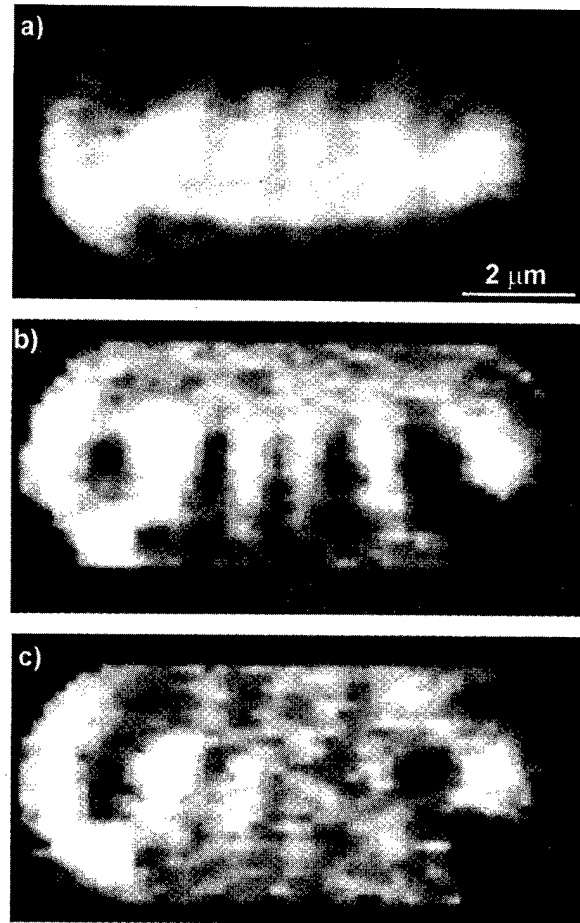


FIG. 9. The nonuniformity of response during the initial flip is shown in this set of magnetic images taken for the $10 \times 4 \mu\text{m}$ bar at $t = +3$ ns, under the conditions of Fig. 8. (a) Longitudinal (x) component. (b) Transverse (y) component. (c) Polar (z) component.

the influence of the closure domains at the ends of the bar on the motion of the wall. Second, at pulse amplitudes above 65 Oe, there is a nearly linear region, possibly preceded by a discontinuity in the curve. The images of the magnetization are qualitatively different in this regime, with the reversal proceeding not by movement of the domain wall but rather through a rotation process which propagates through the center of the domain after nucleating near the closure domain boundaries at the ends. This is clearly evident in Fig. 6(c), where change in the longitudinal Kerr signal is seen to begin not at the wall but closer to the center of the domain, and to develop symmetrically about this point. The distinct asymmetry arising from wall motion in Fig. 6(b) is notably absent. Therefore the reversal rates found at higher fields in Fig. 7 cannot correctly be interpreted as velocities because of this change in reversal mechanism. Normalizing the data as described above, the maximum wall speed we find before this phenomenological change is 650 m/s at 60 Oe.

A great richness of phenomena is observed upon pursuit of these investigations to higher fields. Beginning from an equilibrium state in which the centers of the bars are uniformly magnetized (static field of -35 Oe), we obtain a view of the speed of reversal by recording the time evolution of the magnetization change with the laser focussed at the center of the structure. Results are shown in Fig. 8 for $4 \mu\text{m}$ wide samples of three different lengths, 4, 10, and 20 μm . The 10 ns duration transient field has amplitude 140 Oe. The rising and falling transitions are markedly asymmetric, particularly for the longest and shortest samples. It is clear from the expanded view of the initial switch in the inset that reversal at the center occurs more rapidly for the shorter bars. The rise time of the pulse itself starts to become significant in limiting the speed for the $4 \times 4 \mu\text{m}$ structure.

Much more information is available in full time-resolved images of the magnetization. We observe that the reversal process starts with a wave-like spatial oscillation of the in-plane magnetization. Figure 9 has panels showing the three components of the magnetization (long. x , long. y , polar) for the $10 \times 4 \mu\text{m}$ particle at $t = 3$ ns after the onset of the field (see the abscissa of Fig. 8). The oscillation is initially quite

symmetric about the equilibrium (x) direction, and shows up most dramatically in the y component. One direction then grows at the expense of the other, culminating in reversal. The relative degree to which this behavior is related to the "concertina" structure seen in static reversal,¹⁴ or is induced by dynamics, remains to be sorted out. The wavelength of the spatial variation appears to be extremely stable and reproducible. At the same time these oscillations are clearly observed only on the rising edge of the pulses. Two effects may be at work to cause different behavior on the trailing edge. The time rate-of-change of the magnetic field is considerably less when the pulse shuts off relative to when it turns on, making it less effective at driving a dynamic instability. In addition the switched state may be more uniformly magnetized because of the unequal amplitudes of the static and transient fields, although the bar may not have completely relaxed into a switched equilibrium state by the end of the 10 ns pulse.

Strong dependences on sample size are also found in imaging. Some results from a more detailed investigation of magnetization reversal in the longer bar are reported in a companion paper.¹⁵

IV. DISCUSSION

The present work only begins to scratch the surface of what is possible with these pulsed optical methods. Many other materials systems and geometries remain to be investigated with our present set-up. Some of the choices will be guided by the desire for convergence between experiment and micromagnetic simulations, an obvious goal for the near term. The immediate goal is to study smaller particle sizes.

The same experimental techniques are well suited to the characterization of devices and media for magnetic recording, particularly when high speed is an issue.^{16,17} The utility of such measurements is further enhanced by time-domain magneto-optical measurements of currents, for direct comparison between the response (e.g., of the magnetization at the pole tips of a recording head) and the input (e.g., the drive signal to the coil). A stroboscopic "movie" of the magnetization at the air bearing surface of a write head in response to a dibit input can be viewed on the internet.¹⁸

In terms of the experimental method, there are many potential improvements that would further broaden the range of significant applications. Although the speed of the technique is more than adequate for our present studies, this is material dependent. Awschalom and co-workers⁴ have studied much faster dynamics in magnetic semiconductors using optical excitation of the sample. Substantial improvement of the speed of pulsed magnetic field generation is required before our approach can enter the sub-picosecond regime. Of even more interest is increasing the amplitude of magnetic field pulses, to open the door to large tipping angle measurements and associated nonlinearities in resonance. Studies of reversal in magnetically harder materials would also be of interest, as in the case of studies of high-speed switching in media by Doyle and co-workers.¹⁹ At present we are unable to pass more than about 300 mA peak current through the photoconductive switches. The corresponding current densities are very high and may be near to intrinsic damage thresholds of the materials, but the fact that the quantum efficiency of the devices is very low suggests that there may still be room for significant improvement here.

It is also imperative to improve spatial resolution in order to investigate the detailed micromagnetic dynamics of much smaller ferromagnetic particles. In the present experiments some information is already lost below the limit of spatial resolution, especially near the edges of the particles. When we attempt to cleanly separate the vector components of the magnetization the demands on resolution increase still further. Because of unwanted "clipping" of the beam which occurs as the focus spot scans over an edge, a small focus

also helps in keeping the entire laser spot on the particle as close to the edge as possible. We have developed a solid immersion lens capability for these experiments offering improvements of a factor of three in spatial resolution over that achieved here.²⁰ This is probably good enough to explore strong size effects and to be useful for the next few generations of magnetic devices, but certainly not for superparamagnetic particles or for such devices as seem certain to exist before the "endpoint" of magnetic recording is reached. In this regard the near-field and second harmonic generation methods of Silva, Rogers, and co-workers²¹ are particularly exciting.

ACKNOWLEDGMENTS

The authors are indebted to the Alberta Microelectronics Centre for access to their deposition and patterning facilities, and to Professor Abdul Elezzabi for his assistance during the early stages of this project. We thank J. Giusti for pointing out Ref. 14. This work is supported by the Natural Sciences and Engineering Research Council, Canada.

¹D. D. Awschalom, J.-M. Halbout, S. von Molnar, T. Siegrist, and F. Holtzberg, *Phys. Rev. Lett.* **55**, 1128 (1985).

²M. R. Freeman, M. J. Brady, and J. F. Smyth, *Appl. Phys. Lett.* **60**, 2555 (1992).

³A. Y. Elezzabi, M. R. Freeman, and M. Johnson, *Phys. Rev. Lett.* **77**, 3220 (1996).

⁴S. A. Crooker, J. J. Baumberg, F. Flack, N. Samarth, and D. D. Awschalom, *Phys. Rev. Lett.* **77**, 2814 (1996).

⁵J. Levy, V. Nikitin, J. M. Kikkawa, A. Cohen, N. Samarth, R. Garcia, and D. D. Awschalom, *Phys. Rev. Lett.* **76**, 1948 (1996).

⁶W. K. Hiebert, A. Stankiewicz, and M. R. Freeman, *Phys. Rev. Lett.* **79**, 1134 (1997).

⁷A. Y. Elezzabi and M. R. Freeman, *Appl. Phys. Lett.* **68**, 3546 (1996).

⁸C. E. Patton, Z. Frait, and C. H. Wilts, *J. Appl. Phys.* **46**, 5002 (1975).

⁹M. Lederman, S. Schultz, and M. Ozaki, *Phys. Rev. Lett.* **73**, 1986 (1994).

¹⁰J. Ding and J.-G. Zhu, *J. Appl. Phys.* **79**, 5892 (1996).

¹¹W. Wernsdorfer, K. Hasselbach, A. Sulpice, A. Benoit, J.-E. Wegrowe, L. Thomas, B. Barbara, and D. Mailly, *Phys. Rev. B* **53**, 3341 (1996).

¹²W. Wernsdorfer, B. Doudin, D. Mailly, K. Hasselbach, A. Benoit, J. Meier, J.-Ph. Ansermet, and B. Barbara, *Phys. Rev. Lett.* **77**, 1873 (1996).

¹³S. T. Chui, *Phys. Rev. B* **55**, 3688 (1997).

¹⁴H. A. M. van den Berg and D. K. Vavani, *IEEE Trans. Magn.* **18**, 880 (1982).

¹⁵A. Stankiewicz, W. K. Hiebert, G. E. Ballentine, K. W. Marsh, and M. R. Freeman, *IEEE Trans. Magn.* (7th Joint MMM-I Proceedings) (submitted).

¹⁶M. R. Freeman and J. F. Smyth, *J. Appl. Phys.* **79**, 5898 (1996).

¹⁷M. R. Freeman, A. Y. Elezzabi, and J. A. H. Stotz, *J. Appl. Phys.* **81**, 4516 (1997).

¹⁸<http://laser.phys.ualberta.ca/~freeman/maghead.mov>

¹⁹L. He, W. E. Doyle, L. Varga, H. Fujiwara, and P. J. Flanders, *J. Magn. Mater.* **155**, 6 (1996).

²⁰J. A. H. Stotz and M. R. Freeman, *Rev. Sci. Instrum.* **68**, 4468 (1997).

²¹T. J. Silva, T. M. Crawford, and C. T. Rogers (these proceedings).

Magnetic force microscopy image restoration technique for removing tip dependence

Jian-Gang Zhu, Xiangdong Lin,^{a)} and Rick C. Shi

Data Storage System Center, Department of Electrical and Computer Engineering, Carnegie Mellon University, Pittsburgh, Pennsylvania 15213

Yansheng Luo

IBM, SSD, San Jose, California

Quantitative interpretation of a magnetic force microscopy (MFM) image usually requires detailed knowledge of the magnetization configuration of the sensing tip. Here, we demonstrated a technique that converts the obtained raw MFM image into the magnetic pole density distribution without explicitly knowing the tip magnetization orientation. By creating an approximate point source of magnetic poles in the same sample imaged, the impulse response function of the MFM tip is obtained for deconvolution of a raw image in the Fourier space. Experimental demonstrations with various tip magnetization orientations were performed on recorded magnetic transitions in a thin film longitudinal medium. © 1998 American Institute of Physics. [S0021-8979(98)53811-X]

I. INTRODUCTION

Magnetic force microscopy (MFM) has been used extensively in imaging magnetic structure in magnetic materials and devices. However, any MFM image depends on magnetization configuration of the sensing tip used, while the tip magnetization configuration can be very complicated. Lack of the knowledge of the tip magnetization orientation often results in difficulties in interpretation of the obtained images. Direct calculations on tip magnetization configuration have been undertaken, however, it is often intensive and requires detailed knowledge of the tip magnetic film microstructure.¹⁻³

A simple deconvolution technique has been proposed previously.⁴ However, using the ends of magnetized elongated narrow bar as an ideal magnetic pole point source presents many difficulties in practice. In this paper, a point source is created on the same sample imaged. The technique to convert a raw MFM image to the corresponding magnetic pole density distribution is presented in detail and demonstrated experimentally.

II. DESCRIPTION OF THE TECHNIQUE

A magnetic force microscope senses the gradient of the magnetic force exerted on the sensing tip due to the stray field of the sample. Assuming the measurement response is linear (which requires the tip magnetization be rigid), the obtained image $I(x,y)$ can be written as the convolution of the tip impulse response function and the magnetic pole density distribution, from which the stray field originates, as follows:⁴

$$I(x,y) = \int \rho(x',y') \cdot h(x-x',y-y') dx' dy', \quad (1)$$

where $\rho(x,y)$ is the magnetic pole density distribution in the sample and $h(x-x',y-y')$ is the tip impulse response func-

tion with tip at (x,y) and point pole source at (x',y') . The image for a point pole source at the origin is the tip impulse response function:

$$I_p(x,y) = h(x,y).$$

Using the impulse response function, a MFM image of a magnetic structure imaged with the same tip at the same imaging conditions, can be deconvolved in the Fourier space with a Wiener's filter:

$$\hat{\rho}(k_x, k_y) = \frac{\hat{I}(k_x, k_y)}{\hat{I}_p(k_x, k_y)} \cdot \frac{\hat{I}_p(k_x, k_y) \cdot \hat{I}_p^*(k_x, k_y)}{\hat{I}_p(k_x, k_y) \cdot \hat{I}_p^*(k_x, k_y) + \text{tiny}(k_x, k_y)}. \quad (2)$$

The final magnetic pole density distribution $\rho(x,y)$ can be obtained by inverse Fourier transformation of $\hat{\rho}(k_x, k_y)$. In all the cases presented here, $\text{tiny}(k_x, k_y)$ is chosen to be a small constant, adjusted for each individual case.

III. SIMULATION RESULTS

In this section, computer simulation results are presented to demonstrate the technique. In corresponding to the experimental demonstration, which will be presented in the later section, recorded transitions in a longitudinal thin film medium were chosen to be an example, as shown in Fig. 1. According to the orientation of the tip magnetization, three cases were shown here: the magnetization of the tip is case A: vertical, case B: horizontal, and case C: canted.

The track width is assumed to be $w = 2.0 \mu\text{m}$ and the intertransition spacing $B = 1.0 \mu\text{m}$. For calculation simplicity, the tip is assumed to be a uniformly magnetized sphere with diameter $D = 30 \text{ nm}$. The point source of the magnetic pole density is approximated by an isolated transition, i.e., $B = 16 \mu\text{m}$, with $W = 0.2 \mu\text{m}$. MFM images were calculated by calculating the gradient of the magnetic force exerted on the tip due to the stray field generated from the recorded transitions. The left height of the tip is $d = 60 \text{ nm}$.

^{a)}Electronic mail: lin@dilbert.ece.cmu.edu

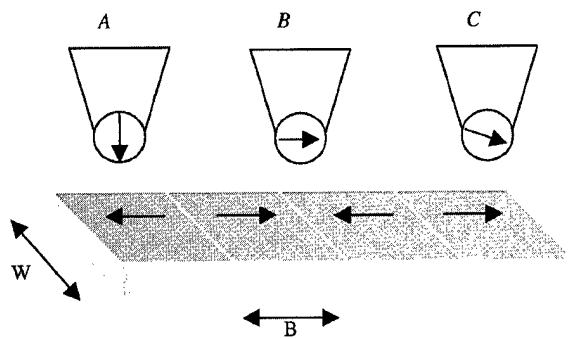


FIG. 1. Recorded transitions for MFM imaging.

A. Case A: Tip magnetized vertically

In this case, the calculated image of the recorded transitions with assuming tip magnetization orientation is perpendicular to the sample surface, as shown in Fig. 2(a). In the image, alternating black and white stripes indicate the locations of the transitions. Since the magnetization in the tip is vertical, only the vertical component of the stray field contributes to the image. The image of the approximate point source is shown in Fig. 2(b). Using this image as the impulse function, the image shown in Fig. 2(a) was deconvolved in the Fourier space according to Eq. (2), shown in Fig. 2(c). The slight broadening of the images is due to the finite size effect of the approximated point source.

B. Case B: Tip magnetized horizontally

When the tip is magnetized horizontally, only the gradient of the horizontal component of the stray field is sensed. The MFM image of the same recorded magnetization structure becomes that shown in Fig. 3(a) as in contrast to that

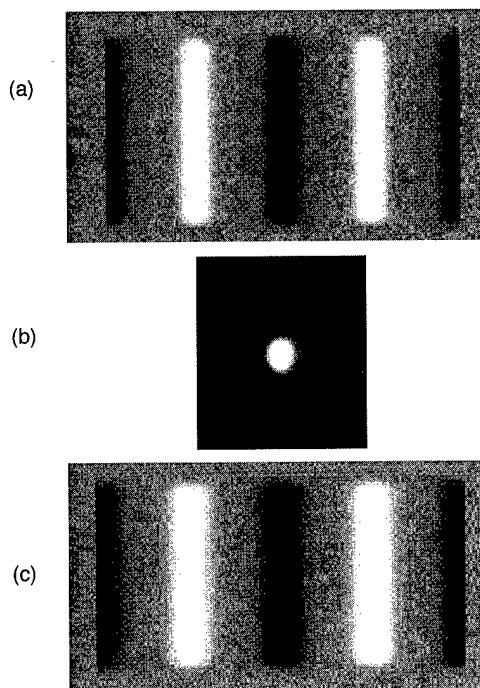


FIG. 2. Calculated images with tip magnetization vertical to the sample surface. (a) Transitions, (b) point source, (c) deconvolved image.

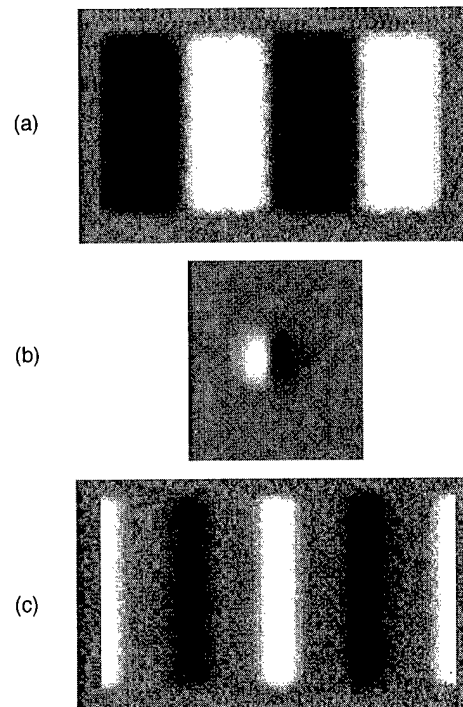


FIG. 3. Calculated images with tip magnetization orientation horizontal. (a) Transitions, (b) point source, (c) deconvolved image.

shown in Fig. 2(a). The image of the approximate point source, shown in Fig. 3(b), also becomes dipolelike instead of a bell-shaped intensity profile as that shown in Fig. 2(b). Using this image of the point source to deconvolve the transition image in the Fourier space, the resulting magnetic pole density distribution is recovered, as shown in Fig. 3(c), almost exactly the same as that shown in Fig. 2(c).

C. Case C: Tip with magnetization canted

Since in practice, it is difficult to assure that the magnetization of the tip is either perfectly vertical or perfectly horizontal, the case of canted magnetization orientation was simulated. The canting angle in this case was set at 10° with respect to the horizontal. The calculated MFM image of the recorded transitions is shown in Fig. 4(a), which is essentially a mixture of Figs. 2(a) and 3(a). Figure 4(b) shows the image of the point source. The restored magnetic pole density distribution is shown in Fig. 4(c). Indeed, it is the same as that shown in both Figs. 2(c) and 3(c). The slight differences among the three restored pole density distributions are due to the finite size of the point source as well as the finite size of the sensing tip.

IV. EXPERIMENTAL RESULTS

Experimental demonstration was performed on a thin film longitudinal disk medium recorded with a thin film head. The track width was $W = 4.5 \mu\text{m}$ and adjacent transition separation was $B = 2.5 \mu\text{m}$. The point source was created by using the same thin film head used in the recording to dc erase the recorded isolated transitions from both sides of the track. For analysis on the effect of finite size point charge, the residual track width, i.e., the width of the point

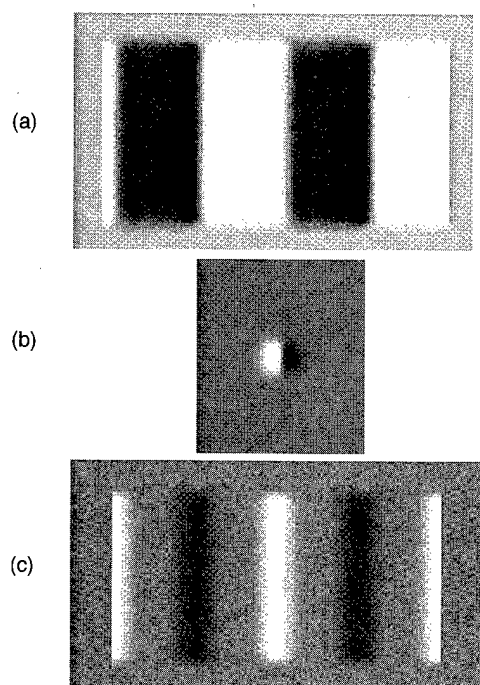


FIG. 4. Calculated images with tip magnetization canted 10° with respect to horizontal. (a) Transitions, (b) point source, (c) deconvolved image.

charge, has been varied. The MFM tip has a magnetic coating thickness of 40 nm. The lift height of the tip during imaging was 60 nm.

Figure 5(a) shows the raw image of the recorded transitions with a vertically magnetized tip. Approximated point charges with various widths were used for image deconvolution. Figures 5(b), 5(c), and 5(d) show the deconvolved images for point charges of image widths 0.3, 0.46, and $0.55 \mu\text{m}$.

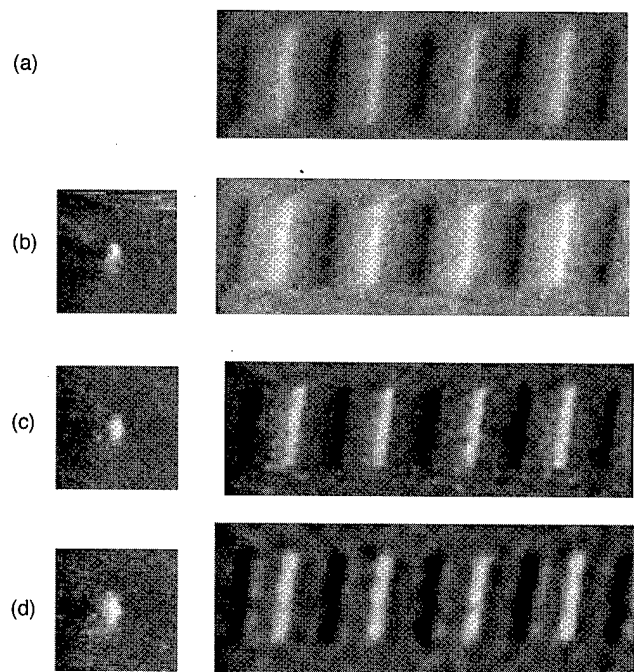


FIG. 5. MFM images with tip magnetized vertically (a) raw image (b)–(d): deconvolved images with different size point charges; (b) $0.30 \mu\text{m}$, (c) $0.46 \mu\text{m}$, (d) $0.55 \mu\text{m}$.

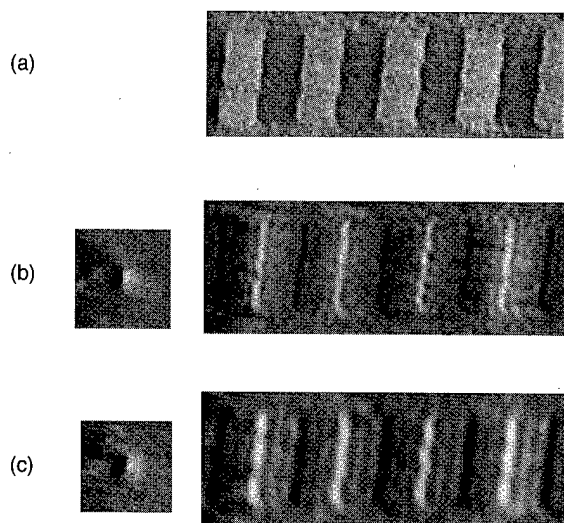


FIG. 6. MFM images with tip magnetized horizontally (a) raw image (b), (c): deconvolved images with different size point charges, (b) $0.30 \mu\text{m}$, (c) $0.55 \mu\text{m}$.

μm , respectively. For the case with the narrowest point charge, the resolution of the features in the deconvolved image is very similar to that in the raw image. Clearly, the wider the point charge width, the broader the feature size in the deconvolved images.

The same recorded transitions were imaged with the tip magnetized horizontally. The raw image is shown in Fig. 6(a). The deconvolved images with two different point charges of widths 0.3 and $0.55 \mu\text{m}$ (image widths), are shown as Figs. 5(b) and 5(c), respectively. The effect of finite size of the point charge is also evident.

V. SUMMARY AND REMARKS

We have experimentally demonstrated the deconvolution technique for removing tip dependence in MFM images and restoring the raw MFM image to the magnetic pole density distribution. By creating a point source on the same sample imaged, the impulse response function of the sensing tip can be obtained at the same imaging conditions. The technique does require that the magnetization of the tip is rigid during imaging. If the size of the point source is greater than the tip resolution, the resolution of the deconvolved pole density distribution will be degraded.

Since the MFM only senses the stray field from a magnetized sample, the formula by Madabhushi *et al.*⁵ is not valid. The divergence free portion of the magnetization M could not be recovered by MFM technique. Only the charge distribution can be imaged.

¹R. P. Ferrier, S. McVitie, A. Gallagher, and W. Nicholson, *IEEE Trans. Magn.* **33**, 4064 (1997).

²G. P. Heydon, A. N. Farley, S. R. Hoon, M. S. Valera, and S. L. Tomlinson, *IEEE Trans. Magn.* **33**, 4059 (1997).

³S. L. Tomlinson and A. N. Farley, *J. Appl. Phys.* **81**, 5029 (1997).

⁴T. Chang, M. Lagerquist, J.-G. Zhu, J. Judy, P. Fischer, and S. Chou, *IEEE Trans. Magn.* **28**, 3138 (1992).

⁵R. Madabhushi, R. D. Gomez, E. R. Burke, and I. D. Mayergoyz, *IEEE Trans. Magn.* **32**, 4147 (1996).

Quantification of magnetic force microscopy images using combined electrostatic and magnetostatic imaging

R. D. Gomez,^{a)} A. O. Pak, A. J. Anderson, E. R. Burke, A. J. Leyendecker,
and I. D. Mayergoyz

*Department of Electrical Engineering and Laboratory for Physical Sciences, University of Maryland,
College Park, Maryland 20742*

A method for calibrating the force gradients and probe magnetic moment in phase-contrast magnetic force microscopy (MFM) is introduced. It is based upon the combined electrostatic force microscopy EFM and MFM images of a conducting non magnetic metal strip. The behavior of the phase contrast in EFM is analyzed and modeled as a finite area capacitor. This model is used in conjunction with the imaging data to derive the proportionality constant between the phase and the force gradient. This calibration is further used to relate the measured MFM images with the field gradient from the same conducting strip to derive the effective magnetic moment of the probe. The knowledge of the phase-force gradient proportionality constant and the probe's effective moment is essential to directly quantify field derivatives in MFM images. © 1998 American Institute of Physics. [S0021-8979(98)27711-5]

I. INTRODUCTION

Magnetic force microscopy (MFM) has become a standard diagnostic workhorse in understanding surface magnetism. In its basic implementation, the technique maps an image which is proportional to the local magnetostatic force gradient between a ferromagnetic sample and a magnetic probe. In an ideal case of a magnetic dipole probe, the force F^m is the gradient of the magnetostatic energy, $(\vec{m} \cdot \vec{B})$, and the force gradient can be expressed as,¹

$$\frac{\partial F^m(x,y)}{\partial z} = \sum_{i=1}^3 \mu_0 m_i \cdot \frac{\partial^2 H_i(x,y)}{\partial z^2}. \quad (1)$$

The image depends upon the direction of the probe's magnetic moment, and contains the contribution of the different components of the surface stray field. In practice, it is customary to premagnetize the probe along the surface normal direction, \hat{z} , which makes the contrast proportional to the second derivative of the normal magnetic field component. By using Eq. (1), it is possible to interpret the images and extract the values of some parameters, such as the transition lengths and zigzag deviation of recorded patterns, the width of the domain wall, and the direction of local surface magnetization of ferromagnetic surfaces, as well as other quantities that are dependent only on the spatial coordinates but are independent of the absolute magnitude of the interaction force.² The difficulty in establishing the absolute values of the interaction force arises since the proportionality constant, K_p , between the measured oscillation phase, $\Delta\phi$ and the force gradient,

$$\Delta\phi = K_p \cdot \frac{\partial F_z}{\partial z} \quad (2)$$

is dependent upon the specific mechanical characteristics of the probe and its environment, and is generally unknown. In addition, the probe's effective magnetic moment, \vec{m} appear-

ing in Eq. (1) is also undetermined. Thus, without the knowledge of these two important probe-dependent parameters, Eq. (1) and Eq. (2) can only be taken as qualitative descriptions of the imaging contrast.

Several research groups have attempted to calibrate the probe and provide estimates for tip-sample interaction force. Unfortunately, due to space constraints in this article, we refer the reader to the literature. Previous approaches have involved the imaging of a standardized system, such as a metal strip^{3,4} or single-crystal surfaces⁵ or the usage of sophisticated methods to measure the magnetic moment of the probe and compare the acquired data with various models for the probe.^{6,7} There are, however, no methods that prescribe a self-contained calibration procedure of both the probe's mechanical and magnetic characteristics by utilizing only the measurements of the instrument itself. In this work, we propose a straightforward method for estimating K_p and m_z , thereby allowing a direct quantification of the MFM response. The basic concept uses the equivalence of the electrostatic (EFM) and magnetic interactions in generating the force gradients on a conducting metal strip. This was accomplished by imaging a test sample, an 11 μm wide Au metal line on silicon, using EFM and MFM with the same probe.

II. EXPERIMENTAL RESULTS AND DISCUSSION

The relationship between the force gradient and phase in Eq. (2) with constant K_p is valid as long as the scanned probe microscope (SPM) operates in a linear regime, which is tacitly assumed in our analysis. The force, F , could be due to either electrostatic or magnetostatic interactions. To determine K_p , we obtained an EFM image of the test sample by biasing the metal structure at voltage V relative to the probe at ground and examined the dependence of the phase contrast versus bias voltage and height. Note that a regular MFM probe was used for this experiment, since the magnetic coating is also electrically conducting. A typical EFM image is shown in Fig. 1 (right), along with a representative cross sectional profile. The electrostatic forces are purely attractive

^{a)}Electronic mail: rdgomez@eng.umd.edu

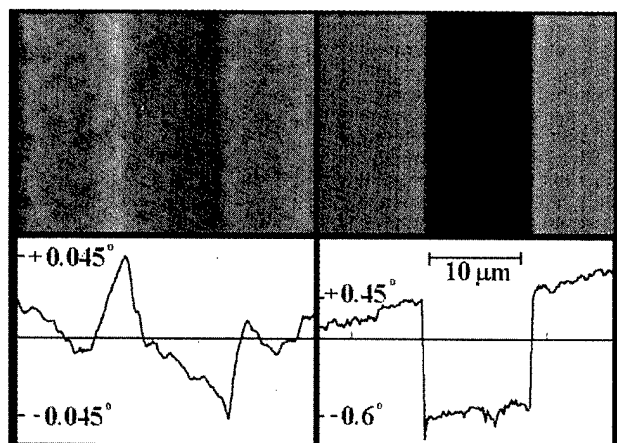


FIG. 1. Right: EFM image of a conducting 11 μm wide metal strip at $V = 2$ V. Left: MFM image of the same strip with 11 mA current. Bottom: Average line profiles across the strip.

so that the EFM contrast appears dark in the regions where the energized metal structure is present. The electrostatic force is a function of the bias voltage, V , as well as its capacitance:

$$F_z^e = -\frac{V^2}{2} \frac{\partial C}{\partial z}, \quad (3)$$

and the force gradient appearing in Eq. (2) can be expressed as

$$\frac{\partial F_z^e(x,y)}{\partial z} = -\frac{V^2}{2} \frac{\partial^2 C(x,y)}{\partial z^2}. \quad (4)$$

Equation (4) shows that the electrostatic force gradients and consequently the EFM images should vary as V^2 and its curvature and spatial variations are dependent only on the capacitance. This is experimentally verified in Fig. 2, which shows the acquired images at different voltages and at a constant height. The contrast has been reversed using software in order to emphasize the changing magnitude of the force gradient. In this experiment, the same area of the sample was continuously scanned at a tip height of 50 nm, as the bias voltage was progressively incremented by 100 mV. The values of the maximum phase contrast in the range from 100 mV to 2 V is shown at the bottom of Fig. 2. The fit to a quadratic function convincingly shows the V^2 dependence. As mentioned previously, all of the spatial variation in the electrostatic contrast is contained in the capacitance term so that the coefficient of the quadratic term in the fit is proportional to the second derivative of the capacitance with respect to z . Furthermore, since there are no dielectric materials in the gap region, the capacitance of the system depends only upon the geometrical arrangement.

To model the capacitance of the system, we considered the dependence of the image on the separation or the lift height, h , between the sample and probe. Figure 3 shows the variation of the image contrast at constant voltage, $V = 1.8$ V, as a function of the height, h . As in Fig. 2, the same region was imaged repeatedly, as the lift height was incremented to the labeled values. The glitch separating each increment is an instrumental artifact and arises due to the finite response time

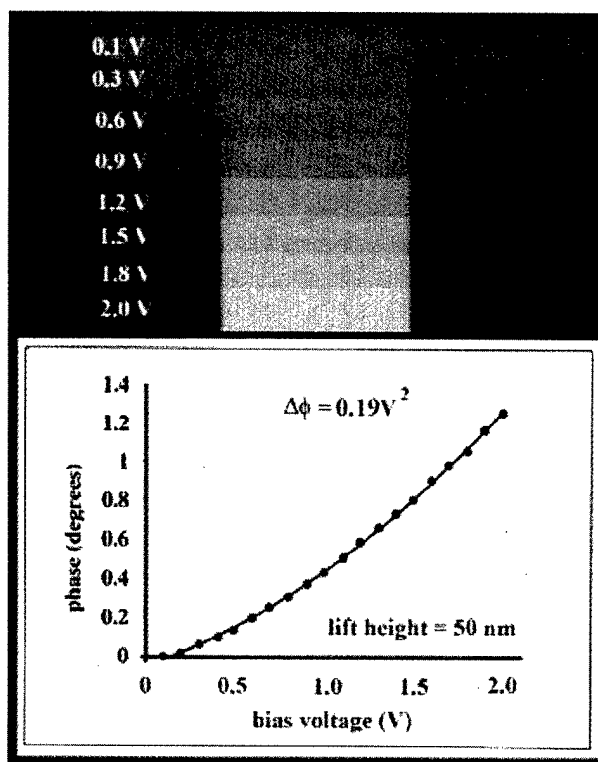


FIG. 2. EFM contrast dependence on bias voltage. Top: EFM image at a lift height of 50 nm with increasing voltage. Bottom: Plot of the maximum contrast as a function of voltage, fitted to a quadratic function $\Delta\phi = 0.19V^2$.

of the feedback system. Nevertheless, the log-log plot of the maximum phase contrast versus h at the bottom of the image clearly shows the strong dependence of the phase image on h . The lines are various power law curves, and the best fit to the data is $\Delta\phi \sim h^{-1.9}$. The nearly h^{-2} dependence suggests that the interaction between the sample and probe can be modeled as a finite area parallel plate capacitor.

III. ANALYSIS

The capacitance for a square parallel plate capacitor can be solved using the Schwarz transformation technique⁸ and the second derivative with respect to the separation distance, h , is given by

$$\frac{\partial^2 C}{\partial h^2} = 2\epsilon_0 A \times \left(\frac{1}{h^3} + \frac{2}{\pi^{3/2} R h^2} \right), \quad (5)$$

where A is the effective surface area and R is the tip radius. In order to relate Eq. (5) with the parameters of the instrument, we assume that the apex of the pyramidal probe can be approximated by a square cross section of width $\sqrt{\pi}R$. The first term in Eq. (5) is identified with an infinite plate capacitor ($R \gg h$), and the second term is due to the fringing effects of the field at the edges. It is clear that as the sample-probe separation, h tends to zero, Eq. (5) is dominated by the first term. However, the relative contribution of the fringe effects increases as $0.36(h/R)$, so that the fringing field contributes about 36% for $R = h$ and significantly more for $h \gg R$. This is precisely the reason why the phase contrast in Fig. 3 follows the h^{-2} power law rather than h^{-3} . Substituting Eq. (5) into

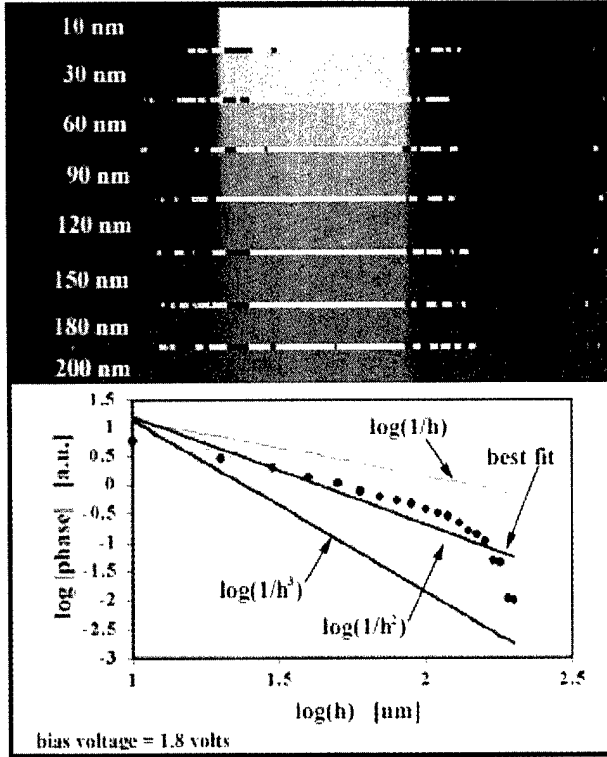


FIG. 3. EFM contrast dependence on lift height. Top: EFM image at a constant bias voltage of 1.8 V at varying lift heights. Bottom: Log-log plot of the maximum contrast as a function of height. Fit corresponds to $\log|\text{phase}| = -1.9 \log(h) + 3.1$; plots for $\log(1/h)$, $\log(1/h^2)$, and $\log(1/h^3)$ are also shown for comparison.

Eq. (4), and using the result into Eq. (2), yields the explicit expression for the calibration for the parameter, K_p .

$$K_p = 2 \left(\frac{|\Delta\phi|}{V^2} \right)_{\text{meas}} \bigg/ 2\epsilon_0 A \times \left(\frac{1}{h^3} + \frac{2}{\pi^{3/2} R h^2} \right), \quad (6)$$

where the numerator is the coefficient of the quadratic term of the data in Fig. 2, and the denominator is calculated directly from the parameters: $R=40$ nm, related to the effective tip curvature, and the lift height, $h=50$ nm. Inserting these numbers into Eq. (6) yields $K_p=369$ degs/Newton/m. Using this derived calibration constant, we can then calculate the effective probe moment along the z direction. In this case, we assume for convenience that the probe is nominally oriented along the z axis, so that only the z component of the surface stray fields contribute to the image. Again, we can make use of Eq. (1) and Eq. (2) to show that

$$m_z = \frac{\partial F^m}{\partial z} \bigg/ \frac{\partial^2 B_z}{\partial z^2} = |\Delta\phi|_{\text{meas}} \bigg/ K_p \frac{\partial^2 B_z}{\partial z^2}. \quad (7)$$

We now image the same current strip at a specific current, and measure the change in phase. A representative image is shown in Fig. 1(left), where the bright and dark contrasts are most pronounced at the edges of the strip as expected for the maximum normal field component. The field from this non-ferromagnetic current strip is well known and the field derivatives in Eq. (7) at a distance of $h=50$ nm and at a current of 11 mA is 5.5×10^{10} T/m². Using this value with the maxi-

mum measured phase of 0.045 degrees in Fig. 1 (left), we obtain the effective moment for the probe, $m_z = 2.22 \times 10^{-15}$ A m² (2.22×10^{-12} emu). This value is consistent with previous estimates,^{4,6} albeit somewhat lower, which could be attributed to differences on the specific probes used. As a plausibility check, we can compute the magnetization of the probe by dividing m_z with effective magnetic volume. If the effective volume is assumed to be that of a half-sphere ($2\pi/3 R^3$) with $R=40$ nm (film thickness at 40 nm as well) then the magnetization is in excess of 18 000 emu/cc, which is much larger than the 400–800 emu/cc remanent magnetization of the CoCr thin film coating. However, as pointed out by previous authors,⁹ the actual magnetic volume can be considerably larger than the volume of the half sphere shell at the apex of tip. In this particular case, if the effective volume were to include magnetic material up to a distance of 200 nm from the apex, then we obtain $M_p = 586$ emu/cc which is closer to the expected saturation magnetization of the CoCr coating.

In conclusion, the value of this calibration method is that the procedure is self-contained, and that all calibrations are derivable from the measurements themselves. It does not necessitate other sophisticated external measurements nor assumptions about the specific mechanical properties of the system. This will save considerable time and effort, and avoid the ever present doubt of whether the externally measured probe characteristics are invariant under actual operation. The procedure outlined in this paper, however, should be considered as an initial step that could be improved considerably. One area for improvement is the replacement of the analytical expression for the finite square area capacitor model with a more accurate numerical calculation involving the actual geometry of the pyramidal apex. This must be accompanied by a deconvolution procedure that takes into account the vertical excursion of the oscillating in the height-dependence measurements. Finally, it should be pointed out that while the calibration procedure here is carried out for phase-detection, a similar procedure can be performed for frequency or amplitude modes of force gradient mapping.

This work was partially supported by NSF MRSEC and ARO Physics Contract No. 36114 PH-RIP. We thank Professor R. Webb for the samples used.

¹P. Grutter, H. J. Mamin, and D. Rugar, in *Scanning Tunneling Microscopy Vol. II*, edited by R. Wiesendanger and H.-J. Guntherodt (Springer, Berlin, 1992), p. 151.

²R. D. Gomez, E. R. Burke, and I. D. Mayergoyz, *J. Appl. Phys.* **79**, 6441 (1996).

³T. Goddenhenrich, H. Lemke, M. Muck, U. Hartmann, and C. Heiden, *Appl. Phys. Lett.* **57**, 2612 (1990).

⁴K. Babcock, V. Elings, J. Shi, D. D. Awschalom, and M. Dugas, *Appl. Phys. Lett.* **69**, 705 (1996).

⁵S. Huo, J. E. Bishop, J. W. Tucker, W. M. Rainforth, and H. A. Davies, *IEEE Trans. Magn.* **33**, 4056 (1997).

⁶G. P. Heydon, A. N. Farley, S. R. Moon, M. S. Valera, and S. L. Tomlinson, *IEEE Trans. Magn.* **33**, 4059 (1997).

⁷R. Proksch, G. D. Skidmore, E. D. Dahlberg, S. Foss, J. J. Schmidt, C. Merton, B. Walsh, and M. Dugas, *Appl. Phys. Lett.* **69**, 2599 (1996).

⁸See, for example, R. S. Elliot, *Electromagnetics* (McGraw-Hill, New York, 1996), p. 180.

⁹K. Babcock, M. Dugas, V. Elings, and S. Loper, *IEEE Trans. Magn.* **30**, 4503 (1994).

Magnetic force microscopy using nonoptical piezoelectric quartz tuning fork detection design with applications to magnetic recording studies

M. Todorovic and S. Schultz^{a)}

Department of Physics and Center for Magnetic Recording Research, University of California, San Diego, La Jolla, California 92093-0401

We have developed a novel form of magnetic force microscopy that uses a commercial piezoelectric quartz tuning fork to detect magnetic forces and force gradients. Such a detection system is extremely simple and inexpensive, compared to conventional optical methods of cantilever vibration detection. The setup is, in addition, characterized by small size, which makes it attractive for studies done in constrained spaces. The instrument is first described, then theoretical comparison of signal to noise ratio and resolution is made with the conventional optical detection techniques of cantilever vibration, and finally, first images of thin film media commercial hard disk magnetic bit transitions, point response of magnetoresistive elements, and field gradients above the write gap of a commercial hard disk head are presented. © 1998 American Institute of Physics.

[S0021-8979(98)28111-4]

I. INTRODUCTION

Magnetic force microscopy (MFM)¹ has become one of the most attractive techniques for studies of microscopic magnetic phenomena, and has found especially wide use in the commercial hard disk industry.² The simplicity of the technique and minimal sample preparation have furthered MFM popularity. In conventional MFM, the magnetic probe vibration is monitored by optical means, the most sensitive being the fiber optic interferometer.³ We have adapted piezoelectric quartz tuning forks (PQTF), first introduced by Karrai and Grober,⁴ as inexpensive and simple, nonoptical excitation and detection devices. The design is similar to the recent reports for near-field optical microscopy distance control,⁴⁻⁶ and dynamic AFM based on PQTF.⁷ We find PQTF are particularly effective for magnetic recording studies when proper modifications are made for detection of magnetic forces and force gradients. In Refs. 4-6, a tapered optical fiber is attached to one leg of the piezoelectric tuning fork, the tuning fork vibrates parallel to the sample surface, and the shear forces between the fiber end and the sample change the resonant properties of the fork. The signal is then mapped with respect to the position over the sample. This technique exploits the high Q of the PQTF, and the simplicity of the nonoptical, small sized, one component design. We have modified this setup by attaching a sharp magnetic tip to the end face of one of the legs of the PQTF, but vibrating in direction perpendicular to the sample, such that magnetic forces and force gradients can be imaged.

II. DESCRIPTION OF THE INSTRUMENT

To obtain maximum sensitivity of the instrument, we used the smallest available quartz tuning forks (Digi-Key Corp., Thief River Falls, Mn). The fork legs are 2 mm long, 200 μm thick, and 100 μm wide. This corresponds to a value of the spring constant, k , of approximately 2000 N/m, which

is an order of magnitude smaller than in previously reported shear force or dynamic AFM instruments. The Q is around 3000 in air and 35 000 in vacuum. To maintain the sensitivity, the magnetic probe is mounted on the end face of one of the tuning fork legs. This serves two purposes: (1) The quality factor, Q , of such a setup remains within a few percent of the initial Q of bare tuning fork, while the resonant frequency is reduced due to the added mass (see Fig. 1); and (2) This probe arrangement does not increase the spring constant of the tuning fork, thus keeping the sensitivity at a maximum. In a shear force microscope, due to specific probe characteristics, the fiber attachment usually reduces the Q from 7000 to 1000 and increases the spring constant, k , due to additional stiffness of the glue. Both of these changes reduce the sensitivity of the instrument.

In our tuning fork MFM, the magnetic probe is a sharp electrochemically etched nickel wire. Such probes are sometimes used in MFM work after being mounted on a piezoelectric bimorph and bent with a pair of sharp razors.⁸ In this new method, there is no need for bending the tip, which is often the hardest part of making such probes. The probe is

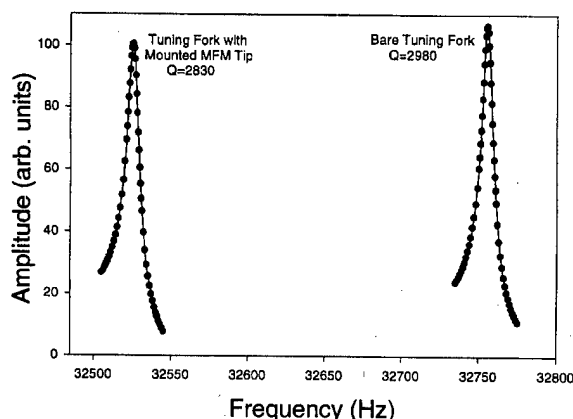


FIG. 1. Resonance curves for piezoelectric quartz tuning fork in air with and without mounted magnetic probe.

^{a)}Electronic mail: sschultz@ucsd.edu

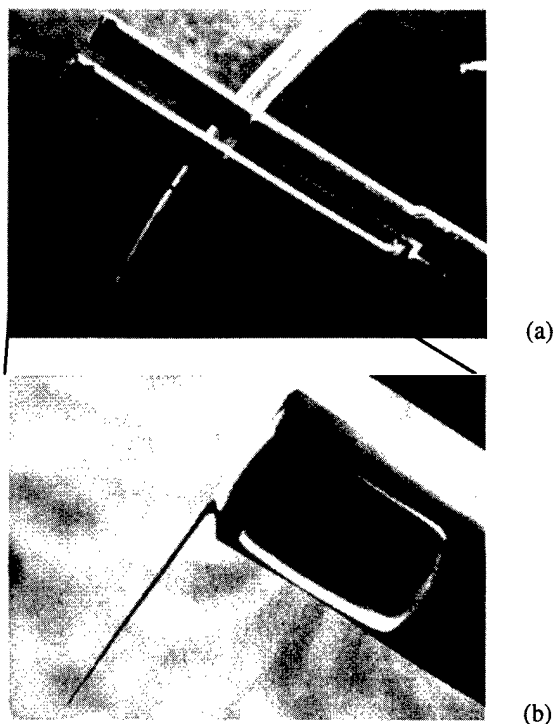


FIG. 2. Scanning electron microscope (SEM) images of (a) tuning fork MFM and (b) nickel probe.

mounted, using micromanipulators under an optical microscope, on the end face of one of the legs of the tuning fork, which is initially covered with a small drop of glue. In addition, a small amount of silver epoxy connects the tip to one of the gold electrodes of the tuning fork in order to avoid electrostatic forces. The probe protrudes 100 to 300 μm from the edge of the tuning fork leg. In this completed form, shown in Fig. 2, the MFM sensor's overall height above the sample surface is less than 1 mm, which makes it very convenient for use in constrained spaces such as vacuum chambers, or under a lens of an optical or scanning electron microscope.

III. SENSITIVITY AND RESOLUTION CONSIDERATIONS

In conventional MFM, the vibration of the cantilever is monitored by optical means, and the signal that is measured is the second derivative of the field in the vibration direction. As the probe is scanned over a surface, the magnetic force gradients change the resonant frequency of the cantilever, and such change is detected in amplitude, phase, or frequency modulation modes, the last one having the largest bandwidth.⁹ The same physical principles apply in the tuning fork MFM design. The tuning fork is driven at the resonant frequency of approximately 32 kHz and magnetic force gradients are detected by monitoring the phase change in the resonant circuit. The sensitivity of the instrument is limited by the thermal noise of the tuning fork oscillator. In such case, previous publications have shown that the minimum detectable force gradient is proportional to¹⁰

$$\sqrt{k/Q\omega}.$$

Since conventional MFM cantilevers and PQTFs operate at similar frequencies, the differences between the two designs lie in spring constants and quality factors of the two respective mechanical oscillators. Regular MFM cantilevers have spring constants between 1 and 10 N/m and Q values of about 100 in air and 1000 in vacuum, while smallest tuning forks have k values of 2000 N/m and Q value of 3000 in air and 35 000 in vacuum.

The resolution of the MFM is determined by the dimensions and magnetic moment value of the probe, as well as the height at which it is scanned. For the highest resolution, minimum height is required, and a trade off is made with the spring constant to avoid tip crashes during the scan.¹¹ These comparisons make the conventional MFM more sensitive by a factor of less than 10, but the tuning fork can be scanned closer to the surface due to the larger spring constant.

IV. RESULTS AND DISCUSSION

Several types of measurements were done to demonstrate the usefulness of the simple design of tuning fork MFM in magnetic recording studies. The commercial hard disk recorded transitions were imaged in air, as shown in Fig. 3. The tuning fork was positioned near the sample surface by a vertical mechanical translator. The fork tines were vibrating at amplitudes between 25 and 50 nm, as confirmed independently by the fiber-optic interferometer³ we use in conventional MFM work. The sample was scanned by a high precision, linearized piezoelectric stage. The image in Fig. 3 was taken in the phase mode and the scan range is 5 μm . As expected, the image shows equivalent resolution to the conventional MFM, since the dimensions of the tip are similar. The signal-to-noise ratio compared to conventional MFM image is lower by an order of magnitude, which is also expected theoretically due to the larger spring constant of the tuning fork.

In addition to imaging magnetic transitions on hard disk media, the tuning fork MFM has also been used for measuring the point response function of commercial magnetoresistive elements,¹² and imaging field gradients above the write gaps of commercial heads.¹ The head was placed on the

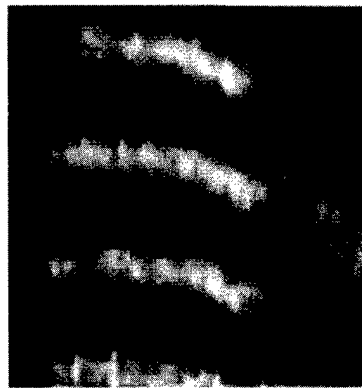


FIG. 3. 5 μm \times 5 μm scan of hard disk magnetic transitions with 2.8- μm -track width.

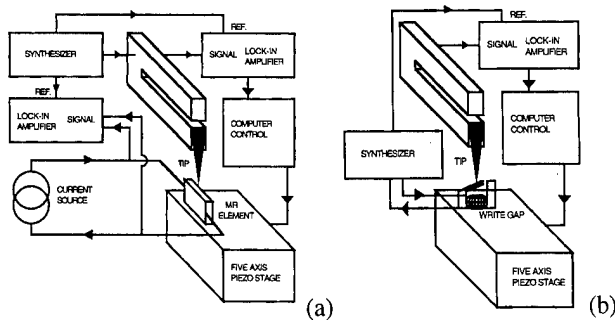


FIG. 4. Block diagrams for (a) MR point response measurement, (b) write gap imaging.

sample holder so that the MR element and write gap face the tip on the tuning fork as shown in Fig. 4. The tuning fork was first driven at resonant frequency while over the MR element, thereby providing a magnetic alternating point flux source. The driving signal to the tuning fork was used as a reference signal for the lock-in amplifier, which monitored the signal from the MR element. Simultaneous with monitoring the ac MR element signal, a second lock-in amplifier monitored the signal from the resonant tuning fork circuit in order to avoid tip crashes during scan. Figure 5 shows the resulting image. The specific features of the MR point response function were repeatable.

Alternatively, the inductive write head was driven at the resonant frequency of the tuning fork, as shown in Fig. 4(b). Alternating field gradients from the gap exerted alternating forces on the tip, and the piezoelectric signal from the tuning fork was monitored with a lock-in amplifier. Figure 6 shows the field gradient gray scale image of the trimmed pole write gap. These techniques provide important information about MR sensor cross track response, field gradients above the gap, and could provide simple and inexpensive diagnosis during fabrication of MR heads.

In conclusion, novel detection technique for magnetic force microscopy is described and applications to magnetic

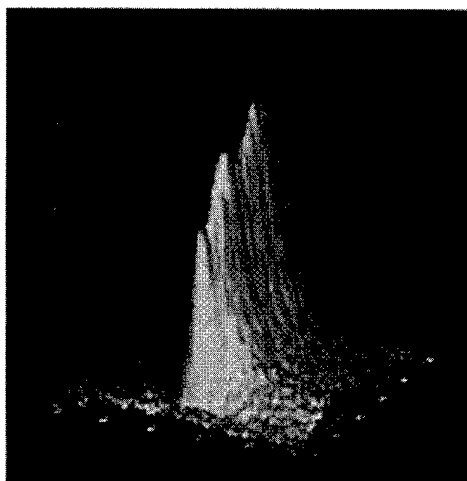


FIG. 5. 4 μm × 4 μm scan of point response function of a MR element.

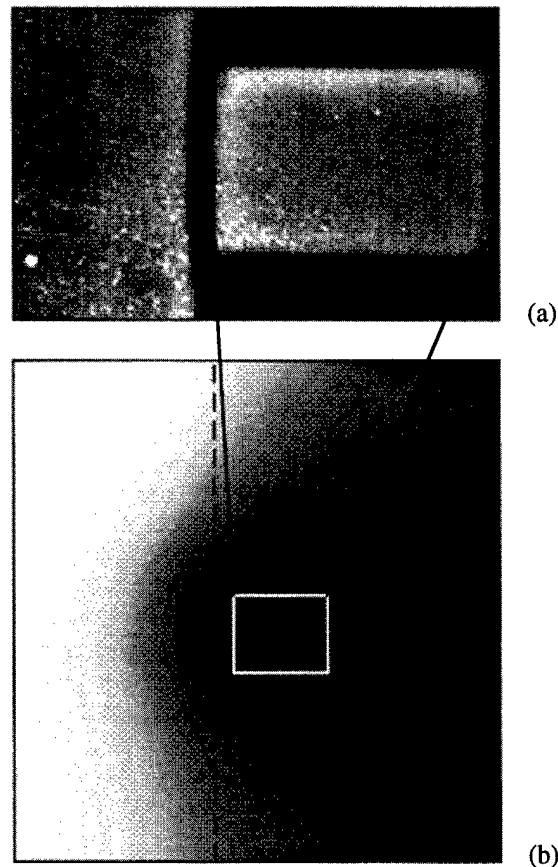


FIG. 6. (a) SEM image of 3-μm-wide write gap of commercial head and (b) 20 μm × 20 μm image of field gradient above the gap.

recording technology are presented. The technique provides an inexpensive, simple, and small sized alternative to conventional MFM.

ACKNOWLEDGMENTS

The authors thank George Kassabian, Sam Hobbs, Ray Descoteaux, and Mark Vojkovich for technical help, and Robert O'Barr and Steven Yamamoto for helpful discussions. This work was supported by the Center for Magnetic Recording Research and NSF-DMR-9400439 (MRSEC) grant.

- ¹Y. Martin and H. K. Wickramasinghe, *Appl. Phys. Lett.* **50**, 20 (1987).
- ²D. Rugar, H. J. Mamin, P. Guethner, S. E. Lambert, J. E. Stern, I. McFadyen, and T. Yogy, *J. Appl. Phys.* **68**, 3 (1990).
- ³D. Rugar, H. J. Mamin, and P. Guethner, *Appl. Phys. Lett.* **55**, 25 (1989).
- ⁴K. Karrai and R. D. Grober, *Appl. Phys. Lett.* **66**, 14 (1995).
- ⁵Y. H. Chuang, C. J. Wang, J. Y. Huang, and C. L. Pan, *Appl. Phys. Lett.* **69**, 22 (1996).
- ⁶W. A. Atia and C. C. Davis, *Appl. Phys. Lett.* **70**, 4 (1997).
- ⁷H. Edwards, L. Taylor, W. Duncan, and A. J. Melmed, *J. Appl. Phys.* **82**, 3 (1997).
- ⁸H. J. Mamin, D. Rugar, J. E. Stern, B. D. Terris, and S. E. Lambert, *Appl. Phys. Lett.* **53**, 1563 (1988).
- ⁹T. R. Albrecht, P. Grutter, D. Horne, and D. Rugar, *J. Appl. Phys.* **69**, 668 (1991).
- ¹⁰Y. Martin, C. C. Williams, and H. K. Wickramasinghe, *J. Appl. Phys.* **61**, 4723 (1987).
- ¹¹H. J. Hug, A. Moser, Th. Jung, O. Fritz, A. Wadas, I. Parashikov, and H. J. Guntherid, *Rev. Sci. Instrum.* **64**, 10 (1993).
- ¹²G. A. Gibson, S. Schultz, T. Carr, and T. Jagielinski, *IEEE Trans. Magn. MAG-28*, 2310 (1992).

Kerr effect enhancement by photon tunneling and possible application to a new scanning probe magnetic microscope

A. Kikitsu^{a)} and C. M. Falco

ARL/Surface Science Division, The University of Arizona, Tucson, Arizona 85721

M. Mansuripur

Optical Sciences Center, The University of Arizona, Tucson, Arizona 85721

Magneto-optical effects are calculated for the film stack consisting of hemisphere glass/magnetic film (10 nm)/air gap (d nm)/glass plate. Polarized light (wave length=800 nm) is irradiated through the hemisphere glass in the total internal reflection configuration. A typical amorphous rare earth-transition metal alloy is used for the magnetic layer. We find a large monotonic change in the figure of merit (product of the reflected amplitude of light and the Kerr rotation angle) as a function of the air gap, ranging from 1 to 800 nm. Similar results are obtained for a magnetic film with a 10 nm SiO₂ protective layer and for a 1-nm-thin magnetic film. This phenomenon is mostly caused by a change in the reflectivity at magnetic film/air interface due to photon tunneling. The difference in the figure of merit between perpendicular and longitudinal magnetization is about 0.6°. These results imply that it might be possible to obtain an image of perpendicular magnetic moment with photon scanning tunnel microscopy (STM). This method can be combined simultaneously with a conventional atomic force microscope or STM. © 1998 American Institute of Physics. [S0021-8979(98)53511-6]

I. INTRODUCTION

In the total internal reflection (TIR) mode, light irradiated from the first medium with refractive index n_1 to the second medium with n_2 ($n_1 > n_2$) is completely reflected at the boundary,¹ and the electromagnetic field in the second medium, which is called an evanescent field, decreases exponentially with the distance from the boundary. However, when a third medium with refractive index n_1 exists close to the first medium, the evanescent wave is converted to a propagating wave at the second boundary. This phenomenon is called photon tunneling.² The photon scanning tunnel microscope (STM)³ utilizes this phenomenon. A scanned fine tip is used as the third medium, and the morphology of the first boundary (distance from the tip) is detected as a change in the intensity of the converted light.

When the incident light is linearly polarized and the first medium is a magnetic film, magneto-optical (MO) effect, that is, a rotation of the polarization angle, will be observed both in the reflected and the converted light and also will be changed with the distance from the tip. This leads to a scanning probe magnetic microscope, which has the advantages of being sensitive to low magnetization materials and having no magnetic interaction between probe and sample. Safarov *et al.* reported such a microscope using a pulsed magnetic field to a Co thin film sample.⁴ However, no static magnetization image was reported. A weak MO signal in the converted light appears to be a problem in this microscope system.

In this article, we calculate MO effects in a hemisphere glass/magnetic film/air gap/glass plate system in the TIR

condition and estimate them from the view point of the figure of merit, which corresponds to the detected intensity. Then we discuss the possibility of a new scanning probe magnetic microscope using the photon tunneling phenomenon.

II. CALCULATION

Numerical calculations were performed by the program MULTILAYER^{TM5} with a configuration shown in Fig. 1. This program solves Maxwell's equations at flat interfaces without any approximations. A linearly polarized light (wave-length 800 nm) irradiated through the hemisphere glass at an angle θ greater than the critical angle. The values of the dielectric tensor of a typical amorphous rare earth-transition metal alloy with perpendicular and longitudinal magnetization were used for the magnetic layer.

III. RESULTS AND DISCUSSION

A change in the figure of merit [(FOM): $E \times \theta_k$, E : amplitude of light, θ_k : Kerr rotation angle] of the reflected light

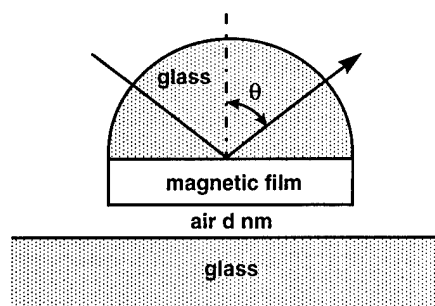


FIG. 1. Configuration used for the calculations.

^{a)}Permanent address: Materials and Devices Research Laboratories, Toshiba Corporation R&D Center, Kawasaki, Kanagawa 210, Japan. Electronic mail: akira.kikitsu@toshiba.co.jp

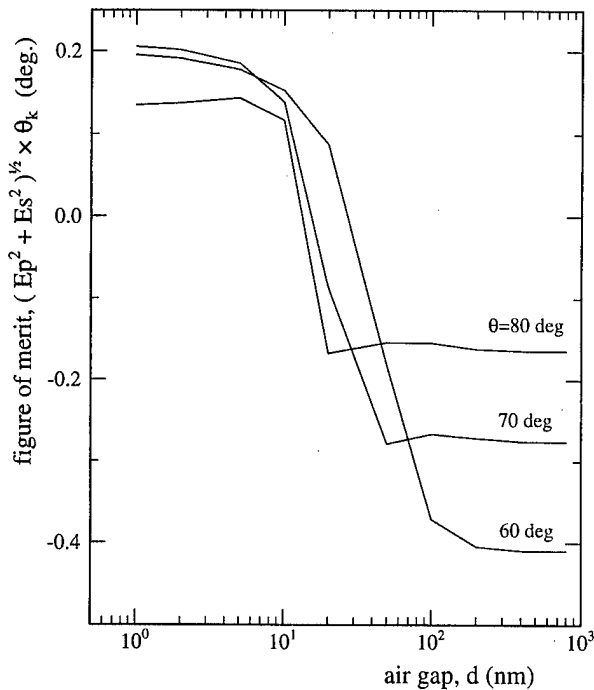


FIG. 2. Figure of merit (=amplitude $\times\theta_k$) of the reflected light vs the air gap for glass/MO material (10 nm)/air (d nm)/glass plate. P -polarized incident light and perpendicular magnetization were assumed.

against the air gap d for $\theta=60^\circ$, 70° , and 80° is shown in Fig. 2. The magnetic film is a perpendicular magnetized MO material with thickness of 10 nm. The incident beam has a unit intensity and is p polarized, that is, the direction of the polarization is perpendicular to the film surface. Although a large θ_k , more than 2° , is obtained at a couple of specific conditions, E tends to be small in such cases, so the FOM is small. As can be seen, the FOM increases monotonically with decreasing d . For $\theta=60^\circ$, the change in the FOM is as large as 0.6° , which is larger than the FOM for the case of normal incidence of 0.13° . The result for the longitudinal magnetization is shown in Fig. 3. FOM has rather complex d dependence but the change in the FOM is less than 0.1.

It is clear that the detected MO signal almost corresponds to the perpendicular magnetic moment from the results of Figs. 2 and 3. A difference in the FOM between perpendicular and longitudinal magnetization cases is shown in Fig. 4. When the direction of an analyzer is set to be crossed to that of the polarization for large d case, the signal intensity becomes large with decreasing d . Therefore, it might be possible to utilize this phenomenon for a new scanning probe magnetic microscope by using a fine glass tip instead of the glass plate.

The change in FOM is caused by the change in the reflectivity at magnetic film/air interface according to the extent of photon tunneling. That is, FOM changes from the value of glass/magnetic film/glass configuration ($d=0$) to that of TIR configuration ($d=\infty$). In the calculation of FOM, a contribution of multiple-beam interference within magnetic film and air gap is included. When a fine glass tip is used for the glass plate in Fig. 1, such an interference does not expect to occur. However, FOM change is not thought to decrease so much even when the tip completely scatters the

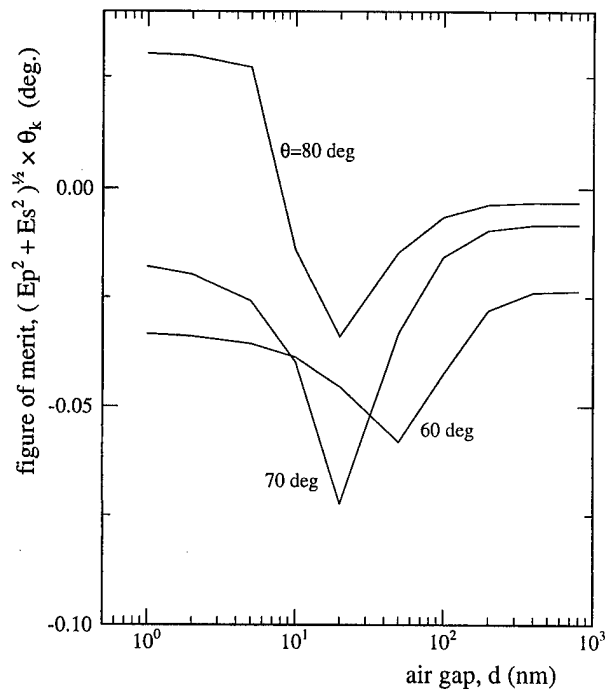


FIG. 3. Figure of merit vs d , for the longitudinal magnetization case.

evanescent wave. FOM from hemisphere glass/magnetic film interface is estimated to be $+0.1^\circ$ and that from magnetic film/glass interface ($d=0$) is estimated to be more than 0.03° for $\theta=60^\circ$. Since FOM for large d value is independent of the occurrence of the scattering, FOM change is expected to be more than 0.57° for $\theta=60^\circ$.

Though a possible problem is that almost all of the detected light comes from the area where the tip is not positioned, this light can be eliminated when the direction of an

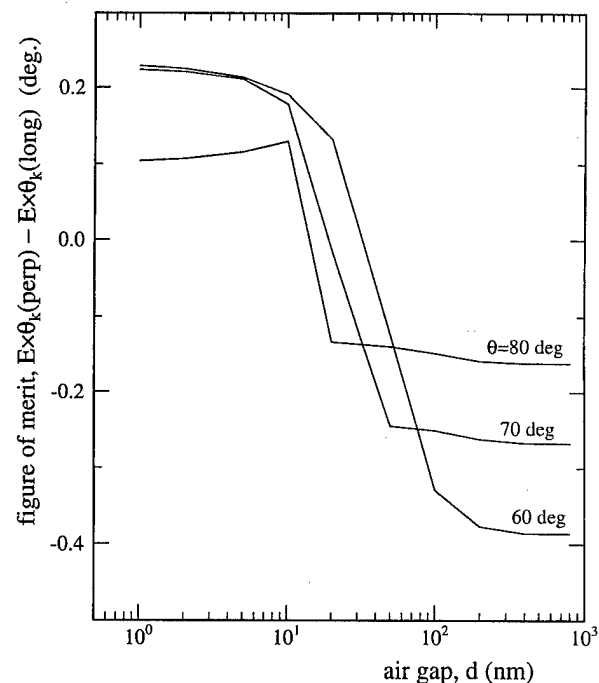


FIG. 4. Difference in FOM between the perpendicular and longitudinal magnetization cases for glass/MO material (10 nm)/air (d nm)/glass.

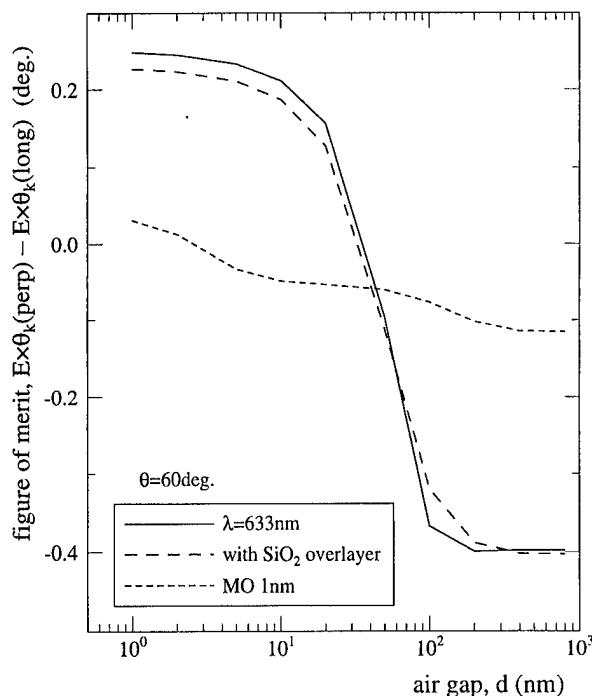


FIG. 5. The difference in FOM between the perpendicular and longitudinal magnetization cases for the case of $\lambda=633$ nm, for magnetic film with 10 nm SiO_2 protective layer and for 1 nm magnetic film. Conditions are p -polarized incident, $\theta=60^\circ$ and perpendicular magnetization.

analyzer is set as mentioned above. As for the case of collecting the evanescent wave, large FOM (about 0.3° at maximum) is obtained but it includes much contribution of the multiple-beam interference in air gap and also this method has a problem of poor coupling efficiency between photon and glass probe. Moreover, our method could employ a couple of signal enhancement method such as an ac method with photoelastic modulation optics⁶ or by vibrating the tip.

Since a tip need not collect the light, a metal tip can be used. A change in FOM with air gap for glass/magnetic film/air/Pt is 0.5° . This means that simultaneous measurement of

magnetization and morphology would be possible by combining our method with a conventional STM or atomic force microscope.

In order to examine the feasibility of this method, MO effects were calculated for various film configurations. Figure 5 shows the results for 633 nm wavelength, for a magnetic film with a 10 nm SiO_2 protective layer and for 1 nm magnetic film. Similar results to that shown in Fig. 4 are obtained. This method is useful for magnetic film with a dielectric overcoat and might have the capability for ultrathin magnetic film.

IV. SUMMARY AND CONCLUSION

A magneto-optical effect for the film stack of hemisphere glass/magnetic film/air gap/glass plate is calculated in the total internal reflection condition. It is found that the figure of merit (FOM) of reflected light changes monotonically as a function of the air gap. This phenomenon is caused by the change in the reflectivity at magnetic film/air interface due to photon tunneling through the air gap. The monotonic air gap dependence of FOM and a FOM difference as large as 0.6° between perpendicular and longitudinal magnetization are found, so it might be possible to apply this phenomenon to a new scanning probe magnetic microscope.

ACKNOWLEDGMENTS

This research was supported in part by US DOE Grant No. DE-FG03-93ER45488.

¹M. Born and E. Wolf, *Principles of Optics*, 6th ed. (Pergamon, Oxford, 1993).

²J. P. Fillard, *Near Field Optics and Nanoscopy* (World Scientific, Singapore, 1996).

³R. C. Reddick, R. J. Warmack, and T. L. Ferrell, *Phys. Rev. B* **39**, 767 (1989).

⁴V. I. Safarov, V. A. Kosobukin, C. Hermann, G. Lampel, C. Marlière, and J. Peretti, *Ultramicroscopy* **57**, 270 (1995).

⁵MULTILAYER™ is a product of MM Research Inc., Tucson, Arizona; also see M. Mansuripur, *J. Appl. Phys.* **67**, 6466 (1990).

⁶K. Sato, *Jpn. J. Appl. Phys., Part 1*, **20**, 2403 (1981).

Design and construction of a sensitive nuclear magnetic resonance force microscope

T. A. Barrett, C. R. Miers, H. A. Sommer, K. Mochizuki, and J. T. Markert^{a)}

Department of Physics, University of Texas, Austin, Texas 78712

We report our progress in the design and construction of a sensitive and versatile nuclear magnetic resonance force microscope. Improvements over previous designs include the use of higher Q ($Q \approx 10^5 - 10^7$), single-crystal double-torsional mechanical oscillators for force detection and the development of extremely convenient positioning and approach capabilities. We describe both a demonstration experiment using large (~ 1 cm) torsional oscillators and the micromachining of the small ($\sim 100 \mu\text{m}$) torsional oscillators. © 1998 American Institute of Physics.

[S0021-8979(98)49711-1]

I. INTRODUCTION

Recently, Rugar *et al.*¹ have reported the force detection of nuclear magnetism. In such an experiment, shown schematically in Fig. 1, the nuclear spins, in a sample mounted on a mechanical oscillator, are first polarized in a large static magnetic field; the z component of the nuclear magnetism is cyclically inverted at the mechanical oscillator resonant frequency by a modulated radio-frequency field from a nearby coil. This time-dependent nuclear moment is coupled to the field gradient of a nearby permanent magnet, producing a resonant force on the mechanical oscillator; the oscillator motion is detected with a fiber-optic interferometer. Here, we first describe the probe that brings these elements together; we then discuss the design sensitivity of this probe. The function of the elements is demonstrated using large single-crystal silicon double-torsional oscillators; finally, the fabrication of the torsional micro-oscillators that will permit the ultimate design sensitivity is discussed.

II. EXPERIMENT

The experimental probe, contained in a vacuum can, fits in a 60-mm-diam variable-temperature cryostat which itself is inserted in the bore of an 8.2 T superconducting magnet. The bottom of the probe is shown in Fig. 2. Rotary motion

from outside the probe drives the three mechanical translators shown, one each for fiber coarse approach positioning, oscillator lateral movement, and permanent magnet positioning. The piezoelectric elements provide finer adjustments: the piezoelectric bimorph swings the fiber optics in and out

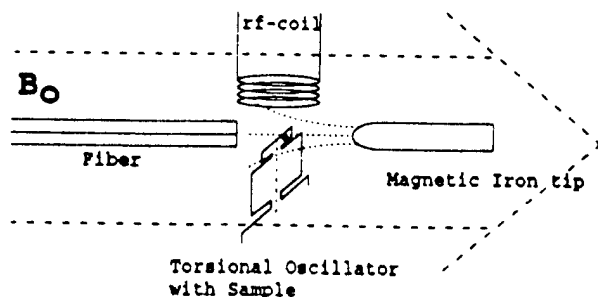


FIG. 1. Experimental setup for the NMR microscope, including static field B_0 , inhomogeneous field magnet, double-torsional oscillator, rf field coil, and fiber-optic interferometer.

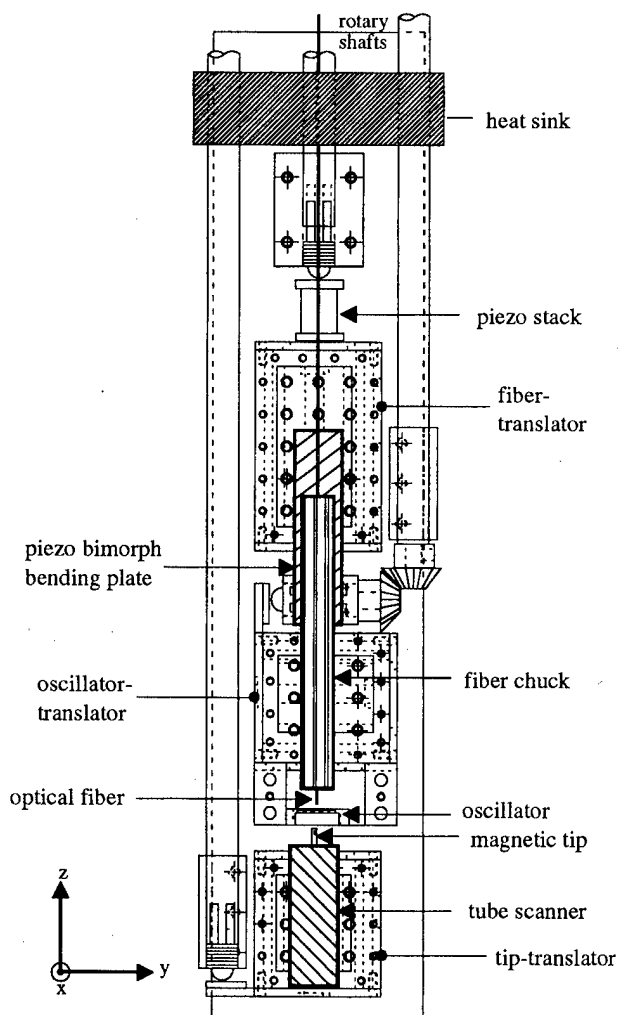


FIG. 2. Probe elements showing manipulation capabilities: three translators for coarse positioning, and piezoelectric bimorph, tube, and stack for fine positioning.

^{a)}Electronic mail: markert@physics.utexas.edu

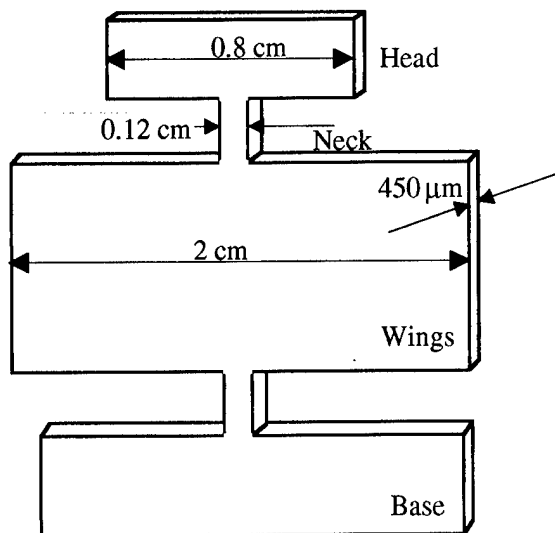


FIG. 3. The single-crystal silicon double-torsional oscillator. In the antisymmetric mode, most of the energy is in the motion of the head.

of the plane of the figure, the stack piezo provides fiber optic fine positioning, and the tube piezo provides fine positioning for the permanent magnet.

Fiber optic interferometers of similar design have been described elsewhere.² Here, a 675 nm laser diode is coupled into one arm of a Gould directional coupler; reflections from the cleaved end of the fiber and from the nearby oscillator interfere and are sensed by a PAR photodiode, the output of which is detected by a lock-in amplifier. For this system, the output current at the photodiode is about 20 pA/Å; the photodiode noise level is less than 0.2 pA/√Hz, thus providing a motion sensitivity of better than 0.01 Å/√Hz.

We refer to Ref. 1 for a discussion of detailed relations between the relevant quantities. Here, we specify the parameters used in our demonstration experiment: the static field was varied (as the permanent magnet approached a paraffin sample at the edge of the oscillator) over the range of 8.50–8.55 T (8.20 T from the superconducting magnet, and 0.30–0.35 T from an iron-wire permanent magnet). An approximately 20 G rf field was turned on 400 kHz off resonance, swept to the NMR frequency of 363.5 MHz over a 0.5 ms period, and then frequency modulated at the oscillator 10.3 kHz frequency with an amplitude of 50 kHz. The static field gradient at the sample was approximately 300 T/m.

For both the demonstration experiment and for the ultimate microscope design, single-crystal double-torsional oscillators are used. To understand why, refer to Fig. 3. Residual losses in single-crystal oscillators occur through coupling to the base; typical cantilever modes have a $Q \approx 10^3$. For a double-torsional oscillator in the antisymmetric mode with a small moment of inertia at the top (the head), most of the energy is stored in the head, effectively isolating its Q . We routinely obtain Q 's of $\sim 10^5$ at room temperature, $\sim 10^6$ at 77 K, and $\sim 10^8$ at 4.2 K. For any mechanical oscillator, the theoretical sensitivity from thermal noise is $F_{\min} = \sqrt{4kk_B T \Delta \nu / Q \omega}$, where ω and k are the frequency and effective spring constant of the oscillator. For our large os-

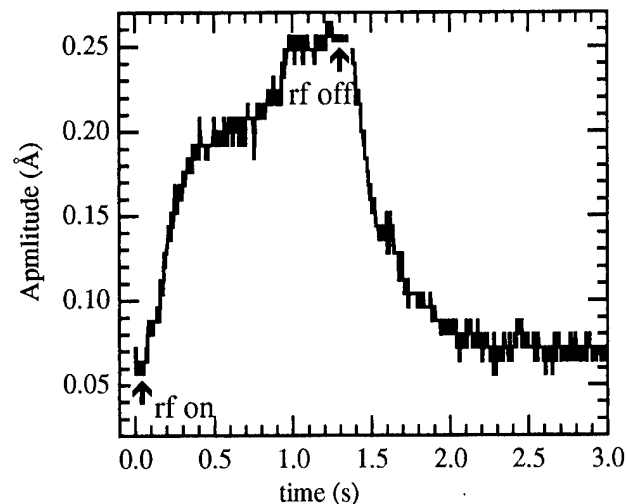


FIG. 4. Amplitude of motion of oscillator head during the NMR experiment described in the text.

cillators at room temperature, the measured parameters indicate $F_{\min} = 3 \times 10^{-13}$ N. However, this produces a motion a factor of five smaller than our photodiode detection limit of 0.01 Å/√Hz; thus the latter sets the noise level. For our small oscillators, we predict $F_{\min} = 2 \times 10^{-18}$ N at 4.2 K; this, however, will result in a motional amplitude of 0.2 Å, well above our photodiode limit; thus for the small oscillators, the noise is thermally limited.

In the one-dimensional experiment using the large oscillators, no signal is observed at the lock-in output when the spins in the sample are far from resonance. As the magnet approaches the sample, there reaches a point where a slice of the spins are resonant, of thickness $\Delta z = \Delta B / (\partial B_z / \partial z)$,¹ where $\Delta B \approx 20$ G is determined by the frequency modulation and the amplitude of the rf field. For our $\partial B_z / \partial z \approx 300$ T/m, we have $\Delta z \approx 7$ μm. Thus for our 2-mm-diam sample, a volume of 0.02 mm³ was resonant, corresponding to 6×10^{17} spins and a moment (via Curie's law) of 6×10^{-14} J/T, and thus a force of $F = M(\partial B_z / \partial z) = 2 \times 10^{-11}$ N, well above our photodiode noise floor. Figure 4 shows a plot of the lock-in output as a function of time for a 1.3 s rf pulse; the oscillator is seen to ring up to an amplitude of approximately 0.25 Å before decaying back to the noise level of approximately 0.01 Å, indicating a force of about 3×10^{-11} N, quite close to the predicted value.

For the small oscillators, the moment sensitivity will be greatly enhanced, both because of the increased force sensitivity and because much larger field gradients can be used (the maximum field gradient simply scales inversely with the diameter of the wire). For example, a 100-μm-diam wire will produce a field gradient of about 10^4 T/m, implying a resolvable moment of 10^{-21} J/T, or about 10^9 proton moments at 4.2 K. Such NMR sensitivity is unprecedented.

III. OSCILLATOR FABRICATION

The oscillators were fabricated by standard photolithographic and micromachining techniques. The large oscillators have been described elsewhere.^{3,4} The small oscillators were fabricated as follows: a silicon wafer was masked with

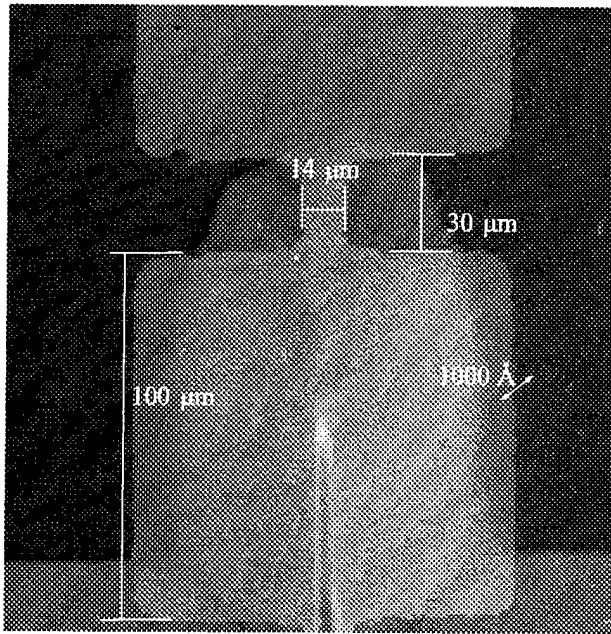


FIG. 5. Scanning electron micrograph of one of the micro-oscillators.

rows of various sizes of micro-oscillators, typically $150\ \mu\text{m}$ high, and implanted with 134 keV boron ions at a dose of at least $1.4 \times 10^{16}/\text{cm}^2$ to provide an etch stop for the final structures. This implant was chosen for a target depth of $4000\ \text{\AA}$ and initial profile thickness of approximately $1000\ \text{\AA}$. The implanted wafers are then annealed at $1000\ ^\circ\text{C}$ for 15

min to 4 h to recrystallize the damaged silicon and spread the profile to any desired thickness up to about $4000\ \text{\AA}$. The annealed wafers were placed in an anisotropic silicon etch consisting of 48% H_2O , 32% ethanol, and 20% KOH for about two days. Once the oscillators were fully undercut from the substrate, a great impediment to completing the fabrication is the drying (surface tension tends to pull the oscillators to the substrate). To overcome this, a freeze-drying technique⁵ was successfully employed, eliminating the surface tension problem completely. Figure 5 shows an scanning electron microscopy (SEM) micrograph of the free-standing single-crystal double-torsional micro-oscillator attached only at the base. Such oscillators are now undergoing characterization and testing for use in the NMR microscope.

ACKNOWLEDGMENTS

This work was supported by the National Science Foundation under Grant No. DMR-9705414, The Welch Foundation under Grant No. F-1191, and the Texas Advanced Technology Program under Project No. 003658-339.

¹D. Rugar, O. Züger, S. Hoen, C. S. Yannoni, H.-M. Vieth, and R. D. Kendrick, *Nature (London)* **264**, 1560 (1994).

²T. R. Albrecht, P. Grütter, D. Rugar, and D. P. E. Smith, *Ultramicroscopy* **42-44**, 1638 (1992).

³A. L. Barr and J. T. Markert, *Phys. Rev. Lett.* **77**, 731 (1996).

⁴G. Kaminsky, *J. Vac. Sci. Technol. B* **3**, 1015 (1985); R. N. Kleiman, G. K. Kaminsky, J. D. Reppy, R. Pindak, and D. J. Bishop, *Rev. Sci. Instrum.* **56**, 2088 (1985).

⁵H. Guckel, J. J. Sniegowski, and T. R. Christenson, *Sens. Actuators* **20**, 117 (1989).

Exchange-spring behavior in epitaxial hard/soft magnetic bilayer films

J. S. Jiang,^{a)} Eric E. Fullerton,^{b)} M. Grimsditch, C. H. Sowers, and S. D. Bader

Materials Science Division, Argonne National Laboratory, Argonne, Illinois 60439

We present results on the magnetic reversal process in epitaxial Sm-Co(1100)/TM (TM=Fe, Co) bilayer films prepared via magnetron sputtering onto Cr-buffered single-crystal MgO substrates. The magnetically hard Sm-Co films have 20 T uniaxial anisotropy and coercivities >3 T at room temperature. The magnetization of the soft layer is pinned at the interface to the hard-magnet layer and switches reversibly as expected for an exchange-spring magnet. With increasing soft layer thickness, the coercive field of the hard layer becomes significantly less than that of a single layer. We also present numerical solutions to a one-dimensional model that provide the spin configuration for each atomic layer. Comparison of the experimental results with the model simulations indicates that the exchange-spring behavior of our bilayer films can be understood from the intrinsic parameters of the hard and soft layers. © 1998 American Institute of Physics.
[S0021-8979(98)42611-2]

The exchange-spring magnets, which are composed of suitably nano-dispersed hard and soft magnetic phases, have been the subject of many recent studies.¹⁻⁸ Exchange interaction between the two magnetic phases results in enhancement of the remanence and the energy-product. Although future application of exchange-spring magnets will most likely be based on nano-dispersed composite geometries,⁸ to obtain greater insights into the coercivity mechanism and magnetization reversal process in these materials, it is advantageous to devise a simpler structure with well-defined properties to isolate the various contributions that are often masked by the structural complexities of a random two-phase system. Theoretical calculations by Skomski and Coey^{6,7} predicted that, in superlattice structures consisting of exchange coupled soft layers and aligned hard-magnet layers, a giant energy-product of 120 MGOe (about three times that of commercially available permanent magnets) is attainable.

It is now possible to fabricate high-quality permanent magnet thin films with well-defined crystallographic orientation and close-to-intrinsic magnetic properties.⁹ For example, epitaxially grown Sm-Co films can have the *c* axis of the hcp structure lying in-plane, giving rise to strong uniaxial in-plane anisotropy.¹⁰ These films, when incorporated into the bilayer structure with transition metal (TM) soft-magnet layers, provide a model system in which the magnetization rotation process of the exchange-coupled TM layers can be studied with the applied field both parallel and perpendicular to the anisotropy axis of the hard layer. In this article we examine the magnetization reversal processes in epitaxial hard/soft Sm-Co(1100)/TM bilayers (TM=Fe and Co). We also use a simple one-dimensional atomic model to simulate

the spin profile and the magnetization hysteresis loops. Comparison of the experimental results with the model simulations indicates that the exchange-spring behavior can be understood from the intrinsic parameters of the hard and soft layers.

The Sm-Co(1100)/TM bilayers are grown via dc magnetron sputtering onto single-crystal MgO(110) substrates coated with an epitaxial 200 Å Cr(211) buffer layer. The 200 Å Sm-Co layers are deposited by co-sputtering from separate Sm and Co sources with a nominally Sm₂Co₇ concentration at a substrate temperature $T_S = 600^\circ\text{C}$ as outlined in Refs. 9 and 10. The TM layers are then grown at $T_S = 300\text{--}400^\circ\text{C}$ with thicknesses of 25–200 Å and capped with a 50 Å Cr layer. The magnetic properties were measured using a 7 T superconducting quantum interference device (SQUID) magnetometer equipped with both longitudinal and transverse coils, and the longitudinal magneto-optic Kerr effect (MOKE) using *p*-polarized, 633 nm light.

The structural and magnetic characterization of Sm-Co(1100) films grown onto Cr(211) buffer layers are described in detail in Ref. 10. The epitaxial relation for the Sm-Co(1100) films is $\text{Sm-Co}[0001] \parallel \text{Cr}[01\bar{1}] \parallel \text{MgO}[001]$, resulting in a uniaxial in-plane structure with the magnetic easy axis parallel to the Sm-Co *c* axis. The films exhibit strong uniaxial in-plane anisotropy consistent with the expected *c*-axis anisotropy. For **H** parallel to the Sm-Co easy axis (MgO[001]), a square loop is observed with a coercive field H_C of 3.4 T. The coercivity increases to 7.3 T at 25 K. For **H** applied in the orthogonal in-plane direction, a sheared hard-axis loop is measured. The anisotropy field, estimated from extrapolating the hard-axis loop to saturation, is ≈ 20 T, close to the known anisotropy value of bulk Sm-Co. These high-quality hard magnetic layers form the basis of this study.

Shown in Fig. 1 are room-temperature easy-axis hysteresis loops of the Sm-Co(200 Å)/Fe bilayers with different

^{a)}Electronic mail: jiang@anl.gov

^{b)}Present address: IBM Almaden Research Center, 650 Harry Rd., San Jose, CA 95120-6099.

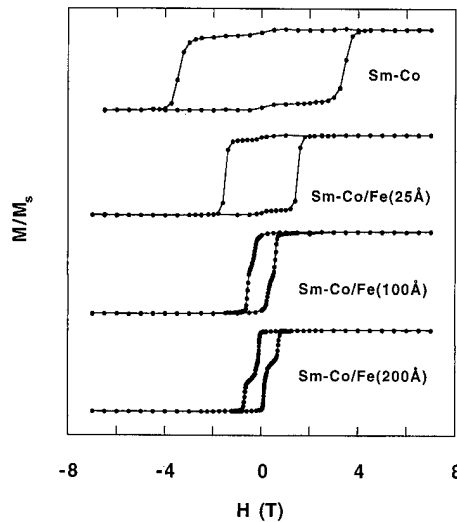


FIG. 1. Room-temperature magnetic hysteresis loops for single layer Sm-Co and Sm-Co/Fe bilayer films with different Fe thickness with H parallel to the easy-axis directions. The loops are offset vertically for clarity.

Fe layer thicknesses. For a 25 Å Fe layer, a square easy-axis loop is measured, indicating that the Fe layer is strongly coupled to the underlying Sm-Co film and that the two layers switch as a unit. As the result of coupling between the layers, the coercivity $H_c = 1.7$ T is only $\sim 50\%$ of that of the isolated Sm-Co film. For the 100 and 200 Å Fe layers the loops change shape quite significantly, and separate switching transitions for the Fe and Sm-Co layers are observed. This is similar to that observed in Refs. 11–14 but with much thinner soft layers in the present samples. The switching fields for the Sm-Co layers (0.6–0.7 T) are similar for the 100 and 200 Å Fe layers and are only 20% of that of the isolated Sm-Co film value. The saturation magnetization M_s increases with increasing Fe layer thickness.

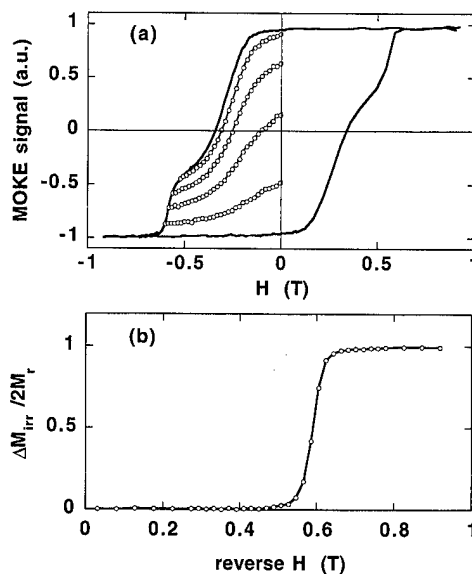


FIG. 2. Room-temperature magnetic properties of Sm-Co/Fe bilayer films measured by MOKE. (a) Hysteresis loop (solid curve) and recoil curves (open circle) measured with H parallel to the easy-axis directions for the 100 Å Fe film. (c) The irreversible magnetization ΔM_{irr} vs reverse field measured with H parallel to the easy axis.

Shown in Fig. 2(a) are the hysteresis loop and recoil curves for the 100 Å Fe layer film measured using the MOKE technique. As a result of the finite penetration of the light, the MOKE measurements are dominated by the top Fe layer. At low reverse fields, the Fe layer is pinned by the underlying Sm-Co layer. The Fe layer starts to switch at the exchange field $H_{ex} = 0.22$ T. Above H_{ex} , a sharp drop in the magnetization occurs as the Fe layer starts to rotate away from alignment with the hard layer. The rotation is fully reversible since the recoil curves coincide with the demagnetization curve. At reverse fields > 0.5 T, the recoil curves deviate from the demagnetization curve as the hard layer begins to switch irreversibly and the Fe does not recover full remanence on recoil. A quantitative assessment of the irreversibility is the irreversible magnetization change $\Delta M_{irr} = M_r - M_d(H)$ where M_r is the remanent magnetization and $M_d(H)$ the field-demagnetization remanence after recoiling from the reversal field H . Shown in Fig. 2(b) is $\Delta M_{irr}/2M_r$ as a function of the reverse field. The magnetization is fully reversible ($\Delta M_{irr} = 0$) up to 0.5 T, where the Sm-Co layer switches and ΔM_{irr} begins to increase sharply.

To obtain greater insight into the switching of both the soft and hard layers, we use a one-dimensional atomic model where the bilayer is treated as a chain of spins normal to the layers and each spin is the sum of total moments in an atomic layer.^{11,13,15} The total energy of the system is given by:

$$E = - \sum_{i=1}^{N-1} \frac{A_{i,i+1}}{d^2} \cos(\theta_i - \theta_{i+1}) - \sum_{i=1}^N K_i \cos^2(\theta_i) - \sum_{i=1}^N H M_i \cos(\theta_i - \theta_H), \quad (1)$$

where the rotation angle for the i th layer θ_i is measured relative to the easy-axis direction of the hard layer, θ_H is the angle between the field and the easy axis, A_i , K_i , M_i , d are the exchange constants, uniaxial anisotropy constants, magnetic moments, and inter-plane distance ($= 2$ Å), respectively. The equilibrium spin configuration for a given field is determined by minimizing Eq. (1). To calculate this configuration we employ an iterative approach outlined by Camley.¹⁶ Details of the modeling will be published elsewhere.¹⁷

Shown in Fig. 3(a) is a comparison of the calculated Sm-Co/Fe(200 Å) demagnetization curves to the ones measured at 25 K. Included are both the longitudinal and transverse magnetization with respect to the applied field. The parameters used in the calculation are, for the hard layer, $A_h = 1.2 \times 10^{-6}$ ergs/cm, $K_h = 5 \times 10^7$ ergs/cm³, $M_h = 550$ emu/cm³; for the soft layer, $A_s = 2.8 \times 10^{-6}$ ergs/cm, $K_s = 10^3$ ergs/cm³, $M_s = 1700$ emu/cm³, the interface exchange constant $A_{int} = 1.8 \times 10^{-6}$ ergs/cm, and $\theta_H = 3^\circ$. The values of K_h and M_h were estimated from magnetization measurements on the Sm-Co films. The calculation reproduces the H_{ex} value, the field dependence of both the longitudinal and transverse magnetization, as well as the switching field of the Sm-Co layer at ≈ 1.5 T. The value of A_{int} , which is intermediate to the exchange coupling of the hard and soft layers, reflects the strong interfacial exchange cou-

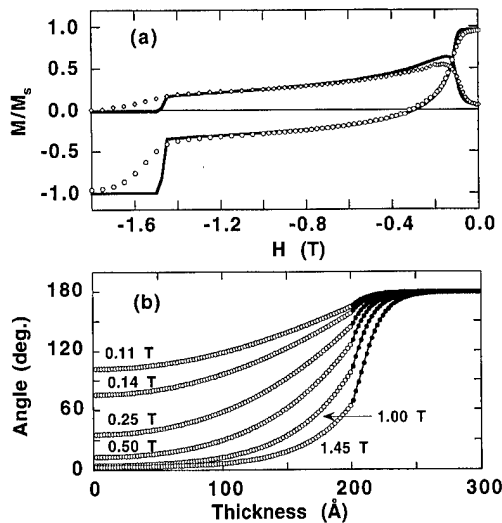


FIG. 3. (a) Low-temperature (25 K) demagnetization curves for the Sm-Co/Fe(200 Å) film compared to the model calculation (solid line). The longitudinal and transverse components of the magnetization are given by the circles and triangles, respectively. (b) Representative spin configuration determined from the model calculation shown in (a). Open circles are Fe spins and filled circles are Sm-Co spins. The free Fe surface is located at zero and the Sm-Co/Fe interface is at 200 Å.

pling between the layers. With a large interfacial exchange energy, the moments in the soft layer near the interface are pinned by the hard layer. Shown in Fig. 3(b) is the spin configuration at various fields for the calculated magnetization in Fig. 3(a). As expected, the distribution of moments is consistent with the expectation that the Fe located away from the interface rotates more. As H increases, the interfacial Sm-Co spin is also increasingly rotated and a domain wall is slowly introduced into the hard layer. At a field such that the domain wall energy density in the soft layer becomes greater than that in the hard layer, the domain wall in the soft layer moves into, and switches, the hard layer.¹

The temperature dependence of the Sm-Co(200 Å)/Co(100 Å) bilayer is shown in Fig. 4. At low temperatures, separate switching transitions are observed for the Sm-Co and Co layers at H_{irr} and H_{ex} , respectively. The exchange field for the bilayer structure with Co layers is significantly higher than that with Fe layers of comparable thickness. This behavior arises from the intrinsic magnetic anisotropy of the Co layer. The c -axis Co anisotropy stabilizes the Co layer either parallel or antiparallel to the Sm-Co film and results in an enhanced Co switching field. The Co layer reverses by nucleating a 180°-domain wall. As long as the Sm-Co does not switch, the H_{ex} is given by the requirement that the energy cost (γ) in creating a domain wall be balanced by the gain in Zeeman energy ($HM_s t$), i.e., $H_{ex} = \gamma/M_s t$, where t is the Co layer thickness. A rough estimate gives $H_{ex} \approx 0.7$ T, in reasonable agreement with the experiment. The exchange field H_{ex} remains rather temperature-insensitive whereas the H_{irr} decreases with increasing temperature, suggesting that the hard layer switches via some thermally assisted reverse domain nucleation and wall de-pinning. At temperatures above 250 K, square easy-axis loops are observed as the Sm-Co and Co layers switch simultaneously a nucleation field H_N .

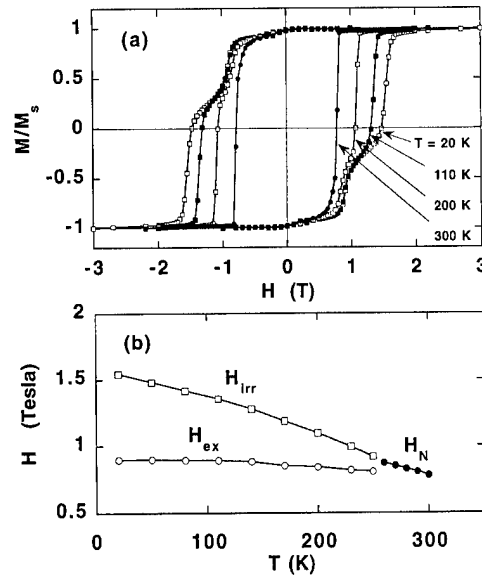


FIG. 4. (a) Easy-axis hysteresis loops for the Sm-Co(200 Å)/Co(100 Å) measured at different temperatures. (b) The switching fields plotted as a function of temperature.

In conclusion, we have presented the experimental results on strongly exchange-coupled Sm-Co(1100)/TM bilayer films. The magnetically hard Sm-Co layers have an in-plane uniaxial anisotropy field as large as 20 T. The magnetization of the soft TM layer is pinned at the interface to the hard-magnet layer and switches reversibly as expected for an exchange-spring magnet. Our model calculation using intrinsic parameters gives quantitative agreement with the experimental data.

This work was supported by the U.S. Department of Energy, Basic Energy Sciences-Materials Science, under Contract No. W-31-109-ENG-38.

- ¹E. F. Kneller and R. Hawig, IEEE Trans. Magn. **27**, 3588 (1991).
- ²J. Ding, P. G. McCormick, and R. Street, J. Magn. Magn. Mater. **124**, L1 (1993).
- ³L. Withanawasam, G. C. Hadjipanayis, and R. F. Krause, J. Appl. Phys. **75**, 6646 (1994).
- ⁴I. A. Al-Omari and D. J. Sellmyer, Phys. Rev. B **52**, 3441 (1995).
- ⁵T. Schrefl, H. F. Schmidts, J. Fidler, and H. Kronmüller, IEEE Trans. Magn. **29**, 2878 (1993).
- ⁶R. Skomski and J. M. D. Coey, Phys. Rev. B **48**, 15 812 (1993).
- ⁷R. Skomski, J. Appl. Phys. **76**, 7059 (1994).
- ⁸J. M. D. Coey, Solid State Commun. **102**, 101 (1997).
- ⁹E. E. Fullerton, C. H. Sowers, J. Pearson, S. D. Bader, X. Z. Wu, and D. Lederman, Appl. Phys. Lett. **69**, 2438 (1996).
- ¹⁰E. E. Fullerton, J. S. Jiang, C. Rehm, C. H. Sowers, S. D. Bader, J. B. Patel, and X. Z. Wu, Appl. Phys. Lett. **71**, 1579 (1997).
- ¹¹K. Mibu, T. Nagahama, and T. Shinjo, J. Magn. Magn. Mater. **163**, 75 (1996).
- ¹²D. Givord, J. Betz, K. Mackay, J. C. Toussaint, J. Voiron, and S. Wüchner, J. Magn. Magn. Mater. **159**, 71 (1996).
- ¹³S. Wüchner, J. C. Toussaint, and J. Voiron, Phys. Rev. B **55**, 11 576 (1997).
- ¹⁴Y. Suzuki, R. B. van Dover, E. M. Gyorgy, J. M. Phillips, and R. J. Felder, Phys. Rev. B **53**, 14 016 (1996).
- ¹⁵E. Goto, N. Hayashi, T. Miyashita, and K. Nakagawa, J. Appl. Phys. **36**, 2951 (1965).
- ¹⁶R. E. Camley, Phys. Rev. B **35**, 3608 (1987).
- ¹⁷E. E. Fullerton, J. S. Jiang, M. Grimsditch, C. H. Sowers, and S. D. Bader, Phys. Rev. B (submitted).

Magnetization reversal of Nd(Dy)–Fe–B thin films on Si(111) or Ta/Si(111)

J. L. Tsai, T. S. Chin,^{a)} and E. Y. Huang

Department of Materials Science & Engineering, Tsing Hua University, Hsinchu 300, Taiwan, Republic of China

S. K. Chen

Department of Materials Science, Feng Chia University, Taichung 407, Taiwan, Republic of China

Nd(Dy)–Fe–B films were prepared by dc magnetron sputtering on a Si(111) wafer with or without a Ta underlayer. The reversal magnetization process of Nd–Fe–B/Ta bilayer was found to be dominated by nucleation control model with the magnetic inhomogeneity coefficient $\alpha_k=0.32$ defined by Kronmuller's formulation of micromagnetic theory. But the coercivity mechanism of Nd(Dy)–Fe–B single layer was fitted well to domain wall pinning behavior. The range factor (half width between pinning sites) r_0 is equal to 6.9 nm as $r_0 > \delta_B$, the width of the domain wall. The magnetization phenomena of the two films are also manifest from initial magnetization curves.

© 1998 American Institute of Physics. [S0021-8979(98)42711-7]

I. INTRODUCTION

Nd–Fe–B films have been prepared by thin film processes such as magnetron sputtering, molecular beam epitaxy, and pulsed laser deposition.^{1–4} These films have potential applications in microelectronics or the micro-electromechanical system (MEMS) due to the high energy product possible even down to a nanometer scale. The magnetic properties depend mainly on microstructure, thus the growth technologies, texture control, and microstructure studies of Nd–Fe–B films have attracted much attention.^{5–11}

Magnetization reversal of Nd₁₅Fe₇₇B₈ sintered magnets and Nd–Fe–B melt spun ribbons has been studied in detail by Kronmuller using the micromagnetic model,^{12–14} and by Hadjipanayis using the Gaunt model,¹⁵ respectively. But that of Nd–Fe–B thin films has not been studied in-depth so far due mainly to the difficulty in structure control and the interface problems.

In this article we applied Kronmuller's formulation to study the coercive mechanism of the sputtered Nd(Dy)–Fe–B films with or without the Ta underlayer, which has been reported to exhibit exchange interaction between the interface.¹⁶

II. EXPERIMENT

Nd(Dy)–Fe–B films, with a thickness of 324 nm, with or without a Ta underlayer (30 nm) were prepared by dc magnetron sputtering carried out in a vacuum chamber with a background pressure of 5×10^{-7} Torr. A commercial Nd₁₂Dy₃Fe₇₇B₈ target and a pure Ta foil, with a diameter of 3.3 cm each, were used. The distance between the target and the substrate was 10 cm. High purity argon (99.999%) was used as a sputtering gas and the working pressure was 8×10^{-3} Torr during sputtering. The Nd(Dy)–Fe–B films were deposited at room temperature and post annealed in a high vacuum (1×10^{-7} Torr) with a temperature between 480 and 600 °C. The phases of films were analyzed by x-ray

diffraction (XRD). The thickness of each film was measured using an α -step thickness probe. The surface roughness of the films was measured with an atomic force microscope (AFM). The initial magnetization curves and magnetic hysteresis loops with different applied fields were measured with a vibrating sample magnetometer (VSM) at room temperature. The magnetic properties of the films were also measured at 5–400 K by a superconducting quantum interference device (SQUID) magnetometer under a maximum field of 55 kOe.

The coercive mechanism was studied by using the modified Brown's micromagnetic theory.¹²

III. RESULTS AND DISCUSSION

A. Microstructure study

Figure 1 shows the x-ray diffraction patterns of Nd(Dy)–Fe–B films with or without Ta underlayer. All peaks are attributed to R₂Fe₁₄B single phase (refer to JCPDS file 39-0473, where R is the rare-earths) for both the (Nd,Dy)₂Fe₁₄B single layer and the (Nd,Dy)₂Fe₁₄B/Ta bilayer. The Ta diffraction cannot be found because of its extreme thinness, about 30 nm. The (Nd,Dy)₂Fe₁₄B peaks are rough and broadened due to the fine grain structure resulting from the lower annealing temperatures at 480–520 °C for 10 min.

To make a quantitative surface morphology, the root mean square surface roughness was taken by an AFM to be 4.8 and 8.9 nm, respectively, for the films with or without Ta underlayer. Samples with roughness below 10 nm appear to have a mirrorlike smoothness which is good for application in lithography.

B. Initial magnetization curves

Figure 2 shows magnetic hysteresis loops of films with or without the Ta underlayer measured parallel to the film plane. The coercive force of the (Nd,Dy)₂Fe₁₄B single layer and the (Nd,Dy)₂Fe₁₄B/Ta bilayer are 14.0 and 11.3 kOe, respectively, while the squareness ratio of the bilayer, 0.72, is higher than that of the single layer, 0.62. The shape of

^{a)}Electronic mail: tschin@mse.nthu.edu.tw

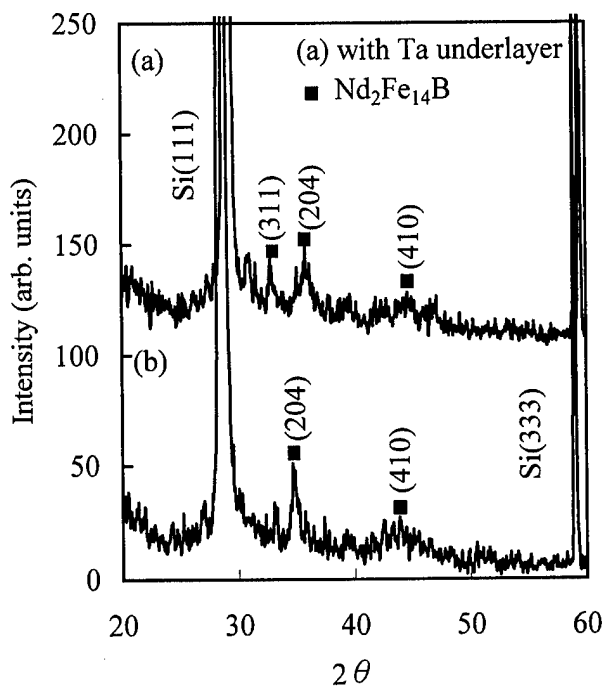


FIG. 1. X-ray diffraction patterns of sputtered (Nd,Dy)₂Fe₁₄B films on Si(III).

hysteresis loops changes as the magnetization field is increased. Initial magnetization curves of the (Nd,Dy)₂Fe₁₄B film with or without the Ta underlayer exhibit two different magnetization reversal processes; that of (Nd,Dy)₂Fe₁₄B/Si(111) film, sustaining nearly the same width before a sharp ascent, is dominated by the domain-wall pinning,¹⁷ while that of the bilayer shows neither a nucleation nor a wall-pinning control process, as shown in Fig. 2(a). Thus further testimony was carried out by the micromagnetics approach.

C. Testimony of the magnetization reversal model

According to the well-known micromagnetic approach, the relationship between coercivity (H_c) and the ideal nucleation field (H_n) is given by Brown's formula¹⁸

$$H_c = \alpha H_n - N_{\text{eff}} M_s. \quad (1)$$

Here α is a form factor and H_n equals $2K_1/M_s$, corresponding to the ratio between the first anisotropy constant and spontaneous magnetization, respectively. N_{eff} means effective local demagnetization factor. A modified relationship about form factor α has been derived from the micromagnetics theory by Kronmüller,^{13,14,19} describing the reduction in nucleation field due to (1) the misalignment of grains α_φ ; and (2) the magnetic inhomogeneity coefficient α_k i.e., $\alpha = \alpha_\varphi \alpha_k$

$$H_c = 2K_1 \alpha_\varphi \alpha_k / M_s - N_{\text{eff}} M_s. \quad (2)$$

For the studied Nd₁₂Dy₃Fe₇₇B₈ films, the R₂Fe₁₄B hard magnetic phase possesses K_1 values from negative to positive in the temperature range 5–400 K. The temperature dependent coercive force of the films could be delineated in two parts:

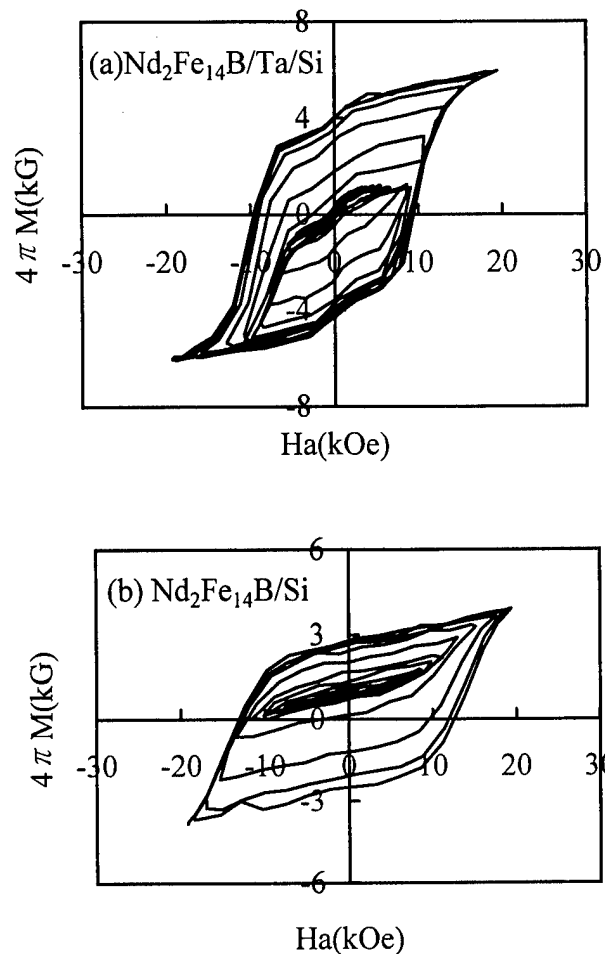


FIG. 2. Hysteresis loops of (Nd,Dy)₂Fe₁₄B films at different applied fields.

one below the spin reorientation temperature ($T_{\text{sr}} \approx 135$ K) and the other above it. Three temperature ranges are distinguishable:²⁰

- (i) In the temperature range of 5–135 K: ($K_1 < 0, K_2 > 0$)

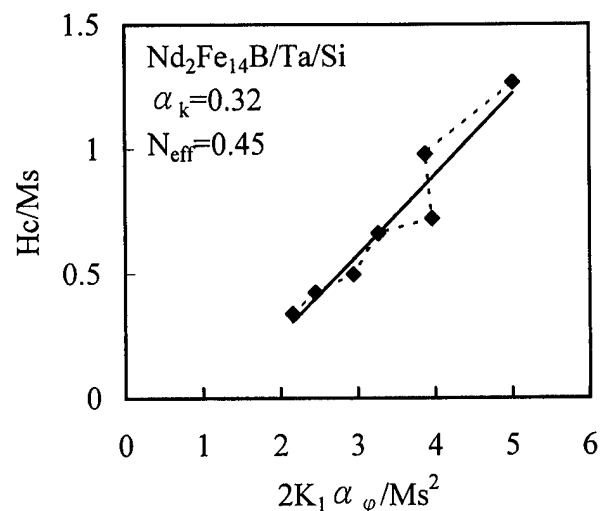


FIG. 3. H_c/M_s vs $2K_1 \alpha_\varphi / M_s^2$ for the sputtered (Nd,Dy)₂Fe₁₄B film with Ta underlayer.

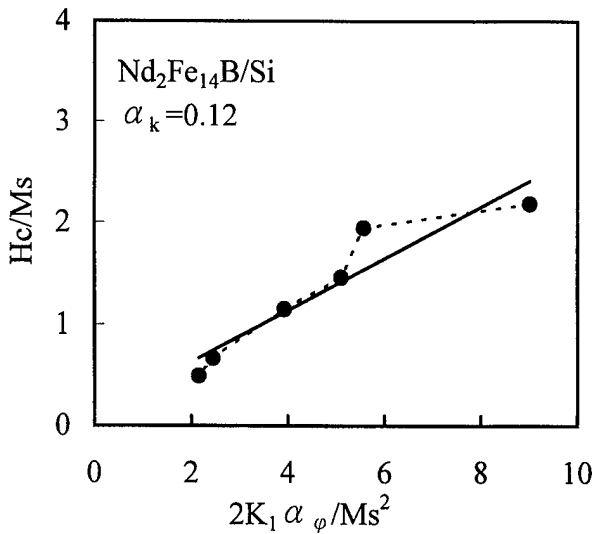


FIG. 4. H_c/M_s vs $2K_1\alpha_\phi/M_s^2$ for the sputtered $(\text{Nd,Dy})_2\text{Fe}_{14}\text{B}$ film without Ta underlayer.

$$H_c = 2K_1\alpha_\phi\alpha_k/M_s - N_{\text{eff}}M_s \quad (2')$$

$$\alpha_\phi = \frac{1}{\cos \delta [1 + (\tan \delta)^{2/3}]^{3/2}} \left(1 + \frac{3K_2(\tan \delta)^{2/3}}{K_1[1 + (\tan \delta)^{2/3}]} \right),$$

where δ is replaced by $\delta = \phi + \theta$ for $K_1 < 0$. Without the external field, the easy magnetization direction deviates from the c axis by an angle $\theta = \arcsin(-K_1/2K_2)^{1/2}$, if spin reorientation occurs for $K_1 < 0$.¹²

In the temperature range of 135–298 K:

$$(K_1 > 0, K_2 > 0, -K_2 < K_1 < 4K_2) \quad (3)$$

$$H_n = \frac{4(K_1 + K_2)}{3M_s} \left(\frac{1}{3} + \frac{K_1}{6K_2} \right)^{1/2}.$$

In the temperature range of 298–400 K:

$$(K_1 \gg K_2, K_2 > 0)$$

$$H_n = 2K_1/M_s \quad (4)$$

$$\alpha_\phi = \frac{1}{\cos \phi [1 + (\tan \phi)^{2/3}]^{3/2}} \left(1 + \frac{3K_2(\tan \phi)^{2/3}}{K_1[1 + (\tan \phi)^{2/3}]} \right),$$

where ϕ is the angle between the c axis of neighboring grains. The α_ϕ is equal to 0.5 for isotropic $\text{Nd}(\text{Dy})\text{-Fe-B}$ thin films.

As indicated in Eqs. (3) and (4), in both case $H_n\alpha_\phi/M_s$ vs H_c/M_s should be fitted in a straight line for a nucleation control magnet. The plot of $H_n\alpha_\phi/M_s$ vs H_c/M_s is shown in Fig. 3. The linearized slope is the value of α_k , which in this case is measured to be 0.32, being larger than the critical value of 0.30. The effective demagnetization field N_{eff} is obtained as 0.45. This means that the coercive mechanism of

$\text{Nd}(\text{Dy})\text{-Fe-B}$ film with the Ta underlayer is dominated by the nucleation control model. By using Eq. (2'), the fitting of H_n/M_s vs H_c/M_s is also a line but with a negative N_{eff} that is out of physical meaning. The data of $\text{Nd}(\text{Dy})\text{-Fe-B}$ film without the Ta underlayer were also fitted by Eqs. (3) and (4).

By measuring magnetic properties of $\text{Nd}(\text{Dy})\text{-Fe-B}$ single layer film from 5 to 400 K, a linear plot of H_c/M_s vs $2K_1\alpha_\phi/M_s^2$ was obtained as shown in Fig. 4. The magnetic inhomogeneity coefficient α_k is measured to be 0.12. This value is less than the critical value of 0.3. Therefore, the magnetization reversal of the $\text{Nd}(\text{Dy})\text{-Fe-B}$ single layer film is determined by domain-wall pinning. A magnet with a thick pinning region of ($r_0 > \delta_B$) should have an α value of ($2\delta_B/3\pi r_0$), where r_0 is a range factor (half-width between pinning sites). The reported data of domain wall width δ_B was equal to 3.9 nm for the $\text{Nd}_{15}\text{Fe}_{77}\text{B}_8$ sintered magnet.²¹ The calculated value of r_0 is 6.9 nm.

ACKNOWLEDGMENT

The authors are grateful for the partial support of this project by the National Science Council of the Republic of China under Grant No. NSC87-2216-E007-043.

- ¹D. J. Keavney, E. E. Fullerton, J. E. Pearson, and S. D. Bader, IEEE Trans. Magn. **32**, 4440 (1996).
- ²B. A. Kapitanov, N. V. Kornilov, Ya. L. Linetsky, and V. Yu. Tsvetkov, J. Magn. Magn. Mater. **127**, 289 (1993).
- ³K. D. Aylesworth, Z. R. Zhao, D. J. Sellmyer, and G. C. Hadjipanayis, J. Magn. Magn. Mater. **82**, 48 (1989).
- ⁴H. Lemke, C. Echer, and G. Thomas, IEEE Trans. Magn. **32**, 4404 (1996).
- ⁵A. J. M. Geurtsen, J. C. S. Kools, L. de Wit, and J. C. Lodder, Appl. Surf. Sci. **96**, 887 (1996).
- ⁶F. J. Cadieu, J. Appl. Phys. **61**, 4105 (1987).
- ⁷S. Parhofer, G. Gieres, J. Wecker, and L. Schulz, J. Magn. Magn. Mater. **163**, 32 (1996).
- ⁸H. Sun, T. Tomida, S. Hirose, and Y. Maehara, J. Magn. Magn. Mater. **164**, 18 (1996).
- ⁹S. Yamashita, J. Yamasaki, M. Ikeda, and N. Iwabuchi, J. Appl. Phys. **70**, 6627 (1991).
- ¹⁰H. Lemke, S. Muller, T. Goddenhenrich, and C. Heiden, Phys. Status Solidi A **150**, 723 (1995).
- ¹¹H. Lemke, T. Lang, T. Goddenhenrich, and C. Heiden, J. Magn. Magn. Mater. **148**, 426 (1995).
- ¹²J. Hu, X. C. Kou, and H. Kronmuller, Phys. Status Solidi B **188**, 807 (1995).
- ¹³J. Hu, X. C. Kou, and H. Kronmuller, Phys. Status Solidi A **138**, K41 (1993).
- ¹⁴J. Hu, H. Gerth, A. Forkl, G. Martinek, X. C. Kou, and H. Kronmuller, Phys. Status Solidi A **137**, 227 (1993).
- ¹⁵G. C. Hadjipanayis, J. Appl. Phys. **63**, 3310 (1988).
- ¹⁶J. L. Tsai, E. Y. Huang, S. K. Chen, and T. S. Chin, IEEE Trans. Magn. **33**, 3646 (1997).
- ¹⁷J. J. Becker, IEEE Trans. Magn. **6**, 965 (1976).
- ¹⁸H. Kronmuller, Phys. Status Solidi B **130**, 197 (1985).
- ¹⁹H. Kronmuller, K. D. Durst, and M. Sagawa, J. Magn. Magn. Mater. **74**, 291 (1988).
- ²⁰X. C. Kou, E. H. C. P. Sinnecker, R. Grossinger, G. Wiesinger, W. Rodewald, and H. Kronmuller, Phys. Rev. B **51**, 16 025 (1995).
- ²¹K. D. Durst, and H. Kronmuller, J. Magn. Magn. Mater. **59**, 86 (1986).

Phase formation and magnetic properties of Co-rare earth magnetic films

Y. Liu

*Center for Materials Research and Analysis, and Department of Mechanical Engineering,
University of Nebraska, Lincoln, Nebraska 68588-0656*

Richard A. Thomas, S. S. Malhotra, Z. S. Shan, S. H. Liou, and D. J. Sellmyer

*Center for Materials Research and Analysis, and Behlen Laboratory of Physics, University of Nebraska,
Lincoln, Nebraska 68588-0111*

Co-Sm and Co-Pr films were deposited by dc magnetron sputtering. Transmission electron microscopy and magnetic measurement were used to study the microstructure and magnetic property relationship. The nanostructure of the as-deposited Co 19 at. % Sm films consists of two phases: the amorphous phase and the crystallite phase. Upon annealing at 600 °C, the Co₅Sm phase with the Cu₅Ca structure, having grain size of about 20 nm, is obtained along with high coercivity (45 kOe). The as-deposited Co 22 at. % Sm films also have nanostructure similar to the Co 19 at. % films except the volume fraction of the crystallite is reduced. This is related to the concentration of Sm which promotes the formation of the amorphous phase. A new metastable phase Co₃Sm is formed upon annealing of the Co 22 at. % Sm film at 500 °C. This phase has the DO₁₉ structure in which the Sm atoms take ordered positions of a triangular pattern in the close-packed planes. A relatively high coercivity value of 29 kOe was obtained from this phase. The as-deposited Co-Pr films show mainly an amorphous phase. Upon annealing at 500 °C for 20 min, Co₂Pr with the Mg₂Cu-type structure was identified in the Co 35 at. % Pr film. Two phases were identified in the Co 16 at. % Pr films. Coercivities up to 3.1 kOe were achieved in these films. © 1998 American Institute of Physics. [S0021-8979(98)30611-8]

I. INTRODUCTION

Hard and semihard Co rare earth films are of increasing interest for magneto-electronic and magnetic-recording applications. The Co-Sm and Co-Pr systems also have high T_c suitable for high temperature magnets. A number of articles on the Co-Sm and Co-Pr systems have been presented.¹⁻⁵ The magnetic properties of materials can be divided into intrinsic properties and extrinsic properties. The intrinsic properties such as magnetization are related to the crystal structure of the magnetic phase while the extrinsic properties such as coercivity are affected by the microstructure. Development of new magnetic materials involves the search for new magnetic phases and the design of microstructure. In this article we report our detailed study on phase formation, microstructure, and magnetic properties relationship in films based on the Co-Sm system and Co-Pr system heat treated at different temperatures.

II. EXPERIMENTAL PROCEDURE

For the Co-Sm system, the films were deposited by dc magnetron sputtering. Two compositions near the Co₅Sm and Co₇Sm₂ were selected. All films have a Cr underlayer of about 90 nm except the one with the composition of Co 19 at. % Sm annealed at 600 °C which is deposited on a quartz substrate. All the films have a Cr cover layer of about 10 nm. For the Co-Pr system multilayers of Co-Pr/Co films were deposited using a multiple-gun dc and rf sputtering chamber. The multilayer microstructure is designed to promote magnetic hard phase and soft phase coupling in order to gain maximum energy product. A 50 nm underlayer and a 10 nm

cover layer of Cr were used for film seeding and protection. Plan-view transmission electron microscopy (TEM) samples were prepared by dimpling and ion milling process. TEM study was conducted using a JEOL 2010 transmission electron microscope.

III. RESULTS AND DISCUSSION

The deposition parameters, film thickness, coercivity, and phase identification results are summarized in Table I.

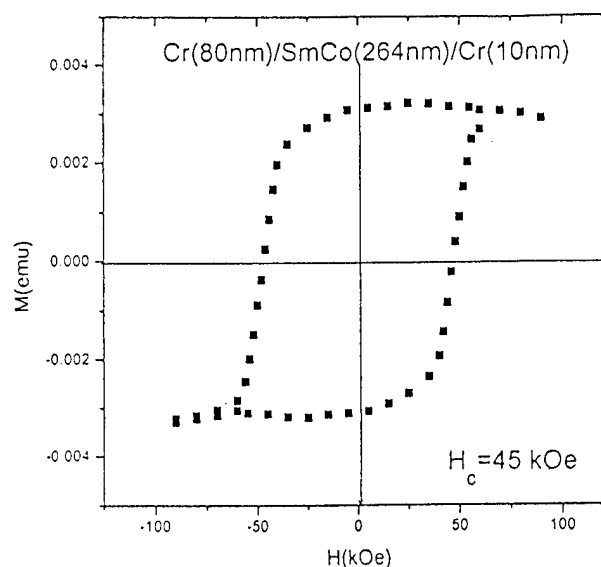


FIG. 1. Magnetization loop of the Co₅Sm film annealed at 600 °C.

TABLE I. Composition, deposition condition, nanostructure, and magnetic properties relation in Co–Sm and Co–Pr films. C indicates crystallite phase and A amorphous phase. Vc is the volume fraction of the crystallite phase against the amorphous phase.

Film com. (at. %)	Ar pressure (mTorr)	Film thickness (nm)	Phases	Vc (%)	Grain size (nm)	Coercivity (kOe)
Co 19 at. % Sm	5	24	C+A	91	5	0.61
Co 19 at. % Sm	12	24	C+A	65	5	2.58
Co 19 at. % Sm	30	24	C+A	54	5	0.92
Co 19 at. % Sm Annealed at 600 °C	20	360	Co ₅ Sm (Cu ₅ Ca)	100	20	45
Co 22 at. % Sm	5	30	C+A	81	5	1.2
Co 22 at. % Sm	17	30	C+A	57	5	4.1
Co 22 at. % Sm	30	30	C+A	48	5	3.4
Co 22 at. % Sm Annealed at 500 °C		394	DO ₁₉	100	15	29

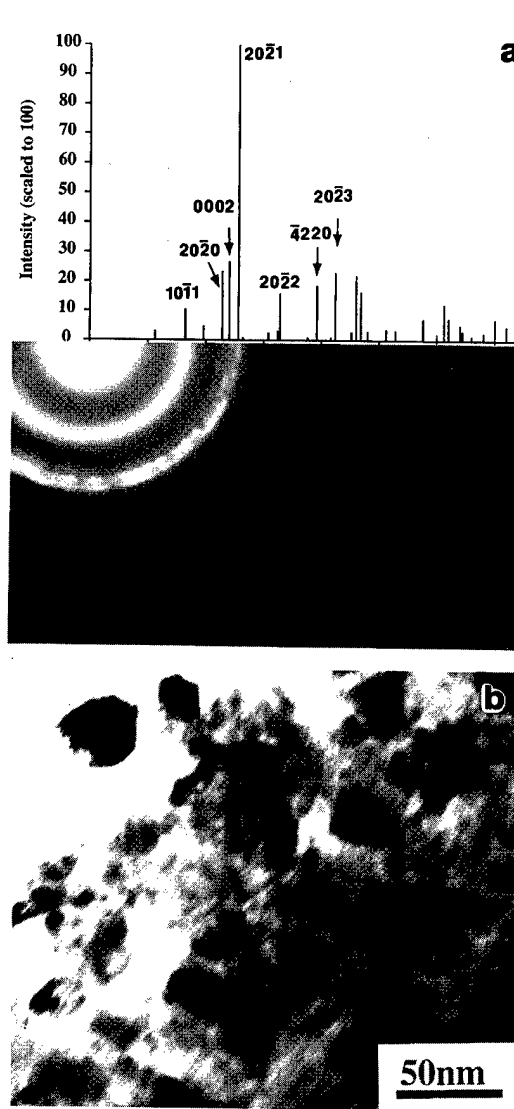
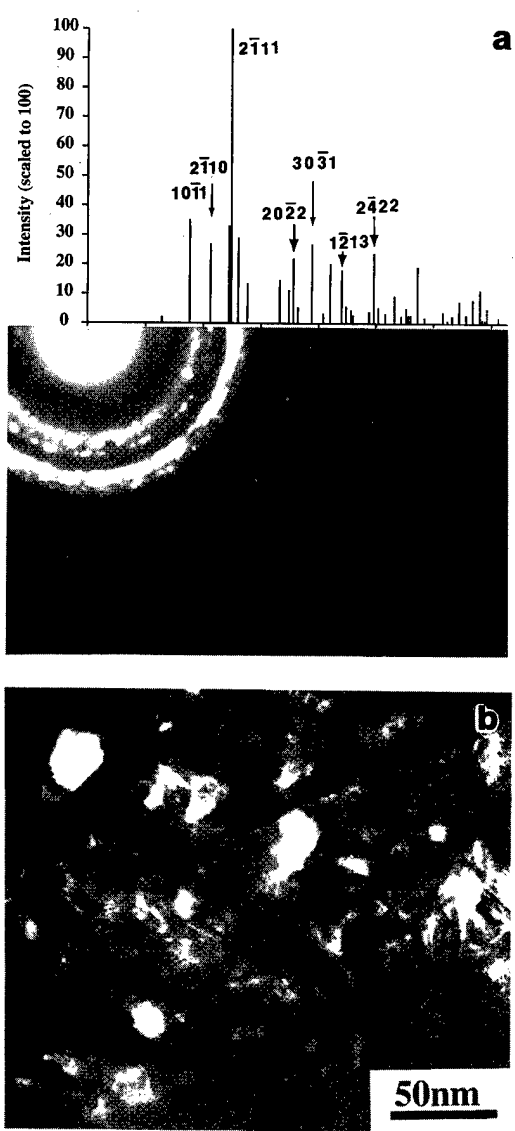


FIG. 2. (a) Comparison of SAD pattern and calculated intensity distribution for the film described in Fig. 1. (b) TEM image of the microstructure.

FIG. 3. (a) Comparison of SAD pattern and calculated intensity distribution for the Co 22 at. % Sm film. (b) TEM image of the microstructure.

The nanostructure of the as-deposited Co 19 at. % Sm films has been studied in earlier work¹ and is included here for comparison. Upon annealing at 600 °C, the equilibrium phase Co₅Sm with the Cu₅Ca structure is obtained along with high coercivity. Figure 1 shows the magnetization loop. Coercivities up to 45 kOe were achieved. Figure 2 shows the selected area diffraction (SAD) pattern and TEM micrograph. The diffraction shows perfect match with the calculated intensity. The grain size is about 20 nm.

The Co 22 at. % Sm films also have a nanostructure similar to the Co 19 at. % films except the volume fraction of the crystalline against amorphous phase is reduced. This is related to the concentration of Sm which promotes the formation of the amorphous phase. Figure 3 shows the SAD pattern and the TEM image of the Co 22 at. % Sm film annealed at 500 °C. A new phase Co₃Sm is formed as indicated by the matching of the TEM pattern and calculation. This phase has the DO₁₉ structure in which the Sm atoms taking the ordering positions of a triangular pattern in the close-packed planes. The close-packed planes are stacked by the sequence of ABAB in the *c* direction. A relatively high coercivity value of 29 kOe was obtained from this phase.

The appearance of the DO₁₉ structure is not a surprise but rather easy to comprehend. In the as-deposited Co–Sm films, the structure of the crystallite is the close-packed structure with Sm atoms randomly distributed in the close-packed planes and short range packing order in the *c* direction. Upon annealing, two things happened: one is that the Sm atoms within each close-packed plane form a triangular ordering pattern, and the second is that the packing in the *c* direction takes the long range ABAB packing. The lattice parameters deduced from this phase are $a=0.256$ nm $c=0.419$ nm compared to the lattice parameters of Co $a=0.2505$ nm, 0.4065 nm. It is interesting to note that the lattice parameters between the DO₁₉ phase and the Co phase are close to each other, suggesting a low energy state at the interphase. It is suggested that two-phase structure composed of Co and DO₁₉ phase could be stable up to 500 °C.

The as-deposited Co–Pr films show largely amorphous phase. Upon annealing at 500 °C for 20 min, Co₂Pr of the Mg₂Cu-type structure was identified in the Co 35 at. % Pr film. Two phases were identified in the Co 16 at. % Pr films. Coercivities up to 3.1 kOe were achieved in these films.

IV. CONCLUSIONS

Three metastable phases were found in the sputtered Co–Sm films: the amorphous phase, the close-packed hexagonal phase with different stacking mode in the as-deposited film, and the DO₁₉ structure phase in the film annealed at 500 °C.

Corresponding to the different phases and microstructure, the coercivities change from about 1–42 kOe. Maximum coercivity was achieved from the Co₅Sm phase with the Cu₅Ca structure. The new metastable phase of DO₁₉ structure found in the Co 22 at. % Sm film also showed relatively high coercivity of 29 kOe.

ACKNOWLEDGMENTS

The authors wish to thank Xueli Zhao for preparing the TEM samples. The TEM work was performed at the Central Facility for Electron Microscopy operated by CMRA. This research is sponsored by the U.S. Department of Energy, Grant No. DE-FG-02-86ER45262, National Science Foundation, Grant No. DMR-9623992, National Storage Industry Consortium, and CMRA. S. H. Liou is supported by the U.S. Army Research Office, Grant No. DAAG55-98-1-0014.

¹Y. Liu, B. W. Robertson, Z. S. Shan, S. Malhotra, M. J. Yu, S. K. Renukunta, S. H. Liou, and D. J. Sellmyer, *IEEE Trans. Magn.* **6**, 4035 (1994).

²Y. Liu, D. J. Sellmyer, B. W. Robertson, Z. S. Shan, and S. H. Liou, *IEEE Trans. Magn.* **31**, 2740 (1995).

³S. S. Malhotra, Y. Liu, Z. S. Shan, S. H. Liou, D. C. Stanford, and D. J. Sellmyer, *J. Magn. Magn. Mater.* **161**, 316 (1996).

⁴E. M. T. Velu and D. N. Lambeth, *IEEE Trans. Magn.* **28**, 3249 (1992).

⁵K. Chen, H. Hegde, S. U. Jen, and F. J. Cadieu, *J. Appl. Phys.* **73**, 5923 (1993).

High coercivity SmCo based films made by pulsed laser deposition

F. J. Cadieu,^{a)} R. Rani, X. R. Qian, and Li Chen

Department of Physics, Queens College of CUNY, Flushing, New York 11367

Films of SmCo based materials exhibiting high intrinsic coercivities and smooth hysteresis loops have been prepared by pulsed laser deposition (PLD) onto moderately heated substrates. Films directly crystallized from SmCo₅ targets onto 375 °C substrates exhibited a maximum $H_c = 11.3$ kOe at a pulse repetition rate of 10 Hz with lower coercivities for both lower and higher pulse repetition rates. In the present case the films were deposited onto polycrystalline substrates. The films exhibited a very small grain size of less than 1 μm diameter, were mirrorlike, and shadow deposited films were relatively particulate free under scanning electron microscope examination. Shadowed PLD deposition was used for the best films. Laser wavelengths of 193 and 248 nm were used with pulse repetition rates from 5 to 50 Hz. Films grown without shadowing exhibited a great deal of particulate contamination. The hysteresis loops of such nonshadowed films were constricted and exhibited drops in the $4\pi M$ values upon demagnetization. To our knowledge this is the first reporting of high coercive force SmCo based films deposited by PLD exhibiting single phase type hysteresis loops. © 1998 American Institute of Physics. [S0021-8979(98)42811-1]

INTRODUCTION

High coercivity films of SmCo based systems have been deposited by sputtering by several distinct variants. Highly textured polycrystalline films have been made by using sputter process control to grow films at thicknesses out to at least 120 μm .¹⁻⁴ Such films have the crystalline c axes nearly randomly aligned onto the substrate plane. Buffer layers are necessary to grow relatively thick films but in principle arbitrarily thick films of highly aligned SmCo deposits can be grown by this method. In contrast to this, highly aligned thin films with thicknesses of less than 0.1 μm have been grown by using substrate film epitaxy.^{5,6} The thicker films as grown by sputter process control are generally more suited to device applications. Such relatively thicker films as grown by sputter process control have been used to bias to saturation YIG substrates,⁴ to bias permalloy films,⁷ and in the construction of a film based magneto-optic waveguide isolator.⁸ In this latter device the textured SmCo films were grown directly onto compliant layers directly deposited onto a Bi-YIG optical waveguide so that epitaxy could not have been used to grow such films. Film scale magnetic devices generally employ a magnetically sensitive material such as a magnetoresistive material, a superconducting film element, or a magnetic field sensitive optical material. In addition soft magnetic films are used as flux paths with permanent magnet films used as magnetic biasing elements. Many of the magnetically sensitive types of materials have been readily deposited by pulsed laser deposition (PLD). Such films include high T_c oxide superconductors, ferrites, and magnetoresistive materials such as the La manganites. It should be noted that these are oxide materials which are generally difficult to sputter deposit with controlled texturing and at appreciable deposition rates. To illustrate the differences in PLD and sputter deposition we have made SmCo based magnetic films by PLD. Although the time averaged deposition rates of

sputter and PLD deposited films are comparable, material is ejected in PLD only during a series of pulses of very short time duration compared to the time between pulses.⁹ This means that the relative mobility of deposited surface atoms is very much less for PLD than for sputtering since a complete monolayer can be deposited per pulse. The growth of PLD deposited permanent magnet films also has direct impact on the fabrication of film scale magnetic devices. There have been only a few reportings of rare earth transition metal films as grown by PLD and mostly confined to Nd₂Fe₁₄B.¹⁰

EXPERIMENT

PLD, utilizing a Lambda Physik 305Fi excimer laser, has been used to deposit SmCo based films from a set of bulk compound targets. Films have been deposited using wavelengths of 248 and 193 nm, pulse energies of 500–650 mJ at 5–50 Hz with an estimated pulse width of 15 ns. A shadow mask has been used to shield part of the substrate during the PLD process. In this manner the magnetic properties, as well as the number of particulates reaching the substrate in and out of the shadow region, could be observed. Most of the films discussed here have been grown using a substrate temperature ranging from 100 to 750 °C in argon pressures from 100 to 240 mTorr. Film compositions were determined using electron excited x-ray analysis in a scanning electron microscope (SEM). The film composition measurements were calibrated against known bulk composition standards.

RESULTS AND DISCUSSION

SmCo based films deposited by PLD in the absence of any shadowing onto heated alumina substrates exhibited a strong dependence of Sm concentration on the argon background gas pressure in the deposition chamber. Figure 1 shows the Sm concentration for a series of films deposited onto polished alumina substrates at 375 °C from SmCo₅ targets, and at 500 °C from SmCo “2–17” targets, as a func-

^{a)}Electronic mail: Fred_Cadieu@QC.EDU

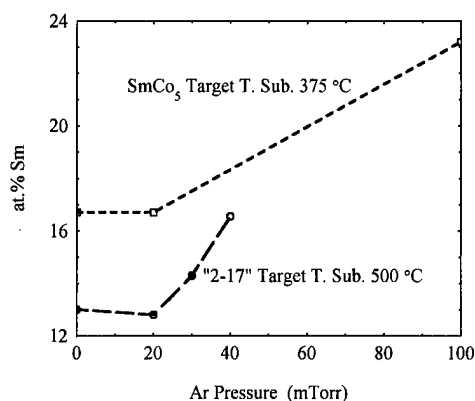


FIG. 1. The Sm at % for a series of PLD films made on to 375 °C substrates from bulk SmCo_5 targets, and films made on to 500 °C substrates from bulk SmCo "2-17" targets, for different Ar pressures during the deposition is shown.

tion of Ar gas pressure. The targets in the latter case consisted of normal bulk type "2-17" magnet material with a composition of Sm 13 at %, Co 58%, Fe 20%, Cu 7%, and Zr 2%. Under vacuum conditions the film Sm concentration corresponded to that of the targets. Films made under vacuum, however, exhibited a large number of particulates causing such films to be unattractive for film device applications. During sputtering large concentration changes can also be effected by using increased sputtering gas pressures and in particular admixtures of Xe as a part of the sputtering gas.² Changes in the sputtering gas pressure could be used to vary the film composition from 12 to 18 at %.¹¹ Higher pressures tend to preferentially scatter the lower mass transition metal atom components relative to the more massive Sm atoms. The net effect is that the lighter transition metal atoms are on the average scattered through larger angles and effectively removed from the deposition beam. Higher pressures in the deposition chamber tend to enrich the Sm concentration in the films.

Room temperature hysteresis loops measured in plane and perpendicular to the plane are shown in Fig. 2 for a shadow region film deposited at 375 °C and 100 mTorr Ar at a laser wavelength of 193 nm with a pulse rate of 14 Hz. The PLD target was bulk SmCo_5 . The in plane H_c was 9.7 kOe and the loop shape was characteristic of single phase material. It should be noted that there is no retracing of the in plane hysteresis loop to the highest measurement magnetic field of 18 kOe. An x-ray diffraction pattern for the film of Fig. 2 is shown in Fig. 3. The evident CaCu_5 -type structure (110) dominant texturing and (111) secondary CaCu_5 -type shoulder are consistent with the relative shapes of the in plane and perpendicular to the plane hysteresis loops.

Films of SmCo based materials made without the use of a shadow mask exhibited an appreciable density of particulates on the substrate. Films made in vacuum, 1.8×10^{-7} Torr, on to 550 °C substrates exhibited a small grain size of 0.17–0.30 μm diameter. The particulates tended to be of two principal sizes, $\approx 0.33 \mu\text{m}$ diameter for the small ones, and $\approx 0.83 \mu\text{m}$ diameter for the larger ones. The particulate density for nonshadowed films increased with pressure even though the number density of the larger sized par-

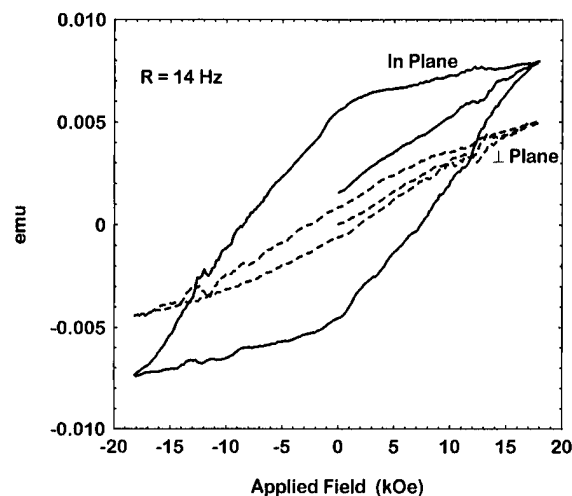


FIG. 2. Room temperature hysteresis loops for a shadow deposited PLD film made from SmCo_5 target at 375 °C on to alumina substrate, pressure 100 mTorr Ar, pulse rate 14 Hz are shown. The key items to note are that the intrinsic coercivity is 9.7 kOe and that the loop shape is smooth.

ticulates remained nearly constant. Nonshadowed films made at 500 °C and 30 mTorr Ar exhibited an average particulate density of $0.21/\mu\text{m}^2$, similar films except at 75 mTorr Ar exhibited $0.33/\mu\text{m}^2$. In order to limit the number of particulates arriving at the substrate a stainless steel sheet metal shadow was located in the deposition plume to block the direct transport of particulates to the substrate. A higher background gas pressure of argon was then required to scatter the atoms to reach the substrate. The shadow mask strip was arranged midway between the target and substrate so that the shadow blocked a 13×50 mm substrate region.

Figure 4 shows hysteresis loops for a SmCo based film shadow deposited at a substrate temperature of 375 °C in 100 mTorr Ar at a laser pulse rate of 10 Hz. The in film plane H_c was 11.3 kOe. The film surface was mirrorlike which is different from directly crystallized textured SmCo films grown onto alumina films by sputtering. The smooth mirrorlike surface was consistent with a small average grain size. The

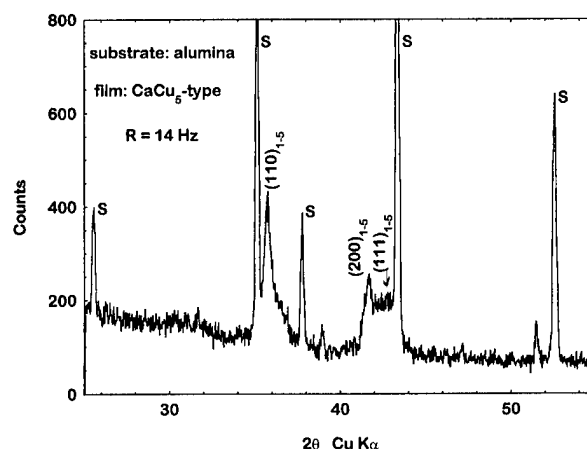


FIG. 3. An x-ray diffraction trace for the film of Fig. 2 is shown which indicates (110) dominant and (111) secondary texturing. The x ray is indexed as CaCu_5 -type structure film. The substrate lines from the polycrystalline Al_2O_3 are indicated by S in the figure.

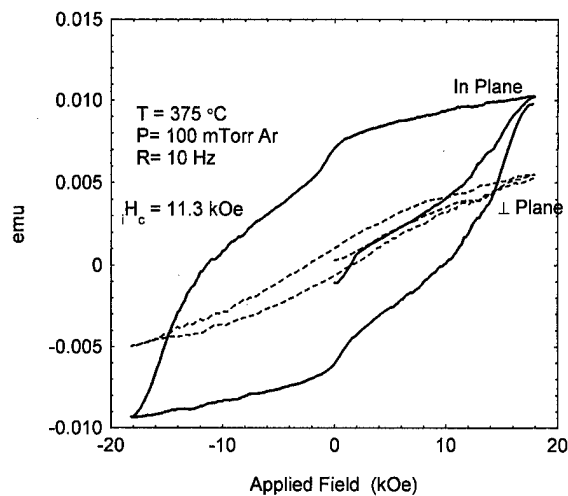


FIG. 4. Room temperature hysteresis loops are shown for a PLD film deposited from bulk SmCo_5 target at 375°C , pressure 100 mTorr Ar, shadowed deposition. The laser settings were 193 nm, 600 mJ pulses, 10 ns pulse width, and 10 Hz.

shadow deposited films replicated polish marks on the underlying substrate that made it difficult to determine a film grain size. The deposit in the shadow region was particulate free.

To study the effects of surface atom mobility a series of films were deposited from bulk SmCo_5 targets in 100 mTorr Ar onto substrates held at 375°C using $\lambda=193$ nm for differing pulse repetition rates from 5 to 50 Hz. This is shown in Fig. 5 where the H_c values versus laser pulse rate are shown for a series of films shadow deposited under the same conditions except for the laser pulse repetition rate. The higher pulse rates result in low coercivities due to insufficient time between pulses for surface atom site adjustments.

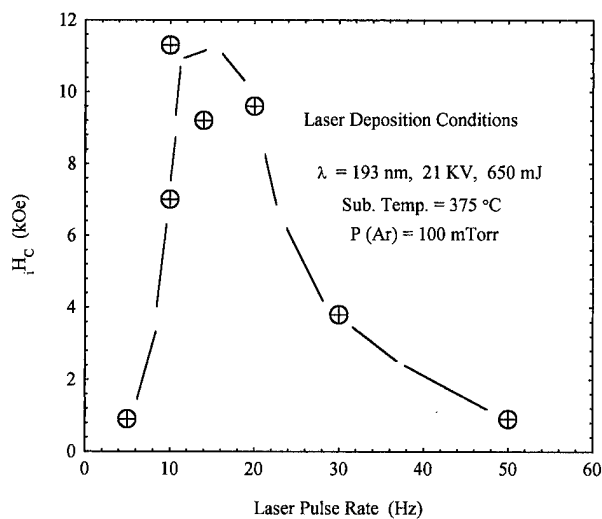


FIG. 5. The coercivity H_c vs laser pulse rate is shown for a series of films shadow deposited from SmCo_5 bulk targets using $\lambda=193$ nm, T substrate $=375^\circ\text{C}$, and $P=100$ mTorr Ar. The values shown were measured at room temperature on as deposited films.

In this series the highest coercivity of 11.3 kOe was obtained for a pulse rate of 10 Hz. The hysteresis loops for films made at laser pulse rates between 10 and 20 Hz were offset in the initial magnetization direction since the maximum applied field of 18 kOe was insufficient to achieve saturation. Lower pulse rates resulted in low coercivities believed to be caused by surface gas contamination due to the longer times between successive pulses.

A key result of this article is that it has been possible to produce SmCo films directly by shadowed PLD onto slightly heated substrates with coercivities up to 11.3 kOe at 10 Hz as a function of the laser pulse repetition rate. Higher laser pulse rates did not allow sufficient site relaxation between pulses, while lower pulse rates lead to film contamination because of the longer time between deposition pulses. An operative deposition condition is that $\sqrt{T}/R = \text{const} \cdot d$, where T is the absolute substrate temperature with the surface atom speed proportional to \sqrt{T} , d is the site relaxation distance, and $1/R$ is the time between laser pulses for the pulse rate R . Higher laser pulse rates can then only be fruitfully used at higher substrate temperatures where the surface atom mobility is increased to provide site relaxation before the surface is buried by the deposit from the next laser pulse. At higher substrate temperatures the film reactivity with contaminating background gases is expected to increase so that higher substrate temperatures would require lower background gas pressures.

ACKNOWLEDGMENTS

The PLD system was purchased with NSF-ARI Grant No. STI-9512308, and with partial support from the NYS Graduate Research Initiative. This work was supported in part by the U.S. Army Research Office, Grant No. DAAH04-94-G-0079, and in part by the Office of Naval Research, Grant No. ONR N00014-96-1-0767. Some support was also derived from the PSC-CUNY Faculty Research Award Program of CUNY.

¹F. J. Cadieu, H. Hegde, and K. Chen, IEEE Trans. Magn. **MAG-25**, 3788 (1989).

²F. J. Cadieu, "Permanent Magnet Thin Films," in *Physics of Thin Films* (Academic, San Diego, 1992), Vol. 16.

³F. J. Cadieu, in *Magnetic Materials, Processes, and Devices IV*, edited by L. T. Romankiw and D. A. Herman, Jr., Proc. Electrochem. Soc. (Electrochemical Society, Pennington, NJ, 1996), paper PV 95-18, pp. 319-335.

⁴F. J. Cadieu, H. Hegde, E. Schloemann, and H. J. Van Hook, J. Appl. Phys. **76**, 6059 (1994).

⁵E. E. Fullerton, C. H. Sowers, J. P. Pearson, S. D. Bader, X. Z. Wu, and D. Lederman, Appl. Phys. Lett. **69**, 2438 (1996).

⁶E. E. Fullerton, J. S. Jiang, C. Rehm, C. H. Sowers, S. D. Bader, J. B. Patel, and X. Z. Wu, Appl. Phys. Lett. **71**, 1579 (1997).

⁷H. Hegde, S. U. Jen, K. Chen, and F. J. Cadieu, J. Appl. Phys. **73**, 5926 (1993).

⁸M. Levy, R. M. Osgood, Jr., H. Hegde, F. J. Cadieu, R. Wolfe, and V. J. Fratello, Photonics Technol. Lett. **8**, 903 (1996).

⁹D. H. Lowndes, D. B. Geohegan, A. A. Poretzky, D. P. Norton, and C. M. Rouleau, Science **273**, 898 (1996).

¹⁰H. Lemke, C. Echer, and G. Thomas, IEEE Trans. Magn. **32**, 4404 (1996).

¹¹F. J. Cadieu, H. Hegde, and K. Chen, Thin Solid Films **193/194**, 857 (1990).

Mechanism of composition change in sputter deposition of barium ferrite films with sputtering gas pressure

E. Suzuki and Y. Hoshi^{a)}

Faculty of Engineering, Tokyo Institute of Polytechnics, Atsugi, Kanagawa 243-02, Japan

M. Naoe

Tokyo Institute of Technology, Meguro-ku, Tokyo 152 Japan

In this study, we used computer simulation to investigate changes in the composition of hexagonal barium ferrite films with sputtering gas pressure obtained by the sputter-deposition processes. The iron content in the film deposited by facing target sputtering increased as the sputtering gas pressure increased and reached a maximum value at a certain gas pressure. These changes in the film composition were explained as follows: sputtered particles scatter when they collide with sputtering gas atoms, and this scattering changes the ratio of the particles reaching the substrate. When the substrate was located to the side of the target, as in a facing target sputtering system, this scattering resulted in an increase in the amount of sputtered particles arriving at the substrate, although too much scattering caused the amount to decrease. When a magnetron sputtering system is used for the film preparation, this gas scattering leads to a decrease in the amount of sputtered particles arriving at the substrate which is located opposite the target. Since this gas scattering depends significantly on the atomic mass of the sputtered particles, the gas pressure dependence of the amount of iron atoms arriving differs considerably from that of the amount of barium atoms arriving. This difference leads to the changes in film composition. © 1998 American Institute of Physics. [S0021-8979(98)46311-4]

I. INTRODUCTION

A hexagonal barium ferrite (BaM) thin film with excellent magnetic properties cannot be obtained unless the film composition is controlled precisely.¹ In the sputter deposition of barium ferrite films, however, the film composition changed significantly when the deposition conditions change,² mainly because high-energy particles, produced from negative oxygen ions emitted from the target, bombarding the film surface caused the composition of the film to differ from that of the target material.^{1,2} This high-energy particle bombardment of the film surface was eliminated in facing target sputtering (FTS), which resulted in only a small change in film composition.¹

The iron content in a BaM film deposited by a FTS system, however, increases with an increase in sputtering gas pressure, reaches a maximum at a certain gas pressure, and decreases with further increases in the gas pressure. To explain these changes in the film composition with sputtering gas pressure, we carried out a computer simulation of the sputter deposition processes and found that changes in the film composition with sputtering gas pressure were mainly caused by the scattering that occurs when sputtered particles in the space between the target and substrate collide with the atoms of the sputtering gas.

In this article, we will show the mechanisms of the composition changes caused by the scattering of sputtered particles through the collisions with sputtering gas atoms in FTS and in conventional magnetron sputtering.

II. SIMULATION OF TRANSPORT PROCESS IN SPUTTERING

A facing target sputtering system and a magnetron sputtering system were assumed to be used for the film deposition (Fig. 1). The trajectory of each of the sputtered particles emitted from the target was calculated and the amount of sputtered particles deposited on the substrate was estimated. This transportation of the sputtered particles was calculated according to the model reported by Motohiro³ and Turner.⁴ The emission angles of sputtered particles from the target

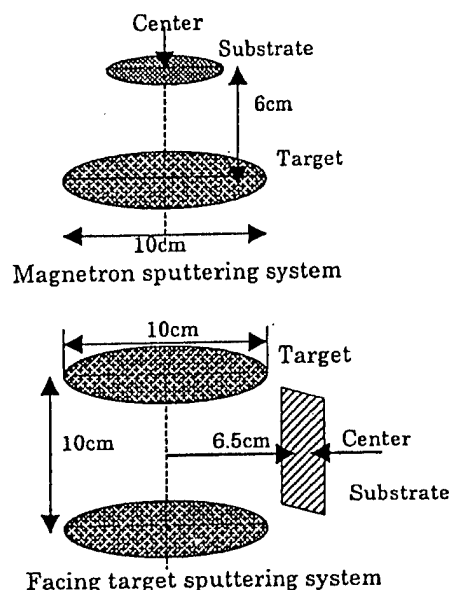


FIG. 1. Target-substrate arrangement in the sputtering systems simulated in this study.

^{a)}Electronic mail: hoshi@ec.t-kougei.ac.jp

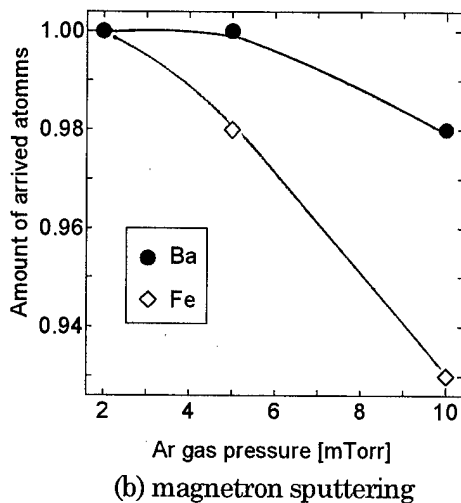
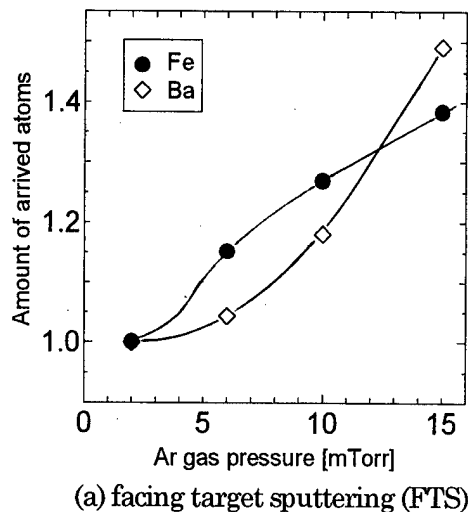


FIG. 2. Relation between sputtering gas pressure and the amounts of iron and barium atoms arriving at the substrate. (a) is obtained for the FTS, and (b) is obtained for the magnetron sputtering system.

were assumed to follow cosine law. The energy distributions of iron atoms emitted from the target were assumed to be emitted from pure metal iron, and calculated by using Thompson's model.⁵ The energy of primary ion which bombards the target surface was assumed to be 780 eV. For barium atoms, the following parameters were used in calculating the energy distribution; atomic number, 56; atomic mass, 137.3; atomic radius, 2.22 Å; length between atoms, 4.35 Å; bonding energy (BaO_2), 8.4 eV in the Thompson's model.⁵ Gas temperature during sputtering was assumed to be 673 K. In the simulation, one million atoms were emitted from the target and the amount of particles incident on the substrate was calculated at various sputtering gas pressures. It should be noted that the sputtering gas, iron, and barium, differ considerably in terms of both atomic radius and atomic mass.

III. RESULTS AND DISCUSSIONS

Figure 2 shows simulated examples of the amount of iron atoms and barium atoms arriving at the substrate in the magnetron sputtering and in the FTS. The amount of atoms arriving in Fig. 2 was normalized by the value obtained with-

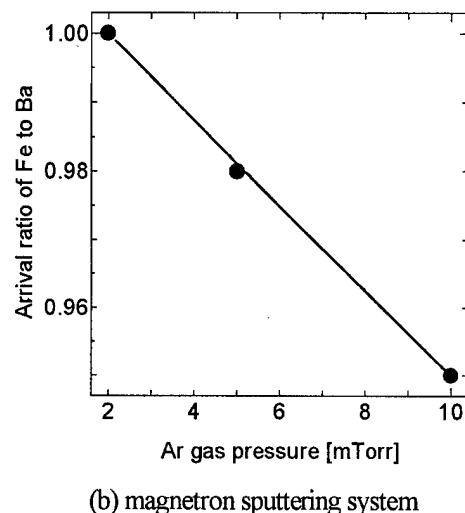
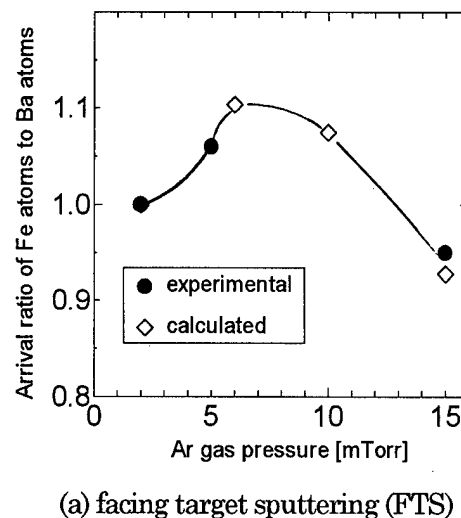


FIG. 3. Changes in the arrival ratio of iron atoms to barium atoms with sputtering gas pressure. (a) is obtained for FTS, and (b) is obtained for the magnetron sputtering.

out gas scattering. It should be noted that the amount of atoms arriving in the FTS increases as the sputtering gas pressure increases. On the contrary, the amount of atoms arriving in magnetron sputtering decreases as the sputtering gas pressure increases. This increase in the FTS and decrease in the magnetron sputtering are explained as follows: in a facing target sputtering system, the substrate is located to the side of the target as shown in Fig. 1. In this target-substrate arrangement, scattering of the sputtered particles because of collisions with sputtering gases leads to an increase in the amount of sputtered particles arriving at the substrate. Too much scattering which will occur at a higher gas pressure, however, causing the amount to decrease.

In the magnetron sputtering system, the scattering causes a decrease in the amount of both iron and barium arriving at the substrate as the sputtering gas pressure increases, since the substrate is located opposite the target.

It should also be noted that the gas pressure dependence of the amount of iron atoms arriving at the substrate differs remarkably from that of barium atoms. This is mainly due to the different atomic masses of iron and barium. These differ-

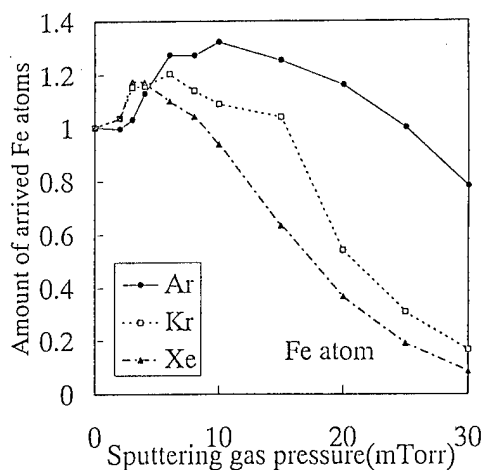


FIG. 4. The amount of iron atoms arriving during sputtering in Ar, Kr, and Xe in FTS.

ences in the amount of deposition particles arriving should cause the film composition to change. The ratio of the amount of the iron atoms to barium atoms arriving at the substrate (arrival ratio) is equivalent to the composition of the deposited film, when the sticking probability is unity. Figure 3 shows the changes in the arrival ratio with sputtering gas pressure in the FTS Fig. 3(a) and in the magnetron sputtering system Fig. 3(b). The arrival ratio of iron to barium estimated from the composition of barium ferrite films deposited by the FTS is also shown in Fig. 3(a). The arrival ratio at 2 mTorr was assumed to be 1. The iron content in the film deposited by FTS increases as the sputtering gas pressure increases, and reaches a maximum at a certain gas pressure. It is clear from the figure that these changes in the arrival ratio obtained from the simulation qualitatively agree with experimental results.

On the other hand, the arrival ratio of iron to barium in the magnetron sputtering system decreases monotonically as the sputtering gas pressure increases, since the amount of arriving iron atoms decreased more steeply than did the amount of barium atoms. This indicates that the iron content in the film should decrease as the sputtering gas pressure

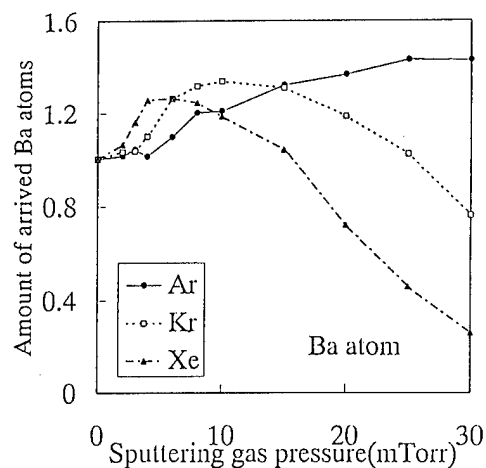


FIG. 5. The amount of barium atoms arriving during sputtering in Ar, Kr, and Xe in FTS.

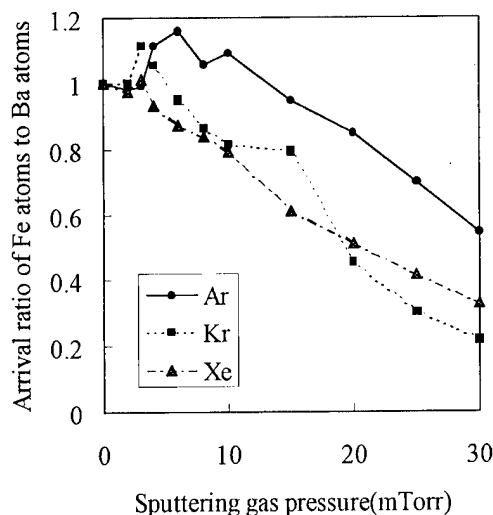


FIG. 6. Arrival ratio of iron atoms to barium atoms sputtered in Ar, Kr, and Xe in FTS.

increases, if the high-energy particle bombardment of the film surface is eliminated during deposition. However, distinguishing the composition change due to the gas scattering of sputtered atoms was difficult, since the high-energy particle bombardment of the film surface during deposition was not eliminated in this sputtering system.

When other sputtering gases (such as Kr and Xe) are used in place of Ar, the gas pressure dependence of the amount of iron and barium atom arriving will differ significantly from that observed in sputtering using argon gas. This difference will result in changes in the pressure dependence of the film composition. Figures 4 and 5 show examples of the amounts of iron and barium atoms arriving during sputtering in various gases in the FTS. It is clear from the figure that the gas pressure where the amount of atoms arriving takes a maximum value shifts to a lower gas pressure area as the mass of sputtering gas increases. From these results, the changes in film composition with the changes in sputtering gas pressure, shown in Fig. 6, can be derived. The sputtering-gas-dependent changes in film composition should thus be taken into consideration to obtain a film with the desired composition.

IV. CONCLUSIONS

The transportation of sputtered particles from the target to the substrate was investigated. The scattering of sputtered particles by collision with the sputtering gas was found to play an important role in changing the film composition. In addition, it should be noted that this gas scattering effect will lead to a quite different gas pressure dependence of the film composition when the arrangement of target and substrate in the sputtering systems is changed.

¹M. Matsuoka, Y. Hoshi, M. Naoe, and S. Yamanaka, *IEEE Trans. Magn.* **18**, 1119 (1982).

²M. Naoe, S. Hasunuma, Y. Hoshi, and Y. Yamanaka, *IEEE Trans. Magn.* **17**, 3184 (1981).

³T. Motohiro, *J. Vac. Sci. Technol.* **4**, 189 (1986).

⁴G. M. Turner, I. S. Falconer, B. W. James, and D. R. McKenzie, *J. Appl. Phys.* **65**, 3671 (1989).

⁵M. W. Thompson, *Philos. Mag.* **18**, 377 (1968).

Magnetic and structural properties of high coercivity Sm(Co, Ni, Cu) sputtered thin films

C. Prados^{a)} and G. C. Hadjipanayis

Department of Physics and Astronomy, University of Delaware, Newark, Delaware 19716

The effects of heat treatments on the structural and magnetic properties of Sm(Co, Ni, Cu) sputtered thin films were investigated. Crystallization of the initially amorphous magnetic films produces a huge enhancement of coercivity (from 100 Oe to more than 40 kOe). The crystallized structure consists of exchange coupled precipitates in the nanometers range. The pinning of the magnetization reversal at the high anisotropy grains is proposed as the origin of such a magnetic behavior. By tuning the coercivity through the annealing conditions, these systems could be used in a number of applications, from longitudinal recording media to thin film permanent magnet. © 1998 American Institute of Physics. [S0021-8979(98)46411-9]

I. INTRODUCTION

In the last years, SmCo/Cr bilayers films have been proposed as an attractive candidate for ultrahigh density recording media.¹⁻⁴ The main driving force for the use of rare-earth based alloys is to attain a recording density as high as 10–20 Gb/in². In general, modifications of the SmCo₅ composition have been used due to its high coercivity and large magnetic anisotropy. In order to obtain appropriate microstructure and crystallographic orientation in these films, extensive studies have been carried out using different deposition conditions and underlayer materials.⁴

On the other hand, the CaCu₅ type compounds, SmCo_{5-x}Ni_x and SmCo_{5-x}Cu_x are known to exhibit huge values of coercivity due to the so-called giant intrinsic magnetic hardness.^{5,6} In spite of the number of studies related to the properties of the bulks alloys, only a few are reported on thin films. In this article, the structural and magnetic properties of SmCo₅, SmCo₂Cu₃, and SmCo₂Ni₃ thin films deposited by dc magnetron sputtering on a Cr underlayer are studied in the as-deposited state and after subsequent heat treatments. The different microstructures which have been obtained lead to a wide range of coercivity values, which make these compounds suitable for a variety of applications, from longitudinal recording media to thin film permanent magnets.

II. EXPERIMENT

Sm(Co, Ni, Cu)/Cr bilayers were deposited on water cooled Si substrates with a dc magnetron sputtering system. Ar at a pressure of 5 mTorr was used as discharge gas. The Cr underlayers were deposited from a pure (99.9%) solid Cr target. The Sm(Co, Ni, Cu) targets were pressed powder type with nominal compositions SmCo₅, SmCo₂Cu₃, and SmCo₂Ni₃. The deposition rates were 1.25 Å/s for Cr and 6 Å/s for Sm(Co, Ni, Cu) and were calibrated by low angle x-ray diffractometry (XRD). The thickness of the Cr underlayer and the Sm(Co, Ni, Cu) film were 300 and 500 nm, respectively. The role of the Cr underlayer is to promote a

c-axis texture along in plane directions in the Sm–Co film in order to increase its in-plane magnetic anisotropy.⁴ The bilayers were annealed in a vacuum of better than 10⁻⁵ Torr at a constant temperature for 30 min. Different pieces of the same as-deposited sample were submitted to this heat treatment, ranging the annealing temperature for each piece from 400 to 650 °C. Each heat treatment has been labelled with the characteristic annealing temperature. The structural properties were determined by XRD. Room temperature hysteresis loops were measured with a superconducting quantum interference device (SQUID) magnetometer at a maximum applied magnetic field of 55 kOe. Principal remanence curves were measured at room temperature using a vibrating sample magnetometer.

III. RESULTS AND DISCUSSION

The high angle XRD diagrams of the samples showed the (110) peak as the single line from the Cr, and revealed that the Sm(Co, Ni, Cu) layers were amorphous in the as deposited state. After subsequent heat treatments, the amorphous hallow around the position corresponding to the SmCo₅ (111) line started to evolve into a broad nanocrystalline peak with an increasing relative intensity. Figure 1 shows the crystalline grain size for the layers of compositions SmCo₂Cu₃ and SmCo₂Ni₃ as a function of the annealing temperature. Grain size has been determined from the full width at half maximum through the Scherrer's formula. The values are around 20 nm for SmCo₂Ni₃ and 10 nm for SmCo₂Cu₃. The effect of the increasing annealing temperature was to increase the Sm–Co crystallized fraction rather than change the grain size, which slightly grew with the annealing temperature. Preliminary transmission electronic microscopy studies showed that the nanocrystallites are embedded in an amorphous matrix.

Figure 2(a) shows the evolution of coercivity with the annealing temperature for the three compositions. All of them exhibit low coercivity in the as deposited state, because of their amorphous structure, which increases more than two orders of magnitude with the heat treatment. The hardening starts at 515 °C for the case of SmCo₅ and at 450 °C for SmCo₂Ni₃ and SmCo₂Cu₃. The highest value of coercivity

^{a)}Electronic mail: celso@fresno.csic.es

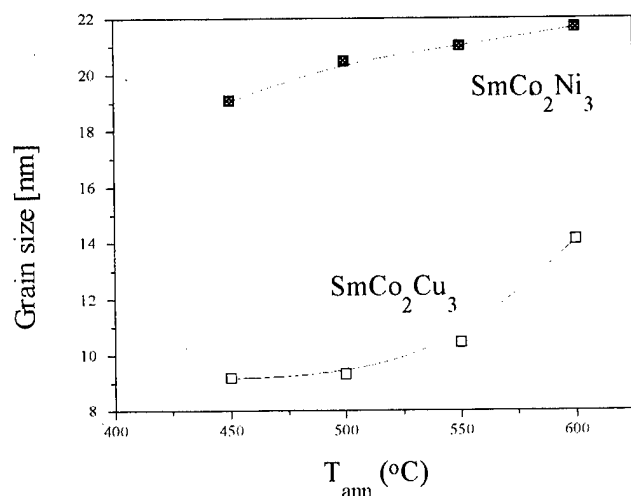


FIG. 1. SmCo_2Cu_3 and SmCo_2Ni_3 grain size as a function of the annealing temperature. Grain size has been determined from the width of the (111) SmCo_5 line using Scherrer's formula.

has been of 42 kOe for the SmCo_2Cu_3 composition, annealed at 550 °C for 30 min (note that coercivity has been determined at room temperature and with a maximum applied field of only 55 kOe). Coercive fields larger than 20 kOe have been obtained for the other two compositions. These values are comparable, and even much larger in the case of SmCo_2Cu_3 , than those reported in epitaxial oriented Sm-Co

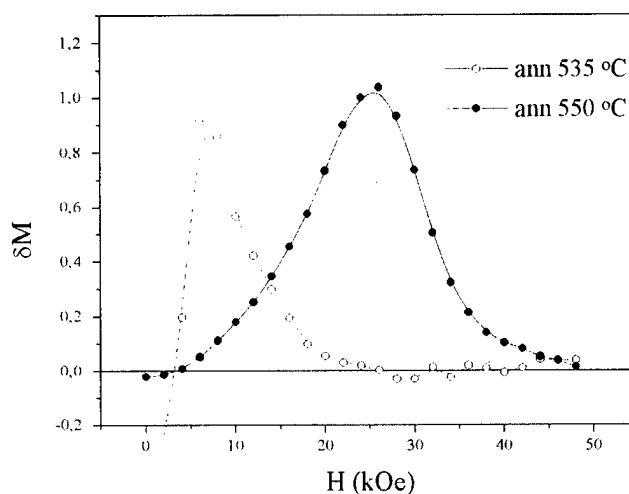


FIG. 3. δM plots of the sample with composition SmCo_5 at two representative annealing conditions, 535 (low coercivity) and 550 °C (high coercivity). $\delta M(H)$ has been obtained from the isothermal magnetization curve, $M_r(H)$ and the dc demagnetization $M_d(H)$ through the expression $dM = M_d - (1 - 2M_r)$.

films measured along the hard axis.⁷ Relative remanence (remanent moment divided by the magnetic moment at the maximum applied field) is displayed in Fig. 2(b) for the three compositions at the different annealing temperatures. In the highest coercivity range the relative remanence is around 0.8.

No steps are observed in the measured hysteresis loops over the range of annealing conditions and subsequent structures. This is indicating that, in spite of the different amorphous and crystalline phases present in the films, they behave magnetically coupled. This point is more deeply analyzed through the principal remanence curves.

δM plots have been constructed from the principal remanence curves measured for the three compositions at different annealing conditions (for the definition of the principal remanence curves and δM plots see, for instance, Ref. 8). Figure 3 shows δM plots for the SmCo_5 sample at two representative annealing conditions, 535 °C where the sample still exhibits a low coercivity, and 550 °C in the high coercivity range. The positive values of the δM are interpreted to result from magnetizing interaction between the particles (exchange coupling). The maximum value of the δM plot does not change substantially with the annealing temperature, indicating that the strength of the interaction between particles is independent of the coercivity. Similar behavior is observed in the other two compositions, intergrain interaction is always magnetizing and of the same order for the different crystallization stages.

The structural and magnetic characterization described above provides insight on the outstanding magnetic properties exhibited by these samples. In the as deposited and low temperature annealing stages, the magnetic layers are basically amorphous with low coercivity. A nanocrystalline structure is developed with the higher temperature heat treatments, with the grain size being rather independent of the annealing temperature. The particles are exchange coupled

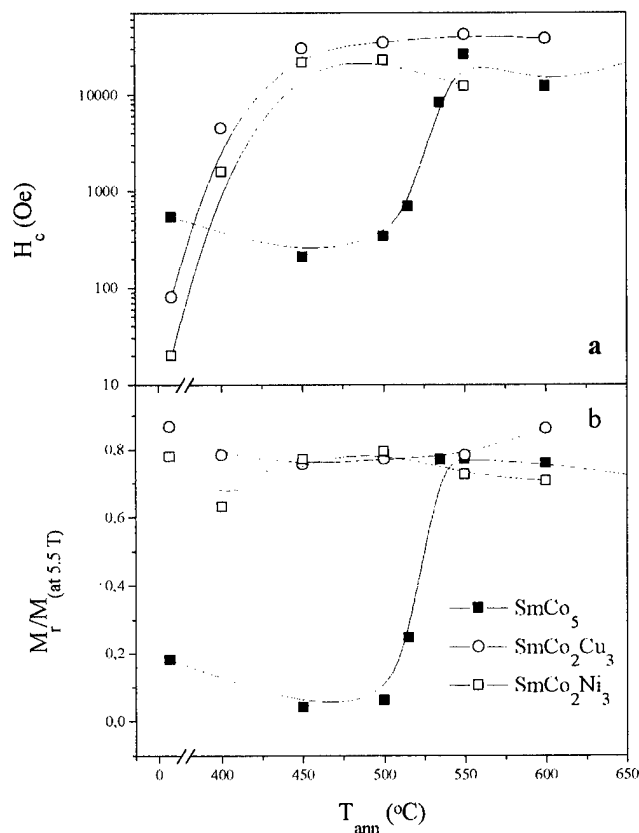


FIG. 2. Evolution of coercivity (a) and relative remanence (b) with the annealing temperature in the films SmCo_2Cu_3 , SmCo_2Ni_3 , and SmCo_5 . Both coercivity and relative remanence have been obtained measuring hysteresis loops with a maximum applied field of 55 kOe.

through the remaining ferromagnetic matrix. The huge enhancement of coercivity may be related to the strong hindrances of the magnetization reversal due to domain wall pinning at the high anisotropy Sm-Co precipitates. The pinning effectiveness improves with the density of crystallites giving rise to such an enhancement of coercivity at annealing temperatures around 500–550 °C.

IV. CONCLUSION

SmCo₅/Cr and giant intrinsic magnetic hardness compounds Sm(Co, Ni, Cu)₅/Cr have been fabricated by dc magnetron sputtering deposition. Heat treatment of the initially amorphous magnetic films results in a refined grain structure with high anisotropy Sm-Co precipitates in the nanometric scale. At the same time, a huge coercivity enhancement (from 100 Oe to 42 kOe in the case of SmCo₂Cu₃) is observed. The nondependence of the strength on the positive magnetic interaction between particles and the average grain size on the crystallization stage, indicated that the coercivity

is related to domain wall pinning at the high anisotropy precipitates. The possibility of tuning the coercivity over a range of more than two orders of magnitude through the annealing conditions, make these films suitable for a variety of applications, from longitudinal recording media to thin film permanent magnets.

¹E. M. T. Velu and D. N. Lambeth, J. Appl. Phys. **69**, 5175 (1991).

²S. S. Malhotra, Y. Liu, Z. S. Shan, S. H. Liou, D. C. Stafford, and D. J. Sellmyer, J. Appl. Phys. **79**, 5958 (1996).

³S. Takei, S. Shomura, A. Morisako, and M. Matsumoto, J. Appl. Phys. **81**, 4674 (1997).

⁴Y. Okumura, H. Fujimori, O. Suzuki, N. Hosoya, X. B. Yang, and H. Morita, IEEE Trans. Magn. **30**, 4038 (1994).

⁵S. Foner, E. J. McNiff, H. Oesterreicher, F. T. Parker, and M. Misroch, J. Appl. Phys. **49**, 2061 (1979).

⁶H. Oesterreicher, F. T. Parker, and M. Misroch, J. Appl. Phys. **50**, 4273 (1979).

⁷E. Fullerton, J. S. Jiang, C. Rehm, C. H. Sowers, S. D. Bader, J. B. Patel, and X. Z. Wu, Appl. Phys. Lett. **71**, 1579 (1997).

⁸R. W. Chatrell, in *Nanomagnetism*, edited by G. C. Hadjipanayis (Kluwer Academic, Dordrecht, 1994), p. 21.

Mechanically alloyed nanocomposite magnets (invited)

P. G. McCormick^{a)}

Special Research Centre for Advanced Mineral and Materials Processing, University of Western Australia, Nedlands 6907, Australia

W. F. Miao

Carnegie Mellon University, Pittsburgh, Pennsylvania 15213

P. A. I. Smith

Department of Physics, Trinity College, Dublin 2, Ireland

J. Ding

Department of Materials Science, National University of Singapore, 119260 Singapore

R. Street

Special Research Centre for Advanced Mineral and Materials Processing, University of Western Australia, Nedlands 6907, Australia

Nanocomposites, consisting of a hard magnetic rare earth-transition metal phase exchange coupled to soft magnetic α -Fe or α -(Fe,Co), exhibit enhancement of the remanent magnetization due to exchange coupling across interfaces between grains. Modeling studies have shown that crystallite sizes of less than 20 nm are generally required for significant remanence enhancement and values of remanent magnetization equal to 70%–80% of saturation magnetization have been reported in mechanically alloyed two phase mixtures of α -Fe and a hard magnetic phase, such as $\text{Nd}_2\text{Fe}_{14}\text{B}$. Studies of microstructural evolution during mechanical alloying have shown that as-milled structures consist of a magnetically soft two phase mixture of α -Fe and an amorphous phase. Similar microstructures are observed regardless of whether mechanical milling or mechanical alloying has been carried out. Heat treatment above a critical temperature is required to crystallize grains of the hard magnetic phase. The formation of metastable intermediate phases with interesting magnetic properties may precede formation of the equilibrium phase. It is found that the crystallization temperature is an important parameter determining the grain size of the soft magnetic phase and, hence, magnetic properties. Recent measurements of the reversible and irreversible magnetization behavior of this novel class of permanent magnet are also discussed. © 1998 American Institute of Physics. [S0021-8979(98)42911-6]

I. INTRODUCTION

Nanocomposite permanent magnetic materials have attracted considerable interest since 1991, when it was recognized¹ that exchange coupled, nanoscale mixtures of a hard magnetic phase such as $\text{Nd}_2\text{Fe}_{14}\text{B}$ and a soft magnetic phase such as α -Fe could potentially provide maximum energy products, $(BH)_{\text{max}}$, in excess of 200 kJ/m³.² In addition to the high values of $(BH)_{\text{max}}$ that may be achieved, nanocomposite magnets are of commercial interest because the costly magnetic alignment step is not required to obtain maximum performance and the alloys require less of the expensive rare earth element.

Remanence enhancement is associated with exchange coupling at interfaces separating nanocrystalline hard and soft magnetic phases, which causes the magnetization vector of the soft phase to be rotated toward that of the hard phase, thus increasing the remanent magnetization in the direction of initial magnetization. As a consequence, the material, although crystallographically isotropic, can exhibit remanence values significantly higher than the isotropic value of 0.5 of the saturation magnetization, M_s , for a material with

uniaxial magnetocrystalline anisotropy, without the necessity of crystallographic alignment.

The basic concepts of exchange coupling and remanence enhancement date back to the studies of Meiklejohn and Bean.³ McCallum, *et al.*⁴ first reported remanence enhancement in single phase nanocrystalline melt spun $\text{Nd}_2\text{Fe}_{14}\text{B}$ containing small amounts of Si and Al. The phenomenon was attributed to exchange coupling between ~ 20 nm $\text{Nd}_2\text{Fe}_{14}\text{B}$ grains. Remanence enhancement in nanocrystalline composites of magnetically hard and soft phases was first reported by Coehoorn and co-workers.^{5,6} Remanence values of up to $0.8 M_s$ were measured in a melt-spun $\text{Nd}_4\text{Fe}_{78}\text{B}_{18}$ alloy consisting of $\text{Nd}_2\text{Fe}_{14}\text{B}$, Fe_3B , and α -Fe. Ding *et al.*^{7,8} first reported remanence enhancement in mechanically alloyed two phase α -Fe/ $\text{Sm}_2\text{Fe}_{17}\text{N}_{2.6}$ alloys containing 5–11 at % Sm. The as-milled structures consisted of two phase mixtures of α -Fe and an amorphous phase. Crystallization at temperatures above 773 K resulted in two phase α -Fe/ $\text{Sm}_2\text{Fe}_{17}$ mixtures which were subsequently nitrided at 673 K to form α -Fe/ $\text{Sm}_2\text{Fe}_{17}\text{N}_{2.6}$. The crystallite size was ~ 15 –20 nm in samples heat treated at 873 K. Remanence enhancement has now been observed in a number of mechanically alloyed and heat treated nanocomposite alloys.

^{a)}Electronic mail: pgm@mech.uwa.edu.au

Micromagnetic modeling studies have shown that the magnetic properties of nanocomposite magnets depend strongly on both the microstructure developed during processing and the intrinsic magnetic properties of the individual phases.⁹⁻¹² Of particular importance, the grain size of the soft phase should be less than the exchange length of the soft magnetic phase.¹¹ The calculations of Fischer *et al.*¹¹ predict that M_r should increase logarithmically with increasing grain size and that the magnetic properties are degraded by a nonuniform microstructure. The values of M_r , H_c and $(BH)_{\max}$ predicted by modeling studies exceed experimental values and it is clear that greater attention needs to be placed on the development of optimum microstructures and phase constitutions during processing to enable property improvements to be realized. In this article recent studies of microstructure-property relationships in mechanically alloyed and heat treated rare-earth nanocomposite magnetic materials are reviewed.

II. STRUCTURAL EVOLUTION DURING MECHANICAL ALLOYING

Mechanical alloying and the related processes of mechanical milling and mechanochemical processing have been applied to the synthesis of a wide range of amorphous and nanocrystalline materials.¹³ The application of mechanical alloying to the synthesis of magnetic materials was first reported by Schultz and co-workers in 1987¹⁴ and subsequently has been applied to a wide range of rare-earth permanent magnet alloys.¹⁵

The metastable nanocrystalline and/or amorphous structures which are inherently obtained in mechanically alloyed powder are developed from the repeated processes of deformation and fracture which accompany ball/powder collision events. Plastic deformation of the powder particles initially occurs by the development of shear bands. When sufficiently high dislocation densities are reached the shear bands decompose into sub-grains separated by low-angle grain boundaries. With further milling the sub-grain size is reduced and the sub-grains become randomly oriented and separated by high angle boundaries. The large surface energy of the nanocrystalline grains has been shown to provide the driving force for a crystalline→amorphous phase transition.¹⁶ The rate of diffusion is also important as the diffusion coefficients may be increased by the deformation induced defect density and high local collision temperatures. In many systems the final structure reflects the competition between deformation induced disorder and diffusion limited recovery processes and is independent of whether the starting material is pre-alloyed or a mixture of elemental powders.

The as-milled structures of a wide range of rare-earth permanent magnet alloys are characterized by nanoscale mixtures of crystalline and amorphous phases.¹⁵ For example, both mechanically alloyed and mechanically milled FeNdB alloys consist of a mixture of nanocrystalline α -Fe and amorphous NdFe phases.^{14,17} Mechanical milling of the $\text{Nd}_2\text{Fe}_{14}\text{B}$ phase has been shown to result in disproportionation into a mixture of α -Fe and amorphous NdFe.¹⁷ The same final phases are formed regardless of whether the starting material has been pre-alloyed.^{17,18}

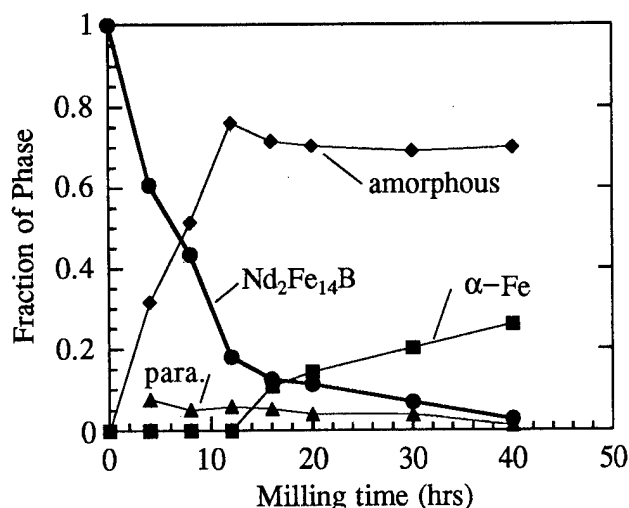


FIG. 1. Phase changes during mechanical milling of $\text{Nd}_2\text{Fe}_{14}\text{B}$ (Ref. 19).

Microstructure evolution in single phase $\text{Nd}_2\text{Fe}_{14}\text{B}$ and two phase α -Fe/ $\text{Nd}_2\text{Fe}_{14}\text{B}$ composites during mechanical milling has been studied in detail using x-ray diffraction, Mössbauer spectroscopy, and transmission electron microscopy (TEM) measurements.¹⁹ Figure 1 shows the effect of milling time on the volume fraction of the phases present in initially single phase $\text{Nd}_2\text{Fe}_{14}\text{B}$. The phase compositions were determined from Mössbauer measurements.¹⁹ In the early stage of milling, the fraction of the amorphous phase increased rapidly at the expense of the $\text{Nd}_2\text{Fe}_{14}\text{B}$ phase. After milling for 12 h the microstructure consisted of ~80% amorphous phase and ~20% $\text{Nd}_2\text{Fe}_{14}\text{B}$. For longer milling times the α -Fe phase began to form, while the fraction of amorphous phase remained approximately constant. For milling times exceeding 40 h the fraction of α -Fe reached a constant value of nearly 0.20. A small fraction of $\text{Nd}_2\text{Fe}_{14}\text{B}$ was still present after milling for 80 h. Miao and co-workers¹⁹ suggested that the α -Fe phase forms from the amorphous phase, thus giving a two-stage reaction $\text{Nd}_2\text{Fe}_{14}\text{B} \rightarrow a1 \rightarrow \alpha\text{-Fe} + a2$, where $a1$ and $a2$ refer to the two amorphous phases. A similar two-stage process has also been observed in two phase α -Fe/ $\text{Nd}_2\text{Fe}_{14}\text{B}$ composites.²⁰

In Sm-Co alloys a single amorphous phase is formed during mechanical alloying.^{21,22} The partial substitution of Fe for Co leads to a mixture of a Sm-Co-Fe amorphous phase and nanocrystalline α -(Fe-Co) in milled samples.²³ As shown in Fig. 2, the formation of α -(Fe-Co) was observed when the Fe content exceeded the Sm concentration. A bright field TEM image and selected area diffraction pattern of an as-milled $\text{Sm}_{9.2}\text{Co}_{49.8}\text{Fe}_{40}$ particle are shown in Fig. 3. The distinct diffraction rings are associated with the α -(Fe-Co) phase. The broad diffuse rings which are also evident are consistent with the presence of an amorphous Sm-Co-Fe phase.

III. EFFECT OF HEAT TREATMENT

In all rare earth-transition metal magnetic alloys studied to date the as-milled structure is magnetically soft and a post-milling heat treatment must be carried out to form the

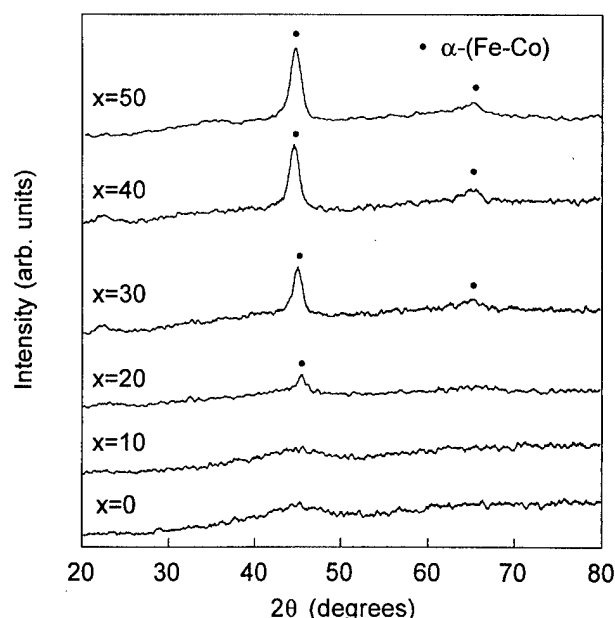


FIG. 2. X-ray diffraction patterns showing effect of Fe content, x , on the phases present in as-milled $\text{Sm}_{10.5}\text{Co}_{89.5-x}\text{Fe}_x$ (Ref. 33).

hard magnetic phase and thus obtain hard magnetic properties. The crystallization temperature in NdFeB alloys has been shown to be a function of the Fe content, increasing from 550 °C to over 600 °C as the equilibrium volume fraction of α -Fe increased from 15% to 75%.²⁰ A two stage crystallization process has been observed to occur in both NdFeB (Ref. 18) and SmCoFe alloys.^{23,24} With NdFeB alloys the first stage involves the crystallization of the amorphous phase with no change in the volume fraction of α -Fe as shown in Fig. 4. No solid state reaction occurred between the amorphous and α -Fe phases during the first stage of crys-

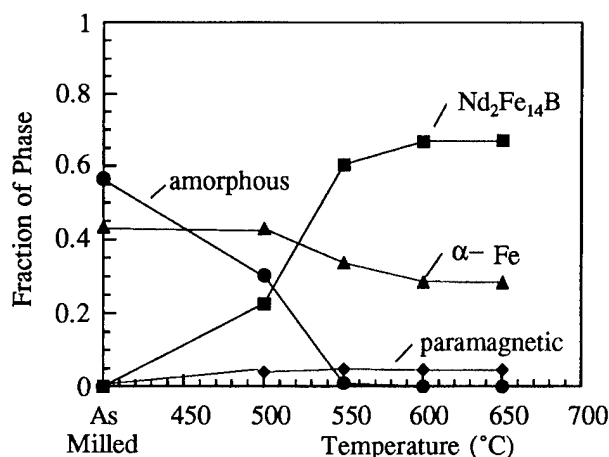


FIG. 4. Phase changes accompanying crystallization in $\text{Nd}_{10}\text{Fe}_{84}\text{B}_6$ (Ref. 18).

tallization. At higher temperatures a decrease in the fraction of α -Fe accompanied further crystallization of $\text{Nd}_2\text{Fe}_{14}\text{B}$. The temperatures required for complete crystallization of the $\text{Nd}_2\text{Fe}_{14}\text{B}$ phase are sufficiently high for grain growth of the α -Fe phase to occur. Minimum grain sizes of 20 nm have been reported for crystallized α -Fe/ $\text{Nd}_2\text{Fe}_{14}\text{B}$ nanocomposite structures, as compared to 5–10 nm in the as-milled powders.²⁰

Similar observations have been reported for SmFeCo alloys.^{21–24} On annealing, the amorphous phase formed during milling initially crystallized to a metastable intermetallic phase or a mixture of intermetallics having the same composition as the amorphous phase. As with α -Fe/ $\text{Nd}_2\text{Fe}_{14}\text{B}$, no solid state reaction occurred between the amorphous phase and the nanocrystalline α -(Fe-Co) phase during crystallization. The initial crystallization reaction occurred between 430 and 530 °C, with the crystallization temperature decreasing with increasing Sm and Fe content of the amorphous phase. A solid state reaction occurs at higher temperatures between the initially crystallized phase and α -(Fe-Co) to form the equilibrium 2–17 phase. It has been found that the intermetallic phase initially crystallized in $\text{Sm}_{10.5}\text{Co}_{49.5}\text{Fe}_{40}[\text{Sm}(\text{Co},\text{Fe})_7]$ has better magnetic properties than formed by solid state reaction at higher temperatures. Since the structure of the initial intermetallic phase is determined by the composition of the amorphous phase, it is clear that control of the as-milled structure is vital for producing a particular combination of soft and hard phases.

IV. MAGNETIC PROPERTIES OF NANOCOMPOSITE MAGNETS

The magnetic properties of nanocomposite magnets characteristically exhibit high values of remanent magnetization and reversible susceptibility. Figure 5 compares the magnetization curves and recoil loops for mechanically alloyed single phase $\text{Sm}_2\text{Fe}_{14}\text{Ga}_3\text{C}_2$ and exchange coupled $\text{Sm}_2\text{Fe}_{14}\text{Ga}_3\text{C}_2 + 40\%$ α -Fe samples, respectively.²⁵ As shown in Fig. 5, the single phase material exhibits a remanent magnetization equal to $0.5 M_s$ and relatively flat recoil loops associated with a low reversible component of the total

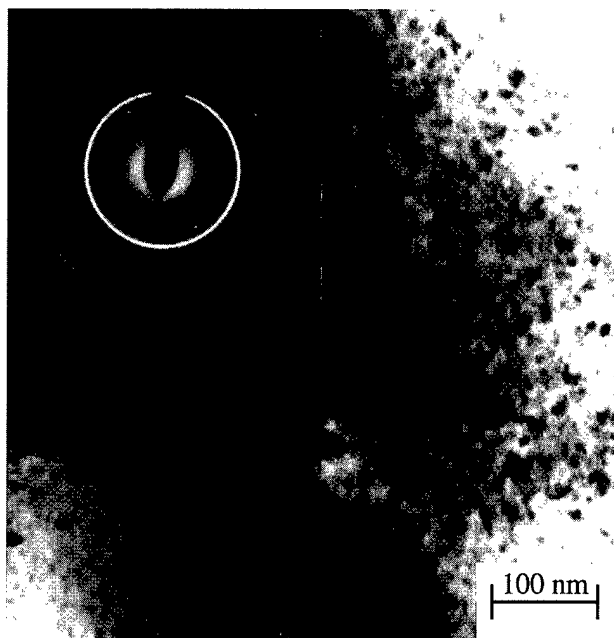


FIG. 3. TEM micrograph of as-milled $\text{Sm}_{9.1}\text{Co}_{49.8}\text{Fe}_{40}$ particle (Ref. 22).

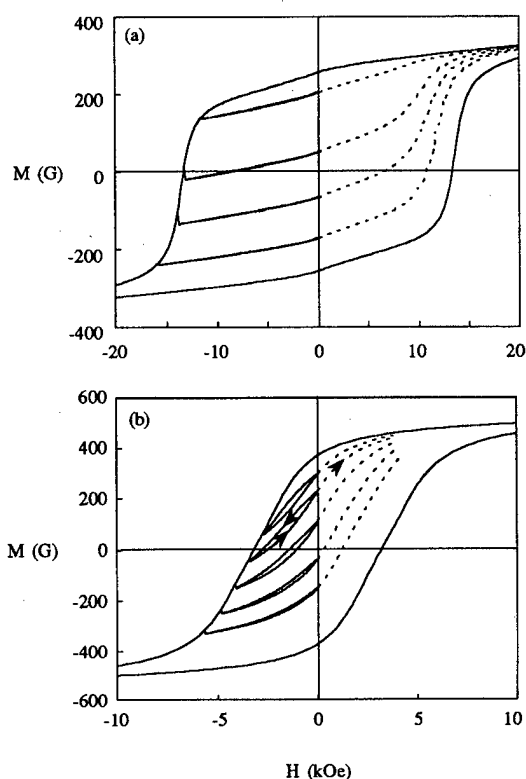


FIG. 5. Magnetization curves and recoil loops for: (a) single phase $\text{Sm}_2\text{Fe}_{14}\text{Ga}_3\text{C}_2$ and (b) $\alpha\text{-Fe}/\text{Sm}_2\text{Fe}_{14}\text{Ga}_3\text{C}_2$ nanocomposite (Ref. 25).

magnetization. In comparison, the two phase material exhibits a higher remanent magnetization ($M_r \sim 0.65 M_s$) and a lower coercivity. The recoil curves exhibit large reversible magnetization.

The high reversible magnetization of exchange coupled nanocomposites is associated with the rotation of the magnetic moments within soft phase grains towards the direction of easy magnetization in neighboring hard grains to which they are exchange coupled. It is important to note that the reversible magnetization changes in the two phase material occur at fields significantly higher than the coercivity of the uncoupled soft phase. This behavior is a clear indication of exchange coupling between nanosized grains of hard and soft phases. Without such exchange coupling irreversible magnetization reversal of the soft phase ($\alpha\text{-Fe}$) would occur at fields of a few Oe, resulting in a reduced remanence and a step in the magnetization curve. The reversible magnetization of the two phase sample is associated almost entirely with the soft phase. Feutrill, McCormick and Street²⁵ have shown that the reversible magnetization in the nanocomposite is limited by the onset of reversal of the hard phase. It is also noted in Fig. 5 that the irreversible relaxation observed at the start of the recoil loops (magnetic viscosity) is significantly reduced in the two phase material as compared with the single phase material. It has been shown that the time dependent magnetic viscosity behavior in exchange coupled magnets is associated with time dependent reversal of the hard phase.²⁵

The nature of the interface between the hard and soft phases in exchange coupled nanocomposites is not well understood. Kneller and Hawig¹ determined that crystallo-

graphic coherence across the interface between hard and soft phases was a necessary condition for exchange coupling and hence remanence enhancement. High resolution TEM studies on nanostructured materials indicate that, while the interfaces take on low energy, highly ordered configurations, there is no crystallographic coherence across interface boundaries.^{26,27} Exchange coupled behavior has been observed in mechanically milled $\text{Nd}_2\text{Fe}_{14}\text{B}$ which consisted of a nanocomposite mixture of $\text{Nd}_2\text{Fe}_{14}\text{B}$ and an amorphous phase.¹⁹ Similar behavior has also been reported in $\text{Sm}_2\text{Fe}_{17}\text{N}_3$, partially disproportionated by mechanical milling to contain a mixture of an amorphous phase and $\text{Sm}_2\text{Fe}_{17}\text{N}_3$.²⁸

Since crystallographic coherence does not exist between the hard and soft phases in these materials, coherence cannot be a necessary condition for exchange coupling and remanence enhancement in nanocomposite magnets. Indeed, significant remanence enhancement has been reported in the melt-spun $\text{Nd}_2\text{Fe}_{14}\text{B}/\alpha\text{-Fe}$ system containing an amorphous intergranular phase.²⁹ Exchange effects between metallic hard and soft magnetic phase components rely on the distributed nature of the electrons involved in cooperative behavior. The range of interaction of collective electrons is of the order of a few interatomic distances. In these circumstances exchange coupling between grains is not critically dependent on crystallographic coherence.

V. FACTORS LIMITING MAGNETIC PROPERTIES

The main factors limiting the performance of mechanically alloyed nanocomposite magnets are microstructure related. The values of a maximum energy product obtained to date are limited by low coercivity, and it is clear that increasing H_c will rely on optimizing the microstructure. In particular, the average grain size and grain size distribution are important parameters determining the magnetic properties. The values of M_r , M_r/M_s , and H_c all decrease with increasing grain size. A number of studies have now shown that the grain size in mechanically alloyed and heat treated nanocomposites exhibiting optimum magnetic properties is typically ~ 20 nm, which is larger than the optimum grain size of ~ 10 nm predicted by modeling studies.^{1,2,9}

As discussed previously, the minimum grain size that can be achieved in mechanically alloyed nanocomposites is limited by the heat treatment conditions employed in the crystallization of the hard magnetic phase. Figures 6 and 7 illustrate the effect of heat treatment time on grain growth and magnetic properties in mechanically alloyed $\text{Sm}_{10.5}\text{Co}_{49.5}\text{Fe}_{40}$ during crystallization at 600°C .^{23,24} The dark field micrographs shown in Fig. 6 were obtained by positioning the objective aperture on the strongest diffraction ring for $\alpha\text{-(Fe-Co)}$. The diffracting grains are thus mainly $\alpha\text{-(Fe-Co)}$, although some bright $\text{Sm}_2(\text{Fe,Co})_7$ grains are also present in the image due to the proximity of the (119) diffraction ring for the 2:7 phase with the (110) diffraction ring of $\alpha\text{-(Fe-Co)}$. In the sample heat treated for 60 min [Fig. 6(b)] the largest grains were identified by energy dispersive spectra (EDS) to be $\alpha\text{-(Fe-Co)}$. Figure 7 shows the decrease in coercivity and M_r/M_s with increasing crystalli-



FIG. 6. Dark field TEM micrographs of mechanically alloyed $\text{Sm}_{10.5}\text{Co}_{49.5}\text{Fe}_{40}$ sample heat treated at 600°C for: (a) 10 min, (b) 60 min (Ref. 23).

zation time. As would be expected, the theoretical density values of $(BH)_{\text{max}}$ decreased significantly with increasing time, from 129 kJ/m^3 for samples crystallized for 5 min to 77 kJ/m^3 for 150 min.²⁴

In $\text{Nd}_2\text{Fe}_{14}\text{B}/\alpha\text{-Fe}$ and SmFeCo nanocomposites crystallization occurs at temperatures of $550\text{--}600^\circ\text{C}$ and $430\text{--}530^\circ\text{C}$, respectively, and grain growth of the soft phase occurs during crystallization. It is clear that to achieve smaller grain sizes it is necessary to reduce grain growth of the soft phase during crystallization. In alloys where a solid state reaction between the amorphous and nanocrystalline phases is required for crystallization of the hard phase, some grain growth of the soft phase is inevitable. Attempts to reduce grain growth of the soft phase through the addition of grain growth inhibitors such as Si, Ta, and Nb have met with mixed success.^{30,31}

The effect of volume fraction of the soft phase in mechanically alloyed nanocomposites has been studied in the $\text{Nd}_2\text{Fe}_{14}\text{B}/\alpha\text{-Fe}$, $\text{Sm}_2\text{Fe}_{17}\text{C}_3/\alpha\text{-Fe}$, and SmFeCo

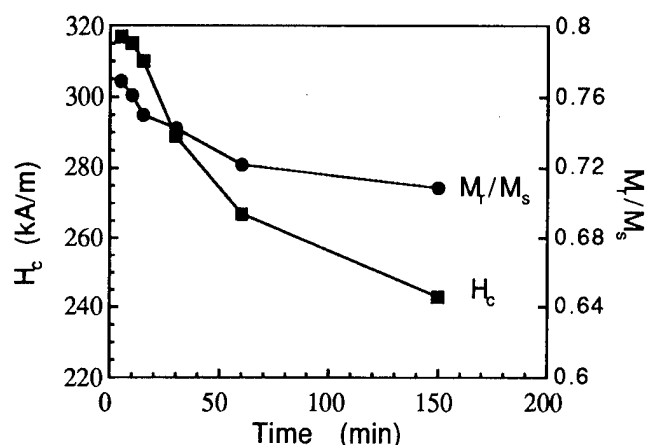


FIG. 7. Effect of crystallization time on coercivity and reduced remanence in $\text{Sm}_{10.5}\text{Co}_{49.5}\text{Fe}_{40}$ heat treated at 600°C (Ref. 23).

systems.^{8,20,22,32,33} Increasing the fraction of the soft phase increases the remanence but decreases the coercivity, consistent with the results of modeling studies.⁹

The uniformity of the microstructure, in particular the distribution of hard and soft grains and the grain size distribution, is also important in determining magnetic properties. If clusters of soft grains are present, exchange coupling will be diminished even if the grain size is small. As a consequence, nonuniform microstructures cause a decrease in both remanence and coercivity.¹¹ The higher values of M_r and H_c observed in mechanically milled $\text{Nd}_2\text{Fe}_{14}\text{B}/\alpha\text{-Fe}$ nanocomposites, as compared to mechanically alloyed powders of the same nominal composition, have been attributed to the finer and more uniform microstructures obtained in the mechanically milled samples.¹⁸ The clustering of $\alpha\text{-Fe}$ grains in hot pressed $\text{Nd}_2\text{Fe}_{14}\text{B}/\alpha\text{-Fe}$ nanocomposites has also been reported.³¹

A further factor limiting the performance of mechanically alloyed nanocomposite magnets is the difficulty of achieving high densities after consolidation. The magnetic properties reported in most studies to date are calculated from experimental measurements assuming samples are 100% dense. Mechanically alloyed powders exhibit low as-pressed densities in comparison to melt spun materials. The as-pressed density of mechanically alloyed powders is generally limited to about 50% of the theoretical density due to the irregular surface morphology of the particles. Density increases up to $\sim 70\%$ may be achieved during heat treatment. However, higher densities can only be obtained by sintering at higher temperatures, resulting in significant grain growth and a loss of exchange coupled behavior. Alternatively, high densities may be achieved by hot pressing with minimal grain coarsening, provided closely controlled processing conditions are used.³¹

VI. CONCLUSIONS

Mechanical alloying has been shown to be a promising method for the production of nanocomposite magnets. The nanocrystalline grain structure inherently developed by milling and heat treatment is essential for effective exchange coupling and remanence enhancement, enabling high values

of $(BH)_{\max}$ to be obtained. Heat treatment of the as-milled structure is required to form hard magnetic phases. The formation of novel metastable hard phases during heat treatment may provide the basis of new nanocomposite phase mixtures with improved magnetic properties. Recent studies have shown that grain growth accompanying crystallization of the hard magnetic phase and the formation of nonuniform grain structures are important factors which currently limit the magnetic properties of mechanically alloyed nanocomposites.

- ¹E. F. Kneller and R. Hawig, IEEE Trans. Magn. **27**, 3588 (1991).
- ²R. Skomski and J. M. D. Coey, Phys. Rev. B **48**, 15812 (1993).
- ³W. H. Meiklejohn and C. P. Bean, Phys. Rev. **102**, 1413 (1956).
- ⁴R. W. McCallum, A. M. Kadin, G. B. Clemente, and J. E. Keem, J. Appl. Phys. **61**, 3577 (1987).
- ⁵R. Coehoorn, D. B. de Mooij, J. P. W. B. Duchateau, and K. H. J. Buschow, J. Phys. (Paris), Colloq. **8**, 669 (1988).
- ⁶R. Coehoorn, D. B. de Mooij, and C. D. de Waard, J. Magn. Magn. Mater. **80**, 101 (1989).
- ⁷J. Ding, P. G. McCormick, and R. Street, J. Magn. Magn. Mater. **124**, 1 (1993).
- ⁸J. Ding, Y. Liu, R. Street, and P. G. McCormick, J. Appl. Phys. **75**, 1032 (1994).
- ⁹T. Schrefl, R. Fisher, J. Fidler, and H. Kronmüller, J. Appl. Phys. **76**, 7053 (1994).
- ¹⁰R. Fisher, T. Schrefl, H. Kronmüller, and J. Fidler, J. Magn. Magn. Mater. **150**, 329 (1995).
- ¹¹R. Fisher, T. Schrefl, H. Kronmüller, and J. Fidler, J. Magn. Magn. Mater. **153**, 35 (1996).
- ¹²H. Kronmüller, Nanostruct. Mater. **6**, 157 (1995).
- ¹³C. C. Koch, Nanostruct. Mater. **2**, 109 (1993).
- ¹⁴L. Schultz, J. Wecker, and E. J. Hellstern, J. Appl. Phys. **61**, 3583 (1987).
- ¹⁵P. G. McCormick, *Handbook on the Physics and Chemistry of Rare Earths*, edited by K. A. Gschneidner and L. Eyring (North-Holland, Amsterdam, 1997), Chap. 16, Vol. 24.
- ¹⁶J. S. C. Jang and C. C. Koch, J. Mater. Res. **5**, 498 (1990).
- ¹⁷T. Alonso, H. Yang, Y. Liu, and P. G. McCormick, Appl. Phys. Lett. **60**, 833 (1992).
- ¹⁸W. F. Miao, J. Ding, P. G. McCormick, and R. Street, J. Appl. Phys. **79**, 2079 (1996).
- ¹⁹W. F. Miao, J. Ding, P. G. McCormick, and R. Street, J. Phys. D: Appl. Phys. **29**, 2370 (1996).
- ²⁰W. F. Miao, J. Ding, P. G. McCormick, and R. Street, J. Alloys Compd. **240**, 200 (1996).
- ²¹J. Ding, P. G. McCormick, and R. Street, J. Magn. Magn. Mater. **135**, 200 (1994).
- ²²P. A. I. Smith, Ph. D. thesis, University of Western Australia, 1997.
- ²³P. A. I. Smith, P. G. McCormick, and R. Street, Mater. Sci. Forum **179-181**, 527 (1995).
- ²⁴P. A. I. Smith, J. Ding, R. Street, and P. G. McCormick, Scr. Mater. **34**, 61 (1996).
- ²⁵E. H. Feuttrill, P. G. McCormick, and R. Street, J. Phys. D: Appl. Phys. **29**, 2320 (1996).
- ²⁶D. H. Ping, T. S. Xie, D. X. Li, and H. Q. Ye, Nanostruct. Mater. **5**, 457 (1995).
- ²⁷A. Manaf, R. A. Buckley, and H. Davies, J. Magn. Magn. Mater. **128**, 302 (1993).
- ²⁸D. Eckert, P. A. P. Wendhausen, B. Gebel, M. Wolf, and K. H. Müller, J. Magn. Magn. Mater. **157-158**, 93 (1996).
- ²⁹A. Inoue, A. Takeuchi, A. Makino, and T. Masumoto, Mater. Trans., JIM **36**, 676 (1995).
- ³⁰K. O'Donnell, C. Kuhrt, and J. M. D. Coey, J. Appl. Phys. **76**, 7068 (1994).
- ³¹J. Wecker, K. Schnitzke, H. Cerva, and W. Grogger, Appl. Phys. Lett. **67**, 563 (1995).
- ³²M. Jurczyk, S. J. Collocott, J. B. Dunlop, and P. B. Gwan, J. Phys. D **29**, 2284 (1996).
- ³³P. A. I. Smith, P. G. McCormick, and R. Street, Proc. Symp. Phase Transformations in Metastable Materials, MRS, Warrendale, PA (unpublished, 1998).

Micromagnetic simulation of magnetizability of nanocomposite Nd-Fe-B magnets

Thomas Schrefl^{a)} and Josef Fidler

Institute of Applied and Technical Physics, Vienna University of Technology, Wiedner Hauptstrasse 8-10, A-1040 Vienna, Austria

Micromagnetic finite element calculations clearly show that the magnetizability of nanocomposite $\text{Nd}_2\text{Fe}_{14}\text{B}$ magnets improves with increasing α -Fe content. The magnetization curves show a steep increase at the domain propagation field in dc demagnetized samples. Thermally demagnetized states store a higher amount of exchange energy, leading to an increase of the initial susceptibility. An applied field of 960 kA/m leads to a saturation of 85% for a two-phase α -Fe/ $\text{Nd}_2\text{Fe}_{14}\text{B}$ magnet, whereas the $\text{Fe}_3\text{B}/\text{Nd}_2\text{Fe}_{14}\text{B}$ magnet and the single-phase $\text{Nd}_2\text{Fe}_{14}\text{B}$ magnets reach a saturation of only 70% and 50%, respectively. The improved saturation behavior of two-phase α -Fe/ $\text{Nd}_2\text{Fe}_{14}\text{B}$ magnets has to be attributed to the exchange field which is provided by α -Fe grains that are already oriented parallel to the field direction. Hard magnetic grains that remain oppositely magnetized after applying the maximum magnetizing field deteriorate the coercive squareness in single-phase $\text{Nd}_2\text{Fe}_{14}\text{B}$ magnets and two-phase $\text{Fe}_3\text{B}/\text{Nd}_2\text{Fe}_{14}\text{B}$ magnets. © 1998 American Institute of Physics. [S0021-8979(98)30711-2]

I. INTRODUCTION

Exchange-spring permanent magnets have become a topic of recent research in permanent magnets.¹⁻⁴ A mixture of a magnetically hard and soft phases reduces the overall rare-earth content, while preserving good hard magnetic properties.^{5,6} In addition to the cost reduction, the improved magnetizability of nanocomposite $\text{Nd}_2\text{Fe}_{14}\text{B}$ magnets is a major advantage as compared to conventional bonded magnets.⁷ Panchanathan⁸ compared the saturation behavior of single phase $\text{Nd}_2\text{Fe}_{14}\text{B}$, two phase $\text{Fe}_3\text{B}/\text{Nd}_2\text{Fe}_{14}\text{B}$, and two-phase α -Fe/ $\text{Nd}_2\text{Fe}_{14}\text{B}$ magnets. The magnetization field of 800–960 kA/m leads to a saturation of 55%–60% for a standard, single phase $\text{Nd}_2\text{Fe}_{14}\text{B}$ powder. The α -Fe/ $\text{Nd}_2\text{Fe}_{14}\text{B}$ composites show a saturation of about 80% with a field of only 960 kA/m, while the corresponding bonded magnet reaches a coercive field of 320 kA/m. Rave and co-workers⁹ investigated the effect of different initial states on the initial magnetization curve of nanocrystalline permanent magnets. They reported a higher susceptibility in thermally demagnetized samples than in dc demagnetized samples. This susceptibility difference was qualitatively reproduced by two-dimensional micromagnetic simulations assuming a brick wall model to represent the grain structure.

This work presents three-dimensional micromagnetic calculations of magnetizability and coercivity of α -Fe/ $\text{Nd}_2\text{Fe}_{14}\text{B}$ and $\text{Fe}_3\text{B}/\text{Nd}_2\text{Fe}_{14}\text{B}$ two-phase magnets. The magnetic properties of single phase $\text{Nd}_2\text{Fe}_{14}\text{B}$ magnets are calculated as reference. The use of the finite element method allows modeling of realistic microstructures.

II. MICROMAGNETIC SIMULATION OF DEMAGNETIZED STATES

The theoretical description of magnetization processes in ferromagnetic materials starts from the total magnetic Gibbs

free energy. Its minimization provides a stable equilibrium state of a ferromagnetic structure. The actual path of the magnetization towards a local minimum can be computed by the time integration of the Gilbert equation of motion. The transient states show how reversed domains nucleate and propagate.¹⁰ In order to reduce the required computation time, a conjugate gradient method is used to minimize the energy in the present study. Details of the finite element algorithm are described Ref. 6. The cubic model magnet with an edge length of 80 nm consists of 125 polyhedral grains generated from grain growth simulation using Voronoi cells. The average grain diameter is 20 nm. The different phases and the anisotropy directions are randomly assigned to the grains. The composite magnet contains 40 vol % $\text{Nd}_2\text{Fe}_{14}\text{B}$ and either α -Fe or Fe_3B as soft magnetic phase. Table I gives the intrinsic material parameters¹¹⁻¹³ used for the calculations.

The magnetization distribution with the lowest energy represents a thermally demagnetized state. The magnetocrystalline anisotropy energy is the dominating energy term in $\text{Nd}_2\text{Fe}_{14}\text{B}$ magnets. To minimize the energy, the magnetization within the hard magnetic grains must be parallel to the anisotropy directions. The requirement to minimize the magnetostatic energy determines the orientation of the magnetization along the easy axes. Thus, an approximation of a thermally demagnetized state can be obtained from simulated annealing¹⁴ to minimize the magnetostatic energy followed by the calculation of equilibrium states for increasing exchange constant. Indeed the total energy of the thermally demagnetized state calculated by the above procedure is about 5% smaller than the total energy of an equilibrium state with grains initialized randomly along their easy axes. This procedure to calculate the thermally demagnetized state adopts the zero exchange formulation of micromagnetics as outlined by DeSimone.¹⁵ The minimization of the total energy leads to a dc demagnetized state assuming an initial

^{a)}Electronic mail: schrefl@email.tuwien.ac.at

TABLE I. Intrinsic magnetic properties used for the calculations. The columns give the spontaneous magnetic polarization $J_s(T)$, the anisotropy constants K_1 and K_2 (MJ/m³), and the exchange constant A (pJ/m).

	J_s	K_1	K_2	A	Reference
Nd ₂ Fe ₁₄ B	1.61	4.5	0.66	12.5	11
Fe ₃ B	1.62	-0.32		12.5	12
α -Fe	2.15	0.046	0.015	25	13

magnetization antiparallel to each other in two halves of the cube. The net magnetization of the calculated demagnetized states is not exactly zero, owing to the limited number of grains.

III. RESULTS AND DISCUSSION

Figure 1 compares the magnetization curves starting from the thermally demagnetized and dc demagnetized states. The solid, dotted, and dashed lines refer to the α -Fe/Nd₂Fe₁₄B, the Fe₃B/Nd₂Fe₁₄B, and the single-phase Nd₂Fe₁₄B magnets. The magnetization curve of the dc demagnetized Nd₂Fe₁₄B magnet clearly shows three different regimes. At low external fields the magnetization rotates reversibly towards the direction of the applied field within the grains originally magnetized oblique to the field direction. At an external field of about 1000 kA/m the region with upward magnetization starts to expand through the entire magnet leading to a steep increase of the dc magnetization curve at 1340 kA/m. At external fields greater than 1400 kA/m the upward magnetization has completely swept through the magnet, and reversible rotations are the only process to increase the magnetization. The thermally demagnetized state stores a higher amount of exchange energy than the dc demagnetized state, which can be released upon saturation. Only a small external field is required to initiate the irreversible switching of entire grains in the thermally demagnetized Nd₂Fe₁₄B magnet, leading to a higher initial susceptibility.

The soft magnetic grains of the two-phase α -Fe/Nd₂Fe₁₄B or Fe₃B/Nd₂Fe₁₄B magnet become oriented parallel to the field direction at low applied fields. Their exchange field helps to reverse neighboring hard magnetic grains. The comparison of the dc magnetization curves of Fig. 1 shows that the external field required to expand the upward domain through the hard magnetic grains decreases to 750 kA/m as 60% of the hard magnetic phase is replaced by Fe₃B, and to 540 kA/m as Fe₃B is substituted by α -Fe. Figure 2 shows the magnetization process of a two-phase α -Fe/Nd₂Fe₁₄B magnet starting from a dc demagnetized state. The plane where the magnetization component parallel to the field direction becomes zero indicates the position of the domain wall. The solid line denotes the trace of this plane on the surface of the cubic magnet. In nanocrystalline permanent magnets the competitive effects of magnetocrystalline anisotropy and intergrain exchange interactions lead to a strongly inhomogeneous magnetization distribution.⁶ Whereas the magnetization remains parallel to the easy axes in the center of the grains, it deviates from the local easy axis in the vicinity of the grain boundaries. As a consequence, the two regions originally oppositely magnetized are not sepa-

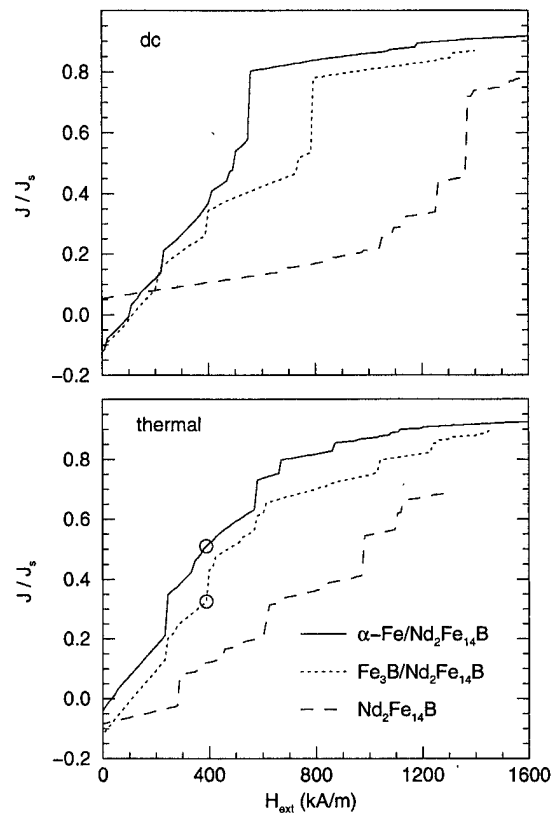


FIG. 1. Calculated magnetization curves starting from a dc-demagnetized state (top) and a thermally demagnetized state (bottom). The solid, dotted, and dashed lines refer to the α -Fe/Nd₂Fe₁₄B, the Fe₃B/Nd₂Fe₁₄B and the single-phase Nd₂Fe₁₄B magnet, respectively. The circles indicate the magnetic states plotted in Fig. 3.

rated by a well-defined domain wall. On both sides of the border between the oppositely magnetized regions, the direction of the magnetization varies on a length scale comparable with the domain wall width. Thus the transition structure is far more complex than in a classical Bloch wall, where the magnetization changes only in the direction perpendicular to the wall. The plot on the left-hand side of Fig. 2 gives the position of the wall for zero applied field. As the external field is increased, the wall bends around Nd₂Fe₁₄B grains following their boundaries. However, the wall may go through α -Fe grains. The plot on the right-hand side of Fig.

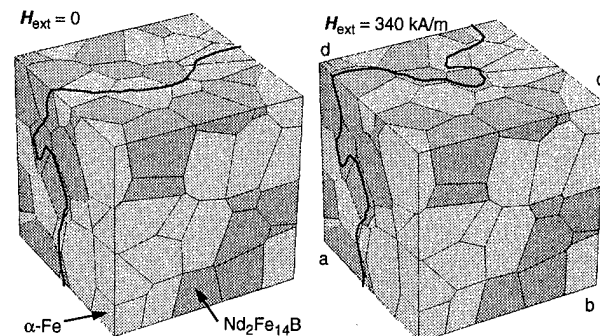


FIG. 2. Domain wall propagation in the dc demagnetized α -Fe/Nd₂Fe₁₄B magnet. The solid line gives the trace of the plane where the component of the magnetization parallel to the direction of the applied field becomes zero.

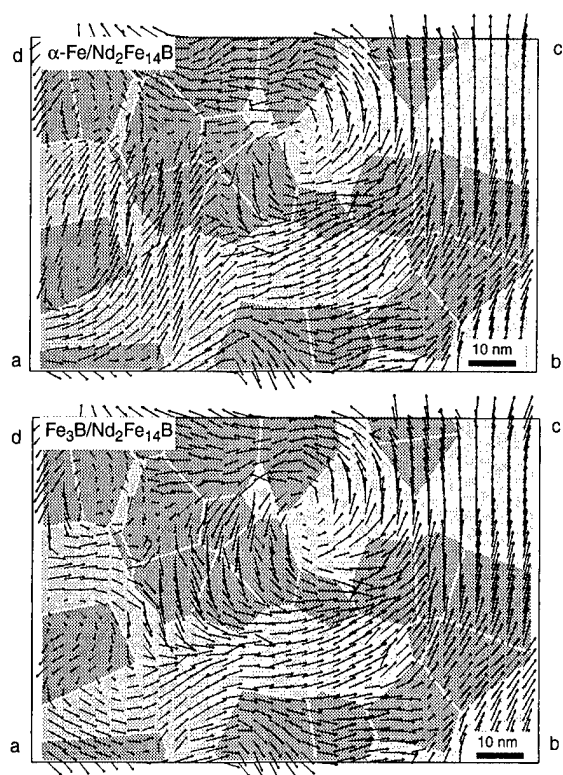


FIG. 3. Magnetization distribution during saturation of the thermally demagnetized α -Fe/Nd₂Fe₁₄B and Fe₃B/Nd₂Fe₁₄B magnet. The magnetization is projected onto a plane parallel to the field direction for an applied field of 390 kA/m. The field is applied parallel to the vector from point b to point c.

2 depicts the trace of the wall for an applied field of 340 kA/m, showing the deflection of the wall around the hard magnetic grains.

The comparison of the magnetization curves of Fig. 1 clearly shows that the magnetizability increases with increasing α -Fe content. In the thermally demagnetized samples, an applied field of 960 kA/m leads to 85% saturation for a two-phase α -Fe/Nd₂Fe₁₄B magnet and to 70% saturation for the Fe₃B/Nd₂Fe₁₄B magnet. For the same applied field, the single phase magnet reaches a saturation of only 50%. The very same mechanism which causes the decrease of the domain propagation field in the dc demagnetized samples with increasing α -Fe content improves the saturation behavior of thermally demagnetized, two-phase magnets. The magnetization of the Fe₃B and α -Fe grains becomes oriented along the saturation direction at an applied field of 400 kA/m. The exchange field provided by the saturated soft magnetic grains facilitates the alignment of neighboring hard magnetic grains. Figure 3 gives the magnetization distribution in a slice plane parallel to the field direction. Fe₃B grains require a larger applied field to become aligned parallel to the field direction than α -Fe grains. Neighboring hard and soft magnet grains already saturated at an applied field of 390 kA/m in the α -Fe/Nd₂Fe₁₄B magnet remain reversed in the Fe₃B/Nd₂Fe₁₄B magnet.

Figure 4 presents the calculated demagnetization curves as a function of the saturation field. Hard magnetic grains

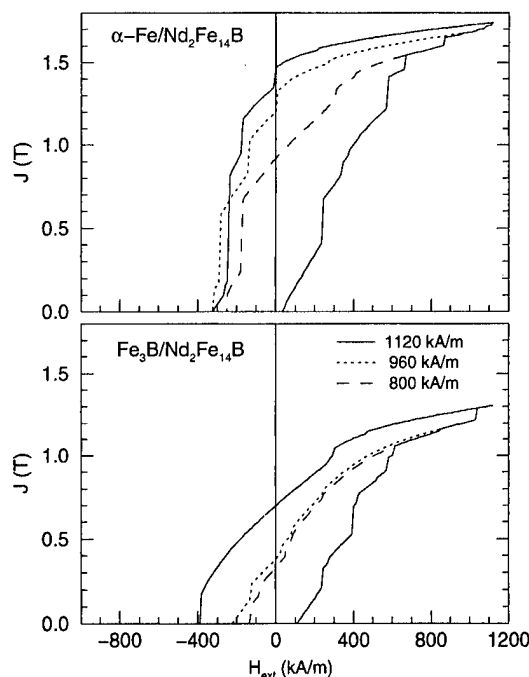


FIG. 4. Influence of the applied field on the loop shape and the coercive field for α -Fe/Nd₂Fe₁₄B and Fe₃B/Nd₂Fe₁₄B magnets. The demagnetization curves were calculated after saturation with an applied field of 800, 960, and 1120 kA/m.

that remain oppositely magnetized deteriorate coercivity and remanence in Fe₃B/Nd₂Fe₁₄B magnets for a saturation field lower than 1000 kA/m. Two phase α -Fe/Nd₂Fe₁₄B magnets show square hysteresis loops. The calculated values for the coercive field and the remanence are 340 kA/m and 1.2 T for a saturation field of 960 kA/m.

ACKNOWLEDGMENTS

This work has been supported by the Austrian Science Foundation FWF (Grant No. P10511-NAW) and the EC-BRITE/EURAM Project BRPR-CT95-0097.

- ¹R. Coehoorn, D. B. DeMooij, and C. DeWaard, *J. Magn. Magn. Mater.* **80**, 101 (1989).
- ²E. F. Kneller and R. Hawig, *IEEE Trans. Magn.* **27**, 3588 (1991).
- ³S. Hirose and H. Kanekiyo, *Mater. Sci. Eng., A* **217/218**, 367 (1996).
- ⁴P. Crespo, V. Neu, and L. Schultz, *J. Phys. D* **30**, 2298 (1997).
- ⁵R. Skomski and J. M. D. Coey, *Phys. Rev. B* **48**, 15812 (1993).
- ⁶T. Schrefl, R. Fischer, J. Fidler, and H. Kronmüller, *J. Appl. Phys.* **76**, 7053 (1994).
- ⁷J. J. Croat, *J. Appl. Phys.* **81**, 4804 (1997).
- ⁸V. Panchanathan, *IEEE Trans. Magn.* **31**, 3605 (1995).
- ⁹W. Rave, D. Eckert, B. Gebel, A. Handstein, R. Schäfer, and K.-H. Müller, *Proceedings of the XIV International Workshop on Rare Earth Magnets and their Application, Sao Paulo, Brasil*, edited by F. P. Missel *et al.* (World Scientific, Singapore, 1996), p. 297.
- ¹⁰T. Schrefl, H. Roitner, and J. Fidler, *J. Appl. Phys.* **81**, 5567 (1997).
- ¹¹M. Sagawa, S. Fujimura, H. Yamamoto, Y. Mastuura, and S. Hirose, *J. Appl. Phys.* **57**, 4094 (1985).
- ¹²W. Coene, F. Hakkens, R. Coehoorn, B. D. de Mooij, C. De Waard, J. Fidler, and R. Grössinger, *J. Magn. Magn. Mater.* **96**, 189 (1991).
- ¹³E. Kneller, *Ferromagnetism* (Springer, Berlin, 1962).
- ¹⁴A. Corana, M. Marchesi, C. Martini, and S. Ridella, *ACM Trans. Math. Softw.* **13**, 262 (1987).
- ¹⁵A. De Simone, *Arch. Ration. Mech. Anal.* **125**, 99 (1993).

Thick $\text{Fe}_3\text{B}/\text{Nd}_2\text{Fe}_{14}\text{B}$ nanocomposite permanent magnet flakes prepared by slow quenching

H. Kanekiyo and S. Hirosawa^{a)}

Research and Development Division, Sumitomo Special Metals Co., Ltd., 2-15-17 Egawa, Shimamoto-cho, Mishima-gun, Osaka 618, Japan

Thick permanent magnet flakes of $\text{Fe}_3\text{B}/\text{Nd}_2\text{Fe}_{14}\text{B}$ nanocomposites have been prepared directly from molten alloys by means of the low surface-velocity melt-spinning technique under a vacuum. Dependence of microstructure and magnetic properties of $\text{Nd}_4\text{Fe}_{77.5}\text{B}_{18.5}$ rapidly solidified alloys have been studied as functions of pressure of a melt-spinner chamber and the surface velocity of a Cu roll. An as-spun alloy of $\text{Nd}_{3.5}\text{Dy}_1\text{Fe}_{73}\text{Co}_3\text{Ga}_1\text{B}_{18.5}$ obtained at a $V_s = 3.3$ m/s under a 1.3 kPa Ar atmosphere has a thickness of 240 μm and the room temperature magnetic properties of $(BH)_{\text{max}} = 131.6$ kJ/m³, $B_r = 1.15$ T, and $H_{cJ} = 400$ kA/m. © 1998 American Institute of Physics. [S0021-8979(98)15611-6]

I. INTRODUCTION

Nanocomposite permanent magnet materials consisting of tetragonal Fe_3B and $\text{Nd}_2\text{Fe}_{14}\text{B}$ have been attracting much interest since they were reported by Coehoorn in 1988.¹ The hard magnetic properties of these alloys have been significantly improved by the present authors by means of modifications of composition,^{2,3} adding a practical importance on these materials as new candidates for hard magnetic ingredients of resin-bonded permanent magnets.

These materials are produced from amorphous alloys prepared by a single-roll melt-spinning technique and a subsequent heat treatment procedure, in which the amorphous alloys crystallize into a nanocomposite composed of the metastable Fe_3B and the hard magnetic $\text{Nd}_2\text{Fe}_{14}\text{B}$ phases with a minor amount of $\alpha\text{-Fe}$.¹

Although it has been known that $\text{Nd}_2\text{Fe}_{14}\text{B}$ melt-spun materials show good hard magnetic properties in the as-spun state,⁴ the effort to obtain the hard magnetic $\text{Fe}_3\text{B}/\text{Nd}_2\text{Fe}_{14}\text{B}$ as-spun alloys has been unsuccessful. However, to make a conclusive verdict, the effects of quenching conditions on the rapidly solidified alloys have not been thoroughly investigated in the vicinity of the $\text{Fe}_3\text{B}/\text{Nd}_2\text{Fe}_{14}\text{B}$ nanocomposite compositions.

This article reports the effects of melt-spinning conditions, particularly the pressure of the chamber atmosphere of a melt spinner and the surface velocity of a Cu roll during melt spinning, on the microstructure and hard magnetic properties of as-spun alloys. The $\text{Fe}_3\text{B}/\text{Nd}_2\text{Fe}_{14}\text{B}$ nanocomposites have been obtained in the as-quenched alloys for the first time by reducing the chamber pressure down to a practically vacuum regime and the roll surface velocity to a range between 3 and 5 m/s. The hard magnetic materials thus obtained are thick flakes. They may be processed either into crushed powder for fabrication of resin-bonded magnets or directly into thin platelet permanent magnets simply by cutting or machining.

II. EXPERIMENTAL PROCEDURES

Alloys of compositions of $\text{Nd}_4\text{Fe}_{77.5}\text{B}_{18.5}$ and $\text{Nd}_{3.5}\text{Dy}_1\text{Fe}_{73}\text{Co}_3\text{Ga}_1\text{B}_{18.5}$ were prepared by the single role melt-spinning technique under an Ar pressure (P) ranging from 1.3 to 95 kPa. About 30 g of alloys were taken from premelted large ingots and remelted in a quartz crucible. Immediately after the temperature of the molten alloys reached approximately 1300 °C, they were injected through an orifice of a diameter of 0.8 mm cut at the bottom of the crucible. The injection pressure was kept to be a constant value of 30 kPa relative to the chamber pressure. The quenching roll was made of Cu and rotated at a surface velocity (V_s) in a range between 2 and 30 m/s.

The rapidly solidified alloys were investigated using differential thermal analysis (DTA) and powder x-ray diffraction (XRD) analysis using the Cu $K\alpha$ radiation. The surfaces of rapidly solidified alloys were investigated by scanning electron microscopy (SEM). Magnetic properties of the materials were measured at room temperature along the widest surface of flake-shaped specimens using a vibrating sample magnetometer (VSM).

III. EXPERIMENTAL RESULTS

When V_s is 5 m/s, which is extremely slow compared to conventional conditions used for Nd-Fe-B melt-spun hard magnets (V_s is typically 20 m/s), rapidly solidified $\text{Nd}_4\text{Fe}_{77.5}\text{B}_{18.5}$ alloys are obtained as crystalline. For a chamber pressure (P) of 75 kPa, the condition used for our previous studies, the existence of $\alpha\text{-Fe}$ in the alloy is readily confirmed by XRD as shown in Fig. 1. This alloy has an intrinsic coercivity of approximately 20 kA/m, which is negligible as a hard magnet. When P is reduced to 1.3 kPa, the $\text{Fe}_3\text{B}/\text{Nd}_2\text{Fe}_{14}\text{B}$ composite structure is realized in the as-spun alloy for the same V_s (Fig. 1). The diffraction peaks are relatively broad, indicating that the material consists of nanometer-sized crystallites.

Observations of the surface morphology of the flakes by SEM reveal that the flakes obtained under a chamber pressure close to atmospheric pressure have shallow dimples of

^{a)}Electronic mail: hirosawa.s@ssmc.co.jp

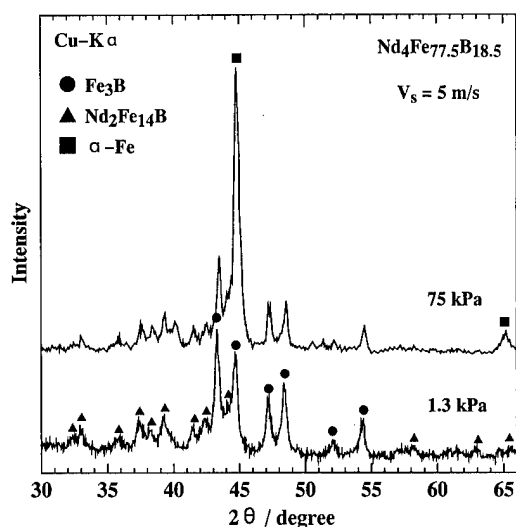


FIG. 1. Comparison of x-ray diffraction patterns of $\text{Nd}_4\text{Fe}_{77.5}\text{B}_{18.5}$ as-spun alloys under different chamber pressures of 75 and 1.3 kPa Ar on a Cu-roll surface moving at $V_s = 5$ m/s.

an approximate diameter of $200\ \mu\text{m}$ on the surface which had contact with the quenching roll ("the roll-side surface" as opposed to the free surface). These are gas pockets created when a strand of the molten alloy had contact with the surface of the quenching roll. On the other hand, the roll-side surfaces are smooth and optically flat when the chamber pressure is lower than 30 kPa. It has been observed that, for these reduced chamber pressures, the quenched alloy is a continuous ribbon or a thin plate.

Figure 2 shows powder XRD patterns of the as-spun $\text{Nd}_4\text{Fe}_{77.5}\text{B}_{18.5}$ alloys for a chamber pressure of 1.3 kPa, showing the effects of V_s on the microstructure. For $V_s = 20$ m/s, an amorphous material is obtained in an agreement with the previous studies. With decreasing V_s , diffraction peaks from Fe_3B and $\text{Nd}_2\text{Fe}_{14}\text{B}$ gradually develop, indicating development of the nanocomposite structure. The dependence of the thickness on V_s of the rapidly solidified

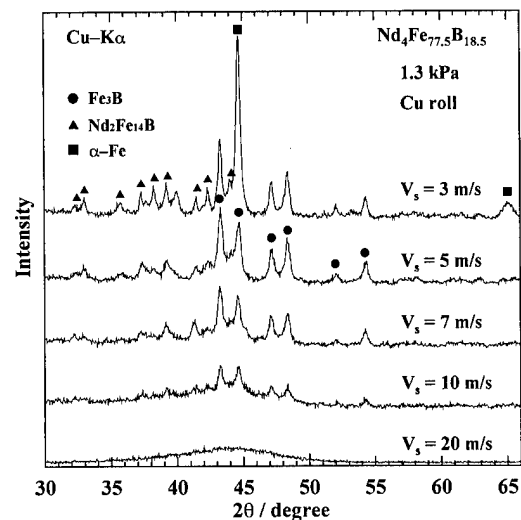


FIG. 2. X-ray diffraction patterns of $\text{Nd}_4\text{Fe}_{77.5}\text{B}_{18.5}$ as-spun alloys obtained under an Ar pressure of 1.3 kPa on a Cu-roll surface moving at different velocities.

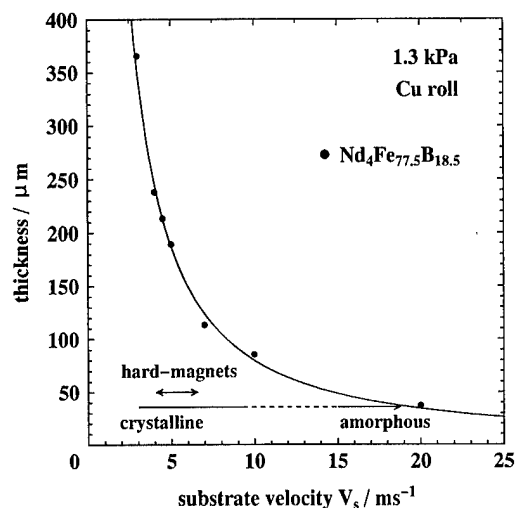


FIG. 3. Dependence of thickness on roll surface velocity for $\text{Nd}_4\text{Fe}_{77.5}\text{B}_{18.5}$ as-spun alloys obtained under an Ar pressure of 1.3 kPa. The width of the ribbons are in a range between 0.7 and 1.2 mm.

$\text{Nd}_4\text{Fe}_{77.5}\text{B}_{18.5}$ ribbons obtained with $P = 1.3$ kPa is shown in Fig. 3. Ribbon widths were in the range between 0.7 and 1.2 mm with the inverse dependence on V_s .

The dependence of magnetic properties of the rapidly solidified $\text{Nd}_4\text{Fe}_{77.5}\text{B}_{18.5}$ alloys on V_s is shown in Fig. 4. Except for the magnetization measured under an external field of 1.2 T ($J_{1.2}$), the intrinsic coercivity, remanence (B_r), and maximum energy product [$(BH)_{\text{max}}$] show strong dependencies on V_s . The optimum hard magnetic properties have been obtained with $V_s = 5$ m/s.

Demagnetization curves of rapidly solidified $\text{Nd}_4\text{Fe}_{77.5}\text{B}_{18.5}$ and $\text{Nd}_{3.5}\text{Dy}_1\text{Fe}_{73}\text{Co}_3\text{Ga}_1\text{B}_{18.5}$ alloys are shown in Fig. 5. The optimal V_s value depends on alloy concentration. The optimal V_s for the latter alloy is 3.3 m/s and the thickness is $240\ \mu\text{m}$. The optimal magnetic properties are $(BH)_{\text{max}} = 118.1\ \text{kJ/m}^3$, $H_{\text{cJ}} = 276\ \text{kA/m}$, and $B_r = 1.25\ \text{T}$ for $\text{Nd}_4\text{Fe}_{77.5}\text{B}_{18.5}$ and $(BH)_{\text{max}} = 131.6\ \text{kJ/m}^3$, $H_{\text{cJ}} = 400\ \text{kA/m}$, and $B_r = 1.15\ \text{T}$ for

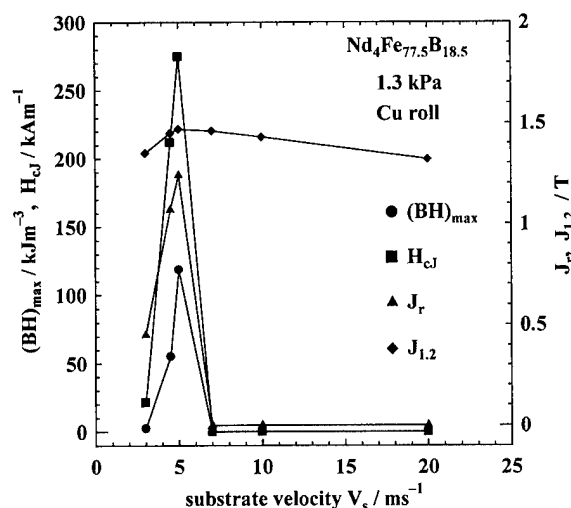


FIG. 4. Dependence of magnetic properties of $\text{Nd}_4\text{Fe}_{77.5}\text{B}_{18.5}$ as-spun alloys obtained under an Ar pressure of 1.3 kPa on the roll surface velocity, V_s .

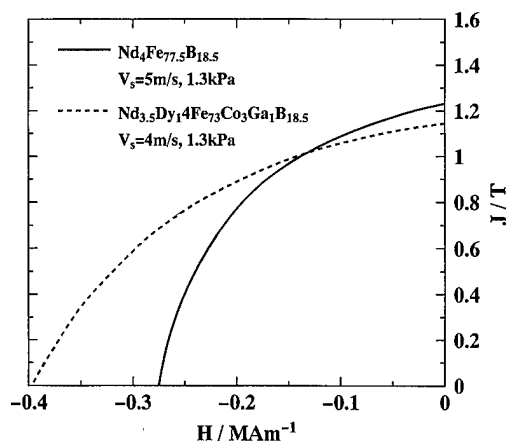


FIG. 5. Demagnetization curves of as-spun $\text{Nd}_4\text{Fe}_{77.5}\text{B}_{18.5}$ and $\text{Nd}_{3.5}\text{Dy}_1\text{Fe}_{73}\text{Co}_3\text{Ga}_1\text{B}_{18.5}$ obtained under an 1.3 kPa Ar atmosphere on Cu-roll surface moving at $V_s = 5$ and 3.3 m/s, respectively.

$\text{Nd}_{3.5}\text{Dy}_1\text{Fe}_{73}\text{Co}_3\text{Ga}_1\text{B}_{18.5}$. These values are equivalent to those obtained previously on alloys crystallized from amorphous precursors.² These materials are magnetically isotropic.

IV. DISCUSSION

In this investigation, it has been clearly demonstrated that the chamber pressure during the melt-spinning procedure has a pronounced effect on microstructure and magnetic properties of as-spun alloys of the $\text{Fe}_3\text{B}/\text{Nd}_2\text{Fe}_{14}\text{B}$ nanocomposite compositions. The presence of gas pockets observed on the roll-side surface of flakes obtained under a near atmospheric chamber pressure would significantly retard heat flow from the molten alloy to the surface of the quenching roll, causing large differences of cooling rates throughout the alloy flakes during solidification. Without the formation of gas pockets in the near vacuum atmosphere, uniform cooling must have been realized. As a result, an unequivocal dependence of microstructure and magnetic properties of these alloys on V_s has been observed, showing the existence of a window in which as-spun hard magnet materials of the $\text{Fe}_3\text{B}/\text{Nd}_2\text{Fe}_{14}\text{B}$ nanocomposite structure can be obtained.

In the Nd-Fe-B system, other types of nanocomposites consisting of α -Fe and $\text{Nd}_2\text{Fe}_{14}\text{B}$ are possible in the Fe-rich composition regime. It has been reported that these nanocomposites are obtainable either directly by a melt-spinning technique or via heat treatment of amorphous precursors,^{5,6} which is not surprising because both α -Fe and $\text{Nd}_2\text{Fe}_{14}\text{B}$ are in equilibrium for compositions of the alloys. In contrast, the $\text{Fe}_3\text{B}/\text{Nd}_2\text{Fe}_{14}\text{B}$ nanocomposites are believed to be metastable because they decompose into a stable mixture of α -Fe and $\text{Nd}_{11}\text{Fe}_{14}\text{B}_4$ when annealed at a temperature above approximately 800 °C.⁷ Therefore, the formation of a metastable composite structure in this type of alloy is not trivial. The possibility of Fe_3B being a high temperature equilibrium phase above 1160 °C was pointed out by Kahn *et al.*⁸ Therefore, Fe_3B may have been formed in the alloy at a high

temperature to consume a substantial amount of boron to allow the formation of $\text{Nd}_2\text{Fe}_{14}\text{B}$ at a lower temperature in the boron-depleted, neodymium-rich region of the alloy. In the present investigation, however, the as-quenched microstructure changed gradually from an amorphous to a $\text{Fe}_3\text{B}/\text{Nd}_2\text{Fe}_{14}\text{B}$ nanocomposite with decreasing rotor surface velocity in a similar manner as the microstructure of a corresponding amorphous alloy does during successive heat treatments.⁷ This observation may possibly indicate that an amorphous solid is formed first and subsequently decomposed into Fe_3B and $\text{Nd}_2\text{Fe}_{14}\text{B}$ in the temperature range in which these phases are metastable when cooling rate is moderate. The elucidation of the rapid solidification behavior of this type of alloy is left for further investigations.

The $\text{Fe}_3\text{B}/\text{Nd}_2\text{Fe}_{14}\text{B}$ hard magnets obtained in relatively slow surface velocities are continuous thick ribbons, the length of which may be as long as a few meters. The limitation of length occurs from a small span of a sample recovery chamber available in the experimental facility. The thickness of the materials is on the order of a few hundred micrometers, for which shaping of most conventional hard magnet materials by machining or polishing is not practical. Although it is known that MnAlC and FeCrCo permanent magnet materials can be fabricated by rolling in their manufacturing process to produce plate-shaped permanent magnets, the former material has a lower saturation magnetization and the latter has only a small coercivity compared to the present materials obtained by direct quenching. Therefore, the thick flake magnets obtained in this investigation are unique and may open new application fields in which thin platelet permanent magnets with a high energy product are desired.

V. CONCLUSION

The $\text{Fe}_3\text{B}/\text{Nd}_2\text{Fe}_{14}\text{B}$ nanocomposite permanent magnets can be obtained directly from the melt via a melt-spinning technique by accomplishing the rapid solidification process under a reduced pressure of 1.3 kPa on a Cu roll moving at a surface velocity significantly slower than conventional melt spinning. Platelet permanent magnets with a thickness of 240 μm and magnetic properties of $(BH)_{\text{max}} = 131.6 \text{ kJ/m}^3$, $H_{\text{cJ}} = 400 \text{ kA/m}$, and $B_r = 1.15 \text{ T}$ have been obtained for $\text{Nd}_{3.5}\text{Dy}_1\text{Fe}_{73}\text{Co}_3\text{Ga}_1\text{B}_{16.5}$.

¹R. Coehoorn, D. B. de Mooij, J. P. W. B. Duchateau, and K. H. J. Buschow, *J. Phys. C* **8**, 669 (1988).

²S. Hiroswa and H. Kanekiyo, *J. Appl. Phys.* **73**, 6488 (1993).

³S. Hiroswa and H. Kanekiyo, *Proceedings of the Thirteenth International Workshop on Rare Earth Magnets and Their Applications* (University of Birmingham, Birmingham, 1994), p. 87.

⁴J. J. Croat, J. F. Herbst, R. W. Lee, and F. E. Pinkerton, *J. Appl. Phys.* **55**, 2078 (1984).

⁵A. Manaf, R. A. Buckley, and H. A. Davies, *J. Magn. Magn. Mater.* **128**, 302 (1993).

⁶G. C. Hadjipanayis, L. Withanwasam, and R. F. Krause, *IEEE Trans. Magn.* **31**, 3596 (1995).

⁷E. F. Kneller and R. Hawig, *IEEE Trans. Magn.* **27**, 3588 (1991).

⁸Y. Kahn, E. Kneller, and M. Sostarich, *Z. Metallkd.* **73**, 553 (1988).

Analysis of magnetic behavior of exchange-enhanced SmFeCo magnets

M. Dahlgren and R. Grössinger

*Institut für Experimentalphysik, Technische Universität Wien,
Wiedner Hauptstrasse 8-10A-1040 Wien, Austria*

D. R. Cornejo and F. P. Missell

Instituto de Física, Universidade de São Paulo, CP 66318, 05315-970 São Paulo, SP, Brazil

A series of densified exchange-enhanced SmFeCo magnets was produced by mechanical alloying, followed by a heat treatment. The nanocrystalline phases and the grain size distribution of the samples were characterized from x-ray diffraction patterns. Magnetic measurements in terms of different models were analyzed for the temperature behavior of the magnetization and coercivity. One analytical formulation was derived from the random anisotropy model predicting that with increasing M_r/M_s ratio a decreasing coercivity occurs. Another numerical approach, which is based on a micromagnetic calculation using finite element techniques was also applied. Attempts were made to improve the existing model derived from the finite element technique. The nucleation model was found to be unsatisfactory for describing the temperature-dependent coercivity. © 1998 American Institute of Physics. [S0021-8979(98)43011-1]

Nanocrystalline hard magnetic materials increasingly form an important area for research on magnetic materials. This development started with the study of low rare earth containing materials like melt-spun $\text{Nd}_4\text{Fe}_{78}\text{B}_{18}$ by Coehoorn *et al.* in 1988.¹ Independently, in 1987 Keem *et al.* reported a remanence enhancement in isotropic rapidly-quenched Nd-Fe-B ribbons containing additions of Al and Si.^{2,3} Since then many different compounds such as Sm-Co⁴ with a maximum coercivity up to 75 kOe or a two-phase $\alpha\text{-Fe/Sm-Fe-N}^5$ were produced in the nanocrystalline or nanocomposite state.

Stoner and Wohlfarth⁶ predicted that the remanence should be half of the saturation magnetization (M_s) for single phase uniaxial materials assuming an isotropic set of noninteracting grains. From this prediction single-phase uniaxial materials are defined as remanence enhanced when the remanence is above half of M_s . In all these materials nanocrystals of the hard magnetic phase with grain sizes between 10 and 35 nm were found. For hard magnetic materials, the anisotropy energy overrides in general the stray field energy. In this case, the length where the extension of spin inhomogeneities is reduced by $1/e$ is referred to as the exchange length $\ell_{\text{ex}} = \sqrt{A/K}$ (where A is the exchange stiffness constant and K is the anisotropy constant). Due to the fact that the grain size is of the same order as the magnetic exchange length, the coupling between the grains becomes extensive enough to considerably enhance the remanence.

All these materials are isotropic due to the production processes generally used (rapidly quenching, mechanical alloying). It was found that the exchange coupling influences intrinsic properties such as the spin reorientation temperature⁷ as well as the Curie temperature.⁸ A simple measure of the exchange coupling is, in addition to the shape of recoil curves⁹ and the hysteresis loop, the ratio remanence M_r to saturation magnetization M_s .

Starting from elementary powders, three compositions, $\text{Sm}_{18.1}\text{Fe}_{11.0}\text{Co}_{70.9}$, $\text{Sm}_{18.4}\text{Fe}_{23.4}\text{Co}_{58.2}$, and

$\text{Sm}_{18.2}\text{Fe}_{33.2}\text{Co}_{48.6}$, were produced by mechanical alloying resulting in a quasi-amorphous matrix. The quasi-amorphous materials were cold pressed into 3 mm diameter cylinder, wrapped in Ta foil, and heated under 10^{-5} mbar vacuum for 15 min at 600–700 °C. So, the quasi-amorphous Sm-Fe-Co can transform into many different nanophases, such as $\text{Sm}_2(\text{Co, Fe})_{17}$, $\text{Sm}(\text{Co, Fe})_5$, $\text{Sm}_2(\text{Co, Fe})_7$, $\text{Sm}(\text{Co, Fe})_3$, and $\alpha\text{-(Fe, Co)}$. Because the phases have similar crystallographic structure it is very difficult to distinguish the different phases from x-ray diffraction. For the compositions used in the present work, the expected hard magnetic phase would be the $\text{Sm}(\text{Co, Fe})_5$ phase. However, according to a previous study¹⁰ the presence of Fe in the quasi-amorphous phase seems to prevent the formation of $\text{Sm}(\text{Co, Fe})_5$. Instead a mixture $\text{Sm}_2(\text{Co, Fe})_{17}$, $\text{Sm}_2(\text{Co, Fe})_7$, $\text{Sm}(\text{Co, Fe})_3$, and $\alpha\text{-(Fe, Co)}$ was found.¹⁰ From our x-ray measurement it seems that $\text{Sm}_2(\text{Co, Fe})_7$ and $\text{Sm}(\text{Co, Fe})_3$ do not exist in the samples. The average grain size and the grain size distribution of the samples were evaluated by analyzing the x-ray diffraction line broadening (Table I).^{11,12}

The determination of the saturation magnetization, M_s , is very important to obtain the characteristic ratio M_r/M_s for exchange enhanced magnets. To determine M_s of isotropic hard magnetic materials accurately, high fields magnetic measurements are necessary in order to exceed the high magnetocrystalline anisotropy of the hard magnetic phases as well as a reliable extrapolation method (e.g., the law of approach to saturation). Therefore magnetization measurements were performed on the SmFeCo magnets in a pulsed field magnetometer with a maximum applied field of 35 T. With this method the temperature dependence of the ratio M_r/M_s as well as the coercivity were measured from 4.2 K up to room temperature. The anisotropy field was estimated from the law of approach to saturation. The estimated anisotropy field for the samples were determined to be between 20 and 30 T at room temperature. This indicates that $\text{Sm}_2(\text{Co, Fe})_7$ ($H_a \approx 30$ T at room temperature) or

TABLE I. The average grain size, D_v (see Refs. 11, 12) for different compositions evaluated by analyzing the x-ray diffraction line broadening. (Sm, Fe, Co) grain corresponds to the grains composed from the hard magnetic (Sm, Fe, Co) phases.

	Sm _{18.1} Fe _{11.0} Co _{70.9}	Sm _{18.4} Fe _{23.4} Co _{58.2}	Sm _{18.2} Fe _{33.2} Co _{48.6}
(Sm, Fe, Co) grain	11.9 nm	17.5 nm	19 nm

Sm₁(Co, Fe)₅ ($H_a \approx 30$ T at room temperature) is more probable instead of Sm₂(Co, Fe)₁₇ ($H_a \approx 10$ T at room temperature).

In Fig. 1 it is evident that the ratio M_r/M_s is increasing with decreasing temperature. This indicates that the coupling is increasing at lower temperature. If the coupling is increasing we would expect that the exchange length should increase with decreasing temperature. This is possible if the anisotropy constant K is decreasing. Blaettner *et al.*¹³ found this behavior for Sm₂Co₇. Therefore those data were used to describe the anisotropy field.

Using the available data, analytical relations between the coercivity and the enhanced remanence can be tested. There exists¹⁴ one analytical prediction relating coercivity and remanence:

$$\frac{M_r}{M_s} = \frac{1}{2} \left[\cos \left(1 - 2 \frac{H_C}{H_A} \right) + \frac{\pi}{2} \sin \left(1 - 2 \frac{H_C}{H_A} \right) \right]. \quad (1)$$

This formula was derived from the random anisotropy model¹⁵ and predicts a decreasing coercivity with increasing M_r/M_s ratio. This analytical relation was tested for our measurements and could not reproduce the temperature behavior. In fact, the results showed a behavior opposite to the prediction of the model. In our measurements both M_r/M_s and the coercivity are increasing (compare Fig. 1 and Fig. 3).

Another numerical approach, which is based on a micro-magnetic calculation using finite element techniques¹⁶ delivers a relation of the type:

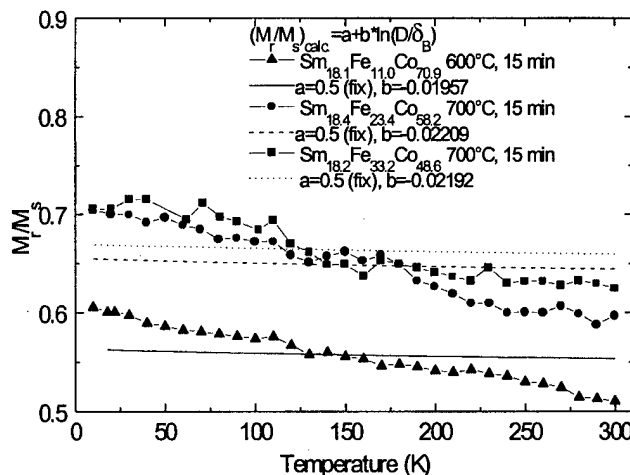


FIG. 1. The temperature behavior of the remanence to saturation magnetization ratio measured using a pulsed field magnetometer. A fit according to the model of Fischer *et al.* (see Ref. 16) is included for comparison.

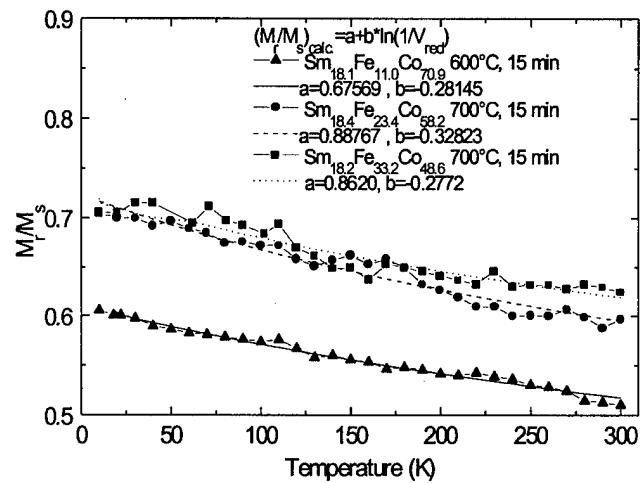


FIG. 2. The modified model of Fischer *et al.* (see Ref. 16) which assumes the exchange coupling to be three dimensional, is compared to the measured data.

$$\frac{M_r}{M_s} = a + b \ln(D/\delta_B^{\text{hard}}) \quad (2)$$

with $M_s = M_s^{\text{hard}} \nu^{\text{hard}} + M_s^{\text{soft}} \nu^{\text{soft}}$, where D is a grain size, $\delta_B = \pi \sqrt{A/K}$ represent the domain wall width of the hard magnetic phase, M_s^{hard} , M_s^{soft} are the saturation polarization of the hard and soft magnetic phases, and ν^{hard} , ν^{soft} are the volume fractions of the hard and soft magnetic phases. In the case of only uncoupled hard magnetic grains $a=0.5$ and $b=0$, whereas in the other cases a increases with the amount of the soft magnetic phase: $0.5 < a < 1$. b is -0.045 without the soft magnetic phase and may increase to -0.15 depending on the amount of the soft magnetic phase.¹⁶

Since, in all of the samples measured, there existed only a small amount of soft magnetic phase, a was fixed to be 0.5. If the parameter a was left free in the fitting procedure it tended to reach values in the range of 0.1–0.3, which have no physical meaning.

This model shows the right tendency when applying it to the measured data, but the fit was not able to reproduce the actual temperature behavior. One disadvantage of Eq. (2) is

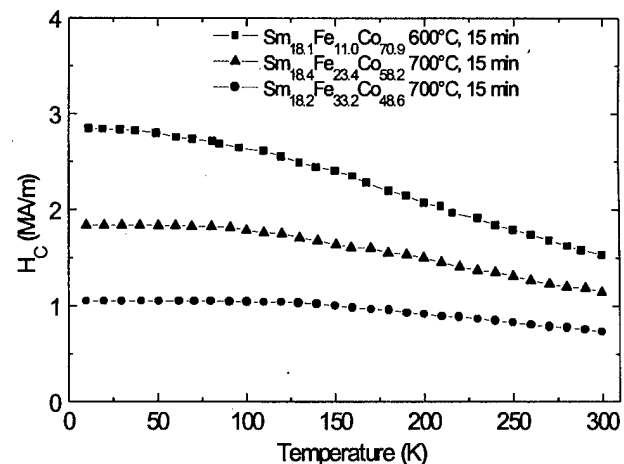


FIG. 3. Temperature dependence of the coercivity measured by using a pulsed field magnetometer.

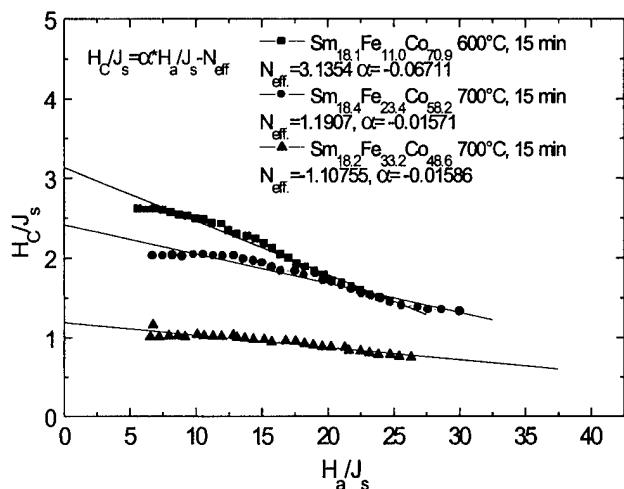


FIG. 4. The nucleation model (see Ref. 17) applied to the measured data.

that D/δ_B describes the coupling of the phases for a one-dimensional model. A 2D model would be able to describe the ratio of the total grain area to the exchange coupled grain area. If, instead of D/δ_B , the ratio of total volume V_{tot} to coupled volume V_{coupl} is used, a 3D model would result. The ratio of coupled volume to total volume can be defined as the reduced volume V_{red} .

$$V_{\text{red}} \equiv \frac{V_{\text{coupl}}}{V_{\text{tot}}} = \frac{(D/2)^3 - (D/2 - \ell_{\text{ex}})^3}{(D/2)^3}. \quad (3)$$

By introducing the reduced volume, the following expression can be defined:

$$\frac{M_r}{M_s} = a + b \ln(1/V_{\text{red}}). \quad (4)$$

If the sample is fully exchange coupled, M_r/M_s in Eq. (4) should be equal to 1 when V_{red} is equal to 1. For the coupled boundary condition M_r/M_s [$\ln(1)=0$] would be equal to a and with $a=1$ the boundary condition is fulfilled. If the grains in the magnet are uncoupled, M_r/M_s in Eq. (4) should be between 0.5 and 1 (depending on the amount of soft magnetic phase), when b and V_{red} are equal to zero. By applying l'Hospital rule on Eq. (4) and letting b and V_{red} approach zero M_r/M_s will be equal to a . Since a can be chosen between 0.5 and 1 also this boundary condition is fulfilled.

In Fig. 2 the modified model of Eq. (4) is tested and indeed the experimental data fit the model. Increasing the amount of Fe in the samples results in a maximum for the parameter a and a minimum for parameter b for the sample with Fe=23 at%. By comparing the values in Fig. 1 with the values in Fig. 2, b seems to be of a factor 10 larger in the modified model. Also the expected values for b ($-0.045 < b < -0.15$) from Fischer *et al.*,¹⁶ are exceeded by a factor of 2 in the modified model.

We also attempted to fit the coercivity using an equation similar to that for the ratio M_r/M_s from Fischer *et al.*:¹⁶

$$H_C = H_a [c + d \ln(D/\delta_B^{\text{hard}})]. \quad (5)$$

However, this formula shows a different behavior than the measured data. Here H_C/H_a has a convex shape and $\ln(D/\delta_B)$ has a concave shape with the temperature.

The nucleation model¹⁷ can be used to describe $H_C(T)/J_s(T)$:

$$\frac{H_C}{J_s} = \alpha \frac{H_a}{J_x} - N_{\text{eff}}. \quad (6)$$

The values obtained from the nucleation model are shown in Fig. 4.

Here the microstructural α parameter has negative values. A negative value of the α parameter has no physical meaning, which indicates that the nucleation model cannot be applied for our samples. However, it is worth noting that an increase of Fe in the samples results in a decrease of the microstructural parameters. One more disadvantage of the nucleation model is that it only indicates if the magnetization processes is nucleation controlled and do not delivers any deeper understanding of the exchange coupling. The same problems arise when applying a similar model such as the nucleus-expansion model.¹⁸

This work was partly supported by Austrian Science Foundation under the project P10945-PHY, by the EC within the framework Alfa (Project No. ALR/B7-3011/94.04-5.0263.8) and also by a traveling grant from Österreichische Forschungsgemeinschaft.

¹R. Coehoorn, D. B. de Mooij, J. P. W. B. Duchateau, and K. H. J. Buschow, *J. Phys. (France)* **C8**, 669 (1988).

²J. E. Keem, G. B. Clemente, A. M. Kadin, and R. W. McCallum, "Hard and Soft Magnetic Materials with Applications including Superconductivity," in *Proceeding Conference on ASM Materials Week 87*, edited by J. A. Salsgiver (American Society for Metals, Metals Park, OH, 1987).

³G. B. Clemente, J. E. Keem, and J. P. Bradsley, *J. Appl. Phys.* **64**, 5299 (1988).

⁴Y. Liu, M. P. Dallimore, P. G. McCormick, and T. Alonso, *J. Magn. Magn. Mater.* **116**, L320 (1992).

⁵J. Ding, Y. Liu, P. G. McCormick, and R. Street, *J. Magn. Magn. Mater.* **123**, L239 (1993).

⁶E. C. Stoner and E. P. Wohlfarth, *Philos. Trans. R. Soc. London, Ser. A* **240**, 599 (1948).

⁷X. C. Kou, M. Dahlgren, R. Grössinger, and G. Wiesinger, *J. Appl. Phys.* **81**, 4428 (1997).

⁸M. Dahlgren, R. Grössinger, E. de Morais, S. Gama, G. Mendoza, J. F. Liu, and H. A. Davies, *Proceedings of Intermag*, New Orleans, 1997 (in print).

⁹E. F. Kneller and R. Hawig, *IEEE Trans. Magn.* **27**, 3588 (1991).

¹⁰P. A. I. Smith Ph.D. thesis, the University of Western Australia, Australia, 1997.

¹¹S. Enzo, G. Fagherazzi, and A. Benedetti, *J. Appl. Crystallogr.* **21**, 536 (1988).

¹²A. Benedetti, G. Fagherazzi, S. Enzo, and M. Battagliarin, *J. Appl. Crystallogr.* **21**, 543 (1988).

¹³H. E. Blaettner, K. J. Strnat, and A. E. Ray, in *The Rare Earths in Modern Science and Technology*, edited by G. J. McCarthy and J. J. Ryhne (Plenum, New York, 1978), p. 421.

¹⁴S. Huo and H. A. Davies, 8th International Symposium on Magnetic Anisotropy and Coercivity, Birmingham, UK, 1994, p. 155.

¹⁵R. Alben, J. J. Becker, and M. C. Chi, *J. Appl. Phys.* **49**, 1653 (1978).

¹⁶R. Fischer, T. Schrefl, H. Kronmüller, and J. Fidler, *J. Magn. Magn. Mater.* **153**, 35 (1996).

¹⁷G. Herzer, W. Fernengel, and E. Adler, *J. Magn. Magn. Mater.* **58**, 48 (1986).

¹⁸D. Givord, A. Lienard, P. Tenaud, and T. Viadieu, *J. Magn. Magn. Mater.* **67**, L281 (1987).

The effect of boron and rare earth contents on the magnetic properties of La and Cr substituted α -Fe/ R_2 Fe₁₄B-type nanocomposites

W. C. Chang,^{a)} D. Y. Chiou, and S. H. Wu

Department of Physics, National Chung Cheng University, Ming-Hsiung, Chia-Yi 621, Taiwan, Republic of China

B. M. Ma, Q. Chen, and C. O. Bounds

Rhodia, Rare Earths and Gallium, CN 7500, Cranbury, New Jersey 08512

The effect of phase transformations on the magnetic properties of rare earth lean ($\text{Nd}_{0.95}\text{La}_{0.05}$)_{9.5}Fe_{82.5-x}Cr₂B_{6+x} ($x=0$ to 4.5) and ($\text{Nd}_{0.95}\text{La}_{0.05}$)_{7.5+y}Fe_{80.5-y}Cr₂B₁₀ ($y=0$ to 4) melt spun ribbons has been investigated. The phase mixture, after optimum thermal processing, was found to be strongly dependent upon the rare earth and boron contents. Two magnetic phases, namely α -Fe and $R_2\text{Fe}_{14}\text{B}$, were found in ($\text{Nd}_{0.95}\text{La}_{0.05}$)_{9.5}Fe_{82.5-x}Cr₂B_{6+x} alloy ribbons with x ranging from 0 to 4.5. For a fixed rare earth content, increases in the boron concentration resulted in a higher volume fraction of the $R_2\text{Fe}_{14}\text{B}$ phase, which led to an increase in the intrinsic coercive force from 7.1 kOe for $x=0$ to 12.6 kOe for $x=4.2$. A $B_r=9.6$ kG, $iH_c=9.5$ kOe, and $(BH)_{\max}=15.5$ MGOe have been obtained in the alloy ribbons with $x=4.5$. On the other hand, the increase in the total rare earth content, or y , was found to suppress the formation of the metastable Fe₃B and/or $R_2\text{Fe}_{23}\text{B}_3$ phases and to yield an α -Fe/ $R_2\text{Fe}_{14}\text{B}$ mixture for $y>1$. This increase in total rare earth content not only increases the volume fraction of both the $R_2\text{Fe}_{14}\text{B}$ and α -Fe phases but also decreases the average grain size of these phases as evidenced by transmission electron microscopy analysis. This decrease in the average grain size may subsequently enhance the intrinsic coercivity and the remanence of the ribbons. A B_r of 9.5 kG, a iH_c of 13.2 kOe, and a $(BH)_{\max}$ of 18 MGOe were achieved in ($\text{Nd}_{0.95}\text{La}_{0.05}$)₁₁Fe₇₇Cr₂B₁₀. © 1998 American Institute of Physics. [S0021-8979(98)20711-0]

Because of their high remanence (B_r) and high maximum energy product [$(BH)_{\max}$], two types of nanocomposite magnets, namely, α -Fe/ $\text{Nd}_2\text{Fe}_{14}\text{B}$ ¹ and Fe₃B/ $\text{Nd}_2\text{Fe}_{14}\text{B}$ ^{2,3} have been widely studied for the bonded magnet application. The B_r of these nanocomposites can be strongly influenced by incorporating group II or IV elements^{4,5} and/or by the controlling of the grain size and volume fraction of α -Fe and $\text{Nd}_2\text{Fe}_{14}\text{B}$ ¹ or Fe₃B and $\text{Nd}_2\text{Fe}_{14}\text{B}$.^{2,3} Similarly, iH_c and squareness of the demagnetization curve are also strongly affected by elemental substitution and microstructure.^{4,5}

Production of precursor materials with an amorphous or nanoscaled structure and precise thermal treatment are the two key processes which determine the magnetic performance of nanocomposite materials. For α -Fe/ $\text{Nd}_2\text{Fe}_{14}\text{B}$ type nanocomposites, it was found that the alloy composition can ease the production of amorphous ribbons by melt spinning.⁶ Furthermore, the size and volume fraction of α -Fe and $\text{Nd}_2\text{Fe}_{14}\text{B}$ can be manipulated by thermal processing.⁷ Although $(BH)_{\max}$ values of 19–21 MGOe have been obtained on α -Fe/ $\text{Nd}_2\text{Fe}_{14}\text{B}$ -type nanocomposites,^{6,7} the corresponding iH_c obtained was normally less than 9 kOe, regardless of the method of fabrication or elemental substitution. Previously, we have shown that La and Cr substitution for Nd and Fe, respectively, in $\text{Nd}_{9.5}\text{Fe}_{81.5}\text{B}_9$ improved the iH_c of the optimized crystallized ribbons.⁸ This increase in iH_c was ascribed to the formation of Cr-rich borides in the grain boundary region which enhance the grain separations, suppress the

grain growth, and/or smooth the grain surface defects. An iH_c of 9.1 kOe and a $(BH)_{\max}$ of merely 12.5 MGOe have been obtained. It is of interest to extend this study to alloys of various boron contents to see if this trend still holds. An alloy series with compositions of (Nd,La)_{9.5}Fe_{82.5-x}Cr₂B_{6+x} ($x=0$ to 4.5) was selected for investigation.

To obtain strong exchange-coupling interaction, the volume fraction of $\text{Nd}_2\text{Fe}_{14}\text{B}$ (the hard magnetic phase) and α -Fe (the soft magnetic phase) phases must be maintained above a critical ratio.^{9–11} Although forming grain boundary phase(s) may increase the iH_c , one usually needs to balance the amount of grain boundary phase to increase iH_c with the requirement to achieve a high saturation magnetization and an effective exchange coupling. For a given boron content, varying the total rare earth content could be one of the ways to adjust the amount of $\text{Nd}_2\text{Fe}_{14}\text{B}$ and α -Fe phase to achieve this goal. For this reason, ($\text{Nd}_{0.95}\text{La}_{0.05}$)_{7.5+y}Fe_{80.5-y}Cr₂B₁₀, where $y=0, 1, 2, 3.5$ and 4, was selected for further study.

Alloy ingots with compositions ($\text{Nd}_{0.95}\text{La}_{0.05}$)_{9.5}Fe_{82.5-x}Cr₂B_{6+x} ($x=0-4.5$) and ($\text{Nd}_{0.95}\text{La}_{0.05}$)_{7.5+y}Fe_{80.5-y}Cr₂B₁₀ ($y=0-4$) were prepared by vacuum induction melting. Ingot pieces of approximately 3 grams were crushed into small pieces to accommodate the size of crucible for melt spinning. Ribbons were produced with wheel speeds (V_s) ranging from 15 to 30 m/s. X-ray powder diffraction with Cu $K\alpha$ radiation was utilized to determine the degree of crystallinity in the ribbons. Selected ribbons were thermally treated at 650–700 °C for 10 min for crystallization and to improve the permanent magnetic prop-

^{a)}Electronic-mail: phywcc@ccunix.ccu.edu.tw

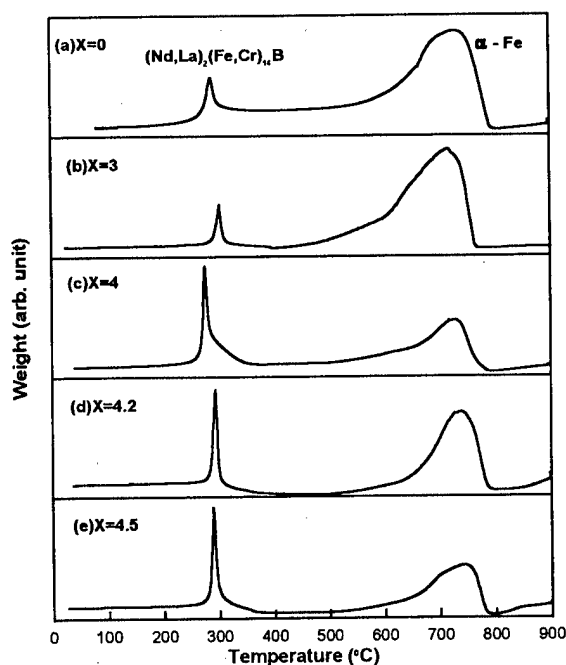


FIG. 1. TMA curves for crystallized $(\text{Nd}_{0.95}\text{La}_{0.05})_{9.5}\text{Fe}_{82.5-x}\text{Cr}_2\text{B}_{6+x}$ ribbons (a) $x=0$, (b) $x=3$, (c) $x=4$, (d) $x=4.2$, and (e) $x=4.5$.

erties. The magnetic phases and the corresponding Curie temperatures (T_c) were identified by a thermal gravimetric analyzer (TGA) with an externally applied magnetic field, i.e., conventionally referred to as the thermo magnetic analysis (TMA). The magnetic properties of the as-quenched ribbons and the thermally treated ribbons were measured by a vibrating sample magnetometer (VSM). Transmission electron microscopy (TEM) with energy dispersion analytical x ray (EDAX) was employed to examine the microstructure and identify the phases of the ribbons obtained.

Shown in Fig. 1 are the TMA scans of $(\text{Nd}_{0.95}\text{La}_{0.05})_{9.5}\text{Fe}_{82.5-x}\text{Cr}_2\text{B}_{6+x}$ ($x=0, 3, 4, 4.2$, and 4.5) ribbons after optimum annealing treatments. Despite the boron content being varied from 6 to 10.5 at. %, only two magnetic phases, namely, α -Fe and $\text{R}_2\text{Fe}_{14}\text{B}$, were detected. The metastable Fe_3B and $\text{R}_2\text{Fe}_{23}\text{B}_3$ phases that usually appear in the ternary boron rich Nd-Fe-B system were not detected. This suggests that La and Cr substitution may be effective in suppressing the formation of Fe_3B and $\text{R}_2\text{Fe}_{23}\text{B}_3$ phases in ribbons at least in the range of boron contents studied. Assuming that α -Fe and $\text{R}_2\text{Fe}_{14}\text{B}$ exhibit the same magnetization during TMA measurement, one may estimate the volume fractions of the α -Fe and $\text{R}_2\text{Fe}_{14}\text{B}$ phases in each ribbon by comparing the relative peak heights. In general, the volume fraction of $\text{R}_2\text{Fe}_{14}\text{B}$ in the ribbons with a higher boron content, $x=4, 4.2$, and 4.5 , is more than those with a lower boron content, $x=0$ and 3 .

Shown in Fig. 2 are the variation of B_r , iH_c , and $(BH)_{\max}$ of $(\text{Nd}_{0.95}\text{La}_{0.05})_{9.5}\text{Fe}_{82.5-x}\text{Cr}_2\text{B}_{6+x}$ ($x=0, 3, 4, 4.2$, and 4.5) ribbons after an optimum annealing treatment. At $x=0$, a B_r of 9.5 kG, a $(BH)_{\max}$ of 15.5 MGOe and an iH_c of merely 7.1 kOe were obtained. Both B_r and $(BH)_{\max}$ decrease initially with increasing boron content, then increase slightly when x was increased above 3. On the contrary, the

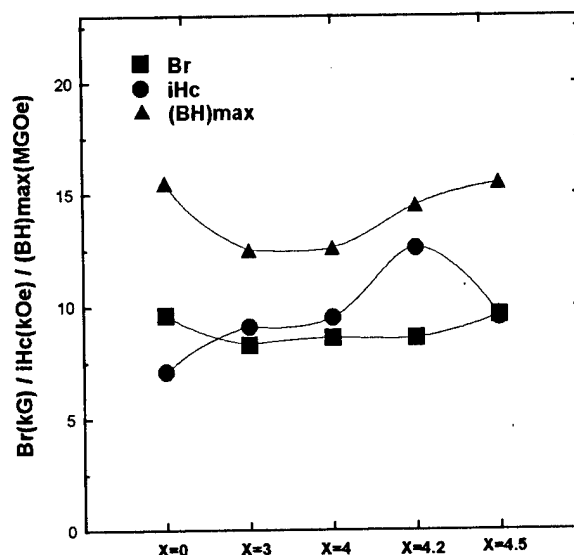


FIG. 2. Comparison of the magnetic properties of $(\text{Nd}_{0.95}\text{La}_{0.05})_{9.5}\text{Fe}_{82.5-x}\text{Cr}_2\text{B}_{6+x}$ ($x=0-4.5$) ribbons annealed at optimum condition.

iH_c increased initially with increasing boron content, reached a maximum of 12.6 kOe at $x=4.2$ then decreased drastically at $x=4.5$ indicating a possible phase transformation or a change of phase mixture. A B_r of 9.6 kG, an iH_c of 9.5 kOe, and a $(BH)_{\max}$ of 15.5 MGOe were obtained at $x=4.5$. This suggests that a B_r of more than 9 kG, $(BH)_{\max}$ of more than 15 MGOe, and iH_c of more than 9 kOe can simultaneously be obtained in $(\text{Nd}_{0.95}\text{La}_{0.05})_{9.5}\text{Fe}_{82.5-x}\text{Cr}_2\text{B}_{6+x}$ ribbons if x is maintained at slightly above 4. Around this boron level, the boron was surmised to react with Cr forming Cr boride(s) in the grain boundary region and freeing some Nd (and La) and Fe to form the desired $\text{R}_2\text{Fe}_{14}\text{B}$ phase. The increase of iH_c with increasing x , presumably, arises from two factors:

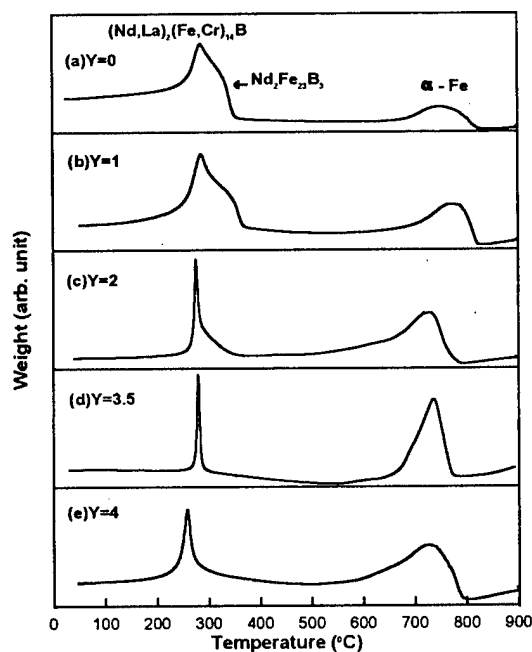


FIG. 3. TMA curves for crystallized $(\text{Nd}_{0.95}\text{La}_{0.05})_{7.5+y}\text{Fe}_{80.5-y}\text{Cr}_2\text{B}_{10}$ ribbons (a) $y=0$, (b) $y=1$, (c) $y=2$, (d) $y=3.5$, and (e) $y=4$.

TABLE I. Estimated volume fraction ratio of magnetic hard and soft phases ($R_2Fe_{14}B$ -type/ α -Fe ratio) of $(Nd_{0.95}La_{0.05})_{7.5+y}Fe_{80.5-y}Cr_2B_{10}$ ribbons ($y = 0$ to 4).

Composition $y =$	Peak height (arb. units)		
	Hard phase ($R_2Fe_{14}B$ type)	Soft phase (α -Fe)	$R_2Fe_{14}B/\alpha$ -Fe Ratio
0	4.498	1.260	3.57
1	2.014	0.968	2.08
2	1.387	0.701	1.98
3.5	0.945	0.736	1.28
4	0.809	0.504	1.61

the increase in the volume fraction of 2:14:1 phase^{8,12} and the increase in the amount of grain boundary phases which serves as grain separator. How to balance these two contributions is the key for successful production of nanocomposites with high iH_c and $(BH)_{max}$.

Shown in Fig. 3 are the TMA scans of $(Nd_{0.95}La_{0.05})_{7.5+y}Fe_{80.5-y}Cr_2B_{10}$ ($y = 0, 1, 2, 3.5$, and 4) ribbons after the crystallization treatment. Three magnetic phases, namely, $(Nd, La)_2(Fe, Cr)_{14}B$, $R_2Fe_{23}B_3$, and α -Fe were found in $y = 0$ and 1. However, only two magnetic phases, $(Nd, La)_2(Fe, Cr)_{14}B$ and α -Fe, were observed on $y = 2, 3.5$, and 4. The peak heights of the hard magnetic phase ($R_2Fe_{14}B$) and soft magnetic phase (α -Fe) measured by TMA scans and the estimated $R_2Fe_{14}B/\alpha$ -Fe ratio of these materials are listed in Table I. The $R_2Fe_{14}B/\alpha$ -Fe ratio decreases from 3.57 for $y = 0$ to 1.28 for $y = 3.5$ then increases again to 1.61 for $y = 4$. It is worth noting that the estimated $R_2Fe_{14}B/\alpha$ -Fe ratio only takes into account the two magnetic phases detected. Phases which were not detected by TMA scans are not included in this consideration. A detailed analytical work by TEM or microprobe is certainly needed along this aspect to confirm our hypothesis.

Shown in Table II are the comparison of B_r , iH_c , and $(BH)_{max}$ obtained for $(Nd_{0.95}La_{0.05})_{7.5+y}Fe_{80.5-y}Cr_2B_{10}$ ($y = 0, 1, 2, 3.5$, and 4) ribbons after optimum crystallization treatments. The B_r and iH_c of the ribbons with $y = 0$ and 1 are extremely low. However, these values are improved significantly when the rare earth content was increased to $y = 2$ or 3.5. A B_r of 9.5 kG, an iH_c of 13.2 kOe, and a $(BH)_{max}$ of 18.0 MGOe have been achieved on $y = 3.5$. Most importantly, an iH_c as high as 13 kOe, a B_r of more than 9.5 kG, and a $(BH)_{max}$ of 18 MGOe have been achieved. These

TABLE II. Magnetic properties of $(Nd_{0.95}La_{0.05})_{7.5+y}Fe_{80.5-y}Cr_2B_{10}$ ($y = 0 - 4$) ribbons after optimum annealing.

Composition $y =$	B_r (kG)	iH_c (kOe)	$(BH)_{max}$ (MGOe)
0	8.1	3.1	4.0
1	10.3	4.0	10.0
2	8.6	9.5	12.6
3.5	9.5	13.2	18.0
4	9.9	5.0	14.0

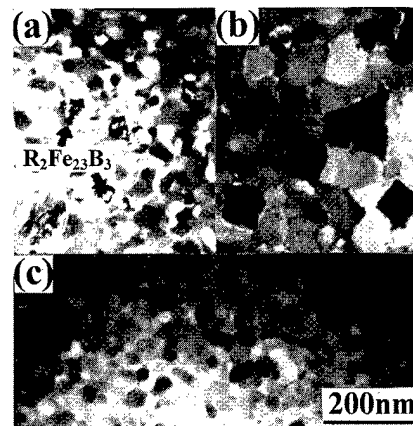


FIG. 4. Transmission electron micrographs of crystallized $(Nd_{0.95}La_{0.05})_{7.5+y}Fe_{80.5-y}Cr_2B_{10}$ ribbons (a) $y = 0$, (b) $y = 2$, and (c) $y = 3.5$.

high values have never been reported in either the α -Fe/ $Nd_2Fe_{14}B$ or the $Fe_3B/Nd_2Fe_{14}B$ nanocomposites.

Shown in Figs. 4(a), 4(b), and 4(c) are the TEM micrographs of ribbons with $y = 0, 2$ and 3.5 , respectively, after optimum thermal treatments. Three distinct phases, namely, $(Nd, La)_2(Fe, Cr)_{14}B$, $R_2Fe_{23}B_3$ (as the arrows indicate), and α -Fe were found in $y = 0$. Only two magnetic phases, $(Nd, La)_2(Fe, Cr)_{14}B$ and α -Fe, were detected in $y = 2$ and 3.5 . These results are consistent with TMA scans. In addition, a thin layer grain boundary phase (nonmagnetic) was found only in $y = 2$ but not in $y = 0$ and 3.5 . Moreover, the grain sizes, both the $(Nd, La)_2(Fe, Cr)_{14}B$ or the α -Fe phases, in $y = 3.5$ and 0 are finer than those in $y = 2$. The sizes of α -Fe and $(Nd, La)_2Fe_{14}B$ are estimated around 20 and 20–30 nm for $y = 3.5$ and 0, and 25 and 70–80 nm for $y = 2$, respectively. This suggests that the presence of the $R_2Fe_{23}B_3$ phase may restrict the grain growth in $(Nd_{0.95}La_{0.05})_{7.5}Fe_{80.5}Cr_2B_{10}$ and the higher La concentration in $y > 2$ may also limit the grain growth. A fine grain size is essential to induce a higher exchange coupling interaction between the 2:14:1 and α -Fe phases, resulting in a high B_r .

This work was supported by National Science Council, Taiwan, R.O.C. under Grant No. NSC-86-2112-M-194-012.

¹ A. Manaf, R. A. Buckley, and H. A. Davies, J. Magn. Magn. Mater. **128**, 302 (1993).

² J. Schneider, D. Eckert, K. H. Muller, A. Handstein, H. Muhlbach, H. Sassik, and H. R. Kirchmayer, Mater. Lett. **9**, 201 (1990).

³ H. Kanekiyo, M. Uehara, and S. Hirokawa, IEEE Trans. Magn. **29**, 2863 (1993).

⁴ A. Manaf, P. Z. Zhang, I. Ahmed, H. A. Davies, and R. A. Buckley, IEEE Trans. Magn. **29**, 2866 (1993).

⁵ A. Manaf, M. Al-Khafaji, P. Z. Zhang, H. A. Davies, R. A. Buckley, and W. Rainforth, J. Magn. Magn. Mater. **128**, 307 (1993).

⁶ W. C. Chang and D. M. Hsing, J. Appl. Phys. **79**, 4843 (1996).

⁷ J. Bauer, M. Seeger, A. Zern, and H. Kronmuller, J. Appl. Phys. **80**, 1667 (1996).

⁸ W. C. Chang, S. H. Wu, B. M. Ma, and C. O. Bounds, J. Appl. Phys. **81**, 4453 (1997).

⁹ T. Schrefl, J. Fidler, and H. Kronmuller, Phys. Rev. B **49**, 6100 (1994).

¹⁰ R. Skomski and J. M. D. Coey, Phys. Rev. B **48**, 1581 (1992).

¹¹ E. F. Kneeller and R. Hawig, IEEE Trans. Magn. **27**, 3588 (1991).

¹² K. O'Donnell, X.-L. Rao, J. R. Cullen, and J. M. D. Coey, IEEE Trans. Magn. (to be published).

Anomalous high-temperature coercivities in hard nanocomposite alloys

L. H. Lewis,^{a)} J.-Y. Wang,^{b)} and D. O. Welch

Department of Applied Science, Brookhaven National Laboratory, Upton, New York 11973-5000

V. Panchanathan

Magnequench International, Inc., 6435 Scatterfield Road, Anderson, Indiana 46013

To elucidate the interphase interactions inherent to nanocomposite magnetic alloys, measurements of remanence B_r , and coercivity H_{ci} were made on a series of four meltspun, remanence-enhanced nanocomposite alloys consisting solely of various amounts of $\text{Nd}_2\text{Fe}_{14}\text{B}$ and $\alpha\text{-Fe}$. The phase constitution and microstructural scale of the alloys were characterized with synchrotron x-ray diffraction. Magnetic measurements were made using superconducting quantum interference device (SQUID) magnetometry on evacuated and encapsulated samples in the temperature range of $300\text{ K} \leq T \leq 750\text{ K}$, in order to characterize the $\alpha\text{-Fe}$ component independently of the $\text{Nd}_2\text{Fe}_{14}\text{B}$ component. The high-temperature coercivities of the samples increase with the amount of $\alpha\text{-Fe}$ present in the samples, ranging from an average value of approximately 75 Oe for the sample with 14 wt % excess Fe to over 400 Oe at 700 K for the sample with 27 wt % excess Fe. The relatively high coercivities of the samples found at elevated temperatures imply that a tabular morphology of the $\alpha\text{-Fe}$ grains is conferring anisotropy to the phase; this conclusion is supported by transmission electron microscopy. It is concluded that while the significant coercivity of the $\alpha\text{-Fe}$ phase likely reduces the room-temperature remanence enhancement of the alloy below its theoretical ideal, the favorable interphase interface orientation promotes exchange coupling. © 1998 American Institute of Physics. [S0021-8979(98)20811-5]

I. INTRODUCTION

A detailed understanding of the nature of the interphase magnetic coupling in exchange-spring nanocomposite alloys is of paramount importance to the modeling and optimization of their performance as permanent magnets. To this end, measurements of magnetization and coercivity H_{ci} were made on a series of four meltspun nanocomposite alloys consisting solely of various amounts of $\text{Nd}_2\text{Fe}_{14}\text{B}$ and $\alpha\text{-Fe}$ using superconducting quantum interference device (SQUID) magnetometry on evacuated and encapsulated samples in the temperature range of $300\text{ K} \leq T \leq 750\text{ K}$, in order to follow the evolution of the magnetic properties as the $\text{Nd}_2\text{Fe}_{14}\text{B}$ passes from the ferromagnetic to the paramagnetic regime. The result thus obtained and expounded upon below elucidate the microstructural evolution of the alloys as increasing amounts of $\alpha\text{-Fe}$ are added to the $\text{Nd}_2\text{Fe}_{14}\text{B}$ system.

II. EXPERIMENTAL DETAILS

The alloys were made from commercial-grade materials by standard melt-quenching techniques and annealed for 4 min at 690 °C to optimize their magnetic properties. To verify the phase composition and average grain size of the alloys, synchrotron x-ray diffraction was performed on powdered samples using radiation of wavelength $0.90\text{ Å} \leq \lambda \leq 1.18\text{ Å}$, well away from the absorption edge of iron and thus preventing fluorescence. Lattice parameters were determined by a least-squares fitting program. Only two phases

were found, $\text{Nd}_2\text{Fe}_{14}\text{B}$ and $\alpha\text{-Fe}$; it is estimated that synchrotron x-ray diffraction would detect minor phases of 0.1–1.0 wt %.¹ The crystallite sizes are determined from the half-width of the Bragg peak at the half-maximum intensity position, corrected for the intrinsic broadening of the synchrotron beam, using the Scherrer formula.² The nominal compositions, lattice parameters, and the average grain size found for each constituent phase are given in Table I. The alloys are identified by their excess iron enrichment δ , defined as $\text{Nd}_2\text{Fe}_{14+\delta}\text{B}$. The specimens studied contained the following amounts of excess Fe: 1 ($\delta=0$), 14 ($\delta=4.6$), 18 ($\delta=7.2$), and 27 wt % ($\delta=9.3$). The amount of excess iron was determined from the ferromagnetic hysteretic response measured at 750 K.³ The magnetic data were obtained on packed samples evacuated to $P \approx 1 \times 10^{-6}$ Torr⁴ using a maximum applied field of 5 T in the temperature range of $300\text{ K} \leq T \leq 780\text{ K}$ with a Quantum Design SQUID magnetometer. The magnetic data were corrected for demagnetization effects, and the paramagnetic response from the 2–14-1 phase was subtracted at each measurement temperature from the corrected data to yield the saturation magnetization of the $\alpha\text{-Fe}$ phase. Room-temperature remanence ratios were calculated from corrected demagnetization extrapolated out to infinite field, Table I. Electron microscopy (TEM) was performed on the sample containing the largest amount of excess $\alpha\text{-Fe}$ ($\delta=9.3$) using a JEOL 2000 FX transmission electron microscope on dimpled and subsequently ion-milled samples.

III. RESULTS

The data in Table I indicate that the scale of the microstructure of all samples is similar, although not identical. The

^{a)}Electronic mail: lhlewis@bnl.gov

^{b)}Present address: Applied Materials, Burton Drive, Bldg. 24, Santa Clara, CA 95054.

TABLE I. Alloy characterization δ characterizes the iron enrichment, defined as $\text{Nd}_2\text{Fe}_{14+\delta}\text{B}$.

Stoichiometry (excess Fe wt %, δ)	Lattice parameters (\AA)	Grain sizes	Remanence (kG) at 300 K	Remanence ratios $B_r/M_s(H=\infty)$, 300 K
$\text{Nd}_{2.39}\text{Fe}_{14}\text{B}_{0.95}$ (1 wt %, $\delta=0$)	2-14-1: $a=8.804\pm0.002$ $c=12.261\pm0.005$	2-14-1: $\approx 340 \text{ \AA}$	6.3	0.53
$\text{Nd}_2\text{Fe}_{18.6}\text{B}_{2.38}$ (14 wt %, $\delta=4.6$)	2-14-1: $a=8.791\pm0.001$ $c=12.170\pm0.002$ $\alpha\text{-Fe: } a=2.86$	2-14-1: $\sim 525 \text{ \AA}$ $\alpha\text{-Fe: } \approx 175 \text{ \AA}$	8.06	0.52
$\text{Nd}_2\text{Fe}_{21.2}\text{B}_{1.65}$ (18 wt %, $\delta=7.2$)	2-14-1: $a=8.787\pm0.002$ $c=12.178\pm0.003$ $\alpha\text{-Fe: } a=2.87$	2-14-1: $\approx 340 \text{ \AA}$ $\alpha\text{-Fe: } \approx 290 \text{ \AA}$	9.21	0.56
$\text{Nd}_2\text{Fe}_{23.3}\text{B}_{1.45}$ (27 wt %, $\delta=9.3$)	2-14-1: $a=8.805\pm0.002$ $c=12.214\pm0.005$ $\alpha\text{-Fe: } a=2.88$	2-14-1: $\approx 235 \text{ \AA}$ $\alpha\text{-Fe: } \approx 180 \text{ \AA}$	10.09	0.60

grain sizes of the $\text{Nd}_2\text{Fe}_{14}\text{B}$ phase are in the range of 25–50 nm, and are always larger than that of the $\alpha\text{-Fe}$ phase, which is smaller than 30 nm in all instances. There is no obvious correlation between the amount of excess iron and the precise scale of the resultant microstructure. Similarly, there is no obvious trend in the lattice parameters of the $\text{Nd}_2\text{Fe}_{14}\text{B}$ phase with excess iron content, and the lattice parameter of the $\alpha\text{-Fe}$ phase agrees well with the JCPDS reference lattice parameter value for $\alpha\text{-Fe}$ of $a=2.8664 \text{ \AA}$.⁵ All samples exhibit moderate remanence enhancement and a smooth second-quadrant demagnetization curve. Figures 1 and 2 illustrate the trends of coercivity and saturation magnetization of the $\alpha\text{-Fe}$ phase, respectively, with temperature. The nominally single-phase $\text{Nd}_2\text{Fe}_{14}\text{B}$ sample exhibits a room-temperature coercivity value of 15 kOe, much higher than the coercivities of the two-phase nanocomposite samples; however, the temperature coefficient of coercivity (i.e., the slope of the coercivity versus temperature curve) is much smaller for the nanocomposite samples than it is for the single-phase sample. The inset of Fig. 1 shows an enlargement of the coercivity trend at high temperatures of the samples studied. The high-temperature coercivity measure-

ments are quite reproducible and are essentially independent of temperature. Both Fig. 1, inset, and Fig. 2 indicate that there is a direct correlation between the amount of excess $\alpha\text{-Fe}$ present in the composite and the resultant remanences and coercivities.

IV. DISCUSSION

The measured saturation magnetizations for the samples at elevated temperatures confirm that the additional Fe added to the starting composition results in the formation of increasing amounts of $\alpha\text{-Fe}$. The coercivities measured at elevated temperatures are much greater than that expected for isotropic grains of $\alpha\text{-Fe}$ with diameters under 300 \AA . If one assumes that the $\alpha\text{-Fe}$ particles are randomly oriented and reverse coherently by rotation under the influence of a demagnetizing field, the maximum coercivity expected at $T=750 \text{ K}$ is equal to $0.64 \cdot (K_1/M_s) \approx 43 \text{ Oe}$, which is approximately an order of magnitude less than the greatest coercivity measured. However, if the assumption that the particles are isotropic is relaxed, the concept of shape anisotropy may be invoked to account for the relatively large measured coercivities. The maximum coercive force that may be obtained in iron from shape anisotropy may be as high as 4300

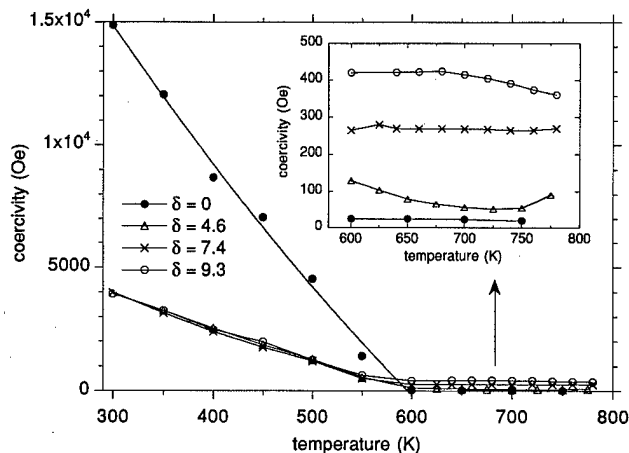


FIG. 1. The variation of coercivity H_{c1} with temperature for the four alloys studied. Inset: Enlargement of the high-temperature portion of the graph.

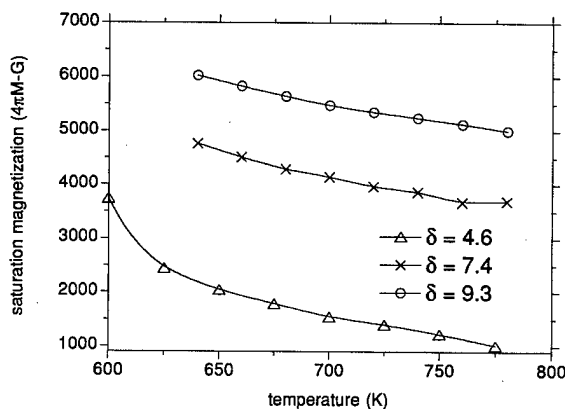


FIG. 2. Saturation magnetizations at elevated temperatures of the ferromagnetic components present in the nanocomposite alloys studied.

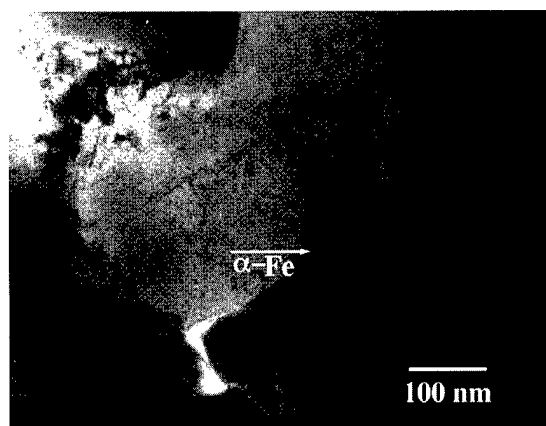


FIG. 3. TEM micrograph of a high-Fe region of microstructure of the sample $\delta=9.3$, containing nominally 27 wt % excess iron. The arrow indicates the blocky α -Fe phase.

Oe at 750 K.⁷ The relative temperature independence of the α -Fe coercivities also supports the hypothesis that the origin of the coercivity is likely to be shape anisotropy.⁷

Electron microscopy investigations also support the conclusion that the α -Fe particles do not have the shape of randomly distributed spheres. Figure 3 is a TEM micrograph of a portion of the $\delta=9.3$ sample that shows a higher relative concentration of iron than the bulk of the sample. The blocky phase, indicated by the arrow in Fig. 3, has been identified by energy-dispersive spectroscopy to largely consist of iron and is thus identified as the α -Fe component. Although the grain size of this region is not typical of the entire sample, it does illustrate the morphology of regions with large concentrations of α -Fe. It is hypothesized that the α -Fe phase develops an increasingly tabular morphology with increasing excess Fe content in the alloys.

The data presented above have two results that are significant for the hard magnetic performance of the nanocomposites. The first result is that the coercivity of the α -Fe

component is not extremely low when both phases are in the ferromagnetic regime, as is desired for optimum exchange coupling and remanence enhancement.^{8,9} If the coercivity measured at 750 K is normalized to the maximum coercivity expected at that temperature from shape anisotropy alone, extrapolation from the high-temperature data implies that the room-temperature coercivity of the α -Fe phase in the most Fe-enriched nanocomposite ($\delta=9.3$) is around 535 Oe. This conclusion implies that the entire volume of the constituent α -Fe grains is not exchange-coupled to the 2-14-1 phase, resulting in both a lower remanence enhancement and complex internal demagnetizing fields. However, the deduced elongated shape of the α -Fe precipitates in the alloy may serve to increase the remanence enhancement by realizing maximum interphase contact.

ACKNOWLEDGMENTS

Research performed under the auspices of the U.S. D.O.E., Division of Materials Sciences, Office of Basic Energy Sciences under Contract No. DE-AC02-76CH00016, and carried out in part at the National Synchrotron Light Source, Brookhaven National Laboratory, which is supported by the U.S. D.O.E., Divisions of Materials and Chemical Sciences.

¹D. Cox (personal communication).

²B. D. Cullity, in *Elements of X-Ray Diffraction* (Addison-Wesley, Reading, MA, 1978), p. 102.

³L. H. Lewis, D. O. Welch, and F. Pourarian, *J. Appl. Phys.* **79**, 5513 (1996).

⁴L. H. Lewis and Konrad M. Bussmann, *Rev. Sci. Instrum.* **67**, 3537 (1996).

⁵JCPDS Powder file #6-696; JCPDS-ICDD Copyright © 1995.

⁶C. Kittel, *Rev. Mod. Phys.* **21**, 541 (1949).

⁷R. M. Bozorth, *Ferromagnetism*, American Telephone and Telegraph Company, 1978, reissued by IEEE Press, Piscataway, NJ, 1993, p. 833.

⁸Eckart F. Kneller and Reinhard Hawig, *IEEE Trans. Magn.* **27**, 3588 (1991).

⁹R. Fischer, T. Schrefl, H. Kronmüller, and J. Fidler, *J. Magn. Magn. Mater.* **150**, 329 (1995).

Magnetic interactions in Fe–Ba hexaferrite nanocomposite materials

M. I. Montero, F. Cebollada, M. P. Morales, J. M. González,^{a)} and A. Hernando^{b)}

Instituto de Ciencia de Materiales de Madrid—C.S.I.C., Cantoblanco, 28049 Madrid, Spain

Results are presented on the hysteretic behavior of Fe-rich, composite Ba hexaferrite–Fe samples prepared by ball milling. The most remarkable feature of these samples was the observation of loops which were displaced in the negative sense of the field axis. Similar to this, the field evolution of the isothermal and the demagnetization remanences evidenced the achievement upon the application of 8 kOe fields of nonequivalent values of both quantities. Our results are discussed considering the different magnetic hardness of the two phases forming the sample and the occurrence of interphase (dipolar) interactions. © 1998 American Institute of Physics. [S0021-8979(98)43111-6]

I. INTRODUCTION

Short range exchange and long range dipolar interactions are crucial in determining the hysteretic properties of many real magnetic materials, for example, the achievement of extreme softness in melt spun, partly crystallized FeSiBCuNb alloys or the induction of remanence enhancement in nanocrystalline, NdFeB-based alloys. In the first case the basic softening mechanism is the average, down to a reduced effective value, of the grain magnetocrystalline anisotropy of large sets of exchange and dipolarly coupled grains.¹ The remanence enhancement, observed in hard isotropic materials, is also related to the occurrence of strong intergranular exchange which helps to keep the magnetization direction of the nanograins away from their local easy axis and close to the internal field direction.² The influence of interactions on the extrinsic properties is specially relevant in the case of composite materials where it has been predicted³ (and experimentally tested in some particular cases) that the coupling of several magnetic phases could result in extremely soft⁴ or hard properties.⁵ There are, however, two relevant obstacles to overcome in order to achieve some degree of control of the interactions and, through this, to improve the behavior of known materials for particular applications. On one hand, the absence of experimental techniques allowing one to measure interactions at a local level⁶ and on the other, the lack of a simple but realistic description of the influence of the dipolar coupling on the magnetization reversal mechanisms⁷ (dipolar interactions have a many-body nature, making them unsuitable to be analyzed in mean field terms). The aim of the present work is to contribute to the description of the phenomenology associated with the presence of interactions. For this purpose we will present data on a composite material formed by nanosized Ba hexaferrite particles and micronsized Fe ones where the interphase interactions are, exclusively, of the dipolar type.

II. PREPARATION OF SAMPLES AND EXPERIMENTAL TECHNIQUES USED

We have prepared nanocomposite samples with nominal compositions given by $\text{Fe}_x/(\text{BaFe}_{12}\text{O}_{19})_{1-x}$, where x (x

$=0.7$ and $x=0.9$) denoted a volume fraction. The samples were prepared by milling for 2 h in ball mill appropriate mixtures of Fe (45 μm average particle size) and Ba hexaferrite [30 nm average particle size, according to the measurement of the (0001) reflection half maximum width] powders. The precursor Ba hexaferrite particles were obtained by synthesis using a water-in-oil microemulsion.⁸ The phase distribution of the as-milled samples was checked through x-ray diffraction (XRD). The study of the hysteretic properties of both the precursor Ba hexaferrite and the composite samples was performed in press-powder cylinders (3 mm height \times 3 mm diameter) by using a vibrating sample magnetometer.

III. EXPERIMENTAL RESULTS

Figure 1 shows the x-ray diffractogram taken in different as-milled Fe–Ba hexaferrite composite samples. As observed in the figure the only detected reflections were those corresponding to α -Fe. (The diffractograms did not show any indication of the presence in the milled materials of phases different from the precursor ones.)

In Fig. 2 we present the room temperature demagnetization branch of the hysteresis loop measured in the starting Ba hexaferrite particles. The inset in that figure shows the field dependence of the associated differential susceptibility. The critical field of the precursor Ba hexaferrite (demagnetizing field for which a differential susceptibility maximum is mea-

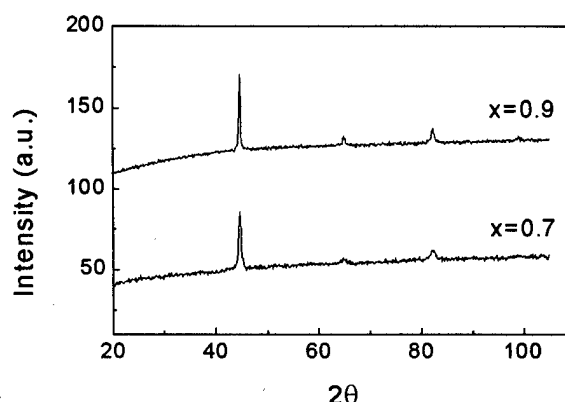


FIG. 1. X-ray diffractograms taken in the $x=0.7$ and $x=0.9$ samples.

^{a)}Electronic mail: jgonzalez@pinar1.csic.es

^{b)}Also with: Instituto de Magnetismo Aplicado “Salvador Velayos”, RENFEUCM, 28230 Las Rozas, Madrid, Spain.

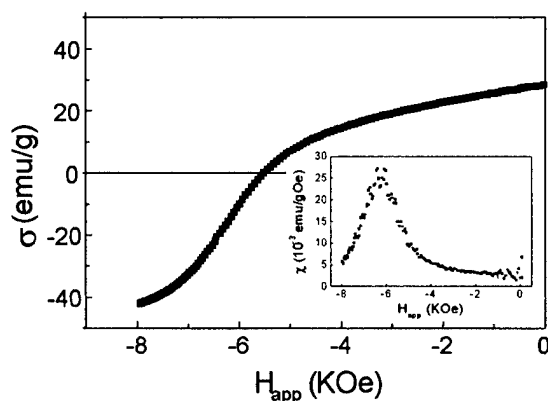


FIG. 2. Demagnetization curve measured, at room temperature, in the starting Ba hexaferrite particles. Inset: field dependence of the associated differential susceptibility.

sured) was of 6225 Oe. Upon milling, the different samples exhibited, at all the considered temperatures, smooth demagnetization curves indicating the occurrence of coupling between the two present magnetic phases. In Fig. 3 we present a loop measured at room temperature and with a maximum applied field of 8 kOe in the $x=0.9$ sample. Very interestingly, the loop was measurably displaced (36 Oe) in the sense of the negative fields (see the inset in Fig. 3). The magnitude of this displacement decreased with the decrease of the Fe volume percentage. In the upper inset in Fig. 3, we present the evolution with the applied demagnetizing field of the room temperature differential susceptibility measured in the $x=0.9$ sample. The demagnetization of the softest (α -Fe) regions of the sample originated from the low field peak after which the susceptibility monotonously decreased. A comparison of the behavior observed in the precursor Ba hexaferrite particles with that measured in the composite samples showed that the field range in which the demagnetization of the hard phase proceeded was, in both cases, clearly different, whereas in the case of the precursor powders (Fig. 2) that range spanned ~ 4000 Oe around the critical field, in the case of the composite samples (Fig. 3) the demagnetization took place due to the Fe-Ba hexaferrite interactions in a much wider field region starting at fields of the order of those involved in the α -Fe reversal and spanning up to 12 kOe.

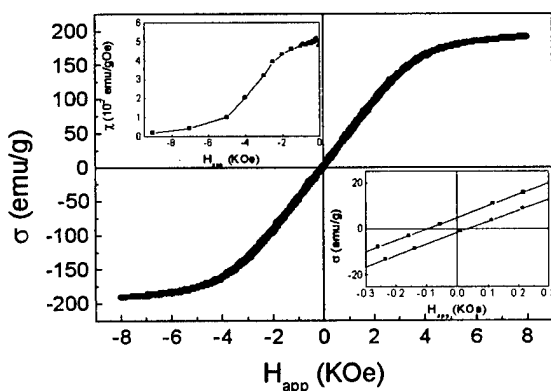


FIG. 3. Hysteresis loop measured, at room temperature, in the $x=0.9$ sample. Upper inset: field dependence of the associated differential susceptibility.

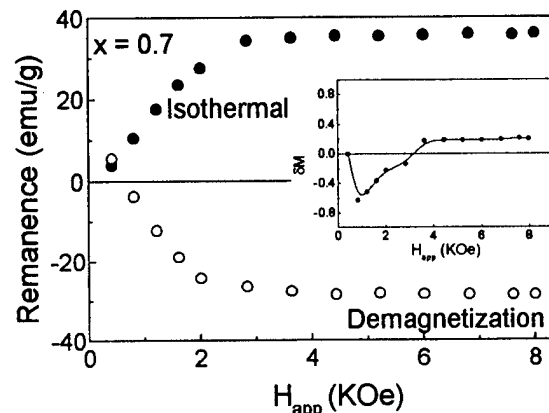
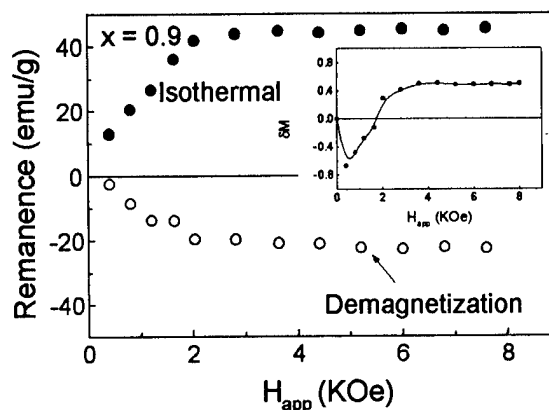


FIG. 4. Isothermal and demagnetization remanences curves measured, at room temperature, in the samples $x=0.9$ and $x=0.7$. Insets: associated δ_M plots.

Our results for the field evolution of the isothermal, M_i , and demagnetization, M_d , remanences are presented in Fig. 4. [M_i was measured by increasing (starting from the demagnetized state) the maximum applied field up to 8 kOe and M_d was obtained by first saturating the sample under a magnetizing 8 kOe field and then applying increasing demagnetizing fields down to -8 kOe.] In Fig. 4 it is observed in both samples that the 8 kOe isothermal and demagnetization remanences are different. As a consequence of this asymmetry, the delta plots (see the insets in Fig. 4 where we have represented the field evolution of the quantity $\delta_M = [M_d(H)/M_i(8 \text{ kOe})] - \{1 - 2[M_i(H)/M_i(8 \text{ kOe})]\}^9$) evidenced the occurrence of positive (magnetizing) interactions in the high field range. The magnitude of the high field δ_M value decreased with the increase of the Ba hexaferrite volume percentage.

IV. DISCUSSION

The preparation procedure and the absence (in the diffractograms taken in the Fe-rich samples) of any Ba hexaferrite reflection led us to suppose that in these samples the Ba hexaferrite particles were fully embedded in the much larger α -Fe ones. We also will assume that the only interaction between both phases was the dipolar one. This assumption was supported by the characteristics of the preparation procedure of the composite samples (which does not result in

intimate phase contact) and by the absence of any milling process-induced secondary phase. In particular we have not detected any Fe oxide which, considering the resolution of the x-ray diffraction, could be nevertheless present in small amounts. We would like to note that our Fe particles are large (they have typical dimensions of the order of tens of μm) and therefore their reversal process should not be significantly influenced by a possible exchange induced anisotropy related to the occurrence of surface oxides. Thus, we propose that the observed loop displacement and remanence asymmetry should result from the local fields, created in the soft regions of the samples by the Ba hexaferrite particles. Let us remark in this sense that the loop in Fig. 3 is not a saturation one: the maximum applied field is smaller than the field for which the demagnetization differential susceptibility of the samples goes to zero (that maximum field and those applied in the remanence measurements are, nevertheless, much larger than the field for which the α -Fe reverses its magnetization). Therefore, for the fields considered in the remanence measurements a substantial fraction of the Ba hexaferrite particles are unreversed, that is, have magnetic moments still pointing along the hemisphere centered along the direction of the initial magnetizing field. Our point is that, when both phases are close to saturation, the stray fields created by the Ba hexaferrite nanoparticles originate significant fluctuations of the local internal field inside the α -Fe particles. The magnitude of those fluctuations depends of the relative orientations of the magnetizations of the α -Fe and Ba hexaferrite particles. If we assume, for instance, that the presence of a single platelet-shaped Ba hexaferrite particle is embedded in the central region of a spherical α -Fe one with the magnetization vectors of both particles perpendicular to the bases of the platelet and pointing in the same sense (see Fig. 5), the (demagnetizing) dipolar field in the α -Fe region close to the bases of the platelet is lower than that existing in the same region if the Ba hexaferrite particle was absent. (There are also regions close to the platelet lateral surface where the local demagnetizing field is increased but, due to the platelet geometry, the volume of these regions is smaller than that corresponding to the regions where the demagnetizing field decreases.) The (predominating) decrease of the local dipolar field results in a coercivity increase (a shift in the negative field sense of the hysteresis loop). Conversely, if the magnetization of the α -Fe particle were already reversed and, as in our remanence experiments, that of the Ba hexaferrite platelet were still pointing along the original saturation direction, the dipolar field created by the hard particle reinforces that associated to the poles in the surface of the

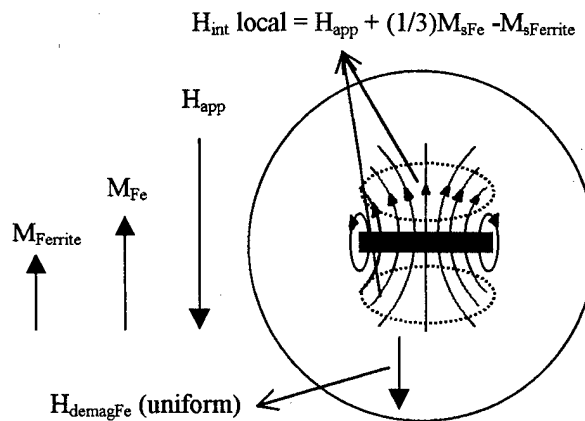


FIG. 5. Simplified scheme of the internal field in a spherical α -Fe particle with a single platelet-shaped Ba hexaferrite particle embedded in its central region.

soft particle, resulting in an easier α -Fe reversal. In terms of energy, our simplified description of the influence of the dipolar interactions in the reversal process can be summarized by stating that when the moments of the α -Fe particle and the Ba hexaferrite platelet point parallel, the dipolar energy of the composite particle is clearly lower than that stored by if both moments point antiparallel. We also would like to propose that, since the Ba hexaferrite particles have typical dimensions corresponding to, approximately, one third of the α -Fe domain wall width, the local dipolar field fluctuations should predominantly influence the nucleation process. The nucleation field is minimized if the wall is originated around defects having transverse dimensions of the order of the 25% of the total domain wall width,¹⁰ whereas the pinning effects should predominantly be linked, for the dimensions of our Ba hexaferrite particles, to the spatial fluctuations of the particle density.

¹G. Herzer, IEEE Trans. Magn. **MAG-26**, 1397 (1990).

²T. Schrefl, H. Roitner, and J. Fidler, J. Appl. Phys. **81**, 5567 (1997).

³J. M. D. Coey, J. Magn. Magn. Mater. **140-144**, 1041 (1995).

⁴J. M. Alameda, L. T. Baczewski, B. Dieny, D. Givord, J. M. Ndjaka, J. P. Nozières, J. J. Préjean, J. P. Rebouillat, and F. H. Salas, J. Magn. Magn. Mater. **104-107**, 1813 (1992).

⁵M. V. P. Altoé, M. S. Lancarotte, H. R. Rechemberg, F. P. Missell, and J. M. González, IEEE Trans. Magn. **31**, 3614 (1995).

⁶C. de Julián, M. Emura, F. Cebollada, and J. M. González, Appl. Phys. Lett. **69**, 4251 (1996).

⁷J. M. González, R. Ramírez, R. Smirnov-Rueda, and J. González, Phys. Rev. B **52**, 16034 (1995).

⁸D. A. Rawlinson and P. A. Sermon, J. Phys. IV **7**, 755 (1997).

⁹D. Richards, J. W. Harrel, and M. R. Parker, J. Magn. Magn. Mater. **120**, 164 (1993).

¹⁰A. Aharoni, Phys. Rev. **119**, 127 (1960); **131**, 1478 (1963).

Infrared studies of magnetic surface modes on antiferromagnets (invited)

R. E. Camley^{a)}

Department of Physics, University of Colorado at Colorado Springs, Colorado Springs, Colorado 80933-7150

M. R. F. Jensen, S. A. Feiven, and T. J. Parker

Department of Physics, University of Essex, Colchester CO4 3SQ, England

In contrast to ferromagnets, where low frequency surface excitations typically have frequencies in the 10 GHz range, surface excitations in antiferromagnets are often in the several hundred GHz to few THz range. Theoretical predictions for surface spin waves on antiferromagnets indicate that they should be highly nonreciprocal, i.e., the properties of a wave with wave vector $+k$ would be very different from those with a reversed wave vector of $-k$. Surface spin waves on antiferromagnets have recently been measured using a high resolution Fourier transform infrared spectrometer. The results show evidence of both true surface modes and surface resonances. The nonreciprocal features of the surface modes are seen in a dramatic nonreciprocal reflection. For example, the reflectivity can be 80% for one orientation, but when the incident and reflected waves are reversed the reflectivity drops to near zero. While the initial measurements were done on a bulk antiferromagnet, we also present calculations showing the results for thin films. © 1998 American Institute of Physics. [S0021-8979(98)36811-5]

The properties of antiferromagnets have recently received renewed attention for a variety of reasons. Many antiferromagnets are insulators and therefore have very different properties from the thoroughly studied ferromagnetic metals of Fe, Ni, and Co. For example, anisotropy fields in antiferromagnets are often in the 100 kG range compared to the 1 kG or less found in the transition metals. Also, antiferromagnets play an important role in the exchange biasing¹ of ferromagnetic films, a feature of current importance in magnetoresistive reading heads.² Again in contrast to ferromagnets, antiferromagnets can have long-wavelength spin excitations in the infrared (IR) frequency regime. This makes antiferromagnets of interest for signal processing in the infrared.

In this paper we report on theoretical and experimental studies of the infrared reflectivity from a bulk antiferromagnet sample of FeF₂. We concentrate in particular on the surface spin waves that propagate in this structure. In contrast to the bulk waves, the surface waves show significant nonreciprocity³ in that reversing the wave vector can significantly change the frequency of the excitation when the system is in the presence of an external magnetic field. In a reflectivity experiment this corresponds to interchanging the incident and reflected waves, and a nonreciprocal reflectivity is also observed.

We also indicate the possibility of IR studies of thin antiferromagnetic films by theoretical calculations. In very thin ferromagnetic films, it is the surface waves which will have the lowest frequencies and which are most easily measured. This is likely to be true in antiferromagnets as well,

and our initial calculations show that it should be possible to see signals from antiferromagnetic films with thicknesses in the 100–1000 Å range.

In the long-wavelength limit the reflectivity of a magnetic insulator is governed primarily by the frequency dependent permeability tensor. For the antiferromagnet, a calculation of this tensor begins with the equations of motion for the spins on the two sublattices:

$$\frac{d\mathbf{M}_1}{dt} = \gamma(\mathbf{M}_1 \times \mathbf{H}_1^{\text{eff}}), \quad (1)$$

and

$$\frac{d\mathbf{M}_2}{dt} = \gamma(\mathbf{M}_2 \times \mathbf{H}_2^{\text{eff}}). \quad (2)$$

In the above equations \mathbf{M}_1 and \mathbf{M}_2 are the magnetizations on the two sublattices, γ is the gyromagnetic ration, and \mathbf{H}^{eff} is an effective field acting either on sublattice 1 or 2.

The effective field is composed of a number of contributions. For example the effective field acting on sublattice 1 is given by

$$\mathbf{H}_1^{\text{eff}} = \mathbf{H}_1^{\text{exchange}} + \mathbf{H}_1^{\text{anisotropy}} + \mathbf{H}_0 + \mathbf{h}_{\text{dipolar}}, \quad (3)$$

with a similar expression for the effective field on sublattice 2. Here H_0 is the applied field. The exchange field is typically the largest of all the fields above with a magnitude on the order of 100–1000 kG. A key point to notice is that the exchange field acting on sublattice 1 comes primarily from the magnetization on sublattice 2, i.e.,

$$\mathbf{H}_1^{\text{exchange}} = \lambda \mathbf{M}_2, \quad (4)$$

where λ is the exchange coupling constant. Even in the long-wavelength limit, the two sublattices do not have to be par-

^{a)}Electronic mail: rcamley@brain.uccs.edu

allel and as a result the large exchange field produced by sublattice 2 influences the motion of sublattice 1 through Eq. (1).

The large exchange field is a significant difference between the ferromagnet and the antiferromagnet and explains why antiferromagnet excitations lie in the infrared while long-wavelength ferromagnetic spin wave frequencies are in the few GHz region. In the ferromagnet—in the long wavelength limit—the exchange field is simply proportional to the magnetization:

$$\mathbf{H}^{\text{exchange}} = \lambda \mathbf{M}. \quad (5)$$

As a result the contribution of the exchange field in the equations of motion is zero since $\mathbf{M} \times \lambda \mathbf{M} = 0$. So even though the exchange field is very large, it does not influence the motion of the spins. In the antiferromagnet, however, the exchange field does play a role, and the resulting frequencies are much higher.

Using the expressions for the exchange field and any external and anisotropy fields, the coupled equations of motion for the two sublattices can be solved to relate the dipolar driving fields to the fluctuating magnetization. We assume a time dependence of $\exp(-i\omega t)$ for all the dynamic fields and obtain the frequency dependent susceptibility tensor defined through the equation

$$\mathbf{M} = \chi(\omega) \mathbf{h}_{\text{dipolar}}. \quad (6)$$

The frequency dependent permeability is then found through the usual definition

$$\mu(\omega) = 1 + 4\pi\chi(\omega). \quad (7)$$

The explicit form for the permeability can be found in Ref. 4. Having found the permeability, the electromagnetic modes for the antiferromagnet may be found in the usual way.⁵ One looks for wavelike solutions which satisfy Maxwell's equations inside and outside the antiferromagnet. These solutions are then matched at the surface of the antiferromagnet and this results in the dispersion relation. The reflectivity may also be calculated similarly.⁶

We note that a number of different structures and geometries have been considered theoretically in the literature. Both easy plane and uniaxial antiferromagnets have been studied, and general geometries with arbitrary directions for the applied magnetic field and for the direction of propagation have been examined. Much of this work is summarized in the review article found in Ref. 7.

We consider a geometry where the surface of the antiferromagnet lies in the xz plane. The results take a particularly simple form for a uniaxial antiferromagnet where the easy axis and the external field are both along the surface and parallel to each other (along the z axis), and the direction of propagation is perpendicular to the external field, i.e., in the xy plane. We look for electromagnetic waves with the electric field parallel to z and the magnetic field in the xy plane (s polarized). With no external field, one may find that the permeability tensor is given by

$$\mu(\omega) = \begin{pmatrix} \mu_1 & 0 & 0 \\ 0 & \mu_1 & 0 \\ 0 & 0 & 1 \end{pmatrix}, \quad (8)$$

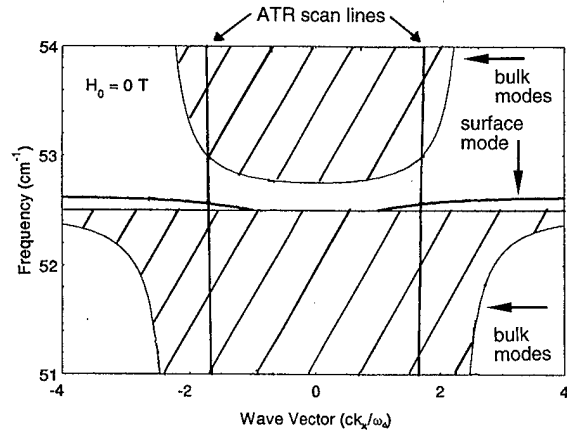


FIG. 1. Dispersion relations for bulk and surface polaritons in FeF_2 . The frequency, $\omega/2\pi c$, is given in wave numbers. The applied field is zero and so both bulk and surface modes are reciprocal, i.e., $\omega(+k_x) = \omega(-k_x)$. Propagation is perpendicular to the easy axis.

where

$$\mu_1(\omega) = 1 + \frac{8\pi H_A M}{\omega_0^2 - \omega^2}. \quad (9)$$

Here ω_0 is the resonance frequency given by

$$\omega_0 = \gamma [H_A(2H_E + H_A)]^{1/2}, \quad (10)$$

and M is the saturation magnetization of one of the sublattices. In FeF_2 the anisotropy field $H_A = 197$ kG and the exchange field $H_E = 533$ kG, and $M = 0.56$ kG. With a gyromagnetic ratio of $\gamma = 0.105$ cm^{-1}/kG this gives a resonance frequency of 52.4 cm^{-1} or about 1500 GHz.

When the applied field is zero the dispersion relations have relatively simple forms. The dispersion relation for the bulk polaritons in zero field is given by the usual relation.

$$k_x^2 + k_y^2 = \epsilon \mu_1 \omega^2 / c^2, \quad (11)$$

where k_x is the component of the wave vector parallel to the surface and k_y is the wave vector component perpendicular to the surface. The dispersion relation for surface polaritons is given by an implicit dispersion relation

$$k_x^2 = \left(\frac{\epsilon - \mu_1}{1 - \mu_1^2} \right) \mu_1 \omega^2 / c^2. \quad (12)$$

The results for the bulk and surface polaritons in FeF_2 with zero applied field are shown in Fig. 1. We see two frequency regions which represent the bulk excitations. Between the bulk bands we see a surface mode which is reciprocal, i.e., the frequency does not depend on the sign of the wave vector.

A very different dispersion curve is found when there is an external magnetic field as can be seen in Fig. 2. Now there are three bulk bands. While the bulk modes are reciprocal, the surface modes are clearly nonreciprocal. For example, one mode which exists at higher frequencies for $-k_x$ has no counterpart for $+k_x$ in the same frequency range. We note that for the geometry considered here reversing the applied field is equivalent to a reversal of the propagation direction. Thus one may determine nonreciprocal propagation and reflectivity characteristics by leaving the optical setup un-

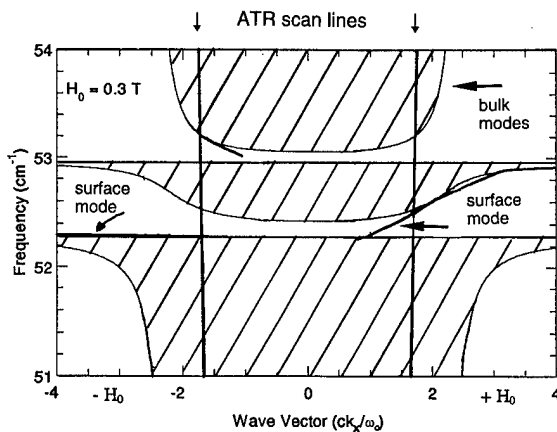


FIG. 2. Dispersion relations for bulk and surface polaritons in FeF_2 with an applied field of 3 kG. In contrast to the $H=0$ case there are now three bulk bands and the surface modes are strongly nonreciprocal.

changed and simply reversing the applied field. This is a much simpler procedure experimentally and we use this method.

Since these excitations are in the infrared, it is natural to use infrared radiation as a probe. We note that this has been done in the past using a laser at a single frequency,^{6,8} and also with a Fourier transform infrared (FTIR) system.⁹ However, none of these experiments truly identified the surface modes. There are several reasons for this. First, the frequency gap between the bulk and the surface modes is quite small, requiring a system with high frequency resolution. Second, an ordinary reflectivity measurement is normally sensitive to bulk modes and not to surface modes.

To overcome the difficulties outlined above, we have used a specially designed FTIR system with a resolution on the order of 0.01 cm^{-1} . This requires the scanning arm of the interferometer to be about 1 m long. Additional information on the interferometer may be found in Ref. 10. In addition we use the attenuated total reflection (ATR) technique which allows the external radiation to couple to the surface modes effectively.¹¹ This technique is illustrated in Fig. 3. External light is incident on a Si prism with dielectric constant $\epsilon = 11.57$. Because of the high index of the prism, the light is totally internally reflected at the base of the prism and the reflectivity, in the absence of a sample, would be unity. However, there is an evanescent wave below the prism base which can couple to electromagnetic modes in the sample. When this occurs, the reflectivity is reduced from unity since some of the energy is transferred to the sample.

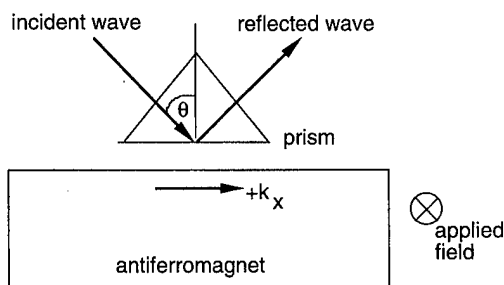


FIG. 3. ATR reflectivity geometry. Reversing the incident and reflected waves reverses the direction of k_x .

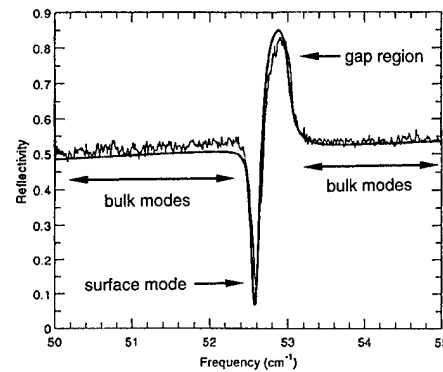


FIG. 4. Experimental and theoretical ATR reflectivity as a function of frequency for FeF_2 in zero field. The broad regions of depressed reflectivity represent losses to bulk modes. The sharp dip in reflectivity represents the loss to the surface mode. The angle of incidence in the prism is 30° and the gap between the prism and the antiferromagnet is $17 \mu\text{m}$.

To understand the ATR curves, it is helpful to plot the dispersion curve representing the incident light in the prism on top of the magnetic polariton dispersion curves. When we write the dispersion relation in terms of the component of the wave vector parallel to the surface we obtain

$$k_x = (\omega/c) \sqrt{\epsilon} \sin \theta. \quad (13)$$

This gives the straight lines shown in Figs. 1 and 2 for positive and negative k_x . Where the dispersion curve (or scan line) of the incident light crosses the bulk or surface modes of the antiferromagnet, there can be a loss of energy from the incident wave to the modes of the antiferromagnet and a corresponding reduction in reflected intensity. Thus a broad region of depressed reflectivity corresponds to the existence of bulk bands, while a sharp dip at one particular frequency corresponds to a surface mode.

In Fig. 4 we plot the ATR reflectivity for the case of zero field. The temperature here and in Fig. 5 is 1.7 K. In this plot we see two broad regions of depressed reflectivity corresponding to the two bulk bands of Fig. 1. In between there is a sharp dip in reflectivity, corresponding to the surface mode, and then an increase in reflectivity corresponding to the gap between the bulk modes. It is clear that the experimental results are in very good agreement with both the theoretical calculations for ATR reflectivity and for the dispersion relations calculated in Fig. 1.

In Fig. 5 we again plot ATR reflectivity presently for a field of $\pm 3 \text{ kG}$. From the dispersion curve in Fig. 2, we expect a total of three regions of reduced reflectivity corresponding to the three bulk bands. In addition we expect sharper dips representing the surface modes. These features are all present in Fig. 5. A key feature to note is that the surface modes appear at different frequencies depending on the sign of applied magnetic field. This clearly demonstrates the expected nonreciprocity of the surface modes. It may be possible to exploit this nonreciprocity for signal processing in the infrared. For example the ATR reflectivity near 52.5 cm^{-1} is close to zero for positive field. In contrast, the wave traveling in the reversed direction (equivalent to reversing the applied field) has a reflectivity of close to 80%. Thus this system might be used as the basis for a nonreciprocal isolator in the infrared.

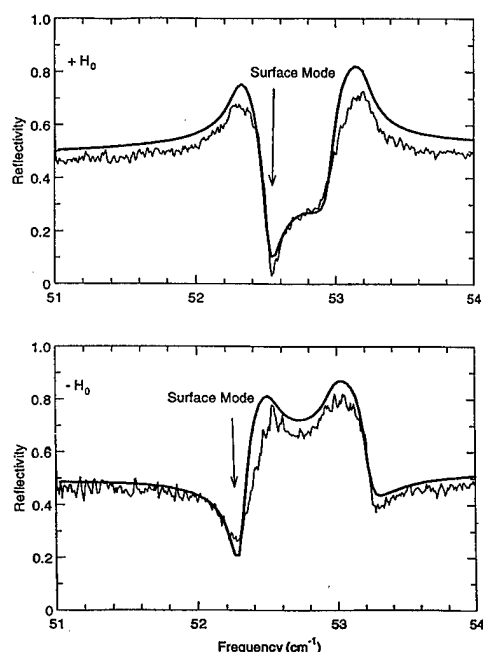


FIG. 5. ATR reflectivity as a function of frequency for FeF_2 with an applied field of 3 kG. The angle of incidence in the prism is 30° and the gap between the prism and the antiferromagnet is $17 \mu\text{m}$. Note the large nonreciprocity in frequency at 52.5 cm^{-1} . The smooth curves are the theoretical results and the thinner, jagged lines are the experimental results.

By doing measurements with different angles of incidence inside the prism, one can trace out the behavior of the edges of the bulk band and the position of the surface mode. In addition one can also use ordinary reflectivity. The results^{12,13} are in excellent agreement with the theoretical calculations shown in Figs. 1 and 2. Other recent reflectivity studies on FeF_2 in a different geometry also show excellent correspondence between theory and experiment.¹⁴

The properties of thin antiferromagnetic films, or of antiferromagnetic films coupled to ferromagnets in an exchange biasing configuration may be quite different from those of bulk antiferromagnets. It is therefore of interest to see whether the infrared studies of bulk materials can be extended to thin films. In Fig. 6 we plot the ordinary infrared reflectivity (not ATR reflectivity) seen from a 1000 \AA FeF_2 film on a Si substrate. If the linewidth is on the order of 500 G, the signal is small. However, if the linewidth is only 50 G the signal is quite substantial with a change in reflectivity on the order of 15%. Linewidths in antiferromagnets can vary substantially depending on the quality of the crystal. Our bulk sample showed a linewidth on the order of 400–500 G at low temperatures. However some samples have been reported with linewidths an order of magnitude or more lower.¹⁵

The current FTIR system is sensitive to about a 1% change in reflectivity. If an antiferromagnetic film has a linewidth on the order of 50 G, this would lead to the conclusion that one should be able to observe a signal from an antiferromagnetic film with a thickness of about 100 \AA . Improvements in the signal to noise ratio might therefore easily allow much thinner films to be studied. Alternatively, one could form a superlattice where the unit cell contained, say, a 100 \AA antiferromagnetic film. Ten repeats of this structure would

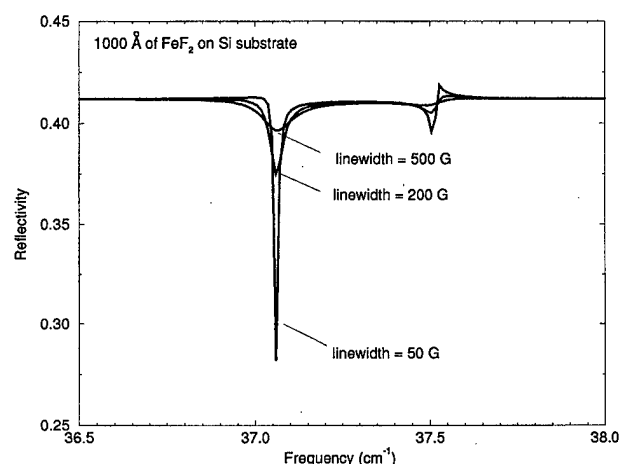


FIG. 6. Ordinary reflectivity from a thin FeF_2 film on a Si substrate for different linewidths. The applied field is 1.5 kG, and the angle of incidence is 45° .

give 1000 \AA of antiferromagnet. In this case a signal should be observable even with the higher linewidths.

What could be expected from studies of thin antiferromagnetic films? We know that in ferromagnets surface anisotropy fields or interfacial exchange fields can substantially change the surface spin wave frequency.¹⁶ Measurements of this frequency can then be used to determine these surface and interface parameters. Initial calculations¹⁷ show that the spin wave modes in antiferromagnets will also be sensitive to surface and interfacial properties. Thus IR probes, either with the FTIR system or with a narrow linewidth laser of thin antiferromagnetic films may be helpful in understanding the exchange biasing effect.

This work was supported by EPSRC through Grant Nos. GR/G54139 and GR/J90831. The work of REC was also supported by U.S. ARO Grant No. DAA H04-94-G-0253.

¹J. Nogues, D. Lederman, T. J. Moran, and I. K. Schuller, *Phys. Rev. Lett.* **76**, 4624 (1996).

²K. M. H. Lenssen, A. E. M. De Veirman, and J. J. T. M. Donkers, *J. Appl. Phys.* **81**, 4915 (1997).

³See the review article on nonreciprocity, R. E. Camley, *Surf. Sci. Rep.* **7**, 103 (1987).

⁴D. L. Mills and E. Burstein, *Rep. Prog. Phys.* **37**, 817 (1974).

⁵R. E. Camley and D. L. Mills, *Phys. Rev. B* **26**, 1280 (1982).

⁶L. Remer, B. Lüthi, H. Sauer, R. Geick, and R. E. Camley, *Phys. Rev. Lett.* **56**, 2752 (1986).

⁷K. Abraha and D. R. Tilley, *Surf. Sci. Rep.* **24**, 129 (1996).

⁸R. W. Sanders, D. Pagnette, V. Jaccarino, and S. M. Rezende, *Phys. Rev. B* **10**, 132 (1974).

⁹R. C. Ohlmann and M. Tinkham, *Phys. Rev.* **123**, 425 (1961).

¹⁰T. Dumelow, D. Brown, and T. J. Parker, *Proc. SPIE* **2104**, 633 (1993).

¹¹M. R. F. Jensen, T. J. Parker, K. Abraha, and D. R. Tilley, *Phys. Rev. Lett.* **75**, 3756 (1995).

¹²M. R. F. Jensen, S. A. Feiven, T. J. Parker, and R. E. Camley, *Phys. Rev. B* **55**, 2745 (1997).

¹³M. R. F. Jensen, S. A. Feiven, T. J. Parker, and R. E. Camley, *J. Phys.: Condens. Matter* **9**, 7233 (1997).

¹⁴K. Abraha, D. E. Brown, T. Dumelow, T. J. Parker, and D. R. Tilley, *Phys. Rev. B* **50**, 6808 (1994).

¹⁵M. Lui, C. A. Ramos, A. R. King, and V. Jaccarino, *J. Appl. Phys.* **67**, 5518 (1990).

¹⁶B. Hillebrands and G. Güntherodt, in *Ultrathin Magnetic Structures II*, edited by J. A. C. Bland and B. Heinrich (Springer, Berlin, 1993).

¹⁷R. L. Stamps and R. E. Camley, *Phys. Rev. B* **54**, 15200 (1996).

Strain induced alteration of the gadolinium surface state

C. Waldfried, D. N. McIlroy, T. McAvoy, D. Welipitiya, and P. A. Dowben^{a)}

*Department of Physics & Astronomy and the Center for Materials Research and Analysis,
University of Nebraska-Lincoln, Lincoln, Nebraska 68588-0111*

E. Vescovo

National Synchrotron Light Source, Brookhaven National Laboratory, Upton, New York 11973

The electronic structure of strained and unstrained Gd(0001) has been studied with photoemission, inverse photoemission, and spin-polarized photoemission. A shift of the occupied majority and unoccupied minority surface states has been observed as a result of the strain, consistent with the phase accumulation model. There is a strain induced shift of the minority spin surface state across the Fermi level. © 1998 American Institute of Physics. [S0021-8979(98)28611-7]

Surface states may experience a shift in binding energy due to strain.¹ For magnetic surfaces the spin dependent shift of the surface majority and minority subbands near the Fermi level can result in a variation of the spin population at different wave vectors k . This will have a substantial influence on the magnetic behavior of the surface. The subject of this article is the effect of strain on the electronic structure of the surface of gadolinium. We show consistency with the effects recently demonstrated by Neuhold and Horn¹ on the surface of Ag(111).

The surface magnetism of gadolinium has been the subject of controversy over the past years, mainly as a result of the proximity of the $5d_{z^2-r^2}$, $6s$ surface states to the Fermi level. Strain substantially alters the electronic structure of gadolinium²⁻⁴ and is expected to result in a shift of the surface state binding energies. We have been able to obtain strained films of gadolinium, with an increased lattice constant of approximately 4% by growing gadolinium on the corrugated surface of Mo(112).²⁻⁴

We investigated the occupied and unoccupied electronic structure of thin films of strained and unstrained Gd(0001). Spin-polarized photoemission experiments were carried out at the new U5UA undulator beamline of the National Synchrotron Light Source (NSLS) at the Brookhaven National Laboratory in Upton, NY. The details of the experimental setups are described elsewhere.^{5,6} Inverse photoemission spectra were acquired in a different UHV system² in the isochromatic mode ($\hbar\omega = 9.4$ eV) with a Geiger-Müller tube and an electron gun based on the Zipf design.⁷ Strained and unstrained thin films of Gd, 10–40 ML thick, were grown by slow thermal deposition on Mo(112) and W(110) substrates, respectively. The surface and bulk character of the bands has been determined from chemisorption studies and photon energy dependence, while the symmetry of the bands has been ascertained from the light polarization dependence as described in detail elsewhere.²

The influence of strain on the surface electronic structure of Gd is illustrated in Fig. 1, which compares two normal emission photoemission spectra that were taken for strained and unstrained Gd(0001). Both spectra have been acquired

with a photon energy of 33 eV for films of similar nominal thickness of approximately 15 ML. The valence band of the strained Gd(0001) films is distinct from that of the relaxed films. The binding energy of the $5d$, $6s$ strained bulk bands at 1.8 eV below E_F differs from the unstrained bulk bands observed at approximately 1.5 and 0.8 eV below E_F at the surface Brillouin zone center. More significant, the narrow surface state near the Fermi level of the unstrained Gd(0001) is shifted towards higher binding energy and appears substantially broadened.

The origin of the clearly altered valence-band states and broader density of states near the Fermi level of strained Gd is revealed by the spin resolved electronic structure, shown in Fig. 2. The unstrained Gd(0001) valence band at the Brillouin zone center ($\bar{\Gamma}$) is characterized⁸ by Stoner-like exchange split $5d$ bulk bands at binding energies of approximately 1.5 (majority) and 0.8 eV (minority) and two sets of

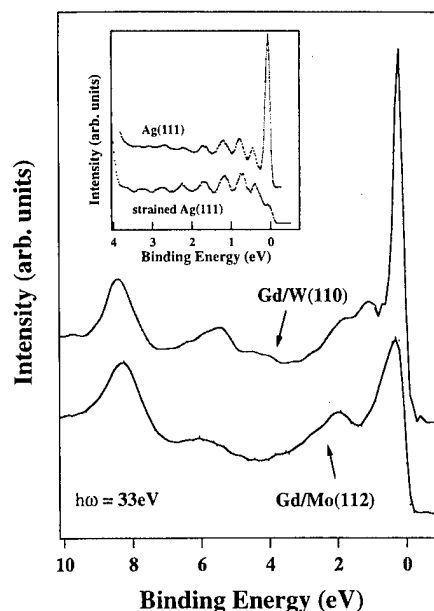


FIG. 1. Normal emission photoemission spectra for strained (bottom) and unstrained (top) films of Gd(0001), acquired with a photon energy of 33 eV. The inset shows a comparison of a strained (bottom) and unstrained (top) Ag(111) surface from Ref. 1.

^{a)}Electronic mail: pdowben@unlinfo.unl.edu

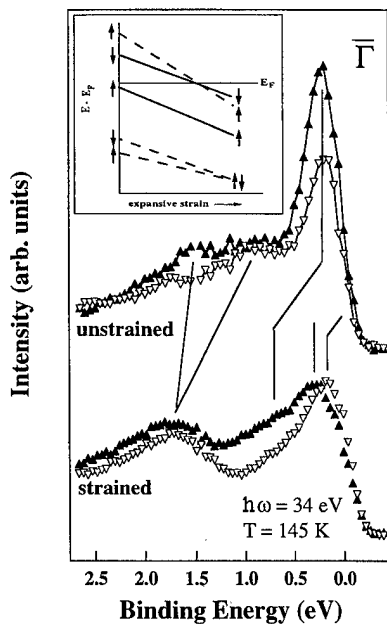


FIG. 2. Spin-polarized photoemission spectra for strained (bottom) and unstrained (top) Gd(0001) at normal emission and approximately 145 K. The spectra were acquired with a photon energy of 34 eV. The inset schematically plots the binding energy shifts of the surface (solid) and bulk (dashed) spin subbands as a function of increased expansive strain.

spin majority and minority subbands of the surface on either side of the Fermi level. The occupied predominantly spin-mixed majority $5d_{z^2-r^2}$, $6s$ surface state is located at approximately 0.1 eV below E_F (Fig. 2) and the unoccupied minority counterpart of the surface state at approximately 0.3 eV above the Fermi level⁹ (Fig. 3) (though this is dependent on temperature well away from T_C).¹⁰

In the strained Gd films the bulk spin majority and minority subbands are found at approximately 1.8 eV binding energy at $\bar{\Gamma}$, with negligible Stoner-like exchange splitting.³ There are three features near the Fermi level (0 to 1 eV binding energy) in the valence band of the strained Gd films. Two features, the spin majority state at 0.7 eV below E_F and the spin minority state at 0.2 eV binding energy are Stoner-

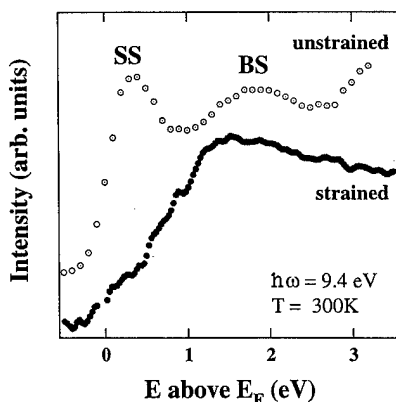


FIG. 3. The unoccupied density of states for strained (bottom) and unstrained (top) films of Gd(0001). The spectra were taken at approximately 300 K. The data for the unstrained Gd has been extracted from Ref. 9. Surface and bulk features are indicated by the surface state (SS) and bulk state (BS), respectively.

like exchange split surface bands.³ The surface character of these two states has been verified by their sensitivity to small amounts of adsorbates and their two dimensionality of state. Both surface sensitive features do not disperse with changing perpendicular momentum² and are therefore confined to the two-dimensional plane at the surface. The third feature in the valence-band region near E_F , an additional bulk band of majority character, is located in the exchange splitting gap at approximately 0.4 eV binding energy at $T/T_C < 0.7$.

The two occupied bands closest to E_F , the spin minority surface subband, and the spin majority bulk band are newly introduced into the occupied density of states as a result of the strain. Both bands are found in the unoccupied region for the unstrained Gd films as seen in Fig. 3. Expansive strain within the Gd films induces a "downward" shift of the unoccupied surface state across the Fermi level. This is consistent with the absence of the surface spin minority state (0.3 eV above E_F)⁹ in the unoccupied density of states of the strained Gd films. The spin majority bulk band at 0.4 eV binding energy of the strained Gd film is postulated to originate from the unstrained bulk band, located approximately 1.5 eV above the Fermi level,⁹ at zone center, crossing the Fermi level about halfway across the zone in unstrained Gd. This shift in binding energy at $\bar{\Gamma}$ is illustrated in the inset of Fig. 2. More detailed studies of the occupied and unoccupied density of states are, nonetheless, necessary to confirm this postulate.

From our data it is clear that the spin majority $5d_{z^2-r^2}$, $6s$ surface state is shifted from 0.2 eV binding energy for the unstrained Gd films to 0.7 eV in the strained Gd(0001). A similar downward shift of 0.5 eV is observed for the spin minority counterpart, which is unoccupied for the "relaxed" Gd(0001) and found at a binding energy of approximately 0.2 eV below E_F due to strain (Fig. 2 inset). Concomitantly, the occupied spin minority (0.8 eV below E_F) and unoccupied spin majority (≈ 1.5 eV above E_F) bulk bands of unstrained Gd experience large shifts of approximately 1.0 and 1.9 eV, respectively.

The shift to higher binding energies of the Gd surface states (majority and minority) under the influence of expansive strain is in agreement with the strain induced shifts of the surface state binding energy for Ag(111),¹ which is shown in the inset of Fig. 1. There, compressive strain results in the upward shift of the sharp Ag(111) surface state across the Fermi level, where it is cut off by the Fermi function and undetectable with photoemission. In both cases the strained induced shift of the surface state(s) can be explained by the phase accumulation model.¹¹⁻¹⁴

Surface states originate from electrons confined to the top most layer of the solid, trapped in between the bulk band gap and the surface potential. A simple one-dimensional (so-called "phase accumulation") model¹¹⁻¹⁴ can be employed to roughly describe the surface state energy. This simple model considers the surface electron in a one-dimensional quantum well, confined by the image potential on the vacuum side and the bulk band gap on the crystal side. The surface state energy is then determined by the lowest allowed quantum mechanical solution of the electron wave function. The energy of the surface state thus varies proportionally to

$1/d^2$, with d being the width of the well. In the phase accumulation formalism, d is dependent, among others, on the bulk band edges¹⁵ and the work function.^{11,13} Thus the strain induced shifts in binding energy of the surface states in gadolinium can be attributed to the altered majority and minority bulk band gaps and the reduced work function of strained Gd, approximately 2.2 eV, as compared to 3.3 eV for the relaxed Gd film.

Our results provide evidence that under expansive strain both spin components of the bulk bands are modified and results in a downward shift of the surface spin subbands. A change of the in-plane lattice constant of approximately 4% yields a surface state energy shift of 0.5 eV (Fig. 2 inset). The strain induced shifts of the bulk band edges (spin majority and spin minority) of approximately 1 to 2 eV are substantially larger than those of the surface bands. The shift of each Gd surface state (one in the spin majority band structure, the other in the spin minority band structure) is consistent with the observations and calculation for Ag(111).¹

This study shows that strain can significantly alter the spin-polarized electronic structure of a ferromagnetic system like gadolinium in much the same way as strain affects a nonmagnetic system like Ag(111). In a ferromagnetic system, we need to consider each surface state spin component in the appropriate spin-resolved band structure. It is only apparent in the spin-resolved band structure how similar the influence of strain is in both Ag(111) and Gd(0001).

ACKNOWLEDGMENTS

This work was supported by NSF through Grant Nos. DMR-92-21655, DMR-94-96131, and DMR-94-07933. The experiments were carried out at the National Synchrotron Light Source which is funded by the DOE and at the Synchrotron Radiation Center which is also funded by NSF.

- ¹G. Neuhold and K. Horn, *Phys. Rev. Lett.* **78**, 1327 (1997).
- ²C. Waldfried, D. N. McIlroy, and P. A. Dowben, *J. Phys.: Condens. Matter* **9**, 10 615 (1997).
- ³C. Waldfried, D. Welipitiya, T. McAvoy, E. Vescovo, and P. A. Dowben, *Phys. Rev. Lett.* (submitted).
- ⁴C. Waldfried, D. N. McIlroy, and P. A. Dowben, *Phys. Rev. B* **54**, 16 460 (1996); **56**, 9973 (1997).
- ⁵E. Vescovo *et al.*, Activity Report 1996, Nat. Synch. Light Source, A-25 (1997).
- ⁶P. D. Johnson *et al.*, *Rev. Sci. Instrum.* **63**, 1902 (1992); J. Unguris, D. T. Pierce, and R. J. Calotta, *Rev. Sci. Instrum.* **57**, 1314 (1986).
- ⁷P. W. Erdmann and E. C. Zipf, *Rev. Sci. Instrum.* **53**, 225 (1982).
- ⁸D. Li, J. Pearson, S. D. Bader, D. N. McIlroy, C. Waldfried, and P. A. Dowben, *Phys. Rev. B* **51**, 13 895 (1995).
- ⁹M. Donath, B. Gubanka, and F. Passek, *Phys. Rev. Lett.* **77**, 5138 (1996).
- ¹⁰M. Bode, M. Getzlaff, S. Heinze, R. Pascal, and R. Wiesendanger, *Phys. Rev. A* (in press).
- ¹¹N. V. Smith, *Phys. Rev. B* **32**, 3549 (1995).
- ¹²N. V. Smith, N. B. Brooks, Y. Chang, and P. D. Johnson, *Phys. Rev. B* **49**, 332 (1994).
- ¹³P. Ahlqvist, *Solid State Commun.* **31**, 1029 (1979).
- ¹⁴P. M. Echenique and J. B. Pendry, *J. Phys. C* **11**, 2065 (1978).
- ¹⁵R. Paniago, R. Matzdorf, G. Meister, and A. Goldmann, *Surf. Sci.* **336**, 113 (1995).

Effect of surface roughness on magnetization reversal of Co films on plasma-etched Si(100) substrates

M. Li,^{a)} Y.-P. Zhao, and G.-C. Wang

Department of Physics, Applied Physics, and Astronomy, Rensselaer Polytechnic Institute, Troy, New York 12180-3590

H.-G. Min

Department of Physics, Hong-Ik University, Seoul 121-791, Korea

Co films ~ 970 Å thick were deposited, *simultaneously*, on ten plasma-etched Si(100) substrates with various etch times t . The surface morphologies and magnetic properties of the Co films were measured by atomic force microscopy (AFM) and magneto-optic Kerr effect (MOKE) technique. The analysis of the AFM images shows that as the etch time t increased from 0 to 100 min, the vertical interface width w increased from ~ 5 to ~ 1400 Å; the lateral correlation length ξ increased from ~ 300 to $\sim 10\,500$ Å. The MOKE measurements provided the in-plane azimuthal angular dependence of the hysteresis loops and the change of loop shapes with the surface roughness. It was found that the magnetization reversal process changed with the surface roughness. Magnetization rotation dominated the magnetization reversal for the smoothest films. As the films roughened, the domain-wall pinning set in, eventually dominating the magnetization reversal for the roughest films. Additionally, the magnetic uniaxial anisotropy in the Co films disappeared as the roughness parameters increased. It was also found from MOKE that the surface roughness strongly affected the coercivity. © 1998 American Institute of Physics. [S0021-8979(98)36911-X]

It is known that surface/interface roughness of magnetic thin films and of superlattices influences magnetic properties, such as magnetic anisotropy, coercivity, magnetoresistance, and magnetic domain structure.¹⁻³ Various works on the relationship between surface roughness and coercivity, of thin and ultrathin films, have been carried out.⁴⁻⁶ For examples, Mal'yutin *et al.*⁴ investigated the effect of surface roughness on the coercivity of chemically etched NiFeCo films (200–1000 Å thick) and found that the coercivity of the film increased with the increase of etch time. During the etching, the thickness of the magnetic film decreased and the surface roughness increased with etch time. Vilain *et al.*⁵ investigated the dependence of coercivity on the surface roughness for electrodeposited NiCo alloy films. For ultrathin films, Jiang *et al.*⁶ investigated the coercivity of ultrathin Co films on Cu(100) substrate versus substrate roughness. The coercivity of the 6–7 ML Co film increases from ~ 70 Oe for deposition on an atomically flat Cu substrate, to ~ 170 Oe for deposition on a Cu substrate roughened by Ar⁺ sputtering to a (vertical) interface width of ~ 1.81 atomic-step heights. This demonstrates the sensitivity of coercivity on the surface roughness.

In addition to the surface roughness, it is known that the thickness, the composition, the crystalline structure of the magnetic film, and the preparation conditions also determine the magnetic properties of the films. Therefore, to understand the interrelationship between roughness and magnetic properties, other factors influencing the magnetic properties must be controlled. In the present study, we deposited ~ 970 Å Co films simultaneously (and thus identically) on ten plasma-

etched Si(100) substrates by thermal evaporation in high vacuum and studied the effect of the surface roughness on the magnetic properties of ~ 970 Å Co films.

Ten *n*-type Si(100) substrates were etched by plasma-etching gases (CF₄ and 4% O₂) with an etch rate of 1500 Å/min to various degrees of roughness in a standard plasma-etching chamber. The etch times t were 0, 1, 5, 10, 20, 30, 40, 60, 80, and 100 min, respectively. The surface morphologies of these roughened Si(100) substrates were imaged by atomic force microscopy (AFM) with a Si₃N₄ tip. Then, these rough Si(100) substrates were arranged on a large supporting plate in another high-vacuum chamber. The Co atoms were thermally evaporated from a crucible onto these ten Si(100) substrates simultaneously. The base pressure was 5×10^{-7} Torr and the pressure increased to 5×10^{-6} Torr during deposition. A quartz crystal monitor indicated a deposition rate of ~ 0.8 Å/s and ~ 970 -Å-thick Co films formed after about 20 min deposition. The starting substrate temperature was at the ambient temperature and the substrate temperature rose during the deposition due to the filament needed to heat the Co source. The characterizations were carried out in ambient air at room temperature. The surface morphology of the Co film was imaged by AFM. The hysteresis loops were measured by the magneto-optic Kerr effect (MOKE) technique.⁷

All of the AFM images from AFM measurements showed islandlike features with a wide distribution of sizes and separations. Figure 1 shows four typical AFM images of the ~ 970 Å Co films deposited on the plasma-etched Si(100) substrates. As illustrated by the increasing scan size for successive etch time t , the average size and separation of the features increased with increasing etch time t . For etch

^{a)}Electronic mail: wangg@rpi.edu

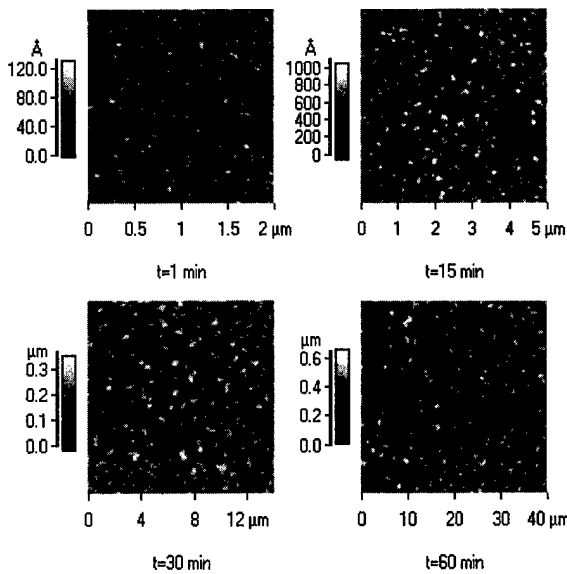


FIG. 1. Four grey-scale AFM images of ~ 970 -Å-thick Co films deposited on Si(100) substrates etched for times $t = 1, 15, 30$, and 60 min. Note, the scan size increases.

times longer than 20 min, the islandlike features connected to form a networklike morphology. The roughness parameters, the (vertical) interface width w , and the (lateral) correlation length ξ can be obtained by analyzing the height-height correlation function $H(r, t)$, which can be calculated from AFM images.⁸ The vertical interface width w increased from ~ 5 to ~ 1400 Å; the lateral correlation length ξ increased from ~ 300 to $\sim 10\,500$ Å. Table I lists the roughness parameters for different etch time t .

The longitudinal hysteresis loops were measured for all of the Co films using an external magnetic field amplitude $H_0 = 128$ Oe with a frequency $f = 1.4$ Hz. For a given sample, the loop was measured as a function of in-plane azimuthal angle φ from 0° to 360° . The results indicate that the easy magnetization direction of the Co films lay in the film plane for all the samples studied here. There was in-plane uniaxial magnetic anisotropy in the Co films for etch times $t < 60$ min, whereas there was no detectable in-plane magnetic anisotropy in the Co films with the etch time $t = 60$ and 100 min.

The directions of the easy axis and the hard axis in the film plane were determined from the azimuthal angle depen-

TABLE I. The surface roughness parameters (vertical interface width w and lateral correlation ξ) of Co films vs etch time t .

t (min)	w (Å)	ξ (Å)
0	5 ± 1.5	335 ± 110
1	15 ± 1.6	310 ± 105
5	30 ± 3	320 ± 108
10	150 ± 5	677 ± 213
15	172 ± 9	765 ± 222
20	453 ± 24	2009 ± 695
30	485 ± 15	2665 ± 932
40	574 ± 18	3207 ± 1160
60	859 ± 30	6795 ± 2342
100	1376 ± 15	10475 ± 3884

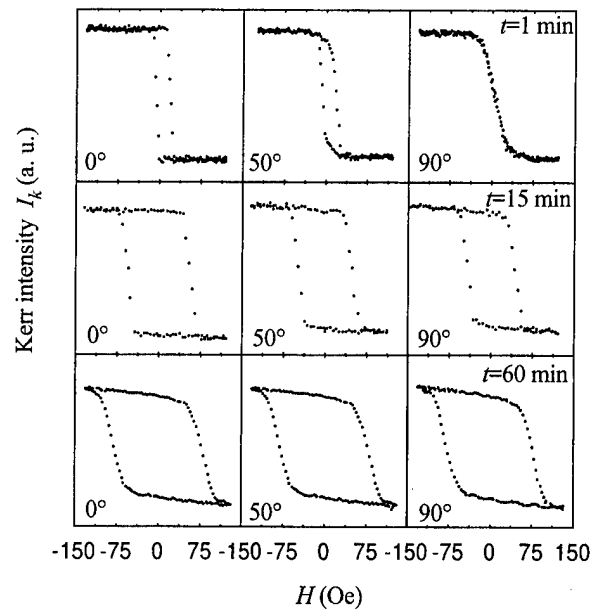


FIG. 2. MOKE hysteresis loops at three in-plane azimuthal angles (0° , 50° , and 90°) for three ~ 970 -Å-thick Co films.

dence of the loop shape. Figure 2 shows the hysteresis loops at different azimuthal angles for three typical samples with etch time $t = 1, 15$, and 60 min. For the samples with etch time $t \leq 5$ min, the shape of the loop changed from squarelike, to spindlelike, to almost a straight line as the in-plane azimuthal angle changes in the range of 0° – 90° . The loop had a squarelike shape, a high coercivity H_c and a high squareness S when the magnetic field was applied along the easy axis. When the magnetic field was applied along the hard axis direction, however, the loop was almost reversible; as a result, both S and H_c were close to zero. This suggests that the magnetization reversal process was dominated by magnetization rotation, and that the contribution to the magnetization reversal from domain wall motion was negligible for samples with $t = 0, 1$, and 5 min. The uniaxial magnetic anisotropy field can be easily obtained from the hysteresis loops.⁹

For samples with etch time $t = 10, 15, 20, 30$, and 40 min, the twofold symmetry in the coercivity versus azimuthal angle still existed, but all of the loop shapes were squarelike. The squareness lost its twofold symmetry, becoming almost constant, independent of φ . Due to the increasing surface roughness, domain-wall pinning started to contribute to the coercivity. The magnetization reversal process was associated with both the domain wall motion and magnetization rotation. To make the magnetization reversal happen in these cases, the applied field H must overcome not only the domain-wall-pinning coercivity, H_{cw} , but also the component of the magnetic anisotropy field in the applied field direction, which is $H'_a = H_a \cos \varphi$. This means that the combined magnetic field should at least equal H_{cw} . Therefore, we have the following relation:

$$H_0^2 = H^2 + H_a'^2 - 2HH'_a \cos \varphi, \quad (1)$$

where φ again is the in-plane angle between the applied

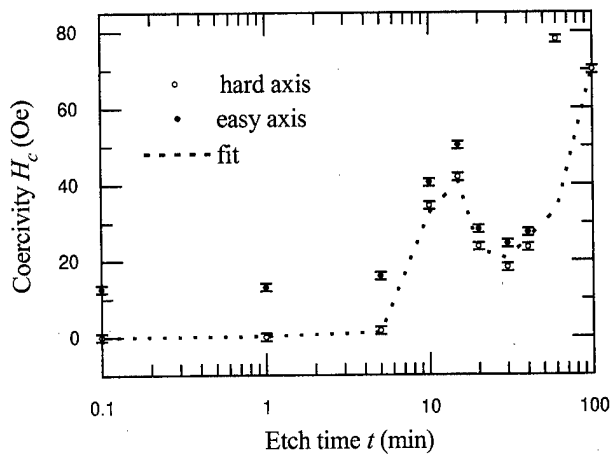


FIG. 3. The easy axis coercivity and hard axis coercivity vs etch time for ~ 970 -Å-thick Co films. The dashed curve is the fit using $H_{cw} = aw^b/\xi^c$.

field and the easy axis of magnetization, and $H'_a = (2K_u/M_s)\cos\varphi$. Letting $H_0 = H_{cw}$, and $H = H_c$, the magnetization reversal will occur, and we have

$$H_c = H'_a \cos\varphi + (H_{cw}^2 - H_a'^2 \sin^2\varphi)^{1/2}. \quad (2)$$

By using this equation, we fitted the measured angular dependence of H_c for samples with $t = 10, 15, 20, 30$, and 40 min, and obtained the magnetic anisotropy field H_a and anisotropy coefficient K_u .

For the samples with $t > 40$ min, the loop shape was squarelike, and there was no detectable in-plane magnetic anisotropy. At this point, the magnetization reversal was controlled mostly by the domain wall motion.

The results of MOKE hysteresis loop measurements suggest that the magnetization reversal process in these Co films depended strongly on the surface roughness. With the increase of the surface roughness, the magnetization reversal process changed from the magnetization rotation ($t < 10$ min) to a combination of magnetization rotation and domain-wall motion ($10 \text{ min} \leq t \leq 40 \text{ min}$), and then to domain-wall motion ($t > 40$ min).

The coercivity determined from MOKE measurements is plotted in Fig. 3 versus etch time t and for samples with $t < 60$ min, both the easy and hard axes coercivity are shown. The easy-axis coercivity H_c was, in general, a monotonically increasing function of the interface width, except for a dip around $t = 30$ min. Specifically, the H_c increased slightly between 13 and 15 Oe for $t \leq 5$ min, peaked at ~ 50 Oe for $t = 15$ min, came down to ~ 25 Oe for $t = 30$ min, then increased again to ~ 80 Oe for $t = 60$ min and ~ 70 Oe for 100 min. The hard-axis coercivity had a similar dependence on the etch time. The difference between easy axis coercivity and hard axis coercivity was due to the in-plane uniaxial anisotropy. The results indicated that H_c increased with the increase of the roughness. This is consistent with the prediction of H_c for a Bloch type of domain wall, for which H_c increases if the surface roughness increases for a given

thickness.⁹ The overall decrease of the absolute values of H_c for $t = 20$ min and $t = 30$ min samples, as compared with those of the $t = 10$ min and $t = 15$ min samples, might be due to the network formation (as in Fig. 1), which would make wall movements easier. As the etch time t increased further, the roughness increased and the H_c increased again for $t > 40$ min. We fitted the hard-axis coercivity, i.e., the domain-wall pinning coercivity by using $H_{cw} = aw^b/\xi^c$, which is shown in Fig. 3 by the dashed line.³ The roughness parameters used in the fit are the measured roughness parameters listed in Table I. The fit parameters obtained are $b = 2.40 \pm 0.05$ and $c = 1.00 \pm 0.01$. The value of fit parameter a was an order of magnitude different in two etch time ranges: $a = 0.135 \pm 0.005$ for $t < 20$ min and $a = 0.019 \pm 0.005$ for $t \geq 20$ min. This change coincides with the formation of the networklike features in the morphology after a 20 min etch. This suggests a quantitative correlation between domain-wall coercivity and surface roughness. It is expected that, as the film thickness decreases, the enhancement of the coercivity due to surface roughness would be more dramatic.

The origin of the in-plane uniaxial magnetic anisotropy is not clear yet. It might be related to the stress built up during the film deposition¹⁰ due to the different thermal expansion coefficients of the substrate and of the Co film. From MOKE measurements, the uniaxial magnetic anisotropy K_u decreased from $1.3 \times 10^3 \text{ J/m}^3$ for $t = 0$ min to 0 J/m^3 (no anisotropy) for $t = 100$ min with the increase of the etch time. A possible reason for the decrease in K_u is that, when the surface became rougher, the stress between the Co film and the Si substrate was more easily relieved. Additionally, since the dispersion of the easy axis is expected to increase with the increase of the surface roughness, the uniaxial anisotropy would average out for differently oriented crystalline grains in a polycrystalline film. It is expected that when the magnetic thin film gets thinner, the effect of the surface roughness on the magnetic properties will be more dramatic and is worth further systematic studies.

This work was supported by the National Science Foundation. H.-G.M. was supported by Korea Research Foundation (KRF) 95-500-648 and KOSEF through ASSRC, Korea. The authors thank K. Mello for the help in the deposition of Co films, and John B. Wedding for reading the manuscript.

¹ *Ultrathin Magnetic Structures I and II*, edited by J. A. C. Bland and B. Heinrich (Springer, Berlin, 1994).

² C.-H. Chang and M. H. Kryder, *J. Appl. Phys.* **75**, 6864 (1994).

³ P. Bruno, G. Bayureuther, P. Beauvillain, C. Chappert, G. Lugert, D. Renard, J. P. Renard, and J. Seiden, *J. Appl. Phys.* **68**, 5759 (1990).

⁴ V. I. Malyutin, V. E. Osukhovskii, Yu. D. Vorobiev, A. G. Shishkov, and V. V. Yudin, *Phys. Status Solidi A* **65**, 45 (1981).

⁵ S. Vilain, J. Ebothe, and M. Troyon, *J. Magn. Magn. Mater.* **157**, 274 (1996).

⁶ Q. Jiang, H.-N. Yang, and G.-C. Wang, *Surf. Sci.* **373**, 181 (1997).

⁷ J.-P. Qian and G.-C. Wang, *J. Vac. Sci. Technol. A* **8**, 4117 (1990).

⁸ H.-N. Yang, T.-M. Lu, and G.-C. Wang, *Diffraction from Rough Surfaces and Dynamic Growth Fronts* (World Scientific, Singapore, 1993).

⁹ R. F. Soohoo, *Magnetic Thin Films* (Harper and Row, New York, 1965).

¹⁰ M. Prutton, *Thin Ferromagnetic Films* (Butterworths, Washington, 1964).

Exploring magnetic roughness in CoFe thin films

J. W. Freeland,^{a)} V. Chakarian, K. Busmann, and Y. U. Idzerda
Naval Research Laboratory, Washington, D.C. 20375

H. Wende
Freie Universität Berlin, D-14195 Berlin-Dahlem, Germany

C.-C. Kao
National Synchrotron Light Source (NSLS), Brookhaven National Laboratory, Upton, New York 11973

The behavior of chemical and magnetic interfaces is explored using diffuse x-ray resonant magnetic scattering (XRMS) for CoFe thin films with varying interfacial roughnesses. A comparison of the chemical versus magnetic interfaces shows distinct differences in the behavior of these two related interfaces as the chemical roughness is increased. Such changes appear to be correlated with the behavior of the magnetic hysteresis of the interface, measured by tracking the diffuse XRMS intensity as a function of applied magnetic field. © 1998 American Institute of Physics. [S0021-8979(98)17511-4]

I. INTRODUCTION

The influence of roughness on the properties of thin film magnetic structures is a question of current interest to many facets of the magnetism community. Current results have shown that direct measurements of magnetic roughness as compared to measurements of the chemical roughness indicate that these interfaces are compositionally rough, but magnetically smooth.^{1,2} Since the magnetotransport of these structures is strongly affected by interfacial scattering and in particular by magnetic disorder at the interface,³⁻⁵ chemical roughness may not be the appropriate parameter for correlation with the degradation of the magnetic properties.

The formalism for the determination of the nature of chemical interfaces and surfaces using specular and off specular (diffuse) scattering is a well established field.^{6,7} However, to probe information about a magnetic interface one needs a significant magnetic scattering signal. One way of providing this is through the resonant enhancement of the magnetic and chemical scattering when an incident circular polarized photon is tuned to an absorption edge, known as x-ray resonant magnetic scattering (XRMS).⁸⁻¹³ Utilization of a circular polarized photon, like its absorption counterpart magnetic circular dichroism (MCD),¹⁴ generates the magnetic scattering component. Recently XRMS has been applied to the study of magnetic roughness. From both specular² and diffuse¹ studies of magnetic thin film structures comes evidence of differing chemical and magnetic interfaces.

To better understand the variation of magnetic versus chemical interfaces we have undertaken a study of thin CoFe films where an increasing chemical roughness was induced through the growth process. The results clearly show that the chemical and magnetic interfaces do not behave in the same manner as the root mean square (rms) chemical roughness is increased. Also, we will demonstrate the possibility of using

variations in the magnetic diffuse intensity as a function of applied field as a probe of interfacial magnetic hysteresis.

II. EXPERIMENT

The reflectivity measurements were conducted at the NRL/NSLS Magnetic Circular Dichroism Facility located at beamline U4B of the National Synchrotron Light Source (NSLS).¹⁵ Details of the experimental apparatus and measurement conditions are described elsewhere.^{13,16} To probe interface roughness via the diffuse intensity we performed a sample rocking curve where the detector angle (2θ) was kept fixed and the sample angle (ω) was varied. In this configuration, a scan over a wave vector in the plane (q_x) is performed while keeping the component perpendicular to the film (q_z) approximately constant. To extract the magnetic information it is necessary to measure the helicity dependent scattering of the magnetic material (denoted as I^+ and I^-). So the magnetic moment of the sample was reversed at each data point to determine I^+ and I^- , which has been shown to be equivalent to alternating the photon helicity.^{17,18}

The CoFe alloys thin films were prepared by the rf sputtering facilities of Nonvolatile Electronics Inc. The samples were grown on atomically flat Si_3N_4 substrates (roughness ~ 1.5 Å rms) with the following structure: $\text{Cu}(30\text{Å})/\text{Co}_{95}\text{Fe}_5(50\text{Å})/\text{Cu}(x\text{Å})/\text{Si}_3\text{N}_4$. Due to growth dynamics the rms roughness of Cu grown on Si_3N_4 increases dramatically as the thickness of the Cu buffer layer, x , is increased. Since the Cu buffer layer thickness can be controlled accurately, the roughness of the surface on which the CoFe is deposited can be tailored. For this study we utilized a series of four films with various Cu buffer layer thicknesses ($x = 200, 400, 800, \text{ and } 1600$ Å) spanning a rms chemical roughness ranging from 2.5 to 32 Å rms as measured by a Digital Instruments Dimension 3000 atomic force microscope (AFM) in tapping mode (resolution 10–50 Å). Since the Cu cap layer is so thin, the topographical information provided by AFM should give an accurate measurement of the chemical roughness of the top CoFe/Cu interface. This will be important

^{a)} Author to whom correspondence should be addressed: Naval Research Laboratory, NSLS Bldg. 725A/U4B, Upton, NY 11973; electronic mail: freeland@bnlls3.nsls.bnl.gov

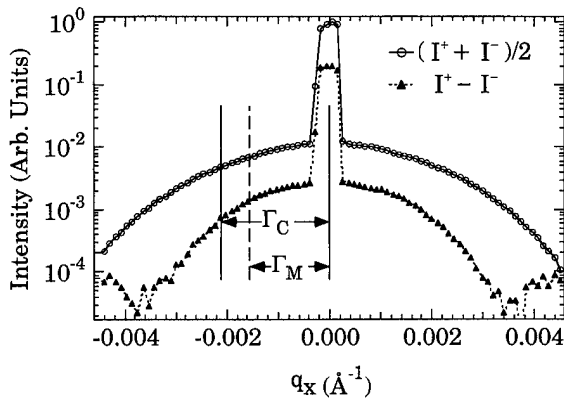


FIG. 1. Sample rocking curve measured at the Co L_3 edge (778 eV) for chemical $[(I^+ + I^-)/2]$ and magnetic $(I^+ - I^-)$ contributions vs q_x . This scan was taken at a detector angle 2θ of 9° ($q_z = 0.062 \text{ \AA}^{-1}$). Notice how the half width of the magnetic diffuse (Γ_M) is smaller than that of the chemical diffuse (Γ_C), indicating a longer correlation length, ξ for the magnetic interface.

when we compare it with the diffuse scattering results because the short mean free path of the photon at the L_3 edge¹⁹ means that measurements made at grazing incidence ($\omega < 10^\circ$) for a 50 \AA CoFe film probe predominately the top CoFe/Cu interface.

III. RESULTS AND DISCUSSION

Figure 1 shows the chemical $[(I^+ + I^-)/2]$ and the magnetic $(I^+ - I^-)$ contributions from a sample rocking (diffuse) scan measured at the Co L_3 edge. The diffuse scan consists of a sharp specular peak around $q_x = 0$, with a broad underlying diffuse component. Since roughness is the mechanism that channels flux from the specular peak into the diffuse component, values for the chemical and magnetic roughness (denoted as σ_C and σ_M , respectively) can be extracted by determining the fraction of total flux that resides in the diffuse part of the spectrum. This is accomplished by comparing the integrated areas of the specular $[S_{\text{specular}}(\mathbf{q})]$ vs diffuse $[S_{\text{diffuse}}(\mathbf{q})]$ components using⁷

$$\frac{\int S_{\text{diffuse}}(\mathbf{q}) d^2 q_{\parallel}}{\int S_{\text{diffuse}}(\mathbf{q}) d^2 q_{\parallel} + \int S_{\text{specular}}(\mathbf{q}) d^2 q_{\parallel}} = 1 - e^{-(q_z \sigma)^2}, \quad (1)$$

where q_{\parallel} denotes integration over the (q_x, q_y) plane, and σ is the roughness perpendicular to the film plane. A second parameter describing the roughness in the film plane, the lateral correlation length, ξ , is determined from the half width (Γ_C and Γ_M) of the diffuse portion of the sample rocking curves using a solution of diffuse structure factor (for a roughness exponent, $h = 1$):^{6,7}

$$S_{\text{diffuse}}(\mathbf{q}) = \frac{2\pi \exp[-(q_z \sigma)^2]}{q_z^2} \times \sum_{m=1}^{\infty} \frac{(q_z \sigma)^{2m}}{m!} \left(\frac{\xi^2}{2m} \right) \exp \left[- \left(\frac{q_x \xi}{2\sqrt{m}} \right)^2 \right]. \quad (2)$$

Results of the analysis of our thickness series are shown in Fig. 2 for both chemical and magnetic data.

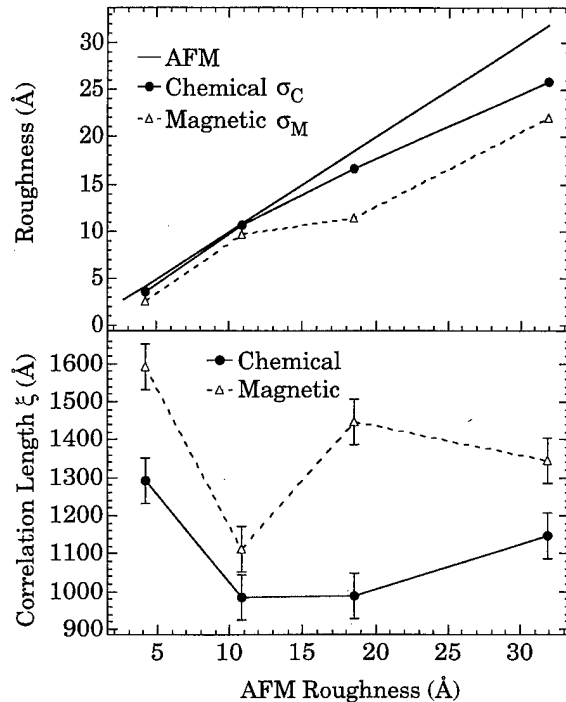


FIG. 2. Roughness parameters derived from the diffuse scattering data. Top panel: Chemical and magnetic rms roughness. Bottom panel: Chemical and magnetic correlation lengths.

The most important general result is the different behavior of both σ and ξ for the chemical versus magnetic interfaces. The magnetic roughness in this series of samples is $\sim 20\%$ – 30% less than the chemical roughness. The same is seen for the behavior of the chemical versus magnetic correlation length (bottom panel of Fig. 2). This indicates that the magnetic interface is typically much smoother than the chemical interface both perpendicular to and in the plane the film. There is good agreement between the σ roughness parameters extracted from the x-ray scattering and from the AFM values (the straight line of the top panel of Fig. 2). The small disagreements can be addressed through a more detailed analysis of the AFM roughness data, which is not shown here due to space limitations.

An interesting application of this technique becomes possible upon examination of the the specular versus diffuse element specific magnetic hysteresis measured by XRMS (see Fig. 3). The reflected intensity as a function of applied field can be utilized as a measure of the magnetic hysteresis since the magnetic portion of the scattering tracks with the magnetic moment of the sample. Since the field dependence specular peak intensity gives a measure of the bulk magnetic hysteresis, we can use the diffuse signal, which only comes from the interfaces, to measure the interfacial magnetic hysteresis. In Fig. 3 the clear difference in the coercive and saturation fields of spins at the interface indicates the different nature of the bulk versus interfacial magnetic environment. For the $x = 400 \text{ \AA}$ film shown in Fig. 3 the difference in coercive fields was $3.5 \pm 0.5 \text{ Oe}$. This was confirmed by measuring at not only several different points in the diffuse, but also in the specular and diffuse at different detector angles. It is worth noting that the sample indicating the large

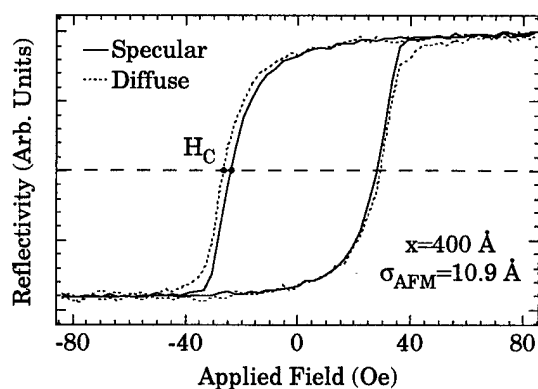


FIG. 3. Comparison of magnetic hysteresis measured by XRMS at specular (bulk) and diffuse (interface) points for the $x=400$ Å film ($\sigma_{\text{AFM}}=10.9$ Å). Differences, such as the coercive field H_C , illustrate the different behavior of the bulk vs interfacial magnetic properties.

est difference the between specular and the diffuse coercive field is also the one exhibiting a roughening of the magnetic interface as noted by the drop in ξ_M and σ_M with respect to ξ_C and σ_C (see Fig. 2).

In conclusion, our results distinctly show that the chemical and magnetic interfaces can have a very different character. In addition, by tracking the diffuse intensity as a function of applied field we find a very different behavior of the interfacial spins, which appears to be correlated with variations of the chemical versus magnetic interface.

ACKNOWLEDGMENTS

This work was supported by the Office of Naval Research. One of the authors (J.W.F.) is a NRC/NRL research

fellow. Brookhaven National Laboratory is supported by the U.S. Department of Energy.

- ¹J. F. MacKay, C. Teichert, D. E. Savage, and M. G. Lagally, *Phys. Rev. Lett.* **77**, 3925 (1996).
- ²Y. U. Idzerda, V. Chakarian, and J. W. Freeland, *Synch. Radiat. News* **10**, 6 (1997).
- ³S. Zhang and P. M. Levy, *Phys. Rev. B* **43**, 11 048 (1991).
- ⁴M. Suzuki and Y. Taga, *Phys. Rev. B* **52**, 361 (1995).
- ⁵Z. J. Zang and M. R. Scheinfein, *Phys. Rev. B* **52**, 4263 (1995).
- ⁶S. K. Sinha, E. B. Sirota, S. Garoff, and H. B. Stanley, *Phys. Rev. B* **38**, 2297 (1988).
- ⁷H.-N. Yang, G.-C. Wang, and T.-M. Lu, *Diffraction From Rough Surfaces and Dynamic Growth Fronts* (World Scientific, River Edge, NJ, 1993).
- ⁸K. Namikawa, M. Ando, T. Nakajima, and H. Kawata, *J. Appl. Phys.* **54**, 4099 (1985).
- ⁹C. Kao, J. B. Hastings, E. D. Johnson, D. P. Siddons, and G. C. Smith, *Phys. Rev. Lett.* **65**, 373 (1990).
- ¹⁰C.-C. Kao, C. T. Chen, E. D. Johnson, D. P. Siddons, H. J. Lin, G. H. Ho, G. Meigs, J.-M. Brot, S. L. Hulbert, Y. U. Idzerda, and C. Vettier, *Phys. Rev. B* **50**, 9599 (1994).
- ¹¹J. M. Tonnerre, L. Seve, D. Raoux, G. Soullie, B. Rodmacq, and P. Wolfers, *Phys. Rev. Lett.* **75**, 740 (1995).
- ¹²V. Chakarian, Y. U. Idzerda, C.-C. Kao, and C. T. Chen, *J. Magn. Magn. Mater.* **165**, 52 (1997).
- ¹³J. W. Freeland, V. Chakarian, Y. U. Idzerda, S. Doherty, J. G. Zhu, J.-H. Park, and C.-C. Kao, *Appl. Phys. Lett.* **71**, 276 (1997).
- ¹⁴V. Chakarian, Y. U. Idzerda, G. Meigs, C. T. Chen, and C. -C. Kao, in *Synchrotron Radiation Techniques in Industrial, Chemical, and Materials Science*, edited by L. J. Terminello, K. L. D'Amico, and D. K. Shuh (Plenum, New York, 1996), pp. 187–205.
- ¹⁵S. Hulbert, D. J. Holly, F. H. Middleton, and D. J. Wallace, *Nucl. Instrum. Methods Phys. Res. A* **291**, 343 (1990).
- ¹⁶E. D. Johnson, C. -C. Kao, and J. B. Hastings, *Rev. Sci. Instrum.* **63**, 1443 (1992).
- ¹⁷C. T. Chen, F. Sette, Y. Ma, and S. Modesti, *Phys. Rev. B* **42**, 7262 (1990).
- ¹⁸Y. U. Idzerda, C. T. Chen, H. -J. Lin, G. Meigs, G. H. Ho, and C. -C. Kao, *Nucl. Instrum. Methods Phys. Res. A* **347**, 134 (1994).
- ¹⁹V. Chakarian, Y. U. Idzerda, and C. T. Chen, *Phys. Rev. B* (to be published).

Soft x-ray resonant magnetic reflectivity study of thin films and multilayers

J. M. Tonnerre,^{a)} L. Sève, A. Barbara-Dechelette, F. Bartolomé, and D. Raoux

Laboratoire de Cristallographie, CNRS/Université Joseph Fourier,
B.P. 166, 38042 Grenoble Cedex 9, France

V. Chakarian

Naval Research Laboratory, Code 6345, Washington, D.C. 20375

C. C. Kao

National Synchrotron Light Source, Brookhaven National Laboratory, Upton, New York 11973

H. Fischer and S. Andrieu

LPM, CNRS/Université Nancy, 54506 Vandoeuvre, France

O. Fruchart

Laboratoire Louis Néel, CNRS/Université Joseph Fourier, B.P. 166, 38042 Grenoble Cedex 9, France

Soft x-ray resonant magnetic reflectivity measurements on thin films and multilayers in a *transverse* geometry using linear polarized photons are presented. Magneto-optic calculations taking into account the layer roughness allows us to reproduce all the experimental features of the angular and energy reflectivity curves as well as the asymmetry ratio in both cases. Application to $\text{Fe}_x\text{Mn}_{1-x}$ alloy films epitaxially grown on Ir(001) brings more insights on the magnetic transition occurring at $x=0.75$. © 1998 American Institute of Physics. [S0021-8979(98)49911-0]

Magnetism in artificially made materials has become an area of intense activity. The study of magnetism of ultrathin films and multilayers has revealed new properties which are different from bulk materials and have technological potential, especially in magnetic memories and magnetic based sensors. Since the devices to be implemented concern multilayered and multielement systems, it is necessary to go beyond the measurements of the macroscopic magnetic properties and to separate out the magnetic signatures of the different species within the different layers. In order to selectively probe the magnetic contributions, we develop the use of the x-ray resonant magnetic scattering (XRMS), especially in the soft x-ray range.

XRMS, which is x-ray magnetic dichroism in a scattering condition, presents the advantage of being atom and shell selective and then allows one to probe the magnetism of the different atomic levels of a specific element in a magnetic material.^{1,2} The angular dependence inherent to a scattering measurement brings furthermore the spatial selectivity. As XRMS is a two photon process, the effects related to magnetic circular dichroism (XMCD) are observable not only with circular polarized photons but also with linear polarized ones.^{3,4} Moreover, they are enhanced in diffraction conditions due to interference effects and, in that case, the magnetization dependent contribution may be of the same order of magnitude as the nonmagnetic one.⁵ This has been shown by using artificial large period structures, like Ag/Ni and Ag/NiFe multilayers, in order to diffract photons of large wavelength ($\lambda \approx 15$ Å at the Ni $L_{2,3}$ edges). These first experiments, where the energy dependence of an asymmetry ratio $R = (I^+ - I^-)/(I^+ + I^-)$ is measured, I^+ and I^- being two Bragg peak intensities collected for two opposite direc-

tions of an applied magnetic field, allowed us on one hand to demonstrate the equivalence between the XMCD and the XRMS⁶ and on the other hand to determine the amplitude of the magnetic moment of both 3d transition metals in a binary alloy.⁷ In order to study thin films, which do not give Bragg peaks at small values, we have to turn to the analysis of magnetic specular reflectivity measurements.

Following the success of XMCD measurements in the soft x-ray range, specular resonant magnetic reflectivity has been mainly measured using circular polarized incident photons in a geometry similar to the *longitudinal magneto-optic Kerr effect*.^{4,8,9} In the simulations, although general trends are well understood,⁴ some discrepancies still remain. One possible reason is related to the difficulty to take into account the roughness at the interfaces when both states of linear horizontal and vertical polarization of the photons are coupled and then to account for its effect on the change of the circular polarization rate at each interface. Therefore, we first focused on the development of the resonant magnetic reflectivity in the *transverse magneto-optic Kerr effect* geometry, using linear *p*-polarized photons. The fact that the photon beam has only one polarization state allows us to straightforwardly extend the Vidal and Vincent formalism to treat the interface roughness.¹⁰

The measurements were conducted at the *U4B* beam line at the National Synchrotron Light Source. A vacuum compatible θ - 2θ spectrometer, working in the horizontal plane, was used.¹¹ The sample was magnetized by using a Bitter electromagnet capable of delivering a field up to 1400 G perpendicular to the diffraction plane. First results were obtained from a bcc W(32 Å)/Fe(91 Å)/W(129 Å) deposited by laser ablation on a Al_2O_3 substrate. Figure 1(a) shows an angular scan where the reflected intensities and the asymmetry ratios R are collected at a selected energy in the vicinity of the L_3 Fe edge. Figure 2(a) displays an energy scan where

^{a)}Electronic mail: tonnerre@polycnrs-gre.fr

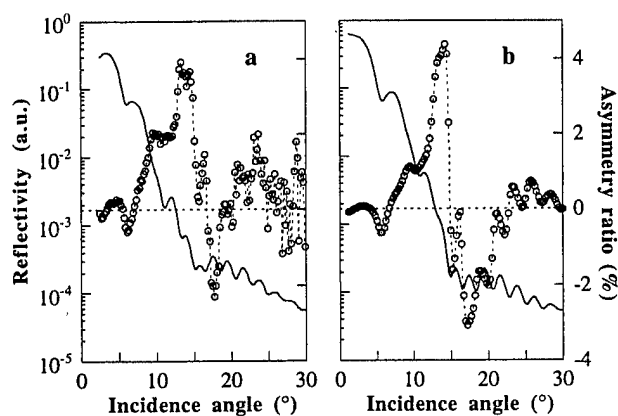


FIG. 1. Fixed energy angle scans (solid line, left side legend) and asymmetry ratio (open circles, right side legend) measured on a W/Fe/W thin film in the vicinity of Fe L_3 edge (703.2 eV): experiment (a) and calculation (b).

the angular position is kept fixed and the incident photon energy is scanned through the Fe $L_{2,3}$ edges. In this transverse geometry, the amplitude at maximum of R are typically of the order of 5% to 15% depending on both the incident angle and energy. Both scans depend on the strong resonance available at the $L_{2,3}$ edges and on the structural features of the layers: thickness and density of the layers as well as interface roughness. The energy scan is more sensitive to the spectroscopic aspect (amplitude of the magnetic moment) and the angular one to the structural aspect (arrangement of the moments).

To analyze the data, we have developed a numerical calculation based on an optical approach, where the Maxwell's equation are solved in a matrix formalism. It allows us to reproduce all the features of the experimental curve [Figs. 1(b) and 2(b)]. The main part is to calculate the dielectric tensor which only diagonal terms in a cubic dielectric and to take into account the magnetic effects through nonvanishing off-diagonal elements. Both the imaginary and real parts of the charge dielectric constant were derived from absorption data and their Kramers-Kronig transformation, respectively. Their magnetic counterparts are determined in the

same way from XMCD data obtained from thin Fe films. That amounts to consider $M_{\text{Fe}} = 2.1 \mu\text{B}$ as derived from sum rules.¹² Since it is usually accepted that XMCD is proportional to the magnetic moment, we use a multiplying factor to reduce or increase the magnetic contribution to the reflectivity in order to fit our data. More details on the calculation will be given in an upcoming article.⁷

We turn next to the discussion of an example where soft x-ray resonant magnetic reflectivity has been used to investigate the magnetic transition occurring in thin $\text{Fe}_x\text{Mn}_{1-x}$ alloy films epitaxially grown on Ir(001). While bulk alloys present a fcc structure and are antiferromagnetic (AF) over the whole range of composition, it has been shown that, in $\text{Fe}_x\text{Mn}_{1-x}/\text{Ir}$ superlattices (SL), the alloy is body-centered tetragonal (bct) and exhibit a magneto-structural transition at $x=0.75$ from a ferromagnetic state ($x>0.75$) to an antiferromagnetic one ($x<0.75$).¹³ In the present study, we focused on two superlattices $\text{Fe}_{0.9}\text{Mn}_{0.1}(27 \text{ \AA})/\text{Ir}(18 \text{ \AA})$ and $\text{Fe}_{0.7}\text{Mn}_{0.3}(27 \text{ \AA})/\text{Ir}(18 \text{ \AA})$, grown on a Ir buffer layer, whose concentrations have been chosen on each sides of the transition. In the 70% Fe sample, the alloy layer is uniformly strained all through the stacking sequence of the superlattice in a bct structure with $c/a=1.23$.¹⁴ In the 90% Fe sample, two phases have been identified.¹⁴ In the first phase, labelled SL1, the alloy and Ir layers undergo the influence of the Ir buffer layer and the alloy layer is bct with $c/a=1.16$. In the second one, SL2, both layers have relaxed the strain imposed by the buffer layer and may be considered as free layers in mutual strain. In that case, the alloy tends to the Fe bcc structure with $c/a=1.08$. The analysis of a series of reciprocal-space maps of the diffracted intensities, collected around the (111) Bragg peak of the buffer layer for different grazing incident angles, allowed us to appreciate their proportion, which corresponds to 60% and 40%, respectively, and their localization.¹⁵ These findings have been supported by the characterization of two thin alloy films of the same composition ($x=0.7$ and 0.9) with similar thicknesses ($\approx 30 \text{ \AA}$) sandwiched between Ir layers, aimed at the determination of the structural properties of the alloy layers at the beginning of the elaboration process. This is of particular interest in order to separate out the magnetic properties of SL1 and SL2.

Figure 3 shows the energy dependence of R measured at 15° on both multilayers around the Fe $L_{2,3}$ edges. The shapes of R are similar and they exhibit two resonances at the L_3 (707 eV) and L_2 edge (720 eV). Fe atoms in the Fe 90% SL give rise to a strong asymmetry ratio of about 40% while for the Fe 70% SL, R values are at most 4%. This reduction of the magnetic signal of the Fe atoms is far beyond the change one would expect from its concentration reduction. The simulation of the energy dependence of R has been carried out using the structural parameters deriving from the structural studies and by assuming that the alloy is a solid solution where the Fe atoms bear the same magnetic moment all through the layers. As in the preceding section, the magnetic moment of Fe is initially assumed to be $2.1 \mu\text{B}$. In the case of the Fe-rich SL, the calculation (solid line) fits quite well the experiment in Fig. 3(b). For the Fe 70% SL, it is required to reduce the dichroism signal by a factor 0.13 in

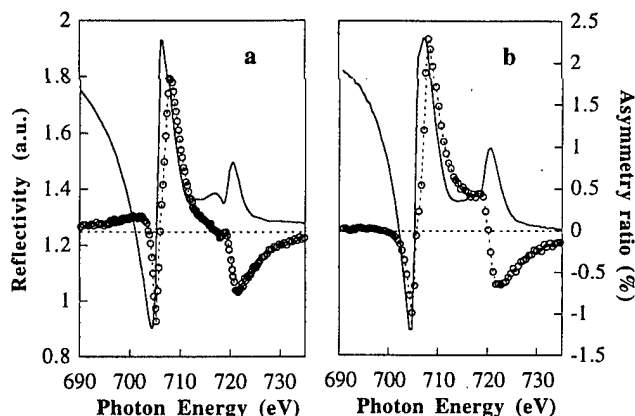


FIG. 2. Fixed angle energy scans (solid line, left side legend) and asymmetry ratio (open circles, right side legend) measured on a W/Fe/W thin film at 5° at the Fe $L_{2,3}$ edges: experiment (a) and calculation (b).

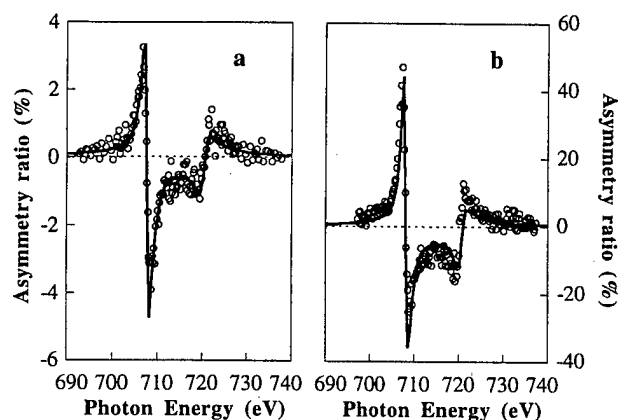


FIG. 3. Energy dependent asymmetry ratio measured at 15° at the Fe $L_{2,3}$ edges on Fe_{0.7}Mn_{0.3}/Ir (a) and Fe_{0.9}Mn_{0.1}/Ir (b): experiment (open circles) and calculation (solid line).

order to fit the data [Fig. 3(a)]. Therefore, we observe a transition for the Fe magnetic moment from 2.1 ± 0.05 to $0.27 \pm 0.05 \mu_B$. The uncertainties derive from the dispersion of the fitting parameters of reflectivity curves measured at other angular positions. It is worth recalling that the value for the Fe-rich SL is an averaged one since two phases have been evidenced in the SL. In order to separately determine the magnetic moment in the SL1 phase, we measured the energy dependence of R for the thin Fe_{0.9}Mn_{0.1} films at different angular positions. Using the same set of structural and magnetic parameters, we obtained a good agreement between experiments and calculations. Figure 4(a) shows the asymmetry ratio values obtained at 26° while the ensemble of R measurements will be published in a full article.¹⁵ Again, a fairly good agreement has been obtained with a Fe magnetic moment of $2.1 \mu_B$, leading us to conclude that the Fe atoms in SL1 and SL2 carry about the same magnetic moments. Gathering the structural and magnetic informations on the three different phases of the alloy thin films, we observe that the magnetic transition is related neither to the

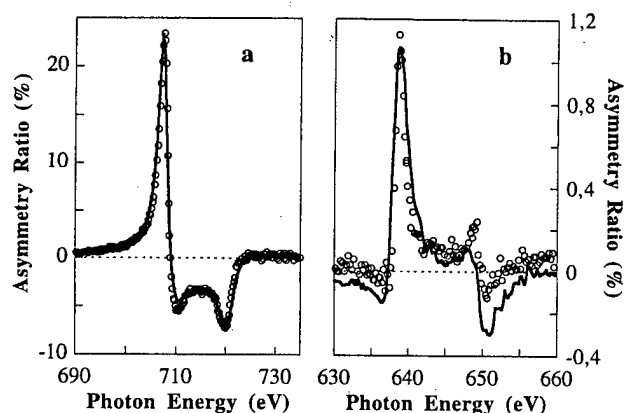


FIG. 4. Energy dependent asymmetry ratio measured on Ir/Fe_{0.9}Mn_{0.1}/Ir thin film at 26° at the Fe $L_{2,3}$ edges (a) and at 20° at Mn $L_{2,3}$ edges (b): experiment (open circles) and calculation (solid line).

hypothetical fcc or bcc structure of the unstrained layer, nor to the Fe magnetic volume. It actually depends on the c/a value and the transition occurs for $c/a=1.2$ ¹⁵ which is in agreement with the theoretical prediction for a bct iron.¹⁶

Work is under progress to understand the magnetic properties of the Mn atoms. Figure 4(b) displays the weak magnetic signal measured at the $L_{2,3}$ edges of Mn in the thin Fe_{0.9}Mn_{0.1} films. It shows that Mn atoms carry a net magnetic moment. We observe the R spectrum has the same shape than that measured at the Fe L edges at the same incident angle. In order to determine the amplitude of the Mn magnetic moment as well as the coupling between Fe and Mn, we have to fit the R values. In the case of Mn, this is not so straightforward, since bulk Mn is antiferromagnetic and shows no circular dichroism. Here, the calculation is performed using the XMCD data from Mn [1 monolayer (ML)]/Fe(001),¹⁷ where the coupling is found to be ferromagnetic and the Mn magnetic moment estimated to be about $1.7 \mu_B$.¹⁸ However, to fit the R values, it has been necessary to change the sign of the XMCD data used in the calculation, which implies to consider an AF coupling of Mn moments to the Fe ones. It appears that the amplitude of the XMCD allows us to simulate the amplitude of R and, hence, we estimate the Mn magnetic moment to be about $1.7 \mu_B$.

In summary, we have shown that XRMS in *transverse mode* allows to investigate quantitatively the magnetic properties of thin films and multilayers. It turns out that it is possible to analyze small changes in the energy dependent magnetic contribution to the reflectivity. This allows us to measure weak magnetic moment (here $0.2 \mu_B$) in a thin buried layer. A refinement procedure applied simultaneously to the angular and energy scans should give more insights about the amplitude of the moments, their distribution inside the layer, and likely about the magnetic roughness at interfaces. Moreover, we show that large magnetic contributions to the reflectivity are available at large angles which should allow developments towards element specific imaging of magnetic domains. This approach could be useful for imaging the behavior of buried magnetic layers.

The authors thank Y. Souche and F. de Bergevin for fruitful discussions on magneto-optic calculations.

¹J. P. Hannon et al., Phys. Rev. Lett. **61**, 1245 (1988); **62**, 2644 (1989).

²P. Carra et al., Phys. Rev. Lett. **64**, 1286 (1990).

³C. C. Kao et al., Phys. Rev. B **50**, 9599 (1994).

⁴C. C. Kao et al., Phys. Rev. Lett. **65**, 373 (1990).

⁵J. M. Tonnerre et al., Nucl. Instrum. Methods Phys. Res. B **97**, 444 (1995).

⁶J. M. Tonnerre et al., Phys. Rev. Lett. **75**, 740 (1995).

⁷L. Sève, Ph.D. thesis, Université Joseph Fourier, 1997 (unpublished).

⁸V. Chakarian et al., J. Magn. Magn. Mater. **165**, 52 (1997).

⁹Y. U. Ydzerda et al., Synchrotron Radiation News **10**, 6 (1997).

¹⁰B. Vidal and P. Vincent, Appl. Opt. **23**, 1784 (1984).

¹¹E. D. Johnson et al., Rev. Sci. Instrum. **63**, 1443 (1992).

¹²C. T. Chen et al., Phys. Rev. Lett. **75**, 152 (1995).

¹³H. Fischer, Ph.D. thesis, Université Nancy, 1995.

¹⁴A. Déchelette-Barbara et al., J. Magn. Magn. Mater. **165**, 87 (1997).

¹⁵A. Déchelette-Barbara, Ph.D. thesis, Université Joseph Fourier, 1997 (unpublished).

¹⁶G. L. Krasko et al., J. Appl. Phys. **67**, 4570 (1990).

¹⁷S. Andrieu et al., Phys. Rev. B **57**, 1985 (1998).

¹⁸S. Andrieu et al., Europhys. Lett. **38**, 459 (1997).

Dependence of anti-Stokes/Stokes intensity ratios on substrate optical properties for Brillouin light scattering from ultrathin iron films

J. F. Cochran,^{a)} M. From, and B. Heinrich

Department of Physics, Simon Fraser University, Burnaby, British Columbia V5A 1S6, Canada

Brillouin light scattering experiments have been used to investigate the intensity of 5145 Å laser light backscattered from spin waves in 20 monolayer thick Fe(001) films. The experiments have shown that the ratio of frequency upshifted light intensity to frequency downshifted light intensity depends upon the material of the substrate used to support the iron films. For a fixed magnetic field and for a fixed angle of incidence of the laser light this intensity ratio is much larger for an iron film deposited on a sulphur passivated GaAs(001) substrate than for an iron film deposited on a Ag(001) substrate. The data have been compared with a calculation that takes into account multiple scattering of the optical waves in the iron film and in a protective gold overlayer. The observations are in qualitative agreement with the theory, except for angles of incidence greater than 60°. © 1998 American Institute of Physics. [S0021-8979(98)37011-5]

The ratio of upshifted scattered light intensity (anti-Stokes line) to downshifted scattered light intensity (Stokes line) in Brillouin light scattering experiments (BLS) performed on ultrathin magnetic films depends on the optical properties of the substrate that support the film.¹ This is illustrated in Fig. 1 for BLS experiments performed on iron films 20 monolayers (ML) thick. Figure 1(a) shows scattered light intensity versus frequency shift for a 20 ML iron film grown on a Ag(001) single crystal by means of molecular beam epitaxy.² The iron film was covered by 18 ML of gold. The BLS measurements were carried out *ex situ*. A magnetic field of 1.00 kOe was applied in the plane of the film and perpendicular to the plane of incidence of the incident 5145 Å laser light. The *p*-polarized laser light was incident at 45°, and the scattered light was collected in the backscattering configuration.³ The data shown in Fig. 1(b) were collected in the backscattering configuration for *p*-polarized light^{4,5} incident at 45°, and using an applied magnetic field of 1.08 kOe. The iron film was 20 ML thick, and was grown by means of molecular beam epitaxy on a sulphur passivated GaAs(001) single crystal.⁶ The iron film was covered by 20 ML of gold and the BLS data were measured *ex situ*. It is clear from a comparison of Figs. 1(a) and 1(b) that (i) the ratio of upshifted to downshifted scattered light intensity is quite different for these two specimens; and (ii) the observed frequency shift is different for the two specimens. Both of these differences can be attributed to the effect of different substrates. The change in frequency between the two specimens can be primarily attributed to a difference in perpendicular uniaxial surface anisotropy, see Table I. The dependence of the intensity ratios on substrate material is a consequence of the dependence of the magnitude and phase of the optical electric field in the iron film on the optical properties of the substrate material. A 20 ML thick iron film is thin compared with the penetration depth of 5145 Å light in iron, consequently the optical electric field amplitudes in the iron film depend very strongly on the optical properties of the substrate.¹

Data for thin iron films grown on Ag and GaAs substrates have been compared with calculations carried out using the formalism described by Cochran and Dutcher.⁷ Relevant parameters used in the calculations are listed in Table I. The magnetic parameters listed in Table I give a good

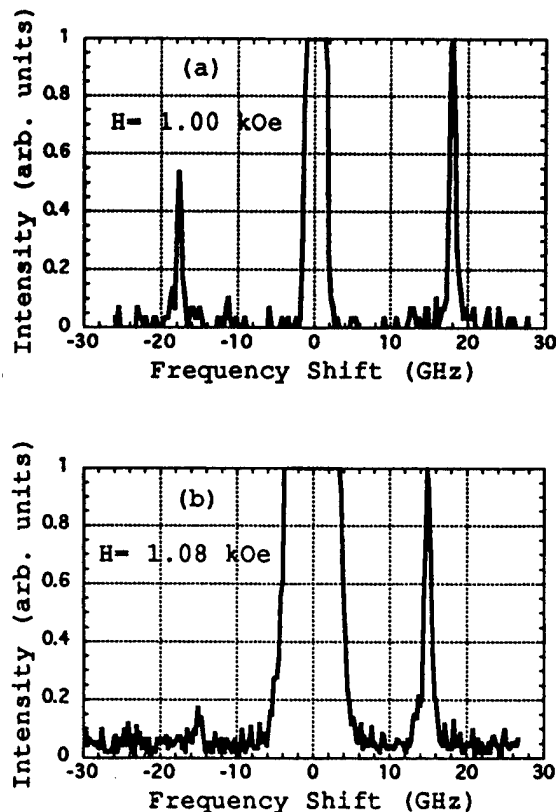


FIG. 1. Light intensity vs frequency shift for 5145 Å light scattered from a 20 ML thick Fe(001) film; the laser light was incident on the specimen at an angle of 45°. The scattered light was collected in the backscattering configuration, and intensities were normalized to the maximum intensity of the frequency upshifted peak. (a) Ag(001)/20 ML Fe/18 ML Au with a field of 1.0 kOe applied in the film plane and directed along (100). (b) GaAs(001)/20 ML Fe/20 ML Au with a field of 1.08 kOe applied in the specimen plane and directed along (110). In both cases the magnetic field was applied perpendicular to the plane of incidence of the laser light.

^{a)}Electronic mail: jcochran@sfu.ca

TABLE I. Parameters used to calculate the frequencies and ratios of upshifted to downshifted scattered light intensities for the Ag(001)/20Fe/18Au and GaAs(001)/20Fe/20Au used for this work. The perpendicular uniaxial anisotropy energy was taken to have the form $E_u = -(K_u/d)(m_z/M_s)^2$ ergs/cc, where d is the iron film thickness and m_z is the magnetization component perpendicular to the plane of the Fe film.

Fe film:	Thickness $d = 20$ monolayers $= 28.6 \text{ \AA}$ Saturation magnetization, $4\pi M_s = 21.4 \text{ kOe}$ Exchange stiffness parameter, $A = 2.03 \times 10^{-6}$ Gilbert damping parameter, $G = 10^8 \text{ Hz}$ Optical dielectric constant, $\epsilon = (-0.40, 16.44)$ Resistivity, $\rho = 1.0 \times 10^{-5} \text{ } \Omega \text{ cm}$
(a) Ag(001)/20Fe/18Au	Cubic anisotropy parameter, $K_1 = 4.0 \times 10^5 \text{ ergs/cc}$ Uniaxial anisotropy parameter, $K_u = 1.04 \text{ ergs/cm}^2$
(b) GaAs(001)/20Fe/20Au	Effective cubic anisotropy parameter for H along (110), $K_1 = 3.7 \times 10^4 \text{ ergs/cc}$ Uniaxial anisotropy parameter, $K_u = 1.42 \text{ ergs/cm}^2$
Au film:	2.04 \AA per monolayer Optical dielectric constant, $\epsilon = (-3.75, 2.75)$ Resistivity, $\rho = 2.35 \times 10^{-6} \text{ } \Omega \text{ cm}$
Ag substrate:	Optical dielectric constant, $\epsilon = (-10.70, 0.33)$ Resistivity, $\rho = 1.59 \times 10^{-6} \text{ } \Omega \text{ cm}$
GaAs substrate:	Optical dielectric constant, $\epsilon = (17.65, 3.19)$ Resistivity, $\rho = 1 \text{ } \Omega \text{ cm}$

description of the dependence of spin-wave frequencies on applied magnetic field, see Fig. 2. The optical dielectric constants listed for 5145 Å light (2.41 eV) were obtained from Johnson and Christy (Iron,⁸ Silver⁹), Joenson *et al.*¹⁰ (gold), and Aspnes and Studna¹¹ (GaAs).

The observed upshifted to downshifted intensity ratios are plotted as a function of applied magnetic field in Fig. 3 for light incident at 45° on the specimens. The solid lines are intensity ratios calculated using the parameters listed in Table I. The data exhibit a decreasing intensity ratio with increasing magnetic field; this decrease with field is repro-

duced by the calculations. However, the calculated intensity ratios tend to be smaller than the observed ratios, especially in the case of the GaAs substrate. The calculated intensity ratios are very sensitive to the amplitudes and phases of the optical electric field components in the iron film, and these field components in turn, especially their phases, are sensitive to the film thicknesses and the dielectric parameters used to describe them.

The ratio of upshifted to downshifted light intensity has been investigated as a function of the angle of incidence of the light for fixed magnetic field. The results of angular mea-

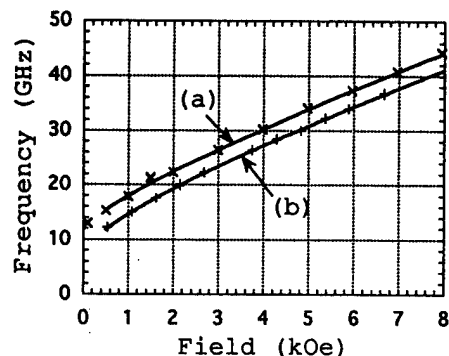


FIG. 2. Spin-wave frequency vs applied magnetic field. The data were obtained from Brillouin light scattering experiments on 20 ML thick films with the field applied in the specimen plane. The angle of incidence of the laser light was 45°. ×—Ag(001)/20 ML Fe(001)/18 ML Au. The field was applied along the (100) direction; (a) calculated using the parameters listed in Table I. +—GaAs(001)/20 ML Fe(001)/20 ML Au. The field was applied along the (110) direction; (b) calculated using the parameters listed in Table I.

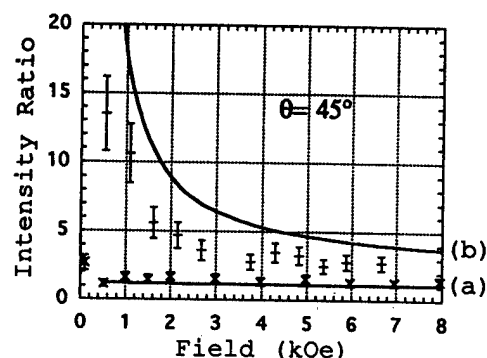


FIG. 3. The ratio of frequency upshifted to frequency downshifted Brillouin backscattered light intensity vs magnetic field applied in the specimen plane. The 5145 Å laser light was incident at 45°. ×—Ag(001)/20 ML Fe(001)/18 ML Au, the field was applied along (100); (a) calculated using the parameters listed in Table I. +—GaAs(001)/20 ML Fe(001)/20 ML Au, the field was applied along (110); (b) calculated using the parameters listed in Table I. The vertical error bars correspond to an estimated 20% uncertainty in the data.

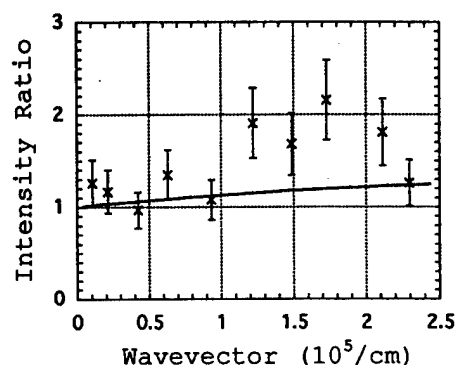


FIG. 4. The ratio of frequency upshifted to frequency downshifted Brillouin backscattered light intensity vs the in-plane component of the spin-wave wave vector for the specimen Ag(001)/20 ML Fe(001)/18 ML Au. A magnetic field of 1.0 kOe was applied in the specimen plane along the (100) direction, and 5145 Å laser light was used for the measurements. The solid line was calculated using the parameters listed in Table I. The vertical error bars correspond to an estimated 20% uncertainty in the data.

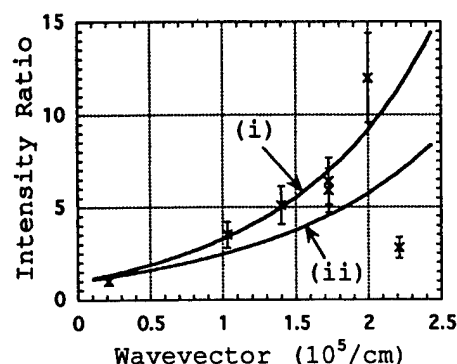


FIG. 5. The ratio of frequency upshifted to frequency downshifted Brillouin backscattered light intensity vs the in-plane component of the spin-wave wave vector for the specimen. GaAs(001)/20 ML Fe(001)/20 ML Au. A magnetic field of 2.2 kOe was applied in the specimen plane along the (110) direction, and 5145 Å laser light was used for the measurements. (i) Calculated for a field of 1.0 kOe and (ii) calculated for a field of 2.2 kOe using the parameters listed in Table I. The vertical error bars correspond to an estimated 20% uncertainty in the data.

measurements on a specimen grown on a silver substrate are shown in Fig. 4, and results for an iron film grown on a GaAs substrate are shown in Fig. 5. The angular variation of the incident light is expressed in terms of the spin-wave wave vector component parallel with the film plane, $Q = (4\pi/\lambda)\sin\theta$, where $\lambda = 5145$ Å is the wavelength of the incident light and θ is the angle of incidence. The data exhibit an increasing intensity ratio with increasing Q , i.e., with increasing angle of incidence. The calculations, indicated by the solid lines in Figs. 4 and 5, also display an increasing intensity ratio with increasing angle of incidence. According to theory, the intensity ratio varies with angle of incidence because of an interference between the scattered light originating from the optical electric field components in the iron film that are parallel and perpendicular to the film plane. In the limit of normal incidence the optical electric field in the iron film has only a component parallel to the plane, there is no interference effect, and therefore the upshifted and downshifted intensity ratio must approach unity in the limit of $Q=0$. This expectation is borne out by the experimental observations. For reasons which we do not understand, the intensity ratio data shown in Fig. 5, and obtained using an applied field of 2.2 kOe, are in better agreement with the ratios calculated for an applied field of 1 kOe [curve (i)] than with the curve calculated using a field of 2.2 kOe [curve (ii)]. This appears to be a coincidence. However, the drop off in intensity ratio observed for Q lying between 2.0 and $2.2 \times 10^5 \text{ cm}^{-1}$ (θ between 55° and 65°), and observed for both the silver substrates and the GaAs substrates, appears to be real. It may be caused by some unknown instrumental effect. For the GaAs substrate the absolute intensity at $\theta = 65^\circ$ was also much reduced over that measured at $\theta = 55^\circ$ contrary to theoretical expectations. The origin of this rather sudden drop off in scattered light intensity is unknown: no such effect was observed for specimens grown on silver substrates. It may be associated with the observed rough iron growth obtained using a GaAs substrate.⁶ A decrease in intensity ratio at large angles of incidence runs counter to the rather sharp increase in the upshifted to down-

shifted intensity ratio for Q approximately equal to $2.25 \times 10^5 \text{ cm}^{-1}$ reported by Moosmüller, Truedson, and Patton for thin permalloy films sputtered on silicon.¹² A monotonic dependence of the intensity ratio on angle of incidence of the laser light was reported by Camley *et al.*⁵ for 100 Å thick polycrystalline iron films.

The authors would like to thank S. Watkins for the sulphur passivated GaAs substrates used in this work, and T. Monchesky for communicating to us the results of his 36 GHz microwave measurements on 20 ML Fe films grown on these GaAs substrates. We would also like to thank the Natural Sciences and Engineering Research Council of Canada for grants that supported this work.

¹M. G. Cottam, J. Phys. C **16**, 1573 (1983).

²Specimens were prepared in a layer-by-layer growth mode using molecular beam epitaxy as described by B. Heinrich, Z. Celinski, J. F. Cochran, A. S. Arrott, and K. Myrtle, J. Appl. Phys. **70**, 5769 (1991).

³J. R. Sandercock, in *Topics in Applied Physics Vol. 51, Light Scattering in Solids III*, edited by M. Cardona and G. Güntherodt (Springer, Berlin, 1982), p. 173.

⁴In the backscattering configuration the intensity of the scattered light is the same for both p - and s -polarized incident light; see R. E. Camley and M. Grimsditch, Phys. Rev. B **22**, 5420 (1980); also Ref. 5.

⁵R. E. Camley, P. Grünberg, and C. M. Mayr, Phys. Rev. B **26**, 2609 (1982).

⁶A buffer layer of GaAs was grown on a GaAs(001) wafer by means of metalorganic chemical vapor deposition and the resulting surfaces were passivated using a H_2S treatment at 400°C . The iron film was deposited on the sulphur passivated GaAs surface at room temperature by means of molecular beam epitaxy. The iron growth was rough and exhibited no RHEED oscillations.

⁷J. F. Cochran and J. R. Dutcher, J. Magn. Magn. Mater. **73**, 299 (1988). There is an error in the last term of R_3 on p. 309; the bracketed term should read $(H_y + H_z + 8\pi M_z)$ not $(H_y + H_z + 4\pi M_z)$.

⁸P. B. Johnson and R. W. Christy, Phys. Rev. B **9**, 5056 (1974).

⁹P. B. Johnson and R. W. Christy, Phys. Rev. B **6**, 4370 (1972).

¹⁰P. Joenson, J. C. Irwin, J. F. Cochran, and A. E. Curzon, J. Opt. Soc. Am. **63**, 1556 (1973).

¹¹D. E. Aspnes and A. A. Studna, Phys. Rev. B **27**, 985 (1983).

¹²H. Moosmüller, J. R. Truedson, and C. E. Patton, J. Appl. Phys. **69**, 5721 (1991).

Critical Phenomena, Spin Glasses, and Frustration

Norm Koon and
Pedro Schottmann, Chairmen

Magnetic phase diagrams of holmium determined from magnetoresistance measurements

Jeffrey R. Gebhardt and Naushad Ali^{a)}

Department of Physics, Southern Illinois University at Carbondale, Carbondale, Illinois 62901

The magnetic phase diagrams of holmium in the magnetic field-temperature plane have been determined using electrical resistance as a function of temperature and electrical resistance as a function of applied magnetic field (magnetoresistance). Two phase diagrams were constructed corresponding to magnetic fields applied along the a and c axes. For temperatures below 80 K and an applied field along the a axis, our H - T phase diagram agrees well with that of Jensen and Mackintosh. In a temperature range of 30–100 K we observe two transitions which correspond to the boundaries of the predicted helifan phase. However, at higher temperatures there are differences with the work of Willis *et al.*, most notably in the behavior of the Néel temperature splitting. We observe a splitting of the Néel temperature above 1 T with one feature remaining nearly constant in temperature as the field is increased. For a c -axis applied field, our phase diagram is very similar to the results of Willis *et al.*, a splitting of the Néel temperature transition above 0.5 T is observed. At temperatures below 18 K and magnetic field less than 1.5 T, an anomaly associated with a devil's staircase is seen. © 1998 American Institute of Physics. [S0021-8979(98)32811-X]

The first detailed studies of the magnetic structures in holmium as a function of temperature and magnetic field, were performed by Koehler *et al.*^{1,2} using neutron diffraction. At temperatures below the Néel temperature ($T_N = 132$ K), holmium orders antiferromagnetically with a helical structure propagating along the hexagonal c axis, and with moments lying in the basal plane. Below the Curie temperature ($T_C = 18$ K), holmium restructures as a commensurate ferromagnetic cone phase. The spiral structures in the region $T_C < T < T_N$ are in general incommensurate, however, a series of commensurate magnetic phases have been found, first by Gibbs *et al.*³ using synchrotron radiation, and later by others.^{4,5} The commensurate structures in holmium are understood in terms of the spin-slip model.^{3,6} The magnetic structures in a basal plane magnetic field were studied by Koehler *et al.*² who identified intermediate phases, termed fans, between the helix and the ferromagnetic phases. Recently, a structure between the fan and helix phases, which they called a helifan, was predicted by Jensen and Mackintosh^{7,8} using mean field calculations. Some experimental evidence of this structure is given by Ohsumi *et al.*⁹ and Gebhardt *et al.*¹⁰ Bulk magnetic properties such as magnetization, Willis *et al.*¹¹ and magnetoresistance^{10,12,13} have also been used to determine magnetic phase transitions. In this article, we present the magnetic phase diagrams of holmium in the H - T plane for applied magnetic fields along the a and c axes using magnetoresistance measurements.

Two single-crystal holmium samples, each in the shape of a long bar were prepared at Ames Laboratory. The first sample has an a -axis length of 10 mm and cross-sectional

area of 0.45 mm², and the second, a c -axis length of 14.9 mm and cross-sectional area of 0.95 mm². The electrical resistance measurements were carried out using the conventional four probe method. A 30 mA longitudinal dc current was provided by a Keithley 220 constant current source, and the voltage measured using a Keithley 181 nanovoltmeter. A constant temperature and applied magnetic field was accomplished by using the temperature control and superconducting magnet of a Quantum Design SQUID magnetometer. For this study, two types of measurements were conducted: (i) the electrical resistance as a function of temperature (5–150 K) at various constant applied magnetic fields (0–5.5 T) and (ii) the electrical resistance as a function of magnetic field, defined as magnetoresistance (MR), at various constant temperatures (2–150 K).

A large number of electrical resistance (R) versus temperature (T) scans and magnetoresistance (MR) versus magnetic field (H) have been carried out for magnetic fields applied along the a and c axes of Ho. In Fig. 1(a), a representative R vs T curve is shown for a field of $H = 2$ T applied along the a axis. The transitions are indicated by arrows. The magnetic transition temperatures are determined by a step change in the R vs T curve, or as a slope change in the R vs T curve. In the inset of Fig. 1(a), the transitions are clearly seen as large spikes in the slope of R vs T curve. The anomaly at 32 K corresponds to the transition from the fan to the ferromagnetic phase. The anomalies at 80 and 86 K bracket the helifan phase predicted by Jensen and Mackintosh.⁸ These two transitions are also clearly seen in MR vs H ($H \parallel a$) curves at a constant temperature. An example is given in Fig. 1(b) for a temperature of $T = 60$ K. The transitions show as step changes in the MR vs H curve

^{a)}Corresponding author.

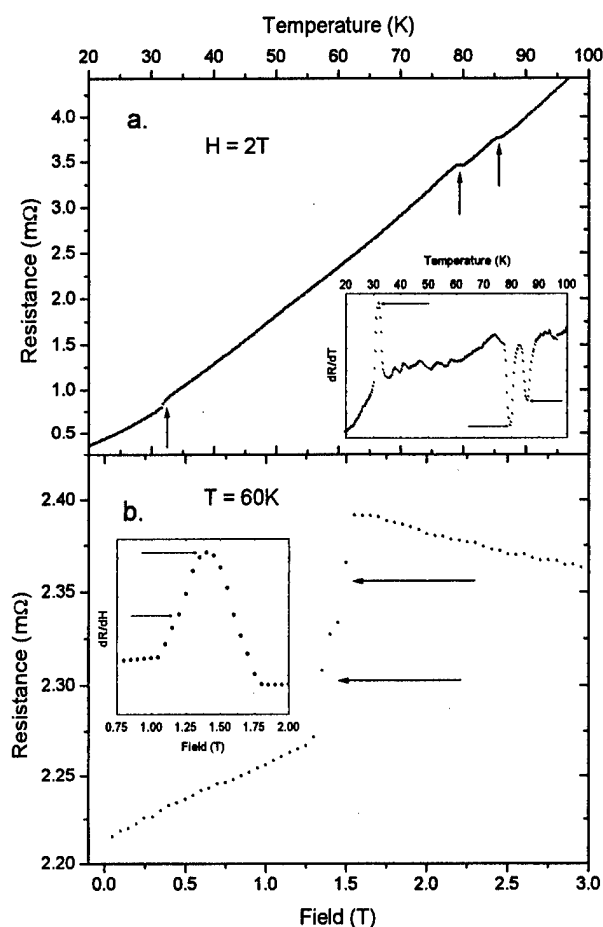


FIG. 1. (a) Resistance vs temperature for a magnetic field of $H = 2$ T applied along the a axis. The inset shows the derivative of the curve. Arrows indicate magnetic transitions. (b) Resistance vs applied field ($H \parallel a$), at a constant temperature of $T = 60$ K. The derivative is given in the inset. Arrows indicate magnetic transitions.

and are indicated by arrows. The inset of Fig. 1(b) shows the $[d(MR)/dH]$ vs H curve where the anomalies are visible in the slope change of the curve. By tabulating the transition temperatures in R vs T curves at a given magnetic field, and the transition fields in MR vs H curves at a given temperature, we are able to construct the H - T phase diagram of holmium for a magnetic field applied along the a axis of Ho.

Figure 2(a) shows a R vs T curve for a magnetic field applied along the c axis. The arrows indicate zero field anomalies at $T = 18, 20$, and 24 K. These transitions are difficult to see in the R vs T curve, but show up clearly in the slope of R vs T curve, which is shown in the inset of Fig. 2(a). The arrow marked by an asterisk refers to an anomaly which is seen in all R vs T data in applied fields from 0 T up to 5.5 T and does not vary with temperature. The anomaly is not observed in MR vs H data and does not correspond to any known magnetic phase transition in Ho. Figure 2(b) shows a MR vs H ($H \parallel c$) curve at a temperature of $T = 5$ K. Although the data is quite noisy, a large transition at $H = 1.25$ T is clearly visible in both the MR vs H , and slope of MR vs H [Fig. 2(b) inset] curves. Again, by tabulating the transition temperatures and fields, we are able to construct the H - T phase diagram of holmium for a magnetic field applied along the c axis.

The H - T phase diagram of Ho for applied field along the a axis is presented in Fig. 3. At lower temperatures, the

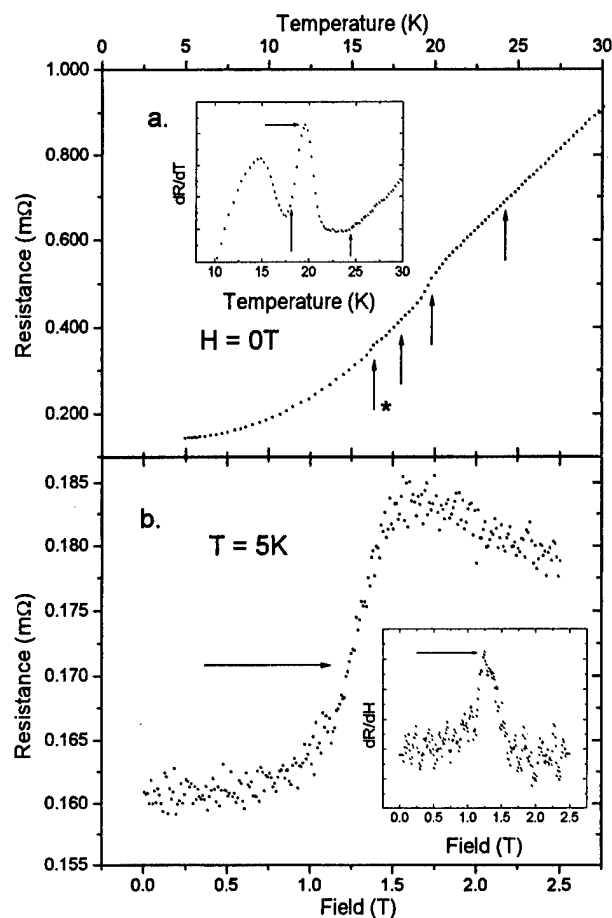


FIG. 2. (a) Resistance vs temperature measured along the c axis in zero applied magnetic field and temperatures below 30 K. The inset shows the derivative of the curve. Arrows indicate magnetic transitions. (b) Resistance vs applied field ($H \parallel c$), at a constant temperature of $T = 5$ K. The large step transition (arrow) shows as a spike in the derivative of the curve given in the inset.

phase diagram is similar to that of Willis *et al.*¹¹ determined from magnetization measurements. The inset of Fig. 3 shows our phase diagram for temperatures below 80 K and field below 2 T. This phase diagram is nearly identical to that of Jensen and Mackintosh⁸ (see Fig. 3), constructed from mean

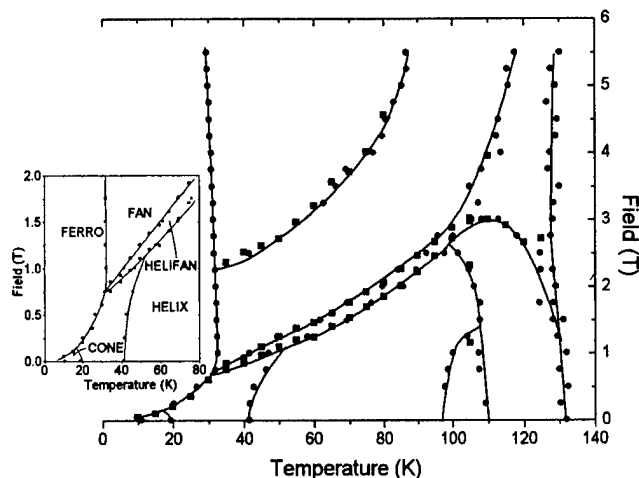


FIG. 3. H - T phase diagram of single-crystal holmium for applied magnetic field along the a axis. Circular symbols (●) indicate data from R vs T measurements, and square symbols (■) indicate data from MR vs H measurements. Solid lines are a visual guide. The inset shows the H - T phase diagram for temperatures below 80 K.

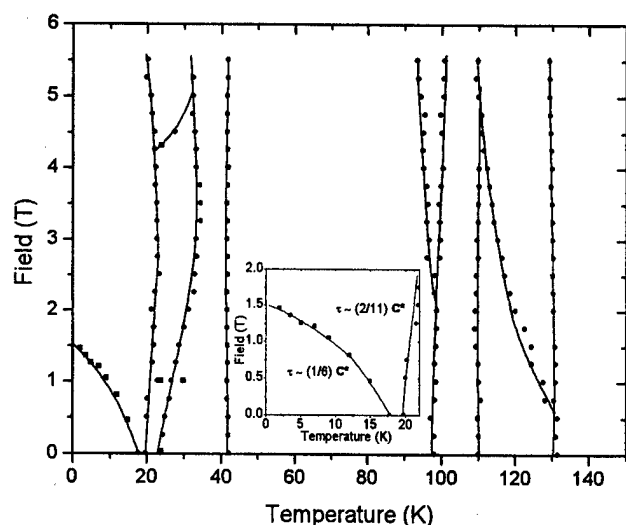


FIG. 4. H - T phase diagram of single-crystal holmium for applied magnetic field along the c axis. Circular symbols (●) indicate data from R vs T measurements, and square symbols (■) indicate data from MR vs H measurements. Solid lines are a visual guide. The inset shows the transition associated with the devil's staircase in Ho.

field calculations and a variety of experimental data. The only exception being a transition at 42 K which merges with the lower helifan line in higher fields. The magnetic structures were labeled using the results of Jensen and Mackintosh.⁸

At higher temperatures, the phase diagram shows similarities to the phase diagram of Gebhardt *et al.*,¹⁰ also constructed from R vs T and MR vs H measurements, for applied field along the b axis of Ho. The most striking similarity is the splitting of the Néel temperature anomaly, at $T_N = 132$ K, above 1 T. This anomaly splits into two parts with one feature changing very little with temperature at higher fields, while the other shifts towards lower temperatures and merges into the lower helifan transition at about 3 T. An anomaly at 110 K shifts slightly to lower temperatures with increasing field until, above 2 T, when this shift becomes more pronounced and it merges with the lower helifan line at 2.5 T. This behavior is similar to that reported by Willis *et al.* (see Fig. 3 of Ref. 11). A transition at 98 K initially has a slight shift to higher temperatures in an increasing field, becoming more pronounced above 1 T and merging with the 110 K anomaly at 1.5 T. This result is consistent with that of Venter *et al.* (see Fig. 14 of Ref. 5), however, the pronounced shift to higher temperatures above 1 T is not evident in their phase diagram. This result also is in contradiction to the result of Willis *et al.*,¹¹ who see the 98 K anomaly shifting to lower temperatures at higher fields.

Figure 4 shows the phase diagram for a c -axis applied magnetic field. This phase diagram is very similar to the one of Willis *et al.* (see Fig. 5 of Ref. 11) determined from magnetization measurements. Zero field anomalies at $T = 18, 20, 24, 42, 98, 110$, and 131 K are observed. The anomaly at $T_C = 18$ K shifts towards lower temperatures as the field is increased, reaching 1.5 T at our lowest attained temperature of 2 K. This transition is shown in the inset of Fig. 4. The dominant wave vectors in the regions above and below the transition are labeled using the results of Venter *et al.* (see

Fig. 8 of Ref. 5), who observed a similar transition using neutron scattering. Higher field transitions for temperatures below 15 K, separating the commensurate structures of a devil's staircase, Cowley *et al.*¹⁴ could not be resolved in this study. The anomaly at 20 K has a slight shift to higher temperatures as the field is increased, until above 4 T when it splits into two parts. One part changing little with temperature, while the other shifts towards higher temperatures in an increasing field. The 24 K transition shifts towards higher temperatures until around 3 T when this shift stops and the anomaly begins a slight shift to lower temperatures as the field is increased. Anomalies at 42 and 110 K were also detected and remain unchanged in fields up to 5.5 T. An anomaly at 98 K was also observed. This anomaly splits into two parts above 2 T, with one part showing little change in temperature as the field is increased, while the other shifts towards lower temperatures. As with fields applied along the a and b axes, for a c -axis applied field, the Néel temperature anomaly at $T_N = 131$ K is seen to split into two parts. This split occurs in fields above 0.5 T which is lower than in the previous two cases. One feature does not change with an increasing field, whereas the other shifts towards lower temperatures, merging with the 110 K anomaly at 5 T.

We have constructed the H - T phase diagrams of Ho for applied magnetic fields along the a and c axes using resistance versus temperature and magnetoresistance versus magnetic field measurements. For temperatures below 80 K, our a -axis phase diagram agrees well with that of Jensen and Mackintosh.⁸ However, at higher temperatures there are discrepancies with that of Willis *et al.*¹¹ Our c -axis phase diagram agrees well with the phase diagram of Willis *et al.*¹¹

This study shows that even complicated magnetic phase diagrams can be established by simple magnetoresistance measurements. Such studies could be very useful for the location of temperature and field ranges for magnetic structure studies by neutron and or x-ray synchrotron scattering.

This work was supported in part by a grant from Consortium for Advanced Radiation Source, University of Chicago, Chicago, Illinois.

¹W. C. Koehler, J. W. Cable, M. K. Wilkinson, and E. O. Wollan, *Phys. Rev.* **151**, 414 (1966).

²W. C. Koehler, J. W. Cable, H. R. Child, M. K. Wilkinson, and E. O. Wollan, *Phys. Rev.* **158**, 450 (1967).

³D. Gibbs, D. E. Moncton, K. L. D'Amico, J. Bohr, and B. H. Grier, *Phys. Rev. Lett.* **55**, 234 (1985).

⁴R. A. Cowley and S. Bates, *J. Phys.* **21**, 4113 (1988).

⁵A. M. Venter and Paul de V du Plessis, *J. Phys.* **9**, 5167 (1997).

⁶J. Bohr, D. Gibbs, D. E. Moncton, and K. L. D'Amico, *Physica (Utrecht)* **140A**, 349 (1986).

⁷J. Jensen and A. R. Mackintosh, *Phys. Rev. Lett.* **64**, 2669 (1990).

⁸J. Jensen and A. R. Mackintosh, *J. Magn. Magn. Mater.* **104-107**, 1481 (1992).

⁹H. Ohsumi, K. Tajima, N. Wakabayashi, Y. Shinoda, K. Kamishima, and T. Goto, *J. Phys. Soc. Jpn.* **66**, 1896 (1997).

¹⁰J. R. Gebhardt, R. A. Baer, and N. Ali, *J. Alloys Compd.* **250**, 655 (1997).

¹¹F. Willis, N. Ali, M. O. Steinitz, M. Kahrizi, and D. A. Tindall, *J. Appl. Phys.* **67**, 5277 (1990).

¹²F. Willis and N. Ali, *J. Alloys Compd.* **181**, 287 (1992).

¹³D. T. Marx and N. Ali, *J. Alloys Compd.* **207**, 304 (1994).

¹⁴R. A. Cowley, D. A. Jehan, D. F. McMorrow, and G. J. McIntyre, *Phys. Rev. Lett.* **66**, 1521 (1991).

Magnetostatic critical point phenomena of ErGa garnet

Toshiro Tanaka^{a)} and Kazuo Miyatani

Department of Materials Science and Engineering, Ehime University, Bunkyocho 3, Matsuyama, 790-8577 Japan

The magnetostatic critical point phenomena of an ErGa garnet, $\text{Er}_3(\text{Fe}_{0.8}\text{Ga}_{0.2})_5\text{O}_{12}$, single crystal sphere were investigated by a computer controlled vibrating sample magnetometer. Subtracting the induced large spin paramagnetic moment of Er^{3+} from the measured values, allowed the Fe-sublattice magnetization $M_{\text{sub}}(H, T)$ to be extracted. M_{sub} data were used to analyze the critical phenomena by eliminating the low field data to avoid the effect of the magnetic inhomogeneity. The spontaneous magnetization and the zero-field susceptibility were obtained from the Arrot plot. The critical temperature and critical indices were obtained to be $T_c = 463.64$ K, $\beta = 0.48 \pm 0.03$, $\gamma = 1.1 \pm 0.1$, and $\delta = 3.1 \pm 0.1$. These results agree well with the predicted values from the molecular field theory. The plot of the critical equation of states $\psi(H, M)$ showed the same function as that found for Fe. Thus, $M_{\text{sub}}(H, T)$ was shown to satisfy the second-order phase transition based on the molecular field theory. © 1998 American Institute of Physics. [S0021-8979(98)23011-8]

I. INTRODUCTION

One of the present authors (K.M.) investigated the magnetostatic critical point phenomena of a yttrium-iron-garnet (YIG) single crystal¹ using the directly measured critical temperature T_c and the spontaneous magnetization $M_0(T)$. In YIG, Y^{3+} is a nonmagnetic ion and the magnetization is given by the ferrimagnetically coupled Fe^{3+} sublattice moments. The magnetostatic critical point phenomena were revealed to be close to those of the Heisenberg ferromagnet CdCr_2Se_4 ² and the metal ferromagnets Ni and Fe which we reported recently.³

The magnetization of the ErIG was explained by the ferrimagnetically coupled Fe^{3+} sublattice moments, and Er^{3+} sublattice moment weakly coupled with them.⁴ In this work, we substituted ErIG with Ga. The substituted nonmagnetic Ga^{3+} diluted the Fe^{3+} sublattice magnetization and the magnetic coupling was lowered. Then, the Er^{3+} moment should become not negligible compared to the Fe^{3+} sublattice moment. It is thus interesting to investigate the magnetostatic critical point phenomena with three sublattice moments.

II. SAMPLE AND EXPERIMENTAL PROCEDURE

A single crystal ErGa garnet, $\text{Er}_3(\text{Fe}_{1-x}\text{Ga}_x)_5\text{O}_{12}$, sphere sample (od = 3.326 ± 0.01 mm) with a polished surface was obtained from a single crystal ingot prepared by a floating zone melting method using an IR imaging furnace at the RCA Laboratories. The sphere sample was annealed at 1273 K for 10 h in air prior to the measurement. The Ga concentration x was estimated to be $x = 0.2$ from the lattice constant, the saturation magnetization at 0 K, and the density measurements.

The magnetization along an easy direction was measured using a computer controlled vibrating sample magnetometer. The temperature of the sample was measured by the cali-

brated PlatinelTM thermocouple directly contacted with its surface. The experimental procedure basically followed our recent work.³

III. RESULTS AND DISCUSSION

The temperature dependence of the magnetization measured at 8 kOe is shown in the inset of Fig. 1. The Curie temperature was about $T_c = 460$ K which was 100 K lower than the reported value of ErIG.⁴ The substituted Ga has thus lowered the average super exchange interaction between Fe^{3+} sublattices. The constant field magnetization was measured in detail from $H_a = 0$ Oe to 8 kOe at the temperatures between 440 and 520 K as shown in Fig. 1. The kink point which corresponds to the spontaneous magnetization was rounded on the curves contrary to the case of YIG¹ and the

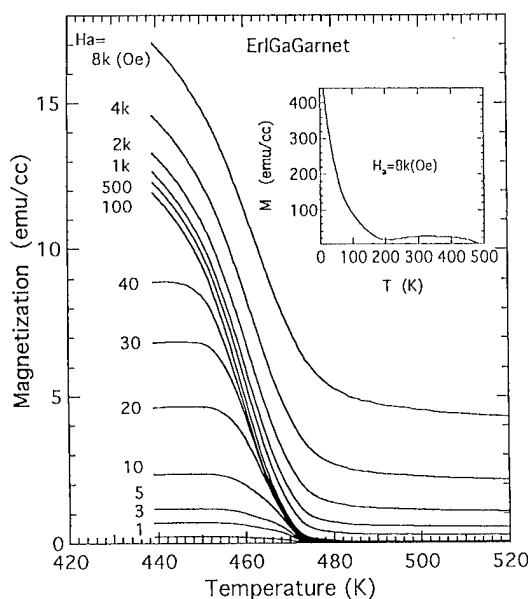
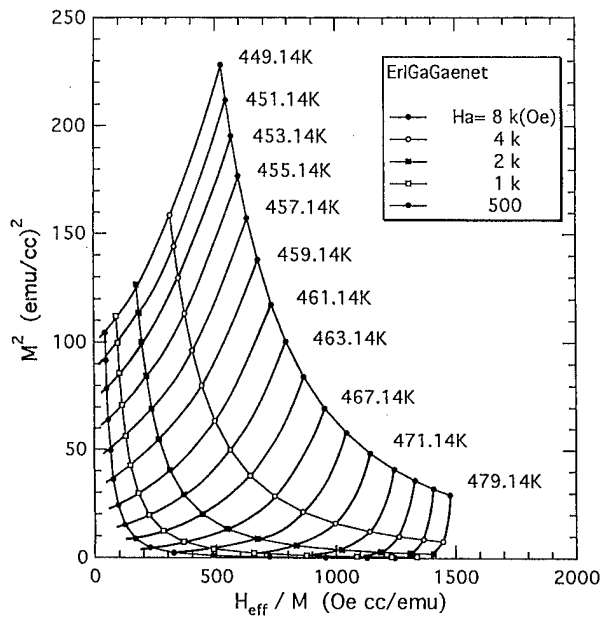
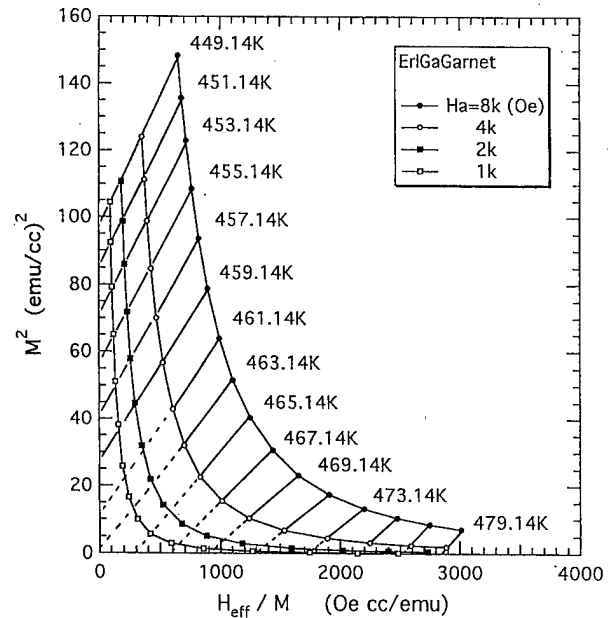


FIG. 1. The temperature dependence of the constant field magnetization near critical temperature. The inset shows the temperature dependence of magnetization measured at 8 kOe from 20 to 500 K.

^{a)}Electronic mail: tanaka@en2.ehime-u.ac.jp

FIG. 2. Arrot plot for the measured magnetization M .FIG. 3. Arrot plot for the Fe-sublattice magnetization M_{sub} .

magnetic transition was broadened. These facts suggest that this single crystal involves a magnetic inhomogeneity which may be caused by the local strain or imperfections associated with the substitution of Fe with Ga and that the low field data are significantly affected by this inhomogeneity.

The Arrot plot, M^2 vs H_{eff}/M , for the measured data M is shown in Fig. 2. H_{eff} was given by $H_{\text{eff}} = H_a - 4\pi nM$ and n was obtained to be 0.3333 from the magnetization measurement. As is seen in the plot, M^2 is not proportional to H_{eff}/M even in high H_{eff} . This shows that the Landau theory for the second-order phase transition does not apply to the present system anymore. To understand the result, we assume that a large paramagnetic magnetization term of the Er^{3+} spin $\chi_{\text{Er}}H_{\text{eff}}$ is involved in M . This term is commonly known to exist in rare-earth iron-garnet (RIG), and should not contribute to the phase transition at T_c . The experimental data M is expressed by

$$M = M_{\text{Fe}} + M_{\text{Er}}(\text{Fe}) + \chi_{\text{Er}}H_{\text{eff}}, \quad (1)$$

where M_{Fe} is the Fe^{3+} sublattice magnetization and $M_{\text{Er}}(\text{Fe})$ is the Er^{3+} sublattice magnetization induced by M_{Fe} .

The susceptibility of Er^{3+} spin paramagnetism $\chi_{\text{Er}} = C_{\text{Er}}/(T - \theta_p)$ was estimated from the paramagnetic susceptibility χ measured at $T > T_c$. χ is given by

$$\chi = C/(T - \theta_p) = (C_{\text{Fe}} + C_{\text{Er}})/(T - \theta_p). \quad (2)$$

C_{Er} was estimated by the ratio of the total Er^{3+} and Fe^{3+} spin magnetic moment in a formula unit. The θ_p was obtained to be -10 K which was close to results of early work.⁴ Now, we can separate the Fe-sublattice magnetization M_{sub}

$$M_{\text{sub}} = M_{\text{Fe}} + M_{\text{Er}}(\text{Fe}) \quad (3)$$

by subtracting $\chi_{\text{Er}}H_{\text{eff}}$ from the experimental data M .

The Arrot plot of M_{sub} was replotted in Fig. 3 for the high field data, $H \geq 1$ kOe, eliminating the low field data. M_{sub}^2 is then found to be proportional to $H_{\text{eff}}/M_{\text{sub}}$. The spontaneous magnetization M_0 and the zero-field inverse

susceptibility χ_0^{-1} were obtained by extrapolation to the M_{sub}^2 axis and the $H_{\text{eff}}/M_{\text{sub}}$ axis, respectively. In Fig. 4, the temperature dependence of M_0 and χ_0^{-1} is shown with $M_{\text{sub}}(T)$.

The critical temperature was assumed to be 463.64 K from the T^* vs T plot⁵ where $T^* \equiv \chi_0^{-1}(T)/(\partial\chi_0^{-1}(T)/\partial T)$. The critical indices β and γ , defined as $M_0(T) = \epsilon^\beta$ and $\chi_0^{-1} = \epsilon^\gamma$ for $\epsilon = |T - T_c|/T_c$, were obtained to be 0.48 ± 0.03 and 1.1 ± 0.1 , respectively. The critical index δ defined as $M_0(H_{\text{eff}}, T_c) = H_{\text{eff}}^{1/\delta}$ was also determined to be 3.1

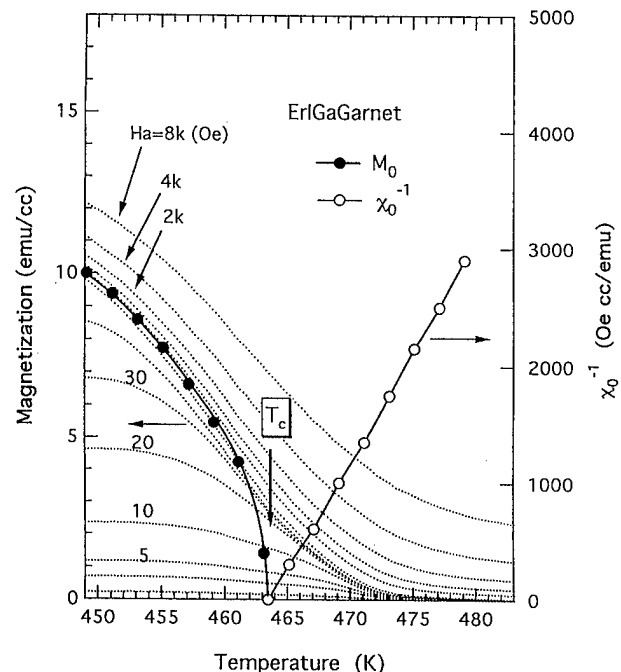
FIG. 4. Temperature dependence of the spontaneous magnetization and zero-field susceptibility. The dotted lines indicate the constant field M_{sub} at 1 Oe–8 kOe.

TABLE I. Critical indices and critical temperature.

	β	γ	δ	T_c (K)	Ref
ErGa garnet	0.48 ± 0.03	1.1 ± 0.1	3.1 ± 0.1	463.46	...
YIG	0.380 ± 0.005	1.312 ± 0.008	4.42 ± 0.05	551.35	^a
Molecular field theory	0.5	1	3	...	^b
3d Ising model	0.312	1.25	5	...	^b

^aReference 1.
^bReference 6.

± 0.1 . The critical indices and the Curie temperature were listed in Table I with those for YIG, and the theoretically predicted values.⁶ The present values do not agree with those for YIG, but are close to those predicted by the molecular field theory.

The Fe-sublattice magnetization at $H_a = 2, 4$, and 8 kOe were plotted in the form of $H_{\text{eff}}/(M(T)\epsilon^\gamma)$ vs $M(T)/\epsilon^\beta$ to check the validity of the critical equation of state $\psi(M, H)$ in Fig. 5. M_{sub} below and above T_c fell on the two separate curves, respectively. This suggests that M_{sub} obeys a second-order phase transition, and $\psi(M, H)$ shows the same function as that for Fe.³

In work on YIG,¹ CdCr_2Se_4 ,² Ni ,^{1,3} and Fe ,³ M_0 and χ_0^{-1} were determined directly from the extremely low field magnetization measurements. This allowed us to investigate the magnetostatic critical point phenomena without approximation. In contrast to this, in the present work, we eliminated the low field data from M to avoid the influence of magnetic inhomogeneity which was enhanced in low fields. The magnetostatic critical point phenomena can be explained approximately by a molecular field theory. Present results show that the magnetization data at the critical region once the low field data was excluded satisfies a molecular field theory.

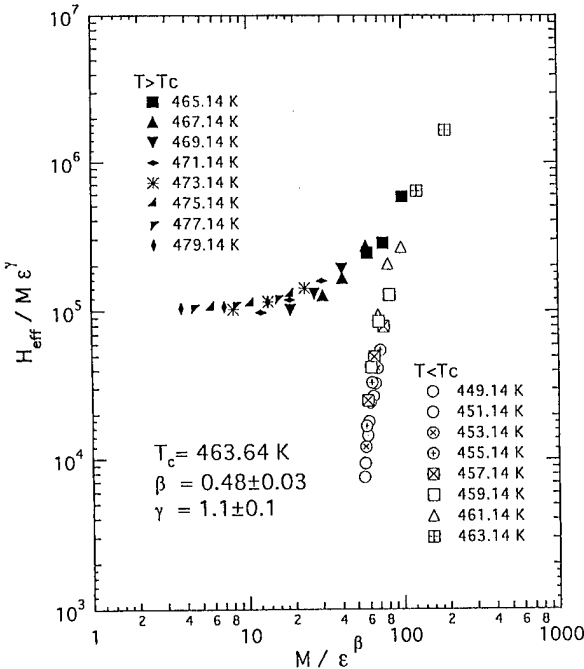


FIG. 5. $H_{\text{eff}}/M\epsilon^\gamma$ vs M/ϵ^β plot of M_{sub} for using $T_c = 463.64$ K in the temperature range from 463.14 to 479.14 K.

ACKNOWLEDGMENT

The authors express their thanks to J. Yamashita for his experimental collaboration during his master's thesis work.

¹K. Miyatani and K. Yoshikawa, J. Appl. Phys. **41**, 1272 (1970).
²K. Miyatani, J. Phys. Soc. Jpn. **28**, 259 (1970).
³T. Tanaka and K. Miyatani, J. Appl. Phys. **82**, 5658 (1997).
⁴R. Pauthenet, Ann. Phys. (Paris) **3**, 424 (1958).
⁵J. S. Kouvel and D. S. Rodbell, J. Appl. Phys. **38**, 979 (1967).
⁶H. E. Stanley, *Introduction to Phase Transitions and Critical Phenomena* (Clarendon, Oxford, 1971), p. 47.

Monte Carlo investigation of the eight-state Potts model on quasiperiodic tilings

D. Ledue^{a)}

Magnétisme et Applications, GMP UMR 6634 CNRS-Université de Rouen, 76821 Mont-Saint-Aignan Cedex, France

D. P. Landau

Center for Simulation Physics, The University of Georgia, Athens, Georgia 30602

J. Teillet

Magnétisme et Applications, GMP UMR 6634 CNRS-Université de Rouen, 76821 Mont-Saint-Aignan Cedex, France

A Monte Carlo investigation of the eight-state Potts model on the two-dimensional (2D) quasiperiodic octagonal tiling with free boundary conditions is performed in order to determine the nature of a temperature-driven transition. It is shown that numerical data suffer from drastic free boundary effects that strongly disturb the probability distributions of the internal energy and, consequently, the scaling behavior of the specific heat. An alternative way consisting in analysing the core of the tilings is applied to pass over free boundary effects. This analysis combined with the Lee-Kosterlitz method allows one to evidence that the system undergoes a first-order transition as in 2D periodic lattices. The first-order type of scaling is observed for the maximum in the susceptibility of the core of the tilings but not for the maximum in the specific heat. © 1998 American Institute of Physics. [S0021-8979(98)23111-2]

I. INTRODUCTION

Recently, it has been shown by theoretical arguments that bond randomness will induce a second-order phase transition in a system that would undergo a symmetry-breaking first-order phase transition.^{1,2} Since these arguments have been derived from an actual renormalization-group calculation¹ and from a rigorous proof of the vanishing of the latent heat,² Chen *et al.*³ have investigated the ability of extensive Monte Carlo (MC) simulations to evidence such a prediction. They have considered the two-dimensional (2D) eight-state Potts model⁴ which undergoes a first-order transition when it is pure. Applying finite-size scaling techniques, they concluded that, under bond randomness, the phase transition changes from first to second order with 2D Ising exponents. These new results have motivated us to study the eight-state Potts model on 2D quasiperiodic tilings⁵ which are less ordered than periodic lattices although they exhibit long range translational order. We have considered an octagonal tiling (Fig. 1) because all octagonal tilings are locally isomorphic,⁶ that is, they exhibit identical phase transitions.

II. BACKGROUND AND NUMERICAL SIMULATIONS

The Hamiltonian of the q -state Potts model is given by⁴

$$H = -\frac{q}{q-1} J \sum_{\langle i,j \rangle} \delta_{S_i S_j} \quad (J > 0),$$

where the spins S_i , which are located at the vertices of the octagonal tiling, take on the values $1, \dots, q$ and δ is the Kronecker delta function (in this study, $q=8$).

The procedure is the importance-sampling MC method based on the standard single spin-flip Metropolis algorithm⁷ combined with the single histogram technique.^{8,9} Our simulations were carried out on finite octagonal tilings of N_{tot} vertices with free boundary conditions. In order to investigate the free boundary effects, two kinds of systems (N vertices) have been considered: systems which are the whole tilings ($N=N_{\text{tot}}=329, 689, 1433, 2481, \text{ and } 5497$), and systems which are the core of the tilings ($N \approx 0.13 \times N_{\text{tot}}=89, 329, \text{ and } 705$). This core is made up of the vertices which are located in a circle centered on the center of the tiling. Between 5×10^5 or 10^6 Monte Carlo steps (MCS)/spin for

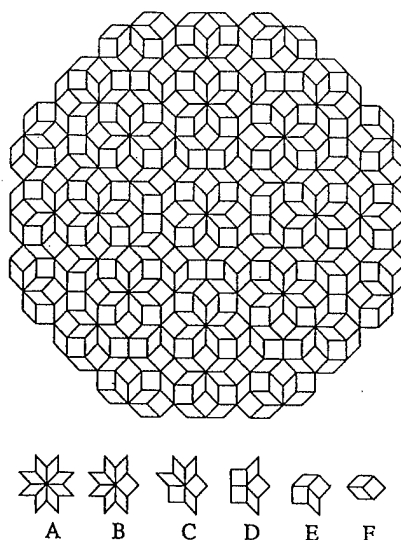


FIG. 1. The octagonal tiling and the six local environments.

^{a)}Electronic mail: Denis.Ledue@univ-rouen.fr

$N_{\text{tot}}=329$ and 5×10^6 MCS/spin for $N_{\text{tot}}=5497$ were performed (the first 2×10^4 MCS/spin were discarded for equilibration).

The nature of a phase transition can be, in principle, determined by looking at the size dependence of some thermodynamic quantities in the vicinity of the transition temperature T_c .¹⁰⁻¹² For example, the scaling forms³ for the specific heat and the susceptibility¹² in 2D systems are, at a first-order transition:

$$C_{\text{max}}(L) \sim L^2 A(tL^2), \quad \chi_{\text{max}}(L) \sim L^2 B(tL^2)$$

and, at a second-order transition:

$$C_{\text{max}}(L) \sim L^{\alpha/\nu} C^0(tL^{1/\nu}), \quad \chi_{\text{max}}(L) \sim L^{\gamma/\nu} \chi^0(tL^{1/\nu}),$$

where $L = \sqrt{N}$ is the linear dimension of the system, α , γ , and ν are three infinite system critical exponents and $t = |T - T_c|/T_c$. However, a pseudodivergent correlation length in weak first-order transition can be responsible for a second-order type of scaling of thermodynamic quantities.¹³ A more powerful method of detecting first-order transitions by numerical simulations on finite systems is the Lee-Kosterlitz method¹⁴ which suggests to look at the size dependence of the free energy, $F_L(E) = -\ln[P_L(E)]$, where $P_L(E)$ is the probability distribution of the internal energy. For a first-order transition, the free energy for large systems at $T_c(L)$ (the location of the maximum in the specific heat) exhibits a maximum $F_L(E_2)$ between two wells of equal depth $F_L(E_1) = F_L(E_3)$. If the free energy barrier, $\Delta F_L = F_L(E_2) - F_L(E_1)$, grows with increasing system size, the transition will be first order in the thermodynamic limit, while the transition will be second order if the barrier decreases with increasing size. In MC simulations using histogram techniques, the free energy barrier can be estimated by the reweighted probability distribution at $T_c(L)$:

$$\Delta F_L = \ln[P_L(E_1)/P_L(E_2)].$$

It has been demonstrated that this method can identify unambiguously weak first-order transitions even when $L \ll \xi$ (ξ is the correlation length), at least for systems with periodic boundary conditions.¹⁴

III. RESULTS AND DISCUSSION

In order to investigate the nature of the phase transition, we plotted the size dependence of the maximum in the specific heat and the susceptibility on a log-log scale (Figs. 2 and 3). Four different linear fits were performed using system sizes $N_{\text{min}} \leq N \leq 5497$ with respectively $N_{\text{min}}=329, 689, 1433$, and 2481 . We were not able to conclude about the nature of the phase transition since the slope increases with N_{min} ($1.30 \pm 0.08, 1.40 \pm 0.09, 1.52 \pm 0.12, 1.61 \pm 0.21$ for C_{max} and $1.76 \pm 0.08, 1.8 \pm 0.1, 1.88 \pm 0.15, 1.93 \pm 0.23$ for χ_{max}) showing a nonanalytic behaviour for the two thermodynamic quantities. Then, one should keep in mind that, for a first-order transition, the L^2 behaviour can be observed only if L is larger than ξ . For example, the asymptotic regime of the 2D pure ten-state Potts model¹³ which is characterized by a small correlation length (≈ 6 lattice spacings) is reached by $L=12$. For the pure 2D eight-state Potts model, the cor-

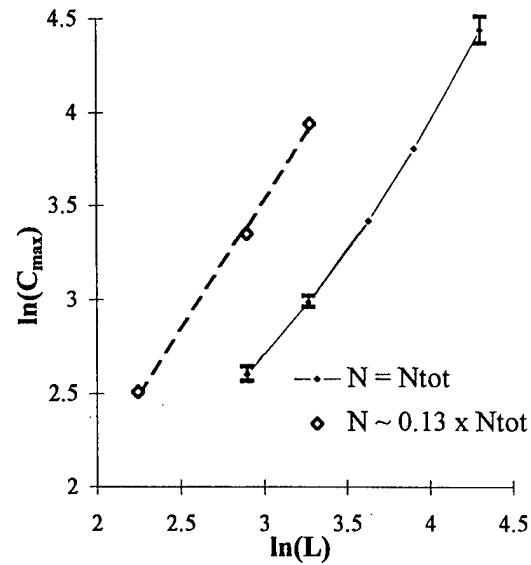


FIG. 2. Log-log plot of the size dependence of C_{max} (the dashed line corresponds to a linear fit; where not shown, the estimated error bars are smaller than the symbols).

relation length is about 15 lattice spacings [$\xi(q=8) \approx 2.5 \times \xi(q=10)$].¹⁵ So, if we assume that the correlation length is roughly the same in the octagonal tiling as in the square lattice, we should observe the L^2 behavior since $L_{\text{max}} \approx 74$ in this study ($N_{\text{max}}=5497$). On the other hand, let us remind that the asymptotic regime of the 2D random-bond eight-state Potts model is reached approximately by $L=28$.³ So, the asymptotic regime should be observed too if our system undergoes a second-order transition. In order to get more information, we plotted the probability distributions of the internal energy at $T_c(L)$ that can be very useful to determine the nature of a transition (even if $L \ll \xi$).¹⁴ Unfortunately, they do not allow to conclude either. Indeed, for $N \leq 1433$, they look like single-Gaussian distributions which should suggest a second-order transition but they clearly exhibit a

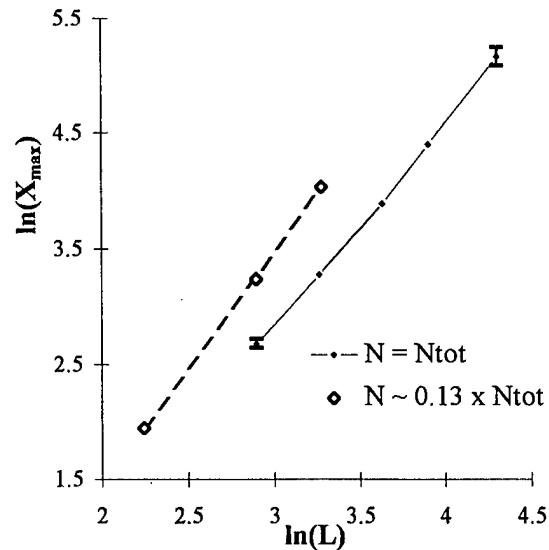


FIG. 3. Log-log plot of the size dependence of χ_{max} (the dashed line corresponds to a linear fit).

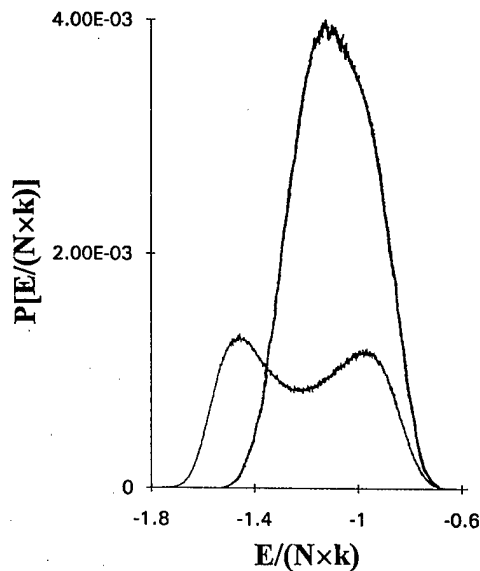


FIG. 4. Probability distributions of the internal energy for $N=N_{\text{tot}}=689$ at $kT/J=0.8550$ (single-Gaussian distribution) and for $N=705$ and $N_{\text{tot}}=5497$ at $kT/J=0.8730$ (double-Gaussian distribution).

shoulder for $N=2481$ and 5497 . These unusual shapes for the probability distributions suggest that our numerical data are strongly disturbed by free boundary effects.

To clarify the question about free boundary effects, MC data from the simulations with $N \approx 0.13 \times N_{\text{tot}}$ are presented below (analysis of the core of the tiling). For a given N , C_{max} , and χ_{max} , increase with N_{tot} (Figs. 2 and 3) indicating that the internal energy and the order parameter fluctuations in the vicinity of the transition are more important as the free boundary effects lower. This can be seen on the probability distributions of the internal energy which evidence that low energy states corresponding to the ordered phases are occupied for the systems with $N \ll N_{\text{tot}}$ but are missing if $N = N_{\text{tot}}$ (Fig. 4). Moreover, the probability distributions look like double-Gaussian distributions. The estimated free energy barrier increases with size N [$\Delta F(N=89)=0.08 \pm 0.03$, $\Delta F(N=329)=0.19 \pm 0.05$, and $\Delta F(N=705)=0.38 \pm 0.05$] indicating that the phase transition is first order as in 2D periodic lattices. Note that the slope of the linear fit of the size dependence of C_{max} and χ_{max} are, respectively, 1.37 ± 0.03 and 2.02 ± 0.02 (Figs. 2 and 3). So, the size dependence for χ_{max} is consistent with a first-order transition whereas the one for C_{max} is difficult to explain.

In order to estimate the infinite tiling transition temperature,^{12,13} we investigated the dependence of the location of χ_{max} vs L^{-2} for the three simulations with $N \approx 0.13 \times N_{\text{tot}}$. Two linear fits, using either the three data points or discarding the point $N=89$, provided, respectively, kT_c/J

$=0.8745 \pm 0.0015$ and 0.8757 ± 0.0006 which are in good agreement. Note that these two estimates are also consistent with those obtained from the size dependence of the location of C_{max} , that is, $kT_c/J=0.875 \pm 0.001$ and 0.8760 ± 0.0007 . So, the transition temperature of the eight-state Potts model on the octagonal tiling (mean coordinence $\langle z \rangle = 4$) is slightly higher than on the square lattice ($kT_c/J=0.8513$).⁴ This higher tendency to ferromagnetic ordering in quasiperiodic tilings has already been observed in previous studies on the Ising and Potts models.¹⁶⁻²⁰

IV. CONCLUSION

Our investigation on the eight-state Potts model on the 2D quasiperiodic octagonal tiling has evidenced drastic free boundary effects in studying first-order transitions by MC simulations. These effects strongly disturb the probability distributions of the internal energy which do not exhibit two peaks in the vicinity of $T_c(L)$ as for systems with periodic boundary conditions. Rather than increasing the size of the tilings, an analysis of the energy probability distributions of the core of the tilings has been used to evidence a first-order transition, as in 2D periodic lattices. From MC data relative to the whole tilings, the L^2 behavior has not been observed, neither for C_{max} nor for χ_{max} , probably because of free boundary effects. Quite surprisingly, MC data for the core of the tilings reveal different scaling behavior for χ_{max} and C_{max} (L^2 behavior for χ_{max} and a nonanalytic form for C_{max}).

¹K. Hui and A. N. Berker, Phys. Rev. Lett. **62**, 2507 (1989).

²M. Aizenman and J. Wehr, Phys. Rev. Lett. **62**, 2503 (1989).

³S. Chen, A. M. Ferrenberg, and D. P. Landau, Phys. Rev. Lett. **69**, 1213 (1992); Phys. Rev. E **52**, 1377 (1995).

⁴F. Y. Wu, Rev. Mod. Phys. **54**, 235 (1982).

⁵D. Gratias, *Du Cristal à l'Amorphe* (Editions de Physique, Paris, 1988).

⁶D. Levine and P. J. Steinhardt, Phys. Rev. B **34**, 596 (1986).

⁷N. Metropolis, A. E. Rosenbluth, M. N. Rosenbluth, A. H. Teller, and E. Teller, J. Chem. Phys. **21**, 1087 (1953).

⁸A. M. Ferrenberg and R. H. Swendsen, Phys. Rev. Lett. **61**, 2635 (1988); **63**, 1195 (1989).

⁹A. M. Ferrenberg, in *Computer Simulation Studies in Condensed Matter Physics III*, edited by D. P. Landau, K. K. Mon, and H. B. Schuttler (Springer, Heidelberg, 1991).

¹⁰M. E. Fisher, in *Critical Phenomena*, edited by M. S. Green (Academic, New York, 1971).

¹¹M. E. Fisher and M. N. Barber, Phys. Rev. Lett. **28**, 1516 (1972).

¹²M. S. S. Challa, D. P. Landau, and K. Binder, Phys. Rev. B **34**, 1841 (1986).

¹³P. Peczak and D. P. Landau, Phys. Rev. B **39**, 11932 (1989).

¹⁴J. Lee and J. M. Kosterlitz, Phys. Rev. Lett. **65**, 137 (1990).

¹⁵J. L. Black and V. J. Emery, Phys. Rev. B **23**, 429 (1981).

¹⁶Y. Okabe and K. Niizeki, J. Phys. Soc. Jpn. **57**, 16 (1988).

¹⁷E. S. Sorensen, M. V. Jaric, and M. Ronchetti, Phys. Rev. B **44**, 9271 (1991).

¹⁸D. Ledue, D. P. Landau, and J. Teillet, Phys. Rev. B **51**, 12523 (1995).

¹⁹D. Ledue, Phys. Rev. B **53**, 3312 (1996).

²⁰D. Ledue, T. Boutry, D. P. Landau, and J. Teillet, Phys. Rev. B **56**, 10782 (1997).

Exact renormalization group equation for systems of arbitrary symmetry free of redundant operators

A. A. Lisiansky

Department of Physics, Queens College of CUNY, Flushing, New York 11367

D. Nicolaides

Natural Sciences and Mathematics, Bloomfield College, Franklin Street, Bloomfield, New Jersey 07003

A generalized exact renormalization group (RG) equation for the Ginzburg–Landau–Wilson functional of an arbitrary symmetry, containing invariants of all orders, with nonlocal vertices is derived. Unlike other RG equations which contain an infinite number of redundant operators, the equation derived is free of them. © 1998 American Institute of Physics. [S0021-8979(98)32911-4]

The new concepts brought about by the renormalization group (RG) theory in the 1970s helped one to understand critical phenomena at continuous phase transitions in magnetic systems.¹ Using RG theory, systematic perturbative RG expansions were developed to calculate critical exponents with a high accuracy.^{2,3} In addition to the perturbation theory, RG has been successful in deriving exact RG equations,⁴ which not only provide a good insight of the theory, but also give a basis for developing new approximation schemes.^{5–9} Working with exact RG equations is a difficult task which has its origin in the fact that an exact RG equation contains an infinite number of redundant operators,^{10–12} which carry no physical meaning. Their exclusion from the RG equation is therefore a necessary but at the same time a complicated task, which requires imposing additional conditions. The problem of eliminating redundant operators for isotropic systems was considered in Ref. 8. In the present article we develop a new RG procedure applicable to arbitrary anisotropic systems. As a result we obtain an exact RG equation free of redundant operators.

We start with the most general kind of Ginzburg–Landau–Wilson functional

$$H_I[\varphi(\mathbf{q})] = \sum_{k=0}^{\infty} 2^{1-2k} \int_{q_1 \dots q_{2k}} \sum_{\alpha_1, \dots, \alpha_{2k}=1}^n \left[g_k^{\alpha_1, \dots, \alpha_{2k}} \times (\mathbf{q}_1, \dots, \mathbf{q}_{2k}) (2\pi)^d \delta \left(\sum_{i=1}^{2k} \mathbf{q}_i \right) \times \prod_{i=1}^{2k} \varphi^{\alpha_i}(\mathbf{q}_i) \right], \quad (1)$$

where φ is an n -component vector and $\int_{\mathbf{q}} \equiv \int d^d q / (2\pi)^d$. The vertices \hat{g}_k have an arbitrary tensorial structure with respect to the space indices α_i . Let us define an RG procedure in the following way. We cut off all momentum integrals at an upper momentum Λ by adding to the functional H_I a term H_0

$$H_0[\varphi] = \frac{1}{2} \int_{\mathbf{q}} G_0^{-1}(q, \Lambda) |\varphi(\mathbf{q})|^2, \quad (2)$$

where the propagator G_0 is defined by

$$G_0(q, \Lambda) = q^{-2} S(q^2/\Lambda^2). \quad (3)$$

Here $S(x)$ is a monotonic function with the properties $S(x=0)=1$ and $\lim_{x \rightarrow \infty} S(x)x^m = 0$ for any m .

We now perform two steps which are standard for RG. First, apply a Kadanoff transformation to thin out the original Hamiltonian by integrating those Fourier components $\varphi(\mathbf{q})$ corresponding to momenta within a spherical shell $\Lambda(1-\xi) < q < \Lambda$ in momentum space with $\xi \ll 1$. The Kadanoff transformation succeeds in bringing down the cut-off momentum to $\Lambda(1-\xi)$. Second, we rescale all the rest momenta in order to restore the original cutoff momentum Λ .

Let us introduce the designation:

$$Z = \int D\varphi \exp(-H[\varphi]) \\ = Z_0 \langle \exp(-H_I[\varphi]) \rangle_{0,\Lambda} \equiv Z_0 \langle w[\varphi] \rangle_{0,\Lambda}, \quad (4)$$

where

$$Z_0 = \int D\varphi \exp(-H_0[\varphi]), \quad (5)$$

and the averaging $\langle \dots \rangle_{0,\Lambda}$ is performed with respect to the functional $H_0[\varphi]$ at a given value of Λ . Note that if $\varphi(\mathbf{q}) = \varphi_1(\mathbf{q}) + \varphi_2(\mathbf{q})$ and $G_0(q, \Lambda) = G_{01}(q, \Lambda_1) + G_{02}(q, \Lambda_2)$, the following identity can be generated:

$$\langle w[\varphi] \rangle_{0,\Lambda} \equiv Z_0^{-1} \int D\varphi w[\varphi] \exp(-H_0[\varphi]) \\ = Z_{01}^{-1} Z_{02}^{-1} \int D\varphi_1 D\varphi_2 w[\varphi_1, \varphi_2] \\ \times \exp(-H_0[\varphi_1, \varphi_2]), \quad (6)$$

where

$$Z_{0i} = \int D\varphi_i \exp \left[-\frac{1}{2} \int_{\mathbf{q}} G_{0i}^{-1}(q, \Lambda_i) |\varphi_i(\mathbf{q})|^2 \right]; \\ H_{0i}[\varphi_1, \varphi_2] = \frac{1}{2} \int_{\mathbf{q}} G_{01}^{-1}(q, \Lambda_1) |\varphi_1(\mathbf{q})|^2 \\ + \frac{1}{2} \int_{\mathbf{q}} G_{02}^{-1}(q, \Lambda_2) |\varphi_2(\mathbf{q})|^2. \quad (7)$$

Choosing $G_{01}(q, \Lambda_1) = G_0(q, \Lambda(1 - \xi))$ with $\xi \ll 1$, makes the function G_{02} of order ξ ,

$$\begin{aligned} G_{02}(q, \Lambda_2) &= G_0(q, \Lambda) - G_{01}(q, \Lambda_1) \\ &\approx \xi \Lambda \frac{\partial G_0(q, \Lambda)}{\partial \Lambda} \equiv 2\xi h(q), \\ h(q) &= q^{-2} \Lambda^2 \frac{dS(q^2/\Lambda)}{d\Lambda^2}. \end{aligned} \quad (8)$$

Modes $\varphi_2(\mathbf{q})$ are those with momenta within a shell $\Lambda(1 - \xi) < q < \Lambda$ which should be integrated out. To do so and have the first step completed we expand $\langle w[\varphi_1, \varphi_2] \rangle$ in Eq. (6) with respect to $\varphi_2(\mathbf{q})$ to obtain

$$\begin{aligned} \langle w[\varphi] \rangle_{0,\Lambda} &= Z_{01}^{-1} Z_{02}^{-1} \int D\varphi_1 D\varphi_2 \left[w[\varphi_1] \right. \\ &\quad + \int_q \sum_\alpha \frac{\delta w[\varphi_1]}{\delta \varphi_1^\alpha(\mathbf{q})} \varphi_2^\alpha(\mathbf{q}) \\ &\quad + \frac{1}{2} \int_{qq'} \sum_{\alpha,\beta} \frac{\delta^2 w[\varphi_1]}{\delta \varphi_1^\alpha(\mathbf{q}) \delta \varphi_1^\beta(\mathbf{q}')} \\ &\quad \left. \times \varphi_2^\alpha(\mathbf{q}) \varphi_2^\beta(\mathbf{q}') + \dots \right] \exp(-H_0[\varphi_1, \varphi_2]). \end{aligned} \quad (9)$$

Having in mind the Gaussian nature of $H_0[\varphi_1, \varphi_2]$ only even terms in the above expansion survive. Keeping terms of the lowest order with respect to ξ the integration yields

$$\begin{aligned} \langle w[\varphi(\mathbf{q})] \rangle_{0,\Lambda} &\approx \left\langle \left(1 + \xi V \int_q h(q) \sum_\alpha \frac{\delta^2}{\delta \varphi^\alpha(\mathbf{q}) \delta \varphi^\alpha(-\mathbf{q})} \right) \right. \\ &\quad \left. \times w[\varphi(\mathbf{q})] \right\rangle_{0,\Lambda(1-\xi)}, \end{aligned} \quad (10)$$

where the averaging $\langle \dots \rangle_{0,\Lambda(1-\xi)}$ is performed with respect to the functional

$$H_0[\varphi, \Lambda(1 - \xi)] = \frac{1}{2} \int_q G_0^{-1}(q, \Lambda(1 - \xi)) |\varphi(\mathbf{q})|^2. \quad (11)$$

Consequently, the right-hand side of Eq. (10) contains effectively only modes with $q < \Lambda(1 - \xi)$. The first step of the RG transformation has been completed.

For the second step, we must rescale the momentum to restore the original cutoff Λ through transformation $\mathbf{q} = \mathbf{q}'(1 - \xi)$. This rescaling changes $H_0[\Lambda]$ to $H_0[\Lambda(1 - \xi)]$ as follows:

$$\begin{aligned} H_0[\varphi, \Lambda(1 - \xi)] &= \frac{1}{2} \int_q G_0^{-1}(q, \Lambda(1 - \xi)) |\varphi(\mathbf{q})|^2, \\ H_0'[\varphi, \Lambda] &= \frac{(1 - \xi)^{d+2}}{2} \int_q G_0^{-1}(q, \Lambda) |\varphi[\mathbf{q}(1 - \xi)]|^2. \end{aligned} \quad (12)$$

However, we must restore this change since it is essential to the restoration of Λ . We do so by substituting $\varphi(\mathbf{q})$,

$$\begin{aligned} \varphi^\alpha(\mathbf{q}) &= \sum_\beta [\delta^{\alpha\beta} + \xi \epsilon^{\alpha\beta}(\mathbf{q})] \varphi'^\beta[\mathbf{q}(1 + \xi)] \\ &= \sum_\beta \left[\delta^{\alpha\beta} + \xi \left(\epsilon^{\alpha\beta}(\mathbf{q}) + \delta^{\alpha\beta} \mathbf{q} \cdot \frac{\partial}{\partial \mathbf{q}} \right) \right] \varphi'^\beta(\mathbf{q}), \end{aligned} \quad (13)$$

where at present $\epsilon^{\alpha\beta}(\mathbf{q})$ is an arbitrary tensor with the only condition $\epsilon^{\alpha\beta}(\mathbf{q}) = \epsilon^{\beta\alpha}(-\mathbf{q})$. Then we apply the above transformation to $\langle w[\varphi(\mathbf{q})] \rangle_{0,\Lambda(1-\xi)}$ of Eq. (10). After keeping terms of the lowest order in ξ and using the relationship $w[\varphi] = \exp(-H_L[\varphi])$ we derive the RG equation for H_L ,

$$\begin{aligned} \dot{H}_L[\varphi] &= Vd \frac{\partial H_L[\varphi]}{\partial V} + \frac{V}{2} \int_q \sum_\alpha \eta^{\alpha\alpha}(\mathbf{q}) \\ &\quad - \frac{1}{2} \int_{q,\alpha,\beta} \eta^{\alpha\beta}(\mathbf{q}) G_0^{-1}(q, \Lambda) \varphi^\alpha(\mathbf{q}) \varphi^\beta(-\mathbf{q}) \\ &\quad + \int_{q,\alpha,\beta} \left[\left(\frac{d+2}{2} \delta^{\alpha\beta} - \frac{\eta^{\alpha\beta}(\mathbf{q})}{2} \right) \varphi^\alpha(\mathbf{q}) + \delta^{\alpha\beta} \mathbf{q} \cdot \frac{\partial \varphi^\alpha(\mathbf{q})}{\partial \mathbf{q}} \right] \frac{\delta H_L[\varphi]}{\delta \varphi^\beta(\mathbf{q})} + \int_q h(q) \\ &\quad \times \sum_\alpha \left[\frac{\delta^2 H_L[\varphi]}{\delta \varphi^\alpha(\mathbf{q}) \delta \varphi^\alpha(-\mathbf{q})} - \frac{\delta H_L[\varphi]}{\delta \varphi^\alpha(\mathbf{q})} \frac{\delta H_L[\varphi]}{\delta \varphi^\alpha(-\mathbf{q})} \right]. \end{aligned} \quad (14)$$

Here $\eta^{\alpha\beta}(\mathbf{q})$ is defined as

$$\eta^{\alpha\beta}(\mathbf{q}) = \delta^{\alpha\beta}(d+2) - 2\epsilon^{\alpha\beta}(-\mathbf{q}). \quad (15)$$

Equation (14) is an exact RG equation for functional (1). It contains an arbitrary function $\eta^{\alpha\beta}(\mathbf{q})$. Note that if we choose $\eta^{\alpha\beta}(\mathbf{q}) = 0$ then the resulting simplified RG equation will be similar to the traditional ones, and as in those cases it will contain redundant operators. Not being physical, these operators must be eliminated by developing a proper procedure. Our goal is to find the correct choice of the tensor $\eta^{\alpha\beta}$ which will make the RG Eq. (14) free of redundant operators. Explicitly, Eq. (14) generates different vertices $g_k^{\alpha\beta}(\mathbf{q})$. Some of the q -dependent part of this renormalization can be incorporated into G_0 of the functional H_0 . This means that the cutoff Λ is affected which should, however, remain unchanged. To avoid so, we define $\eta^{\alpha\beta}(\mathbf{q})$ such that it cancels out the q -dependent renormalization of the vertex $g_1^{\alpha\beta}(\mathbf{q})$. To achieve this, we use Eq. (14) to write explicitly the change of vertices $g_1^{\alpha\beta}$ corresponding to zeroth and first order in $\varphi^\alpha(\mathbf{q}) \varphi^\beta(-\mathbf{q})$. Then we require that $g_1^{\alpha\beta}$ is momentum independent initially and must remain so after the transformation so that H_0 which controls the cutoff remains intact. This requirement finds a momentum dependent expression for the tensor $\eta^{\alpha\beta}(\mathbf{q})$. First, we extract an explicit equation for the vertex $g_1(\mathbf{q})$ from Eq. (14),

$$\begin{aligned} \dot{g}_1^{\alpha\beta}(\mathbf{q}) = & -\eta^{\alpha\beta}(q)G_0^{-1}(q, \Lambda) + \sum_{\gamma} \left[2\delta^{\alpha\gamma} - \eta^{\alpha\gamma}(\mathbf{q}) \right. \\ & \left. - \delta^{\alpha\gamma} \mathbf{q} \cdot \frac{\partial}{\partial \mathbf{q}} \right] g_1^{\gamma\beta}(\mathbf{q}) + \sum_{\gamma} Q^{\alpha\beta\gamma\gamma}(\mathbf{q}) \\ & - 2 \sum_{\gamma} g_1^{\alpha\gamma}(\mathbf{q}) g_1^{\gamma\beta}(\mathbf{q}) h(q), \end{aligned} \quad (16)$$

where

$$Q^{\alpha\beta\gamma\delta}(\mathbf{q}) = 3 \int_p h(p) g_2^{\alpha\beta\gamma\delta}(\mathbf{q} - \mathbf{q}, \mathbf{p}, -\mathbf{p}). \quad (17)$$

We can now split Eq. (16) into two equations: one for \hat{g}_{10} , which is the momentum independent part of $\hat{g}_1(\mathbf{q})$, and another for $\hat{g}'_1(\mathbf{q}) = \hat{g}_1(\mathbf{q}) - \hat{g}_{10}$,

$$\begin{aligned} \dot{g}_{10}^{\alpha\beta} = & \sum_{\gamma} [2\delta^{\alpha\gamma} - \eta^{\alpha\gamma}(0)] g_{10}^{\gamma\beta} + \sum_{\gamma} Q^{\alpha\beta\gamma\gamma}(0) \\ & - 2 \sum_{\gamma} g_{10}^{\alpha\gamma} g_{10}^{\gamma\beta} h(0); \end{aligned} \quad (18)$$

$$\begin{aligned} \dot{g}'_1{}^{\alpha\beta}(\mathbf{q}) = & -\eta^{\alpha\beta}(\mathbf{q})G_0^{-1}(q, \Lambda) + \sum_{\gamma} \left\{ \left[2\delta^{\alpha\gamma} - \eta^{\alpha\gamma}(\mathbf{q}) \right. \right. \\ & \left. - \delta^{\alpha\gamma} \mathbf{q} \cdot \frac{\partial}{\partial \mathbf{q}} \right] g_1^{\gamma\beta}(\mathbf{q}) - [\eta^{\alpha\gamma}(\mathbf{q}) - \eta^{\alpha\gamma}(0)] g_{10}^{\gamma\beta} \\ & + Q^{\alpha\beta\gamma\gamma}(\mathbf{q}) - Q^{\alpha\beta\gamma\gamma}(0) - 2g_{10}^{\alpha\gamma} g_{10}^{\gamma\beta} [h(q) \\ & - h(0)] - 2[g_{10}^{\alpha\gamma} g_1^{\gamma\beta}(\mathbf{q}) + g_1^{\alpha\gamma}(\mathbf{q}) g_{10}^{\gamma\beta} \\ & \left. + g_1^{\alpha\gamma}(\mathbf{q}) g_1^{\gamma\beta}(\mathbf{q})] h(q) \right\}. \end{aligned} \quad (19)$$

Using Eq. (19) we can define the function $\eta^{\alpha\beta}(\mathbf{q})$ such that the derivative of $\hat{g}'_1(\mathbf{q})$ is equal to zero. This means that if the vertex $\hat{g}_1(\mathbf{q})$ of the initial functional H_I is a constant then a q -dependent part of this vertex will not be generated and the functional H_0 will be intact within the renormalization procedure. The requirement $\hat{g}'_1(\mathbf{q}) = 0$ implies that

$$\begin{aligned} \eta^{\alpha\beta}(\mathbf{q}) = & \eta^{\alpha\beta}(0) - \sum_{\nu} \left\{ \eta^{\alpha\nu}(0) G_0^{-1}(q, \Lambda) \right. \\ & + \sum_{\gamma} [2[h(q) - h(0)] g_{10}^{\alpha\gamma} g_{10}^{\gamma\nu} - Q^{\alpha\nu\gamma\gamma}(\mathbf{q}) \\ & \left. + Q^{\alpha\nu\gamma\gamma}(0)] \right\} [g_{10}^{\nu\beta} + G_0^{-1}(q, \Lambda) \delta^{\nu\beta}]^{-1}. \end{aligned} \quad (20)$$

Equation (20) defines the momentum dependent part of the function $\eta^{\alpha\beta}(\mathbf{q})$. We still have to define n^2 components of the tensor $\eta^{\alpha\beta}(0)$. We can use these values to simplify the RG equation and clarify the physical meaning of $\eta^{\alpha\beta}$. To do this, let us diagonalize the vertex \hat{g}_{10} in the initial functional H_1 . This can always be done without loss of generality. The diagonal components of this tensor are trial critical

temperatures for the corresponding components of the order parameter $\varphi(\mathbf{q})$. However, as one can see from Eq. (18), even if the nondiagonal part of the tensor $g_{10}^{\alpha\beta}$ does not exist in the initial functional, it will be generated within the renormalization process. We can use the arbitrariness of tensor $\eta^{\alpha\beta}$ to keep the tensor $g_{10}^{\alpha\beta}$ diagonal. In order to do this, let us split Eq. (18) into two separate equations, for diagonal and nondiagonal parts of the vertex $g_{10}^{\alpha\beta}$. Defining $g_{10}^{\alpha\beta} = \delta^{\alpha\beta} r^{\alpha} + (1 - \delta^{\alpha\beta}) r^{\alpha\beta}$, we have

$$r^{\alpha} = (2 - \eta^{\alpha}) r^{\alpha} + Q^{\alpha}(0) - 2(r^{\alpha})^2 h(0); \quad (21)$$

$$\begin{aligned} r^{\alpha\beta} = & (2 - \eta^{\alpha}) r^{\alpha\beta} - \sum_{\gamma} \tilde{\eta}^{\alpha\gamma} r^{\gamma\beta} + \tilde{Q}^{\alpha\beta}(0) - \tilde{\eta}^{\alpha\beta} r^{\beta} \\ & - 2 \left[r^{\alpha} r^{\alpha\beta} + r^{\alpha\beta} r^{\beta} + \sum_{\gamma} r^{\alpha\gamma} r^{\gamma\beta} \right] h(0), \end{aligned} \quad (22)$$

where η^{α} , Q^{α} and $\tilde{\eta}^{\alpha\beta}$, $\tilde{Q}^{\alpha\beta}$ are diagonal and nondiagonal elements of tensors $\eta^{\alpha\beta}$ and $\sum_{\gamma} Q^{\alpha\beta\gamma\gamma}$, respectively,

$$\begin{aligned} \eta^{\alpha\beta}(0) = & \delta^{\alpha\beta} \eta^{\alpha} + (1 - \delta^{\alpha\beta}) \tilde{\eta}^{\alpha\beta}; \\ \sum_{\gamma} Q^{\alpha\beta\gamma\gamma}(\mathbf{q}) = & \delta^{\alpha\beta} Q^{\alpha}(\mathbf{q}) + (1 - \delta^{\alpha\beta}) \tilde{Q}^{\alpha\beta}(\mathbf{q}). \end{aligned} \quad (23)$$

Now by choosing

$$\tilde{\eta}^{\alpha\beta} = \tilde{Q}^{\alpha\beta} / r^{\beta}, \quad (24)$$

it is guaranteed that if the initial functional does not contain nondiagonal parts of the vertex \hat{g}_1 , then this vertex remains diagonal after the renormalization. If at last we require that the expansion of $\eta^{\alpha\beta}(\mathbf{q})$ does not contain q^2 terms, then the diagonal part of the tensor $\eta^{\alpha\beta}(0)$ is

$$\eta^{\alpha} = \frac{d}{dq^2} [Q^{\alpha}(\mathbf{q}) - 2h(q)(r^{\alpha})^2]_{q=0}. \quad (25)$$

Function $\eta^{\alpha\beta}(\mathbf{q})$ is now completely defined and there is no more freedom in the exact RG Eq. (14), therefore it must contain no redundant operators. The physical meaning of the function $\eta^{\alpha\beta}$ is suggested by Eq. (21): at the stable fixed point of the functional (1), η^{α} is equal to the critical exponent η of the corresponding critical mode φ^{α} .

¹S.-K. Ma, *Modern Theory of Critical Phenomena* (Benjamin, New York, 1976).

²S. G. Gorishny, S. A. Larin, and F. V. Tkachov, *Phys. Lett. A* **101**, 120 (1978).

³J. C. Le Guillon and J. Zinn-Justin, *J. Phys. (France)* **48**, 19 (1987).

⁴K. G. Wilson and J. Kogut, *Phys. Rep.* **12**, 75 (1974).

⁵G. R. Golner and E. K. Reidel, *Phys. Lett.* **58A**, 11 (1976).

⁶E. K. Reidel, G. R. Golner, and K. E. Newman, *Ann. Phys. (N.Y.)* **161**, 178 (1985).

⁷G. R. Golner, *Phys. Rev. B* **33**, 7863 (1986).

⁸Yu. M. Ivanchenko and A. A. Lisyansky, *Phys. Rev. A* **45**, 8525 (1992).

⁹Yu. M. Ivanchenko, A. A. Lisyansky, and A. E. Filippov, *Phys. Lett. A* **150**, 100 (1990).

¹⁰F. J. Wegner and A. Houghton, *Phys. Rev. A* **8**, 401 (1973).

¹¹T. L. Bell and K. G. Wilson, *Phys. Rev. B* **10**, 3935 (1974).

¹²F. J. Wegner, in *Phase Transitions and Critical Phenomena*, edited by C. Domb and M. S. Green (Academic, New York, 1976), Vol. 6, p. 7.

Random-exchange and random-field Ising model-like behaviors in $\text{Fe}_{0.48}\text{Zn}_{0.52}\text{F}_2$

E. P. Raposo^{a)}

Laboratório de Física Teórica e Computacional, Universidade Federal de Pernambuco, 50670-901, Recife, PE, Brazil and Lyman Laboratory of Physics, Harvard University, Cambridge, Massachusetts 02138

M. D. Coutinho-Filho

Laboratório de Física Teórica e Computacional, Universidade Federal de Pernambuco, 50670-901, Recife, PE, Brazil

By using a local mean-field microscopical numerical approach, we investigate the role of frustration, random vacancies, and magnetic field cycles on the random-exchange and random-field Ising model-like behaviors of the diluted antiferromagnet $\text{Fe}_{0.48}\text{Zn}_{0.52}\text{F}_2$. The analysis includes studies on microscopic configurations, distribution of local effective fields, and the crossover exponent ϕ , which were found to be in good agreement with the experimental results. © 1998 American Institute of Physics. [S0021-8979(98)23211-7]

Much progress has been achieved¹ in the last few years on the characterization of the phase diagram of the insulating diluted antiferromagnet (DAF) $\text{Fe}_x\text{Zn}_{1-x}\text{F}_2$. Nevertheless, a complete understanding of the relative influence of its microscopic ingredients, namely, the local density fluctuations, the presence of a small magnetic frustration, and the short range of the spin interactions, is still lacking. In the following, we investigate the roles of these elements in the presence of magnetic field cycles by using a local mean field (LMF) microscopical numerical approach.^{2,3}

The DAF compound $\text{Fe}_x\text{Zn}_{1-x}\text{F}_2$ has a strong single-ion anisotropy in the easy-magnetization direction which makes it a nearly ideal experimental realization of an Ising system.⁴ All its important microscopic ingredients can be found in the DAF Hamiltonian in the presence of a uniform magnetic field H ,

$$\mathcal{H} = \sum_{\langle i, \delta_l \rangle} J_l \mathcal{E}_i \mathcal{E}_{i+\delta_l} S_i S_{i+\delta_l} - \mu_0 \sum_i \mathcal{E}_i S_i H, \quad (1)$$

where $S_i = \pm 2$ (Fe^{+2}), $\mathcal{E}_i = 0, 1$, and l is summed over the three short-range exchange interactions between nearest neighbors in a centered tetragonal lattice. By fitting the Néel temperature which marks the onset of the AF phase for the pure system, $T_N(x=1) \approx 78$ K, we fixed the exchange constants so that the experimental ratios $j_1 = J_1/J_2 = -0.013$ and $j_3 = J_3/J_2 = +0.053$ measured for the pure compound FeF_2 are kept unaltered.⁴ Disorder and frustration are present respectively in the form of local density fluctuations due to the random quenched substitution of magnetic ions Fe^{+2} by nonmagnetic ones Zn^{+2} ("vacancy" sites), and in the presence of a small frustrated super-exchange planar interaction j_3 with respect to the dominant AF coupling j_2 .

The LMF method^{2,3} consists in solving iteratively the self-consistent equations involving the thermally averaged spins, $m_i \in [-2, 2]$,

$$m_i = \langle S_i \rangle_T = 2 \tanh\{h_i / K_B T\}, \quad \mathcal{E}_i = 1, \quad (2)$$

where the local field effectively seen by this spin is

$$h_i = - \sum_{\delta_l} J_{i+\delta_l} \mathcal{E}_{i+\delta_l} m_{i+\delta_l} + \mu_0 H. \quad (3)$$

The numerical procedure starts by choosing an initial random configuration $\{S_i, \mathcal{E}_i\}$ in the high-temperature ($T = 150$ K) paramagnetic (PM) phase. The system is then cooled in a rate $\Delta T = 0.05$ K and, at each temperature, Eqs. (2) and (3) are iterated for every magnetic site until a convergence criterium^{2,3} is satisfied. The cooling procedure is repeated until reaching the minimum temperature $T = 2$ K from which the system is heated by using the same amount ΔT , and then the measurements are done. We have followed the experimental procedures in $\text{Fe}_x\text{Zn}_{1-x}\text{F}_2$ as close as possible. In a zero-field cycle (ZFC) the system is cooled in $H = 0$ to the minimum temperature and a magnetic field is applied along the heating process. On the other hand, in a field cycle (FC) both cooling and heating procedures are performed in the presence of H . We simulate bcc lattices with two sublattices of 30^3 sites each and periodic boundary conditions. In order to eliminate any possible dependence of the results on some initial configuration, we average over 50 independent samples $\{S_i, \mathcal{E}_i\}$.

The compound $\text{Fe}_{0.48}\text{Zn}_{0.52}\text{F}_2$ presents a random-exchange Ising model (REIM)-like behavior at zero field.^{1,5} In $H \neq 0$, it experiences^{1,5} a field-induced crossover upon ZFC from the REIM to the random-field Ising model (RFIM)-like behavior. The LMF results indicate⁶ that the combined action of random vacancies and magnetic field induces an AF long-range order (LRO) that exist up to the neighborhood of the critical temperature, and is essentially constituted by two large slightly-interacting interpenetrating structures with AF internal arrangements, each one occupying approximately half of the sample, in agreement with some very recent experiments.^{1,7} The domain walls are strongly pinned along the vacancies⁸ and can minimize the energy cost by avoiding as much as possible to embody frustrated magnetic bonds so that a different picture emerges

^{a)}Electronic mail: raposo@cmt.harvard.edu

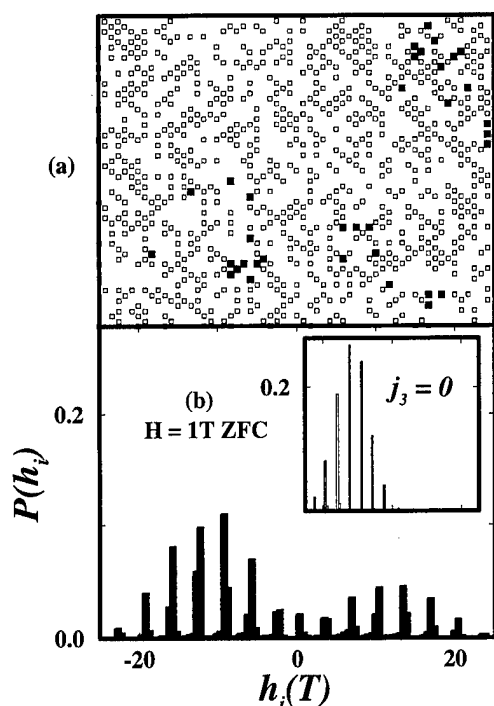


FIG. 1. (a) Few isolated clusters (full squares) represent spins reversed by a ZFC magnetic field, $H=1$ T, with respect to the $H=0$ frustrated configuration close to the ground state, $T/T_N(x=1)=0.06$. Odd (even) horizontal lines correspond to consecutive layers of sublattice A (B). (b) Correspondent local effective field distribution $P(h_i)$ of one sublattice. The nonfrustrated case is presented in the inset.

with respect to the usual Imry–Ma argument,⁹ including the existence of fractal domains.¹⁰

The microscopic states for low and moderate ZFC fields are similar to those obtained in $H=0$, except for the presence of some small isolated clusters, as also experimentally probed.^{1,7} In Fig. 1(a), two consecutive layers (one of each sublattice) randomly chosen in the bulk of the system are projected onto a plane so that spins belonging to the sublattice A (B) are displayed by squares in the odd (even) horizontal lines. Full squares represent reversed spins in the frustrated systems after $H=1$ T ZFC, relative to the $H=0$ case at the very proximity of the ground state, $T/T_N(x=1)=0.06$. Figure 2(a) displays the associated field distributions for one sublattice of these samples, with the nonfrustrated case shown in the inset. A very similar picture is also found in $H=0$. Furthermore, we notice that frustration plays an important role for the nucleation process upon ZFC by inducing the presence of competitive local fields. Indeed, the presence of frustration introduces more important changes on the properties of the system than low and moderate magnetic fields do after ZFC.

On the other hand, a FC procedure at $x=0.48$ leads to a very distinct domain state without AF LRO at low temperatures even for low fields.¹⁰ In Fig. 1(b), a very small field $H=1$ G was applied upon FC and the differences with respect to the zero-field configuration at $T/T_N(x=1)=0.06$ are represented by full squares. Figure 2(b) displays the associated field distributions for one sublattice. Notice from Fig. 2(b) that frustration is unimportant in the FC regime.

The field-induced crossover upon ZFC from the REIM

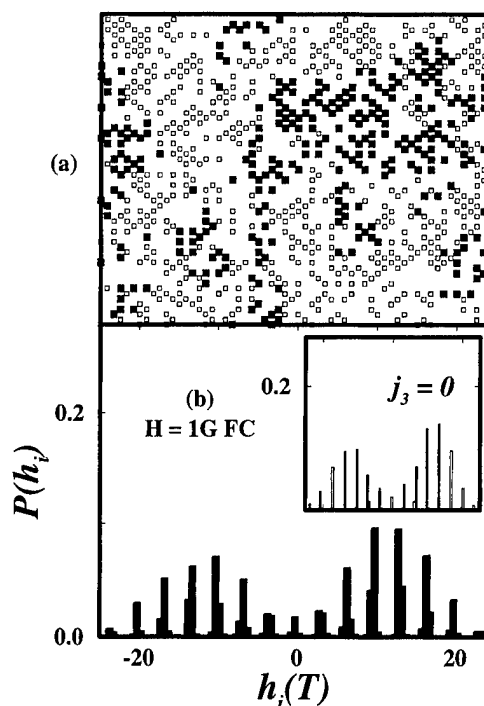


FIG. 2. (a) Even a very low magnetic field $H=1$ G upon FC induces a remarkably distinct low- T configuration (differences indicated by full squares) relative to the AF LRO $H=0$ and ZFC states. The correspondent local effective field distributions of one sublattice are depicted in (b) for the frustrated and nonfrustrated (inset) cases.

to the RFIM-like behavior is described by the crossover exponent ϕ ,¹¹

$$T^* - T_i(H) = AH^{2/\phi}. \quad (4)$$

Above, the same scaling dependence experimentally¹¹ and numerically¹⁰ seen for the critical $[T_c(H)]$ and equilibrium $[T_{eq}(H)]$ lines is accounted by considering both cases, $T_i(H)=T_c(H)$ and $T_i(H)=T_{eq}(H)$. In the former, $T^*=T_N(x=0.48)$, whereas in the latter T^* is the highest temperature below which the total magnetizations measured after ZFC and FC begin to differ. The LMF results for the exponents in the presence of frustration, $\phi_c=1.28\pm0.06$ and $\phi_{eq}=1.30\pm0.08$, nearly agree with the experimental¹¹ and Monte Carlo¹⁰ ones, $\phi\approx1.40$ – 1.46 , if the range of concordance between independent measurements is considered. Notice that the equivalent scaling dependence in the critical and equilibrium lines is also probed by the LMF method. It is remarkable that the exponents do not depend (within the error bars) on the presence of frustration for both $T_{eq}(H)$ and $T_c(H)$ lines. Figure 3 displays the numerical data along with the best-fitting curves and the most generally accepted experimental value, $\phi=1.42$.^{1,11} The LMF approach causes an enlargement of the region where the $T_{eq}(H)$ and $T_c(H)$ lines differ. We have also observed a reentrant behavior in $T_{eq}(H)$ for extremely low fields, $H<0.01$ T, as detailed in the inset of Fig. 3(b). However, the absence of experimental data in this range of fields prevent us to comment on the reality of this reentrance. It would be interesting to probe it in the real compound.

From the H vs T diagrams one can also speculate about the irreversibility and stability of the AF LRO at $x=0.48$. In

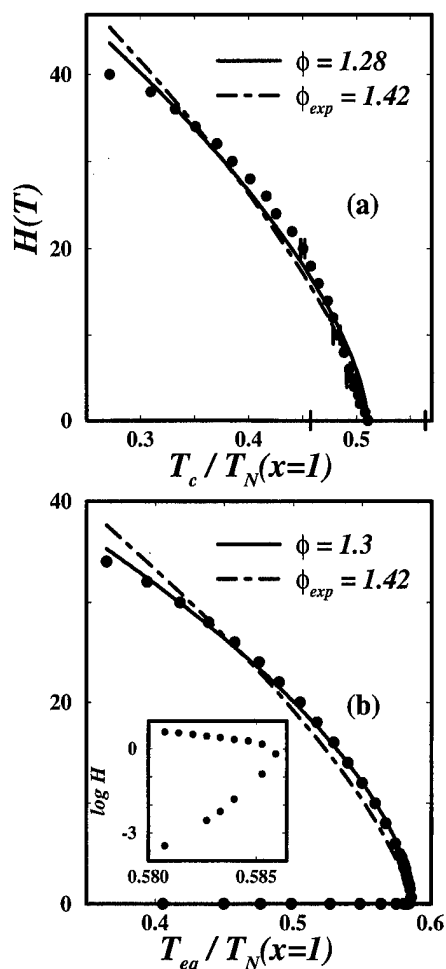


FIG. 3. (a) Critical and (b) equilibrium lines at $x=0.48$. The respective best-fitting plots $\phi=1.28$ and $\phi=1.3$ are shown along with the experimental value $\phi=1.42$ (see Ref. 1) characteristic of the RFIM-like behavior. Inset in (b) displays the numerical reentrance observed for very low magnetic fields, $H \leq 0.1$ T.

the free energy surface, irreversibility is related to the displacement or disappearance of local minima due to changes in H or T .² After ZFC to a low-temperature state, when the uniform magnetic field is turned on and kept fixed, the system initially exhibits an irreversible AF phase whose LRO is broken down when the critical line $T_c(H)$ is crossed during the heating process. The system thus enters an irreversible close-PM regime in which spin correlations still exist.⁶ Below $T_c(H)$ the difference between the ZFC and FC measures means that the FC domain state cannot reach its equilibrium configuration within the characteristic LMF or experimental times. In this sense only the ZFC states are quasi-

equilibrated. On the contrary, in the vitreous intermediate phase, $T_c(H) < T < T_{eq}(H)$, it has been shown² that the domain-like states without fully developed AF LRO have less free energy than those ones associated with the AF LRO. The high- T reversible behavior is restored only after crossing the $T_{eq}(H)$ line above which the equilibrium measurements from both ZFC and FC procedures coincide.

Finally, we would like to mention that the consistency of the LMF results was also attested by applying the same numerical procedure for the system at $x=0.25$. The value obtained,¹² $\phi_{eq}=3.8 \pm 0.6$, is in good agreement with the experimental one, $\phi=3.4 \pm 0.2$, measured¹ for $\text{Fe}_{0.25}\text{Zn}_{0.75}\text{F}_2$, which is associated with the presence of a spin-glass-like phase without AF LRO. The independence of frustration in the crossover exponents has been also observed.¹²

One of the authors (E.P.R.) would like to acknowledge the hospitality of the Condensed Matter Theory group at Harvard University. The authors are deeply grateful to D. P. Belanger for many stimulating discussions. This work was supported by CNPq, FINEF, CAPES, and FACEPE (Brazilian Agencies).

¹For recent reviews, see D. P. Belanger, in *Experiments on the Random Field Ising Model*, edited by A. P. Young (World Scientific, Singapore, 1997), and references therein. See also, D. P. Belanger and A. P. Young, *J. Magn. Magn. Mater.* **100**, 272 (1991); W. Kleemann, *Int. J. Mod. Phys.* **7**, 2469 (1993).

²C. M. Soukoulis, K. Levin, and G. S. Grest, *Phys. Rev. Lett.* **48**, 1756 (1982); *Phys. Rev. B* **33**, 7659 (1986), and references therein.

³E. P. Raposo, M. D. Coutinho-Filho, and F. C. Montenegro, *Europhys. Lett.* **29**, 507 (1995).

⁴M. T. Hutchings, B. D. Rainford, and H. J. Guggenheim, *J. Phys. C* **3**, 307 (1970); A. R. King, V. Jaccarino, T. Sakakibara, M. Motokawa, and M. Date, *Phys. Rev. Lett.* **47**, 117 (1981).

⁵D. P. Belanger, S. M. Rezende, A. R. King, and V. Jaccarino, *J. Appl. Phys.* **57**, 3294 (1985); S.-J. Han, D. P. Belanger, W. Kleemann, and U. Nowak, *Phys. Rev. B* **45**, 9728 (1992).

⁶E. P. Raposo and M. D. Coutinho-Filho (unpublished).

⁷D. P. Belanger, J. Wang, Z. Slănic, S.-J. Han, R. M. Nicklow, M. Lui, C. A. Ramos, and D. Lederman, *Phys. Rev. B* **54**, 3420 (1996).

⁸P. Pollak, W. Kleemann, and D. P. Belanger, *Phys. Rev. B* **38**, 4773 (1988).

⁹Y. Imry and S. K. Ma, *Phys. Rev. Lett.* **35**, 1399 (1975).

¹⁰U. Nowak and K. D. Usadel, *Phys. Rev. B* **39**, 2516 (1989); **43**, 851 (1991); **44**, 7426 (1991); **46**, 8329 (1992); *Physica A* **191**, 203 (1992).

¹¹Although $\phi \approx 1.42$ is the most generally accepted experimental value (see Ref. 1), some of the reported crossover exponents in different measurements are: $\phi=1.40 \pm 0.05$ [A. R. King, V. Jaccarino, D. P. Belanger, and S. M. Rezende, *Phys. Rev. B* **32**, 503 (1985)], $\phi=1.42 \pm 0.03$ [I. B. Ferreira, A. R. King, and V. Jaccarino, *J. Appl. Phys.* **69**, 5246 (1991)], $\phi=1.44 \pm 0.04$ [W. Kleemann, A. R. King, and V. Jaccarino, *Phys. Rev. B* **34**, 479 (1986)], and $\phi=1.46 \pm 0.02$ [M. Lederman, J. Hamman, and R. Orbach, *J. Appl. Phys.* **69**, 5249 (1991)]. The equivalence (within error bars) between the values of ϕ measured from critical and equilibrium lines has been always probed.

¹²E. P. Raposo and M. D. Coutinho-Filho, *J. Appl. Phys.* **81**, 5279 (1997).

Magnetic structures of the triangular lattice magnets $A\text{Fe}(\text{SO}_4)_2$ ($A=\text{K}, \text{Rb}, \text{Cs}$)

H. Serrano-González

School of Chemistry, University of Birmingham, Edgbaston, Birmingham, B15 2TT, United Kingdom

S. T. Bramwell^{a),b)}

Department of Chemistry, University College London, Christopher Ingold Laboratories, 20 Gordon Street, London WC1H 0AJ, United Kingdom

K. D. M. Harris^{a)} and B. M. Kariuki

School of Chemistry, University of Birmingham, Edgbaston, Birmingham, B15 2TT, United Kingdom

L. Nixon and I. P. Parkin

Department of Chemistry, University College London, Christopher Ingold Laboratories, 20 Gordon Street, London WC1H 0AJ, United Kingdom

C. Ritter

Institute Max von Laue-Paul Langevin, BP156, F-38042 Grenoble 09, France

In the crystal structures of $\text{CsFe}(\text{SO}_4)_2$, $\text{RbFe}(\text{SO}_4)_2$, and $\text{KFe}(\text{SO}_4)_2$, the magnetic Fe^{3+} ions form a triangular array in well separated layers. $\text{CsFe}(\text{SO}_4)_2$ and $\text{RbFe}(\text{SO}_4)_2$ may be regarded as realizations of the highly frustrated triangular lattice antiferromagnet, whereas $\text{KFe}(\text{SO}_4)_2$ is a suspected realization of the row model. The latter model is characterized by two couplings J' and J , and for $J'/J > 0.5$ forms a helical spin structure with an incommensurate repeat distance. The regular triangular lattice magnet may be described by the row model with $J' = J$, and its “120°” spin structure may be regarded as a special case of this helical structure. We have determined the low temperature (1.3 K) magnetic structures adopted by $\text{CsFe}(\text{SO}_4)_2$, $\text{RbFe}(\text{SO}_4)_2$, and $\text{KFe}(\text{SO}_4)_2$ by powder neutron diffraction. $\text{CsFe}(\text{SO}_4)_2$ and $\text{RbFe}(\text{SO}_4)_2$ adopt the expected 120° helical spin structure of the triangular lattice magnet, but $\text{KFe}(\text{SO}_4)_2$ does not adopt the expected incommensurate helical structure of the row model. Rather, it adopts a sine wave modulated structure. Possible reasons for this behavior are discussed. © 1998 American Institute of Physics. [S0021-8979(98)50511-7]

The triangular lattice antiferromagnet¹ is the prototypical two-dimensional frustrated magnet. It exhibits a wealth of unusual properties, such as novel critical exponents,² large quantum fluctuation effects,³ and anomalous percolation properties.⁴ Recently we showed that the materials with layered crystal structures related to that of the mineral Yavapaiite $\text{KFe}(\text{SO}_4)_2$ are of interest as realizations of a model quasi-two-dimensional triangular lattice antiferromagnet.⁵ With regard to their magnetic properties, the Yavapaiite materials can be classified into two major groups, depending on the symmetry of the triangular net occupied by the magnetic atoms. The materials in the first group, which includes $\text{CsFe}(\text{SO}_4)_2$ and $\text{RbFe}(\text{SO}_4)_2$, have an equilateral triangular lattice, and approximate very well to the two-dimensional Heisenberg model antiferromagnet on the triangular lattice. Those in the second group, which includes $\text{KFe}(\text{SO}_4)_2$, have an isosceles triangular (i.e., centered rectangular) lattice. They may thus be considered realizations of the “row” model.^{6–8} The relationship between the regular triangular lattice model and the row model is illustrated in Fig. 1; in the regular triangular lattice model all magnetic bonds are of the same strength (J), whereas in the row model “horizontal”

bonds are of different strength (J') to the remaining bonds (J). Zhang *et al.*⁶ and Kawamura⁷ have studied the XY row model and shown that for $J'/J > 1/2$ the ground state is a spin helix propagating along the row direction, with period determined by the ratio J'/J . The regular triangular lattice, with $J'/J = 1$, may be regarded as a special case of the row model, in which the turn angle of the helix is 120°; however, for general J'/J , the period of the helix is incommensurate with the lattice. The stacked row model, with unfrustrated interlayer coupling, was introduced by Kawamura⁷ to explain the magnetic structure of RbMnBr_3 .⁹ However, the model can potentially be used to describe any C -centered spin lattice in which $a \approx b\sqrt{3}$. Thus, the class of C -centered orthorhombic compounds MXO_4 , such as MnSO_4 ¹⁰ and $\beta\text{-CrPO}_4$,¹¹ may also be regarded as realizations of this system; they indeed exhibit the expected incommensurate helical structure.

In this work we determine the low temperature magnetic structures adopted by the title compounds, and compare these with theoretical expectations for the row and triangular models. The magnetic susceptibility versus temperature curves of all three compounds show anomalies in the region of 4–5 K,⁵ which can be attributed to magnetic ordering transitions. Using the *D1B* powder diffractometer at the Institut Max von Laue—Paul Langevin, Grenoble, France, we

^{a)}Authors to whom correspondence should be addressed.

^{b)}Electronic mail: s.t.bramwell@ucl.ac.uk

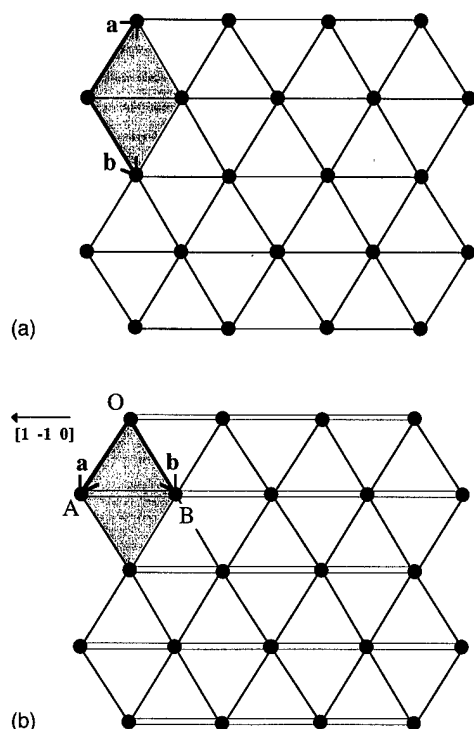


FIG. 1. (a) The regular (equilateral) triangular lattice, showing a unit cell (shaded area with vectors \mathbf{a} and \mathbf{b}); (b) the row model lattice, in which horizontal bonds (double lines) have a different strength to other bonds (single lines). In the crystal structures of $\text{CsFe}(\text{SO}_4)_2$ and $\text{RbFe}(\text{SO}_4)_2$ the magnetic Fe ions occupy a lattice of the type shown in (a), whereas in the crystal structure of $\text{KFe}(\text{SO}_4)_2$ the magnetic Fe atoms occupy a lattice of the type shown in (b). In (b) the primitive unit cell shown (shaded area with vectors \mathbf{a} and \mathbf{b}) describes the magnetic structure of $\text{KFe}(\text{SO}_4)_2$. The lattice sites labeled O , A , and B are referred to in the text.

have measured diffraction patterns both above ordering transition¹² and at 1.3 K, and subtracted these to create a magnetic-only diffraction pattern (in this temperature range thermal effects on the nuclear diffraction pattern are negligible). All the magnetic diffraction patterns show Bragg peaks arising from three-dimensional magnetic order. Magnetic structures were determined using the GSAS¹³ and FULLPROF¹⁴ program packages, assuming a pseudo-Voigt line shape, and zero point corrections and scale factors derived from fits to the nuclear structure. The magnetic form factor for Fe^{3+} was calculated from Ref. 15.

Crystallographic data for the three title compounds are given in Table I. In the case of $\text{CsFe}(\text{SO}_4)_2$ and $\text{RbFe}(\text{SO}_4)_2$, the magnetic diffraction pattern was indexed on a unit cell with $a_m = b_m = a\sqrt{3}$, $c_m = 2c$, $\alpha_m = \beta_m = 90^\circ$, $\gamma_m = 60^\circ$,

TABLE I. Crystallographic data for $\text{CsFe}(\text{SO}_4)_2$, $\text{RbFe}(\text{SO}_4)_2$, and $\text{KFe}(\text{SO}_4)_2$. The magnetic Fe^{3+} ions occupy the (0,0,0) position in each case, and so the Fe sublattice is uniquely defined by the centering symbol (P or C) of the space group. For full crystallographic details see Ref. 5.

Compound	Space group	Lattice parameters
$\text{CsFe}(\text{SO}_4)_2$	$P\bar{3}$	$a = b = 4.8612(5) \text{ \AA}$, $c = 8.7081(1) \text{ \AA}$ (20 K)
$\text{RbFe}(\text{SO}_4)_2$	$P\bar{3}$	$a = b = 4.8189(5) \text{ \AA}$, $c = 8.2248(2) \text{ \AA}$ (8 K)
$\text{KFe}(\text{SO}_4)_2$	$C2/m$	$a = 8.0926(8) \text{ \AA}$, $b = 5.1401(5) \text{ \AA}$, $c = 7.8026 \text{ \AA}$, $\beta = 95.155(11)^\circ$ (15 K)

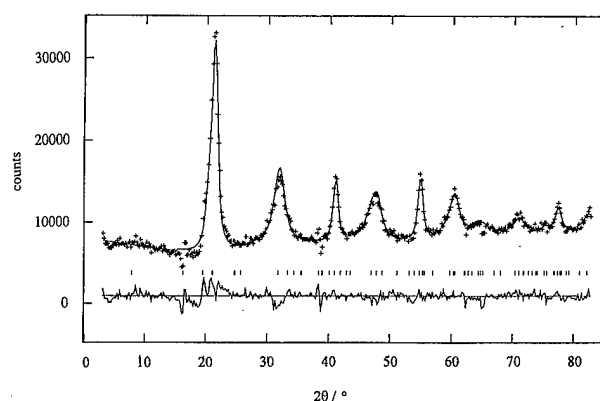


FIG. 2. Fit of the magnetic model described in the text to the experimental magnetic-only powder diffraction pattern of $\text{CsFe}(\text{SO}_4)_2$ at 1.3 K. The figures show experimental (+ marks), calculated (upper solid line), and difference (observed—calculated, lower solid line) magnetic diffraction profiles.

where a , b , and c denote the crystallographic unit cell parameters. The diffraction data are well described by a model in which the spins form a three sublattice “120°” structure in the basal (ab) plane, and there are two basal planes per magnetic unit cell. Spins in adjacent layers are rotated by an angle ϕ , which was found to have the value $180^\circ \pm 10^\circ$ for $\text{CsFe}(\text{SO}_4)_2$ and $150^\circ \pm 10^\circ$ for $\text{RbFe}(\text{SO}_4)_2$. Note that powder neutron diffraction cannot give the in-plane spin direction for the high symmetry structures of $\text{CsFe}(\text{SO}_4)_2$ and $\text{RbFe}(\text{SO}_4)_2$.¹⁶ The refined values of the magnetic moments were $\mu = 4.2 \pm 0.2 \mu_B$ for $\text{CsFe}(\text{SO}_4)_2$ and $\mu = 4.5 \pm 0.2 \mu_B$ for $\text{RbFe}(\text{SO}_4)_2$, which are close to the maximum expected value $\mu = 5 \mu_B$ for Fe^{3+} . The fit to the experimental magnetic diffraction pattern for $\text{CsFe}(\text{SO}_4)_2$ is shown in Fig. 2.

In the case of $\text{KFe}(\text{SO}_4)_2$, the magnetic Bragg peaks could be indexed on the unit cell illustrated in Fig. 1(b). This cell is primitive in the basal ab plane, but contains two basal planes along the c axis.

With respect to this unit cell, the magnetic Bragg peaks could all be indexed by the wave vector $(0.73, -0.73, 0)$. This implies that neighboring spins along the row direction are approximately antialigned, but that the antiferromagnetic

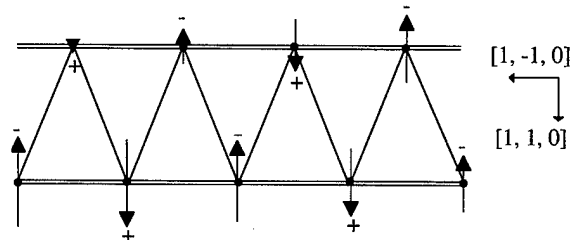


FIG. 3. Sine-wave modulated magnetic structure used to describe the magnetic diffraction pattern of $\text{KFe}(\text{SO}_4)_2$, as described in the text. The figure shows two “rows” in the ab plane of the $\text{KFe}(\text{SO}_4)_2$ structure (not drawn to scale), with the projection of the magnetic structure into the ab plane. The spins shown lie along the $[1, 1, 1/2]$ and $[-1, -1, -1/2]$ directions, which are denoted as (+) or (−) on the diagram. The spin amplitude is modulated along $[1, -1, 0]$ (indices refer to the unit cell shown in Fig. 1). Note that the spins in the upper row may look more strongly modulated than those in the lower row, but in fact the modulation is the same. In the adjacent layer the spins similarly lie along either $[1, 1, -1/2]$ or $[-1, -1, 1/2]$.

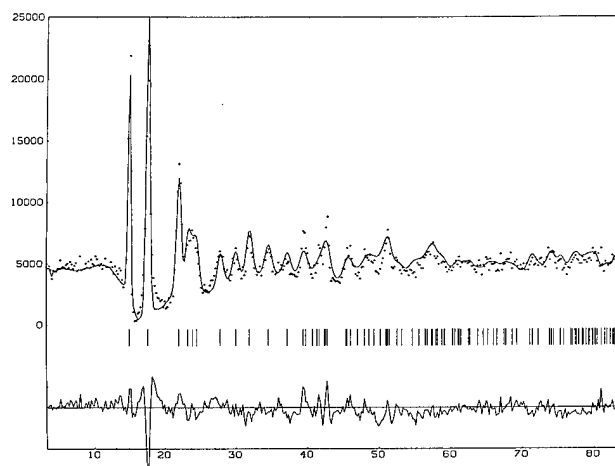


FIG. 4. Fit of the magnetic model described in the text and shown in Fig. 3 to the experimental magnetic-only powder diffraction pattern of $\text{KFe}(\text{SO}_4)_2$ at 1.3 K. The figures show experimental (+ marks), calculated (upper solid line), and difference (observed—calculated, lower solid line) magnetic diffraction profiles.

rows are modulated with a long repeat distance which is incommensurate with the crystal structure (ratio of periodicities approximately equal to 0.73). The modulation may be of the sine wave or helical type, but the indexing imposes severe limitations on the possible magnetic models. All plausible models were tested. Helical structures were tested first, and it was found that none of these described the data, even assuming an elliptical, rather than circular, helix (and thereby introducing an extra fitting parameter). In contrast, one particular sine wave modulated model was found to describe the magnetic diffraction pattern well, with a maximum magnetic moment of $4.3 \pm 0.2 \mu_B$, again close to the maximum expected value for Fe^{3+} . In this model, shown in Fig. 3, the spins in a given layer are uniaxial, but the spin axis alternates from layer to layer. Thus, in the first layer the spins lie along $\pm[1, 1, 1/2]$ and in the second layer they lie along $\pm[-1, -1, 1/2]$. The spin amplitude is modulated perpendicular to this direction along $[1, -1, 0]$, i.e., the row direction, as shown in Fig. 3. The fit of the model to the experimental data is illustrated in Fig. 4.

These results may be discussed in terms of the Heisenberg row model. It is easy to show that its $T=0$ ground state is coplanar, and is the same as that of the XY row model.^{6,7} For $J/J' < 2$, this consists of a helical spin structure with a magnetic unit cell consisting of two rows, and an incommensurate repeat distance along the row direction. This magnetic structure minimizes the energy of every elementary triangular plaquette of spins OAB , where spins A and B lie in the same row and spin O lies in the adjacent row [see Fig. 1(b)]. Let θ_O , θ_A , and θ_B denote the orientation, in the XY plane, of the spins on sites O , A , and B , respectively. If θ_O is set equal to 0° , then $\theta_A = 180^\circ - \cos^{-1}(J/2J')$ and $\theta_B = -\theta_A$. The wave vector of this magnetic structure, referred to the primitive unit cell defined in Fig. 1, is $(\theta_A/360^\circ, -\theta_A/360^\circ)$.

The magnetic structures of $\text{CsFe}(\text{SO}_4)_2$ and $\text{RbFe}(\text{SO}_4)_2$ have $\theta_O = 0^\circ$, $\theta_B = 120^\circ$, and $\theta_A = 240^\circ$, corresponding, as expected, to $J/J' = 1$. The magnetic structure adopted by $\text{KFe}(\text{SO}_4)_2$ has wave vector $(0.73, -0.73, 0)$, corresponding to $\theta_A \approx 97^\circ$, $J/J' \approx 0.25$. However, rather than adopting this helical structure, $\text{KFe}(\text{SO}_4)_2$ adopts a sine wave modulated structure with the same wave vector. This structure can be derived from the expected helical structure by suppression of one of its two orthogonal spin components. The adoption of this partially disordered spin structure is consistent with the fact that helical structures cannot develop in a system with lower than tetragonal symmetry at a second order phase transition.¹⁷ In fact, Sólyom¹⁸ showed that for the C -centered orthorhombic structure of MnSO_4 , the helical spin structure can only arise via three second-order transitions. The observation of a sine wave modulated structure well below the ordering temperature in $\text{KFe}(\text{SO}_4)_2$ is nevertheless surprising, as it implies both substantial anisotropy to fix the spin direction, and also large-amplitude spin fluctuations persisting to low temperature. The origin of this spin structure leaves an intriguing problem for future investigation.

ACKNOWLEDGMENT

It is a pleasure to thank Dr. J. P. Attfield for bringing to our attention the work on the C -centered orthorhombic compounds.^{10,11}

- ¹K. Kawamura and S. Miyashita, J. Phys. Soc. Jpn. **53**, 4138 (1984); S. Miyashita, J. Phys. Soc. Jpn. **55**, 3605 (1986); S. Miyashita and H. Shiba, J. Phys. Soc. Jpn. **53**, 1145 (1984); S. Miyashita and H. Kawamura, J. Phys. Soc. Jpn. **54**, 3385 (1985).
- ²H. Kawamura, Phys. Rev. B **47**, 3415 (1993).
- ³P. W. Anderson, Mater. Res. Bull. **8**, 153 (1973).
- ⁴A. Harrison and T. E. Mason, J. Appl. Phys. **67**, 5424 (1990).
- ⁵S. T. Bramwell, S. G. Carling, C. J. Harding, K. D. M. Harris, B. M. Kariuki, L. Nixon, and I. P. Parkin, J. Phys.: Condens. Matter **8**, L123 (1996).
- ⁶W. M. Zhang, W. M. Saslow, and M. Gabay, Phys. Rev. B **44**, 5129 (1991).
- ⁷H. Kawamura, Prog. Theor. Phys. Suppl. **101**, 545 (1990).
- ⁸M. E. Zhitomirsky, Phys. Rev. B **54**, 353 (1996).
- ⁹C. J. Glinka, V. J. Minkiewicz, D. E. Cox, and C. P. Khattak, AIP Conf. Proc. **18**, 659 (1973).
- ¹⁰G. Will, B. C. Frazer, G. Shirane, D. E. Cox, and P. J. Brown, Phys. Rev. A **140**, 2139 (1965).
- ¹¹J. P. Attfield, P. D. Battle, and A. K. Cheetham, J. Solid State Chem. **57**, 357 (1985).
- ¹²The diffraction patterns were measured at the following temperatures: $\text{CsFe}(\text{SO}_4)_2$, 20 K; $\text{RbFe}(\text{SO}_4)_2$, 8 K; $\text{KFe}(\text{SO}_4)_2$, 15 K.
- ¹³A. C. Larson and R. B. Von Dreele, Los Alamos Laboratory Report No. LA-UR-86-748, 1987.
- ¹⁴J. Rodríguez-Carvajal, "FULLPROF: A program for Rietveld Refinement and Pattern Matching Analysis," Abstracts of the Satellite Meeting on Powder diffraction of the XV Congress of the International Union of Crystallography, Toulouse, France, 1990 (unpublished), p. 127.
- ¹⁵E. J. Lisher and J. B. Forsyth, Acta Crystallogr. **A27**, 545 (1971).
- ¹⁶G. Shirane, Acta Crystallogr. **12**, 282 (1959).
- ¹⁷J. Rossat-Mignod, *Methods of Experimental Physics: Neutron Scattering* (Academic, New York, 1987), Vol. 3, p. 131.
- ¹⁸J. Sólyom, Physica (Amsterdam) **32**, 1243 (1966).

Phase transition and phase diagram of the $J_1 - J_2$ Heisenberg model on a simple cubic lattice

C. Pinettes and H. T. Diep

Laboratoire de Physique Théorique et Modélisation, Université de Cergy-Pontoise 2, Avenue Adolphe Chauvin, 95302 Cergy-Pontoise Cedex, France

By extensive standard and histogram Monte Carlo simulations, we show that the magnetic phase transition is of first order in the frustrated $J_1 - J_2$ Heisenberg model on a simple-cubic lattice.

Despite the infinite ground-state degeneracy, the system is shown to retain only the collinear spin configurations at low temperatures. © 1998 American Institute of Physics.

[S0021-8979(98)38211-0]

I. INTRODUCTION

Various properties of frustrated spin systems have been extensively investigated during the last 15 years.¹ Nevertheless, several questions remain controversial. In particular, the nature of the phase transition from a noncollinear ground state (GS) to the paramagnetic state is not yet understood at present.

In a frustrated system with vector spins (XY or Heisenberg), the frustration is uniformly distributed on all spins, generally causing a noncollinear GS with very high or infinite degeneracy. Some well-known examples are the antiferromagnetic face-centered cubic (fcc) lattice,^{2,3} the so-called fully frustrated simple-cubic (SC) lattice,⁴ the antiferromagnetic hexagonal-close-packed (hcp) lattice,⁵ the stacked triangular antiferromagnets,⁶ the two-dimensional Villain XY model,⁷ and the XY model on the check-board lattices.⁸ This great degeneracy with a noncollinear ground state gives rise to both a rich behavior on the finite temperature properties such as the nature of ordering and on the phase transition.

The purpose of this work is to study the frustrated SC lattice with antiferromagnetic nearest neighbors (NN) and next-nearest-neighbor (NNN) interactions, J_1 and J_2 , respectively. We are particularly interested in the frustrated region of the phase diagram, when J_2 is strong. Extensive Monte Carlo (MC) simulations, including histogram calculations, have been performed to clarify the nature of the ordering and of the phase transition.

II. MODEL

For this purpose, we consider a classical Heisenberg model with the Hamiltonian

$$H = \sum_{\langle ij \rangle} J_1 \mathbf{S}_i \cdot \mathbf{S}_j + \sum_{\langle\langle ij \rangle\rangle} J_2 \mathbf{S}_i \cdot \mathbf{S}_j, \quad (1)$$

where \mathbf{S}_i is a vector spin of unit length occupying the i th lattice site and the sums $\langle \rangle$ and $\langle\langle \rangle\rangle$ run over NN and NNN pairs, respectively. All interactions are antiferromagnetic (>0). Hereafter, the energy and temperature will be measured in units of J_1 .

For Heisenberg spins, the classical ground state can be determined numerically by an iterative procedure minimizing the local energies until the internal energy is stabilized.⁴

It is given as follows: for $0 < J_2 < 0.25 J_1$, the classical GS is the antiferromagnetic structure. For $0.25 J_1 < J_2$ the classical GS has an infinite degeneracy, apart from the global rotation. It is divided into eight sublattices, the elementary cubes containing two tetrahedra formed by the NNN sites and stacked as in Fig. 1(a). The spin configurations a, b, c, and d of the NNN tetrahedra are those of the elementary tetrahedra in the GS of the fcc antiferromagnets:² each NNN tetrahedron is characterized by two angles, θ , formed by two up spins (or two down spins) and ϕ , formed by the plane containing the two up spins and the plane containing the two down spins (see Ref. 2). The three collinear configurations (one line up, one line down) are particular GS configurations in this range of parameters [see Fig. 1(b)].

We have performed standard MC simulations using the sample sizes of $N = 12^3 - 18^3$ spins with periodic boundary conditions. Starting from a random spin configuration as the initial condition for the MC simulations, we have calculated: the internal energy per spin U , the specific heat per spin C_v , the magnetic susceptibility per spin $\langle \chi \rangle$, and the average sublattice magnetization m_s , as functions of temperature T . At a given T , 10 000 MC steps per spin have been discarded for equilibrating and 10 000 MC steps per spins have been used for averaging. Random initial conditions and such long runs

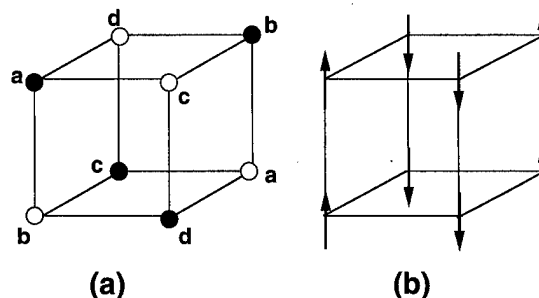


FIG. 1. (a) The general GS spin configurations for $0.25 J_1 < J_2$. It is decomposed into two NNN tetrahedra, defined by the void and solid circles. The spin orientations of the four sublattices a, b, c, and d are the same as in the antiferromagnetic face-centered cubic lattice: it is given by two angles θ and ϕ (see Ref. 2). (b) The collinear configurations (one line up, one line down) are particular GS configurations for $0.25 J_1 < J_2$. There are two other equivalent configurations with lines along the two other directions of the cubic lattice.

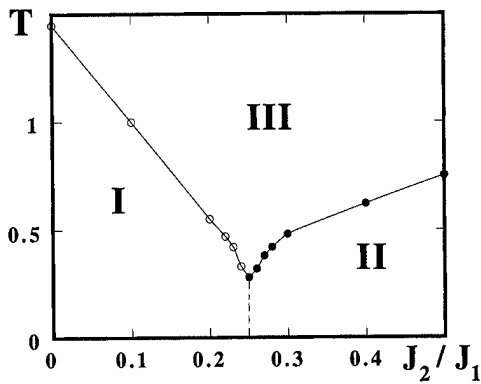


FIG. 2. Phase diagram of the SC J_1 - J_2 lattice in the space $(T, J_2/J_1)$. I, II, and III design antiferromagnetic, collinear [see Fig. 1(a)], and paramagnetic phases, respectively. First-order transitions are shown by black circles for $0.25 J_1 < J_2$. Void circles indicate second-order transitions for $0 < J_2 < 0.25 J_1$. The dashed line indicates the critical value $J_2/J_1 = 0.25$.

were used in order to detect the nature of ordering at finite T as seen below.

III. RESULTS

Figure 2 displays the phase diagram in the phase space $(T, J_2/J_1)$. For $0 < J_2 < 0.25 J_1$, there is a second-order transition from the antiferromagnetic structure to the paramagnetic state at finite temperature. When $0.25 J_1 < J_2$, there is a first-order like transition between the infinitely degenerated GS and the paramagnetic state. At the limit $J_1 = 0$ or $J_1 = \infty$, the SC lattice is decoupled into two independent fcc sublattices. The different physical quantities are shown in Fig. 3 in this range of parameters. They all show a discontinuity at $T_c = 0.33$ for $J_2/J_1 = 0.26$. In order to confirm the nature of the phase transition, we have used the histogram MC simulations.⁹ We discarded 500 000 MC steps per spin for equilibrating and calculated the energy histogram $P(E)$ at the transition temperature over the next one million MC steps. $P(E)$ is shown in Fig. 4 where two peaks are observed at $T_0 = 0.330$ for $J_2/J_1 = 0.26$. This bimodal distribution is a clear evidence of the first-order character of the transition suggested above. Note that long run is necessary to observe the two-peak structure. Less than one million MC steps per spin, the two peaks are not equally developed.

Another interesting point in Fig. 2 is the nature of ordering at low temperature in the frustrated range $0.25 J_1 < J_2$. A natural way to find the nature of ordering at finite temperature is to use the heating procedure from a disordered state and to analyze the spin structure. We used in our runs as order parameters the three staggered magnetizations defined for the collinear configuration shown in Fig. 1(a) and the two other equivalent configurations with lines along the two other directions of the cubic lattice. The results show (see Fig. 5) that just below T_c the system is ordered in one of these three collinear configurations. Thermal (or quantum) fluctuations lift the degeneracy and select collinear configurations. This verifies the conjecture by Henley,¹⁰ in analogy with what was called "order by disorder" in the Ising case,¹¹ as the Heisenberg fcc antiferromagnets,^{2,3} the hcp antiferromagnets,⁵ and the stacked triangular antiferromagnets.⁶

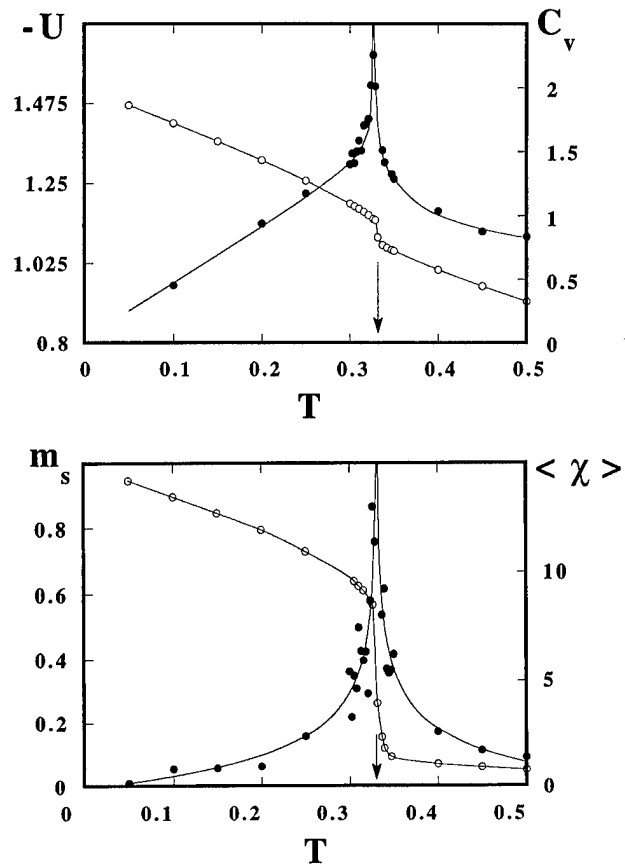


FIG. 3. Thermodynamical quantities as functions of temperature T for $J_2/J_1 = 0.26$. (a) On the left-hand scale, the internal energy per spin U (void circles) and on the right-hand scale, the specific heat per spin C_v (black circles); (b) on the left-hand scale, the average sublattice magnetization m_s (void circles) and on the right-hand scale, the magnetic susceptibility per spin $\langle \chi \rangle$ (black circles). The full curves are a fit to the MC data. The vertical arrows indicate $T_c = 0.33$.

Finally, let us notice that the first-order transition between the collinear phase and the paramagnetic phase can be explained as follows: in the collinear configuration, the infinite degeneracy is reduced to three (apart from the global

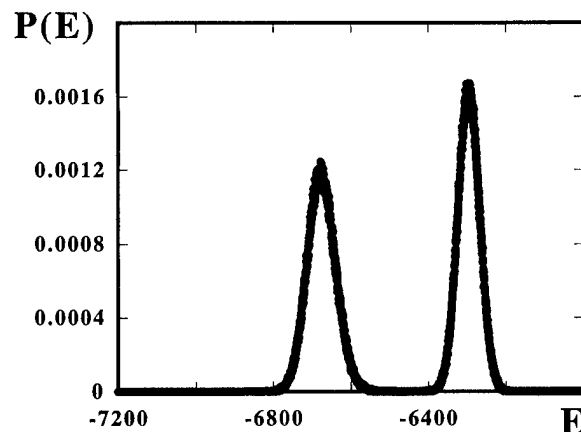


FIG. 4. The energy histogram $P(E)$, E being the total energy, for $J_2/J_1 = 0.26$ at a temperature very close to the transition temperature, $T_0 = 0.330$. The energy E is given for the total number of spins $N = 18^3$. The bimodal distribution is a signature of a first-order transition.

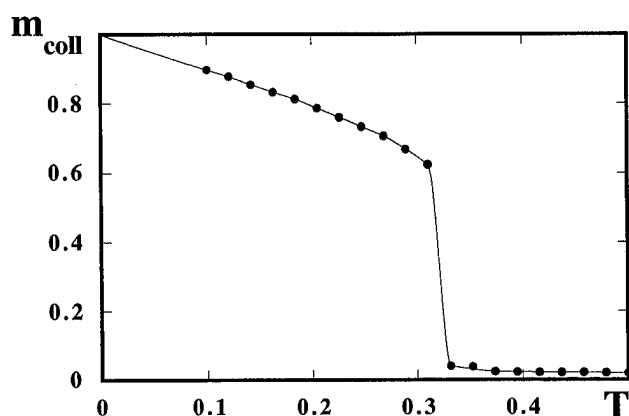


FIG. 5. The three staggered magnetizations defined for the collinear configuration shown in Fig. 1(a) are reported as functions of temperature T for $J_2/J_1 = 0.4$. The full curve is a fit to the MC data.

rotation) since there are three ways to choose the antiparallel spin pairs in a tetrahedron. This threefold degeneracy is reminiscent of the three-state Potts model in three dimensions which is known to undergo a first-order transition. This may be the origin of the first-order line observed here, as in the Heisenberg fcc antiferromagnets^{2,3} and the hcp antiferromagnets.⁵

Nevertheless, the nature of the phase transition in non-collinear spin systems (including helimagnets) is not yet clear since some of them exhibit first-order^{2,3,5,8} character and others show a second-order transition unknown universality class.⁶

IV. CONCLUSION

In conclusion, we note that the different thermodynamical quantities determined as functions of temperature suggest

a first-order character of the phase transition in the frustrated J_1-J_2 simple-cubic lattice with vector spins. This first-order character is confirmed by histogram MC simulations. Finally, we have shown that there is an order by disorder effect in these systems: the thermal fluctuations lift the infinite degeneracy and select collinear configurations.

ACKNOWLEDGMENT

The "Laboratoire de Physique Théorique et Modélisation" is an "équipe postulante" (EP 0127) of CNRS.

- ¹*Magnetic Systems with Competing Interactions (Frustrated Spin Systems)*, edited by H. T. Diep (World Scientific, Singapore, 1994).
- ²T. Oguchi, H. Nishimori, and Y. Taguchi, *J. Phys. Soc. Jpn.* **54**, 4494 (1985).
- ³H. T. Diep and H. Kawamura, *Phys. Rev. B* **40**, 7019 (1989); C. Henley, *J. Appl. Phys.* **61**, 3962 (1987); W. Minor and T. Gielbultowicz, *J. Phys. (Paris)* **49**, C8-1551 (1988).
- ⁴P. Lallemand, H. T. Diep, A. Ghazali, and G. Toulouse, *J. Phys. Lett.* **46**, L-1087 (1985); H. T. Diep, A. Ghazali, and P. Lallemand, *J. Phys. C* **18**, 5881 (1985).
- ⁵H. T. Diep, *Phys. Rev. B* **45**, 2863 (1992).
- ⁶D. Loison and H. T. Diep, *Phys. Rev. B* **50**, 16453 (1994); T. Bhattacharya, A. Billoire, R. Lacaze, and Th. Jolicoeur, *J. Phys. I* **4**, 122 (1994); E. H. Boubekeur, D. Loison, and H. T. Diep, *Phys. Rev. B* **54**, 4165 (1996).
- ⁷B. Berge, H. T. Diep, A. Ghazali, and P. Lallemand, *Phys. Rev. B* **34**, 3177 (1986), and references therein.
- ⁸E. H. Boubekeur, R. Quartu, H. T. Diep, and O. Nagai, *Phys. Rev. B* (submitted).
- ⁹A. M. Ferrenberg and R. H. Swendsen, *Phys. Rev. Lett.* **61**, 2635 (1988); **63**, 1195 (1989).
- ¹⁰C. Henley, *J. Appl. Phys.* **61**, 3962 (1987); *Phys. Rev. Lett.* **62**, 2056 (1989).
- ¹¹J. Villain, R. Bidaux, J. P. Carton, and R. Conte, *J. Phys. (Paris)* **41**, 1263 (1980).

Spin fluctuations and thermal expansion of $\text{La}(\text{Ni}_x\text{Al}_{1-x})_{13}$ amorphous alloys

A. Fujita^{a)} and K. Fukamichi

Department of Materials Science, Graduate School of Engineering, Tohoku University,
Sendai 980-77, Japan

The influences of spin fluctuations on the magnetization M and thermal expansion for $\text{La}(\text{Ni}_x\text{Al}_{1-x})_{13}$ amorphous alloys have been investigated. The spontaneous magnetization obeys a $M^2 - \xi T^{4/3}$ relation and the coefficient ξ is concerned with the dynamical spin fluctuation spectrum. The spontaneous volume magnetostriction in the ferromagnetic state appears due to the thermal variation of the local spin amplitude. The change in the linear thermal expansion coefficient in paramagnetic temperature regions is caused by the saturation of amplitude of the spin fluctuations.

© 1998 American Institute of Physics. [S0021-8979(98)23311-1]

Recently, influences of spin fluctuations on magnetic properties in amorphous weakly itinerant ferromagnetic alloys have been extensively studied.¹⁻⁶ In amorphous alloys, the magnetic properties are changed by the concentration without the limitation of stoichiometry in contrast with that in crystalline compounds.⁵ Therefore, the characteristics of spin fluctuations can be studied more closely in connection with the stability of the ferromagnetic state. Strictly speaking, however, it should be noted that the atomic short-range order varies with the concentration in amorphous alloys⁷ and the recent theoretical studies point out that the stability of ferromagnetism is drastically influenced by the change of the atomic short-range order.^{8,9} The structure of $\text{La}(\text{Ni}_x\text{Al}_{1-x})_{13}$ amorphous alloys can remove the problem mentioned above, namely, the local structure in the present amorphous alloys is well defined by the icosahedral clusters consisting of Ni and Al atoms as observed in NaZn_{13} -type crystalline compounds in a wide concentration range.¹⁰ The present amorphous alloys are useful, therefore, to investigate explicitly spin fluctuation characteristics.

$\text{La}(\text{Ni}_x\text{Al}_{1-x})_{13}$ ($0.90 \leq x \leq 0.95$) amorphous alloys were prepared by high-rate dc sputtering on a water-cooled Cu substrate. The substrate was mechanically removed before the magnetization measurement. The temperature and magnetic field dependences of the magnetization were measured with a SQUID magnetometer.

Temperature dependence of the spontaneous magnetization $M(0, T)$ for $x=0.925$ and 0.95 is plotted in the form of $M(0, T)^2 - T^{4/3}$ in Fig. 1. The value of $M(0, T)$ is deduced from the isothermal magnetization $M(H, T)$ curves. The linear relation is observed in the temperature range above about $T_c/2$ for $x=0.95$ and $0.3 T_c$ for $x=0.925$. According to the theory on exchange enhanced spin fluctuations with mode-mode coupling, the $M^2 - T^{4/3}$ relation is explained as a result of a strong renormalization effect of paramagnon-like modes of spin fluctuations to the magnetic free energy.¹¹⁻¹³ The coefficient ξ in the $M^2 - \xi T^{4/3}$ relation is associated with the dynamical properties of spin fluctuations and expressed by the following expression^{14,15}:

$$\xi = K \frac{1}{T_A T_0^{1/3}}, \quad (1)$$

where K is the constant and the parameters T_A and T_0 characterize the dispersion of the static q -dependent susceptibility and the dynamical spin fluctuation spectrum. The following relation between these parameters and magnetization curve is derived by assuming that the sum of amplitudes of thermal and zero-point spin fluctuations is conserved at finite temperatures.¹⁶

$$-2c \left(\frac{T_c}{T_0} \right)^{4/3} k_B T_A p_s + \frac{4k_B T_A^2}{15T_0} \frac{p_s^3}{8} = 2\mu_B H, \quad (2)$$

where k_B and μ_B are the Boltzmann constant and the Bohr magneton, respectively, p_s equals $2M(0, 0)$, and c is 0.335. The parameters T_A and T_0 for the present amorphous alloys have been evaluated from the Arrott plots in our previous paper² by using Eq. (2). In Fig. 2, the coefficients ξ for $x=0.90, 0.925$, and 0.95 are plotted against $1/(T_A T_0^{1/3})$, and the proportional relation is confirmed. Therefore, the relation (1) is well established in the present amorphous alloys. It should be emphasized that the relations (1) and (2) are valid even in amorphous alloys, although these were originally applied to crystalline systems.¹³

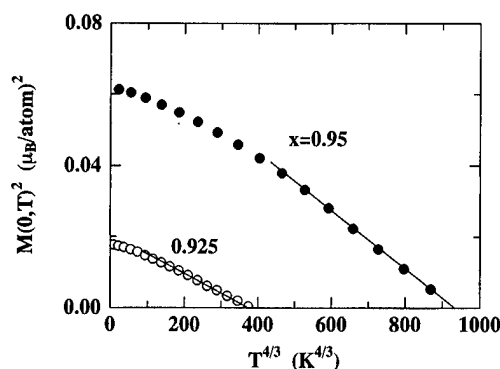


FIG. 1. Temperature dependence of the spontaneous magnetization plotted in the form of $M(0, T)^2 - T^{4/3}$ for $\text{La}(\text{Ni}_x\text{Al}_{1-x})_{13}$ ($x=0.95$ and 0.925) amorphous alloys.

^{a)}Electronic mail: afujita@material.tohoku.ac.jp

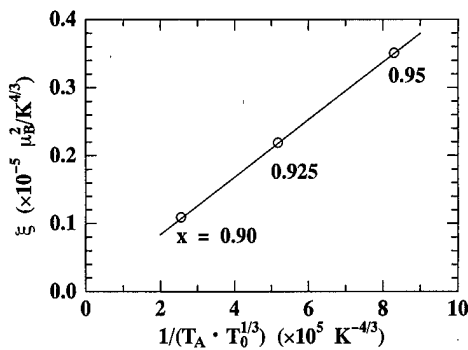


FIG. 2. The coefficient ξ plotted against $1/(T_A T_0^{1/3})$ for $\text{La}(\text{Ni}_x\text{Al}_{1-x})_{13}$ amorphous alloys. The parameters ξ , T_A , and T_0 are explained in the text.

Thermal variation of the amplitude of spin fluctuations is reflected on the thermal expansion.¹⁷ Figure 3 shows the temperature dependence of the spontaneous volume magnetostriction $\omega_m(T)$ for $x=0.925$ and 0.95 . The value of $\omega_m(T)$ is obtained from the comparison between the observed and hypothetical nonmagnetic thermal expansion curves, as shown in the inset in Fig. 3. The hypothetical nonmagnetic thermal expansion curve, represented by a dashed line, is obtained from the Grüneisen relation with referring the Debye model and the free-electron model for phonon and electron contribution, respectively. The Debye temperature θ_D is assumed to be the same value of $\theta_D = 280$ K for $\text{La}(\text{Fe}_x\text{Al}_{1-x})_{13}$ amorphous alloys obtained from the Brillouin scattering.¹⁸ The magnitude of $\omega_m(T)$ continuously decreases with increasing temperature and smears around the Curie temperature. Such behavior is an indication that the amplitude of local spin density varies with temperature and continuously decreases up to the Curie temperature.^{13,17} Detailed influence of spin fluctuations on $\omega_m(T)$ will be discussed elsewhere.¹⁰

Theories on spin fluctuations in itinerant ferromagnets predict that the amplitude of spin fluctuations increases with the temperature and the thermal variation of spin fluctuations gives a positive contribution to the thermal expansion coefficient in paramagnetic temperature ranges.^{13,17} Figure 4

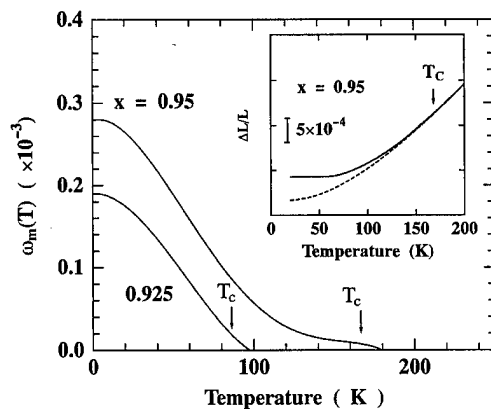


FIG. 3. Temperature dependence of the spontaneous volume magnetostriction $\omega_m(T)$ for $\text{La}(\text{Ni}_x\text{Al}_{1-x})_{13}$ ($x=0.95$ and 0.925) amorphous alloys. The inset shows the thermal expansion curve of $x=0.95$, together with a hypothetical dashed curve in a nonmagnetic state. The Curie temperature is indicated by the arrows.

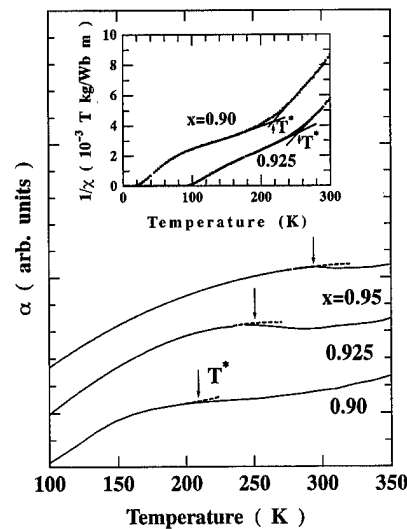


FIG. 4. Temperature dependence of the linear thermal expansion coefficient for $\text{La}(\text{Ni}_x\text{Al}_{1-x})_{13}$ amorphous alloys in the paramagnetic temperature region. The inset shows the temperature dependence of the inverse magnetic susceptibility for $x=0.90$ and 0.925 . The characteristic temperature T^* is given by the arrows.

shows the linear thermal expansion coefficient (TEC) in paramagnetic temperatures for $x=0.95$, 0.925 , and 0.90 . For itinerant weakly ferromagnets, the contribution of spin fluctuations to TEC, α_m , is represented as

$$\alpha_m = \kappa C_m \frac{dS_L^2(T)}{dT}, \quad (3)$$

where $S_L^2(T)$ is the mean square of the amplitude of local spin fluctuations, C_m and κ are the magnetovolume coupling coefficient and the compressibility, respectively.¹⁷ Generally speaking, S_L^2 increases linearly and hence α_m is almost constant in weakly itinerant ferromagnets.^{11,13,19} The electron contribution is proportional to the temperature.¹⁹ In the temperature region higher than the Debye temperature, the phonon contribution to TEC behaves as the Dulong–Petit law. As mentioned in the preceding section, the Debye temperature of the present amorphous alloys is assumed to be 280 K.¹⁸ Therefore, TEC around room temperature should increase monotonically with the temperature. However, as seen in Fig. 4, a change in the increase occurs in all the curves, shifted to lower temperatures with decreasing x . Because of an apparent concentration dependence, the origin of this anomaly neither is phonons nor electrons but spin fluctuations. Thus, the anomalous temperature dependence of S_L^2 occurs in paramagnetic temperature ranges.

The information on the paramagnetic spin fluctuations in itinerant weakly ferromagnets can be obtained from temperature dependence of paramagnetic susceptibility.¹¹ The inverse magnetic susceptibility $1/\chi$ is proportional to S_L^2 , and a linear thermal variation of S_L^2 gives a Curie–Weiss-like behavior even in itinerant ferromagnets.^{11,13} The inset in Fig. 4 shows the temperature dependence of the inverse magnetic susceptibility for $x=0.90$ and 0.925 . For the present amorphous alloys, $1/\chi$ becomes convex upwards just above T_c and subsequently shows an upturn.² The curving of $1/\chi$ con-

vex upwards is interpreted as a significant increase of S_L^2 .^{13,20} A sudden increase in the slope of $1/\chi$ suggests that the magnitude of S_L^2 arrives at its upper limit because of charge neutrality.^{20,21} After the amplitude of spin fluctuations is saturated at the upper limit value, the spin fluctuations give no contribution to $1/\chi$, resulting in a large slope of $1/\chi$ due to the directional fluctuations of magnetic moments. The starting temperature of the saturation phenomenon, T^* , is obtained from the intersection of the straight lines before and after the change in the slope as indicated by the arrows in Fig. 4. Apparently, TEC changes its magnitude at around T^* , revealing that the saturation of the amplitude of spin fluctuations is its origin.

In summary, the influences of spin fluctuations on the magnetization and thermal expansion are observed in $\text{La}(\text{Ni}_x\text{Al}_{1-x})_{13}$ amorphous alloys. In the ferromagnetic state, the $M^2 - \xi T^{4/3}$ relation appears and the coefficient ξ is closely correlated with the spin fluctuation spectrum. The spontaneous volume magnetostriction is caused by the thermal variation of the local spin amplitude. The linear thermal expansion coefficient in paramagnetic temperature regions changes its magnitude due to the saturation of the amplitude of spin fluctuations.

The present work was partially financed by a Grant-in-Aid for Scientific Research from Ministry of Education, Science, Sports and Culture, Japan, No. (B) (2) 08455287. One

of the author (A.F.) would like to thank the JSPS Research Fellowships for Young Scientists.

- ¹A. Fujita, T. H. Chiang, N. Kataoka, and K. Fukamichi, J. Phys. Soc. Jpn. **62**, 2579 (1993).
- ²A. Fujita, K. Fukamichi, H. A. Katori, and T. Goto, J. Phys.: Condens. Matter **7**, 401 (1995).
- ³A. Fujita, K. Suzuki, K. Fukamichi, Y. Obi, and H. Fujimori, Mater. Trans., JIM **36**, 852 (1995).
- ⁴V. S. Amaral and B. Barbara, J. Magn. Magn. Mater. **140-144**, 2011 (1995).
- ⁵A. L. Dawson and D. H. Ryan, Phys. Rev. B **54**, 12238 (1996).
- ⁶P. D. Babu and S. N. Kaul, J. Phys.: Condens. Matter **9**, 3625 (1997).
- ⁷A. Fujita, M. Matsuura, and K. Fukamichi (unpublished).
- ⁸H. Tanaka and S. Takayama, J. Phys.: Condens. Matter **4**, 8203 (1992).
- ⁹Y. Kakehashi, Phys. Rev. B **43**, 10820 (1991).
- ¹⁰A. Fujita, K. Fukamichi, E. Matsubara, and Y. Waseda (unpublished).
- ¹¹T. Moriya and A. Kawabata, J. Phys. Soc. Jpn. **34**, 639 (1973); **35**, 669 (1975).
- ¹²K. Makoshi and T. Moriya, J. Phys. Soc. Jpn. **38**, 10 (1975).
- ¹³T. Moriya, *Spin Fluctuations in Itinerant Electron Magnetism* (Springer, Berlin, 1985).
- ¹⁴Y. Takahashi and T. Moriya, J. Phys. Soc. Jpn. **54**, 1592 (1985).
- ¹⁵G. G. Lonzarich and L. Taillefer, J. Phys. C **18**, 4339 (1985).
- ¹⁶Y. Takahashi, J. Phys. Soc. Jpn. **55**, 3553 (1986).
- ¹⁷T. Moriya and K. Usami, Solid State Commun. **34**, 95 (1985).
- ¹⁸A. Yoshihara, Y. Shimada, T. H. Chiang, and K. Fukamichi, J. Appl. Phys. **75**, 1733 (1994).
- ¹⁹S. Ogawa, Physica B & C **119**, 68 (1983).
- ²⁰T. Moriya and Y. Takahashi, J. Phys. Soc. Jpn. **45**, 397 (1978).
- ²¹T. Moriya, Solid State Commun. **26**, 483 (1978).

Magnetic relaxation in $\text{Ga}_{0.6}\text{Mo}_2\text{S}_4$ spinel

T. Taniyama^{a)} and I. Nakatani

National Research Institute for Metals, Tsukuba 305-0047, Japan

Magnetization measurements on $\text{Ga}_{0.6}\text{Mo}_2\text{S}_4$ cluster compound of modified spinel were performed at temperatures from 2 to 30 K. Temperature irreversibility of the magnetization develops just below the ferromagnetic transition temperature. Relaxation isotherms of the thermoremanent magnetizations can be described by a superposition of a stretched exponential and a constant term, and shows distinctive aging effects. This implies the presence of the orientational spin freezing in the ferromagnetic regime of the $\text{Ga}_{0.6}\text{Mo}_2\text{S}_4$. © 1998 American Institute of Physics.

[S0021-8979(98)50611-1]

The molybdenum cluster compound $\text{Ga}_x\text{Mo}_2\text{S}_4$ ($x = 0.5-0.67$) demonstrates fruitful magnetic properties owing to the tetrahedral molybdenum clustering induced by the order of Ga atoms and vacancies on the tetrahedral sites in spinel structure.¹⁻³ In this kind of compound, imperfections of the Ga-vacancy ordering yields significant modification of electronic properties. Recently, Sahoo *et al.* reported the signature of variable-range hopping between the localized states of clusters induced by such imperfections.^{4,5} However, comparatively little attention has been paid to the magnetic properties intrinsically affected by the random atomic arrangement.

The intrigue magnetic properties due to such random effects can be sensitively probed by the thermoremanent magnetization (TRM). In particular, time evolution of the TRM gives distinguishable dynamic response caused by the different physical mechanism. Thus, we employ the time dependent TRM measurements on the $\text{Ga}_{0.6}\text{Mo}_2\text{S}_4$ to elucidate the magnetic nature in the view of the randomness. In this article, we present temperature irreversibility of the magnetization and waiting time dependence of the magnetic relaxation in the ferromagnetic regime.

The method of sample preparation has been described in our previous article.⁶ The x-ray diffraction pattern was indexed on the basis of the lower symmetric spinel structure (space group $F\bar{4}3m$) having $a = 9.737 \text{ \AA}$ and revealed a homogeneity of the prepared sample. With decreasing temperature, splitting of the $h00$ diffraction peaks was observed below the temperature of 43 K, reflecting the structural transition from a space group $F\bar{4}3m$ to $R\bar{3}m$. This is consistent with the results previously reported by Shamrai *et al.*^{2,3} The pellet used for the x-ray diffraction measurement was cut into a size of $1 \text{ mm} \times 1 \text{ mm} \times 5 \text{ mm}$ for the magnetic measurements. Magnetic data were collected using a magnetometer (PPMS, Quantum Design) at temperatures from 2 to 30 K. Temperature dependent magnetizations were measured with increasing temperature under both zero field cooled (ZFC) and field cooled conditions. The time dependent TRM was recorded over four decades of observation time after switching off the cooling magnetic field.

Figure 1 shows the temperature dependent magnetization

and the ac susceptibility at temperatures from 2 to 30 K. The ZFC magnetization exhibits a shallow maximum structure and the maximum temperature shifts towards lower temperatures as the magnetic field increases. The temperature irreversibility of the magnetization also develops just below the ferromagnetic transition temperature T_c , which has been defined to be 17.4 K by the previous nonlinear susceptibility measurements.⁶ The significant irreversibility and the peak structure of the temperature dependent magnetization are typical of the disordered materials, e.g., spin glasses and random ferromagnets. We note that the magnetic feature of the $\text{Ga}_{0.6}\text{Mo}_2\text{S}_4$ is quite similar to that of the reentrant ferromagnetic semiconductor of the indium-doped chalcogenide spinel $\text{CdCr}_2\text{Se}_4:\text{In}$.⁷

Relaxation isotherms were collected after a sequence of waiting for a time of $t_w = 60 \text{ s}$ at the measurement temperature and switching off the cooling fields of 50 Oe and 1 kOe, from which the temperature dependent relaxation rates (Fig. 2) are extracted simply using the logarithmic relaxation decay form:

$$M = M_0 - S \log t, \quad (1)$$

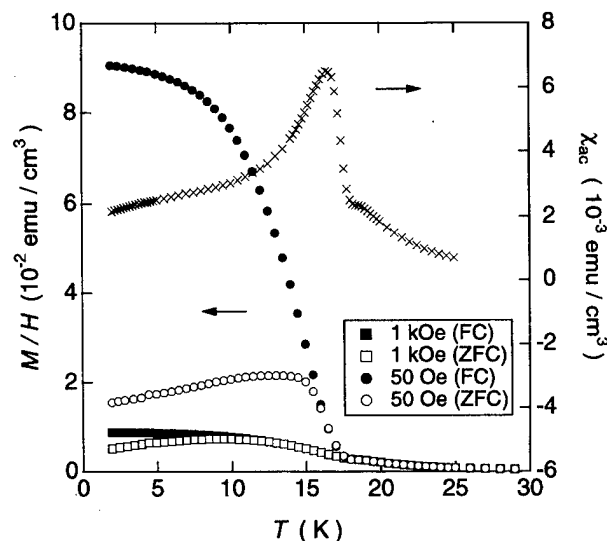


FIG. 1. Temperature dependent zero field cooled and field cooled magnetization in a field of 50 Oe. Temperature dependent ac susceptibility in a modulation field of 2 Oe is also depicted.

^{a)}Electronic mail: taniyama@hagi982.nrim.go.jp

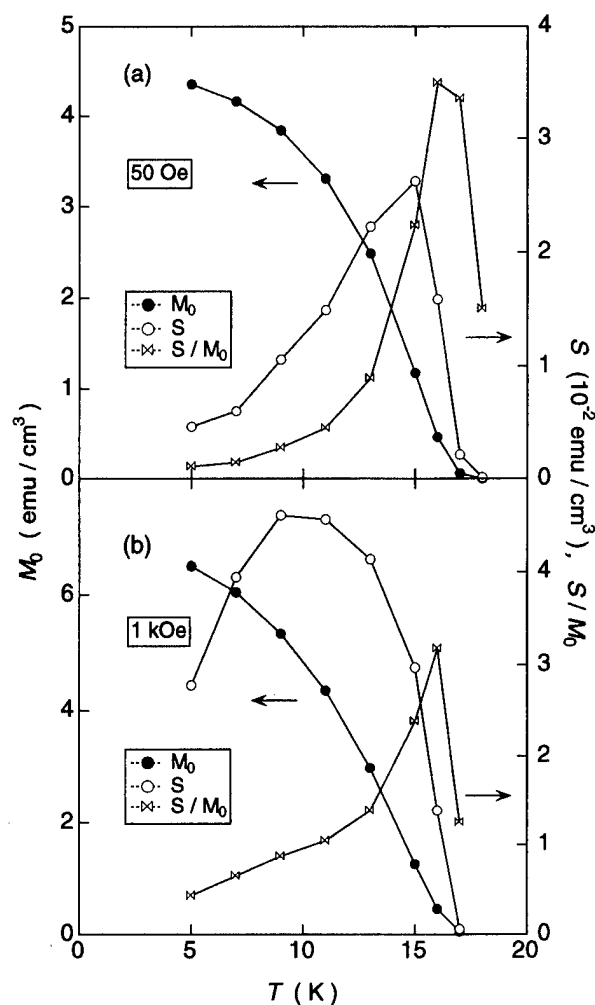


FIG. 2. Temperature dependent relaxation rate S and initial magnetization M_0 in a cooling field of (a) 50 Oe and (b) 1 kOe.

where the S is the relaxation rate and M_0 is the initial magnetization. Although the maximum in the temperature dependent relaxation rate shifts towards lower temperatures with increasing magnetic fields, the normalized relaxation rate S/M_0 hardly shows the field dependence.

Figure 3 illustrates the relaxation dynamics for two extreme waiting times $t_w = 60$ s and $t_w = 10\,800$ s, at 15 K on a logarithmic time scale. In contrast to the concave up profile for $t_w = 60$ s, the relaxation isotherm concaves down after waiting for $t_w = 10\,800$ s in a magnetic field. Such behavior has been frequently observed in the reentrant ferromagnet and the relaxation isotherms can be represented by a superposition of a stretched exponential and a constant term.^{8,9}

$$M = M_0 + M_1 \exp[-(t/\tau)^{1-n}]. \quad (2)$$

The additional constant term has been interpreted on the basis of the reliable picture introduced by Gabay and Thoulouse,¹⁰ in which the longitudinal spontaneous magnetization coexists with the frozen transverse spin component. Within this framework, we fit the experimental data using Eq. (2) over the entire observation time scale (Fig. 3). The best fit parameters are listed in Table I. The values of the fitted parameters τ and n closely correspond to those of FeNiMn reentrant ferromagnet.¹¹

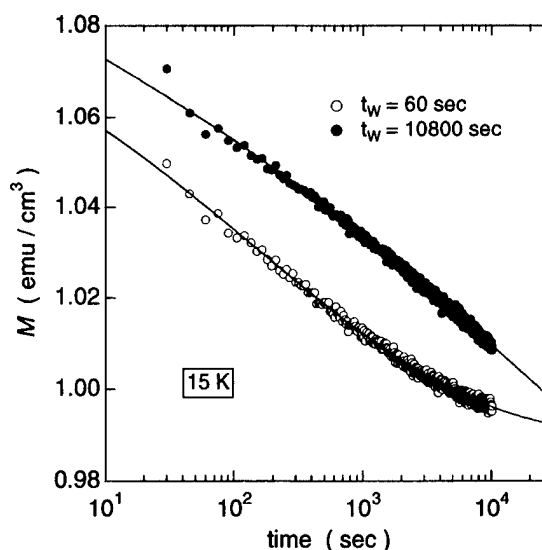


FIG. 3. Time dependent thermoremanent magnetization recorded at 15 K after a sequence of waiting for a time t_w and switching off the cooling magnetic field of 50 Oe. The solid lines are fitted curves in terms of a superposition of a stretched exponential and a constant term.

Mitchler *et al.* carefully investigated the analytical functional forms of the relaxation isotherm in the random ferromagnet PdFe and the reentrant ferromagnet CrFe, and found that the relaxation responses are divided into two groups: a power law and a stretched exponential decay. The former functional form accurately represents the relaxation of the random ferromagnets such as PdFe, while the latter case characterizes the orientational collapse into random spin configurations in the reentrant ferromagnet. Further, the reentrant phase exhibits the system age dependent relaxation although the random ferromagnet shows no measurable aging effects on the relaxation dynamics reflecting the equilibrium aging limit. In the present case, the relaxation isotherms are represented by a stretched exponential superposed on a constant term and show the discernible aging effects. This persuasively indicates that the glassy freezing occurs in the ferromagnetic phase of the $\text{Ga}_{0.6}\text{Mo}_2\text{S}_4$, although the presence of the aging effects on the relaxation isotherms does not offer a definitive criterion for distinguishing the microscopic spin configurations in the disordered materials.

It is not clear whether or not the orientational collapse simultaneously evolves as the ferromagnetic ordering is established. In our previous article, the ferromagnetic transition temperature was determined to be 17.4 K based on the nonlinear susceptibility measurements.⁶ The obtained transition temperature exactly coincides with the temperature below which the dc susceptibility M/H exhibits the field dependence as shown in Fig. 1. On the contrary, the irreversibility in a field of 50 Oe develops below a slightly lower tempera-

TABLE I. Best-fit parameters to a stretched exponential in Eq. (2).

t_w (s)	M_0 (emu/cm³)	M_1 (emu/cm³)	τ (s)	n
60	0.99	0.12	135	0.76
10 800	0.91	0.22	39 000	0.87

ture of 16.5 K. If we assign the glassy freezing with the onset of the irreversibility, the freezing process may sequentially occur after the ferromagnetic transition. Although one may suspect that the irreversibility temperature possibly approaches the T_c with reducing the applied field, we emphasize the coincidence between the irreversibility temperature and the peak temperature of the ac susceptibility in zero bias field. Thus, our picture of the sequential collapse into the randomly orientational spin configurations is plausible.

Finally, we make a brief comments on the origin of the spin-glass-like dynamics. As we have stated before, the magnetic disorder would be mainly driven by the random molybdenum clustering due to the imperfection of the Ga-vacancy ordering. However, we have to claim the instability of the cubic lattice structure at 43 K. Shamrai *et al.* proposed the displacement of the molybdenum atoms to form a Mo_3 complex with a shorter distance in the low-temperature $R3m$ phase and suggested the resultant mixed type of interactions, i.e., indirect exchange interaction and superexchange interaction between molybdenum ions. Thus, the distortion of the crystal lattice should be partly responsible for the frustrating interactions which promote the glassy behaviors in the $\text{Ga}_{0.6}\text{Mo}_2\text{S}_4$.

We summarize the magnetic feature of the $\text{Ga}_{0.6}\text{Mo}_2\text{S}_4$

deduced from the magnetic measurements. The random orientational freezing is inferred from the temperature irreversibility and the relaxation dynamics described by a superposition of a stretched exponential and a constant term, which is further reinforced by the specific aging effects in the ferromagnetic regime. In order to get the convincing evidence for the spin configurations, further microscopic measurements such as neutron scattering or nuclear magnetic resonance measurements are required.

¹A. K. Rastogi, A. Berton, J. Chaussy, R. Tournier, M. Potel, R. Chevrel, and M. Sergent, *J. Low Temp. Phys.* **52**, 539 (1983).

²V. Shamrai, H. Mäde, T. Mydlarz, and G. Leitus, *J. Low Temp. Phys.* **49**, 123 (1982).

³V. F. Shamrai and G. M. Leitus, *Sov. Phys. Solid State* **29**, 1312 (1987).

⁴Y. Sahoo and A. K. Rastogi, *J. Phys.: Condens. Matter* **5**, 5953 (1993).

⁵S. Lamba, A. K. Rastogi, and D. Kumar, *Phys. Rev. B* **56**, 3251 (1997).

⁶T. Taniyama and I. Nakatani, *J. Magn. Magn. Mater.* **177-181**, 263 (1998).

⁷M. Lubecka, L. J. Maksymowicz, R. Szymczak, and W. Powroźnik, *Phys. Rev. B* **55**, 6460 (1997).

⁸P. D. Mitchler, R. M. Roshko, and W. Ruan, *Philos. Mag. B* **68**, 539 (1993).

⁹G. Sinha, R. Chatterjee, M. Uehara, and A. K. Majumdar, *J. Magn. Magn. Mater.* **164**, 345 (1996).

¹⁰M. Gabay and G. Thoulouse, *Phys. Rev. Lett.* **47**, 201 (1981).

¹¹D. Li, R. M. Roshko, and G. Yang, *Phys. Rev. B* **49**, 9601 (1994).

New bulk amorphous Fe-(Co,Ni)-M-B (M=Zr,Hf,Nb,Ta,Mo,W) alloys with good soft magnetic properties

Akihisa Inoue, Tao Zhang, and Hisato Koshida

Institute for Materials Research, Tohoku University, Katahira 2-1-1, Aoba-ku, Sendai 980-77, Japan

Akihiro Makino

Central Research Laboratory, Alps Electric Co. Ltd., Higashi-Takami 1-3-5, Nagaoka 940, Japan

We have found that an amorphous phase with a wide supercooled liquid region reaching 85 K before crystallization is formed in Fe-(Co, Ni)-(Zr, Nb, Ta)-B, Fe-Co-(Zr, Nb)-(Mo, W)-B and Co-Fe-Zr-B systems. The high stability of the supercooled liquid enabled the production of bulk amorphous alloys with diameters up to 5 mm by copper mold casting. These amorphous Fe-(Co, Ni)-M-B alloys exhibit good soft magnetic properties, i.e., saturation magnetization of 0.95 to 1.1 T, low coercivity of 1 to 8 A/m, Curie temperature of 560 to 590 K and low magnetostriction of $8-14 \times 10^{-6}$. The effective permeability of the Co-based alloys exceeds 25 000 at 1 kHz and keeps high values above 5000 at the high frequency of 1 MHz. The permeability at 1 MHz is much higher than those for any kinds of soft magnetic materials. The frequency at which the imaginary part of permeability shows a maximum is also about 1 MHz. The success of synthesis of new Fe- and Co-based amorphous alloys with good soft magnetic properties and high glass-forming ability is promising for future development of a new type of soft magnetic material. © 1998 American Institute of Physics. [S0021-8979(98)47111-1]

It is well known that Fe- and Co-based amorphous alloys exhibit good soft magnetic properties. The soft magnetic properties have been characterized as the achievement of high saturation magnetization for Fe-based alloys and high permeability (μ_e) and zero magnetostriction for Co-based alloys.¹ However, these soft magnetic amorphous alloys have usually been prepared in a thin sheet form with a thickness below 50 μm and in a wire form with a diameter below 120 μm .² The small maximum thickness resulting from the low glass-forming ability has prevented the further extension of application fields as magnetic materials. Consequently, great effort has been devoted to search new ferromagnetic amorphous alloys with higher glass-forming ability for the last two decades. Recently, Inoue *et al.* have succeeded in finding a number of amorphous alloys with high glass-forming ability in Ln-Al-TM,³ Mg-Ln-TM,⁴ Zr-Al-TM⁵ and Pd-Cu-Ni-P⁶ (Ln=lanthanide metal, TM=transition metal) systems and in preparing bulk amorphous alloys with maximum diameters up to about 72 mm by copper mold casting.⁶ Although these bulk amorphous alloys have been limited to the nonferrous alloys without ferromagnetism, the findings of the above-described bulk amorphous alloys have enabled the derivation of the three empirical rules for achievement of large glass-forming ability.⁷⁻¹⁰ That is, (1) multicomponent alloys systems consisting of more than three elements, (2) significant difference in atomic size ratios above 12% among the main constituent elements, and (3) negative heats of mixing among their elements. Based on the three empirical rules, we have subsequently searched ferromagnetic Fe- and Co-based amorphous alloys with large glass-forming ability

leading to the production of bulk amorphous alloys. As a result, we have found that multicomponent Fe-(Co, Ni)-(Zr, Nb, Ta)-B, Fe-Co-(Zr, Nb)-(Mo, W)-B and Co-Fe-(Zr, Nb)-B amorphous alloys exhibit a wide supercooled liquid region reaching 80 K before crystallization¹¹⁻¹³ and can be produced in a cylindrical form with diameters up to about 5 mm by copper mold casting.¹⁴ This is believed to be the first evidence on the preparation of ferromagnetic Fe- and Co-based bulk amorphous alloys. This paper aims to present the composition range in which amorphous alloys in Fe-(Co, Ni)-M-B (M=Zr, Hf, Nb, Mo, W) systems, are formed either by copper mold casting or by melt spinning and to examine the compositional dependence of the thermal stability and magnetic properties of the Fe- and Co-based amorphous alloys.

Multicomponent alloys with composition $\text{Fe}_{56}\text{Co}_7\text{Ni}_7\text{Zr}_{10}\text{B}_{20}$, $\text{Fe}_{56}\text{Co}_7\text{Ni}_7\text{Zr}_8\text{Nb}_2\text{B}_{20}$, $\text{Fe}_{60}\text{Co}_8\text{Zr}_{10}\text{Mo}_5\text{W}_2\text{B}_{15}$, and $\text{Co}_{56}\text{Fe}_{16}\text{Zr}_8\text{B}_{20}$ were prepared by arc melting a mixture of pure metals and pure B crystal in an argon atmosphere. These compositions were chosen because of the appearance of a supercooled liquid region of 35 to 85 K. From these prealloyed ingots, cylindrical samples with a constant length of about 50 mm and different diameters in the range of 0.5 to 6 mm were prepared by injection casting of the molten alloy into copper molds with cylindrical cavities. For comparison, amorphous ribbons with a cross section of $1 \times 0.02 \text{ mm}^2$ were produced by melt spinning. The amorphicity was examined by x-ray diffractometry and optical microscopy (OM). The OM sample was etched for 10 s at 293 K in a solution of 0.5% hydrofluoric acid and 99.5%

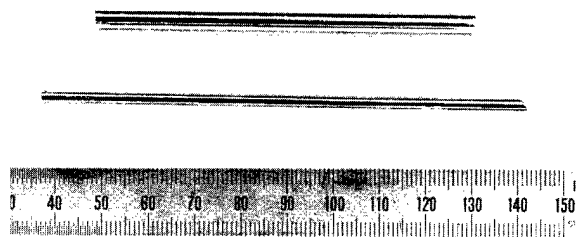


FIG. 1. Outer morphology and surface appearance of cast $\text{Fe}_{60}\text{Co}_8\text{Zr}_{10}\text{Mo}_5\text{W}_2\text{B}_{15}$ alloy cylinders with diameters 3 and 5 mm.

distilled water. The specific heat associated with glass transition, supercooled liquid region and crystallization was measured at a heating rate of 0.67 K/s with a differential scanning calorimeter (DSC). Saturation magnetization (I_s) and coercivity (H_c) under a field of 800 kA/m were measured at room temperature with a vibrating sample magnetometer (VSM). Hysteresis B-H loop under a magnetic field of 1.6 kA/m was also measured for the melt-spun ribbons with a B-H loop tracer. Permeability (μ_e) was evaluated in a frequency range of 1 to 10^4 kHz with an impedance analyzer. Saturated magnetostriction (λ_s) was measured under a field of 240 kA/m by a three-terminal capacitance method. Curie temperature (T_c) was determined by extrapolating the I - T curve in the constant coupling approximation manner. Electrical resistivity measurement was made by the four-probe method at room temperature.

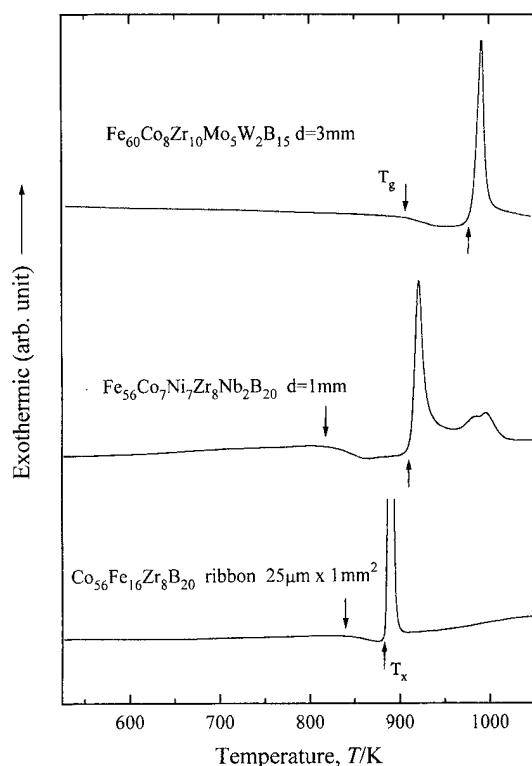


FIG. 2. DSC curves of the cast amorphous $\text{Fe}_{56}\text{Co}_7\text{Ni}_7\text{Zr}_8\text{Nb}_2\text{B}_{20}$, $\text{Fe}_{60}\text{Co}_8\text{Zr}_{10}\text{Mo}_5\text{W}_2\text{B}_{15}$, and $\text{Co}_{56}\text{Fe}_{16}\text{Zr}_8\text{B}_{20}$ alloys.

TABLE I. Maximum sample thickness (t_{max}) and thermal stability (T_g , ΔT_x , and T_g/T_m) of the $\text{Fe}_{56}\text{Co}_7\text{Ni}_7\text{Zr}_{10}\text{B}_{20}$, $\text{Fe}_{56}\text{Co}_7\text{Ni}_7\text{Zr}_8\text{Nb}_2\text{B}_{20}$, $\text{Fe}_{60}\text{Co}_8\text{Zr}_{10}\text{Mo}_5\text{W}_2\text{B}_{15}$, and $\text{Co}_{56}\text{Fe}_{16}\text{Zr}_8\text{B}_{20}$ amorphous alloys.

Alloy	Maximum sample thickness	Thermal stability		
	t_{max} (mm)	T_g (K)	ΔT_x (K)	T_g/T_m
$\text{Fe}_{56}\text{Co}_7\text{Ni}_7\text{Zr}_{10}\text{B}_{20}$	2	814	73	0.60
$\text{Fe}_{56}\text{Co}_7\text{Ni}_7\text{Zr}_8\text{Nb}_2\text{B}_{20}$	2	828	85	-
$\text{Fe}_{60}\text{Co}_8\text{Zr}_{10}\text{Mo}_5\text{W}_2\text{B}_{15}$	6	898	64	0.63
$\text{Co}_{56}\text{Fe}_{16}\text{Zr}_8\text{B}_{20}$	-	839	39	-

Figure 1 shows the outer morphology of the bulk $\text{Fe}_{60}\text{Co}_8\text{Zr}_{10}\text{Mo}_5\text{W}_2\text{B}_{15}$ cylinders with diameters of 3 and 5 mm. These samples have smooth surface and metallic luster. No contrast of a crystalline phase is seen over the outer surface. The x-ray diffraction patterns showed a main halo peak with a wave vector $K_p (=4\pi \sin \theta/\lambda)$ around 29.6 nm^{-1} and no crystalline peak is observed even for the 5 mm ϕ sample. The optical micrographs of the cross section of the two samples also revealed a featureless contrast in an etched state using a hydrogen fluoride acid. These results indicate that the bulk cylinders are composed of an amorphous phase in the diameter range up to 5 mm. It is to be noticed that the maximum thickness (t_{max}) is about 3 times larger than the largest value (2 mm for $\text{Fe}_{72}\text{Al}_5\text{Ga}_2\text{P}_{10}\text{C}_6\text{B}_4\text{Si}_1$) for Fe-based amorphous alloys reported up to date. Figure 2 shows the DSC curves of the bulk amorphous $\text{Fe}_{56}\text{Co}_7\text{Ni}_7\text{Zr}_8\text{Nb}_2\text{B}_{20}$ and $\text{Fe}_{60}\text{Co}_8\text{Zr}_{10}\text{Mo}_5\text{W}_2\text{B}_{15}$ cylinders of 1 to 3 mm in diameter and $\text{Co}_{56}\text{Fe}_{16}\text{Zr}_8\text{B}_{20}$ of 1 mm in width. These amorphous alloys exhibit the sequential transition of glass transition, supercooled liquid and crystallization. The supercooled liquid region, ΔT_x , defined by the difference between the glass transition temperature (T_g) and the onset temperature of crystallization (T_x) is as large as 39 to 85 K and the crystallization from the supercooled liquid occurs through a distinct

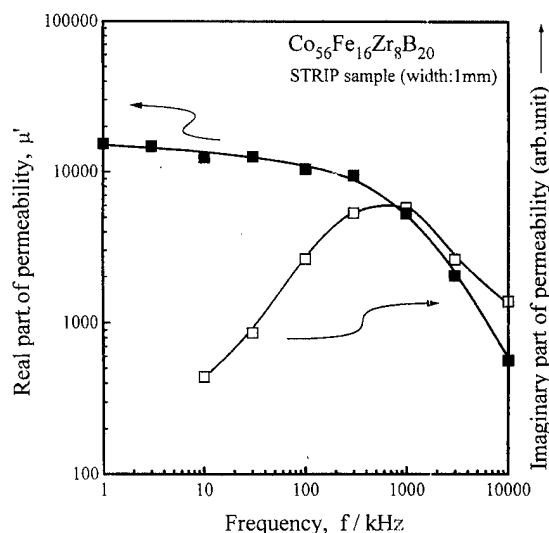


FIG. 3. Frequency dependence of real (μ') and imaginary (μ'') parts of permeability for amorphous $\text{Co}_{56}\text{Fe}_{16}\text{Zr}_8\text{B}_{20}$ alloys of 1 mm in width subjected to annealing for 600 s at 750 and 800 K.

TABLE II. Magnetic properties (I_s , H_c , μ_e at 1 kHz and λ_s) of $\text{Fe}_{56}\text{Co}_7\text{Ni}_7\text{Zr}_{10}\text{B}_{20}$, $\text{Fe}_{56}\text{Co}_7\text{Ni}_7\text{Zr}_8\text{Nb}_2\text{B}_{20}$, and $\text{Co}_{56}\text{Fe}_{16}\text{Zr}_8\text{B}_{20}$ amorphous alloys.

Alloy	Soft magnetic properties					
	I_s (T)	H_c (A/m)	μ_e (1 kHz)	μ_e (1 MHz)	λ_s (10^{-6})	T_c (K)
$\text{Fe}_{56}\text{Co}_7\text{Ni}_7\text{Zr}_{10}\text{B}_{20}$	0.96	2.0	19 100	-	10	594
$\text{Fe}_{56}\text{Co}_7\text{Ni}_7\text{Zr}_8\text{Nb}_2\text{B}_{20}$	0.75	1.1	25 000	-	13	531
$\text{Co}_{56}\text{Fe}_{16}\text{Zr}_8\text{B}_{20}$	0.77	8.3	17 100	5500	14	-

exothermic reaction. The crystallites were identified to consist of α -Fe, Fe_2Zr , Fe_8B , MoB , and W_2B phases for the $\text{Fe}_{60}\text{Co}_8\text{Zr}_{10}\text{Mo}_5\text{W}_2\text{B}_{15}$ sample heated to the temperature just above the exothermic peak. Thus, the crystallization is due to the simultaneous precipitation of the five crystalline phases. This crystallization mode is in agreement with that⁸ for other bulk amorphous alloys. The largest ΔT_x is 85 K for $\text{Fe}_{56}\text{Co}_7\text{Ni}_7\text{Zr}_8\text{Nb}_2\text{B}_{20}$, being larger than the largest values (57 to 67 K) for Fe-(Al, Ga)-(P, C, B, Si)^{14,15} and nonferrous Pd- and Pt-based amorphous alloys.^{16,17}

Table I summarizes the t_{\max} , T_g , ΔT_x and T_g/T_m of the Fe-(Co, Ni)-M-B amorphous alloys. We also evaluated the reduced glass transition temperature (T_g/T_m). The T_m was 1420 K for $\text{Fe}_{56}\text{Co}_7\text{Ni}_7\text{Zr}_{10}\text{B}_{20}$ and 1416 K for $\text{Fe}_{60}\text{Co}_8\text{Zr}_{10}\text{Mo}_5\text{W}_2\text{B}_{15}$ and the T_g/T_m was evaluated to be 0.60 for the former alloy and 0.63 for the latter alloy. Considering that T_g/T_m is 0.54 for $\text{Fe}_{80}\text{P}_{12}\text{B}_4\text{Si}_4$ ¹⁸ and 0.57 for $\text{Fe}_{73}\text{Al}_5\text{Ga}_2\text{P}_{11}\text{C}_4\text{B}_4\text{Si}_1$,¹⁸ the present T_g/T_m values are believed to be the highest among all Fe-based amorphous alloys.

Figure 3 shows the real and imaginary parts of permeability (μ' and μ''), respectively, as a function of frequency (f) for the $\text{Co}_{56}\text{Fe}_{16}\text{Zr}_8\text{B}_{20}$ amorphous ribbon of 1 mm width. The μ' of the $\text{Co}_{56}\text{Fe}_{16}\text{Zr}_8\text{B}_{20}$ ribbon keeps high values of 17 100 to 5500 in the high frequency range up to 1 MHz and decreases with a further increase in frequency to 10 MHz. It is to be noticed that the frequency at which the maximum μ'' is obtained for the ribbon is as high as about 1 MHz. The $\mu''(f)$ data indicate that the Co-Fe-Zr-B alloy can keep high μ' values up to 1 MHz of the maximum μ'' point. The μ' value is much higher than those for the Fe-Si-B amorphous ribbon with the same width of 1 mm over the whole frequency range. Furthermore, the μ' values of the $\text{Co}_{56}\text{Fe}_{16}\text{Zr}_8\text{B}_{20}$ alloy is higher than those for the Co-Fe-Ni-Mo-Si-B amorphous alloy with zero λ_s in the high frequency range above 10 kHz. The electrical resistivity (ρ_{RT}) of the $\text{Co}_{56}\text{Fe}_{16}\text{Zr}_8\text{B}_{20}$ alloy is $1.70 \mu\Omega \text{ m}$, which is higher as compared with $1.34 \mu\Omega \text{ m}$ for $\text{Co}_{70.3}\text{Fe}_{4.7}\text{B}_{10}\text{Si}_{15}$, $1.37 \mu\Omega \text{ m}$ for $\text{Fe}_{78}\text{B}_{13}\text{Si}_9$ (METGLAS 2605S-2) and $1.42 \mu\Omega \text{ m}$ for the Co-Fe-Ni-Si-B METGLAS 2714A alloy.¹⁹ Consequently, the excellent high-frequency permeability for the present alloys is probably due to the decrease in eddy current loss resulting from the higher ρ_{RT} . It is concluded that the present Co-based amorphous alloys have good soft magnetic properties and high stability of supercooled liquid against crystallization.

Table II summarizes the t_{\max} , I_s , H_c , μ_e at 1 kHz and λ_s for the new amorphous Fe-(Co, Ni)-M-B alloys. These amorphous alloys exhibit good soft magnetic properties in an

annealed (800 K, 300 s) state, i.e., high I_s of 0.74 to 0.96 T, low H_c of 1.1 to 3.2 A/m, high μ_e of 12 000 to 25 000 and low λ_s of 10×10^{-6} to 14×10^{-6} . The H_c and μ_e are superior to those for conventional Fe-Si-B amorphous ribbons,²⁵ presumably because of the lower λ_s .

Finally, the reason for the large ΔT_x and t_{\max} for the Fe-based amorphous alloys is discussed in the framework of the three empirical rules for the achievement of high glass-forming ability. The base composition is the Fe-Zr-B system which satisfies the three empirical rules. The addition of Nb, Ta, Mo, and W is effective for the increase in the degree of the satisfaction of the empirical rules. That is, the addition of these elements causes the more sequential change in the atomic size in the order of $\text{Zr} \gg \text{Nb} > \text{W} > \text{Mo} > \text{Fe} > \text{Co} > \text{B}$ as well as the generation of new atomic pairs with various negative heats of mixing. In the supercooled liquid in which the three empirical rules are satisfied at a high level, the topological and chemical short-range orderings are enhanced, leading to the formation of a highly dense random packed structure with low atomic diffusivity. The largest ΔT_x is 85 K for $\text{Fe}_{56}\text{Co}_7\text{Ni}_7\text{Zr}_8\text{Nb}_2\text{B}_{20}$ and 35 K for $\text{Co}_{56}\text{Fe}_{16}\text{Zr}_8\text{B}_{20}$ and the t_{\max} reaches 5 mm for $\text{Fe}_{60}\text{Co}_8\text{Zr}_{10}\text{Mo}_5\text{W}_2\text{B}_{15}$. Furthermore, these bulk amorphous alloys exhibit good soft magnetic properties. These novel characteristics allow us to expect that the new Fe- and Co-based bulk amorphous alloys are used as engineering materials.

¹ *Materials Science of Amorphous Metals*, edited by T. Masumoto (Ohmu, Tokyo, 1982).

² M. Hagiwara, A. Inoue, and T. Masumoto, *Met. Trans. A* **13**, 373 (1982).

³ A. Inoue, T. Zhang, and T. Masumoto, *Mater. Trans. JIM* **30**, 965 (1989).

⁴ A. Inoue, K. Ohtera, K. Kita, and T. Masumoto, *Jpn. J. Appl. Phys., Part 2* **27**, L2248 (1988).

⁵ A. Inoue, T. Zhang, and T. Masumoto, *Mater. Trans. JIM* **31**, 177 (1990).

⁶ A. Inoue, N. Nishiyama, and T. Matsuda, *Mater. Trans. JIM* **37**, 181 (1996).

⁷ A. Inoue, T. Zhang, and T. Masumoto, *J. Non-Cryst. Solids* **156-158**, 473 (1993).

⁸ A. Inoue, *Mater. Trans. JIM* **36**, 866 (1995).

⁹ A. Inoue, *Mater. Sci. Forum* **179-181**, 691 (1995).

¹⁰ A. Inoue, *Mater. Sci. Eng. A* **226-228**, 357 (1997).

¹¹ A. Inoue and J. S. Gook, *Mater. Trans. JIM* **36**, 180 (1995).

¹² A. Inoue and J. S. Gook, *Mater. Trans. JIM* **36**, 1282 (1995).

¹³ A. Inoue and J. S. Gook, *Mater. Trans. JIM* **37**, 32 (1996).

¹⁴ A. Inoue, Y. Shinohara, and J. S. Gook, *Mater. Trans. JIM* **36**, 1427 (1995).

¹⁵ A. Inoue, A. Takeuchi, T. Zhang, A. Murakami, and A. Makino, *IEEE Trans. Magn.* **32**, 4866 (1996).

¹⁶ H. S. Chen, *Mater. Sci. Eng.* **25**, 151 (1976).

¹⁷ H. S. Chen, *J. Appl. Phys.* **9**, 3289 (1978).

¹⁸ A. Inoue and R. E. Park, *Mater. Trans. JIM* **37**, 1715 (1996).

¹⁹ C. H. Smith, *Rapidly Solidified Alloys*, edited by H. H. Lieberman (Marcel Dekker, New York, 1993), p. 617.

Influence of Si addition on thermal stability and soft magnetic properties for Fe–Al–Ga–P–C–B glassy alloys

T. Mizushima and A. Makino

Central Research Laboratory, Alps Electric Co., Ltd., 1-3-5 Higashitakami, Nagaoka 940, Japan

A. Inoue

Institute for Materials Research, Tohoku University, 2-1-1 Katahira, Aoba-ku, Sendai 980-77, Japan

The thermal stability of the supercooled liquid region (ΔT_x), defined by the difference between crystallization temperature (T_x) and glass transition temperature (T_g), and soft magnetic properties were investigated for $\text{Fe}_{70}\text{Al}_5\text{Ga}_2\text{P}_{12.65-x}\text{C}_{5.75}\text{B}_{4.6}\text{Si}_x$ ($x=0-4$) and $\text{Fe}_{77}\text{Al}_{2.14}\text{Ga}_{0.86}\text{P}_{11-x}\text{C}_5\text{B}_4\text{Si}_x$ ($x=0-3$) glassy alloys. The thermal stability, glass forming ability and effective permeability (μ_e) at 1 kHz are improved with the replacement of P by 1–3 at. % Si for $\text{Fe}_{70}\text{Al}_5\text{Ga}_2\text{P}_{12.65-x}\text{C}_{5.75}\text{B}_{4.6}\text{Si}_x$ and by 1–2.6 at. % Si for $\text{Fe}_{77}\text{Al}_{2.14}\text{Ga}_{0.86}\text{P}_{11-x}\text{C}_5\text{B}_4\text{Si}_x$. The ΔT_x and the maximum thickness for glass formation (t_{\max}) reach maximum values of 60 K and 280 μm , respectively, for $\text{Fe}_{70}\text{Al}_5\text{Ga}_2\text{P}_{12.65-x}\text{C}_{5.75}\text{B}_{4.6}\text{Si}_x$ and 34 K and 220 μm , respectively, for $\text{Fe}_{77}\text{Al}_{2.14}\text{Ga}_{0.86}\text{P}_{11-x}\text{C}_5\text{B}_4\text{Si}_x$ at $\text{Si(at. \%)} / (\text{Si(at. \%)} + \text{P(at. \%)}) = 0.24$. Core losses for $\text{Fe}_{77}\text{Al}_{2.14}\text{Ga}_{0.86}\text{P}_{8.4}\text{C}_5\text{B}_4\text{Si}_{2.6}$ glassy alloy is much lower than that for amorphous Fe–Si–B alloy at the sheet thickness more than 70 μm . Therefore, it can be said that the Fe–Al–Ga–P–C–B–Si glassy alloys are useful for inductive applications because of their bulky shape and good soft magnetic properties. © 1998 American Institute of Physics. [S0021-8979(98)47211-6]

Since the discovery of good soft magnetic properties for Fe-based amorphous alloys,^{1,2} the development of thicker ferromagnetic amorphous alloy sheets has been desired for further extension of application fields for these alloys. The thicker sheets have been also desired because the reduction of lamination process for transformers and/or inductors is expected by using thicker sheets. Furthermore, lamination factor will be improved with use of thicker sheets. However, to date, it has been known that the preparation of amorphous sheets with thicknesses over 100 μm was very difficult because of the necessity of high cooling rates resulting from their low glass-forming ability.³ Recently, bulk glassy alloys have been formed in multicomponent Mg-,^{4,5} Ln-,^{6,7} Zr-,⁸⁻¹¹ and Pd-¹² based (Ln=lanthanide metal) alloy systems. These bulk glassy alloys have a wide supercooled liquid region above 60 K before crystallization. There is a clear tendency for the glass-forming ability to increase with increasing ΔT_x . The above mentioned glassy alloys always satisfy the following three empirical rules¹³⁻¹⁵ for achievement of a large glass-forming ability; i.e., (1) multicomponent alloy systems consisting of more than three elements, (2) significantly differential atomic size ratios above about 12% among the main constituent elements, and (3) negative heats of mixing among their elements. Based on the three empirical rules, we have searched for new Fe-based glassy alloys with a wide supercooled liquid region before crystallization. As a result, we have already reported that the Fe-based glassy alloy sheets with thicknesses up to 190 μm were prepared by using a melt spinning technique in Fe–(Al, Ga)–(P, C, B, Si) where the three group elements satisfied the three empirical rules.¹⁶ We have tried to further investigate the composition to prepare a much thicker sample. This paper investigates the influence of Si addition on the thermal stability of the supercooled liquid region and the soft magnetic properties for Fe–

Al–Ga–P–C–B glassy alloys with various Fe concentrations and possibility of producing a thick glassy alloy sheet with good soft magnetic properties.

Multicomponent $\text{Fe}_{70}\text{Al}_5\text{Ga}_2\text{P}_{12.65-x}\text{C}_{5.75}\text{B}_{4.6}\text{Si}_x$ ($x=0-4$) and $\text{Fe}_{77}\text{Al}_{2.14}\text{Ga}_{0.86}\text{P}_{11-x}\text{C}_5\text{B}_4\text{Si}_x$ ($x=0-3$) alloys were used in the present study because the highest permeability (μ_e) at 1 kHz and the largest saturation magnetization (σ_s) for alloys having a supercooled liquid region in the Fe–Al–Ga–P–C–B system were obtained for $\text{Fe}_{70}\text{Al}_5\text{Ga}_2\text{P}_{12.65}\text{C}_{5.75}\text{B}_{4.6}$ and $\text{Fe}_{77}\text{Al}_{2.14}\text{Ga}_{0.86}\text{P}_{11}\text{C}_5\text{B}_4$, respectively.¹⁷ The alloy ingots were prepared by induction melting the mixtures of pure Fe, Al, and Ga metals, premelted Fe–P and Fe–C and pure crystalline boron in an argon atmosphere. Rapidly solidified alloy sheets with various thicknesses ranging from 15 to 320 μm were prepared, through the control of roll velocity, by a single roll melt spinning method. The amorphous nature was confirmed by x-ray diffraction. The thermal stability associated with the glass transition, the supercooled liquid region and crystallization were examined by differential scanning calorimetry (DSC) of a heating rate of 0.67 K/s. The magnetic properties: saturation magnetization (σ_s), coercive force (H_c), permeability (μ_e) at 1 kHz, saturation magnetostriction (λ_s) and core loss (W) were measured at room temperature with a vibrating sample magnetometer (VSM), a B – H loop tracer, an impedance analyzer, a three-terminal capacitance apparatus and a single sheet tester (SST), respectively.

Figure 1 shows the DSC curves for the melt-spun $\text{Fe}_{70}\text{Al}_5\text{Ga}_2\text{P}_{12.65-x}\text{C}_{5.75}\text{B}_{4.6}\text{Si}_x$ ($x=0-4$) and $\text{Fe}_{77}\text{Al}_{2.14}\text{Ga}_{0.86}\text{P}_{11-x}\text{C}_5\text{B}_4\text{Si}_x$ ($x=0-3$) alloy sheets with a thickness of about 30 μm as a function of Si content. One can see an increase in specific heat (endothermic reaction) due to a glass transition, followed by a supercooled liquid region for the samples containing $x=0$ to 3 at. % for

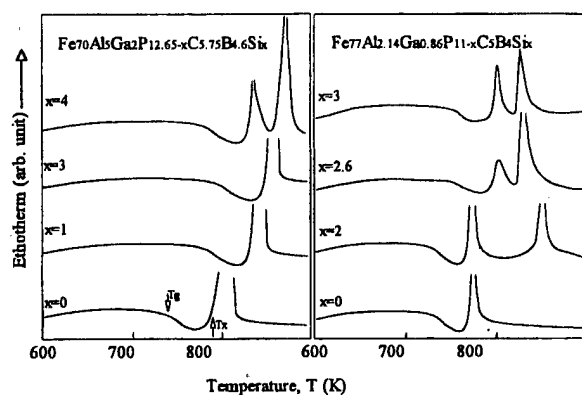


FIG. 1. Changes in DSC curves for the $\text{Fe}_{70}\text{Al}_5\text{Ga}_2\text{P}_{12.65-x}\text{C}_{5.75}\text{B}_{4.6}\text{Si}_x$ and $\text{Fe}_{77}\text{Al}_{2.14}\text{Ga}_{0.86}\text{P}_{11-x}\text{C}_5\text{B}_4\text{Si}_x$ alloy sheets with a thickness of about $30\text{ }\mu\text{m}$ as a function of Si content.

$\text{Fe}_{70}\text{Al}_5\text{Ga}_2\text{P}_{12.65-x}\text{C}_{5.75}\text{B}_{4.6}\text{Si}_x$ and $x=0\text{ at. }\%$ for $\text{Fe}_{77}\text{Al}_{2.14}\text{Ga}_{0.86}\text{P}_{11-x}\text{C}_5\text{B}_4\text{Si}_x$ and then an exothermic reaction, indicating that crystallization of the amorphous phase takes place through a single stage. The latter leads to simultaneous precipitation of more than two kinds of crystalline phase, including $\alpha\text{-Fe}$, Fe_3B , Fe_3P , Fe_2B , and Fe_3C . A supercooled liquid region and two exothermic peaks due to the two-stage crystallization are observed for the samples containing 4 at. % Si for $\text{Fe}_{70}\text{Al}_5\text{Ga}_2\text{P}_{12.65-x}\text{C}_{5.75}\text{B}_{4.6}\text{Si}_x$ and $\geq 2\text{ at. }\%$ Si for the $\text{Fe}_{77}\text{Al}_{2.14}\text{Ga}_{0.86}\text{P}_{11-x}\text{C}_5\text{B}_4\text{Si}_x$. The first and second peaks are due to the crystallization of $\alpha\text{-Fe}$ and Fe_3B and of Fe_3P , Fe_2B and Fe_3C for both alloy series.

Figures 2(a) and 2(b) plot the ΔT_x and t_{max} as a function of Si content. The ΔT_x increases with increasing Si content up to 3 at. % for $\text{Fe}_{70}\text{Al}_5\text{Ga}_2\text{P}_{12.65-x}\text{C}_{5.75}\text{B}_{4.6}\text{Si}_x$ and up to 2.6 at. % for $\text{Fe}_{77}\text{Al}_{2.14}\text{Ga}_{0.86}\text{P}_{11-x}\text{C}_5\text{B}_4\text{Si}_x$, then decreases rapidly. There is a clear tendency for t_{max} to increase with increasing ΔT_x .

Figure 3 shows the relation between the ratio of ΔT_x to ΔT_x at $x=0\text{ at. }\%$ ($\Delta T_x/\Delta T_x(\text{Si}=0\text{ at. }\%)$) and the ratio of Si content to total Si and P content ($\text{Si}/(\text{Si}+\text{P})$). The $\Delta T_x/\Delta T_x(\text{Si}=0\text{ at. }\%)$ increases with increasing $\text{Si}/(\text{Si}+\text{P})$, and reaches the maximum value at $\text{Si}/(\text{Si}+\text{P})=24\%$, then decreases with increasing ($\text{Si}/(\text{Si}+\text{P})$) for both alloy series. This fact indicates that the replacement of P by Si as $\text{Si}/(\text{Si}+\text{P})=24\%$ causes the greatest increase in ΔT_x and t_{max} for Fe-Ga-Al-P-C-B-Si glassy alloys.

It is important to achieve high thermal stability of the supercooled liquid for increase in the glass forming ability. That is, the necessity of long-range rearrangements of the constituent elements causes the retardation of the crystallization reaction, leading to the high stability of the supercooled liquid region and the large glass forming ability. It is therefore presumed that the atomic rearrangements are most difficult in case of $\text{Si}/(\text{Si}+\text{P})=24\%$ for these alloys. The atomic sizes of the metalloids change in the order $\text{Si}>\text{P}>\text{B}>\text{C}$. The increase in the variety of atomic sizes also implies that the atomic rearrangement for the precipitation reaction becomes difficult. Furthermore, the similarity of the atomic sizes and the large negative heats of mixing¹⁸ between P and Si allow us to presume that Si is preferentially dissolved into Fe_3P and the precipitation of the $\text{Fe}_3(\text{P}, \text{Si})$ phase becomes more

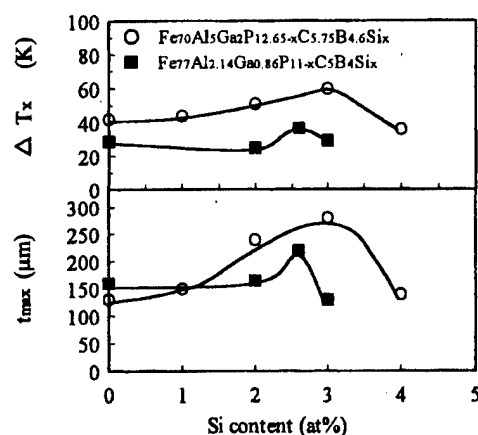


FIG. 2. The changes of (a) the ΔT_x and (b) the t_{max} for the $\text{Fe}_{70}\text{Al}_5\text{Ga}_2\text{P}_{12.65-x}\text{C}_{5.75}\text{B}_{4.6}\text{Si}_x$ and $\text{Fe}_{77}\text{Al}_{2.14}\text{Ga}_{0.86}\text{P}_{11-x}\text{C}_5\text{B}_4\text{Si}_x$ alloy sheets with a thickness of about $30\text{ }\mu\text{m}$ as a function of Si content.

difficult as a results of the need for the rearrangements of two kinds of metalloid atoms. This mechanism is thought to cause the most effective extension of the supercooled liquid region when the P element in these glassy alloys is replaced by Si such that $\text{Si}/(\text{Si}+\text{P})=24\%$.

Figures 4(a), 4(b), and 4(c) show the dependence of H_c , μ_e and λ_s on Si content for $\text{Fe}_{70}\text{Al}_5\text{Ga}_2\text{P}_{12.65-x}\text{C}_{5.75}\text{B}_{4.6}\text{Si}_x$ and $\text{Fe}_{77}\text{Al}_{2.14}\text{Ga}_{0.86}\text{P}_{11-x}\text{C}_5\text{B}_4\text{Si}_x$ glassy alloys for a sample thickness of $30\text{ }\mu\text{m}$. The H_c of these glassy alloys are below 3 A/m up to 3 at. % Si for $\text{Fe}_{70}\text{Al}_5\text{Ga}_2\text{P}_{12.65-x}\text{C}_{5.75}\text{B}_{4.6}\text{Si}_x$ and up to 2.6 at. % Si for $\text{Fe}_{77}\text{Al}_{2.14}\text{Ga}_{0.86}\text{P}_{11-x}\text{C}_5\text{B}_4\text{Si}_x$. On the other hand, the H_c drastically increases beyond 3 at. % Si and 2.6 at. % Si, respectively, for the two systems. The μ_e increases with increasing Si content up to 3 at. % Si for $\text{Fe}_{70}\text{Al}_5\text{Ga}_2\text{P}_{12.65-x}\text{C}_{5.75}\text{B}_{4.6}\text{Si}_x$ and up to 2.6 at. % Si for $\text{Fe}_{77}\text{Al}_{2.14}\text{Ga}_{0.86}\text{P}_{11-x}\text{C}_5\text{B}_4\text{Si}_x$, then decreases for higher Si contents. The influence of Si addition on H_c and μ_e is not reflected in the data for λ_s , and may be related to the glass forming ability. It is, therefore, speculated that the alloys of higher glass forming ability have a more homogeneous structure thus giving superior soft magnetic properties. A detailed investigation of the microstructure is expected to shed some light on the reason for the effect of Si addition on the soft magnetic properties.

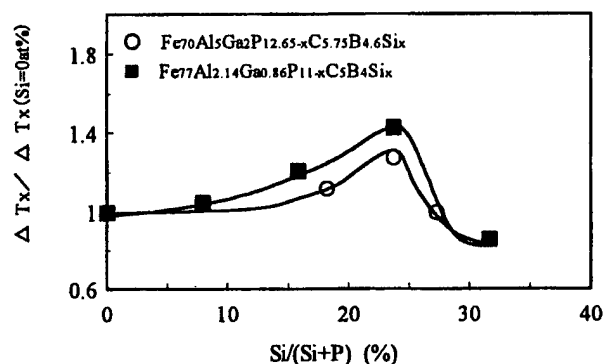


FIG. 3. The relation between the ratio of ΔT_x to ΔT_x at Si free ($\Delta T_x/\Delta T_x(\text{Si}=0\text{ at. }\%)$) and the ratio of Si content total Si and P content ($\text{Si}/(\text{Si}+\text{P})$).

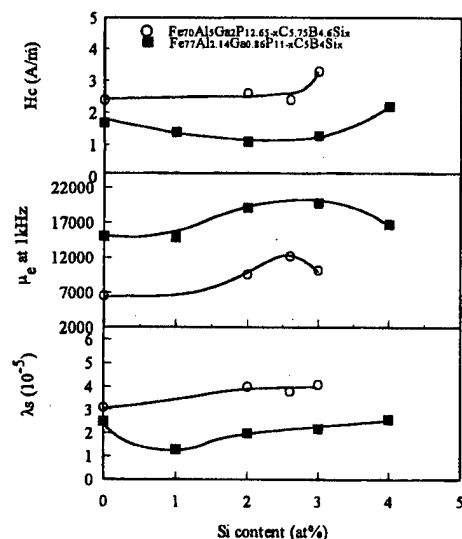


FIG. 4. The influence of Si content on (a) H_c , (b) μ_e and (c) λ_s for the $\text{Fe}_{70}\text{Al}_5\text{Ga}_2\text{P}_{12.65-x}\text{C}_{5.75}\text{B}_{4.6}\text{Si}_x$ and $\text{Fe}_{77}\text{Al}_{2.14}\text{Ga}_{0.86}\text{P}_{11-x}\text{C}_5\text{B}_4\text{Si}_x$ alloy sheets with a thickness of about 30 μm .

Figure 5 shows the changes in core losses at $f=50$ Hz and $B_m=1.0$ T as a function of sample thickness for $\text{Fe}_{77}\text{Al}_{2.14}\text{Ga}_{0.86}\text{P}_{8.4}\text{C}_5\text{B}_4\text{Si}_{2.6}$ glassy alloy and amorphous $\text{Fe}_{78}\text{Si}_9\text{B}_{13}$ alloy. The structure of both samples confirmed by x-ray diffractometry are also shown in Fig. 5. The core loss for the $\text{Fe}_{77}\text{Al}_{2.14}\text{Ga}_{0.86}\text{P}_{8.4}\text{C}_5\text{B}_4\text{Si}_{2.6}$ is under 0.3 W/kg at the thickness up to 210 μm . However, that for amorphous $\text{Fe}_{78}\text{Si}_9\text{B}_{13}$ alloy is over 0.3 W/kg at the thickness over 70 μm , and rapidly increase over 100 μm , because of precipitation of Fe_3B crystalline phase. It is well known that the precipitation of crystalline makes the soft magnetic proper-

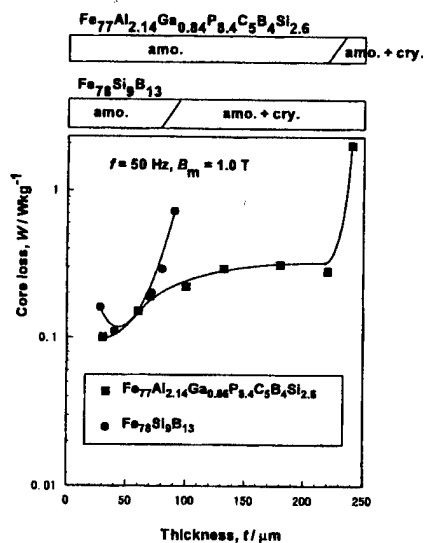


FIG. 5. Changes in core losses at $f=50$ Hz and $B_m=1.0$ T as a function of sample thickness for $\text{Fe}_{77}\text{Al}_{2.14}\text{Ga}_{0.86}\text{P}_{8.4}\text{C}_5\text{B}_4\text{Si}_{2.6}$ glassy alloy and amorphous $\text{Fe}_{78}\text{Si}_9\text{B}_{13}$ alloy. The structure of both sample confirmed by x-ray diffractometry are also shown.

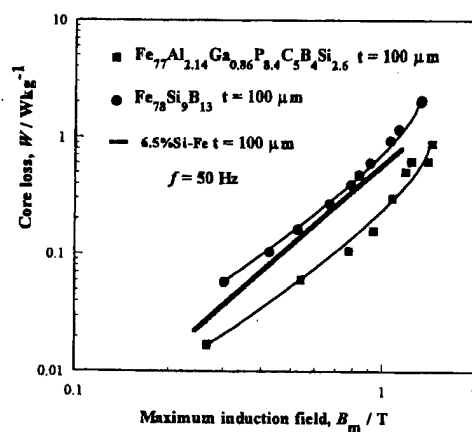


FIG. 6. Changes in core losses at 50 Hz for $\text{Fe}_{77}\text{Al}_{2.14}\text{Ga}_{0.86}\text{P}_{8.4}\text{C}_5\text{B}_4\text{Si}_{2.6}$ alloy sheet, $\text{Fe}_{78}\text{Si}_9\text{B}_{13}$ amorphous ribbon and 6.5% Si-steel with a thickness of about 100 μm as a function of B_m .

ties inferior.¹⁹ Therefore, it can be said that the amorphousness of Fe–Al–Ga–P–C–B–Si glassy alloy is much higher than that of amorphous Fe–Si–B alloy.

Figure 6 shows the core losses at 50 Hz for $\text{Fe}_{77}\text{Al}_{2.14}\text{Ga}_{0.86}\text{P}_{8.4}\text{C}_5\text{B}_4\text{Si}_{2.6}$ glassy alloy, amorphous $\text{Fe}_{78}\text{Si}_9\text{B}_{13}$ alloy and for 6.5% silicon steel,²⁰ having in each case a thickness of 100 μm , as a function of maximum magnetic flux density (B_m). The core loss for $\text{Fe}_{77}\text{Al}_{2.14}\text{Ga}_{0.86}\text{P}_{8.4}\text{C}_5\text{B}_4\text{Si}_{2.6}$ glassy alloy is much lower than those of other magnetic alloys for the whole range of B_m . Viewed in this light, Fe–Al–Ga–P–C–B glassy alloys containing Si can be regarded as having good potential as bulk soft magnetic materials.

¹T. Mizoguchi, K. Yamauchi, and H. Kiyajima, *Amorphous Magnetism* (Plenum, New York, 1973), p. 325.

²H. Fujimori, T. Masumoto, Y. Obi, and M. Kikuchi, *Jpn. J. Appl. Phys.* **13**, 1889 (1974).

³M. Hagiwara, A. Inoue, and T. Masumoto, *Sci. Rep. Res. Inst. Tohoku Univ. A* **29**, 351 (1981).

⁴A. Inoue, K. Ohtera, K. Kita, and T. Masumoto, *Jpn. J. Appl. Phys., Part 2* **30**, L2248 (1988).

⁵A. Inoue, M. Kohinata, A. P. Tsai, and T. Masumoto, *Mater. Trans., JIM* **30**, 378 (1989).

⁶A. Inoue, T. Zhang, and T. Masumoto, *Mater. Trans., JIM* **30**, 965 (1989).

⁷A. Inoue, H. Yamaguchi, T. Zhang, and T. Masumoto, *Mater. Trans., JIM* **31**, 104 (1990).

⁸A. Inoue, T. Zhang, and T. Masumoto, *Mater. Trans., JIM* **31**, 177 (1990).

⁹T. Zhang, A. Inoue, and T. Masumoto, *Mater. Trans., JIM* **32**, 1005 (1991).

¹⁰A. Pekar and W. L. Johnson, *Appl. Phys. Lett.* **63**, 2342 (1993).

¹¹T. Zhang, A. Inoue, and T. Masumoto, *Mater. Trans., JIM* **32**, 1005 (1991).

¹²A. Inoue, N. Nishiyama, and T. Matsuda, *Mater. Trans., JIM* **37**, 181 (1996).

¹³A. Inoue, *Mater. Sci. Forum* **179–181**, 691 (1995).

¹⁴A. Inoue, *Mater. Trans., JIM* **36**, 691 (1995).

¹⁵A. Inoue, *Sci. Rep. Res. Inst. Tohoku Univ. A* **42**, 1 (1996).

¹⁶T. Mizushima, A. Makino, and A. Inoue, *IEEE Trans. Mag.* (in press).

¹⁷T. Mizushima, A. Makino, and A. Inoue, *Sci. Rep. Res. Inst. Tohoku Univ. A* **43**, 123 (1997).

¹⁸F. R. de Boer, R. Boom, W. C. M. Mattens, A. R. Miedema, and A. K. Niessen, *Cohesion in Metals* (Elsevier Science, Amsterdam, 1988), p. 236.

¹⁹H. N. Ok and Morrish, *J. Appl. Phys.* **52**, 1835 (1981).

²⁰Y. Takada, M. Abe, S. Masuda, and J. Inagaki, *J. Appl. Phys.* **64**, 5367 (1988).

Application of nanocrystalline soft magnetic Fe-M-B (M=Zr, Nb) alloys to choke coils

Y. Naitoh, T. Bitoh, T. Hatanai, and A. Makino
Central Res. Lab., Alps Electric Co., Ltd., Nagaoka 940, Japan

A. Inoue
Institute for Materials Research, Tohoku University, Sendai 980-77, Japan

We have developed a choke coil made of new nanocrystalline soft magnetic Fe-M-B (M=Zr, Nb) alloys ("NANOPERM™" material) which exhibit high saturation magnetic induction (B_s), above 1.5 T, excellent soft magnetic properties and zero magnetostriction. A choke coil made of NANOPERM™ material exhibits good dc bias characteristics of inductance because of the high B_s . Furthermore, the choke coil made from NANOPERM™ material showed 1/3rd the temperature rise shown by a core made from Fe-Si-B amorphous alloy. The low core loss and high B_s of NANOPERM™ material allow the reduction of the core size. It is concluded that NANOPERM™ is suitable as a core material for choke coils. © 1998 American Institute of Physics. [S0021-8979(98)36611-6]

I. INTRODUCTION

In increasing instances the reactors of phase modifying equipment are disabled by line current which contains higher harmonic distortion generated by switching regulators, etc. Line current correction to sinusoidal wave by using active filters is a useful method to prevent distortion in the reactors. High saturation magnetic induction (B_s) and low core loss are required for the core material of choke coils as active filters because high frequency current with large amplitude superimposed on direct current flows into the choke coil. It has been reported by us that new nanocrystalline soft magnetic Fe-M-B (M=Zr, Nb) alloys ("NANOPERM™" material) show high B_s above 1.5 T, excellent soft magnetic properties, low core losses and sufficiently small magnetostriction.¹⁻⁴ Figure 1 shows the relation between B_s and permeability (μ_e) at 1 kHz for NANOPERM™ material and other soft magnetic materials. NANOPERM™ material is found to be situated in the top right corner of the figure. NANOPERM™ material is therefore expected to be used as core material for choke coils as active filters. In this article, we report the characteristics of the choke coil made of NANOPERM™ material.

II. EXPERIMENTAL PROCEDURE

The $\text{Fe}_{84}\text{Zr}_{3.5}\text{Nb}_{3.5}\text{B}_8\text{Cu}_1$ alloy was selected an example of NANOPERM™ material in this study. The NANOPERM™ ribbon with 20 μm in thickness was produced by using a single-roller melt-spinning method in an Ar atmosphere. In order to compare the magnetic properties, a commercial $\text{Fe}_{78}\text{Si}_9\text{B}_{13}$ amorphous alloy (METGLAS® alloy 2605 S-2) ribbon with the same thickness as the NANOPERM™ material was prepared. Table I shows typical magnetic properties for the alloys.^{3,6}

Toroidal samples were prepared as follows. A mixture of MgO powders and sodium silica solution (water glass) was applied to both sides of the ribbons to prevent electrical contact between the ribbons. The ribbons were wound into toroidal

cores with 38 mm in outer diameter, 23 mm in inner diameter and 15 mm in height. The annealing treatment of the cores was carried out in vacuum by keeping the cores at 953 K for 600 s (NANOPERM™) or at 643 K for 7.2 ks (Fe-Si-B amorphous alloy). The annealed cores were encapsulation in an epoxy resin. Then the cores were processed by cutting a 2 mm air gap and inserting an insulating material in the gap.

Measurements of core losses were carried out using an ac B - H analyzer after annealing, after encapsulation, and after introducing an air gap. dc bias characteristics were measured after introducing an air gap.

III. RESULTS AND DISCUSSION

Table II shows the size, the lamination factor and the effective cross section of the cores. The size of the cores is almost the same. Figure 2 shows the change in core loss of the cores after annealing, encapsulation, and introducing an

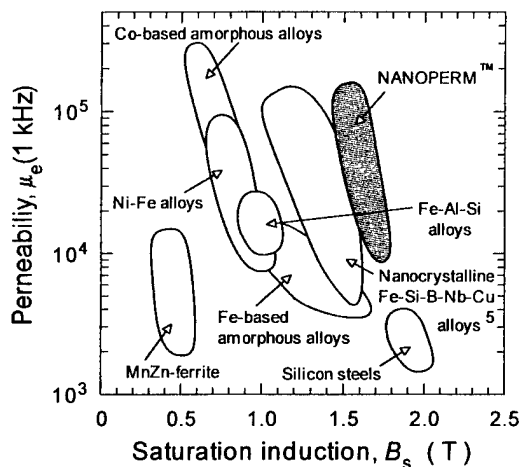


FIG. 1. Relationship between B_s and μ_e at 1 kHz for NANOPERM™, the nanocrystalline Fe-Si-B-Nb-Cu alloys (Ref. 5) and conventional soft magnetic materials.

TABLE I. Typical example of the saturation induction (B_s), permeability (μ), core loss (W), and saturation magnetostriction (λ_s) for the alloys (Refs. 3 and 6).

Alloys	$B_s(T)$	$ \mu $		W (W/kg)		$\lambda_s(10^{-6})$
		1 kHz	100 kHz	1 kHz, 1 T	100 kHz, 0.1 T	
NANOPERM™	1.53	100 000	18 000	1.1	15	~0
Fe-Si-B amorphous alloy	1.56	10 000	5 000	4.0	48	+27

TABLE II. Outer diameter (OD), inner diameter (ID), height (H), lamination factor (K), and effective cross section (S).

Alloys	OD (mm)	ID (mm)	H (mm)	K (%)	S (mm ²)
NANOPERM™	37.1	23.2	15.5	77.1	79.0
Fe-Si-B amorphous alloy	36.9	22.9	15.5	65.8	71.4

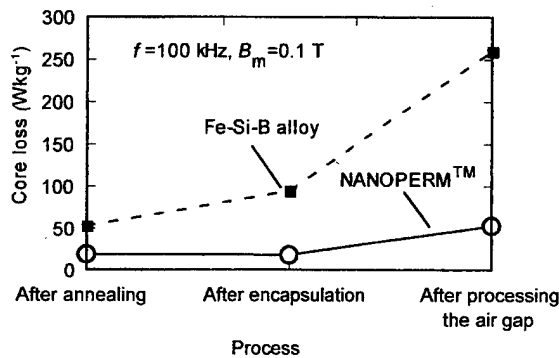
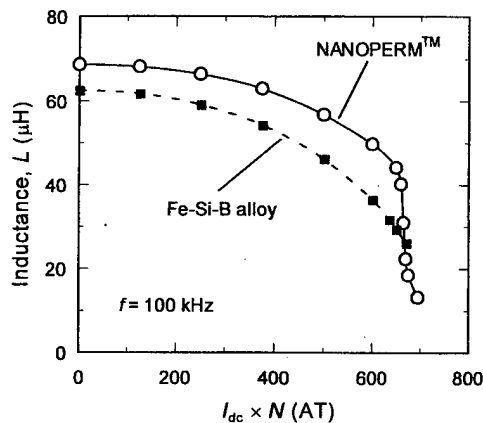


FIG. 2. Change in the core loss of the cores with annealing, encapsulation, and processing the air gap.

FIG. 3. Change of inductance as a function of dc bias current (I_{dc}) times number of turns (N) for choke coils made of NANOPERM™ and Fe-Si-B alloy.

air gap. The core loss of NANOPERM™ core after annealing is about 1/3rd as large as that of the Fe-Si-B core. After encapsulation in the epoxy resin, the core loss of the Fe-Si-B core showed a large increase due to stress from the resin. Since the magnetostriction of the Fe-Si-B amorphous alloy is large, the soft magnetic properties are inferior in the stressed state. On the other hand, the NANOPERM™ core exhibits almost the same low core loss value as that of the core before encapsulation because of its zero magnetostriction. The encapsulation treatment is necessary to cut an air gap. It can be said that the zero magnetostriction is necessary for the toroidal core with a gap to exhibit a low core loss. After introducing an air gap, the core loss increase in both NANOPERM™ and Fe-Si-B alloys. However, the NANOPERM™ core exhibits smaller core loss which is only 1/5th that of the Fe-Si-B core.

Figure 3 shows dc bias characteristics of the gapped cores with 25 turn coil. The inductance of the NANOPERM™ and the Fe-Si-B cores show a decrease around $N \times I = 700$ AT because the saturation magnetic inductions of both the core materials are almost equal. When leakage flux from the air gap can be neglected, inductance (L) of the gapped core can be written as

$$L = N^2 S / \left(\frac{l - l_g}{\mu} + \frac{l_g}{\mu_0} \right), \quad (1)$$

where l_g is gap length, l is length of magnetic path, μ is permeability of material, and μ_0 is permeability of vacuum. When μ is much larger than μ_0 , a term of $(l - l_g)/\mu$ can be neglected. Therefore, the inductance of the gapped core is independent of μ . However, although the NANOPERM™ and the Fe-Si-B cores have the same size and the same gap length, the inductance of the NANOPERM™ core is 10% larger than that of the Fe-Si-B core at a dc bias current of zero. The difference in inductances is caused by the difference in effective cross sections of the cores. As shown in Table II, the effective cross section of the NANOPERM™ core is 14% larger than that of the Fe-Si-B core, which is in good agreement with the difference in inductances.

Next, we have examined the relation between the choke coil loss and temperature rise (ΔT) of the choke cores. The miniaturization of the core is limited by B_s and by the core loss of the core material. If the core loss is large, the core volume should be increased because maximum magnetic induction (B_m) should be decreased to reduce ΔT . Figure 4 shows the B_m dependence of the choke coil loss which consists of the core loss and the copper loss. The operating frequency is 50 kHz and B_m is changed from 0.01 to 0.1 T. The choke coil loss is 4.2 W for Fe-Si-B alloy, and is 1.3 W for

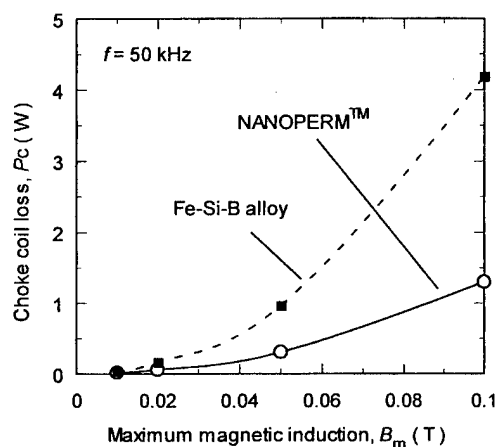


FIG. 4. B_m dependence of the choke coil loss, which consists of the core loss and the copper loss.

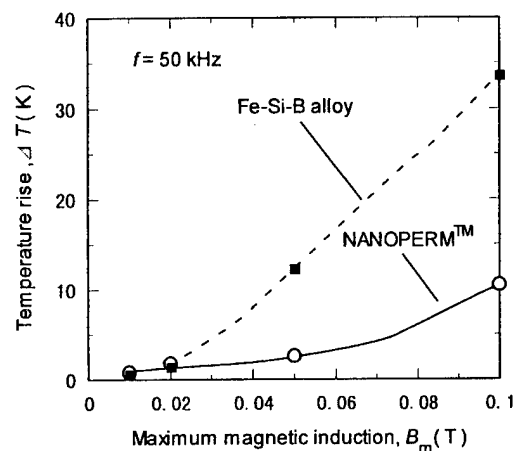


FIG. 5. ΔT of the choke coils as a function of B_m .

NANOPERM™ material at $B_m = 0.1$ T. Figure 5 shows ΔT of the choke coils as a function of B_m . When $B_m = 0.1$ T, ΔT is 34 K for the Fe-Si-B choke coil and 11 K for the NANOPERM™ choke coil, respectively. The ΔT of the NANOPERM™ choke coil is only 32% that of the Fe-Si-B one. In order to achieve a small ΔT of 11 K for Fe-Si-B core, it is necessary to reduce the B_m value to 0.05 T. This means that core volume should be doubled for the Fe-Si-B choke coil.

NANOPERM™ shows a high B_s which is comparable to that of Fe-Si-B amorphous alloys and its choke coil loss is only 1/3rd that of Fe-Si-B amorphous alloys. The very low loss allows a reduction in core size. It is concluded that the

size of the choke coils can be significantly reduced by replacing the core material from Fe-Si-B amorphous alloys to NANOPERM™. Therefore, NANOPERM™ material is suitable as core material for the choke coils of active filters.

¹K. Suzuki, N. Kataoka, A. Inoue, A. Makino, and T. Masumoto, *Mater. Trans., JIM* **31**, 743 (1990).

²A. Makino, K. Suzuki, A. Inoue and T. Masumoto, *Mater. Trans., JIM* **32**, 551 (1991).

³A. Makino, A. Inoue, and T. Masumoto, *Mater. Trans., JIM* **36**, 924 (1995).

⁴A. Makino, T. Hatanai, A. Inoue, and T. Masumoto, *Mater. Sci. Eng., A* **226-228**, 594 (1997).

⁵Y. Yoshizawa, S. Oguma, A. Hiraki and K. Yamauchi, *Hitachi Metals Tech. Rev.* **5**, 13 (1989).

⁶R. Hasegawa, *J. Non-Cryst. Solids* **61-62**, 725 (1984).

Soft magnetic properties and structures of nanocrystalline Fe-Al-Si-B-Cu-Nb alloy ribbons

B. J. Tate, B. S. Parmar, I. Todd, and H. A. Davies^{a)}

Department of Engineering Materials, University of Sheffield, Mappin Street, Sheffield S1 3JD, United Kingdom

M. R. J. Gibbs

Department of Physics, University of Sheffield, Hounsfield Road, Sheffield S3 7RH, United Kingdom

R. V. Major

Telcon Limited, Napier Way, Crawley, West Sussex RH10 2RB, United Kingdom

The effects of Al on the magnetic properties of nanocrystalline $\text{Fe}_{73.5-X}\text{Al}_X\text{Si}_{13.5}\text{B}_9\text{Cu}_1\text{Nb}_3$ alloy ribbons, where $0 \leq X \leq 10$, are reported for the first time. The evolution of the structure and magnetic properties of the ribbons, which were initially cast into the amorphous state in an inert gas environment at subatmospheric pressure, were studied as a function of annealing temperature T_{ann} . The minimum dc coercivity developed during annealing, H_c^{min} , was found to decrease significantly with increasing Al content from 0.5 A/m at $X=0$ to 0.3 A/m at $X=2$ and to remain at approximately this level over the range $2 < X \leq 8$ before rising to 0.4 A/m at $X=10$. The saturation polarization, J_s , was, however, found to decrease linearly over this range from $J_s=1.5$ T at $X=0$ to $J_s=0.9$ T at $X=10$ for samples exhibiting H_c^{min} . As there was little significant reduction in the mean crystallite size, d_g , at H_c^{min} with increasing X , this decrease in coercivity was considered to result from a reduction of the magnetocrystalline anisotropy, K_1 , of the crystallites as a result of the incorporation of Al. © 1998 American Institute of Physics. [S0021-8979(98)49811-6]

I. INTRODUCTION

Nearly a decade ago Yoshizawa *et al.*¹ of Hitachi Research Laboratories showed that small additions of Nb and Cu to a base FeBSi glass forming composition induce the initially amorphous as-spun ribbon to devitrify, on controlled annealing, to a nanocomposite structure of FeSi crystallites, of mean diameter 10–15 nm in a glassy matrix which is enriched in Nb and B. The Cu and Nb act, respectively, to maximize the number density of crystal nuclei and to retard grain growth, thus promoting the formation of an ultrafine grain structure. Contrary to classical behavior of pinning of domains at grain boundaries, for grain diameters (d_g) ≤ 50 nm the coercivity H_c diminishes with decreasing d_g down to $\sim 0.5 \text{ Am}^{-1}$ at ~ 10 nm while, correspondingly, the initial permeability μ_i increases to a peak value of $\sim 10^5$. These properties are better than for amorphous Fe-based alloys and are comparable with those of Co-based metallic glasses which has significant technoeconomic significance. Thus, this so-called Finemet® alloy has stimulated the curiosity of a large body of magnetic and materials scientists.

A number of workers have investigated the effects on the soft magnetic properties of the substitution of additional alloying elements for Fe in the $\text{Fe}_{73.5}\text{Si}_{13.5}\text{B}_9\text{Cu}_1\text{Nb}_3$ alloy composition to further improve the properties [e.g., Co,² Al³] as well as the substitution of Cr, V, Ta, etc., for Nb.⁴ No significant improvements in soft magnetic properties were reported over those of the base composition with the exception of the study of Lim *et al.*³ which found that substitution

of Al for Fe in $\text{Fe}_{73.5-X}\text{Al}_X\text{Si}_{13.5}\text{B}_9\text{Cu}_1\text{Nb}_3$ in the range $0 \leq X \leq 1$ improved the dc coercivity (H_c) but caused other soft magnetic properties, i.e., relative ac permeability (μ) and saturation magnetostriction (λ_s) to deteriorate. In this article we present initial data from an extensive study of $\text{Fe}_{73.5-X}\text{Al}_X\text{Si}_{13.5}\text{B}_9\text{Cu}_1\text{Nb}_3$ with $0 \leq X \leq 10$. The rationale behind this work is that ternary FeSiAl crystals exhibit lower K_1 than those of the binary FeSi system and that the saturation magnetostriction λ_s of the nanocrystallites can be readily controlled⁵ thus leading to the possibility of the development of alloys with lower λ_s than Finemet®.

II. EXPERIMENT

A series of $\text{Fe}_{73.5-X}\text{Al}_X\text{Si}_{13.5}\text{B}_9\text{Cu}_1\text{Nb}_3$ alloy ingots with compositions in the range $0 \leq X \leq 10$ were prepared by rf melting of high purity elements in a flowing Ar atmosphere. Ribbons of cross section typically $20 \mu\text{m} \times 2.0 \text{ mm}$ and surface roughness less than $1.5 \mu\text{m}$ were prepared by melt spinning these ingots in helium at 1/3 atm ambient pressure. The resultant ribbons were cut into 100 mm lengths and thermal treatments were performed in an inert Ar atmosphere in a conventional furnace for 1 h after which the samples were allowed to air cool. The structure of the alloys, both in the as-cast state and after subsequent heat treatment, was confirmed by x-ray diffraction using Co $K\alpha$ radiation, and the mean crystallite size (d_g) for the Fe-Si phase estimated from the half peak breadth of the (110) x-ray diffraction peak via the Scherrer equation. TEM was also employed for selective studies of the nanostructure and grain size. The saturation polarization (J_s), H_c , and λ_s were measured using a vibrating sample magnetometer (VSM) hysteresis loop

^{a)}Electronic mail: h.a.davis@sheffield.ac.uk

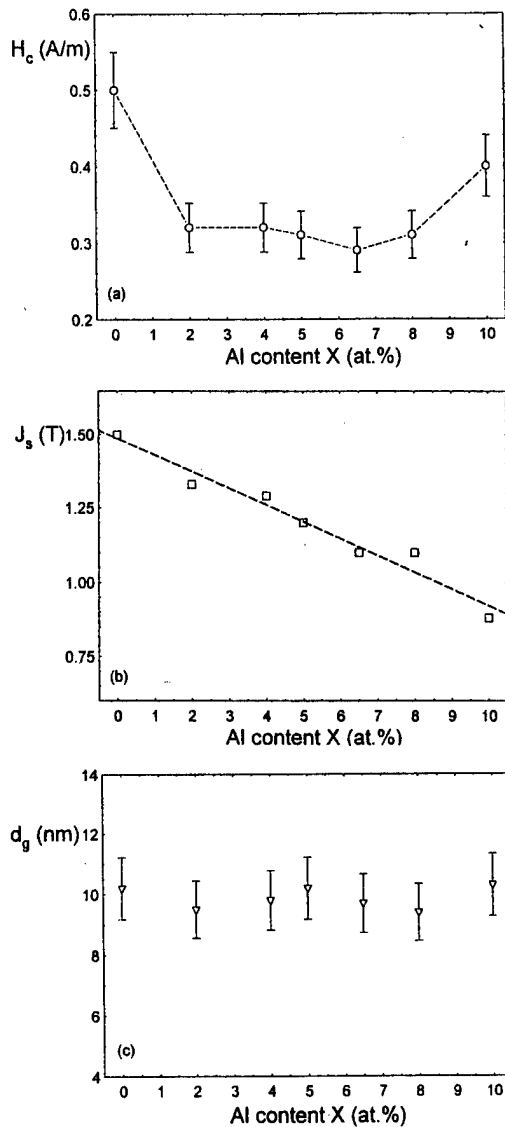


FIG. 1. Variation in (a) the minimum coercivity (H_c^{\min}), (b) saturation polarization (J_s), and (c) crystallite diameter (d_g) for optimally annealed samples as a function of Al content X.

tracer⁶ and the small angle magnetisation rotation (SAMR) method,⁷ respectively. The loop tracer has been specifically designed for reliable and reproducible measurements of high μ low H_c materials.

III. RESULTS AND DISCUSSION

The results presented in this section are for samples heat treated at an optimum annealing temperature ($T_{\text{ann}}^{\text{opt}}$) to develop the minimum dc coercivity H_c^{\min} for each of the compositions investigated. This was found to be 540 °C for $X=0$ and 520 °C for all of the Al-containing compositions. Figure 1(a) shows the dependence of minimum coercivity H_c^{\min} as a function of Al substitution X. Following a substantial (40%) initial decrease, from 0.5 A/m at $X=0$ to 0.3 A/m for $X=2$, H_c^{\min} remains approximately constant at 0.3 A/m up to $X=8$ at. %; it then increases to 0.4 A/m at $X=10$ at. %. The effect of substituting Fe for Al on the magnitude of J_s can be seen in Fig. 1(b). The linear decrease in J_s , from 1.5

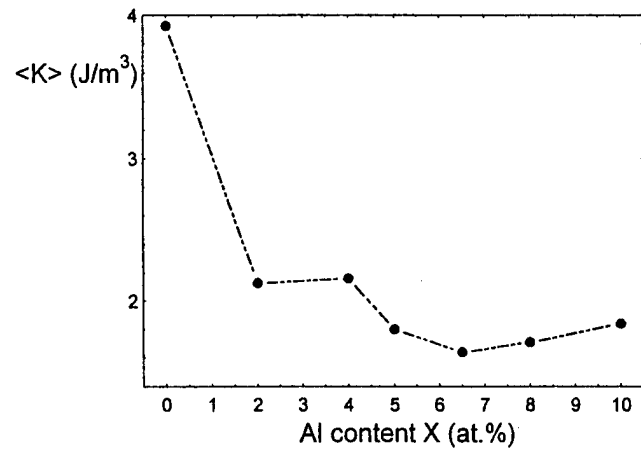


FIG. 2. Variation in the effective anisotropy $\langle K \rangle$, derived from Eq. (2), as a function of the aluminum content X of the alloys.

T for the base composition to 0.9 T at $X=10$ (a rate of ~ 0.06 T/at. % Al) is as might be expected for replacement of Fe by a nonferromagnetic component. Figure 1(c) shows that the aluminium content does not influence significantly the mean crystallite diameter for alloys in their optimum condition, i.e., d_g remains constant at 10 ± 1 nm. This was also confirmed by direct observation of the alloy nanostructure by TEM. This observation contrasts with that of Lim *et al.*³ who reported d_g to decrease upon the addition of 0.1 at. % Al and to remain constant thereafter although the magnitude of this decrease was not disclosed.

These values of H_c^{\min} and J_s allow the variation in effective magnetocrystalline anisotropy $\langle K \rangle$ to be estimated as a function of X. By using the random anisotropy model (RAM) developed by Alben *et al.*⁸ for amorphous ferromagnets Herzer⁹ showed that, for d_g less than the exchange length L_{ex} (~ 40 nm), $\langle K \rangle$ could be approximated by

$$\langle K \rangle \approx K_1^4 d_g^6 / A^3 \quad (1)$$

and that H_c and $\langle K \rangle$ were related thus

$$H_c = p_c \times \frac{\langle K \rangle}{J_s} \quad (2)$$

which leads to the following relationship between coercivity and grain diameter:

$$H_c \approx p_c \times \frac{K_1^4 d_g^6}{A^3 J_s}, \quad (3)$$

where p_c is a constant and A is the exchange stiffness inside the crystal with all other symbols as previously defined. Assuming⁹ that the composition of the crystallites is Fe \sim 20 at. % Si and $A = 1 \times 10^{-11}$ J m⁻¹ and $K_1 = 8 \times 10^3$ J m⁻³ and using the measured values of H_c^{\min} , J_s and d_g for the $X=0$ alloy in Eq. (3) yields a value of 0.19 for the constant p_c . Assuming that this value is applicable for the range of aluminium contents studied we can use the experimentally determined values of H_c^{\min} and J_s to estimate $\langle K \rangle$ from Eq. (2). The variation in $\langle K \rangle$ with respect to X, derived in this way, is shown in Fig. 2.

Equation (1) shows $\langle K \rangle$ to be strongly dependent upon both d_g and K_1 and, as such, both of these factors must be

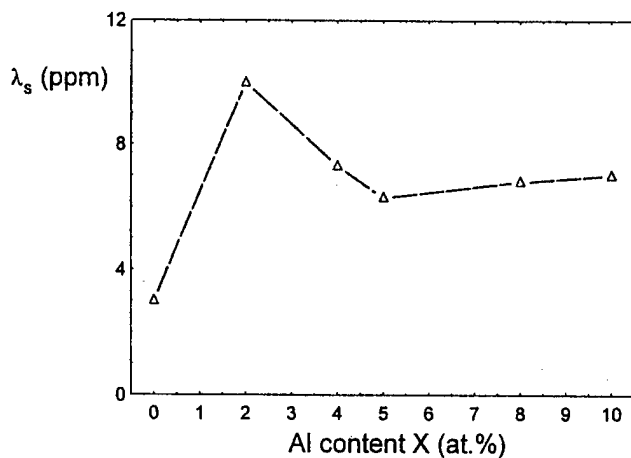


FIG. 3. Variation in the saturation magnetostriction (λ_s) as a function of alloy aluminium content, X .

considered as possible reasons for the observed decrease. $\langle K \rangle$ varies as a d_g^6 so that a 1 nm decrease in d_g could account for the change in $\langle K \rangle$ shown in Fig. 2. As ± 1 nm is estimated to be the precision of the x-ray line broadening determination of d_g it cannot be stated, on this basis, that it is the principal contribution to the decrease in $\langle K \rangle$. However, although it is difficult to establish the absolute value of d_g to better than ± 1 nm by TEM owing to crystallite overlapping effects in the thin foil image, the observations indicated that no change occurred over the range of X studied and thus it is considered that the observed decrease in H_c^{\min} result primarily from a decrease in the magnetocrystalline anisotropy K_1 .

The measured magnetostriction of the Al-alloys exhibiting minimum dc coercivity (Fig. 3) is significantly greater than that of the Al-free alloy, measured at optimum H_c , rising to a maximum of 10×10^{-6} at $X=2$ from 3×10^{-6} at $X=0$ and falling as X increases further to a value of $\lambda_s = 6 \times 10^{-6}$ in the range of $4 \leq X \leq 10$ and are in good agreement with the results of Lim *et al.*³ for $0 \leq X \leq 1$. Figure 4 compares the dependence on annealing temperature of λ_s for the $X=2$ alloy of the present work and those of Yoshizawa *et al.*¹ for the Finemet® composition. Clearly λ_s is very sensitive to T_{ann} in both alloys. In the case of the alloy containing 2 at. % Al, for example, λ_s falls to approximately zero after annealing at 550 °C for 1 h which is significantly smaller than the minimum value of 2.1×10^{-6} developed by the Al-free composition.¹ An advantage of the Al containing alloys is that an ultralow coercivity is developed over a wider range of annealing temperatures than is the case for the Al-free composition, meaning that, if the $X=2$ alloy is optimized with respect to magnetostriction, for example, the coercivity exhibited in this condition is comparable with that of Finemet, i.e., $H_c = 0.5$ A/m.

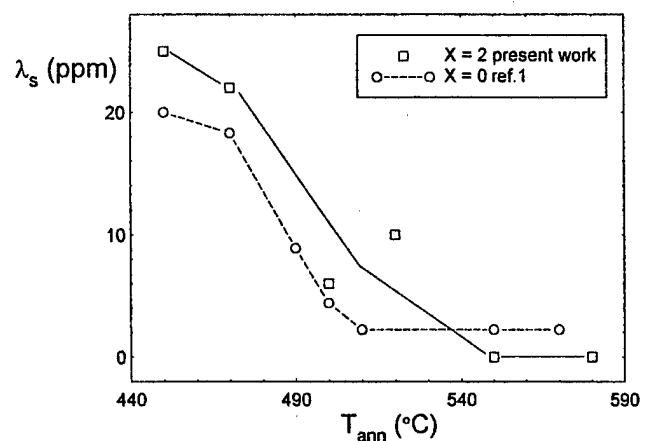


FIG. 4. Comparison of the response of saturation magnetostriction (λ_s) to annealing temperature (T_{ann}) for $X=0$ (Ref. 1) and $X=2$ (present work).

IV. CONCLUSIONS

The soft magnetic properties of nanocrystalline $\text{Fe}_{73.5-X}\text{Al}_X\text{Si}_{13.5}\text{B}_9\text{Cu}_1\text{Nb}_3$ have been investigated in the range of $0 \leq X \leq 10$. It was found that the minimum dc coercivity developed on annealing of the initially amorphous as-spun ribbons showed an initial decrease from 0.5 A/m at $X=0$ to 0.3 A/m at $X=2$ after which H_c^{\min} shows little variation up to $X=8$ beyond which it increases to 0.4 A/m at $X=10$. Over this same range of X the saturation polarization decreases linearly while d_g was determined by x-ray methods to remain at a constant 10 ± 1 nm and TEM confirmed that there was no change in the structure with increasing aluminium substitution. The saturation magnetostriction shows a marked increase over this range of X compared with the base alloy composition. The improvement in the dc coercivity has been attributed to a decrease in the effective anisotropy $\langle K \rangle$ of the alloy and this decrease has been ascribed, on the basis of available evidence, to a decrease in the magnetocrystalline anisotropy of the nanocrystallites. We have also established that, by the optimization of the heat treatment temperature for the $X=2$ material a zero magnetostrictive alloy with a dc coercivity comparable with that of Finemet is achieved.

¹Y. Yoshizawa, S. Oguma, and K. Yamauchi, J. Appl. Phys. **64**, 6044 (1988).

²S. C. Yu, K. S. Kim, Y. S. Cho, and T. K. Kim, IEEE Trans. Magn. **28**, 2421 (1992).

³S. H. Lim, W. K. Pi, T. H. Noh, H. J. Kim, and I. K. Kang, J. Appl. Phys. **73**, 6591 (1993).

⁴Y. Yoshizawa and K. Yamauchi, Mater. Sci. Eng. A **133**, 176 (1991).

⁵M. Takahashi, S. Nishimaki, and T. Wakiyama, J. Magn. Magn. Mater. **66**, 55 (1987).

⁶P. T. Squire, S. M. Sheard, C. H. Carter, and M. R. J. Gibbs, J. Phys. E **21**, 1167 (1988).

⁷K. Narita, J. Yamasaki, and H. Fukunaga, IEEE Trans. Magn. **MAG-16**, 435 (1980).

⁸R. Alben, J. J. Becker, and M. C. Chi, J. Appl. Phys. **49**, 1653 (1978).

⁹G. Herzer, IEEE Trans. Magn. **MAG-26**, 1397 (1990).

Compositional dependence of the effective magnetic anisotropy in nanocrystalline Fe–Zr–B–(Cu) alloys

P. García Tello and J. M. Blanco

Departamento Física Aplicada I, UPV/EHU, 20011, San Sebastián, Spain

N. Murillo, J. González, and R. Zuberek

Departamento Física de Materiales, Facultad de Químicas, UPV/EHU, 20009, San Sebastián, Spain

A. Slawska-Waniewska

Institute of Physics, Polish Academy of Sciences, Warsaw, Poland

J. M. González

Instituto de Ciencia de Materiales de Madrid, CSIC, Cantoblanco, 28049, Madrid, Spain

Results are presented on the evolution with the thermal treatment parameters of the effective anisotropy and dispersion fields and of the saturation magnetostriction of samples having nominal compositions given by $\text{Fe}_{93-x}\text{Zr}_7\text{B}_x\text{Cu}_y$ ($x=6-8$ and $y=0-2$). From these data we conclude that the enhancement of the soft magnetic character of the samples induced by the anneals carried out in the temperature range 480–600 °C could be linked both to the decrease of the anisotropy field and to the reduced magnetostriction values resulting from the thermal treatments. © 1998 American Institute of Physics. [S0021-8979(98)36711-0]

I. INTRODUCTION

$\text{FeZrB}(\text{Cu})$ crystalline alloys with ultrafine microstructures show excellent soft magnetic properties and are regarded as promising candidates for practical uses. These alloys are prepared by partial crystallization of melt spun precursors resulting in the precipitation, from the amorphous matrix, of bcc Fe grains having a typical diameter of 10 nm.¹ The basic mechanism responsible for the outstanding magnetic properties of these nanocrystalline alloys is the averaging (over regions containing a large number of grains) of the easy directions of the local magnetocrystalline anisotropy.² From a study of the effective anisotropy in FINEMET-type nanocrystalline alloys,³ it was possible to deduce that this averaging was based on the occurrence of intergranular coupling. It was also possible to evaluate the typical dimensions of the coupled units. Nevertheless, and since the reduction of the magnetic anisotropy from the value obtained in the amorphous precursor down to that obtained in the nanocrystalline alloy was not sufficient to account for the reduction of the coercive force accompanying the nanocrystallization, the enhancement of the magnetic softness was proposed to be also linked to the decrease of the microstructure–magnetization interactions.³ On the basis of these interactions there is the magnetoelastic coupling, and therefore, a reduced magnetostriction value is considered to be a crucial property to achieve extremely soft magnetic behavior.

In the present work, we report on the dependence of the effective magnetic anisotropy on the annealing temperature for nanocrystalline $\text{FeZrB}(\text{Cu})$ alloys. Our results will be correlated with the evolution of the saturation magnetostriction, λ_s , during heat treatment.

II. PREPARATION OF SAMPLES AND EXPERIMENTAL TECHNIQUES

Amorphous alloys of nominal compositions $\text{Fe}_{93-x}\text{Zr}_7\text{B}_x\text{Cu}_y$ ($x=6-8$ and $y=0-2$) were prepared by

the single-roller melt-spinning method and were annealed under an Ar atmosphere for 1 h at temperatures ranging from 480 up to 650 °C.

The anisotropy field, H_k , associated with the effective anisotropy, K_{eff} , and the dispersion field, H_d , associated with the inhomogeneities of the magnetization distribution, were determined, both in the as-quenched and the treated samples, from measurements of the transverse biased initial

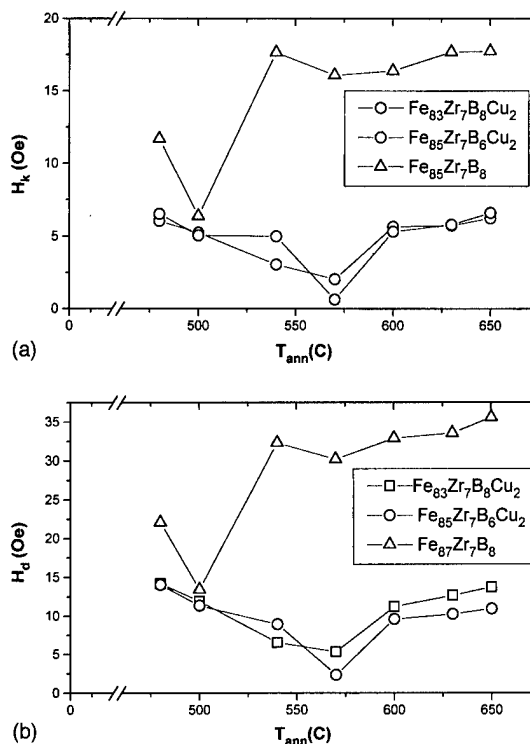


FIG. 1. (a) Temperature dependence of the anisotropy field of the samples. (b) Temperature dependence of the dispersion field of the samples.

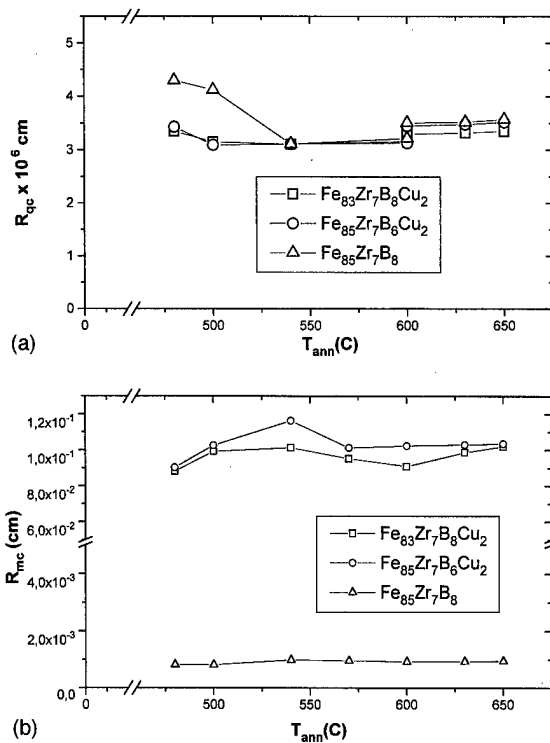


FIG. 2. (a) Temperature dependence of the R_{qc} parameter. (b) Temperature dependence of the R_{mc} parameter in the studied samples.

susceptibility, χ_t .³ For that purpose the original ribbons (3 mm wide, 20 mm thick) were cut by acid etching into disks having diameter 3 mm.

The transverse biased initial susceptibility, χ_t , was measured by applying simultaneously a saturating dc field, H_1 , along the directions of the easy and hard axes of the effective anisotropy and a small ac field, H_2 , directed perpendicular to H_1 . We measured the magnetization component parallel to H_2 . The transverse biased initial susceptibility can be written as

$$1/X_t = H_{\text{eff}}/M_s, \quad (1)$$

where M_s is the saturation magnetization and H_{eff} is given by

$$H_{\text{eff}} = H_1 + (-)H_k + H_d. \quad (2)$$

In (2) the plus (minus) signs stand for the cases in which the saturating field is applied along the easy (hard) axes. In order to identify the macroscopic easy (hard) axis of our samples, the transverse biased initial susceptibility was measured in all of them by applying the saturating field along different in-plane directions. The saturation magnetostriction was measured, at room temperature, by means of the strain modulated ferromagnetic resonance (SMFMR) method with the magnetic field parallel to the ribbon plane.

III. RESULTS

Figures 1(a) and 1(b) show the treatment temperature, T_{ann} , dependence of H_k and H_d , respectively, corresponding to all the samples studied. From our results it is apparent that the anisotropy field exhibited a minimum value (occurring at

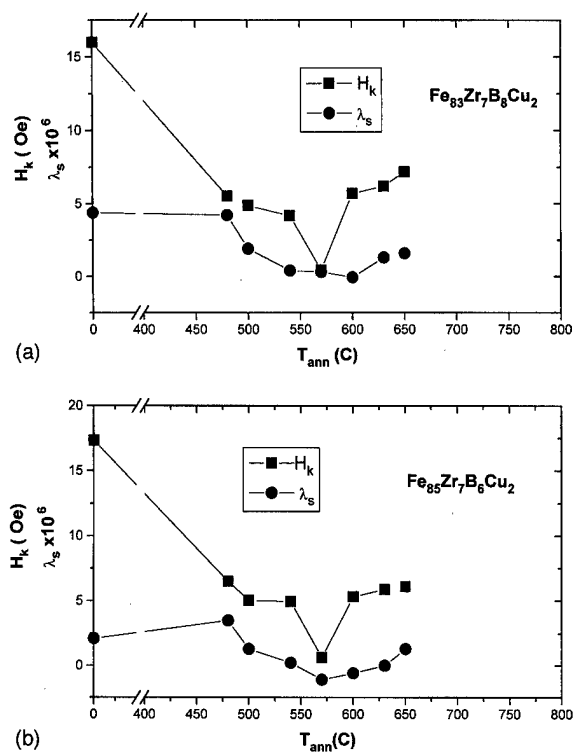


FIG. 3. (a) and (b) Temperature dependence of the anisotropy field and the saturation magnetostriction of the Cu-containing samples.

temperatures coinciding with those of the onset of the crystallization process). The minima measured in the Cu-containing samples coincide at 570 °C whereas that corresponding to the Cu-free sample is observed at 500 °C. Regarding the H_d results, it is important to remark that this parameter shows minima at temperatures coinciding with those observed in the $H_k(T_{\text{ann}})$ curves. The very small H_d value obtained in the Cu-containing samples could result from strong intergranular exchange coupling promoted by a high degree of homogeneity of the grain size distribution.

The micromagnetic analysis of the transverse biased initial susceptibility results, allows a further quantification of the coupling between the microstructure and the magnetization. According to Hoffmann,⁴ the minor, R_{qc} , and major, R_{mc} , semiaxis of the elliptical regions in which the magnetization is coupled, resulting in a reduction of the effective anisotropy, can be expressed as

$$R_{qc} = [AH_k/K_{\text{eff}}(H_1 + (-)H_k)] \quad (3)$$

and

$$R_{mc} = 2^{3/2}d^{1/2}A^{1/4}K_{\text{eff}}^{3/4}M_s[H_k(H_1 + (-)H_k)], \quad (4)$$

where A is the exchange constant, H_1 is the saturating field (our data were evaluated for an H_1 value corresponding to $30H_k$), and d is the thickness of the samples. In Figs. 2(a) and 2(b) we present the annealing temperature dependence of R_{qc} and R_{mc} measured in the heat treated samples. Our results are almost independent of the annealing parameters and composition, except for the fact that the R_{mc} values obtained in the Cu-containing samples are two orders of magnitude larger than those measured in the Cu-free sample. This result clearly shows that the intergranular exchange coupling, that

induces anisotropy averaging, is not the only source of the magnetic softening for these samples. In order to check the influence of the magnetoelastic coupling, we present in Figs. 3(a) and 3(b) the evolution of the saturation magnetostriction constant with heat treatment temperature and, for the sake of comparison, that of the anisotropy field. As can be seen in these figures, the saturation magnetostriction decreases down to a minimum value coinciding with the minimum of the anisotropy field. Since these decreases take place simultaneously with the bcc Fe precipitation, the soft magnetic character should be related to the two-phase nature of the partly crystallized samples.

IV. CONCLUSIONS

The enhancement of the soft magnetic properties in the FeZrB(Cu) alloys occurs due to the combination of two factors both of them associated with the onset of the nanocrys-

tallization process: the low values of the effective anisotropy field and the decrease of the saturation magnetostriction. The intergranular coupling leading to the anisotropy reduction is clearly favored by the Cu addition, presumably due to the larger number of bcc Fe grains involved in the coupled units, compared with those present in the Cu-free sample. Optimum heat treatment conditions (540 °C, 1 h) result, in the case of the Cu-containing samples, in a large degree of intergranular coupling as evidenced [Figs. 3(a) and 3(b)] by the minimum value of the magnetization inhomogeneities related to the dispersion field.

¹K. Suzuki, A. Makino, A. Inoue, and T. Masumoto, *J. Appl. Phys.* **70**, 6232 (1991).

²G. Herzer, *IEEE Trans. Magn.* **26**, 1397 (1990).

³J. M. González, N. Murillo, J. González, J. M. Blanco, and J. Echeberría, *J. Mater. Res.* **11**, 512 (1996).

⁴H. Hoffmann, *IEEE Trans. Magn.* **4**, 32 (1968).

Approach to the magnetic saturation in nanocrystalline ferromagnets in the random anisotropy model

G. R. Aranda and J. González^{a)}

Departamento de Física de Materiales, Facultad de Químicas, Universidad del País Vasco, 20009 San Sebastián, Spain

K. Kulakowski

Faculty of Physics and Nuclear Techniques, University of Mining and Metallurgy, 30059 Cracow, Poland

Recent experimental data on the magnetization curve $M(H)$ of magnetically soft nanocrystalline $\text{Fe}_{73.5}\text{Cu}_1\text{Nb}_3\text{Si}_{13.5}\text{B}_9$ sample are analyzed in terms of the random anisotropy model. Numerical calculations of magnetization are supplemented by a high-field expansion. Near the saturation we get $M(H)/M_s = 1 - 4\langle K \rangle^2 / (15M_s^2 H^2)$, where $\langle K \rangle$ is the averaged anisotropy of crystalline grains, contained in large magnetic domains. Section I is an introduction. In Sec. II, reference data on the model parameters of the nanocrystalline system $\text{Fe}_{73.5}\text{Cu}_1\text{Nb}_3\text{Si}_{13.5}\text{B}_9$ are collected in order to justify the model approximations and to prepare the comparison with experimental results. In the two subsequent sections, the results of the calculations are described and discussed. © 1998 American Institute of Physics. [S0021-8979(98)28211-9]

I. INTRODUCTION

Nanocrystalline Fe-based materials are interesting for their superior magnetic softness.¹ A prominent example of these materials is $\text{Fe}_{73.5}\text{Cu}_1\text{Nb}_3\text{Si}_{13.5}\text{B}_9$ and their magnetic behavior can be explained by the random anisotropy model.² Their low coercive field (≈ 1 A/m) and high initial permeability ($\approx 10^5$) are related to a new magnetic phase. Moreover, new relations can be deduced^{2,3} between the magnetic properties of the system and its micromagnetic structure.

The shape of the magnetization curve in $\text{Fe}_{73.5}\text{Cu}_1\text{Nb}_3\text{Si}_{13.5}\text{B}_9$ was investigated experimentally⁴ both for amorphous and nanocrystalline state. The relevant process of magnetization was the reversible rotation of magnetic moments. The results were fitted to the law

$$M(H) = M_s(1 - a_1/H - a_2/H^2) + bH^{1/2}. \quad (1)$$

The last term in Eq. (1) was responsible for a change of M_s and it was expected to be relevant in very high magnetic fields. The term a_1/H was ascribed to macroscopic inhomogeneities and it was expected to appear for fields below 2 kOe. The constant a_2 is known⁵ to describe the curvature of energy of local magnetic moments at the equilibrium direction. In Ref. 4, a_2 was interpreted as due to magnetoelastic anisotropies of internal stresses. Thus a_2 was expected to be proportional to the squared magnetostriction constant λ_s . This interpretation was based on the theory of stress fields of dislocation dipoles in amorphous systems.^{6,7}

We will demonstrate, that the term $1/H^2$ is a direct consequence of the random anisotropy model.^{2,8}

II. PARAMETERS OF THE NANOCRYSTALLINE SYSTEM

In Ref. 3, the size L_{ex} of magnetic domains in soft magnetic phase of $\text{Fe}_{73.5}\text{Cu}_1\text{Nb}_3\text{Si}_{13.5}\text{B}_9$ is of the order of

10^{-6} m, and the density of the magnetic anisotropy energy $\langle K \rangle$ of a magnetic domain is about 2 J/m^3 . So the energy of a virtual thermal excitation of a domain of the order of $\langle K \rangle \times L_{\text{ex}}^3 \approx 12 \text{ eV}$, almost three orders of magnitude larger than the thermal energy at room temperature.

For large domains, magnetic coupling between them is limited to domain surfaces and neglectable. The energy of a domain in its ground state is

$$VE(\theta, \phi) = \langle K \rangle V \sin^2(\theta - \phi) - HM_s V \cos \phi, \quad (2)$$

where $\langle K \rangle$ is the same as above, θ the angle between a local easy axis of a magnetic domain and the applied magnetic field H , ϕ is the angle between the magnetic moment of the domain and the applied field, and V is the domain volume. Minimizing the energy E as a function of ϕ , we get the ground state value ϕ_0 as a function of θ . Macroscopic magnetic moment is the average $\langle \cos \phi_0 \rangle$ over all directions of the local easy axis. To avoid hysteresis and limit our considerations to reversible rotations of local magnetic moments, only positive contribution to magnetization is taken into account.

As we see, at $T=0$ the only relevant parameter of the model is $x = M_s H / \langle K \rangle$.

After Ref. 3 we take M_s to be 1.2 T. For fields $H \approx 2$ kOe we get the Zeeman energy of the order of 10^5 J/m^3 . Note that in Ref. 4, measurements were performed for fields up to 60 kOe. As noted above, the local anisotropy energy for nanocrystalline grains is of the order of 2 J/m^3 . So x for the soft nanocrystalline phase is of the order of 10^5 .

For amorphous as-quenched state, internal stresses around 40 MPa⁹ combined with the magnetostriction $\lambda_s = 20 \times 10^{-6}$ produce anisotropy energy of the order of 800 J/m^3 . Finally, for uncorrelated crystalline grains above the Curie temperature of the amorphous matrix, the local anisotropy energy of the grains is known³ to be about 8000 J/m^3 . In all three cases, we obtain x above ten.

^{a)}Electronic mail: wabroarg@scxol.sc.ehu.es

Does the argument on the ground state of the beginning of this section hold for the as-quenched amorphous state? In this case, the exchange length L_{am} can be evaluated as

$$L_{\text{am}} = \{2A/(3\lambda\sigma)\}^{1/2}, \quad (3)$$

where A is the exchange stiffness of the order of 10^{-11} J/m³. Keeping the above-noted value of 40 MPa for annealed samples, we get $L_{\text{am}} \approx 100$ nm, and the temperature necessary for thermal excitations of amorphous system of the order of $A^{3/2}/k_B/(3\lambda\sigma/2)^{1/2} = 10^5$ K. Obviously, this is much more than the Curie temperature for grains (about 880 K³).

For the turning field H_1 where the $1/H^2$ law starts to be relevant was found to be 1 to 2 kOe nanocrystalline systems. For amorphous ribbons H_1 is known to be 0.3 kOe.

III. CALCULATIONS AND RESULTS

After Eq. (2), with $\epsilon = 1/x$ the condition of the minimum of energy is $\sin \phi_0 = \epsilon \sin[2(\theta - \phi_0)]$. For high magnetic fields, when $x \geq 10$, small ϵ , the angle between the magnetic moment of a domain and the applied magnetic field in the equilibrium, ϕ_0 , is small and can be developed in ϵ powers

$$\phi_0 = \epsilon \sin(2\theta) - \epsilon^2 \sin(2\theta)\cos(2\theta). \quad (4)$$

For $T > 0$, the magnetization $M(H)$ can be written as

$$M(H)/M_s = 1/(2\pi) \int_0^{\pi/2} \sin \theta d\theta \int_0^{2\pi} d\zeta \langle m(\theta, \zeta, T) \rangle, \quad (5)$$

where

$$\langle m(\theta, \zeta, T) \rangle = 1/Z \int_0^{\pi/2} \sin \phi d\phi \int_0^{2\pi} d\psi \cos \phi \times \exp[-\beta V E(\theta, \zeta, \phi, \psi)], \quad (6)$$

the angles θ and ζ denote the direction of a local easy axis, ϕ and ψ denote the direction of a local magnetic moment, and Z is the partition function. For $T = 0$,

$$\exp[-\beta V E(\theta, \zeta, \phi, \psi)] = \delta(\phi - \phi_0) \delta(\psi - \zeta), \quad (7)$$

$$M(H)/M_s = 1/(2\pi) \int_0^{\pi/2} \sin \theta d\theta \int_0^{2\pi} d\zeta \cos \phi_0. \quad (8)$$

Expanding $\cos \phi_0 \approx 1 - \phi_0^2/2$ and substituting $\phi_0 = \epsilon \sin 2\theta$ [see Eq. (4)], we get

$$M(H)/M_s = 1 - 4\epsilon^2/15 = 1 - 4\langle K \rangle^2/(15M_s^2 H^2) \quad (9)$$

which is the $1/H^2$ law, derived for high field and $T = 0$.

A low-temperature approximation is also justifiable for soft nanocrystalline phase. For $T \neq 0$ but very small (Sec. II), the deviations from the ground state are much smaller than the ground state angle ϕ_0 . Thus

$$M(H)/M_s = 1 - 4\langle K \rangle^2/(15M_s^2 H^2) - 3K_B T/(2VM_s H). \quad (10)$$

Equation (10) is valid if $VM_s H \gg V < K \gg K_B T$. As was justified in Sec. II. On the contrary, in the limit $\epsilon \rightarrow 0$, $t \rightarrow \infty$, $t\epsilon = \text{const}$ we get $M(H)/M_s = 1 - t\epsilon + (t\epsilon)^2$. However, this limit is not appropriate for our system.

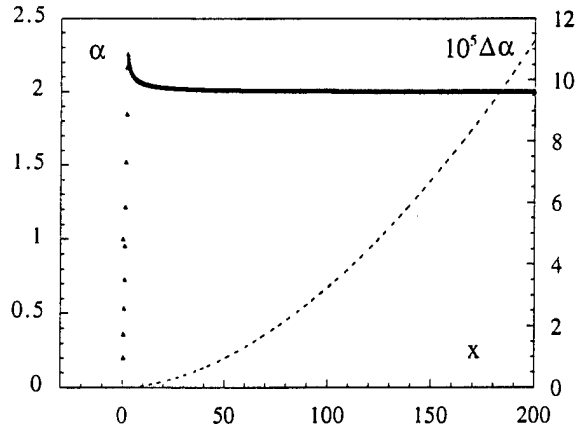


FIG. 1. The coefficient α , (points) and its numerical error (dotted line), as dependent on the parameter $x = M_s H / \langle K \rangle$.

Numerical calculations on the curve $M(H)$ for zero temperature show that the term $1/H^2$ arises as soon as the value of the parameter $x = M_s H / \langle K \rangle$ exceeds 2.0.

This result can be shown in several different ways. In Fig. 1 we show the value of the exponent α , as defined in $M(H) = M_s(1 - a/H^\alpha)$. In our numerical calculations, $M_s = 1$. The numerical error $\Delta\alpha$ of α is due to the error ΔM of M , and we calculate it from $\Delta\alpha = \Delta(M/M_s) / \{ [1 - (M/M_s)] \ln(H/H_0) \}$, where H_0 is a field unit. This result is included in Fig. 1. ΔM is determined numerically by varying the step of integration, and it is found to be 3×10^{-9} . As can be seen in Fig. 1, the value $\alpha = 2.0$ is the asymptotic one for large values of x . Simultaneously, the numerical error $\Delta\alpha$ exceeds 10^{-4} at $x \approx 200$.

Numerical calculations for $T > 0$ contain triple integration, and the accuracy for $M(T, H)$ is near 10^{-4} . Also, the exponential Gibbs factors in Eq. (6) disable the low temperature range to be investigated numerically. Still, we have made an attempt to evaluate a_1 and a_2 of Eq. (1) as dependent on x for various temperatures. For $T = 0$, the coefficient a_1 is found to be maximal near $x = 1$, and above $x = 3$ its absolute value is less than 2×10^{-2} . The coefficient a_2 increases with x from zero to a maximum value near $x = 2.0$, and then it decreases to about 0.27. Analytical calculations give the asymptotic value $a_2 = 4/15 = 0.266(5)$ for large x [Eq. (10)]. For $T > 0$ the plots of $a_1(x)$ and $a_2(x)$ are smoother. The results are given in Figs. 2(a) and 2(b). Clearly in Fig. 2(b), the coefficient a_2 is close to a constant. Numerical calculations for a_1 (checked from $t = 0.03$ to 0.066, t being $K_B T / \langle K \rangle V$), yield $a_1 = K_B T / VM_s H$. In Eq. (10), $a_1 = 3K_B T / 2VM_s H$. It is possible that this change of the coefficient occurs in the range of lower temperatures, which cannot be captured numerically.

In Fig. 3, numerical plots are shown of $y = x^2 [1 - M(x)]$ for different temperatures. As we see, the values of y below $x \approx 2$ and the value of x , where the $1/H^2$ law starts to be valid, do not depend on temperature.

IV. DISCUSSION

In the nanocrystalline state, the magnetostriction is known³ to be reduced by at least a factor of 4, if compared

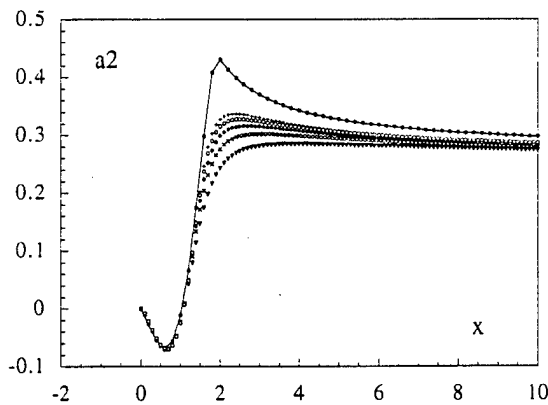
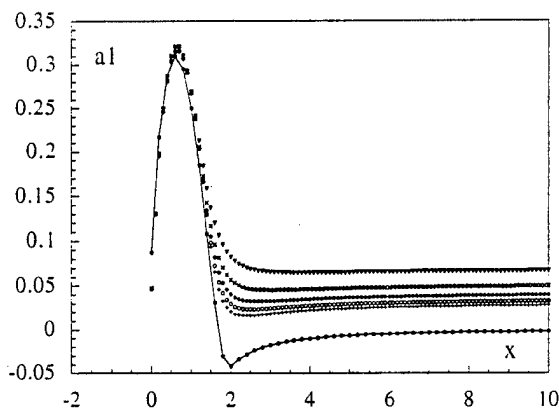


FIG. 2. The coefficients (a) a_1 , (b) a_2 as dependent on x , calculated numerically for various temperatures. Temperature is expressed as $t = k_B T / \langle K \rangle V$. The plots are: (●) $t=0$, (+) $t=0.028$, (○) $t=0.33$, (◆) $t=0.04$, (×) $t=0.05$, and (▽) $t=0.066$. Guide-eye solid line is drawn through the points for $t=0$. Note that for $\langle K \rangle = 2.7 \text{ J/m}^3$ and $V = 10^{-18} \text{ m}^3$ the value $t=0.028$ means that $T=5400 \text{ K}$.

with that for the amorphous matrix. It was pointed out in Ref. 4, that if the coefficient a_2 from Eq. (1) is proportional to the second power of the magnetostriction, it should be much smaller for the nanocrystalline state. Experimental data show that this coefficient is only twice smaller than that for the as-quenched amorphous sample.

We think a_2 for amorphous and nanocrystalline samples are of different origin. In amorphous systems, the fluctuations of local magnetic anisotropy are due to local stresses and the magnetoelastic coupling. On the contrary, in soft nanocrystalline phase the local magnetic anisotropy is due to crystalline grains of bcc-FeSi, and it is partially averaged out within magnetic domains.² The experimental value of a_2 is about $2 \times 10^{-4} \text{ Oe}^2$.⁶ With this result and Eq. (10), we get $\langle K \rangle \approx 2.7 \text{ J/m}^3$, close to the value 2 J/m^3 , accepted for the soft nanocrystalline phase.⁶

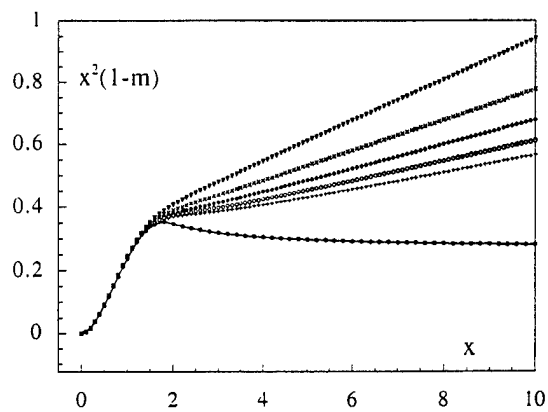


FIG. 3. The quantity $x^2[1-M(x)]$ as dependent on x for various temperatures $t = k_B T / \langle K \rangle V$. The plots are: (●) $t=0$, (+) $t=0.028$, (○) $t=0.33$, (◆) $t=0.04$, (×) $t=0.05$, and (▽) $t=0.066$. Guide-eye solid line is drawn through the points for $t=0$.

On the contrary, if we apply Eq. (10) to an amorphous as-quenched system, we get the local anisotropy $3/2 \lambda \langle \sigma \rangle$ near 4 J/m^3 . Keeping $\lambda = 20 \times 10^{-6}$, we get the average amplitude of stress to be about 0.1 MPa , which is more than two orders of magnitude smaller than the values in Ref. 9.

The experimentally observed value of the coefficient a_1 for the soft nanocrystalline phase was 4 to $5 \times 10^{-3} \text{ Oe}$. As it was pointed out in Ref. 3, the origin of the $1/H$ term is due to macroscopic inhomogeneities. Substituting $V = L_{\text{ex}}^3$ into Eq. (10), we get the coefficient a_1 much smaller than the experimental value. The $1/H$ term of Eq. (10), if observed experimentally for nanocrystalline phase, should be only a small correction to the contributions of other effects.

In conclusion, the $1/H^2$ law of approach to the magnetic saturation, which was observed in the soft nanocrystalline phase of $\text{Fe}_{73.5}\text{Cu}_1\text{Nb}_3\text{Si}_{13.5}\text{B}_9$, can be entirely assigned to the FeSi crystalline grains. The coefficient a_2 is found to be temperature independent, as it was shown experimentally.

ACKNOWLEDGMENTS

The authors are grateful to the Spanish MEC (project PB96-0899-C02-02) and to the Polish Scientific Committee for financial support.

¹Y. Yoshizawa, S. Oguma, and K. Yamauchi, J. Appl. Phys. **64**, 6044 (1988).

²G. Herzer, IEEE Trans. Magn. **26**, 1397 (1990).

³G. Herzer, Scr. Metall. Mater. **33**, 1741 (1995).

⁴J. Gonzalez, M. Vazquez, E. du Tremolet de Lacheisserie, and G. Herzer, in *Ordering and Disordering in Alloys*, edited by A. R. Yavari (Elsevier Applied Science, London, 1992), p. 473.

⁵S. Chikazumi, *Physics of Magnetism* (Krieger, Malabar, 1964).

⁶H. Grimm and H. Kronmüller, Phys. Status Solidi B **117**, 663 (1983).

⁷M. Vazquez, W. Fernengel, and H. Kronmüller, Phys. Status Solidi A **115**, 547 (1989).

⁸R. Alben, J. J. Becker, and M. C. Chi, J. Appl. Phys. **49**, 1653 (1978).

⁹J. Gonzalez, M. Vazquez, and J. M. Barandiaran, Phys. Status Solidi A **93**, K165 (1986).

Multigrid methods for computation of magnetostatic fields in magnetic recording problems

Igor Tsukerman and Alexander Plaks

Electrical Engineering Department, The University of Akron, Akron, Ohio 44325-3904

H. Neal Bertram

Center for Magnetic Recording Research, University of California, San Diego, La Jolla, California 92093-0401

Calculation of magnetostatic fields is usually the most time-consuming stage of micromagnetic simulations. In this article, the Bramble-Pasciak-Xu multilevel preconditioners (MP) are applied to the computation of magnetostatic fields in media such as magnetic tapes or thin films. The asymptotic number of arithmetic operations is optimal and proportional to the number of nodes in the finite element mesh. Unlike the fast Fourier transform, MP are applicable to irregular meshes. Local (adaptive) mesh refinement can be implemented by switching to the hierarchical basis.

© 1998 American Institute of Physics. [S0021-8979(98)38311-5]

I. INTRODUCTION

Magnetization of media in micromagnetic problems is usually simulated by minimizing the sum of the magnetostatic energy, the exchange energy, the anisotropy energy, etc. Calculation of the magnetostatic field is the crucial stage of the overall numerical process of energy minimization. The objective of this study is to develop efficient magnetostatic field algorithms for micromagnetic simulations. The focus is on media such as magnetic tapes or thin films where the nonuniform arrangement of the magnetic particles or grains is of particular interest.

Various linear system solvers are currently in use in magnetostatic finite element (FE) analysis.¹³ The incomplete Cholesky conjugate gradient (ICCG) method⁹ is probably the most popular among iterative methods. Direct methods, such as nested dissection⁵ (ND) or quotient minimum degree,⁵ for two-dimensional (2D) problems are usually faster¹³ and more robust than ICCG. Linear 2D magnetostatic problems of moderate size (say, up to 10 000 unknowns) can be solved easily using either of the methods mentioned.

However, performance of these methods deteriorates, especially in three-dimension (3D), when finite element meshes are refined and thus the number n of unknowns in the system increases. The number of arithmetic operations for ICCG and ND grows as $n^{3/2}$ in 2D and as $n^{4/3}$ and n^2 , respectively, in 3D.

Multigrid methods are asymptotically much faster. Typically for these methods, the number of arithmetic operations per unknown is independent or almost independent of the size of the linear system being solved. This behavior is on a par with the fast Fourier transform (FFT) and the Greengard-Rokhlin multipole method.⁶ FFT, however, is applicable only to regular FE meshes (or a spatially uniform particle arrangement),¹⁶ while multigrid methods can be applied to

arbitrary tetrahedral meshes. Comparison with the multipole method is interesting and is planned for future work.

II. THE MAGNETOSTATIC MULTIPARTICLE PROBLEM

The magnetic scalar potential u of a system of magnetized particles satisfies the Poisson equation

$$\Delta u = \nabla \cdot \mathbf{M}, \quad (1)$$

where \mathbf{M} is the magnetization vector. For the purpose of computing the magnetostatic field, the magnetization of each of the particles is assumed to be known. Particles may have arbitrary orientation in space and, in principle, arbitrary shapes, although practical restrictions may be imposed by the capabilities of an FE mesh generator. The direction of magnetization may also be arbitrary.

In the weak (variational) form Eq. (1) can be written as

$$a(u, u') \equiv \langle \nabla u, \nabla u' \rangle = \langle \mathbf{M}, \nabla u' \rangle, \quad (2)$$

where the angle brackets denote an L_2 -type inner product of two vector functions in a given computational domain Ω , and u' is an arbitrary trial function from the appropriate Sobolev space. Different types of boundary conditions can be considered with Eqs. (1) or (2); for unbounded problems, the potential is assumed to be zero at infinity.

The FE method has already been successfully applied to multiparticle problems by Koehler, Yang, and Fredkin,^{1,2,8} but multigrid solvers have not been tried.

III. MULTILEVEL PRECONDITIONERS

The Bramble-Pasciak-Xu (BPX) multilevel preconditioners (MP)^{4,14,15,18,12} are among the least restrictive and the most efficient multigrid methods. The method is applicable to 2D and 3D magnetostatic problems (and to linear elliptic problems in general) and is suitable for highly irregular

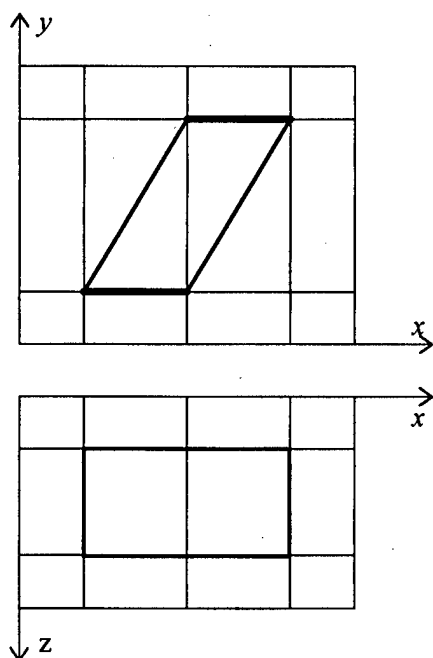


FIG. 1. Mesh generation.

meshes and inhomogeneous materials. For the magnetostatic multiparticle problem on a mesh with n nodes, the asymptotic number of arithmetic operations for BPX-MP is¹⁵ $O(n)$. In addition, the BPX preconditioner is a double sum which can be computed in parallel.

A few levels of nested tetrahedral meshes are generated. In the simplest case of global refinement, each of the tetrahedral elements is subdivided into eight tetrahedra, thus obtaining the next level of triangulation. Associated with each level k ($k=1,2,\dots,m$) is a set of FE basis functions $\psi_i^{(k)}$ ($i=1,2,\dots,n_k$), where n_k is the number of nodes at level k , and a finite dimensional space P_k (of dimension n_k) spanned by these basis functions. Then $P_1 \subset P_2 \subset \dots \subset P_m$.

One of the simplest versions of the BPX preconditioner can be written as follows:^{14,4}

$$Br = \sum_{k=1}^m 4^{-k} \sum_{i=1}^{n_k} (r, \psi_i^{(k)}) \psi_i^{(k)}, \quad r \in P_m. \quad (3)$$

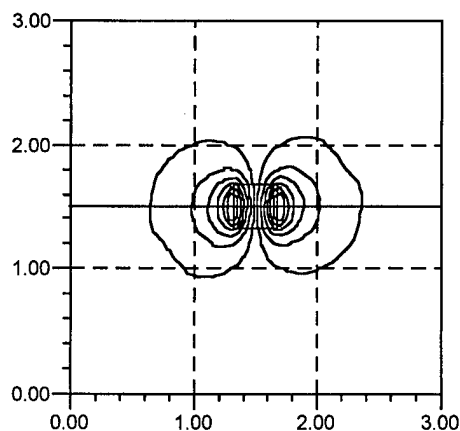


FIG. 2. Lines of equal scalar magnetic potential of one particle.

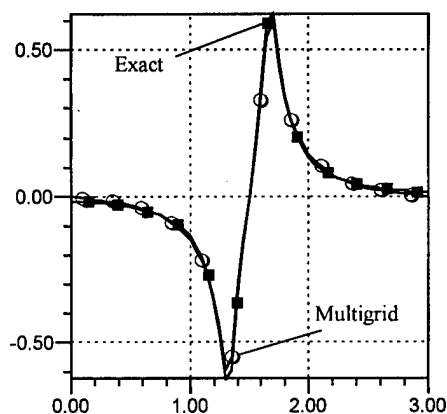


FIG. 3. Exact and multigrid solutions for one particle. (Tetrahedral mesh with over 600 000 elements.)

For the Poisson equation, the conjugate gradient method with the preconditioner B requires only $O(1)$ iterations to converge and $O(n)$ arithmetic operations. For inhomogeneous problems and/or highly irregular grids the preconditioner B in Eq. (3) needs to be modified, as proposed by Yserentant¹⁸ and further explained by Bornemann *et al.*³

$$Br = A_0^{-1}r + \sum_{k=1}^m \sum_{i=1}^{n_k} \frac{(r, \psi_i^{(k)})}{a(\psi_i^{(k)}, \psi_i^{(k)})} \psi_i^{(k)}, \quad (4)$$

where the operator A_0 corresponds to the FE representation of the bilinear form $a(u, u')$ on the coarsest mesh.

Adaptive refinement of the FE mesh may be needed to achieve the desirable accuracy of the numerical solution. Two main problems arise in connection with such refinement. First, if one of two elements having a common boundary is refined, the FE basis becomes nonconforming and the continuity of the solution must be explicitly imposed. Second, effective error estimates are needed in order to determine where the local refinement is needed.

Both of these problems can be solved simultaneously by using *hierarchical* FE bases,¹⁷ as proposed by Mitchell¹⁰ and R  de.¹¹ By setting the *hierarchical basis* value of an FE function at nonconforming ("slave") nodes to zero, the continuity of the function can be assured. At the same time, the hierarchical basis representation provides means of error estimation and control. The method is known as "fully adaptive multigrid" (FAM).^{10,11}

TABLE I. Number of iterations and solution time for the problem with one particle.

Level of refinement	Number of elements	Number of iterations ^a	Solution time (seconds) ^b
0	162	7	<1
1	1296	25	<1
2	10 368	40	<1
3	82 944	56	8
4	663 552	78	88

^aThe norm of the residual was reduced by a factor of 10–5.^bThe computations were performed on a personal computer with a Pentium II 300 MHz processor and 64 M RAM.

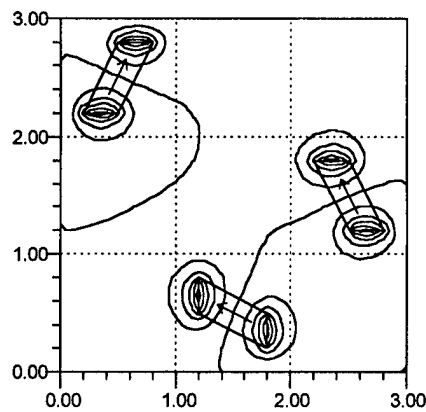


FIG. 4. The scalar magnetic potential for a model problem with three magnetized particles.

Our implementation of the multigrid algorithm is based on the BPX preconditioner transformed to the hierarchical basis. This approach combines the high convergence rate of BPX with the flexibility of local refinement provided by FAM. Representation of the magnetic scalar potential in the hierarchical basis ensures the continuity of the potential over nonconforming tetrahedral elements. In order to combine the hierarchical basis representation essential for FAM with BPX-MP, all vector variables and the BPX preconditioner are converted into the hierarchical basis.

IV. TESTING THE METHOD

Several test problems with magnetized particles were solved. To simplify mesh generation, the particles were considered to be parallelepipeds oriented parallel to the xy plane. The mesh initially consists of a set of prisms which are then subdivided into tetrahedra (Fig. 1).

The problem is solved on the finest mesh; the auxiliary coarser levels are needed only to construct the preconditioner. Since the domain properties are homogeneous (the Poisson equation is being solved), coarser meshes need not represent the exact geometry of the particles; rather, finer levels can be adaptively adjusted to the shape of the particles. (However, our current mesh generator exactly represents the geometry starting from the coarse mesh level.) Results for two of the model problems are presented below.

Problem 1. The main purpose of this test example was to compare the FE-multigrid solution with the analytical one. A cubic particle in free space is magnetized along the x axis. The analytical solution for the magnetic scalar potential is $u(r) = (1/4\pi) \int_S (\vec{M} \cdot d\vec{s}') / |r - r'|$. In FE analysis, the domain was bounded and homogeneous Dirichlet conditions were imposed on the boundary. The lines of equal magnetic potential are shown in Fig. 2. The magnetic potential distribution along the central line of the domain is shown in Fig. 3. The computational statistics are shown in Table I.

Problem 2. Three particles are magnetized along their axes (Fig. 4). Homogeneous Dirichlet boundary conditions are imposed on the external boundary. Computational statistics are shown in Table II.

TABLE II. Number of iterations and solution time for the problem with three particles.

Level of refinement	Number of elements	Number of iterations ^a	Solution time (seconds) ^b
0	1296	8	1
1	10 368	25	1
2	82 944	38	6
3	663 552	50	62

^aThe norm of the residual was reduced by a factor of 10^{-5} .

^bThe computations were performed on a personal computer with a Pentium II 300 MHz processor and 64 M RAM.

V. FUTURE WORK

The multigrid solver is to be incorporated into the overall micromagnetic simulation process. A straightforward approach would be to use the BPX preconditioner within the usual iterative procedure of minimizing the free energy. Whether or not energy minimization can be more fully integrated in the multigrid method remains an open question.

For open boundary problems, the modification of the multigrid method proposed by Hsiao and Zhang⁷ is promising. The asymptotic number of arithmetic operations remains the same as in a bounded problem. Comparison with the Greengard-Rokhlin fast multipole method, which has similar asymptotic characteristics, would be interesting.

It is anticipated that *a posteriori* error estimates will be implemented and used in the mesh refinement process.

VI. CONCLUSIONS

Magnetostatic fields in micromagnetic simulations are efficiently computed using multilevel preconditioners. A finite element problem with half a million elements can be solved in about a minute on a modern personal computer.

ACKNOWLEDGMENTS

The work of I. Tsukerman and A. Plaks was supported in part by the National Science Foundation.

- ¹B. Yang, Ph.D. thesis, University of California, San Diego, 1997.
- ²B. Yang and D. R. Fredkin, J. Appl. Phys. **79**, 5755 (1996).
- ³F. Bornemann, B. Erdmann, and R. Kornhuber, Int. J. Numer. Methods Eng. **36**, 3187-3203 (1993).
- ⁴J. H. Bramble, J. E. Pasciak, and J. Xu, Math. Comput. **55**, 1 (1990).
- ⁵A. George and G. Liu, *Computer Solution of Large Sparse Positive Definite Systems* (Prentice-Hall, Englewood Cliffs, NJ, 1981).
- ⁶L. Greengard and V. Rokhlin, J. Comput. Phys. **73**, 325 (1987).
- ⁷G. C. Hsiao and S. Zhang, SIAM (Soc. Ind. Appl. Math.) J. Numer. Anal. **31**, 680 (1994).
- ⁸T. R. Koehler and D. R. Fredkin, IEEE Trans. Magn. **28**, 1239 (1992).
- ⁹J. A. Meijerink and H. A. van der Vorst, Math. Comput. **31**, 148 (1977).
- ¹⁰W. F. Mitchell, SIAM (Soc. Ind. Appl. Math.) J. Sci. Stat. Comput. **13**, 146 (1992).
- ¹¹U. Rüde, SIAM (Soc. Ind. Appl. Math.) J. Numer. Anal. **30**, 230 (1993).
- ¹²I. Tsukerman, IEEE Trans. Magn. **29**, 2365 (1993).
- ¹³I. A. Tsukerman, A. Konrad, G. Bedrosian, and M. V. K. Chari, IEEE Trans. Magn. **29**, 1711 (1993).
- ¹⁴J. Xu, Ph.D. thesis, Cornell University, 1989.
- ¹⁵J. Xu, SIAM (Soc. Ind. Appl. Math.) Rev. **34**, 581 (1992).
- ¹⁶S. W. Yuan and H. N. Bertram, IEEE Trans. Magn. **28**, 2031 (1992).
- ¹⁷H. Yserentant, Numer. Math. **49**, 379 (1986).
- ¹⁸H. Yserentant, Numer. Math. **58**, 163 (1990).

Modified scalar potential solution for three-dimensional magnetostatic problems

K. Sivasubramaniam,^{a)} S. Salon, and M. V. K. Chari

Department of Electric Power Engineering, Rensselaer Polytechnic Institute, Troy, New York 12180-3590

I. D. Mayergoyz

Department of Electrical Engineering, University of Maryland, Maryland 20742

A novel three-dimensional magnetostatic solution based on a modified scalar potential method has been developed. This method has significant advantages over the traditional total scalar, reduced scalar, or vector potential methods. The new method was successfully applied to a three-dimensional geometry of an iron core inductor and a permanent magnet motor. The results obtained are in close agreement with those obtained from traditional methods. © 1998 American Institute of Physics. [S0021-8979(98)38411-X]

I. INTRODUCTION

Solutions for two-dimensional magnetostatic field problems using a vector potential have been extensively reported in the literature.¹ However, there is a need for a computationally robust method particularly for three-dimensional field problems. Total scalar and reduced scalar^{2,3} potential solutions, and to a lesser extent three-dimensional vector potential⁴ solutions, or a combination of scalar and vector methods,⁵ have been presented by researchers. The scalar potential solutions do not suffer from the uniqueness problem that are encountered in the vector potential methods, although elaborate vector potential schemes of overcoming this difficulty have been described in the literature. The reduced scalar potential method allows current sources to be accurately represented and has, thus, found a wider application than the total scalar method because of the limitations of current sheet representation of sources and the need for branch cuts in the latter. However, even in the traditional reduced scalar potential method, the forcing function is evaluated over the entire solution domain and the zero divergence of the magnetic field due to current sources in free space is needlessly implemented resulting in numerical errors.

In this article, a three-dimensional modified scalar potential solution is described which minimizes numerical inaccuracies. In the new method, the forcing function is evaluated only in the iron region, and the zero divergence of the source magnetic field is eliminated from the computation.

II. THEORY

The fundamental theory behind the new method has been presented in an earlier paper,⁶ but is summarized here for completeness.

Since magnetic induction is divergence-free, the following equation may be written in terms of a reduced scalar potential formulation

$$\nabla \cdot [\mu(\bar{H}_c - \nabla\Phi)] = 0, \quad (1)$$

where \bar{H}_c is the magnetic field due to current sources (i.e., the rotational part of H), Φ is the scalar potential, μ is the permeability, and μ_0 is the free space permeability.

Since \bar{H}_c is divergence-free in free space,

$$\nabla \cdot (\mu_0 \bar{H}_c) = 0. \quad (2)$$

Subtracting Eq. (2) from eq. (1),

$$\nabla \cdot [(\mu - \mu_0)\bar{H}_c] - \nabla \cdot (\mu \nabla \Phi) = 0. \quad (3)$$

Applying the Galerkin weighted residual process to Eq. (3) using shape functions $\zeta_k (k=1,2,\dots,n)$,

$$\int_v \zeta_k \nabla \cdot [(\mu - \mu_0)\bar{H}_c] dv - \int_v \zeta_k \nabla \cdot (\mu \nabla \Phi) dv = 0. \quad (4)$$

This equation can be solved using the traditional finite element formulation for three-dimensional problems.

III. THREE-DIMENSIONAL APPLICATION TO AN IRON-CORE INDUCTOR

Figure 1 shows an octant of an iron core inductor excited by a current source (not shown in the figure) surrounding the central limb. The field H_c due to this current source is evaluated by Biot-Savart law separately. Equation (5) was solved

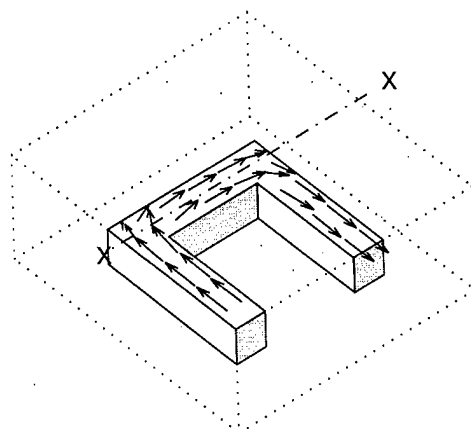


FIG. 1. Iron core inductor.

^{a)}Electronic mail: sivask@rpi.edu

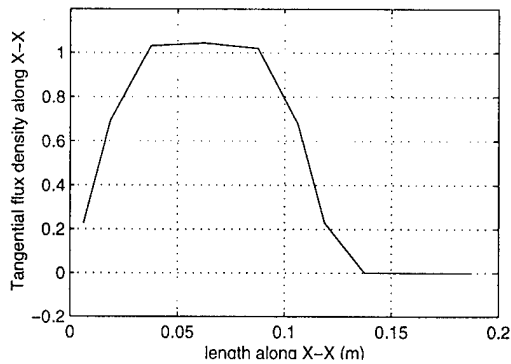


FIG. 2. Flux density variation along X-X.

using a nonlinear finite element procedure with second-order isoparametric bricks. The field in the iron core was then computed as the sum of H_c and the negative gradient of the solution Φ . The flux density variation along X-X, obtained by this procedure is illustrated in Fig. 2.

IV. PERMANENT MAGNET FORMULATION

The flux density, \bar{B} , the magnetizing force \bar{H} and the intrinsic magnetization, \bar{M} , of a permanent magnet material are related by

$$\bar{B} = \mu \bar{H} + \mu_0 \bar{M}_0. \quad (5)$$

Since $\bar{H} = \bar{H}_c - \nabla \Phi$, Eq. (5) can be written as

$$\bar{B} = \mu (\bar{H}_c - \nabla \Phi) + \mu_0 \bar{M}_0. \quad (6)$$

Taking the divergence on both sides of Eq. (6), and setting it to zero yields

$$\nabla \cdot \bar{B} = 0 = \nabla \cdot \mu (\bar{H}_c - \nabla \Phi) + \nabla \cdot (\mu_0 \bar{M}_0). \quad (7)$$

Also,

$$\nabla \cdot (\mu_0 \bar{H}_c) = 0. \quad (8)$$

Substituting Eq. (8) into Eq. (7), as before, gives

$$\nabla \cdot [(\mu - \mu_0) \bar{H}_c] - \nabla \cdot (\mu \nabla \Phi) + \nabla \cdot (\mu_0 \bar{M}_0) = 0. \quad (9)$$

The weighted Galerkin formula yields

$$\begin{aligned} \int_v \zeta_k \nabla \cdot [(\mu - \mu_0) \bar{H}_c] dv - \int_v \zeta_k (\nabla \cdot \mu \nabla \Phi) dv \\ + \int_v \zeta_k \nabla \cdot (\mu_0 \bar{M}_0) dv = 0. \end{aligned} \quad (10)$$

Equation (10) is then solved by the three-dimensional finite element method in the traditional manner.

V. THREE-DIMENSIONAL PERMANENT MAGNET APPLICATIONS

Figure 3 shows a three-dimensional section of a six-pole permanent magnet motor. The rotor poles are of linear permanent magnet pieces, and the stator is of conventional design with one conductor per slot. The flux path is shown in

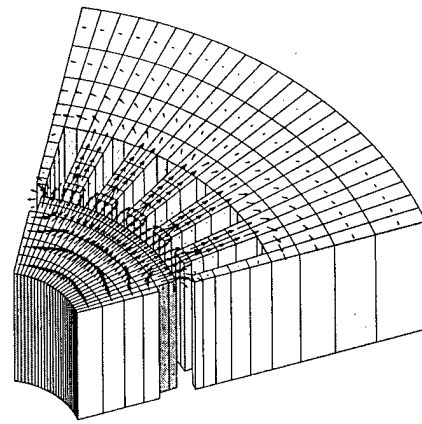


FIG. 3. Permanent magnet motor under no-load condition.

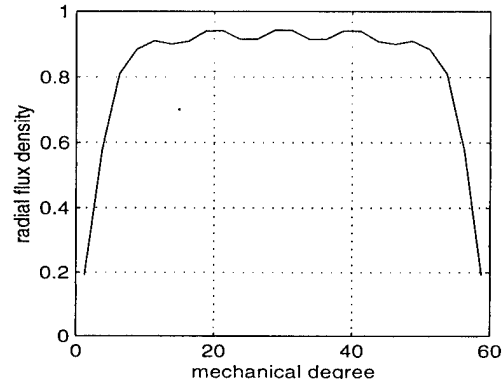


FIG. 4. Airgap flux density (no load).

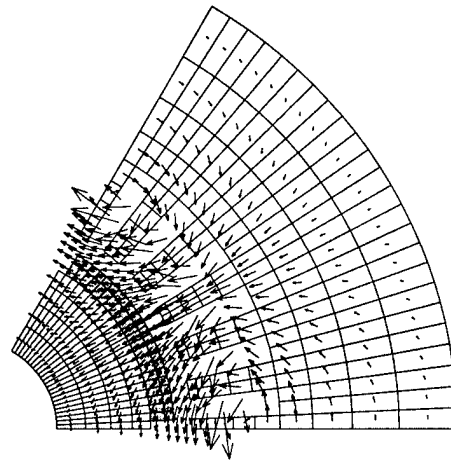
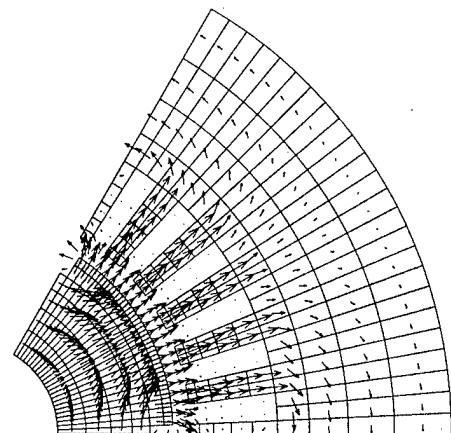
FIG. 5. H_c —Flux due to current sources without effect of iron.

FIG. 6. Flux due to permanent magnet.

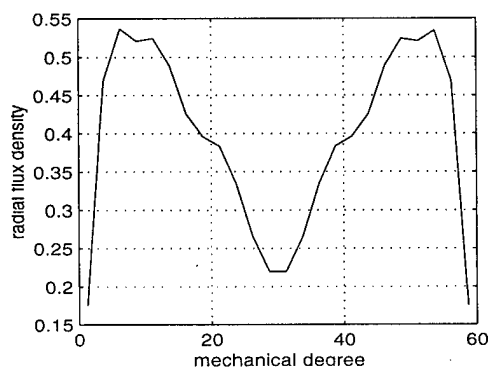


FIG. 7. Airgap flux density under load (directly demagnetizing case).

the figure by arrows representing the magnetic field intensity vectors. The flux density profile in the airgap is illustrated in Fig. 4 for the open circuit condition.

The short circuit condition with stator currents directly demagnetizing the rotor field is illustrated by the flux pattern in a cross section as shown in Figs. 5 and 6. The corresponding flux density variation in the airgap is given in Fig. 7.

The potentials obtained from these solutions are then used to compute engineering quantities like forces and inductances.

VI. CONCLUSIONS

An economical and efficient method for solving three-dimensional magnetostatic problems has been developed. The method has been applied to solve various three-dimensional problems including permanent magnet applications. The new method minimizes numerical inaccuracies by implementing the zero divergence of \vec{H}_c only in the iron parts. It also reduces the amount of computation necessary to solve the problem.

¹P. P. Silvester, *Finite Elements for Electrical Engineers* (Cambridge University Press, Cambridge, 1983).

²J. Simkin and C. W. Trowbridge, *IEE Proc.*, vol. 1.27, part B, No. 6, pp. 238–347, 1980.

³O. C. Zienkiewicz, J. Lynnes, and D. J. R. Owen, *IEEE Trans. Magn.* **13**, 1649 (1977).

⁴M. V. K. Chari, Z. J. Cendes, P. P. Silvester, A. Konrad, and M. A. Palmo, *IEEE Trans. Power Appar. Syst.* **100**, 40 007 (1981).

⁵R. Wang and N. A. Demerdash, *IEEE Trans. Magn.* **27**, 3971 (1991).

⁶M. V. K. Chari, S. Salon, G. Bedrosian, and J. Joseph, *IEEE Trans. Magn.* **31**, 1468 (1995).

Numerical simulation of the magnetization structures in thin polycrystalline films with the random anisotropy and intergrain exchange

D. V. Berkov^{a)} and N. L. Gorn

INNOVENT e.V., Göschwitzer Str. 22, D-07745, Jena, Germany, and Institute of Physical High Technologies, Helmholtzweg 4, D-07743, Jena, Germany

We have developed a new algorithm which enables a fast and exact evaluation of the dipolar interaction field for lattice systems of magnetic moments when periodic boundary conditions should be applied. The method uses the combination of (i) the fast Fourier transformation technique for the dipolar field evaluation and (ii) the modified version of the Ewald method known from the calculations of the Coulomb lattice sums. The algorithm enabled us to perform large-scale numerical simulations of the remagnetization processes in polycrystalline thin magnetic films with the random single-grain anisotropy and the intergrain exchange. The well known ripple-like structures forming during the remagnetization process were observed. The dependence of the ripple correlation lengths and the hysteresis loop parameters on the intergrain exchange coupling and the film thickness was studied. © 1998 American Institute of Physics. [S0021-8979(98)23411-6]

I. INTRODUCTION

The most time-consuming part of any micromagnetic algorithm for the simulation of the equilibrium magnetization structures — including simulations of the quasistatic remagnetization processes — is the calculation of the dipolar interaction field (also called the demagnetizing or stray field) due to its long-range character.^{1–5} For finite samples or aperiodic magnetization structures with fixed boundary conditions, the application of the convolution theorem allows the usage of the fast Fourier transformation (FFT) technique with zero padding^{1,2} resulting in the operation count $\sim N \log N$ (where N is the total number of lattice sites or discretization cells), which is only slightly worse than for systems with the short-range interaction. However, in lattice systems with periodic boundary conditions direct application of the convolution theorem is not possible due to the already mentioned long-range character of the dipolar field. Various methods were suggested to overcome these difficulty,^{3–6} but all of them encounter serious problems: (i) cut-off of the dipolar interaction at some prescribed distance^{5,6} can be applied only to 2D models and introduces small but significant errors which can strongly influence the result especially in low external fields (see below); (ii) the so called hierarchical model⁴ suffers from the same drawback and, in addition, its implementation is quite complicated; (iii) direct solution of the Poisson equation for “magnetic charges,”^{3,7} enables to calculate the Fourier components of the dipolar field analytically, but the cut-off of the corresponding Fourier spectrum — even at arbitrary large frequency — introduces strong artificial oscillations into the calculated dipolar field, because Fourier components of, e.g., the stray field of the point dipole do not tend to zero for large wave vectors.

In this contribution we propose a method which combines advantages of the FFT technique for the computation of the long-range interaction field ($\sim N \log N$ operation

count) and of the Ewald method normally used for the calculation of the lattice sums for the Coulomb potential (the error by the field evaluation may be reduced to a vanishingly small value with only a minor — of order $\sim N$ — computational effort). Thus we obtain an algorithm which allows fast and exact evaluation of the dipolar interaction field in lattice systems with periodic boundary conditions.

II. METHOD FOR THE DIPOLAR FIELD EVALUATION

We are going to calculate the stray field created by the lattice of point-like dipoles. Following the basic idea of the Ewald method,^{8,9} we add and subtract at each lattice node $\mathbf{r}_{ij} \equiv (i, j)$ (which carries the dipole moment $\boldsymbol{\mu}_{ij}$) an artificial “Gaussian dipole” with total moment $-\boldsymbol{\mu}_{ij}$ and “magnetic charge” density given by

$$\rho_{ij}^G(\mathbf{r}) = -\frac{\delta(z)}{(2\pi)^{3/2}a^5}[(x-x_{ij})\mu_{ij}^x + (y-y_{ij})\mu_{ij}^y] \times \exp\left[-\frac{(\mathbf{r}-\mathbf{r}_{ij})^2}{2a^2}\right], \quad (1)$$

where the choice of the “dipole width” a will be discussed elsewhere.¹⁰ The charge density of the system can then be written as the sum $\rho(\mathbf{r}) = \rho_A(\mathbf{r}) + \rho_B(\mathbf{r})$, where the first part

$$\rho_A(\mathbf{r}) = \sum_{i,j=1}^{N_x, N_y} [\boldsymbol{\mu}_{ij} \cdot \nabla \delta(\mathbf{r}-\mathbf{r}_{ij})] + \sum_{i,j=1}^{N_x, N_y} \rho_{ij}^G(\mathbf{r}) \quad (2)$$

is the sum of the point dipoles [$\rho(\mathbf{r})$ of the initial system] and the contribution of the “negative” Gaussian dipoles (1). The second part

$$\rho_B(\mathbf{r}) = -\sum_{i,j=1}^{N_x, N_y} \rho_{ij}^G(\mathbf{r}) \quad (3)$$

represents the density of the “positive” Gaussian dipoles which should cancel the second sum in Eq. (2).

^{a)}Electronic mail: DBerkov@t-online.de

The advantage of this transformation is the following. For the first part, $\rho_A(\mathbf{r})$ the total moment attached to each lattice site is zero, because the total moment of the negative Gaussian dipole— μ_{ij} exactly compensates the moment of the corresponding point dipole of the initial system μ_{ij} . Hence the field created by magnetic charges of this first part $\rho_A(\mathbf{r})$ associated with each lattice site tends to zero faster than exponentially [to be more precise, as $\exp(-r^2/2a^2)$] and may be treated as a short-range interaction field, so it can be evaluated in $\sim N$ operations for the whole lattice. On the other hand, the second part $\rho_B(\mathbf{r})$ of the charge density is smooth, because it is given not by the point dipoles, but by the smooth Gaussian distribution at each lattice site. This means that the field created by $\rho_B(\mathbf{r})$ can be safely calculated using the solution of the corresponding Poisson equation and the FFT technique (see Introduction). Further details of the method will be reported elsewhere.¹⁰

III. NUMERICAL SIMULATIONS

We consider a thin magnetic film consisting of single-domain grains (crystallites) with saturation magnetization M_s forming a 2D hexagonal lattice. The magnetization \mathbf{M}_i inside each grain (cell) is assumed to be homogeneous, and hence is completely described by the unit vector $\mathbf{m}_i \equiv \mathbf{M}_i/M_s$. To calculate the equilibrium magnetization structure for the given external field we minimize a total system energy E taking into account, as usual, four energy contributions: (i) energy in the external field, (ii) energy due to the exchange between the neighboring crystallites, (iii) single-crystallite magnetic anisotropy energy and (iv) stray field energy:

$$\frac{E}{M_s^2 V_0} = - \sum_i \mathbf{m}_i \mathbf{h}_0 - \frac{C_{\text{exch}}}{2M_s^2 V_0 \langle ij \rangle} \sum_i \mathbf{m}_i \mathbf{m}_j - \frac{K}{M_s^2} \sum_i (\mathbf{m}_i \mathbf{n}_i)^2 - \frac{1}{2} \sum_i \mathbf{m}_i \mathbf{h}_i^{\text{dem}}, \quad (4)$$

where V_0 is the cell volume, reduced fields are defined as $\mathbf{h} \equiv \mathbf{H}/M_s$, K is the anisotropy constant. The constant C_{exch} which characterizes the strength of the exchange interaction can be evaluated from the exchange stiffness of the bulk material A , the hexagonal cell side b , the intergrain separation δ , the film thickness d , and the exchange weakening κ on the grain boundaries using the method described, e.g., in Ref. 11: $C_{\text{exch}} = \kappa \cdot A b d / \delta$; in the exchange term the sum is taken over the nearest neighbors $\langle ij \rangle$ only. Random space orientation of the crystallite anisotropy axes \mathbf{n}_i and periodic boundary conditions are assumed. To minimize the energy (4) we have used the simplest version of the relaxation method described in Ref. 2.

Numerical simulations which results are presented below were performed for a system with magnetic parameters corresponding to Co films ($A = 10^{-6}$ erg/cm, $M_s = 1400$ emu/cc, $K = 4 \times 10^6$ erg/cm³), film thickness $d = 10$ nm (when not stated otherwise), hexagonal cell side $b = 5$ nm, intergrain boundary thickness $\delta = 1$ nm. The magnetic structures shown in Fig. 1 and Fig. 4 are $N_x \times N_y = 64 \times 128$ cuts out of a lattice with 128×256 cells actually simulated (physical sys-

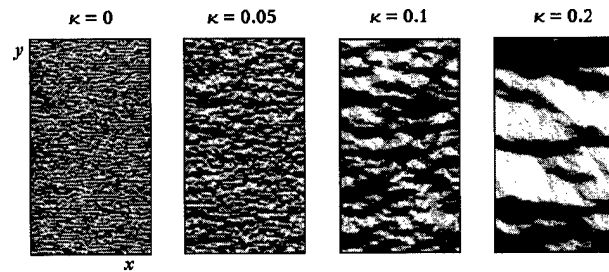


FIG. 1. Magnetization configuration (m_x -gray-scale maps) of the thin film near the coercivity for various exchange weakening degrees κ as indicated in the figure.

tem size $\approx 1.1 \times 1.9 \mu\text{m}$). All simulations were performed on the IBM Pentium PC 133 MHz. A typical run for a complete hysteresis loop (~ 40 values of the external field, $\sim 2 \times 10^4$ iterations totally) took about 10 hours.

IV. RESULTS AND DISCUSSION

Due to the limited paper length we present here in some detail only the dependence of the system behavior on the exchange coupling strength C_{exch} . Figure 1 demonstrates the magnetization structures at the coercivity point obtained by the simulation of the hysteresis loops for thin films with various values of the exchange weakening on the grain boundaries κ as indicated in the figure ($\kappa = 0$ means exchange decoupled grains, whereby, e.g., $\kappa = 0.1$ means that the exchange through a grain boundary is 10 times weaker than in the bulk). Initial direction of the external field was chosen parallel to the y direction in Fig. 1). The gray-scale map is used to present the x projection of the magnetization vectors $-1 < m_x < 1$, so Fig. 1 is supposed to simulate a standard Kerr-microscopy image. As expected, the average scale of the observed ripple structure (with stripes mostly perpendicular to the initial field direction) increases strongly with the exchange coupling at grain boundaries.

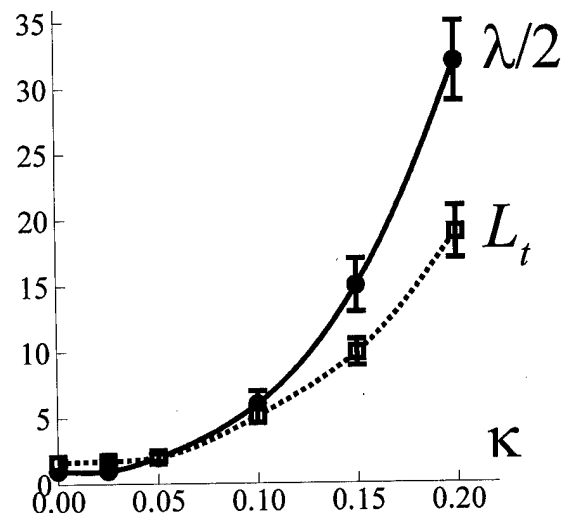


FIG. 2. Dependencies of the average ripple wavelength λ and the transverse correlation length L_t on the exchange weakening κ (statistical errors, where not shown, are smaller than the symbol size.)

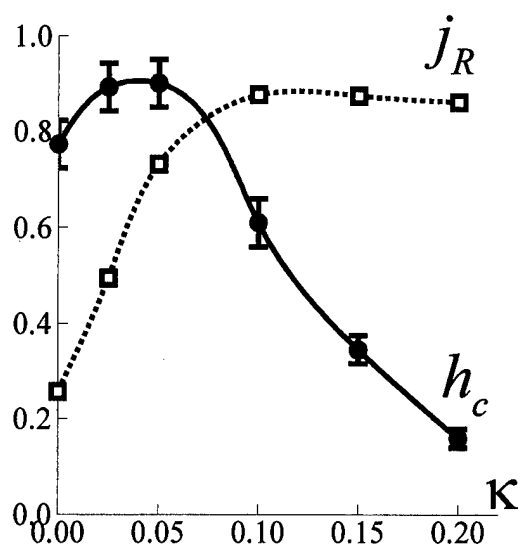


FIG. 3. Dependencies of the reduced remanent magnetization j_R and the coercivity h_c on the exchange weakening κ .

To investigate this dependence qualitatively, we have studied the average ripple wavelength λ and the transverse correlation length of the m_x -component L_t (defined as the decay distance of the spatial m_x -correlation function in the direction perpendicular to the external field) as functions of κ . Corresponding dependencies are shown in Fig. 2. The growth of both correlation lengths with the exchange coupling is evidently faster than a linear one predicted by the linear and even by the nonlinear ripple theories (see, e.g., Ref. 12).

The exchange dependence of the most important hysteresis loop parameters — reduced remanent magnetization $j_R = M_z(H=0)/M_s$ and reduced coercivity $h_c = H_c/M_s$ — is presented in Fig. 3. First of all, we point out that the remanence j_R for low exchange coupling differs significantly from that obtained using the cut-off method^{5,6} and the hierarchical model.⁴ This discrepancy is probably due to the small errors introduced by these both latter methods. Indeed, performing special test runs we have found that adding random errors with the relative magnitude ~ 0.01 – 0.02 to the exact stray field values evaluated by our method leads to a significant increase of the remanence especially in the case of small exchange coupling where the dipolar interaction is of a major importance. The second difference with the known results^{4–6} is the stronger decrease of the coercivity for large values of the exchange coupling obtained in our simu-

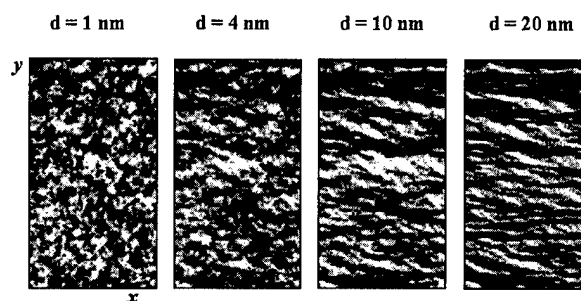


FIG. 4. Remanent magnetization states shown as m_x -gray-scale maps for various film thicknesses d as indicated in the figure.

lations which may be due to the much larger system size used by us. Namely, large correlation lengths occurring for strong exchange couplings (see Fig. 2) may lead to substantial finite-size effects for smaller system sizes.

We have also studied the dependence of the parameters discussed above on the film thickness d . Remanent magnetization states obtained for various film thicknesses are shown in Fig. 4. Here we would like only to point out that for a very thin film (where the intergrain interaction is almost negligible) the almost random magnetization pattern is formed (see image for $d=1$ nm) whereby for the thicker films the ripple structure became more and more pronounced. Detailed results of these studies, discussion of their relation to the available experimental data and of the applicability of our method to numerical simulations by finite temperatures will be presented elsewhere.¹⁰

ACKNOWLEDGMENTS

The authors are very grateful to Professor W. Andrä and Dr. R. Mattheis for helpful discussions.

- ¹ S. W. Yuan and H. N. Bertram, IEEE Trans. Magn. **MAG-28**, 2031 (1992).
- ² D. V. Berkov, K. Ramstoeck, and A. Hubert, Phys. Status Solidi A **137**, 207 (1993).
- ³ M. Mansuripur and R. Giles, IEEE Trans. Magn. **AG-24**, 2326 (1989).
- ⁴ J. J. Miles and B. K. Middleton, J. Magn. Magn. Mater. **95**, 99 (1991).
- ⁵ J.-G. Zhu and H. N. Bertram, J. Appl. Phys. **63**, 3248 (1988).
- ⁶ J. J. Miles and B. K. Middleton, IEEE Trans. Magn. **MAG-26**, 2137 (1990).
- ⁷ M. Mansuripur and R. C. Giles, Comput. Phys. **4**, 291 (1990).
- ⁸ C. Kittel, *Introduction to Solid State Physics* (Wiley, New York, 1953).
- ⁹ J. C. Slater, *Insulators, Semiconductors and Metals* (McGraw-Hill, New York, 1967).
- ¹⁰ D. V. Berkov, Phys. Rev. B (submitted).
- ¹¹ C. Kittel, Rev. Mod. Phys. **21**, 541 (1949).
- ¹² K. J. Harte, J. Appl. Phys. **37**, 1295 (1966).

Finite element analysis of the influence of a fatigue crack on magnetic properties of steel

Y. Shi and D. C. Jiles

Center for Nondestructive Evaluation, Iowa State University, Ames, Iowa 50011

Fatigue can affect the magnetic properties of materials due to microstructural changes. Previous investigations have shown that several structure sensitive magnetic properties, such as coercivity H_c and remanence B_r , changed systematically as a result of fatigue. When approaching failure the accumulated changes in microstructure resulted in the occurrence of fatigue cracks and the magnetic properties showed dramatic changes which mainly resulted from the geometrical changes in samples due to the cracks. It was found that the remanence B_r followed the changes in stress, while the coercivity H_c sometimes showed different trends. In this article the influence of the size and the position of a fatigue crack on magnetic field and magnetic induction were studied using finite element modeling. Models were constructed to simulate the geometry of the test sample and sensor. It was found that, for a given coil current in the exciting coil, the magnetic induction was mainly determined by the geometry of the crack, while the magnetic field was influenced by both the size and the position of the crack. © 1998 American Institute of Physics. [S0021-8979(98)50711-6]

I. INTRODUCTION

In recent years there has been increased interest in correlating magnetic properties of ferromagnetic materials with their mechanical properties.^{1,2} The evolution of the magnetic properties during fatigue is of particular interest because of the relation between the fatigue and magnetic properties of materials.³⁻⁵ It has been shown that the measured magnetic properties change systematically throughout the fatigue lifetime. When approaching failure, the cumulative stress results in the occurrence of cracks, which normally start from the outer surface. After cracks appeared there was little overall change in the microstructure of the materials because most stresses then concentrated at the tip of the crack and the main change subsequently was the growth of the crack. During this period, the corresponding changes of magnetic properties mainly resulted from geometrical changes in the samples because of crack growth. It was found during this period that the remanence B_r still depended primarily on the crack geometry although the coercivity H_c sometimes showed different trends.

To explain the above observations magnetic finite element modeling (FEM) work was conducted to establish the relation between the fatigue crack geometry and the surrounding magnetic field distribution. Finite element analysis techniques, although yielding only approximate solutions to the classical partial differential equations of the electromagnetic field, are particularly attractive for the study of field distribution within magnetic structures having complex boundary configurations. This property makes the method very suitable for the analysis of the interaction between the magnetic field and defects within materials, and thus it has been applied to magnetic leakage field inspection⁶⁻⁸ and creep damage detection.⁹ In this article, it is shown that the method can be extended to fatigue analysis.

II. FINITE ELEMENT MODELING

The general geometry of the FEM solid model is shown in Fig. 1. The shape of the fatigue sample on which experimental measurements were made was a cylindrical rod which was subjected to a uniaxial cyclic stress. An inductive magnetic sensor consisting of a search coil wound on a magnetic C core was used to measure the magnetic properties of the sample during the fatigue lifetime. The magnetic field was measured using a Hall probe which was located at the center of the C core and on the surface of the sample. Magnetic induction was measured using a detection coil which was wound on the core of the sensor. To simplify the modeling two-dimensional representations were constructed to simulate the geometry of the sample and sensor. The magnetic field values were calculated at the location of the Hall probe and the magnetic induction values were calculated from the throughout the volume of the detection coil.

The amplitude of the excitation current was small enough that the sensor operated in the low field hysteresis

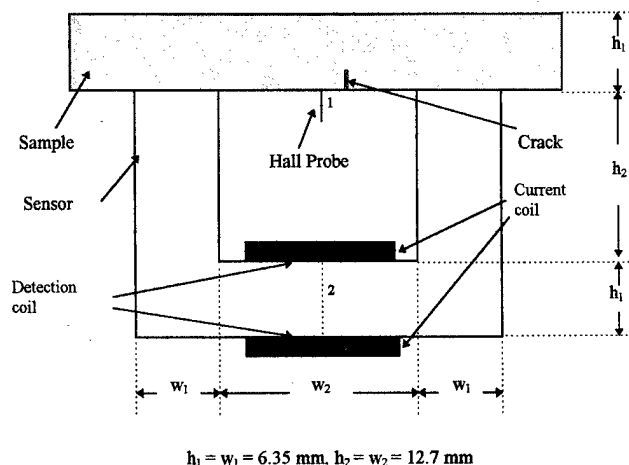


FIG. 1. Geometry for the finite element model calculation.

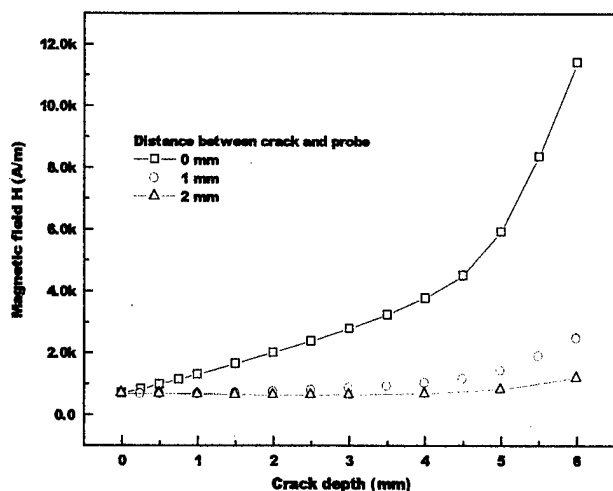


FIG. 2. Calculated magnetic field H vs crack depth in the position with the crack on the side of the specimen facing the C core and positioned at the center of the sensor.

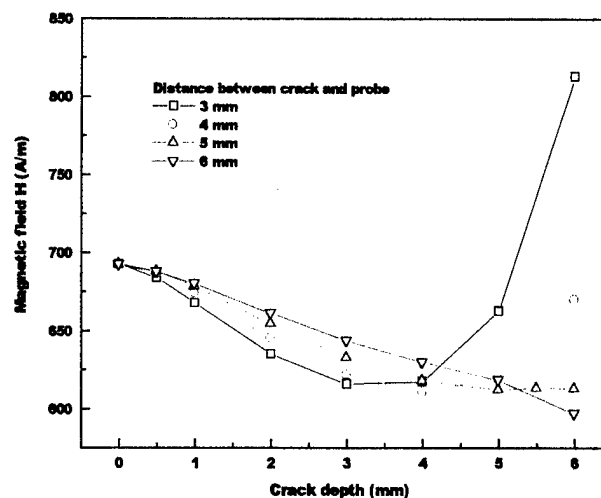


FIG. 3. Calculated magnetic field H vs crack depth in the position with the crack on the side of the specimen facing the C core and positioned away from the center of the sensor.

region which can be considered as approximately linear. So the magnetic properties of the sensor material were assumed linear to simplify the problem. However, nonlinear B - H data, which were measured experimentally, were used for the sample material, because different regions would have different magnetic states during fatigue after the crack generated.

The vector potential formulation was employed to conduct calculations.¹⁰ With this method it is possible to calculate the flux passing through a predefined line contour. At first calculations were conducted to determine the magnetic field distribution of the whole system for different crack sizes and positions under a fixed excitation current. Then the magnetic field value at the Hall probe (location 1 in Fig. 1) and the magnetic induction at the detection coil (location 2 in Fig. 2) were calculated.

III. RESULTS AND DISCUSSION

The magnetic field in the specimen was influenced by both the crack size and its position as shown in Figs. 2–4. This is because the magnetic field distribution in the space between the sample and the C core was mainly determined by two factors: the leakage field of the corners and tips of the crack and the demagnetizing effect generated by the crack surfaces. The leakage field increased as the crack grew, which resulted in a larger field amplitude. However growth of the crack also increased its surface area which led to an increase in the demagnetizing effect and hence reduction of the magnetic field. When the crack was located below the C core at the center of the sample, the leakage field dominated. The resultant field increased with the crack size as shown in Fig. 2. When the crack did not occur at the midpoint, the demagnetizing effect of crack surfaces altered the magnetic field. Therefore, as the crack was initiated, the magnetic field at first decreased because of the demagnetizing field from the crack surface. Later it increased because of the leakage field introduced by the corners of the crack as shown in Fig. 3. As the distance between the probe and the crack increased, the

influence of the demagnetizing effect on the resultant amplitude of the magnetic field became greater, and the influence of the leakage field became less.

A similar explanation can be applied to the case when the crack is on the side of the specimen opposite from the C core. The only difference is that the leakage field generated by the tip of the crack dominated in most cases. The demagnetizing effect hardly influenced the magnetic field in the immediate vicinity of the crack. Only when the crack was farther away from the center of the sample did the influence of demagnetizing effect on the magnetic field become apparent as shown in Fig. 4.

Compared with the magnetic field H , the resultant magnetic induction B exhibited much smaller changes with the crack geometry as shown in Fig. 5. This result can be explained because the detection coil measured the flux change in the sensor, which was distant from the crack region. Therefore, the measured magnetic induction was an average

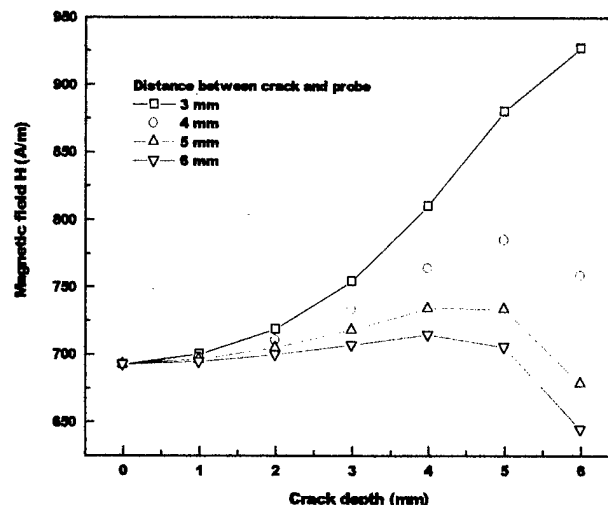


FIG. 4. Calculated magnetic field H vs crack depth in the position with the crack on the opposite side of the specimen from the C core and away from the center of the sensor.

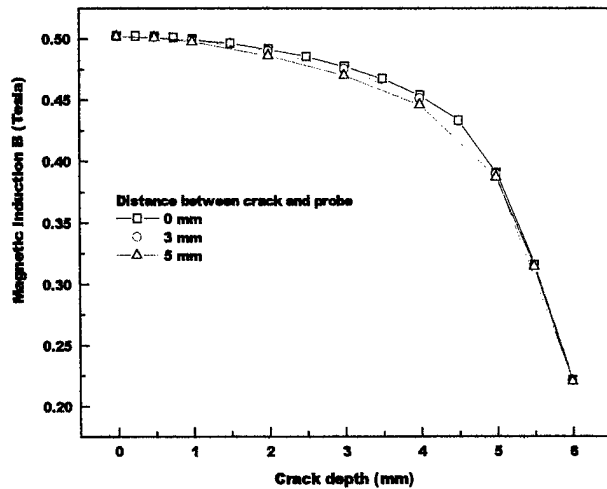


FIG. 5. Calculated magnetic induction B vs crack depth in the position with the crack on the opposite side of the specimen from the C core and away from the center of the sensor.

which was much less influenced by the two effects than was the highly localized magnetic field. The main factor influencing the resultant magnetic induction was the size of the air gap which was introduced by the crack into the magnetic circuit. This increased the magnetic reluctance around the flux path and resulted in a decrease in magnetic induction with crack size under the same magnetomotive force as shown in Figs. 5 and 6.

IV. CONCLUSIONS

The interactions of the magnetic field and the fatigue crack were modeled using finite element techniques. It was found that the detected magnetic field was determined principally by two factors: the leakage field of the corners and tips of the crack and the demagnetizing effect of the crack surfaces. These two factors had opposite effects on the detected magnetic field amplitudes. On the other hand, the calculated magnetic induction appeared to be only determined by the crack geometry.

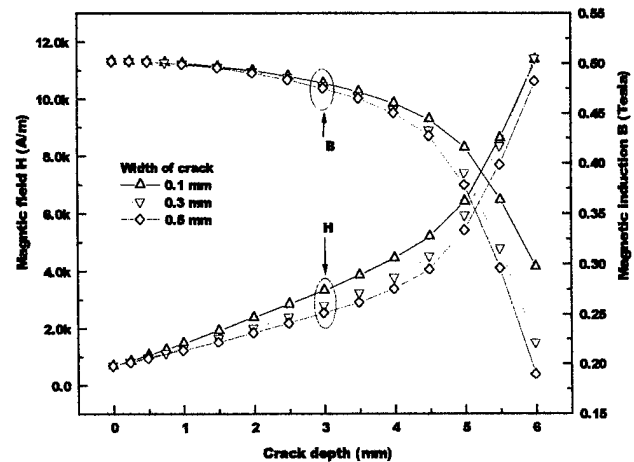


FIG. 6. Calculated magnetic field H and magnetic induction B vs crack width and depth with the crack on the side of the specimen facing the C core and located at the center of the sensor.

ACKNOWLEDGMENT

This research was supported by the National Science Foundation, Division of Civil and Mechanical Structures, under Grant No. CMS-9532056.

- ¹D. C. Jiles, *NDT & E Int.* **21**, 311 (1988).
- ²M. K. Devine, D. C. Jiles, D. A. Kaminski, and D. Chandler, *Rev. Prog. Quantitative NDE* **11**, 1771 (1992).
- ³M. S. C. Bose, *NDT & E Int.* **19**, 83 (1986).
- ⁴M. K. Devine, D. A. Kaminski, L. B. Sipahi, and D. C. Jiles, *J. Eng. Performance* **1**, 249 (1992).
- ⁵Y. Bi, M. R. Govindaraju, and D. C. Jiles, *International Magnetics Conference*, New Orleans, 1–4 April 1997 (unpublished).
- ⁶F. Forster, *NDT & E Int.* **19**, 3 (1986).
- ⁷J. H. Hwang and W. Lord, *ASTM J. Testing Evaluation* **21** (1975).
- ⁸W. Lord, J. M. Bridges, W. Yen, and R. Palanisamy, *Mater. Eval.* **47** (1978).
- ⁹M. J. Sablik, S. W. Rubin, D. C. Jiles, D. Kaminski, and Y. Bi, *IEEE Trans. Magn. Int.* **32**, 4290 (1996).
- ¹⁰Electromagnetic field analysis guide, ANSYS Inc., Release 5.3, 1996.

Magnetohydrodynamic calculation for free surfaces

Keisuke Fujisaki and Takatsugu Ueyama

Process Research Tech Labs. Nippon Steel Corp., 20-1 Shintomi, Futtsu-city, Chiba 293-8511, Japan

A magnetohydrodynamic calculation for free surface is used in the design and evaluation of a cold-crucible or initial solidification such as stirring phenomena commonly found in the metal processing industry. A direct calculation of both the electromagnetic field and the fluid dynamics field for the surface of a molten metal that changes with time requires significant computing times, especially for three-dimensional models. An approximate calculation method, the shadow method, is one which uses a fixed mesh. Results obtained by the shadow method show that the shape of molten metal does not collapse under gravity as observed experimentally. © 1998 American Institute of Physics. [S0021-8979(98)33011-X]

I. INTRODUCTION

A magnetohydrodynamic calculation for free surface is used in the design and evaluation of cold-crucible or initial solidification such as stirring phenomena commonly found in the metal processing industry.¹⁻³ The magnetohydrodynamic calculation is necessary for an electromagnetic field calculation based on Maxwell equations and a flow dynamics calculation based on the Navier–Stokes equations. A direct calculation method that allows for the surface of the molten metal to change with time requires significant computing times, especially for three-dimensional models. Hence an approximate scheme of calculation is desirable.

In a free surface calculation, the shape of molten metal changes with time and the numerical solutions are iterated to within a certain error. Since the shape of the molten metal changes, a moving mesh calculation method is used.⁴ However, using a moving mesh requires extra calculations needed to solve for the mesh positions. Moreover, the influence of the flow dynamics on the free surface shape is ignored. Only the balance of electromagnetic and gravitational forces is considered. Here, we propose a shadow method on a fixed mesh.

II. CALCULATION METHOD

A. Direct method

Figure 1 shows the results of a magnetohydrodynamic calculation using the direct method. Through an electromagnetic analysis, the electromagnetic force is calculated, and the fluid dynamics is analyzed using the condition that the electromagnetic force is the driving force for the fluid dynamics. During the fluid dynamic analysis, the velocity and the mesh shape are calculated, and the electromagnetic forces are analyzed using the condition that the velocity makes the electromotive force, and the mesh shape provides the new boundary condition.

Here, the eddy current field and the quasistationary field are assumed in the electromagnetic analysis.⁵ Turbulent flow in the fluid dynamic analysis is assumed, because the Reynolds number is as large as 10^5 – 10^6 . The direct method has been used for a two-dimensional model using a static condition.^{6,7} However, calculations of the electromagnetic

fields and fluid dynamics in the case of a three-dimensional model or one with transient dynamics requires a lot of computation. Hence an approximate shadow method is described and tested in this article.

B. Shadow method

Figure 2 shows the results of a magnetohydrodynamic calculation using the shadow method proposed here. The shadow method is used to model the electromagnetic fields in a flow dynamic calculation. The problem to be solved is how to calculate the new electromagnetic forces when the shape of molten metal changes as a result of the old electromagnetic forces. Usually, the new electromagnetic forces are different from the old electromagnetic forces whenever the shape of molten metal changes. In the shadow method, it is assumed that the electromagnetic field is the same when the clearance between the coil and the molten metal is the same.

In the shadow method, we consider one line in the molten metal to be solved. The line could be selected to be along a direction in which the molten metal shape changes. Along this line, we can make any point of the molten metal which does not change shape corresponds to a certain point of the molten metal which changes under the influence of the old electromagnetic force distribution. Then the new electromagnetic force in the molten metal can be obtained from this one to one correspondence.

The flow dynamics calculation for a free surface uses a fixed mesh. The mesh in free surface is expressed as the occupation rate of the molten metal. The curve of the free surface is made smooth on the mesh, where the pressure is equal.⁸

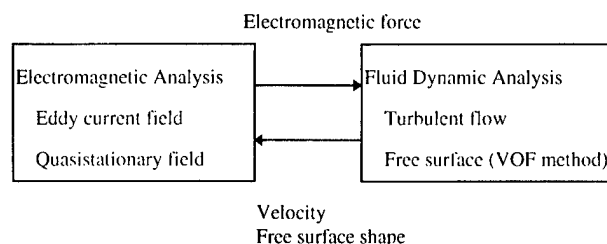


FIG. 1. Magnetohydrodynamic calculation by direct method.

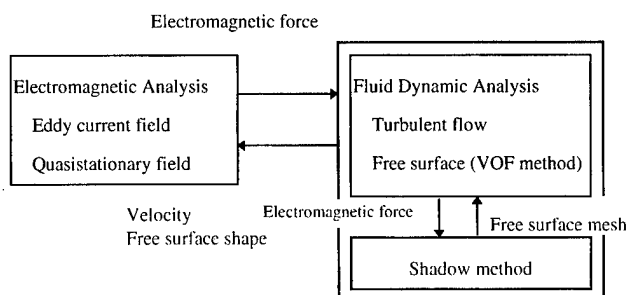


FIG. 2. Magnetohydrodynamic calculation by shadow method.

The shadow method is based on a modeling method called MORDY, which stands for moving reference frame model for multibody.⁹ The MORDY approach is used in dynamic calculations such as in electromagnetic levitated vehicles.¹⁰

III. CALCULATION RESULTS

A. Calculation method

Figure 3 shows the calculation model here. To test the validity of the shadow method, we use a cylindrical two-dimensional non-static model. The z direction is the line that is selected. Along this line, the electromagnetic force is shadowed from the old molten metal to the new molten metal. This model is used in the initial solidification in continuous casting.⁶

The electromagnetic forces are calculated using a general solver of electromagnetic fields called FLEDY.¹¹ The

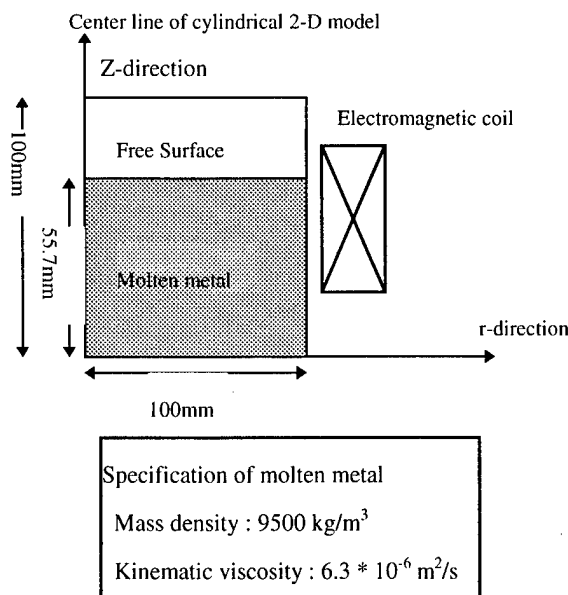


FIG. 3. Calculation model (cylindrical 2D model).

electromagnetic force is applied to the molten metal for the first 0.1 s. The calculation time of fluid dynamics is 2.0 s.

B. Calculation results

Figure 4 shows the calculated results without the shadow method. For $z > 0.0557$ m, no electromagnetic forces are applied to the molten metal as shown in (2-1) of Fig. 4 (the

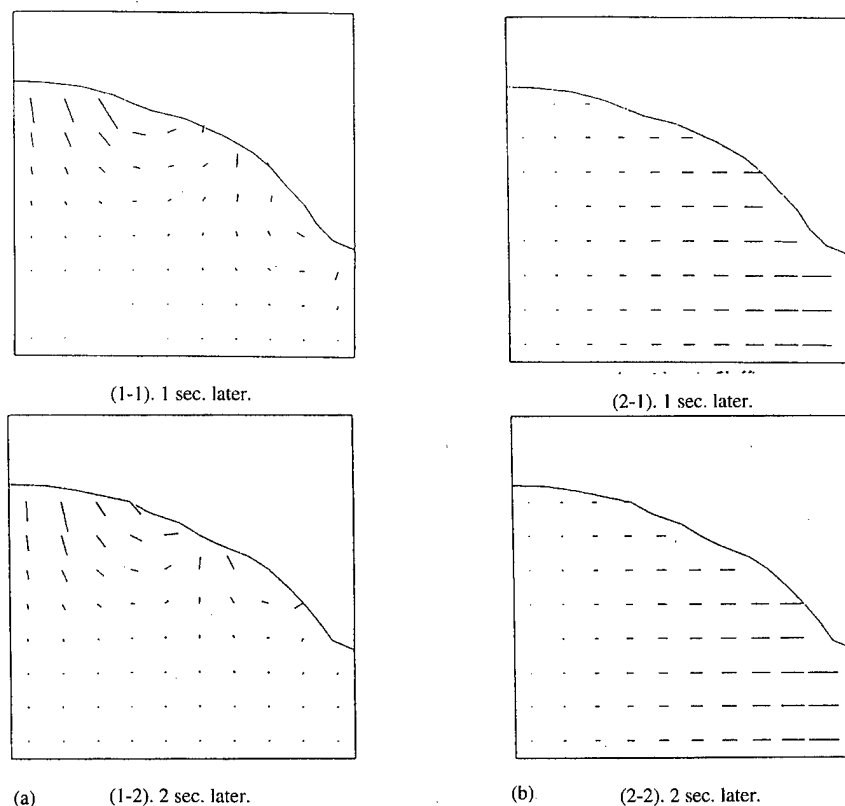


FIG. 4. Calculation results by no shadow method. (a) Velocity distribution. (b) Electromagnetic force distribution.

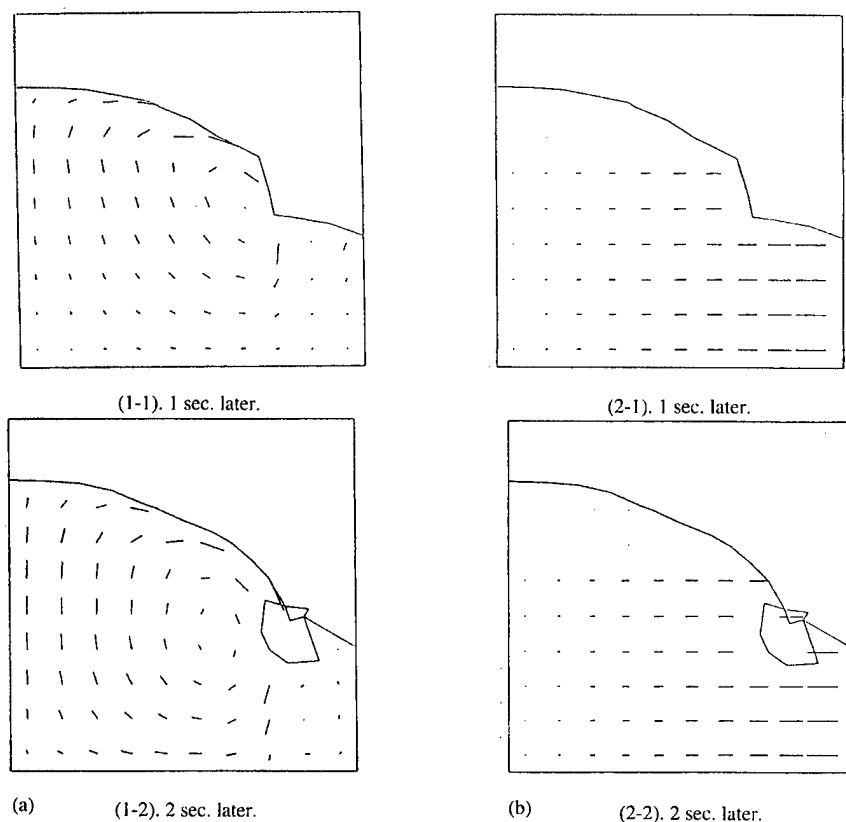


FIG. 5. Calculation results by shadow method. (a) Velocity distribution. (b) Electromagnetic force distribution.

electromagnetic force distribution after 1.0 s). The molten metal near the center line rises, and then falls down because there is no electromagnetic force to support it, as shown in (1-2) of Fig. 4 (the velocity after 2.0 s). This contradicts experimental observations during initial solidification,⁶ in which collapse of the metal does not occur. The electromagnetic force only supports the molten metal in the first few seconds.

On the other hand, Fig. 5 shows the calculated results with the shadow method. In contrast to the direct calculation, for $z > 0.0557$ m electromagnetic forces are applied to the molten metal as shown in the corresponding panel (2-1) of Fig. 5. The molten metal near the center line also rises up. However, the molten metal does not fall down because the electromagnetic forces support the molten metal, as shown in (1-2) of Fig. 5.

IV. CONCLUSION

A shadow method is proposed here as the modeling method for free surface magnetohydrodynamic calculations.

The results obtained by the shadow method show that the shape of molten metal does not collapse under gravity in accordance with experimental observations.

¹K. Fujisaki, J. Nakagawa, and H. Misumi, *IEEE Trans. Magn.* **30**, 4764 (1994).

²S. Sato, *Proceedings of Japan Industry Applications Society Conference, International Sessions of 7-th Annual Conference, S.11-5, August 1993*, pp. 240–243.

³A. J. Mestel, *Proceedings of the International Union of Theoretical and Applied Mechanics*, 1982, pp. 197–204.

⁴Y. Kawase, Y. Murai, and N. Hayashi, *Trans. Inst. Electron. Inf. Commun. Eng. D11*, J72 271 (1989).

⁵K. Fujisaki, T. Ueyama, and K. Okazawa, *IEEE Trans. Magn.* **33**, 1642 (1996).

⁶T. Toh, E. Takeuchi, J. Sakane, M. Hojo, H. Takeuchi, H. Kawai, and S. Matsumura, *International Symposium on Electromagnetic Processing of Materials*, October 1994, pp. 254–259.

⁷H. Ohsaki, *Proceedings of Japan Industry Applications Society Conference, International Sessions of 7-th Annual Conference, J.93-A-6, August 1993*, pp. 117–122.

⁸C. W. Hirt and B. D. Nichols, *J. Comput. Phys.* **39**, 201 (1981).

⁹K. Fujisaki and E. Masada, *Simulation (Japanese)* **3**, 88 (1984).

¹⁰E. Masada and K. Fujisaki, "Untersuchung am dynamischen Verhalten des elektromagnetischen Schwebefahrzeugs durch die Simulation," *VDI-Berichte, Nr.510, S.223*, March 1984.

¹¹T. Ueyama, K. Shinkura, and R. Ueda, *IEEE Trans. Magn.* **25**, 4153 (1989).

Differential Preisach model for the description of dynamic magnetization processes

P. Andrei, Al. Stancu,^{a)} and O. Caltun

"Al. I. Cuza" University, Faculty of Physics, Iasi, 6600, Romania

A differential dynamic Preisach model developed by us and introduced as an idea suggested by Bertotti is generalized. The starting point of this model is that the instantaneous excess field due to the moving and dynamic processes can be approximated as a function of M and its variation rate dM/dt : $F(M, dM/dt)$. Thus, we determine a differential equation for the magnetic susceptibility. The model's parameters are found by an original identification method. As an application we simulate a simple electrical circuit and compare the results with the experimental data. A very good agreement between the measured and simulated data is observed. © 1998 American Institute of Physics. [S0021-8979(98)33111-4]

I. INTRODUCTION

Generally, the actual phenomenological models for the magnetic hysteresis¹⁻⁴ are given by a differential equation for the magnetization (or induction) and they try to fit theoretical curves to experimental data. Usually, this differential equation (the model equation) is of the first order and one can determine the susceptibility χ (or permeability) as a function of the magnetization M , of the applied field H , and of their variation rate (\dot{M} and \dot{H}). If χ depends on all these variables then the model is called a dynamic model and if χ is only a function of M and H , the model is a static one. Integrating $\chi(H, M, \dot{H}, \dot{M})$ one obtains the magnetization M as a function of time. There have also been a few attempts^{3,4} to present some dynamic Preisach models in a mathematical form but none of them gives a differential equation. This makes it very difficult to use the Preisach model in many applications where the dynamic effects must be taken into account such as: simulation of electrical circuits that contain a coil with a nonlinear core or prediction of some magnetization processes where H is given by a differential equation.

In this article we have generalized a dynamic Preisach model (DPM) recently developed by us.⁵ It is known⁶ that the dynamic effects in a magnetic core (such as the effects produced by eddy currents) can be taken into account by supposing that the effective magnetic field is the sum between the applied field and an excess instantaneous field which depends on the variation rate of M . To consider a classical moving term depending on M as well, we suppose that the effective field is the sum of the applied field, H , and a general moving term, $F(M, \dot{M})$, depending on M and \dot{M} :

$$H_{\text{eff}} = H + F(M, \dot{M}). \quad (1)$$

Due to the symmetry of the major loop the general moving function F must satisfy the condition $F(M, \dot{M}) = -F(-M, -\dot{M})$.

II. DYNAMIC PREISACH MODEL

In order to find an analytical expression for the magnetic susceptibility in DPM we will employ a method developed

by us previously.⁵ We consider the generalized moving Preisach model with the effective field given by (1). The Preisach distribution function is assumed to be the product of a Gaussian distribution in the interaction field and a log-normal distribution in the coercive field:

$$P(H_\alpha, H_\beta) = P_0 P_i \left(\frac{H_\alpha + H_\beta}{\sqrt{2}} \right) P_c \left(\frac{H_\alpha - H_\beta}{\sqrt{2}} \right), \quad (2)$$

with (P_0 is a normalization factor):

$$P_0 = \frac{SM_s H_0}{2\pi H_{\sigma i} H_{\sigma c}}, \quad P_i(h) = \exp\left(-\frac{h^2}{2H_{\sigma i}^2}\right), \quad (3)$$

$$P_c(h) = \frac{1}{h} \exp\left[-\frac{\ln^2(h/H_0)}{2(H_{\sigma c}/H_0)^2}\right],$$

where $H_{\sigma i}$ and $H_{\sigma c}$ are distribution standard deviations, H_0 is the center of the distribution after coercivities and M_s is the saturation value of the magnetization. The factor S represents the weight of the irreversible part in the total magnetization of the sample. The reversible component of the model is given by:

$$R(H_\alpha) = \frac{(1-S)M_s}{2H_{\sigma r}} \exp\left(-\frac{|H_\alpha|}{H_{\sigma r}}\right), \quad (4)$$

where $H_{\sigma r}$ is a fit parameter.

In order to find the susceptibility in DPM, we differentiate the total magnetization of the generalized moving Preisach model with respect to the magnetic field. Using the same method presented earlier⁵ one finds the differential equation:

$$\frac{d\chi}{dt} = \frac{1}{F'_{\partial M}(M, \dot{M})} + \frac{[F'_M(M, \dot{M})\dot{H} - F'_{\partial M}(M, \dot{M})\ddot{H}](I+J) - \dot{H}}{(I+J)F'_{\partial M}(M, \dot{M})\dot{H}} \chi, \quad (5)$$

where we have introduced the notations:

^{a)}Electronic mail: alstancu@uaic.ro

$$I = \begin{cases} 2 \frac{\partial E(H_{N \text{ eff}}, H_{\text{eff}})}{\partial H_{\text{eff}}} = 2 \int_H^{H_{N \text{ eff}}} P(h, H_{\text{eff}}) dh, & \text{if } H \text{ is increasing;} \\ 2 \frac{\partial E(H_{\text{eff}}, H_{N \text{ eff}})}{\partial H_{\text{eff}}} = 2 \int_{H_{N \text{ eff}}}^H P(H_{\text{eff}}, h) dh, & \text{if } H \text{ is decreasing;} \end{cases} \quad (6)$$

(H_{eff} is the value of the effective field, $H_{N \text{ eff}}$ is the last extreme value of the effective field in the Preisach plane), and

$$J = 2R(H_{\text{eff}}). \quad (7)$$

The functions $F'_M(M, \dot{M})$ and $F'_{\dot{M}}(M, \dot{M})$ represent the partial derivatives of F with respect to M and \dot{M} , respectively. The function E is the Everett integral defined as:

$$E(H_x, H_y) = \int_{-H_0}^{-H_0 + (H_x - H_y)/2} \left[\operatorname{erf}\left(\frac{H_x - H_0 - h}{H_{oi}}\right) - \operatorname{erf}\left(\frac{H_y + H_0 + h}{H_{oi}}\right) \right] P_c(h + H_0) dh, \quad (8)$$

where erf is the error function.⁷ The functions I and J represent the irreversible and the reversible part of the susceptibility in the generalized Preisach model, respectively.

The choice of the function F is a quite intricate problem. Bertotti⁶ has shown that the average excess field in a half hysteresis loop depends on the average magnetization rate as $H_{\text{exc}} = -\beta \operatorname{sgn}(\dot{M})(\sqrt{1 + \gamma|\dot{M}|} - 1)$, where β and γ are two parameters that depend on the material. In this article we suppose that at each point of the hysteresis loop the instantaneous excess field is given by the same equation where \dot{M} is the instantaneous magnetization rate. Thus, the generalized moving function is:

$$F(M, \dot{M}) = \alpha M - \beta \operatorname{sgn}(\dot{M})(\sqrt{1 + \gamma|\dot{M}|} - 1), \quad (9)$$

where α is the moving parameter.³ The existence of the excess magnetic field H_{exc} that adds to the applied magnetic field implies an important variation of the coercive field of the major hysteresis loop with the frequency of the applied field. Thus one can determine the parameters β and γ by measuring the coercive field for different \dot{M} .

III. IDENTIFICATION METHOD

There are some identification methods for the Preisach distribution but all of them are quite intricate and need many experimental data (e.g., Mayergoyz³). In this section we propose a robust identification method for the Preisach distribution's parameters (M_s , H_{oc} , H_{oi} , H_{oc} , H_0 , and S) and for the moving parameter α from the experimental major hysteresis loop and the experimental remanent major loop, respectively.

In order to determine the distribution's parameters we have used the following method. First, one determines from the static hysteresis loop: the coercive field H_c , the remanent magnetization M_r , the magnetization at the upper branch of the loop for the coercive field M_c , and the energy lost per cycle (the surface of the loop) w , the closure field (the field where the upper branch of the major loop touches the lower

branch) H_{cl} , the saturation field H_s and the susceptibility at H_{cl} and H_s [$\chi(H_{cl})$ and $\chi(H_s)$, respectively]. Then, one determines the parameters M_s (as the saturation value of the major loop) and H_{oc} from the equation:

$$H_{\text{oc}} = \frac{H_s - H_{cl}}{\chi(H_{cl}) - \chi(H_s)}, \quad (10)$$

(the susceptibility for field greater than H_{cl} is given by the reversible part of the susceptibility). Finally, one follows the iteration:

- (1) One starts from two "first guess" values of the parameters H_0 and H_{oc} (in our simulation we have always started from $H_0 = H_c$ and $H_{\text{oc}} = H_c$).
- (2) One determines S from the condition that the surface of the major loop is w :

$$S = \frac{\sqrt{\pi} w H_{\text{oc}}}{4 M_s H_0} \left[\int_0^\infty P_c(\sqrt{2}h) h dh \right]^{-1}. \quad (11)$$

- (3) The H_{oi} parameter is determined from the remanent magnetization M_r by solving the next transcendental equation:

$$M_r = \frac{S M_s H_0}{\sqrt{\pi} H_{\text{oc}}} \int_0^\infty P_c(\sqrt{2}h) \operatorname{erf}\left(\frac{h}{H_{oi}}\right) dh. \quad (12)$$

- (4) The H_0 parameter is determined from the coercive field H_c by solving the transcendental equation:

$$\frac{S M_s H_0}{\sqrt{\pi} H_{\text{oc}}} \int_0^\infty P_c(\sqrt{2}h) \operatorname{erf}\left(\frac{H_c - h}{H_{oi}}\right) dh + 2 \int_0^{H_c} R(h) dh = 0. \quad (13)$$

- (5) One repeats steps 2, 3 and 4 until the convergence is attained (in our simulations we imposed that the actual values of the S , H_{oi} , and H_0 differ from the old ones with a relative error of 10^{-3}).
- (6) One determines the actual value of M_c from the upper branch of the major loop (we denote this value by M'_c):

$$M'_c = \frac{S M_s H_0}{\sqrt{\pi} H_{\text{oc}}} \int_0^\infty P_c(\sqrt{2}h) \operatorname{erf}\left(\frac{H_c + h}{H_{oi}}\right) dh + 2 \int_0^{H_c} R(h) dh. \quad (14)$$

- (7) If $|M'_c - M_c| < \epsilon$ (where ϵ is a small parameter that ensures the convergence; we considered $\epsilon = 10^{-3} M_s$) then one stops the iteration; else one pass to the next step.
- (8) One determines the new value of H_{oc} by adding to the old value of H_{oc} the term $\xi(M'_c - M_c)$, where ξ is an appropriate relaxation factor. This constant has to be sufficiently great in order to increase the convergence rate of the algorithm but not so large that it causes the algorithm to diverge (in our simulations we considered $\xi = 1/M_s$). Then one passes to step 2 and one repeats the algorithm.

In order to determine the moving parameter α we used the following algorithm. One starts with a "first guess" value for the moving parameter α (in our simulations we have started with $\alpha = 0$) and transforms the experimental major loop in the operational plane (the operational plane is the plane $(M, H + \alpha M)$). One determines the distribution's parameters using the method presented above and then the new value of the moving parameter by adding to the old value, the quantity:⁸

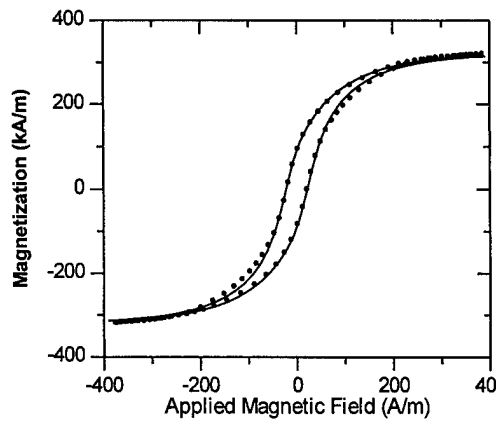


FIG. 1. Static hysteresis loops: experimental (points) and simulated (continuous line).

$$\Delta\alpha = \frac{H_c'(\text{rem}) - H_c(\text{rem})}{M(H_c'(\text{rem}))}, \quad (15)$$

where $H_c(\text{rem})$ and $H_c'(\text{rem})$ are the coercive fields of the experimental and the simulated remanent major hysteresis loops, respectively, and $M(H_c'(\text{rem}))$ is the simulated magnetization corresponding to $H = H_c'(\text{rem})$. One continues the iteration until $\Delta\alpha$ is negligible.

IV. RESULTS AND DISCUSSIONS

The experimental setup consists of a RL circuit in series with an ac generator. The inductance L is a MnZn soft magnetic torus (A-41) having the inner radius $r_1 = 23$ mm, the outer radius $r_2 = 35$ mm, and the high $h = 20$ mm. The experimental magnetic hysteresis loop is determined using a digital storage oscilloscope.⁹

Using the identification method presented above we have obtained the next set of parameters: $M_s = 3.2 \times 10^{-5}$ A/m, $S = 0.23$, $H_{\sigma 1} = 27.5$ A/m, $H_{\sigma 2} = 67.1$ A/m, $H_{\sigma 3} = 111.0$ A/m, $H_0 = 74.4$ A/m, and $\alpha = 1.13 \times 10^{-4}$. The experimental and the simulated static hysteresis loops are shown in Fig. 1. In Fig. 2 is shown the dc demagnetization (which is used in the identification of α) and the isothermal remanent magnetization curves. The identification method ensures that the coercive field H_c , the magnetizations M_r and M_c and the losses (the area) in one major hysteresis loop are the same as the experimental ones. The dynamic parameters β and γ are

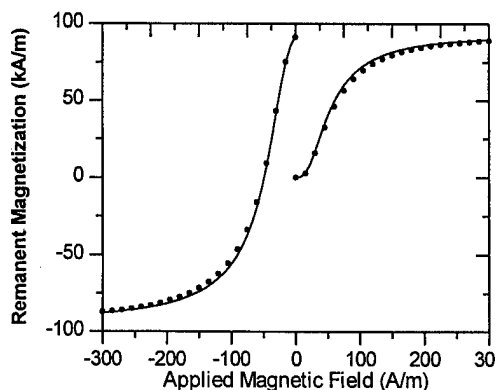


FIG. 2. Experimental (points) and simulated (continuous line) remanent magnetization curves: IRM for positive fields and DCD for negative fields.

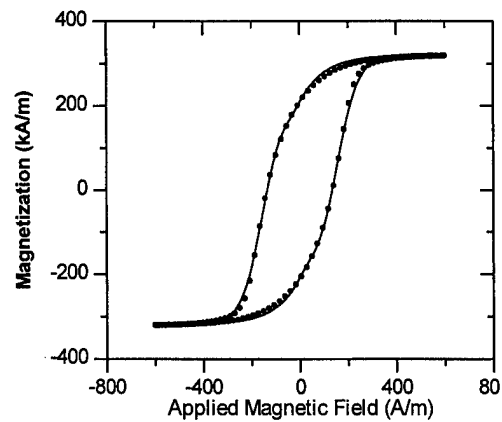


FIG. 3. Dynamic hysteresis loops for $\nu = 1$ kHz: experimental (points) and simulated (continuous line).

calculated from least-squares criteria applied to the simulated and experimental wave form magnetization in the dynamic loop. We present in Fig. 3 the dynamic hysteresis loop, obtained for the frequency of the applied field $\nu = 1$ kHz. One observes a substantial increase of the coercive field (approximately five times) that is characteristic to the soft ferrites.

V. CONCLUSIONS

Various magnetization processes were simulated with a differential Preisach model. The dynamic processes were taken into account using a simple phenomenological assumption: the effective field in the Preisach plane is the sum of the applied field and a generalized moving field depending on the instantaneous magnetization and its variation rate. The same method can be applied to all the phenomenological models of hysteresis (e.g., the Jiles–Atherton model and Hodgdon model). We have deduced a differential equation for the magnetic susceptibility, analogous to that previously presented.

In order to determine the model's parameters we have developed a robust identification method that needs the experimental major hysteresis loop (for the distribution parameters) and the experimental dc demagnetization curve (for the moving parameter). A very good agreement is observed between the simulated and experimental curves.

ACKNOWLEDGMENTS

Petru Andrei extends his gratitude to Prince Dimitrie Sturdza for financial support. The authors also wish to acknowledge IEEE Magnetics Society and “Al. I. Cuza” University for financial support.

¹D. C. Jiles and D. L. Atherton, J. Appl. Phys. **55**, 2115 (1984).

²C. D. Boley and M. L. Hodgdon, IEEE Trans. Magn. **MAG-25**, 3922 (1989).

³I. D. Mayergoyz, *Mathematical Models of Hysteresis* (Springer, New York, 1991).

⁴G. Bertotti, F. Fiorillo, and M. Pasquale, IEEE Trans. Magn. **29**, 3496 (1993).

⁵P. Andrei, O. Caltan, and Al. Stancu, IEEE Trans. Magn. **34**, 231 (1998).

⁶G. Bertotti, J. Appl. Phys. **57**, 2118 (1985).

⁷M. Abramovitz and I. A. Stegun, *Handbook of Mathematical Functions* (National Bureau of Stand. Appl. Math. Series) (NBS, Washington, DC, 1964), Vol. 55.

⁸J. Oti, F. Fajda, and E. Della Torre, J. Appl. Phys. **69**, 4826 (1991).

⁹N. Schmidt and H. Güldner, IEEE Trans. Magn. **32**, 489 (1996).

Influence of the permanent magnet overhang on the performance of the brushless dc motor

J. P. Wang and D. K. Lieu

University of California, Berkeley, California 94720

W. L. Lorimer and A. Hartman

Quantum Corporation, Milpitas, California 95035

Axial overhang of the permanent magnets has been used to enhance the performance of radial flux brushless dc motors, but its precise contribution to performance is not well known. This article aims at the investigation of the overhang effects by finite element and lumped parameter modeling. An empirical formula which allows two-dimensional analysis to account for overhang effects is proposed. A three-dimensional equivalent magnetic circuit model is developed and its ability to accurately predict overhang effects is assessed. Results of finite element and lumped parameter models are compared and a design methodology is forwarded. © 1998 American Institute of Physics. [S0021-8979(98)46911-1]

I. INTRODUCTION

High performance and low power brushless dc motors continue to be the trend in the hard disk drive (HDD) industry. Axial overhang of the permanent magnets has been used to enhance the performance of radial flux brushless dc motors, but its precise contribution to performance is not well known. Besides adding cost, there are three other reasons why it is not wise to use overhang without knowing its proper length. First, not all the extra magnetic flux produced by magnet overhang produces useful torque. Second, the originally preferred trapezoidal back EMF shape will be distorted if the flux increment is not uniform at all rotor positions. Third, magnet overhang is not effective in improving performance unless the stator has been sized to accommodate the additional flux. The purpose of this paper is to investigate the overhang effects by three-dimensional (3D) finite element (FEM) and lumped parameter modeling (LPM). The former is favored for its high accuracy in handling highly nonlinear magnetic field in electrical machines. The latter is popular for its fair accuracy but quick repetition of computation.

To account for magnet overhang and end leakage effects, which can be significant in low-profile motors, a 3D model is required. The data storage space and CPU time required for a 3D finite element model, however, may be prohibitive.

Lumped parameter modeling, an alternative to FEM, has a good capability in predicting magnetic flux and back EMF in 2D problems.¹ The model is extended to 3D by adding permeances representing extra flux and leakage paths to the original magnetic circuit built for 2D problem.

A typical 8-pole 12-slot spindle motor used in the HDD is used in this analysis. To illustrate three-dimensional effects, magnetic flux and back EMF are computed for different overhang lengths as a function of rotor position. Different permanent magnet strength (remanence) is applied to achieve different saturation levels. Overhang effects predicted by FEM and LPM are compared, and recommenda-

tions for accurately predicting optimum magnet overhang without a full 3D finite element analysis are forwarded.

II. 3D MODEL DESCRIPTION

A. Finite element model

The top view of a typical 8-pole 12-slot spindle dc spindle motor and a description of the finite element mesh is shown in Fig. 1 (and Table I, respectively). The aspect ratio (airgap diameter divided by stator height) for this motor is a moderate 2.5, but ratios as high as 10 are common in HDD motors. Permanent magnets are modeled with radial magnetization, materials are assumed isotropic and hysteresis effects are ignored. The size of analyzed domain can be reduced to one octant by taking advantage of the symmetry and imposing the proper boundary conditions. The angular size of the elements in the airgap are chosen to be the same as that of rotor step angle in order to maintain mesh uniformity and in turn improve accuracy. In selecting axial mesh density, models of increasing coarseness are solved. The coarsest mesh to produce the converged (fine mesh) solution is chosen for speed considerations. Solution time for a single rotor position ranges from 2 hours to 8 hours in the nonlinear cases.

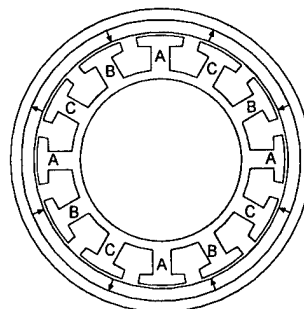


FIG. 1. Top view of 8-pole 12-slot spindle motor.

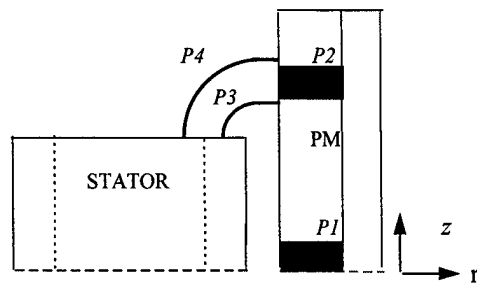


FIG. 2. 3D lumped parameter model permeances.

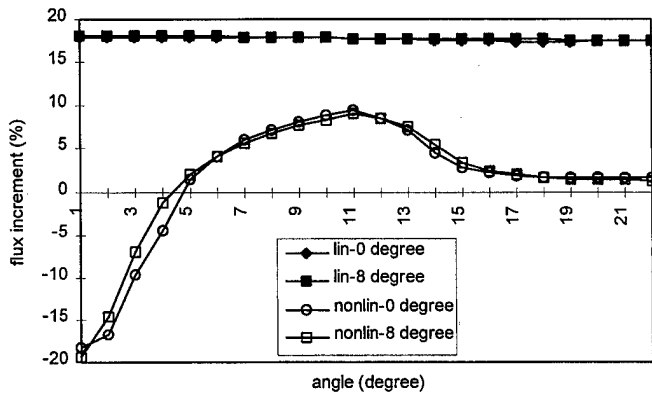


FIG. 3. The effect of the size of magnet deadzone on the flux increment, 15% overhang.

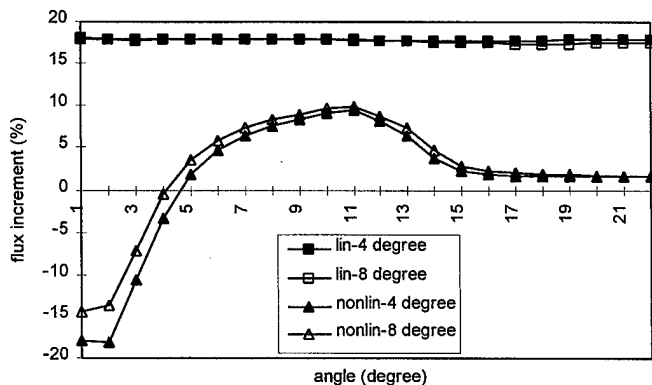


FIG. 4. The effect of the size of slot opening on the flux increment, 15% overhang.

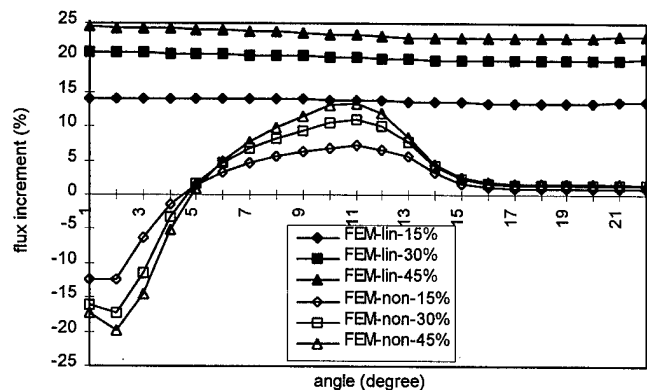
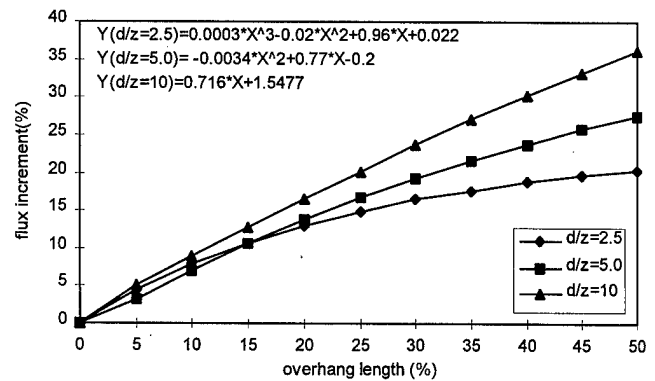
FIG. 5. The effect of the saturation level and overhang on the flux increment, $B_r=0.71$ in nonlinear cases.

FIG. 6. Flux increments for motors with various aspect ratios and overhang lengths in linear cases.

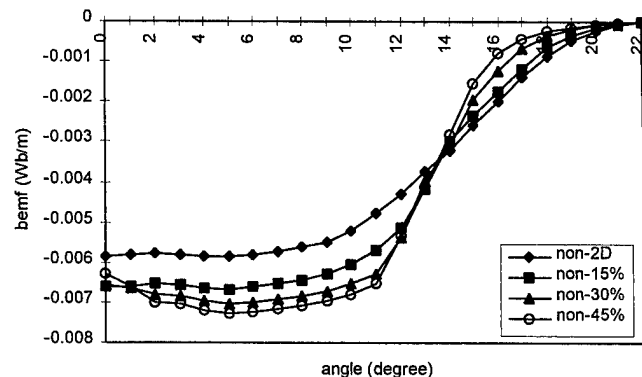
B. Lumped parameter model

Three-dimensional LPM is developed by modifying 2D model described in Ref. 1. Permeances modeling extra flux and leakage paths are added and properly connected to the 2D model. Figure 2 shows part of the modification. Instead of a single path in 2D model, one additional path is added to lead flux originating from the overhang part to the stator tooth through its top. Three permeances, P_2 , P_3 , and P_4 are added to account for this axial flux. As in the 2D case, permanent magnets are modeled as constant potential sources and their permeances are determined by a periodic function of θ .² In the 3D model, the 2D magnet permeance used to represent the internal resistance of one magnet is split into two, P_1 and P_2 . P_2 has the same angular distribution as P_1 (original 2D magnet permeance) and is computed by (1).

$$P_2 = P_1 * (\text{rotor height} - \text{stator height}) / \text{stator height}. \quad (1)$$

Conventional straight-line and circular-arc technique is used for modeling permeances P_3 and P_4 . P_3 models the flux linking to the tooth foot from its top, P_4 models the flux going directly to the tooth stem and equals to zero for a short overhang.

Unlike FEM, where there is a significant computational cost associated with 3D solutions, the addition of 3D permeances in LPM has a much smaller impact. End-to-end leakage permeances can be numerically superposed to existing 2D permeances according to electrical circuit theory. The additional 3D permeances are all linear, and consequently

FIG. 7. The effect of the overhang length on the back EMF, $B_r=0.5$.

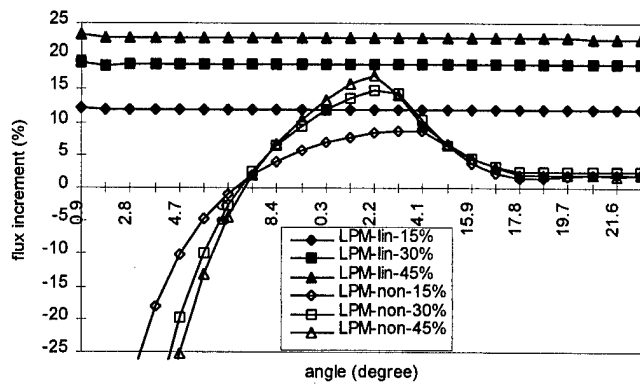


FIG. 8. Flux increment of different overhang lengths predicted by LPM.

have a minimal impact on computation time. Computation time consumed in 2D and 3D LPM simulation are of the same order.

III. RESULTS AND DISCUSSION

Figures 3–8 show results over one-half pole pitch, starting from the zero flux (peak back EMF) position. Flux increment is defined as the difference between effective tooth flux predicted by 3D and 2D models divided by that of the 2D model. With this definition, flux increment at 0° is undefined. Magnet overhang is defined as the difference between magnet height and stator height divided by stator height.

Intuitively, several factors such as the size of the slot opening and magnet dead zone, as well as the overhang length, rotor position, and saturation level of stator teeth may influence the overhang effects. The first two factors are examined first. Figure 3 and Fig. 4, respectively, illustrate the influence of the magnet deadzone and slot opening on the flux increment. Both linear and nonlinear cases are investigated. It is seen that the sizes of magnet dead zone and slot opening have no (slight) influence on the flux increment in the linear (highly saturated) cases.

Figure 5 shows how the flux increment changes with magnet overhang. In the linear cases, the flux increment is positive and uniform through the cycle, but it is not proportional to the overhang length. Being independent of the rotor position, the flux increment can be simply related to the overhang length. As shown in Fig. 6, motors with lower aspect ratio require higher order polynomial functions of overhang length to approximate the flux increment. The back EMF (the derivative of flux) is also magnified proportionally. Thus, in the linear case, only magnet overhang and motor aspect ratio influence the flux increment.

Magnetic saturation complicates the flux increment behavior. The nonlinear results shown in Fig. 5 are for a severely saturated design ($B_r=0.71$ T). The flux increment associated with the position where the magnet transition is aligned with a tooth edge is comparable to the linear case, i.e., flux is increased by the introduction of magnet overhang.

TABLE I. Motor dimensions and mesh details.

Gap diameter	19.5 mm
Stator z-height	7.66 mm
Gap	0.25 mm
Element type	8-node brick
Mesh size	1° angular
Gap elements	4 radial
No. nodes	30 000–64 000

As the rotor moves away from this position, however, the flux increment decreases, and near the peak back EMF position (0°), the flux is actually lower than in the 2D case. Figure 7 shows that the detrimental effect of excess overhang occurs even under conditions of moderate saturation ($B_r=0.5$ T). Some overhang (up to 15%) is beneficial to the back EMF its magnitude is increased and shape is preserved. As overhang is increased, the back EMF dip becomes evident. This tendency is more pronounced in highly saturated designs and in configurations with pole pitch longer than slot pitch. The complicated behavior exhibited in the nonlinear case encourages the construction of 3D LPM rather than the simple correction factor applicable to linear cases.

To test the capability of the 3D LPM, flux increments due to different overhang lengths are computed and compared with FEM results. It is observed by comparing Fig. 5 and Fig. 8, the 3D LPM successfully predicts the trends, but tends to overpredict the flux decrement in the vicinity of 0° . This discrepancy may be tolerable for design if the impact on rms back EMF is small. The reason for the discrepancy between LPM and FEM is the subject of current research, and an improved LPM is expected.

IV. CONCLUSION

A typical 8-pole 12-slot spindle motor used in the HDD is used to investigate overhang effects. In the case of mild saturation, magnet overhang always enhances motor performance, increasing back EMF without changing its shape. A series of polynomial functions of overhang length approximate the flux increment of motors with various stator heights and can be used together with 2D FEM in lieu of a full 3D model. Under saturating conditions, however, the simple relationship does not hold. Furthermore, excessive overhang is shown to be detrimental to back EMF. To properly design for magnet overhang, a 3D lumped parameter model using straight-line and circular-arc technique to model axial flux is proposed. Although there is some discrepancy in the magnitude of flux increment at certain rotor positions under severe saturation, the 3D LPM well predicts the trend of flux increment, and seems a better tool for the searching of optimal overhang length in terms of the accuracy and CPU time.

¹J. P. Wang and D. K. Lieu, IEEE Trans. Magn. **33**, 4092 (1997).

²Z. Q. Zhu and D. Howe, IEEE Trans. Magn. **29**, 124 (1993).

Optimization of coils for detecting initial rotor position in permanent magnet synchronous motor

S. Wakao,^{a)} T. Onuki, K. Tatematsu, and T. Iraha

Department of Electrical, Electronics and Computer Engineering, Waseda University, 3-4-1 Ohkubo Shinjuku-ku, Tokyo 169-8555, Japan

This article describes the shape optimization of detective coils for initial rotor position estimation in the drive system of permanent magnet synchronous motors. The characteristics of magnetic circuits in rotating machinery are very complicated. The magnetic flux distribution in the air gap is nonsinusoidal due to the influence of slots, magnets, and magnetic saturation, etc. By utilizing the slot ripple influence and taking the effects of both magnetic saturation and permanent magnets into consideration, an optimization of the detective coil by means of a genetic algorithm combined with a hybrid finite element and boundary element method is reported. This produces a global optimal solution in a shorter time. © 1998 American Institute of Physics. [S0021-8979(98)50811-0]

I. INTRODUCTION

There is a growing interest in permanent magnet synchronous motors (PMSMs) owing to their high power density and efficiency. Recent efforts are directed toward developing the sensorless drive system for PMSM applications, and various algorithms of rotor-position estimation have been proposed. However, these algorithms, which are generally based on the measurement of terminal voltages and currents of the motor, have some difficulties to detect the rotor position at standstill because the terminal quantities cannot be measured. This results in unstable starting with counter rotation.

To overcome these difficulties in PMSM sensorless drives at standstill, the authors propose to attach additional coils to the motor for detecting the initial rotor position. The proposed detection scheme is based on the voltage induced in the additional coil owing to the small displacement of the rotor with permanent magnets. Applying an impulse input to the armature results in the small displacement of the rotor, and the displacement is transformed into induced voltages. Thus, we can estimate the initial rotor position, and hence sensorless operation follows by using the detected position. It is desirable that the wave form of the induced voltage be a square wave that is suitable for digital processing. This results in both a decrease of the dead zone and an increase in accuracy of the initial rotor-position estimation. This article is aimed at designing the additional coil to obtain the desirable wave form of the induced voltage. Taking the characteristics of magnetic circuits in rotating machinery, e.g., magnetic saturation, into consideration, the authors perform an optimization procedure by means of the genetic algorithm (GA) combined with the hybrid finite element and boundary element (FE-BE) method.

Finally, the numerical example of a concrete model (a four-pole PMSM) is presented to indicate the validity of the proposed optimization procedure.

II. INVESTIGATED SYSTEM

The configuration of the investigated model is shown in Fig. 1. The stator is made of isotropic silicon steel, and the rotor of carbon steel (S45C). Figure 2 represents the $B-H$ curves of the steel. Rare-earth magnets of Sm-Co type are attached to the rotor, and their remanence B_r and coercive force H_c are 0.9 T and 7.0×10^5 A/m, respectively.

The additional coils are thin and placed in the air gap along the stator surface. The voltage induced in the additional coil is amplified and transformed into the rotor position data by a signal processing circuit. A signal processing circuit is usually composed of some logic-integrated circuits of complementary metal-oxide semiconductor type that have two logic states, i.e., H -level and L -level. The boundary between H -level and L -level is called the threshold voltage. The variation of output voltage in the detective coil is illustrated in Fig. 3. If the induced voltage rises slowly, the L -level region becomes larger than that of the fast rise case as in Fig. 3. The dead zone of detective coil increases with the L -level region, which causes the detection capability of the proposed scheme to decrease. Hence it is desirable that the wave form of the induced voltage changes in the rectangular form with rotation. This article describes a shape opti-

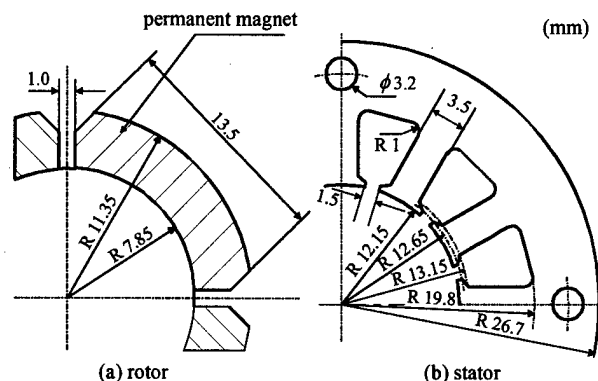
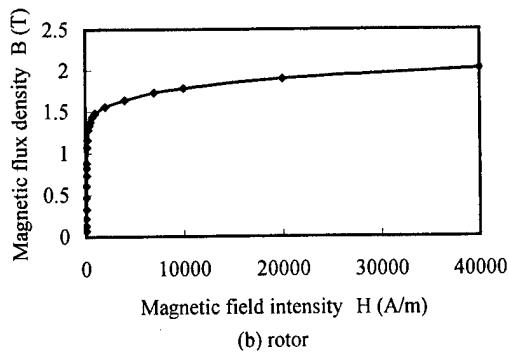
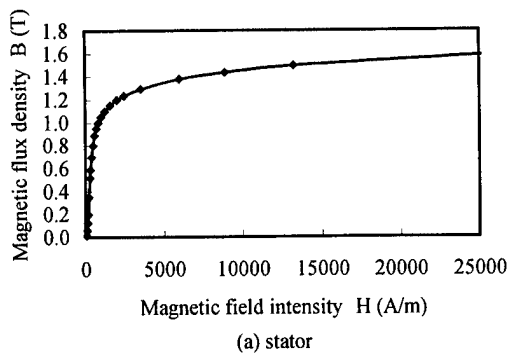


FIG. 1. Four-pole permanent magnet synchronous motor.

^{a)}Electronic mail: wakao@mn.waseda.ac.jp

FIG. 2. B - H curve of steel.

mization procedure to give the detective coil with the above-mentioned characteristics.

III. OPTIMIZATION PROCEDURE

The finite element method (FEM) and the boundary element method (BEM), which have entirely different features from each other, are very useful for numerical analysis of the physical phenomena described by partial differential equations. Both methods seem to be complementary partners and not opponents. Therefore, taking into account of the advantages in these methods, the authors adopt the hybrid FE-BE method as a field calculation tool in this article.¹⁻⁴ By applying the FEM to the rotor and stator regions and the BEM to the air-gap region, a two-dimensional analysis of magnetic field with moving boundaries is naturally implemented without remeshing. This also allows easy consideration of material nonlinearity by the FEM, and enables the precise estimation of air-gap field by the BEM.

The fundamental equation of the magnetic field in terms of the magnetic vector potential A can be obtained as follows:

$$\nabla \times (\nu \nabla \times A) = J_0 + \nabla \times \nu_0 M, \quad (1)$$

where ν is the reluctivity, J is the current density, and M is the magnetization density. The demagnetization characteristic of the permanent magnet is approximated by a straight line, and M is described as

$$M = B - \mu_0 H = B - \mu_0 (B - B_r) (H_c / B_r), \quad (2)$$

where μ is the permeability. The reluctivity is not constant but dependent on the applied magnetic field. Therefore, the distribution of the magnetic field is calculated by the iteration method including a nonlinear analysis. In this article, the

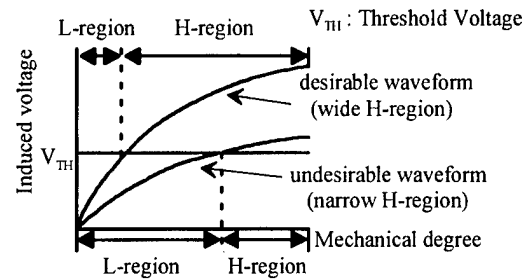


FIG. 3. Wave form of induced voltage.

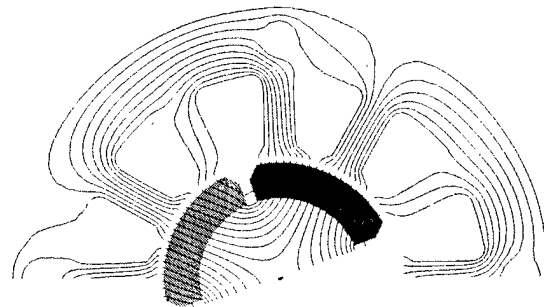


FIG. 4. Magnetic flux distribution.

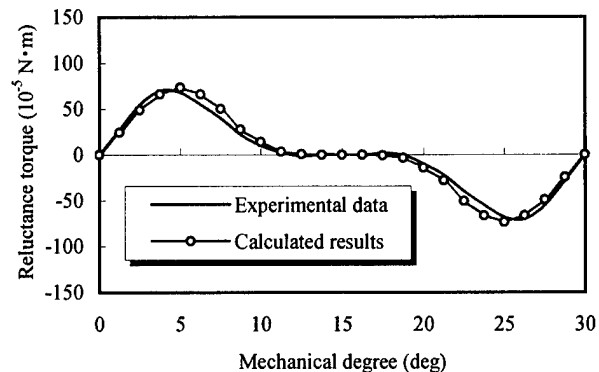


FIG. 5. Reluctance torque characteristic.

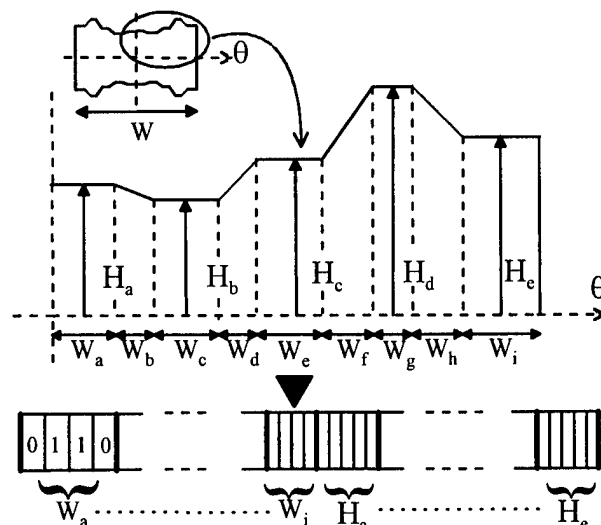


FIG. 6. Coding for string structure.

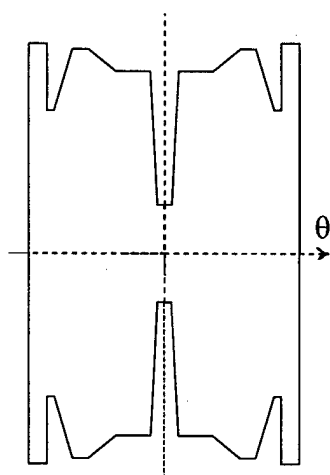


FIG. 7. Optimized configuration of additional coil.

Newton-Raphson method⁵ is used in considering the nonlinear characteristics as in Fig. 2. The magnetic field distribution and the reluctance torque characteristic of the investigated model are shown in Figs. 4 and 5, respectively. On the whole, the calculated values of the reluctance torque agree with the experimental data. Finally, regarding the flux distribution in the shaft direction as uniform, we estimate the magnetic flux interlinkage of the detective coil and derive the wave form of the induced voltage by inner field calculation of the BEM.

As regards to a search algorithm, the genetic algorithm (GA) is adopted.^{6,7} The GA is a powerful search method based on probabilistic evolution through generations, which consists of three fundamental operators upon the string structures; reproduction, crossover, and mutation. These string structures called chromosomes represent different design parameters, respectively, (see Fig. 6). Calculating the objective function value, i.e., the length of L -level region, by the hybrid FE-BE method, the GA estimates the fitness of each string structure and creates a new generation from the previous one by the three above-mentioned operators. This results in the survival of the strings that better suit the environment, i.e., the decrease of L -level region, along the future generations.

TABLE I. Optimization results.

Design variable	Result (\times pole pitch)	Design variable	Result (\times pole pitch)
Wa	0.021	Wh	0.000
Wb	0.021	Wi	0.056
Wc	0.104	Ha	0.144
Wd	0.083	Hb	0.544
We	0.049	Hc	0.611
Wf	0.056	Hd	0.428
Wg	0.021	He	0.628

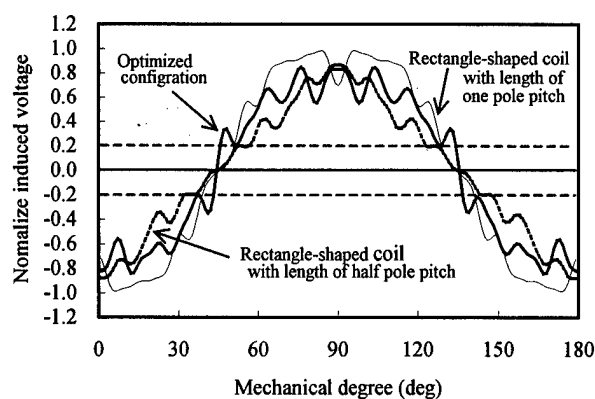


FIG. 8. Voltage induced in additional coil.

IV. NUMERICAL RESULTS

An optimization procedure using a GA combined with a hybrid FE-BE method is reported. The initial population of the search has 40 members. The members of the initial population are created by randomly placing the binary code of $\{0, 1\}$ into the bit positions of the chromosomes. Each of the 14 design variables is coded into a four- or five-bit string segment as shown in Fig. 6. Both the roulette wheel and elite technique are implemented for the reproduction operator. The uniform crossover, where each bit in the string has a probability of 0.6 to be swapped, is adopted for the crossover operator. The occurrence probability for mutation is 0.05. The decision on the convergence of solutions is based on the fitness, i.e., the objective function value, of the population. The search is terminated in 937 generations in this example. The whole CPU time required for the optimization procedure is about two days under typical workstation-implementing conditions. The optimization results are shown in Fig. 7 and Table I. Figure 8 indicates the computational results of the normalized voltage wave form induced in the shape-optimized coil. For a comparison, the wave forms of the rectangle-shaped coils with lengths W of one or half pole pitch are also computed and shown in Fig. 8. In this example, setting the threshold voltage of 0.2, we can find the L -level region, i.e., the dead-zone, of the shape-optimized coil is reduced to about 20% of that of the rectangle-shaped coils.

¹T. Onuki, IEEE Trans. Magn. **26**, 582 (1990).

²S. Wakao and T. Onuki, IEEE Trans. Magn. **29**, 1487 (1993).

³T. Onuki, S. Wakao, and T. Hattori, IEEE Trans. Magn. **30**, 2908 (1994).

⁴T. Onuki, S. Wakao, and T. Yoshizawa, IEEE Trans. Magn. **31**, 1436 (1995).

⁵T. Nakata, N. Takahashi, K. Fujiwara, N. Okamoto, and K. Muramatsu, IEEE Trans. Magn. **28**, 1048 (1992).

⁶D. E. Goldberg, *Genetic Algorithm in Search, Optimization and Machine Learning* (Addison-Wesley, 1989).

⁷F. G. Uler, O. A. Mohamed, and C. S. Koh, IEEE Trans. Magn. **30**, 4296 (1994).

Temperature analysis of induction motors using a hybrid thermal model with distributed heat sources

S. C. Mukhopadhyay^{a)} and S. K. Pal

Department of Electrical Engineering, Jadavpur University, Calcutta 700032, India

The article presents a hybrid thermal model for the accurate estimation of temperature distribution of induction motors. The developed model is a combination of lumped and distributed thermal parameters which are obtained from motor dimensions and other constants such as material density, specific heats, thermal conductivity, etc. The model is especially suited for the derating of induction motors operating under distorted and unbalanced supply condition. The model have been applied to a small (2hp, 415 V, 3-phase) cage rotor induction motor. The performance of the model is confirmed by experimental temperature data from the body and the conductor inside the slots of the motor. © 1998 American Institute of Physics. [S0021-8979(98)23511-0]

I. INTRODUCTION

Prediction of temperature distribution of induction motors is very important to the design engineers as well as motor manufacturers. To have a good knowledge of temperature rise, studies on thermal model of induction motors started quite a long time back. Thermal circuit have been used in the past for electric machinery analysis. An equivalent thermal circuit for non-ventilated induction motors was reported by Kotnik.¹ The different parts of the machine had been considered as lumped parameters interconnected with each other. This just gives some ideas of average temperature rise of motors which was sufficient during that time. Many papers have dealt with the temperature estimation method of the induction motor by using finite element (FE) analysis. In FE analysis usually only a part of stator core and rotor core is considered in the model.² It is difficult to know the temperature distinction along the motor lamination unless a whole model is taken into consideration, particularly under unbalanced voltage operation. This article has described the development of a hybrid thermal model for the analysis of motor temperature distribution. The model can be used during the unbalanced and distorted supply operation of the motors.

II. THERMAL MODEL FORMULATION

The nonsteady conduction equation of heat flow in two dimensions is known to be

$$K_x \frac{\partial^2 t}{\partial x^2} + K_y \frac{\partial^2 t}{\partial y^2} + q^* = \rho C_p \frac{\partial T}{\partial t}, \quad (1)$$

where K_x and K_y are the thermal conductivities along X and Y direction, respectively, q^* is the internal generated heat per unit volume, ρ is the density, and C_p is the specific heat. Equation (1) can be expanded and the equation for the central node, a , in terms of adjacent nodes b , c , d , and e as shown in Fig. 1, can be expressed as

$$\frac{T_b - T_a}{R_{ab}} + \frac{T_c - T_a}{R_{ac}} + \frac{T_d - T_a}{R_{ad}} + \frac{T_e - T_a}{R_{ae}} + q_a = \frac{C_a}{\partial t} (T'_a - T_a), \quad (2)$$

where T_a and T'_a represent current and future temperature of node "a," respectively, q_a is the rate of heat addition to node a , C_a is the thermal capacitance associated with node a ; R_{ab} , R_{ac} , R_{ad} , and R_{ae} represent the thermal resistance between nodes $a-b$, $a-c$, $a-d$, and $a-e$, respectively.

Based on this idea the nodes are assumed throughout the motor cross section, while the thermal capacitances are considered to be lumped at each node and thermal resistances between two consecutive nodes. The thermal model developed for the determination of temperature condition along the motor cross section is shown in Fig. 2. The nodes lying extreme outside represent the ambient temperature and the next inside ones are lying on the motor surface. Adequate number of nodes are assumed to know the detailed temperature distribution of the motor.

The thermal resistances are given by

$$R_t = \frac{1}{K_t} \cdot \frac{L}{A}, \quad (3)$$

where K_t is the thermal conductivity, L is the length of heat flow path and A is the area normal to heat flow path. The thermal conductivities of different materials are chosen as: iron=73, air=0.0241, copper=386, aluminium=202, and

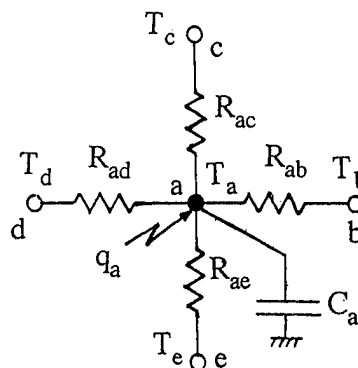


FIG. 1. Nodal network representation for two-dimensional heat flow.

^{a)}Electronic mail: chandra@magstar.ec.t.kanazawa-u.ac.jp

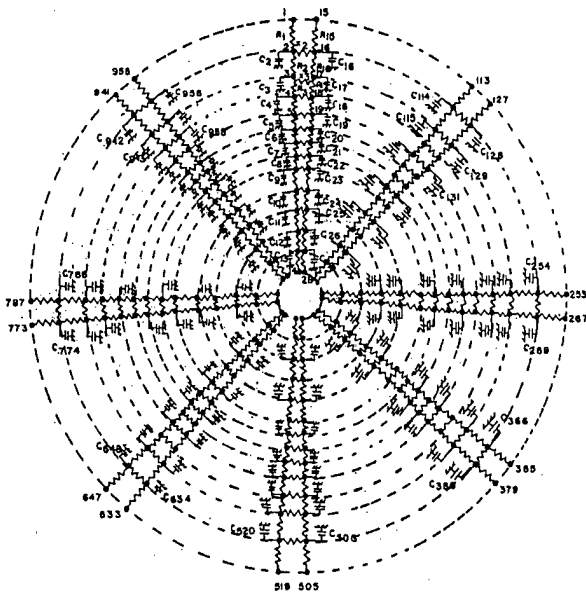


FIG. 2. Thermal model of induction motor.

insulation=0.05. Using Eq. (3) the thermal resistances of the following sections are calculated: (i) frame, (ii) stator core, (iii) stator teeth, (iv) stator slot to stator core, (v) stator slot to stator teeth, (vi) rotor slot to rotor teeth, (vii) rotor slot to rotor core, (viii) rotor teeth, (x) rotor core, and (x) shaft. The following resistances are calculated separately: (i) between frame and ambient, (ii) contact resistance between frame to stator laminations, and (iii) airgap between stator and rotor.

The thermal resistance between frame and ambient (such as R_1, R_{15} , etc. are calculated by $R_{\text{frame}} = \Delta t / P_{\text{node}}$, where Δt is the frame temperature rise over ambient and P_{node} is the power dissipated from each node. The approximate value of Δt is obtained by $\Delta t = W / (AK)$, where W is the total power loss of the machine in W , A is the surface area in m^2 , and K is a constant chosen as $97.1 \text{ W/m}^2/^{\circ}\text{C}$.

Using Eq. (4) the heat dissipated by radiation, W_r , is obtained, where e is relative emissivity, assumed to be 0.9.

$$W_r = 5.72Ae \left[\left(\frac{273 + T_{\text{amb}} + \Delta t}{100} \right)^4 - \left(\frac{273 + T_{\text{amb}}}{100} \right)^4 \right]. \quad (4)$$

The rest power $W_c = W - W_r$ is dissipated by convection. From Eq. (5) Δt is obtained, where D is the outer surface diameter of the machine in meter.

$$W_c = 12.02A \left(\frac{1}{D} \right)^{0.5} (\Delta t)^{1.25}. \quad (5)$$

If Δt obtained from Eq. (5) does not match to that obtained earlier, by slight adjustment Δt is obtained by repeating (4) and (5).

Due to imperfect contact between stator lamination and frame, the thermal resistance is calculated by $R_{1c} = r_{1c} / A_c$, where r_{1c} is thermal contact resistance and depends on the metals involved, the surface roughness, the contact pressure, the materials occupying void spaces and temperature. The value of r_{1c} has been chosen as $0.0005 \text{ m}^2/^{\circ}\text{C/W}$ in the model.

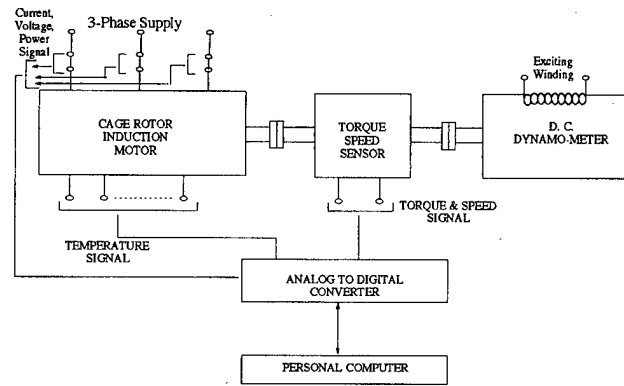


FIG. 3. Experimental setup.

The thermal resistance of airgap between stator and rotor is defined in terms of a dimensionless Nusselt number, N_{Nu} , the airgap length, l_g , and is given by Eq. (6). N_{Nu} to be properly chosen.³

$$R_{\text{ag}} = \frac{l_g}{N_{\text{Nu}} K_{\text{air}} A_{\text{ag}}}. \quad (6)$$

The lumped thermal capacitance at each node is defined as

$$C_a = V_a \rho C_p, \quad (7)$$

where $V_a = \delta x * \delta y * \text{length}$ (δx and δy being the average length between two consecutive nodes along X and Y direction, respectively), ρ is the density, and C_p is the specific heat of the material on which it lies.

In order to model accurately, the heat input to each node must be allocated properly. The dissipated power are: ohmic losses in stator and rotor winding, iron losses in stator core and teeth, flux pulsation loss in stator and rotor teeth, and frictional windage loss. The ohmic losses are calculated from the ohmic resistance and current. Ohmic resistance should be properly adjusted to take into account of temperature rise.

The iron losses are calculated from Eq. (8).

$$p = afB_p^2 + b(\nabla f B_p)^2, \quad (8)$$

where p is the power loss per kg, f is frequency, ∇ is the thickness of lamination in mm, B_p is the peak value of flux density; a and b are two constants and are assumed to be 0.057 and 0.00282 in the model.

In machines with slots both on stator and rotor, the flux density in the teeth varies as the relative position of the teeth varies. The amplitude of the flux fluctuation in the stator teeth is

$$B_{p1} = \frac{\tau_{s2}}{2\tau_{s1}} \cdot \frac{K_{c2} - 1}{K_{c2}} \cdot B_{tm1}, \quad (9)$$

where τ_{s1} and τ_{s2} are the slot pitches of stator and rotor, respectively. K_{c2} is the Carter factor of the rotor, and B_{tm1} is the maximum value of flux density in the middle of the tooth.

The frequency is given by $f_1 = Q_2^* (\text{rpm}/60)$, where Q_2 is the number of slots in the rotor. For the rotor teeth the indices 1 and 2 should be interchanged.

The pulsation loss in watts per unit weight of the teeth is given by

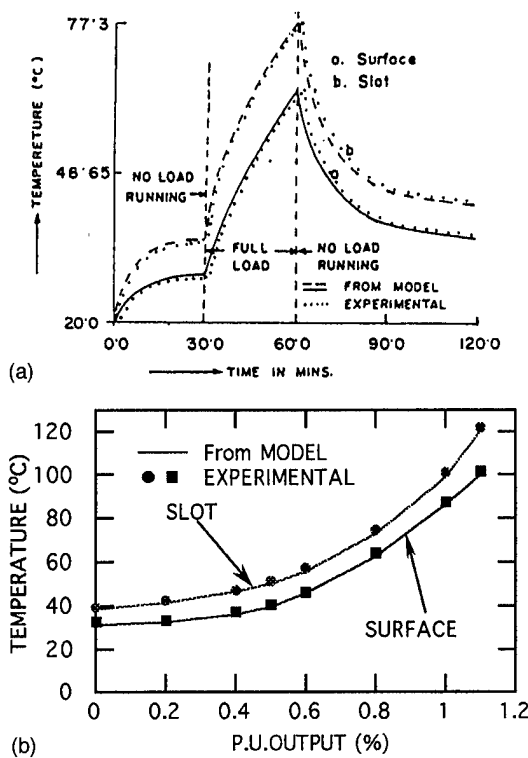


FIG. 4. Thermal characteristic (a) at continuous running with short time load, (b) steady-state temperature with power output.

$$P_p = b(\nabla f B_p)^2. \quad (10)$$

The mechanical loss due to friction of the bearing and windage loss are

$$P_{F+W} = 5.4 \times 10^5 (\text{rpm})^{0.7} P_R, \quad (11)$$

where P_R is the rated power of the machine in watts.

After calculating all the thermal resistances and capacitances and allocating the losses to each node, the temperature of each node is calculated by

$$t'_i = t_i + \partial\tau \left(\sum_j \frac{t'_j - t'_i}{R_{ij}C_i} + \frac{q_i}{C_i} \right). \quad (12)$$

Starting values of all the nodes are taken to be equal to ambient temperature. The time step $\partial\tau$ should be critically selected so that

$$\partial\tau \leq \left[\frac{1}{\sum_{i=1}^n 1/(R_{ij}C_i)_{\min}} \right]. \quad (13)$$

The solution is assumed to reach steady-state values when

$$|T(j)_{n+1} - T(j)_n| \leq \epsilon \quad (14)$$

is satisfied for each and every node, where ϵ is a convergence criterion.

III. PERFORMANCE OF THE MODEL AND EXPERIMENTAL VERIFICATION

The model is applied to a small 4 pole motor. The detailed specifications of the motor are: Three-phase cage-rotor induction motor; power output=2hp, voltage=415 V, current=3.2 A, frequency=50 Hz, speed=1425 rpm, insulation=Class B, no of stator slots=36, no of rotor slots=44, stator outer diameter=190 mm, rotor outer diameter=114.5 mm, core length=100 mm, stator resistance per phase=6.8 Ω , rotor resistance referred to stator=6.4 Ω .

The experiments are conducted using the setup as shown in Fig. 3. The load on the motor is changed by varying the excitation. The surface and slot temperatures are measured by temperature sensors.

Figure 4(a) shows the simulated and experimental thermal characteristic at continuous running with short time load. Figure 4(b) shows the variation of steady-state temperature of surface and slot with power output. It is seen that the difference of the experimental and simulated values are less than 2 °C.

IV. CONCLUSION

This article has reported the development of a thermal model for the temperature analysis of induction motors. The model is based on distributed thermal resistances and capacitances with properly allocated heat sources to each node. The model can predict both steady state and transient temperature rise of motors. Predicted results were compared with measurements showing good agreement, thus proving the validity of the model.

¹R. L. Kotnik, AIEE Trans. Feb. 1955, pp. 1604–1608.

²A. F. Armor and M. V. K. Chari, IEEE Trans. Power Appar. Syst. PAS-95, (1976).

³S. C. Mukhopadhyay, Ph.D. thesis, Jadavpur University, India, 1994.

Bifurcation phenomena and chaotic attractors in a six-dimensional nonlinear system

T. Sutani^{a)}

Kanazawa Institute of Technology, 7-1 Ogigaoka, Nonoichi, Ishikawa 921-8812, Japan

T. Czaszejko

Monash University, 900 Dandenong Road, Caulfield East, Victoria, Australia 3145

A. Nafalski

University of South Australia, Warrendi Road, The Levels, Adelaide, South Australia 5095

Some chaotic properties of a six-dimensional nonlinear dynamic system are investigated. Equations describing the system are based on the equivalent circuit of a magnetic frequency tripler. Numerical solutions are obtained using the fourth-order Runge–Kutta algorithm. Simulation results reveal the presence of Hopf and a period-doubling bifurcations. Phase space projections at points before and after bifurcations show the existence of three symmetrical and four asymmetric regions. Poincaré maps reveal six different chaotic attractors within the asymmetric regions. The correlation dimension of the sea horse attractor is found to be 2.37. © 1998 American Institute of Physics. [S0021-8979(98)23611-5]

I. INTRODUCTION

Studies of bifurcation phenomena in the Van der Pol–Duffing oscillator as well as in two coupled Duffing oscillators were described recently in Refs. 1 and 2. A similar behavior can be observed in an electromagnetic circuit of a frequency tripler. This circuit can be described as a six-dimensional nonlinear dynamic system and it can be simulated on a computer using the fourth-order Runge–Kutta algorithm. In the previous attempt to depict bifurcation diagrams of the magnetic frequency tripler using voltage of the saturable reactor as a parameter, a period-doubling (PD) bifurcation and the presence of a chaotic attractor were revealed. These results were presented in Refs. 3 and 4.

This article describes equations of state for a six-dimensional nonlinear system based on the equivalent circuit of a magnetic frequency tripler. Numerical solution of these equations enable further analysis. Characteristic sequences of transitions are studied using bifurcation diagram. The phase space projections obtained from the numerical solution verify existence of chaotic attractors in the regions after bifurcations as well as the presence of symmetry in the phase space. Then, the correlation dimension of the phase space trajectory is performed in the region of sea horse attractor.

II. EQUATIONS OF STATE

The six-dimensional nonlinear system described in this article is obtained from the equivalent circuit of a magnetic frequency tripler with series-connected reactors.⁵ Figure 1 shows the six-dimensional nonlinear system for computer simulations. This system was presented in detail previously in Refs. 3 and 4. Here, we bring only its short description. If

magnetizing characteristics of the saturable reactors are approximated by third-order polynomials, equations of state for this system become

$$\begin{aligned}\dot{x}_1 &= -k_1 x_1 - k_2 x_2 + f \sin \tau, \\ \dot{x}_2 &= k_3 x_1 - \alpha_1 x_3 - \beta_1 x_3^3 - \alpha_2 x_4, \\ \dot{x}_3 &= k_4 (x_2 + x_6), \\ \dot{x}_4 &= k_5 (x_2 - x_6), \\ \dot{x}_5 &= k_6 x_6, \\ \dot{x}_6 &= \alpha_{20} x_4 - \alpha_{10} x_3 - \beta_{11} x_3^3 - \alpha_{00} x_5 - \beta_{00} x_5^3 - k_7 x_6,\end{aligned}\quad (1)$$

where $(x_1, x_2, \dots, x_6, \tau) \in R^6 \times S^1, \tau \in S^1$.

These equations are solved numerically using the fourth-order Runge–Kutta algorithm with double precision. The system is iterated 36 000 times (200 periods, 400π). A step size of 3.4906585×10^{-2} ($2\pi/180$) ensured converged numerical results.

III. BIFURCATION DIAGRAM

Bifurcation diagrams are obtained by setting the coefficient k_4 (voltage across C_{in} and C_o) as a parameter and by plotting solutions for x_5 obtained at 2π radian intervals. In order to exclude initial transient solutions for $0 \leq \tau < 100\pi$ are ignored, and then, solutions for $100\pi \leq \tau \leq 400\pi$ are plotted.

Figure 2 shows bifurcation diagram obtained by incrementing parameter k_4 by 0.002 units. It can be seen from the

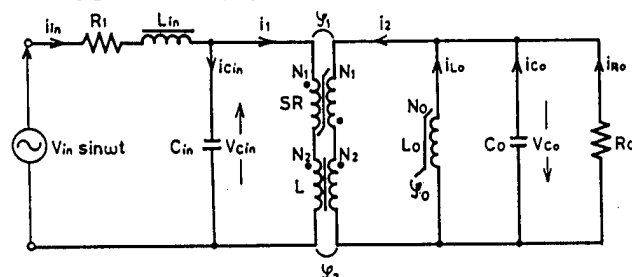


FIG. 1. Six-dimensional nonlinear system for computer simulations.

^{a)}Electronic mail: t-sutani@neptune.kanazawa-it.ac.jp

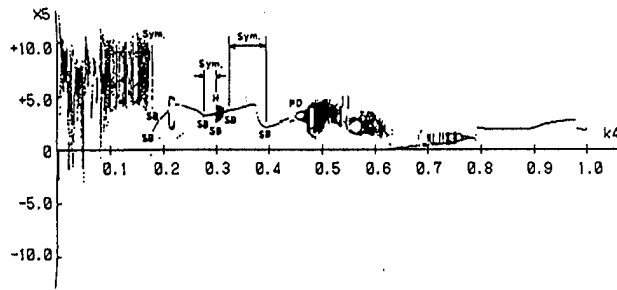


FIG. 2. Bifurcation diagram with $\alpha_{1i} = \alpha_{10} = \alpha_{00} = 0$, $\alpha_{2i} = 5.0 \times 10^{-6}$, $\alpha_{20} = 6.0 \times 10^{-6}$, $\beta_{1i} = 1.5$, $\beta_{00} = 1.8$, $\beta_{10} = 1.3$, $f = 12.5$, $k_1 = 0.05$, $k_2 = 0.011$, $k_3 = 20.0$, $k_5 = 0.2$, $k_6 = k_7 = 0.5$, $x_{10} = 1.1$, $x_{20} = 1.0$, $x_{30} = 5.0$, $x_{40} = 2.0$, $x_{50} = 3.0$, and $x_{60} = 4.0$.

diagram that the region $k_4 < 0.1$ is chaotic. This chaotic region is followed by a sequence of period-one, period-two, and period-one solutions. The Hopf bifurcation takes place at $k_4 = 0.3$ followed by another band of period-one solutions. The PD bifurcation occurs at $k_4 = 0.448$, followed by another chaotic region. Later, for $0.63 < k_4 < 0.79$, period-one solutions dominate except for a few chaotic regions appearing sporadically. The bifurcation diagram converges finally to stable period-one solutions for $k_4 > 0.8$.

IV. PHASE SPACE PORTRAITS

All period-one solutions of the analyzed system return generally identical phase space trajectories if the initial transients are ignored. Phase space trajectories for chaotic solutions, on the other hand, assume several characteristic shapes. Figure 3 shows some examples of the phase space diagrams obtained for $100\pi < \tau \leq 102\pi$ before and after Hopf bifurcation points.

The orbit shown in Fig. 3(a) is obtained for $k_4 = 0.272$. This orbit is asymmetric. Figure 3(b) shows the orbit for the parameter k_4 increased to 0.284. The resulting orbit becomes symmetrical with respect to origin, i.e., $f(-x) = -f(x)$. Figure 3(c) shows an asymmetric orbit at an upper symmetry-breaking (SB) point which occurs for $k_4 = 0.298$. The transition from the upper SB point leads to the onset of the Hopf bifurcation. This transition can be identified as Hopf bifurcation following Sparrow's work on the Lorenz system⁶ and Kozłowski's work on two-coupled Duffing oscillators. From there, it is concluded that Hopf bifurcation is always accompanied by SB in the phase space diagram.

Figure 4 shows examples of orbital trajectories from the third and the widest region on the bifurcation diagram in which symmetry is maintained. Figure 4(b) shows the orbit

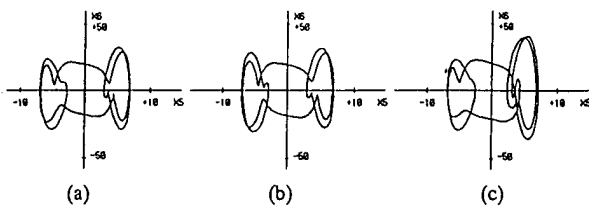


FIG. 3. Phase space projections: (a) $k_4 = 0.272$, (b) $k_4 = 0.284$, and (c) $k_4 = 0.298$.

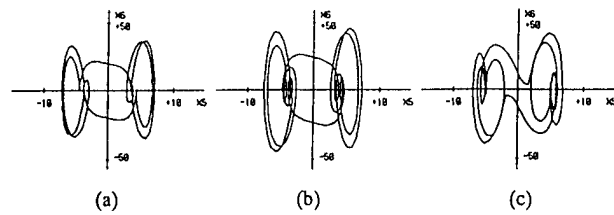


FIG. 4. Phase space projections: (a) $k_4 = 0.320$, (b) $k_4 = 0.360$, and (c) $k_4 = 0.390$.

at $k_4 = 0.360$ with its typical shape for this symmetrical region. In comparison with Fig. 3(b), the orbit has similar inverse structure except that this time it has more loops which, in turn, indicates the presence of higher harmonics. Further, symmetric trajectories become asymmetric at $k_4 = 0.390$, but here the SB point does not precede a PD bifurcation.

In the analyzed system, there are no further symmetrical regions observed for $k_4 \geq 0.390$. In such a case, a question arises whether phase space portraits at points prior and after PD bifurcation present the same asymmetric structure. In order to clarify this question, orbital projections of the phase space are investigated around this PD bifurcation point. Figure 5(a) shows an orbit for τ between 100π and 102π for $k_4 = 0.4465$, i.e., just prior the bifurcation. This orbit is asymmetric. Figure 5(b) shows an orbit for $k_4 = 0.4466$. The orbit also appears to be asymmetric. However, comparison of the shape of orbits prior to bifurcation with that after the bifurcation reveals that they are in central symmetry with each other with respect to origin. For the first time it is shown that a reversal of phase space occurs in order to preserve asymmetry at the PD bifurcation point.

V. CHAOTIC ATTRACTORS

There have been several types of chaotic attractors defined in multidimensional dynamic systems.⁷ In order to find the types of attractors existing in the frequency tripler analyzed in this paper, Poincaré maps are constructed for chaotic regions identified previously on the bifurcation diagram. Six maps, consisting of 2000 periods ($\tau = 4000\pi$) each, are shown in Figs. 6(a)–6(f). These maps are obtained for $k_4 = 0.05, 0.16, 0.30, 0.50, 0.59$, and 0.74 , respectively. Figures 6(a) and 6(b) show two slightly different Poincaré sets but both displaying characteristics of hyperchaos.⁸ Figure 6(c) shows a chaotic attractor obtained at a point after Hopf bifurcation. This attractor does not represent a limit cycle and

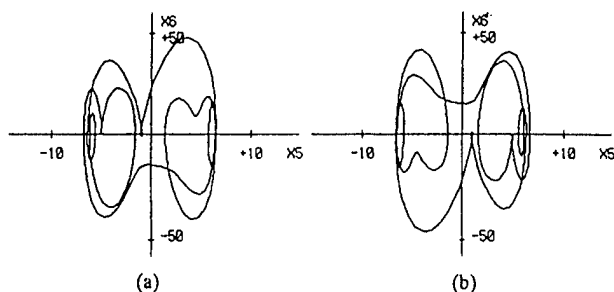


FIG. 5. Phase space projections: (a) $k_4 = 0.4465$ and (b) $k_4 = 0.4466$.

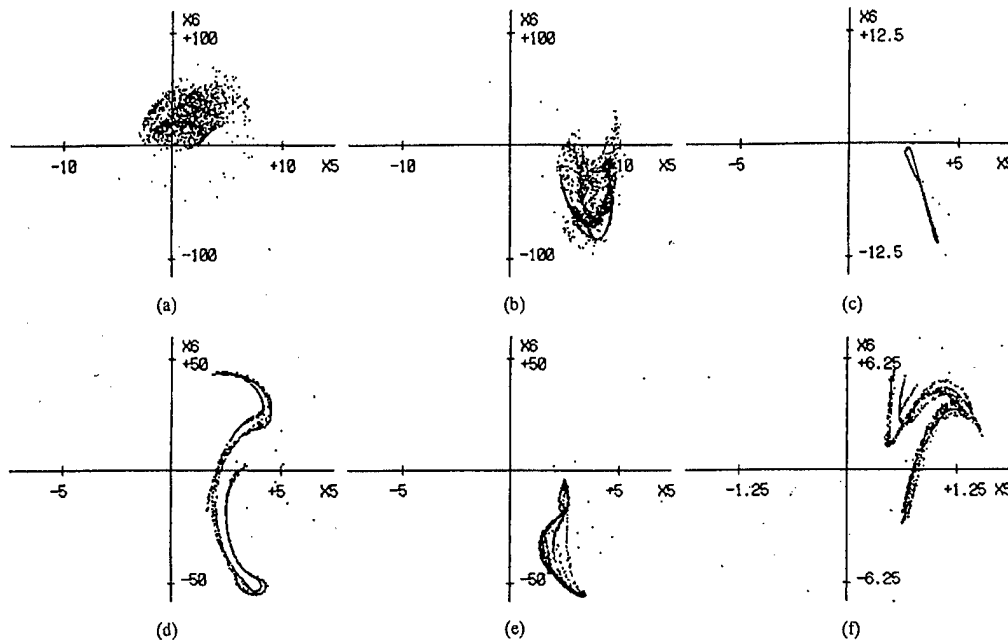


FIG. 6. Two hyperchaos: (a) $k_4=0.05$ and (b) $k_4=0.16$, and four chaotic attractors: (c) $k_4=0.30$, (d) $k_4=0.50$, (e) $k_4=0.59$, and (f) $k_4=0.74$.

it can be called a string attractor. Figure 6(d) shows a shape of the before-presented sea horse attractor. The harp attractor is also identified within the region of the PD cascade and it is shown in Fig. 6(e). It should be noted that the harp attractor is not a part of the sea horse attractor, as it may appear, but it is another type of attractor. Figure 6(f) shows a sparrow attractor which appears in the narrow chaotic regions after the PD cascade. In summary, two hyperchaos and four other chaotic attractors are identified in the six-dimensional system investigated in this article.

In order to determine dimensionality of a dynamic system the correlation method is used. Following the work of Grassberger and Procaccia,⁹ the correlation dimension D_c can be defined as

$$D_c = \lim_{\delta \rightarrow 0} [\log C(\delta) / \log \delta], \quad (2)$$

where $C(\delta)$ is a correlation integral as a function of the diameter δ , of the phase space volume element in which the integral is evaluated.

Computations of the correlation dimension for the frequency tripler are performed on the phase space trajectory assuming the shape of a sea horse attractor on the Poincaré map. As the result, the value of $D_c=2.37$ is obtained. This outcome indicates that our original six-dimensional system can be described with a substantially smaller number of variables, possibly as low as three.

VI. CONCLUSION

Bifurcation phenomena and chaotic attractors in a six-dimensional nonlinear system based on the equivalent circuit of a magnetic frequency tripler have been analyzed in this article. The main results are as follows.

- (1) Phase space projections are asymmetric at regions where hyperchaos, period-two solutions, the Hopf bifurcation and the period-doubling bifurcation occur.
- (2) The occurrence of the Hopf bifurcation is accompanied by symmetry breaking of the phase space trajectory.
- (3) The phase space trajectory reverses at the point of the period-doubling bifurcation to preserve asymmetry.
- (4) The existence of two hyperchaos and four chaotic attractors is found in the system.
- (5) The correlation dimension of the sea horse attractor is 2.37.

Our next subjects are investigation on mechanics of development of chaotic attractors and controlling chaos in the six-dimensional system.

¹G. P. King and S. T. Gaito, Phys. Rev. A **46**, 3092 (1992).

²J. Kozłowski, U. Parlitz, and W. Lauterborn, Phys. Rev. E **51**, 1861 (1995).

³T. Sutani and K. Bessho, Trans. IEE Jpn. **115-D**, 936 (1995) (in Japanese).

⁴T. Sutani and A. Nafalski, Australasian Universities Power Engineering Conference, AUPEC'96, 1, 1996, pp. 263–267.

⁵T. Sudani and K. Bessho, IEEE Trans. Magn. **MAG-23**, 1956 (1987). T. Sudani changed the expression of his family name to T. Sutani in 1993.

⁶C. Sparrow, *The Lorenz Equations: Bifurcations, Chaos, and Strange Attractors* (Springer, New York, 1982), p. 11.

⁷M. Franaszek, Phys. Rev. E **49**, 3927 (1994).

⁸O. E. Rossler, Phys. Lett. A **71**, 155 (1979).

⁹P. Grassberger and I. Procaccia, Physica D **9**, 189 (1983).

Symposium on Layered Manganites

J. D. Jorgensen, Chairman

Two-dimensional ferromagnetic correlations above T_C in the naturally layered CMR manganite $\text{La}_{2-2x}\text{Sr}_{1+2x}\text{Mn}_2\text{O}_7$ ($x=0.3-0.4$) (invited)

D. N. Argyriou and T. M. Kelley

Los Alamos Neutron Science Center, Los Alamos National Laboratory, Los Alamos, New Mexico 87545

J. F. Mitchell

Materials Science Division, Argonne National Laboratory, Argonne, Illinois 60439

R. A. Robinson

Los Alamos Neutron Science Center, Los Alamos National Laboratory, Los Alamos, New Mexico 87545

R. Osborn and S. Rosenkranz

Materials Science Division, Argonne National Laboratory, Argonne, Illinois 60439

R. I. Sheldon

Los Alamos Neutron Science Center, Los Alamos National Laboratory, Los Alamos, New Mexico 87545

J. D. Jorgensen

Materials Science Division, Argonne National Laboratory, Argonne, Illinois 60439

Neutron diffuse scattering in the form of rod-like features has been observed in single crystals of the layered CMR material $\text{La}_{2-2x}\text{Sr}_{1+2x}\text{Mn}_2\text{O}_7$ ($x=0.4, 0.36$), consistent with the presence of 2D ferromagnetic spin correlations. These diffuse features are observed over a wide temperature region. However, their coherence length does not appear to diverge at T_C , although there is evidence of the development of three-dimensional correlations around ferromagnetic reflections of the 3D-ordered magnetic structure close to T_C . Quasi-elastic neutron scattering on a ceramic sample of $x=0.3$ shows that the lifetime of these ferromagnetic correlations increases at $T \rightarrow T_C$. They exhibit a spin-diffusion constant above T_C of $\sim 5 \text{ meV } \text{\AA}^2$, much lower than that reported for $\text{La}_{2/3}\text{Ca}_{1/3}\text{MnO}_3$. We discuss the relationship of these magnetic correlations to models of the ferromagnetic transition in CMR compounds. © 1998 American Institute of Physics.

[S0021-8979(98)43211-0]

The close interplay among charge, spin, and lattice degrees of freedom in the colossal magnetoresistive (CMR) manganite oxides is widely believed to play an important role in the mechanism of transport in these itinerant ferromagnets. Among the current models of transport in the three-dimensional perovskite materials is that magnetic polarons—mobile lattice distortions carrying spin—are the fundamental charge-carrying entity, at least above the Curie temperature (T_C).^{1,2} Indeed, localized lattice distortions have been observed above and below T_C ,^{3,4} in the (La, Ca) MnO_3 perovskite system. DeTeresa *et al.* have extended this work by inferring that these lattice distortions carry spin (magnetic polarons) from recent in-field small angle neutron scattering (SANS) experiments on the perovskite $\text{La}_{2/3}\text{Ca}_{1/3}\text{MnO}_3$.⁵

While current attention is centered on perovskite manganites, the discovery of layered compounds $\text{La}_{2-2x}\text{Sr}_{1+2x}\text{Mn}_2\text{O}_7$ as another class of CMR oxides provides a rich opportunity to explore structure-property relationships on varying length and time scales in reduced dimensions. The material of interest, is comprised of perovskite bi-layers of corner-linked MnO_6 octahedra forming infinite sheets. Bi-layers of (La, Sr) MnO_3 are separated

along the c -axis by insulating (La, Sr)O layers. We have shown that although below T_C Mn-spins order ferromagnetically within the ab -plane⁶ in a certain compositional range, a competition between super- and double-exchange may result to a canting of Mn-spins between adjacent ferromagnetic sheets, within the perovskite bi-layer.⁷ There is evidence to show that this competition may be reflected within ferromagnetic correlations above T_C , as reported recently by Osborn *et al.*⁸ Perring *et al.* also report that weak antiferromagnetic and ferromagnetic spin fluctuations coexist in these layered materials above T_C .⁹ Clearly, understanding both long and short range magnetism—structure and dynamics—is an essential ingredient in developing a coherent picture of the physics of this class of transition metal oxides.

In this paper we report neutron scattering results from single crystals with $x=0.4$ and 0.36 that demonstrate that 2D ferromagnetic correlations exist in these layered CMR materials, as high as $2.8T_C$. Their size increases as $T \rightarrow T_C$ reaching a size of $\sim 10 \text{ \AA}$ at T_C . The coherence length of these ferromagnetic correlations does not appear to diverge at T_C . Quasielastic neutron scattering from a polycrystalline x

=0.3 sample, reproduce the single crystal results and find a spin diffusion constant of $5 \text{ meV } \text{\AA}^2$, lower than that recently determined for the 3D perovskite materials.

Single crystals of $\text{La}_{2-2x}\text{Sr}_{1+2x}\text{Mn}_2\text{O}_7$ were melt-grown in flowing 100% O_2 in a floating zone optical image furnace (NEC SC-M15HD). The crystals were characterized using inductively coupled plasma spectroscopy (ICP), d.c. magnetization, and resistivity. Two single crystals were prepared and characterized by these methods; ICP measurement of their composition was determined to be consistent with a doping of $x=0.40(1)$ ($\text{La}_{1.2}\text{Sr}_{1.8}\text{Mn}_2\text{O}_7$) and $x=0.36(1)$ ($\text{La}_{1.28}\text{Sr}_{1.72}\text{Mn}_2\text{O}_7$). These samples exhibit transitions from a paramagnetic insulator (PI) to a ferromagnetic metal (FM) at 133 K for $x=0.36$ and 116 K for $x=0.4$. Diffraction data were obtained as a function of temperature from these single crystals, using the neutron time-of-flight single crystal diffractometer (SCD) located at the Manuel Lujan Jr., Neutron Scattering Center (MLNSC) at the Los Alamos National Laboratory. Quasi-elastic neutron scattering data were measured as a function of temperature from a polycrystalline sample with $x=0.3$ ($\text{La}_{1.4}\text{Sr}_{1.6}\text{Mn}_2\text{O}_7$) synthesized via standard ceramic techniques exhibiting coupled PI to FM transitions at 116 K, using the time-of-flight chopper spectrometer PHAROS,¹⁰ also located at the MLNSC. Data were recorded using an incident energy of 12.1 meV, except for data measured at 115 K where incident energies of 12.1 and 8.1 meV were used to extend the Q range of the measurement. Neutron powder diffraction data were measured as a function of temperature from 20–300 K, using the Special Environment Powder Diffractometer (SEPD)¹¹ at the Intense Pulsed Neutron Source at the Argonne National Laboratory.

Single crystal time-of-flight neutron diffraction is ideally suited for the broad survey of reciprocal space for both Bragg reflections (long range structure) and also diffuse scattering which reflects structural features on a local scale. For both $x=0.36$ and $x=0.4$ single crystals, we observe a diffuse rod-like feature along c^* centered at $(0,1,0)$ and $(1,0,0)$. An example of these rod-like features is shown in Fig. 1, measured at 120 K from the $x=0.36$ crystal. The diffuse scattering is strongly temperature dependent, becoming more intense as $T \rightarrow T_C$, while below T_C it decreases, consistent with scattering from magnetic correlations. For the $x=0.4$ crystal we do observe rod-like features for higher orders of h and k [$(h,0,0)$ or $(0,k,0)$ with h or k as high as 7], where the magnetic form factor is expected to decrease substantially the magnetic scattering. These features have a smaller FWHM than the scattering at $h=1$, or $k=1$, suggesting that there is an additional nuclear component to the observed magnetic scattering. This nuclear scattering may arise from a low density of perovskite intergrowths in the crystal as proposed by Potter *et al.*¹² and also observed in high resolution electron microscopy.¹³ For the $x=0.36$ crystal we observed no diffuse scattering at higher orders of h and k , suggesting a significantly lower concentration of intergrowths than in the $x=0.4$ crystal.

Figure 2 shows the variation of the intensity of the magnetic rod scattering in both $x=0.36$ and $x=0.4$ crystals as a function of temperature. These values were obtained by fitting data perpendicular to the rod, along the $[010]$ direction,

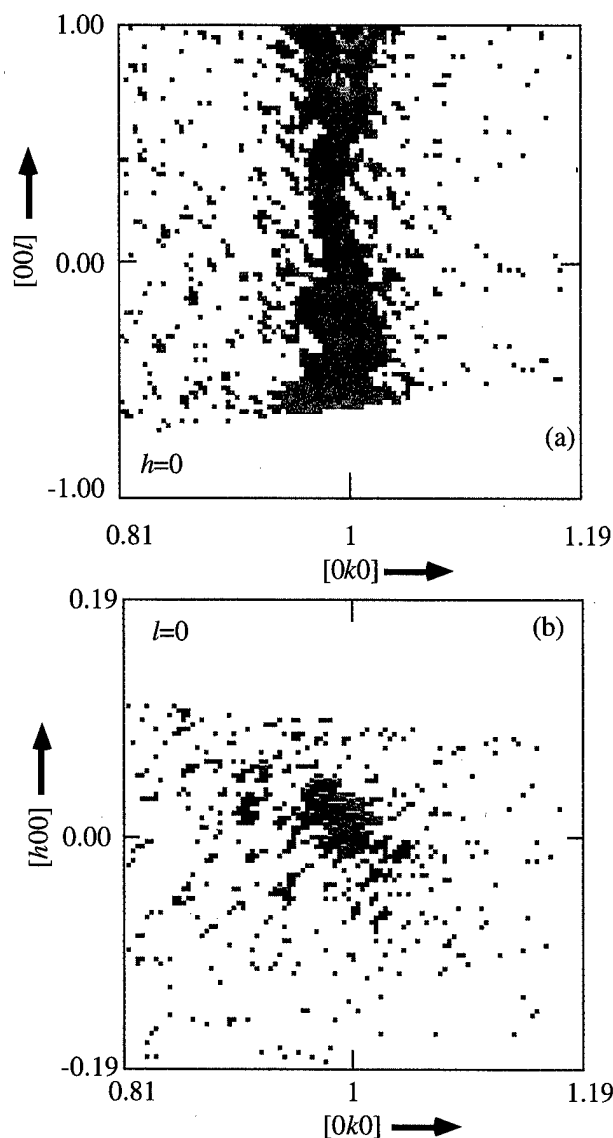


FIG. 1. Time-of-flight neutron diffraction data measured from a single crystal of $\text{La}_{1.28}\text{Sr}_{1.72}\text{Mn}_2\text{O}_7$ at 120 K. The observed scattering is shown as a section through reciprocal space (a) perpendicular to $[100]$ and (b) perpendicular to $[001]$. The small peak just below the (011) reflection corresponds to a much smaller second crystal in the sample with a relative intensity of the main (011) reflection of $1/5000$.

with a Lorentzian function and accounting for the nuclear scattering with a narrower Lorentzian with its width fixed at a value determined at 20 K. We find that the intensity of the magnetic diffuse scattering increases as $T \rightarrow T_C$ from above, while below T_C its intensity decreases, vanishing for $T < 0.5T_C$. That this scattering appears as a diffuse rod along c^* and with a finite width along $[h00]$ or $[0k0]$, clearly shows that the spin correlations are 2D. We find that these modulations are ferromagnetic but do not strictly obey a $\cos^2(\pi\Delta z/l)$ dependence (where Δz is the difference of the fractional z coordinate between neighboring Mn atoms); we have proposed a model where these modulations are described in terms of spin-canting in these ferromagnetic correlations resulting from a competition between super- and double-exchange which is reported elsewhere.⁸ On Fig. 2 we also show the variation of intensity of the $(0,1,1)$ ferromag-

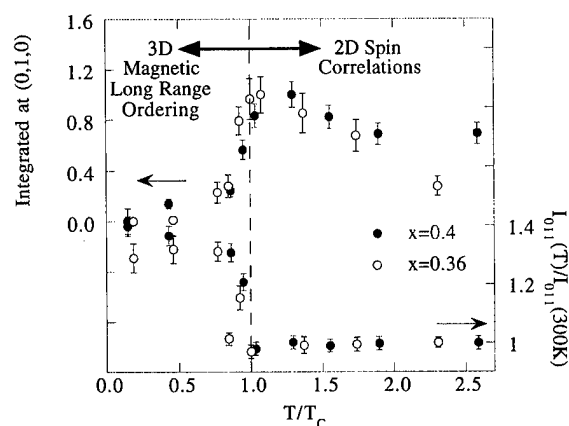


FIG. 2. Temperature dependence of diffuse scattering intensity at (0,1,0) and the intensity of the ferromagnetic (0,1,1) measured from single crystals of $x=0.4$ and 0.36 . The intensity of the (0,1,1) reflection has been normalized to its intensity measured at 300 K.

netic reflection as a function of temperature. This demonstrates that peak in the intensity of the ferromagnetic 2D fluctuations is correlated with the onset of 3D magnetic ordering. The observed ferromagnetic reflections below T_C were consistent with ordered Mn spins aligned ferromagnetically within the ab plane as reported previously.⁶

The coherence length of the ferromagnetic correlations within the perovskite bilayers, ξ_{2D} , is $\sim 4-5$ Å at 300 K, and increases to ~ 10 Å at T_C . Surprisingly ξ_{2D} does not appear to diverge at T_C (see Fig. 3). It is unclear where the critical region for these 2D ferromagnetic correlations lies,

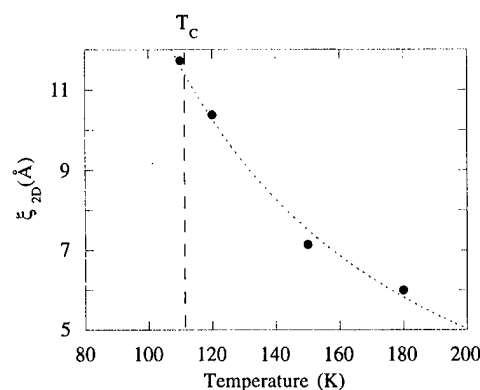


FIG. 3. The planar coherence length ξ_{2D} as a function of temperature.

however, from a more detailed study on the same $x=0.4$ crystal we find that power law scaling of ξ_{2D} suggests a much lower critical temperature for these correlations than actually observed; a $T_C^{2D}=98$ K is obtained using a mean field exponent $\nu=0.5$, or a $T_C^{2D}=63$ K for a 2D-Ising exponent of $\nu=1$.⁸ Interestingly, measurement of the critical scattering close to the (004) ferromagnetic reflection suggests that there is a buildup of three-dimensional correlations below 120 K resulting in a coherence length that appears to diverge at T_C .⁸ These data suggest that there may be a cross-over close to T_C from 2D to 3D critical scaling. However, we also note that in the same temperature region we have reported significant electron-phonon coupling in these materials.⁶ As discussed below, these localized lattice distortions

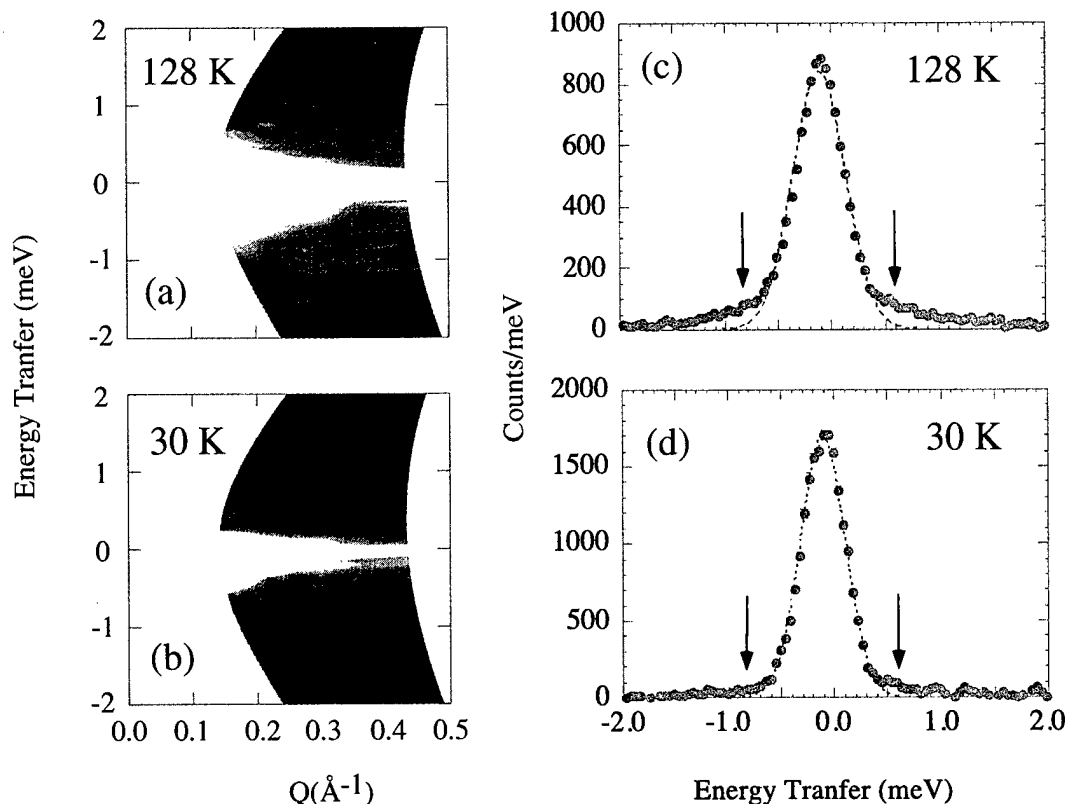


FIG. 4. Inelastic neutron data in Q, ω space measured at 128 K (a) and 30 K (b) using an incident neutron energy of 12.1 meV. The same data measured at 128 K (c) and 30 K (d) plotted as a function of energy integrated over the accessible Q -range of this measurement. See text for details.

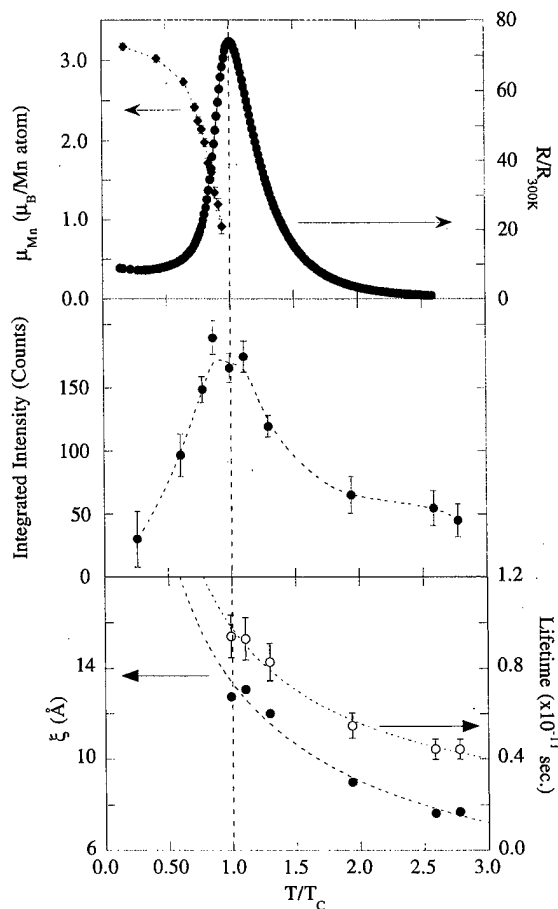


FIG. 5. (a) Temperature dependent resistivity and magnetization (determined from full profile Rietveld refinement of neutron powder data) from the polycrystalline sample $\text{La}_{1.4}\text{Sr}_{1.6}\text{Mn}_2\text{O}_7$, (b) integrated intensity of the quasi-elastic Lorentzian component, and (c) coherence length as a function of reduced temperature T/T_C . In (c) the dashed lines are a fit to a power law function. Magnetic reflections from the $x=0.3$ sample were consistent with a ferromagnetic alignment of Mn spins in the a - b plane.⁶

tions may contribute to the lack of divergence in the 2D coherence length. Theoretical considerations suggest that this coupling arises from local Jahn-Teller effects in these mixed valent materials.^{1,2}

To investigate the spin dynamics of these 2D ferromagnetic correlations we have measured quasi-elastic neutron scattering from a large polycrystalline sample of $x=0.3$. (The need for a large sample mass to yield sufficient signal-to-noise prohibited the use of a single crystal specimen for this experiment.) We have deliberately selected a Q, ω range to measure ferromagnetic scattering as l or $Q \rightarrow 0$ without the measurement being perturbed by spin waves and 3D spin correlations at lower Q . Figures 4(a) and 4(b) show data measured at 128 and 30 K in Q, ω space, while panels (c) and (d) show the same data, integrated over the accessible Q range, as a function of energy. On panels (c) and (d) we show a fit to the elastic incoherent peak using a Gaussian function with a fixed FWHM that reflects the resolution of the spectrometer (dashed line). At 30 K we find no significant deviations from the fit, as seen in Fig. 4(d). This contrasts with the scattering at higher temperatures, and especially close to T_C , where we find an additional broad Lorentzian component superimposed on the Gaussian elastic

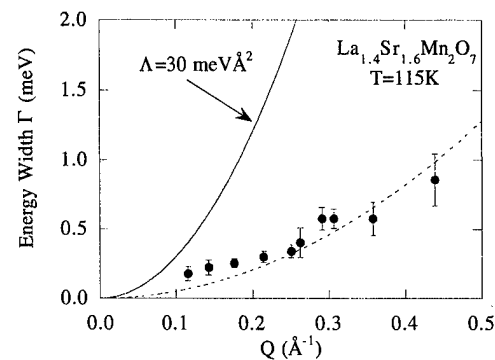


FIG. 6. The Q -dependence of the Lorentzian quasielastic width (Γ) at 115 K measured from a ceramic sample of $\text{La}_{1.4}\text{Sr}_{1.6}\text{Mn}_2\text{O}_7$. The dashed line represents a fit to $\Gamma = \Lambda Q^2$, while the solid line represents the behavior observed in $\text{La}_{2/3}\text{Ca}_{1/3}\text{MnO}_3$ reported by Lynn *et al.*¹⁵

incoherent peak. This feature is clearly shown in Figs. 4(a) and 4(c). The intensity of the Lorentzian component diverges as $Q \rightarrow 0$, as expected for ferromagnetic correlations.

Both quantitatively and qualitatively this ceramic $x=0.3$ sample behaves similarly to the single crystals discussed above. A broad Lorentzian component is observed as high as $2.8T_C$ [Fig. 5(b)], while with decreasing temperature and approaching T_C , the intensity of the quasi-elastic scattering increases and reaches a maximum at T_C . Below T_C the quasi-elastic scattering decreases linearly with temperature suggesting that it may result from soft c -axis spin wave scattering.¹⁴ The peak in the quasi-elastic scattering at T_C strongly correlates with a sharp decrease in the resistivity of the sample, and the development of three-dimensional ordering of Mn spins determined from neutron powder diffraction, as shown in Fig. 5(a). These observations resemble those reported from inelastic scattering experiments on three-dimensional perovskite materials.¹⁵ The spatial extent of the ferromagnetic correlations—computed from the Q dependence of the Lorentzian signal—yields an overall ξ of $\sim 5 \text{ \AA}$ ($\sim 1.30a$), increasing to $\sim 12 \text{ \AA}$ at T_C ($\sim 3.1a$), similar to that found for the single crystal samples described above [see Fig. 5(c)].

The lifetime of these ferromagnetic correlations, obtained from the width of the quasi-elastic scattering integrated over the accessible Q range of the measurement, increases $T \rightarrow T_C$, reaching a value of $1.1(1) \times 10^{-11} \text{ s}$ at T_C . Interestingly like the correlation length, the lifetime does not diverge suggesting that even close to T_C , there are 2D ferromagnetic spins that are rapidly fluctuating [see Fig. 5(c)]. Lynn *et al.*¹⁵ have suggested that the magnetic transition in CMR perovskites is unusual as the spin waves stiffness constant D does not collapse close to T_C . Instead they describe the magnetic transition in the perovskite $\text{La}_{2/3}\text{Ca}_{1/3}\text{MnO}_3$ in terms of spin-diffusion due to slow polaronic hopping of e_g carriers with a spin diffusion constant, Λ , of 30 meV \AA^2 , a quantity that is analogous to the spin-stiffness constant for a magnetically ordered system. From the Q dependence of the Lorentzian width we estimate a spin-diffusion constant $\Lambda \sim 5 \text{ meV \AA}^2$ at 115 K for our sample (see Fig. 6), a value substantially lower than the perovskite material

(30 meV Å²). Presumably, this reduced Λ is a consequence of the low dimensionality of these naturally layered manganites.

The results presented here clearly demonstrate that in these naturally layered materials 2D ferromagnetic correlations exist at temperatures as high as $\sim 2.8 T_C$. As $T \rightarrow T_C$, their size and lifetime increases but these quantities do not appear to diverge at T_C . Clearly there is a need to reconcile the behavior of these ferromagnetic correlations with the 3D ferromagnetic transition at T_C , where critical behavior and a divergent coherence length is observed about magnetic reflections. The data support a model where the 3D magnetic transition interrupts 2D fluctuations that would otherwise order over a long range at a lower T_C (see also Ref. 8). That the measured T_C occurs at a higher temperature than the estimate of T_C^{2D} suggests that at a critical size ξ_{2D} , Mn spins in adjacent perovskite bilayers may start ordering ferromagnetically in three dimensions. This implies a crossover to 3D critical scaling close to T_C . Indeed the underlying physics of these 2D ferromagnetic correlations may be competing antiferromagnetic super-exchange and ferromagnetic double-exchange; in a previous paper we have reported that this competition may result in a canted Type-A ferromagnetic structure in $x=0.4$ below T_C .⁷ As pointed out by Osborn *et al.* these ferromagnetic correlations may arise from the same competition above T_C .⁸

Alternatively the observation of nondivergent ferromagnetic correlations over a wide temperature region, may lend support to the small polaron model put forward to explain CMR in the manganite perovskites.^{1,2} Röder *et al.*¹ have calculated the magnetic behavior of localized phenomena such as Jahn–Teller polarons associated with localized e_g carriers and argue that the magnetic transition in the CMR manganites is accompanied by a crossover of length scales from a quasi-self-trapped small polaron to a large polaronic state below T_C . At T_C their calculation predicts a magnetic coherence length of ~ 3 –4 Mn sites or ~ 12 –16 Å. As magnetic polarons have a finite size, their coherence length is not necessarily expected to diverge as in a second-order magnetic transition. That is, the coherence length of the 2D magnetic correlations may be constrained by the lattice degrees of freedom (localized Jahn–Teller effects), which are in turn influenced by the electronic state. Our values of ξ_{2D} are in reasonable agreement with the prediction of Röder *et al.* and the size measurements of magneto-elastic polarons by DeTeresa *et al.* in $\text{La}_{2/3}\text{Ca}_{1/3}\text{MnO}_3$,⁵ while the lower value of Λ observed here may reflect polaronic mobility in reduced dimensions compared to the 3D octahedral network of perovskite materials. However, since the degree of electron-phonon coupling (via the Jahn–Teller effect) and T_C are closely coupled in the CMR materials,^{1,2,16} the difference between the two possible explanations put forward here may be subtle.

In conclusion, we have demonstrated the existence of 2D ferromagnetic correlations in layered CMR materials over a wide temperature range, with a coherence length ξ_{2D} and lifetime that do not diverge at T_C . These 2D ferromagnetic correlations accompany the ferromagnetic transition at T_C , which appears to exhibit critical scattering and a divergent coherence length. Quasi-elastic neutron scattering shows these ferromagnetic correlations still fluctuate rapidly close to T_C , while the spin diffusion constant is much lower than the perovskite materials. Importantly, the naturally layered manganites provide a unique opportunity to examine in detail the mechanism of this crossover between 2D and 3D magnetism.

This work was supported by the U.S. Department of Energy, Basic Energy Sciences-Materials Sciences under contract W-7405-ENG-36 (D.N.A., T.M.K., R.A.R.) and W-31-109-ENG-38 (JFM, RO, JDJ, SR). D.N.A. also thanks R. Heffner, H. Röder, H. N. Bordallo, and P. G. Radaelli for stimulating discussions on this subject, and the Institut Laue Langevin for financial support during the preparation of this manuscript.

- ¹H. Röder, J. Zang, and A. R. Bishop, *Phys. Rev. Lett.* **76**, 1356 (1996).
- ²A. J. Millis, P. B. Littlewood, and B. I. Shraiman, *Phys. Rev. Lett.* **74**, 5144 (1995).
- ³S. J. L. Billinge, R. G. Difrancesco, G. H. Kwei, J. J. Neumier, and J. D. Thompson, *Phys. Rev. Lett.* **77**, 515 (1996).
- ⁴P. G. Radaelli, D. E. Cox, M. Marezio, S.-W. Cheong, P. E. Schiffer, and A. P. Ramirez, *Phys. Rev. Lett.* **75**, 4488 (1995).
- ⁵J. M. DeTeresa, M. R. Ibarra, P. A. Algarabel, C. Ritter, C. Marquina, J. Blasco, J. Garcia, A. Delmoral, and Z. Arnold, *Nature (London)* **386**, 256 (1997).
- ⁶J. F. Mitchell, D. N. Argyriou, J. D. Jorgensen, D. G. Hinks, C. D. Potter, and S. D. Bader, *Phys. Rev. B* **55**, 63 (1996).
- ⁷D. N. Argyriou, J. F. Mitchell, J. B. Goodenough, O. Chmaissem, S. Short, and J. D. Jorgensen, *Phys. Rev. Lett.* **78**, 1568 (1997).
- ⁸R. Osborn, S. Rosenkranz, D. N. Argyriou, L. Vasilii-Doloc, J. W. Lynn, S. K. Sinha, J. F. Mitchell, K. E. Gray, and S. D. Bader, *Phys. Rev. Lett.* (submitted).
- ⁹T. G. Perring, G. Aeppli, Y. Morimoto, and Y. Tokura, *Phys. Rev. Lett.* **78**, 3197 (1997).
- ¹⁰R. A. Robinson, M. Nutter, R. L. Ricketts, E. Larson, J. P. Sandoval, P. Lysaght, and B. J. Olivier, in *Proceedings of the International Collaboration on Neutron Scattering XII, Rutherford Appleton Laboratory, 1994* (Rutherford Appleton Laboratory, RAL 94-025), Vol. 1, p. 44.
- ¹¹J. D. Jorgensen, J. J. Faber, J. M. Carpenter, R. K. Crawford, J. R. Hagemann, R. L. Hitterman, R. Kleb, G. E. Ostrowski, F. J. Rotella, and T. G. Worton, *J. Appl. Crystallogr.* **22**, 321 (1989).
- ¹²C. D. Potter, S. D. Bader, J. F. Mitchell, and D. N. Argyriou, *Phys. Rev. B* **57**, 72 (1988).
- ¹³D. Miller, private communication (1997).
- ¹⁴K. Hirakawa, H. Yoshizawa, and K. Ubukoshi, *J. Phys. Soc. Japan* **51**, 2151 (1982).
- ¹⁵J. W. Lynn, R. W. Erwin, J. A. Borchers, Q. Huang, A. Santoro, J.-L. Peng, and Z. Y. Li, *Phys. Rev. Lett.* **76**, 4046 (1996).
- ¹⁶G.-M. Zhao, K. Conder, H. Keller and K. A. Müller, *Nature (London)* **381**, 676 (1996).

Chemistry of naturally layered manganites (invited)

P. D. Battle,^{a)} N. Kasmir, J. E. Millburn, M. J. Rosseinsky, R. T. Patel, L. E. Spring, and J. F. Vente

Inorganic Chemistry Laboratory, Oxford University, South Parks Road, Oxford OX1 3QR, United Kingdom

S. J. Blundell, W. Hayes, A. K. Klehe, A. Mihut, and J. Singleton

Department of Physics, Clarendon Laboratory, Oxford University, Parks Road, Oxford OX1 3PU, United Kingdom

Experiments on three double-layer ($n=2$) Ruddlesden–Popper (RP) systems are reported. Doping $\text{Sr}_{1.8}\text{La}_{1.2}\text{Mn}_2\text{O}_7$ ($T_c=126$ K) with Nd to form $\text{Sr}_{1.8}\text{La}_{1.2-x}\text{Nd}_x\text{Mn}_2\text{O}_7$ leads to a reduction in Curie temperature for low doping levels ($x=0.2$), and to behavior reminiscent of $\text{Sr}_{1.8}\text{Nd}_{1.2}\text{Mn}_2\text{O}_7$ for $x\geq 0.7$. This suggests that it may be possible to control the temperature of maximum magnetoresistance chemically in these phases. The application of pressure ($0 < P/\text{GPa} \leq 1.8$) is shown to modify the magnetotransport properties of $\text{Sr}_2\text{NdMn}_2\text{O}_7$ to resemble those of $\text{Sr}_{1.9}\text{Nd}_{1.1}\text{Mn}_2\text{O}_7$. The changes can be explained by considering the relative strength of ferromagnetic and antiferromagnetic interactions within the material. Finally, the need for careful phase analysis of $n=2$ RP materials is demonstrated by the misleading magnetization data recorded for a sample of $\text{Sr}_{1.8}\text{Sm}_{1.2}\text{Mn}_2\text{O}_7$ containing $\sim 2.8\%$ of an $n=\infty$ perovskite phase. © 1998 American Institute of Physics. [S0021-8979(98)20911-X]

I. INTRODUCTION

Compounds of manganese have played a central role in recent studies of the magnetotransport properties of mixed metal oxides. It has been shown that the electrical resistivity of oxides containing Mn in a nonintegral oxidation state ($\text{Mn}^{3+/4+}$) can decrease dramatically in an applied magnetic field, an observation that may lead to applications in the area of data storage. The effect has been most widely studied^{1,2} in perovskites of the general form $\text{Ln}_{1-x}\text{A}_x\text{MnO}_3$, where the presence of both lanthanide (Ln) and alkaline earth (A) cations results in the adoption of a mixed-valence state by the Mn cation. Perovskite can be regarded as the $n=\infty$ member of the Ruddlesden–Popper (RP)³ family of compounds $(\text{Ln}, \text{A})_{n+1}\text{B}_n\text{O}_{3n+1}$, with the K_2NiF_4 structure being at the opposite ($n=1$) extreme (Fig. 1). RP phases can be considered to consist of perovskite-like blocks of vertex sharing BO_6 octahedra which extend to infinity in the xy plane and have a thickness of n octahedra parallel to the z axis; neighboring blocks are separated by a rock-salt layer such that the overall composition can be described as $[(\text{Ln}, \text{A})\text{BO}_3]_n(\text{Ln}, \text{A})\text{O}$. Following the observation of colossal magnetoresistance (CMR) in $n=\infty$ RP phases, the electronic properties of other members of the series have been studied. CMR is not observed in samples of the $n=1$ system $\text{Sr}_{2-x}\text{La}_x\text{MnO}_4$ which, for $x\sim 0.5$, show charge ordering on the Mn sublattice.^{4–7} However, CMR has been detected around the Curie temperature (126 K)⁸ of the $n=2$ (Fig. 1) composition $\text{Sr}_{1.8}\text{La}_{1.2}\text{Mn}_2\text{O}_7$, which does not show charge ordering. The majority of the data collected to date for $n=1, 2$, and ∞ suggest that CMR is incompatible with charge ordering on the Mn sublattice, and that it is closely linked to the appearance of a spontaneous magnetization in the sample. There are, however, a number of ex-

ceptions to this sweeping generalisation. $\text{Sr}_{2-x}\text{Nd}_{1+x}\text{Mn}_2\text{O}_7$, for example, shows^{9,10} CMR in the absence of a spontaneous magnetization. Studies of this system have demonstrated that the nature and behavior of the sample are very sensitive to the conditions used in the chemical synthesis.¹¹ More specifically, samples with the composition $x=0.0$ or 0.1 appear to contain two $n=2$ phases with the same stoichiometry, as

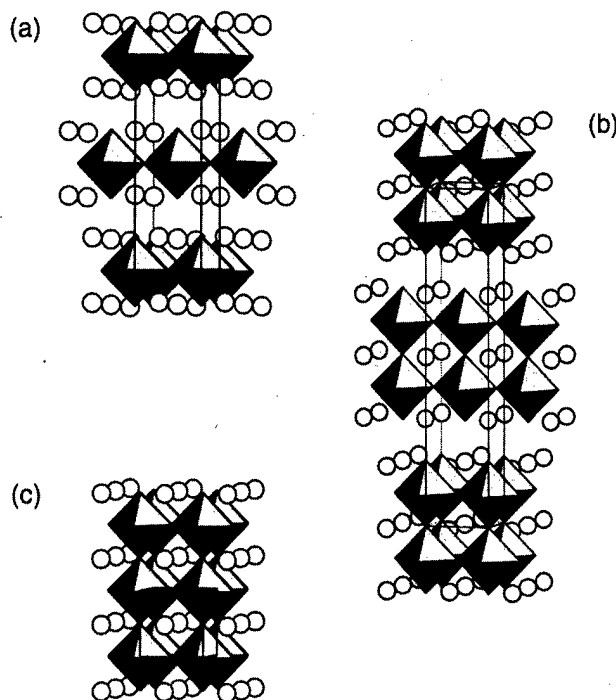


FIG. 1. Ruddlesden–Popper structures: (a) K_2NiF_4 ($n=1$), (b) $\text{Sr}_2\text{LnMn}_2\text{O}_7$ ($n=2$), (c) perovskite ($n=\infty$). MnO_6 octahedra are shaded, hollow circles represent Sr/Ln atoms.

^{a)}Electronic mail: peter.battle@chem.ox.ac.uk

TABLE I. Unit cell parameters for $\text{Sr}_{1.8}\text{La}_{1.2-x}\text{Nd}_x\text{Mn}_2\text{O}_7$.

x	% phase 1	a_1	c_1	% phase 2	a_2	c_2
0.2	40.0(5)	3.8684(2)	20.138(2)	60.0(5)	3.8698(2)	20.117(1)
0.7	53.2(6)	3.8532(2)	20.145(2)	46.8(6)	3.8551(2)	20.124(2)
1.1	96.6(7)	3.84191(1)	20.149(1)	3.4(7)	3.8372(8)	20.093(7)

judged by the unit cell volume, but with a different distribution of Sr^{2+} and Nd^{3+} cations over the available sites,¹² whereas $\text{Sr}_{1.8}\text{Nd}_{1.2}\text{Mn}_2\text{O}_7$ can be prepared to contain a single $n=2$ phase, albeit contaminated by $n=\infty$ perovskite.¹³ The difference between the Nd- and La-containing $n=2$ compounds demonstrates that the electronic properties are very sensitive to elemental composition, and diffraction experiments^{12,14,15} have indicated that the sensitivity can be traced to the subtle structural changes which are brought about by the variations in composition. We have previously shown^{16,17} that the introduction of smaller Ln cations (Ho^{3+} , Y^{3+}) into the $n=2$ structure results in the formation of a spin-glass phase at low temperatures, and also in the loss of CMR. In this article, we describe the magnetic behavior of $\text{Sr}_{1.8}\text{La}_{1.2-x}\text{Nd}_x\text{Mn}_2\text{O}_7$, a system which can be thought of as a solid solution between the "conventional" Mn-containing CMR compound $\text{Sr}_{1.8}\text{La}_{1.2}\text{Mn}_2\text{O}_7$ and the "unconventional" $\text{Sr}_{1.8}\text{Nd}_{1.2}\text{Mn}_2\text{O}_7$. We also discuss the pressure dependence of the CMR in $\text{Sr}_{2-x}\text{Nd}_{1+x}\text{Mn}_2\text{O}_7$ and show how the application of pressure can mimic the effect of changes in chemical composition. Finally, we discuss the consequences for the magnetic and magnetotransport properties of introducing the Sm^{3+} cation, intermediate in size between Nd^{3+} and Ho^{3+} , into the $n=2$ structure.

II. EXPERIMENT

The $n=2$ RP system $\text{Sr}_{1.8}\text{La}_{1.2-x}\text{Nd}_x\text{Mn}_2\text{O}_7$ could not be prepared free of perovskite impurity by traditional ceramic techniques. A synthetic strategy which involved the use of a Bi_2O_3 flux¹⁰ was more successful. Stoichiometric quantities of SrCO_3 , Nd_2O_3 , La_2O_3 , and MnO_2 were ground together with a small amount of Bi_2O_3 such that the initial cation composition was $\text{Sr}_{1.8}\text{La}_{1.2-x}\text{Nd}_x\text{Mn}_2\text{Bi}_{0.1}$. The reaction mixture, contained in an alumina crucible, was heated at 900 (12 h) and 1200 °C (12 h) before being pelletized and heated at 1500 °C for a total of 36 h. X-ray powder diffraction measurements, carried out on a Siemens D5000 diffractometer using $\text{Cu K}\alpha_1$ radiation, showed that the products were free of $n=\infty$ and $n=1$ impurity phases. The $\{0\ 0\ 10\}$ reflection of all samples in the composition range $0.1 \leq x \leq 1.1$ had a full width at half maximum (FWHM) of $\Delta 2\theta \sim 0.1^\circ$. We have previously shown^{11,13} that values less than this are characteristic of unstrained, monophasic samples, whereas larger values indicate that the sample either has a high degree of strain or is actually biphasic, possibly in a very subtle way.¹² The quality of the new samples was thus uncertain, and structure refinement by Rietveld profile analysis^{18,19} was carried out in order to determine their true nature. Analysis by ICP emission spectroscopy established that the metal content of the samples was in agreement with

the expected values and iodometric titrations established $y = 7.00(2)$ for the oxygen content in $\text{Sr}_{1.8}\text{La}_{1.2-x}\text{Nd}_x\text{Mn}_2\text{O}_y$. The temperature dependence of the magnetization of three selected samples ($x=0.2, 0.7, 1.1$) was measured in an applied field of 1 kG using a Quantum Design MPMS superconducting quantum interference device (SQUID) magnetometer.

The synthesis of $\text{Sr}_{2-x}\text{Nd}_{1+x}\text{Mn}_2\text{O}_7$ ($x=0.0, 0.1$) has been described previously.⁹ These samples both contain two $n=2$ RP phases, but no $n=\infty$ perovskite was detectable by x-ray or neutron diffraction. The pressure dependence of the resistance of $\text{Sr}_{2-x}\text{Nd}_{1+x}\text{Mn}_2\text{O}_7$ ($x=0.0, 0.1$) was measured using currents $21 \leq I/nA \leq 210$. No current dependence of the resistance was detected. The magnetoresistance was measured using standard, low-frequency (30 Hz), four-wire ac techniques in magnetic fields up to 15 T, with the current perpendicular to the magnetic field. Field reversal verified that the Hall contribution to the magnetoresistance was negligible. The measurements were restricted to (P, T, B) regions where the sample resistance was less than $10^5 \Omega$. They were performed on two different pieces of ceramic sample to verify the sample independence of the observed signal. All resistance values were normalized to the sample resistance at ambient pressure, 275 K and 0 T. A standard piston-cylinder cell with petroleum spirit as pressure medium was used²⁰ to apply pressure at room temperature. The pressure inside the cell, which was monitored with a calibrated manganin wire,²¹ decreased by ~ 0.3 GPa during cooling from room temperature to 4.2 K; all pressures quoted are room temperature values.

A sample of $\text{Sr}_{1.8}\text{Sm}_{1.2}\text{Mn}_2\text{O}_7$ was prepared by firing a stoichiometric mixture of SrCO_3 , Sm_2O_3 , and MnO_2 in air at 800 (24 h), 1000 (24 h), and 1350 °C (10 days). Initial x-ray characterization was carried out using a Siemens D5000 diffractometer, and the sample was then examined under higher resolution using the diffractometer 2.3 at the SRS, Daresbury Laboratory ($\lambda = 1.3997 \text{ \AA}$, $\Delta 2\theta = 0.01^\circ$). The zero field cooled (ZFC) and field cooled (FC) magnetic susceptibility of the sample was measured in a field of 500 G. Ambient pressure magnetoresistance measurements on $\text{Sr}_{1.8}\text{Sm}_{1.2}\text{Mn}_2\text{O}_7$ were accomplished using a four-terminal dc technique in fields of up to 14 T.

III. RESULTS

Analysis of the x-ray diffraction patterns of the compositions $\text{Sr}_{1.8}\text{La}_{1.2-x}\text{Nd}_x\text{Mn}_2\text{O}_7$ showed (Table I) that they all contain more than one $n=2$ RP phase, as do $\text{Sr}_2\text{LaMn}_2\text{O}_7$ and $\text{Sr}_2\text{NdMn}_2\text{O}_7$.^{12,14} The relative proportions of the two phases varied in an irregular manner as a function of x . In the compositions that were selected for further study (x

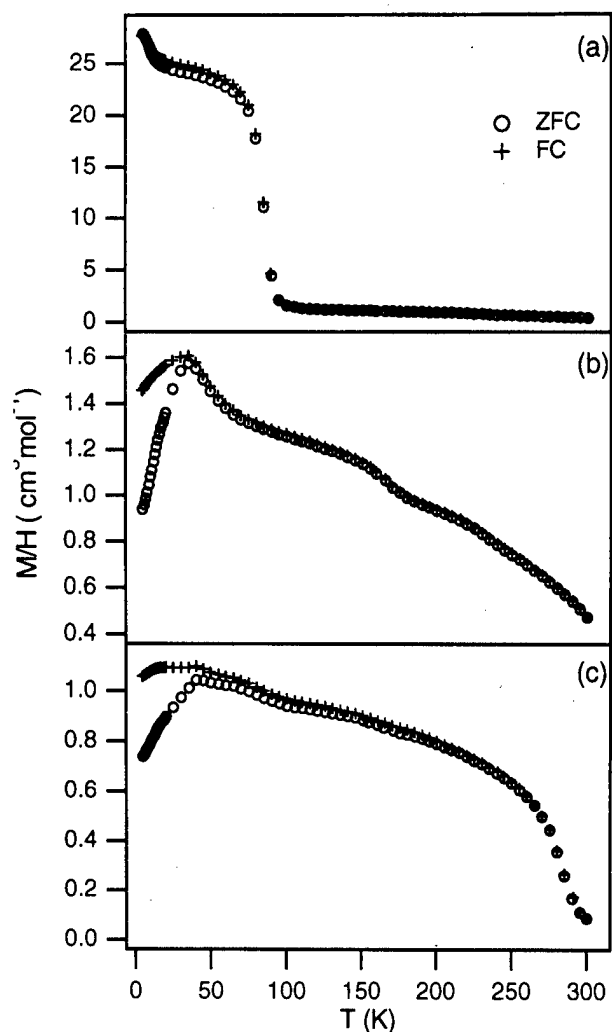


FIG. 2. Magnetic susceptibility of $\text{Sr}_{1.8}\text{La}_{1.2-x}\text{Nd}_x\text{Mn}_2\text{O}_7$ measured in an applied field of 1 kG for x = (a) 0.2, (b) 0.7, and (c) 1.1.

=0.2, 0.7, 1.1) the phase fractions were 40/60, 53/47, and 97/3; thus the composition $\text{Sr}_{1.8}\text{La}_{0.1}\text{Nd}_{1.1}\text{Mn}_2\text{O}_7$ appeared to be almost monophasic at the resolution of our powder diffraction apparatus. The data gave no indication of (Sr, La, Nd) cation ordering over the two crystallographically distinct sites available—one in the perovskite blocks and the other in the rock-salt layers. As expected, the unit cell volume showed a general decrease as the concentration of the smaller Nd^{3+} cation increased. The magnetic susceptibility, measured in a field of 1 kG, of the three chosen compositions is plotted as a function of temperature in Fig. 2. The composition $x=0.2$ shows a rise in susceptibility below 20 K, but otherwise shows qualitatively similar behavior to $x=0.0$ ⁸ (Fig. 3), with a Curie point apparent at 85 K and a suggestion of short range or two dimensional ordering below 230 K (cf. 126 and 250 K for $x=0.0$). A saturation magnetic moment of $2.23 \mu_B$ per Mn cation was measured in a field of 1 kG. The Curie point is not visible in the data collected on $x=0.7$, and the susceptibility of $x=1.1$ is very similar to that of the composition $x=1.2$, although the marked rise in the magnetization occurs at 290 K (270 K) in the former (latter); neu-

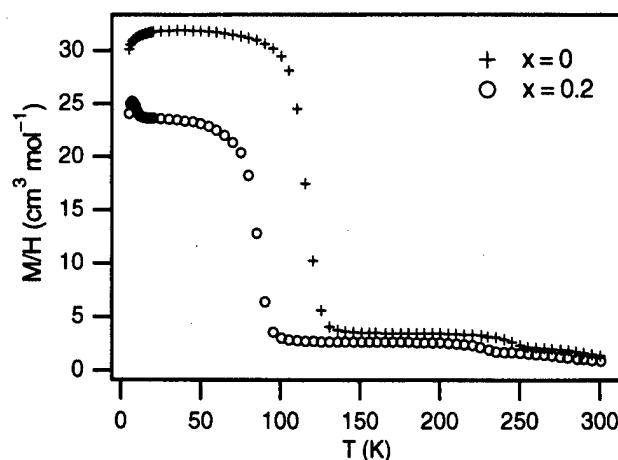


FIG. 3. Magnetic susceptibility of $\text{Sr}_{1.8}\text{La}_{1.2-x}\text{Nd}_x\text{Mn}_2\text{O}_7$ measured in 100 G for $x=0.0$ and 0.2.

tron diffraction experiments have previously failed to detect any long-range magnetic order in $\text{Sr}_{1.8}\text{Nd}_{1.2}\text{Mn}_2\text{O}_7$.¹³

The normalized resistance of $\text{Sr}_2\text{NdMn}_2\text{O}_7$ between 50 and 300 K is shown in Fig. 4 as a function of pressure and applied field. The zero-field resistance is seen to increase by over three orders of magnitude between room temperature and 80 K. Neither the absolute value nor the temperature dependence of the zero-field resistance are affected significantly by the application of pressure. The temperature dependence of the zero-field resistance under pressure for $170 \leq T/K \leq 300$ can be fitted as an activated process, $\rho = \rho_0 e^{(E/kT)}$, with an activation energy of 110 ± 5 meV, independent of the applied pressure. This implies that the activa-

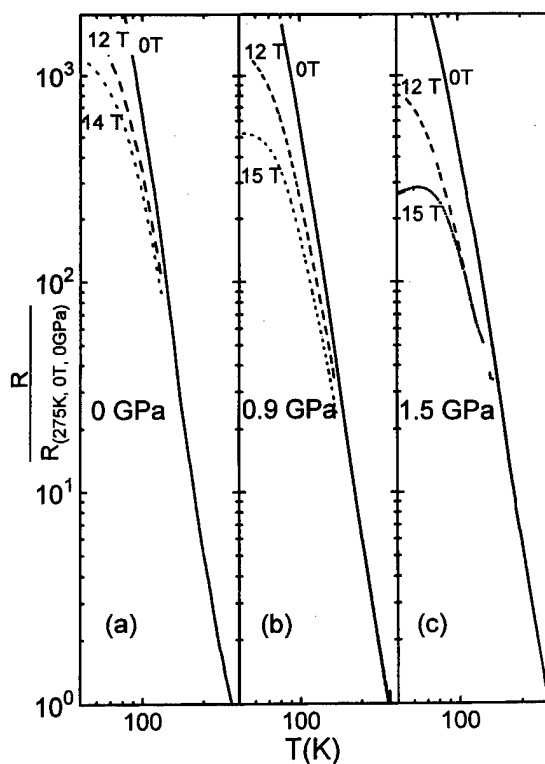


FIG. 4. Normalized resistance of $\text{Sr}_2\text{NdMn}_2\text{O}_7$ for $50 \leq T/K \leq 300$ at different magnetic fields and (a) ambient pressure, (b) 0.9, and (c) 1.5 GPa.

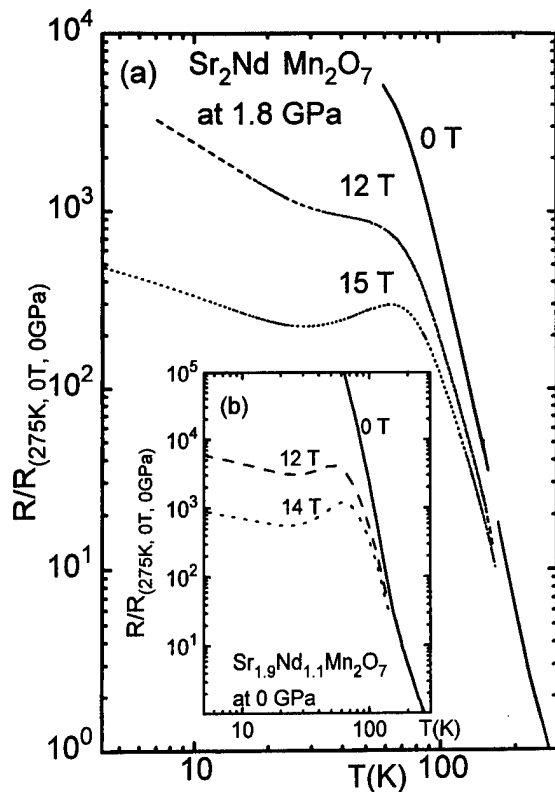


FIG. 5. (a) Normalized resistance of $\text{Sr}_2\text{NdMn}_2\text{O}_7$ at 1.8 GPa for different magnetic fields. (b) Normalized resistance of $\text{Sr}_{1.9}\text{Nd}_{1.1}\text{Mn}_2\text{O}_7$ at ambient pressure for comparison purposes.

tion energy of this system cannot depend sensitively on the unit cell dimensions. This is a surprising result, particularly in view of the decrease in activation energy observed when $n=\infty$ perovskites are subjected to pressure.^{22,23} The magnetoresistance, however, is strongly dependent on the pressure applied, as illustrated in Fig. 4. Even at temperatures as high as 100 K, the magnetoresistance ratio at 12 T, $(\rho_B - \rho_0)/\rho_B$, changes from $\sim -90\%$ at 0 GPa to $\sim -200\%$ at 1.5 GPa, and there is a marked similarity between the behavior of $\text{Sr}_2\text{NdMn}_2\text{O}_7$ under pressure and $\text{Sr}_{1.9}\text{Nd}_{1.1}\text{Mn}_2\text{O}_7$ at ambient pressure.⁹ This becomes particularly noticeable (Fig. 5) at pressures in excess of 1.5 GPa and in high magnetic fields ($B > 12$ T). In this regime, $\text{Sr}_2\text{NdMn}_2\text{O}_7$ develops a local resistivity maximum at ~ 70 K, similar to that observed in $\text{Sr}_{1.9}\text{Nd}_{1.1}\text{Mn}_2\text{O}_7$ at high fields and ambient pressure [Fig. 5(b)]. It is interesting to note that once this maximum has developed, its position and height are almost pressure independent. This could be an indication that the maximum is due to the completion of a pressure-field assisted ordering process among the Mn spins.

The x-ray diffraction data collected on $\text{Sr}_{1.8}\text{Sm}_{1.2}\text{Mn}_2\text{O}_7$ using a laboratory-based diffractometer indicated that we had been successful in preparing a monophasic, tetragonal $n=2$ RP sample, despite the fact that our previous attempts to prepare $\text{Sr}_2\text{SmMn}_2\text{O}_7$ had resulted in the formation of two $n=2$ phases with similar but different structural characteristics.²⁴ However, close scrutiny of the high resolution data collected at the synchrotron radiation source showed that the new sample was contaminated with

TABLE II. Structural parameters of $\text{Sr}_{1.8}\text{Sm}_{1.2}\text{Mn}_2\text{O}_7$ determined at SRS.

Atom	Site	x	y	z	u_{iso} (\AA^2)	Occup. %
Sr/Sm (1)	2b	0	0	1/2	0.0053(7)	81/19(1)
Sr/Sm (2)	4e	0	0	0.317 32(5)	0.0057(4)	50/50(1)
Mn	4e	0	0	0.0976(1)	0.0038(5)	
O (1)	2a	0	0	0	0.018(4)	
O (2)	4e	0	0	0.2001(5)	0.032(3)	
O (3)	8g	0	1/2	0.0981(3)	0.013(1)	

Space group $14/mmm$, $R_{\text{wpr}}=4.59\%$, reduced $\chi^2=1.56$ for 32 variables
 $\text{Mn}-\text{O}(1)=1.965(2)$, $\text{Mn}-\text{O}(2)=2.06(1)$, $\text{Mn}-\text{O}(3)=1.912 59(4)$,
 $\text{Mn}(z)-\text{Mn}(-z)=3.931(5)$ \AA .

~ 2.8 wt % of a perovskite ($n=\infty$) phase. The unit cell parameters refined to the following values: for $n=2$, $a=3.825 13(2)$, $c=20.1269(1)$ \AA ; for $n=\infty$, $a=5.4205(5)$, $b=7.6840(6)$, $c=5.4130(5)$ \AA . The Sr^{2+} and Sm^{3+} cations order in the $n=2$ phase such that 84% of the smaller Sm^{3+} cations are nine coordinate in the rock-salt layer [$\text{Sr}/\text{Sm}(2)$], with the majority of the Sr^{2+} cations being twelve coordinate within the perovskite blocks [$\text{Sr}/\text{Sm}(1)$]. The refined values of the atomic coordinates are presented in Table II, along with the most important bond lengths; note that O(1) lies at the center of the perovskite block, the bond $\text{Mn}-\text{O}(2)$ is directed along z into the rock-salt layer, and $\text{Mn}-\text{O}(3)$ lies within the xy sheets; we have used the same labeling scheme previously.^{12,14} Although it is not ideal to determine these parameters by x-ray diffraction, the high absorption cross section of Sm renders a neutron diffraction study impractical. The magnetization of $\text{Sr}_{1.8}\text{Sm}_{1.2}\text{Mn}_2\text{O}_7$ is plotted as a function of temperature in Fig. 6. There is a sharp rise at 140 K, and some hysteresis is apparent below this temperature; a maximum is observed at ~ 35 K. A weak magnetization of $\sim 0.06 \mu_B$ per formula unit is seen at 5 K. The resistivity is plotted as a function of temperature and magnetic field in Fig. 7. The smooth curves are characteristic of an insulator, and no phase transition is apparent at 140 K. The magnetoresistance $[(\rho_B - \rho_0)/\rho_0] \times 100\%$ apparently increases throughout the measured temperature range and reaches a maximum value of $\sim -10\%$.

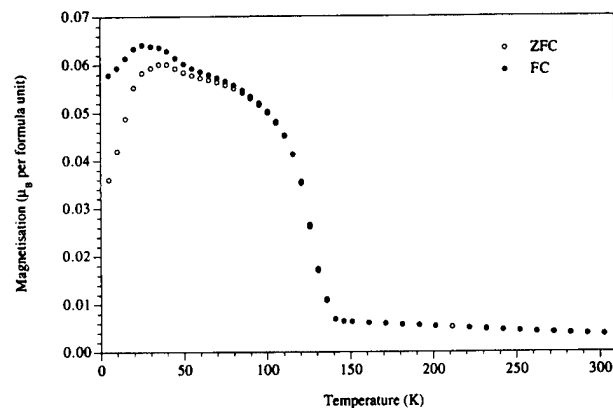


FIG. 6. FC and ZFC magnetization of $\text{Sr}_{1.8}\text{Sm}_{1.2}\text{Mn}_2\text{O}_7$, measured in 500 G.

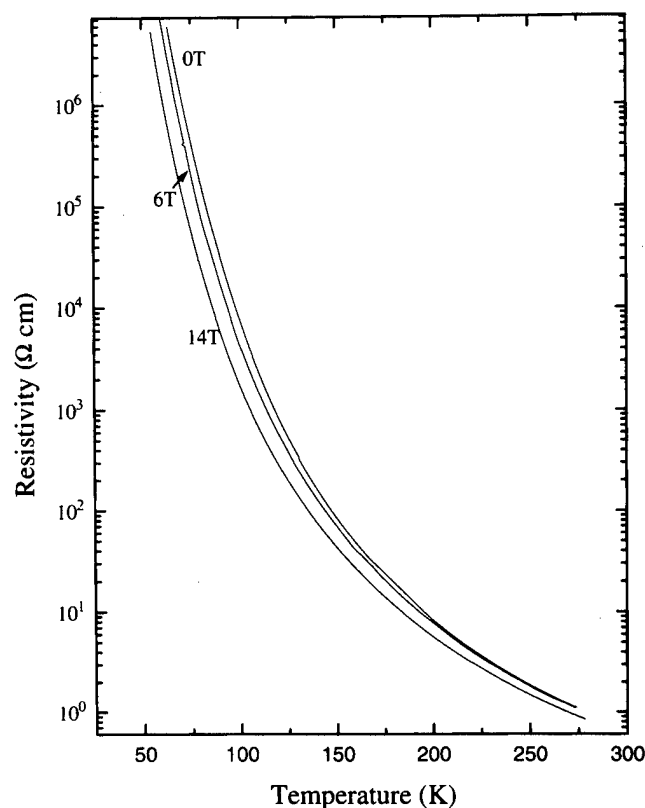


FIG. 7. Resistivity of $\text{Sr}_{1.8}\text{Sm}_{1.2}\text{Mn}_2\text{O}_7$ as a function of temperature and magnetic field.

IV. DISCUSSION

The data described above suggest that it is possible to dope $\text{Sr}_{1.8}\text{La}_{1.2}\text{Mn}_2\text{O}_7$ with Nd, thereby weakening the strength of the interactions producing long-range ferromagnetic ordering. Previous structural studies^{13,15} suggest that this is likely to involve a lengthening of the Mn–O(2) distance, which will decrease the coupling between neighboring perovskite blocks and reduce the three-dimensional nature of the magnetic interactions. It is interesting to note that the change from one type of magnetic behavior to another occurs gradually with changing composition. As the Nd-content increases, the susceptibility begins to resemble that of $\text{Sr}_{1.8}\text{Nd}_{1.2}\text{Mn}_2\text{O}_7$, which does not show long-range magnetic ordering.¹³ However, this neat description is too simplistic because it does not take into account the fact that our x-ray data show that the samples are biphasic, and without a more detailed neutron diffraction study we cannot confidently describe the differences in crystal structure and composition between the two phases, and we therefore cannot account fully for the weakening of the ferromagnetic interactions and the generally complex susceptibility behavior shown in Fig. 2. It is likely, for example, that the ferromagnetic transition and the low temperature rise in susceptibility seen for $x = 0.2$ in Fig. 2(a) are attributable to the two different components of the sample. Nevertheless, Nd-doping clearly influences the magnetic properties of this system, and our data give reason to believe that, for relatively low, but as yet badly defined ($x < 0.7$), levels of Nd doping it may be possible to tune T_c in this system chemically by controlling the

elemental distribution over the A sites within either the perovskite blocks or the rock-salt layers. This implies that it will also be possible to tune the temperature of maximum magnetoresistance, but more magnetotransport measurements are needed to prove this point. The suggestion that the properties can be controlled by the La/Nd ratio should sound a warning to those who treat these compounds as a Mn–O network with benign lanthanide cations playing only a space-filling role in the structure.

The results of our high pressure experiments suggest that the application of hydrostatic pressure to $\text{Sr}_2\text{NdMn}_2\text{O}_7$ has a similar effect, with regard to CMR, to increasing the Nd:Sr ratio. At ambient pressure, increasing the Nd content produces a contraction of the unit cell parameter a , but an increase in c , and, given that pressure and increasing Nd content have the same effect on CMR and that pressure will decrease both unit cell parameters, it is reasonable to assume that the change in a is of greater significance. Our samples of both $\text{Sr}_2\text{NdMn}_2\text{O}_7$ and $\text{Sr}_{1.9}\text{Nd}_{1.1}\text{Mn}_2\text{O}_7$ are biphasic, and we have described them as containing both an antiferromagnetic phase and a spin-glass phase, with the spin-glass fraction being more significant in the Nd-rich sample. The occurrence of the latter phase was attributed to frustration caused by the presence of both ferromagnetic and antiferromagnetic interactions. Furthermore, the lower ordered magnetic moment per Mn cation and the lower Néel temperature of $\text{Sr}_{1.9}\text{Nd}_{1.1}\text{Mn}_2\text{O}_7$ indicate that frustration-induced magnetic disorder is relatively large even in the magnetically ordered component of the Nd-rich sample. Our new results can then be taken to suggest that pressure produces an increase in the degree of frustration in antiferromagnetic $\text{Sr}_2\text{NdMn}_2\text{O}_7$ by enhancing the relative strength of any ferromagnetic interactions in the ordered phase. This is consistent with the magnetic structure¹² which consists of ferromagnetic sheets perpendicular to z ; the decrease in a will increase the strength of the ferromagnetic coupling and hence increase the degree of frustration in the antiferromagnetic structure. Susceptibility or neutron measurements under pressure are necessary to test this proposal further.

Finally, our data on $\text{Sr}_{1.8}\text{Sm}_{1.2}\text{Mn}_2\text{O}_7$ demonstrate the need for careful diffraction studies in order to identify the phases present in manganate samples. Damay *et al.*²⁵ have reported that perovskite compositions $\text{Sm}_{1-x}\text{Sr}_x\text{MnO}_3$ show a Curie temperature at ~ 140 K, with a saturation moment per Mn cation of $\sim 1 \mu_B$ for $x = 0.44$ in a field of 500 G. Thus the magnetization of our sample can be attributed to the presence of 3% of the perovskite $\text{Sm}_{0.56}\text{Sr}_{0.44}\text{MnO}_3$, essentially the fraction estimated from our x-ray study. This would not have been observed had we relied on our laboratory-based powder diffractometer, although it is a relatively modern, high-resolution machine. Indeed, the presence of this phase was not taken into account in our discussion of magnetic data collected before high resolution x-ray studies had been performed,¹⁶ and our earlier discussion is therefore flawed. The perovskite phase dominates the magnetization data, but it is present at too low a concentration to influence the magnetotransport data, as can be seen from a comparison of our data with those of Damay *et al.*, which show a metal-insulator transition. We can conclude that the majority, n

$n=2$ phase does not show magnetoresistance on the scale of the La and Nd analogs, even though we cannot describe the temperature dependence of the susceptibility. As in $\text{Sr}_2\text{HoMn}_2\text{O}_7$, the preferential occupation of the perovskite block site by the larger Sr^{2+} cation results in a large Mn–Mn distance (3.931 Å) along z within a double layer, and this is likely to weaken the interatomic interactions along the axis in comparison to those within the xy plane; it is also likely to prevent the exchangestriction which stabilizes the antiferromagnetic phase in $\text{Sr}_2\text{NdMn}_2\text{O}_7$. Although we cannot draw any firm conclusions about the magnetic properties of the $n=2$ phase from our susceptibility data, the similarity between the structural data described above and those reported previously for $\text{Sr}_2\text{HoMn}_2\text{O}_7$ and $\text{Sr}_2\text{YMn}_2\text{O}_7$ ¹⁷ leads us to predict spin glass behavior at low temperatures (<50 K) in $n=2$ $\text{Sr}_{1.8}\text{Sm}_{1.2}\text{Mn}_2\text{O}_7$. It is possible that the susceptibility maximum at 35 K (Fig. 6) corresponds to the glass transition temperature. It should be noted that the Ho- and Y-containing compounds show a slight distortion from the ideal RP structure. This involves oxide ion displacements arising from the rotation of MnO_6 octahedra, and is easily detected in neutron diffraction experiments. However, we would not expect to have detected it in our x-ray experiments on the Sm compound.

Finally, we wish to emphasise that, having attempted to prepare a number of $n=2$ RP phases, and having paid careful attention to synthesis conditions, we have never succeeded in preparing a monophasic material. We have prepared samples free of $n=\infty$ perovskite, but they have always contained two $n=2$ phases, for example $\text{Sr}_2\text{NdMn}_2\text{O}_7$. We have made highly crystalline $n=2$ phases, but they have always been contaminated by perovskite, for example $\text{Sr}_{1.8}\text{Sm}_{1.2}\text{Mn}_2\text{O}_7$ as described above. Furthermore, even samples which appear to contain only one $n=2$ phase show a relatively high concentration of intergrowths of other RP phases.²⁶ Our final conclusion is thus that any attempt to make an unambiguous interpretation of the physical properties of these materials is fraught with difficulty. The problems may diminish if single crystals become available, but they are unlikely to disappear altogether.

ACKNOWLEDGMENTS

This research is supported by EPSRC and the Donors of the Petroleum Research Fund, administered by the American Chemical Society.

- ¹A. Urushibara, Y. Moritomo, T. Arima, A. Asamitsu, G. Kido, and Y. Tokura, *Phys. Rev. B* **51**, 14 103 (1995).
- ²C. N. R. Rao, A. K. Cheetham, and R. Mahesh, *Chem. Mater.* **8**, 2421 (1996).
- ³S. N. Ruddlesden and P. Popper, *Acta Crystallogr.* **11**, 541 (1958).
- ⁴W. Bao, C. H. Chen, S. A. Carter, and S.-W. Cheong, *Solid State Commun.* **98**, 55 (1996).
- ⁵J. C. Bouloux, J. L. Soubeyroux, A. Daoudi, and G. L. Flem, *Mater. Res. Bull.* **16**, 855 (1981).
- ⁶Y. Moritomo, Y. Tomioka, A. Asamitsu, and Y. Tokura, *Phys. Rev. B* **51**, 3297 (1995).
- ⁷B. J. Sternlieb, J. P. Hill, U. C. Wildgruber, G. M. Luke, B. Nachumi, Y. Moritomo, and Y. Tokura, *Phys. Rev. Lett.* **76**, 2169 (1996).
- ⁸Y. Moritomo, A. Asamitsu, H. Kuwahara, and Y. Tokura, *Nature (London)* **380**, 141 (1996).
- ⁹P. D. Battle, S. J. Blundell, M. A. Green, W. Hayes, M. Honold, A. K. Klehe, N. S. Laskey, J. E. Millburn, L. Murphy, M. J. Rosseinsky, N. A. Samarin, J. Singleton, N. A. Sluchanko, S. P. Sullivan, and J. F. Vente, *J. Phys.: Condens. Matter* **8**, L427 (1996).
- ¹⁰R. Seshadri, C. Martin, A. Maignan, M. Hervieu, B. Raveau, and C. N. R. Rao, *J. Mater. Chem.* **6**, 1585 (1996).
- ¹¹P. D. Battle, S. J. Blundell, D. E. Cox, M. A. Green, J. E. Millburn, P. G. Radaelli, M. J. Rosseinsky, J. Singleton, L. E. Spring, and J. F. Vente, *Mater. Res. Soc. Symp. Proc.* **453**, 331 (1997).
- ¹²P. D. Battle, M. A. Green, N. S. Laskey, J. E. Millburn, P. G. Radaelli, M. J. Rosseinsky, S. P. Sullivan, and J. F. Vente, *Phys. Rev. B* **54**, 15 967 (1996).
- ¹³P. D. Battle, J. Hepburn, J. E. Millburn, P. G. Radaelli, M. J. Rosseinsky, L. E. Spring, and J. F. Vente, *Chem. Mater.* **9**, 3215 (1997).
- ¹⁴P. D. Battle, D. E. Cox, M. A. Green, J. E. Millburn, L. E. Spring, P. G. Radaelli, M. J. Rosseinsky, and J. F. Vente, *Chem. Mater.* **9**, 1042 (1997).
- ¹⁵J. F. Mitchell, D. N. Argyriou, J. D. Jorgensen, D. G. Hinks, C. P. Potter, and S. D. Bader, *Phys. Rev. B* **55**, 63 (1997).
- ¹⁶P. D. Battle, M. A. Green, N. S. Laskey, N. Kasmir, J. E. Millburn, L. E. Spring, S. P. Sullivan, M. J. Rosseinsky, and J. F. Vente, *J. Mater. Chem.* **7**, 977 (1997).
- ¹⁷P. D. Battle, J. E. Millburn, M. J. Rosseinsky, L. E. Spring, and J. F. Vente, and P. G. Radaelli, *Chem. Mater.* **9**, 3136 (1997).
- ¹⁸A. C. Larson and R. B. von-Dreele, *General Structure Analysis System (GSAS)*, 1990, Los Alamos National Laboratories (unpublished).
- ¹⁹H. M. Rietveld, *J. Appl. Crystallogr.* **2**, 65 (1969).
- ²⁰M. Eremets, *High Pressure Experimental Methods* (Oxford University Press, Oxford, 1996).
- ²¹D. L. Decker, W. A. Bassett, L. Merrill, H. T. Hall, and J. D. Barnet, *J. Phys. Chem. Ref. Data* **1**, 773 (1972).
- ²²J. J. Neumeier, M. F. Hundley, J. D. Thompson, and R. H. Heffner, *Phys. Rev. B* **52**, 7006 (1995).
- ²³K. Khazeni, Y. X. Jia, L. Lu, V. H. Crespi, M. L. Cohen, and A. Zettl, *Phys. Rev. Lett.* **76**, 295 (1996).
- ²⁴P. D. Battle, M. A. Green, N. S. Laskey, J. E. Millburn, L. Murphy, M. J. Rosseinsky, S. P. Sullivan, and J. F. Vente, *Chem. Mater.* **9**, 552 (1997).
- ²⁵F. Damay, N. Nguyen, A. Maignan, M. Hervieu, and B. Raveau, *Solid State Commun.* **98**, 997 (1996).
- ²⁶P. Laffez, G. VanTendloo, R. Seshadri, M. Hervieu, C. Martin, A. Maignan, and B. Raveau, *J. Appl. Phys.* **80**, 5850 (1996).

Role of intergrowths in the properties of naturally layered manganite single crystals (invited)

S. D. Bader,^{a)} R. M. Osgood III, D. J. Miller, J. F. Mitchell, and J. S. Jiang
Materials Science Division, Argonne National Laboratory, Argonne, Illinois 60439

Two-layered Ruddlesden–Popper phase $\text{SrO}(\text{La}_{1-x}\text{Sr}_x\text{MnO}_3)_2$, with $x=0.3$ and 0.4 , exhibits colossal magnetoresistance, a magnetic anisotropy which is strongly composition-dependent, very little remanence, and an anomalous low-field magnetization (M) plateau between the Curie temperature (T_C) and $T^* \sim 300$ K. The resistivity peaks near T_C for both in-plane and out-of-plane currents. The magnetization plateau is not intrinsic to the crystal, but is attributed to intergrowth defects, consisting of one additional or missing SrO blocking layers, as observed in transmission electron micrographs. The intergrowths exhibit interesting two-dimensional magnetic behavior, for both the $x=0.3$ and 0.4 compositions. For $x=0.4$, M scales as $(1-T/T^*)^\beta$, with $\beta=0.25 \pm 0.02$. For $x=0.3$, the intergrowths exhibit an easy axis in the a - b plane due to the shape anisotropy, while for $T < T_C$, M lies along the c axis. © 1998 American Institute of Physics. [S0021-8979(98)43311-5]

I. INTRODUCTION

Manganites, based on the perovskite structure type, are a fascinating class of materials, exhibiting both the colossal magnetoresistance (CMR) phenomenon¹ and a host of interesting magnetic properties.^{2,3} Recently, Moritomo *et al.* fabricated these materials in the two-layered form;² i.e., the $n=2$ variant of the Ruddlesden–Popper series $(\text{La}, \text{Sr})_{n+1}\text{Mn}_n\text{O}_{3n+1}$, and there have been a number of subsequent investigations of this material.^{3–9} Figure 1 illustrates the $n=1, 2, \infty$ members of this family. The unit cell may be written: $\text{SrO}(\text{La}_{1-x}\text{Sr}_x\text{MnO}_3)_2$, where it is clear that two MnO_6 octahedra are separated from one another by an insulating layer of SrO . The structure is tetragonal, with the a - b plane parallel to the layers of MnO_6 and the c axis perpendicular.³ The $n=2$ variant of this family was found to have a $\sim 20\,000\%$ CMR at 129 K with $H=7$ T, while at low fields (0.3 T), a CMR of $\sim 200\%$ was found (at 129 K).² These materials (including the $n=\infty$ variety) exhibit a competition between antiferromagnetism due to superexchange, and ferromagnetism due to double exchange. For $x=0$, the material is antiferromagnetic, while in the region $x \approx 0.2$ – 0.4 , the materials are ferromagnetic and exhibit a metal–insulator transition at T_C . T_C moves appreciably in an external field H , which in turn shifts and broadens the metal–insulator transition and causes CMR. An external field is thought to align the Mn sites and therefore allow the electron (via the double exchange mechanism) to delocalize and “hop” between the Mn sites.

As in the cuprate superconductors,¹⁰ not all of the interesting physics for the manganites is confined in the temperature region $T < T_C$. Several studies have reported short-range magnetic order for $T > T_C$ in these layered materials (both $x=0.3$ and 0.4).^{3,4,11,12} One naturally asks the question: “to what extent is this magnetic order intrinsic to the layered structure of the material?” We find that the CMR occurs at low fields at $T=T_C$ for the current both in the a - b plane and

along the c axis. The high temperature magnetization is, however, interesting in its own right; it is attributed to intergrowth defects extrinsic to the crystal, which exhibits novel, two-dimensional magnetic behavior.

II. EXPERIMENT

Crystals of $\text{La}_{2-2x}\text{Sr}_{1+2x}\text{Mn}_2\text{O}_7$ ($x=0.3, 0.4$) were grown from polycrystalline rods of the same nominal composition using the traveling-floating-zone technique in an optical image furnace (NEC model SC-M15HD). The precursor rods were prepared by solid-state synthesis from high purity ($>99.99\%$) starting materials: La_2O_3 (prefired in flowing O_2 at 1000°C for 12 h), MnO_2 , and SrCO_3 . After several firings at 1000 – 1350°C , the powders were isostatically pressed into rods suitable for zone melting. The growth atmosphere was 20% O_2 for $x=0.3$ and 0.4 . In each case, the crystals grew with the c axis normal to the zone travel direction. The resulting highly textured polycrystalline boules can be cleaved readily to yield shiny black crystals of layered manganite. Typical dimensions of the cleaved crystals are $2 \times 2 \times 0.1$ mm³. Back-reflection x-ray Laue photographs establish that in all cases the cleaved crystals have the c axis oriented normal to the thin plates. Magnetization and suscep-

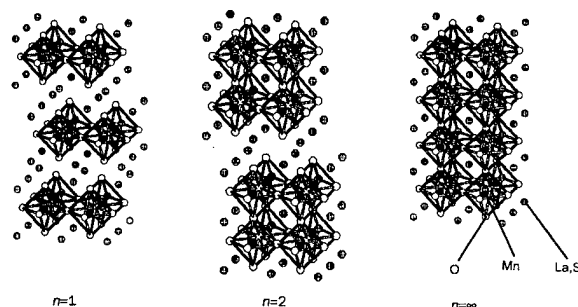


FIG. 1. Diagram of the structure $\text{SrO}(\text{La}_{1-x}\text{Sr}_x\text{MnO}_3)_2$, reproduced from Ref. 2. The variable n refers to the number of MnO_6 octahedra layers in the bilayer. The shaded atoms are the La, Sr cations, the white atoms are O, and the black atom in the center of the O_6 octahedron is the Mn atom.

^{a)}Electronic mail: bader@anl.gov

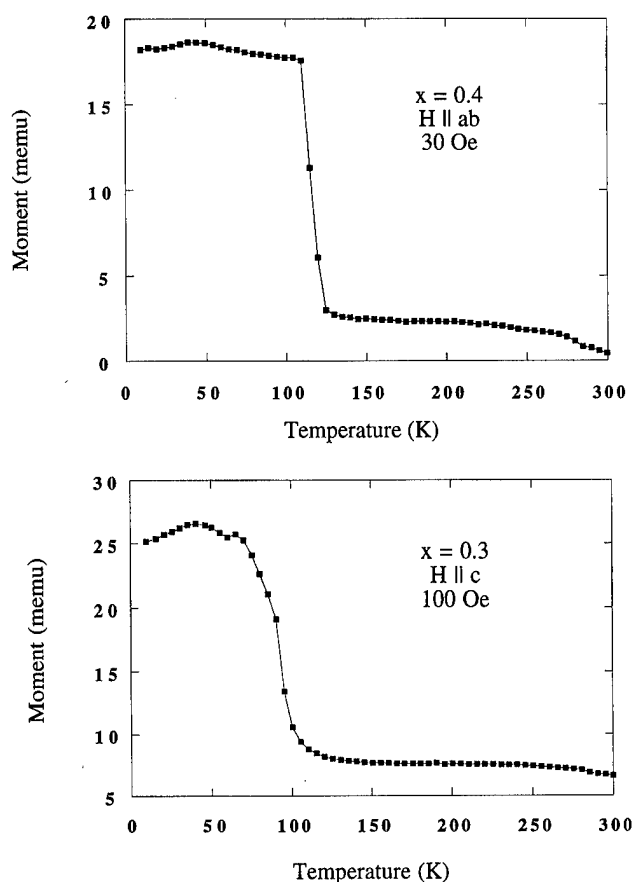


FIG. 2. Magnetic moment vs temperature for (a) $x=0.4$ ($H=30$ Oe $\parallel ab$); (b) $x=0.3$ ($H=50$ Oe $\parallel c$).

tibility (χ) measurements were made on both a superconducting-quantum interference device (SQUID) and an extraction magnetometer from Quantum Design, equipped with a 7 and 9 T superconducting solenoid, respectively. The trapped flux in the solenoid (~ 10 Oe) was monitored, so that the field values given are correct to within ± 0.5 Oe. Measurements were made with the applied field both parallel to the a - b plane ($H \parallel ab$) and parallel to the c axis ($H \parallel c$). Resistivity measurements were made on thin platelets obtained by crushing the boule; leads were connected by attaching Cu wires to sputtered Au contacts. Another platelet from the same boule was ion-milled and used for transmission electron microscope (TEM) measurements.

III. MAGNETIZATION AND TRANSPORT

Figure 2(a) displays M vs T ($H=30$ Oe $\parallel ab$) for $x=0.4$; Figure 2(b) illustrates M vs T ($H=100$ Oe $\parallel ab$) for $x=0.3$. For both compositions, there are two plateaux below the two transitions. The lower transition is T_C (~ 94 K for $x=0.3$ and 116 K for $x=0.4$); the upper transition is at $T=T^* \sim 300$ K. In Fig. 2b, T^* is not as visible for the $x=0.3$ sample as it is for $x=0.4$ because of the higher field employed for this measurement (100 Oe), which tends to smear out the transition. A measurement of M vs T with $H=15$ Oe near T^* is displayed in Fig. 3. Measurements of M vs H below T_C yield a ferromagnetic hysteresis loop, albeit one with virtually no remanence [see Fig. 4(a) for $H \parallel ab$ and

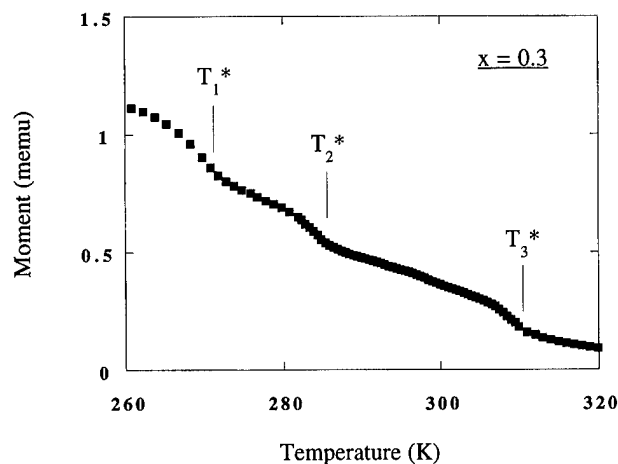


FIG. 3. Magnetic moment vs temperature for $x=0.3$ ($H=15$ Oe $\parallel ab$, $T \approx T^*$). Three transitions are identified.

$H \parallel c$ in $x=0.4$; see Fig. 4(b) for $H \parallel ab$ and $H \parallel c$ in $x=0.3$, all at 5 K]. The easy axis, determined by the saturation field, lies in the a - b plane for $x=0.4$ and along c for $x=0.3$, in agreement with Ref. 3. Measurements of M vs H for $T_C < T < T^*$ yield a small ferromagnetic loop superimposed on a

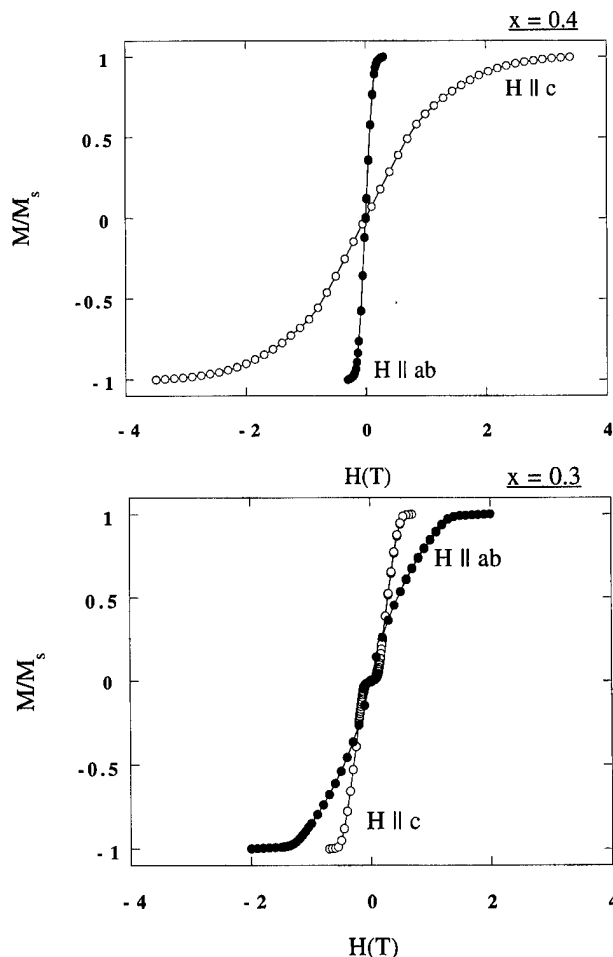


FIG. 4. Magnetization (normalized to the saturation magnetization M_s) vs H for (a) $x=0.4$, (b) $x=0.3$ ($H \parallel ab$: filled symbols, $H \parallel c$: clear symbols, $T=5$ K for both compositions). Measurements were made sweeping H from negative to positive values and back to $M=0$.

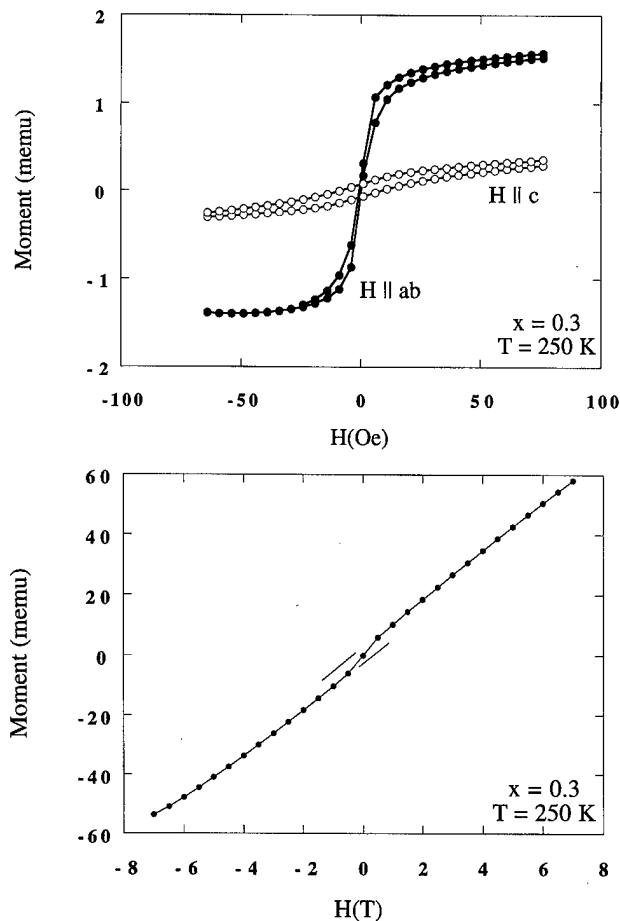


FIG. 5. (a) Magnetic moment vs applied field (H) at 250 K for $H||ab$ (filled symbols) and $H||c$ (clear symbols). Both measurements are superimposed on a linear paramagnetic background from the intrinsic portion of the crystal, which is displayed in (b) for $H||ab$. Two lines in (b) indicate the kink near $H=0$ which is due to the ferromagnetic response of the extrinsic material. All measurements in this figure are from the same sample.

paramagnetic background, in agreement with neutron diffraction experiments, which have been able to sense moments only for $T < T_C$.⁵ The high-temperature paramagnetism therefore must represent short range order. Figure 5(a) displays M vs $H||ab$ and M vs $H||c$ in $x=0.3$, while Fig. 5(b) displays the M vs $H||ab$ data on a larger scale; the ferromagnetic part of the signal manifests itself here as a kink near $H=0$. These measurements are all from the same sample. Note the scales on Figs. 5(a) and 5(b); the ferromagnetic signal is masked by the paramagnetic signal from the intrinsic material.

Associated with the T_C illustrated in Fig. 2 for $x=0.3$ are peaks in the resistivity ρ and in the CMR, displayed in Fig. 6 for two different directions of the current j . There was a slight difference in $T_C \approx 90$ K between the two separate samples measured in Fig. 6; this difference has been normalized out. Note that the resistance was much higher along the c axis, in agreement with Ref. 3. Note that peaks for both ρ_{ab} and ρ_c at $H=0$ are at $T \approx T_C$. The authors of Ref. 3 observed a large peak in ρ_{ab} , the resistivity measured in the $a-b$ plane, for $T > T_C$. This was considered a sign of ferromagnetic correlations within the MnO_6 planes and lack of correlation between the planes. Below T_C , where M lies

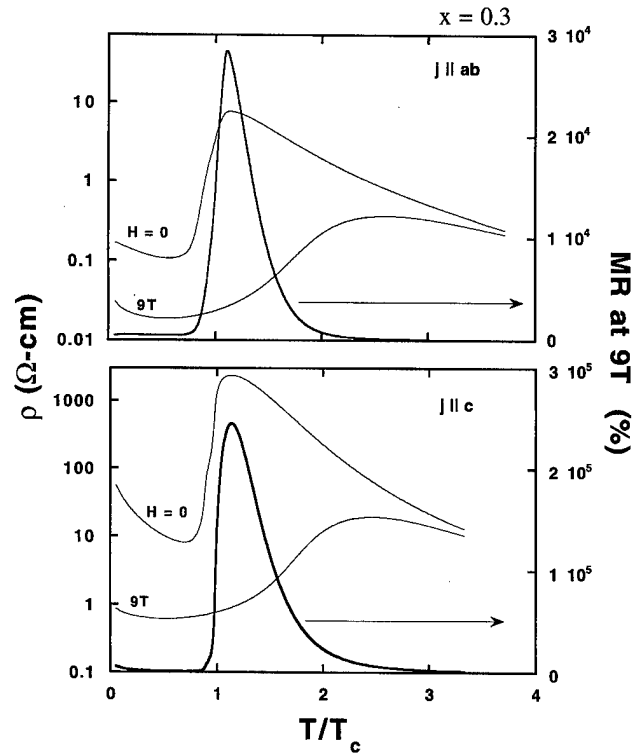


FIG. 6. Measurement of resistivity vs applied field for (a) $j||ab$ and (b) $j||c$ for the $x=0.3$ composition. Measurements were made on separate samples, both of whom had $T_C \approx 90$ K; the minor difference between the T_C 's has been normalized out.

only along c , Kimura *et al.* rationalized the drop in ρ_{ab} they observed as being due to the disappearance of spin disorder in the $a-b$ plane.³ We did not observe such a peak in ρ_{ab} for $T > T_C$ for $x=0.3$. We conclude that the high-temperature magnetism is an extrinsic phenomenon, due to an intergrowth phase, which was presumably also present in the similarly prepared samples used in Ref. 3.

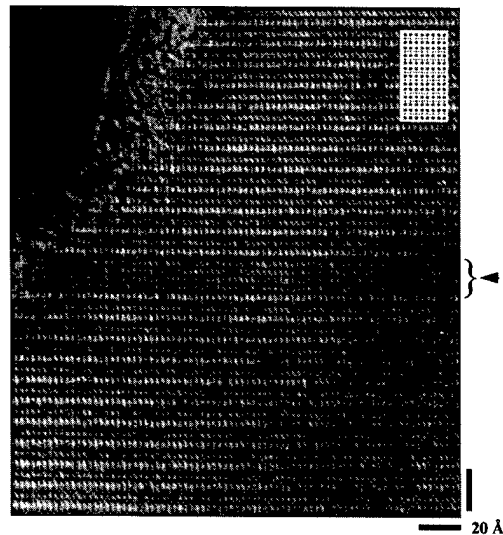


FIG. 7. High-resolution TEM micrograph showing one intergrowth (marked with a pointer) with $n=5$ for the $x=0.4$ composition.

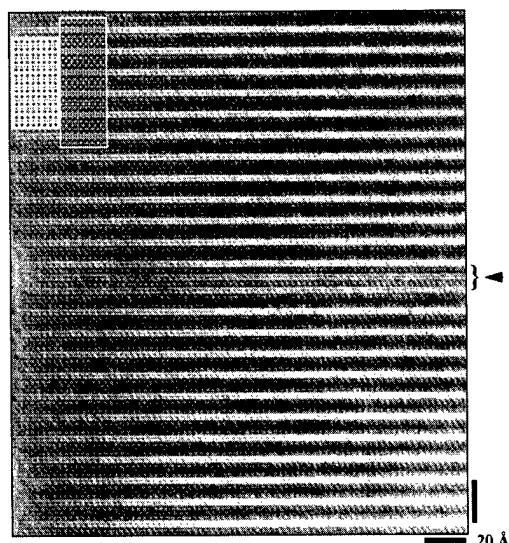


FIG. 8. High-resolution TEM micrograph showing two intergrowths (marked with a pointer) with $n=1$ for the $x=0.4$ composition.

IV. INTERGROWTHS

Seshadri *et al.* have demonstrated the presence of intergrowths in these materials, using TEM.⁷ Intergrowths can be due to missing or extra layers of SrO atoms between the MnO_6 octahedra. Such defects represent $n \neq 2$ variants of the Ruddlesden–Popper series. Figures 7 and 8 display high-resolution TEM images from samples with $x=0.4$. The insulating double SrO layer is the white band. In Fig. 7, the regular series of white bands is interrupted by a $n=5$ intergrowth; in Fig. 8, an extra white band divides two $n=1$ intergrowths. Such intergrowths are also observed in the $x=0.3$ samples (see Fig. 9). An estimate of the intergrowth volume fraction can be made by dividing the height of the hysteresis loop measured at 250 K by the saturation magnetic moment (measured with H large enough to saturate M at $T < T_C$). We obtain a volume fraction of $\sim 0.1\%$ intergrowths in the $x=0.4$ samples and $\sim 0.6\%$ intergrowths in the x

$=0.3$ samples, although there was a variation of $\pm 0.3\%$ among samples with $x=0.3$ (four with this composition were measured).

Potter *et al.*⁴ have given evidence that the magnetism of the intergrowths is two dimensional. For $T \approx T^*$, M scales as $(1 - T/T^*)^\beta$, where $\beta = 0.25 \pm 0.02$ for the $x=0.4$ composition, which is reminiscent of two-dimensional (2D) behavior. For the $x=0.3$ composition, three transitions in the M vs T data are observed, as displayed in Fig. 3, indicating the presence of three different distributions of intergrowths. It was therefore not possible to obtain an exponent for $x=0.3$.

Another experimental observation that strongly supports the influence of the intergrowths above T_C is the fact that hysteresis loops measured with the field along the c axis are much harder than those measured with the field in the a - b plane [see Fig. 5(a)]. This is consistent with the picture of two-dimensional intergrowths running parallel to the a - b plane. Such inclusions are magnetically hard along the c axis, due to shape anisotropy, in contrast with the easy axis anisotropy along the c axis observed below T_C for the intrinsic material. Were the magnetic signal above T_C to be due to intralayer correlations only (the model proposed in Ref. 3), there would not necessarily be an anisotropy in the magnetization loops.

V. CONCLUSIONS

The two-layered Ruddlesden–Popper phase $\text{SrO}(\text{La}_{1-x}\text{Sr}_x\text{MnO}_3)_2$, with $x=0.3$ and 0.4 , exhibits CMR at T_C at low H and a magnetic anisotropy which is strongly composition-dependent. The magnetic order observed for $T > T_C$ includes not only the short-range order response of the intrinsic material, but a minor ferromagnetic signal evident at low fields due to intergrowths. These intergrowths are clearly visible in TEM images and exhibit novel two-dimensional magnetism. The intergrowths are magnetically hard along the c axis in the $x=0.3$ material, despite the fact that the c axis is easy for this composition. We find that the $x=0.3$ and

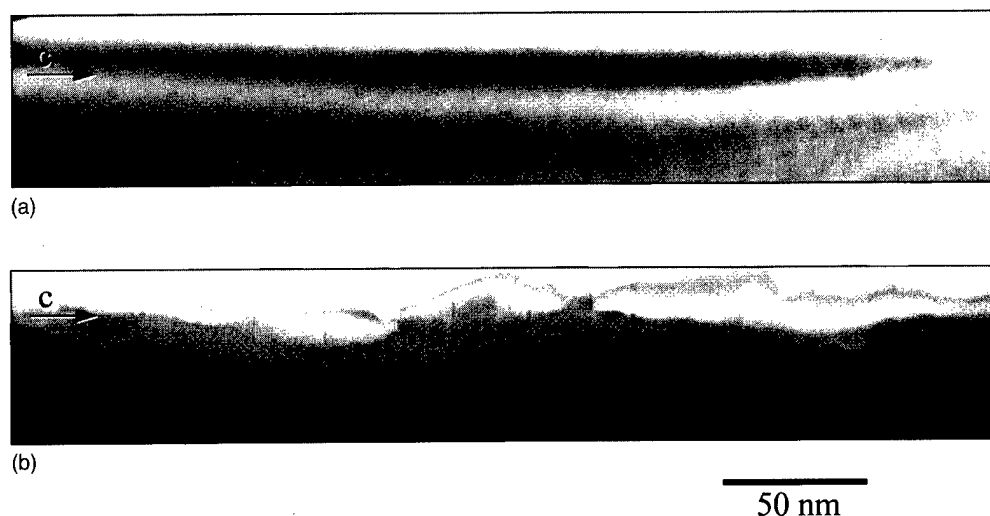


FIG. 9. Bright-field micrograph of the $x=0.3$ composition showing (a) perfect crystal, (b) crystal with intergrowths. In (b) the intergrowths are visible as vertical streaks in the photograph running parallel to the a - b plane.

0.4 compositions differ strongly only in the magnetic anisotropy of the intrinsic material, not in the temperature dependence of the resistivity or magnetization.

- ¹R. van Helmolt, J. Wecker, B. Holzapfel, L. Schultz, and K. Samwer, *Phys. Rev. Lett.* **71**, 2331 (1993).
- ²Y. Moritomo, A. Asamitsu, H. Kuwahara, and Y. Tokura, *Nature (London)* **380**, 141 (1996).
- ³T. Kimura, Y. Tomioka, H. Kuwahara, A. Asamitsu, M. Tamura, and Y. Tokura, *Science* **274**, 1698 (1996).
- ⁴C. D. Potter, M. Swiatek, S. D. Bader, D. N. Argyriou, J. F. Mitchell, D. J. Miller, D. G. Hinks, and J. D. Jorgensen, *Phys. Rev. B* (in press).
- ⁵J. F. Mitchell, D. N. Argyriou, J. D. Jorgensen, D. G. Hinks, C. D. Potter, and S. D. Bader, *Phys. Rev. B* **55**, 63 (1997).
- ⁶D. N. Argyriou, J. F. Mitchell, J. B. Goodenough, O. Chmaissem, S. Short, and J. D. Jorgensen, *Phys. Rev. Lett.* **78**, 1568 (1997).
- ⁷R. Seshadri, M. Hervieu, C. Martin, A. Maignan, B. Domenges, B. Raveau, and A. N. Fitch, *Chem. Mater.* **9**, 1778 (1997).
- ⁸P. D. Battle, M. A. Green, N. S. Laskey, J. E. Millburn, P. G. Radaelli, M. J. Rosseinsky, S. P. Sullivan, and J. F. Vente, *Phys. Rev. B* **54**, 15967 (1996).
- ⁹P. Laffez, G. Van Tendeloo, R. Seshadri, M. Hervieu, C. Martin, A. Maignan, and B. Raveau, *J. Appl. Phys.* **80**, 5850 (1996).
- ¹⁰H. Ding, T. Yokoya, J. C. Campuzano, T. Takahashi, M. Randeria, M. R. Norman, T. Mochiku, K. Hadowaki, and J. Giapintzakis, *Nature (London)* **382**, 51 (1996).
- ¹¹T. G. Perring, G. Aeppli, Y. Moritomo, and Y. Tokura, *Phys. Rev. Lett.* **78**, 3197 (1997).
- ¹²J. B. MacChesney, J. F. Potter, and R. C. Sherwood, *J. Appl. Phys.* **40**, 1243 (1969).

The development of high performance Nd-Fe-Co-Ga-B die upset magnets

T. Saito^{a)}

Department of Metallurgical Engineering, Chiba Institute of Technology, 2-17-1 Tsudanuma, Narashino, Chiba 275, Japan

M. Fujita and T. Kuji

Corporate R&D Center, Mitsui Mining and Smelting Co. Ltd., 1333-2 Haraichi, Ageo, Saitama 362, Japan

K. Fukuoka and Y. Syono

Institute for Materials Research, Tohoku University, Katahira, Sendai 980, Japan

The magnetic properties and the microstructure of Nd-Fe-B and Nd-Fe-Co-Ga-B die upset magnets produced from amorphous materials were studied. The Nd-Fe-B die upset magnets had fine polygonal Nd₂Fe₁₄B grains and showed magnetic anisotropy. The compositional modification and optimization of the die upset condition led to the increase in the remanence and coercivity values of the Nd-Fe-B die upset magnets. The optimally deformed Nd-Fe-Co-Ga-B die upset magnets showed the maximum energy product of 54.4 MGOe. © 1998 American Institute of Physics. [S0021-8979(98)15011-9]

INTRODUCTION

The maximum energy products of Nd-Fe-B magnets, which are usually produced by sintering and melt-spinning,^{1,2} are dependent on the degree of the crystallographic alignment of the Nd₂Fe₁₄B phase. In the sintered magnets, alignment of the Nd₂Fe₁₄B phase is achieved by the prior green compaction of the crushed ingot powders in an applied magnetic field.¹ Nd-Pr-Dy-Fe-B sintered magnets with the highest maximum energy product of 54.2 MGOe have been reported.³ On the other hand, alignment of the Nd₂Fe₁₄B phase is achieved by die upsetting in the melt-spinning approach.⁴ Amorphous melt-spun ribbons are comminuted and then are consolidated into bulk form by hot pressing before die upsetting. Although as-hot-pressed magnets have randomly oriented Nd₂Fe₁₄B grains, subsequent die upsetting gives rise to the crystallographic alignment of the Nd₂Fe₁₄B phase.^{5,6} Even though the die upset magnets have some advantages such as the finer Nd₂Fe₁₄B grains and lower oxygen content than the sintered counterparts, the maximum energy product of the die upset magnets are not yet comparable to those of the sintered counterparts. The optimization of the processing will lead to further improvement of the crystallographic alignment of the Nd₂Fe₁₄B phase in the die upset magnets, thereby enhancing the maximum energy product.

In the die upset magnets, the inhomogeneity of the as-hot-pressed magnets deteriorates the crystallographic alignment of the Nd₂Fe₁₄B phase during the die upsetting.⁷ It has been reported that the Nd-Fe-B die upset magnets produced from the amorphous materials with the homogeneous micro-

structure exhibit the higher maximum energy products than those produced from the as-hot-pressed magnets.⁸ In this study, we are trying to improve the maximum energy products of the die upset magnets produced from the amorphous materials by optimizing the composition and the processing conditions. The magnetic properties and the crystallographic alignment of the die upset magnets produced from the amorphous materials are compared to those of the die upset magnets produced from the as-hot-pressed magnets.

EXPERIMENT

Nd_{13.5}Fe_{80.5}B₆, Nd_{13.5}(Fe_{0.975}Co_{0.025})_{80.5}B₆, and Nd_{13.5}(Fe_{0.975}Co_{0.025})₈₀Ga_{0.5}B₆ alloy ingots were melt-spun in argon onto a copper substrate rotating at a surface velocity of 52 m s⁻¹. The melt-spun ribbons were comminuted and filled into a steel container. The powders were dynamically compacted at a shock pressure of 21 GPa by the impact of a flyer launched by a 25 mm propellant gun. The propellant gun facilities and process have been described in detail elsewhere.⁹ The consolidated powders were taken out from the container by lathing. Typical dimensions of the bulk materials were 20 mm thick and 25 mm in diameter. For comparison, the melt-spun ribbons were consolidated into bulk form by hot pressing. The bulk materials and the as-hot-pressed materials were deformed by die upsetting at a reduction rate of about 5 × 10⁻² mm s⁻¹. The thicknesses of the specimens were successfully reduced from 20 to 4 mm at temperatures between 963 and 1073 K in an argon atmosphere.

The specimens were examined by x-ray diffraction (XRD) using Cu K_α radiation. The microstructures of the specimens were examined under a transmission electron mi-

^{a)}Electronic mail: tetsuji@cc.it-chiba.ac.jp

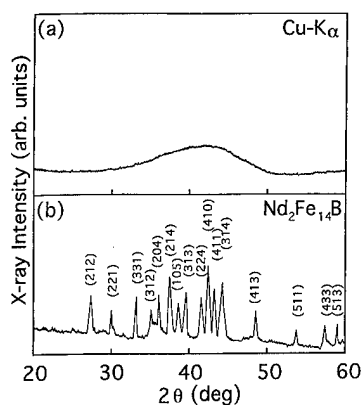


FIG. 1. XRD patterns of (a) bulk materials of $\text{Nd}_{13.5}\text{Fe}_{80.5}\text{B}_6$ alloy and (b) those die upset at 1023 K.

croscope (TEM). In the die upset specimen, the cross-sectional microstructures parallel to the die upset direction were investigated. The magnetic properties of the specimens were determined by a recording fluxmeter with a maximum applied field of 25 kOe after premagnetization in a field of 150 kOe.

RESULTS AND DISCUSSION

Figure 1 shows the XRD patterns of the bulk materials of the $\text{Nd}_{13.5}\text{Fe}_{80.5}\text{B}_6$ alloy and those die upset at 1023 K. The XRD pattern of the bulk materials shows only a fairly broad peak at around 40° , which is a characteristic of an amorphous structure. This indicates that the bulk material produced from the melt-spun ribbons maintains the amorphous state. On the other hand, the XRD pattern of the die upset specimen is well indexed according to the tetragonal $\text{Nd}_2\text{Fe}_{14}\text{B}$ phase. This suggests that the heat exposure during the die upsetting of the amorphous bulk materials results in the crystallization of the $\text{Nd}_2\text{Fe}_{14}\text{B}$ phase as is the case for the die upsetting of the as-hot-pressed magnets.^{4,6}

Figure 2 shows the TEM micrographs of the bulk materials of the $\text{Nd}_{13.5}\text{Fe}_{80.5}\text{B}_6$ alloy and those die upset at 1023 K. The microstructure of the bulk material is featureless, and the corresponding selected area diffraction (SAD) pattern of the specimen shows a diffuse halo. This suggests that the bulk material consists of the amorphous phase. In the die upset specimen, the polygonal crystallites with an average

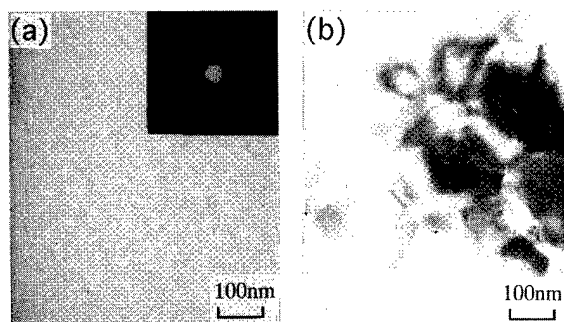


FIG. 2. TEM micrographs of (a) bulk materials of $\text{Nd}_{13.5}\text{Fe}_{80.5}\text{B}_6$ alloy and (b) those die upset at 1023 K.

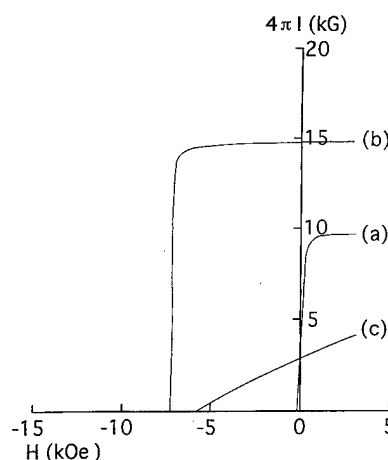


FIG. 3. Demagnetization curves of (a) bulk materials of $\text{Nd}_{13.5}\text{Fe}_{80.5}\text{B}_6$ alloy and those die upset at 1023 K. The die upset specimens were measured in the (b) parallel and (c) normal to the die upset direction.

diameter of about $0.1 \mu\text{m}$ are seen in the microstructure. This indicates that the die upset magnets produced from the amorphous bulk materials consists of fine $\text{Nd}_2\text{Fe}_{14}\text{B}$ grains with the polygonal shape.

Figure 3 shows the demagnetization curves of the bulk materials of the $\text{Nd}_{13.5}\text{Fe}_{80.5}\text{B}_6$ alloy and those die upset at 1023 K. The coercivity of the bulk material remains as low as that of amorphous melt-spun ribbons. The die upset specimen shows the high coercivity value. This is due to the fine $\text{Nd}_2\text{Fe}_{14}\text{B}$ grains of the die upset magnets. The anisotropy of the die upset magnets is characterized by the significantly higher remanence in the parallel direction than in the normal direction. The $\text{Nd}_{13.5}\text{Fe}_{80.5}\text{B}_6$ die upset magnets show a maximum energy product of 47.7 MGOe with an intrinsic coercivity of 7.3 kOe. The increase in the coercivity value of $\text{Nd}_{13.5}\text{Fe}_{80.5}\text{B}_6$ die upset magnets would give the magnets with the excellent high maximum energy products.

Figure 4 shows the dependence of the maximum energy product of the die upset magnets on the die upset temperature. The substitution of Co or Ga for Fe of the $\text{Nd}_{13.5}\text{Fe}_{80.5}\text{B}_6$ alloy results in the increase of the optimal die upset temperature to obtain the high maximum energy prod-

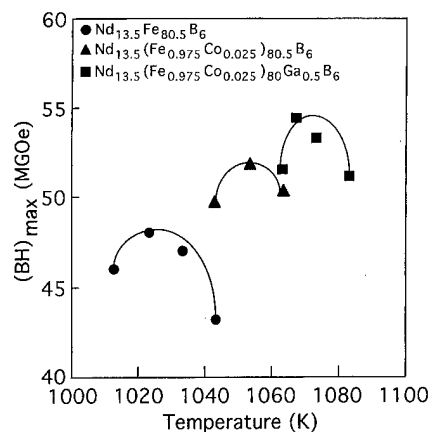


FIG. 4. Dependence of the maximum energy product, $(BH)_{\text{max}}$, of the die upset magnets on the die upset temperature.

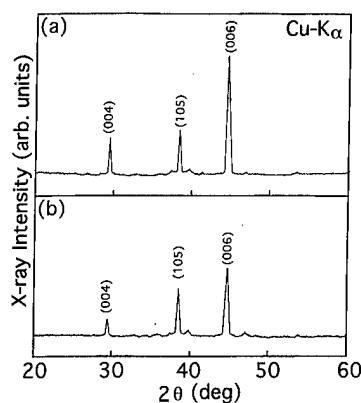


FIG. 5. XRD patterns of $\text{Nd}_{13.5}(\text{Fe}_{0.975}\text{Co}_{0.025})_{80}\text{Ga}_{0.5}\text{B}_6$ die upset magnets produced from (a) amorphous bulk materials and (b) as-hot-pressed magnets.

ucts. The TEM studies revealed that the resultant die upset magnets consisted of the polygonal $\text{Nd}_2\text{Fe}_{14}\text{B}$ grains as fine as the $\text{Nd}_{13.5}\text{Fe}_{80.5}\text{B}_6$ die upset magnets. The substitution of Co or Ga for Fe of the $\text{Nd}_{13.5}\text{Fe}_{80.5}\text{B}_6$ die upset magnets led to the improvement of the coercivity and the maximum energy products of the Nd-Fe-B die upset magnets as is the case for the die upset magnets produced from the as-hot-pressed magnets.⁶ The resultant $\text{Nd}_{13.5}(\text{Fe}_{0.975}\text{Co}_{0.025})_{80}\text{Ga}_{0.5}\text{B}_6$ die upset magnets exhibit a maximum energy product of 54.4 MGOe with an intrinsic coercivity of 12.5 kOe.

The XRD patterns of the $\text{Nd}_{13.5}(\text{Fe}_{0.975}\text{Co}_{0.025})_{80}\text{Ga}_{0.5}\text{B}_6$ die upset magnets produced from the amorphous bulk materials and the as-hot-pressed magnets are shown in Fig. 5. The polished surfaces of the die upset specimens were examined. Even though both XRD patterns show the pronounced *c*-axis alignment of the $\text{Nd}_2\text{Fe}_{14}\text{B}$ phase, which is characterized by the prominent (004) and (006) peaks, the die upset magnets produced from the amorphous bulk materials have the higher ratio of the (006) to (105) peaks than those produced from the as-hot-pressed magnets. This indicates that the die upset magnets produced from the amorphous bulk materials have the higher crystallographic alignment of the $\text{Nd}_2\text{Fe}_{14}\text{B}$ phase than those produced from the as-hot-pressed magnets, which are characterized with the platelike $\text{Nd}_2\text{Fe}_{14}\text{B}$ grains.⁵

The demagnetization curves of these die upset magnets are shown in Fig. 6. The $\text{Nd}_{13.5}(\text{Fe}_{0.975}\text{Co}_{0.025})_{80}\text{Ga}_{0.5}\text{B}_6$ die upset magnets produced from the as-hot-pressed magnets show a maximum energy product of 50.2 MGOe with an intrinsic coercivity of 13.2 kOe. This value is almost comparable to that of the best die upset magnets.¹⁰ The observed higher remanence value of the die upset magnets produced

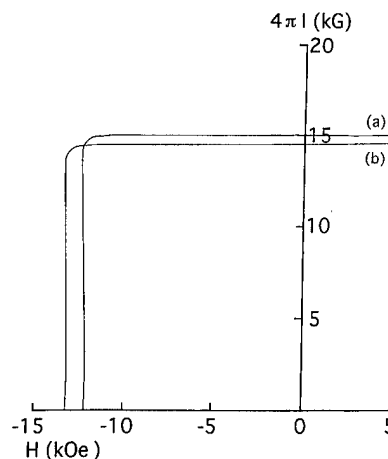


FIG. 6. Demagnetization curves of $\text{Nd}_{13.5}(\text{Fe}_{0.975}\text{Co}_{0.025})_{80}\text{Ga}_{0.5}\text{B}_6$ die upset magnets produced from (a) amorphous bulk materials and (b) as-hot-pressed magnets.

from the amorphous bulk materials is due to the higher crystallographic alignment of the polygonal $\text{Nd}_2\text{Fe}_{14}\text{B}$ grains. The detailed TEM studies revealed that the die upset magnets produced from the as-hot-pressed magnets contained similar polygonal $\text{Nd}_2\text{Fe}_{14}\text{B}$ grains together with the typical platelet shaped grains.¹¹ Therefore, the further optimization of the hot pressing and die upsetting conditions would lead to an increase in the maximum energy product of the die upset magnets produced from the as-hot-pressed magnets.

ACKNOWLEDGMENTS

This work was performed under the Research and Development Program on "Advanced Chemical Processing Technology," conducted under a program set by New Energy and Industrial Technology Development Organization.

- ¹M. Sagawa, S. Fujimura, N. Togawa, H. Yamamoto, and Y. Matsuura, *J. Appl. Phys.* **55**, 2083 (1984).
- ²J. J. Croat, J. F. Herbst, R. W. Lee, and F. E. Pinkerton, *J. Appl. Phys.* **55**, 2078 (1984).
- ³K. Kaneko, K. Tokuhara, and N. Ishigaki, *J. J. Soc. Powder Powder Metallurgy* **41**, 695 (1994).
- ⁴R. W. Lee, E. G. Brewer, and N. A. Schaffel, *IEEE Trans. Magn.* **MAG-21**, 1958 (1985).
- ⁵R. K. Mishra, E. G. Brewer, and R. W. Lee, *J. Appl. Phys.* **63**, 3528 (1988).
- ⁶C. D. Fuerst and E. G. Brewer, *J. Appl. Phys.* **73**, 5751 (1993).
- ⁷Y. Nozawa, S. Tanigawa, and M. Tokunaga, *IEEE Trans. Magn.* **MAG-26**, 1724 (1990).
- ⁸T. Harada, M. Fujita, and T. Kuji, *J. Alloys Compd.* **243**, 139 (1996).
- ⁹T. Harada, T. Kuji, K. Fukuoka, and Y. Syono, *J. Mater. Sci. Lett.* **11**, 1072 (1992).
- ¹⁰V. Panchanathan, *J. Mater. Eng. Performance* **4**, 423 (1995).
- ¹¹R. K. Mishra, T. Y. Chu, and L. K. Rabenberg, *J. Magn. Magn. Mater.* **84**, 88 (1990).

Plastic deformation modeling of die-upset process for magnequench NdFeB magnets

S. Guruswamy and Y. R. Wang

Department of Metallurgical Engineering, University of Utah, Salt Lake City, Utah 84112

V. Panchanathan

Magnequench International, Anderson, Indiana 46013

The die upset of hot pressed NdFeB magnets modifies the equiaxed grains to platelets, develops the *c*-axis texture parallel to press direction, and improves magnetic properties. The mechanism of *c*-axis alignment has been suggested to be a combination of grain-boundary sliding and anisotropic grain growth in a direction normal to the applied stress. To clearly understand the role of deformation process in grain-boundary sliding or anisotropic grain growth simulations of the die-upset process were performed using ANATARES, a three-dimensional finite element method based deformation modeling software. The stresses and strains in the different regions of a cylindrical Nd-Fe-B magnet at different stages of the die-upset process were determined. The average value of the maximum principal stress (parallel to the upset direction) and total effective strain increased as the upset increased from 50% to 70%. The maximum principal stress and total effective strain show a maximum at the center and decrease in both the thickness and the radial direction due to friction at the die-wall/magnet interface. The stress and effective strain uniformity improves with increase in upset. The data agree well with the variations of texture in the magnet observed using pole figure measurements in this study and texture studies using a synchrotron source. © 1998 American Institute of Physics. [S0021-8979(98)16511-8]

I. INTRODUCTION

The magnequench process for the production of Nd-Fe-B-based magnets consists of melt spinning the alloy to produce ribbons, milling of melt-spun ribbons to powder, followed by hot pressing and die upsetting.¹⁻⁴ The optimally quenched melt-spun ribbons have equiaxed and randomly oriented Nd₂Fe₁₄B (2-14-1) grains. Hot pressing of ribbon powder achieves complete densification and a desired shape while maintaining essentially an isotropic structure and magnetic properties. The subsequent hot deformation process modifies the equiaxed grains to platelets with increase in grain size. These platelets are stacked with the *c* axis perpendicular to the face of the grains. The mechanism of *c*-axis alignment has been suggested to be by a combination of grain-boundary sliding and anisotropic grain growth in a direction normal to the applied stress.^{5,6} The amount of *c*-axis alignment with the press direction, measured using x-ray diffraction techniques, has been shown to depend on the amount of deformation. In addition, the strain distribution in a magnet deformation at a given level is expected to be non-uniform due to friction between the die wall and the magnet. The friction coefficient between the die wall and magnet is sensitive to the surface conditions, deformation temperature, the lubricant, and the load. Thus, depending on the die-upset process conditions, the stress and strain distribution will vary and this is expected to influence the texture, and hence, the magnetic properties. The nature of the strain and stress distribution in the magnet during the different stages of the upset deformation is very critical in understanding the texture development in these magnets. To the best of our knowledge, no detailed analysis of how the local stress and strain

influence the crystallographic alignment by grain-boundary sliding and anisotropic grain growth has thus far been performed. In this work, an assessment of stresses and strains in the magnet is made by a simulation of the die-upset process and is correlated with texture measurements made using x-ray diffraction.

II. EXPERIMENTAL WORK

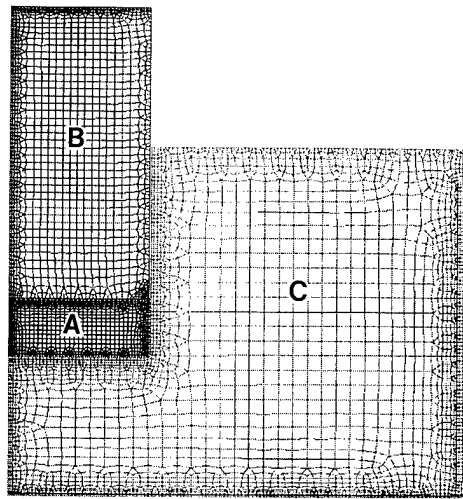
NdFeB magnets were die upset to 50%, 60%, and 70% deformation and the texture in these magnets were evaluated using x-ray pole figures. Simulation of the die-upset process for NdFeB magnets was done using "ANTARES," a finite-element-based plastic deformation modeling software for the cases of 50%, 60%, and 70% upsets. An initial strain rate of 2×10^{-2} and a temperature of deformation of 800 °C was assumed. The material was assumed to exhibit a deformation behavior by the equation

$$\sigma = \sigma^0 + k \epsilon^n \dot{\epsilon}^m,$$

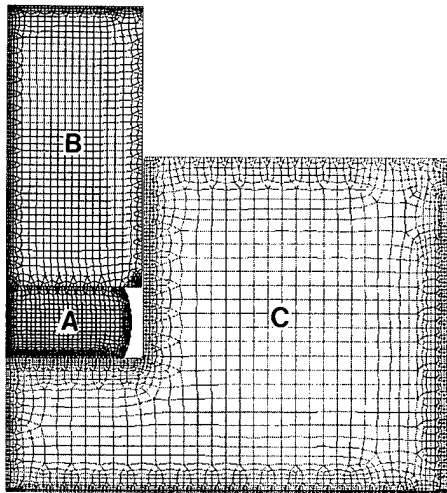
where σ^0 = flow stress at $\epsilon=0$, k =constant, ϵ =strain, $\dot{\epsilon}$ = strain rate, n =strain hardening factor, and m =strain rate sensitivity factor. For the die material, the property data used corresponded to H-11 tool steel. The data for Nd-Fe-B used were obtained from the work of Yoshikawa *et al.*⁷ A friction coefficient of 0.3 was used for the magnet/die interface lubricated with graphite.

III. RESULTS AND DISCUSSION

Typical deformation geometry used for die-upset simulation is shown in Fig. 1(a). The diameter of the billet is 18 mm and the length of the billet varies slightly depending on



(a)



(b)

FIG. 1. Typical deformation (a) at the end of the die upset and (b) at an intermediate stage of the die upset. Axis of symmetry is along the left edge. A, B, and C refer to the magnet, top punch, and bottom die, respectively.

the die upset required. Each % upset requires a different die set with appropriate diameter and depth of the cavity. The geometry of the billet at each incremental step of the punch movement can be obtained, and Fig. 1(b) presents the billet mesh geometry at an intermediate stage of the die-upset process. The barreling of the billet results from (i) the friction at the top punch/billet interface and the die/billet interface, and (ii) the temperature variation across the billet due to heat transfer across the die-billet interfaces and billet/protective gas interface. Near the end of the deformation process, the barreled surface of the billet makes contact with the lateral faces of the die, and the flow patterns in peripheral regions become complex. The values of different stress, strain, strain energy, temperature, and other parameters are obtained at every stage of the process. Of importance are the principal stress and effective strain values. The principal stress is nearly parallel to the axis of the magnet and the effective strain is proportional to the strain in the direction parallel to

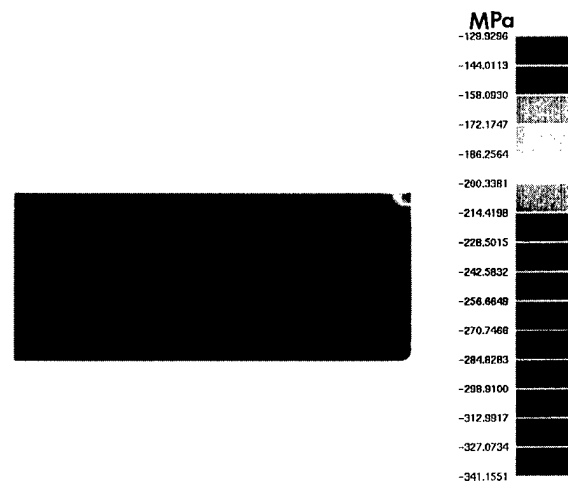


FIG. 2. Principal stress contours at the end of 60% die-upset deformation.

the axis of the billet (ϵ_{zz}). Figures 2 and 3 present the principal stress and effective strain contours in the magnets at the end of deformation for the 60% die-upset magnets. It has been observed that grain growth along the a axes that are normal to the applied stress is favored. The principal stress-time-temperature profile is thus important in assessing the contribution of the anisotropic growth. The effective strain could also be more directly correlated with the grain rotation and anisotropic grain growth, and the crystalline alignment. For the case of the 50% die-upset magnet (Fig. 4), the effective plastic strain varies from 53.27% at the center of the bottom and top face to a value of 79.81% at the central region of the magnet. This suggests that the crystalline texture must vary significantly across the magnet. For the case of 60% deformation (Fig. 3), the effective strains at all the different locations have increased. At the center of the bottom and top faces, the effective strain is 59.29% compared to the value of 53.27% for 50% deformation. The center of the magnet experienced an effective strain of 107.62%. For the 70% upset magnet (Fig. 5), these values increased to 71.74% for the center of the top and bottom faces and 145.91% for the central region of the magnet. In these three figures, the lateral confinement by the cylindrical bottom die face, and



FIG. 3. Effective strain contour at the end of 60% die-upset deformation.

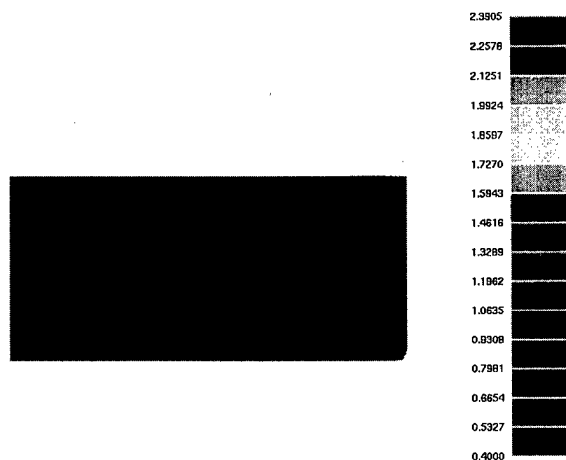


FIG. 4. Effective strain contour at the end of 50% die-upset deformation.

the extrusion of the magnet through the clearance between the punch and bottom die result in a highly nonuniform strain distribution in the corner regions. The average strain level increases with the increase in the percentage of the die upset, and therefore, the overall texture should increase with percentage of the die upset. However, the large variation in the effective strain should also lead to extensive variation in texture across the magnet, and therefore, the magnetic properties are expected to be nonuniform. There may, however, be a critical effective strain level above which there is no further improvement in texture. If this critical level is exceeded at all the locations of the magnet, then a complete or limiting (006) texture would have been achieved. The effective strain variation in the radial direction is much less compared to the variation in the thickness direction, except for the region near the edge of the magnet.

The deformation modeling work is consistent with the texture measurements made in these die-upset magnets. The

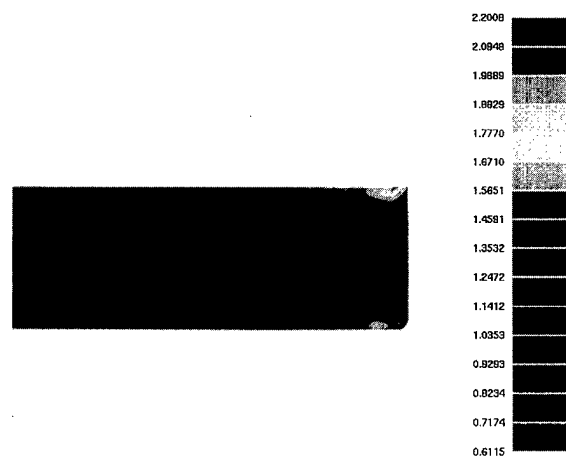


FIG. 5. Effective strain contour at the end of 70% die-upset deformation.

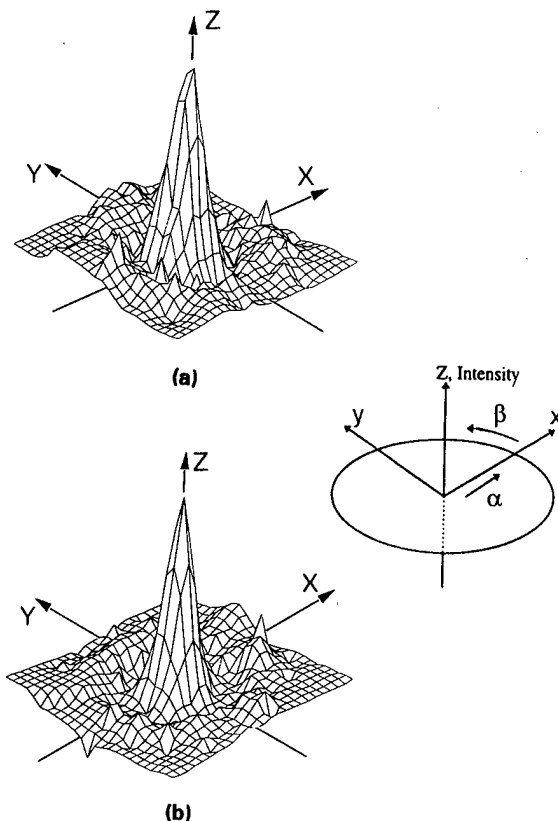


FIG. 6. Three-dimensional partial (006) pole figure from (a) 0.5 mm depth and (b) 1.0 mm depth of the 60% die-upset magnet.

(006) pole figures from a 0.5 mm depth are shown in Fig. 6(a) and those for a 1.0 mm depth are shown in Fig. 6(b). Their W_{50} values are 26.3° and 24.0° for the 0.5 and 1.0 mm depths, respectively. They again show that the crystallographic alignment is enhanced as one moves from the surface toward the center of the magnet. This observation is as expected from the deformation modeling. The larger strain produced a stronger (006) texture. It also suggests that friction between the sample and punch affects the crystal alignment near the sample surface. The results from the modeling work are also consistent with the study of texture variation across the die-upset magnets by Lewis *et al.*⁸

¹J. Croat, J. F. Herbst, R. W. Lee, and F. E. Pinkerton, Appl. Phys. Lett. **44**, 148 (1984).

²J. Croat, J. F. Herbst, R. W. Lee, and F. E. Pinkerton, J. Appl. Phys. **55**, 2078 (1984).

³R. W. Lee, Appl. Phys. Lett. **46**, 790 (1985).

⁴R. W. Lee, N. Schaffel, and L. Brewer, IEEE Trans. Magn. **MAG-21**, 1958 (1985).

⁵R. K. Mishra, Mater. Sci. Eng. B **7**, 297 (1991).

⁶K. Ohmori, L. Li, and C. D. Graham, Jr., IEEE Trans. Magn. **MAG-28**, 2139 (1992).

⁷N. Yoshikawa, Y. Kasai, T. Watanabe, S. Shibata, V. Panchanathan, and J. J. Croat, J. Appl. Phys. **69**, 6049 (1991).

⁸L. H. Lewis, W. O. Welch, T. R. Thurston, and V. Panchanathan, Proceedings of the 9th International Symposium on Magnetic Anisotropy and Coercivity in RE-TM Alloys (1996), p. 278.

Microstructural analysis of strip cast Nd–Fe–B alloys for high $(BH)_{\max}$ magnets

J. Bernardi^{a)} and J. Fidler

Institute of Applied and Technical Physics, University of Technology, A-1040 Wien, Austria

M. Sagawa

Intermetallics Company Ltd., Nishikyo-ku, Kyoto 615, Japan

Y. Hirose

Showa Denko K.K., Chichibu Research Laboratory, Saitama 369-18, Japan

High energy density magnets $>400 \text{ kJ/m}^3$ are increasingly used in many applications. Conventional casting techniques for sintered magnets reveal the formation of a high quantity of α -Fe and large Nd-rich regions. New techniques, like strip casting, produce homogeneous and fine scaled microstructures and are already used for producing high $(BH)_{\max}$ magnets. The fast cooling rate during strip casting suppresses the formation of α -Fe dendrites and of large Nd-rich pockets. Directional solidification causes a formation of columnar grains containing a typical arrangement of hard magnetic $\text{Nd}_2\text{Fe}_{14}\text{B}$ regions and Nd-rich regions. The Nd regions occur as intragranular platelets as well as intergranular phases. Intragranular lamellae show a periodicity which corresponds to a eutectoidal solidification according to the composition of the liquid and are directed parallel to the temperature gradient during solidification. The lamellae show an average width of 150 nm, a spacing of 3 μm , and a length up to the size of the hard magnetic grains. The fine separation of the hard magnetic and Nd phases is advantageous for the milling of the alloy after hydrogen decarburization and improves sinterability of magnets. Although the microstructure of strip cast alloys is much finer than that of ordinary cast alloys, the alignment of the powder is not deteriorated and B_r is not reduced due to a sufficient large interlamellar spacing between the Nd-rich platelets that enables the formation of single crystal powder particles after milling. © 1998 American Institute of Physics. [S0021-8979(98)18911-9]

I. INTRODUCTION

Sintered Nd–Fe–B-type permanent magnets are widely used in applications that require a high energy product/volume ratio in order to reduce weight.¹ In addition there is a rising demand for magnets with $(BH)_{\max}$ higher than 400 kJ/m^3 . This goal can be reached by shifting the alloy composition more towards the stoichiometric $\text{Nd}_2\text{Fe}_{14}\text{B}$ composition as well as by improving the alignment of the hard magnetic grains during compacting. In addition the distribution of phases in the starting alloy can be significantly improved. Conventional casting techniques reveal the formation of a high quantity of precipitated α -Fe that deteriorates the powder alignment² and large Nd-rich regions that are very sensitive to oxidation. The α -Fe is formed according to the pseudo-binary Fe–(Nd,B) phase diagram, with Nd:B = 2:1, where the solidification path passes through a region (Liq. + Fe) and Fe particles are formed within the liquid.³ The formation of dendritic α -Fe in cast alloys can be reduced by additives like M2=Ti, Nb, Zr, V, Mo, or W that form M2–Fe–B borides⁴ as well as by optimizing the casting technique. It has been previously shown that flat cast ingots consist of fine grains near the mold surface, columnar grains in the central portions, and coarse grains near the free surface.⁵ Reducing the thickness of the ingots from 8.7 to 4.4 mm resulted in an increase of the amount of columnar grains

and in a decrease of dendritic α -Fe in the ingot. An improvement of B_r by 5% and $(BH)_{\max}$ by 10% of magnets produced from that ingot were attributed to a significantly reduced presence of dendritic α -Fe causing a better grindability of the powder and a better grain alignment. In this article we report on the effect of strip casting on the microstructure of Nd–Fe–B magnetic material. Materials produced by strip casting are already used for high $(BH)_{\max}$ magnets. This new technique allows large scale production of ingots with a homogeneous and fine scaled microstructures without a significant precipitation of α -Fe. The fine dispersion of the rare earth-rich phase is important not only for high energy magnets having $(BH)_{\max}$ of over 400 kJ/m^3 , but also for high coercivity magnets that include high Dy concentrations. In such strip cast high Dy alloys B_r and $(BH)_{\max}$ are improved keeping the coercive field high because the total rare earth content can be substantially decreased without the formation of rare earth depleted regions that can deteriorate the squareness of the demagnetization curve of sintered magnets.

II. EXPERIMENT

The investigated samples with the composition $(\text{Nd,Dy})_{14.1}(\text{Fe,Al})_{80}\text{B}_{5.9}$ were produced by strip casting, a technique similar to melt spinning, using a wheel speed of 1 m/s. The platelike casted alloy shows a typical thickness of 250–350 μm and a width of several centimeters. The samples were investigated by optical microscopy with polar-

^{a)}Electronic mail: bernardi@email.tuwien.ac.at

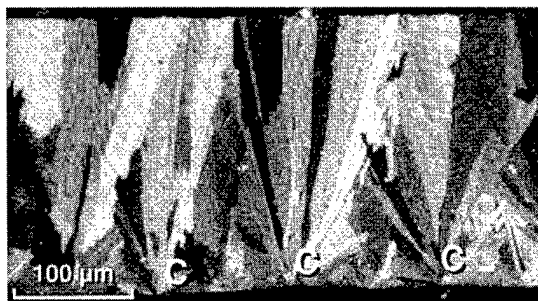


FIG. 1. Optical micrograph of the cross section of strip cast $(\text{Nd,Dy})_{14.1}(\text{Fe,Al})_{80}\text{B}_{5.9}$ showing the columnar growth of hard magnetic grains starting at nucleation centers (C) and the magnetic domains structure inside the columnar grains.

ized light as well as by scanning electron microscopy (SEM) and transmission electron microscopy (TEM).

III. RESULTS AND DISCUSSION

The typical microstructure of the strip cast alloy parallel to the direction of solidification observed with polarized light is shown in Fig. 1. Solidification of the melt starts at nucleation centers (C) at the wheel side of the strips. The distance between individual centers is 50–120 μm . Starting from these nucleation sites, a columnar structure of hard magnetic grains is formed due to directional solidification. The growth direction of the grains is typically the direction of the heat flow during solidification. The columns grow within a cone with an opening angle 60°–80° towards the free surface of the strips. The diameter of the individual grains perpendicular to the growth direction is 5–25 μm close to the wheel side and 25–60 μm close to the free surface side (Fig. 2), respectively.

The columnar grains consist of a hard magnetic phase, which is proven by the existence of the magnetic domain pattern in that structure. The orientation of the domain walls visible with polarized light indicates that the growth direction of these columns within the cone does not correspond with either $\langle 100 \rangle$, the easy growth axis of the tetragonal 2:14:1 structure,^{6,7} or $\langle 001 \rangle$. A columnar dendritic 2:14:1 structure with a growth direction parallel to $\langle 001 \rangle$ was pre-

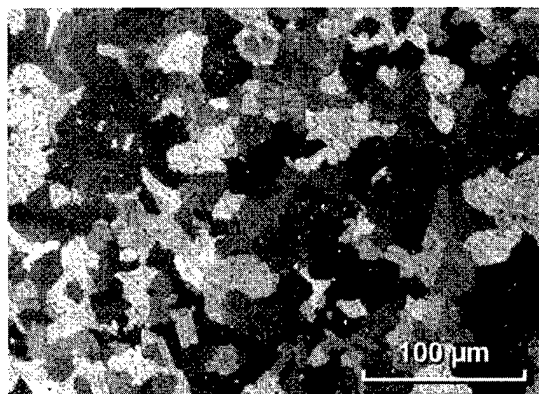


FIG. 2. Optical micrograph taken parallel to the surface of the strips near the free surface side.

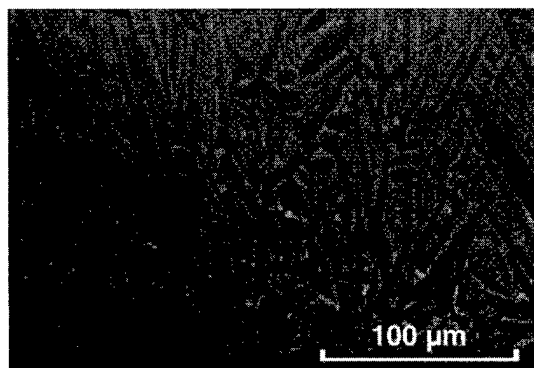


FIG. 3. SEM micrograph of the polished cross section of the strip cast alloy showing the distribution of hard magnetic phase (dark) and Nd-rich phase (bright) in backscattered mode.

viously observed in splat cooled $\text{Nd}_{15}\text{Fe}_{77}\text{B}_8$ magnets.⁸ A preferred c axis texture normal to the ribbon plane was also observed in melt spun $\text{Nd}_{16}\text{Fe}_{76}\text{B}_8$ ribbons.⁹ Close to the wheel side between the nucleation sites, smaller elongated grains are formed with a growth direction more parallel to the surface. In these grains the domain walls tend to be oriented perpendicular to the surface, indicating a preferred $\langle 100 \rangle$ growth direction of the magnetic grains in that region. Within the large dendritic columns of the 2:14:1 phase a thin plateletlike phase is formed parallel to the growth direction. The occurrence of this intragranular layered structure does not usually influence the domain structure of the hard magnetic grains (compare Fig. 1). Figure 3 shows a SEM backscattered electron micrograph of a strip cast sample perpendicular to the wheel side. The hard magnetic grains appear as dark areas. Thin bright regions which occur with a certain periodicity within the hard magnetic grains and at grain boundaries consist of the Nd-rich phase. There is no indication for the formation of dendritic $\alpha\text{-Fe}$ or a significant amount of additional phases like $\text{Nd}_{1+x}\text{Fe}_4\text{B}_4$ formed during solidification. The lamellar arrangement of the two phases that are oriented parallel to the temperature gradient is characteristic for a eutectoidal solidification. The interlamellar spacing between the Nd-rich platelets is about 3 μm and is controlled by the temperature gradient during solidification as well as the composition of the liquid.

The orientation relationship between the Nd-rich intragranular platelets and hard magnetic matrix grains was further investigated by TEM. Figure 4 shows the typical microstructure of a columnar 2:14:1 grain in the center of a strip viewed perpendicular to the direction of solidification. Hard magnetic grains are separated by intragranular Nd-rich lamellae with a thickness of 60–150 nm. Within a grain all hard magnetic regions show the same crystallographic orientation. Close to grain boundaries the Nd-rich intragranular regions are also found with more irregular shapes.

At grain boundaries and especially at grain boundary junctions, intergranular Nd-rich phases are found. Selected area electron diffraction (SAD) confirms that the Nd-rich platelets as well as the intergranular Nd-rich phases mainly occur as fcc Nd and less frequently as Nd oxide. X-ray spectra show that there is usually a significant amount of Fe



FIG. 4. TEM micrograph of strip cast $(\text{Nd,Dy})_{14.1}(\text{Fe,Al})_{80}\text{B}_{5.9}$ showing intragranular Nd-rich platelets embedded in a hard magnetic grain. The diffraction pattern of the marked region shows diffraction spots from the tetragonal $\text{Nd}_2\text{Fe}_{14}\text{B}$ phase and of the fcc Nd-rich lamella.

dissolved within the Nd-rich phases. During the TEM investigation no $\alpha\text{-Fe}$ or $\text{Nd}_{1+x}\text{Fe}_4\text{B}_4$ was detected. The analysis of various diffraction patterns revealed that most of the lamellae are formed parallel to the $\{1,1,-1\}$ plane of the tetragonal 2:14:1 phase.

Good magnetic properties require a homogeneous distribution of all phases and dopant elements throughout the cast material. Traditional casting techniques can cause a segregation of individual phases depending, e.g., on the geometry of the casting mold, composition, or cooling rate, and therefore lead to strong inhomogeneities of the microstructure and the chemical composition.^{2,5,10} The strip casting technique enables a fine separation of hard magnetic and rare earth-rich phases in the cast alloys. The merits of using strip cast alloys as a starting material for high performance Nd-Fe-B magnets are as follows:

(1) The rapid solidification process prevents the formation of large dendritic $\alpha\text{-Fe}$ grains in the cast alloy without the need of isothermal annealing even if the total rare earth content is reduced in order to produce high $(\text{BH})_{\text{max}}$ mag-

nets. The sufficiently large interlamellar spacing of about $3\text{ }\mu\text{m}$ between the Nd-rich platelets in the columnar $\text{Nd}_2\text{Fe}_{14}\text{B}$ grains is crucial in order to enable the formation of single crystal powder particles after HD treatment and jet milling necessary for optimum alignment of the particles and for high Br in the magnets.

(2) The homogeneous fine scale microstructure, containing a high amount of thin rare earth-rich platelets, leads to a high density of fine pre-cracks after hydrogen decrepitation. That and the lack of large dendritic $\alpha\text{-Fe}$ grains improves the crushability of strip cast alloys significantly.

(3) The good dispersion of rare earth-rich phases in the strip cast alloys leads to an optimum distribution of liquid phase during sintering and enables the production of high density magnets with high coercive fields even at lower sintering temperatures. The total rare earth content can be decreased by using strip casting without the formation of rare earth depleted zones in the magnets. That is essential for high $(\text{BH})_{\text{max}}$ magnets but also in the case of magnets with high Dy content in order to improve the remanence and $(\text{BH})_{\text{max}}$ while keeping high iH_c .

¹H. Nagel and W. E. Krönert, *Proceedings of the 13th International Workshop on Rare Earth Magnets and their Applications*, Birmingham, UK, 1994, edited by C. A. F. Manswaring, D. G. R. Jones, A. J. Williams, and I. R. Harris (University of Birmingham, Birmingham, UK, 1994), p. 391.

²D. W. Scott, B. M. Ma, Y. L. Liang, and C. O. Bounds, *J. Appl. Phys.* **48**, 4830 (1996).

³G. Schneider, E. T. Henig, H. H. Stadelmaier, and G. Petzow, *Proceedings of the 5th International Symposium on Magnetic Anisotropy and Coercivity in Rare Earth Transition Metal Alloys, Part II, Bad Soden, Germany, 1987*, edited by C. Herget, H. Kronler, and R. Poerschke (Deutsche Physikalische Gesellschaft, Bad Honnef, FRG 1987), p. 347.

⁴J. Fidler, J. Bernardi, and T. Schrefl, *Scri. Metall. Mater.* **33**, 1781 (1995).

⁵B. M. Ma and C. O. Bounds, *J. Appl. Phys.* **70**, 6471 (1991).

⁶G. Schneider, E. Th. Henig, F. P. Missell, and G. Petzow, *Z. Metallkd.* **81**, 322 (1990).

⁷A. Fujita and I. R. Harris, *IEEE Trans. Magn.* **29**, 2803 (1993).

⁸T. Harada, T. Ando, R. C. O'Handley, and N. J. Grant, *J. Appl. Phys.* **70**, 6468 (1991).

⁹D. Dadon, Y. Gefen, and M. P. Dariel, *IEEE Trans. Magn.* **23**, 3605 (1987).

¹⁰H. Lemaire, P. Tenaud, F. Vial, and B. Labulle, *J. Magn. Magn. Mater.* **83**, 234 (1990).

Extension of the primary solidification region of $\text{Nd}_2\text{Fe}_{14}\text{B}$ by levitation of undercooled melts

R. Hermann^{a)} and W. Löser

Institute of Solid State and Materials Research (IFW), Institute of Metallic Materials, Helmholtzstrasse 20, D-01069 Dresden, Germany

Undercooled Nd–Fe–B melts with compositions near the $\text{Nd}_2\text{Fe}_{14}\text{B}$ phase (Φ phase) were studied by the electromagnetic levitation technique. *In situ* measurements of the solidification kinetics were accomplished and melt drops with controlled undercooling were quenched onto chill substrates in order to reveal the solidification sequence and microstructure formation processes. Crystal growth velocities of the Φ phase of the order of 1 mm s^{-1} were estimated from *in situ* measurements. Consistent with the nucleation theory, which predicts primary γ -Fe phase crystallization up to 650 K undercooling for the stoichiometric alloy, γ -Fe nucleation could not be avoided during undercooling but the quenching of the melt drops led to dissolution of the γ -Fe nuclei during Φ -phase formation. The γ -Fe phase growth was suppressed in a seam adjacent to the chill surface, whereas Fe dendrites occurred in the remaining parts of the quenched samples. Reduced solute rejection on growth is believed to be responsible for the preferred metastable Φ -phase formation from the undercooled melt on chill substrates. The investigation gives some clues to understand different microstructures and magnetic properties of powder precursors for permanent magnets obtained from different rapid solidification routes. © 1998 American Institute of Physics. [S0021-8979(98)15111-3]

I. INTRODUCTION

Commercial Nd–Fe–B permanent magnets are usually prepared by sintering or rapid quenching methods.^{1,2} The $\text{Nd}_2\text{Fe}_{14}\text{B}$ compound exhibits a high saturation magnetization and a strong magnetocrystalline field. These properties are the physical conditions for excellent permanent magnets. However, different magnetic properties are obtained using various processing techniques due to different microstructure. The determination of the crystallization behavior and the resulting microstructure are still under study. Detailed knowledge of the solidification behavior is essential especially for the development of alloys with novel properties. The solidification processes in rapid solidification techniques are hardly accessible to direct observation. Therefore, the purpose of this article was a study of crystallization processes of Nd–Fe–B melts by the containerless electromagnetic levitation method. This technique permits *in situ* measurements of the solidification kinetics of undercooled melt drops during the recalescence stage. Moreover, melt drops with controlled undercooling levels have been quenched onto copper substrates and copper–tin-coated substrates, respectively, in order to reveal the as-solidified microstructure.

II. EXPERIMENT

Three different Nd–Fe–B master alloys were prepared from pure Nd and Fe–B alloy by arc melting under argon atmosphere. Composition A is the stoichiometric $\text{Nd}_{11.8}\text{Fe}_{82.3}\text{B}_{5.9}$ alloy. Composition B is a hypostoichiometric $\text{Nd}_{11}\text{Fe}_{83.5}\text{B}_{5.5}$ alloy and composition C is a hyperstoichiometric $\text{Nd}_{15.8}\text{Fe}_{76.3}\text{B}_{7.9}$ alloy. Spheres of about 6 mm

in diameter and about 1.2 g mass were containerless melted and solidified in an electromagnetic levitation facility under helium gas atmosphere. The melted samples were cooled by a gas stream enabling cooling rates of about 10 K s^{-1} . The temperature of the sample was monitored by a two-colorpyrometer with a sampling rate of 50 Hz and a relative accuracy of $\pm 3 \text{ K}$. For measuring and resolving the fast recalescence time a modified single-reflex camera with a silicon diode in its focal plane was used enabling sample rates of 500 MHz. The sampling rate of the transient recorder was 1.5 MHz. A detailed description of the facility is given elsewhere.³ Melt drops of well defined undercooling level were quenched on a copper substrate and a copper substrate which was coated with tin to enhance the interfacial heat transfer. Immediately after nucleation the drops solidify with a preferred heat flow into the undercooled melt but with a heat transfer into the chill substrate as well. The as-solidified melt drops were investigated by digitally enhanced Kerr microscopy and scanning electron microscopy.

III. RESULTS

A. Time-temperature characteristic

The solidification of the undercooled melt drop starts by spontaneous nucleation or can be initiated by triggering at a well defined undercooling level. The photodiode does not, in principle, allow one to determine an absolute temperature, but the two-color pyrometer could be used to set the temperature scale in order to compare the results with the equilibrium phase diagram. Figure 1 shows typical temperature-time profiles of the three investigated Nd–Fe–B compounds. The stoichiometric sample [Fig. 1(a)] was melted at $T_m = 1520 \text{ K}$ and initially superheated. After cooling down be-

^{a)}Electronic mail: R.Hermann@IFW-Dresden.de

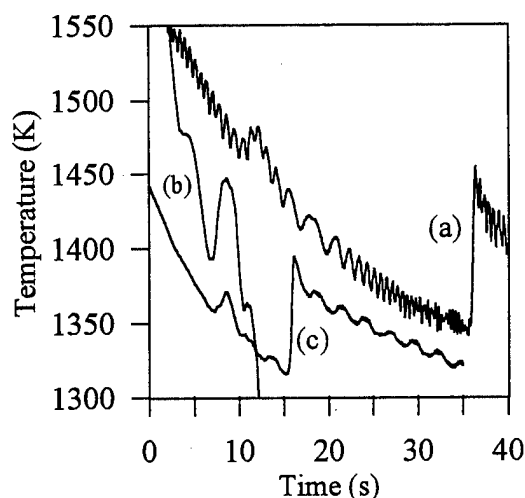


FIG. 1. Temperature-time characteristic of double recalescence events of: (a) a stoichiometric Nd-Fe-B alloy at an undercooling level of 170 K (with respect to the liquidus temperature), (b) a hypostoichiometric Nd-Fe-B alloy at an undercooling level of 165 K, (c) a hyperstoichiometric Nd-Fe-B alloy at an undercooling level of 130 K.

low the melting temperature, the solidification of the sample occurs at 1350 K, corresponding to an undercooling level of $\Delta T = 170$ K. The solidification process consists of two steps. The first step can be attributed to a small amount of γ -Fe phase nuclei at about 1460 K, whereas the drop is still under undercooling. The second step starts with the solidification of the Φ phase. Assuming that the solidification front is planar, the growth velocity of the Φ phase can be estimated to 1.2 mm s^{-1} . The resulting time of crossing the planar front through the viewing field of the diode ($0.88 \text{ mm} \times 0.88 \text{ mm}$) was measured to 720 ms. Figures 1(b) and 1(c) show the corresponding temperature-time profile of the hypostoichiometric and hyperstoichiometric sample, respectively. It is of interest to note that all three alloys show the small recalescence step of γ -Fe phase nucleation independent of the achieved undercooling level.

B. Phase analysis of as-solidified samples

The *in situ* observation of undercooled melts is an important tool for investigation of rapid solidification. Nevertheless, the microstructure of the as-solidified sample has to be investigated. The arc-melted master alloys show different microstructures. In alloys A and B γ -Fe dendrites are clearly visible whereas alloy C does not contain any γ -Fe dendrites. Figure 2 shows the backscattering electron (BSE) micrographs of a sample of alloy B, undercooled at about 150 K prior to solidification and subsequently quenched on a copper-tin-coated substrate. Immediately on the strongly separated tin layer a nonfeatured layer of about $100 \mu\text{m}$ has been developed, responsible for pure metastable Φ phase electron probe microanalysis investigation, Fig. 2(a)]. The relatively sudden transition to the structured layer shows the beginning decomposition into Fe-rich phases and the growth of $\text{Nd}_2\text{Fe}_{14}\text{B}$ needles [see Figs. 2(a) and 2(b)]. Finally, the growth of Fe dendrites and the separation of Nd-rich phases in the interdendritic region indicate the transition to equilibrium solidification [Fig. 2(c)].

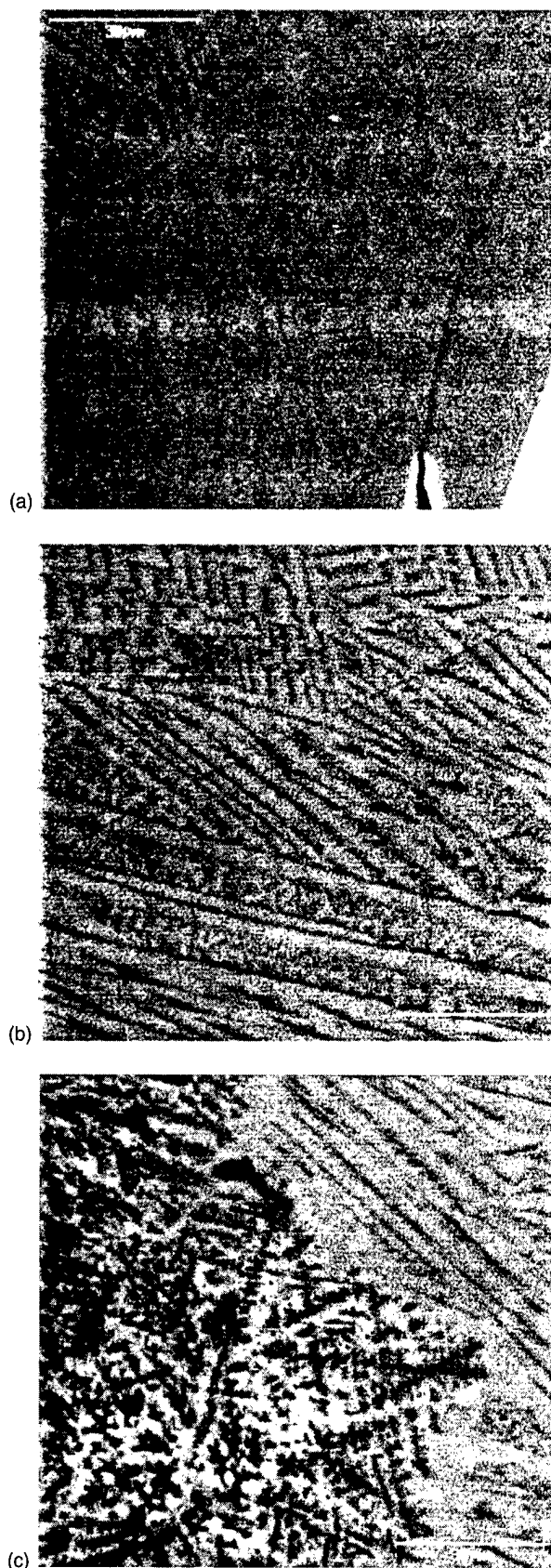


FIG. 2. BSE micrographs of alloy B, undercooled at about 150 K prior to chilling on a copper-tin-coated substrate: (a) featureless $\text{Nd}_2\text{Fe}_{14}\text{B}$ phase layer near the chill substrate, (b) growth of $\text{Nd}_2\text{Fe}_{14}\text{B}$ needles and Fe-rich phases, (c) growth of Fe dendrites near the top of the sample.

On the other hand BSE micrographs of samples quenched on a copper substrate prior to solidification, show that Fe dendrites have been grown directly in the quenched region. The heat transfer was not sufficient for the formation of pure metastable Φ phase even at the stoichiometric alloy. These microstructures indicate that both critical undercooling and rapid quenching are necessary for the growth of the metastable Φ phase.

IV. DISCUSSION

The as-solidified microstructure of Nd-Fe-B alloys is determined by nucleation and growth processes of the competitive phases, notably γ -Fe and Φ phase, and post-solidification transformations as well. The homogeneous nucleation rates of γ and Φ phase, I_γ and I_Φ , respectively were estimated as functions of melt undercooling on the basis of thermodynamic and kinetic data given by Clavaguera and Diego.⁴ For the stoichiometric melt composition, the nucleation of the peritectic γ -Fe phase dominates in a wide undercooling range below the liquidus temperature $T_{l,\gamma}$. The crossing point with the I_Φ is about 650 K below the liquidus temperature, outside the range of experimental accessibility. In principle, the nucleation and growth of the Φ phase can arise in the primary γ -Fe phase field well above the peritectic temperature if a critical undercooling below the metastable liquidus temperature $T_{l,\gamma}$ is achieved.^{5,6} The time-temperature characteristics of levitated samples indicate that γ -Fe nucleation could not be avoided on slow cooling of the levitated samples. This becomes apparent from the small dip near the liquidus temperature $T_{l,\gamma}$. The residual melt, however could be undercooled by a considerable amount of >170 K below $T_{l,\gamma}$. Accordingly a very distinct recalescence event was obtained due to the growth of the Φ phase from the undercooled melt. The microstructural features indicate that both melt undercooling and fast cooling were necessary for the growth of the metastable Φ phase. Quenching of the undercooled melt drops onto the copper-tin-coated substrate led to a wide seam of more than $100\ \mu\text{m}$ thickness free of γ -Fe dendrites even for hypostoichiometric melt alloys. More distant from the chill surface the growth of $\text{Nd}_2\text{Fe}_{14}\text{B}$ needles continued with apparent Fe segregation in the interdendritic regions before γ -Fe dendrites indicate the transition to the equilibrium solidification mode. The reason

for the possible suppression of the γ -Fe equilibrium phase dendrites and preferred growth of the metastable Φ phase is its smaller composition deviation from the melt, which leads to less solute rejection at the growth front.⁶ This behavior is typical of various peritectic alloys.⁷ This first attempt of Nd-Fe-B melt undercooling experiments shed some light onto the obvious differences in microstructure and magnetic properties of powder precursors for Nd-Fe-B hard magnetic materials obtained from different rapid solidification techniques. In hyperstoichiometric inert-gas-atomized Nd-Fe-B particles peritectic γ -Fe precipitations depending on droplet size were found,⁸ whereas thin melt spun ribbons often exhibit an overquenched amorphous state from which the Φ phase can evolve. There is an apparent difference in the thermal history of both rapid solidification techniques. IGA particles are exposed to moderate cooling rates of 10^3 – $10^5\ \text{K s}^{-1}$ by the gas stream. High undercooling of droplets prior to solidification is expected, which is a behavior similar to levitated samples. In melt spinning there is a vigorous heat transfer from a thin melt film to the chill substrate, which can lead to a dynamic undercooling and finally quenching the melt into the amorphous state before nucleation of crystalline phases because of cooling rates as high as $10^6\ \text{K s}^{-1}$.

ACKNOWLEDGMENTS

The authors wish to thank H.-G. Lindenkreuz, M. Frömmel, S. Schinnerling, and I. Bäcker for carrying out undercooling experiments and microstructure investigations. The support of the Deutsche Forschungsgemeinschaft is gratefully acknowledged.

¹M. Sagawa, S. Fujimura, N. Togawa, H. Yamamoto, and Y. Matsuura, J. Appl. Phys. **55**, 2083 (1984).

²J. J. Croat, J. F. Herbst, R. W. Lee, and F. E. Pinkerton, J. Appl. Phys. **55**, 2078 (1984).

³W. Löser, H. Genest, and H.-G. Lindenkreuz, Ann. Report, IFW Dresden, 27 (1994).

⁴N. Clavaguera and J. A. Diego, Intermetallics **1**, 187 (1993).

⁵G. Schneider, E.-T. Henig, G. Petzow, and H. H. Stadelmaier, Z. Metallkd. **77**, 755 (1986).

⁶T. Umeda, T. Okane, and W. Kurz, Acta Mater. **44**, 4209 (1996).

⁷H. W. Kerr and W. Kurz, Int. Mater. Rev. **41**, 129 (1996).

⁸C. H. Sellers, T. A. Hyde, D. J. Braggan, L. H. Lewis, and V. Panchanathan, J. Appl. Phys. **81**, 1351 (1997).

High performance Nd-Fe-B sintered magnets made by the wet process

M. Takahashi,^{a)} K. Uchida, and F. Taniguchi

Magnetic and Electronic Materials Research Laboratory, Hitachi Metals, Ltd. 5200 Mikajiri, Kumagaya, Saitama 360, Japan

T. Mikamoto

Production System Laboratory, Hitachi Metals, Ltd., 6010 Mikajiri, Kumagaya, Saitama 360, Japan

The wet process for the fabrication of Nd-Fe-B sintered magnets has been developed on the mass production scale. In this process, mineral oil is used as a solvent to prevent the milled powder and green bodies from oxidation. It is removed before sintering. As a result, the oxygen uptake during storage is less than 0.01 wt %/day. By reducing the oxygen content and the total rare earth (TRE) content in sintered magnets to less than 0.2 and 29.3 wt %, respectively, magnets with $(BH)_{\max}/H_c$ greater than 50 MGOe/10 kOe, 45 MGOe/15 kOe, and 32 MGOe/32 kOe were obtained with high reliability. The magnets produced by this wet process also show better corrosion resistance and 20% higher mechanical strength than those made by conventional methods. These characteristics may be explained by a smaller grain size, smaller TRE content, and higher density produced by the wet process. © 1998 American Institute of Physics. [S0021-8979(98)15211-8]

I. INTRODUCTION

Nd-Fe-B sintered magnets with higher magnetic properties have been required as their applications decrease in size. Minimizing nonmagnetic secondary phases (rare earth oxide, B-rich phase etc.), maximizing grain alignment, and optimizing alloy design are ways to increase $(BH)_{\max}$ of Nd-Fe-B sintered magnets, and concrete methods based on these principles have been presented.^{1,2} Improving the magnetic properties by minimizing nonmagnetic secondary phases requires a reduction in the oxygen content in sintered magnets. To reach this goal, various methods have been developed for the powder metallurgy process. However, it is difficult to prevent oxidation in chemically active fine powder and green compacts that are exposed to the air with conventional methods. A low oxygen content of around 0.2 wt % in a sintered body could be achieved only on the laboratory scale by a wet process using an organic solvent such as *n*-hexane or a dry process using oxygen-free chambers and containers.

We have developed a wet process (HILOP, HITACHI low oxygen process) using mineral oil as a solvent and have obtained Nd-Fe-B sintered magnets with less than 0.2 wt % oxygen in sintered bodies on the production scale. In this article, the procedure of the developed wet process and the characteristics of the resultant magnets will be presented.

II. EXPERIMENT

The developed wet process is based on conventional powder metallurgy techniques, but is distinguished from the conventional technique by handling the milled powders and green bodies in oil from milling to sintering. The wet process procedure is illustrated in Fig. 1 in comparison with the conventional dry process. Cast alloys were annealed at 1100 °C for 6 h, and then ground to less than 500 μm after the hy-

drogen decrepitation process. The oxygen content in the nitrogen gas used in the mill chamber for conventionally processed materials is commonly around 1000 ppm to stabilize the surface of the fine powder to prevent rapid oxidation in air. In the wet process, however, the prepared coarse powders were jet milled with no oxygen (less than the detection limit, i.e., <0 ppm). Milled powders were put in mineral oil without being exposed to the air, mixed into slurries, and stored for pressing. The slurries were die-pressed in a magnetic field of 14 kOe applied perpendicular to the axis of the press. The extremely low vaporization rate of the oil compared to that of organic solvents such as *n*-hexane enables the green bodies to be handled in air. The oil present in the green bodies was removed in the temperature range 100 °C $\leq T \leq$ 300 °C for 1 h in a vacuum of 10^{-1} Torr before sintering. Sintering was carried out at temperatures from 1050 to 1080 °C in a vacuum of 10^{-5} Torr for 5 h. Sintered bodies were heat-treated at 900 °C for 2 h followed by another heat treatment at temperatures from 460 to 560 °C for 1 h. Magnetic properties were measured by a *B-H* tracer. Corrosion rates were determined by measuring the weight losses after exposing the magnets in an autoclave under conditions of 120 °C, 100% relative humidity, and 2 atm.

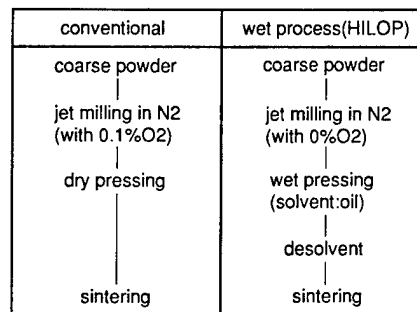


FIG. 1. A comparison of the wet process (HILOP) with the conventional dry process.

^{a)}Electronic mail: Masahiroj_Takahashi@po.hitachi-metals.co.jp

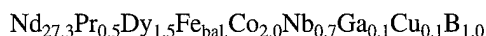
TABLE I. Typical oxygen and carbon contents of HILOP-processed and conventionally processed materials.

Process	Oxygen (wt %)	Carbon (wt %)
HILOP	0.16	0.061
Conventional	0.58	0.055

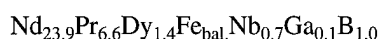
III. RESULTS AND DISCUSSION

A. Oxygen contents and magnetic properties

The typical oxygen and carbon contents of magnets with compositions of



and



in wt % produced by the wet process and the conventional dry process, respectively, are shown in Table I. The final carbon content of the wet-processed magnets is only around 0.01 wt % greater than that of conventionally processed magnets. This indicates that the oil remaining in the green body was well removed by the desolvent process. The oxygen content of wet-processed materials is less than a third of that of the magnets produced by the conventional process. The oxygen content increased by only 0.02 wt % from the starting coarse powder with 0.14 wt % oxygen during jet milling, pressing, desolventing, and sintering process steps. The oxygen uptake rate for wet-processed powders stored in oil was much lower than that for powders stored in organic solvent (*n*-hexane): 0.007 and 0.016 wt %/day, respectively. The characteristics of oxidation prevention and low vaporization rate of the oil contribute to the adaptation of the wet process to mass production with high reliability. The low final oxygen levels provided by the wet process raised the possibility of a reduction of total rare earth (TRE) content.

Figure 2 shows variations of iH_c with oxygen content for sintered magnets with different TRE contents. The coercivity iH_c decreased with the increase of oxygen content. As TRE decreased from 29.8 to 28.9 wt %, the iH_c decrease rate for the oxygen content in the range 0.15 wt % \leq O \leq 0.25 wt % became higher and iH_c was deteriorated to zero with a lower

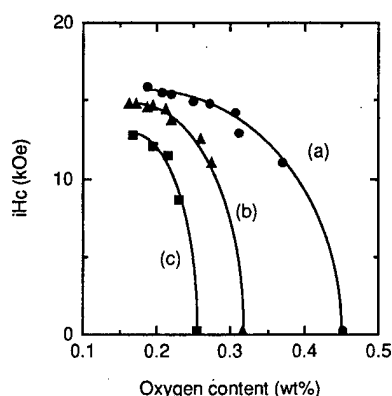


FIG. 2. Variations of iH_c with oxygen content for sintered magnets with different TRE contents: (a) 29.8 wt %, (b) 29.3 wt %, (c) 28.9 wt %.

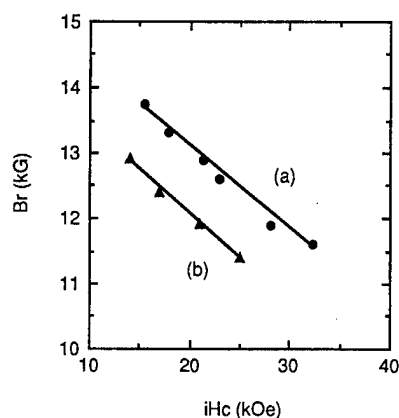


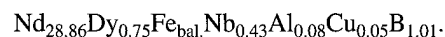
FIG. 3. Magnetic properties of HILOP materials (a) in comparison with conventionally processed materials (b).

oxygen content. This is due to a reduction of the Nd-rich phase caused by the change from Nd to Nd oxide. To obtain a high enough iH_c for practical use, a TRE of more than 29.3 wt % is required.

Figure 3 shows the magnetic properties of HILOP materials for 29.3 wt % TRE



($x = 1.5, 3.0, 4.5, 5.5, 7.5, 9.5$) in wt %] in comparison with conventional compositions (TRE = 31.5–32.5 wt %) on the production scale. From high Br to high iH_c , Br of HILOP materials is 800 G higher than that of conventionally processed materials, due to lower oxygen content and lower TRE content. The HILOP process is also applicable to materials with a much higher $(BH)_{\text{max}}$. The magnetic properties of $(BH)_{\text{max}} = 51.0$ MGOe with $iH_c = 13.1$ kOe were obtained for the composition of



B. Corrosion resistance

The corrosion resistance of the HILOP materials containing less than 0.2 wt % oxygen was investigated. The weight loss of the HILOP material ($\text{Nd}_{27.1}\text{Pr}_{0.6}\text{Dy}_{1.5}\text{Fe}_{\text{bal.}}\text{Co}_{2.1}\text{Nb}_{0.7}\text{Ga}_{0.1}\text{Cu}_{0.1}\text{B}_{1.1}$) is shown in Table II in comparison with a conventionally processed material ($\text{Nd}_{23.9}\text{Pr}_{6.6}\text{Dy}_{1.4}\text{Fe}_{\text{bal.}}\text{Nb}_{0.7}\text{Ga}_{0.1}\text{B}_{1.0}$) and a reference material ($\text{Nd}_{28.2}\text{Pr}_{2.2}\text{Dy}_{1.2}\text{Fe}_{\text{bal.}}\text{Nb}_{0.5}\text{Ga}_{0.1}\text{B}_{1.1}$) that has almost the same TRE as the conventionally processed material and almost the same oxygen content as HILOP material. The weight loss rate of the magnet with a TRE of around 32 wt % increased with decreased oxygen content. This trend is in agreement with those reported by Kim³ and Camp.⁴ How-

TABLE II. Weight loss of HILOP material by pressure cooker test (P.C.T.) for 96 h in comparison with the conventionally processed material. The materials' compositions are given in the text.

Process	TRE (wt %)	Oxygen (wt %)	Weight loss (mg/cm ²)
Conventional	31.7	0.75	0.67
Ref.	31.9	0.15	21.12
HILOP	29.2	0.15	0.53

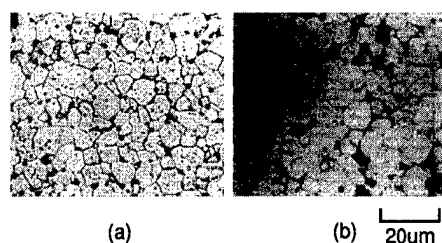


FIG. 4. Photos showing the microstructure of HILOP material (a) in comparison with a conventionally processed magnet (b).

ever, the HILOP material shows a lower weight loss rate even compared to that of the conventionally processed material in spite of its low oxygen content.

Figure 4 shows optical micrographs of the HILOP material and the conventional material. Compared to the conventional material, the HILOP material has a smaller and more homogeneous grain size, so the Nd-rich phases (black or gray regions in the micrographs) at the triple junctions are smaller and more homogeneously distributed. According to the article by Scott *et al.*,⁵ the weight loss rate decreases with the decrease of grain size. Since the corrosion of Nd-Fe-B sintered magnets is initiated in the Nd-rich grain boundary phase,^{6,7} the above result may be explained by the fact that the magnet possesses a lower TRE and that the Nd-rich phases are more evenly distributed, with smaller grain size.

C. Mechanical strength

Table III shows the three-point bending strength and the density of sintered bodies of HILOP material ($\text{Nd}_{21.3}\text{Pr}_{0.5}\text{Dy}_{7.5}\text{Fe}_{\text{bal.}}\text{Co}_{2.0}\text{Nb}_{0.7}\text{Ga}_{0.1}\text{Cu}_{0.1}\text{B}_{1.0}$) and the conventionally processed material



The mechanical strength of HILOP material is improved by around 25%. This result may be attributed to the smaller

TABLE III. Three-point bending strengths and densities (ρ s) of HILOP material in comparison with those of the conventionally processed material.

Process	ρ s (g/cm ³)	Three-point bending strength (kgf/mm ²)
Conventional	7.62	26.2
HILOP	7.70	32.8

grain size mentioned above, higher density (i.e., fewer voids) and fewer inclusions in the Nd-rich phase, such as rare-earth oxides. This issue requires further investigation.

IV. CONCLUSION

The wet process using mineral oil to prevent milled powder and green bodies from oxidation has been established. As a result, magnets with oxygen content of less than 0.2 wt % and $(BH)_{\text{max}}$ of higher than 45 MGOe were obtained in production. The above magnets also have a better corrosion resistance and a higher mechanical strength mainly due to a smaller grain size and a smaller TRE content in the sintered bodies. This process has produced a reduction in the final oxygen content during production, and is one approach for the production of high performance Nd-Fe-B sintered magnets. Additional improvements in the crystallographic alignment of the magnets will produce magnets with much higher magnetic properties.

¹E. Otuki, T. Otsuka, and T. Imai, in *Proceedings of the 11th Workshop on RE Magnets and their Applications*, edited by S. G. Sanker (Carnegie Mellon University Press, Pittsburgh, PA, 1990), pp. 328–340.

²M. Sagawa and H. Nagata, *IEEE Trans. Magn.* **MAG-29**, 2747 (1993).

³A. S. Kim, F. E. Camp, and E. J. Dulis, *IEEE Trans. Magn.* **MAG-26**, 1936 (1990).

⁴F. E. Camp and A. S. Kim, *J. Appl. Phys.* **70**, 6348 (1991).

⁵D. W. Scott, B. M. Ma, Y. L. Liang, and C. O. Bounds, *J. Appl. Phys.* **79**, 5501 (1996).

⁶K. Tokuhara and S. Hirose, *J. Appl. Phys.* **69**, 5521 (1991).

⁷A. S. Kim and F. E. Camp, *J. Mater. Eng.* **13**, 175 (1991).

Hydrogen absorption and desorption behavior in Pr-Fe-B type alloys

Yoon B. Kim and W. Y. Jeung

Center for Metal Processing, Korea Institute of Science and Technology, P.O. Box 131 Cheongryang, Seoul 130-650, Korea

In this study, the hydrogen absorption and desorption behavior of Pr-Fe-B type alloys with addition of Co, Ga, and Zr was investigated focusing on the disproportionation and recombination reaction in HDDR process. In $\text{Pr}_{13}\text{B}_6\text{Fe}_{\text{bal}}$ alloy, the second hydrogen absorption reaction which corresponds to the disproportionation reaction in HDDR process occurs at about 620 °C, and the recombination reaction was not observed below 1000 °C in hydrogen atmosphere. In alloys with Co content of 12 at.%, the second hydrogen desorption reaction, which corresponds to the recombination reaction in HDDR process, occurs at about 955 °C and the occurring temperature of the recombination reaction is further decreased with increasing Co content. The Ga addition to $\text{Pr}_{13}\text{B}_6\text{Fe}_{\text{bal}}$ alloy also reduces the recombination reaction temperature and has no significant influence on the disproportionation reaction. Moreover, the lowering of the recombination reaction temperature is remarkable when Ga and Co are added simultaneously. On the contrary, Zr addition to $\text{Pr}_{13}\text{B}_6\text{Fe}_{\text{bal}}$ alloy may not cause the recombination reaction but make the disproportionation reaction sluggish. The Pr-Fe-B type magnet powder which has a remanence of 9.8 kG and coercivity of 4.8 kOe, was obtained by HDDR treatment. © 1998 American Institute of Physics. [S0021-8979(98)34611-3]

I. INTRODUCTION

Hydrogen treatment such as hydrogenation, disproportionation, desorption, and recombination (HDDR) process is now well established as a method of producing Nd-Fe-B type anisotropic magnetic powder through a hydrogen induced phase transformation.¹⁻⁴ The effects of such minor elements as Co, Ga, and Zr on the HDDR process of Nd-Fe-B type alloy have been intensively studied.⁵⁻⁷ However, the research on applying the HDDR treatment to Pr-Fe-B type alloy and HDDR phenomena with such additive elements in Pr-Fe-B type alloy were not available.

In Pr-Fe-B based alloys where Pr is used as the rare earth instead of Nd, $\text{Pr}_2\text{Fe}_{14}\text{B}$ compound may disproportionate into the mixture of PrH_2 , Fe_2B , and $\alpha\text{-Fe}$ at the disproportionation reaction stage of HDDR treatment. At the recombination reaction stage in HDDR treatment, these decomposed mixtures could be recombined into the fine grained $\text{Pr}_2\text{Fe}_{14}\text{B}$ phase. In the present study, the effects of such minor elements as Co, Ga, and Zr on the hydrogen absorption and desorption behavior of Pr-Fe-B type alloys were investigated focusing on the disproportionation and recombination reaction in HDDR process. In addition to this, magnetic properties of HDDR treated Pr-Fe-B type alloy were investigated.

II. EXPERIMENT

Pr-Fe-B alloy ingots of various composition were prepared by arc melting and induction melting weighed amounts of constituent elements. The alloy ingots were then homogenized at 1000 °C for 20 h in vacuum. After homogenization, alloy ingots were mechanically crushed down to powders of under 200 μm . These powders were used for investigating

the hydrogen absorption and desorption behavior. The chemical composition of alloys used in this study are shown in Table I.

For investigating the hydrogen absorption and desorption characteristics, the samples were heated from room temperature to 1000 °C at an initial hydrogen pressure of 760 Torr and then the pressure changes as well as temperature changes were monitored. At each measurement, an 8 g sample was used and the heating rate was 5 °C/min. The expansion of hydrogen at an elevated temperature was taken into account by performing blank test. The phase changes during hydrogen absorption and desorption were examined using a x-ray diffractometer with $\text{Cu-}k\alpha$ radiation.

The samples for HDDR treatment were prepared by hydrogen decrepitation at room temperature and subsequent milling. For HDDR treatment, the disproportionation treatment was carried out at 800 °C and subsequent evacuating was performed at 820 °C. The disproportionation time was varied. The bonded magnets were made by aligning and pressing after mixing the HDDR treated powders with solid phenol. This compacts were then cured at 120 °C for 2 h. The magnetic properties of bonded magnets were measured by a D.C Fluxmeter.

TABLE I. The chemical composition of alloys (at.%).

No.	Pr	B	Co	Zr	Ga	Fe
1	13.0	6.0				bal.
2	13.0	6.0	6.0-35.0			bal.
3	13.0	6.0		0.1-1.0		bal.
4	13.0	6.0			0.5-1.5	bal.
5	13.0	6.0	12.0	0.5-1.0		bal.
6	13.0	6.0	12.0		1.5	bal.

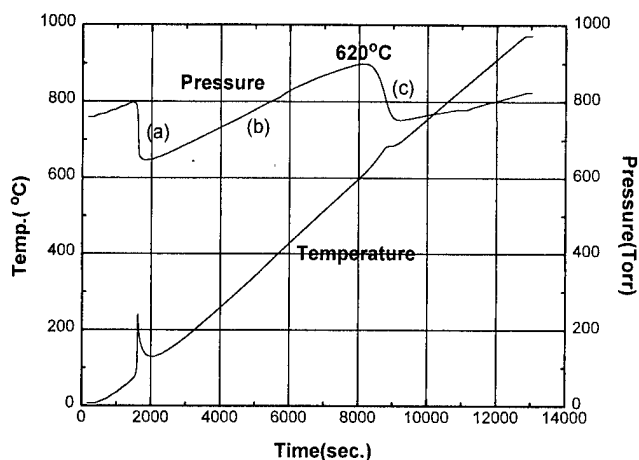


FIG. 1. The hydrogen absorption and desorption behavior in $\text{Pr}_{13}\text{B}_6\text{Fe}_{\text{bal.}}$ type alloys.

III. RESULT AND DISCUSSION

The pressure and the temperature changes in $\text{Pr}_{13}\text{B}_6\text{Fe}_{\text{bal.}}$ alloy, which is the standard composition in this study, on heating from room temperature to 1000 °C is shown in Fig. 1. The pressure change curve for this alloy consists of three regions, two hydrogen absorption regions (designated as a and c) and one hydrogen desorption region (designated as b). The first hydrogen absorption reaction of this alloy, which correspond to hydrogen absorption into Pr-rich and $\text{Pr}_2\text{Fe}_{14}\text{B}$ phases, starts at about 80 °C. This is followed by broad hydrogen desorption reaction. Another hydrogen absorption reaction corresponding to disproportionation reaction in HDDR process occurs at around 620 °C. The recombination reaction was not observed below 1000 °C in hydrogen atmosphere in Pr-Fe-B three component system. The two exothermic peaks on the temperature change curve correspond to the hydrogen absorption reaction.

Figure 2 shows the hydrogen absorption and desorption behavior of Co added Pr-Fe-B alloys. In order for investigation of effect of Co addition on the hydrogen absorption and desorption behavior, the contents of Co addition was varied from 6 to 24 at.%. The starting temperature of first

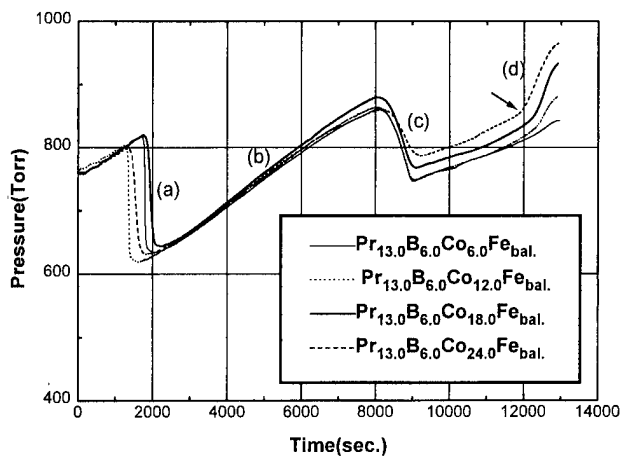


FIG. 2. The hydrogen absorption and desorption behavior in $\text{Pr}_{13}\text{B}_6\text{Co}_x\text{Fe}_{\text{bal.}}$ ($x=6, 12, 18, 24$) type alloys.

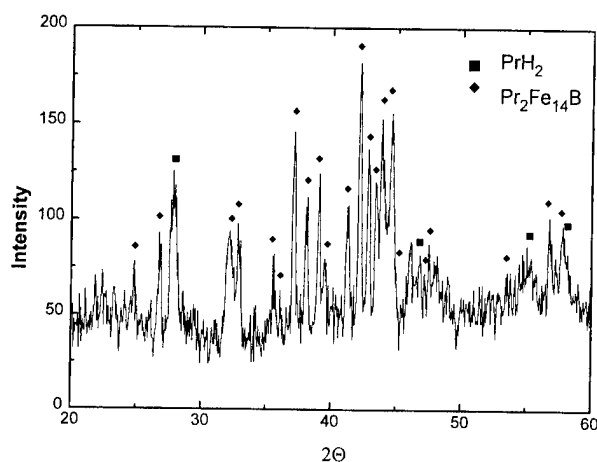


FIG. 3. X-ray diffraction pattern of powders after second hydrogen desorption reaction in $\text{Pr}_{13}\text{B}_6\text{Co}_{12}\text{Fe}_{\text{bal.}}$ type alloys.

hydrogen absorption reaction were varied 70 to 100 °C with the addition of Co. However, the occurring temperatures of second hydrogen absorption reaction corresponding to disproportionation reaction are almost the same as those in the alloys with or without Co, which is around 620 °C. So, the addition of Co to Pr-Fe-B type alloy may not affect the disproportionation reaction. On the contrary, in the alloy with Co content of 12 at.%, the second hydrogen desorption reaction (designated as d) occurs at 955 °C, which corresponds to the recombination reaction in HDDR process. The x-ray diffraction pattern of the powder after this desorption reaction in Fig. 3 shows that the diffraction peaks of $\text{Pr}_2\text{Fe}_{14}\text{B}$ phase, which were recombined from the decomposed mixture of PrH_2 , Fe_2B , and $\alpha\text{-Fe}$, are dominant. The second hydrogen desorption reaction in $\text{Pr}_{13}\text{B}_6\text{Co}_{18}\text{Fe}_{\text{bal.}}$ and $\text{Pr}_{13}\text{B}_6\text{Co}_{24}\text{Fe}_{\text{bal.}}$ alloys occurred at 940 and 925 °C, respectively. So, the occurring temperature of recombination reaction is further decreased with increasing Co content. The recombination reaction was not observed in the alloys with Co content below 6 at.%.

Figure 4 shows the hydrogen absorption and desorption behavior of Ga added Pr-Fe-B alloys. Ga was added from 0.5 to 1.5 at.%. The Ga addition to $\text{Pr}_{13}\text{B}_6\text{Fe}_{\text{bal.}}$ alloy also

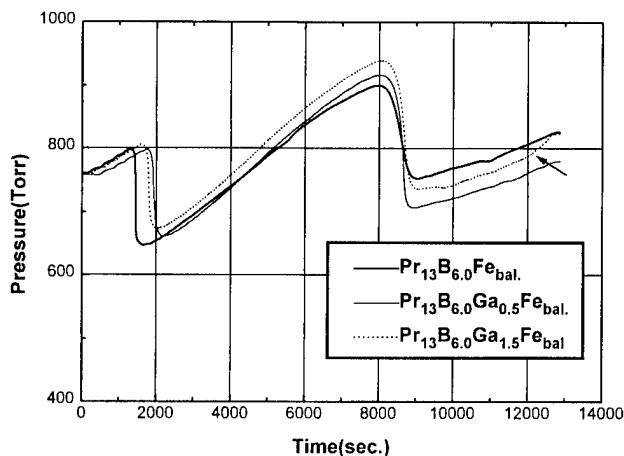


FIG. 4. The hydrogen absorption and desorption behavior in $\text{Pr}_{13}\text{B}_6\text{Ga}_x\text{Fe}_{\text{bal.}}$ ($\text{Ga}=0.5, 1.5$) type alloys.

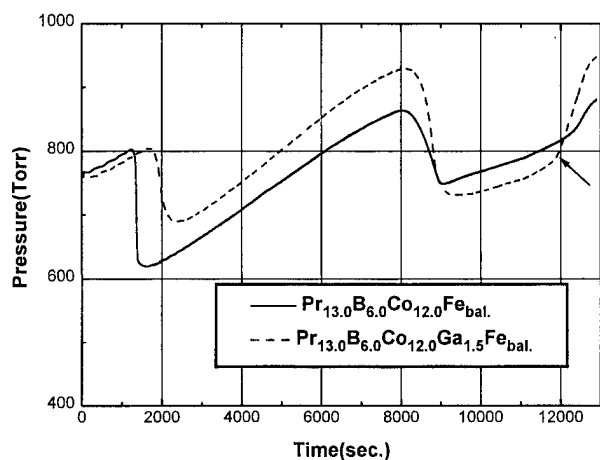


FIG. 5. The hydrogen absorption and desorption behavior in $\text{Pr}_{13}\text{B}_6\text{Co}_{12}(\text{Ga}_{1.5})\text{Fe}_{\text{bal.}}$ type alloys.

causes the recombination reaction below 1000 °C in hydrogen atmosphere, which is the same behavior as that observed in Co added alloys. In $\text{Pr}_{13}\text{B}_6\text{Ga}_{1.5}\text{Fe}_{\text{bal.}}$ the recombination reaction was occurred at about 940 °C, but small addition of Ga (0.5 at.%) does not cause the recombination reaction. The addition of Ga to $\text{Pr}_{13}\text{B}_6\text{Fe}_{\text{bal.}}$ has no significant influence on disproportionation reaction.

As shown in Fig. 2 and Fig. 4, the most distinct effects of Co and Ga addition to Pr-Fe-B system is the lowering of the recombination reaction temperature below 1000 °C in comparison with $\text{Pr}_{13}\text{B}_6\text{Fe}_{\text{bal.}}$ alloy. The decomposed mixture is considered to be less stable by the addition of Co and Ga and hence the recombination reaction starts at a lower temperature. This result indicates that the addition of Co and Ga to Pr-Fe-B alloy enhances the recombination reaction by lowering the recombination reaction temperature.

Figure 5 shows the hydrogen absorption and desorption behavior of $\text{Pr}_{13}\text{B}_6\text{Co}_{12}\text{Ga}_{1.5}\text{Fe}_{\text{bal.}}$ alloy. In this alloy, the recombination reaction starts at about 890 °C. In comparison with $\text{Pr}_{13}\text{B}_6\text{Co}_{12}\text{Fe}_{\text{bal.}}$, the starting temperature of recombination reaction was further decreased by Ga addition. The lowering of the occurring temperature is remarkable when Ga and Co are added simultaneously.

The hydrogen absorption and desorption behavior of Zr added Pr-Fe-B alloys is shown in Fig. 6. The Zr content was varied from 0.1 to 1.0 at. %. The shape of second hydrogen absorption curve corresponding to disproportionation reaction for alloy with 0.1 at. % Zr is broadened in comparison with $\text{Pr}_{13}\text{B}_6\text{Fe}_{\text{bal.}}$ alloy. This disproportionation curve is further broadened with increasing Zr content and both the starting and finishing temperature of disproportionation reaction were changed. So, it can be said that the addition of Zr to Pr-Fe-B alloy may retard the disproportionation reaction. In opposition to Co and Ga added Pr-Fe-B alloys, Zr addition to $\text{Pr}_{13}\text{B}_6\text{Fe}_{\text{bal.}}$ alloy does not cause the recombination reaction below 1000 °C in hydrogen atmosphere.

HDDR treatment was employed to the $\text{Pr}_{13}\text{B}_6\text{Zr}_{0.1}\text{Ga}_{1.0}\text{Co}_{24}\text{Fe}_{\text{bal.}}$ alloy. The samples for HDDR treatment were prepared by hydrogen decrepitation at room

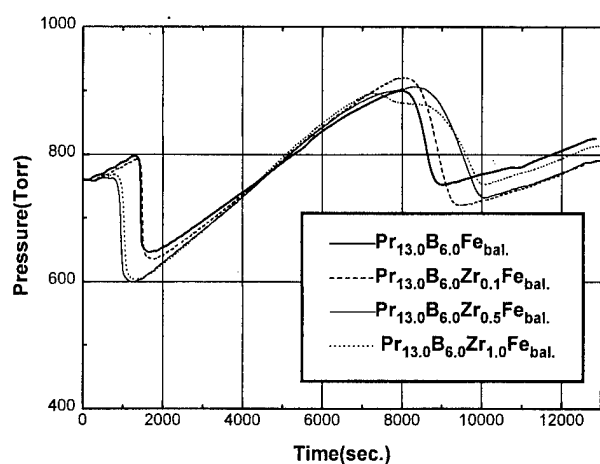


FIG. 6. The hydrogen absorption and desorption behavior in $\text{Pr}_{13}\text{B}_6\text{Zr}_x\text{Fe}_{\text{bal.}}$ ($\text{Zr} = 0.1, 0.5, 1.0$) type alloys.

temperature and subsequent milling. HDDR treatment was carried out by keeping the sample at 800 °C in hydrogen and evacuating hydrogen from the sample at 820 °C. As a result, $\text{Pr}_{13}\text{B}_6\text{Zr}_{0.1}\text{Ga}_{1.0}\text{Co}_{24}\text{Fe}_{\text{bal.}}$ magnet powder having a remanence of 9.8 kG and a coercivity of 4.8 kOe was obtained by employing the HDDR treatment to Pr-Fe-B system.

IV. CONCLUSION

From the investigation of hydrogen absorption and desorption behavior of Pr-Fe-B type alloys and magnetic properties of HDDR treated Pr-Fe-B type magnetic powder, the following conclusions can be drawn.

The second hydrogen desorption reaction, which corresponds to recombination reaction in HDDR process, occurs at about 955 °C in $\text{Pr}_{13}\text{B}_6\text{Co}_{12}\text{Fe}_{\text{bal.}}$ alloy and the occurring temperature of recombination reaction is further decreased with increasing Co content. The Ga addition to $\text{Pr}_{13}\text{B}_6\text{Fe}_{\text{bal.}}$ alloy also reduces the recombination reaction temperature. So, the addition of Co and Ga to Pr-Fe-B alloy enhances the recombination reaction. Moreover, the lowering of the recombination reaction temperature is remarkable when Ga and Co are added simultaneously. The addition of Co and Ga to $\text{Pr}_{13}\text{B}_6\text{Fe}_{\text{bal.}}$ alloy has no significant influence on disproportionation reaction. On the contrary, Zr addition to $\text{Pr}_{13}\text{B}_6\text{Fe}_{\text{bal.}}$ alloy may not cause the recombination reaction but make the disproportionation reaction sluggish. The Pr-Fe-B type magnet powder which has a remanence of 9.8 kG and coercivity of 4.8 kOe, was obtained by HDDR treatment.

¹ T. Takeshita and R Nakayama, in Proc. of the 12th Int. Workshop on Rare-Earth Magnets and Their Application, Canberra, July 670 (1992).

² I. R. Harris and P. J. McGuiness, J. Less-Common Met. **172**, 1273 (1991).

³ R Nakayama and T. Takeshita, J. Appl. Phys. **74**, 2719 (1993).

⁴ I. R. Harris, in Proc. of the 12th Int. Workshop on Rare-Earth Magnets and Their Application, Canberra, July, 347 (1992).

⁵ R Nakayama and T. Takeshita, J. Alloys Compd. **193**, 259 (1993).

⁶ T. Takeshita and R Nakayama, in Proc. of the 11th Int. Workshop on Rare-Earth Magnets and Their Application, Pittsburgh, Oct. 49 (1990).

⁷ M. Uehara, P. Choi, T. Tomida, U. Tomizawa, S. Hirose, and Maehara, IEEE Trans. Magn. **31**, 3632 (1995).

Coercivity of sintered $\text{Nd}(\text{Fe}_{0.92-x}\text{Ga}_x\text{B}_{0.08})_{5.5}$ permanent magnets

X. C. Kou^{a)} and F. R. de Boer

Van der Waals-Zeeman Institute, University of Amsterdam, 1018 XE Amsterdam, The Netherlands

H. Kronmüller

Max-Planck Institut für Metallforschung, Institut für Physik, Heisenbergstraße 1, 70569 Stuttgart, Germany

The temperature dependence of the coercive field of $\text{Nd}(\text{Fe}_{0.92-x}\text{Ga}_x\text{B}_{0.08})_{5.5}$ compounds with $x = 0$ and 0.01 has been measured from 10 K up to the Curie temperatures in fields applied parallel or perpendicular to the magnetic alignment direction and has been analyzed in terms of a micromagnetic model. Two temperature ranges in which different mechanisms control the coercivity can clearly be distinguished. At temperatures above 170 K , a nucleation process of reversed domains determines the coercivity mechanism. From the micromagnetism point of view, partial substitution of Fe by Ga into NdFeB magnets leads to a reduction of the local effective demagnetization field ($-N_{\text{eff}}M_s$) which makes the nucleation of reversed domains more difficult, and therefore enhances the coercivity. © 1998 American Institute of Physics.

[S0021-8979(98)15311-2]

Anisotropic NdFeB permanent magnets are mainly produced by the sintering technique.¹ The magnetic phase in NdFeB magnets is the tetragonal $\text{Nd}_2\text{Fe}_{14}\text{B}$ phase which has exciting intrinsic magnetic properties. However, the coercive field realized in NdFeB magnets depends strongly on the microstructure. The main disadvantage of the NdFeB magnet is its large temperature coefficient of the coercivity. The way to reduce the temperature coefficient of a magnet is to increase either its coercive field or its Curie temperature. Partial substitution of Nd in NdFeB magnets by Tb and/or Dy results in a large enhancement of the coercive field. This is because of the huge uniaxial magnetic anisotropy of $\text{Tb}_2\text{Fe}_{14}\text{B}$ or $\text{Dy}_2\text{Fe}_{14}\text{B}$. However, substitution of Tb and/or Dy leads to a drastic reduction of the saturation magnetization. On the other hand, the Curie temperature of NdFeB magnets can be drastically increased by partial substitution of Fe by Co, however, at a cost of the coercive field. Ga is the only nonmagnetic element which simultaneously raises the Curie temperature² and the coercive field of NdFeB magnets. It is one of the main subjects of the present article to understand why the coercive field is enhanced in Ga-containing NdFeB magnets. In addition, the mechanism which controls the magnetization reversal process in NdFeB and $\text{Nd}(\text{Fe,Ga})\text{B}$ magnets will be studied with the main emphasis on the comparison of the temperature dependence of the coercive field measured with the field applied parallel and perpendicular to the magnetic-alignment direction.

Much effort was made to obtain magnets with a high degree of the grain alignment. A number of cylindrical samples with a diameter of 4 mm and a length of 6 mm were cut out from the bulk $\text{Nd}(\text{Fe}_{0.92}\text{B}_{0.08})_{5.5}$ and $\text{Nd}(\text{Fe}_{0.91}\text{Ga}_{0.01}\text{B}_{0.08})_{5.5}$ sintered magnets with the cylindrical axis parallel or perpendicular to the magnetic alignment direction. Magnetic hysteresis loops were measured from 10 to 800 K in a vibrating-sample magnetometer equipped with a

superconducting coil providing a maximum field strength of 6.4 MA/m . The value of the coercive field H_c is defined as the field where the irreversible susceptibility of the demagnetization curve has a maximum. According to this definition, the coercive field corresponds to the field where most domains reverse their magnetization direction under the action of the applied inverse field.

Figure 1 shows the magnetic hysteresis loops of $\text{Nd}(\text{Fe}_{0.91}\text{Ga}_{0.01}\text{B}_{0.08})_{5.5}$ measured at 300 K in external fields applied parallel and perpendicular to the magnetic-alignment direction. The presence of a fairly good grain alignment follows from the very pronounced difference of the magnetic hysteresis loops measured in the two directions. The hysteresis loop in the parallel measurements is predominantly due to magnetization reversal of the grains which are magnetically aligned. However, the hysteresis loop in the perpendicular measurements is only due to the presence of grains which are misaligned. This is because the magnetic moments of the aligned grains will be rotated to the direction of the applied field only when the external field exceeds the anisotropy field, which is about 7 MA/m at 300 K for $\text{Nd}_2\text{Fe}_{14}\text{B}$. According to the micromagnetic model of coercivity,^{3,4} the presence of misaligned grains in permanent magnets leads to lowering coercivity. This is because the nucleation field is lower in misaligned single-domain particles. From the present measurement, however, it becomes evident that the coercive field is larger when the magnetic hysteresis loop is measured in a perpendicular field. This experimental fact suggests the coercivity in misaligned grains to be larger than in perfectly aligned grains. It must be noted that it is a common feature of NdFeB sintered magnets that an improvement of the degree of grain alignment results in a reduction of the coercivity. To understand this seeming paradox between the experimental results and the theoretical prediction forms another main subject of the present article.

In Fig. 2, the temperature dependence of the coercive field of $\text{Nd}(\text{Fe}_{0.92}\text{B}_{0.08})_{5.5}$ and $\text{Nd}(\text{Fe}_{0.91}\text{Ga}_{0.01}\text{B}_{0.08})_{5.5}$ magnets is shown. It can be seen that the coercive fields mea-

^{a)}Author to whom correspondence should be addressed; electronic mail: kou@phys.uva.nl

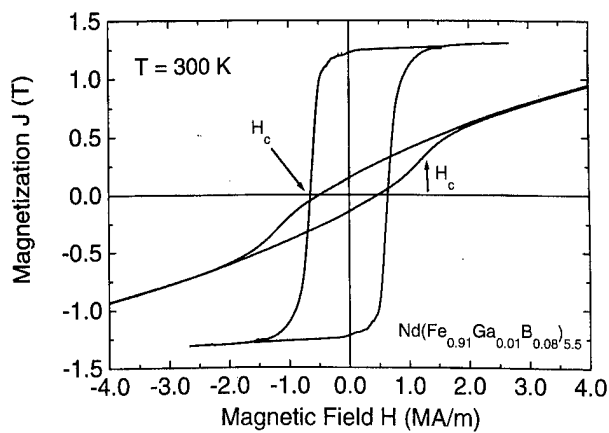


FIG. 1. Magnetic hysteresis loops of $\text{Nd}(\text{Fe}_{0.91}\text{Ga}_{0.01}\text{B}_{0.08})_{5.5}$ sintered magnets measured in external fields applied parallel or perpendicular to the magnetic-alignment direction.

sured in a perpendicular field are higher at all temperatures where magnetic order exists. In the parallel measurements, compared to the pure NdFeB magnets, the Ga-containing magnets show a higher coercive field at higher temperature. In order to understand from the micromagnetic point of view why the coercive field changes upon Ga addition and why the perpendicular measurements give a higher coercive field, the intrinsic magnetic properties of $\text{Nd}_2\text{Fe}_{14}\text{B}$, e.g., the anisotropy constants, K_1 , K_2 , and the spontaneous magnetization M_s should be known. The values of K_1 , K_2 , and M_s of NdFeB magnets at various temperatures, corresponding to the measuring temperatures of H_c , were obtained by interpolating from the data of Hock,⁵ which have been obtained by measuring the magnetization of a $\text{Nd}_2\text{Fe}_{14}\text{B}$ single crystal.

Within the theory of micromagnetism, the coercive field H_c of a permanent magnet can be expressed as^{4,6}

$$H_c = \alpha_K \alpha_\phi H_n - N_{\text{eff}} M_s, \quad (1)$$

where H_n is the nucleation field of a spherical single-domain particle of a hard magnetic phase if the external field is applied exactly antiparallel to the magnetization vector. M_s is the spontaneous magnetization of the hard magnetic phase. α_K , α_ϕ , and N_{eff} are micromagnetic parameters which describe the deviation of the coercivity in real magnets from

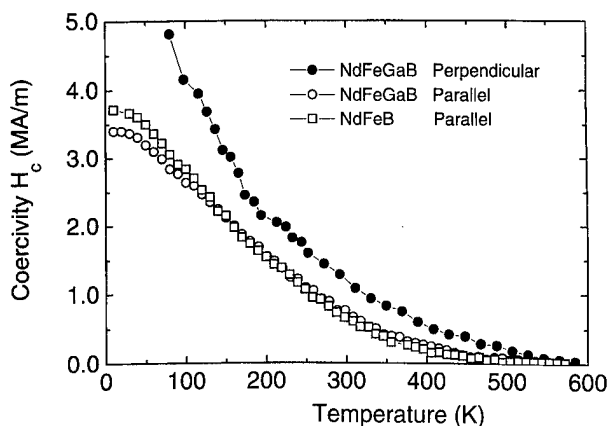


FIG. 2. Temperature dependence of the coercive field H_c of $\text{Nd}(\text{Fe}_{0.92}\text{B}_{0.08})_{5.5}$ and $\text{Nd}(\text{Fe}_{0.91}\text{Ga}_{0.01}\text{B}_{0.08})_{5.5}$ sintered magnets.

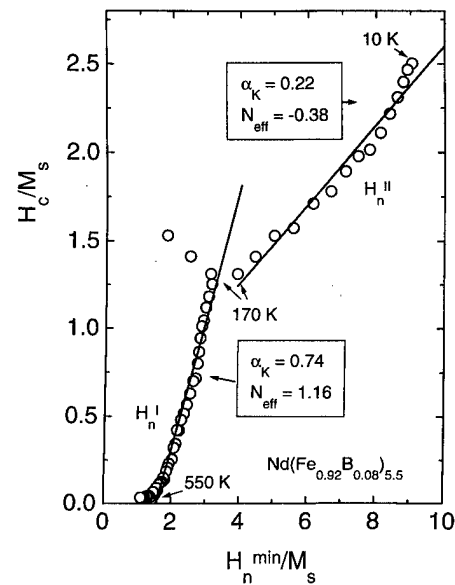


FIG. 3. Least-square linear fit of the H_c/M_s vs H_n^{min}/M_s curves of $\text{Nd}(\text{Fe}_{0.92}\text{B}_{0.08})_{5.5}$ in two temperature ranges. The H_c values were obtained from magnetic hysteresis loops measured in a field parallel to the magnetic-alignment direction.

the nucleation field in a spherical single-domain particle. α_K is the parameter which describes the reduction of the nucleation field caused by the low magnetic anisotropy at the grain surface. α_ϕ represents the reduction of the nucleation field due to the presence of the misaligned grains. This is because the misaligned single-domain particles have a low nucleation field and the nucleated reversed domains in the grains should have the same easy magnetization direction (EMD) as the grains themselves. Theoretically, both α_ϕ and α_K are temperature dependent. The micromagnetic parameter, N_{eff} , determines the locations where the reversed domains are preferentially nucleated.

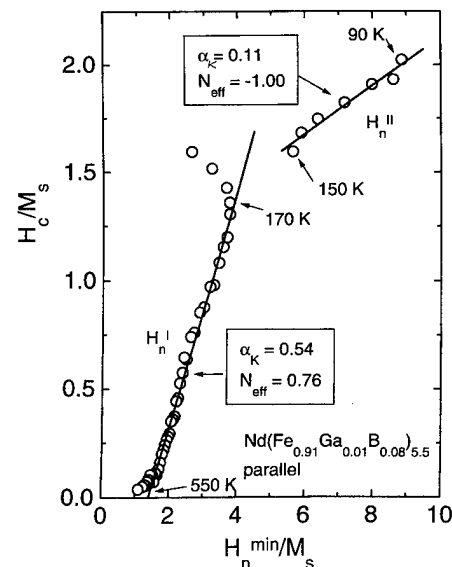


FIG. 4. Least-square linear fit of the H_c/M_s vs H_n^{min}/M_s curves for $\text{Nd}(\text{Fe}_{0.91}\text{Ga}_{0.01}\text{B}_{0.08})_{5.5}$ magnets at two temperature ranges. The H_c values were obtained from magnetic hysteresis loops measured in a field parallel to the magnetic-alignment direction.

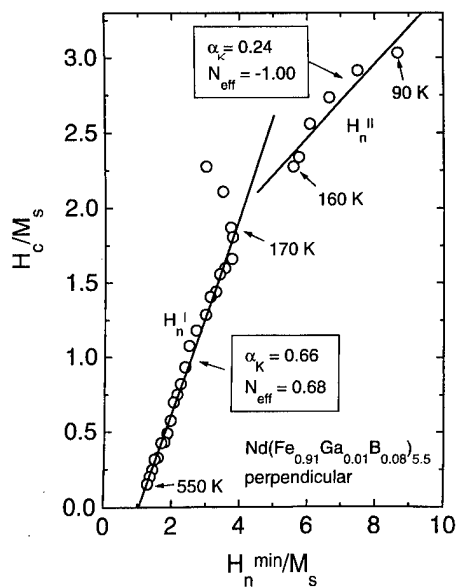


FIG. 5. Least-square linear fit of the H_c/M_s vs H_n^{\min}/M_s curves for $\text{Nd}(\text{Fe}_{0.91}\text{Ga}_{0.01}\text{B}_{0.08})_{5.5}$ magnets at two temperature ranges. The H_c values were obtained from magnetic hysteresis loops measured in a field perpendicular to the magnetic-alignment direction.

The value of the nucleation field, H_n , is determined only by the intrinsic magnetic properties of the hard-magnetic phase, i.e., of $\text{Nd}_2\text{Fe}_{14}\text{B}$. From the data on the anisotropy constants obtained by Hock,⁵ it follows that at temperatures above 170 K the conditions $K_1 \gg K_2$ and $K_1 \neq 0$ hold. The nucleation field H_n and the parameter α_φ can be calculated by means of the expressions:

$$H_n^1 = \frac{2K_1}{\mu_0 M_s}$$

and

$$\alpha_\varphi = \frac{1}{\cos \varphi} \frac{1}{(1 + \tan^{2/3} \varphi)^{3/2}} \left(1 + \frac{2K_2}{K_1} \frac{\tan^{2/3} \varphi}{1 + \tan^{2/3} \varphi} \right),$$

where φ is the angle between the EMD of the grain and the direction of the applied magnetic field. At temperatures below 170 K, the condition $-2K_2 < K_1 < 4K_2$ holds. In this case, α_φ can only be obtained by numerical calculation. The minimum of H_n^{II} has been calculated by Martinek *et al.*⁷ to be:

$$H_n^{\text{II min}} = \frac{1}{\mu_0 M_s} \frac{1}{2\sqrt{2}} \left[K_1 + \frac{K_2}{4} \left(W - \frac{K_1}{K_2} + 3 \right) \right] \\ \times \sqrt{\left[W \left(\frac{K_1}{K_2} + 1 \right) - \left(\frac{K_1}{K_2} \right)^2 - \frac{2K_1}{K_2} + 3 \right]},$$

where

$$W = \sqrt{\left(\frac{K_1}{K_2} + 1 \right)^2 + 8}.$$

In a real magnet, misalignment is inevitable and a distribution of the grain alignment exists. The nucleation field differs therefore from one grain to the other. For simplicity,

it is assumed that the coercive field of the bulk magnet is determined by the grains which have the minimum nucleation field ($H_n^{\min} = \alpha_\varphi^{\min} H_n$).

In Fig. 3, H_c/M_s is plotted as the function of H_n^{\min}/M_s for $\text{Nd}(\text{Fe}_{0.92}\text{B}_{0.08})_{5.5}$ permanent magnets. Similar to what was found previously,⁸ two clearly distinguishable temperature ranges can be seen. At temperatures above 170 K, H_n^{I} is the nucleation field, whereas H_n^{II} is the nucleation field below 170 K. The mechanism which controls the coercivity may be different in these two temperature ranges. A least-square linear fitting program was applied to fit separately the H_c/M_s vs H_n^{\min}/M_s curves in two temperature ranges. The fitting parameters, α_K and N_{eff} , are included in the figure. A large difference in values of N_{eff} is evident in these two temperature ranges. In the temperature range where H_n^{I} is the nucleation field, the value of N_{eff} is rather large. This implies that the magnetization reversal process in this temperature range is realized through expansion of reversed domains which are nucleated preferentially in the region of the grain surface where the local effective demagnetizing field ($-N_{\text{eff}}M_s$) is the largest. On the other hand, in the temperature range where H_n^{II} is the nucleation field, the value of N_{eff} is rather small or even negative. This suggests that reversed domains in this temperature range are not nucleated due to a large local effective demagnetizing field. In the present analysis, the main emphasis will be on the temperatures above 170 K.

In Figs. 4 and 5, plots of H_c/M_s vs H_n^{\min}/M_s are shown for measurements parallel and perpendicular to the magnetic-alignment direction, respectively. Similar to what was found for $\text{Nd}(\text{Fe}_{0.92}\text{B}_{0.08})_{5.5}$, there are two temperature ranges which manifest themselves by different mechanisms in the magnetization reversal process. Let us first compare the results in the temperature range above 170 K, as shown in Figs. 3 and 4, which should reveal the influence of the Ga additive. Compared to the $\text{Nd}(\text{Fe}_{0.92}\text{B}_{0.08})_{5.5}$ magnet, the $\text{Nd}(\text{Fe}_{0.91}\text{Ga}_{0.01}\text{B}_{0.08})_{5.5}$ magnet has a lower value of α_K and a much lower value of N_{eff} . The low value of α_K leads to a reduction of coercivity, whereas the low value of N_{eff} results in a large coercivity. This result suggests that the enhancement of the coercivity in $\text{Nd}(\text{Fe}_{0.91}\text{Ga}_{0.01}\text{B}_{0.08})_{5.5}$ is mainly due to the reduction of the local effective demagnetization field ($-N_{\text{eff}}M_s$). A similar conclusion can be drawn from a comparison of Figs. 4 and 5. The misaligned grains have a lower nucleation field which reduces the coercivity. On the other hand, the much lower local effective demagnetization field drastically enhances the coercivity.

One of the authors (X.C.K.) would like to thank the European Commission for a grant in the TMR program.

¹M. Sagawa, S. Fujimura, H. Yamamoto, N. Togawa, and Y. Matsuura, J. Appl. Phys. **55**, 2083 (1984).

²X. C. Kou, X. K. Sun, Y. C. Chuang, T. S. Zhao, R. Grössinger, and H. R. Kirchmayr, J. Magn. Magn. Mater. **82**, 327 (1989).

³H. Kronmüller, Phys. Status Solidi B **130**, 197 (1985).

⁴H. Kronmüller, K.-D. Durst, and G. Martinek, J. Magn. Magn. Mater. **69**, 149 (1987).

⁵S. Hock, thesis, University of Stuttgart, 1988.

⁶W. F. Brown, Jr., Rev. Mod. Phys. **17**, 15 (1945).

⁷G. Martinek and H. Kronmüller, J. Magn. Magn. Mater. **86**, 177 (1990).

⁸X. C. Kou and H. Kronmüller, J. Phys.: Condens. Matter **6**, 6691 (1994).

The origin and interpretation of fine scale magnetic contrast in magnetic force microscopy: A study using single-crystal NdFeB and a range of magnetic force microscopy tips

M. Al-Khafaji,^{a)} W. M. Rainforth,^{a)} M. R. J. Gibbs,^{b),c)} J. E. L. Bishop,^{b)} and H. A. Davies^{a)}
Sheffield Centre for Advanced Magnetic Materials and Devices, Sheffield, United Kingdom

We have used an oriented single crystal of Nd₂Fe₁₄B₁ as a test sample to explore contrast and resolution as a function of magnetic force microscopy tip coating, tip scan height, and sample history. We find that resolution is independent of tip type; that contrast is greater at low scan heights and for higher moment tips; and that the fine length scale structure of order 25 nm can be resolved. We further show how the surface structure is a function of state (demagnetized or remanent), demonstrating the ability of well-characterized studies to give high-resolution information on carefully prepared samples. © 1998 American Institute of Physics. [S0021-8979(98)16611-2]

INTRODUCTION

In magnetic force microscopy (MFM) the interaction between the tip magnetic moment and the stray field gradient (SFG) above a sample raises a number of issues. The SFG includes contributions from surface and subsurface domain structure, and surface topology. The response of the tip depends on the magnetization process within the tip, on the local SFG (dominated by contributions from local structure), and also, depending on the tip susceptibility, on the magnitude and direction of the field itself. While the SFG is strongly dominated by local contributions, the field will include significant long-range contributions, and indeed, may strongly reflect the gross magnetic state of the tip. A fully quantitative interpretation of the MFM signal must remain a distant goal.

Systematic observations, with sufficiently close control of the variables, are required in order to establish MFM performance. Convention has it that the spatial resolution limit is the tip-sample spacing or the tip radius, whichever is the greater. We have previously reported¹ fine scale magnetic-force gradient contrast in MFM images taken on a plane orthogonal to the easy axis of a large single crystal of as-grown Nd₂Fe₁₄B, having high *c*-axis texture. This single-crystal sample constitutes a stable test sample, with a large area for scanning, and high coercivity and high anisotropy energy. Magnetic contrast was clearly observed on a scale of order 25 nm, less than the tip-sample spacing and of the order of the tip radius. We now extend this study in three ways: we explore the resolution limit; the image formation for different tip coatings; and the NdFeB sample in a number of magnetic states.

EXPERIMENTAL DETAILS

A Digital Instruments Dimension 3000 scanning probe microscope was used in the Tapping/Lift™ mode, using sili-

con cantilevers with integral pyramidal tips and commercial coatings (Digital Instruments) of CoCr (high coercivity) and NiFe (low coercivity).²

THE RESOLUTION LIMIT

Figure 1 shows MFM images of the NdFeB single crystal (as-grown) using a NiFe coated tip. Registration of the images (gross features are the same on all images) was maintained using features in the associated topographic scan (not shown). A remarkable feature of the 25 nm scale fine structure is a distinct pattern of fine curved lines that repetitively decorate the bends of the rick-rack domain pattern. The con-

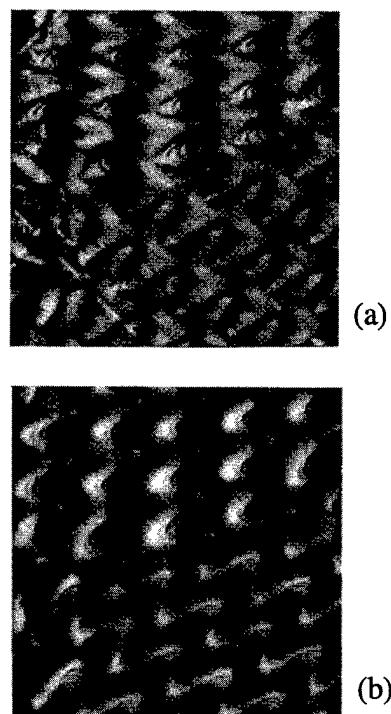


FIG. 1. 5 $\mu\text{m} \times 5 \mu\text{m}$ MFM images from the surface of an as-grown NdFeB single crystal on a face orthogonal to the easy axis. Scan heights (a) 25 nm and (b) 100 nm. Tip NiFe. Contrast=phase shift of 20°.

^{a)}Also with Department of Engineering Materials, University of Sheffield, Sheffield S1 3JD, UK.

^{b)}Also with Department of Physics, University of Sheffield, Sheffield S3 7RH, UK.

^{c)}Electronic mail: M.R.Gibbs@Sheffield.ac.uk

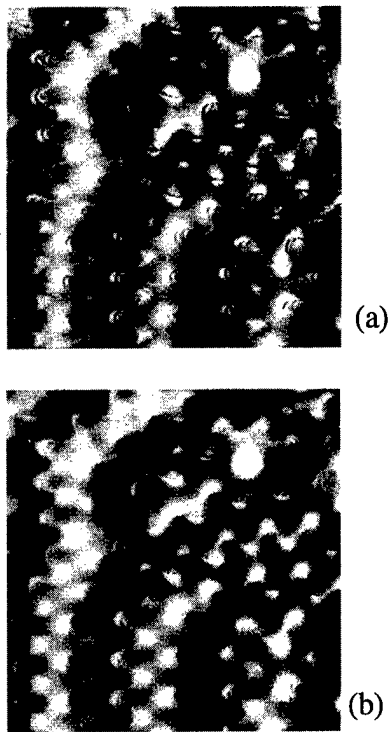


FIG. 2. $7\text{ }\mu\text{m}\times 7\text{ }\mu\text{m}$ MFM images from the surface of an as-grown NdFeB single crystal on a face orthogonal to the easy axis. Scan heights (a) 100 nm and (b) 200 nm. Tip CoCr. Contrast=phase shift of 60° .

trast and resolution vary with scan height, but gross features are maintained. Analysis shows that the image is influenced primarily by features near the surface to a depth proportional to the scan height. Thus, increasing the scan height does not simply blur the details, but enhances the relative sensitivity to deeper structures. Scanning with a second NiFe tip produced identical results.

Figure 2 shows analogous images for a CoCr coated tip from another area of the sample, again in register for the series. As for the NiFe tip, the gross features are reproduced, only the contrast and resolution decrease with increasing scan height.

Of particular significance is the fine scale structure observed in both of the low scan height images, including the repetitive pattern discussed above. The resolution limit is practically tip independent, and also scanning in an orthogonal direction produces an essentially identical image. It must be deduced that the simple rule for the resolution limit given in the Introduction is not adequate, and that many finer scale features can be reproducibly observed.

COMPARISON OF TIP COATINGS

According to earlier studies² on such tips, the magnetic characteristics should be very different, the CoCr presenting a high moment, high coercivity behavior, while the NiFe is lower moment and lower coercivity. Comparing images between tips for the same scan height, it is clear that the resolution is largely independent of tip character.

A simple comparison of Figs. 1 and 2 demonstrates that the nature of the contrast is, as expected, somewhat different

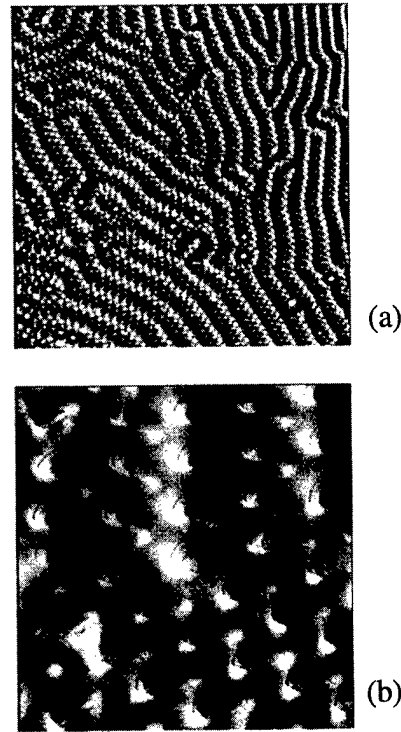


FIG. 3. MFM images orthogonal to the c axis of a thermally demagnetized single crystal of $\text{Nd}_2\text{Fe}_{14}\text{B}$. CoCr tip. (a) $35\times 35\text{ }\mu\text{m}$:100 nm scan height and (b) $5\times 5\text{ }\mu\text{m}$:100 nm scan height. Black-white contrast= 50° phase shift.

for the two tip coatings. This can be interpreted in terms of the CoCr tip behaving essentially as a fixed dipole, whereas the moment of the NiFe is controlled by the field of the Nd-Fe-B. Thus, the CoCr tip primarily delineates the domains, while the NiFe tip primarily delineates the domain walls.³ It is important to emphasize that the fine scale structure is visible with both tips, that is, it must reflect the underlying magnetic domain structure and is, therefore, no artifact.

STUDY OF NdFeB SINGLE CRYSTAL IN DIFFERENT MAGNETIC STATES

Two distinct types of features are visible in Fig. 3 (a thermally demagnetized state); closure spike domains (bright spots dispersed across the image),⁴ and rick-rack domains.¹ The fine scale line structure associated with the rick-rack pattern is again observed, with the rick-rack domains parallel to each other over distances long compared to their separation and wavelength. For the remanent state after magnetization to 5 T in a hard direction (Fig. 4), this long-range structure is not present, the rick-rack pattern has become much more convoluted, and the incidence of spike domains has decreased. There is now an absence of the fine line structure associated with the rick-rack pattern.

For the remanent state after magnetization to 5 T in the easy direction (Fig. 5), the convolution of the rick-rack pattern is similar to the other remanent state. The incidence of spike domains remains low, but the fine line structure associated with the rick-rack domains is more pronounced.

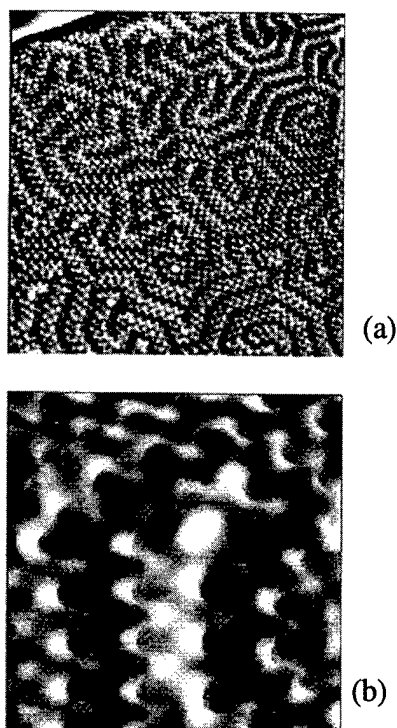


FIG. 4. MFM images orthogonal to the c axis of a single crystal of $\text{Nd}_2\text{Fe}_{14}\text{B}$, in a remanent state after magnetization to 5 T with the field in the sample plane. CoCr tip. (a) $35 \times 35 \mu\text{m}$ at 100 nm scan height and (b) $5 \times 5 \mu\text{m}$ at 100 nm scan height. Black-white contrast $\equiv 50^\circ$ phase shift.

From these detailed comparisons it is possible to conclude that the rick-rack pattern represents a closure structure on the surface of a sample of high uniaxial anisotropy constant $K_1 > 2\pi M_s^2$.¹ The gross features of this pattern are unaffected by previous magnetic history, except in the case of thermal demagnetization. Figure 3(a) demonstrates that the convolution is much less after demagnetization. A reasonable interpretation is that in achieving the thermally demagnetized state, the fundamental underlying domain structure is more ordered and less complex. The long-range quasiparallel orientation of the rick-rack walls suggests the underlying structure approximates the well-known stripe domain structure.

The fine scale line structure parasitic on the rick-rack pattern is clearly influenced by the magnetic history. In the case of Fig. 4 where a field of 5 T has been applied and then removed in plane, this fine detail is not evident. This suggests that in these regions, close to the sample surface, further energy minimization is possible, when the remanent state is along the easy direction (Fig. 5), by division into

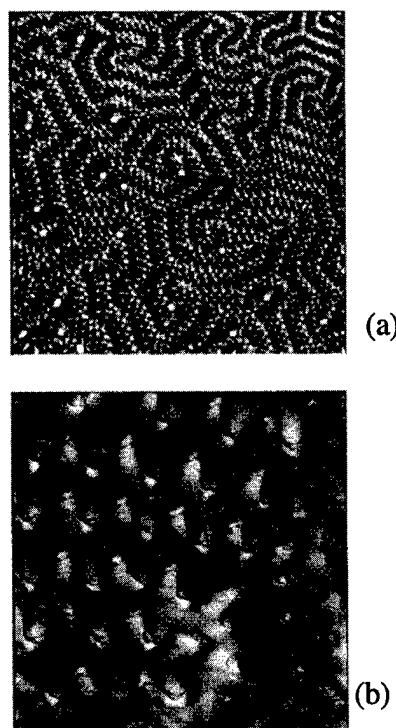


FIG. 5. MFM as in Fig. 4 in a remanent state after magnetization to 5 T with the field orthogonal to the sample plane. CoCr tip. (a) $35 \times 35 \mu\text{m}$ at 100 nm scan height and (b) $5 \times 5 \mu\text{m}$ at 100 nm scan height. Black-white contrast $\equiv 50^\circ$ phase shift.

smaller closure domains at regions of high wall curvature. It is certainly also true that this fine scale contrast is magnetic in origin, although the length scale is so short.

CONCLUSIONS

The fine scale structure on a scale of 25 nm, much less than the tip-sample spacing, and of the order of the tip radius, is clearly resolved and of magnetic origin. Its existence is independent of tip materials. It is seen in thermally demagnetized samples and in samples remanent after magnetization in the easy direction normal to the surface, but not when the remanent state is reached after magnetization in a hard direction.

¹M. Al-Khafaji, W. M. Rainforth, M. R. J. Gibbs, J. E. L. Bishop, and H. A. Davies, *IEEE Trans. Magn.* **32**, 4138 (1996).

²K. Babcock, V. Elings, J. Shi, D. Awschalom, and M. Dugas, *Appl. Phys. Lett.* **69**, 705 (1996).

³M. Al-Khafaji, W. M. Rainforth, M. R. J. Gibbs, H. A. Davies, and J. E. L. Bishop, *J. Magn. Magn. Mater.* (in press).

⁴L. Folks, R. Street, R. C. Woodward, and K. Babcock, *J. Magn. Magn. Mater.* **159**, 109 (1996).

Off-axis electron holographic mapping of magnetic domains in $\text{Nd}_2\text{Fe}_{14}\text{B}$

M. R. McCartney

Center for Solid State Science, Arizona State University, Tempe, Arizona 85287-1704

Yimei Zhu

Department of Applied Sciences, Brookhaven National Laboratory, Upton, New York 11973

Off-axis electron holography employing a field-free Lorentz lens has been used to provide direct imaging of magnetic induction in $\text{Nd}_2\text{Fe}_{14}\text{B}$ with nanometer-scale resolution and high signal-to-noise. Using this technique, reconstructed phase images have been used to measure domain wall widths for 90° and 180° walls in a sintered sample were measured to be no greater than 7 and 9 nm, respectively. Induction maps show an unusual array of 90° domains in a hot-press sample, with singularities at the intersections of the domains. *In situ* thermal annealing of the hot-pressed sample resulted in magnetization rotation accompanied by domain wall movement and evidence for pinning at a structural defect. Heating of the sample above 400°C resulted in the accumulation of small particles in thin regions and decrease in magnetic contrast. © 1998 American Institute of Physics. [S0021-8979(98)41411-7]

Hard magnetic materials such as NdFeB alloys have high remanence and coercivity that potentially lead to many practical applications.^{1,2} Magnetic force microscopy (MFM) and scanning electron microscopy with polarization analysis (SEMPA)³ can provide quantitative information about surface features such as domain walls that intersect the surface of bulk magnetic materials. Transmission electron microscopy techniques for imaging thin magnetic films include Foucault imaging⁴ and differential phase contrast⁵ imaging which give direction-dependent magnetization contrast, and out-of-focus, Fresnel or Lorentz imaging which gives contrast at domain wall positions.⁶ Off-axis electron holography is a technique that is sensitive to electrostatic and magnetic potentials within solid materials. In particular, the magnetic induction strength and direction can be imaged at high resolution and with high sensitivity.⁷ In this work, we describe the use of off-axis electron holography to map the induction distribution of magnetic domains in $\text{Nd}_2\text{Fe}_{14}\text{B}$ alloys at nanoscale spatial resolution.

The electron holograms and Lorentz images were recorded with a Philips CM200 transmission electron microscope equipped with a field emission electron source.⁸ This instrument has a (Lorentz) mini-lens in the region below the lower objective polepiece which provides a line resolution of 1.2 nm with only a small residual field at the sample. The microscope is equipped with an electrostatic biprism in the plane of the selected area aperture holder for off-axis electron holography. Holograms and Fresnel images were recorded digitally with a Gatan 679 slow-scan CCD camera. A double-tilt heating holder was used to investigate the effects of heating cycles on the induction distribution.

A pair of Fresnel images from a sintered sample of $\text{Nd}_2\text{Fe}_{14}\text{B}$ recorded under field-free conditions are shown in Figs. 1(a) and 1(b). The contrast at the domain walls (arrowed) has inverted upon going from underfocus to overfocus. Figure 1(c) shows a contoured phase image that was reconstructed from an off-axis electron hologram of the indicated region of Fig. 1(a). The equispaced contours within each domain indicate uniform magnetization that gives rise

to a constant phase plane. The normal to this plane is related to the direction and magnitude of the induction. Ridges and valleys in the phase image can be directly related to the bright and dark lines in the underfocus Fresnel image. These abrupt changes in slope are associated with changing magnetization and correspond to the domain wall positions. In order to map the magnetic induction within the sample, simple gradients of the phase image can be calculated by displacing the phase image, followed by subtraction.⁹ Figure 1(d) shows the vertical gradient of the phase and reveals the horizontal component of the induction.

Two perpendicular gradient images can be combined into a vector map to produce a direct image of magnetic structure within the domains, as shown in Fig. 2(a). The vector map is divided into $10\text{ nm} \times 10\text{ nm}$ squares, and shows three distinct domains with the top and middle domains ori-

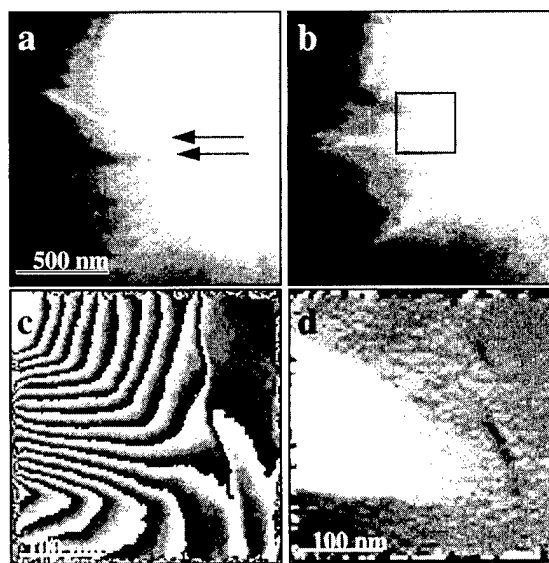


FIG. 1. (a) Over-focus and (b) under-focus Fresnel images of non-parallel domain walls in $\text{Nd}_2\text{Fe}_{14}\text{B}$. Box indicates area used for off-axis holography. (c) Reconstructed phase image from outlined region contoured at 0.5π radian intervals. (d) Vertical gradient of (c).

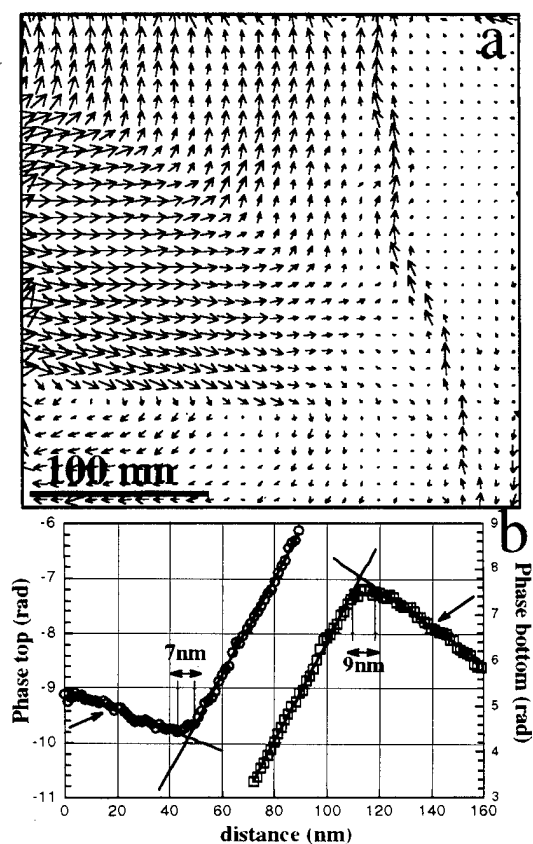


FIG. 2. (a) Induction map derived from phase gradients in Fig. 1 with 90° and 180° domain walls. (b) Domain wall width measurements from phase profiles. Circles (top wall) and squares (bottom wall) are phase data, solid lines are linear fits.

ented at approximately 90° and the middle and lower oriented at approximately 180° to each other. The minimum vector length indicates out-of-plane or vanishing induction. The vectors which delineate the edge of the sample are an artefact due to the rapid increase in mean potential at the sample-vacuum interface. Within the sample, the vector length corresponds to the product of the in-plane magnetization and the thickness. Using an estimate of 60 nm for the thickness^{10,11} for thicker areas of the sample (on the left of Fig. 2), the vector lengths calculated from the modulus of the gradients correspond to magnetizations, $4\pi M_s = B = 0.8$ T, 1.2 T, and 0.5 T for the top, middle, and bottom domains, respectively. Care should be taken when interpreting details of the induction maps, particularly because of undetermined fringing fields immediately above and below the sample surface. For example, such demagnetizing fields, visible as curved contour lines extending into vacuum at the lower right of Fig. 1(c) may be responsible for the apparent reduction of the magnetization in the bottom domain. In addition, it should be noted that the technique is only sensitive to the in-plane component so that any crystal tilt toward the c -axis normal will reduce the measured magnetization.

An estimate for domain wall width can be made directly from the phase image by measuring the distance over which the phase slope abruptly changes. Figure 2(b) shows phase profiles taken perpendicular to the top (90°) and bottom (180°) domain walls. The open circles (squares) are the

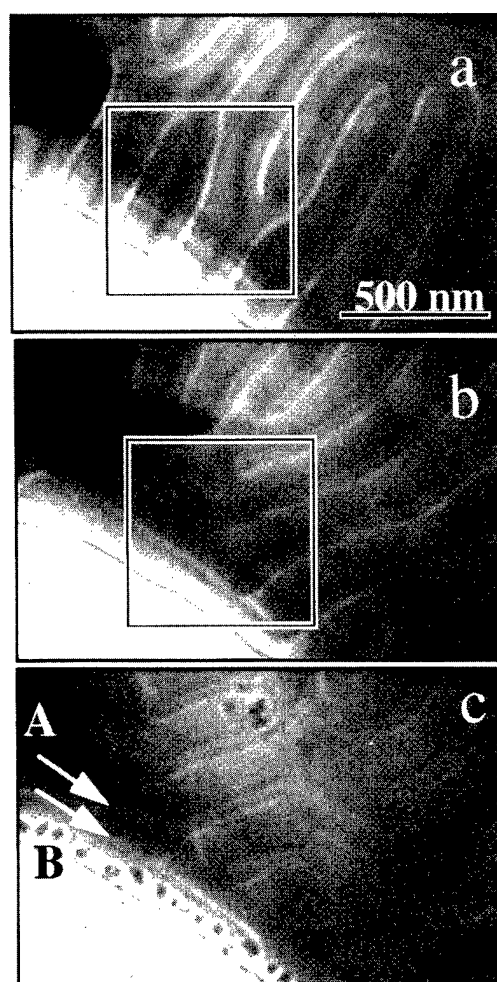


FIG. 3. Fresnel under-focus images of die-upset $\text{Nd}_2\text{Fe}_2\text{B}$ as function of temperature: (a) room temperature; (b) heated to 300°C and then cooled to room temperature; (c) heated above the Curie temperature, then cooled. "A" indicates domain wall associated with crystal defect, "B" is a grain boundary.

phase data averaged over 20 nm and the solid lines are least square linear fits to the data. These measurements indicate a maximum¹² width of 6.7 ± 1.4 nm and 9.2 ± 1.4 nm for the upper and lower domain walls, respectively.

Under-focus Lorentz images of a sample of die-upset¹³ $\text{Nd}_2\text{Fe}_{14}\text{B}$ are shown in Fig. 3. The characteristic lines of light and dark contrast in Fig. 3(a) correspond to serpentine and "Y"-shaped domains that extend to the sample edge. The shape of these domains is similar to that previously reported near grain boundaries in sintered Nd-Fe-B .¹⁴ In addition, two features are noted, one dark and one bright, which are labeled "A" and "B," that lie parallel to the vacuum edge and intersect the domains which form the stems of the Y domains. Analysis of these features, reported elsewhere, indicates that feature A is associated with an unidentified planar defect while B is a grain boundary.⁹

Domain rearrangement resulted from heating the sample *in situ* to a nominal 300°C followed by cooling to room temperature, as shown in Fig. 3(b). The domain walls have been released from the thin sample edge although some domains still interact with features A and B. Subsequent heat-

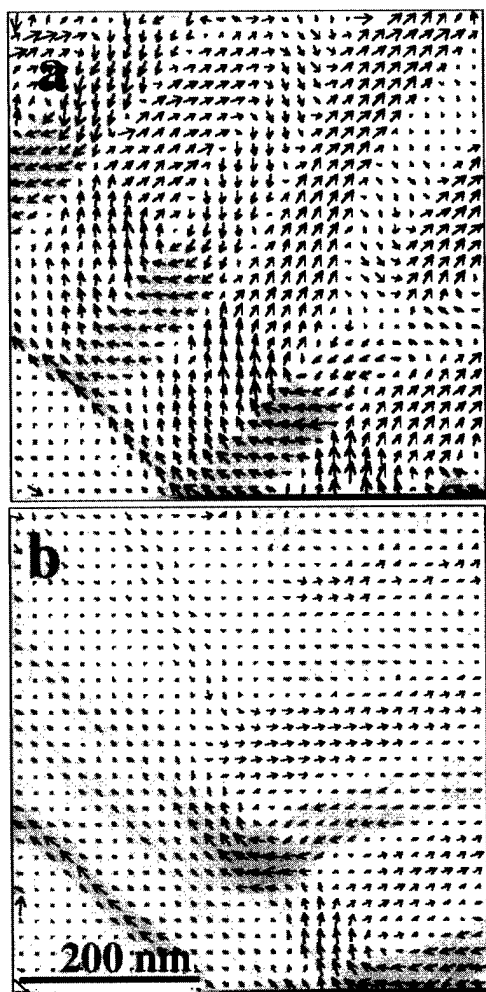


FIG. 4. Induction map from outlined areas of Fig. 3 showing change in domain structure before (a) and after (b) heating to 300 °C.

ing to 400°C (above the Curie temperature of 585 K¹⁵) resulted in complete disappearance of the domain structure. A new domain structure was then visible after cooling to room temperature, as shown in Fig. 3(c). The domain boundaries again interact with features A and B but none of the domain walls extend to the thin edge of the annealed sample. The sample has accumulated dark particles in areas near the edge and on the surface of thinner parts of the specimen. The presence of the particles is correlated to an absence of domain walls and a marked reduction in the Fresnel contrast of the domain walls in the interior of the sample.

Electron holograms were recorded at various stages of this treatment cycle, and then later processed to obtain phase and phase gradient images. The vector map shown in Fig. 4(a), which has been superimposed on a low contrast image of the x gradient, is divided into 20 nm×20 nm squares. The map shows that the magnetizations of the domains in this region of the sample are oriented at approximately 90° to each other rather than the expected 180°. The region of the sample between A and the vacuum edge is comprised of a series of domains which appear to close the in-plane induction more or less parallel to the thin edge, and give rise to

pairs of singularities at the intersection with the striped domains. This structure is reminiscent of cross-tie walls that contain periodic arrays of Bloch lines of alternating polarity.^{7,16} The grain boundary has a limited effect on the magnetization, and the magnetization across the two grains is coupled. Effects at the grain boundary itself may arise not only from changes in the induction but also from preferential thinning or changes in composition at the boundary. Between this grain boundary and the sample edge, the vectors show decreasing length which may be due to rapidly decreasing specimen thickness rather than an increased out-of-plane component.

Figure 4(b) is an induction map of the same area [see Fig. 1(b)] after heating to 300° and subsequent cooling to room temperature. The well-defined domains on the left-hand side have disappeared, and the reduced phase gradients may indicate that the remaining structure has a large out-of-plane component. The domains which had previously been oriented perpendicular to the edge of the sample have rotated by approximately 90° and the magnetizations of adjacent domains are now oriented at approximately 180°. The magnetizations on either side of the grain boundary are no longer strongly coupled. However, the domains in the lower part of the figure appear to be pinned between the grain boundary and the defect which have impeded the movement of domains away from the thin edge of the sample and preserved the original orientation.

ACKNOWLEDGMENTS

The electron holography was performed at the Arizona State University Center for High Resolution Electron Microscopy. This work was supported in part by the U.S. Department of Energy, Division of Materials Sciences, Office of Basic Energy Sciences under Contract No. DE-AC02-76CH00016.

¹ *Rare-Earth Iron Permanent Magnets*, edited by J. M. D. Coey (Clarendon, Oxford, 1996).

² J. F. Herbst, *Rev. Mod. Phys.* **63**, 819 (1991).

³ M. R. Scheinfein, J. Unguris, J. L. Blue, K. J. Coakley, D. T. Pierce, and R. J. Celotta, *Phys. Rev. B* **43**, 3395 (1991).

⁴ J. P. Jakubovics, in *Electron Microscopy in Materials Science*, Part IV, edited by U. Valdre and E. Ruedl (Commission of the European Communities, Brussels, 1976), pp. 1303.

⁵ J. N. Chapman, P. E. Batson, E. M. Waddell, and R. P. Ferrier, *Ultramicroscopy* **3**, 203 (1978).

⁶ L. Reimer, *Transmission Electron Microscopy*, 2nd ed. (Springer, Berlin, 1989).

⁷ A. Tonomura, *Rev. Mod. Phys.* **59**, 639 (1987).

⁸ M. R. McCartney, D. J. Smith, R. F. C. Farrow, and R. F. Marks, *J. Appl. Phys.* **82**, 2461 (1997).

⁹ M. R. McCartney and Yimei Zhu, *Appl. Phys. Lett.* **72**, 1380 (1997).

¹⁰ M. R. McCartney and M. Gajdardziska-Josifovska, *Ultramicroscopy* **53**, 283 (1994).

¹¹ P. A. Crozier, *Philos. Mag. B* **61**, 311 (1990).

¹² The minimum width of any measurement in this microscope operating mode is limited to 3 nm by the point resolution of the imaging lens.

¹³ C. D. Fuerst and E. G. Brewer, *J. Appl. Phys.* **73**, 5751 (1993).

¹⁴ H. Kronmüller, in *Science and Technology of Nanostructured Materials*, edited by G. C. Hadjipanayis and G. Prinz (Plenum, New York, 1990), p. 657.

¹⁵ J. F. Herbst and J. J. Croat, *J. Magn. Mater.* **100**, 57 (1991).

¹⁶ B. O. Cullity, *Introduction to Magnetic Materials* (Addison-Wesley, New York, 1972).

Improvement of protective coating on Nd-Fe-B magnet by pulse nickel plating

C. W. Cheng and F. T. Cheng^{a)}

Department of Applied Physics, The Hong Kong Polytechnic University, Hung Hom, Hong Kong

H. C. Man

Department of Manufacturing Engineering, The Hong Kong Polytechnic University, Hung Hom, Hong Kong

Sintered Nd-Fe-B magnets were coated by pulse nickel plating at different plating conditions. Optimal pulse plating condition was established (average current density = 1 A/dm², peak current density = 6 A/dm² with $T_{\text{on}}:T_{\text{off}} = 1:2$). In order to make a comparison, magnets with similar nickel coating thickness plated by dc were also prepared. The corrosion resistance of the coated magnets was evaluated by (i) Normal Salt Spray Test (5% NaCl, 35 °C) and (ii) potentiodynamic polarization measurement (3.5% NaCl solution). It was found that the corrosion resistance of the pulse nickel plated magnet was significantly improved as compared with that of the conventional dc plated ones, with negligible deterioration in magnetism. The microstructure of the coating was examined by optical microscopy and scanning electron microscopy. It was found that the porosity was much lower, and the grains much finer in the pulse-plated layer as compared with the dc plated ones.

© 1998 American Institute of Physics. [S0021-8979(98)15411-7]

I. INTRODUCTION

The neodymium-iron-boron (Nd-Fe-B) permanent magnet, being one of the most popular magnets nowadays, derives its attractiveness and popularity from its well known excellent magnetic properties, including high remanence, high coercivity, and large energy product.¹ However, the applications of the Nd-Fe-B magnets are greatly hindered by their poor corrosion resistance in humid environments, especially when the magnets are of the sintered type.² The corrosion attack arises from the preferential oxidation of the Nd-rich phase in the grain boundary region.³ Such an intergranular mode of corrosion results in irreversible loss in flux and coercivity,⁴ contamination, and even total disintegration. The employment of coatings on the Nd-Fe-B magnets has been proven to be one feasible way to enhance the corrosion resistance without leading to significant deterioration of the magnetic properties. Among the various types of coatings applied to the Nd-Fe-B magnets, metallic coatings of Ni, Ni/Cr, Al, Zn, Cu, etc., have achieved different degrees of corrosion protection.⁵⁻⁹ Such metallic coatings were applied to Nd-Fe-B by dc electroplating, electroless plating, or immersion coating. On the other hand pulse plating, a technique which is well known for producing coatings which are more uniform, less porous, more wear-resistant and more corrosion-resistant (although with higher equipment cost, about twice that of the dc ones), has not been used on the Nd-Fe-B magnets. Thus it is the purpose of the present study to investigate the possibility of pulse plating the Nd-Fe-B magnets with Ni, to establish the optimal plating conditions, and to assess the coating properties.

II. EXPERIMENTAL PROCEDURE

Commercial Nd-Fe-B magnets composed of 15% Nd, 77% Fe, and 8% B were used in the present study. They

were in disk form with diameter and thickness of 15.7 and 2.2 mm, respectively. The samples were fabricated by conventional sintering and supplied by a local manufacturer. The magnetic properties were given as $B_r = 11.4$ kG, $H_{ci} = 12.4$ kOe, and $(BH)_{\text{max}} = 34$ MGOe.

The samples were cleaned by electrodegreasing in an alkaline solution, and then immersed in 10% hydrochloric acid at room temperature for 30 s for activation. The samples were pretreated with Ni striking at a current density of 2 A/dm² for 1 min, followed by dc plating of semi-bright Ni at 50 °C for 5 min using 1 A/dm². The samples were subsequently pulse plated with Ni using unipolar pulse in a bath having the composition and conditions listed in Table I. Four selected combinations of on and off times ($T_{\text{on}}:T_{\text{off}} = 1:1, 1:2, 1:4, 1:10$) were prepared. The mean thickness of the Ni coating film was in the range of 12–15 μm. For comparison, dc plated Ni coatings of similar thickness were also prepared using similar current densities.

The corrosion resistance of Ni coatings was investigated by (i) normal salt spray (NSS) test and (ii) electrochemical measurement. The NSS test (35 °C, 5% NaCl) was performed for 136 h using a standard chamber in accordance with ASTM G85 practice.

TABLE I. Composition and conditions for pulse nickel plating.

Nickel sulphate (NiSO ₄ ·6H ₂ O)	300 g/l
Nickel chloride (NiCl ₂ ·6H ₂ O)	60 g/l
Boric acid (H ₃ BO ₃)	40 g/l
Wetting agent	0.5 ml/l
Brightener	3 ml/l
Anode	Nickel
Average current density	1 A/dm ²
Peak current density	6 A/dm ²
Temperature	50 °C
Agitation	Moderate to vigorous

^{a)}Electronic mail: apaftche@polyu.edu.hk

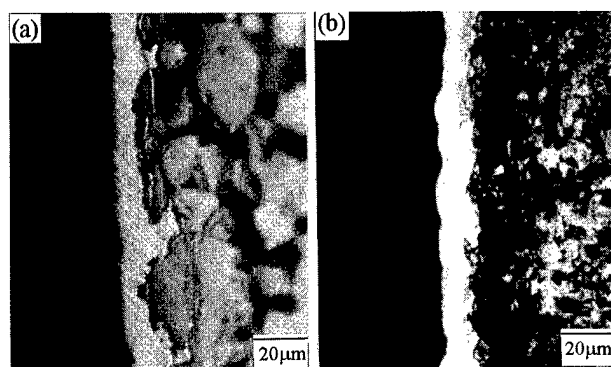


FIG. 1. Cross section of pulse Ni-plated samples (a) with pretreatment, (b) without pretreatment.

The time of initial formation of brown rust on the samples was recorded. Samples were removed at regular intervals from the chamber, carefully cleaned with de-ionized water, and dried thoroughly with warm air and weighed. The mass gain per unit surface area exposed due to the formation of corrosion product was also recorded and plotted against the exposure time.

In the electrochemical measurement of the samples, an EG&G PARC 273 potentiostat was used to obtain the potentiodynamic polarization scans. Two parallel graphite rods were used as the counter electrode and the saturated calomel electrode (SCE) was used as the reference electrode. Potentiodynamic polarization scans were carried out according to ASTM G5 practice, using deaerated 3.5% NaCl solution as the electrolyte at a scan rate of 0.6 V/h, scanning from -1 to $+1.2$ V. The corrosion potential E_{corr} and the corrosion current density i_{corr} were determined from the polarization curves using Tafel extrapolation.

Magnetic measurements were performed after 136 h of exposure in the salt spray test. The samples were pulse magnetized in a field of 35 kOe and demagnetized in a vibrating sample magnetometer (VSM) to obtain the demagnetization curves. The remanence B_r and the coercivity H_{ci} were determined.

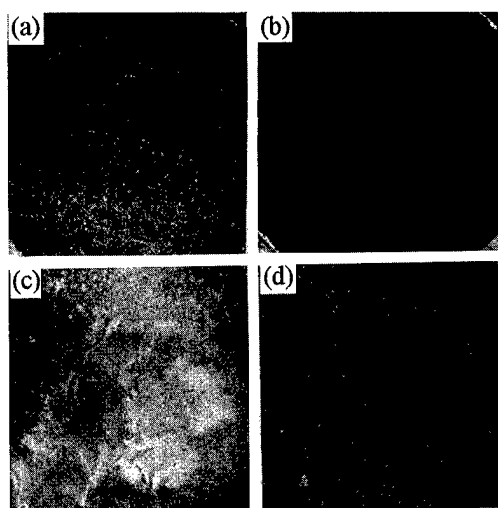


FIG. 2. Surfaces of samples before and after 16 h of exposure in salt spray test: dc-plated (a)(c); pulse-plated (b)(d). (3.5X).

TABLE II. Time of initial formation of brown rust in NSS test for different settings.

Plating technique	T_{on} (μs)	T_{off} (μs)	Time of initial formation of brown rust (h)
Pulse-plated	200	200	15
	200	400	16
	200	800	8
	200	2000	10
dc-plated	8

III. RESULTS AND DISCUSSION

Pulse Ni coating having a thickness of 12–15 μm was obtained and the cross section is shown in Fig. 1(a). The coating was smooth and good adhesion was observed between the substrate and the coating. Pretreatment using dc plated semi-bright Ni was found to have greatly improved the adhesion of the coating to the substrate. The pretreatment prevented direct attack of the acidic bath on the magnet surface and hence prevented disintegration of the grains at the interlayer. Figure 1(b) revealed voids and pores appearing between the substrate and the coating without pretreatment. To achieve a high quality coating at a reasonable deposition rate, proper selection of current density is of primary importance. In the present study the optimal average current density was 1 A/dm² at 50 °C, with a peak current density of 6 A/dm². An on time of 200 μs was employed since it is the most common selection for ferrous material with a reasonable deposition rate.

The corrosion resistance of four different pulse-plated Ni coatings, together with dc-plated Ni coating and the bare sample was assessed in the salt spray environment. The surfaces of dc-plated and pulse-plated samples before and after 16 h of salt spray test are shown in Fig. 2. It could be seen that the dc coating was seriously damaged [Fig. 2(c)] while for the pulse coating, the corrosion product just began to form [Fig. 2(d)]. The time of initial formation of brown rust was recorded and listed in Table II. It was found that the initial time for rust formation in pulse-plated samples was retarded by a factor of 2 as compared with that for the dc

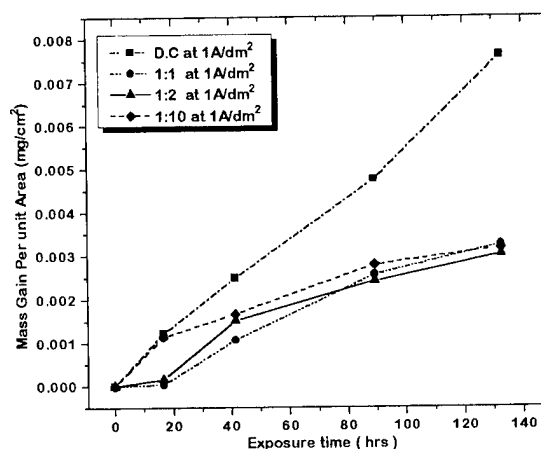


FIG. 3. Mass gain per unit sample area exposed at different exposure times in NSS test.

TABLE III. E_{corr} and i_{corr} from potentiodynamic polarization measurement of different plated samples.

Samples	E_{corr} (mV)	i_{corr} ($\mu\text{A}/\text{cm}^2$)
Pulse-plated Ni ($T_{\text{on}}:T_{\text{off}}=1:2$)	-440	0.12
dc plated Ni	-530	0.98
Uncoated Nd-Fe-B	-940.7	115.7

plated samples, extending up to 16 h for coatings with an on-off time ratio of 1:2. For bare samples, corrosion products were visible after 2 h of exposure.

The mass gain due to the formation of rust at different times of exposure is shown in Fig. 3. It was found that the mass increased at a faster rate after initial formation of rust, indicating breakdown of coating and exposure of the substrate to the salt mist environment.

Potentiodynamic polarization test of the pulse Ni-plated, dc Ni-plated and the bare samples in 3.5% NaCl deaerated solution at room temperature was performed and the corresponding corrosion potential E_{corr} and the corrosion current density i_{corr} were listed in Table III. The i_{corr} of the bare Nd-Fe-B was much greater than those of the coated ones, in fact greater by a few orders of magnitude. The i_{corr} of the pulse-plated samples was lower than that of the dc-plated samples by about an order of magnitude. The reduction in corrosion rate is probably due to the removal of discontinuities and pores which are usually present in dc plating. The more noble value of E_{corr} for pulse Ni coating indicated that the coating was more stable as compared with that of the conventional dc plating. Thus both the salt spray test and electrochemical test showed that the pulse-plated samples were more corrosion resistant than the dc plated ones. The improvement in corrosion resistance may be attributed to the structure of the coating in pulse plating, which is characterized by finer grains and lower porosity, as shown in Fig. 4(a)

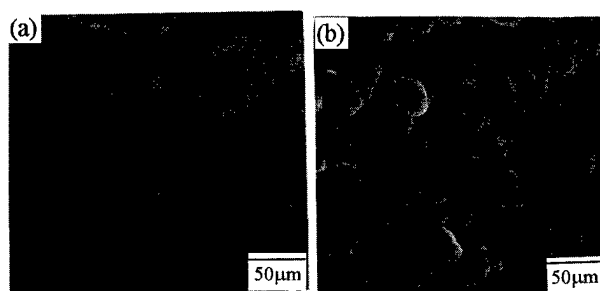


FIG. 4. Scanning electron microscope (SEM) micrographs of surfaces of pulse-plated (a) and dc-plated (b) samples.

TABLE IV. Magnetic properties before and after salt spray test.

	Before NSS test		After NSS test		Loss in B_r (%)
	B_r (kG)	H_{cl} (kOe)	B_r (kG)	H_{cl} (kOe)	
Pulse-plated Ni	11.3	12.4	11.2	12.3	0.88%
dc-plated Ni	11.3	12.3	11.1	12.3	1.77%
Uncoated	11.6	12.3	10.9	12.2	6.51%

versus the case of dc plating, Fig. 4(b).¹⁰

After 136 h of exposure in the salt spray test, the magnetic properties of the coated samples remained almost unchanged, whereas those of the bare samples decreased by about 6.5% (Table IV).

IV. CONCLUSIONS

Ni coating of thickness 12–15 μm has been successfully applied to the magnets by pulse plating. The set of conditions used was: average current density = 1 A/dm², peak value = 6 A/dm², temperature = 50°C, on-off times = 200 μs :400 μs . The coating obtained was fine-grained and low in porosity, and adhered well to the substrate. Corrosion data from both the salt spray test and electrochemical test indicated that for similar coating thickness, the corrosion resistance of the pulse Ni-plated samples was at least doubled as compared with the dc-plated ones. Magnetic measurements revealed that the remanence and the coercivity of the magnets were unaffected by the Ni coating.

ACKNOWLEDGMENTS

The authors would like to acknowledge the Research Committee of The Hong Kong Polytechnic University for the provision of a research grant (No. 350/631). Thanks are also due to F. Lau, Manager of the Industrial Centre, HKPU, for providing pulse plating equipment.

¹M. Sagawa, S. Fujimura, N. Togawa, H. Yamamoto, and Y. Matsuura, J. Appl. Phys. **55**, 2083 (1984).

²J. Jacobson and A. S. Kim, J. Appl. Phys. **61**, 3763 (1987).

³A. S. Kim and F. E. Camp, J. Mater. Eng. **13**, 175 (1991).

⁴C. J. Willman and KSVL Narasimhan, J. Appl. Phys. **61**, 3766 (1987).

⁵H. H. Man, H. C. Man, and L. K. Leung, J. Magn. Magn. Mater. **152**, 40 (1996).

⁶C. W. Cheng, H. C. Man, and F. T. Cheng, IEEE Trans. Magn. **33**, 3910 (1997).

⁷P. Mitchell, IEEE Trans. Magn. **26**, 1933 (1990).

⁸T. Minowa, M. Yoshihawa, and M. Honshima, IEEE Trans. Magn. **25**, 3776 (1989).

⁹C. D. Qin, A. S. Li, and D. H. L. Ng, J. Appl. Phys. **79**, 4854 (1996).

¹⁰J. C. Puipe, American Electroplaters & Surface Finishers Society 3rd Int. Pulse Plating Symposium, Orlando, FL, 1986, Paper A.

A pump with flat-ring-shaped magnets

H. Saotome,^{a)} T. Hagiwara, and Y. Sato

Faculty of Engineering, Chiba University, Inage, Chiba 263, Japan

Previously, authors developed a novel linear actuator with flat-ring-shaped magnets and applied it to a pump. In this article, the output power of the actuator and the efficiency of the pump are obtained by experiments. A pair of flat-ring-shaped Nd-Fe-B magnets having *N* and *S* poles on the surface are put on the same axis and face each other. Rotating one of the ring magnets in the direction of its circumference, an oscillating force occurs on the other magnet. When this magnet is restricted to linear motion along the axis, the mechanical power driving the rotating magnet is transferred to the linear motion power. A pump was made with this mechanism. The efficiency of the pump is experimentally obtained, where water pressure difference between the intake and the outlet has been changed. As a result, the efficiency of the pump attains to about 45%. The efficiency of the actuator itself is very high, because the actuator has no copper and iron losses, and a negligibly small eddy current loss. © 1998 American Institute of Physics. [S0021-8979(98)19011-4]

I. INTRODUCTION

With the development of strong metal magnets, various types of magnetic actuators have been proposed.¹⁻³ Comparing electromagnetic solenoids and linear actuators with metal magnets, the actuators have some advantages. Metal magnets make positive and negative magnetic forces while the magnetic force in solenoids is only attractive. No hysteresis loss occurs in a metal magnet when the alternate magnetic field intensity around the magnet is less than a certain value. If a linear actuator has no winding for the exciting current, the linear actuator causes no copper loss which yields a large amount of heat in solenoids. If a linear actuator is driven at low frequency, the eddy current loss in a metal magnet is very small. We have proposed a linear actuator which satisfies all the conditions and has all the benefits mentioned above. And the actuator was applied to a pump.³

In this article, the efficiency of the pump is estimated with the output power of the actuator. Also, the output characteristics of the pump, which have been obtained by experiments, are shown.

II. FUNDAMENTAL MECHANISM

Figure 1 shows the fundamental mechanism of the proposed actuator. Two flat-ring-shaped magnets are facing each other with the distance *d*. Each magnet has two magnetic poles on both sides. For example, the opposite side of *N*-pole surface is *S* pole. By rotating the left magnet in the θ direction, push and pull forces occur on the right magnet. When the right magnet is restricted to linear motion, the magnet moves left and right alternately. As a result, the mechanical power driving the rotating magnet is transferred to the linear motion power. In order to make the magnetic field intensity yielding the forces large, the iron yoke is fixed to the rotating magnet on the left side. The push-pull force *f* occurring between the magnets in Fig. 1 is measured as a function of *d*

and θ (Fig. 2). The outer and inner diameters of the magnets are 27 and 15 mm, respectively. The thicknesses of the magnet and the iron yoke are 1.6 and 2 mm, respectively. The force pattern with respect to θ is like a triangular wave when the distance *d* is small.

A pump was made with the mechanism shown in Fig. 1. Figure 3 shows its structure. In order to have large output power of the pump, two pairs of rotating and linear motion magnets are used. The pump has two cylinders separated by a wall with two linear motion magnets. The force on each linear motion magnet is given by both of the rotating magnets.

III. OUTPUT CHARACTERISTICS

Figure 4 shows the experimental results of reciprocal linear motions of the wall in the pump, with respect to θ , when water pressure difference between the intake and the outlet has been changed from 0 mm H_g to 5.88 mm H_g. The origin of the wall position is the center between two rotating magnets in Fig. 3. The rotating speed is kept at 30 rpm in Fig. 4. The maximum displacement of the wall is restricted to ± 2.8 mm by stoppers.

In order to obtain the output power of the wall motion, *x-f* relation is calculated with the experimental results of Figs. 4 and 2, as shown in Fig. 5. Each area of the *x-f* loop corresponds to the output energy of one period of the wall motion for each pressure at 30 rpm. Figure 2 is used to transform θ in Fig. 4 to *f* in Fig. 5. The output power of the wall motion, *P*₁, is plotted in Fig. 6 with respect to the pressure *p*. The output power *P*₁ (mW) is obtained by dividing the output energy (mJ), the area of the *x-f* loop in Fig. 5, by 0.5 Hz (=30 rpm). The measured water flow from the pump, *Q*, is also plotted in Fig. 6. It is found from Fig. 6 that *P*₁ variation is between 20 and 25 mW at a constant speed of 30 rpm. On the other hand, water flow output is decreased with an increase of the pressure.

*P*₁ versus the rotating speed *n* is plotted in Fig. 7 for each pressure. Except for the case of *p* = 5.88 (mm H_g) over

^{a)}Electronic mail: saotome@cute.te.chiba-u.ac.jp

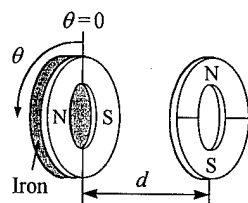


FIG. 1. Fundamental mechanism of the actuator.

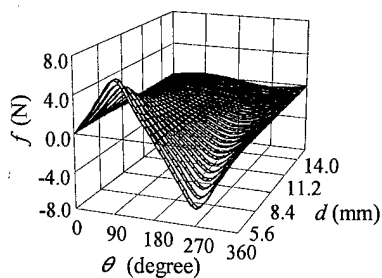


FIG. 2. The push-pull force between the magnets.

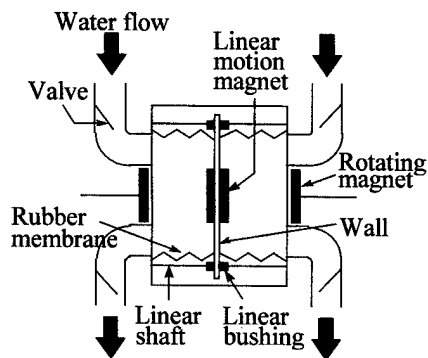


FIG. 3. Pump structure.

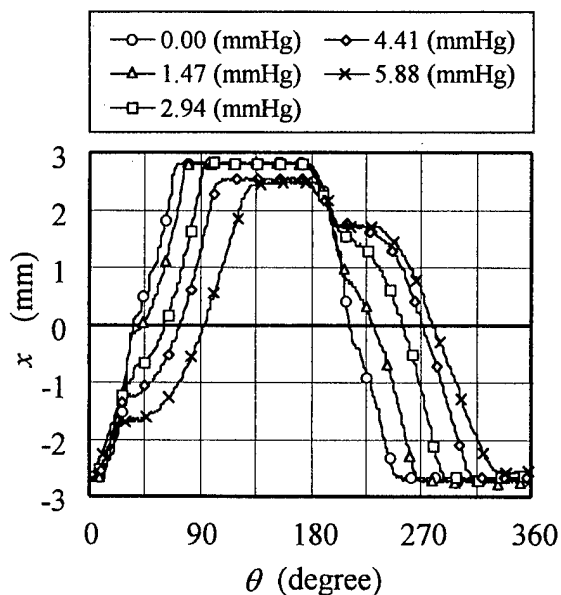
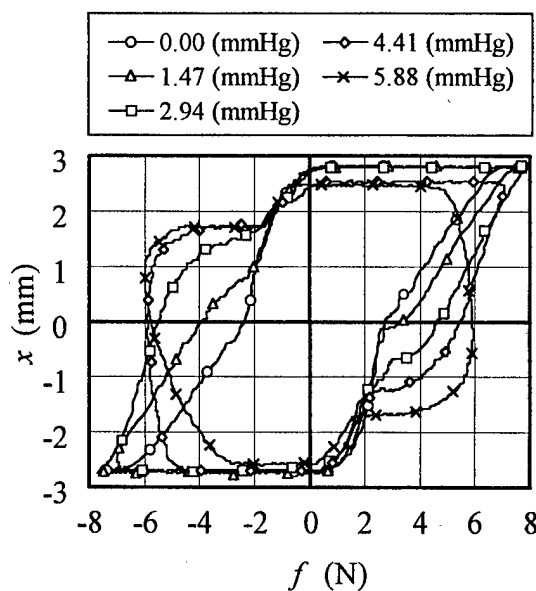
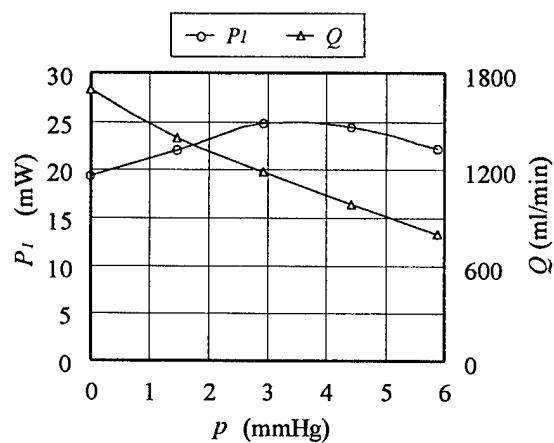
FIG. 4. Wall motions of the pump with respect to θ (30 rpm).FIG. 5. The x - f loops of the wall motion (30 rpm).

FIG. 6. The output characteristics of the wall motion and the water flow characteristics of the pump, with respect to the pressure (30 rpm).

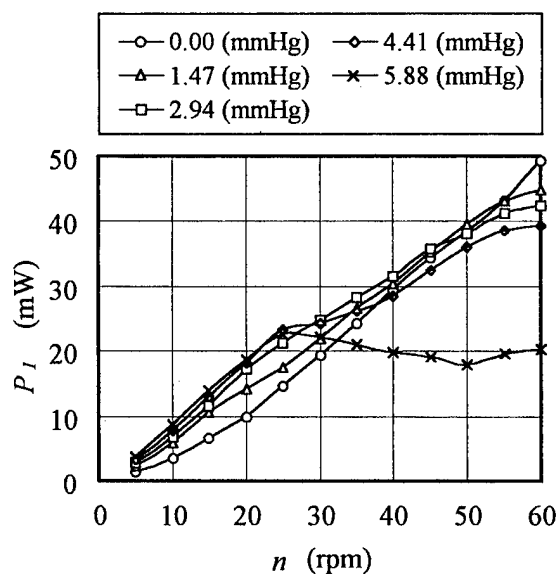


FIG. 7. The output characteristics of the wall motion with respect to the rotating speed.

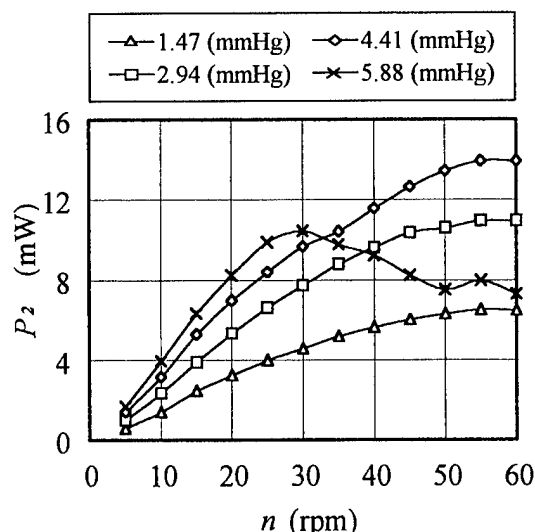


FIG. 8. The output characteristics of the pump with respect to the rotating speed.

30 rpm, P_1 varies linearly with n ; also it is nearly the same for all the pressures studied. This result implies that each area of the x - f loop, corresponding to each P_1 , does not change considerably with respect to n and p .

Figure 8 shows the output characteristics of the pump with respect to n , obtained by the product of the measured pressure and the measured water flow. It is found from the figure that the pump output P_2 is approximately proportional to the rotating speed of the pump, n , except for the case of $p = 5.88$ (mm Hg) over 30 rpm.

From Figs. 7 and 8, we have the efficiency of the pump, as $\eta = P_2/P_1$, because the output power of the wall motion, P_1 , is regarded as the output power of the actuator. Figure 9 shows the efficiency characteristics of the pump with respect to the rotating speed n for each pressure. The efficiency η increases with an increase of the pressure and reaches about 45% when $p = 5.88$ (mm Hg).

IV. CONCLUSION

The efficiency of the proposed actuator itself is very high, because the actuator has no copper and iron losses, and

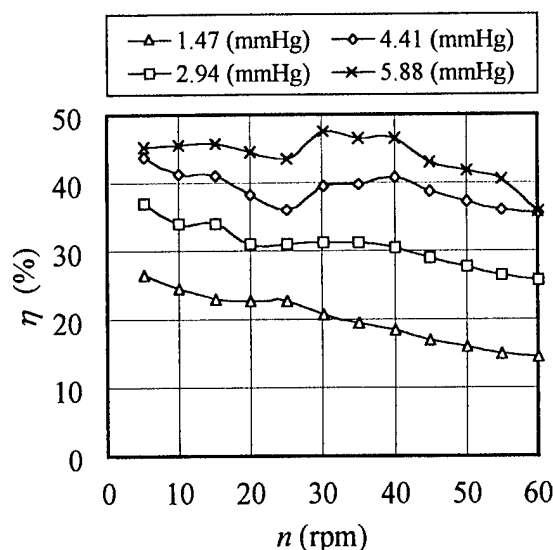


FIG. 9. The efficiency characteristics of the pump with respect to the rotating speed.

a negligibly small eddy current loss. We have experimentally obtained the output power of the actuator with the x - f loop given by the x - θ and f -(x, θ) relations. And we have evaluated the efficiency of the pump with the output power ratio between the pump and the actuator. As a result, approximately 45% efficiency is obtained. More than half of the output power of the actuator, $P_1 - P_2$, is supposed to be transformed to the fluid and mechanical losses of the pump.

ACKNOWLEDGMENTS

This study was financially supported by the Grant-in-Aid for Fundamental Scientific Research from the Japanese Ministry of Education, Science and Culture; and the Electro-Mechanical Technology Advancing Foundation.

¹TDK Corp. Catalogue of REC Pump.

²T. Honda, K. Arai, and J. Yamazaki, Technical Meeting of Magnetic Society, IEE Japan, MAG 97, 68 (1997).

³H. Saotome, K. Saito, M. Ueda, and Y. Sakaki, T. IEE Japan 117-A, 118 (1997).

New phase boundary between magnetic and non-Fermi-liquid in $\text{Ce}(\text{Rh}_{1-x}\text{Ru}_x)_3\text{B}_2$, for $0 \leq x \leq 0.4$

E. Bauer, R. Hauser, A. Galatanu, A. Lindbaum, G. Hilscher, H. Sassik, and H. Kirchmayr

Institut für Experimentalphysik, TU Wien, Wiedner Hauptstr. 8-10, Austria

J. G. Sereni

Centro Atómico Bariloche CNEA, 8400 S.C. de Bariloche, Argentina

P. Rogl

Institut für Physikalische Chemie, Universität Wien, Währingerstraße 42, Austria

A study of the temperature-dependent magnetic susceptibility and electrical resistivity $\rho(T)$ (0.5–300 K) on single-phase alloys (CaCu₅ type), prepared by argon arc melting, reveals a magnetic phase transition with a nonmonotonous decrease of the ordering temperature from $T_c = 115$ K for $x = 0$ to $T_c \approx 0$ for $x = 0.40$. A kink in the susceptibility at about 70 K indicates that ferromagnetism (at $x < 0.1$) transforms to a complex magnetic order for $0.125 \leq x \leq 0.35$. Above that concentration $\rho(T) = \rho_0 + AT^n$ changes from $n \approx 2$ to $n \approx 1.5$, a characteristic for non-Fermi-liquid behavior. Under pressure T_c stays almost constant for $x = 0.125$ but dT_c/dp grows with increasing Ru content. On the contrary, applied fields up to 12 T do not affect T_c . Low-temperature specific heat and ac susceptibility for $x = 0.40$ confirm the absence of long-range magnetic order down to 0.5 K. For $x = 0.35$ $C_p/T = 62$ mJ/mol K at 1.5 K, a value which is three times larger than that of CeRh_3B_2 .

© 1998 American Institute of Physics. [S0021-8979(98)46511-3]

I. INTRODUCTION

With respect to our general interest in the CaCu₅-type rare-earth intermetallics, the system $\text{Ce}(\text{Rh}_{1-x}\text{Ru}_x)_3\text{B}_2$ has attracted our attention because its low-temperature magnetic phase boundary is hitherto still uncertain. Former studies (e.g., Refs. 1–4) reported a rather drastic decay of ferromagnetic order from $T_c = 115$ K at $x = 0$ to $T_c = 40$ K at $x = 0.1$ followed by a paramagnetic phase. However, there is no detailed analysis of the critical region, where T_c is expected to approach zero. Knowing that magnetic instabilities usually are accompanied by non-Fermi-liquid (NFL) behavior, the present article is devoted to a thorough exploration of the above-mentioned phenomena.

II. EXPERIMENT

Alloys with the composition $x = 0.08, 0.125, 0.15, 0.2, 0.25, 0.3, 0.32, 0.35, 0.375$, and 0.4 were prepared by argon arc melting and were found to be single-phase CaCu₅ type from x-ray powder diffraction analysis. Physical properties like electrical resistivity under pressure (< 10 kbar) and fields (< 12 T), dc- and ac-magnetic susceptibility as well as specific heat, were investigated in the temperature region from 500 mK to 300 K; the low-temperature region below 10 K was studied using a ^3He cryostat.

III. RESULTS AND DISCUSSION

The volume change in $\text{Ce}(\text{Rh}_{1-x}\text{Ru}_x)_3\text{B}_2$ is found to be nonlinear and anisotropic with the a parameter increasing

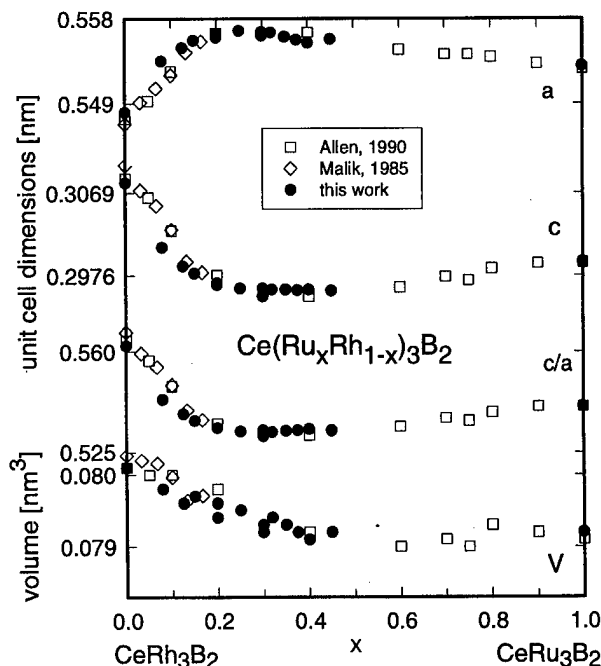


FIG. 1. Unit cell dimensions for $\text{Ce}(\text{Rh}_{1-x}\text{Ru}_x)_3\text{B}_2$ as function of x .

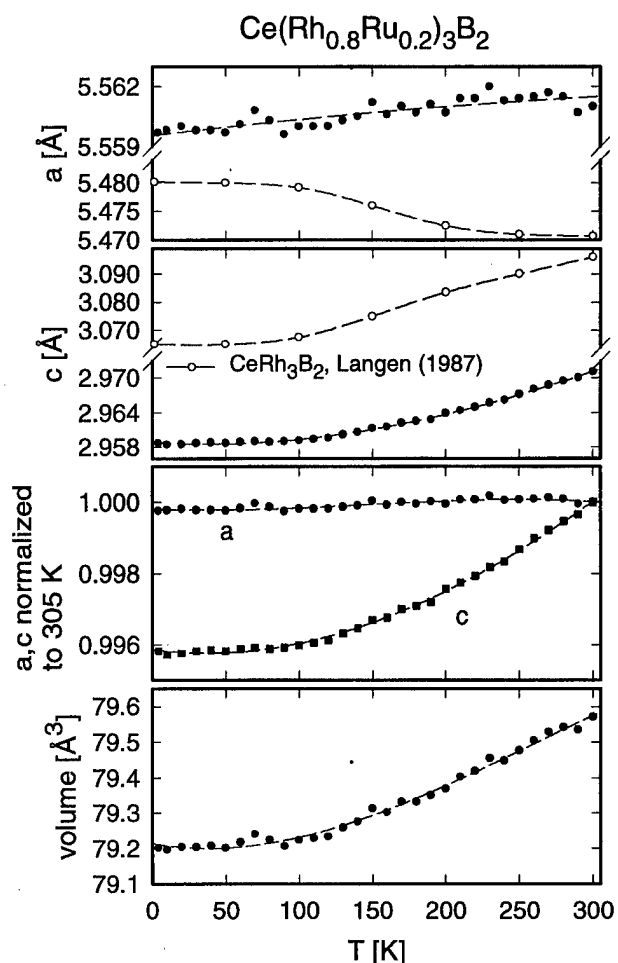


FIG. 2. Unit cell dimensions for $\text{Ce}(\text{Rh}_{1-x}\text{Ru}_x)_3\text{B}_2$ as function of temperature for $x=0.2$ in comparison with data for CeRh_3B_2 (Ref. 4).

and c parameter decreasing with respect to pure CeRh_3B_2 (Fig. 1). Similarly, the temperature variation of c is much more pronounced than that of a . While a remains practically

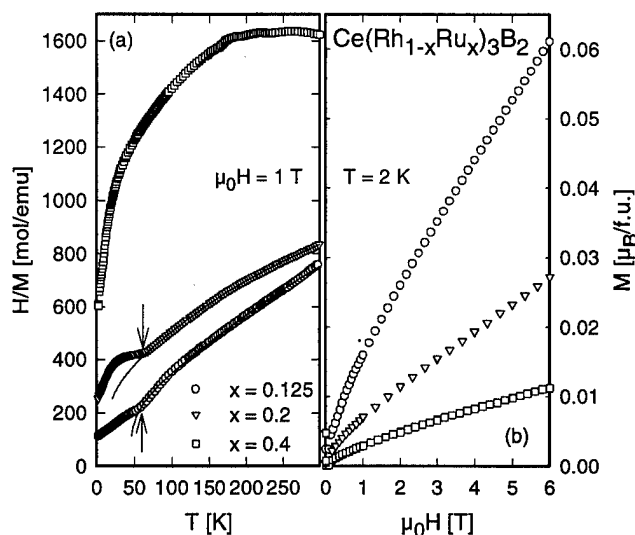


FIG. 3. (a) Temperature dependence of the inverse susceptibility H/M at T for $x=0.125, 0.2$, and 0.4 . The arrows indicate the onset of magnetic order. (b) Magnetization vs field at 2 K .

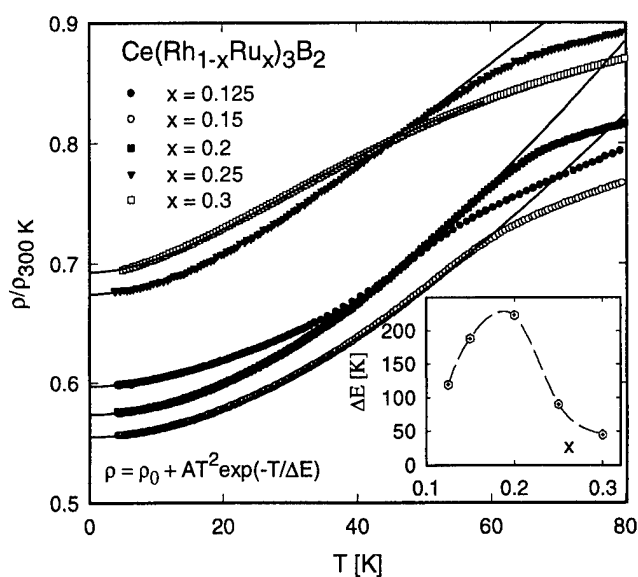


FIG. 4. Temperature dependence of the electrical resistivity for $x=0.125, 0.15, 0.2, 0.3, 0.35$, and 0.4 . Solid lines are the fit to $\rho(T) = \rho_0 AT^2 \times \exp(-T/\Delta E)$. Inset: energy gap ΔE as a function of the Rh/Ru substitution.

constant, c increases significantly with increasing temperature. This observation refers to CeRh_3B_2 (Ref. 4) as well as to $\text{Ce}(\text{Rh}_{0.65}\text{Ru}_{0.35})_3\text{B}_2$ (Fig. 2).

A study of the temperature-dependent magnetic susceptibility M/H and electrical resistivity (Figs. 3 and 4) reveals a magnetic phase transition with a nonlinear decrease of the ordering temperature from $T_c = 115\text{ K}$ for $x=0$ to $T_c \approx 0$ for $x=0.40$. While in literature¹ $T_c \approx 0$ is extrapolated to $x \approx 0.13$, we still observe an anomaly in magnetic susceptibility and resistivity within the concentration range for $0.125 \leq x \leq 0.35$. This suggests the presence of magnetic correlations which peak at $T_m^{\text{max}} = 67\text{ K}$ and $x=0.2$. Above this temperature, the susceptibilities, recorded for the alloys with $x=0.125, 0.2$ can be analyzed in terms of a modified Curie-

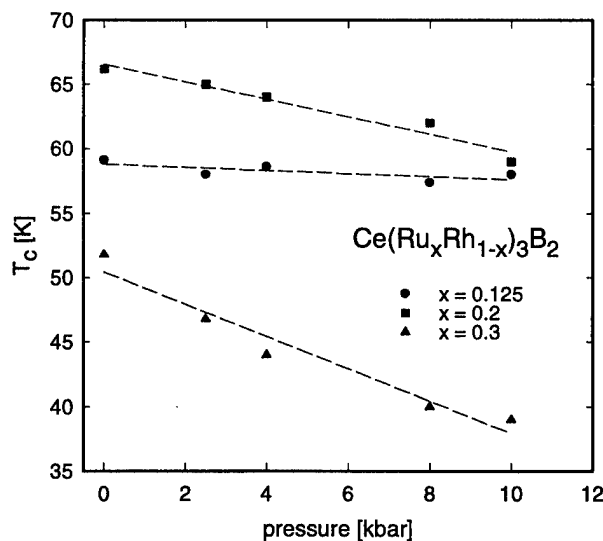


FIG. 5. Pressure dependence of magnetic ordering temperature up to 10 kbar for $x=0.125, 0.2$, and 0.3 .

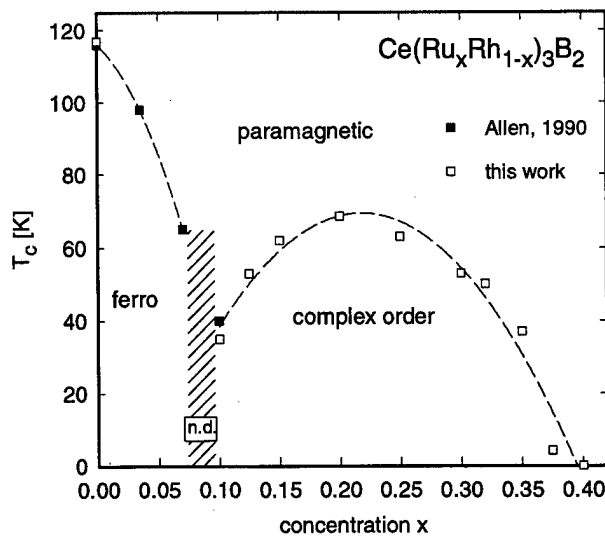


FIG. 6. Tentative magnetic phase diagram for the system $\text{Ce}(\text{Rh}_{1-x}\text{Ru}_x)_3\text{B}_2$. The magnetic state of the shaded region is not determined yet.

Weiss law yielding effective magnetic moments $\mu_{\text{eff}} = 1.5\mu_B$ ($\Theta_p = -16$ K) and $1.3\mu_B$ ($\Theta_p = -56$ K), respectively. The temperature-dependent susceptibility may alternatively be accounted for by crystal field contributions and indeed is well fitted [solid line in Fig. 3(a)] assuming a pure $|\pm 1/2\rangle$ doublet ground state and a first excited $|\pm 5/2\rangle$ level at 850 and 1090 K, respectively (Fig. 3). The $|\pm 3/2\rangle$ state as uppermost level is at substantially higher energies. For such a level scheme, no contribution from hybridization was adopted. Figure 3(b) displays isothermal magnetization measurements at $T = 2$ K for $x = 0.125, 0.2$, and 0.4 . As the Ru content increases, the magnetization diminishes, however, the observed overall values are extremely small.

Within the ordered region, the concentration dependent variation of the magnetic contribution to the electrical resistivity corresponds to a crossover from long-range ferromagnetism (low Ru content) to a complex magnetic order. The latter conclusion is drawn from the low-temperature behavior of the resistivity according to $\rho(T) = \rho_0 + AT^n \times \exp(-T/\Delta E)$, where $n = 2$ and ΔE accounts for a gap in the spin wave spectrum. A least-squares fit to the data indicates that the energy gap correlates with the magnetic ordering temperature, again with a maximum value of $\Delta E/k_B \approx 225$ K at $x = 0.2$. Furthermore, $\rho(T)$ is almost independent on fields up to 12 T.

The pressure dependence of the ordering temperature of $\text{Ce}(\text{Rh}_{1-x}\text{Ru}_x)_3\text{B}_2$ has been evaluated from resistivity measurements (Fig. 5). While T_c stays almost constant for $x = 0.125$, increasing Ru content invokes a higher influence

of pressure upon T_c . On the contrary, applied fields do not affect T_c .

As the magnetic order vanishes due to Rh/Ru substitution ($x > 0.35$), the temperature dependence of the electrical resistivity changes to a power law with an exponent close to 1.5 (for $T < 30$ K). Such a dependence is inconsistent with Fermi liquid behavior.

A low-temperature study of the specific heat for $x = 0.40$ confirmed the absence of long-range magnetic order and revealed a C_p/T value for $T = 1.5$ K of about 66 mJ/mol K^2 , which is about three times larger than that of CeRh_3B_2 .

A tentative fit of the specific heat data of $\text{Ce}(\text{Rh}_{0.6}\text{Ru}_{0.4})_3\text{B}_2$ below about 1.5 K according to $C_p/T = a \ln(T/T_0)$ yields a logarithmic divergence ($a < 0$) and a characteristic temperature $T_0 \approx 300$ K. In agreement with the resistivity results and according to a universal scaling² of the form $(C_p/T - E)T_0 = -7.2 \log(T/T_0)$, where E accounts for the conduction electron system, a NFL state of this alloy is confirmed. In the scope of Doniach's model for Kondo lattices the Rh/Ru substitution is responsible for a shift of the system from a region with low values of $J \cdot N(E_F)$ to large values of this parameter (here J is the s - f coupling constant and $N(E_F)$ is the electronic density of states at the Fermi energy). Hence, magnetic order vanishes and the dependence of T_c on pressure becomes significant. A tentative version of the magnetic phase diagram for the region $0 < x < 0.4$ is shown in Fig. 6.

In summary, the presented results on the physical behaviour in the alloy system $\text{Ce}(\text{Rh}_{1-x}\text{Ru}_x)_3\text{B}_2$ define the appearance of an additional magnetic state with rather small ordered moments in the concentration range $0.12 < x < 0.35$. Above this composition a non-Fermi-liquid behavior is observed.

ACKNOWLEDGMENTS

This research was sponsored by the FWF under Grant No. P8218, No. S5605 as well as by the FWF (project 10947)-CONICET (project 811) in the form of a bilateral Austrian/Argentinian research cooperation.

¹S. A. Shaheen, J. S. Schilling, and R. N. Shelton, Phys. Rev. B **31**, 656 (1985).

²J. Sereni, C. Geibel, M. G. Berisso, P. Hellmann, O. Trovarelli, and F. Steglich, Physica B **230-232**, 580 (1997).

³J. W. Allen, M. B. Maple, J. S. Kang, K. N. Yang, M. S. Torikachvili, Y. Lassailly, W. P. Ellis, B. B. Pate, and L. Lindau, Phys. Rev. B **41**, 9013 (1990).

⁴J. Langen, G. Jackel, W. Schlätz, M. Veit, and D. Wohlleben, Solid State Commun. **64**, 169 (1987).

⁵S. K. Malik, A. M. Umarji, G. K. Shenoy, P. A. Montano, and M. E. Reeves, Phys. Rev. B **31**, 4728 (1985).

Magnetic ordering of Ce in the heavy-fermion compound Ce_3Al

W.-H. Li,^{a)} J. C. Peng, Y.-C. Lin, and K. C. Lee

Department of Physics, National Central University, Chung-Li, Taiwan 32054, Republic of China

J. W. Lynn

NIST Center for Neutron Research, NIST, Gaithersburg, Maryland 20899

Y. Y. Chen

Institute of Physics, Academia Sinica, Taipei, Taiwan 115, Republic of China

Neutron diffraction and specific heat measurements have been performed to study the magnetic ordering of the Ce ions in the heavy-fermion compound Ce_3Al . Detailed crystal structure analysis, determined using high resolution neutron diffraction patterns and Rietveld method, shows that the Ce ions may be grouped into two types: one in the Ce–Al chain, the other in the Ce–Ce chain. The specific-heat data reveal an anomaly at $T \approx 2.2$ K, but the calculated magnetic entropy is much smaller than the expected $R \ln 2$ if all Ce spins ordered. Low temperature neutron diffraction measurements confirm that the transition at 2.2 K is magnetic and is associated with the ordering of the Ce spins. The magnetic unit cell is double the nuclear one along the a and c axes, and contains 48 Ce ions. Only the Ce ions in the Ce–Al chains participate in the ordering at 2.2 K, and they are coupled antiferromagnetically. © 1998 American Institute of Physics. [S0021-8979(98)21011-5]

The unusual properties found in heavy-fermion systems continue to generate renewed interest in the f -electron materials. Their physical origin is believed to effectively arise from the strong coupling between the conduction electrons and the fluctuating f -electron moments.^{1,2} Among the Ce-based compounds, the family Ce_xAl_y has attracted considerable attention. On the magnetic side, antiferromagnetic order has been observed in CeAl and CeAl_2 , whereas no ordering was found down to 0.6 K in CeAl_3 . Previous studies^{3,4} have shown that the thermodynamic, magnetic, and transport properties of intermetallic Ce_3Al behaves as a heavy-fermion system. Above 520 K, Ce_3Al crystallizes into the cubic Cu_3Au type of structure (β - Ce_3Al), below which it transforms into the hexagonal Ni_3Sn type of structure (α - Ce_3Al). Another structural transition occurs at 115 K, below which monoclinic (but very close to orthorhombic) symmetry was found (γ - Ce_3Al).⁵ A Kondo effect develops below 20 K, and antiferromagnetic ordering is expected at ~ 2.5 K. In this article, we report studies made on the ordering of the Ce spins in γ - Ce_3Al , by using specific heat and neutron diffraction measured at low temperatures. A relatively small value for the magnetic entropy was observed, and only a portion of the Ce spins orders in a simple antiferromagnetic arrangement at $T_N \approx 2.2$ K.

A polycrystalline sample of Ce_3Al was prepared by arc melting high-purity cerium (99.99%) and aluminum (99.9999%) in a helium atmosphere. The arc-melting process was repeated 20 times to obtain a more homogeneous sample. After arc melting, the ingot was sealed in vacuum, followed by annealing at 500 °C for 3 days and then 200 °C for another three weeks to relieve strains and promote conversion from the cubic to hexagonal phase. Ce_3Al is highly ductile, and is quite stable against oxidation. The fabricated

sample was characterized using high resolution neutron diffraction and Rietveld analysis,⁶ covering a range in temperature from 300 to 12 K. At 300 K, α - Ce_3Al was found with essentially no unexpected peaks present. We estimated the impurity levels to be less than 1%. Below 110 K, both α - Ce_3Al and γ - Ce_3Al were present, with the γ phase gradually becoming dominate with reducing temperature. At 12 K, it shows 92% γ - Ce_3Al phase and 8% α - Ce_3Al phase, with monoclinic lattice parameters $a = 6.8212(6)$ Å, $b = 12.458(1)$ Å, $c = 5.3587(4)$ Å, and the angle between the a and b axes $\gamma = 89.96(1)^\circ$.

The specific heat data were taken on a 9 mg thin specimen employing the time constant technique.⁷ Shown in Fig. 1 is the temperature dependence of the specific heat below 25 K. The main feature seen is the peak at $T = 2.2$ K, which is associated with the ordering of the Ce spins (see below).

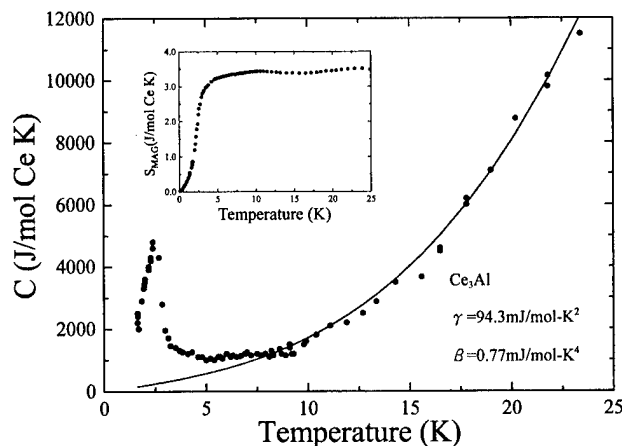


FIG. 1. Temperature dependence of the specific heat. The peak at 2.2 K is associated with the ordering of the Ce spins. The solid curve shows the contributions from phonons and conduction electrons. Shown in the inset is the magnetic entropy calculated from the magnetic specific heat data.

^{a)}Electronic mail: whli@joule.phy.ncu.edu.tw

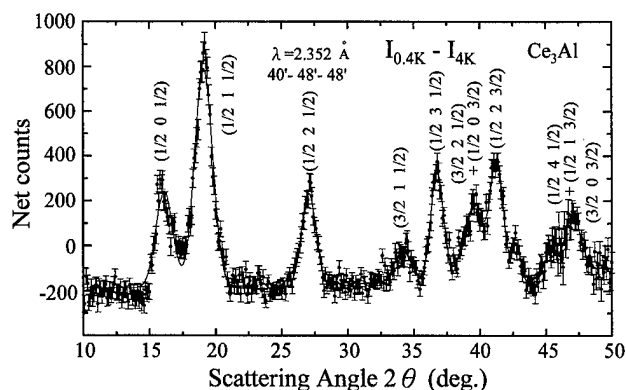


FIG. 2. Magnetic diffraction pattern obtained at $T=0.4$ K, where the indices shown are based on the nuclear unit cell. The solid curves are fits of the peaks to the Gaussian instrumental resolution function.

Above 10 K, the contribution from phonons becomes dominant. The solid curve shown is a fit of the data obtained between $15 \text{ K} \leq T \leq 40 \text{ K}$ (not shown) to the expression $C(T) = \gamma T + \beta T^3$, with $\gamma = 95 \text{ mJ/mol-Ce-K}^2$ for the contribution from electrons and $\beta = 0.77 \text{ mJ/mol-Ce-K}^4$ from phonons. The value obtained for the linear coefficient γ is about two orders of magnitude larger than that for ordinary metals. It is, however, still smaller than what is usually obtained for heavy-fermion compounds.

The magnetic contribution to the specific heat C_m may be isolated by subtracting the phonon and electron terms discussed above from the observed data. Shown as an inset in Fig. 1 is the magnetic contribution to the entropy, determined by calculating the area beneath the C_m/T versus T curve. We may expect that the low crystal symmetry of monoclinic $\gamma\text{-Ce}_3\text{Al}$ should split the $J=5/2$ line for Ce into three doublets. An integrated entropy of $R \ln 2 = 5.76 \text{ J/mol K}$ is then anticipated for the ground state. The observed value, however, is substantially smaller at all temperatures shown. This may indicate only a fraction of the entropy of a doublets is liberated at the magnetic phase transition.

Neutron diffraction experiments were conducted at the US NIST Research Reactor. Data were collected on the BT-9 triple-axis spectrometer operated in double-axis mode without using an analyzer crystal. The incoming neutrons had a wavelength of 2.352 \AA defined by a pyrolytic graphite (PG) (002) monochromator, with a PG filter placed in front of the monochromator to suppress higher-order wavelength contaminations. Collimators with horizontal divergences of $40'$, $48'$, and $48'$ full width at half maximum acceptance were used for the in-pile, monochromatic, and diffracted beams, respectively. The samples were mounted in an aluminum can filled with helium exchange gas to facilitate thermal conduction at low temperatures. A pumped ^3He cryostat was used to cool the sample, and the lowest temperature achieved was 0.4 K .

Figure 2 shows the magnetic diffraction peaks that develop as the temperature is reduced from 4 to 0.4 K . These data are obtained by subtracting the diffraction pattern taken at 4 K from the one taken at 0.4 K . This magnetic diffraction pattern originates from the Ce spin ordering. The solid

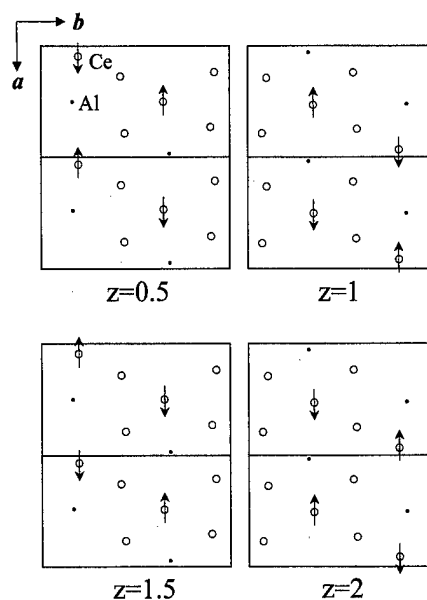


FIG. 3. The proposed spin configuration. Only the Ce in the Ce-Al chains order, with $T_N \approx 2.2 \text{ K}$.

curves shown are fits of the data to the Gaussian instrumental resolution function, and the peaks may all be indexed (as shown) based on the monoclinic nuclear unit cell. A half-integer value for the Miller's index means that the length of the magnetic unit cell along the corresponding axis is double that of the nuclear one. The magnetic unit cell is then double the nuclear one along both the a and b axis directions. It contains 48 Ce ions, since there are 12 in each nuclear unit cell.

The arrangement of the Ce spins can be determined from the relative intensities of the magnetic peaks.⁸ Although the structure of the γ phase is complicated, it, however, can be viewed as consisting of slightly tilted Ce-Al and Ce-Ce chains (hence Ce_3Al) along the a axis alternately stacked along both the b and c axis directions, as shown in Fig. 3. Finding the spin arrangement is not a simple matter in the present case, since there are 48 Ce ions in the magnetic unit cell. We tried over 80 models, each with a different spin arrangement, considering essentially all possible arrangements including collinear and noncollinear structures. Starting with the assumption that all Ce spins are ordered, we found two models that could describe the correct d spacings for the observed magnetic pattern. However, the spin direction was found to be arbitrary, leading us to believe that the models were not physical. We next tried models assuming either only the Ce in the Ce-Ce chains or those in the Ce-Al chains order. No satisfactory models were found in the former case, while the model in which the Ce spins in the Ce-Al chains are aligned antiparallel with no moments on the Ce in the Ce-Ce chains, was found to describe the observed pattern fairly well. The spin structure of this proposed model is shown in Fig. 3, and comparisons between the observed and calculated intensities are listed in Table I. We note that the goodness of the fit of this proposed model is the best among all models studied. This result of only a portion of the Ce spins participates in the magnetic order at this

TABLE I. Observed and calculated magnetic integrated intensities at 0.4 K. The intensities are normalized with respect to the $\{1/2\ 2\ 1/2\}$ intensity.

Miller index (<i>h k l</i>)	Scattering angle (deg.)		Integrated intensity	
	Observed	Calculated	Observed	Calculated
(1/2 0 1/2)	16.1	15.9	1.18	1.29
(1/2 1 1/2)	19.1	19.3	2.81	2.98
(1/2 2 1/2)	27.1	27.1	1	1
(3/2 1 1/2)	34.1	34.4	0.30	0.27
(1/2 3 1/2)	36.8	36.8	0.96	0.90
(3/2 2 1/2)+(1/2 0 3/2)	39.2	39.5	1.04	0.76
(1/2 2 3/2)	45.4	45.7	1.05	1.19
(3/2 3 1/2)	47.0	46.9	0.19	0.26
(1/2 4 1/2)+(1/2 1 3/2)	47.5	47.5	0.23	0.58

transition is consistent with the conclusion made in a separate study⁴ based on specific heat and resistivity measurements. Dividing the rare-earth ions into two sublattices has been suggested for the Ce in CeAl as well, where different magnetizations (magnitude and direction) were proposed for the two sublattices.⁹

The variations of the $\{\frac{1}{2}0\frac{1}{2}\}$ and $\{\frac{1}{2}1\frac{1}{2}\}$ peak intensities with temperature are shown in Figs. 4(a) and 4(b), respectively. Both plots reveal basically the same temperature dependence, and a typical order-parameter curve for polycrystalline samples. On cooling, the intensity starts to grow around 2.5 K, increasing in the usual way, and reaching saturation around 1 K. The ordering temperature for the Ce spins, as determined by the inflection point of the $\{\frac{1}{2}1\frac{1}{2}\}$ curve, is $T_N \approx 2.2$ K. This ordering temperature matches the temperature at which the peak in $C(T)$ occurs. By comparing the $\{\frac{1}{2}2\frac{1}{2}\}$ integrated intensity to the $\{110\}$ nuclear one, we obtained the low temperature saturated moment of $\langle \mu_z \rangle = 1.24(3) \mu_B$ for each Ce ions.

In summary, we have performed specific heat and neutron diffraction measurements to study the ordering of the Ce spins in a polycrystalline Ce₃Al. Intermetallic Ce₃Al may be classified as a heavy-fermion system, as its electronic specific heat is much larger than that of ordinary metals. However, the electrons in Ce₃Al are not as heavy as those in other heavy-fermion systems like CeAl₃ and UPt₁₃. Below 110 K, Ce₃Al transforms gradually from hexagonal α phase into monoclinic γ phase with reducing temperature. A magnetic

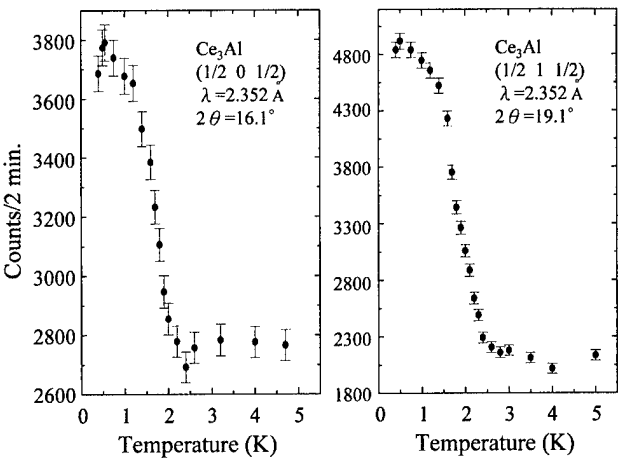


FIG. 4. Temperature dependence of the $\{\frac{1}{2}0\frac{1}{2}\}$ and $\{\frac{1}{2}1\frac{1}{2}\}$ peak intensities, showing the variation of the square of the staggered magnetization with temperature.

transition associated with the ordering of the Ce spins was observed to occur at $T_N \approx 2.2$ K. Only those Ce ions located on the Ce–Al chains participate in this ordering. The coupling is antiferromagnetic in nature, and a simple collinear antiferromagnetic spin arrangement was found. However, the calculated entropy is about 40% smaller than the observed value. We believe that crystalline electric field effect plays an important role in this issue, and inelastic neutron scattering measurements are needed to resolve this point.

ACKNOWLEDGMENT

The research at the NCU was supported by the National Science Council of the Republic of China under Grant No. NSC 87-2112-M-008-017.

¹G. R. Stewart, *Rev. Mod. Phys.* **56**, 755 (1984).
²P. Fulde, J. Keller, and G. Zwicknagl, *Solid State Physics*, edited by H. Ehrenreich and D. Turnbull (Academic, New York, 1988), Vol. 41, p. 1.
³Y. Y. Chen, J. M. Lawrence, J. D. Thompson, and J. O. Willis, *Phys. Rev. B* **40**, 10 766 (1989).
⁴Y. Y. Chen, Y. D. Yao, B. C. Hu, C. H. Jamg, J. M. Lawrence, H. Huang, and W.-H. Li, *Phys. Rev. B* **55**, 5937 (1997).
⁵A. C. Lawson, J. M. Lawrence, J. D. Thompson, and A. Williams, *Physica B* **163**, 587 (1990).
⁶H. M. Rietveld, *J. Appl. Crystallogr.* **2**, 65 (1969).
⁷G. R. Stewart, *Rev. Sci. Instrum.* **54**, 1 (1983).
⁸G. E. Bacon, *Neutron Diffraction*, 3rd ed. (Clarendon, Oxford, 1975).
⁹J. M. Lawrence, K. Parvin, and S. M. Shapiro, *J. Phys. C* **19**, 2021 (1986).

Size and dimensionality effect in single-impurity Anderson model

Feng Chen and Nicholas Kioussis^{a)}

Department of Physics, California State University Northridge, Northridge, California 91330-8268

The dimensionality and the size effect on the magnetic properties of the single-impurity symmetric Anderson model in three-, two-, and one-dimensional lattices has been studied using the quantum Monte Carlo method. We have considered clusters with odd number of sites with the impurity placed at the center of the cluster and have employed open boundary conditions. In 3D and 1D lattices, we find that at sufficiently low temperatures, the system can be in either a spin compensated or noncompensated state as the cluster size is reduced. On the other hand, in 2D the system is always in a spin-compensated state independent of the cluster size. These results imply physics beyond that contained in the simplest Kondo model and may explain the discrepancy between two recent experimental results. © 1998 American Institute of Physics. [S0021-8979(98)30811-7]

The Kondo effect involves the interaction of a localized moment with an electron gas and is relevant to the behavior of dilute magnetic alloys, as well as concentrated systems such as the heavy-fermion materials. The ground state of the single-impurity Kondo problem is a singlet in which the local moment is "compensated" by the conduction electrons due to the antiferromagnetic exchange interaction between the local moment and the conduction electrons.¹ Several calculations predict that the length scale of the compensation cloud is of the order $R_K \approx \hbar v_F / 2\pi k_B T_K$.² On the other hand, several experiments suggest that the length scale is of an order of magnitude smaller than the theoretical value or that the polarization cloud may not even exist.³ Thus surprisingly, despite the large amount of work on the Kondo problem, it appears that the question of length scale is far from settled.

Nearly all of the work on the single-impurity Kondo problem has involved bulk, i.e., three-dimensional systems. However, in recent years the behavior and the properties of the spin-compensation cloud in lower-dimensional (quasi-one and quasi-two dimensional) systems have attracted much attention both experimentally⁴⁻⁸ and theoretically.^{9,10} Since a length scale (R_K) is associated with the Kondo effect, one might expect the Kondo behavior to be different in a small system (as compared to a "bulk" sample), provided that one or two dimensions are small compared to the relevant length scale R_K . The experimental results can be summarized as follows: (i) A large size dependence was found for Au(Fe) and Cu(Fe) thin films (for film thickness less than 2000 Å), where the Kondo contribution to the resistivity is suppressed;⁴ (ii) no size dependence of the Kondo resistivity was found in Au(Fe) wires when the width dependence of the electron-electron interaction contribution to the resistivity was taken into account;⁷ and (iii) the Kondo temperature T_K shows no size dependence.⁶

The purpose of this paper is to investigate the effect of: (1) the size of the system and (2) the dimensionality on the ground-state properties of the single-impurity Anderson model. Although the effect of size on the Friedel resonance

was studied recently by Bergmann,¹² to our knowledge, the effect of dimensionality on the ground-state properties has not been studied theoretically. In reduced dimensions, systems may exhibit anomalous properties. For example, the Van Hove singularities in the density of states and the nested Fermi surface in a two-dimensional lattice or the charge-density instability in one dimension may effect the ground state properties of the Kondo problem.

Quantum Monte Carlo methods have been used previously to study the single-impurity Anderson model and have provided great insight into the magnetic properties.^{13,14} However, while in all previous simulations the magnetic impurity is placed in a three-dimensional infinite sea of conduction electrons, in the present work the conduction electrons are confined on a regular lattice. In order to study the size effect, we employ open boundary conditions and place the magnetic impurity in the middle of the lattice. In open boundary conditions, conduction electrons that reach the boundary sites can hop only back to interior sites. We have changed the dimensionality and the size of the lattice and have studied the local moment and the temperature dependent impurity susceptibility. The results of the numerical simulations indicate that the properties of the ground state are quite different than those for the bulk systems depending on the dimensionality and the size of the lattice, and may explain the discrepancy between two recent experimental results.⁵⁻⁷

The single-impurity Anderson model is

$$H = -t \sum_{\langle i,j \rangle \sigma} (c_{i\sigma}^+ c_{j\sigma} + H.c.) + E_d \sum_{\sigma} d_{\sigma}^+ d_{\sigma} + U n_{d\uparrow} n_{d\downarrow} + V (c_{i_0\sigma}^+ d_{\sigma} + h.c.), \quad (1)$$

where $c_{i,\sigma}^+$ creates a conduction electron on site i with spin σ , d_{σ}^+ creates a localized electron on the impurity site i_0 with spin σ , E_d is the energy of a singly occupied impurity level, U is the Coulomb interaction between two d electrons on the impurity site, and V is the on-site hybridization energy between the conduction-electron orbital and the impurity-electron orbital.

We have used a finite-temperature Monte Carlo technique with an exact updating procedure. A typical Monte

^{a)}Electronic mail: nkoussi@newton.csun.edu

Carlo run involved 5000 sweeps through the lattice and the statistical error for the quantity measured was negligible except where shown. The finite time slice $\delta\tau$ introduces a systematic error. Simulations with $\delta\tau=0.125$ and 0.25 give results which differ only by a few percent. As a check on our Monte Carlo algorithm we have done extensive comparison with exact diagonalization results for an impurity interacting with a two-site conduction-electron lattice. We consider the symmetric case with $E_d = -U/2$, which is the most favorable for the formation of an impurity magnetic moment, and the case of half-filled conduction band and one localized d electron. This choice ensures particle-hole symmetry. The Monte Carlo simulations were carried out in the intermediate parameter regime, where the correlation effects are comparable in size to the hybridization interaction, i.e., $U/t = V/t = 1$. In the intermediate regime Monte Carlo simulations provide essentially exact results, whereas analytic approaches are most likely to fail or be inaccurate.

In order to investigate the effect of size and dimension on the spin-compensation cloud, we have calculated the impurity local moment:

$$\langle(\sigma_z^d)^2\rangle = \langle(n_{d\uparrow} - n_{d\downarrow})^2\rangle. \quad (2)$$

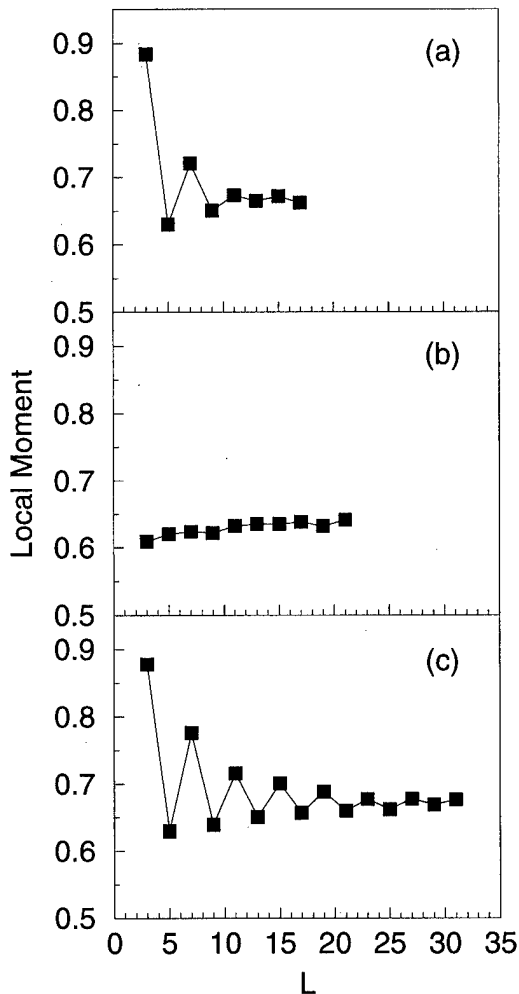


FIG. 1. Local magnetic moment, $\langle(\sigma_z^d)^2\rangle$, vs cluster size L^n for $U=1$, $V=1$, and $\beta=16$ in (a) a 3D cubic lattice, (b) a 2D square lattice, and (c) a 1D lattice.

In Fig. 1 we show the local moment, $\langle(\sigma_z^d)^2\rangle$, versus the cluster size (L^n for n dimension) for three [Fig. 1(a)] two, [Fig. 1(b)] and one dimension [Fig. 1(c)] at low temperatures $\beta=16/t$. One can see that the local moment in one and three dimensions oscillates as the lattice size is reduced. This result indicates that for 3D and 1D there are two different types of ground states, a compensated one (for $L=5$, nine sites) and an uncompensated one (for $L=3$, seven sites). The local magnetic moment associated with the uncompensated ground state is larger than that of the compensated state and shows a larger size effect. The moment decreases exponentially with lattice size, $\mu \propto e^{-L/L_0}$, where L_0 is 7.6 for 3D and 12.8 for the 1D lattice. On the other hand, the local moment in 2D varies monotonically with lattice size, indicating the existence of one type of ground state only, the compensated one.

The size effect in 1D can be understood by examining the Anderson-Hamiltonian for $U=0$ which can be diagonalized exactly. The eigenfunctions in 1D can either be of odd or even parity depending on the number of sites in the system. The eigenfunctions of even (odd) parity have a large (small) spectral weight on the impurity site which gives rise

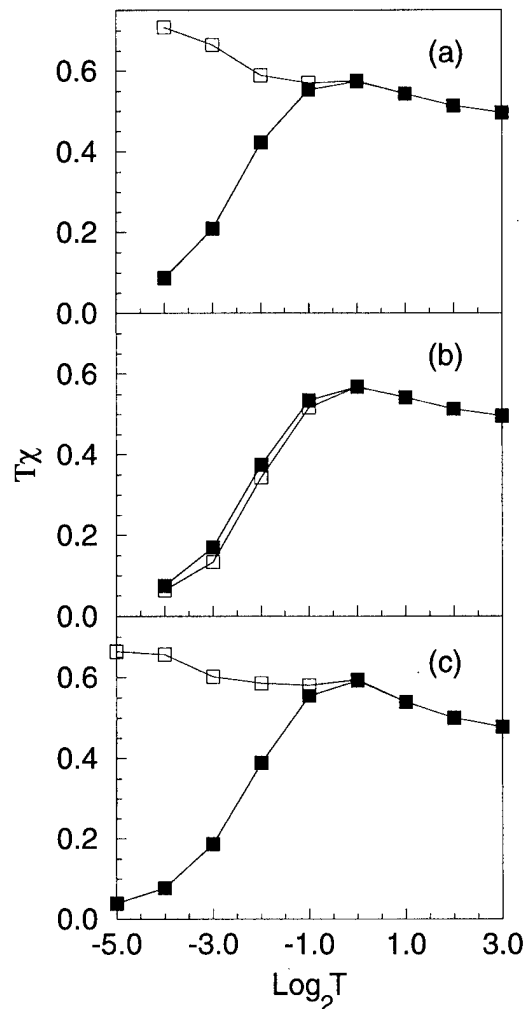


FIG. 2. Impurity magnetic susceptibility vs $\log_2 T$ for $U=1$ and $V=1$ for (a) 3D lattice, (b) 2D lattice, and (c) 1D lattice, for the cluster size $L^n = 3^n$ and $L^n = 5^n$, respectively.

to a strong (weak) antiferromagnetic interaction between the local and conduction electrons. Thus, for cluster size of $L = 3, 7, \dots$ the states at the Fermi energy are of odd parity giving rise to an "uncompensated" state, whereas for $L = 5, 9, \dots$ the states at the Fermi energy are of even parity giving rise to a "compensated" ground state.

In order to gain further insight of the nature of the ground state, we have calculated the impurity d -spin magnetic susceptibility

$$T_\chi = \int_0^\beta d\tau \langle \sigma_z^d(\tau) \sigma_z^d(0) \rangle, \quad (3)$$

as a function of temperature. In Fig. 2, we plot the "effective moment," T_χ , vs $\log_2 T$ for three [Fig. 2(a)], two [Fig. 2(b)], and one dimension [Fig. 2(c)] for the cluster size $L^n = 3^n$ and $L^n = 5^n$ (n is the dimension), respectively. If the ground state is compensated, the effective moment, T_χ , should decrease to zero at lower temperatures, signaling the quenching of the local moment. In Fig. 2, we plot these calculations with $L = 3$ and 5. It is clear that in 3D and 1D, the ground state can be either a compensated ($L = 5$) state or an uncompensated ($L = 3$) state, while the ground state in the 2D lattice can only be a compensated state.

In order to check the effect of boundary conditions on the ground state properties, we have also carried out Monte Carlo simulations for systems with even number of sites employing periodic and antiperiodic boundary conditions. The results for the size and dimensionality effect on the ground state properties are similar to those reported in this work for the case of systems with odd number of sites with open boundary conditions.

The absence of a size effect in our calculations for the 2D lattice is consistent with the experimental results of Chandrasekhar *et al.*⁷ On the other hand, the presence of a size effect in 3D is consistent with the experimental results of Giordano *et al.*^{5,6} The Kondo temperature inferred from the temperature dependence of the impurity magnetic susceptibility does not depend on the system size in 1D, 2D, and

3D lattices, which is consistent with the experimental results.⁵⁻⁸ It is interesting to consider the case of a magnetic impurity doped quantum dot, although no experimental results are currently available. Our results in 1D suggest that the ground state of the quantum dot can be a compensated or an uncompensated state as the size of the wire is reduced.

In conclusion, the dimensionality of the conduction electrons affect their interaction with the impurity resulting in a compensated or an uncompensated ground state for the case of 3D and 1D depending on the lattice size, and to a compensated ground state for the case of 2D. The dimensionality and size effect are consistent with the experimental results for the Kondo resistivity anomalies in doped films and wires. We predict that there should be a large size effect in doped quantum dots.

The research at California State University Northridge (CSUN) was supported through the National Science Foundation under Grant No. DMR-9531005 and the Office of Research and Sponsored Projects at CSUN.

¹K. Fischer, in *Springer Tracts in Modern Physics*, edited by G. Höhler (Springer, Berlin, 1970), Vol. 54, p. 1.

²H. Ishii, *Prog. Theor. Phys.* **55**, 1373 (1976).

³C. P. Slichter, in *Magnetism and Magnetic Materials*, AIP Conf. Proc. No. 29, edited by J. J. Becker, G. H. Lander, and J. J. Rhyne (AIP, New York, 1976), p. 306.

⁴M. A. Blachly and N. Giordano, *Phys. Rev. B* **51**, 12537 (1995).

⁵G. Chen and N. Giordano, *Phys. Rev. Lett.* **66**, 209 (1991).

⁶M. A. Blachly and N. Giordano, *Phys. Rev. B* **49**, 6788 (1994).

⁷V. Chandrasekhar, P. Santhanam, N. A. Penebre, R. A. Webb, H. Vloeberghs, C. Van Haesendonck, and Y. Bruynseraede, *Phys. Rev. Lett.* **72**, 2053 (1994).

⁸J. F. DiTusa, K. Lin, M. Park, M. S. Isaacson, and J. M. Parpia, *Phys. Rev. Lett.* **58**, 678 (1992).

⁹O. Ujsaghy, A. Zawadowski, and B. L. Gyorffy, *Phys. Rev. Lett.* **76**, 2378 (1996).

¹⁰I. Martin, Y. Wan, and P. Phillips, *Phys. Rev. Lett.* **78**, 114 (1997).

¹¹K. G. Wilson, *Rev. Mod. Phys.* **47**, 773 (1975).

¹²G. Bergmann, *Phys. Rev. Lett.* **67**, 2545 (1991).

¹³J. E. Hirsch and R. M. Fye, *Phys. Rev. Lett.* **56**, 2521 (1986).

¹⁴J. E. Gubernatis, J. E. Hirsch, and D. J. Scalapino, *Phys. Rev. B* **35**, 8478 (1987).

***f*-Electron delocalization/localization and the abrupt disappearance of uranium magnetic ordering with dilution alloying**

B. R. Cooper^{a)} and Y.-L. Lin

Department of Physics, West Virginia University, Morgantown, West Virginia 26506-6315

We have applied the model and technique previously applied to the change of Curie temperature with pressure for correlated-electron uranium systems to predict the change in Curie temperature and ordered moment with dilution alloying. The theory is remarkably successful in its predictions, and this success has important implications for the overall understanding of magnetic ordering in correlated-electron systems including heavy fermion systems. For US, the dilution alloying behavior found experimentally is dramatic. In $U_xLa_{1-x}S$, the magnetic ordering abruptly disappears at about 55% uranium. Our *ab initio*-based theory quantitatively predicts this abrupt disappearance while also quantitatively predicting the monotonic decrease of Curie temperature with pressure for undiluted US. In addition, in agreement with experiment, the theory predicts the correct trend for the magnetic ordering to disappear with dilution, while at the same time absolutely and quantitatively predicting the nonmonotonic variation of Curie temperature with pressure, for USe and UTe. The *ab initio*-based model gives absolute material-specific predictions using input from the local density approximation paramagnetic uranium *f*-electron-projected density of states plus *ab initio* calculated values of the correlation energy U . The key physics of the model is the recognition and quantification of the concept that the *f* spectral density in the vicinity of a specific uranium nucleus (so-to-speak in the muffin-tin sphere) can either be in a stable f^3 configuration for a long enough period of time that, through coupling to other such stable f^3 sites, it can magnetically order, or can be in a situation such that the configuration fluctuates rapidly between f^3 and f^2 , and for purposes of magnetic ordering acts like a hole in the *f*-electron lattice in the same way that substitution of lanthanum for uranium creates a hole. Both pressure and dilution alloying, by causing an increase in *f*-delocalization, increase the fraction of uranium sites in the rapidly fluctuating, magnetically ineffective, condition. For dilution alloying, at a certain point this increase in fluctuations causes the stable f^3 component to fall abruptly below a critical value necessary to sustain any magnetic ordering, and hence brings about a catastrophic collapse in magnetic ordering. © 1998 American Institute of Physics. [S0021-8979(98)21111-X]

I. INTRODUCTION AND PHYSICAL PICTURE

The magnetic ordering of the NaCl-structure uranium monochalcogenides under high pressure and upon dilution alloying experimentally provides extremely interesting physics. This includes the nonmonotonic variation of the Curie temperature (T_c) under pressure¹⁻³ for USe and UTe and the abrupt disappearance of magnetic ordering in $U_xLa_{1-x}S$ at about 55% uranium (far above the percolation limit)^{4,5} and similar behavior for⁶ diluted USe and UTe. By dilution alloying, we mean alloying as in the case of $U_xLa_{1-x}S$, where one can alter the magnetic interactions among the *f*-electron ions by an alloying process that keeps the background non-*f* chemical environment essentially unchanged. Except for a small change in lattice constant, magnetically this simply creates "holes" at those lattice sites where, e.g., lanthanum replaces uranium in US. Understanding this physics, as described below, provides us with valuable insight into the mechanisms controlling magnetic ordering in systems of partially delocalized *f* electrons (cerium and light actinides) that hybridize with non-*f* band electrons in the presence of on-site coulomb repulsion. This understanding and the method-

ology developed, in fact, gives us a quantitative material-predictive theory for the magnetic ordering aspects of heavy fermion behavior.

The central problem of treating magnetism in cerium and light actinide compounds with metals and metalloids is how to deal with the *f* delocalization in energy and space and the associated hybridization of the *f* electrons with *p* or *d* electrons coming from other atoms. To improve this treatment, in effect, means improving the treatment of correlation effects.

In past work,⁷⁻⁹ we have discussed how the physics can be captured by including two-electron correlations involving a single on-site *f* electron and a single *l* (*p/d*) electron of off-site parentage as well as on-site *f*-*f* correlations. In model calculations,⁷ we have shown that this leads to the possibility of narrow singlet (nonmagnetic) and triplet (magnetic) bands "competing" to be the ground state of the system. This then reproduces the range of specific heat and susceptibility behavior characteristic of heavy fermion systems, where it is essential to include the temperature dependence of the Fermi energy in the calculations. In effect, the essential feature of the Kondo effect, the possible formation of a spin-singlet state as the ground state and the competition with a magnetic state to provide the ground state, is already present at the level of including only two-electron correla-

^{a)}Electronic mail: bcooper@wvu.edu

tions. Thus the use of the impurity Kondo model and the resulting Kondo resonance (see Ref. 10 for a discussion) is not required to explain heavy fermion phenomenology. We have also shown^{8,9} that essentially the same singlet/magnetic state picture arises when we include two-electron $f-l$ and $f-f$ correlations for actinides, which have atomic f^n configurations with $n > 1$. We have outlined⁹ a practical electronic structure scheme for real materials based on a sequence in which a conventional one-electron electronic structure calculation is followed by a calculation for the lattice with a heliumlike two-electron hamiltonian at the f -atom sites. This procedure will reconstruct the LDA bands to include two-electron texturing, i.e., will impose a substructure of extremely narrow nonmagnetic and magnetic bands leading to the phenomena modeled in Ref. 7 depending on where the Fermi energy falls with respect to this extreme narrow-band substructure.

In order to treat specific observable spectral features and their thermodynamic (e.g., specific heat, susceptibility) and transport property consequences, we would have to carry out the two-electron computational procedure outlined in Ref. 9. At present, we have not yet carried out calculations using the procedure outlined in Ref. 9. However, because they are global properties (i.e., involve the spectral density in an integrated sense), we can nevertheless perform *ab initio*-based calculations for the Curie temperature and ordered moment. Such calculations were first described in Ref. 11 for the Curie temperature variation with pressure and here are refined and extended to treat the Curie temperature and ordered moment change with dilution alloying as well as the change of T_c with pressure.

The *ab initio*-based model of Ref. 11, as refined and extended here, gives absolute material-specific predictions using input from the uranium f -electron-projected paramagnetic LDA density of states from supercell calculations plus the *ab initio*-calculated correlation energy U . There is one arbitrary feature: how to separate the localized f spectral density from the delocalized f spectral density. We adopt a boundary defined by the energy where, upon decreasing energy from the $j = 5/2$ peak in the density of states, there is a distinct difference between the total and the f -projected density of states. (In effect, this is the energy where significant hybridization begins to occur between the f electrons and the non- f band electrons. Operationally, we define this as the energy where the density of states first stops dropping monotonically from the peak, i.e., the first local minimum in the density of states.) Once this is done, there is only one non-*ab initio* number that must be provided for a given material, e.g., US. This is setting the starting (baseline) division between occupation of uranium states where an f^3 (magnetic) configuration exists for long enough for those sites to be able to magnetically order and those states which fluctuate between an f^2 configuration and an f^3 configuration sufficiently rapidly to, in effect, provide magnetic holes in much the same way as a La site. We choose that single number (i.e., the baseline fraction of uranium sites with stable f^3 configuration) for the pure (unalloyed) material (e.g., US) at ambient pressure.

The catastrophic ordered magnetic moment collapse that occurs at 55% uranium for $U_x\text{La}_{1-x}\text{S}$ is then a consequence of three effects providing an extremely nonlinear magnetic response to the dilution: most importantly, the increased delocalization acts wholly to reduce the stable f^3 component, secondarily that f^3 component becomes more localized, hence giving less coupling for a given f^3-f^3 separation, and in addition the f^3 sites are spread further apart with increasing lanthanum dilution. While probably secondary in triggering the ordered moment collapse, the extreme localization, as it disappears, of the remaining f^3 component, may be central to the observation of heavy fermion effects.

II. CALCULATIONAL PROCEDURE

Using the Hubbard model, following the procedure described in Ref. 11, the coupling (J) between localized moments on an fcc lattice is obtained from the width of the localized peak in the uranium f -electron-projected density of states and the calculated correlation energy (U). If t is the interatomic interaction, then for an fcc lattice, the localized peak width Γ is related to t through $\Gamma = 1.04t$ and $J = t^2/U$. The magnetic ordering is then calculated exactly as in Ref. 11 for an Ising lattice (used to mimic the very large magnetic anisotropy) with holes.

The key point is to identify the number of holes, i.e., the average number of sites not occupied by stable f^3 uranium. We do this by first establishing a baseline fraction of stable f^3 sites for the pure unalloyed material at atmospheric pressure. This is the one point at which we either insert a physically motivated guess or use one piece of experimental data or use a value to balance between fitting several pieces of data. The obvious choices for this purpose are the low-temperature ordered moment, the Curie temperature, or the LDA f -electron count. For US all three of these indicate very closely the same baseline value. The experimental low-temperature ordered moment per uranium of US from the recent neutron measurements of Ref. 5 is $1.60 \mu_B$, and from the magnetization measurements of Ref. 4 is $1.55 \mu_B$. This is slightly less than half the ordered moment expected for U^{3+} (f^3 uranium) ($3.27 \mu_B$). This would give a baseline fraction of stable f^3 of 0.49. The LDA f count is close to 2.5 for US, indicating a baseline f^3 fraction of 0.5. In addition, for US as discussed below with that choice of 0.5, the calculated T_c is 183 K compared to the experimental value of^{4,5} 180 K. So we take the baseline value of holes as 50% for pure US at atmospheric pressure. (This is a different baseline than in Ref. 11, and there are also some changes in the technical details. Thus the predicted variation of Curie temperature with pressure shown below differs somewhat from that of Ref. 11.)

For US and UTe, our choice of the starting baseline fraction of stable f^3 uranium guided by the data of Ref. 12 and the LDA f counts is 0.67 and 0.80, respectively. It is this greater degree of localization, of having more stable f^3 , on going from US to USe to UTe that gives rise to the dramatically different variation of T_c with pressure.

Then the key input information from the LDA calculations is how this baseline number of holes increases with pressure and dilution alloying as the hybridization with the

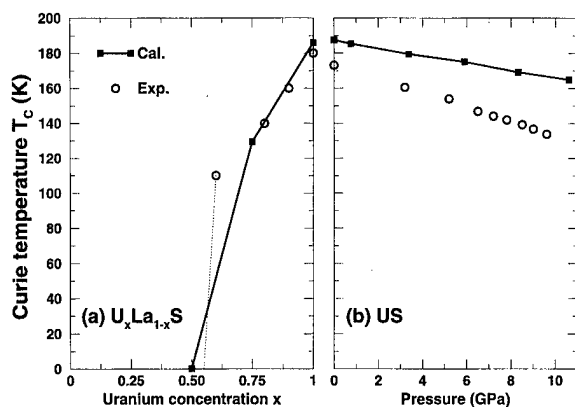


FIG. 1. Calculated Curie temperature for US compared to experiment for change with La dilution in (a) (experimental results from Ref. 5) and for change with pressure in (b) (experimental results from Ref. 3).

p/d electrons increases. We do this by calculating the decrease in integrated f -spectral weight per uranium contained in the localized peak of the LDA density of states. Thus for US, for pressure effects, the increase in holes comes wholly from the size of that spectral transfer, which decreases the 0.5 electron per uranium that on average defines the baseline fraction of well ordered f^3 uranium.

For dilution alloying, there are two ways in which the number of holes increases, by the shift of spectral weight per uranium from the localized peak to the itinerant tail (an illustrative figure and illustrative numerical results for the previous pressure calculation can be seen in Ref. 11), i.e., the same effect as caused by pressure. In addition, substitution of a lanthanum by itself gives a hole. Thus dilution alloying has a much enhanced effect on magnetic ordering. The actual LDA calculations for dilution alloying have been carried out using supercells containing four uranium/lanthanum sites and four anion sites. Thus, at present, we can predict alloying effects only at intervals of 25% dilution.

III. RESULTS AND DISCUSSION

The predicted variation of Curie temperature with pressure and dilution alloying is compared to experiment^{3,5} for US in Fig. 1. We emphasize that the predictions are absolute. All input information is *ab initio* except for the baseline specification of the fraction of stable f^3 uranium for unalloyed US at atmospheric pressure. In Fig. 2, we show the comparison between the predicted and experimental⁵ low temperature ordered moment for $U_xLa_{1-x}S$. The remarkable agreement of prediction with experiment shown in Figs. 1 and 2, including the collapse of magnetic ordering somewhat above 50% uranium, provides strong confirmation of the correctness of the physical picture used. We have also calculated the predicted normalized ordered moment and Curie temperature behavior for diluted USe and UTe and reproduce the experimentally observed⁶ trend. For the baseline f^3 fractions used (0.50, 0.67, and 0.80 for US, USe, and UTe, respectively), the predicted Curie temperature and ordered moment are 183 K and $1.64 \mu_B$ (experimentally 180 K and $1.6 \mu_B$) for US, 149 K and $2.19 \mu_B$ (experimentally 160 K

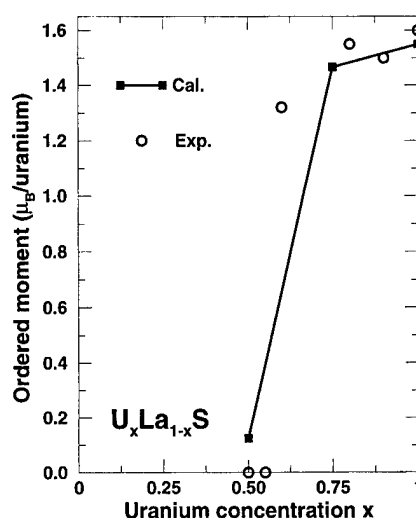


FIG. 2. Calculated low-temperature ordered moment per uranium compared to experiment (from Ref. 5) for $U_xLa_{1-x}S$.

and $2.0 \mu_B$) for USe, and 91 K and $2.6 \mu_B$ (experimentally 104 K and $2.25 \mu_B$) for UTe. In addition find nonmonotonic variation of T_c for USe and UTe with pressure in excellent agreement with experiment.

In conclusion, we want to emphasize that the collapse of magnetic ordering in US is a catastrophic consequence of the existence of two kinds of occupied uranium, states and of the change in this mixture by increasing the f delocalization with pressure or dilution alloying. This picture is equivalent to that provided by the competing nonmagnetic and magnetic correlated ultranarrow band picture of Refs. 7–9 and contains all the essential physics of correlated f -electron behavior, including all aspects of heavy fermion behavior.

ACKNOWLEDGMENTS

This research was supported by National Science Foundation Grant No. DMR-91-20333. We have appreciate discussion of their data with F. Bourdarot, P. Burlet, and O. Vogt, and permission to quote their results.

- ¹ P. Link, U. Benedict, J. Wittig, and H. Wühl, J. Phys.: Condens. Matter **4**, 5585 (1992).
- ² P. Link, U. Benedict, J. Wittig, and H. Wühl, Physica B **190**, 68 (1993).
- ³ A. L. Cornelius, J. S. Schilling, O. Vogt, K. Mattenberger, and U. Benedict, J. Magn. Magn. Mater. **161**, 169 (1996).
- ⁴ J. Schoenes, O. Vogt, J. Löhle, F. Hulliger, and K. Mattenberger, Phys. Rev. B **53**, 14 987 (1996).
- ⁵ F. Bourdarot, P. Burlet, R. Calemczuk, F. Lapiere, M. Mattenberger, and O. Vogt, 27th Journées des Actinides, Dijon, France, April, 1997 (unpublished), paper 08.2.
- ⁶ O. Vogt (private communication).
- ⁷ Q. G. Sheng and B. R. Cooper, Philos. Mag. Lett. **72**, 123 (1995).
- ⁸ B. R. Cooper, Y.-L. Lin, and Q. G. Sheng, Physica B **230–232**, 27 (1997).
- ⁹ B. R. Cooper, Y.-L. Lin, and Q. G. Sheng, J. Appl. Phys. **81**, 3856 (1997).
- ¹⁰ N. E. Bickers, D. L. Cox, and J. W. Wilkins, Phys. Rev. B **36**, 2036 (1987).
- ¹¹ Q. G. Sheng and B. R. Cooper, J. Magn. Magn. Mater. **164**, 335 (1996).
- ¹² See Table 19 on page 105 of Chapter 2 "Bulk Properties of the Actinides" by J.-M. Fournier and R. Troc' in *Handbook on the Physics and Chemistry of the Actinides*, edited by A. J. Freeman and G. H. Lander (Elsevier Science, Amsterdam, 1985), Vol. 2.

Evidence for an extended critical region near the metamagnetic transition of UCoAl

A. V. Kolomiets, L. Havela,^{a)} and V. Sechovský

Department of Metal Physics, Charles University, Ke Karlovu 5, 121 16 Prague 2, The Czech Republic

L. E. DeLong and D. B. Watkins

Department of Physics and Astronomy, University of Kentucky, Lexington, Kentucky 40506-0055

A. V. Andreev

Institute of Physics, Academy of Sciences of the Czech Republic, Na Slovance 2, 180 40 Prague 8, The Czech Republic

Electrical resistivity and ac magnetic susceptibility studies of the 5*f*-metamagnet UCoAl reveal the presence of strong spin fluctuation effects for temperatures below 30 K and magnetic fields below the critical metamagnetic field $\mu_0 H_c \approx 1$ T, where a non-Fermi liquid term $\sim T^{3/2}$ is prominent in the electrical resistivity. A step-wise increase of the residual resistivity and an increasingly prominent Fermi liquid T^2 term of the resistivity is observed as the field is increased through the metamagnetic transition. © 1998 American Institute of Physics. [S0021-8979(98)43411-X]

INTRODUCTION

UCoAl is a 5*f*-band metamagnet with a remarkably low critical magnetic field ($\mu_0 H_c \approx 1$ T). It crystallizes in the hexagonal ZrNiAl-type structure, which consists of alternating U-Co and U-Al layers stacked along the *c* axis. These structural features and hybridization between the uranium 5*f* and conduction electron states result in a strong uniaxial anisotropy with the easy-magnetization axis along the (001) direction.¹ A lack of anomalies in specific heat and resistivity¹⁻³ suggests that UCoAl has a nonmagnetic ground state. The temperature dependence of the magnetic susceptibility for the applied field along the *c* axis exhibits a broad maximum near $T = 17$ K.^{2,4} A weak spontaneous magnetization of the order of $0.01 \mu_B/\text{U}$ is observed below $T \approx 15$ K, especially for samples with a slight excess of Co.⁴ The absence of magnetic order at low fields is corroborated by a μ^+ -SR experiment.⁵ The 5*f* origin of the field-induced magnetization (about $0.3 \mu_B/\text{U}$) was demonstrated in polarized neutron diffraction experiments.^{6,7}

Previously, only polycrystalline resistivity data were available for UCoAl,^{2,3,8} although the strong anisotropy of the transport properties of UTX compounds requires experiments on single crystals to deduce basic characteristics of the low temperature behavior.

Because the crystal structure of UCoAl allows some off-stoichiometry and a Co excess apparently affects magnetic properties at low temperatures, we investigated two Co-deficient single crystals $\text{UCo}_{1-x}\text{Al}_{1+x}$ of slightly different compositions ($x = 0.05$ and 0.10), which were prepared by a mineralization method.⁴ The transport and magnetic behavior of these two compositions are quite similar.

Here we present the first results of electrical resistivity measurement with magnetic field up to 5 T and electrical current both applied along the *c* axis.

RESULTS AND DISCUSSION

Figure 1 shows the metamagnetic transition of

$\text{UCo}_{0.90}\text{Al}_{1.10}$ and its shift towards higher fields with increasing T . The data for $\text{UCo}_{0.95}\text{Al}_{1.05}$ are similar, but exhibit a slightly lower critical field H_c . Corresponding susceptibility χ (M/H vs T) data are displayed in Fig. 2. The data for $\mu_0 H = 0.5$ T are representative of the low-field region. Note that for $\mu_0 H = 2$ T, the $\chi(T)$ dependence resembles that of a ferromagnet. A magnetic field $\mu_0 H = 1$ T is sufficient to induce the metamagnetic transition below $T \approx 5$ K. The increase of H_c with increasing T is the reason why the sample reverts to the low-field state for higher temperatures.

General features of resistivity are similar for both compositions, although the residual resistivity ρ_0 is somewhat lower for $\text{UCo}_{0.95}\text{Al}_{1.05}$ (Figs. 3 and 4). $\rho(T)$ gradually saturates at high T , which is characteristic of spin-fluctuation materials such as USn_3 or UAL_2 .⁹

A prominent feature of the low temperature resistivity is a $T^{3/2}$ term that is present up to 17 K. This behavior is distinct from a Fermi-liquid T^2 dependence, which is expected for electron quasiparticle scattering. The upper limit of the

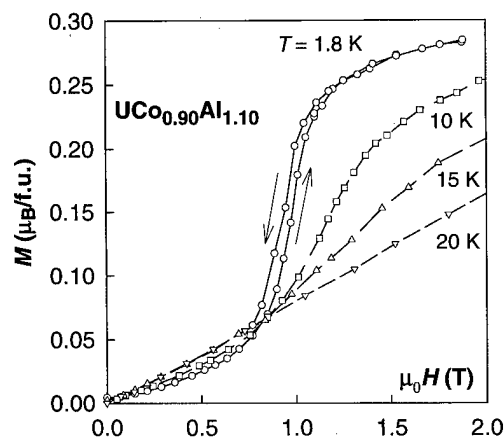


FIG. 1. Field dependence of magnetization M for the single crystal $\text{UCo}_{0.90}\text{Al}_{1.10}$ with field $H \parallel c$ axis at various temperatures T . The data for $T < 4.2$ K show a weak hysteresis. The arrows indicate the direction of the field sweep for $T = 1.8$ K. (After Ref. 4).

^{a)}Electronic mail: havela@apollo.karlov.mff.cuni.cz

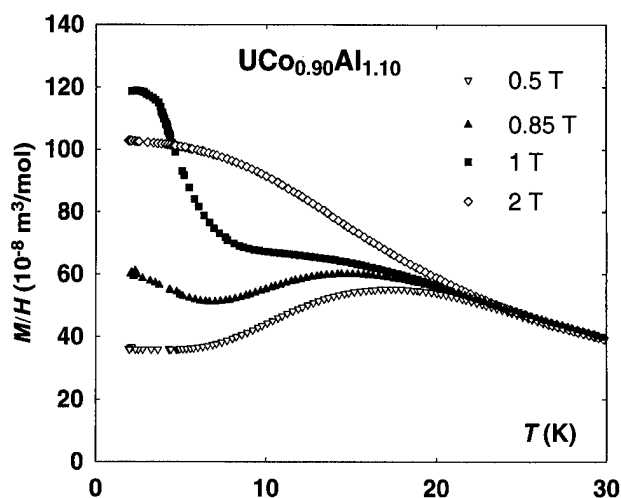


FIG. 2. Temperature dependence of M/H measured in several fields $H||c$ for the single crystal $\text{UCo}_{0.90}\text{Al}_{1.10}$.

$T^{3/2}$ law is dependent upon magnetic field, and coincides with the onset of a strong low-temperature upturn in the dc magnetic susceptibility (see Fig. 2 for $\mu_0 H = 1$ T).

The $T^{3/2}$ law is predicted¹⁰ for a system with strong spin fluctuations due to incipient magnetic order. The extent of the $T^{3/2}$ region is gradually reduced as the applied field approaches H_c , and a knee develops near 10 K for $\mu_0 H \approx 1$ T. This knee broadens and slowly moves to higher temperatures when the magnetic field is increased above 1 T, and roughly follows the temperature dependence of $H_c(T)$. The Fermi liquid aT^2 dominates $\rho(T)$ for high fields and lower temperatures up to about 10 K; but in the range 10–30 K (above the knee) $\rho(T)$ is still best described by a $T^{3/2}$ dependence. It is noteworthy that the evolution of $\rho(T)$ with field is remarkably similar to comparable data¹¹ for weak ferromagnets like Sc_3In and ZrZn_2 .

A Quantum Design (SQUID) magnetometer was used to measure the ac susceptibility at various ac frequencies $0 \leq f \leq 1$ kHz and driving fields $0.01 \leq h_0 \leq 3.9$ Oe. Data for both the real [$\chi'(T)$] and imaginary [$\chi''(T)$] parts of the ac mag-

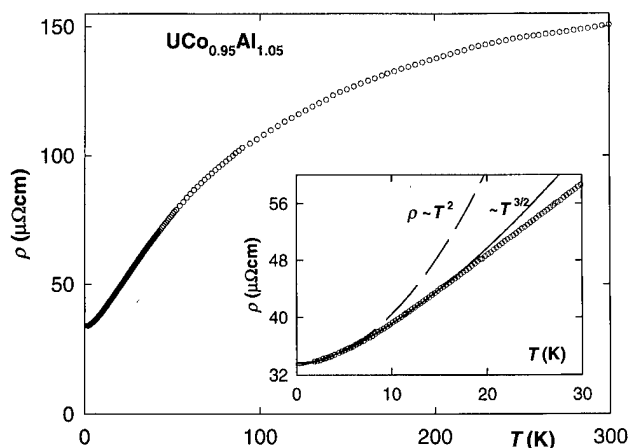


FIG. 3. Temperature dependence of electrical resistivity ρ (current i along the c axis) for $\text{UCo}_{0.95}\text{Al}_{1.05}$ single crystal in zero magnetic field. The inset shows the low temperature detail as well as the fits to $\rho \sim bT^{3/2}$ and $\rho \sim aT^2$, the latter yielding somewhat lower ρ_0 .

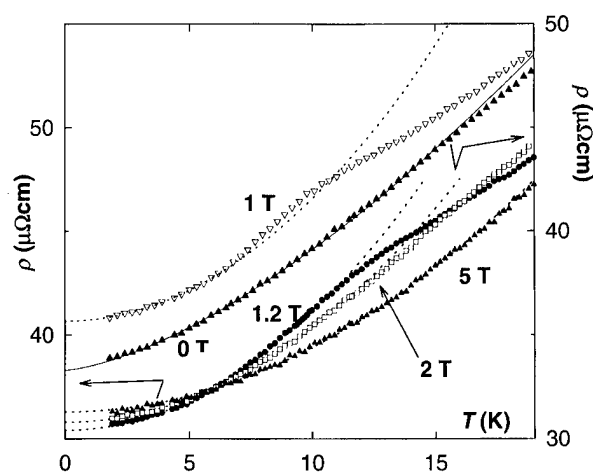


FIG. 4. Temperature dependencies of resistivity ρ for $\text{UCo}_{0.95}\text{Al}_{1.05}$ in various fields. The dotted lines represent the fits to the T^2 law, the full lines fits to the $T^{3/2}$ law. Note two different ρ scales (left and right).

netic susceptibility of $\text{UCo}_{0.95}\text{Al}_{1.05}$ ($\text{UCo}_{0.90}\text{Al}_{1.10}$ is analogous) are shown in Fig. 6. $\chi'(T)$ exhibits a broad maximum at $T \approx 16$ K in zero field, similar to the dc susceptibility. At magnetic fields just below H_c , a second, sharper peak appears and grows near 7 K, and is most pronounced at $\mu_0 H \approx 0.7$ T for $\text{UCo}_{0.95}\text{Al}_{1.05}$, and at $\mu_0 H \approx 1$ T for $\text{UCo}_{0.90}\text{Al}_{1.10}$. This feature is undoubtedly connected with the rapid variation of the dc susceptibility in this temperature range; it is clear that both a broad anomaly (10–20 K) and a sharp upturn (7 K) are visible in the dc susceptibility for $\mu_0 H = 1$ T, as seen in Fig. 2. Further increase of field leads to a broadening, and an apparent shift of the second peak to higher temperatures make a separation of the two anomalies

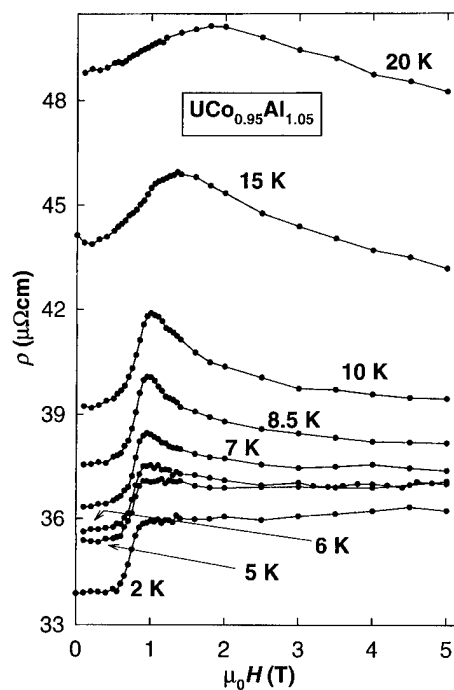


FIG. 5. Field dependence of resistivity ρ for $\text{UCo}_{0.95}\text{Al}_{1.05}$ at various temperatures. The lines are guides to the eye.

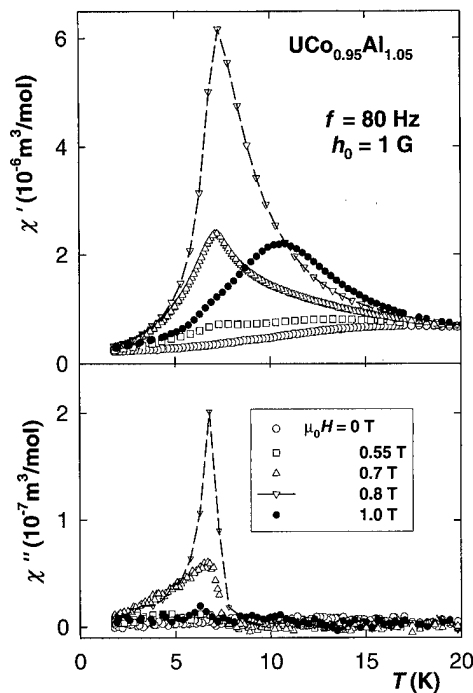


FIG. 6. Temperature dependencies of real χ' and imaginary χ'' parts of the ac susceptibility for $\text{UCo}_{0.95}\text{Al}_{1.05}$ at various static external fields. The line is the guide to the eye.

difficult. $\chi''(T)$ exhibits a narrow peak coinciding with the more prominent maxima in $\chi'(T)$, possibly reflecting the skin effect (i.e., permeability) variations, and dissipation accompanying the hysteresis at lowest temperatures (shown in Fig. 1). The peak in $\chi''(T)$ abruptly terminates at $T \approx 7$ K, which may be interpreted as an upper limit of a first-order phase transition.

The character of the ac susceptibility data provides evidence against the existence of a spin-glass or cluster-glass ground state induced by crystallographic disorder, in which case one typically observes a low-field cusp in $\chi_{ac}(T)$ that broadens with moderate applied dc field.

The shift of the maximum in $\chi'(T)$ with increasing T is similar to the behavior of band metamagnets (such as YCo_2),¹² but is in clear contrast with the metamagnetic fields of typical antiferromagnets. The latter typically decrease with increasing T , reflecting a higher entropy in the metamagnetic state. Thermodynamic considerations, based on the Clausius–Clapeyron equation, show that the metamagnetic transition in UCoAl reduces the entropy of the system.

The occurrence of the $3/2$ resistivity exponent strongly suggests that the behavior of UCoAl at low temperatures is dominated by critical spin fluctuations attendant with incipient magnetic order. The magnitude of the resistivity coefficient b increases with applied field up to H_C . The suppression of critical fluctuations in the metamagnetic state removes the non-Fermi liquid temperature dependence in favor of the Fermi liquid aT^2 term, with an a value that decreases gradually with field.

As seen in Fig. 5, the residual resistivity ρ_0 jumps at the metamagnetic transition from 35 to 38 $\mu\Omega \text{ cm}$ for $\text{UCo}_{0.95}\text{Al}_{1.05}$ and can be associated with a decrease of density

of states at the Fermi level $N(E_F)$ due to a Fermi surface reconstruction accompanying the formation of the $5f$ moment. This change is actually smaller than expected, because the spin-orbit interaction should result in a very strong coupling of the U magnetic moments to the electronic structure.¹³

A decrease of the total density of states at the Fermi level $N(E_F)$ is consistent with the observed reduction of the Sommerfeld specific heat coefficient γ in the metamagnetic state (from 75 to 55 mJ/mol K^2),¹⁴ and can also reflect the suppression of spin fluctuations. However, using the Kadowaki–Woods¹⁵ relation between the resistivity coefficient a and γ^2 , we would expect a value of the a coefficient even lower than our observed $a \approx 0.03 \mu\Omega \text{ cm K}^{-2}$ in the high field state. This discrepancy could simply result from anisotropy of the T^2 term, which is under investigation.

CONCLUSIONS

The low temperature behavior of UCoAl is strongly influenced by critical spin fluctuations due to incipient magnetic ordering, as reflected by a $T^{3/2}$ dependence over approximately 1 decade of the low-temperature resistivity below the critical metamagnetic field. The spin fluctuations are suppressed when the material enters the high field regime above the metamagnetic transition, where a Fermi liquid T^2 behavior of the resistivity is recovered. The residual resistivity for current along the c axis exhibits a step-wise increase at the metamagnetic transition ascribed to a Fermi surface reconstruction.

ACKNOWLEDGMENTS

This work was supported by the joint Czech-US grant of MSMT CR and NSF under Grant No. ES 011 and by the Czech Grant Agency (Grant No. 202/95/0008).

- ¹ V. Sechovsky, L. Havela, F. R. de Boer, J. J. M. Franse, P. A. Veenhuizen, J. Sebek, J. Stehno, and A. V. Andreev, *Physica B & C* **142B**, 283 (1986).
- ² L. Havela, L. Neuzil, V. Sechovsky, A. V. Andreev, C. Schmitzer, and G. Hilscher, *J. Magn. Magn. Mater.* **54–57**, 551 (1986).
- ³ V. Sechovsky, L. Havela, L. Neuzil, A. V. Andreev, G. Hilscher, and C. Schmitzer, *J. Less-Common Met.* **121**, 169 (1986).
- ⁴ L. Havela, A. V. Andreev, V. Sechovsky, I. K. Kozlovskaya, K. Prokes, P. Javorsky, M. I. Bartashevich, T. Goto, and K. Kamishima, *Physica B* **230–232**, 98 (1997).
- ⁵ L. Havela, P. Svoboda, and K. Prokes (unpublished results).
- ⁶ M. Wulff, J. M. Fournier, A. Delapalme, B. Gillon, V. Sechovsky, L. Havela, and A. V. Andreev, *Physica B* **163**, 331 (1990).
- ⁷ R. J. Papoular and A. Delapalme, *Phys. Rev. Lett.* **72**, 1486 (1994).
- ⁸ V. H. Tran, R. Troc, A. J. Zaleski, F. G. Vagizov, and H. Drulis, *Phys. Rev. B* **54**, 15907 (1996).
- ⁹ V. Sechovsky and L. Havela, in *Ferromagnetic Materials*, edited by E. P. Wohlfarth and K. H. J. Buschow (North-Holland, Amsterdam, 1988), pp. 309–491.
- ¹⁰ T. Moriya and T. Takimoto, *J. Phys. Soc. Jpn.* **64**, 960 (1995).
- ¹¹ S. Ogawa, *J. Phys. Soc. Jpn.* **40**, 1007 (1976).
- ¹² H. Mitamura, T. Sakakibara, G. Kido, and T. Goto, *J. Phys. Soc. Jpn.* **64**, 3459 (1995).
- ¹³ V. A. Antonov, A. Ya. Perlov, P. M. Oppeneer, A. N. Yaresko, and S. V. Halilov, *Phys. Rev. Lett.* **77**, 5253 (1996).
- ¹⁴ Y. Aoki, T. D. Matsuda, H. Sugawara, H. Sato, H. Ohkuni, R. Settai, Y. Onuki, E. Yamamoto, Y. Haga, A. V. Andreev, V. Sechovsky, L. Havela, H. Ikeda, and K. Miyake, *J. Magn. Mater.* **177–181** (1998) (in press).
- ¹⁵ K. Kadowaki and S. B. Woods, *Solid State Commun.* **58**, 507 (1986).

Electronic structure and magnetic properties of URhSi

M. Galli and F. Marabelli

INFM and Department of Physics, "A. Volta," University of Pavia, via Bassi 6, I-27100 Pavia, Italy

A. Continenza and P. Monachesi

INFM and Department of Physics, University of L'Aquila, via per Coppito, I-67010 L'Aquila, Italy

F. Canepa and M. L. Fornasini

INFM and Department of Chemistry and Industrial Chemistry, University of Genova, via Dodecaneso 31, I-16146 Genova, Italy

Orthorhombic URhSi orders ferromagnetically below $T_c = 9.5$ K, with an ordered magnetic moment $\mu = 0.11\mu_B$ per U atom and has a relatively enhanced value of the specific heat $c_p/T = 186$ mJ/mol K². U-U atomic distances fall in a critical region around the Hill limit so that it is thought to be an itinerant magnet. Our present investigation includes: (i) preparation of high purity crystalline samples further analyzed by single crystal x-ray diffraction and magnetization measurements; (ii) band structure calculations performed with self-consistent full potential linearized Augmented plane wave method within the local density approximation; (iii) optical measurements at room and at low temperature over a large spectral range (2 meV–6 eV). As a result, the details of the crystal structure of URhSi have been refined with respect to previous measurements on powdered samples. The comparison of electronic structure calculations and optical results show: (a) a low mobility of free carriers and a large dielectric screening at the lowest frequencies, connected with excitation of f states hybridized with d states at the Fermi level; (b) smooth spectral features due to the huge number and density of states (the main contribution being due to occupied Rh d states). The whole amount of information obtained would suggest the presence of Kondo-like behavior in this compound, independently on the magnetic order. © 1998 American Institute of Physics. [S0021-8979(98)43511-4]

I. INTRODUCTION

Intermetallic ternary uranium alloys have been studied during the latest years due to their interesting interplay between magnetic and electronic structure. Both localized and itinerant magnetism have been observed in this class of compounds, often coexisting with heavy fermion properties.^{1–3} One of the most investigated material was URu₂Si₂ that is an itinerant antiferromagnet with heavy fermion properties.^{1,4,5} URhSi is a compound with orthorhombic structure apparently not too different from URu₂Si₂. On the other hand, URh₂Si₂ is a normal magnet with transition temperature and magnetic moment expected from a Curie Weiss behavior.⁶ The first characterization of the physical properties of URhSi has been performed by Prokes *et al.*⁷ Neutron diffraction experiment, electrical resistivity, magnetic susceptibility, and specific heat measurements evidenced a ferromagnetic transition at 9.5 K with a reduced magnetic moment of $0.11\mu_B$ and itinerant character.

Stimulated by the possible interplay of crystallographic structure and electronic bonding (there are two different U-U distances in the structure) we undertaken a thorough investigation of this compound. The results of crystallographic, magnetic, optical, and theoretical investigations are detailed below.

II. EXPERIMENT

Samples of about 2 grams each were prepared by direct synthesis of the elements (U depleted 99.8 wt % purity, Rh

99.9 wt % purity, and Si 99.999 wt % purity. The Rh metal was outgassed under dynamic vacuum for 5 h. at 800 °C.) pressed together in form of pellets and then melted in a semi-levitation high-frequency induction furnace on a water-cooled tantalum heart under an atmosphere of pure and dry argon. The samples were inverted and remelted three times to ensure complete homogenization and then slowly cooled to room temperature.

A metallographic examination showed that the samples were single phase, well crystallized, and compact with little grain separation (1% at most). The phase of URhSi was examined by single crystal and powder methods. Intensity data of a single crystal with dimensions $20 \times 50 \times 70 \mu\text{m}^3$ were collected with a CAD-4 diffractometer using graphite monochromated Mo $K\alpha$ radiation in the θ range 2–30°. A total of 1309 reflections measured in the ω - θ scan mode gave 352 independent reflections with $R_{\text{int}}(F_0^2) = 0.158$. Both spherical and semiempirical absorption corrections based on the azimuthal scan data of a top reflection were applied, with a linear absorption coefficient of 83.7 mm^{-1} and a ratio between maximum and minimum transmission factors of 3.5. Lattice constants were obtained from a diffractometer powder pattern, using Cu $K\alpha$ radiation and Si as an internal standard.

Refinement of 19 parameters was made with SHELXL-93,⁸ applying anisotropic displacement parameters and weights $w = 1/[\sigma(F_0^2) + (0.1293P)^2]$, where $P = (F_0^2 + 2F_c^2)/3$. The final agreement factors were $wR(F^2) = 0.169$ for all data and $R = 0.064$ for 245 reflections with

TABLE I. Interatomic distances in URhSi as obtained by x-ray diffraction. Standard deviations are indicated in brackets.

U-Rh (Å)	U-Si (Å)	U-U (Å)
2.9421(2)	2.944(8)	3.424(2)
3.048(3)	2.95(1)	3.629(2)
3.118(3)	2.955(7)	...
3.299(2)

$F_0 > 4\sigma(F_0)$. Interatomic distances for U atoms calculated by the program SEXIE⁹ are listed in Table I.

The phase, orthorhombic, space group Pnma, $a = 6.990(1)$ Å, $b = 4.114(1)$ Å, $c = 7.427(1)$ Å, resulted to be isotypic with TiNiSi. From magnetization measurements, performed at 4.2 K in a Faraday balance in magnetic fields up to 1 Tesla on randomly oriented crystals, a saturation value (at 1 Tesla) of $0.56 \mu_B/f.u.$ was obtained, in agreement with the results of Prokeš *et al.*⁷

The electronic properties for the paramagnetic phase of URhSi have been determined using the self-consistent full potential linearized augmented plane wave (FLAPW) method within local density approximation (LDA). The calculated total and partial density of states (DOS) are shown in Fig. 1. U- f states result to be placed just above the Fermi energy (E_F) mixed with U- d , Si- p and, particularly, with Rh- d states. Due to the well known failure of LDA in correctly reproducing exchange-correlation effects in strongly localized states as the f states, the real energy position of these states can be quite different. However, it should be pointed out that the major contribution to the DOS of the occupied states (from E_F down to about -6 eV, which is the energy region of interest) comes from the Rh d states (see Fig. 1), which are very well reproduced by LDA. Si- s and U- p states lie practically unhybridized well below E_F (-8 eV and -19 eV, respectively).

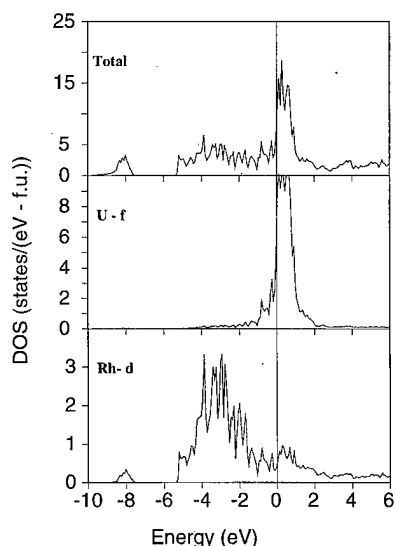


FIG. 1. Electronic density of states (DOS) as calculated by FLAPW+LDA in URhSi. (Top: total DOS; middle: partial U- f DOS; bottom: partial Rh- d DOS).

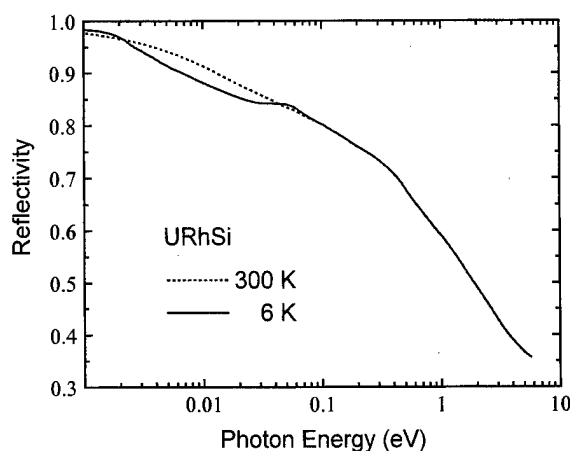


FIG. 2. Optical reflectivity of URhSi measured at room temperature (dashed line) and at 6 K (full line).

Near normal optical reflectance measurements were performed on a polycrystalline disk of material with a diameter of about 7 mm and 2 mm thick. The sample surface was optically polished with diamond powder of decreasing size down to $0.25 \mu\text{m}$. The shining surface so obtained is crossed by some fracture lines which, anyway, affect only a small fraction of the measured area. ellipsometric measurements (ellipsometry is almost unaffected by roughness, but it is very sensitive to oxidation) performed at several different angles of incidence in the spectral region between near infrared and ultraviolet (1.4–5 eV) confirmed that the residual roughness only slightly affects the optical results at energies above 3 eV. A thin oxide layer due to air exposure of the sample is probably present, but it practically does not affect the near normal reflectance, particularly in the infrared.

The measurements were performed over a very broad spectral range from 2 meV up to 6.5 eV, using a Fourier transform infrared spectrometer, equipped with a Si bolometer, and a high precision grating spectrometer in the UV-visible spectral region. In the medium- and far-infrared the sample was also put on the cold finger of a helium flow cryostat and measured at several different temperatures between 6 K and room temperature.

The spectra so obtained exhibit an almost structureless, monotonically decreasing reflectivity from far infrared to ultraviolet (Fig. 2). A smooth change of curvature occurs in the medium infrared whereas a small structure emerges around 20 meV by lowering the temperature.

Kramers–Kronig transformation was applied to the reflectivity data in order to obtain the dielectric function and the optical conductivity. A small correction of the reflectivity data above 3 eV and a common extrapolation of the data as ω^{-s} above 6.5 eV were introduced (s was chosen in such a way as to ensure the consistence with the ellipsometric results). At energies below 2 meV an extrapolation was obtained by the Hagens–Rubens relation $R = 1 - \sqrt{2\omega/\pi\sigma_{dc}}$, where σ_{dc} is the static conductivity of the material, and assuming a Drude like behavior of the free carrier.

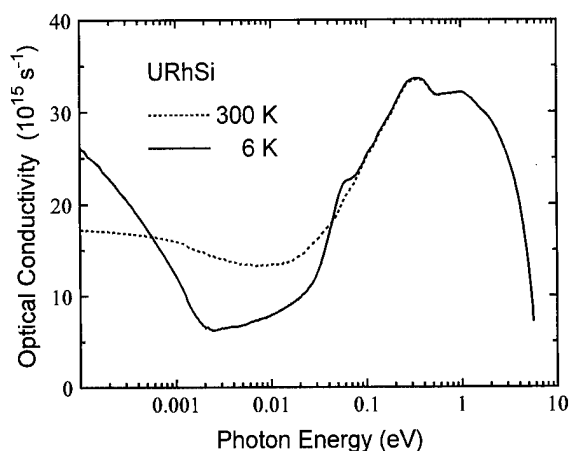


FIG. 3. Optical conductivity of URhSi obtained by Kramers–Kronig analysis at room temperature (dashed line) and at 6 K (full line).

III. DISCUSSION

The structure determination of URhSi by single crystal methods confirms its isotypism with the ordered TiNiSi type, as already reported by Prokes *et al.*⁷ by neutron diffraction measurements. However, the lattice constants found in the present work are all smaller than those determined by neutron diffraction at 80 K. A slightly higher fraction of U and a slightly lower fraction of Rh in the sample were hypothesized by Prokes *et al.* for both improving the fit of the neutron diffraction spectrum and matching the electron microprobe analysis; that could be partially responsible for the higher values of the lattice constants. Examining the interatomic distances in URhSi we see that the U–U, U–Rh, and U–Si distances are always larger than the sum of the elemental radii, but this is probably due to a scarce transferability of the uranium radius from elemental to alloyed states.

Kramers–Kronig analysis yield to an optical conductivity showing a smooth maximum at about 0.2 eV followed by a shoulder around 1 eV and an almost linear decrease for increasing energies (Fig. 3).

The smoothness of the optical structures is usually related to disorder effects, but in our case it is actually consistent with the calculated band structure, being related to the almost constant and large DOS below the Fermi level produced by the *d* states. The huge number of levels involved in the electronic structure is therefore responsible for the structureless and continuous behavior of the optical conductivity. As a matter of fact, very peculiar features appear at the lowest frequencies, reminiscent of heavy fermion behavior: Below 0.2 eV the optical conductivity decreases for decreasing

frequencies down to a smooth minimum around 10 meV; below this energy Drude like behavior is present. Due to the lack of exact information of the static conductivity, and than the difficulty in calibrating the low energy extrapolation for Kramers–Kronig transformations, it has not been possible to assign a defined value for the plasma frequency ω_p . Anyway, optical values impose some constraints to the possible ω_p value which could be in the order of a few tenths of eV, even at room temperature. At low temperature the features are even more clear: a well defined structure emerges at 20 meV, the minimum at 10 meV is further depressed and heavy fermion Drude behavior with a low plasma frequency is necessarily growing up at the lowest frequencies. A prudent estimate gives a value of $\omega_p \approx 0.2$ eV. The comparison of such a value with the available data of specific heat⁷ yields to an effective mass of about $60m_e$, in the range of values observed in similar compounds.^{2,5}

It is interesting to notice that such a behavior is unaffected by the onset of magnetic order at 9.5 K, being observed both above and below such a temperature. Moreover, the low temperature features begin to emerge in the reflectivity spectra already at 120 K. On the other hand, since the ferromagnetic transition does not open any gap at the Fermi surface, no changes can be expected in the optical response.^{3,5} A similar behavior has been observed in $\text{URu}_{2-x}\text{Re}_x\text{Si}_2$, where, for increasing amount of Re content, the material pass from itinerant anti ferromagnetism to itinerant ferromagnetism.^{1,5}

In conclusion crystallographic parameters of URhSi have been exactly determined and heavy fermion behavior has been identified which is not affected by the magnetic transition.

¹Y. Dalichaouch, M. B. Maple, M. S. Torikachvili, and A. L. Giorgi, Phys. Rev. B **39**, 2423 (1989).

²L. Degiorgi, M. Dressel, G. Grüner, P. Wachter, N. Sato, and T. Komatsubara, Europhys. Lett. **25**, 311 (1994).

³L. Degiorgi, H. R. Ott, M. Dressel, G. Grüner, and Z. Fisk, Europhys. Lett. **26**, 221 (1994).

⁴D. A. Bonn, J. D. Garrett, and T. Timusk, Phys. Rev. Lett. **61**, 1305 (1988).

⁵St. Thieme, P. Steiner, L. Degiorgi, P. Wachter, Y. Dalichaouch, and M. B. Maple, Europhys. Lett. **32**, 367 (1995).

⁶Y. Miyako, S. Kawai, H. Amitsuka, C. C. Paulsen, and K. Hasselbach, J. Appl. Phys. **70**, 5791 (1991).

⁷K. Prokeš, E. Bruk, K. H. J. Buschow, F. R. De Boer, V. Sechovsky, P. Svoboda, X. Hu, H. Maletta, and T. J. Gortenmulder, J. Appl. Phys. **79**, 5221 (1996).

⁸G. M. Sheldrick, SHELXL-93, Program for the Refinement of Crystal Structures, University of Göttingen, Germany, 1993.

⁹B. Rupp, B. Smith, and J. Wong, J. Appl. Crystallogr. **24**, 263 (1991).

Weighted minimum-norm source estimation of magnetoencephalography utilizing the temporal information of the measured dataSunao Iwaki^{a)} and Shoogo Ueno^{b)}*Department of Biomedical Engineering, University of Tokyo, 7-3-1 Hongo, Bunkyo-ku, Tokyo 113, Japan*

The weighted minimum-norm estimation (wMNE) is a popular method to obtain the source distribution in the human brain from magneto- and electro-encephalographic measurements when detailed information about the generator profile is not available. We propose a method to reconstruct current distributions in the human brain based on the wMNE technique with the weighting factors defined by a simplified multiple signal classification (MUSIC) prescanning. In this method, in addition to the conventional depth normalization technique, weighting factors of the wMNE were determined by the cost values previously calculated by a simplified MUSIC scanning which contains the temporal information of the measured data. We performed computer simulations of this method and compared it with the conventional wMNE method. The results show that the proposed method is effective for the reconstruction of the current distributions from noisy data. © 1998 American Institute of Physics. [S0021-8979(98)38511-4]

I. INTRODUCTION

Sophisticated techniques to provide functional imaging of information processing in the human brain are needed for clinical applications and for tools of investigation of higher brain functions. Many methods have been developed to reconstruct the internal electrical current distributions in the human brain from magneto- and electro-encephalographic (MEG/EEG) measurements.¹ Among those, the minimum-norm estimation (MNE)^{2,3} is a popular technique to obtain the internal primary current distributions if the detailed information about the generator profile was not available. Because the sensitivity of the sensors decreases as the distance from the source increases, the MNE tends to introduce a bias towards superficial sources.⁴ To avoid this problem, the weighted MNE (wMNE) method, which minimizes the weighted norm of the solution (depth normalization), has been widely applied.^{4,5} However, because the conventional wMNE method deals with only the instantaneous distribution of MEG/EEG data, reconstructed currents could be seriously distorted when the method is applied to noisy data. To reduce the distortion of the reconstructed current distribution, a method to include temporal information of the MEG/EEG data into the wMNE method using simplified multiple signal classification (MUSIC)⁶ prescanning is proposed in this article.

II. METHODS**A. Weighted minimum norm estimation**

Here, we define the primary current distribution at time instant t_i as $\mathbf{p}(t_i) = [\mathbf{p}_1(t_i), \mathbf{p}_2(t_i), \dots, \mathbf{p}_N(t_i)]^T$ and the measured field distribution as $\mathbf{f}(t_i) = [\mathbf{f}_1(t_i), \mathbf{f}_2(t_i), \dots, \mathbf{f}_M(t_i)]^T$, where N is the number of possible current source locations and M is the number of sensors. The relationship between \mathbf{f} and \mathbf{p} is described as

$$\mathbf{f} = L\mathbf{p} + \mathbf{n}, \quad (1)$$

where L is a gain matrix called the lead field matrix and \mathbf{n} is the additive measurement noise. The conventional wMNE method can be written as follows.⁷

$$\mathbf{p} = L^{-}\mathbf{f}, \quad (2)$$

where L^{-} is given by

$$L^{-} = (L^T L + \gamma \mathbf{W}_c)^{-1} L^T, \quad (3)$$

which minimizes the cost $E_c = \|\mathbf{f} - \mathbf{f}_c\|^2 + \gamma^2 \|\mathbf{W}_c \mathbf{p}\|^2$, (\mathbf{f}_c : calculated value of field distribution).⁷ The diagonal matrix \mathbf{W}_c contains the weighting factors for depth normalization, and γ is a regularization parameter, which controls the degree of regularization, determined in accordance with the signal-to-noise ratio (SNR). In this article, we use the simplest weighting factors for depth normalization ($\mathbf{W}_c = \text{diag}\{\|L_i\|_2\}$).

B. Weighted minimum norm estimation with MUSIC prescanning

Because the conventional wMNE method deals with only instantaneous distributions of MEG/EEG data, results of current reconstruction could be seriously distorted when

^{a)}Electronic mail: iwaki@medes.m.u-tokyo.ac.jp

^{b)}Electronic mail: ueno@medes.m.u-tokyo.ac.jp

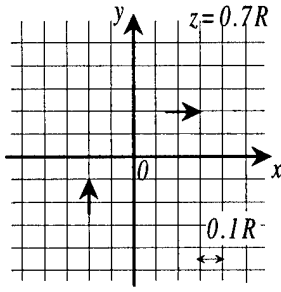


FIG. 1. Assumed source locations for the computer simulations. Two dipolar current sources were located at $(-0.2R, -0.2R, 0.7R)$ and $(0.2R, 0.2R, 0.7R)$.

applied to noisy (low SNR) data. To reduce the distortion of the reconstructed current distributions, we propose a method to include temporal information in the wMNE using simplified MUSIC prescanning.

First, to separate signal and noise subspaces of $M \times l$ spatio-temporal measured data matrix $\mathbf{F} = [\mathbf{f}(t_1), \mathbf{f}(t_2), \dots, \mathbf{f}(t_l)]$ using an eigen-decomposition of the auto-correlation matrix of \mathbf{F} . Here, we denote Λ_s, Λ_n as a diagonal matrix containing signal and noise eigenvalues, and Φ_s, Φ_n as signal and noise eigenvectors, respectively. Then, for each scanning grid j located in the head model, we calculate the cost values c_j ,

$$c_j = 1/\lambda_{\min}\{\mathbf{U}_{Lj}^T \Phi_n \Phi_n^T \mathbf{U}_{Lj}\}, \quad (4)$$

where $\lambda_{\min}\{\cdot\}$ denotes the minimum eigenvalue of $\{\cdot\}$, and \mathbf{U}_{Lj} denotes the principal left eigenvector of L_j . Then c_j becomes 0 at the correct source location when the source is modeled as a single current dipole,⁸ and c_j approximates the relative values of time-averaged current intensity if the source can be modeled as a few current dipoles.⁹

We use the cost values c_j to determine the weighting factors of wMNE as follows.

$$\mathbf{W} = \mathbf{W}_c + \mathbf{W}_m = \text{diag}\{\|\mathbf{L}_i\|_2\} + \alpha \text{diag}\{I - \tilde{c}_j\}, \quad (5)$$

$$\mathbf{L}^- = (\mathbf{L}^T \mathbf{L} + \gamma \mathbf{W})^{-1} \mathbf{L}^T, \quad (6)$$

where \tilde{c}_j is a normalized value of c_j , and α is a alteration parameter of weighting factors. This method minimizes the cost $E_m = \|\mathbf{f} - \mathbf{f}_c\|^2 + \gamma^2 \|(\mathbf{W}_c + \mathbf{W}_m)\mathbf{p}\|^2$ that causes the reconstructed current distribution to be biased towards the regions with the largest c_j values calculated by the simplified MUSIC prescanning. When $\alpha=0$, the proposed method becomes identical to the conventional wMNE method.

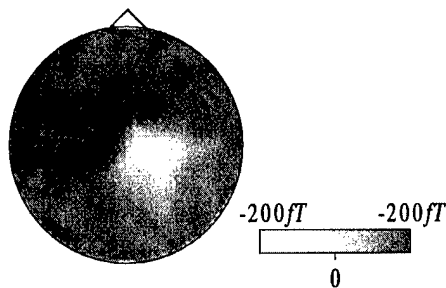


FIG. 2. Example of the spatial distribution of the MEG. The SNR of the simulated data was set to 4 dB.

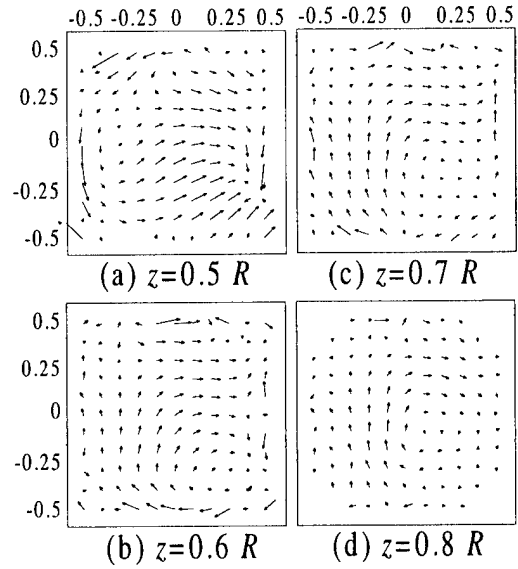


FIG. 3. Results of current reconstruction using the conventional wMNE method. Axial views of the reconstructed current distributions in the x - y plane are displayed with (a) $z=0.5R$, (b) $z=0.6R$, (c) $z=0.7R$, and (d) $z=0.8R$. The SNR of the simulated data was 4 dB, and the regularization parameter γ was set to 0.4.

This method utilizes not only the instantaneous spatial distribution but also the temporal properties of the measured data. It is possible to reconstruct current distribution properly even if the SNR of the measured data were so low that the conventional wMNE method might fail to reconstruct.

III. RESULTS AND DISCUSSION

We performed computer simulations of the proposed method and compared the results with the results from the conventional wMNE method.

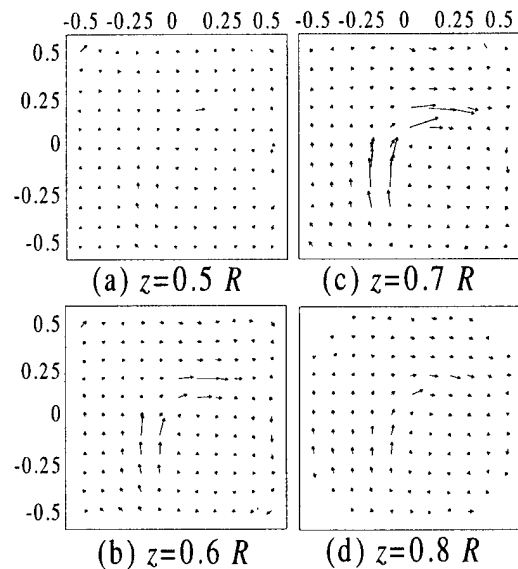


FIG. 4. Results of current reconstruction using the proposed method. Axial views of the reconstructed current distributions in the x - y plane are displayed with (a) $z=0.5R$, (b) $z=0.6R$, (c) $z=0.7R$, and (d) $z=0.8R$. The SNR and γ were the same as for Fig. 3, and the alteration parameter α was set to 0.06.

Figure 1 shows an assumed source configuration for these simulations. Two current dipoles were located in the x - y plane [(a) $(x,y,z)=(-0.2R,-0.2R,0.7R)$, (b) $(x,y,z)=(0.2R,0.2R,0.7R)$, R : radius of the head model]. The y component of the assumed source (a) and the x component of the source (b) were assumed to alter synchronously. Magnetic fields generated by these sources were assumed to be measured at 80 points on the upper hemisphere of the head model, and white noise was added. The SNR of the simulated data was approximately 4 dB, which was relatively low when compared with actual MEG measurements of large evoked responses with an adequate number of signals averaged. However, the SNR was not low when compared with that of spontaneous brain activities without averaging or evoked responses with a limited number of data sets. An example of the instantaneous spatial distribution of simulated data is shown in Fig. 2.

The results of the current reconstruction using the conventional wMNE method and the proposed method are shown in Fig. 3 and Fig. 4, respectively. In each figure, axial views of reconstructed current distributions in the x - y plane are displayed with (a) $z=0.5R$, (b) $z=0.6R$, (c) $z=0.7R$, and (d) $z=0.8R$. In these simulations, the regularization parameter γ and alteration parameter α were set to $\gamma=0.4$, $\alpha=0.06$ empirically. The reconstructed current distribution was severely distorted in the conventional wMNE method under noisy measurement condition as SNR equals to 4 dB. In the proposed method, current distributions corresponding to two assumed sources were clearly reconstructed. These results indicated the effectiveness of the proposed method for the reconstruction of internal current distributions under the noisy measurement condition. In these cases, the increase of the amount of calculation in the proposed method was less than 10% of that required in the conventional wMNE method.

Further consideration must be given to develop algorithms to obtain optimum values of the regularization and alteration parameters.

IV. CONCLUSION

We proposed a method to reconstruct current distributions in the human brain based on the weighted minimum-norm estimation technique with the weighting factors defined by simplified MUSIC prescanning. With this method, in addition to the conventional depth normalization technique, weighting factors of the wMNE were determined by the cost values previously calculated by simplified MUSIC scanning which contains the temporal information of the measured data. We performed computer simulations of this method and compared it with the conventional wMNE method. The results show that the proposed method is effective for the reconstruction of the current distributions from noisy data.

¹M. S. Hamalainen, R. Hari, R. J. Ilmoniemi, J. Knuutila, and O. V. Lounasmaa, *Rev. Mod. Phys.* **65**, 413-497 (1993).

²R. J. Ilmoniemi, M. S. Hamalainen, and J. Knuutila, *Biomagnetism: Application and Theory*, edited by H. Weinberg, G. Stroink, and T. Katila (Pergamon, New York, 1985), pp. 278-282.

³J. Z. Wang, S. J. Williamson, and L. Kaufmann, *IEEE Trans. Biomed. Eng.* **39**, 665-675 (1992).

⁴B. Jeffs, R. M. Leahy, and M. Singh, *IEEE Trans. Biomed. Eng.* **34**, 713-723 (1987).

⁵A. A. Ioannides, J. P. R. Bolton, and C. J. S. Clarke, *Inverse Probl.* **6**, 523-542 (1990).

⁶J. C. Mosher, P. S. Lewis, and R. M. Leahy, *IEEE Trans. Biomed. Eng.* **39**, 541-557 (1992).

⁷H. C. Andrews and B. R. Hunt, *Digital Image Restoration* (Prentice-Hall, Eaglewood Cliffs, NJ, 1977).

⁸R. O. Schmidt, *IEEE Trans. Antennas Propag.* **34**, 276-280 (1986).

⁹K. Sekihara and B. Scholz, *IEEE Trans. Biomed. Eng.* **43**, 281-291 (1996).

A comparative study of the magnetic separation characteristics of magnetotactic and sulphate reducing bacteria

A. S. Bahaj,^{a)} P. A. B. James, and F. D. Moeschler

University of Southampton, Southampton, Hampshire, SO17 1BJ, United Kingdom

Many microorganisms have an affinity to accumulate metal ions onto their surfaces which results in metal loading of the biomass. Microbial biomineralization of iron results in a biomass which is often highly magnetic and can be separated from water systems by the application of a magnetic field. This article reports on the magnetic separation of biomass containing microbial iron oxide (Fe_3O_4 , present within *magnetotactic* bacteria) and iron sulphide (Fe_{1-x}S , precipitated extracellularly by sulphate reducing bacteria) in a single wire cell. Since such bacteria can be separated magnetically, their affinity to heavy metal or organic material accumulation render them useful for the removal of pollutants from waste water. The relative merits of each bacterium to magnetic separation techniques in terms of applied magnetic field and processing conditions are discussed. © 1998 American Institute of Physics. [S0021-8979(98)38611-9]

I. INTRODUCTION

Magnetotactic bacteria (MTB)¹ which biomineralize magnetite (Fe_3O_4) and sulphate reducing bacteria (SRB) present within sediments, contrast in their utilization of iron which is based on the oxide and sulphide forms, respectively. A magnetotactic spirillum and a sulphate reducing vibroid have been isolated from brackish sediments near Southampton, UK and grown in pure culture. The MTB possess a magnetic moment along their line of length due to a chain of membrane enveloped magnetite crystals called *magnetosomes*. Transmission electron microscopy utilizing electron dispersive x-ray analysis confirmed that the magnetosomes within Southampton MTB were iron oxide based. This magnetite chain acts as a dipole, enabling magnetic orientation of the bacteria with the earth's magnetic field (magnetotaxis). This results in flagellar driven motion downwards towards the oxic-anoxic transition near the sediment-water interface of their salt marsh pan environment.

Unlike magnetotactic bacteria, sulphate reducing bacteria do not, in general, exhibit magnetotaxis. Ferrous (Fe^{2+}) and ferric (Fe^{3+}) sulphate ions are taken up by SRB in a process known as "dissimilatory sulphate reduction" where the sulphate ions act as an oxidizing agent for the dissimilation of organic matter, as oxygen does in conventional respiration.² A small amount of the reduced sulphur is assimilated by the organism, and the iron ions are then precipitated onto the bacterium surface. In a magnetic field, this coating gives rise to a randomly orientated magnetic dipole, as opposed to the specific direction of the permanent dipole found in MTB.

Recently, a sulphate reducing bacterium has been discovered which is magnetotactic, containing intracellular magnetosomes of magnetite and extracellular iron sulphide precipitation.³ Moreover, magnetotactic bacteria which form magnetosomes of iron sulphide, such as greigite (Fe_3S_4) and pyrite (FeS_2) have been found.⁴ It must be remembered

therefore, that the relationship between iron sulphide/oxide and sulphate reducing/magnetotactic bacteria is not as clear cut as considered here.

Many microorganisms have an affinity to accumulate metal ions into their surfaces which results in metal-loading of the biomass. Hence water systems can be purged of metal pollutants when the biomass is removed. This article reports on the separation approach for removing the loaded biomass from a metal polluted system. In the case of magnetotactic bacteria there are two conditions for separation: Case (a) represents the removal of *motile* MTB and the utilization of their magnetotaxis property. In this case orientational magnetic separation can be applied where direction of motion is imposed externally whilst the motion is due to the flagella effect of the bacteria. Case (b) applies to the removal of *non motile* MTB as well as the sulphate reducing bacteria using high gradient magnetic separation (HGMS). The article also discusses the various conditions under which each type of bacteria can be utilized for enhanced magnetic separation processes.

II. EXPERIMENT

The experimental setup for single wire cell studies consists of a dedicated analysis workstation coupled to an optical microscope. On the microscope stage is mounted a small iron yoke to which pairs of boron-iron-niodymium magnets are attached. Between the magnets is placed a glass cuvette containing an 8.3 μm nickel wire. The wire is aligned perpendicular to the magnetic field, producing magnetic gradients up to 10^{10} Tm^{-1} , enabling capture of magnetic material from the surrounding medium. A sample of MTB or SRB is added to the cuvette and a recording of the resulting motion is made onto a VCR for subsequent analysis. A specialized hardware/software package enables sampling of the VCR recording to generate a sequence of frames marking the position and time of a cell as it is captured onto the wire.⁵

Magnetotactic bacteria were grown in 100 ml batch cultures incubated at 30 °C for ten days using standard magnetospirillum growth medium.⁶ Single wire cell measure-

^{a)}Electronic mail: bahaj@soton.ac.uk

ments were made on individual motile and nonmotile bacteria. To render MTB nonmotile specific metal ions were added to a culture 15 min prior to addition to the single wire cell.

Sulphate reducing bacteria were grown at room temperature in a 2 ℓ chemostat, operated at a dilution rate of 0.028 through which nitrogen was bubbled to maintain anaerobic conditions and provide mixing. The medium used was a development of a Freke and Tate preparation for the culture of sulphate reducing bacteria from soil.⁷ Single wire cell measurement of the motion of disordered "clumps" of iron sulphide rich biomass, ranging in size from 1.6 to 12 μm across, were made.

To observe particle motion, small volumes of biomass were pipetted into a cuvette which was half filled with distilled water. Single wire cell measurement of the motion of disordered clumps of iron sulphide rich biomass, ranging in size from 1.6 to 12 μm across, were made.

To observe cell motion, small volumes of biomass were pipetted into a cuvette which was half filled with distilled water. Measurements were made in effectively no flow conditions (quasistatic). Single wire cell experiments were carried out at three different magnetic field strengths (0.110 T, 0.284 T, and 0.688 T). In each case the motion of 50 MTB was analyzed to produce an average capture profile of a bacterium onto the wire.

The experimental conditions used allowed for cells up to an initial distance of 9 wire diameters (70 μm from the wire) to be imaged. The width of the imaging area being determined by the magnification of the camera/microscope system. The capture limit of several iron sulphide rich SRB was found to be in excess of 70 μm at 0.110 T. The magnification of the microscope was therefore halved, and single wire cell capture repeated at both 0.110 T and 0.284 T enabling capture profiles at much greater distances to be studied (18 wire diameters, 150 μm). At both field strengths the capture below 70 μm produces average paths which are independent of the microscope magnification used. The average capture paths shown for the SRB are therefore, the result of two sets of 50 profiles at different magnifications. Measurements on iron sulphide rich biomass were made at the two lower fields. At 0.688 T the high speed of cell-field interaction made accurate measurement ineffective.

III. RESULTS AND DISCUSSION

A typical magnetotactic bacterium studied here was found to have the following characteristics: length=2.9 μm , width=0.6 μm , determined using transmission electron microscope techniques—number of magnetosomes=15, diameter=30 nm.

The results depicted in Fig. 1 illustrate a comparison of high gradient magnetic separation, in a single wire cell, of motile magnetotactic bacteria and iron sulphide rich SRB biomass. The curves show the paths of the cells as they approach the wire in the cell and represent the average of 50 trajectories for MTB and 100 trajectories in the case of SRB.

The capture of motile MTB was found to be effectively independent of the applied magnetic field at distances greater

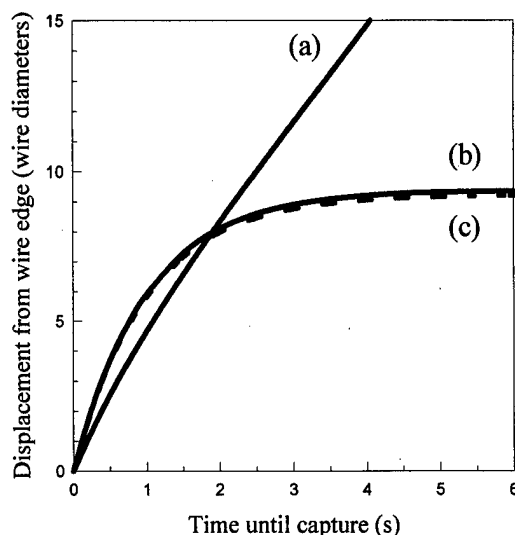


FIG. 1. Comparison of high gradient magnetic separation, in a single wire cell. Motile magnetotactic bacteria average trajectory; (a) 0.284 T and iron sulphide rich SRB biomass trajectories, (b) 0.284 T and (c) 0.110 T are shown.

than several wire diameters from the center of the wire. Away from the close proximity of the wire the flagellar force dominates over the magnetic field force producing an effectively linear capture profile. For the current experimental setup, it can be seen from the results that a cross-over point occurs in which the capture of iron sulphide rich SRB is more effective than MTB. For example, at 0.284 T, for cells initially, less than 7.2 wire diameters (60 μm from the wire) SRB material will be captured more rapidly. Furthermore, the point at which this cross-over occurs increases in distance from the wire as the applied magnetic field is increased.

Figure 2 shows the average capture profiles of 50 non-motile MTB and iron sulphide rich SRB at a various applied

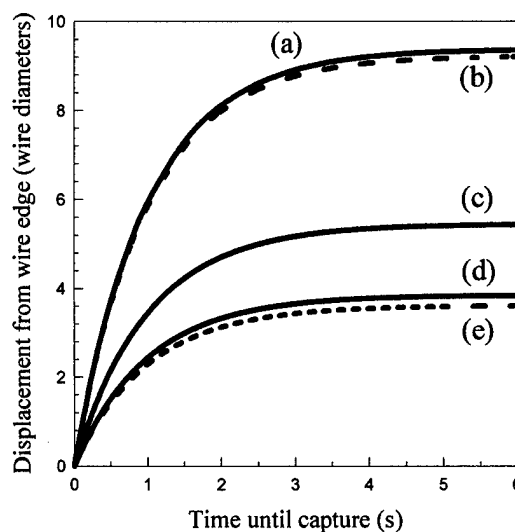


FIG. 2. High gradient magnetic separation of iron sulphide rich SRB biomass; (a) 0.284 T, (b) 0.110 T and nonmotile magnetotactic bacteria, (c) 0.688 T, (d) 0.284 T, (e) 0.110 T. Graph depicts the average trajectories of 50 MTB and 100 SRB.

magnetic fields. Previously⁸ the magnetic moment of MTB was estimated from analysis of the trajectories of nonmotile bacteria using single wire theory.⁹ The analysis is repeated for this work and gives an average bacterium magnetic moment of $1.1 \times 10^{-15} \text{ Am}^2$, similar to that obtained previously. Determination of the magnetic moment of the disordered structure of the SRB material is rather complex and is not undertaken under this study. However, for this case, the results give a clear indication of the separation profiles that are likely to occur. It can be seen that at 0.284 T for example, the capture range of nonmotile MTB (less than four wire diameters) is less than the SRB material at 0.110 T (more than nine wire diameters). MTB are first orientated by the field, to give an "end-on" alignment trajectory of capture onto the wire. Despite the drag minimization that results from this alignment, the randomly orientated SRB material is captured at higher speed or more efficiently, indicating its significantly higher magnetic moment.

Motile magnetotactic bacteria, which are magnetically orientated by the applied field to swim in a required direction, can offer a pragmatic processing alternative. Motile MTB recovery is a relatively slow process. A typical bacterium swims at approximately $40 \mu\text{ms}^{-1}$, the separation time of bacteria from a wire mesh matrix is dependant only on the distance to the nearest suitably magnetized site. Therefore, for an efficient separation, it is necessary to process such MTB in a system where the site proximity is close to the bacterium which would minimize time of travel and hence the residence time.

Another approach is to separate motile MTB using magnetic poles positioned around a separation chamber. MTB accumulate at the north and south magnetic foci on the separation chamber walls for subsequent recovery from the system. This process when applied to metal/organic recovery will require static treatment chambers or slow moving waste streams of bacteria leading to long processing times. This contrasts with HGMS recovery of SRB material which, with suitable matrix, flow and field conditions rapid separation

can be achieved. The only penalty with HGMS being the moderately high magnetic field that is required (1–2 T for most conditions).

IV. CONCLUSIONS

This study depicts aspects of magnetic separation techniques applied to two distinct microbial systems. The single wire cell work illustrates that the magnetic iron sulphide coating present on SRB enables efficient separation using HGMS. The magnetic interaction of nonmotile MTB is weak in comparison to SRB. Despite the minimized drag effect of magnetically aligned, end-on capture, high gradient capture of nonmotile MTB was shown to be less effective when compared with SRB recovery regardless of the conditions used.

In contrast, orientation magnetic separation of MTB provides a simpler approach which can potentially be integrated into the process circuit of numerous processes (e.g., nuclear power stations, tanning plants, steel works, etc.). In this way contamination can be removed prior to discharge producing a truly "clean" technology. The separation conditions for a process have been well defined but significant metal/organic loading and continued viability of the biomass under a sufficiently wide variety of conditions has yet to be achieved.

¹R. P. Blakemore, *Science* **190**, 377 (1975).

²J. R. Postgate, *The Sulphate-Reducing Bacteria*, 2nd ed. (Cambridge University, Cambridge, UK, 1984).

³T. Sakaguchi, J. G. Burgess, and T. Matsunaga, *Nature* **365**, 6411, 47 (1993).

⁴S. Mann, N. H. C. Sparks, R. B. Frankel, D. A. Bazylinski, and H. W. Jannasch, *Nature* **343**, 6255, 258 (1990).

⁵A. S. Bahaj and P. A. B. James, *IEEE Trans. Magn.* **29**, 3358 (1993).

⁶R. P. Blakemore, D. Maratea, and R. S. Wolfe, *J. Bacteriol.* **140**, 720 (1979).

⁷M. Freke and D. Tate, *J. Biochem. Microbio. Technol. Eng.* **3**, 29 (1961).

⁸A. S. Bahaj, P. A. B. James, and F. D. Moeschler, *IEEE Trans. Magn.* **32**, 5106 (1996).

⁹*High Gradient Magnetic Separation*, edited by R. Gerber and R. R. Birss (Research Studies, Chichester, UK, 1983).

Magnetoelectrolysis of copper

G. Hinds and J. M. D. Coey

Department of Physics, Trinity College, Dublin 2, Ireland

M. E. G. Lyons

Department of Chemistry, Trinity College, Dublin 2, Ireland

The effect of a uniform static magnetic field on processes occurring at Cu/acidified CuSO₄ interfaces is examined by analysis of potentiodynamic polarization curves. The mass transport controlled deposition current is increased by as much as a factor of 2 in a 0.6 T field, independent of field direction and electrode orientation. The extent of current enhancement is greatest at low *pH* (<1), where it is associated with diffusional rather than migrational transport of the copper ions.

© 1998 American Institute of Physics. [S0021-8979(98)38711-3]

I. INTRODUCTION

The processes of electrochemical metal deposition and dissolution¹ are of fundamental scientific and technological interest. They involve interfacial electron transfer which is strongly influenced by the magnitude of the electric field present at the electrode/solution interface. The rates of metal deposition/electrodissolution may be expressed in terms of current densities and kinetics quantified by analysis of steady state current/voltage curves, with recourse to phenomenological electrode kinetic models. Heterogeneous electrochemical processes involve, in general, two coupled sequential processes: diffusional mass transport to the surface of the electrode and potential-induced interfacial electron transfer between an electron donor/acceptor species in the solution and the electrode surface. Either interfacial electron transfer (activation control) or reactant logistics (mass transfer control) can be rate determining. For a sequential electrochemical process involving the transfer of a single electron, the steady state current density is given by²

$$j = \frac{Fk_E k_D c^\infty}{k_E + k_D}, \quad (1)$$

where *F* is the Faraday constant, *k_E* is the heterogeneous electrochemical rate constant, *k_D* is the diffusional rate constant, and *c[∞]* represents the concentration of electroactive reactant species in the bulk solution. If we utilize the Nernst diffusion layer approximation³ the diffusional rate constant *k_D* is given by *D/δ*, where *D* is the diffusion coefficient of the reactant and *δ* denotes the diffusion layer thickness. Also the heterogeneous electron transfer rate constant is given by the Butler-Volmer equation:

$$k_E = k_E^0 \exp(\pm \alpha \theta), \quad (2)$$

where *k_E⁰* denotes a potential independent rate constant and *α* is the transfer coefficient. Note that *θ* is a normalized potential and is related to the Galvanic potential drop *Δψ* across the electrode/solution interface by *θ* = *FΔψ/RT*, where *R* is the gas constant.

Clearly when *k_E* ≫ *D/δ*, the electron transfer kinetics are rapid and the electron transfer current will be controlled by the rate of mass transport to the electrode surface. Under such circumstances Eq. (1) reduces to

$$j = \frac{FDc^\infty}{\delta}. \quad (3)$$

In contrast when *k_E* ≪ *D/δ*, the rate of reactant supply is rapid and the electron transfer kinetics are slow and the reaction is activation controlled. Here Eq. (1) reduces to

$$j = Fk_E^0 c^\infty \exp\left(\pm \frac{\alpha F \Delta \psi}{RT}\right). \quad (4)$$

There are few well-documented examples of uniform static magnetic fields influencing the rates of chemical reactions, although there have been several previous reports of a field effect on the electrodeposition of copper.^{4,5} The effect of an applied magnetic field on a heterogeneous electrochemical process at an electrode/solution interface is termed magnetoelectrolysis. The applied *B* field might effect the transport of reactants to the electrode surface,⁴ accelerate the electron transfer kinetics at the electrode/solution interface,⁶ or indeed modify the transport rate of solvated ions in the bulk electrolytic solution.⁷ Here we focus on the effect of magnetic fields on reactant species located in regions close to the electrode surface, with specific reference to copper electrodes in contact with acidified copper sulfate solutions.^{5,8}

II. EXPERIMENTAL METHODS

All experiments were performed in a standard one compartment three electrode cell containing an Ag/AgCl (satd. KCl) reference electrode, a large surface area graphite counter electrode and a copper working electrode. The copper electrode was constructed by spot welding a copper wire to a copper plate (thickness 1 mm) of geometric surface area 85 mm². The wire was encased in a glass tube and the sides and rear surface of the copper plate electrode were sealed with epoxy. The electrode was polished before each experiment using fine grain sandpaper and then washed with 2 M sulfuric acid followed by thorough rinsing with triply distilled water. The electrochemical experiments were controlled using an EG&G Model 273 potentiostat. Potentiodynamic current/voltage curves were recorded using an XY plotter. A Magnetic Solutions Model HC600-54 Halbach cylinder with a 54 mm bore was used to apply a static magnetic field of magnitude 0.6 T to the electrochemical cell

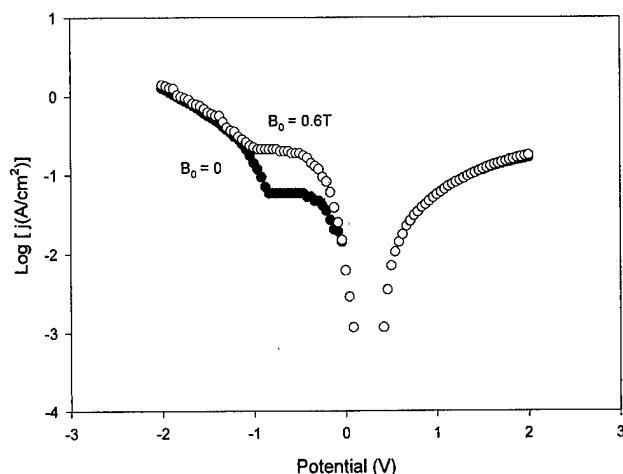


FIG. 1. Tafel plot for copper sulfate in acidified aqueous solution at $pH = 0.8$ with (a) no external applied magnetic field, (b) an external applied field of 0.6 T.

which was placed centrally within the cylinder. In all experiments the electrolyte was an aqueous solution of 0.75 M copper (II) sulfate. The pH of the copper sulfate medium was varied by the addition of 2 M sulfuric acid. Solution pH values were measured using a digital pH meter.

III. RESULTS

The electrochemical behavior of the system was examined by applying a slow (10 mV s^{-1}) potential sweep to the copper electrode and examining the resultant current response profile. Typical potentiodynamic curves at $pH = 0.8$ with and without the field are presented in Fig. 1. The current response recorded at negative potentials corresponds to copper deposition and other reduction processes, whereas that obtained at positive potentials corresponds to electrodisolution of copper. The curves comprise a number of clearly defined regions. First we consider the cathodic portion. A narrow Tafel type region, where $\log j$ varies linearly with potential, may be identified at low negative potentials, from -200 to -100 mV . Here the electron transfer kinetics at the interface are slow and rate determining. It is seen from Fig. 1 that the magnetic field has some effect on the magnitude of the current response in the Tafel region. But the current plateau which extends from -200 to -900 mV increases very considerably when the field is present. This feature of curve can be ascribed to the diffusion controlled transport of aquo Cu^{2+} species to the electrode surface. The rise in current at potentials more cathodic than the current plateau region is due to the electroreduction of water to form molecular hydrogen. This process also remains unaffected by the imposition of a static magnetic field. The current response at anodic potentials is due to the electrodisolution of copper. The application of the field appears to have little effect here.

We have observed that the plateau of current enhancement due to the magnetic field depends to a marked extent on the pH of the solution. In Fig. 2(a) we show the variation of the mass transport controlled limiting current for copper electrodeposition in the absence and in the presence of the 0.6 T field, with changes in solution pH . Both the “field

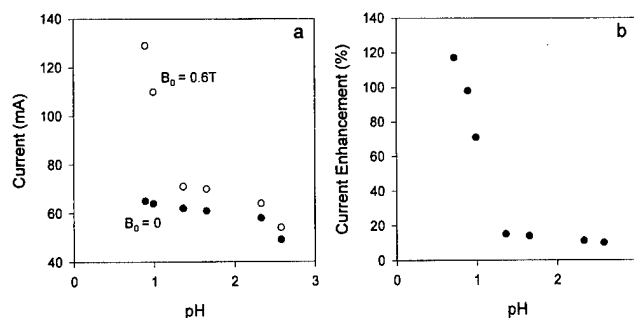


FIG. 2. Current enhancement at -500 mV as a function of pH : (a) effect of external applied field, (b) percentage enhancement.

off” and “field on” currents increase with decreasing solution pH , but the enhancement increases markedly with decreasing pH , as shown in Fig. 2(b). The extent of current enhancement is typically 10–15% over the pH range 1.5–2.5, whereas a very rapid increase in current enhancement is observed when the solution becomes strongly acidic. For example, at pH 0.7 the current enhancement is 117%. This effect had not been noted previously in the literature. Furthermore, in a series of experiments where we varied the electrode orientation and field direction relative to the cell we could detect no significant variations, leading to the conclusion that the effect is independent of the direction of magnetic field.

The mass transfer enhancement induced by the magnetic field was confirmed by weighing the copper electrode. When the potential was held at -500 mV for a fixed interval at pH 0.8, 11 mg of copper was deposited when the magnetic field was applied compared to 5 mg with no applied field.

Figure 3 shows the Tafel plots obtained for the cathodic copper electrodeposition process at $pH = 0.72$. Plots of $\log j$ vs V are presented in Fig. 3(a). The curvature indicates that the potential region where deposition is kinetically controlled is quite narrow. Mass transport effects become important at quite low potentials. Hence we use the following modified form of the Tafel equation to extract values for the transfer coefficient α :

$$\log\left(\frac{j j_L}{j - j_L}\right) = K + \log c^\infty - \frac{\alpha F V}{2.303 R T}, \quad (5)$$

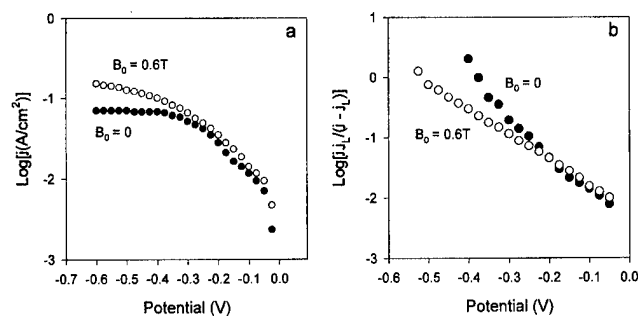
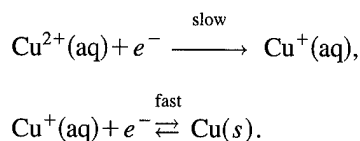


FIG. 3. (a) Tafel plot for copper sulfate in acidified aqueous solution at $pH = 0.72$. (b) Modified Tafel plot showing effect of the magnetic field on the transfer coefficient.

where j_L denotes the limiting plateau current density, j is the measured current density at any applied potential V . Modified Tafel plots presented in Fig. 3(b) are linear. The transfer coefficient α in the absence of a static magnetic field is 0.38, whereas in the presence of the 0.6 T field we obtain $\alpha = 0.24$. These values are lower than the theoretically expected value of 0.5. However, our current/voltage data have not been corrected for uncompensated solution IR errors which can be significant when large currents flow at the interface.

The value of the transfer coefficient α is an indicator of the copper deposition process. Our values are in good agreement with the mechanism proposed by Mattsson and Bockris.⁸ Hence we assign the following sequential mechanism:



The rate-determining step is the formation of an aquo $\text{Cu}(\text{I})$ species, which rapidly accepts a second electron to form metallic copper.

IV. DISCUSSION

It appears that the primary effect of the magnetic field is to alter the rate of transport of ions to the surface of the working electrode. The effect of magnetic fields on the kinetics of interfacial electron transfer processes (manifested as currents in the Tafel region of the potentiodynamic response curve) is relatively small. In addition to the entropic and viscous forces which control diffusion of hydrated ions in aqueous solution, electric and magnetic fields will generate a force on the electroactive ions which can be expressed in terms of the Lorentz equation:

$$\mathbf{F} = q(\mathbf{E} + \mathbf{v} \times \mathbf{B}), \quad (6)$$

where q denotes the charge on the ion and \mathbf{v} is the ionic velocity. The net magnetic force generated per unit volume \mathbf{F}_M is related to the net current density \mathbf{j} associated with ion transport through the solution by $\mathbf{F}_M = j\mathbf{B} \sin \theta$, where θ is the angle between the current vector and the field. Taking $j \sim 0.1 \text{ A cm}^{-2}$, we obtain $F_M \sim 600 \text{ N m}^{-3}$. We then compare this force to the gravitational force on the copper ions in the same volume, $F_G \sim 470 \text{ N m}^{-3}$, justifying the idea that the magnetic field might influence convection.

Striking features of our data are the independence of the current enhancement on the angle θ , and the pH dependence, with the sharp increase below a pH of 1.4. The Pourbaix diagram for the sulfur/water system at 298 K indicates that the predominant anionic species changes from SO_4^{2-} to HSO_4^- at a solution pH value close to 1.5.

Hence the composition of the ionic atmosphere surrounding the copper ion changes in this critical pH region. Furthermore, as the pH is reduced, the solution becomes more conducting, which reduces the electric field in the diffusion layer and cuts down transport of ions by direct migration to the cathode.⁹ The transport process at low pH is essentially diffusive, which means that the velocity to consider in Eq. (4) is the instantaneous velocity of the ion, rather than the velocity associated with the net current density. As a result, it is the effective diffusion coefficient D in the boundary layer, or possibly the thickness δ of the layer itself which is influenced by the magnetic field.

It has been noted in recent literature^{10,11} that the rate of transport of electrically neutral species can also be significantly enhanced by an applied magnetic field. Since the Lorentz force acting on a neutral species is zero, the field-induced enhancement of the flux of a neutral molecule must occur indirectly. One possibility is that experimentally observed current and material flux enhancement is due to convective solution flow induced by the field. This approach can be quantified in the context of magnetohydrodynamic theory.¹² Microscopically, the solution flow results from a momentum transfer from electric-field-accelerated ions to neighboring ions and solvent molecules. Hence, as noted by White and co-workers,^{10,11} the MHD analysis describes current enhancement in terms of a magnetic body force acting on a solution element through which a distributed and continuous current passes, rather than in terms of the direct interaction of the field on discrete current carrying ions.

ACKNOWLEDGMENTS

This work was supported by FORBAIRT. One of the authors (J.M.D.C.) is grateful to Dr. F. E. Spada for helpful discussions.

- ¹J. O'M. Bockris and S. U. M. Khan, *Surface Electrochemistry: A Molecular level Approach* (Plenum, New York, 1993), Chap. 8.
- ²C. M. A. Brett and A. M. Oliveira Brett, *Electrochemistry: Principles, Methods and Applications* (Oxford Science, Oxford, 1993), Chap. 6.
- ³V. G. Levich, *Physicochemical Hydrodynamics* (Prentice-Hall, New York, 1962), Sec. 15, p. 87.
- ⁴T. Z. Fahidy, *Electrochim. Acta* **18**, 607 (1973).
- ⁵E. Chassaing and R. Wiart, *Electrochim. Acta* **29**, 649 (1984); J. P. Chopard, J. Dougdale, P. Fricoteaux, and A. Olivier, *ibid.* **36**, 459 (1991); V. C. Noninski, *ibid.* **42**, 251 (1997).
- ⁶E. J. Kelly, *J. Electrochem. Soc.* **124**, 987 (1977).
- ⁷J. B. Hubbard and P. G. Wolynes, *J. Chem. Phys.* **75**, 3051 (1981).
- ⁸E. Mattsson and J. O'M. Bockris, *Trans. Faraday Soc.* **55**, 1586 (1959).
- ⁹J. S. Newman, *Electrochemical Systems* (Prentice-Hall, Englewood Cliffs, NJ, 1972), Chap. 19.
- ¹⁰S. R. Ragsdale, J. Lee, X. Gao, and H. S. White, *J. Phys. Chem.* **100**, 5913 (1996); J. Lee, X. Gao, L. D. A. Hardy, and H. S. White, *J. Electrochem. Soc.* **142**, L90 (1995).
- ¹¹S. R. Ragsdale, J. Lee, and H. S. White, *Anal. Chem.* **69**, 2070 (1997).
- ¹²P. G. Wolynes, *J. Chem. Phys.* **68**, 473 (1978); P. Colonos and P. G. Wolynes, *ibid.* **71**, 2644 (1979).

Impedance magnetic resonance imaging: A method for imaging of impedance distributions based on magnetic resonance imaging

S. Ueno^{a)}

Department of Biomedical Engineering, Graduate School of Medicine, University of Tokyo, 7-3-1 Hongo, Bunkyo-ku, Tokyo 113, Japan

N. Iriguchi

Siemens-Asahi Medical Technologies Limited, Tokyo 141, Japan

Magnetic resonance imaging (MRI) techniques have become important tools in medicine and biology. Conventional MRI, however, produces no information about the electrical properties of the body. This article proposes a new and noninvasive method for imaging electrical properties such as conductivity and impedance based on MRI techniques. The basic idea is to use the shielding effects of induced eddy currents in the body on spin precession. Two types of methods are introduced; (i) a large flip angle method, and (ii) a third coil method. The large flip angle method enhances the shielding effects of conducting tissues at the given Larmor frequency. The third coil method detects the shielding effects of conducting tissues at an arbitrary frequency. Both phantom and animal experiments have been carried out to verify this concept using a MRI system of 7.05 T with a bore size of 183 mm in diameter. © 1998 American Institute of Physics. [S0021-8979(98)23711-X]

I. INTRODUCTION

Since electrical properties are important characteristics of living organisms, techniques for impedance tomography to visualize impedance distribution have been developed with great interests.^{1,2} The previously proposed techniques require that electrodes are attached to the surface of the human body. Meanwhile, magnetic resonance imaging (MRI) techniques have become important tools in medicine and biology. Conventional MRI, however, produces no information about the electrical properties of the body. This article proposes new methods to visualize electrical impedance distribution based on MRI techniques.

When conductive tissues are subjected to an excitation rf field in MRI, eddy currents are induced in the tissues. In this article, a new method for impedance tomography is introduced based on MRI techniques. The basic idea is to use shielding effects of induced eddy currents in the body on spin precession. Two types of methods are proposed.

One proposed method to visualize the conductivity distribution of living organisms is to use very large flip angles. The method is used to obtain conductivity-enhanced MR images at the given Larmor frequency.

Another proposed method is to apply an additional time-varying magnetic field parallel to the main static field B_0 . The magnetic field is produced by the third coil, named “ B_c ” coil. The method is used to obtain conductivity-enhanced MR images at an arbitrary frequency. Experiments have been carried out to verify these concepts using a 7.05 T, 18.3 cm system.

II. PRINCIPLES

When conductive tissues are exposed to rf magnetic fields, eddy currents are induced in the conductive tissues,

which results in the reduction of the net rf fields into the tissues. By the shielding effects, the flip angles, (i.e., nutation angles of the macroscopic magnetization of excited spins from the axis of the main static field B_0 .) are reduced in varied degrees, depending on the electrical characteristics of the tissues.

When a precise 180° , 360° , or 540° excitation pulse is applied to conductive tissues, the tissues do not yield a signal due to the absence of the transversal components of magnetization. Meanwhile, resistive tissues yield signals because they are less electrically shielded than conducting tissues and simultaneously undergo different flip angles. Also, the resistive tissues leave transversal components with magnitudes determined by the sine wave functions of flip angles. The difference in signal, therefore, reflects the conductivity of tissues. By applying very large flip angles, conductivity-enhanced MR images can be obtained, yet, only at the given Larmor frequency, and in the direction perpendicular to the applied rf field.

To obtain conductivity-enhanced images at an arbitrary frequency, an additional time-varying field parallel to the main static field B_0 is introduced. The perturbing field is produced by the third coil hereby named B_c coil. By the perturbing field or B_c field, slice positioning of the image is affected, and the slice selection fluctuates. Spatial information in the read-out and phase-encoded directions are also affected. Conducting tissues are less affected by B_c field, because of the shielding effects. Since the frequency of B_c field is independent of the given Larmor frequency,

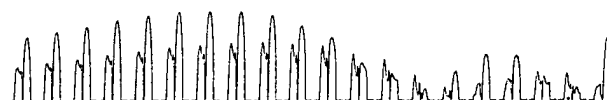


FIG. 1. Series of image projections of water and saline solution phantom obtained with excitation power increased stepwise from the left to the right.

^{a)}Electronic mail: ueno@medes.m.u-tokyo.ac.jp



FIG. 2. Proton density reference image of the mouse head.

conductivity-enhanced images can be obtained at any frequency but in the direction perpendicular to the B_c field.

III. MATERIALS AND METHODS

Experiments were first performed on a distilled water phantom and a saline solution phantom. Both phantoms were columnar, 2 cm in diameter, and 4 cm long. A conventional spin echo (SE) sequence was used to obtain MR images. By varying the excitation rf power level stepwise, image projections in the read-out direction were obtained. A 7.05 T, 18.3 cm machine was used. The proton Larmor frequency of magnetic resonance at 7.05 T is 300 MHz. To eliminate the longitudinal T_1 relaxation effects, the repetition time T_r was set as $T_r = 10$ s. Next, a series of image projections of the head of a four-week old mouse were obtained. The SE images of the head were obtained by applying excitation pulses which were 160° , 180° , and 200° selective to the cerebrospinal fluid (CSF) of the head.

A four-turn solenoidal coil of 6 cm in diameter was fabricated as the B_c coil to produce a low-frequency sinusoidal magnetic field of 10 mT in amplitude. The amplitude of the field was comparable to the amplitudes of the reading-out gradient field and the maximum phase-encoding field. An eight-week old rat was subjected to SE imaging with a constant B_c field of sinusoidal 1 kHz.

IV. RESULTS AND DISCUSSION

Figure 1 shows a series of image projections obtained with the excitation power increased stepwise from the left to the right. The larger projections, to the right of each image, are the water phantoms, and to the left are, smaller projections of the saline solution phantom. The saline solution

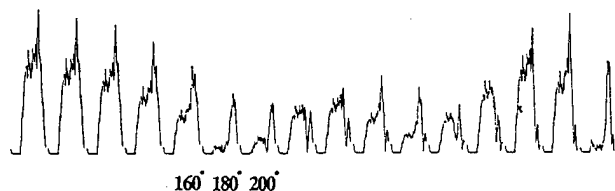


FIG. 3. Series of image projections of the mouse head obtained with the excitation power increased stepwise from the left to the right.



(a)



(b)



(c)

FIG. 4. Images of the mouse head obtained with different excitation flip angles to cerebrospinal fluid (CSF). (a) 160° , (b) 180° , (c) 200° .

phantom contained air as a marker. The maximum projection intensity resulted from a 90° , 270° , or 450° excitation, and the minimum projection intensity resulted from a 180° , 360° , or 540° excitation. It should be noted that the saline solution phantom requires more power for excitation than does the water phantom.

Figure 2 is a sagittal SE reference image of the mouse head obtained with 90° excitation pulses, a repetition time T_r ,



(a)



(b)

FIG. 5. Images of the rat head. (a) Flash reference image of the rat head. (b) Reference image subtracted by a B_c -applied image.

of 3000 ms, and an echo time T_e of 10 ms. The horizontal ($F1$) axis denotes the phase-encoded direction and the vertical ($F2$) axis denotes the read-out direction. Figure 3 shows a series of image projections of the same mouse head obtained in the read-out ($F2$) direction with the excitation power increased stepwise from the left to the right. The flip angle degrees 160°, 180°, and 200° were selective to the CSF of the head. The three images of Fig. 4 are head images with excitation flip angles of (a) 160°, (b) 180°, and (c) 200°. Also, the flip angles were selective to the brain CSF and all angles corresponded to the image projections (Fig. 3). All

scan parameters were identical to those of the reference image (Fig. 2) but different in flip angles. The 180° image [Fig. 4(b)] shows a slight signal from the brain and muscle tissues because there were almost no transversal components of magnetization. On the other hand, in the same 180° image, the resistive fatty tissues, which were transparent to the rf field, yielded a specific signal. By applying 180° pulses to the conducting CSF and muscle tissues, resistive fatty tissues simultaneously received excitation of the flip angles larger than 180° and produced an image signal.

Figure 5(a) is a sagittal, flash (fast low angle shot) reference image of the rat head, and Fig. 5(b) is the reference image subtracted by a continuous B_c -applied image. The signals of Fig. 5(b) are mainly from the spinal discs, ligaments, and fatty tissues. Using a continuous B_c field, more spins were perturbed in resistive tissues than in conducting tissues, and the image signal from resistive tissues fluctuated and disappeared. The possible blurring effects of B_c field in the read-out direction and phase-encoded direction can be eliminated by triggering the B_c field.

There are prior studies on B_1 field mapping³⁻⁵ but, those studies have not specifically targeted impedance distribution based on MRI techniques without electrodes. Both the large flip angle method and B_c field method are sensitive to rf inhomogeneity. In addition, both the Larmor frequency B_1 field and the low frequency B_c field are easily transmitted, absorbed, and reflected by biological tissue boundaries in varying degrees. The variance depends on the geometry of the subject, tissue properties, frequency, and the direction of B_1 or B_c field. However, in spite of these difficulties, the methods of this study are useful to obtain tomographic images of electrical impedance distributions of living organisms.

V. CONCLUSIONS

By applying large flip angles, conductivity-enhanced MR images were obtained at the Larmor frequency. By applying an additional time-varying magnetic B_c field parallel to the main static field B_0 , conductivity-enhanced images were obtained at an arbitrary frequency. The development of these methods is currently at a qualitative stage, but these are noninvasive methods used for visualization of electrical conductivity distribution *in vivo*.

¹B. H. Brown and A. D. Seagar, Clin. Phys. Physiol. Meas. A **8**, 91 (1987).

²P. Metherall, D. C. Barger, R. H. Smallwood, and B. H. Brown, Nature (London) **380**, 509 (1996).

³J. P. Hornak, J. Szumowski, and R. G. Bryant, Magn. Reson. Med. **6**, 158 (1988).

⁴E. K. Insko and L. Bolinger, J. Magn. Reson., Ser. A **103**, 82 (1993).

⁵R. Stollberger and P. Wach, Magn. Reson. Med. **35**, 246 (1996).

Polymerization and dissolution of fibrin under homogeneous magnetic fields

M. Iwasaka, M. Takeuchi, S. Ueno, and H. Tsuda^{a)}

Department of Biomedical Engineering, Graduate School of Medicine, University of Tokyo, Tokyo 113, Japan

We investigated whether or not a mutually compensating state of coagulation and fibrinolysis is changed by homogeneous magnetic fields. We used a superconducting magnet which produced magnetic fields of up to 14 T at its center. Fibrin polymerization over time, and the subsequent dissolution of the fibrin fiber network, were observed by measuring the optical absorbance of the mixture at 350 nm. A spectrophotometer with an external optical cell box in a superconducting magnet was used. We observed that the optical absorbance of the mixture at 350 nm increased during the fibrin-polymerization process, and decreased during the fibrinolytic processes. The optical absorbance was stable in the transient state between fibrin-polymerization and fibrinolytic processes. A magnetic field of 14 T increased the rate of the polymerization process by 55%–70% compared to the control group. On the other hand, the rate of the fibrinolytic process under a magnetic field at 14 T, increased by 27%–140% compared to the control. The results indicate that the magnetic orientation of fibrin fibers accelerated both the polymerization and the dissolution of fibrin fibers. © 1998 American Institute of Physics. [S0021-8979(98)38811-8]

I. INTRODUCTION

In the final process of blood coagulation, fibrinogen molecules change to fibrin monomers through the action of protease thrombin. Fibrin monomers are polymerized and form various sizes of fibers to become a gel. The fibrinogen molecule is composed of diamagnetic material which has diamagnetic anisotropy. In the course of polymerization, the fibrin fibers orient parallel to the magnetic fields.^{1–3} Past studies have focused on the mechanisms of the polymerization process using the magnetic orientation of fibrin. To investigate the fibrin structure and the mechanism of fibrin assembly, effects of coagulation factors such as Ca^{2+} , factor XIIIa, and fibrinopeptides on magnetic orientation of fibrin were clarified.^{4–6} We reported the clotting ability of various sizes of fibrinogen fractions using a magnetic orientation technique.⁷

In this study, we carried out an experiment to investigate whether or not a mutually compensating state of coagulation and fibrinolysis is changed by static magnetic fields. We measured the sophisticated process of enzymatic reactions of thrombin and plasmin under a 14 T homogeneous magnetic field. When blood coagulation occurs, the enzyme plasmin dissolves fibrin fibers, and the blood vessel remains in a normal state. The effects of magnetic fields on enzymatic reactions, which involve enzymes such as thrombin and plasmin, are interesting because each of these enzymes has opposing roles in the process of fibrin clot formation.

II. METHODS

We used a horizontal superconducting magnet which produced magnetic fields of up to 14 T at its center. First, 3

ml of fibrinogen solution (2.4–10.7 mg/ml) was incubated for 2 min at 37 °C. Next, plasmin and thrombin were added into the fibrinogen solution, and the mixture was incubated in an optical cell both with and without a constant magnetic field at 14 T.

Fibrin polymerization over time and the resulting dissolution of the fibrin fiber network were observed by measuring the optical absorbance of the mixture at 350 nm. A polymerized fibrin fiber has an optical turbidity. The period to reach a maximum level of absorbance at 350 nm is a conventional parameter for the evaluation of fibrin formation. In the present study, we evaluated the absorbance rate at 350 nm.

We used a spectrophotometer (JASCO, model V570) which has an external optical cell box in a superconducting magnet. Two optical fibers connected the external optical cell with the spectrophotometer, as shown in Fig. 1.

III. RESULTS AND DISCUSSION

The optical absorbance of fibrin gel at 350 nm shows the level of polymerization of fibrin fibers. Thick and large fibrin fibers have large optical absorbance at 350 nm.

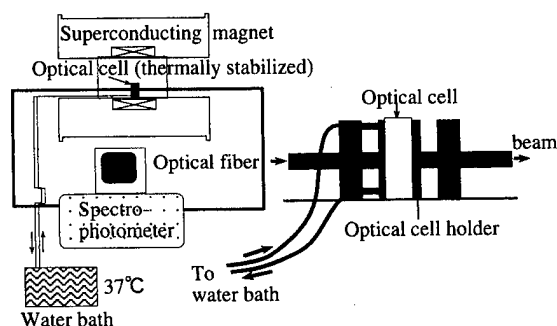


FIG. 1. Experimental setup for real-time measurement of the processes of fibrin formation and dissolution under strong magnetic fields.

^{a)}Clinical Laboratory, Kyushu University Hospital, Kyushu University, Fukuoka 812, Japan.

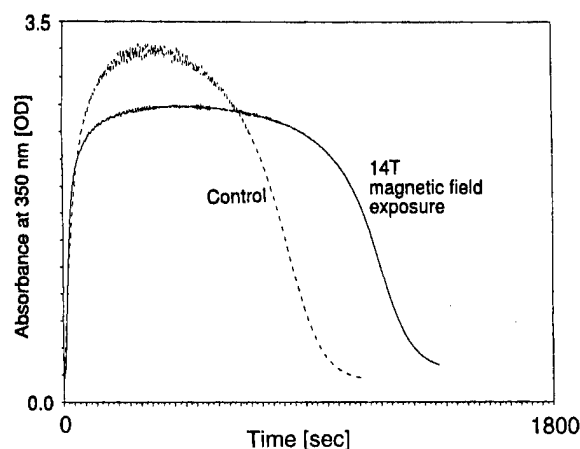


FIG. 2. Time course of the optical absorbance of the mixture at 350 nm during a fibrin polymerization process. The concentrations of fibrinogen, plasmin, and thrombin were 10.8 mg/ml, 0.28 units/ml, and 0.13 NIH units/ml, respectively.

The optical absorbance of the mixture at 350 nm increased during fibrin polymerization and decreased during the fibrinolysis, as shown in Fig. 2. The concentrations of fibrinogen, plasmin, and thrombin were 10.8 mg/ml, 0.28 units/ml, and 0.13 NIH units/ml, respectively. The optical absorbance was stable during the transient state between fibrin polymerization and the fibrinolytic processes. The experiments were carried out four times, and each time similar results were obtained.

We analyzed the time course of the optical absorbance of the mixture at 350 nm, and obtained absorbance rates for both fibrin polymerization and fibrinolysis, as shown in Fig. 3. The absorbance rates in both polymerization and fibrinolysis were calculated using a kinetics program of the spectrophotometer system. The concentration of fibrinogen was 10.8 mg/ml. The bar in positive area shows the rate of polymerization, and the bar in negative area shows the rate of fibrinolysis. A magnetic field at 14 T increased the rate in the polymerization process by 70% compared to the control group. In contrast, the rate in the fibrinolytic process under a magnetic field at 14 T decreased by 7% compared to the control. Also, a magnetic field at 14 T prolonged the duration of the transient state between fibrin polymerization and fibrinolytic processes.

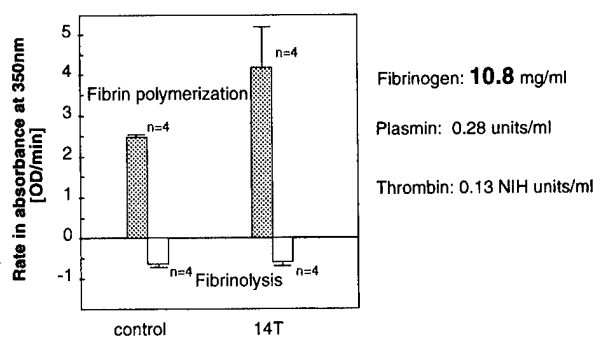


FIG. 3. Absorbance rate at 350 nm under both fibrin polymerization and fibrinolytic process. The concentrations of fibrinogen, plasmin, and thrombin were 10.8 mg/ml, 0.28 units/ml, and 0.13 NIH units/ml, respectively.

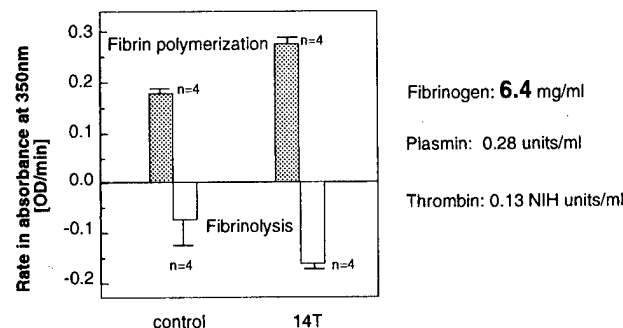


FIG. 4. Absorbance rate at 350 nm under both fibrin polymerization and fibrinolytic process. The concentrations of fibrinogen, plasmin, and thrombin were 6.4 mg/ml, 0.28 units/ml, and 0.13 NIH units/ml, respectively.

Figure 4 shows the results with a fibrinogen concentration of 6.4 mg/ml. The rate of fibrin polymerization also increased under a 14 T magnetic field. The maximum levels of the absorbance and the rate of fibrinolysis, increased under a 14 T magnetic field.

Figure 5 shows the results with a fibrinogen concentration of 2.4 mg/ml. The effects of the applied magnetic field were similar to the results shown in Fig. 4.

We also obtained the enhancement of both polymerization and dissolution processes of fibrin with a low concentration of enzymes, as shown in Fig. 6.

In the case of high fibrinogen concentration, 50 mg/ml, magnetic field effects were not significant in fibrin polymerization, as shown in Fig. 7. Fibrinolysis of the polymerized fibrin did not occur due to the high density of fibrin fibers.

The results of our study indicate that the magnetic orientation of fibrin fibers accelerated the polymerization of fibrin fibers.

The complete orientation of fibrin is obtained when the magnetic energy of fibrin fibers exceeds thermal energy kT ,

$$-\frac{\Delta\chi N}{2\mu_0} B^2 > kT, \quad (1)$$

where $\Delta\chi$ is the diamagnetic anisotropy of a fibrin monomer, and N is the number of fibrin monomers in a fibrin fiber.

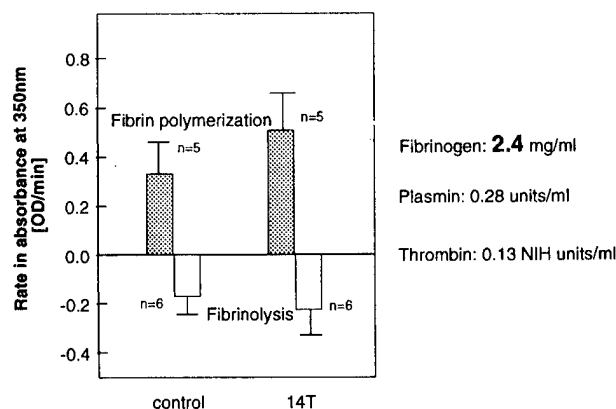


FIG. 5. Absorbance rate at 350 nm under both fibrin polymerization and fibrinolytic process. The concentrations of fibrinogen, plasmin, and thrombin were 2.4 mg/ml, 0.28 units/ml, and 0.13 NIH units/ml, respectively.

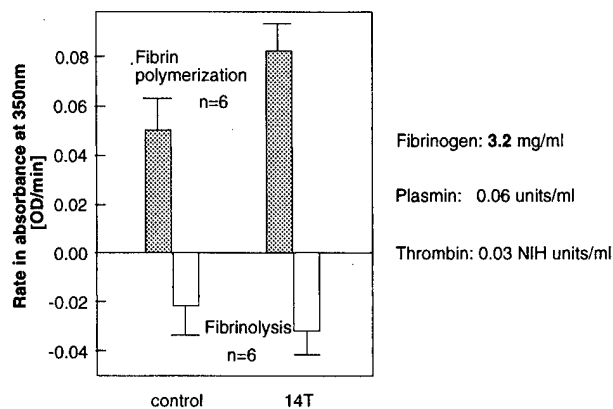


FIG. 6. Absorbance rate at 350 nm under both fibrin polymerization and fibrinolytic process. The concentrations of fibrinogen, plasmin, and thrombin were 3.2 mg/ml, 0.06 units/ml, and 0.03 NIH units/ml, respectively.

A fibrin fiber with more than 10^7 fibrin monomers has enough energy for complete magnetic orientation under an 8 T magnetic field at 298 K. Fibrin fibers orient parallel to the field direction.

We proposed a model for the magnetic field effect on fibrin polymerization enhancement which is shown in Fig. 8. Figure 8(a) shows the formation of fibrin fibers, so-called "protofibrils," in the early stages. Later, smaller fibrin polymers with 10^5 – 10^7 fibrin monomers aligned along the magnetic field direction. Thus, fibrins under magnetic fields form a thick and dense mass and show a high rate of optical turbidity increase.

In a previous study, we carried out an experiment to understand how the fibrin, oriented in a magnetic field, dissolves.³ Fibrin gels formed in a magnetic field were more soluble than those formed without a magnetic field. It was observed that the shapes of holes in dissolved fibrin changed to ellipsoidal patterns when fibrin plates were formed in a magnetic field at 8 T. The transverse axis of the ellipse was parallel to the magnetic fields.

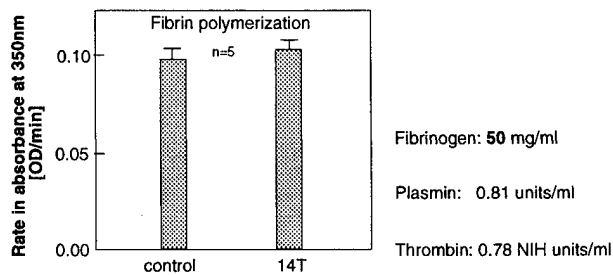


FIG. 7. Absorbance rate at 350 nm under both fibrin polymerization and fibrinolytic process. The concentrations of fibrinogen, plasmin, and thrombin were 50 mg/ml, 0.81 units/ml, and 0.78 NIH units/ml, respectively.

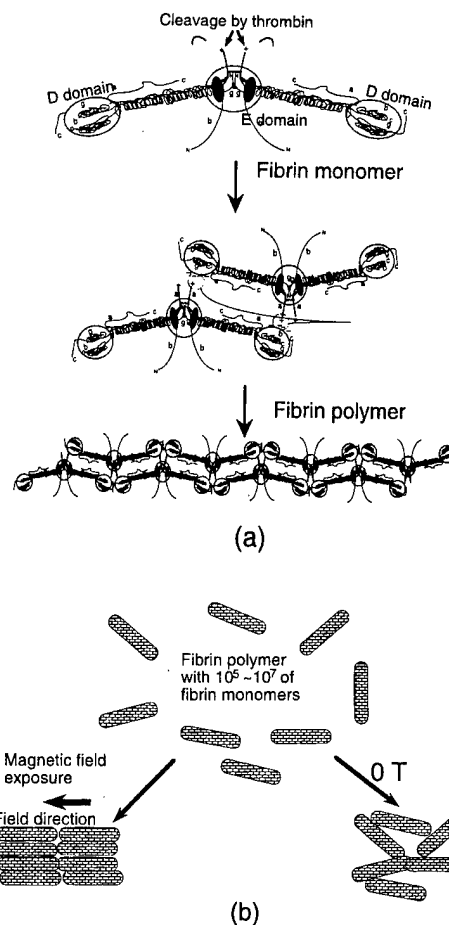


FIG. 8. A model for the magnetic field effect on fibrin polymerization enhancement.

The present results of optical turbidity measurement also show that the oriented fibrin fibers dissolve at a high rate. It is possible that the magnetic orientation of the fibrin fibers enhanced the dissolution of fibrin by plasmin for low fibrinogen concentration. However, for high fibrinogen concentration, it was suggested that plasmin embedded in oriented fibrin gel lost its ability to dissolve the fibrin fibers.

ACKNOWLEDGMENT

This work was supported in part by grants from the Ministry of Education, Science and Culture.

- ¹J. Torbet, M. Freyssinet, and G. Hudry-Clergeon, *Nature (London)* **289**, 91 (1981).
- ²A. Yamagishi, T. Takeuchi, T. Higashi, and M. Date, *J. Phys. Soc. Jpn.* **58**, 2280 (1989).
- ³S. Ueno, M. Iwasaka, and H. Tsuda, *IEEE Trans. Magn.* **29**, 3352 (1993).
- ⁴J. M. Freyssinet, J. Torbet, G. Hudry-Clergeon, and G. Maret, *Proc. Natl. Acad. Sci. USA* **80**, 1616 (1983).
- ⁵G. Hudry-Clergeon, J. M. Freyssinet, J. Torbet, and J. Marx, *Ann. (N.Y.) Acad. Sci.* **408**, 380 (1983).
- ⁶J. Torbet, *Biochem. J.* **244**, 633 (1987).
- ⁷M. Iwasaka, S. Ueno, and H. Tsuda, *J. Appl. Phys.* **79**, 4708 (1996).

Bioluminescence under static magnetic fields

M. Iwasaka^{a)} and S. Ueno

Department of Biomedical Engineering, Graduate School of Medicine, University of Tokyo,
Tokyo 113, Japan

In the present study, the effect of magnetic fields on the emission of light by a living system was studied. The fireflies *Hotaria parvula* and *Luciola cruciata* were used as the bioluminescence systems. The firefly light organ was fixed at the edge of an optical fiber. The emitted light was introduced into a single-channel photon-counting system using an optical fiber. We measured both the spectrum of a constant light emission and, the time course of bioluminescence pulses. Two horizontal-type superconducting magnets, which produced 8 and 14 T magnetic fields at their center, were used as the magnetic-field generators. We also carried out an *in vitro* study of bioluminescence. The enzymatic activity of luciferase was measured under a 14 T magnetic field. We measured emission spectra of bioluminescence over the interval 500–600 nm at 25 °C in a stable emission state. It was observed that the peak wavelength around 550 nm shifted to 560 nm under a 14 T magnetic field. However, the effects of magnetic fields were not significant. Also, we measured the time course of emissions at 550 nm in a transient emission state. The rate in the light intensity under a 14 T magnetic field increased compared to the control. There is a possibility that the change in the emission intensities under a magnetic field is related to a change in the biochemical systems of the firefly, such as the enzymatic process of luciferase and the excited singlet state with subsequent light emission. © 1998 American Institute of Physics.

[S0021-8979(98)38911-2]

I. INTRODUCTION

The question of whether magnetic fields affect enzymatic activities or not is of considerable interest in biochemistry and in biomagnetics. Possible biomagnetic and chemical effects can be expected when biological systems are exposed to both static magnetic fields and other energy such as light and radiation.¹ Photochemical reactions produced by a radical-pair intermediate in solution, can be exposed to show magnetic-field effects that arise from an electron-Zeeman interaction, an electron-nuclear hyperfine interaction, or a hyperfine interaction mechanism including an electron-exchange interaction in a radical-pair intermediate. A common mechanism of magnetic-field effects on photochemical processes is that a chemical yield of the cage or escape product shows a magnetic-field dependence when a single-triplet intersystem crossing is subject to magnetic perturbations. The magnetic-field effects on photochemical reactions were verified in previous studies.²

To clarify the effect of magnetic fields on enzymatic reactions in living systems, it is important to study the enzymatic reactions that involve radicals generated from nonphotochemical processes. Haberditzl reported that magnetic fields of up to 6 T enhanced the activity of catalase 4.9%–52%.³ We examined the possible effects of static magnetic fields on biochemical reactions catalyzed by xanthine oxidase and by catalase.^{1,4} It was reported that magnetic fields of 0.10–0.15 T affected B₁₂ ethanolamine ammonia lyase.⁵ While several enzymatic processes have radical pairs, it is not easy to examine the products of a radical reaction *in vivo*. However, if the products could be measured by light

emission, the real-time measurement of the radical reaction could be available in an *in vivo* system. The use of bioluminescence to investigate the interaction of magnetic fields with *in vivo* biochemical processes involving the radical pairs is effective. In the present study, the effect of magnetic fields on the emission of light by a living system was studied.

II. METHODS

A. Magnetic-field exposure systems

We used two horizontal types of superconducting magnets. The magnet 700 mm long with a bore of 100 mm in

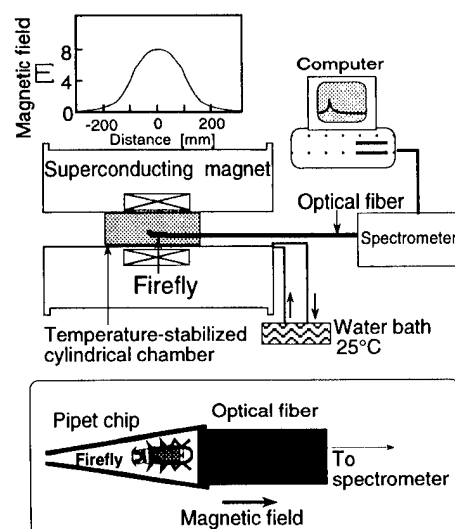


FIG. 1. Experimental setup for the bioluminescence of a firefly.

^{a)}Electronic mail: iwasaka@medes.m.u-tokyo.ac.jp

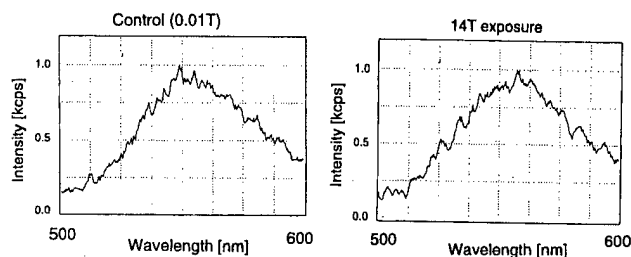


FIG. 2. Emission spectra of firefly *Hotaria parvula* over the intervals 500–600 nm at 25 °C with and without magnetic field at 14 T.

diameter produced 8 T at its center. The magnet 480 mm long with a bore of 50 mm in diameter produced 14 T at its center. All experiments were carried out under homogeneous magnetic fields of 8 and 14 T.

B. In vivo experiments

The fireflies *Hotaria parvula* and *Luciola cruciata* were used as the bioluminescence systems. The firefly light organ was fixed at the edge of an optical fiber. The emitted light was introduced into a single-channel photon-counting system using an optical fiber, as shown in Fig. 1. We measured both the spectrum of a constant light emission and the time course of bioluminescence pulses.

C. In vitro experiments

We carried out an *in vitro* study of bioluminescence by means of a luciferin–luciferase reaction. The enzymatic activity of luciferase was measured under a 14 T magnetic field. We prepared a reaction mixture, which contained 0.1 mM of d-luciferin (RD systems Co.), 1.5–4.0 m units/ml of luciferase, 5 mM of magnesium sulfate, and 20 mM of HEPES (pH 7.7). The luciferase was a recombinant of *Luciola cruciata*.

The reaction was started by the addition of 50 μ l of ATP solution. The final concentration of ATP was changed in the range of 0.2 μ g/ml–0.2 mg/ml. Reaction mixtures were exposed to a magnetic field of 14 T for 2000 s at 25 \pm 0.1 °C. The emission of bioluminescence was stable at low intensity emissions where the optical intensity decreased below 1000 counts per second (cps). However, the emission was unstable

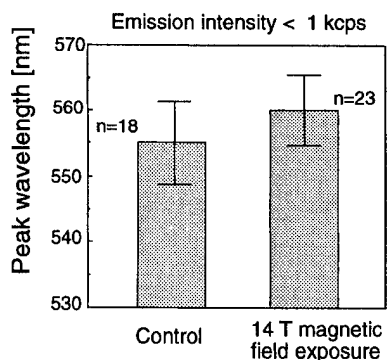


FIG. 3. The effects of a 14 T magnetic field on the peak wavelength at 550 nm.

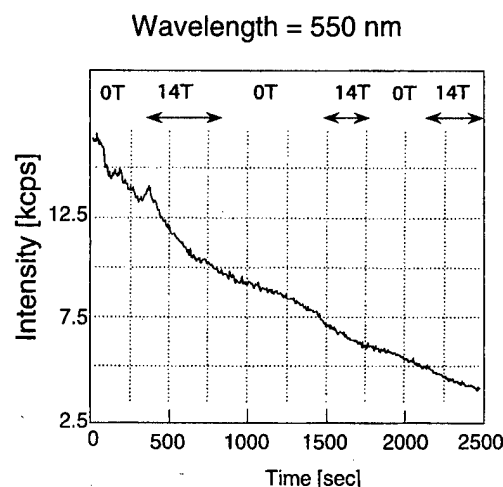


FIG. 4. The effects of a 14 T magnetic field on the time course of the transient emission of the firefly *Hotaria parvula* at 550 nm.

when the optical intensities were \sim 10 kilocounts per second (kcps). We measured the spectra of bioluminescence under stable emission conditions.

III. RESULTS AND DISCUSSION

We measured the emission spectra of *in vivo* experiments of the bioluminescence of the firefly *Luciola cruciata* in an 8 T magnetic field. In the range of 25–37 °C, the peak intensity and wavelength at 435 nm changed significantly. However, the two peak wavelengths, at 435 and 550 nm, did not change in an 8 T magnetic field. The effects of an 8 T magnetic field on the emission spectrum are negligible compared to the effects of temperature.

We measured the low-intensity (<1 kcps) emission spectra of bioluminescence of *Hotaria parvula* over the interval 500–600 nm at 25 °C under a 14 T magnetic field. It was observed that the peak wavelength around 550 nm shifted to 560 nm under a 14 T magnetic field, as shown in Fig. 2. Figure 3 shows the effects of a 14 T magnetic field on the peak wavelength at 550 nm. The effects of magnetic fields were not significant.

The emission spectra of the *in vitro* luciferin–luciferase reactions were also measured under the stable states. In our experiment, the light intensities were stable at approximately

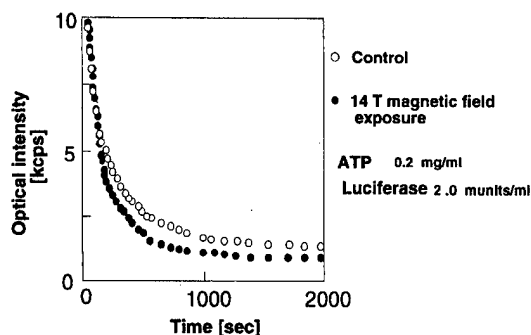


FIG. 5. Time course of the emitted light of the luciferin–luciferase *in vitro* reaction at 550 nm under a 14 T magnetic field.

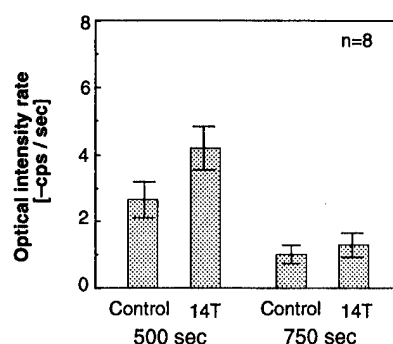


FIG. 6. Rate in the emitted light intensity of the luciferin reaction at 550 nm under a 14 T magnetic field after the addition of an ATP solution.

2000 s after the addition of an ATP. A distinct effect of the magnetic field on the peak wavelength at 550 nm was not observed.

Furthermore, we measured the time course of the emission of firefly *Hotaria parvula* in a transient emission state. Figure 4 shows a time course of high-intensity (5–10 kcps) emissions at 550 nm. During the experiment, the light intensity gradually decreased; the firefly was exposed to a 14 T magnetic field, three times. It was observed that a 14 T magnetic field enhanced the inclination of emission intensity.

Figure 5 shows the time course of the emitted light of the luciferin–luciferase *in vitro* reaction at 550 nm under a 14 T magnetic field. After the addition of an ATP solution, the light intensity rapidly increased. The reaction mixture in an optical cell was inserted into the superconducting mag-

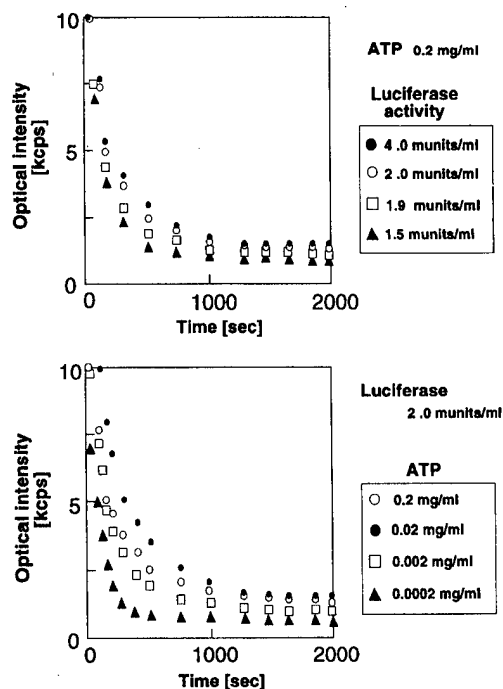


FIG. 7. Effects of the concentrations of ATP and luciferase on the time course of bioluminescence at 550 nm.

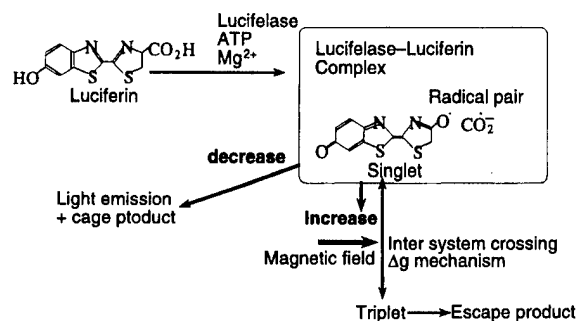


FIG. 8. The mechanism of the luciferin–luciferase reaction.

net's bore, and the decreasing light intensity was observed. The light intensity under a 14 T magnetic field decreased rapidly compared to the control. Figure 6 shows the rate of emitted light intensities at 14 T. A 14 T magnetic field affected the transient state of the time course of the light intensity.

In order to investigate the mechanism of the observed effects, we measured the time course of the emitted light, by changing the concentration of ATP and luciferase, as shown in Fig. 7. The upper figure of Fig. 7 shows results with a constant concentration of ATP and four types of luciferase activities. When the activity of luciferase decreased, optical intensities also decreased. Similarly, lowering the ATP concentration for a constant concentration of luciferase reduced the optical intensity. Decreasing the luciferase activity, the ATP concentration and a 14 T magnetic field exposure have the same effect, an optical intensity drop.

There is a possibility that the change in the emission intensities under a magnetic field is related to the change in the biochemical systems of the firefly, such as the enzymatic process of luciferase and the excited singlet state with subsequent light emission. Figure 8 shows the mechanism of the luciferin–luciferase reaction.⁶ The luciferin and luciferase form an enzyme–substrate complex, and an intermediate dioxetane produces a radical pair in the singlet state, oxyln. The excited singlet state of oxyln generates a cage product and yellow-green light. On the other hand, the triplet state generates only an escape product. It is possible that the magnetic fields affect the single–triplet intersystem crossing by electron–Zeeman interactions, i.e., Δg mechanism.²

IV. CONCLUSION

In conclusion, it was found that the bioluminescence of the luciferin–luciferase reaction was changed under a magnetic field at 14 T. The static magnetic fields of 14 T enhanced the decrease of emission intensity. The static magnetic fields of 8–14 T had no distinct effects on the peak wavelength at 400–600 nm.

¹ S. Ueno and K. Harada, IEEE Trans. Magn. **22**, 868 (1986).

² S. Nagakura and Y. Molin, Chem. Phys. **162**, 1 (1992).

³ W. Haberditzl, Nature (London) **213**, 72 (1967).

⁴ S. Ueno and M. Iwasaka, J. Appl. Phys. **79**, 4705 (1996).

⁵ T. T. Harkins and C. B. Grissom, Science **263**, 958 (1994).

Structure of water molecules under 14 T magnetic field

M. Iwasaka^{a)} and S. Ueno

Department of Biomedical Engineering, Graduate School of Medicine, University of Tokyo,
Tokyo 113, Japan

In this study, we investigated the effects of strong magnetic fields of up to 14 T on the near-infrared spectrum of water molecules. We used a near-infrared spectrophotometer, which has an external optical cell box in a 14 T superconducting magnet. We measured the near-infrared spectrum of water in the range of 900–2000 nm by changing the optical path lengths from 0.1 to 100 mm. The peak wavelengths in the near-infrared spectrum in the range of 900–2000 nm of water, increased in length by 1–3 nm under a 14 T magnetic field. Also, we measured a near-infrared spectrum of glucose solutions under a magnetic field at 14 T to investigate the hydration of sugar. In contrast to the case of water, the peak wavelength of glucose solutions showed blueshift under a 14 T magnetic field. When the magnetic fields were changed from 0 to 14 T, the differential optical absorbance of the glucose solution at 958 nm increased compared to the controls. There is a possibility that the 14 T magnetic field affects the formation of hydrogen bonds of water molecules and the hydration of glucose molecules. © 1998 American Institute of Physics. [S0021-8979(98)39011-8]

I. INTRODUCTION

Water, an important material for living systems, is a diamagnetic material. We have observed the phenomenon that the surface of water was parted by magnetic fields and the bottom of the water chamber appeared when water was exposed to magnetic fields up to 8 T.^{1,2} It is important to know whether or not magnetic fields affect the property of water molecules. As water is an essential material in the living body, the understanding of the behavior of water under magnetic fields provides information to discuss the effects of magnetic fields on living systems.

The so called ‘Moses’ effect’ can be explained by the diamagnetic property of water. Since water is diamagnetic, when a magnetic force acting on water reaches a high enough value, it presses back the water. Also, it is important to understand the mechanism of the interaction of magnetic fields with organic and water molecules. A diamagnetic macromolecule such as fibrin is a good model for studying biomagnetic effects because fibrin polymers are oriented parallel to the direction of magnetic fields.³ Compared to paramagnetic inorganic materials, solutions of biological materials such as proteins and amino acids are mostly diamagnetic, and their magnetic susceptibility is small.

We reported the effect of magnetic fields up to 8 T on the enzymatic reaction of glucose oxidase with *D*-glucose using an electrochemical technique.⁴ We observed that electric currents decreased by 10%–20% after a magnetic-field exposure for 1–2 h. We conjecture that the diffusion process of glucose in aqueous solution, into the pore of the electrode, appeared to be inhibited by the magnetic field. Also, it is important to investigate the effects of dissolved oxygen concentration on the properties of aqueous solution.^{5,6} The reported effect of a magnetic field on the diffusion of saccharides through a porous membrane was obtained at 1.1 T.⁷ It

is possible for a strong magnetic field to affect the hydration of sugar.

In this study, we investigated the effects of strong magnetic fields of up to 14 T on the near-infrared spectrum of water and a sugar solution.

II. METHODS

We investigated the near-infrared spectrum of aqueous solutions using a horizontal type of superconducting magnet, which produces 14 T at its center. We used a near-infrared spectrophotometer, which has an external optical cell box in a superconducting magnet, as shown in Fig. 1. Two optical fibers connected the external optical cell with the spectrophotometer.

We measured the near-infrared spectrum of aqueous solutions in the range of 900–2000 nm. Each of the spectra was obtained from 100 to 600 measurements. The optical

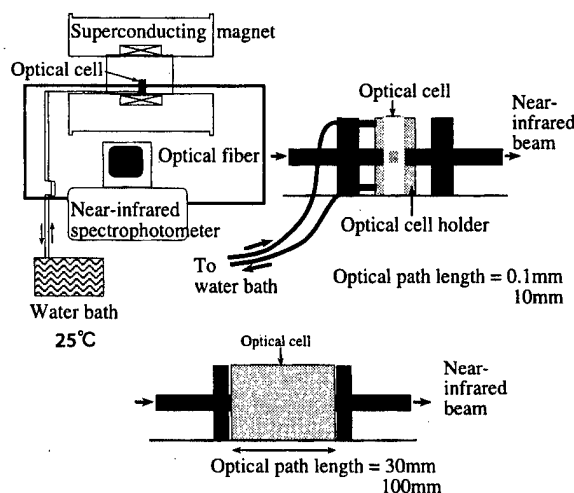


FIG. 1. Experimental setup for near-infrared absorbance measurement of water and glucose solutions under magnetic fields of up to 14 T.

^{a)}Electronic mail: iwasaka@medes.m.u-tokyo.ac.jp

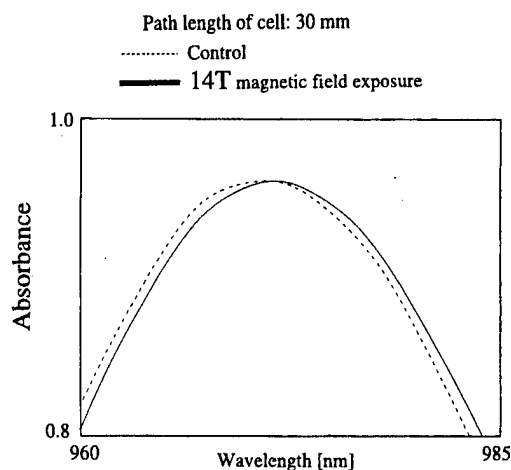


FIG. 2. Effects of a 14 T magnetic field on near-infrared spectrum of water at 900–1000 nm. Optical length is 30 mm.

path lengths of the cells were 0.1, 10, 30, and 100 mm. All measurements were carried out in a temperature-stabilized holder at 25 °C.

Also, we measured the near-infrared absorbance of a sugar solution under a magnetic field at 14 T to investigate the hydration of the solute in aqueous solution. The hydration of *D*-glucose was investigated by the absorbance of solutes at 958 nm.⁸ We measured the absorbance of 2.3, 1, and 0.1 M of *D*-glucose solution and water.

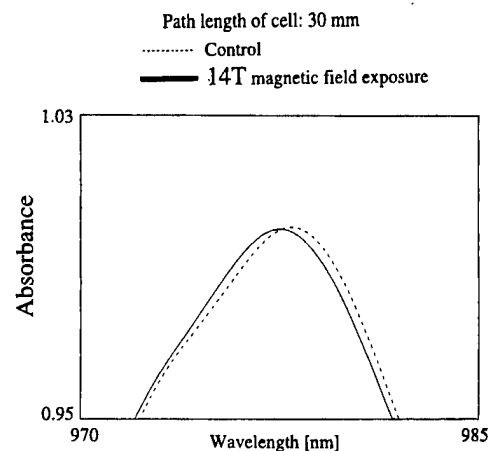
III. RESULTS AND DISCUSSION

Figure 2 shows the effect of a 14 T magnetic field on the near-infrared spectrum of water at 900–1000 nm. The optical path length of the cell was 30 mm. A peak wavelength at 970 nm shifted to a longer wavelength in a 14 T magnetic field. Each of the spectra was the average of 600 measurements.

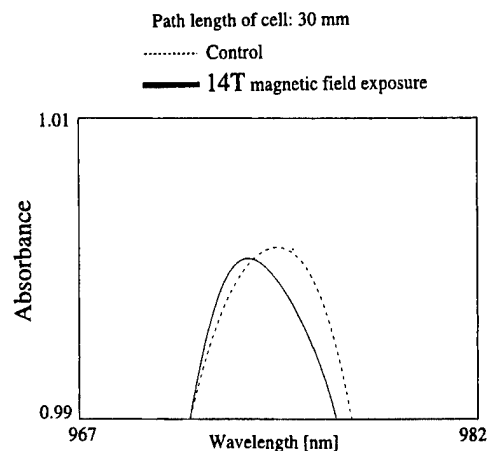
We measured spectra of two types of glucose solution, 2.3 and 1.0 M, in the 30 mm optical path. Each of the spectra was obtained from 600 measurements. Figure 3(a) shows the spectrum of 2.3 M of the *D*-glucose solution. The peak wavelength of 2.3 M glucose shifted to a longer wavelength compared to the water without magnetic-field exposures. In contrast to the case of water, the peak wavelength of 2.3 M glucose showed blueshift under a 14 T magnetic field. The effect of magnetic fields on 1.0 M of the *D*-glucose solution was the blueshift of a peak wavelength, as shown in Fig. 3(b).

Figure 4 shows the effects of magnetic fields of up to 14 T on the near-infrared absorbance of *D*-glucose solutions and water at 958 nm. Figures 4(a) and 4(b) show the results in the optical paths of 10 and 100 mm, respectively.

The optical absorbance at 958 nm in the 10 mm optical path was adjusted to zero when an empty cell was put in the optical cell holder. When the magnetic fields were changed from 0 to 14 T, the absorbance of 1 M of the *D*-glucose solution increased by 0.006 [optical density (OD)], as shown in Fig. 4(a). The absorbance at 958 nm of 1 M of the *D*-glucose solution was stable in the range of 0–14 T. How-



(a) 2.3M of *D*-glucose solution



(b) 1.0M of *D*-glucose solution

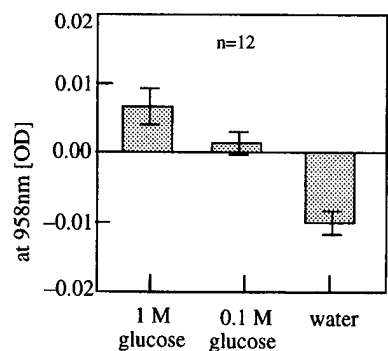
FIG. 3. Effects of a 14 T magnetic field on near-infrared spectra of *D*-glucose solutions at 900–1000 nm. (a) 1.0 M of *D*-glucose solution, and (b) 2.3 M of *D*-glucose solution. Optical length is 30 mm.

ever, when we measured the absorbance at 958 nm of distilled water under magnetic fields, the absorbance decreased by 0.010 (OD).

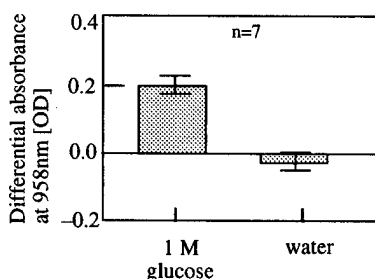
In the experiments with the 100 mm optical path cell, the absorbance level was adjusted to zero by water. As shown in Fig. 4(b), when the magnetic fields were changed from 0 to 14 T, the absorbance of 1 M of the *D*-glucose solution increased by 0.2 (OD). When we measured the absorbance of distilled water at 958 nm under magnetic fields, distinct changes in the absorbance were not observed.

The results of Figs. 3 and 4 indicate that the increase in the optical absorbance at 958 nm under magnetic fields was because a property of the glucose solution, such as the hydration of glucose, changed under magnetic fields of up to 14 T.

We investigated the property of near-infrared absorbance of water by changing the optical path length for a second time. Figure 5 shows the time course of the change in the peak wavelength of water at 977 nm. The optical path length was 10 mm. Each of the spectra was obtained from 100 measurements. Before magnetic-field exposure, the peak wavelength was 977.0–977.1 nm. The peak shifted to 978.0 nm under a 14 T magnetic field, and gradually shifted to the



(a) Optical path length = 10mm



(b) Optical path length = 100mm

FIG. 4. Near-infrared absorbance of *D*-glucose solutions and water at 958 nm under magnetic fields of up to 14 T.

shorter wavelength after the magnetic field was turned off.

Figure 6 shows the effects of a 14 T magnetic field on the peak wavelength of water at 1920–1940 nm. The optical length was 0.1 mm. Each of the spectra was obtained from 900 measurements. The peak wavelength of water shifted from 1927.2 ± 0.9 nm to 1929.4 ± 0.8 nm under the 14 T magnetic field.

An enhancement of the formation of hydrogen bonds in water molecules under high pressure was reported.⁹ The bottom figures of Fig. 6 show an enhancement of the formation of hydrogen bonds in water molecules. The near-infrared

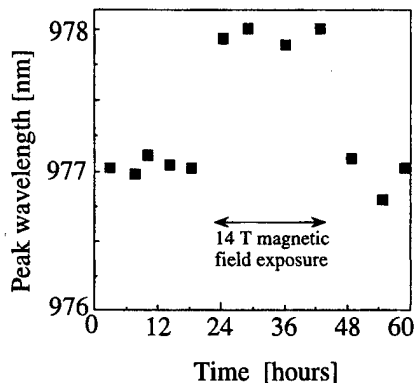


FIG. 5. Effects of a 14 T magnetic field on the peak wavelength of water at 978–980 nm. Optical length is 10 mm.

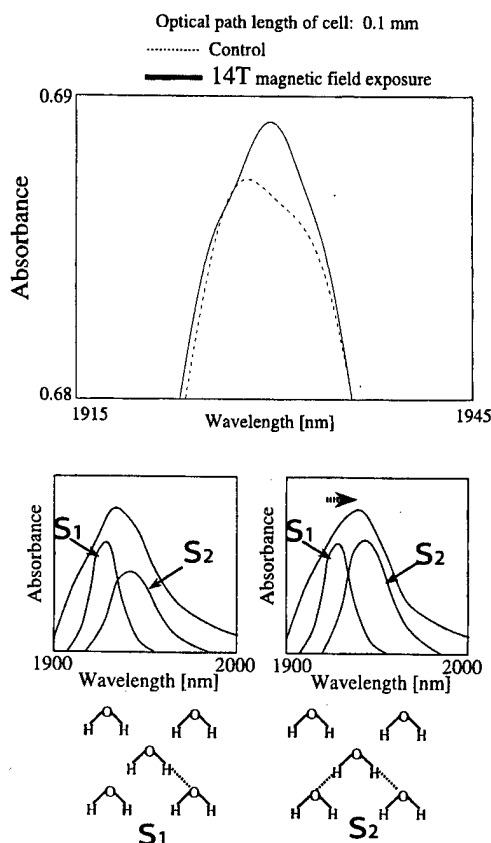


FIG. 6. Effects of a 14 T magnetic field on the peak wavelength of water at 1920–1940 nm. Optical length is 0.1 mm. The lower figure shows an enhancement of the formation of hydrogen bonds in water molecules (Ref. 9). The species of water molecules, which have two hydrogen bonds, increased in number, and the peak wavelength shifts to longer wavelengths.

spectrum of water around 1900 nm originates from the species of water molecules S1 and S2.⁹ The species of water molecules, (S2) which have two hydrogen bonds, increased in number, and the peak wavelength shifts to longer wavelengths. There is a possibility that the species of water molecules, which have two hydrogen bonds between water molecules, increased in number under the 14 T magnetic field. Also, we need to investigate the effects of dissolved oxygen on the optical properties of aqueous solutions.^{5,6}

¹S. Ueno and M. Iwasaka, J. Appl. Phys. **75**, 7177 (1994).

²S. Ueno and M. Iwasaka, IEEE Trans. Magn. **30**, 4698 (1994).

³J. Torbet, M. Freyssinet, and G. Hudry-Clergeon, Nature (London) **289**, 91 (1981).

⁴M. Yaoita, M. Iwasaka, and S. Ueno, *Nonlinear Electromagnetic Systems, Studies in Applied Electromagnetics and Mechanics* (IOS, 1996), Vol. 10, p. 314.

⁵S. Ueno and K. Harada, IEEE Trans. Magn. **18**, 1704 (1982).

⁶S. Ueno, M. Iwasaka, and G. Furukawa, IEEE Trans. Magn. **31**, 4259 (1995).

⁷J. Liemezs, V. Atwal, and H. Aleman, J. Electrochem. Soc. **137**, 3809 (1990).

⁸J. L. Hollenberg and J. B. Ifft, J. Phys. Chem. **86**, 1938 (1982).

⁹M. Kato, Y. Taniguchi, S. Sawamura, and K. Suzuki, in *Physics and Chemistry of Ice*, edited by N. Maeno and T. Hondoh (Hokkaido University Press, 1992), p. 83.

Estimation of multiple sources using a three-dimensional vector measurement of a magnetoencephalogram

Koichiro Kobayashi^{a)} and Yoshinori Uchikawa

Tokyo Denki University, Ishizaka Hatoyama Hiki-gun, Saitama, 350-0394 Japan

We developed a three-dimensional (3D) second-order gradiometer connected to three superconducting quantum interference devices (SQUIDs) for vector measurement of a magnetoencephalogram (MEG) that can detect magnetic-field components perpendicular and tangential to the scalp simultaneously. Each coil is orthogonally wound with Nb-Ti wire on a rectangular solid $3 \times 3 \times 6$ cm. To assess discrimination and separation of multiple sources, we carried out a 3D vector measurement of the MEG with a mixed auditory evoked field (AEF) and a somatosensory evoked field (SEF) overlapping in time. The magnetic-field distribution perpendicular to the scalp was not helpful in estimating the location and number of sources, owing to the lack of a dipole pattern. But the magnetic-field distribution tangential to the scalp can provide information about constraint conditions by visual inspection. We estimated multiple sources of the mixed AEF and SEF from the MEG data of the magnetic field tangential to the scalp and confirmed by comparison with magnetic resonance imaging (MRI) of a subject's head superimposed source locations. We conclude that this 3D second-order gradiometer can provide constraint conditions by visual inspection for calculating the inverse problem with multiple sources. © 1998 American Institute of Physics. [S0021-8979(98)39111-2]

INTRODUCTION

Magnetoencephalogram (MEG) measurement of the magnetic field perpendicular to the scalp is widely used. There are problems of separating multiple sources overlapping in time when many distinct areas of the cortex are active.¹⁻⁴ We developed a three-dimensional (3D) second-order gradiometer connected to three superconducting quantum interference devices (SQUIDs) for vector measurement of the MEG that can detect magnetic-field components perpendicular (Br) and tangential ($B\theta, B\phi$) to the scalp simultaneously.⁵ The magnetic-field distribution tangential to the scalp can provide information about constraint conditions by visual inspection. This paper presents a 3D vector measurement of the MEG with a mixed auditory evoked field (AEF) and a somatosensory evoked field (SEF) overlapping in time, and also presents an estimation of multiple sources using the MEG data of the magnetic-field components perpendicular and tangential to the scalp.

METHOD

A 3D vector measurement of the MEG was carried out using a 3D second-order gradiometer shown in Fig. 1(a). The coordinate system is shown in Fig. 1(b). The 3D second-order gradiometer is orthogonally wound with Nb-Ti wire on a rectangular solid $3 \times 3 \times 6$ cm. The magnetic-field output of this gradiometer is expressed as follows:

$$Br = B(r, \theta, \phi) - 2B(r + \Delta r, \theta, \phi) + B(r + 2\Delta r, \theta, \phi), \quad (1)$$

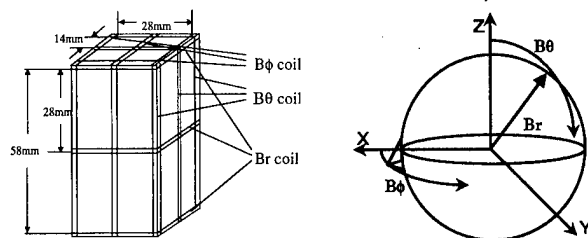
$$B\theta = B(r, \theta, \phi) - 2B(r, \theta + \Delta \theta, \phi) + B(r, \theta + 2\Delta \theta, \phi), \quad (2)$$

$$B\phi = B(r, \theta, \phi) - 2B(r, \theta, \phi + \Delta \phi) + B(r, \theta, \phi + 2\Delta \phi), \quad (3)$$

where (r, θ, ϕ) indicates the lowest place of the Br component coil shown in Fig. 1(a). Δr is a base line (2.8 cm) of a Br coil. $\Delta \theta$ and $\Delta \phi$ indicate a base line (1.4 cm) of a coil for $B\theta$ and $B\phi$.

A multiple source estimation study was done using the moving dipole inverse solution with a spherical homogeneous conductor model (85 mm radius) as a human head. Multiple sources are estimated by minimizing the cost function, which is the least-squares fit between the measured magnetic field and calculated magnetic field. In this method, source parameters such as amplitude and orientation were varied, and the minimum cost function was obtained by iterative calculation. The cost function f is defined as

$$f = \frac{\sum_{i=1}^n (Bm_i - Be_i)^2}{\sum_{i=1}^n (Bm_i)^2}, \quad (4)$$



(a) 3-D second-order gradiometer

(b) coordinate system

FIG. 1. Configuration of a 3D second-order gradiometer and the coordinate system.

^{a)}Electronic mail: kobaya@f.dendai.ac.jp

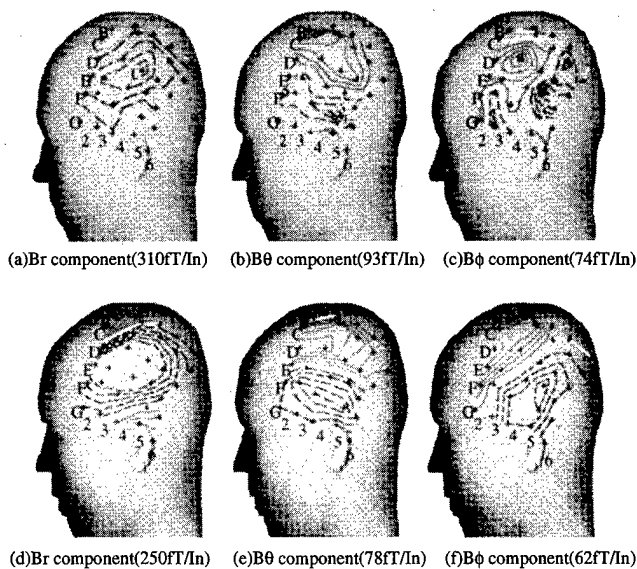


FIG. 2. Isofield contour maps consisting of the mixed AEF (120 ms) and SEF (80 ms) overlapping in time. (a), (b), and (c) measured MEG; and (d), (e), and (f) calculated MEG.

where Bm_i is the measured magnetic field at i th position, and Be_i is the calculated field. The goodness-of-fit G is defined as

$$G = \sqrt{1 - f} \times 100 \quad (\%). \quad (5)$$

The main elements of the calculation process for the inverse solution are as follows. The initial parameters of the multiple dipoles are determined by topographical features of the tangential magnetic-field distribution ($B\theta, B\phi$). Namely, the number and the location of the dipoles are given from tangential magnetic-field extremes since the tangential magnetic field shows maximum or minimum field just above the location of a single dipole.⁵ The amplitudes of the dipoles are also given by the magnetic-field extremes. Then, a least-squares calculation [Eq. (4) of the cost function] was performed for the perpendicular magnetic field (Br) using these initial parameters of sources obtained from the tangential magnetic field ($B\theta, B\phi$). A unique characteristic of this inverse calculation is the use of the initial parameters obtained from the tangential field as the constraint conditions.

MEG MEASUREMENT AND SOURCE ESTIMATION

We carried out a 3D MEG measurement of mixed AEF and SEF overlapping in time. The AEF was elicited by 1 kHz tone bursts of 50 ms duration to the right ear. The SEF was elicited by electric pulses of 0.2 ms duration with 6–8 mA to the median nerve of the right wrist. The interval of stimulation was 500 ms. Stimulation to the median nerve was delivered 40 ms later than to the ear. There were two evoked fields, namely, the mixed AEF and SEF, overlapping in time. There were 30 measurement positions on the scalp. All magnetic data were averaged for 400 measurements at each position. The sampling interval was 0.5 ms. A band-pass filter was used in the range of 0.5–40 Hz.

Figures 2(a), 2(b), and 2(c) show an example of isofield contour maps at 120 ms latency of the AEF and at 80 ms

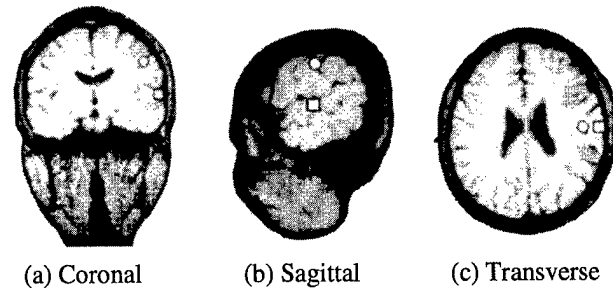


FIG. 3. MRI of a subject's head showing the superimposed source localization of the AEF (open square) and the SEF (open circle).

latency of the SEF. Solid lines (positive field) of the Br component shows the outflow of the magnetic flux from the scalp. These lines (positive field) of $B\theta$ and $B\phi$ show a magnetic flux directed along the latitudes and longitudes shown in Fig. 1(b). As shown in Fig. 2(a), the contour map of Br shows one extremum at measurement position D4 that is not a dipole pattern. This map was not helpful in estimating the location and the number of sources. By referring to the contour maps of $B\theta$ and $B\phi$ shown in Figs. 2(b) and 2(c), we can clearly see two extremes with opposite polarity on both contour maps. Namely, these magnetic fields consist of two sources with opposite polarity underlying each extreme.⁶ We can obtain the initial parameters of the number, the locations, and the directions of the sources by visual inspection from these contour maps. We carried out source estimation using these initial parameters. Figures 2(d), 2(e), and 2(f) show calculated isofield contour maps. The calculated maps $B\theta$ and $B\phi$ were estimated from the result of the inverse solution from Br . The goodness of fit (G) of Br is 92.4%, and the goodness of fit (G) of $B\theta$ and $B\phi$ are 88.7% and 88.6%, respectively.

Figure 3 shows the magnetic resonance imaging (MRI) of a subject's head. Estimated sources are superimposed on the MRI. The localization of the AEF source (open square) at 120 ms latency on the MRI was estimated at the gyrus of the sylvian sulcus with a depth of 1.8 cm below the scalp, which is in the auditory area. Localization of the SEF source (open circle) at 80 ms latency on the MRI was estimated at the gyrus of the central sulcus with a depth of 1.4 cm from the scalp, which is the somatosensory area. The results of this study, analyzing magnetic fields over the human primary cortices, agree in general terms with the related findings in previous human studies.^{7,8}

CONCLUSION

We developed a 3D second-order gradiometer connected to three SQUIDS for vector measurement of the MEG that can detect magnetic-field components perpendicular and tangential to the scalp simultaneously. To assess discrimination and separation of multiple sources, we carried out 3D vector measurements of the MEG with the mixed AEF and SEF overlapping in time. We estimated multiple sources from the MEG data and confirmed source locations are reasonable by comparison with the MRI of the subject's head. We conclude

that this 3D vector magnetic-field measurement can provide information on constraint conditions, which can be obtained from the tangential magnetic field when we calculate the inverse problem with multiple sources. Up to the present time, we have used only the magnetic field perpendicular to the scalp.

ACKNOWLEDGMENTS

This study has been supported by a grant from the Center for Research of Tokyo Denki University and the Japan Ministry of Education.

- ¹C. Baumgartner, W. W. Sutherling, S. Di, and D. S. Barth, *Electroencephalogr. Clin. Neurophysiol.* **79**, 27 (1991).
- ²A. Achim, F. Richer, and J. S. Hilaire, *Electroencephalogr. Clin. Neurophysiol.* **79**, 227 (1991).
- ³J. C. Mosher, P. S. Lewis, and R. M. Leahy, *IEEE Trans. Biomed. Eng.* **39**, 541 (1992).
- ⁴S. Supek and C. J. Aine, *IEEE Trans. Biomed. Eng.* **40**, 529 (1993).
- ⁵Y. Uchikawa, F. Matsumura, K. Kobayashi, and M. Kotani, in *Biomagnetism: Fundamental Research and Clinical Applications*, edited by C. Baumgartner, L. Deecke, G. Stroink, and S. J. Williamson (Elsevier Science, Amsterdam the Netherlands, 1995), p. 389.
- ⁶M. Muluaka, Y. Uchikawa, M. Kotani, and Y. Yamashita, *Frontiers Med. Biol. Eng.* **8**, 35 (1997).
- ⁷W. Penfield and T. Rasmussen, *The Cerebral Cortex of Man* (Macmillan, New York, 1950).
- ⁸Y. C. Okada, R. Tanenbaum, S. J. Williamson, and L. Kaufman, *Exp. Brain Res.* **56**, 197 (1984).

Measurements of biomagnetic fields using a high-resolution dc superconducting quantum interference device magnetometer

K. Iramina,^{a)} B. Hong, S. Uchida, K. Goto, and S. Ueno

Department of Biomedical Engineering, Graduate School of Medicine, University of Tokyo,
Tokyo 113-0033, Japan

S. Nakayama

Seiko Instruments Inc., Matsudo, Chiba 271, Japan

We have developed a multichannel high-resolution superconducting quantum interference device magnetometer for measuring biomagnetic fields produced by small animals. We measured the magnetocardiogram produced by a rat. Topographies of the *P* wave, *QRS* wave, and *T* wave of the rat magnetocardiogram were obtained. We also measured the magnetoretinogram, visually evoked magnetic fields, and auditory evoked magnetic fields of the rat. The signals of the magnetoretinogram appeared at 60 ms latency and the field intensities were about 0.6 pT. It was not possible to obtain the clear visually evoked fields because those signals were hidden behind the magnetoretinogram. It was possible to obtain auditory evoked magnetic fields of the rat. The significant differences of the wave forms were observed in both sides of the right ear, which are separated by 15 mm. Our system has adequate spatial resolution for measurement of the magnetocardiogram and auditory evoked magnetic fields produced by small animals. © 1998 American Institute of Physics. [S0021-8979(98)39211-7]

INTRODUCTION

A dc superconducting quantum interference device (SQUID) system is desired for the study of biomagnetism. It is especially necessary for use in medical diagnosis and the study of higher brain functions. The main aim of measurement of biomagnetic fields is to estimate the sources of electrical activity in the brain. Many studies of functional organization of the human brain have been made through a technique using the magnetoencephalogram (MEG). Most of these investigations were concerned with estimation of localization in evoked magnetic fields. Sources of these evoked fields are assumed as a single current dipole. It is sufficient to assume a single current dipole as the source within the limits of sources in the primary sensory cortex of the brain. However, concerning higher brain functions such as memory, perception, and learning, a single dipole is not sufficient as the electrical activities of the brain are complex. It is important to consider spatially distributed multiple dipoles or spreading dipoles as the sources of magnetic fields. But, it is difficult to solve the inverse problem using this type of source model. Knowledge about the nature of the generator of magnetic fields is required for advancing source estimation. Besides, for the advancement of clinical applications of the MEG and magnetocardiogram (MCG), it is necessary to investigate the relationship between diseases and induced biomagnetic fields using an experimental animal model. Typical SQUID magnetometers are constructed with 15–25 mm diameter pickup coils and the distance between each coil is 30–40 mm. This type of coil configuration is designed for the human brain. Because of limited spatial resolution, this configuration cannot be used for the MEG measurements of

small animals such as the rat. A high-resolution magnetometer is needed to measure the biomagnetic fields produced by small animals in conjunction with more invasive physiologic measurements.

Buchanan *et al.*¹ and Wikswo *et al.*² developed a high-resolution SQUID magnetometer, called a micro-SQUID, which was designed for the experiments on *in vitro* preparations such as isolated nerves and muscles and slices of brain tissue. Measurement of *in vitro* preparations would benefit from 1 to 2 mm resolution. Using the micro-SQUID, magnetic evoked fields from an *in vivo* preparation were recorded by Okada *et al.*³ and Kyuhou and Okada.⁴ Experiments on small animals such as the rat or the cat would benefit from 3 to 5 mm resolution. In this study, we have designed a high-resolution SQUID magnetometer for measurement of the biomagnetic fields produced by small animals.

We measured the MCG produced by a rat. The magnetoretinogram (MRG) of the rat, which is produced by the retina in response to photic stimulation and the auditory evoked magnetic fields, were also recorded. Our system has adequate spatial resolution for the measurement of biomagnetic fields produced by small animals.

SYSTEM

The system consists of a 12-channel SQUID gradiometer installed in a five-layer magnetically shielded room. A pickup coil with a diameter of 5 mm was selected. Twelve pickup coils were located on a 7.5 mm grid. Each pickup coil consisted of a first-order gradiometer, which has a 15 mm base line as shown in Fig. 1. The distance between the pickup coil and the outside surface of the dewar was 5 mm. The field sensitivity was $100 \text{ fT}/\sqrt{\text{Hz}}$ in the frequency of the white-noise region. While the absolute sensitivity of this sys-

^{a)}Electronic mail: iramina@medes.m.u-tokyo.ac.jp

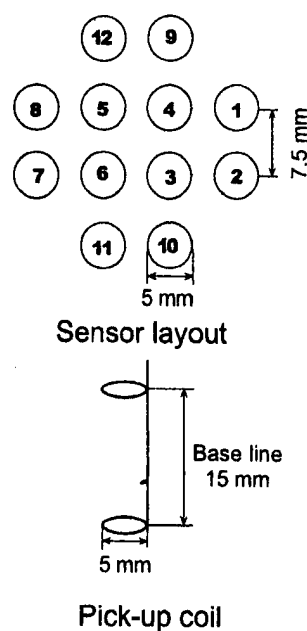


FIG. 1. Sensor layout and pick-up coil of a 12-channel high-resolution SQUID system.

tem is lower than in a conventional SQUID system, the relative sensitivity compares favorably to the conventional SQUID because of the reduced coil-to-source spacing.

MEASUREMENT OF MAGNETOCARDIOGRAM OF THE RAT

Four adult rats, ranging in weight from 0.2 to 0.3 kg, were used in the study. They were anesthetized with urethane (0.4 mg/100 g) intraperitoneally. Figure 2 shows the MCG signals and electrocardiogram (ECG) signal recorded simultaneously from a rat. The MCG signals are filtered from 0.5 to 100 Hz and averaged 100 times at the *QRS* wave of the ECG as the trigger. Significant differences are observed in the wave-form shape between the points separated by only 15 mm. We measured the MCG at 63 points over the breast of the rat and made isocountour maps at several time points as shown in Fig. 3. Each pattern shows the dipole pattern.

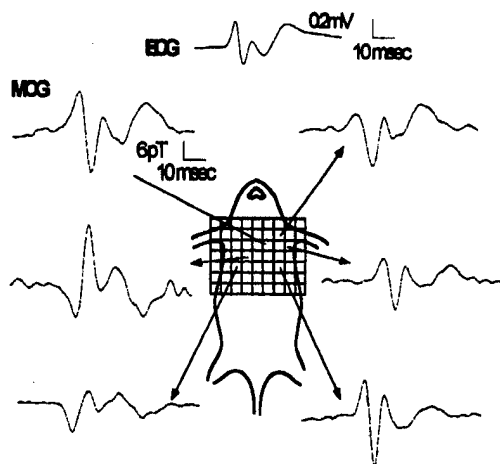


FIG. 2. MCGs and ECG of a rat (100 average). The MCGs were measured at 63 points on the grid as shown in the figure.

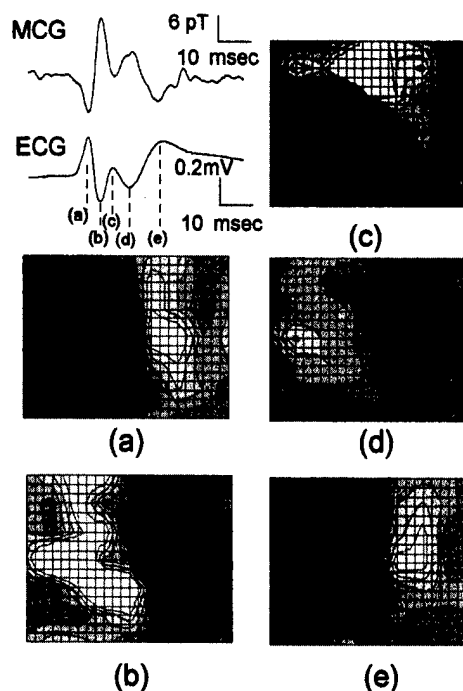


FIG. 3. Topographies of the MCGs during the (a), (b), (c), (d), and (e) periods, which are shown in the wave form of the ECG.

MEASUREMENT OF VISUALLY EVOKED MAGNETIC FIELDS

Three adult rats, ranging in weight from 0.25 to 0.3 kg, were used in the study. They were anesthetized with urethane (0.4 mg/100 g) intraperitoneally. Visual stimuli were presented unilaterally with a strobe light. Concentrated points of light were delivered to the right eye through an optical fiber. The ends of the optical fiber was placed 0.1 m from the eye. The left eye was covered by an eye mask. In order to investigate the effect of the magnetic fields produced from the retina, the electroretinogram (ERG) was measured using a contact-lens-type electrode. Figure 4 shows visually evoked

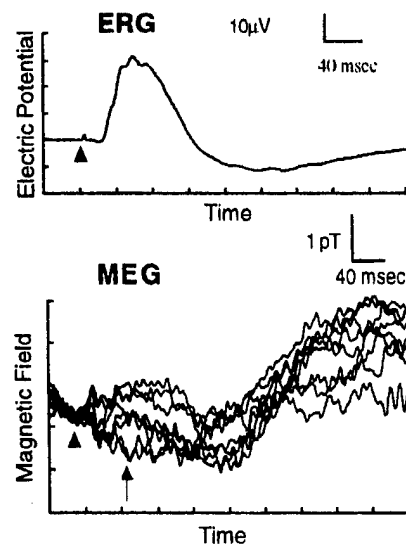


FIG. 4. Visual evoked magnetic fields of the rat. Measurement points are shown by the black dot in Fig. 5.

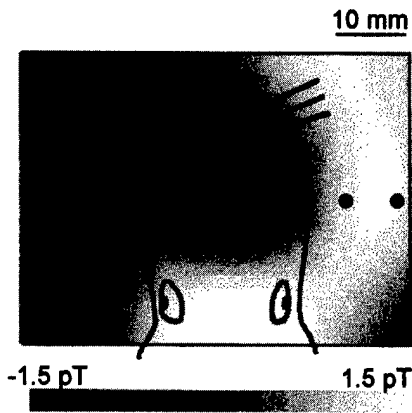


FIG. 5. Topography of the VEF and the estimated dipole.

fields (VEFs), which were measured at six points along a straight line over both eyes, and the ERG of the right eye of the rat. In the ERG, the negative peak appeared at 60 ms and the ERG signal changed slowly. The VEF signal had a slow component similar to the ERG signal. The VEF and MRG were superposed together because the ERG of the rat was a large signal and the eyes and the brain were close together. It is difficult to discriminate the VEF signals from the MRG signals using this SQUID magnetometer. The topography at 60 ms latency is obtained as shown in Fig. 5. From this topography one dipole, which was located at the point of right eyeball, was estimated as the source of the ERG.

MEASUREMENT OF AUDITORY EVOKED MAGNETIC FIELDS

Three adult rats, ranging in weight from 0.25 to 0.3 kg, were used in the study. They were anesthetized with urethane (0.4 mg/100 g) intraperitoneally. We used tone bursts of 3 kHz with 10 ms duration as the auditory stimuli. The stimuli were presented to the left ear of the rat through a plastic tube. Figure 6 shows the superimposed superposition of all ten wave forms of the auditory evoked magnetic fields. Magnetic signals were filtered from 1 to 100 Hz and averaged 4000 times. The small peak of the magnetic fields appeared at a

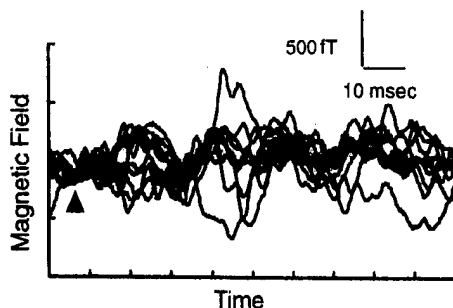


FIG. 6. The superposition of ten curves of evoked magnetic fields in the stimulation of tone bursts to the left ear of the rat.

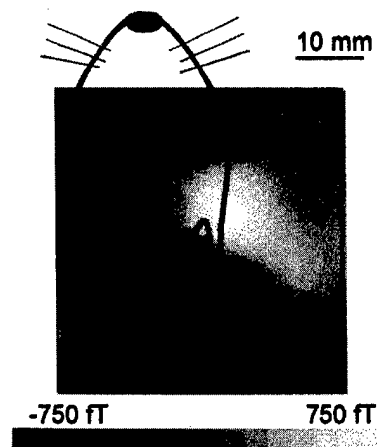


FIG. 7. Topography of the peak at 34 ms latency and the estimated dipole.

latency about 10 ms and the large peak appeared at a latency 34 ms. Figure 7 shows the isocontour map over the head of the rat at 34 ms latency. The peak of the emerging flux is anterior to the right ear, and the peak of the entering flux is posterior to the right ear. The source of this peak is estimated at a point, which is 3 mm lateral from the meatus acusticus externus.

DISCUSSION

In this study, we were able to measure the MCG and the MEG of the rat with adequate spatial resolution. Animal experiments using a high-resolution SQUID in conjunction with more invasive physiological measurements, may contribute to the further understanding of the physiological basis of the MEG, and the advancement of solving the inverse problem. We used normal healthy rats in this study. However, in animal experiments it is possible to make abnormal rat models with diseases such as myocardial infarction or cerebral infarction. Using the abnormal rat model, we can investigate the relationships between the disease and biomagnetic fields with the possibilities of making diagnoses of abnormal activity. Hence, the MCG and MEG may become useful noninvasive diagnostic procedures for the investigation of abnormal cardiac or brain activity.

ACKNOWLEDGMENTS

The authors thank Professor Kaga for providing useful advice for the measurement of the auditory and visually evoked magnetic fields.

¹D. S. Buchanan, D. B. Crum, D. Cox, and J. P. Wikswo, in *Biomagnetism*, edited by S. J. Williamson, M. Hoke, G. Stroink, and M. Kotani (Plenum, New York, 1989), pp. 677–679.

²J. P. Wikswo, R. N. Friedman, A. W. Kilroy, J. M. Egwratt, and D. S. Buchanan, in *Biomagnetism*, edited by S. J. Williamson, M. Hoke, G. Stroink, and M. Kotani (Plenum, New York, 1989), pp. 681–684.

³Y. C. Okada, S. Kyuhou, A. Lähteenmäki, and C. Xu, in *Biomagnetism: Clinical Aspects*, edited by M. Hoke, Y. Okada, and G. Romani (Elsevier, Amsterdam, The Netherlands, 1992), pp. 375–383.

⁴S. Kyuhou and Y. Okada, *J. Neurophysiol.* **70**, 2665 (1993).

Crystalline Soft Magnetic Materials

R. F. Krause, Chairman

Magnetic properties and ordering in C-coated $\text{Fe}_x\text{Co}_{1-x}$ alloy nanocrystals

Z. Turgut, J. H. Scott, M. Q. Huang, S. A. Majetich, and M. E. McHenry
*Department of Materials Science and Engineering, Carnegie Mellon University, Pittsburgh,
Pennsylvania 15213*

C-coated $\text{Fe}_x\text{Co}_{1-x}$ ($x=0.50, 0.45, 0.40, 0.35, 0.30, 0.25$) nanoparticles were produced using a rf plasma torch. The only C source was acetylene used as a carrier gas. Structural determination by x-ray diffraction indicated a single disordered bcc α -FeCo phase along with graphitic C for all compositions. A Scherrer analysis of the peak widths revealed particles to have an average diameter of 50 nm. A broad log-normal size distribution was found from transmission electron microscopy observations. Magnetic hysteresis loops have been measured to temperatures exceeding 1050 K and revealed relatively high room temperature coercivities (200–400 Oe), with a strong compositional variation similar to that observed in bulk alloys. Larger coercivities are consistent with particles near the monodomain size for these alloys. The temperature dependence of the magnetization revealed the effects of atomic ordering. The variation of the saturation magnetization as a function of temperature showed a discontinuity near the bulk order–disorder ($\alpha \rightarrow \alpha'$) transformation temperature, as well as loss of magnetization at the $\alpha \rightarrow \gamma$ structural phase transition temperature. Other features of $M(T)$ near 500–550 °C are consistent with prior observations of a “550 °C structural anomaly” which has been observed in bulk alloys with less than perfect order. © 1998 American Institute of Physics. [S0021-8979(98)28711-1]

I. INTRODUCTION

The technical importance of FeCo alloys arises from their high saturation magnetization and Curie temperature which cannot be matched by any other alloy system. The high saturation magnetization of up to 2.4 and the Curie temperature about 950 °C are characteristics for the FeCo alloys with compositions 25%–50% Co. Alloys near equiatomic compositions are particularly soft and exhibit large permeabilities¹ which can be attributed to a zero crossing of the first order magnetic anisotropy constant, K_1 near this composition. We have described our initial attempts to produce FeCo[C] nanoparticles as precursors for the eventual production of a dense compacted nanocrystalline soft alloy.²

FeCo alloys in the composition range of about 30%–70% Co undergo a continuous (i.e., higher than first order) order–disorder phase transformation at a maximum temperature of 730 °C at the equiatomic composition. The change in the structure from the disordered α -bcc(A1) to the ordered α' -CsCl(B2) appears as a λ type anomaly in the heat temperature spectra. The composition dependence of this order–disorder transformation of bulk FeCo alloys is well established by specific heat measurements³ and neutron diffraction.⁴

It has been reported by many workers that in the specific heat curve of the ordered FeCo superlattice alloy, there is a peak of unknown origin at about 550 °C in addition to that for the order–disorder transformation which occurs at higher temperatures. A complete explanation of this so called 550 °C anomaly in bulk FeCo alloy which has also been observed in discontinuities in the T dependence of the electrical resistance, saturation magnetization, specific heat hardness, and thermo electromotive force has not been given yet.⁵

It has, however, been concluded that the 550 °C anomaly does not exist in equilibrium and is rather associated with metastable disordered FeCo.⁶

In previously reported work⁷ we have given magnetic evidence for the order–disorder transformation in a nanocrystalline $\text{Fe}_{50}\text{Co}_{50}$ alloy produced in carbon-arc. The compositional dependence of this structural transformation has not been studied until now in nanocrystalline alloy particles. Here we report our success to synthesis this nanocrystalline powders by a rf plasma torch route and our investigation of the compositional dependence of the ordering temperature for $\text{Fe}_x\text{Co}_{1-x}[\text{C}]$ ($x=0.55, 0.60, 0.65, 0.70$, and 0.75) nanocrystalline alloy compositions. We briefly discuss the existence of 550 °C anomaly in our nanocrystalline systems and results of measurements of the ordering transformation kinetics.

II. EXPERIMENT

We have employed a radio frequency plasma system (Fig. 1) consisting of a TEKNA PL 50 type plasma torch head and a gas expansion-reaction vessel connected to a filtering unit. A 50 kW, 3 MHz power supply (Ilepel) was used. Argon gas flowing at 40 standard liters per minute (slpm) was used as plasma gas and the sheath gas was consisted of 80 slpm Ar mixed with 9 slpm of hydrogen. A 6–10 μm Fe powder and 1.6 μm Co powder mixture was used as a starting feedstock and injected axially into the plasma stream through an injection probe with the aid of a screw driven powder feeder and 3 slpm Ar as a carrier gas. Acetylene was introduced into the carrier gas and powder mixture between powder feeder and injection probe as a carbon source for coating purposes.

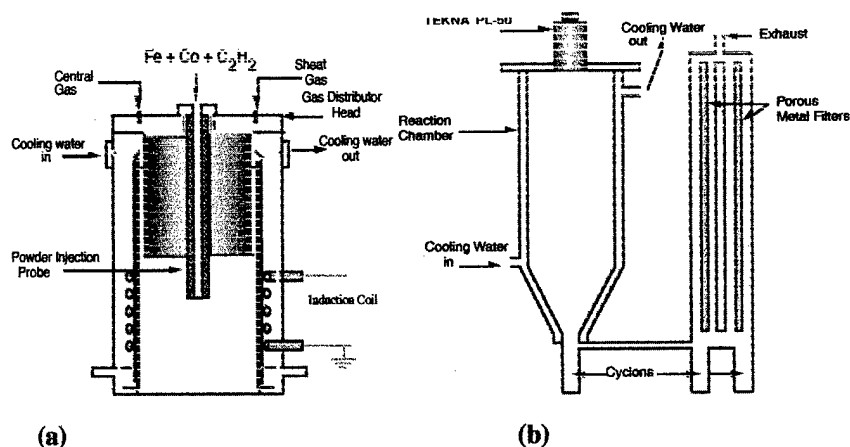


FIG. 1. (a) A detailed schematic representation of plasma torch head. (b) The rf plasma torch reaction with reaction chamber and porous metal filters.

X-ray diffraction characterization of the as-synthesized nanoparticles was carried out on a Rikagu θ - θ diffractometer using Cu $K\alpha$ radiation. Transmission electron microscopy (TEM) on a JEOL 4000 EX was used to examine the coating morphology. A high temperature vibrating-sample magnetometer (with a Lake Shore Model 7300 controller) was employed for the magnetic measurements up to 1000 °C.

III. RESULTS AND DISCUSSION

We have only observed disordered bcc (α -Fe), fcc Co, and graphitic carbon by x-ray diffraction with no observation of carbides, oxides, or the hcp ϵ -Co phase. A Scherrer analysis of the peak broadening indicated an average particle diameter of $d \sim 50$ nm which is in reasonable agreement with TEM observations of particle size with a Gaussian type size distribution. High temperature magnetic measurements revealed that the bcc (α -Fe) structure is in disordered metastable state as produced.

Figure 2(a) shows saturation magnetization as a function of composition before and after annealing at 800 °C. The highest M_s value is observed at composition 70% Fe as predicted by the Slatter-Pauling curve. After annealing reordering of the initially disordered particles results in an increase of the saturation magnetization as was detected by neutron

diffraction studies. Figure 2(b) shows coercivity as a function of composition. The initial permeability measurements for bulk Fe give lower values at compositions close to the 70% Fe-30% Co which can be thought because of the higher coercivities at this composition.

Figure 3(a) illustrates the thermomagnetic data at $H = 500$ Oe for various $\text{Fe}_x\text{Co}_{1-x}[\text{C}]$ alloy nanoparticles. Heating rate was 4 °C/min for these series of experiments. It is surprising that no compositional dependence of the reordering temperature was observed. It is possible to argue that, nanocrystalline materials are composed of randomly arranged surface atoms and increased temperature leads to the relaxation of interfacial atoms which makes the surface of the particles more compact and surface atoms more ordered, so that magnetization increases. But the differential thermal analysis results in a previous work⁷ convinced us that the peak in the heating branch corresponds to the reordering phenomena. From this it may be suggested that contribution of reordering to an increase in magnetization is greater than that of surface relaxation. No compositional dependence, on the other hand, can be related to a faster kinetic nature of the nanocrystalline particles. In nanocrystalline particles an enormous enhancement of diffusivity has been reported.⁸

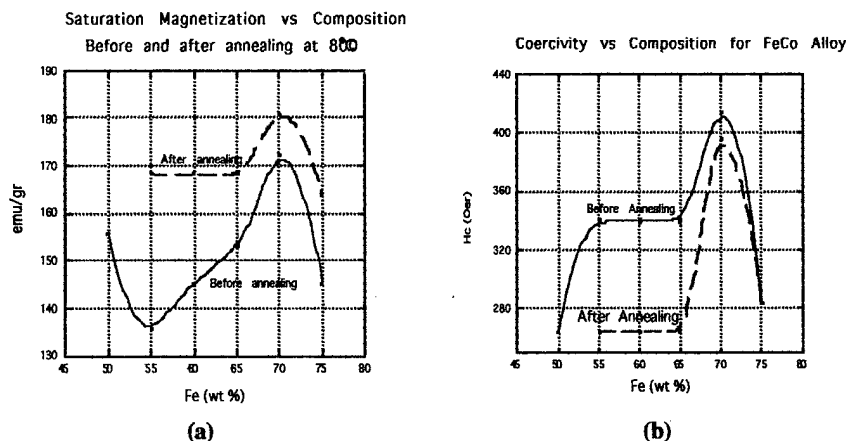


FIG. 2. (a) Composition dependence of saturation magnetization for as-produced disordered and annealed-ordered nanocrystals. (b) Coercivity change as a function of composition for the same nanocrystals.

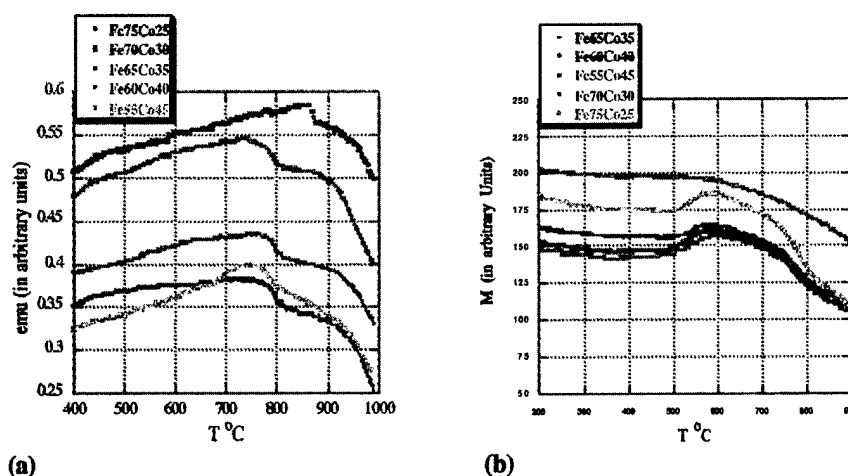


FIG. 3. (a) Magnetization vs temperature data taken at 500 Oe and 4 °C/min. heating rate for various $\text{Fe}_x\text{Co}_{1-x}[\text{C}]$ nanoparticles. (b) Same response taken at 10 kOe and 2 °C/min heating rate.

Figure 3(b) shows high field thermomagnetic data for $\text{Fe}_x\text{Co}_{1-x}[\text{C}]$ alloy nanocrystals where $H=10$ kOe with a heating rate of 2 °C/min. Again no compositional dependence of the reordering temperature was observed for the saturation magnetization. Another observation was that the presence of 550 °C anomaly which occurs as a decrease in saturation magnetization with increasing temperatures up to 510 °C. The $\text{Fe}_{70}\text{Co}_{30}$ composition leaves the characteristics of other compositions with the presence of very small anomalous effect of temperature. This result is in good agreement with Velisek,⁹ showed that based on the calorimetric studies, while $\text{Fe}_{50}\text{Co}_{50}$ composition shows 550 °C anomaly accompanied with the change of specific heat at this temperature, Fe_3Co composition shows a small degree of anomaly at this temperature. Our measurements on annealed samples showed that while the anomaly is observed in compositions (rather than $\text{Fe}_{70}\text{Co}_{30}$ composition) not depending on the initial structure is ordered or metastable disordered, initially ordered $\text{Fe}_{70}\text{Co}_{30}$ composition revealed no anomaly. In nanocrystalline materials the anomaly occurs at temperatures well below 550 °C which can be concluded from the fact of high diffusivity in this particles.

A large amount of work based on resistivity measurements concluded that the 550 °C anomaly does not exist in equilibrium. Yokoyama⁶ has reported that it takes about 15 h

for initially disordered FeCo bulk sample to reach the equilibrium at temperature 475 °C. Figure 4 shows the time response of magnetization of $\text{Fe}_{50}\text{Co}_{50}$ nanocrystalline alloy at 400 °C and 500 Oe. For a nanocrystalline material it takes about 1 h to reach the equilibrium at a given temperature even at relatively lower temperatures. As the temperature is further increased faster time response is observed, i.e., 30 min at temperature 650 °C. Having this high diffusivity in nanocrystalline system, we should not have observed the 550 °C anomaly based on the conclusion mentioned earlier. This result may lead to reconsideration of Goman'kovs'¹⁰ suggestion which propose that anomaly arises by the appearance of magnetic dispersion in the superstructural reflection caused by the difference in partial magnetic moments at temperatures above the anomaly temperature.

IV. CONCLUSION

We have successfully produced $\text{Fe}_x\text{Co}_{1-x}[\text{C}]$ nanoparticles with a disordered bcc structure by plasma torch synthesis. Reordering of this as-quenched nanoparticles was observed with thermomagnetic measurements. No compositional dependence of this reordering temperature was observed due to the fact that high diffusivity in this particle dominates over the compositional effect. The so-called 550 °C anomaly was observed as a decrease in saturation magnetization even with the lower heating rates, i.e., 2 °C/min.

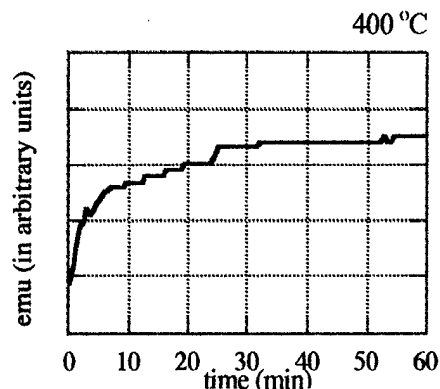


FIG. 4. Time-dependent response of low field magnetization at 400 °C where $H=500$ Oe.

- ¹K. Gallagher, F. Johnson, E. Kirkpatrick, J. H. Scott, S. Majetich, and M. E. McHenry, *Intermag* (1996).
- ²R. Boll, *Soft Magnetic Metals and Alloys* (1994), Vol. 3b, Chap. 14, p. 339.
- ³H. Asano, Y. Bando, N. Nakanishi, and S. Kachi, *Trans JIM* **8**, 180 (1967).
- ⁴J. A. Oyedele and M. F. Collins, *Phys. Rev. B* **16**, 3208 (1997).
- ⁵T. Nishizawa and K. Ishida, *Bull. Alloy Phase Diagrams* **5**, (1984).
- ⁶T. Yokoyama, T. Takezawa, and Y. Higashida, *Trans. JIM*, **2**, 30 (1971).
- ⁷Z. Turgut, M.-Q. Huang, K. Gallagher, S. A. Majetich, and M. E. McHenry, *J. Appl. Phys.* **81**, 4039 (1997).
- ⁸J. Horwath, R. Birringer, and H. Gleiter, *Solid State Commun.* **62**, 319 (1987).
- ⁹J. Velisek, *Czech. J. Phys. B* **20**, 250 (1970).
- ¹⁰V. I. Goman'kov, D. P. Litvin, A. A. Loshmanov, B. G. Lyashchenko, and I. M. Puzei, *Sov. Phys. Crystallogr.* **637** (1962).

Soft magnetic properties of LaCo_{13} and $\text{La}(\text{Co}, \text{Fe})_{13}$ alloys

M. Q. Huang,^{a)} W. E. Wallace, and M. E. McHenry

Department of Materials Science and Engineering, Carnegie Mellon University, Pittsburgh, Pennsylvania, 15213

Q. Chen and B. M. Ma

Rhone-Poulenc, Rare Earths and Gallium, CN 7500, Cranbury, New Jersey, 08512

LaCo_{13} and $\text{La}(\text{Co}, \text{Fe})_{13}$ alloys have been prepared and studied as high temperature, high performance soft magnetic materials. The dc magnetic properties have been measured over a temperature range of 10–1273 K in fields of 0 to 5 T. Data obtained show that the dc magnetic properties (H_c, K_1) of the $\text{La}(\text{Co}, \text{Fe})_{13}$ bulk alloys are comparable with Fe bulk alloy and $T_c = 1021\text{--}1297$ K are higher than that of Fe and Hipercor; ac magnetic properties are first time reported in a bulk LaCo_{13} alloy, showing a reasonably higher power loss than that of commercial Hipercor alloy. The ac magnetic properties can be improved by making LaCo_{13} alloys as laminated thin sheets. © 1998 American Institute of Physics. [S0021-8979(98)29311-X]

I. INTRODUCTION

LaCo_{13} has a high content of the 3d element Co which leads to a large magnetization (1.3 T) and a high T_c (1297 K).¹ Because of these properties, this alloy has attracted attention in regard to high temperature applications. It had been studied in this laboratory some years ago as a hard magnetic material. Results were negative in that regard.² In the present investigation, LaCo_{13} -based alloys have been studied as soft magnetic materials. Their cubic structure leads to the low anisotropy and coercivity, which is required by a soft magnetic material. This article provides information in regard to the basic soft magnetic properties, both dc and ac, for LaCo_{13} -based alloy systems. LaCo_{13} and $\text{La}(\text{Co}, \text{Fe})_{13}$ alloys have been synthesized and characterized in a bulk form. The dc magnetic properties have been measured over the temperature range of 10 to 1273 K in fields from 0 to 5 T. The ac magnetic properties are established at room temperature in the frequency range of 50 Hz to 100 kHz. The magnetocrystalline anisotropy constant K_1 has been estimated based on the law of approach to saturation.

II. EXPERIMENTAL DETAILS

The alloys were prepared by arc melting under argon, after which they were heat treated at 1273 K for about one week. X-ray diffraction (XRD) with Cu radiation was used to determine crystal structure and lattice parameters. The dc magnetic properties (M , T_c , H_c , and K_1) were established using a vibrating sample magnetometer (VSM) and a superconducting quantum interference device magnetometer (SQUID) with a chunk sample. The ac magnetic properties were established using a hysteresisgraph (Walker AMH-401) with a toroidal sample which was cut from a bulk ingot. The dimensions of the toroidal sample are o.d. (1.5 cm), i.d. (0.9 cm), path (3.77 cm), and area ($0.3 \times 0.3 \text{ cm}^2$).

^{a)}Electronic mail: mh8f@andrew.emu.edu

III. RESULTS AND DISCUSSIONS

A. Structure and dc magnetic properties

The structure and dc magnetic properties M_s , H_c , and T_c are given in Table I and Fig. 1. The results show that the LaCo_{13} sample is single phase with the fcc NaZn_{13} structure. It exhibits no phase transition between RT and 1300 K, except a magnetic transition (ferro to para) at the Curie temperature (1297 K). The coercivity, H_c , for a polycrystal bulk sample of the LaCo_{13} alloy is ~ 8 Oe at RT and ~ 10 Oe at 10 K. It is comparable with a pure Fe sample, the H_c of which is around 5 Oe for a bulk material. Above room temperature, H_c of the LaCo_{13} alloy decreases almost linearly with increasing temperature. At 800 °C, it is about 30% reduced from that at room temperature (see Fig. 1). This behavior can be ascribed to the decrease of magnetocrystalline anisotropy energy with increasing temperature. The moment of LaCo_{13} alloy at RT, 130 emu/g, is lower than that of Fe and Fe–Co alloys. However, the moment can be enhanced by partial replacement of Co with Fe. As shown in Table I, a sample with $\sim 40\%$ Fe substitution, has a moment of 153 emu/g at RT and 159 emu/g at 10 K. This alloy retains the fcc structure of the LaCo_{13} alloy and shows a similar low H_c , around ~ 8 Oe at RT and ~ 10 Oe at 10 K.

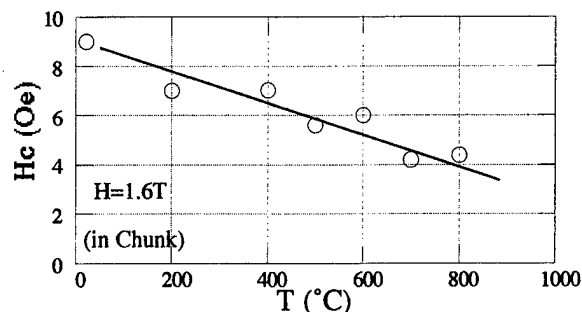
B. Magnetocrystalline anisotropy constant K_1

Making use of the law of approach to saturation for polycrystalline material with crystals oriented at random and also in cubic structure,³

TABLE I. Structure and dc magnetic Properties of LaCo_{13} -type alloys.

Compound	Structure	a (Å)	M (emu/g) ^a		H_c (Oe)		T_c (K)
			RT	10 K	RT	10 K	
LaCo_{13}	NaZn_{13}	11.340	130	135	~ 8	~ 10	1297
$\text{La}(\text{Co}_{0.6}\text{Fe}_{0.4})_{13}$	NaZn_{13}	11.469	153	159	~ 8	~ 10	1021

^{a)}Measured at $H = 5$ T.

FIG. 1. The dc-coercivity H_c vs temperature T for LaCo_{13} ($H=1.6$ T).

$$I_s = I_s \left(1 - \frac{a}{H} - \frac{b}{H^2} - \dots \right) + \chi_0 H,$$

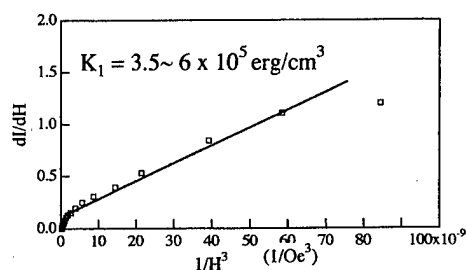
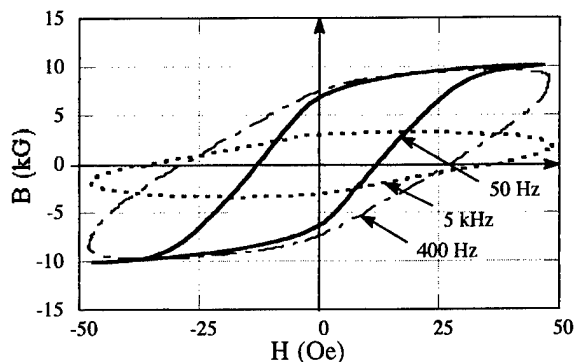
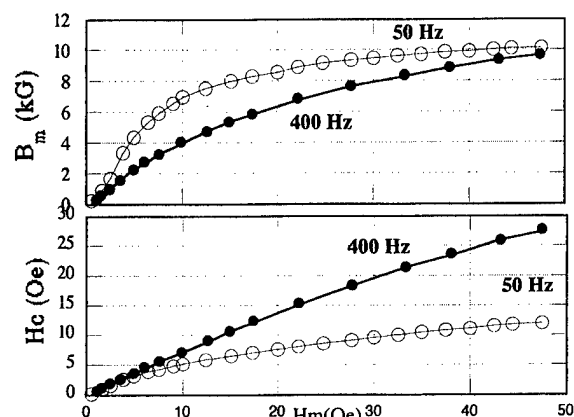
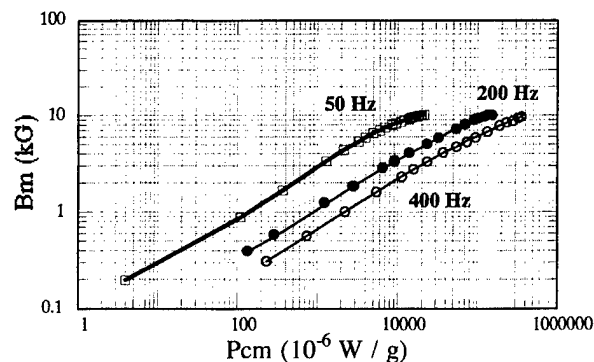
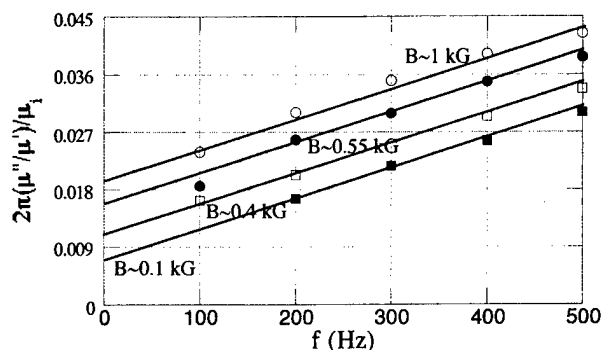
$$\frac{dI}{dH} = I_s \left(\frac{a}{H^2} + \frac{2b}{H^3} + \dots \right) + \chi_0, b = \frac{8}{105} \frac{K_1}{I_s^2}$$

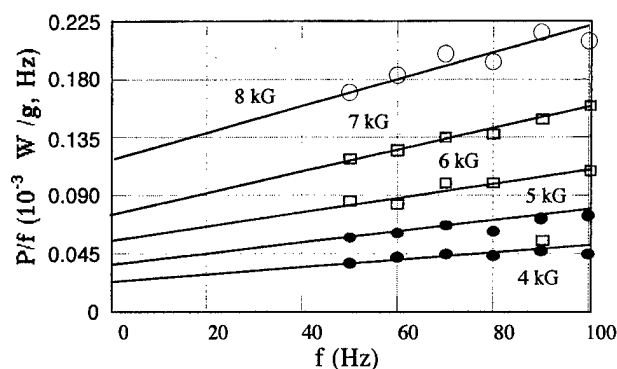
we have estimated a magnetocrystalline anisotropy constant K_1 for a LaCo_{13} sample. The sample is in a cube shape. Considering the effect of a demagnetizing field created by the magnetic poles of this cube sample on our measurement, a demagnetizing factor $N=0.27$ has been used. It is taken from Bozorth's demagnetizing factor calculation data for a rod-shape sample with length/diameter=1.⁴ From experiment results of moment I (G) vs field H (Oe), we can obtain dI/dH vs $1/H^3$ (see Fig. 2). Then, from the slope of this curve, $2bI_s = 16K_1^2/105I_s$, we have estimated a value of $K_1 \sim 3.5\text{--}6 \times 10^5$ erg/cm³, which is comparable with K_1 of Fe, 4.5×10^5 erg/cm³.

C. The ac magnetic properties

The information about the ac magnetic properties of the LaCo_{13} toroidal sample are given in Figs. 3–8.

Figure 3 shows typical ac-(BH) loops, measured at different frequencies (50 Hz–5 kHz). Maximum induction B_m , coercivity H_c vs maximum field H_m at 50–400 Hz and total core loss per unit mass P_{cm} vs B_m are given in Figs. 4 and 5. The B_m is around 10 kG at 50 and 400 Hz. The H_c increases from ~ 12 to ~ 27 Oe when frequency increases from 50 to 400 Hz. The total power loss at 400 Hz is around 0.2 W/g for $B_m = 10$ kG (see Fig. 5). It is much higher than that of a current commercial Hiperco 50 sample, which is 0.01 W/g for $B_m = 10$ kG at 400 Hz.⁵ This high power loss was expected, especially due to the eddy current loss. As we know,^{4,6} the macroscopic eddy current loss is proportional to

FIG. 2. dI/dH vs $1/H^3$ for LaCo_{13} . (I -moment per volume).FIG. 3. ac-BH loops measured at 50 Hz–5 kHz for LaCo_{13} .FIG. 4. B_m , H_c vs H_m at 50 and 400 Hz for LaCo_{13} .FIG. 5. P_{cm} (core loss per gram) vs B_m (flux density) at 50–400 Hz for LaCo_{13} .FIG. 6. $2\pi(\mu''/\mu')/\mu_i$ (specific loss factor) vs f at B_m of 0.1–1 kG.

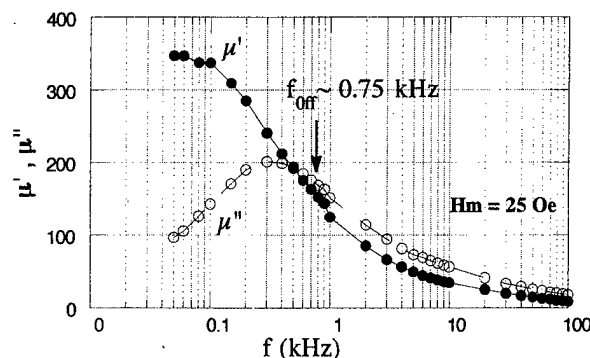
FIG. 7. P_{cm}/f (core loss per cycle) vs f (frequency) at $B_m=4-8$ kG.

$(fBr)^2/\rho$, where f is the frequency, B is the induction, ρ is the resistivity, and r is the radius of the cylinder or the thickness of the plate of the materials. Comparing the dimensions of the LaCo_{13} sample with the Hiperco sample, which is made of laminated thin sheets and the thickness of the each sheet is ~ 0.015 cm, the $r \sim \sqrt{(0.09)\text{cm}^2/\pi} \sim 0.17$ cm for the LaCo_{13} sample is almost 11 times larger than that of the Hiperco sample. By this factor, the eddy-current loss for the LaCo_{13} sample could be 100 times higher than that of the Hiperco sample. Except for the eddy current loss, the total power loss also involves a hysteresis loss and a residual loss.⁴ By using classic methods,⁴ we can analyze and separate these three type of losses.

1. Power losses analysis

a. *Losses in low inductions:* ($B_m=0.1-1$ kG, $f \leq 500$ Hz): Legg⁷ gave an empirical equation expressing the losses in low fields: $2\pi(\mu''/\mu')/\mu_i = ef + aB + c$, where $(\mu''/\mu')/\mu_i$ is the specific loss factor, μ' is the real part, and μ'' is the imaginary part of the complex permeability, μ_i is the initial permeability, 167, which was obtained from dc measurement by using Walker dc hysteresisgraphy in a cylinder sample at this lab, e is the eddy-current resistance coefficient, a is the hysteresis resistance constant, and c is residual loss constant. We have measured the frequency dependence of $2\pi(\mu''/\mu')/\mu_i$ at different B_m , 0.1–1 kG (in Fig. 6). The values of e , a , and c can be established as follows: (1) $e \sim 4.8 \times 10^{-5}$ s, which is around four orders of magnitude higher than that of Hiperco 80 alloys (10^{-9}).⁸ (2) $a \sim 1.3 \times 10^{-5}$ G⁻¹, which is a same order of magnitude with that of the Hiperco 80 (10^{-5}). (3) $c \sim 5600 \times 10^{-6}$, which is a same order of magnitude as ferrite materials.⁸

b. *Losses at intermediate and high inductions:* ($B_m=0.3-0.8$ kG, and $f \leq 100$ Hz). Using the Steinmetz equation for hysteresis losses,⁴ the total power losses are as follows: $P = \eta B^{1.6}f + eB^2f^2$, or P/f (power losses per cycle) $= \eta B^{1.6} + eB^2f$, where $\eta B^{1.6}$ is the hysteresis loss per cycle and eB^2f is the eddy current loss per cycle. We have measured the frequency dependence of core loss per cycle at $B_m=4-8$ kG and plotted P/f vs f for different B_m , (in Fig. 7). From these experimental curves, one can established η and e . The results are: $e \sim 1.2 \times 10^{-6}$ s, and $\eta \sim 6 \times 10^{-3}$ Oe. Using these two constants, we can analyze the relative loss of eB^2f^2 and $\eta B^{1.6}f$. For example, to obtain

FIG. 8. Frequency dependence of the real (μ') and imaginary (μ'') parts of the complex permeability at $H_m \sim 25$ Oe.

$B_m \sim 8$ kG at $f \sim 400$ Hz for the LaCo_{13} sample, the eddy current loss, eB^2f^2 , is 79% of the total loss, which dominates the power loss, and the hysteresis loss is only 21%. Usually, η is related to coercivity H_c of materials, i.e., $\eta \sim 10^{-3} H_c$. Our experimental results, H_c , measured at $B_m \sim 8$ kG and $f \leq 100$ Hz, are 7–8 Oe, which agree with the above estimation.

2. Magnetic spectrum (μ' , μ'' vs f)

At the ac magnetic field, the magnetic induction B is generally delayed by the phase angle δ from the magnetic field H due to various types of power losses and resonances. $B = \mu H = (\mu' - j\mu'')H$, where μ' and μ'' express the real and imaginary parts of the complex permeability μ , respectively. The physical mechanism of this lag due to different types of resonances can be studied by analyzing a magnetic spectrum (μ' and μ'' vs f at a low ac field). Figure 8 shows a magnetic spectrum of the LaCo_{13} sample, which was measured at a lower field (~ 25 Oe). This curve shows a relaxation type of magnetic spectrum.⁹ At ~ 400 Hz, the μ' drops and μ'' increases rapidly and reaches a maximum, as well as the energy loss of the sample. It can be suggested that a resonance of domain wall motion occurs at ~ 400 Hz. A maximum application frequency (cutoff f) for the LaCo_{13} sample is around ~ 750 Hz, where μ' drops to \sim half of μ_{\max} , and it is lower than that of the Hiperco alloys (~ 1 kHz).

ACKNOWLEDGMENT

This work was supported by the Air Force Office of Scientific Research, AirForce Materiel Command, USAF, under Grant No. F49620-96-1-0454.

¹K. H. J. Bushow, Rep. Prog. Phys. **40**, 1179 (1977).

²M. Q. Huang, W. E. Wallace, R. T. Obermyer, S. Simizu, M. Mchenry, and S. G. Sankar, J. Appl. Phys. **79**, 5949 (1996).

³S. Chikazumi, *Physics of Ferromagnetism* (1964), p. 274.

⁴R. M. Bozorth, *Ferromagnetism* (1951), pp. 778–782.

⁵Sample was made by Carpenter Technology Corporation.

⁶Chih-Wen Chen, *Magnetism and Metallurgy of Soft Magnetic Materials* (1977), p. 138.

⁷V. E. Legg, Bell System Tech. J. **16**, 39 (1936).

⁸D. F. Fan and S. H. Lo, *Physics of Magnetism* (China, 1987), p. 270.

⁹P. A. Miles, W. E. Westphal, and A. Vonb Hippel, Rev. Mod. Phys. **29**, 1 (1957).

Effects of heat treatment on the magnetic properties of polymer-bound iron particle cores

M. Namkung, B. Wincheski, and R. G. Bryant
NASA Langley Research Center, Hampton, Virginia 23681

A. Buchman
Old Dominion University, Norfolk, Virginia 23529

Spherical iron particles of three different size distributions, 6–10 μ in diameter, 100 mesh and 30–80 mesh, were mixed with 2.0 wt % of soluble imide and compression molded at 300 °C under 131 MPa. Post-fabrication heat treatments were performed at 960 °C for 6 h resulting in a significant enhancement of the permeability in low field region for all the specimens except for the one made of 30–80 mesh particles. The rate of core loss of these specimens at a magnetic induction of 5 kG measured up to 1 kHz shows a noticeable increase after heat treatment which, along with the permeability enhancement, can be explained by the coalescence of particles forming a network of conductivity paths in the specimens. The scanning electron micrographs taken for the 6–10 μ particle specimens show no evidence of heat treatment-induced grain growth. The untreated specimens show a very weak f^2 -dependence of the core loss which clearly indicates a negligible contribution from the eddy current loss. In particular, an almost perfect linearity was found in the frequency dependence of the core loss of the untreated specimen made of 100 mesh iron particles.

© 1998 American Institute of Physics. [S0021-8979(98)34711-8]

I. INTRODUCTION

Our previous study has shown that the permeability of polymer-bound cores of spherical iron particles of 6–10 μ can be enhanced by a factor of 30–40 through a simple post-fabrication heat treatment at 960 °C for 6 h.¹ The low field portion of the magnetization curves of these heat treated specimens showed clear evidence of contributions from reversible and irreversible domain wall motions which were absent in the untreated specimens. The most probable reason for such a heat treatment-induced permeability enhancement is the coalescence of iron particles forming a network connecting bare metal particles since the temperature of heat treatment was within the range of the typical sintering temperature of metallic particles.

Unlike the case of sintered powder metallurgy components, the presence of polyimide in these core specimens does not allow a clear visualization of interparticle contacts in the scanning electron micrographs. An alternate way of investigating the formation of such a network structure is to measure the core loss which is sensitive to the range of eddy current flow. Hence, the purpose of the present study is to systematically investigate the effect of heat treatment on the core loss for specimens of different size distributions since it is one of the major factors controlling the structure² upon which the magnetic properties of interest depend.

II. EXPERIMENTS

Spherical iron particles of 6–10 μ in diameter, 30–80 mesh (0.59–0.17 mm in diameter) and 100 mesh (diameter less than 0.14 mm) were mixed with 2.0 wt % of high temperature soluble thermoplastic adhesive known as LaRC™-SI and molded into cubic blocks under 131 MPa of external compressive load at 300 °C for 30 min.³ Two pic-

ture frame specimens of identical geometry having a cross-section of 6.35×6.35 mm², and outer edges of lengths 12.7 mm and 19.05 mm were cut from each block for core loss measurements. One of the two picture frame specimens of each particle size distribution was heat treated at 960 °C for 6 h. The rate of heating and cooling before and after heat treatment in the furnace was approximately 0.5 °C/min. The core loss was measured at the magnetic induction amplitude of 5 kG up to 1 kHz except the heat treated specimens of 6–10 μ and 30–80 mesh particles which were tested to 500 Hz. Two identical square rod specimens with the same cross-section of 6.35×6.35 mm² and 19.05 mm length were prepared from each block for the characterization of permeability, mass density and conductivity before and after an identical heat treatment.

III. RESULTS AND DISCUSSION

Figure 1 summarizes the magnetization curves of untreated and heat treated specimens of the three particle size distributions. The magnetization of the three untreated specimens increases very slowly but maintains its slope in the high field region, i.e., roughly 170–500 Oe, which is steeper than that of heat treated specimens of 6–10 μ and 100 mesh particles. This indicates that a certain level of domain wall motion is present in the untreated specimens in this field region. This is readily explainable since most iron particles are coated and well isolated in these untreated specimens providing strong barriers impeding the domain wall movement such that it takes a stronger driving force to complete the domain wall motion.⁴ The effect of heat treatment on the 6–10 μ particle specimen is seen to be dramatic. A close examination of the initial stage reveals the domain wall mobility for reversible motion is even higher in the heat treated

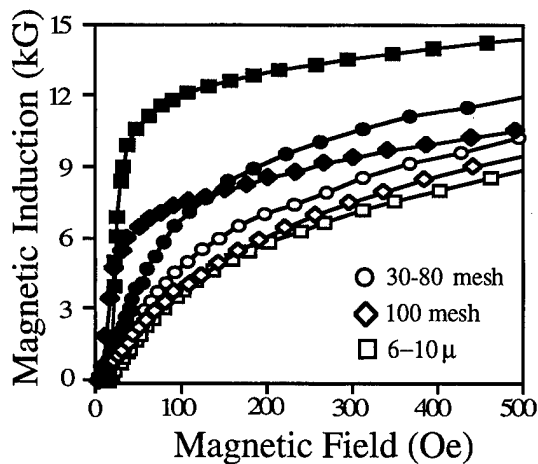


FIG. 1. Magnetization curves of heat treated (filled symbols) and untreated (unfilled symbols) specimens of three different iron particle size distributions.

specimen of 100 mesh particles than it is in that of 6–10 μ particles but the overall induction being much lower in the former is not immediately explainable. It is evident that the effect of heat treatment on the dc magnetic properties of the 30–80 mesh particle specimens is merely to increase the magnetization.

Speed and Elman showed that prefabrication annealing of the iron particles increase the maximum permeability by a factor of 2–5⁴ which is presumably due to relieving of the surface residual stress in each particle that tends to limit the magnetization activity. The temperature of molding in the present work, i.e., 300 °C, is not high enough for residual stress relief. The temperature of post-fabrication heat treatment, 960 °C, is in the range of typical sintering temperature and it is safely assumed that the individual particles are stress-relieved and coalesced with the neighboring ones forming a channel which enhances the domain wall mobility. Hence, the post-fabrication heat treatment provides two major effects enhancing the initial magnetization processes observed in the 6–10 μ and 100 mesh specimen. An indirect evidence of coalescence of particles is the brittle-ductile transition introduced by the heat treatment as reported in our previous study.¹ The behavior of initial magnetization of the heat treated 30–80 mesh specimen is not readily explainable and the rupture test of this specimen, which is yet to be performed, may provide useful information.

Table I summarizes the density and resistivity of the test

TABLE I. Density and resistivity of test specimens.

Specimens ^a	Density ^b (gm/cc)	Resistivity (Ω cm)
6–10 μ	6.3 ^c /6.22 ^d	0.467/0.043
100 mesh	5.88/7.41	1.686/0.057
30–80 mesh	5.75/6.92	0.161/0.064

^aSpecimen designation based on the iron particle sizes.

^bDensity measured using the weight of an object measured immediately after it was submerged in water. (It changes as water fills up the voids. See Ref. 1 for details.)

^cValues for untreated specimens.

^dValues for heat treated specimens.

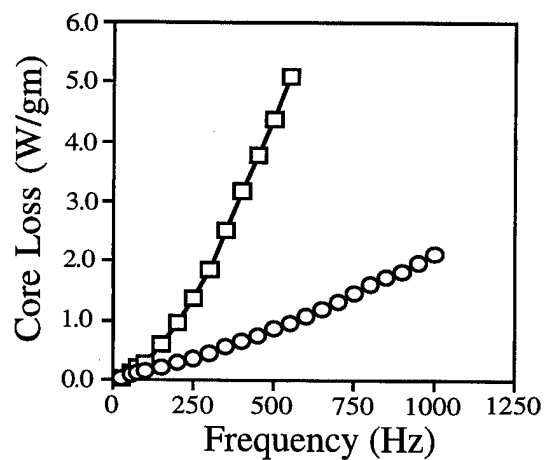


FIG. 2. Frequency dependent core loss/unit mass of heat treated (square) and untreated (circle) specimens of 6–10 μ iron particle cores.

specimens measured before and after heat treatment. The density of the 6–10 μ specimen in this work was reduced by heat treatment which is a trend that is consistent with that reported in the previous work.¹ Such a reduction in the density is thought to be due to the bubbling up of the binder material, i.e., polyimide, creating voids but why it is limited to 6–10 μ particles only is yet to be studied further. The resistivity of the 6–10 μ particle specimen is seen to decrease by a factor of 10 due to heat treatment. Such a reduction in the resistivity can be clearly explained. The individual particles were originally coated with polyimide. During the fabrication process, at 300 °C under 131 MPa of compressive load, however, a certain fraction of particles rub against each other establishing bare metal to metal contacts forming an initial stage of network through the specimen. The heat treatment causes the neighboring particles in direct contact to coalesce into each other to drastically reduce the resistivity in the conduction network. In addition, the carbonization of polyimide, which begins to occur around 500 °C, transforms the insulating layers among the particles into a conducting matrix.

The density and dc magnetic properties are closely related to the particle size distribution and the fabrication condition. For certain simplified conditions, it is possible to numerically predict both properties.⁵ The presence of the binder, however, causes significant complication and no particular correlation can be found. Nevertheless, all the heat treated specimens display consistently low resistivity values. It is to be noted that the resistivity of the untreated 100 mesh particle specimen is much higher than those of the other specimens. Figure 2 shows the core loss of heat treated and untreated 6–10 μ particle specimens. It is immediately clear that the nonlinear frequency dependence is very weak in the loss curve of the untreated specimen, whereas a noticeable nonlinearity is present in the curve of the heat treated specimen. The simplest model of frequency dependence of core loss includes two terms; first and second order terms of frequency. The former is due to the hysteresis loss and the latter is due to the eddy current loss assuming the absence of the domain structure. Figure 3 shows a nonlinear curve of core loss per kg-cycle as a function of frequency of the heat

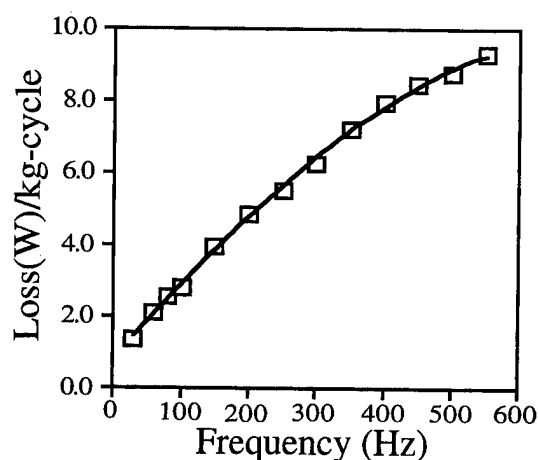


FIG. 3. Nonlinearity in core loss/unit mass-cycle in 6–10 μ iron particle core indicating the effect of anomalous eddy current loss due to a nonuniform distribution of magnetization across the cross-section.

treated 6–10 μ particle specimen displaying the effect of anomalous eddy current loss caused by the presence of domain wall motion.⁴

Figure 4 shows the core loss of heat treated and untreated specimens of 100 mesh particles. The core loss of the untreated specimen is seen to be a remarkably linear function of frequency which is a clear evidence of the absence of eddy current loss in this material. When fitted to a second order polynomial, the coefficients of the second and first order of frequency terms are $5.8149 \times 10^{-8} \text{ W s}^2/\text{gm}$ and $1.4975 \times 10^{-6} \text{ W s}/\text{gm}$, respectively. Compared to $1.269 \times 10^{-6} \text{ W s}^2/\text{gm}$ and $2.187 \times 10^{-6} \text{ W s}/\text{gm}$ for the curve of heat treated specimen, the linearity in the untreated specimen can be considered nearly perfect. The lack of eddy current loss is a strong evidence of the absence of macroscopic eddy current flow in the material since the effect of microscopic

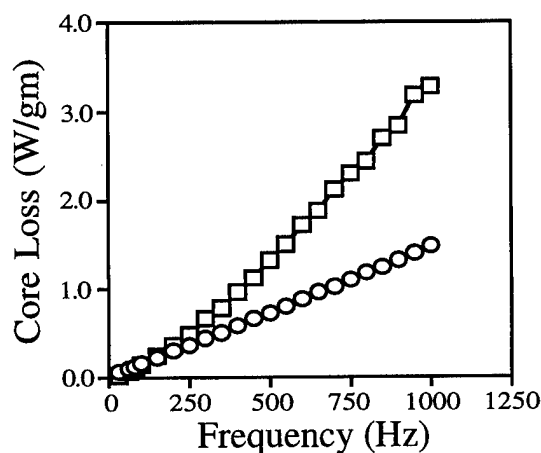


FIG. 4. Frequency dependent core loss/unit mass of heat treated (square) and untreated (circle) specimens of 100 mesh particles displaying a nearly perfect linearity in the latter due to the absence of eddy current loss.

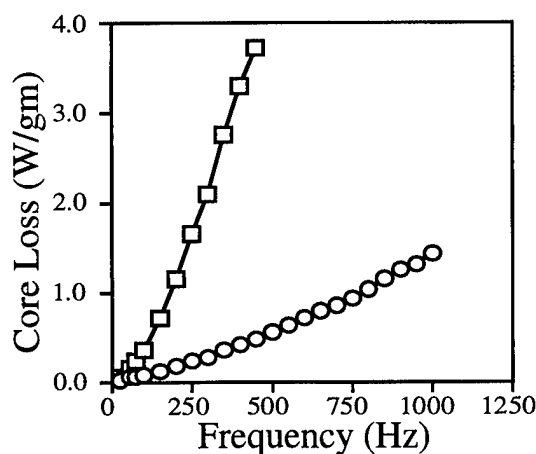


FIG. 5. Frequency dependent core loss/unit mass of heat treated (square) and untreated (circle) specimens of 30–80 mesh iron particles.

eddy current contribution is linearly proportional to the frequency.⁶ Figure 5 shows the results of core loss measurements in 30–80 mesh particle specimens. The difference in core loss between heat treated and untreated states in these specimens is as pronounced as in the specimens of 6–10 μ particles.

It is evident that the core loss is noticeably lower in the untreated specimens than in the heat treated specimens as the frequency increases. Apparently, the major contributing factor for this is the resistivity. The resistivity of the untreated 100 mesh iron particle specimen, in particular, is unusually high and it contributes to the elimination of eddy current loss. At the same time, the magnetization curve of this specimen is comparable to those of the two other untreated specimens. As high resistivity and magnetization are essential requirements for a transformer core material, the untreated 100 mesh iron particle specimen provides a clear direction for the further development.

IV. CONCLUSION

The effect of heat treatment on the magnetization and core loss properties were investigated in polymer-bound iron particle cores of three different particles size distributions. It was found that the iron particle size distribution strongly affects the heat treatment-induced enhancement of magnetization as well as the frequency dependence of core loss which was investigated up to 1 kHz. The absence of eddy current loss, which was attributed to high resistivity, was observed in the untreated 100 mesh iron particle specimen.

¹M. Namkung, R. G. Bryant, B. Wincheski, and A. Buchman, *J. Appl. Phys.* **81**, 4112 (1997).

²R. M. German, *Sintering Theory and Practice* (Wiley, New York, 1996).

³R. G. Bryant, M. Namkung, B. Wincheski, J. P. Fulton, and R. L. Fox, NASA Patent Disclosure, LAR 15463-1-SB (1995).

⁴B. D. Cullity, *Introduction to Magnetic Materials* (Addison-Wesley, Reading, MA, 1972).

⁵H. How and C. Vittoria, *J. Appl. Phys.* **70**, 5915 (1991).

⁶R. M. Bozorth, *Ferromagnetism* (Van Nostrand, New York, 1952).

Alternating current magnetic properties of cores made from pressed acicular steel particles

R. F. Krause,^{a)} J. H. Bularzik, and H. R. Kokal
Magnetics International, Inc., Burns Harbor, Indiana 46304

This article describes results of magnetic testing of cores made from a composite material that yields powder metallurgically pressed compacts of high density suitable for a variety of ac magnetic applications. Small acicular steel particles are annealed, individually insulated, and uniaxially pressed using standard powder metallurgical techniques. The ac losses and permeability of the pressed compacts are strongly dependent upon particle geometry. The variations of the core loss among the different particle geometries was found to be a function of the cross sectional area of the acicular particles as well as the strain imparted to the particles during the pressing operation. The core loss, when measured at 60 Hz, exhibits a minimum at a certain cross sectional area. The shape of the curve is attributed to a decrease in eddy current loss with decreasing particle cross sectional area, while the hysteresis loss increases with decreasing particle cross sectional area. At a test frequency of 400 Hz, the eddy current component of core loss predominates, and the core loss decreases steadily with decreasing particle cross sectional area. Permeability was also found to depend upon particle geometry. The smaller the demagnetizing factor of the individual particles, the higher the permeability, while the increased strain in the smaller particles overwhelms the smaller demagnetizing factor resulting in a decrease in permeability. The net result is a maximum in permeability for the mid-sized particles. © 1998 American Institute of Physics. [S0021-8979(98)22211-0]

I. INTRODUCTION

Pressed cores made from insulated iron powders have been used for many years for ac magnetic applications.¹ These “dust cores” and similar flake iron cores are particularly applicable for very high frequency applications, up to 1 MHz. Unfortunately, because of the nature of the very fine particle size, the density of both dust cores and flake iron cores is rather low, therefore, the magnetic properties are not suitable for power frequency applications. Recently, there has been a resurgence of interest in the development of “composite” materials consisting of iron powders with organic coatings.²⁻⁶ Unfortunately, the low density and low frequency properties are still insufficient for use in most devices that operate at power frequencies.

This article discusses results of magnetic testing of a composite soft magnetic material that has been developed for power and low frequency ac magnetic applications.⁷⁻⁹ This composite material consists of acicular steel particles that are annealed, individually insulated with an organometallic insulation, lubricated to enable pressing using conventional powder metallurgical techniques, and pressed to final shape in a die. The resultant cores have a very high density ($7.50\text{--}7.70\text{ g/cm}^3$), approximately equivalent to the density of a stack of steel laminations.

Variables that can influence the magnetic properties include particle properties such as composition, size, and shape, and the processing parameters such as coating thickness, annealing conditions, and pressing pressure. It has been found that the geometry of the particles is particularly important if acceptable ac properties are to be obtained. Specifically,

these acicular particles are roughly triangular in cross section and several orders of magnitude larger than typical powdered iron. This article discusses the effect of particle geometry on the magnetic properties.

II. EXPERIMENTAL PROCEDURE

Steel particles were produced with different cross sectional areas but with the same particle length ($\sim 0.2\text{ cm}$). The cross sectional areas ranged from about $4.6 \times 10^{-4}\text{ cm}^2$ for the smallest particle to about $2.5 \times 10^{-3}\text{ cm}^2$ for the largest particle. All particles were annealed, received the same amount of insulative coating, the same amount of lubricant, and the same pressing pressure (860 MPa) when pressed into test cores. The test cores are approximately 1.1 cm in height with an inside diameter of approximately 2.5 cm and an outside diameter of approximately 5.0 cm. After pressing, the lubricant was baked out of the cores at 315°C . The compact density was approximately 7.70 g/cm^3 or about 98% of the theoretical density of iron. The ac magnetic properties, core loss and permeability, were measured at frequencies of 60, 100, and 400 Hz.

From a classical point of view, the total core loss consists of hysteresis loss and eddy current loss. The hysteresis loss is considered to vary linearly with frequency, while the eddy current loss varies with the square of the magnetizing frequency. Plotting the loss per cycle versus frequency allows one to separate the loss into the classical components.

III. RESULTS AND DISCUSSION

The effect of the cross sectional area of the particles on the core loss is shown in Fig. 1. A minimum in 15 kG, 60 Hz core loss occurs at a particle cross sectional area of about $1.4 \times 10^{-3}\text{ cm}^2$. The 15 kG, 400 Hz core loss does not exhibit a similar minimum within the range of particle sizes

^{a)}Electronic mail: Krause@inland.com

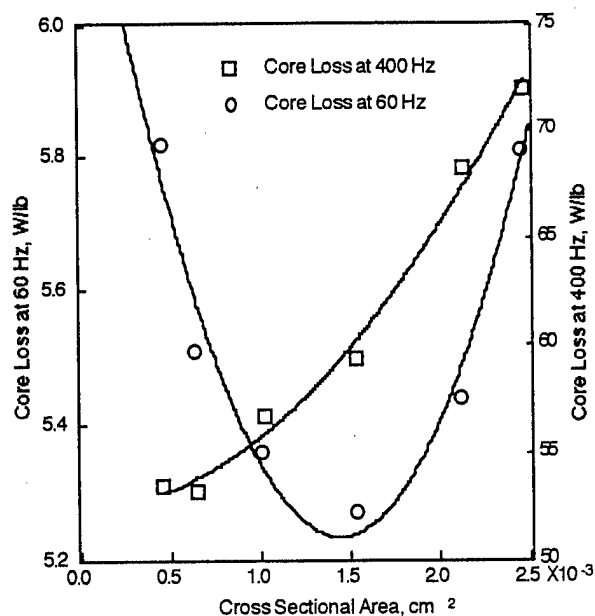


FIG. 1. Effect of cross sectional area on 15 kG, 60 Hz, and 400 Hz core loss.

studied. Instead, the core loss steadily decreases as the particle cross sectional area decreases. The 15 kG, 100 Hz core loss, which is not shown, exhibits a minimum at a particle cross sectional area of approximately $1.2 \times 10^{-3} \text{ cm}^2$. Thus, within the range studied, the minimum core loss occurs with ever decreasing particle size as the test frequency increases. These results can be explained by understanding the contribution of both the hysteresis losses and the eddy current losses in the different sized particles.

Using an analogy between lamination steels where the eddy current loss is proportional to the sheet thickness squared,¹⁰ the eddy current loss of these small particles would be expected to decrease as the thickness (or cross sectional area) of the particles decreases. Figure 2 presents the slope of the eddy current loss with frequency versus the cross sectional area of the particles. The eddy current loss

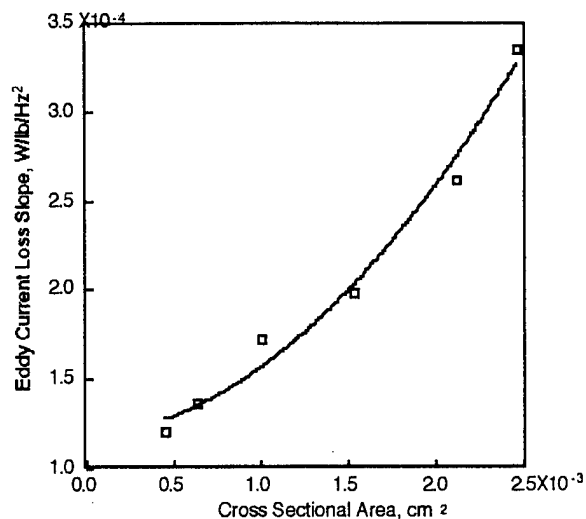


FIG. 2. The dependence of 15 kG eddy current loss on particle cross sectional area.

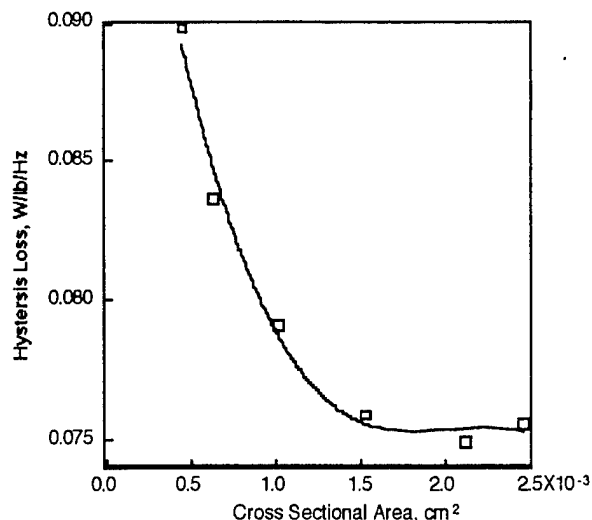


FIG. 3. The dependence of 15 kG hysteresis loss on particle cross sectional area.

steadily declines with decreasing particle cross sectional area. Thus, the analogy between lamination steel and these small particles appears justified.

The hysteresis loss is dependent upon many factors. Some of these factors, such as chemical composition, are the same for all particle sizes in this experiment. Yet other factors can be different, such as the degree of plastic deformation that occurs in the particles during the pressing operation and the surface area of the individual particles. Again, drawing an analogy with lamination steel where the hysteresis loss increases as the thickness of the sheet decreases (or as the surface-to-volume ratio increases) we would expect that the hysteresis loss would increase as the particle cross sectional area decreases. Figure 3 presents the 15 kG hysteresis loss as a function of particle cross sectional area. The hysteresis loss does in fact decrease as the particle cross sectional area increases and appears to level off for the very large particles. As discussed above, this behavior is not unexpected.

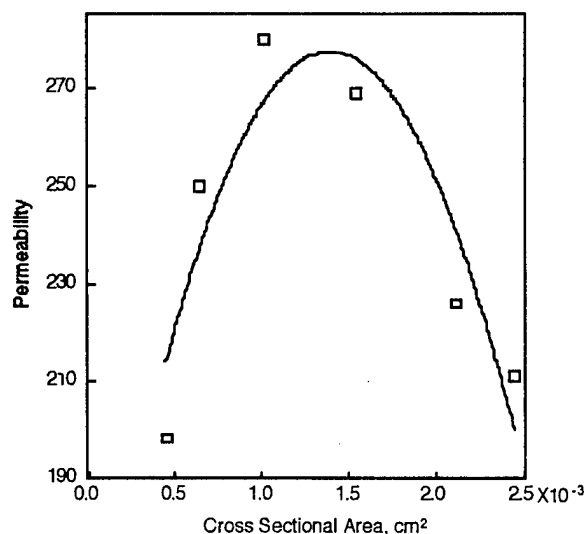


FIG. 4. Effect of cross sectional area on 15 kG permeability.

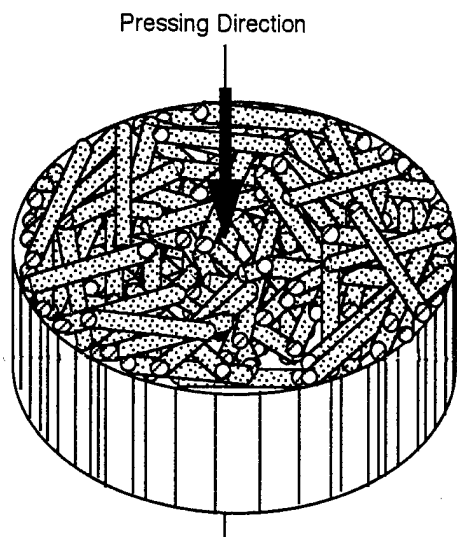


FIG. 5. Planar anisotropy (highly stylized).

If Figs. 2 and 3 are compared, it is now evident why the core loss behavior illustrated in Fig. 1 is observed. Typically, hysteresis loss is said to increase linearly with frequency while classical eddy current loss increases with the square of frequency.¹⁰ Thus, in the low frequency regime, a minimum in core loss occurs. However, as the test frequency increases, this minimum shifts to ever decreasing particle cross sectional areas as the eddy current component of the total losses begins to predominate.

The effect of particle cross sectional area on the 15 kG permeability is illustrated in Fig. 4. A maximum in permeability occurs at a particle cross sectional area of about $1.5 \times 10^{-3} \text{ cm}^2$. This behavior is thought to be dependent upon two competing processes: (1) the shape anisotropy of the individual particles and (2) either the strain induced by pressing or the surface-to-volume ratio of the individual particles. Hysteresis loss and permeability should be closely related since both measure the "softness" of a magnetic material. That is, the lower the hysteresis loss, the higher the permeability. Previously, it was hypothesized that the hysteresis loss increases with decreasing particle cross sectional area because the degree of plastic deformation that occurs in the particles during the pressing operation might be more severe in the smaller particles, and the surface-area-to-volume ratio of the individual particles is greater in the smaller particles. Thus, if this hypothesis is true, the permeability should decrease with decreasing particle size.

Competing with the behavior described above is thought to be the shape anisotropy of the individual particles. Since the particles are acicular in shape, they will tend to have their major axes lie perpendicular to the pressing direction when they are placed (or fall) into the pressing cavity, Fig. 5. Thus, an overall shape anisotropy is created in the pressed compact. This anisotropy will affect the apparent permeability of the compact.¹¹ For simplicity, we can think of these acicular particles as small rods, each with a shape anisotropy related directly to their aspect ratio. Since all particles are of the same length, the particles with the smallest cross sectional

area will exhibit the lowest demagnetizing factor. Thus, if a single particle is magnetized along its axis the apparent permeability will be dependent upon the demagnetizing factor of that particle, i.e., the smaller the cross sectional area of the particle, the higher the apparent permeability. Translating the effect into the pressed compact would suggest that the compacts made from the particles with the smallest cross sectional area would exhibit the highest permeability. It is suggested that these competing effects account for the behavior exhibited in Fig. 4.

IV. SUMMARY

The ac magnetic properties of composite cores pressed from insulated acicular particles have been measured. It has been found that the size of the particles strongly influences the magnetic properties of the pressed cores. Particles with a small cross sectional area exhibit a small eddy current loss but a high hysteresis loss, while particles with a large cross sectional area exhibit just the opposite. Thus, the minimum core loss as a function of frequency is strongly dependent on particle geometry. Permeability was also observed to be dependent on particle geometry and this can be explained qualitatively in terms of a net shape anisotropy in the pressed cores and plastic deformation during pressing.

ACKNOWLEDGMENTS

The help of W. Bolton, J. Kaczur, and F. Keim in preparing the samples and conducting the magnetic tests is greatly appreciated.

- ¹F. Brailsford, *Magnetic Materials* (Wiley, New York, 1960), pp. 123–125.
- ²D. E. Gay, "High Performance Microencapsulated Powders for Various P/M Applications," *Advances in Powder Metallurgy and Particulate Materials—1995* (compiled by M. Phillips and J. Porter) (Metal Powder Industries Federation, Princeton, New Jersey, 1995), Vol. 3, Part 11, pp. 103–126.
- ³C. Gelinas, F. Chagnon, and S. Pelletier, "Development of an Iron-Resin Composite Material for Soft Magnetic Applications," *Advances in Powder Metallurgy and Particulate Materials—1996* (compiled by T. M. Cadle and K. S. Narasimhan) (Metal Powder Industries Federation, Princeton, New Jersey, 1996), Vol. 6, Part 20, pp. 85–97.
- ⁴C. G. Oliver and H. G. Rutz, "Powder Metallurgy in Electromagnetic Applications," in Ref. 2, pp. 87–102.
- ⁵B. Weglinski, "Soft Magnetic Powder Composites—Dielectromagnetics and Magnetodielectrics," *Reviews on Powder Metallurgy and Physical Ceramics*, Vol. 4, No. 2 (1990), pp. 79–154.
- ⁶C. H. Sellers, T. A. Hyde, and D. E. Gay, "Soft Magnetic Composites for Application in AC Electrical Components," in Ref. 3, pp. 99–113.
- ⁷R. F. Krause, J. H. Bularzik, and H. R. Kokal, "High density metal components manufactured by powder metallurgy," US Patent No. 5,594,186 (14 January 1997).
- ⁸R. F. Krause, J. H. Bularzik, and H. R. Kokal, "A New Soft Magnetic Material for ac and dc Motor Applications," *Proceedings of the Symposium on Incremental Motion Control Systems and Devices*, edited by B. C. Kuo, 25th Annual Conference, San Jose, California (1996), pp. 9–16.
- ⁹H. R. Kokal, J. H. Bularzik, and R. F. Krause, "High-Density Pressed Soft Magnetic Components for ac and dc Applications," *Advances in Powder Metallurgy and Particulate Materials—1997* (compiled by R. A. McKotch and R. Webb) (Metal Powder Industries Federation, Princeton, New Jersey, 1997), Vol. 1, Part 1, pp. 61–75.
- ¹⁰B. D. Cullity, *Introduction to Magnetic Materials* (Addison-Wesley, Reading, Massachusetts, 1972), pp. 497–502.
- ¹¹R. M. Bozorth, *Ferromagnetism* (Van Nostrand, Princeton, New Jersey, 1951) (reprinted IEEE Press, Piscataway, New Jersey, 1993), pp. 845–849.

Magnetic induction and surface segregation in thin-gauged 3% Si steel

N. H. Heo

Materials and Corrosion Laboratory, Korea Electric Power Research Institute, Taejeon 305-380, Korea

K. H. Chai and J. G. Na

Division of Metals, Korea Institute of Science and Technology, Seoul 136-791, Korea

J. S. Woo

Research Laboratory, Pohang Iron and Steel Company, Pohang 790-785, Korea

A correlation between magnetic induction and surface phenomena has been investigated in a 3% Si steel 0.1 mm thick. During final annealing at several temperatures, the saturation level in magnetic induction increased with increasing final annealing temperature, and reached 1.93 T after final annealing at 1300 °C for 4.9 ks. This is attributed to the formation of complete (110)[001] Goss texture. During final annealing, the magnetic induction of the thin-gauged 3% Si strip was inversely proportional to the sulfur concentration on the surface. The surface segregation of sulfur occurred after a critical time the silicon concentration on the surface dropped to the level obtained from the α -iron matrix containing 3% Si. The drop in silicon level on the thin-gauged strip surface is due to the volatile silicon monoxide, which arises from the reaction between the silicon dioxide and the silicon segregated, or between the silicon segregated and the oxygen from the high vacuum condition. © 1998 American Institute of Physics. [S0021-8979(98)41511-1]

I. INTRODUCTION

A 3% Si steel with (110)[001] Goss texture, which results in high magnetic induction, is usually used as core materials of power and distribution transformers. There are indications that adsorption of sulfur, and possibly oxygen, on silicon steels can lead to the development of (100)[001] texture in thin sheets by a surface-energy induced recrystallization process.¹⁻³ For a clean surface (i.e., the absence of sulfur or oxygen) (110)[001] texture develops. It is the purpose of this study to investigate the correlation between surface phenomena during final annealing and the magnetic induction in a 3% Si steel 0.1 mm thick.

II. EXPERIMENTAL PROCEDURE

A 3% Si steel was prepared through vacuum induction melting. The chemical composition of the steel is shown in Table I. The ingot was hot-rolled to 2.5 mm plates after holding at 1200 °C for 3.6 ks. The thickness of the plates were finally reduced to 0.1 mm through three-steps cold rolling process with a reduction ratio of 80%–50%–60%. During cold rolling process intermediate annealing was performed at 800 °C for 1.8 ks. The final annealing was given the thin strips in the temperature range of 1000–1300 °C for 0.02 to 184.2 ks. All the annealing treatments were carried out under a vacuum of approximately 10^{-6} Torr. Auger electron spectroscopy (AES) was used for surface analyses. Surface phenomena on the thin-gauged 3% Si strips during final annealing were investigated with ion sputtering technique after final annealing, although this method is not accurate in finding the real Auger peaks because the ion sputtering technique tends to spread out artificially the solute atom distribution in the direction of the beam.⁴

III. RESULTS AND DISCUSSION

Figure 1 shows a change in magnetic induction of the thin-gauged 3% Si strip with final annealing time at 1200 °C. Here, one sample was only used, and was repeatedly annealed to 14.4 ks in order to obtain the magnetic induction values shown in Fig. 1. During final annealing, the magnetic induction [$B_{10}(T)$] passed through a maximum and a minimum, and then increased up to 1.90 T after final annealing to 14.4 ks. The magnetic induction, however, amounted to 1.98 T after one-step final annealing for 14.4 ks. The result of ion-sputtering is shown in Fig. 2, which has been obtained from the sample finally annealed at 1200 °C for 0.06 ks. Prior to ion-sputtering, strong oxygen and carbon peaks were observed while sulfur peak was very weak. After ion-sputtering for 0.015 ks, the carbon adsorbed on the surface from atmosphere was removed, but the oxygen peak became stronger, relatively. This result may imply the presence of an iron oxide layer of atomic scale on the surface, which can be supported by the data.⁵ A sulfur peak appeared with increasing ion-sputtering time, and showed a maximum after ion-sputtering for 0.045 ks. It is suggested that the position corresponding to the maximum is approximately located at the real surface of the thin-gauged strip exposed to the final annealing condition. Figure 3 shows a change in sulfur concentration on the thin-gauged strip with final annealing time at 1200 °C. After final annealing for 0.18 ks, the sulfur concentration reached a maximum, and then decreased to a low level with increasing annealing time. It is shown from a com-

TABLE I. The chemical composition of the thin-gauged 3% Si steel.

Si	C	S	N	Mn
2.92	0.002	0.0006	0.0013	<0.001

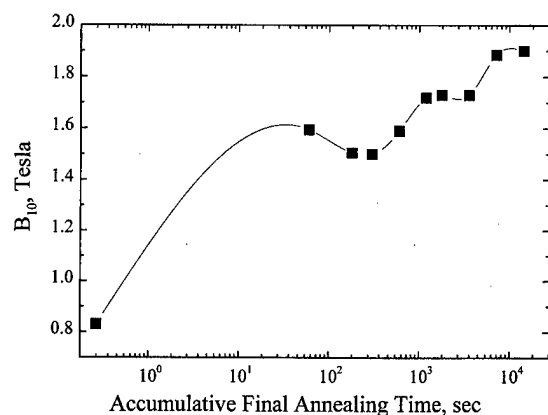


FIG. 1. A change in magnetic induction of the thin-gauged 3% Si steel strip 0.1 mm thick with accumulative final annealing time at 1200 °C.

parison between Figs. 1 and 3 that the maximum in sulfur concentration corresponds to the minimum in magnetic induction, and the magnetic induction increases to the saturation point with decreasing sulfur. This result is in good agreement with the results of some other researches,^{6,7} which reported that the segregated sulfur on surface was the main factor inhibiting the formation of (110)[001] Goss texture.

It has been reported that the segregation kinetics of a species is largely influenced by a precipitation reaction related to the segregating species^{8,9} or by evaporation occurring at a solid-vapor or solid-vacuum interface.^{10,11} Lea and Seah¹¹ found evaporation of tin to be significant in their Auger study of surface segregation kinetics in an Fe–Sn system, and treated the free surface segregation including evaporation theoretically. Following their result, the surface coverage at short times increases as if there were no evaporation. With increasing time, the evaporative loss term becomes dominant so that the surface coverage passes through a maximum, and then decreases to a very low value. Likewise, such a maximum appears also in segregation kinetics accompanying a precipitation reaction.^{8,9} Considering the extremely high vapor pressure of sulfur,¹² such an evaporation phenomenon can possibly occur in the present annealing condition. As a result, the maximum point in sulfur concentration, as shown in Fig. 3, means a turning point, after which the evaporation of sulfur becomes dominant, relatively.

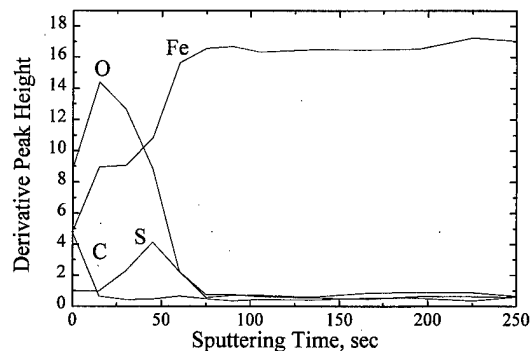


FIG. 2. Ion-sputtering result obtained from the sample finally annealed at 1200 °C for 0.06 ks.

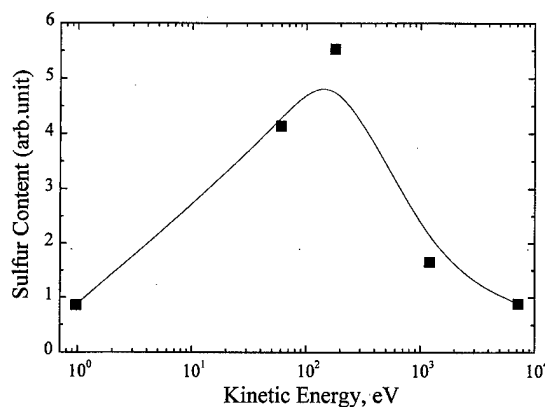


FIG. 3. A change in sulfur peak with accumulative final annealing time at 1200 °C.

Figure 4 shows changes in magnetic induction of the thin-gauged strips during final annealing at several temperatures. At early annealing stage of each temperature, the abrupt increase in magnetic induction can mainly be attributed to the effect of stress relief. The saturation level in magnetic induction increased with increasing final annealing temperature, and amounted to 1.93 T after annealing at 1300 °C for 4.9 ks. However, the saturation value in magnetic induction, 1.71 T, obtained after final annealing at 1000 °C for 184.2 ks was much lower than that at 1300 °C. Ion-sputtering results obtained from the samples finally annealed at 1000 °C for 3.6 and 91.7 ks are shown in Figs. 5(a) and 5(b). As shown in Fig. 5(a), the sulfur segregated is not observed within the ion-sputtering time range, while the silicon and oxygen peaks are strong and decrease gradually with ion-sputtering time. The silicon peak decreased with final annealing time at 1000 °C and dropped to the level obtained from the bulk matrix after final annealing for 91.7 ks as shown in Fig. 5(b). The sulfur peak appeared after the drop of the silicon peak. Based on the results,^{13–15} the drop in the silicon peak during final annealing at 1000 °C can be explained as follows. During heating to the final annealing temperature, the silicon segregated reacts rapidly with oxygen in the high vacuum, resulting in silicon dioxide. Subsequently, during final annealing at the temperature, the silicon dioxide reacts with the silicon segregated from the matrix, giving the

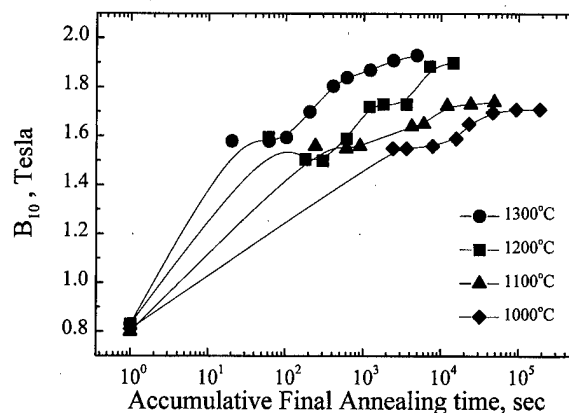


FIG. 4. Changes in magnetic induction of thin-gauged strips with accumulative final annealing time at several temperatures.

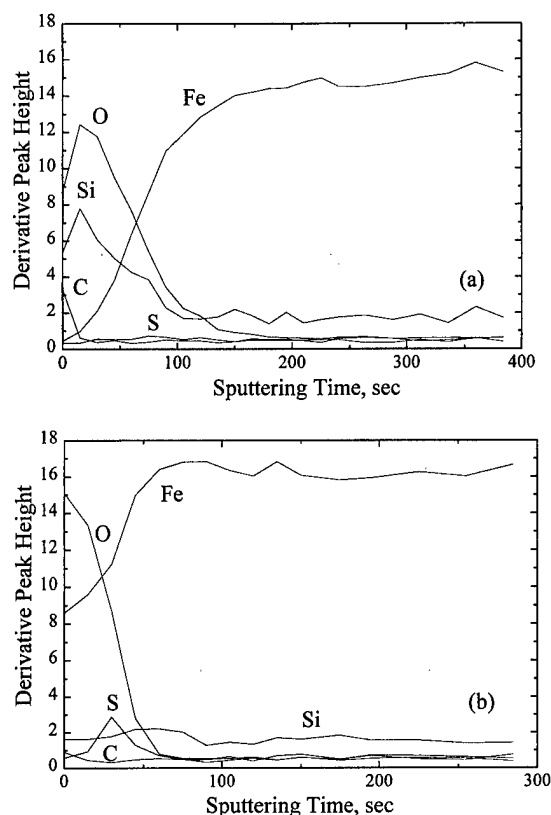


FIG. 5. Ion-sputtering results obtained from the samples finally annealed at 1000 °C: (a) 3.6 and (b) 91.7 ks.

volatile silicon monoxide. As a result, the thickness of the silicon dioxide decreases with final annealing time, and is, as a result, removed on the thin-gauged strip surface. In addition, it is suggested that because the additional silicon segregated on the bare surface without the silicon dioxide also reacts with oxygen¹³⁻¹⁵ in the high vacuum and forms the volatile silicon monoxide, the silicon segregated is not observed on the surface, as shown in Fig. 5(b). On the other hand, the sulfur segregation after the drop of the silicon peak, as shown in Fig. 5(b), can be attributed to a competition between sulfur and silicon in segregation behavior.¹⁶⁻¹⁸

IV. SUMMARY

A correlation between magnetic induction and surface phenomena has been investigated in a 3% Si steel 0.1 mm

thick. During final annealing at 1200 °C, the magnetic induction amounted to 1.98 T after one-step final annealing at 1200 °C for 14.4 ks. This is attributed to the formation of complete (110)[001] Goss texture. The magnetic induction of the thin-gauged 3% Si strip was inversely proportional to the sulfur concentration on the surface. During final annealing at several temperatures, the saturation level in magnetic induction increased with increasing final annealing temperature, and reached 1.93 T after final annealing at 1300 °C for 4.9 ks. However, even after final annealing at 1000 °C for 184.2 ks the saturation level in magnetic induction, 1.71 T, was much lower than that at 1300 °C. During final annealing at 1000 °C, the surface segregation of sulfur occurred after a critical time the silicon concentration on the surface dropped to the level obtained from the α -iron matrix containing 3% Si. The drop in silicon level on the thin-gauged strip surface is due to the volatile silicon monoxide, which arises from the reaction between the silicon dioxide and the silicon segregated, or between the silicon segregated and the oxygen from the high vacuum condition.

¹D. Kohler, J. Appl. Phys. **31**, 4085 (1960).

²K. Foster, J. J. Kramer, and G. W. Wiener, Trans. TMS-AIME **227**, 185 (1963).

³C. G. Dunn and J. L. Walter, Trans. TMS-AIME **224**, 518 (1962).

⁴E. D. Hondros, J. Phys. **36**, Colloque C-4, 117 (1975).

⁵D. R. Gaskell, *Introduction to Metallurgical Thermodynamics*, 2nd ed. (1981), p. 287.

⁶D. Kohler, J. Appl. Phys. **31**, 4085 (1960).

⁷K. Foster, J. J. Kramer, and G. W. Wiener, Trans. TMS-AIME **227**, 185 (1963).

⁸N. H. Heo and H. C. Lee, Metall. Trans. **27A**, 3059 (1996).

⁹N. H. Heo, Acta Mater. **44**, 1581 (1996).

¹⁰C. L. Lea and C. Molinari, J. Mater. Sci. **19**, 2336 (1984).

¹¹C. L. Lea and M. P. Seah, Philos. Mag. **35**, 213 (1977).

¹²R. E. Honig and D. A. Kramer, RCA Rev. **30**, 285 (1969).

¹³C. Wagner, J. Appl. Phys. **30**, 1295 (1958).

¹⁴C. Gelain, A. Cassuto, and P. Le Goff, Oxidation Metals **3**, 139 (1971).

¹⁵J. W. Hinze and H. C. Graham, J. Electrochem. Soc. **123**, 1066 (1976).

¹⁶M. Es-Souni and A. Mosser, Scr. Metall. **22**, 1469 (1988).

¹⁷J. C. Kim, N. H. Heo, J. G. Na, J. S. Woo, and G. M. Kim, Scr. Mater. (in press).

¹⁸N. H. Heo, Met. Mater. **2**, 49 (1996).

New method to predict the magnetic properties of thin gauged Si-Fe sheets

J. G. Na, C. H. Park, J. Kim,^{a)} N. H. Heo,^{b)} S. R. Lee^{c)} C. S. Lee,^{d)} and J. S. Woo^{d)}

Korea Institute of Science and Technology, Seoul 136-791, Korea

A tertiary crystal growth method was used to fabricate thin gauged 3% Si-Fe sheets in order to reduce the thickness of the sheets without deteriorating soft magnetic properties. During the investigation, the magnetic properties of final annealed sheets were found to be directly related to the magnetic properties of final cold rolled sheets. X-ray and transmission electron microscopy were used to understand the above relation. It was found that the fraction of (110) grains at the surface of the final cold rolled sheets significantly affected the final magnetic properties of the final annealed sheets. On the basis of the above argument, the final magnetic properties of the thin gauged Si-Fe sheets can be predicted by the B_{10} values of the final cold rolled sheets. © 1998 American Institute of Physics. [S0021-8979(98)34811-2]

I. INTRODUCTION

Due to excellent soft magnetic characteristics, i.e., low energy losses and high saturation magnetization at low magnetic fields, usually expressed in B_{10} (induced magnetic flux at 10 Oe), grain oriented 3% Si-Fe sheets have been extensively studied and are currently used as core materials of large transformers, large rotating machines, and pole transformers where energy losses during magnetization are of critical concern.^{1,2} The magnetic characteristics of 3% Si-Fe sheets arise from a preferred orientation, i.e., (110)[001] Goss texture formed after cold rolling followed by secondary recrystallization.^{3,4}

It is well known that the energy losses significantly decrease with decreasing thickness of Si-Fe sheets.⁴ Therefore, there have been many investigations to reduce the thickness of the Si-Fe sheets with good (110)[001] texture. After Walter and Dunn,⁵ who reported that a difference in surface energy induced a tertiary recrystallization, thin gauged 3% Si-Fe sheets with good magnetic properties were developed using the tertiary recrystallization in a vacuum.^{6,7}

The production of thin gauged 3% Si-Fe sheets are composed of several procedures including melting and casting, preannealing, 3 times cold-rolling, intermediate annealing, and final annealing, and the magnetic properties of the final annealed sheets are very sensitive to the parameters of each procedure. It is, therefore, very helpful to find a method to predict the final magnetic properties of the thin gauged sheets. During investigating the effect of reduction ratio/pass in the cold rolling processes on the magnetic properties and the microstructures of the sheets, it was found that the final cold rolled sheets that had high B_{10} values showed the high B_{10} values after final annealing. For example, the final cold rolled sheets with B_{10} of 0.83 and 0.76 T exhibited the B_{10}

values of 1.98 and 1.84 T in the final annealed sheets, respectively.

In this paper, the relationship between the magnetic properties of the cold rolled and final annealed sheets was investigated using x-ray and transmission electron microscopy (TEM).

II. EXPERIMENTAL METHODS

100 μm thick 3% Si-Fe sheets were prepared via conventional metallurgical processes including melting and casting, hot rolling to 2.5 mm, preannealing at 800 °C for 30 min, first cold rolling to 0.5 mm, intermediate annealing at 800 °C for 30 min, second cold rolling to 0.25 mm, intermediate annealing at 800 °C for 30 min, final cold rolling to 100 μm and final annealing at 1200 °C for 1 h in a vacuum of 10^{-6} Torr. Detailed processes for the sheets are published elsewhere.⁸

The compositions of the thin 3% Si-Fe sheets, shown in Table I, were analyzed by a chemical method. The microstructures of thin 3% Si-Fe sheets were analyzed by TEM and optical microscope specimens. 10% nital solution was used as an etchant for the optical microscopes. Philips CM-30 was used for TEM analysis and a jet thinning method utilizing 8% perchloric acid + 92% acetic acid was used to perforate TEM specimens. A Seifert XRD-3000PTS was used for x-ray analysis.

The magnetic properties of 3% Si-Fe sheets were measured using a dc flux meter (Toei model TRF-5AH1) and an open circuit method.

III. RESULTS AND DISCUSSION

Figure 1 shows the variations of the B_{10} values of final cold rolled and final annealed thin gauged 3% Si-Fe sheets,

^{a)}Department of Metallurgy and Materials Science, Hanyang University, Ansan 425-171, Korea.

^{b)}KEPRI, Taejon 305-380, Korea.

^{c)}Department of Metals Engineering, Korea University, Seoul 136-701, Korea.

^{d)}Pohang Iron and Steel Co., Pohang 790-785, Korea.

TABLE I. Composition of a thin gauged 3% Si-Fe sheet (wt %).

Si	C	S	N	Mn
2.92	0.002	0.0006	0.0013	<0.001

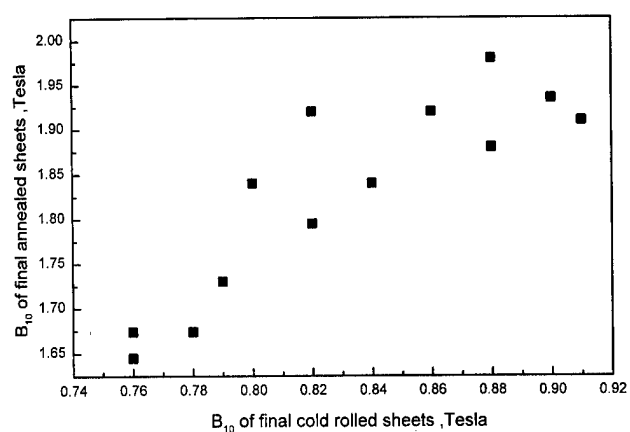


FIG. 1. Variations of the B_{10} values of final cold rolled and final annealed 3% Si-Fe sheets.

prepared by a tertiary recrystallization method. It shows that the annealed sheets with high B_{10} values also have high B_{10} values in the final cold rolled condition. This simple relationship provides an effective method to predict the final magnetic properties of thin gauged 3% Si-Fe sheets and makes

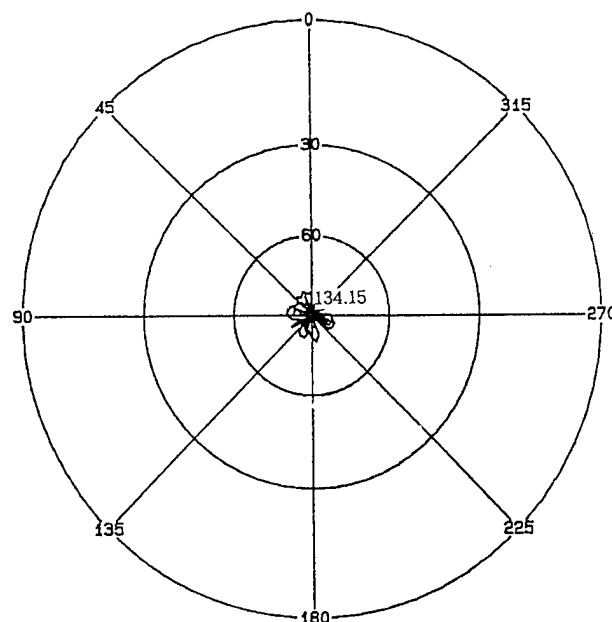


FIG. 2. (110) pole figure of a final annealed 3% Si-Fe sheet.

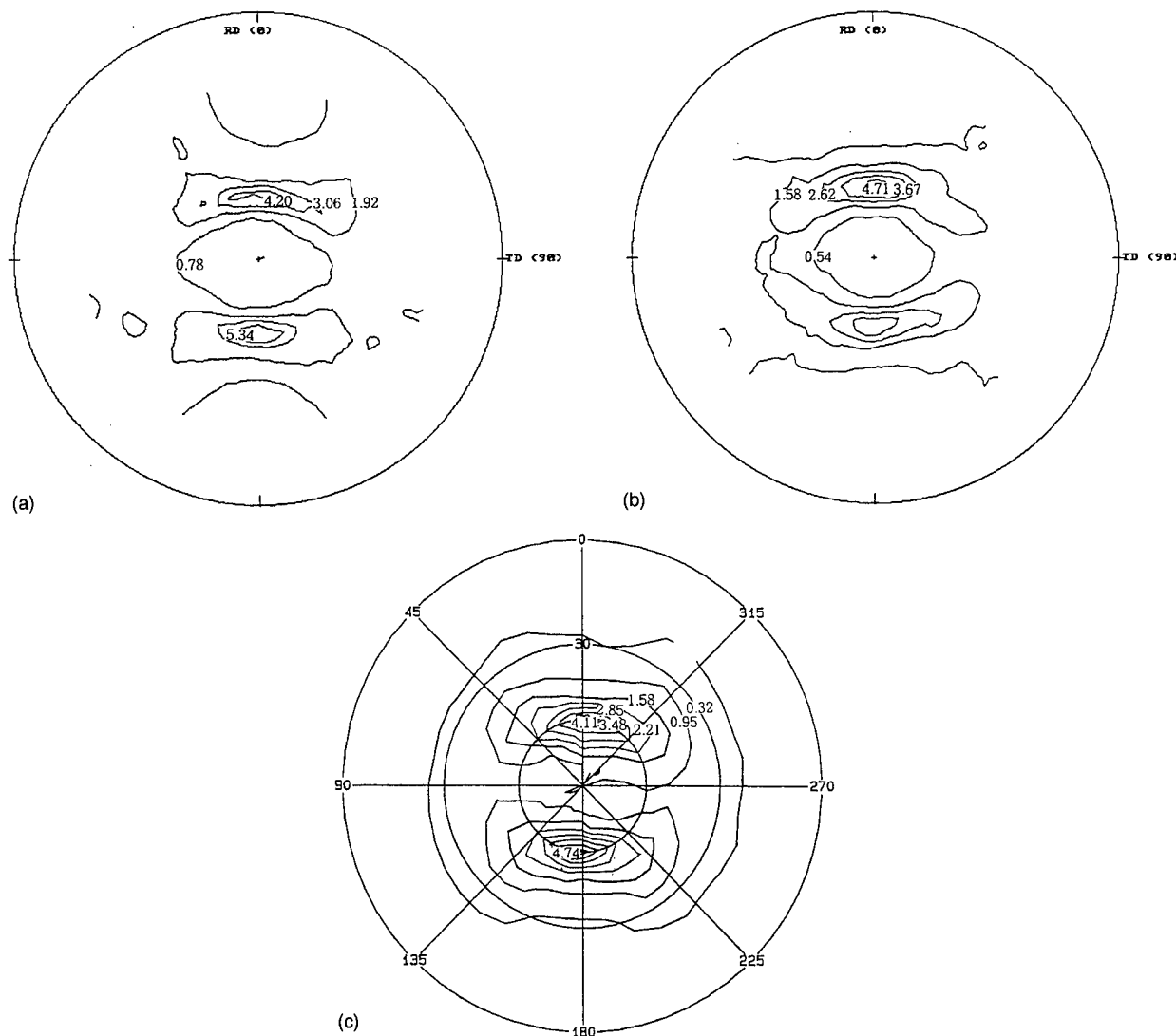


FIG. 3. (110) pole figures of final cold rolled 3% Si-Fe sheets. (a) At the surface; (b) at the surface; (c) at the center.

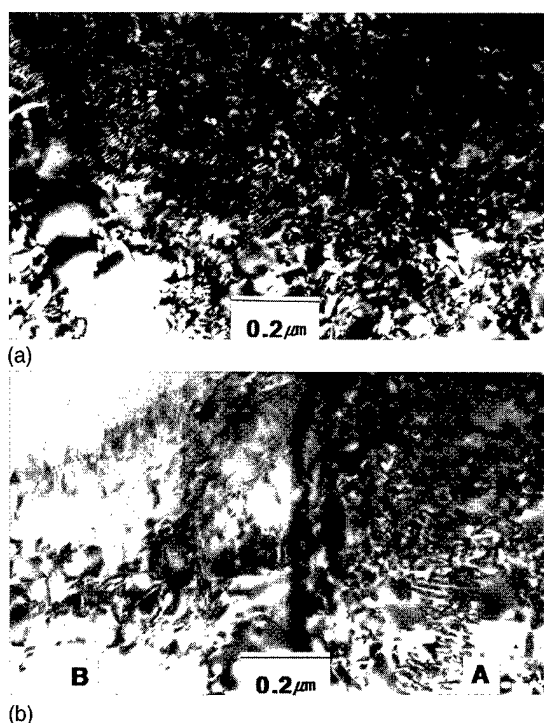


FIG. 4. TEM images of final cold rolled sheets annealed 3% Si-Fe sheet. (a) At the center; (b) at the surface.

possible the avoidance of the high cost final treatment when the sheets will not produce good final properties.

In order to understand the above relationship, the grain orientation and the microstructures of the final cold rolled and the annealed sheets are investigated. Figure 2 shows the $[110]$ pole figure in an annealed sheet, having 1.98 T. It proves that the annealed sheet has excellent $(110)[001]$ texture. Figures 3(a) and 3(b) shows the (110) pole figure of the surface of the cold rolled sheets, which have final B_{10} values of 1.98 T (specimen 1) and 1.84 T (specimen 2), respectively. Both of the specimens have $(111)[112]$ texture but the cold rolled sheet of specimen 1 has more $(110)[001]$ grains compared to the cold rolled sheet of specimen 2. This means that the cold rolled sheet of specimen 1 has a larger area covered with (110) grains than that of specimen 2. Figure 3(c) shows the (110) pole figure of the final cold rolled sheet of specimen 1, obtained in the middle of the specimen by removing top surfaces by chemical etching ($40\text{ }\mu\text{m}$ final thickness). At the center region, the cold rolled sheet of specimen 1 has a $(111)[112]$ texture, which is also found in specimen 2, and a very low fraction of $(110)[001]$ grains compared to the top surfaces.

Figures 4(a) and 4(b) show the TEM images of the cold rolled sheets of specimen 1, which are taken in the middle and top surface, respectively. In Fig. 4(a), a grain is aligned close to the $[111]$ zone axis and the dislocation density is very high. At the center of the cold rolled sheet of specimen 2, the grain orientation and the dislocation density are similar to specimen 1. In Fig. 4(b), there exist two grains; one is aligned close to $[111]$ (representing region A) and the other close to the $[110]$ zone axis (representing region B). It is difficult to quantize the dislocation density of these severely deformed structures because the deformed sheets are relaxed

and continuously change the orientation in their TEM specimens. This makes it too difficult to apply two beam diffraction analyses. In spite of the dislocation density quantization problem, it clearly shows that the dislocation density of region A is much higher than that of region B. In specimen 2, (110) grain was not found due to $(111)[112]$ preferred orientation and (111) grains also have very high dislocation density.

The magnetic easy axis of 3% Si-Fe sheets is located in the $[001]$ direction.⁹ This means that $(110)[001]$ structures could be easily magnetized in the longitudinal direction compared to the $(111)[112]$ structures. There is a significant portion of (110) grains at the surface of the final cold rolled sheet, specimen 1, with high B_{10} as shown in Fig. 3(a). Additionally, the dislocation density of (110) grains at the surface of specimen 1 is quite low as shown in Fig. 4(b). These two factors make specimen 1 have higher magnetization in cold rolled sheets, taking into account that the middle of the sheet with high dislocation density contributes little to B_{10} . Therefore, the (110) grains of the cold rolled sheets are expected to be the dominant factor deciding the magnetization. And the (110) grains also act as seeds for tertiary grain growth. Therefore, specimens having high magnetization values will show high B_{10} values after final annealing. This relation between B_{10} values of the cold rolled and the final annealed sheets gives a critical guideline to predict the magnetic properties after the tertiary recrystallization.

IV. CONCLUSION

Thin gauged 3% Si-Fe sheets show excellent soft magnetic properties after tertiary recrystallization. It was found that high B_{10} values of final cold rolled sheets result in high B_{10} values in final annealed sheets. From pole figure and TEM analyses it was shown that the final cold rolled sheets with high B_{10} had a significant portion of (110) grains having low dislocation density at the surface, while a portion of (110) grains in the cold rolled sheets with low B_{10} was small. At the center of both cold rolled sheets, on the other hand, grains are aligned close to the $[111]$ zone axis and had a very high dislocation density. Thus, the difference in amount of (110) surface grains results in the different magnetic properties of the final cold rolled sheets. These (110) grains are known to be nuclei for a tertiary recrystallization. Therefore, the final magnetic properties of the thin gauged Si-Fe sheets are determined by the portion of (110) grains with low dislocation density. On the basis of the above argument, the final magnetic properties of the thin gauged Si-Fe sheets can be predicted by the B_{10} values of the final cold rolled sheets.

¹M. F. Littmann, IEEE Trans. Magn. **MAG-7**, 48 (1971).

²B. Fukuda, K. Satoh, Y. Shimizu, and Y. Ito, J. Appl. Phys. **55**, 2130 (1984).

³M. F. Littmann, J. Appl. Phys. **38**, 1104 (1967).

⁴E. T. Stephenson, J. Appl. Phys. **55**, 2142 (1984).

⁵J. L. Walter and C. G. Dunn, Trans. AIME **215**, 465 (1959).

⁶K. I. Arai and K. Ishiyama, J. Appl. Phys. **64**, 5352 (1988).

⁷K. I. Arai, H. Satoh, S. Agatsuma, and K. Ishiyama, IEEE Trans. Magn. **MAG-26**, 1969 (1990).

⁸N. H. Heo, Y. J. Kim, J. G. Na, S. R. Lee, D. R. Son, C. S. Lee, and J. S. Woo, Scr. Mater. **37**, 279 (1997).

⁹H. J. Williams, Phys. Rev. **52**, 747 (1937).

Local distribution on magnetic properties in grain-oriented silicon steel sheet

Masato Enokizono and Ikuo Tanabe

Faculty of Engineering, Oita University, 700 Dannoharu, Oita 870-11, Japan

Takeshi Kubota

Steel Research Laboratories, Nippon Steel Corporation, 20-1 Shintomi, Futaba, Chiba 293, Japan

Grain-oriented silicon steel is the most important soft magnetic material used as core material of large transformers, large rotating machines, and pole transformers. Total loss of grain-oriented silicon steel tends to become lower with an increasing degree of texture. However, the material which has a higher degree of texture ordinarily contains larger grains, and the materials which have larger grains show higher total loss due to increased eddy current loss. As the gauge is reduced, the rate of decrease in total loss becomes lower for the thinner gauge due to increased hysteresis loss. However, the investigation of local magnetic properties due to grain situation in this sheet was not discussed from the viewpoint of the distribution of localized magnetic properties, for example, iron loss, hysteresis loop, behavior H vector (magnetic field strength) and B vector (Magnetic flux density). This paper describes the distribution of magnetic properties in high oriented silicon steel sheet, which are loss, hysteresis loop, and locus of field strength. © 1998 American Institute of Physics. [S0021-8979(98)34911-7]

I. INTRODUCTION

Magnetic properties in electrical steel sheets are usually measured by using the single sheet tester or the Epstein's tester in order to evaluate the materials. In these measurements, the permeability is estimated as a scalar value, that is, the relationship between the magnetic flux density B and the magnetic field intensity H in only the rolling direction. Therefore, the measured property represents an average value in the specimens. However, it is well known that the local distributions of B and H are not uniform in grain-oriented silicon steel sheet. These phenomena are closely related to not only the magnetic properties, but also the local loss distributions. Thus it is necessary to measure the local B and H as vector valuables and to estimate the local iron losses with those vector relations in constructed cores. We have measured the two-dimensional magnetic properties in a grain-oriented sheet by using a small sensor which can be

applied to the local measurement. The result shows the relationship between the magnetic properties and the grain structure in a specimen.

II. MEASURING SYSTEM

Figure 1 shows the measuring apparatus and the measuring points. The specimen used in the experiment was a grain-oriented 3% silicon steel sheet (23 ZH: 100 mm×500 mm×0.23 mm) without insulator coating. The distribution of the grain structure can be observed directly, using the sample sheet without insulator coating. The measuring points were distributed in a 100 mm×100 mm area near the center of specimen and the total number of points were assumed to be 143 as shown in Fig. 1. The points were defined with 13 lines in the rolling direction ($D-P$) and 11 lines in the transverse direction (1-11). The yoke was also constructed with the grain-oriented steel sheet (23 ZH) as shown in Fig. 1. The number of lamination was equal to 7.

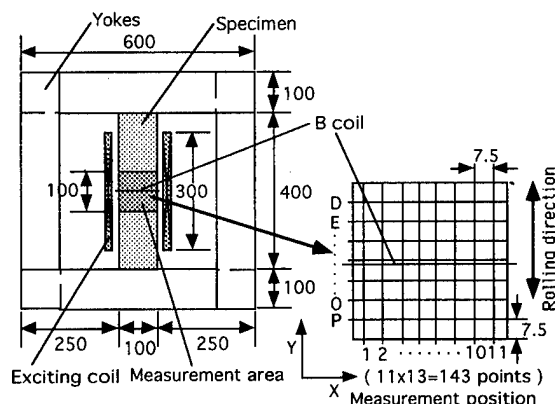


FIG. 1. Measuring apparatus.

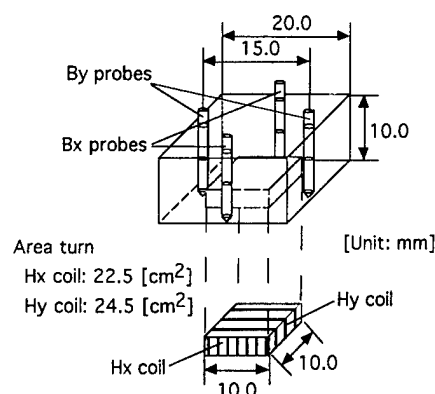


FIG. 2. Two-dimensional magnetic sensor.

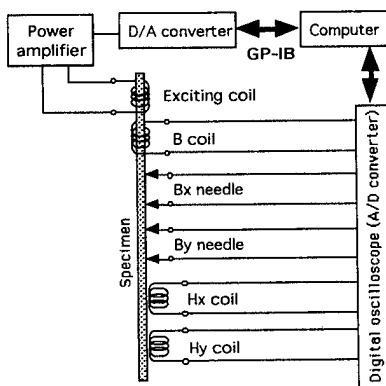


FIG. 3. Measuring system.

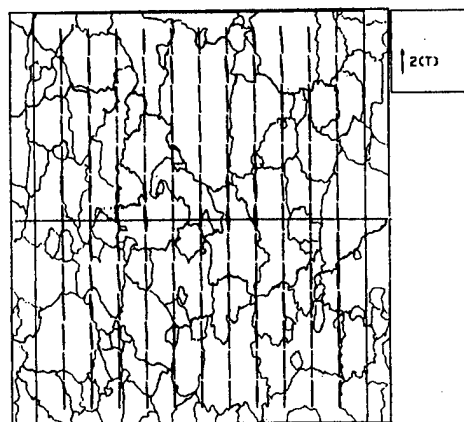
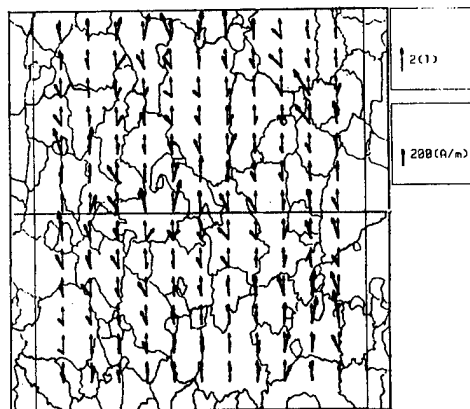
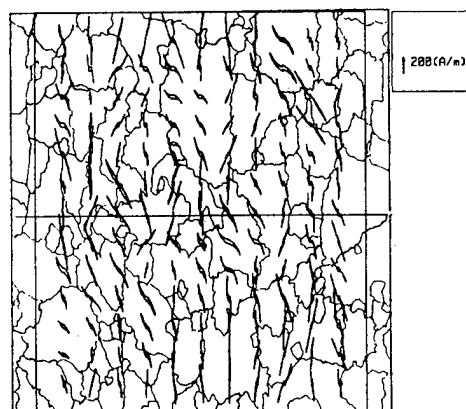
FIG. 5. The loci of B vector.

Figure 2 shows the construction of the two-dimensional magnetic sensor.^{1,2} The sensor has two sets of double needles to measure the component of the flux density vector in each direction. The distance between the facing needles was equal to 15 mm. To absorb the vibration of the specimen, a spring was fixed inside the needles. This method, because making a hole array in the specimen is needless, is useful in comparison with the conventional search-coil method. Furthermore, the field changes due to holes are prevented which expands the limit of measuring points. The double H coil was used in measuring the magnetic field intensity vector. The H_x coil was wound around a bakelite plate and the H_y coil was wound over the H_x coil with formal wire 0.04 mm in diameter. The area turns of the H_x coil and H_y coil were 22.5 and 24.5 cm², respectively. Figure 3 shows the measuring system in this experiment. The average flux density in the specimen was controlled to be 1.7 T in sinusoidal waveform by using the output signal from the B coil (1 turn) which was wound at the center of the specimen. The exciting frequencies were 50 and 100 Hz, and the sampling frequencies were 20 and 50 kHz, respectively. The output signals from the sensor were handled with a computer after passing through a digital oscilloscope.

III. RESULTS AND DISCUSSION

Figure 4 shows the relationship between the B vector and H vector at each measuring point at $\omega t = 90$ degrees. As shown in this figure, almost all B vectors were parallel to the rolling direction of the specimen, but most H vectors were not parallel to the B vectors. This phenomenon influences the estimations of iron loss of the grain-oriented silicon steel sheet. It can be observed that the relationships between the B vector and H vector at each measuring position in the same grain were almost similar. Figures 5 and 6 show the loci of the B vector and H vector at each measuring position, respectively. Most loci of the B vectors were alternating, but some of the loci became a slender rotational shape. The loci of the H vectors were quite different from those of the B vectors, and the shapes were dependent on the grain size and its location. Figure 7 shows the loci of the B , H vectors and the hysteresis loop for the X , Y components at some measuring points. Because the measuring area of the sensor at each part was larger than the size of most grains, we could not measure the properties in each grain. However, we can discuss properties at most inner parts of grains or near the boundaries of grains. There were large differences in loci of H vectors at each position. The position D_{-05} was located near the boundary of the neighboring grains and the positions F_{-06} and O_{-07} were almost located in the comparatively

FIG. 4. The relationship between B vector and H vector.FIG. 6. The loci of H vector.

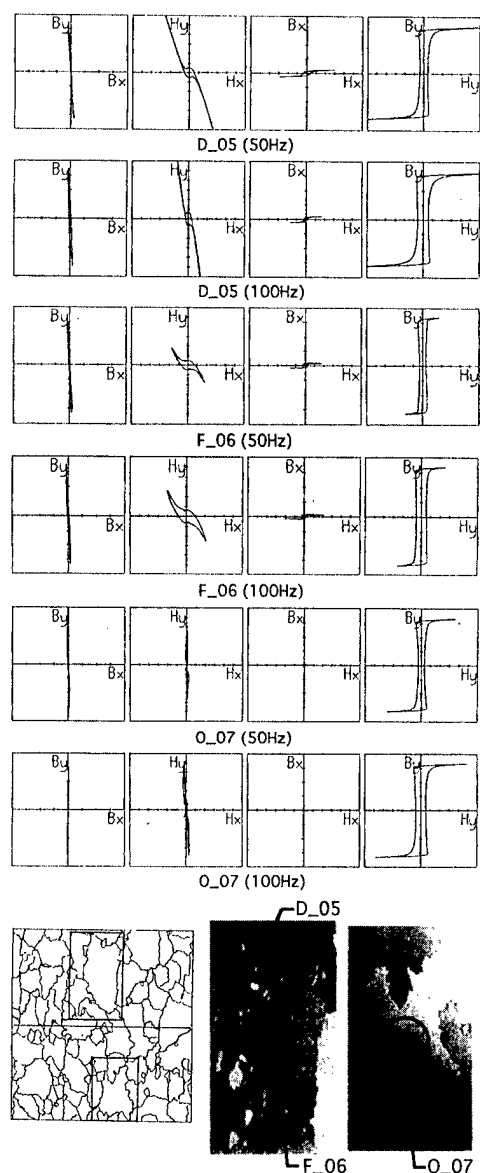


FIG. 7. The loci of the B , H vectors and the hysteresis loop for the X , Y components. The axis of B is 0.5 [T/Div.]. The axis of H is 50 [(A/m)/Div.].

large grains. At D_{-05} and F_{-06} , the loci of H vectors were not parallel to the loci of B vectors, however, the loci of H vectors and B vectors at the O_{-07} position became nearly parallel. One can observe in Figs. 5 and 6 that the H vectors were not locally parallel to the B vectors. This phenomena can be caused by the two following reasons: The demagnetizing field of each grain having different size and shape, influenced each other; there were a few very small grains, which were not consumed after recrystallization, in the large

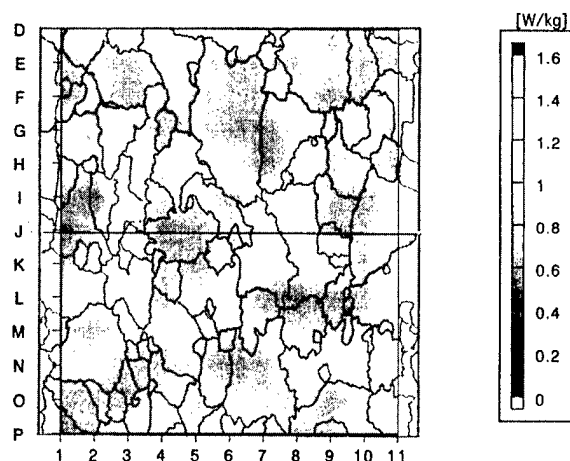


FIG. 8. The local iron loss distribution. Exciting frequency is 50 [Hz].

grains whose deviation of the $[100]$ direction from the rolling direction was small (F_{-06}). To reduce the iron loss of the silicon steel sheet, it is necessary to remove such small grains that have the $[100]$ direction different from the rolling direction. The changing rate of the loci of H vectors depending on frequency was different at each position. It can be said that those differences in the shape of the hysteresis loops were obviously due to the difference in anisotropy at each grain.

Figure 8 shows the local iron loss distribution in the specimen. The distribution was calculated with the values in both the rolling and transverse direction at each measuring position, and was illustrated with a linear interpolation. The result showed that the loss distributions were not uniform in the sample sheet due to the influence of the grain structure.

IV. CONCLUSION

In this paper, the local iron loss distribution measured by using a two-dimensional magnetic measurement sensor has been presented. The results showed that the distribution of iron loss and the field strength were not uniform in the sample sheet due to the influence of grain structure and its local anisotropy. Because the phenomena widely influence the efficiency of the transformer, the evaluation of such local magnetic properties is very important in improving the characteristics of grain-oriented silicon steel sheet. We intend to clarify the relationship between the local magnetic properties and the domain structure.

¹T. Kanada, M. Enokizono, and K. Kawamura, IEEE Trans. Magn. **32**, 4797 (1996).

²M. Enokizono, M. Morikawa, K. Kawamura, and J. Sievert, IEEE Trans. Magn. **32**, 4989 (1996).

Anisotropy design in magnetic media: A micromagnetics study

J. H. Kaufman, T. Koehler,^{a)} A. Moser, D. Weller, and B. Jones

IBM Research Division, Almaden Research Center, 650 Harry Road, San Jose, California 95120-6099

We have investigated the characteristics of model magnetic media using different strategies for the "anisotropy design." We modeled media with intragrain anisotropy oriented random in the plane of the media, random in 3D, and aligned along the track direction, and for a large range of anisotropy field H_k and intergranular exchange J . We report a possible scaling function which collapses data for all three geometries onto a single universal curve. The rescaled data were then analyzed along with the signal-and-noise functions from the various model materials. For any geometry, we find a relation between exchange and anisotropy which maximizes the signal-to-(media) noise function.

© 1998 American Institute of Physics. [S0021-8979(98)33211-9]

I. INTRODUCTION

Magnetic storage media consists of thin hard granular magnetic films.^{1,2} By design these grains are granular and weakly coupled.^{3,4} One can conceive different "designs" of the magnetic anisotropy of these grains. Typically the easy magnetic axis is aligned in the plane of the film by use of appropriate underlayers and deposition temperature. However, one can also allow the easy axis to be random in 3D or perhaps, through underlayer texture, to be oriented in the track direction. It is not clear, *a priori*, which is the best strategy to optimize the overall performance of a recording media. In this work we investigated the effect of anisotropy design on coercivity, and we report a universal scaling function which relates coercivity to exchange, anisotropy, and saturation magnetization, for each of the different geometries.

II. PROCEDURES

The micromagnetics code used in this calculation was written by Koehler and Fredkin.^{5,6} The code uses quasi-static relaxation and a hybrid FEM-BEM method to determine the magnetic state of an arbitrary three dimensional object. The meshing algorithm creates quasi-random tetrahedral elements of the three-dimensional object (film) to be investigated. Each of the tetrahedral elements is treated as an individual "grain." The exchange coupling, J , between grains may be varied along with the remnant magnetization, m_s , and the direction and magnitude of the magnetocrystalline anisotropy field H_k . The calculation was done for a "film" with dimensions $|x| = 1 \mu\text{m}$, $|y| = 2 \mu\text{m}$, $|z| = 200 \text{ \AA}$. This volume was divided into 2878 tetrahedral elements. For each of three anisotropy geometries, the microscopic parameters were varied over a range that produced coercivities and squareness typical of magnetic media. We used $m_s = 500$ (emu/cc), $H_k = 6000, 8000, 10\,000, 12\,000$ (Oe), and

varied the exchange, A , between 1.6×10^{-8} and 4.7×10^{-7} (erg/cm). The input to the model for exchange strength is in terms of the variable J which is dimensionless and model dependent. For a model using a simple cubic mesh, the corresponding constant, J^* , is defined by^{3,4,7}

$$J^* = \frac{2A}{4\pi m_s^2 a^2}, \quad (1)$$

where a is the linear size of the mesh elements in cm. In the Koehler model J also sets an internal scale factor ($l_i = I$) for the computation, and it determines the overall physical length scale (l_p) for the meshed object,

$$J = \frac{2A}{4\pi m_s^2} \left(\frac{l_i^2}{l_p^2} \right) = \frac{2A}{4\pi m_s^2 a^2 (2n^2)} = \frac{1}{(2n^2)} J^*, \quad (2)$$

where $(2n^2)$ is the number of "effective" cubic elements which would fill the $2 \times 1 (\times .02) \mu\text{m}$ slab using a cubic mesh. The number of tetrahedral elements is $5-6 \times$ the number of effective cubic elements.

For each of these "materials," the coercivity was then measured by applying, and switching, an external field in small steps between 10^4 and -10^4 (Oe) in the x direction. The remnant magnetization and coercivities were obtained from the resulting $M-H$ loops.⁸

III. RESULTS AND DISCUSSION

As expected, the coercivity was found to increase with H_k and decrease with increasing A .^{1-4,8,9} The squareness, S^* , increases with A . We looked for a scaling function which would collapse the data (for all values of H_k , A , and for all anisotropy designs) onto a single universal curve. By superposition we expected this function $H_c(J, H_k, \dots)$ to be linear in the anisotropy field and an effective exchange field. The scaling function obtained is shown in Fig. 1. The variables are rescaled by

$$H_c^* = \gamma H_c \quad (3)$$

^{a)}Present address: DAS Devices, 1504 McCarthy Blvd., Milpitas, CA 95035.

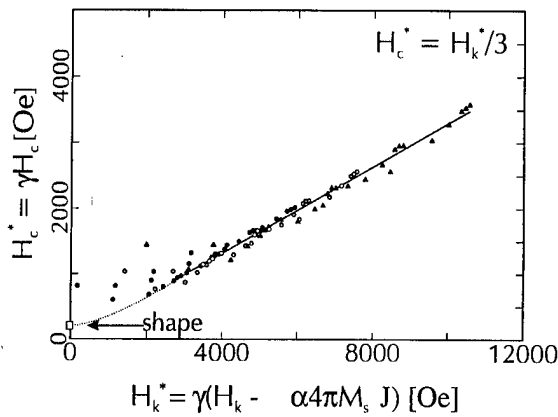


FIG. 1. Scaling function for coercivity of granular magnetic media.

and

$$H_k^* = \gamma(H_k - \alpha 4\pi m_s J^*), \quad (4)$$

where we use the more common J^* defined above (J^* differs from J in the Koehler program by a scale factor).

There is only one adjustable parameter, α in this rescaling. The dimensionless variable α represents the number of neighbors which contribute, on average, to the effective exchange field. For the tetrahedral mesh $0 < \alpha < 7$. We find the data collapses onto the scaling function when $\alpha = 4$ for both the random in plane and aligned in plane anisotropy geometries and $\alpha = 6$ for the 3D random anisotropy geometries. Note that in all cases the tetrahedral elements have the same number of geometric neighbors (6–7) and that the same geometric mesh is used in all of the calculations. The other (dimensionless) parameter, γ , in the scaling function is a geometry factor defined by, $\gamma = m_r/m_s$, the ratio between the remnant and saturation magnetization. For each of the geometries, γ may be calculated exactly in the case of weak exchange and large H_k . For the case with anisotropy random in plane,

$$\gamma = \frac{1}{\pi} \int_{-\pi/2}^{\pi/2} d\theta \cos(\theta) = \frac{2}{\pi} = 0.64. \quad (5)$$

For anisotropy distribution random in 3D,

$$\gamma = \frac{1}{2\pi} \int_0^\pi \sin(\theta) d\theta \int_{-\pi/2}^{\pi/2} d\varphi \cos(\varphi) = \frac{1}{2}. \quad (6)$$

A similar analytic expression may be solved for the case with anisotropy aligned in plane using an elliptic distribution of easy axis directions. We created the anisotropy distribution with a ratio of minor to major axes $a/b = 0.2$ and obtained $\gamma = 0.89$. For a perfect orientation of H_k along \hat{X} , $a/b = 0$ and $\gamma = 1$.

For large H_k and small J , the rescaled data asymptotically approaches $H_c^* = H_k^*/3$. Note that the scaling function does not intercept the origin ($H_c^* = H_k^* = 0$). The γ intercept is determined by the shape anisotropy of the finite slab used in the calculation. We measured this separately by performing an $M-H$ loop with low H_c and large exchange and found $H_c^{\text{shape}} \sim 220$ (Oe).

IV. CONCLUSIONS

We found a universal scaling function to relate coercivity to the microscopic parameters m_s , H_k , and J . The function applies in general for all possible designs of anisotropy (random in plane, random in 3D, and aligned in the track direction). In future work we plan to apply this scaling function to the analysis of signal-to-noise data calculated from simulated data tracks using the same parameter space. This holds the promise of providing a recipe to optimize signal to noise as a function of microscopic parameters at any value of coercivity and for arbitrary geometry's of anisotropy.

¹H. N. Bertram, *Theory of Magnetic Recording* (Cambridge University, Cambridge, 1994).

²K. E. Johnson, P. R. Ivett, D. R. Timmons, M. Mirzamaani, S. E. Lambert, and T. Yogi, *J. Appl. Phys.* **67**, 4688 (1990).

³J-G Zhu, *IEEE Trans. Magn.* **MAG-27**, 5040 (1991).

⁴J-G Zhu and I. Beardslery, *IEEE Trans. Magn.* **MAG-27**, 3553, 5037 (1991).

⁵D. R. Fredkin and T. R. Koehler, *J. Appl. Phys.* **67**, 5544 (1990).

⁶T. R. Koehler and D. R. Fredkin, *IEEE Trans. Magn.* **MAG-28**, 1239 (1992).

⁷H. N. Bertram and J-G Zhu, *Solid State Phys., Adv. Res. Appl.* **46** (1992).

⁸B. D. Cullity, *Introduction to Magnetic Materials* (Addison-Wesley, Reading, MA, 1972).

⁹S. Chikazumi and S. H. Charap, *Physics of Magnetism* (Krieger, 1978).

A variational approach to exchange energy calculations in micromagnetics

M. J. Donahue

National Institute of Standards and Technology, Gaithersburg, Maryland 20899

This article presents a magnetization interpolation method for micromagnetic exchange energy calculations using a variational procedure to relax spins on a supplemental (refined) lattice. The approximations implicit in standard micromagnetic discretization schemes fail when angles between neighboring spins in the model become large, but the proposed approach effectively reduces the angle between neighboring spins, alleviating many of the associated problems. Moreover, this method does not introduce excessive discretization-induced vortex pinning observed with some large angle exchange energy formulations. This article includes details on proper post-interpolation exchange torque calculation, bounds on nearest-neighbor angles for interpolated lattices, a simple model predicting discretization-induced Néel wall collapse, and an example of a collapsed (1 cell wide) domain wall that can be restored by the proposed technique. [S0021-8979(98)33311-3]

I. INTRODUCTION

Many difficulties arise in micromagnetic simulations when angles between neighboring spins become large. Nonetheless, computational limitations often prevent many interesting micromagnetic problems from being discretized at a scale fine enough to resolve all the details of the magnetization structure. In particular, models of thin magnetic films often contain vortices and crossties with unresolved cores measuring only a few nanometers across. As discussed below, such undersampled core regions can collapse during model evolution into one cell wide 180° domain walls, even in settings where the Néel wall width is many cells wide. Once formed, these structures are stable, because they tend to be supported by magnetostatic and crystalline anisotropy fields, and the usual exchange energy formulation provides zero torque across 180° spins. One can introduce an exchange energy formulation modified for large angles, but simple approaches result in strong artificial pinning of vortices to the computation grid.¹

One solution to these problems is to base the exchange energy formulation on a continuous interpolation of the magnetization that respects the constraint that the reduced magnetization $\|m\| = 1$. In this article, an interpolatory "supplemental" lattice is introduced, and a variational procedure is used to relax the spins on this lattice to achieve a smooth interpolation. It is shown that a simple half-step interpolation suffices to avoid the aforementioned one cell wide 180° domain walls, without introducing excessive false pinning of vortices.

II. NÉEL WALL COLLAPSE

Figure 1 shows an example of a situation where an underresolved structure produces errors at a larger scale. This is a simulation of the first μMag standard problem,² a 20 nm thick, $1\ \mu\text{m} \times 2\ \mu\text{m}$ rectangle of $\text{Ni}_{80}\text{Fe}_{20}$ ($M_s = 8.0 \times 10^5\ \text{A/m}$, $A = 1.3 \times 10^{-11}\ \text{J/m}$, $K_u = 500\ \text{J/m}^3$). The weak uniaxial magnetocrystalline anisotropy is directed along the long axis of the film. The computation cells are 25 nm squares, 20 nm thick, with 3D spins. The exchange energy is given by the eight-neighbor dot product formula E_i

$= (A/3) \sum_{n=1}^8 (1 - m_i \cdot m_n)$, detailed in Ref. 1, though similar results are obtained using the more common four-neighbor expression. The magnetostatic fields are calculated via an FFT-based scalar potential method on an offset grid, described in Ref. 3. The magnetization is relaxed using heavily damped Landau-Lifshitz-Gilbert equations of motion. For more details on the calculation technique, see Ref. 4.

The configuration in Fig. 1 is the relaxed state just past the coercive point, after saturation to the left along the long axis of the film. The 180° domain wall in the lower right-hand portion of Fig. 1 was formed in an intermediate (non-relaxed) state as part of a vortex+crosstie pair. The vortex drifted upward (behind the inset, but symmetric with the vortex in the opposite corner), and the crosstie flattened out into the observed 1-cell wide domain wall. It is difficult to predict how wide this wall should be, given the restricted spatial dimensions and the complicated magnetic structure, but one certainly expects it to be wider than a single 25 nm cell.

Figure 2 presents a simple illustrative 1D model of a coarsely discretized Néel wall. (See Refs. 5 and 6 for more on 1D wall models, and Ref. 7 for a numerical study of 2D wall structures.) In this 4 cell model, each cell is a constant magnetization region, infinite along the y axis, with width a

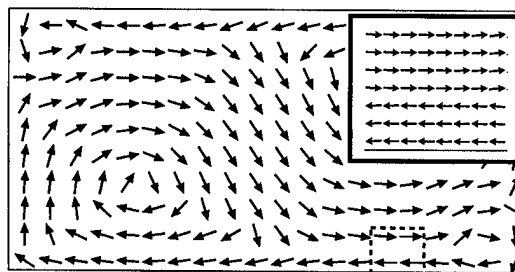


FIG. 1. Simulation results of the μMag first standard problem, using 25 nm square, 20 nm thick calculation cells (4×4 subsample). This is a relaxed state with an applied field of $\mu_0 H = 4.5\ \text{mT}$ directed towards the right. The inset displays all the calculation spins in the dashed box region, showing a collapsed Néel wall.

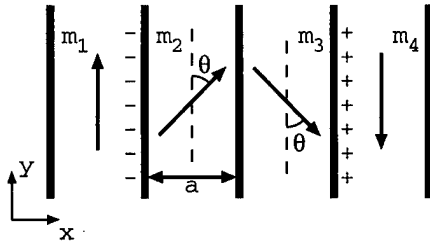


FIG. 2. Illustration of a simple 1D model to study discretization-induced Néel wall collapse. The outer spins \mathbf{m}_1 and \mathbf{m}_4 are fixed and antiparallel.

as shown, and a thickness t small enough to force the spins to lie in the xy plane. Material parameters are saturation magnetization M_s and exchange constant A . Magnetocrystalline anisotropy is ignored. The outer spins \mathbf{m}_1 and \mathbf{m}_4 are held fixed and antiparallel as shown, while the inner spins \mathbf{m}_2 and \mathbf{m}_3 are allowed to rotate, with θ denoting the angle between the inner spins and their outside neighbor. We make the simplifying assumption that the inner spins are symmetric about the midpoint, as illustrated, because then there are no free poles along the center line, greatly reducing the magnetostatic energy. (This alignment of the center of a Néel wall between discretization nodes is observed in practice.) We also assume that $\theta < 90^\circ$.

Magnetic poles collect along the infinite strip between the two leftmost cells, and between the two rightmost cells. This produces a field at spin \mathbf{m}_2 that acts against the exchange torque produced on \mathbf{m}_2 from \mathbf{m}_3 . If we include the exchange torque at \mathbf{m}_2 from \mathbf{m}_1 , and solve for 0 torque, we find a unique energy minimum at

$$\sec \theta = 2 - \frac{\mu_0 a^2 M_s^2 \{ \arctan(t/a) + \arctan[t/(3a)] \}}{2A\pi},$$

provided the right-hand side is > 1 . Note that as $a \rightarrow 0$, $\theta \rightarrow 60^\circ$ as expected. If the right-hand side is ≤ 1 , then the antiparallel state ($\theta = 0$) is the only stable configuration, and the Néel wall collapses completely. If M_s , A , and t are fixed, then for a sufficiently large the wall will collapse. For a $\text{Ni}_{80}\text{Fe}_{20}$ film with $t = 20$ nm, this works out to a larger than about 7.1 nm, lending credence to the conjecture that a mechanism of this sort is responsible for the wall collapse observed in Fig. 1.

It seems likely that the under-resolved crosstie formed during the evolution to the relaxed state of Fig. 1 produces a local condition not unlike that modeled in Fig. 2, and seeds the collapse of the entire wall. A similar situation can also arise through grid refinement.

Regardless of its origins, the observed Néel wall collapse is made possible by the disappearance of the exchange torque in the antiparallel state. One can try a modified exchange field formulation appropriate for large angles, but simple attempts yield unacceptably strong vortex pinning.¹ More sophisticated interpolations of \mathbf{m} between grid points are made difficult by the apparent importance of the $\|\mathbf{m}\| = 1$ constraint, and the need to produce an interpolation that is consistent across neighboring discretization cells.

A different approach is to interpolate the coarse grid spins $\mathbf{m}_1, \dots, \mathbf{m}_N$ with a differentiable function $\mathbf{m}(x, y, z)$ that minimizes the variational integral

$$E(\mathbf{m}) = A \int (\nabla m_x)^2 + (\nabla m_y)^2 + (\nabla m_z)^2 dV, \quad (1)$$

subject to some constraints. A discrete version of this is developed in the next section. But let us first examine how large an interpolated spin angle can be. As a simple estimate, suppose we are trying to align an interpolating spin $\tilde{\mathbf{m}}$ between neighboring spins $\mathbf{m}_1, \dots, \mathbf{m}_n$. Consider all of these spins as points in S^2 , the unit sphere in \mathbf{R}^3 . If the angle between $\tilde{\mathbf{m}}$ and spin \mathbf{m}_i is to be less than θ , then $\tilde{\mathbf{m}}$ must lie outside the circular disk symmetrically opposite to \mathbf{m}_i on S^2 with diameter $2\pi - 2\theta$. The area of such a disk is $2\pi(1 + \cos \theta)$. This is true for each i , so if the total area of n such disks is less than the total area of the sphere, then there exists a $\tilde{\mathbf{m}}$ that is no farther than θ from each of the spins $\mathbf{m}_1, \dots, \mathbf{m}_n$. Solving for θ we find $\theta \leq \arccos(-1 + 2/n)$. As an example, if we are trying to fit $\tilde{\mathbf{m}}$ between four fixed spins, then there is a direction for $\tilde{\mathbf{m}}$ that is at most $\arccos(-1 + 2/4) = 120^\circ$ from each of the fixed spins.

III. THEORY

We now develop a discrete analog to (1). Given the coarse grid spins $\mathbf{m} = (\mathbf{m}_1, \dots, \mathbf{m}_N)$, we want to find interpolating spins $\tilde{\mathbf{m}} = (\tilde{\mathbf{m}}_1, \dots, \tilde{\mathbf{m}}_K)$ solving

$$\min_{\tilde{\mathbf{m}}} F(\mathbf{m}; \tilde{\mathbf{m}}) \quad \text{subject to} \quad \Phi(\tilde{\mathbf{m}}) = \mathbf{0}, \quad (2)$$

where $\Phi = (\phi_k)$ is a collection of constraints, $k = 1, \dots, K$. (In Sec. IV we will use $\phi_k(\tilde{\mathbf{m}}) = \|\tilde{\mathbf{m}}_k\| - 1$.) We will assume that both the objective function F and the constraints are differentiable.

Let us assume for the moment that the interpolated spins $\tilde{\mathbf{m}}$ are differentiable with respect to \mathbf{m} , and use the extended discretization set $(\mathbf{m}, \tilde{\mathbf{m}})$ to evaluate the exchange energy $E(\mathbf{m}) = \tilde{E}[\mathbf{m}, \tilde{\mathbf{m}}(\mathbf{m})]$.

To relax our solution over \mathbf{m} , whether by integrating the Landau-Lifshitz-Gilbert equations, or through direct energy minimization, we needed to know $\partial E / \partial \mathbf{m}$:

$$\frac{\partial E}{\partial \mathbf{m}_i} = \frac{\partial \tilde{E}}{\partial \mathbf{m}_i} + \sum_{j=1}^N \frac{\partial \tilde{E}}{\partial \tilde{\mathbf{m}}_j} \frac{\partial \tilde{\mathbf{m}}_j}{\partial \mathbf{m}_i}. \quad (3)$$

We have only an implicit relation for $\tilde{\mathbf{m}}$ in terms of \mathbf{m} , so the last term above is difficult to evaluate. However, suppose we use \tilde{E} as the objective function F in (2). It follows from the theory of Lagrange multipliers that if $(\partial \phi_k / \partial \tilde{\mathbf{m}}_j)_{k,j}$ has full rank $K < \tilde{N}$, then at a local minimum $\tilde{\mathbf{m}}$ we can write $\partial \tilde{E} / \partial \tilde{\mathbf{m}}$ as a linear combination of $\partial \phi_k / \partial \tilde{\mathbf{m}}$ i.e.,

$$\frac{\partial E}{\partial \mathbf{m}_i} = \frac{\partial \tilde{E}}{\partial \mathbf{m}_i} + \sum_{k=1}^K \lambda_k \sum_{j=1}^{\tilde{N}} \frac{\partial \phi_k}{\partial \tilde{\mathbf{m}}_j} \frac{\partial \tilde{\mathbf{m}}_j}{\partial \mathbf{m}_i}.$$

If the constraints Φ are independent of \mathbf{m} , then the last sum is zero, and we get the simple relation

$$\frac{\partial E(\mathbf{m})}{\partial \mathbf{m}} = \frac{\partial \tilde{H}[\mathbf{m}, \tilde{\mathbf{m}}(\mathbf{m})]}{\partial \mathbf{m}}.$$

The one difficulty is that we cannot guarantee the differentiability of $\tilde{\mathbf{m}}$ with respect to \mathbf{m} . More work needs to be done to identify and handle those spin configurations for which differentiability is lost, but in practice such occurrences appear to be relatively uncommon.

IV. RESULTS AND CONCLUSIONS

To test this interpolation technique, we introduced a supplemental lattice to the simulation described in Sec. II. The supplemental lattice interpolated the main grid at half the cell dimension, i.e., with 12.5 nm square cells. The eight-neighbor dot product exchange energy formulation was minimized to determine the spins on the supplemental lattice (holding fixed the spins on the original lattice), subject to the constraint $\|\mathbf{m}\|=1$ for all spins. (For this initial study, we employed a simple gradient descent minimization algorithm, which required computation time comparable to that of the demagnetization calculation. We expect a sophisticated minimization algorithm will be much faster.) The refined lattice is used only for the exchange energy and exchange torque calculations.

The magnetization configuration in Fig. 1 is not a stable state under the new scheme, but using it as an initial state and allowing the simulation to evolve to a new energy minimum yields Fig. 3. Note that the interpolation has allowed the crosstie to reform, and the domain wall is now a resolved Néel wall. These results are similar to those obtained using the standard exchange scheme and a “real” refinement with 12.5 nm cells. Conversely, using the proposed method the Néel wall does not collapse even with 50 nm cells (and a 25 nm supplemental lattice).

As another test, we repeated the vortex pinning simulations detailed in Ref. 1, and found no increase in the vortex pinning field.

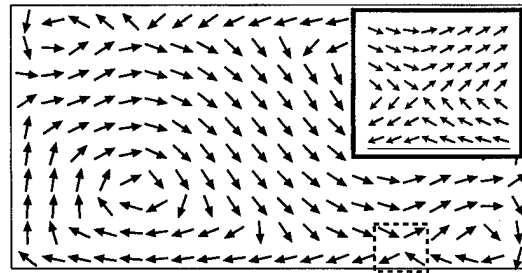


FIG. 3. Simulation results using the described interpolation technique, with Fig. 1 as the initial state ($\mu_0 H = 4.5$ mT). The collapsed wall in that figure has expanded into a crosstie and a resolved Néel wall.

It is important to distinguish this interpolation technique from a straightforward grid refinement. In the proposed technique the interpolated spins affect only the exchange energy, and at each step the interpolated spins are relaxed completely to an exchange energy minimum (holding fixed the spins on the coarse mesh). Because of this, the angle between neighboring spins on the refined mesh cannot collapse to 180° , as described in Sec. II. Instead, this technique effectively produces an exchange energy formulation that does not break down in the case of large angles between neighboring spins, yet does not increase vortex pinning.

¹M. J. Donahue and R. D. McMichael, *Physica B* **233**, 272 (1997).

²Round-robin results for a $2 \times 1 \times .02 \mu\text{m}$ $\text{Ni}_{80}\text{Fe}_{20}$ computational problem are available at <http://cobalt.nist.gov/mumag/prob1/prob1report.html>

³D. V. Berkov, K. Ramstöck, and A. Hubert, *Phys. Status Solidi A* **137**, 207 (1993).

⁴R. D. McMichael and M. J. Donahue, *IEEE Trans. Magn.* **33**, 4167 (1997).

⁵A. Aharoni, *J. Appl. Phys.* **37**, 3271 (1966).

⁶W. F. Brown, Jr. and S. Shtrikman, *Phys. Rev.* **125**, 825 (1962).

⁷K. Ramstöck, W. Hartung, and A. Hubert, *Phys. Status Solidi A* **155**, 505 (1996).

Hysteresis loop areas in kinetic Ising models: Effects of the switching mechanism

S. W. Sides^{a)} and P. A. Rikvold

Center for Materials Research and Technology and Department of Physics, and Supercomputer Computations Research Institute, Florida State University, Tallahassee, Florida 32306-4130 and Colorado Center for Chaos and Complexity, University of Colorado, Boulder, Colorado 80309-0216

M. A. Novotny

Supercomputer Computations Research Institute, Florida State University, Tallahassee, Florida 32306-4130

Experiments on ferromagnetic thin films have measured the dependence of the hysteresis loop area on the amplitude and frequency of the external field, $A=A(H_0, \omega)$, and approximate agreement with numerical simulations of Ising models has been reported. Here we present numerical and theoretical calculations of A in the low-frequency regime for two values of H_0 , which bracket a temperature and system-size dependent crossover field. Our previous Monte Carlo studies have shown that the hysteretic response of the kinetic Ising model is qualitatively different for amplitudes above and below this crossover field. Using droplet theory, we derive analytic expressions for the low-frequency asymptotic behavior of the hysteresis loop area. In both field regimes, the loop area exhibits an extremely slow approach to an asymptotic, logarithmic frequency dependence of the form $A \propto -[\ln(H_0\omega)]^{-1}$. Our results are relevant to the interpretation of data from experiments and simulations, on the basis of which power-law exponents for the hysteresis-loop area have been reported. © 1998 American Institute of Physics. [S0021-8979(98)23811-4]

When a ferromagnet is subject to an oscillating external field, $H(t)=H_0 \sin \omega t$, the time-dependent magnetization, $m(t)$, typically lags behind the field. The area of the resulting hysteresis loop, $A=-\oint m(H)dH$, equals the energy dissipated per period. It is therefore frequently measured in studies of periodically driven magnetic systems. Recent experiments on ultrathin ferromagnetic films,^{1,2} as well as numerical simulations of two-dimensional Ising models,³⁻⁶ have been interpreted in terms of a low-frequency power law, $A \propto H_0^a \omega^b$, with a range of exponent values having been reported.⁴⁻⁶ This interpretation is not fully consistent with the fluctuation-free mean-field result,^{7,8} $A=A_0 + \text{const}[\omega^2(H_0^2 - H_{sp}^2)]^{1/3}$ with positive constants A_0 and H_{sp} , which has been successfully applied to analyze experiments on ultrathin films of Co on Cu(001).⁹ Nor does the single power-law dependence agree with the logarithmic dependence expected if thermally activated nucleation is the rate-determining process.¹⁰⁻¹² Here we present analytical and numerical results that indicate a resolution of this puzzling situation.

Theoretical arguments and numerical simulations reveal parameter regimes in which, following instantaneous field reversal, a uniaxial single-domain ferromagnet switches to the stable magnetization direction via two distinct mechanisms. This magnetization reversal occurs either by nucleation of a *single* critical droplet of the stable phase [the single-droplet (SD) regime] or by simultaneous nucleation and growth of *many* critical droplets [the multi-droplet (MD) regime].¹²⁻¹⁴ The SD (MD) regime corresponds to weaker (stronger) fields and/or smaller (larger) systems. In this extension of our previous studies of hysteresis,¹⁵ we present

analytical and Monte Carlo results for the hysteresis-loop area for a kinetic Ising model at low frequencies; both in the SD regime and in the MD regime. The derivations are based on time-dependent extensions of classical homogeneous nucleation theory and “Avrami’s law” for the decay of a metastable phase.¹⁶ For both decay mechanisms, we show how an extremely slow approach of A to an asymptotic logarithmic dependence on $H_0\omega$ as $\omega \rightarrow 0$ gives “effective exponents” which superficially appear to describe a power law, even for data extending over several decades in frequency.

The model used here is a kinetic, nearest-neighbor Ising ferromagnet on a square lattice with Hamiltonian $\mathcal{H} = -J \sum_{\langle ij \rangle} s_i s_j - H(t) \sum_i s_i$ and periodic boundary conditions. Here $s_i = \pm 1$ are the local spin variables, $\sum_{\langle ij \rangle}$ runs over all nearest-neighbor pairs, and \sum_i runs over all $N=L^2$ lattice sites. The ferromagnetic exchange coupling is $J>0$, and $H(t)$ is a time-dependent external field. The dynamic is the Glauber single-spin-flip algorithm, with updates at randomly chosen sites. It is defined by the spin-flip probability $W(s_i \rightarrow -s_i) = \exp(-\beta \Delta E_i) / (1 + \exp(-\beta \Delta E_i))$, where ΔE_i is the change in the energy of the system if the spin flip is accepted, and $\beta^{-1} = k_B T$ is the temperature in energy units. Time is given in units of Monte Carlo steps per spin (MCSS). The average lifetime, $\langle \tau(|H|) \rangle$, of the unfavorably magnetized phase in a *static* field of magnitude $|H|$ is defined as the average time it takes the magnetization to reach zero, following instantaneous field reversal. The frequency, ω , of the applied sinusoidal field, is chosen by specifying the ratio $R = (2\pi/\omega) / \langle \tau(H_0) \rangle$.

^{a)}Electronic mail: sides@scri.fsu.edu

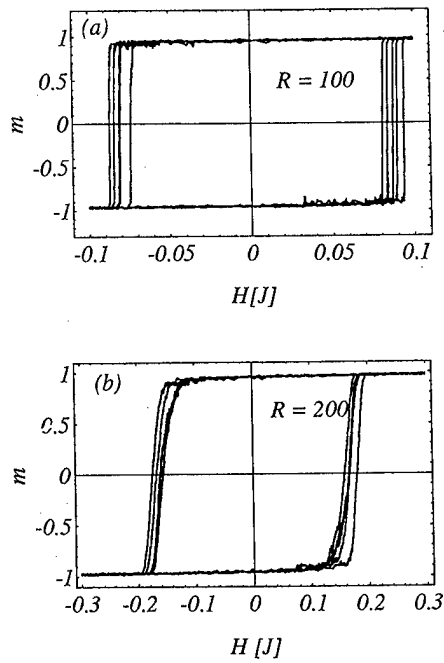


FIG. 1. Low-frequency hysteresis loops from simulations of a kinetic Ising model. For both regimes five loops are shown, representing short portions of the entire simulation time series. (a) Loops from the single-droplet (SD) regime, using $H_0 = 0.1$ J at a scaled frequency of $1/R = 0.01$. (b) Loops from the multi-droplet (MD) regime, using $H_0 = 0.3$ J at a scaled frequency of $1/R = 0.005$.

We initially prepare a system of size $L = 64$ at $T = 0.8T_c$ with all spins down, i.e., $m(0) = -1$. Then the sinusoidal field $H(t) = H_0 \sin \omega t$ is applied, and $m(t)$ is recorded for a fixed number of MCSS, n_{\max} . For the simulations in the SD regime, the field amplitude is $H_0 = 0.1$ J (which gives $\langle \tau \rangle = 2058$ MCSS) with $n_{\max} = 16.9 \times 10^6$ MCSS. For the MD regime, the amplitude is $H_0 = 0.3$ J (which gives $\langle \tau \rangle = 75$ MCSS) with $n_{\max} = 5.9 \times 10^5$ MCSS. For the values of L and T used here, the crossover field [called the Dynamic Spinodal¹⁴ (DSP)] between these two regimes is $H_{\text{DSP}} \approx 0.11$ J. For large systems H_{DSP} vanishes slowly with L as $H_{\text{DSP}}(L) \sim (\ln L)^{-1/(d-1)}$. Figure 1 shows representative hysteresis loops from simulations in both the SD and MD regimes. The large relative fluctuations in the loop area in Fig. 1(a) indicate the stochastic nature of the switching mechanism in the SD regime.¹⁷ The relative fluctuations in the loop area are smaller in the MD regime [Fig. 1(b)]. The stochastic nature of magnetization reversal in the SD regime allows one to treat the switching as a variable-rate Poisson process. For low frequencies, this variable switching rate is the system volume times the nucleation rate obtained from classical droplet theory,

$$L^d I(H(t), T) \propto L^d |H(t)|^K \exp \left[-\frac{\Xi_0(T)}{|H(t)|^{d-1}} \right], \quad (1)$$

where d is the spatial dimension of the system, and K and $\Xi_0(T)$ are known from theory and simulations.^{13,14} The quantity $\Xi_0(T)$ is the field-independent part of the free-energy cost of a critical droplet, divided by $k_B T$. The time dependence of the nucleation rate enters solely through $H(t)$. Using Eq. (1) one can derive an expression for the cumula-

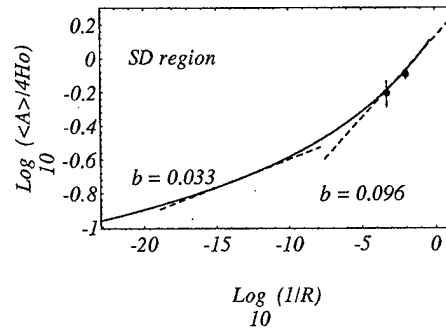


FIG. 2. Log-log plot of $\langle A \rangle / 4H_0$ vs $1/R$ in the SD regime. The solid curve is obtained from the numerical solution of Eq. (2), the derivation of which is outlined in the text. The dashed line segments represent linear least-squares fits to different portions of the numerical solution data. The data that yield the effective exponent $b = 0.096$, are centered around $\log(1/R) = -2.05$; those that yield $b = 0.033$ are centered around $\log(1/R) = -13.38$. The two solid dots are MC simulation data. The vertical lines are not error bars; they represent the standard deviation of the loop-area distribution.

tive probability that a switch has taken place by time t , $F(t)$.¹⁷ The median switching time, t_s , is given by $F(t_s) = 1/2$. To obtain an analytic result we use the low-frequency approximation $H(t) \approx H_0 \omega t$. Then the median switching field, $H_s = H_0 \omega t_s$, is given by the solution of the equation,

$$\ln 2 = \rho_0 \frac{e^{\frac{\Xi_0(T)}{H_0^{d-1}} \frac{K+1}{d-1}}}{H_0^{K+1} (d-1) \omega} \times \Gamma \left(1 - \frac{K+d}{d-1}, \frac{\Xi_0}{H_s^{d-1}} \right), \quad (2)$$

where $\Gamma(a, x)$ is the incomplete gamma function, and ρ_0 is the switching rate in a static field of magnitude H_0 , which has been measured in field-reversal simulations.¹⁷

Due to the square shape of the hysteresis loop in both regimes, the loop area is given by $\langle A \rangle / 4H_0 \approx m_{\text{eq}} H_s(\omega) / H_0$, where m_{eq} is the spontaneous zero-field magnetization. Figure 2 is a log-log plot of the hysteresis-loop area versus the frequency, $1/R$, in the SD regime. The solid curve is calculated by numerical solution of Eq. (2) with $d=2$, $K=3$, $\Xi_0 = 0.506192$ J, and $\rho_0 = 6.62 \times 10^{-4}$ MCSS⁻¹. Hence, this calculation involves no adjustable parameters. The solid dots are data from MC simulations. Each of the two dashed lines is obtained from a linear least-squares fit to the numerical solution for the loop area over nearly four decades in frequency. The effective exponents obtained from this fitting procedure appear valid over a frequency range that would be considered large from the viewpoint of experiments or even simulations. Over a very large frequency range however, the effective exponent depends on the frequency range in which data are analyzed. Expanding $\Gamma(a, x)$ in Eq. (2) for large values of $x = \Xi_0 / H_s^{d-1}$ gives the asymptotic low-frequency result $\langle A \rangle_{\text{SD}} \propto [\ln(H_0 \omega)]^{-1/(d-1)}$.

The details of the theoretical derivation of the loop area in the MD regime are different than in the SD regime. However, two basic features are the same: the form of the time-dependent nucleation rate, $I(H(t), T)$ from Eq. (1), and the linear approximation for the field used to obtain asymptotic

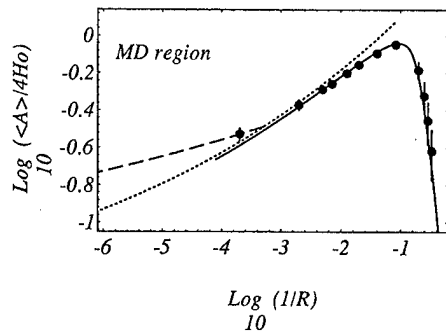


FIG. 3. Log-log plot of $\langle A \rangle / 4H_0$ vs $1/R$ in the MD regime. The solid curve is obtained from a full numerical integration of the time-dependent Avrami's law result for $m(t)$, using a sinusoidal field, $H(t) = H_0 \sin \omega t$. (This calculation could not be extended to lower frequencies than those shown due to numerical difficulties.) The dotted curve is obtained from a numerical solution of an analytic expression whose derivation uses a linear approximation for the field, $H(t) \approx H_0 \omega t$. The solid dots represent MC simulations. The vertical bars denote the standard deviation in the loop-area distributions as in Fig. 2. The dashed curve represents the SD result (the solid curve in Fig. 2) after rescaling so that the SD and MD results may be compared.

analytic results for very low frequencies. Figure 3 is a log-log plot of the hysteresis-loop area versus $1/R$ in the MD regime. The solid curve results from a full numerical integration (NI) of an analytic expression for $m(t)$, obtained from Avrami's law,¹⁶ with the sinusoidal form of $H(t)$. The dotted curve results from a numerical solution (NS) of an analytic expression obtained from a linear approximation for $H(t)$, as for the SD regime. The transcendental equation that must be solved is analogous to Eq. (2), but contains a sum of three incomplete gamma functions.¹⁷ The MC data (solid dots), NI and NS results are in excellent agreement. For $d=2$ and *extremely* low frequencies, an asymptotic expansion of the analytic expression used to obtain the NS result gives $\langle A \rangle_{\text{MD}} \propto -[\ln(H_0 \omega)]^{-1}$. As in the SD case, from a log-log plot of the loop area versus frequency one can extract effective exponents from the data over nearly two decades in $1/R$. However, these effective exponents depend strongly on the frequency range in which the fit is performed. Similarly, if A is plotted vs $-\ln(H_0 \omega)$ as in Ref. 10, the slow crossover will result in a significant overestimate of the asymptotic exponent $1/(d-1)$.

A change from MD to SD behavior should appear not only as $H_0 \rightarrow H_{\text{DSP}}$, but for finite systems it should be observed when ω becomes sufficiently low that $H_s < H_{\text{DSP}}(L)$. The frequency of this crossover should be given by the intersection of the results for the loop areas in the SD and MD regions. The dashed curve in Fig. 3 represents the solid curve in Fig. 2, which has been rescaled so that the two results may be plotted together. The value of the loop area at the intersection is that of a loop with $H_s \approx H_{\text{DSP}}(L)$. While $m(t)$ and A do not depend on system size in the MD regime, A in the

SD region, and hence the location of the crossover, depends on L .

In conclusion, we have shown that the hysteresis-loop areas for kinetic Ising ferromagnets driven by oscillating external fields vanish logarithmically with $H_0 \omega$ for asymptotically low frequencies. This result should be valid for all fields and temperatures such that magnetization switching proceeds via a homogeneous nucleation-and-growth mechanism,^{10,11} in particular for both the single-droplet and multidroplet regimes considered here. For both of these regimes we stress that the asymptotic low-frequency behavior would only be seen for *extremely* low frequencies. For frequencies in a more "realistic" range, we find a wide crossover, extending over many decades in frequency. Power law fits to the loop areas over as much as four frequency decades give good agreement within the fitting range, but the resulting effective exponents depend strongly on the fitting interval. We believe our results are significant to the interpretation and comparison of results from experimental^{1,2,9} and numerical⁴⁻⁶ studies of hysteresis in ferromagnetic systems, in which power-law dependences of the loop areas have been reported with a variety of exponents.

The authors (S.W.S.) and (P.A.R.) thank P. D. Beale, G. Brown, W. Klein, M. Kolesik, and R. A. Ramos for useful discussions and the Colorado Center for Chaos and Complexity for hospitality and support during the 1997 Workshop on Nucleation Theory and Phase Transitions. Research supported in part by FSU-MARTECH, by FSU-SCRI under DOE Contract No. DE-FC05-85ER25000, and by NSF Grants Nos. DMR-9315969, DMR-9634873, and DMR-9520325.

¹Y. He and G. Wang, Phys. Rev. Lett. **70**, 2336 (1993).

²J. S. Suen and J. Erskine, Phys. Rev. Lett. **78**, 3567 (1997).

³M. Rao, H. Krishnamurthy, and R. Pandit, Phys. Rev. B **42**, 856 (1990).

⁴W. Lo and R. A. Pelcovits, Phys. Rev. A **42**, 7471 (1990).

⁵S. Sengupta, Y. Marathe, and S. Puri, Phys. Rev. B **45**, 7828 (1992).

⁶M. Acharyya and B. K. Chakrabarti, Phys. Rev. B **52**, 6550 (1995), and references cited therein.

⁷P. Jung, G. Gray, and R. Roy, Phys. Rev. Lett. **65**, 1873 (1990).

⁸C. Luse and A. Zangwill, Phys. Rev. E **50**, 224 (1994).

⁹Q. Jiang, H.-N. Yang, and G.-C. Wang, Phys. Rev. B **52**, 14911 (1995).

¹⁰P. B. Thomas and D. Dhar, J. Phys. A **26**, 3973 (1993).

¹¹P. D. Beale, Integr. Ferroelectr. **4**, 107 (1994).

¹²M. Kolesik, M. A. Novotny, and P. A. Rikvold, Phys. Rev. B **56**, 11791 (1997).

¹³H. L. Richards, S. W. Sides, M. A. Novotny, and P. A. Rikvold, J. Magn. Magn. Mater. **150**, 37 (1995); H. L. Richards *et al.*, Phys. Rev. B **54**, 4113 (1996); **55**, 11521 (1997).

¹⁴P. A. Rikvold, H. Tomita, S. Miyashita, and S. W. Sides, Phys. Rev. E **49**, 5080 (1994).

¹⁵S. W. Sides, R. A. Ramos, P. A. Rikvold, and M. A. Novotny, J. Appl. Phys. **79**, 6482 (1996); **81**, 5597 (1997).

¹⁶K. Sekimoto, Physica A **135**, 328 (1986).

¹⁷S. W. Sides, P. A. Rikvold, and M. A. Novotny, Phys. Rev. E (in press); (unpublished).

Domain-wall motion in random potential and hysteresis modeling

M. Pasquale,^{a)} V. Basso, and G. Bertotti

IEN Galileo Ferraris and INFN C. so M. D'Azeglio 42, 10125 Torino, Italy

D. C. Jiles and Y. Bi

Ames Laboratory, Iowa State University, 50011 Ames, Iowa

Two different approaches to hysteresis modeling are compared using a common ground based on energy relations, defined in terms of dissipated and stored energy. Using the Preisach model and assuming that magnetization is mainly due to domain-wall motion, one can derive the expression of magnetization along a major loop typical of the Jiles–Atherton model and then extend its validity to cases where mean-field effects and reversible contributions are present. © 1998 American Institute of Physics. [S0021-8979(98)39311-1]

I. INTRODUCTION

The Preisach¹ and Jiles–Atherton² models are two widely used approaches to the description of magnetic hysteresis. They have been applied to a wide range of static and dynamic conditions, ranging from the solution of circuits containing hysteretic components to microstructural analysis.^{3–5} Their physical significance can be best appreciated when modeling features are reduced to fundamental energetic aspects, and this result is particularly helpful in the clarification of the relations between different approaches to hysteresis modeling. In this paper, we show that by referring to fundamental energy relations, which can be used to describe the models in terms of stored and dissipated energy, one is able to derive the fundamental expression of magnetization laws of the Jiles–Atherton model by applying a physically meaningful set of assumptions to the Preisach model.

When work is performed by external sources on a system displaying hysteresis, part of the energy is stored and part is dissipated. This energy balance can be described using a model which takes into account a minimum set of relevant physical quantities. Considering, for example, a homogeneous magnetic system and assuming, for the sake of simplicity, that the bulk magnetization M is aligned to the applied magnetic-field H_α , the general expression for the balance between stored and dissipated energy can be expressed as

$$-\mu_0 M dH_\alpha = dg + \delta Q, \quad (1)$$

where dg corresponds to the change in free energy per unit volume and δQ is the dissipated energy term. In this paper, we show how one can express the terms of Eq. (1) with quantities easily recognized in each of the modeling schemes, and furthermore, how this can be used as a common reference for the quantitative comparison of the Jiles–Atherton and Preisach models.

^{a)}Electronic mail: pasquale@ien.it

II. JILES–ATHERTON MODEL

In the case of the Jiles–Atherton model, it is assumed that the free-energy term dg of Eq. (1) can be expressed in terms of the anhysteretic curve $M_{an}(H_\alpha)$; the idea is that the energy supplied coincides with the change in magnetostatic energy in the absence of hysteresis:

$$dg = -\mu_0 M_{an} dH_\alpha. \quad (2)$$

The other term of Eq. (1), δQ , corresponding to the dissipated energy, will be the difference between the energy supplied and the change in magnetostatic energy. This can be taken to be proportional to the change in magnetization,

$$\delta Q = \mu_0 k dM, \quad (3)$$

since dM can be thought to be proportional to the number of pinning sites seen by a moving domain wall; and each pinning event giving rise to Barkhausen jump, when integrated over the entire specimen, will produce a dissipation contribution proportional to the pinning site density k . The dissipation is always positive, that is, there can be loss of energy only, and therefore, in Eq. (3) and the subsequent analysis it is implicitly assumed that dM is positive. The equations can easily be modified to take into account a negative dM . Using these assumptions, Eq. (1) becomes then,

$$-\mu_0 M dH_\alpha = -\mu_0 M_{an} dH_\alpha + \mu_0 k dM, \quad (4)$$

which can be directly written as

$$\frac{dM}{dH_\alpha} = \frac{M_{an}(H_\alpha) - M(H_\alpha)}{k}, \quad (5)$$

which is the simplest expression of the basic magnetization law of the Jiles–Atherton model² in the absence of an internal coupling field.

III. PREISACH MODEL

In the Preisach model, hysteresis is described starting from the hypothesis that a free-energy profile characterized by multiple local minima and metastable states can be decomposed into a set of many elementary bistable contributions. Each bistable unit can occupy one of two states, which we shall call (+) and (−) states and is characterized by two

fields h_c and h_u , respectively proportional to the height of the barrier separating the (+) and (−) states and to the energy difference of the (+) and (−) states. The basic relation of the magnetization in the Preisach model is

$$M = 2M_s \int_0^\infty dh_c \int_0^{b(h_c)} dh_u p(h_c, h_u), \quad (6)$$

obtained by integration on the plane defined by the ensemble of bistable units. The integration upper limit $b(h_c)$ consists of a chain of segments of alternating slope $db/dh_c = +1$ and $db/dh_c = -1$ generated by the past field history. This line defines the partition of the Preisach plane in only one (+) and one (−) region.¹ In the case of the saturation loop branch with peak-field H_α , $b(h_c)$ becomes simply $H_\alpha - h_c$, a segment of slope $db/dh_c = -1$. The physical meaning of the Preisach model emerges clearly when one considers the properties of domain walls (DW) moving in this complex energy profile, which is rich in metastable states. It has been proved⁶ that the hysteresis properties of a DW moving in a Wiener-like pinning field profile can be described by the Preisach hysteresis model, where the Preisach distribution $p(h_c, h_u)$, weighting the elementary contributions, is proportional to

$$p(h_c, h_u) \propto \exp(-h_c/k), \quad (7)$$

independent of h_u where k describes the statistical properties of the pinning field. This result pertains to indefinite wall motion and contains no description of magnetic saturation. Saturation can then be taken into account by modifying Eq. (7) into

$$p(h_c, h_u) \propto u(h_c) \nu(h_u), \quad (8)$$

where the ν function is an integrable even function of h_u . This generalization corresponds again to the physical picture where stored energy (represented by the h_u variable) and dissipated energy (represented by h_c) can be factorized as $u(h_c) \nu(h_u)$ for a proper description of the system.

In the case of a saturation loop branch, by applying Eq. (8) to Eq. (6) for the calculation of the saturation loop branch, one will obtain a relation identical to the Jiles–Atherton hysteresis model² where the integral of $\nu(h_u)$ coincides with the anhysteretic curve. This curve represents the nondissipation limit of the magnetization process, and it can be obtained for any value of applied-field H_α by applying an oscillating field history with decreasing peak amplitude in order to demagnetize the material in the bias field H_α . The anhysteretic curve is closely connected with the function $\nu(h_u)$. In fact, the upper integration limit $b(h_c)$ associated with the anhysteretic state assumes the particularly simple form $b(h_c) = H_\alpha$ when the demagnetization is performed using an arbitrarily large number of decreasing steps.¹ In this case, Eq. (8) can be written as

$$M_{an}(H_\alpha) = 2M_s \int_0^\infty dh_c \int_0^{H_\alpha} dh_u u(h_c) \nu(h_u), \quad (9)$$

and if the dissipation term is normalized so that

$$\int_0^\infty dh_c u(h_c) = 1, \quad (10)$$

the anhysteretic magnetization can simply be expressed as

$$M_{an}(H_\alpha) = 2M_s \int_0^{H_\alpha} dh_u \nu(h_u), \quad (11)$$

and $\nu(h_u)$ must, therefore, be the derivative of M_{an} with respect to h_u rescaled by some constant. This result follows directly from the chosen factorization Eq. (7) of the Preisach distribution. Considering now the expression for magnetization of Eq. (6), one obtains an expression for dM ,

$$\frac{dM}{dH_\alpha} = 2M_s \int_0^\infty \frac{dh_c}{k} \exp(-h_c/k) \nu(H_\alpha - h_c), \quad (12)$$

that integrated by parts gives

$$\frac{dM}{dH_\alpha} = \frac{1}{k} [M_{an}(H_\alpha) - M(H_\alpha)], \quad (13)$$

which demonstrates the actual equivalence between the Preisach and Jiles–Atherton models in the calculation of a saturation branch, under the hypothesis of DW dominance and saturation approach according to an anhysteretic law. The result in Eq. (13) can be used to clarify the equivalence through the direct comparison of the terms appearing in Eq. (1) derived from the two models, and to this end we will write Eq. (13) for later use as

$$\mu_0 k dM = \mu_0 M_{an} dH_\alpha - \mu_0 M dH_\alpha. \quad (14)$$

It has also been shown in Ref. 7 that through the Preisach operator of Eq. (6) one can obtain an expression for the terms δQ and g appearing in Eq. (1):

$$\delta Q = \left| 2\mu_0 M_s \int_0^\infty dh_c h_c p[h_c, b(h_c)] \delta b(h_c) \right|, \quad (15)$$

and

$$g = 2\mu_0 M_s \int_0^\infty dh_c \int_0^{b(h_c)} dh_u (h_u - H_\alpha) p(h_c, h_u), \quad (16)$$

where $\delta b(h_c)$ represents a small variation of the integration limit, i.e., a small variation of the state of the system consequent to a small field variation dH_α . Now, if δQ is written using Eqs. (7) and (8) and then it is integrated by parts, one obtains

$$\begin{aligned} \delta Q = & 2\mu_0 M_s \int_0^\infty dh_c \exp(-h_c/k) \nu(H_\alpha - h_c) dH_\alpha \\ & - 2\mu_0 M_s \int_0^\infty dh_c h_c \exp(-h_c/k) \\ & \times \left[\frac{d\nu(x)}{dx} \right]_{x=H_\alpha-h_c} dH_\alpha, \end{aligned}$$

where substituting

$$\begin{aligned} \mu_0 X dH_\alpha = & 2\mu_0 M_s \int_0^\infty dh_c h_c \exp(-h_c/k) \\ & \times \left[\frac{d\nu(x)}{dx} \right]_{x=H_\alpha-h_c} dH_\alpha, \end{aligned}$$

one will be able to write

$$\delta Q = \mu_0 H_0 dM - \mu_0 X dH_\alpha. \quad (17)$$

Finally, Eqs. (14) and (17) can be combined with Eq. (1) to obtain an expression of dg :

$$dg = -\mu_0 M_{\text{an}} dH_\alpha + \mu_0 X dH_\alpha, \quad (18)$$

and this result, when compared with Eqs. (2) and (3) shows that both the Preisach and Jiles–Atherton models are fully consistent with the energy balance expressed in Eq. (1), even though a deviation term is observed.

A. Irreversible and reversible magnetization

In Eq. (13) it has been shown that the expressions for magnetization derived in the Preisach framework can be used to obtain an expression for magnetization along the major loop as in the Jiles–Atherton model. The general expression for total magnetization M is usually given as the sum of two contributions M_{irr} and M_{rev} . Equations (6) and (8) refer to the irreversible part only, so that

$$M_{\text{irr}}(H_\alpha) = \frac{2M_s}{k} \int_0^\infty dh_c \int_0^{H_\alpha - h_c} dh_u \exp(-h_c/k) \nu(h_u), \quad (19)$$

and the Jiles–Atherton relation (5) becomes

$$\frac{dM_{\text{irr}}(H_\alpha)}{dH_\alpha} = \frac{1}{k} [M_{\text{an}}(H_\alpha) - M_{\text{irr}}(H_\alpha)]. \quad (20)$$

Reversible magnetization processes can be quite naturally introduced in the Preisach model by association with elementary hysteresis loops with no energy dissipation, e.g., where $h_c = 0$. These objects will be distributed along the h_u axis and they can be defined using Dirac's delta function $\delta(h_c)$. The Preisach distribution referring to total magnetization is then the sum of two parts, both multiplied by the same function $\nu(h_u)$,

$$[(1-c)u(h_c) + c\delta(h_c)]\nu(h_u), \quad (21)$$

where $\delta(h_c)$ is the Dirac function.

Using Eq. (21) and referring to the general expression for magnetization in Eq. (6) and (9), where one can substitute $p(h_c)$ with $\delta(h_c)$, the reversible contribution to magnetization can be written as

$$\begin{aligned} M_{\text{rev}}(H_\alpha) &= c2M_s \int_0^\infty dh_c \int_0^{H_\alpha} dh_u \delta(h_c) \nu(h_u) \\ &= cM_{\text{an}}(H_\alpha), \end{aligned} \quad (22)$$

having made use of Eq. (13). With this result, total magnetization can be written both for the Preisach and the Jiles–Atherton models as

$$dM = [(1-c)dM_{\text{irr}} + cdM_{\text{an}}]. \quad (23)$$

B. Mean-field contributions

Wishing to express the same quantities in the presence of a mean-field interaction, one has to distinguish the applied-field H_α from the internal-field H_{eff} , which is equal to the sum of the applied field and a coupling term proportional to magnetization through a coefficient $\alpha \neq 0$:

$$H_{\text{eff}} = H_\alpha + \alpha M, \quad (24)$$

taking the derivative of H_α with respect to internal-field H_{eff} one obtains,

$$\frac{dH_\alpha}{dH_{\text{eff}}} = 1 - \alpha \frac{dM}{dH_{\text{eff}}}, \quad (25)$$

which can be used to write the derivative of M with respect to H_α ,

$$\frac{dM}{dH_\alpha} = \frac{dM}{dH_{\text{eff}}} \bigg/ \frac{dH_\alpha}{dH_{\text{eff}}} = \frac{dM}{dH_{\text{eff}}} \bigg/ \left(1 - \alpha \frac{dM}{dH_{\text{eff}}} \right). \quad (26)$$

Now one is able to write Eq. (20) using H_{eff} instead of H_α ,

$$\frac{dM(H_{\text{eff}})}{dH_{\text{eff}}} = \frac{1}{k} [M_{\text{an}}(H_{\text{eff}}) - M_{\text{irr}}(H_{\text{eff}})],$$

and transform it to a derivative with respect to H_α :

$$\frac{dM(H_\alpha)}{dH_\alpha} = \frac{M_{\text{an}}(H_\alpha) - M_{\text{irr}}(H_\alpha)}{k - \alpha [M_{\text{an}}(H_\alpha) - M_{\text{irr}}(H_\alpha)]}, \quad (27)$$

which gives the Jiles–Atherton law for irreversible magnetization.

ACKNOWLEDGMENT

This work was supported by NATO, Division of Scientific Affairs, under Collaborative Research Grant No. CRG 960765.

¹I. D. Mayergoyz, *Mathematical Models of Hysteresis* (Springer, New York, 1991).

²D. C. Jiles and A. L. Atherton, *J. Appl. Phys.* **55**, 2115 (1984).

³D. A. Philips, L. R. Duprè, and J. A. A. Melkebeek, *IEEE Trans. Magn.* **30**, 4377 (1994).

⁴S. Bobbio, M. De Magistris, G. Miano, C. Visone, and E. Zamparelli, *IEEE Trans. Magn.* **30**, 3367 (1994).

⁵V. Basso, G. Bertotti, F. Fiorillo, and M. Pasquale, *IEEE Trans. Magn.* **30**, 4893 (1994).

⁶G. Bertotti, V. Basso, and G. Durin, *J. Appl. Phys.* **79**, 5764 (1996).

⁷G. Bertotti, *Phys. Rev. Lett.* **76**, 1739 (1996).

The field-space perspective on hysteresis in uniaxial ferromagnets

Y. T. Millev^{a)}

Max Planck Institute of Mathematics in the Sciences, Inselstr. 22-26, D-04103 Leipzig, Germany

J. R. Cullen

Physics Department, Trinity College of Dublin, Dublin 2, Ireland

H. P. Oepen

Max Planck Institute of Microstructure Physics, Weinberg 2, D-06120 Halle, Germany

A procedure for the analysis of hysteresis in the \mathbf{H} space of a uniaxial ferromagnet with higher-order anisotropy is put forward. The formulation is valid to any order n in the anisotropy expansion. The critical boundaries separating stable from metastable states are cast in a formally decoupled parametric way as $H_x = H_x(M_x)$, $H_z = H_z(M_z)$. The analytic expressions provide the basis for the construction of generalized astroids to any order. For $n > 1$, new features are found and interpreted in their relation to rotational hysteresis and possible spin-reorientation transitions in uniaxial materials. The shape and symmetry of the critical boundaries depend crucially on up to $n-1$ independent ratios of the anisotropy constants against a suitable normalizing quantity; the normalizer can be any from among the set of constants or any linear combination thereof. Self-crossing of an astroid indicates the existence of additional extrema and, hence, of complicated hystereses. © 1998 American Institute of Physics. [S0021-8979(98)23911-9]

I. INTRODUCTION

Hysteresis is a complex nonlinear phenomenon of delicate sensitivity to the past states of the system.¹ In ferromagnets whose anisotropy could be reasonably well characterized by a phenomenologic free energy expansion $F(\theta, \phi)$ in the angular variables of the saturation magnetization \mathbf{M} , hysteresis holds place even if one allows for homogeneous rotation of \mathbf{M} only.² There are certain advantages with the analysis of a uniaxial system in its field space. For instance, one can determine the boundaries of stability of states corresponding to different minima of the anisotropy energy for any field direction and not only for the two principal configurations with field parallel or perpendicular to the axis of symmetry. The case with only the lowest term in the anisotropy expansion has been systematically discussed and implemented.^{1,3} The only exceptions dealing with astroids in higher orders are Refs. 4 and 5 concerning a system with two anisotropy constants. In the following, we demonstrate that this type of analysis is easily extended to any order in the anisotropy expansion due to a special feature of the problem at hand, so that the first two orders are deduced as particular cases. The procedure gives rise to field-space diagrams which will be referred to as generalized astroids. Self-crossing of the boundaries of stability, found already in the second order,^{4,5} arises over large domains of values of the anisotropy constants and is the most pronounced feature of this generalization. It signals the existence of complicated hysteresis behavior due to the emergence of additional competing energy minima.

II. GENERALIZED ASTROIDS: ANALYTICAL AND EXAMPLES

One carries out the field-space analysis with the phenomenological thermodynamic potential of the type $g_A = f_A + \epsilon_Z$, where $\epsilon_Z = -\mathbf{M} \cdot \mathbf{H}$ is the Zeeman term, while

$$f_A(\theta; \{a_j\}) = \sum_{k=1}^{\infty} a_k \sin^{2k} \theta \quad (1)$$

is the full expansion for the anisotropy energy density of a uniaxial ferromagnet.³ The $\{a_j\}$'s are the anisotropy constants of order j , while θ is the angle between \mathbf{M} and the crystallographic axis of cylindrical symmetry \mathbf{n} .

In the assumed symmetry, all three relevant vectors \mathbf{n} , \mathbf{H} , and \mathbf{M} lie in the same plane, since there is no torque to drive the magnetization out of the plane (\mathbf{H}, \mathbf{n}). The remagnetization processes are confined to this plane. This makes all results directly applicable to situations, typical of thin ferromagnetic films, where the magnetization vector is confined within the plane of the film because of the strong dipolar contribution.⁶ We choose the z axis along \mathbf{n} with $\mathbf{M} = (M_x, 0, M_z)$ and $\mathbf{H} = (H_x, 0, H_z)$. To find the stable directions of \mathbf{M} under applied field, one has to look for extrema of $g_A(\theta)$ by solving $g'(\theta) = 0$ and requiring that $g''(\theta) \geq 0$ at the eventual solutions of the extremal equation. In zero field, there is always more than one stable solution, while in sufficiently high fields, the Zeeman energy favors conforming alignment of \mathbf{M} and \mathbf{H} . So the boundaries between perfectly aligned and competing equilibrium states are at some finite magnitude of field which may vary with field direction. It is determined by the simultaneous consideration of the conditions $g'(\theta) = g''(\theta) = 0$ by inserting the expansion from Eq. (1). One observes that this system of two equations is linear in the components of the field, so that, solving for H_x and H_z , one obtains

^{a)}On leave from the CPCS Lab, Inst. Solid State Phys., Sofia; electronic mail: millev@mis.mpg.de

$$H_x = \frac{2}{M} \sum_{k=1}^{\infty} k a_k \sin^{2k-1} \theta [2(1-k) + (2k-1) \sin^2 \theta],$$

$$H_z = \frac{2}{M} \sum_{k=1}^{\infty} k a_k (1-2k) \sum_{p=0}^{k-1} \binom{k-1}{p} (-1)^p \cos^{2p+3} \theta. \quad (2)$$

This is obviously a parametric solution of the type $H_x = H_x(\theta)$, $H_z = H_z(\theta)$ which describes the boundaries of stability in the field space of the uniaxial system to arbitrary order. A seemingly redundant complication has arisen in passing from $\sin \theta$ to $\cos \theta$ in Eqs. (2). This was motivated by the desire to cast the parametric solution in a formally decoupled way as $H_x = H_x(M_x)$, $H_z = H_z(M_z)$. The form serves to identify correspondence rules between the particular principal cases of fields applied along \mathbf{n} or perpendicularly to it. The rules come about by comparing identical powers in M_x and M_z in the two equations for the respective field components. They save half of the labor in exploring the phase diagrams in \mathbf{H} space, since features of given symmetry for a given set of anisotropy constants $\{a_k\}$ must be identical, up to permutation of H_x and H_z axes, for the *corresponding set* of constants. This is in fact a symmetry argument which has escaped attention in the earlier field-space (astroid) studies; here, one deduces it from the general solution to arbitrary order.

A further general observation, valid to any order, is borne out by looking in turn at the two principal configurations $\mathbf{H} \parallel \mathbf{n}$ and $\mathbf{H} \perp \mathbf{n}$. In the first case, the conforming solution ($\mathbf{H} \parallel \mathbf{M}$) is $\sin \theta = 0$ and is stable, to any order, for $H \geq H_{A1}$ with the anisotropy field $H_{A1} = 2|a_1|/M$ depending on a_1 alone despite of considering the contributions from all orders. In the second case, the conforming solution is $\cos \theta = 0$ and is stable for $H \geq H_{A2}$ with $H_{A2} = 2|\sum_{k=1}^{\infty} k \cdot a_k|/M$. As a very interesting consequence, in a system with a spin-reorientation transition, which would occur in a given anisotropic ferromagnet if $a_1 \rightarrow 0$ under variation of some parameter like temperature etc., the anisotropy in the direction of the symmetry axis \mathbf{n} becomes soft ($H_{A1} \rightarrow 0$) which gives rise to a number of peculiarities. Either H_{A1} or H_{A2} may serve as natural normalizing quantities for the generalized astroids to arbitrary order, but the choice is not restricted and may be varied, should particular considerations of simplicity hold in a particular system. Generally, the precise shape of the boundaries in \mathbf{H} space depends on up to $n-1$ constitutive ratios to order n . In principle, the part of a normalizing quantity may be played by any linear combination of anisotropy constants.

The predictive power of the \mathbf{H} -space analysis to higher orders depends crucially on the fact that the tangent construction¹ for the determination of the hysteresis along any route in field space remains valid even with anisotropy constants of higher orders. It is indeed a substitute for the numerical solution of a high-degree polynomial equation. The existence of more competing states as one goes to higher orders in the anisotropy energy gives rise to rather complex generalized astroids whose generation by Eqs. (2) can, however, be performed pretty easily.

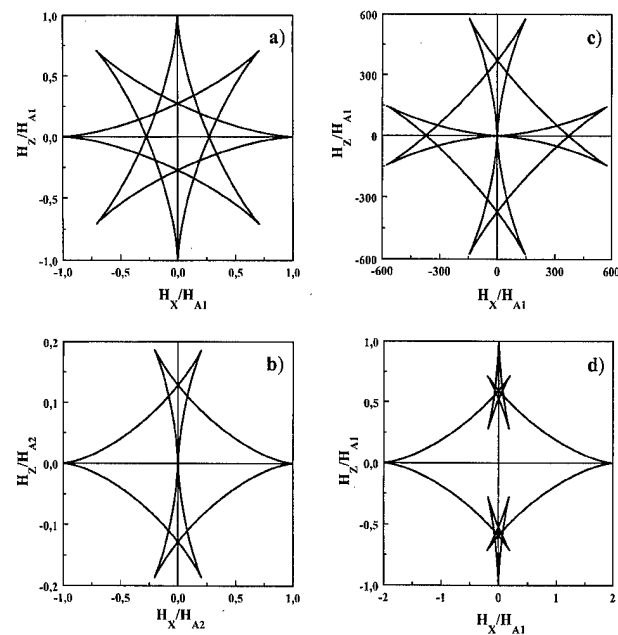


FIG. 1. (a) The octopole astroid ($a_1 = -a_2$, $a_3 = 0$). The exceptionally high eightfold symmetry derives from the exchange of stability along this special line in the anisotropy space of the system (Ref. 8). (b) Swallow tails due to softening of the anisotropy axis \mathbf{n} for a system with a spontaneous orientational transition. (c) Generalized astroid for a system with both anisotropy fields gone soft ($a_1 \approx 0$, $a_1 + 2a_2 + 3a_3 = 0$). Note the squarelike aspect of the "mainframe." (d) A generalized astroid with all $|a_{1,2,3}|$ equal ($a_{1,3} < 0$, $a_2 > 0$). Self-crossings of this type imply complicated secondary hystereses.

We proceed to illustrate the general method by several examples up to order $n=3$ in the anisotropy expansion. For bulk systems, the necessity of considering three orders in the expansion for a uniaxial system arises in the analysis of the behavior of the rather important group of highly anisotropic rare-earth-transition-metal compounds.⁷ The examples are indicative of the variety of nontrivial cases which are in store when higher-order anisotropies are non-negligible. Consider the case with $a_3 = 0$ first. A symmetric astroid results when $a_1 = -a_2$ [Fig. 1(a)]. This condition corresponds to the line in the anisotropy space along which a stable canted solution exists ($a_1 < 0$) or there is a pair of coexisting minima of equal depth ($a_1 > 0$).³ The symmetry is exceptionally high with the vertices of the octopolelike astroid lying on a circle.⁸ All cases which are of the self-crossing type may be viewed as resulting from continuous deformations of the most symmetric case upon variation of the ratio a_2/a_1 . Generalizing these observations, the most symmetric astroids to any given order of the expansion will be realized on the manifolds where, in zero field, the eventual minima transform into each other continuously or exchange stability, while coexisting. Now consider the case with $a_2 \neq 0$, $a_1 = a_3 = 0$. This is a two-constant approximation where, additionally, the lowest order contribution goes to zero as would be the case in systems exhibiting orientational transitions in zero field. The behavior in the principal field configurations has been elucidated in great detail.⁹ The astroid in Fig. 1(b) sheds light on the behavior of such a system under an applied field of arbitrary direction. One observes the "softening" of the anisotropy field H_{A1} in that the swallow tails adjacent to

the \mathbf{n} axis run smoothly down to the origin. By the same token, the direction perpendicular to \mathbf{n} will become soft whenever the linear combination of constants defining H_{A2} goes to zero. Thus, swallow tails along the H_x axis will run to the origin on the hyperplanes in the anisotropy space defined by $\sum_{k=1}^n k \cdot a_k = 0$ in order n . This is corroborated by Fig. 1(c) where the condition $a_1 + 2a_2 + 3a_3 = 0$ is imposed. Since a_1 is intentionally very small for this plot, the same figure typifies also the situation at an orientational transition [unlike Fig. 1(b), here $a_3 \neq 0$]. Now both H_{A1} and H_{A2} are zero, hence, the symmetric outlook of the cross between the two complete swallow tails. Note that the "mainframe" of the astroid in Fig. 1(c) is very nearly square-shaped. This last feature comes up also with sets of constants which do not lead to self-crossing; we have observed it, e.g., with $a_2/a_1 \approx -1/8$, $a_3/a_1 \approx 1/2$. The outcome of all constants being equal is presented in Fig. 1(d) ($|a_1| = |a_2| = |a_3|$, $a_{1,3} < 0$, $a_2 > 0$). Complicated self-crossings imply nontrivial secondary hystereses as one already knows from the lower-order treatments.^{4,5}

III. DISCUSSION

The method described above can be used to study the possibility of eliminating undesirable hysteresis in uniaxial materials by applying stress in a suitable direction. The idea has been put forward in the context of cubic magnetostrictive materials,¹⁰ but it applies to any symmetry, in principle. The advantage of the uniaxial setting is that there is a single angular degree of freedom, while in cubic symmetry two such degrees are relevant and the analysis relies on an expansion in small deviations from the symmetry axis. The analysis can be performed most easily for stresses along or perpendicular to \mathbf{n} . Since the stress-induced contribution is always of the lowest order, it shifts a_1 by an amount \tilde{a}_1 . For stress σ along \mathbf{n} , the shift is $\tilde{a}_1 = -\sigma\lambda^{\alpha,2}$ for both tetragonal and hexagonal symmetry; here, $\lambda^{\alpha,2}$ is the magnetostrictive coefficient for the mode of change of length along \mathbf{n} .¹¹ Note that the sign of the shift can be controlled, for a given material (i.e., for a given $\lambda^{\alpha,2}$) by applying tensile or compressive stress. The hysteresis for driving fields along one of the two principal directions can be diminished and, eventually, eliminated if the anisotropy field along the other (conjugate) axis is much smaller than along the direction of the driving field. That is, make one of the axes (say, \mathbf{n}) anisotropically soft by applying stress; then the axis perpendicular to \mathbf{n} is automatically the (relatively) harder one; hence, remagnetization along it would be as closely hysteresis-free as the \mathbf{n} -axis is soft. Since there are two options for the quantities to be modified by stress, H_{A1} and H_{A2} , and two further

options for the sign of \tilde{a}_1 , one recognizes four generic possibilities as a framework for selecting suitable material parameters for prospective applications.

The study of hysteresis by the described generalized-astroid construction is readily applicable to ultrathin ferromagnets as well. In these, there is a strong enhancement of the lowest-order anisotropy due to broken crystallographic symmetry at the surface whereby the anisotropy per surface atom is typically about an order of magnitude larger than in the bulk.¹² In both bulk and thin-film uniaxial systems, the consideration of generalized astroids in applied field may offer valuable insights, especially when a spin-reorientation transition is to be analyzed [cf. Figs. 1(b) and 1(c)]. In the vicinity of such transition points, higher-order anisotropies come into play.

Apart from the prospective applications described in the above paragraphs, the general solution to arbitrary order given in Eq. (2) provides for an overview on the whole problem by: (i) reducing the calculation in any particular order to a *deductive* procedure whereas the $n=1$ and $n=2$ solutions appear as special, *ad hoc* constructions independent of each other; (ii) leading straightforwardly to correspondence rules valid to any order by virtue of the formally decoupled solutions $H_x(M_x)$ and $H_z(M_z)$; and (iii) uncovering to any desired order the possibility for, and the mechanism of, making one of the principal axes anisotropically soft and thus allowing the identification of hysteresis-free conditions. Finally, the field-space perspective should be viewed as complementary to stability analyses in the anisotropy space of the system¹³ whereby only the union of both approaches may yield as detailed description as possible and/or required.

¹I. D. Meyergoyz, *Mathematical Models of Hysteresis* (Springer, New York, 1984).

²E. C. Stoner and E. P. Wohlfarth, *Philos. Trans. R. Soc. London, Ser. A* **240**, 599 (1948).

³L. D. Landau and E. M. Lifshitz, *Electrodynamics of Continuous Media* (Pergamon, Oxford, 1960), Chap. 5.

⁴A. I. Mitsek *et al.*, *Fiz. Met. Metalloved.* **38**, 35 (1974).

⁵C.-R. Chang and D. R. Fredkin, *J. Appl. Phys.* **63**, 3435 (1988); C.-R. Chang, *J. Appl. Phys.* **69**, 2431 (1991).

⁶O. Fruchart *et al.*, *J. Magn. Magn. Mater.* **165**, 508 (1997).

⁷J. F. Herbst, *Rev. Mod. Phys.* **63**, 819 (1991).

⁸The symmetric octopole was given as *typical* for cases VII and VIII of Ref. 5 whereas it only occurs for the *particular* ratio of $a_1/a_2 = -1$.

⁹Y. T. Millev *et al.*, *Phys. Rev. B* (in press).

¹⁰J. R. Cullen *et al.*, *J. Appl. Phys.* **81**, 5417 (1997).

¹¹E. du Tremolet, *Magnetostriction* (CRC, Boca Raton, 1993).

¹²U. Gradmann, in *Handbook of Magnetic Materials*, edited by K. H. J. Buschow (North-Holland, Amsterdam, 1993), Vol. 7, Chap. 1; M. Farle *et al.*, *Phys. Rev. B* **55**, 3708 (1997).

¹³G. Asti, in *Ferromagnetic Materials*, Vol. 3, edited by K. H. J. Buschow and E. Wohlfarth (Elsevier, Amsterdam, 1990), pp. 398–464.

Micromagnetic localization

Ralph Skomski^{a)}

Max-Planck-Institut für Mikrostrukturphysik, Weinberg 2, 06120 Halle, Germany

The localization of nucleation modes in inhomogeneous ferromagnets and its influence on the coercivity are investigated. From the formal analogy between quantum mechanics and micromagnetics follows that anisotropy inhomogeneities may cause localization. The nucleation modes of one-dimensional arrays, such as multilayers composed of hard and soft magnetic materials, are localized even if the superlattice exhibits a nearly ideal periodicity. Gaussian distributions of the layer thicknesses lead to Urbach tails and very low coercivities, but a maximum thickness l_m of the soft layers suppresses the Urbach tails. The related problem of magnetic viscosity leads to a supersymmetric Fokker-Planck description where the time dependence of the magnetization is given by the ground-state mode of a fermionic potential. © 1998 American Institute of Physics. [S0021-8979(98)50911-5]

I. INTRODUCTION

Localization means that the eigenfunctions of a partial differential equation are concentrated in a small volume. A well-known problem is electron localization: metallic wave functions, such as free-electron plane waves, are delocalized, whereas electrostatic correlations and disorder may give rise to Mott and Anderson localization, respectively.¹⁻³ Mott localization is a many-body effect and occurs, for example, if the interatomic distance of a metal exceeds a threshold above which metallic conductivity vanishes. Here we are concerned with the Anderson localization in a random potential.

As discussed for example in Ref. 4, there is a formal analogy between micromagnetics and quantum mechanics. Nuclei in homogeneous ellipsoids of revolution are delocalized, but localization may be caused by magnetic inhomogeneities. This micromagnetic localization is of practical importance because it determines the nucleation of reverse domains and therefore affects the coercivity. An example is oriented nanostructured two-phase permanent magnets such as $\text{Nd}_2\text{Fe}_{14}\text{B}/\text{Fe}$, where very high energy products are expected.⁴⁻⁷ In these structures, the rare-earth-containing hard regions act as a skeleton which stabilize the high magnetization of the soft phase, but nucleation modes localized in extended soft regions tend to destroy coercivity.

A related problem is the time dependence of quantities such as the remanent magnetization (magnetic viscosity). On an atomic level, magnetic viscosity arises from the interaction of the magnetic moments with other degrees of freedom such as lattice vibrations. As emphasized in Ref. 8, the heat bath associated with the nonmagnetic degrees of freedom leads to a Fokker-Planck diffusion of the magnetic moments in the zero-temperature potential E_m . However, even for one-dimensional problems such as the motion of a domain wall in a disordered potential there exists no exact solution.

Here we present an interpretation of micromagnetics in terms of the localization problem. Particular emphasis is put on nucleation modes and long-time magnetic relaxations.

II. LOCALIZATION OF NUCLEATION MODES

For simplicity, we will restrict ourselves to the energy functional

$$E_m = \int \left(A \frac{\nabla \mathbf{M}^2}{M_s^2} + K_1(\mathbf{r}) \frac{M_z^2}{M_s^2} - \mu_0 M_z H \right) d\mathbf{r}, \quad (1)$$

where A is the exchange stiffness and $K_1(\mathbf{r})$ denotes the lowest-order uniaxial anisotropy constant. The magnetostatic self-interaction is approximated by a demagnetizing field, because anisotropy fields $2K_1/\mu_0 M_s$ tend to be much larger than stray fields in hard magnets such as ultrathin films and rare-earth permanent magnets.^{4,9,10} Typical microstructures of interest are shown in Fig. 1.

To obtain nucleation modes we rewrite \mathbf{M} as

$$\mathbf{M}(\mathbf{r}) = M_s \sqrt{1 - m(\mathbf{r})^2} \mathbf{e}_z + M_s \mathbf{m}(\mathbf{r}) \quad (2)$$

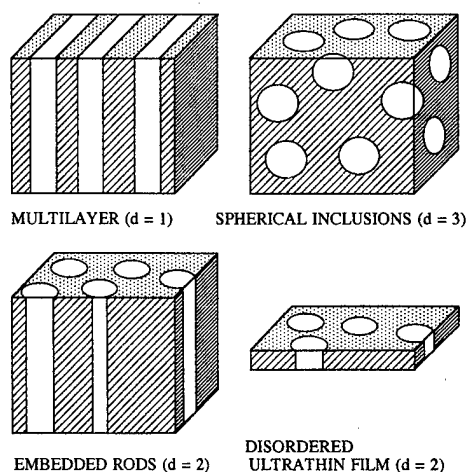


FIG. 1. Inhomogeneous structures consisting of magnetically hard (dark) and soft (white) regions. The orientation of the common easy axis is irrelevant as long as it is parallel to the applied magnetic field.

^{a)}Present address: Department of Physics and Astronomy, University of Nebraska, Lincoln, Nebraska 68588-0111.

and expand E_m into powers of the small transverse magnetization component $\mathbf{m} = m_x \mathbf{e}_x + m_y \mathbf{e}_y$. Minimizing E_m then yields

$$-A \nabla^2 \mathbf{m} + 2K_1(\mathbf{r}) \mathbf{m} = -\mu_0 M_s H \mathbf{m}. \quad (3)$$

This equation is degenerate with respect to m_x and m_y , so that we restrict ourselves to any direction in the xy plane. In practice, small deviations from the common c -axis anisotropy (grain misalignment) and magnetostatic interactions break the symmetry and fix the direction of \mathbf{m} .

Equation (3) is reminiscent of Schrödinger's equation for an electron in an electrostatic potential V . In this quantum-mechanical analogy, A , K_1 , and $-\mu_0 M_s H/2$ are analogous to \hbar^2/m_e , V , and E , respectively. The ground-state energy E_0 corresponds to the nucleation field $H = -H_N$, which determines the coercivity of nucleation-controlled magnets.⁴ In the ordered limit, Eq. (3) has been solved for a number of cases.^{4,11-13}

Lowest-order perturbation theory yields^{4,5,9}

$$H_N = \frac{2\langle K_1(\mathbf{r}) \rangle_v}{\mu_0 M_s} \quad (4)$$

so that the nucleation field is given by the volume-averaged anisotropy constant $\langle K_1(\mathbf{r}) \rangle_v = K$. In the quantum-mechanical analogy, this approach is known as the *virtual crystal* approximation.¹⁴

There are various methods to solve the random-potential band structure problem.^{3,14} Here we restrict ourselves to *second-order perturbation theory*. Applying the quantum-mechanical expression

$$E = E_0 + \langle \psi_0 | V | \psi_0 \rangle - \sum_k \frac{|\langle \psi_k | V | \psi_0 \rangle|^2}{E_k - E_0} \quad (5)$$

to Eq. (3) yields

$$\mu_0 H_N = \frac{2K}{M_s} - \frac{4}{(2\pi)^d A M_s} \int \frac{1}{k^2} G(\mathbf{k}) d^d \mathbf{k}. \quad (6)$$

Here $G(\mathbf{k}) = \int \exp(i\mathbf{k} \cdot \mathbf{r}) \cdot \langle [K_1(\mathbf{r}) - K][K_1(0) - K] \rangle_v d\mathbf{r}$ is the Fourier-transformed autocorrelation function of the disorder. For example, the isotropic distribution $\langle [K_1(\mathbf{r}) - K][K_1(0) - K] \rangle_v = K_0^2 \exp(-r^2/2R^2)$ yields $G(\mathbf{k}) = (2\pi R^2)^{d/2} K_0^2 \exp(-k^2 R^2/2)$. In these equations, R is the average radius of the hard and soft regions and $K_0 = K_h \sqrt{f_s(1-f_s)}$, where K_h is the anisotropy constant of the hard phase and f_s is the volume fraction of the soft phase.

Localization depends on the *dimensionality* of the problem and is most pronounced in one and two dimensions.^{1,14} Figure 1 shows some one-, two-, and three-dimensional structures of interest. In Eq. (6), the $1/k^2$ term causes the corrections to diverge in less than two dimensions. This result is related to the absence of metallic conduction in less than two dimensions.^{3,14} For $d > 2$, Eq. (6) yields

$$\mu_0 H_N = \frac{2K}{M_s} - \frac{4R^2}{(d-2)AM_s} K_0^2. \quad (7)$$

The $1/(d-2)$ dependence in this equation shows that three-dimensional configurations of soft and hard regions are not very much affected by minor inhomogeneities. As a rule,

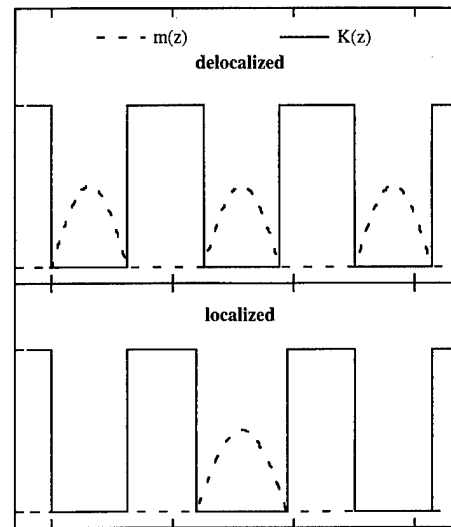


FIG. 2. Nucleation modes in (a) ideally periodic and (b) nearly periodic multilayers. The solid lines show the K_1 profiles in the z direction, while the nucleation modes $|\mathbf{m}(z)|$ are given by the dashed lines.

coercivity breaks down if the size of the soft regions is larger than the domain-wall width $\pi\sqrt{A/K_h} \approx 4$ nm of the hard phase (compare also Refs. 4 and 9).

In one dimension, for example in multilayers, arbitrary small disorder leads to localization. Figure 2 compares delocalized and localized nucleation modes $\mathbf{m}(z)$ in (a) periodic and (b) nearly periodic multilayers. In Fig. 2(b), one soft layer is thicker by about 15% than the others, and the nucleation mode is localized. As in quantum mechanics, there is a small resonance interaction (tunneling) between the potential minima,⁴ but in fair approximation this contribution can be neglected here and following Ref. 4 we estimate that the nucleation field of Fig. 2(b) is smaller by about 30% than that of the periodic lattice Fig. 2(a).

In most cases, disorder leads to extended soft regions which destroy coercivity. In the context of electron localization, the low-lying states responsible for this behavior are known as *Urbach tails*, and asymptotically the density of states of the Urbach tail is given by the probability distribution of the structural disorder.³ In multilayers, a Gaussian distribution of thicknesses l_s of the soft layers yields a logarithmic dependence of the nucleation field on the total film thickness t and yields $H_N = 0$ for $t \rightarrow \infty$.¹⁸ However, if the thicknesses obey $l_s \leq l_m$ then the Urbach tails are cut off and the nucleation field scales as $1/l_m^2$, as sketched for example in Refs. 4 and 13.

III. SUPERSYMMETRY

An atomic approach towards magnetic viscosity is to consider random thermal forces $\xi(t)$ acting on the magnetization vector. For simplicity, we will restrict ourselves to a single magnetization degree of freedom s . Examples are $s = \sin \theta$ and $s = x$ in fine-particle and pinning-type magnets, respectively. This leads to the *magnetic Langevin equation*

$$\frac{\partial s}{\partial t} = -\frac{\Gamma_0}{k_B T} \frac{\partial E_m}{\partial s} + \sqrt{2\Gamma_0} \xi(t), \quad (8)$$

where $\Gamma_0 = 1/\tau_0$ is an atomic attempt frequency.^{8,15,16} The random forces obey $\langle \xi(t) \rangle = 0$ and $\langle \xi(t)\xi(t') \rangle = \delta(t-t')$, where $\delta(x)$ is the delta or "needle" function defined by $\delta(x) = 0$ for $x \neq 0$ and $\int \delta(x)dx = 1$. At low temperatures, the $\partial s/\partial t$ and ξ terms are negligible and Eq. (8) reduces to the trivial minimization problem $\partial E_m/\partial s = 0$.

The probability distribution $P(s, t)$ obeys the magnetic Fokker-Planck equation^{8,15}

$$\Gamma_0^{-1} \partial P/\partial t = (k_B T)^{-1} \partial (P \partial E_m/\partial s)/\partial s + \partial P^2/\partial s^2. \quad (9)$$

As Eq. (1), the Fokker-Planck equation implies that macroscopic magnetization jumps consist of a chain of microscopic events. A simple one-dimensional example are small patches of (111) transition-metal films with easy-plane anisotropy but without in-plane anisotropy, that is $E_m(\phi) = \text{const}$. For the initial condition $\mathbf{M} = \mathbf{M}_s \mathbf{e}_x$ we obtain $P(\phi, t) = (4\pi\Gamma_0 t)^{-1/2} \exp(-\phi^2/4\Gamma_0 t)$ and $\langle \cos \phi \rangle = \exp(-\Gamma_0 t)$. There is, however, no general solution of the one-dimensional Fokker-Planck equation.^{8,15}

In equilibrium, where $\partial P/\partial t = 0$, Eq. (9) yields the relaxation rate $\Gamma = 0$ and $P(s) = Z^{-1} \exp(-E_m/k_B T)$. However, to understand the long-time magnetic-viscosity limit we have to consider the smallest nonzero relaxation rate $\Gamma_1 = 1/\tau_1$. A conceptionally very simple solution of this problem is provided in terms of supersymmetric quantum mechanics, which unifies bosonic and fermionic properties of matter. The observed particle masses indicate a strong breaking of the supersymmetry in elementary particle physics, but the concept is a useful idea not only in elementary particle physics but also in solid-state physics.^{15,17} The formal ansatz $P(s, t) = \exp(-\Gamma t) \exp(-E_m/2k_B T) \Psi(s)$ transforms Eq. (9) into

$$\frac{\Gamma}{\Gamma_0} \Psi = -\frac{\partial^2 \Psi}{\partial s^2} + V_+ \Psi, \quad (10)$$

where the so-called bosonic potential V_+ and its fermionic counterpart V_- are given by

$$V_{\pm} = (\partial E_m/\partial s)^2/4k_B^2 T^2 \mp (\partial E_m/\partial s^2)/2k_B T. \quad (11)$$

In supersymmetric quantum mechanics, replacing V_+ by V_- transforms the "bosonic" differential Eq. (10) into a fermionic equation. Since the first excited eigenvalue of the bosonic problem is equal to the lowest eigenvalue for the fermionic potential,¹⁷ the long-time limit of magnetic viscos-

ity is a ground-state property of the fermionic problem. However, the localization behavior of the fermionic ground-state mode is more complicated than that shown in Fig. 2 and requires further analysis.

IV. DISCUSSION AND CONCLUSIONS

In conclusion, we have analyzed the localization behavior of nucleation and magnetic-viscosity modes in terms of the new concepts of micromagnetic Urbach tails and supersymmetric magnetic viscosity. Nucleation modes in one-dimensional structures, such as multilayers, are localized, even if the structure is nearly periodic. Gaussian disorder destroys coercivity, but a maximum thickness l_{max} of the soft-magnetic layers achieved by careful processing assures a finite nucleation field. On the other hand, we have shown that the long-time limit of magnetic viscosity is equivalent to the ground-state localization in a fermionic supersymmetric potential.

ACKNOWLEDGMENTS

The author is indebted to F. P. Liu, J. Kirschner, Ch. Kuhrt, and S. M. Parhofer for stimulating discussions.

- ¹P. W. Anderson, Phys. Rev. **109**, 1492 (1958).
- ²N. F. Mott, *Metal-Insulator Transitions* (Taylor and Francis, London, 1974).
- ³C. M. Soukoulis and N. M. Economou, in: *Encyclopedia of Applied Physics*, Vol. 5 (VCH, Weinheim, 1993), p. 549.
- ⁴R. Skomski and J. M. D. Coey, Phys. Rev. B **48**, 15 812 (1993).
- ⁵R. Skomski, J. Appl. Phys. **76**, 7059 (1995).
- ⁶S. M. Parhofer, J. Wecker, Ch. Kuhrt, G. Gieres, and L. Schultz, IEEE Trans. Magn. **32**, 4437 (1996).
- ⁷D. J. Keavney, E. E. Fullerton, J. E. Pearson, and S. D. Bader, IEEE Trans. Magn. **32**, 4440 (1996).
- ⁸W. F. Brown, Phys. Rev. **130**, 1677 (1963).
- ⁹R. Skomski and J. M. D. Coey, IEEE Trans. Magn. **29**, 2860 (1993).
- ¹⁰*Ultrathin Magnetic Structures I*, edited by J. A. C. Bland and B. Heinrich (Springer, Berlin, 1994).
- ¹¹H. Kronmüller, Phys. Status Solidi B **144**, 385 (1987).
- ¹²S. Nieber and H. Kronmüller, Phys. Status Solidi B **153**, 367 (1989).
- ¹³R. Skomski, Phys. Status Solidi B **174**, K77 (1992).
- ¹⁴E. N. Economou, *Green's Functions in Quantum Physics* (Springer, Berlin, 1979).
- ¹⁵H. Risken, *The Fokker-Planck Equation* (Springer, Berlin, 1989).
- ¹⁶K. H. Fischer and J. A. Hertz, *Spin Glasses* (University Press, Cambridge, 1991).
- ¹⁷M. Bernstein and L. S. Brown, Phys. Rev. Lett. **52**, 1933 (1984).
- ¹⁸In practice, there is a minor deterioration of the hysteresis loops with increasing total film thickness [F. P. Liu (private communication)].

Computational micromagnetic investigation of magnetization reversal in Nd-Fe-B nanocomposite magnets

S. David,^{a)} B. Kevorkian, J. C. Toussaint, and D. Givord

Laboratoire de Magnétisme Louis Néel-CNRS, BP 166, 38042 Grenoble Cedex 9, France

As a complement to the experimental analysis of magnetization reversal in a two-phase system, a numerical micromagnetic three-dimensional calculation is developed and tested. It is applied to a set of 64 nanometer-scale hard ($\text{Nd}_2\text{Fe}_{14}\text{B}$) and soft (Fe_3B) cubic grains. Calculations reproduce qualitatively the experimentally observed processes and allow the relation between the structure and the coercivity mechanism in nanocomposite hard magnetic materials to be better understood.

© 1998 American Institute of Physics. [S0021-8979(98)51011-0]

I. INTRODUCTION

In nanocomposite magnets, a hard medium-magnetization phase and a soft high-magnetization phase are closely intermixed. With the constituent crystallites being of nanometer size, exchange coupling between them allows both high remanence and medium coercivity to be obtained.¹ Due to their high potential for applications, recent investigations were aimed at improving coercivity in these compounds by optimization of the preparation procedures and the compositions.² Moreover, numerical micromagnetic approaches were developed³ to appraise and predict the influence of microstructural features such as grain size on basic magnetic properties such as remanence, coercivity, and $(\text{BH})_{\text{max}}$. But achievement of both high remanence and sufficient coercivity in nanocomposite hard materials remains unrealized.

Recently methods and models which have been developed to interpret coercivity in other hard magnetic materials were employed to identify the relevant physical parameters and mechanisms involved in magnetization reversal in such materials.^{4,5} To gain deeper understanding and with an eye toward quantitative prediction of magnetic performance, a three-dimensional (3D) computational micromagnetic tool was developed to complement these experimental investigations. In this article it is applied to a simple system which models the structure and interactions within the material. The magnetization reversal process which is deduced from calculation is then qualitatively compared with the experimental results; this is considered a fundamental criterion by which to validate the numerical approach.

II. EXPERIMENTAL BACKGROUND

In a recent study,⁵ the magnetic properties of two-phase nanocrystalline magnets were investigated on several alloys. Reversible and irreversible reversal processes were separated by extracting the corresponding susceptibilities from the magnetic measurements. In contrast with the mechanisms found in single-phase magnets, this study revealed that reversal in these systems can be schematically interpreted as a two-step process: the initial magnetization reversal is dominated by reversible processes while irreversible processes,

which characterize the coercivity mechanism, occur at larger field values. Furthermore, the field at which the maximum of irreversible reversal occurs is the relevant physical parameter to be considered in analyzing coercivity; as shown in Fig. 4(b), it is found to be higher than H_c^M (the field at which the magnetization vanishes).

In the following, we use, as a basis for comparison with calculation, the hysteresis cycle (Fig. 3) and magnetic susceptibilities (Fig. 4) measured at 300 K on a material containing approximately 50% (volume) hard $\text{Nd}_2\text{Fe}_{14}\text{B}$ and 50% soft Fe_3B , with a crystallite size ranging between 10 and 30 nm as characterized by transmission electron microscopy (TEM).⁶ A model structure was defined according to these structural features.

III. MODEL SYSTEM

We consider a 3D chessboard arrangement where 32 hard phase grains and 32 soft phase grains are stacked up alternatively (Fig. 1). The main advantage of such a model system compared with others³ is that it allows better control over the numerical errors that are observed using a finite difference approach. A 15 nm grain size was chosen for the both hard and soft phases. The intrinsic parameters common to the two magnetic phases (at 300 K) are the spontaneous magnetization $\mu_0 M_s = 1.61$ T and the exchange constant $A = 12.5 \times 10^{-12}$ J/m. In each grain, the magnetocrystalline anisotropy is assumed to be uniaxial; the anisotropy constants are $K_1 = 4.5 \times 10^6$ J/m³ and $K_2 = 0.66 \times 10^6$ J/m³ for the $\text{Nd}_2\text{Fe}_{14}\text{B}$ phase and $K_1 = -0.322 \times 10^6$ J/m³ for the Fe_3B phase. The distribution of the easy axis for the hard grains is chosen randomly and is constrained to be isotropic ($\langle \cos \theta \rangle = 1/2$).

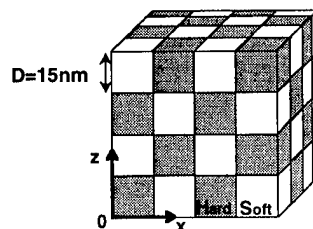


FIG. 1. The chessboard model system.

^{a)}Electronic mail: david@labs.polycnrs-gre.fr

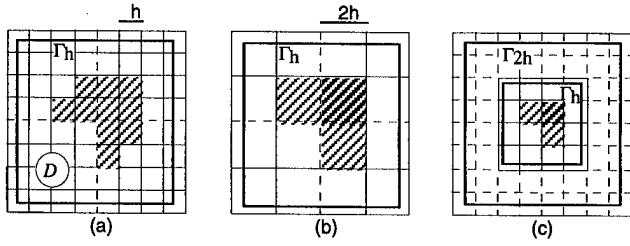


FIG. 2. Scaling transformation of a 2D mesh with a factor $b=2$; the dashed squares correspond to the physical system. (a), (b), and (c) illustrate the different steps involved in the transformation.

IV. NUMERICAL BACKGROUND

In the continuous medium approximation, the Gibbs free energy density $F\{\mathbf{m}(\mathbf{r})\}$ of a ferromagnetic system of magnetization vector $\mathbf{M}(\mathbf{r}) = M_s \cdot \mathbf{m}(\mathbf{r})$ can be written as

$$F\{\mathbf{m}(\mathbf{r})\} = \int_V d^3r \{ A[\nabla \mathbf{m}(\mathbf{r})]^2 - P_k[\mathbf{u}_k \cdot \mathbf{m}(\mathbf{r})] - \mu_0 \times M_s \mathbf{H}_{\text{ext}} \cdot \mathbf{m}(\mathbf{r}) - \frac{1}{2} \mu_0 \cdot M_s \mathbf{m}(\mathbf{r}) \cdot \mathbf{H}_S\{\mathbf{m}(\mathbf{r})\} \}, \quad (1)$$

where P_k is a polynomial which expresses the magnetocrystalline anisotropy energy; $\mathbf{H}_S\{\mathbf{m}(\mathbf{r})\}$ is the stray field due to the magnetostatic volume charges $\rho_m = -M_s \nabla \cdot \mathbf{m}(\mathbf{r})$ and to the surface charges $\sigma_m = M_s \mathbf{m}(\mathbf{r}) \cdot \mathbf{n}$ (\mathbf{n} is the surface normal, pointing outwards). \mathbf{H}_S is derived from a scalar potential ϕ which satisfies the Poisson equation inside the material and the Laplace equation outside it. We used the finite difference method to calculate the potential ϕ associated with a given magnetization distribution $\{\mathbf{m}(\mathbf{r})\}$. The values of $\phi(\mathbf{r})$ and $\{\mathbf{m}(\mathbf{r})\}$ were sampled at the cell centers of a regular cubic mesh with grid spacing h .

Accurate estimates of the potential ϕ normally require the grid to be extended over a large region outside the physical system. A multigrid method has therefore been developed to reduce the size of the external mesh and save calculation time. Let us consider a two-dimensional (2D) bounded square domain D , in which the physical system is enclosed, that is placed on a square mesh of parameter h . We note Γ_h the contour joining the set of outer nodes where ϕ is calculated [Fig. 2(a)]. Let us apply a scaling transformation defined by a factor b (in this case $b=2$). The dilatation of the grid gives a coarse mesh of parameter $2h$ [Fig. 2(b)]. In each of the new cells the magnetization vector is determined as a vectorial average of the magnetization vectors. A contraction of this grid is then performed by the same factor [Fig. 2(c)]. The superposition of the two views of domain D before [Fig. 2(a)] and after transformation [Fig. 2(c)] shows that the boundary Γ_h is now located inside the mesh limited by the contour Γ_{2h} .

By imposing $\phi_{2h}=0$ on Γ_{2h} in the fine mesh of Fig. 2(c), the Poisson equation is solved and a coarse estimation of the solution $\{\phi_{2h}\}$ in each cell is obtained. $\{\phi_h\}$ on Γ_h is then calculated by a linear interpolation of $\{\phi_{2h}\}$. The system is then re-expanded to its initial size keeping constant the estimate values of $\{\phi_h\}$ on Γ_h . By again solving the Poisson equation, a better estimate of $\{\phi_h\}$ than that for the

case $\phi_h=0$ on Γ_h is obtained. The method illustrated here for 2D systems have been applied to 3D systems. Our simulations use a grid spacing $h=12.5 \text{ \AA}$ such that $h < \delta_w$ and $h < \delta_{\text{ex}}$ are verified. The nanocomposite structure, made of 64 grains, is discretized by $32 \times 32 \times 32$ elements centered within a box of width $48h$ that surrounds it.

In static field calculations, magnetization configurations in the equilibrium state are determined by integrating the dynamic Landau-Lifshitz-Gilbert (LLG) equation:

$$\frac{d\mathbf{m}}{dt} = -\mathbf{m} \times \mathbf{H}_{\text{eff}}(t), \quad (2)$$

with

$$\mathbf{H}_{\text{eff}}(t) = \mathbf{H}(t) + \alpha \cdot \mathbf{m}(t) \times \mathbf{H}(t), \quad (3)$$

where α is the Gilbert damping constant and $\mathbf{H}(t)$ denotes the functional derivatives of the magnetic energy $F\{\mathbf{m}(\mathbf{r})\}$ with respect to \mathbf{m} . At equilibrium, the torque created by the effective field on the magnetization vector must vanish at each point in the physical system. The evolution of \mathbf{m} turning around the vector field $\mathbf{H}_{\text{eff}}(t)$, governed by Eq. (2), may be described by

$$\begin{aligned} \mathbf{m}(t + \delta t) = & \mathbf{m}(t) \cos(H_{\text{eff}}(t) \delta t) \\ & + \frac{\sin[H_{\text{eff}}(t) \delta t]}{H_{\text{eff}}(t)} [\mathbf{H}_{\text{eff}}(t) \times \mathbf{m}(t)] + [1 \\ & - \cos(H_{\text{eff}}(t) \delta t)] \frac{\mathbf{H}_{\text{eff}}(t) \cdot \mathbf{m}(t)}{H_{\text{eff}}^2(t)} \mathbf{H}_{\text{eff}}(t). \end{aligned} \quad (4)$$

This relation tends towards an exact integration of the LLG equation in the limit of a weakly time-dependent effective field \mathbf{H}_{eff} . This scheme of integration is at least as accurate as the modified Euler method, in which the Taylor expansion must be truncated at second order. It is also more efficient, since it requires only that the first order time derivative be evaluated and, moreover, it allows the magnetization modulus to be maintained constant. As with any explicit method,⁷ numerical instabilities may be encountered and may lead to mistaken solutions to the LLG equations. A stability criterion may be determined for ferromagnetic systems which are mainly governed by exchange interactions. Let us consider a chain of spins located on a Ox axis and directed along Oz . When the system is weakly perturbed, the LLG equations may be linearized. The Von Neumann analysis of the stability consists in developing any numerical fluctuation into a Fourier series and to examine the time evolution of the amplitude $\epsilon_k(t)$ of each mode k . The integrating scheme for a given time step δt is considered to be stable as the gain $G = |\epsilon_k(t + \delta t)/\epsilon_k(t)|$ remains lower than 1. The analysis shows that a time step limit exists and is defined by

$$\delta t_{\text{lim}}^{\text{1D}} = \frac{h^2}{8A} \mu_0 M_s \frac{2\alpha}{1 + \alpha^2}. \quad (5)$$

For 3D systems, a similar analysis leads to $\delta t_{\text{lim}}^{\text{3D}} = \frac{1}{3} \delta t_{\text{lim}}^{\text{1D}}$. An upper limit of $\delta t_{\text{lim}}^{\text{3D}}$ is obtained by choosing $\alpha=1$. This value was chosen in our calculations in order to save computational time.

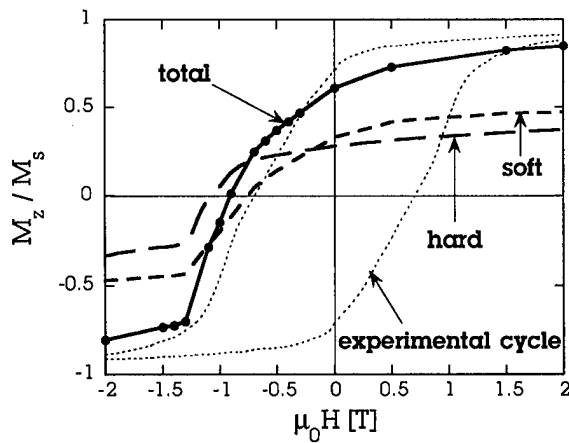


FIG. 3. Calculated (bold lines) and experimental (dotted line) hysteresis curves in the range $[-2, +2]$ T. The black dots correspond to the calculated equilibrium states of magnetization.

V. RESULTS

The hysteresis curve (Fig. 3) was obtained after calculating the initial polarization of the system in a 4 T external field applied along the Oz axis. The black dots represent the equilibrium magnetization states within the field range $[-2, +2]$ T. A continuous curve was then defined by interpolating it from calculated points; it was used to evaluate the total magnetic susceptibility χ_{tot} as the derivative of magnetization with respect to the applied field [Fig. 4(a)]. Since the simulation enables the contributions to the total magnetization by the two magnetic phases to be distinguished, the hysteresis curve and the susceptibility were also obtained for both hard (χ_{hard}) and soft (χ_{soft}) phases. Moreover, the reversible contribution to the total susceptibility, χ_{rev} , was determined using a procedure which mimicks the experimental method, i.e., by evaluating the slope of the magnetization on successive recoil loops (10 mT) along the major cycle. The quantity $\chi_{\text{tot}} - \chi_{\text{rev}}$,⁴ which is predominantly associated with irreversible reversal phenomena, can thus be deduced.

The calculated ratio M_r/M_s (0.68) is found to be close to the experimental value (0.73). In addition, the calculated hysteresis curves of the hard and soft phases (Fig. 3) clearly show that the reversal process in the second and third quadrants is not homogeneous: the reversal of the soft phase dominates at low field ($H \leq H_c^M$) and that of the hard phase at higher fields ($H > H_c^M$).

The susceptibilities that were derived from simulation [Fig. 4(a)] reveal that (i) the maxima of the reversible and irreversible reversals occur at distinct field values, leading to the fact that (ii) H_c^M is lower than the field value corresponding to the maximum of irreversible reversals. These features are in agreement with the experimental results [Fig. 4(b)] and Sec. II. However, the calculated ratio $\chi_{\text{rev}}/(\chi_{\text{tot}} - \chi_{\text{rev}})$ is much smaller than the experimental values. This result means that a lower proportion of magnetic moments reverse reversibly within the model system than in the real one. From the field dependence of χ_{soft} and χ_{hard} , it appears that about half of the soft moments and the majority of the hard

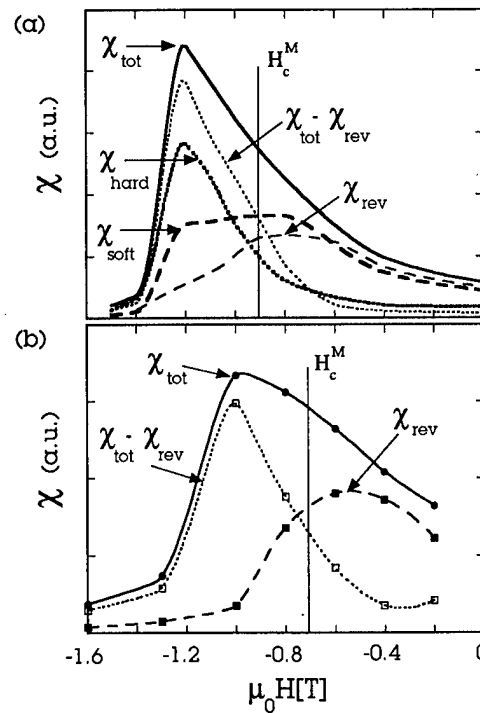


FIG. 4. Calculated (a) and measured (b) magnetic susceptibilities.

moments reverse around the same field value of 1.2 T. This shows that the majority of the soft moments is strongly exchange coupled to the hard moments and is forced to follow their rotation. This phenomenon can be ascribed to the fact that the grain size taken in the present calculation ($D = 15$ nm) tends to be smaller than experimental values (D ranging between 10 and 30 nm, from TEM). Thus, the coupling between the hard and soft phases is stronger than it is in the real system. In turn, the calculated coercivity is larger than it is in the real system and this result suggests that the coercivity of nanocomposite materials can be improved by favoring a small and homogeneous size of the constituent crystallites. This observation is in agreement with the optimal grain size for both coercivity and remanence enhancement that was determined numerically by different authors,⁸ and which is close to 10 nm.

ACKNOWLEDGMENT

This work has been supported by the European Union within the Brite-Euram project EMERGE (Grant No. BRPR-CT23-0097).

- ¹E. F. Kneller and R. Hawig, IEEE Trans. Magn. **MAG-27**, 3588 (1991).
- ²S. Hirose, H. Kanekiyo, and M. Uehara, J. Appl. Phys. **73**, 6488 (1993).
- ³R. Fisher, T. Schrefl, H. Kronmüller, and J. Fidler, J. Magn. Magn. Mater. **153**, 35 (1996).
- ⁴E. H. Feuttrill, P. G. McCormick, and R. Street, J. Phys. D: Appl. Phys. **29**, 2320 (1996).
- ⁵S. David and D. Givord, J. Alloys Compd. (to be published).
- ⁶J. Bernardi and S. David (unpublished).
- ⁷Y. Nakatani, Y. Uesaka, and N. Hayashi, Jpn. J. Appl. Phys., Part 1 **28**, 2485 (1989).
- ⁸W. Rave and K. Ramstöck, J. Magn. Magn. Mater. **171**, 69 (1997).

Influence of the system parameters on the non-Arrhenius magnetic relaxation of systems having distributed properties

R. Smirnov-Rueda, O. A. Chubykalo, and J. M. González

Instituto de Ciencia de Materiales de Madrid-C.S.I.C., Cantoblanco, 28049 Madrid, Spain

J. González

Departamento de Física de Materiales, Facultad de Química, UPV/EHU. Apartado 1072, 20080 San Sebastián, Spain

We have investigated, in the framework of the micromagnetic approximation, the relaxation behavior of both simple systems and systems having distributed properties. In the case of single-particle-type systems, our study focused on the exchange constant dependence of the so-called "waiting time" for the onset of the relaxation to conclude that this parameter linearly increased with the increase of the exchange constant. Our results for the relaxation of polycrystalline-type systems having distributed anisotropy easy axes showed the occurrence in limited time ranges of a magnetization decrease which was adequately fitted by the $M(t) - M(0) \propto \ln(t+t_0)$ law. The exchange constant dependence of the additive fitting parameter in the logarithmic law qualitatively reproduced that of the waiting time indicating that both parameters were linked to the same underlying characteristic of the demagnetization process: the coupling of the magnetic moments forming the domain-wall-like structures through which the system reversed its magnetization. © 1998 American Institute of Physics. [S0021-8979(98)33411-8]

The occurrence of magnetic relaxation¹ is typically identified with the observation of a time variation of the magnetization of a sample which is kept under constant applied demagnetizing field and temperature. The interest on magnetic relaxation is related to two main problems: the experimental study of the behavior of systems having high structural homogeneity and reduced dimensionality (as thin films, multilayers, and sets of nanoparticles^{2,3}); and the analysis of the behavior of very simple systems as isolated particles.⁴ Whereas the first point is of major relevance for the magnetic recording technology, the second one could allow the understanding of the basic relaxation mechanisms of systems having many degrees of freedom.⁵ The conventional analysis of the magnetic relaxation processes⁶ assumes that (i) the system can be replaced by a set of noninteracting subsystems with two-level-type behavior, and (ii) each subsystem relaxes according to the Arrhenius kinetics. This treatment has some relevant limitations: (i) it ignores the fact that the field induced magnetization reversal involves several stages in the nucleation-expansion-propagation-pinning sequence,⁷ (ii) it does not provide any explicit relationship between the relaxation behavior and the defect distribution of the sample, (iii) it ignores any exchange and dipolar interactions, and (iv) arbitrarily assumes a particular relaxation kinetics mainly invoked to account for the quasilogarithmic relaxations ubiquitously observed in hard magnetic materials.⁸ Regarding these limitations the authors have recently discussed in several works⁹ the behavior of simple systems in terms of free energy micromagnetic models. In these works it is shown that the thermally activated magnetization reversal cannot be described in terms of the Arrhenius predictions since, similarly to hysteresis, it takes place through a nucleation-propagation process and involves a "waiting time" during which the macroscopic state of the system varies slowly.

Recent experimental results,¹⁰ obtained in highly homogeneous thin films, evidence the actual occurrence of the basic relaxation features predicted in Ref. 9. Our purpose in the present work was to investigate the system parameter dependence of the relaxation behavior of model polycrystalline systems and to compare the obtained results with those corresponding to simple systems. The considered models⁹ consist of a long chain of infinite parallel planes. The internal energy of the systems includes anisotropy, Zeeman, exchange, and magnetostatic interactions.⁹ The intrinsic properties of our system are described by the following parameters: (i) the exchange energy-to-anisotropy energy ratio, $a = Ad^{-2}/2K$ (where A is the exchange constant, d is the interplanar distance, and K the uniaxial anisotropy constant); (ii) the square of the magnetization-to-anisotropy energy ratio, $m = \mu_0 M_s^2/2K$ (where M_s is the saturation magnetization), and (iii) the reduced applied field, $h = \mu_0 M_s H/2K$ (where H is the applied field directed along the z direction of our reference system). We have considered two different types of systems: (a) single-grain-like systems having homogeneous easy anisotropy axis and (b) polycrystalline-like systems which are divided in 100 "grains" (each one having 50 planes). In the case of the polycrystalline-like systems the easy directions corresponding to the different grains are uniformly distributed in a cone having an apex angle of α degrees and a symmetry axis parallel to the Z . In the single-grain systems the easy axis is contained in the YZ plane and forms a 10° angle with the Z direction. Our simulations were carried out at a temperature corresponding to 10^{-4} of the maximum anisotropy energy per unit surface attainable by the system. The field and time evolution of the system configurations was followed by minimizing their energy by means of a Monte Carlo algorithm implemented with Metropolis dynamics. In this context, we define a Monte Carlo

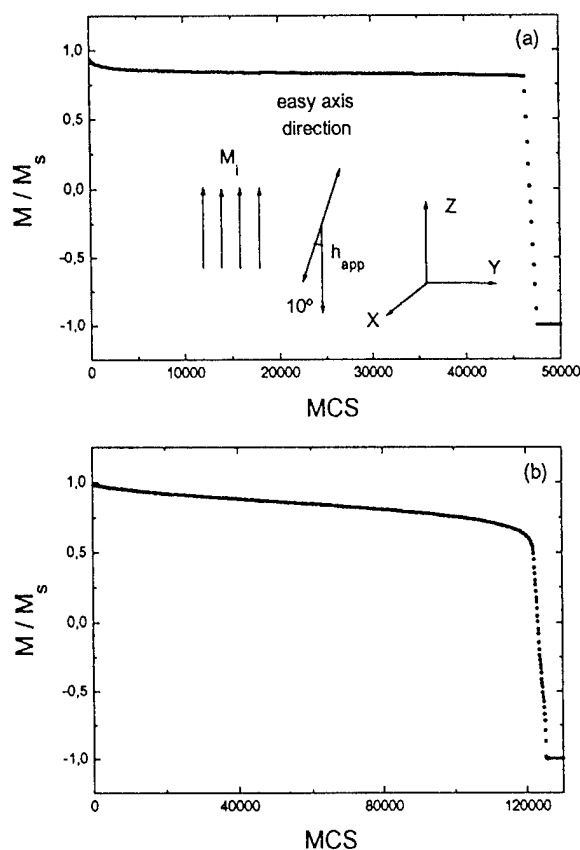


FIG. 1. Typical evolution, at constant applied field, of the reduced magnetization with the number of MCS. Single-grain systems: (a) $a=2$, (b) $a=20$ ($m=0.15$).

step (MCS) as the process corresponding to the introduction of a random modification in all degrees of freedom of the system. If the attempt frequency for those modifications is known (through an independent argument), the number of MCS can be converted in real-time units. In Figs. 1(a) and 1(b) we present results corresponding to the (time) MCS evolution of the magnetization of two single-grain-like systems having exchange-to-anisotropy ratios of 2 and 20, respectively (see the other system parameters in the caption). The relaxation curves were obtained under a constant reduced field $h=0.99h_c$ (h_c being the coercive force of the system, evaluated from the $+Z$ saturated state, by considering a field decrement of $\Delta h=10^{-3}$ and a relaxation stage of 1500 MCS). In both systems, the occurrence of a waiting time and that of a complete magnetization reversal in a finite number of MCS are apparent. As previously discussed⁹ both facts are related to the accomplishment of magnetic relaxation through a process involving the nucleation and propagation of domain-wall-like structures. Figure 2 presents our results for the dependence on the exchange-to-anisotropy ratio of the waiting time observed in single-grain-like systems. The observed linear increase of the waiting time is related to the increase, with the parameter, of the number of moments involved in the wall structures responsible for the magnetization reversal (the typical number of moments forming these structures varies with a as $a^{1/2}$). Figures 3(a) and 3(b) present relaxation results corresponding to polycrystalline-like systems having different exchange-to-anisotropy ratios.

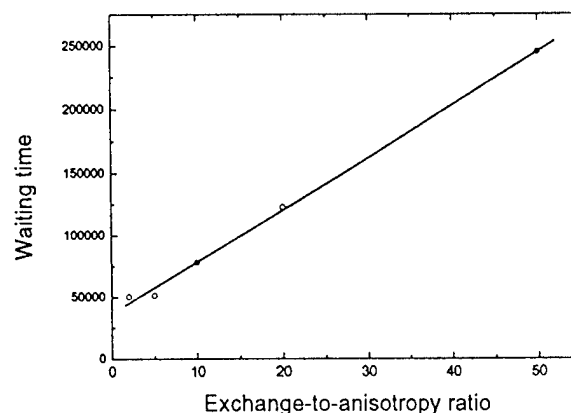


FIG. 2. Single-grain system. Variation of the waiting time with the exchange-to-anisotropy ratio.

These results were obtained under a reduced applied field $h=0.97h_c$ (h_c was evaluated as detailed above). Similarly to the case of the single-grain-like systems, it is possible to observe in these figures a time interval of slow demagnetization rate and the accomplishment of complete relaxation in a finite time. In Figs. 4(a) and 4(b) we have plotted in a logarithmic scale the relaxation data presented in Figs. 3(a) and 3(b). As it is possible to observe in these figures a logarithmic law is not adequate to describe the whole relaxation process (as, for instance, a stretched exponential would be) but it describes reasonably well the (time) MCS region cor-

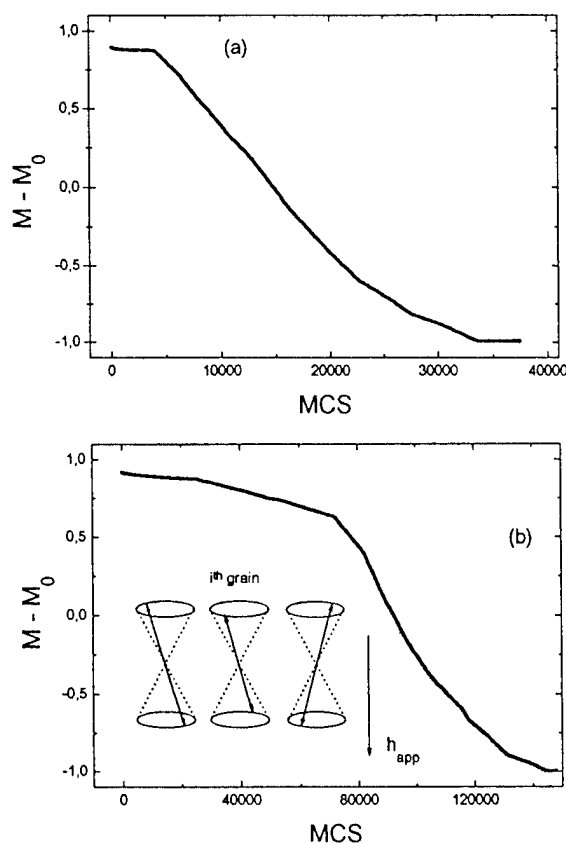


FIG. 3. Typical evolution, at constant applied field, of the reduced magnetization with the number of MCS. Polycrystalline system: (a) $a=2$, (b) $a=20$ ($m=0.15$).

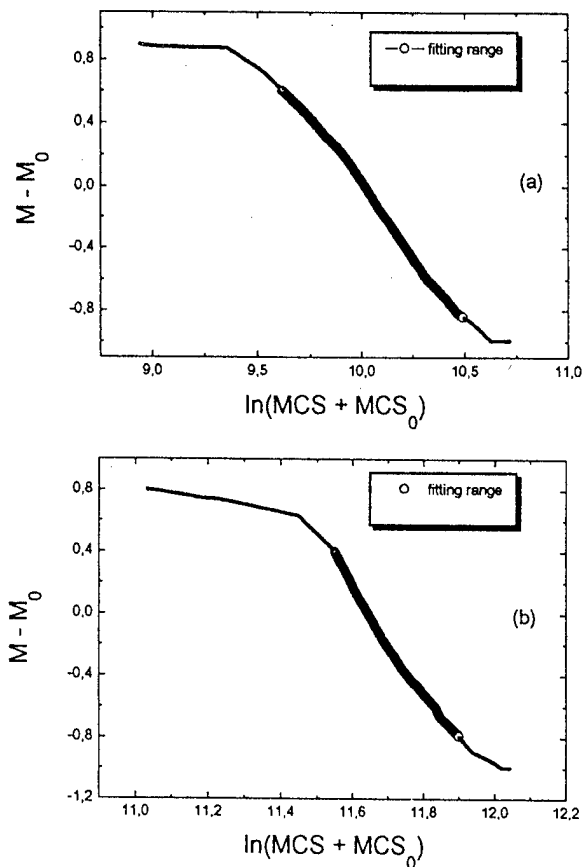


FIG. 4. Data shown in Fig. 3 plotted as a function of $\ln(\text{MCS} + \text{MCS}_0)$: (a) $a=2$, (b) $a=20$.

responding to the highest demagnetization rates (indicated in the figures by large symbols). In fact, the law giving the best fit to our data in these regions is given by $M(\text{MCS}) - M(0) = -S \ln(\text{MCS} + \text{MCS}_0)$, where the MCS_0 fitting parameter translates the occurrence of a slow demagnetization regime. This point has been evidenced through to different simulations. In Fig. 5 we present the MCS_0 dependence on the exchange-to-anisotropy ratio which qualitatively repro-

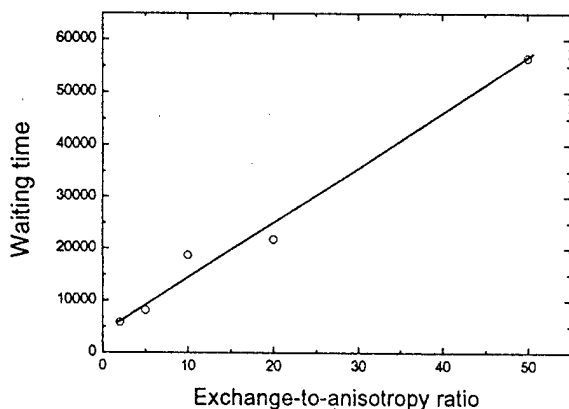


FIG. 5. Polycrystalline system. Variation of the MCS_0 parameter with the exchange-to-anisotropy ratio.

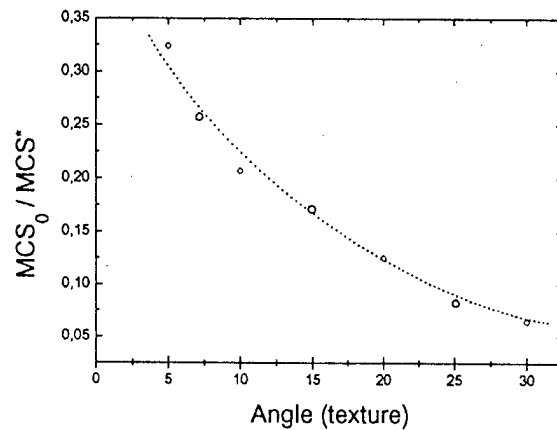


FIG. 6. Variation of MCS_0 with the degree of texture (MCS_0 is normalized to MCS^*), the waiting time value corresponding to a single-grain system having the same model parameters.

duces that observed in the case of the single-grain-like systems. The magnitude of MCS_0 is about five times smaller than that obtained for the waiting time (considering the same system parameters) in the case of the single-grain-like systems. Nevertheless, direct comparison of both sets of results is not possible due to the fact that in the polycrystalline-like systems significant inhomogeneities are present, due to the easy axes distribution, in the magnetic moment configurations corresponding to the remanent states and these inhomogeneities are effective as wall nucleation centres.⁹ Figure 6 shows our results for the MCS_0 dependence on α (the parameter measuring the degree of texture of the polycrystalline-like systems). The data in the figure (obtained for $h = 0.95h_c$, $a=2$, $m=0.15$) were normalized to MCS^* , the waiting time corresponding to a single-grain system having the same model parameters. MCS_0 increases with the decrease of α (that is with the increase of the degree of texture) evidencing its relationship to the degree of order of the remanence moment configuration from which the thermally activated reversal proceeds.

¹F. Preisach, Z. Phys. **94**, 277 (1935).

²D. K. Lottis, E. D. Dahlberg, J. A. Christner, J. I. Lee, R. L. Peterson, and R. M. White, J. Appl. Phys. **63**, 2920 (1988).

³R. D. Kirby, J. X. Shen, R. D. Hardy, and D. J. Sellmeyer, Phys. Rev. B **49**, 10810 (1994).

⁴M. Lederman, S. Schultz, and M. Ozaki, Phys. Rev. Lett. **73**, 1986 (1994); W. Wernsdorfer, K. Hasselbach, A. Benoit, G. Cernicchiaro, D. Mailly, B. Barbara, and L. Thomas, J. Magn. Magn. Mater. **151**, 38 (1995).

⁵J. M. González, R. Ramírez, R. Smirnov-Rueda, and J. González, J. Magn. Magn. Mater. **157-158**, 363 (1996).

⁶R. Street and S. D. Brown, J. Appl. Phys. **76**, 6386 (1994).

⁷D. W. Taylor, V. Villas-Boas, Q. Lu, M. F. Rossignol, F. P. Missell, D. Givord, and S. Hirose, J. Magn. Magn. Mater. **130**, 225 (1994).

⁸J. C. G. Martinez, F. P. Missell, and F. J. G. Landgraf, J. Magn. Magn. Mater. **73**, 267 (1988).

⁹J. M. González, R. Ramírez, R. Smirnov-Rueda, and J. González, Phys. Rev. B **52**, 16034 (1995).

¹⁰G. Suran, J. I. Arnaudas, M. Ciria, C. de la Fuente, M. Rivoire, O. A. Chubykalo, and J. M. Gonzalez, Europhys. Lett. (to be published).

Voltage dependence of magnetoresistance in spin dependent tunneling junctions

J. Zhang and R. M. White^{a)}

*Data Storage Systems Center, Department of Electrical and Computer Engineering,
Carnegie Mellon University, Pittsburgh, Pennsylvania 15213*

The voltage dependence of magnetoresistance in spin dependent tunneling (SDT) junctions was studied experimentally and theoretically. Different magnetoresistance (MR)- V dependence in various patterned junctions was observed and correlated with other technologically important parameters, including the magnitude of the MR, linearity of the current-voltage characteristic, temperature dependence of the junction resistance, and the MR. A phenomenological model based on a spin-independent two-step tunneling via defect states in the barrier, in addition to the spin-dependent direct tunneling, is proposed to account for the MR- V dependence. The MR ratio is determined by the ratio of the two currents. The MR- V dependence results from a stronger voltage dependence of the two-step tunneling current compared to that of the direct tunneling current. The same model also satisfactorily predicts other properties of SDT junctions. A high quality barrier is required to minimize the MR- V dependence and improve other junction properties. The approach to achieving desirable junction impedance for data storage applications is discussed. © 1998 American Institute of Physics. [S0021-8979(98)28311-3]

I. INTRODUCTION

Tremendous progress has been made recently in achieving high room temperature magneto (MR) ($\sim 20\%$) in microstructure spin dependent tunneling (SDT) junctions at low field.^{1,2} However, there is a lack of understanding for one of the most puzzling features of SDT junctions, i.e., the voltage dependence of the MR. Although the detailed voltage dependence of the MR varies from junction to junction, the MR generally decreases as the voltage increases and falls to half of the low bias MR at a voltage of several hundred millivolts.³ Understanding this effect is not only critical to optimize SDT device performance for potential data storage applications, but also provides critical insights into magnetotransport properties of SDT junctions. This article studies the MR- V dependence experimentally and theoretically. A simple yet effective model based on a second tunneling mechanism, in addition to the ideal direct tunneling, is proposed for the first time to interpret the MR- V dependence and its correlation with other technologically important properties of SDT junctions.

II. EXPERIMENTS AND RESULTS

SDT trilayers with the structure ferromagnetic (FM)/FM were sputter deposited on Si substrates with a thermally oxidized surface in a Perkin-Elmer 2400-8L sputtering system. The insulating barrier AlO_x was formed by oxidizing an ultrathin Al layer in an Ar/O_2 plasma. A magnetic field was applied during deposition to define a uniaxial anisotropy of the FM layers. Sheet films show clear magnetic

loop separation, indicating a weak interlayer coupling. They were subtractively patterned into SDT junctions using a photolithographic process similar to other reported approaches.⁴ Precautions were taken during the processing to avoid shorting of top and bottom electrodes near junction edges, breakdown of oxide barriers, and unreliable contact between leads and electrodes. These actions guarantee that subsequent measurements reveal the intrinsic junction properties.

Two groups (A and B) of SDT junctions were studied for comparison. Both groups have the structure $\text{Si}/\text{SiO}_2/\text{FM1}(125 \text{ \AA})/\text{Al}-\text{AlO}_x/\text{FM2}(150 \text{ \AA})$, where FM1 can be NiFe or NiFeCo, and FM2 can be Co or CoFe. The major difference between the two groups lies in the oxide barrier. The 17 Å barrier in group A was formed by glow discharge⁵ with a high cathode voltage of around -1000 V . The 20 Å barrier in group B was formed by oxygen plasma etching⁶ with a low substrate voltage of -40 V . Sheet films in group A were deposited at Nonvolatile Electronics, Inc. (NVE) and patterned into devices at CMU. The MR was measured using a dc four-probe method. Most junctions show a clean MR- H response. The room temperature MR at low voltage ranges from below 1% to as high as 17%. The current-voltage (I - V) characteristics and the MR- V dependence were obtained by sweeping the voltage from 10 to up to 500 mV. The temperature dependence data were acquired by heating the junction with flexible heaters to up to 100°C .

The junctions in these two groups show very different behavior. Junctions in group A show a high MR of up to 17% at room temperature, while junctions in group B show a much lower MR. On the other hand, the MR of group B junctions show a much stronger voltage dependence than group A junctions. Typical MR- V dependencies are plotted

^{a)}Electronic mail: white@gauss.ece.cmu.edu

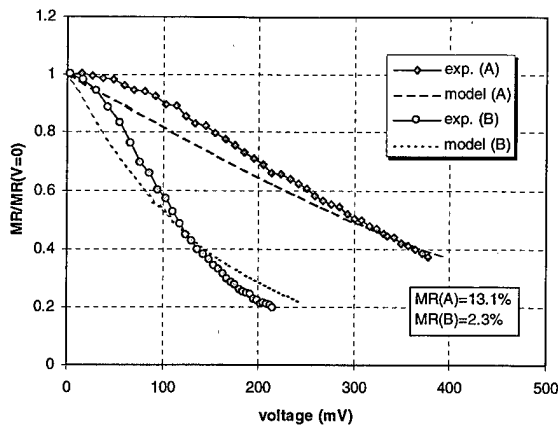


FIG. 1. Typical room temperature MR-V dependence of junctions in groups A and B. MR is normalized to low bias MR for comparison. Dashed lines show model predicted MR-V dependence.

in Fig. 1. This is consistent with the correlation of MR-V dependence and MR observed by other groups.¹ Unlike other reported results,³ however, no large asymmetry with regard to the bias polarity was observed. The I - V characteristics of group B junctions are more nonlinear than group A junctions, as shown in Fig. 2. A decrease of the MR at increased bias is accompanied by the onset of pronounced nonlinearity. In addition, the resistance and the MR of group B junctions show a much stronger temperature dependence compared to group A junctions, as shown in Figs. 3 and 4. This experimental data indicates a correlation between the MR, the I - V characteristic, and the MR-V, MR-T, and R-T dependencies. We shall propose a simple yet effective theory to explain these correlations.

III. A PHENOMENOLOGICAL MODEL

The spin dependent tunneling theory by Julliere⁷ at low temperature and voltage is widely accepted. The theory assumes direct tunneling with no spin flipping. However, the theory based on this assumption fails to explain the voltage and temperature dependence of junction properties. For example, the predicted temperature coefficient of the junction resistance is on the order of $-0.1\%/^{\circ}\text{C}$, much less than observed for group B junctions. The calculated MR-V and

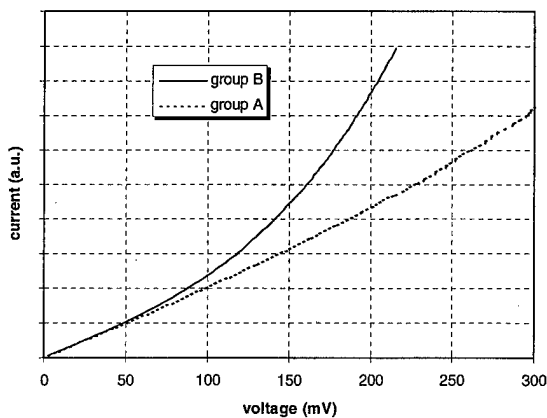


FIG. 2. Typical I - V characteristics of junctions in two groups. The resistance is normalized to the low bias resistance for nonlinearity comparison.

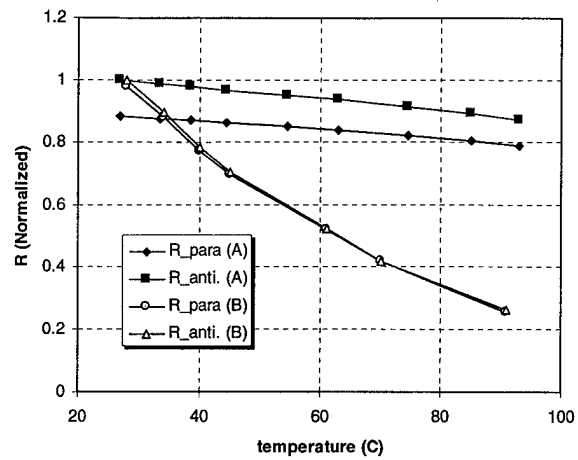


FIG. 3. Temperature dependence of junction resistance. The resistance is normalized to R_{T1} at room temperature.

MR-T dependence is also much weaker than experimental results. The discrepancy suggests that other factors, such as other tunneling mechanisms or spin flipping processes, must be considered to complete the description.

The strong R-T dependence shown by group B junctions, which is not predicted by the conventional tunneling theory, suggests a thermal activation process. We suggest that there exist localized defect states in the barrier. Excitation of electrons from these states, either thermally or by hot electron impact, create states available for two-step tunneling,⁸ as shown in Fig. 5. Because these thermally generated states are not polarized, the two-step tunneling is spin independent and does not contribute to MR. The MR is reduced by this spin-independent current and can be expressed as

$$MR = \frac{(I_{\text{para}} - I_{\text{anti}})/I_{\text{anti}}}{1 + I_2/I_{\text{anti}}} \sim \frac{MR_{\text{max}}}{1 + I_2/I_{\text{anti}}}, \quad (1)$$

where I_2 is the current carried by the two-step tunneling. I_{para} and I_{anti} are spin dependent currents carried by the direct tunneling when magnetic moments are parallel and antiparallel, respectively. $MR_{\text{max}} \sim (I_{\text{para}} - I_{\text{anti}})/I_{\text{anti}}$ is approximately the MR given by Julliere's model⁷ when there is no

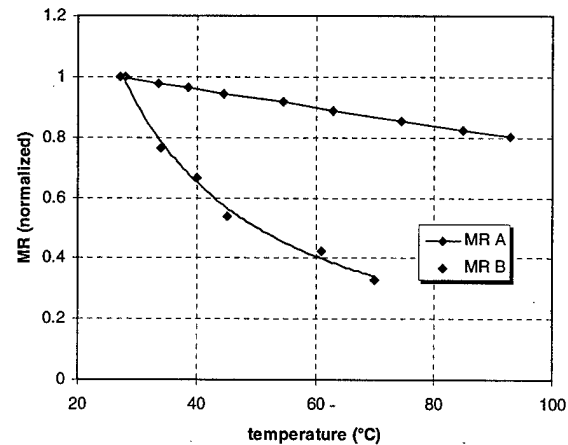


FIG. 4. Temperature dependence of MR normalized to room temperature MR.

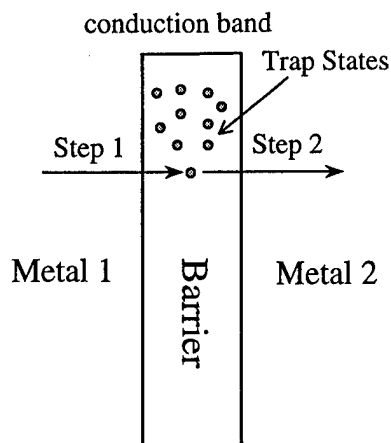


FIG. 5. Schematic view of the two-step tunneling via defect states.

spin mixing. It is clear that the ratio of the spin-dependent and spin-independent currents determines the MR. If the tunneling current is mainly carried by the two-step tunneling, a low MR is expected. It should be pointed out that other factors, such as a thick layer of unoxidized Al layer, also lead to a low MR. However, this possibility has been ruled out in our case by the process control.

The voltage and temperature dependence of the two-step tunneling current is the key to understanding the voltage and temperature dependence of junction properties. For simplicity, it is assumed that the defect states in the barrier are uniformly distributed, both spatially and energetically. The energetic distribution of the available defect states is governed by a Fermi-Dirac function

$$f(E) = \frac{1}{1 + \exp[(E_c - E)/kT_{\text{eff}}]}, \quad (2)$$

where E is the energy level of the defect state, E_c is the energy level of the barrier conduction band edge, k is the Boltzmann constant, and T_{eff} is the effective barrier temperature. As suggested by Eq. (2), the density of available states increases exponentially as the energy level increases. Therefore, the two-step tunneling current, which is proportional to the vacant defect state density, increases quickly at an increased bias voltage. The two-step tunneling current calculated by this model quickly exceeds the direct tunneling current at increased voltage. This leads to a decrease in the MR, according to Eq. (1). This model also indicates that the two-step tunneling is mainly responsible for the nonlinearity of the I - V characteristic. Therefore, the observed correlation of MR, MR- V dependence, and I - V characteristic can be explained.

T_{eff} is a parameter in this model. It determines the nonlinearity of the I - V characteristic of the two-step tunneling, and therefore, the MR- V dependence. Our fit to the MR- V dependence data at room temperature in Fig. 1 gives a value of kT_{eff} of the order of 0.2 eV. This T_{eff} is higher than the ambient temperature, and is possibly due to the presence of hot electrons in the barrier. In metal-oxide-semiconductor (MOS) devices, trap state generation in the gate oxide is enhanced by high electric fields and temperature.⁹ Similarly, T_{eff} for SDT barriers is expected to increase with the voltage

bias and the temperature. Based on the results from hot electron studies, we have assumed a form for $T_{\text{eff}}(V, T)$ given by

$$kT_{\text{eff}} = \sqrt{(CkT)^2 + [eV_1 \exp(V/V_2)]^2}, \quad (3)$$

where V_1 , V_2 , and C are free parameters which depend on the material properties of the barrier. The first and the second term in the square root represent the effect of temperature and voltage, respectively. C represents the indirect effect of temperature on the excitation process¹⁰ and can be determined from the temperature dependence data, while V_1 and V_2 can be determined from the voltage dependence data. This expression was found to fit the experimental data reasonably well for voltages between 10 and 500 mV. The predicted MR- V dependence based on this model is plotted in Fig. 1. The parameters used are $C=3.0$, $V_1=0.2$ V, and $V_2=10.0$ V. Different ratios of the spin-dependent and the spin-independent currents are required for junctions in group A and B.

It can be shown that the two-step tunneling has a stronger temperature dependence than the direct tunneling. Therefore, the temperature dependence of the junction properties can also be explained by this model. These details are covered elsewhere.¹⁰

IV. DISCUSSIONS AND CONCLUSIONS

Based on the model discussed in Sec. III, the current in group A (B) junctions with a high (low) MR is mainly carried by the spin-dependent direct tunneling (spin-independent two-step tunneling). Though other factors might lead to the observed voltage and temperature dependence of junction properties,¹ it is believed that this dependence is mainly attributed to the nonperfect nature of the barrier and the strong voltage and temperature dependence of the two-step tunneling. Therefore, the key to improving the MR and minimizing the voltage and temperature dependence is high quality barriers with low defect state density. In particular, a thin barrier is preferred to a low barrier as this will also reduce the resistance of the junction.

ACKNOWLEDGMENTS

Authors thank Dr. J. M. Daughton and Dr. D. Wang at NVE for their help in depositing some of the films used in this work. This work was supported by the National Science Foundation under Grant No. ECD-8907086. U.S. Government has certain rights to this material.

¹J. S. Moodera and L. R. Kinder, J. Appl. Phys. **79**, 4724 (1996).

²W. J. Gallagher, S. S. P. Parkin, Y. Lu, X. P. Bian, A. Marley, K. P. Roche, R. A. Altman, S. A. Rishton, C. Jahnes, T. M. Shaw, and G. Xiao, J. Appl. Phys. **81**, 3741 (1997).

³A. C. Marley and S. S. P. Parkin, J. Appl. Phys. **81**, 5526 (1997).

⁴R. S. Beech, J. Anderson, J. Daughton, B. A. Everitt, and D. Wang, IEEE Trans. Magn. **32**, 4713 (1996).

⁵W. Schroen, J. Appl. Phys. **39**, 2671 (1968).

⁶J. H. Greiner, J. Appl. Phys. **42**, 5151 (1971).

⁷M. Julliere, Phys. Lett. A **54**, 225 (1975).

⁸E. L. Wolf, *Principles of Electron Tunneling Spectroscopy* (Oxford University Press, Oxford, 1985).

⁹P. P. Apte and K. C. Saraswat, IEEE Trans. Electron Devices **41**, 1595 (1994).

¹⁰J. Zhang, Ph.D. dissertation, Carnegie Mellon University, 1997.

Bias voltage and temperature dependence of magnetotunneling effect

Yu Lu,^{a)} X. W. Li, and Gang Xiao
Brown University, Providence, Rhode Island 02912

R. A. Altman and W. J. Gallagher
IBM, Yorktown Heights, New York 10698

A. Marley, K. Roche, and S. Parkin
IBM Almaden, San Jose, California 95120

We have studied systematically the magnetotunneling properties of several metallic magnetic-tunnel-junction systems ($\text{Ni}_{80}\text{Fe}_{20}$ -insulator- $\text{Ni}_{80}\text{Fe}_{20}$, $\text{Ni}_{80}\text{Fe}_{20}$ -I-Co, Co-I-Co, $\text{Ni}_{40}\text{Fe}_{60}$ -I-Co). The room-temperature magnetoresistance MR value at zero-bias ranges between 16% and 27%, depending on the spin polarization of the electrodes. There seems to be a general bias dependence of MR in all of these systems. In particular, it requires a bias in the range of 0.22–0.23 V to suppress the maximum MR value by half. We have also measured the bias dependence of MR as a function of barrier parameters (thickness and oxidation time). At low temperature, a sharp cusplike feature appears near zero bias. In some cases, low-temperature MR values substantially exceed expectations from established spin-polarization. © 1998 American Institute of Physics.
[S0021-8979(98)47311-0]

Magnetic-tunnel junctions (MTJs) are emerging as a new class of magnetoresistive (MR) devices.^{1–7} MTJs have demonstrated a number of technical advantages over the existing giant magnetoresistance (GMR) devices. Metallic GMR structures are inherently highly conductive, so a large current density is required to generate enough voltage signal. For a tunnel junction, however, device resistance can in principle be controlled by barrier parameters.

Magnetic-tunnel junctions have been studied since the 1970s.¹ One of the perplexing properties observed since then is a strong suppression of magnetoresistance with bias voltage on a junction.^{5,8–10} This bias voltage dependence could convey information about the detailed process of spin-polarized tunneling. In this paper, we present an on-going study of the bias voltage and temperature dependence of MTJs particularly with transition metals and alloys as both electrodes.

The magnetic-tunnel junctions employed in this study are made by magnetron sputtering. The base pressure of the deposition system is lower than 1×10^{-8} Torr. A typical layer sequence is represented in Fig. 1(a). A thin layer of Al was deposited and subsequently plasma oxidized in the chamber to form the tunnel barrier. The nominal thickness of this Al layer is in the range of 5–15 Å. The oxygen pressure during oxidation is 100 mTorr, and oxidation times range from 30 s to 7 mins. A ferromagnet–antiferromagnet–ferromagnet (FM–AFM–FM) sandwich structure is deposited to provide exchange biasing for the bottom electrode. This technique separates the magnetic response of the top electrode from that of the bottom, and enables us to attain saturated antiparallel configurations of the junction. After the deposition, a lithographical patterning procedure was used to fabricate the MTJ devices as small as $1 \times 1 \mu\text{m}^2$. The details of this process have been described elsewhere.^{5–7}

The blanket multilayer films are examined by a

vibrating-sample magnetometer at room temperature after the deposition. Figure 1(b) shows a typical result. Three distinct hysteresis loops of varying sizes can be clearly seen, corresponding to the three ferromagnetic layers in the FM–AFM–FM sandwich structure of the bottom electrode, and have been shifted due to the exchange biasing effect. The centered hysteresis loop is generated by the top electrode. For more details about the magnetic properties of MTJs, refer to Refs. 5 and 6.

The hysteresis loops of the two electrodes are well reproduced by the tunneling resistance of the junction, as shown in Fig. 2(a). Between the hysteresis loops, the magnetization of the electrodes are antiparallel to each other, and junction resistance is maximized due to the mismatch of spin-polarized bands across the tunnel barrier. At higher field in either direction, the electrodes are aligned to be parallel and junction resistance reduces to a minimum value. This magnetoresistance effect can be understood qualitatively in the framework of the two-current model, first proposed by

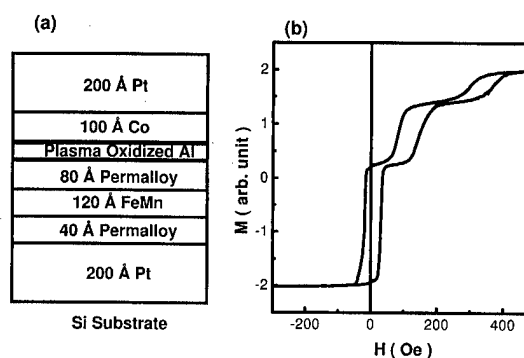


FIG. 1. (a) Layer sequence of a typical MTJ junction with exchange biased bottom electrode, and (b) the magnetization curves of one blanket multilayer film consisting of the MTJ structure. Three distinctive hysteresis loops can be seen corresponding to the three ferromagnetic layers in the film.

^{a)}Electronic mail: yulu@watson.ibm.com

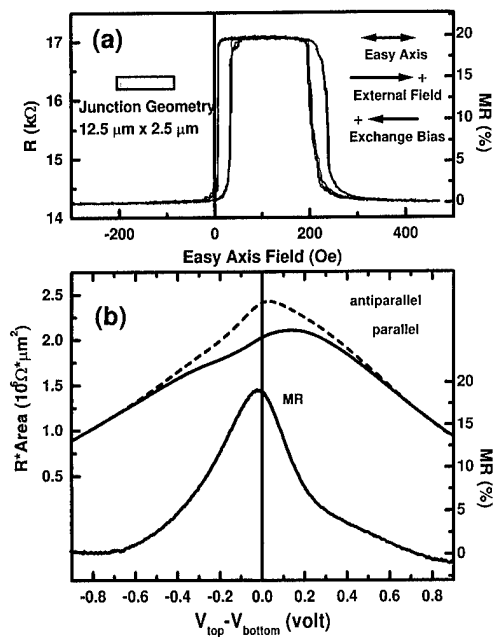


FIG. 2. (a) Resistance vs magnetic-field curves of a typical MTJ device at room temperature; the geometry of the junction as well as the relative orientation of exchange bias, easy axis, and external field are shown in the inset. (b) Differential junction resistance in parallel (solid) and antiparallel (dashed) configurations as a function of dc bias voltage on the junction. (c) Magnetoresistance, calculated using the differential resistance data, as a function of dc bias.

Julliere.¹ Assuming the two spin species of electrons tunnel through the barrier independently, the two-current model predicts the magnetoresistance, defined as the difference in resistance divided by the minimum value, as

$$\frac{\Delta R}{R_P} = \frac{R_{\uparrow\downarrow} - R_{\uparrow\uparrow}}{R_{\uparrow\uparrow}} = \frac{J_P}{J_{AP}} - 1 = \frac{1 + P_1 P_2}{1 - P_1 P_2} - 1 = \frac{2 P_1 P_2}{1 - P_1 P_2}, \quad (1)$$

where P_1 and P_2 are the spin-polarization factor of the two electrodes. The spin polarization of a number of materials has been measured in a series of tunneling experiments between ferromagnets and superconductor (FM-I-S) by Meservey and Tedrow.¹¹ We will later assemble a comparison of our results with these spin-polarization factors.

The simple two-current model does not take into consideration the effects of electron band structure, tunnel barrier transmission, and spin-flipping excitations into consideration, and thus, predicts no bias voltage dependence for the magnetoresistance. Experimenters,¹⁻⁴ however, have always observed a substantial decrease in MR with the application of bias. The differential resistance in parallel (solid) and antiparallel (dashed) states as well as the MR of one of our junctions are plotted versus dc bias in Fig. 2(b). The bias dependence of the differential resistance has the general feature of a metal-insulator-metal tunnel junction in that resistance decreases with bias and has a smooth maxima close to zero bias. The detailed shape of the curve shows deviations from simple calculations such as Simmons's formula.

We have measured the bias dependence of R and MR in MTJs with various electrode material and barrier parameters. The results are summarized in Figs. 3(a) and 3(b). Figure

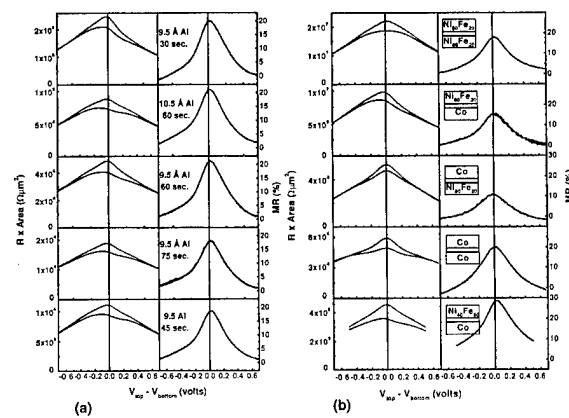


FIG. 3. (a) Bias dependence (room temperature) of junction resistance in both parallel (solid) and antiparallel (dashed) configurations and MR in a series of junctions with a Co base electrode and $\text{Ni}_{80}\text{Fe}_{20}$ counter electrode, but different barrier fabrication conditions (shown in the insets). (b) Same plots as (a) for a series of junctions with various electrode material combinations (shown in the insets).

3(a) plotted the bias dependence of R and MR in a series of junctions all with a Co base electrode and permalloy ($\text{Ni}_{80}\text{Fe}_{20}$) counter electrode, but differing barrier fabrication conditions. The junction conductance has been normalized by junction area, and thus, provides a measure of the barrier transmission coefficient. The graphs are ordered such that the parameter R^* area (inverse unit-area conductivity) decreases from the top graph. Nominal thicknesses of the Al layer as well as oxidation times are indicated in the insets with each pair of curves. Due to the exponential dependence of tunneling conductance on barrier thickness and height, R^* area of these samples vary by more than a factor of 20 even though the barriers are very similar. It is evident from this set of curves that little if any change in the bias dependence of tunneling resistance and MR is incurred by changing the barrier transmission, within the range of our data.

Figure 3(b) shows the same representative bias dependence for a series of junctions with different electrode material combinations. Although the material combinations are far from complete, the data seem to suggest a correlation between the bias dependence of the junction resistance with the material of the negatively biased electrode. Particularly, when the Co electrode is negatively biased there is a dip in the resistance curve at about 150 mV, and when $\text{Ni}_{80}\text{Fe}_{20}$ is negatively biased this feature is not present. This observation is consistent with the band-structure effect. Since the tunneling current comes mostly from electrons near the Fermi level of the positive electrode, which are closest in energy to the barrier top, variation in their tunneling probability as a function of bias is a mapping of the negative electrode's density of states above its Fermi level. Differences in the electrode-barrier interface cannot be ruled out as another possible cause of this correlation. The bias dependence of the MR ratio, however, does not vary as much as the resistance itself. Although the maximum MR ratio changes from 12% to 28%, the bias voltage needed to suppress the MR to half of its maximum value within each junction falls within the narrow range of 220–230 mV. We have not identified any correlation between electrode material and variations in the half-

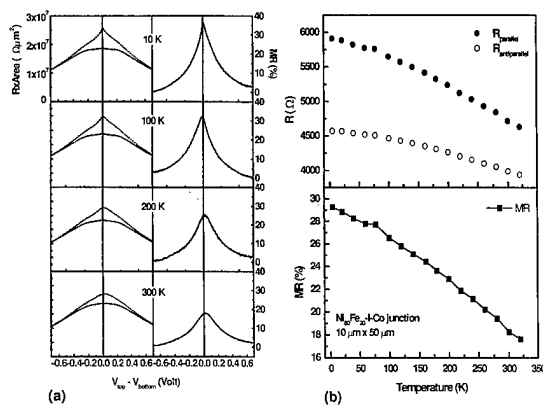


FIG. 4. (a) Bias dependence of R and MR of one MTJ at reduced temperatures. Plots follow the same convention used in Figs. 3(a) and 3(b). (b) Junction resistance and MR plotted as a function of temperature.

maximum bias voltage or the slight asymmetry in the MR curves. This surprisingly “universal” behavior is difficult to understand considering the close relationship between the spin polarization of the material and the MR. Since all these measurements are carried out at room temperature, the underlying mechanism should have a correspondingly high-energy scale. This is also indicated by the size of half-maximum bias.

We have also measured the bias dependence of MTJs at reduced temperature. The results are summarized in Fig. 4(a). As the samples are cooled from room temperature, a cusplike peak gradually develops at zero bias. This peak is limited within about ± 100 mV, and is much more pronounced in the antiparallel configuration than in parallel case. This zero-bias peak and the difference in peak height for the two magnetic configurations account for most of the increase in both junction resistance and MR at zero bias, which are plotted in the Fig. 4(b). This cusplike peak has been attributed to magnon excitations at the electrode-barrier interface by Zhang *et al.*¹² This theory has predicted some significant characteristics of the zero-bias peak, such as the cusplike shape and the size difference in the two magnetic configurations. We have not been able to distinguish the predicted $T \log T$ functional form of the temperature dependence of the zero-bias resistance from other possibilities. Aside from the zero-bias peak just discussed, the general bias dependence at higher voltage ranges does not change significantly with temperature.

Figure 5 compares our results with those of Meservey and Tedrow. The horizontal position of the points shows the MR values calculated using formula (1). The vertical positions then indicate the highest MR measured in each group of junctions, at room temperature (filled) and liquid-helium temperature (open). The room-temperature MR (black square) is generally 70%–90% of the predicted value, while low-temperature values have less dependence on electrode material and, for low P materials, are much higher than predicted. The reduction of MR at room temperature could come from the smearing of the Fermi surface or from thermally activated conduction that is spin independent. Another

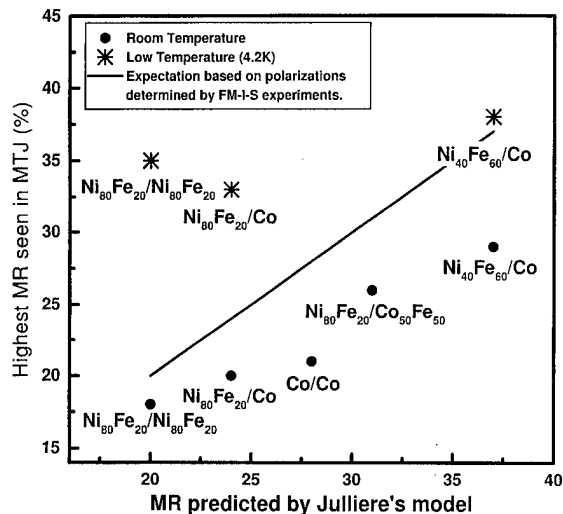


FIG. 5. Maximum MR values measured for MTJs with several electrode material combinations vs predicted values using the two-current model and spin-polarization factors measured in FM-I-S tunneling experiments. Room-temperature data are plotted as filled circles and liquid-helium temperature data as open circles, and solid lines indicate the prediction.

factor to be concerned is the loss of magnetization at elevated temperature, i.e., magnon excitation in the material or at the interface. Although the low-temperature data are not as extensive as those at room temperature, the continuity in temperature dependence and consistency in different junctions clearly precludes defects as the reason for the higher MR observed. Whether this discrepancy is due to some subtle difference between FM-I-S and FM-I-FM tunneling or other spin-dependent effects beyond the two-current model is unknown. It is also possible that the polarization values determined 20 years ago may need to be refined.

The authors wish to thank J. Z. Sun, J. C. Slonczewski, P. L. Trouilloud, and J. C. Connolly for help and discussions. Work supported in part by DARPA Contract No. MDA972-96-C-0014 and by NSF Contract No. DMR-9414160.

¹M. Julliere, Phys. Lett. **54**, 225 (1975).

²T. Yaoi, S. Ishio, and T. Miyazaki, J. Magn. Magn. Mater. **126**, 430 (1993).

³J. S. Moodera, L. R. Kinder, T. M. Wong, and R. Meservey, Phys. Rev. Lett. **74**, 3273 (1995).

⁴J. S. Moodera and L. R. Kinder, J. Appl. Phys. **79**, 4724 (1996).

⁵W. J. Gallagher, S. S. P. Parkin, Yu Lu, X. P. Bian, A. Marley, K. P. Roche, R. A. Altman, S. A. Rishton, C. Jahnes, T. M. Shaw, and Gang Xiao, J. Appl. Phys. **81**, 3741 (1997).

⁶Y. Lu, R. A. Altman, A. C. Marley, S. A. Rishton, P. L. Trouilloud, Gang Xiao, W. J. Gallagher, and S. S. P. Parkin, Appl. Phys. Lett. **70**, 2610 (1997).

⁷S. A. Rishton, Yu Lu, R. A. Altman, A. C. Marley, X. P. Bian, C. Jahnes, R. Viswanathan, G. Xiao, W. J. Gallagher, and S. S. P. Parkin, Microelectron. Eng. **35**, 249 (1997).

⁸Y. Lu, X. W. Li, G. Q. Gong, G. Xiao, A. Gupta, P. Lecoeure, J. Z. Sun, Y. Y. Wang, and V. P. Dravid, Phys. Rev. B **54**, R15 629 (1996).

⁹J. Z. Sun, W. J. Gallagher, P. R. Duncombe, L. Krusin-Elbaum, R. A. Altman, A. Gupta, Y. Lu, G. Q. Gong, and G. Xiao, Appl. Phys. Lett. **69**, 3266 (1996).

¹⁰C. T. Tanaka, J. Nowak, and J. S. Moodera, J. Appl. Phys. **81**, 5515 (1997).

¹¹R. Meservey and P. M. Tedrow, Phys. Rep. **239**, 174 (1994).

¹²S. Zhang, P. M. Levy, A. C. Marley, and S. S. P. Parkin, Phys. Rev. Lett. (to be published).

Finite bias spin dependent tunneling: A nonequilibrium Green's function approach

Xindong Wang^{a)}

Metals and Ceramics Division, Oak Ridge National Laboratory, Oak Ridge, Tennessee 37831-6114

The nonequilibrium Green's function theory is applied to a model spin dependent tunneling system at finite bias. In the limit of zero bias, the present result agrees with that of Landauer's formula. For finite bias, it is found that as the bias increases, the magnetoresistance ratio decreases. © 1998 American Institute of Physics. [S0021-8979(98)28811-6]

I. INTRODUCTION

Spin dependent tunneling has attracted ever growing attention due to its vast potential applications. It was recently reported by Marley and Parkin¹ that the magnetoresistance ratio (MR) decreases as the voltage bias increases. The MR is defined here to be $R_{\uparrow\downarrow} - R_{\uparrow\uparrow} / R_{\uparrow\uparrow} + R_{\uparrow\downarrow}$, where $R_{\uparrow\uparrow}$ is the resistance of the magnetic-metal-insulator-magnetic-metal tunnel junction when the magnetizations on both sides of the junction are parallel, and $R_{\uparrow\downarrow}$ is the resistance of the tunnel junction when the magnetizations are antiparallel to each other. In this article, the nonequilibrium Green's function approach² is applied to a model for finite bias spin dependent tunneling. In the zero-bias limit, the present result agrees with Landauer's formula.² It is found that the observed bias dependence of the MR can be explained within a simple model without evoking more complicated mechanisms.

In the next section, a brief derivation of the formalism based on the nonequilibrium Green's function theory is presented. The formalism is applied to a simplified model for finite bias spin dependent tunneling and numerical results are presented.

II. NONEQUILIBRIUM GREEN'S FUNCTION APPROACH TO TUNNELING

In order to make clear the notation used in this article, we will outline the main results of nonequilibrium Green's function theory here. A detailed exposition of the theory can be found in Ref. 2. The three Green's functions used in this article are the correlation function $G^n(\mathbf{r}, \mathbf{r}'; t, t')$, the retarded Green's function $G^r(\mathbf{r}, \mathbf{r}'; t, t')$, and the advanced Green's function $G^a(\mathbf{r}, \mathbf{r}'; t, t')$. They are defined as

$$G^n(\mathbf{r}, \mathbf{r}'; t, t') = i \langle \Psi^\dagger(\mathbf{r}', t') \Psi(\mathbf{r}, t) \rangle, \quad (1)$$

$$G^r(\mathbf{r}, \mathbf{r}'; t, t') = -i \theta(t - t') \langle \{ \Psi(\mathbf{r}, t), \Psi^\dagger(\mathbf{r}', t') \}_+ \rangle, \quad (2)$$

and

$$G^a(\mathbf{r}, \mathbf{r}'; t, t') = i \theta(t' - t) \langle \{ \Psi(\mathbf{r}, t), \Psi^\dagger(\mathbf{r}', t') \}_+ \rangle, \quad (3)$$

where $\hbar = 1$ is adopted throughout this article. Since only steady states are considered in this article, the time depen-

dence of all the Green's functions is just on $t - t'$. We will only need to work with their time Fourier transformations defined as

$$G(\omega) = \frac{1}{2\pi} \int dt G(t) \exp(i\omega t).$$

The retarded (advanced) Green's function satisfies

$$[\omega - T - V - \Sigma^{r(a)}(\omega)] G^{r(a)}(\omega) = \mathbf{I}, \quad (4)$$

where the $\Sigma^{r(a)}$ is the self-energy operator and $\Sigma^a = (\Sigma^r)^\dagger$.

For steady state, the correlation function G^n is related to the other two Green's functions as

$$G^n = G^r \Sigma^n G^a, \quad (5)$$

where Σ^n is the self energy for G^n .

For fermions in equilibrium, Σ^n is related to Σ^r through

$$\Sigma^n = -2if(\omega)\text{Im}(\Sigma^r), \quad (6)$$

where $f(\omega)$ is the Fermi-Dirac distribution function.

For the tunneling devices to be modeled in this article, the system is separated into three regions, left reservoir (infinite lead), device region, and right reservoir (infinite lead). In the reservoirs, quasithermal equilibrium is assumed so that we have $f_L(\omega)$ and $f_R(\omega)$ for the left and right reservoir, respectively. Accordingly, Σ^n is decomposed into three parts:

$$\Sigma^n = \Sigma_L^n + \Sigma_R^n + \Sigma_D^n, \quad (7)$$

where locality of the three parts are assumed so that

$$\Sigma_{L(R)}^n(\omega) = -2if_{L(R)}(\omega)\text{Im}[\Sigma^r(\omega)], \quad (8)$$

and Σ_D^n originates in the dissipative processes within the device region. Since in the two-probe setup, the reservoir is taken to be the infinite lead with infinitesimal $\text{Im} \Sigma^r = -\eta < 0$, we have

$$\Sigma_{L(R)}^n = 2i\eta f_{L(R)}(\omega) \theta_{L(R)}(\mathbf{r}) \delta(\mathbf{r} - \mathbf{r}') \quad (9)$$

with the limit $\eta \rightarrow 0^+$ to be taken last. Here $\theta_{L(R)}(\mathbf{r})$ is a step function which is one when \mathbf{r} is inside the left(right) reservoir and zero otherwise.

Once G^n is known, the tunneling current density is

$$\mathbf{J} = -\frac{e}{m} \int \frac{d\omega}{2\pi} \lim_{\mathbf{r}' \rightarrow \mathbf{r}} \nabla G^n(\mathbf{r}, \mathbf{r}'; \omega). \quad (10)$$

In the following, we will adopt Rydberg units in which the electron mass, m , is 1/2. For a laterally uniform system,

^{a)}Electronic mail: yxw@ornl.gov

the following two-dimensional Fourier transformation simplifies the problem to an effective one-dimensional problem

$$G(\Sigma)(\mathbf{r}, \mathbf{r}') = \frac{1}{(2\pi)^2} \int d^2\mathbf{q} e^{i\mathbf{q} \cdot (\mathbf{r} - \mathbf{r}')} G(\Sigma)(z, z'; \omega). \quad (11)$$

Substituting these Fourier transformations into Eq. (4), we have

$$\left(\frac{d^2}{dz^2} + \omega - q^2 - V(z) \right) G_q^{r(a)}(z, z'; \omega) - \int dz_1 \Sigma_q^{r(a)}(z, z_1; \omega) G_q^{r(a)}(z_1, z'; \omega) = \delta(z - z'). \quad (12)$$

From Eq. (5), we have

$$G_q^n(z, z'; \omega) = \int dz_1 \int dz_2 G_q^r(z, z_1; \omega) \Sigma_q^n(z_1, z_2; \omega) G_q^a(z_2, z'; \omega). \quad (13)$$

Let the device region be within $[Z_L, Z_R]$, and

$$V(z) = V_L \quad \text{when } z < Z_L, \quad (14)$$

$$V(z) = V_R \quad \text{when } z > Z_R. \quad (15)$$

Let us further assume that

$$\Sigma(z, z') = \delta(z - z') \Sigma(z) \quad (16)$$

for all Σ .

With this local self energy, the retarded and advanced Green's functions have simple forms as given below. Define the following function:

$$\left(\frac{d^2}{dz^2} + \omega - q^2 - V(z) - \Sigma_q^\pm(z; \omega) \right) \psi_q^\pm(z; \omega) = 0 \quad (17)$$

with the following boundary conditions:

$$\psi_q^+(z; \omega) = \exp(ik_R z) \quad \text{when } z > Z_R \quad (18)$$

and

$$\psi_q^-(z; \omega) = \exp(-ik_L z) \quad \text{when } z < Z_L \quad (19)$$

with $k_{R(L)}^2 = \omega - q^2 - V_{R(L)}$.

Then we have for the retarded Green's function,

$$G_q^r(z, z'; \omega) = \frac{\psi_q^+(z_{>}; \omega) \psi_q^-(z_{<}; \omega)}{W(\psi^+, \psi^-)}, \quad (20)$$

and for the advanced Green's function,

$$G_q^a(z, z'; \omega) = \frac{\psi_q^+(z_{>}; \omega)^* \psi_q^-(z_{<}; \omega)^*}{W(\psi^+, \psi^-)^*}, \quad (21)$$

where $z_{>(<)}$ is the larger(smaller) argument of z and z' and the wronskian is

$$W(\psi^+, \psi^-) \equiv \frac{d\psi^+}{dz} \psi^- - \frac{d\psi^-}{dz} \psi^+ = \text{constant}.$$

Substituting Eq. (20), Eq. (21) into Eq. (13) and using the locality assumptions in Eq. (16), and taking the limit of $\eta \rightarrow 0^+$, we have for z and z' within $[Z_L, Z_R]$,

$$G_q^n(z, z'; \omega) = C_q^L(z, z'; \omega) f_L(\omega) + C_q^R(z, z'; \omega) f_R(\omega) + \int_{Z_L}^{Z_R} dz_1 G_{q^r}(z, z_1; \omega) \Sigma_q^n(z_1, z'; \omega) \times G_q^a(z_1, z'; \omega), \quad (22)$$

where

$$C_q^L(z, z'; \omega) = i \frac{\psi_q^+(z; \omega) (\psi_q^+(z'; \omega))^*}{|W(\psi^+, \psi^-)|^2} 2k_L \theta(k_L^2) \quad (23)$$

and

$$C_q^R(z, z'; \omega) = i \frac{\psi_q^-(z; \omega) (\psi_q^-(z'; \omega))^*}{|W(\psi^+, \psi^-)|^2} 2k_R \theta(k_R^2). \quad (24)$$

Here $\theta(x)$ is the step function which is one when $x > 0$ and zero otherwise, and k_L and k_R are real and are defined in Eqs. (18) and (19), respectively. Note that from the factor $2k_{L(R)} \theta(k_{L(R)}^2)$ comes the following limit [cf. Eq. (16)]:

$$\lim_{\eta \rightarrow 0^+} 2\eta \int_{-\infty(Z_R)}^{Z_L(\infty)} dz |\psi_q^{-(+)}(z; \omega + i\eta)|^2. \quad (25)$$

If the dissipation within the device can be neglected, we have the ballistic current density for channel \mathbf{q} (note that $m = 1/2$)

$$I_q(\omega) = -2e \lim_{z' \rightarrow z} \frac{d}{dz} G_q^n(z, z'; \omega), \quad (26)$$

which can be evaluated at Z_L or Z_R to be

$$I_q(\omega) = \frac{4ek_L k_R}{|W(\psi^+, \psi^-)|^2} \theta(k_L^2) \theta(k_R^2) [f_L(\omega) - f_R(\omega)]. \quad (27)$$

Since we have for ψ^+ in the region $z < Z_L$ the following,

$$\psi_q^+(z) = \frac{1}{t_q^+(\omega)} (\exp(ik_L z) + r_q^+(\omega) \exp(-ik_L z)) \quad \text{for } z < Z_L, \quad (28)$$

we have

$$W(\psi^+, \psi^-) = \frac{2ik_L}{t_q^+(\omega)}. \quad (29)$$

Alternatively, we can write the Wronskians in terms of k_R ,

$$W(\psi^+, \psi^-) = \frac{-2ik_R}{t_q^-(\omega)}. \quad (30)$$

So the current density for channel \mathbf{q} is

$$I_q(\omega) = e(1 - R_q) [f_L(\omega) - f_R(\omega)] \theta(k_R^2) \theta(k_L^2), \quad (31)$$

where

$$R_q = |r_q^+(\omega)|^2 = |r_q^-(\omega)|^2. \quad (32)$$

And the total current density is

$$I = \frac{1}{(2\pi)^3} \int d\mathbf{q} d\omega I_q(\omega). \quad (33)$$

In the limit of zero bias, we have the two-probe Landauer formula.² Equation (31) can be viewed as a generalized Landauer formula at finite bias.

III. APPLICATION TO FINITE BIAS SPIN DEPENDENT TUNNELING

For finite bias spin dependent tunneling, the following simplified model is used in this article: Let the bias be $U = \mu_L - \mu_R$, where $\mu_{L(R)}$ is the chemical potential in the left(right) reservoir. Assume the barrier for both spin components of the electrons is V_b and the exchange splitting for the magnetic metal is Δ_{ex} . Then when the magnetizations are parallel to each other, the following tunneling potential is used:

$$\begin{aligned} V_L^\sigma &= -\frac{\sigma}{2} \Delta_{ex} + U, \\ V_R^\sigma &= -\frac{\sigma}{2} \Delta_{ex}, \end{aligned} \quad (34)$$

$$V(z \in [Z_L, Z_R]) = V_b,$$

and when the magnetizations are antiparallel to each other, the following tunneling potential is used:

$$\begin{aligned} V_L^\sigma &= -\frac{\sigma}{2} \Delta_{ex} + U, \\ V_R^\sigma &= +\frac{\sigma}{2} \Delta_{ex}, \end{aligned} \quad (35)$$

$$V(z \in [Z_L, Z_R]) = V_b,$$

where $\sigma = \pm$ is the spin index.

For $V_b = 1.0$ Ryd, $\Delta_{ex} = 0.2$ Ryd, $\mu_R = 0.3$ Ryd, and $Z_R - Z_L = 5.0$ a.u., the MR versus V_b is shown in Fig. 1. It is clear that MR decreases as the bias increases. However, it is surprising that for large bias, MR even changes sign (not

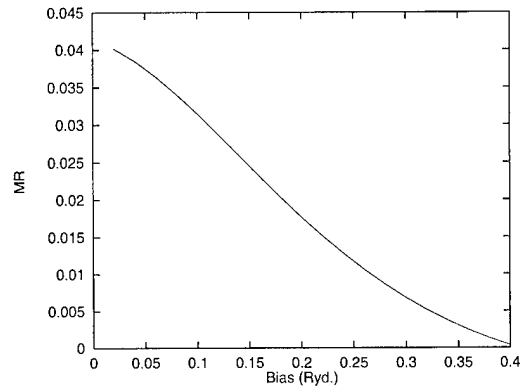


FIG. 1. MR vs bias for $V_b = 1.0$ Ryd, $\Delta_{ex} = 0.2$ Ryd, $\mu_R = 0.3$ Ryd, and $Z_R - Z_L = 5.0$ a.u.

shown in Fig. 1). To understand the MR decrease as the bias increases in our model, we note that as the bias increases, the effect of the exchange splitting is relatively decreased. Whether this is an artifact due to the oversimplified model used here will have to be resolved in the future.

ACKNOWLEDGMENTS

The author thanks Dr. W. H. Butler for constant support and a critical reading of the manuscript. Research performed as an Eugene P. Wigner Fellow and staff member at the Oak Ridge National Laboratory and sponsored by the Division of Materials Sciences, Office of Basic Energy Sciences, U.S. Department of Energy under Contract No. DE-AC05-96OR22464 with Lockheed Martin Energy Research Corporation.

¹A. C. Marley and S. S. P. Parkin, J. Appl. Phys. **81**, 5526 (1997).

²S. Datta, *Electronic Transport in Mesoscopic Systems* (Cambridge University Press, Cambridge, 1995).

Spin-dependent tunneling in epitaxial systems: Band dependence of conductance

J. M. MacLaren^{a)}

Department of Physics, Tulane University, New Orleans, Louisiana 70118

W. H. Butler and X.-G. Zhang

Oak Ridge National Laboratory, Oak Ridge, Tennessee 37831-6114

We present first principles based calculations of the tunneling conductance between iron electrodes separated by semiconducting ZnSe. We assume that Fe (100) and ZnSe (100) atomic planes are epitaxed. We find that the conductance depends strongly on the relative alignment of the magnetic moments in the two Fe electrodes. The relative change in conductance increases dramatically as the thickness of the semiconductor increases. We show that this effect is due to the fact that electrons from a particular majority spin band are injected efficiently into the ZnSe from the Fe and also that electrons are ejected efficiently from the ZnSe into this band. Our calculations are based upon the Landauer-Büttiker expression for the conductance which is expressed in terms of the transmission matrix elements. © 1998 American Institute of Physics. [S0021-8979(98)20311-2]

Recently, it has been observed¹⁻⁵ that the tunneling current through a FM|S|FM sandwich (where FM represents a ferromagnet and S represents a semiconductor or an insulator) may depend on the relative orientation of the moments in the two ferromagnetic layers. Although most experimental observations of spin-dependent tunneling have involved non-epitaxial systems with uncharacterized or amorphous interlayers, there have been recent observations of large spin-dependent tunneling effects in epitaxial systems.^{4,5} Epitaxial systems have the advantage for a first-principles theoretical study that the nominal physical structure is well defined.

Although many treatments of tunneling⁶⁻⁹ and even of spin-dependent tunneling^{10,11} have been proposed, we suggest that a useful understanding of this phenomenon must be based on a realistic approximation to the electronic structure of the ferromagnets, the nonconducting interlayer and especially the interfaces which separate them. As first steps towards that goal we have calculated the self-consistent electronic structure of epitaxial FM|S|FM sandwiches using first principles techniques and we have used these electronic structures to calculate the tunneling conductance for both parallel and antiparallel alignment of the magnetic moments of the ferromagnetic layers.

Both the self-consistent electronic structures¹² and the techniques for calculating the tunneling conductance^{13,14} have been described previously. We have considered the case in which the ferromagnetic layers consist of bcc Fe with (100) atomic planes parallel to the interfaces and the semiconducting layer consists of (100) atomic planes of ZnSe epitaxed to the Fe. For this case we showed¹⁴ that for reasonably thick films the conductance is much larger in the majority channel for parallel alignment of the moments than for the minority moment for the same alignment and that it is also much larger than the conductance of either of the chan-

nels for antiparallel alignment. This leads to a large magnetoconductance which increases with increasing film thickness.

In this article we point out that the tunneling conductance may vary dramatically from band to band. The contribution from one particular majority channel band at the Fe Fermi energy is responsible for the large majority conductance and ultimately for the large calculated change in conductance when the alignment of the moments in the two magnetic layers is changed. The band in question was singled out previously by Stearns.¹⁰

The Layer Korringa Kohn Rostoker (LKKR) technique¹⁵ was used to solve the equations of density functional theory in the local density approximation. The LKKR technique assumes that the system consists of atoms that are arranged in periodic layers, but it allows the treatment of systems which are not periodic in the direction perpendicular to these layers. We took advantage of this feature to calculate the self-consistent electronic structure of 9 atomic layers of ZnSe embedded in bcc iron.¹² The calculations showed a large peak in the minority Fermi energy density of states localized on the interfacial Fe layer, and the formation of a dipole layer at the interface which correctly places the Fermi energy of the semiconductor interlayer relative to that of the bulk iron.

We also calculated the tunneling conductance as a function of the thickness of the ZnSe using between 9 and 33 layers of Zn and Se. The tunneling conductance was calculated using the Landauer-Büttiker formalism¹⁶ implemented for Bloch electrons.^{13,14} In this formalism the conductance is expressed as a sum of the transmission probability over "channels." In this case the channels are the Bloch states which are enumerated by k_{\parallel} , the component of the momentum in the plane of the layers (taken to be the $x-y$ plane), by a propagation index, \pm , which indicates the direction of propagation of the Bloch wave perpendicular to the layers, and by a band index which distinguishes between the bands for a given value of k_{\parallel} . Thus the conductance for a given

^{a)}Electronic mail: james@maclaren.phy.tulane.edu

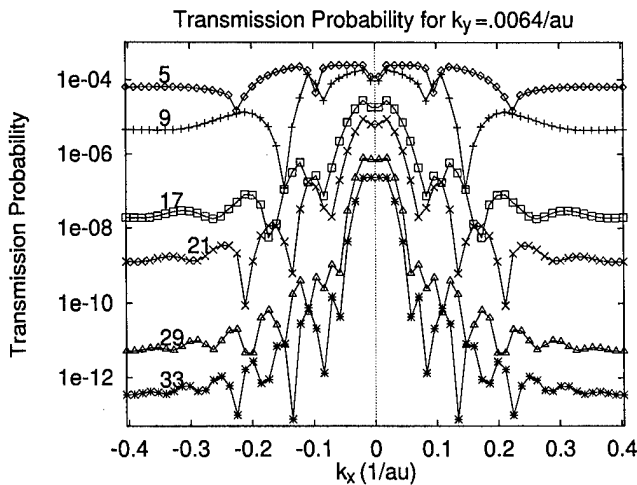


FIG. 1. Dependence of current on k_x for fixed $k_y \approx 0$ for majority electrons for the case of parallel alignment of the moments in the two ferromagnetic layers. The numbers near each curve indicate the number of Zn and Se layers in the interlayer.

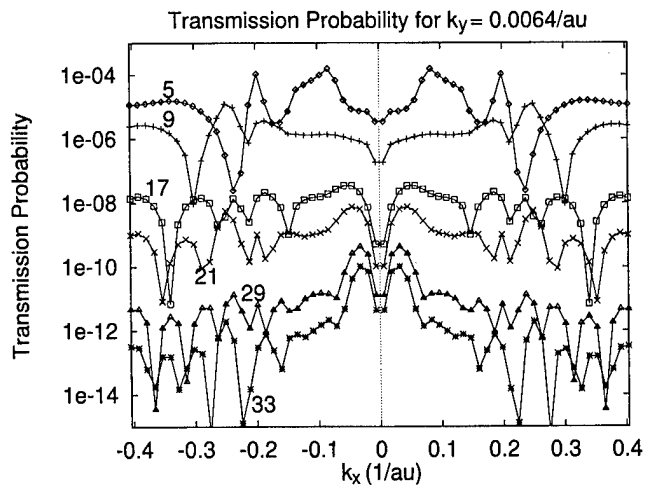


FIG. 2. Dependence of current on k_x for fixed $k_y \approx 0$ for minority electrons for the case of parallel alignment of the moments in the two ferromagnetic layers.

spin channel is given by $G = (e^2/h) \sum_{k_{\parallel}, i, j} T^{i+, j+}(k_{\parallel})$, where $T^{i+, j+}(k_{\parallel})$ is the transmission probability for a right going Bloch state $i+$ with the given value of k_{\parallel} on the left hand side of the semiconductor to be transmitted into the right going Bloch state $j+$ with the same value of k_{\parallel} on the right hand side of the barrier. In our calculations k_{\parallel} is conserved in the tunneling processes because of the assumed two-dimensional periodicity of the system.

Three-dimensional plots which show the conductance as a function of k_{\parallel} over the entire two-dimensional Brillouin zone for 9 and for 33 layers of Zn and Se were presented in Ref. 14. In Fig. 1 we show plots of the conductance along a line in the two-dimensional zone which runs approximately along the line from $\bar{\Gamma}$ to \bar{H} . As the thickness increases it can be seen that the current becomes more strongly peaked near $k_x = 0$. Superposed on this general behavior is a thickness dependent structure of the current as a function of k_x . The wavelength of at least some of this structure decreases as the thickness of the interlayer increases. Little of the structure is present in the current calculated for a simple spatially uniform barrier. The origin of this structure lies partly in the band structure of the Fe since there can only be transmission for those values of k_x for which there are bands to inject the electrons into the ZnSe and bands to receive the electrons that are ejected from the ZnSe. We suggest, however, that most of the structure, especially that part that depends on the interlayer thickness arises, from the “interference” of electron waves reflected off of the interfaces between the Fe and ZnSe.

Similar “interference” effects can be seen in the minority current as a function of k_{\parallel} which is displayed in Fig. 2. The major differences between the majority and minority transmission probabilities are the smaller maximum values in the minority channel and the pronounced minimum near $k_{\parallel} = 0$. The pronounced minimum near $k_{\parallel} = 0$ for the minority and the smaller minimum near $k_{\parallel} = 0$ for the majority seem to be related to the Fe bands since similar structure is seen in the current calculated for a simple spatially constant barrier.

The suggestion of “interference” effects in the tunneling conductance may seem strange since tunneling electrons are generally perceived to be tunneling through a “barrier.” It should be realized however that the ZnSe layers do not present a classical barrier to electrons, only a quantum mechanical one. Electrons at the Fermi energy find all of space except a small region near the interstitial points classically accessible, i.e., $E_F > V(\mathbf{r})$. If the electrons were classical particles almost all of them would be transmitted. Although Bloch waves cannot propagate at the Fermi energy in the ZnSe because destructive interference leads to a band gap, this same interference leads to the rapid changes in transmission probability with k_x that is seen in Figs. 1 and 2.

In order to gain a better understanding of the difference between the conductance in the majority channel and the minority channel and to better understand the change in conductance when the moment alignment is switched from parallel to antiparallel, we calculated the density of states (DOS)

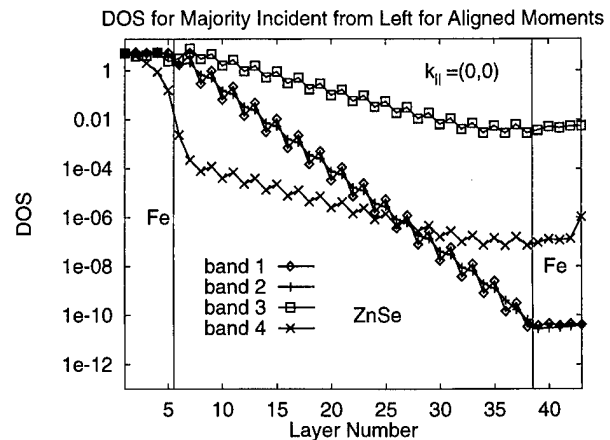


FIG. 3. Density of states for majority electrons incident from the left for the case of aligned moments. The DOS is shown for each majority band at the Fermi energy for $k_{\parallel} = 0$. This corresponds to bands in the three-dimensional zone that intersect the Fermi energy along the line $\bar{\Gamma} \rightarrow \bar{H}$. The sawtooth shape of the DOS in the ZnSe interlayer is due to alternate layers being Zn and Se.

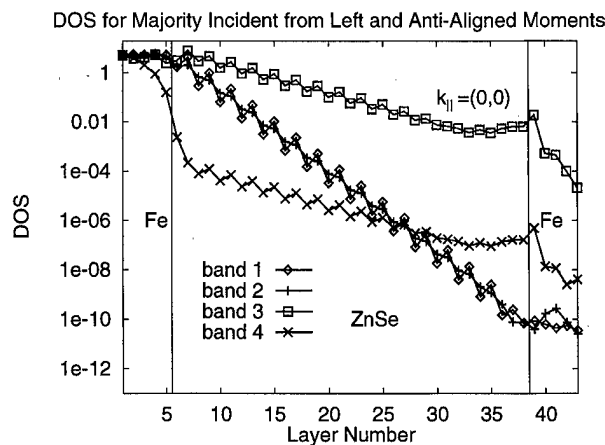


FIG. 4. Density of states at $k_{\parallel}=0$ for majority electrons incident from the left for the case of antialigned moments.

for Bloch electrons incident on the semiconducting interlayer. Imagine calculating the density of states of Bloch electrons in Fe with a given value of k_{\parallel} . Let us further restrict the DOS to those Bloch electrons with a given k_{\parallel} and whose z component of Fermi velocity is greater than zero, i.e., electrons traveling from left to right. Now imagine that we insert the ZnSe interlayer into the Fe. Most of the Bloch electrons will be reflected, but a few will penetrate into the semiconductor where we expect the DOS to decay exponentially and a few will be transmitted. This DOS is shown in Fig. 3 for each band in Fe at the Fermi energy with $k_{\parallel}=0$.

The most salient feature of Fig. 3 is the relatively large DOS for band 3 inside the semiconductor. The electrons from this particular Bloch wave are able to penetrate easily into the semiconductor. They also exit the semiconductor easily when the moments are aligned. However, they are not so easily ejected when the moments are antialigned as is shown in Fig. 4. There is a surprising variability in the rate of decay of the wave function within the ZnSe interlayer. After about 20 atomic layers only electrons from band 3 of the Fe contribute significantly to the DOS. The DOS from band 3 decays only about 1/3 as fast as the other majority states. If the decay for band 3 is fit to $e^{-z/\ell}$, ℓ is approximately 9 Å.

Figure 5 shows the DOS for minority electrons incident from the left. The DOS for all of the minority bands is seen to decay rapidly to zero. The decay length for these states is approximately the same as for the majority electrons other than band 3.

The distinguishing characteristic of majority band 3 compared to the other bands at the Fermi energy is that it has much more s and p character. This particular band was described by Stearns¹⁰ as "itinerant" d . Stearns also argued that this band would be important for spin-dependent tunneling.

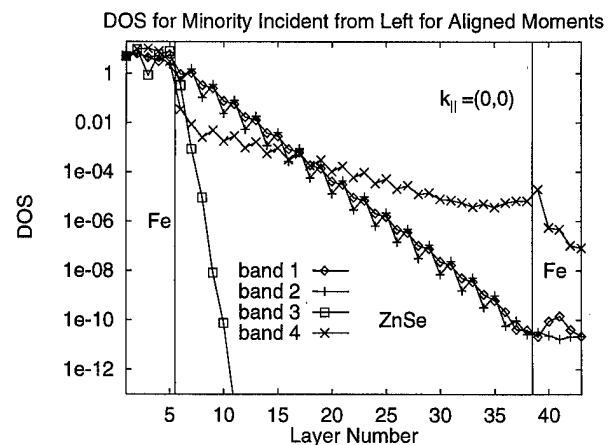


FIG. 5. Density of states at $k_{\parallel}=0$ for minority electrons incident from the left for the case of aligned moments.

Work at Oak Ridge was sponsored by the Division of Materials Sciences Office of Basic Energy Sciences of the USDOE under Contract No. DE-AC05-96OR22464 with Lockheed Marietta Energy Research Corp. Work at Tulane University was funded by the NSF Center for Photoinduced Processes, the Louisiana Board of Regents, and by DARPA Grant No. MDA 972-97-1-003. One of the authors (J.M.M.) acknowledges support from DARPA grant No. MDA 972-97-1-003. W.H.B. and X.G.Z. acknowledge support from Laboratory Directed Research and Development funds at ORNL and from the Office of Basic Energy Sciences, Division of Materials Sciences of the U.S. Department of Energy under Contract No. DE-AC05-96OR22464 with Lockheed Martin Energy Research Corp.

- ¹J. S. Moodera, L. R. Kinder, T. M. Wong, and R. Meservey, *Phys. Rev. Lett.* **74**, 3273 (1995).
- ²T. Miyazaki, T. Yaoi, and S. Ishio, *J. Magn. Magn. Mater.* **98**, L7 (1991); **126**, 430 (1993).
- ³T. Miyazaki and N. Tezuka, *J. Magn. Magn. Mater.* **139**, 4231 (1995).
- ⁴X. W. Li, Yu Lu, G. Q. Gong, Gang Xiao, A. Gupta, P. Lecoeur, J. Z. Sun, Y. Y. Wang, and V. P. Dravid, *J. Appl. Phys.* **81**, 5509 (1997).
- ⁵T. Kimura, Y. Tomioka, H. Kuwahara, A. Asamitsu, M. Tamura, and Y. Tokura, *Science* **274**, 1698 (1996).
- ⁶J. G. Simmons, *J. Appl. Phys.* **34**, 1793 (1963).
- ⁷I. Giaever, *Phys. Rev. Lett.* **5**, 147,464 (1960).
- ⁸J. Bardeen, *Phys. Rev. Lett.* **6**, 57 (1961).
- ⁹W. A. Harrison, *Phys. Rev.* **123**, 85 (1961).
- ¹⁰M. B. Stearns, *J. Magn. Magn. Mater.* **5**, 167 (1977).
- ¹¹J. C. Slonczewski, *Phys. Rev. B* **39**, 6995 (1989).
- ¹²W. H. Butler, X.-G. Zhang, X.-D. Wang, J. van Ek, and J. M. MacLaren, *J. Appl. Phys.* **81**, 5518 (1997).
- ¹³J. M. MacLaren, X.-G. Zhang, and W. H. Butler, *Phys. Rev. B* **56**, 8970 (1997).
- ¹⁴J. M. MacLaren, X.-G. Zhang, W. H. Butler, and X.-D. Wang, *Phys. Rev. B* (submitted).
- ¹⁵J. M. MacLaren, S. Crampin, D. D. Vvednsky, R. C. Albers, and J. B. Pendry, *Comput. Phys. Commun.* **60**, 365 (1990).
- ¹⁶R. Landauer, *IBM J. Res. Dev.* **1**, 223 (1957); R. Landauer, *Philos. Mag.* **21**, 863 (1970); M. Büttiker, *IBM J. Res. Dev.* **32**, 317 (1988).

Anomalous behavior of temperature and bias-voltage dependence of tunnel-type giant magnetoresistance in insulating granular systems

S. Mitani,^{a)} K. Takanashi, K. Yakushiji, and H. Fujimori
Institute for Materials Research, Tohoku University, Sendai 980-77, Japan

We have investigated temperature and bias-voltage dependence of tunnel-type giant magnetoresistance (MR) in Co–Al–O insulating granular films. A remarkable enhancement of MR which is larger than the theoretical value by a simple model is observed for Co–Al–O granular films at low temperatures, and it steeply decreases with increasing temperature. On the other hand, the MR does not decrease with increasing bias voltage although the resistivity decreases by a few orders of magnitude. Furthermore, it has been found that the effect of temperature is definitely different from that of bias voltage. The anomalous behavior is in contrast to that of macroscopic tunnel junctions, suggesting the significant effect of Coulomb blockade in granular systems. © 1998 American Institute of Physics. [S0021-8979(98)28911-0]

I. INTRODUCTION

Spin-dependent transport phenomena in artificial nanostructures have attracted much attention in the fields of physics and electronics.¹ The tunnel-type giant magnetoresistance (GMR) in insulating granular systems, e.g., Co–Al–O sputtered films, is one of such novel phenomena.^{2,3} The insulating granular systems consist of magnetic metal granules (e.g., Co) and nonmagnetic insulating matrix (e.g., Al oxide), and the magnetoresistance (MR) is caused by the tunneling current between magnetic metal granules depending on their magnetization directions. In a previous article, we reported a preliminary result on the enhancement of MR at low temperatures in Co–Al–O and Fe–Al–O granular films.⁴ This article provides further investigations including the anomalous behavior of temperature and bias-voltage dependence of MR in Co–Al–O granular films.

II. EXPERIMENTAL PROCEDURE

Co–Al–O granular films (1 to 2 μm in thickness) were prepared on glass substrates using a reactive-sputtering technique with mixed gas of Ar+O₂. Details of the sample preparation and the structural characterization were described previously in our articles.^{3,5} Electrical resistivity (ρ) were measured using a dc four-terminal method, as a function of the temperature between 2 and 300 K, and of the applied magnetic field up to 12 kOe. Magnetization curves were measured by a superconducting quantum interference device (SQUID) magnetometer with the field applied up to 50 kOe. On the basis of the proportional relation between MR and square of the normalized magnetization,³ i.e., $\Delta\rho/\rho_{\text{max}} \propto (M/M_s)^2$, it was confirmed that the MR at 12 kOe almost reaches the saturated state. In case that MR did not saturate at 12 kOe, the saturation values of MR were extrapolated using $\Delta\rho/\rho_{\text{max}} \propto (M/M_s)^2$.

The bias-voltage (V_b) dependence of MR was measured at 12 kOe and 4.2 K in the current-perpendicular-to-plane (CPP) geometry where the Co–Al–O granular films were

sandwiched with upper and lower electrodes of Au–Cr alloy, as shown in Fig. 1. The source dc current was controlled in order to adjust V_b between voltage electrodes to a constant value in the accuracy of less than 0.01% because the resistivity varies drastically via the change of the bias-voltage V_b .

III. RESULTS AND DISCUSSION

Figure 2 shows the temperature dependence of MR for the Co–Al–O films with different compositions: Co₅₄Al₂₁O₂₅, Co₅₂Al₂₀O₂₈, and Co₃₆Al₂₂O₄₂. It is clearly seen that the MR is remarkably enhanced at low temperatures. The MR reaches up to 24% around 2 K for the Co₃₆Al₂₂O₄₂ film, and the MR decreases dramatically with increasing temperature. The dashed line of $P_{\text{Co}}^2/(1+P_{\text{Co}}^2)$ shown in Fig. 2 is the magnitude of MR calculated theoretically using a simple model of tunneling transport,⁶ where P_{Co} is the spin polarization of conduction electrons in Co granules. $P_{\text{Co}}^2/(1+P_{\text{Co}}^2)$ is calculated to be about 10% using the value of P_{Co} (34%) obtained by means of tunnel spectroscopy experiments.⁷ This simple model was originally proposed for MR effect in ferromagnetic tunnel junctions and gave the result of $\text{MR} = 2P^2/(1+P^2)$, where P is the

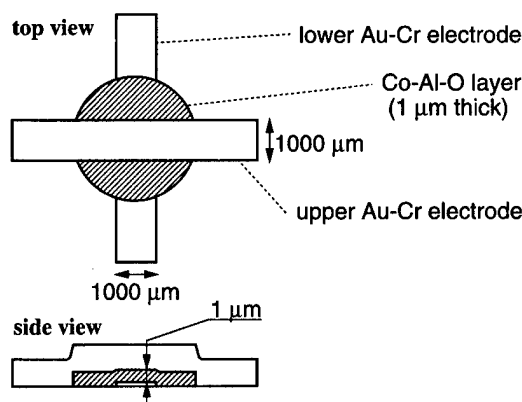


FIG. 1. Schematic illustration of a Co–Al–O film for the measurement in current-perpendicular-to-plane (CPP) geometry.

^{a)}Electronic mail: mitani@magmate.imr.tohoku.ac.jp

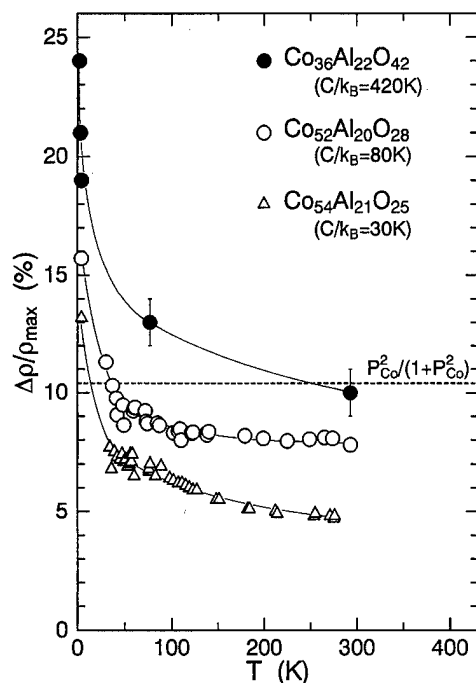


FIG. 2. Temperature dependence of MR for $\text{Co}_{54}\text{Al}_{21}\text{O}_{25}$, $\text{Co}_{52}\text{Al}_{20}\text{O}_{28}$, and $\text{Co}_{36}\text{Al}_{22}\text{O}_{42}$ films. $P^2/(1+P^2)$ is the theoretical value of MR in Co-based insulating granular systems by a simple model. The values of C/k_B are also shown for the films (see the text).

spin polarization for ferromagnetic metal.⁶ The factor of 2 is just due to the difference between the random magnetization alignment in granular systems and antiparallel magnetization alignment in ferromagnetic tunnel junctions. The magnitudes of MR reported so far for ferromagnetic tunnel junctions with a macroscopic size were always smaller than the theoretical value of $2P^2/(1+P^2)$. For insulating granular films, however, Fig. 1 indicates that the MR can be much larger than the theoretical value.

Figures 3(a) and 3(b) show ρ and MR, respectively, as functions of bias-voltage V_b for the $\text{Co}_{36}\text{Al}_{22}\text{O}_{42}$ film. The magnitude of MR is 19%, and it is almost constant in the range of $V_b=0$ to 600 mV although ρ decreases by three orders of magnitude. For the results of the temperature and bias-voltage dependence of MR, we would like to emphasize the two following points which are characteristic of granular systems: The first is that the MR as a function of bias voltage is independent of the dramatic change in ρ . This is in clear contrast to the case of ferromagnetic tunnel junctions with a macroscopic size, where both MR and ρ decrease gradually with increasing bias voltage.⁸ The second point is the difference between the temperature and bias-voltage dependence of MR. We can estimate the number of Co granules aligned between the upper and lower electrodes, using the mean diameter of granules (20–30 Å),⁵ the mean thickness of insulating barriers (~ 10 Å),⁵ and the film thickness (1.0 μm), and it is calculated to be 250–300. Therefore, the applied bias voltage per one microjunction between two neighboring Co granules is estimated to be approximately 2 mV at $V_b=600$ mV. The 2 mV corresponds to 23 K in temperature. Therefore, it is shown that the MR does not decrease up to the bias voltage corresponding to 23 K. On the other hand, as

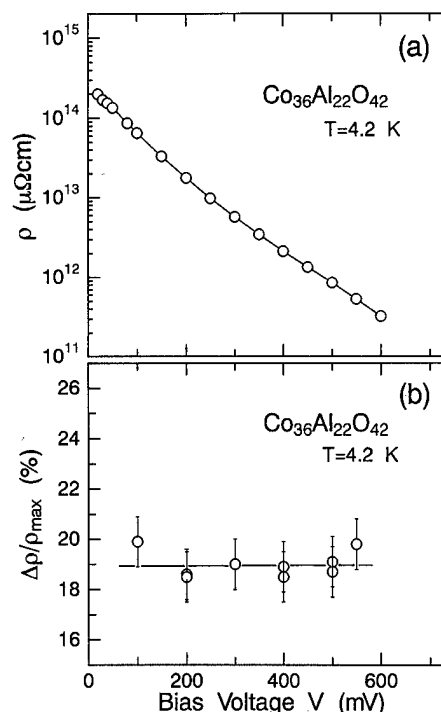


FIG. 3. Bias-voltage (V_b) dependence of ρ and MR for a $\text{Co}_{36}\text{Al}_{22}\text{O}_{42}$ film at 4.2 K; (a) ρ and (b) MR.

shown in Fig. 2, MR decreases with increasing temperature up to 23 K. This indicates that the effect of temperature is different from that of bias voltage. This is also in clear contrast to the case of ferromagnetic tunnel junctions with a macroscopic size. The effect of bias voltage is not so different from that of temperature.⁹

We will discuss the above-mentioned remarkable features of MR in granular systems in relation to the effect of Coulomb blockade. Figure 4 shows $\log \rho$ as a function of $T^{-1/2}$ for $\text{Co}_{54}\text{Al}_{21}\text{O}_{25}$, $\text{Co}_{52}\text{Al}_{20}\text{O}_{28}$, and $\text{Co}_{36}\text{Al}_{22}\text{O}_{42}$ films. The linear relationship is seen, showing $\log \rho = \alpha T^{-1/2}$ (α : constant). The characteristic behavior of $\log \rho = \alpha T^{-1/2}$ appears due to the combination of (i) the tunneling effect of electrons between metallic granules through intergranular insulating barriers and (ii) the electrical charging effect of metallic granules (Coulomb blockade). The constant α is expressed as

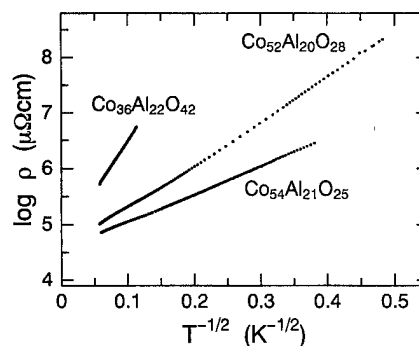


FIG. 4. $\log \rho$ as a function of $T^{-1/2}$ for $\text{Co}_{54}\text{Al}_{21}\text{O}_{25}$, $\text{Co}_{52}\text{Al}_{20}\text{O}_{28}$, and $\text{Co}_{36}\text{Al}_{22}\text{O}_{42}$ films.

$$\alpha = 2(C/k_B)^{1/2}, \quad (1)$$

where the constant C is called tunnel-activation energy¹⁰ and k_B is Boltzmann constant. C is given by¹⁰

$$C = (2m\phi)^{1/2}(h/2\pi)sE_c, \quad (2)$$

where m is the effective electron mass, ϕ is the effective potential height of insulating barrier, h is Planck's constant, s is the barrier thickness, and E_c is the charging energy of a metallic granule. The coefficient between C and E_c , i.e., $(2m\phi)^{1/2}/(h/2\pi)s$, can be determined to be the order of 1, using $m = 9.11 \times 10^{-28}$ g (free electron's mass), $\phi \sim 1$ eV (the order of potential height of Al_2O_3), and $s \sim 10$ Å.^{5,10} Therefore, C is considered to be roughly equal to E_c . The magnitudes of C/k_B obtained from the experiments are shown in Fig. 2, i.e., 30, 80, and 420 K for the $\text{Co}_{54}\text{Al}_{21}\text{O}_{25}$, $\text{Co}_{52}\text{Al}_{20}\text{O}_{28}$, and $\text{Co}_{36}\text{Al}_{22}\text{O}_{42}$ films, respectively. The $\text{Co}_{36}\text{Al}_{22}\text{O}_{42}$ film has the largest charging energy, and hence it may show the largest effect associated with Coulomb blockade. The $\text{Co}_{36}\text{Al}_{22}\text{O}_{42}$ film shows the largest MR effect, and we find in Fig. 2 that the MR is larger as C/k_B is larger. Furthermore, the enhancement of MR for each film appears below the temperature which corresponds approximately to the charging energy of granules. This suggests that the enhancement of MR appears in relation to the Coulomb blockade effect. Ono *et al.* reported enhanced MR associated with Coulomb blockade in microfabricated ferromagnetic tunnel junctions.¹¹

Recently, Takahashi and Maekawa calculated temperature and bias-voltage dependence of MR for a ferromagnetic double-junction system with a small island electrode in Coulomb blockade regime.¹² The behavior of temperature and bias-voltage dependence of MR in the theoretical work is similar to our experimental results for granular systems. It is suggested that the theory in Coulomb blockade regime would elucidate the origin of the difference of the temperature and bias-voltage dependence in granular systems.

IV. CONCLUSION

The remarkable enhancement of MR which is larger than the theoretical values, $P^2/(1+P^2)$, is observed for Co-Al-O granular films at low temperatures, and it steeply decreases with increasing temperature. On the other hand, the MR does not decrease with increasing bias voltage although ρ decreases by a few orders of magnitude. Furthermore, it has been found that the effect of temperature is definitely different from that of bias voltage. The anomalous behavior is in contrast to that of macroscopic tunnel junctions, suggesting the significant effect of Coulomb blockade in granular systems.

ACKNOWLEDGMENTS

The authors are grateful to Professor Inoue, Nagoya University, and Professor Maekawa and Dr. Takahashi, IMR, Tohoku University, for helpful discussions. This work was partly supported by a Grant-In-Aid of Japanese Ministry of Education, Science, Sport, and Culture for Scientific Research (No. 07405030).

¹For example, G. A. Prinz, *Phys. Today* **48**, 58 (1995).

²H. Fujimori, S. Mitani, and S. Ohnuma, *Mater. Sci. Eng. B* **31**, 219 (1995).

³S. Mitani, H. Fujimori, and S. Ohnuma, *J. Magn. Magn. Mater.* **165**, 141 (1997).

⁴S. Mitani, H. Fujimori, and S. Ohnuma, *J. Magn. Magn. Mater.* (in press).

⁵M. Ohnuma, K. Hono, E. Abe, H. Onodera, S. Mitani, and H. Fujimori, *J. Appl. Phys.* **82**, 5646 (1997).

⁶J. Inoue and S. Maekawa, *Phys. Rev. B* **53**, R11 927 (1996).

⁷R. Meservey and P. M. Tedrow, *Phys. Rev. B* **7**, 318 (1973), R. Meservey and P. M. Tedrow, *Phys. Rev.* **238**, 173 (1994).

⁸J. S. Moodera, L. R. Kinder, T. M. Wong, and R. Meservey, *Phys. Rev. Lett.* **74**, 3273 (1995); N. Tezuka and T. Miyazaki, *J. Phys. D* (to be published).

⁹N. Tezuka and T. Miyazaki, *Jpn. J. Appl. Phys., Part 2* **37**, L221 (1998).

¹⁰B. Abeles, P. Sheng, M. D. Coutts, and Y. Arie, *Adv. Phys.* **24**, 407 (1975).

¹¹K. Ono, H. Shimada, S. Kobayashi, and Y. Ootuka, *J. Phys. Soc. Jpn.* **65**, 3449 (1996).

¹²S. Takahashi and S. Maekawa, *Phys. Rev. Lett.* **80**, 1758 (1998).

High perpendicular anisotropy and magneto-optical activities in ordered Co₃Pt alloy films

Y. Yamada,^{a)} W. P. Van Drent, E. N. Abarra, and T. Suzuki

Information Storage Materials Laboratory, Toyota Technological Institute, 2-12-1, Hisakata, Tempaku, Nagoya 468, Japan

The origin of the large perpendicular magnetic anisotropy constant K_u of Co₃Pt alloy thin films is discussed. The films deposited onto Al₂O₃(0001), Al₂O₃(1120), and MgO(111) substrates held at 230–450 °C during deposition exhibit K_u of the order of 10^7 erg/cm³ at room temperature. While the one dimensional long range order parameter S estimated by x-ray diffraction is very consistent with the development of the perpendicular magnetic anisotropy in the films deposited at 380–450 °C, very little evidence is found to suggest the correlation between S and K_u for the lower deposition temperature range (230–380 °C). To explain this, a short range ordering is suggested to be responsible for the origin of K_u , similar to the cases in Pt₇₂Co₂₈ alloys. The magneto-optical polar Kerr activity of ordered Co₃Pt film is found to be enhanced for both θ_K and η_K in the photon energy range from 2 to 4 eV. © 1998 American Institute of Physics. [S0021-8979(98)43611-9]

I. INTRODUCTION

Recently, several different workers reported large perpendicular magnetic anisotropy constants K_u on the order of 10^7 erg/cm³ in Co–Pt and Fe–Pt alloy thin films of various composition.^{1–5} The origin of such a high perpendicular magnetic anisotropy has been the subject for many workers. Tyson *et al.*⁶ have shown that the anisotropic distribution of the Co–Co bonds is responsible for the magnetic anisotropy in Co_{1–x}Pt_x alloys ($x \sim 0.7$), similar to the orientational asymmetry in the Fe–Fe, Tb–Tb, and Tb–Fe bonds in amorphous TbFeCo alloy films.⁷ Harp *et al.*⁸ showed the existence of the ordered phase of Co₃Pt alloy films, which had not been in the phase diagram for a long time. However, no magnetic anisotropy of this ordered phase had been reported. Recently, Yamada *et al.*^{1,2} reported for the first time on a large perpendicular anisotropy in Co-rich CoPt alloys, and suggested the possible correlation of the order phase of Co₃Pt with the origin of the magnetic anisotropy. However, the detailed mechanism of the magnetic anisotropy has not been understood. The present article describes a further result of the perpendicular magnetic anisotropy in Co_{1–x}Pt_x ($x \sim 0.2–0.3$) alloy thin films.

II. EXPERIMENT

Co_{1–x}Pt_x ($0 \leq x \leq 0.5$) alloy thin films were deposited onto fused silica, MgO(111), Al₂O₃(0001), and (1120) substrates by electron beam evaporation using separate Co and Pt sources. The detailed deposition condition was described elsewhere.^{5,6} The film thickness was approximately 1000 Å for all cases. Measurements of magnetic properties were carried out by using vibrating sample magnetometer, alternative gradient force magnetometer, and torque magnetometer in

fields up to 20 kOe. The magneto-optical Kerr effect was measured using an ultrawide range Kerr spectrometer in a photon energy range from 1.4 to 6.8 eV.⁹ The measurement was made from the sample surface side.

III. RESULTS AND DISCUSSION

The intrinsic perpendicular anisotropy constant K_u (defined as $K_u = K_\infty + 2\pi M_s^2$, where K_∞ is the torque amplitude as $H \rightarrow \infty$) at different compositions of Co–Pt alloy films was studied. Figure 1 shows the dependence of K_u on film composition at various substrate deposition temperatures T_s . One can see that K_u values of the films deposited onto Al₂O₃(0001) and MgO(111) substrates at $T_s = 400$ °C ex-

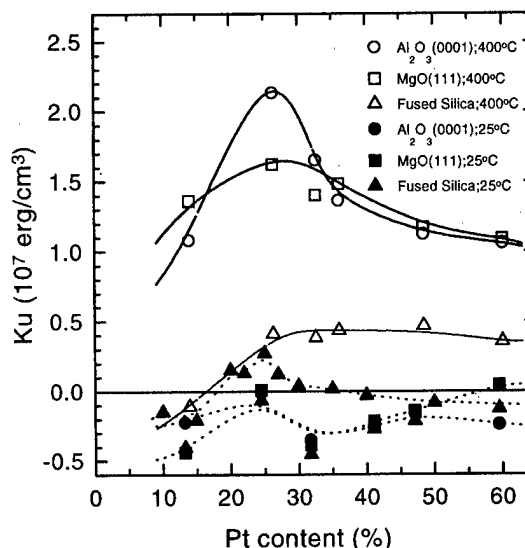


FIG. 1. Dependence of the perpendicular anisotropy constant K_u on Pt content.

^{a)}Electronic mail: d2syosi@ypcfs1.toyota-ti.ac.jp

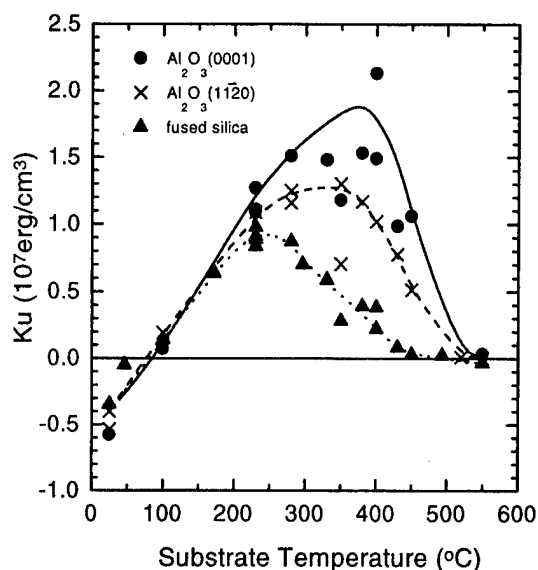


FIG. 2. Dependence of the perpendicular anisotropy constant K_u on substrate deposition temperature for $\text{Co}_{75}\text{Pt}_{25}$ films.

hibit a maximum at about 25 at % Pt. On the other hand, a very small change of K_u with film composition for the samples deposited at 25 °C and deposited onto fused silica was observed. The maximum values of K_u are 2.1×10^7 and 1.6×10^7 erg/cm³ for $\text{Al}_2\text{O}_3(0001)$ and $\text{MgO}(111)$ substrates, respectively.

Figure 2 shows the dependence of K_u on T_s for 25 at % Pt thin films deposited onto various substrates. The K_u becomes zero at about 500 °C for all the samples. The maximum value of K_u for samples on $\text{Al}_2\text{O}_3(0001)$ is 2.1×10^7 erg/cm³, and those on $\text{Al}_2\text{O}_3(1120)$ and fused silica are 1.2×10^7 and 1.0×10^7 erg/cm³ at room temperature, respectively. It is clearly seen that for all the substrates cases, there is a broad maximum of K_u at $T_s = 250$ – 400 °C for both the Al_2O_3 cases, and 200–300 °C for the fused silica case.

The x-ray diffraction analysis indicates that all these samples deposited onto the Al_2O_3 and MgO substrates exhibit the hcp structure for T_s from the ambient temperature to about 450 °C with the textured (0001) along the film normal. Furthermore, the hcp (0001) superlattice peak is observed for the samples deposited onto $\text{Al}_2\text{O}_3(0001)$, $\text{MgO}(111)$, and $\text{Al}_2\text{O}_3(1120)$ at approximately 380–450 °C.

The one dimensional order parameter S is defined as

$$S = \frac{r_A - F_A}{1 - F_A} \propto \left(\frac{I_{0001}}{I_{0002}} \right)^{1/2},$$

where r_A is the fraction of A sites occupied by A atoms, F_A is the fraction of A atoms in the alloy, I_{0001} and I_{0002} are the integrated intensities of the fundamental peaks and the superlattice peak, respectively. Thus, the one dimensional order parameter S can be estimated by measuring the integrated intensity ratio.¹⁰

Figure 3 shows the dependence of S on T_s . It shows a sharp peak at ~ 400 °C for both the $\text{Al}_2\text{O}_3(0001)$ and (1120) cases, where K_u becomes maximum. This result is consistent with the work by Harp *et al.*⁸

Figure 4 shows the relation between K_u and order pa-

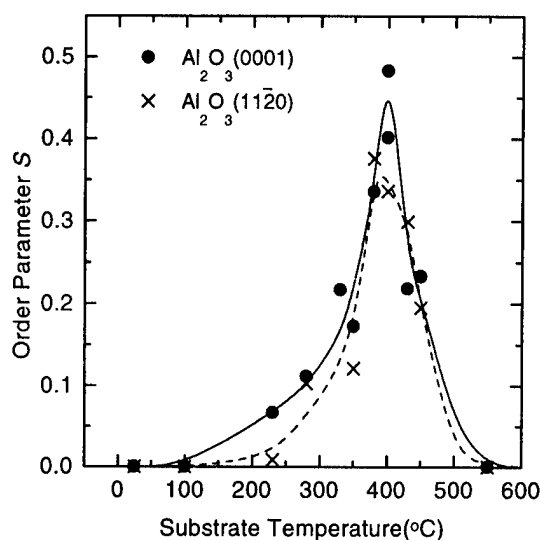


FIG. 3. Dependence of the order parameter S on substrate deposition temperature for $\text{Co}_{75}\text{Pt}_{25}$ films.

rameter S for the thin film deposited onto the $\text{Al}_2\text{O}_3(0001)$ substrate. The numbers close to the data points correspond to T_s . K_u is found to vary linearly with S for T_s between 380 °C and 450 °C, indicating that the ordering is a primary factor governing K_u in this temperature range. One would expect K_u of 4×10^7 erg/cm³ for a perfectly order state. On the other hand, there is no clear correlation between K_u and S for T_s less than 380 °C. This situation is similar to the case of CoPt_3 alloy films.¹¹ Tyson *et al.*⁶ have shown evidence for a directional anisotropy in the number of Co–Co bonds in $\text{Co}_{28}\text{Pt}_{72}$ alloy films by using x-ray absorption fine structure (XAFS). To clarify this matter, an experiment was performed in which case a deposition rate was changed to a lower rate at $T_s = 230$ °C for $\text{Al}_2\text{O}_3(0001)$ substrates. One sample was deposited at 1.6 Å/s, which is the same as all other experiments. The deposition rate for the other sample was lowered to 1/5 of the original. It was found that both K_u

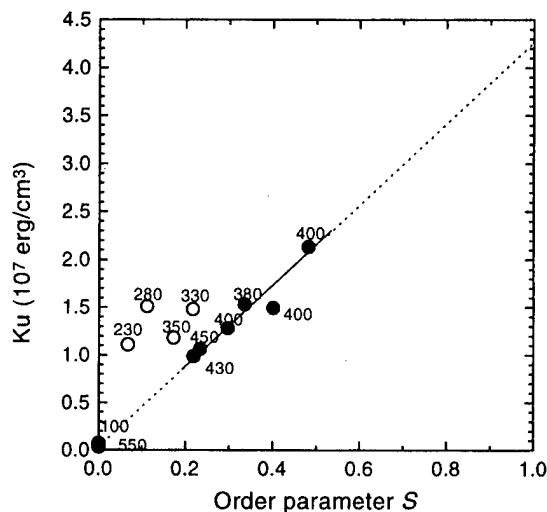


FIG. 4. Relation between K_u and the order parameter S for the films deposited onto $\text{Al}_2\text{O}_3(0001)$. The numbers close to the data points corresponds to T_s .

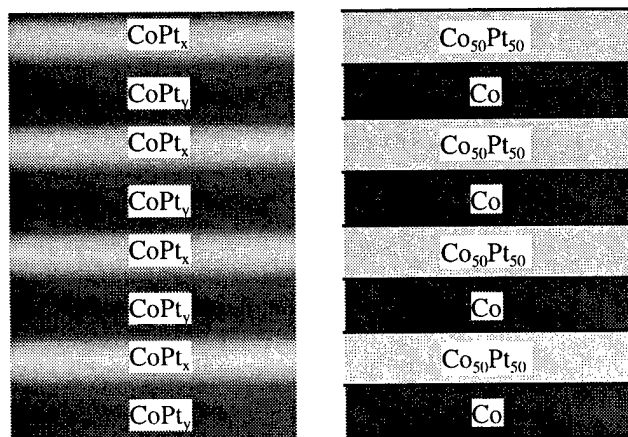


FIG. 5. A model for the origin of the large K_u ; short range ordering for low T_s (left) and Co_3Pt ordered structure for high T_s (right).

and S increased with lowering a deposition rate ($K_u = 1.3 \times 10^7 - 1.8 \times 10^7 \text{ erg/cm}^3$, $S = 0$ to 0.12). This result seems to support the model put forward by Tyson *et al.*⁶ A model of a short range ordering to account for large K_u is shown in Fig. 5(a). In this model, atomic layers of CoPt_x and CoPt_y are alternately present, as ABAB stacking. The origin of the large perpendicular magnetic anisotropy is believed to result from the anisotropic bonding distribution of Co–Co atoms in the film plane with respect to the film thickness direction, as proposed by Tyson *et al.*⁶ This situation may also be similar to Co/Pt multilayers.

Figure 6 shows the Kerr rotation and ellipticity spectra for $\text{Co}_{75}\text{Pt}_{25}$ alloy thin films deposited onto an $\text{Al}_2\text{O}_3(0001)$ substrate at $T_s = 25^\circ\text{C}$ (disordered) and 400°C (ordered) in a photon energy range from 1.4 to 6.8 eV. The Kerr rotation spectrum, which was obtained by Harp *et al.* for $\text{Co}_{75}\text{Pt}_{25}$ thin film deposited at 375°C ,⁸ is also shown. The spectrum for the sample deposited at 400°C shows slightly larger θ_K and η_K for photon energies less than 4 and 6 eV, respectively. The present result for the ordered structure ($T_s = 400^\circ\text{C}$) does exhibit the peak around 3 eV, consistent with their result.

IV. CONCLUSION

The very large perpendicular magnetic anisotropy constant K_u values are found in $\text{Co}_{75}\text{Pt}_{25}$ alloy thin films deposited at $T_s = 230$ – 450°C . The relation between K_u and the order parameter S is investigated in detail for Co–Pt alloy thin films. When the substrate deposition temperature is high (380 – 450°C), the magnitude of K_u is linearly correlated with S . However, when T_s is not high enough (230 – 380°C), no clear correlation is found. To account for these high K_u values, a short range ordering is suggested for the origin of the large K_u at lower T_s , where the films exhibit a large K_u without ordering. The magneto-optical activities of these

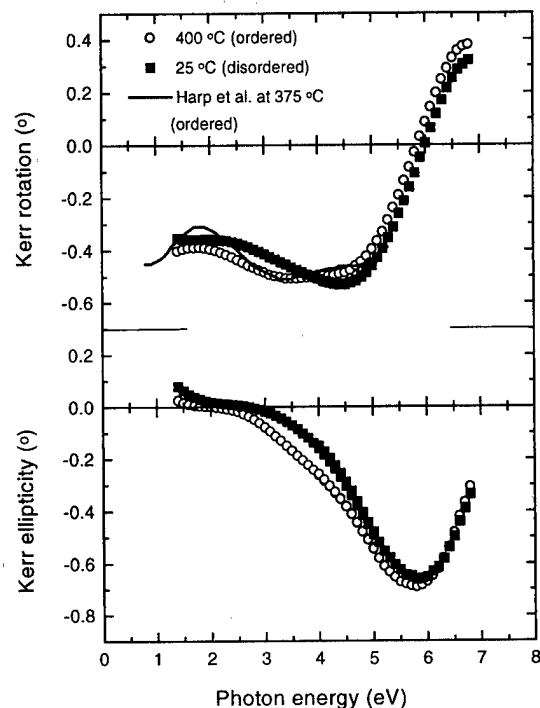


FIG. 6. Magneto-optical spectra for the samples deposited onto $\text{Al}_2\text{O}_3(0001)$ at various T_s .

Co–Pt alloy thin films were measured. The enhancement in Kerr rotation at $\sim 3.0 \text{ eV}$, which is characteristic for Co_3Pt ordered structure, is observed.

ACKNOWLEDGMENTS

The work has been partially supported by the Storage Research Consortium and the Original Industrial Technology R & D Promotion Program from the New Energy and Industrial Technology Development Organization (NEDO) of Japan (Contract No. 8C-039-1). One of the authors acknowledges the support by DENSO CORPORATION for x-ray diffraction analysis and chemical compositional analysis.

- ¹Y. Yamada, T. Suzuki, and E. N. Abarra, *IEEE Trans. Magn.* **34**, 343 (1998).
- ²Y. Yamada, T. Suzuki, and E. N. Abarra, *IEEE Trans. Magn.* **33**, 3622 (1997).
- ³R. A. McCurrie and P. Gaunt, *Philos. Mag.* **19**, 339 (1969).
- ⁴A. Z. Men'shikov, Y. A. Dorofeyev, V. A. Kazantsev, and S. K. Sidorov, *Phys. Met. Metallogr.* **38**, 47 (1974).
- ⁵B. M. Lairson, M. R. Visokay, E. E. Marinero, R. Sinclair, and B. M. Clemens, *J. Appl. Phys.* **74**, 1922 (1993).
- ⁶T. A. Tyson, S. D. Conradson, R. F. C. Farrow, and B. A. Jones, *Phys. Rev. B* **54**, 3702 (1996).
- ⁷V. G. Harris, K. D. Aylesworth, B. N. Das, W. T. Elam, and N. C. Koon, *Phys. Rev. Lett.* **69**, 1939 (1992).
- ⁸G. R. Harp, D. Weller, T. A. Rabedeau, R. F. C. Farrow, and M. F. Toney, *Phys. Rev. Lett.* **71**, 2493 (1993).
- ⁹W. P. Van Drent and T. Suzuki, *J. Magn. Magn. Mater.* **175**, 53 (1997).
- ¹⁰B. D. Cullity, *Elements of X-ray Diffraction*, 2nd ed. (Addison-Wesley, Massachusetts, 1998), p. 383.
- ¹¹P. W. Rooney, A. L. Shapiro, M. Q. Tran, and F. Hellman, *Phys. Rev. Lett.* **75**, 1843 (1995).

Thermopower studies of percolating magnetic metallic nanostructures

X. N. Jing^{a)} and X. Yan^{b)}

Department of Physics, Hong Kong University of Science and Technology,
Clearwater Bay, Kowloon, Hong Kong

We have observed a small and temperature insensitive thermal electric power S as well as a large resistivity following $\rho \sim -\log(T)$ dependence, in percolating magnetic metal-insulator nanocomposites, irrespective to the sign of the carrier. Upon annealing, however, a normal metallic behavior with a linear temperature dependence for both S and ρ was recovered. We propose that the large charging energy of the nanometer sized particles in the percolation conduction channels is responsible for this observation as well as the giant Hall effect or the loss of the effective carrier density in these nanostructures. © 1998 American Institute of Physics. [S0021-8979(98)52211-6]

There is renewed interest in magnetic metal-insulator nanocomposite materials, or magnetic nanostructures, due to the recent discoveries of giant magnetoresistance (5%–10%) when tunneling conduction exists between the adjacent magnetic metal particles,¹ and giant Hall effect (GHE), or a 10 000-fold enhancement of Hall resistivity when the nanometer-sized magnetic metal particles form percolation conduction channels.² GHE cannot be explained via a simple percolation theory that predicts a maximum enhancement factor of ~ 20 (Ref. 3) based on the percolation critical exponent of Hall resistivity $g \sim 0.4$ (Ref. 4) for a 1 μm thick film. From our systematic studies of Ni-rich NiFe–SiO₂ and Fe–SiO₂ nanocomposite films, having carrier dominated by electrons and holes, respectively, a few unique properties were identified near the percolation threshold.^{2,5–8} Namely, the giant enhancement of Hall resistivity exists if and only if there exist a large resistivity (0.1–1 Ωcm) with a temperature dependence following $\rho(T) \sim -\log(T)$, and nanometer-sized particles in the percolating channels,⁵ which are independent of the sign of the conduction carrier. In the following discussion, we use the term “percolating magnetic nanostructure” to refer to a system with the above-mentioned novel properties. Understanding of these properties is limited.⁹ Particularly the apparent dramatic loss of “effective carrier” still lacks an important clue for its origin.^{9,10} A measure of “entropy per carrier,” thermal electric power was chosen to help identify the origin of the carrier loss.¹¹

Percolating (NiFe)_x(SiO₂)_{1-x} and Fe_x(SiO₂)_{1-x} nanostructured films were prepared using a magnetron rf co-sputtering system as described elsewhere.^{2,5,9} Samples used for this work were from the same batch in which giant Hall effect was found. The saturation Hall resistivity are about $-200\ \mu\Omega\text{cm}$ and $+500\ \mu\Omega\text{cm}$ for (NiFe)_x(SiO₂)_{1-x} and Fe_x(SiO₂)_{1-x}, indicating that giant Hall effect exists irrespective to the sign of the conduction carrier. The thickness and the deposition temperatures were 1 and 0.5 μm and 150 and 25 $^{\circ}\text{C}$ for the two systems, respectively. The metal volume fraction x were determined by energy-dispersive

x-ray spectroscopy using a Philips EDAX XL30. For NiFe–(SiO₂), the relative Fe content in NiFe, was determined to be 0.15, 0.14, and 0.14, for $x = 0.58, 0.61$, and 0.63 , respectively.⁵ For annealing, samples were placed in a quartz tube that was evacuated for half an hour and purged six times using high-purity helium gas. The quartz tube was heated at 520 $^{\circ}\text{C}$, and pulled out to room temperature after 1 h.⁵ 520 $^{\circ}\text{C}$ was chosen because from previous studies it is known that the giant Hall effect will disappear to a normal metallic behavior⁵ in a conventional metal-insulator composite system above the percolation threshold.

Thermal electric power (thermopower or TEP) measurements were performed on narrow strips of the sample (typically $12 \times 1.5\text{ mm}$) by using a pulsed heating method.¹² While the resistance was measured using a four-probe technique. Gold wires of $\phi 25\ \mu\text{m}$ were served as both current and voltage leads. Chromel/constantan thermocouple (type E) with diameters of 25 μm , connected in a differential mode, were fixed onto the sample with the thermal contact close to the two voltage electrodes. Resistance and TEP data on the same sample were taken in sequence with the temperature decreasing at a rate controlled at $\sim 3\text{ mK/s}$. A temperature gradient $\Delta T \sim 1\text{--}2\text{ K}$, generated by a small carbon film heater, was applied along the sample. Care was taken to null the offset values by turning the heater on and off periodically. The voltage drop on the sample and that for temperature gradient were obtained by the voltage difference with the heat on and off by using two Keithley 182 nanovoltmeters. For each on or off voltage, 30 repeated readings were averaged after reaching a thermally static state. The absolute thermopower of gold wire was calibrated against a pure lead, and the calibration was in agreement with that in Ref. 12. All the TEP data shown in this article are the absolute thermopower by subtracting off the contribution of the gold wires.

Figure 1 shows TEP S as functions of temperature of (NiFe)_x(SiO₂)_{1-x} films for (a) various volume fraction, $x = 0.58, 0.60, 0.63$, and 1 , and (b) for one percolating sample, $x = 0.58$ for various annealing conditions. All these samples are above the percolation threshold x_c of 0.53 .² Compared with a homogeneous metallic sample, the TEP near the percolation appears to be quite insensitive to the temperature, as is often the case in typical disordered metals.¹³ Since TEP is

^{a)}Also at Institute of Physics, Chinese Academy of Science, Beijing, China.

^{b)}Electronic mail: phxyan@ust.hk

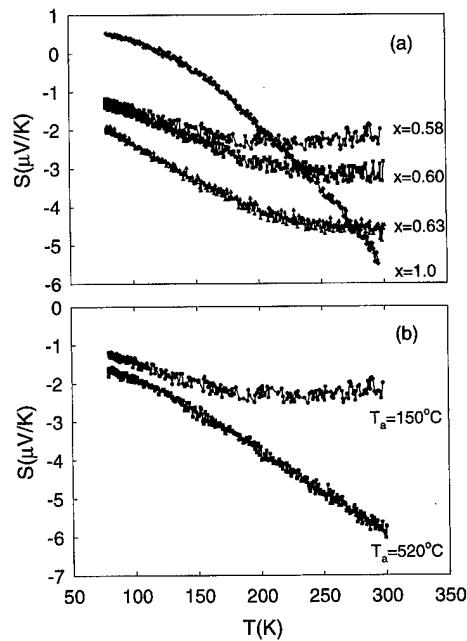


FIG. 1. Thermopower as functions of temperature of $(\text{NiFe})_x(\text{SiO}_2)_{1-x}$ films for (a) as-deposited films with different volume fractions and (b) different annealing conditions for $x=0.58$.

a measure of "entropy per carrier," such a temperature insensitive TEP indicates that the entropy of the carrier is determined by another energy scale that is either much larger or much smaller than kT in such a disordered percolating system. Another striking finding is a similar linear temperature dependent TEP for both a pure metallic case ($x=1$) and the percolating samples after annealing, suggesting that neither the thermal power in a two-component composite model¹⁴ nor the percolating geometry alone is sufficient to give rise to a temperature independent TEP. A linear temperature dependent TEP indicates that the electron conduction in the classical percolating system is similar to liquid metals or semimetals where electron states near the Fermi surfaces are nonlocalized despite the disorder.

Shown in Fig. 2 is the temperature dependence of the resistivity (normalized to 79 K), for $x=0.58$ with $T_a=150^\circ\text{C}$, and 520°C , and for $x=1$ (as-deposited). The dashed line is a fit to a $-\log(T)$ dependence. For the as-

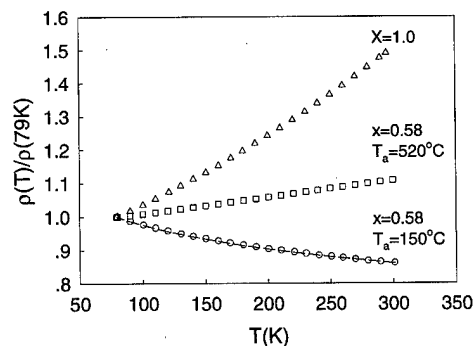


FIG. 2. Temperature dependent resistivity of $(\text{NiFe})_x(\text{SiO}_2)_{1-x}$ films for various volume fraction and annealing conditions. The dashed line is a $-\log(T)$ fit.

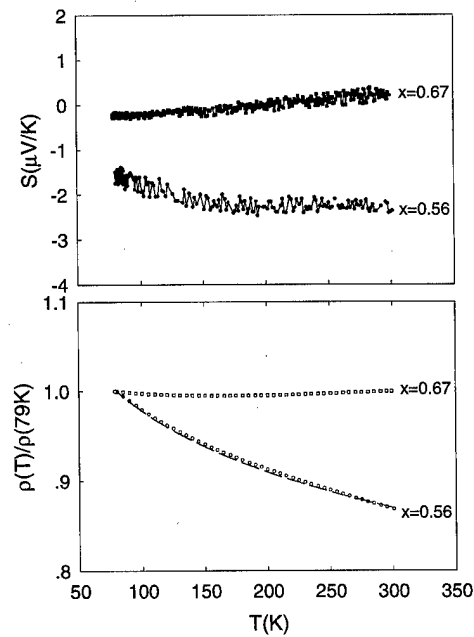


FIG. 3. Temperature dependence of thermopower (a) and resistivity (b) for as-deposited $\text{Fe}_x(\text{SiO}_2)_{1-x}$ films.

deposited sample near the percolation, the temperature coefficient of resistivity is negative, and the temperature dependence of the resistivity is close to logarithmic. Annealed at high temperature, the large resistivity with a $-\log(T)$ dependence changes to a small metalliclike resistivity, while the giant Hall effect disappears.² Upon annealing at 520°C , the resistivity decreases more than one order of magnitude, in agreement with the previous measurements.^{2,5}

Similar TEP and resistivity were measured in Fe-SiO_2 films near the percolation where there is a giant Hall effect. Shown in Fig. 3 are (a) TEP and (b) resistivity as functions of temperature for $x=0.56$ and 0.67 , respectively. The dashed line in (b) is a fit to $-\log(T)$ dependence. Again, a similar $-\log(T)$ dependence of resistivity was observed in Fe-SiO_2 films for $x=0.56$ which is slightly above the percolation threshold ($x_c \sim 0.51$). Associated with a weak temperature dependent resistivity, there is a weak temperature dependent TEP. These results suggest that whenever there is a giant Hall effect, the conduction mechanism is such that it gives rise to a rather small and temperature insensitive TEP, independent of the sign of the carrier. The annealing process was failed to perform on the Fe-SiO_2 due to the easy oxidation of iron. However, a small and temperature insensitive TEP characterizes the as-deposited percolating magnetic nanostructures having giant Hall effect, in addition to a large resistivity having a $-\log(T)$ dependence in both systems.

To our knowledge, there are no materials that have such unusually combined transport behavior, namely a large Hall resistivity and a small TEP. A large Hall effect usually indicates a small effective carrier. A loss of carrier in originally a metallic system is often associated with the opening of a gap at the Fermi surface.¹⁵ Associated with an existence of a gap, thermal electric power should behave like a semiconductor, with its value increasing as decreasing temperature. Failure to observe such a behavior indicates that the system

is not like a doped semiconductor and that the disorder plays a crucial role in the electron transport process. It is important to note that the temperature insensitive TEP is a signature of mixed valence conductors¹⁰ including cuprate superconductors,¹⁶ or amorphous and quasicrystalline metals.¹³ In the mixed valence metals, the value of the temperature insensitive TEP is governed by the entropy per carrier according to $S = (k/e) \ln[c/(1-c)]$, if the relevant disorder energy W for the carrier is either much smaller or much larger than kT , where c and $1-c$ are the probability of the two disordered states.

If the disorder can give rise to a temperature insensitive TEP, what types of disorder could give rise to a virtually zero TEP and a zero carrier density at the same time? In order to answer this question, let us first concentrate on one small nanometer-sized particle in the conduction channel.¹⁷ There are two additional energy scales when the metal particle reduces its size. One is the quantized energy level spacing that is inversely proportional to the number of the atoms in the particle. The other is the charging energy, or the energy required to add one more electron into the particle, which is inversely proportional to the capacitance or the size of the particle. From previous transmission electron microscope, Hall, and resistivity studies upon annealing, particles size of order 2–3 nm were identified to be crucial in determining the effective carrier and thus the conduction mechanism.⁵ In terms of the characteristic energy, 2 and 3 nm particles correspond to the level spacing ΔE of 3 meV and 1 meV assuming Fermi energy of 8 eV,¹⁸ or the charging energy E_c of 150 meV and 100 meV assuming a dielectric constant of 4.¹⁷ It is clear that the charging energy E_c is much larger than both the level spacing ΔE and thermal energy kT at room temperature. When there is a large charging energy E_c , such small nanometer-sized particles will generally not carry current. However, at some special size, the small particle can have an equal ground state energy for holding N and $N+1$ electrons, and hence could freely add and subtract one electron without causing energy. Only these special “conducting” particles can then carry current. Such a physical picture on a single nanometer-sized metal particle was firmly established via conductance measurements at low temperature.¹⁷ Moreover, Thermopower studies in such a quantum dot system showed both experimentally¹⁹ and theoretically²⁰ that whenever there is a peak in the conductance, there is a zero thermopower. This suggests that carriers via these special “conducting” nanometer particles do not carry entropy.

In percolating magnetic nanocomposites, there are nanometer-sized particles in the conduction channels. These nanometer-sized particles play the role of quantum dots in controlling the conduction mechanism of the system. Because there is a smooth size distribution, only a fraction of them “conducting,” correspond to a particular particle size having the same energy for N and $N+1$ electrons. As a result, the effective carrier is reduced. This picture explains the loss of the effective carrier when there are nanometer particles in the percolating channels. For these special conducting particles, there is an equal probability ($c \sim 1-c$

~ 0.5) for holding N and $N+1$ electrons, and hence the entropy per carrier is simply $(k/e) \ln[1/(1-c)]$ which is close to 0, similar to the quantum dot system.^{17,18} Upon annealing, these nanometer-sized particles grow. When small particles disappear eventually in the percolation channels, the conductors are all determined by the metallic ones, and the carrier returns to the typical metallic value. As a result, the giant Hall effect disappears, and both the resistivity and the TEP changes to a linear temperature dependence, indicative of the recovery of the normal metallic behavior.

The present physical picture of a large charging energy of nanometer particles in the percolation channels is not limited to the magnetic nanostructure. It could have a general impact in understanding the transport behavior in percolating metal-insulating nanocomposites. Many materials near percolation show a $-\log(T)$ dependence from room temperature.^{19,20} Specifically, we predict that in these nanostructures having $-\log(T)$ dependence, there could be enhanced Hall resistivity and reduced thermal electric power, compared to their corresponding macroscopic composites or homogeneous conducting materials.

The author wishes to acknowledge Yingfan Xu, Jie Xhie, and Silas Hung for their contribution to sample preparations, and the support from Hong Kong RGC-CERG Grant HKUST692/96P. In particular, X. Y. would like to thank Paul McEuen and Michael Heaney for useful discussion that stimulated the explanation of TEP in this article.

- ¹M. Fujimori, S. Mitani, and S. Ohnuma, *Mater. Sci. Eng.*, B **31**, 219 (1995); *J. Magn. Magn. Mater.* **156**, 311 (1996).
- ²A. B. Pakhomov, X. Yan, and B. Zhao, *Appl. Phys. Lett.* **67**, 3497 (1995).
- ³A. B. Pakhomov and X. Yan, *Solid State Commun.* **99**, 139 (1996); A. B. Pakhomov, X. Yan, N. Wang, X. N. Jing, B. Zhao, K. K. Fung, J. Xhie, T. F. Hung, and S. K. Wong, *Physica A* (in press).
- ⁴D. J. Bergman and D. Stroud, *Solid State Phys.* **46**, 149 (1992).
- ⁵X. N. Jing, N. Wang, A. B. Pakhomov, K. K. Fung, and X. Yan, *Phys. Rev. B* **53**, 14 032 (1996).
- ⁶Y. Xu, B. Zhao, and X. Yan, *J. Appl. Phys.* **79**, 6137 (1996).
- ⁷Y. Xu and X. Yan, *J. Mater. Res.* **11**, 2506 (1996).
- ⁸B. Zhao and X. Yan, *Physica A* (in press).
- ⁹B. Zhao, T. K. Ng, X. N. Jing, X. Yan, and B. Hui *Phys. Rev. Lett.* (unpublished).
- ¹⁰F. Brouers, A. Granovsky, A. K. Sarychev, and A. Kalitsov, *Physica A* **241**, 284 (1997).
- ¹¹F. J. Blatt, P. A. Schroeder, C. L. Foiles, and D. Greig, *Thermoelectric Power of Metals* (Plenum, New York, 1976), pp. 4 and 5.
- ¹²P. M. Chaikin and J. F. Kwak, *Rev. Sci. Instrum.* **46**, 218 (1975); M. J. Burns and P. M. Chaikin, *Phys. Rev. B* **27**, 5924 (1983).
- ¹³H. V. Lohneysen, *Mater. Sci. Eng.*, A **133**, 51 (1991).
- ¹⁴M. Khodja and M. Mostefa, *Solid State Commun.* **79**, 427 (1991); G. Hurvits, R. Rosenbaum, and D. S. McLachlan, *Physica A* **207**, 391 (1994).
- ¹⁵Xiao Yan, Ph.D. thesis, University of Pennsylvania, 1989, and references therein (unpublished).
- ¹⁶R. C. Yu, X. Yan, M. J. Naughton, P. M. Chaikin, and P. Davis, *Rev. Solid State Sci.* **1**, 181 (1987).
- ¹⁷For review of quantum dots, see H. van Houten, C. W. J. Beenakker, and A. A. M. Staring, *Single Electron Tunneling*, edited by H. Grabert and M. H. Devoret, NATO ASI series B, Vol. 294 (Plenum, New York, 1992).
- ¹⁸A. Carl, G. Dumpich, and E. F. Wassemann, *Phys. Rev. B* **50**, 4802 (1994).
- ¹⁹C. W. J. Beenakker and A. A. M. Staring, *Phys. Rev. B* **46**, 9667 (1992).
- ²⁰A. A. M. Staring, L. W. Molenkamp, B. W. Alphenaar, H. von Houten, O. J. A. Buyk, M. A. A. Mabeoone, C. W. J. Beenakker, and C. T. Foxon, *Europhys. Lett.* **22**, 57 (1993).

Structural and magnetic properties of Fe_xSe_y thin films during their selenization process

T. Takahashi, S. Kuno, N. Honda, Y. Takemura,^{a)} and K. Kakuno

Division of Electrical and Computer Engineering, Yokohama National University, Tokiwadai, Hodogaya, Yokohama, 240-8501, Japan

K. Saito

Department of Electronics and Information Sciences, Teikyo University of Science and Technology, Yatsuzawa, Uenohara, Yamanashi, 409-0133, Japan

Fe_xSe_y films were prepared on GaAs(001) substrates by a selenization of Fe films using molecular beam epitaxy equipment. Structural and magnetic properties of Fe_xSe_y thin films during their selenization process were studied. The selenized films obtained consisted of polycrystalline grains of 100–700 nm. A magnetic anisotropy of in-plane/perpendicular to the films was weakened by increasing the selenization ratio of the samples, which was interesting in contrast to the fact that the grain size of the films became larger. © 1998 American Institute of Physics.

[S0021-8979(98)43711-3]

I. INTRODUCTION

Recently, there has been increased research activity in the area of diluted magnetic semiconductors and ferromagnet/semiconductor heterostructures such as $\text{Fe}/\text{ZnSe}/\text{GaAs}$,¹ MnAs/GaAs ,² or MnGa/GaAs .³ Fe_xSe_y is expected as an interlayer of the Fe/ZnSe system or a new magnetic material. Characterizations of bulk crystals of FeSe have been reported with Fe_3Se_4 and Fe_7Se_8 structures.^{4,5} Although $\text{Zn}_x\text{Fe}_y\text{Se}$ and FeSe epilayers grown on GaAs(001) have been reported,⁶ Fe_xSe_y thin films have not been studied much. The lattice structure of bulk Fe_3Se_4 and Fe_7Se_8 is NiAs type with ordered Fe vacancies. The origin of the ferromagnetism in these materials associated with Fe vacancies is similar to the case of Fe_7S_8 pyrrhotite. A saturation magnetization of Fe_7Se_8 is 65 emu/cc at room temperature. Curie temperatures of Fe_3Se_4 and Fe_7Se_8 are 314 and 455 K, respectively. Because of their lattice structures, they have a strong magnetocrystalline anisotropy along the c axis.

In our study, Fe_xSe_y thin films were prepared by a selenization of Fe films using molecular beam epitaxy (MBE) equipment.⁷ As previously reported, the Fe/Se composition ratio x/y of the obtained Fe_xSe_y films measured by an energy dispersive x-ray spectroscopy (EDX) was 2/3 or 1/3.⁸ It was different from those of the reported stable structures of bulk Fe_3Se_4 , Fe_7Se_8 , and FeSe epilayers. In this article, structural and magnetic properties of Fe_xSe_y thin films during their selenization process are reported.

II. EXPERIMENTS

Fe_xSe_y thin films were prepared on GaAs substrates by a selenization technique. Semi-insulating nondoped GaAs (001) substrates were used. Fe thin films deposited by a vacuum evaporation on GaAs substrates were selenized in a MBE chamber. Conventional MBE equipment with solid sources was used. The thickness of the Fe films was 600 nm.

The selenization was performed by supplying a Se beam from a K cell for 30–240 min. The Se beam intensity was varied from 2×10^{-8} to 4×10^{-8} Torr. The beam intensity was monitored by an ion gauge which was positioned outside of the growth area. It was found that Fe_xSe_y compound films were obtained by this technique above a substrate temperature of 380 °C.⁷

Depth profiles of the selenized thin films were measured by using Auger electron spectroscopy (AES). Surface images of the films were observed by a scanning electron spectroscopy (SEM). The magnetization of the films was measured by a vibrating sample magnetometer (VSM) at room temperature.

III. RESULTS AND DISCUSSION

Fe thin films were selenized from their surfaces in the selenization process as shown in inserts in Fig. 1. Figure 1 shows depth profiles of Fe, Se, Ga, and As measured by the AES from the sample selenized with Se beam intensity of 4×10^{-8} Torr for 60 min at a substrate temperature of 380 °C. It is found that a partial region from the surface of the sample is selenized and that the sample consists of a $\text{Fe}_x\text{Se}_y/\text{Fe}/\text{GaAs}$ structure. The intensities of signals of Fe and Se are constant in the selenized region of the sample. It indicates that the layer consists of an Fe_xSe_y compound with a constant composition ratio of Fe/Se. A selenized ratio of $\text{Fe}_x\text{Se}_y/\text{Fe}$ is defined as a ratio of Fe_xSe_y layer thickness against a total film thickness of $\text{Fe}_x\text{Se}_y + \text{Fe}$. The selenized ratio of the sample shown in Fig. 1 is calculated to be 35%.

Samples with various selenized ratios were prepared by varying the selenization time and Se beam intensity at a substrate temperature of 380 °C. In this article, samples with selenized ratios in the range of 6%–74% were investigated.

From the observed SEM surface images of the films, it was found that the films consisted of polycrystalline grains. A dependence of the grain size of the films on the selenized ratio is indicated in Fig. 2. The grain size became larger with the increase of the selenized ratio of the films. The Fe thin

^{a)}Electronic mail: takemura@dnj.ynu.ac.jp

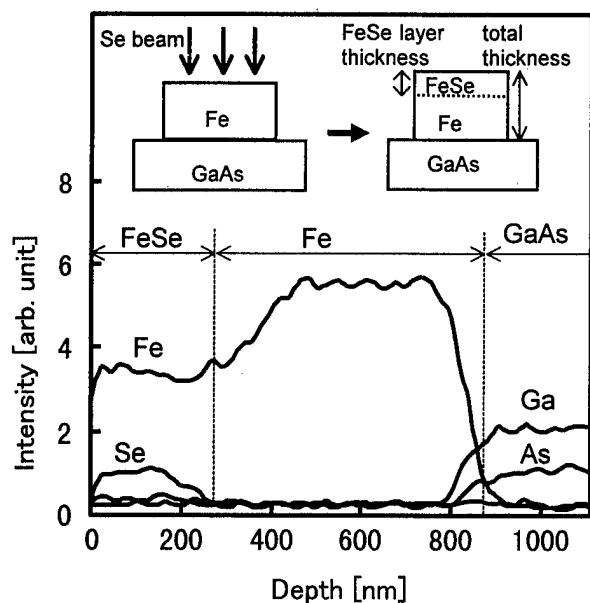


FIG. 1. Depth profiles of Fe, Se, Ga, and As of the selenized thin film measured by Auger electron spectroscopy. The sample was selenized for 60 min with a Se beam intensity of 4×10^{-8} Torr at a substrate temperature of 380 °C. The inserts are schematic diagrams of the selenization process of Fe film on GaAs(001) substrate on molecular beam epitaxy equipment.

films before selenization were polycrystalline with a smooth surface. The grain size was assumed to be of the order of film thickness (600 nm).

Figure 3 shows M - H curves of the selenized films measured by the VSM. An external magnetic field, H was applied along the GaAs [110] axis which was the in-plane direction of the film. Similar M - H curves were obtained from these samples in measurements with the applied magnetic field along [100] and [010] axes. The samples exhibited isotropic magnetic properties in the in-plane direction of the films. The coercive force calculated from the measured in-plane M - H curves of these samples was about 250 Oe, which did not depend on their selenized ratio. A saturation magnetization (M_s) of the samples decreased with the increase in the selenized ratio as shown in Fig. 4. This decrease in the saturated magnetization was attributed to a decrease of Fe atomic concentration in the films. The saturation magne-

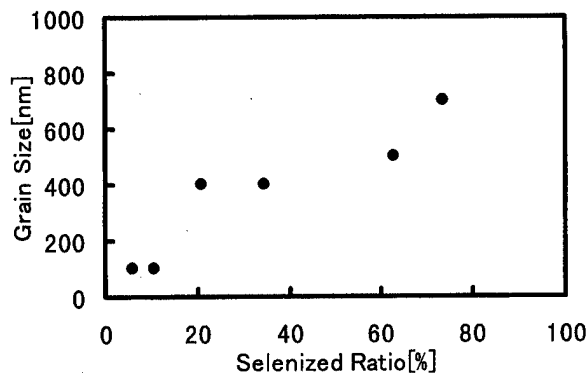


FIG. 2. Dependence of grain size obtained from the SEM observations of the selenized films on their selenized ratio.

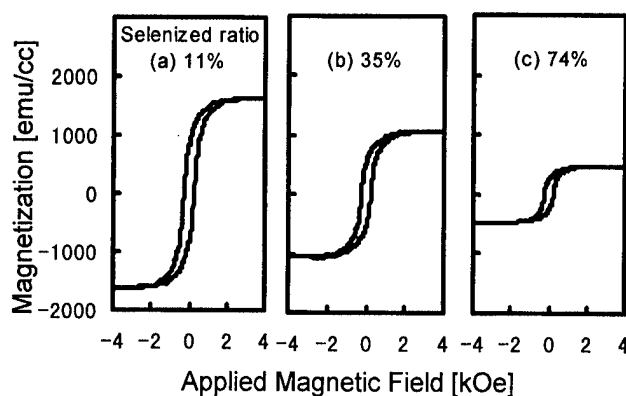


FIG. 3. In-plane magnetic properties (M - H curve) of the selenized films measured by VSM. The external magnetic field, H was applied along GaAs[110] axis, which was the in-plane direction of the films. The selenized ratios of the samples are 11%(a), 35%(b), and 74%(c), respectively.

tization M_s of the Fe_xSe_y film was 120 emu/cc, which was larger than the reported value of M_s in bulk Fe_7Se_8 (65 emu/cc at 290 K).⁴

Figure 5 shows the M - H curves of the selenized films recorded by applying the magnetic field along the GaAs [001] axis, perpendicular to the films. The magnetic anisotropy between the in-plane and perpendicular directions of the film was weakened with the increase of the selenized ratio of the samples. This is because the thickness of the Fe layer decreases and that the Fe_xSe_y thin films exhibit an isotropic magnetization both in-plane and perpendicular to the film. The grain size of the samples increased with the increase in their selenized ratio, whereas the magnetic anisotropy in-plane/perpendicular to the films was weakened. As the structure of the obtained Fe_xSe_y thin films is different from the reported structures of both bulk and epilayer, it has been difficult to determine a crystal structure of the Fe_xSe_y samples from x-ray diffraction measurements at this moment. A further study on structural analysis by using transmission electron microscopy is required.

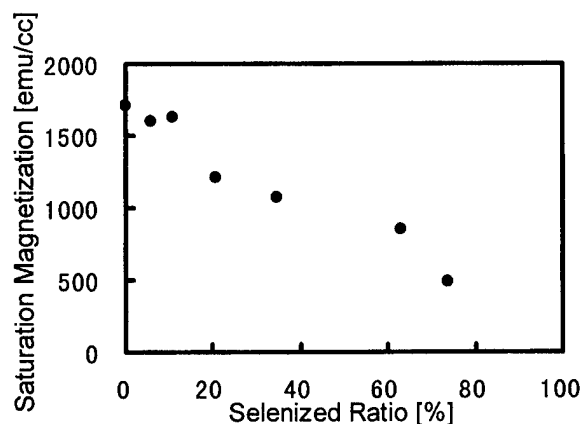


FIG. 4. Dependence of saturation magnetization (M_s) on the selenized ratio calculated from the in-plane M - H curves of the selenized films.

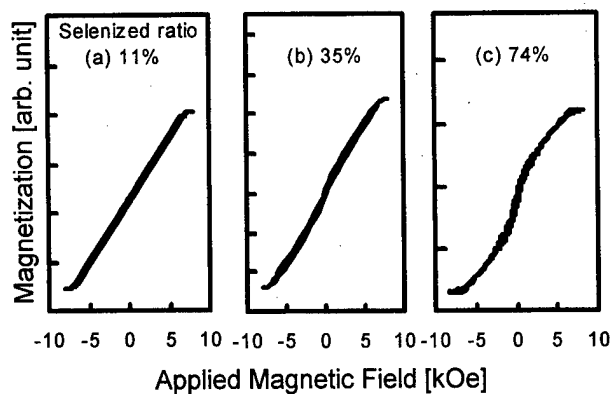


FIG. 5. Perpendicular magnetic properties (M - H curve) of the selenized films measured by VSM. The external magnetic field H was applied along the GaAs[001] axis, perpendicular to the films. The selenized ratios of the samples are 11%(a), 35%(b), and 74%(c), respectively.

IV. CONCLUSION

Structural and magnetic properties of the selenized Fe thin films prepared on GaAs(001) substrates were studied. The films consisted of polycrystalline grains 100–700 nm. The size of the grains became larger with the increase in the

selenized ratio defined by the thickness ratio of $\text{Fe}_x\text{Se}_y/(\text{Fe}_x\text{Se}_y + \text{Fe})$. The saturation magnetization of the selenized films decreased with the increase in selenized ratio. It was also found that the magnetic anisotropy of in-plane/perpendicular to the films was weakened with the increase in selenization ratio, which was interesting in contrast to the fact that the grain size of the films became larger.

ACKNOWLEDGMENT

This work was partly supported by a Grant-in-Aid for science research from the Ministry of Education, Science, Sports and Culture, Japan.

- ¹G. A. Prinz, *Science* **250**, 1092 (1990).
- ²M. Tanaka, J. P. Harbison, M. C. Park, Y. S. Park, T. Shin, and G. M. Rothberg, *J. Appl. Phys.* **76**, 6278 (1994).
- ³M. Tanaka, J. P. Harbison, J. DeBoeck, T. Sands, B. Philips, T. L. Cheeks, and V. G. Keramidas, *Appl. Phys. Lett.* **62**, 1565 (1993).
- ⁴T. Kamimura, K. Kamigaki, T. Hirose, and K. Sato, *J. Phys. Soc. Jpn.* **22**, 1235 (1967).
- ⁵A. Okazaki, *J. Phys. Soc. Jpn.* **16**, 1162 (1961).
- ⁶B. T. Jonker, J. J. Krebs, S. B. Qadri, G. A. Prinz, F. Volkening, and N. C. Koon, *J. Appl. Phys.* **63**, 3303 (1988).
- ⁷Y. Takemura, H. Suto, N. Honda, K. Kakuno, and K. Saito, *J. Appl. Phys.* **81**, 5177 (1997).
- ⁸Y. Takemura, N. Honda, T. Takahashi, H. Suto, and K. Kakuno, *J. Magn. Mater.* **181**, 1319 (1998).

Magnetic behavior of the new low- T_c phase of SrRuO_3

P. A. Joy^{a)} and S. K. Date^{b)}

Physical and Materials Chemistry Division, National Chemical Laboratory, Pune 411008, India

P. S. Anil Kumar

Centre for Advanced Studies in Material Science and Solid State Physics, Department of Physics, University of Pune, Pune 411007, India

Magnetic properties of the new phase of SrRuO_3 having a magnetic ordering temperature of 140 K (low- T_c phase) is compared against that of the normal ferromagnetic phase of $T_c = 160$ K (high- T_c phase). The symmetric ac susceptibility curve and an S-shaped M vs H curve of the low- T_c phase suggests a spin-glasslike behavior. However, the value of M at 80 K is comparable for both the phases and the low- T_c phase shows no magnetic aging effect expected for a spin glass. The low- T_c phase is thus a ferromagnetic phase, the difference in the magnetic behavior of the low- T_c phase from that of the high- T_c phase probably originates from the domain structure. © 1998 American Institute of Physics. [S0021-8979(98)30911-1]

I. INTRODUCTION

The ferromagnetic perovskite oxide, SrRuO_3 , offers wide technological applications owing to its high electrical conductivity and the fact that thin films of high thermal and chemical stability can be fabricated.¹ Polycrystalline and single crystal samples of SrRuO_3 , usually synthesized at or above 1200 °C, undergo a paramagnetic to ferromagnetic transition below $T_c = 160$ K.² The Curie temperature of SrRuO_3 is known to decrease linearly with an increase in the applied pressure.³ Identical behavior is observed with increasing x in $\text{Sr}_{1-x}\text{Ca}_x\text{RuO}_3$; the T_c decreases with x and CaRuO_3 with $x = 1$ is an antiferromagnetic metal.⁴ Studies on transport and magnetic properties of thin film samples of SrRuO_3 showed that T_c for some of the films is 140 K (Ref. 1) and if the film thickness is increased further, $T_c = 160$ K is obtained (no intermediate T_c value is reported).⁵ We have shown recently that polycrystalline samples also show similar magnetic behavior.⁶ Polycrystalline SrRuO_3 when synthesized below 1150 °C showed a magnetic transition at 140 K (low- T_c phase) and if the processing temperature is increased above 1150 °C, the phase with $T_c = 160$ K (high- T_c phase) is obtained without any drastic modification of crystal structure. The crystal structure of the high- T_c phase of SrRuO_3 is related to the orthorhombic GdFeO_3 structure with lattice parameters $a = 5.57$ Å, $b = 5.53$ Å, and $c = 7.85$ Å.⁷ The low- T_c phase also has the same structure with only a marginal difference in the basal plane lattice parameters, $a \approx b \approx 5.6$ Å.⁶

The observed difference between the shape of the ac susceptibility curves of the low- and high- T_c phases was initially ascribed to a different type of magnetic ordering for the low- T_c phase compared to the ferromagnetic ordering of the high- T_c phase.⁶ In this paper we report the results of a comparison of the magnetic behavior of the two phases of SrRuO_3 .

II. EXPERIMENT

The synthesis of the low- and high- T_c phases of SrRuO_3 was previously reported.⁶ Initial studies showed that a small fraction of the high- T_c phase is always present in the low- T_c phase (as evidenced from a small hump in the ac susceptibility curve at 160 K) which could not be eliminated by varying the synthesis or processing conditions. Formation of the compounds was checked by powder x-ray-diffraction measurements. The microstructural features of both the samples were obtained using a Leica-Cambridge 440 scanning electron microscope (SEM). SEM revealed that the particles were almost spherical with comparable particle sizes, ~ 300 nm and ~ 500 nm for the low- and high- T_c phases, respectively. ac susceptibility was measured using mutual inductance method in an APD close cycle helium cryostat in the temperature range 15–300 K at 27 Hz and 10 Oe. High field dc magnetization and the field cooled (FC) and zero field cooled (ZFC) magnetization studies (80–300 K) at 100 Oe were performed using a PAR EG&G vibrating sample magnetometer, Model 4500. All the experiments on both phases were carried out under identical conditions.

III. RESULTS AND DISCUSSION

Temperature variation of the inverse magnetic susceptibility of the two different phases of SrRuO_3 are shown in Fig. 1. From the magnetization data, T_c is obtained as ~ 160 K and ~ 140 K for the two phases. In the paramagnetic region, above 225 K, both the $\chi^{-1}(T)$ curves follow Curie-Weiss behavior. The calculated effective magnetic moment, μ_{eff} , and the paramagnetic Curie temperature, Θ , for the high- T_c phase are $2.78\mu_B$ and 165 K, and the corresponding values for the low- T_c phase are $2.73\mu_B$ and 144 K, respectively. The μ_{eff} values are close to that expected for an $S = 1$ system (in SrRuO_3 , Ru^{4+} which is a d^4 ion is present in the low spin state $S = 1$). The lower value of T_c for the new phase is due to the larger distortion of the RuO_6 octahedra which in turn changes the Ru-Ru exchange integral

^{a)}Electronic mail: joy@dalton.ncl.res.in

^{b)}Electronic mail: skdate@ems.ncl.res.in

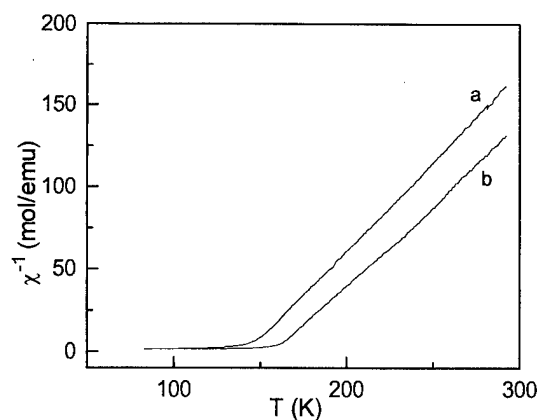


FIG. 1. $\chi^{-1}(T)$ curves of the two different phases of SrRuO_3 showing Curie-Weiss behavior above 225 K, (a) low- T_c phase, $T_c = 140$ K and (b) high- T_c phase, $T_c = 160$ K.

compared to that of the high- T_c phase and not due to the difference in particle size as the particle sizes of both phases are comparable.

Figure 2 shows the ac magnetic susceptibility curves of the two phases of SrRuO_3 . The high- T_c phase shows a sharp peak corresponding to the ferromagnetic transition at 160 K whereas for the low- T_c phase, a symmetric peak is obtained at 140 K apart from the small hump at 160 K which is due to the contribution from the high- T_c phase. The difference between the shape of the two curves indicates that the type of magnetic ordering of the low- T_c phase is probably different from that of the other phase. Symmetric ac susceptibility curves are usually expected for a spin glass⁸ whereas the behavior observed for the high- T_c phase is similar to that reported previously³ for SrRuO_3 and is assigned to the Hopkinson effect,⁹ or to that of cluster-glass-type compounds.¹⁰

Figure 3 shows the M vs H curves of the two phases recorded at 80 K up to a field strength of 15 kOe. Interestingly, the low- T_c phase shows a behavior different from that of the high- T_c phase. The magnetization curve is more or less S shaped and the total magnetization at 15 kOe is slightly less for this phase though the value is very high compared to spin glasses. The symmetric ac susceptibility curve with the S-shaped $M-H$ curve is indicative of a spin-

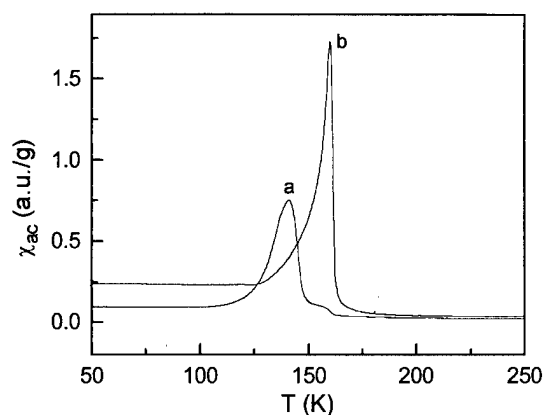


FIG. 2. χ_{ac} vs T curves of (a) low- T_c phase and (b) high- T_c phase of SrRuO_3 .

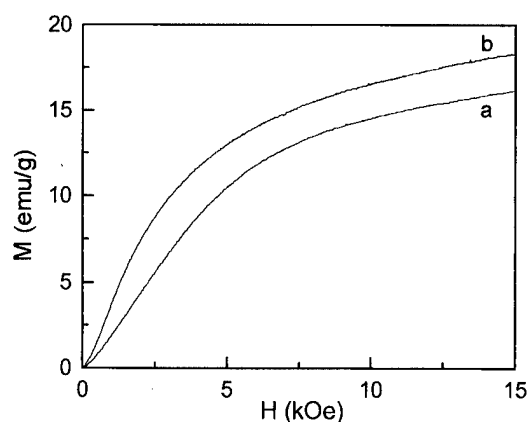


FIG. 3. The magnetization curves of (a) low- T_c phase and (b) high- T_c phase of SrRuO_3 .

glasslike behavior⁸ of the low- T_c phase. The reduced remanent magnetization, $R_M = M_r/M_s$, where M_r and M_s are the remanence and saturation magnetization (at 15 kOe), is identical for both the phases (~ 0.77). For polycrystalline ferromagnetic samples, this ratio is a measure of the anisotropy energy and the observed value is in the range expected for such specimens.¹¹ This indicates that the low- T_c phase is another ferromagnetic phase of SrRuO_3 . The above value of R_M is close to that calculated [using $R_M = 0.25n \sin(\pi/n) \approx 0.74$, where n is the number of equivalent directions] for a planar distribution of four easy directions in which two types of uniaxial anisotropies act simultaneously.¹²

In Fig. 4, the FC and ZFC curves of the two phases are compared. For the high- T_c phase, the irreversibility starts at the T_c . Both the low- and high- T_c phases show large and comparable differences between the FC and ZFC magnetization values at 80 K and show identical behavior. Owing to the presence of a small fraction of the high- T_c phase in the low- T_c phase, the FC and ZFC curves start deviating at 160 K for the low- T_c phase as well. This suggests that the low- T_c

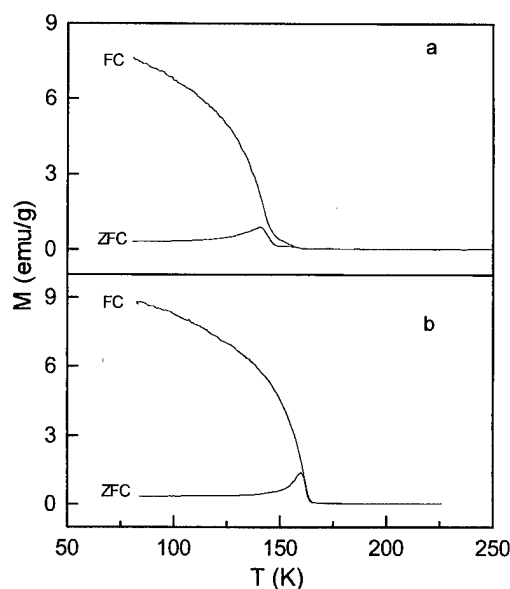


FIG. 4. The temperature dependence of FC and ZFC magnetization of SrRuO_3 measured at 100 Oe, (a) low- T_c phase and (b) high- T_c phase.

phase is not related to a spin-glass or cluster-glass system. It may also be noted that the total magnetization of the low- T_c phase is only slightly smaller than that of the high- T_c phase, in contrast to the very small magnetization expected for a true spin-glass system.

We have performed magnetic relaxation experiments on both phases to find whether there is any difference in the behavior between the two systems. For this, the samples were cooled across T_c in a magnetic field of 100 Oe to a temperature, $t=0.7T_c$, and the magnetic field was switched off after a waiting period $t_w=100$ s. The residual magnetization was recorded as a function of time (for 10^5 s) keeping the temperature constant. The experiment was also performed with $t_w=3000$ s. Both the low- and high- T_c phases behaved in a similar manner, with no aging effect. Absence of aging effect for both the phases then indicates that the low- T_c phase is also undergoing a ferromagnetic transition at 140 K. The observed difference in the shape of the ac susceptibility curve as well as the S-shaped $M-H$ curve of the low- T_c phase is then probably a manifestation of the difference in the domain structure or the inequality of the two types of uniaxial anisotropies, which needs to be investigated further.

ACKNOWLEDGMENT

P.S.A.K. is grateful to UGC, India for financial assistance.

- ¹C. B. Eom, R. J. Cava, R. M. Fleming, J. M. Phillips, R. B. Van Dover, J. H. Marshall, J. W. P. Hsu, J. J. Krajewski, and W. F. Peck, Jr., *Science* **258**, 1766 (1992); S. Y. Hou, J. Kwo, R. K. Watts, J.-Y. Cheng, and D. K. Fork, *Appl. Phys. Lett.* **67**, 1387 (1995); M. Izuka, K. Abe, M. Koike, S. Takeno, and N. Fukushima, *Appl. Phys. Lett.* **70**, 1405 (1997).
- ²A. Kanbayasi, *J. Phys. Soc. Jpn.* **41**, 1876 (1976); A. Callaghan, C. W. Moeller, and R. Ward, *Inorg. Chem.* **5**, 1572 (1966).
- ³M. Shikano, T.-K. Huang, Y. Inaguma, M. Itoh, and T. Nakamura, *Solid State Commun.* **90**, 115 (1994).
- ⁴A. Kanbayashi, *J. Phys. Soc. Jpn.* **44**, 108 (1978); G. Cao, S. McCall, M. Shepard, J. E. Crow, and R. P. Guertin, *Phys. Rev. B* **56**, 321 (1997).
- ⁵J. H. Cho, Q. X. Jia, X. D. Wu, S. R. Foltyn, and M. P. Maley, *Phys. Rev. B* **54**, 37 (1996).
- ⁶P. A. Joy, S. K. Date, and P. S. Anil Kumar, *Phys. Rev. B* **56**, 2324 (1997).
- ⁷C. W. Jones, P. D. Battle, P. Lighfoot, and W. T. A. Harrison, *Acta Crystallogr., Sect. C: Cryst. Struct. Commun.* **45**, 365 (1989).
- ⁸J. A. Mydosh, *Spin Glasses: An Experimental Introduction* (Taylor & Francis, London, 1993).
- ⁹J. Hopkinson, *Proc. R. Soc. London* **48**, 1 (1890).
- ¹⁰S. Mukherjee, R. Ranganathan, P. S. Anil Kumar, and P. A. Joy, *Phys. Rev. B* **54**, 9267 (1996).
- ¹¹D. J. Craik and R. S. Tebble, *Ferromagnetism and Ferromagnetic Domains* (North-Holland, Amsterdam, 1965), p. 294.
- ¹²E. P. Wohlfarth and D. G. Tonge, *Philos. Mag.* **2**, 1333 (1957).

Growth and characterization of epitaxial thin films of conductive ferromagnetic oxide SrRuO₃

C. B. Eom,^{a)} R. A. Rao, Q. Gan, and D. B. Kacedon

Department of Mechanical Engineering and Materials Science, Duke University, Durham, North Carolina 27708

We have grown epitaxial thin films of the conductive ferromagnetic oxide SrRuO₃ on vicinal (001) SrTiO₃ substrates with different miscut angles and miscut direction. Scanning tunneling microscopy and x-ray diffraction studies indicate that when the miscut angle of the substrate is small ($\alpha \leq 1^\circ$), the films grow by a combination of two-dimensional nucleation and step flow leading to a two domain in-plane texture. As the miscut angle of the substrate is increased, complete step flow growth occurs resulting in single domain thin films if the miscut direction is close to the [010] direction. When the miscut direction of the substrate is changed towards the in-plane [110] direction, two directional step flow growth occurs leading to two domain texture with both domains being present in equal volume fraction. Such differences in the growth mechanism and domain structure of the films lead to significant differences in their magnetization and magnetotransport behavior. © 1998 American Institute of Physics. [S0021-8979(98)31011-7]

Epitaxial thin films and heterostructures of magnetic oxide materials have great potential for novel electronic and magnetic device applications. However, the properties of these devices are sensitive to the surface morphology and microstructure of the thin films. Furthermore, atomic scale control of the surface morphology and interfaces is very important in the fabrication of spin-polarized tunneling¹ in colossal magnetoresistive (CMR) manganites² and other multilayered heterostructure devices. Therefore, controlling the growth mechanisms of magnetic oxide thin films is essential for device applications. Recently, we have controlled the growth of magnetic metallic oxide SrRuO₃ thin films³ in three different growth modes and studied the influence of the growth mechanism on domain structure⁴ by using substrate miscut and lattice mismatch as additional growth parameters. In this report, we elaborate on the influence of miscut angle and direction of vicinal (001) SrTiO₃ substrates on the step flow growth, the resulting domain structure, and the magnetotransport properties of SrRuO₃ thin films.

SrRuO₃ is an itinerant ferromagnet with a Curie temperature of about 160 K in the bulk material. It has a GdFeO₃-type pseudocubic perovskite structure with a bulk lattice parameter of 3.93 Å. This material exhibits strong magnetocrystalline anisotropy in single crystal bulk^{5,6} and single domain thin film⁷ samples. Single crystal epitaxial SrRuO₃ thin films have been grown on miscut (001) SrTiO₃ substrates,⁸ which allows us to study intrinsic anisotropic materials behavior.

The SrRuO₃ thin films were deposited from a 2 in. diameter stoichiometric composite target using a 90° off-axis sputtering technique^{9,10} on vicinal (001) SrTiO₃ substrates. During deposition, the operating pressure was held at 200 mTorr (60%Ar/40%O₂) and the substrate block temperature was in the range of 600–680 °C. After deposition, the samples were cooled down to room temperature in an oxygen pressure of 300 Torr. Films with thickness in the range

of 1000–3000 Å were deposited. At these growth conditions, the SrRuO₃ (110) plane grows readily on the SrTiO₃ (001) face, as the energetically favorable direction for fast growth. All the miller indices for SrRuO₃ referred to in this work are based on the orthorhombic unit cell.

Vicinal (001) SrTiO₃ substrates with miscut angle (α) in the range of 0°–4° and miscut direction varying from and towards the in-plane [010] direction ($\beta \approx 0^\circ$) to close to in-plane [110] direction ($\beta \approx 45^\circ$), were used to investigate the effect of miscut angle and direction. The growth mechanism and surface morphology of the films were studied by STM and atomic force microscopy (AFM). All the films were scanned such that the scan direction (one edge of the image) was parallel to the substrate [010] direction. The crystallographic domain structure was studied by four circle x-ray diffraction. Due to the small lattice mismatch between the film and substrate ($\sim 0.64\%$), all the films had a coherent growth resulting in a strained lattice with in-plane lattice parameters close to that of the substrate (3.91 Å) and an out-of-plane lattice parameter of 3.96 Å. Furthermore, all the films had a purely (110) texture normal to the substrate.

The influence of α was studied by comparing films deposited on substrates with similar β values ($\beta \leq 12^\circ$) but different α . On 0° miscut or exact (001) SrTiO₃ substrates, the film grows by two-dimensional nucleation resulting in a smooth surface and a two domain in-plane texture as described in Ref. 3. As the miscut angle of the substrate is increased, the substrate surface shows a periodic step terrace structure with the terrace width being determined by the miscut angle of the substrate. For vicinal substrates with miscut direction close to the in-plane [010] axis ($\beta \sim 0^\circ$), the (010) plane of SrTiO₃ is also preferentially exposed at the steps on the substrate which leads to a step flow growth mechanism.¹¹ If the miscut angle is too small, then the terrace width on the substrate is larger than the critical surface diffusion length of the film adatoms. As a result, the supersaturation of the adatoms reaches a critical value on the terraces and two-

^{a)}Electronic mail: eom@acpub.duke.edu

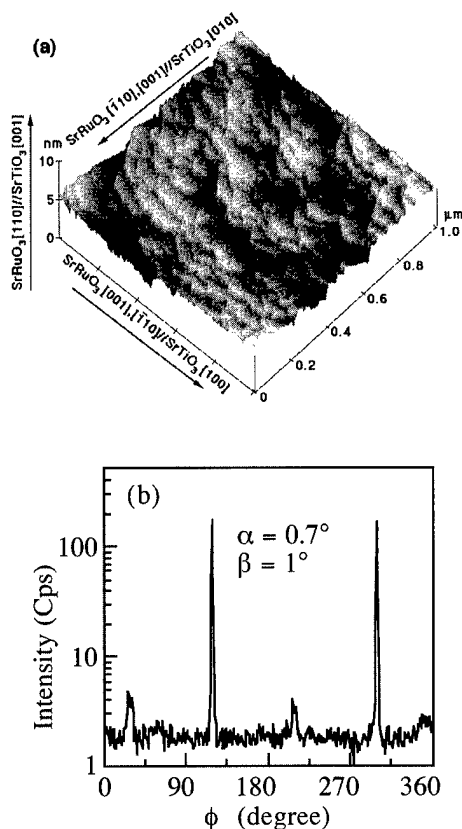


FIG. 1. SrRuO₃ thin film on (001) SrTiO₃ substrate with $\alpha=0.7^\circ$ and $\beta=1^\circ$: (a) STM image showing meandering steps and (b) x-ray ϕ scan of the off-axis (221) reflection.

dimensional nucleation occurs on the terrace. The film growth then proceeds by a combination of step flow and two-dimensional nucleation.

Figure 1(a) shows the STM image of a SrRuO₃ film deposited on vicinal (001) SrTiO₃ substrate with $\alpha=0.7^\circ$ and $\beta=1.0^\circ$. The film surface shows meandering semicircular shaped steps, which indicate that the growth did indeed proceed by a combination of step flow and two-dimensional nucleation, as expected. The step height on the film varies between 4 and 12 Å. This film has a smooth surface with a root mean square (rms) roughness of 5 Å over a $1\ \mu\text{m}\times 1\ \mu\text{m}$ scan area. The x-ray ϕ scans of the (221) reflection of the film is shown in Fig. 1(b). Four peaks are observed indicating a two domain structure with an in-plane alignment of SrRuO₃[$\bar{1}10$], [001]//SrTiO₃[010] and SrRuO₃[001], [$\bar{1}10$]//SrTiO₃[100]. However, due to the partial step flow growth, the [$\bar{1}10$] direction of SrRuO₃ tends to align along the miscut direction or [010] direction of the substrate. Therefore, the domain with an epitaxial arrangement of SrRuO₃[$\bar{1}10$]/SrTiO₃[010] and SrRuO₃[001]/SrTiO₃[100] is found to be predominant.

As the miscut angle of the substrate is increased to greater than 2° the film grows completely by step flow growth and no two-dimensional nucleation is observed. The film surface typically shows straight steps with step bunching, although half and single unit cell high steps can be distinguished in some of the bunched steps. Figure 2(a) shows the STM image and section analysis of a SrRuO₃ film grown on a vicinal (001) SrTiO₃ substrate with $\alpha=4.1^\circ$ and $\beta=11^\circ$. The step height on the film surface varied between 10

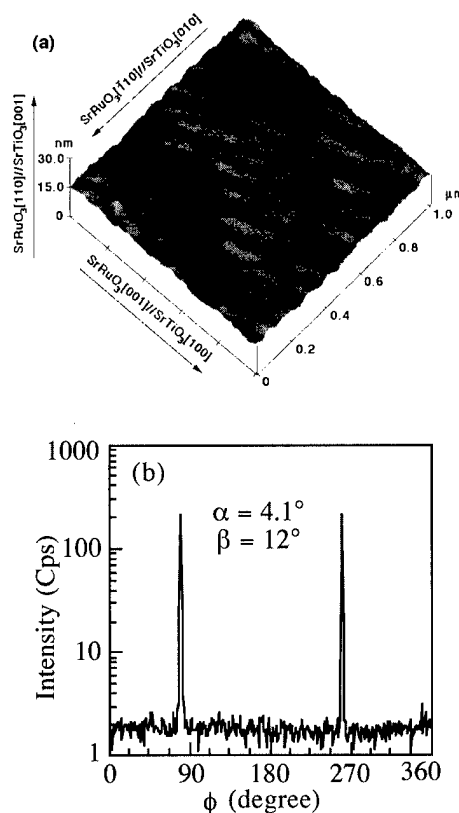


FIG. 2. SrRuO₃ thin film on (001) SrTiO₃ substrate with $\alpha=4.1^\circ$ and $\beta=11^\circ$: (a) STM image showing straight steps and (b) x-ray ϕ scan of the off-axis (221) reflection.

and 37 Å. The rms surface roughness was found to be 9.2 Å over a $1\ \mu\text{m}\times 1\ \mu\text{m}$ scan area. The complete one directional step flow growth led to a single domain texture as evidenced by two peaks separated by 180° in the x-ray ϕ scans of the (221) reflection shown in Fig. 2(b). The in-plane epitaxial arrangement is SrRuO₃[$\bar{1}10$]/SrTiO₃[010] and SrRuO₃[001]/SrTiO₃[100]. As the miscut angle is further increased, the step height on the film surface increases leading to a corresponding increase in the rms surface roughness of the films. The increase in the step height with the miscut angle is consistent with the bunching phenomenon observed in the step flow growth model.

We have also investigated the effect of changing the miscut direction, β , on the growth mechanism and domain structure, by comparing films deposited on 2° miscut SrTiO₃ substrates with $\beta=12^\circ$ and $\beta=45^\circ$. The SrRuO₃ film deposited on the former substrate showed a straight step pattern. The film surface shows step bunching with the bunched step height varying between 10 and 30 Å. The rms surface roughness is 8 Å over a $1\ \mu\text{m}\times 1\ \mu\text{m}$ scan area. Although the miscut direction is 12° away from the in-plane [010] direction, the film surface shows only a few kink sites, indicating that the step flow is dominated by the majority planes exposed at the step sites. This one directional step flow leads to a single domain texture with the same in-plane epitaxial alignment as the film on 4.1° the miscut substrate, as shown in Fig. 2(b).

However, on the latter substrate ($\beta\sim 45^\circ$) both the (010) and (100) plane are exposed in equal proportions at the step sites. Therefore, it is expected that step flow growth occurs-

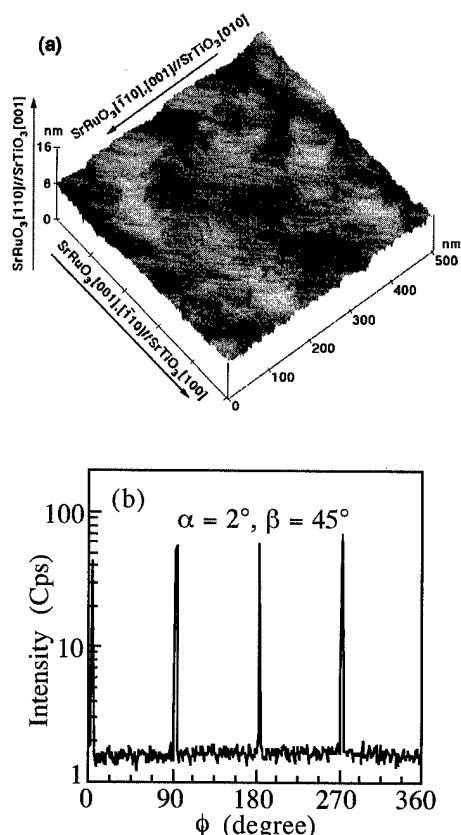


FIG. 3. SrRuO₃ thin film on (001) SrTiO₃ substrate with $\alpha=2.0^\circ$ and $\beta=45^\circ$: (a) STM image showing two directional step flow and (b) x-ray ϕ scan of the off-axis (221) reflection.

equally along both directions with no single direction dominating the growth. This should lead to a two domain in-plane texture.

Figure 3(a) shows the STM image of a SrRuO₃ film deposited on the substrate with $\beta=45^\circ$. As expected, the film surface shows a step pattern indicating step flow growth in two orthogonal directions. The bunched step height on the film surface varies between 8 and 25 Å. Single and half unit cell high steps can be distinguished in the bunched steps. Due to the two directional step flow, several kink sites are observed on the film surface. The film surface has a rms surface roughness of 6.4 Å over a $1\mu\text{m}\times 1\mu\text{m}$ scan area. Figure 3(b) shows the x-ray diffraction ϕ scans of the (221) reflection for this film. Four peaks separated by 90° from each other are observed, indicating a two domain in-plane alignment. Furthermore, the four peaks are of equal intensity which implies that the two domains are present in equal volume fraction.

Such changes in the growth mechanism and domain structure can lead to significant differences in the magnetization and magnetotransport properties of the film.

Figure 4 shows the magnetoresistance (MR) as a function of field for the single domain film obtained on miscut substrate with $\alpha=2^\circ$, $\beta=12^\circ$ and the two domain film obtained on miscut substrate with $\alpha=0.7^\circ$, $\beta=1^\circ$, respectively. The magnetoresistance is calculated as: $\text{MR} = [\rho(H) - \rho(0)] / \rho(0)$, where $\rho(H)$ and $\rho(0)$ are the resistivity at a field H and at zero field, respectively. As is evident from Figs. 4(a) and 4(b), the single domain film shows anisotropic behavior when the field is applied along the two

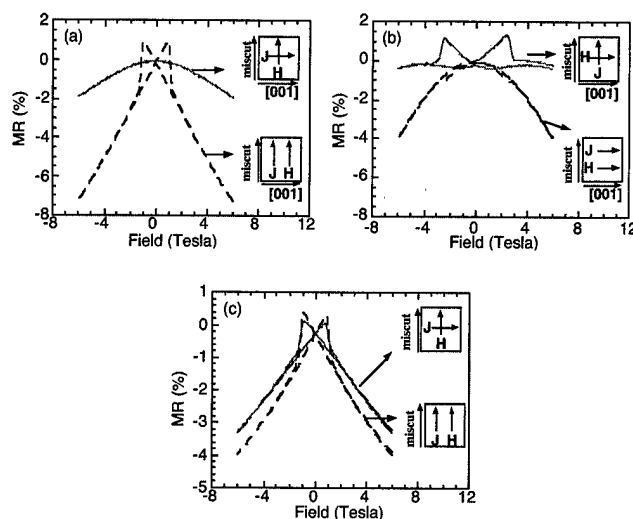


FIG. 4. The magnetoresistance (MR) as a function of applied field at 5 K for (a) and (b) single domain film on (001) SrTiO₃ substrate with $\alpha=2^\circ$ and $\beta=12^\circ$ along the two different directions of applied field and (c) two domain film on (001) SrTiO₃ substrate with $\alpha=0.7^\circ$ and $\beta=1^\circ$. The inset shows the field (H) and current (J) directions with respect to the miscut direction of the substrate.

different in-plane directions. This anisotropic behavior is attributed to the inherent magnetocrystalline anisotropy of SrRuO₃ which is a result of the large spin-orbit coupling of Ru. Figure 4(c) shows the MR versus field behavior for the two domain film with field applied along the miscut direction. An almost identical MR behavior is expected when the field is also applied perpendicular to the miscut direction as observed in multidomain films deposited on (001) LaAlO₃ substrates.¹² Thus, the anisotropy in the magnetic and magnetoresistance properties of SrRuO₃ thin films are dependent on the crystallographic domain structures of the films.

This work was supported by the David and Lucile Packard Fellowship (CBE), the NSF Young Investigator Award (CBE), the ONR Grant No. N00014-95-1-0513, and the NSF Grant No. DMR 9421947.

- ¹J. Z. Sun, W. J. Gallagher, P. R. Duncombe, L. Krusin-Elbaum, R. A. Altman, A. Gupta, Y. Lu, G. Q. Gong, and G. Xiao, Appl. Phys. Lett. **69**, 3266 (1996).
- ²S. Jin, T. H. Tiefel, M. McCormack, R. A. Fastnacht, R. Ramesh, and L. H. Chen, Science **264**, 414 (1994).
- ³R. A. Rao, Q. Gan, and C. B. Eom, Appl. Phys. Lett. **71**, 1171 (1997).
- ⁴Q. Gan, R. A. Rao, and C. B. Eom, Appl. Phys. Lett. **70**, 1962 (1997).
- ⁵A. Kanbayashi, Jpn. J. Appl. Phys. **41**, 1879 (1976); G. Cao, S. McCall, M. Shepard, and J. E. Crow, Phys. Rev. B **56**, 321 (1997).
- ⁶G. Cao, S. McCall, M. Shepard, J. E. Crow, and R. P. Guertin, Phys. Rev. B **56**, 321 (1997).
- ⁷L. Klein, J. S. Dodge, C. H. Ahn, J. W. Reiner, L. Mievill, T. H. Geballe, M. R. Beasley, and A. Kapitulnik, J. Phys.: Condens. Matter **8**, 10111 (1996).
- ⁸C. B. Eom, R. J. Cava, R. M. Fleming, J. M. Phillips, R. B. van Dover, J. H. Marshall, J. W. P. Hsu, J. J. Krajewski, and W. F. Peck, Science **258**, 1766 (1992).
- ⁹C. B. Eom, J. Z. Sun, K. Yamamoto, A. F. Marshall, K. E. Luther, S. S. Laderman, and T. H. Geballe, Appl. Phys. Lett. **55**, 595 (1989).
- ¹⁰C. B. Eom, J. Z. Sun, S. K. Streiffer, A. F. Marshall, K. Yamamoto, B. M. Lairson, S. M. Anlage, J. C. Bravman, T. H. Geballe, S. S. Laderman, and R. C. Taber, Physica C **171**, 351 (1990).
- ¹¹W. K. Burton, N. Cabrera, and F. C. Frank, Philos. Trans. R. Soc. London, Ser. A **243**, 299 (1951).
- ¹²D. B. Kacedon, R. A. Rao, and C. B. Eom, Appl. Phys. Lett. **71**, 1724 (1997).

A field induced ferromagnetic-like transition below 2.8 K in Li_2CuO_2 : An experimental and theoretical study

R. J. Ortega,^{a)} P. J. Jensen,^{b)} and K. V. Rao

Department of Condensed Matter Physics, Royal Institute of Technology, S-100 44 Stockholm, Sweden

F. Sapiña and D. Beltrán

Institut de Ciència dels Materials, Universitat de València, C/Doctor Moliner 50, E-46 100 Burjassot, Spain

Z. Iqbal

Allied Signal Inc., 101 Columbia Road, Morristown, New Jersey 07962

J. C. Cooley and J. L. Smith

Los Alamos National Laboratory, Mail Stop K763, Los Alamos, New Mexico 87545

The low temperature magnetic properties of the Li_2CuO_2 compound have been investigated by means of superconducting quantum interference device magnetometry. We find in addition to an antiferromagnetic phase below 9.5 K a ferromagnetic-like steep rise of the magnetization around 2.8 K. The observed low temperature behavior is discussed by considering second and fourth order magnetocrystalline effective anisotropy coefficients, in addition to the exchange couplings reported in the literature. © 1998 American Institute of Physics. [S0021-8979(98)31111-1]

The magnetic properties of ternary copper oxides are currently of considerable interest, in particular with respect to high T_c superconducting compounds. Unlike these perovskite systems the Li_2CuO_2 compound investigated here exhibits an orthorhombic structure consisting of CuO_2 planes stacked along the crystallographic c axis, and separated by Li-rich layers. Within a CuO_2 plane the Cu ions are lined up in chains.^{1,2} Thus this compound was expected to exhibit magnetic properties reminiscent to a one dimensional magnet.³ The magnetic structure of this compound as determined by neutron diffraction² may be described as follows: the magnetic moments within the CuO_2 planes are ferromagnetically ordered, whereas neighboring planes are coupled antiferromagnetically (AF) along the c axis. In addition to an AF ordering transition at $T_N = 9.5$ K, we observe at temperatures below 2.8 K the appearance of a ferromagnetic component along the direction of the applied magnetic field. We argue that the observed magnetic behavior corresponds to a noncollinear arrangement of the spin layers due to competing magnetocrystalline anisotropies and interlayer exchange coupling. Experimental evidence supporting this argument is presented.

The procedure for fabricating the polycrystalline Li_2CuO_2 compound has been described elsewhere.² The x-ray diffraction patterns of the sample corresponds to a *single crystallographic phase*. The magnetic properties have been measured by means of superconducting quantum interference device (SQUID) magnetometry with applied magnetic fields up to 10 kOe, and in the temperature range between 2 and 300 K. In all our experiments the temperature dependence of the magnetization is measured during warming

scans. It is important to point out that independent samples fabricated and measured at two different places yield identical structural and magnetic properties.

As has already been reported in the literature,^{1,2} the magnetic properties of the Li_2CuO_2 compound (i) exhibits an AF ground state with a Néel temperature $T_N \approx 9$ K, and (ii) shows a Curie-Weiss behavior of the paramagnetic susceptibility above T_N , with a paramagnetic Curie temperature of about $\Theta \approx -40$ K. In addition we have observed the appearance of a *ferromagnetic* component of the magnetization oriented along the applied magnetic field for temperatures below 2.8 K, cf. Fig. 1. The samples were field cooled (FC) in an applied field of 10 Oe, as well as zero field cooled (ZFC) down to 2.0 K. With increasing temperatures the magnetization for both ZFC and FC conditions were measured by applying a magnetic field of 10 Oe. We notice that both curves overlap above 2.8 K, and show the characteristic kink at the Néel temperature T_N . Note also the change of scale of the magnetization for the data taken above 4 K, cf. Fig. 1(b). In

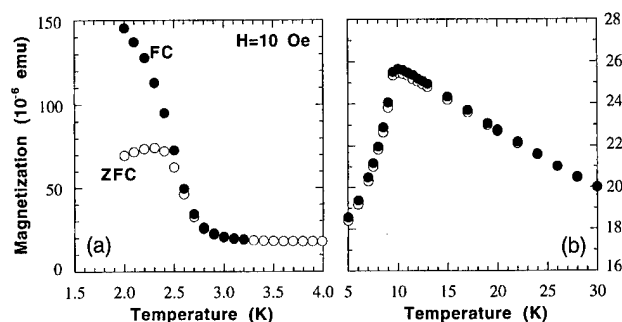


FIG. 1. Temperature dependence of the magnetization of a Li_2CuO_2 sample (67.3 mg). ZFC denotes cooling the sample down to 2.0 K in zero applied field; FC is cooled in a magnetic field of about 10 Oe. (a) Transition from a noncollinear arrangement of the spin layers to a purely AF phase above 2.8 K. (b) Transition from the AF to the paramagnetic phase, with the Néel temperature $T_N \approx 9.5$ K.

^{a)}Permanent address: Departamento de Física, Universidad Pública de Navarra, Campus de Arrosadía, E-31 006 Pamplona, Spain.

^{b)}Permanent address: Hahn-Meitner Institut, Bereich Theorie (TV), Glienicke Str. 100, D-14 109 Berlin, Germany; electronic mail: jensen@hmi.de

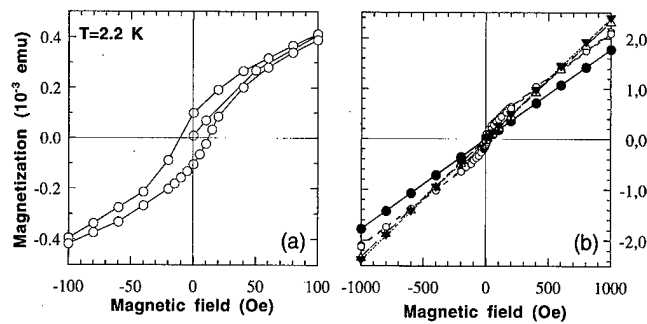


FIG. 2. Magnetic loops of a Li_2CuO_2 sample (67.3 mg) as a function of applied magnetic field. The samples are cooled in zero applied field (ZFC) down to 2.2 K. (a) $T=2.2$ K; first the virgin curve is measured, then the sample is cycled between $H=\pm 10$ kOe. (b) Linear magnetic loops measured at $T=5$ K (\bullet), $T=9$ K (Δ), and $T=14$ K (\blacktriangledown). The hysteresis loop obtained for $T=2.2$ K (\circ) is also shown for comparison.

addition we have monitored the magnetic hysteresis loops $M(H)$ below and above 2.8 K. In the former case we observe a small *remanent magnetization*, cf. Fig. 2(a) for $T=2.2$ K, and a resulting coercive field of about $H_c \approx 12$ Oe. Within these measurements the samples were cooled in ZFC down to 2.2 K. First the virgin magnetization curve $M(H)$ is monitored, then the complete hysteresis loop is measured by cycling the external field through ± 10 kOe. We find that the loops close and the reversible part of the magnetization $M(H)$ is reached for magnetic fields above $|H|=100$ Oe.

No remanence was observed for temperatures above 2.8 K, as shown in Fig. 2(b) for temperatures of about 5, 9, and 14 K. However, for all temperatures investigated the magnetization curves $M(H)$ stay in the linear regime and do not saturate at even the strongest available applied fields, resulting in a high field susceptibility $\chi_{\text{hf}} \approx 2.6 \times 10^{-5}$ emu/gOe at $T=2.2$ K. We note that a complete saturation of the Cu^{2+} ions would render a specific magnetization of about $\sigma_s = 51$ emu/g, assuming $J=1/2$ spins.

In addition we have measured the susceptibility in the paramagnetic phase. A Curie-Weiss behavior was observed, yielding a Curie constant $C_M \approx 0.41$ emu K/mol Oe and the paramagnetic Curie temperature $\Theta \approx -15$ K, which differs from the one reported previously.² From our data we conclude a magnetic moment $\mu \approx 1.05 \mu_B$ per Cu ion, which is consistent with a recent neutron diffraction study yielding a magnetic moment of $\mu \approx 0.96(4) \mu_B$.²

The above results can be explained in terms of a uniaxial magnetocrystalline anisotropy determining the direction of the magnetization with respect to the c axis. Commonly, the uniaxial anisotropy is given as a series in powers of $\cos \theta$, θ being the angle between the magnetization and the c axis. The anisotropic part of the free energy per spin pair may be written as

$$F(T, \theta_1, \theta_2) = -J_c(T) \cos(\theta_1 - \theta_2) - K_2(T) (\cos^2 \theta_1 + \cos^2 \theta_2) - K_4(T) (\cos^4 \theta_1 + \cos^4 \theta_2).$$

$K_2(T)$ and $K_4(T)$ are the second and fourth order *effective*, i.e., temperature dependent, lattice anisotropy coefficients. Expressions of these coefficients as calculated by, e.g., a thermodynamic perturbational expansion of the free energy

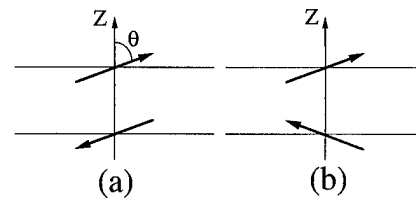


FIG. 3. Sketch of the spin arrangements of two neighboring CuO_2 layers for (a) the purely AF phase, and (b) the noncollinear phase. Note that the latter is metastable since it refers to a local minimum of the free energy. It exhibits a finite remanent magnetization, and may vanish above some temperature T_x . θ is the canting angle between the magnetization and the crystallographic c axis.

are given in Ref. 4. Note that for $K_{2,4} > 0$ a magnetization parallel to the c axis is favored ($\theta=0$), and a perpendicular orientation ($\theta=\pi/2$) for $K_{2,4} < 0$. $J_c(T) < 0$ is the *effective* interlayer exchange coupling connecting q nearest neighbors in adjacent CuO_2 layers, and favoring an AF alignment. Minimization of $F(T, \theta_1, \theta_2)$ with respect to θ_1 and θ_2 reveals the equilibrium canting angles. The most stable state is always the purely AF spin arrangement with $\theta_2 = \theta_1 + \pi$ and a vanishing total magnetization. The case of competing anisotropies $K_2 > 0$ and $K_4 < 0$ may result in a canted magnetization,⁴ i.e., $0 < \theta < \pi/2$, cf. Fig. 3(a).

Most importantly, two additional metastable states may occur corresponding to a noncollinear spin arrangement, cf. Fig. 3(b), which may be in parts thermally populated. The respective canting angles θ_1 and $\theta_2 = -\theta_1$ are determined by $J_c(T)$, $K_2(T)$, and $K_4(T)$ (and also by an applied magnetic field if present), and should be close to $\pi/2$. Quite interestingly, due to the *effective* temperature variation of the involved interactions, the metastable state may *vanish* above some temperature T_x , probably around 2.8 K in the present case. However, below T_x and in the absence of an applied field the two metastable states refer to oppositely oriented magnetizations. Since these two states have the same free energy, they are equally populated, but less populated than the purely AF state. The occupation ratio may be given by $\propto \exp(-\Delta F/k_B T)$, where ΔF is the free energy difference between the stable and the two metastable states. An applied magnetic field may cause a different thermal population of these two metastable states, yielding a small but finite remanent magnetization, cf. the hysteresis loop shown in Fig. 2(a). Also shown in this figure is the virgin curve, i.e., the sample was cooled down to 2.2 K in vanishing magnetic field, resulting in equally populated metastable minima and thus in a vanishing remanence. Furthermore, the ZFC magnetization should vanish at temperatures close to $T=0$, since then the equilibrium thermal population of the metastable states would be vanishingly small. A complete description of the model and the theoretical results will be presented elsewhere.

We do not think that T_x refers to a blocking temperature as present in superparamagnetic systems, since our systems exhibit infinitely extended and strongly coupled ferromagnetic layers. Of course each layer may break up into magnetic domains which will determine essentially the behavior of the hysteresis loops, cf. Fig. 2(a).

In conclusion, the low temperature magnetic properties

of the Li_2CuO_2 compound have been investigated by experimental and theoretical means. At temperatures below 2.8 K the pure AF arrangement of the spin layers is disturbed by the appearance of metastable minima of the free energy, referring to a noncollinear spin arrangement. The origin of such spin configuration is the competition between the AF interlayer exchange coupling, and the magnetocrystalline anisotropy causing a canted magnetization. The thermal population of such minima is observed by the appearance of a finite remanence and coercivity below 2.8 K. Above this temperature the metastable states vanish due to the effective temperature dependence of the involved interactions. At elevated temperatures the compound is an antiferromagnet with Néel temperature $T_N \approx 9.5$ K. The high temperature paramagnetic susceptibility, which closely obeys the Curie-Weiss law, reveals a magnetic moment of about $1 \mu_B$ per Cu ion.

P. J. Jensen wishes to acknowledge the hospitality by the members of the Department of Condensed Matter Physics at

the Royal Institute of Technology. It is a privilege to acknowledge a Gustafsson Stiftelse Visiting Scientist grant, which made this visit possible. Work at Los Alamos was performed under the auspices of the U.S. Department of Energy. Work at the Institut de Ciència dels Materials was supported by the Spanish Comisión Interministerial de Ciencia y Tecnología (Grant No. CICYT MAT 96-1037). Research in Stockholm has been supported by the Swedish funding agencies NFR and NUTEK. It is our pleasure to acknowledge fruitful discussions with Professor V. Madurga and J. Vergara.

¹K. Sreedhar and P. Ganguly, *Inorg. Chem.* **27**, 2261 (1988).

²F. Sapiña, J. Rodríguez-Carvajal, M. J. Sanchís, R. Ibáñez, and A. Beltrán, *Solid State Commun.* **74**, 779 (1990), and references therein.

³S. A. Carter, B. Batlogg, R. J. Cava, J. J. Krajewski, W. F. Peck, Jr., and T. M. Rice, *Phys. Rev. Lett.* **77**, 1378 (1996).

⁴H. B. Callen and E. R. Callen, *J. Phys. Chem. Solids* **27**, 1271 (1966); P. J. Jensen and K. H. Bennemann, *Ann. Phys. (Leipzig)* **2**, 475 (1994); Y. Millev and M. Fähnle, *Phys. Rev. B* **51**, 2937 (1995).

Magneto-optic study of Ni-based diluted magnetic semiconductors

K. Ando^{a)}

Electrotechnical Laboratory, Tsukuba, Ibaraki 305, Japan

A. Chiba

Tsukuba University, Tsukuba, Ibaraki 305, Japan

H. Tanoue

Electrotechnical Laboratory, Tsukuba, Ibaraki 305, Japan

After establishing the usefulness of ion implantation to synthesize diluted magnetic semiconductors (DMSs) for the case of $\text{Zn}_{1-x}\text{Co}_x\text{Te}$, we apply this technique to obtain Ni-based DMS which has not been reported before. Ni ions are implanted into a ZnTe film with acceleration energies from 30 to 390 keV to achieve a Ni density of $3 \times 10^{20}/\text{cm}^3$. Magnetic circular dichroism (MCD) spectra show that the Ni ions substitute Zn ions and induce sizable Zeeman splittings of the optical transitions. Analyses of the MCD spectra show that the p - d exchange in $\text{Zn}_{1-x}\text{Ni}_x\text{Te}$ is antiferromagnetic. © 1998 American Institute of Physics. [S0021-8979(98)43811-8]

I. INTRODUCTION

Diluted magnetic semiconductors (DMSs)¹ are solid solutions of II-VI semiconductors with some cations replaced by 3d transition-metal ions. DMS shows a variety of interesting phenomena such as the giant Faraday effect. These anomalous spin-dependent properties of DMS arise from a strong hybridization between the sp band carriers of the host semiconductors and the localized d orbitals of the transition-metal ions in the tetrahedral (T_d) symmetry. Therefore, the properties of DMS should sensitively depend on the transition-metal ions. The sp - d exchange interactions in DMS with different transition-metal ions ranging from Sc to Cu have been investigated theoretically.²⁻⁴ However, only Mn-, Fe-, and Co-based DMS have been studied experimentally. Recently Cr-based new DMS was also synthesized.⁵ But there have been no experimental reports on DMS with Sc, Ti, V, Ni, or Cu ions. These ions do not substitute the cations of the host II-VI semiconductor under the thermoequilibrium conditions in which the bulk crystals were grown. One must develop nonthermoequilibrium synthesis methods to break the solubility limit of the transition metal ions into the host semiconductor materials. We already know such examples. Zinc-blende type $\text{Cd}_{1-x}\text{Mn}_x\text{Te}$ with a Mn concentration higher than $x=0.7$ cannot be obtained as bulk crystals. But epitaxial films of these metastable DMSs have been obtained by the molecular beam epitaxy (MBE).^{6,7} The MBE method was also used to expand the Cr concentration limit in Cr-based DMS⁸ up to at least $x=0.08$. But the MBE method has not successfully synthesized Ni-based DMS.

In this article, we report on the first successful synthesis of Ni-based DMS by using ion implantation method.⁹ We demonstrate that DMS can be synthesized by ion implantation by showing the case of Co-based DMS which has been well-studied. Next we show the synthesis of $\text{Zn}_{1-x}\text{Ni}_x\text{Te}$ and discuss its sp - d exchange interactions.

II. EXPERIMENT

ZnTe films were epitaxially grown on sapphire (0001) substrates by MBE. The typical thickness of the film was about 200 nm. ZnTe films were implanted with ions of energy 30–390 keV to doses up to $1 \times 10^{16}/\text{cm}^2$ at room temperature. The implanted depths estimated for the energy of 200 keV were about 100 nm. Therefore, for the dose of $1 \times 10^{16}/\text{cm}^2$, the concentration of the transition metal ions can be a few percent of the total cations.

Magnetic circular dichroism (MCD) measurements¹⁰ were used to detect the synthesized DMS. MCD measures the relative difference of the circular polarization dependent optical absorption under the applied magnetic field, i.e., $2(K_- - K_+)/ (K_+ + K_-)$, where K_- and K_+ are optical absorption coefficient for σ_- and σ_+ polarizations, respectively. The optical absorption depends on the circular polarization due to the Zeeman splittings of the band structures. Because the strong sp - d exchange interaction of DMS should lead to sizable Zeeman splittings of the optical transitions, the MCD spectroscopy sensitively detects the DMSs and explores their electronic structures. We measured the MCD spectra with alternating σ_+ and σ_- circularly polarized light (50 kHz) produced by a quartz stress-modulator. One degree of MCD corresponds to a 7% difference of optical absorption. The magnetic field was applied along the light propagation direction (i.e., Faraday configuration).

III. SYNTHESIS OF $\text{Zn}_{1-x}\text{Co}_x\text{Te}$ BY ION IMPLANTATION

Figure 1 shows the MCD spectra of ZnTe films with and without the ion implantations. The ZnTe film showed a small positive peak at its band-gap energy E_0 of 2.40 eV [Fig. 1(a)]. This is due to the diamagnetic Zeeman effect of the exciton at the Γ point. This peak became weaker and broader by the defects induced by Zn implantation of the dose of $5 \times 10^{16}/\text{cm}^2$ at 200 keV [Fig. 1(b)]. This shows that the defects do not induce the magneto-optic effect. Therefore we can attribute the appearance of new MCD structures in the

^{a)}Electronic mail: ando@etl.go.jp

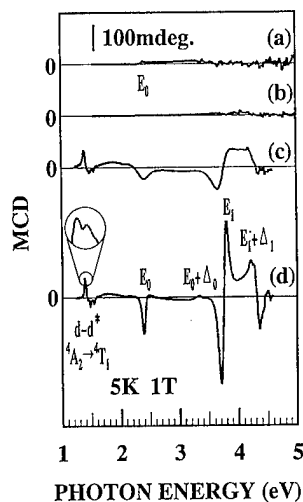


FIG. 1. MCD spectra at 5 K and 1 T of (a) pure ZnTe, (b) as-implanted ZnTe:Zn(5×10^{16} Zn/cm²), (c) as-implanted ZnTe:Co(1×10^{16} Co/cm²), and (d) ZnTe:Co(1×10^{16} Co/cm²) after annealing at 500 °C for 1 min. A part of (d) is magnified for clarity.

transition-metal ion implanted films to the change of the electronic states caused by the transition-metal ions. Figure 1(c) is a spectrum of the Co implanted ZnTe film of the dose of 1×10^{16} /cm² at 200 keV. Sharp MCD peaks appeared in a spectral range of 1.4–1.5 eV. Near the band-gap energy E_0 of ZnTe, a broad negative peak appeared. At the photon energy range between 3.5 and 4.5 eV, a complex structure also appeared. A thermal annealing of the Co implanted film at 500 °C for 1 min in a forming gas (90% N₂, 10% H₂) sharpened the spectral structures especially at an energy range higher than 2 eV. It becomes clear that the complex structure near 4 eV is composed of the two dispersion-type structures centered at 3.76 and 4.32 eV. These photon energies are exactly coincident with the energies of the spin-orbit split E_1 and $E_1 + \Delta_1$ optical transitions of ZnTe.

The $d-d^*$ intraionic transitions of the Co²⁺ ion in the T_d symmetry have been experimentally studied in Cd_{1-x}Co_xTe,¹¹ Zn_{1-x}Co_xS,¹² and Zn_{1-x}Co_xSe crystals.¹² Two strong optical transitions from the ground state $^4A_2(^4F)$ to the excited state $^4T_1(^4P)$ were reported at 1.348 and 1.362 eV in Cd_{1-x}Co_xTe. These energies correspond to the two positive MCD peaks at 1.370 and 1.384 eV as shown in the magnified part of Fig. 1(d). The $d-d^*$ transitions are also known to accompany weaker absorption lines at about 0.1–0.2 eV higher energies.¹² The small negative MCD peaks at 1.468 and 1.538 eV of Fig. 1(d) correspond to the weaker absorption lines of the $^4A_2(^4F) \rightarrow ^4T_1(^4P)$ transitions. Therefore the MCD peaks at 1.4–1.5 eV are the fingerprints of Co²⁺ in the T_d symmetry. This is clear evidence that the implanted Co ions substituted Zn ions, at least partly, and that Zn_{1-x}Co_xTe was successfully synthesized.

Appearances of the strong MCD structures at the energies corresponding E_0 , E_1 , and $E_1 + \Delta_1$ critical points are due to a well known strong $sp-d$ exchange interaction in Co-based DMS.¹ At present it is not clear what percentage of the implanted Co ions substituted Zn ions. Only the transition-metal ions in the T_d symmetry sites can induce the

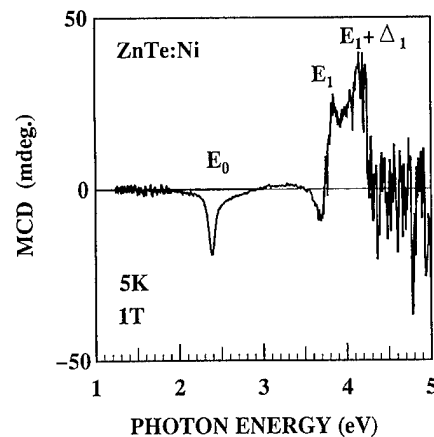


FIG. 2. MCD spectra at 5 K and 1 T of a Ni implanted ZnTe film with Ni density of 3×10^{20} /cc after annealing at 300 °C for 1 min.

$sp-d$ exchange interaction.¹³ The MCD selectively detects the synthesized part of Zn_{1-x}Co_xTe.

IV. Zn_{1-x}Ni_xTe AND ITS $sp-d$ EXCHANGE INTERACTION

We applied the ion implantation method to obtain a heretofore unknown new DMS, Zn_{1-x}Ni_xTe. Ni ions were implanted with five different acceleration energies ranging from 30 to 390 keV to obtain a 200 nm thick implanted layer with a uniform Ni ion density of 3×10^{20} /cm³. The ZnTe:Ni sample annealed at 300 °C for 1 min shows the characteristic MCD structures (Fig. 2) of DMS to be the same as Zn_{1-x}Co_xTe [Fig. 1(d)]. This indicated that Zn_{1-x}Ni_xTe was successfully synthesized.

The polarities of the MCD peaks strongly correlate with the polarity of the $p-d$ exchange interaction. In DMS the $p-d$ exchange interaction is much stronger than the $s-d$ exchange.¹ Then the $p-d$ exchange interaction determines the polarity of the Zeeman split, which in turn determines the polarity of MCD. We have shown that at the E_0 band edge the antiferromagnetic (AF) $p-d$ exchange induces the negative MCD peak, and the ferromagnetic (F) $p-d$ exchange induces the positive MCD peak.⁸ Then the negative MCD peaks at E_0 in ZnTe:Co and ZnTe:Ni films strongly suggest the AF $p-d$ exchange in Zn_{1-x}Co_xTe and Zn_{1-x}Ni_xTe. Indeed, it is well known that the $p-d$ exchange in Co-based DMS is antiferromagnetic.¹

This conclusion of AF $p-d$ exchange interaction in Zn_{1-x}Ni_xTe was also supported from the MCD structures at the E_1 and $E_1 + \Delta_1$ optical transitions (Fig. 3). The spectra of ZnTe, ZnTe:Co, and ZnTe:Ni samples are shown together with that of a MBE grown Zn_{0.95}Cr_{0.05}Te film.⁸ Two peak structures of the pure ZnTe film are both positive at E_1 and $E_1 + \Delta_1$. The ZnTe:Co film clearly shows the inverted polarity of the E_1 MCD peak. The polarity of the $E_1 + \Delta_1$ MCD peak remained the same as that of ZnTe. It has been shown that the hybridization between the d orbitals and the p valence band causes the Zeeman splittings of the E_1 and $E_1 + \Delta_1$ transitions in opposite directions.¹⁴ The E_1 inverted and $E_1 + \Delta_1$ noninverted MCD structures correspond to the AF $p-d$ exchange. If the $p-d$ exchange is ferromagnetic,

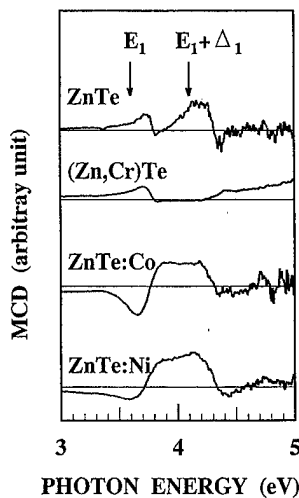


FIG. 3. MCD spectra at E_1 and $E_1 + \Delta_1$ of MBE grown ZnTe, MBE grown $\text{Zn}_{0.95}\text{Cr}_{0.05}\text{Te}$ samples, as-implanted $\text{ZnTe:Co}(1 \times 10^{16} \text{ Co/cm}^2)$ and as-implanted $\text{ZnTe:Ni}(1 \times 10^{16} \text{ Ni/cm}^2)$ samples measured at 5 K and 1 T.

we expect the reversed polarities, i.e., noninverted E_1 edge and inverted $E_1 + \Delta_1$ edge. Indeed $\text{Zn}_{0.95}\text{Cr}_{0.05}\text{Te}$, which has a ferromagnetic p - d exchange, showed the expected MCD structures. Judging from these correspondences, the MCD structures at the E_1 and $E_1 + \Delta_1$ edges also indicate the AF p - d exchange in $\text{Zn}_{1-x}\text{Ni}_x\text{Te}$.

The AF p - d exchange in $\text{Zn}_{1-x}\text{Ni}_x\text{Te}$ is reasonable.²⁻⁴ The Γ_8 Luttinger states of the valence band only couple with the three one-electron d states belonging to the t_{2g} representation of the point group T_d . The Ni^{2+} ion has eight d electrons which occupy four e_g and four t_{2g} one-electron orbitals. The spin-up t_{2g} electron states are all occupied. There is only one available vacant spin-down t_{2g} electron state for the electron jump from the valence band. The absence of the spin-up electron jump into the t_{2g} state may be a common reason for the AF p - d exchange in Mn-, Fe-, Co-, and Ni-based DMS. For Ni-based DMS, a huge AF p - d exchange was theoretically predicted.⁴ Quantitative evaluation of the p - d exchange interaction requires information on the mag-

nitude of the Zeeman splitting and numbers of Ni ions which substitute Zn ions. This evaluation is now in progress.

V. CONCLUSIONS

We have shown that the ion implantation technique is a powerful method to synthesize diluted magnetic semiconductors. By using this method Ni-based DMS $\text{Zn}_{1-x}\text{Ni}_x\text{Te}$ has been successfully synthesized for the first time. From the magnetic circular dichroism spectra, the p - d exchange interaction in $\text{Zn}_{1-x}\text{Ni}_x\text{Te}$ is shown to be antiferromagnetic.

ACKNOWLEDGMENT

The authors wish to thank Professor S. Onari of Tsukuba University for his encouragement and support.

- ¹(a) J. K. Furdyna, J. Appl. Phys. **64**, R29 (1988); (b) *Diluted Magnetic Semiconductors*, edited by J. K. Furdyna and J. Kossut (Academic, New York, 1988).
- ²A. K. Bhattacharjee, Phys. Rev. B **46**, 5266 (1992).
- ³J. Blinowski and P. Kacman, Phys. Rev. B **46**, 12 298 (1992).
- ⁴T. Mizokawa and A. Fujimori, Phys. Rev. B **56**, 6669 (1997).
- ⁵W. Mac, N. Khoi, A. Twardowski, J. A. Gaj, and M. Demianiuk, Phys. Rev. Lett. **71**, 2327 (1993).
- ⁶S. M. Durbin, J. Han, S. O. M. Kobayashi, D. R. Menke, R. L. Gunshor, Q. Fu, N. Pelekanos, A. V. Nurmikko, D. Li, J. Gonsalves, and N. Otsuka, Appl. Phys. Lett. **55**, 2087 (1989).
- ⁷K. Ando and H. Akinaga, J. Magn. Magn. Mater. **140-144**, 2029 (1995).
- ⁸K. Ando and A. Twardowski, in *Proceedings 23rd International Conference on the Physics of Semiconductors*, Berlin 1996, edited by M. Scheffler and R. Zimmermann (World Scientific, Singapore, 1996), p. 285.
- ⁹G. H. Braunstein, D. Heimann, S. P. Withrow, and G. Dresselhaus, in *Diluted Magnetic (Semimagnetic) Semiconductors*, edited by R. L. Aggarwal, J. K. Furdyna, and S. von Molnar (Materials Research Society, Pittsburgh, 1987), Vol. 89, p. 237.
- ¹⁰K. Ando, K. Takahashi, T. Okuda, and M. Umehara, Phys. Rev. B **46**, 12289 (1992).
- ¹¹S. V. Mel' nichuk, A. I. Savchuk, and D. N. Trifonenko, Phys. Solid State **38**, 731 (1996) [Fiz. Tverd. Tela (St. Petersburg) **38**, 1320 (1996)].
- ¹²A. Ehlert, J. Dreyhsig, and H.-E. Gumlich, Mater. Sci. Forum **182-184**, 635 (1995).
- ¹³K. Ando and K. Takahashi, in *Proceedings 23rd International Conference on the Physics of Semiconductors*, Berlin 1996, edited by M. Scheffler and R. Zimmermann (World Scientific, Singapore, 1996), p. 457.
- ¹⁴A. K. Bhattacharjee, Phys. Rev. B **41**, 5696 (1990).

Magneto-optic effect of the ferromagnetic diluted magnetic semiconductor $\text{Ga}_{1-x}\text{Mn}_x\text{As}$

K. Ando^{a)}

Electrotechnical Laboratory, 1-1-4 Umezono, Tsukuba, Ibaraki 305, Japan

T. Hayashi

Department of Electronic Engineering, The University of Tokyo, 7-3-1 Hongo, Bunkyo-ku, Tokyo 113, Japan

M. Tanaka

Department of Electronic Engineering, The University of Tokyo, 7-3-1 Hongo, Bunkyo-ku, Tokyo 113, Japan and PRESTO(Sakigake-21), Japan Science & Technology Corporation

A. Twardowski

Institute of Experimental Physics, Warsaw University, Hoza 69, 00681 Warsaw, Poland

Magnetic circular dichroism (MCD) of a ferromagnetic diluted magnetic semiconductor $\text{Ga}_{1-x}\text{Mn}_x\text{As}$ films was measured to clarify their electronic structure. Strong enhancement of MCD by Mn substitution indicated a strong $sp-d$ hybridization. The $p-d$ exchange interaction was concluded to be antiferromagnetic, which was in contrast with the reported ferromagnetic $p-d$ exchange in very diluted paramagnetic GaAs:Mn bulk crystals. The change of the character of the $p-d$ exchange interaction is due to the unique feature of $\text{Ga}_{1-x}\text{Mn}_x\text{As}$ that the relative abundance of the neutral and ionized Mn acceptors controls the $p-d$ exchange. © 1998 American Institute of Physics. [S0021-8979(98)43911-2]

I. INTRODUCTION

$\text{Ga}_{1-x}\text{Mn}_x\text{As}$ is a new III-V based diluted magnetic semiconductor (DMS).¹⁻⁴ Single-phase zinc-blende type epitaxial films can be obtained with manganese concentration x up to 0.08. Ferromagnetic ordering was observed by magnetic and magnetotransport measurements. However, little is known of their electronic structure, especially how the Mn d electrons interact with the sp -band electrons in this Mn containing DMS. In this article, we show magnetic circular dichroism (MCD) spectra of $\text{Ga}_{1-x}\text{Mn}_x\text{As}$ epitaxial films, and discuss their electronic structure.

II. EXPERIMENT

$\text{Ga}_{1-x}\text{Mn}_x\text{As}$ thin films were grown on (001) GaAs substrates by the molecular beam epitaxy method at 200–300 °C under As rich conditions.^{2,4} Reflection high energy electron diffraction and x-ray diffraction showed that they are single phase zinc-blende type epitaxial films. No MnAs precipitation was detected by x-ray diffraction. Two $\text{Ga}_{1-x}\text{Mn}_x\text{As}$ samples of $x = 0.005$ (thickness 1.0 μm) and 0.074 (thickness 1.4 μm) were used for this study. Their hole concentrations at room temperature are 1.93×10^{19} and $2.58 \times 10^{20} \text{ cm}^{-3}$, respectively. Ferromagnetic ordering was observed below ≈ 10 K for $x = 0.005$ and below ≈ 60 K for $x = 0.074$.

MCD measures the difference between the reflectance for left and right polarizations.⁵ Alternating polarized light (50 kHz) was produced by a quartz stress-modulator. The direction of input and reflected lights deviate from the film

normal by 10° . One degree of MCD corresponds to 7% difference of reflectivity.

III. RESULTS AND DISCUSSIONS

Figure 1(a) shows the MCD spectrum of GaAs substrate. The structures appear at the energies of the critical points (CPs) of the zinc-blende type band structure, E_0 , $E_0 + \Delta_0$, E_1 and $E_1 + \Delta_1$. The signal between 1.51 and 1.60 eV is the oscillation by the Landau quantization effect. With incorporating manganese ions, the MCD signals near CP are significantly enhanced as shown in Figs. 1(b) and 1(c). This clearly

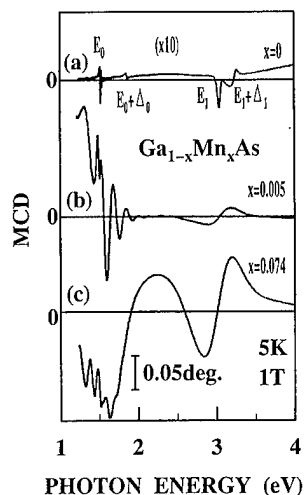


FIG. 1. Magnetic circular dichroism (MCD) spectra of (a) nondoped semi-insulating GaAs substrate and (b),(c) the epitaxial $\text{Ga}_{1-x}\text{Mn}_x\text{As}$ films at $T = 5$ K and $H = 1$ T. The spectrum of GaAs is magnified ten times because the signal is weaker than that of $\text{Ga}_{1-x}\text{Mn}_x\text{As}$.

^{a)}Electronic mail: ando@etl.go.jp

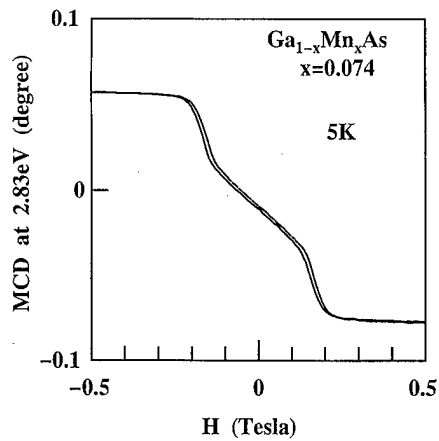


FIG. 2. Magnetic field dependence of E_1 MCD at 2.83 eV of $\text{Ga}_{1-x}\text{Mn}_x\text{As}$ ($x=0.074$) at $T=5$ K.

shows that $\text{Ga}_{1-x}\text{Mn}_x\text{As}$ has a typical band structure of the zinc-blende type semiconductors and the strong $sp-d$ mixing occurs at each CP.

The magnetic field dependence of the MCD intensity of the $\text{Ga}_{1-x}\text{Mn}_x\text{As}$ ($x=0.074$) sample at 2.83 eV shows the apparent ferromagnetic behavior (Fig. 2). The MCD signal originates from the E_1 CP of $\text{Ga}_{1-x}\text{Mn}_x\text{As}$, and the MCD spectrum of MnAs (Ref. 6) has no common feature with that of $\text{Ga}_{1-x}\text{Mn}_x\text{As}$. Therefore, we can exclude the possibility that the observed ferromagnetism comes from possible small clusters of MnAs precipitations. The observed ferromagnetism comes from the $\text{Ga}_{1-x}\text{Mn}_x\text{As}$ ternary alloy semiconductor.

The MCD near E_0 CP for the $x=0.005$ sample is shown in Fig. 3. This oscillating structure arises from the optical interference effect within the film. The oscillating period (≈ 160 meV) agrees with the expected period calculated from the film thickness and the refractive index of GaAs. We noted that near the band-gap energy E_0 of GaAs, 1.52 eV, a sharp negative MCD peak is superimposed on the interference pattern. This indicates that the MCD is negative at E_0 in $\text{Ga}_{1-x}\text{Mn}_x\text{As}$. From the negative polarity of MCD at E_0 , we can estimate the character of the $p-d$ exchange. The polarity of MCD is a good indicator of the polarity of the $p-d$ ex-

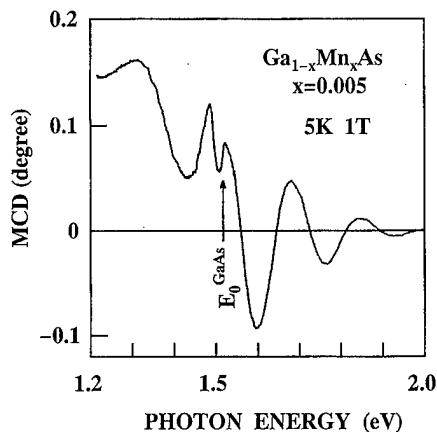


FIG. 3. MCD spectrum of $\text{Ga}_{1-x}\text{Mn}_x\text{As}$ ($x=0.005$) film near the E_0 critical point. The E_0 point energy of GaAs is shown for comparison by an arrow.

change constant $N_0\beta$. For example, at E_0 CP, the antiferromagnetic (AF) $p-d$ exchange ($N_0\beta < 0$) in $\text{Cd}_{1-x}\text{Mn}_x\text{Te}$ showed a negative MCD peak, and the ferromagnetic (F) $p-d$ exchange ($N_0\beta > 0$) in $\text{Zn}_{1-x}\text{Cr}_x\text{Se}$ showed a positive MCD peak.⁷ This is due to a relation⁵ of MCD with $N_0\beta$ and the $s-d$ exchange constant $N_0\alpha$,

$$\text{MCD} = -(1/4)(N_0\alpha - N_0\beta) \times \langle Sz \rangle (1/R) dR/dE, \quad (1)$$

where $\langle Sz \rangle$ is the average spin per Mn ion, and E is the photon energy. Mn ions in DMS occupy the tetrahedrally (T_d) coordinated sites, and their d orbits mix with the p valence band, not with the s conduction band.⁸ Then the absolute value of $N_0\beta$ should be larger than that of $N_0\alpha$, and the polarity of MCD is determined by the polarity $N_0\beta$. The negative MCD at E_0 CP of $\text{Ga}_{1-x}\text{Mn}_x\text{As}$ corresponds to the AF $p-d$ exchange, $N_0\beta < 0$.

The MCD structures at the E_1 CP and $E_1 + \Delta_1$ CP are also strongly enhanced by the Mn substitution (Fig. 1), although the E_1 and $E_1 + \Delta_1$ structures are merged into a broad structure. The broadening of the MCD structures due to Mn substitution is generally observed in II-VI based DMS,⁹ and can be attributed to the strong $sp-d$ hybridization. Note that the polarity of the MCD of $\text{Ga}_{1-x}\text{Mn}_x\text{As}$ remains the same as that of GaAs. The effective g values of the GaAs at the E_1 edge were reported by Fujimori *et al.*¹⁰ as $g_{\text{eff}} = -1.63$. So g_{eff} of $\text{Ga}_{1-x}\text{Mn}_x\text{As}$ should be negative also at the Λ CP. In DMS, polarity of g_{eff} depends on the polarity of $-(N_0\alpha - N_0\beta/4)$.¹¹ Because $N_0\alpha$ should be always positive,¹² our conclusion of the negative $N_0\beta$ is compatible with the negative g_{eff} .

The AF $p-d$ exchange in $\text{Ga}_{1-x}\text{Mn}_x\text{As}$ presents a sharp contrast to the ferromagnetic $p-d$ exchange reported by Szczytko *et al.*¹² who studied the Zeeman splitting of heavily doped paramagnetic GaAs:Mn bulk crystals. We believe this discrepancy may be explained by taking into account variation of neutral (A^0) and ionized (A^-) Mn acceptors abundance with increasing Mn concentration. We recall that a neutral acceptor center is formed by substitutional Mn^{3+} (d^4) ion, which tightly binds an electron (yielding d^5 configuration) and then weakly (0.113 eV) binds a hole ($d^5 + h$ configuration).¹³ The hole is spin polarized and provides an additional, ferromagnetic exchange channel as pointed out in Ref. 12. This exchange path was suggested as responsible for F $p-d$ exchange reported for heavily doped (10^{17} – 10^{18} cm^{-3}) bulk samples.¹² On the other hand ionization of the hole leads to the ionized Mn acceptor A^- , which is equivalent to the Mn^{2+} (d^5) ion. For such center only AF $p-d$ exchange is possible, as established both experimentally¹⁴ and theoretically^{8,15,16} for Mn based II-VI DMS. For very diluted GaAs:Mn both A^0 and A^- centers were observed in the electron paramagnetic resonance (EPR) experiment.¹³ The EPR spectra of the paramagnetic bulk GaAs:Mn crystals used in Ref. 12 were compared with that of the ferromagnetic $\text{Ga}_{1-x}\text{Mn}_x\text{As}$ ($x=0.005$) epitaxial film.¹⁷ At 3.5 K the bulk GaAs:Mn sample showed two strong lines corresponding to A^0 and A^- . The A^0 line disappears with increasing temperature, while the A^- line is observed up to 300 K. On the contrary, the EPR spectrum of the $\text{Ga}_{1-x}\text{Mn}_x\text{As}$ ($x=0.005$) epilayer showed in the entire

temperature range only a signal corresponding to the A^- center. No A^0 signal was detected. Based on these observations we conclude that the concentration of neutral Mn acceptor centers A^0 in GaAs:Mn decreases with increasing Mn concentration, so for $x=0.005$ only A^- centers are left in the crystal. The reason for the disappearance of A^0 centers may be high hole concentration (10^{19} cm^{-3} for $x=0.005$ and 10^{20} cm^{-3} for $x=0.074$), which yields screening of the A^- attractive potential, so the hole can be hardly bound. We note that ionization of A^0 to A^- should supply the free holes, which contribute to the measured p -type conductivity of the epilayer. Effectively the absence of A^0 centers means that no F p - d exchange channels are available and one is left only with AF p - d exchange, typical for Mn^{2+} ions. This way the system of GaAs doped with Mn presents an interesting (and unique among DMS) case where concentration of A^0 centers (roughly inversely proportional to Mn concentration) controls the character of p - d exchange interaction. It changes from ferromagnetic at a very dilute limit to antiferromagnetic at a more concentrated range.

IV. CONCLUSIONS

In summary, we observed the strong enhancement of the magneto-optic effect at the critical points of the $\text{Ga}_{1-x}\text{Mn}_x\text{As}$. This indicates that $\text{Ga}_{1-x}\text{Mn}_x\text{As}$ has a zinc-blende type band structure, and it shows the strong sp - d exchange interaction. The magnetic field dependence of the MCD signal at the critical point showed that ferromagnetism is an inherent property of the zinc-blende type $\text{Ga}_{1-x}\text{Mn}_x\text{As}$. From the polarities of the MCD structure, the antiferromagnetic p - d exchange interaction was indicated. Comparisons with the electron paramagnetic resonance data revealed a unique feature of $\text{Ga}_{1-x}\text{Mn}_x\text{As}$ among DMS that the relative abundance of the neutral and ionized Mn acceptors changes the polarity of p - d exchange interaction.

ACKNOWLEDGMENTS

The authors wish to thank Professor T. Nishinaga for encouragement and support. This work was partly supported by the PRESTO project of Japan Science & Technology Corporation, and by a Grant-in-Aid for Scientific Research from the Ministry of Education, Science, Sports & Culture, Japan.

- ¹H. Ohno, A. Shen, F. Matsukura, A. Oiwa, A. Endo, S. Katsumoto, and H. Iye, *Appl. Phys. Lett.* **69**, 363 (1996).
- ²T. Hayashi, M. Tanaka, T. Nishinaga, H. Shimada, H. Tsuchiya, and Y. Otuka, *J. Cryst. Growth* **175/176**, 1063 (1997).
- ³J. De Boeck, A. Van Esch, and G. Borghs (unpublished).
- ⁴T. Hayashi, M. Tanaka, T. Nishinaga, and H. Shimada, *J. Appl. Phys.* **81**, 4865 (1997).
- ⁵K. Ando, K. Takahashi, T. Okuda, and M. Umehara, *Phys. Rev. B* **46**, 12 289 (1992).
- ⁶K. Ando, T. Hayashi, and M. Tanaka (unpublished).
- ⁷K. Ando and A. Twardowski, in *Proceedings of the 23rd International Conference on the Physics of Semiconductors*, Berlin 1996, edited by M. Scheffler and R. Zimmermann (World Scientific, Singapore, 1996), p. 285.
- ⁸S.-H. Wei and A. Zunger, *Phys. Rev. B* **35**, 2340 (1987).
- ⁹K. Ando and H. Akinaga, *J. Magn. Magn. Mater.* **140-144**, 2029 (1995).
- ¹⁰A. Fujimori, H. Fukutani, and G. Kuwabara, *J. Phys. Soc. Jpn.* **45**, 910 (1978).
- ¹¹A. K. Bhattacharjee, *Phys. Rev. B* **41**, 5696 (1990).
- ¹²J. Szczytko, W. Mac, A. Stachow, A. Twardowski, P. Becla, and J. Tworzydło, *Solid State Commun.* **99**, 927 (1996).
- ¹³J. Schneider, U. Kaufmann, W. Wilkening, M. Baeumler, and F. Kohl, *Phys. Rev. Lett.* **59**, 240 (1987).
- ¹⁴J. K. Furdyna, *J. Appl. Phys.* **64**, R29 (1988); "Diluted Magnetic Semiconductors" in *Semiconductors and Semimetals*, edited by J. K. Furdyna and J. Kossut (Academic, New York, 1988), Vol. 25; *Diluted Magnetic Semiconductors*, edited by M. Balkanski and M. Averous (Plenum, New York, 1991); J. Kossut and W. Dobrowolski, in *Handbook of Magnetic Materials*, edited by K. H. J. Buschow (North Holland, Amsterdam, 1993), Vol. 7, p. 231.
- ¹⁵B. E. Larson, K. C. Hass, H. Ehrenreich, and A. E. Carlsson, *Phys. Rev. B* **37**, 4137 (1988).
- ¹⁶J. Blinowski and P. Kacman, *Phys. Rev. B* **46**, 12 298 (1992).
- ¹⁷J. Szczytko, K. Swiatek, and A. Twardowski (unpublished).

Hall effect and magnetic properties of III-V based $(\text{Ga}_{1-x}\text{Mn}_x)\text{As}/\text{AlAs}$ magnetic semiconductor superlattices

T. Hayashi, M. Tanaka,^{a)} K. Seto, and T. Nishinaga

Department of Electronic Engineering, The University of Tokyo, 7-3-1 Hongo, Bunkyo-ku, Tokyo 113, Japan

H. Shimada

Cryogenic Center, The University of Tokyo, 2-11-16 Yayoi, Bunkyo-ku, Tokyo 113, Japan

K. Ando

Electrotechnical Laboratory, 1-1-4 Umezono, Tsukuba 305, Japan

We present magnetotransport properties, with emphasis on Hall effect, of a new class of III-V based magnetic $(\text{GaMnAs})/\text{nonmagnetic (AlAs)}$ semiconductor superlattices (SLs) grown by low-temperature molecular beam epitaxy. The SLs having relatively wide $(\text{GaMn})\text{As}$ layers ($\geq 70 \text{ \AA}$) are ferromagnetic at low temperatures, and their hole concentrations and Curie temperatures are estimated through the analysis of Hall measurements. The dependence of the magnetic and transport properties on the GaMnAs well width is discussed. © 1998 American Institute of Physics. [S0021-8979(98)21211-4]

I. INTRODUCTION

Diluted magnetic semiconductors (DMSs), containing a large fraction of magnetic ions in compound semiconductors, offer interesting opportunities to explore spin-related phenomena caused by the interaction of carriers and local magnetic moments. Recent progress in epitaxial growth techniques made it possible to grow III-V based DMSs, $(\text{InMn})\text{As}$,^{1,2} and $(\text{GaMn})\text{As}$.³⁻⁶ These III-V based DMSs, especially $(\text{GaMn})\text{As}$ which is based on the most widely used III-V semiconductor GaAs, provide new potential applications as well as unique opportunities for basic research, because carrier control is much easier in such III-V based systems than in traditional II-VI based DMSs.

We have successfully grown GaMnAs by low-temperature molecular beam epitaxy (LT-MBE) and have studied its magnetic, transport, and magneto-optic properties.^{3,4,7} Very recently, we have extended our study to III-V based magnetic quantum heterostructures, and have successfully grown magnetic $(\text{GaMnAs})/\text{nonmagnetic (AlAs)}$ semiconductor superlattices (SLs).^{8,9} The feasibility of preparing such magnetic semiconductor SLs will open up the unique possibility of coupling the spin-related phenomena with the well established band engineering in III-V semiconductors. In this article, we report magnetotransport properties, especially Hall effect, of the $(\text{Ga}_{1-x}\text{Mn}_x)\text{As}/\text{AlAs}$ magnetic semiconductor SLs.

II. EPITAXIAL GROWTH AND STRUCTURAL PROPERTIES

We have grown $(\text{Ga}_{1-x}\text{Mn}_x)\text{As}/\text{AlAs}$ SLs on semi-insulating (001) GaAs substrates by molecular beam epitaxy

(MBE) using solid sources of Ga, As, Mn, and Al. After growing a GaAs buffer layer at 600°C under normal growth conditions, the substrate temperature was cooled to 250°C . The As_4 flux was kept on throughout the growth. During the cooling process, the reflection high energy electron diffraction (RHEED) pattern changed from (2×4) to $c(4 \times 4)$. On this $c(4 \times 4)$ -(001) GaAs surface, an AlAs layer was first grown at a growth rate of $0.3 \mu\text{m/h}$, and then a $(\text{GaMn})\text{As}$ layer was grown at $0.5 \mu\text{m/h}$. This cycle was repeated 31 times to grow a SL structure at 250°C . The film-thicknesses of the $(\text{GaMn})\text{As}$ and AlAs were $45\text{--}120 \text{ \AA}$ and $30\text{--}68 \text{ \AA}$, respectively. The Mn content x in $(\text{Ga}_{1-x}\text{Mn}_x)\text{As}$ of the SLs studied here was $0.05\text{--}0.06$.

RHEED patterns during the growth of both $(\text{GaMn})\text{As}$ and AlAs were fairly streaky despite low-temperature growth. Clear twofold streaks were observed in the RHEED on the $(\text{GaMn})\text{As}$ surface, whereas almost no reconstruction was seen on the AlAs surface. Structural characterizations by x-ray diffraction and transmission electron microscopy showed that the SL structures were formed as intended with fairly abrupt interfaces.⁸

III. MAGNETOTRANSPORT PROPERTIES

Magnetization measurements using superconducting quantum interference device (SQUID) were done on the SLs, and it was found that the SLs with wider GaMnAs layers ($\geq 70 \text{ \AA}$) were ferromagnetic, whereas the SLs with narrower GaMnAs layers ($\leq 65 \text{ \AA}$) were not ferromagnetic but paramagnetic even at 2 K. In all the ferromagnetic SLs, the easy axis of magnetization lies in-plane, like the thick ($\sim 1 \mu\text{m}$) GaMnAs films.³ The magnetic properties of $(\text{GaMn})\text{As}$ and related heterostructures can be studied through transport measurements, since all the samples show p -type conduction. Holes are supplied by Mn acceptors with which Ga sites in the GaAs zincblende structure are replaced.¹⁰ Since the ferromagnetic order of $(\text{InMn})\text{As}$ is

^{a)}Also at: PRESTO(Sakigake-21), Japan Science & Technology Corporation, 4-1-8 Honcho, Kawaguchi 332, Japan; electronic mail: masasaki@ee.t.u.-tokyo.ac.jp, t: 011-81-3-3812-2111 ext 6729, f: 011-81-3-3816-4996

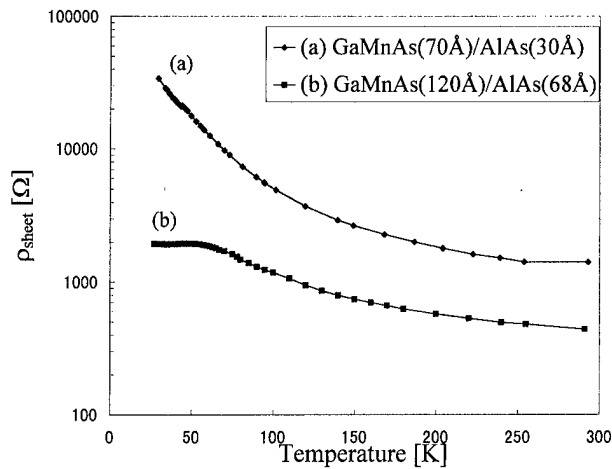


FIG. 1. Temperature dependence of the sheet resistance of the SLs; (a) sample A: (GaMn)As(70 Å)/AlAs(30 Å), (b) sample B (GaMn)As(120 Å)/AlAs(68 Å).

considered to be induced by holes,^{2,11} it is interesting to study the transport properties in such GaMnAs magnetic heterostructures.

First we have done transport measurements on the ferromagnetic (GaMn)As/AlAs SLs with relatively wider well widths (≥ 70 Å). The measurements were performed at various temperatures (2–300 K) on photolithographically patterned Hall bars with a width and a length of 200 μm and 1.3 mm, respectively. We present the results of two SL samples; one is sample A [(Ga_{0.95}Mn_{0.05})As(70 Å)/AlAs(30 Å)], and the other is sample B [(Ga_{0.94}Mn_{0.06})As(120 Å)/AlAs(68 Å)]. Magneto-optic spectra using magnetic circular dichroism (MCD) on these SLs have shown the clear evidence for quantum confinement effect and the formation of subbands.⁸ Figure 1 shows the temperature dependence of their sheet resistivity ρ_{sheet} . Sample A shows a nonmetallic (semiconducting) behavior, where the resistance increases with lowering temperature. On the other hand, the behavior of sample B is more like a metallic conduction, where the resistance is almost constant below 50 K. Since the characteristics of thick (GaMn)As films (~ 1 μm) with similar Mn content was similar to that of sample B, the difference between the two SL samples can be attributed to the difference of the GaMnAs well width. Also, there is a broad hump for sample B, which roughly corresponds to the Curie temperature T_C (~ 60 K). Such a hump is not observed in sample A, whose T_C is around 46 K, as will be estimated by our magnetotransport study below.

Next, we measured Hall effect on these ferromagnetic SLs. In general, the Hall resistivity of magnetic materials is expressed as $\rho_{\text{Hall}} = R_0 B + R_s M$, where R_0 is the normal Hall coefficient, B the magnetic flux density, R_s the extraordinary Hall coefficient, and M the magnetization. The first term represents the ordinary Hall effect caused by Lorentz force, and the second term does the extraordinary Hall effect (EHE) caused by the anisotropic scattering between carriers and local moments. When the materials are ferromagnetic (at low temperature), one can neglect the first term because the second term is much larger; $\rho_{\text{Hall}} = R_0 B$. On the other hand, at

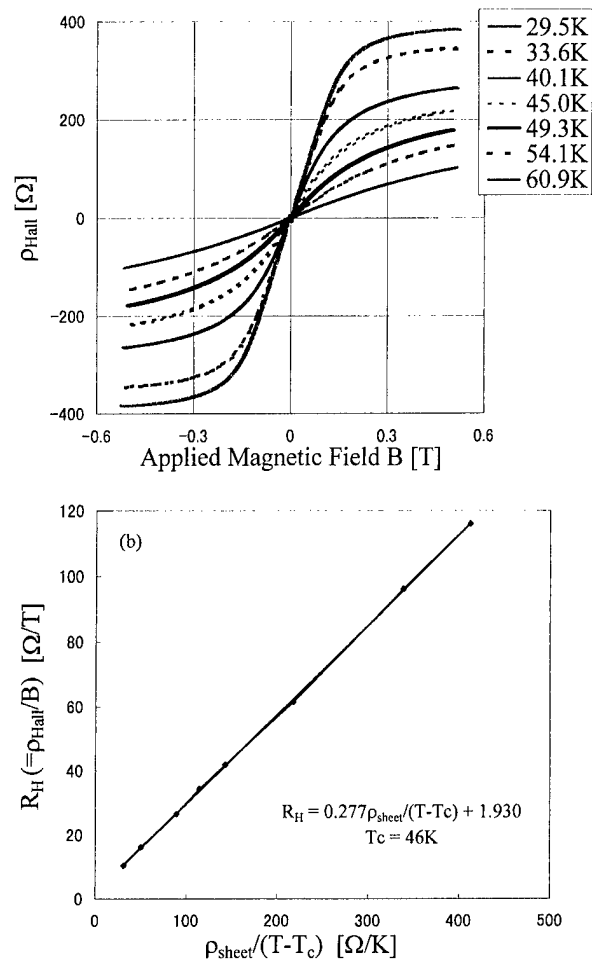


FIG. 2. (a) Hall effect of sample A (GaMn)As(70 Å)/AlAs(30 Å) SL at relatively low temperature range. (b) Temperature dependence of Hall coefficient R_H of sample A. The horizontal axis is $\rho_{\text{sheet}}/(T-T_C)$, where T_C is fitted as 46 K.

high temperature where the materials are paramagnetic, the Hall coefficient $R_H (= \rho_{\text{Hall}}/B)$ is given by

$$R_H = R_0 + \frac{c \rho_{\text{sheet}}}{\mu_0} \frac{C}{(T - T_C)} \quad (1)$$

because the magnetization M is expressed as $M = \chi H$, where χ is the magnetic susceptibility which follows the Curie-Weiss law. Here C is the Curie constant and R_s is represented as $c \rho_{\text{sheet}}$ (c : constant) for simplicity.

Figure 2(a) shows the Hall effect of sample A at low temperature range. The clear ferromagnetic behavior was observed at low temperature (< 46 K). Here only very little hysteresis loops appeared, because the easy axis of magnetization lies in-plane and the field is applied perpendicular along the hard axis. The Hall resistivity is proportional to the magnetization in ferromagnetic materials as describe above, $\rho_{\text{Hall}}/\rho_{\text{sheet}} = A M_s$ (A is constant). Then one can calculate the spontaneous magnetization M_s near the Curie temperature (low temperature range) by making the Arrott plot, $(\rho_{\text{Hall}}/\rho_{\text{sheet}})^2$ versus $B/(\rho_{\text{Hall}}/\rho_{\text{sheet}})$. Thus we have estimated the Curie temperature T_C of sample A to be 49 K.

On the other hand, from the temperature dependence of the Hall coefficient R_H at high temperature range, we can

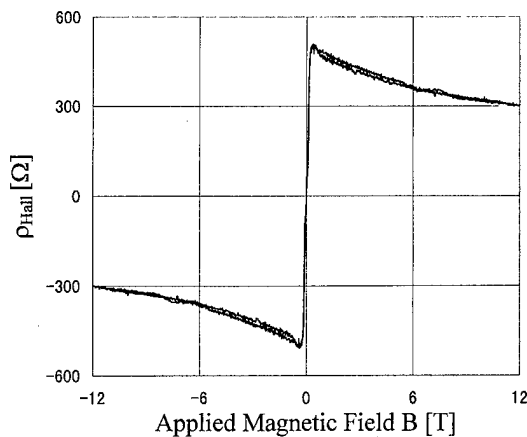


FIG. 3. Magnetic field dependence of Hall resistivity ρ_{Hall} of sample A measured at 10 K.

also estimate T_C and R_0 . We measured R_H at various temperatures and made the plot of $R_H (= \rho_{\text{Hall}}/B)$ near zero field versus $\rho_{\text{sheet}}/(T - T_C)$, as shown in Fig. 2(b), which is linear as expected from the Eq. (1). In making this plot, the value of T_C was best fitted to be 46 K, in good agreement with the estimation by the Arrott plot. Also, R_0 was estimated from Fig. 2(b) and the hole concentration p of this sample is estimated to be $1.3 \times 10^{13} \text{ cm}^{-2}$ per (GaMn)As quantum well.

Then we have done the Hall measurements of this sample under higher magnetic field (up to 12 T) at lower temperature (10 K), as shown in Fig. 3. The negative slope of Hall resistance at higher field is due to the contribution of resistivity ρ_{sheet} through $R_s = c\rho_{\text{sheet}}$. In fact, very large negative magnetoresistance (MR) was observed at high field in this sample. Assuming that the magnetization at 10 K saturates at sufficiently low field and becomes constant at high field, we can estimate R_0 , i.e., the hole concentration p , by excluding the negative MR contribution of the $\rho_{\text{sheet}}(B)$ data from the $\rho_{\text{Hall}}(B)$ data and by estimating the remaining slope of $\rho_{\text{Hall}}(B)$ at high field ($B > 10$ T). In this way, the hole concentration p of sample A is estimated to be $2.3 \times 10^{13} \text{ cm}^{-2}$ per (GaMn)As quantum well at 10 K. Although the estimation of carrier concentration of ferromagnetic samples is generally very difficult due to the strong contribution of extraordinary Hall effect, we have analyzed the magnetotransport data and have estimated it by low field and high field measurements.

We have also done the same magnetotransport measurements of sample B with wider (GaMn)As quantum wells. From the Arrott plot at low temperature range, T_C was estimated to be 63 K. From the temperature dependence of the Hall coefficient at high temperature range, T_C and hole concentration p of this sample is estimated to be also 63 K and $6.2 \times 10^{14} \text{ cm}^{-2}$ per (GaMn)As layer. Both T_C and p of sample B are higher than those of sample A.

Although both samples A and B are ferromagnetic at low temperatures, SQUID measurements revealed that no ferromagnetic phase appeared in the SL samples whose well width is less than 70 Å even at low temperature ($T = 2$ K).

The SL samples with no ferromagnetic order became high resistive at low temperature and transport measurements were difficult. This is probably because carriers are localized due to some structural fluctuations such as interface roughness. The fluctuations of the quantized energy due to interface roughness becomes rapidly large with the decrease of the quantum well width. These experimental facts strongly suggest that the ferromagnetic order in (GaMn)As is induced by carriers (holes), and the hole concentration of sample A ($1 - 2 \times 10^{13} \text{ cm}^{-2}$) gives the critical value for the ferromagnetic order in (GaMn)As quantum wells.

IV. SUMMARY

We have shown the magnetotransport properties, with emphasis on Hall effect, of a new class of III-V based magnetic (GaMn)As/nonmagnetic (AlAs) semiconductor superlattices (SLs). The SLs having relatively wide (GaMn)As layers (≥ 70 Å) are ferromagnetic at low temperature, and their hole concentrations and Curie temperatures are estimated. The hole concentrations of the (GaMn)As(70 Å)/AlAs(30 Å) SL and the (GaMn)As(120 Å)/AlAs(68 Å) SL are estimated to be $1.3 - 2.3 \times 10^{13} \text{ cm}^{-2}$ and $6.23 \times 10^{14} \text{ cm}^{-2}$ per (GaMn)As layer, and the Curie temperatures are estimated to be 46 K and 63 K, respectively.

ACKNOWLEDGMENTS

The authors wish to thank H. Tsuchiya and Professor Y. Otuka of the University of Tokyo for their help in SQUID measurements. This work is supported by the PRESTO Program of JST, Grant-in-Aid for Scientific Research on Priority Areas "Spin Controlled Nanostructures" from the Ministry of Education, Science, Sports and Culture, and the JSPS Research for the Future Program (Project No. JSPS-RFTF97P00202). Thanks are also due to the partial support from Asahi-Glass Foundation and Mitsubishi Foundation. One of the authors (T.H.) thanks the financial support from the JSPS fellowship.

¹H. Munekata, H. Ohno, S. von Molnar, A. Segmuller, L. L. Chang, and L. Esaki, Phys. Rev. Lett. **63**, 1849 (1989).

²H. Ohno, H. Munekata, T. Penny, S. von Molnar, and L. L. Chang, Phys. Rev. Lett. **68**, 2664 (1992).

³T. Hayashi, M. Tanaka, T. Nishinaga, H. Shimada, H. Tsuchiya, and Y. Otuka, J. Cryst. Growth **175/176**, 1063 (1997).

⁴T. Hayashi, M. Tanaka, T. Nishinaga, and H. Shimada, J. Appl. Phys. **81**, 4865 (1997).

⁵H. Ohno, A. Shen, F. Matsukura, A. Oiwa, A. Endo, S. Katsumoto, and Y. Iye, Appl. Phys. Lett. **69**, 363 (1996).

⁶A. Shen, H. Ohno, F. Matsukura, Y. Sugawara, N. Akiba, T. Kuroiwa, A. Oiwa, A. Endo, S. Katsumoto, and Y. Iye, J. Cryst. Growth **175/176**, 1069 (1997).

⁷K. Ando, M. Tanaka, T. Hayashi, and A. Twardowski, J. Appl. Phys., these proceedings.

⁸T. Hayashi, M. Tanaka, K. Seto, T. Nishinaga, and K. Ando, Appl. Phys. Lett. **71**, 1825 (1997).

⁹M. Tanaka, 8th International Conference on Modulated Semiconductor Structures, Santa Barbara, July 1997; J. Phys. (in press).

¹⁰R. Shioda, K. Ando, T. Hayashi, and M. Tanaka (unpublished).

¹¹S. Koshihara, A. Oiwa, S. Katsumoto, H. Hirasawa, Y. Iye, and H. Munekata, Phys. Rev. Lett. **78**, 4617 (1997).

¹²L. Berger and G. Bergmann, in *The Hall Effect and Its Applications*, edited by C. L. Chien and C. R. Westgate (Plenum, New York, 1980), p. 55.

Long-range antiferromagnetic couplings in [ZnTe|MnTe] superlattices

J. Lin and J. J. Rhyne^{a)}

University of Missouri, Columbia, Missouri 65211

J. K. Furdyna

University of Notre Dame, Notre Dame, Indiana 46556

T. M. Giebutowicz

Oregon State University, Corvallis, Oregon 97330

Magnetic semiconductor superlattices consisting of x monolayers of ZnTe alternated with y monolayers of MnTe $[(\text{ZnTe})_x(\text{MnTe})_y]$ have been grown in the zinc-blende structure by molecular beam epitaxy. For relative thin ZnTe nonmagnetic interlayers ($3 \leq x \leq 6$), neutron diffraction data show long range order within the MnTe layers and also an interlayer magnetic coupling across the semiconducting ZnTe interlayer extending over multiple bilayers. For the $x = 5$, $y = 10$; and $x = 4$, 5 , $y = 20$ superlattices at low temperature (10 K), the spins in adjacent MnTe layers couple in an inphase antiferromagnetic structure with identical spin orientations in all MnTe layers. As the temperature is raised, this ordering slowly transforms into an antiphase coupling in which alternate MnTe layers have spin directions reversed. For increasing ZnTe layer thickness, a systematic reduction in the magnetic correlation range is observed, with the correlation range reducing to approximately one MnTe layer for $x = 6$ and 7. © 1998 American Institute of Physics. [S0021-8979(98)21311-9]

I. INTRODUCTION

Magnetic semiconductor II–VI compounds grown as single crystal epitaxial structures by molecular beam epitaxy (MBE) techniques exhibit a number of unique magnetic phenomena associated with their crystal structure and exchange interactions.^{1–4} In this article, we report results on superlattices consisting of alternate layers of MnTe and nonmagnetic ZnTe [i.e., $[\text{ZnTe}|\text{MnTe}]$] that exhibit long range order within the magnetic layers, and for thin ZnTe interlayers also show magnetic coupling along the growth axis extending over several bilayers.

These MBE structures crystallize in the cubic zinc-blende (ZB) crystal structure in which the antiferromagnetic (AFM) interactions are typically close idealizations of the Heisenberg fcc model. The coupling is dominated by nearest neighbor (NN) superexchange between magnetic cations that are arranged in a tetrahedron with the mediating anion sited at the center. Because of exchange paths that involve more than one anion, the next nearest neighbor (NNN) exchange is typically reduced^{2,5} by a factor of 5 to 10. The dominance of NN AFM coupling and the tetrahedral atomic arrangement leads to near perfect exchange frustration in the intrinsic ZB AFM structure. This frustration can be removed by selective dilution, strain, or local atomic distortions.

In the $[\text{ZnTe}|\text{MnTe}]$ superlattices, the approximately 4% lattice parameter mismatch strain between layers effectively eliminates the tetrahedral spin frustration. The result is a long range ordering of the MnTe layers in a three dimensional type III AFM structure that is consistent with the dominant NN exchange and a weaker but antiferromagnetic NNN exchange. There are three possible orthogonal domain

orientations in this structure; however the epitaxial strain energies favor the single domain for which the AFM doubling of the unit cell is along the superlattice growth direction [001]. This domain preference² is temperature dependent with about 67% of the domains of [001] orientation at low temperature rising to near 100% [001] domains near T_N .

It should be noted that in bulk form MnTe crystallizes in the nonspin-frustrated NiAs structure; however it can be forced into the cubic zinc-blende (ZB) structure by alloying with a nonmagnetic constituent such as ZnTe or CdTe. In these cases, the ZB cell can be stabilized for Mn concentrations as high as 70% and the Mn spins show moderate-range antiferromagnetic correlations extending out to 30–70 Å, but no long-range order.^{2,3} MBE growth techniques extend the range of stability of the ZB structure up to 100% MnTe.

II. SUPERLATTICE MAGNETIC SCATTERING

Superlattices $[(\text{ZnTe})_x(\text{MnTe})_y]_n$ have been prepared by MBE on (001) GaAs substrates over a significant range of MnTe and ZnTe layer thicknesses. For moderately thick ZnTe interlayers (e.g., $x = 18$), long-range AFM order exists within each MnTe layer. However, neutron scattering results show no evidence of coupling between the spin structures in adjacent Mn layers.

In sharp contrast to these results on superlattices with thick ZnTe nonmagnetic interlayers, recent neutron diffraction studies on superlattices with relatively thin ZnTe interlayers (e.g., $3 \leq x \leq 7$) show interlayer exchange couplings that extend across multiple bilayers (for $x = 3, 4$, and 5). This result was quite unexpected due to the short range nature of conventional superexchange interactions.

The neutron diffraction data were taken at the University of Missouri Research Reactor using a triple axis spectrom-

^{a)}Electronic mail: jrhyne@showme.missouri.edu

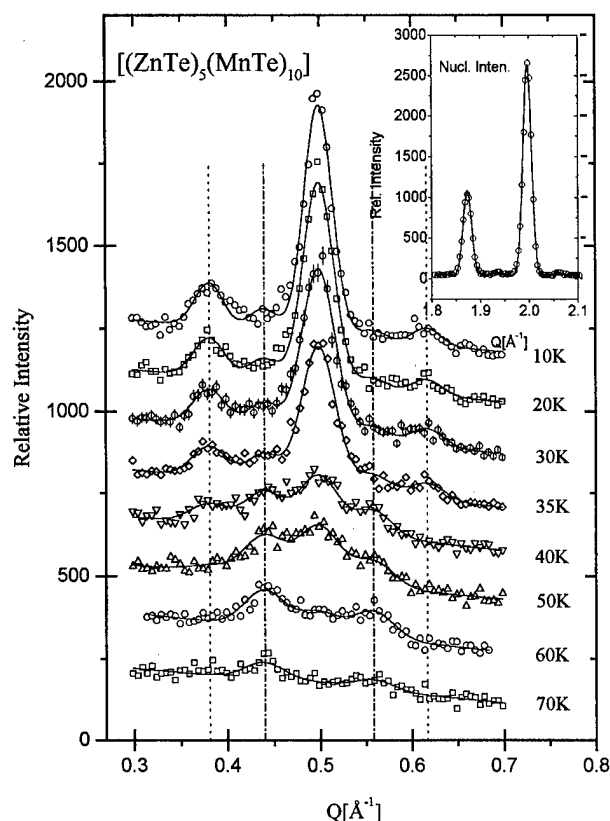


FIG. 1. Neutron scattering intensity at the $(0,1,\frac{1}{2})$ AFM reflection as a function of wave vector transfer Q in a $[(\text{ZnTe})_5(\text{MnTe})_{10}]$ superlattice at temperatures below the Néel temperature. The inset shows a scan across the nuclear principal peak. The dotted lines indicate the peak positions of the in-phase magnetic domain structure and the dot-dashed (inner set) lines the antiphase structures.

eter with an analyzer set for elastic scattering to reduce unwanted background signals. Neutrons with $E=14.7$ meV from a (002) pyrolytic graphite focusing monochromator were used with a flat analyzer and $40'-20'-20'-40'$ Soler slit collimation. This gave a q resolution for longitudinal scans of 0.018 \AA^{-1} . Longitudinal [001] scans through nuclear structure peak positions (see inset of Fig. 1) exhibited multiple bilayer harmonics that were essentially resolution limited in width, reflecting the excellent crystal quality, and a structural coherence essentially equal to the sample thickness. Transverse scans were also made through both nuclear and magnetic principal peaks to confirm the in-plane ordering. The thickness of a bilayer, Γ in Angstroms, that was obtained from the separation of the superlattice structural harmonic peaks ($\Delta Q = 2\pi/\Gamma$) was in satisfactory agreement with that determined from the growth parameters. However, the bilayer spacings obtained from the magnetic superlattice reflections was generally larger by several percent than that obtained from the nuclear harmonics. This discrepancy is currently not understood.

The type III antiferromagnetic spin ordering gives rise to purely magnetic peaks with coordinates $\{(0,k,n/2), \text{ where } n=2\ell+1\}$ corresponding to the single domain for which the doubling of the unit cell is along the growth axis. Longitudinal scans through the $(0,1,\frac{1}{2})$ AFM peak for a $[(\text{ZnTe})_5(\text{MnTe})_{10}]$ superlattice in Fig. 1 at low tempera-

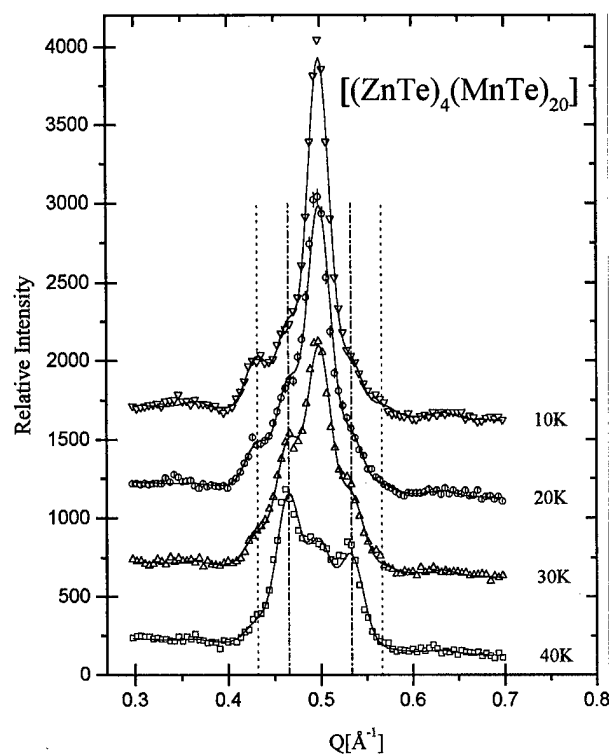


FIG. 2. Scattered intensity at the AFM reflection in a $[(\text{ZnTe})_4(\text{MnTe})_{20}]$ superlattice. In-phase and antiphase magnetic peak positions are indicated by the vertical dotted and dot-dashed lines as in Fig. 1.

ture reveal a fundamental magnetic peak and harmonic sidebands, thus demonstrating conclusively the existence of antiferromagnetic coupling extending over multiple bilayer periods. The scattering data further show the existence of two types of interlayer long range coupling, and a gradual transfer of intensity (net magnetization) from one type to the other as temperature is increased. Each MnTe layer retains the type III AFM spin configuration; however, in the first coupling scheme (in-phase), the spin direction on each site of the first atomic plane of adjacent MnTe layers is identical. In the second coupling arrangement (antiphase), the spin directions on each site of the first atomic plane are reversed between adjacent MnTe layers. The in-phase magnetic structure has the same repeat sequence as the atomic structure and results in the formation of a central magnetic peak and bilayer harmonics (indicated by the outer pair of vertical dotted lines in the figure) each with the same spacing ($\Delta Q = 2\pi/\Gamma$) as the structural peaks. The antiphase structure introduces a new set of bilayer harmonics, into the structure that are located midway between the in-phase structure harmonics as shown by the inner set of dot-dashed lines in the figure. The occurrence of both AFM structures was reproducible and also observed in superlattices from a different series,⁶ $[(\text{ZnTe})_x(\text{MnTe})_{20}]$ as shown for $x=4$ in Fig. 2. Only the in-phase structure was observed, however, in the $[(\text{ZnTe})_4(\text{MnTe})_{10}]$ superlattice.

The magnetic intensity in Figs. 1 and 2 is proportional to the square of a Mn order parameter. Figure 3 shows separately the temperature dependence of the order parameters for the "in-phase" and the "antiphase" antiferromagnetic states for the $x=5, y=10$ superlattice. The in-phase compo-

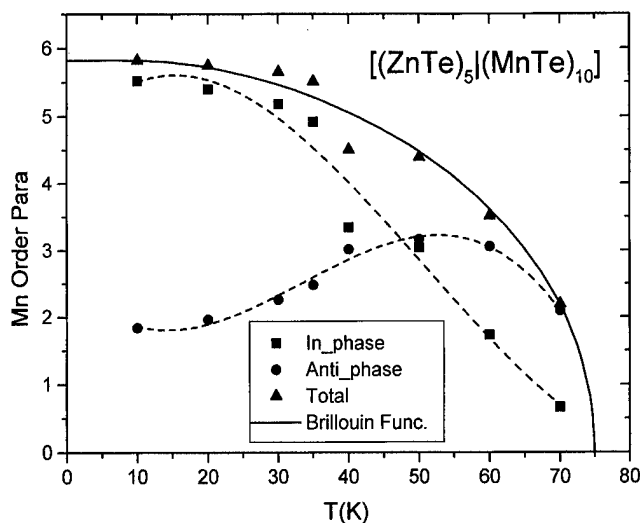


FIG. 3. Temperature dependence of the in-phase and antiphase magnetic domain intensities and the total magnetic intensity as a function of temperature. The solid line is a fit to the Brillouin function for $S=5/2$. The dotted lines are guides to the eye.

ment represents the square root of the integrated intensity of the central peak plus its two side bands separated by $2\Delta Q$, while the antiphase order is the square root of the sum of the integrated intensities of only the two intervening peaks separated by ΔQ . The total order parameter is derived from the square root of the total magnetic intensity and is well represented by a $S=5/2$ Brillouin function. The agreement with the Brillouin mean field result is worse if applied to the sum of the individual in-phase and antiphase magnetizations, which is consistent with the assumed uncorrelated nature of the two types of antiferromagnetic orderings. The results in Fig. 2 clearly show that the in-phase order predominates at low temperature, but, as the temperature is raised, it is gradually replaced by the antiphase ordering before both vanish at a common Néel temperature near 75 K. The 75 K value for the Néel temperature was essentially identical for all the superlattices studied. It should be remarked that the behavior of the two antiferromagnetic orderings reflects a change of the number of Mn spins involved in each phase with temperature; however the temperature dependence of the full Mn sublattice moment is mean field as confirmed by the Brillouin fit to the total magnetic intensity. Whether the temperature dependence of the two AFM structures is related to the temperature dependent relative population of domains parallel to and perpendicular to the growth axis is not known.

The coherence range of the magnetic order has been obtained from the width in \AA^{-1} of the principal magnetic peak after deconvoluting the resolution width. The net width ΔQ

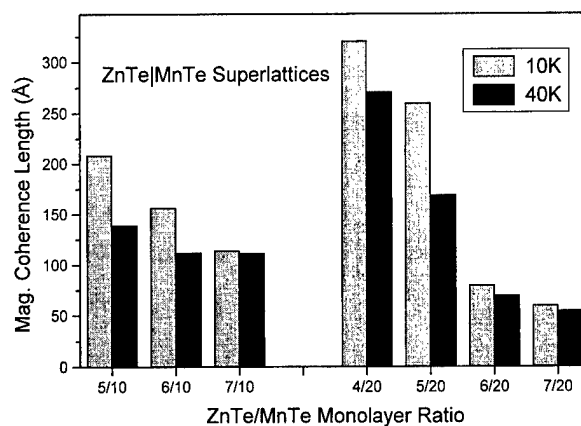


FIG. 4. Magnetic coherence lengths obtained from the width of the principal magnetic peaks for the compositions studied. Results are shown for two temperatures below the 75 K Néel temperature.

$=2\pi/\xi$ where ξ is the coherence range in \AA . Coherence ranges for the series of superlattices with 5, 6, and 7 ML ZnTe layers are shown in Fig. 4 for the series with MnTe thickness of 10 ML. Essentially the same results were obtained for the $y=20$ ML series that are also given in the figure. The results show that the coherence range drops with increasing thickness of the diamagnetic ZnTe layer and also shows a weaker dependence on temperature. For the $[\text{ZnTe}_5\text{MnTe}_{10}]$ superlattice, the correlation range at 10 K corresponds to magnetic order coherent over approximately 70 ML (nearly five bilayers), and it drops to about 35 ML (only somewhat more than 1 bilayer) for the $[\text{ZnTe}_7\text{MnTe}_{20}]$ superlattice, indicating that long range order is destroyed by ZnTe interlayer thicknesses of 6 to 7 ML. A precise determination of ξ in the samples with $(x=6,7)$ ZnTe layers is complicated by the partially unresolved main peak and bilayer harmonics.

ACKNOWLEDGMENT

The authors gratefully acknowledge the support of the National Science Foundation through Grant No. DMR95-10241.

¹D. D. Awschalom, J. M. Hong, L. L. Chang, and G. Grinstein, Phys. Rev. Lett. **64**, 2438 (1990).

²T. M. Giebultowicz, P. Klosowski, N. Samarth, T. H. Luo, J. K. Furdyna, and J. J. Rhyne, Phys. Rev. **48**, 12 817 (1993).

³T. M. Giebultowicz, P. Klosowski, N. Samarth, H. Luo, J. J. Rhyne, and J. K. Furdyna, Phys. Rev. B **42**, 2582 (1990).

⁴N. Samarth, P. Klosowski, H. Luo, T. M. Giebultowicz, J. K. Furdyna, B. Larson, and N. Otsuka, Phys. Rev. B **44**, 4701 (1991).

⁵A. Lewicki, J. Spalek, J. K. Furdyna, and R. R. Galazka, Phys. Rev. B **37**, 1860 (1988).

⁶Additional details are in J. J. Rhyne, J. Lin, J. K. Furdyna, and T. M. Giebultowicz, J. Magn. Magn. Mater. (to be published).

Magnetic measurements on the III-VI diluted magnetic semiconductor $\text{Ga}_{1-x}\text{Mn}_x\text{Se}$

T. M. Pekarek^{a)}

Department of Natural Sciences, University of North Florida, Jacksonville, Florida 32224

B. C. Crooker

Department of Physics, Fordham University, Bronx, New York 10458

I. Miotkowski and A. K. Ramdas

Department of Physics, Purdue University, West Lafayette, Indiana 47907

We have investigated the magnetic properties of $\text{Ga}_{1-x}\text{Mn}_x\text{Se}$, which represent a new class of diluted magnetic semiconductors based on a III-VI semiconductor. These are layered materials; however the local environment is tetrahedral as in the II-VI materials. In contrast to the II-VI semiconductors, the Mn substitutional atoms have direct bonds to three Se atoms and to either a Ga or Mn atom. This leads to a complex temperature dependent magnetization. In fields of 100 G and below, a broad peak is observed in the magnetization centered at 160 K. In addition, a sharp change in magnetization is observed at 119 K. In a field of 100 G, the peak has a magnitude of 3×10^{-5} emu/g above the background of 7×10^{-5} emu/g. With increasing magnetic fields, these features are broadened which is suggestive of some type of short-range antiferromagnetic ordering. At 5 K we observe a magnetization which increases linearly with field up to 6 T similar to the Van Vleck paramagnetic behavior observed in the Fe substituted II-VI semiconductors. © 1998 American Institute of Physics. [S0021-8979(98)44011-8]

I. INTRODUCTION

The new class of III-VI diluted magnetic semiconductors (III-VI DMS) include systems of the form $\text{A}_{1-x}^{\text{III}}\text{M}_x^{\text{VI}}$, where $\text{A}_{1-x}^{\text{III}}\text{B}^{\text{VI}}$ is a III-VI semiconductor and M is a transition metal ion. The III-VI semiconductors GaSe ,¹⁻⁴ InSe ,^{1,5,6} GaTe ,⁷ and GaS (Ref. 8) have received considerable interest in the last few years because they have remarkable nonlinear optical properties and are promising materials for photoelectronic applications. Although Mn has been incorporated into GaSe up to ~ 1 at. % nominal level (in samples grown from the melt), this work is focused on photoluminescence,^{3,9,10} photoconductivity,^{5,10} Hall effect,³ electron spin resonance,^{11,12} and deep-level transient spectroscopy measurements.³ No magnetization studies have been reported.

Like the II-VI DMS,¹³ substitutional magnetic ions in the III-VI DMS are in a tetrahedral environment. However, in sharp contrast to the II-VI DMS, the III-VI semiconducting host is two dimensional (Fig. 1). Each $\text{Ga}_{1-x}\text{Mn}_x\text{Se}$ layer is comprised of a top two-dimensional layer of Se ions, two middle layers of Ga ions, and a bottom layer of Se ions as shown in Fig. 1(a). Within each four atom thick layer, the bonds are covalent.¹⁴ The weak van der Waals bonding between the stacked four atom thick layers further enhances the two-dimensional nature of this crystal.¹⁴

Because each Ga ion has three neighboring Se ions as well as another Ga ion, substitutional magnetic ions would experience a host of different local environments. In III-VI DMS, directly bonded Mn-Mn pairs [shown as a dotted line in Fig. 1(a)] are expected which opens a channel for a direct

exchange between magnetic ions. In addition, both Mn-Se-Mn superexchange interactions (common in II-VI DMS), and Mn-Ga-Se-Mn pairings are also possible [Figs. 1(a) and 1(b)].

In this article we present magnetization measurements taken on bulk $\text{Ga}_{1-x}\text{Mn}_x\text{Se}$. The crystal structure of $\text{Ga}_{1-x}\text{Mn}_x\text{Se}$ is analyzed in terms of several distinct configurations of the magnetic ions within the III-VI lattice structure leading to a complex magnetic behavior.

II. EXPERIMENTAL DETAILS

Single-crystalline $\text{Ga}_{1-x}\text{Mn}_x\text{Se}$ samples were taken from a boule with a nominal concentration of $x=0.05$. Typically, samples grown by the vertical Bridgman method yield actual concentrations less than the nominal value. Atomic absorption spectroscopy (AAS) was performed yielding a value for the concentration of $x=0.012$. It is expected that the solubility limit for Mn in GaSe is higher than the amount of Mn incorporated into this sample and that higher concentrations will be achieved as the crystal growing technology for this system develops further.

Magnetic measurements were made between 1.5 and 324 K in fields up to 6 T using a commercial superconducting quantum interference device (SQUID) magnetometer. The diamagnetic susceptibility -2.0×10^{-7} emu/g G for GaSe has been subtracted from the data.¹⁵

III. EXPERIMENTAL RESULTS AND DISCUSSION

$\text{Ga}_{1-x}\text{Mn}_x\text{Se}$ exhibits magnetic behavior that is significantly different from that observed in II-VI DMS. Magnetization versus temperature measurements taken in a 0.01, 0.05, 0.1, 1, and 6 T field are shown in Fig. 2. Focusing on

^{a)}Electronic mail: tpekarek@gw.unf.edu

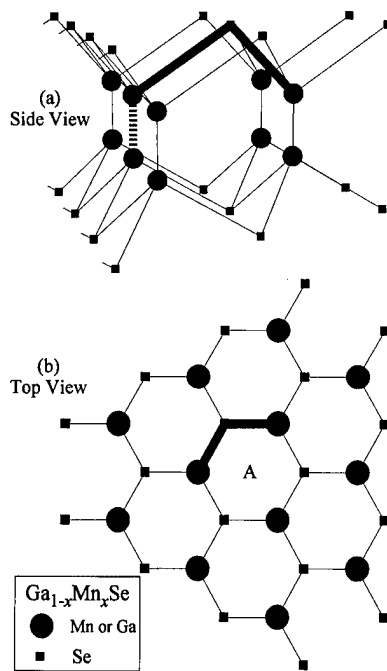


FIG. 1. Crystal structure for $\text{Ga}_{1-x}\text{Mn}_x\text{Se}$. The big solid circles are the Ga lattice sites in GaSe or the substitutional Mn lattice sites in $\text{Ga}_{1-x}\text{Mn}_x\text{Se}$. The small squares are the Se lattice sites. (a) Cross section of a four atom thick layer. The tetrahedral environment of the Ga or Mn lattice sites is emphasized with three neighboring Se ions as well as another Ga or Mn ion. The direct Mn-Mn bond is shown by the bold dotted line. The bold solid line emphasizes the bonds in a Mn-Se-Mn pair. A Mn-Ga-Se-Mn pair can be seen where the bold dotted line is the bond between the Ga and the first Mn ions and the bold solid lines then completes the Ga-Se-Mn bonds. (b) Top view of a single four atom thick layer. The top and bottom Mn ions are in a vertical line as are the Se ions. The bold solid lines are the bonds in the Mn-Se-Mn pair. The pair Mn~Se-Mn (where ~ denotes a van der Waals bond between layers) would have a van der Waals bond between the Mn (in the four atom thick layer shown) and a Se ion directly above followed by a covalent bond to a Mn ion located at position A. The second layer would then be offset to the right by one half of the hexagon width.

the 0.01 T data, the key features are a broad peak between 120 and 195 K with an apex at 160 K and a sharp change in magnetization at 119 K. With increasing field, the peak appears to broaden and shift to lower temperatures, until it is barely visible above a rising background signal by 6 T. The sharp drop at 119 K is also rapidly broadened by the magnetic field.

Given the observed broadening of these features in increasing magnetic fields, the expected antiferromagnetic interactions between the magnetic ions, and the two-dimensional crystal structure, our data is suggestive of short-range two-dimensional antiferromagnetic ordering.¹⁶ The sharp drop in magnetization at 119 K could then be interpreted as a transition to three-dimensional order as the inter-layer coupling becomes important. Given the low concentration of magnetic ions ($x=0.012$) as well as the increasing low temperature magnetization discussed below, it is likely that any order is short-range.

We also cannot rule out the possibility that microcrystals of MnSe exist within our samples and are producing the observed magnetization signal. We note that the Néel temperature of thin films of MnSe was found to be 115 K by

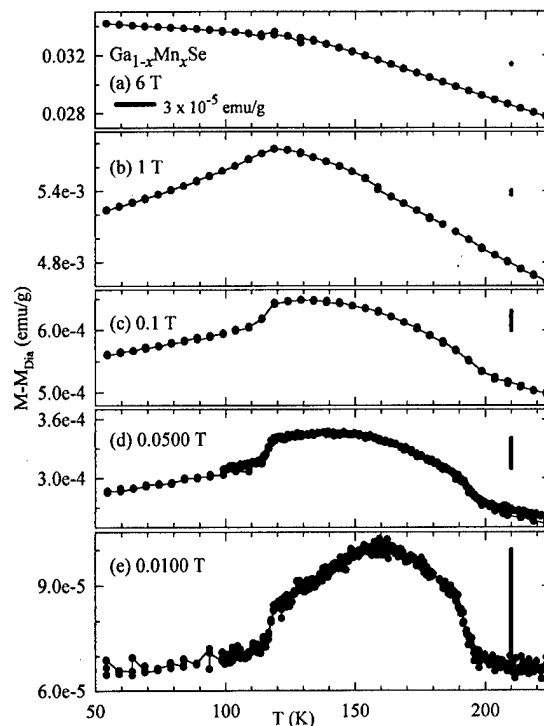


FIG. 2. Magnetization vs temperature for $\text{Ga}_{1-x}\text{Mn}_x\text{Se}$ in a 0.0100, 0.0500, 0.1, 1, or 6 T field. The diamagnetic contribution due to GaSe has been subtracted. The solid vertical bar at 210 K in each graph is 3×10^{-5} emu/g tall to aid in a quick comparison of scales.

Samarth *et al.*¹⁷ which is very close to the observed sharp feature at 119 K.

However, Ishchenko and co-workers^{11,12} found that the bulk of the manganese in their GaSe:Mn crystals did go in as substitutional Mn^{2+} ions at the gallium lattice sites and have the ϵ -GaSe layer structure.¹⁴ The ϵ -GaSe layer structure has a two-layer basis. The top layer is offset to the right by one half of the hexagon width [i.e., one pair of Ga/Mn lattice sites is directly above position A in Fig. 1(b)]. Lee *et al.* also found the ϵ -GaSe structure for their GaSe:Mn crystals.¹⁰ Shigetomi argued from conductivity measurements that a small fraction of their Mn was located in the interstices or between the layers of GaSe.³

Turning now to the low temperature behavior of these samples, we show in Fig. 3(a) the temperature dependence of the magnetization in $\text{Ga}_{1-x}\text{Mn}_x\text{Se}$ at 1 T between 5 and 325 K. As can be seen, there is a background magnetization that monotonically increases, in addition to the broad peak discussed above. The background rises above the peak at low temperatures and is rapidly increasing.

To further investigate this background we show in Fig. 3(b) data on magnetization versus field taken at 5 K, which is well below the broad peak discussed above. As can be seen the increase in magnetization is nearly linear in magnetic field with $M/H=6.2 \times 10^{-7}$ emu/g G. This is much weaker than a $S=5/2$ Brillouin function represented in the figure as a dotted and dashed lines for $x=2 \times 10^{-4}$ and $x=0.012$, respectively. Further, even at 6 T there is no evidence that the magnetization is saturating. The linear field dependence is similar to that seen in Fe based II-VI semiconductors. In that case it is attributed to Van Vleck paramagnetism.¹⁸

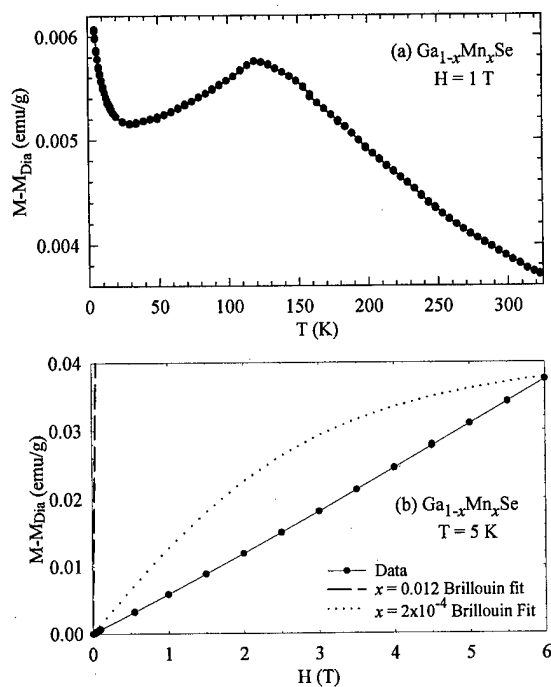


FIG. 3. The magnetization data for $\text{Ga}_{1-x}\text{Mn}_x\text{Se}$ are shown by solid circles. (a) Magnetization vs temperature in a 1 T field. (b) Magnetization versus field at 5 K. The dotted and dashed lines are a $S = 5/2$ Brillouin response for $x = 2 \times 10^{-4}$ and $x = 0.012$, respectively. The diamagnetic contribution due to GaSe has been subtracted from the data.

Some of the magnetic behavior of the II-VI DMS has been successfully understood assuming that the transition metal ions are randomly incorporated into the host lattice. The theory was then developed taking into consideration the fraction of magnetic ions incorporated as singlets, doublets, triplets, etc., assuming only the shortest-range interactions.¹³ Looking within a single layer in Fig. 1 we see that if Mn substitutionally replaces Ga in this material, then the probability p of a Mn being a singlet is $p = (1 - x)$.¹³ There is one Mn-Mn neighbor [$p = x(1 - x)$], six Mn-Se-Mn neighbors [$p = 6x(1 - x)$], and six Mn-Ga-Se-Mn neighbors [$p = 6x(1 - x)$] (note that there are two equivalent exchange channels between the two Mn ions). If we also consider interlayer couplings, with one Mn ion in each layer there are three Mn~Se-Mn neighbors, three Mn-Ga~Se-Mn neighbors, and three Mn~Se-Ga-Mn neighbors (note that ~ denotes a van der Waals bond between layers).

For a concentration of $x = 0.012$ this leads to 1% of the Mn atoms having direct bonds with a second Mn atom. We expect this interaction to be much stronger than the superexchange interactions and would tentatively ascribe the peak at 160 K to these pairs and larger clusters. We note that the

saturation magnetization of the directly bonded Mn with $S = 5/2$ spins would be roughly 0.025 emu/g. The fact that this number is a factor of 700 larger than the observed peak height, might be expected if the peak arises from antiferromagnetic ordering of the Mn-Mn pairs. The remaining 99% of the Mn atoms, which are not involved in direct bonds with a second Mn atom, would then contribute to the low temperature behavior.

IV. CONCLUSIONS

Mn substituted III-VI semiconductors represent a new class of diluted magnetic semiconductors. We have studied $\text{Ga}_{1-x}\text{Mn}_x\text{Se}$ and found a magnetization peak at 160 K that is not observed in the II-VI DMS. We tentatively ascribe this peak to direct Mn-Mn bonds in this material. In addition, we find a linear magnetization as a function of field at low temperatures which is reminiscent of the Fe based II-VI materials.

ACKNOWLEDGMENTS

The authors wish to thank R. Sensemeier for his work on the AAS measurements. This work was supported by the National Science Foundation (NSF) under Material Research Group Grant Nos. DMR-92-21390 and DMR-94-00415.

- ¹A. Segura, J. Bouvier, M. V. Andrés, F. J. Manjón, and V. Muñoz, Phys. Rev. B **56**, 4075 (1997).
- ²S. Nüsse, P. H. Bolivar, H. Kurz, V. Klimov, and F. Levy, Phys. Rev. B **56**, 4578 (1997).
- ³S. Shigetomi, T. Ikari, and H. Nakashima, J. Appl. Phys. **76**, 310 (1994).
- ⁴L. T. Vinh, M. Eddrief, J. E. Mahan, A. Vantomme, J. H. Song, and M. A. Nicolet, J. Appl. Phys. **87**, 7289 (1997).
- ⁵S. Nüsse, P. H. Bolivar, H. Kurz, F. Levy, A. Chevy, and O. Lang, Phys. Rev. B **55**, 4620 (1997).
- ⁶D. Errandonea, A. Segura, J. F. Sánchez-Royo, V. Muñoz, P. Grima, A. Chevy, and C. Ulrich, Phys. Rev. B **55**, 16217 (1997).
- ⁷J. Z. Wan, J. L. Brebner, and R. Leonelli, Phys. Rev. B **53**, 15413 (1996).
- ⁸F. J. Manjón, A. Segura, and V. Muñoz, J. Appl. Phys. **81**, 6651 (1997).
- ⁹Yu P. Gnatenko, Yu I. Zhirko, and P. A. Skubenko, Sov. Phys. Solid State **30**, 1540 (1988).
- ¹⁰S. Lee, S. Hahn, C. Chung, S. Yun, and W. Kim, Solid State Commun. **60**, 453 (1986).
- ¹¹V. I. Kononov, S. S. Ishchenko, and S. M. Okulov, Sov. Phys. Solid State **22**, 1070 (1980).
- ¹²S. S. Ishchenko, S. M. Okulov, G. B. Abdullaev, G. L. Belen'kii, V. G. Grachev, M. F. Deigen, R. Kh. Nani, E. Yu. Salaev, and Yu. G. Samenov, Sov. Phys. Solid State **17**, 1168 (1975).
- ¹³See, for example, in *Semiconductors and Semimetals*, edited by J. K. Furdyna and J. Kossut (Academic, Boston, 1988), Vol. 25.
- ¹⁴S. Jandl, J. L. Brebner, and B. M. Powel, Phys. Rev. B **13**, 686 (1976).
- ¹⁵K. Dobleto, Yu A. Markhuda, A. V. Anikin, and A. Ashirov, Bull. Acad. Sci. SSSR, Inorg. Mater. (English Transl.) **14**, 246 (1978).
- ¹⁶L. J. de Jongh and A. R. Miedema, Adv. Phys. **23**, 1 (1974).
- ¹⁷N. Samarth, P. Kłosowski, H. Luo, T. M. Giebutowicz, J. K. Furdyna, J. J. Rhyne, B. E. Larson, and N. Otsuka, Phys. Rev. B **44**, 4701 (1991).
- ¹⁸R. M. Villeret, S. Rodriguez, and E. Kartheuser, J. Appl. Phys. **67**, 4221 (1990).

Second harmonic spectroscopy and control of domain size in antiferromagnetic YMnO_3

M. Fiebig,^{a)} D. Fröhlich, and S. Leute

Institut für Physik, Universität Dortmund, 44221 Dortmund, Germany

R. V. Pisarev

Ioffe Physical Technical Institute of the Russian Academy of Sciences, St. Petersburg 194021, Russia

A novel technique for the visualization of antiferromagnetic domains making use of second harmonic generation is used to study the easy-plane antiferromagnet YMnO_3 . Domain states characterized by small, medium, or large domains are observed. Switching from one state to another can be achieved by a heat treatment *above* T_N and subsequent cooling *below* T_N . Contributions to the mechanism of this unusual behavior of domains are discussed. © 1998 American Institute of Physics. [S0021-8979(98)21411-3]

Domains, domain walls, and their behavior as a function of external fields and material parameters is one of the most fundamental and technologically important problems of magnetic solids. The configurational details of domains in substances with a spontaneous magnetization, as arising from the competition of various contributions to the total energy, are discussed in many articles,¹ and a large number of experimental methods for the investigation of ferro- or ferrimagnetic domains have been developed.²⁻⁴ There are, however, merely a few publications on the formation of domains and domain walls in antiferromagnets.^{1,5,6} One of the reasons for this is the very limited number of experimental techniques for the visualization of antiferromagnetic (AFM) domains.⁷

In this article, we report the study of the afm domain structure and its variation with temperature in YMnO_3 using a recently developed method of nonlinear optical spectroscopy.⁷⁻⁹ Domains in YMnO_3 show a behavior drastically different from that in any other known AFM crystal. We have found that by suitable annealing *above* T_N samples can be switched into different states characterized by small, medium, or large domains *below* T_N .

At low temperature, hexagonal YMnO_3 is antiferromagnetic and ferroelectric. The crystal structure below the ferroelectric Curie temperature $T_C = 930$ K is described by the noncentrosymmetric point group $6mm$.¹⁰ The magnetic properties of YMnO_3 arise from the $\text{Mn}^{3+}(3d^4)$ ions in the high-spin state, $S = 2$. Below $T_N = 74$ K, the spins of the six Mn^{3+} ions in the unit cell are ordered antiferromagnetically in a triangular structure with all spins perpendicular to the polar axis. The corresponding magnetic point group is $6mm$.^{11,12}

Above T_N , second harmonic (SH) generation in YMnO_3 is allowed in the electric-dipole approximation due to the time-invariant (*i* type) susceptibility $\chi_{ijk}(i)$. This contribution, which is solely related to the symmetry of the crystal lattice, vanishes for propagation of light along the C_6 axis ($\mathbf{k} \parallel \mathbf{z}$). Below T_N , electric-dipole contributions to SH are

also allowed due to the time-noninvariant (*c* type) susceptibility $\chi_{ijk}(c)$,¹³ which is related to the magnetic structure of the crystal

$$P_x(2\omega) = \epsilon_0 \chi_{xxx}(c) [E_x^2(\omega) - E_y^2(\omega)], \quad (1)$$

$$P_y(2\omega) = -2\epsilon_0 \chi_{xxx}(c) E_x(\omega) E_y(\omega). \quad (2)$$

The nonlinear polarizations $P_x(2\omega)$ and $P_y(2\omega)$ change phase by 180° when passing from one AFM domain to another, which is accompanied by a sign reversal of any AFM order parameter and thus of $\chi_{xxx}(c)$.

Flux-grown (0001) single crystals, both as-grown and polished, with a thickness of 0.1–0.5 mm along the (0001) axis and lateral dimensions 1–4 mm were used in the experiments. Optical absorption spectra were found to be in agreement with previously reported data.¹⁴ In order to find the SH energy most suitable for imaging of domains, the SH spectrum was measured at low temperature (Fig. 1). In accordance with Eqs. (1) and (2), there was no difference in the spectra for right and left circularly polarized light. As expected, no SH was observed for $T > T_N$.

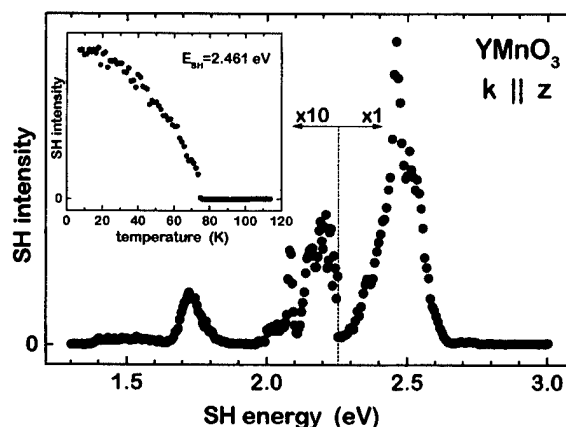


FIG. 1. SH spectrum of YMnO_3 at $T = 8$ K for light propagating along the optical axis $C_6(z)$. The spectra with right and left circularly polarized light are identical. The inset shows the temperature dependence of the SH signal at 2.461 eV.

^{a)}Electronic mail: fiebig@ap.t.u-tokyo.ac.jp

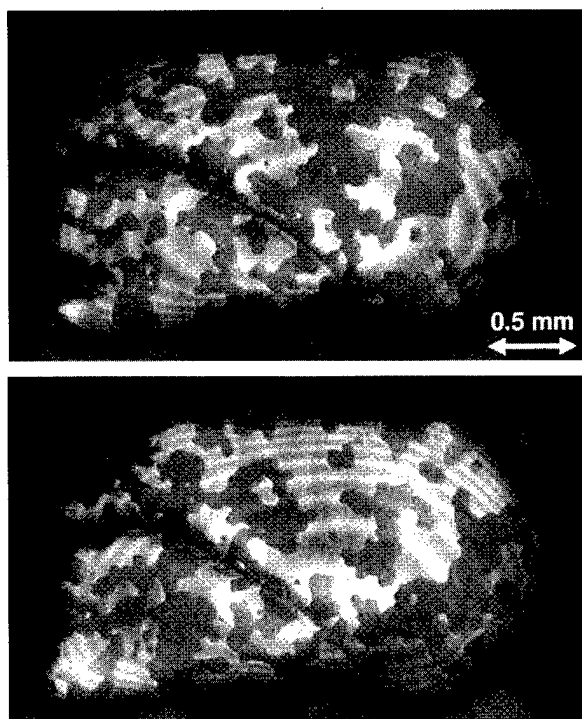


FIG. 2. Image of 180° AFM domain in a polished sample at $T = 8$ K showing the interchange of the contrast between domains by shifting the phase between time-invariant and time-noninvariant SH contributions by 180° . This large domain state can be obtained via path 5 in Fig. 4.

Recently, a new optical method for topography of AFM domains was introduced. It was shown that visualization of 180° AFM domains is possible when there is interference of c - and i -type contributions to the SH.⁷⁻⁹ If both contributions are (1) *intrinsically* present and (2) of the same order of magnitude, domains can be visualized just by projecting the SH light emitted from the sample on a CCD camera, where the phase shift between the c - and i -type light field is converted into an intensity contrast. Due to restriction (1), this method is suitable only for substances with a favorable point symmetry and only in those spectral regions which meet restriction (2). In most substances, the conditions (1) and (2) are not met, and in order to visualize the domain structure the time-noninvariant SH signal originating in the magnetic ordering of the crystal has to be superimposed with an *externally* generated time-invariant SH light field, e.g., from a crystalline quartz plate. By proper adjustment of phases and amplitudes of the c - and the i -type light fields, their interference on the camera can lead to a high contrast between the brightness of different domains. With circularly polarized light, the phase of the reference light field can be controlled by rotating the quartz plate whereas the amplitude can be adjusted by making use of optical filters and spectral oscillations of the SH intensity from the quartz plate known as Maker fringes.¹⁵ Details of this novel technique and the experimental setup are given in Ref. 7. The information on the spatial distribution of domains is contained in the phase and the amplitude of the c -type SH field from the sample, which is different for domains with different orientations of the AFM order parameter. By the invention of the *external ref-*

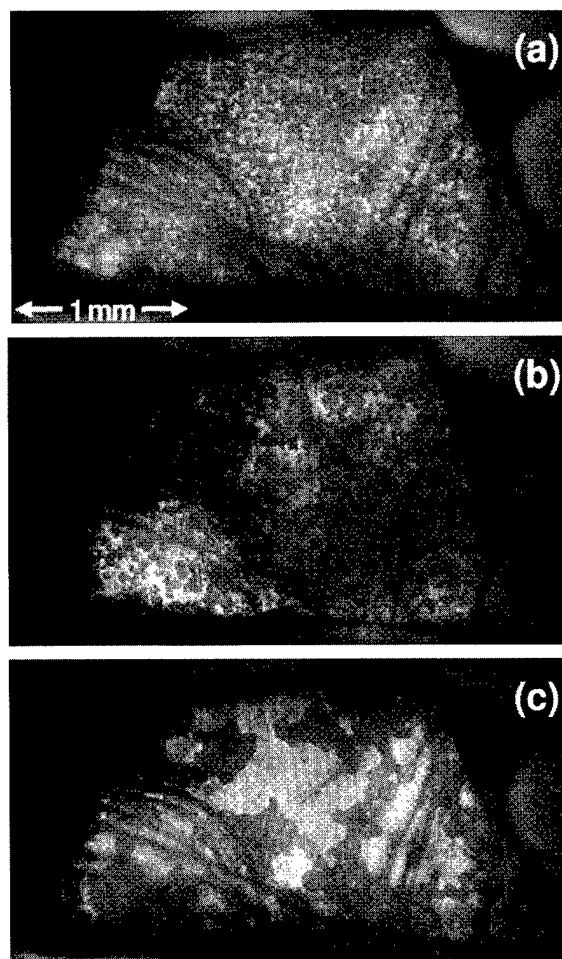


FIG. 3. Three images of small (a), medium (b), and large (c) domain states in an as-grown sample. Access to each of these states can be achieved via heat treatment processes shown in Fig. 4.

erence, SH domain topography can now be applied to *any* antiferromagnet exhibiting a sufficiently strong time-noninvariant contribution to the SH signal.

Figure 2 shows two images of AFM domains in a polished sample at $T = 8$ K. Dark and bright regions correspond to the respective 180° domains. Instead of straight or slightly curved planes which are typical for most antiferromagnets,^{3,16-18} the walls in YMnO_3 look like patchwork with some small domains surviving inside larger ones. The contrast in the two images is interchanged by changing the phase of the reference field from the quartz plate by π . Images with a contrast of 3:1 up to 20:1 between neighboring domains are obtained with exposure times of 3–5 min. Without external SH reference, the contrast between domains vanishes, although domain walls remain visible.

No changes of the domain structure were observed when the temperature was varied below T_N . However, striking changes occurred after heating and cooling the sample through T_N . Figure 3 shows three images of AFM domains in an as-grown sample, which are characterized by small- (a), medium- (b), and large-domain states (c). Here we refer to the average size of the domains throughout the whole sample. Each cycle of the sample through T_N resulted in a

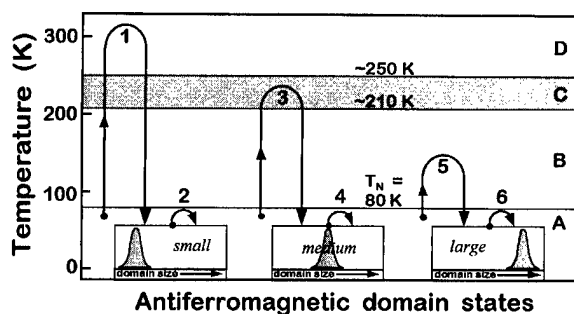


FIG. 4. Diagram showing thermal routes to different AFM states, characterized by domains of small, medium, and large size. Distribution functions of domain size for each state are shown schematically.

different domain pattern even if the distribution function did not change. Cooling rates from 1 to 20 K/min and dwell times of 0–20 min at the annealing temperature $T_a > T_N$ were found to have no influence on the achievement of different domain states. In the small-domain state, the dimension of domains was about 20–40 μm . Smaller domains ($< 10 \mu\text{m}$) which were not resolved by the optical system might have been present. In the large-domain state, the average dimension of domains was larger by an order of magnitude with some of the domains extending over the entire sample. No pronounced difference was noticed between polished and as-grown samples. Domain patterns are different in detail on opposite sides of the sample, but they both belong to the same domain state.

The AFM domain patterns look different in large- and small-domain states after each cycle through T_N . This indicates that memory effects are absent or very small. Furthermore it disproves correlations to ferroelectric domains.¹⁹ YMnO_3 exhibits a rather large electric coercive field $E_C = 2.5 \times 10^6 \text{ V/m}$ at $T = 300 \text{ K}$.¹⁰ Thus no change of the ferroelectric domain structure is expected below room temperature.

Figure 4 shows how different states can be achieved via different heat treatments: The temperature is uniformly increased from below T_N up to a certain temperature T_a above T_N and then decreased again below T_N . The final domain state solely depends on T_a . Samples can be transformed into small- (path 1), medium- (path 3), or large-domain states (path 5) for values of temperatures $T_a > 250 \text{ K}$ (region D), $210 \text{ K} < T_a < 250 \text{ K}$ (region C), and $T_N < T_a < 210 \text{ K}$ (region B), respectively. Cooling or warming within region A does not change the domains (paths 2, 4, 6).

This is the first observation of such behavior of AFM domains. The most surprising result is that the average size of domains is sensitive to the annealing temperature T_a (larger than T_N) in the sense that the smaller the domains the higher T_a has been. The case of YMnO_3 thus contrasts with all previous observations, and the mechanism behind the observed behavior of domains remains rather unclear. Since the domain structure does not change at all below T_N , pinning effects are without any doubt strong and have to be taken

into account. Furthermore, the average domain size is influenced by various competing contributions to the free energy of the sample describing the formation of domain walls. Exchange and anisotropy energy, entropy and the bending of walls may be mentioned.^{5,6}

In conclusion, by use of nonlinear optical spectroscopy and a novel imaging technique for AFM domains, we have observed an unusual behavior of 180° domains in the easy-plane triangular antiferromagnet YMnO_3 . Depending on the annealing temperature $T_a > T_N$, the sample can be transformed into different states below T_N which are characterized by domains of small, medium, or large average size. The small-domain state with a large density of AFM domain walls is formed in crystals annealed at a sufficiently high temperature. This result contrasts with all previous observations of domains in antiferromagnets.

The wide applicability of nonlinear optical domain topography should stimulate further experimental studies, which should help to develop a plausible model for the observed static and dynamic properties of AFM domains and domain walls.

ACKNOWLEDGMENTS

The crystals used in this study were grown by I. E. Mylnikova. The financial support by the Deutsche Forschungsgemeinschaft and the Graduiertenkolleg "Festkörperspektroskopie" is greatly appreciated. The work of R.V.P. was supported in part by the Russian Basic Research Foundation and by the INTAS.

- ¹ A. Hubert, *Theorie der Domänenwände in geordneten Medien* (Springer, Berlin, 1974); A. P. Malozemoff and J. C. Slonczewski, *Magnetic Domain Walls in Bubble Materials* (Academic, New York, 1979).
- ² D. J. Craik and R. S. Tebble, *Ferromagnetism and Ferromagnetic Domains* (North-Holland, Amsterdam, 1965).
- ³ M. Schlenker and J. Baruchel, *Ferroelectrics* **162**, 299 (1994); J. Baruchel, *Physica B* **192**, 79 (1993).
- ⁴ L. Dobrzynski and K. Blinowski, *Neutrons and Solid State Physics* (Ellis Horwood, London, 1994).
- ⁵ Y.-Y. Li, *Phys. Rev.* **101**, 1450 (1956).
- ⁶ I. M. Lifshitz, *Sov. Phys. JETP* **15**, 939 (1962); *J. Exptl. Theor. Phys.* **42**, 1354 (1962).
- ⁷ M. Fiebig, D. Fröhlich, and S. Leute, *Appl. Phys. B* (in press).
- ⁸ M. Fiebig, D. Fröhlich, G. Sluyterman, and R. V. Pisarev, *Appl. Phys. Lett.* **66**, 2906 (1995).
- ⁹ M. Fiebig, D. Fröhlich, B. B. Krichevskov, and R. V. Pisarev, *Phys. Rev. Lett.* **73**, 2127 (1994).
- ¹⁰ Landolt-Börnstein, *Numerical Data and Functional Relationships, New Series, III/16a*, edited by K.-H. Hellwege (Springer, New York, 1981).
- ¹¹ G. M. Nedlin, *Sov. Phys. Solid State* **6**, 2156 (1965).
- ¹² E. F. Bertaut, M. Mercier, and R. Pauthenet, *J. Phys. (Paris)* **25**, 550 (1965).
- ¹³ R. R. Birss, *Symmetry and Magnetism* (North-Holland, Amsterdam, 1966).
- ¹⁴ K. Kiritayakirana, P. Berger, and R. V. Jones, *Opt. Commun.* **1**, 95 (1969).
- ¹⁵ Y. R. Shen, *The Principles of Nonlinear Optics* (Wiley, New York, 1984).
- ¹⁶ P. J. Brown, *Physica B* **192**, 14 (1993).
- ¹⁷ V. V. Eremenko, N. F. Kharchenko, Y. G. Litvinenko, and V. N. Naumenko, *Magneto-Optics and Spectroscopy of Antiferromagnets* (Springer, New York, 1992).
- ¹⁸ W. L. Roth, *J. Appl. Phys.* **32**, 2000 (1960).
- ¹⁹ M. Safrankova, J. Fousek, and S. A. Kizhaev, *Czech. J. Phys., Sect. B* **17**, 173 (1967).

Giant Magnetoimpedance

Floyd B. Humphrey, Chairman

High frequency behavior of soft magnetic wires using the giant magnetoimpedance effect

P. Ciureanu,^{a)} M. Britel, D. Ménard, and A. Yelon*Département de Génie Physique and Groupe de Recherche en Physique et Technologie des Couches Minces, École Polytechnique, Montréal, C.P. 6079, succ. C-V, Québec H3C 3A7, Canada*

C. Akyel

Département de Génie Électrique, École Polytechnique, Montréal, C.P. 6079, succ. C-V, Québec H3C 3A7, Canada

M. Rouabhi and R. W. Cochrane

Département de Physique and Groupe de Recherche en Physique et Technologie des Couches Minces, Université de Montréal, Montréal, Québec H3C 3J7, Canada

P. Rudkowski and J. O. Ström-Olsen

MXT Inc., 1744 William St., Suite 104, Montréal, Québec H3J 1R4, Canada

We have investigated the high frequency properties of several amorphous and polycrystalline wires mounted as inner conductors in coaxial lines. A static magnetic field was applied along the wire axis. The impedance spectra of the wires, measured using a network analyzer, show peaks in the real part of the impedance, which shift to higher frequency with the strength of the static field, a behavior typical of ferromagnetic resonance. The theoretical resonance condition predicts a straight line on an $f_0^2 - H_0$ plot, where f_0 is the resonance frequency and H_0 is the resonant field, whose slope depends only on the saturation magnetization, M_s , of the material. All our wires obey this relation, and the values of M_s calculated from the slopes are in good agreement with those measured directly using a vibrating sample magnetometer. © 1998 American Institute of Physics.

[S0021-8979(98)24011-4]

I. INTRODUCTION: GIANT MAGNETOIMPEDANCE AT SATURATION

The giant magnetoimpedance (GMI) at saturation is a magnetotransport effect recently observed in soft magnetic wires driven by ac current. It consists of a large change in the voltage drop across a wire subject to an axial dc magnetic field. As the voltage drop is proportional to the wire impedance when the current amplitude is fixed, the relative change in impedance, $\Delta Z/Z$, which occurs is:

$$\frac{\Delta Z}{Z} = \frac{|Z(H)| - |Z(H_{\text{ref}})|}{|Z(H_{\text{ref}})|},$$

where H is the axial magnetic field, $H_{\text{ref}}=0$, and $Z(H, \omega) = \text{Re } Z + j \text{Im } Z$. The GMI effect relies on phenomena known for many years: the skin effect and ferromagnetic resonance. GMI became noticed only after recent advances in materials technology resulted in the fabrication of ultrathin ferromagnetic wires.

The oscillating magnetic field created by the drive current in the wire is circumferential, as is the magnetic field in a transverse electromagnetic (TEM) propagating mode coaxial line. These fields are present in the wire only in a thin outer shell. A circumferential permeability, μ_ϕ , can be as-

sociated with these fields and the circumferential magnetization of the wire.

In the case of a permalloy wire at low to moderate frequencies (0.1–100 MHz), the GMI effect is negative and shows a significant decrease of the wire impedance when a saturating (200 Oe) magnetic field is applied. This phenomenon was explained by the influence of the technical saturation on the skin effect.^{1,2} In fact, the effective skin depth $\delta = \sqrt{2/\omega \mu_\phi \sigma}$ increases when the circumferential permeability

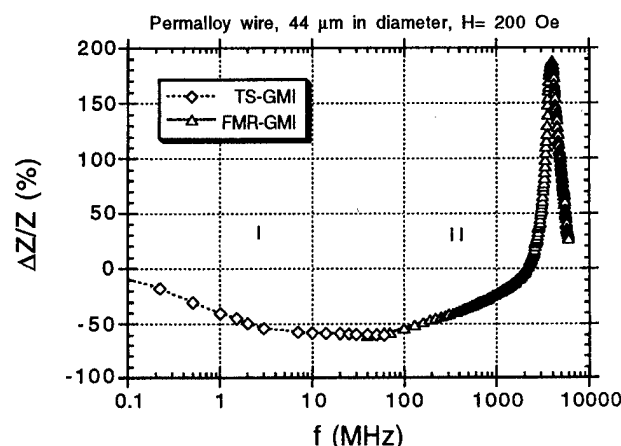


FIG. 1. Skin-effect in the TS and FMR regimes of GMI for a HyMu80 wire, plotted using an oscilloscope and microwave techniques, respectively.

^{a)}Electronic mail: ciureanu@lisa.polymtl.ca

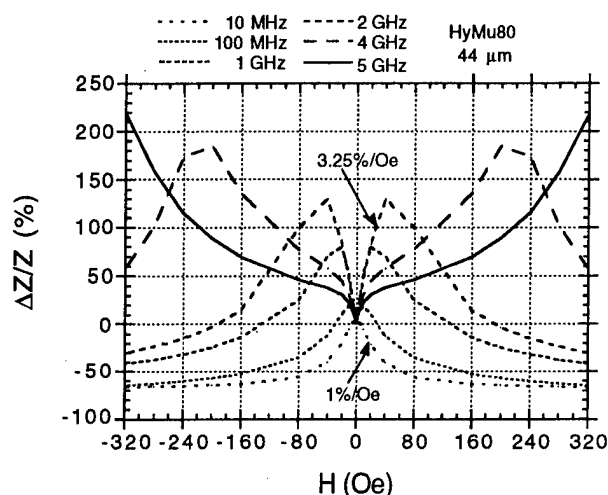


FIG. 2. GMI responses of a HyMu80 wire determined using the technique described in Sec. II.

decreases upon the application of a longitudinal magnetic field. The real part of the wire impedance thus decreases, producing a 60% decrease of the voltage drop across the wire.

At high frequencies (1–10 GHz), the GMI effect is positive and shows a significant increase of the wire impedance when a saturating (200 Oe) magnetic field is applied. This phenomenon was explained by the ferromagnetic resonance occurring in the wire.³ The large circumferential permeability at resonance strongly decreases the effective skin depth and increases the impedance of the wire by up to 200%. Technical saturation (TS) dominates the skin effect in the radio frequency range (region I in Fig. 1), whereas ferromagnetic resonance (FMR) dominates the skin effect in the microwave range (region II).

The GMI effect has a very strong potential for sensing purposes. As shown in Fig. 2, the sensitivity of the permalloy wire depends on frequency, ranging between 1%/Oe at 10 MHz and 3.25%/Oe at 2 GHz. The purpose of this article is to show that, apart from sensing devices, the GMI effect can be useful for determining the intrinsic properties of magnetic materials.

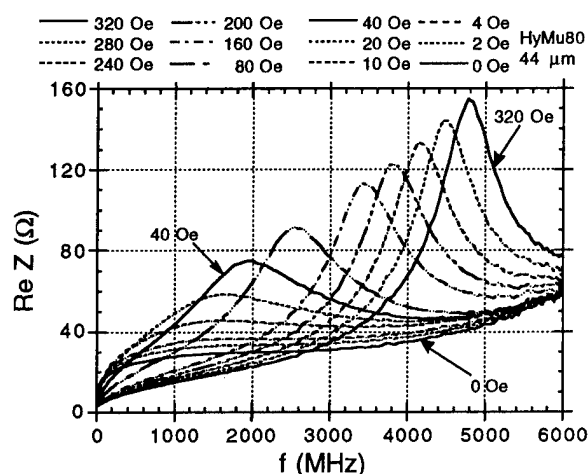


FIG. 3. Impedance spectra of a HyMu80 wire.

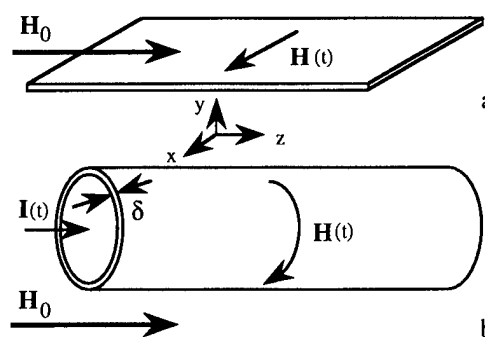


FIG. 4. Magnetic field configurations in a thin planar film and in the thin outer shell of a cylindrical conductor.

II. EXPERIMENTAL DETAILS

Impedance spectra of soft magnetic wires were measured in the 10 MHz–6 GHz frequency range using a shorted coaxial line in the presence of a longitudinal magnetic field. The inner conductor of the line was replaced, in turn, by three different types of magnetic wire: polycrystalline HyMu80 permalloy ($\text{Ni}_{80}\text{Fe}_{16}\text{Mo}_4$) wires, amorphous NiCo-rich ($\text{Ni}_{45}\text{Co}_{25}\text{Fe}_6\text{Si}_9\text{B}_{13}\text{Mn}_2$) wires and amorphous CoFe-rich ($\text{Co}_{71}\text{Fe}_4\text{Si}_{14.5}\text{B}_{6.5}\text{Nb}_4$ and $\text{Co}_{68.2}\text{Fe}_{4.3}\text{Si}_{12.5}\text{B}_{15}$ -Unitika) wires. The HyMu80 wires were 44 or 118 μm in diameter and were cold drawn. The amorphous wires were 30 and 125 μm in diameter and were cast by rapid solidification. The length, l , of the wires was less than 1 cm. The input impedance per unit length of the coaxial line was measured using a network analyzer. The condition $l < \lambda/4$, where λ is the wavelength of the signal generated by the analyzer, is satisfied over the entire measurement range, so this impedance is close to that of the magnetic wire. Details of the experimental technique are given in Ref. 4.

The variation with frequency of the real part of the impedance of a permalloy wire, $\text{Re } Z$, for several static field strengths is shown in Fig. 3. $\text{Re } Z$, which is related to the magnetic losses, peaks at higher frequency for higher fields. The imaginary part of the impedance, $\text{Im } Z$, crosses zero at the same frequency where the maximum of the real part occurs, a behavior typical for ferromagnetic resonance. A resonance frequency, f_0 , can be determined for each value of the static field, H_0 .

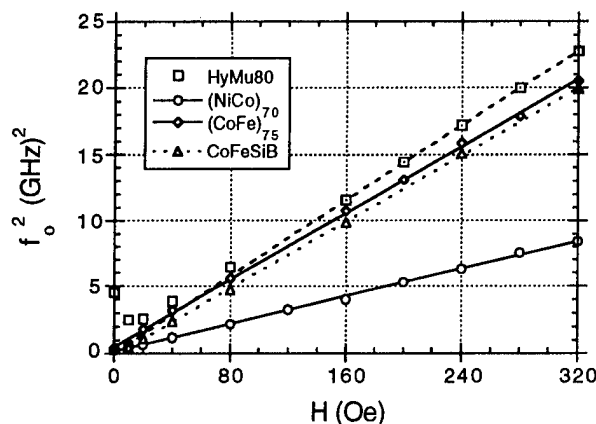


FIG. 5. The square of the resonance frequency vs the resonance field for several soft magnetic wires. A linear fit of the experimental data was made in all cases (only data for $H_0 \geq 160$ Oe have been used in the case of the HyMu80 wire).

TABLE I. Saturation magnetization of several magnetic wires.

Wire alloy	Diameter (μm)	Length (mm)	R_{dc} (Ω)	ρ ($\mu\Omega\text{ cm}$)	M_s (10^6 A/m) GMI	M_s (10^6 A/m) VSM
(NiCo) ₇₀	33	2.76	3.2	100	0.250	0.27
(CoFe) ₇₅	28	6.5	17.2	160	0.628	0.68
HyMu80	44	7	2.1	46	0.691	0.71
CoFeSiB	125	5.5	0.7	156	0.644	0.64

III. FERROMAGNETIC RESONANCE

Ferromagnetic resonance occurs in samples submitted simultaneously to a longitudinal static field, which causes saturation of the sample and precession of the spins, and a perpendicular oscillating field, which provides the energy to maintain the precession and produces the resonance. In the presence of these fields, the dynamic equation of the magnetization of a ferromagnetic material (where damping has been neglected) is:⁵

$$\frac{d\mathbf{M}}{dt} = \gamma \mathbf{M} \times \mathbf{B} = \gamma \mu_0 \mathbf{M} \times \mathbf{H}, \quad (1)$$

where

$$\mathbf{H} = \mathbf{H}_0 + \mathbf{H}(t) \quad \text{and} \quad \mathbf{M} = \mathbf{M}_s + \mathbf{M}(t). \quad (2)$$

In Eq. (2), \mathbf{H}_0 is a large static field applied parallel to the z axis, whereas $\mathbf{H}(t) = H e^{j\omega t}$ is a small oscillating field perpendicular to the static one. \mathbf{M}_s is the saturation magnetization aligned in the static field direction, whereas $\mathbf{M}(t) = M e^{j\omega t}$ adds a small oscillating component normal to \mathbf{M}_s . The resonance frequency for a thin ferromagnetic film containing the z axis in its plane [Fig. 4(a)] can thus be written as⁶

$$\omega_0 = \gamma \mu_0 \sqrt{\mathbf{H}_0(\mathbf{H}_0 + \mathbf{M}_s)}, \quad (3)$$

where $\gamma = 0.176 \times 10^{12} (\text{Ts})^{-1}$ is the gyromagnetic ratio of the electron. When $H_0 \ll M_s$, which applies well for all the wires, Eq. (3) simplifies to

$$\omega_0 \approx \gamma \mu_0 \sqrt{\mathbf{H}_0 \mathbf{M}_s}. \quad (4)$$

The field geometry for the giant magnetoimpedance effect in a magnetic wire driven by a rf current or used as a central conductor in a coaxial line in which a microwave signal is propagating [Fig. 4(b)] may be mapped onto that of the ferromagnetic resonance in a thin magnetic film submitted to fields \mathbf{H}_0 and $\mathbf{H}(t)$. For the wire, the oscillating field $\mathbf{H}(t)$ created by the oscillating current $\mathbf{I}(t)$ is circumferential, as is the magnetic field in a TEM propagating mode coaxial line. Due to the skin effect, these fields are present only in a thin outer shell of the wire. By unrolling the outer shell into a plane, we obtain the same field configuration as for a planar film: the oscillating field is perpendicular to the static field. Thus, when the skin depth is small compared to the wire radius (for example, permalloy wires 44 μm in diameter have a skin depth of 0.22 μm at 4.5 GHz), Eq. (4) applies also to the wires,⁷ and can be written in SI units as

$$f_0^2 = \left(\frac{\gamma \mu_0}{2\pi} \right)^2 M_s H_0 \approx 1.24 \times 10^9 M_s H_0. \quad (5)$$

Equation (5) predicts a straight line with zero intercept for a plot of f_0^2 vs H_0 , whose slope is determined by the

saturation magnetization of the material. Figure 5 indicates that data for all three materials obey such a linear relation and, in all cases, the straight lines pass through the origin. The saturation magnetization can be calculated as

$$M_s = 0.805 \times 10^{-9} \frac{df_0^2}{dH_0} (\text{A/m}), \quad (6)$$

where f_0^2 is expressed in $(\text{GHz})^2$ and H_0 in A/m.

IV. DISCUSSION

Using the values of the slopes calculated from Fig. 5 in Eq. (6), the saturation magnetizations of NiCo-rich, CoFe-rich, and permalloy wires were determined and compared in Table I with the results obtained using a vibrating sample magnetometer (VSM). A good agreement was found for the M_s values obtained through the two methods.

In calculating the slope of the $f_0^2 - H_0$ line for permalloy using only high field data, the contribution of the anisotropy field was neglected.

One source of possible differences between GMI and VSM measurements of M_s may be the inhomogeneity of M_s through the cross section of the magnetic wire. GMI-related phenomena take place only in a thin outer layer of the wire, where permeability inhomogeneity, oxidation and surface defects may occur, whereas VSM provides average values of M_s . Another possible source of disagreement is the error in determining the sample volume, necessary for the VSM.

Thus, we have demonstrated that the giant magnetoimpedance effect of magnetically soft wires at high frequencies is a result of skin depth variations produced by the ferromagnetic resonance occurring in the material. This approach permitted us to determine the saturation magnetization of different samples using GMI measurements, which offer accurate data over a much broader frequency range than ferromagnetic resonance measurements, for example.

ACKNOWLEDGMENT

This work was supported by a grant of the Natural Sciences and Engineering Research Council of Canada.

¹L. V. Panina and K. Mohri, Appl. Phys. Lett. **65**, 1189 (1994).

²R. S. Beach and A. E. Berkowitz, Appl. Phys. Lett. **64**, 3652 (1994).

³A. Yelon, D. Ménard, M. Britel, and P. Ciureanu, Appl. Phys. Lett. **69**, 3084 (1996).

⁴D. Ménard, M. Britel, P. Ciureanu, A. Yelon, V. P. Paramonov, A. S. Antonov, P. Rudkowski, and J. O. Ström-Olsen, J. Appl. Phys. **81**, 4032 (1997).

⁵C. Kittel, Phys. Rev. **73**, 155 (1958).

⁶D. Craik, *Magnetism* (Wiley, New York, 1995), p. 282.

⁷The equivalence of the thin film uniform mode and the cylindrical spin wave mode can be demonstrated rigorously [D. Ménard *et al.* (unpublished)].

Modeling of domain structure and anisotropy in glass-covered amorphous wires

D. Ménard,^{a)} D. Frankland, P. Ciureanu, and A. Yelon

Groupe de Recherche en Physique et Technologie des Couches Minces, Dép. de génie physique, École Polytechnique, C.P. 6079, succ. Centre-ville, Montréal H3C 3A7, Canada

M. Rouabhi and R. W. Cochrane

Groupe de Recherche en Physique et Technologie des Couches Minces, Dép. de physique, Université de Montréal, Montréal, Québec, H3C 3J7, Canada

H. Chiriac and T. A. Óvári

Institute of Technical Physics, 47 Mangeron blvd., 6600 Iasi 3, Romania

Giant magnetoimpedance (GMI) at 10 MHz and longitudinal magnetization curves are used to investigate the anisotropy of $\text{Co}_{68.15}\text{Fe}_{4.35}\text{Si}_{12.5}\text{B}_{15}$ wires, glass-covered and after glass removal. The high resolution GMI response to the field shows hysteresis and large Barkhausen jumps, in good agreement with those observed in the magnetization curves. These are modeled through superposition of the response of the inner core and outer shell of the wires. The GMI response is calculated using the differential susceptibility deduced from the model, thus relating the domain structure to the observed magnetoimpedance. © 1998 American Institute of Physics. [S0021-8979(98)24111-9]

I. INTRODUCTION

The anisotropy in soft amorphous magnetic wires is due partly to exchange and magnetostatic effects, and partly to magnetoelastic effects. The latter are quite effective in amorphous glass-covered wires (AGCW), due to large residual stresses.¹ Removal of the glass, leading to significant stress relief, produces a major change in the magnetic structure of these wires.

Recent reports^{2,3} have discussed the effect of applied tensile and torsional stresses on the anisotropy of Co-rich and Fe-rich AGCW and wires after glass removal (WAGR). For instance, dynamic axial hysteresis loops were measured to investigate the remanence, the coercivity and the occurrence and disappearance of large Barkhausen jumps, from which possible domain structure was inferred.

Here, high resolution giant magnetoimpedance (GMI) and magnetometry are compared to investigate the magnetic structure of these wires. A quasistatic model due to Nowak⁴ is applied to interpret the results, yielding interesting insights into the magnetic structure and the GMI response of wires.

II. PHENOMENOLOGICAL MODELING

The model is based on a core-shell domain structure consisting of a cylindrical inner core (IC) with an axial easy axis, surrounded by an outer shell (OS) with a circumferential easy axis. The quasistatic magnetic hysteresis of each part of the wire is described using a modification, proposed by Nowak,⁴ of the Stoner-Wolfarth model for thin ferromagnetic films with in-plane anisotropy. The model is adapted to the cylindrical geometry by considering that the circumferential direction of the wires is equivalent to the transverse direction of the films.

The global magnetization of the wire is the sum of the magnetizations of the IC and the OS

$$M = \alpha M_{\text{IC}} + (1 - \alpha) M_{\text{OS}}, \quad (1)$$

where α is the relative volume of the IC. The axial magnetization of the IC and the OS region as a function of the longitudinal applied field H are given by⁴

$$M_i(H) = M_s \cos[\varphi_i(H)], \quad (2)$$

where

$$\varphi_i(H) = \tan^{-1} \left(\frac{T_i}{H + L_i} \right) + p\pi \quad (3)$$

is the equilibrium angle between the local magnetization and the applied axial field. In Eq. (2), M_s is the saturation magnetization and p (equal to either 0 or 1) is required to select the appropriate argument of the cosine function. The parameters L_i and T_i are the longitudinal and transverse components of an effective internal field with respect to the direction of the applied field for the two regions. The longitudinal field L_i gives the width of the loop, while the transverse field T_i is responsible for the squareness and the slope of this loop.

It is useful to establish a link between the magnetization curves and the giant magnetoimpedance, which is currently explained by the significant variation of the skin depth due to the sensitive dependence of the circumferential permeability μ_φ upon the application of the longitudinal field.⁵

The impedance of a magnetic wire⁵

$$Z = R_{\text{dc}} \frac{ka J_0(ka)}{2 J_1(ka)}, \quad \text{with} \quad k = \frac{1-i}{\delta}, \quad (4)$$

is a function of the effective skin depth, $\delta = \sqrt{c^2/2\pi\omega\sigma\mu_\varphi}$, where c is the velocity of light, σ the electrical conductivity, ω the angular frequency of the drive current, R_{dc} the dc re-

^{a)}Electronic mail: menard@lisa.polymtl.ca

sistance, $J_0(ka)$ and $J_1(ka)$ are Bessel functions and a is the radius of the wire. Obviously, any attempt to model the GMI requires an expression for the circumferential permeability

$$\mu_\phi = \frac{\partial B_\phi}{\partial H_\phi} = 1 + 4\pi \frac{\partial M_\phi}{\partial H_\phi}. \quad (5)$$

In the present context, M_ϕ is the circumferential magnetization with a form similar to Eq. (2), with $\cos(\varphi_i)$ replaced by $\sin(\varphi_i)$. The differential susceptibility, for a given region of the wire, is then calculated by adding the small circumferential driving field h_ϕ to T_i in the numerator of Eq. (3), and taking the derivative of M_ϕ with respect to h_ϕ . This results in

$$\mu_\phi = 1 + 4\pi M_s \frac{H + L_i}{(H + L_i)^2 + T_i^2} \cos[\varphi_i(H)] \quad (6)$$

from which we obtain the skin depth, and therefore the GMI response to the applied field.

III. EXPERIMENTAL METHOD

GMI and longitudinal magnetization curves were measured in nearly-zero magnetostrictive $\text{Co}_{68.15}\text{Fe}_{4.35}\text{Si}_{12.5}\text{B}_{15}$ glass-covered wires and in the same wires after glass removal. The 20 mm-long metallic samples, with a nominal diameter of $27 \mu\text{m}$ ($R_{dc} \approx 50 \Omega$) were initially covered by a glass sheet about $6 \mu\text{m}$ thick. The chemical glass removal process is described in Ref. 1.

The longitudinal magnetization curves were obtained in the -10 – $+10$ Oe range with a vibrating sample magnetometer (VSM) operating in high resolution field regime. The GMI was measured at 10 MHz using a HP4192A impedance analyzer. The drive current was kept below 0.6 mA, producing a maximum rf field of 0.03 Oe at the surface of the samples. The longitudinal static magnetic field was produced with a pair of Helmholtz coils connected to a programmable current source and controlled by a computer. Automatic data acquisition was performed in cycles ranging between -4 and $+4$ Oe with a resolution of 0.01 Oe.

IV. RESULTS AND DISCUSSION

Hysteresis curves for the AGCW and WAGR are shown in Figs. 1(a) and 1(b), respectively, along with calculations based upon Eq. (1). A small correction due to the demagnetizing field has been applied to the external field. Figure 1(a) clearly shows the presence of two distinct mechanisms. The large Barkhausen jump (LBJ) observed for $H \approx \pm H_c = 0.1$ Oe, gives evidence for a domain structure with axial easy axis, while the external part of the curve ($|H| > H_c$) is dominated by rotational mechanisms relating to the transverse anisotropy. The WAGR sample [Fig. 1(b)] has a lower $H_c = 0.05$ Oe and a larger LBJ.

The intrinsic material parameters extracted from these curves are summarized in Table I. The saturation magnetization M_s , is defined here as the magnetization for a 10 Oe applied field. The difference between the M_s value for the two types of wire is primarily attributed to uncertainties in determination of the volume. The anisotropy fields, H_K ,

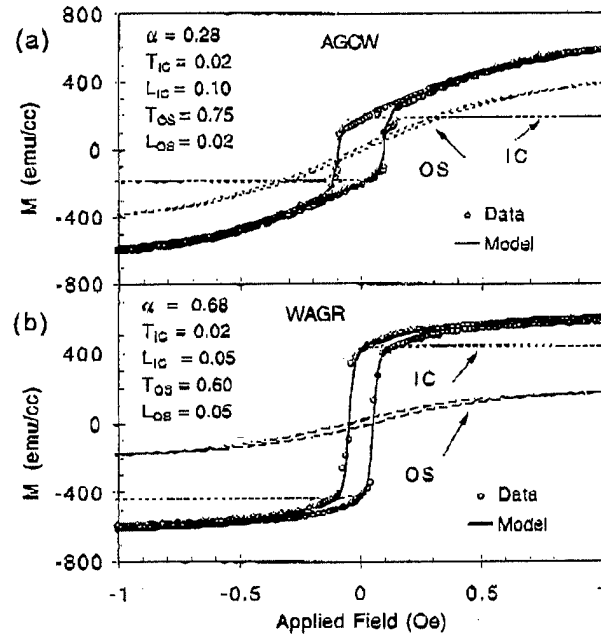


FIG. 1. Comparison between experimental data and a simple model for hysteresis loops in (a) AGCW and (b) WAGR.

were estimated from the slopes of the external part of the curves close to the origin $H=0$, and from first magnetization curves.

The agreement between the model and the experimental data in Fig. 1 is good. The parameters used for the fit are shown in the figure. The effective fields give an indication of the anisotropy in each region of the wire. The longitudinal field L_{IC} corresponds to the coercive field H_c of the IC region, while the transverse field T_{OS} reflects the anisotropy field H_K of the OS.

The factor α was estimated by the reduced remanent magnetization M_r/M_s which gives a direct estimation of the relative volume occupied by the axial domains, that is $M_r/M_s = r_{IC}^2/a^2$, where r_{IC} is the inner core radius. The data of Table I indicate that the removal of the stress provided by the glass cladding results in a significant expansion of the inner core from 53% to 83% of the wire radius. This behavior is due to stress relief, which results in the increased importance of the exchange and magnetostatic energies (facilitating axial magnetization) compared to the magnetoelastic term (facilitating circumferential magnetization).

The GMI responses for both wires, presented in Fig. 2(a) and Fig. 2(b), reflect the circumferential bias permeability ($Z \sim \mu_\phi^{1/2}$). The AGCW wire has a double-peaked response, typical of the permeability of a magnetic layer measured along the easy axis in the presence of a bias field along the hard axis, while the WAGR shows a single peak at the ori-

TABLE I. Magnetic parameters of the wires.

Sample	M_s (emu/cc)	M_r/M_s (%)	H_c (Oe)	H_K (Oe)
AGCW	675	28	0.10	0.8
WAGR	645	68	0.05	0.5

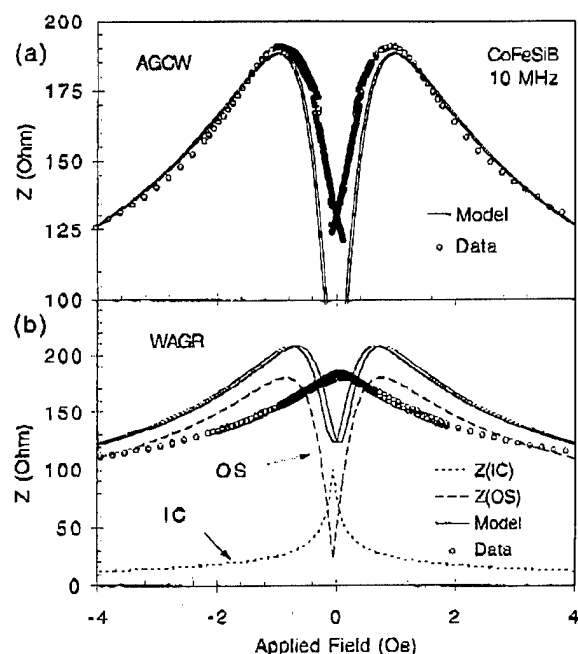


FIG. 2. Comparison between experimental data and a simple model of the modulus of the impedance as a function of the static field for (a) AGCW and (b) WAGR. The data were collected from -4 to $+4$ Oe and then back to -4 Oe.

gin, typical of the bias field parallel to the easy axis.⁴ For the field range under study, the effective skin depth calculated from Eq. (6), is found to vary between 15% and 30% of the wire's radius, so that the GMI response is dominated by the OS in both wires.

The modeling of the AGCW, in Fig. 2(a), based on the parameters of the OS calculated from the magnetization curves, shows good agreement with the experimental data, except at very low fields. This behavior suggests that the sample breaks up into a complicated domain structure in this range. However, using the parameters of the OS region for the WAGR [Fig. 2(b)], the model is unable to fit the experimental data. Including a contribution from both regions,

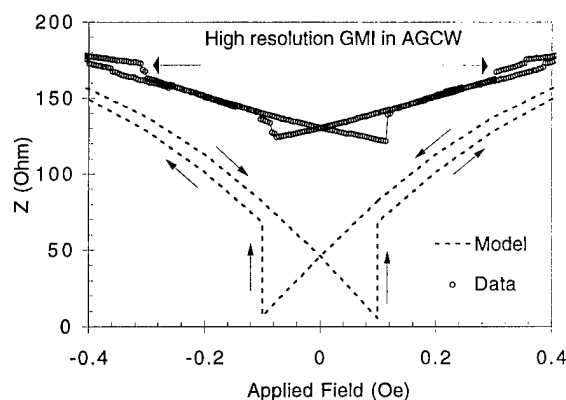


FIG. 3. Details of the low field behavior of the GMI response for the data shown in Fig. 2. The thin arrows show the direction of the sweeping field.

weighted by an appropriate factor, also fails to accurately describe the results, as shown in Fig. 3. Indeed, from the value of the skin depth at different fields and the relative volume occupied by the two regions, we find that 2% to 10% of the IC is within the skin depth. This may correspond to a transition region between the inner and outer regions, for which the domain structure remains unclear.

The detailed response of the GMI near the origin (Fig. 3) shows an asymmetric and hysteretic cycle in the low field range ($H < 0.5$ Oe) for the AGCW, characterized by discontinuities at the coercive points observed in the magnetization curves. Repeated measurements verify the reproducibility of the jumps. They appear consistently at the same field as it is swept back and forth, so that they must reflect reproducible features of the domain structure. Similar jumps were also observed in the WAGR sample.

It is somehow puzzling to observe LBJ, which were previously attributed to the IC, in the GMI response of the OS. However, this feature can be reasonably explained by introducing an additional effective field $\pm H_x$ in the OS due to an exchange coupling with the IC, whose sign depends upon the state of the IC. When the applied field reaches the critical field for which the magnetization of the IC reverses ($H \sim H_c$), the effective field in the OS jumps from $H - H_x$ to $H + H_x$, thus producing a discontinuity in the GMI response. The model for the AGCW is in qualitative agreement with this behavior as shown in Fig. 3.

The additional smaller jumps at ± 0.3 Oe for the AGCW shown by the broad arrows in Fig. 3 have no equivalent in the magnetization curves, reflecting the fact that the real domain structure is more complicated.

V. CONCLUSION

We have used a simple yet plausible model to describe the anisotropy of soft magnetic wires. The model gives a reasonable interpretation of the hysteresis loops and provides interesting insights into the GMI effect. In particular, the large Barkhausen jumps are correctly explained by the introduction of an exchange coupling between the inner core and the outer shell regions. In addition, the model yields an analytic expression for the GMI which works well in AGCW, but fails to describe the response in the WAGR. However, a more realistic approach based on a calculated quenched-in stress distribution is required to clearly establish the effect of the stress on the GMI response.

This work was supported by grants from FCAR (Quebec) and NSERC (Canada).

¹H. Chiriac, T. A. Ovari, and Gh. Pop, *Prog. Mater. Sci.* **40**, 333 (1997).

²H. Chiriac, T. A. Ovari, and Gh. Pop, *IEEE Trans. Magn.* **33**, 782 (1997).

³H. Chiriac, G. Pop, T. A. Ovari, and F. Barariu, *IEEE Trans. Magn.* **32**, 4872 (1996).

⁴J. Nowak, *J. Appl. Phys.* **72**, 1490 (1992).

⁵See, for example, L. V. Panina and K. Mohri, *Appl. Phys. Lett.* **65**, 1189 (1994) or R. S. Beach and A. E. Berkowitz, *Appl. Phys. Lett.* **64**, 3652 (1994).

⁶A. Yelon, D. Ménard, M. Britel, and P. Ciureanu, *Appl. Phys. Lett.* **69**, 3084 (1996).

Phenomenological model for magnetoimpedance in soft ferromagnets

D. Atkinson and P. T. Squire^{a)}

Department of Physics, University of Bath, Bath BA2 7AY, United Kingdom

The dependence of magnetoimpedance (MI) on transverse susceptibility in soft ferromagnets is used in conjunction with an existing phenomenological domain structure model to study the relative importance of moment rotation and domain-wall motion in MI. It is shown that moment rotation is predominantly responsible for the observed behavior in amorphous wires at frequencies above 1 MHz. It is also necessary to include anisotropy distributions in both magnitude and direction.

© 1998 American Institute of Physics. [S0021-8979(98)39411-6]

INTRODUCTION

Very large magnetoimpedance (MI) is observed in soft ferromagnets at frequencies upwards of 10 kHz.¹ The origin of this behavior is recognized as magnetoinductance and skin-depth effects, and the link between the domain structure and anisotropy and the magnitude of the MI is also established.² However, efforts to model MI in terms of magnetization processes associated with a particular domain structure are limited.³ Notably, the relative importance of domain-wall motion and magnetization rotation processes and the effect of easy axis orientation have not been clearly addressed.

In this work, a phenomenological model relating the domain structure and magnetization processes of a ferromagnet to the transverse susceptibility and the MI response is presented.

PHENOMENOLOGICAL MODEL

The relationship between the impedance and the magnetic permeability of a conductor is understood through classical electromagnetism and described in terms of the skin-depth effect.⁴ The complex impedance of a cylindrical conductor can be described in the form

$$Z = R_{dc}kaJ_0(ka)/2J_1(ka), \quad (1)$$

where R_{dc} is the dc resistance of the wire, a its radius, J_0 and J_1 are Bessel functions of the first kind, and $k = (1+j)/\delta$, where δ is the skin depth. At higher frequencies ($|ka| \gg 1$), the asymptotic form of the Bessel functions allows the impedance to be expressed as

$$Z = R + jX, \quad (2)$$

where

$$R \approx X \approx R_{dc} \left(\frac{a}{2\delta_0} \right) \sqrt{\mu_r}, \quad (3)$$

δ_0 is the skin depth when the relative permeability $\mu_r = 1$, and is given by

$$\delta_0 = \sqrt{\frac{2\rho}{\mu_0\omega}}, \quad (4)$$

where ρ is the resistivity and ω is the angular frequency.

For a ferromagnetic material, the magnetic-field dependence of the permeability, therefore, controls the MI behavior of the conductor.

It follows that magnetoimpedance can be understood by expressing the permeability along an appropriate axis as a function of the magnetic field. For cylindrical (wire) geometry the appropriate permeability is circumferential and for planar geometry (ribbons and thin films) it is transverse, with respect to the axis of current flow. The permeability depends on many factors, including the domain configuration, anisotropy, stress, and the mode of magnetization (domain-wall motion or magnetization rotation). These factors can be complex in real materials, making accurate modeling very difficult.

This work is based on the model of Squire⁵ for magnetization and magnetoelastic effects in soft ferromagnets. The model assumes a simplified domain structure, consisting of antiparallel domains separated by 180° domain walls; a single, arbitrary easy axis orientation; and magnetization processes which are anhysteretic. Both domain-wall motion and magnetization rotation are included in the model, allowing their relative contributions to the transverse permeability to be investigated. Figure 1 schematically illustrates the domain structure and angles used in the model. The model excludes domain-wall bowing and rotational damping.

The model is applicable to both cylindrical and planar geometries, which differ only in terms of the magnitude of the transverse demagnetizing energy. For cylindrical geometry, the circumferential demagnetizing field is very small

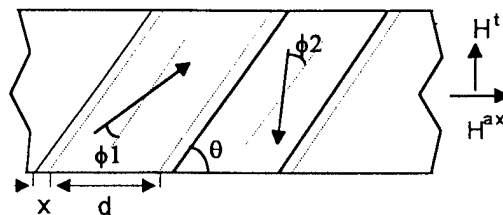


FIG. 1. Geometry assumed for the domain model. The easy axis makes an angle θ with the dc field axis. Moments in the two types of domains make angles of ϕ_1 and ϕ_2 with the easy axis under the combined influence of the axial field H^{ax} and the transverse field H^t . The domain widths are both taken as d in zero applied field; x denotes the field-induced domain-wall movement.

^{a)}Electronic mail: p.t.squire@bath.ac.uk

since the circumferential magnetization is essentially continuous. In the case of a planar geometry, the transverse demagnetizing field depends on the width of the sample.

The model is used to calculate the transverse susceptibility χ^t , which is simply related to the relative permeability ($\mu_r = \chi^t + 1$). The transverse susceptibility is derived from the magnitude of the transverse magnetization developed by the magnetic field due to the current in the material.

Modeling involves minimization of the free-energy density to determine the domain structure (domain-wall positions and magnetization rotation angles) obtained when the material is subject to both transverse and axial magnetic fields. The free-energy density includes the following terms:

$$U_{\text{tot}} = U_K + U_H^{\text{ax}} + U_H^t + U_W, \quad (5)$$

where U_K is the uniaxial anisotropy energy density, taken as

$$U_K = K[\alpha \sin^2 \phi_1 + (1 - \alpha) \sin^2 \phi_2], \quad (6a)$$

where K is the anisotropy constant. The parameter α is the fraction of material occupied by domains magnetized towards the applied axial field (Fig. 1). U_H^{ax} is the Zeeman energy due to the axial magnetic field H^{ax} :

$$U_H^{\text{ax}} = \mu_o M_s H^{\text{ax}}[(1 - \alpha) \cos(\theta + \phi_2) - \alpha \cos(\theta - \phi_1)], \quad (6b)$$

U_H^t is the Zeeman energy due to the transverse magnetic field, H^t :

$$U_H^t = \mu_o M_s H^t[(1 - \alpha) \sin(\theta + \phi_2) - \alpha \sin(\theta - \phi_1)], \quad (6c)$$

and U_W is the magnetostatic energy, which depends on the domain-wall position. A parabolic potential is used to represent this contribution:

$$U_W = \beta u^2, \quad (6d)$$

where $u = x/d$ and β is a measure of the domain-wall stiffness.⁵ The procedure is to choose the values of moment angle ϕ_1 , ϕ_2 , and domain-wall position α that minimize U_{tot} in a given axial field H^{ax} with the transverse field H^t equal to zero; then, to find the changes in these parameters induced by a small transverse field. The difference ΔM between the transverse magnetization with and without a transverse field allows the transverse susceptibility $\chi^t = \Delta M/H^t$ to be calculated.

Here, the model is addressed to three aspects of the relationship between magnetoimpedance and the domain structure. (Previous results concerning the effect of applied stress on MI have been reported elsewhere⁶). The first aspect addressed is the relationship between the magnetization processes and the MI effect. It is clear from many observations of magnetoimpedance that the shape of the MI (H) curve is a function of the frequency of the excitation current. It is also established from permeability studies that domain-wall motion becomes increasingly heavily damped due to eddy currents at high frequencies.⁷ The model has, therefore, been applied to calculate the transverse susceptibility for a material in which the amount of domain-wall motion due to the transverse field was made progressively smaller.

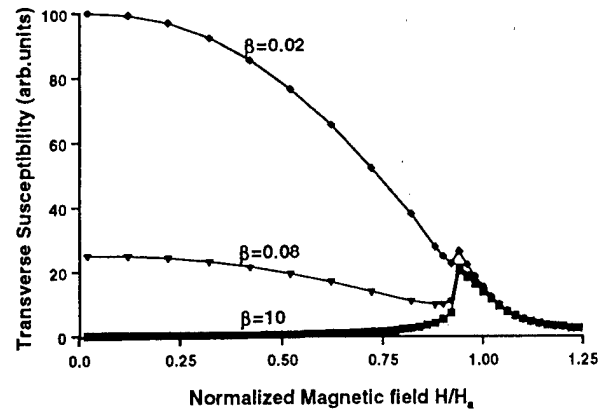


FIG. 2. Transverse susceptibility calculated for $\theta=90^\circ$ as a function of the applied-field H , normalized to the anisotropy-field H_a . The parameter β controls domain-wall movement: large values of β inhibit wall motion [see Eq. 6(d)].

The second aspect studied here is the relationship between the anisotropy easy-axis orientation θ and the MI response. Observations have shown that the shape of the MI (H) curves depends on the easy axis orientation. Finally, the effects of a distribution in anisotropy magnitude on the MI response of materials has been studied.

RESULTS AND DISCUSSION

Figure 2 shows the effect of increasingly restricted wall motion on the transverse susceptibility of a material with a perpendicular ($\theta=90^\circ$) anisotropy. For small β values [Eq. 6(d)], domain walls move easily under the influence of the transverse field. In this case, the transverse susceptibility falls as the axial field increases because the transverse magnetization in each domain is reduced as the moments rotate towards the axial field. This behavior is to be expected at relatively low frequencies where eddy-current damping of domain-wall motion is negligible. For intermediate values of β , the relative contribution of domain-wall motion to the transverse susceptibility decreases. For high values of β , domain-wall motion is negligible and the transverse susceptibility is due only to magnetic-moment rotation. In this case, the transverse susceptibility is zero when the axial field is zero and increases with axial field until close to the anisotropy field. The transverse susceptibility then falls with a further increase of the axial field. This behavior is expected at higher frequencies, when eddy currents severely damp domain-wall motion. This indicates, therefore, that for MI of amorphous wires and transverse-field annealed ribbons observed at ≥ 1 MHz magnetic-moment rotation is the dominant mechanism responsible for the magnetoimpedance. Figure 2 also shows that above the anisotropy field the three curves converge. This occurs because for axial fields greater than the anisotropy field the moments are aligned with the axis; the transverse susceptibility is due only to a small perturbation of the moments from this axis.

Figure 3 illustrates the influence of the anisotropy easy-axis angle θ on the transverse susceptibility due to magnetization rotation (appropriate to high frequencies). The shape of the transverse susceptibility curve evolves from the high

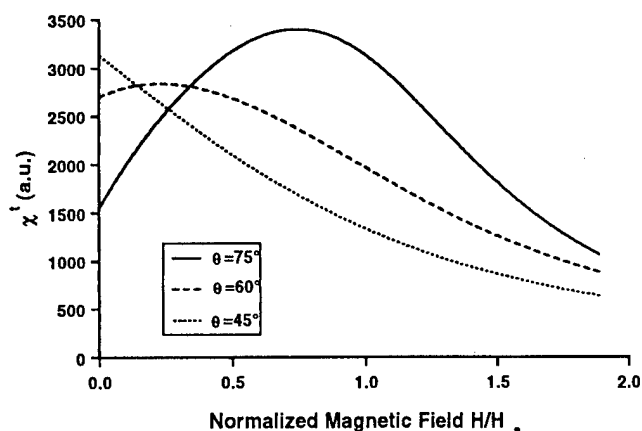


FIG. 3. Effect of different easy-axis orientations on the transverse susceptibility.

angle case, in which the susceptibility rises from a low value to a peak and then falls with further increase of the axial field, to the lower angle case in which the transverse susceptibility falls monotonically with the axial magnetic field. This result is again consistent with experimental MI observed in as-quenched and annealed amorphous ribbons and wires.^{2,6}

It is known from modeling of magnetic and magnetoelastic effects that some level of distribution in the anisotropy magnitude and easy-axis orientation is required to rep-

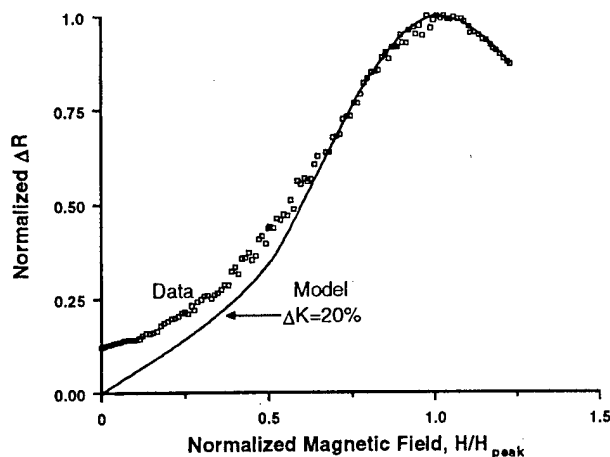


FIG. 4. Comparison of the experimental field dependence of the resistive component of magnetoimpedance with the model. Optimum fit is obtained by assuming a Gaussian distribution of anisotropy magnitude with 3σ limits equal to 20% of the mean.

resent the behavior of amorphous alloys.⁵ Figure 4 shows the resistive component of the impedance for an as-quenched $\text{Co}_{72.5}\text{Si}_{12.5}\text{B}_{15}$ amorphous wire, subject to axial, tensile stress of 170 MPa, and a modeled curve which assumes rotational magnetization processes, an easy-axis orientation of $\theta=90^\circ$, and a Gaussian distribution of the anisotropy constant. There is good agreement between the data and the model except at low fields, supporting the presence of an anisotropy distribution in the wire. The anisotropy distribution can be attributed to variations of the internal stress in the wire. The discrepancy between the model and the data at low fields most probably arises from a distribution of the easy-axis orientation around the assumed value of 90° .

CONCLUSIONS

A static, phenomenological model, developed originally for the calculation of magnetic and magnetoelastic properties, has been effectively extended to calculate the transverse susceptibility, and hence, magnetoimpedance in soft ferromagnets. The model includes domain-wall motion and magnetic-moment rotation, but excludes domain-wall bowing and rotational damping.

Modeling shows that the basic shape of the MI as a function of applied field is governed by the easy-axis orientation and the magnetization processes contributing to the transverse susceptibility. Comparison of the model with published experimental data indicates that at frequencies of about 1 MHz and above magnetization rotation is largely responsible for the MI response in CoFeSiB wires and ribbons. The model also suggests that the MI response of amorphous alloys reflects a distribution of the magnitude of the anisotropy.

ACKNOWLEDGMENT

This work has been supported in part by the Structural Materials Centre of the U.K. DERA.

¹L. V. Panina, K. Mohri, K. Bushida, and M. Noda, *J. Appl. Phys.* **76**, 6198 (1994).

²M. Tejedor, B. Hernando, M. L. Sanchez, and A. Garcia-Arribas, *J. Magn. Magn. Mater.* **157/158**, 141 (1996).

³F. L. A. Machado and S. M. Rezende, *J. Appl. Phys.* **79**, 6558 (1996); L. V. Panina, K. Mohri, T. Uchiyama, and M. Noda, *IEEE Trans. Magn.* **31**, 1249 (1995).

⁴L. D. Landau and E. M. Lifshitz, *Electrodynamics of Continuous Media* (Pergamon, Oxford, 1960).

⁵P. T. Squire, *J. Magn. Magn. Mater.* **87**, 299 (1990); **140-144**, 1829 (1995).

⁶D. Atkinson and P. T. Squire, *IEEE Trans. Magn.* **3**, 3364 (1997).

⁷H. Okuno and T. Homma, *IEEE Trans. Magn.* **29**, 2506 (1993).

Field and stress dependence of the irreversible magnetization changes in pure iron

J. Pearson and P. T. Squire^{a)}

Department of Physics, University of Bath, Bath, BA2 7AY, United Kingdom

Measurements of the irreversible magnetization changes accompanying the application and removal of stress to a sample of 99.99% pure iron have been made as a function of applied field and stress magnitude for both compressive and tensile stress. The fields for peak change have been compared with those for the peak difference $M_{AN} - M_{INI}$ between the anhysteretic and initial magnetization curves and the field derivative of the magnetostriction. It is shown that at low tensile stress the magnetostrictive contribution is dominant, as found by Pravdin. At higher stress the wall pinning term is dominant, and the magnetization changes are proportional to $M_{AN} - M_{INI}$, in accordance with the Jiles–Atherton model. © 1998 American Institute of Physics. [S0021-8979(98)24211-3]

I. INTRODUCTION

There have been numerous studies exploring the effects of stress on the magnetic properties of ferromagnetic materials. A good review has been given by Robertson.¹ Despite the extensive study there has never been an adequate explanation of the complicated history-dependent effects that have been observed. Early work by Brown² suggested that, on the initial magnetization curve, stress should act as an additional pressure on a domain wall. This pressure varies for different domain wall types, but gives equal magnetization changes in tension and compression. This approach had some success for field and stress changes within the Rayleigh region, but not beyond. Later work by Birss,³ Faunce and Isaac,⁴ and Craik and Wood⁵ showed that the experimental results could only be explained if stress affected the magnetization in three ways:

- altered the pinning site energies;
- induced preferential occupancy of a particular axis, encouraging domain creation and or annihilation;
- produced direct pressure on non-180° domain walls.

Jiles and Atherton⁶ (JA) have developed a theory based on domain wall motion. In the JA model the change in magnetization induced by the application and release of an applied stress (ΔM_{IRR}) was proportional to the difference between the initial (M_{INI}) and anhysteretic magnetization curves (M_{AN}). It proposes that an applied stress acted to help a domain wall overcome its local pinning sites, allowing a domain wall to move towards its thermal equilibrium position, which is assumed to be the anhysteretic. Figure 12 in Ref. 6 compares the difference $M_{AN} - M_{INI}$ with ΔM_{IRR} as a function of applied field for a stress of 140 MPa. Although there are qualitative similarities, the peak change in ΔM_{IRR} clearly occurs at a higher field value than the difference $M_{AN} - M_{INI}$. Pravdin^{7,8} looked at the effect of low-magnitude cyclic stress, separating the irreversible and reversible changes after many cycles. Although not mentioned in his work, it is clear from Fig. 5 in Ref. 7 that ΔM_{IRR} in tension peaked at a higher field value than ΔM_{IRR} in com-

pression. Pravdin showed that these changes were not proportional to χ or $M_{AN} - M_{INI}$ (Jiles–Atherton) but corresponded to the differential magnetostriction ($\partial\lambda/\partial H$).

The present study extends the work of Pravdin to higher magnitude stresses. We will show how the peak position of ΔM_{IRR} varies with the magnitude and sign of the applied stress and explore the possible reasons for this variation.

II. EXPERIMENTAL DETAILS

Experiments were carried out on a 2 mm diameter, 150 mm long piece of 99.99% pure iron rod. Magnetization of the sample was measured using the ballistic method with software integration of the induced voltage. The magnetic field was provided by a solenoid. The stress was applied using an electromagnetic actuator and a lever system for mechanical advantage. The rate of application of stress was maintained constant throughout the experiment. Demagnetization of the sample was by the alternating field method with a 1% reduction in the peak field value per cycle. Comparison with a 0.1% reduction per cycle showed a negligible difference in the data. A typical measurement occurred as follows. The sample was demagnetized under zero stress. A known bias field was applied. The required stress was applied and released in several steps, measuring the induced search coil voltage at each step. The whole process was repeated for bias fields ranging from 0 to 6000 A/m with the same applied peak stress. The anhysteretic data were produced by demagnetizing the sample in a dc bias field, then saturating the sample and measuring ΔM . Experimental uncertainty was estimated from three measurements at each data point. Variations in the applied stress introduced most of the uncertainty in the data. For example, applying 9.5 MPa instead of 10 MPa could introduce a 5% difference in consecutive measurements. The error bars are therefore proportionally larger as the applied stress decreases. Errors in software integration drift have been minimized to less than 0.01 mT per point and are therefore negligible in these measurements.

^{a)}Electronic mail: pypspts@bath.ac.uk

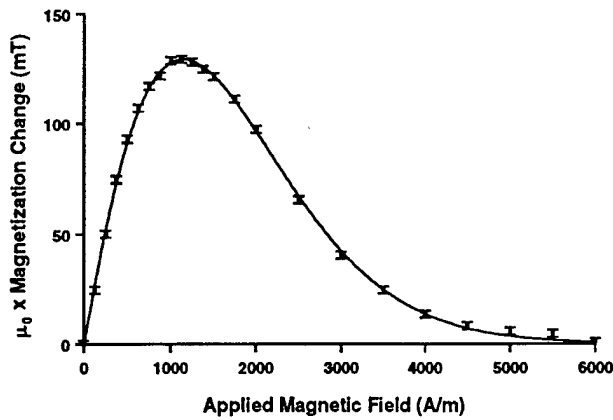


FIG. 1. Irreversible magnetization change as a function of the applied field after application and release of 47 MPa tension.

Magnetostriction was measured as a function of applied field by means of a fiber-optic dilatometer.⁹ The quantity $(\partial\lambda/\partial H)$ was derived in software from the experimental $\lambda(H)$ data.

III. RESULTS AND DISCUSSION

Figure 1 shows ΔM_{IRR} as a function of applied field due to the application and release of 47 MPa tension. This is typical of the data sets at various peak stresses, from which the peak positions and magnitudes were derived by curve fitting. Figure 2 shows how $(\partial\lambda/\partial H)$ varies with applied field. Curve fitting shows that this peaks at 2035 ± 35 A/m. Figure 3 shows how the peak position of ΔM_{IRR} varies with absolute applied stress. The extrapolated value at $\sigma=0$ is 1720 ± 240 A/m. Figure 4 shows how $\Delta M_{\text{IRR}}(\text{max})$ varies as a function of applied stress. Values have been calculated from curve fitting parameters obtained from data sets like Fig. 1. Figure 5 shows the difference $M_{\text{AN}} - M_{\text{INI}}$ as a function of applied field. Figure 6 shows how the peak position of $M_{\text{AN}} - M_{\text{INI}}$ varies with absolute applied stress.

On average, no moment direction is preferred in the demagnetized state and hence stress has no macroscopic effect on the magnetization. Increasing the field from the demag-

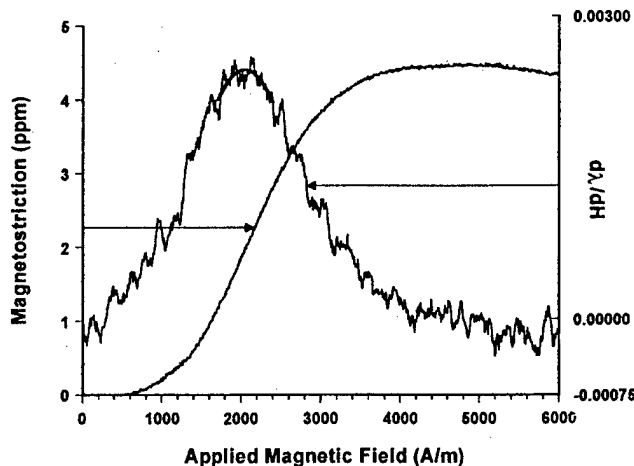


FIG. 2. Magnetostriction and its field derivative.

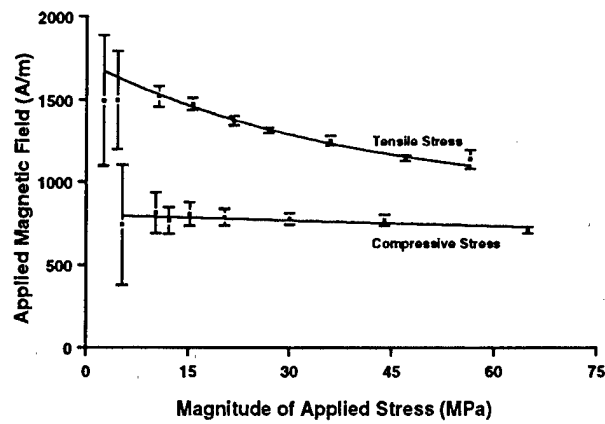


FIG. 3. Variation of the peak position of irreversible magnetization as a function of magnitude of peak stress. The error bars are obtained from curve fitting parameters.

netized state induces a preferred direction and hence the application of a *small tensile* stress changes the magnetization by the methods outlined in the introduction.

We write

$$P_{\sigma} \propto \frac{\partial \lambda}{\partial H},$$

$$P_H \propto \mu_0 H M_S,$$

and

$$P_{\text{PIN}} \propto \frac{\partial E_{\text{PIN}}}{\partial x},$$

for the pressures on the domain wall due to the applied stress and field respectively. P_{PIN} is the restoring pressure due to the wall pressure energy density gradient. In simple terms a pinned domain wall will “jump” from its pinning site when

$$P_H + P_{\sigma} > P_{\text{PIN}}.$$

If some of the pinning sites are magnetostrictive and of both tensile and compressive types,¹⁰ then tensile stress raises and lowers an equal number of pinning site energies. In a planar wall system consider the effect of P_{PIN} only. If tensile stress has the effect of increasing P_{PIN} at a pinned domain wall, then to compensate there will be a small, usually reversible,

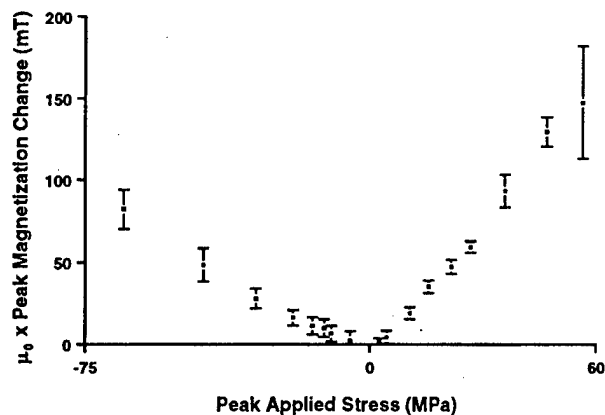


FIG. 4. Peak magnetization change as a function of applied stress. Error bars are obtained from curve fitting parameters.

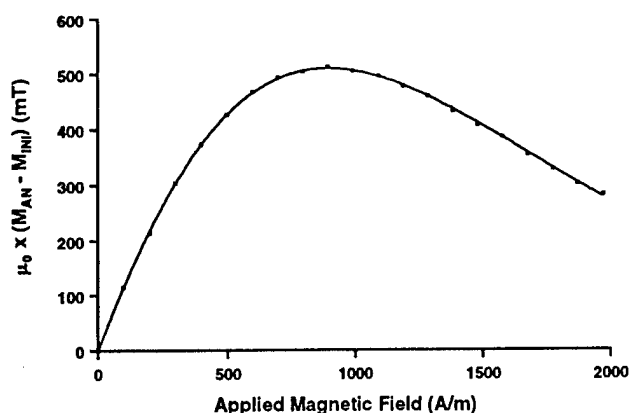


FIG. 5. Difference between the anhysteretic and initial magnetization curves, $M_{AN} - M_{INI}$, as a function of applied field at zero stress.

decrease in magnetization. However, if the restoring pressure, P_{PIN} decreases, then the magnetization will increase, and a fraction of the pinned domain walls will irreversibly jump to the next local energy minimum. The irreversible increases will be larger than the reversible decreases in magnetization. In this way, on average, ΔM_{IRR} due to changes in P_{PIN} should always increase the magnetization towards the anhysteretic value. This change will be at a maximum when most domain walls are pinned, that is at the peak in $M_{AN} - M_{INI}$. However, this does not consider the P_σ term which, to first order, only affects non-180° domain walls. Therefore, at low tensile stress, the peak in ΔM_{IRR} due to changes in P_σ and P_{PIN} occurs at a higher field value than the peak in $M_{AN} - M_{INI}$, closer to the peak in $(\partial\lambda/\partial H)$ shown in Fig. 2. As the stress value increases, the change in P_{PIN} begins to dominate the changes in ΔM_{IRR} and hence we see a shift in the peak position of ΔM_{IRR} towards the peak in $M_{AN} - M_{INI}$ as seen in Fig. 2. In compression the situation is more complicated, in that the change in P_{PIN} increases, while the change in P_σ decreases the magnetization. For this iron sample the net result is an increase in magnetization but very little change in the peak position of ΔM_{IRR} with applied field.

Figure 4 gives an indication of why accurate measurement of the peak positions are difficult at low stress due to the low induction change. Hence on this sample it is impossible to say whether the peak in ΔM_{IRR} coincides exactly with the peak in $(\partial\lambda/\partial H)$ as $\sigma \rightarrow 0$, or only that it approaches it. These trends cannot be attributed to changes in M_{AN} under stress as would be the case in the JA model. Figure 6 shows that the positions of the peak in $M_{AN} - M_{INI}$, as seen in Fig. 3, diverge as the applied stress increases.

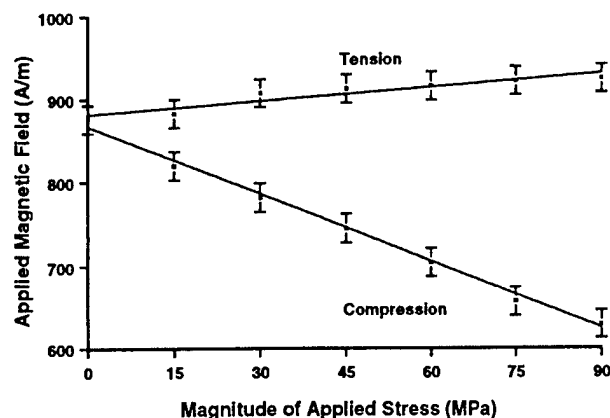


FIG. 6. Variation of the peak position of $M_{AN} - M_{INI}$ as a function of absolute applied stress.

IV. CONCLUSIONS

We have shown that the peak position of ΔM_{IRR} cannot be explained by the JA model at low stress. At low tensile stress the peak in ΔM_{IRR} is closer to the peak in $(\partial\lambda/\partial H)$, as suggested by Pravdin. As the magnitude of the applied stress increases, the peak in ΔM_{IRR} moves towards the peak in $M_{AN} - M_{INI}$, as predicted in the JA model. We have shown that this change is due to stress affecting the magnetization by different mechanisms at different stress magnitudes. At low stress the primary change is due to P_σ which is proportional to $(\partial\lambda/\partial H)$. As the stress increases, changes in P_{PIN} begin to dominate, which are proportional to $M_{AN} - M_{INI}$.

In further work we hope to establish that these trends are true for other materials. (Such as Ni, SiFe, and steel.)

ACKNOWLEDGMENTS

This work has been supported in part by the Structural Materials Centre of the UK DERA and the UK EPSRC. The encouragement of Dr. Mark Maylin of DERA has been valuable.

¹I. M. Robertson, Mater. Forum **15**, 117 (1991).

²W. F. Brown, Phys. Rev. **75**, 147 (1949).

³R. R. Birss, IEEE Trans. Magn. **MAG-7**, 113 (1971).

⁴R. R. Birss, C. A. Faunce, and E. D. Isaac, J. Phys. D **4**, 1040 (1971).

⁵D. J. Craik and M. J. Wood, J. Phys. D **4**, 1009 (1971).

⁶D. C. Jiles and D. L. Atherton, J. Phys. D **17**, 1265 (1984).

⁷L. S. Pravdin, K. B. Vlasov, and V. G. Kuleyev, Phys. Met. Metallogr. **47**, 60 (1980).

⁸K. B. Vlasov and L. S. Pravdin, Phys. Met. Metallogr. **48**, 101 (1981).

⁹P. T. Squire, J. Phys. E **20**, 54 (1987).

¹⁰D. Hull, Introduction to Dislocations (Pergamon, Oxford, 1965).

Temperature dependence of magnetoimpedance effect in amorphous $\text{Co}_{66}\text{Fe}_4\text{NiB}_{14}\text{Si}_{15}$ ribbon

Y. K. Kim, W. S. Cho, T. K. Kim, and C. O. Kim

Division of Material Science, Chungnam National University, Taejeon 305-764, Korea

Heebok Lee^{a)}

Department of Physics Education, Kongju National University, Kongju 314-701, Korea

The temperature dependence of the magnetoimpedance (MI) effect is important both for scientific study and for thermal stability of MI sensors. We have performed the measurement of MI effect in amorphous $\text{Co}_{66}\text{Fe}_4\text{NiB}_{14}\text{Si}_{15}$ (Metglas 2714A) ribbon from a cryogenic chamber where the temperature of the sample can vary from 10 to 300 K. The ac current was fixed at 10 mA for all measured frequencies ranging from 100 kHz to 10 MHz. The magnetoimpedance ratio (MIR) was revealed the drastic increment as a function of $\text{MIR}(T) = \text{MIR}(0)\exp(cT^2)$, where c is a constant. The measured MIR values at room temperature are usually 2–3 times larger than the data measured at 10 K for all measured frequencies. However, the shapes of the MIR curves are remained. This result shows the potential application of the MI effect for a temperature sensor. © 1998 American Institute of Physics. [S0021-8979(98)24311-8]

I. INTRODUCTION

Recently, large and sensitive changes in the alternating current magneoresistance, called as magnetoimpedance (MI) effect, as a function of applied field in nearly zero magnetostriction amorphous wires and ribbons have been studied intensively, because of the increasing perspectives of novel applications in magnetic sensors.^{1–3}

The MI effect has a classical electromagnetic behavior where the impedance is changing under the application of a longitudinal magnetic field. The electromagnetic origin of MI effect has been conjectured to the combination of a skin effect and field dependence of the circumferential magnetic permeability associated with the circular motion of magnetic moments.⁴

The impressive sensitivities of a magnetoimpedance effect at room temperature were observed up to 1700%/Oe after proper thermal treatments.⁵ We have found that the maximum magnetoimpedance ratio (MIR) of amorphous $\text{Co}_{66}\text{Fe}_4\text{NiB}_{14}\text{Si}_{15}$ ribbons annealed at 250 °C for 1 h reached to as much as 750% at large current of 60 mA with a high frequency of 5 MHz. Despite MIR is large enough to use for magnetic sensor, the stability of the MI sensors remains questionable. When we measured the magnetoimpedance of this sample several times, we found that MIR was changed slightly at each measurement. Therefore, we have started to investigate the temperature dependence of the MI effect in the sample. The investigation of the temperature dependence of the MI effect seems to be important for scientific interests, technical applications for a temperature sensor, and thermal stability of MI sensors.

In this work, we have used amorphous $\text{Co}_{66}\text{Fe}_4\text{NiB}_{14}\text{Si}_{15}$ (Metglas 2714A) ribbon, which is a well known amorphous ferromagnet with a nearly zero magnetostriction constant and a high magnetic permeability, to study the temperature dependence of MI effect at low temperature (10–300 K).

II. EXPERIMENT

The MI measurements were carried out along the ribbon axis with longitudinal magnetic field. The sample was cut out 15 mm in length and 2.5 mm in width with 19 μm in thickness. The schematic diagram of MI measurement system is shown in Fig. 1. The sample was attached in the cold finger of a closed cycle cryostat (10–300 K). For the four-terminal MI measurement, a silver paint has been used to attach the terminals where the separation between the current leads and the voltage leads are about 15 and 10 mm, respectively. A computer controlled rf signal generator with its power amplifier was connected to the sample in series with a resistor for monitoring the driving ac current. An ac current and a voltage across the sample for calculating the impedance, can be measured by digital multimeters (DMM) with rf/V probes. The external field applied by a solenoid on the top of a cryogenic chamber can be swept through the entire cycle equally divided by 800 intervals from –150 to 150 Oe. Averaging MIR with sweeping fields, changing frequencies,

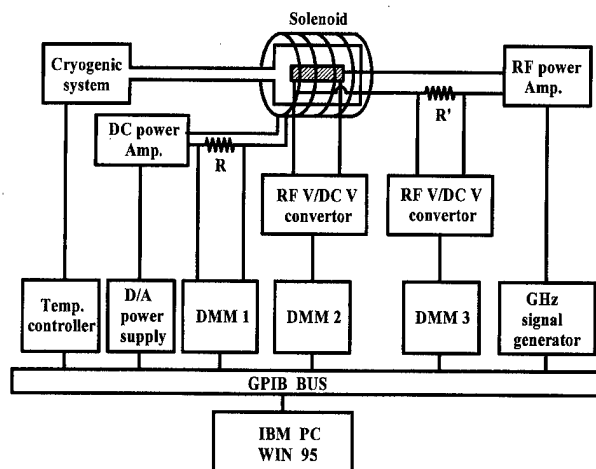


FIG. 1. Schematic diagram of the magnetoimpedance measurement system.

^{a)}Electronic mail: Heebok@knu.kongju.ac.kr

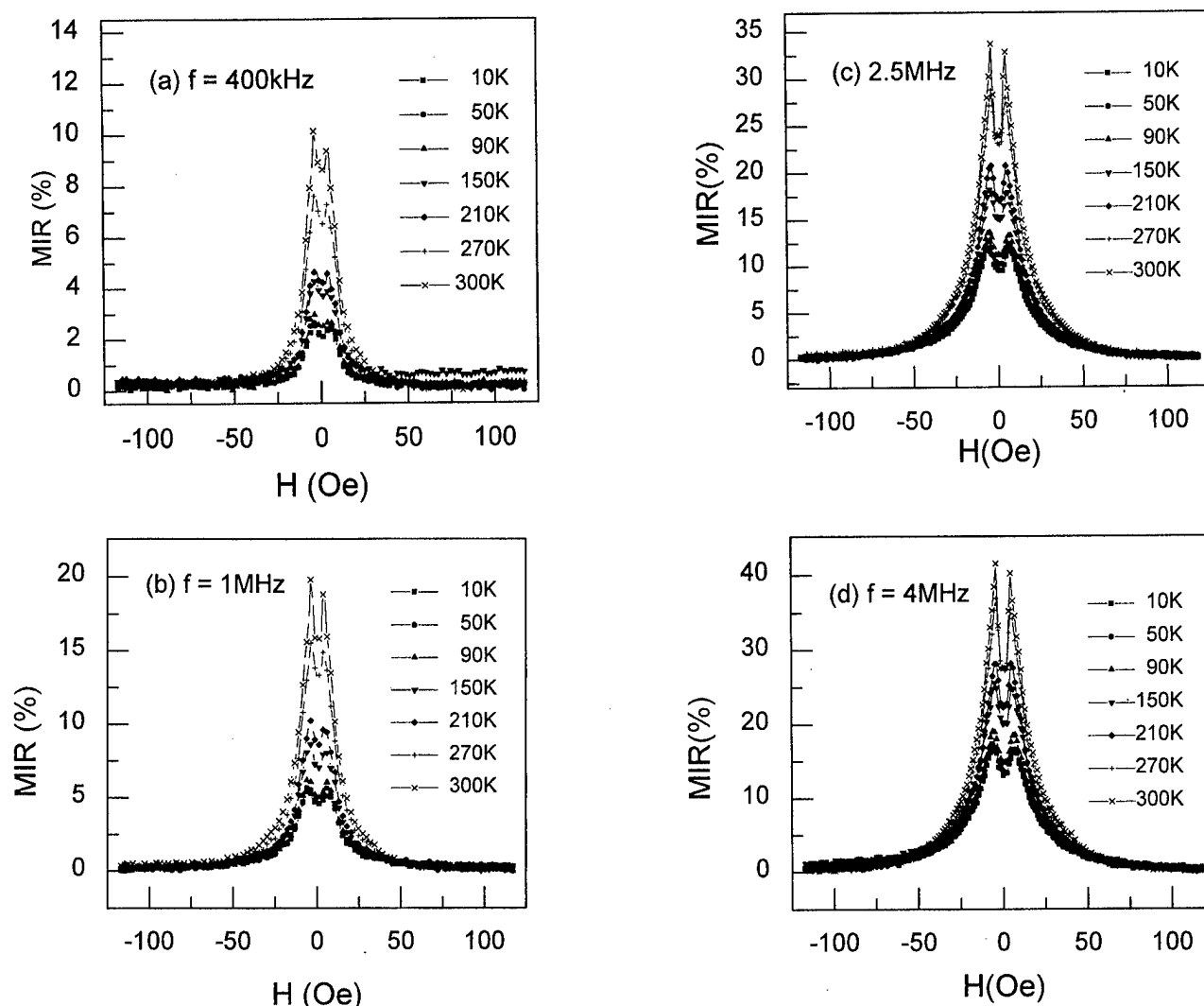


FIG. 2. The MIR vs the external field H for various temperatures at the frequency of (a) 400 kHz, (b) 1 MHz, (c) 2.5 MHz, and (d) 4 MHz.

and keeping a constant ac current, are activities performed by a Windows 95 program. Because of capacitive interferences between wires in the cryogenic chamber, the measured MI values diminished by a factor. The effect of the earth's magnetic field has been minimized by suitable positioning of the sample.

III. RESULTS AND DISCUSSION

The MIR can be defined as $MIR(H) = \Delta Z / Z(H_{\max}) = 1 - |Z(H)/Z(H_{\max})|$, where H_{\max} is an external magnetic field sufficient for saturating the magnetoimpedance. $H_{\max} = 150$ Oe was taken in our experiment.

The frequency dependence of MIR in the sample has shown a typical behavior where the maximum values of MIR are increased and also the shapes of MIR curves are getting broader with the increment of the frequency as observed in the Co-based amorphous wires and ribbons.¹

The MI effect at a high frequency can be explained in terms of an external field dependence of impedance as a result of the transverse magnetization with respect to the current direction flowing through the sample, and the skin effect of an ac current. Because an alternating current tends to be

concentrated near the surface of a conductor, the impedance Z is changing according to the current distribution and the shape of a conductor. For magnetic materials, the transverse circumferential permeability μ_ϕ affects the penetration depth since in magnetic materials it depends on permeability; $\delta_m = \delta / \sqrt{\mu_\phi}$, where δ is $c / \sqrt{2\pi\omega\sigma}$ nonmagnetic penetration depth.⁶ We can expect that with increasing frequency the dependence of the impedance, in case of a skin effect $a/\delta_m \gg 1$, is proportional to $(\omega\mu_\phi)^{1/2}$.

The experimental results are plotted selectively in Fig. 2 due to lack of space. As shown in the Fig. 2, MIR is increasing as frequency increases and MIR is decreasing rapidly as the external field increases producing the bell-shaped curves coincided with the above discussion. Since H_{ex} is a hard axis field with respect to the circumferential anisotropy, the magnetic field applied along the ribbon axis suppresses the circular magnetization by domain wall movements at low frequency regions, or the motion of localized magnetic moments at high frequency regions. Our experiment was performed in the high frequency region (100 kHz–10 MHz) where domain wall movements are highly damped by eddy currents. As the circumferential permeability decreases rap-

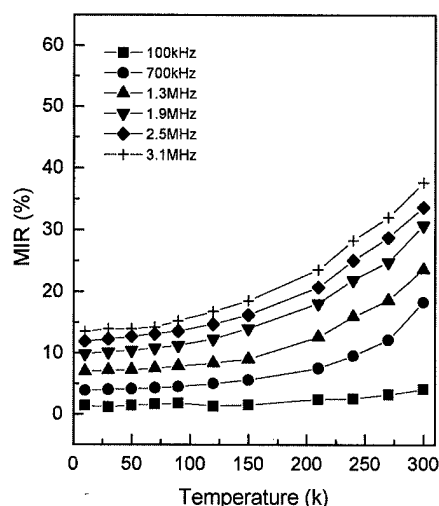


FIG. 3. Temperature dependence of maximum MIR values at various frequencies.

idly with the increment of the external field, it is responsible for MI effects in ribbons.

This process accompanied by rapid reduction in the circumferential soft magnetic properties of amorphous $\text{Co}_{66}\text{Fe}_{4}\text{NiB}_{14}\text{Si}_{15}$ ribbons as the external field increases affects the voltage across the ribbon ends. Therefore MIR can be measured directly from the changes of this voltage.

The ac current flowing through the sample generates an easy axis driving field which causes a circular magnetization field H_ϕ . The external longitudinal field H_{ex} is a hard axis field with respect to circular flux change. Therefore, MIR is linearly proportional to the driving current and becomes saturated at a current larger than about 65 mA due to the saturation of the circular magnetization M_ϕ .

One may adapt a model for the transverse biased permeability in thick ferromagnetic films where eddy current damping and the ripple field H_R incorporating with the anisotropy field H_K give rise to the peak of permeability at an external field as well as the broadening of the permeability changes as a function of the external field to explain broadening MIR curves at high frequency.⁷ It is worthily noting that the magnetoimpedance is increasing as frequency increases because the impedance is proportional to $(\omega\mu_\phi)^{1/2}$ even in case of the decrement of the transverse permeability at high frequency. The ripple field can give us further explanation of the changes in the field at the MIR peak with the increment of the current frequency.

The MIR values measured at room temperature are usually 2–3 times larger than the data measured at 10 K for all measured frequencies. For the comparison of MIR curves at different temperatures, the driving currents were fixed at 10 mA. The shapes of the MIR curves were not changed at temperature variation except MIR values. Especially, the changes of the field at the peak MIR curves were not sensitive to the variation of temperature indicating that the anisotropy field H_K was not function of temperature.

The temperature dependance of maximum MIR values at various frequencies are shown in Fig. 3, where the MIR values are increased exponentially as the temperature increases.

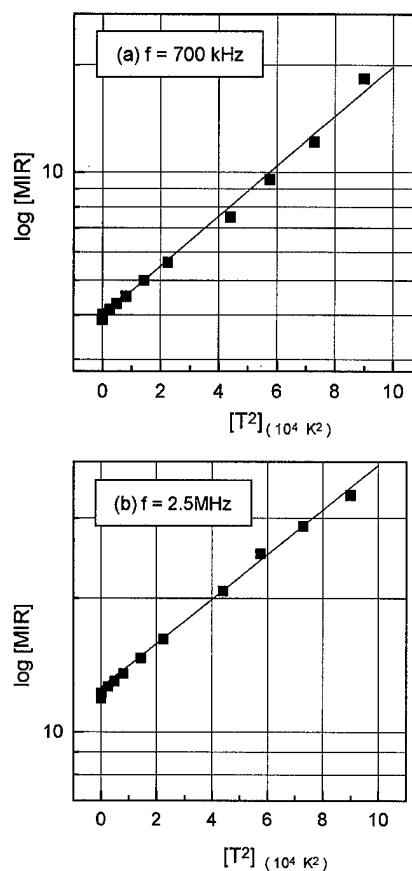


FIG. 4. Temperature dependence of maximum MIR values plotted in logarithm graphs for the frequency of (a) 700 kHz and (b) 2.5 MHz.

The maximum MIR values vs temperatures are plotted in a logarithm graph as shown in Fig. 4. The measured $\text{MIR}(T)$ data are very well fit with the function $\text{MIR}(T) = \text{MIR}(0)\exp(cT^2)$, where $\text{MIR}(0)$ is MIR at $T=0$ K and c is the constant.

Because the magnetic permeability is sensitive to the temperature, the MIR is changing rapidly as a function of temperature. The exchange energy between magnetic moments at low temperature is larger than that at high temperature. Therefore, the circular motion of magnetic moments will be frozen at low temperature resulting in lower permeabilities thereby reducing MIR values. Further research should be done for the exact explanation of the exponential increment of $\text{MIR}(T)$.

ACKNOWLEDGMENT

This work was supported by the Korean Ministry of Education Research Fund for Advanced Materials in 1996.

- ¹L. V. Panina and K. Mohri, J. Magn. Soc. Jpn. **19**, 265 (1995).
- ²K. V. Rao, F. B. Humphry, and J. L. Coasta-Krämer, J. Appl. Phys. **76**, 6204 (1994).
- ³M. Knobel, M. L. Sánchez, C. Gómez-Polo, P. Marin, M. Vázquez, and A. Hernando, J. Appl. Phys. **79**, 1646 (1995).
- ⁴L. V. Panina and K. Mohri, Appl. Phys. Lett. **65**, 1189 (1994).
- ⁵J. L. Coasta-Krämer and K. V. Rao, IEEE Trans. Magn. **31**, 1261 (1995).
- ⁶L. D. Landau and E. M. Lifshitz, *Electro-dynamics of Continuous Media* (Pergamon, Oxford, 1975).
- ⁷W. D. Doyle, X. He, P. Tang, T. Jagielinski, and N. Smith, J. Appl. Phys. **73**, 5995 (1993).

Magneto-impedance effect in high permeability NiFeMo permalloy wires

M. Vázquez,^{a)} J. M. García-Beneytez, and J. P. Sinnecker

*Instituto de Magnetismo Aplicado-UCM-RENFE and Instituto de Ciencia de Materiales-CSIC,
P.O. Box 155, 28230 Las Rozas, Madrid, Spain*

Lin Li^{b)}

Carpenter Technology Corporation, Reading, Pennsylvania 19612

The giant magneto-impedance effect (GMI) has been measured in commercial HyMu80® permalloy wires, submitted to different treatments (annealing and cold-drawing). Although hysteresis measurements show quasibistable magnetic behavior, GMI variations as high as 160% can be found in the frequency range 1–10 MHz. The frequency dependence of the GMI is also analyzed in terms of a nonhomogeneous anisotropy distribution. © 1998 American Institute of Physics.

[S0021-8979(98)24411-2]

I. INTRODUCTION

The change in the high frequency impedance of very soft ferromagnetic materials upon the action of external dc fields, has been intensively studied over the last few years.^{1–3} This effect, known as magneto-impedance (MI) is attractive for technological applications, as it combines the appearance of large changes of the impedance ratio for applied fields of few kA/m in strength,² opposite to magnetoresistance effect,⁴ where large fields are required to achieve very small variations of the resistance. The giant magneto-impedance (GMI) effect is interpreted as arising from a classical electrodynamic origin^{2,3} depending on the interaction between the magnetic field created by the ac current flowing through the sample and its magnetic domain structure. When the frequency of the current becomes high enough, the skin effect plays an important role,⁵ diminishing the effective section of the conductor and thus increasing its impedance. As the skin effect depends on the circular magnetic permeability, the sensitivity of the impedance of the sample to the action of an external field can be explained in terms of the variations of this circular permeability.

GMI has been measured in a wide range of materials, with particular interest focused on amorphous and nanocrystalline wires, ribbons, and films.^{6–8} The highest MI effect is observed for Co-rich amorphous wires, with nearly zero magnetostriction constant, where the internal stresses distribution created during quenching couple with magnetostriction to generate a relative small circular anisotropy and a circular domain pattern which enhances the value of the circular permeability. In this work we present measurements of the MI effect in commercially produced wires made with Carpenter HyMu80® alloy (Ni₈₀Mo_{4.2}Fe_{bal} permalloy). This magnetically soft alloy wire exhibits quite interesting properties regarding its magnetization processes.⁹ MI variations as high as 150% are reported, and the evolution of MI ratio with different treatments is also analyzed.

II. EXPERIMENT

Magneto-impedance measurements have been carried out in commercial Carpenter HyMu80® wires (nominal composition Ni₈₀Mo_{4.2}Fe_{bal}). Three different samples were used for the experiment, obtained submitting the initial as-cast wire to different treatments. The initial as-cast sample is produced with a diameter of 140 μm, but does not show good soft magnetic properties and special treatments are then required in order to observe magneto-impedance effect. Sample A is obtained after annealing the as-cast sample at 925 °C for 40 min in a dry H₂ atmosphere, followed by fast cooling. The diameter of the wire can be reduced to 44 μm if a cold-drawn process is carried out in the as-cast wire, leading to sample B. Further annealing of this sample is applied to obtain sample C. In each case, pieces of 20 cm length were chosen for the experiment.

Measurements were carried out in a specially designed experimental setup, similar to one described elsewhere.¹⁰ Impedance variations with respect to a dc-magnetic field are determined by measuring the voltage drop over the sample when an ac current is flowing. Frequency range analyzed sweeps from 1 to 10 MHz. The current intensity is kept constant and equal to 10 mA (rms value) by monitoring the voltage drop over a high frequency resistance connected in series with the sample. Data are acquired using a HP3589A Spectrum Analyzer. An external Helmholtz coil system is used to apply dc magnetic fields up to 11 kA/m parallel to the axis of the sample. The magneto-impedance ratio, which depends on the applied magnetic field, is defined as $\Delta Z/Z(H) = 100 \times [Z(H) - Z(H_{\max})]/Z(H_{\max})$, where H_{\max} is the maximum applied magnetic field. The system is computer controlled through a GPIB interface.¹⁰ Quasistatic hysteresis loops have been measured using a conventional induction technique.

III. RESULTS AND DISCUSSION

Sample A has a characteristic loop of a soft magnetic material with a coercivity of 15 A/m, while in sample B a significant hardening was observed, with an increase of the coercive field up to 400 A/m as a consequence of the cold

^{a)}Electronic mail: VAZQUEZV@FENIX.IMA.CSIC.ES

^{b)}Present Address: YBM Magnex Inc., 110 Terry Drive, Newtown, PA 18940.

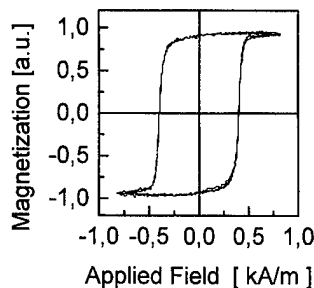


FIG. 1. Quasistatic axial hysteresis loops for cold-drawn sample (sample B).

drawing process that induces quite strong stresses in the sample. Figure 1 shows the hysteresis loop measured in this sample. Further annealing on sample B results in a decrease of the coercivity to a value of 30 A/m in sample C as a consequence of the significant relief of the internal stresses. A common feature of all the loops (samples A, B, and C) is their quasibistable magnetic behavior: there is a critical field below which it is not possible to observe remagnetization. Above this field, hysteresis loops appear, as shown in Fig. 1. This behavior, typical of amorphous wires, can be explained considering that the main contribution to the magnetization process arises from domain wall motion.

GMI measurements for samples B and C are shown in Fig. 2, where the relative variation in the impedance, $\Delta Z/Z$, is plotted as a function of the applied magnetic field. Different curves correspond to different frequencies of the ac current, in the range from 1 to 10 MHz. The general trend is the decrease of $\Delta Z/Z$ for increasing dc field as a consequence of the decrease of the circular permeability.²

The largest MI ratio of 150% is found for sample C, at a frequency of 3 MHz, while the maximum variation of sample B is of 50% and takes place at a higher frequency of 7 MHz. Results for sample A (not shown) are very similar to those of sample C. For this sample, a maximum value of 130% is found at 1 MHz.

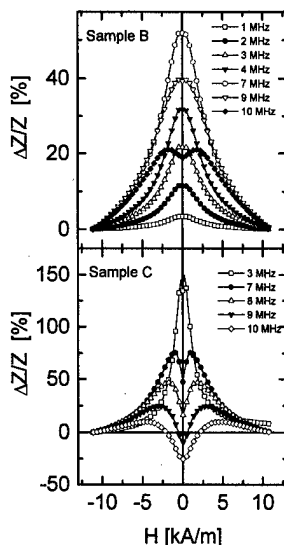
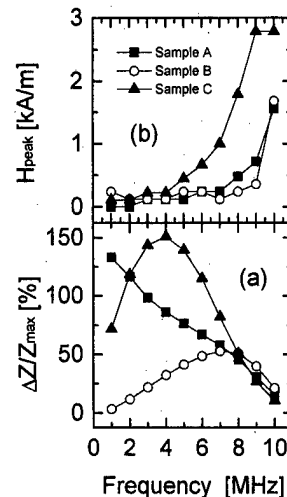


FIG. 2. Variations of the impedance of samples B (a) and C (b) with axial magnetic field for different frequencies.

FIG. 3. (a) Evolution with frequency of the maximum value of MI ratio with the frequency of the ac current and (b) evolution of the magnetic field H_{peak} where the maximum of the MI ratio takes place as a function of the frequency of the current.

The fact that sample B shows a smaller GMI ratio than samples A and C can be explained in terms of the relative magnetic softness of each sample. It is anyway remarkable the large magneto-impedance effect of sample B in spite of its much larger coercivity. As is well known, MI depends on variations of the circular permeability induced by external axial fields. These changes modify the penetration depth of the ac current and then the impedance of the sample. A softer magnetic material will, in general, present a higher variation of the circular permeability.

The evolution of the field dependence of the impedance with frequency is a common feature of all measurements performed. The maximum value of MI ratio changes with the frequency of the ac current as shown in Fig. 3(a). Samples B and C show a maximum located at 4 and 7 MHz, respectively, while sample A reaches its maximum for the lower frequency considered.

The magnetic field where the maximum value of the impedance is measured (H_{peak}) also changes with frequency. The initial peak, located at $H=0$ (for sample A), evolves into two symmetric peaks which tend to move towards higher values as the frequency increases. The same tendency has been observed for the three samples under consideration. This effect can be seen in Fig. 3(b).

The maximum in the MI ratio is usually explained in terms of the existence of a circular anisotropy. For a fixed value of the external field (equal to the anisotropy field), the anisotropy is compensated, and a maximum in the permeability (and then in the MI ratio) is expected. The observation of this maximum in wires with a bistable behavior indicates that domain wall motion cannot be the only mechanism taking part in the magnetization process, as could be deduced from the shape of the hysteresis loops (Fig. 1). Instead, magnetization rotation from the circular to the longitudinal direction must be considered, as pointed out by Atkinson and Squire,¹¹ in order to account for a variation in the circular permeability of the sample.

On the other side, the shift of the maximum towards higher fields as the frequency increases [Fig. 3(b)] can be explained considering the existence of a radial anisotropy profile in the wire. An increase in the frequency is associated with a decrease in the penetration depth of the ac current through the sample. Then, for very high frequencies, the current is flowing only through a layer close to the surface of the material. As the transport properties (impedance in this case) depend on the behavior of this region of the material, the measurement of the impedance allows us to get information of the region close to the surface. The observed increase with frequency of the field where MI ratio is maximum (the circular anisotropy field) can be explained considering that the anisotropy is not homogeneous in all the wire section, but increases as one approaches the surface. As the local anisotropy is higher, the peak moves toward higher values. For very high frequencies, the anisotropy can be so large that the maximum applied field is not enough to saturate the sample. In this case, the impedance can have a smaller value for $H = 0$ than for $H = 11$ kA/m. This is the case observed for sample C at 10 MHz.

IV. CONCLUSION

High values of MI are reported for a Ni-rich permalloy wire presenting a quasibistable behavior. The analysis of the frequency evolution of the curves reveals the existence of a

radial profile of anisotropies, and proposes MI measurements as a useful tool to study the magnetic behavior of regions close to the surface of the wire.

ACKNOWLEDGMENTS

The financial support of the Spanish CICYT under project MAT95/0273 is acknowledged. J. P. Sinnecker thanks the Brazilian agency FAPESP for the post-doctoral fellowship.

- ¹K. Mohri, T. Kohzawa, K. Kawashima, H. Yoshida, and L. V. Panina, *IEEE Trans. Magn.* **28**, 3150 (1992).
- ²L. V. Panina, K. Mohri, K. Bushida, and M. Noda, *J. Appl. Phys.* **76**, 6198 (1994).
- ³R. S. Beach and A. E. Berkowitz, *Appl. Phys. Lett.* **64**, 3652 (1992).
- ⁴M. N. Baibich, J. M. Broto, A. Fert, F. Nguyen van Dau, F. Petroff, P. Etienne, G. Creuzet, A. Fiederich, and J. Chazeles, *Phys. Rev. Lett.* **61**, 2472 (1988).
- ⁵Landau and Lifshitz, *Electrodynamics of Continuous Media* (Pergamon, Oxford, 1975), p. 195.
- ⁶F. L. A. Machado, C. S. Martins, and S. M. Rezende, *Phys. Rev. B* **51**, 3926 (1995).
- ⁷J. Velázquez, M. Vázquez, D. X. Chen, and A. Hernando, *Phys. Rev. B* **50**, 16 737 (1994).
- ⁸R. L. Sommer and C. L. Chien, *Appl. Phys. Lett.* **67**, 3346 (1995).
- ⁹L. Li, *J. Appl. Phys.* **81**, 4287 (1997).
- ¹⁰J. P. Sinnecker, M. Knobel, M. L. Sartorelli, J. Shonmaker, and F. C. S. Silva, *Proceedings of the Soft Magnetic Materials Conference SMM13*, Grenoble, Sept. 1997.
- ¹¹D. Atkinson and P. T. Squire, *IEEE Trans. Magn.* **33**, 3364 (1997).

The influence of field- and stress-induced magnetic anisotropy on the magnetoimpedance in nanocrystalline FeCuNbSiB alloys

G. V. Kuryandskaya,^{a)} J. M. García-Beneytez, M. Vázquez, and J. P. Sinnecker^{b)}

*Instituto de Magnetismo Aplicado UCM-RENFÉ and Instituto de Ciencia de Materiales-CSIC,
P.O. Box 155, Las Rozas 28230 Madrid, Spain*

V. A. Lukshina and A. P. Potapov

Institute of Metal Physics, UD RAS GSP-170, Ekaterinburg 620219, Russia

The correlation between magnetic anisotropy and magnetoimpedance has been studied in field- and stress-annealed Fe_{73.5}Cu₁Nb₃Si_{13.5}B₉ ribbons. As-cast and previously nanocrystallized samples were submitted to different annealing conditions ($T=500, 530$, and 560°C and tensile stress $\sigma=150$ MPa) in order to induce different magnetic anisotropy. The magnetoimpedance ratio $[\Delta Z/Z]$ was measured at 3 MHz using a driving current $I_{\text{rms}}=10$ mA. An hysteretic behavior of the magnetoimpedance ratio is observed. This hysteretic behavior is interpreted considering the magnetization process for samples exhibiting different magnetic anisotropies. © 1998 American Institute of Physics. [S0021-8979(98)39511-0]

INTRODUCTION

It is well known that a suitable annealing ($T=540^\circ\text{C}$, $t=1$ h) of the amorphous FeSiBNbCu alloys (known as FINEMET) leads to a nanoscale grain-size multiphase structure, which has excellent soft magnetic properties.^{1,2} A magnetic anisotropy can be induced if this annealing is performed under the application of a magnetic field, an external stress, or both of them.³⁻⁵

The so-called giant magnetoimpedance (GMI) has been extensively studied in the last few years due to its technological impact.^{6,7} This effect arises from a field-induced change in the classical skin depth that follows the changes in the magnetic circular permeability when a high-frequency current flows through the sample. The effect is also sensitive to the anisotropies of the material and can exhibit hysteretic behavior.⁸⁻¹⁰ Some results on the giant magnetoimpedance of field-annealed FINEMET ribbons were presented recently,^{6,10} but up to now an analysis of the role of field and stress annealing for the GMI ratio, i.e., of induced anisotropies, to the best of our knowledge is still missing.

The aim of this paper is to study the influence of different heat treatments, like field and/or stress annealing, on the giant magnetoimpedance in Fe_{73.5}Cu₁Nb₃Si_{13.5}B₉ samples and its hysteretic behavior. The results show that the hysteretic behavior is related to the irreversible magnetization processes of the samples.

EXPERIMENTAL PROCEDURE

Amorphous ribbons of the composition Fe_{73.5}Cu₁Nb₃Si_{13.5}B₉ were prepared by a conventional melt spinner. The dimensions of the samples chosen for magnetic measurements were 100 mm×0.2 mm×18 μm . Field an-

nealing was done in two regimes: (i) IF: annealing of as-cast samples for 1 h at 540°C with a magnetic transverse field of 240 kA/m, and (ii) IIF: annealing the as-cast samples for 1 h at 540°C and subsequent annealing at the same conditions but under a magnetic transverse field of 240 kA/m. Stress annealing was carried out in a vertical furnace as described in detail elsewhere.⁴ The sample is suspended inside a furnace and a load is fastened to the ribbon edge using a special clamp. This stress annealing was also performed in two ways: (i) IS: annealing of an as-cast sample at $T=530^\circ\text{C}$ for $t=2$ h under a tensile stress of $\sigma=150$ MPa, and (ii) IIS: using a previously nanocrystallized sample (annealed at $T=530^\circ\text{C}$, $t=1$ h) and then submitting this sample to a stress annealing at temperatures $T=500, 530$, and 560°C under a tensile stress of $\sigma=150$ and 290 MPa. Samples annealed $T=530^\circ\text{C}$ for $t=1$ h without field or stress (conventional annealing) were also used.

Hysteresis loops of the samples were measured by the conventional flux method. The anisotropy constants induced by field or stress annealing, K_u , were deduced from the axial hysteresis loops as $K_u = \mu_0 M_s H_k / 2$, where $\mu_0 M_s$ is the saturation magnetic polarization and H_k is the anisotropy field. The magnetoimpedance was measured using a fully computer-controlled setup.¹¹ The change of ac impedance of the sample was evaluated by measuring the ac voltage drop across the sample while passing a constant ac current through it. The GMI ratio was defined as $\Delta Z/Z(H) = 100 \times [Z(H) - Z(H_{\text{max}})]/Z(H_{\text{max}})$, for a maximal field $H_{\text{max}} = \pm 10.5$ kA/m. The constant current $I_{\text{rms}}=10$ mA was supplied by a HP 3589A spectrum/network analyzer and the frequency was fixed at 3 MHz. The axial dc field was produced by a pair of Helmholtz coils.

In all the cases here discussed, the annealings induce a transverse magnetic anisotropy besides the magnetic softening (i.e., coercivity) typical of the nanocrystallization process of those samples.

^{a)}Permanent address: Institute of Metal Physics UD RAS GSP-170, Kovalenskaya str. 18, Ekaterinburg 620219, Russia.

^{b)}Corresponding author: J. P. Sinnecker, Instituto de Magnetismo Aplicado RENFE-UCM. P.O. Box 155, Las Rozas 28230 Madrid, Spain.

Electronic mail: sinn@arrakis.es

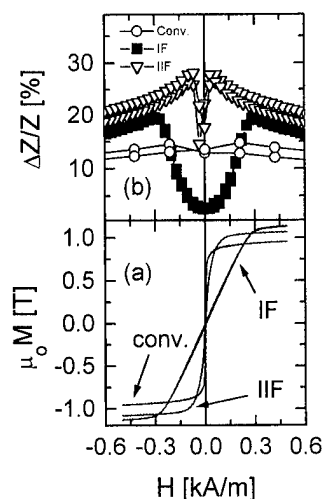


FIG. 1. (a) Hysteresis loops and (b) giant magnetoimpedance ratio ($\Delta Z/Z$) measured in field- (IF and IIF) and conventional- (conv.) annealed $\text{Fe}_{73.5}\text{Si}_{13.5}\text{B}_9\text{Nb}_3\text{Cu}_1$ ribbons.

RESULTS AND DISCUSSION

Figure 1 shows the hysteresis loops and GMI ratio curves for the samples after IF and IIF annealings, and also after the conventional one. Both treatments in a magnetic field induce a transversal magnetic anisotropy, the one corresponding to annealing in one step (IF) being higher than that in two steps (IIF). The GMI curve for the conventional annealing shows a maximum about 15% with a typical GMI behavior. The IF annealing gives rise to a nonhysteretic GMI curve with maximum $\Delta Z/Z$ of about 19% for an applied dc field of ± 300 A/m, which corresponds to the anisotropy field H_k of this sample. The IIF annealing promotes $\Delta Z/Z$ values as large as 28%, with a GMI curve characterized by a two-peak shape and its hysteretic character. Although the obtained GMI value is higher, the observed hysteresis may be unsuitable for technological applications.

Figure 2 shows the axial hysteresis loops and GMI curves after IS and IIS stress annealing. In this case, the higher the temperature of the stress annealing the higher the value of the induced magnetic anisotropy and the coercive field. IS annealing leads to the state with a smaller GMI ratio (about 7.5%) and also shows a hysteretic behavior in the field interval ± 1.5 kA/m.

The hysteresis of the GMI is observable exactly within the same field region as the axial hysteresis (see the hysteresis loop in Fig. 2).^{9,12} Figure 3 shows the hysteresis of the GMI ratio observed for the sample submitted to IIS at 560 °C.

These curves can be explained considering the corresponding magnetization processes that take place in the samples. The samples are submitted to two kinds of magnetic fields, i.e., the ac field generated from the ac current flowing for the GMI measurement and the superimposed dc axial field to the last one. At the saturation, the dc field determines the magnetization direction, and the ac field has only a minor role, being unable to affect the magnetization vector inside the sample. When the dc field is decreased, the magnetization starts to sense the presence of the ac field, and

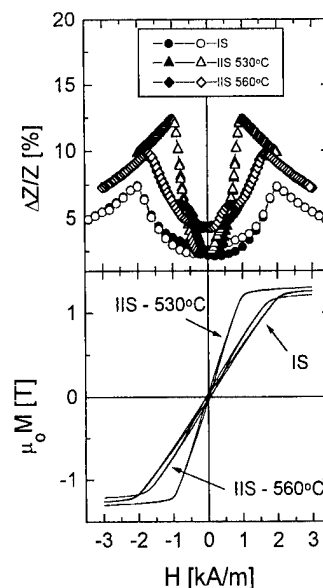


FIG. 2. (a) Hysteresis loops and (b) giant magnetoimpedance ratio ($\Delta Z/Z$) measured in stress-annealed $\text{Fe}_{73.5}\text{Si}_{13.5}\text{B}_9\text{Nb}_3\text{Cu}_1$ ribbons according to procedures IS and IIS. Open and solid symbols in (b) refer to decreasing and increasing field, respectively.

the magnetization vector starts to rotate, increasing thus the circular permeability, and thus the impedance. When the anisotropy field is reached, the magnetization vector is more free to rotate under the influence of the ac field, and the circular permeability exhibits a maximum. At this point, there is a maximum in the GMI. As the field is further decreased, domain-wall irreversible processes start to take place, as clearly seen by the axial hysteresis loops, which results in irreversible contributions to the circular magnetization processes, and thus, a hysteretic GMI can be observed. The different GMI behavior of the different samples can be explained considering that the differences in the induced an-

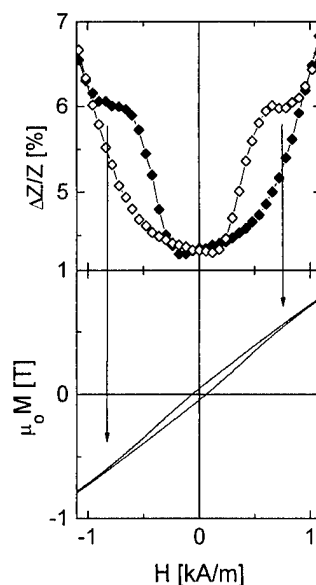


FIG. 3. (a) Hysteresis loop and (b) GMI ratio ($\Delta Z/Z$) measured in a stress-annealed $\text{Fe}_{73.5}\text{Si}_{13.5}\text{B}_9\text{Nb}_3\text{Cu}_1$ ribbon according to procedure IIS. Open and solid symbols in (b) represent decreasing and increasing field, respectively.

isotropy, imposed by the distinct annealing conditions, produce specific domain structures with particular magnetization processes and GMI.

In view of this, magnetoimpedance measurements can be considered as a valid and alternative tool to investigate the magnetic behavior of ferromagnetic samples. On one side, it is possible to obtain information on the efficiency of different annealing methods to induce transverse anisotropy. On the other side, the appearance of hysteresis in the GMI curves denotes the irreversibility of the dynamic process of circular magnetization. As shown in Fig. 3, the magnetic field where hysteresis in the impedance appears, roughly corresponds with the field where hysteresis in the axial magnetization is found. Thus, this irreversibility, associated with the behavior of the circular permeability under the action of an axial field, can be studied through the analysis of the shape of the GMI curves.

CONCLUSIONS

Transverse magnetic anisotropy induced by different field and stress annealing in nanocrystalline FINEMET changes the domain structure, modifying the magnetization processes and the GMI behavior. Field annealing at 540 °C for 1 h combined with nanocrystallization produces a transversal anisotropy with $K_u = 75 \text{ J/m}^3$, which is characterized by nonhysteretic magnetoimpedance curves. Field annealing on previously nanocrystallized samples produce higher GMI values, but extremely hysteretic in the field interval applied during the measurements.

Stress annealings at 500, 530, or 560 °C with tensile stress $\sigma = 150 \text{ MPa}$ for 1 h give rise to a higher stress-induced magnetic anisotropy but a smaller GMI maximum ratio. All these states are characterized by a hysteretic GMI in the low-field region near zero field, where some irreversibility of the magnetization process appears. It was found

also that for the higher stress-induced magnetic anisotropy, a more complex shape of the GMI curves is observed, with a final appearance of additional peaks in a field which nearly corresponds to the point of the inflection of the axial hysteresis loop. Maximum $\Delta Z/Z$ was always observed for applied dc fields corresponding to the induced anisotropy field. Hysteretic behavior of the magnetoimpedance in nanocrystalline FINEMET ribbons after different regimes of dc field and stress annealing can be a critical parameter from the point of view of technological applications of this material as GMI sensors.

ACKNOWLEDGMENTS

One of the authors (G.V.K.) acknowledges the Spanish Ministerio de Educación y Cultura for supporting Project No. SAB95-0421. One of the authors (J.P.S.) thanks the Brazilian agency FAPESP for the postdoctoral fellowship. This work was supported by the Spanish CICYT under Project No. MAT95/0273.

¹Y. Yoshisawa, S. Oguma, and K. Yamauchi, *J. Appl. Phys.* **64**, 6044 (1988).

²G. Herzer, *IEEE Trans. Magn.* **25**, 3327 (1989).

³B. Hoffmann and H. Kronmüller, *J. Magn. Magn. Mater.* **152**, 91 (1996).

⁴V. A. Lukshina, N. V. Dmitrieva, and A. P. Potapov, *Phys. Met. Metallogr.* (in Russian) **N4**, 376 (1996).

⁵G. Herzer, *J. Magn. Magn. Mater.* **157-158**, 133 (1996).

⁶G. V. Kurlyandskaya, M. Vázquez, E. H. C. P. Sinnecker, A. P. Zhukov, J. P. Sinnecker, A. Hernando, and M. El Ghannami, *Proceedings of the VI International Workshop on Non-Crystalline Solids* (World Scientific, to be published).

⁷R. S. Beach and E. Berkowitz, *Appl. Phys. Lett.* **64**, 3652 (1994).

⁸L. V. Panina and K. Mohri, *Appl. Phys. Lett.* **65**, 1189 (1994).

⁹J. P. Sinnecker, P. Tiberto, G. V. Kurlyandskaya, E. H. C. P. Sinnecker, M. Vázquez, and A. Hernando, *J. Appl. Phys.* (submitted).

¹⁰R. L. Sommer and C. L. Chien, *Appl. Phys. Lett.* **67**, 857 (1995).

¹¹J. P. Sinnecker, M. Knobel, M. L. Sartorelli, J. Shonmaker, and F. C. S. Siva, *J. Phys.* (to be published).

¹²L. V. Panina and K. Mohri, *J. Magn. Magn. Mater.* **157/157**, 137 (1996).

Giant magneto-impedance effect in nanocrystalline glass-covered wires

H. Chiriac,^{a)} T. A. Óvári, and C. S. Marinescu

National Institute of R&D for Technical Physics, 47 Mangeron Boulevard, 6600 Iași 3, Romania

We investigate the evolution of the magneto-impedance (MI) response of $\text{Fe}_{73.5}\text{Cu}_1\text{Nb}_3\text{Si}_{13.5}\text{B}_9$ glass-covered wires with the annealing temperature, starting from the as-cast amorphous state up to 600 °C. As-cast FeCuNbSiB amorphous glass-covered wires display a MI ratio of about 1%, this value increasing with the annealing temperature to about 5% for 550 °C when the nanocrystalline phase appears. For wires which have had the glass removed, the MI ratio increases from 5% for the as-cast amorphous state up to 28% after the appearance of the nanocrystalline phase. The MI is larger than that found in CoFeSiB amorphous wires after glass removal. Annealing over 550 °C leads to a decrease of the MI ratio for both glass-covered samples and samples with the glass coating removed. The results demonstrate the role of soft magnetic properties on the sensitivity of the MI effect. © 1998 American Institute of Physics. [S0021-8979(98)51111-5]

I. INTRODUCTION

The giant magneto-impedance (GMI) effect, that consists of a variation of the high frequency impedance of a magnetic conductor when it is subjected to a dc magnetic field, was extensively studied over the last few years and was found to be useful for sensing applications.^{1,2} The largest GMI effect was obtained in $\text{Co}_{68.15}\text{Fe}_{4.35}\text{Si}_{12.5}\text{B}_{15}$ amorphous wires with diameters reduced down to 30 μm by cold drawing in several steps. The wires were subsequently tension annealed in order to obtain a circumferential domain structure in the entire volume, since it was shown that this is the most favorable case for a sensitive GMI response.¹ The impedance behavior is strongly related to the basic magnetic properties of the materials, and to the changes in the dynamic magnetization processes as the frequency increases.

The aim of this article is to study the sensitivity and magnitude of the GMI effect in $\text{Fe}_{73.5}\text{Cu}_1\text{Nb}_3\text{Si}_{13.5}\text{B}_9$ nanocrystalline glass-covered wires. Changes induced when the glass coating is removed by chemical etching are also considered. The results are discussed by taking into account the specific magnetic properties and behavior of these wires.

The results obtained are important from the point of view of the applications of these materials in magnetic sensors working on the GMI principle.

II. EXPERIMENT

We prepared $\text{Fe}_{73.5}\text{Cu}_1\text{Nb}_3\text{Si}_{13.5}\text{B}_9$ amorphous glass-covered wires by glass-coated melt spinning. For our experimental investigations we have chosen wires with a metallic core diameter of 15 μm and a glass cover thickness of 5 μm . The amorphous state was checked by x-ray diffraction. $\text{Fe}_{73.5}\text{Cu}_1\text{Nb}_3\text{Si}_{13.5}\text{B}_9$ amorphous glass-covered samples and samples obtained after glass removal were annealed in vacuum for 1 h at temperatures up to 600 °C. Each stage of annealing was performed starting from an amorphous wire, which was annealed for 1 h at a given annealing temperature, T_a , e.g., 500, 550 °C, etc.

GMI measurements were performed on glass-covered samples and on samples after glass removal after each stage of annealing at frequencies up to 10 MHz, using a digital oscilloscope coupled with a computer that allowed data acquisition and processing. We studied the impedance behavior as function of frequency, f , and axial dc field, H_{dc} .

III. RESULTS AND DISCUSSION

We analyze in the following the sensitivity of the GMI effect in FeCuNbSiB glass-covered wires and wires after glass removal, starting from the amorphous state after different stages of annealing. Figure 1 shows the frequency dependence of the MI ratio, $\Delta Z/Z$, defined as $[Z(H_{dc}=0) - Z(H_{dc}=1000 \text{ A/m})]/Z(H_{dc}=0)$, where Z is the impedance for glass-covered FeCuNbSiB wires with the annealing temperature, T_a , as a parameter.

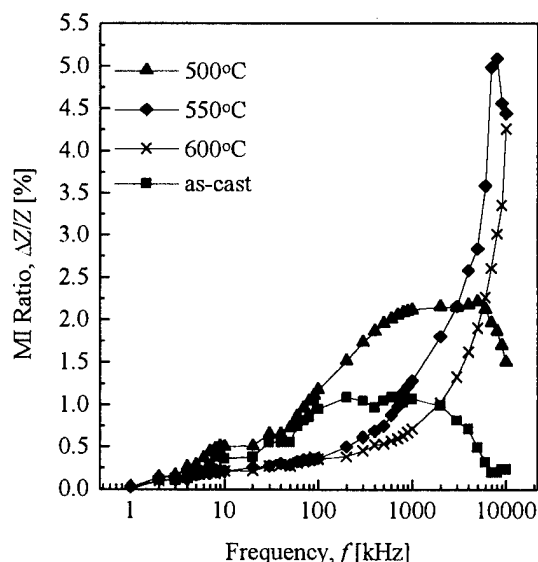


FIG. 1. Frequency dependence of the magneto-impedance ratio, $\Delta Z/Z = [Z(H_{dc}=0) - Z(H_{dc}=1000 \text{ A/m})]/Z(H_{dc}=0)$, for glass-covered FeCuNbSiB wires with the annealing temperature as a parameter.

^{a)}Electronic mail: hchiriac@phys-iasi.ro

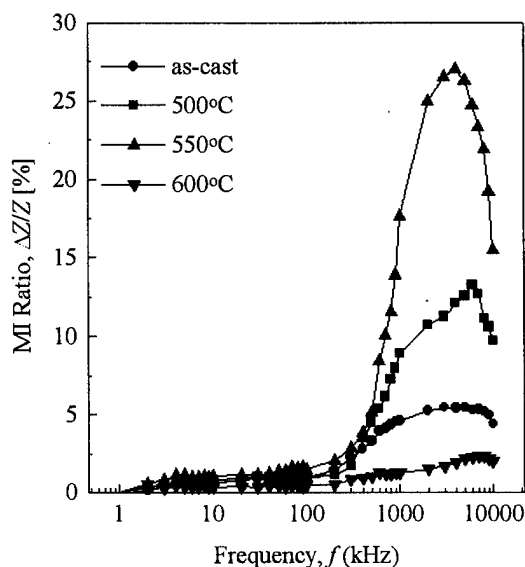


FIG. 2. Frequency dependence of the magneto-impedance ratio, $\Delta Z/Z$, for FeCuNbSiB wires after glass removal with the annealing temperature as a parameter.

The MI ratio is directly related to the sensitivity of the GMI effect since it indicates the behavior of Z at two extreme values of the axial field H_{dc} : 0 A/m, where Z is affected only by the frequency f of the ac driving current, and 1000 A/m, which is a high value field that completely damps the magnetization processes in the circumferential direction of a soft magnetic wire. The circumferential magnetization processes play a decisive role in determining the magnitude and sensitivity of the GMI effect. The GMI effect is directly related to the magnitude of the skin effect, since the dynamics of the magnetization in the circumferential direction—domain wall movements or rotations—affects the behavior of the circumferential permeability μ_θ , which, in turn, influences the magnetic penetration depth $\delta_m = (\rho / \pi \cdot f \cdot \mu_\theta)^{1/2}$, where ρ is the resistivity of the wire.

One observes that as-cast amorphous FeCuNbSiB displays a GMI effect with a maximum MI ratio of 1%. This very small value of $\Delta Z/Z$ is due to the high positive magnetostriction of amorphous FeCuNbSiB glass-covered wires ($\lambda \approx 25 \times 10^{-6}$) that leads through magnetomechanical coupling with internal stresses to a domain structure with axially magnetized inner core and radially magnetized outer shell. After annealing at 500 °C, the wires become magnetically softer due to stress relief, and the maximum MI ratio increases to about 2%. After annealing for 1 h at 550 °C, the nanocrystalline phase appears,³ and consequently the wires become magnetically softer, the maximum MI ratio increasing to more than 5%. Annealing over 550 °C leads to a dimensional increase of the α -FeSi crystalline grains and consequently to a deterioration of the soft magnetic properties, resulting in a decrease of the maximum MI ratio to less than 4.5%.

Figure 2 shows the frequency dependence of the MI ratio, $\Delta Z/Z$, for FeCuNbSiB wires after glass removal, with the annealing temperature, T_a , as a parameter.

One observes that amorphous FeCuNbSiB wires after glass removal display a maximum MI ratio of 5% before any

annealing. This behavior is expected to be due to the stress relief produced by glass removal. After annealing at 500 °C, the maximum MI ratio increases to about 14% due to further stress relief produced by annealing. Once the nanocrystalline phase appears (annealing at 550 °C), the maximum MI ratio reaches about 28%. Annealing over 550 °C has the same result as that in the case of the glass-covered wires: the good soft magnetic properties suffer deterioration due to the increase in size of the crystalline grains.

Nanocrystalline wires without glass have a much more sensitive GMI response as compared to glass-covered ones since they are magnetically softer (the coercive force is about 100 A/m for the former and almost 400 A/m for the latter). The GMI response of nanocrystalline wires without glass is even better than that of CoFeSiB amorphous wires after glass removal,⁴ with their maximum MI ratio being about 20%. In addition, the maximum MI ratio of nanocrystalline wires after glass removal is obtained at lower frequencies (~ 4 MHz) as compared to CoFeSiB amorphous ones after glass removal (~ 9 MHz). Both aspects can be explained by noting that at high frequencies, where circumferential magnetization is achieved by spin rotations, the differences in the soft magnetic properties from the outer shells of the two materials play an essential role. Thus, in CoFeSiB amorphous wires after glass removal a larger energy, provided by the circumferential ac field, is required in order to rotate the magnetic moments from the easy axis direction toward any other direction, since in this case, the circumferential magnetoelastic anisotropy from the outer shell, determined by the coupling between magnetostriction and large compressive circumferential stresses is important.⁵ On the other hand, nanocrystalline wires without glass are magnetically softer due to their vanishing magnetostriction.³ Thus, a larger μ_θ of nanocrystalline wires without glass, compared to the amorphous ones without glass, is expected. The direct consequence of this fact is a shift toward lower values of the frequency where the maximum MI ratio is detected in nanocrystalline wires, and is a more sensitive effect in this case. Under these circumstances, we can state that good soft magnetic properties are essential in obtaining a sensitive GMI response of a given material. Furthermore, the presence of good soft magnetic properties may be considered as a second criterion in the choice of an appropriate material for a GMI-based application, together with the already widely accepted criterion that requires an appropriate domain structure, e.g., a circumferential one for wires and a transverse one for ribbons and thin films.

This statement is supported by the fact that in the discussed frequency range the sensitivity of the GMI response of nanocrystalline wires after glass removal is very close to that of cold-drawn amorphous CoFeSiB ones.⁴ The tendency of these thin wires (15 μm in diameter) to reach a similar magnitude of the GMI effect ($\sim 28\% - 30\%$) like the cold-drawn ones (30 μm in diameter), emphasizes once again the close relationship between good soft magnetic properties and a sensitive GMI effect, since at close values of the resistivities, it is obvious that the differences in μ_θ play an important role in the magnitude of the skin effect.

The above results allow us to suggest a new application of the GMI effect, namely, its use for directly monitoring the structural changes that occur in amorphous ferromagnets during annealing, and especially those during specific annealing for nanocrystallization.

IV. CONCLUSION

We investigated the GMI effect in $\text{Fe}_{73.5}\text{Cu}_1\text{Nb}_3\text{Si}_{13.5}\text{B}_9$ nanocrystalline glass-covered wires and wires after glass removal. Nanocrystalline wires without glass display the more sensitive GMI response. The results are explained by considering the structural changes that occur during annealing and their effect on the magnetic properties of both glass-covered wires and wires after glass removal. The results obtained

indicate the importance of good soft magnetic properties for a sensitive GMI response. Our study is important with regard to the selection of a proper material for the achievement of GMI-based magnetic sensors.

¹L. V. Panina, K. Mohri, K. Bushida, and M. Noda, J. Appl. Phys. **76**, 6198 (1994).

²L. V. Panina, K. Mohri, T. Uchiyama, K. Bushida, and M. Noda, in *Nanostructured and Non-Crystalline Materials*, edited by M. Vázquez and A. Hernando (World Scientific, Singapore, 1995), p. 461.

³H. Chiriac, T. A. Óvári, Gh. Pop, and F. Barariu, J. Appl. Phys. **81**, 5817 (1997).

⁴H. Chiriac, T. A. Óvári, and C. S. Marinescu, IEEE Trans. Magn. **33**, 3352 (1997).

⁵H. Chiriac, Gh. Pop, T. A. Óvári, and F. Barariu, IEEE Trans. Magn. **32**, 4872 (1996).

High frequency properties of glass-coated microwire

A. N. Antonenko,^{a)} E. Sorkine, A. Rubshtein, V. S. Larin,^{b)} and V. Manov

Advanced Metal Technologies Ltd., 1 Ha'atmaut St., P.O.B. 2903, Even Yehuda 40500, Israel

Static and high-frequency 1–30 MHz properties of the $(\text{Co}_{100-x}\text{Mn}_x)_{75}\text{B}_{15}\text{Si}_{10}$ microwires cast using the modified Taylor's technique are reported. The hysteresis loop and the frequency dependence of permeability indicate that the longitudinal magnetization process occurs by coherent rotation of the moments. The values of static permeability are in good agreement with those predicted by the theory of ferromagnetic resonance where damping is taken into account. We observed a close correlation between the static permeability and the high-frequency limit (the frequency up to which the real part of permeability is still constant). For glass-coated CoMn microwires, this limit is considerably higher than that given by the Snoek equation. © 1998 American Institute of Physics. [S0021-8979(98)39611-5]

INTRODUCTION

Glass-coated amorphous microwires, cast by a modified Taylor's technique is a comparatively scarcely studied magnetic material. Hereafter, we will adhere to the term "microwire" to distinguish this material from amorphous wires produced by other methods, for example, by rotating water quenching. Recently, several papers devoted to the investigation of microwires were published.^{1,2} It was shown that microwires demonstrate unique magnetic properties. In particular, Fe-based microwires with positive magnetostriction demonstrate bistable behavior, with the critical length as small as 2 mm.² The natural ferromagnetic resonance in the 2–12 GHz frequency range was observed in Fe-based microwires.³ The permeability of microwires reaches an extremely high value (up to 1000) in this frequency range, that suggest that microwires may be a promising material for super-high-frequency applications.

Co-based microwires with negative magnetostriction are studied very scarcely. Static magnetic properties of such microwires were reported in Ref. 4. The investigation of the GMI effect indicates that Co-based microwires have a high permeability in a radio-frequency range of 1–100 MHz, however, there are no relevant publications relating to the direct measurement of permeability in this frequency range.

The present work reports the measurement of the complex permeability of Co-based microwires in the 1–30 MHz frequency range. The correlation between static and high-frequency magnetic properties of microwires are studied too. Another aspect of this work is an attempt to provide a theoretical description of microwire behavior. The dynamic behavior of a magnetic material such as ferrite or amorphous ribbon is rather complicated. In high-frequency magnetic fields, both moment rotation and domain wall motion can take place. Calculations of permeability and of energy losses with different modes of remagnetization are extremely difficult. From this point of view, the microwire seems to be

easier to model. Unlike other materials, it is possible to use a simple model for the description of its dynamic properties.

EXPERIMENT

We have investigated microwires of $(\text{Co}_{100-x}\text{Mn}_x)_{75}\text{B}_{15}\text{Si}_{10}$ alloys, where x lies in the range from 4 to 8. In this range of Mn content, the alloy magnetostriction passes through zero. The microwires were cast by Taylor's technique. The diameter of the metal was in the 6–10 μm range, and the glass coating was 2–4 μm thick.

We have measured static hysteresis loops as well as real and imaginary parts of the permeability in the 1–30 MHz frequency range. The static hysteresis loop was plotted using a conventional hysteresisgraph. The microwire was placed in the alternating magnetic field of a long solenoid. A signal proportional to the solenoid current was applied to the X channel of an oscilloscope, while remagnetization signal was detected by a small pickup coil and, after integrating, was applied to the Y channel.

The permeability was measured at high frequency using the LC resonance method. First, the circuit with a coreless coil was adjusted to resonance at certain frequency by changing the capacitance. The value of the capacitance, C_1 and the quality factor, Q_1 were measured. The sample consisting of several microwires was placed into the coil, and then the circuit was adjusted to resonance again by changing the value of the capacitor. The new values, C_2 and Q_2 , were measured. Real and imaginary parts of permeability were calculated as follows:

$$\mu' = 1 + \left(\frac{C_1}{C_2} - 1 \right) \cdot \frac{D^2}{nd^2}, \quad (1)$$

$$\mu'' = \left(\frac{1}{Q_2} - \frac{1}{Q_1} \right) \cdot \frac{D^2}{nd^2}, \quad (2)$$

where D is the diameter of coil, d is the diameter of microwire core, and n is the number of microwires.

The static hysteresis loop depends substantially on the Mn content of the microwire material. Mn-rich microwires feature a rectangular hysteresis loop. With decreasing Mn

^{a)}On leave from «AmoTec» Ltd., bd Dachia 15/78, 2038 Kishinev, Moldova.

^{b)}«AmoTec» Ltd, bd Dachia 15/78, 2038 Kishinev, Moldova.

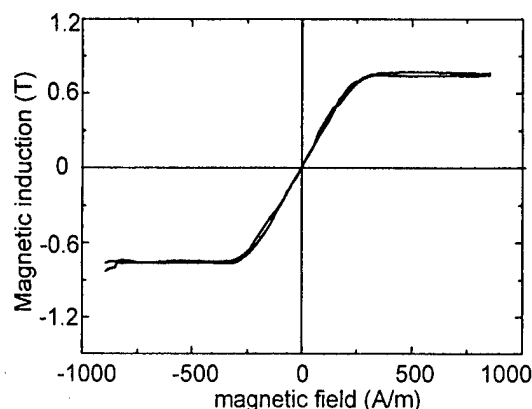


FIG. 1. The typical hysteresis loop of microwire with Mn<6%.

content, the value of coercivity decreases and the loop becomes gradually unhysteretic. Further decreasing of the Mn content does not change the shape of the loop, only its slope, which decreases. The anisotropy field of the material thus increases with the decreasing in the Mn content. The typical loop of microwires with less than 6% Mn is presented in Fig. 1. This loop has an inflection point approximately corresponding to the anisotropy field H_k .

The frequency dependences of real and imaginary parts of the permeability for different values of the anisotropy field are presented in Figs. 2 and 3. The real part of permeability is nearly constant in a certain frequency range, and it decreases rapidly as the frequency increases over a critical value f_r . The frequency dependence of the imaginary part shows a maximum at f_r . The static permeability as well as f_r depend on anisotropy field H_k . Table I summarizes the obtained results.

DISCUSSION

The hysteresis loops we obtained are typical for the case of an external magnetic field applied perpendicular to the plane of easy magnetization. In our experiments, this plane is perpendicular to the microwire axis. The magnetic anisotropy is induced by the stresses quenched in the microwire core. These stresses arise during the process of microwire

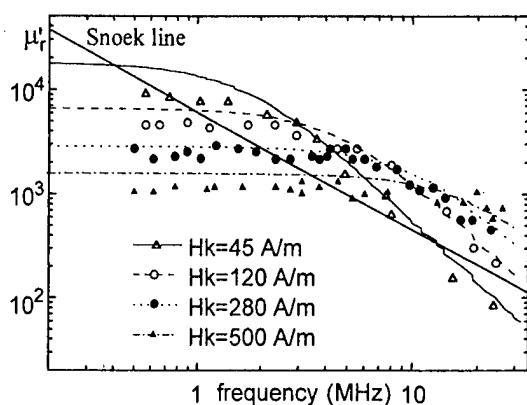


FIG. 2. Frequency dependence of the real part of the permeability. The symbols mean experimental data, continuous curves were obtained from the proposed model.

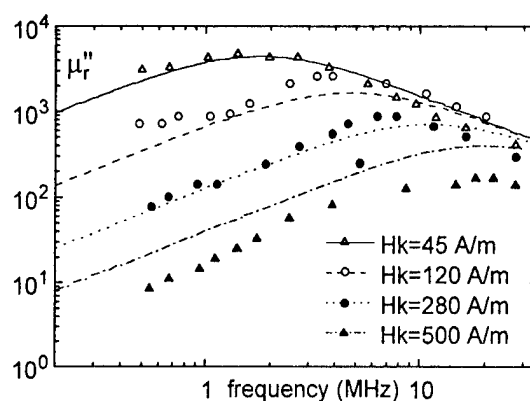


FIG. 3. Frequency dependence of the imaginary part of the permeability. The symbols mean experimental data, continuous curves were obtained from the proposed model.

fabrication as a result of difference in thermal expansion coefficient between glass and metal. As shown in Ref. 5, the value of internal stresses σ may reach 1 GPa. If the Mn content is lower than approximately 6%, the magnetostriction constant λ becomes negative. Due to the effect of magnetoelastic anisotropy, which is proportional to $\lambda\sigma$, the moments will lie in a plane perpendicular to the microwire axis, and the external magnetic field applied along the microwire axis will produce a coherent rotation of moments.

At present time, there is not a definite picture of the magnetic structure in the Co-based microwires. The appearance of circumferential anisotropy like in the conventional amorphous wires seems to be the most probable, however, there is no direct confirmation of this supposition. Nevertheless, the magnetic properties of microwires may be described without knowing the definite magnetic structure. The further consideration is based on the following assumptions:

(a) The axis of easy magnetization lies in the plane perpendicular to the microwire axis. In each point of microwire the magnetic anisotropy has the same value H_k and magnetization vector \mathbf{M} coincides with the direction of magnetic anisotropy.

(b) The coherent moments rotation is the only mechanism of remagnetization.

The Gilbert equation for this mechanism is⁶

$$\frac{d\mathbf{M}}{dt} = \nu \cdot \left\{ \mathbf{M} \times \left(\mathbf{H} - \frac{\alpha}{\nu M} \cdot \frac{d\mathbf{M}}{dt} \right) \right\}, \quad (3)$$

where \mathbf{M} is the magnetization vector, \mathbf{H} is the magnetic field vector, ν is the gyromagnetic factor, and α is the parameter which describes losses.

TABLE I. μ_{st} is the static permeability and μ'_r , μ''_r is the permeability measured at f_r .

H_k (A/m)	f_r (MHz)	μ_{st}	μ'_r	μ''_r
45	5	8000	4000	3000
120	12	4000	2000	1200
280	25	2500	1200	400
500	30	1000	500	60

The \mathbf{M} and \mathbf{H} vectors include static ($\mathbf{M}_0, \mathbf{H}_k$) and alternating (\mathbf{m}, \mathbf{h}) components and we can write:

$$\mathbf{M} = \mathbf{M}_0 + \mathbf{m}, \quad \mathbf{H} = \mathbf{H}_k + \mathbf{h}. \quad (4)$$

Let us divide the microwire on elements which are small enough to consider that the direction of local anisotropy in each element is uniform. The assumption (b) means that the component m_z has the same value for each element. So, from the solution of Eq. (3) for a small element, it is possible to obtain the permeability of the whole microwire. We take a local coordinate system for a small element of the microwire such that the X axis is directed along the local \mathbf{M}_0 and \mathbf{H}_k vectors, while the Z axis is directed along the microwire axis. The effect of neighboring elements may be taken into account by introducing the demagnetization factor, N , so \mathbf{h} transforms to $\mathbf{h} - N\mathbf{m}$. The components of N for the long cylinder are $N_x = 1/2$, $N_y = 1/2$, $N_z \sim (l/r)^2 \ll 0$ (l is the length of microwire, r is the radius of microwire). We confine ourselves to the consideration of dynamic processes in the low external field, such that $h \ll H_k$ and $m \ll M_0$. So, we may neglect terms including products of mh , mm , and hh . With these assumptions, Eq. (3) may be rewritten as

$$\frac{dm_y}{dt} = \nu \cdot \left[m_z H_k - M_0 h + M_0 N m_z + \frac{\alpha}{\nu} \cdot \frac{dm_z}{dt} \right], \quad (5)$$

$$\frac{dm_z}{dt} = \nu \cdot \left[M_0 N m_y + H_k m_y + \frac{\alpha}{\nu} \cdot \frac{dm_y}{dt} \right]. \quad (6)$$

By solving these equations, it is possible to find an expression for the frequency-dependent complex permeability:

$$\tilde{\mu} = \mu_{st} \cdot \frac{\omega_r (\omega_r (1 + \mu_{st} N) + i \omega \alpha)}{\omega_r^2 (1 + \mu_{st} N) - \omega^2 - \omega^2 \alpha^2 + 2i \omega \omega_r \alpha (1 + \mu_{st} N)}, \quad (7)$$

where $\omega_r = \nu H_k$, $\mu_{st} = M_0 / H_k$ (initial permeability).

The term $(\alpha/\nu) \cdot (dm_z/dt)$ in Eq. (5) expresses the demagnetization field occurring due to eddy currents. According to Ref. 7 the moment rotation in the cylinder of radius r induces a demagnetization field $H_d = (r^2/4\rho) \cdot (dM/dt)$. The loss factor α is equal to $(\nu M r^2)/4\rho$, where ρ is the resistivity of the microwire. The frequency dependences of the real and imaginary parts of the permeability are presented in Figs. 2 and 3. These were calculated using the following parameters:

$$r = 4 \times 10^{-6} \text{ m}, \quad \rho = 1.6 \times 10^{-6} \Omega \text{ m},$$

$$M = 0.8 \text{ T}, \quad \text{and} \quad \nu = 2.2 \times 10^5 \text{ m(A s)}^{-1}.$$

The experimental results obtained are in a good agreement with the above theoretical considerations. The experimental values of static permeability and permeability at the critical frequency, as well as the values of critical frequency differ less than 20% from the values predicted by the proposed theoretical model. It is worth to note that CoMn microwires show a lower value of μ_r'' than that predicted by the theoretical model especially for the alloys with high anisotropy field. It is also interesting that a certain part of the frequency dependence of μ_r' lies above the so-called Snoek limit line which is described by the equation $\omega\mu = 2\nu M/3\mu_0$.⁸ The Snoek line confines the area in which the dependences $\mu(f)$ would lie if we take a bulk material with a single magnetic anisotropy. There are two kinds of considerably different magnetic anisotropies in the microwire. A rather low magnetoelastic anisotropy is responsible for the high value of static permeability while a strong shape anisotropy provides the extension of the frequency range where the real part of the permeability stays near constant.

CONCLUSION

The Mn content of Co Mn microwires strongly affects the magnetic properties. While the Mn content is less than the critical value of about 6.5% the microwire shows easy axes in a plane perpendicular to its axis. The remagnetization of the microwires occurs by moment rotation, which provides a fast response to the applied external magnetic field. The proposed model of the dynamic magnetization process is in a good agreement with the experimental results. Microwires exhibit low values of eddy current loss factor and an extended frequency range where the real part of the permeability is near constant.

¹ J. Gonzalez, N. Murillo, V. Larin, J. M. Barandiaran, M. Vazquez, and A. Hernando, *Sens. Actuators A* **59**, 97 (1997).

² A. Zhukov, M. Vazquez, J. Velazquez, H. Chiriac, and V. Larin, *J. Magn. Mater.* **151**, 132 (1995).

³ A. N. Antonenko, S. A. Baranov, V. S. Larin, and A. V. Torcunov, *Proceedings of the Ninth International Conference on Rapidly Quenched and Metastable Materials, Bratislava, 1996* (Supplement) (Elsevier, Amsterdam, 1997), pp. 248–250.

⁴ S. A. Baranov, V. S. Larin, A. V. Torcunov, A. Zhukov, and M. Vazquez, in *Proceedings of the Fourth International Workshop on Non-Crystal. Solids, 1994*, edited by M. Vazquez and A. Hernando (World Scientific, Singapore, 1995), p. 567.

⁵ S. A. Baranov et al., *Fiz. Met. Metalloved.* **67**, 73 (1989).

⁶ T. L. Gilbert, *Phys. Rev.* **100**, 1243 (1955).

⁷ S. Tikadzumy, *Fiz. Ferromagnetizma* (Russo, translated from Jap.), "MIR," Moscow, 1987, p. 324 (1987).

⁸ W. Gorter, *Proc. IRE* **43**, 245 (1955).

Frequency versus Lyapunov exponent map: A new approach to investigate dynamics of nonlinear magnetic systems

N. Y. Piskun^{a)} and P. E. Wigen

Department of Physics, The Ohio State University, Columbus, Ohio 43210

The complex Lyapunov exponent λ plays a vital role in characterizing the dynamics of a physical system. The real part of λ has frequently been related to as just the Lyapunov exponent and has been used for decades to characterize the stability of the system. The imaginary part or the frequency of oscillations can also give valid information about the dynamics of the system, particularly how it behaves near the equilibrium points. In this article we will show that the frequency versus Lyapunov exponent map can give additional information about the very nature of the system and provide background for detailed analysis concerning the applicability of the control technique and its robust nature. As an example of the applicability of the map, an appropriate model to investigate the origin and growth of the auto-oscillations are the circular YIG films. Starting with the low power ferromagnetic resonance spectrum and analyzing the behavior as a function of power the creation and evolution of "shoots" in the map have been demonstrated. The resulting map gives new insights about the relationship between the underlying dynamics of the system and the "growth" of the shoots into auto-oscillation fingers. This approach can explain many features of the auto-oscillation behavior and gives new insights into investigating techniques to control and synchronize chaos as well as to explain desynchronization bursts. © 1998 American Institute of Physics. [S0021-8979(98)51211-X]

INTRODUCTION

The field of controlling chaos has had a profound effect in different areas of science. The ability to eliminate chaotic behavior as well as the ability to "control" it can increase not only the ranges of stable regions but also can find new areas of applicability.¹ One of the main features of the chaotic system is sensitivity to initial conditions. A small perturbation to a system parameter can lead to large modifications of the behavior of the system. In this manner it is possible to influence the system behavior and obtain a desired periodic or "controlled" response from the system.

From the beginning of the chaos investigations the Lyapunov exponents were widely used to investigate the stability of the system around a position of equilibrium points or near stable or unstable manifolds. The ability to bring the system from the chaotic region to a stable region actually involves the ability to change the sign of the positive Lyapunov exponent λ . On the other hand, the imaginary part of the complex Lyapunov exponent or frequency describes the dynamic properties or the frequency of the oscillations around the equilibrium point.

Even though plots of the Lyapunov exponent and frequency versus system parameters can give some basic information about stability regions and system oscillations, they do not answer questions about the controlling techniques and the robustness of the controlled region. On the contrary, the frequency versus Lyapunov exponent map can provide im-

portant information about the "controlling" properties of the system that explains its behavior near the equilibrium points as well as provide background for detailed analysis concerning the applicability of the control technique and its robustness.

ORIGIN OF THE AUTO-OSCILLATIONS IN CIRCULAR THIN YIG FILMS

As an example of the applicability of the map, the model appropriate to investigate the origin and growth of the auto-oscillations in circular yttrium-iron-garnet (YIG) films at perpendicular resonance² has been used. In a small disk the boundary conditions introduce normal modes whose energies are shifted slightly above the bottom of the spin-wave band. The ferromagnetic resonance spectrum consists of a series of resonances with separations of typically 1 or 2 Oe. At higher powers, these modes exhibit nonlinear behavior leading to periodic and then chaotic auto-oscillations. It has been shown³ that in the case of thin circular YIG films the dynamics of the system can be approximated by the system of first-order nonlinear differential equations, representing the coupled magneto-static modes C_i :

$$\frac{dC_i}{dt} = -i\gamma \left[(H - H_i^{\text{res}} - i\Gamma_i) C_i + \left(\frac{h_p}{2} \right) I_i^* + 2\pi M_s \sum_{jkl} A_{ijkl} C_j^* C_k C_l \right], \quad (1)$$

where A_{ijkl} are the nonlinear coupling coefficients whose magnitudes are determined from the original Hamiltonian.

^{a)}Electronic mail: piskun@mps.ohio-state.edu

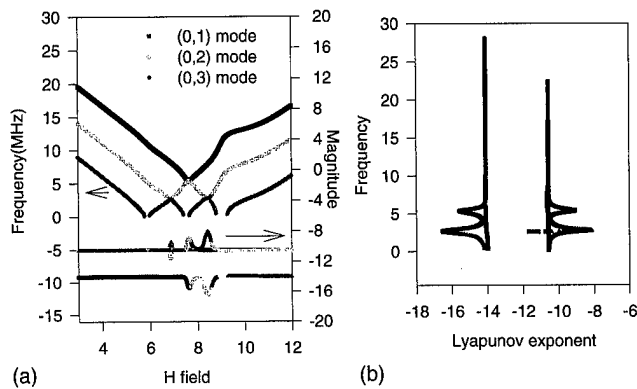


FIG. 1. (a) Plots of frequency (upper) and the Lyapunov exponent (lower) as a function of the magnetic field. The power was fixed at $ATT = -18$ a.u. and the magnetic field H was varied from 2 to 12 Oe. (b) The Lyapunov exponent vs the frequency map for the same sweep.

The constant characteristics of the system are M_s —the sample magnetization and I_i^* —the coupling with the rf field. H_i^{res} and Γ_i are the resonant field and half-width of the i th magneto-static mode and are taken directly from the low power FMR experiment. The variable parameters of the system are H —the magnetic field and h_p —the rf input power [expressed in attenuation (ATT) level units].

In the linear case the equations can be easily solved analytically giving the solution for each mode C in the form:

$$C = C_0 e^{\lambda t + i\omega t} - \frac{h_p I_i^*}{2(H - H_i^{\text{res}} - i\Gamma)}, \quad (2)$$

where $\lambda = -\gamma\Gamma$ and $\omega_\lambda = (H - H_i^{\text{res}})\gamma$.

As we can see, the Lyapunov exponent is negative and does not depend on the system variables H and h_p . The frequency depends linearly on the deviation of H from the resonant field position. The steady-state solution gives ordinary low-power FMR-type behavior. Despite its simplicity the linear approximation can serve as a starting point to future nonlinear investigation of Lyapunov exponents and frequencies.

In order to explore nonlinear properties of the system the equations were solved numerically to find corresponding Lyapunov exponents λ and frequencies ω as a function of the magnetic field H and power ATT for three magneto-static modes C_i . The plots of $\lambda(H)$ and $\omega(H)$ for small fixed power are shown on Fig. 1(a). Figure 1(b) is the single map of ω vs λ for the same H sweep. From Fig. 1, we can clearly observe that the increase in the Lyapunov exponent occurs when the frequencies of the magneto-static modes coincide or, in other words when the modes couple to each other. For the three-mode model we can obtain three possible couplings: (0,1) with (0,2) or (0,3) and (0,2) with (0,3). Two of them (0,1)–(0,2) and (0,2)–(0,3) are off-resonant couplings whereas (0,1)–(0,3) is a resonant coupling. The different position leads to different properties of couplings or “shoots” at high power resonance. The increase of power will only increase the magnitude of the Lyapunov exponent and only weakly affect the shape of “shoots.” This is particularly true for the first (0,1)–(0,2) shoot. To the contrary, the shape of a resonant shoot is strongly affected by the corresponding

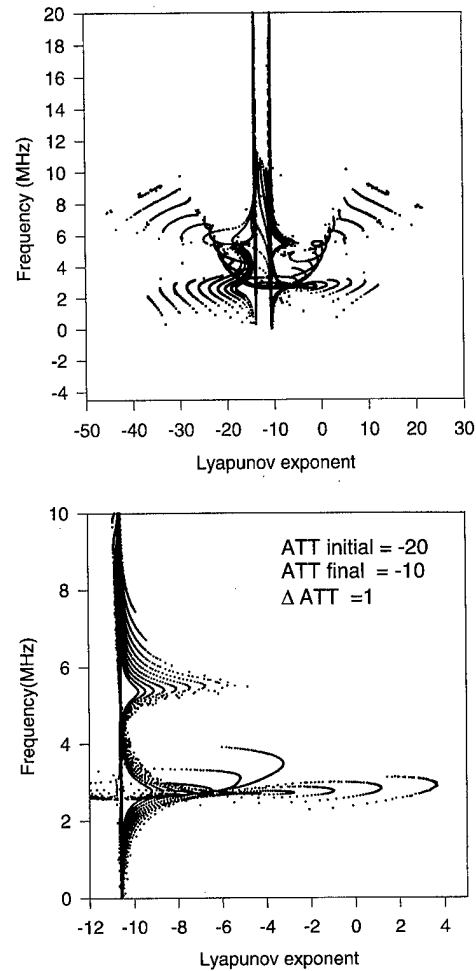


FIG. 2. (a) The Lyapunov exponent vs frequency map for 20 different H field sweeps. The power level has been varied from -20 to 0 a.u. in 1 a.u. steps. The first finger appears at a frequency of 2.5 MHz. The second finger is created by two colliding shoots at a frequency of 5.5 MHz. (b) The Lyapunov exponent vs the frequency map for 10 different H field sweeps. The power level has been varied from -20 to -10 a.u. in 1 a.u. steps.

FMR resonance. As can be seen from Figs. 2(a) and 2(b), as the power increases, it will shrink first at $ATT = -13$ [Fig. 2(b)] and then reappear again at $ATT = -10$.

When the Lyapunov exponent is equal to or greater than zero, the auto-oscillations start to be observed. This process is best seen from a global Lyapunov versus frequency map as presented on Fig. 2(b) where the magnetic field was swept through the resonance at 10 different attenuation levels. From this map the evolution of the mode coupling shoots into the auto-oscillation fingers can be observed. The first finger is obtained from the first nonresonant shoot as it crosses zero of the Lyapunov exponent. On the other hand, the analysis shows that the second finger is created by two colliding shoots: resonant (0,1)–(0,3) and nonresonant (0,2)–(0,3), which introduce additional complexities into the system.

STABILITY AND ROBUSTNESS ANALYSIS

In order to analyze the properties of our system a more extensive map is presented in Fig. 3 where the Lyapunov exponent is near zero. This map offers a unique opportunity

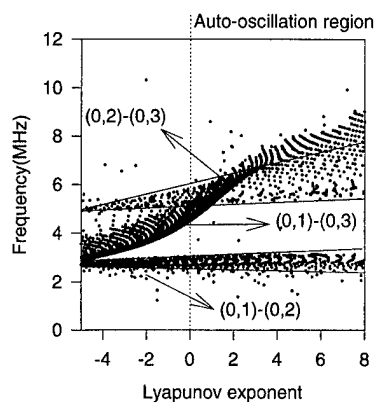


FIG. 3. The Lyapunov exponent vs the frequency map expanded in the region where the Lyapunov exponent is near zero.

to visualize and analyze the behavior of the system from the stability point of view. Figure 3 clearly shows that the lowest branch, which corresponds to the first auto-oscillation finger in the experiments, is very narrow in the frequency band and for small changes in the frequency during a given field sweep there is a large change in the Lyapunov exponent. It suggests that chaos can be suppressed very efficiently by applying a small periodic perturbation with a frequency near this value in an open loop control, or the chaotic state can be controlled relatively easily by driving the system into the

region of the map having a negative or zero Lyapunov exponent. Furthermore, the narrow frequency band might be related to the robust features of the system. In this case, we would expect it to be easier to bring the system into the controlled state but perhaps more difficult to maintain that control.

On the other hand, the analysis of the second finger, which was created by two colliding branches seems to give some promising insights. This branch has an increasing dependence of frequency on power and exhibits a much wider frequency band. As a result, it would be expected that it would be more difficult to establish a controlled state but once in that state the controlling process would be more robust.

The map also gives quantitative estimates for the auto-oscillation frequency for the first and the second finger. As shown on Fig. 3, the region of the map with positive Lyapunov exponent corresponds to the auto-oscillations. The experimental results at the onset of the auto-oscillations⁴ are in good agreement (within 10%) with the numerical estimations.

¹“Special issue: Controlling Chaos,” edited by T. Kapitaniak and M. El Naschie, *Chaos Solitons Fractals* **8** (1997).

²D. Peterman, Dissertation, The Ohio State University, 1996.

³R. McMichael and P. Wigen, *Phys. Rev. Lett.* **64**, 64 (1990).

⁴N. Y. Piskun and P. Wigen, *J. Appl. Phys.* **81**, 5731 (1997).

Coupling of reversal modes for an infinite ferromagnetic cylinder

Ching-Ray Chang^{a)}

Department of Physics, National Taiwan University, Taipei, Taiwan, Republic of China

Ching-Ming Lee

Division of Electrical Engineering, Chung Chou Junior College of Technology and Commerce, ChangHwa, Taiwan, Republic of China

We used amplitude equations to study the dynamic behavior of magnetization nucleation. Under certain conditions, the amplitudes of higher modes become dominant at large field and the reversal process moves to a new metastable state. Mode-mode coupling excites a cascade of nucleation modes and indicates that a common single-mode analysis is invalid. © 1998 American Institute of Physics. [S0021-8979(98)24511-7]

The magnetization reversal mechanism of a single-domain ferromagnetic particle has been studied for decades.¹⁻⁴ However, the experimental behavior of an isolated particle was only reported recently, and some of the data are inconsistent with the predictions of single-domain theory.^{5,6} An understanding of this problem is important from both fundamental interests and high-density data storage applications. According to the micromagnetics theory, the magnetization reverses through certain spatial modes when the external field reaches the nucleation field. Both the nucleation field and its corresponding mode can be obtained by solving the linearized Brown's equation.² However, it does not consider the possibility that an intermediate stable state may exist to trap the reversal process. Only a few attempts have studied the reversal process beyond the linear stability theory.^{4,7} Most of the theories are based on the assumption that a single mode is involved in the reversal process. However, there usually exist many intermediate metastable states during the reversal process and many different growing modes may arrive the same metastable state. Muller⁷ has also shown that in the case of a thick slab the state with finite deviation from saturation involves four different spatial modes. Therefore, conclusions based on the single-mode consideration are not sufficient and it is necessary to incorporate the equation of motion of magnetization to give a more satisfactory description on magnetization reversal.

We use a perturbative approach to investigate the dynamic behavior of the magnetization after nucleation in an infinite cylinder. Our studies can be briefly described as follows. The deviation of magnetization from its saturation state, i.e., the component perpendicular to the cylinder axis, is assumed to be a small quantity. In order to study the non-linear behavior, we keep the Landau-Lifshitz (L-L) equation to the third order of the deviation from the saturation. The deviated magnetization is separated as the spatial modes and time-dependent amplitudes. Using the spatial mode-expansion technique, we transform the partial differential L-L equation into a set of coupled ordinary differential

equations for the spatial mode amplitudes. By solving the amplitude equations we can then study the validity of the single-mode analysis.

For an infinite uniaxial ferromagnetic cylinder with radius R , $|\mathbf{M}(\mathbf{r})|$ is usually assumed to be conserved. Following the usual convention, the z axis is parallel to the cylinder axis and the external field is along its axis. Then \mathbf{m} can be written as $\mathbf{m}_0 + \mathbf{v}$, where \mathbf{m}_0 is the initially saturated state (0,0,1) and $\mathbf{v} = (v_x, v_y, \sqrt{1-v_x^2-v_y^2}-1)$ represents the deviation from the saturation state. Substituting \mathbf{m} into L-L equation and keeping terms up to third order of v_x and v_y , we have

$$\begin{aligned} \frac{\partial v_+}{\partial t} = & (\alpha - i\gamma) \left(\frac{2A}{M_s} \nabla^2 v_+ + H_+^{(1)} - H v_+ \right) + (\alpha - i\gamma) \\ & \times (H_+^{(2)} - H_z^{(1)} v_+) - (\alpha - i\gamma) v_+ \left[H_{\text{ex}}^{(2)} + H_K^{(2)} \right. \\ & \left. + H_z^{(2)} + \frac{1}{2} v_- \left(\frac{2A}{M_s} \nabla^2 v_+ + H_+^{(1)} \right) \right] \\ & - \frac{1}{2} \alpha v_+^2 \left(\frac{2A}{M_s} \nabla^2 v_- + H_-^{(1)} - H v_- \right), \end{aligned} \quad (1)$$

where γ is the gyromagnetic ratio and α is the damping parameter for dissipative effect, and $v_{\pm} = v_x \pm i v_y$,

$$H_{\text{ex}}^{(2)} = \frac{2A}{M_s} \nabla^2 \left(-\frac{1}{2} v_+ v_- \right), \quad H_K^{(2)} = \left(-\frac{1}{2} \frac{2K}{M_s} \right) v_+ v_-,$$

$H_{\pm}^{(1)} = H_x' \pm H_y'$. Further, $H_+^{(1)}$, $H_-^{(2)}$ are demagnetizing fields due to the magnetization $M_s(v_x, v_y, 0)$ and $M_s[0, 0, -\frac{1}{2}(v_x^2 + v_y^2)]$, respectively, and H is the sum of external field H_{ext} and $2K/M_s$.

It is natural to choose the solutions of the linearized Brown's equation,^{2,3} i.e., $\{\mathbf{v}_i(\mathbf{r})\}$, as our basis. Then we can write $v_+ = \sum_i C_i(t) v_{i+}(r)$, where C_i 's are the temporal amplitudes. With the same dimensionless units of Aharoni and Shtrikman,³ the first unstable mode for reduced cylinder radius $S \equiv R/(\sqrt{A/M_s}) \geq 1.1$ is the curling mode and this is the

^{a)}Electronic mail: crchang@phys.ntu.edu.tw

condition used in this article. In the z direction all eigenmodes have the form of $\cos(kz/R)$, and the eigenfield (normalized by $2\pi M_S$) for curling modes with different wave number k can be written as $h(k, S) = -1.08/S^2 - k^2/\pi S^2$. Hence the spectrum of eigenfield is continuous. The assumption of infinite length is a simplification for particles with negligible end effects.⁸ Thus we take the periodical boundary condition $v_+(z+2L) = v_+(z)$ for convenience, and $k_n = n\pi R/L$, $n \in N$. The value of L/R is interpreted as the aspect ratio of the particle. The first two curling modes $v_{1+}(\mathbf{r})$, $v_{2+}(\mathbf{r})$ can be written as $v_{1+}(\mathbf{r}) = N_1 i J_1(1.841r/R) e^{i\varphi}$, $v_{2+}(\mathbf{r}) = N_2 i J_1(1.841r/R) e^{i\varphi} \cos(\pi z/L)$, where J_1 is the first-kind Bessel function of order one and the normalization constants N_1 and N_2 satisfy the condition

$$\frac{1}{\pi R^2 2L} \int_{-L}^L dz \int_0^{2\pi} d\varphi \int_0^R dr r |v_{i+}(\mathbf{r})|^2 = 1.$$

Let $v_+ = \sum_i C_i(t) v_{i+}(\mathbf{r})$ in Eq. (1), we obtain the equations for the amplitudes C_i 's. The amplitude equations can be written as $\dot{C}_i = (\alpha - i\gamma)(H_i - H)C_i + N_i(C_i, C_j)$, where H_i is the eigenfield of mode i , and N_i represents the nonlinear mode-mode coupling. The linear instability (nucleation) occurs when external field H is equal to the largest eigenfield H_1 . To study the evolution of system after nucleation, we must solve the infinite coupled nonlinear equations. By the adiabatic elimination method,⁹ modes with large $|H_i - H|$ decay rapidly for the negative linear term $H_i - H < 0$ for $i \geq 2$ near the nucleation point. Therefore, a truncation is reasonable and we keep only the first few active modes (or "slow modes") to simplify the problem. The number of active modes depends on the periodicity L in z direction. For large L the eigenfields are very close for adjacent modes and hence the characteristic times are also of the same order of magnitude. We arbitrarily choose $p \equiv L/R = 10$ (to represent a needle particle with aspect ratio 10) and $S = 3$ (about 0.1 mm for $\gamma\text{-Fe}_2\text{O}_3$) in our calculations. To demonstrate the effect of mode-coupling we consider only the first two modes. In general C_i 's are complex amplitudes: pure imaginary amplitude C_i corresponds to the "flower state,"¹⁰ and pure real C_i represents the conventional curling mode (or the "vortex state,"¹⁰). Thus the amplitude equations contain four dynamic variables, but the number of variables can be further reduced for the imaginary parts of C_1 and C_2 are much smaller than their real parts.⁸ Therefore let X_1 and X_2 be the real part of C_1 and C_2 respectively, and the long-term behavior of the magnetization will be determined by:⁸

$$\dot{X}_1 = \frac{\alpha}{\gamma} \omega_0 \{ (h_1 - h)X_1 + AX_1^3 + BX_1X_2^2 \}, \quad (2)$$

$$\dot{X}_2 = \frac{\alpha}{\gamma} \omega_0 \{ (h_2 - h)X_2 + CX_2^3 + DX_1^2X_2 \}, \quad (3)$$

where $\omega_0 = 2\pi M_S \gamma$ and the coefficients are

$$A = 0.584(h_K + h - 2h_1) - \frac{0.393}{S^2},$$

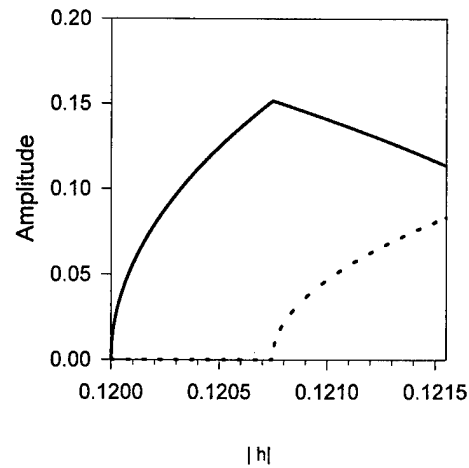


FIG. 1. The bifurcation diagram of the amplitudes X_1 and X_2 of the two excited curling modes. The solid curve represents X_1 , and the dotted curve represents X_2 . For $|h| \in (0.12, 0.12075)$ only the first mode X_1 is excited, growing with increasing $|h|$; $X_2 = 0$. For $|h| \in (0.12075, 0.12155)$ X_2 grows with $|h|$, i.e., the second mode is excited; but X_1 decreases with $|h|$. As $|h| > 0.12155$ no stable stationary (X_1, X_2) exists.

$$B = 3 \left(0.584h_K - \frac{0.393}{S^2} \right) - 0.584(3h_2 + 2h_1 - 3h),$$

$$C = \frac{3}{2} 0.584(h_K + h - 3h_2) - \frac{1}{S^2} \left(0.5895 + \frac{1.168\pi}{p^2} \right),$$

$$D = 1.752(h_K + h - h_2 - 2h_1) - \frac{1.179}{S^2},$$

where $h_K = K/\pi M_S^2$. Time-independent solutions of (2) and (3) are: $(X_1=0, X_2=0)$, $(X_1 = \pm \sqrt{(h-h_1)/A}, X_2=0)$, $(X_1 = \pm \sqrt{-E/F}, X_2 = \pm \sqrt{(h-h_2+DE/F)/C})$, and $(X_1=0, X_2 = \pm \sqrt{(h-h_2)/C})$, here $E = h_1 - h - B(h_2 - h)/C$ and $F = A - BD/C$. The actual state of the magnetization depends on values of the parameters, especially on the effective anisotropic field h_K and the external field h .

For a positive or zero uniaxial anisotropy, i.e., $h_K \geq 0$, the only possible stationary solution is the saturation state, i.e., $(X_1=0, X_2=0)$. As the reverse external field h exceeds the nucleation field h_1 this solution becomes unstable. Any perturbative deviation from this state will grow without limit. Thus it seems that the magnetization reverses in a single step and it is consistent with earlier single-mode analysis.^{3,4} On the other hand, for negative h_K the magnetization can exhibit entirely different behavior. With a variation of the external field, the magnetization bifurcates from one solution to another. The bifurcation diagram is shown in Fig. 1 where we choose $h_K = -0.1$. The saturation state can only be stable for $|h| \leq |h_1| = 0.12$. For fields $|h| \in (0.12, 0.12075)$, nucleation takes place, and the saturation state is replaced by the stationary solution $(X_1 = \pm \sqrt{(h-h_1)/A}, X_2=0)$. After reduction to its normal form it can be easily shown that here occurs the supercritical pitchfork bifurcation.¹¹ From the figure we see that the amplitude of the curling mode grows with increasing $|h|$. Within this field range the single-mode approximation is valid because that the second curling mode with nontrivial z dependence is not excited. If the reverse

external field increases further above another threshold, $|h| \geq 0.12075$, then the previous single-mode solution becomes unstable and the $v_{2+}(\mathbf{r})$ is excited through the mode coupling. The stable solution changes to $(X_1 = \pm \sqrt{-E/F}, X_2 = \pm \sqrt{(h-h_2+DE/F)/C})$. Again the bifurcation is the supercritical pitchfork type. The second mode gradually becomes dominant with increasing $|h|$. For $|h| > 0.12155$, the solution of double-mode coupling also loses its stability and a perturbation of this mixed state grows without limit. Beyond this critical field the magnetization may transit to another stationary state involving more than two nucleation modes. The symmetry of the system lowers with increasing $|h|$. At the nucleation field $h=h_1$ the formation of the first curling mode removes the isotropy of magnetization. Continuous translation symmetry in z direction also breaks as the second curling mode is excited with further increasing $|h|$. We have also calculated the change of volume averaged z -component of the magnetization \bar{m}_z with $|h|$. Due to an increase of the amplitude X_1 of the first curling mode for $|h| \in (0.12, 0.12075)$, \bar{m}_z decreases as the applied field increases in this region. However, for $|h| \in (0.12075, 0.12155)$, because of the modulation factor $\cos[(\pi/L)z]$ in the second curling mode, \bar{m}_z will increase a little bit for the increasing amplitude of X_2 . Another stationary solution ($X_1=0$, $X_2 = \pm \sqrt{(h-h_2)/C}$) is always unstable to any perturbation in X_2 and thus it will not occur in reality.

We use the mode expansion and amplitude equations to analyze the response of magnetization deviated from saturation at nucleation. This study shows the reversal process of a single-domain particle can be much more complicated than that of the single-mode analysis predicated. Here only two cylindrical modes are considered and multimode analysis can be extended by including more modes to the amplitude equa-

tions. For an infinite ferromagnetic cylinder with positive or zero uniaxial anisotropy, we found that the curling mode grows without limit, with no other modes involved. In the case of negative anisotropy the stable stationary curling states exist even as the reverse external field exceeds the nucleation field. However, from the symmetry consideration, magnetization cannot only reverse with the curling modes of different axial periodicity discussed here.¹² Therefore, other kinds of modes, e.g., the buckling modes or the coherent mode should be excited by mode-mode coupling during the reversal. These noncylindrical modes should break the cylindrical symmetry as the deviation grows large. Our studies suggest that a cascade of nucleation modes occurs during the reversal process and the discrepancy between experimental data and single-domain theory can be attributed to the mode coupling.

This research has been partially supported by NSC-87-2112-M002-006, ROC.

¹E. C. Stoner and E. P. Wohlfarth, *Philos. Trans. R. Soc. London* **A240**, 599 (1948).

²W. F. Brown, Jr., *Phys. Rev.* **105**, 1479 (1957).

³A. Aharoni and S. Shtrikman, *Phys. Rev.* **109**, 1522 (1958).

⁴W. F. Brown, Jr., *J. Appl. Phys.* **29**, 470 (1958).

⁵M. Lederman, S. Schultz, and M. Ozaki, *Phys. Rev. Lett.* **73**, 1986 (1994).

⁶W. Wernsdorfer, E. Bonet Orozco, K. Hasselbach, A. Benoit, B. Barbara, N. Demoncy, A. Lorseau, H. Pascard, and D. Mailly, *Phys. Rev. Lett.* **78**, 1791 (1997).

⁷M. W. Muller, *Phys. Rev.* **122**, 1485 (1961).

⁸C.-M. Lee and C.-R. Chang (unpublished).

⁹H. Haken, *Synergetics: an Introduction* (Springer, New York, 1977).

¹⁰M. E. Schabes, *J. Magn. Magn. Mater.* **95**, 249 (1991).

¹¹J. Guckenheimer and P. Holmes, *Nonlinear Oscillations, Dynamical Systems and Bifurcations of Vector Fields* (Springer, New York, 1983), Chap. 3.

¹²C.-R. Chang, C. M. Lee, and J. S. Yang, *Phys. Rev. B* **50**, 6461 (1994).

Magnetism and Jahn-Teller effect in LaMnO₃

M. Z. Li

Institute of Solid State Physics, Academia Sinica, P.O. Box 1129, Hefei 230031, People's Republic of China

Liang-Jian Zou

CCAST (World Laboratory), P.O. Box 8730, Beijing 100083, People's Republic of China;

Institute of Solid State Physics, Academia Sinica, P.O. Box 1129, Hefei 230031,

People's Republic of China; and Department of Physics, Chinese University of Hong Kong, Shatin, N.T., Hong Kong

Q. Q. Zheng

Institute of Solid State Physics, Academia Sinica, P.O. Box 1129, Hefei 230031,

People's Republic of China and Department of Physics, Chinese University of Hong Kong, Shatin, N.T., Hong Kong

Combining charge transfer with the Jahn-Teller electron-phonon coupling, the magnetic properties of LaMnO₃ and the influence of the Jahn-Teller effect are studied. The interaction parameters of super exchange coupling between manganese spins are obtained. In the ground state, manganese spins are antiferromagnetically ordered but canted by a small angle. The spectrum of the low-energy spin excitation is very close to that observed experimentally. Behaviors of magnetization and spin correlation functions of LaMnO₃ exhibit certain two-dimensional ferromagnetic characters, even though it is an A-type antiferromagnet with anisotropic super exchange coupling. These results agree with several experiments. Furthermore, it is expected that the super exchange interactions depend on the electron-phonon coupling strength exponentially, and the Néel temperature will exhibit isotope shift. © 1998 American Institute of Physics. [S0021-8979(98)39711-X]

The discovery of colossal magnetoresistance (CMR) in hole-doped perovskite manganese oxides R_{1-x}A_xMnO₃ (R = La, Pr, Nd, ... and A = Ca, Sr, Ba, Pb, ...) has renewed wide interest in these compounds. Properties of these compounds could qualitatively be explained within the framework of Zener's double exchange model,¹ in which the presence of the Mn³⁺ - Mn⁴⁺ mixed valence is responsible for both the ferromagnetic ordering and charge transport. Nevertheless, it is shown recently that, in addition to the double exchange interaction, the influence of the Jahn-Teller (JT) electron-phonon coupling is also important.^{2,3} Undoped LaMnO₃ exhibits distinct electronic and magnetic properties which relate to the magnetic and transport properties of hole-doped LaMnO₃. In order to fully understand the nature of CMR effect and related phenomena of doped manganese oxides, it is essential to clarify the magnetic properties and the influence of the JT effect in their parent compounds.

The electronic configuration of the LaMnO₃ is 3d⁴(t_{2g}³e_g¹), where three localized t_{2g} electrons form a core spin with S_c=3/2 while the one e_g electron is paralleled to the core spin due to strong Hund coupling J_H. With cubic symmetry, t_{2g} and e_g orbitals are threefold and twofold degenerate, respectively. Orbital degeneracy leads to a JT instability which causes the oxygen octahedra to distort, lowers its site symmetry to tetragonal and orthorhombic, and removes orbital degeneracy. In LaMnO₃, both t_{2g} and e_g orbitals hybridize with O 2p orbitals but the t_{2g} orbitals hybridize mainly with the 2p_π orbitals while the e_g orbital hybridizes mainly with the 2p_σ orbital. Therefore, the π-bonding orbitals t³-O:2p_π-t³ and σ-bonding orbitals e¹-O:2p_σ-e⁰ are formed.⁴ A virtual t³-p_π-t³=t²-p_π-t⁴ charge transfer and a real e¹-p_σ-e⁰ charge transfer

occur and cause super exchange interactions between manganese spins. With this picture in mind, we consider an effective JT electron-phonon mode together with the two kinds of charge transfer between Mn 3d and O 2p orbitals and write down the following Hamiltonian:

$$H = H_0 + H_{JT}, \quad (1)$$

$$H_0 = \sum_{i\alpha} \epsilon_d^\alpha d_{ie\alpha}^\dagger d_{ie\alpha} + \sum_{i\alpha} \epsilon_d^t d_{it\alpha}^\dagger d_{it\alpha} + \sum_{l\alpha} \epsilon_p p_{l\alpha}^\dagger p_{l\alpha} + \frac{U_\sigma}{2} \sum_{i\alpha} n_{ie\alpha} n_{ie\bar{\alpha}} + \frac{U_\pi}{2} \sum_{i\alpha} n_{it\alpha} n_{it\bar{\alpha}} - t^\sigma \times \sum_{\langle il \rangle \alpha} (d_{ie\alpha}^\dagger p_{l\alpha} + h.c.) - t^\pi \sum_{\langle il \rangle \alpha} (d_{it\alpha}^\dagger p_{l\alpha} + h.c.), \quad (2)$$

$$H_{JT} = \sqrt{\beta \hbar \omega} \sum_i n_i (b_i^\dagger + b_i) + \hbar \omega \sum_i \left(b_i^\dagger b_i + \frac{1}{2} \right). \quad (3)$$

Here d_{ieα}[†](d_{itα}[†]) and p_{lα}[†] are electron creation operators with spin α in the e_g(t_{2g}) orbital(s) on the ith Mn site and the p orbital on the lth O site, respectively. Their corresponding energy levels are ε_d^e, ε_d^t, and ε_p. The term t^σ(t^π) is the hopping matrix between 2p_σ(2p_π) and e_g(t_{2g}) orbitals. U_π and U_σ are electrostatic energies required to add an electron to a half-filled t_{2g} orbital and to an empty e_g orbital, respectively. The term n_i is the number operator of electrons on site R_i. β is the electron-phonon coupling constant and ħω is the phonon frequency. For LaMnO₃, these parameters are chosen as t^σ ≈ t^π ≈ 1.8 eV, U_π ≈ 7 eV, U_σ ≈ 4.5 eV, J_H ≈ 2.0 eV, ε_σ ≈ 4.5 eV, and ε_π ≈ 6.5 eV.⁵⁻⁷

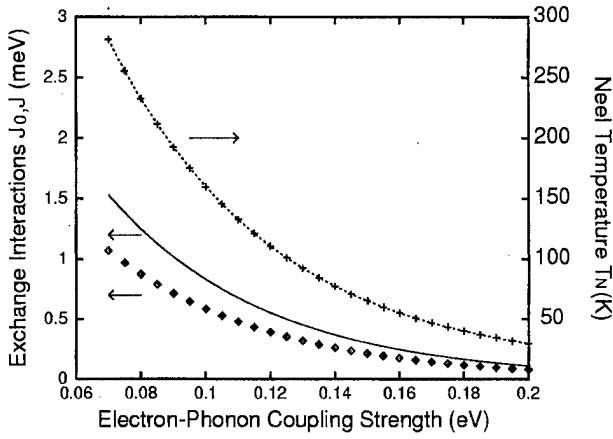


FIG. 1. The electron-phonon coupling strength β dependence of super exchange coupling parameters J_0 (solid), J (diamond) and Néel temperature T_N (dash) for LaMnO_3 .

Making use of a canonical transformation, $\bar{H} = e^{-S} H e^S$ where $S = \sqrt{\beta/N\hbar\omega} \sum_i n_i (b_i - b_i^\dagger)$, we eliminate the linear term of phonon operators in Eq. (3). We then average \bar{H} over thermal equilibrium states of phonons and use Fröhlich's canonical transformation to remove operators $p_{l\alpha}$ and $p_{l\alpha}^\dagger$. Thus the effective transfer integral between the nearest neighbor Mn on the ab plane, t_{eff}^σ , and along the c axis, t_{eff}^π , are obtained,

$$t_{\text{eff}}^\sigma = (t^\sigma e^{-S_T})^2 / (\epsilon_\sigma + \beta), t_{\text{eff}}^\pi = (t^\pi e^{-S_T})^2 / (\epsilon_\pi + \beta), \quad (4)$$

where $\epsilon_\sigma = \epsilon_p - \epsilon_d^\sigma$ and $\epsilon_\pi = \epsilon_p - \epsilon_d^\pi$. $S_T = \sum_q |\lambda_q|^2 (\langle n_q \rangle + \frac{1}{2})$, $\lambda_q = \sqrt{\beta/N\hbar\omega} e^{iq \cdot r_i}$, and $n_q = 1/[\exp(\hbar\omega/k_B T) - 1]$. According to Goodenough's super exchange argument,⁵ the effective magnetic interactions can be obtained,

$$H_{\text{eff}} = -J_0 \sum_{\langle ii' \rangle} \mathbf{S}_i \cdot \mathbf{S}_{i'} - J \sum_{\langle ij \rangle} \mathbf{S}_i \cdot \mathbf{S}_j - D \sum_i (S_i^z)^2. \quad (5)$$

Here $J_0 = (t_{\text{eff}}^\sigma)^2 J_H / (8U_\sigma^2) (>0)$ and $J = -(t_{\text{eff}}^\pi)^2 / (8U_\pi) (<0)$ ⁵ are intralayer ferromagnetic interaction and interlayer antiferromagnetic interaction, respectively. $\langle ii' \rangle$ denotes the nearest neighbors within the layer and $\langle ij \rangle$ denotes the nearest neighbors between the two nearest layers. The third magnetic anisotropy term is introduced due to the anisotropic magnetic coupling of LaMnO_3 as mentioned above. The anisotropy constant $D \approx 0.15$ meV. Experimental results showed that LaMnO_3 is an A-type antiferromagnetic (AFM) insulator.⁸

Apparently, J_0 and J decrease with the increase of electron-phonon coupling strength β as shown in Fig. 1. Choosing $\beta = 0.105$ eV, which is within the range listed in the review article by Sturge,⁹ we obtain $J_0 \approx 0.748$ meV and $J \approx -0.53$ meV. These values are somewhat smaller than the experimental fitted values¹⁰ $J_0 \approx 0.83$ meV and $J \approx -0.58$ meV, but the ratio of J_0 to J is very close.

Applying a variational method to Eq. (5) in the semiclassical approximation of spin operators, it is found that spin cants a small angle to the c direction in the ground state. The angle between the spin moment and the c axis is about 86° . So the magnetic ground state is a canted structure and with a

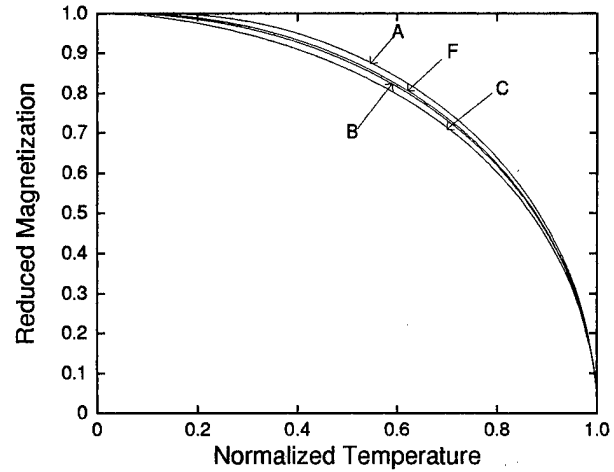


FIG. 2. The reduced magnetization of GAFM (A), LaMnO_3 (B), Q2DFM (C) and A-type AFM without JT effect (F) are plotted as a function of the normalized temperature (T/T_N).

net moment ($\sim 0.13 \mu_B/\text{Mn}$) along the c axis, in agreement with the experimental data.¹¹ So the weak ferromagnetism is an intrinsic property of undoped LaMnO_3 .

The magnetic properties of LaMnO_3 can be studied by using the double-time Green's Function method. Within the random phase decoupling scheme, the spectrum of low-energy spin excitation is obtained,

$$E_{kk'} = \sqrt{A_k^2 - B_{k'}^2} \langle S^z \rangle, \quad (6)$$

$$A_k = 2J_0 z(1 - \gamma_k) - 2Jz' + 2D \quad B_{k'} = -2Jz' \gamma_{k'}, \quad (7)$$

where $\gamma_k = \cos(k_x a) \cos(k_y b)$, $\gamma_{k'} = \cos(k_z c)$; $z = 4$ and $z' = 2$ are coordinate numbers in the ab plane and along the c axis, respectively. At low temperature region, $\langle S^z \rangle \approx S$, the spin-wave spectrum agrees very well with experiment.¹² As can be seen from the energy spectrum, the magnetic interactions exhibit strong anisotropic dispersion.

In terms of the expression of sublattice magnetization for the case of $S = 2$,¹³ Néel temperature can be expressed as $T_N = S(S+1)/(3k_B C_1)$, where $C_1 = (2/N) \sum_{kk'} (A_k/E^2)$. It is found that T_N decreases with the increase of electron-phonon coupling strength β as shown in Fig. 1. For $\beta = 0.105$ eV, $T_N \approx 145$ K which is in good agreement with experimental data (140 K).^{11,12} The spin correlation functions $\langle S_j^- S_i^+ \rangle_{\parallel}$ in the ab plane and $\langle S_j^- S_i^+ \rangle_{\perp}$ along the c axis are also obtained,

$$\langle S_j^- S_i^+ \rangle_{\parallel} = \frac{2\langle S^z \rangle}{N} \sum_{k,k'} \left[\frac{A_k}{E} \coth \left(\frac{E_{kk'}}{2k_B T} \right) - 1 \right] e^{i\mathbf{K} \cdot (\mathbf{R}_i - \mathbf{R}_j)}, \quad (8)$$

$$\langle S_j^- S_i^+ \rangle_{\perp} = -\frac{2\langle S^z \rangle}{N} \sum_{k,k'} \left[\frac{B_{k'}}{E} \coth \left(\frac{E_{kk'}}{2k_B T} \right) \right] e^{i\mathbf{K}' \cdot (\mathbf{R}_i - \mathbf{R}_j)}, \quad (9)$$

where $E = \sqrt{A_k^2 - B_{k'}^2}$. Sublattice magnetization and correlation functions can be calculated self-consistently.

In Fig. 2, the reduced magnetization of LaMnO_3 is calculated and compared with those of quasi-two-dimensional ferromagnets (Q2DFM) and G-type antiferromagnets

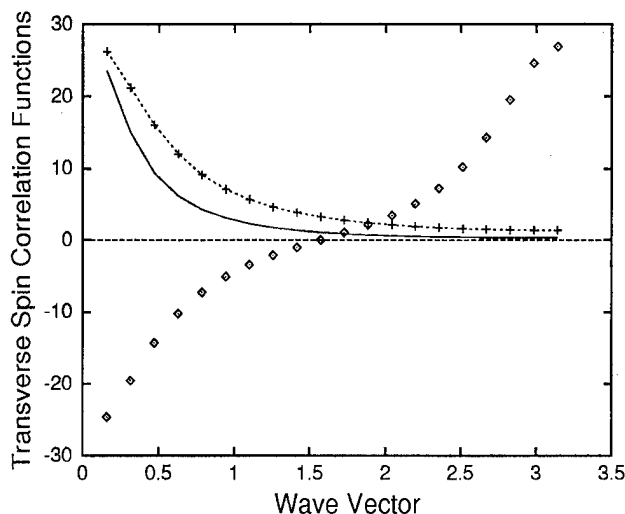


FIG. 3. Wave-vector dependence of the transverse spin-spin correlation functions. The solid line and diamond represent the correlations of LaMnO_3 in $[100]$ and $[001]$ directions, respectively. The dashed line represents the correlation of GAFM in $[001]$ direction.

(GAFM) with the same parameters. A, B and C represent reduced magnetization curves of GAFM, LaMnO_3 and Q2DFM, respectively. The reduced magnetization of LaMnO_3 lies between those of Q2DFM and GAFM. It is obvious that LaMnO_3 exhibits a certain two-dimensional (2D) ferromagnetic character, which is in agreement with the experiment.¹² Furthermore, the reduced magnetization of A-type AFM without JT effect is also calculated (see the curve F in Fig. 2). The curves B and F are very close to each other, but the reduced magnetization of LaMnO_3 is smaller than that without JT effect at the same normalized temperature, which shows that the presence of JT effect weakens the magnetic coupling of the spins.

In Fig. 3, wave-vector dependence of the transverse spin-spin correlation functions of LaMnO_3 in the $[100]$ and $[001]$ directions are shown. In the $[100]$ direction, the transverse correlation decreases to zero with the increase of k_x in the first Brillouin zone (BZ), but in the $[001]$ direction, the transverse correlation increases when the wave vector k_z increases in the first BZ, while at $k_z = \pi/2$, the correlation is zero. The behavior of correlation of LaMnO_3 in the $[001]$ direction is different from that of GAFM which decreases with increasing of k_z as shown in Fig. 3. Due to the distinct ferromagnetic coupling in the ab plane and antiferromagnetic coupling along the c direction, the behavior of spin correlation exhibits anisotropy. The anisotropic super exchange coupling in the undoped LaMnO_3 may be the origin of anisotropic magnetoresistance recently discovered in the doped LaMnO_3 .¹⁴

According to Eq. (4), the magnetic coupling in LaMnO_3 depends on the JT phonon frequency which is proportional to $M^{-1/2}$, mass of the oxygen. Therefore isotope substitution of oxygen may affect the effective magnetic interactions between neighboring Mn cations, and the Néel temperature will exhibit isotope effect. From Eq. (4) and the formulas of J_0 , J and T_N , the isotope shift of Néel temperature in LaMnO_3 , denoted as $\Delta T = T_N^{16} - T_N^{18}$, can be calculated numerically. For LaMnO_3 , the phonon frequency $\hbar\omega \approx 0.05$ eV;¹⁵ thus the isotope shift of the Néel temperature is estimated to be $\Delta T \approx 17$ K. So the isotope substitution of heavy oxygen reduces the phonon frequency, and the Néel temperature by about 17 K. Therefore, the isotope shift of T_N should be able to be observed in further experiment.

In summary, the magnetic properties of LaMnO_3 and the influence of the JT effect on it are studied. It is found that in the ground state of LaMnO_3 , spins cant a small angle. The magnetization and the spin correlation functions show that LaMnO_3 possesses certain 2D ferromagnetic characters with anisotropic super exchange coupling. The JT effect substantially reduces the theoretical estimate of the Néel temperature, and the Néel temperature is expected to exhibit an isotope shift.

This work is supported in part by the Grants of CAS and the NSF of China, and in part by the Direct Grant for Research from the Research Grants Council (RGC) of the Hong Kong Government.

¹C. Zener, Phys. Rev. **82**, 403 (1951); P. W. Anderson and H. Hasegawa, *ibid.* **100**, 675 (1955); P.-G. de Gennes, *ibid.* **118**, 141 (1960).

²A. J. Millis, P. B. Littlewood, and B. I. Shraiman, Phys. Rev. Lett. **74**, 5144 (1995).

³M. C. Martin, G. Shirane, Y. Endoh, K. Hirota, Y. Moritomo, and Y. Tokura, Phys. Rev. B **53**, 14285 (1996).

⁴J. B. Goodenough, J. Appl. Phys. **81**, 5330 (1997).

⁵J. B. Goodenough, in *Progress in Solid State Chemistry*, edited by H. Reiss (Pergamon, New York, 1971), Vol. 5.

⁶T. Saitoh, A. E. Bocquet, T. Mizokawa, H. Namatame, A. Fujimori, M. Abbate, Y. Takeda, and M. Takano, Phys. Rev. B **51**, 13942 (1995).

⁷J. H. Chung, K. H. Kim, D. J. Eom, E. J. Choi, J. Yu, Y. S. Kwon, and Y. Chung, Phys. Rev. B **55**, 15489 (1997).

⁸E. O. Wollan and W. C. Koehler, Phys. Rev. **100**, 545 (1955).

⁹M. D. Sturge, in *Solid State Physics*, edited by F. Seitz, H. Turnbull, and H. Ehrenreich (Academic, New York, 1967), Vol. 20.

¹⁰F. Moussa, M. Hennion, J. Rodriguez-Carvajal, and H. Moudden, Phys. Rev. B **54**, 15149 (1996).

¹¹G. Matsumoto, J. Phys. Soc. Jpn. **29**, 606 (1970).

¹²K. Hirota, N. Kaneko, A. Nishizawa, and Y. Endoh, J. Phys. Soc. Jpn. **65**, 3736 (1996).

¹³A. S. Chakravarty, *Introduction to the Magnetic Properties of Solid* (Wiley-Interscience, New York, 1980).

¹⁴Y. Fei, Z. Liu, A. R. Meng, and H. K. Wong (to be published).

¹⁵A. J. Millis, Phys. Rev. B **53**, 8434 (1996).

Application of spin-dynamics methods to a study of magnetization tunneling in many-spin systems

V. V. Dobrovitski and B. N. Harmon^{a)}

Ames Laboratory and Department of Physics and Astronomy, Iowa State University, Ames, Iowa 50011

Spin-dynamics methods were applied for the numerical study of magnetic tunneling in many-spin systems. A numerical technique based on the instanton approach was developed and the zero-temperature case as well as finite-temperature effects were considered. We show that even for a two-spin system results can differ considerably from those of a corresponding reduced one-spin (or collective spin) system. Moreover, it is argued that such a difference can take place for real materials such as magnetic molecules (e.g., Mn_{12}). Thus, consideration of the many-spin nature of some systems is shown to be important. © 1998 American Institute of Physics.

[S0021-8979(98)51311-4]

The phenomenon of magnetization tunneling is a fundamental property of mesoscopic magnetic systems. It has been studied for more than a decade and much progress has been achieved.¹ But most of the studies have been restricted by one important approximation: instead of systems where each spin is individually treated, reduced systems were considered, with the coupled separate spins forming a single collective degree of freedom. For example, tunneling in small ferromagnetic (FM) grains (as well as in molecular magnets such as Mn_{12}) was treated as tunneling of a single large spin representing the collective degree of freedom of all the small spins comprising the grain.¹ Analogously, the Néel vector is the corresponding collective degree of freedom in a small antiferromagnetic (AFM) particle.^{1,2} Such an approximation works well if the exchange interactions between spins are much stronger than the anisotropy energies governing the motion of the collective degree of freedom (collective spin). Thus the question arises, How strong does the exchange need to be to make the collective spin method valid and what can be expected if the ratio of exchange to anisotropy is not very large?

The primary goal of this article is to show that, even if exchange is considerably larger than anisotropy (say, five times larger), many-spin effects are important. We identify one of the parameters governing the tunneling rate in the many-spin case and give a qualitative explanation of its dependence on exchange and anisotropy constants. Our aim is to elucidate basic principles, so here we present results only for simple two-spin systems. For the same reason, we consider only systems with collinear ordering.

We use the instanton approach^{1,3} to describe the tunneling process quasiclassically. Thus, we consider systems consisting of several large spins (two spins for the cases presented below) where anisotropy is of the same order as the exchange coupling between the large spins. Our results can be applied qualitatively to such systems as assemblies of certain f ions (those possessing large spin on each ion) or Mn_{12} high-spin molecules, as described below.

We consider a system consisting of easy-axis spins

coupled by exchange interactions. The easy axis is chosen to be directed along the x axis. In general, if the total spin projection onto the easy axis is not zero, an additional easy-plane anisotropy should exist to allow tunneling.¹ Thus, introducing spherical angles θ and ϕ , the Hamiltonian of the system under consideration is

$$H = \sum_i K_i \sin^2 \theta_i \sin^2 \phi_i + \sum_i K'_i \cos^2 \theta_i + \sum_{i < j} J_{ij} [\cos \theta_i \cos \theta_j + \sin \theta_i \sin \theta_j \cos(\phi_i - \phi_j) \pm 1], \quad (1)$$

where K_i and K'_i ($K'_i \geq K_i$ for all i) are the easy-axis and easy-plane anisotropy constants, respectively, and J_{ij} are the exchange couplings. In third sum we add ± 1 (depending on the mutual direction of i th and j th spins) to provide normalization of the energy.

As we mentioned above, only systems with collinear ordering are considered, so the Hamiltonian (1) possesses two degenerate minima: $\theta_i = \pi/2$, $\phi_i = 0$ and $\theta_i = \pi/2$, $\phi_i = \pi$. These minima are separated by a potential barrier (the barrier height is governed by the easy-axis anisotropies K_i of all spins), and tunneling is possible between them. Within the instanton approach, we introduce imaginary time $\tau = it$ ($i = \sqrt{-1}$). Equations of motion for the system in imaginary time define the instanton trajectory, which starts at $\tau \rightarrow -\infty$ at the point corresponding to one minimum of the Hamiltonian (1) and ends at the other minimum at $\tau \rightarrow +\infty$. The value of imaginary-time action functional on the instanton trajectory \mathcal{S}_E defines the tunneling rate Γ :

$$\Gamma = \Gamma_0 \exp(-\mathcal{S}_E/\hbar), \quad (2)$$

where Γ_0 is the prefactor. The value of Γ is essentially determined by the instanton action \mathcal{S}_E (due to exponential dependence), so our analysis will be focused only on the quantity \mathcal{S}_E .

To solve the problem (both for zero- and finite-temperature cases) the following numerical scheme was used. We find the instanton as a solution of the boundary

^{a)}Electronic mail: harmon@ameslab.gov

value problem for a finite interval τ_0 of imaginary time; the boundary conditions are $\cos \theta_i = 0$ at both ends of the interval, $\tau = +\tau_0/2$ and $\tau = -\tau_0/2$. The quantity τ_0 is defined by the temperature: $2\tau_0 = \beta\hbar = \hbar/(k_B T)$, where k_B is Boltzmann's constant. The Newton quasilinearization method with step correction was used with an analytical initial approximation. If the analytical initial approximation is too far from the actual solution to attain convergence, a preliminary computation is performed, with another set of parameters chosen to attain convergence to the solution directly from analytical initial approximation. Then, results of this preliminary computation are used as an initial approximation for the calculation with the set of parameters we are interested in. Finally, integration of the Lagrangean along the instanton path gives the value of the action \mathcal{S}_E .

In calculations we use dimensionless energies normalized to some characteristic energy of the system E_0 and dimensionless imaginary time (using substitution $\tau \rightarrow E_0 \tau / \hbar$). Such a normalization does not change the value of the instanton action. Values of individual spins S_i are also normalized to some characteristic large spin S_0 ; in doing so the instanton action \mathcal{S}_E becomes S_0 times smaller.

To understand qualitatively the role of interaction between spins, let us analyze the Hamiltonian (1). Due to the lack of space it will be done briefly, omitting some details.

The easy-axis (first) term defines the potential barrier height and thus basically determines a general energy scale for the i th spin. The easy-plane (second) term permits the tunneling: both easy-axis and exchange terms conserve the projection of the total spin onto the easy axis. Thus, the rate of change of the projection of i th spin is governed by the quantity $K'_i - K_i$. The exchange (third) term transfers the rotation of i th spin to j th spin, so even if $K'_j - K_j$ is zero, the j th spin can tunnel: the i th spin (having nonzero $K'_i - K_i$) makes the j th spin rotate. The rate of rotation of j th spin in this case is governed by J_{ij} (if J_{ij} is small enough) or by $K'_i - K_i$ (if J_{ij} is strong, so that i th and j th spins rotate as a one collective spin).

The total energy of the system is conserved; since the energy at each minimum is zero, we obtain for the instanton action:

$$\mathcal{S}_E = - \int d\tau \sum_i S_i p_i \dot{\phi}_i, \quad (3)$$

where $p_i = i \cos \theta_i$ are canonical momenta conjugated to coordinates ϕ_i . It can be shown that \mathcal{S}_E is always positive in spite of the negative sign in (3).

Thus, the instanton action is defined by the rate of spin rotation. The exact solution for a single spin (see Ref. 1) predicts that the value \mathcal{S}_E is smaller when spins rotate faster. It holds also for the systems under consideration. Thus, rotation rate is one of the main parameters governing the instanton action. If the rotation rate of all spins is the same, there is no additional contribution from exchange term and the instanton action is the same as for noninteracting spins.

If spins rotate with different rates, exchange tends to unify rotation, i.e., push trajectories of individual spins closer to each other (for FM exchange) or pull them apart (for AFM exchange). Therefore, the exchange interaction

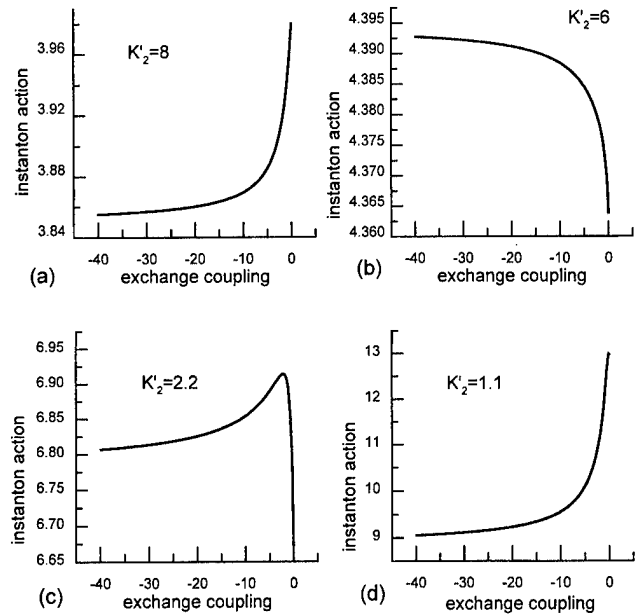


FIG. 1. Dependence of instanton action vs exchange for different values of the parameter K'_2 (governing the rotation rate of the second spin): (a) $K'_2 = 8$; (b) $K'_2 = 6$; (c) $K'_2 = 2.2$; (d) $K'_2 = 1.1$. All the other parameters are the same for all plots: $K_1 = K_2 = 1$, $S_1 = 1$, $S_2 = 3$, $K'_1 = 2$. Spins are FM coupled (exchange integral is negative).

slows down rotation of faster spins and accelerates rotation of slower spins. Thus, the contribution to the instanton action from faster spins increases and for slower spins it decreases. However, the contribution to the total action is larger for larger spins, so that accelerating the larger spins will increase the tunneling probability.

Following these guidelines, we can understand the curves shown in Fig. 1 for the system of two FM-coupled spins, $S_1 = 1$ and $S_2 = 3$. Dependences of instanton action versus coupling are presented there for different values of easy-plane anisotropy of the second spin K'_2 ; the other anisotropies are kept unchanged: $K_1 = K_2 = 1$, $K'_1 = 2$. When K'_2 is large [Fig. 1(a)], S_2 rotates faster, and exchange mainly accelerates the first spin, decreasing the instanton action. The contribution from slowing second spin is less, so the total action decreases with increased coupling. When we reduce K'_2 , rotation rates for both spins become equal, so exchange has almost no impact on instanton action [Fig. 1(b)]. Further reduction of K'_2 leads to a competition between acceleration of the second spin and slowing of the first one, so the peak appears [Fig. 1(c)]. For lower values of K'_2 , an increase in exchange leads predominantly to acceleration of the second spin, lowering the total action. These curves are quite characteristic for a rather large variation of parameters and the analysis remains qualitatively the same.

Nonzero temperature T can be accommodated quite naturally within the instanton approach using the theory developed by Affleck.⁴ In this case the tunneling rate is given by the same formula (2), but the instanton is the periodic trajectory with the finite period $2\tau_0$ (which is defined by the temperature, see above). With increasing temperature, the instanton action remains almost unchanged until some tem-

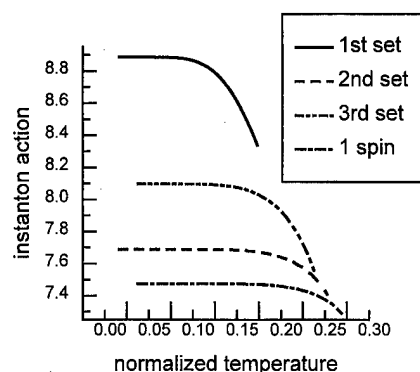


FIG. 2. Temperature behavior of instanton action for the two-spin model system of a Mn_{12} molecule. Results are shown for different sets of anisotropy constants: 1st set— $K_1=2$, $K'_1=2.2$, $K_2=K'_2=0$; 2nd set— $K_1=K'_1=0$, $K_2=2$, $K'_2=2.2$; 3rd set— $K_1=K_2=1$, $K'_1=K'_2=1.1$. Spin values are $S_1=1$, $S_2=3$. Spins are AFM coupled, and the coupling strength is $J=10$. The plot for the single spin $S=2$ is also shown; anisotropies are $K=2$ and $K'=2.2$. Note that this single spin is “equivalent” to all parameter sets of two-spin system presented here.

perature region, called the crossover region, is reached. At the crossover region the instanton action starts to decrease; it means that the thermal effects, instead of tunneling, govern the relaxation rate.

The present study can serve as a qualitative model of the extensively investigated molecular magnet Mn_{12} . We consider a Mn_{12} molecule as consisting of two AFM-coupled spins, $S_1=6$ and $S_2=16$. Individual anisotropies for these spins are not known, but the equivalent single spin is known⁵ to have the value $S=10$ and the easy-axis anisotropy equivalent to about 60 K. We assume that the tunneling in Mn_{12} is provided by a small easy-plane anisotropy, $|K'-K|\ll K$.⁶ The value of coupling J can be estimated to be about 300 K.

Thus, we consider the model system consisting of two AFM-coupled spins $S_1=1$ and $S_2=3$ ($1:3\approx 6:16$). Energy is normalized to have $K=2$, so individual easy-axis anisotropies obey $K_1+K_2=2$. Normalized coupling J is 10. Below we present results for $K'=2.2$ (so individual easy-plane anisotropies obey $K'_1+K'_2=2.2$); calculations for the values down to $K'=2.02$ give qualitatively the same results.

Results of computations for such a model system are shown in Fig. 2. Temperature dependencies of instanton action are shown for different easy-axis and easy-plane anisotropies. Normalized temperature is used: $T(\text{K})=12\text{ K}\times T(\text{dimensionless})$. The ideas described above can be used to understand these curves: to get larger instanton action we

slow down the larger spin by making the easy-plane anisotropy of this spin equal to zero (along with the easy-axis anisotropy, since $K_i\leq K'_i$). A zero anisotropy of the smaller spin gives smaller instanton action (we increase K'_2 up to the limiting value 2.2 thus accelerating S_2 as much as possible). It is easy to see that instanton action varies considerably, and can be 20% higher than that of “equivalent” single spin (the lowest curve in Fig. 2). If we estimate the difference in relaxation times (using $S_0\approx 6$), we find that the relaxation rate is about 2000 times smaller for the two-spin system in comparison with the “equivalent” single-spin system. This result could offer an alternative explanation for the unusually small value of the pre-exponential factor⁷ observed for Mn_{12} . The crossover temperature for the two-spin system also decreases considerably and achieves a value almost two times less than that for the “equivalent” single spin. Thus, even if exchange is five times larger than anisotropy, many-spin effects are important for determining the crossover temperature.

In summary, for two-spin systems with collinear ordering we demonstrated that many-spin effects are important even if exchange is considerably larger than anisotropy. We have shown that qualitative understanding of our results can be achieved by analysis of the spin rotation rates which are governed by easy-plane terms in the Hamiltonian. Finite-temperature effects were also studied for the two-spin model of the magnetic molecule Mn_{12} . We demonstrated that in this case the temperature dependence of the tunneling probability for the two-spin system can differ considerably from the corresponding collective spin system.

The authors would like to thank V. Antropov for formulating the problem. This work was carried out at the Ames Laboratory, which is operated for the U.S. Department of Energy by Iowa State University under Contract No. W-7405-82, and was supported by the Director for Energy Research, Office of Basic Energy Sciences of the U.S. Department of Energy.

¹P. C. E. Stamp, E. M. Chudnovsky, and B. Barbara, *Int. J. Mod. Phys. B* **6**, 1355 (1992).

²B. Barbara and E. M. Chudnovsky, *Phys. Lett. A* **145**, 205 (1990).

³C. G. Callan, Jr. and S. Coleman, *Phys. Rev. D* **16**, 1762 (1977).

⁴I. Affleck, *Phys. Rev. Lett.* **46**, 388 (1981).

⁵D. Gatteschi, *Adv. Mater.* **6**, 635 (1994).

⁶B. Barbara, V. V. Dobrovitski, A. K. Zvezdin, and E. R. Rakhmetov, *Acta Phys. Pol. A* **92**, 336 (1997).

⁷F. Hartmann-Boutron, P. Politi, and J. Villain, *Int. J. Mod. Phys. B* **10**, 2577 (1995).

Spin dynamics in $S=1/2$ chains and ladders from NMR and susceptibility measurements in $\text{Sr}_{14-x}\text{Na}_x\text{Cu}_{24}\text{O}_{41}$

P. Carretta and M. Corti

Department of Physics "A. Volta", Unità INFN di Pavia, Via Bassi 6, 27100-I Pavia, Italy

P. Ghigna

INCM, Department of Physical Chemistry, Via Taramelli 16, 27100-I Pavia, Italy

A. Lascialfari

Department of Chemistry, Via Maragliano 75/77, 50144-I Firenze, Italy

The authors report on NMR and susceptibility measurements in $\text{Sr}_{14-x}\text{Na}_x\text{Cu}_{24}\text{O}_{41}$ for $0 \leq x \leq 2$. The analysis of the susceptibility evidences that only a small fraction of Cu^{2+} spins are involved in the dimerization of $\text{Cu}(1)\text{O}_2$ chains. The introduction of extra holes by Na^+ doping is found to decrease the $\text{Cu}(1)^{2+}$ uniform static susceptibility without affecting the amplitude of the dimerization gap. On the other hand, the amplitude of the spin gap in the $\text{Cu}(2)_2\text{O}_3$ two-leg-ladders and the resistivity are reduced by doping. The origin of the discrepancy in the amplitude of the gap estimated by means of nuclear spin-lattice relaxation and susceptibility measurements is briefly discussed. © 1998 American Institute of Physics. [S0021-8979(98)39811-4]

I. INTRODUCTION

The discovery of high-temperature superconductivity has brought renewed interest in the study of low-dimensional cuprates,¹ and the search for superconductivity in the quasi-one-dimensional (quasi-1D) ones [$(\text{Sr}, \text{Ca})_{14}\text{Cu}_{24}\text{O}_{41}$] has recently been proven to be successful.² This fact is of major interest and could lead to a reexamination of the properties of high- T_c superconductors (HT_cSC) in the frame of a quasi-1D scenario, particularly if a phase separation takes place.³ Therefore an extensive investigation of either pure or hole doped quasi-1D cuprates and a comparison with the normal-state properties of HT_cSC is required. $\text{Sr}_{14}\text{Cu}_{24}\text{O}_{41}$ is the parent of this new family of quasi-1D superconductors and its structure comprises $\text{Cu}(1)\text{O}_2$ chains and $\text{Cu}(2)_2\text{O}_3$ 2-leg-ladders.⁴ $\text{Cu}(1)^{2+}$ spins dimerize around 80–100 K and the origin of this dimerization is still under debate.⁵ On the other hand, the comprehension of the properties of spin excitations in the 2-leg-ladders could be considered almost complete if the discrepancy in the value of the gap derived from DC susceptibility and NMR measurements is not concerned.¹² The chains are intrinsically doped by six holes due to the three excess O^{2-} ions present in the stoichiometry. By a substitution of Sr^{2+} with Ca^{2+} , an increase in the chemical pressure is obtained, a more efficient transfer of holes to the ladders is achieved, and a superconducting state is realized.² In this paper we report on the modifications of the spin dynamics in the chains and in the 2-leg-ladders of $\text{Sr}_{14}\text{Cu}_{24}\text{O}_{41}$ after an introduction of extra holes by substituting Sr^{2+} with Na^+ . By varying the Na^+ content we expect to vary the hole concentration in the ladders due both to an increase of the chemical pressure and to the heterovalent nature of the substitution.

II. RESULTS AND DISCUSSION

For all samples the resistivity was observed to increase on cooling and two different activated regimes, with energy

barriers decreasing with doping (see Fig. 3 later on), were evidenced. The two regimes are separated by a crossover temperature $T_p \approx 130$ K where an anomaly, possibly related to structural distortions,⁶ is observed. These distortions could be relevant to the dimerization of $\text{Cu}(1)\text{O}_2$ chains since they modify the $\text{Cu}(1)\text{--O--Cu}(1)$ bonding angle and the corresponding superexchange coupling.⁷

The temperature dependence of the susceptibility is dominantly contributed from $\text{Cu}(1)^{2+}$ spins and is similar to the one expected for the case of spin dimerization with an activation energy around 140 K as explained below.⁵ $\text{Cu}(2)^{2+}$ spins in the ladder are strongly coupled by forming a spin singlet state and their contribution is rather small, although not negligible for $T \geq 200$ K. The total spin susceptibility is $\chi = (10/24)\chi_D + (14/24)\chi_L$, with χ_D the susceptibility of the dimerized $\text{Cu}(1)\text{O}_2$ chains and χ_L that of the ladder. The coefficient in front of each term gives the relative occupation of $\text{Cu}(1)^{2+}$ and $\text{Cu}(2)^{2+}$ spins per formula unit. $\chi_{D,L}$ can be written in the form

$$\chi_{D,L} = \frac{N_A g^2 \mu_B^2}{k_B T} \frac{z_{D,L}(T, \Delta_{D,L})}{1 + 3z_{D,L}(T, \Delta_{D,L})}. \quad (1)$$

For a chain of noninteracting dimers⁸ one has $z_D = \exp(-\Delta_D/T)$, while for a 2-leg-ladder in the isotropic limit ($J_{\parallel} = J_{\perp} = J = 2\Delta_L$, J_{\parallel} being the superexchange coupling along the chains and J_{\perp} in the rungs) and for $J \gg T$, one has $z_L \approx 0.4 \sqrt{T/2\Delta_L} \exp(-\Delta_L/T)$.⁹ From a quantitative analysis of the susceptibility data at low temperatures ($T \leq 200$ K), it turned out that only 35% of $\text{Cu}(1)^{2+}$ spins per formula unit contributes to the susceptibility. As first suggested by Carter *et al.*¹⁰ this reduction should be associated to the possible formation of Zhang–Rice (ZR)¹¹ singlets between the extra-holes intrinsically present in this compound and the $\text{Cu}(1)^{2+}$ spins in the chains. If one considers that there are n_h of these

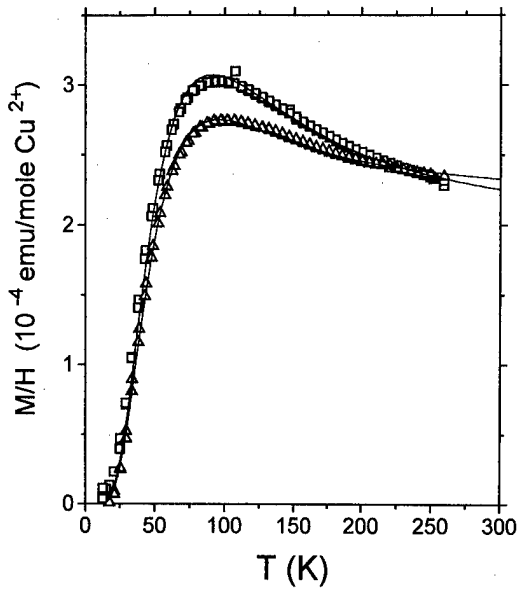


FIG. 1. Temperature dependence of the DC susceptibility for the $x=0$ (squares) and $x=2$ (triangles) samples. A low-temperature Curie-Weiss contribution $\chi_{CW} = C/(T - \Theta)$ has been subtracted from the raw data, with $C(x=0) = 0.015$ emu K/mol Cu^{2+} , $C(x=0.02) = 0.0167$ emu K/mol Cu^{2+} , $\Theta(x=0) = -1.23$ K and $\Theta(x=0.02) = -1.14$ K. The solid lines give the best fit according to Eqs. (1) and (2) over all the temperature range.

localized holes in the chain, per formula unit, the DC susceptibility should be reduced by a factor $(10 - n_h)/10$. Then one has

$$\chi = \frac{10 - n_h}{24} \chi_D + \frac{14}{24} \chi_L. \quad (2)$$

By fitting the low-temperature (for $T < 130$ K χ_L is negligible) data with just the first term of Eq. (2) one can derive n_h and Δ_D . One finds $\Delta_D \approx 140$ K and weakly sample dependent, while the number of localized holes in the chain increases from $n_h \approx 6.4$ to $n_h \approx 7$ on increasing x . Keeping these two parameters fixed one can estimate Δ_L from the fit of the data over all the temperature range with Eqs. (1) and (2) (see Fig. 1). One finds $\Delta_L \approx 500$ K for $x=0$, while $\Delta_L \approx 420$ K for $x=2$. The value for n_h derived for the pure compound is in good agreement with the value $n_h = 6$ that one would expect on the basis of considerations on the oxygen stoichiometry. From the same considerations, for $x=2$ one would expect a stronger increase of n_h . The fact that only a slight increase is observed suggests that part of the holes start to be doped into the $\text{Cu}(2)_2\text{O}_3$ ladders, causing the observed decrease in Δ_L .

Now we turn to the discussion of the NMR measurements. The temperature dependence of ^{23}Na $1/T_1$ for $H \parallel b$ is shown in Fig. 2(b). One observes an increase on decreasing temperature and then a sharp activated decrease at low temperatures. The low-temperature dependence is characterized by an activation energy $\Delta_D \approx 130$ K, very close to the one derived from susceptibility measurements, implying that ^{23}Na nuclei below ~ 130 K probe essentially $\text{Cu}(1)^{2+}$ spin dynamics. Only at high temperatures the contribution from $\text{Cu}(2)^{2+}$ spin fluctuations to the relaxation can be observed, causing a smooth increase in ^{23}Na $1/T_1$. On the other hand,

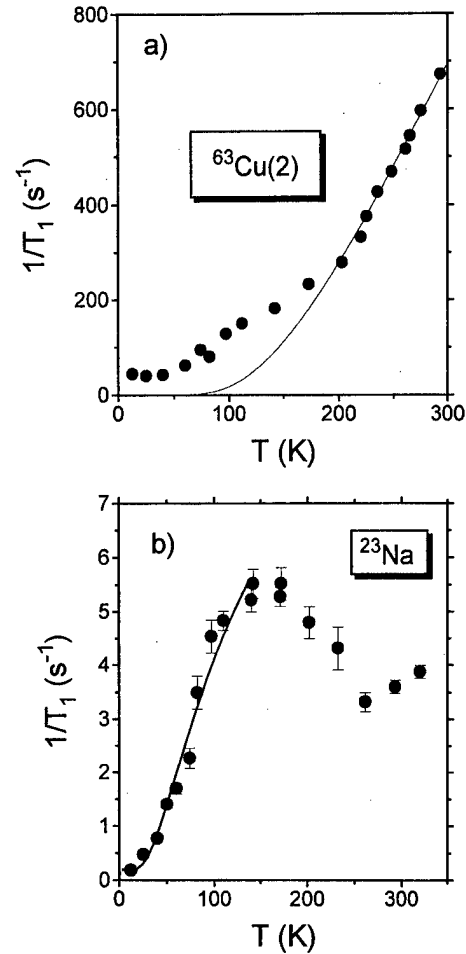


FIG. 2. (a) Temperature dependence of $^{63}\text{Cu}(2)$ $1/T_1$ for the $x=2$ oriented powder sample in the magnetic field $H = 5.9$ T along the b axis. The solid line describes the high-temperature activated behavior. (b) Temperature dependence of ^{23}Na $1/T_1$ for the same sample in a magnetic field $H = 5.9$ T along the b axis. The solid line shows the activated behavior for $\Delta_D = 130$ K.

this is the dominant contribution to $^{63}\text{Cu}(2)$ relaxation at high temperatures, where an activated trend [see Fig. 2(a)], characterized by activation energies decreasing with doping from around 650 to ≈ 500 K, is observed. We remark that these values are higher by a factor ~ 1.4 than the ones derived from DC susceptibility measurements, a situation similar to the one found in other 2-leg-ladders,¹² but not in all of them.¹³ Around 90 K a bump in $^{63}\text{Cu}(2)$ $1/T_1$ superimposed to the activated behavior is obviously seen. This extra contribution is strongly field dependent and possibly related to the slowing down of the fluctuations associated to the diffusive motions of the holes.¹⁴

In $S = 1/2$ 2-leg-ladders and dimerized chains, at low temperatures and low magnetic fields ($g\mu_B H/k_B \ll T \ll \Delta_{D,L}$), only the low part of the triplet magnon branch is occupied. Then¹⁵ the nuclear relaxation is driven by indirect $q \approx 0$ processes involving triplet excitations, its temperature dependence is related to the population of these excitations and one finds that $1/T_1 \propto \exp(-\Delta/T)$. For $T \gg \Delta_{D,L}$ $1/T_1$ reaches asymptotically a constant value related to Heisenberg exchange frequency. This is indeed the behavior observed for $^{63}\text{Cu}(2)$ in the $S = 1/2$ AF 2-leg-ladder⁷ and in S

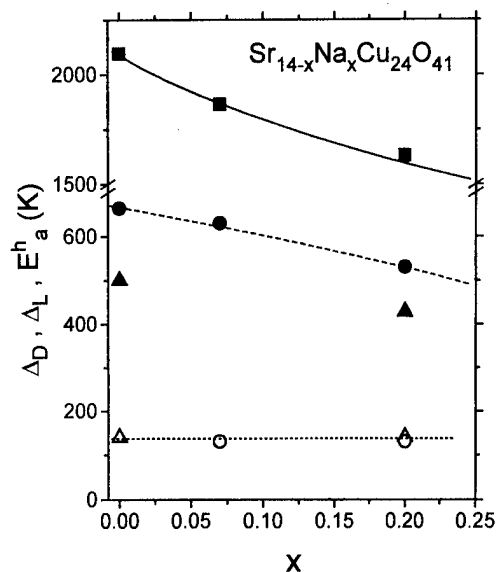


FIG. 3. Doping dependence of the high-temperature transport activation energy E_a (solid squares), Δ_L derived from $^{63}\text{Cu}(2)$ $1/T_1$ (solid circles), Δ_L derived from DC susceptibility measurements (solid triangles), Δ_D estimated from ^{23}Na $1/T_1$ (open circles), and Δ_D from DC susceptibility measurements (open triangles). The lines are guides to the eye.

$S=1/2$ dimerized chains,¹⁶ however, it is not the one observed for ^{23}Na $1/T_1$ in $\text{Sr}_{14-x}\text{Na}_x\text{Cu}_{24}\text{O}_{41}$ which between these two regimes shows a broad maximum. The origin of this maximum is still unclear and a systematic study of the field dependence of ^{23}Na $1/T_1$ is required to understand whether it has a dynamical origin or if it is due to a modification in the hyperfine coupling constants on cooling, related to the occurrence of lattice distortions.

III. SUMMARIZING REMARKS AND CONCLUSIONS

We have presented a series of NMR and susceptibility measurements aiming at clarifying the modifications of the spin dynamics in $\text{Cu}(1)\text{O}_2$ chains and in $\text{Cu}(2)_2\text{O}_3$ ladders as a function of temperature and doping. The magnetic properties in the chains are essentially the ones expected for weakly interacting dimers. In fact, the analysis of the susceptibility supports the presence of a rather small number of spins which dimerize while the other $\text{Cu}(1)^{2+}$ spins form ZR singlets with localized holes. The presence of this isolated dimers separated by ZR singlets could also explain the presence of neutron scattering peaks at wave vectors around $1/4$ – $1/6$ reciprocal lattice units.¹⁷ The amplitude of the dimerization gap was estimated $\Delta_D \approx 140$ K either from DC susceptibility or ^{23}Na $1/T_1$ data and was found not to vary with doping (see Fig. 3), suggesting that the dimers are weakly interacting, thus supporting our analysis of the DC susceptibility. The structural distortions evidenced in NQR spectra⁷ and resistivity measurements are believed to modify the superexchange coupling along the chains.

As for the $\text{Cu}(2)_2\text{O}_3$ 2-leg-ladders we observe that the amplitude of the gap Δ_L , derived both from DC susceptibility and $1/T_1$ measurements decreases with increasing doping

(Fig. 3). This behavior is analogous to that of the activation barrier E_a measured through resistivity (Fig. 3) and evidences a frustration of the AF correlations on increasing the hole itineracy, analogous to the one observed in underdoped HTcSC. It is interesting to point out that the initial suppression rate for the gap $s = -d\Delta_L/dx$ is higher for Na-doped ($s \approx 70$ K/ Na^+ ion) than for Ca-doped samples ($s \approx 45$ K/ Ca^{2+} ion),^{18,19} as expected for the heterovalent nature of the Sr^{2+} for Na^+ substitution. On the other hand, we remark that the amplitude of the gap derived from $1/T_1$ and DC susceptibility differs by a factor ~ 1.4 . Sachdev and Damle,²⁰ on the basis of a semiclassical model for the spin excitations in quasi-1D systems with a gap, which should be valid for $T \ll \Delta$, found that the gaps probed by $1/T_1$ and χ differ by a factor of 1.5, very close to what is experimentally measured. However, one should notice that in other quasi-1D gapped quantum antiferromagnets (dimerized chains or in other ladder compounds with $J_\perp > J_\parallel$), where this model should still apply, the gap derived from susceptibility and $1/T_1$ is the same. A possible origin of the discrepancy is that excitations around $q \approx \pi$, involving 3-magnons,¹⁵ can become more important for $J_\parallel > J_\perp$. In that case the continuum of spin excitations moves to lower energies and there is a higher density of states with energies $2\Delta_L$ which are involved in the 3-magnon processes. Then one should have an extra contribution of the form $(1/T_1)_{(3)} \propto \exp(-2\Delta_L/T)$. An agreement with the susceptibility measurements can be found in this case provided the amplitude of 3-magnon terms is six times larger than that of 2-magnon processes. The fact that the disagreement in the estimate of Δ_L is absent for $J_\perp > J_\parallel$ suggests that the origin of the discrepancy is inherent to the form of the magnon dispersion curve.

¹E. Dagotto and T. M. Rice, *Science* **271**, 619 (1995).

²M. Uehara *et al.*, *J. Phys. Soc. Jpn.* **65**, 2764 (1996).

³V. J. Emery, S. A. Kivelson, and O. Zachar, *Phys. Rev. B* **56**, 6120 (1997); C. Castellani, C. Di Castro, and M. Grilli, *Z. Phys. B* **103**, 137 (1997).

⁴E. M. McCarron *et al.*, *Mater. Res. Bull.* **23**, 1355 (1988).

⁵M. Matsuda and K. Katsumata, *Phys. Rev. B* **53**, 12201 (1996); M. Kato *et al.*, *Physica C* **235–240**, 1327 (1994); M. W. McElfresh *et al.*, *Phys. Rev. B* **40**, 825 (1989).

⁶See, for example, R. W. Vest and J. M. Honig in *Conductivity in Ceramics and Glass*, edited by N. M. Tallan (Marcel Dekker, New York, 1974), p. 343 and references therein.

⁷P. Carretta *et al.*, *Phys. Rev. B* **56**, 14587 (1997).

⁸For interacting dimers one would obtain the same expression as for the ladders. The estimated value for the gap Δ_D would then decrease from 140 to 120 K. See Ref. 13 for more details.

⁹M. Troyer, H. Tsunetsugu, and D. Würtz, *Phys. Rev. B* **50**, 13515 (1994); G. Chaboussant, Ph.D. thesis, University Joseph Fourier (Grenoble I), 1997.

¹⁰S. A. Carter *et al.*, *Phys. Rev. Lett.* **77**, 1378 (1996).

¹¹F. C. Zhang and T. M. Rice, *Phys. Rev. B* **37**, 3759 (1988).

¹²M. Azuma *et al.*, *Phys. Rev. Lett.* **73**, 3463 (1994).

¹³G. Chaboussant *et al.*, *Phys. Rev. Lett.* **79**, 925 (1997).

¹⁴P. Carretta and M. Corti, and A. Rigamonti, *Phys. Rev. B* **48**, 3433 (1993).

¹⁵J. Sagi and I. Affleck, *Phys. Rev. B* **53**, 9188 (1996).

¹⁶Y. Furukawa *et al.*, *J. Phys. Soc. Jpn.* **65**, 2393 (1996).

¹⁷M. Matsuda *et al.*, *Phys. Rev. B* **54**, 12199 (1996).

¹⁸H. Kumagai *et al.*, *Phys. Rev. Lett.* **78**, 1992 (1997).

¹⁹K. Magishi *et al.*, *Physica C* (to be published).

²⁰S. Sachdev and K. Damle, *Phys. Rev. Lett.* **78**, 943 (1997).

²¹Y. Fagot-Revurat *et al.*, *Phys. Rev. B* **55**, 2364 (1997); P. Gaveau *et al.*, *Europhys. Lett.* **12**, 647 (1990).

Magnetic properties and spin dynamics in hole-doped $S=1$ AF chain: ^{89}Y NMR and susceptibility in $\text{Y}_{2-x}\text{Ca}_x\text{BaNiO}_5$

F. Tedoldi, A. Rigamonti, C. Brugna, and M. Corti^{a)}

INFN-Department of Physics "A. Volta", University of Pavia, I-27100 Pavia, Italy

A. Lascialfari

Department of Chemistry, University of Firenze, I-50144 Firenze, Italy

D. Capsoni and V. Massarotti

Department of Physical Chemistry, University of Pavia, I-27100 Pavia, Italy

Hole-doping effects in Haldane chain have been studied by means of magnetic susceptibility and ^{89}Y nuclear magnetic resonance in $\text{Y}_{2-x}\text{Ca}_x\text{BaNiO}_5$ for $x=0$, $x=0.06$ and $x=0.18$. In nominally pure YBNO detailed information on this prototype of Haldane systems is extracted. In the charge-doped compounds the ^{89}Y relaxation rates indicate that holes induce low-energy excitations with an effective spectral density having a structure characterized by a narrow central peak.

© 1998 American Institute of Physics. [S0021-8979(98)24611-1]

I. INTRODUCTION

The compound Y_2BaNiO_5 (YBNO) is characterized by the presence of weakly coupled chains of strongly interacting Ni^{2+} ($S=1$) ions.¹ The ratio of interchain/intrachain coupling ($|J'/J| \leq 5 \times 10^{-4}$,^{2,3} indicates that YBNO can be considered a good realization of $S=1$ one-dimensional Heisenberg antiferromagnet (1D-HAF). The magnetic properties of YBNO are well described by the Hamiltonian

$$H = J \sum_i S_i \cdot S_{i+1} + D \sum_i (S_i^z)^2 + E \sum_i [(S_i^x)^2 - (S_i^y)^2] \quad (1)$$

with $J \approx 285$ K, $D \approx -8$ K, and $E \approx 3$ K.^{2,3}

YBNO has triggered a great deal of interest, since the relatively high gap ($\Delta \approx 100$ K) and the small values of the anisotropy terms D and E allow one to study the Haldane⁴ ground state in a wide temperature range. Furthermore, the heterovalent substitutions of Ca^{2+} for Y^{3+} introduce holes mainly residing in the Ni-O chains⁵ and induce relevant modifications in the magnetic properties of this prototype of 1D-HAF. The possible itinerancy of the holes can induce novel features in the spin liquid state, with low-energy excitations lying into the gap.^{5,6}

Here we present magnetic susceptibility χ , ^{89}Y shift K , T_1 , and T_2 measurements in $\text{Y}_{2-x}\text{Ca}_x\text{BaNiO}_5$.

II. EXPERIMENTALS AND EXPERIMENTAL RESULTS

Solid state reaction has been used to obtain $\text{Y}_{2-x}\text{Ca}_x\text{BaNiO}_5$ in the compositions: $x=0$, $x=0.06$, $x=0.18$. X-ray diffraction indicated a single-phase compound and was used also to estimate the real amount of doping. The susceptibility measurements have been performed by SQUID magnetometer, in field cooled and zero field cooled conditions. No appreciable difference between the two cases have been detected, in the temperature range 3–250 K. The mag-

netization curves appear linear, in all samples, up to $H_0 = 0.5$ T. The experimental data of $\chi = M/H_0$ are reported in Fig. 1 after subtraction of a core-diamagnetic term $\chi_d = 1.28 \times 10^{-4}$ emu/mole.

Standard pulse NMR techniques have been used to obtain ^{89}Y spectra and relaxation times in external magnetic fields $H_0 = 5.9$ T and $H_0 = 9.4$ T. In pure YBNO, as already noticed,⁷ the spectrum results from the powder distribution of an hyperfine field h of cylindrical symmetry. Due to the orthorhombic symmetry at the Yttrium site, this cylindrical symmetry has to be related to a compensation with the anisotropy in the single ion susceptibility.⁸ A shift parameter $K = \frac{1}{3}K_{\parallel} + \frac{2}{3}K_{\perp}$ can then be defined (\parallel and \perp to the x -chain axis). The powder distribution of the dipolar part of h is responsible of the structure of the NMR line, centered at the frequency $\nu = \gamma H_0(1 + K)$. In $\text{Y}_{2-x}\text{Ca}_x\text{BaNiO}_5$ the homogeneous broadening of the line prevents the same type of analysis of the spectra. Then K has been obtained from the

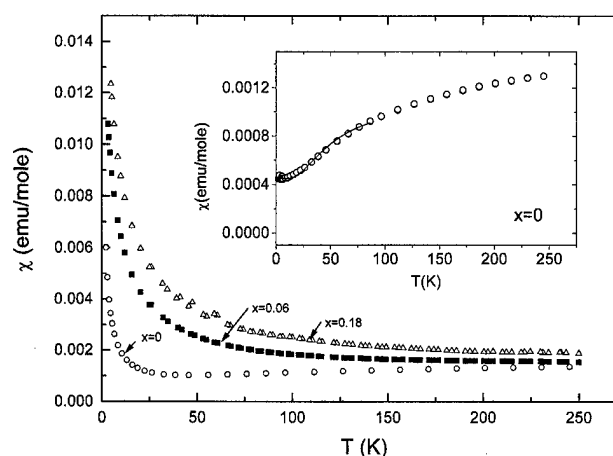


FIG. 1. Magnetic susceptibility χ in $\text{Y}_{2-x}\text{Ca}_x\text{BaNiO}_5$ as a function of temperature. In the inset the behavior of χ in pure YBNO after subtraction of the Curie-Weiss term is shown. The solid line is the best fit of the data according to Eq. (2) in the temperature range $T \leq 100$ K, where it is expected to hold.

^{a)}Electronic mail: CORTI@PV.INFN.IT

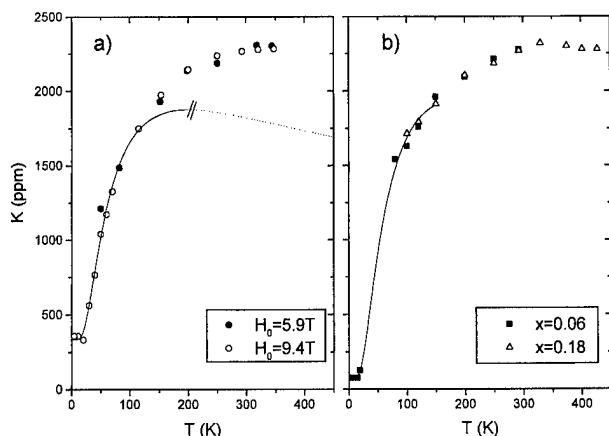


FIG. 2. Shift K of the ^{89}Y NMR line (with respect to a solution of YCl_3) in pure YBNO, for two values of the external magnetic field H_0 [part (a)]. In part (b) the shift for the Ca-doped compounds are reported (no field dependence was noted). The solid lines are the best fit behaviors, for $T \leq 150$ K, according to the function $K(T) = K(0) + (B/\sqrt{T})e^{-\Delta_K/T}$. The lack of experimental data for $30 \text{ K} \leq T \leq 80 \text{ K}$ in (b) corresponds to the disappearing of the echo signal due to the divergence in T_2^{-1} .

position of the maximum in the resonance peak ($\approx K_{\perp}$). In Fig. 2 the temperature behaviors of K are reported, for different values of the external field, in pure and doped YBNO.

The recovery of the nuclear ^{89}Y magnetization $M_z(t)$ in the doped compounds has a stretched-exponential form, particularly at low temperatures ($T \leq 250$ K). Therefore all the recovery plots have been fitted by the law $M_z(t) = M_z(0)\exp[-(t/T_1)^\beta]$ (see Fig. 3).

The decay of the ^{89}Y echo signal has a gaussian behavior, for $T \geq 250$ K. Instead, in the latter case and for $T \leq 150$ K, the decay of the echo turns to an exponential form, with a tendency to become stretched. In Fig. 4 the values of the spin decay rates are reported.

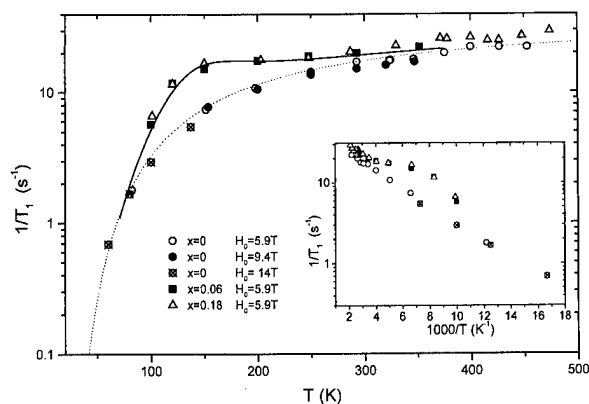


FIG. 3. ^{89}Y spin-lattice relaxation rates as a function of temperature in $\text{Y}_{2-x}\text{Ca}_x\text{BaNiO}_5$. The values of β in the stretched exponential are $\beta \approx 1$ for $x=0$, while in the doped compounds β is close to 1 in the high temperature range and becomes $\beta \approx 0.8$ for $T < 200$ K. In the inset the semilogarithmic plot of T_1^{-1} as a function of $1000/T$ is shown. The dotted lines are the best fit of the data according to a gapped behavior, with $\Delta_{T_1} = 250$ K. The solid line is the best fit according to the model discussed in the text for the extracontribution due to Ca doping.

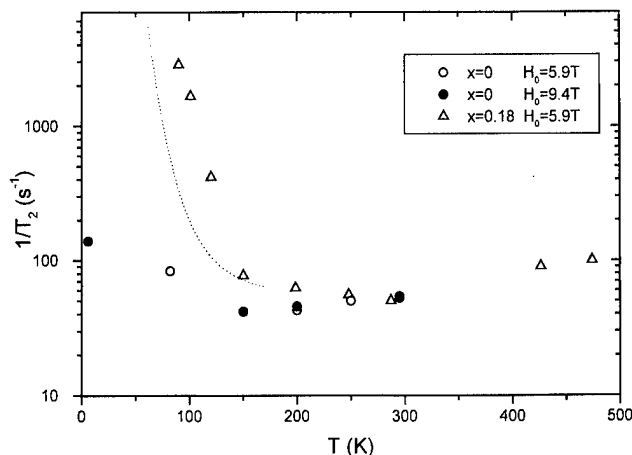


FIG. 4. ^{89}Y spin-spin relaxation rates in $\text{Y}_{2-x}\text{Ca}_x\text{BaNiO}_5$. The dotted line represents the theoretical behavior for T_2^{-1} derived from the single-Lorentzian spectral density of the excitations which describes the doping-related extracontribution to T_1^{-1} (see Fig. 3).

III. ANALYSIS OF THE RESULTS AND CONCLUSIONS

The behavior of χ in nominally pure YBNO is typical of $S=1$ HAFs containing a small percent of magnetic impurities, most likely are due to oxygen nonstoichiometry.⁸ One can try to account for the experimental results, for $T < 100$ K, by means of the expression^{9,10}

$$\chi(T) = \chi(0) + \frac{C}{T - \Theta} + \frac{A(\Delta_\chi)}{\sqrt{T}} e^{-\Delta_\chi/T}. \quad (2)$$

$\chi(0)$ takes into account the possible orbital contribution (Van Vleck paramagnetism) and/or the one related to the anisotropy in the magnetic Hamiltonian.^{9,11} Furthermore, in Eq. (2) we have added a Curie-Weiss term to describe the effects of paramagnetic impurities, dominant at low temperatures ($T < 20$ K). By fitting the data (Fig. 1) with Eq. (2), one derive $\chi(0) = 4.5 \times 10^{-4}$ emu/mole, $C = 1.56 \times 10^{-2}$ emu K/mole, $\Theta = 0.5$ K, $A = 1.2 \times 10^{-2}$ emu K/mole, and $\Delta_\chi = 92$ K. From the value of C , for $s=1/2$ defects (as it is the case either for O^- or Ni^{3+} in the low-spin state) one can estimate a concentration of 3×10^{-2} impurities for Ni ion.

After subtraction of the Curie contribution (inset in Fig. 1), $\chi(T)$ shows the behavior described by the third term in Eq. (2). The value of Δ_χ is not far from the separation between the singlet ground state and the first excited magnetic state, obtained by neutron scattering $\Delta_{\text{NS}} = 102$ K.^{2,3} It should be noted that Δ_χ , as well as Δ_{NS} , are smaller than the gap theoretically expected ($\Delta_{\text{Th}} \approx 117$ K) if one uses $J = 285$ K (Ref. 12) and sets $\Delta_{\text{Th}} \approx 0.4105$ J, as suggested by numerical techniques^{9,10} for Heisenberg Hamiltonian [$D=E=0$ in Eq. (1)]. On the other hand, the presence of easy-axis anisotropy (namely, $D < 0$) increases the energy separation between the ground state and the first excited magnetic state. If one assumes for the prefactor A in the third term of Eq. (2) the expression derived in the free boson approach,⁹ i.e., $A_{\text{Th}} = 2(g\mu_B)^2/\nu\sqrt{2\pi}$ and a spin wave velocity $v = 2.49$ J, then $A_{\text{Th}} \approx 1.8 \times 10^{-2}$ emu $\sqrt{\text{K}}$ /mole, again larger than the experimental result.

TABLE I. Curie constants and temperatures extracted from the best fit of the data in Fig. 1. n is the number of magnetic impurities for Ni ion deduced from C.

x	C (emu K/mole)	θ (K)	n
0	1.56×10^{-2}	-0.5	3×10^{-2}
0.06	1×10^{-1}	-6.5	2×10^{-1}
0.18	1.6×10^{-1}	-9.1	3×10^{-1}

Since the Curie-like term in Eq. (2) does not contribute to the ^{89}Y NMR shift, one can confidently use the data for K to derive reliable information on the gap-related term. The best fit of the data for $T \leq 150$ K [solid line in Fig. 2(a)] yields $\Delta_K = 102 \pm 5$ K, in agreement with Δ_{NS} . The measurements of K are particularly useful in the doped samples, where the increase in the Curie term prevents reliable estimates of Δ and A from bulk susceptibility. From the data in Fig. 2(b) one derives $\Delta_K = 98 \pm 10$ K for $x = 0.06$ (the large error is due to the lack of data for $30 \text{ K} \leq T \leq 80$ K, see caption). The susceptibility measurements can be used to derive the x dependence of C and θ [Eq. (2)]. By assuming that A and Δ_K do not change dramatically with doping (as indicated by K), reliable fittings of χ below 100 K yield the results reported in Table I. It is noted that for $x = 0.06$ the value for the number n of $s = 1/2$ paramagnetic sites for Ni ion, is compatible with the model of three paramagnetic moments for each heterovalent substitution.¹³ The departure for $x = 0.18$ is an obvious consequence of the breakdown of the assumption of dilute magnetic moments.

The relaxation rates in pure YBNO, down to $T \approx 40$ K, are well fitted by a law of the form $T_1^{-1} \propto (-\Delta/T)$ (Fig. 3, inset) typical of gapped systems. One derives a field-independent gap $\Delta_{T_1} = 250$ K, of the order of the one expected for a dominant contribution to the relaxation involving staggered process.¹⁴

In doped compounds an extra contribution to the relaxation rate is observed in the temperature range 50–250 K, yielding a broad maximum in T_1^{-1} for $T \approx 150$ K (Fig. 3). The occurrence of novel spin excitations upon heterovalent substitutions is more evident in the divergence of the spin-spin relaxation rate T_2^{-1} (Fig. 4). In the following we qualitatively discuss these features in the ^{89}Y relaxation, by referring to a simple model of fluctuating effective field $h^e(t)$ at the Y site, that we attribute to extra magnetic moments induced by the hole along the chain. Then

$$\frac{1}{T_1} = \frac{\gamma^2}{2} \int e^{-i\omega_L t} \langle h_z^e(0) h_z^e(t) \rangle dt, \quad (3a)$$

$$\frac{1}{T_2} = \frac{1}{2T_1} + \frac{\gamma^2}{2} \int \langle h_z^e(0) h_z^e(t) \rangle dt. \quad (3b)$$

If one tentatively assumes for the components of $h^e(t)$ an exponential correlation function, with an effective correla-

tion time τ_e of the form $\tau_0 \exp[E/T]$, then the T_1 data in doped compounds, in the temperature range $50 \leq T \leq 250$ K, can be approximately fitted with $\tau_0 = 3 \times 10^{-10}$ s and $E \approx 580$ K (solid line in Fig. 3). It is interesting to observe that the holes contribution to T_1^{-1} seems to be only little dependent on x for $x \geq 0.06$. From the maximum in T_1^{-1} at $T_m \approx 150$ K, that occurs when $\tau_e \approx \omega_L^{-1}$, one can estimate $\langle |h_e|^2 \rangle$ at the Y site. One has $\sqrt{\langle |h_e|^2 \rangle} \approx 30$ G, about 30% of the intrinsic linewidth.

One can try to discuss the temperature dependence of T_2 (Fig. 4) by assuming $\langle |h_z^e|^2 \rangle \approx \langle |h_\pm|^2 \rangle$ and for $\int \langle h_z^e(0) h_z^e(t) \rangle dt$ the same correlation time τ_e used for T_1 . As it appears in Fig. 4 the behavior of T_2^{-1} is far from being fitted by this theoretical prediction. The discrepancy indicates that the spectral density of the spin excitations in the doped compounds cannot be taken of the form $J(\omega) = 2\tau_e / (1 + \omega^2 \tau_e^2)$. The results for T_2 point out that $J(\omega)$ is structured, with a central peak centered at $\omega \approx 0$, superimposed on the diffusive contribution of width τ_e^{-1} . This is a typical feature of systems characterized by nonlinear dynamics, e.g., in strongly anharmonic double-well potential, as widely discussed at structural phase transitions.¹⁵ In some cases the width of the correspondent central peak can be written¹⁶ in terms of the static correlation length and of an average velocity of propagation of solitonlike excitations. Then a divergence in T_2^{-1} can be expected, while T_1 is controlled by the regular diffusive component of the spin dynamics.

¹D. J. Buttrey, J. D. Sullivan, and A. L. Rheingold, J. Solid State Chem. **88**, 291 (1990).

²T. Sakaguchi, K. Kakurai, T. Yokoo, and J. Akimitsu, J. Phys. Soc. Jpn. **65**, 3025 (1996).

³G. Xu, J. F. DiTusa, T. Ito, K. Oka, H. Takagi, C. Broholm, and G. Aeppli, Phys. Rev. B **54**, R6827 (1996).

⁴F. D. M. Haldane, Phys. Lett. **93A**, 464 (1983); Phys. Rev. Lett. **50**, 1153 (1983).

⁵J. F. Di Tusa, S. W. Cheong, J. H. Park, G. Aeppli, C. Broholm, and C. T. Chen, Phys. Rev. Lett. **73**, 1857 (1994).

⁶E. Dagotto, J. Riera, A. Sandvik, and A. Moreo, Phys. Rev. Lett. **76**, 1731 (1996).

⁷T. Shimizu, D. E. MacLaughlin, P. C. Hammel, J. D. Thompson, and S. W. Cheong, Phys. Rev. B **52**, R9835 (1995).

⁸T. Yokoo, T. Sakaguchi, K. Kakurai, and J. Akimitsu, J. Phys. Soc. Jpn. **64**, 3651 (1995).

⁹I. Affleck, Phys. Rev. B **41**, 6697 (1990); Eq. 2.14 has an error [see Takigawa, T. Asano, Y. Ajiro, and M. Meketa, Phys. Rev. B **52**, R13087 (1995)].

¹⁰T. Jolicoeur and O. Golinelli, Phys. Rev. B **50**, 9265 (1994), and references therein.

¹¹A. M. Tsvelik, Phys. Rev. B **42**, 10499 (1990).

¹²J. Darricet and L. P. Regnault, Solid State Commun. **86**, 409 (1993).

¹³M. Hagiwara, K. Katsumata, I. Affleck, B. I. Halperin, and J. P. Renard, Phys. Rev. Lett. **65**, 3181 (1990).

¹⁴J. Sagi and I. Affleck, Phys. Rev. B **53**, 9188 (1996).

¹⁵See, for example, K. A. Muller, J. C. Fayet, F. Borsa, and A. Rigamonti, in *Structural Phase Transitions II*, edited by K. A. Muller and H. Thomas (Springer, Berlin, 1991).

¹⁶J. P. Boucher, Hyperfine Interact. **49**, 423 (1989).

Exchange and Film Hard Magnets

R. W. McCallum, Chairman

Coercivity and exchange coupling in PrCo:Co nanocomposite films

J. P. Liu,^{a),b)} Y. Liu,^{c)} and D. J. Sellmyer^{b)}*Center for Materials Research and Analysis, University of Nebraska, Lincoln, NE 68588*

Magnetic hysteresis and intergrain exchange coupling in nanostructured PrCo:Co composite films have been investigated. The composite thin films were made by multilayer sputtering and subsequent annealing. It is found that the coercivity mechanism is related to film morphology, especially the Co phase fraction. Evidence for the hard-soft-phase exchange coupling has been found and high energy products have been obtained. © 1998 American Institute of Physics. [S0021-8979(98)26011-7]

I. INTRODUCTION

Theoretical calculations have predicted giant energy products in exchange-coupled nanostructured hard-soft-phase composites.^{1,2} However, it is difficult to obtain an ideal nanostructure experimentally. Grain growth during heat treatment and distribution of the second phases cannot be controlled and tailored easily. In addition, it is found that coercivity usually decreases dramatically as the soft phase is added. Among various methods of making nanostructured composites, physical vapor deposition has advantages in controlling grain size and distribution of second phase. We have obtained clear evidence of intergrain exchange coupling and remanence enhancement in SmCo/Co multilayer³ and FePt-based nanocomposites.^{4,5} In a recent investigation,⁶ we have successfully inserted the soft Co phase into the hard hexagonal PrCo phase thin films to enhance the remanent magnetizations without losing coercivity within a certain thickness of the Co layers. However, the domain structure remained unclear and direct evidence of exchange coupling was not found. In this investigation we study the grain morphology, domain structure, coercivity mechanism, and exchange-coupling behavior in the PrCo:Co nanocomposite films (In this article we use notation PrCo/Co to represent the as-deposited multilayers and PrCo:Co the composites after annealing.)

II. EXPERIMENT

The PrCo/Co multilayer thin films with Cr underlayer and cover layer were prepared with a multiple-gun dc- and rf-sputtering system by depositing the targets onto glass or silicon substrates. The PrCo target was made by compressing Co and Pr powders with the atomic ratio 7:2 and sintering at 1050 °C for 1 h. Flowing high-purity argon gas was used for sputtering and the pressures were varied from 5 to 20 mTorr. The sputtering parameters in this investigation (including the

argon pressure, the power rates of sputtering targets, and the distance between the targets and the substrates) were chosen to produce films with maximum coercivity. The thickness of each film was calculated by measuring the mass gain upon deposition. The as-deposited films were then heat treated in a furnace with vacuum 6×10^{-7} Torr at temperatures up to 500 °C.

Magnetization loops were measured by an alternating gradient force magnetometer and a superconducting quantum interference device (SQUID) magnetometer. Magnetic force

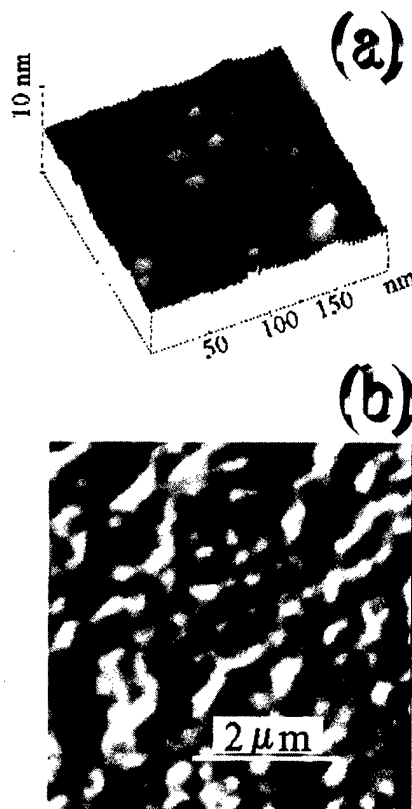


FIG. 1. The AFM (a) and MFM (b) images of a (PrCo30 nm/Co11 nm) $\times 10$ sample with heat treatment at 500 °C.

^{a)}Electronic mail: cmra@unlinfo.unl.edu

^{b)}Also at: Behlen Laboratory of Physics.

^{c)}Also at: Department of Mechanical Engineering.

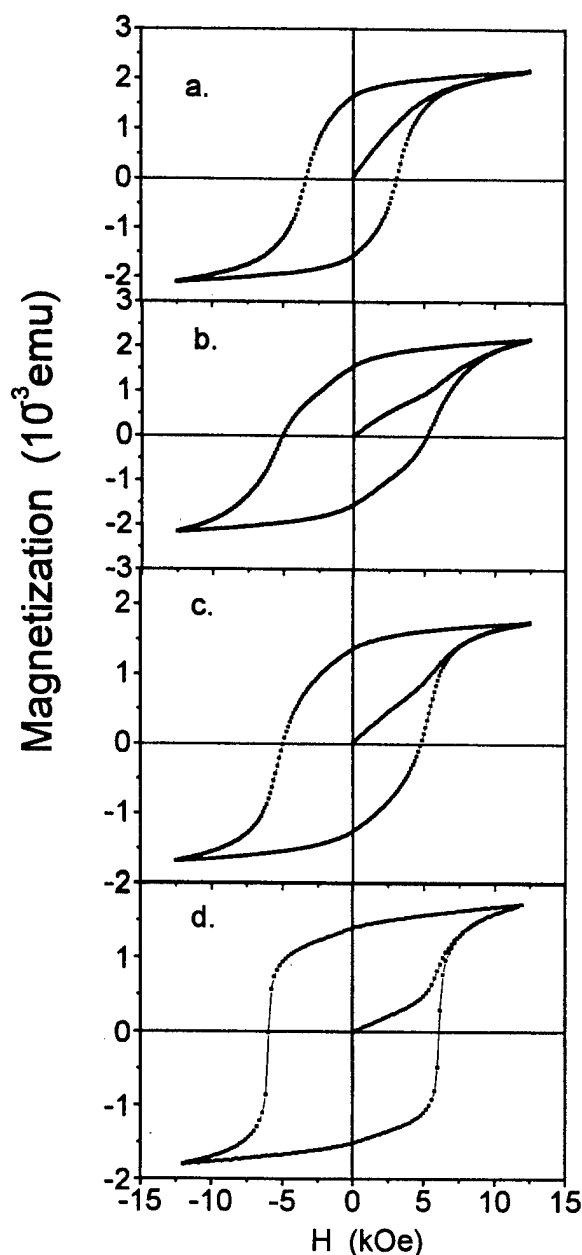


FIG. 2. Hysteresis loops of the heat treated multilayers with structure (PrCo30 nm/Co nm) \times 10. In a, $x = 11$ nm, in b, $x = 10$ nm, c, $x = 8$ nm, and in d, $x = 5$ nm. The magnetization was measured with the field in the film plane.

microscopy (MFM) and atomic force microscopy (AFM) were used to observe the domain structures and the surface morphology. More details about the crystal structure and anisotropy of the films are given in Ref. 6.

III. RESULTS AND DISCUSSION

Figure 1 shows the AFM image of nanostructured PrCo:Co grain morphology (a) and the MFM image of the domain pattern (b). It can be seen that the average size of a domain is about ten times larger than an average grain size (about 20 nm, consistent with our early TEM observation),⁶ indicating that in one domain, many grains are included. As discussed in our previous study,⁶ the PrCo:Co composite consists of the PrCo grains with a disordered hexagonal

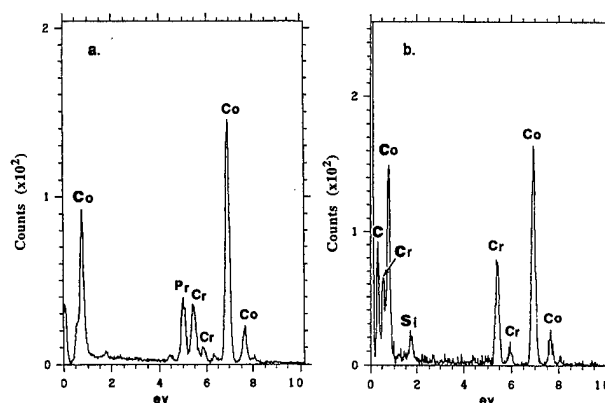


FIG. 3. EDX spectra of a heat treated PrCo:Co film. (a) from the matrix grain and (b) from the second phase grain.

structure and elemental Co with the hexagonal close-packed structure. It is important to note that Co grains have much smaller grain size than the PrCo grains because the Co layers are much thinner than the PrCo layers when the multilayers were sputtered. The grain size we observe in Fig. 1 is basically for the matrix PrCo grains. According to theoretical calculation,² for effective intergrain exchange coupling the dimension of the soft phase should not be bigger than twice that of the domain-wall thickness of the hard phase. In rare-earth transition-metal compounds, the typical thickness of domain walls is 3–5 nm. Therefore if the grain size of the soft phase is less than 10 nm, effective intergrain exchange coupling should exist. The grain size of Co phase in the annealed samples can be controlled by controlling the Co layer thickness in the multilayers. This has been demonstrated in our previous experiments.⁶ The critical point is how to deal with the trade-off between coercivity and remanent magnetization as the amount of soft phase is increased. To optimize the energy product the effect of the soft phase on coercivity must be investigated.

Figure 2 shows the initial magnetization curves and the hysteresis loops of a group of samples with decreasing Co layer thicknesses from sample a to sample d. It is interesting to see the change of the initial magnetization curves. For sample a with multilayer structure (PrCo30 nm/Co11 nm) \times 10, the initial curve is similar to that expected in a nucleation-type mechanism of coercivity; whereas for sample d with multilayer structure (PrCo30 nm/Co5 nm) \times 10, the initial curve is typical for wall-pinning controlled reversal. However, in case of nanoscale morphology, one may have to consider interaction domains,^{7,8} because simple nucleation and pinning models might not adequate for describing the coercivity mechanism. A study of the details of coercivity mechanism is underway and will be reported later. One point clearly seen from Fig. 2 is that the increase in thickness of the soft Co layers, therefore the Co phase fraction in the annealed samples has changed the magnetization-reversal process.

It is also seen from Fig. 2 that with increasing concentration of Co phase, squareness of the loops become smaller and so does the coercivity. The change in the squareness is associated with a change in the film's morphology and the

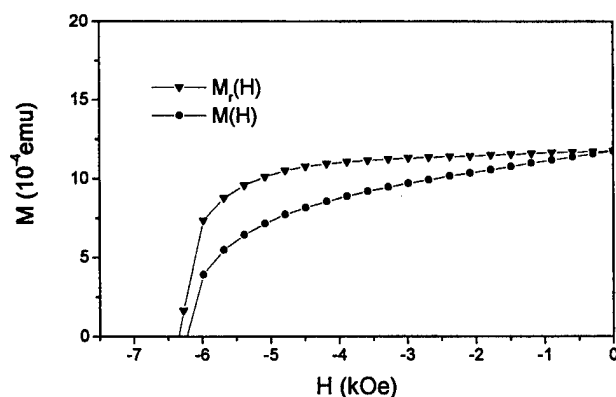


FIG. 4. The demagnetizing curve $M(H)$ and the remanence curve $M_r(H)$ of an annealed sample (PrCo30 nm/Co8 nm) $\times 10$.

coercivity mechanism. It has been found in our experiment that the squareness and the coercivity is also strongly dependent on heat treatment. In the as-deposited films, the PrCo layer is amorphous which is magnetically soft. Heat treatment produces the magnetically hard hexagonal phase and the coercivity reaches its maximum at heat treatment temperature of 500 °C for a half-hour annealing. In order to minimize grain growth during the heat treatment, rapid thermal processing has been adopted in this investigation with heating rates up to 100 °C/s. It is found that a two-step treatment is better than a single-step treatment in obtaining greater squareness and coercivity.

Another important feature observed from Fig. 2 is that in all the cases, the ratio of remanence M_r to saturation M_s (M_r/M_s) is larger than 0.5. This is an indication that there is intergrain exchange interactions between the grains, as discussed in Ref. 6. To verify that the exchange coupling takes place between the soft phase and the hard phase, we checked the nanostructure by TEM with energy dispersive x-ray (EDX) spectroscopy and by measuring remanence curve to see the exchange-spring behavior. Figure 3 shows the EDX spectra measured in a film in two adjacent grains. One is the matrix grain (a) and another is the soft-phase grain (b). Except for Cr peaks which are from the cover layer and bottom layer and a trace of Si and C which may be from the substrate and the contamination during the specimen preparation, in (a) we detected Co and Pr elements, and in (b) we only detected Co. This shows clearly that there are two phases, the hard PrCo phase and soft Co phase existing in the composite. No third phase has been found. Figure 4 shows

the remanent magnetization curve $M_r(H)$ (also called as dc-demagnetization curve) and the demagnetizing curve $M(H)$ (the part in the second quadrant of the hysteresis loop) of a heat-treated sample. The flatness of the upper curve is equivalent to the behavior Kneller and Hawig¹ demonstrated for the exchange-spring magnets.

With the understanding of morphology and properties of the PrCo/Co composite films discussed above, we have been able to optimize the sputtering and the heat-treatment processes. We added up to 25% Co into the composite which leads to enhanced remanent magnetization without losing coercivity significantly. By a carefully controlled processing, we have succeeded in obtaining films with coercivity as high as 20 kOe and maximum energy products as high as 25 MGOe at room temperature.

IV. CONCLUSION

Magnetization behavior of PrCo:Co composite films has been studied including the initial curves and hysteresis loops. The results show that increasing the amount of soft phase appears to change the coercivity mechanism from wall-pinning-like to nucleation-like. It is also found that the coercive force and the shape of the loops are very sensitive to heat treatment. Compared with any single-step treatment, a combination of two or more steps in the heat treatment can raise coercivity markedly and improve the squareness of the loops. Optimizing the heat treatment and composite nanostructure leads to high energy products.

ACKNOWLEDGMENT

We are grateful to Professor S. W. Liou for his help in the MFM and AFM observations. Research sponsored by the U.S. Department of Energy under Grant Nos. DOE-DE-F602-86ER45262 and DOE/ANL-95-47DH-007.

¹E. F. Kneller and R. Hawig, IEEE Trans. Magn. **27**, 3588 (1991).

²R. Skomski and J. M. D. Coey, Phys. Rev. B **48**, 15 812 (1993).

³I. A. Al-Omari and D. J. Sellmyer, Phys. Rev. B **52**, 3441 (1995).

⁴J. P. Liu, Y. Liu, C. P. Luo, and D. J. Sellmyer, J. Appl. Phys. **81**, 5644 (1997).

⁵J. P. Liu, C. P. Luo, Y. Liu, and D. J. Sellmyer, Appl. Phys. Lett. (in press).

⁶J. P. Liu, Z. S. Shan, and D. J. Sellmyer, IEEE Trans. Magn. **33**, 3709 (1997).

⁷W. Rave, D. Eckert, R. Schäfer, B. Gebel, and K.-H. Miller, IEEE Trans. Magn. **32**, 4362 (1996).

⁸R. K. Mishra and R. W. Lee, Appl. Phys. Lett. **48**, 733 (1986).

Nanostructured NdFeB films processed by rapid thermal annealing

M. Yu,^{a),b)} Y. Liu,^{c)} S. H. Liou,^{a)} and D. J. Sellmyer^{a)}

Center for Materials Research and Analysis, University of Nebraska, Lincoln, Nebraska 68588-0113

Nanostructured NdFeB films were prepared by magnetron sputtering followed by rapid thermal annealing at a ramp rate of 200 °C/s. Isotropically oriented Nd₂Fe₁₄B crystallites were formed in the films and coercivities up to 20 kOe and remanence ratios up to 0.8 were obtained. Transmission electron microscopy analysis shows that the majority phase of the magnetic layer in the high coercivity films consists of Nd₂Fe₁₄B nanocrystallites with an average size of about 50 nm. These nanocrystallites are believed to be single-domain particles, which are responsible for the high coercivities. MFM measurements show that the domain size is about 500 nm. It is thus indicated that the 50 nm Nd₂Fe₁₄B nanocrystallites are strongly exchange-coupled into the 500 nm domains and the high remanence ratio originates from this exchange coupling. © 1998 American Institute of Physics. [S0021-8979(98)44111-2]

I. INTRODUCTION

Since the discovery of Nd₂Fe₁₄B in 1984,¹⁻³ numerous studies on NdFeB-based materials have been conducted to obtain a better understanding of their excellent intrinsic properties and develop better fabrication processes for permanent magnets.⁴ Most of this research was on bulk NdFeB materials and relatively only a little work has been done on thin film NdFeB materials.⁵⁻¹³ With the rapid development of micromechanical devices, microelectronics, and integrated magnetoelectronic devices, applications of permanent magnet films are becoming more significant. Furthermore, better knowledge of NdFeB films also can help one to understand the exchange coupling in nanostructured magnetic materials because films thickness and grain sizes can be controlled to some extent to test some recent theoretical calculations.^{14,15}

In this article we report our systematic study of the magnetic properties of nanostructured NdFeB films prepared from amorphous state by rapid thermal annealing (RTA). RTA features a very high ramp rate (200 °C/s) and thus is able to anneal films for a very short effective annealing time (tens of seconds), which is essential in forming isotropic nanostructured NdFeB films with high coercivities (H_c) and high remanence ratios (M_r/M_s).

II. EXPERIMENTAL METHODS

All NdFeB films were deposited directly onto water-cooled 7059 glass substrates at room temperature by dc magnetron sputtering with base pressure of better than 3×10^{-7} Torr and Ar pressure of 10 mTorr. The NdFeB layer has a thickness of 500 nm and is protected by a 40 nm Cr overcoat. The Nd₁₅Fe₇₇B₈ target was provided by Electron Energy Company and some Nd chips were added to adjust the Nd concentration. The composition of the films is Nd₃₀Fe₆₃B₇, which was estimated by the area ratio of Nd chips and the target and verified by energy-dispersive x-ray measurements. The as-deposited films were all processed by

RTA technique (unless specified otherwise) in flowing Ar with a ramp rate of 200 °C/s. The structure and microstructure were characterized by x-ray diffraction (XRD) and transmission electron microscopy (TEM) measurements. The magnetic properties at room temperature were determined by a SQUID magnetometer and the magnetic domain size was estimated by MFM measurements.

III. RESULTS AND DISCUSSION

The XRD pattern of an as-deposited NdFeB film is shown in Fig. 1. Magnetic measurements showed that the as-deposited films are magnetically soft. It is thus indicated as expected that the as-deposited films are amorphous except for the presence of a little α -Fe. Figure 1 also shows the XRD pattern of the NdFeB film annealed at 500 °C for 60 s. Nd₂Fe₁₄B crystallites were formed and they were found to be isotropically oriented in the annealed film, as indicated by the peaks in Fig. 1. In fact all properly annealed films (i.e.,

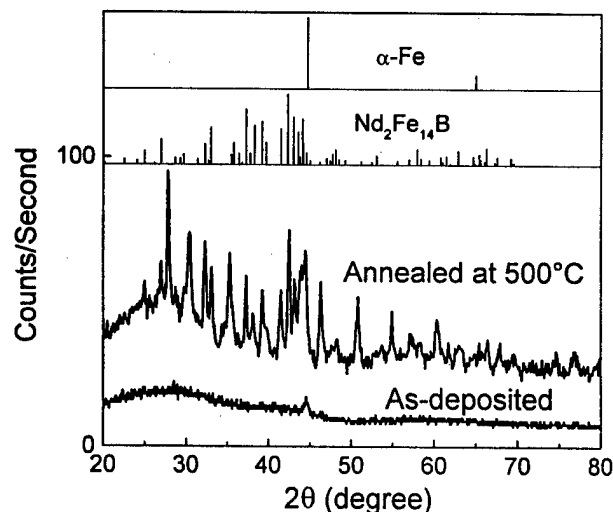


FIG. 1. X-ray diffraction patterns of as-deposited and annealed (500 °C, 60 s) NdFeB films. The standard diffraction patterns of α -Fe and Nd₂Fe₁₄B phases are also shown for comparison.

^{a)}Department of Physics and Astronomy.

^{b)}Electronic mail: myu@unlinfo.unl.edu

^{c)}Department of Mechanical Engineering.

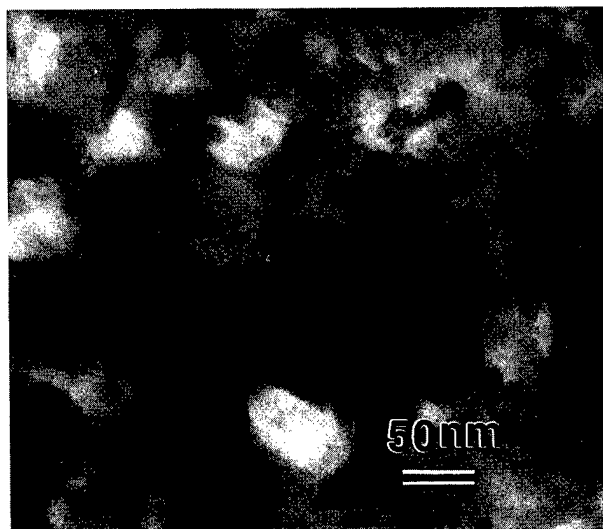
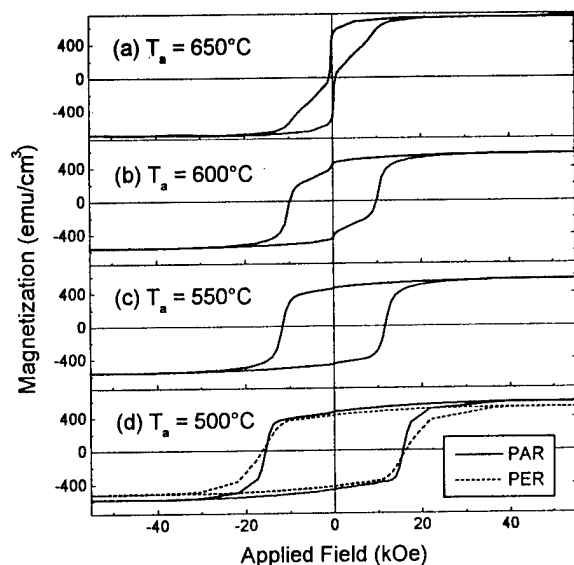
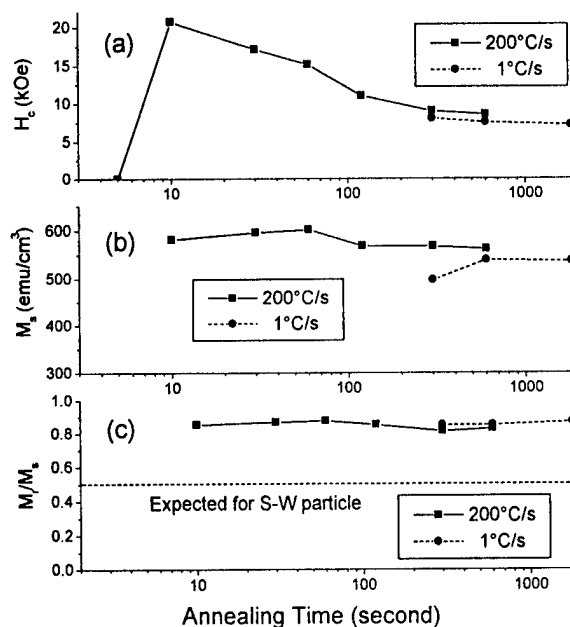


FIG. 2. TEM picture of a NdFeB film annealed at 500 °C for 60 s.

those with $H_c > 5$ kOe) consist of isotropically oriented $\text{Nd}_2\text{Fe}_{14}\text{B}$ crystallites, as confirmed by both XRD and magnetic measurements (see later discussion).

The XRD pattern of the annealed NdFeB film has peaks other than those of $\text{Nd}_2\text{Fe}_{14}\text{B}$. They can all be indexed to Nd_2O_3 and NdO phases. The oxygen was mainly introduced in the RTA process which in our case can be done only in flowing Ar.

The formation of the $\text{Nd}_2\text{Fe}_{14}\text{B}$ phase is only one necessary condition to have high H_c and M_r/M_s in NdFeB films. The other is that appropriate microstructure must be developed. Figure 2 is the bright field TEM picture of the NdFeB film annealed at 500 °C for 60 s. Electron diffraction analysis indicates that the grains shown in Fig. 2 are $\text{Nd}_2\text{Fe}_{14}\text{B}$ crystallites. The size of these crystallites is about 50 nm. This means that these nanocrystallites are single-domain particles because the critical single-domain particle diameter of

FIG. 3. Hysteresis loops of NdFeB films annealed for 60 s at various temperatures (T_a).FIG. 4. (a) H_c , (b) M_s , and (c) M_r/M_s of NdFeB films annealed at 550 °C for various times with ramp rates of 200 and 1 °C/s.

$\text{Nd}_2\text{Fe}_{14}\text{B}$ is about 300 nm.⁴ The composition of the film indicates that there should be a thin Nd-rich layer between the nanocrystalline $\text{Nd}_2\text{Fe}_{14}\text{B}$ particles, although it cannot be seen due to limited resolution. The high ramp rate may also introduce some defects other than the Nd-rich layer.

With the change of structure and microstructure in Nd-Fe-B films, the magnetic properties are also changed completely after annealing. Figure 3(d) shows the parallel and perpendicular hysteresis loops of the NdFeB film annealed at 500 °C for 60 s. The large H_c (~ 16 kOe) and the similarity of the two loops also indicate the formation of isotropically oriented $\text{Nd}_2\text{Fe}_{14}\text{B}$ nanocrystallites in a Nd-Fe-B system. In addition to the formation of the $\text{Nd}_2\text{Fe}_{14}\text{B}$ phase, the microstructure (the 50 nm nanocrystallites and the associated defects) also plays an important role in developing high H_c .

Annealing temperature (T_a) and time (t_a) can strongly affect the magnetic properties. Figure 3 shows the hysteresis loops of the NdFeB films annealed for 60 s at various T_a . We observed that no H_c can be developed if $T_a < 500$ °C. After T_a reaches 500 °C, H_c is developed but decreases and the saturation magnetization M_s changes slightly as T_a increases. If $T_a > 650$ °C, H_c decreases sharply with a moderate increase of M_s . These results have the following implications. First, the crystallization of $\text{Nd}_2\text{Fe}_{14}\text{B}$ can occur only when $T_a \geq 500$ °C, which is less than 627 °C, the crystallization temperature of $\text{Nd}_2\text{Fe}_{14}\text{B}$.⁴ This is reasonable because the crystallization temperature decreases when Nd concentration increases.¹⁶ Second, when $T_a > 500$ °C, presumably the $\text{Nd}_2\text{Fe}_{14}\text{B}$ nanocrystallites grow and the defects are reduced. This is the most probable reason for the decrease of H_c with the increase of T_a . Finally when $T_a \geq 650$ °C, most Nd is oxidized and α -Fe is left as the main magnetic phase, causing the sharp decrease of H_c and the increase of M_s .

Another batch of NdFeB films was annealed at 550 °C for various t_a and the resulting H_c , M_s , and M_r/M_s are

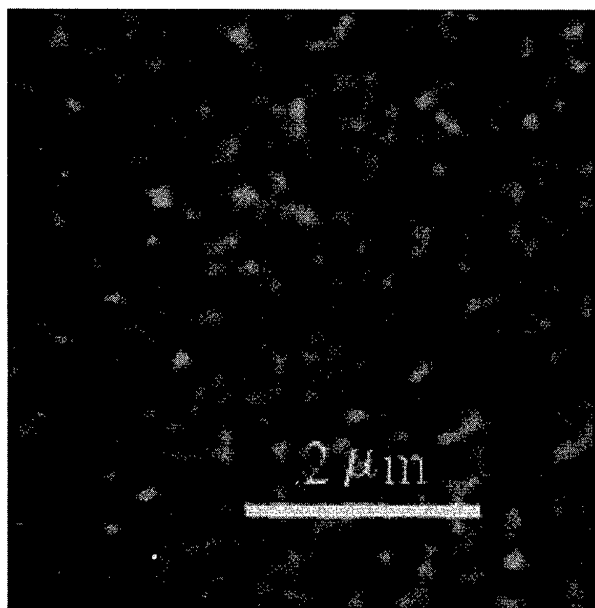


FIG. 5. MFM image of a thermally demagnetized NdFeB film annealed at 500 °C for 60 s. The CoCr MFM tip was magnetized parallel to the sample surface.

plotted in Fig. 4. It is noted that t_a has a strong effect on H_c but a weak one on M_s . Short t_a is critical to obtain high H_c , but $t_a < 10$ s is too short to achieve the proper crystallization of Nd₂Fe₁₄B for high H_c . When $T_a > 500$ °C, longer t_a has essentially the same effect as higher T_a on the microstructure, i.e., the Nd₂Fe₁₄B nanocrystallites grow and the defects are reduced. In turn H_c decreases and M_s changes slightly as t_a increases. The general effects of T_a and t_a on H_c are in agreement with the results obtained in melt-spun NdFeB materials.¹⁶

For comparison we also annealed the as-deposited films at 550 °C in a conventional oven with a ramp rate of 1 °C/s. The resulting H_c , M_s , and M_r/M_s are also shown in Fig. 4. Because of the low ramp rate, the total effective annealing time of the conventional oven is longer than that of RTA for the same t_a . Thus the H_c obtained by the conventional oven is smaller than that obtained by RTA. This result clearly demonstrates the importance of high ramp rate when very short annealing time is needed.

We have shown that the Nd₂Fe₁₄B nanocrystallites are isotropically oriented in the annealed films. According to Stoner–Wohlfarth theory¹⁷ such a system should have a M_r/M_s of 0.5 if there is no interaction among the Nd₂Fe₁₄B nanocrystallites. But Fig. 4(c) shows that these isotropic NdFeB films have $M_r/M_s > 0.8$. The high M_r/M_s must come from the strong exchange coupling among the Nd₂Fe₁₄B nanocrystallites. This phenomenon was observed in melt-spun isotropic NdFeB materials¹⁸ and predicted in theoretical

calculations.¹⁹ A MFM image of a thermally demagnetized NdFeB film annealed at 500 °C for 60 s is shown in Fig. 5. It can be estimated that the domain size is about 500 nm. This means that in one domain there are many Nd₂Fe₁₄B nanocrystallites aligned by exchange coupling. Such a micromagnetic structure (sometimes called “an interaction domain”) provides a direct explanation for the high M_r/M_s . The exchange coupling here is so strong that M_r/M_s is changed slightly when H_c is changed dramatically.

IV. CONCLUSIONS

By using the RTA technique we are able to fabricate isotropic nanocrystalline NdFeB films with high H_c and high M_r/M_s . H_c is very sensitive to annealing temperature and time. Low temperature and short time, which are just enough to crystallize the amorphous NdFeB into single-domain Nd₂Fe₁₄B nanocrystallites, are critical to obtain the proper microstructure for high H_c . We also found that these high coercivity, nanocrystalline NdFeB films have very high M_r/M_s , which originates from the strong exchange coupling among the Nd₂Fe₁₄B nanocrystallites.

ACKNOWLEDGMENTS

The authors would like to thank Professor R. D. Kirby and Dr. Z. S. Shan for their generous help. This work was supported by DOE and CMRA. S. H. Liou was also supported by ARO/DAAG55-98-1-0014.

- ¹J. J. Croat, J. F. Herbst, R. W. Lee, and F. E. Pinkerton, J. Appl. Phys. **55**, 2078 (1984).
- ²M. Sagawa, S. Fujimura, M. Togawa, H. Yamamoto, and Y. Matsuura, J. Appl. Phys. **55**, 2083 (1984).
- ³D. J. Sellmyer, A. U. Ahmed, and G. C. Hadjipanayis, J. Appl. Phys. **55**, 2088 (1984).
- ⁴J. F. Herbst, Rev. Mod. Phys. **63**, 819 (1991).
- ⁵F. J. Cadeu, T. D. Cheung, and L. Wickramasekara, J. Magn. Magn. Mater. **54–57**, 535 (1986).
- ⁶K. D. Aylesworth, Z. R. Zhao, D. J. Sellmyer, and G. C. Hadjipanayis, J. Appl. Phys. **64**, 5742 (1988).
- ⁷J. F. Zasadzinski, C. U. Segre, and E. D. Rippert, J. Appl. Phys. **61**, 4278 (1987).
- ⁸H. Homburg, Th. Sinnemann, S. Methfessel, M. Rosenberg, and B. X. Gu, J. Magn. Magn. Mater. **83**, 231 (1990).
- ⁹B. A. Kapitanov, N. V. Komilov, Ya. L. Linestsky, and V. Yu. Tsvetkov, J. Magn. Magn. Mater. **127**, 289 (1993).
- ¹⁰H. Lemke, S. Müller, T. Göddenhenrich, and C. Heiden, Phys. Status Solidi A **150**, 723 (1995).
- ¹¹S. Parhofer, G. Gieres, J. Wecker, and L. Schultz, J. Magn. Magn. Mater. **163**, 32 (1996).
- ¹²H. Sun, T. Tomida, S. Hirasawa, and Y. Maehara, J. Magn. Magn. Mater. **164**, 18 (1996).
- ¹³D. J. Keavney, E. E. Fullerton, J. E. Pearson, and S. D. Bader, J. Appl. Phys. **81**, 4441 (1997).
- ¹⁴R. Skomski and J. M. D. Coey, Phys. Rev. B **48**, 15812 (1993).
- ¹⁵I. A. Al-Omari and D. J. Sellmyer, Phys. Rev. B **52**, 3441 (1995).
- ¹⁶J. Wecker and L. Schultz, J. Appl. Phys. **62**, 990 (1987).
- ¹⁷W. C. Stoner and E. P. Wohlfarth, Philos. Trans. R. Soc. London, Ser. A **240**, 599 (1948).
- ¹⁸G. C. Hadjipanayis and W. Gong, J. Appl. Phys. **64**, 5559 (1988).
- ¹⁹R. Fischer and H. Kronmüller, Phys. Rev. B **54**, 7284 (1996).

Magnetic and structural properties of $(\text{Co}_{1-x}\text{Fe}_x)\text{Pt}$ thin films

P. W. Jang,^{a)} D. W. Kim, C. H. Park,^{b)} J. G. Na,^{c)} and S. R. Lee^{c)}

Department of Physics, Chongju University, Cheongju 360-764, Korea

$(\text{Co}_{1-x}\text{Fe}_x)\text{Pt}$ films were grown on a glass substrate by a rf sputtering and then annealed at 650–700 °C in a high vacuum. All the as-sputtered $(\text{Co}_{1-x}\text{Fe}_x)\text{Pt}$ films deposited below 400 °C had a disordered structure and showed very low coercivities. With increasing the deposition temperature and Fe contents, the (111) texture was weakened in as-deposited $(\text{Co}_{1-x}\text{Fe}_x)\text{Pt}$ ternary films. Vibrating sample magnetometer and x-ray diffraction data show that Co atoms in the $L1_0$ CoPt phase were substituted with Fe atoms. In-plane coercivities of these films decreased almost linearly with increasing Fe content which seemed to be due to the decrease of a crystalline anisotropy energy. © 1998 American Institute of Physics. [S0021-8979(98)31211-6]

I. INTRODUCTION

FePt and CoPt binary alloy films with a tetragonal $L1_0$ structure have received a significant attention because of their very high crystalline anisotropy, and thus their potential as magnetic or magneto-optic recording materials.^{1–4} Because both compounds have a tetragonal $L1_0$ structure substitution of Co atoms with Fe atoms or vice versa can give interesting properties. However, no experimental data about these ternary alloy films have not been published yet.

In this article we deposited $(\text{Co}_{1-x}\text{Fe}_x)\text{Pt}$ thin films by sputtering, annealed at 650–700 °C in a high vacuum, and investigated their magnetic and structural properties.

II. EXPERIMENTAL PROCEDURE

All films were prepared on Corning 7059 glass substrates using a rf magnetron sputter system from 10 cm diam sources at 100 W with a source to substrate distance of 6 cm. For CoPt and FePt binary films, Co–Pt or Fe–Pt composite targets were used, for which 5×10 mm Pt sheets were placed on an erosion track of pure Co or Fe targets, respectively. 100–300 nm thick $(\text{Co}_{1-x}\text{Fe}_x)\text{Pt}$ films were deposited from Co–Fe–Pt composite targets, for which additional 5×10 mm Fe or Co sheets were placed on preset Co–Pt or Fe–Pt binary composite targets. The chamber base pressure was better than 6×10^{-7} Torr and sputtering pressure was 1 mTorr. Deposition temperature was room temperature, 300 and 400 °C for the films which were deposited from Co–Pt composite targets. Films using Fe–Pt composite targets were deposited at room temperature. As-sputtered films were annealed in a high vacuum better than 7×10^{-6} Torr at 650 and 700 °C for 0.5 and 1 h. For the structural analysis, x-ray diffraction was performed on a Philips X'Pert-MPD diffractometer with a thin film attachment and Cu K_α radiation source. Film compositions were analyzed by energy disper-

sive spectroscopy (EDS). Magnetic properties were investigated by a vibrating sample magnetometer (VSM), with a maximum field of 10 kOe.

III. RESULTS AND DISCUSSION

Normally films deposited at low temperatures show a fiber texture with a close packed plane parallel to the film plane while films deposited at high temperatures show a texture with a low index plane parallel to the film plane. Because disordered CoPt films have a face centered cubic system, CoPt films deposited at room temperature showed the (111) texture and higher deposition temperatures weakened the (111) texture. Figure 1 shows x-ray diffraction patterns of CoPt binary films deposited at different temperatures. With increasing the deposition temperature well developed (111) textures became weaker and (200) and (311) peaks were clearly seen.

Figure 2 shows x-ray diffraction patterns of $(\text{Co}_{0.72}\text{Fe}_{0.28})\text{Pt}$ thin films deposited at different temperatures. Compared with Fig. 1 of CoPt binary films, the (111) texture became apparently weak and the (220) texture was devel-

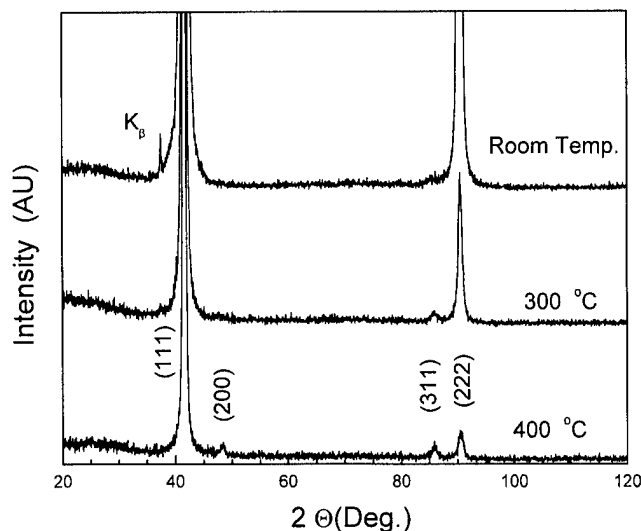


FIG. 1. X-ray diffraction patterns of CoPt binary alloy films deposited at different temperatures.

^{a)}Electronic mail: pwjang@alpha94.chongju.ac.kr

^{b)}Also with: Department of Metals Eng., Korea University, Seoul 136-701, Korea.

^{c)}Also with: Div. of Metals, Korea Inst. of Sci. & Tech., Seoul 136-791, Korea.

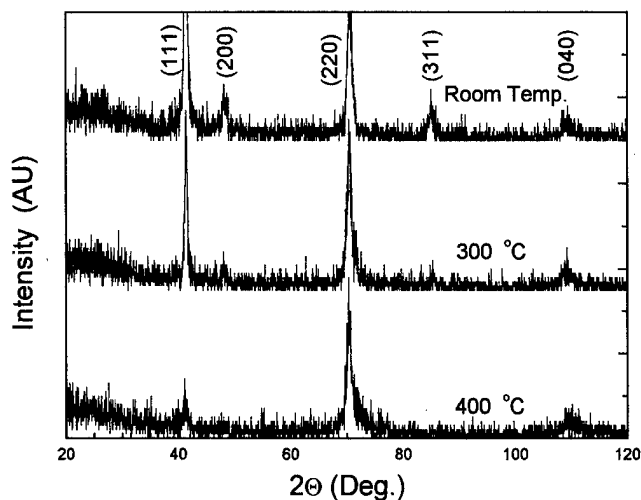


FIG. 2. X-ray diffraction patterns of $(\text{Co}_{72}\text{Fe}_{28})\text{Pt}$ ternary alloy films deposited at different temperatures.

oped with the addition of Fe. Also the (220) texture was shown in $(\text{Co}_{0.72}\text{Fe}_{0.28})\text{Pt}$ films deposited at high temperatures. In Figs. 1 and 2 there were no peaks related to superlattices such as (001) and (003) peaks, meaning the formation of a disordered structure below 400 °C deposition temperature leads to very low coercivities.

Figure 3 shows x-ray diffraction patterns of $(\text{Co}_{1-x}\text{Fe}_x)\text{Pt}$ films deposited at 400 °C and annealed at 700 °C for 1 h. With increasing Fe content almost all peaks of fundamental as well as (001) superlattice peaks were clearly seen. When Fe atoms are added to the $L1_0$ CoPt structure, there would be two possibilities for phase formation. One possibility is the formation of the $L1_0$ FePt structure and another is the substitution of Co atoms with Fe atoms. If a mixture of the CoPt and FePt structure existed, there would be two peaks diffracted from (222) planes of each phase which are around 1.1° apart from each other. In Fig. 3 there are single (222) diffraction peaks and no hints of the superposition of two peaks. Therefore it can be con-

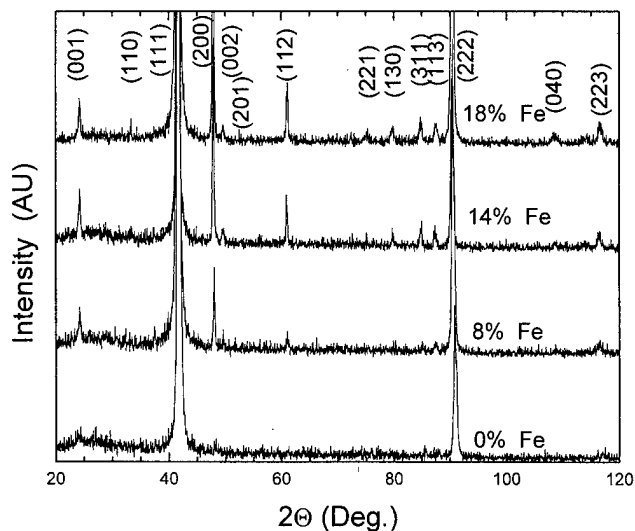


FIG. 3. X-ray diffraction patterns of $(\text{Co}_x\text{Fe}_{1-x})\text{Pt}$ films deposited at 400 °C and annealed at 700 °C for 1 h.

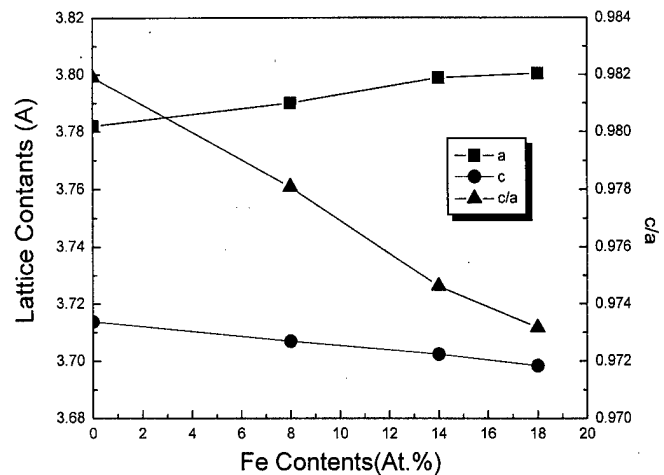


FIG. 4. Variation of lattice constants of ordered $(\text{Co}_{1-x}\text{Fe}_x)\text{Pt}$ films with Fe content.

cluded that Co atoms in the $L1_0$ CoPt structure were substituted with Fe atoms, thus leading to an ordered structure. It can also be seen that (111) texture becomes weaker with increasing Fe content.

Figure 4 shows the variation of lattice constants of ordered $(\text{Co}_{1-x}\text{Fe}_x)\text{Pt}$ films with Fe content. CoPt binary data were fitted because there were only (111) and (222) peaks diffracted from the same plane as shown in Fig. 3. The c/a ratio decreased with increasing Fe content, which also excluded the possibility of the mixture of the $L1_0$ CoPt and FePt phases.

Figure 5 shows the variation of in-plane coercivities of ordered $(\text{Co}_{1-x}\text{Fe}_x)\text{Pt}$ films deposited at different temperatures and annealed at 700 °C for 1 h. With increasing Fe content coercivities of all films decreased linearly. The reason for the decreased coercivity seems to be associated with the decrease of anisotropy energy, reversal mechanism change, or crystallographic texture change. It seems that there is no possibility of the reversal mechanism changing because both in-plane and perpendicular coercivities of films were almost the same, suggesting the spin rotation mecha-

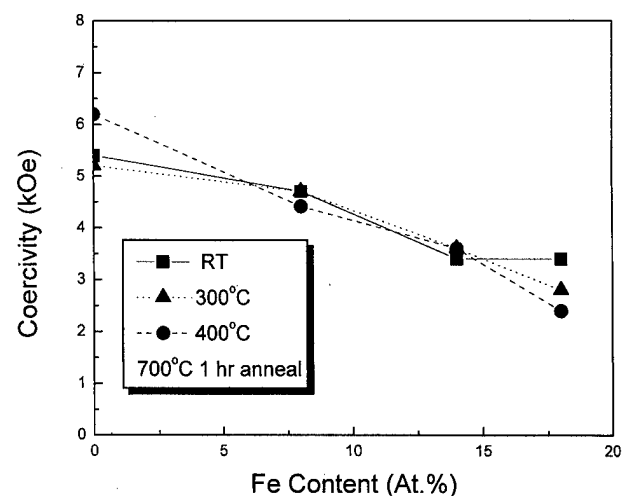


FIG. 5. Dependence of Fe contents on the coercivity of $(\text{Co}_{1-x}\text{Fe}_x)\text{Pt}$ films.

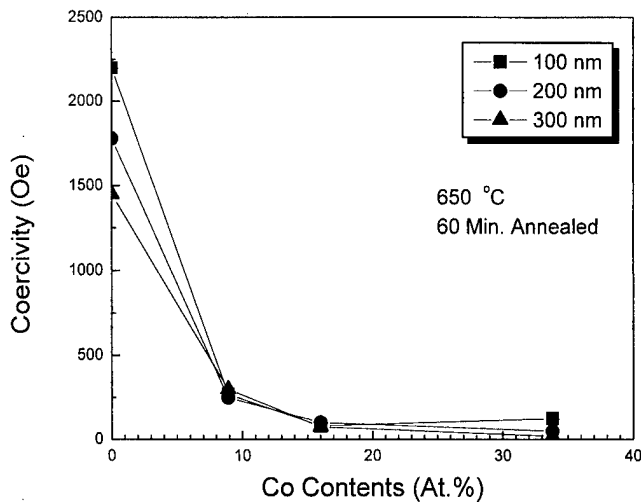


FIG. 6. Dependence of Co content on coercivities of $(\text{Co}_x\text{Fe}_{1-x})\text{Pt}$ films.

nism. Effects of the texture on the coercivity should be excluded because films deposited at different temperatures and annealed had almost the same coercivities even though the degree of the (111) texture is quite different. Therefore the decrease of coercivities in Fig. 5 seems to be due to the decrease of anisotropy energy.

Figure 6 shows the coercivities of $(\text{Co}_{1-x}\text{Fe}_x)_{0.55}\text{Pt}_{0.45}$ films sputtered from the Fe–Pt composite target for which Pt and Co sheets were placed on a pure Fe target. The binary film had an equiatomic composition while Pt contents of ternary films were 4–6 at % lower than that of the stoichiometric FePt phase. In Fig. 6 coercivities decreased rapidly with increasing Co content. The ordered FePt $L1_0$ phase has been known to be formed in a wide Pt range of 22–50 at %.⁵ We tried to find superlattice peaks of $(\text{Co}_{1-x}\text{Fe}_x)_{0.55}\text{Pt}_{0.45}$ films, but it was very difficult to analyze it by x-ray diffraction (XRD) because of a high degree of the (111) texture as shown in Fig. 7. In Fig. 7 there was a very broad peak around $2\theta = 24^\circ$, but the peaks seemed to be unrelated to the superlattice (001) peak because same broad peaks could be observed in as-sputtered films. Further, if we consider the results of Figs. 4 and 5, and Ref. 5, the possibility for forming the ordered $(\text{Co}_{1-x}\text{Fe}_x)_{0.55}\text{Pt}_{0.45}$ phase was very low.

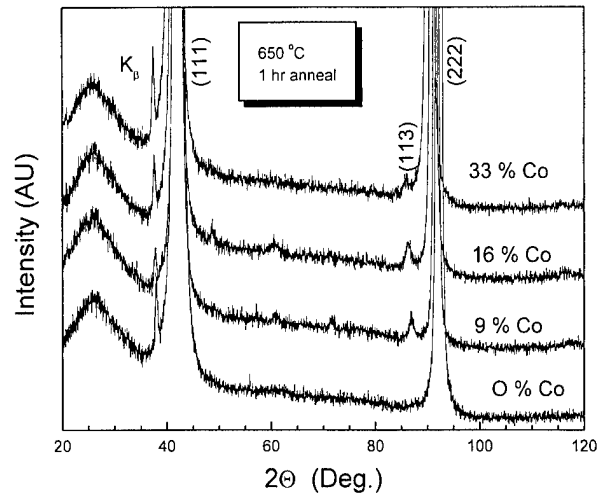


FIG. 7. X-ray diffraction patterns of $(\text{Fe}_{1-x}\text{Co}_x)_{0.55}\text{Pt}_{0.45}$ films annealed at 650°C for 1 h.

These are very unexpected results; the reason is not clear yet and more experimental results are needed.

IV. CONCLUSION

$(\text{Co}_{1-x}\text{Fe}_x)\text{Pt}$ films were grown on a glass substrate by a rf sputtering and then annealed at $650\text{--}700^\circ\text{C}$ in a high vacuum. All as-sputtered $(\text{Co}_{1-x}\text{Fe}_x)\text{Pt}$ films deposited below 400°C had a disordered structure and showed very low coercivities. With increasing deposition temperature and Fe content, the (111) texture was weakened in as-deposited $(\text{Co}_{1-x}\text{Fe}_x)\text{Pt}$ ternary films. Vibrating sample magnetometer (VSM) and x-ray diffraction pattern data show that Co atoms in the $L1_0$ CoPt phase could be substituted with Fe atoms. In-plane coercivities of these films decreased almost linearly with increasing Fe content which seemed to be due to the decrease of crystalline anisotropy energy.

¹M. Watanabe and M. Homma, Jpn. J. Appl. Phys., Part 2 **35**, L1264 (1996).

²B. M. Laison, M. R. Visokay, E. E. Mariero, R. Sinclair, and B. M. Clemens, J. Appl. Phys. **74**, 1992 (1993).

³B. M. Laison and B. M. Clemens, Appl. Phys. Lett. **63**, 1438 (1993).

⁴D. Weller, H. Brandel, G. Gorman, C.-J. Lin, and H. Notays, Appl. Phys. Lett. **61**, 2726 (1992).

⁵S. W. Yung, Y. H. Chang, T. J. Lin, and M. P. Hung, J. Magn. Magn. Mater. **116**, 411 (1992).

Magnetocrystalline anisotropy in (111) CoPt₃ thin film with growth-induced chemical anisotropy investigated by x-ray magnetic circular dichroism

W. Grange, J.-P. Kappler, and M. Maret
IPCMS-GEMME, 23 rue du Loess, 67037 Strasbourg, France

J. Vogel and A. Fontaine
Laboratoire de Magnétisme Louis Néel, CNRS, Boîte Postale 166, 38042 Grenoble, France

F. Pétroff
Unité Mixte CNRS-Thomson CSF, Domaine de Corbeville, 91404 Orsay, France

G. Krill
Laboratoire pour l'Utilisation du Rayonnement Electromagnétique (LURE), Bâtiment 209D, Université Paris-Sud, 91405 Orsay, France

A. Rogalev,^{a)} J. Goulon, M. Finazzi, and N. B. Brookes
European Synchrotron Radiation Facility (ESRF), Boîte Postale 220, 38043 Grenoble, France

Angle-dependent x-ray magnetic circular dichroism (XMCD) experiments performed at both the Co and Pt $L_{2,3}$ edges for a cubic CoPt₃ thin film, which exhibits growth-induced chemical anisotropy, are used to determine the element specific magnetic anisotropy. The large decrease of the 3d orbital moment, observed when the spins are forced out the easy axis of magnetization by the applied magnetic field, is a consequence of a strong magnetocrystalline anisotropy (MCA). In addition, a weak but systematic variation of the Pt orbital moment indicates that the 5d atoms could play an important role in the MCA. These results correlate the microscopic XMCD evaluation of the MCA and the local structural anisotropy as observed with x-ray absorption fine structure (XAFS).

© 1998 American Institute of Physics. [S0021-8979(98)53911-4]

Compared to classical bulk methods, alloy growth by the ultrahigh vacuum evaporation methods such as molecular beam epitaxy (MBE) benefits of surface diffusion controlled by an appropriate choice of temperature growth and deposition rates. It is an appealing route to "fabricate" materials with specific properties, and is of prime importance for the development of magnetic and magneto-optic materials. In this respect, Co_xPt_{1-x} thin alloy films, that are characterized by large Kerr rotations at short wavelengths and strong magnetocrystalline anisotropy (MCA), appear as good candidates to substitute the current TbFeCo media.¹ Recently, strong perpendicular magnetic anisotropy (as large as 10^7 erg cm⁻³) as well as 100% perpendicular remanence has been observed in (111)-oriented fcc CoPt₃ alloy films.^{2,3} This was unexpected for a cubic lattice and was attributed to the existence of an anisotropic local chemical order.³ MCA is known to be a microscopic effect,⁴ but the evidence of MCA comes mainly from macroscopic measurements (either torque or magnetization).^{2,3} To demonstrate unambiguously the correlation between MCA and this growth-induced chemical anisotropy, angle-dependent x-ray magnetic circular dichroism measurements (XMCD) were performed at both the Co and Pt $L_{2,3}$ edges. XMCD is obviously a good probe to provide new information: the sum rules for XMCD⁵ show a correlation between orbital momentum and MCA through separate spin and orbital magnetic moment evaluations.⁶ In addition, the site selectivity of XMCD allows one to investigate the role of the Pt orbital moment in the MCA: this role has not yet been considered, although calculations argue that the

large anisotropy observed in Co-Pt or Co-Pd systems results mainly from the large spin-orbit interaction on the 5d (4d) atoms.⁷

The (111) CoPt₃ thin film alloy was deposited by MBE in a 10^{-10} Torr pressure onto a 150 Å Ru (0001) buffer layer grown at 900 K onto a mica (001) substrate. The 500 Å thick film was co-evaporated at 690 K using deposited rates of 0.2 Å/s for Pt and 0.05 Å/s for Co, respectively. Finally a 15 Å protective Pt layer was deposited. The film exhibits a fcc disordered structure, slightly compressed along the growth direction [111].³ Such a deformation was attributed to an anisotropic local order, which was confirmed by XAFS measurements performed at the Co K and Pt L_3 edges, revealing the existence of preferential CoPt pairs along the growth direction.⁸ This structural anisotropy is mainly the result of two effects: (i) the surface diffusion which at 690 K is large compared to the bulk mobility, and (ii) the Pt surface segregation during deposition. This film may be seen as surface alloys stacked above each other and frozen-in as the free surface advances. Finally, this surface chemical ordering yields an anisotropic alloy with a large MCA. The magnetization hysteresis loops show an easy axis of magnetization perpendicular to the film plane (i.e., the [111] direction) with roughly $K_u = (1 \pm 0.2)10^7$ erg cm⁻³ at 30 K. It is worth noting that the growth temperature is the key parameter in fabricating such systems, since a completely disordered fcc film grown at room temperature and a L1₂-type ordered fcc film grown at 800 K do not exhibit perpendicular anisotropy.³

XMCD experiments were carried out at the ESRF beamlines ID 12A (Pt $L_{2,3}$ edges) and ID 12B (Co $L_{2,3}$ edges). The straight section ID 12 is equipped with two helical un-

^{a)}Electronic mail: rogalev@esrf.fr

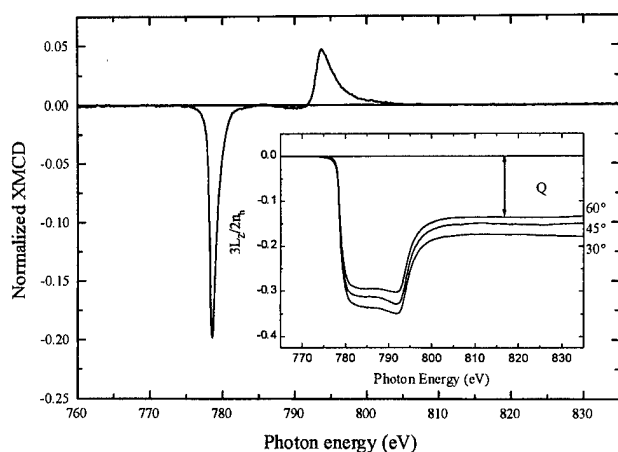


FIG. 1. Normalized XMCD signal measured in the total electron yield detection mode at the Co $L_{2,3}$ edges for a CoPt₃ thin film alloy ($\gamma=60^\circ$). In the inset the result of the integration of the XMCD signal is shown [i.e., $3L_z/2n_h$ (in units of \hbar)] for $\gamma=30^\circ$, 45° , and 60° , respectively.

dulators (Helios-I and Helios-II) which cover two complementary energy ranges from soft (0.5 to 1.6 keV) to hard (3.0 to 22.0 keV) x rays.^{9,10} Helical undulators provide a highly circular polarization rate, which is well transferred by the optical elements for the two present investigations, and allow to alternate easily the helicity of the photons. For the energy range requested for the Pt $L_{2,3}$ edges (11.0–13.5 keV), the third harmonic of the undulator Helios-II was chosen and the double-crystal monochromator was equipped with a pair of Si (111) crystals. For the measurements at the Co $L_{2,3}$ edges, the ID 12B branch was equipped with a grating spectrometer (1200 1/mm). The circular polarization rate was estimated to be 0.9 (ID 12A) and 0.85 (ID 12B), respectively. The XAS spectra were recorded at room temperature (i) in the fluorescence detection mode, using a Si photodiode associated with a digital lock-in exploiting square waves modulated x-ray beam, for the measurements at the Pt $L_{2,3}$ edges, and (ii) in the total electron yield detection (TEY) mode for the measurements at the Co $L_{2,3}$ edges. For both experiments, the XMCD signal was monitored by keeping the helicity of the incoming x rays fixed and flipping the direction of the applied magnetic field generated by a superconducting magnet (± 4 T, i.e., parallel or antiparallel to the direction of the incoming light). No sizable self-absorption effect is expected using the fluorescence mode at the Pt $L_{2,3}$ edges since the film is very thin with respect to the penetration depth of the incoming photons; and to avoid saturation effects in the measurements performed at the Co $L_{2,3}$ edges (TEY mode), the analysis has been restricted to $0^\circ < \gamma < 60^\circ$, where γ denotes the angle between the direction of the incoming light (i.e., the direction of the applied magnetic field) and the normal to the surface. Let us emphasize that due to the small absorption coefficient of the 500 Å CoPt₃ film (about 3% at the Pt $L_{2,3}$ edges), these experiments were rather challenging.

Co $L_{2,3}$ edges

Figure 1 shows a typical XMCD spectrum recorded in the TEY mode at $\gamma=60^\circ$. The XMCD signal is normalized to the isotropic absorption cross section (i.e., approximately,

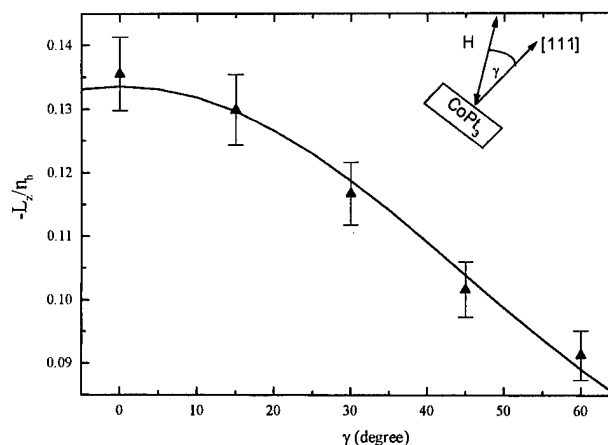


FIG. 2. $-L_z/n_h$ (in units of \hbar) as a function of the incident angle γ . The full curve represents the fitting assuming that the 3d orbital moment varies (at lowest order) as $m_{\text{orb}}^\perp + (m_{\text{orb}}^\parallel - m_{\text{orb}}^\perp) \sin^2 \gamma$, where m_{orb}^\perp and m_{orb}^\parallel denote, respectively, the orbital moment measured along and perpendicular to the [111] direction.

the half-sum of the absorption cross section recorded for left- and right-handed circularly polarized light) corresponding to the $2p-3d$ transitions and is corrected for the finite rate of circular polarization. Using the notation of Arvanitis *et al.*,¹¹ the angle-dependent orbital sum rule for XMCD takes the form:

$$m_{\text{orb}}^\gamma = -(2Q^\gamma/3)(10 - n_{3d}), \quad (1)$$

where m_{orb}^γ is the orbital moment measured at the angle γ , n_{3d} is the number of electrons in the 3d shell and Q^γ is the normalized integrated dichroism intensity at the angle γ . The

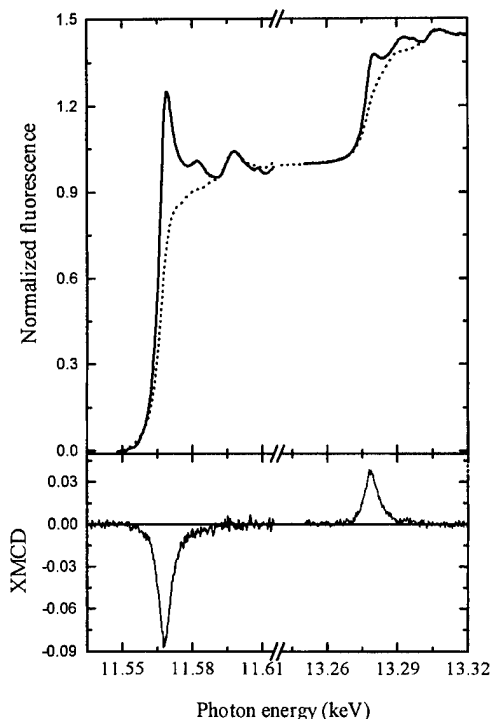


FIG. 3. Upper panel: $L_{2,3}$ isotropic absorption edges of Pt in a CoPt₃ thin alloy film (500 Å) and of Au (dashed line) in a CuAu₃ bulk sample. Lower panel: difference between the spectra recorded for left- and right-circular polarized light (XMCD signal). The XMCD is corrected for the rate of circular polarization.

magnetic field was sufficient to saturate the magnetic moment, so no additional data corrections are needed.

According to (1), the integral Q^γ of each XMCD signal shown in the inset of Fig. 1 is directly proportional to the orbital moment. The drastic diminution of the orbital moment when the spins are forced out of the [111] direction by the 4 T applied magnetic field is the microscopic signature of strong MCA.¹² In the case of a uniaxial anisotropy, it has been found that the 3d orbital moment varies (at lowest order) as $m_{\text{orb}}^\perp + (m_{\text{orb}}^\parallel - m_{\text{orb}}^\perp) \sin^2 \gamma$, where m_{orb}^\perp and m_{orb}^\parallel denote, respectively, the orbital moment measured along and perpendicular to the easy axis of magnetization (i.e., the normal to the surface).⁴ Figure 2 shows the good agreement between our experiments and this theoretical prediction (full curve) supporting the present model. Taking 7.75 for the 3d electron occupation number,¹³ we found $m_{\text{orb}}^\perp - m_{\text{orb}}^\parallel = 0.13 \mu_B$ and $m_{\text{orb}}^\perp = (0.30 \pm 0.02) \mu_B$. This enhancement of the orbital moment [the value measured for bulk hcp Co [0001] is $m_{\text{orb}}^\perp = 0.15 \mu_B$ (Ref. 14)] is consistent with previous XMCD experiments that have found an obvious connection between orbital moment, MCA and the breaking of symmetry at interfaces.^{14,15}

Pt $L_{2,3}$ edges

According to calculations, the strong MCA observed in Co-Pt (Pd) systems is the consequence of the strong 5d (4d) spin-orbit coupling ($\xi_{\text{Pt}}/\xi_{\text{Co}} \approx 8$):⁷ roughly speaking, the 3d atoms would play a minor role in the MCA, acting only as a "source of magnetism." We recently found in Pd/Co multilayers an anisotropy of the 4d orbital moment of $m_{\text{orb}}^\perp - m_{\text{orb}}^\parallel = 0.07 \mu_B$, which demonstrates the important role played by the 4d atoms in the MCA.¹⁶ Figure 3 shows the isotropic absorption and the corresponding XMCD signal recorded in the fluorescence detection mode at the Pt $L_{2,3}$ edges. The XMCD signal is corrected for the incomplete polarization of the x rays and the applied magnetic field was tilted at 30° away from the normal to the surface. To separate the transitions to unoccupied 5d states from the continuum ($2p \rightarrow nd, s$), a steplike function (or an arctangent function) can be subtracted from the isotropic absorption cross section. This procedure has been extensively used for the determination of the 3d near-edge resonance (the "white line"); however the L_3 and L_2 Pt edges do not exhibit a strong white line and the errors in the determination of the steplike background, negligible for the $L_{2,3}$ Co edges, might now be as large as 40%. For an accurate analysis, we have compared the L_3 and L_2 Pt edges with those of Au, measured in a CuAu₃ bulk alloy under the same experimental conditions. The energy scale of the Au spectra was expanded with a factor 1.07 to account for the difference in the lattice parameter, aligned in energy with the Pt spectra on the fine structure and finally normalized to the edge jump.¹⁷ According to this procedure, the angle-dependent orbital sum rule takes the following form:

$$m_{\text{orb}}^\gamma = -2(\Delta A_{L_3}^\gamma + \Delta A_{L_2}^\gamma) \times \{3[\sigma_{\text{tot}}(\text{Pt}) - \sigma_{\text{tot}}(\text{Au})]/[n_{5d}(\text{Pt}) - n_{5d}(\text{Au})]\}^{-1}, \quad (2)$$

where $\Delta A_{L_3}^\gamma$ and $\Delta A_{L_2}^\gamma$ are the integrals over the dichroism at the L_3 and L_2 edges, respectively, $\sigma_{\text{tot}}(\text{Pt}) - \sigma_{\text{tot}}(\text{Au})$ is the integral of the isotropic absorption cross section over the difference curve and $[n_{5d}(\text{Pt}) - n_{5d}(\text{Au})]$ is the electron number difference, calculated to be 1.06.¹³ The application of the sum rule gives $m_{\text{orb}} = 0.052, 0.049$, and $0.044 \mu_B$ for $\gamma = 30^\circ, 45^\circ$, and 60° , respectively. Despite the uncertainties in the determination of the orbital moment (typically 10%), it appears that the anisotropy of the 5d orbital moment exists. Reminding that the MCA energy is proportional to the spin-orbit constant, the anisotropy of the Pt orbital moment itself, as weak as it may be, should also play an important role in the MCA.

Angle-dependent XMCD experiments at the Co and Pt $L_{2,3}$ edges in a fcc (111) CoPt₃ thin film give evidence for a strong correlation between the chemical anisotropic local order and the MCA. In agreement with previous experiments, we found a large anisotropy of the 3d orbital moment ($m_{\text{orb}}^\perp - m_{\text{orb}}^\parallel = 0.13 \mu_B$) and have confirmed the validity of the model developed by Bruno,⁴ who has shown theoretically that the 3d orbital moment varies as $m_{\text{orb}}^\perp + (m_{\text{orb}}^\parallel - m_{\text{orb}}^\perp) \sin^2 \gamma$ for a uniaxial symmetry. Thanks to the high quality of the data recorded, we were able to measure a weak but systematic decrease of the 5d orbital moment when the spins are forced out of the easy direction. These findings support the idea that the 5d orbital moment itself could play an important role in the MCA.

¹D. Weller, H. Brändle, G. L. Gorman, C. J. Lin, and H. Notarys, Appl. Phys. Lett. **61**, 2726 (1992).

²P. W. Rooney, A. L. Shapiro, M. Q. Tran, and F. Hellman, Phys. Rev. Lett. **75**, 1843 (1995).

³M. Maret, M. C. Cadeville, R. Poinso, A. Herr, E. Baurepaire, and C. Monier, J. Magn. Magn. Mater. **166**, 45 (1997).

⁴P. Bruno, Phys. Rev. B **39**, 865 (1989).

⁵B. T. Thole, P. Carra, F. Sette, and G. van der Laan, Phys. Rev. Lett. **68**, 1943 (1992); P. Carra, B. T. Thole, M. Altarelli, and X. Wang, *ibid.* **70**, 694 (1993).

⁶D. Weller, J. Stöhr, R. Nakajima, A. Carl, M. G. Samant, C. Chappert, R. Mégy, P. Beauvillain, P. Veillet, and G. Held, Phys. Rev. Lett. **75**, 3752 (1995).

⁷I. V. Solov'yev, P. H. Dederichs, and I. Merting, Phys. Rev. B **52**, 13419 (1995).

⁸C. Meneghini, M. Maret, M. C. Cadeville, and J. L. Hazemann, J. Phys. IV France **7**, Colloq. C2 1115 (1997).

⁹J. Goulon, N. B. Brookes, C. Cautier, J. Goedkoop, C. Goulon-Ginet, M. Hagelstein, and A. Rogalev, Physica B **208&209**, 199 (1995).

¹⁰C. Gauthier, G. Goujon, S. Feite, E. Moguiline, L. Braicovich, N. Brookes, and J. Goulon, Physica B **208&209**, 232 (1995).

¹¹D. Arvanitis, M. Tischer, J. Hunter Dunn, F. May, N. Mårtensson, and K. Baberschke, in *Spin-Orbit-Influenced Spectroscopy of Magnetic Solids*, edited by H. Ebert and G. Schütz (Springer, Herrschin, Germany, 1995).

¹²H. Dürr and G. van der Laan, Phys. Rev. B **54**, R760 (1996).

¹³D. Stoeffler (private communication).

¹⁴Y. Wu, J. Stöhr, B. D. Hermsmeier, M. G. Samant, and D. Weller, Phys. Rev. Lett. **69**, 2307 (1992).

¹⁵H. A. Dürr, G. Y. Guo, G. van der Laan, J. Lee, G. Lauhoff, and J. A. C. Bland, Science **277**, 213 (1997).

¹⁶J. Vogel, A. Fontaine, V. Cross, F. Petroff, W. Grange, J.-P. Kappler, G. Krill, A. Rogalev, and J. Goulon, Proceedings of the Grand-Est Meeting, edited by J.-P. Kappler (Strasbourg, France, 1997).

¹⁷J. Vogel, A. Fontaine, V. Cross, F. Petroff, J.-P. Kappler, G. Krill, A. Rogalev, and J. Goulon, Phys. Rev. B **55**, 3663 (1997).

Magnetic properties of NdFeB thin films synthesized via laser ablation processing

ChoongJin Yang,^{a)} SangWon Kim, and Jong Seog Kang

Electromagnetic Materials Laboratory, Research Institute of Industrial Science & Technology (RIST),
P.O. Box 135, 790-600 Pohang, Korea

High energy product $\text{Nd}_2\text{Fe}_{14}\text{B}$ films have been grown onto Si(100) substrate by KrF pulsed laser ablation using the targets of $\text{Nd}_x\text{Fe}_{90.98-x}\text{B}_{9.02}$ ($x = 17.51-27.51$). The films exhibit no preferred texture, however, good hard magnetic properties were produced from as-deposited condition: $4\pi M_s \approx 7$ kG, $4\pi M_r \approx 4$ kG, and $H_c = 300-1000$ Oe. The beam density of 3 J/cm^2 gave the optimal condition to have the highest $4\pi M_r$ and H_c for a substrate T of 650°C . The higher content of Nd induces a higher coercivity and $4\pi M_r$ at the same time without prominent change in $4\pi M_s$. The films grown at elevated temperature ($620-700^\circ\text{C}$) are understood to suggest a magnetically coupled interaction between $\text{Nd}_2\text{Fe}_{14}\text{B}$ and $\alpha\text{-Fe}$ grains by taking into account the monotonously decreasing $4\pi M_r$ values accompanying with a broad peak regime in H_c at around $550-625^\circ\text{C}$.
© 1998 American Institute of Physics. [S0021-8979(98)21511-8]

If high field strength permanent magnets in film forms can be easily synthesized, those film magnets can then be used to fabricate integrated electromagnetic components. Circulators and isolators are the typical hybrid type microwave devices using the ferrite disks for a biasing field. Magnetoresistive heads are another area in which permanent magnetic films can play a significant role to obtain the magnetoresistive sensitivity. Miniaturized magnetic sensors, actuators, and motors are other areas that can benefit from the development of film type magnets.

In spite of these expectations the magnetic field strength of the films must be comparable to the energy product term in bulk magnets. In addition hard magnetic films in microdevices and data storage technology must be cost effective, yet produces smooth hard magnetic films with high values of $4\pi M_s$, $4\pi M_r$, and H_c . Furthermore, a popular film substrate, such as Si wafer, must be proven to be an appropriate material showing no mismatch with the magnetic film materials for volume production in future. Nd-Fe-B compounds of suitable composition and nanostructure is a good candidate for the above requirements. NdFeB magnetic films have been studied during the past years by sputtering a cast target.¹⁻⁴ Recently, a high coercive NdFeB films grown on MgO(100) by molecular beam epitaxy (MBE) was reported.⁵

In this article we report a laser ablation technique for synthesizing $\text{Nd}_2\text{Fe}_{14}\text{B}$ base films using a KrF excimer laser. Our interest is on controlling the microstructure in nanoscale to obtain a high field strength films which presumably will consist of magnetically coupled soft and hard grains.

The magnetic films were prepared by a KrF excimer laser (248 nm wave) ablation. The lasing energy density ranged from 2.75 to 5.99 J/cm^2 at a constant repetition rate of 10 Hz was employed using $\text{Nd}_x\text{Fe}_{90.98-x}\text{B}_{9.02}$ ($x = 17.5-27.5$) targets. The films were deposited onto Si(100) wafer at various substrate temperatures ranging $620-700^\circ\text{C}$. Targets were made by induction arc melting and repeated

homogenization treatment. The film thickness was controlled by total pulse of $2500-3000 \text{ \AA}$ for all the samples which exhibited an optimal magnetic properties. The average deposition rate was identified after pulsation for ten minutes for each lasing condition, and the thickness was checked by the scanning electron microscope and "α-Step" as well.

Characterization was performed as functions of various ablation parameters such as laser beam density, Nd contents of targets and substrate temperatures. The film samples were pulsed to have about 300 nm thick with a rate of 10 Hz . As the lasing beam density increases linearly from 2.75 to 5.99 J/cm^2 , the deposition rate of film varied linearly from 0.038 to 0.13 nm/s .

Figure 1 shows the typical magnetic properties as a function of beam energy density. The target composition was

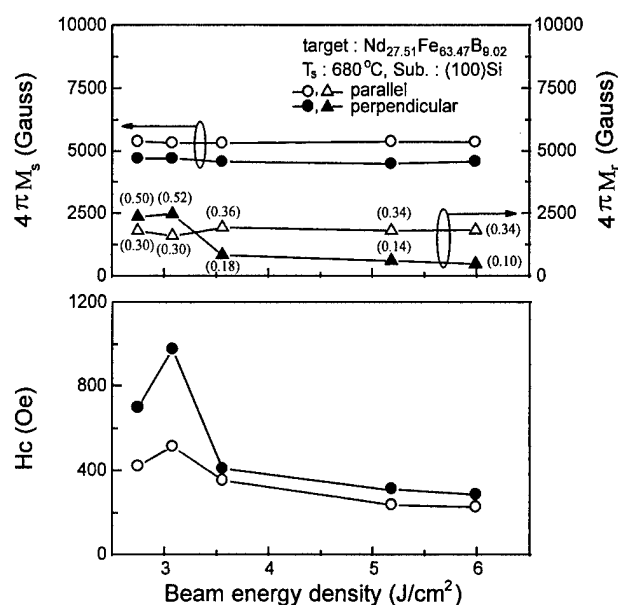


FIG. 1. Laser beam energy dependency on the magnetic properties of $\text{Nd}_{27.51}\text{Fe}_{63.47}\text{B}_{9.02}$ film on (100)Si deposited at a substrate temperature of 680°C .

^{a)}Electronic mail: cjyang@risnet.rist.re.kr

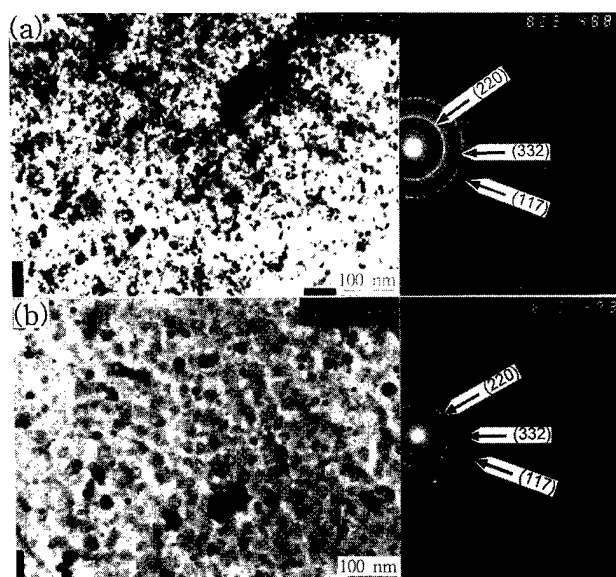


FIG. 2. TEM micrographs and electron diffraction patterns of $\text{Nd}_{27.51}\text{Fe}_{63.47}\text{B}_{9.02}$ films deposited at a laser beam energy density of (a) 3.08 J/cm^2 and (b) 5.99 J/cm^2 , respectively, at 680°C .

$\text{Nd}_{27.51}\text{Fe}_{63.47}\text{B}_{9.02}$, and the film was grown at 680°C . The open circles denote data measured along the in-plane, and the solid circles for out-of-plane direction. The experimentally saturated magnetic moments ($4\pi M_s$) along parallel direction ranged about 5300–5700 G, while those of 1000 G lower values were exhibited along the out-of-plane direction. Saturation magnetization was found to be almost constant regardless of the laser energy density. However, remanence values along the out-of-plane were measured to be much higher for laser energy density $2.75\text{--}3.08 \text{ J/cm}^2$ as shown in Fig. 1(b). The numbers in round brackets, which are reduced remanence (M_r/M_s) values, for the samples grown with the laser energy density of $2.75\text{--}3.08 \text{ J/cm}^2$ are at most $0.5\text{--}0.52$. The laser energy density higher than 3.5 J/cm^2 gave poor shape of hysteresis curves resulted in low values of both the $4\pi M_r$ and H_c . Although the magnetic properties of the films decrease with higher beam densities, the microstructure of all films indicated the presence of $\text{Nd}_2\text{Fe}_{14}\text{B}$ without any minor phase clarified by x-ray diffraction (XRD) and TEM. Only the difference in the microstructure between the films at lower (3.08 J/cm^2) and higher beam density (6.0 J/cm^2) is the grain size as shown in Fig. 2. The grain size of $\text{Nd}_2\text{Fe}_{14}\text{B}$ phase of the film at a higher beam density (6.0 J/cm^2) is measured to be doubled (36 nm) that of film at 3.08 J/cm^2 .

Figure 3 shows the variation of magnetic properties as a function of substrate temperature (T_s) for the films grown at a laser beam density of 3.08 J/cm^2 . For $T_s < 640^\circ\text{C}$, the hysteresis behaves like a soft magnet which shows $4\pi M_r \leq 330 \text{ G}$ and $H_c \leq 180 \text{ Oe}$. If T_s is raised above 640°C , however, both the $4\pi M_r$ and H_c increase resulting from a very coercive hysteresis curve, and the M_r/M_s becomes more than 0.5 . X-ray pattern indicated that T_s below 640°C let the films largely amorphous without any minor phase. One interesting thing regarding the substrate temperature is that the

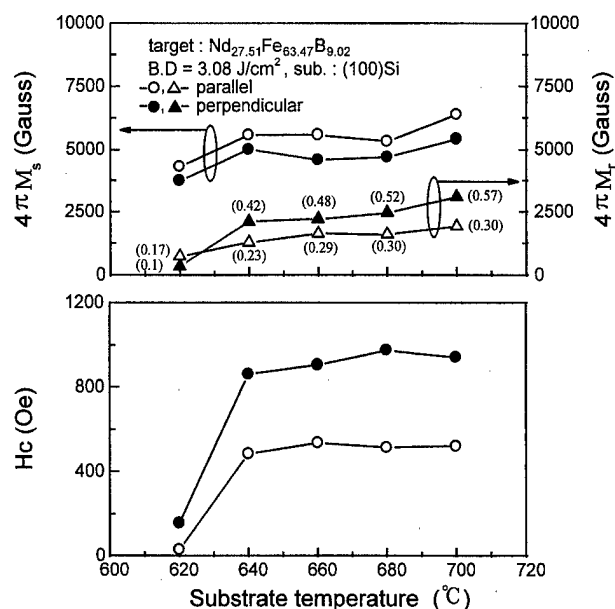


FIG. 3. Substrate temperature dependency on the magnetic properties of $\text{Nd}_{27.51}\text{Fe}_{63.47}\text{B}_{9.02}$ film on (100)Si deposited at a laser beam energy density of 3.08 J/cm^2 .

deposition rate of film was found to be more than 0.6 Å/s below 640°C , while above that temperature the rate was less than 0.5 Å/s .

The variation of $4\pi M_r$ and H_c depend strongly upon the concentration of Nd of the targets. Figure 4 shows the magnetic properties of $\text{Nd}_x\text{Fe}_{90.98-x}\text{B}_{9.02}$ films grown at T_s of 680°C with the beam density of 3.08 J/cm^2 . The variation of $4\pi M_s$ as a function of Nd content is low along the both in-plane and out-of-plane directions. However, the $4\pi M_r$ and H_c exhibit different behaviors. The films grown from the targets of $x = 17.51$ and 22.51 shows the M_r/M_s along in-

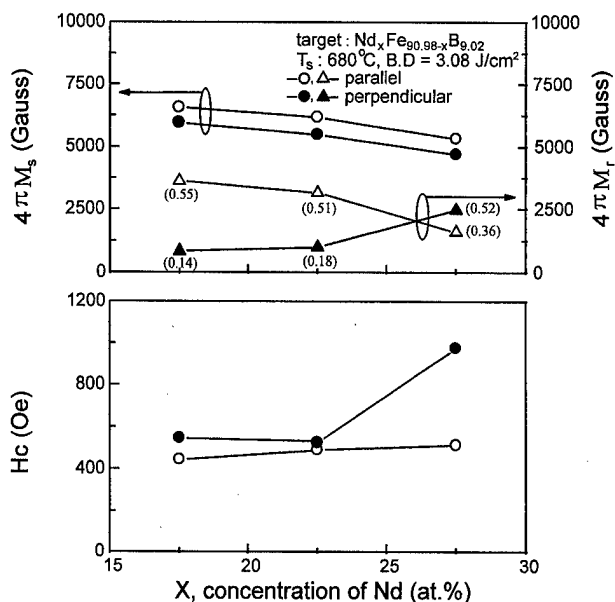


FIG. 4. The effect of Nd content on the magnetic properties of $\text{Nd}_x\text{Fe}_{90.98-x}\text{B}_{9.02}$ films on (100)Si deposited at the substrate temperature of 680°C at a laser density of 3.08 J/cm^2 .

plane of 0.51–0.55, and along out-of-plane of 0.14–0.18 with a low value of $4\pi M_r$ and H_c as well. For the films $x = 27.51$, however, the $4\pi M_r$ and H_c along out-of-plane change abruptly to have $M_r/M_s = 0.52$ and $H_c = 900$ Oe, respectively. X-ray diffraction patterns of $x = 17.51$, 22.51, and 27.51 clearly show that the spectrum of lower Nd contents indicates the poor formation of $\text{Nd}_2\text{Fe}_{14}\text{B}$ crystallite, while the pattern of $x = 27.51$ shows well developed crystallites. In spite of the variation of Nd content the films formed at T_s of 620–680 °C consist of single phase of $\text{Nd}_2\text{Fe}_{14}\text{B}$, while the films grown at room temperature to indicate the presence of amorphous and crystalline. The previous studies on NdFeB films processed by sputtering^{1,3,4,6} exhibited the anisotropic texture aligning the c axis perpendicular to the film plane.

The high-resolution micrographs of the films $\text{Nd}_{17.51}\text{Fe}_{73.47}\text{B}_{9.02}$ and $\text{Nd}_{27.51}\text{Fe}_{63.47}\text{B}_{9.02}$, respectively, indicate that the basic difference between those Nd concentrations is the grain size. The films of Nd=27.51 at. % shows the finer grains less than 15 nm of $\text{Nd}_2\text{Fe}_{14}\text{B}$ which resulted in a higher coercivity than those of Nd=17.51 or 22.51 at. % whose grain size was found to be around 20 nm. In the course of ablation around the eutectic temperature some excess of Nd might oust out of the alloy, and the formation of Nd-rich grainboundary would take place to anchor the motion of magnetic domains.

Figures 5(a) and 5(b) shows the typical variations of magnetic properties of $\text{Nd}_{17.51}\text{Fe}_{73.47}\text{B}_{9.02}$ films grown at room temperature and 680 °C, respectively. The data were for the samples measured along in-plane direction taking into account the applicability of the film type permanent magnets exhibiting the high field strength along the in-plane direction of the end devices. In Fig. 5(a) both the $4\pi M_s$ and $4\pi M_r$ of as-deposited films are high due to the presence of abundant amorphous phase which also shows the lower coercivity. By post annealing at *in situ* substrate the $4\pi M_r$ values drop prominently to a certain value (4000 G) and then stabilized thereafter. Almost the same behavior is denoted for $4\pi M_s$. As was mentioned above the post annealing seems to induce the fusion of Nd and oust out the grain boundaries. However, as the annealing temperature is increased, the H_c value enhances considerably up to 600 Oe around 600–650 °C. The formation of $\text{Nd}_2\text{Fe}_{14}\text{B}$ crystallites developed by crystallizing amorphous phase appears to be responsible for the enhancement of H_c . At higher temperatures, H_c decreases due to the extended growth of $\text{Nd}_2\text{Fe}_{14}\text{B}$ grains. The above rationalization for the magnetic properties seems to also be true for the films grown at 680 °C in Fig. 5(b).

The high values of $4\pi M_s$ and $4\pi M_r$ for the as-deposited films grown at 680 °C tend to decrease with increasing the annealing temperature. At the same time, H_c values increase to the maximum value (550 Oe) around 550–600 °C and then decrease thereafter [Fig. 5(a)]. In this case, it should be understood that if the film samples exhibit the

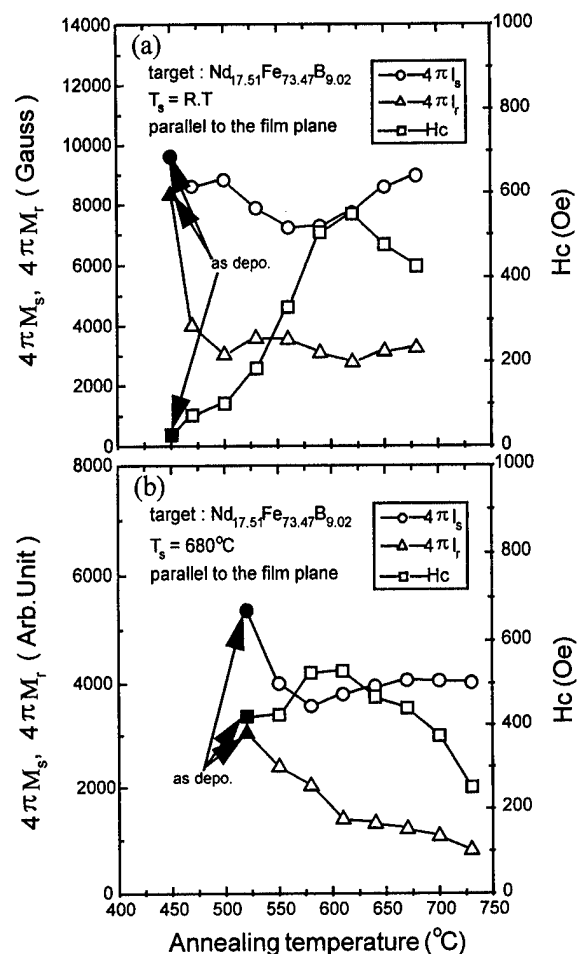


FIG. 5. The variation of magnetic properties as a function of annealing temperature for $\text{Nd}_{17.51}\text{Fe}_{73.47}\text{B}_{9.02}$ films deposited at (a) room temperature and (b) 680 °C.

same demagnetization effect at each temperature, the decreasing $4\pi M_r$ should be accompanied with decreasing H_c values due to the slender hysteresis curve. In addition, the $\text{Nd}_2\text{Fe}_{14}\text{B}$ grains developed during the previous temperature regime will grow, losing their coercivity. However, in Fig. 5(b) H_c still shows a broad maximum over a small temperature range. These films indicate a coupling interaction between $\text{Nd}_2\text{Fe}_{14}\text{B}$ grains and magnetically soft $\alpha\text{-Fe}$ grains which inevitably will form during post annealing.

¹F. J. Cadieu, T. D. Cheung, L. Wickramasekara, and N. Kamprath, IEEE Trans. Magn. **MAG-22**, 752 (1986).

²K. D. Aylesworth, Z. R. Zhao, D. J. Sellmyer, and G. C. Hadjipanayis, J. Appl. Phys. **64**, 5742 (1988).

³M. Shindo, M. Ishizone, and T. Miyazaki, J. Appl. Phys. **81**, 4444 (1996).

⁴S. M. Parhofer, J. Wecker, G. Gieres, and L. Schultz, IEEE Trans. Magn. **MAG-32**, 4437 (1996).

⁵D. J. Keavney, E. E. Fullerton, J. E. Pearson, and S. D. Bader, J. Appl. Phys. **81**, 4441 (1996).

⁶B. A. Kapitanov, N. V. Kornilov, Ya. L. Linetsky, and V. Tsvetkov, J. Magn. Magn. Mater. **127**, 289 (1993).

Maximum energy product of isotropic Nd-Fe-B-based nanocomposite magnets

J. Kuma, N. Kitajima, Y. Kanai, and H. Fukunaga

Department of Electrical Engineering and Computer Science, College of Engineering, Nagasaki University, 1-14 Bunkyo, Nagasaki 852 Japan

The maximum energy products, $(BH)_{\max}$, of isotropic Nd-Fe-B-based nanocomposite magnets were calculated by a three dimensional model ($10 \times 10 \times 10$) that incorporated non-uniform magnetization reversals by subdivisions of the grains. Based on the results of our simulation, the largest obtainable $(BH)_{\max}$ for a sample with 60% soft and 40% hard grains is about 290 kJ/m^3 . This value is lower than the previous crude estimate of 400 kJ/m^3 but is almost twice as large as the experimental measured maximum of 160 kJ/m^3 suggesting that further improvement in $(BH)_{\max}$ is possible if the nanostructure of an actual magnet can be made close to the theoretically ideal structure.

© 1998 American Institute of Physics. [S0021-8979(98)44211-7]

I. INTRODUCTION

In developing isotropic Nd-Fe-B nanocomposite magnets, it is important to obtain the maximum energy product, $(BH)_{\max}$, that is close to the theoretical upper bound. Based on numerical calculations, the theoretically obtainable $(BH)_{\max}$ of those magnets were estimated to be around 400 kJ/m^3 .^{1,2} On the contrary, experimentally measured $(BH)_{\max}$ have not exceeded 160 kJ/m^3 .³ Part of the difference may be caused by the two-dimensional nature of the model² or by the suppression of nonuniform magnetization reversals.¹ Hence we have attempted to improve the estimate of $(BH)_{\max}$ by subdividing the grains to incorporate nonuniform magnetization reversals while maintaining the three-dimensional configuration of the grains.

After the effects of the subdivision were studied and 64 elements per grain was found to be sufficient for accurate calculation of $(BH)_{\max}$, the calculation was repeated with $n=64$ to investigate the theoretically ideal nanostructures. The ratio of soft and hard grains and a relative exchange strength were varied and the conditions for the maximum $(BH)_{\max}$ were obtained.

II. SIMULATION MODEL AND METHOD

Our simulation model is shown in Fig. 1. 1000 magnetically soft and hard cube-shaped grains were arranged in an array of $10 \times 10 \times 10$. Periodic boundary conditions are used in three directions to eliminate the necessity of demagnetizing-field correction. After the fractions of the magnetically soft and hard grains were specified, the locations of the grains were determined by pseudorandom numbers. The magnetically hard grains represent Nd-Fe-B with a uniaxial anisotropy constant, $K_u^{(H)} = 4.5 \times 10^6 \text{ J/m}^3$ and saturation magnetization $M_s^{(H)} = 1.61 \text{ T}$. Moreover, their easy axes are randomly distributed in space to model an isotropic material. The magnetically soft grains are assumed to be iron with no anisotropy ($K_u^{(S)} = 0$) and saturation magnetization $M_s^{(S)} = 2.16 \text{ T}$.

In order to study the effects of nonuniform magnetization reversals, all the grains were subdivided into $n=1, 8,$

27, or 64 cubic elements. The magnetization inside each element is assumed to be uniform, but this scheme allowed to approximate nonuniform magnetization reversals within the grain.

The total energy W of the magnet, when an external field \mathbf{H} is applied, is given by

$$W = - \sum_{i=1}^{n \times 1000} \left\{ K_{ui} \frac{V}{n} (\mathbf{u}_i \cdot \mathbf{m}_i)^2 + \frac{J_e S}{6n^{2/3}} \left(\sum_{j=1}^6 \mathbf{m}_i \cdot \mathbf{m}_j \right) + M_{si} V (\mathbf{m}_i \cdot \mathbf{H}) \right\} + W_m, \quad (1)$$

where the terms in the brackets represent the anisotropy energy, the exchange interaction energy caused by the six neighboring elements and the applied field energy in that order. W_m represents the magnetostatic energy due to the local demagnetization field.

K_{ui} and M_{si} are the anisotropy constant and the saturation magnetization of the i th element, and their values de-

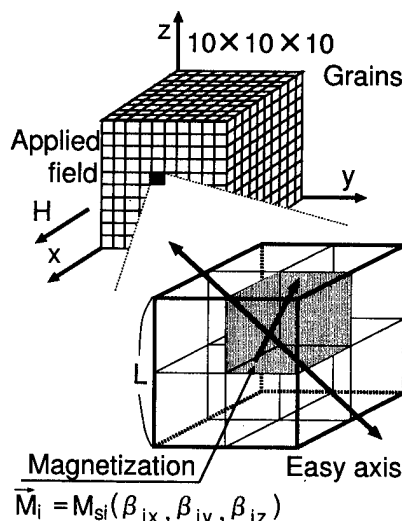


FIG. 1. Model of a magnet.

pend on the kind of grain in which the element is located. S and V are the surface area and the volume of each grain and are converted into those of each element by dividing by n or $n^{2/3}$, where n is the number of elements per grain. J_e is the exchange interaction constant per unit surface area, and a single value was assumed for all the boundaries.

\mathbf{u}_i is a unit vector in the direction of the easy axis of the i th element. \mathbf{m}_i and \mathbf{m}_j are the magnetizations in the i th and the j th elements and are reduced by the saturation magnetization of the corresponding grain.

To find the directions of the magnetizations in response to an applied field, the following form of Gilbert's equation⁴ is numerically integrated.

$$\frac{d\mathbf{m}_i}{dt} = \frac{\gamma}{(1 + \alpha^2)M_{si}V} \mathbf{A} \frac{\delta W}{\delta \mathbf{m}_i}, \quad (2)$$

$$\mathbf{A} = \begin{pmatrix} \alpha(\beta_{ix}^2 - 1) & \alpha\beta_{ix}\beta_{iy} - \beta_{iz} & \beta_{iy} + \alpha\beta_{iz}\beta_{ix} \\ \beta_{iz} + \alpha\beta_{ix}\beta_{iy} & \alpha(\beta_{iy}^2 - 1) & \alpha\beta_{ix}\beta_{iy} - \beta_{iz} \\ \alpha\beta_{ix}\beta_{iy} - \beta_{iz} & \beta_{ix} + \alpha\beta_{iy}\beta_{iz} & \alpha(\beta_{iz}^2 - 1) \end{pmatrix}$$

where γ and α are the gyromagnetic constant and the damping parameter, respectively. β 's are the direction cosines of the magnetization in the i th element so that $\mathbf{m}_i = (\beta_{ix}, \beta_{iy}, \beta_{iz})$.

The variation of the total energy with respect to \mathbf{m}_i can be written as

$$\frac{\delta W}{\delta \mathbf{m}_i} = -2K_u^{(H)} \frac{V}{n} \left\{ \frac{K_{ui}}{K_u^{(H)}} \mathbf{u}_i (\mathbf{u}_i \cdot \mathbf{m}_i) + \frac{J_e S n^{1/3}}{6K_u^{(H)} V} \left(\sum_{k=1}^6 \mathbf{m}_k \right) + \frac{M_{si}}{2K_u^{(H)}} (\mathbf{H} + \mathbf{H}_{di}) \right\}. \quad (3)$$

Here the ratio of the exchange energy to the anisotropy energy of a magnetically hard grain, $J_e S / 6K_u^{(H)} V$, is defined as the exchange parameter η . The calculated magnetic properties depend solely on η and the fraction of the soft grains once K_u and M_s of two kinds of grains are specified.

\mathbf{H}_{di} is the local demagnetizing field acting on the i th element and is calculated in the following manner. First, we calculate the distribution of the magnetic charges according to the magnetization of each element. These results are used to calculate the magnetic potential by means of FFT (fast Fourier transform) and the inverse FFT. \mathbf{H}_{di} is calculated as the gradient of the magnetic potential at the i th element.

After the directions of the magnetizations were determined, the reduced magnetization m of the model is calculated as the sum of the in-field component of $\mathbf{M}_i (= M_{si} \mathbf{m}_i)$ divided by the sum of the saturation magnetizations of all the elements.

III. RESULTS

In order to examine the effects of the subdivisions of the grains, five different configurations of 60% soft and 40% hard grains were generated with $\eta = 0.118$, and the simulation was repeated. The value of η and the fraction of the soft grains were so selected that the largest $(BH)_{\max}$ was obtained for a single cubic element.

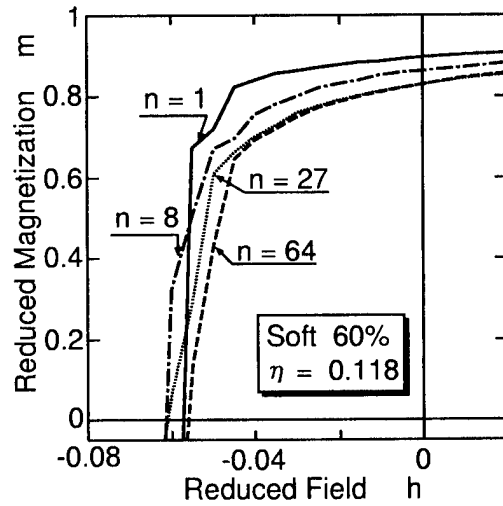


FIG. 2. Demagnetization curves for magnets containing 60% soft grains.

Figure 2 shows the calculated demagnetization curves that were close to the average of those five simulations. In the figure, h is the reduced applied field defined as $h = H / (M_s^{(H)} / 2K_u^{(H)})$. As the number of elements in a grain, n , is increased, the remanence, m_r , decreases and approaches 0.8. At the same time the hysteresis loops deviate more from a square loop.

The directions of the magnetizations are shown in Fig. 3 for $n=27$ with a reversal field of $|h|=0.055$ applied in the negative x direction. A cross-sectional plane parallel to the x - y plane was selected, and the magnetizations of the grains contained in that plane were projected onto the x - y plane. The darker arrows represent the magnetizations in magnetically hard elements and lighter arrows represent those in the soft elements. The directions of magnetizations in the hard grains are relatively uniform, because their anisotropic en-

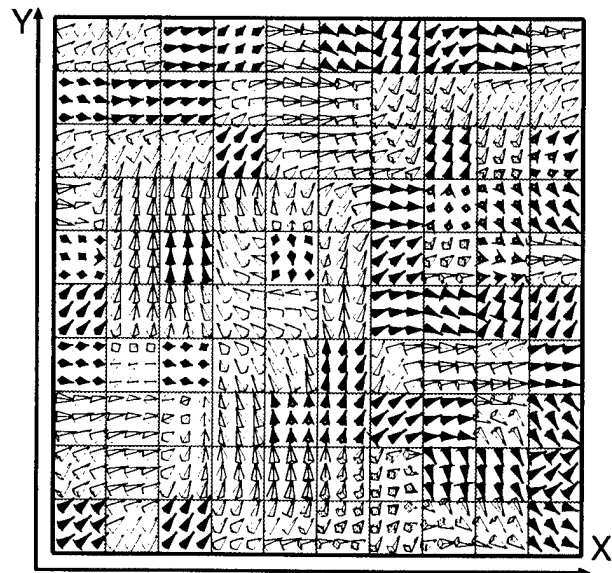


FIG. 3. Directions of magnetizations projected onto x - y plane. $h = -0.055$ is applied to a sample containing 60% soft grains. Each darker arrow represents the magnetization in a magnetically hard element, and a lighter arrow represents the magnetization in a soft element. ($n=27$).

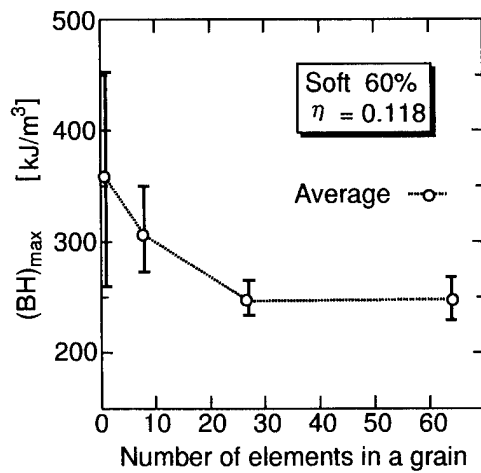


FIG. 4. Dependence of $(BH)_{\max}$ on the number of elements in a grain. The average value and the range of $(BH)_{\max}$ of 5 simulations are shown at each n .

ergy is about 9 times larger than the exchange energy. The magnetizations in the soft grains, on the other hand, show non-uniform behavior because of the lack anisotropy.

Figure 4 shows the dependence of $(BH)_{\max}$ on the number of elements per grain. As n increases, the calculated $(BH)_{\max}$ decreases and approaches about 250 kJ/m^3 . The range of $(BH)_{\max}$ also diminishes as expected.

The calculation of $(BH)_{\max}$ was repeated for $n=64$ with various ratios of soft and hard grains and a range of η . As shown in Fig. 5, the largest $(BH)_{\max}$ was observed when the ratio of the soft grains was 60%, which was same as the case of $n=1$. When n was increased from 1 to 64, however, the the largest $(BH)_{\max}$ increased from 250 to 290 kJ/m^3 and the corresponding values of η shifted from 0.118 to a larger value (or a smaller grain size). If we assume $J_e = 16 \times 10^{-2} \text{ J/m}^2$, $\eta=0.177$ corresponds to the optimum grain size of 20 nm.

IV. CONCLUSIONS

The magnetic properties of isotropic Nd-Fe-B-based nanocomposite magnets were calculated by computer simulation based on a micromagnetic theory. Each grain was subdivided into 1 to 64 elements to study the effects of nonuniform magnetization reversals within the grain. As the number of elements per grain increased, both the calculated

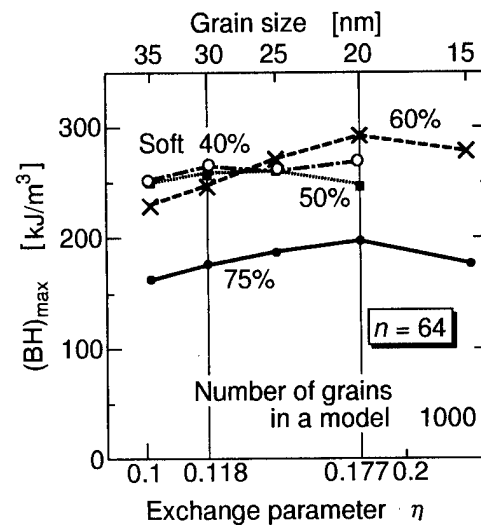


FIG. 5. $(BH)_{\max}$ as a function of the exchange interaction parameter η with the ratio of the soft grains varying from 40 to 75%. The grain sizes are calculated assuming $J_e = 1.6 \times 10^{-2} \text{ J/m}^2$.

$(BH)_{\max}$ and m_r decreased and approached constant values. Thus $n=64$ appears to be sufficient for an accurate estimate of $(BH)_{\max}$.

The simulation was repeated by varying the exchange interaction parameter η and the fraction of the soft grains. The largest $(BH)_{\max}$ was obtained when the ratio of the soft grains was 60% as reported before. However, the value of $(BH)_{\max}$ obtained with $n=64$ was 290 kJ/m^3 . This value is about 28% lower than the previous estimate of 400 kJ/m^3 . It was also noted that the largest $(BH)_{\max}$ corresponded to a grain size of 20 nm which is smaller than the estimate made without non-uniform magnetization reversals.

The remaining difference between the experimentally measured maximum $(BH)_{\max}$ of 160 kJ/m^3 and this simulation is probably caused by the differences in the nanostructures. In other words the magnetic properties may be further improved by fabricating magnets whose nanostructures are closer to the theoretically ideal structures.

¹H. Fukunaga, N. Kitajima, and Y. Kanai, Mater. Trans., JIM **37**, 864 (1996).

²T. Schrefl, J. Fidler, and H. Kronmüller, Phys. Rev. B **49**, 6100 (1994).

³J. F. Liu and H. A. Davies, J. Magn. Magn. Mater. **157/158**, 29 (1996).

⁴T. L. Gilbert, Phys. Rev. **100**, 1243 (1955).

Remanence enhancement in mechanically alloyed isotropic Nd(Fe, Mo)₁₂N_x compounds

Yiaofu Xiao,^{a)} Qi Zeng, Shengzhi Dong, and Run Wang

Institute of Materials Science and Engineering, University of Science and Technology, Beijing 100083, People's Republic of China

The structure and magnetic properties of Nd(Fe, Mo)₁₂N_x compounds prepared by mechanical alloying have been studied using x-ray diffraction, transmission electron microscopy, and magnetic measurements. After heat treatment and nitriding, it is found that almost single-phase Nd(Fe, Mo)₁₂N_x can be obtained. Electron microscopy revealed a nanometer grain size of 10–30 nm and the magnets have a remanence enhancement of approximately 60% of the saturation.

© 1998 American Institute of Physics. [S0021-8979(98)31311-0]

I. INTRODUCTION

In structurally isotropic magnetic materials the ratio of remanent magnetization M_r and saturation magnetization, M_r/M_s , is at 0.5.¹ Recently enhanced magnetically isotropic properties have been observed in single-phase materials^{2,3} and two-phase materials containing both hard and soft magnetic phase. In these materials, M_r is significantly greater than $1/2M_s$. As to single-phase materials, there are two necessary conditions for the remanent enhancement phenomenon happening:² (1) a substantial absence of an intergranular phase between the crystallites, and (2) a specific grain size range.

Due to a relatively high Curie temperature, high saturation magnetization and a large (easy *C* axis) anisotropy field, Nd(Fe, M)₁₂N_x (M=Mo, Ti, V) compounds are promising candidates for permanent magnet application.^{4,5} Nd(Fe, Mo)₁₂N_x especially, has the advantage of easy formation of its single phase and the realization of high coercivity. So in this article, we report on the occurrence of remanence enhancement in mechanically alloyed Nd–Fe–Mo–N powders.

II. EXPERIMENT

Alloys of NdFe₁₀Mo₂ compounds were prepared by induction melting of 99.9 wt. % pure materials in a water cooled crucible under purified argon atmosphere. An additional amount of Nd (3 wt. %) was added to compensate for the loss during the process. The ingots were annealed at 950 °C for 100 h. For mechanical alloying (MA), the annealed compounds were crushed into particles with a diameter of less than 50 μm and sealed into a vial with several 10 and 12 mm stainless steel balls in a ratio of powder to ball of 1 to 20 under argon atmosphere. MA was done in a high-energy ball mill designed by our laboratory for 24 h. All handling was conducted in a glove box filled with argon gas. Crystallization was carried out in the temperature range from 700 to 900 °C for 0.5 h in a vacuum atmosphere. The recrystallized compounds were nitrided at 500 °C for 2 h in pure nitrogen atmosphere. X-ray diffraction (XRD) analysis was

conducted using Cu *Kα* radiation with a Rigaku D/max-rA diffractometer equipped with a graphite crystal monochromator. Transmission electron microscope (TEM) observation was performed with an H-800 electron microscopy, and magnetic measurement was performed with a magnetometer operating in a field of 2 T.

III. RESULTS AND DISCUSSION

X-ray diffraction patterns of a mechanically alloyed NdFe₁₀Mo₂ sample are shown in Fig. 1. It can be seen from Fig. 1(a) that the mechanically alloyed materials show a mixture of amorphous and α-Fe. On subsequent isothermal aging at 1073 K, the mechanically alloyed powders were converted into Nd(Fe, Mo)₁₂ with the ThMn₁₂ structure [Fig. 1(b)]. The nitrided ThMn₁₂ crystalline structure was obtained by following nitrogenation, and it is composed of single-phase 1:12 [Fig. 1(c)].

Figure 2 show the hysteresis loop of a NdFe₁₀Mo₂N_x compound measured in a field of 2 T. The sample was crystallized at 1073 K for 0.5 h and nitrided at 773 K for 2 h. It can be seen that $M_s=70.7$ emu/g, $M_r=44.5$ emu/g, and $M_r/M_s=0.63$. However, the sample was unable to be satu-

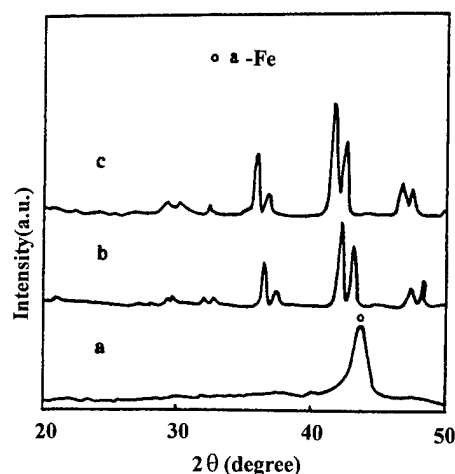


FIG. 1. X-ray diffraction patterns of the MA NdFe₁₀Mo₂ sample: (a) milled for 24 h; (b) annealed at 1073 K for 0.5 h after MA; (c) nitrided at 773 K for 2 h.

^{a)}Electronic mail: bkg.mag@public3.bta.net.cn

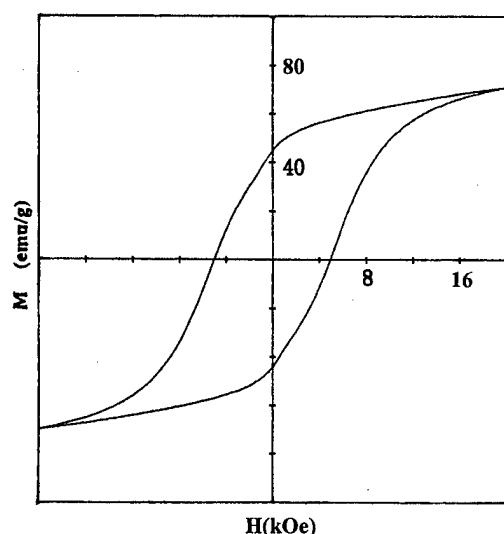


FIG. 2. Hysteresis loop of $\text{NdFe}_{10}\text{Mo}_2\text{N}_x$ powder measured in a field of 2 T.

rated at the field of 2 T, so we use the “law of approach”⁶ to calculate the M_s for $H \rightarrow \infty$, which is approximately 75.4 emu/g and corresponding to $M_r/M_s = 0.60$.

The crystal size of the aged, MA powder was found to be approximately 15 nm by X-ray diffraction analysis. The TEM micrograph of an individual powder particle, which has the size of 300 nm, is shown in Fig. 3. It is comprised of randomly oriented equiaxed crystallites with the tetragonal ThMn_{12} structure. The crystallite size of the nanocrystalline phase ranges from 10 to 30 nm, being in good agreement with the x-ray diffraction analysis. In addition, the crystallites are substantially free of any intergranular phase—crystalline or amorphous. The employment of dark-field techniques verified that there is intimate contact between ThMn_{12} grains.

The exchange interaction tends to align all the magnetic moments parallel, and conversely the anisotropy interaction lines up the magnetic moments in each grain with its crystallographic C -axis direction. The exchange energy grows with the increasing intergrain contact surface area. On the other hand the anisotropy energy grows with increasing grain volume. Hence, at sufficiently small grain sizes accommodation between the two types of magnetic interaction arises. The remanence enhancement phenomenon results from this accommodation of the two competing interactions. The direction of each grain's magnetization deviates from its C axis towards the direction of the neighboring grains' magnetization; hence, the resultant magnetization of the entire magnet is greater than if each grain acted independently. However, the grain sizes are so small that the coercivity becomes

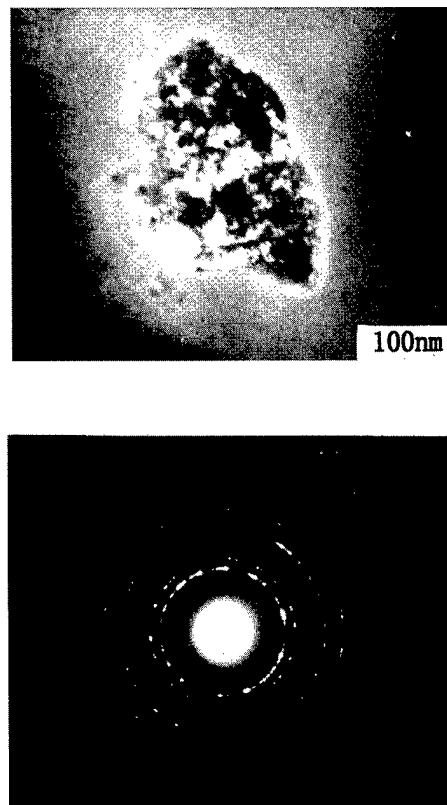


FIG. 3. TEM bright-field image and the corresponding diffraction pattern of MA $\text{NdFe}_{10}\text{Mo}_2$ powder which had been milled for 24 h, aged, and nitrided.

lower, only 5.0 kOe was obtained in our study, which is lower than the result reported by Gong and Hadjipanayis.⁷

IV. CONCLUSION

MA has been successfully used in the preparation of $\text{Nd}(\text{Fe}, \text{Mo})_{12}\text{N}_x$ permanent magnets with remanence enhancement, $M_r/M_s \approx 0.6$. The reasons for the exchange interaction to give rise to the magnetic enhancement are: (1) the mean grain size of 20 nm; (2) the substantial absence of any intergranular phase.

¹E. C. Stoner and E. P. Wohlfarth, *Philos. Trans. R. Soc. London, Ser. A* **240**, 599 (1948).

²G. B. Clemente, J. E. Keem, and J. P. Bradley, *J. Appl. Phys.* **64**, 5299 (1988).

³R. W. McCallum, A. M. Kadin, G. B. Chemeate, and J. E. Keem, *J. Appl. Phys.* **61**, 3577 (1987).

⁴J. Yang and Sh. Zh. Dong, *J. Appl. Phys.* **78**, 1140 (1995).

⁵M. Anagnoston and C. Christides, *J. Appl. Phys.* **70**, 6012 (1991).

⁶B. Bleaney, *Proc. Phys. Soc. London* **82**, 469 (1963).

⁷W. Gong and G. C. Hadjipanayis, *IEEE Trans. Magn.* **28**, 2563 (1992).

Magnetic properties of $\text{Nd}_8\text{Fe}_{77}\text{Co}_5\text{B}_6\text{CuNb}_3$ melt-spun ribbons

H. Chiriac^{a)} and M. Marinescu

National Institute of R&D for Technical Physics, 47 Mangeron Boulevard, 6600 Iasi 3, Romania

$\text{Nd}_8\text{Fe}_{77}\text{Co}_5\text{B}_6\text{CuNb}_3$ amorphous ribbons were obtained by the melt spinning method using a large range of the wheel circumferential speed (18–40 m/s). For 10 min time of heat treatment at 700 °C the following values of the magnetic characteristics were achieved: $H_c = 3.95$ kOe, $B_r = 11.25$ kG, and $(BH)_{\text{max}} = 15$ MGOe. The 13% increase of the remanent ratio $M_r/M_{1.5\text{T}}$ by applying a magnetic field during annealing suggests an improvement of the exchange coupling effect. The Curie temperature of both hard and soft magnetic component phases increases with about 50 °C due to the Co content but it is not affected by the magnetic field annealing. © 1998 American Institute of Physics. [S0021-8979(98)31411-5]

I. INTRODUCTION

The most attractive alloys which exhibit hard magnetic properties are the NdFeB based alloys. Two methods are known to produce NdFeB magnets: powder metallurgy and rapid quenching from the melt. The former leads to a microstructure that was found to consist of large grains (4–10 μm) of $\text{Nd}_2\text{Fe}_{14}\text{B}$ phase embedded in a matrix of Nd-rich phase.¹ The main advantage of the second route is that it allows the possibility of lowering the Nd content without affecting the magnetic properties. In this case two phases are separated: a soft magnetic Fe-based phase having high saturation ($4\pi M_s = 2.2$ T) and a hard magnetic $\text{Nd}_2\text{Fe}_{14}\text{B}$ phase having a high anisotropy constant ($K_1 = 4.3 \times 10^6$ J/m³). The properties of each individual magnetic phase contribute to the properties of the entire ensemble due to their ferromagnetic exchange coupling. The optimum hard magnetic properties are obtained when the crystallites behave as single domain ($d_g < 40$ nm) and there exist a uniform distribution of the magnetically soft and hard phases.² The nanoscale grain refinement can be obtained directly during the quenching process but in this case the presence of the metastable phases cannot be controlled,³ or from amorphous precursors by annealing. In order to obtain a “clean” magnetic structure we preferred to use the second method.

The quenchability⁴ and the nanostructured phase formation are improved by adding various elements at the basic composition. The most known addition used in soft magnetic materials is the pair of the atomic species (Cu, Nb) which promote the formation of the grains and act as a grain growth inhibitor. For this reason we studied the $\text{Nd}_8\text{Fe}_{77}\text{Co}_5\text{CuNb}_3\text{B}_6$ composition. The Co was added in order to increase the Curie temperature of the hard phase, thus enlarging the temperature range in which the magnets could be used.

We also present the influence of the magnetic field annealing on the exchange coupling between the magnetic phases evaluated in terms of $M_r/M_{1.5\text{T}}$.

II. EXPERIMENT

An alloy ingot of $\text{Nd}_8\text{Fe}_{77}\text{Co}_5\text{CuNb}_3\text{B}_6$ was prepared by arc melting pure constituents (99.9% purity). Amorphous flakes up to 20–25 cm in length and 20–25 μm in thickness were produced in an inert atmosphere by the melt spinning technique. For wheel circumferential speed of 18–40 m/s, the samples were obtained in an amorphous state. The nanocrystalline structure has been induced by annealing the samples at 700 °C for different periods of time in a range of 2–20 min. Other samples were subjected to an external applied magnetic field of 0.8 T during the same heat treatments. In order to evaluate the effect of the magnetic field annealing after each treatment the hysteresis loops were measured using a vibrating sample magnetometer (VSM), and the strength of the magnetic interactions was evaluated by means of the remanence ratio $M_r/M_{1.5\text{T}}$. The structure of both as-cast and annealed ribbons was investigated by the x-ray diffraction (XRD) method. The Curie temperatures of the hard and soft magnetic phases were pointed out by the thermomagnetic curve.

III. RESULTS AND DISCUSSION

X-ray diffraction studies performed on as-cast ribbons present a broad maximum, which is specific to the amorphous structure even using a wheel circumferential speed $v_{\text{circ}} = 18$ m/s.

Influence of the annealing time of the amorphous ribbons obtained for $v_{\text{circ}} = 26$ m/s, on coercivity, reduced remanence and maximum energy product is presented in Fig. 1. It seems that the most adequate time for heat treatment is that performed for 10 min, when the best magnetic properties of the investigated ribbons have achieved the following values: $H_c = 3.95$ kOe, $B_r = 11.25$ kG, and $(BH)_{\text{max}} = 15$ MG Oe. We applied the magnetic field during heat treatment in order to induce a uniform nucleation of the grains and thus to improve the ferromagnetic exchange coupling effect between them. The exchange distance was deduced to be of the order of about 4 nm for the hard phase and of the order of at least 40 nm for the soft Fe-based phase. If this latter distance exceeds the size of the grains, then strong interactions occur not only between the contacting hard grains but also between

^{a)}Electronic mail: hchiriac@phys-iasi-ro

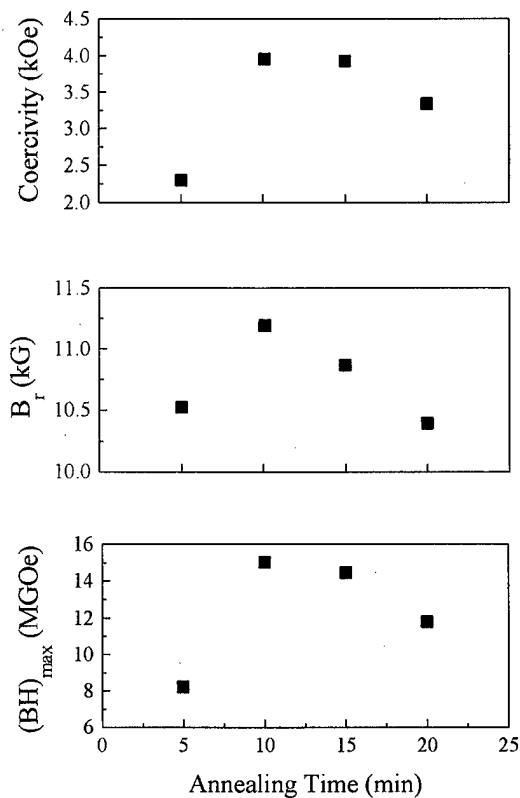


FIG. 1. Influence of the annealing time at 700 °C on the magnetic properties of the melt-spun $Nd_8Fe_{77}Co_5B_6CuNb_3$ ribbons.

those which are not in contact, via neighboring soft particles.² The effect of the magnetic field treatment on the magnetic properties of the $Nd_8Fe_{77}Co_5B_6CuNb_3$ ribbons at different temperatures of annealing is illustrated in Fig. 2. Ribbons subjected to the magnetic field and heat treated at 700 °C for different duration present different behavior of the magnetic characteristics. One can note that the magnetic

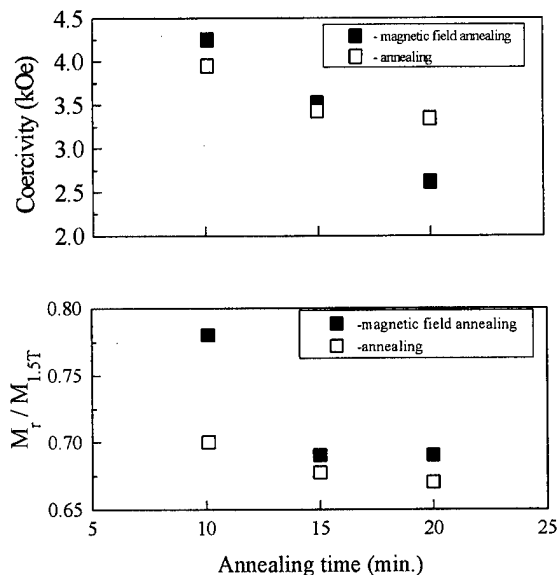


FIG. 2. Coercivity and remanent ratio $M_r/M_{1.5T}$ of the melt-spun $Nd_8Fe_{77}Co_5B_6CuNb_3$ ribbons as a function of annealing time with and without applied magnetic field.

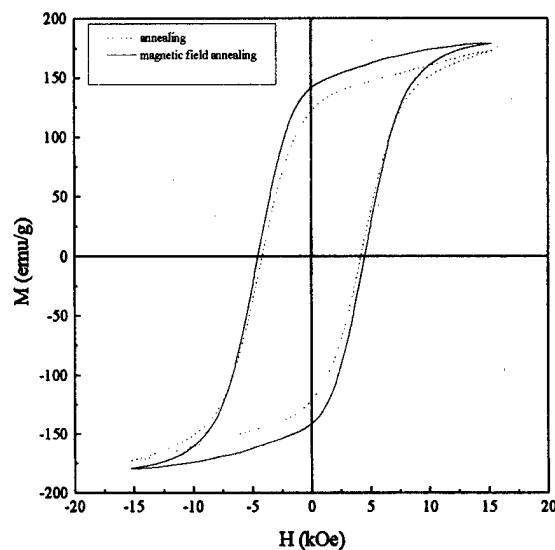


FIG. 3. Hysteresis loops of the melt-spun $Nd_8Fe_{77}Co_5B_6CuNb_3$ ribbons annealed at 700 °C for 10 min with and without applied magnetic field.

properties obtained by performing heat treatments are improved by applying simultaneously a magnetic field.

The remanence ratio is enhanced by applying a magnetic field. This result supports the assumption that the exchange coupling between magnetic phases is increased. The biggest enhancement in the $M_r/M_{1.5T}$ values is of 13% and corresponds to the treatment for which the maximum in coercivity is reached meaning that the grains behave as single-domain particles (see Fig. 1).

Figure 3 illustrates the effect of the magnetic field applied during the heat treatment at 700 °C for 10 min on a hysteresis loop. The enhancement of the $M_r/M_{1.5T}$ ratio by the applied magnetic field supports the assumption that the exchange coupling between magnetic phases is increasing. Figure 4 presents the thermomagnetic curve for the $Nd_8Fe_{77}Co_5B_6CuNb_3$ ribbons. It follows that Co atoms are simultaneously diffused in $Nd_2Fe_{14}B$ as well as in α -Fe and increase the corresponding Curie temperatures from the characteristic values of the above mentioned phases (316 °C and 770 °C) up to about 360 °C and 820 °C, respectively. This increase is due only to the Co content.

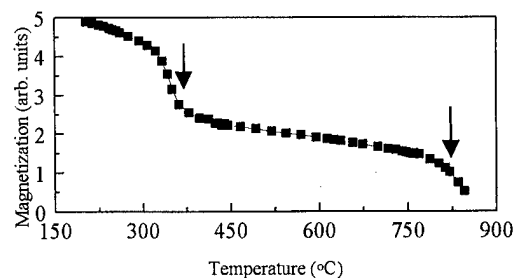


FIG. 4. Thermomagnetic curve of $Nd_8Fe_{77}Co_5B_6CuNb_3$ ribbons magnetic field annealed at 700 °C for 10 min.

IV. CONCLUSION

Summarizing, the addition of Cu and Nb leads to the improvement of the magnetic properties as a result of the nanocrystalline structure. The addition of Co results in an $\sim 50^\circ\text{C}$ increase in the Curie temperature of both hard and soft magnetic phases. The magnetic field annealing of the melt-spun $\text{Nd}_8\text{Fe}_{77}\text{Co}_5\text{B}_6\text{CuNb}_3$ amorphous ribbons leads to improvement of the hard magnetic properties. The obtained

results suggest that the magnetic field applied during annealing determines a uniform mixture of the soft and hard component magnetic phases.

¹G. H. Hadjipanayis, *Rare Earth Iron Permanent Magnets*, edited by J. M. D. Coey (Clarendon, Oxford, 1996), pp. 303–319.

²A. Manaf, R. A. Buckley, and H. A. Davis, *J. Magn. Magn. Mater.* **128**, 302 (1993).

³L. Withanawasam, I. Panagiotopoulos, and G. C. Hadjipanayis, *IEEE Trans. Magn.* **32**, 4422 (1996).

⁴M. J. Kramer, C. P. Li, K. W. Dennis, R. W. McCallum, C. H. Sellers, D. J. Branagan, and J. E. Shield, *J. Appl. Phys.* **81**, 4459 (1997).

Effect of TiC additions to the microstructure and magnetic properties of $\text{Nd}_{9.5}\text{Fe}_{84.5}\text{B}_6$ melt-spun ribbons

M. J. Kramer,^{a)} C. P. Li, K. W. Dennis, and R. W. McCallum
39 Wilhelm Hall, Ames Laboratory, Ames, Iowa 50011

C. H. Sellers and D. J. Branagan

Lockheed Martin Idaho Technologies Company, and Idaho National Engineering and Environmental Laboratory, Idaho Falls, Idaho 83415-2218

L. H. Lewis and J. Y. Wang

Department of Applied Science, Brookhaven National Laboratory, Upton, New York 11973

Rapidly solidified samples of $\text{Nd}_{9.5}\text{Fe}_{84.5}\text{B}_6$ with and without 3 at. % TiC were prepared by melt spinning and melt extraction and then annealed in vacuum (3×10^{-6} Torr) at temperatures from 600 to 750 °C. For alloys melt spun under similar conditions, the overquenched state was achieved at wheel speeds >10 m/s for the TiC added alloy while >20 m/s was necessary without TiC. The overquenched samples contained a smaller fraction of α -Fe in smaller grains than the undercooled samples where Fe dendrites formed near the free surface during solidification. These Fe dendrites were not removed by annealing. In addition, large orientated 2-14-1 grains nucleated on the Fe dendrites. This combination is detrimental to the magnetic properties. The addition of TiC results in improved control of the microstructure over a larger fraction of the ribbon volume enhancing the magnetic properties. © 1998 American Institute of Physics. [S0021-8979(98)31511-X]

I. INTRODUCTION

To achieve enhanced remanence in Nd-Fe-B alloys, numerous groups have shown that adding excess Fe and B improves the exchange coupling effect.¹⁻⁴ The formation of secondary phases is dependent on the initial composition, melt-spinning parameters, and subsequent heat treatment. Additions of TiC have been shown to improve the quenchability and inhibit grain growth during subsequent annealing for stoichiometric 2-14-1.⁵ A study of the effect of TiC addition on a high remanence alloy was undertaken to see if TiC addition provides better quenchability and microstructural control during subsequent annealing. The effect of processing and composition on microstructure will be discussed in light of a new model for rapid solidification in peritectic systems.^{6,7}

II. EXPERIMENTAL TECHNIQUES

$\text{Nd}_{9.5}\text{Fe}_{84.5}\text{B}_6$ with and without 3 at. % TiC was melt spun from 5 to 25 m/s in Ar then annealed in vacuum (3×10^{-6} Torr) at temperatures from 600 to 750 °C. The TiC added alloy is designated HRT, the alloy without TiC, HR1. The microstructure of these samples was compared to samples of $\text{Nd}_{9.5}\text{Fe}_{84.5}\text{B}_6$ melt-extracted at 45 m/s and annealed in a similar manner. The samples were analyzed using differential thermal analysis (DTA) to determine glass fraction, dc superconducting quantum interference device (SQUID) magnetometry to determine energy product, and vibrating sample magnetometry (VSM) to characterize Fe content. Microstructure and phase composition were studied

by transmission electron microscopy (TEM) and x-ray diffraction (XRD). TEM samples were prepared by mounting the ribbons onto Cu ovals and Ar ion milling at 5 keV using a liquid nitrogen cooled stage. XRD was performed on ground and sieved ($<38 \mu\text{m}$) powder and on ribbon surfaces. XRD on the wheel and free surfaces was previously shown to indicate variations in phase compositions and the presence of texturing in underquenched ribbons of stoichiometric 2-14-1 composition.⁷ The optimally quenched state as a function of wheel speed was determined by the maximum in the energy products before heat treatment while the overquenched state was achieved when the energy product was effectively zero (i.e., primarily glass).

III. BACKGROUND

To explain the evolution in microstructures in melt-spun Nd-Fe-B, the following model, based upon previous work on eutectic alloys, was developed.⁸ The microstructure predicted by this model depends on the degree of undercooling achieved before nucleation occurs on the wheel surface. For the slightly undercooled condition, γ -Fe dendrites solidify under a relatively low driving force which results in thick dendrites with numerous side-arms. When the material cools below the peritectic temperature, 2-14-1 nucleates epitaxially on the Fe with $(111)_{\gamma\text{-Fe}} \parallel (330)_{2-14-1}$ and $[1-10]_{\gamma\text{-Fe}} \parallel [001]_{2-14-1}$. Due to nucleation on the side-arms as well as the dendrite trunks, no significant texture of the 2-14-1 is observed. Under moderate undercooling conditions, 2-14-1 nucleates and grows rapidly. But before the growth front reaches the free side of the ribbon, growth front temperature recedes to the peritectic temperature. Since $T_{\text{peritectic}}$ is significantly below T_{liquid} , Fe dendrites then grow

^{a)}Electronic mail: mjkrmer@ameslab.gov

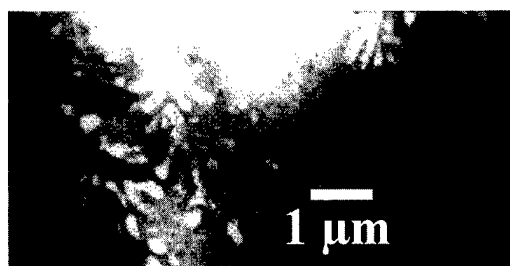


FIG. 1. TEM bright field image of melt-extracted alloy annealed for 10 min at 600 °C. Note the large Fe dendrites with secondary branches.

rapidly into the remaining liquid in the direction of the temperature gradient without side-arm formation. At the same time the initial 2-14-1 dendrites break up forming a layer seeded with 2-14-1 nuclei. The solidified ribbon consists of two layers, an equiaxed fine-grained 2-14-1 layer and an oriented coarse-grained 2-14-1 structure which nucleated from the Fe dendrites. At optimum undercooling, the 2-14-1 dendrites grow through enough of the ribbon to seed the entire ribbon so that when the dendrite breakup occurs following recalescence, a fine-grained equiaxed microstructure is formed. If the undercooling is sufficiently high, the critical undercooling rate for glass formation is reached in the layer of the ribbon on the wheel surface. The undercooling rate in the interior of the ribbon is lower and hence nucleation may occur after a finite thickness of glass is formed. On the other hand, at sufficiently high rates, the entire ribbon is glassy.

IV. RESULTS

Based on TEM and XRD results, the melt-extracted alloy obviously formed in the slightly undercooled state. The XRD and VSM data show a large fraction of free Fe phase as expected from the stoichiometry (~ 17 vol % as determined by VSM). Large Fe dendrites were also observed in the TEM (Fig. 1). This is also supported by the low energy product which was not substantially changed with annealing. Higher undercooling was achieved with melt-spinning wheel speeds >10 m/s. Based on magnetization data and XRD, HR1 was near its optimal quench at 15 m/s while it took only 10 m/s for HRT (Table I). Previous work showed that optimal as-spun magnetic properties are achieved with moderate undercooling.⁹ After annealing, the magnetic properties of both samples showed a slight decrease, most likely due to grain growth of the grains near optimal size. The XRD shows a substantial Fe peak for both samples. This is predicted in the model since a small fraction of the ribbon will recalescence to the $T_{\text{peritectic}}$, where primary Fe will form.

The overquenched state was achieved at wheel speeds >10 m/s for HRT while >20 m/s was necessary for HR1. The largest energy product for a given wheel speed was obtained using a 700 °C anneal for 10 min for both alloys. For the various wheel speeds, the highest energy product was obtained for those alloys melt-spun in the over quenched state, 15 m/s for TiC added (14.1 MGOe) and 20 m/s without TiC (12.4 MGOe), regardless of the annealing temperature. For the TiC added alloy, there is a drop in energy product with increasing wheel speed much beyond the optimal

TABLE I. Maximum energy product (BH_{max}) measured on B rich, high remanence alloys in the as-spun state and after 700 °C anneal for 10 min.

Wheel speed (m/s)	HR1 (without TiC)		HRT (with TiC)	
	As-spun (MGOe)	700 °C (MGOe)	As-spun (MGOe)	700 °C (MGOe)
5	0.36	0.18	0.5	0.6
10	3.04	1.85	2.5	4.6
15	10.1	6.26	0	14.13
20	3.29	12.43	0	12
25	0	11	0	12.3

quench rate. The largest difference in magnetic properties between HRT and HR1 alloys after annealing was at 15 m/s while at 20 and 25 m/s the alloys showed similar properties. Here the improved energy product of the HRT alloy is primarily due to an increase in its coercivity compared to HR1. In fact, the remanence for HR1 at 20 and 25 m/s is better than HRT (Table II).

While 700 °C is high enough to crystallize the amorphous fraction, it is not high enough to cause substantial diffusion over a short time period. This is brought out in the XRD of the free surface of the ribbons (Fig. 2). Note that the HRT alloy shows a typical random pattern for 2-14-1 for both optimal (15 m/s) and overquenched (20 m/s) conditions, while the moderately undercooled HR1 alloy shows distinct texturing of the 2-14-1. As discussed above, the texturing of the 2-14-1 comes about from the growth of Fe during solidification in underquenched ribbons when recalescence raises the temperature of the growth front above the peritectic temperature.

TEM was performed to determine if there are any distinct microstructural differences between the optimally to overquenched and annealed alloys. Dark field images showed little differences in either grain size or percentages of grain boundary (GB) phases except for HRT at 20 m/s which had slightly larger grains and increased GB phases (Fig. 3). The TiC particles were only observed in the GB region. As we expect a microstructural variation through the ribbon thickness, the regions observed may not be representative of the entire ribbon due to the selective nature of TEM. Thus we cannot rule out the existence of significant differences near the ribbon surfaces as demonstrated in the XRD of the free surfaces.

From the solidification model, the formation of γ -Fe occurs after the temperature of the solidification front reaches

TABLE II. Remanence and coercivity for 700 °C annealed ribbons.

Wheel speed (m/s)	HR1 (without TiC)		HRT (with TiC)	
	Remanence (G)	Coercivity (Oe)	Remanence (G)	Coercivity (Oe)
5	2183	378	4343	676
10	6000	1410	7809	3867
15	5810	3911	8980	6336
20	9616	5686	9362	6566
25	9195	4666	8714	5337

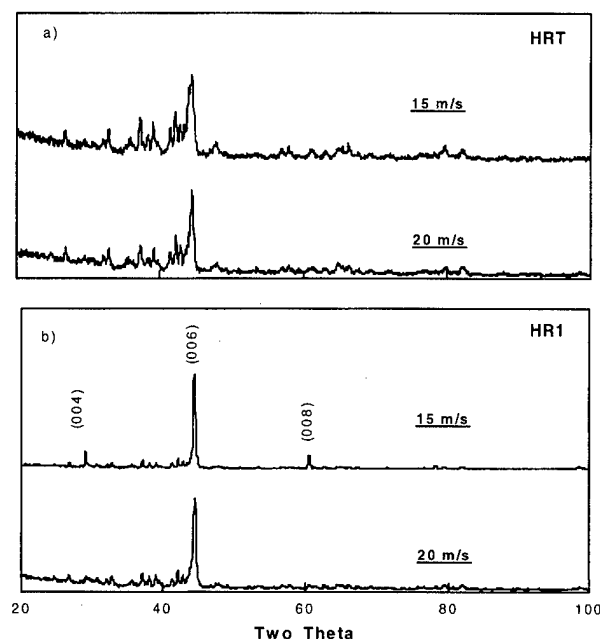


FIG. 2. XRD patterns on free sides of (a) HRT alloy and (b) HR1 alloy melt-spun at 15 and 20 m/s then annealed at 700 °C. Note the strong enhancement of the (001) lines for the 2-14-1 phase in the underquenched HR1 alloy which is absent in HRT.

the peritectic temperature but before the liquid composition reaches the composition of the peritectic liquid. If the Fe forms primarily under conditions of high undercooling, fine dendrites form. These dendrites may easily be partially dissolved into the liquid during the solidification of 2-14-1 from the pseudo-equilibrium liquid. This will result in a fine dispersion of small Fe particles which will result in remanence enhancement. If the Fe dendrites form under low undercooling conditions, the dendrites are coarser. As a result the Fe which remains after solidification is larger than the optimum size and possibly large enough to promote reverse domain formation. It appears that for Fe rich compositions, the undercooling required to ensure rapid dendritic growth is such that a limited amount of glass is formed during initial solidification. A short term anneal is sufficient to crystallize this glass without promoting significant grain growth. As in the stoichiometric material, the addition of TiC alters the growth kinetics so that more uniform microstructure may be obtained throughout the ribbon.

Selection of elemental additions and processing conditions to modify the microstructure can be guided by the model presented here. Additions must show considerable solubility in the melt, yet limited solubility in the primary solidification phase, 2-14-1. Appropriate additions can provide solute drag on the primary solidification features, providing more time for the growth front to reach the free boundary. Solidification conditions must provide sufficient undercooling below the peritectic temperature so the dendrites of the primary solidification phase will reach the free boundary before recalescence raises the temperature above peritectic temperature.

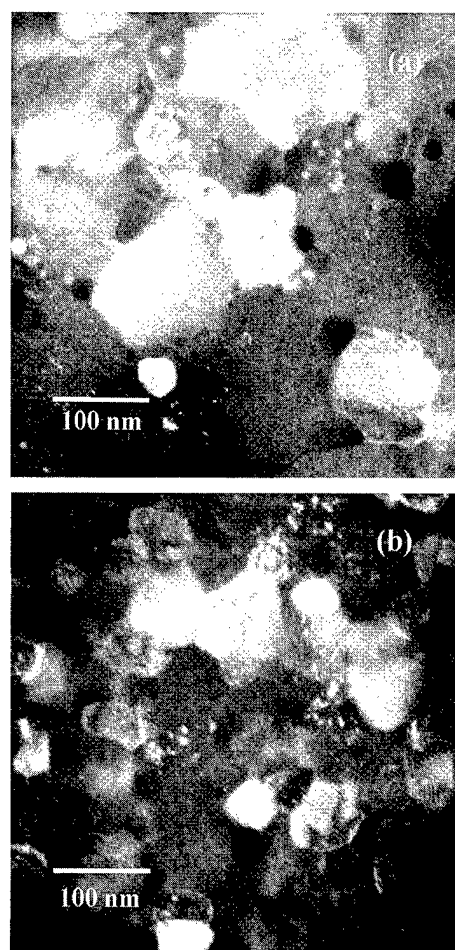


FIG. 3. TEM dark field images of samples melt-spun at 20 m/s and then annealed for 10 min: (a) HRT, (b) HR1. The 2-14-1 grain size is approximately 80 nm. The smaller bright grains at the grain boundaries are mostly T/C [as determined by electron energy-loss spectra (EELS)] while the grain boundary phases were predominately Fe and Nd.

ACKNOWLEDGMENTS

This work was supported by the DOE Division of Materials Science, Office of Basic Energy Sciences at Ames Laboratory through Iowa State University under Contract No. W-7405-Eng-82, at INEEL under DOE Idaho Operations Office Contract No. DE-AC07-94ID13223, and at BNL under Contract No. DE-AC02-76CH00016.

- ¹A. Manaf, R. A. Buckley, and H. A. Davies, *J. Magn. Magn. Mater.* **128**, 302 (1993).
- ²R. K. Mishra and V. Panchanathan, *J. Appl. Phys.* **75**, 6652 (1994).
- ³A. Manaf, M. Al-Khafaji, P. Z. Zhang, H. A. Davies, R. A. Buckley, and W. M. Rainforth, *J. Magn. Magn. Mater.* **128**, 307 (1993).
- ⁴W. C. Chang, D. M. Hsing, B. M. Ma, and C. O. Bounds, *IEEE Micro-wave Guid. Wave Lett.* **MAG-32**, 4425 (1995).
- ⁵D. J. Branagan and R. W. McCallum, *J. Alloys Compd.* **218**, 143 (1995).
- ⁶M. J. Kramer, C. P. Li, K. W. Dennis, R. W. McCallum, C. H. Sellers, D. J. Branagan, and J. E. Shields, *J. Appl. Phys.* **81**, 4459 (1997).
- ⁷M. J. Kramer, C. P. Li, K. W. Dennis, and R. W. McCallum, submitted to the 1998 TMS Symposium on Rapid Solidification.
- ⁸M. Schwarz, A. Karma, K. Eckler, and D. M. Herlach, *Phys. Rev. Lett.* **73**, 1380 (1994).
- ⁹D. J. Branagan and R. W. McCallum, *J. Alloys Compd.* **218**, 143 (1995).

Application of the shock compaction technique for consolidation of hard magnetic powders

M. Leonowicz,^{a)} W. Kaszuwara, E. Jezierska, and D. Januszewski
*Faculty of Materials Science and Engineering, Warsaw University of Technology, Narbutta 85,
02-524 Warszawa, Poland*

G. Mendoza and H. A. Davies
Department of Engineering Materials, The University of Sheffield, Sheffield S1 3JP, United Kingdom

J. Paszula
*Faculty of Armament and Aviation, Military University of Technology, Kaliskiego 2, 02-524 Warszawa,
Poland*

A shock compaction technique has been successfully applied for the consolidation of hard magnetic powders without appreciable changes in the phase structure and grain size. Pr-Fe-B and Sm-Fe-N materials, prepared with the application of melt spinning and mechanical alloying, respectively, were shock compacted with a shock wave speed of 1200 m/s and a pressure of 4.4 GPa. We found that the coercivity of high RE containing material, for which the magnetic hardness is controlled by good magnetic separation of magnetic grains by a RE-rich paramagnetic phase, decreases slightly, by $\sim 5\%$, due to the closer proximity of the crystallites in a dense material. For low RE, exchange coupled materials, the densification does not change the coercivity. © 1998 American Institute of Physics. [S0021-8979(98)21611-2]

I. INTRODUCTION

Fully dense, RE-based, permanent magnets are usually made either by liquid phase sintering¹ or by hot working of melt-spun ribbon or mechanically alloyed powder^{2,3}. Recently, a new type of nanocomposite material containing hard and soft magnetic phases (RE-Fe-B- α Fe, Sm-Fe-N- α Fe) with nanoscale grain size have been developed⁴⁻⁶. The improved magnetic properties of these materials are derived from ferromagnetic exchange coupling between the highly refined hard magnetic grains and from the presence of the α Fe, which in both alloys has a higher saturation magnetization than the respective phase. Hard magnetic phases for these materials are Nd₂Fe₁₄B and Sm₂Fe₁₇N₃, respectively. Their crystal structures are tetragonal for the former and rhombohedral for the latter with the easy magnetization directions parallel to the crystallographic *c* axes. The nanocrystalline materials are isotropic. However, hot working at high temperatures, which is usually used for consolidation and texture formation for microcrystalline materials, deteriorates the nanocrystalline microstructure and leads to decomposition of low temperature stability phases such as Sm₂Fe₁₇N₃. Thus, the commonly used method of consolidation of nanophase materials is currently based on resin or metal bonding which substantially reduces the remanence due to the presence of, typically, ~ 20 vol. of nonferromagnetic binder.

Shock compaction of powders is one of the alternative consolidation techniques which enables production of bulk solids while avoiding prolonged heating⁷. This relatively new method involves a variety of processes which utilize rapid deposition of energy in the powder by shock waves.

The application of shock compaction was already reported for the processing of bulk Sm-Fe-N magnets^{8,9}. Promising results were achieved by Mashimo *et al.*¹⁰ who produced shock compressed Sm-Fe-N anisotropic specimens having the magnetic properties: coercivity, $J_H = 450$ kA/m and remanence, $J_r = 1.14$ T.

In this study shock compaction was applied to the consolidation of both crushed melt-spun ribbon and mechanically alloyed powders. The magnetic properties and microstructures of the resulting consolidated magnets are presented and discussed.

II. EXPERIMENTAL PROCEDURE

Rapidly quenched Pr-Fe-B alloys were prepared as ribbon by melt spinning (MS) of molten alloy on a rotating copper roll at speeds of 18–20 m/s in an argon atmosphere. The meltspun ribbon was pulverized to a fine powder. (Sm_{16.5}Fe_{83.5})_{1-x}N_x and (Sm_{13.5}Fe_{86.5})_{1-x}N_x dense compacts were processed by mechanical alloying (MA) in a ball mill, in an argon atmosphere for 50 h. The mechanically alloyed powder was annealed at 700 °C for 1 h and subsequently nitrided at 460 °C for 3 h. The powders were initially cold pressed up to 80% density (specimens - 8 mm diameter by 6 mm height) and subsequently shock compacted using explosives at a pressure of 4.4 GPa within a time of 0.1–1 μ s. The shock wave speed was 1200 m/s¹¹.

The magnetic properties were measured using a vibrating sample magnetometer (VSM) and a pulsed field hysteresisgraph in magnetic fields up to 5 T. Microstructural investigations were carried out using a Jeol 3010 transmission electron micrograph (TEM) equipped with an energy dispersive spectrometer.

^{a)}Electronic mail: mkil@inmat.pw.edu.pl

TABLE I. Magnetic properties (coercivity J_H , remanence J_r and maximum energy product $(BH)_{\max}$) of green compacts and shock compressed specimens.

Composition	Green compacts (80% of full density)		Shock compressed (89%–97% of full density)			Fully dense material
	J_H (kA/m)	J_r (T)	J_H (kA/m)	J_r (T)	$(BH)_{\max}$ (kJ/m ³)	J_r (T)
Pr ₁₀ Fe ₈₄ B ₆	200	0.85	214	0.96	70	1.08
Pr ₁₂ Fe ₈₂ B ₆	599	0.81	482	0.91	97	1.02
Pr ₁₅ Fe ₇₉ B ₆	1490	0.59	1376	0.67	71	0.75
Pr ₁₈ Fe ₇₆ B ₆	1348	0.62	1138	0.70	74	0.79
(Sm _{13.5} Fe _{86.5}) _{1-x} N _x	2040	0.52	1900	0.64	58	0.66
(Sm _{16.5} Fe _{83.5}) _{1-x} N _x	1900	0.42	1860	0.51	40	0.53

III. RESULTS AND DISCUSSION

The major shock compaction parameter, wave speed, was 1200 m/s in this study and was selected on the basis of published data¹⁰. Thus, the difference in a final density observed can be explained by the lack of the wave speed optimisation for particular powder precursor. The mechanically alloyed powder had a mean particle size of $\sim 10 \mu\text{m}$ and a mean crystallite size of $\sim 50 \text{ nm}$. For crushed melt-spun ribbon the mean particle and grain sizes were $\sim 100 \mu\text{m}$ and $\sim 50 \text{ nm}$, respectively. Generally, better densification, $\sim 97\%$ of full density, was achieved for mechanically alloyed Sm–Fe–N powder. A lower value of $\sim 89\%$ of full density was obtained for the Pr–Fe–B crushed melt-spun alloy ribbon. This difference we attribute to the smaller mean particle size for the former. Higher densities were also achieved for alloys having higher RE contents.

The magnetic properties of materials before and after shock compaction are shown in Table I and Fig. 1. Hysteresis loops for low and high Pr containing magnets are shown in Fig. 2. The coercivity (J_H) of shock compressed specimens did not differ significantly from their powder precursors. The remanence (J_r), normalized to a fully dense material, does not change for specimens before and after compressing which indicates that the processing does not significantly affect the phase constitution of the material. This suggestion was further confirmed by x-ray analysis which showed the same phase structures before and after

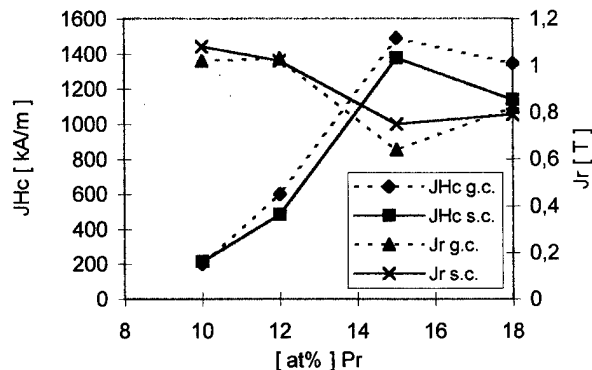


FIG. 1. Magnetic properties of green compacts (g.c.) and shock compressed (s.c.) Pr_xFe_{94-x}B₆ specimens.

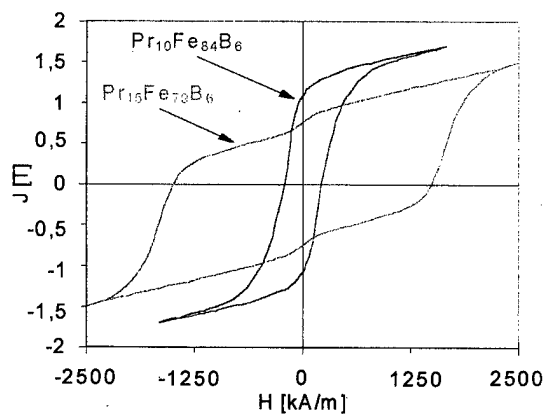


FIG. 2. Hysteresis loops for low and high Pr containing magnets.

compressing (Fig. 3). This is especially important for Sm–Fe–N alloys because the Sm₂Fe₁₇N₃ phase decomposes at $\sim 600^\circ\text{C}$ and the material thus cannot be processed at elevated temperatures. However, the actual remanence depends on the density; it is low for green compacts (about 80% of full density) and increases for shock compressed specimens. This increase was greater for the MA than for the MS specimens, which in the present study showed insufficient density. This was reflected in rather low values of remanence and energy product for the melt-spun specimens.

The effect of shock compaction on the microstructure was studied in detail for (Sm_{13.5}Fe_{86.5})_{1-x}N_x mechanically alloyed powder using TEM (Fig. 4). Following annealing and nitriding the powder had a mean particle size of $\sim 50 \mu\text{m}$ consisting of mainly crystallites of diameter 30–60 nm; however, some isolated large grains of diameter 300–500 nm were also visible. After shock compaction the grains had a greater size distribution with diameters 10–100 nm and a mean diameter of 60 nm. However, the very large grains had disappeared so that the microstructure appeared more homogeneous, evidently due to the fragmentation of the large grains during the rapid compaction. Dark field images showed for larger crystallites, $>50 \text{ nm}$ diameter, the existence of 5 nm sized substructure arising either from local misorientation (microtwins) or chemical inhomogeneities. The major phase was Sm₂Fe₁₇N₃; however, small propor-

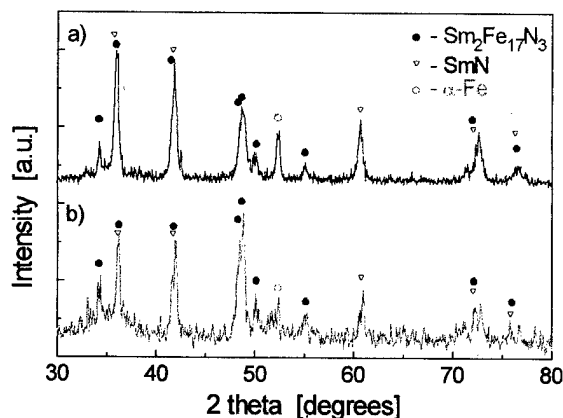


FIG. 3. X-ray patterns for MA (Sm_{13.5}Fe_{86.5})_{1-x}N_x material before (a) and after (b) shock compressing.

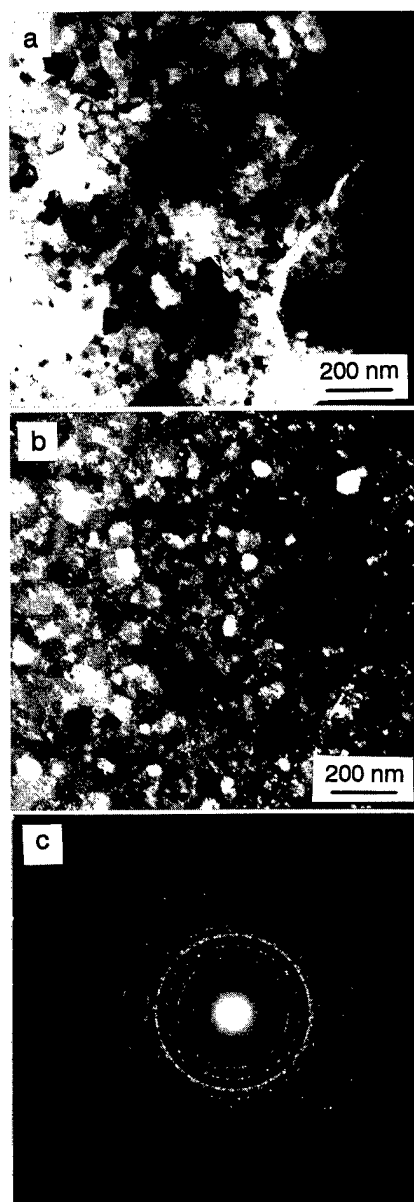


FIG. 4. TEM micrographs of $(\text{Sm}_{13.5}\text{Fe}_{86.5})_{1-x}\text{N}_x$ shock compressed magnet: (a) and (b) bright and dark field images, respectively, (c) electron diffraction.

tions of SmN and αFe were also visible. The energy dispersive spectra (EDS) for this alloy indicated that the average chemical composition was $\text{Sm}_{14.8}\text{Fe}_{80.5}\text{N}_{4.7}$. The higher nitrogen content in the material (4.7 at%) consistent with the

$\text{Sm}_2\text{Fe}_{17}\text{N}_3$ compound reflects the measurement of average N content for both the $\text{Sm}_2\text{Fe}_{17}\text{N}_3$ and the small inclusions of SmN phase. Dark field images revealed also the existence of thinner areas which could have arisen from dense inhomogeneities in the shock compacted samples.

We investigated the possibility of influencing the microstructure of magnets by the addition of Zn powder. For this experiment we used two $(\text{Sm}_{13.5}\text{Fe}_{86.5})_{1-x}\text{N}_x$ samples having different coercivities; low J_H (360 kA/m) — large grain milled ingot (particle and crystallite sizes both 3 μm) and high J_H (1900 kA/m) — nanocrystalline MA material (particle and crystallite sizes 50 μm and 30–60 nm, respectively). The addition of Zn to the powders before shock compaction resulted in a substantial increase of the coercivity for the former (up to 520 kA/m) and almost unchanged J_H for the latter (1930 kA/m). We relate the increase of J_H to better magnetic isolation of hard magnetic grains by a nonferromagnetic Zn-rich phase; however the coercivity of MA powder is apparently close to a maximum level for this composition and cannot be further improved.

ACKNOWLEDGMENTS

Financial support from NATO under the Collaborative Science Program “Priority Area on High Technology” (Grant No. CRG/961146) and from the Polish Committee for Scientific Research (Grant No. 7T08A01113) are gratefully acknowledged. The authors wish to thank S. Jezierski for TEM sample preparation.

- ¹M. Sagawa, S. Fujimura, M. Togawa, and Y. Matsuura, J. Appl. Phys. **55**, 2083 (1984).
- ²J. J. Croat, J. F. Herbst, R. W. Lee, and F. E. Pinkerton, J. Appl. Phys. **50**, 2078 (1994).
- ³R. W. Lee, Appl. Phys. Lett. **46**, 790 (1985).
- ⁴H. A. Davies, A. Manaf, M. Leonowicz, Z. P. Zhang, S. J. Dobson, and R. A. Buckley, J. Nanostr. Mater. **2**, 197 (1993).
- ⁵J. Ding, G. P. McCormick, and R. Street, J. Magn. Magn. Mater. **124**, L1 (1993).
- ⁶H. A. Davies, J. F. Liu, and G. Mendoza, Proceedings of the IXth International Symposium on Magnetic Anisotropy and Coercivity in RE-TM Alloys, Sao Paulo, Brazil, 1996, edited by F. P. Missell *et al.* (unpublished), p. 251.
- ⁷R. Prümmer, Mat. Wiss. Werkstofftech. **20**, 410 (1989).
- ⁸T. Mashimo, S. Tashiro, S. Hirose, and T. Ikegami, Trans. Mater. Res. Soc. Jpn. **14B**, 1079 (1994).
- ⁹H. Oda, K. Kondo, H. Uchida, Y. Matsumura, S. Tachibana, and T. Kawanabe, Jpn. J. Appl. Phys., Part 2 **34**, L35 (1995).
- ¹⁰T. Mashimo, X. S. Huang, S. Hirose, K. Makita, H. Kato, S. Mitsudo, and M. Motokawa, Proceedings of the International Conference EXPLOMET 95, El Paso, TX, 6–10 August 1995 (unpublished).
- ¹¹W. Kaszuwara, M. Leonowicz, D. Januszewski, G. Mendoza, J. Paszula, and H. A. Davies, J. Mater. Sci. (in press).

Reversible processes and magnetic viscosity of nanocrystalline permanent magnets

D. R. Cornejo,^{a)} V. Villas-Boas, and F. P. Missell

Instituto de Física, Universidade de São Paulo, C. P. 66318, 05315-970 São Paulo S.P., Brazil

The accurate determination of the magnetic viscosity parameter S_v requires the calculation of a new parameter $\eta = (\partial M_{\text{rev}} / \partial M_{\text{irr}})_{H_i}$ which describes the dependence of reversible magnetization on irreversible magnetization. Measurements of the magnetic viscosity were performed at 300 K on the major demagnetization curves of two different nanocrystalline permanent magnetic materials: (i) melt-spun and flash-annealed $\text{Pr}_4\text{Fe}_{78}\text{B}_{18}$ and (ii) mechanically alloyed and heat-treated $\text{Sm}_{18}\text{Fe}_{33}\text{Co}_{49}$. We show that η is proportional to the intrinsic reversible susceptibility χ_{rev}^i , in good agreement with predictions of the moving Preisach model. Measurements of the reversible susceptibility were made in order to determine η . Experimental values of η are positive on the major demagnetization curve in both materials, resulting in substantial corrections to S_v near H_c .

© 1998 American Institute of Physics. [S0021-8979(98)44311-1]

I. INTRODUCTION

The problem of separating the magnetization M into reversible (M_{rev}) and irreversible (M_{irr}) components arises naturally in studies of the time dependence of M . In many materials, the time dependence of M in a constant field H can be described by the relation

$$M(t) = M_0 + S \ln(1 + t/t_0), \quad (1)$$

where M_0 and t_0 are constants and $S = S(D)$ is the magnetic viscosity, with D the demagnetization factor of the sample. Since S is sample shape dependent, another quantity S_v , the magnetic viscosity parameter, is more often used to characterize the time dependence of M . S_v is obtained in terms of S and the irreversible susceptibility χ_{irr} (also shape dependent) from the relation¹

$$S_v = S / \chi_{\text{irr}}. \quad (2)$$

However, χ_{irr} is a time-dependent quantity and care must be exercised in its determination. There are two common methods for obtaining χ_{irr} . In the DCD method, χ_{irr} is taken to be the derivative of the dc demagnetization curve that is obtained by measuring the remanence after applying progressively larger reverse fields after positive saturation. Alternatively, χ_{irr} can be determined as the difference of χ_{tot} and χ_{rev}^i , where χ_{tot} is the total susceptibility measured on the major hysteresis loop and the intrinsic reversible susceptibility χ_{rev}^i is measured by defining it as the mean slope of a small minor loop performed after determining the time dependence of M .

Schumann² has shown, however, that the two methods for determining χ_{irr} can result in substantially different values for this quantity. Crew *et al.*³ studied the resulting differences in S_v in terms of the Stoner–Wohlfarth model. They explained the differences in S_v in terms of a dependence of

M_{rev} on the configuration of domains in the material. This was expressed phenomenologically by Cammarano *et al.*⁴ using the equation

$$dM_{\text{rev}} = \chi_{\text{rev}}^i dH_i + \eta dM_{\text{irr}}, \quad (3)$$

where $H_i = H_{\text{ap}} - DM$ is the internal magnetic field. The quantities χ_{rev}^i and η are given by

$$\chi_{\text{rev}}^i = (\partial M_{\text{rev}} / \partial H_i)_{M_{\text{irr}}}$$

and

$$\eta = (\partial M_{\text{rev}} / \partial M_{\text{irr}})_{H_i}. \quad (4)$$

The parameter η measures the change in M_{rev} when the domain configuration, represented by M_{irr} , is changed. The relation between the reversible, irreversible, and total susceptibilities is then altered when $\eta \neq 0$:

$$dM_{\text{irr}} / dH_i = \chi_{\text{irr}} = (\chi_{\text{tot}} - \chi_{\text{rev}}^i) / (1 + \eta). \quad (5)$$

Using this relation, the relation between S and S_v becomes

$$\eta S_v = S(1 + D\chi_{\text{tot}} + \eta D\chi_{\text{irr}}) / (1 + \eta)\chi_{\text{irr}}. \quad (6)$$

This formalism has been used to discuss magnetic viscosity measurements in NdFeB ⁵ and in exchange-coupled $\text{Sm}_2\text{Fe}_{14}\text{Ga}_3\text{C}_2/\alpha\text{-Fe}$.⁶

In this article we consider two exchange-coupled materials with very different values of the reversible susceptibility: (i) melt-spun and flash-annealed $\text{Pr}_4\text{Fe}_{78}\text{B}_{18}$ and (ii) mechanically alloyed and heat-treated $\text{Sm}_{18}\text{Fe}_{33}\text{Co}_{49}$. For $\text{Pr}_4\text{Fe}_{78}\text{B}_{18}$, χ_{rev}^i is about 30% of χ_{tot} , while for $\text{Sm}_{18}\text{Fe}_{33}\text{Co}_{49}$, χ_{rev}^i is less than 5% of χ_{tot} . We derive a relation between η and χ_{rev}^i which is in agreement with predictions of the moving Preisach model.⁷ This relation allows us to determine η and ηS_v for both materials.

II. EXPERIMENT

Partially amorphous ribbons of $\text{Pr}_4\text{Fe}_{78}\text{B}_{18}$ were produced by melt spinning in He on a mild steel wheel. They were annealed for 20 s at $T = 640^\circ\text{C}$ by passing current

^{a)}Electronic mail: cornejo@macbeth.if.usp.br

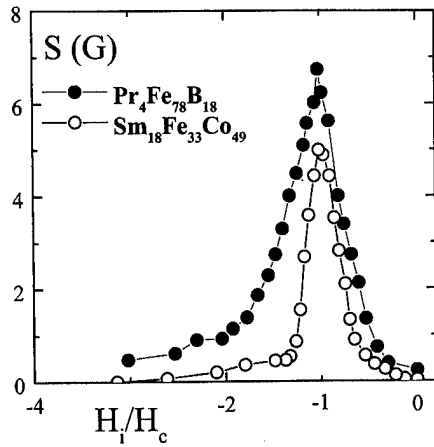


FIG. 1. Magnetic viscosity S as a function of the internal magnetic field H_i for $\text{Pr}_4\text{Fe}_{78}\text{B}_{18}$ and $\text{Sm}_{18}\text{Fe}_{33}\text{Co}_{49}$.

through the sample, a process known as flash annealing.⁸ Previously, a Mössbauer analysis⁹ of flash-annealed $\text{Nd}_4\text{Fe}_{78}\text{B}_{18}$ showed 80% of the absorption to be due to magnetically soft Fe_3B . The flash-annealed ribbons of $\text{Pr}_4\text{Fe}_{78}\text{B}_{18}$ had $H_c = 4.0$ kOe and $M_r/M_s = 0.77$, thus showing enhanced-remanence behavior. Mechanical alloying of elementary Sm, Fe, and Co powders was carried out for 30 h with hardened steel balls in a hardened steel vial using a Fritsch Pulverisette-5 mill. As-milled powders composed of $\text{Sm}_{18}\text{Fe}_{33}\text{Co}_{49}$ were cold pressed into 3 mm diam cylinders and heated in vacuum for 15 min at 700 °C. The x-ray diffraction pattern indicated that a mixture of the hard magnetic phases $\text{Sm}(\text{Fe}, \text{Co})_5$ and $\text{Sm}(\text{Fe}, \text{Co})_7$ had been formed. This alloy also presents remanence enhancement ($M_r/M_s = 0.6$) and $H_c = 9.6$ kOe.

All magnetization measurements were carried out at room temperature using a vibrating sample magnetometer (VSM) mounted in a 90 kOe superconducting solenoid. Magnetization measurements for times between 20 and 300 s were fitted to Eq. (1) to determine the magnetic viscosity S . From the fits to Eq. (1) we typically obtained values of $t_0 \approx 1.5$ s. After the viscosity measurement, the magnetic field was varied by 200 Oe to measure χ_{rev}^i .

III. RESULTS AND DISCUSSION

The magnetic viscosity (S) results in both $\text{Pr}_4\text{Fe}_{78}\text{B}_{18}$ and $\text{Sm}_{18}\text{Fe}_{33}\text{Co}_{49}$ are presented in Fig. 1. In both materials we see that S presents a well-defined peak, centered at the coercive field H_c , the field at which χ_{irr} has its maximum value. Both sets of S values determined here are about the same order of magnitude as those encountered in two-phase $\text{Nd}_2\text{Fe}_{14}\text{B}/\alpha\text{-Fe}$ (Ref. 10) and exchange-coupled $\text{Sm}_2\text{Fe}_{14}\text{Ga}_3\text{C}_2/\alpha\text{-Fe}$.⁶ The authors of Ref. 10 observed a systematic decrease in S as the fraction of soft magnetic phase present was increased. Here the larger viscosity is associated with $\text{Pr}_4\text{Fe}_{78}\text{B}_{18}$, the material with more soft magnetic phase. A proper comparison, however, should involve materials containing the same phases. A systematic study of the behavior of S with the fraction of soft phase in SmFeCo will be presented elsewhere.

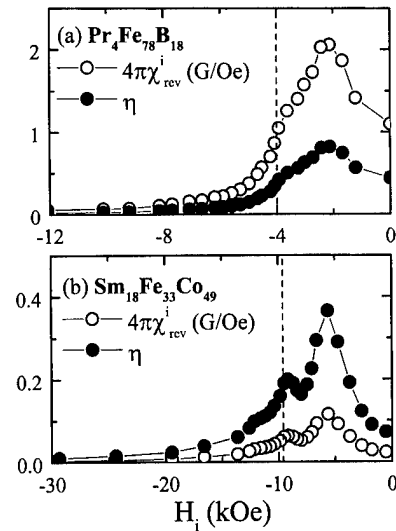


FIG. 2. The reversible susceptibility $4\pi\chi_{\text{rev}}^i$ and parameter η as a function of the internal field along the major hysteresis loop for (a) $\text{Pr}_4\text{Fe}_{78}\text{B}_{18}$ and (b) $\text{Sm}_{18}\text{Fe}_{33}\text{Co}_{49}$.

In order to determine S_v from S using Eq. (6), χ_{irr} was determined using Eq. (5) from the difference $\chi_{\text{tot}} - \chi_{\text{rev}}^i$, where χ_{tot} was derived from the major hysteresis loop and χ_{rev}^i was measured by defining it as the mean slope of a small minor loop performed after determining the time dependence of M . Measurements of $4\pi\chi_{\text{rev}}^i$ for the two samples are shown in Fig. 2. We note that the maximum value of χ_{rev}^i is about 30% of χ_{tot} for $\text{Pr}_4\text{Fe}_{78}\text{B}_{18}$. On the other hand, in $\text{Sm}_{18}\text{Fe}_{33}\text{Co}_{49}$, χ_{rev} is small, about 5% of χ_{tot} . For $\text{Sm}_{18}\text{Fe}_{33}\text{Co}_{49}$, we clearly observe a secondary peak in $4\pi\chi_{\text{rev}}^i$ at H_c . This occurs because χ_{rev}^i is a function of both H_i and M_{irr} , as will be discussed below. The larger peak is associated with the inversion of the soft phase, while the smaller peak reflects the inversion of the hard magnetic phase.

In order to determine η from the measured susceptibility, one must integrate the identity $(\partial\eta/\partial H_i)_{M_{\text{irr}}} = (\partial\chi_{\text{rev}}^i/\partial M_{\text{irr}})_{H_i}$. In Ref. 6, the authors apparently used $\delta M_{\text{irr}} = \chi_{\text{irr}} \Delta H_i$ to evaluate the right-hand side of that identity. But the right-hand side must be calculated with constant H_i . Using Eq. (4), the variation δM_{irr} for the H_i constant can be written as $\delta M_{\text{irr}} = \delta M_{\text{rev}}/\eta$, while the variation δH_i for the M_{irr} constant is given by $\delta H_i = \delta M_{\text{rev}}/\chi_{\text{rev}}^i$. The above identity then becomes

$$\chi_{\text{rev}}^i (\partial\eta/\partial M_{\text{rev}})_{M_{\text{irr}}} = \eta (\partial\chi_{\text{rev}}^i/\partial M_{\text{rev}})_{H_i}. \quad (7)$$

One can show that $(\delta M_{\text{rev}})_{M_{\text{irr}}} = (\delta M_{\text{rev}})_{H_i}$ in the limit that $\delta H_i \rightarrow 0$. Then, for $\delta H_i \rightarrow 0$, we have the relation $d\eta/\eta = d\chi_{\text{rev}}^i/\chi_{\text{rev}}^i$, which can be integrated to give

$$\eta = (\eta_0/\chi_{\text{rev}0}^i) \chi_{\text{rev}}^i. \quad (8)$$

Recently we applied the moving Preisach model to the problem of separating the magnetization into its reversible and irreversible components. We obtained⁷ a simple relation between η and the reversible susceptibility χ_{rev}^i : $\eta = k\chi_{\text{rev}}^i$, where k is the moving parameter of the moving Preisach model. In that model, the effective magnetic field acting on

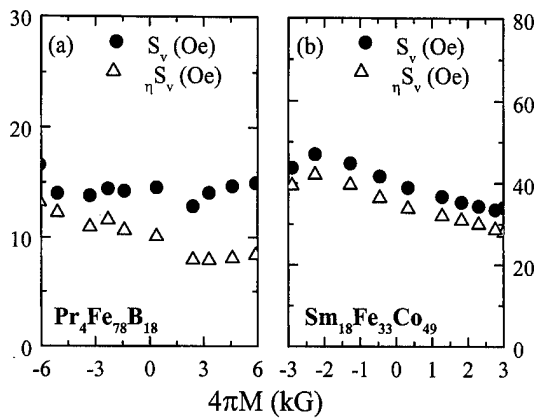


FIG. 3. The magnetic viscosity parameters S_v and ηS_v as a function of sample magnetization for (a) $\text{Pr}_4\text{Fe}_{78}\text{B}_{18}$ and (b) $\text{Sm}_{18}\text{Fe}_{33}\text{Co}_{49}$.

the system is $H = H_i + kM$, where H_i is the internal field and kM is a mean field term associated with the total magnetization M . This result suggests that the simple relation between η and χ_{rev}^i of Eq. (8) is, in fact, indicative of a collective behavior of the system.

There then remains the problem of choosing the initial values of η and χ_{rev}^i for use in Eq. (8). We take $\eta_0 = \eta(H_i = 0) = M_{R_{\text{rev}}} / (M_R - M_{R_{\text{rev}}})$, where $M_{R_{\text{rev}}}$ is the reversible magnetization at remanence ($H_i = 0$) and M_R is the total magnetization at remanence ($H_i = 0$). Our choice of η_0 would reduce to zero with $M_{R_{\text{rev}}} = 0$ at remanence. However, Cammarano *et al.*⁴ and Crew *et al.*³ have noted that M_{rev} is not a reversible function of the internal field as is generally assumed, but instead exhibits a small hysteresis. We have observed the same behavior in our materials. Thus $M_{R_{\text{rev}}}$ was determined by integrating χ_{rev}^i between $H_i = 0$ and the value of H_i corresponding to $M_{\text{rev}} = 0$. For $\text{Pr}_4\text{Fe}_{78}\text{B}_{18}$, we obtained $\eta_0 = 0.43 \pm 0.07$. Using $4\pi\chi_{\text{rev}_0}^i = (1.1 \pm 0.1) \text{ G/Oe}$, we obtained $k = (5 \pm 2) \text{ Oe/G}$. For $\text{Sm}_{18}\text{Fe}_{33}\text{Co}_{49}$, $\eta_0 = 0.07 \pm 0.01$. Using $4\pi\chi_{\text{rev}_0}^i = (0.020 \pm 0.005) \text{ G/Oe}$, we obtained $k = (40 \pm 30) \text{ Oe/G}$. We have not yet completed a moving Preisach model analysis of the materials studied in this article and, therefore, have not yet determined values of k for these materials. However, our Preisach analysis¹¹ of $\text{Sm}_{18}\text{Fe}_{11}\text{Co}_{71}$ yielded a moving parameter $k = 39 (4\pi M_s / H_c) \text{ Oe/G} \approx 18 \text{ Oe/G}$ for that material, which is in reasonable agreement with the value found here for $\text{Sm}_{18}\text{Fe}_{33}\text{Co}_{49}$. The calculated curves of η for the two materials are shown in Fig. 2.

The magnetic viscosity parameters S_v and ηS_v are shown as a function of the magnetization in Fig. 3 for $\text{Pr}_4\text{Fe}_{78}\text{B}_{18}$ and $\text{Sm}_{18}\text{Fe}_{33}\text{Co}_{49}$. For $\text{Pr}_4\text{Fe}_{78}\text{B}_{18}$, the correction to S_v due to η approaches 40% for positive values of M , while for $\text{Sm}_{18}\text{Fe}_{33}\text{Co}_{49}$ the correction is less than 20%. We note that smaller values of S_v and ηS_v are observed in $\text{Pr}_4\text{Fe}_{78}\text{B}_{18}$ which contains a large fraction of the soft mag-

netic phase Fe_3B . Insofar as S_v or ηS_v is related to the coercive field, then we would expect larger values for these quantities in $\text{Sm}_{18}\text{Fe}_{33}\text{Co}_{49}$ where H_c is larger.

Finally, we would like to comment on the origin of the hysteresis observed in M_{rev} . Using the relation $\eta = k\chi_{\text{rev}}^i$ in Eq. (3), we obtain

$$dM_{\text{rev}}(1 + k\chi_{\text{rev}}^i) = \chi_{\text{rev}}^i(dH_i + k dM). \quad (9)$$

We define the total internal field as $H_{it} = H_i + kM$ and the total reversible susceptibility as $\chi_{\text{rev}}^i = dM_{\text{rev}}/dH_{it} = \chi_{\text{rev}}^i / (1 + k\chi_{\text{rev}}^i)$. (This total internal field H_{it} is analogous to the effective field acting in the moving Preisach model.¹²) We note that χ_{rev}^i is a function of both H_i and M_{irr} and, therefore, is not reversible with regard to variations in H_i . On the other hand, χ_{rev}^i is a single-valued function of H_{it} and is completely reversible with regard to that field.⁷

IV. CONCLUSIONS

We have determined the magnetic viscosity parameter ηS_v for the nanocrystalline exchange-coupled alloys $\text{Pr}_4\text{Fe}_{78}\text{B}_{18}$ and $\text{Sm}_{18}\text{Fe}_{33}\text{Co}_{49}$, two materials for which the reversible contributions to the susceptibility are quite different. The dependence of the reversible magnetization on the magnetic domain structure (irreversible magnetization), as expressed through the parameter η , was determined and was used to correct S_v . In both cases the parameter η was determined from χ_{rev}^i using the relation $\eta = (\eta_0 / \chi_{\text{rev}_0}^i) \chi_{\text{rev}}^i$, which is similar in form to a relation derived previously⁷ within the context of the moving Preisach model: $\eta = k\chi_{\text{rev}}^i$. The systematic relationship, observed previously,¹⁰ between S and the amount of soft magnetic phase present could not be investigated here but will be considered in the SmFeCo system.

ACKNOWLEDGMENTS

The authors thank FAPESP, CNPq, CAPES, and FINEP who provided financial support.

- ¹D. Givord, P. Tenaud, and T. Viadieu, *IEEE Trans. Magn.* **24**, 1921 (1988).
- ²R. Schumann, *J. Magn. Magn. Mater.* **150**, 349 (1995).
- ³D. C. Crew, S. H. Farrant, P. G. McCormick, and R. Street, *J. Magn. Magn. Mater.* **163**, 299 (1996).
- ⁴R. Cammarano, P. G. McCormick, and R. Street, *J. Appl. Phys.* **75**, 5481 (1994).
- ⁵D. C. Crew, P. G. McCormick, and R. Street, *IEEE Trans. Magn.* **32**, 4356 (1996).
- ⁶E. H. Feutrell, P. G. McCormick, and R. Street, *J. Phys. D* **29**, 2320 (1996).
- ⁷D. R. Cornejo and F. P. Missell (unpublished).
- ⁸V. Villas-Boas, S. A. Romero, and F. P. Missell, *J. Appl. Phys.* **81**, 4434 (1997).
- ⁹M. V. P. Altoé, M. S. Lancarotte, H. R. Rechenberg, F. P. Missell, and J. M. González, *IEEE Trans. Magn.* **31**, 3614 (1995).
- ¹⁰E. H. Feutrell, P. G. McCormick, and R. Street, *Magnetic Anisotropy and Coercivity in Rare-Earth Transition Metal Alloys* (World Scientific, Singapore, 1996), pp. 457–463.
- ¹¹D. R. Cornejo, M. Lo Bue, V. Basso, G. Bertotti, and F. P. Missell, *J. Appl. Phys.* **81**, 5588 (1997).
- ¹²V. Basso and G. Bertotti, *IEEE Trans. Magn.* **30**, 64 (1994).

Magnetic properties of $RFe_{10.5}Mo_{1.5}C_x$ and their nitrides

Weihoa Mao,^{a)} Jinbo Yang, Benpei Cheng, and Yingchang Yang

Department of Physics, Peking University, Beijing 100871, People's Republic of China

$RFe_{10.5}Mo_{1.5}C_x$ ($R=Y, Nd, \text{ and } Dy; x=0-0.6$) have been successfully synthesized by arc melting, then followed by a gas-solid phase reaction to form $YFe_{10.5}Mo_{1.5}C_xN_y$. X-ray diffraction studies and thermomagnetic analysis show that all samples are of good single phase, and carbides and carbon nitrides remain the $ThMn_{12}$ -type structure. The addition of carbon atoms has an effect of improving the magnetic properties. Both Curie temperature and saturation magnetization are found to be increased with carbon concentration x in the $RFe_{10.5}Mo_{1.5}C_x$ series, and the carbon atoms also affect the magnetocrystalline anisotropy. The easy axial anisotropy of $NdFe_{10.5}Mo_{1.5}C_x$ and $DyFe_{10.5}Mo_{1.5}C_x$ is enhanced. As to the nitrides, the results indicate that $YFe_{10.5}Mo_{1.5}C_xN_y$ possess a higher Curie temperature and a larger saturation magnetization than $YFe_{10.5}Mo_{1.5}N_y$, which is of significance in the technical applications. © 1998 American Institute of Physics. [S0021-8979(98)21711-7]

I. INTRODUCTION

It has been found that the magnetic properties of the $ThMn_{12}$ -type compounds can be drastically improved by introducing of nitrogen or carbon atoms into the structure.¹⁻⁴ Owing to their excellent intrinsic magnetic properties, the nitrides and carbides of the $ThMn_{12}$ -type compounds have been regarded as promising candidates for permanent magnet applications. Unfortunately the nitrides or carbides prepared by gas-solid phase reaction are metastable compounds and they will disproportionate at temperature higher than 700 °C in general. Thus the conventional high-temperature powder metallurgy is not applicable to these materials.

Besides gas-solid phase reaction, there are many preparation techniques for carbides: (a) melting of constituents in arc or induction furnace,⁵⁻⁸ (b) synthesis from heavy hydrogencarbon compounds,⁹ and (c) solid-solid phase reaction.^{10,11} Above all, the advantage of carbides prepared by melting method is stability in high temperature. However, the single phase carbides with $ThMn_{12}$ -type structure are difficult to be synthesized by melting method, especially when the carbon content is larger than 0.3.

Yang *et al.* studied the effects of carbon on the structural and magnetic properties of $RTiFe_{10.75}C_{0.25}$.⁵ It was found that introducing the carbon atoms by arc melting have no effect on the Curie temperature, but the saturation magnetization is increased and the unit cell volume is decreased slightly with carbon content. They also reported that introducing the carbon atoms by arc melting increases the planar anisotropy for rare-earth ions with the negative second-order Stevens constant α_J such as Nd^{3+} and Dy^{3+} , and strengthens the axial anisotropy for those with positive α_J such as Sm^{3+} . The effect of arc-melting additions of carbon atoms is different from that of the interstitial nitrogen or carbon atoms introduced by the gas-solid phase reaction. Zhang *et al.*⁷ and Hu *et al.*⁸ published their results of neutron diffraction experiment carried out on $YFe_{11}TiC_{0.3}$ and $ErFe_{11}TiC_{0.25}$ prepared by arc melting. They found that all of the carbon atoms

introduced by arc-melting method occupy $8i$ sites, not the interstitial $2b$ sites. Hu *et al.* also studied the structure of $YFe_{10.5}Mo_{1.5}C_{0.3}$ prepared by arc melting, and he found it is different from $R(Fe,Ti)_{12}C_x$ compounds though all of the carbon atoms introduced by arc melting. He reported that only about 40% carbon atoms occupy $8i$ sites and the others occupy $2b$ sites in $YFe_{10.5}Mo_{1.5}C_{0.3}$. Since the location of arc melting introduced carbon atoms in the compounds $Y(Fe,Mo)_{12}C_x$ is different from that of $R(Fe,Ti)_{12}C_x$, the effect of carbon on the magnetic properties of $R(Fe,Mo)_{12}C_x$ would be different from that of $R(Fe,Ti)_{12}C_x$. But no systematic studies on magnetic properties of the $R(Fe,Mo)_{12}C_x$ prepared by arc-melting method are reported in literature. Since a part of carbon atoms occupy the $2b$ interstitial sites in the $RFe_{12-x}Mo_xC_y$ compounds, the interstitial modification might be significant if carbon content is large enough. It is imperative to study the magnetic properties of arc-melting $RFe_{12-x}Mo_xC_y$ with a high carbon content.

In this article, the magnetic properties of $RFe_{10.5}Mo_{1.5}C_x$ ($R=Y, Nd, \text{ and } Dy; x=0-0.6$) are reported. The combination effects of carbon and nitrogen in the $YFe_{10.5}Mo_{1.5}C_xN_y$ compounds are also investigated.

II. EXPERIMENTAL METHOD

$YFe_{10.5}Mo_{1.5}C_x$ ($x=0, 0.2, 0.4, 0.6$), $NdFe_{10.5}Mo_{1.5}C_x$ ($x=0, 0.2, 0.4$), and $DyFe_{10.5}Mo_{1.5}C_x$ ($x=0, 0.2, 0.4, 0.6$) were prepared by arc melting of 99.5% pure materials in a purified argon atmosphere. The carbon was introduced as Fe-C alloy. Carbon nitrides were prepared by passing purified nitrogen gas at atmospheric pressure over finely ground carbides powder samples (about 10–30 μm) at 400–600 °C for 2–6 h, then rapidly cooling to room temperature. The nitrogen content (y) of $YFe_{10.5}Mo_{1.5}C_xN_y$ was determined by weight increment upon nitrogenation. X-ray diffraction was used to determine the structure. The powder sample of cylindrical shape was aligned in a 20 kOe field in epoxy resin. Magnetic measurements are performed with a field of up to 20 kOe in a temperature range from 80 to 1000 K by using a vibrating sample magnetometer (VSM).

^{a)}Electronic mail: wmao@ibm320h.phy.pku.edu.cn

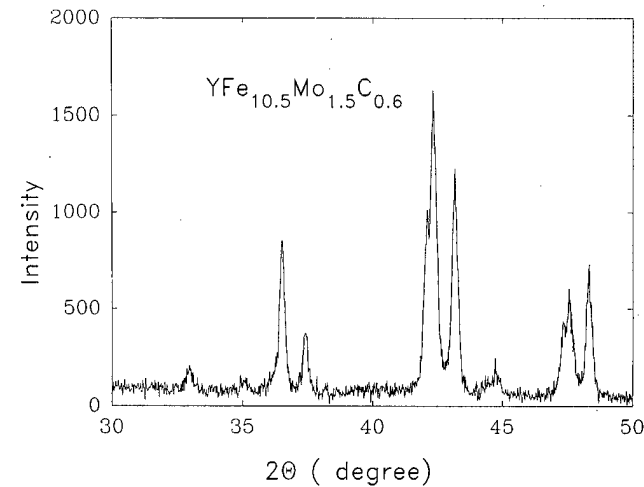


FIG. 1. The x-ray diffraction pattern of YFe_{10.5}Mo_{1.5}C_{0.6}.

III. RESULTS AND DISCUSSION

A. Crystallographic structure

According to the x-ray diffraction studies and thermo-magnetic analysis, all samples are found to remain the ThMn₁₂-type tetragonal structure, and, no α -Fe phase is observed. Figure 1 illustrates the x-ray diffraction patterns of YFe_{10.5}Mo_{1.5}C_{0.6}. The lattice parameters are listed in Table I. The cell volume increases with the carbon content, which is different from the case of R(Fe,Ti)₁₂C_x.⁵ These results suggest that a significant part of carbon atoms are introduced into the interstitial sites.

B. Curie temperature and saturation magnetization

The Curie temperature (T_c) and saturation magnetization (σ_s) of RFe_{10.5}Mo_{1.5}C_x (R=Y, Nd, and Dy) are indicated in Table I. The carbon atoms have an effect of increasing both Curie temperature and saturation magnetization. Since yttrium is nonmagnetic, the moment of yttrium compounds represents that of the Fe sublattice. The carbon increases the average magnetization of Fe atoms in the lattice.

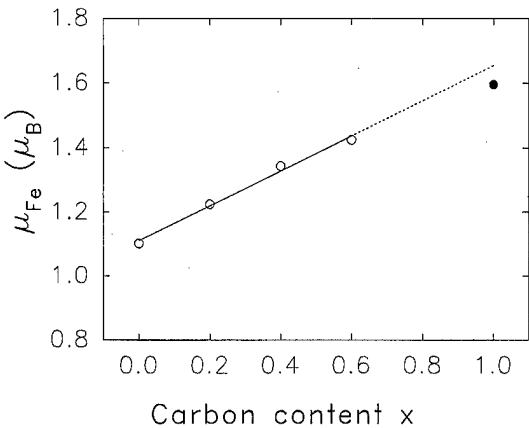


FIG. 2. Average Fe moments of YFe_{10.5}Mo_{1.5}C_x vs carbon content (the solid dot is the average Fe moment of YFe_{10.5}Mo_{1.5}N).

The variation of average Fe magnetic moments as a function the carbon content (x) is illustrated in Fig. 2. The results could be extrapolated to $x=1$, and at that point, average Fe moment is about $1.65\mu_B$ at room temperature. The average Fe moment in the YFe_{10.5}Mo_{1.5}N is $1.60\mu_B$ (the solid dot in Fig. 2). It indicates that the arc melting introduced carbon atoms have a similar effect on the average Fe magnetic moments to that of nitrogen atoms.

C. Magnetocrystalline anisotropy

The anisotropy field H_A is calculated by using Sucksmith–Thompson method.¹² The results are listed in Table I.

The carbon effect on the magnetocrystalline anisotropy of the Fe sublattice can be deduced from the yttrium compounds YFe_{10.5}Mo_{1.5}C_x. There is a slight decrease trend with the carbon content, which is similar to the interstitial nitrogen effect.

The arc melting introduced carbon atoms also have a drastic effect on the magnetocrystalline anisotropy of the rare-earth sublattice. The H_A of RFe_{10.5}Mo_{1.5}C_x (R=Nd and

TABLE I. The lattice parameters a and c , unit-cell volume V , Curie temperature T_c , saturation magnetization σ , magnetic anisotropy field H_A , and nitrogen content y of RFe_{10.5}Mo_{1.5}C_x (R=Y, Nd, and Dy) and YFe_{10.5}Mo_{1.5}C_xN_y.

	a (Å)	c (Å)	V (Å ³)	T_c (K)	σ_s (emu/g)	H_A (kOe)	y
YFe _{10.5} Mo _{1.5}	8.540	4.791	349.4	433	78.66	9.33	...
YFe _{10.5} Mo _{1.5} C _{0.2}	8.546	4.792	350.0	460	87.41	9.69	...
YFe _{10.5} Mo _{1.5} C _{0.4}	8.560	4.794	351.3	480	95.95	8.05	...
YFe _{10.5} Mo _{1.5} C _{0.6}	8.584	4.800	353.7	488	101.74	6.81	...
NdFe _{10.5} Mo _{1.5}	8.609	4.799	355.7	427	102.6	4.46	...
NdFe _{10.5} Mo _{1.5} C _{0.02}	8.613	4.798	355.9	444	108.6	6.03	...
NdFe _{10.5} Mo _{1.5} C _{0.4}	8.613	4.803	356.3	452	110.4	8.64	...
DyFe _{10.5} Mo _{1.5}	8.543	4.793	349.8	457	52.60	17.3	...
DyFe _{10.5} Mo _{1.5} C _{0.2}	8.551	4.790	350.2	479	57.63	21.7	...
DyFe _{10.5} Mo _{1.5} C _{0.54}	8.556	4.790	350.7	488	63.78	32.5	...
DyFe _{10.5} Mo _{1.5} C _{0.6}	8.560	4.794	351.3	490	66.96	35.5	...
YFe _{10.5} Mo _{1.5} N _y	8.666	4.810	361.2	614	113.9	7.36	1.03
YFe _{10.5} Mo _{1.5} C _{0.1} N _y	8.659	4.805	360.3	616	117.4	7.43	0.90
YFe _{10.5} Mo _{1.5} C _{0.2} N _y	8.670	4.807	361.3	629	117.0	7.00	0.77

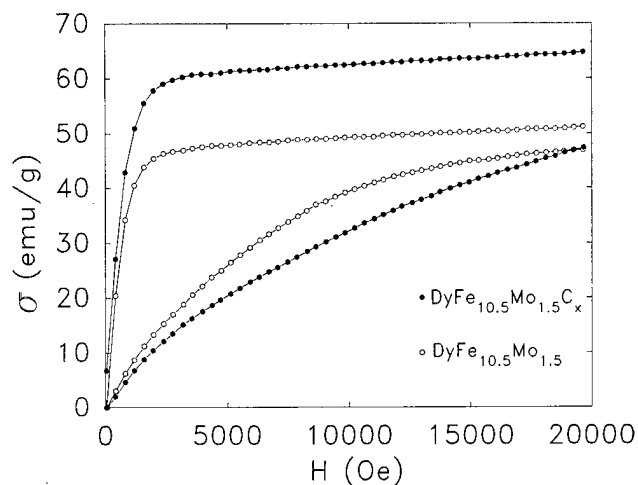


FIG. 3. Magnetization curves of $\text{DyFe}_{10.5}\text{Mo}_{1.5}\text{C}_x$ ($x=0$ and 0.6) at 300 K , parallel and perpendicular to the orientation direction.

Dy) increases with the carbon content (see Table I). The easy axial anisotropy of $\text{DyFe}_{10.5}\text{Mo}_{1.5}\text{C}_x$ is significantly enhanced, as shown in Fig. 3, in which the magnetization curves of $\text{DyFe}_{10.5}\text{Mo}_{1.5}\text{C}_x$ ($x=0$ and 0.6) are illustrated. In the case of $\text{R}=\text{Nd}$, the similar results are observed. A spin reorientation occurs in $\text{NdFe}_{10.5}\text{Mo}_{1.5}\text{C}_x$, when $x=0$ and 0.2 . The spin reorientation results from the competition between the easy-plane anisotropy of the Nd^{3+} sublattice and the easy-axial anisotropy of Fe sublattice. The spin reorientation temperature (SRT) of $\text{NdFe}_{10.5}\text{Mo}_{1.5}$ is 170 K , while it decreases to 135 K with $\text{NdFe}_{10.5}\text{Mo}_{1.5}\text{C}_{0.2}$. In the case of $\text{NdFe}_{10.5}\text{Mo}_{1.5}\text{C}_{0.4}$, no spin reorientation is detected above 80 K . It could be concluded that the addition of carbon leads to a change in the anisotropy of the Nd^{3+} ions, which have a tendency to transform their easy magnetization direction from easy plane to easy axis.

As to the magnetocrystalline anisotropy, the effect of the arc melting introduced carbon atoms of the $\text{RFe}_{10.5}\text{Mo}_{1.5}\text{C}_x$ is similar to that of interstitial nitrogen and carbon atoms which are introduced by gas-solid phase reaction. These results indicate that there is a significant part of carbon atoms introduced into the interstitial $2b$ site. When the carbon atoms occupy $2b$ site, they could change the second-order crystal-field coefficient A_{20} from negative to positive. As a result, the easy magnetization direction of rare-earth ions with the negative second-order Stevens constant α_J such as Nd^{3+} and Dy^{3+} may change from easy plane to easy axis.

D. Combination effect of carbon and nitrogen

After nitrogenation, the x-ray diffraction studies and thermomagnetic analysis indicate that all nitrides of $\text{YFe}_{10.5}\text{Mo}_{1.5}\text{C}_x$ remain ThMn_{12} -type structure and no α -Fe phase is observed. The lattice parameters and unit cell volume are listed in Table I.

The Curie temperature and saturation magnetization of carbon nitrides increase rapidly. This is due to the effect of

interstitial modification. It should be noted that the Curie temperature and saturation magnetization of carbon nitrides are larger than those of carbon free nitride ($x=0$). The saturation magnetization of carbon nitrides is larger than simple nitride by 3–4%. It proves a method to enhance the saturation magnetization of nitrides, which is of significance in the technical applications.

The nitrogen content (y) in the $\text{YFe}_{10.5}\text{Mo}_{1.5}\text{C}_x\text{N}_y$ is listed in Table I. The average error of y is 0.05 . It is very interesting that the nitrogen contents decrease with the increasing of carbon content and their sums ($x+y$) approximate 1. In order to characterize carbon location in the $\text{R}(\text{Fe}, \text{Mo})_{12}$ compounds and its effect on the local magnetic moments, the neutron diffraction experiments with the relative carbides are in progress.

IV. CONCLUSION

In conclusion, the carbon atom introduced by arc melting not only have an effect of increasing both Curie temperature and saturation magnetization of $\text{R}(\text{Fe}, \text{Mo})_{12}$ compounds, but also give rise to an change in the magnetocrystalline anisotropy. Their effects are similar to those of the nitrogen or carbon atoms introduced by gas-solid phase reaction, but the arc-melting carbides are much more stable in the high temperature than those prepared by gas-solid phase reaction.

ACKNOWLEDGMENTS

This work was supported by National Target Basic Research Project of China and National Science Foundation of China. The x-ray diffraction experiment was carried out in the Materials Physics Lab, State Key Lab. of Artificial Microstructure and Mesoscale Physics, Department of Physics, Peking University.

¹Y.-C. Yang, X.-D. Zhang, S.-L. Ge, L.-S. Kong, and Q. Pan, in *Proceedings of the Sixth International Symposium on Magnetic Anisotropy and Coercivity in Rare Earth Transition Metal Alloys*, edited by S. G. Sankar (Carnegie Mellon University, Pittsburgh, 1990), p. 190.

²D. P. F. Hurley and J. M. D. Coey, *J. Phys.: Condens. Matter* **4**, 5573 (1992).

³Q. Qi, Y. P. Li and J. M. D. Coey, *J. Phys.: Condens. Matter* **4**, 8209 (1992).

⁴Z. X. Tang, E. W. Singleton, and G. C. Hadjipanayis, *IEEE Trans. Magn.* **28**, 2572 (1992).

⁵Y. C. Yang, X. D. Zhang, S. Z. Dong, and Q. Pan, *J. Appl. Phys.* **74**, 6847 (1993).

⁶X. F. Xu, Y. X. Sun, Z. X. Liu, and C. Lin, *Solid State Commun.* **89**, 409 (1994).

⁷B. Zhang, J. Yang, Y. Ding, C. Ye, H. Du, Y. Yang, X. Zhang, S. Dong, and Q. Pan, *Physica B* **213&214**, 297 (1995).

⁸Z. Hu, W. B. Yelon, X. Zhang, and W. J. James, *J. Appl. Phys.* **79**, 5522 (1996).

⁹D. Fruchart, O. Isnard, S. Miraglia, L. Pontonnier, J. L. Soubeyroux, and R. Fruchart, *J. Alloys Compd.* **203**, 157 (1994).

¹⁰R. V. Skolozdra, E. Tomey, D. Gignous, D. Fruchart, and J. L. Soubeyroux, *J. Magn. Mater.* **139**, 65 (1995).

¹¹H. Izumi, Y. Seyama, K. Machida, and G. Adachi, *J. Alloys Compd.* **233**, 231 (1996).

¹²W. Sucksmith and J. E. Thompson, *Proc. R. Soc. London, Ser. A* **225**, 362 (1954).

Microstructure and magnetic properties of FeCoN thin films

P. C. Kuo, S. S. Chang, and C. M. Kuo

Institute of Materials Science and Engineering, National Taiwan University, Taipei, Taiwan

Y. D. Yao

Institute of Physics, Academia Sinica, Taipei 115, Taiwan

H. L. Huang

Department of Physics, National Taiwan University, Taipei, Taiwan

Effects of nitrogen contents and substrate temperatures to the microstructure and magnetic properties of the FeCoN films have been investigated. According to the TEM and x-ray Scherrer's equation analyses, we found that the grain size of films with substrate temperature below 200 °C is roughly about 13 nm, however, it increases very fast for films with substrate temperature above 300 °C. N content in the films is saturated to 30 at. %, as N_2 flow ratio $N_2/(Ar+N_2)$ is higher than 5 vol. %. From the magnetization studies, we have found that the saturation magnetization $4\pi M_s$ of the optimum samples (with the substrate temperature near 200 °C) is 23.9 kG. The improvement of the magnetic properties is attributed to the combination of α -Fe with N to form the high magnetic moment FeN phases. © 1998 American Institute of Physics. [S0021-8979(98)35011-2]

I. INTRODUCTION

A soft magnetic film with high saturation magnetization $4\pi M_s$ is required for use in a high-density magnetic recording head. Recently, extensive efforts have been made to improve the soft magnetic properties of Fe-based films.¹⁻⁷ According to the Pauling-Slater curve, Fe-Co alloys have the highest magnetization of iron alloy. Takahashi *et al.*⁸ prepared FeCo nitride film onto a polyimide substrate by ion-assisted normally vapor deposition method. They found that the film was columnar structure with large grains of about 500 Å and maximum $4\pi M_s$ occurred at the Co content of about 32 at. %. Their films have large perpendicular magnetic anisotropy and N content of the film is unknown. On the other hand, Liao⁹ reported that electrodeposited Fe₉₀Co₁₀ films show a high $4\pi M_s$ value of 19 kG and good soft magnetic properties. Recently, Nakagawa *et al.*¹⁰ examined the FeCoN and FeCoTaN films which prepared by facing targets sputtering with N_2 +Kr mixture gas. They found that $4\pi M_s$ of the film was decreased with increasing N_2 partial pressure. Pure Fe₉₀Co₁₀ alloy film has an extremely large $4\pi M_s$ of about 24 kG. In this report, we investigate the effect of substrate temperature and N content on the magnetic properties and microstructures of sputtered FeCoN films.

II. EXPERIMENT

(Fe_{0.9}Co_{0.1})_{100-x}N_x films with $x=0-30$ were prepared on a precleaned glass substrate by reactive RF magnetron sputtering in N_2 and Ar mixed atmosphere. The flow ratio of nitrogen to argon and nitrogen, i.e., $N_2/(Ar+N_2)$, during sputtering was varied between 0 and 10 vol. %. The substrate temperature was varied between 25 and 400 °C. Composite

target consisting of pure Fe disk overlaid with Co pieces was used in this experiment. The base pressure in the system with a turbo pump was 1×10^{-6} Torr, and after the high purity Ar- N_2 mixed gas was introduced, sputtering pressure was 1×10^{-3} Torr. Thickness of the films was about 200 nm.

Structure and grain size of the films were determined by using x-ray diffractometer (XRD). Thickness of the films was measured by a Sloan DEKTAK-3-0305ST α -step profilometer. Magnetic properties of the films were measured with vibrating sample magnetometer (VSM) at room temperature with maximum applied field of 12 kOe. Composition, N content, and homogeneity of the films were determined by depth profiling analysis of Auger electron spectroscopy (AES).

III. RESULTS AND DISCUSSION

Figure 1 shows the N contents in pure Fe, Co, and Fe₉₀Co₁₀ films as a function of N_2 flow ratio during sputtering, i.e., $(N_2/Ar+N_2) \times 100\%$, with the substrate temperature T_s kept at 25 °C. It can be seen that N content in the films increases dramatically with increasing N_2 flow ratio when N_2 flow ratio is lower than 5 vol. %. This is because N atoms can easily occupy interstitial sites of crystal lattice during deposition as N_2 flow ratio is lower than 5 vol. %. N content in the film is saturated as N_2 flow ratio is higher than 5 vol. % for all films. This is due to that all interstitial sites of crystal lattices in the film are occupied. Saturated N content of Fe film is about 32 at. % which is equal to the N content of ζ -Fe₂N phase.¹¹ ζ -Fe₂N phase is nonmagnetic and has maximum equilibrium N content in Fe-N binary system.¹² The maximum N contents of Fe₉₀Co₁₀ and Co films are 30 and 23 at. %, respectively. Figure 2 presents a

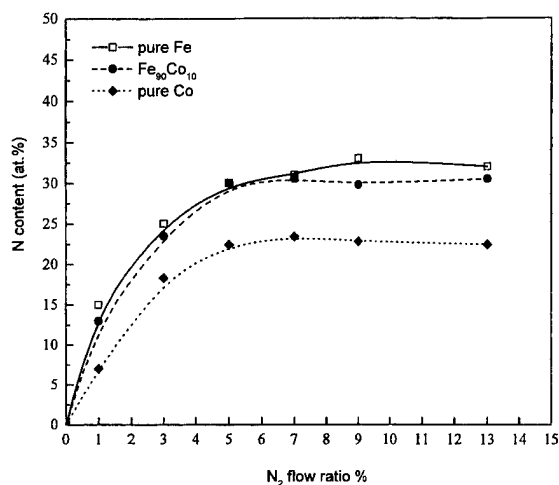


FIG. 1. Variation of N content with N₂ flow ratio of Fe, Fe₉₀Co₁₀ and Co films. The substrate temperature is kept at 25 °C.

typical depth profile of a FeCoN film analyzed by Auger electron spectroscopy (AES). We can see that the composition of this film is approximately (Fe_{0.9}Co_{0.1})₇₀N₃₀. It is calibrated by a standard of bulk Fe₅₀Co₅₀ alloy. Because the films were exposed to air prior to AES analysis, near the surface of the films, O and C were always observed as shown in Fig. 2.

Typical microstructure of the (Fe_{0.9}Co_{0.1})_{100-x}N_x films is shown in Fig. 3. Figure 3(a) is a TEM photograph of the (Fe_{0.9}Co_{0.1})₇₇N₂₃ film with substrate temperature of 25 °C. We can see that the film has a nanocrystalline structure and its average grain size is about 13 nm. In Fig. 3(b), from the diffraction lines of the electron diffraction pattern of this film, we noticed that ϵ -Fe₂₋₃N, Co₂N, γ' -Fe₄N, and ζ -Fe₂N phases are included.

Figure 4 shows the saturation magnetization $4\pi M_s$ and coercivity H_c as a function of N content in (Fe_{0.9}Co_{0.1})_{100-x}N_x films with its substrate temperature at 25 °C. It is clear that $4\pi M_s$, and both in-plane coercivity $H_{c\parallel}$ and perpendicular coercivity $H_{c\perp}$ of the films increase slowly from 22 to 22.8 kG, 12 to 18 Oe, and 22 to 30 Oe, respectively, for N less than roughly 13 at. %. However,

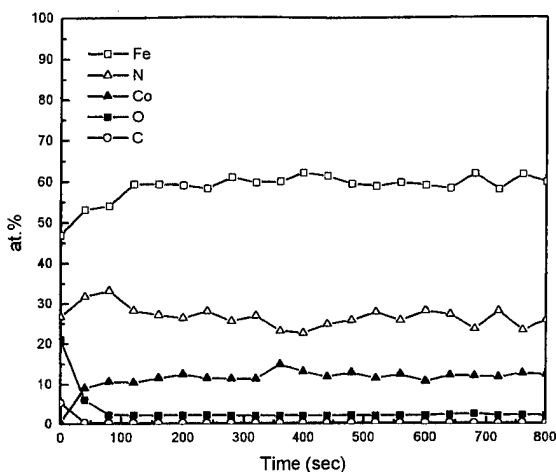


FIG. 2. Auger depth profile of a (Fe_{0.9}Co_{0.1})₇₀N₃₀ film.

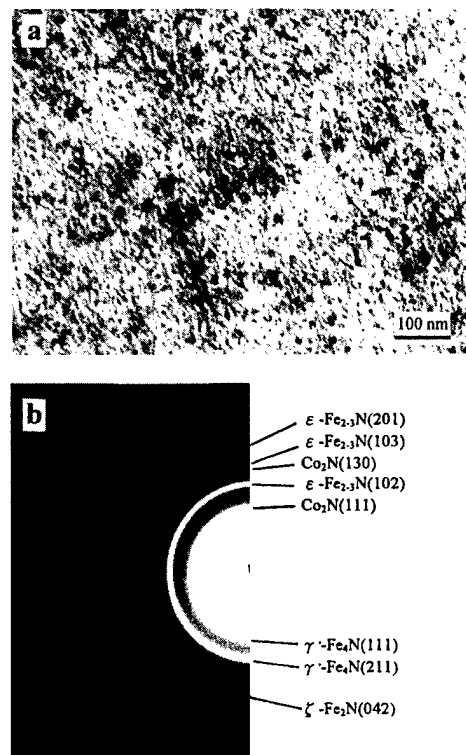


FIG. 3. TEM micrograph and electron diffraction pattern of (Fe_{0.9}Co_{0.1})₇₇N₂₃ film with $T_s = 25$ °C. (a) is the microstructure of planar section and (b) is the corresponding electron diffraction pattern.

$4\pi M_s$ decreases and both H_c 's increase rapidly as N content is larger than 13 at. %. When N content is approached to 30 at. %, both H_c increase to about 150 Oe and $4\pi M_s$ decreases to about 2 kG due to the formation of ζ -Fe₂N phase in the film. The perpendicular coercivity $H_{c\perp}$ is slightly higher than that of the in-plane coercivity $H_{c\parallel}$. This indicates that the film is almost magnetic isotropy as substrate temperature is kept at 25 °C.

Figure 5 shows the relation between $4\pi M_s$, $H_{c\parallel}$, $H_{c\perp}$ and substrate temperature T_s of the (Fe_{0.9}Co_{0.1})_{100-x}N_x films prepared with the flow ratio of N₂ at 1 vol. % during sputtering. According to the AES analysis, the N content of the

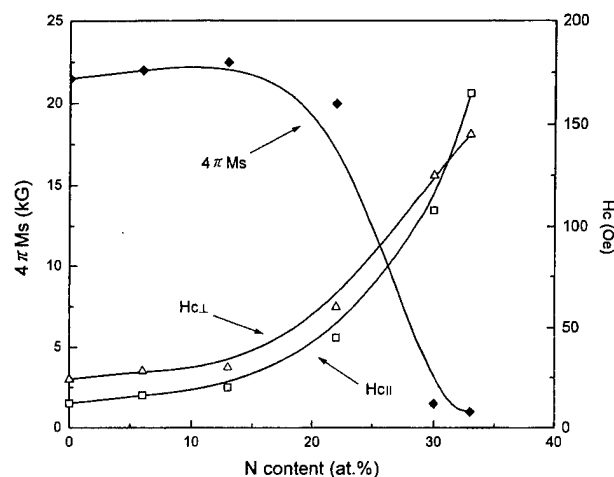


FIG. 4. Effect of N content on the $4\pi M_s$, $H_{c\parallel}$, and $H_{c\perp}$ of (Fe_{0.9}Co_{0.1})_{100-x}N_x films. The substrate temperature is kept at 25 °C.

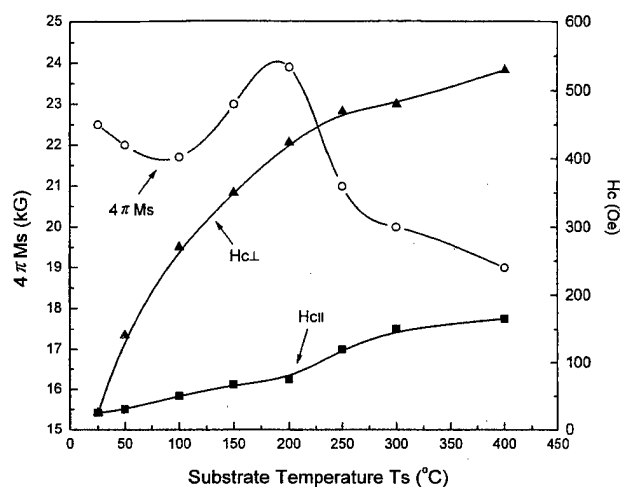


FIG. 5. The change of $4\pi M_s$, H_{cL} , and H_{cH} against T_s for $(\text{Fe}_{0.9}\text{Co}_{0.1})_{100-x}\text{N}_x$ films. N_2 flow ratio is 1 vol. % during sputtering.

film was found to decrease from 13 at. % for $T_s = 25^\circ\text{C}$ to 10 at. % for $T_s = 100^\circ\text{C}$, 8 at. % for $T_s = 200^\circ\text{C}$, and 3 at. % for $T_s = 400^\circ\text{C}$. It can be seen that H_{cL} increases monotonously from 25 to 165 Oe when T_s increasing from 25 to 400°C , but H_{cH} of the film is increased rapidly from 25 to 530 Oe. It is obvious that magnetic easy axis is in the film plane, as T_s is higher than 25°C . The increasing of coercivities with T_s is owing to that N content of the film is decreased with increasing T_s . From the x-ray diffraction patterns study of the films at various T_s , we found that the amount of high coercivity FeCo phase is increased with T_s . For example, Fig. 6 shows curves (a) to (c) with their substrate temperatures at 25, 100, and 200°C , respectively. When T_s is higher than 300°C , only the FeCo peak can be detected by x-ray diffractometer. According to the x-ray Scherrer's equation analysis from the diffraction peak of FeCo(100), we found that the grain size of the films with substrate temperature below 200°C is roughly about 13 nm, however, it increases very fast for films with substrate temperature above 300°C .

The $4\pi M_s$ in Fig. 5 shows a minimum value of 21.7 kG around 100°C , and a maximum value of 24 kG at $T_s \approx 200^\circ\text{C}$. Comparing with the x-ray diffraction peaks of Figs. 6(a), 6(b), and 6(c), we can see that these films all contain high moment FeCo and $\alpha' - \text{Fe}_{6-10}\text{N}$ phases.¹³ From this point of view, variation of the $4\pi M_s$ of film with T_s is due to the change of N content in the film, i.e., amounts of various FeN, FeCo, CoN, α -Fe phases in the film are changed.

IV. CONCLUSIONS

In conclusion, effects of nitrogen contents and substrate temperatures to the microstructure and magnetic properties of the $(\text{Fe}_{0.9}\text{Co}_{0.1})_{100-x}\text{N}_x$ films with $x=0-30$ films have been investigated. TEM observation found that they have nanocrystalline structure. When N content of the film is

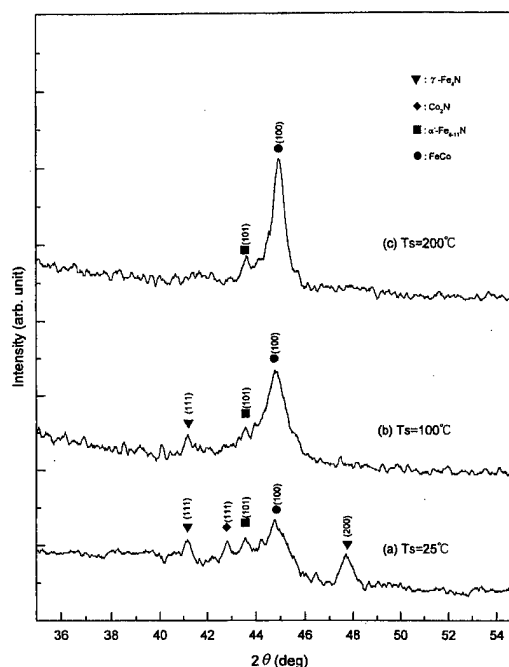


FIG. 6. X-ray diffraction patterns of various $(\text{Fe}_{0.9}\text{Co}_{0.1})_{100-x}\text{N}_x$ films. N_2 flow ratio is 1 vol. % during sputtering and substrate temperatures are (a) $T_s = 25^\circ\text{C}$, (b) $T_s = 100^\circ\text{C}$, and (c) $T_s = 200^\circ\text{C}$.

lower than 13 at. %, it contains high moment $\alpha' - \text{Fe}_{6-10}\text{N}$, FeCo, and $\gamma' - \text{Fe}_4\text{N}$ phases. The $(\text{Fe}_{0.9}\text{Co}_{0.1})_{92}\text{N}_8$ film which prepared at substrate temperature of about 200°C and N_2 flow ratio of 1 vol. % has maximum $4\pi M_s$ of 23.9 kG. As N content of the film is higher than 20 at. %, $4\pi M_s$ of the film decreases rapidly due to the formation of nonmagnetic $\zeta - \text{Fe}_2\text{N}$ phase in the film.

ACKNOWLEDGMENTS

This work was supported by the National Science Council of ROC through Grant Nos. NSC 86-2216-E-002-029 and NSC 86-2112-M001-020.

- ¹ K. Nago, H. Sakahima, K. Ihara, and K. Osano, IEEE Trans. Magn. **28**, 2943 (1992).
- ² B. Viala, M. K. Minor, and J. A. Bamard, IEEE Trans. Magn. **32**, 3506 (1996).
- ³ B.-II Cho, W. Win, Eui-Jung Yun, and R. M. Walser, IEEE Trans. Magn. **31**, 3859 (1995).
- ⁴ P. Pain, J. P. Eymery, M. F. Denanot, and J. F. Dinhut, J. Magn. Mater. **133**, 493 (1994).
- ⁵ D. J. Rogers, S. Wang, D. E. Laughlin, and M. H. Kryder, IEEE Trans. Magn. **28**, 2418 (1992).
- ⁶ J. Ching, L.-J. Chen, and C.-J. Chen, IEEE Trans. Magn. **30**, 3912 (1994).
- ⁷ M. Takahashi, H. Shoji, H. Takahashi, H. Nashi, and T. Wakiyama, J. Appl. Phys. **76**, 6642 (1994).
- ⁸ S. Takahashi, M. Kume, and K. Matsuura, IEEE Trans. Magn. **36**, 1632 (1992).
- ⁹ S. H. Liao, IEEE Trans. Magn. **MAG-23**, 2981 (1987).
- ¹⁰ S. Nakagawa, S. Tanaka, K. Sumitsu, and M. Naoe, J. Appl. Phys. **79**, 5156 (1996).
- ¹¹ G. Hagg, Nature (London) **122**, 962 (1928).
- ¹² O. Kubaschewski, *Iron-Binary Phase Diagrams* (Springer, Berlin, 1982), p. 67.
- ¹³ K. H. Jack, Proc. R. Soc. London, Ser. A **208**, 200 (1951).

Structure and magnetic properties of a Fe–Zr–N thin film

Jong-Sung Baek and Seong-Cho Yu

Department of Physics, Chungbuk National University, Cheongju 361–763, Korea

Woo-Young Lim

Department of Physics, Korea University, Chochiwon 339–700, Korea

Chul-Sung Kim

Department of Physics, Kookmin University, Seoul 136–702, Korea

Taek-Soo Kim and Chong-Oh Kim

Department of Material Engineering, Chungnam National University, Taejeon 302–764, Korea

Fe–Zr–N thin films were deposited in an argon and nitrogen mixed atmosphere using a rf magnetron reactive sputtering apparatus at room temperature. The x-ray diffraction pattern of the $\text{Fe}_{76}\text{Zr}_{8}\text{N}_{16}$ thin film obtained at room temperature indicates that the as-sputtered film consists of amorphous and crystalline phases. The mixed structure of the sample was also confirmed by the temperature dependence of the saturation magnetic flux density. The as-sputtered film exhibited soft magnetic properties with a saturation magnetic flux density of 1.1 T and effective permeability of 1400 or more at 1 MHz. The film also showed good thermal stability, sustaining the effective permeability of 3000 at temperatures up to 550 °C. The film annealed in a magnetic field of 500 Oe at 450 °C showed a permeability of 2200 or more up to 40 MHz. The conventional Mössbauer spectrum of the kapton substrate sample obtained at room temperature could be fitted by a mixture of three kinds of six-line hyperfine splittings. © 1998 American Institute of Physics. [S0021-8979(98)16711-7]

I. INTRODUCTION

Recently various investigations have been performed on the development of soft magnetic materials with high saturation magnetic flux densities that would be useful for high density magnetic recording systems.^{1–3} High saturation magnetic flux densities and excellent soft magnetic properties at high frequencies are essential for magnetic recording head materials. To reduce the magnetocrystalline anisotropy of Fe, most of these investigations on Fe-based alloy films are concentrated on research to reduce the grain size of magnetically coupled α -Fe. It is reported that the addition of a B, N, or C element to Fe-based alloy reduces the grain size, but high temperature treatments often prevent the fine grain size to be maintained.^{4–6}

Fe–M–N (M=Zr, Hf, Ta, Nb) ternary systems⁷ also exhibit excellent soft magnetic properties even after heat treatments above 550 °C. The Fe–Zr–N ternary alloy, especially, has merits for practical use, such as low material cost and a wide range of composition in which desirable soft magnetic properties can be achieved.

In this work, Fe–Zr–N thin films were made using a rf magnetron sputtering technique, and the dependence of the magnetic properties of the samples, such as the saturation magnetic flux density and the effective permeability, on the annealing temperature were examined. In order to investigate the thermal stability of the film, the temperature dependence of the saturation magnetic flux density of the sample was studied. Also, the magnetic hyperfine field of Fe particles in the sample was examined by conventional Mössbauer spectroscopy.

II. EXPERIMENT

Fe–Zr–N thin films were deposited on various substrates (Corning glass No. 7059, a Si wafer, and kapton) in an argon and nitrogen mixed atmosphere using a rf magnetron reactive sputtering apparatus at room temperature. In order to avoid oxidation of the films during annealing, the silicon dioxide film was coated with a thickness of 1000 Å. The as-sputtered film was annealed at 200–700 °C for 30 min in a nitrogen atmosphere. The background pressure was lower than 7.0×10^{-7} Torr. A mixture of argon and nitrogen with a purity 99.999% was used as the sputtering gas. The deposition gas pressure was fixed at 6 mTorr, and the partial pres-

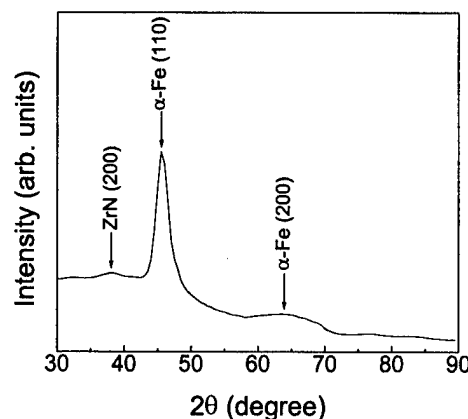
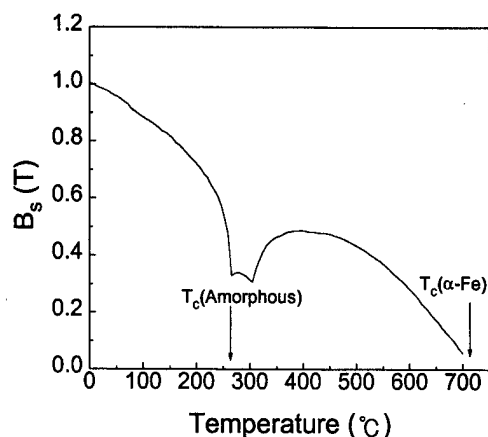


FIG. 1. The x-ray diffraction pattern of the as-sputtered $\text{Fe}_{76}\text{Zr}_{8}\text{N}_{16}$ thin film.

FIG. 2. Thermomagnetic diagram of the $\text{Fe}_{76}\text{Zr}_8\text{N}_{16}$ thin films.

sure of the nitrogen was 5%. The thickness and the composition of the films were about 900 Å and $\text{Fe}_{76}\text{Zr}_8\text{N}_{16}$, respectively.

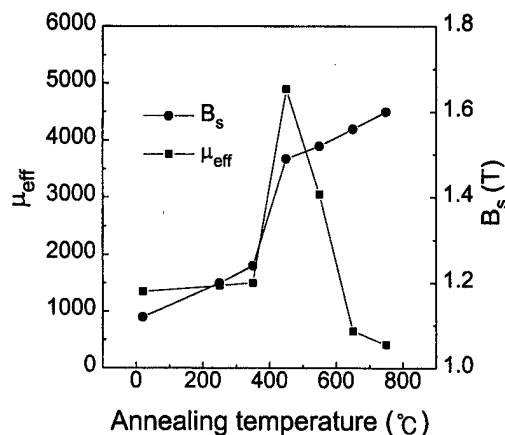
The composition of the sample was examined by electron probe microanalysis (EPMA), Auger electron spectroscopy (AES), and Rutherford backscattering spectroscopy (RBS). The crystallographic characteristics and the microstructure of the films were analyzed by x-ray diffractometry (XRD) and scanning electron microscope (SEM), respectively. The saturation magnetic flux density, the coercive force, and the thermomagnetic properties were measured with a vibrating sample magnetometer. Conventional Mössbauer spectroscopy for ^{57}Fe for as-sputtered film was carried out using an electron detector of gas (He 90%– CH_4 10%) flow type at room temperature.

III. RESULTS AND DISCUSSIONS

The x-ray diffraction pattern of the as-sputtered $\text{Fe}_{76}\text{Zr}_8\text{N}_{16}$ thin film obtained at room temperature is shown in Fig. 1. The full width at half maximum of the peak appeared at $2\theta=45.5^\circ$ is about 2.5° .

Figure 2 represents the saturation magnetic flux densities B_s as a function of temperature for the $\text{Fe}_{76}\text{Zr}_8\text{N}_{16}$ thin films. The saturation magnetic flux density decreases slowly with increasing temperature up to 240 °C, and it decreases significantly in and around 280 °C, which is considered to be Curie temperature of the amorphous phase. And then, the saturation magnetic flux density increases abruptly at 310 °C. This phenomenon is possibly due to the crystallization of the amorphous film. Finally, it behaves like a typical ferromagnetic material in the range above 450 °C, and the value approaches zero at 710 °C, which is the Curie temperature for $\alpha\text{-Fe}$.

Figure 3 shows the saturation magnetic flux densities B_s and the effective permeabilities μ_{eff} as a function of annealing temperature for the $\text{Fe}_{76}\text{Zr}_8\text{N}_{16}$ thin film. The saturation magnetic flux density of the film increases slightly with increasing annealing temperature up to 350 °C, and then increases abruptly at 350 °C. This effect is associated with the increased phase transition from the amorphous to the crystal state with annealing temperature. We suppose therefore that the x-ray diffraction pattern shown in Fig. 1 indicates a com-

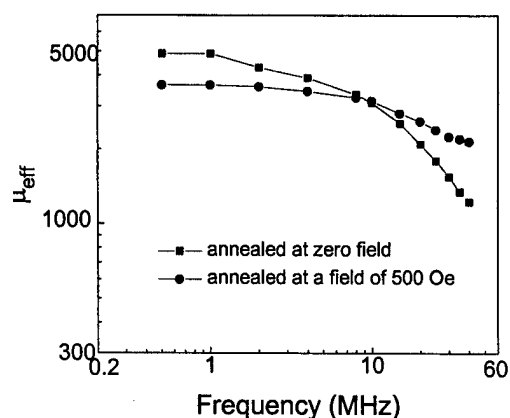
FIG. 3. Dependence of saturation magnetic flux density (B_s) and effective permeability (μ_{eff}) (at 1 MHz) on the annealing temperature of the $\text{Fe}_{76}\text{Zr}_8\text{N}_{16}$ thin films.

bination of these states. The phase transition appears to decrease with annealing temperature in the range above 450 °C. The effective permeability increases slightly with increasing annealing temperature up to 350 °C with a maximum value of 4800, but decreases rapidly with increasing annealing temperature in the range above 450 °C, while maintaining the effective permeability of 3000 at temperatures up to 550 °C. This result indicates that the $\text{Fe}_{76}\text{Zr}_8\text{N}_{16}$ thin film has good thermal stability up to 550 °C.

The coercive force of the as-sputtered film was 0.4 Oe, and it decreases slowly with increasing annealing temperature in the range up to 550 °C. It has the minimum value of 0.2 Oe at 550 °C and increases abruptly above 600 °C.

SEM micrographs show that the as-sputtered film has an amorphouslike structure, and that the sample annealed at 450 °C is slightly crystallized. With further annealing above 650 °C, a columnar structure was formed, possibly resulting in the observed abrupt increase in coercive force of the annealed sample.

Figure 4 represents the effective permeabilities of the $\text{Fe}_{76}\text{Zr}_8\text{N}_{16}$ thin films as a function of frequency. The sample annealed (in no field) at 450 °C has a permeability of 4800 at 1 MHz and 4000 at 5 MHz, but it decreases rapidly with increasing frequency in the range above 5 MHz. However,

FIG. 4. Frequency characteristics of effective permeability (μ_{eff}) for the $\text{Fe}_{76}\text{Zr}_8\text{N}_{16}$ thin films annealed at 450 °C.

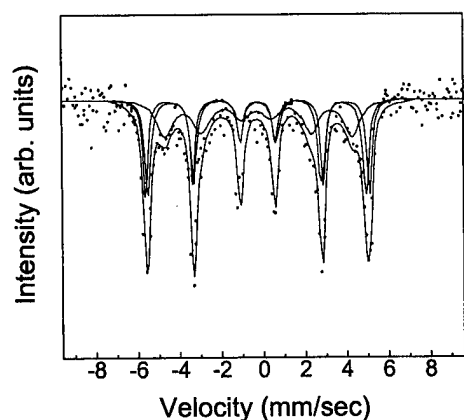


FIG. 5. Mössbauer spectrum at room temperature for the as-deposited $\text{Fe}_{76}\text{Zr}_8\text{N}_{16}$ thin film.

the film annealed in a 500 Oe magnetic field at 450 °C, perpendicular to the film plane, has a permeability of 2200 or more up to 40 MHz. This is due to a decrease of the in-plane uniaxial anisotropy of the film during annealing in the magnetic field.

The Mössbauer spectrum at room temperature for the kapton substrate sample is shown in Fig. 5. This spectrum was fitted by a sum of three kinds of six-line hyperfine splittings with fairly good quality. The three kinds of iron sites (I), (II), and (III) have values of magnetic hyperfine fields (H_i) of 331, 321, and 276 kOe, respectively. The Fe(I) state with a hyperfine field of 331 kOe corresponds to α -Fe and the Fe(II) state with $H_i = 321$ kOe corresponds to iron atoms surrounded by interstitial nitrogen atoms. On the other hand, the Fe(III) iron site with 276 kOe seems to correspond to iron atoms surrounded by zirconium atoms. The substitutional zirconium atoms will interact chemically with iron atoms, which leads to a decrease in the saturation magnetic flux

density of α -Fe, i.e., the decrease in H_i of iron atoms in α -Fe. The resonant areas of each iron site, calculated from the intensity of each subspectrum, were almost same.

IV. CONCLUSION

In this article, the influence of annealing temperature on the structure and magnetic properties of a $\text{Fe}_{76}\text{Zr}_8\text{N}_{16}$ thin film made using a rf magnetron sputtering at room temperature was studied. The as-sputtered film exhibited soft magnetic properties with a saturation magnetic flux density of 1.1 T and an effective permeability of 1400 or more at 1 MHz. The film also showed good thermal stability by sustaining the effective permeability of 3000 up to 550 °C. The film annealed in a magnetic field of 500 Oe at 450 °C showed permeability of 2200 or more up to 40 MHz. The Mössbauer spectrum at room temperature indicated that some of the nitrogen and zirconium atoms are incorporated into α -Fe interstitially and substitutionally, respectively.

ACKNOWLEDGMENTS

The research was supported by the Basic Science Research Institute Program, Korean Ministry of Education, 1997, under Project No. 2410 and also by the Korean Science and Engineering Foundation under Grant No. 975-0200-004-2.

¹T. Kobayashi, R. Nakatani, S. Ootomo, and N. Kumasaka, J. Appl. Phys. **63**, 3203 (1988).

²F. W. A. Dirne, J. A. M. Tolboom, H. J. de Wit, and C. H. M. Witmer, J. Appl. Phys. **66**, 748 (1989).

³H. J. de Wit, F. W. A. Dirne, and C. H. M. Witmer, J. Appl. Phys. **67**, 5131 (1990).

⁴N. Hasegawa and M. Saito, J. Magn. Soc. Jpn. **14**, 313 (1990).

⁵N. Hasegawa, M. Saito, A. Kojima, A. Makino, Y. Misaki, and T. Watanabe, J. Magn. Soc. Jpn. **14**, 319 (1990).

⁶K. Nakanishi, O. Shimizu, and S. Yoshida, J. Magn. Soc. Jpn. **15**, 371 (1991).

⁷O. Kohmoto, IEEE Trans. Magn. **MAG-27**, 3640 (1991).

An effect of nitrogen on magnetic properties and microstructure of Fe-Nb-B-N nanocrystalline thin films

J. Y. Park and S. J. Suh

Department of Metallurgical Engineering, Sungkyunkwan University, 440-746 Suwon, Korea

T. H. Noh

Department of Metallurgical Engineering, Andong National University, 760-749 Andong, Korea

K. Y. Kim and H. J. Kim

Thin Film Technology Research Center, Korea Institute of Science and Technology, 136-791 Seoul, Korea

Fe-Nb-B-N films with good soft magnetic properties were fabricated by Ar+N₂ reactive sputtering. The quaternary films have better soft magnetic properties than that of Fe-Nb-B films. The best magnetic properties are saturation magnetization of 16.5 kG, coercivity of 0.13 Oe and effective permeability of about 5000 up to 10 MHz. It was observed by transmission electron microscopy that the Fe-Nb-B-N thin film annealed at 590 °C consisted of three phases: a fine α -Fe phase whose grain size is around 7 nm, a Nb-B rich amorphous phase and NbN precipitates with the size of less than 3 nm. The fine grained α -Fe structure, together with finely dispersed NbN precipitates and the amorphous boundary phase are considered to be a main factor for the good magnetic properties. © 1998 American Institute of Physics. [S0021-8979(98)35111-7]

I. INTRODUCTION

Recently, Fe-Nb-B thin films¹ with nanometer-scale grain size were reported to exhibit good soft magnetic properties. The microstructures of Fe-Nb-B film are composed of a major part of α -Fe grains and a small part of residual intergranular amorphous layer. The nanoscale α -Fe grains contain a small amount of Nb and B elements, which results in the small magnetostriction. The intergranular amorphous phase has high T_c resulting from a larger amount of Nb and B elements in the phase, which cause the strong magnetic exchange coupling of bcc grains. Nitrogen addition in Fe-Hf-C thin films was known to be an effective method to obtain good soft magnetic properties, which result from α -Fe phase refinement by Hf(C,N) precipitates.² Thus, it is expected that good soft magnetic properties can be obtained by means of the nitrogen addition in Fe-Nb-B system.

In this work, we studied the effect of nitrogen addition in Fe-Nb-B system on soft magnetic properties such as high saturation magnetization and high effective permeability in high frequency ranges.

II. EXPERIMENTAL PROCEDURE

Fe-Nb-B-N films were fabricated in Ar+N₂ plasma by a rf magnetron sputtering apparatus. The target consisted of an Fe-10 at. % B disk with small pieces of Nb. The partial pressure of N₂ gas was controlled in the range of 0%-4% keeping the total gas pressure of 2 mTorr constant. The films which were deposited onto Corning 7059 glass substrates were disk shaped with 10 mm diameter and about 1 μ m thickness. The composition of film was analyzed by Auger electron spectroscopy (AES). The films were annealed at 450–700 °C for 1 h in vacuum of 10⁻⁶ Torr. The saturation magnetization ($4\pi M_s$) and coercivity (H_c) were measured using a vibrating sample magnetometer (VSM). The effective permeability (μ_{eff}) was measured at the frequency range

of 0.5–100 MHz by a figure-8 coil method. The electrical resistivity (ρ) was determined by a four point probe method. The microstructures were investigated by x-ray diffractometry (XRD) using Cu-K α radiation and transmission electron microscopy (TEM) combined with nanobeam electron diffraction.

III. RESULTS AND DISCUSSION

Figure 1 shows the compositional diagrams for μ_{eff} and $4\pi M_s$ of Fe-Nb-B-N films annealed at optimum tempera-

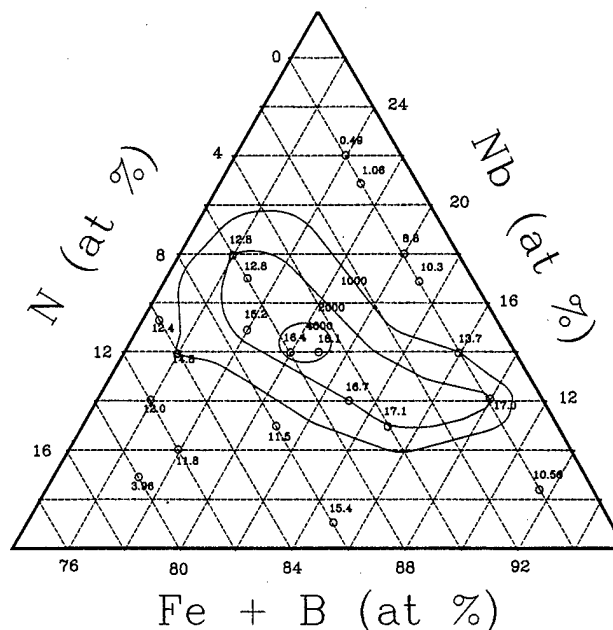


FIG. 1. Compositional diagrams of effective permeability (μ_{eff}) and saturation magnetization ($4\pi M_s$) for Fe-Nb-B-N films annealed at optimum temperatures for 1 h.

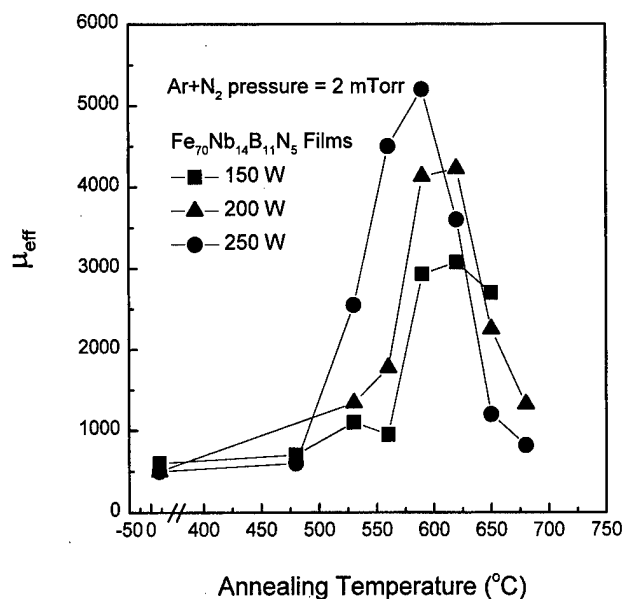


FIG. 2. The changes of effective permeability (μ_{eff}) according to rf input power for $\text{Fe}_{70}\text{Nb}_{14}\text{B}_{11}\text{N}_5$ film with annealing temperature.

tures, obtained from systematic heat treatment experiments. The Fe-Nb-B-N films exhibited high μ_{eff} of more than 4000 and $4\pi M_s$ of above 16 kG in the composition range where the Fe, Nb, and N content are 70–72, 13–14, and 5–6 at. %, respectively. It was investigated that $\text{Fe}_{70}\text{Nb}_{14}\text{B}_{11}\text{N}_5$ film was the optimum composition for the best magnetic properties in a Fe-Nb-B-N system.

Figure 2 shows the changes of μ_{eff} at 10 MHz as a function of annealing temperature at various rf input powers. At the input power of 250 W, μ_{eff} is significantly high as 5000 compared to the other conditions. From the results of Fig. 2, it was considered that the film deposited at 250 W and annealed at 590 °C was the optimum condition for the best magnetic properties in $\text{Fe}_{70}\text{Nb}_{14}\text{B}_{11}\text{N}_5$ film.

The dependence of annealing temperature (T_a) on magnetic properties for $\text{Fe}_{70}\text{Nb}_{14}\text{B}_{11}\text{N}_5$ film were studied. Figure 3 shows the changes of $4\pi M_s$, H_c , and μ_{eff} at 10 MHz for $\text{Fe}_{70}\text{Nb}_{14}\text{B}_{11}\text{N}_5$ film as a function of annealing temperature. $4\pi M_s$ was small, below 480 °C, but it increased drastically with increasing T_a and showed the maximum of 16.5 kG at 590 °C. The rapid increase of $4\pi M_s$ is due to the structural change from the amorphous phase with low M_s showing an Invar effect to the α -Fe phase with high M_s . The lowest H_c in the crystallized state was 0.13 Oe at 590 °C, and it increased rapidly above 600 °C. The μ_{eff} at 10 MHz increased with increasing annealing temperature and reached a maximum value of 5000 at 590 °C. With the further increase of annealing temperature, effective permeability decreased rapidly. This behavior of μ_{eff} vs T_a in the present work is similar to that of annealed nanocrystalline alloys reported elsewhere.^{3,4}

Figure 4 shows the frequency dependence of the effective permeability (μ') and μ'' for $\text{Fe}_{70}\text{Nb}_{14}\text{B}_{11}\text{N}_5$ film annealed at 590 °C. Higher permeabilities of 5000 were maintained up to 10 MHz.

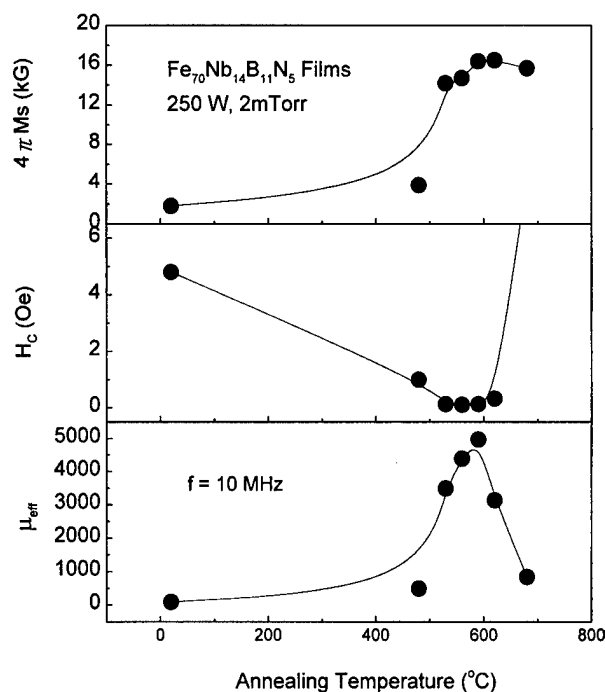


FIG. 3. The changes of saturation magnetization ($4\pi M_s$), coercivity (H_c), and effective permeability (μ_{eff}) for $\text{Fe}_{70}\text{Nb}_{14}\text{B}_{11}\text{N}_5$ film with annealing temperature.

The above-mentioned magnetic properties of Fe-Nb-B-N thin film are expected to be related to some microstructural modifications. Figure 5 shows the variation of x-ray diffraction patterns with annealing temperatures for $\text{Fe}_{70}\text{Nb}_{14}\text{B}_{11}\text{N}_5$ films. Up to 480 °C, typical broad peaks suggest the amorphous state appeared. However, an α -Fe (110) main peak sharpened at 530 °C, indicating the occurrence of crystallization. When T_a reached 590 °C, clear (110), (200), and (211) peaks of the α -Fe phase appeared. From this result, it was concluded that the increase of μ_{eff} and $4\pi M_s$,

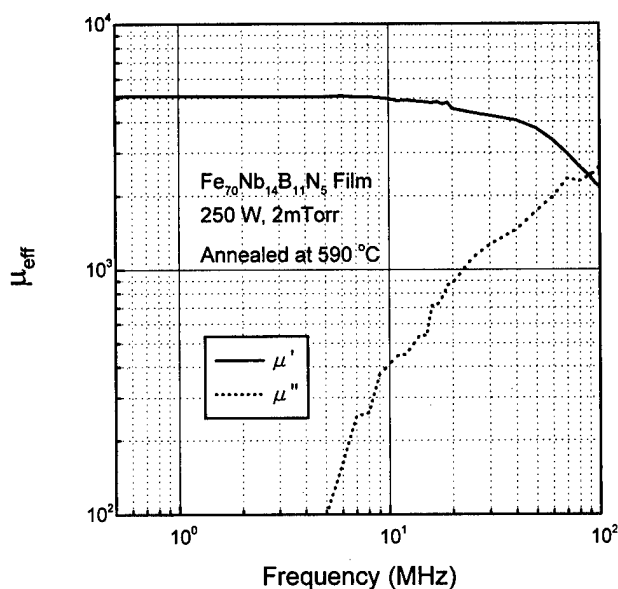


FIG. 4. Frequency dependence of effective permeability (μ') and μ'') for $\text{Fe}_{70}\text{Nb}_{14}\text{B}_{11}\text{N}_5$ film annealed at optimum annealing temperature.

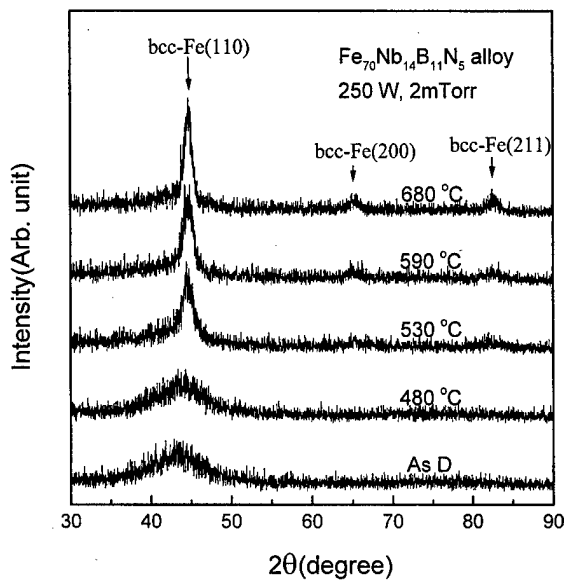


FIG. 5. The variations of XRD patterns for $\text{Fe}_{70}\text{Nb}_{14}\text{B}_{11}\text{N}_5$ film as a function of annealing temperature.

and the decrease of H_c in the T_a range of 500–600 °C resulted from the formation of α -Fe phase. And the variations of α -Fe grain size for $\text{Fe}_{70}\text{Nb}_{14}\text{B}_{11}\text{N}_5$ film with annealing temperature were shown in Table I. These values were calculated by the Scherrer's formula using XRD main peaks shown in Fig. 5.

In order to investigate the effect of nitrogen on microstructure of the thin film, TEM images (bright field, diffraction pattern, α -Fe dark field and NbN dark field) of $\text{Fe}_{70}\text{Nb}_{14}\text{B}_{11}\text{N}_5$ film annealed at 590 °C were observed as shown in Fig. 6. The results show the formation of mixed phase of α -Fe and NbN precipitates. And it is expected that excess Nb and B of about 20 at. % form Nb–B rich intergranular amorphous layer, if all the nitrogen combine with Nb to form NbN precipitates, presumably. Thus, it was considered that the film consisted of three phases: a fine crystalline α -Fe phase whose grain size is 5–10 nm, a Nb–B rich amorphous phase and Nb–nitride precipitates with a size of less than 3 nm. On the other hand, it was reported that annealed Fe–Nb–B films⁴ have two phases: α -Fe grains with the size of about 10 nm and Nb–B amorphous phase. The finer α -Fe grains were obtained in Fe–Nb–B–N film as compared to Fe–Nb–B film. It results from suppressing the growth of α -Fe grains by the intergranular amorphous phase

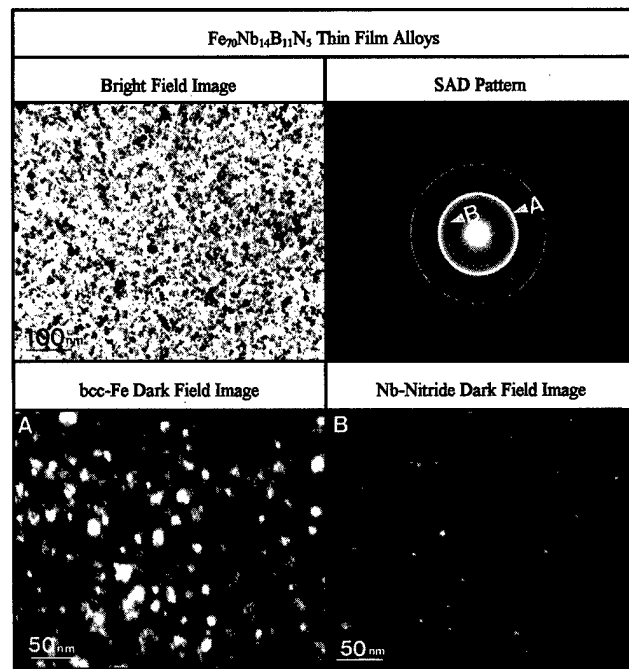


FIG. 6. TEM microstructure (bright field, bcc-Fe dark field and NbN dark field) and SAD patterns of $\text{Fe}_{70}\text{Nb}_{14}\text{B}_{11}\text{N}_5$ film annealed at 590 °C. (A): α -Fe (110) diffraction pattern. (B): NbN diffraction pattern.

as well as Nb–nitride precipitates. From above results, it is concluded that nitrogen addition in Fe–Nb–B system was effective on α -Fe grain refinement. Herzer⁵ suggested that the effective permeability increases in proportion with the inverse of D^6 (D : grain diameter) through the decrease in effective magnetocrystalline anisotropy. Therefore, the high permeability for annealed $\text{Fe}_{70}\text{Nb}_{14}\text{B}_{11}\text{N}_5$ film as shown in Fig. 4 can be considered to be mainly due to the reduction of grain size of α -Fe.

IV. CONCLUSIONS

The effects of nitrogen addition in Fe–Nb–B system on magnetic properties and microstructure were investigated. Considerably enhanced soft magnetic properties were obtained by adding nitrogen. The saturation magnetization, coercivity and effective permeability at 10 MHz were 16.5 kG, 0.13 Oe and 5000, respectively. These good soft magnetic properties of the $\text{Fe}_{70}\text{Nb}_{14}\text{B}_{11}\text{N}_5$ film were mainly due to the decrease of the grain size of a α -Fe phase by the mixed effect of the intergranular amorphous phase as well as Nb–nitride precipitates. Therefore, nitrogen addition to a Fe–Nb–B system was considered to be an effective method for improving soft magnetic properties.

TABLE I. Grain size variation for $\text{Fe}_{70}\text{Nb}_{14}\text{B}_{11}\text{N}_5$ film with annealing temperature calculated from (110) α -Fe main peak by Scherrer's formula.

Annealing temperature (°C)	As depo.	480	530	590	680
Average grain size (nm)	Amorphous	Amo+ α -Fe	6	7	15

¹ A. Makino, T. Hatanai, A. Inoue, and T. Masumoto, Mater. Sci. Eng. A **A226-228**, 594 (1997).

² J. O. Choi, H. J. Kim, and I. K. Kang, J. Appl. Phys. **75**, 106 (1994).

³ A. Makino, A. Inoue, and T. Masumoto, J. Jpn. Inst. Metals **58**, 58 (1994).

⁴ Y. Yoshizawa, S. Oguma, and K. Yamauchi, J. Appl. Phys. **64**, 6044 (1988).

⁵ G. Herzer, IEEE Trans. Magn. **25**, 3327 (1989).

Soft magnetic properties of as-deposited Fe–Hf–C–N and Fe–Hf–N nanocrystalline thin films

J. Y. Song^{a)} and J. J. Lee

Department of Metallurgical Engineering, Seoul National University, 151-742 Seoul, Korea

S. H. Han and H. J. Kim

Thin Film Technology Research Center, Korea Institute of Science and Technology, P.O. Box 131, 130-650 Seoul, Korea

J. Kim

Department of Metallurgy and Materials Science, Hanyang University, Ansan, 425-791 Kyungki, Korea

As-deposited Fe–Hf–C–N nanocrystalline thin films are investigated to improve soft magnetic properties by controlling both the compositions of the films and sputtering conditions, such as input power and N₂ partial pressure. As-deposited Fe–Hf–N thin films are also investigated for the applications to simplify the fabrication of magnetic devices. The as-deposited Fe–Hf–C–N and the as-deposited Fe–Hf–N thin films are fully nanocrystallized during deposition by controlling the composition and sputtering condition. The thin films show the excellent soft magnetic properties of saturation magnetization ~ 17.5 kG/ ~ 16.5 kG and coercivity ~ 0.5 Oe/ ~ 0.5 Oe when the compositions of each film are 6.8–7.2 at % Hf, 2.0–2.5 at % C, 9.8–10.8 at % N, and balanced Fe/6.3–7.0 at % Hf, 13.2–14.0 at % N, and balanced Fe, respectively. Both of the thin films exhibit an outstanding frequency dependence of permeabilities, i.e., the effective permeabilities of the films remain flat over 3000 up to 100 MHz. © 1998 American Institute of Physics.

[S0021-8979(98)15511-1]

I. INTRODUCTION

A demand for high performances in miniaturized electronic/electrical equipment forces soft magnetic materials to play an important role in micromagnetic devices including thin film inductors or transformers operating at high frequency (≥ 10 MHz). Thus soft magnetic thin films with excellent frequency dependence are strongly required as core materials. Soft magnetic thin films based on iron-rich Fe–Ta, Fe–Nb, Fe–Zr, and Fe–Hf have been investigated, and the enhancement of soft magnetic properties are obtained by adding B, C, and N.^{1–3} However, the excellent soft magnetic properties of Fe-based thin films are only obtained after post heat treatment which nanocrystallizes the deposited films at a temperature of 300–600 °C.

We reported that as-deposited Fe–Hf–C–N thin films have nanocrystalline structures and good soft magnetic properties, coercivity (H_c) of 0.5 Oe, saturation magnetization ($4\pi M_s$) of 13 kG, and effective permeability (μ_{eff}) over 3000 up to 100 MHz.⁴ The as-deposited films are applicable to magnetic devices which have not been heat treated, since heat treating deteriorates components and materials that are sensitive to the high temperature exposure. Thin films with higher $4\pi M_s$ are more favorable in practical applications. Thus, the magnetic properties of as-deposited Fe–Hf–C–N thin films are investigated to increase $4\pi M_s$ by controlling the deposition conditions and as-deposited ternary Fe–Hf–N thin films are also investigated for easy fabrication.

II. EXPERIMENTAL PROCEDURE

As-deposited Fe–Hf–C–N and Fe–Hf–N thin films have been prepared by a reactive magnetron sputtering method in a nitrogen atmosphere. The pellets of Hf and C are put on the pure Fe target to control thin film compositions. The flow of Ar gas is maintained at 20 sccm, and N₂ partial pressure is regulated in the range from 0% to 10% in order to obtain the films with various nitrogen contents. Both the mixed gases are introduced into the chamber after it has been evaluated to a pressure below 1×10^{-6} Torr. The working pressure is maintained at 1 mTorr. The distance between the target and the water-cooled Si(001) substrate is 6 cm. The rf input power varies from 150 to 550 W. The film thickness is 1 ± 0.2 μm , measured by a stylus profiler. The compositions and the microstructures of the films are analyzed by Auger electron spectroscopy (AES), Rutherford backscattering spectroscopy (RBS), x-ray diffraction with Cu K_α , and transmission electron microscopy (TEM). The magnetic properties of the films are measured by a vibrating sample magnetometer (VSM) and the magnetic easy/hard directions in plane are determined by a B - H loop tracer. The frequency dependence of μ_{eff} is obtained in the hard direction by using an eight-figure coil method. The electrical resistivity of the films is measured by a four-point probe method.

III. RESULTS AND DISCUSSION

The saturation magnetization of as-deposited Fe–Hf–C–N and Fe–Hf–N thin films varies with the rf input power as shown in Fig. 1(a). At 150 W, as-deposited films are not saturated by the external field up to 1 kOe. The $4\pi M_s$ of the as-deposited films are relatively small because of an Invar

^{a)}Electronic mail: hijkim@kistmail.kist.re.kr

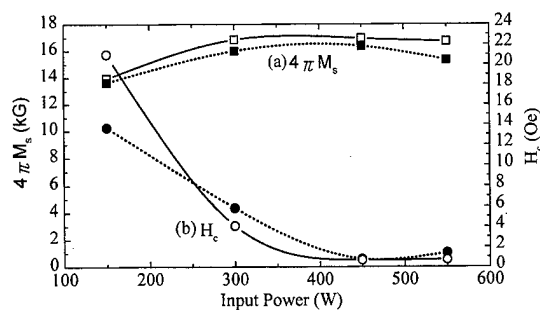


FIG. 1. (a) Saturation magnetization ($4\pi M_s$) and (b) coercivity (H_c) as a function of rf input power. [An applied field (H_a) of 100 Oe but in case of input power of 150 W, the films are saturated by $H_a = 1$ kOe, $4\pi M_s$: (□) Fe-Hf-C-N, (■) Fe-Hf-N, H_c : (○) Fe-Hf-C-N, (●) Fe-Hf-N, the error range of data points is $\pm 5\%$.]

effect. Above 300 W, the $4\pi M_s$ of the films are coincident with Fe content. The maximum values of $4\pi M_s$ are 17.5 and 16.5 kG, respectively. The H_c of both the films decrease as the rf input power increases as shown in Fig. 1(b), and the minimum in H_c , $H_c = 0.5$ Oe, is obtained at 450 W. The μ_{eff} of the as-deposited films shows a good flat dependence on frequency, which remains around 3000 up to 100 MHz. As shown in Fig. 3(b), the μ_{eff} decreases slightly at the input power of 550 W. The best soft magnetic properties are observed at 450 W.

Figure 2 shows the effect of N_2 partial pressure on the soft magnetic properties of Fe-Hf-C-N and Fe-Hf-N thin films. All the films with different N contents are saturated at an applied field of 100 Oe. At low N_2 partial pressure (3%–4% and 4%–6%), $4\pi M_s$ are relatively small, which is presumed to be due to an Invar effect. Nitrogen, introduced during deposition, enhances the $4\pi M_s$ of the films. The maximum values for both the films are ~ 17.5 and ~ 16.5 kG at 6%–8% and 7%–8.5% of P_{N_2} , respectively. The coercivities of both the films have a minimum value at 5%–6.5% and 7%–8% of P_{N_2} . The minimum coercivities of both the films are about 0.5 Oe, as shown in Fig. 2(b). The addition of nitrogen strongly affects the μ_{eff} as shown in Fig. 3(a). The μ_{eff} of both the films increases with the introduction of nitrogen and reaches the maximum of 3000 in the range of 5.5%–6% and 7.5%–8% of P_{N_2} for Fe-Hf-C-N and Fe-Hf-N, respectively, and remain flat up to 100 MHz without any loss until several 10 MHz. However, excessive N con-

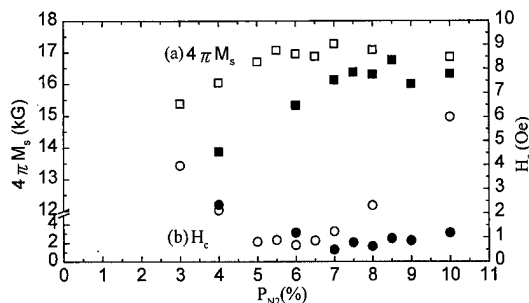


FIG. 2. (a) Saturation magnetization ($4\pi M_s$) and (b) coercivity (H_c) as a function of N_2 partial pressure. [An applied field (H_a) of 100 Oe, $4\pi M_s$: (□) Fe-Hf-C-N, (■) Fe-Hf-N, H_c : (○) Fe-Hf-C-N, (●) Fe-Hf-N, the error range of data points is $\pm 5\%$.]

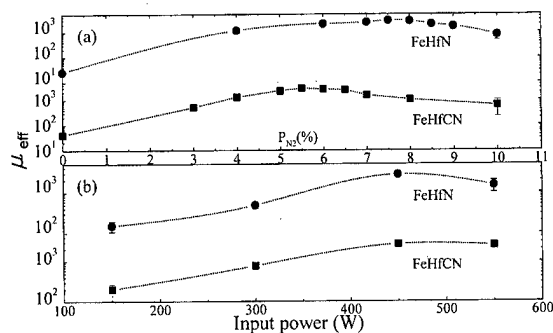


FIG. 3. Effective permeability at 100 MHz (measured in the hard direction) with (a) N_2 partial pressure and (b) rf input power. The films show a flat frequency spectrum in optimum condition.

tent in the films decreases the μ_{eff} near $P_{N_2} = 10\%$. On the other hand, the μ_{eff} measured in the easy direction is not constant and very small (about several 10–100). As a result of AES and RBS analysis, the $\text{Fe}_{79.9-81.1}\text{Hf}_{6.8-7.2}\text{C}_{2.0-2.5}\text{N}_{9.8-10.8}$ and $\text{Fe}_{79.0-80.6}\text{Hf}_{6.0-7.0}\text{N}_{13.2-14.0}$ thin films have the best soft magnetic properties. Actually, the films with the content of 70–82 at % Fe in the case of Fe-Hf-C-N and Fe-Hf-N exhibit such excellent soft magnetic properties when the ratio of C+N/Hf and N/Hf is 1.8–1.9 and 2.0–2.2, respectively.⁴ The value of N/Hf is larger than that of C+N/Hf for optimum compositional condition, because the solubility of nitrogen in α -Fe is larger than that of carbon in α -Fe.

The variations of x-ray diffraction patterns with the addition of N and rf input power are shown in Figs. 4 and 5, respectively. Figures 4(a) and 5(a) show that the films deposited at the input power of 150 W are amorphous or mixed phase of amorphous and crystal, and that high input power generally crystallizes the films during deposition. Figures 4(b) and 5(b) show that nitrogen enhances the crystallization of the films from a mixed phase of crystal and amorphous,

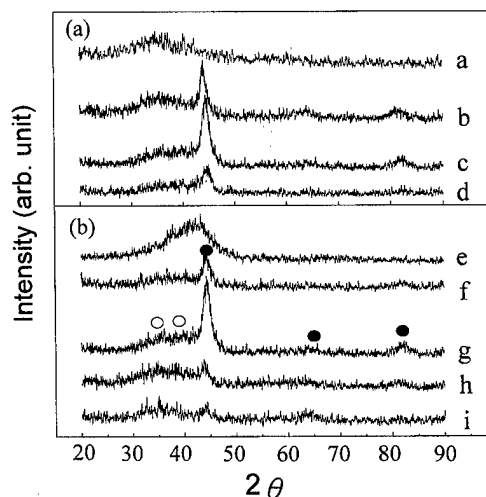


FIG. 4. X-ray diffraction patterns [(●) α -Fe (110), (200), (211) and (○) Hf precipitates (111), (200) in order] of Fe-Hf-C-N thin films with rf input power [(a)=150 W, (b)=300 W, (c)=450 W, (d)=550 W] and N_2 partial pressure [(e)=0%, (f)=3%, (g)=6%, (h)=8%, (i)=10%].

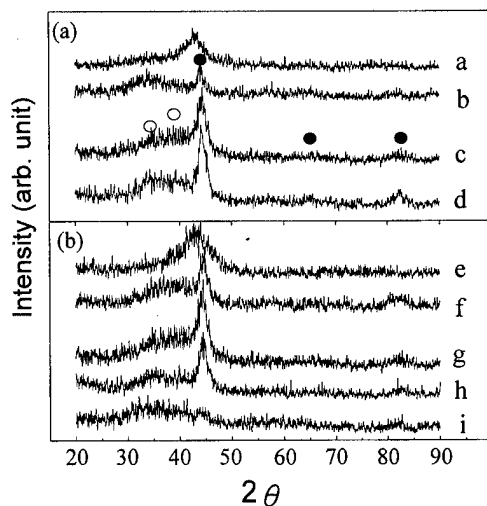


FIG. 5. X-ray diffraction patterns [(●) α -Fe (110), (200), (211) and (○) Hf precipitates (111), (200) in order] of Fe-Hf-N thin films with rf input power [(a)=150 W, (b)=300 W, (c)=450 W, (d)=550 W] and N_2 partial pressure [(e)=0%, (f)=4%, (g)=7.5%, (h)=8%, (i)=10%].

which is confirmed by TEM analysis. They also show that the excessive addition of nitrogen breaks the crystallinity of the films. Thus, as-deposited Fe-Hf-C-N and Fe-Hf-N thin films are completely crystallized in the case where the rf input power and N_2 partial pressure are well controlled. Figure 6 shows the high resolution TEM image of Fe-Hf-C-N film deposited at 450 W and $P_{N_2}=6\%$. The Fe-Hf-C-N films consist of finely grained α -Fe with a diameter of ~ 5 nm and Hf(C,N) precipitates of smaller size. The morphology of exceptionally small grains surrounded by Hf precipitates contributes to the excellent soft magnetic properties. The soft magnetic properties of the films are little affected, after annealing at 823 K for 30 min. It is explained by the morphology that Hf precipitates prevent α -Fe grains from growing during annealing.

In order to understand the excellent high frequency permeability, the electrical resistivities of the films are measured. The resistivities are around $100 \mu\Omega$ cm which is similar to those of other Fe-nanocrystalline films.^{2,3} It means that the excellent dependence of effective permeability is not mainly due to the decrease of eddy current loss by the decrease of electrical resistivity. The excellent dependency appears when the permeability is measured in the hard direction, which means the existence of in-plane magnetic anisotropy at the as-deposited films. A B - H loop tracer shows that the frequency dependence of effective permeability is more excellent when the anisotropy is well aligned in the hard direction than widely dispersed. It means that the degree of magnetic anisotropy dispersion is related with permeability dependence. However, magnetocrystalline anisotropy is known to be averaged out by the refinement of α -Fe grains (random anisotropy model).⁵ The existence of in-plane anisotropy of the films could be due to the stray field from magnetron ring and interstitial insertion of C and N in α -Fe.⁶ Due to fast deposition, carbon and nitrogen remain in

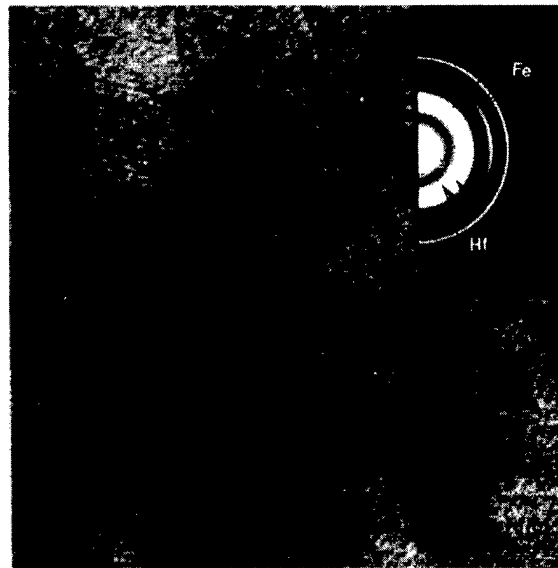


FIG. 6. High resolution TEM image of Fe-Hf-C-N thin film deposited at $P_{N_2}=6\%$ and 450 W shows the nanocrystallized α -Fe grains (white area) and Hf precipitates (dark area). In the ring pattern, the notation of Fe represents 110, 200, 211 of α -Fe and the notation of Hf does 111, 200, 220 of Hf(C,N), respectively, from the center.

the octahedral sites of the α -Fe lattice, which contributes to uniaxial anisotropy.⁷ Even though the uniaxial anisotropy due to the solute atoms leads to an increase of the net anisotropy, the softness of the films is still maintained; i.e., the resultant coercivity is low (0.5 Oe), but it is larger than that (≤ 0.1 Oe) of other Fe-based thin films.^{2,3}

IV. SUMMARY

Fe-Hf-C-N and Fe-Hf-N thin films can be completely crystallized by controlling N_2 partial pressure and input power. As-deposited $Fe_{79.9-81.1}Hf_{6.8-7.2}C_{2.0-2.5}N_{9.8-10.8}$ and $Fe_{79.0-80.6}Hf_{6.3-7.0}N_{13.2-14.0}$ nanocrystalline thin films exhibit such excellent soft magnetic properties of $4\pi M_s$ (17 and 16.5 kG) and H_c (0.5 Oe). The films show especially excellent frequency dependence of high permeability of about 3000 up to 100 MHz without any loss until several 10 MHz. As-deposited Fe-Hf-C-N and Fe-Hf-N thin films are composed of finely dispersed α -Fe (~ 5 nm) and smaller Hf precipitates. Thus, the exceptionally small grains and precipitates enhance the soft magnetic properties and show thermal stability up to 823 K.

¹N. Hasegawa, M. Saito, A. Kojima, A. Makino, Y. Misaki, and T. Watanabe, J. Magn. Soc. Jpn. **14**, 319 (1990).

²H. J. Ryu, J. O. Choi, J. J. Lee, S. H. Han, H. J. Kim, and I. K. Kang, IEEE Trans. Magn. **31**, 3868 (1995).

³J. O. Choi, J. J. Lee, S. H. Han, H. J. Kim, and I. K. Kang, J. Appl. Phys. **75**, 5785 (1994).

⁴J. Y. Song, J. Kim, H. J. Kim, and J. J. Lee, J. Phys. III (to be published).

⁵G. Herzer, IEEE Trans. Magn. **26**, 1397 (1990).

⁶B. D. Cullity, *Introduction to Magnetic Materials* (Addison-Wesley, Reading, MA, 1972), Chap. 10.

⁷E. van de Riet, W. Klaassens, and F. Roozeboom, J. Appl. Phys. **81**, 806 (1997).

Microstructure and soft magnetic properties of FeSiAl(Ti/Ta)(O)N

M. Hiramoto,^{a)} N. Matsukawa, H. Sakakima, Y. Ichikawa, and K. Ijima

Central Research Lab, Matsushita Electric Industrial Co., Ltd., Seika-cho, Kyoto 619-0237, Japan

The microstructure and magnetic properties of FeSiAl(Ti/Ta)(O)N films prepared by rf magnetron reactive sputtering were studied. The microstructure was controlled by changing the N₂ gas flow rate ratio [$\eta = N_2/(Ar+N_2)$] in the sputtering gas. The soft magnetic properties were observed after thermal treatment at around η of 2% and η of 20%, where the saturation magnetostrictions and the intrinsic stresses took small values. The film with η of 20% had a granular structure as mostly observed on nanocrystalline materials. On the other hand, the film prepared with η of 2% had the structure which consisted of needle shaped grains or dendritic grains. The composition of the granular grains and needle shaped grains were mainly Fe and FeSi, respectively. The film with η of 2% exhibited B_s of 1.3 T, permeability of 3000–8000 at 1 MHz, respectively, and realized a high corrosion resistance. The soft magnetic properties of the films with needle shaped grains are explained by two-dimensional random anisotropy effect. © 1998 American Institute of Physics. [S0021-8979(98)48711-5]

I. INTRODUCTION

Nanocrystalline soft magnetic materials with high saturation magnetic flux density (B_s) and/or high electrical resistivity have been intensively investigated.^{1,2} Generally speaking, nanocrystalline materials have a granular structure obtained from the amorphous state by thermal treatment. The soft magnetic properties are affected by the mean grain size and intergranular magnetic properties. The softness is explained by a three-dimensional random anisotropy model^{3,4} and/or magnetic ripple theory.⁵ However, there were few reports about the dependence of magnetic properties on grain shape as well as grain size. We investigated the magnetic, structural, and corrosive properties of sputtered FeSiAl(Ti/Ta)(O)N films, whose grain structures were controlled by introducing N₂ gas during sputtering. The films are expected to be sensitive on the grain structures because of the small magnetocrystalline anisotropy (K_1) of the FeSiAl system (i.e., the films have a relatively long ferromagnetic correlation length, L_0 , compared with that of Fe). In this article, we report on the nanocrystalline materials, which have new types of the granular structure.

II. EXPERIMENT

FeSiAl(Ti/Ta)(O)N films of 3 μ m in thickness were prepared onto ceramic substrates by rf magnetron sputtering using alloy targets with a dimension of 3 in in diameter or 5 \times 15 in. The sputtering gas was a mixture of Ar+N₂ or Ar+N₂+O₂. The flow rate ratio of N₂, $\eta = N_2/(Ar+N_2)$, was varied from 0% to 23% and the flow rate ratio of O₂ was kept at 0% or 0.5%. Thermal treatment was performed in a vacuum at 520 °C. The B_s , initial permeability along the hard axis (μ_i), and the saturation magnetostriction (λ_s) were measured by using a vibrating sample magnetometer (VSM), a figure-8 coil apparatus, and an optical cantilever method, respectively. The microstructure was observed by

using a transmission electron microscopy (TEM) and x-ray diffraction, (XRD). The internal stress was evaluated by the change in the bending of the substrate. The film composition was determined by using an electron probe microanalysis (EPMA) and a Rutherford backscattering spectrometry (RBS). The corrosion resistance of the films was evaluated by the change in B_s of the films immersed in the 0.5 N NaCl solution for 50 h. All the measurements were carried out at room temperature.

III. RESULTS AND DISCUSSION

A. Magnetic properties and magnetostrictive anisotropy

The compositions of the FeSiAl(Ti/Ta) films sputtered with Ar gas were determined by EPMA as Fe₇₆Si₁₉Al₃Ti₂ and Fe₇₆Si₁₉Al₂Ta₃. Figure 1 shows the dependence of initial permeability (μ_i) on the flow rate ratio of N₂ (η). The μ_i has two peaks at around η of 2% and η of 20%. In order to clarify the origin of the two peaks of μ_i , several properties were precisely studied as follows. Figure 2(a) shows dependence of the internal stress (σ) of the films on η . The plotted

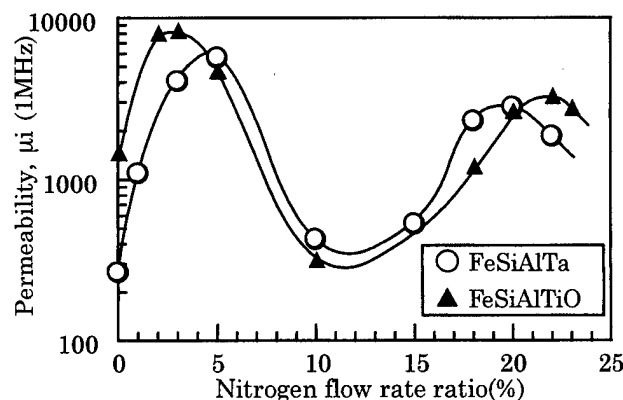


FIG. 1. Initial permeability (μ_i) of the FeSiAl(Ti/Ta) films with changing the nitrogen flow rate ratio (η).

^{a)}Electronic mail: hiramoto@crl.mei.co.jp

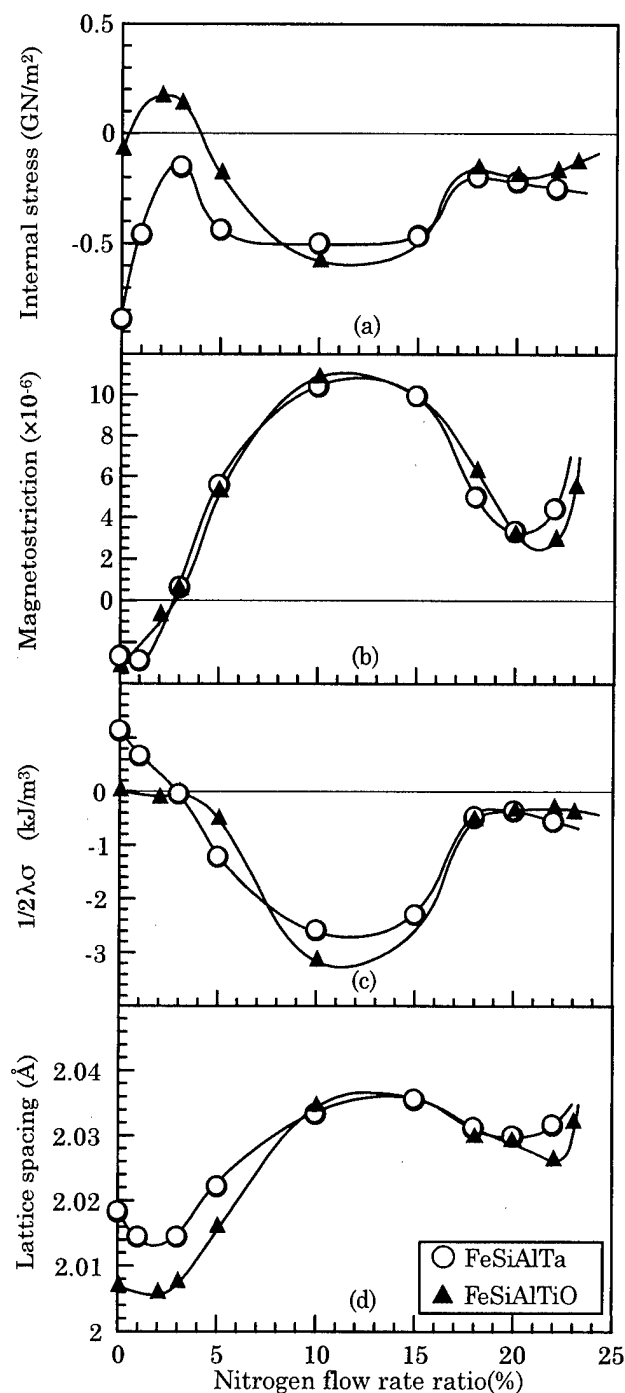


FIG. 2. Internal stress (σ), saturation magnetostriction (λ_s), magnetostrictive anisotropy energy due to the internal stress ($1/2\lambda_s \times \sigma$), and the lattice spacing of (110) plane ($d_{(110)}$) of the FeSiAl(Ti/Ta) films with changing the nitrogen flow rate ratio (η).

σ includes the thermal stress caused by thermal treatment. The negative sign denotes compressive stress. Figure 2(b) shows the dependence of the saturation magnetostriction (λ_s) on η . The relationship between λ_s and η is very similar to that of λ_s and the concentration of Si in α -Fe.⁶ Using the value of σ and λ_s , the magnetostrictive anisotropy energy due to the internal stress ($1/2\lambda_s \times \sigma$) was calculated. The result is illustrated in Fig. 2(c). Compared with Fig. 1, the magnetostrictive energy for the films prepared with η of 3%–18% may explain the deteriorations of μ_i . Figure 2(d) shows the

dependence of the lattice spacing of the (110) plane, $d_{(110)}$, on η . The value of $d_{(110)}$ with increasing η of these films approaches 2.0268 Å, which is the value of α -Fe, though it includes the affection of the lattice strain caused by σ . Considering that the stress affection and the $d_{(110)}$ of Fe₃Si is 2.005 Å, it is clear that the main grain compositions of the prepared films are changed from FeSi to Fe by changing the η 's from 0% to 20%. This result agrees with the consideration of the magnetostriction change as mentioned above. Further, in the range over 20%, the expansion of $d_{(110)}$ and the increasing of λ_s are observed. It may suggest that the Fe grains of the films with an η of over 20% contained the interstitial N atoms and the concentration of the N atoms is considered to be larger than that of Fe–N films which were widely known to show soft magnetic properties. Accordingly, the excess N atoms cause the deterioration of the soft magnetic property over an η of 20%.

B. Magnetic properties and microstructure

As mentioned above, the soft magnetic properties of FeSiAl(Ti/Ta)(O)N films are strongly affected by the magnetostrictive anisotropy energy. However, observing more precisely, it is noted that μ_i of the FeSiAlTiON film changes drastically from the μ_i of 1500 to 8000 with increasing the η from 0% to 3%, though the magnetostrictive energy is almost constant, μ_i of the prepared Fe₇₇Si₂₀Al₃ film was only 1800 at 1 MHz under the zero stress condition. Therefore, a μ_i of over 8000 of the FeSiAlTiON film cannot be explained only by the compositional change of FeSiAlTi grains by selective nitriding of Ti. Further, the reduction of K_1 caused by lattice strain⁷ is not expected because the change of $d_{(110)}$ in the η 's range of 0%–3% is small.

In order to investigate the influence of the microstructure on soft magnetic properties, TEM observations of the films were performed. Figures 3(a), 3(b), and 3(c) show the cross sectional dark field TEM images of FeSiAlTiON films prepared with an η of 20% and 2% using a 3 in target. The film prepared with an η of 20% [see Fig. 2(a)] consisted of the granular structure having a grain size smaller than 10 nm as observed in other nanocrystalline materials.^{1,2} It is clearly observed that the interparticle regions are in an amorphous state. On the other hand, the microstructure of the film prepared with an η of 2% [see Figs. 2(b) and 2(c)] consists of needle shaped fine grains grown perpendicularly to the film plane. The grain size is over 200 nm in length and 20 nm in width. Contrary to the film with an η of 20%, interparticle regions are not clearly observed. In other words, the film with an η of 2% is composed of mainly magnetic grains. A perpendicular anisotropy, which could be expected by the shape anisotropy of the needle shaped grains, was not observed in the hysteresis curve. The result is owing to the film structure mainly composed of magnetic grains as mentioned above. That is, the grains may have a strong exchange interaction with each other in the plane. The electron diffraction showed that the grains were randomly orientated crystallographically in the plane.

From the analysis of EPMA and RBS, the composition of the FeSiAlTiON film with an η of 2% was determined as

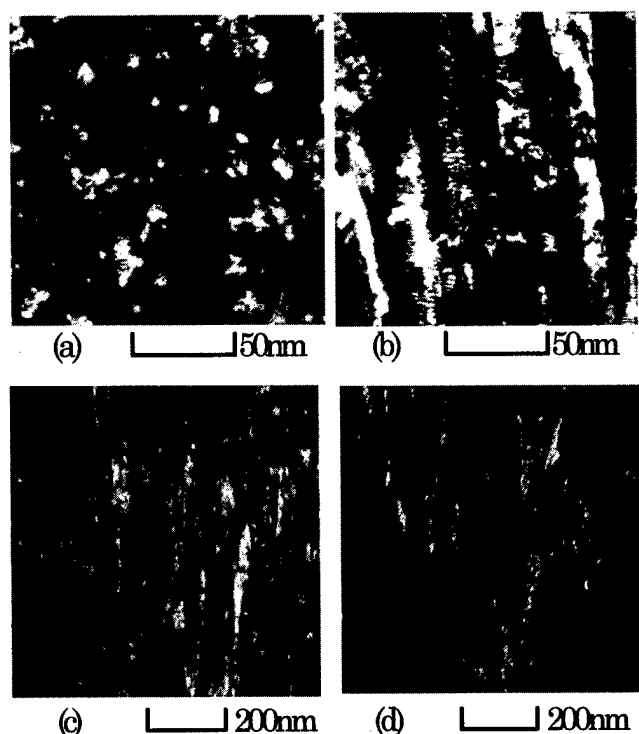


FIG. 3. The cross sectional dark field TEM micrographs of FeSiAlTiON films. (a) with an η of 20% and using a 3 in target. (b) and (c) with an η of 2% and using a 3 in target. (d) with an η of 2% and using a 5×15 in target.

($\text{Fe}_{76}\text{Si}_{19}\text{Al}_3\text{Ti}_2$) $_{94}\text{O}_1\text{N}_5$. Assuming that the grains are composed of a $\text{Fe}_{80}\text{Si}_{20}$ alloy, the ferromagnetic correlation length, L_0 is estimated³ as 35 nm. Taking a grain size of 20 nm in width, which is smaller than L_0 , and the random orientation of grains in the plane into consideration, the film satisfied the random anisotropy condition only in the plane. Therefore, we concluded that the good softness of the film with an η of 2% was caused by a two-dimensional random anisotropy effect in the plane as was observed in magnetic/nonmagnetic multilayered films.⁸

The shape of fine grains is interesting from the viewpoint of the film formation process. Generally speaking, a thick columnar structure is obtained by the condensation of several islandlike nucleuses with the surface diffusion. However, in the case of FeSiAlTiON with an η of 2%, only the needle shaped grain structure was observed instead of the thick columnar structure. This may indicate that the surface diffusion length is suppressed. Figure 3(d) shows a cross sectional TEM image of the FeSiAlTiON film prepared with an η of 2% using a wider target (5×15 in). The microstructure consisted of unique dendritic grains. The growth directions of "branches" of the dendrite are consistent with the directions of the oblique incident particles. The thin dendritic grain is good evidence of the suppressing of the surface diffusion in the plane. Compared with the needle shaped grain film, the dendritic grain film showed a stronger uniaxial magnetic anisotropy in the plane. The anisotropy may be due to the difference of the exchange correlation length in the

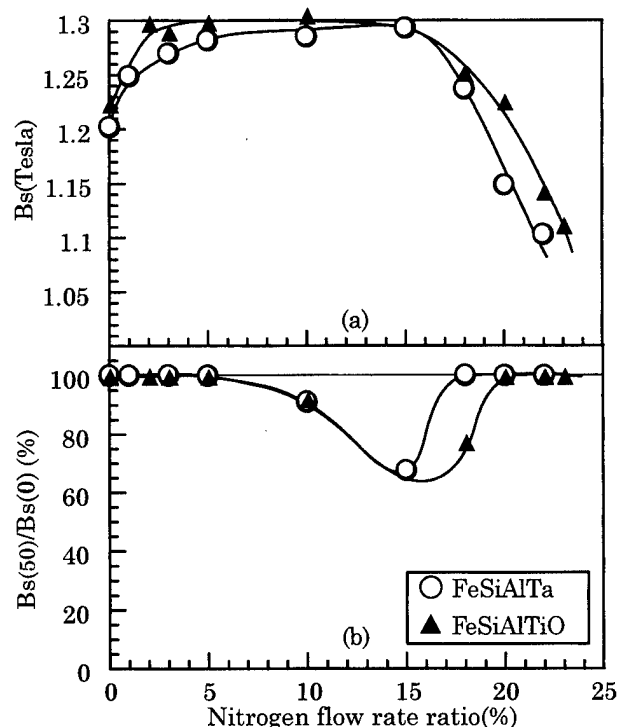


FIG. 4. B_s and the change of $B_s(50)/B_s(0)$ of the FeSiAlTiON films with changing the nitrogen flow rate ratio (η).

plane direction caused by the size and the shape of dendritic grains grown anisotropically owing to the oblique incident.

C. Corrosion resistance

Figures 4(a) and 4(b) show the dependence of B_s and the corrosion resistance, $B_s(50)/B_s(0)$ which is estimated with the change of B_s of the films on η . Whereas $B_s(50)$ denotes the B_s of the films after immersing the films in the 0.5 N NaCl solution for 50 h. The B_s shows a broad maximum at around an η of 5–15%. The increment of B_s is due to the segregation of the additive element out of α -Fe. The $B_s(50)/B_s(0)$ takes a minimum value at around an η of 15%. The high corrosion resistance in the low η 's range is realized by an additive which passivates the grain surface. On the other hand, in the high η 's range, the interparticle region in the amorphous state prevents the α -Fe grains from corrosion.

ACKNOWLEDGMENT

This research was supported by NEDO, under the Synergy Ceramics Project of ISTF program.

- ¹K. Nago, H. Sakakima, and K. Ihara, IEEE Trans. Magn. **7**, 119 (1992).
- ²S. Omura, J. Appl. Phys. **79**, 5130 (1996).
- ³G. Herzer, IEEE Trans. Magn. **26**, 1397 (1990).
- ⁴G. Herzer, Phys. Scr. **T49**, 307 (1993).
- ⁵H. Hoffmann, J. Appl. Phys. **35**, 1790 (1964).
- ⁶M. Takahashi, S. Suwabe, T. Narita, and T. Wakiyama, J. Magn. Soc. Jpn. **10**, 307 (1986).
- ⁷M. Takahashi, H. Shoji, T. Simatsu, H. Omaba, and T. Wakiyama, IEEE Trans. Magn. **26**, 1503 (1990).
- ⁸M. Hiramoto, O. Inoue, and K. Kugimiya, IEEE Trans. Magn. **30**, 4884 (1994).

New applications of nanocrystalline Fe(Co-Fe)-Hf-O magnetic films to micromagnetic devices

T. Sato,^{a)} Y. Miura, S. Matsumura, and K. Yamasawa

Department of Electrical and Electronic Engineering, Shinshu University, Nagano 380, Japan

S. Morita, Y. Sasaki, T. Hatanai, and A. Makino

Central Research Laboratory, Alps Electric Co., Nagaoka 940, Japan

New applications of high resistivity magnetic films, such as Fe-Hf-O and Co-Fe-Hf-O as thin film inductors and flux gate magnetic sensors, were investigated. These soft magnetic films with nanocrystalline structure and high resistivity were deposited on glass substrate by using the oxygen reactive sputtering method. Planar sandwich thin film inductors developed by using Fe-Hf-O or Co-Fe-Hf-O films had a higher quality factor than that of an amorphous Co-Ta-Hf film inductor. The dc-dc converter using the Fe(Co-Fe)-Hf-O film inductor had higher conversion efficiency. These high resistivity magnetic films were also applied to a flux gate magnetic sensor operated at high frequencies over 1 MHz. Both high frequency excitation and high permeability (owing to the low eddy current loss) enabled us to increase the sensitivity, e.g., 39 mV/Oe/turn at 5 MHz when using a 3 μm thick Fe-Hf-O film (12 \times 6 mm² area). © 1998 American Institute of Physics. [S0021-8979(98)22311-5]

I. INTRODUCTION

In recent years, the micromagnetic devices, such as magnetic thin film inductors¹ (transformers²) and thin film flux gate sensors,³ have been developed to miniaturize the magnetic components in electronic equipment. Both high frequency excitation and thin film structure enable us to make the passive component smaller. However, in order to develop the high performance magnetic thin film devices, it is necessary to suppress the excess losses due to eddy currents. The authors developed the nanocrystalline Fe(Co-Fe)-Hf-O films with good soft magnetic properties and high electrical resistivity,⁴ and reported the planar inductor application.⁵

In this study, new applications of the Fe(Co-Fe)-Hf-O magnetic films were investigated. First, in order to make planar sandwich inductors smaller than the already reported inductors⁵ using a meander coil pattern and magnetic films, a square spiral pattern was used in the inner coil, which was sandwiched by top and bottom magnetic films. In the developed 10 \times 10 mm² size inductors, 0.53–0.80 μH inductances and the maximum quality factor of 16 at 10 MHz were obtained. Second, a flux gate magnetic field sensor was developed, which had the outer exciting coil, outer detecting coil, and the inner magnetic film. High resistivity magnetic films enabled us to increase the sensor sensitivity with increasing frequency, due to small eddy currents.

II. EXPERIMENTAL PROCEDURE

High resistivity nanocrystalline Fe(Co-Fe)-Hf-O films were produced on a glass substrate using oxygen rf sputter deposition method. Some properties of the 3 μm thick magnetic films are shown in Table I. For a comparison, the amorphous Co-Ta-Hf metal film is also shown in Table I. In order to induce uniaxial anisotropy, the Fe-Hf-O film was

annealed in the presence of a magnetic field of 2 kOe, and a temperature of 573 K for a time of 1 h, in vacuum. Uniaxial anisotropy was also induced in the Co-Fe-Hf-O film, by carrying out the deposition in the presence of the dc magnetic field applied to the substrate. From results of the transmission electron microscopy (TEM) and nano-beam energy dispersive x-ray (EDX) analyses, the high resistivity magnetic films had a nanocrystalline structure consisting of nanoscale Fe(Co-Fe) rich grains and Hf-O rich amorphous matrix. Consequently, these films exhibited high resistivity due to the Hf-O rich matrix.

First, high resistivity magnetic films were used to make small size planar inductors used for 5 MHz operation, dc-dc converters. Figure 1 shows a schematic illustration of the developed inductor, which had the multilayered structure composed of 10 \times 10 mm² square spiral coil sandwiched by the top and bottom magnetic layers. These materials were held together by synthetic resin, so planar sandwich structure is preserved.

Second, the flux gate magnetic sensor was developed by using high resistivity magnetic films. Figure 2 is the sensor structure. The exciting coil (Ne) and detecting coil (Nd) were wound together (Ne=10, Nd=10) to form the solenoid structure. The 3 μm thick rectangular magnetic film (12 \times 6 mm²) was inserted into the inner cavity of the solenoid to excite to the hard magnetization direction (short axis of rectangular film).

III. RESULTS AND DISCUSSION

The frequency dependence of permeability of these films was measured by using the parallel line method,⁶ and this is shown in Fig. 3. High resistivity magnetic films such as Fe(Co-Fe)-Hf-O had good frequency response (permeability) and low loss tangent ($\tan \delta$).

^{a)}Electronic mail: labyaml@gipwc.shinshu-u.ac.jp

TABLE I. Some properties of Fe-Hf-O, Co-Fe-Hf-O, and Co-Ta-Hf films.

Magnetic film	Fe-Hf-O	Co-Fe-Hf-O	Co-Ta-Hf
Composition (at. %)	Fe ₆₁ Hf ₁₃ O ₂₆	Co ₄₄ Fe ₁₉ Hf ₁₅ O ₂₂	Co ₈₃ Ta ₆ Hf ₁₁
Saturation magnetization	13 kG	10.9 kG	8.1 kG
Anisotropy field	7.5 Oe	60.3 Oe	10.3 Oe
Resistivity	500 μΩ cm	1700 μΩ cm	170 μΩ cm

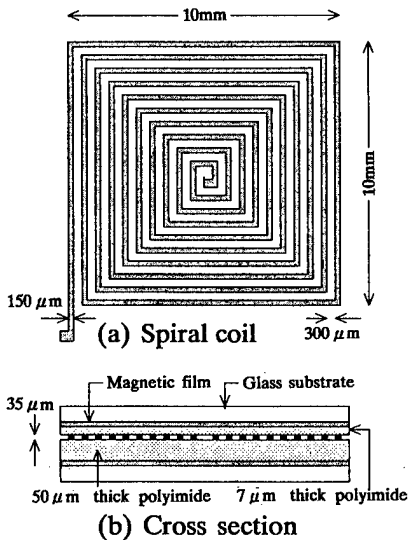


FIG. 1. Schematic illustration of planar sandwich inductor.

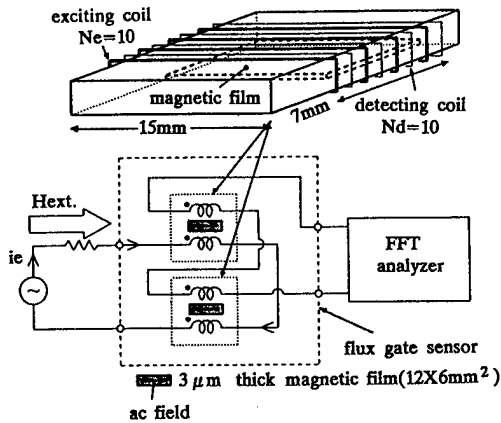


FIG. 2. Schematic illustration of flux gate sensor.

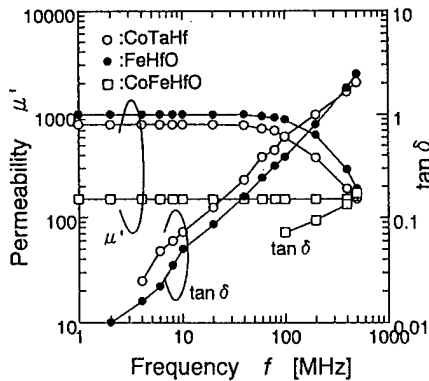


FIG. 3. Frequency dependence of permeability.

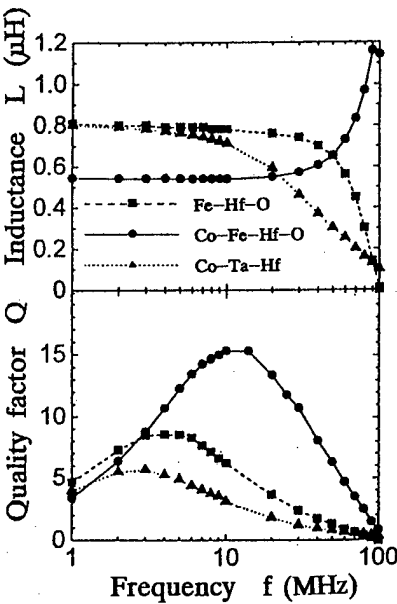


FIG. 4. Frequency characteristic of planar sandwich inductors.

Figure 4 shows the frequency characteristics of the planar sandwich inductors using Fe-Hf-O, Co-Fe-Hf-O, and Co-Ta-Hf film. The inductances at 1 MHz were 0.53–0.80 μH, and these were nearly constant up to 10 MHz, except for the Co-Ta-Hf film inductor. Though the cutoff frequency of μ' was about 90 MHz in 3 μm thick Co-Ta-Hf film, the inductance was gradually decreasing in the MHz band. This is mainly due to its low electrical resistivity. As shown in Fig. 5, the eddy currents in the top and bottom magnetic layers are not only due to the in-plane flux component, but also due to the perpendicular flux component. In particular, the latter component causes larger in-plane eddy current than that due to the former component. Therefore, it is important to increase the resistivity of the magnetic layer. In fact, the maximum quality factor of up to 16 was obtained through the inductor using the highest resistivity Co-Fe-Hf-O film.

Figure 6 shows the load current versus efficiency curves in the 5 MHz switching boost converter using planar sandwich inductor. The converter using Fe(Co-Fe)-Hf-O film inductors had higher efficiencies than those in case of Co-Ta-Hf film inductor. When the load current was large, the

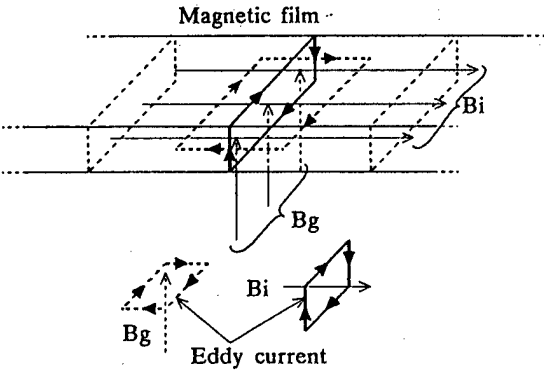


FIG. 5. In-plane eddy current due to perpendicular flux.

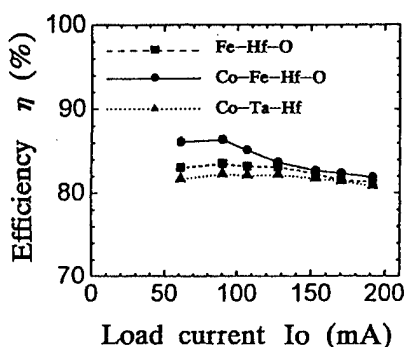


FIG. 6. Efficiency vs load current curves measured in 5 MHz switching boost converter using planar sandwich inductor, with 3.6 V input and 4.6 V output condition.

efficiencies were nearly the same. This is owing to the large dc copper losses in the inductors.

The flux gate sensors were produced by using Fe-Hf-O and Co-Ta-Hf films, since both films had relatively high permeability. Figure 7 is the relationship between second harmonic amplitude V_{2p} across the differential detecting coil and the external dc field H_{ext} , where frequency f was 1 MHz, and exciting current amplitude I_{max} was 700 mA. The field sensitivities S ($=dV_{2p}/dH_{ext}$) were about 100 mV/Oe and 77 mV/Oe in the Fe-Hf-O and Co-Ta-Hf, respectively. The Fe-Hf-O film flux gate sensor had higher sensitivity than that of the Co-Ta-Hf film sensor. In order to get higher sensor sensitivity, it is important not only to have high permeability, but also to have high resistivity, in the magnetic films used in the sensors. Figure 8 shows the frequency dependence of the sensor sensitivity S . The sensitivities were nearly proportional to the $f^{0.9}$. However, the sensitivity of the Co-Ta-Hf film sensor didn't become higher over 4

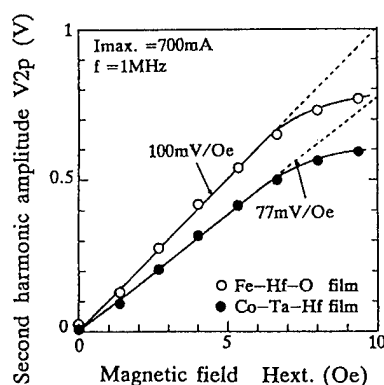


FIG. 7. Relationship between external magnetic field H_{ext} and second harmonic amplitude V_{2p} in flux gate sensor.

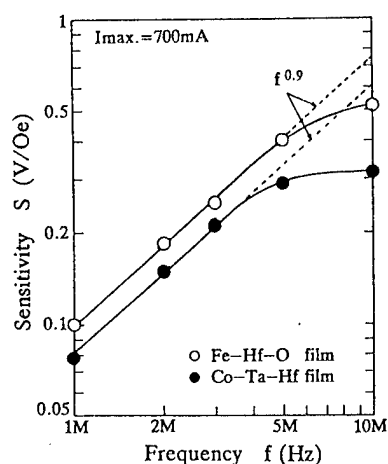


FIG. 8. Frequency dependence of sensitivity in flux gate sensor.

MHz. The similar sensitivity saturation was also observed over 6 MHz in the Fe-Hf-O film. The saturation frequency relates to the high frequency loss, that is, the magnetic loss due to the eddy current and winding loss due to the skin and proximity effects. Since the high frequency loss, which is described as the equivalent parallel resistance in the equivalent parallel circuit, gives rise to the degradation of the core excitation, it is necessary not only to use high permeability and low loss magnetic material, but also to establish the optimum device structure to reduce the excess losses (to get high sensitivity).

IV. SUMMARY

To develop high performance micromagnetic devices, some applications of high resistivity nanocrystalline magnetic films Fe(Co-Fe)-Hf-O were investigated. The results obtained were as follows.

(1) Planar sandwich inductors using high resistivity magnetic films had higher quality factor exceeding 10 in the MHz band, and enabled us to increase efficiency in the high frequency energy conversion.

(2) Solenoid flux gate sensor using high resistivity and high permeability magnetic film had higher sensitivity.

¹T. Sato, T. Inoue, H. Tomita, S. Yatabe, K. Nishijima, Y. Tokai, M. Nameki, N. Saito, and T. Mizoguchi, in *IEEE International Telecommunications Energy Conference 1996 Proceedings* (IEEE, Boston, 1996), pp. 485-490.

²C. R. Sullivan and S. R. Sanders, *IEEE Power Electronics Specialists Conference 1996 Proceedings* (unpublished), p. 287.

³S. Kawahito, Y. Sasaki, H. Satoh, T. Nakamura, and Y. Tadokoro, *Sens. Actuators A* **43**, 128 (1994).

⁴Y. Hayakawa and A. Makino, *Nanostruct. Mater.* **6**, 989 (1995).

⁵T. Sato, E. Komai, K. Yamasawa, T. Hatanai, and A. Makino, *IEEE Trans. Magn.* **33**, 3310 (1997).

⁶T. Kimura, M. Mitara, M. Terasaka, M. Nose, F. Matsumoto, H. Matsuki, H. Fujimori, and T. Masumoto, *J. Magn. Soc. Jpn.* **17**, 497 (1993).

Study on the in-plane uniaxial anisotropy of high permeability granular films

W. D. Li, O. Kitakami, and Y. Shimada

Research Institute for Scientific Measurements, Tohoku University, 2-1-1 Katahira, Aoba, Sendai 980-77, Japan

We have investigated the uniaxial magnetic anisotropy of the high resistivity Fe–Al–O granular films prepared by sputtering. It is found that application of external dc field during film deposition and post-annealing treatments give rise to no serious effects on the magnetic anisotropy. In contrast, the incident angle of sputtered particles to the substrate greatly affects the strength and the direction of the anisotropy. These results suggest that the magnetic anisotropy is induced by a shape anisotropy due to anisotropic morphology in the films. The temperature dependence of the anisotropy constant, however, does not obey the usual shape anisotropy relationship $K_u(T) \propto M_s(T)^2$. In the present article, we propose an anisotropic coupling model in order to explain the uniaxial anisotropy found in these granular films, where the magnetic coupling between Fe grains is assumed to be anisotropic in the film plane due to the presence of low T_c intergranular phase which bridges the gap between Fe grains in one direction but not in the orthogonal direction. This model satisfactorily explains the temperature dependence of $K_u(T)$ and $M_s(T)$ for all Fe–Al–O granular films prepared in the present experiment. This agreement between the experiments and the theory implies that the magnetic anisotropy of the granular films is remarkably influenced by the magnetism and spatial distribution of the low T_c intergranular phase. © 1998 American Institute of Physics. [S0021-8979(98)35211-1]

I. INTRODUCTION

High resistivity granular films receive much attention from the standpoint of low core-loss films for high frequency use.^{1–4} Since the high frequency behavior of the permeability is mainly dominated by the magnetic anisotropy of the films, it is essential to accurately control the anisotropy. However, the anisotropic field present in the granular films is so high (from $H_k=20$ Oe to about 300 Oe) that the conventional theories of induced anisotropy are inapplicable. Moreover, appearing in very fine Fe or Co crystals with no preferential crystal orientation, it cannot be explained by contribution from the crystalline anisotropy either. It has been reported that the anisotropy can be induced by magnetic field annealing in Co-based granular films,⁵ but not in Fe-based ones.

The origin of high uniaxial anisotropy appeared in the granular films still remains unclear to date.

In this article we mainly present the experimental procedure, the anisotropic exchange coupling model, the calculation of the microscopic shape anisotropy, and a possible method of controlling the anisotropy in order to improve the high frequency characteristics of the high resistivity granular films.

II. EXPERIMENT

Fe–Al–O granular films were prepared on glass substrates in a rf magnetron sputtering system at ambient temperature, with the base pressure less than 2×10^{-6} Torr and argon gas pressure of 4 mTorr. For some samples, a static field of 200 Oe was applied parallel to the substrate surface during the film deposition in order to check the effect of the field on the magnetic anisotropy. The film composition was

varied by changing the number of Al_2O_3 chips on an Fe target and were determined by wavelength dispersive x-ray analysis. The film thickness was kept constant at 2 μm . Three kinds of substrate holders were utilized to change the incident angle of sputtered particles to the film normal (0° , 20° , 30°).⁶ Thus obtained Fe–Al–O films were annealed in vacuum at 200–450 $^\circ\text{C}$ for 4 h under the dc field (1000 Oe) applied along either the easy or hard axis of the samples in the film plane. The crystalline structures and the magnetic properties were evaluated by an x-ray diffractometer (XRD) and a vibrating sample magnetometer (VSM), respectively.

III. RESULTS AND DISCUSSION

We found that both the direction and the strength of uniaxial anisotropy strongly depended on the substrate positions, namely, the easy axis lies along radial direction from the center of the substrate holder⁴ and its magnitude drastically increases with the average incident angle $\langle \theta \rangle$ of sputtered particles (see the inset in Fig. 2). On the other hand, the external field during film deposition gave rise to little changes in the distribution and the strength of the uniaxial magnetic anisotropy, indicating that the anisotropy is not induced by the magnetic annealing effect. In order to make this clear, the change of anisotropy constant (K_u) was measured after annealing in 1000 Oe dc magnetic field parallel or perpendicular to the easy direction of the samples. Figure 1 shows the dependence of K_u on annealing temperature and magnetic field direction. From this figure, it is clear that the anisotropy does not depend on the magnetic field direction. Therefore, it can be concluded that the anisotropy of Fe–Al–O film is not field induced. Figure 2 shows the anisotropy field (H_k) of the as-deposited Fe–Al–O films as a func-

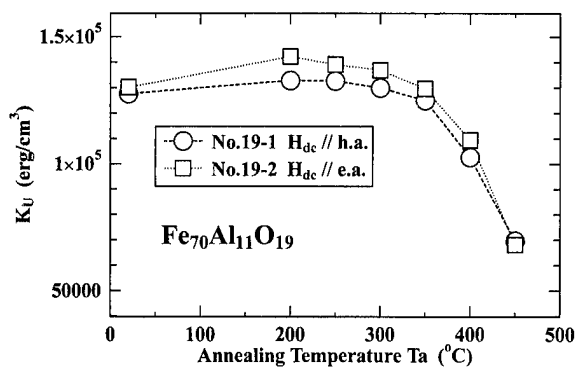


FIG. 1. Anisotropy dependence on annealing temperature and magnetic field direction for Fe-Al-O granular films.

tion of average incident angle $\langle\theta\rangle$. The magnitude of the uniaxial anisotropy is exclusively governed by $\langle\theta\rangle$ irrespective of other deposition conditions such as different substrate shapes and dc magnetic field. These results lead us to think that oblique incidence of sputtered particles causes the uniaxial anisotropy of the Fe-Al-O films. If an anisotropic film morphology develops by the oblique incidence effect,⁷ one may expect a magnetic anisotropy due to shape anisotropy. Then, the magnetic anisotropy would be proportional to the square of M_s . We measured $M_s(T)$ and $K_u(T)$ as a function of temperature in the range of 77–673 K, as shown in Fig. 3 with \circ and \triangle , respectively. We note that $K_u(T)$ drops off more rapidly than $M_s(T)^2$ (\square). Therefore, it is unlikely that a simple anisotropic morphology plays a dominant role for the occurrence of uniaxial magnetic anisotropy in the granular films. Moreover, as seen in Fig. 3, the M_s - T curve is quite different from that of pure α -Fe⁸ (—), indicating that the granular film contains a certain amount of low T_c phase in addition to α -Fe. Since we only observed the diffractions due to α -Fe in the XRD scans of the granular films, the unknown low T_c phase seems to be amorphous or severely disordered. Thus, it is reasonable to assume that the granular film consists of α -Fe grains and a low T_c disordered phase.⁹

Based on the above experimental results, we propose an anisotropic coupling model schematically shown in Fig. 4(a). In this model, the magnetic coupling between Fe grains is assumed to be anisotropic in the film plane due to the pres-

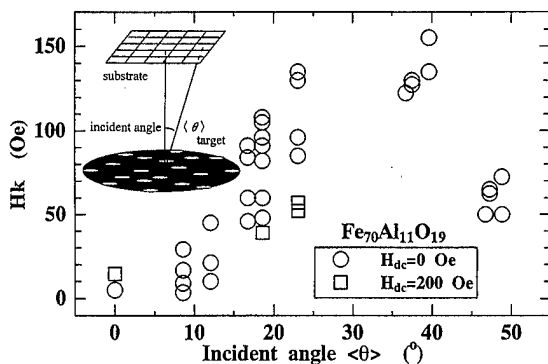


FIG. 2. Incident angle dependence of anisotropy field H_k for Fe-Al-O granular films.

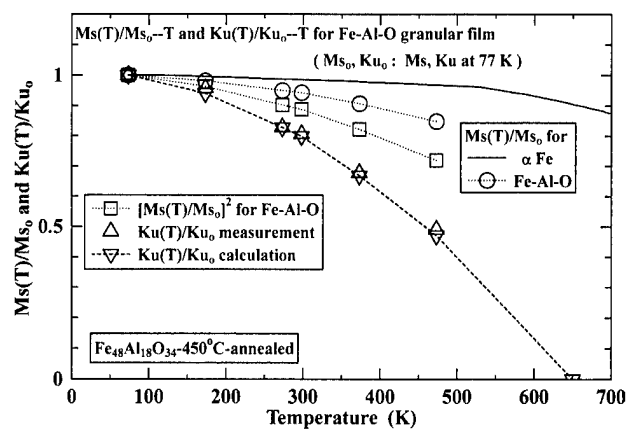


FIG. 3. Temperature dependence of M_s and H_k for an Fe-Al-O granular film.

ence of the low T_c intergranular phase, which anisotropically bridges the gap between Fe grains. This situation can be realized if the Fe content in the boundaries along the x direction is larger than along y direction. A simplified model for calculation is shown in Fig. 4(b). This model assumes rectangular shaped Fe grains and boundaries. The main difference of this model from that in Fig. 4(a) is that the exchange coupling appears only in the boundaries distributed along the x direction. In the actual films, the boundaries along the y direction may also be ferromagnetic, but this model assumes the exchange coupling along the x direction is strong enough to neglect them. According to the microscopic shape anisotropy model proposed by Fujiwara,¹⁰ the magnetostatic energies when the film is fully magnetized in the x and y directions are, respectively, given by

$$\epsilon_x = 2\pi M_s^\alpha (M_s^\alpha - M_s') \delta / a, \quad (1)$$

$$\epsilon_y = 2\pi (M_s^\alpha)^2 \delta / a, \quad (2)$$

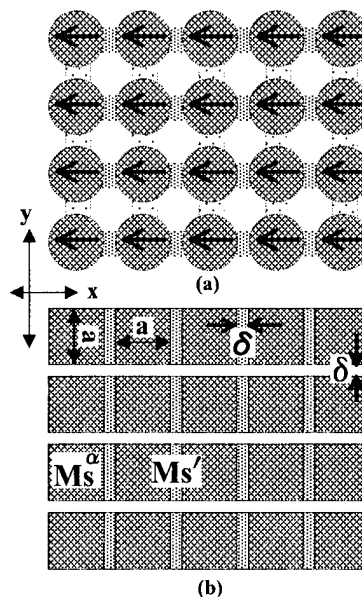


FIG. 4. Anisotropy model for Fe-Al-O granular films.

for $\delta \ll a$, where δ and a are the size of intergranular space and Fe granule, M_s^α and M_s' are the saturation magnetizations for the α -Fe phase and the low T_c boundary phase. The anisotropy energy is then given by the magnetostatic energy difference between Eqs. (1) and (2):

$$K_u = \Delta \epsilon = \epsilon_y - \epsilon_x = 2 \pi M_s^\alpha M_s' \delta / a. \quad (3)$$

Thus, the shape anisotropy is determined by the microscopic structural parameters δ/a and M_s' . From Eq. (3), the temperature dependence of the normalized anisotropy energy can be rewritten as

$$\frac{K_u(T)}{K_{u0}} = \frac{M_s^\alpha(T)}{M_{s0}^\alpha} \times \frac{M_s'(T)}{M_{s0}'}, \quad (4)$$

where K_{u0} , M_{s0}^α , and M_{s0}' are the values at liquid nitrogen temperature. When the volumetric ratios for α -Fe grains and low T_c phase are, respectively, V^α and V' , $M_s(T)$ of the film can be expressed as

$$M_s(T) = M_s^\alpha(T) V^\alpha + M_s'(T) V'. \quad (5)$$

At the Curie temperature of the low T_c intergranular phase ($T = T_c'$), Eq. (5) becomes

$$M_s(T_c') = M_s^\alpha(T_c') V^\alpha. \quad (6)$$

According to Eq. (3), the in-plane uniaxial anisotropy K_u vanishes at $T = T_c'$. Therefore, T_c' is defined as the temperature at which K_u becomes zero. Using Eqs. (5) and (6), Eq. (4) can be rewritten as

$$\frac{K_u(T)}{K_{u0}} = \frac{M_s^\alpha(T)}{M_{s0}^\alpha} \times \frac{M_s(T) - M_s(T_c') M_s^\alpha(T) / M_s^\alpha(T_c')}{M_{s0} - M_s(T_c') M_{s0}^\alpha / M_s^\alpha(T_c')}. \quad (7)$$

Substituting the magnetization values at various temperatures into Eq. (7), one can predict the temperature dependence of $K_u(T)$. Thus the predicted $K_u(T)$ perfectly coincides with the experimental results for all Fe-Al-O granular films prepared in the present study as shown in Fig. 5. We also found that the temperature dependence of $M_s(T)$ was well fitted by Eq. (5). Thus, the present anisotropic coupling model is appropriate to explain the uniaxial anisotropy of the Fe-Al-O granular films.

This model is also supported by measurement of the frequency dependence of permeability for Fe-Al-O films with various anisotropy fields H_k .^{3,4} By fitting the frequency dependence of permeability for Fe-Al-O films using the Landau-Lifshitz equation for magnetic films with uniaxial anisotropy, it is found that the damping constant becomes bigger for weak H_k . This implies the exchange coupling between the Fe grains becomes weaker, giving rise to a spin fluctuation to which the Landau-Lifshitz model is inapplicable.

As mentioned above, it is clarified that the magnetism of the boundary phase plays an important role for the magnetic anisotropy of the granular films. Therefore, one can optimize the magnetic anisotropy of the granular films for high frequency use by controlling the magnetism of the boundaries. For Fe-Al-O granular films, adjusting the slope of substrate surface is effective to control it.

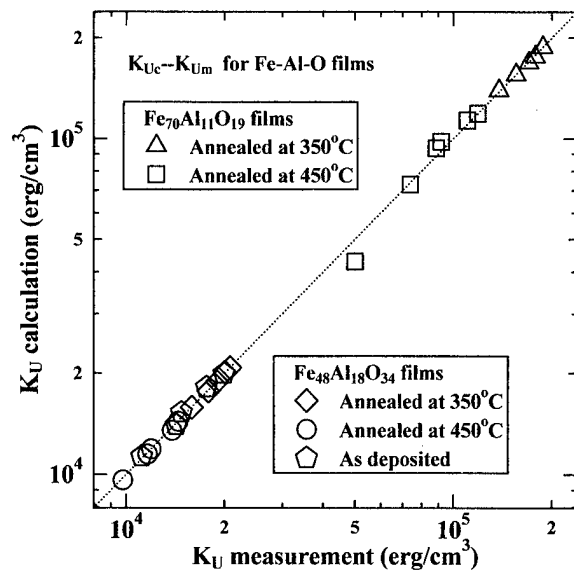


FIG. 5. Comparison of measured and calculated K_u for Fe-Al-O granular films.

IV. SUMMARY

We have investigated the uniaxial magnetic anisotropy of Fe-Al-O granular films. The main results can be summarized as follows:

- (1) The high uniaxial anisotropy found in Fe-Al-O granular films is not field induced, because the application of a static field during film deposition and post-annealing give rise to no significant changes in the anisotropy.
- (2) The behavior of the magnetic anisotropy can be satisfactorily explained by the proposed anisotropic coupling model in which the magnetic coupling between Fe grains is anisotropic in the film plane due to the presence of the low T_c intergranular phase. The good agreement between the experiment and the theory indicates that the magnetic anisotropy is dominated by the magnetism and spatial distribution of the low T_c intergranular phase.

ACKNOWLEDGMENT

This research was partly supported by the Storage Research Consortium (SRC) in Japan.

¹A. Makino and Y. Hayakawa, J. Magn. Soc. Jpn. **18**, 411 (1994).

²S. Ohnuma, H. Fujimori, S. Mitani, and T. Masumoto, J. Appl. Phys. **79**, 5130 (1996).

³W. D. Li, O. Kitakami, and Y. Shimada, J. Magn. Soc. Jpn. **20**, 461 (1996).

⁴W. D. Li, O. Kitakami, and Y. Shimada, J. Magn. Soc. Jpn. **22** (to be published).

⁵S. Mitani and S. Ohnuma, J. Magn. Soc. Jpn. **19**, 19 (1995).

⁶R. E. Jones, Jr., C. J. Spector, J. L. Williams, and C.-J. Lin, IEEE Trans. Magn. **32**, 4588 (1996).

⁷K. Kato, Y. Takeno, O. Kitakami, and Y. Shimada, J. Magn. Soc. Jpn. **21**, 1088 (1997).

⁸A. H. Morrish, *The Physical Principles of Magnetism* (Krieger, New York, 1980), p. 264.

⁹G. Herzer, IEEE Trans. Magn. **25**, 3327 (1989).

¹⁰H. Fujiwara, J. Phys. Soc. Jpn. **20**, 2092 (1965).

Soft magnetic properties of Co–Cr–O granular films

Takeshi Morikawa,^{a)} Motofumi Suzuki, and Yasunori Taga

Toyota Central R & D Laboratories, Inc., 41-1, Yokomichi, Nagakute, Aichi 480-11, Japan

Excellent soft magnetic properties have been achieved for Co–Cr–O granular films with nanoscaled grains of Co distributed in the amorphous intergranular regions of Cr_2O_3 . A rapid decrease in coercivity has been observed with the volume fraction of Co, and the minimum value of 0.39 Oe was obtained at 75.5 vol % of Co without postannealing. This value is one order of magnitude smaller than those of Co–Al–O and Co–Si–O sputtered films. The saturation magnetization, in-plane anisotropy field, and permeability below 800 MHz are 11.8 kG, 80 Oe, and 141, respectively. Because of its large saturation magnetization and in-plane anisotropy, the resonance frequency is estimated at 2.9 GHz. Therefore, Co–Cr–O granular films can be used in the high frequency devices operating over 2 GHz. © 1998 American Institute of Physics. [S0021-8979(98)29411-4]

I. INTRODUCTION

In recent years, soft ferromagnetic properties of granular thin films have attracted much attention for applications to magnetic devices operated in the GHz region such as micro-inductors, noise filters, and microsenors. High ferromagnetic resonance (FMR) frequency, large electrical resistivity ρ , and low coercivity H_c are required to reduce magnetic losses by FMR, eddy currents, and hysteresis. Up to now, soft magnetic properties of Fe–M–N,^{1,2} Fe–M–O,³ and Co–M–O⁴ films have been reported, where M are nonmagnetic materials such as B, Hf, Al, Si, Zr, etc. Among them, the Co–Al–O film⁴ shows a large FMR frequency of over 2 GHz and a high electrical resistivity of over 300 $\mu\Omega$ cm. Thus, they can be used in the GHz region. The mechanism of the soft magnetic properties of the Co–Al–O films is quantitatively understood by the random anisotropy model proposed by Herzer.⁵ The randomized magnetocrystalline anisotropy of each Co grain is effectively canceled within the ferromagnetic exchange length in the entire film. Therefore, the interaction between Co grains through the intergranular regions plays an important role in the soft magnetic properties.

On the other hand, the magnetic properties of Co-based granular films can be modified or enhanced, if the intergranular materials include 3d transition metals. However, such systems have not been investigated to date. In the present work, therefore, we have selected chromium oxide as the intergranular phase and achieved both a low coercivity and a high resonance frequency in the Co–Cr–O granular films.

II. EXPERIMENT

The Co–Cr–O thin films were deposited on glass and silicon (100) substrates in a magnetron sputtering system with a base pressure of $(4-8) \times 10^{-7}$ Torr. Co and Cr_2O_3 targets were sputtered in an Ar atmosphere of 3.0×10^{-3} Torr. In order to change the composition of the

samples, the deposition rate of Cr_2O_3 was varied over a wide range from 0 to 10 nm/min, while that of Co was kept constant at 16 nm/min. The thicknesses of films were 550 nm for all the samples. In order to induce unidirectional magnetic anisotropy, the films were deposited in the presence of a static in-plane magnetic field of 100–150 Oe. The substrate temperatures were below 50° during the deposition.

The structural and compositional characterization and the measurements of the electromagnetic properties were performed for the samples without any postannealing. Direct current resistivity was measured by the four-probe method. The structure was analyzed by x-ray diffractometry (XRD) with Cu $K\alpha$ radiation. The composition and chemical bonding were analyzed by x-ray photoemission spectroscopy (XPS) using a Mg $K\alpha$ x-ray source. Saturation magnetization $4\pi M_s$, coercivity H_c , and in-plane magnetic anisotropy field H_k were measured by a vibrating sample magnetometer (VSM). The complex permeability ($\mu = \mu' - j\mu''$) below 100 MHz was measured by the commercial permeance meter (Ryowa Electronics Inc.)⁶ together with a HP4194A impedance analyzer and that from 100 to 800 MHz was measured by the parallel line method^{7,8} using a HP8510C network analyzer. For the latter measurement, the measurement fixture was carefully designed to set its resonance frequency above 3 GHz.

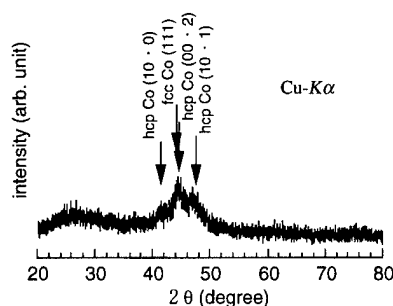


FIG. 1. X-ray diffraction pattern of 75.5 vol % Co ($\text{Co}_{77}\text{Cr}_9\text{O}_{14}$) film.

^{a)}Electronic mail: morikawa@iclab.tytlabs.co.jp

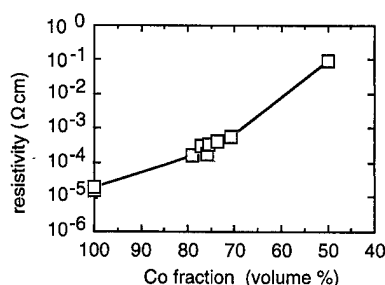


FIG. 2. Dependence of dc electrical resistivity on Co fraction.

III. RESULTS AND DISCUSSIONS

A. Film structure

In the XPS spectra for our samples, only the peaks due to the metallic Co and Cr–O bond were observed, while peaks due to Co–O, Co–Cr bonds and metallic Cr were not detected. It is also confirmed by XPS that the target composition of Cr_2O_3 is preserved in the films. In the present article, we use a nominal volume fraction of Co to denote the composition of the samples.

Figure 1 shows a typical x-ray diffraction pattern for the Co–Cr–O film of 75.5 vol % of Co. The film shows broad diffraction peaks corresponding to hcp (10•0), (00•2), (10•1), and fcc (111) of Co. The average diameter of Co grains is estimated to be 4 nm by Scherrer's formula. These diffraction peaks are observed in the films of 70.7–100.0 vol % of Co. On the other hand, no diffraction peaks due to the crystalline of Cr_2O_3 are observed. A (110) peak of Cr at $2\theta = 44.39^\circ$ is negligible because no metallic Cr was observed by XPS. Consequently, in our samples, nanoscaled metallic Co grains less than 4 nm in diameter are distributed in the amorphous intergranular region of Cr_2O_3 .

B. Electric and magnetic properties

Figure 2 shows a dependence of dc resistivity ρ on the volume fraction of Co. The resistivity increases exponentially with decreasing volume fraction of Co. The values of ρ are 300–400 $\mu\Omega \text{ cm}$ around 75 vol % of Co, where the films exhibit soft ferromagnetism as discussed below. These values of ρ are comparable with those of the Co–Al–O films.

Figure 3(a) shows a dependence of coercivity on the Co volume fraction. It is remarkable that the coercivity strongly depends on the volume fraction of Co. The minimum coercivity is smaller by three orders of magnitude than that of pure Co film. As shown in Table I, the films including Co of 73.8–75.5 vol % have coercivities less than 2 Oe which are

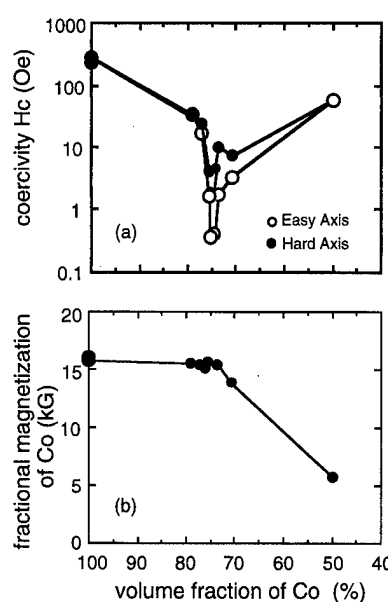


FIG. 3. Dependence of (a) coercivity and (b) fractional magnetization of Co on the volume fraction of Co.

superior to those of Co–Al–O.⁴ Particularly, the sample of 75.5 vol % of Co exhibits a small coercivity and a large unidirectional anisotropy field of 80 Oe as shown in Fig. 4. The minimum coercivity in the easy axis is 0.39 Oe. This value is one order of magnitude smaller than the value of Co–Al–O.⁴ The coercivity in the hard axis is 1.8 Oe. The reason for the larger hard axis coercivity is likely to be due to the magnetic anisotropy dispersion. However, the coercivity in the hard axis is also smaller than that of Co–Al–O.

Figure 3(b) shows a dependence of the fractional saturation magnetization on the volume fraction of Co. Here, the fractional saturation magnetization is defined as the ratio of the total saturation magnetizations of the samples to the volume fraction of Co. The fractional saturation magnetizations show a plateau of 15.7 kG within the region of 100–75.5 vol % of Co. This suggests that the Co grains in the Co–Cr–O films maintain the same magnetization as that of pure Co film. Below 75.5 vol % of Co, the fractional magnetizations begin to decrease with decreasing the volume fraction of Co, while the coercivity begins to increase. Hence, excellent soft magnetic properties are dominated by the nanoscaled Co grains with the same magnetizations as pure Co and the minimum coercivity appears near the boundary where magnetizations of Co grains begin to decrease.

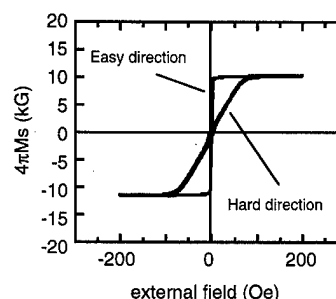
FIG. 4. In-plane M - H curves for 75.5 vol % of Co ($\text{Co}_{77}\text{Cr}_9\text{O}_{14}$).

TABLE I. Properties of Co–Cr–O films.

Composition		H_c (Oe)		$4\pi M_s$ (kG)	ρ ($\mu\Omega \text{ cm}$)
(vol % of Co)	(at. %)	Easy axis	Hard axis		
77.2	$\text{Co}_{80}\text{Cr}_8\text{O}_{12}$	17.0	24.6	11.9	310
75.5	$\text{Co}_{77}\text{Cr}_9\text{O}_{14}$	0.39	1.8	11.8	326
73.8	$\text{Co}_{74}\text{Cr}_{11}\text{O}_{16}$	1.7	10.2	11.4	396

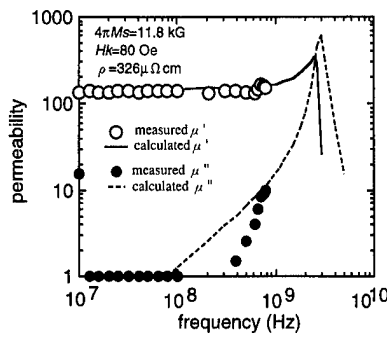


FIG. 5. Dependence of hard-axis complex permeability $\mu = \mu' - j\mu''$ on frequency for film of 75.5 vol % Co. Solid and dotted lines are calculated μ' and μ'' , respectively.

The drastic change in coercivity above 75.5 vol % of Co is due to the decrease in grain size⁵ from 26 to 4 nm. On the other hand, below 75.5 vol %, it is considered that the change is caused by the gradual decrease in ferromagnetic coupling between Co grains as expected in Fig. 3(b). Compared with previously reported Co-based films,⁴ the present Co-Cr-O film shows small coercivity. It is considered that the ferromagnetic exchange length may be effectively modified by the intergrains. However, a detailed investigation is necessary to clarify the mechanism of the small coercivities of Co-Cr-O films.

Figure 5 shows the dependence of hard-axis complex permeability $\mu = \mu' - j\mu''$ on frequency for the film of 75.5 vol % of Co. Open and solid circles represent the real and imaginary part of the measured permeability, respectively. The real part of measured permeability keeps constant at $\mu' = 141$ below 800 MHz. On the other hand, the imaginary part is $\mu'' = 1$ below 300 MHz and then increases with frequency. The solid and dotted lines represent μ' and μ'' , respectively, calculated by using the solution of Landau-Lifshitz equations taking account of the coherent spin rotation as follows:^{9,10}

$$\mu = \frac{4\pi M_s \omega_0^2 ((\omega_0^2 - \omega^2) - j4\pi\lambda\omega)}{H_k((\omega_0^2 - \omega^2)^2 + (4\pi\lambda\omega)^2)}, \quad (1)$$

$$\omega_0^2 = 4\pi|\gamma|^2 M_s H_k, \quad (2)$$

where, ω_0 is the FMR frequency, γ is the gyromagnetic constant (here, 2.34×10^5 m/As), and λ is the relaxation frequency.

The calculated permeability agrees well with the measured ones. This indicates that the domain wall motion is

eliminated because of the operation at very high frequency. Furthermore, since the Co-Cr-O film has a large $4\pi M_s$ and H_k , the FMR frequency is estimated at about 2.9 GHz [Eq. (2)]. The skin depth of the film is estimated at 1.4 μm at 2.9 GHz and eddy current loss is negligible in this frequency region because of large ρ . In consequence, it is expected that the real permeability μ' keeps constant up to 2 GHz so that the present Co-Cr-O system is applicable to the high frequency devices operated over 2 GHz.

IV. CONCLUSION

Soft magnetic properties of Co-Cr-O granular films prepared by codeposition of Co and Cr_2O_3 are investigated. In the resulting films, nanocrystalline Co grains distributed in the amorphous intergranular regions of Cr_2O_3 . A drastic change in coercivity is observed depending on the volume fraction of Co. The excellent soft magnetic property has been achieved at 75.5 vol % of Co. The $4\pi M_s$ of 11.8 kG, H_k of 80 Oe, and H_c of 0.39 Oe are obtained. The value of H_c is one order of magnitude smaller than the previously reported Co-based films. The dc resistivity is 326 $\mu\Omega\text{cm}$. The real part of the permeability keeps constant at 141 up to 800 MHz and the FMR frequency is estimated at 2.9 GHz. Therefore, Co-Cr-O granular films can be used in the high frequency devices operated over 2 GHz.

ACKNOWLEDGMENTS

We are very thankful to N. Takahashi and K. Dohmae for their help in measuring XPS.

- ¹H. Karamon, T. Masumoto, and Y. Makino, J. Appl. Phys. **57**, 3527 (1985).
- ²S. Jin, W. Zhu, R. B. van Dover, T. H. Tiefel, and V. Korenivski, Appl. Phys. Lett. **70**, 3161 (1997).
- ³Y. Hayakawa, A. Makino, H. Fujimoto, and A. Inoue, J. Appl. Phys. **81**, 3747 (1997).
- ⁴S. Ohnuma, S. Mitani, H. Fujimori, and T. Masumoto, J. Magn. Soc. Jpn. **20**, 489 (1996).
- ⁵G. Herzer, IEEE Trans. Magn. **26**, 1397 (1990).
- ⁶T. Kawazu, M. Yamaguchi, and K. I. Arai, IEEE Trans. Magn. **30**, 4641 (1994).
- ⁷T. Kimura, M. Mitera, M. Terasaka, M. Nose, F. Matsumoto, H. Matsuki, H. Fujimori, and T. Masumoto, J. Magn. Soc. Jpn. **17**, 497 (1993).
- ⁸V. Korenivski, R. B. van Dover, P. M. Mankiewich, Z. X. Ma, A. J. Becker, P. A. Polakos, and V. J. Fratello, IEEE Trans. Magn. **32**, 4905 (1996).
- ⁹Y. Maehata, S. Tsunashima, and S. Uchiyama, J. Magn. Soc. Jpn. **9**, 207 (1985).
- ¹⁰A. Hosono and Y. Shimada, J. Magn. Soc. Jpn. **12**, 295 (1988).

Magnetic properties of Fe films deposited by Ar, Kr, and Xe ion beam sputtering

S. Iwatsubo, T. Takahashi,^{a)} and M. Naoe^{b)}

Toyama Industrial Technology Center, Takaoka, Toyama 933, Japan

Fe films have been deposited by ion beam sputtering using Ar, Kr, and Xe gases. The sputtering voltage V_S was varied in the range of 900–1800 V. The magnetic properties of the films had the significant relationship with the element of the sputtering gas. The saturation magnetization $4\pi M_S$ was 21 kG for Ar and 20 kG for Kr or Xe. The coercivity H_C took the minimum value of 5 Oe at V_S of 1200 V for Ar. The energy/the number of the energetic particles, such as the sputtered atoms and the recoiled ions bombarding to the substrate was calculated by Monte-Carlo simulation in the sputtering system with an amorphous Fe target. The average energy of the sputtered atoms E_S was 40–60 eV for Ar, 30–34 eV for Kr and 24–34 eV for Xe. The average energy of the recoiled ions E_R was 200–370 eV for Ar, 60–100 eV for Kr, and 25–50 eV for Xe. The energy was remarkably different among their sputtering gases with different atomic mass. The bombardment by the recoiled ions at the high energy reduced the coercivity H_C of the Fe films. © 1998 American Institute of Physics. [S0021-8979(98)35311-6]

I. INTRODUCTION

Pure Fe is one of the most representative materials with soft magnetism such as a low coercivity and a large saturation magnetization of 21.5 kG. So far, when Fe films were deposited by sputtering, their structure and properties significantly depended on the preparation condition.^{1–3} For the film preparation with good reproducibility it should be required to control the energy of the arrival particles to the substrate. The energy may be the most significant factor to characterize the properties of the deposited films.

In sputtering, both the energy and the flux of the sputtered atoms and the recoiled ions depends on the difference in atomic mass between the component elements of target and the sputtering gas. So, the sputtering using the gas with different atomic mass is an effective method to control the parameters. Therefore, the magnetic properties of Fe films may be controlled by sputtering with Kr and Xe instead of Ar.

In this study, the difference of magnetic properties of the Fe films among Ar, Kr, and Xe gases has been investigated using an ion-beam sputtering apparatus with the features of plasma-free deposition and good controllability. The Monte-Carlo simulation TRIM⁴ was used to estimate the energy and flux of the arriving particles, that is, the sputtered atoms and the recoiled ions, to the substrate plane.

II. EXPERIMENTAL PROCEDURE

The Fe films were deposited on water-cooled glass substrates using an ion beam sputtering apparatus with an ion source. It was Kaufman-type and the grid had a diameter of 2.5 cm. The target was a Fe disk of 99.9% in purity and 120 mm in diameter. The distance between the target and the

substrate was 200 mm. Pure Ar, Kr, and Xe with the different atomic mass were used as the sputtering gas. After the chamber was evacuated to the residual gas pressure lower than 6×10^{-5} Pa, the sputtering gas at flow rate of 2 sccm was introduced into the sputtering ion source. Gas pressure was 5.0, 11, and 30 mPa for Ar, Kr, and Xe, respectively. The current of the sputtering ion beam was fixed at 50 mA. Film thickness was approximately 300–350 nm. The internal stress σ was calculated from the measured value of the curvature of cantilever samples. The electrical resistivity ρ was measured by the four-terminal method. The saturation magnetization $4\pi M_S$ and the coercivity H_C of the Fe films were measured using a vibrating sample magnetometer (VSM).

III. RESULTS AND DISCUSSION

A. Simulation results and deposition rate

Figure 1 shows the schematic layout of the ion beam sputtering (IBS) apparatus used in this study and the angular distribution in energy of the Ar ions recoiled from the Fe target at the sputtering voltage V_S of 1200 V, as calculated by Monte-Carlo simulation TRIM. The TRIM calculations

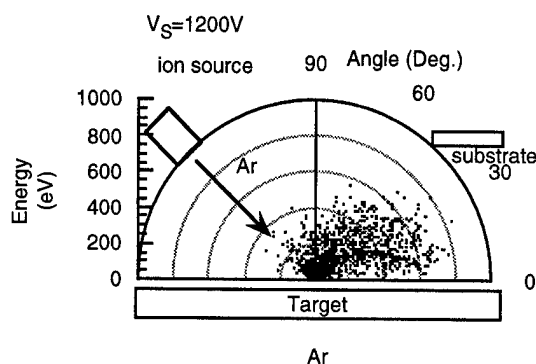


FIG. 1. Layout of IBS apparatus and angular distribution in energy of Ar recoiled ions.

^{a)}Faculty of Engineering, Toyama University, Toyama, Toyama 930, Japan.

^{b)}Faculty of Engineering, Tokyo Institute of Technology, Meguroku, Tokyo 152, Japan.

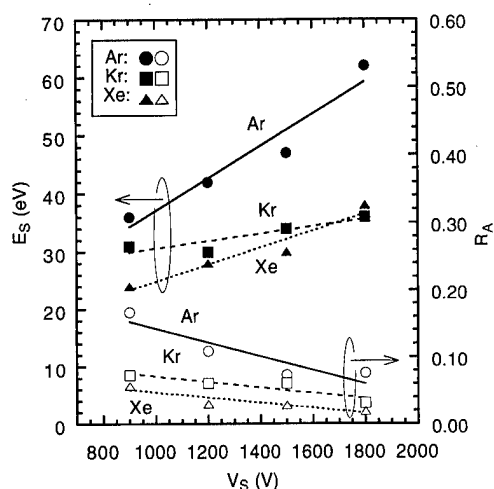


FIG. 2. V_S dependence of average energy of sputtered atoms E_S and ratio in arrival number R_A for Ar, Kr, and Xe as sputtering gas.

are based on a direct Monte-Carlo method applied to the transport of ions and recoils in an amorphous Fe target. The incident angle of the sputtering ion beam to target plane was equal to 45° . The substrate was parallel to the target plane. The calculation at 10 000 events was executed. The small dots in the figure correspond to the energy and the angular direction of recoiled ions. In this figure, the substrate was bombarded by the recoiled Ar ions at the high energy up to 800 eV. The flux of a large number of the recoiled ions was reflected from the ion source in the direction of the target plane to the substrate.

Figure 2 shows the V_S dependence of the average energy E_S of the sputtered atoms and the ratio in arrival number R_A of the recoiled ions to the sputtered Fe atoms to the substrate. Namely, R_A was given by

$$R_A = \frac{\text{Number of recoiled ions}}{\text{Number of sputtered Fe atoms}}.$$

The energy of the sputtered atoms and the recoiled ions was estimated from taking statistics of the particles arrived at the substrate surface as shown in Fig. 1. For Ar, E_S monotonically increased from 40 to 60 eV with an increase of V_S . For Kr and Xe, E_S gradually increased from 24 to 35 eV. On the other hand, R_A decreased with an increase of V_S . R_A was in the range of 0.07–0.16 for Ar, 0.03–0.07 for Kr, and 0.02–0.06 for Xe. The values of E_S and R_A for Kr and Xe were remarkably different from those for Ar.

Figure 3 shows the V_S dependence of the average energy E_R of the recoiled ions. E_R increased in proportion to an increase of V_S . The value of E_R was in the range of 200–380 eV for Ar, 60–100 eV for Kr, 20–50 eV for Xe. The magnitude in variation of E_R was larger than that of E_S . For Xe, E_R was at the almost same value. On the other hand, E_R for Ar was very high. Especially for Ar, the film surface was bombarded by the recoiled ions with E_R of 380 eV and R_A of 0.07 at V_S of 1800 V. It seems that the bombarding effect by the recoiled Ar ions is very serious for the growing Fe films.

Figure 4 shows the V_S dependence of the deposition rate R_D . R_D linearly increased with increase of V_S for Kr and Xe. On the other hand, R_D for Ar was almost constant value

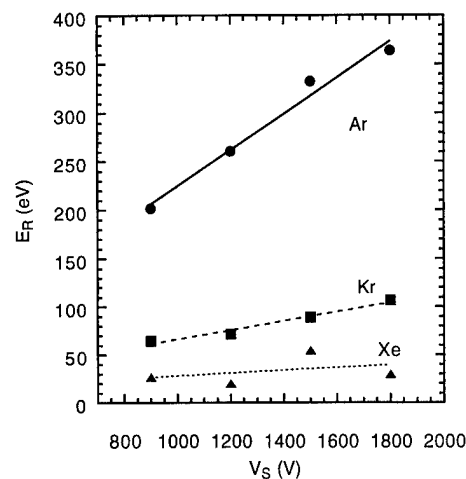


FIG. 3. V_A dependence of average energy of recoiled ions E_R .

of 2.2 nm/min. This difference may be due to the re-sputtering effect by the recoiled ions to the substrate. Because the recoiled ions for Ar possess a high energy enough to sputter the surface region of film. The extent of R_D reduction by resputtering effect corresponded to the value estimated from R_A and the sputtering yield of Fe at each E_R .

B. Properties

Figure 5 shows the V_S dependence of the internal stress σ . The negative value of σ indicates compressive stress. σ monotonically decreased from -0.02 to -0.1 GPa with increase of V_S for Kr and Xe. On the other hand, for Ar, σ took the minimum value of -0.14 GPa at V_S of 1200 V. The absolute value of σ for Ar was larger than that for Kr and Xe. It was caused from the atom peening effect due to bombardment by the recoiled ions with the high energy. As a result, the films deposited under the Ar bombardment, that is, a bias sputtering,⁵ exhibited high internal stress.

Figure 6 shows the V_S dependence of the electrical resistivity ρ of the films. The film exhibited higher ρ than bulk pure Fe (about $10 \mu\Omega \text{ cm}$). ρ was almost constant for Kr and Xe. On the other hand, for Ar, ρ increased from 24 to 56

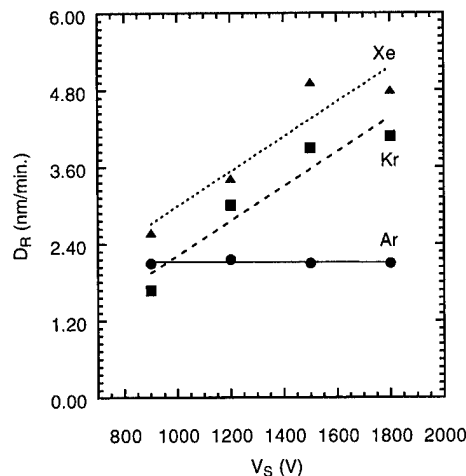
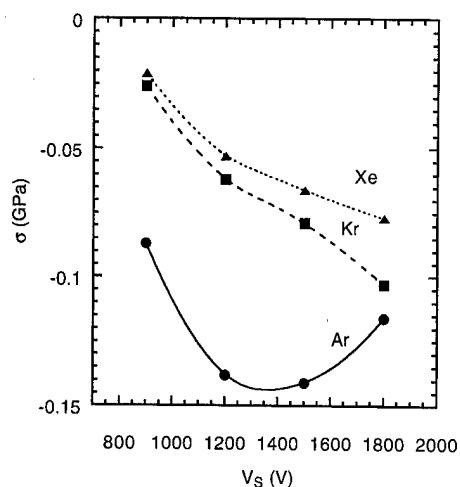
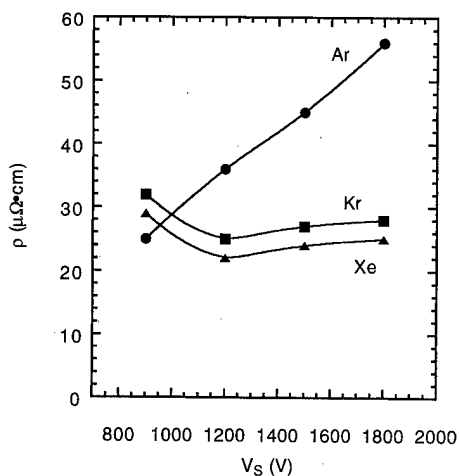
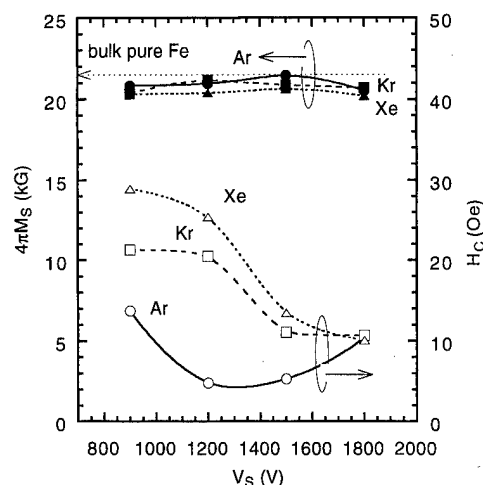


FIG. 4. V_A dependence of deposition rate D_R .

FIG. 5. V_A dependence of internal stress σ .

$\mu\Omega$ cm in proportion to V_s . Generally, the value of ρ strongly depended on the film structure. The variation of ρ may be attributed to electron scattering at the grain boundary of the microstructure in the films. The grain size of films for Ar seems to be smaller than that for Kr and Xe.

Figure 7 shows the V_s dependence of the saturation magnetization $4\pi M_s$ and the coercivity H_C . $4\pi M_s$ was nearly equal to that of bulk pure Fe for all gases. On the other hand, H_C decreased with increase of V_s for Kr and Xe. H_C was in the range from 10 to 20 Oe for Kr and from 10 to 30 Oe for Xe. For Ar, H_C took the minimum value of 5 Oe at V_s of 1200 V. H_C was remarkably different among sput-

FIG. 6. V_A dependence of electrical resistivity ρ .FIG. 7. V_A dependence of saturation magnetization $4\pi M_s$ and coercivity H_C .

tering gases, where for Ar was lowest. This result agreed exactly with the fact that the Fe films deposited with the ion bombardment such as bias sputtering¹ and double ion beam sputtering^{2,3} had lower H_C . Therefore, the decrease of H_C may be caused by the bombardment of the recoiled ions with high energy.

IV. CONCLUSION

The energy of the recoiled ions E_R from the target plane was related to the change of V_s . E_R was very different among the sputtering gases. For Ar, E_R was in the range of 200 to 380 eV. For Kr and Xe, E_R was in the range from 40 to 110 eV. The bombardment by the high energy recoiled ions changed the electrical and magnetic properties of the Fe films. The Fe films with good soft magnetism such as $4\pi M_s$ of about 21.5 kG and H_C of 5 Oe were deposited at V_s of 1200 V for Ar. For the Fe films deposited by Kr and Xe sputtering, $4\pi M_s$ and H_C were about 20 kG, and 10–30 Oe, respectively. The Fe films with lower H_C was obtained by bombardment of the recoiled ions with the high energy.

Consequently, it was found that the recoiled ions played a very important role to deposit the good soft magnetic Fe films by ion-beam sputtering. The energy of the recoiled ions, in other words, the mass of the sputtering gas may be an important parameter to characterize the properties of the Fe films.

¹A. Fukizawa and M. Naoe, IEEE Trans. Magn. **MAG-23**, 140 (1987).

²M. Naoe, Y. Yamaga, and N. Terada, IEEE Trans. Magn. **MAG-21**, 1900 (1985).

³N. Ishiwata, C. Wakabayashi, and T. Matsumoto, IEEE Trans. Magn. **24**, 3078 (1988).

⁴J. P. Biersack and W. Eckstein, Appl. Phys. A: Solids Surf. **34**, 73 (1984).

⁵R. D. Bland, G. J. Kominiak, and D. M. Mattox, J. Vac. Sci. Technol. **11**, 671 (1974).

Effects of plasma and bias power on magnetic properties of sendust films

M. S. Araghi, R. E. Hurley, and H. S. Gamble

Northern Ireland Semiconductor Research Centre, Department of Electronic and Electrical Engineering, The Queen's University of Belfast, Belfast, BT7 1NN, United Kingdom

P. M. Dodd and R. Atkinson

Department of Pure and Applied Physics, The Queen's University of Belfast, Belfast, BT7 1NN, United Kingdom

Thin films of Sendust (wt. 85% Fe, 10% Si, 5% Al) were deposited by rf diode and dc magnetron sputtering. The objective was the production of soft magnetic films without post deposition annealing. Films were deposited on both glass and $\text{Al}_2\text{O}_3/\text{TiC}(\text{AlTiC})$ ceramic substrate. Coercivities in the range 45 to 50 Oe for rf diode deposited and 25 to 35 Oe for dc magnetron deposited films were measured. Application of rf bias to the substrate reduced this further to 7 to 12 Oe together with a reduction in grain size. The value of magnetic flux at the surface of the sputtering target was controlled by an electromagnet and found to be an important parameter for the production of soft magnetic films, low flux densities producing the softest layers. This may be related to deposition rate and/or the influence of the target magnetic field penetrating into the substrate region. The softer magnetic layers produced as a result of applying a low rf bias to the substrate is believed to be due to ion bombardment during deposition resulting in smaller grain size. © 1998 American Institute of Physics. [S0021-8979(98)41611-6]

I. INTRODUCTION

Sendust thin films have applications in both metal-in-gap (MIG) and thin film recording heads due to their soft magnetic properties and high degree of mechanical hardness. Generally, sendust films deposited by rf diode sputtering do not possess soft magnetic properties, a post-deposition anneal step being necessary to achieve a sufficiently low value of coercivity.¹ The process annealing step is normally carried out by either conventional furnace methods and/or rapid thermal annealing;² it would be a major advantage to eliminate this in production applications. In the present study, the effects of deposition parameters on magnetic properties of Sendust films have been investigated, the final objective being the optimization of process parameters in order to obtain magnetically soft films without the need for a process annealing step.

II. EXPERIMENTAL PROCEDURES

Films were produced in a CVC AST 304 sputtering system employing a 20 cm diameter, 6 mm thick Sendust target.

TABLE I. Process parameters for rf diode sputtered films.

Base pressure	$7-9 \times 10^{-7}$ Torr
Argon gas pressure	8×10^{-3} Torr
RF input power	750 W
Target/substrate separation	55 mm
Substrate temperature	10–30 °C
Deposition rate	500 nm/h
Coercivity	55–90 Oe
Grain size	55–80 nm

Rf diode sputtered films of Sendust 2–2.2 μm thick were deposited on both glass and AlTiC substrates which were thermally anchored to the substrate holder's cooling mechanism. Process conditions and parameters are shown in Table I. Dc magnetron sputtered films were produced using a 20 cm, 6 mm thick Sendust target and a backing assembly employing an electromagnet which was designed and con-

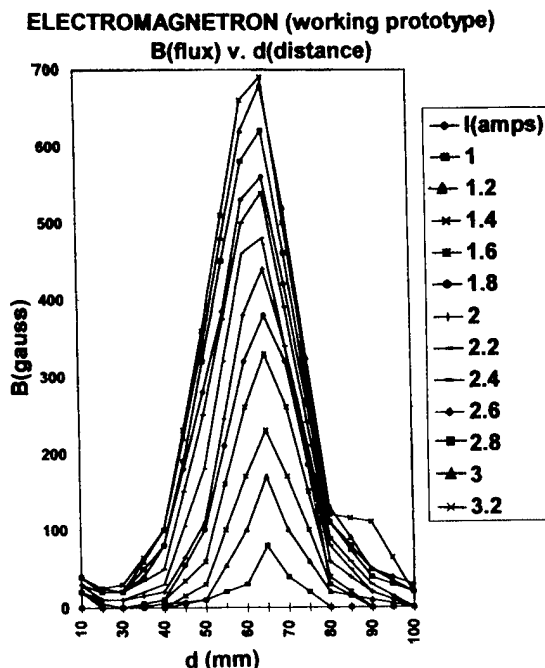


FIG. 1. Flux produced by the electromagnet as a function of applied current.

TABLE II. Process parameters for dc magnetron sputtered films.

Base pressure	$7-9 \times 10^{-7}$ Torr
Argon gas pressure	8×10^{-3} Torr
DC input power	750 W
Target/substrate separation	55 mm
Substrate temperature	10–23 °C
Deposition rate	4 $\mu\text{m/h}$
Coercivity	25–35 Oe
Grain size	25–50 nm

structed in-house. By altering the coil current, the magnetic flux at the surface of the target was varied by saturating the flux within the target in the radial direction. Figure 1 shows the radial component of flux parallel to and immediately above the target surface as a function of the distance from the outer edge of the target for various coil currents.

For certain experiments, rf bias was applied to the substrates. The crystalline structure of films were characterized using x-ray diffraction (XRD). Grain size and surface roughness measurements were carried out using atomic force microscopy (AFM). Magnetic properties of films were studied using a BH hysteresis loop tracer and a magneto-optical looper utilizing the longitudinal Kerr effect. Electron microprobe analysis was used to determine the composition of films.

III. RESULTS AND DISCUSSION

A. Rf diode sputtered films

As shown in Table I, deposited layers had measured coercivities in the range 45–50 Oe, grain size varying between 60–80 nm. Film adhesion was good. Low coercivity films could only be produced from rf sputtered layers by post-deposition annealing. Deposition rates were low as expected from an rf diode configuration. These results are similar to those quoted in the literature, and verify the effect of high energy secondary electrons which are produced in rf diode configurations and are known to produce high coercivity layers.³ Film structure and properties could also be affected by reflected high energy neutrals⁴ and negative ion⁵ bombardment from impurity ions which could be significant in the current experimental conditions.

TABLE III. Optimal process parameters for dc magnetron sputtered films.

Base pressure	$7-9 \times 10^{-7}$ Torr
Argon gas pressure	20×10^{-3} Torr
DC input power	250 W
Target/substrate separation	55 mm
Substrate temperature	10–13 °C
Deposition rate	1 $\mu\text{m/h}$
Coercivity	22–30 Oe
Grain size	25–40 nm

TABLE IV. Optimal process parameters for dc magnetron sputtered films plus bias power.

Base pressure	$7-9 \times 10^{-7}$ Torr
Argon gas pressure	20×10^{-3} Torr
DC input power	250 W
RF bias power	90 W
Substrate temperature	10–17 °C
Target/substrate separation	55 mm
Deposition rate	1 $\mu\text{m/h}$
Coercivity	7–12 Oe
Grain size	10–25 nm

B. Dc-magnetron films

Table II shows that coercivities in the range 25–30 Oe were typical in the case where no rf substrate bias was applied. Adhesion was good, but AFM analysis indicated large grain sizes. Variations in process parameters were investigated and it was found that a reduction in the deposition power from 750 to 250 W as shown in Table III, together with an increase in process gas pressure from 8 to 20 mTorr did result in marginally softer films. The plasma in front of the target had a “hollow cone” shape and it was observed that where it was in contact with the surface of the substrate, deposited film surfaces appeared much smoother due to smaller grain sizes which was verified by AFM measurements. In addition, a slight decrease in coercivity was observed. A more uniform distribution of plasma was achieved by applying rf bias to the substrate during deposition with a resulting smoothness of the surface of the deposited films. This resulted in a further reduction in grain size and produced films which had much improved soft magnetic properties (7–12 Oe) as shown in Table IV. Argon was the only process gas, but incorporation of N_2 has been reported to result in further reductions in coercivity.⁶ The composition of films was very close to that of the bulk sendust target. Experiments showed that the optimum value of rf bias power for soft films was in the range 90–100 W. At higher powers a marked decrease in film adhesion and an increase in coercivity was observed. The dependence of coercivity on bias power for optimum process conditions is shown in Fig. 2. Figure 3 shows the relationship between grain size and co-

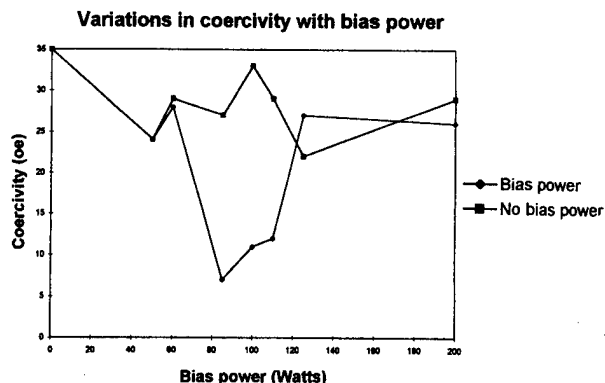


FIG. 2. Effect of bias power on coercivity.

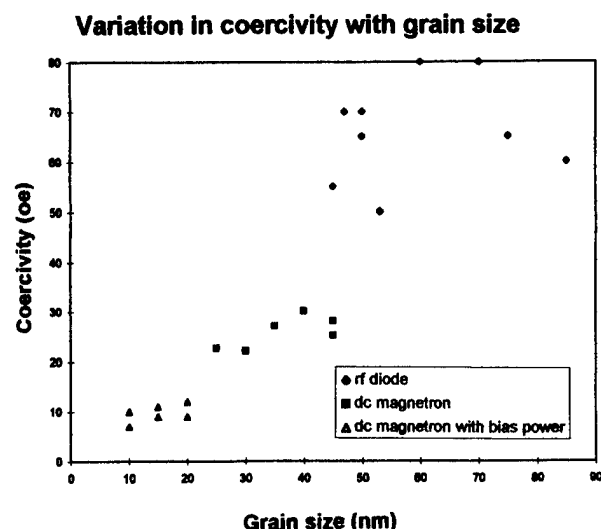


FIG. 3. Variations in coercivity as a function of grain size.

ercivity, coercivity decreasing as expected with grain size.⁷ In Figs. 4(a) and 4(b) AFM micrographs of the surfaces of two typical films are shown. Figure 4(a) shows films deposited without the application of a bias power whereas in Fig. 4(b) the bias power is present and smaller grains have been formed.

When electromagnet coil current was increased to produce flux densities of 500–600 Gauss at the target surface and a more intense confined plasma, the deposited films had a more crystalline structure as indicated by XRD analysis and were magnetically harder. The effect may be caused in the present experiments by the increased deposition rate upsetting the balance between the atom arrival and bombardment from the substrate plasma. This allows large grains to grow with increased deposition rate and hence the production of harder layers. Further work could profitably investigate the role of nitrogen which has been reported to result in further reductions in coercivity.

IV. CONCLUSIONS

The optimum process conditions and parameters for achieving soft magnetic properties without the need for annealing and/or N₂ reactive sputtering have been determined. Soft magnetic properties were found to be dependent mainly on small grain size which was achieved by the application of rf bias power during deposition. It is believed that the plasma

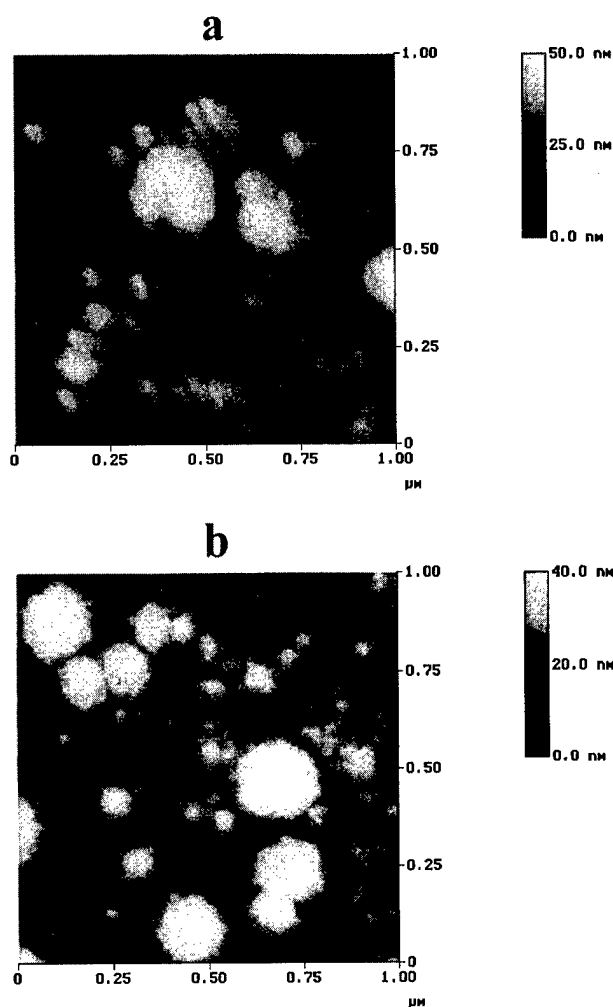


FIG. 4. Atomic force micrographs showing grains in (a) a hard film (b) a soft film.

induced bias provides an energy input by ion bombardment which during deposition results in reduced grain size and softer layers.

¹J. Daval, B. Bechevet, J. Arroyo, B. Vallon, M. F. Armand, and H. Joisten, *IEEE Trans. Magn.* **30**, 3930 (1994).

²P. M. Dodd, R. Atkinson, P. Papakonstantinou, M. S. Araghi, and H. S. Gamble, *J. Appl. Phys.* **81**, 4104 (1997).

³M. I. Ullah, K. R. Coffey, M. A. Parker, and J. K. Howard, *IEEE Trans. Magn.* **30**, 3927 (1994).

⁴R. E. Hurley, *Thin Solid Films* **86**, 241 (1981).

⁵J. A. Thornton, *Thin Solid Films* **54**, 23 (1978).

⁶Y. Chen, P. J. Ryan, J. F. Dolcisi, G. Al-Jumaily, Z. Yang, D. R. Louder, T. J. McKay, D. Macken, and M. H. Kryder, *Conference Proceedings, Digest of Intermag 97, GD/06* (1997).

⁷G. Herzer, *IEEE Trans. Magn.* **26**, 1397 (1990).

Preparation of soft magnetic films of nanocrystalline Fe–Cu–Nb–Si–B alloy by facing targets sputtering

Masahiko Naoe, Hiroaki Matsumiya, Takayuki Ichihara, and Shigeki Nakagawa

Department of Physical Electronics, Tokyo Institute of Technology, 2-12-1, O-okayama, Meguro, Tokyo 152, Japan

Soft magnetic thin films of nanocrystalline Fe–Cu–Nb–Si–B alloy were deposited using the facing targets sputtering (FTS) apparatus. It was found that the Fe–Cu–Nb–Si–B single layers thinner than 100 nm revealed good soft magnetic properties, of which the saturation magnetization $4\pi M_s$ and the relative permeability μ_r were 11.3 kG and 500, respectively. However, when these films were thicker than 100 nm, their soft magnetic properties degraded due to the perpendicular magnetic anisotropy. On the other hand, the soft magnetic properties of the post-annealed films were improved owing to the release of stress in the films. Especially, μ_r of the post-annealed films with thickness of 120 nm increased drastically up to around 6200. Furthermore, Fe–Cu–Nb–Si–B/Al multilayers revealed superior soft magnetic properties due to the magnetostatic coupling between the two ferromagnetic layers. These multilayers post-annealed at 300 °C revealed softer magnetic properties than single layers. They exhibited very low coercivity H_c of 0.63 Oe, large $4\pi M_s$ of 13.2 kG and high μ_r of 4600. © 1998 American Institute of Physics. [S0021-8979(98)41711-0]

I. INTRODUCTION

Nowadays, the very soft magnetic thin films with large saturation magnetization are required for the development of various magnetic components in new electronic devices. Therefore, amorphous magnetic alloys have been studied and they are used for many applications. Although amorphous magnetic Fe–Si–B alloys exhibit large saturation magnetization, their soft magnetic properties tend to degrade in the high-frequency range comparing with amorphous Co-based alloys. However, it has been reported that Fe–Cu–Nb–Si–B alloys exhibit excellently soft magnetic properties and large saturation magnetization due to the formation of fine bcc Fe crystallites by adding Cu and Nb.¹ In addition, they exhibit relatively high resistivity comparing with other soft magnetic materials, such as Ni–Fe, and superior soft magnetic properties in high-frequency range. For these reasons, thin films of Fe–Cu–Nb–Si–B alloy, which are also anticipated to reveal such superior soft magnetic properties and nanocrystalline microstructure, are expected for the materials of core layers in the magnetic recording heads.

In this study, the Fe–Cu–Nb–Si–B thin films were deposited using the facing targets sputtering (FTS) apparatus at lower substrate temperature. And then, the films were post-annealed at 300 °C in order to improve the soft magnetic characteristics of them. Furthermore, the Fe–Cu–Nb–Si–B/Al multilayers were fabricated in order to improve soft magnetic characteristics of Fe–Cu–Nb–Si–B thin films with large thickness.

II. EXPERIMENT

The Fe–Cu–Nb–Si–B thin films were deposited on glass substrates at the substrate temperature T_s of 30 and 300 °C using the FTS apparatus with the targets of commercial Fe₇₅Cu₁Nb₃Si₁₄B₇ alloy under the background pressure lower than 1.0×10^{-6} Torr. The sputtering Ar gas pressure

P_{Ar} was fixed at 1.0 mTorr, and the input power P_{in} and the deposition rate R_d were set at 160 W and 4.5 nm/min, respectively. In addition, the films deposited at T_s of both 30 and 300 °C were heated at the annealing temperature T_A of 300 °C in vacuum for 2 h without the magnetic field and then, the magnetic characteristics of them were compared with those of the as-deposited films.

In addition, the Fe–Cu–Nb–Si–B/Al multilayers, as shown in Fig. 1(b), were deposited at T_s of 30 °C. Fe–Cu–Nb–Si–B layers in the multilayer were deposited under the same condition as those for the single layers, as shown in Fig. 1(a). Al layers were deposited in the same evacuated chamber at P_{in} and R_d of 180 W and 10 nm/min, respectively. The thickness of each Fe–Cu–Nb–Si–B layer was fixed at 70 nm, and the thickness of Al intermedialayer t_{Al} was changed in the range from 0 to 10 nm. And then, these multilayers were post-annealed under the same condition as those of single layers.

The crystallographic characteristics of these films were evaluated by x-ray diffractometry (XRD). The magnetic characteristics of these films, such as the saturation magnetization $4\pi M_s$ and the coercivity H_c were determined on the M – H hysteresis loops measured by the vibrating sample magnetometer (VSM). The relative permeability μ_r was measured by shunt core method at frequency of 1.0 MHz.

III. RESULTS AND DISCUSSION

A. Fe–Cu–Nb–Si–B single layers

Figure 2 shows the XRD diagrams of the Fe–Cu–Nb–Si–B single layers deposited at T_s of 30 and 300 °C, and the ones post-annealed at T_A of 300 °C, respectively. These diagrams of three kinds of films had weak peak corresponding to bcc Fe crystallites, of which the grain size was estimated to be 2–3 nm. This suggests that relatively high temperature process had little effects to the growth of Fe grains, which

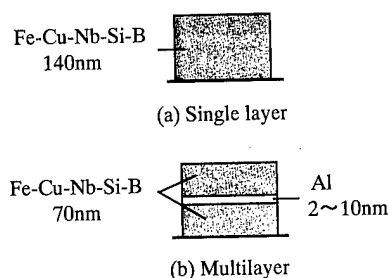
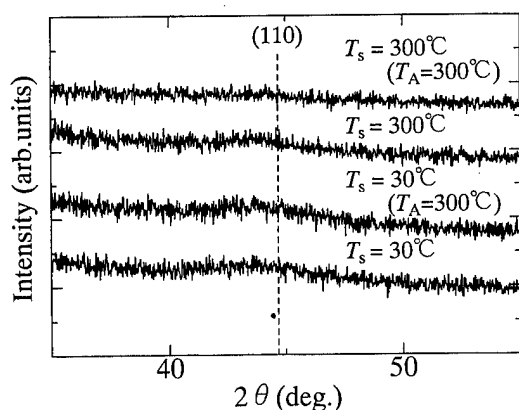
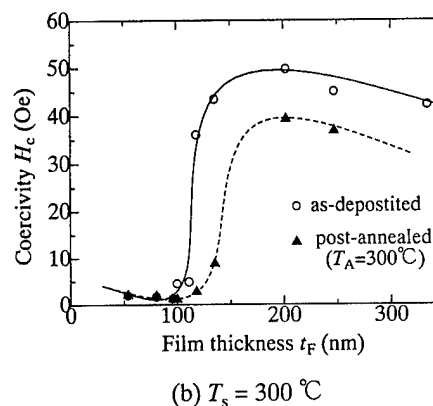
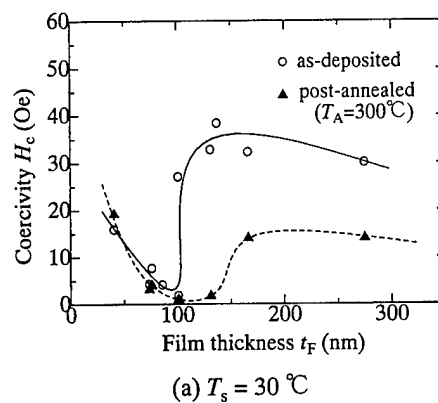


FIG. 1. Schematic illustration of (a) single layer and (b) multilayer.

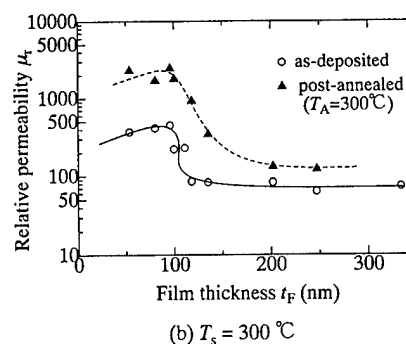
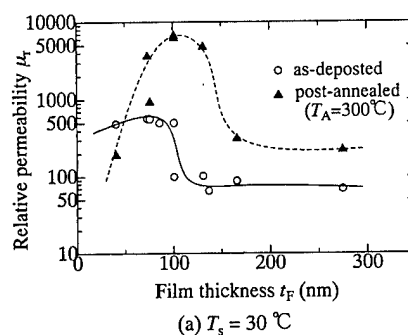
seem to be uniformly dispersed in these films. Figures 3 and 4 show the dependence of H_c and μ_r on the film thickness t_F for the Fe-Cu-Nb-Si-B single layers deposited at T_s of 30 and 300 °C, and the ones post-annealed at T_A of 300 °C, respectively. These characteristics were measured along the hard axis of the films. It was found that Fe-Cu-Nb-Si-B single layers as-deposited at T_s of both 30 and 300 °C thinner than 100 nm exhibited low H_c and high μ_r , of which the values of the layers as-deposited at 30 °C were 1.84 Oe and 500, respectively. However, when these films were thicker than 100 nm, their soft magnetic properties degraded drastically, so that H_c and μ_r were 40 Oe and 90, respectively. This degradation seems to be originated from the difficulty of the magnetization reversal by the appearance of perpendicular magnetic anisotropy, which is observed in the evaporated thick Ni-Fe films.² In addition, there were not any significant differences for this tendency between the films deposited at T_s of 30 and 300 °C. This result indicates that the T_s of 300 °C should not be high enough to change the microstructure of the films during deposition.

On the other hand, the soft magnetic properties of the films with t_F of 90–120 nm were improved drastically by post-annealing. Especially, the films with t_F of 100 nm deposited at 30 °C exhibited low H_c of 1.05 Oe and extremely high μ_r of 6200. The improvement of the characteristics by post-annealing seems to be originated from the release of the internal stress in the films, which makes it ease to reverse the magnetization vector in the films.

FIG. 2. X-ray diffraction diagrams of Fe-Cu-Nb-Si-B single layers deposited at T_s of 30 and 300 °C, and ones post-annealed at T_A of 300 °C.FIG. 3. t_F dependence of H_c of Fe-Cu-Nb-Si-B single layers.

B. Fe-Cu-Nb-Si-B/Al Multilayers

Figure 5 shows the dependence of H_c and μ_r on the thickness of Al layer t_{Al} for Fe-Cu-Nb-Si-B/Al multilayers deposited at T_s of 30 °C, where the film with t_{Al} of 0 nm

FIG. 4. t_F dependence of μ_r of Fe-Cu-Nb-Si-B single layers.

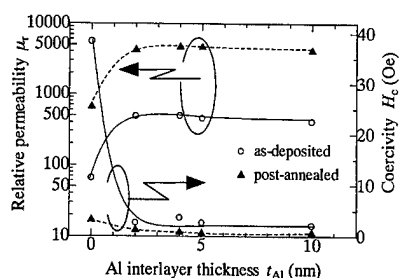


FIG. 5. t_{Al} dependence of μ_r and H_c of Fe-Cu-Nb-Si-B/Al multilayers deposited at T_s of 30 °C.

corresponds to the 140 nm-thick single layer as shown in Fig. 1(a). The multilayers constructed by inserting Al intermedialayer with thickness thicker than 2 nm revealed much softer magnetic properties than the thicker single layers. For example, the as-deposited films with t_{Al} of 10 nm exhibited low H_c of 2.1 Oe and high μ_r of 410, of which the value were same as those of as-deposited single layers thinner than 100 nm. These results indicate that the appearance of the perpendicular anisotropy in the ferromagnetic layer was suppressed by insertion of Al intermedialayer and that the soft magnetic characteristics were improved because of the magnetostatic coupling between the two ferromagnetic layers.

Furthermore, the soft magnetic properties of these multilayers were improved by the post-annealing process, as found for single layers. Especially, μ_r increased up to 4600

and H_c attained at the value as very low as 0.63 Oe for the multilayers with t_{Al} of 2 nm.

IV. CONCLUSIONS

Nanocrystalline Fe-Cu-Nb-Si-B thin films were deposited using the FTS apparatus. As a result, it was found that Fe-Cu-Nb-Si-B single layers thinner than 100 nm deposited at T_s of 30 and 300 °C exhibited relatively large $4\pi M_s$ of 11.3 kG and high μ_r of 500. However, when these films became thicker than 100 nm, their soft magnetic properties degraded drastically.

On the other hand, μ_r of the films thinner than 120 nm post-annealed at T_A of 300 °C were improved drastically. Especially the films with t_F of 100 nm deposited at 30 °C revealed extremely high μ_r of 6200.

In addition, the soft magnetic characteristics of Fe-Cu-Nb-Si-B/Al multilayers were improved drastically up to the same value as the single layers thinner than 100 nm. Furthermore the post-annealed multilayers exhibited very lower H_c and higher μ_r of 0.63 Oe and 4600, respectively.

Therefore, these films with such excellently soft magnetic properties seem to be suitable for the core layers in the magnetic recording heads.

¹Y. Yoshizawa, S. Oguma, and K. Yamauchi, J. Appl. Phys. **64**, 6044 (1988).

²N. Saito, H. Fujiwara, and Y. Sugita, J. Phys. Soc. Jpn. **19**, 1116 (1964).

Measurement of the magnetostriction constants of amorphous thin films on kapton substrates

C. Ouyang, T. W. Kim, and R. J. Gambino^{a)}

Department of Materials Science and Engineering, SUNY at Stony Brook, Stony Brook, New York 11794

C. Jahnes

IBM Thomas J. Watson Research Center, Yorktown Heights, New York 10598

The saturation magnetostriction constants of thin films of amorphous $\text{Co}_{39}\text{Ni}_{31}\text{Fe}_8\text{Si}_8\text{B}_{14}$ and CoZrTb have been measured either by the small angle magnetization rotation (SAMR) method or by the initial susceptibility method. The SAMR method is used for the soft materials. When the material is magnetically hard or has a strong perpendicular anisotropy, the initial susceptibility method is used. It is found that the amorphous $\text{Co}_{39}\text{Ni}_{31}\text{Fe}_8\text{Si}_8\text{B}_{14}$ prepared by ion beam deposition from an alloy target shows very soft magnetic properties and has a very small negative saturation magnetostriction, λ_s , of -1×10^{-7} . Sputtered films of CoZrTb show a strong perpendicular anisotropy when the concentration of Tb is high. We have found that the SAMR method can be applied to CoZrTb films when the Tb content is low. The saturation magnetostriction constant of a sputtered film of $\text{Co}_{78.4}\text{Zr}_{20.8}\text{Tb}_{0.8}$ is 2×10^6 . When the Tb content is high, however, the initial susceptibility method is used to measure magnetostriction. © 1998 American Institute of Physics. [S0021-8979(98)18311-1]

I. INTRODUCTION

The saturation magnetostriction constant of amorphous thin films has been measured by the capacitance method.¹ However, this method is usually used to measure the magnetostriction of the thin film on a hard substrate like glass. The film and substrate form a bimorph, so the deflection of the sample in an applied field is measured and is used to obtain the magnetostriction constant. Clearly, this method is not practical for thin film samples on soft substrates like kapton. As shown in this article, the alternative indirect measurement method, small angle magnetization rotation (SAMR)² can be used for soft thin films such as $\text{Co}_{39}\text{Ni}_{31}\text{Fe}_8\text{Si}_8\text{B}_{14}$ which have a very small magnetostriction constant. Films of CoZrTb amorphous alloy are not always soft. When the Tb content is not too high, the SAMR method can still be used to measure the saturation magnetostriction constants. When the content of Tb is high, however, the magnetostriction constants were measured using a magneto-elastic technique, the initial susceptibility method.

II. THEORY

The theory of the methods are introduced briefly here. Consider a ribbon with a tensile stress applied parallel to the ribbon axis, subjected simultaneously to a small ac magnetic field (H_{\perp}) perpendicular to the sample axis but in the plane of the ribbon and a high strength dc field (H_{\parallel}) parallel to the sample axis. The dc bias field H_{\parallel} is high enough that the sample is in the saturated state. Hence a vibration of the magnetization vector is induced about the dc field direction in the sample. The magnetization rotation produces an induced voltage e_{2f} in a sensing coil around the sample

$$e_{2f} = -4\pi NS \times d(M_s \cos \theta)/dt, \quad (1)$$

where N is the number of turns of the sense coil, S is the cross sectional area of the ribbon sample, M_s is the saturation magnetization of the sample, and θ is the angle between the magnetization and the ribbon axis. The magnetization oscillates in the plane of the ribbon around the direction of the dc bias field. The magnetization rotation angle is derived by minimizing the total energy of the sample.

$$\sin \theta = H_{\perp} / (H_{\parallel} + H_k + H_s), \quad (2)$$

where H_k is the stress induced anisotropy field, and H_s is the shape anisotropy field. The magnetocrystalline anisotropy and growth induced anisotropy fields are assumed to be very small compared to H_k and H_s . When a uniform external stress σ is applied, the signal e_{1f} changes. If the change of e_{2f} is compensated by changing the parallel field H_{\parallel} , then λ_s can be calculated from the value of ΔH_{\parallel} using the relation

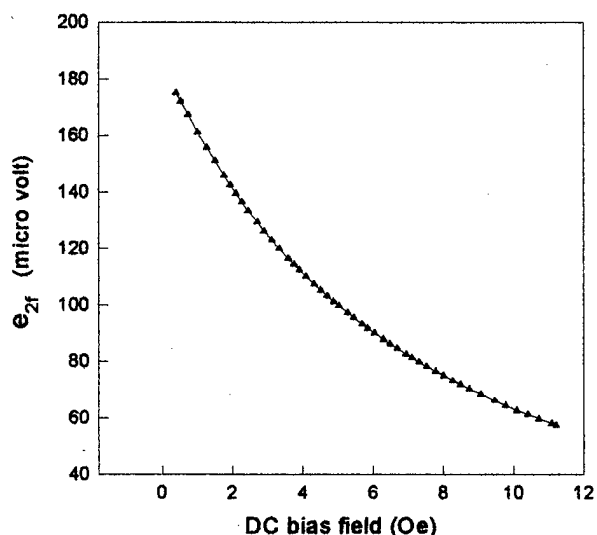
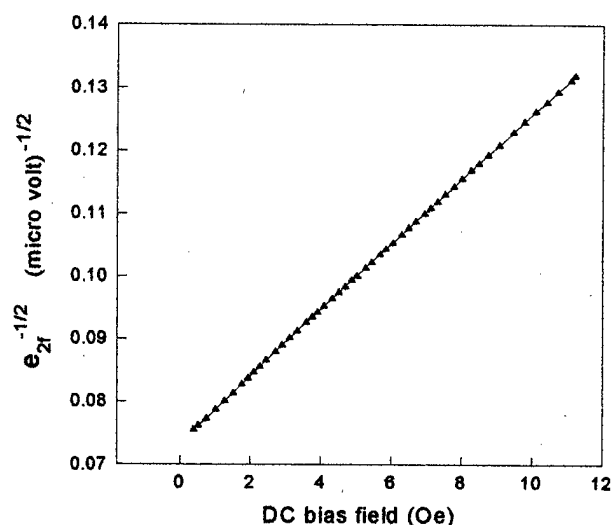
$$\lambda_s = \Delta H_{\parallel} M_s / (3\sigma). \quad (3)$$

Similar to the above analysis, the SAMR method is extended to measure the saturation magnetostriction constant of amorphous magnetic thin films. A force is applied to the substrate and the film by means of a pulley and weight system and the stress condition of the film is analyzed conventionally.³ The magnitude of the stress is below the yield point of both the substrate and magnetic film in order to prevent irreversible deformation or fracture of the film. The condition of the film is monitored by measuring the resistivity of the thin film. It is found that the resistivity of the film does not change before and after the SAMR experiment.

By applying a ac field along the long axis of the sample and with no magnetic field applied perpendicular to the sample, the change of the initial susceptibility with stress can be calculated using the following formula:

$$\chi = -M_s^2 / (3\lambda_s \sigma), \quad (4)$$

^{a)}Electronic mail: rgambino@ccmail.sunysb.edu

FIG. 1. The output signal e_{2f} as a function of dc bias field.FIG. 2. The output signal $e_{2f}^{-1/2}$ as a function of dc bias field.

where χ is the initial susceptibility. From Eq. (4) it can be seen that the inverse of the susceptibility depends linearly on the stress with slope $(-3\lambda_s/M_s^2)$. The method is particularly suitable for hard magnetic thin films or the films with strong perpendicular anisotropy, because the method measures the saturation magnetostriction constants without saturating the sample.

The large parallel dc field and the ac field used in the SAMR method are supplied by two pairs of Helmholtz coils. Two nearly identical, flat sensing coils are put inside the middle of the dc and ac coils and are carefully matched to compensate each other when the sample is absent. Complete compensation is difficult to achieve, so a mutual inductor is connected between the ac Helmholtz coil and the sensor coil to get better compensation.⁴ The output voltage e_{2f} is detected by means of a lock-in amplifier. A frequency of 1 kHz is chosen so that the system is less susceptible to background noise, and can supply a distinguishable signal. This setup is also used for the initial susceptibility measurement.

III. SAMR MEASUREMENT OF $\text{Co}_{39}\text{Ni}_{51}\text{Fe}_8\text{Si}_8\text{B}_{14}$ THIN FILM SAMPLE

The thin film samples were prepared by ion beam sputtering of a target of composition $\text{Co}_{39}\text{Ni}_{31}\text{Fe}_8\text{Si}_8\text{B}_{14}$. This alloy has been reported to have extremely small magnetostriction and occurs in a composition region where magnetostriction is weakly dependent on composition.^{5,6} The thickness of the film is 0.5 μm on a kapton substrate, with thickness 75 μm , supplied by the DuPont company. Figures 1 and 2 are the graphs of e_{2f} and $e_{2f}^{-1/2}$ against the dc bias field H_{\parallel} . The relation between signal e_{2f} and tensile stress σ was measured as shown in Fig. 3. It shows that the signal increases with increasing tensile stress which implies that the saturation magnetostriction constant is negative in the sample.

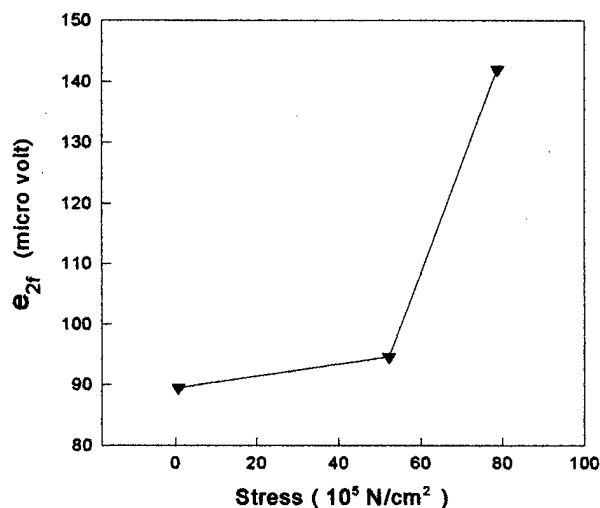
In Fig. 4, the perpendicular ac magnetic field H_{\perp} and the signal output e_{2f} are kept unchanged by varying the applied stress with respect to the dc bias field. The magnetostriction

constant, as determined using Eq. (3), is -1×10^{-7} . The Young's modulus of the kapton substrate was obtained from the DuPont company and it is $2.62 \times 10^5 \text{ N/cm}^2$. The Young's modulus of the thin film is one parameter that is very difficult to determine. It has been determined for some amorphous ribbon samples.⁷ The Young's modulus of amorphous film here is approximated as $1.7 \times 10^7 \text{ N/cm}^2$.

IV. SATURATION MAGNETOSTRICTION MEASUREMENT OF CoZrTb THIN FILMS

The CoZrTb thin films were investigated following a similar procedure. The Tb is a rare earth (RE) metal and the Zr element was incorporated in order to obtain a well defined amorphous state even for low RE concentration.

In the present experiment, the amorphous transition metal-rare earth (TM-RE) CoZrTb thin films are prepared using facing target magnetron sputtering from composite targets. Film composition was determined using energy disper-

FIG. 3. The output signal e_{2f} as a function of the applied stress.

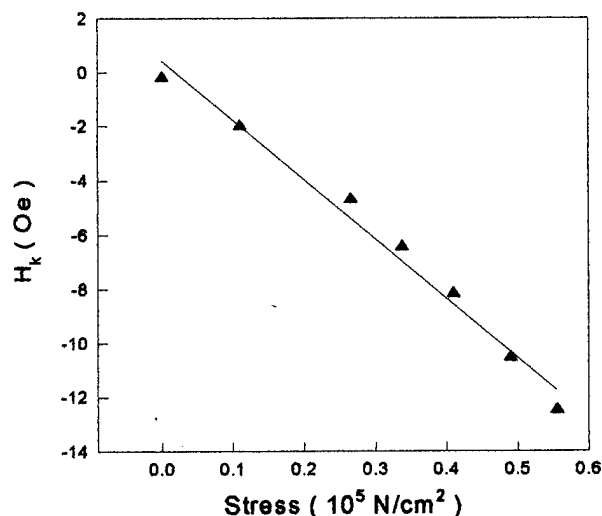


FIG. 4. The induced anisotropy field as a function of the applied stress.

sive x-ray (EDX) analysis. It has been shown that, when the composition of Tb is high, in spite of their amorphous structure, the films can exhibit an anisotropy perpendicular to their plane. If the magnetization is sufficiently low, the lowest energy orientation for the magnetization is perpendicular to the film plane.⁸ The origins of this perpendicular anisotropy have been the subject of a number of investigations. Short-range pair ordering,⁹ single-ion anisotropy produced by non-*s*-state rareearth ions,¹⁰ stress-induced anisotropies produced during the growth process,¹¹ and atomic scale structural anisotropy¹² have all been suggested as playing a role. However, if only a small amount of Tb is alloyed with the CoZr, the easy axis is in plane and the SAMR is applicable. By measuring the change of anisotropy field as a function of the applied stresses, the saturation magnetostriction constant of the $\text{Co}_{78.4}\text{Zr}_{20.8}\text{Tb}_{0.8}$ thin film is obtained by the SAMR measurement and it is found to be 2×10^{-6} .

Using the initial susceptibility method, the data in Fig. 5 are obtained for a film of composition $\text{Co}_{77.2}\text{Zr}_{20.4}\text{Tb}_{2.4}$. The saturation magnetostriction constant measured for this composition is 6×10^{-6} . What is important is that the magnitude of the magnetic field has to be controlled in the linear range of the in-plane $M-H$ curve. It is assumed that, in this linear range, the magnetization process is reversible.

One important factor which determines if the material is hard or soft is the coercivity. The coercivity is greatly affected by the roughness of the substrates. Although the kap-

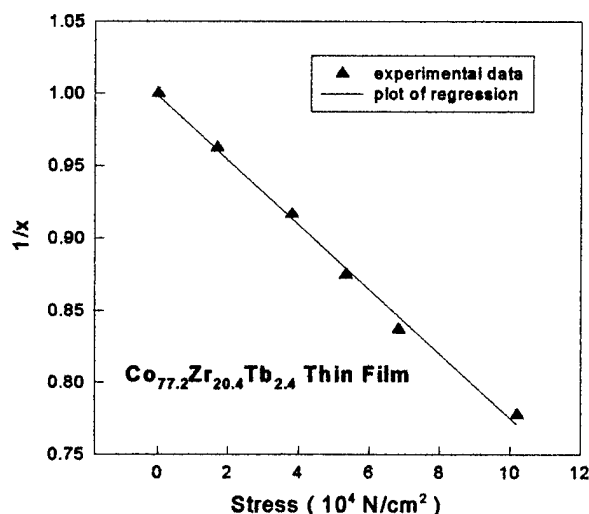


FIG. 5. The inverse of the susceptibility as a function of the stress.

ton substrate provides an easy way to apply the stress to the film, at the same time, a compromise has to be made with respect to substrate roughness. The roughness of the kapton is higher than that of glass by about an order of magnitude.

The saturation magnetostriction of amorphous $\text{Co}_{39}\text{Ni}_{31}\text{Fe}_8\text{Si}_8\text{B}_{14}$ and CoZrTb thin films is measured either by the SAMR or by the initial susceptibility methods. The saturation magnetostriction constants of $\text{Co}_{39}\text{Ni}_{31}\text{Fe}_8\text{Si}_8\text{B}_{14}$, $\text{Co}_{78.4}\text{Zr}_{20.8}\text{Tb}_{0.8}$, and $\text{Co}_{77.2}\text{Zr}_{20.4}\text{Tb}_{2.4}$ thin films are -1×10^{-7} , 2×10^{-6} , and 6×10^{-6} , respectively.

¹E. Klokholm, IEEE Trans. Magn. **MAG-12**, 819 (1976).

²K. Narita, J. Yamasaki, and H. Fukunaga, IEEE Trans. Magn. **MAG-16**, 435 (1980).

³J. Huang, C. Prados, J. E. Evetts, and A. Hernado, Phys. Rev. B **51**, 297 (1995).

⁴L. Kraus, J. Phys. E **22**, 943 (1989).

⁵T. Jagielinski, K. I. Arai, N. Tsuya, S. Ohnuma, and T. Masumoto, IEEE Trans. Magn. **MAG-13**, 1553 (1977).

⁶G. Suran and R. J. Gambino, J. Appl. Phys. **50**, 7671 (1979).

⁷J. C. M. Li, in *Treatise on Materials Science and Technology, Ultra-Rapid Quenching of Liquid Alloys*, edited by H. Herman (Academic, New York, 1982), Vol. 20, p. 325.

⁸G. Suran, K. Roky, J. Sztern, F. Machizaud, and J. M. Mackowski, IEEE Trans. Magn. **MAG-30**, 4770 (1994).

⁹R. J. Gambino and J. J. Cuomo, J. Vac. Sci. Technol. **15**, 296 (1978).

¹⁰Y. Suzuki, S. Takayama, F. Kirino, and N. Ohta, IEEE Trans. Magn. **MAG-23**, 2275 (1987).

¹¹S.-C. N. Cheng, M. H. Kryder, and M. Naoe, IEEE Trans. Magn. **MAG-25**, 4018 (1989).

¹²V. G. Harris, K. D. Aylesworth, B. N. Das, W. T. Elam, and N. C. Koon, Phys. Rev. Lett. **69**, 1939 (1992).

Longitudinal-transverse resonance and localization related to the random anisotropy in *a*-CoTbZr films

G. Suran^{a)} and E. Boumaiz

Laboratoire Louis Néel CNRS BP 166, 38042 Grenoble, France

The properties of a resonance mode, the existence of which is related to the random local anisotropy of the sample, are reported. It was detected in amorphous CoZrTb thin films of low Tb content, in which there exists an in-plane uniaxial anisotropy field. Here the angular dependence of the mode is shown. In agreement with theory, it changes from a pure longitudinal to a mixed longitudinal transverse and a pure transverse state as a function of the orientation of the external field. The process is accompanied by the development of a very pronounced Anderson localization process due to the high value of the Tb related local anisotropy K_l . © 1998 American Institute of Physics. [S0021-8979(98)18411-6]

Theoretical calculations¹ predicted that a ferromagnet which possesses a random magnetic anisotropy should exhibit a resonance mode (RAR for random anisotropy resonance) specific to this state.

Very recently we reported that in CoZr rare earth (RE) amorphous thin films^{2,3} a resonance mode with completely new properties can be detected, apart from the so-called uniform resonance (UR). The theoretical computation showed that for a given configuration a longitudinal resonance mode should be observed, while in a crystalline material only a transverse resonance can be excited. The first period of our investigations was devoted to the demonstration that for certain configurations of the external dc field H and of the microwave field h_{rf} this new resonance mode presents a pure longitudinal character so that it is a RAR mode.

Here we report the variations of the properties of the RAR when the field H is rotated from the longitudinal to the transverse configuration. These measurements showed that in conformity with the theory the nature of the RAR mode changes and progressively takes up a transverse character. The variations of the RAR are accompanied by a very spectacular Anderson-type localization process, which is the first direct experimental observation in magnetism of this type of process.

The RAR mode was detected in amorphous $\text{Co}_{93-x}(\text{RE})_x\text{Zr}_7$ thin films. The films were prepared by rf sputtering. The mode could be observed for RE=Nd, Pr, Dy, and Tb and for $0 < x < 4$. For this small RE substitution the films possess a rather high $4\pi M_s$ and a small coercive field. The results presented here are those obtained for RE=Tb. A necessary condition for the observation of the RAR mode is that the films display a very well defined in-plane uniaxial anisotropy H_k with a negligible skew. H_k , having a magnitude of $50 < H_k < 150$ Oe, was induced during the deposition of the films by applying a dc field parallel to the film plane. Other details were reported in Refs. 2 and 3. The ferromagnetic resonance measurements (FMR) were made with a standard spectrometer at 9.8 GHz.

In the previous investigations the properties of the RAR mode were presented for the configurations which corre-

spond to the pure longitudinal resonance. This was the case when H was applied in the plane (P) defined by H_k and the film normal n , and h_{rf} was applied along H_k ($\alpha=0^\circ$) and for H in the plane P at any angle θ' with respect to n . The longitudinal nature of the RAR mode was formally demonstrated, since it could be excited for the theoretical configuration, i.e., when $H \parallel h_{rf} \parallel M_s$ and at various working frequencies. These experiments showed also that, contrary to the UR which is a collective process in which all spins participate, only a limited number of spins contribute to the RAR. This fact made it possible to explain both the small intensity of the RAR mode as compared to the UR one, and the result that the resonance field and linewidth related to the RAR mode are wholly independent of the angle θ' . This last property is due to the negligible values of the demagnetizing fields involved in the RAR process.

Let us consider now the variations of the RAR and the UR when the direction of H is changed by angle θ in the plane perpendicular to both P and the film plane, and the microwave field h_{rf} is applied in the film plane along H_k ($\alpha=0$). The results obtained on a typical sample are presented in Figs. 1 and 2. The properties of the UR are consistent with the classical models. The value of $4\pi M_s$, computed from the resonance fields in perpendicular ($\theta=0^\circ$ or H_\perp) and parallel ($\theta=90^\circ$ or H_\parallel) configuration, agree well with static measurements. The resonance field is maximal and minimal for H_\perp and H_\parallel , respectively, and for intermediate values of θ it follows the theoretical curve established for the resonance field of the UR (Fig. 2). The resonance linewidth ΔH_0 increases with increasing Tb content in the film.² ΔH_0 is of the same order of magnitude for H_\perp and H_\parallel and exhibits a well defined maxima for an intermediate value of θ . Such a behavior is archetypal for ΔH_0 of UR in thin films and is attributed mainly to geometrical effects.⁴

The variations with θ of the resonance field related to the RAR mode are opposite to that of the UR (Fig. 2): It is minimal for H_\perp and maximal for H_\parallel . The variations of the linewidth, the shape, and the intensity of the RAR mode are also specific. For $\theta=0^\circ$ the resonance field H_r and linewidth ΔH_r were minimal and the intensity I_r of the mode was maximal. The shape of the line is very close to a Lorentzian one. When θ is increased both H_r and ΔH_r increase fairly

^{a)}Electronic mail: suran@labs.polycnrs-gre.fr

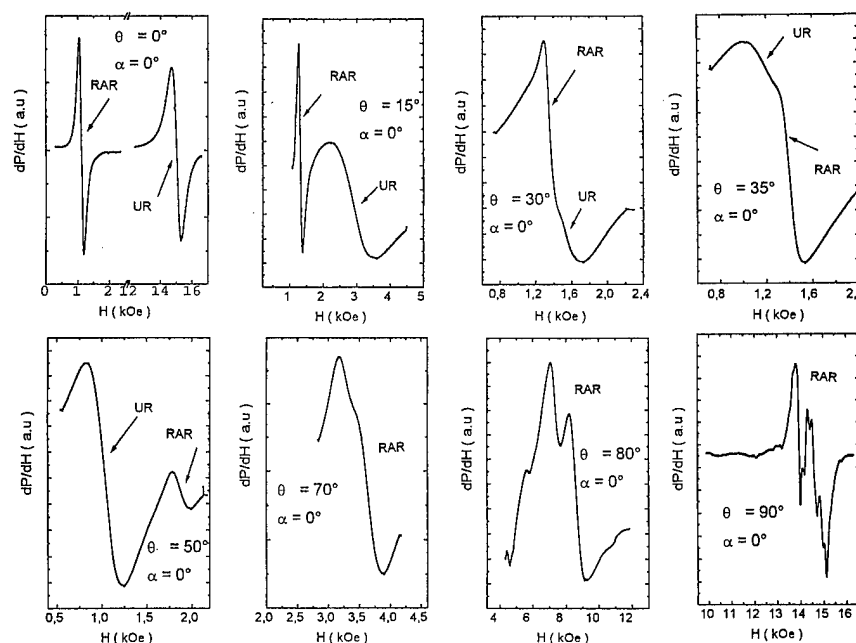


FIG. 1. Spectra of the the uniform (UR) and the random anisotropy resonance (RAR) modes at various angles θ . For $\theta \geq 70^\circ$ only the RAR mode is reported.

spectra. This process is most pronounced when $\theta=90^\circ$. In this case the spread of the spectra is the greatest and extends from $H_r \sim 9-11$ kOe up to $H_r \sim 14.5-15.5$ kOe. The intensity of the individual peaks is the smallest and their line-widths are in the range of 150–300 Oe. The results reported here correspond to a film of composition $x=1.6$ but this type of data was observed for a large number of samples.

The present results can be explained using the following assumptions: (a) the direction of H_k displays a dominant role as only those clusters (or group of spins) can participate in the RAR mode that have their easy local axis K_l oriented sufficiently close to H_k . (b) The magnetic state is determined by the ferromagnetic correlation length which is specific to a ferromagnetic thin film which possess a H_k .⁵ Such a film exhibits longitudinal and transverse ferromagnetic correlation lengths proportional to the exchange forces and a transverse magnetostatic field, respectively, so the coupling length, when no field is applied, is an order of magnitude bigger along the transverse direction than along the longitudinal one.⁵

Using these hypotheses, the variations can be explained as follows: for $\theta=0^\circ$, as shown by the previous studies, an RAR which is purely longitudinal is detected. When the external field is rotated perpendicular to the plane P , a transverse component is developed, the magnitude of which changes as a function of θ .⁶ It is fairly small for relatively small values of θ , increases when θ increases, and becomes predominant for sufficiently high θ . The fact that each mode has both longitudinal and transverse components allows to explain the variations versus θ of the resonance field H_r and of the linewidth ΔH_r . In conformity with theoretical computations, H_r is much bigger for the transverse than for the longitudinal case, which explains the increases of H_r when θ , and so the transverse component of the mode, increases. The relaxation process which corresponds to the two configura-

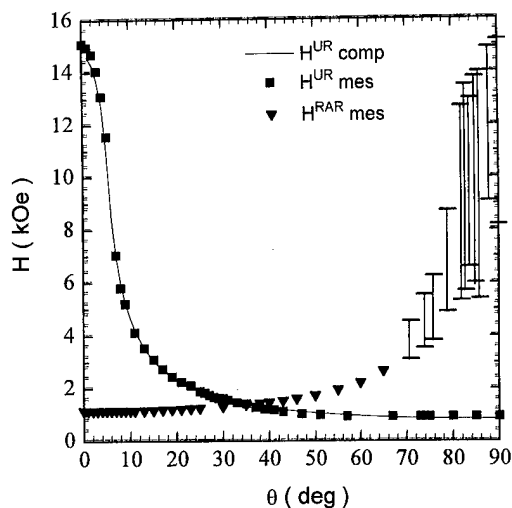


FIG. 2. Variations, as a function of θ , of the resonance fields related to the UR (■) and the RAR (▼) mode, respectively. (—): computed curve. (I): spread of the RAR spectra.

tions differs also in accordance with the present results: it is much stronger for the transverse case.⁷ The variations of the transverse ferromagnetic correlation length, which decreases continuously as H_r increases, is at the origin of the localization process. This localization changes from a weak to a very strong one as H_r is increased. Now the wavelength of the excited modes is limited by the volume of the ferromagnetically correlated regions, which diminishes when H_r is increased. This process makes it possible to explain the splitting of the mode into several modes. For $\theta=90^\circ$ the transverse correlation length is the smallest, the various peaks are spinwaves excited at the level of clusters, and their very short wavelength is controlled by the ferromagnetic correlation length. The configuration $\theta=90^\circ$ obviously corresponds to the pure transverse case, because the applied field H is perpendicular to the plane P which defined the pure longitudinal one. The high value of H_r and the strong localization process are due to the high value of K_l related to Tb. In conformity with the theoretical computations the transverse resonance should occur for¹

$$\omega/\gamma = H + K_l/M_s. \quad (1)$$

If one takes for $H \sim 14\text{--}15$ kOe one finds for K_l about $(1\text{--}3) \times 10^7$ erg/cm³, a result which agrees well with that obtained previously.⁸ Another series of studies, only briefly discussed here, confirmed the as proposed mechanism. It consists of investigating the variations of the spectra as a function of α while θ is kept constant. As one increased α from 0° to 90° , both H_r and ΔH_r decreased. Simultaneously the intensity of the mode diminished and finally became undetectable for a critical value of α , i.e., α_{crit} . These variations of H_r and ΔH_r are due to the progressive suppression of the transverse component of the RAR which recovers its longitudinal character. The range of α for which the mode can be detected presents spectacular variations as one approaches the pure transverse configuration. Now α_{crit} becomes fairly small so the propagation of the RAR mode is highly directional. This means that, for example, when $\theta=80^\circ$ the mode can be detected for $|\alpha| < 2^\circ\text{--}4^\circ$ and at $\theta=90^\circ$ for $|\alpha| < 1^\circ\text{--}2^\circ$. This effect results from the very important localization process as the angle along which the propagation is permitted is fairly small.

It is very instructive to study the variations of the spectra versus α at the angle θ for which the UR and RAR modes exhibit the same resonance fields (Fig. 3). It occurs for $30^\circ < \theta < 33^\circ$. For $\alpha=0^\circ$ a single, strongly distorted resonance line is detected and the related linewidth is minimum. As α is increased the overall linewidth of the mode increases and becomes maximum for $\alpha=90^\circ$, while its shape tends toward a Lorentzian one. This result confirms that when h_{rf} is oriented along H_k , only a part of the spins follow the RAR process, while all the spins contribute practically to the UR when the nonresonant condition ($\alpha=90^\circ$) for the RAR mode is settled down.

In conclusion, in amorphous thin films, apart from the UR, if the film exhibits an in-plane uniaxial anisotropy field a resonance mode is detected, the properties of which are

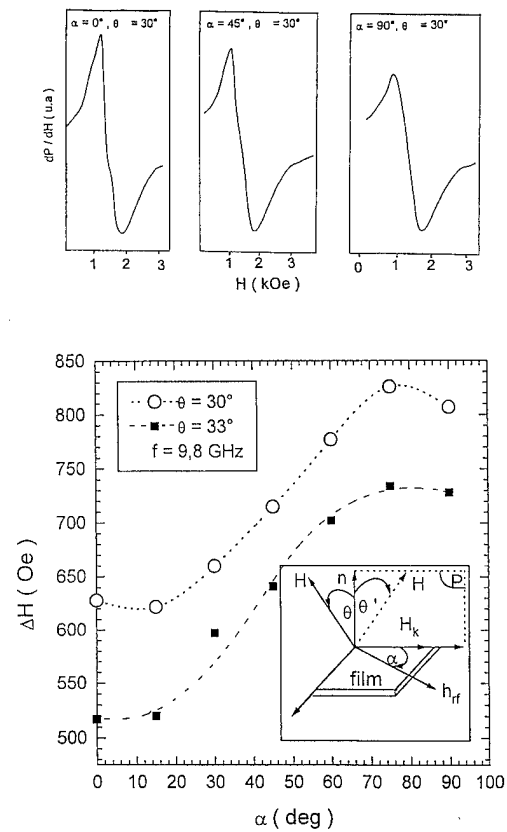


FIG. 3. Variations of the overall linewidth of the spectra as a function of α for $\theta=30^\circ$ and $\theta=33^\circ$, respectively. The definition of the various angles is in the inset.

determined by K_l . The necessity of H_k is related to the basic mechanism involved in the RAR process. The computation was based on the hypothesis that the static equilibrium axis must vary in space due to the disorder. This effect has been simulated by a spin-space rotation angle as a dynamical variable in the equations of motion. The present results, and calculations reported elsewhere, show that this angle can be a dynamical variable only for spins whose local axis is oriented sufficiently close to h_{rf} . The existence of H_k is necessary in order to obtain an RAR mode which has a sufficiently strong intensity. H_k arises from an anisotropic distribution of the local easy axis. So the number of clusters which participate in the RAR is much higher when h_{rf} is directed along the easy axis H_k as compared to the isotropic case.

¹W. M. Saslow, Phys. Rev. Lett. **50**, 1320 (1983).

²G. Suran and E. Boumaiz, Europhys. Lett. **35**, 615 (1996).

³G. Suran, Z. Frait, and E. Boumaiz, Phys. Rev. Lett. **55**, 11 076 (1997).

⁴C. Vittoria, C. Barker, and A. Yelon, Phys. Rev. Lett. **19**, 792 (1967).

⁵H. Hoffmann, IEEE Trans. Magn. **4**, 32 (1968).

⁶These variations are qualitatively similar to that exhibited by a spin glass with uniaxial anisotropy as shown in a theoretical computation. See C. L. Henley, H. Sompolsky, and B. I. Halperin, Phys. Rev. B **25**, 5849 (1982).

⁷No theoretical predictions actually exist about the mechanism which should govern these relaxation processes, but recently we could confirm this difference experimentally on another group of amorphous thin films which exhibit an RAR mode but do not contain RE.

⁸J. F. Calleja, J. A. Corrales, M. Rivas, I. Iglesias, M. N. Contreras, and G. Suran, J. Appl. Phys. **79**, 3168 (1996).

Influence of barrier impurities on the magnetoresistance in ferromagnetic tunnel junctions

R. Jansen and J. S. Moodera

Francis Bitter Magnet Laboratory, Massachusetts Institute of Technology, Cambridge, Massachusetts 02139

The effect of barrier impurity atoms on the magnetoresistance of ferromagnetic tunnel junctions has been investigated. For that purpose, $\text{Co}/\text{Al}_2\text{O}_3/\text{Ni}_{80}\text{Fe}_{20}$ junctions were prepared with submonolayer amounts of Co, Pd, Cu, or Ni incorporated into the middle of the insulating oxide. The junction magnetoresistance (JMR) was measured at 77 and 300 K and referenced to that of simultaneously prepared control junctions without impurities. The JMR decays approximately linearly with increasing impurity content, the slope depending sensitively on the type of element. The decrease is most pronounced for Ni, with the normalized JMR going down at a rate of 0.39 \AA^{-1} of material (at 77 K), whereas Co shows a relatively weak decay of only 0.08 \AA^{-1} . Pd and Cu represent intermediate cases. At 300 K, the suppression of JMR is slightly higher. Results are interpreted in terms of spin-flip scattering of tunneling electrons by the impurities. © 1998 American Institute of Physics. [S0021-8979(98)17611-9]

INTRODUCTION

Tunneling of electrons between two ferromagnetic electrodes, separated by a thin insulator, is dependent on the spin orientation of the electrons. As a consequence, the resistance of a ferromagnetic tunnel junction changes when the relative orientation of the electrode magnetizations is altered, an effect already known since pioneering experiments by Julliere¹ in 1975. Large values of this so-called junction magnetoresistance (JMR), however, were only recently obtained^{2,3} and the potential for application in low-power magnetic field sensors or memory devices has been recognized.

Essential to the existence of JMR is the conservation of electron spin during the tunneling process. Indeed, barrier spin scattering has probably been one of the factors contributing to the low JMR values obtained in early attempts. Scattering of tunneling electrons by localized spins and the resulting effect on the tunnel conductance have been analyzed by Appelbaum^{4,5} and by Anderson.⁶ With respect to the JMR, the reduction due to spin scattering may be understood with the help of the following simple picture. In the absence of spin flips, the tunnel conductances G_p and G_{ap} , respectively, for parallel and antiparallel orientations of the electrode magnetizations can be written as¹

$$G_p = G(1 + P_1 P_2), \quad (1)$$

$$G_{ap} = G(1 - P_1 P_2), \quad (2)$$

where P_1 and P_2 are the electron polarizations of electrodes 1 and 2, while G is a constant. The JMR is then defined as

$$\text{JMR} = (G_p - G_{ap})/G_p. \quad (3)$$

Next consider a spin-up electron tunneling from electrode 1 to 2. When a spin-flip event occurs in the barrier, it has to enter a spin-down empty state in electrode 2. In other words, for electrons that change their spin during tunneling, it is as

if the magnetization of electrode 2 has been reversed, i.e., they exhibit an inverse magnetoresistance. Denoting their fraction by f , the conductance for parallel magnetization becomes $(1-f)G_p + fG_{ap}$ and similarly for the antiparallel case. Simple algebra then shows that the JMR is now equal to

$$\text{JMR} = \frac{(1-2f) \cdot \text{JMR}^0}{1-f \cdot \text{JMR}^0}, \quad (4)$$

where JMR^0 is the magnetoresistance in the absence of spin-flip scattering ($f=0$). In first approximation, the JMR is thus expected to go down linearly with the fraction f , since the denominator is close to unity for ferromagnetic tunneling with $\text{JMR}^0 \leq 0.3$.

High quality Al_2O_3 tunnel barriers can be prepared with great reproducibility.³ This allows us to study electron spin scattering in a systematic and controlled manner, i.e., by introducing a well-defined amount of known foreign elements into the barrier, and recording the resulting decrease of the JMR. Note that scattering at the Fermi energy is of importance here, as tunneling electrons generally originate from states in a narrow energy interval around the Fermi level. Moreover, barrier layers are usually oxides (mostly Al_2O_3) such that the incorporated impurity atoms are in an oxygen environment. Traditionally, these are studied with optical absorption, spin resonance, and Mössbauer spectroscopy. However, in the present experiment, their effect on spin-polarized transport is studied, providing an interesting comparison with the spin-scattering properties of their metallic counterparts.

In this article we present JMR measurements at 77 and 300 K for $\text{Co}/\text{Al}_2\text{O}_3/\text{Ni}_{80}\text{Fe}_{20}$ tunnel junctions with submonolayer amounts of Co, Pd, Cu, or Ni incorporated into the oxide barrier. We show that the JMR decays in a linear fashion, with the strongest decrease for Ni and only a minor

JMR reduction for Co at 77 K. Results are discussed in terms of spin-flip scattering on the basis of the possible magnetic configurations of the impurities.

EXPERIMENT

Ferromagnetic tunnel junctions were prepared by thermal evaporation in a high vacuum system with a base pressure of 1×10^{-7} mbar. Initially, a 10 Å Si seed layer was deposited onto a 5×5 cm², liquid-nitrogen-cooled glass substrate. A total of 12 Co strips, typically 80 Å thick and 0.2 mm wide, were deposited as bottom electrodes. The tunnel barrier was then prepared as follows. First all Co strips were covered with a 7 Å thick Al film. Over one half of each Co strip, a submonolayer amount of impurities (thickness t) was then evaporated, leaving the other half uncoated. The complete structure was then overcoated with another 7 Å of Al. Thus, half of each Co strip has a total of 14 Å of Al without impurities; in the other half the submonolayer of impurities is sandwiched between two 7 Å thick Al layers. Impurities are either Co, Pd, Cu, or Ni. Subsequently, the substrate was warmed to room temperature and oxidized in a glow discharge in oxygen at 7×10^{-2} mbar and a dc voltage of 1.8 kV for 110–120 s. This ensures complete transformation of all Al into Al₂O₃. After pumping down again, cross strips of the Ni₈₀Fe₂₀ top electrode (100–150 Å thick and 0.3 mm wide) are deposited at room temperature. For each individual Co bottom strip, three Ni₈₀Fe₂₀ cross strips are located in the half section that contains impurities, while three others are deposited in the part with $t=0$. For the ferromagnetic top and bottom electrodes, an in-plane magnetic field (100 Oe) was applied during growth. Film thicknesses are determined with a quartz crystal monitor with an absolute accuracy of 8%.

The prepared junctions have an area of 6×10^{-4} cm² and room temperature resistance between 1 and 25 kΩ. Magnetoresistance was measured at 77 and 300 K with an ac resistance bridge (Linear Research, LR700), using a four-terminal method.

RESULTS AND DISCUSSION

Before describing the magnetoresistance data, a few remarks about the tunneling resistance itself are appropriate. Due to the presence of incorporated foreign elements in the oxide barrier, additional transport mechanisms may be present. For example, tunneling may occur via metallic inclusions/clusters⁷ or impurity induced defect states in the barrier.⁸ If such effects are present, they should be reflected in the junction resistance, since they provide extra current channels. Also, they will contribute to a decreased JMR.⁹ For the junctions studied here, the resistance is generally comparable to that of control samples, while in extreme cases the resistance differs by no more than a factor of 2.5. This shows that the formation of the oxide barrier is not inhibited. The resistance ratio, $R_{77\text{ K}}/R_{300\text{ K}}$, is only slightly higher for some sets of impurity containing junctions, with ratios ranging from 1.2 to 1.5, compared to 1.2–1.35 for the control junctions. However, no correlation with the drop of the JMR was evident, although it may account for part of the scatter in

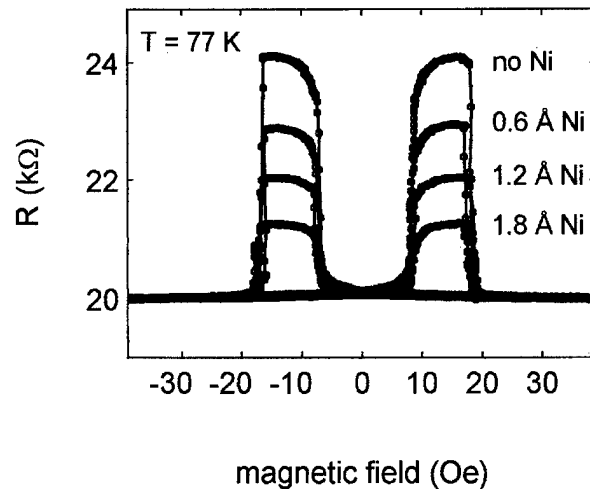


FIG. 1. Magnetoresistance curves for tunnel junctions containing 0.6, 1.2, and 1.8 Å of Ni, respectively, together with the corresponding control junction without Ni. Data are obtained at 77 K and the resistances are multiplied by a constant factor for each curve to have an equal value of 20 kΩ at high fields.

the JMR data presented below. Only for Co at $t=1.8$ Å was a substantially higher resistance ratio of about 1.75 found. In short, we found no major changes in the tunneling transport properties of the junctions used here, with the exception of Co at higher thickness.

As an example, magnetoresistance curves for Ni-containing junctions are presented in Fig. 1, for 0, 0.6, 1.2, and 1.8 Å of Ni, respectively. Data were obtained at 77 K and, for ease of comparison, resistances are multiplied by a constant factor for each curve to have an equal value of 20 kΩ in the high magnetic field state. We observe a significant reduction of the JMR with increasing Ni content, from 17.6% for the control junction to 13.3%, 9.6%, and 6.1%, respectively, for $t=0.6$, 1.2, and 1.8 Å of Ni. Note that the shape of the JMR curves remains practically unchanged.

Figure 2 shows JMR versus thickness t obtained at 77 K for Co, Pd, Cu, and Ni, normalized to the JMR of the corre-

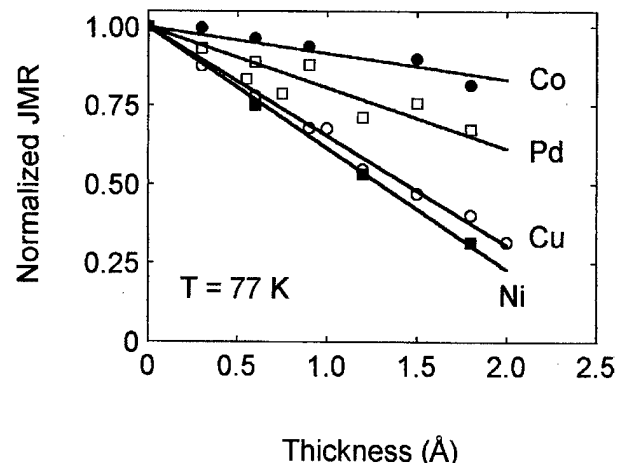


FIG. 2. Normalized JMR vs thickness t of the layer of impurities present in the tunnel barrier. Data, measured at 77 K, are shown for Co (filled circles), Pd (open squares), Cu (open circles), and Ni (filled squares), together with a linear fit (solid lines).

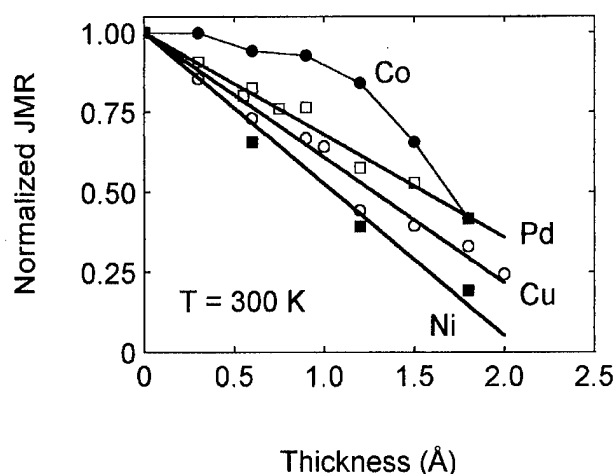


FIG. 3. The same as Fig. 2, but measured at 300 K. For Co no linear fit is given.

sponding control junctions. Similar data acquired at 300 K are given in Fig. 3. We observe an approximately linear decrease of JMR with t , with the strongest decay for Ni (0.39 Å^{-1} at 77 K). Interestingly, for Co only a very weak suppression of the JMR is found (decay of 0.08 Å^{-1} at 77 K), while elements like Pd and Cu that are nonmagnetic in metal form have a much larger influence than Co. The same applies at 300 K, where for all materials the reduction is somewhat enhanced, most notably for Pd and Ni. Note that only in case of Co at 300 K, a clear deviation from a linear dependence is found at higher values of t . We will come back to this point below.

The linear behavior can be understood with help of Eq. (4) by assuming that, for the submonolayer thicknesses used here, the covered junction area increases linearly with t . This is a reasonable assumption considering the fact that the impurity atoms were deposited with the substrate cooled with liquid nitrogen, thereby minimizing surface diffusion and clustering effects. The net result is that the fraction f of tunneling electrons that experience a spin flip, scales linearly with t , provided that the spin-scattering properties of the impurities are not affected by the increasing interaction among the impurities at higher coverage.

Comparing different elements, the weak reduction for Co is remarkable. However, a possible explanation may be found by considering the most frequently encountered oxidation states.¹⁰ The Co^{2+} ion has a $3d^7$ electron configuration, with a corresponding spin¹¹ of $S=3/2$. The Co^{3+} ion has a $3d^6$ configuration and is generally found in a low-spin state¹⁰ with no magnetic moment, as in Al_2O_3 .^{12,13} We may therefore tentatively ascribe the weak influence of Co to the dominant presence of Co in a trivalent oxidation state. For Ni^{2+} and Ni^{3+} ions, respectively, $S=1$ and $S=1/2$ are expected¹¹ in Al_2O_3 . A magnetic moment is thus present irrespective of

the oxidation state, which would provide a qualitative explanation of the observed difference in behavior between Ni and Co.

Along the same line of reasoning, Cu is mostly found¹⁰ as Cu^+ with a nonmagnetic $3d^{10}$ closed-shell configuration (as in Cu_2O) or as Cu^{2+} with $S=1/2$ (as in CuO). It however also exists as Cu^{3+} with $S=1$ in some ternary oxides and as impurities¹¹ in Al_2O_3 . The case of Pd is a special one, since it is only known to appear in a divalent oxidation state (as in PdO), with a $4d^8$ configuration. For an octahedral oxygen coordination Hund's rules would lead to a $S=1$ state. However, for other oxygen geometries like the square planar one found in PdO , a nonmagnetic state results due to crystal field effects.¹⁰ More detailed information about the magnetic properties of Pd in Al_2O_3 is thus required.

Finally, we discuss the behavior of Co at 300 K, for which we did not find a linear relationship between JMR and t . This may be related to a change in the magnetic structure at higher Co content or to an increased interaction of the Co atoms at higher thickness. However, since also a stronger temperature dependence of the resistance was found, the faster decrease of JMR might also be caused by the presence of an additional current mechanism, such as temperature activated tunneling through Co-derived states. To clarify this, further investigations are underway.

In conclusion, the incorporation of submonolayer amounts of impurities in the barrier of ferromagnetic tunnel junctions leads to a linear decrease in the JMR. The effect is most pronounced for Ni and relatively weak for Co. The results show that tunneling magnetoresistance can be severely reduced as a result of spin scattering.

ACKNOWLEDGMENTS

This work was supported by ONR Crant No. N00014-92-J-1847 and NSF Grant No. DMR 9423013. One of the authors (R.J.) was partially supported by ONR Grant No. N00014-92-J-1847 and a research grant from Hewlett-Packard Company.

¹M. Julliere, Phys. Lett. A **54**, 225 (1975).

²J. S. Moodera, L. R. Kinder, T. M. Wong, and R. Meserve, Phys. Rev. Lett. **74**, 3273 (1995).

³J. S. Moodera and L. R. Kinder, J. Appl. Phys. **79**, 4724 (1996).

⁴J. Appelbaum, Phys. Rev. Lett. **17**, 91 (1966).

⁵J. Appelbaum, Phys. Rev. **154**, 633 (1967).

⁶P. W. Anderson, Phys. Rev. Lett. **17**, 95 (1966).

⁷H. R. Zeller and I. Giaever, Phys. Rev. **181**, 789 (1969).

⁸A. I. Larkin and K. A. Matveev, Zh. Eksp. Teor. Fiz. **93**, 1030 (1987) [Sov. Phys JETP **66**, 580 (1987)].

⁹A. M. Bratkovsky, Phys. Rev. B **56**, 2344 (1997).

¹⁰P. A. Cox, *Transition Metal Oxides. An Introduction to their Electronic Structure and Properties* (Clarendon, Oxford, 1992).

¹¹S. Geschwind and J. P. Remeika, J. Appl. Phys. **33**, 370 (1962).

¹²C. J. Delbecq, S. A. Marshall, and P. H. Yuster, Phys. Status Solidi B **99**, 377 (1980).

¹³D. S. McClure, J. Chem. Phys. **36**, 2757 (1962).

Spin-dependent tunneling junctions with hard magnetic layer pinning

J. F. Bobo, F. B. Mancoff,^{a)} and K. Bessho

Materials Science and Engineering, Stanford University, Stanford, California 94305-2205

M. Sharma

Electrical Engineering, Stanford University, Stanford, California 94305

K. Sin and D. Guarisco

Materials Science and Engineering, Stanford University, Stanford, California 94305-2205

S. X. Wang

Electrical Engineering, Stanford University, Stanford, California 94305

B. M. Clemens

Materials Science and Engineering, Stanford University, Stanford, California 94305-2205

We have fabricated ferromagnet-insulator-ferromagnet tunnel junctions with Co and NiFe electrodes, where the Co electrodes are pinned with a hard magnetic $\text{Co}_{81}\text{Pt}_{19}$ alloy layer. This approach gives a coercivity of about 300 Oe for the Co layer, while that of the NiFe is about 80 Oe, so we obtain antiparallel magnetization over a wide field range. The Al_2O_3 tunneling barrier layers were formed by *in situ* plasma oxidation of elemental Al layers with thicknesses from 10 to 25 Å. For the junctions, we find room temperature magnetoresistance ratios as high as 13% and nonlinear current-voltage curves that are well fit by the Simmons tunneling theory. Depth profiling x-ray photoelectron spectroscopy of oxidized Al barrier layers on Co underlayers reveals a stoichiometry of nearly Al_2O_3 . © 1998 American Institute of Physics. [S0021-8979(98)50011-4]

I. INTRODUCTION

Recent progress in the deposition of high quality ferromagnet-insulator-ferromagnet trilayers has led to sizable spin-dependent tunneling magnetoresistance effects.¹⁻⁸ The size of the magnetoresistance makes spin-dependent tunnel junctions of interest for device applications, including magnetic random access memories and magnetic recording read heads. In order to approach the maximum achievable magnetoresistance $\Delta R/R_p = 2p_1p_2/(1-p_1p_2)$, where p_1 and p_2 are the spin polarizations of the two ferromagnetic electrodes and $\Delta R = R_a - R_p$ is the resistance difference between the antiparallel and parallel magnetization states,^{9,10} the tunnel barrier layer must be a continuous, smooth, homogeneous insulator with very clean interfaces with the ferromagnetic layers. Spin-dependent tunneling also requires a mechanism to switch between parallel and antiparallel alignment of the two ferromagnetic layers' magnetizations. Previous work has achieved antiparallel alignment of the magnetizations by choosing ferromagnetic materials with sufficiently different coercivities,¹⁻⁴ pinning with exchange anisotropy from an antiferromagnet,^{6,8} or altering the deposition temperature to create a difference in coercivities.⁵

In this article, we study the tunneling magnetoresistance effect for junctions in which we magnetically bias the bottom ferromagnetic electrode with a hard ferromagnetic layer to allow an antiparallel alignment of magnetizations on the two sides of the insulating barrier. We have fabricated $\text{Co}_{81}\text{Pt}_{19}/\text{Co}/\text{Al}_2\text{O}_3/\text{NiFe}$ spin-dependent tunnel junctions in which the hard magnetic $\text{Co}_{81}\text{Pt}_{19}$ alloy layer pins the Co layer, effectively increasing its coercivity well above that of the NiFe layer. The Al_2O_3 barrier layer is formed by expos-

ing a thin Al film, grown on the $\text{Co}_{81}\text{Pt}_{19}/\text{Co}$ bilayer, to an oxygen plasma. The junctions show nonlinear current-voltage ($I-V$) curves, indicative of tunneling across the Al_2O_3 . Our best room temperature magnetoresistance results of $\Delta R/R_p = 13\% - 16\%$, obtained for a 15–20 Å Al film oxidized for 30 s–2 min, are close to values from previous work on Co–NiFe tunnel junctions.⁴ X-ray photoelectron spectroscopy (XPS) studies of the tunneling barrier reveal nearly stoichiometric Al_2O_3 for different oxidation conditions.

II. EXPERIMENT

The tunnel junctions were deposited by dc magnetron sputtering at room temperature on Si(001) wafers with the following layer structure: Si/500 Å Pt/200 Å $\text{Co}_{81}\text{Pt}_{19}$ /200 Å Co/ Al_2O_3 /500 Å NiFe. The base pressure prior to deposition was $< 5 \times 10^{-9}$ Torr, and sputtering was done in 1.5 mTorr Ar. The $\text{Co}_{81}\text{Pt}_{19}$ layers were deposited by cosputtering from separate elemental targets. The Al_2O_3 was formed by first depositing Al films with thicknesses of 10–25 Å followed by *in situ* exposure to an oxygen plasma for durations between 30 s–10 min, at powers of 5–30 W and oxygen pressures of 23–200 mTorr. All layers were deposited prior to removing the sample from the vacuum chamber. After deposition of the structure, tunnel junctions with areas from $10 \times 20 \mu\text{m}^2$ to $50 \times 50 \mu\text{m}^2$ were patterned by standard optical lithography and wet chemical etching. The 500 Å Pt layer served as a seed layer for junction deposition as well as an unpatterned bottom electrode in the final devices. Magnetoresistance loops and $I-V$ curves were measured at room temperature using a probing station with dc current in two point geometry. Magnetic hysteresis loops were measured prior to patterning of the wafers using a vibrating sample magnetometer

^{a)}Electronic mail: fred.mancoff@stanford.edu

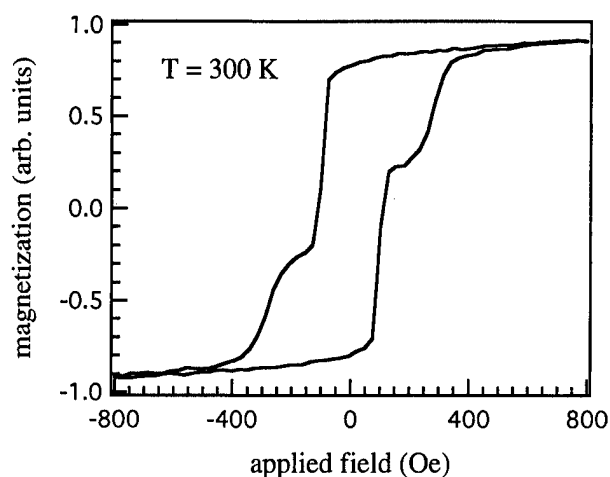


FIG. 1. Room temperature magnetization vs applied magnetic field for the Si/500 Å Pt/200 Å Co₈₁Pt₁₉/200 Å Co/Al₂O₃/500 Å NiFe spin-dependent tunneling structure.

(VSM) at room temperature. Also, the chemical composition of the oxide layers was examined by *ex situ* XPS with sputter etch depth profiling on samples with a Al–O layer grown on a Co film with a glass substrate and a Pt capping layer. The XPS spectra were recorded around the Al 2s, O 1s, Co 2p_{3/2}, and Pt 4f peaks.

III. RESULTS AND DISCUSSION

Figure 1 shows the magnetic hysteresis loop at room temperature for a Co–Al₂O₃–NiFe tunnel junction using a Co₈₁Pt₁₉ alloy layer to magnetically bias the Co. The magnetizations of the Co and NiFe layers reverse direction separately, with coercivities ~ 80 Oe for the NiFe and ~ 300 Oe for the Co. In the magnetic field range between these coercivities, the antiparallel alignment of the ferromagnets' magnetizations is expected to lead to a decrease in the tunneling current across the barrier and a corresponding increase in the resistance of the device.⁹ Magnetic hysteresis loops for similar Co–Al₂O₃–NiFe junctions grown without the Co₈₁Pt₁₉ layer displayed a single coercivity of ~ 20 Oe, without separate reversal of the Co and NiFe layer magnetizations. Thus, the Co₈₁Pt₁₉ layer increases the coercivity of the Co, with which it is in direct contact, as well as the coercivity of the NiFe to a lesser degree. This change from 20 to 80 Oe can be explained in terms of ferromagnetic orange peel coupling across the barrier. Cross-sectional transmission electron microscopy (TEM) images reveal a continuous Al₂O₃ barrier that is conformal with the ~ 25 Å amplitude roughness of the Co electrode. Using this roughness value along with the ~ 450 Å mean lateral size of the roughness features observed by TEM, Néel's model¹¹ for orange peel coupling gives an exchange field ~ 40 Oe. When added to the original 20 Oe NiFe coercivity, the result is comparable to the observed 80 Oe NiFe coercivity in the presence of the Co₈₁Pt₁₉.

Shown in Fig. 2(a) is the room temperature magnetoresistance curve versus applied magnetic field for a $30 \times 50 \mu\text{m}^2$ area device fabricated on a wafer with a 15 Å Al film oxidized for 30 s in 23 mTorr of oxygen with 30 W applied power. The resistance of the device as a function of

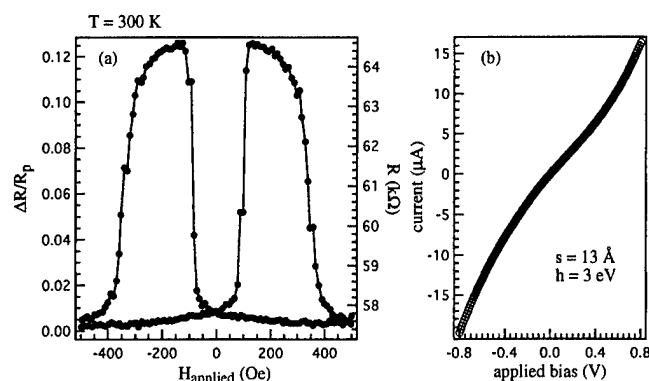


FIG. 2. (a) Room temperature resistance (R) and magnetoresistance ratio ($\Delta R/R_p$) vs applied magnetic field for tunneling between Co₈₁Pt₁₉/Co and NiFe electrodes across a Al₂O₃ barrier, formed from a plasma oxidized 15 Å Al film. Resistance was measured with a 3 mV voltage bias across the $30 \times 50 \mu\text{m}^2$ junction. (b) Tunneling current vs applied voltage (open circles) is well fit by the Simmons tunneling theory (solid line) with barrier thickness $s = 13$ Å and height $h = 3$ eV.

applied field was measured for a constant low voltage bias of 3 mV applied across the device. The maximum magnetoresistance for our devices $\Delta R/R_p \sim 13\% - 16\%$ is close to the room temperature values for previous studies of Co–Al₂O₃–NiFe spin-dependent tunnel junctions.⁴ The peaks in the magnetoresistance for this and other devices are relatively flat, indicating the presence of an antiparallel alignment of the Co and NiFe magnetizations over a wide applied field range due to the Co₈₁Pt₁₉ hard biasing layer. Figure 2(b) shows the results of an I – V measurement at zero applied magnetic field for this device. The nonlinear shape of the curve is characteristic of electron tunneling as the method of conduction across the barrier layer. A fit of this curve to the form given by the Simmons tunneling theory [Fig. 2(b), solid line] describes the data well.¹² The thickness parameter resulting from the fit is around ~ 13 Å, in reasonable agreement with the thickness of the original 15 Å Al film for the barrier, and the barrier height given by the fit of ~ 3 eV is consistent with typical values for Al₂O₃ tunnel junction barriers.^{2,4}

We have investigated the junction area dependence of the tunneling conductance at zero applied field and low voltage bias for devices from this wafer with nominal junction areas of 30×30 , 30×50 , and $50 \times 50 \mu\text{m}^2$. The devices were all located close to each other on the wafer. The conductance increases linearly with area as expected, indicating that electrons tunnel uniformly over the area of the junction. The line extrapolates to zero conductance at a finite, nonzero junction area, indicating an offset between the nominal and actual junction areas, likely due to an undercut of the junction stack from the chemical etch step during lithography.

We used *ex situ* XPS with sputter etching to investigate the chemical composition depth profile of plasma oxidized Al layers, capped with 20 Å Pt, grown on 200 Å Co underlayers on glass substrates. We discuss the results for two samples, each with 20 Å Al originally deposited and oxidized for 1 and 5 min in 23 mTorr oxygen with 30 W applied power. Tunnel junctions on a similarly prepared 1 min oxidized wafer showed tunneling magnetoresistance up to 12%,

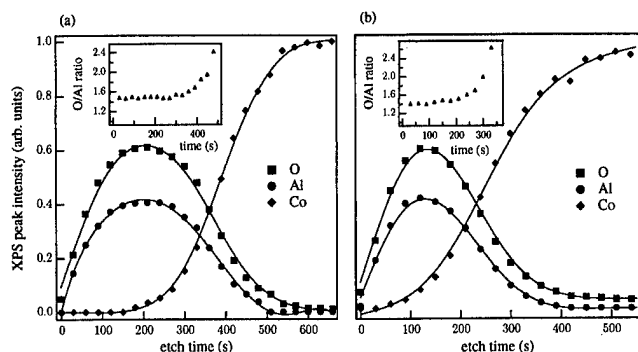


FIG. 3. XPS intensities vs depth profile sputter etch time for Al 2s (circles), O 1s (squares), and Co 2p_{3/2} (diamonds) peaks for 20 Å Al films, grown on 200 Å Co underlayers and capped with 20 Å Pt, oxidized for (a) 5 and (b) 1 min. Similarly prepared 1 min oxidized tunnel junctions displayed up to 12% tunneling magnetoresistance, and 5 min oxidized junctions showed no magnetoresistance. Inset: The ratio of atomic percent O to Al vs etch time indicates the stoichiometry of the oxidized Al layer is nearly Al₂O₃ for both 5 and 1 min oxidized samples through the majority of the oxidized Al layer.

while junctions on a 5 min oxidized wafer displayed no magnetoresistance. Figures 3(a) and 3(b) show the development of the XPS peak integrated intensities with etch time for the 5 and 1 min oxidized samples, respectively. The Pt 4f intensity from the capping layer decreases rapidly, while the Al 2s (circles) and O 1s (squares) intensities first increase and then decrease. The Co 2p_{3/2} intensity (diamonds) increases after etching through the majority of the oxidized Al layer. The ratio of O to Al atomic percent [Figs. 3(a) and 3(b), insets] is calculated by first normalizing the observed peak intensities using tabulated O 1s and Al 2s XPS sensitivities. The solid lines in Fig. 3 are guides to the eye, and there is a slight difference between Figs. 3(a) and 3(b) in etch times required to profile all the layers. For both samples, the oxidized Al layer stoichiometry is within a few percent of the desired Al₂O₃, with the exception of the initial etch step (when oxygen contamination is removed from the surface) and a tail of excess O that extends a few Å into the Co region. This residual oxygen tail could result in part from sputter yield differences between Al and O for the etch process.

The tunneling magnetoresistance is typically sensitive to oxidation time for a given thickness of Al. The magnetoresistance will decrease with either over oxidation of the barrier, leading to formation of Co-oxide at the interface with the bottom Co electrode, or underoxidation, leaving a layer of pure Al at this interface.^{1,4} XPS energy resolution is typically sufficient to detect the ~1 to 2 eV energy shift in an element's spectrum due to formation of a chemical bond in a compound versus the pure element, making this technique useful to search for an oxidized Co or unoxidized Al layer. For both samples, we detect a single Al peak, corresponding to Al₂O₃, through the thickness of the barrier. We observe a shoulder on the high energy side of the Co 2p_{3/2} peak, as expected for formation of CoO¹³ and consistent with the observed oxygen tail [Figs. 3(a) and 3(b)]. For the 1 and 5 min oxidized samples, we fit the spectra in the Co 2p_{3/2} energy region using separate Gaussian peaks for Co and CoO, offset by ~2 eV in position. The 5 min oxidized sample displays a

slightly more prominent CoO peak, relative to the Co, than the 1 min oxidized sample at the start of the Co layer. This effect is consistent with the decreased magnetoresistance in the 5 min oxidized sample compared to the 1 min oxidized sample. Thus, we conclude from the XPS data that the stoichiometry of the barrier layers is very nearly Al₂O₃ as desired, with increased CoO formation at longer oxidation time leading to decreased magnetoresistance.

IV. CONCLUSION

We have fabricated Co/Al₂O₃/NiFe spin-dependent tunnel junctions using a hard magnetic Co₈₁Pt₁₉ alloy to bias the Co layer coercivity well above that of the NiFe layer. With this approach, we can achieve antiparallel alignment of the Co and NiFe magnetizations over a wide range of applied magnetic field. The coercivity of the NiFe is affected by ferromagnetic orange peel coupling across the tunnel barrier. The tunnel barrier layers are formed by exposing a thin layer of elemental Al on top of the Co and Co₈₁Pt₁₉ layers to an oxygen plasma. The junctions show nonlinear *I*-*V* curves well described by the tunneling model and spin-dependent tunneling magnetoresistances as large as 13%. The conductance of the junctions, measured at low applied voltage bias, depends linearly on the junction area as expected. Depth profiling XPS measurements indicate that the insulating barrier layers have nearly the correct Al₂O₃ stoichiometry for a range of plasma oxidation times. The utilization of a hard magnetic layer to bias one of the ferromagnetic electrodes offers a new technique for switching between parallel and antiparallel alignment of magnetizations in the tunnel junction.

ACKNOWLEDGMENTS

The authors thank T. Clark for TEM micrographs. This work is supported by the NSF-MRSEC Program through the Center for Materials Research at Stanford University, the NSF under Grant No. ECS-9700168, CNRS and NATO (J.F.B.), the Hertz Foundation (F.B.M.), and Sony (K.B.). The lithography of spin-dependent tunneling devices was performed at the Stanford Nanofabrication Facility supported by NSF and industrial members.

¹J. S. Moodera, L. R. Kinder, T. M. Wong, and R. Meservy, Phys. Rev. Lett. **74**, 3273 (1995).

²J. S. Moodera and L. R. Kinder, J. Appl. Phys. **79**, 4724 (1996).

³C. L. Platt, B. Dieny, and A. E. Berkowitz, Appl. Phys. Lett. **69**, 2291 (1996).

⁴J. S. Moodera, E. F. Gallagher, K. Robinson, and J. Nowak, Appl. Phys. Lett. **70**, 3050 (1997).

⁵T. Miyazaki and N. Tezuka, J. Magn. Magn. Mater. **139**, 231 (1995).

⁶W. J. Gallagher, S. S. P. Parkin, Y. Lu, X. P. Bian, A. Marley, K. P. Roche, R. A. Altman, S. A. Rishton, C. Jahnke, T. M. Shaw, and G. Xiao, J. Appl. Phys. **81**, 3741 (1997).

⁷Y. Lu, X. W. Li, G. Q. Gong, G. Xiao, A. Gupta, P. Lecoeur, J. Z. Sun, Y. W. Wang, and V. P. Dravid, Phys. Rev. B **54**, 8357 (1996).

⁸Y. Lu, R. A. Altman, A. Marley, S. A. Rishton, P. L. Trouilloud, G. Xiao, W. J. Gallagher, and S. S. P. Parkin, Appl. Phys. Lett. **70**, 2610 (1997).

⁹M. Julliere, Phys. Lett. A **54**, 225 (1975).

¹⁰J. C. Slonczewski, Phys. Rev. B **39**, 6995 (1989).

¹¹L. Néel, C. R. Hebd. Seances Acad. Sci. **255**, 1676 (1962).

¹²J. G. Simmons, J. Appl. Phys. **34**, 1793 (1963).

¹³T. J. Chuang, C. R. Bundle, and D. W. Rice, Surf. Sci. **59**, 413 (1976).

Picotesla field sensor design using spin-dependent tunneling devices

Mark Tondra,^{a)} James M. Daughton, Dexin Wang, Russell S. Beech, Anita Fink, and John A. Taylor

Nonvolatile Electronics, 11409 Valley View Rd., Eden Prairie, Minnesota 55344

Pinned spin-dependent tunneling devices were fabricated and tested in a mode suited for low-field sensing. The basic structure of the devices was NiFeCo125/Al₂O₃25/CoFe70/Ru9/CoFe70/FeMn125 (in Å). This structure had a tunneling resistivity of 110 MΩ μm² and exhibited a 20% magnetoresistance when a field was swept along the easy direction of the soft electrode. High sensitivity, low hysteresis operation was achieved by applying a bias field orthogonal to the easy axis. A sensitivity of 3%/Oe with negligible hysteresis was observed using this mode of operation. A sensor using this type of material was designed to achieve a minimum resolvable field in the picotesla range. The sensor consists of a bridge with four elements, each having 16 tunnel junctions in series. A signal-to-noise ratio of 1:1 at 1 pT (10⁻⁸ Oe) is possible assuming achievable values for the tunneling resistivity, device size, bias level, and sensitivity. © 1998 American Institute of Physics. [S0021-8979(98)52611-4]

I. INTRODUCTION

Tunneling devices have been used for many years as a way to study spin polarization in ferromagnetic thin films.¹⁻³ Typically, the experiments were carried out at low temperature since one of the electrodes was superconducting Al. Sizeable room temperature tunneling magnetoresistance in similar structures was first reported in 1995 by Moodera⁴ and Miyazaki,⁵ though that of Ref. 5 was overstated due to non-uniform current distribution effects.⁶ These recent reports demonstrated the utility of spin dependent tunneling (SDT) structures for a number of practical applications. Several papers have been published discussing their use in magnetoresistive memory and read head applications.⁷⁻⁹ The present work shows results from recently constructed SDT elements which are designed to be used in a low magnetic field sensor.

Data from these elements show about 20% junction magnetoresistance (JMR) at room temperature. When these elements are operated in a special orthogonally biased mode, they have 3%/Oe sensitivity with little hysteresis and a bipolar linear response (excellent for low field sensing). A general calculation of the minimum detectable field for a given element sensitivity is given, showing that the signal-to-noise ratio of an N -element array of SDT devices goes as \sqrt{N} . It is shown that 1 pT (10⁻⁸ Oe) sensitivity is achievable using these elements in a design which is practical from both a size and power standpoint. A complete sensor design applying these principles is described below, and is followed by a discussion of design tradeoffs in sensor power, size, and sensitivity.

II. SDT ELEMENT DESIGN AND FABRICATION

The material structure is NiFeCo 125/Al₂O₃ 25/CoFe 70/Ru 9/CoFe 70/FeMn 125, as shown in Fig. 1. The SDT material was deposited using rf diode sputtering. The Al₂O₃ layer was formed by reactively sputtering Al. Once the ma-

terial is deposited on 4 in. Si wafers, the SDT devices are patterned using standard semiconductor lithography techniques as described in previous work.⁸ A finished device is depicted in Fig. 2.

It is possible to achieve 25% junction magnetoresistance (JMR, defined as $\Delta V/V_{\min}$ and expressed as a percentage) at room temperature with a simpler structure (for instance, NiFeCo 125/Al₂O₃ 25/CoFe 125) as long as the two magnetic electrodes have different coercivities. However, the R vs H characteristics of such a device are not very good for sensor applications due to high hysteresis and nonlinearity. Consequently, we have incorporated an antiferromagnetic (AF) pinning mechanism (an FeMn pinned Co/Ru/Co/AF coupled sandwich) for the top electrode and an orthogonal biasing scheme for the bottom. Together, the resulting R vs. H behavior is nonhysteretic, very sensitive at zero field, and has usable linearity at zero field. The top electrode is designed to be the "hard" layer. Its magnetization remains rigidly fixed in small fields. The soft layer, whose easy axis is parallel to the pinning axis of the hard layer, is free to rotate under the influence of an applied field. The resistance response due to an applied field along the easy axis is shown in Fig. 3. These data show that the soft layer switches very quickly and uniformly. Data collected with a denser field spacing indicate that the entire switch takes place in less than

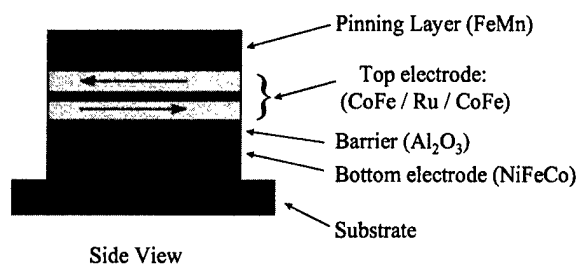
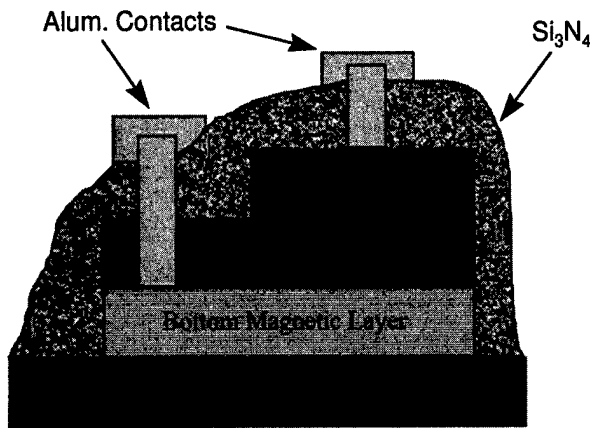


FIG. 1. Cross section of a pinned SDT device with the top electrode being a CoFe/Ru sandwich.

^{a)}Electronic mail: markt@nve.com



Side View

FIG. 2. Cross section of a lithographically patterned SDT device. The lateral dimensions can range from $2.5 \times 2.5 \mu\text{m}$ to $1 \times 1 \text{ mm}$.

100 mOe. Unfortunately, this switching is dominated by domain wall motion and is inherently noisy. A quieter, more linear mode of operation is required for a low field sensor.

It can be shown that a low dispersion film is very sensitive to magnetic fields in the easy direction when it is biased in the hard direction with a field just over the anisotropy field. Not only is the film sensitive, but it also rotates as a single domain with little or no hysteresis. When this is done to the soft layer of a pinned SDT element, the element's resistance is also very sensitive because 90° is the angle at which $dR/d\theta$ is highest.

The data in Fig. 4 were collected from a device biased in this way. The device was on the wafer, and the biasing was done with a permanent magnet positioned about 50 mm above the wafer. The magnitude of the field was about 20 Oe. The magnet was oriented such that most of the field was perpendicular to the sensitive axis, but rotated just enough so that the interlayer coupling was canceled by the easy axis component. One can see that the region near zero field has a very steep slope (3%/Oe) with minimal hysteresis. It is be-

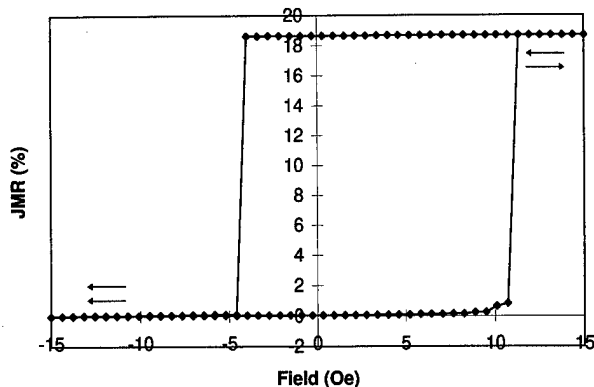


FIG. 3. Magnetoresistive data from a pinned SDT device. The absolute voltage in the parallel state is about 60 mV. JMR is defined as $\Delta V/V_{\min}$ and expressed as a percentage. The field is being applied parallel to the direction of the pinned layer's magnetization.

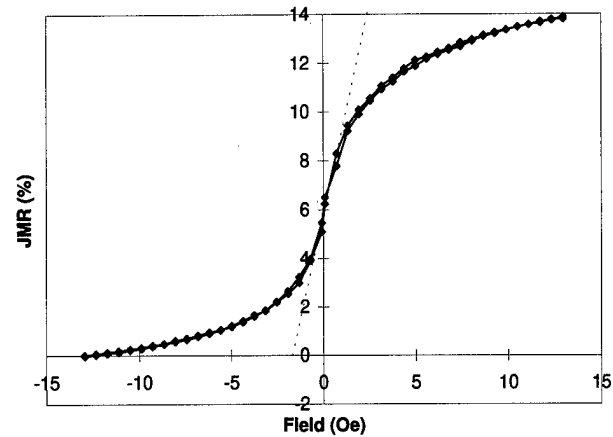


FIG. 4. Magnetoresistance as a function of field for pinned SDT device with an externally applied hard axis bias. The field is being swept along the easy axis of the soft layer, and the hard layer is pinned in the negative direction, parallel to the easy axis. The dotted line, inserted as a guide to the eye, corresponds to a sensitivity of roughly 3%/Oe.

lieved that this is the highest reported sensitivity for a magnetoresistive sensor with no flux concentrators.

III. SENSOR DESIGN

This section will first develop a sensitivity calculation based on fundamental signal-to-noise considerations. In doing so it will be shown that, within the context of this work, hooking N SDT elements together to make a sensor increases the fundamental signal to noise ratio by \sqrt{N} , whether the elements are in series or in parallel. Then, reasonable values will be plugged in to determine the required sensor configuration for a given SDT material.

The noise voltage, V_n , for a single SDT element is taken as the Johnson noise for a resistor of equal value, R . It is assumed that each element will be operated at some fixed voltage, V_e . And each element has an intrinsic sensitivity, S , to an applied field with units of V/Oe.

The Johnson noise is given by

$$V_n = \sqrt{4kTR\Delta f} \text{ V rms}, \quad (1)$$

where k is the Boltzmann's constant, T is the absolute temperature in K, R is the resistance in ohms, and Δf is the noise bandwidth in Hz. Assuming a constant temperature and bandwidth, the noise of a single element may be written as

$$V_n = C\sqrt{R},$$

where

$$C = \sqrt{4kT\Delta f}. \quad (2)$$

The signal in a single element with sensitivity S , due to an applied field, H , is $V_e = SH$, so the signal-to-noise ratio for a single element is

$$S:N_1 = \frac{SH}{V_n} = \frac{SH}{C\sqrt{R}}. \quad (3)$$

The noise of N elements in series is then

$$V_n(N \text{ in series}) = C\sqrt{RN}, \quad (4)$$

while the noise of N elements in parallel is

$$V_n(N \text{ in parallel}) = C\sqrt{\frac{R}{N}}. \quad (5)$$

The signal of N elements in series is NS , while the signal from N elements in parallel is still S . So the $S:N$ ratios at a field H for N elements in series and parallel are

$$S:N_{\text{series}} = \frac{NSH}{V_n(N \text{ in series})} = \frac{NSH}{C\sqrt{RN}} = \frac{SH}{C} \sqrt{\frac{N}{R}}. \quad (6)$$

$$S:N_{\text{parallel}} = \frac{SH}{V_n(N \text{ in parallel})} = \frac{SH}{C} \sqrt{\frac{N}{R}}. \quad (7)$$

So the $S:N$ ratio of N elements increases as \sqrt{N} whether the elements are in series or in parallel. The $S:N$ ratio of one element may be calculated using the following values in Eq. (3):

$$\begin{aligned} S &= 0.02 \text{ V/Oe} \quad (20\%/Oe \text{ at } 100 \text{ mV bias voltage}), \\ H &= 1 \times 10^{-8} \text{ Oe (desired minimum detectable field,} \\ &\quad 1 \text{ pT} = 10^{-8} \text{ Oe)}, \\ \Delta f &= 1 \text{ Hz}, \\ T &= 300 \text{ K}, \\ k &= 1.38 \times 10^{-23} \text{ J/K}, \\ C &= 1.29 \times 10^{-10} \text{ V}, \\ R &= 100 \text{ } \Omega, \\ S:N_1(10^{-8} \text{ Oe}) &= 0.155. \end{aligned} \quad (8)$$

By using an array of 49 elements (7×7) the $S:N$ ratio at 10^{-8} Oe would increase by a factor of 7 to 1.05. To have a $S:N$ ratio of 10:1, roughly 5000 elements would be required. While this is a lot of elements, the area they require is still small. We have made high sensitivity SDT material with a tunnel resistivity (ρ_T) of $0.1 \text{ M}\Omega \mu\text{m}^2$. A $100 \text{ } \Omega$ device out of this material has an area of $1000 \mu\text{m}^2$ ($25 \times 40 \mu\text{m}$). An array of 5000 devices, then, requires $5 \times 10^6 \mu\text{m}^2$ or 5 mm^2 . Since each element is operating at 0.1 V with a resistance of $100 \text{ } \Omega$, each element consumes 0.1 mW for a total of 500 mW for the array.

We have designed and fabricated sensors using SDT elements in such an array. The sensor elements are arranged in a Wheatstone bridge configuration with each leg consisting of 16 elements in series for a total of 64 elements. The orthogonal biasing mode is achieved with on-chip current straps. A second set of straps are included for the purpose of setting the pinning direction of the bridge elements prior to use. This setting coil is arranged so that the field from it is in opposite directions over opposite legs of the bridge.

The pinning is set by warming the sample to just above the Néel temperature of the antiferromagnetic pinning layers and then cooling back to room temperature while passing current through the coil.

IV. DISCUSSION AND CONCLUSION

Looking at Eq. (3) it is clear that increasing the number of elements is not the only way to increase the fundamental signal-to-noise ratio. Decreasing the resistance per element will also have a square root dependence. This may be done by increasing the size of elements or by decreasing ρ_T . The lowest value we have made is $0.1 \text{ M}\Omega \mu\text{m}^2$, though $0.01 \text{ M}\Omega \mu\text{m}^2$ SDT materials appear to be achievable. There is certainly a limit to how low this parameter can go. The $0.1 \text{ M}\Omega \mu\text{m}^2$ material has a barrier of roughly $15 \text{ } \text{\AA}$, and every $2 \text{ } \text{\AA}$ thinner corresponds to roughly a factor of 10 decrease in ρ_T . But as its thickness decreases, the barrier is harder to make with no pinholes and becomes more fragile. Another practical limitation is that contact resistance will degrade the percentage signal if it is on the same order as the element barrier resistance.

Assuming a fixed voltage across each tunneling element, the power consumption increases linearly with both N and $1/\rho_T$. So signal-to-noise goes as \sqrt{P} whether the signal is being increased through more elements or lower resistivity.

While this work uses the thermal noise to calculate signal to noise ratios, preliminary results indicate some excess noise above the thermal noise in SDT devices. It is current dependent and primarily $1/f$ in nature. It is not yet clear how the excess noise varies with device shape and size, and barrier thickness. Further results will be reported as they become available.

SDT elements have been shown to have excellent prospects as transducers for low field magnetometers. The sensitivity and impedance are high enough to allow a multiple element array to be fabricated on a chip which would fit in a small standard integrated circuit package. This sensor would consume at most several hundred mW and much less if expected material improvements are made.

ACKNOWLEDGMENTS

The authors wish to thank J. Moodera for his helpful suggestions and the Office of Naval Research for financial support of this work.

¹P. M. Tedrow, R. Meservey, and P. Fulde, Phys. Rev. Lett. **25**, 1270 (1970).

²P. M. Tedrow and R. Meservey, Phys. Rev. Lett. **26**, 192 (1971).

³P. M. Tedrow and R. Meservey, Phys. Rev. B **7**, 318 (1973).

⁴J. S. Moodera, L. R. Kinder, T. M. Wong, and R. Meservey, Phys. Rev. Lett. **74**, 16 3273 (1995).

⁵T. Miyazaki and N. Tezuka, J. Magn. Magn. Mater. **139**, L231 (1995).

⁶J. S. Moodera, L. R. Kinder, J. Nowak, P. LeClair, and R. Meservey, Appl. Phys. Lett. **69**, 708 (1996).

⁷Z. Wang and Y. Nakamura **19**, 108 (1995).

⁸R. S. Beech, J. Anderson, J. Daughton, B. A. Everitt, and D. Wang, IEEE Trans. Magn. **32**, 4713 (1996).

⁹J. M. Daughton, J. Appl. Phys. **81**, 3758 (1997).

Ferromagnetic tunnel junctions with plasma-oxidized Al barriers and their annealing effects

M. Sato,^{a)} H. Kikuchi, and K. Kobayashi

Fujitsu Laboratories Ltd., 10-1 Morinosato-Wakamiya, Atsugi 243-0197, Japan

Cross-geometrical Ni-Fe/Co/Al-AIO/Co/Ni-Fe/Fe-Mn/Ni-Fe tunnel junctions were fabricated by magnetron sputtering. To form the insulating layer, an Al layer was reverse sputtered in an atmosphere of either oxygen or oxygen-argon mixture at low power after deposition. The oxidization time necessary to form an AIO barrier was much shorter than that by natural oxidization, lasting for only a half to a few minutes. By adding argon to oxygen, the oxidization was slowed down and high MR ratios were obtained for a wide range of time. A magnetoresistance (MR) ratio of 16% was observed in the as-deposited junction when the barrier was oxidized in oxygen plasma for 35 s. In addition, the MR ratio increased to 24% by annealing at 300 °C. In as-deposited junctions, the tunnel resistances were increased by increasing the plasma oxidization time, but the MR ratios gradually decreased. The estimated tunnel barrier width increased and the barrier height decreased with the plasma oxidization time. After annealing, the MR ratio increased only for those junctions oxidized for short times. This suggests that the remaining Al between the AIO and the Co surface plays an important role in the effects of annealing. © 1998 American Institute of Physics. [S0021-8979(98)47411-5]

I. INTRODUCTION

The tunnel resistances of ferromagnetic tunnel junctions with the structure of two ferromagnetic layers separated by a thin insulating barrier are known to change according to the relative angle of the magnetizations within the two layers.^{1,2} Such a junction could be applicable as a further generation magnetic read-head sensor, because theoretically, the magnetoresistance (MR) ratios of 20%–50% can be achieved with a low magnetic field. We fabricated ferromagnetic junctions with spin-valve-like MR properties and in which the tunnel barrier was naturally oxidized in Al for over 500 h.³ In addition, the MR ratios have been found to increase up to 24% after annealing at 300 °C.⁴ However, it takes a longer time to form a good barrier with almost no pinholes by natural oxidization, which is also affected by humidity and temperature and not so clean. Plasma oxidization is considered to be promising for fabricating barriers speedily with greater controllability than natural oxidization.⁵ In this study, we investigated the properties of ferromagnetic tunnel junctions having plasma-oxidized Al barriers and the effect of annealing upon them.

II. EXPERIMENT

Cross-geometrical spin-valve-like NiFe (171 Å)/Co(33 Å)/Al-AIO(13 Å)/Co(33 Å)/NiFe(171 Å)/FeMn(450 Å)/NiFe(86 Å) junctions were patterned by metal masks using magnetron sputtering on 4 in. Si wafers with 1 μm thermally oxidized surfaces. The bottom Ni-Fe/Co layer was the free layer, the center Al-AIO layer was the tunnel barrier layer, and the top Co/Ni-Fe layer was the pinned layer in which the magnetization was pinned to one direction by the exchange field from the Fe-Mn antiferromagnetic layer. Thin

Co layers having a larger polarization than the Ni-Fe layer were inserted to increase the MR changes. The top Ni-Fe layer was a cover layer to prevent oxidization. The argon pressure was 0.2 Pa and the incident power was about 2–3 W/cm².

The junction areas were 9×10^{-4} – 9×10^{-2} mm². To change the metal masks, the surfaces of the lower Co and the oxidized Al were exposed to the air for a few minutes. To form the insulating layer, a 13 Å Al layer was first deposited. Then, the process gas was introduced to the chamber at a pressure of 0.5 Pa, and samples were rf reverse sputtered for a few seconds to a few minutes at a power density of 0.01 W/cm². Oxygen or oxygen-argon mixtures were used for the process gas. Some of the samples were also annealed at a pressure of below 1×10^{-5} Torr at 200–350 °C for 1 h with an applied field of 1 kOe. Annealing and measurements were done repeatedly for each sample. The electrical properties were measured at room temperature by the four-probe method while applying a field of ± 100 Oe in the same direction as the magnetization of the pinned layer.

III. RESULTS AND DISCUSSION

Figure 1 shows the dependence of tunnel resistivity on the plasma oxidization time. The process gas used was pure oxygen. The tunnel resistances increased rapidly with an increase of plasma oxidization time. This indicates that as oxidization progresses with time, the barrier gets thicker. Though a few hundreds of hours were necessary to achieve a tunnel resistivity of 10 Ω mm² in our previous work,⁴ only about 1 min is necessary to achieve the same value.

Figure 2 shows the dependence of the barrier width and height on the plasma oxidization time. The barrier width and height were estimated by fitting the nonlinear voltage-current characteristics to the Simmons' equation.⁶ The fitting was done over the voltage range of below about 200 mV in

^{a)}Electronic mail: satoma@flab.fujitsu.co.jp

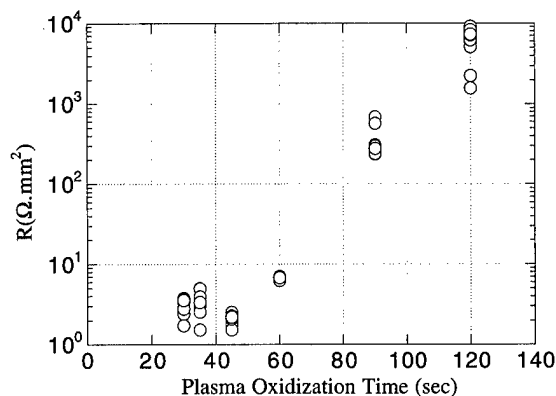


FIG. 1. Dependence of tunnel resistivity on plasma oxidation time. The thickness of the Al layer was fixed at 13 Å and the processed gas was pure oxygen.

the magnetic field of 150 Oe, which value is enough to align the magnetizations. Though the fitted values have a little spread, there are tendencies for the barrier widths to increase and for the barrier heights to decrease with the oxidation time. For the junctions with the barrier oxidized for 120 s, the barrier width is much thicker than the deposited Al thickness. Though the Al layer is thickened by oxidizing, the surface of the Co layer is probably oxidized in such samples.

MR changes were observed in almost all samples. Figure 3 shows the dependence of the MR ratio on the plasma oxidation time. The MR ratios gradually decreased when increasing oxidation time. The maximum MR ratio for an as-deposited junction was 16% achieved by plasma oxidizing for 35 s, which is a much shorter time than that required by natural oxidation. We believe that the barriers with almost no pinholes are formed by plasma oxidation.

Figure 4 shows the dependence of the MR ratios for different oxidation times on the annealing temperature. The values of the same samples, which were repeatedly annealed, are expressed in the same symbols connected by lines. In samples in which the barrier was oxidized for 35 s in pure oxygen plasma, the MR ratio increased by annealing at 300 °C. But, in the samples having barriers oxidized for 45 s, the MR ratio increased at 250 °C. In the samples having

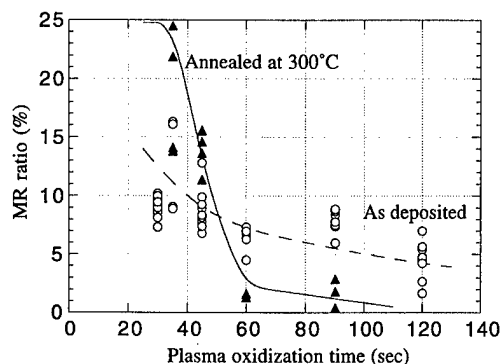


FIG. 3. Dependence of MR ratio on oxygen plasma oxidation time. Open circles show the as-deposited values and the closed triangles show the values after annealing at 300 °C for 1 h.

barriers oxidized for over 60 s, the as-deposited MR ratios vanished by annealing at only 200 °C. In Fig. 4(a) there is a dip at 250 °C. The reason for this dip is still not clear, but it can be seen in some samples. The MR ratios after being

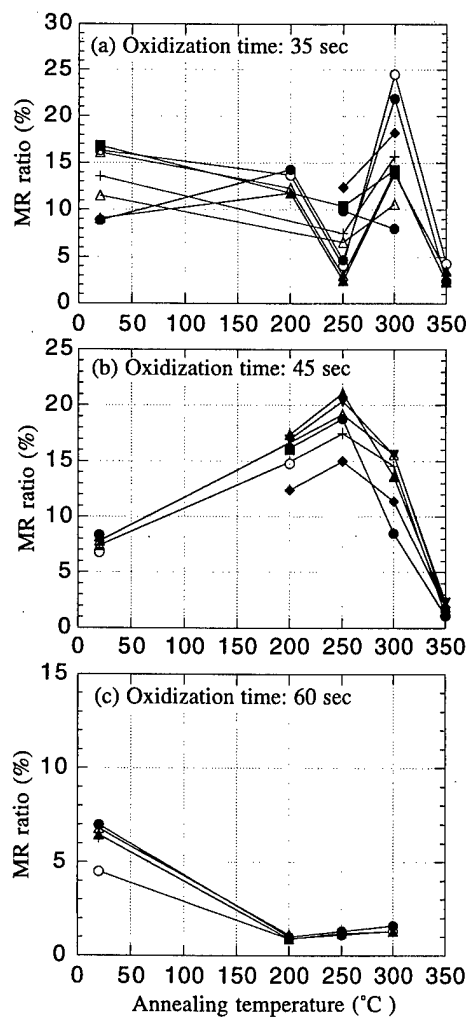


FIG. 4. Dependence of MR ratios for different oxidation times in oxygen plasma on annealing temperature. The values of the same samples which were repeatedly annealed are expressed in the same symbols connected by lines.

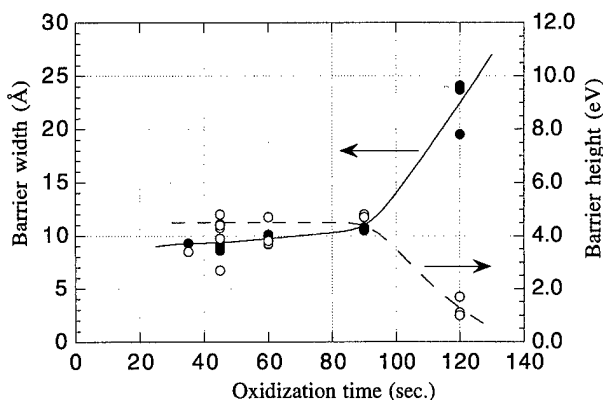


FIG. 2. Evaluated barrier width and height as related to plasma oxidation time in oxygen. Fittings for I-V curves in magnetic field according to Simmons' equation.

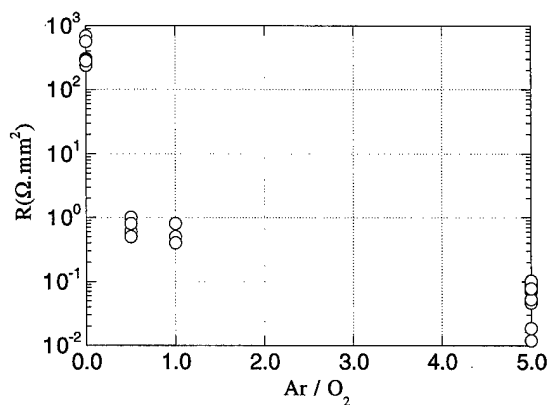


FIG. 5. Dependence of tunnel resistivity on the ratio of oxygen to argon. The plasma oxidation time was fixed at 90 s.

annealed at 300 °C for 1 h are also shown in Fig. 3. The MR ratios of the junctions with oxidation times of under 60 s increase and those with oxidation times of over 60 s decrease by annealing.

This is assumed to occur due to the following mechanism. In samples with oxidation times of under 60 s, the Al layer is gradually oxidized from the surface, and the bottom of the layer still remains unoxidized. In these samples, oxygen atoms at the Co surface move into the Al layer by annealing, and the polarization of electrons at the interface of Co and Al increases. In long oxidation times of over 60 s, however, the whole Al layer and the inside of the Co layer become oxidized. In these samples, the oxygen atoms at the Co surface move into the Co layer and reduce the polarization of electrons in the Co layer, therefore, disturbing the spin-preserved tunneling.

Figure 5 shows the dependence of tunnel resistivity on the ratio of oxygen to argon. The plasma oxidation time was fixed at 90 s. The tunnel resistivity rapidly decreases by adding a little argon to the oxygen. Figure 6 shows the dependence of the MR ratios of the junctions after being annealed at 300 °C for 1 h on the plasma oxidation time. The process gases for oxidation are pure oxygen and an oxygen-argon mixture at a ratio of 1:5. Pure oxygen plasma

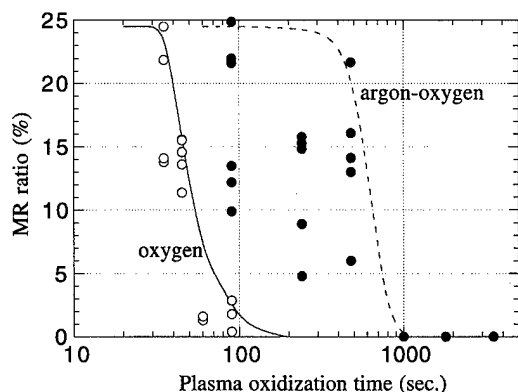


FIG. 6. Dependence of MR ratios of junctions after being annealed at 300 °C for 1 h. The processed gases for oxidation are pure oxygen and an oxygen-argon mixture at a ratio of 1:5.

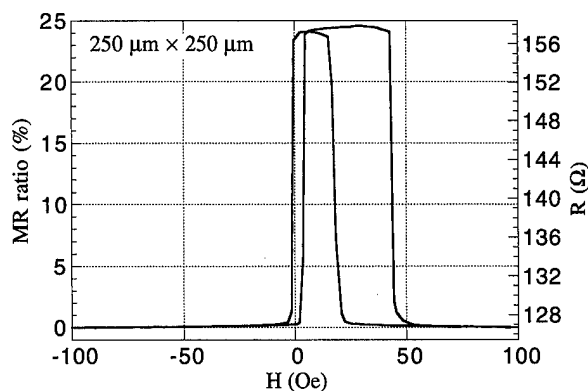


FIG. 7. MR curve of the NiFe(171 Å)/Co(33 Å)/Al-AIO(13 Å)/Co(33 Å)/NiFe(171 Å)/FeMn(450 Å)/NiFe(86 Å) junction after annealing at 300 °C for 1 h. The Al-AIO barrier layer was oxidized in oxygen plasma for 35 s.

oxidizes the Al layer so fast that the MR ratios decrease rapidly with time and it is a little hard to control. On the other hand, for the samples oxidized in the oxygen-argon mixture plasma, the oxidation was slowed down and high MR ratios were obtained for a wide range of time under 1000 s.

Figure 7 shows the MR curve of the junction after being annealed at 300 °C for 1 h and in which the barrier layer was oxidized for 35 s in oxygen plasma. The spin-valve-like MR property is clearly observed, in which the MR ratio is 24%, and its properties are almost the same as those of junctions with a naturally prolonged oxidation of the Al barrier after annealing at 300 °C.⁴

Though we expected to obtain junctions which have constant high MR ratios with better reproducibility by oxidizing in a closed chamber, the present data still have large spreads of resistances and MR ratios. These are thought to be caused by the exposure to air when the mask was changed or by the roughness of the bottom layer.

IV. CONCLUSION

We fabricated ferromagnetic tunnel junctions with barriers formed by plasma oxidation. MR ratios of 16% were observed in the as-deposited junctions with barriers oxidized in oxygen plasma for 35 s, which is a much shorter time than that needed in natural oxidation. In these samples, furthermore, the MR ratio increased to 24% by annealing at 300 °C. In the as-deposited junctions, tunnel resistances increased by increasing the plasma oxidation time, but the MR ratios gradually decreased. By adding argon to oxygen, the oxidation is slowed down and high MR ratios are obtained for a wide range of time. After annealing, the MR ratio increased only for junctions oxidized for a short time. This suggests that the remaining Al between the AIO and the Co surface plays an important role in the effects of annealing.

¹M. Julliere, Phys. Lett. **54A**, 225 (1975).

²S. Maekawa and U. Gafvart, IEEE Trans. Magn. **MAG-18**, 707 (1982).

³M. Sato and K. Kobayashi, Jpn. J. Appl. Phys., Part 2 **36**, L200 (1997).

⁴M. Sato, H. Kikuchi, and K. Kobayashi, IEEE Trans. Magn. **33**, 3553 (1997).

⁵J. S. Moodera, L. R. Kinder, T. M. Wong, and R. Meservy, Phys. Rev. Lett. **74**, 3273 (1995).

⁶J. G. Simmons, J. Appl. Phys. **34**, 2581 (1963).

Tunneling magnetoresistance and current distribution effect in spin-dependent tunnel junctions

J. J. Sun,^{a)} R. C. Sousa, T. T. P. Galvão,^{b)} V. Soares, T. S. Plaskett, and P. P. Freitas^{b)}
INESC, Rua Alves Redol 9-1, 1000 Lisbon, Portugal

In this paper, spin-dependent tunnel junctions fabricated by shadow mask (junction area 0.25 mm^2) and by lithography (junction area down to $9 \times 2 \mu\text{m}^2$) were studied. The junctions have NiFe and CoFe electrodes and the insulating barrier Al_2O_3 is formed by depositing a $10\text{--}30 \text{ \AA}$ thick Al layer, followed by a 1–3 min plasma oxidation in an O_2 atmosphere. The mm^2 -size junctions show tunneling magnetoresistances (TMR) of $10\%\text{--}13.5\%$ at room temperature (RT), with 50% decrease in TMR for a bias voltage of 220 mV. The junction resistances range from hundreds of Ω to tens of $\text{k}\Omega$. The analysis of current distribution indicates that no geometrically enhanced magnetoresistance occurs in the cross-shaped mm^2 -size junctions when the measured junction resistance is five times larger than the electrode resistance over junction area. The μm^2 -size junctions show TMR of $17\%\text{--}24\%$ at RT, independent of the junction area, and have a resistance between $90 \text{ k}\Omega$ and $1 \text{ M}\Omega$ for the $9 \times 2 \mu\text{m}^2$ size (resistance-area products of $\sim 3 \text{ M}\Omega \times \mu\text{m}^2$). The μm^2 -size junctions show 50% decrease in TMR for a bias voltage of 430 mV, and high sensitivity ($>20\%/\text{Oe}$). © 1998 American Institute of Physics. [S0021-8979(98)37111-X]

I. INTRODUCTION

Large tunneling magnetoresistances (TMR) have been recently observed at room temperature (RT) in magnetic tunnel junctions.^{1–4} The TMR signal and junction resistance depend mainly on the insulating layer quality (pinholes and defects), bottom electrode roughness, and single domain state for the ferromagnetic electrodes with high polarization. Junctions with large room temperature TMR use Al_2O_3 as insulating barrier, which is prepared by deposition of a thin Al layer followed by oxidation^{1–4} (plasma or natural oxidation). Insulating layers, like MgO , HfO_2 , and AlN , prepared by sputtering or reactive sputtering,^{5,6} normally lead to low or no TMR at RT, due to incorporation of defects in the barrier, and resulting in a strong temperature dependence of TMR. AlN barriers prepared by reacting an Al layer have been reported,⁷ but junction resistance is too low (a few hundred $\text{m}\Omega$). In this case, the junction resistance is comparable to the electrode resistance over junction area, the current flows nonuniformly through the insulating layer, leading to an enhancement of the magnetoresistance (MR) effect.⁷ For memory or head applications, TMR device resistance should not exceed a few $\text{k}\Omega$. In this paper, junctions fabricated by shadow masks and by lithography are studied, where either the bottom or top electrode is pinned to ensure single domain state for one of the electrodes. The μm -size junctions show a TMR of 24% at RT, with the lowest resistance of $90 \text{ k}\Omega$ in a $9 \times 2 \mu\text{m}^2$ size junction. The current distribution in low resistance junctions is analyzed with a finite element program to distinguish true TMR from the geometrically enhanced effect.

II. EXPERIMENTAL METHOD

Two types of junction structures were studied, where either the bottom or top ferromagnetic electrode is pinned by a TbCo ferromagnetic exchange layer. Junctions have the following structure $\text{Ta}(80 \text{ \AA})/\text{NiFe}(100 \text{ \AA})/\text{CoFe}(20 \text{ \AA})/\text{Al}_2\text{O}_3/\text{CoFe}(50 \text{ \AA})/\text{TbCo}(150 \text{ \AA})/\text{Ta}(80 \text{ \AA})$ with pinned top electrode, and the ones with pinned bottom electrode $\text{Ta}(80 \text{ \AA})/\text{Cu}(40\text{--}200 \text{ \AA})/\text{Ta}(80 \text{ \AA})/\text{NiFe}(60 \text{ \AA})/\text{TbCo}(120 \text{ \AA})/\text{NiFe}(60 \text{ \AA})/\text{CoFe}(20 \text{ \AA})/\text{Al}_2\text{O}_3/\text{CoFe}(6\text{--}20 \text{ \AA})/\text{NiFe}(120 \text{ \AA})$. The magnetic layers were deposited in a Nordiko 2000 high vacuum magnetron sputtering system with a base pressure of 5×10^{-8} Torr. An aligning field of 20 Oe was applied to induce parallel easy axis in each electrode. The Al_2O_3 barrier was formed in a different setup, depositing a thin Al layer ($10\text{--}30 \text{ \AA}$, dc magnetron sputtering, 3 mTorr, $0.25 \text{ W}/\text{cm}^2$) followed by a 1–3 min plasma oxidation ($P_{\text{O}_2} = 5 \text{ mTorr}$, $4\text{--}8 \text{ mW rf}/\text{cm}^2$). For mm^2 -size junctions, both electrodes were deposited using a shadow mask, originating nine junctions each with an area of 0.25 mm^2 . For μm^2 -size junctions, the full junction structure is deposited on a blank glass substrate, and subsequently a self-aligned microfabrication process is used to achieve junction areas down to a few μm^2 . In this process, bottom electrode dimensions are $250 \times 20 \mu\text{m}^2$ or $250 \times 125 \mu\text{m}^2$, and different top electrode dimensions, consequently different junction areas down to a few μm^2 , are defined on the same mask.

III. RESULTS AND DISCUSSION

Figure 1(a) shows the room temperature MR curve for mm^2 -size $\text{CoFe}/\text{Al}_2\text{O}_3/\text{CoFe}$ junction where the top electrode is pinned, with a TMR signal of 13.5% , and $3.17 \text{ k}\Omega$ junction resistance. The inset shows the minor loop, where only the free bottom electrode is reversing its magnetization. The junction shows 7.5 Oe coercivity (H_c) for the free bot-

^{a)}Electronic mail: jjsun@pseudo.inesc.pt

^{b)}Also at IST, Av. Rovisco Pais, 1096 Lisbon, Portugal.

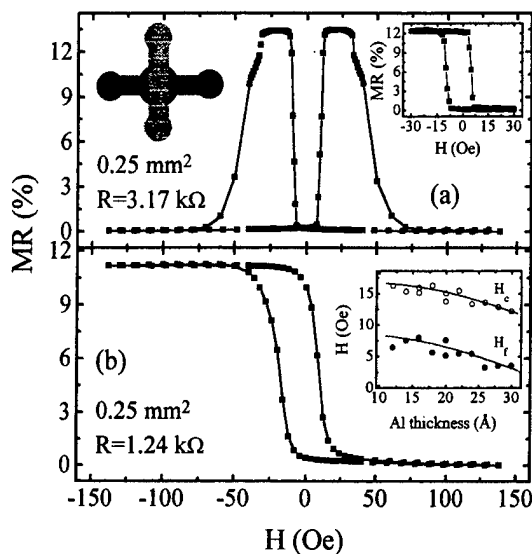


FIG. 1. Room temperature MR curves of CoFe/Al₂O₃/CoFe 0.25 mm² junctions with pinned top electrode (a) and pinned bottom electrode (b). The insets show a minor loop and the relationship of H_c and H_f with the thickness of Al layer.

tom layer and a 2.5 Oe coupling field (H_f). The field was always applied parallel to the easy axis of electrodes.

Figure 1(b) shows equivalent data for the mm²-size junction with pinned bottom electrode and 11.3% TMR signal, where only the minor loop is measured in this field range. The inset highlights the relationship between H_f and H_c of the free top electrode, and the thickness of the Al layer. As the Al thickness is increased from 12 to 30 Å, H_c decreases from 17 to 12 Oe and H_f is reduced from 8 to 3 Oe. These values are always larger than the equivalent values for junctions with pinned top electrode [in Fig. 1(a)]. The H_f value is probably related to the Néel "orange-peel" coupling due to the correlated interface roughness.

The TMR decrease with increasing bias voltage is shown in Fig. 2(a) for a junction with CoFe electrodes as described previously and in Fig. 2(b) for a junction with different electrodes (NiFe, CoFe). At very low bias voltage the TMR is constant or just decreases slightly, decreasing rapidly with higher bias. The TMR is reduced to half its initial value at about 220 mV. This strong decrease of TMR with bias voltage may indicate that the junction is not perfect. This decrease may arise from the reduction of the barrier height with increasing bias, resulting in a decrease in spin polarization of the tunneling current, as discussed by Slonczewski.⁸ Looking carefully at the distinct MR fall-off curves, the curves in Fig. 2(a) are symmetric when the bias voltage is applied in different directions (i.e., from top to bottom or from bottom to top). However, the MR fall-off curves in Fig. 2(b) are asymmetric. According to the Simmons model,⁹ the potential barrier should be asymmetric for NiFe/Al₂O₃/CoFe junctions due to the different work functions of NiFe and CoFe as indicated by the asymmetric $I-V$ curves in the inset of Fig. 2(b), thereby resulting in asymmetric fall-off curves. The effective barrier height (Φ) and effective thickness (t_{eff}) were obtained, respectively, 1.4 eV and 18 Å (deposited Al thickness $t_{\text{Al}} = 20$ Å, oxidation time 2 min) for this junction from

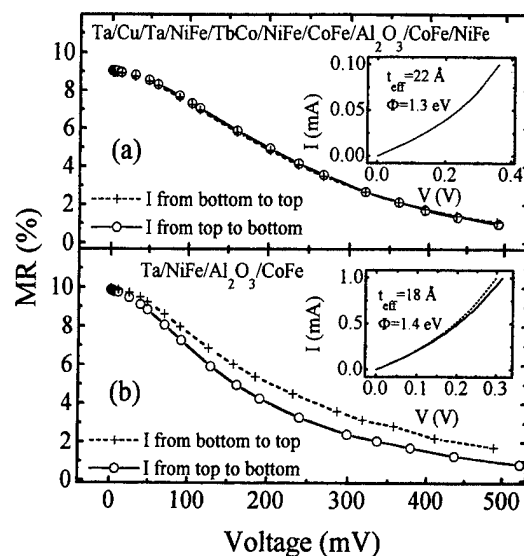


FIG. 2. MR fall-off curves for a pinned bottom electrode CoFe/Al₂O₃/CoFe 0.25 mm² junction (a), and a NiFe/Al₂O₃/CoFe 0.25 mm² junction (b). The $I-V$ curves are represented in the insets.

fitting $I-V$ curves to Simmons model. In the case of the CoFe/Al₂O₃/CoFe junctions with pinned bottom electrode, the potential barrier should be symmetric, which is confirmed by the symmetric $I-V$ curves in the inset of Fig. 2(a) ($\Phi = 1.3 \text{ eV}$, $t_{\text{eff}} = 22 \text{ Å}$, $t_{\text{Al}} = 25 \text{ Å}$, oxidation time 2.5 min), leading to symmetric fall-off curves. This indicates that the bias dependence of TMR may be related to the tunnel barrier characteristics. This bias dependence of TMR could also be due to the spin excitations localized at the interface between the magnetic electrodes and the tunnel barrier.¹⁰

The dependence of TMR on junction resistance is now addressed. Junction resistances ranging from hundreds of mΩ to tens of kΩ can be produced varying Al thickness and plasma oxidation conditions. When the plasma oxidation of the Al layer is carried out for a short time, the junctions have relatively small resistance or negative resistance, leading to MR values up to 80%. This is a consequence of the geometrical enhancement of the MR effect.⁷ An existing program¹¹ was adapted to analyze the current distribution in these junctions. The model consists of two electrode planes connected by 26×26 equal valued resistors. The simulated MR curves for our cross shaped 0.25 mm² junctions are plotted in Fig. 3. Resistivities of 20.8 and 26 μΩ cm were used for the CoFe and NiFe layers, and theoretical TMR values of 10% and 20% are used to compare with experimental results. It can be seen that in our junction structures the geometrical enhancement effect occurs when the measured resistance in the cross, R_M , is smaller than 200 Ω. This value is about six times the electrode resistance over the junction area (in-plane resistance). For a value of 500 mΩ, this effect causes a measured MR of 100%, while the TMR is only 10%. In the experimental data also shown in this figure, it is observed that the measured MR of 10%–13.5% for R_M values ranging from hundreds of Ω to tens of kΩ is true TMR. The inset shows the measured junction resistance R_M versus real junction resistance, R_J , as simulated from our model. It can be seen that, R_M is equal to R_J when $R_J > 200 \text{ Ω}$, smaller than

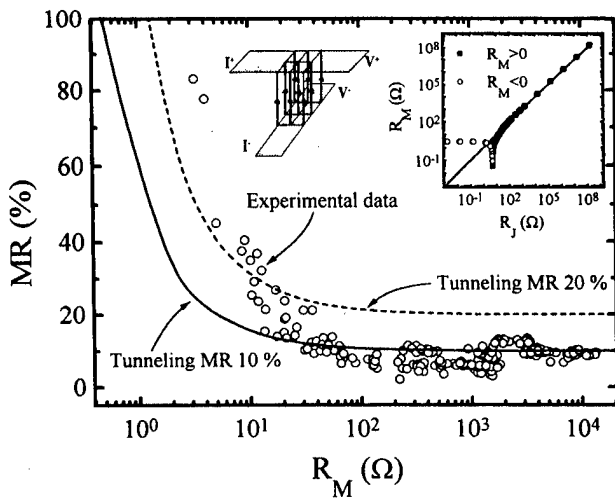


FIG. 3. Simulated MR and experimental MR data as a function of the measured resistance R_M . The inset shows the values of R_M vs junction resistance R_J resulting from the simulation. Junction area is 0.25 mm^2 .

R_J when $R_J < 200 \Omega$, and changes its sign when R_J is smaller than a few Ω , due to the inhomogeneous current flow through the insulating layer.

Figure 4(a) shows the MR curve for a CoFe/Al₂O₃/CoFe junction ($12 \times 2 \mu\text{m}^2$) with pinned top electrode fabricated by lithography. The TMR signal is 23.1% at RT, with a junction resistance of 551 k Ω . Compared with Fig. 2, an improved bias dependence of TMR is shown in the inset, where TMR drops 50% at 430 mV. These small area junctions have less defects, higher effective barrier height (2.6 eV), and smaller effective thickness (13 Å) ($t_{\text{Al}} = 15 \text{ Å}$, oxidation time 2 min). Figure 4(b) shows the MR curve of a CoFe/Al₂O₃/CoFe junction ($12 \times 2 \mu\text{m}^2$) with pinned bottom electrode, with 18.2% TMR signal at RT and 131 k Ω resistance. In both cases the easy axis is parallel to the longer dimension of the top electrode and the field is applied parallel to the easy axis.

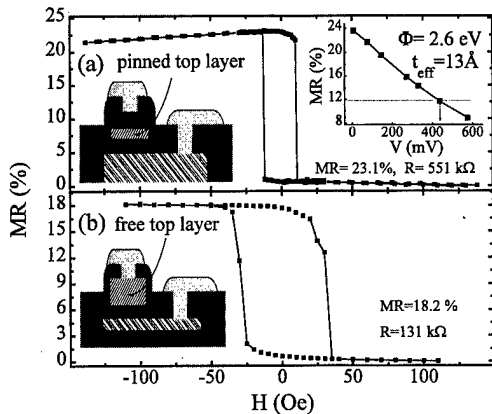


FIG. 4. Room temperature MR curves of $12 \times 2 \mu\text{m}^2$ CoFe/Al₂O₃/CoFe junctions with pinned top electrode (a), and pinned bottom electrode (b). The inset shows the bias voltage dependence of TMR for junction (a).

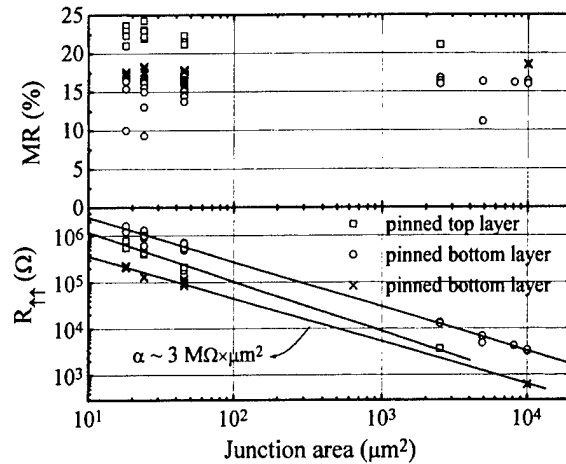


FIG. 5. MR and junction resistance R_{11} vs junction area for junctions with pinned top and pinned bottom electrode fabricated by lithography.

The dependence of the TMR signal and junction resistance R_{11} (parallel state) on the junction area is shown in Fig. 5. Most junctions with sizes from 100×100 to $9 \times 2 \mu\text{m}^2$ have about 17%–24% TMR at RT with resistances from 600 Ω to 1 M Ω (resistance-area products $\alpha \sim 3 \text{ M}\Omega \times \mu\text{m}^2$). The lowest resistance for the smallest junction area ($9 \times 2 \mu\text{m}^2$) is 90 k Ω .

It is worth mentioning that the free top electrode normally has larger coercivity than the free bottom electrode, and then the MR curves for the latter show sharper switching behavior for both mm² and μm^2 size junctions ($> 20\%/Oe$ for small junctions) as shown in Figs. 1 and 4.

In conclusion, magnetic tunnel junctions with mm² and μm^2 sizes were fabricated. The mm²-size junctions show 10%–13.5% TMR at RT. The μm^2 -size junctions show 17%–24% TMR at RT, independent of the junction area, and weaker TMR dependence on bias voltage, where TMR drops 50% at 430 mV.

ACKNOWLEDGMENT

J. J. Sun would like to thank the support of a grant from PRAXIS Project PRAXIS/2/2.1/FIS/348/94.

- ¹T. Miyazaki and N. Tezuka, J. Magn. Magn. Mater. **139**, L231 (1995).
- ²J. S. Moodera, L. R. Kinder, T. M. Wong, and R. Meservey, Phys. Rev. Lett. **74**, 3273 (1995).
- ³W. J. Gallagher, S. S. P. Parkin, Y. Lu, X. P. Bian, A. Marley, R. A. Altman, S. A. Rishton, K. P. Roche, C. Jahnes, T. M. Shaw, and G. Xiao, J. Appl. Phys. **81**, 3741 (1997).
- ⁴M. Sato and K. Kobayashi, IEEE Trans. Magn. **33**, 3553 (1997).
- ⁵T. S. Plaskett, P. P. Freitas, J. J. Sun, R. C. Sousa, F. F. Silva, T. T. P. Galvao, N. M. Pinho, S. Cardoso, and J. C. Soares, Mater. Res. Soc. Symp. Proc. **475**, 469 (1997). T. S. Plaskett, P. P. Freitas, N. P. Barradas, M. F. Silva, and J. C. Soares, J. Appl. Phys. **76**, 6104 (1994).
- ⁶C. L. Platt, B. Dieny, and A. E. Berkowitz, J. Appl. Phys. **81**, 5523 (1997).
- ⁷J. S. Moodera, L. R. Kinder, J. Nowak, P. Leclair, and R. Meservey, Appl. Phys. Lett. **69**, 708 (1996).
- ⁸J. C. Slonczewski, Phys. Rev. B **39**, 6995 (1989).
- ⁹J. C. Simmons, J. Appl. Phys. **34**, 1793 (1963).
- ¹⁰S. Zhang, P. M. Levy, A. C. Marley, and S. S. P. Parkin, Phys. Rev. Lett. **79**, 3744 (1997).
- ¹¹M. Kamon, L. M. Silveira, C. Smithhisler, and J. White, FastHenry User's Guide, MIT (1996).

High conductance magnetoresistive tunnel junctions with multiply oxidized barrier

P. K. Wong, J. E. Evetts, and M. G. Blamire

Department of Materials Science, University of Cambridge, Pembroke Street, Cambridge CB2 3QZ, United Kingdom

We have fabricated $8 \times 8 \mu\text{m}^2$ mesa junctions from ultrahigh vacuum magnetron sputter-deposited Nb/Fe/Al₂O₃/Al/CoFe/Nb heterostructures. The Al₂O₃ barrier was prepared by the technique of multiple oxidation. The effect of multiple oxidation on the junction magnetoresistance (JMR) was investigated. JMR up to 6.2% at room temperature and 9.2% at 77 K was obtained. Junctions with the highest JMR have resistance-area products in the range required for device applications.

© 1998 American Institute of Physics. [S0021-8979(98)52711-9]

I. INTRODUCTION

Magnetoresistance in ferromagnetic tunnel junctions (MTJs), which essentially consist of an insulating tunnel barrier sandwiched between two ferromagnetic electrodes, was first observed in Fe-Ge-Fe heterostructures by Julliere,¹ who explained the magnetic field dependent tunneling conductance by a simple model relating the tunneling probability to the relative orientation of the magnetizations of the ferromagnetic electrodes. In Julliere's model, the junction magnetoresistance (JMR) at zero bias can be calculated from the electron spin polarizations of the ferromagnetic electrodes. In general, the JMR of junctions having ferromagnetic metals and/or their alloys as electrodes is predicted to have a magnitude of a few tens of percent. JMR here is defined as the maximum percentage change in junction resistance with respect to the resistance in high magnetic field. Such magnitude of JMR, together with a relatively low switching field between high and low junction resistance, make MTJ potentially applicable in sensor devices and especially in magnetic read heads.

Studies on MTJ have been focused on the fabrication of junctions having high JMR. Since JMR can be reduced by the presence of leakage current, a high quality barrier is of paramount importance. Various methods of barrier fabrication have been reported. Table I summarizes various barrier preparation methods, the corresponding resistance-area (RA) products, and the JMR of the resulting MTJ.²⁻⁷ Until recently, JMR values comparable to the predictions of Jul-

liere's model have not been observed. However Moodera *et al.*⁶ have obtained a magnetoresistance of 11.8% at room temperature and 24% at 4.2 K with CoFe/Al₂O₃/Co cross-strip junctions. JMR of 25% at room temperature has been reported recently by Parkin *et al.*⁷ in MTJ having an Al₂O₃ barrier prepared by plasma oxidation of sputter-deposited Al at room temperature. Although a high JMR comparable to the theoretical value was achieved, the RA products of the junctions were too high for device applications. It is generally easier to obtain high JMR with junctions having low leakage, i.e., high resistance. A RA product of $10^3 \Omega \mu\text{m}^2$ is required for device applications.⁸ In this article, we report a study of Fe/Al₂O₃/CoFe tunnel junctions with the barrier prepared by multiple oxidation technique. The junctions have RA products in the range suitable for device applications.

II. FABRICATION

A. Deposition of the Nb/Fe/Al₂O₃-Al/CoFe/Nb heterostructure

The Nb/Fe/Al₂O₃-Al/CoFe/Nb multilayer was deposited by ultrahigh vacuum dc magnetron sputtering in a liquid N₂ cooled chamber. The Nb layers which will be superconducting at liquid He temperature served as wiring for the accurate measurement of RA product. In the preparation of the Al₂O₃ barrier, an ≈ 1 nm Al layer was first deposited and partially oxidized in 1 kPa of O₂ for 10 min; then extra layers of about

TABLE I. Summary of the barrier preparation methods, the corresponding RA products, and the JMR values in reported work.

Barrier	Preparation method	RA product ($\Omega \mu\text{m}^2$)	JMR (Temp) (%)	Ref.
GdO _x	Oxidation in atmosphere	5×10^8	5.6(4.2 K)	2
GdO _x	Oxidation in 10^{-3} Pa during Gd deposition	1.3×10^9	7.7(4.2 K)	2
Al ₂ O ₃	Oxidation in atmosphere for 30 h	3.1×10^6	2.7(300 K)	3
Al ₂ O ₃	Oxidation in atmosphere for 24 h	6.4×10^3	18(300 K)	4
Al ₂ O ₃ /MgO	Al/Mg sputter deposited in 2%-10% O ₂ in Ar	1.2×10^8	0.2(300 K)	5
Al ₂ O ₃	Oxidation with an O ₂ glow discharge	$10^6 - 10^8$	11.8(300 K)	6
Al ₂ O ₃	Plasma oxidation of Al layer	2×10^7	25(295 K)	7
Al ₂ O ₃	Multiple oxidation technique	9.6×10^2	6.2(300 K)	This work

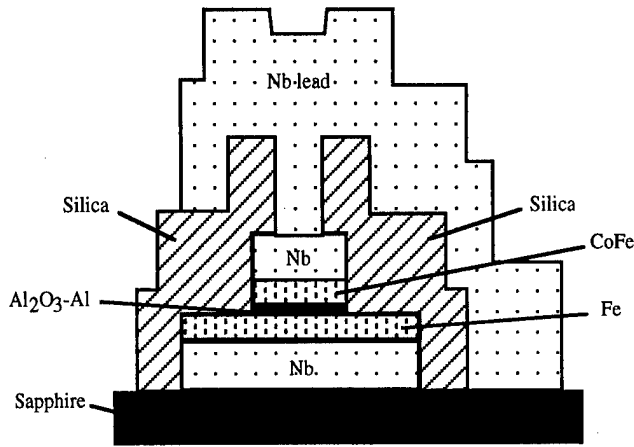


FIG. 1. Schematic cross section of a $8 \times 8 \mu\text{m}^2$ mesa junction fabricated from a Nb/Fe/Al₂O₃-Al/CoFeNb heterostructure.

0.1 nm Al were deposited on top and each layer was oxidized in 1 kPa of O₂ for 10 min before the deposition of others. After the deposition of the last Al layer, the barrier was oxidized in 1 kPa O₂ for 1 h. Three types of barriers, with one, three, and no extra Al layers, have been studied. A further layer of Al was deposited onto the barrier to protect it from resputtering during counter electrode deposition. A similar method has been used in superconducting tunneling device fabrication for producing a lower leakage tunnel barrier.⁹

B. Fabrication of the MTJ

In the junction fabrication process, the base circuitry including the bottom electrodes was first patterned for the entire heterostructure by standard photolithography and Ar/2% O₂ ion milling at 500 V and 0.36 mA/cm². Mesas, $8 \times 8 \mu\text{m}^2$, which defined the junction areas, were then CF₄ plasma etched into the top Nb layer using a photoresist mask, followed by ion milling the CoFe layer down to the barrier. To isolate the junction, a smaller photoresist mask was defined at the center of each of the mesas, followed by rf magnetron sputter deposition of 350 nm silica. Silica deposited onto the smaller mesa mask was later removed by dissolving the photoresist in an acetone bath, i.e., the "lift-off" process, leaving a small window in the silica layer to access the top Nb. Nb wiring 450 nm thick, was finally deposited by the lift-off process to connect the top electrode to the rest of the circuit. Figure 1 shows the cross section of a finished mesa junction.

III. MEASUREMENT

Magnetoresistance of the junctions was measured by a four-point probe inserted between a Helmholtz pair with a LN₂ insert, so that measurement can be made down to 77 K. Figure 2 shows plots of JMR against applied field for the three types of barrier. In all the three cases, the hysteretic JMR peaks occurred at about 9 mT, i.e., 90 Oe, while cohesivity of CoFe and Fe are found to be 78 Oe and 160 Oe, respectively, indicating antiferromagnetic coupling of the electrodes at the peak field. The highest measured JMR of

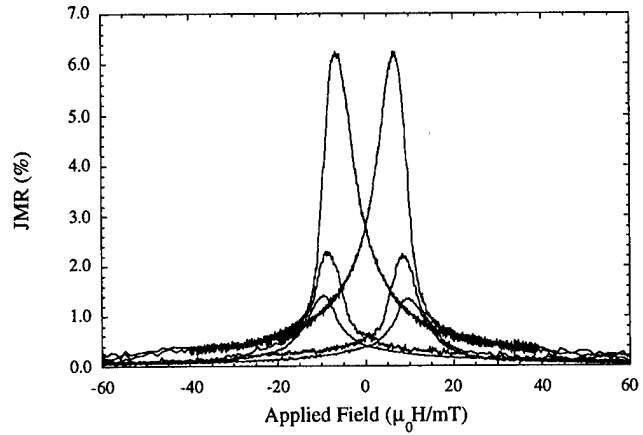


FIG. 2. Hysteretic MR vs H curves of the three types of samples. Peak JMR increases with the number of extra Al layers N , $N=0, 1$, and 3 .

junctions at room temperature with zero, one, and three extra Al layers were 1.4%, 2.3%, and 6.2%, respectively, with junction resistance of 3.5, 5.6, and 15 Ω measured at 4.2 K. This progressive increase in JMR and resistance with the number of extra Al layers is in agreement with a simple model in which each extra Al layer (which is much less than a monolayer) sealed a certain fraction of pinholes in the oxide barrier which are the main source of leakage current. As derived in Ref. 10, the observed JMR in a MTJ, m_{obs} is related to the junction conductance by

$$m_{\text{obs}} = \frac{m_0 G_p}{(G_p + G_l)}, \quad (1)$$

where m_0 is the maximum possible JMR of a leakage-free junction. G_p is the conductance of the leakage-free junction at the hysteretic peak field, and G_l is the leakage conductance due to the presence of pinholes which is considered to be independent of applied field. We assume that G_l is directly proportional to the total area of the pinholes. If each extra Al layer can seal a fraction a of total pinhole area in the lower layer, then for N extra Al layers,

$$G_l(N) = G_l(0)(1-a)^N. \quad (2)$$

Here $G_l(0)$ is the leakage conductance when there is no extra Al layer, i.e., when $N=0$. Substituting Eq. (2) into Eq. (1), a relation between the observed JMR, m_{obs} , and the number of extra Al layers, N , is obtained,

$$m_{\text{obs}} = \frac{m_0}{1 + \frac{G_l(0)}{G_p} (1-a)^N}. \quad (3a)$$

When $G_l(0)(1-a)^N \gg G_p$,

$$m_{\text{obs}} \approx \frac{m_0 G_p}{G_l(0)(1-a)^N} = \frac{m_0 G_p}{G_l(0)} \exp \left[N \times \ln \frac{1}{1-a} \right]. \quad (3b)$$

In Fig. 3, we present a semilogarithmic plot of m_{obs} (%) against N , as well as a plot of resistance of junctions showing highest JMR against N . The distribution of JMR for junctions with the same number of Al layers in their barriers is probably due to defects caused during the junction fabrication process. The data points with highest JMR, corre-

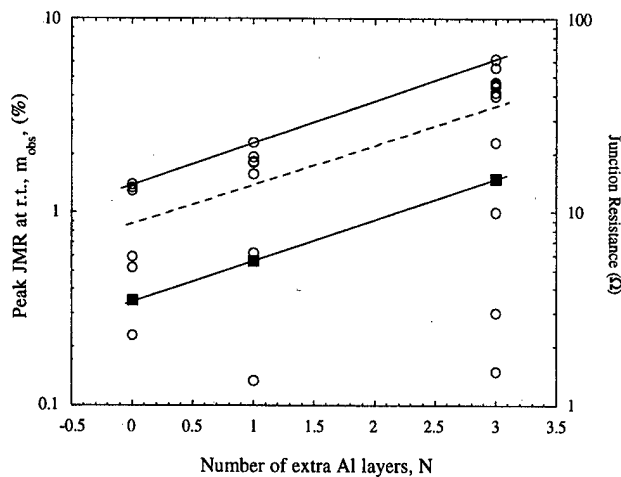


FIG. 3. Observed peak JMR at room temperature, m_{obs} (circles), and the resistance of junctions having highest peak JMR (squares) plotted against the number of extra Al layers N . A straight line is fitted for the samples showing highest JMR for each N , implying having best quality. The dashed line is the fitting for average JMR values.

sponding to junctions with the best quality, i.e., least defeat, lie well on a straight line of $1.400 \exp(0.496N)$. The linearity of the points indicates that $a \approx 0.39$ and $G_I(0)/G_p \gg 1$ when $N \leq 3$. In other words, each extra Al layer can seal about 39% of the total pinhole area in the lower layer. Taking the average data (dashed line in Fig. 3) also gives the same result for a . From the interception of Fig. 3, we deduced that $m_0 G_p / G_I(0) = 1.400$. To estimate the value of m_0 , the dependence of JMR on temperature must be considered. The theoretical JMR predicted by Julliere's model is 42% for a Fe-insulator-CoFe junction, which does not take into account the temperature dependence of JMR. With the temperature dependence factor 2.03 from Ref. 6, defined as the ratio between JMR at 4.2 K and at room temperature, m_0 can estimated to be equal to $42\%/2.03$, i.e., 20.7%. The JMR at 77 K in our junctions showing 6.2% magnetoresistance at room temperature ($N=3$) was found to be 9.2%, i.e., 1.5 times the value at room temperature. This ratio is similar to the temperature dependence factor between 77 K and room temperature reported in Ref. 6. Thus it is reasonable to as-

sume a value for m_0 , 20.7%, which allows us to estimate $G_p/G_I(0)$ as 0.068. Thus $G_I(0)/G_p \gg 1$ which is consistent with our assumption in the beginning of the analysis.

IV. CONCLUSIONS

We have fabricated and studied Fe/Al₂O₃/CoFe MTJ with barriers formed by a multiple oxidation technique. JMR up to 6.2% at room temperature and 9.2% at 77 K was obtained and the RA product is $9.6 \times 10^2 \Omega \mu\text{m}^2$, suitable for device applications. We have demonstrated an analysis which relates the increase in JMR with the number of extra Al layers. The model agrees well with our data. It is demonstrated that the multiple oxidation barrier preparation technique gives more control to the conductance and magnetoresistance of the MTJ which is important in applications. In particular, it allows the minimization of the unoxidized Al base layer thickness which is likely to suppress the JMR achievable.¹¹

ACKNOWLEDGMENT

P. K. Wong would like to thank The Croucher Foundation of Hong Kong for supporting his research in the University of Cambridge.

- ¹M. Julliere, Phys. Lett. A **54**, 225 (1975).
- ²J. Nowak and J. Rauluszkiewicz, J. Magn. Magn. Mater. **109**, 79 (1992).
- ³T. Yaoi, S. Ishio, and T. Miyazaki, J. Magn. Magn. Mater. **126**, 430 (1993).
- ⁴T. Miyazaki and N. Tezuka, J. Magn. Magn. Mater. **139**, L231 (1995).
- ⁵T. S. Plaskett, P. P. Freitas, N. P. Barradas, M. F. Dasilva, and J. C. Soares, J. Appl. Phys. **76**, 6104 (1994).
- ⁶J. S. Moodera, L. R. Kinder, T. M. Wong, and R. Meservey, Phys. Rev. Lett. **74**, 3273 (1995).
- ⁷S. S. P. Parkin, R. E. Fontana, and A. C. Marley, J. Appl. Phys. **81**, 5521 (1997).
- ⁸J. S. Moodera, L. R. Kinder, J. Nowak, P. LeClair, and R. Meservey, Appl. Phys. Lett. **69**, 708 (1996).
- ⁹E. P. Houwman, D. Veldhuis, J. Flokstra, and H. Rogalla, J. Appl. Phys. **67**, 1992 (1990).
- ¹⁰P. K. Wong, J. E. Evetts, and M. G. Blamire, Appl. Phys. Lett. (submitted).
- ¹¹J. S. Moodera, E. F. Gallagher, K. Robinson, and J. Nowak, Appl. Phys. Lett. **70**, 3050 (1997).

Area scaling of planar ferromagnetic tunnel junctions: From shadow evaporation to lithographic microfabrication

H. Boeve^{a)}

IMEC, Kapeldreef 75, B-3001 Leuven, Belgium

R. J. M. van de Veerdonk

Department of Appl. Physics, Eindhoven University of Technology and COBRA, Eindhoven, The Netherlands and Francis Bitter Magnet Laboratory, Massachusetts Institute of Technology, Cambridge, Massachusetts 02139

B. Dutta and J. De Boeck

IMEC, Kapeldreef 75, B-3001 Leuven, Belgium

J. S. Moodera

Francis Bitter Magnet Laboratory, Massachusetts Institute of Technology, Cambridge, Massachusetts 02139

G. Borghs

IMEC, Kapeldreef 75, B-3001 Leuven, Belgium

In order to meet the requirements for applications in magnetoelectronics (e.g., read heads and magnetic random access memory), a processing scheme for micron-scale ferromagnetic tunnel junctions has been developed. A comparative study of junctions defined by shadow evaporation and by lithographic processing was made, where a similar resistance-area product of nearly $1 \text{ G}\Omega \mu\text{m}^2$ and a high tunnel magnetoresistance of up to 15% at room temperature were observed for $\text{Co}/\text{Al}_2\text{O}_3/\text{Ni}_{80}\text{Fe}_{20}$ junctions patterned by both methods. A bipolar sensor characteristic at zero field was realized by inducing anisotropies in the two ferromagnetic layers that are orthogonal to each other. © 1998 American Institute of Physics. [S0021-8979(98)50111-9]

INTRODUCTION

Spin-dependent tunneling between ferromagnetic materials has recently been generating much interest. A planar tunnel junction consists of two ferromagnetic layers separated by a thin insulating spacer layer. Changes in the relative orientation of the magnetization of the ferromagnetic films causes a resistance variation which is due to the change in the tunneling probability between the ferromagnetic electrodes. These magnetoresistance values can be considerably higher than for state-of-the-art spin valve structures.

Initially barrier properties and deposition conditions were studied using structures defined by shadow evaporation.^{1,2} This is unsuitable for integration and further miniaturization. Furthermore, as a vertical structure, microstructured tunnel junctions have a high potential in applications based on a high areal density, e.g., in high density nonvolatile solid-state magnetic memories.³

To date there have been few reports on micron-scale tunnel junctions⁴⁻⁶ although size and geometrical effects combined with intrinsic magnetic properties will strongly affect the performance of tunnel devices. Uniformity over a larger area is another key issue for further device applications. In this article tunnel junctions were patterned using a photolithographic process. The main properties will be compared with those of shadow evaporated junctions.

MULTILAYER FILM PREPARATION

The preparation of the multilayer film used in the microfabrication process has been performed by evaporation at liquid nitrogen temperatures,¹ without breaking the vacuum. On a pre-cooled glass substrate an adhesion layer of 1 nm Si was deposited. A 10 nm Co film was then deposited which later serves as the bottom electrode. During the growth of this layer a magnetic field of a few kA/m was applied to induce uniaxial magnetocrystalline anisotropy. On top of the bottom electrode an Al film was deposited; this film varied in thickness between 1.0 and 1.4 nm. The substrate was then heated to room temperature. The barrier was formed by oxidizing the Al in an oxygen dc glow discharge for 100 s at a pressure of 70 mTorr.⁷ A 17 nm thick $\text{Ni}_{80}\text{Fe}_{20}$ top electrode was deposited next. Also during the growth of this layer a magnetic field was applied to induce uniaxial magnetocrystalline anisotropy, in this case oriented perpendicular to that applied during growth of the bottom layer. Finally, the multilayer was covered by a 4 nm protective Al layer.

MICROFABRICATION PROCESS

The multilayer films were patterned using a four-mask lithographic process, as schematically illustrated in Fig. 1.

First the bottom electrode geometry was defined by Xe ion milling leaving isolated mesas containing the full multilayer stack on the glass substrate [Fig. 1(a)]. During a second ion milling step the active junction area was further defined by etching into the parts of the mesa that were not covered by resist [Fig. 1(b)]. The resulting junctions have a square geometry, ranging from 64×64 down to $2 \times 2 \mu\text{m}^2$.

^{a)}Electronic mail: boeve@imec.be

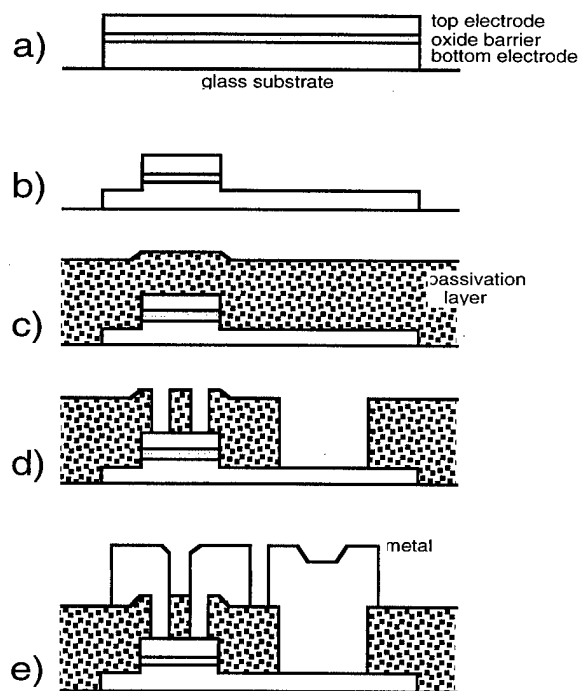


FIG. 1. Schematic of the cross section of the multilayer during microfabrication showing the different steps in the process.

The ion milling was timed to stop under the Al_2O_3 barrier. Nevertheless, some depth nonuniformity over bigger areas seems unavoidable and this can drastically increase the series resistance of the bottom electrode. The junctions were then passivated with 75 nm of Si_3N_4 followed by another lithographic step and opening of the contact holes in the nitride using a CF_4 rf plasma [Figs. 1(c) and 1(d)]. The final step consists of the deposition of a 15 nm TiW/155 nm Au metallization [Fig. 1(e)].

During the Si_3N_4 deposition the substrate temperature was raised to 250 °C, which does not allow the use of a self-aligned process, which would save one mask level and is better suited to reach the smallest dimensions.

An optical microscope image of the completed devices is shown in Figs. 2(a) and 2(b). Also visible are the well-defined top and bottom contacting schemes. In the middle of the bottom electrode two contacts are patterned in order to measure the resistance of the bottom electrode and the double top contacts for the bigger structures [Fig. 2(b) shows a $16 \times 16 \mu\text{m}^2$ junction) are used to control the nitride opening.

RESULTS AND DISCUSSION

The series resistances of the contacts were estimated by measuring the junctions with different contacting schemes. The resistance of the bottom electrode is around 100 Ω , while the resistance of the top electrode connection depends on the cross section of the via between the contact pad and the top electrode, and is generally much lower.

In order to investigate whether the processing scheme described above influences the barrier properties, $I(V)$ char-

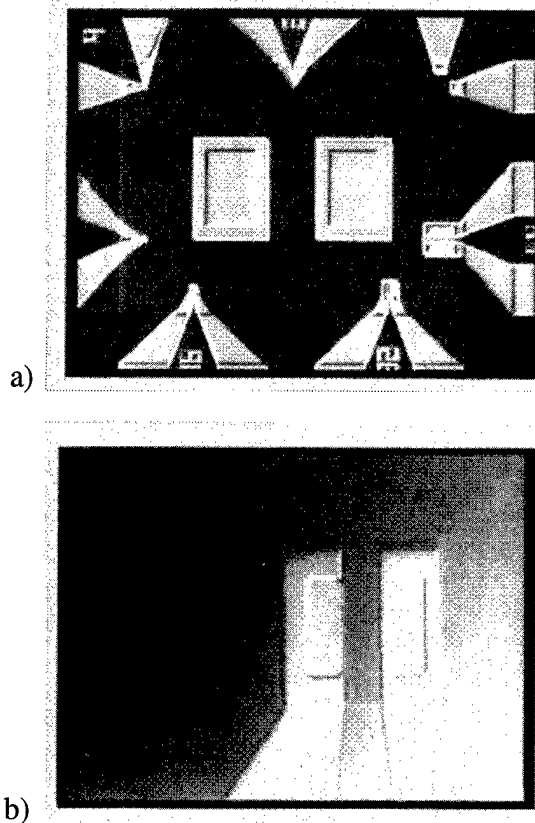


FIG. 2. (a) Layout of the final tunnel devices. Along the sides of the main mesa, several junctions are defined, ranging from 64×64 down to $2 \times 2 \mu\text{m}^2$ for the smallest junctions. The contacts for the bottom electrode are situated in the middle of the mesa. (b) A junction of $16 \times 16 \mu\text{m}^2$ which clearly shows the double top metal contact.

acteristics were measured for several junctions having different areas and they were compared with known results of junctions defined by shadow evaporation.

Curves taken from 0 to 0.75 V show the quality of the barrier after processing. At low bias, the behavior is ohmic while at higher bias it shows a nonlinear dependence. Simmons' general theory of tunneling⁸ was used to estimate the barrier height and thickness for junctions with different areas. Independent of the original Al thickness in the sample, all junctions give a barrier height of 3 eV, while the barrier thickness varies from 1.30 to 1.36 nm. For junctions with a 1.0 nm Al layer a slight asymmetry was seen in the $I(V)$ curves which corresponds to an asymmetric barrier caused by some oxide formation in the Co bottom layer.⁹

The resistance scaled from typically 200 k Ω for a junction area of $64 \times 64 \mu\text{m}^2$ up to 14 M Ω for $4 \times 4 \mu\text{m}^2$. This leads to a resistance-area product of nearly 1 G $\Omega \mu\text{m}^2$, as represented in Fig. 3, which is in excellent agreement with previous results obtained for similar junctions prepared by shadow evaporation.

Magnetoresistance measurements at room temperature were performed in an adapted probe station. A maximum magnetic field of 8 kA/m could be applied using a set of Helmholtz coils. Generally two-point measurements were

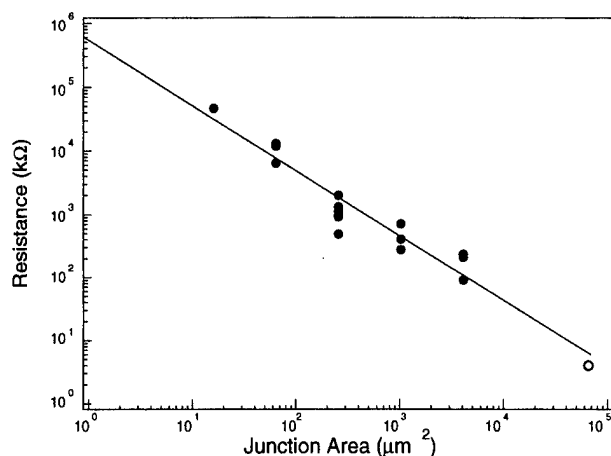


FIG. 3. Area dependence of the junction resistance. Open symbols represent junctions made by shadow evaporation, and closed symbols represent microfabricated junctions.

done, justified by the enormous difference between the junction and possible contact resistance. Tunnel current variations due to the magnetic field were monitored by both ac and dc techniques using a SR830 lock-in amplifier and a HP4145B semiconductor parameter analyzer. Different magnetoresistance values were measured for different Al thicknesses, even though the barrier height and thickness in Simmons' model gave similar results. For the case of 1.0 nm Al, the maximum magnetoresistance value at room temperature was 14% for a $64 \times 64 \mu\text{m}^2$ junction. A thicker Al layer (1.4 nm) resulted in a lower magnetoresistance value of 10% but in this case that value has been measured for junction areas down to $4 \times 4 \mu\text{m}^2$. Compared to the smaller barrier thickness, some unoxidized Al might be left over, which would result in a decrease of spin polarization of the current from the Co electrode and therefore the lower magnetoresistance value.

The magnetoresistance curve shows a different switching behavior for both ferromagnetic layers, which is confirmed by the hysteresis loop before patterning. Figure 4 shows the magnetoresistance curves for a magnetic field applied along a different anisotropy axis. Since the Co has a higher coercivity and anisotropy field than the $\text{Ni}_{80}\text{Fe}_{20}$ layer, the full signal can only be reached along the easy axis of the Co layer. Thus, in this configuration the (nearly) antiparallel alignment of the magnetization in the ferromagnetic layers can be reached, as can be seen by the formation of a plateau on the magnetoresistance peaks. In addition, the orthogonal anisotropies create a bipolar sensor characteristic around zero field.

CONCLUSION

We have successfully patterned ferromagnetic tunnel junctions with areas ranging from 64×64 down to $4 \times 4 \mu\text{m}^2$. The properties of these are very similar to the properties of junctions prepared by shadow evaporation. The

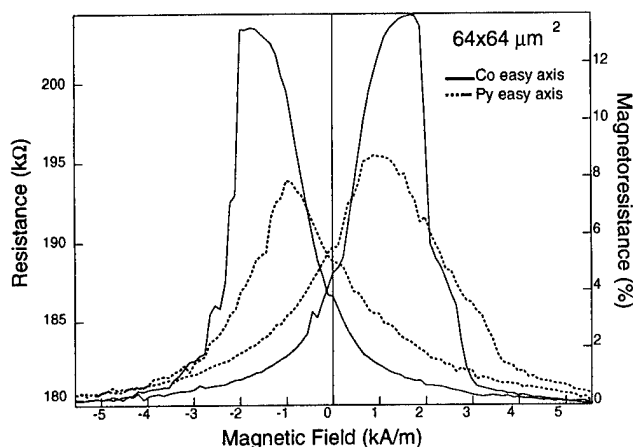


FIG. 4. Magnetoresistance response along both the Co and the NiFe easy axes. The difference in relative height can be explained by the relative orientation of the magnetization of the ferromagnetic layers for a magnetic field being applied along a different axis.

resistance-area product of the junctions is nearly $1 \text{ G}\Omega \mu\text{m}^2$, which seems very high for further device applications.

We have started studying the effect of intrinsic magnetic properties on the performance of the tunnel junction. A bipolar sensor characteristic can be achieved by using a perpendicular anisotropy axis orientation for the different ferromagnetic layers. Further scaling towards smaller dimensions is under investigation as is the influence of the different processing steps on tunnel junction properties. Smaller dimensions will require a self-aligned processing scheme.

ACKNOWLEDGMENTS

The authors wish to thank S. Peeters for the technical assistance. One of the authors (H.B.) acknowledges the financial support of the I.W.T. This work was supported in part by the ESPRIT research project, Novel Magnetic Nanodevices and Artificially Layered Materials (NM)², by ONR Grant No. N00014-92-J-1847 and by NSF Grant No. DMR 9423013.

¹J. S. Moodera, L. R. Kinder, T. M. Wong, and R. Meservy, *Phys. Rev. Lett.* **74**, 3273 (1995); J. S. Moodera and L. R. Kinder, *J. Appl. Phys.* **79**, 4724 (1996).

²T. Miyazaki and N. Tezuka, *J. Magn. Magn. Mater.* **151**, 403 (1995).

³J. M. Daughton, *J. Appl. Phys.* **81**, 3758 (1997).

⁴Y. Lu, R. A. Altman, A. Marley, S. A. Rishton, P. L. Trouilloud, G. Xiao, W. J. Gallagher, and S. S. P. Parkin, *Appl. Phys. Lett.* **70**, 2610 (1996); S. A. Rishton, Y. Lu, R. A. Altman, A. C. Marley, X. P. Bian, C. Jahnes, R. Viswanathan, G. Xiao, W. J. Gallagher, and S. S. P. Parkin, *Microelectron. Eng.* **35**, 249 (1997); W. J. Gallagher, S. S. P. Parkin, Y. Lu, X. P. Xian, A. Marley, K. P. Roche, R. A. Altman, S. A. Rishton, C. Jahnes, T. M. Shaw, and G. Xiao, *J. Appl. Phys.* **81**, 3741 (1997).

⁵T. Miyazaki, S. Kumagai, and T. Yaoi, *J. Appl. Phys.* **81**, 3753 (1997); S. Kumagai, T. Yaoi, and T. Miyazaki, *J. Magn. Magn. Mater.* **166**, 71 (1997).

⁶R. S. Beech, J. Anderson, J. Daughton, B. A. Everitt, and D. Wang, *IEEE Trans. Magn.* **32**, 4713 (1996).

⁷J. L. Miles and P. H. Smith, *J. Electrochem. Soc.* **110**, 1240 (1963).

⁸J. C. Simmons, *J. Appl. Phys.* **34**, 1793 (1963).

⁹J. S. Moodera, E. F. Gallagher, K. Robinson, and J. Nowak, *Appl. Phys. Lett.* **70**, 3050 (1997).

Nanometric cartography of tunnel current in metal-oxide junctions

V. Da Costa,^{a)} F. Bardou, C. Béal, Y. Henry, J. P. Bucher, and K. Ounadjela

Institut de Physique et Chimie des Matériaux de Strasbourg, UMR 46 CNRS, F-67037 Strasbourg Cedex, France

Recently, ferromagnet/insulator/ferromagnet trilayer junctions were shown to exhibit large magnetoresistance effects. However, these effects proved to be poorly reproducible from sample to sample. To get a nanoscopic insight on the origin of these fluctuations, we have used a combined atomic force microscope/scanning tunneling microscope setup to map the tunnel current that flows through metal/oxide stacks. The current histogram, which extends over 1–2 orders of magnitude, is found to be well described by a simple model which takes into account tiny spatial fluctuations of tunnel barrier thickness (typically, 0.1 nm). Moreover, our analysis shows that the total conductance of imperfect metal/oxide junctions tends to be dominated by very few sites. This result allows us to relate the sample-to-sample conductance fluctuations to slight local variations of the tunnel barrier parameters. © 1998 American Institute of Physics. [S0021-8979(98)47511-X]

Spin-polarized tunneling has been extensively studied since the discovery of large magnetoresistance effects in magnetic tunnel junctions (MTJ's) consisting of ferromagnet/insulator/ferromagnet trilayers.^{1,2} Because of their remarkable magnetotransport properties, these MTJ's appeared as good candidates for technological applications in devices such as magnetic sensors or nonvolatile data storage memories. The advantage of using such junctions is, however, significantly altered by the large fluctuations of tunnel resistance (up to four orders of magnitude) that are currently observed from junction to junction,^{2–5} and which make them not yet usable as industrial products. At the present time, the irreproducibility of the electrical characteristics of MTJ's is assumed to be mostly related to large changes in local electron barrier transmission, which may result from defects providing localized electron states, from fluctuations in barrier thickness, as well as from pinholes in the insulating films.^{3,5} All of these defects being normally buried within the core of the MTJ's, hence, hard to investigate, no attempt has yet been made to verify these assumptions.

One way to study the role played in the tunneling process by localized defects inside the insulating layers is to investigate, at a nanoscopic scale, the tunnel current transmitted through the insulating layers while not yet covered by the second ferromagnetic layers. For studying locally this current, we applied the technique first developed by Morita *et al.*⁶ and later improved by Houzé *et al.*⁷ for measuring local contact resistance. An atomic force microscope (AFM) equipped with a conducting tip was used to simultaneously record the usual topographical information and map the current flowing through a tunnel barrier consisting of an insulating oxide layer naturally grown on a ferromagnetic film. Our experimental results show that the tunnel current can vary from place to place by more than one order of magnitude. A statistical analysis involving a fit of the current distributions according to a simple model reveals that the large

fluctuations of current are probably induced by rather small fluctuations of tunnel barrier thickness (or of other tunnel parameters such as barrier height).

The samples studied consisted of superficially oxidized Co films. The initial films were prepared by ultrahigh vacuum e-beam evaporation. 10 nm thick hcp (0001) Co layers were first grown at room temperature on 25 nm thick single-crystal (0001) Ru buffer layers previously deposited at 700 °C on freshly cleaved mica substrates. The oxidation of the top Co surface was later accomplished by leaving the films under atmospheric conditions for three months. X-ray photoelectron spectroscopy (XPS) revealed that the average thickness of the capping oxide was (2 ± 1) nm.

The current measurements were carried out using a commercial atomic force microscope operated in a dc contact mode. The deflection of the cantilever supporting the tip, and thus the force exerted on the tip (a few 10^{-9} N), was maintained at some constant value by a feedback loop that continuously adjusted the cantilever height as the tip was scanned over the sample surface, which allowed us to determine the topography of the investigated sample. Furthermore, using a conducting tip and applying a bias voltage of, typically, 1 V between the bottom ferromagnetic electrode and the tip permitted us to record simultaneously the current flowing through the insulating layer. This led to a cartography of the electrical features of the insulator surface.

The probes were common Si_3N_4 cantilevers with integrated tips having an apex radius of, typically, 30 nm. These probes were coated with 30 nm thick conducting films deposited under high-vacuum conditions. The quality of the experimental results strongly depended on the nature of the conducting material.⁷ We obtained the best results with probes covered with TiN_x compounds, which exhibit ultrahardness, good corrosion resistance, as well as electrical conductivities comparable to those of pure transition metals.⁸ Indeed, the current images obtained with TiN_x coated probes proved to be reproducible as successive scans were performed.

Figures 1(a) and 1(b) show typical topographical and current images recorded simultaneously while exploring a

^{a)}Electronic mail: victor@michelangelo.u-strasbg.fr.

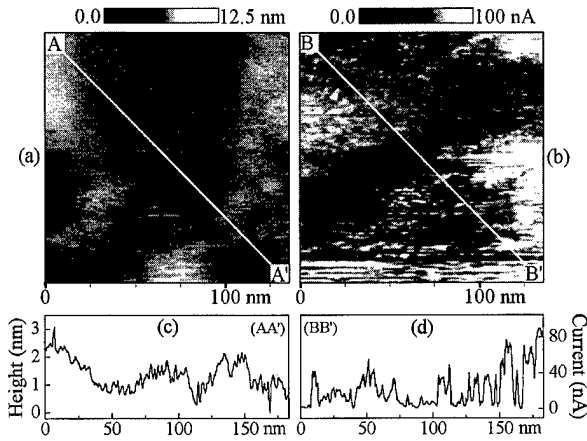


FIG. 1. (a) $136 \times 136 \text{ nm}^2$ topographical and (b) electrical images of the same area of an epitaxial Co film oxidized in air. (c) Topography profile along AA'. (d) Profile of the tunnel current intensity along BB'=AA'.

$136 \times 136 \text{ nm}^2$ region of an oxidized Co surface. The AFM image of Fig. 1(a) reveals that the oxidation in air of our Co films gives rise to a relatively flat top surface, the standard deviation of the height data being 0.5 nm within the displayed area. However, no atomic steps and terraces can be distinguished.

The currents that were measured in the different parts of the investigated region [Fig. 1(b)] range from almost zero or undetectable values to nearly 100 nA. As we checked by investigating (oxide-free) Au surfaces with the same experimental setup, currents that are measured in the case of a metal/metal contact between the tip and sample are no less than a few microamperes. Furthermore, one can check using (for example) Simmons' model⁹ that the most probable current values, which range from a few tenths of nanoampere to a few nanoamperes, are consistent with tunneling through a 1–2 nm thick barrier of height 1–2 eV and an effective contact area of about 20 nm^2 , as inferred from the size of the smallest electrical features that were imaged. Therefore, we attribute the low currents that are obtained on CoO_x films to tunneling. Moreover, no pinholes are found in the CoO_x cap (we have unambiguously observed such pinholes as we investigated other kinds of samples). Following this line of thought, the bright (respectively, dark) zones in the current image correspond to high (respectively, low) tunneling currents, and hence, to sites where the barrier thickness might be locally smaller (respectively, larger) than the average value. Notice that a comparison of the topographical [Figs. 1(a) and 1(c)] and electrical [Figs. 1(b) and 1(d)] data does not reveal a strong correlation between the two kinds of features.

The electrical images were analyzed statistically by calculating the distribution of tunnel currents $P_i(i)$. The distribution computed from the image shown in Fig. 1(b) is presented in Fig. 2. It exhibits a highly asymmetric shape with a pronounced maximum at 3 nA and a very slow decrease for large currents. From this distribution, it appears that the tunnel current varies from place to place by 1–2 orders of magnitude and that relatively high currents are only transmitted through very few sites.

These observations can be connected to the statistical

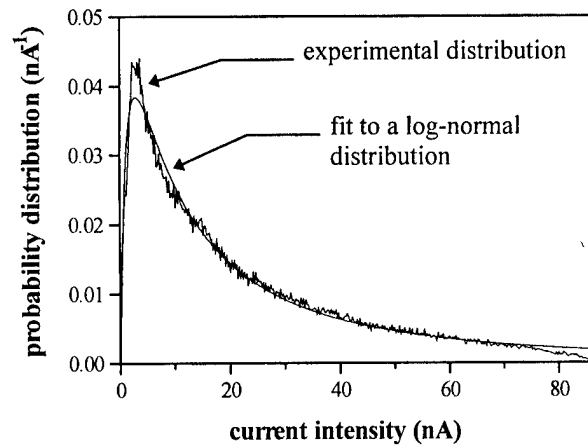


FIG. 2. Experimental and theoretical distributions of tunneling current. The experimental data were calculated from the image of Fig. 1(b).

analysis of tunneling through a barrier with fluctuating parameters presented in Ref. 10. As a simple model, one may consider a rectangular potential barrier of height V_0 and thickness l . The tunneling probability t for particles of mass M and kinetic energy $E < V_0$ is given by $t = 1/\{1 + B^{-1} \sinh^2[l/(2\lambda)]\}$ where $\lambda = \hbar/[2\sqrt{2M(V_0 - E)}]$ is the attenuation length within the barrier and $B^{-1} = V_0^2/[4E(V_0 - E)]$. To take into account the fluctuations in the barrier thickness, one may introduce a Gaussian distribution of average value l_0 and standard deviation σ . This results, for $t \ll 1$, in a log-normal distribution $P_i(t)$ of the transmission coefficient t

$$P_i(t) \approx \frac{1}{\beta\sqrt{2\pi}} \frac{1}{t} \exp\left[-\frac{1}{2\beta^2} [\ln(t) - \alpha]^2\right], \quad (1)$$

where $\alpha = \ln(4B) - l_0/\lambda$ and $\beta = \sigma/\lambda$. As shown in Ref. 10, the transmission t exhibits very different behaviors, depending on σ . For very small σ , $P_i(t)$ is close to a narrow Gaussian distribution. For larger σ , $P_i(t)$ becomes much "broader" and has a tail at large t , which allows the transmission t to fluctuate from place to place by as much as several orders of magnitude. One can show that the current may then flow so inhomogeneously through the tunnel barrier that the total transmission is dominated by very few sites. Thereby, one can predict very large sample-to-sample conductance fluctuations. Interestingly, these results are robust and similar behaviors would be obtained for non-Gaussian fluctuations of barrier thickness, more complicated barrier shapes, or fluctuations in the barrier height.

This model has been used to achieve a quantitative determination of the statistical properties of the Co/CoO_x junctions. As shown in Fig. 2, the current distribution is reasonably well fit using Eq. (1). This is remarkable since the latter contains only two parameters, α and β , and results from a simple model (rectangular barrier; Gaussian fluctuations). As currents i are measured and not directly the transmissions t , a scaling parameter η was introduced to give $t = \eta i$. This transformation, implying $P_i(i) = \eta P_i(\eta i)$, leads to an expression for the current distribution $P_i(i)$ similar to that obtained for the transmission t , the α parameter in Eq. (1) being simply replaced by $\alpha' = \alpha - \ln(\eta)$. The proportionality

factor η is related to the contact area between the tip and the sample, and hence, depends upon the tip radius, since the latter determines the size of the surface area from which the current is collected.

For all data, however, there is a small residual discrepancy between the experimental data and the distribution fit for values of i larger than 75 nA and smaller than 5 nA, which may be attributed to the finite size of the probing tip. Indeed, the rather large radius of the tip prevents access to the small holes that exist in the sample surface. One may reasonably think that in these holes the tunnel barrier is thinner and the current, which could be transmitted, is higher. Not probing them results in an underestimate of the amount of surface associated with large currents. Correspondingly, sharp asperities that would correspond to low transmissions tend to keep the tip away from the surface, thus artificially increasing the proportion of low currents. This explanation accounts for the weak correlation that exists between the surface topography and barrier thickness.

The best fit of our experimental data [Fig. 2] was obtained with $\alpha' = 3.0$ and $\beta = 1.4$. To our knowledge, no experimental value has been reported for the effective barrier height $\phi = V_0 - E$ of cobalt oxide. However, typical values of ϕ available in the literature range from 1 to 4 eV, depending on the insulating material.¹¹ This corresponds to attenuation lengths λ ranging from 0.05 to 0.1 nm. Combining these limiting values with the parameter $\beta = \sigma/\lambda$ deduced from our fit, we can estimate the variance of the barrier thickness distribution σ , to be between 0.07 and 0.14 nm. This value ($\sigma \approx 0.1$ nm) is smaller than the topographical roughness (≈ 0.5 nm). We, thus, interpret the latter as being due mostly to the underlying Co film. This film would be covered by a CoO_x layer of nearly constant thickness.

From the distribution $P_i(i)$ determined experimentally, it is concluded that the tunnel current flows in an inhomogeneous manner through the CoO_x barrier. Indeed, we calculate that 50% of the total current that gets through the barrier is transmitted by only 9% of the sample area. Concomitantly, the average transmission $\langle t \rangle$ is 15 times larger than the most probable transmission t_i , which is associated with the peak of the distribution. This shows that the usual integrated conductance or resistance measurements that yield only average values fail to characterize imperfect tunnel junctions. Indeed, for broad distributions as opposed to narrow distributions, such as Gaussian, the random variable fluctuates so much around its average value that the average value in itself ceases to be a relevant parameter.^{10,12} This statement is reinforced by the fact that our sample is a very good one from the point of view of the tunnel barrier homogeneity since fluctuations of barrier thickness amount to less than one atomic layer ($\sigma \approx 0.1$ nm). For $\sigma = 0.2$ nm ($\beta = 2.8$), which would still be good according to usual thin-film standards, 50% of the current would be transmitted through only 0.3% of the sample surface. The average transmission $\langle t \rangle$ would be 2×10^5 times the most probable transmission t_i , thus ut-

terly ruining the meaningfulness of measurement techniques yielding average values.

In conclusion, we have demonstrated the possibility of reproducibly mapping, at a nanoscopic scale the tunnel currents. As predicted in Ref. 10, the distribution of currents tends to exhibit a shape similar to that of Lévy distributions, characterized by a long tail extending to large current values. This shows that broad distributions, widely known in complex systems such as turbulent flows or spin glasses,¹² also appear in the theoretical description of simpler phenomena such as quantum tunneling through insulating layers.

Moreover, the statistical properties of these Lévy-like distributions imply dramatic practical consequences. First, for thin insulating films, very small thickness fluctuations ($\sigma = 0.1$ nm) give rise to tunnel current fluctuations greater than one order of magnitude. Second, usual measurements of average conductance performed on imperfect tunnel junctions yield incomplete information about the tunnel barrier, since the current flows in such an inhomogeneous way that the total conductance is often dominated by contributions from a few localized sites having very high transmissions. Third, the statistical properties discussed here could naturally account for the large fluctuations of integrated conductance observed from sample to sample. Finally, we can take advantage of the results of our statistical analysis to propose a strategy for making more reproducible tunnel junctions, in the same way as previously used to improve the lowest temperatures achieved by laser cooling.¹³ Apart from the trivial argument of reducing σ , Eq. (1) shows that one could drastically reduce the current fluctuations by increasing λ , i.e., using lower tunnel barriers.¹⁴

The authors thank J. Hommet for performing the XPS measurements. This work was partially supported by the European Community Brite Euram project BE96-3407 and the Société de Secours des Amis des Sciences.

¹P. M. Tedrow and R. Meserve, Phys. Rev. B **7**, 318 (1973).

²J. S. Moodera, L. R. Kinder, T. M. Wong, and R. Meserve, Phys. Rev. Lett. **74**, 3273 (1995).

³E. L. Wolf, *Principles of Electron Tunneling Spectroscopy* (Oxford University Press, New York, 1985), pp. 68 and 486.

⁴J. S. Moodera, L. R. Kinder, J. Nowak, P. LeClair, and R. Meserve, Appl. Phys. Lett. **69**, 708 (1996).

⁵N. Tezuka and T. Miyazaki, J. Appl. Phys. **79**, 6262 (1996).

⁶S. Morita, T. Ishizaka, Y. Sugawara, T. Okada, S. Mishima, S. Imai, and N. Mikoshiba, Jpn. J. Appl. Phys., Part 2 **28**, L1634 (1989).

⁷F. Houzé, R. Meyer, O. Schneegans, and L. Boyer, Appl. Phys. Lett. **69**, 1975 (1996).

⁸See, for instance, L. E. Toth, *Transition Metal Carbides and Nitrides* (Academic, New York, 1971), Vol. 7.

⁹J. G. Simmons, J. Appl. Phys. **34**, 1793 (1963).

¹⁰F. Bardou, Europhys. Lett. **39**, 239 (1997).

¹¹J. S. Moodera and L. R. Kinder, J. Appl. Phys. **79**, 4724 (1996).

¹²*Lévy Flights and Related Topics in Physics*, edited by M. F. Schlesinger, G. M. Zaslavsky, and U. Frisch (Springer, Berlin, 1995).

¹³J. Reichel, F. Bardou, M. Ben Dahan, E. Peik, S. Rand, C. Salomon, and C. Cohen-Tannoudji, Phys. Rev. Lett. **75**, 4575 (1995).

¹⁴A measure of the relative fluctuations is given by $\langle t \rangle / t_i = e^{3\sigma^2/(2\lambda^2)}$.

Hard Magnets I

G. Hadjipanayis, Chairman

Sm₂(Co,Fe,Cu,Zr)₁₇ magnets for use at temperature $\geq 400^\circ\text{C}$

C. H. Chen, M. S. Walmer, and M. H. Walmer

Electron Energy Corporation, 924 Links Ave., Landisville, Pennsylvania 17538

S. Liu and E. Kuhl

University of Dayton, 300 College Park Ave., Dayton, Ohio 45469

G. Simon

Air Force Research Laboratory, Wright Patterson Air Force Base, Ohio 45433

Sintered Sm₂(Co,Fe,Cu,Zr)₁₇ magnets with improved high temperature performance have been obtained by reducing the iron content in the magnet alloys. A record intrinsic coercive force, iH_C , of 8.3 kOe at 400 °C was obtained when the iron content was decreased to 7 wt%. At 400–600 °C, 2:17 magnets with low iron content have demonstrated lower irreversible loss of magnetic flux, higher maximum energy product, and lower temperature coefficient of iH_C . A temperature coefficient of $iH_C = -0.12\%/^\circ\text{C}$ (20–400 °C) was obtained for the low Fe magnets, compared to $-0.23\%/^\circ\text{C}$ for commercial 2:17. Reducing iron content increases both Curie temperature and anisotropy field. Therefore, it is anticipated that new 2:17 magnet materials capable of operating at 400 °C or higher temperatures can be developed by reducing or eliminating the iron content and making other adjustments in composition and heat treatment. © 1998 American Institute of Physics. [S0021-8979(98)19111-9]

I. INTRODUCTION

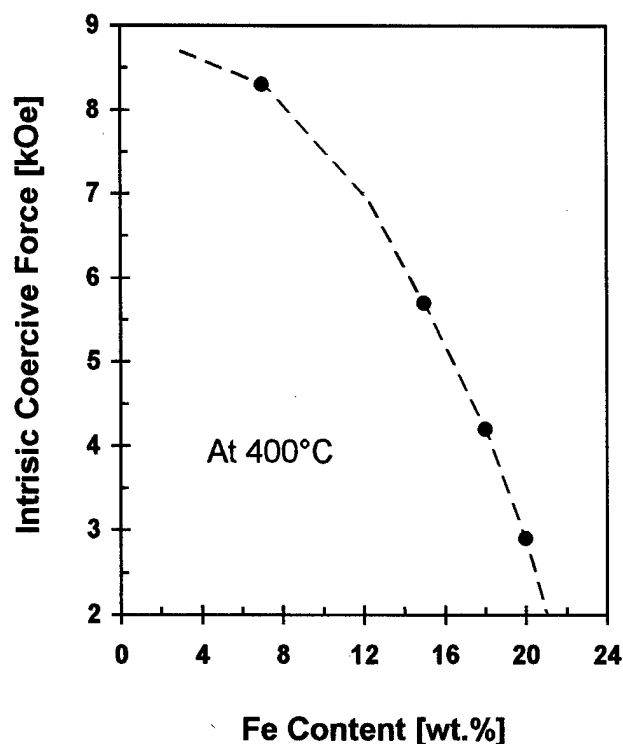
The power system in a new generation of aircraft requires magnetic materials capable of operating at temperatures higher than 400 °C. The More Electric Aircraft (MEA) initiative proposed by the U.S. Air Force is a driving force in high temperature requirements for magnetic materials. In the MEA, all hydraulic-mechanical components will be replaced by electric-magnetic components, and the centralized hydraulic heat sink will also be eliminated. This will significantly enhance the reliability, reduce maintenance, and greatly decrease support and logistics cost. However, the high temperature properties of magnetic materials must be substantially improved to satisfy MEA requirements.

The best existing high energy density, high temperature permanent magnet material, Sm₂(Co_wFe_xCu_yZr_z)₁₇ (2:17), has been satisfying many applications at temperatures up to 300 °C. For applications at temperatures higher than 400 °C, magnetic materials with improved high temperature properties must be developed. Prior to the Air Force MEA initiative, there was little demand or need for magnets capable of operation above 300 °C. Accordingly, magnet performance at temperatures $>300^\circ\text{C}$ has not been a principal concern in magnetic materials R&D. In the last 14 years, permanent magnet material R&D has been focused primarily on the following three topics: (1) Nd₂Fe₁₄B based materials and other ternary rare earth (RE)-transition metal (TM) systems; (2) New RE-TM permanent magnet materials containing interstitial atoms (N or C); and (3) New nanocrystalline composite magnet materials containing the magnetically hard phase with high crystalline anisotropy and the magnetically soft phase with high saturation magnetization.^{1–3} These ef-

forts, however, have not yet led to the next generation of rare earth permanent magnets (REPM).

Because most RE-TM binary systems have been extensively studied, it is more likely that the new promising compounds will be found in ternary or quaternary systems. Based on today's knowledge of thermodynamics, kinetics, crystallography, and magnetism, it is still impossible to predict or calculate crystalline structures and basic magnetic properties. In the foreseeable future the empirical approach will be our principal method to search for new promising compounds in more complicated systems. Therefore, it will take more time than one might expect before another breakthrough occurs. Since the appearance of Nd₂Fe₁₄B magnets in 1983, the worldwide study of 2:17 magnets has been slowed considerably. Actually, there is still room for significant improvement. We believe that, in addition to studying new materials, we can continue to improve the best existing high temperature 2:17-type magnets.

Recent studies have shown that the thermal stability of 2:17 magnets is related to the iron content in the 2:17 magnet alloys.^{4–6} In order to increase the long-term reliable operating temperature from the current 300 °C to higher temperatures, two important magnetic parameters of the existing commercial 2:17 magnets must be improved. The first one is iH_C . Our high temperature characterization of the best commercial high-coercivity-type 2:17 magnets showed that at 400 °C, iH_C dropped from the room temperature value of >30 to 5.7 kOe and the second-quadrant induction demagnetization curve is not straight.⁴ In order to keep the induction demagnetization curve a straight line, which is important for dynamic applications, iH_C at 400 °C has to be increased

FIG. 1. iH_C vs Fe content in 2:17 magnets at 400 °C.

to at least > 8 kOe. The second magnetic parameter which needs to be improved is the long-term thermal stability. Our previous application-oriented characterization showed that after aging at 400 °C for 4300 h, the maximum energy product, the best commercial 2:17 magnet, dropped as much as about 40%.⁶ Obviously, the long-term high temperature stability of the current 2:17 magnets must be significantly improved before they can be used at 400 °C or higher.

Previous studies on the $\text{Sm}_2(\text{Co}_{1-x}\text{Fe}_x)_{17}$ system indicated that when $x < 0.5$, the compound retains the easy-axis magnetic symmetry. And, on further reduction of x , both the anisotropy field and the Curie temperature are substantially increased.^{7,8} Therefore, it is possible that the above mentioned two problems can be resolved by reducing the iron content and by making other adjustments in composition and heat treatment.

II. EXPERIMENT

New 2:17 magnets with compositions of $\text{Sm}(\text{Co}_{0.9}\text{Fe}_{0.1}\text{Cu}_{0.06}\text{Zr}_{0.02})_{7.6}$ with $v = 0-0.28$ (0–20 wt%) were prepared by vacuum induction melting and conventional powder metallurgy processing. Magnetic characterizations from room temperature up to 300 °C were performed using a hysteresigraph, while magnetic properties at 400 °C and higher were determined using a vibrating sample magnetometer (VSM). Because the VSM characterization is an open-circuit measurement, careful calibration was made so that the result of VSM measurement was in excellent agreement with that of closed-circuit hysteresigraph measurement. An aging experiment was carried out up to 845 °C, in which the flux was determined using a fluxmeter. Curie temperatures of 2:17 magnets with various iron contents were determined

TABLE I. $(\text{BH})_{\text{max}}$ and β of 2:17 magnets vs Fe wt% at different temperatures.

Fe [wt%]	$(\text{BH})_m$ at various temperatures [MGoe]					β [%/°C] 20–400 °C
	20 °C	300 °C	400 °C	500 °C	600 °C	
20	30.5	20.7	14.6	6.2	2.9	...
15	28.2	21.5	17.4	8.4	3.2	−0.23
8 [A] ^a	24.6	18.8	15.8	11.6	5.6	−0.21
8 [B] ^a	22.6	17.2	14.5	10.2	4.9	−0.12
0	21.4	16.4	Samples in test for 400–600 °C			

^a8% Fe [A] and 8% Fe [B] have different iH_C at room temperature.

using thermal magnetic analysis (TMA). A Siemens Gaddis Hi Start Area Detector x-ray diffraction was used to determine lattice constants of 2:17 materials with different iron contents. Curie temperatures and lattice constants are shown in Table III.

III. RESULTS AND DISCUSSION

Figure 1 shows the iH_C versus the iron content in 2:17 magnets at 400 °C. The data show that reducing iron content enhances the iH_C at 400 °C. A record iH_C of 8.3 kOe at 400 °C was obtained when the iron content was decreased to 7 wt%. It is also significant that the second-quadrant induction demagnetization curve of this magnet is a straight line at 400 °C. Decreasing iron content in 2:17 magnet alloys also resulted in magnets with low temperature coefficient of $iH_C(\beta)$. A very low β of $-0.12\%/^{\circ}\text{C}$ (20–400 °C) was achieved in the magnets with 8 wt% iron. This is about half of the value of commercial 2:17 magnets. The 2:17 magnets with low iron content demonstrate not only higher iH_C and lower temperature coefficient of iH_C , but also greater maximum energy product $(\text{BH})_M$ at high temperatures. Table I lists the $(\text{BH})_{\text{max}}$ of three 2:17 magnets with different iron contents at different temperatures. Figure 2 shows the

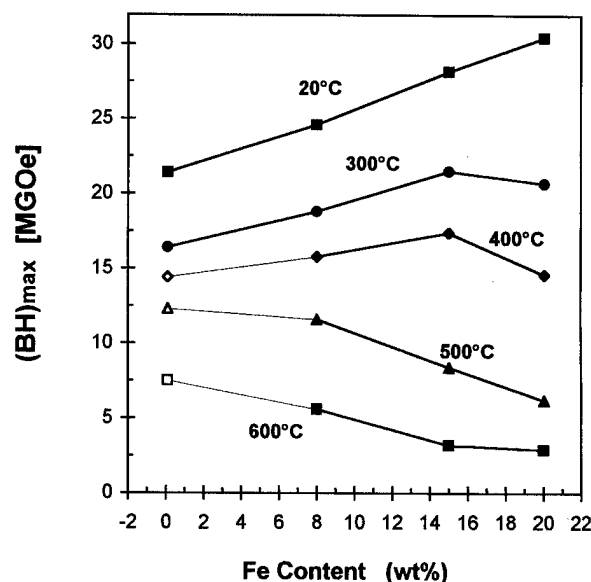


FIG. 2. Energy product vs Fe content at different temperatures: solid marks-measured data, hollow marks-estimated.

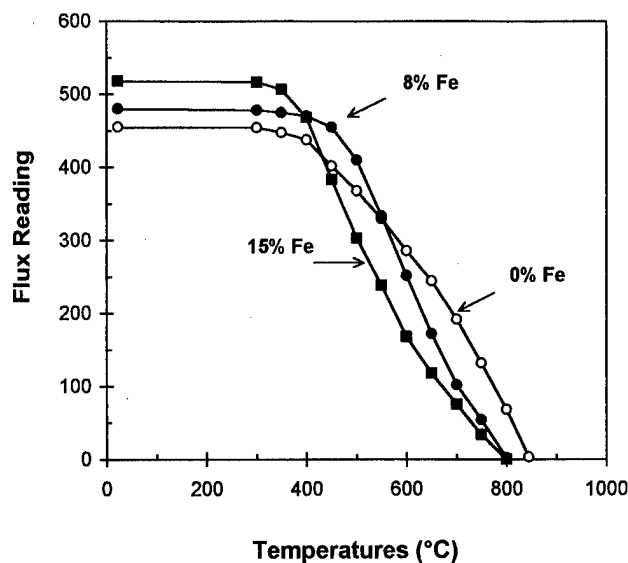


FIG. 3. Room temperature magnetic flux of the magnets with different % Fe after 2 h at the temperatures shown. Sample dimensions: ϕ 1.0 cm \times 0.635 cm.

$(BH)_{\max}$ vs Fe content at different temperatures. It is evident that at high temperatures 2:17 magnets with lower iron demonstrate better magnetic performance than that of commercial 2:17. With adjustments in chemical compositions and heat treatment, further improvement is anticipated.

Figure 3 compares the magnet flux change of 2:17 magnets in an aging experiment up to 845 °C. Three 2:17 magnets with various iron contents were used in this experiment as shown in Table II. The dimensions of the samples for this experiment were 1.00 cm in diameter, and 0.635 cm in thickness. In this experiment, 2:17 magnet samples were heated to a specific temperature between room temperature and 845 °C, kept at that temperature for 2 h, cooled to room temperature, and then the magnetic flux was measured using a Helmholtz coil. It can be seen from Fig. 3 that after the short-term aging, the magnet with 15 wt% Fe retained the highest flux when aged below 400 °C. When aged between

TABLE III. T_c , lattice constants, and unit cell volumes of the 2:17 magnets.

Fe [wt%]	T_c [°C]	a [Å]	c [Å]	v [Å ³]
15	810	8.493	12.244	764.94
8 [B]	...	8.471	12.218	759.31
0	855	8.459	12.206	756.27

400° and 550 °C, the magnet with 8: wt% Fe showed the highest flux. When aged from >550 to 845 °C, the magnet with 0 wt% Fe demonstrated the highest flux. The sample with 0 wt% Fe had lower μH_C at room temperature, which might affect the losses at <550 °C.

One reason why 2:17 magnets with low iron content demonstrate improved high temperature stability is their higher Curie temperature. The Curie temperature of a 2:17 magnet with 0 wt% Fe is 855 °C, or 45 °C higher than that of a 2:17 magnet with 15 wt% Fe (Table III). We anticipate that these new 2:17 magnets with low (or zero) iron content will demonstrate improved long-term high temperature stability because of their increased Curie temperature and the increased crystalline anisotropy. Results of x-ray diffraction showed that the new 2:17 magnet materials containing 8 wt% Fe and 0 wt% Fe have rhombohedral crystalline symmetry and the crystal lattice constants shrank slightly upon reducing iron content as shown in Table III.

These new promising results show that it is possible to develop new 2:17 magnet materials capable of operating at temperatures of 400 °C or higher by reducing or eliminating the iron content and making other adjustments in composition and heat treatment.

ACKNOWLEDGMENTS

This work was supported by the U.S. Air Force under Contract No. F33615-96-C-54. The authors also wish to thank W. Gong and B.M. Ma of Rhone-Poulenc for their assistance in TMA and x-ray diffraction.

TABLE II. Three 2:17 magnet samples used in the aging experiment.

Fe [wt%]	μH_C^a [kOe]	Saturated Flux	450 °C/2 h		600 °C/2 h	
			Flux	Loss	Flux	Loss
15	>30	518	383	26%	168	68%
8 [A]	>30	480	455	5%	252	48%
0	17	455	403	11%	286	37%

^a μH_C At room temperature. All the samples have 1.00 cm in diameter and 0.635 cm in thickness.

¹K. H. J. Buschow, *Ferromagnetic Materials*, edited by E. P. Wohlfarth and K. H. J. Buschow (Elsevier, New York, 1988), Vol. 4, p. 7.

²J. M. D. Coey and H. Sun, *J. Magn. Magn. Mater.* **87**, L251 (1990).

³E. F. Kneller and R. Hawig, *IEEE Trans. Magn.* **27**, 3588 (1991).

⁴S. Liu and E. P. Hoffman, *IEEE Trans. Magn.* **MAG-32**, 5091 (1996).

⁵B. M. Ma, Y. L. Liang, J. Patel, D. Scott, and C.O. Bounds, *IEEE Trans. Magn.* **MAG-32**, 4377 (1996).

⁶S. Liu, E. P. Hoffman, and J. R. Brown, *IEEE Trans. Magn.* **MAG-33**, 3859 (1997).

⁷A. E. Ray and K. J. Strnat, *IEEE Trans. Magn.* **MAG-8**, 516 (1972).

⁸R. S. Perkins, S. Gaiffi, and A. Menth, *IEEE Trans. Magn.* **MAG-11**, 1431 (1975).

Phase transformation and magnetic properties of $\text{Sm}(\text{Co}_{0.91-x}\text{Fe}_x\text{Cu}_{0.07}\text{Zr}_{0.02})_z$ powders for bonded magnet applications

W. Gong, B. M. Ma,^{a)} and C. O. Bounds

Rhodia, Rare Earths and Gallium, CN 7500, Cranbury, New Jersey 08512

Structural and magnetic properties of $\text{Sm}(\text{Co}_{0.91-x}\text{Fe}_x\text{Cu}_{0.07}\text{Zr}_{0.02})_{8.0}$, where $x = 0, 0.12, 0.21, 0.29$, and 0.32 , and $\text{Sm}(\text{Co}_{0.64}\text{Fe}_{0.28}\text{Cu}_{0.06}\text{Zr}_{0.02})_z$, where z ranged from 6.9 to 8.6 , have been systematically investigated by x-ray powder diffraction. It was found that most of these alloys exhibit a hexagonal $\text{Th}_2\text{Ni}_{17}$ structure with a space group $\text{P6}_3/\text{mmc}$ after an optimum solid solution treatment with rapid quench. The fully processed materials (after precipitation hardening) all exhibit a rhombohedral $\text{Th}_2\text{Zn}_{17}$ structure with a space group of $\text{R}\bar{3}\text{m}$ as the primary phase. For $\text{Sm}(\text{Co}_{0.91-x}\text{Fe}_x\text{Cu}_{0.07}\text{Zr}_{0.02})_{8.0}$, the lattice parameters, a and c , and cell volume, V , increase slightly at first with increasing x , and then more sharply when x is increased above 0.28 . The latter drastic increase in lattice parameters and cell volume results in a sharp decrease in the H_{ci} , H_c , and H_k values of fully processed materials. For $\text{Sm}(\text{Co}_{0.64}\text{Fe}_{0.28}\text{Cu}_{0.06}\text{Zr}_{0.02})_z$, the lattice parameters, a and c , and cell volume increase slightly when z is varied from 6.8 to 7.8 , then exhibit a drastic decrease when z is further increased beyond 8.0 . A B_r of 11.3 kG, H_{ci} of 27 kOe, and BH_{max} of 30 MGOe have been obtained on $\text{Sm}(\text{Co}_{0.63}\text{Fe}_{0.28}\text{Cu}_{0.07}\text{Zr}_{0.02})_{8.0}$ after a solid solution at 1160°C and aging at 850°C . © 1998 American Institute of Physics. [S0021-8979(98)15711-0]

I. INTRODUCTION

The phase transformations of $\text{Sm}(\text{Co}, \text{Fe}, \text{Cu}, \text{Zr})_z$ alloys of commercial interest have been studied by many researchers.¹⁻³ There are many models to explain the relationship between transitional phases and the mechanism, microstructure, and magnetic properties obtained on finished magnets. One model suggests that a single phase precursor (after a solid solution treatment and quenching) with a rhombohedral $\text{Th}_2\text{Zn}_{17}$ structure with a space group of $\text{R}\bar{3}\text{m}$ (Space Group No. 166) is critical to obtaining the desired final microstructure.⁴ A second model indicates that the precursor phase must be a metastable TbCu_7 structure with a space group of $\text{P6}/\text{mmm}$ (Space Group No. 191).⁵ Since both structures are metastable derivations of the CaCu_5 structure, lattice parameters and their relationship with nominal compositions are of scientific interest and technological importance.

To clarify the structural transitions, we studied a narrowly defined composition range and conducted a series of experiments with various thermal treatments to compare the structure, lattice parameters, and magnetic properties of $\text{Sm}(\text{Co}_{0.91-x}\text{Fe}_x\text{Cu}_{0.07}\text{Zr}_{0.02})_z$, where $x = 0.21$ to 0.32 and $z = 6.9$ to 8.6 . Our focus was on how the alloy composition affected the microstructural, lattice parameters, and the magnetic properties, namely B_r , H_c , H_{ci} , BH_{max} , and H_k .

II. EXPERIMENT

$\text{Sm}(\text{Co}_{0.91-x}\text{Fe}_x\text{Cu}_{0.07}\text{Zr}_{0.02})_z$, where $x = 0.21$ to 0.32 and $z = 6.9$ to 8.6 , were prepared by conventional vacuum induction melting and mold casting. Alloy ingots were solu-

tion treated over a temperature range of 1130 to 1200°C for 4 to 24 h and quenched to room temperature, precipitation hardened at 800 – 900°C for 4 to 10 h, slowly cooled to 400°C at a rate of $1^\circ\text{C}/\text{min}$, and then quenched to room temperature. Alloy ingots were pulverized by a jaw crusher and a cross-beater mill to obtain powder with top size of $75\ \mu\text{m}$. A Perkin Elmer differential thermal analyzer (DTA) was employed to determine magnetic phase transformations. A Siemens x-ray diffractometer with a $\text{Co } K\alpha$ radiation and a Hi-Star area detector were utilized to measure the lattice parameters and to determine the structure of the alloy powders. Magnets of 3 mm in diameter were prepared by mixing powders with molten paraffin, aligned under a 30 kOe peak magnetic field then solidified. The magnetic properties were determined by measuring the second quadrant demagnetization curves using a vibrating sample magnetometer (VSM). A theoretical density of $8.4\ \text{gm}/\text{cm}^3$ and a demagnetization factor of 0.29 were used to obtain the normalized $4\pi M$, B_r , and BH_{max} values of powders.

III. RESULTS AND DISCUSSION

Shown in Fig. 1 are the x-ray powder diffraction patterns of $\text{Sm}(\text{Co}_{0.69}\text{Fe}_{0.22}\text{Cu}_{0.07}\text{Zr}_{0.02})_{8.0}$ alloy quenched from solid solution treatment temperature [patterns (a) and (b)] and after an isothermal aging at 850°C [patterns (c) and (d)]. In order to obtain a more precise structural indexing, the x-ray diffraction (XRD) was performed on powder samples with and without magnetic field alignment. Diffraction patterns (a) and (b) in Fig 1 are XRD patterns of samples quenched from solid solution temperature with and without magnetic field alignment, respectively. These samples had a hexagonal $\text{Th}_2\text{Ni}_{17}$ structure with $a = 8.489$, $c = 8.176$, and $V = 510.22\ \text{\AA}^3$. The enhanced intensity of the (004) peaks for

^{a)}Electronic mail: bma@us.rhodia.com

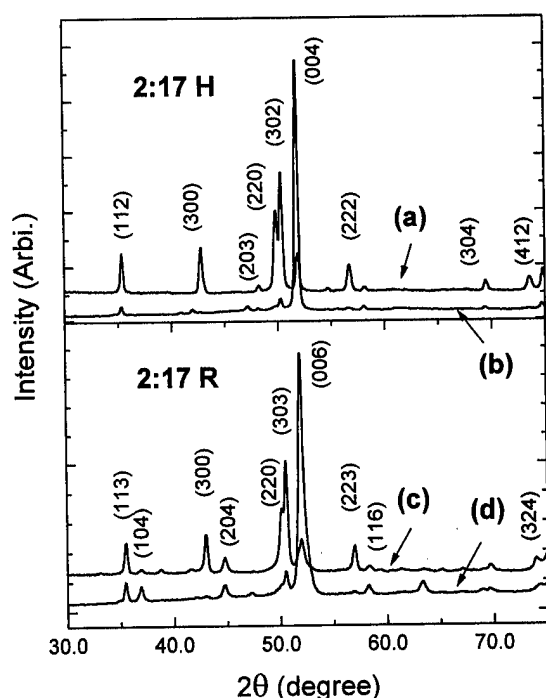


FIG. 1. X-ray powder diffraction of $\text{Sm}(\text{Co}_{0.69}\text{Fe}_{0.22}\text{Cu}_{0.07}\text{Zr}_{0.02})_{8.0}$ after a solid solution treatment (a) without and (b) with magnetic alignment and fully processed materials (c) without and (d) with magnetic alignment.

the powder aligned with a magnetic field suggests that the alloy is magnetically anisotropic with easy magnetization direction (EMD) parallel to the c axis of the hexagonal structure. Similarly, XRD patterns (c) and (d) in Fig. 1 correspond to the patterns of fully processed powders with and without magnetic alignment, respectively. A rhombohedral $\text{Th}_2\text{Zn}_{17}$ structure with space group of $\text{P6}_3/\text{mmc}$ was identified. Again, the enhanced intensity of (006) peaks with the magnetic alignment suggests that it is magnetically anisotropic with EMD parallel to the c axis of the rhombohedral structure.

Shown in Fig. 2 are the variations of H_{ci} , B_r , H_c , BH_{\max} , and H_k of optimally processed $\text{Sm}(\text{Co}_{0.91-x}\text{Fe}_x\text{Cu}_{0.07}\text{Zr}_{0.02})_{8.0}$ with Fe content, where $x=0.12, 0.21, 0.29$, and 0.32 . As shown, the H_{ci} remains relatively constant when the x was increased from 0.21 to 0.28 then decreases sharply when x reached values above 0.28. Unlike H_{ci} , the B_r increases linearly with the Fe content. The BH_{\max} increases initially then approaches a maximum value of nearly 30 MGOe when x was increased above 0.25. It is of interest to note that both H_c and H_k increase linearly at low Fe content then decrease sharply when the Fe content was increased beyond 0.28. The sharp decrease in H_c , H_{ci} , and H_k may result from a structural change but further study is required to be precise.

Shown in Fig. 3 are the variations of the lattice parameters, both a and c , and the cell volumes of the fully processed $\text{Sm}(\text{Co}_{0.91-x}\text{Fe}_x\text{Cu}_{0.07}\text{Zr}_{0.02})_{8.0}$ with Fe content, where $x=0, 0.12, 0.21, 0.29$, and 0.32 . At $x=0$ (without Fe substitution), an a of 8.459 Å, c of 12.206 Å, and V of 756.27 Å³ were obtained when indexed to the $\text{Th}_2\text{Zn}_{17}$ structure. The lattice parameters, a and c , and cell volume, V , increase gradually with increasing Fe content initially. Sharp

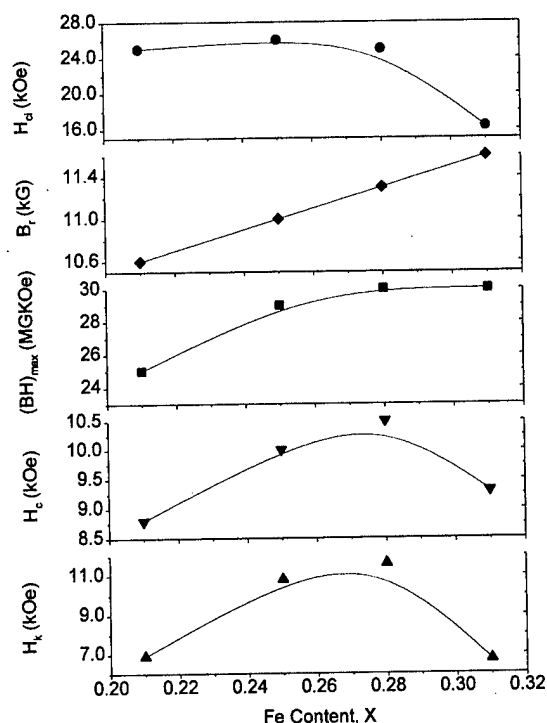


FIG. 2. The variations of H_{ci} , B_r , BH_{\max} , H_c , and H_k of $\text{Sm}(\text{Co}_{0.91-x}\text{Fe}_x\text{Cu}_{0.07}\text{Zr}_{0.02})_{8.0}$ with Fe content, where $x=0.12, 0.21, 0.29$, and 0.32 .

increases in a and c and V can be observed when the x was increased above 0.29. The increase in lattice parameters and cell volume may hinder atomic diffusion and the development of the desired cellular structure with appropriate precipitated phase for domain wall pinning.⁶ The increase in the lattice parameter and cell volume also stretch the distance

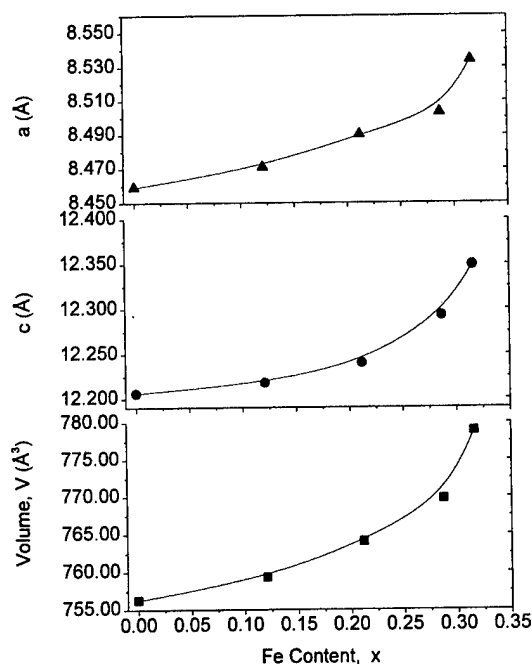


FIG. 3. The variations of lattice parameters a , c and cell volume V of $\text{Sm}(\text{Co}_{0.91-x}\text{Fe}_x\text{Cu}_{0.07}\text{Zr}_{0.02})_{8.0}$ with Fe content, where $x=0, 0.12, 0.21, 0.29$, and 0.32 .

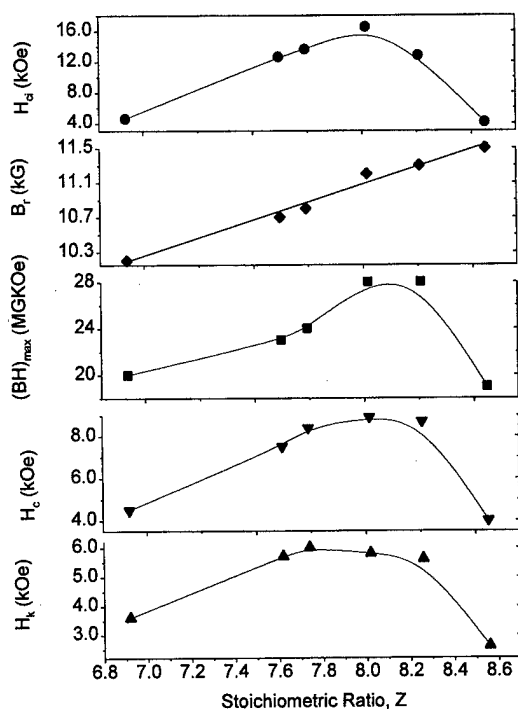


FIG. 4. The variations of H_{ci} , B_r , BH_{max} , H_c , and H_k of $\text{Sm}(\text{Co}_{0.64}\text{Fe}_{0.28}\text{Cu}_{0.06}\text{Zr}_{0.02})_z$ with z , where z ranges from 6.9 to 8.6.

between transition metals, and enhance the exchange interaction, which may explain the magnetization increase with increasing Fe content.

Shown in Fig. 4 are the variations of H_{ci} , B_r , BH_{max} , H_c and H_k of $\text{Sm}(\text{Co}_{0.64}\text{Fe}_{0.28}\text{Cu}_{0.06}\text{Zr}_{0.02})_z$, where z ranges from 6.9 to 8.6. Initially, the H_{ci} increases linearly with the stoichiometric ratio z , reaches a peak at $z=8.0$, then decreases drastically when z is increased beyond 8.0. Unlike H_{ci} , the B_r increases linearly with the z value. The BH_{max} , H_c and H_k all increase gradually with increasing z , reach a maximum at z near 8.0 to 8.2 then decrease sharply when z is increased beyond 8.2. Again, the decrease in H_{ci} and H_k may be caused by the lattice parameters and cell volume which inhibit the formation of desired microstructure.

Shown in Fig. 5 are the variations of lattice parameters, a and c , and the cell volume, V , of fully processed $\text{Sm}(\text{Co}_{0.64}\text{Fe}_{0.28}\text{Cu}_{0.06}\text{Zr}_{0.02})_z$, where z ranged from 6.9 to 8.6. The trends of the lattice parameters, a and c , and cell volume are very similar. They all increase slightly with increasing z then decrease drastically when z is increased beyond 8.0 indicating a structural change. A higher z value may cause an imbalance of the 2:17 ($\text{Th}_2\text{Zr}_{17}$) and 1:5 (CaCu_5) mixture in the cellular structure,⁷ and result in a drastic decrease in H_{ci} , H_c , and H_k when z was over 8.2.

IV. CONCLUSIONS

Structural and magnetic properties of $\text{Sm}(\text{Co}_{0.91-x}\text{Fe}_x\text{Cu}_{0.07}\text{Zr}_{0.02})_{8.0}$, where $x=0, 0.12, 0.21$,

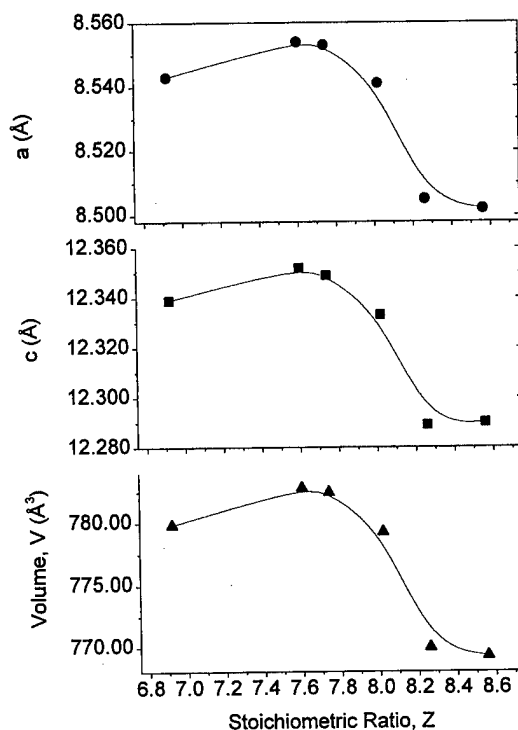


FIG. 5. The variations of lattice parameters a , c and cell volume V of $\text{Sm}(\text{Co}_{0.64}\text{Fe}_{0.28}\text{Cu}_{0.06}\text{Zr}_{0.02})_z$ with z , where z ranges from 6.9 to 8.6.

0.29, and 0.32, and $\text{Sm}(\text{Co}_{0.64}\text{Fe}_{0.28}\text{Cu}_{0.06}\text{Zr}_{0.02})_z$, where z ranged from 6.9 to 8.6, have been systematically investigated. It was found that most of these alloys exhibit a hexagonal $\text{Th}_2\text{Ni}_{17}$ structure with a space group $P6_3/\text{mmc}$ after solid solution treatment. The fully processed materials all exhibit a rhombohedral $\text{Th}_2\text{Zr}_{17}$ structure with a space group of $R\bar{3}m$. For $\text{Sm}(\text{Co}_{0.91-x}\text{Fe}_x\text{Cu}_{0.07}\text{Zr}_{0.02})_{8.0}$, the lattice parameters, a , and c , and cell volume, V , increase slightly with increasing x then increase more sharply when x is increased above 0.28. This drastic increase in lattice parameters and cell volume results in a sharp decrease in H_{ci} , H_c , and H_k values of fully processed materials. For $\text{Sm}(\text{Co}_{0.64}\text{Fe}_{0.28}\text{Cu}_{0.06}\text{Zr}_{0.02})_z$, the lattice parameters, a and c , and cell volume increase slightly when z was varied from 6.8 to 7.8 then decrease drastically when z was increased beyond 8.0. Higher z value may cause an imbalance of the 2:17 and 1:5 mixture in the cellular structure, and result in a drastic decrease in H_{ci} , H_c , and H_k when z was over 8.2.

¹A. E. Ray, J. Appl. Phys. **55**, 2094 (1984).

²Y. Morita, T. Umeda, and Y. Kimura, IEEE Trans. Magn. **MAG-23**, 2702 (1987).

³K. J. Strnat, in *Ferromagnetic Materials*, edited by E. P. Wohlfarth and K. H. J. Bushnow (Elsevier Science, New York, 1988), Vol. 4, Chap. 2, pp. 131–209.

⁴A. E. Ray, J. Appl. Phys. **67**, 4972 (1990).

⁵Y. Morita, T. Umeda, and Y. Kimura, in MRS International Meeting On Adv. Mater. **11**, 97 (1988).

⁶B. Y. Wong, M. Willard, and D. E. Laughlin, J. Magn. Magn. Mater. **169**, 178 (1997).

⁷J. D. Livingston and D. L. Martin, J. Appl. Phys. **48**, 1350 (1977).

The effect of particle size and consolidating pressure on the magnetic properties of $\text{Sm}(\text{Co}, \text{Fe}, \text{Cu}, \text{Zr})_2$ bonded magnets

B. M. Ma,^{a)} W. Gong, and C. O. Bounds

Rhodia, Rare Earths and Gallium, CN-7500 Cranbury, New Jersey 08512

C. H. Chen and M. S. Walmer

Electron Energy Corporation, 924 Links Avenue, Landisville, Pennsylvania 17538

The effect of particle size on the B_r , BH_{\max} , and specific density of $\text{Sm}(\text{Co}_{0.62}\text{Fe}_{0.29}\text{Cu}_{0.07}\text{Zr}_{0.02})_{8.0}$ and $\text{Sm}(\text{Co}_{0.70}\text{Fe}_{0.21}\text{Cu}_{0.07}\text{Zr}_{0.02})_{8.0}$ bonded magnets has been systematically investigated. It was found that magnets made of powders with a top size less than $53\ \mu\text{m}$ have a low specific density and, hence, low B_r and BH_{\max} values. Magnets made of powders of about $250\ \mu\text{m}$ top size, with a composition of $\text{Sm}(\text{Co}_{0.62}\text{Fe}_{0.29}\text{Cu}_{0.07}\text{Zr}_{0.02})_{8.0}$, yield a specific density of $7.0\ \text{gm/cc}$ (84% of theoretical density), a B_r of more than $8.1\ \text{kG}$, and a BH_{\max} of about $15\ \text{MGOe}$. A slight decrease in B_r and BH_{\max} was noticed when the particle top size was increased beyond $710\ \mu\text{m}$. This decrease in B_r and BH_{\max} may be attributed to the imperfect grain alignment arising from the fact that each particle may consist of multigrain grains with a random orientation. Because of the slightly lower Fe content, magnets with a composition of $\text{Sm}(\text{Co}_{0.70}\text{Fe}_{0.21}\text{Cu}_{0.07}\text{Zr}_{0.02})_{8.0}$ exhibit slightly lower B_r and BH_{\max} values when compared to those of $\text{Sm}(\text{Co}_{0.62}\text{Fe}_{0.29}\text{Cu}_{0.07}\text{Zr}_{0.02})_{8.0}$. However, the relationships of B_r and BH_{\max} to particle size are nearly identical for both compositions. When the powder top size was fixed at about $250\ \mu\text{m}$, a consolidating pressure of $8\ \text{T/cm}^2$ appears to be sufficient to obtain magnets with a specific density of $6.9\ \text{gm/cc}$ and with a reasonable grain alignment. For $\text{Sm}(\text{Co}_{0.62}\text{Fe}_{0.29}\text{Cu}_{0.07}\text{Zr}_{0.02})_{8.0}$ bonded magnets, a B_r of $8.5\ \text{kG}$, H_c of $8.5\ \text{kOe}$, H_{ci} of $23.0\ \text{kOe}$, BH_{\max} of $16.7\ \text{MGOe}$, and H_k of $8.0\ \text{kOe}$ were obtained. © 1998 American Institute of Physics. [S0021-8979(98)22411-X]

I. INTRODUCTION

$\text{Sm}(\text{Co}, \text{Fe}, \text{Cu}, \text{Zr})_2$ -type bonded magnets have been used commercially for many years.¹ Because of their high operational temperature and potentially high BH_{\max} values, $\text{Sm}(\text{Co}, \text{Fe}, \text{Cu}, \text{Zr})_2$ bonded magnets have generated significant interest for anisotropic applications.²

Anisotropic bonded magnet applications with high BH_{\max} values require the use of powders with high intrinsic BH_{\max} values and/or the optimization of grain alignment and packing density (ρ) during magnet fabrication. In our previous work,³ we have established the effects of particle size and size distribution on the magnetic properties of fully processed $\text{Sm}(\text{Co}, \text{Fe}, \text{Cu}, \text{Zr})_2$ alloy powders. For a given batch of powder, particle alignment and packing density are two interrelated factors that determine the BH_{\max} of bonded magnets. Large particles ($>250\ \mu\text{m}$) are usually multi-grain with random orientation and incapable of being fully aligned. The lower surface to volume ratio of large particles also implies that a high packing density can be obtained without using an excessive amount of binder. Unlike large particles, nearly single crystal grains can readily be obtained on small particles which can result in a nearly perfect grain alignment under an externally applied magnetic field of reasonable strength. However, the increase in surface to volume ratio of powders of small sizes also suggests that a higher percentage of binder may be necessary to achieve reasonable mechanical strength. Moreover, the increase in the volume fraction of

binder will result in a lower packing density and, hence, reduce the B_r and BH_{\max} values of bonded magnets.

The consolidating pressure applied during molding is also an important factor in determining the particle alignment and packing density of bonded magnets. A higher consolidating pressure, for a fixed batch, usually leads to a higher packing density but may cause grain misalignment. Thus, powder particle size and distribution as well as consolidating pressure are important parameters that affect grain alignment and packing density and need to be compromised for obtaining bonded magnets with the highest BH_{\max} .

In this article, we report on the relationships of the magnetic properties obtained on anisotropically bonded $\text{Sm}(\text{Co}, \text{Fe}, \text{Cu}, \text{Zr})_2$ magnets with the particle size distribution and consolidating pressure during molding.

II. EXPERIMENT

$\text{Sm}(\text{Co}_{0.70}\text{Fe}_{0.21}\text{Cu}_{0.07}\text{Zr}_{0.02})_{8.0}$ and $\text{Sm}(\text{Co}_{0.62}\text{Fe}_{0.29}\text{Cu}_{0.07}\text{Zr}_{0.02})_{8.0}$ alloys were prepared by conventional vacuum induction melting and mold casting. Alloy ingots were solution treated, precipitation hardened, followed by a slow cooling, and then quenched to optimum conditions. A jaw crusher was utilized to break ingots into millimeter size chunks. Ingot pieces were then fed into a cross-beater mill with various screen sizes to produce powders with various maximum sizes from 53 to $720\ \mu\text{m}$ size sieves. A rotary sieve was used to assure that all powders pass through the predetermined sieve size. A Horiba LA-910 laser particle size analyzer was used to measure the particle size distribution of the powders. Magnets of $10\ \text{mm}$ in diameter and $6.4\ \text{mm}$ in length were

^{a)}Electronic mail: bma@us.rhodia.com

TABLE I. Magnetic properties and specific density of $\text{Sm}(\text{Co}_{0.62}\text{Fe}_{0.29}\text{Cu}_{0.07}\text{Zr}_{0.02})_{8.0}$ and $\text{Sm}(\text{Co}_{0.70}\text{Fe}_{0.21}\text{Cu}_{0.07}\text{Zr}_{0.02})_{8.0}$ bonded magnets made from powders of various particle size when compacted with a consolidating pressure of 10 T/cm^2 .

Sample	Particle size (μm)	B_r (kG)	H_c (kOe)	H_{ci} (kOe)	BH_{\max} (MGOe)	H_k (kOe)	Specific density (gm/cc)
$\text{Sm}(\text{Co}_{0.62}\text{Fe}_{0.29}\text{Cu}_{0.07}\text{Zr}_{0.02})_{8.0}$							
1	<710	7.6	6.9	29.3	13.6	7.4	7.01
2	<425	7.7	7.1	29.3	13.8	7.8	7.00
3	<250	8.5	7.4	29.5	16.7	7.8	6.92
4	<180	7.9	7.3	29.0	14.2	7.7	6.88
5	<106	7.7	7.1	29.0	14.0	7.6	6.72
6	<53	7.2	6.3	28.3	11.8	5.2	6.40
$\text{Sm}(\text{Co}_{0.70}\text{Fe}_{0.21}\text{Cu}_{0.07}\text{Zr}_{0.02})_{8.0}$							
7	<425	7.2	6.9	28.8	12.3	8.6	6.91
8	<250	7.6	7.1	28.8	13.7	10.0	7.01
9	<180	7.6	7.0	28.8	13.4	8.2	6.89
10	<106	6.9	6.4	25.6	11.0	7.6	6.72
11	<53	6.7	6.0	25.0	10.1	5.8	6.40

prepared by mixing powders of the desired size with 2 wt% of epoxy, aligned under a 60 kOe magnetic field, and consolidated with a mechanical press under a maximum load of 10 T/cm^2 . To study the effect of consolidating pressure on bonded magnets, the load of the press was controlled from 4 to 10 T/cm^2 .

III. RESULTS AND DISCUSSION

Listed in Table I are the remanence (B_r), coercive force (H_c), intrinsic coercivity (H_{ci}), maximum energy product (BH_{\max}), squareness factor (H_k), and specific density (ρ) of $\text{Sm}(\text{Co}_{0.62}\text{Fe}_{0.29}\text{Cu}_{0.07}\text{Zr}_{0.02})_{8.0}$ and $\text{Sm}(\text{Co}_{0.70}\text{Fe}_{0.21}\text{Cu}_{0.07}\text{Zr}_{0.02})_{8.0}$ bonded magnets made from powders of various sizes (from 53 to about $710 \mu\text{m}$ top size) using a consolidating pressure of 10 T/cm^2 . In general, the trends of the two magnet compositions are nearly identical. The variation of ρ , B_r , BH_{\max} , H_c , and H_k of $\text{Sm}(\text{Co}_{0.62}\text{Fe}_{0.29}\text{Cu}_{0.07}\text{Zr}_{0.02})_{8.0}$ bonded magnets with powder particle sizes are shown in Figs. 1(a)–1(e), respectively. A magnet made from powders of less than $53 \mu\text{m}$ yielded a specific density of 6.40 gm/cc (76% of theoretical density). The ρ increased significantly from 6.40 to 7.00 gm/cc when the powder size was increased from less than 53 to less than $425 \mu\text{m}$ and approached, asymptotically, 7.01 gm/cc (84% of the theoretical density) when the particle size was further increased to nearly $710 \mu\text{m}$. Unlike ρ , the B_r , BH_{\max} , and H_c of $\text{Sm}(\text{Co}_{0.62}\text{Fe}_{0.29}\text{Cu}_{0.07}\text{Zr}_{0.02})_{8.0}$ magnets all exhibit sharp initial increases, then decrease slightly when the particle top size is increased from 53 to beyond $250 \mu\text{m}$.

Shown in Figs. 2(a) and 2(b) are the optical micrographs of an as-cast and fully processed alloy ingot with a nominal composition of $\text{Sm}(\text{Co}_{0.62}\text{Fe}_{0.29}\text{Cu}_{0.07}\text{Zr}_{0.02})_{8.0}$. As can be seen, the as-cast ingot consists of three phases: the matrix phase, a Sm-rich boundary phase and a Zr-rich needlelike phase. The average grain size is about $80 \mu\text{m}$. Significant grain growth can be observed on the fully processed ingot; the average grain size of the fully processed ingot is about $200 \mu\text{m}$. This suggests that powders of small sizes should be

nearly single crystal in each individual particle and, in principle, should yield a better alignment during compaction and result in a high B_r value. Nevertheless, for actual bonded magnets, the B_r is determined by two factors; the grain alignment and the packing density (ρ). The low B_r and BH_{\max} obtained on bonded magnets made from $53 \mu\text{m}$ top size powders suggests that the low ρ was more important than grain alignment. The higher B_r and BH_{\max} values obtained

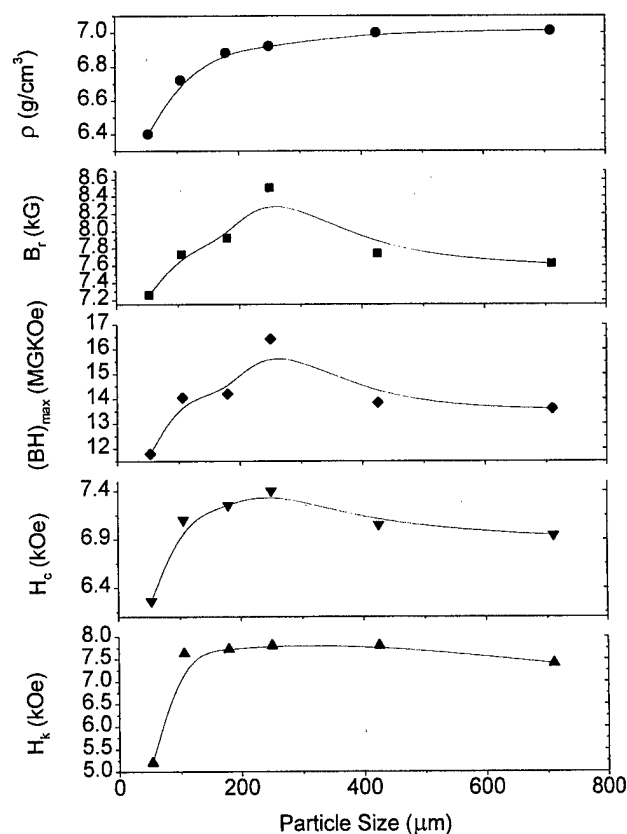


FIG. 1. Variation of specific density (ρ), B_r , BH_{\max} , H_c , and H_k of $\text{Sm}(\text{Co}_{0.62}\text{Fe}_{0.29}\text{Cu}_{0.07}\text{Zr}_{0.02})_{8.0}$ bonded magnets with precursor powder particle size.

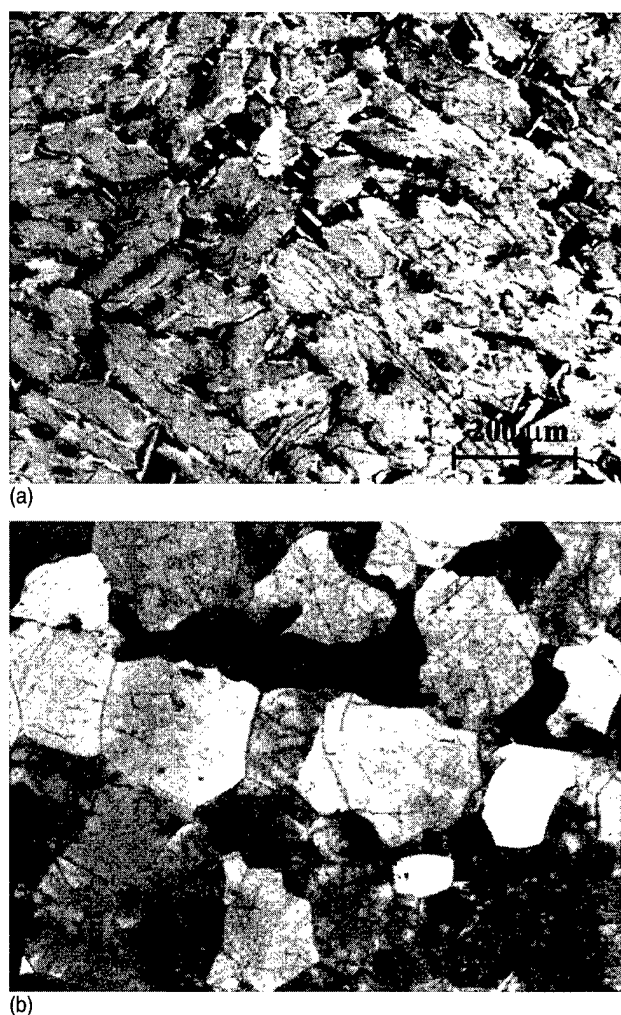


FIG. 2. Optical micrographs of (a) as-cast and (b) fully processed $\text{Sm}(\text{Co}_{0.62}\text{Fe}_{0.29}\text{Cu}_{0.07}\text{Zr}_{0.02})_{8.0}$ ingot.

on magnets made from powders of 250 μm top size may be explained by the combination of a reasonable grain alignment and higher ρ obtained. Combining the high ρ and the decreases in B_r and BH_{max} values, one may conclude that imperfect grain alignment (or grain misalignment) may have occurred when the particle size was increased above a 450 μm top size. A similar trend, but less pronounced, was also observed on H_k . Based on these plots, it appears that powders with a top size of 250 μm may yield the highest B_r and BH_{max} values for the magnet fabrication method employed.

TABLE II. The variation of the magnetic properties and specific density of $\text{Sm}(\text{Co}_{0.62}\text{Fe}_{0.29}\text{Cu}_{0.07}\text{Zr}_{0.02})_8$ bonded magnets made from powder of less than 250 μm and with various consolidating pressures.

Sample	Consolidating pressure (T/cm ²)	B_r (kG)	H_c (kOe)	H_{ci} (kOe)	BH_{max} (MGoe)	H_k (kOe)	Specific density (gm/cc)
A	4	7.5	6.7	28.7	12.9	7.2	6.55
B	6	7.7	6.9	28.7	13.6	7.3	6.75
C	8	8.1	7.2	28.8	14.8	7.4	6.88
D	10	8.5	7.4	29.5	16.7	7.8	6.92

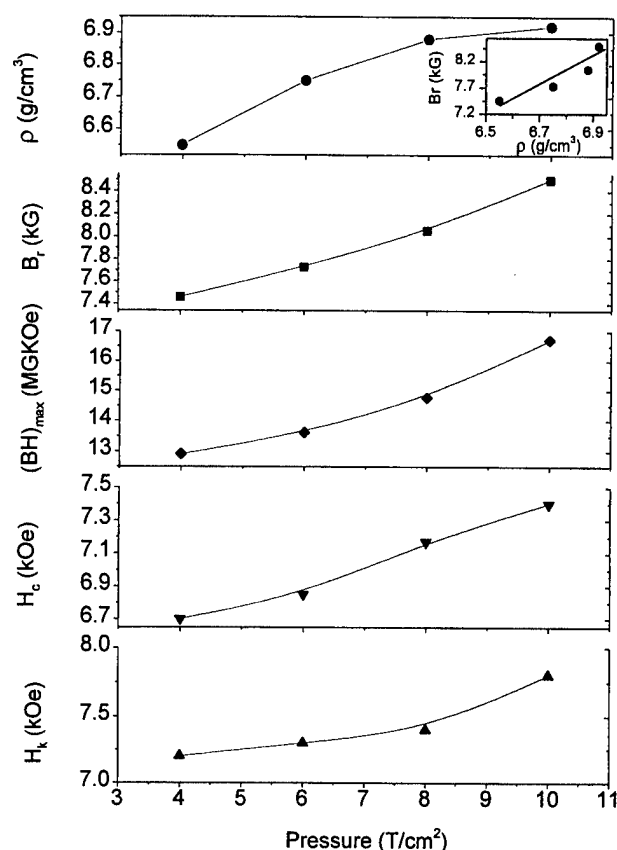


FIG. 3. Variation of specific density (ρ), B_r , BH_{max} , H_c , and H_k of $\text{Sm}(\text{Co}_{0.70}\text{Fe}_{0.21}\text{Cu}_{0.07}\text{Zr}_{0.02})_{8.0}$ bonded magnets with consolidating pressure.

In addition to the particle top size, particle size distribution also plays an important role in determining the impact on ρ , B_r , and BH_{max} of the bonded magnets. The distribution is nearly Gaussian with a mean at 120 μm and a standard deviation of 70 μm . Powders of the other top sizes have a similar distribution as reported elsewhere.⁴

Listed in Table II are the B_r , H_c , H_{ci} , BH_{max} , H_k and ρ of $\text{Sm}(\text{Co}_{0.62}\text{Fe}_{0.29}\text{Cu}_{0.07}\text{Zr}_{0.02})_{8.0}$ magnets made of powders with a particle top size of 250 μm using various consolidating pressures. The variations of ρ , B_r , BH_{max} , H_c , and H_k with consolidating pressure are shown in Fig. 3. A nearly linear relationship between ρ and consolidating pressure can be observed, and shown in the inset of Fig. 3, suggesting that ρ , for the fixed particle size studied, of bonded magnets is a simple function of the consolidating pressure. Using the 250 μm top size powder and the type of binder used in this study, a minimum consolidating pressure of 6 T/cm² is necessary to achieve an 80% theoretical density.

¹T. Shimoda, K. Kasai, and K. Teraishi, *Proceedings of the Fourth International Workshop on Rare Earth-Cobalt Permanent Magnets and Their Applications*, edited by K. Strnat (University of Dayton, Dayton, OH, 1979), pp. 335–345.

²T. Shimoda, E. Natori, and C. Tomita, in *Proceedings of the Eighth International Workshop on Rare-Earth Magnets and Their Applications*, edited by K. Strnat (University of Dayton, Dayton, OH, 1985), pp. 297–308.

³W. Gong, B. M. Ma, and C. O. Bounds, *J. Appl. Phys.* **81**, 5640 (1997).

⁴W. Gong, B. M. Ma, and C. O. Bounds, in *Rare Earths, Science, Technology & Applications III*, edited by R. G. Bautista, C. O. Bounds, T. W. Ellis, and B. T. Kilbourn (Society of Minerals, Metals, and Materials, Warrendale, PA, 1997), pp. 259–272.

High temperature stability of SmTM magnets

A. S. Kim

YBM Magnex, Inc., 110 Terry Drive, Newtown, Pennsylvania 18940

To meet the demand for permanent magnet materials usable up to 450–500 °C, we investigated and reported that a SmTM magnet with a low temperature coefficient of coercivity and a moderately high coercivity has substantially lower irreversible losses at elevated temperatures than conventional Sm₂TM₁₇ magnets. We have continued our studies on the high temperature magnetic behavior of these magnets. The magnetic properties, particularly coercivity, of the SmTM₇ alloy magnets are reduced much more slowly than the Sm₂TM₁₇ alloy magnets as temperature increases. As a result, the H_{ci} of SmTM₇ remains greater than 5 kOe at 500 °C and thus maintains its high-energy product, while the Sm₂TM₁₇ magnet has only about 1.7 kOe at the same temperature and has a low energy product. SmTM₇ alloy magnets undergoing a long-term stability test at 500 °C exhibit irreversible flux losses of less than 5% after 1240 h. These results indicate that SmTM₇ alloy magnets can be usable up to 500 °C for an extended period of time. This will expand the application temperature range of high performance permanent magnets. © 1998 American Institute of Physics. [S0021-8979(98)41811-5]

I. INTRODUCTION

To fulfill recent requirements for high temperature applications,¹ it is necessary to expand the temperature range of permanent magnet materials from the current maximum operating temperature of 300 °C to 450–500 °C. To meet this demand, we calculated the necessary conditions and designed a magnet satisfying those conditions.²

The operating temperature (OT) of the magnet is expressed as

$$OT = RT + \frac{H_{ci,RT} - H_{ci,OT}}{H_{ci,RT} \times (-\beta)} \times 100\%, \quad (1)$$

where R.T. stands for room temperature, $H_{ci,RT}$ and $H_{ci,OT}$ stand for intrinsic coercivities at room temperature and operating temperature, respectively, and β stands for the temperature coefficient of H_{ci} .

Since the maximum energy product can be obtained when $H_{ci,OT} \geq \frac{1}{2} B_{r,OT}$, it is generally safe to set the minimum $H_{ci,OT} = 5$ kOe at temperature range of 450–500 °C for the maximum operating temperature, as described elsewhere.² Therefore, the Eq. (1) can be rewritten as

$$MOT = RT + \frac{H_{ci,RT} - 5 \text{ kOe}}{H_{ci,RT} \times (-\beta)} \times 100\%. \quad (2)$$

The maximum operating temperature (MOT) is a function of coercivity at room temperature ($H_{ci,RT}$) and the temperature coefficient of coercivity (β). It is noted that the MOT is much more effectively increased by a β decrease than by an $H_{ci,RT}$ increase. This suggests changing our research direction from increasing $H_{ci,RT}$ to lowering the β value while maintaining a moderately high $H_{ci,RT}$ and a high Curie temperature. To develop a magnet meeting such a concept, it is necessary to find out what controls the temperature coefficient of coercivity. Nesbitt *et al.*³ reported that a partial substitution of Cu for Co in SmCo₅ formed a nonmagnetic Cu-rich precipitate in the SmCo₅ matrix, which could impede domain wall motion. Senno *et al.*⁴ reported that the addition

of Cu in Sm₂(Fe,Co)₁₇ exhibited domain wall pinning, and Nagel⁵ reported that Mn and Cr addition in Sm₂(Fe,Co)₁₇ exhibited nucleation controlled magnetization reversal. The former has a much smaller β than the latter. In other words, Cu addition to SmCo₅ or Sm₂(Fe,Co)₁₇ changes the magnetization reversal from nucleation control to domain wall pinning and reduces the β value. With this knowledge, it is possible to predict a further reduction of β by the optimum control of Cu in relation to other elements. Alloy compositions of Sm(Co,Fe,Cu,Zr)_z were varied to find the optimum composition with the lowest β value. We found and reported² that a magnet made from a Cu enriched SmTM₇ alloy possesses a low temperature coefficient of coercivity ($-\beta \leq 15\%/^{\circ}\text{C}$) and moderately high coercivity ($H_{ci,RT} \geq 15$ kOe).

In this study, we will discuss the high temperature magnetic behavior of this magnet compared to a conventional Sm₂TM₁₇ magnet. The possible mechanism for the lower temperature coefficient of coercivity will also be discussed.

II. EXPERIMENT

Two predetermined alloy charges were melted in a vacuum induction-melting furnace. They are

2:17 alloy: Sm(Co_{0.677}Fe_{0.232}Cu_{0.068}Zr_{0.023})₈,

1:7 alloy: Sm(Co_{0.687}Fe_{0.202}Cu_{0.090}Zr_{0.021})₇.

The alloy melts were cast into a copper mold and sintered magnets were prepared from them by a conventional powder metallurgy method described elsewhere.² The magnetic properties were measured at room temperature (21 °C) and at 150 °C with a hysteresigraph and a high temperature search coil. The temperature coefficient of H_{ci} (β) was determined from the magnetic properties measured at 21 and 150 °C. The high temperature magnetic properties were measured up to 600 °C with a VSM equipped with a furnace. The irreversible magnetic flux loss was estimated at a permeance

TABLE I. Magnetic properties at room temperature.

Alloy	B_r , kG	H_{ci} , kOe	H_k , kOe	$(BH)_{max}$, MGOe
2:17	10.16	27.51	9.41	24.71
1:7	8.38	18.68	14.82	17.10

coefficient=1.0 by measuring the flux difference with a Helmholtz coil before and after exposing the magnet to elevated temperatures for 6 h in an argon environment. The microstructure was examined in a transmission electron microscope at the University of Delaware.

III. RESULTS AND DISCUSSION

The magnetic properties at room temperature of the aged magnets are listed in Table I. The magnet made from 2:17 alloy exhibits much higher B_r , H_{ci} , and $(BH)_{max}$ than the magnet made from 1:7 alloy. It is noted, however, that the 1:7 alloy has much better loop squareness (H_k) than the 2:17 alloy. These magnets were measured at 150 °C with the same hysteresisgraph.

The H_{ci} values at 21 and 150 °C, and temperature coefficient of coercivity (β) calculated between 21 and 150 °C are listed in Table II. The 2:17 alloy magnet has $\beta = -0.27\%/^{\circ}\text{C}$, while that of the 1:7 alloy magnet is $-0.14\%/^{\circ}\text{C}$. Since the latter satisfies the necessary conditions described in the Introduction, we examined the thermomagnetic behavior of it at temperatures between 21 and 600 °C by comparing with 2:17 alloy magnets. The coercivities of two 2:17 alloy magnets and one 1:7 alloy magnet measured at 21, 150, 300, 400, 500, and 600 °C are plotted against temperature in Fig. 1. The 2:17 alloy magnets show much higher room temperature coercivities than the 1:7 alloy magnet. However, as temperature increases, the coercivities of 2:17 alloy magnets decrease much faster than that of the 1:7 alloy magnet. This reflects the difference in the temperature coefficient of coercivity. As predicted in the Introduction, the 2:17 alloy magnets reach their maximum operating temperature (MOT) at just above 300 °C ($H_{ci} \geq 5$ kOe), while the 1:7 alloy magnet reaches its MOT at about 500 °C ($H_{ci} \geq 5$ kOe) as shown in Fig. 1.

The magnetic properties measured at 500 °C for both magnets are compared in Fig. 2(a) and Fig. 2(b). The 1:7 alloy magnet exhibits a fairly wide hysteresis loop having a coercivity of 5.1 kOe at 500 °C while the 2:17 alloy magnet exhibits a narrow loop with a low coercivity (~ 1.7 kOe). We also compared the temperature stabilities of these magnets by measuring the irreversible flux losses after exposure to elevated temperatures for 6 h. The irreversible losses of 2:17 and 1:7 alloy magnets are plotted against temperature in

TABLE II. Coercivities at 21 and 150 °C, and temperature coefficient of H_{ci} .

Alloy	H_{ci} , 21 °C, kOe	H_{ci} , 150 °C, kOe	$\beta(21-150\text{ }^{\circ}\text{C})$, %/ $^{\circ}\text{C}$
2:17	27.51	17.80	-0.27
1:7	18.68	15.36	-0.14

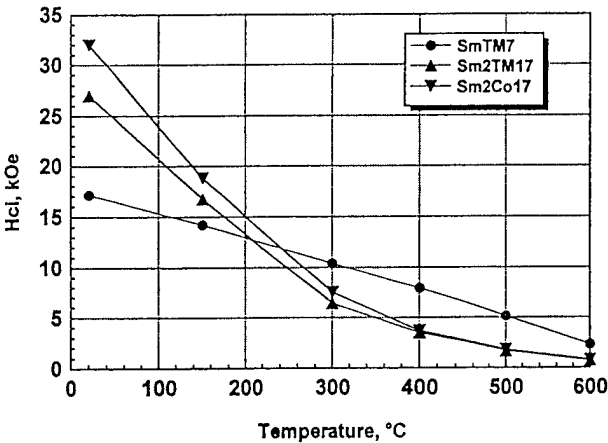


FIG. 1. Temperature dependence of coercivity of 2:17 and 1:7 alloy magnets.

Fig. 3. The 2:17 alloy magnet (A) starts to increase irreversible losses at about 300 °C, and the 1:7 alloy magnet (D) at about 500 °C. These temperatures agree well with the MOT values (300 °C for the 2:17 magnet and 500 °C for the 1:7 magnet with $-\beta \leq 0.15\%/^{\circ}\text{C}$) predicted in the Introduction.

The 1:7 alloy magnets undergoing a long term stability test at 500 °C exhibit irreversible flux losses of less than 5% after 1240 h. This indicates that the MOT is dramatically increased by lowering the β value rather than raising the H_{ci}

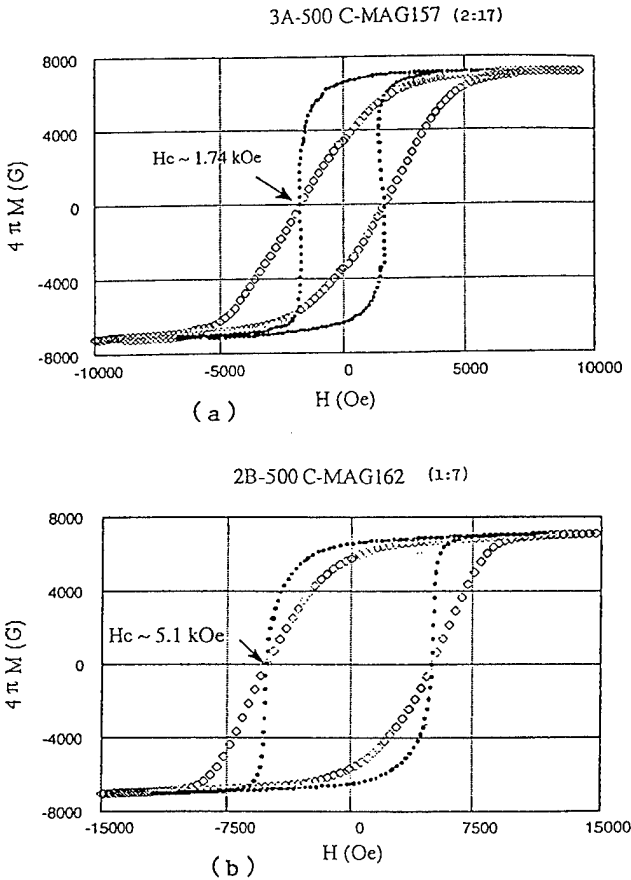


FIG. 2. Hysteresis loops for 2:17 (1) and 1:7 (2) alloy magnets measured with a VSM at 500 °C.

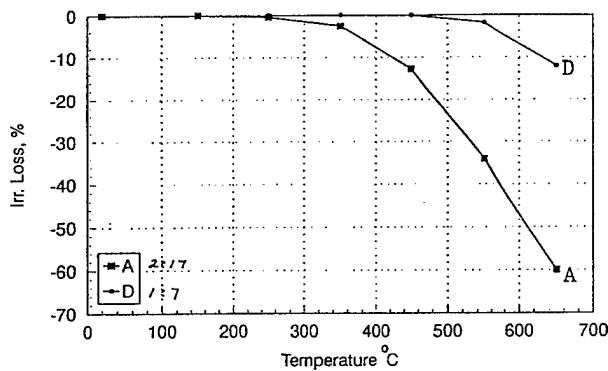


FIG. 3. Irreversible flux losses of magnets A (2:17) and D (1:7) as a function of temperature

value. It is therefore predicted that a further increase in MOT is possible by either further reducing the β value or a combination of lower β and higher H_{ci} values.

To understand the mechanism for the lower temperature coefficient of coercivity of the 1:7 alloy magnet, we compared the microstructures of the 2:17 and 1:7 alloy magnets in a transmission electron microscope. As shown in Figs. 4(a) and 4(d), the 1:7 alloy magnet exhibit a somewhat smaller cell size (2:17 phase) and thicker cell boundaries (1:5 phase) than the 2:17 alloy magnet. The former exhibits a little Z phase, while the latter exhibits much more Z-phase

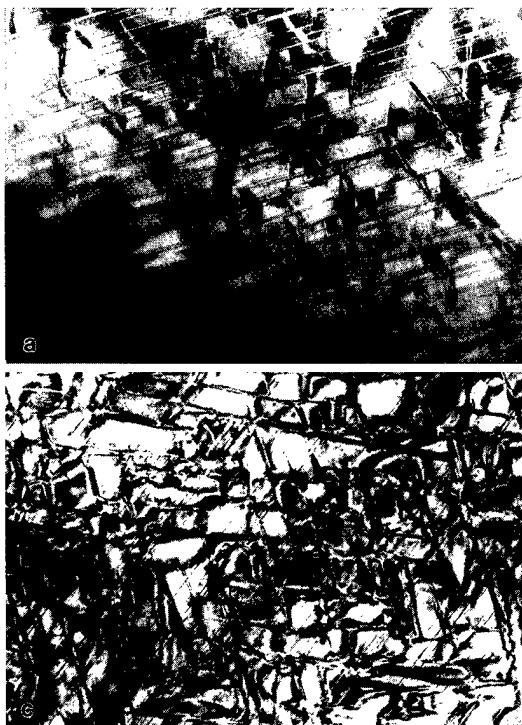


FIG. 4. TEM micrographs of 2:17 alloy magnet (a) and 1:7 alloy magnet (c).

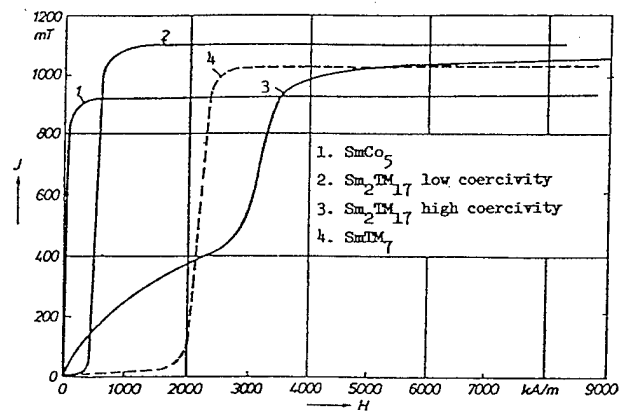


FIG. 5. Virgin magnetization curves for various sintered SmTM magnets.

precipitation. This microstructural difference may affect the temperature behavior.

We also compared the magnetization curves of these magnets. As shown in Fig. 5, the 2:17 alloy magnet exhibits mixed pinning (strong inhomogeneities), while the 1:7 alloy magnet exhibits homogeneous wall pinning. While a low coercivity 2:17 alloy magnet exhibits weak homogeneous wall pinning,⁶ the 1:7 alloy magnet exhibits much stronger wall pinning. This may originate from the Cu-enriched microstructural change described above and may therefore be responsible for the low temperature coefficient of H_{ci} .

IV. CONCLUSION

We have designed a temperature stable SmTM magnet having a low temperature coefficient of coercivity ($-\beta \leq 0.15\%/^{\circ}\text{C}$) and a moderately high coercivity ($H_{ci} \sim 20$ kOe). A Cu-enriched 1:7 alloy was discovered that effectively reduces the β . High temperature magnetic measurements reveal that the 2:17 alloy magnet can be used up to about 300 $^{\circ}\text{C}$, while the 1:7 alloy magnet whose $-\beta$ is lower than $0.15\%/^{\circ}\text{C}$ can be used up to 500 $^{\circ}\text{C}$. The magnetization curve of the 2:17 alloy magnet exhibits mixed pinning, while that of the 1:7 alloy magnet exhibits strong homogeneous wall pinning. This may be responsible for the low β and for the high temperature stability.

ACKNOWLEDGMENTS

This work was partially supported by a grant from the Air Force Wright Laboratory/Universal Technology Corporation (F33615-94-C-5800/5402-2-04-01) and a grant from the Air Force Office of Scientific Research/University of Delaware (F49620-96-1-0434/B238460-6). I would like to acknowledge R. A. Hohowski for his technical assistance.

¹R. Fingers, "Airforce applications of advanced magnetic materials," U. of Delaware MURI Overview, Sept. 1996.

²A. S. Kim, J. Appl. Phys. **81**, 5609 (1997).

³E. A. Nesbitt, R. H. Willens, R. C. Sherwood, F. Buehler, and J. H. Wernick, Appl. Phys. Lett. **12**, 361 (1968).

⁴H. Senno and Y. Tawara, IEEE Trans. Magn. **Mag-10**, 313 (1974).

⁵H. Nagel, AIP Conference Proceedings 29, edited by J. J. Becker *et al.* (American Institute of Physics, New York, 1976), p. 643.

⁶K. J. Strnat and R. M. W. Strnat, J. Magn. Magn. Mater. **100**, 38 (1991).

Structure and magnetic properties of $\text{SmCo}_{7-x}\text{Zr}_x$ alloys ($x=0-0.8$)

M. Q. Huang, W. E. Wallace, and M. McHenry

Department of Materials Science and Engineering, Carnegie Mellon University, Pittsburgh, Pennsylvania 15213

Q. Chen and B. M. Ma

Rhone-Poulenc, Rare Earths and Gallium, CN7500, Cranbury, New Jersey 08512

The alloys with composition of $\text{SmCo}_{7-x}\text{Zr}_x$ ($x=0-0.8$) were synthesized and characterized in the temperature range of 10–1273 K and at fields up to 5 T. The experimental results show that a small amount of Zr substitution can contribute to a stabilization of the TbCu_7 structure, and improve magneto-anisotropy H_a from 90 kOe for $x=0$ –180 kOe for $x=0.5$ at room temperature, and from 140 kOe for $x=0$ –300 kOe for $x=0.5$ at 10 K. It is probable that Zr may partly replace a dumbbell of Co atom pair in these alloys. The phase transition between CaCu_5 , TbCu_7 , $\text{Th}_2\text{Zn}_{17}$, and Ce_2Ni_7 at different heat treatment conditions was also discussed. © 1998 American Institute of Physics. [S0021-8979(98)29511-9]

I. INTRODUCTION

SmCo_7 is a metastable phase at room temperature with the TbCu_7 structure. The structures of SmCo_7 and $\text{Sm}_2\text{Co}_{17}$ are both derived from the structure of SmCo_5 .^{1,2} The metastable phase SmCo_7 can be obtained by splat cooling,³ meltspinning,² or mechanical alloying.⁴ Some magnetic properties have been reported by Saito *et al.*² They reported that $\text{Sm}_2(\text{Co}, \text{Mn})_{17}$ with the TbCu_7 structure exhibits an anisotropy of 105–140 kOe, which is 1.2–1.4 times larger than that of $\text{Sm}_2(\text{Co}, \text{Mn})_{17}$ with the $\text{Th}_2\text{Zn}_{17}$ structure. In regard to magnet fabrication, it was found that the 1:7 phase plays an important role for developing the cellular structure and the high coercivity in 2:17-type magnets.^{5,6} Interestingly, in 1982, Strnat *et al.* observed that the $\text{Sm}(\text{Co}, \text{Fe}, \text{Cu}, \text{Zr})_{7+x}$ magnets with $x=0$ exhibited less temperature dependence of coercivity than that of magnets with $x>0$.⁷

Currently there is an intense search to find new magnets or to improve existing magnets specifically for high temperature application. A systematic study of the SmCo_7 system will be of use in this regard. In order to stabilize this metastable phase and increase its anisotropy, third element doping is needed. Zr will be the first candidate in this regard, since it was the most effective element for increase of anisotropy in R_2Co_{17} systems.⁹ In the present study, the alloys with a composition of $\text{SmCo}_{7-x}\text{Zr}_x$ ($x=0-0.8$) were synthesized and characterized in the temperature range 10–1273 K and at fields up to 5 T. The structure, magnetic properties, and some phase transformations during heat treatment are reported.

II. EXPERIMENT

Alloys were prepared by arc melting under argon atmosphere. Some of the alloys were then annealed for 72–96 h at various temperatures (600–1100 °C), followed by a water quench. X-ray diffraction (XRD) with Cu radiation, optical microscopy, and scanning electron microscopy (SEM) were used to determine the crystal structure, lattice parameters, and phases present. Magnetic properties (M , H_c , H_a and T_c) were measured in the temperature range of 10–1273 K

and at fields up to 5 T, by using a vibrating sample magnetometer (VSM) and a superconducting quantum interference device (SQUID) magnetometer. The measured samples were in the forms of chunk, loose or aligned powder ($\leq 38 \mu\text{m}$). The anisotropy field (H_a) was determined by measuring the easy and hard axis magnetization on powder aligned in a field of 1.6 T and fixed in a epoxy.

III. RESULTS AND DISCUSSION

A. Structure information of as-cast alloys

Information in regard to the structure and phases present is shown in Figs. 1–3 and Table I.

It was found that the crystal structures of as-cast alloys $\text{SmCo}_{7-x}\text{Zr}_x$ vary significantly with Zr content, x . As shown in Fig. 1, a typical superlattice line for the $\text{Th}_2\text{Zn}_{17}$ structure, 015 and 204, disappears when $x \geq 0.2$. This indicates that the structure of the main phase changes from rhombohedral ($\text{Th}_2\text{Zn}_{17}$ -type) ($x=0$) to hexagonal (TbCu_7 -type) when $x \geq 0.2$. This is also evident from the XRD of aligned samples and a thermomagnetic analysis (TMA). As shown in Fig. 2, the sample with $x=0$ shows two Curie temperatures, $T_{c1} \sim 920$ °C for the 2:17 phase and $T_{c2} \sim 780$ °C for the 1:7

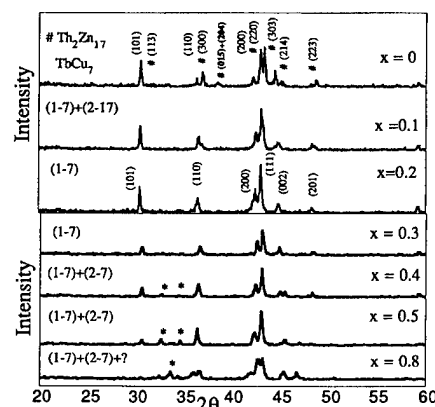
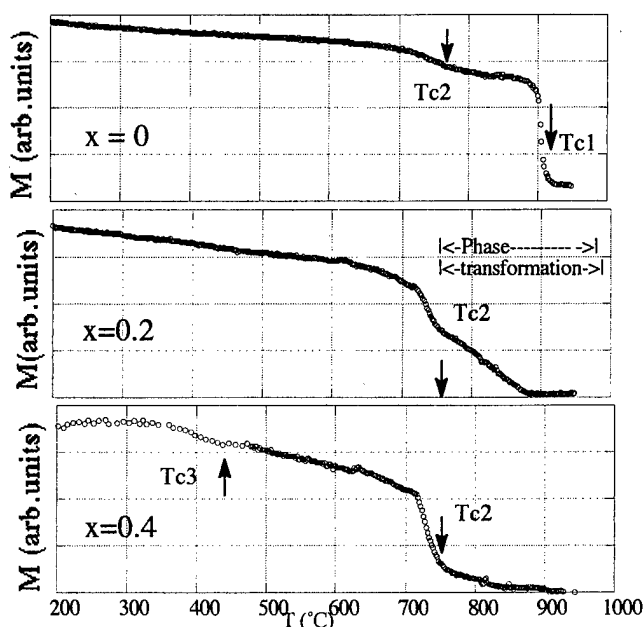
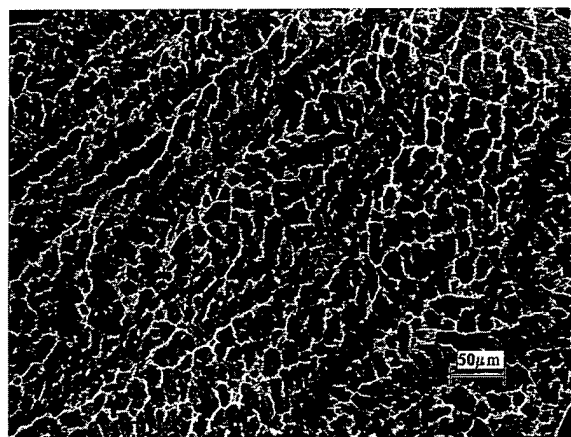


FIG. 1. XRD of $\text{SmCo}_{7-x}\text{Zr}_x$ as-cast alloys ($x=0-0.8$).

FIG. 2. M vs T of $\text{SmCo}_{7-x}\text{Zr}_x$ as-cast alloys ($H=500$ Oe).

phase. For $x=0.2$, it shows one $T_c \sim 760^\circ\text{C}$ for the 1:7 phase (some phase transformations occur above 750°C , which will be discussed later). The sample with $x=0.2$ is nearly a single phase, which was also confirmed by a microstructure examination (SEM). As shown in Fig. 3, its composition was detected to be $\text{Sm} \sim 12.5$, $\text{Co} \sim 85$, $\text{Zr} \sim 2.5$ (at. %) for the main phase (in gray domain), which is very close to $\text{Sm}(\text{Co,Zr}_7)$ and $\text{Sm} \sim 12.7$, $\text{Co} \sim 84.4$, $\text{Zr} \sim 2.9$ (at. %) for the minor phase (in white boundary part). Clearly, Zr stabilizes the hexagonal structure. The lattice parameters c and c/a decrease as x increases. This can be ascribed to a substitution of Zr for Co dumbbells. When the Zr content exceeds 0.4, the XRD intensity of line 101 decreases and some other extra lines, which do not belong to the 1:7 phase, appear. The two T_c is detected by TMA, $T_{c2} \sim (730-750^\circ\text{C})$ for the 1:7 phase and $T_{c3} \sim (430-450^\circ\text{C})$ for the other magnetic phase. Perhaps, this lower T_c phase is an R-rich phase with the hexagonal Ce_2Ni_7 structure or a 1:3 phase. It is to be noted that the above

FIG. 3. Microstructure of $\text{SmCo}_{6.8}\text{Zr}_{0.2}$ as-cast alloy.TABLE I. Phases present and crystal structure of $\text{SmCo}_{7-x}\text{Zr}_x$ as-cast alloys ($x=0-0.8$).

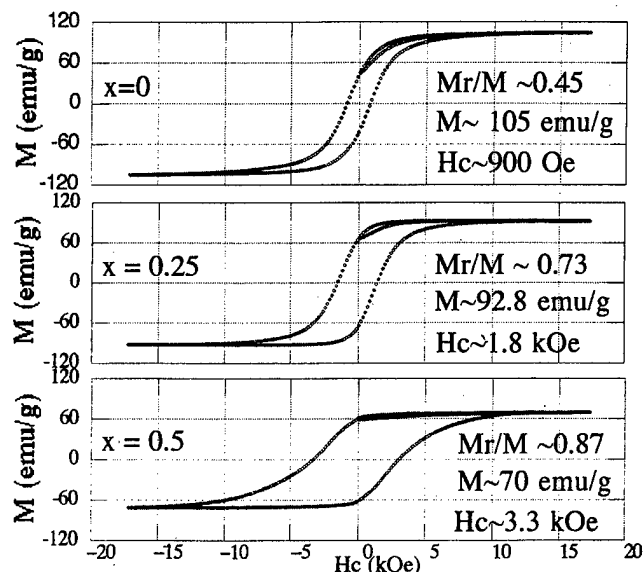
X	Phases		a (Å)	c (Å)	c/a	T_c ($^\circ\text{C}$)		
	(main)	(minor)				T_{c1}	T_{c2}	T_{c3}
0	2:17 ^a	1:7	4.856	4.081	0.84	920	~ 780	
0.1	1:7	2:17	4.869	4.079	0.84	905	~ 770	
0.2	1:7 ^b		4.916	4.049	0.83		~ 762	
0.3	1:7		4.923	4.035	0.82		~ 760	
0.4	1:7 2:7 ^c	4.932	4.040	0.82			~ 752	~ 439
0.5	(1:7)+(2-7)		4.947	4.025	0.81		~ 736	~ 428
0.8	(1:7)+(2-7)+?							~ 420

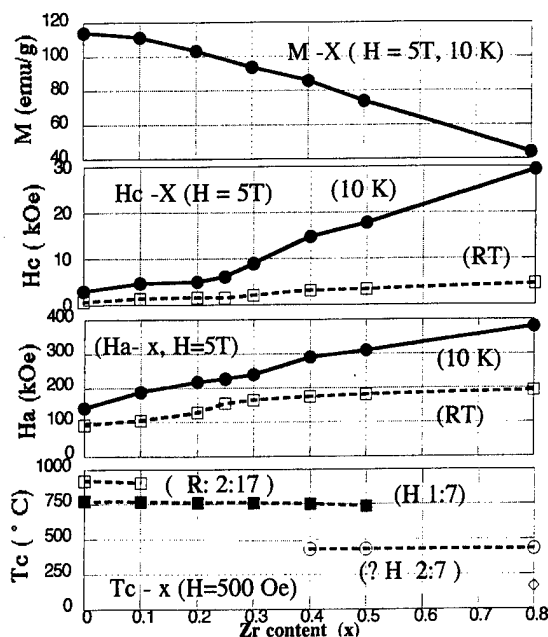
^a $\text{Th}_2\text{Zn}_{17}$ -type structure.^b TbCu_7 structure.^c Ce_2Ni_7 -type structure or other R-rich R-Co phases.

information about the phases present in $\text{SmCo}_{7-x}\text{Zr}_x$ as-cast alloys match nicely with the phase diagram of Derkaui *et al.* of the Sm-Co-Zr system at 1150°C .⁸

B. Magnetic properties of as-cast alloys

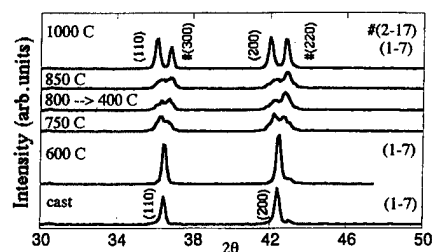
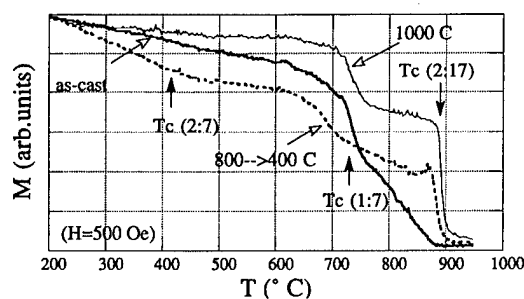
The magnetic properties M_s , H_c , H_a , and T_c are given in Figs. 4 and 5. Figure 4 shows the hysteresis loops of loose powder samples with $x=0$, 0.25, and 0.5 at room temperature. The Mr/M and coercivity increase substantially with increase of Zr content. The former may relate to a strengthened interaction between the magnetic particles and the latter should be ascribed to strengthening magnetocrystalline anisotropy fields H_a . As seen in Fig. 5, the H_a increases from 90 kOe ($x=0$) to 160 kOe for $x=0.25$ at room temperature and from 140 kOe ($x=0$) to 230 kOe for $x=0.25$ at 10 K. A decrease of M is reasonable, due to an increase in the amount of nonmagnetic element Zr. The H_c and H_a of the $\text{SmCo}_{7-x}\text{Zr}_x$ compounds increase significantly by an increase of the Zr content. This behavior is very similar to that

FIG. 4. M - H loops of $\text{SmCo}_{7-x}\text{Zr}_x$ as-cast alloys (RT) in loose powder.

FIG. 5. M , H_c , H_a , and T_c vs x (Zr content).

of substitution of Co by Mn or Zr in $\text{Sm}_2(\text{Co}, \text{Mn})_{17}$ ² or $\text{Sm}_2(\text{Co}, \text{Zr})_{17}$ systems.⁹ Deportes *et al.*¹⁰ have pointed out that the Co anisotropy in RCO_5 systems comes primarily from the $2c$ sites. When the Co dumbbells are inserted in place of R, the environment changes in such a way as to reduce the Co anisotropy and also that of the compound. When Zr replaces the dumbbells, the lost anisotropy is restored.

Information about the Curie temperatures of $\text{SmCo}_{7-x}\text{Zr}_x$ (T_c vs Zr content) is given in Fig. 5. As mentioned before, for $x=0$, two T_c , $T_{c1} \sim 920^\circ\text{C}$ for $\text{Sm}_2\text{Co}_{17}$ phase and $T_{c2} \sim 780^\circ\text{C}$ for SmCo_7 phase are observed. As $x > 0$, i.e., Zr doping, the amount of 1:7 phase increases and the 2:17 phase decreases and disappears. The T_{c2} for 1:7 phase slightly decreases with increasing Zr content x from 780°C for $x=0$ to $\sim 730^\circ\text{C}$ for $x=0.5$. The decrease of T_{c2} is not as rapid as that in the case of $\text{Sm}_2(\text{Co}, \text{Zr})_{17}$ system.⁹ For $x \geq 0.4$, another magnetic phase, with $T_{c3} = 430\text{--}450^\circ\text{C}$, was detected. As mentioned before, this lower T_c , but high H_a phase may belong to $(\text{Sm}, \text{Zr})_2(\text{Co}, \text{Zr}_7)$ phase. Further investigations are continuing.

FIG. 6. XRD of aligned powders ($H \sim 1.6$ T) of annealed $\text{SmCo}_{6.8}\text{Zr}_{0.2}$ alloys.FIG. 7. M vs T of annealed $\text{SmCo}_{6.8}\text{Zr}_{0.2}$ alloys.

C. Information about the phase transformation

Figure 6 shows the XRD of aligned powder ($H \sim 1.6$ T) of annealed $\text{SmCo}_{6.8}\text{Zr}_{0.2}$ alloys. Two strengthened lines, 110 and 200, which belong to the 1:7 phase, begin to broaden after annealing above 750°C , and the 1:7 phase begins to decompose. When the annealing temperature increased to 1000°C , two other strengthened lines, 300 and 220, which belong to the 2:17 phase, are clearly showing up and the 2:17 phase precipitates out. The above phase transformation was also observed by TMA measurement as seen in Fig. 7. The T_c for the 1:7 phase varies slightly at different annealing temperatures, which may be associated with a shift in composition. It was found that H_c (loose powder) at room temperature increases from 1.5 kOe for the as-cast sample, to 2.5 kOe when the sample was heated at 800°C followed by a slow cooling to 400°C and decreases to 1.1 kOe after annealing at 1000°C . The increase of H_c may be related to precipitation of a strong anisotropy 2:7 phase, as seen in Fig. 7. The decrease of H_c can be ascribed to the formation of a weak anisotropy 2:17 phase. Similar behavior was also observed in the other alloys ($x=0 \sim 0.5$). Further studies about the effects of heat treatment on magnetic properties are in process.

ACKNOWLEDGMENT

This work was supported by the U.S. Army Research Office and the Air Force Office of Scientific Research, Air Force Material Command, USAF, under Grant No. F49620-96-1-0454).

- W. E. Wallace and K. S. Narasimhan *Science and Technology of Rare and Earth Materials* (1980), p. 395.
- H. Saito, M. Takahashi, T. Wakiyama, G. Kodoand, and H. Nakagawa, *J. Magn. Magn. Mater.* **82**, 322 (1989).
- K. H. Buschow and F. J. A. den Broeder, *J. Less-Common Met.* **3**, 191 (1973).
- J. Yang, O. Mao, and Z. Altounian, *IEEE Trans. Magn.* **32**, 4390 (1996).
- Y. Morita, T. Umeda, and Y. Kimura, *IEEE Trans. Magn.* **23**, 2702 (1987).
- Y. Fukui, T. Nishio, and Y. Iwama, *IEEE Trans. Magn.* **23**, 2705 (1987).
- S. Liu, H. F. Mildrum, and K. J. Strnat, *J. Appl. Phys.* **53**, 2383 (1982).
- S. Derkaui, N. Valignat, and C. H. Allibert, *J. Alloys Compd.* **232**, 296 (1996).
- H. Fujii, M. V. Satyanaryana, and W. E. Wallace, *Solid State Commun.* **41**, 445 (1982).
- J. Deportes, D. Givord, J. Schweizer, and F. Tasset, *IEEE Trans. Magn.* **12**, 1000 (1976).

Coercivity calculation of $\text{Sm}_2(\text{Co,Fe,Cu,Zr})_{17}$ magnets

M. Katter

Vacuumschmelze, Grüner Weg 37, D-63450 Hanau, Germany

The coercivity of $\text{Sm}_2(\text{Co,Fe,Cu,Zr})_{17}$ is calculated on the basis of a two dimensional model. To find local minima of the sum of the domain wall energy and the magnetostatic energy, the domain wall is divided into 1 nm long segments which are allowed to fluctuate randomly. With increasing field strength the domain wall is heavily bowed, forming the well known zig-zag domains. At higher field strengths, the domain wall is depinned first, from the edges of the 2/17 cells and later, from the intersection lines of the Z phase with the 1/5 boundary phase. For these two sites, the widths and the heights of the energy barriers for the movement of the domain walls are calculated in dependence of the applied magnetic field and compared with the thermal activation energy. As a result, the stronger pinning site is stable up to a local field strength of about 40 kA/cm. Since the domain wall generates a demagnetizing field of about 11 kA/cm at the critical position, the coercivity correlated to the stronger pinning site is reduced to 29 kA/cm at room temperature. © 1998 American Institute of Physics. [S0021-8979(98)41911-X]

I. INTRODUCTION

The microstructure of fully heat treated $\text{Sm}_2(\text{Co,Fe,Cu,Zr})_{17}$ magnets consists of rhombohedral $\text{Sm}_2(\text{Co,Fe})_{17}$ (2/17 phase) cells with a diameter of about 100 nm. These cells are surrounded by the Cu-rich cell boundary phase $\text{Sm}(\text{Co,Cu})_5$. Additionally, in magnets with high coercivity there appears a Zr-rich platelet phase (Z-phase) which is precipitated perpendicular to the *c*-axis.^{1,2}

It is well established that the coercivity mechanism of such magnets is of the pinning type. In the past it has been assumed that the domain walls are pinned at the Cu-rich boundary phase.³ In order to explain the fact that magnets with Zr show an about three times larger coercivity than magnets without Zr, a new model for the coercivity mechanism of $\text{Sm}_2(\text{Co,Fe,Cu,Zr})_{17}$ magnets has been proposed recently.⁴ According to this model, the domain walls are pinned at two different pinning sites: in low magnetic fields at the edges of the 2/17 cells and in higher magnetic fields at the intersection lines between the Z phase and the Cu-rich boundary phase. This model was supported by the observation that in $\text{Sm}_2(\text{Co,Fe,Cu,Zr})_{17}$ magnets with high coercivity there exist two distinct demagnetization processes which show different temperature dependences.⁵

So far, this model could only explain that there exist two different pinning sites and that the second one is about 2–3 times stronger than the first one. Assuming plain domain walls, the absolute coercivity was calculated to be only about 1 kA/cm which is more than 10 times smaller than the experimental values.⁶ To overcome this problem, it is the aim of this paper to calculate the coercivity of $\text{Sm}_2(\text{Co,Fe,Cu,Zr})_{17}$ magnets in detail, including the effect of domain wall curvatures and thermal activations.

II. SIMULATION OF DOMAIN WALL MOVEMENT

In a magnetic field, *H*, a domain wall in $\text{Sm}_2(\text{Co,Fe,Cu,Zr})_{17}$ magnets will move and deform to increase the volume fraction where the magnetization is paral-

lel to the applied magnetic field. The final shape and position is determined by local minima of the sum of the magnetostatic energy and the domain wall energy.

For the present calculation, the cellular microstructure of $\text{Sm}_2(\text{Co,Fe,Cu,Zr})_{17}$ magnets is approximated by a two dimensional model, see Figs. 1 and 2.⁴ Following parameters are used: length of the rhombohedral 2/17 cells, *L* = 100 nm; thickness of the 1/5 boundary phase, *d* = 5 nm; inclination angle of the 1/5 phase, $\alpha = 60^\circ$, radius at the edges of the 2/17 cell, *r* = 1 nm; thickness of the Z-phase platelets, *z* = 3 nm; saturation polarization, *J_s*, and domain wall energy, γ , of the phases, $J_{s,2/17} = 1.3$ T, $\gamma_{2/17} = 35$ mJ/m², $J_{s,1/5} = 1.1$ T, $\gamma_{1/5} = 58$ mJ/m², $J_{s,z} = 0.5$ T, $\gamma_z = 11$ mJ/m². The model is set to be periodic parallel to the *c* axis with a periodicity of *L*.

First it is assumed that without applied field, a plain domain wall crosses the 1/5 boundary phase at the edges of the 2/17 cells. For this configuration the magnetostatic energy is zero and the domain wall energy is easily calculated to be $(l_{2/17}\gamma_{2/17} + l_{1/5}\gamma_{1/5} + l_z\gamma_z)1m/L$, where *l*_{2/17}, *l*_{1/5}, and *l_z* are the lengths of the domain wall in the 2/17, 1/5, and Z phase. The factor 1*m/L* is a result of the periodicity of the model. In order to find the local energy minima for an applied magnetic field, the domain wall is divided into short 1 nm long segments which are allowed to fluctuate randomly. After each fluctuation the total energy is calculated by summing up all contributions of the single segments to the domain wall energy and the magnetostatic energy

$$E_{\text{total}} = \sum [l_{2/17}\gamma_{2/17} + l_{1/5}\gamma_{1/5} + l_z\gamma_z - 2H(J_{s,2/17}a_{2/17} + J_{s,1/5}a_{1/5} + J_{s,z}a_z)]1m/L. \quad (1)$$

Here *a*_{2/17}, *a*_{1/5} and *a_z* are the areas of the 2/17, 1/5, and Z phase which have been reversed by the movement of the wall compared to the position at *H* = 0. Due to the two dimensional model, the unit of *E*_{total} is J/m. If this new total energy is lower than the former value then it is taken as

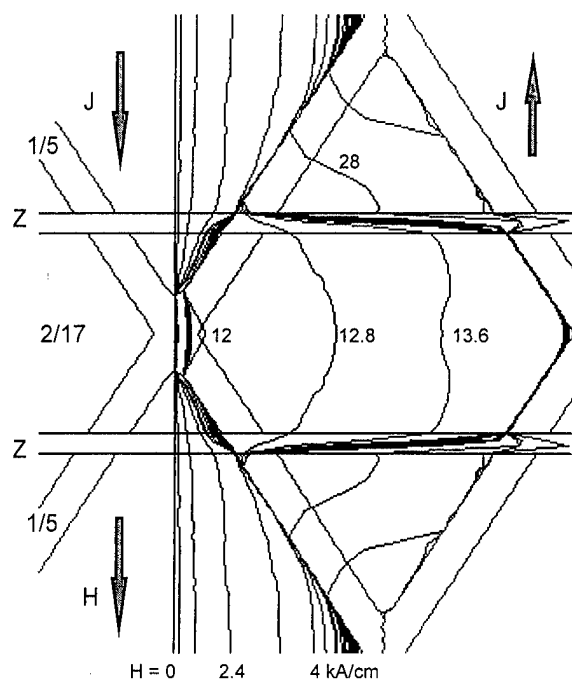


FIG. 1. Shape and position of domain walls in $\text{Sm}_2(\text{Co,Fe,Cu,Zr})_{17}$ magnets for various magnetic field strengths.

starting point for the next iteration. This procedure simulates the effect of the thermal fluctuations in magnets.

For the calculation shown in Fig. 1, wedge-shaped fluctuation volumes were chosen. The length of the wedges were varied randomly between 0 and 10 nm, the width varied from 0 to 2 nm and the position was also determined randomly. The applied magnetic field strength was increased in steps of 0.8 kA/cm and at every new field value, 2000 iterations were tried to find the new equilibrium.

With increasing magnetic field strength the wall bows out in the 2/17 phase quickly and is pressed towards the 1/5 boundary phase. Already at a field strength of about 4 kA/cm, the wall forms the well known zig-zag domains.^{7,8} Additionally, the wall is bowed a little bit in the 1/5 phase too, but it is pinned at the edges of the 2/17 cell. At a field strength of 12 kA/cm, the wall is bowed so strong that it reaches the neighboring 2/17 cell. The wall is depinned and moves up to the next 1/5 boundary. The intermediate positions for 12.8 and 13.6 kA/cm are only a result of the limited number of 2000 iterations per field value. In this state, because of the low domain wall energy of the Z phase, the domain wall preferably follows the Z phase forming domain walls which are almost perpendicular to the c axis. Such wall segments have been recently observed by high resolution Foucault mode Lorentz microscopy.⁸ For field strengths up to 28 kA/cm, the domain wall is still pinned at the intersection line of the Z phase with the 1/5 boundary phase. At this field strength the domain wall is depinned from the second pinning center and the magnet will be completely reversed.

III. ENERGY BARRIERS

In order to be depinned from one of the two pinning sites, the domain wall must overcome an energy barrier. The field dependence of the height and the width of these energy barriers will be calculated below.

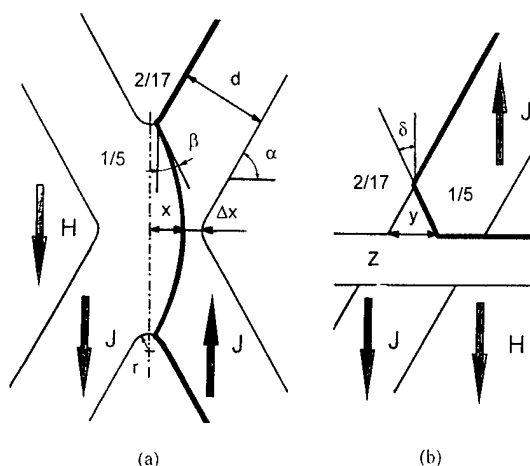


FIG. 2. Geometry of the two pinning sites in $\text{Sm}_2(\text{Co,Fe,Cu,Zr})_{17}$ magnets. The domain wall is marked by the thick line.

For the first pinning site at the edges of the 2/17 cell it is assumed, that in the 2/17 cell the domain wall follows the phase boundary to the 1/5 phase, see Fig. 2(a). The section through the 1/5 phase is approximated by an arc segment which intersects the border to the 2/17 phase at an angle β . In the center, the wall deviates by a distance x . For the second pinning site, it is assumed that a straight segment of the domain wall intersects the 1/5 phase at an angle δ , see Fig. 2(b). The width of the cut triangle is y . For the Z phase it is assumed that the domain wall is perpendicular to the c axis.

The total energy is calculated in dependence of the magnetic field strength and the parameters, x and β for the first pinning site, or y and δ for the second pinning site, respectively. The energy is set to zero for the starting positions $x = 0$, $\beta = 0$ or $y = 0$, $\delta = 0$.

Figure 3 shows an example for the second pinning site, calculated for a magnetic field strength of 16 kA/cm. For $\delta = 0$, the total energy initially increases with increasing y and reaches at $y = 3.5$ nm a maximum of about 3.5×10^{-11} J/m. This maximum is a little bit lower for an angle δ of about 20° . So the actual energy barrier for this pinning site has a

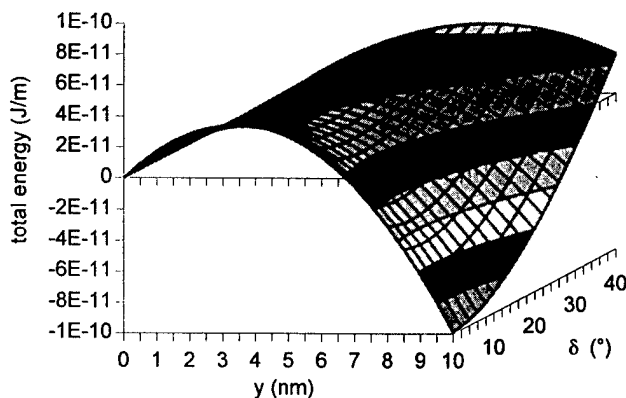


FIG. 3. Total energy for the pinning site at the intersection line of the Z phase and the 1/5 boundary phase in dependence of the displacement, y , and the inclination, δ , of the domain wall.

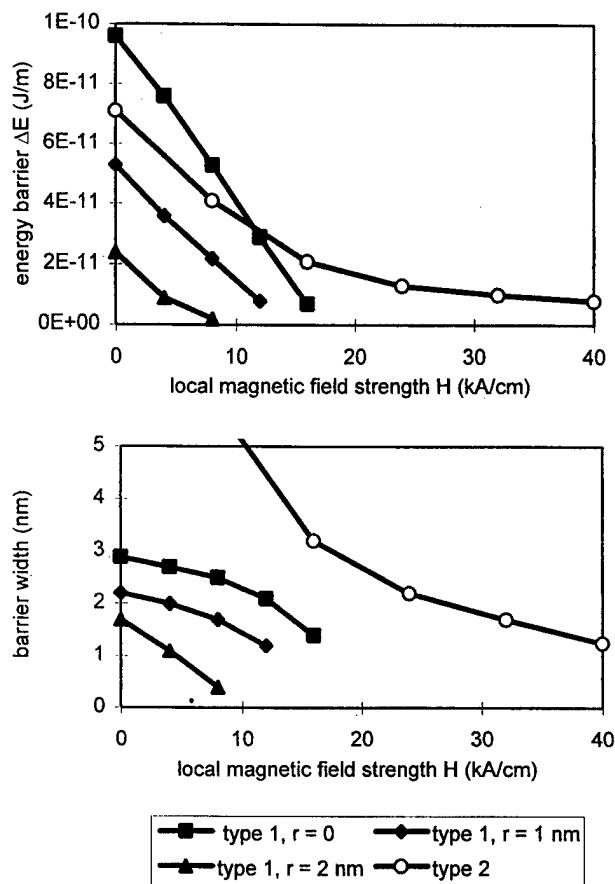


FIG. 4. Field dependence of the width and the height of the energy barriers for various pinning sites in $\text{Sm}_2(\text{Co,Fe,Cu,Zr})_{17}$ magnets.

width of about 3.5 nm and a height of slightly above 2×10^{-11} J/m for an applied magnetic field strength of 16 kA/cm.

Similar calculations were performed for the first pinning site. In this case the width of the energy barrier is determined by the distance between the domain wall and the neighbouring 2/17 cell, Δx , see Fig. 2(a). Hence, the height of the energy barrier is correlated to the total energy at the position where the domain wall reaches the neighbouring cell.

The result of these calculations are shown in Fig. 4. With increasing magnetic field strength both the width and the height of the energy barrier decrease. For the first pinning site, the energy barrier cannot be wider than 3 nm, even for sharp edges. If the edges have a radius of 1 or 2 nm then the width and also the height of the energy barrier is strongly reduced. Depending on this radius, the energy barrier vanishes between about 8 and 17 kA/cm.

The situation is different for the second pinning site. Here the width and the size of the energy barrier decrease slower with increasing magnetic field strength. In particular, at a magnetic field strength of 40 kA/cm, the width of the energy barrier is still 1.2 nm and its height is about 1×10^{-11} J/m.

IV. THERMAL ACTIVATION AND COERCIVITY

The energy necessary to overcome the energy barriers is usually provided by the thermal activation. The thermal activation energy for magnetization states is about $\Delta E_{\text{th}} = 25 \text{ kT}$.⁹ For 300 K this results in $\Delta E_{\text{th}} \approx 1 \times 10^{-19}$ J. This energy is large enough to depinn the domain wall at a length of 10 nm if the energy barrier is 1×10^{-11} J/m. It is assumed that 10 nm is just the length which is necessary to form a stable depinning nucleus. If such a nucleus is once formed then it will expand over the whole length of the pinning site and the domain wall is completely depinned.

Taking 1×10^{-11} J/m as the minimum necessary energy barrier, it turns out that the pinning site at the intersection line of the Z phase and the 1/5 boundary phase is stable up to a local magnetic field strength of 40 kA/cm. The weaker pinning site at the edges of the 2/17 cell is only stable up to 15 kA/cm. If the edges of the 2/17 cell are not sharp, this limit is further reduced, see Fig. 4.

So far the magnetic dipolar interaction has not been taken into account. Therefore, the local magnetic field strengths calculated must be corrected by the demagnetizing field which is generated by the domain wall itself. These demagnetizing fields were calculated by summing up the contributions from each wall segment. Due to the favorable geometry, for the weaker pinning site at the edges of the 2/17 cell the demagnetizing fields almost cancel. Hence the critical fields calculated above are almost identical to the coercivities.

For the stronger pinning site, the demagnetizing field at the critical position is calculated to be about 11 kA/cm. This field strength has to be added to the applied magnetic field. Hence the coercivity of the stronger pinning site in $\text{Sm}_2(\text{Co,Fe,Cu,Zr})_{17}$ magnets is reduced to about 29 kA/cm and determines the coercivity of the magnet.

ACKNOWLEDGMENTS

The author thanks E. Adler, W. Rodewald, P. Schrey, and, in particular, A. Hubert for many stimulating discussions and suggestions.

¹A. E. Ray and S. Liu, *J. Mater. Eng. Perform.* **1**, 183 (1992).

²C. Maury, L. Rabenberg, and C. H. Allibert, *Phys. Status Solidi A* **140**, 57 (1993).

³K. D. Durst, H. Kronmüller, and W. Ervens, *Phys. Status Solidi A* **108**, 403,705 (1988).

⁴M. Katter, J. Weber, W. Assmus, P. Schrey, and W. Rodewald, *IEEE Trans. Magn.* **32**, 4815 (1996).

⁵M. Katter, J. Weber, W. Assmus, P. Schrey, and W. Rodewald, *Proceedings of the 14th International Workshop on Rare Earth Magnets and their Applications, 1996*, edited by F. P. Missell *et al.*, (unpublished), Vol. 1, 194.

⁶R. Skomski, *J. Appl. Phys.* **81**, 5627 (1997).

⁷J. Fidler, *J. Magn. Magn. Mater.* **30**, 58 (1982).

⁸B. Y. Wong, M. Willard, and D. E. Laughlin, *J. Magn. Magn. Mater.* **169**, 178 (1997).

⁹D. Givord and M. F. Rossignol, in *Rare-Earth Iron Permanent Magnets*, edited by J. M. D. Coey (Clarendon, Oxford, 1996), p. 241.

Finite-temperature behavior of anisotropic two-sublattice magnets

Ralph Skomski

Department of Physics and Astronomy, University of Nebraska, Lincoln, Nebraska 68588-0111

The finite-temperature magnetism of rare-earth transition-metal intermetallics is investigated by extending the n -component vector spin model to two-sublattice magnets. Mean-field analysis shows that the influence of the rare-earth anisotropy on the mean-field Curie temperature is much smaller than expected from the low-temperature rare-earth anisotropy. The use of ultraspherical polynomials yields a generalization of the famous $m(m+1)/2$ power-law exponent to $m(m+n-2)/(n-1)$.

© 1998 American Institute of Physics. [S0021-8979(98)48811-X]

I. INTRODUCTION

Two-sublattice ferro- and ferrimagnets such as $\text{Nd}_2\text{Fe}_{14}\text{B}$, $\text{Dy}_3\text{Fe}_5\text{O}_{12}$, and SmCo_5 are physically interesting and technologically important materials.¹⁻⁴ A particular feature of these materials is that their two-sublattice character is associated with nonequivalent crystallographic sites.⁵⁻⁷ This has to be contrasted to antiferromagnets having equivalent sublattices.^{8,9} For example, the square-lattice Ising antiferromagnet can be mapped onto the square-lattice Ising ferromagnet by simultaneously changing the sign of the exchange and reversing the spins of one sublattice.¹⁰

Rare-earth transition-metal compounds consist of transition-metal and rare-earth sublattices coupled by a comparatively weak intersublattice interaction.^{3,11} For the late iron-series elements the intersublattice exchange between rare-earth and transition-metal spins is antiferromagnetic¹¹ so that, according to Hund's rules, light and heavy rare earths yield ferromagnetic and antiferromagnetic intersublattice coupling, respectively.

Atomic anisotropy energies are small, typically of order $E_a/k_B T \approx 1$ K, but due to interatomic exchange their influence on the magnetic properties is not restricted to low temperatures. Note that the theoretical description of the finite-temperature anisotropy of itinerant electrons is still in its initial stage, whereas the Heisenberg-type magnetism of localized electrons is comparatively well understood. Here we use a generalized n -vector model to investigate anisotropic two-sublattice magnets. Emphasis is put on two questions: (i) the effect the two-sublattice anisotropy on the Curie temperature, and (ii) the finite-temperature behavior of the net anisotropy.

II. MODEL AND CALCULATION

The n -component vector-spin or n -vector model (Fig. 1) is defined in terms of quasiclassical local magnetization vectors obeying $\mathbf{s}^2 = s_1^2 + \dots + s_n^2 = 1$.^{9,12} This definition includes the Ising model ($n=1$, so that $\mathbf{s} = s\mathbf{e}_z$), the planar model ($n=2$, $\mathbf{s} = s_y\mathbf{e}_y + s_z\mathbf{e}_z$), the classical Heisenberg model ($n=3$, $\mathbf{s} = s_x\mathbf{e}_x + s_y\mathbf{e}_y + s_z\mathbf{e}_z$), and the spherical model ($n=\infty$). The $n=0$ model is known as the polymer model.¹³ The n -vector model is widely used to study finite-temperature magnetism.^{9,12} For example, the critical exponents of the spherical model are known exactly.⁹

To generalize the n -vector model we have to introduce separate transition-metal and rare-earth sublattice magnetizations \mathbf{s} and \mathbf{S} , respectively, so that $\mathbf{s}^2 = 1$ and $\mathbf{S}^2 = 1$. The spontaneous sublattice magnetizations are then given by $\mathbf{M}_{sT} = s\mathbf{M}_{0T}$ and $\mathbf{M}_{sR} = S\mathbf{M}_{0R}$, where the index 0 refers to the zero-temperature moment. Let us, for the moment, consider the mean-field Hamiltonian

$$\mathcal{H} = -J_{TT}S_z\langle s_z \rangle - J_{RT}S_z\langle s_z \rangle - J_{TR}S_z\langle S_z \rangle - J_{RR}S_z\langle S_z \rangle - K_T s_z^2 - K_R S_z^2. \quad (1)$$

For the materials of interest, the transition-metal intrasublattice coupling J_{TT} dominates the intersublattice exchange described by J_{RT} and J_{TR} , whereas the rare-earth intrasublattice exchange J_{RR} is negligibly small. K_T and K_R are the lowest-order uniaxial transition-metal and rare-earth sublattice anisotropy constants, respectively, and refer to the magnetic energy per atom. Due to the pronounced rare-earth spin-orbit coupling, $K_R \gg K_T$ for typical magnets. An exception are rare earths whose $4f$ electron cloud is spherical, such as gadolinium. Note that putting $J_{RT} = J_{TR} = K_R = 0$ and $K_T = K_R = 0$ yields, for $n=3$, the well-investigated limits of the anisotropic one-sublattice¹⁴ and isotropic two-sublattice^{6,7} Heisenberg models, respectively.

The equilibrium behavior of the model Eq. (1) is given by the partition function

$$Z = \int' \exp(-\mathcal{H}/k_B T) d\mathbf{s} d\mathbf{S}. \quad (2)$$

Here, the dash indicates that the conditions $\mathbf{s}^2 = 1$ and $\mathbf{S}^2 = 1$ restrict the integration to the surfaces of n -dimensional spheres. The thermally averaged sublattice magnetizations

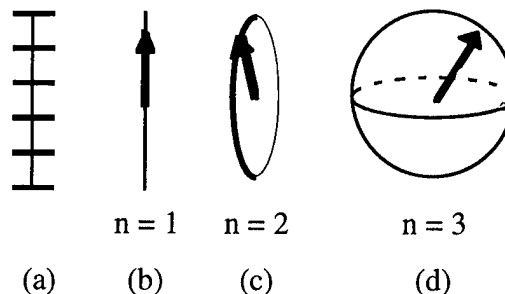


FIG. 1. Spin configurations: (a) $J=5/2$ Heisenberg model, (b) Ising model, (c) planar model, and (d) classical Heisenberg model.

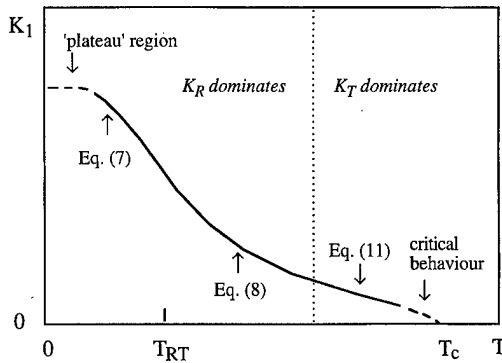


FIG. 2. Temperature dependence of magnetocrystalline anisotropy if both K_T and K_R are positive (schematic).

$M_{sT}\langle s_z \rangle$ and $M_{sR}\langle S_z \rangle$ and anisotropies $K_T\langle s_z^2 \rangle$ and $K_R\langle S_z^2 \rangle$ are obtained by direct integration or, more conveniently, by differentiating Eq. (2) with respect to $\langle s_z \rangle$ and $\langle S_z \rangle$. The resulting self-consistent equations are, in general, coupled and nonlinear. Mathematically, the calculation involves surface averages such as $\langle z^m \rangle_0 = \int' z^m d\mathbf{x} / \int d\mathbf{x}$. In particular, $\langle z^2 \rangle_0 = 1/n$ and $\langle z^4 \rangle_0 = 3/n(n+2)$.

A. Curie temperature

In the vicinity of the Curie temperature it is possible to expand Z into powers of the small quantities $\langle s_z \rangle$ and $\langle S_z \rangle$. As in the case of isotropic two-sublattice magnets,^{6,7} the determination of the Curie temperature reduces to the calculation and diagonalization of a 2×2 secular matrix equation. In the present case,

$$\begin{pmatrix} \langle s_z \rangle \\ \langle S_z \rangle \end{pmatrix} = \begin{pmatrix} A_{TT} & A_{TR} \\ A_{RT} & A_{RR} \end{pmatrix} \begin{pmatrix} \langle s_z \rangle \\ \langle S_z \rangle \end{pmatrix}, \quad (3)$$

where

$$A_{ik} = (J_{ik}/nk_B T) \{1 + [2(n-1)K_i]/[n(n+2)k_B T]\}. \quad (4)$$

Neglecting J_{RR} and taking into account the smallness of J_{RT} , K_T , and K_R , we obtain by eigenvalue analysis

$$T_c = T_T + T_{RT}^2/T_T + \{2(n-1)/[n(n+2)k_B]\} (K_T + K_R T_{RT}^2/T_T^2), \quad (5)$$

where $T_T = J_{TT}/nk_B$ and $T_{RT} = \sqrt{J_{RT}J_{TR}/n^2 k_B^2}$.

The first two terms on the right-hand side of Eq. (5) are well known and describe the isotropic transition-metal and rare-earth contributions to the Curie temperature, respectively.^{3,7} The third term on the right-hand side of Eq. (5) is the anisotropy contribution to T_c . We see that the influence of the rare-earth anisotropy is smaller than expected from the value of K_R by a factor T_{RT}^2/T_T^2 , that is of order 0.05 for iron-rich rare-earth intermetallics.

Note that the anisotropy of the ideally anisotropic Ising model ($n=1$) does not contribute to the Curie temperature, but from the leading term $T_T = J_{TT}/nk_B$ we see that the Ising Curie temperature is about three times larger than the Heisenberg Curie temperature.

B. Anisotropy

Figure 2 gives a schematic idea of the temperature dependence of the total anisotropy. Here we neglect the low-temperature and critical limits (dashed lines) and focus on the intermediate regimes $T < T_{RT}$ and $T_{RT} < T < T_c$. In the classical Heisenberg model, the temperature dependence of m th-order anisotropy contributions is proportional to the thermal average of the Legendre polynomials $\langle P_m(S_z) \rangle_0$, where the index 0 refers to the isotropic Hamiltonian.¹⁴ For the n -vector model we have to use ultraspherical polynomials $P_m^{(n)}(x)$.¹⁵ The first ultraspherical polynomials are $P_{0(n)} = 1$, $P_{1(n)} = x$,

$$P_{2(n)} = \frac{1}{n-1} (nx^2 - 1), \quad (6a)$$

$$P_{3(n)} = \frac{1}{n-1} [(n+2)x^3 - 3x], \quad (6b)$$

and

$$P_{4(n)} = \frac{1}{n^2-1} [(n+2)(n+4)x^4 - 6(n+2)x^2 - 1]. \quad (6c)$$

For $n=2$, the ultraspherical polynomials are also known as Tchebicheff polynomials.

At low temperatures, the magnetization dependence of the Heisenberg anisotropy constants $K_{m/2}$ is given by the famous power-law $K(T)/K(0) = (M_s/M_0)^{m(m+1)/2}$ (Ref. 14). For example, $K_1(T)/K_1(0) = (M_s/M_0)^3$. Let us now generalize this power law to arbitrary spin dimensionalities, which is of some interest because statistical considerations often simplify in the limit of large spin dimensionalities. The starting point is the "low-temperature" expression $\int' \exp(z/t) z^m d\mathbf{x} = 1 - m(n-1)t/2$. By expressing the ultraspherical polynomials in terms of hypergeometric functions,¹⁵ we find after short calculation

$$K_1(T)/K_1(0) = (M_s/M_0)^{m(m+n-2)/(n-1)}. \quad (7)$$

Note that the exponent in this equation equals m in the spherical model and $2n/(n-1)$ for the lowest-order anisotropy constant ($m=2$).

Equation (7) is restricted to one-sublattice magnets, but at very low temperatures $T < T_{RT}$ it remains valid if M_s and M_0 refer to the rare-earth sublattice magnetization. In the practically important intermediate region $T_{RT} < T < T_c$, one has to consider the rare-earth sublattice in the exchange field of the transition-metal sublattice,^{3,17} which yields the approximate $1/T^4$ power-law

$$\frac{K_R(T)}{K_R(0)} = \frac{J_{RT}^2}{n(n+2)k_B^2 T^2}. \quad (8)$$

This prediction agrees fairly well with numerical studies on a quantum-mechanical single-ion model¹⁶ and the estimate $A = 1.7 \pm 0.4$ deduced from literature data on $\text{Sm}_2\text{Fe}_{17}\text{N}_x$ and $\text{Sm}_2\text{Fe}_{17}\text{C}_x$.⁴

C. Transition-metal sublattice

The itinerant character of the 3d electrons means that not only the spontaneous magnetization but also the mag-

netic moment are temperature dependent.¹⁷⁻¹⁹ However, in most cases the thermal reduction of the magnetic moment does not exceed a few percent so that its neglect is a fair assumption.¹⁷⁻¹⁹ As a very crude approximation, we consider the mean-field Hamiltonian

$$\mathcal{H} = -J_{TT}s_z\langle s_z \rangle - K_T s_z^2 - U_0 s^2, \quad (9)$$

where $n=3$ and $s^2 \leq 1$ and the parameter $U_0 \propto I - 1/D(E_F)$ is a Stoner-type single-site energy.¹⁹ Typically, $U_0 \gg J \gg K_T$, so that in lowest-order $T_c = T_T(1 + 4K_T/15k_B T_T - 2T_T/U_0)$. The reduction of T_c is small in the region where Eq. (9) applies, but may nevertheless be larger than the K_1 contributions discussed in this paper.

In lowest order, the transition-metal anisotropy is given by the linear relation¹⁴

$$K(T) = K(0)(1 - T/T_c). \quad (10)$$

Note that this temperature dependence is even simpler than that of the spontaneous magnetization, which exhibits an implicit dependence on the Langevin function.

III. DISCUSSION AND CONCLUSIONS

The ultimate reason for the weak K_R dependence in Eq. (5) is that the two sublattices are largely decoupled above T_{RT} . In the vicinity of T_c , the sublattice magnetizations are given by the eigenmode

$$\langle m_z \rangle = \langle s_z \rangle + \frac{T_{RT}}{T_c} \langle S_z \rangle, \quad (11)$$

showing that the mean-field magnetization near T_c is dominated by the transition-metal sublattice. Of course, the mean-field approximation is incorrect in the vicinity of T_c .¹⁰ However, the thermal sublattice decoupling is a mean-field effect starting far below T_c and being most pronounced at high temperatures. As a consequence, even for $K_T=0$ the rare-earth critical behavior is difficult to observe.

The key advantage of the n -vector model, namely its transparent physical meaning, is paid by an incorrect description of quantum-mechanical spin excitations. In particular, the classical n -vector model neglects the nonzero energy spacing between the quantum levels [Fig. 1(a)] and does not work very well at low temperatures (the "plateau" region in Fig. 2).¹⁶ Furthermore, Eq. (1) neglects exchange

anisotropy²⁰ and magnetostatic dipole interactions. For this reason, our predictions are only semiquantitative.

In conclusion, we have analyzed the finite-temperature behavior of a generalized n -vector model. The influence of transition-metal and rare-earth anisotropies on the Curie temperature is treated in a mean-field approximation. Due to the weakness of the intersublattice coupling, the anisotropy contribution to the Curie temperature is determined by the transition-metal sublattice. The temperature dependence of the anisotropy may be approximated by a hierarchy of power laws.

ACKNOWLEDGMENTS

The author is indebted to J. M. D. Coey and J. Cullen for stimulating discussions.

- ¹J. F. Herbst, Rev. Mod. Phys. **63**, 819 (1991).
- ²K. N. R. Taylor and M. I. Darby, *Physics of Rare-earth Solids* (Chapman and Hall, London, 1972).
- ³*Rare-earth Iron Permanent Magnets*, edited by J. M. D. Coey (Oxford University Press, Oxford, 1996).
- ⁴R. Skomski and N. M. Dempsey, in *Interstitial Intermetallic Alloys*, edited by F. Grandjean *et al.* (Kluwer, Dordrecht, 1995), p. 653.
- ⁵L. Néel, Ann. Phys. (Paris) **3**, 137 (1948).
- ⁶J. S. Smart, *Effective Field Theories of Magnetism* (Saunders, Philadelphia, 1966).
- ⁷A. Herpin, *Théorie du Magnétisme* (Institut National des Sciences et Techniques Nucléaires, Saclay, 1968).
- ⁸L. J. de Jongh and A. R. Miedema, Adv. Phys. **23**, 1 (1975).
- ⁹D. C. Mattis, *The Theory of Magnetism II* (Springer, Berlin, 1985).
- ¹⁰L. P. Kadanoff, W. Götzke, D. Hamblen, R. Hecht, E. A. S. Lewis, V. V. Palciauskas, M. Rayl, J. Swift, D. Aspnes, and J. Kane, Rev. Mod. Phys. **39**, 395 (1967).
- ¹¹I. A. Campbell, J. Phys. F **2**, 147 (1972).
- ¹²K.-H. Fischer and A. J. Hertz, *Spin Glasses* (Cambridge University Press, Cambridge, 1991).
- ¹³P.-G. de Gennes, *Scaling Concepts in Polymer Physics* (Cornell University Press, Ithaca, 1979).
- ¹⁴R. Callen, J. Appl. Phys. **33**, 832 (1962).
- ¹⁵H. Hochstadt, *The Functions of Mathematical Physics* (Wiley, New York, 1971).
- ¹⁶M. D. Kuz'min, Phys. Rev. B **46**, 8219 (1992).
- ¹⁷P. Fulde, *Electron Correlations in Molecules and Solids* (Springer, Berlin, 1991).
- ¹⁸T. Moriya, *Spin Fluctuations in Itinerant Electron Magnetism* (Springer, Berlin, 1985).
- ¹⁹R. Skomski, J. Magn. Magn. Mater. **140-144**, 2003 (1995).
- ²⁰R. M. White, *Quantum Theory of Magnetism* (McGraw-Hill, New York, 1970).

Magnetic properties of DyCo₁₀V₂

C. Zhang, X. C. Kou, Z. G. Zhao, E. Brück, K. H. J. Buschow, and F. R. de Boer
*Van der Waals-Zeeman Institute, University of Amsterdam, Valkenierstraat 65,
 1108 XE Amsterdam, The Netherlands*

The easy magnetization direction of DyCo₁₀V₂ is parallel to the *c* axis at room temperature. The magnetization hysteresis loops of magnetically aligned samples were measured from 5 to 300 K with fields applied parallel and perpendicular to the alignment direction. For samples field-cooled to below the compensation temperatures, shifts of the loop centers into the range of negative magnetizations were observed. These features and the occurrence of negative remanences are explained in terms of the magnetization reversal when passing the compensation temperature upon cooling. From measurements of the temperature dependence of the magnetization, it was derived that a spin-reorientation transition takes place at about $T_{SR} = 41$ K. © 1998 American Institute of Physics. [S0021-8979(98)35411-0]

I. INTRODUCTION

The RCo₁₀V₂ compounds have the tetragonal ThMn₁₂ structure and it was shown by neutron diffraction that the V atoms occupy almost exclusively the 8*i* site, leaving only small occupancies for the 8*f* and 8*j* sites.¹ Magnetic measurements have shown that the Curie temperatures are well above 400 K and that the atomic Co moments in these compounds are about 0.8 μ_B .² The Co-sublattice anisotropy favors an easy magnetization direction perpendicular to the *c* axis.³ Depending on the nature of the rare-earth component and the concomitant second order Stevens factor, the rare-earth sublattice anisotropy may favor an easy magnetization direction parallel to the *c* axis at low temperatures and lead to a spin-reorientation transition in the low-temperature range. Such behavior is expected for the compound DyCo₁₀V₂. In addition, due to the ferrimagnetic coupling between the Dy and Co moments, the magnetization reversal process is expected to be different in the temperature ranges above and below the compensation temperature. For this reason, we have studied the magnetic properties of this compound in more detail, including hysteresis loops at different temperatures.

II. EXPERIMENT

The DyCo₁₀V₂ compound was prepared by melting stoichiometric proportions of the constituent metals (purity at least 99%) in an argon-arc furnace. Subsequently, the sample was wrapped in Ta foil and annealed for three weeks at 1050 °C in an evacuated quartz tube. After annealing, the sample was investigated by x-ray diffraction. Inspection of the x-ray diagram showed that a single-phase compound of the ThMn₁₂-type structure had formed.

The field and temperature dependences of the magnetization of the DyCo₁₀V₂ compound were studied by means of a SQUID magnetometer. The magnetic isotherms were measured on magnetically aligned powders with the measuring fields applied parallel and perpendicular to the alignment direction.

III. RESULTS AND DISCUSSION

From x-ray diffraction made on a magnetically aligned powder sample of the DyCo₁₀V₂ compound, it is derived that the easy magnetization direction is parallel to the *c* axis. The x-ray diagram of the aligned sample can be compared in Fig. 1 with the diagram measured on a powder sample in which the particles are oriented at random.

Measurements of the temperature dependence of the magnetization were made in various fields with increasing temperature on a piece of bulk material containing a statistical distribution of grain orientations. Results are shown in Fig. 2. The measurements were made after cooling the sample to 5 K in zero field. The minimum in the upper two curves at about 120 K corresponds to the compensation temperature (T_{comp}). Below this temperature, the magnetization is Dy dominated and above this temperature Co dominated. This means that the total magnetization, in order to become oriented parallel to the field direction, has to revert its direction when passing through T_{comp} . Alternatively, one could say that the applied field is parallel to the total magnetization below T_{comp} and antiparallel to it above T_{comp} . Because of the presence of a large coercivity, the total magnetization is not able to revert its direction when the measuring fields are too small. This is the case for the lower three curves shown

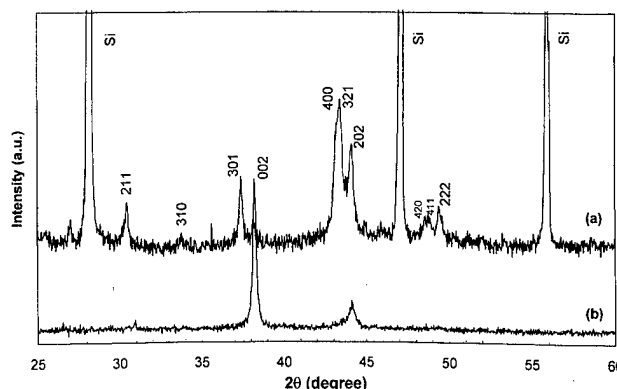


FIG. 1. X-ray diagrams of (a) an unaligned sample, and (b) a magnetically aligned sample of DyCo₁₀V₂.

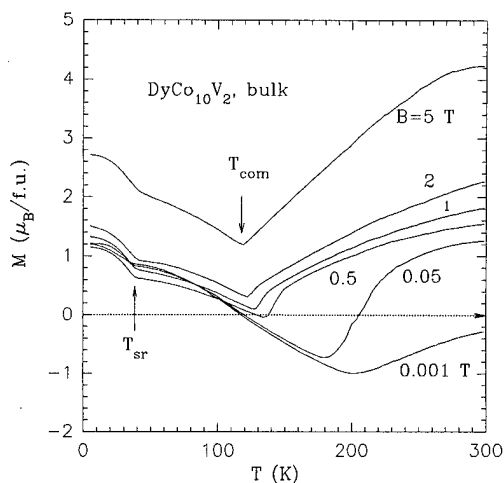


FIG. 2. Temperature dependence of the magnetization of a piece of bulk material of $\text{DyCo}_{10}\text{V}_2$, fixed with epoxy, measured in various applied fields with increasing temperature from 5 K to room temperature.

in Fig. 2. We will show below that the coercivity strongly decreases with increasing temperature. This means that the higher the applied field, the sooner will the total magnetization be able to revert its direction above T_{comp} . This may explain why the sample, when measured with comparatively low fields, retains its original magnetization with negative values even up to room temperature for $B = 0.001$ T.

It can be seen in Fig. 2 that all the curves show a discontinuity at about 41 K. This discontinuity is attributed to a spin reorientation. The Co-sublattice anisotropy favors an easy magnetization direction perpendicular to the c axis.³ We have shown above that the easy magnetization direction in the $\text{DyCo}_{10}\text{V}_2$ compound is parallel to the c axis at room temperature. This means that the Dy-sublattice anisotropy, which depends much stronger on temperature than the Co-sublattice anisotropy, has been able to overcompensate the Co-sublattice anisotropy already at room temperature. This excludes the possibility for a type of spin reorientation that might originate from a competition between these two sublattices below room temperature. Because the Dy-sublattice anisotropy is crystal-field induced, anisotropy contributions due to higher order crystal-field terms gain in importance upon decreasing temperature and may be responsible for the spin reorientation at $T_{\text{SR}} \approx 41$ K. This spin reorientation may lead to an easy-cone configuration, allowing for a small component of the magnetization perpendicular to the c axis. Because the anisotropy within the basal plane is commonly only very small, this cone configuration leads to a small enhancement of the magnetization for statistically oriented grains below T_{SR} . A similar type of spin reorientation transition has been observed at cryogenic temperatures, for instance, in the compound $\text{Nd}_2\text{Fe}_{14}\text{B}$.

It is well known that the coercivity depends strongly on the magnetic anisotropy. The anisotropy field can be expressed in terms of the anisotropy constant K_1 (neglecting higher-order terms for the sake of simplicity) and the saturation magnetization M_s via the relation $H_A(T) = 2K_1(T)/\mu_0 M_s(T)$. This means that the anisotropy field of the $\text{DyCo}_{10}\text{V}_2$ compound will be particularly strong in the

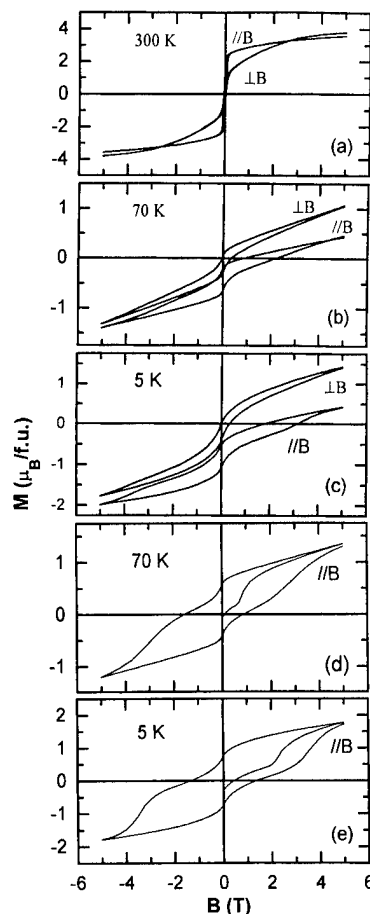


FIG. 3. Coercive behavior of $\text{DyCo}_{10}\text{V}_2$ particles, magnetically aligned and fixed at room temperature (a) when measured at room temperature, when measured after cooling in 5 T to the measuring temperature of (b) 70 K, (c) 5 K. Coercive behavior of particles magnetically aligned parallel to the c direction, fixed with epoxy, and measured with the applied field parallel to the alignment direction after cooling in zero field, (d) first to 70 K, (e) then to 5 K.

low-temperature region, not only because K_1 increases strongly with decreasing temperature but also because of the mutual compensation of the magnetization of the two sublattices. The room-temperature hysteresis loops for magnetically aligned powder particles are shown in Fig. 3(a). The mutually antiparallel Dy and Co sublattice moments can bend towards each other in the applied field when the latter is perpendicular to the alignment direction. For this reason, the net moment can become higher in comparatively high fields than when measurements are made with the field applied parallel to the alignment direction. This may explain the crossing of the two isotherms shown in Fig. 3(a).

Measurements of the hysteresis loops at 70 and 5 K are shown in Figs. 3(b) and 3(c), respectively. These were obtained by applying a field of 5 T in the alignment direction and, subsequently, cooling the sample to 5 K and/or 70 K in the same field. It can be derived from the shape of the loops measured at 5 and 70 K that these are minor hysteresis loops. When interpreting the results shown in Figs. 3(b) and 3(c) one has to bear in mind that the applied field is much higher than the coercivity at high temperatures. This means that the domain walls are removed from the particles by the applied field and that the magnetization of the particles corresponds

to a location on the upper branch of a hysteresis loop. This situation is basically retained when cooling the sample to lower temperatures in the presence of the same field. However, because the compensation temperature is passed when cooling down, the magnetization has changed its direction. The applied field is now opposite to the magnetization direction. This is the reason why the loops measured in parallel direction have their center at negative values of the magnetization. Furthermore, the fact that the remanence is still negative makes it clear that fields substantially higher than 5 T would be required for reaching complete magnetization reversal and for reaching the maximum coercivity. In fact, for perfectly aligned particles one would have expected a magnetization behavior corresponding to the quasilinear behavior when traversing the lower branch rather than upper branch of an extremely wide hysteresis loop. However, superimposed on this quasilinear behavior is probably the loop behavior of less well aligned particles. Computer simulations and model calculations^{4,5} have shown that the coercivity can become strongly reduced when the particle alignment deviates from the parallel direction. This is very likely also the reason for the comparatively small coercivities found in the loops in Figs. 3(b) and 3(c) measured with the field perpendicular to the alignment direction. Note that the magnetization reversal associated with T_{comp} should not have any influence when the measurements are made perpendicular to the magnetization direction, but the less ideal alignment already mentioned may shift the centers of these loops somewhat into the region of negative magnetizations.

The results displayed in Figs. 3(d) and 3(e) describe experiments made on samples aligned parallel to the c axis and cooled to 70 and 5 K in zero field. At room temperature the

sample can be regarded as demagnetized, a situation that will not have changed much by the small field of 0.04 T used for positioning the sample in the magnetometer. The demagnetized state is retained when cooling to 5 and 70 K. Because we expect the maximum coercivity to be higher than 5 T, the hysteresis loops measured up to the latter field have to be regarded as minor loops, which obviously is the case.

Finally, we wish to comment on the wasp-tailed shape of the various loops shown in Fig. 3. This shape suggests the presence of particles having different coercivities. We mentioned already the influence of particle misalignment on the loop behavior. However, one has also to take into consideration that the particle size is not uniform, and that the samples may contain very small particles with single-domain character and high coercivities as well as a whole gamut of larger sized particles with multidomain character and lower coercivities.

ACKNOWLEDGMENT

The present investigation has been carried out within the scientific exchange program between China and The Netherlands.

¹O. Moze, R. M. Ibberson, and K. H. J. Buschow, *J. Alloys Compd.* **196**, L1 (1993).

²J. H. V. J. Brabers, G. F. Zhou, F. R. de Boer, and K. H. J. Buschow, *J. Magn. Magn. Mater.* **118**, 339 (1993).

³F. R. de Boer, Z. G. Zhao, and K. H. J. Buschow, *J. Magn. Magn. Mater.* **157/158**, 504 (1996).

⁴K. Kronmüller, in *Proc. NATO-ASI Supermagnets, Hard Magnetic Materials*, edited by G. J. Long and F. Grandjean (Kluwer Academic, Dordrecht, 1991).

⁵J. Fidler and T. Schrefl, *J. Appl. Phys.* **79**, 5029 (1996).

Investigation of the magnetic properties of $\text{ErFe}_{11}\text{Ti}$ and $\text{ErFe}_{11}\text{TiH}$ in high magnetic field

O. Isnard^{a)}

Laboratoire de Cristallographie, CNRS, BP 166X, 38042 Grenoble, France

M. Guillot

Laboratoire des Champs Magnétiques Intenses CNRS/MPI 38042 Grenoble, France

Marked changes of the main structural and magnetic properties of the RFe_{11}Ti phases are induced by hydrogen insertion. High field magnetization measurements are reported on magnetically oriented $\text{ErFe}_{11}\text{Ti}$ and $\text{ErFe}_{11}\text{TiH}$ samples under a field up to 240 kOe (24 T) in the 4.2–300 K temperature range. A raise of the Curie temperature and room temperature saturation magnetization upon hydrogen insertion is observed. The $M(H)$ curves show a significant susceptibility is observed even at room temperature. The magnetic anisotropy constants are determined. Isofield magnetization curves reveal broad maxima in the 230 K range which reflect the fast decrease of the Er sublattice under high field. © 1998 American Institute of Physics. [S0021-8979(98)29611-3]

I. INTRODUCTION

The seek for permanent magnet materials has led to the discovery of compounds of the type $\text{RFe}_{12-x}\text{M}$ (R=rare earth or yttrium and M=transition metal element). These intermetallic compounds stabilize with the ThMn_{12} structure type whose space group is $I4/mmm$. For selected R or M, potentially hard magnetic materials are obtained among which one can cite $\text{SmFe}_{11}\text{Ti}^{1-3}$ and $\text{SmFe}_{11}\text{TiH}^{4,5}$ where insertion of hydrogen induces an enhancement of the magnetic features. RFe_{11}Ti phases have also attracted much attention for fundamental research. Many of these RFe_{11}Ti compounds are exhibiting spin reorientation (SR) at low temperatures.^{3,6,7} Till now the $\text{RFe}_{11}\text{TiH}$ phases have been less studied, here we focus on the magnetic properties of $\text{ErFe}_{11}\text{Ti}$ and $\text{ErFe}_{11}\text{TiH}$.

The sample preparation and sample analysis have been described in Ref. 4. The amount of absorbed hydrogen estimated by the gravimetric, as well as the volumetric method was one H atom per $\text{ErFe}_{11}\text{Ti}$ formula unit. This content has been confirmed by neutron diffraction. Thermomagnetic analysis was performed using a home-made Faraday type balance by recording magnetization (M) versus temperature (T). High field magnetization measurements have been performed on both $\text{ErFe}_{11}\text{Ti}$ and $\text{ErFe}_{11}\text{TiH}$ in a continuous magnetic field up to 240 kOe. Magnetic measurements over the temperature range 4.2–300 K were performed using an automatic system provided with a cryostat associated with a calorimeter and described in Ref. 8. The experimental accuracy on M is estimated to be $\pm 2\%$.

No single crystals of the hydrogen containing compound were available, thus, in order to work in the same conditions, both compounds have been studied on a polycrystalline sample. The samples were made from oriented powders with a particle size smaller than 25 μm . The magnetic field was applied either parallel or perpendicular to the alignment direction. The powder was aligned at room temperature using

an orientation field of typically 10 kOe and fixed in epoxy resin. Magnetization isofield curves have been measured between 50 and 300 K in order to obtain the thermal variation of the magnetization. The saturation magnetization has been obtained from extrapolation of the $M(H)$ curve with H parallel to the alignment direction according to $M(H) = M_{\text{sat}} + a/H^2$. The magnetocrystalline anisotropy of uniaxial crystals is given by $K_1 \sin^2 \theta + K_2 \sin^4 \theta$, where θ is the angle between the easy direction of magnetization and the magnetization (anisotropy constants of higher order than K_2 being neglected). The anisotropy constants K_j has been deduced from the fitting of the magnetization curves: Refs. 9 and 10. This approach was successfully used to determine the constants for the $\text{SmFe}_{11}\text{Ti}$ compound,⁴ leading to values equivalent to that obtained from single crystals.¹¹ The analysis of the x-ray diffraction pattern shows that the $I4/mmm$ symmetry is kept after hydrogen insertion. The lattice parameters of the hydride are larger than that of the host alloy. This is a rather common features in the rare-earth-iron intermetallics. The estimated H uptake (1 atom per formula unit) is in good agreement with the localization of hydrogen deduced from neutron diffraction experiments.^{12,13} In $\text{ErFe}_{11}\text{TiH}$, hydrogen atoms are found to be exclusively located in the octahedral $2b$ site. In this site, H atoms are surrounded by two erbium atoms and four iron atoms.

II. RESULTS AND DISCUSSION

The ordering temperatures are 518 and 574 K for $\text{ErFe}_{11}\text{Ti}$ and $\text{ErFe}_{11}\text{TiH}$, respectively. This is clearly evidenced in an enhancement of the exchange interaction and has to be related to the unit cell increase mentioned above. According to the Néel–Slater curve, in the range of interatomic distances observed in RFe_{11}Ti compounds, an increase of the Fe–Fe interatomic distance produces an enhancement of the Fe–Fe exchange interaction. According to x-ray diffractometry performed on magnetically aligned powder, both $\text{ErFe}_{11}\text{Ti}$ and $\text{ErFe}_{11}\text{TiH}$ compounds exhibit an uniaxial easy magnetization at room temperature. This is not

^{a)}Electronic mail: isnard@labs.poly.cnrs-gre.fr.

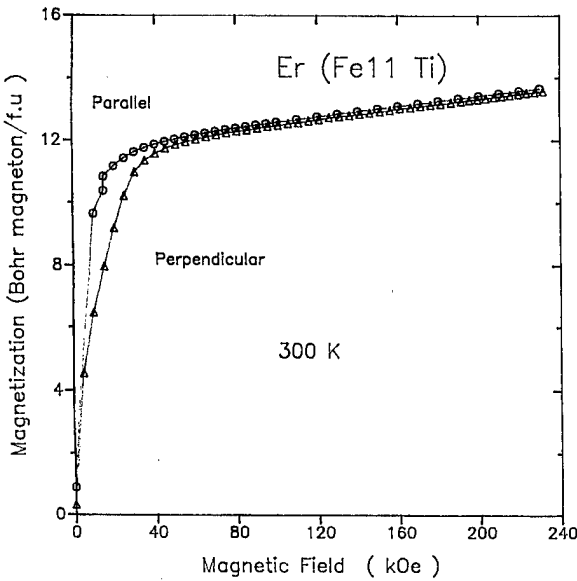


FIG. 1. Isothermal magnetization curves at 300 K on oriented ErFe₁₁Ti up to 240 kOe.

that surprising since previous investigations on RFe₁₁Ti alloys and hydrides R=Y, Lu, and Gd^{4,5,13} have shown that, in this structure, the iron sublattice anisotropy favors an alignment of the magnetic moment along the *c* axis and that for rare earth elements having a positive second order Stevens coefficient, α_J (Sm,Er,Tm), the easy axis is also the *c* axis.

Nevertheless, a spin reorientation (SR) phenomenon has been observed for cooling below room temperature.^{1,3,14} Neither Tm, nor Sm containing compounds are exhibiting such a SR, it was thus suggested that in the RFe₁₁Ti structure the first order crystal electric field parameter A_0^2 is not sufficient to understand the low temperature magnetic features, higher order parameters have to be taken into account, in particular with different behaviors of comparison with Sm and Tm, one may arise from the highest value of the γ_J Stevens coefficient in the case of erbium.¹⁵

This evidenced in the RFe₁₁Ti families of compounds that higher than two order crystal electric field parameters have to be taken into consideration to understand the contribution of the rare earth sublattice to the magnetocrystalline anisotropy. This conclusion was also drawn from the analysis of RFe₁₁Ti compounds (i.e., Dy).^{6,15} The magnetization curves recorded at room temperature on oriented powder are given in Figs. 1 and 2 for ErFe₁₁Ti and ErFe₁₁TiH, respectively. Unlike what was measured for other rare earth elements, a significant susceptibility is observed for the ErFe₁₁Ti and ErFe₁₁TiH even at room temperature and a rather high magnetic field. This feature was not pointed out by Andreev *et al.*¹⁴ but is also present on their single crystal data. The main magnetic features deduced from these curves are summarized in Table I. The purity of the sample is confirmed by the magnetization obtained from our sample which is very close to the ErFe₁₁Ti single crystal data.¹⁴ M_{sat} is found to be slightly higher for the alloy 15.7 μ_B / formula unit against 15.0 for the hydride. Since the iron sublattice magnetization is almost insensitive to the presence of

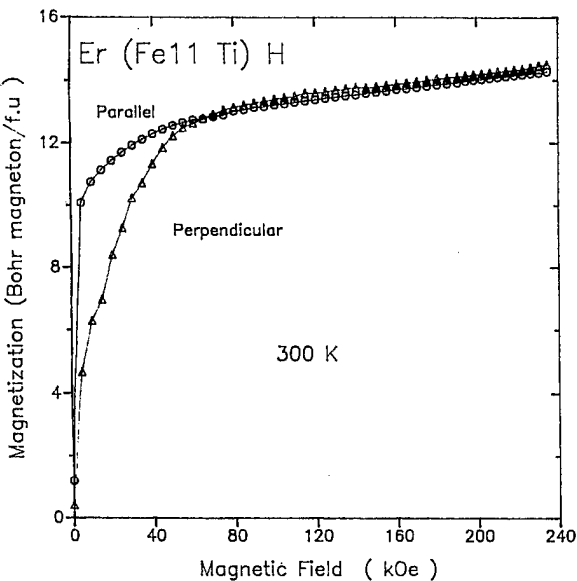


FIG. 2. Isothermal magnetization curves at 300 K on oriented ErFe₁₁TiH up to 240 kOe.

hydrogen,^{4,5,13} the observed decrease of the overall magnetization induced by hydrogen insertion reflects an increase of the Er sublattice magnetization at room temperature.

The anisotropy constants K_1 and K_2 are in agreement with an alignment of the total magnetization along the *c* axis. A slight decrease of the parameter K_1 is found after hydrogenation. The low temperature magnetization curves (4.2 K) are plotted in Fig. 3. M_{sat} is found to be 11.6 μ_B / formula for ErFe₁₁Ti; this value agrees with that obtained on a single crystal.¹⁴ If one subtracts the Fe sublattice magnetization (about 17 μ_B / formula) deduced from the study on LuFe₁₁Ti or YFe₁₁Ti,¹² about 5.4 μ_B is obtained for Er. Note that this value reflects the projection of the Er magnetization along the *c* axis. It is worth noting that since the Er atoms are located on a fourfold axis (position 2*a* of space group I4/mmm) one may expect four equivalent directions of the Er magnetic moment each tilted on a angle θ with respect to the *c* axis and a pyramidal arrangement seems more probable than that of a simple cone as usually proposed. A continuous rotation (decrease of the angle θ) has been observed on a ErFe₁₁Ti single crystal when the temperature increases.¹⁴ The same thing may be expected for the corresponding hydride, nevertheless the θ angle can be different from that

TABLE I. Magnetic features of ErFe₁₁Ti and ErFe₁₁TiH.

	T_C (K)	M_{sat} (μ_B /f.u.)	K_1 (MJ/m ³)	K_2 (MJ/m ³)
300 K	518	15.7	3.2±0.4	-0.40±0.05
ErFe ₁₁ Ti				
4.2 K		11.6	4.0±0.2	-0.60±0.10
300 K	574	15.0	2.4±0.2	-0.40±0.05
ErFe ₁₁ TiH				
4.2 K		13.0		

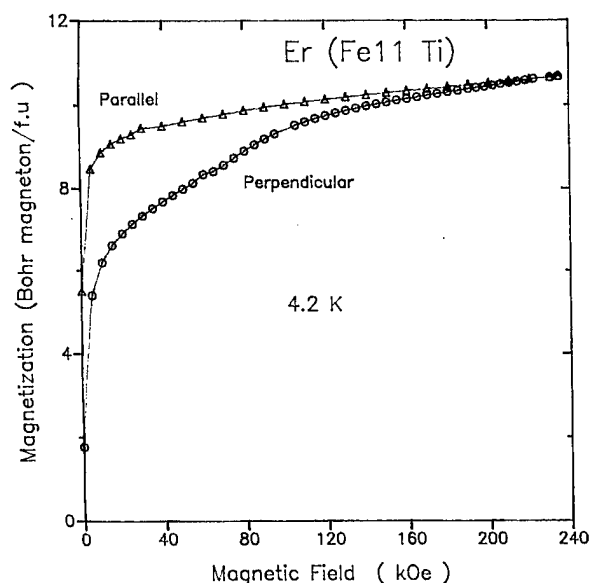


FIG. 3. Isothermal magnetization curves at 4.2 K on oriented $\text{ErFe}_{11}\text{Ti}$ up to 240 kOe.

observed for the alloy since hydrogen insertion modifies the crystal field parameters at the rare earth site.¹⁶

The magnetization curve recorded for $\text{ErFe}_{11}\text{Ti}$ at 4.2 K evidences a peculiar behavior at about 70 kOe where a change of the slope is observed on the curve measured when applying the field perpendicularly to the alignment direction. Since such peculiar behavior is not observed at high temperatures, we suggest that from 70 kOe all the magnetic moments are titled in respect to the c axis, whereas at higher magnetic fields the magnetization is along the c axis (the θ angle has vanished). Following this interpretation, the anisotropy constant have been extracted from the magnetization curve obtained at field between 70 and 240 kOe (Table I).

The isofield magnetization curves given in Fig. 4 are characterized by a broad maximum which decreases when the applied field increases; this maximum is found at 248 and 228 K for $\text{ErFe}_{11}\text{Ti}$ at 10 and 230 kOe, respectively. In $\text{ErFe}_{11}\text{TiH}$, the maximum is observed at slightly higher temperatures, typically 265 and 236 K on an applied field of 10 and 230 kOe, respectively. Whatever the magnetic field, a sharp raise of the magnetization is observed as the temperature increases towards the maximum. This reflects the fast decrease of the Er magnetic moment versus temperature while the Fe sublattice remains almost constant in this temperature range. After this broad maximum of the magnetization, the total magnetization decreases due to the decrease of the Fe sublattice magnetization.

Hydrogen insertion in $\text{ErFe}_{11}\text{Ti}$ does not modify the magnitude of the Fe sublattice magnetization much as discussed elsewhere.^{4,12,5} The displacement of the maximum towards the higher temperature indicates an enhancement of the Er magnetization upon H insertion in $\text{ErFe}_{11}\text{Ti}$. This observation corroborates the lower M_{sat} value obtained at 300 K in the hydride. Another feature of the isofield magnetization curves is the minimum observed at low temperature.

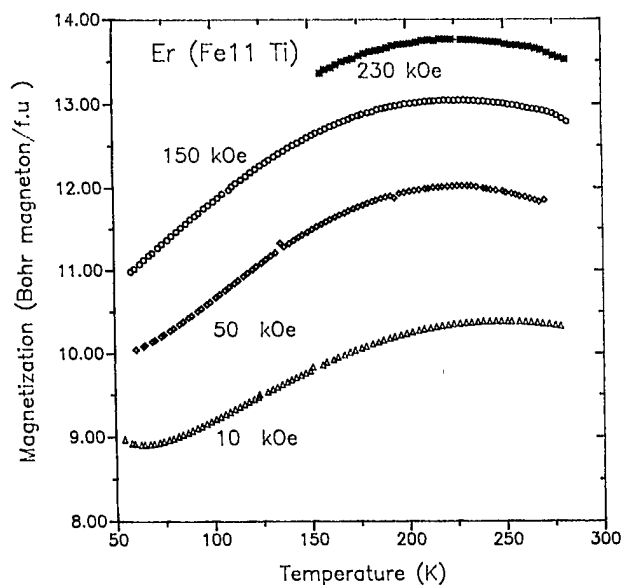


FIG. 4. Isofield magnetization curves at different magnetic field on oriented c axis $\text{ErFe}_{11}\text{Ti}$ compounds in the 50–275 K temperature range.

This minimum occurs in the same temperature range as the spin reorientation T_{SR} does. The increase of the magnetization when cooling below T_{SR} may be associated to the progressive tilting of the Er magnetic moment apart from the c axis, thus leading to an increase of the net magnetization ($M_{\text{Fe}} - M_{\text{Er}}$). Another possibility would be a coherent rotation of M_{Fe} and M_{Er} , both remaining antiferromagnetically coupled, but with such a phenomena, a decrease of the projection of the magnetization along the c axis and a non-negligible remanent magnetization would be expected unlike what is experimentally observed. The proposed interpretation for the rotation of the Er magnetization will be checked by low temperature neutron diffraction experiments.

¹B. P. Hu, H. S. Li, J. P. Gavigan, and J. M. D. Coey, *J. Phys.: Condens. Matter* **1**, 755 (1989).

²T. Kaneko, M. Yamada, K. Ohoshi, Y. Tawara, R. Osagi, H. Yoshida, G. Kido, and Y. Natagawa, *Proceedings of the 10th International Workshop on Rare-Earth Magnets and their Applications*, Kyoto, Japan, 1989 (unpublished), p. 191–200.

³R. Grossinger, X. C. Kou, and G. Wiesinger, *IEEE Trans. Magn.* **30**, 1018 (1994).

⁴O. Isnard, M. Guillot, S. Miraglia, and D. Fruchart, *J. Appl. Phys.* **78**, 5542 (1996).

⁵L. Y. Zhang and W. E. Wallace, *J. Less-Common Met.* **149**, 371 (1989).

⁶X. C. Kou, T. S. Zhao, R. Grossinger, H. R. Kirchmayr, X. Li, and F. R. de Boer, *Phys. Rev. B* **47**, 3231 (1993).

⁷K. H. J. Buschow, *J. Magn. Magn. Mater.* **100**, 79 (1991).

⁸J. C. Picoche, M. Guillot, and A. Marchand, *Physica B* **155**, 407 (1987).

⁹O. Isnard, S. Miraglia, M. Guillot, and D. Fruchart, *J. Appl. Phys.* **75**, 5988 (1994).

¹⁰K. D. Durst and H. Krommüller, *J. Magn. Magn. Mater.* **59**, 86 (1986).

¹¹V. Ya. Bodiakov, T. I. Ivanova, G. A. Nikitin, and I. S. Tereshina, *J. Alloys Compd.* **253**, 265 (1997).

¹²O. Isnard and M. Guillot (unpublished).

¹³O. Isnard, S. Miraglia, M. Guillot, and D. Fruchart, *J. Alloys Compd.* (to be published).

¹⁴A. V. Andreev, S. Sechvsky, N. V. Kudrevatykh, S. S. Sigaev, and E. N. Tarasov, *J. Less-Common Met.* **144**, L21 (1988).

¹⁵B. P. Hu, Ph. D. thesis, Trinity College, Dublin, 1990.

¹⁶O. Isnard, P. Vuillet, J. P. Sanchez, and D. Fruchart, *J. Magn. Magn. Mater.* (to be published).

Magnetic properties of TbCo_3B_2 studied by neutron diffraction, magnetization, and ac-susceptibility measurements

El'ad N. Caspi

*Nuclear Research Centre-Negev, P. O. Box 9001, 84190 Beer-Sheva, Israel
and Ben-Gurion University of the Negev, P. O. Box 653, 84105 Beer-Sheva, Israel*

Haim Pinto, Moshe Kuznietz, Hanania Ettegui, and Mordechai Melamud

Nuclear Research Centre-Negev, P. O. Box 9001, 84190 Beer-Sheva, Israel

Israel Felner

Racah Institute of Physics, The Hebrew University, 91904 Jerusalem, Israel

Hagai Shaked

Ben-Gurion University of the Negev, P. O. Box 653, 84105 Beer-Sheva, Israel

Neutron-diffraction measurements on TbCo_3B_2 , with the isotope ^{11}B , show ferromagnetic structure below 35(2) K. Ordered magnetic moments of Tb and Co were found to be in the basal planes directed parallel to each other. The Tb ordered moment is significantly smaller than its free-ion value. The Co ordered moment is nearly zero. Ac-susceptibility and SQUID magnetometer measurements agree with the neutron results. © 1998 American Institute of Physics. [S0021-8979(98)35511-5]

TbCo_3B_2 belongs to the $\text{R}_{n+1}\text{Co}_{3n+5}\text{B}_{2n}$ (R =lanthanide, $n=0, 1, 2, 3$, and ∞) family of compounds with $n=\infty$, which crystallize in the hexagonal CaCu_5 -type structure¹ (P6/mmm space group). In this compound cobalt atoms in the $2c$ site of the isostructural TbCo_5 are replaced by boron atoms (Fig. 1).

Magnetic and specific heat measurements on some of the RCO_3B_2 compounds (mainly $\text{R}=\text{Gd}$, Sm , and Dy)²⁻⁶ show ferromagnetic behavior. In these measurements the magnetic structure, as well as the relative contributions of the atoms to the ferromagnetic moment, cannot be deduced. In this work we determine the magnetic moments on the Tb and Co atoms using neutron-diffraction measurements. The magnetic values obtained from the neutron-diffraction data are compared with ac-susceptibility and SQUID magnetometer measurements.

Polycrystalline TbCo_3B_2 sample was prepared by arc melting the elements, using the ^{11}B isotope (99.5 a/o) in an argon atmosphere. The obtained button was annealed at 1073 K in vacuum for 120 h. A specimen from the sample was examined by x-ray diffraction and was found to be single phase. Neutron ($\lambda=240$ pm) diffraction measurements of ~ 16 g sample were performed at the IRR-2 reactor at RT (~ 295 K) and LT (~ 18 K). The diffractograms were analyzed using the Rietveld profile analysis (the FULLPROF program).⁷ Ac-susceptibility measurements were carried out from 8 K up to RT on a 0.126 g sample. The applied ac field is ~ 10 Oe. Magnetization measurements were carried out using a SQUID magnetometer from 5 K up to RT on a 0.028 g sample. Magnetic fields ranging from zero up to 50 kOe, were used in the magnetization measurements.

The RT neutron diffractogram of TbCo_3B_2 [Fig. 2(a)] is consistent with the hexagonal CaCu_5 -type structure. The lattice parameters, $a=505.3(5)$ pm, and $c=301.1(3)$ pm are in agreement with previous x-ray diffraction data.¹

The LT neutron diffractogram of TbCo_3B_2 shows an in-

crease in the intensities of the reflections in comparison with the RT diffractogram [Fig. 2(b)]. This increase in intensity is consistent with a ferromagnetic structure. Rietveld analysis of the LT diffractogram results in the existence of both Tb and Co ordered magnetic moments in the basal plane, parallel to each other. The magnetic form factors of the Tb and Co atoms are approximated by the exponentially decreasing function, $\exp[-C(\sin \theta/\lambda)^2]$. The C values used in the refinements were fixed to be 4.8×10^4 pm² for Tb, and 8.3×10^4 pm² for Co (Ref. 8). The refined Tb and Co ordered magnetic moments are $5.4(2) \mu_B$ and $0.13(7) \mu_B$, respectively.

The temperature dependence of the neutron integrated intensity of the $\{010\}$ reflections was measured (Fig. 3). The ordering temperature, T_f^{neut} , at which the intensity of the magnetic contribution to the $\{010\}$ reflections vanishes, is 35(2) K (Fig. 3).

In the measurement of the molar ac-susceptibility, χ_M , vs temperature, a large maximum in χ_M is shown, charac-

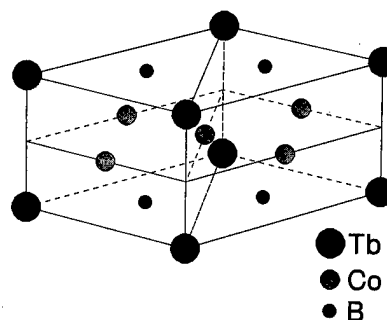


FIG. 1. Crystallographic unit cell of TbCo_3B_2 . The Tb, Co, and B atoms occupy the $1a$, $3g$, and $2c$ sites, respectively, in the space group P6/mmm (CaCu_5 -type structure).

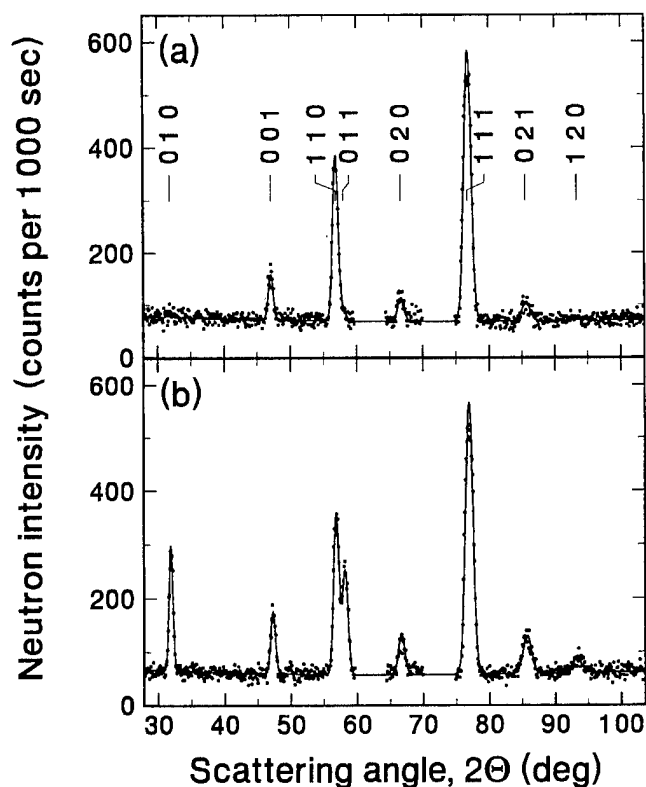


FIG. 2. Neutron ($\lambda \approx 240$ pm) powder diffraction data (dots) and Rietveld refinement profile (line) of TbCo_3B_2 at (a) RT and (b) LT. RT reflections are consistent with the hexagonal CaCu_5 -type structure. Increase of these reflections at LT is consistent with ferromagnetic ordering of Tb and Co atoms in the basal plane, parallel to each other. Observed peaks due to Al sample holder contribution (at $\sim 62^\circ$ and 74°) were omitted.

teristic of ferromagnetic transition at T_f^{susc} (Fig. 4; Table I). Another transition is observed at T_o^{susc} (Fig. 4; Table I). Above 150 K the sample is paramagnetic, and the susceptibility adheres to the Curie-Weiss law (Fig. 4). The effective

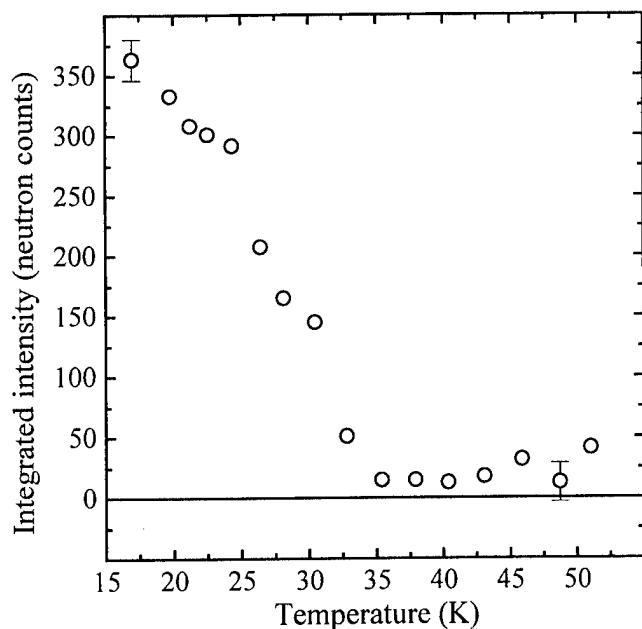


FIG. 3. Integrated intensity of the $\{010\}$ reflections as a function of temperature for TbCo_3B_2 . The magnetic contribution vanishes at 35(2) K.

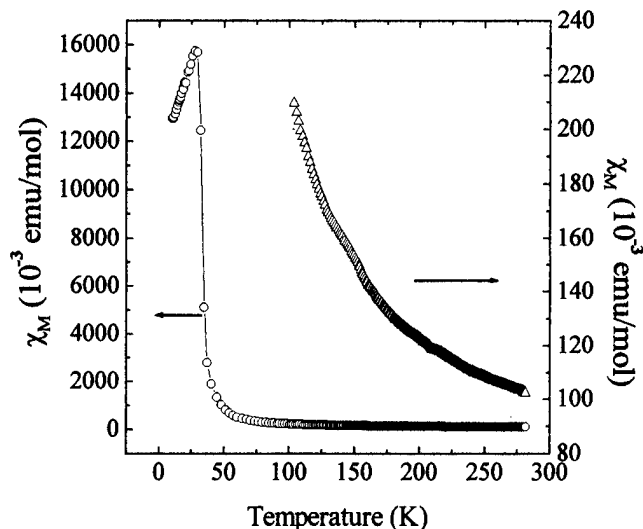


FIG. 4. Ac-magnetic-susceptibility of TbCo_3B_2 as a function of temperature (left ordinate) and its expansion in the temperature range 100–280 K (right ordinate).

magnetic moments, μ_{eff} , the paramagnetic Curie temperature, θ , and the enhanced Pauli paramagnetic susceptibility,⁵ χ_0 , are obtained by fitting the Curie-Weiss law, $(\chi_M - \chi_0)^{-1} = (2.83/\mu_{\text{eff}})^2 (T - \theta)$, to the observed data (Table I).

SQUID magnetometer measurements of the magnetic moment, M , vs temperature, in applied magnetic field $H = 1$ kOe, show similar results. Two transitions, at T_f^{SQUID} and at T_o^{SQUID} , are observed (Table I). Above 150 K the Curie-Weiss law is observed with the refined parameters summarized in Table I.

SQUID magnetometer measurements of M vs the magnetic field, H , show ferromagnetic behavior of the sample at 5 K (Fig. 5). The observed magnetic moment at $H = 50$ kOe is $6.2 \mu_B$. This moment is not saturated. The estimated saturated value is $\sim 6.9 \mu_B$. The linear relation between M and H at 90 K indicates a non-ferromagnetic state (Fig. 5).

The neutron diffraction method as a powerful tool for determination of the magnetic structure and the magnitude of magnetic moment is demonstrated in this work. Previously, the determination of the lanthanide and Co magnetic moments was achieved by using different assumptions about the moments in the family $\text{R}_{n+1}\text{Co}_{3n+5}\text{B}_{2n}$ (Refs. 2–6). Mainly, it was assumed that the Co atom is either nonordered magnetically² or has a small moment, which is antiparallel to the lanthanide moment.^{4,5} The latter assumption is based on results for heavy lanthanides in RCO_5 (Ref. 9).

TABLE I. Enhanced Pauli paramagnetic susceptibility,⁵ χ_0 , paramagnetic Curie temperature, θ , effective magnetic moment, μ_{eff} , and transition temperatures, T_f , and T_o , as obtained from ac-susceptibility (applied field $H = 10$ Oe) and SQUID ($H = 1$ kOe) magnetometer measurements.

Method	χ_0 (emu/mol)	θ (K)	μ_{eff} (μ_B)	T_f (K)	T_o (K)
ac-susceptibility	0.071(1)	40(4)	7.7(1)	35(5)	150(5)
SQUID	0.022(1)	14(7)	7.8(2)	35(5)	130(5)

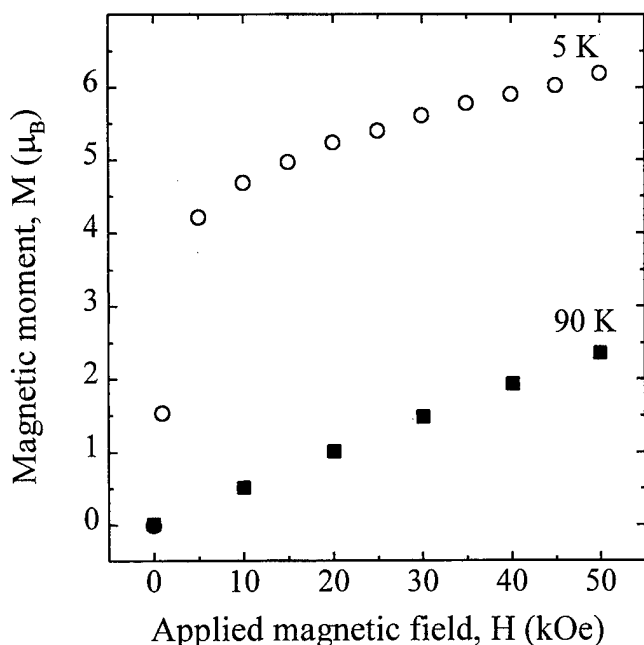


FIG. 5. Magnetic moment as a function of magnetic field as measured using SQUID magnetometer at 5 and 90 K.

Our LT (18 K) neutron diffraction data requires $5.4(2) \mu_B$ for the magnetic moment of Tb, and $0.13(7) \mu_B$ for Co, with the moments aligned parallel to each other. Attempts to refine the neutron diffraction data using Co magnetic moment which is either zero or antiparallel to the Tb magnetic moment resulted in significantly worse agreement factors. Moreover, attempts to increase the Tb magnetic moment up to its free-ion value (i.e., $9 \mu_B$) show a clear disagreement with the experimental data.

The SQUID magnetometer measurements of M vs H (Fig. 5) agree with the reduced magnetic moment of Tb. Extrapolating $M \propto 1/H$ to $1/H=0$ resulted in $\sim 6.9(2) \mu_B$ for the saturated moment at 5 K. This value is higher than the neutron value [total moment of $5.8(2) \mu_B$] at LT (18 K). This is expected from the difference in the temperatures at which the moments were measured. Similar reduction of the lanthanide magnetic moment has been previously^{3,4} estimated from magnetization measurements for other lanthanides in this structure (e.g., Dy and Sm). This reduction was associated with crystalline electric field effects.^{3,4}

Above 150 K the TbCo_3B_2 compound exhibits the paramagnetic behavior, as determined from the SQUID and ac-susceptibility measurements (Table I). The discrepancy in χ_o and θ is ascribed to the difference in the applied field. The best-fitted effective magnetic moment is small in comparison with the free-ion Tb^{3+} effective moment ($9.72 \mu_B$). This result can probably be related to the reduction in the ordered magnetic moment discussed above.

The nature of the higher temperature transition, T_o , observed by both SQUID and ac-susceptibility measurements (Table I), is yet to be studied.

¹K. Niihara and S. Yajima, Bull. Chem. Soc. Jpn. **46**, 770 (1973).

²H. H. A. Smit, R. C. Thiel, and K. H. J. Buschow, J. Phys. F **18**, 295 (1988).

³H. Ogata, H. Ido, and H. Yamauchi, J. Appl. Phys. **73**, 5911 (1993).

⁴H. Ido, M. Nanjo, and M. Yamada, J. Appl. Phys. **75**, 7140 (1994).

⁵R. Ballou, E. Burzo, and V. Pop, J. Magn. Magn. Mater. **140-144**, 945 (1995).

⁶W. Perthold, N. M. Hong, H. Michor, G. Hilscher, H. Ido, and H. Asano, J. Magn. Magn. Mater. **157-158**, 649 (1996).

⁷J. Rodríguez-Carvajal, Physica B **192**, 55 (1993).

⁸H. Pinto, M. Melamud, and H. Shaked, in *Neutron Scattering—1981*, edited by J. Faber, AIP Conf. Proc. **89** (AIP, New York, 1982), p. 315.

⁹R. Lemaire, Cobalt **32**, 132 (1966).

A Mössbauer spectral study of $\text{Tb}_2\text{Fe}_{17}$ and the $\text{Tb}_2\text{Fe}_{17-x}\text{Si}_x$ solid solutions

Dimitri Hautot, Gary J. Long, and P. C. Ezekwenna

Department of Chemistry, University of Missouri–Rolla, Rolla, Missouri 65409-0010

F. Grandjean

Institute of Physics, B5, University of Liège, B-4000 Sart-Tilman, Belgium

D. P. Middleton

Philips Research Laboratories, NL-5600 JA Eindhoven, The Netherlands

K. H. J. Buschow

Van der Waals-Zeeman Laboratory, University of Amsterdam, NL-1018 XE Amsterdam, The Netherlands

The Mössbauer spectra of a series of rhombohedral $\text{Tb}_2\text{Fe}_{17-x}\text{Si}_x$ solid solutions, with x equal to 0, 1, 2, and 3, have been measured as a function of temperature. Although the spectra of $\text{Tb}_2\text{Fe}_{17}$ change substantially upon cooling from 295 to 85 K, it has been possible to fit them with a consistent seven sextet model corresponding to a basal magnetization. The spectral analysis yields reasonable hyperfine parameters and the expected changes with temperature. The resulting weighted average effective iron recoil mass of 66 g/mol and the Mössbauer temperature of 395 K are typical of this type of intermetallic compound. In addition, the isomer shifts and the hyperfine fields observed for the crystallographically distinct iron sites in $\text{Tb}_2\text{Fe}_{17}$ agree well with those expected from the differences in the Wigner–Seitz cell volumes and the near-neighbor environments of the four sites. The spectra of the silicon substituted solid solutions have been fit with the same model and similar hyperfine parameters, but with a binomial distribution of near-neighbor environments. The weighted average hyperfine field decreases slowly with increasing silicon content, whereas the isomer shift increases. © 1998 American Institute of Physics. [S0021-8979(98)35611-X]

R_2Fe_{17} is a very common intermetallic phase whose magnetic properties can be modified by replacing part of the iron by a substitutional metal such as aluminum,^{1–4} gallium,^{5,6} or silicon.^{7,8} Often the Curie temperatures increase up to a maximum at $x \approx 3$ in these $\text{R}_2\text{Fe}_{17-x}\text{M}_x$ solid solutions. Thus a systematic study of these compounds may lead to improved permanent magnet materials as a result of a better understanding of the influence of the substitutional metal.

Herein, we report on the magnetic properties of $\text{Tb}_2\text{Fe}_{17}$ and its silicon substituted solid solutions, $\text{Tb}_2\text{Fe}_{17-x}\text{Si}_x$, with $x = 1, 2$, and 3 , by Mössbauer spectroscopy between 85 and 295 K. We are interested in these solid solutions because their lattices contract with increasing x , contractions which are rather surprising because it has generally been believed that such contractions would lead to an increase in the anti-ferromagnetic coupling between some of the iron atoms. Such an increase should lead to a decrease in the Curie temperature in contrast to the observed increase with x . Thus a study of these compounds, which seem to be an exception to this general belief, may help to better understand the magnetic behavior of such substituted intermetallic compounds.

The $\text{Tb}_2\text{Fe}_{17-x}\text{Si}_x$ solid solutions, with $x = 0, 1, 2$, and 3 , were prepared as described previously.⁵ Powder x-ray diffraction results indicate that all of these compounds are virtually single phase and crystallize with the rhombohedral $\text{Tb}_2\text{Zn}_{17}$ -type structure. Three silicon atoms per formula unit are the most that can be introduced into $\text{Tb}_2\text{Fe}_{17}$ and still yield a single phase solid solution.

The Mössbauer spectral absorbers contained 27 mg/cm² of powder¹⁰ which had been sieved to a particle diameter of

0.045 mm or less. The Mössbauer spectra were measured on a constant acceleration spectrometer which utilized a rhodium matrix cobalt-57 source and was calibrated at room temperature with an α -iron foil.

A preliminary study¹¹ of the Mössbauer spectra of $\text{Tb}_2\text{Fe}_{17}$ at 78 and 295 K has revealed a distinct difference in the shape of the spectra at these two temperatures. Further, the reported temperature dependence of the spectral hyperfine parameters was unusual. In order to better understand these changes, the $\text{Tb}_2\text{Fe}_{17}$ Mössbauer spectra were remeasured at several temperatures between 85 and 295 K. Figure 1, which shows several of these spectra, reveals a continuous change in the shape of the spectrum upon cooling. At 85 K the spectrum shows a very distinct absorption at ca. -5.3 mm/s as well as two distinct shoulders at ca. -2.5 and 4.5 mm/s, absorptions which begin to converge with others above 175 K such that at 295 K there is little if any sign of these three spectral features.

Because the magnetization of $\text{Tb}_2\text{Fe}_{17}$ is basal, we have fit its Mössbauer spectra with a seven sextet model⁹ in which the hyperfine parameters are consistent with both the near-neighbor environment and the Wigner–Seitz cell volume of each iron site. The seven sextets correspond to the seven inequivalent magnetic sites,⁹ $6c, 9d_6, 9d_3, 18f_{12}, 18f_6, 18h_{12}$, and $18h_6$, respectively, and the isomer shifts for the crystallographically equivalent, but magnetically inequivalent, sites were constrained to be equal. Further, in this model the isomer shift increases with the cell volume of a crystallographic site because of a reduced s -electron density at the iron-57 nucleus. The results of these fits are given in Table I along with the 295 K Wigner–Seitz cell volume for each site.^{12,13}

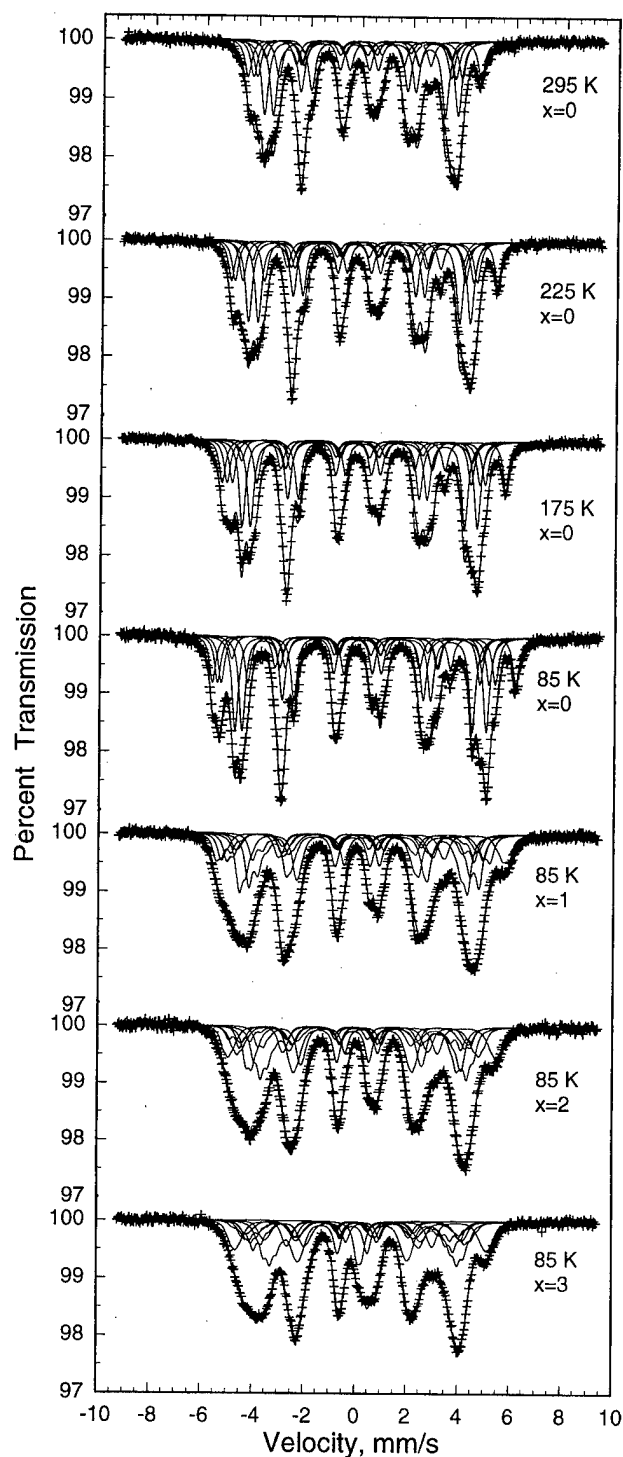


FIG. 1. The Mössbauer spectra of $\text{Tb}_2\text{Fe}_{17}$ measured at 295, 225, 175, and 85 K, and the 85 K Mössbauer spectra of the $\text{Tb}_2\text{Fe}_{17-x}\text{Si}_x$ solid solutions with $x=1, 2$, and 3.

As already observed⁹ in many related R_2Fe_{17} compounds, the hyperfine fields increase with the number of iron near neighbors for each crystallographic site, see Fig. 2. As expected, the hyperfine fields decrease with increasing temperature and the quadrupole shifts are independent of temperature. The effective mass, M_{eff} , of each iron site can be calculated¹⁴ from the temperature dependence of the isomer shift. Table I reveals that the 9d site has the largest, the 18f and 18h sites have similar intermediate, and the 6c site has

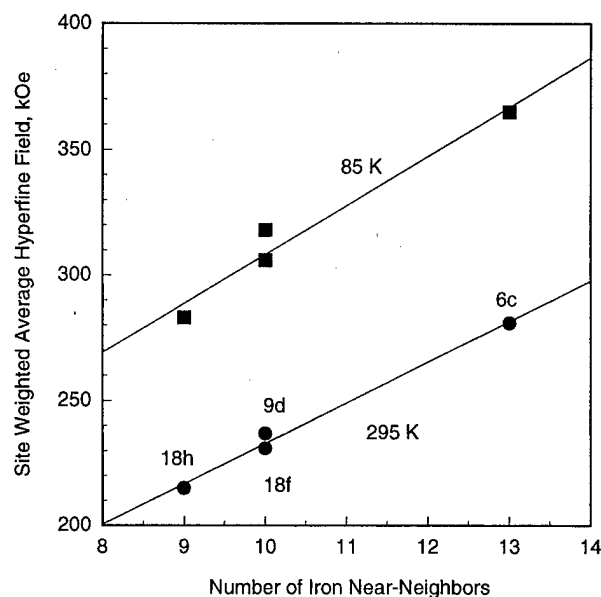


FIG. 2. The correlation between the $\text{Tb}_2\text{Fe}_{17}$ site weighted average hyperfine fields and the number of iron near-neighbors.

the smallest effective masses. This indicates that the 9d site is more covalently bound than the other sites, as is expected for the site with the smallest Wigner-Seitz cell volume. The temperature dependence of the isomer shift and the logarithm of the spectral absorption area may be used to calculate¹⁴ the Mössbauer temperature, θ_M , for each site. The resulting values, of ca. 400 K, see Table I, are typical for this type of intermetallic compound.¹⁵

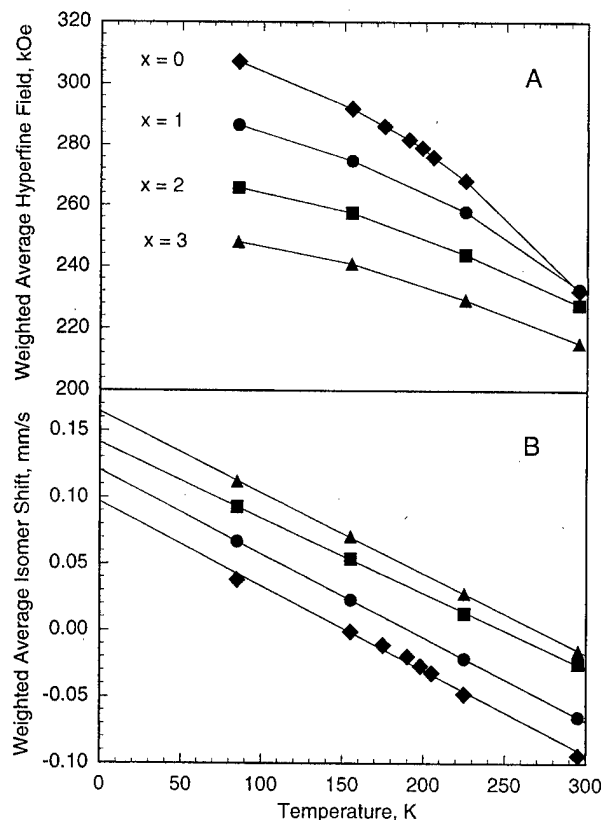


FIG. 3. The temperature dependence of the weighted average hyperfine fields, A, and the weighted average isomer shifts, B, for the $\text{Tb}_2\text{Fe}_{17-x}\text{Si}_x$ solid solutions with $x=0$, \diamond ; 1, \bullet ; 2, \blacksquare ; and 3, \blacktriangle .

TABLE I. Mössbauer spectral hyperfine parameters^a and Wigner-Seitz cell volumes for Tb₂Fe₁₇.

	T, K	6c	9d ₆	9d ₃	18f ₁₂	18f ₆	18h ₁₂	18h ₆	Wt. ave.
H, kOe	295	281	244	223	223	247	218	208	232
	85	365	327	300	294	330	285	279	307
δ, mm/s ^b	295	0.066	-0.180	-0.180	-0.084	-0.084	-0.113	-0.113	-0.094
	85	0.229	-0.063	-0.063	0.041	0.041	0.021	0.021	0.038
δ ₀ , mm/s ^c		0.304	0.082	0.082	0.095	0.095	0.080	0.080	0.112
dδ/dT ^c		-7.55	-5.55	-	-6.15	-	-6.43	-	-6.36
M _{eff} , g/mol		55	74	-	67	-	64	-	66
θ _M , K		433	371	-	390	-	399	-	395
QS, mm/s	295	0.05	-0.21	0.04	0.45	-0.01	-0.33	0.45	0.06
	85	0.06	-0.20	0.04	0.45	-0.02	-0.33	0.45	0.06
V _{WS} , Å ³ ^d	295	12.55	11.28	-	11.77	-	11.88	-	11.81

^aThe linewidth is 0.32 mm/s at 295 K and 0.29 mm/s at 85 K and $d(\ln \text{Area})/dT$ is $-7.51 \times 10^{-4} \text{ K}^{-1}$.

^bRelative to room temperature α -iron foil.

^c δ_0 is the zero Kelvin intercept and the slope, $d\delta/dT$, is $\times 10^{-4} \text{ (mm/s)/K}$.

^dCalculated with the structural parameters given in Ref. 13 and BLOKJE, Ref. 12, with the 12 coordinate atomic radii of 1.80 and 1.26 Å for terbium and iron, respectively.

The Mössbauer spectra of Tb₂Fe_{17-x}Si_x, with $x = 1, 2$, and 3, were measured between 85 and 295 K, and the 85 K spectra are shown in Fig. 1. These spectra are clearly much broader than those of Tb₂Fe₁₇ and thus must be fit with a distribution of hyperfine fields resulting from the binomial distribution of silicon near neighbors, a fitting procedure which has been described in detail elsewhere.^{8,11} To carry out these fits, the amount of silicon on each iron site must be known. Unfortunately, at this time, no neutron diffraction results are available for these compounds, and thus the silicon occupancies reported⁸ for Ce₂Fe_{17-x}Si_x were used herein. Indeed, earlier work¹⁻⁸ has shown that the M site occupancies are rather independent of the nature of the rare earth in R₂Fe_{17-x}M_x. Further, for low silicon content even less variation with the rare earth is expected. A single linewidth, between 0.29 mm/s at 85 K and 0.32 mm/s at 295 K, was used in the fits.

The resulting isomer shifts follow the sequence $9d < 18f < 18h < 6c$ as observed in Tb₂Fe₁₇. Figure 3 shows the temperature dependence of the average isomer shift for the four compounds studied herein. It is clear that the 85 K weighted average isomer shift increases with silicon content from 0.038 mm/s at $x = 0$ to 0.112 mm/s at $x = 3$. A similar variation was observed^{7,8} in Nd₂Fe_{17-x}Si_x and Ce₂Fe_{17-x}Si_x. Figure 3 shows the temperature dependence of the weighted average hyperfine field. The decrease in the hyperfine field, ΔH , due to each silicon near neighbor at a given site, is ca. 16 kOe, a value^{7,8} which is typical of these solid solutions.¹⁵

The temperature dependence of the spectral hyperfine parameters, and their changes with x in Tb₂Fe_{17-x}Si_x, show an internal consistency in the series, agree well with previous results¹⁻⁸ obtained for similar R₂Fe_{17-x}M_x solid solutions, and agree with the magnetization measurements,¹³ measurements which indicate a maximum Curie temperature of 520 K for Tb₂Fe₁₄Si₃. This consistency will be discussed in detail in a future paper.¹³

In the experimental section, it was noted that a maximum of three silicon atoms per formula unit can be introduced into Tb₂Fe₁₇. In the fits of Tb₂Fe₁₄Si₃, a doublet with an isomer shift of 0.2 mm/s, a quadrupole splitting of 0.19

mm/s, and a relative area of 4%, had to be included at 85 K. Its parameters are consistent with the iron-silicon phase previously observed⁷ in Nd₂Fe_{17-x}Si_x. Both the formation of this stable impurity phase and the contraction of the unit cell lattice with increasing x may explain why no more than three silicon atoms can be substituted into Tb₂Fe₁₇.

The authors acknowledge with thanks the financial support of the Division of Materials Research of the U. S. National Science Foundation for Grant No. DMR-9521739, the Belgian *Fonds National de la Recherche Scientifique*, and the Dutch Technology Foundation (STW).

¹G. J. Long, G. K. Marasinghe, S. Mishra, O. A. Pringle, Z. Hu, W. B. Yelon, D. P. Middleton, K. H. J. Buschow, and F. Grandjean, *J. Appl. Phys.* **76**, 5383 (1994).

²G. K. Marasinghe, S. Mishra, O. A. Pringle, G. J. Long, Z. Hu, W. B. Yelon, F. Grandjean, D. P. Middleton, and K. H. J. Buschow, *J. Appl. Phys.* **76**, 6731 (1994).

³S. R. Mishra, G. J. Long, O. A. Pringle, D. P. Middleton, Z. Hu, W. B. Yelon, F. Grandjean, and K. H. J. Buschow, *J. Appl. Phys.* **79**, 3145 (1996).

⁴S. R. Mishra, G. J. Long, O. A. Pringle, G. K. Marasinghe, D. P. Middleton, K. H. J. Buschow, and F. Grandjean, *J. Magn. Magn. Mater.* **162**, 167 (1996).

⁵Z. Hu, W. B. Yelon, S. Mishra, G. J. Long, O. A. Pringle, D. P. Middleton, K. H. J. Buschow, and F. Grandjean, *J. Appl. Phys.* **76**, 443 (1994).

⁶G. J. Long, S. R. Mishra, O. A. Pringle, Z. Hu, W. B. Yelon, F. Grandjean, D. P. Middleton, and K. H. J. Buschow, *J. Magn. Magn. Mater.* **176**, 217 (1997).

⁷G. J. Long, G. K. Marasinghe, S. Mishra, O. A. Pringle, F. Grandjean, K. H. J. Buschow, D. P. Middleton, W. B. Yelon, F. Pourarian, and O. Isnard, *Solid State Commun.* **88**, 761 (1993).

⁸D. P. Middleton, S. R. Mishra, G. J. Long, O. A. Pringle, Z. Hu, W. B. Yelon, F. Grandjean, and K. H. J. Buschow, *J. Appl. Phys.* **78**, 5568 (1995).

⁹G. J. Long, O. A. Pringle, F. Grandjean, and K. H. J. Buschow, *J. Appl. Phys.* **72**, 4845 (1992).

¹⁰G. J. Long, T. E. Cranshaw, and G. Longworth, Mössbauer Effect Reference Data J. **6**, 42 (1983).

¹¹S. R. Mishra, Doctoral dissertation, University of Missouri-Rolla, 1996.

¹²L. Gelato, *J. Appl. Crystallogr.* **14**, 141 (1981).

¹³O. A. Pringle, G. J. Long, D. Hautot, H. Luo, W. B. Yelon, and K. H. J. Buschow, *J. Magn. Magn. Mater.* (in preparation).

¹⁴R. H. Herber, in *Chemical Mössbauer Spectroscopy*, edited by R. H. Herber (Plenum, New York, 1984), p. 199.

¹⁵B. Kolk, in *Dynamic Properties of Solids*, Vol. 5, edited by G. K. Horton and A. A. Maradudin (North Holland, Amsterdam, 1984), p. 5.

Asymmetric nonlinear magneto-optic effects in PtMnSb thin films

R. Carey,^{a)} D. M. Newman, and M. L. Wears

Centre for Data Storage Materials, Coventry University, Coventry CV1 5FB, United Kingdom

Nonlinear magneto-optic measurements on thin films of PtMnSb exhibit asymmetric behavior in both the transverse and longitudinal Kerr configurations. Second harmonic generation under magnetization reversal is asymmetric about the state of zero magnetization with the degree of asymmetry dependent on the angle of incidence. The origin of the asymmetry arises from simultaneous detection of even ($\propto M^2$) and odd ($\propto M$) magneto-optic effects. In principle such effects exist in both the optical linear and nonlinear regimes but in most materials even effects are very small and only observed in specific experimental arrangements where the linear effects in M vanish (such as the Voigt configuration). This is not the case with PtMnSb in which the band structure produces total polarization of the majority and minority spin carriers giving rise to unusually strong magneto-optic interactions. © 1998 American Institute of Physics.

[S0021-8979(98)44411-6]

INTRODUCTION

Pustogowa, Hubner, and Bennemann^{1,2} calculate magneto-optic effects in second harmonic generation (SHG) arising from the nonlinear interaction between an optical field and a magnetized medium. They show that such effects may be significantly larger than their linear counterparts. From quite general results they consider the possibility that materials with large spin-orbit coupling or large magnetic moments as in the Heusler alloys might exhibit large Kerr rotations in the second harmonic. Such expectations were subsequently confirmed experimentally for single crystals of Fe,³ Fe/Cu,⁴ and Rh/Co/Cu (Ref. 5) multilayers and also for the Heusler alloy PtMnSb.⁶

PtMnSb is a half-metallic ferromagnet that, in its crystalline stoichiometric form, exhibits the largest magneto-optic effects yet recorded at room temperature. In most experimental configurations the changes observed in a linear optical field reflected from or transmitted through the medium being subjected to magnetization reversal are typically an order of magnitude greater than those observed for iron. Following Pustogowa *et al.* magneto-optic effects observed in the SHG field from PtMnSb are expected to be larger still. Reif, Rau, and Matthias,⁶ reporting the only nonlinear magneto-optic studies of PtMnSb to date, investigated circular magnetic dichromism and the longitudinal Kerr effect at one angle of incidence (75°) for the (111) surface of a single crystal. On reversal of the magnetization they recorded a 7% change in detected SHG intensity for circularly polarized radiation and a Kerr rotation of 14° for linearly polarized radiation.

Following our previous extended studies of thin films of PtMnSb,⁷⁻¹⁰ this article reports our recent investigation of

the nonlinear magneto-optic behavior of thin films of PtMnSb in the transverse Kerr configuration. In addition, the circular dichroism measurements reported by Reif *et al.* are repeated and extended to other angles of incidence.

In the linear optical regime it is usual to describe the magneto-optic interaction, in the transverse Kerr configuration, in terms of δ , the fractional change in the detected reflected intensity, defined as

$$\delta = \frac{I_{Ms}^{\uparrow} - I_{Ms}^{\downarrow}}{I_{Ms}^{\uparrow} + I_{Ms}^{\downarrow}},$$

where I_{Ms}^{\uparrow} and I_{Ms}^{\downarrow} are the intensities associated with opposite states of in-plane magnetic saturation, normal to the plane of incidence. This definition can similarly be used to describe transverse Kerr effects nonlinear in the optical field:

$$\delta_{\text{SHG}} = \frac{Y_{Ms}^{\uparrow} - Y_{Ms}^{\downarrow}}{Y_{Ms}^{\uparrow} + Y_{Ms}^{\downarrow}}$$

where Y_{Ms}^{\uparrow} and Y_{Ms}^{\downarrow} are now the detected SHG yields associated with the opposite states of magnetic saturation. In both the linear and nonlinear cases the detected intensity changes are expected to be symmetrical about the reflected intensity or SHG yield when the sample magnetization is zero along a direction perpendicular to the plane of incidence, $I_{M=0}$ and $Y_{M=0}$, respectively. Note that because the structure of PtMnSb is noncentrosymmetric the SHG yield will contain both bulk and surface contributions.

EXPERIMENT

The PtMnSb films used in this study were prepared by magnetron sputtering from individual targets of Pt and MnSb (50:50 at. %) onto a rotating substrate. As deposited, the films were amorphous and were subsequently crystallized by rapid thermal processing (RTP) in vacuum using a

^{a)}Electronic mail: r.carey@coventry.ac.uk

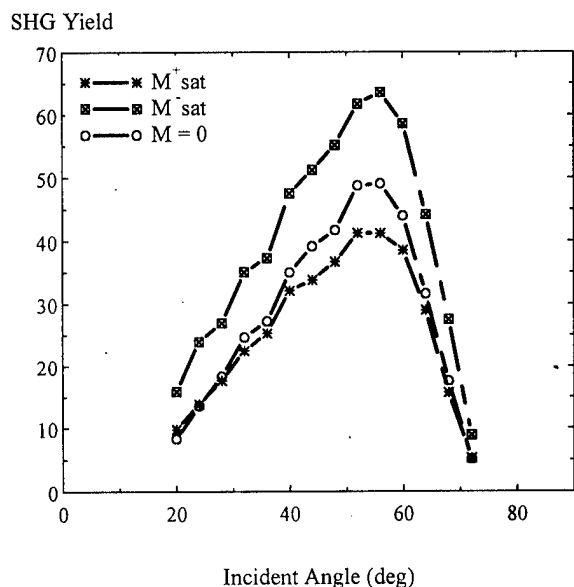


FIG. 1. Asymmetry in the SHG yield under magnetization reversal in the transverse Kerr configuration.

60 W CO₂ laser. X-ray diffraction analysis showed the resulting samples to be composed of very fine crystallites with the (111) surface predominant. With a thickness of 190 nm the films were just semitransparent. In the linear magneto-optic regime they exhibited a polar Kerr rotation of 1.8° at a wavelength (λ) of 670 nm and in the transverse Kerr configuration a fractional change in reflected intensity of 2.5% at $\lambda = 532$ nm.

Nonlinear magneto-optic measurements were made using a Minilite Nd:Yag ($\lambda = 1064$ nm) laser emitting Q-switched 5 ns, 25 mJ pulses at a repetition rate of 10 Hz to produce a power density of 70×10^6 W cm⁻² at the film surface. Appropriate filters were used to block SHG signals produced by the input optical train and also to isolate the fundamental from the photomultiplier detector.

Prior to making magneto-optic measurements the polarization of the SHG signal from a demagnetized sample was studied as a function of the polarization of the 1064 nm (fundamental) beam. The SHG yields Y_{Ms}^{\uparrow} , Y_{Ms}^{\downarrow} , and $Y_{M=0}$ were then recorded as a function of the angle of incidence using *p*-polarized radiation in the transverse configuration and both left and right circularly polarized beams in the longitudinal configuration. The values presented for these parameters are averages obtained over 500 pulses recorded using a Lecroy digital oscilloscope.

RESULTS AND DISCUSSION

In the polarization studies from demagnetized samples we found, as previously observed by Reif, Rau, and Matthias,⁶ that the SHG output beam was *p* polarized for both *p* and *s* input polarization. The efficiency of the SHG process was, however, greatly reduced when the fundamental input beam was *s* polarized.

Figure 1 shows the behavior of the SHG ($\lambda = 532$ nm) yield under magnetization reversal in the transverse Kerr configuration as a function of angle of incidence. The yield

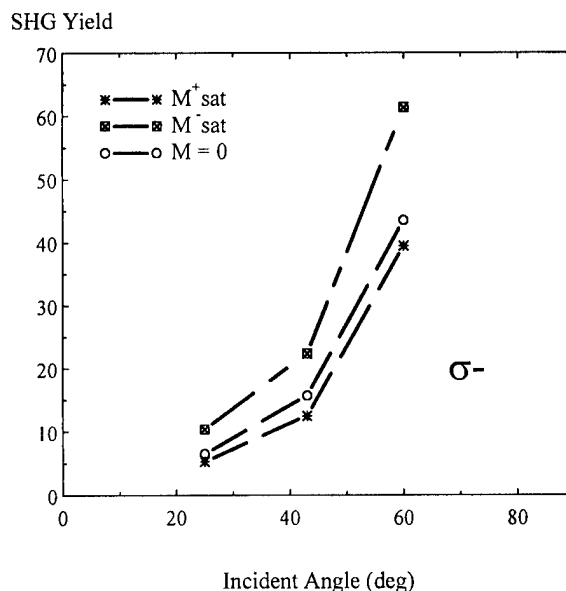


FIG. 2. Asymmetric changes in SHG yield for left circularly polarized radiation in the longitudinal Kerr configuration.

for the two states of magnetic saturation is seen to be quite asymmetrical about that of the demagnetized state. The transverse effect with *s*-polarized input radiation is not actually forbidden in the SHG field as it is for the linear field but no measurable magneto-optic interaction was observed.

The asymmetry is also apparent in the longitudinal configuration. Figure 2 shows the results taken using left circularly polarized input radiation. Essentially identical results are obtained using right circularly polarized radiation. A similar asymmetry is just discernible in the raw data of Reif, Rau, and Matthias.⁶ Using the definition of Reif *et al.* for the fractional change (Δ) in detected intensity due to circular magnetic dichroism we obtain values for Δ greater than 42% at 60° angle of incidence. This is considerably larger than the 7% they reported at a wavelength of 266 nm and a 75° angle of incidence. The difference is probably a conse-

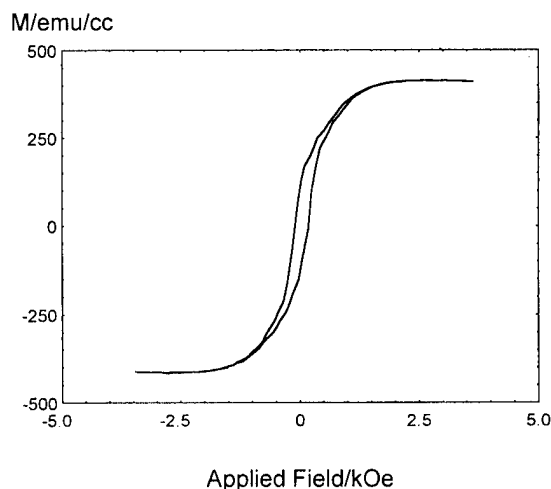


FIG. 3. Magnetic hysteresis loop of the sample used for the nonlinear magneto-optic experiments.

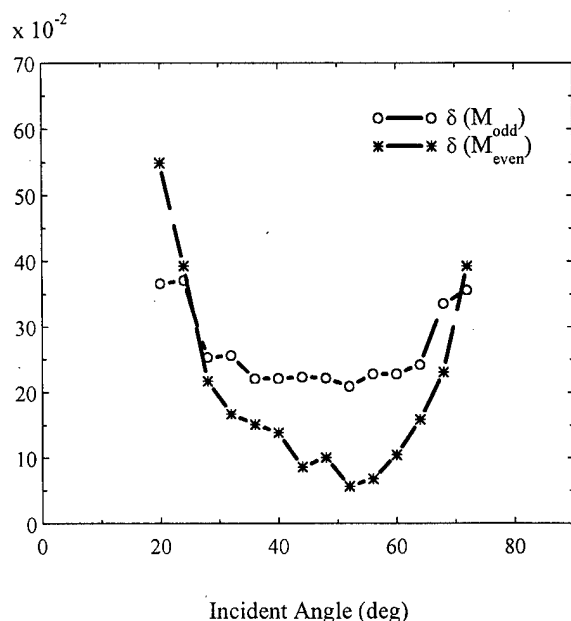


FIG. 4. Odd and even contributions to the fractional intensity change in the SHG field as a result of magneto-optic interactions observed in the transverse Kerr configuration.

quence of the different wavelengths at which the measurements are made and of possible enhancement within the thin film structure of our samples.

In discussing nonlinear magneto-optic effects most workers assume quadrupole interactions to be negligible and, following Pan, Wei, and Shen,¹¹ separate the geometry dependent elements of the dipole nonlinear susceptibility tensor into two classes, odd and even with respect to magnetization (\mathbf{M}) reversal about a given direction. There is often a tendency to assume that even susceptibility elements are small and may be ignored or incorporated with the nonmagnetic contribution to the nonlinear susceptibility.³ With most of the simple ferromagnetics the former assumption is valid as evidenced by the magnetic hysteresis loops recorded for Fe (Ref. 3) and Co/Cu (Ref. 12) multilayers using the nonlinear Kerr effect. Any significant \mathbf{M}^2 or higher (even) order in \mathbf{M} contribution to the detected SHG signal would distort the hysteresis loops obtained. For the PtMnSb films reported here it is clear that, although the magnetic behavior of the samples is perfectly conventional (see Fig. 3), the detected SHG signal is not a simple linear function of sample magnetization for either the transverse or the longitudinal configurations. The presence of a significant even ($\propto \mathbf{M}^2$) contribution to the detected signal immediately explains the

asymmetric nature of the results of Figs. 1 and 2. Assuming the odd ($\propto \mathbf{M}$) contribution to the yield is symmetrical about the $Y_{M=0}$ yield, separation of the odd and even contributions is straightforward and fractional changes in the SHG yield of each component are readily achieved. These are shown in Fig. 4 where odd ($\delta(M_{\text{odd}})$) and even ($\delta(M_{\text{even}})$) contributions to the observed δ_{SHG} are plotted as a function of angle of incidence.

It can be seen that the odd and even contributions are very large (cf. 25%) and of similar magnitude. Both the odd and even contributions in the nonlinear (SHG) field are at least an order of magnitude greater than those observed in linear field measurements. To our knowledge values $>50\%$ for the fractional change in any even (\mathbf{M}) magneto-optic effects are hitherto unreported. It therefore seems very likely that even (\mathbf{M}) magneto-optic effects in the linear field measurements for PtMnSb will also be large. Our initial measurements indicate that this is indeed the case and odd and even effects again contribute to the detected signal.

CONCLUSION

Asymmetry in the magneto-optic transverse Kerr effect in second harmonic generation from PtMnSb thin films has been shown to originate in signals that are odd and even in the sample magnetization and comparable in size. Magneto-optic effects in PtMnSb are measured to be at least an order of magnitude greater in the SHG field than in the normal linear field as was predicted by Pustogowa *et al.*¹ The measurements of the even (\mathbf{M}) components in the SHG field are believed to be the first of their kind to be reported.

¹U. Pustogowa, W. Hubner, and K. H. Bennemann, Phys. Rev. B **49**, 10 031 (1994).

²U. Pustogowa, W. Hubner, and K. H. Bennemann, Appl. Phys. A: Solids Surf. **59**, 611 (1994).

³R. Vollmer, M. Straub, and J. Kirschner, J. Magn. Soc. Jpn. **20**, 29 (1996).

⁴B. Koopmans, M. G. Koerkamp, and T. Rasing, Phys. Rev. Lett. **74**, 3692 (1995).

⁵R. Stolle, K. J. Veenstra, F. Manders, T. Rasing, H. Van den Berg, and N. Persat, Phys. Rev. B **55**, R4925 (1997).

⁶J. Reif, C. Rau, and E. Matthias, Phys. Rev. Lett. **71**, 1931 (1993).

⁷G. S. Bains, R. Carey, D. M. Newman, and B. W. J. Thomas, Jpn. J. Appl. Phys., Part 1 **6**, 46 (1991).

⁸G. S. Bains, R. Carey, D. M. Newman, and B. W. J. Thomas, J. Magn. Mater. **104-107**, 1011 (1992).

⁹R. Carey, H. Jenniches, D. M. Newman, and B. W. J. Thomas, J. Magn. Soc. Jpn. **17**, 290 (1993).

¹⁰R. Carey, H. Jenniches, D. M. Newman, and B. W. J. Thomas, J. Appl. Phys. **75**, 7081 (1994).

¹¹R.-P. Pan, H. D. Wei, and Y. R. Shen, Phys. Rev. B **39**, 1229 (1989).

¹²H. A. Wierenga, W. de Jong, M. W. J. Prins, Th. Rasing, R. Vollmer, A. Kirilyuk, H. Schwabe, and J. Kirschner, Phys. Rev. B **74**, 1362 (1995).

Anisotropic third-order magneto-optical Kerr effect

A. V. Petukhov^{a)} and Th. Rasing

Research Institute for Materials, 6525 ED Nijmegen, The Netherlands

T. Katayama

Electrotechnical Lab. Tsukuba-shi, Ibaraki 305, Japan

N. Nakajima

Photon Factory, National Laboratory, High Energy Physics, Tsukuba-shi, Ibaraki 305, Japan

Y. Suzuki

JRCAT-NAIR, Tsukuba-shi, Ibaraki 305, Japan

The magnitude of the polar magneto-optical Kerr effect in reflection from thick iron epitaxial films is experimentally found to strongly depend on the crystallographic orientation of the film, with variations of more than 20%. Similar results are obtained on the (001) and (110) faces of a bulk Fe crystal. It is shown that this anisotropy can be described as a third-order effect in the magnetization \mathbf{M} on the optical response $\epsilon(\omega, \mathbf{M})$. Our analysis can also be used to understand the transversal Kerr effect at normal incidence recently observed by Gridnev *et al.* © 1998 American Institute of Physics. [S0021-8979(98)46611-8]

Magneto-optics provides a simple and quite universal way to probe the magnetization \mathbf{M} of a ferromagnetic medium.¹⁻⁴ Most of the magneto-optical phenomena arise due to the effect of \mathbf{M} on the dielectric constant of a medium $\epsilon(\mathbf{M})$. Assuming that this effect is weak, the $\epsilon(\mathbf{M})$ dependence is often expanded in powers of \mathbf{M} yielding⁵

$$\vec{\epsilon}(\mathbf{M}) = \vec{\epsilon}^{(0)} + 4\pi i \mathbf{f} \cdot \mathbf{M} + 4\pi \mathbf{g} : \mathbf{M}\mathbf{M} + 4\pi i \mathbf{h} : \mathbf{M}\mathbf{M}\mathbf{M} + \dots, \quad (1)$$

where $\epsilon^{(0)}$ denotes the magnetization-independent part of $\epsilon(\mathbf{M})$ and the tensors \mathbf{f} , \mathbf{g} , and \mathbf{h} describe the linear-, second-, and third-order magnetization-induced corrections to the dielectric function of the magnetic medium. So far the main attention has been paid to the magneto-optical effects arising via the second and third term in Eq. (1). For instance, to describe magnetic circular dichroism (MCD) it is usually enough to account for the term $4\pi i \mathbf{f} \times \mathbf{M}$ that is linear in the magnetization. Upon light reflection, MCD results in the magneto-optical Kerr effect (MOKE) which is used to study magnetism in opaque media.¹ The second-order magnetization-induced term $4\pi \mathbf{g} : \mathbf{M}\mathbf{M}$ results in the linear birefringence.² Higher order terms in \mathbf{M} in Eq. (1) are usually neglected. However, they may result in new magneto-optical effects and thus become important. In particular, a third-order contribution ($\propto \mathbf{h}$) to Eq. (1) has been recently observed by Gridnev *et al.*⁶ to contribute to the transversal magneto-optical Kerr effect upon light reflection from the (111) face of LiFe_5O_8 .

In this work we analyze novel magneto-optical effects that can originate via higher-order (and anisotropic) contributions in the magnetization dependence of the dielectric response in cubic media. In particular, these contributions can describe experimentally observed anisotropy of the magneto-optical Kerr rotation in reflection from (001) and

(110) oriented iron epitaxial films and (001) and (110) faces of a bulk Fe crystal. A similar effect has also been observed on epitaxial hcp Co films,³ where the anisotropy is linear in the magnetization.^{3,4} For cubic bcc iron, however, this linear effect is forbidden by symmetry and the anisotropy can be understood as a third-order effect of the magnetization. We also demonstrate how the orientation dependence of the polar MOKE is related to the transversal third-order MOKE observed in Ref. 6.

The epitaxial Fe(001) and (110) films with the thickness 700–1000 Å were grown on Au(001) and Au(111) buffer layers as described in Ref. 7. The bulk samples were prepared by cutting an iron single crystal along (001) and (110) planes with subsequent polishing by a diamond paste. The MOKE spectra of epitaxial Fe films were measured in the range of 4–10 eV using the synchrotron facility described in Ref. 8. Similar measurements in the range 1.55–6 eV on epitaxial films and bulk samples were done on a Kerr spectrometer.

In Fig. 1 we show the spectra of the Kerr rotation angle ϕ_K and the Kerr ellipticity η_K measured on thick Fe epitaxial films with the (001) and (110) orientation. A strong anisotropy $\Delta\phi_K = \phi_K^{(001)} - \phi_K^{(110)}$ and $\Delta\eta_K = \eta_K^{(001)} - \eta_K^{(110)}$ is

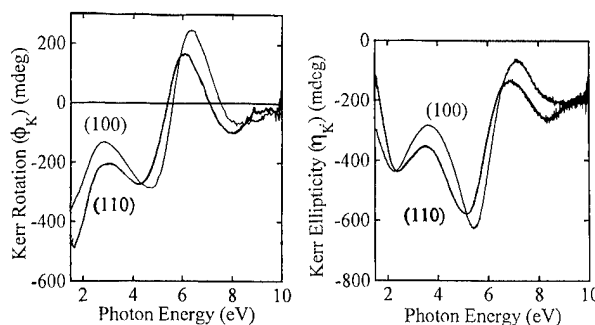


FIG. 1. The Kerr rotation (left panel) and Kerr ellipticity (right panel) spectra measured on epitaxial Fe(001) and Fe(110) films.

^{a)}On leave from the Institute of Crystallography, Moscow, Russia; electronic mail: petukhov@sci.kun.nl

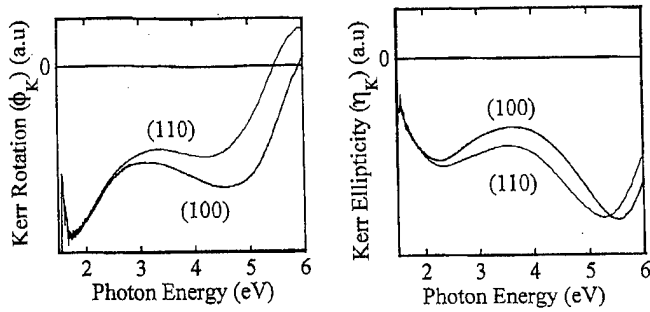


FIG. 2. The same as in Fig. 1 but measured on two faces of a bulk iron crystal.

clearly seen. For the thick Fe films the effect of quantum well states should be negligible and the natural explanation of this anisotropy could then be a difference in the structure of the two studied films. For instance, a different strain of the Fe lattice may affect the magneto-optical parameters. Alternatively, one can think about a different roughness of the different film surfaces as a possible source of the orientation dependence of MOKE.

However, an additional study performed on different faces of iron bulk single crystals contradicts this simple explanation. In Fig. 2 we show the MOKE spectra measured upon light reflection from Fe(001) and Fe(110). In this case the effect of the lattice strain should be much smaller, if not negligible, in comparison to that expected in epitaxial films. The surface (micro-) roughness of the faces of the bulk crystal, which can result from the sample polishing, is obviously expected to be distinctly different from the surface (micro-) roughness of epitaxial films which can arise during the film growth. However, the great similarity between the results presented in Figs. 1 and 2 is obvious. Only at small photon energies $\hbar\omega \leq 2$ eV there is a clear anisotropy found for the epitaxial films while the single crystal faces do not show this. This observation strongly suggests that the MOKE anisotropy at $\hbar\omega > 2$ eV is an intrinsic effect of a perfect Fe crystal rather than related to the mechanisms described above.

For cubic media the first two tensors $\vec{\epsilon}^{(0)}$ and \mathbf{f} in the expansion (1) reduce to scalars ϵ_0 and f_0 times the unity symmetric and antisymmetric tensors, respectively. Therefore, up to the term linear in the magnetization, the relation between the induction $\mathbf{D}(\omega)$ and the electric field $\mathbf{E}(\omega)$ of the light wave can be written in a vector form:

$$\mathbf{D} = \epsilon_0 \mathbf{E} + 4\pi i f_0 \mathbf{E} \times \mathbf{M}. \quad (2)$$

Although MCD depends on the mutual orientation of the light propagation direction and the magnetization \mathbf{M} , within the approximation of Eq. (2) MCD is isotropic in a sense that it does not depend on the orientation of \mathbf{E} and \mathbf{M} relative to the crystallographic axes. Therefore, to describe the anisotropic MCD effect in a cubic medium one has to account for the higher-order terms in the expansion (1), which are *anisotropic* even in high-symmetry cubic media. The second-order term $4\pi g_{ijkl} M_k M_l$ is even in the magnetization and therefore cannot contribute to MCD. In order to account for the anisotropy of MCD one therefore has to consider the third-order term.

In general, an axial fifth-rank tensor in a cubic medium has ten independent nonvanishing elements.⁹ The permutation symmetry of h_{ijklm} with respect to the last three indices and the Onsager symmetry $h_{ijklm} = -h_{jiklm}$ reduces this number to only 2. In the following it is convenient to introduce a contracted notation. We define a ten-dimensional vector \mathbf{MMM} with components

$$\mathbf{MMM} = \begin{pmatrix} M_1^3 \\ M_2^3 \\ M_3^3 \\ 3M_2 M_3^2 \\ 3M_3 M_1^2 \\ 3M_1 M_2^2 \\ 3M_3 M_2^2 \\ 3M_1 M_3^2 \\ 3M_2 M_1^2 \\ 6M_1 M_2 M_3 \end{pmatrix}, \quad (3)$$

where M_1 , M_2 , and M_3 denote the projections of \mathbf{M} on the principal crystallographic axes [100], [010], and [001]. The axial fifth-rank tensor \mathbf{h} can then be written as a third-rank tensor κ_{ijk} where the last index K runs from 1 to 10. The nonvanishing elements of κ_{ijk} are

$$\kappa_1 \equiv \kappa_{123} = \kappa_{231} = \kappa_{312} = -\kappa_{132} = -\kappa_{213} = -\kappa_{321}, \quad (4)$$

$$\begin{aligned} \kappa_2 \equiv \kappa_{127} = \kappa_{238} = \kappa_{319} = -\kappa_{139} = -\kappa_{328} = -\kappa_{217} \\ = \kappa_{125} = \kappa_{236} = \kappa_{314} = -\kappa_{134} = -\kappa_{326} = -\kappa_{215}. \end{aligned}$$

For isotropic media the same elements of κ_{ijk} are nonvanishing but the number of independent elements is reduced to one because of an extra relation $\kappa_1 = 3\kappa_2$ between the κ_1 and κ_2 elements. In cubic media the anisotropic element $\kappa_{an} = \kappa_1/3 - \kappa_2 \neq 0$ leads to the anisotropy in MCD.

Now we introduce the laboratory coordinate system (xyz), where the z axis is normal to the surface and along the magnetization vector $\mathbf{M} = \mathbf{e}_z M$. The transformation matrix \mathbf{A} from the crystallographic (123) to the laboratory (xyz) frame is taken in the form

$$\mathbf{A} = \begin{pmatrix} \cos \theta \sin \psi & \cos \theta \cos \psi & -\sin \theta \\ -\cos \psi & \sin \psi & 0 \\ \sin \theta \sin \psi & \sin \theta \cos \psi & \cos \theta \end{pmatrix}, \quad (5)$$

where the angles θ and ψ determine the orientation of the surface normal \mathbf{e}_z with respect to the crystallographic axes. Using Eqs. (4) and (5) one can find the xy element of $\vec{\epsilon}(\mathbf{e}_z M)$:

$$\begin{aligned} \epsilon_{xy}(\mathbf{e}_z M) = 4\pi i [f_0 M + \kappa_1 M^3 - 6\kappa_{an} \sin^2 \theta (\cos^2 \theta \\ + \sin^2 \theta \cos^2 \psi \sin^2 \psi) M^3] \end{aligned} \quad (6)$$

that determines the MCD for light propagating along z . The last term in Eq. (6) is *anisotropic*, i.e., it depends on the orientation of the surface relative to the cubic frame. For the (001) face $\theta = 0$ and Eq. (6) yields

$$\epsilon_{xy}^{(001)}(\mathbf{e}_z M) = 4\pi i [f_0 M + \kappa_1 M^3] \quad (7)$$

while for the (110) face $\theta = \pi/4$, $\psi = 0$ and

$$\epsilon_{xy}^{(110)}(\mathbf{e}_z M) = 4\pi i [f_0 M + \kappa_1 M^3 - \frac{3}{2} \kappa_{an} M^3]. \quad (8)$$

Obviously, $\epsilon_{xy}^{(001)} \neq \epsilon_{xy}^{(110)}$ and the third-order term in expansion (1) can describe the observed anisotropy.

The analysis above can also be used to describe the observed third-order *transversal* ($\mathbf{k} \perp \mathbf{M}$, where \mathbf{k} denotes the light wave vector) Kerr effect reported in Ref. 6. We take the light incident along the surface normal z and the magnetization parallel to the surface $\mathbf{M} = \mathbf{e}_x M$. In cubic media the linear in the magnetization contribution $i f_0 \mathbf{E} \times \mathbf{M}$ to the induced polarization is then always along \mathbf{k} and, therefore, does not radiate into the direction of light propagation. The second-order contribution $\mathbf{g}:\mathbf{M}\mathbf{M}$ is reciprocal and cannot contribute to the MCD and one again arrives to the third-order term which gives rise to the transversal MCD via

$$\epsilon_{xy}(\mathbf{e}_x M) = h_{xyxxx} M^3, \quad (9)$$

where $h_{xyxxx} = \kappa_{an} f(\theta, \psi, \phi)$ denotes the magnitude of the corresponding tensor element in the laboratory coordinate system which depend on the relative orientation of the two frames given by the Euler angles θ , ψ , and ϕ , where the additional angle ϕ describes the azimuthal orientation of the sample which becomes important for the transversal geometry. We note that this transversal MCD vanishes on the even-fold rotation symmetry (001) and (110) faces of cubic fcc and bcc crystals. Indeed, the rotation of the sample by π reverses the direction of $\mathbf{M} = \mathbf{e}_x M$ while ϵ_{xy} and h_{xyxxx} should be unchanged since $(x, y) \rightarrow (-x, -y)$ is a symmetry operation for these faces and $\epsilon_{xy}(\mathbf{e}_x M)$ should therefore vanish for any ϕ . For other faces the transversal MCD is present. For instance, for the (111) face one can calculate the function $f(\theta, \psi, \phi)$ to obtain

$$\epsilon_{xy}(\mathbf{e}_x M) = -\frac{4\pi i}{\sqrt{2}} \kappa_{an} M^3 \sin 3\phi. \quad (10)$$

Note that this effect is anisotropic during azimuthal rotation

of the sample. It vanishes every time when the magnetization is normal to one of the mirror symmetry planes (011), (101), and (110) of the (111) face. Comparing Eqs. (7), (8), and (10) one can see that a measurement of the transversal MOKE on Fe(111) similar to that done by Gridnev *et al.*⁶ can be used for an unambiguous verification of the mechanism of the anisotropy of the polar Kerr effect proposed in this work.

In conclusion, we have observed a strong surface orientation dependence of the magneto-optical Kerr effect in the polar configuration that can be understood as a third-order effect in the magnetization on the optical response. We give a phenomenological description of this effect, which can also explain the transversal Kerr effect at normal incidence on odd-fold symmetry faces of a cubic crystal observed by Gridnev *et al.*

Fruitful discussions with Roman V. Pisarev and Andrei Kirilyuk are acknowledged. The present work was partially supported by the HCM fellowship ERBCHICT-941761 and TMR network "NOMOKE."

¹U. Gradmann, J. Magn. Magn. Mater. **100**, 481 (1991); D. Bader, *ibid.* **100**, 440 (1991).

²See, e.g., J. Ferré and G. A. Gehring, Rep. Prog. Phys. **47**, 513 (1984).

³D. Weller, G. R. Harp, R. F. C. Farrow, A. Cebollada, and J. Sticht, Phys. Rev. Lett. **72**, 2097 (1994).

⁴P. M. Oppeneer, T. Kraft, and H. Eschrig, Phys. Rev. B **52**, 3577 (1995).

⁵L. D. Landau and E. M. Lifshitz, *Electrodynamics of Continuous Media* (Pergamon, New York, 1960).

⁶V. N. Gridnev, B. B. Krichevskii, V. V. Pavlov, and R. V. Pisarev, Pis'ma Zh. Eksp. Teor. Fiz. **65**, 65 (1997) [JETP Lett. **65**, 68 (1997)]. Note that the magnetoelectric contribution to the optical response, which is also observed in this work, is forbidden in centrosymmetric iron.

⁷T. Katayama, N. Nakajima, N. Okusawa, Y. Miyauchi, T. Koide, T. Shidara, Y. Suzuki, and S. Yuasa, J. Magn. Magn. Mater. (in press).

⁸T. Sugimoto, T. Katayama, Y. Suzuki, T. Koide, T. Shidara, M. Yuri, A. Itoh, and K. Kawanishi, Phys. Rev. B **48**, 16 432 (1993).

⁹A. V. Petukhov, I. L. Lyubchanskii, and Th. Rasing, Phys. Rev. B **56**, 2680 (1997).

Magneto-optical properties of MnPt_3 : LDA+ U calculations

R. F. Sabiryanov and S. S. Jaswal^{a)}

*Department of Physics and Astronomy and Center for Materials Research and Analysis,
University of Nebraska, Lincoln, Nebraska 68588-0111*

Our recent first-principle LMTO-ASA calculations of the magneto-optical properties of MnPt_3 are in good agreement with the experimental data. However, the calculated positions of the Kerr-rotation peaks are shifted by approximately 0.5 eV with respect to the experimental results. An interesting feature in the density of states (DOS) of MnPt_3 is the narrow unoccupied peak in the minority Mn d DOS signifying the fairly localized nature of these states. Usually the study of the optical properties of systems with localized states requires the inclusion of correlation effects beyond the LDA through the Hubbard U parameter. We report here a study of the effect of U and the energy expansion parameter E_v in LMTO for the minority Mn d states on the calculated Kerr spectra of MnPt_3 . It is found that a reasonable choice of E_v gives the Kerr effect in good agreement with the experimental data without the need to use the U parameter. © 1998 American Institute of Physics. [S0021-8979(98)21811-1]

I. INTRODUCTION

Ferromagnetic compounds containing manganese and platinum have attracted considerable interest recently because of their large Kerr rotation. MnPt_3 and MnPtSb have Kerr rotation of 1.2° at 1.2 and 1.7 eV photon energies, respectively. The first-principle calculations of the Kerr effect in these compounds have been performed by a number of authors during the last three years using the local density approximation (LDA).¹⁻³ The calculated Kerr rotation as a function of the photon energy is in good agreement with the experiment. However, the position of the main peak, mentioned above, is shifted to the lower photon energy by 0.4–0.7 eV. The reasons for this shift are not well understood. The densities of states (DOS) of these compounds are similar. Both have large localized peaks of unoccupied states above the Fermi energy in the minority Mn d DOS well separated from the occupied states. The results of the electronic structure calculations show that MnPtSb in the ground state is half-metallic, i.e., it has a gap at the Fermi energy (E_F) in the minority spin states and no gap for majority spin states.¹⁻³ MnPt_3 is almost half-metallic with very low minority DOS around E_F .¹ It is well known that LDA fails to describe properly the optical properties of systems with highly localized states. Recently, LDA+ U approach has been used to get an improved description of the properties of some of the systems with localized states, where the Hubbard parameter U simulates correlations beyond the LDA.⁴ Another important parameter is the energy E_v about which expansion is carried out in the linear-muffin-tin-orbital (LMTO) method. Normally, E_v corresponds to the center of mass of the occupied states for a given orbital. Since the minority Mn d DOS primarily consists of a fairly localized and unoccupied band, the E_v should be the center of mass of the whole minority d band. This was not done in our earlier calculations. Therefore we study here the effect of U and E_v

for the minority Mn d band on the calculated Kerr rotation of MnPt_3 and the results are compared with the experimental data.

II. METHOD

The LMTO method in the atomic sphere approximation (LMTO-ASA) is used to perform the self-consistent spin-polarized electronic structure calculations for all results presented here, where the spin-orbit interaction is included in quasiperturbative manner.⁵ The details of the electronic structure calculations and procedure to calculate the Kerr effect are given in Ref. 1. The lifetime parameter for the interband contribution (\hbar/τ) is 0.4 eV. The collision frequency parameter (\hbar/γ) and the plasma frequency ($\hbar\omega_p$) are 0.3 and 4.4 eV, respectively. The procedure to calculate the U parameter is quite standard and a complete description can be found in Ref. 6. The calculated U parameter is included in the LMTO code to take into account the correlation effects beyond the LDA.^{4,6}

III. RESULTS AND DISCUSSION

Our recently calculated Kerr spectra for MnPt_3 obtained using the LDA show a good agreement with experimental data except for an overall shift of about 0.5 eV.¹ The present study is an attempt to improve upon this disagreement by the modifications to the calculational procedure commensurate with the electronic structure of this system. As mentioned in the introduction, we explore here the effect of E_v and U on the Kerr spectra of MnPt_3 .

The main contribution to Kerr effect at low energies is due to the p – d transitions on Pt sites. The effect of the Mn atoms is to provide large exchange splitting. If the spin-flip transitions are neglected, the contributions from minority and majority spin channels can be found and this analysis shows that the Kerr effect is determined mostly by the majority spins for energies below 1.3 eV and by the minority spins above this energy. This effect is due to the peculiarities of

^{a)}Electronic mail: sjaswal@unlinfo.unl.edu

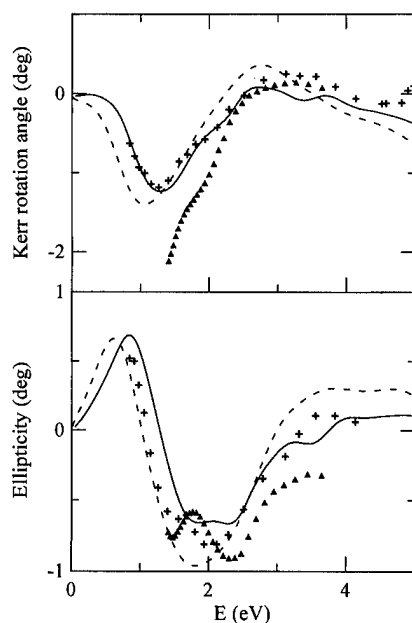


FIG. 1. Kerr rotation and ellipticity of MnPt_3 : Theory—solid line gives the results with E_v at the center of mass of the whole minority Mn d band and dashed line with E_v at the center of mass of the occupied band; experiment—triangles represent the 95 K data from Ref. 1 and crosses represent the room temperature experimental results from Ref. 7.

the electronic structure. Minority band has a very narrow localized peak about 1.5 eV above the Fermi energy. This peak is determined mainly by the Mn d states, but Pt p and d states also have peaks at this energy due to the hybridization effect. Majority spins have very small DOS in this energy region.

The calculated Kerr spectra for two values of E_v are compared with the experimental data in Fig. 1. The dashed line corresponds to our earlier spectra that are shifted with respect to the experimental data by ~ 0.5 eV. This is based on the E_v that is the center of mass of the occupied minority Mn d band. Because this band is mostly unoccupied, a better choice of E_v is the center of mass of the whole band. This produces an upward shift of E_v by 3.44 eV. The solid line in Fig. 1 is based on this value of E_v and is in much better agreement with the experimental data than that based on the previous choice of E_v . With the new E_v magnetic moment changes from 3.6 to $3.66\mu_B$.

In an attempt to further improve the agreement between theory and experiment, we use the LDA+ U Hamiltonian where U is for the Mn d states. The U parameter is calculated using constrained LMTO formalism in the atomic limit.⁶ The value of U for the d^5 and d^6 configurations are 5.7 and 4.7 eV, respectively, while $J \sim 0.8$ eV for both configurations. Since the Mn d occupancy in MnPt_3 is about 5.4, we use a value of 5 eV for U in one of the calculations. The calculated Kerr spectra are shown in Fig. 2. As can be seen

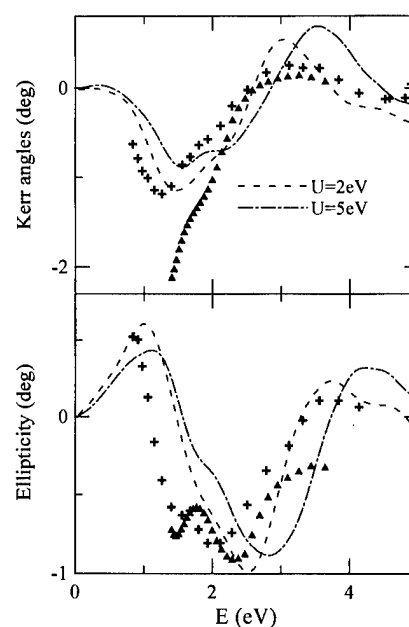


FIG. 2. Kerr rotation and ellipticity of MnPt_3 as a function of U obtained in LDA+ U calculations. Experimental curves are the same as in Fig. 1.

in Fig. 2, the disagreement between theory and experiment gets worse than before. A lower value of U (2 eV) improves the result somewhat (Fig. 2) but the agreement with the experiment is still worse than that without U . It can be seen from Figs. 1 and 2 that a small value of U can be chosen to remove the wiggle around 3.5 eV in the Kerr spectra without affecting the rest of the spectra.

In conclusion, the Kerr spectra of MnPt_3 are better described by LDA if LMTO linearization is done about the center of mass of the whole minority Mn d band instead of the occupied part only. The correlation effects beyond LDA introduced by the Hubbard term in the Hamiltonian do not play a significant role in this system. This should also be true for the Mn-based Heussler alloys with similar electronic structure.

ACKNOWLEDGMENT

This work is supported by the National Science Foundation under Grant Nos. OSR-9255225 and DMR-9705044.

¹K. W. Wierman, J. N. Hilfiker, R. F. Sabiryanov, S. S. Jaswal, R. D. Kirby, and J. A. Woollam, Phys. Rev. B **55**, 3093 (1997).

²P. M. Oppeneer, V. N. Antonov, T. Kraft, H. Eschrig, A. N. Yaresko, and A. Ya. Perlov, J. Phys.: Condens. Matter **8**, 5769 (1996).

³J. van Ek and J. M. Maclaren, Phys. Rev. B **56**, R2924 (1997).

⁴V. I. Anisimov, I. V. Solovyev, M. A. Korotin, M. T. Czyzyk, and G. A. Sawatzky, Phys. Rev. B **48**, 16929 (1993).

⁵O. K. Andersen, Phys. Rev. B **12**, 3060 (1975).

⁶I. V. Solovyev, P. H. Dederichs, and V. I. Anisimov, Phys. Rev. B **50**, 16861 (1994).

⁷T. Kato, H. Kikuzawa, S. Iwata, S. Tsunashima, and S. Uchiyama, J. Magn. Magn. Matter. **140–144**, 713 (1995).

Thickness dependence of interfacial magneto-optic effects in Pt/Co multilayers

Xiang Gao,^{a)} Michael J. DeVries, Daniel W. Thompson, and John A. Woollam
*Center for Microelectronic and Optical Materials Research and Department of Electrical Engineering,
 University of Nebraska, Lincoln, Nebraska 68588-0511*

Spectroscopic ellipsometry and magneto-optic Kerr effects are measured on Pt/Co multilayers with a series of Co layer thicknesses from 0.08 to 1 nm. An electromagnetic theory of multilayered structures allows regression analysis fits between acquired data and parameter dependent model analysis. Recently, we determined the single layer Co magneto-optic Voigt parameter and found that it depends on Co layer thickness. In the present work, we report an in-depth study of interfacial magneto-optic effects for a large number of Pt/Co multilayer samples. Kerr rotation and ellipticity were measured over the spectral range from 200 to 1700 nm. Voigt parameters of the magnetic layers for these Pt/Co multilayer samples with different thicknesses were compared, and the Pt-Co interface thicknesses were determined in terms of the material dielectric tensor. © 1998 American Institute of Physics. [S0021-8979(98)46711-2]

I. INTRODUCTION

Metallic multilayers of Pt/Co are very promising magneto-optic (MO) media, especially for the short wavelength range.¹ Our recent studies have shown that the Pt-Co interface regions and the Co rich regions contribute differently to the magneto-optic response, with the Pt-Co interface making the greater contribution.² That is, off-diagonal components of the complex dielectric tensor for the Pt-Co interface are greater in magnitude than those of the Co rich regions. In the study reported in Ref. 2, the thicknesses of the interfaces were assumed to be equal to one atomic layer of Pt, since the growth was at room temperature, resulting in minor atom mixing. Also in our previous work, magneto-optic response studies were limited to the spectral range from 300 to 700 nm.

Due to the larger contribution of the Pt-Co interface to the total MO response, the actual thickness of this interface is very important for the optimum design of Pt/Co multilayer structures. In this article, MO data from a much wider spectral range for two sets of ten Pt/Co multilayer samples are presented. Each set has the same Pt layer thickness and a series of ten magnetic layer thicknesses from very thin to reasonably thick. The magnetic layer (denoted as "mag-opt" layer) includes the Co rich regions as well as the Pt-Co interface regions. The off-diagonal components of the mag-opt layer's dielectric tensor are determined from experiments using electromagnetic magneto-optic theory,^{3,4} in an effort to decide the beginning of the Co rich region and the thickness of Pt-Co interface.

II. THEORY AND EXPERIMENT

An electromagnetic theory (originally proposed by Lissberger and others)⁵ was developed and simplified by McGahan and He for the case of normal incidence polar Kerr

effects.^{3,4} A Jones matrix was used to describe the optical properties of the multilayer structure, as given by

$$\mathbf{J} = \begin{pmatrix} R_x & K_y \\ K_x & R_y \end{pmatrix}. \quad (1)$$

The reflected light beam is related through this Jones matrix to the incident beam by $\mathbf{E}^r = \mathbf{J} \cdot \mathbf{E}^i$, where r and i denote "reflected" and "incident." Kerr rotation and ellipticity θ_k and η_k are defined by $\theta_k = \text{Re}\{K_x/R_x\}$ and $\eta_k = \text{Im}\{K_x/R_x\}$.

For multilayer systems, each of the four elements in the Jones matrix is a function of the thickness and dielectric tensors of the individual layers. The uniaxially symmetric dielectric tensor is given by

$$\tilde{\epsilon} = \begin{pmatrix} \tilde{\epsilon}_{xx} & -\tilde{\epsilon}_{xy} & 0 \\ \tilde{\epsilon}_{xy} & \tilde{\epsilon}_{xx} & 0 \\ 0 & 0 & \tilde{\epsilon}_{zz} \end{pmatrix} \quad (2)$$

and the Voigt parameters are defined as $\tilde{Q} = Q_1 + jQ_2 = -i\tilde{\epsilon}_{xy}/\tilde{\epsilon}_{xx}$. The Q value is a direct indication of the magnitude of the MO response, which increases with increasing Voigt parameter.^{3,4}

To determine the MO responses of the multilayer structures, *in situ* spectroscopic ellipsometry (*in situ* SE) analysis was used to determine the layer thicknesses and diagonal components of the dielectric tensor for each individual layer. In this article these are Pt and mag-opt layers. MO Kerr rotation and ellipticity data were then taken on the samples. The Voigt parameters were determined by regression fitting the MO data to models using Voigt parameters as variables.¹ The layer thicknesses and diagonal dielectric components were obtained from *in situ* SE.

III. EXPERIMENTAL RESULTS AND ANALYSIS

Two series of Pt/Co multilayer structures were deposited using dc magnetron sputtering. *In situ* SE data were taken during the depositions. The thicknesses for the Pt and mag-opt layers in the multilayer structures were determined using

^{a)}Electronic mail: xgao@engr.unl.edu

TABLE I. Thicknesses of samples 1 through 10 (a), and samples 11 through 20 (b) for two series of 50 period multilayers.

(a)										
Sample No. (50 periods)	1	2	3	4	5	6	7	8	9	10
Pt layer thickness (nm)	1.02	1.02	1.02	1.02	1.02	1.02	1.02	1.02	1.02	1.02
Mag-opt layer thickness (nm)	0.08	0.16	0.24	0.32	0.40	0.47	0.55	0.71	0.87	1.03
(b)										
Sample No. (50 periods)	11	12	13	14	15	16	17	18	19	20
Pt layer thickness (nm)	2.04	2.04	2.04	2.04	2.04	2.04	2.04	2.04	2.04	2.04
Mag-opt layer thickness (nm)	0.08	0.16	0.24	0.32	0.40	0.47	0.55	0.71	0.87	1.03

in situ ellipsometric analysis. Meanwhile, the optical constants (diagonal components of the dielectric tensor) of the Pt and mag-opt layer were determined. The thicknesses of the Pt and mag-opt layers of all samples are listed in Table I.

Magneto-optic Kerr rotation and ellipticity data were taken using a modified *ex situ* ellipsometer system.⁶ The spectral ranges of the measurements were from 200 to 1700 nm (0.73 to 6.2 eV). The MO data taken from all samples listed in Table I are shown in Fig. 1. As one can see from Figs. 1(a) and 1(b), the magnitudes of the MO Kerr rotation and ellipticity data increase as the mag-opt layer thickness increases from 0.08 to 0.87 nm, when the Pt layer thickness is fixed at 1.02 nm. There is almost no rotation or ellipticity change between samples 9 and 10. Likewise, for the data in Figs. 1(c) and 1(d), the responses increase as the mag-opt layer thickness increases from 0.08 to 0.71 nm when the Pt layer thickness is fixed at 2.04 nm. The effect saturates for mag-opt layers thicker than 0.71 nm, since the thicker Pt layer prevents the incident light from reaching the bottom mag-opt layers. (Note that there are 50 periods of the multilayers.)

Using the MO analysis described above, the Voigt parameters for the mag-opt layers of each sample were determined by regression fits.⁶ Fits were not unique for the samples with mag-opt layer thicknesses smaller than 0.32 nm, likely because it is too thin to form an actual layer. Fits were excellent and unique for samples with mag-opt layer thicknesses equal to or thicker than 0.32 nm. The spectral range for Voigt parameter fits were limited to 280 to 760 nm, the same as the *in situ* SE spectral range. During the regression fits, equal values of Voigt parameters were assumed for samples with the same mag-opt layer thicknesses but different Pt layer thicknesses.²

In Fig. 2, the Voigt parameters at a wavelength of 350 nm for samples with mag-opt layer thicknesses equal to or larger than 0.32 nm are plotted. We see that, starting from the sample with a 0.40 nm mag-opt layer thickness, the magnitudes of Voigt parameters decrease as the mag-opt layer thicknesses increase. However, the results are almost identical for the sample with 0.32-nm-thick mag-opt layer and 0.40-nm-thick mag-opt layer. As described in the Intro-

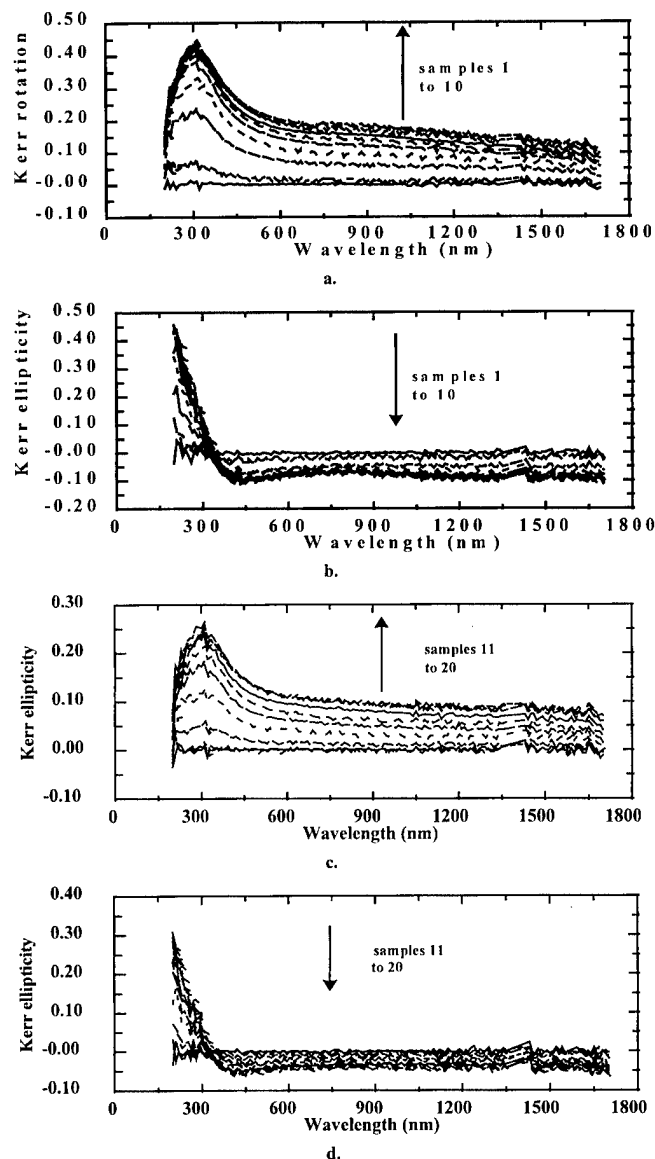


FIG. 1. (a) Kerr rotation data for samples 1 to 10 listed in Table I. (b) Kerr ellipticity data for samples 1 to 10 listed in Table I. (c) Kerr rotation data for samples 11 to 20 listed in Table I. (d) Kerr ellipticity data for samples 11 to 20 listed in Table I.

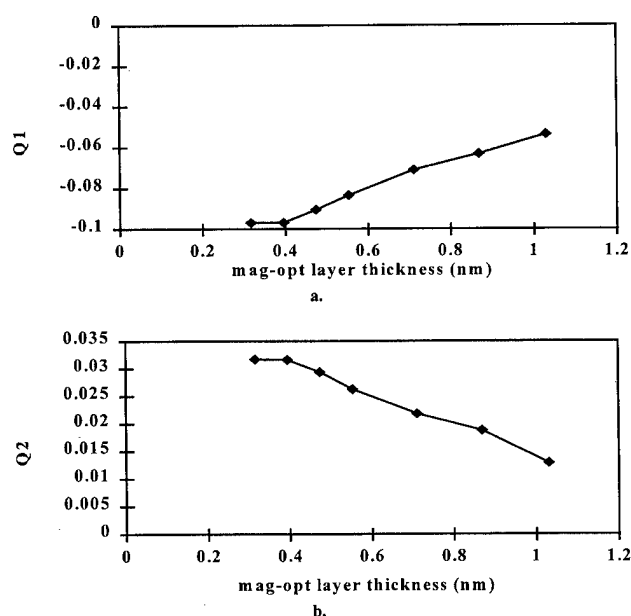


FIG. 2. Voigt parameters Q_1 (a), and Q_2 (b) determined from regression fits for the MO responses in Fig. 1 on samples 4 to 10 and samples 14 to 20.

duction, there are actually two regions, the Co rich region and the Pt-Co interface, in the Pt/Co multilayer structure, and the Voigt parameters for the Pt-Co interface region are larger. Therefore, the pseudo-Voigt parameters (the Voigt parameter determined if there were only one homogeneous region) for both the Co rich region, and the Pt-Co interface should decrease with increase in mag-opt layer thickness. The equal Q values for the sample with 0.32-nm-thick mag-opt layers and 0.40 nm mag-opt layers indicate that the Co rich regions have disappeared. On the other hand, the de-

crease of the Voigt parameters for samples with mag-opt layer thicknesses larger than 0.4 nm indicates that the formation of Co rich regions begins at a thickness of around 0.4 nm (smaller than 0.47 nm). This is very close to the value we assumed in earlier research.²

IV. SUMMARY

Wide spectral range magneto-optic Kerr rotation and ellipticity responses from two series of Pt/Co multilayer structures were measured. An optimal choice between Co layer thicknesses and number of multilayer periods can be made, thus maximizing the magneto-optic Kerr response for practical applications. Finally, by comparing the Voigt parameters of the magnetic layer for samples with mag-opt layer thickness greater than 0.32 nm, a Pt-Co interface thickness of around 0.40 nm was determined.

ACKNOWLEDGMENTS

Research was supported by the National Science Foundation under Grant No. DMR-9623992, and by the State of Nebraska funded Center for Microelectronic and Optical Materials Research.

¹K. Sato, in *Magneto-optical Spectra in Multilayers (Magnetic Multilayers)*, edited by L. H. Bennett and R. E. Watson (World Scientific, Singapore, 1994), p. 277.

²X. Gao, S. D. W. Thompson, and J. A. Woollam, *Appl. Phys. Lett.* **70**, 3292 (1997).

³W. A. McGahan and J. A. Woollam, *Appl. Phys. Commun.* **9**, 1 (1989).

⁴P. He, W. A. McGahan, and J. A. Woollam, *SPIE Optical Data Storage* **1499**, 401 (1991).

⁵P. H. Lissberger, *Rep. Prog. Phys.* **33**, 197 (1970).

⁶X. Gao, D. W. Glenn, S. Heckens, D. W. Thompson, and J. A. Woollam, *J. Appl. Phys.* **82**, 4525 (1997).

Optical and magneto-optical properties of Co/Pt/AlN multilayers

R. Atkinson,^{a)} P. M. Dodd, and I. W. Salter

Department of Pure and Applied Physics, The Queen's University of Belfast, Belfast BT7 1NN, Northern Ireland, United Kingdom

P. J. Grundy and C. J. Tatnall

Department of Physics, University of Salford, Salford M5 4WT, United Kingdom

The optical and polar Kerr magneto-optical properties of a series of Co/Pt/AlN multilayers have been determined in the photon energy range 1.4–4 eV. Observations of the spectral variation of reflectivity are discussed in terms of the optical properties of the constituent materials using multilayer theory. Magneto-optic polar Kerr spectra over the same energy range are also discussed taking into account the modified magnetic properties resulting from undesirable structural changes in the films. © 1998 American Institute of Physics. [S0021-8979(98)44511-0]

INTRODUCTION

The potential of Co/Pt multilayered media for magneto-optic (MO) data storage is widely recognized. However, the magnetic properties of Co/Pt are not ideal. The inclusion of a third material into the system has potential for changing magnetic properties such as the coercivity, anisotropy constant, and Curie temperature. Recently it has been shown¹ that, providing the additional material is a dielectric, the MO potential of the multilayered material remains unchanged, as judged by the figure of merit (FOM),²

$$\text{FOM} = |Q|(\Gamma + \Gamma^{-1}), \quad (1)$$

where Q is the Voigt parameter and $\Gamma (=n/k)$ is the ratio of the real and imaginary parts of the complex refractive index $(n+ik)$. Although Q and Γ may vary on the inclusion of the dielectric component the FOM, in principle, does not. And performance can always be optimized to that of Co/Pt by the use of a carefully designed trilayer structure. We have attempted to fabricate multilayer systems consisting of Co, Pt, and AlN using a multisource, cluster magnetron sputter-deposition system.

We present the results of a series of optical, MO, and magnetic measurements on several multilayers, where the thickness of the AlN layer was varied systematically. The spectral variation of reflectivity is discussed on the basis of the optical properties of the component materials and the MO properties, specifically, the polar Kerr rotation and ellipticity are considered in comparison with the known MO properties of Co, Pt, and Co/Pt. It will be shown, using magnetic and structural data, that changes in MO activity are not due solely to the inclusion of a transparent medium but suffer significant deterioration due to interdiffusion of the AlN into the Pt layers and through the poor stoichiometry of the nitride layer.

EXPERIMENT

All samples were deposited using a multisource, cluster magnetron sputter-deposition system. Sputtering took place

in argon at a partial pressure of 5 mTorr, with a previous base pressure of less than 2×10^{-7} Torr. Both Co and Pt were deposited using dc magnetron sources with deposition rates of 0.06 and 0.11 nm s⁻¹, respectively, onto glass substrates at room temperature.

The AlN was rf sputtered from a stoichiometric target. The deposition rates for Co and Pt were calculated using a TFOS software package in a scanning electron microscope (SEM). The AlN calibrated films could not be accurately measured owing to specimen charging in the SEM, hence a low angle x-ray diffraction was employed. The dielectric layer was multilayered with a thick (2 nm) layer of platinum and the bilayer repeated 20 times. By analyzing the diffraction data the mean bilayer and dielectric thickness were evaluated and hence the associated AlN deposition rate was calculated as 0.78 nm s⁻¹ at an applied power of 150 W.

Two series of films were fabricated on glass substrates with a 5 nm Pt underlayer to induce preferred crystallographic texture in the multilayer that is known to be beneficial for high remanence and anisotropy.³ Series (I) consisted of $10 \times (0.4 \text{ nm Co}/Z \text{ nm AlN}/1 \text{ nm Pt})$ and series (II) was $10 \times (0.4 \text{ nm Co}/0.5 \text{ nm Pt}/Z \text{ nm AlN}/0.5 \text{ nm Pt})$, where Z ranged from 0 to 2 nm.

RESULTS

Using a normal incidence spectroscopic photometer the intensity reflectance (R) was determined for each sample in the two series. The results of these simple measurements are shown in Fig. 1. Generally, the behavior of R for both series is similar and this is to be expected since in the case of $Z = 0.8$ and 1.2 nm the structures contain the same amounts of each material. Moreover, because these are in the form of very thin layers they should have the same effective optical constants.⁴ What is particularly surprising is the magnitude of R , which increases with increasing AlN content and is higher than that for the pure Co/Pt multilayer. The latter is calculated on the basis of the optical constants of Co/Pt multilayered structures.⁵ This result is totally unexpected since the addition of a transparent dielectric like AlN should reduce the reflectivity below that of the pure metallic component. To illustrate what would be expected on the basis of the

^{a)}Electronic mail: ronald.atkinson@qub.ac.uk

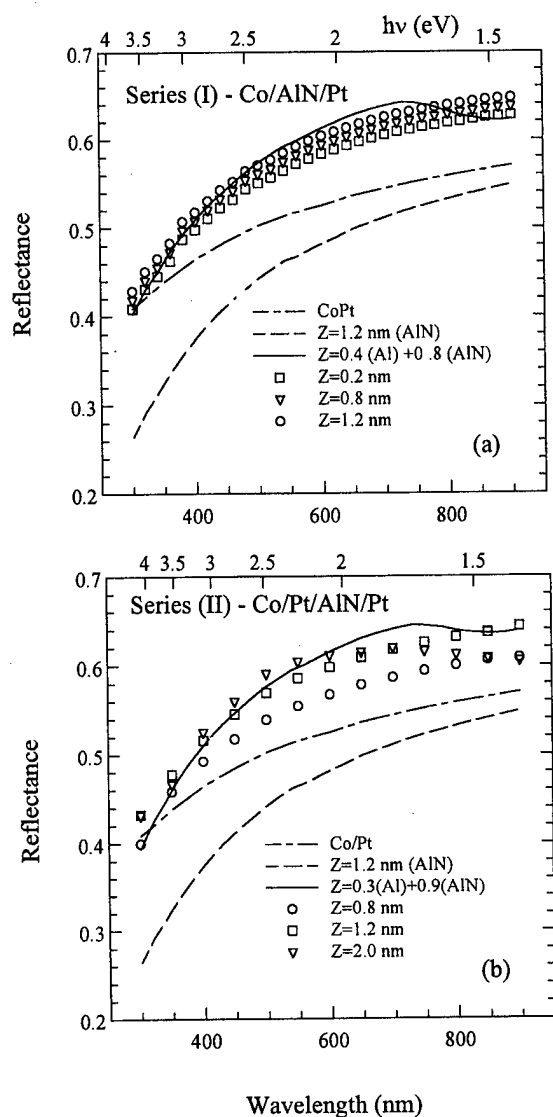


FIG. 1. Normal incidence reflectance for (a) series (I) and (b) series (II). The solid and dashed curves are calculated and the points are measured data.

optical constants of Co, Pt, and AlN we have calculated the reflectivity spectrum for the perfect structures. These are shown as the lower dashed curves in the two cases. In order to explain this anomalous result we considered the possibility that the AlN layer consisted of both AlN and free Al. By varying the proportion of free Al in the sublayers we were able to account for the increased reflectance. To illustrate the improvement we consider the samples with $Z = 1.2$ nm. In Fig. 1(a) with each AlN layer made up from the equivalent of 0.4 nm of Al and 0.8 nm of AlN and in Fig. 1(b), 0.3 nm Al and 0.9 nm AlN there is a much improved agreement with the measured values. Calculations were made using classical electromagnetic theory of multilayers as a first approximation in dealing with this problem. In light of the complex structures involved here and the uncertainties in the stoichiometry and form of the AlN layer the improvement is quite remarkable. Readers may note a reflectance shoulder at long wavelengths in these calculated curves. This is due to the rapidly changing optical constants of Al at a wavelength of 800 nm. In general this is not seen in the

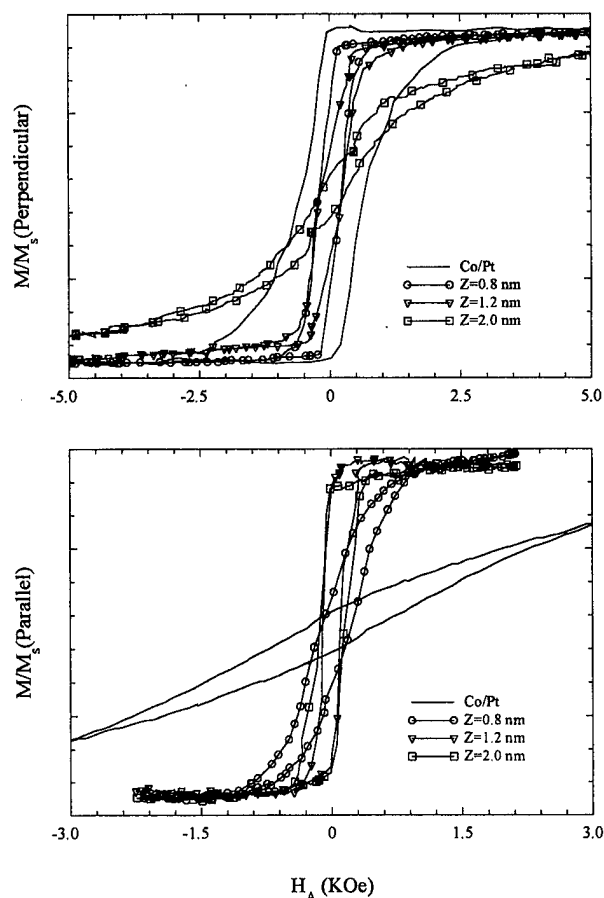


FIG. 2. Perpendicular and parallel hysteresis loops for film series (I).

measured data except for that corresponding to the film with the thickest AlN layer [Fig. 1(b), $Z = 2$ nm] which shows a turning point similar to that seen in the calculated curves. This is consistent with the above arguments, favoring the existence of significant amounts of free Al in the layers.

Figure 2 show the perpendicular and in-plane hysteresis loops for the films in series (II). Similar loops can be observed for series (I). It is quite clear that the addition of AlN to this system results in a gradual decrease in perpendicular anisotropy and coercivity with the result that there is a pronounced shearing of the loop. In the case of $Z = 2$ nm any residual anisotropy has been overcome by the demagnetizing fields and the easy axis of the sample lies in the plane of the film. Since it is known that the perpendicular anisotropy in Co/Pt multilayers arises due to interactions at the interfaces between Co and Pt, the loss of anisotropy is not surprising for the films of series (I) where the AlN layer separates the Co and Pt. However, since the AlN layer in series (II) is located between two Pt layers, one might expect the anisotropy to remain. Evidently this is not the case.

The polar Kerr rotation and ellipticity were obtained with the films in a magnetically saturated state, at normal incidence, using a rotating analyzer Kerr polarimeter with a precision of $\pm 0.005^\circ$. The results are shown in Fig. 3 for both series of films, (I) and (II). For comparison the curves corresponding to Co/Pt are also shown.

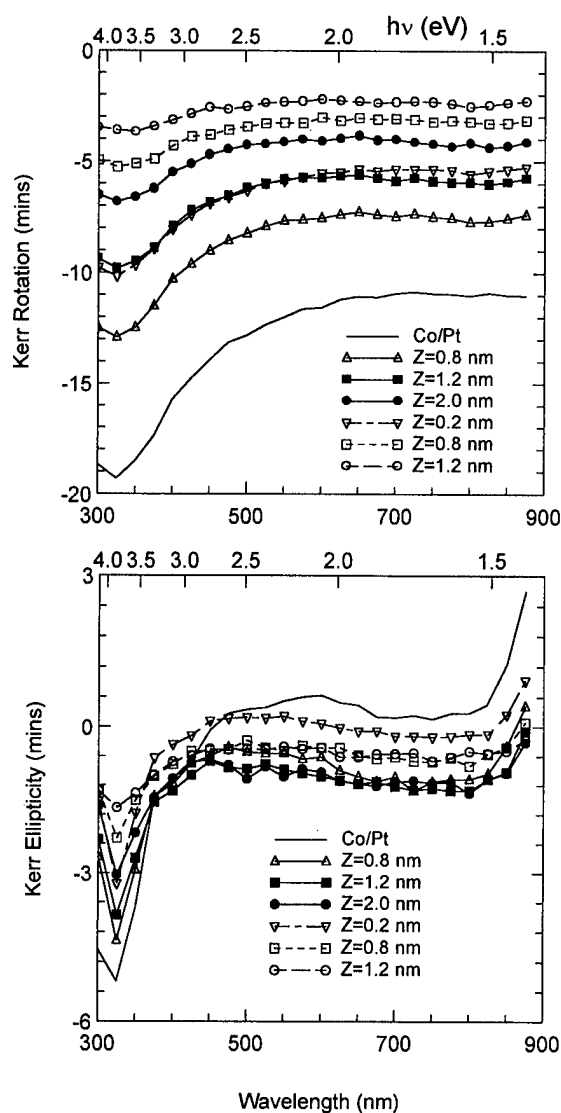


FIG. 3. Measured complex Kerr rotation and ellipticity. Dashed lines—series (I); solid lines—series (II).

It should be noted that the dominant component of the MO activity is associated with the Kerr rotation rather than with the ellipticity that is approximately a factor of 4 smaller over the whole spectral range. It is clear that as the amount of AlN increases the MO activity decreases. This is to be expected, even under ideal conditions since we are diluting the system with a nonmagnetic component. However, in this case the decrease is accelerated. On the basis of multilayer calculations, the variations seen in Fig. 3 cannot be reproduced in detail, although some aspects of the curve shapes can be generated. The reasons for the deteriorating performance of both sets of films are complex and will be discussed below.

One can observe that the Kerr rotations produced by series (I) are significantly lower than those in series (II) for the same AlN thickness. The reason for this is that in the former the dielectric layer directly interrupts the Co–Pt interface. This has the effect of reducing the perpendicular

interfacial anisotropy. This is clearly indicated by the magnetic properties of the films. In addition, since the polarization of the Pt layers has its origins at this interface,⁶ this too is reduced and the magneto-optic contribution of the Pt component is lost. The result is a massive decrease in magneto-optic activity. In the case of the second series the AlN layer is situated between the two Pt layers each of which forms an interface with Co. Nevertheless the MO activity is less what might be expected. This may be caused by the existence of the free Al component referred to in the discussion of the optical properties. The intimate mixing of an optically absorbing nonmagnetic element to any magneto-optic structure like this will cause a decrease in magneto-optic effects. In addition, it is clear that perpendicular anisotropy is also being lost. The implication is that, despite the fact that the AlN layer is deposited between Pt, there is a disruption of the Co/Pt interfaces, resulting in lost anisotropy and hence reduced polarization of the Pt and even perhaps lost magnetization within the Co layers. Some evidence for interdiffusion of the elements of these structures caused by the presence of the AlN has been reported in an earlier paper.⁷ Clearly, if this interfacial mixing occurs in the case of series (II), then it is also likely to be present in series (I), and with even greater effect.

SUMMARY

Two series of Co–AlN–Pt multilayer samples were fabricated by magnetron sputtering in an attempt to demonstrate that MO potential is not a function of the thickness of the dielectric layer. However, the magnetic perpendicular anisotropy normally associated with Co/Pt multilayers is gradually reduced with increasing AlN content whether the AlN is located between the Co and Pt or between two Pt layers. Measurements of optical reflectivity suggest that free Al is present in the structures and may indicate that nitrogen diffuses through the structure gradually disrupting the multilayer structure. This causes a severe reduction in MO activity through the loss of polarization of the Pt and perhaps lowering the magnetization of the Co layers. The deteriorating film properties make further meaningful analysis unprofitable.

ACKNOWLEDGMENT

The authors wish to thank the EPSRC for funding this research through Grant Nos. GR/J27322 and GR/H65320.

¹R. Atkinson, *J. Magn. Magn. Mater.* **124**, 333 (1993).

²R. Gamble, P. H. Lissberger, and M. R. Parker, *IEEE Trans. Magn.* **21**, 1651 (1985).

³C. J. Tatnall, R. J. Pollard, and P. J. Grundy, *J. Magn. Magn. Mater.* **156**, 61 (1996).

⁴R. Atkinson, *J. Magn. Magn. Mater.* **95**, 61 (1991).

⁵R. Atkinson, S. Pahirathan, I. W. Salter, P. J. Grundy, C. J. Tatnall, J. C. Lodder, and Q. Meng, *J. Magn. Magn. Mater.* **162**, 131 (1996).

⁶R. Atkinson and W. R. Hendren, *J. Magn. Soc. Jpn.* **20**, 291 (1996).

⁷C. J. Tatnall, G. J. Sinclair, P. J. Grundy, and R. Atkinson, *J. Magn. Soc. Jpn.* **20**, 259 (1996).

Effect of Pt in TbFeCo on magnetic and magneto-optical properties

Y. Itoh,^{a)} W. P. Van Drent, and T. Suzuki

Information Storage Materials Laboratory, Toyota Technological Institute, 2-12-1, Hisakata, Tempaku-ku, Nagoya 468, Japan

The effect of Pt additives in TbFeCo(Pt)/Pt multilayers on magnetic properties and magneto-optical Kerr effect is investigated. The perpendicular magnetic anisotropy K_u of the multilayer becomes larger ($\sim 2 \times 10^6$ erg/cm³) than that of the TbFeCo(Pt) single layer. Pt layers are found to contribute significantly to the polar Kerr spectra at ultraviolet photon energies beyond 4 eV. The largest enhancement in the Kerr rotation θ_K is found at about 5 eV. The Kerr rotation θ_K and ellipticity η_K are enhanced with increasing Pt layer-thickness t_{Pt} , and become saturated at $t_{Pt} = 12$ Å. This result implies that Pt atoms up to about 6 Å from the interfaces are contributing to the Kerr activity.

© 1998 American Institute of Physics. [S0021-8979(98)21911-6]

I. INTRODUCTION

Future high density optical recording technology requires novel materials with high polar Kerr activities at short wavelengths. TbFeCo amorphous films currently used exhibit a substantial reduction in Kerr activity with decreasing wavelength¹ and therefore, it is desirable to enhance it by adding some elements. Pt is known to be effective in enhancing the magneto-optical Kerr effect at short wavelengths, as demonstrated in Co/Pt multilayers.²⁻⁴ Awano *et al.* indicated that the Kerr rotation of the rare-earth transition-metal (RE-TM)/Pt multilayer was larger than that of the RE-TM single layer at λ down to 300 nm.⁵

In order to clarify the effect of Pt in the TbFeCo/Pt multilayer, a systematic study of the dependence of magnetic and magneto-optical properties on Pt layer thickness has been made. The magneto-optical Kerr effect of the multilayers was examined in ultraviolet photon energies (~ 6.8 eV) for the first time.

II. EXPERIMENT

Multilayered films of TbFeCo(Pt)/Pt were fabricated by sputter deposition in Ar atmosphere. The base pressure of the sputtering chamber is better than 5×10^{-8} Torr. Ar gas pressure during the deposition is 5 mTorr. The samples were fabricated by depositing TbFeCo and Pt onto glass substrates. The deposition rate for both was 0.5–1 Å/s. The Pt mixture in the TbFeCo layer was detected at a level of less than 1 at % by electron probe microanalyzer (EPMA), although the attempt was made so that the vapor streams were interrupted alternately for programmed times with shutters. The composition of the TbFeCo(Pt) layer exhibited to be TM rich. The thicknesses of TbFeCo ($=t_{TbFeCo}$) and Pt layers ($=t_{Pt}$) were varied from 10 to 50 Å and 0 to 24 Å, respectively. The total thickness of the multilayer was designed for 250 and 500 Å. Measurements of magnetic properties were carried out using a vibrating sample magnetometer (VSM), an alternating gradient field magnetometer (AGFM), and a torque magnetometer. The magneto-optical Kerr effect and

optical constants were measured using a Kerr spectroscopy in a photon energy from 1.4 to 6.8 eV ($\lambda = 182$ –886 nm). Details of the setup are described elsewhere.⁶

III. RESULTS AND DISCUSSION

A. Magnetic property

Samples with a total thickness of the multilayer between 450 and 500 Å were prepared by sputter deposition. A 30 Å thick Pt layer was used as an overcoat on each film for protection. Hysteresis loops measured for these samples by AGFM are shown in Fig. 1. This figure indicates the dependence of hysteresis loops on Pt layer-thickness t_{Pt} for a constant TbFeCo(Pt) layer-thickness t_{TbFeCo} of 50 Å. The TbFeCo(Pt) single layer of the same total thickness, i.e., $t_{Pt} = 0$, is also given in Fig. 1 for comparison. For all the Pt thicknesses under consideration, the hysteresis loops maintain the perfect squareness, though a small kink is observed at very small fields. As t_{Pt} increases, the saturation magnetization M_s also increases, and the coercivity H_c decreases except for the case of $t_{Pt} = 1$ Å.

Figure 2 shows the coercivity H_c as a function of t_{Pt} for various t_{TbFeCo} . At $t_{Pt} = 0.5$ Å, H_c increases drastically for the cases of $t_{TbFeCo} = 30$ and 50 Å, and then decreases monotonously. The increase in H_c is not due to a compensation point because the polarity of the Kerr effect does not change on both sides. The Barkhausen volume V_B was measured through the apparent coercivity as a function of the sweeping speed for the magnetization curves.⁷ It was found that the V_B values are indeed the smallest for this t_{Pt} region. Therefore, the rapid increase of H_c is due to an increase in pinning sites over the interfacial regions.

Figure 3 shows the dependence of K_u on t_{Pt} for various t_{TbFeCo} . K_u is the intrinsic perpendicular magnetic anisotropy constant, defined as $K_0 + 2\pi M_s^2$, where K_0 is the torque amplitude extrapolated to an infinite field strength. As seen in this figure, K_u increases with t_{Pt} for all the cases. K_u becomes significantly larger for $t_{Pt} > 3$ Å at $t_{TbFeCo} = 50$ Å, and for $t_{Pt} > 1$ Å at $t_{TbFeCo} = 30$ Å. For the case of $t_{TbFeCo} = 10$ Å, it seems that $t_{Pt} < 1$ Å is enough to increase K_u . The small K_u at $t_{Pt} = 0$ is due to the Pt dilution (~ 1 at %) in the TbFeCo. Katayama *et al.* also reported that the Pt addition

^{a)}Electronic mail: d2syito@ypcfs1.toyota-ti.ac.jp

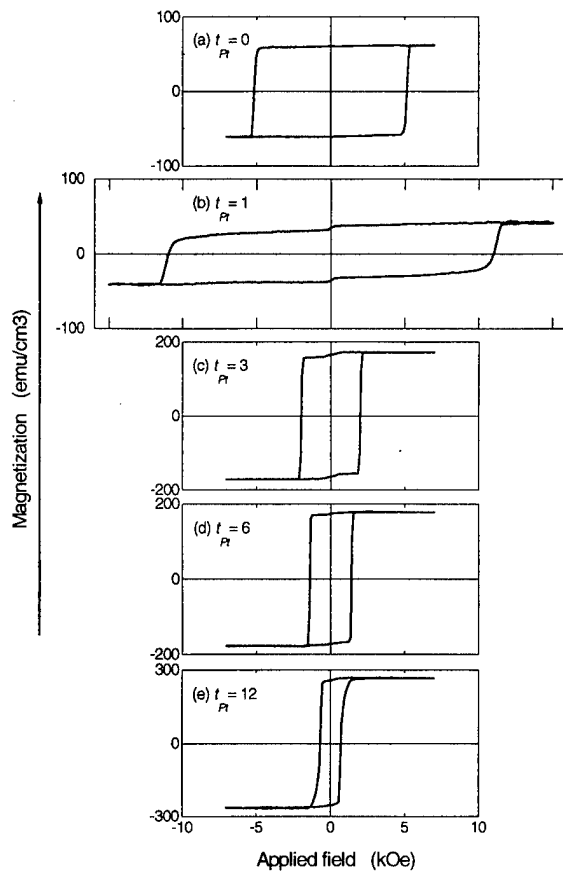


FIG. 1. Hysteresis loops for TbFeCo(Pt)/Pt multilayers. (a) TbFeCo(Pt) single layer, (b) $9 \times [50 \text{ Å TbFeCo(Pt)/1 Å Pt}]$, (c) $9 \times [50 \text{ Å TbFeCo(Pt)/3 Å Pt}]$, (d) $8 \times [50 \text{ Å TbFeCo(Pt)/6 Å Pt}]$, and (e) $8 \times [50 \text{ Å TbFeCo(Pt)/12 Å Pt}]$.

decreases K_u in amorphous RE-TM films.⁸ From this point of view, the multilayered film has an advantage. The critical point, at which each K_u becomes saturated, seems to be related to the $t_{\text{Pt}}/t_{\text{TbFeCo}}$ ratio.

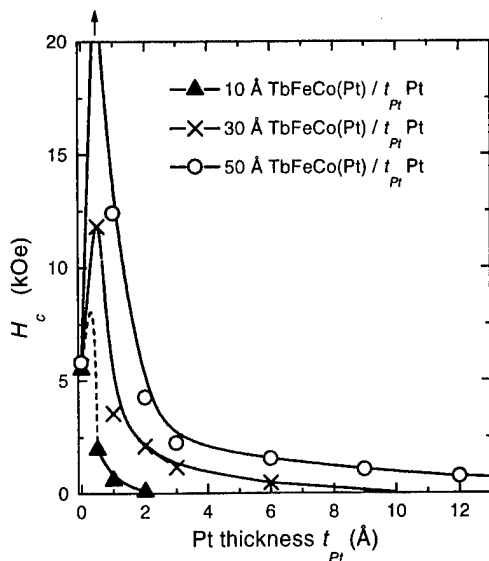


FIG. 2. Coercivity H_c as a function of t_{Pt} for various t_{TbFeCo} .

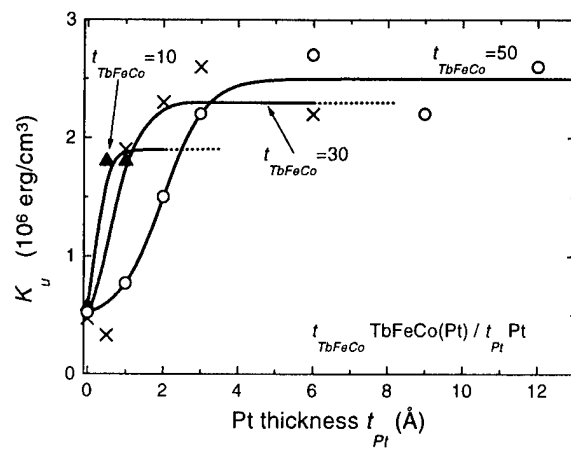


FIG. 3. Dependence of K_u on t_{Pt} for various t_{TbFeCo} .

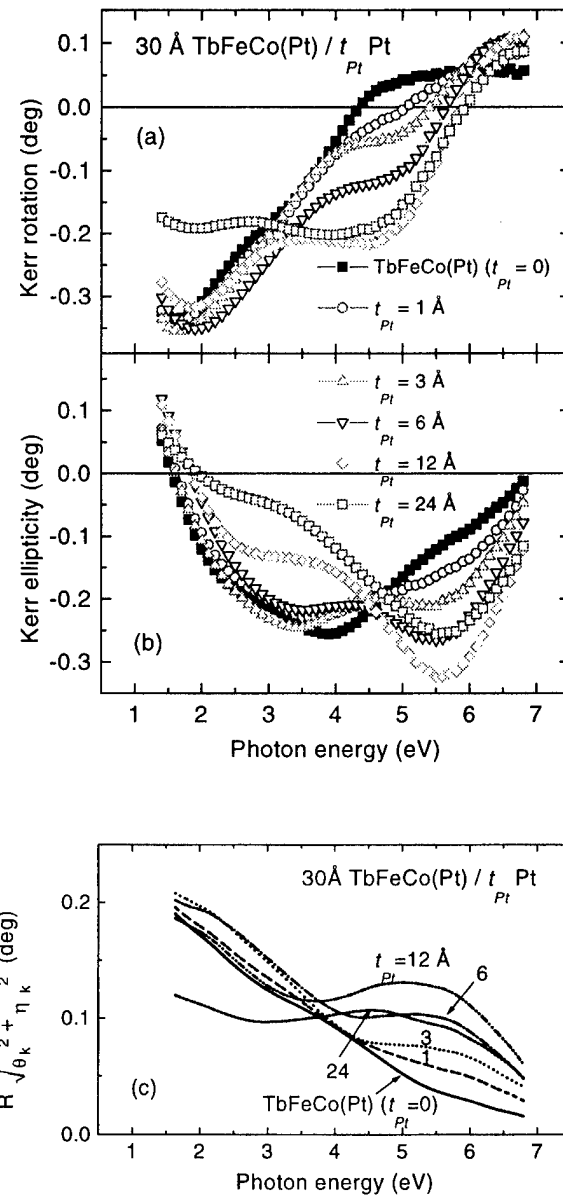


FIG. 4. The Kerr rotation angle (a) ellipticity (b) and $R(\theta_k^2 + \eta_k^2)^{1/2}$ (c) of $30 \text{ Å TbFeCo(Pt)/}t_{\text{Pt}}$ multilayers ($t_{\text{Pt}} = 0\text{--}24 \text{ Å}$) as a function of photon energy.

B. Magneto-optical property

Very thin multilayers, of which a total thickness is about 250 Å, were deposited on a 750 Å thick Pt reflector for this measurement. Neither any overcoat nor enhancing layer was deposited on each multilayer. This structure is suitable for obtaining an intrinsic Kerr spectrum of a multilayer without optical interference effects. The magneto-optical Kerr effect just after the deposition was measured.

Figure 4 shows the photon energy dependence of (a) the Kerr rotation angle θ_K , (b) ellipticity η_K , and (c) Kerr signal $S = R(\theta_K^2 + \eta_K^2)^{1/2}$, where R is the reflectivity calculated by measured optical constants, for various Pt layer-thicknesses t_{Pt} and a 30 Å thick TbFeCo(Pt). As seen in this figure, the absolute value of Kerr rotation increases with increasing Pt layer thickness. This implies the enhancement is due to Pt. The enhancement becomes evident at ultraviolet photon energies beyond 4 eV. The peak position of the θ_K enhancement is about 5 eV. Pt layers have a negative effect for the enhancement on η_K at photon energies <5 eV and a positive effect at >5 eV. It is found that the enhancements of both θ_K and η_K become saturated at $t_{Pt} = 12$ Å. This result is of interest since one can estimate a range from the interface to be 6 Å (half the t_{Pt}), under which Pt atoms are likely being polarized, giving rise to the higher Kerr activity. As a result, the difference (enhancement) of θ_K value at 5 eV reaches 0.23°. The Kerr signal in Fig. 4(c) reflects those results, and it becomes larger to 2.5 times at 5 eV.

IV. SUMMARY

A systematic experimental study to examine the effect of Pt on both magnetic and magneto-optical properties is presented. The large H_c (>20 kOe) is obtained at about t_{Pt}

= 0.5 Å for 50 Å thick TbFeCo(Pt)/Pt multilayers. K_u initially increases with t_{Pt} , and then remains constant ($\sim 2 \times 10^6$ erg/cm³) for thicker values. From this point of view, the multilayered film has an advantage for enhancing H_c and K_u . The effect of the addition of Pt layers on the Kerr spectra becomes evident at ultraviolet photon energies beyond 4 eV. The largest enhancement in θ_K takes place at around 5 eV. The θ_K is enhanced with increasing t_{Pt} . In the case of $t_{TbFeCo} = 30$ Å multilayers, the enhancements of both the Kerr rotation θ_K and ellipticity η_K become saturated at about $t_{Pt} = 12$ Å. This result implies that Pt atoms up to about 6 Å from the interfaces are contributing to the Kerr activity.

ACKNOWLEDGMENTS

This work was partially supported by the Original Industrial Technology R&D Promotion Program from the New Energy and Industrial Technology Development Organization (NEDO) of Japan (8C-039-1). One of the authors wishes to thank Toyota Motor Corporation for the assistance in acquiring the composition data.

- ¹D. Weller, J. Hurst, H. Notarys, H. Brandle, R. F. C. Farrow, R. Marks, and G. Harp, J. Magn. Soc. Jpn. **17**, 72 (1993).
- ²W. B. Zeper, F. J. A. M. Greidanus, P. F. Carcia, and C. R. Fincher, J. Appl. Phys. **65**, 4971 (1989).
- ³W. B. Zeper, F. J. A. M. Greidanus, and P. F. Carcia, IEEE Trans. Magn. **25**, 3764 (1989).
- ⁴S. Hashimoto, Y. Ochiai, and K. Aso, J. Appl. Phys. **67**, 2136 (1990).
- ⁵H. Awano, T. Niihara, and M. Ojima, J. Magn. Magn. Mater. **126**, 550 (1993).
- ⁶W. Van Drent and T. Suzuki, IEEE Trans. Magn. **33**, 3223 (1997).
- ⁷G. Bayreuther, P. Bruno, G. Lugert, and C. Turtur, Phys. Rev. B **40**, 7399 (1989).
- ⁸T. Katayama, M. Miyazaki, H. Awano, and H. Masuda, Digests of the 8th Annual Conference, J. Magn. Soc. Jpn., 1984, p. 123 (in Japanese).

Magneto-optical properties of Sc-substituted erbium-iron-garnet single crystals

J. Ostoréro^{a)}

CNRS, UPR 209, 92195 Meudon Cedex, France

M. Guillot

CNRS-LCMI/MPI, 38042 Grenoble Cedex, France

The magneto-optical properties of $\text{Er}_3\text{Fe}_{5-z}\text{Sc}_z\text{O}_{12}$ ($z=0.10$ and 0.30) single crystals are presented and compared to those of pure ErIG. Faraday rotation (FR) measurements at 1152 nm wavelength were performed in the 6–600 K temperature range under a magnetic field of up to 20 kOe applied parallel to the [100] and [111] crystallographic axes of the crystals. The compensation temperature T_{comp} is shifted from 80 ($z=0$) to 51 K ($z=0.30$). Below T_{comp} , the diamagnetic Sc^{3+} substitution in the octahedral Fe^{3+} sublattice also has a strong influence on FR anisotropy: both spontaneous FR Φ_s and FR susceptibility $\chi_F = d\Phi/dH$ show that the “easy” FR axis changes from [111] in ErIG ($z=0$) to [100] for $z=0.30$. The FR isotherms ($z=0.30$) for the [111] direction show a nonlinear behavior in the 20 K– T_{comp} temperature region. © 1998 American Institute of Physics. [S0021-8979(98)44611-5]

I. INTRODUCTION

In ferrimagnetic rare earth-iron-garnet, formula of $\text{RE}_3\text{Fe}_5\text{O}_{12}$ (REIG), the magnetic ions are distributed over three crystallographic sites: octahedral site $16a[\text{Fe}^{3+}]$, tetrahedral site $24d(\text{Fe}^{3+})$, and dodecahedral site $24c\{\text{RE}^{3+}\}$.¹ The $\text{Fe}[a]$ – $\text{Fe}(d)$ superexchange interactions determine the Néel temperature ($T_N=560$ K) for all REIGs. In heavier rare earth garnets, the influence of the rare earth is manifested by a compensation temperature T_{comp} at which the bulk magnetization vanishes. In pure ErIG, T_{comp} is equal to 80 K.²

At low temperature ($T < T_{\text{comp}}$), ErIG presents anisotropic physical properties which were studied using different techniques, particularly magnetization,² neutron diffraction,³ and magneto-optical (MO) properties.^{4–6} These different results, sometimes confusing or contradictory due in part to the sensitivity of the anisotropy properties to magnetic and thermal sample history,³ enable one to distinguish between the magnetic and MO Faraday rotation (FR) anisotropy properties performed on the same monocrystalline samples.

MO results indicate that [111] is the “easy” axis of ErIG corresponding to the greatest FR absolute values.^{6,7} Concerning the magnetic anisotropy, the spontaneous magnetic properties show that a spin reorientation occurs at ~50 K (Ref. 2) and that the easy magnetic axis is [100] at low temperature. Nevertheless, the spontaneous magnetization along [100] and [111] is only slightly different as was shown for rare earth-iron-garnets where the rare earth (here Er^{3+}) is a Kramers ion.⁸ Moreover, below ~75 K in ErIG, in the rare earth sublattice, when both crystal field effects and exchange Fe^{3+} – RE^{3+} interaction anisotropies become of the same order of magnitude, the ferrimagnetic order is destroyed and an onset of a noncollinear ordering takes place in the $\{c\}$ sublattice as shown by neutron diffraction

experiments.^{2,3} Finally, an anomaly in the magnetic anisotropy near 6 K has been observed recently⁹ which was related to the splitting of the lowest Kramers doublet of Er^{3+} by the anisotropic exchange interaction with the iron sublattices.

An effective mean of modifying the exchange interaction between RE and Fe sublattices is to substitute Fe^{3+} ions by diamagnetic ones in $\text{RE}_3\text{Fe}_{5-z}\text{M}_z\text{O}_{12}$ garnets ($\text{M}=\text{Al}, \text{Ga}, \text{Sc}$). In contrast to Al^{3+} and Ga^{3+} ions which substitute to Fe^{3+} ions on both tetrahedral (d) and octahedral [a] sites with a large tetrahedral preference, Sc^{3+} ions substitute almost exclusively to Fe^{3+} on octahedral sites¹⁰ and have a stronger influence on the RE–Fe exchange interaction than Al^{3+} or Ga^{3+} .^{10,11} However, the influence of the diamagnetic scandium substitution on the magnetic and MO properties of garnets has been limited mainly to yttrium-iron-garnet compounds $\text{Y}_3\text{Fe}_{5-z}\text{Sc}_z\text{O}_{12}$.¹⁰ We present here for the first time, to the best of our knowledge, the MO properties of $\text{Er}_3\text{Fe}_{5-z}\text{Sc}_z\text{O}_{12}$ ($z=0.10$ and 0.30) single crystals and in particular Faraday rotation at 1152 nm wavelength. In order to emphasize the influence of Sc substitution on the MO properties of ErIG, FR measurements were performed for the same experimental conditions as a function of temperature and magnetic field oriented along the principal crystallographic axes [100] and [111] and compared to previous results on pure ErIG.^{4–6} The magnetic properties of these compounds will be described in a forthcoming paper.

Using the method of flux growth under 10 bar of oxygen pressure, single crystals of $\text{Er}_3\text{Fe}_{5-z}\text{Sc}_z\text{O}_{12}$ with $z=0.10$ and 0.30 were synthesized. The scandium content was determined by electron microprobe analysis to within $\pm 2\%$ accuracy. X-ray diffraction measurements were in agreement with the garnet Ia $3d$ structure, the lattice parameters being 1.2347, 1.2358, and 1.2379 nm for $z=0, 0.10$, and 0.30 , respectively. Polished platelets ~0.4 mm thick oriented perpendicular to the [111] and [100] axes were obtained from the same “as grown” crystal to avoid the slight Sc concen-

^{a)}Electronic mail: ostorero@cnrs-bellevue.fr

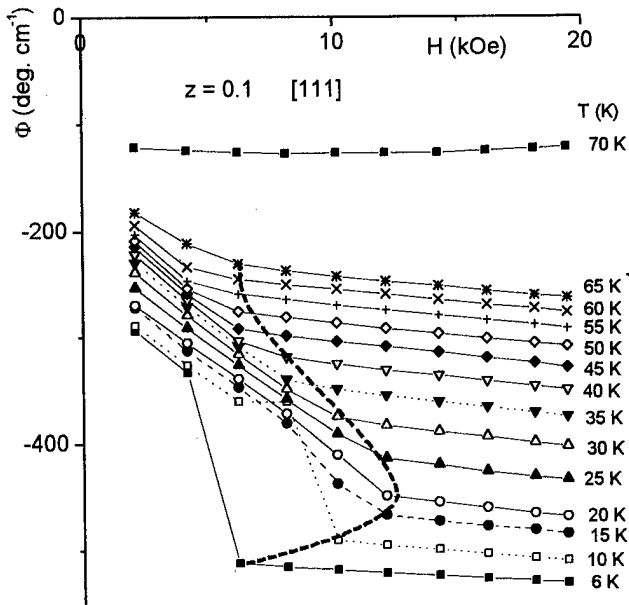


FIG. 1. FR isotherms of ErIG:Sc ($z=0.10$) at 1152 nm for $T < T_{\text{comp}}$ ($T_{\text{comp}} = 71$ K) and H parallel to [111]. The saturation field H_{sat} is indicated by the dashed curve. When H is parallel to [100], $H_{\text{sat}} \leq 4$ kOe in the whole temperature range.

tration difference which can occur between different crystals of the same batch. FR measurements Φ were performed at temperatures between 6 and 600 K under a magnetic field of up to 20 kOe applied parallel to the [111] or [100] direction at a wavelength of 1152 nm using a modulation technique. This wavelength is in the transparency window of the garnet—the nearest Er absorption lines are located at about 6500 cm^{-1} ($^4I_{15/2} \rightarrow ^4I_{13/2}$ transition) and at about 10000 cm^{-1} ($^4I_{15/2} \rightarrow ^4I_{11/2}$ transition)¹²—and the MO properties presented in this article are mainly dispersive. The experimental accuracy is estimated to $\pm 2\%$ for Φ . It is to be noted that the samples are cooled to the lowest temperature in the absence of a magnetic field prior to FR measurements.

II. RESULTS AND DISCUSSION

FR isotherms $\Phi(H)$ are plotted in Fig. 1 ($z=0.10$) and Fig. 2 ($z=0.30$). They present a linear part when $H \geq H_{\text{sat}}$. A least-squares fit of these linear isotherms using $\Phi = \Phi_s + \chi_F H$ gives the spontaneous FR $\Phi_s(T, z)$ and FR susceptibility $\chi_F(T, z)$. For all Sc concentrations, two different temperature regions are evidenced according to T_{comp} of the samples. In the vicinity of T_{comp} , FR isotherms are no longer linear and the FR changes its sign within $T_{\text{comp}} \pm 2$ K, keeping the same absolute values. The values of T_{comp} are 71 and 51 K for $z=0.10$ and 0.30 , respectively.

Below T_{comp} , H_{sat} is strongly dependent on the Sc concentration, orientation, and temperature of the sample and a strong FR anisotropy is observed. When $z=0.10$ and H parallel to [111] (Fig. 1), H_{sat} is a complex function of temperature and presents a maximum $H_{\text{sat}} = 12$ kOe in the 15–25 K temperature region. This is in contrast with the FR isotherms for $z=0.10$ and H parallel to [100]: in this case, H_{sat} is at most 4 kOe at 6 K. Concerning the linear part of the isotherms, they are identical within experimental accuracy for

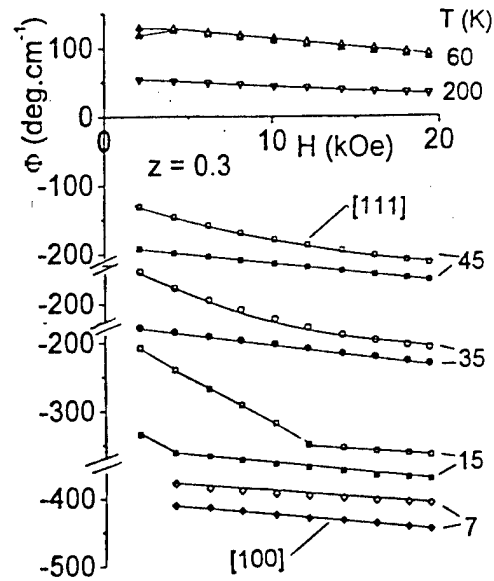


FIG. 2. FR isotherms of ErIG:Sc ($z=0.30$) at 1152 nm. To avoid confusion, the Φ axis is broken according to different isotherms. Closed symbols: H parallel to [100]. Open symbols: H parallel to [111].

$z=0.10$ and H parallel to [100] and [111] giving the same FR spontaneous values, Φ_s , and FR susceptibilities, χ_F . When $z=0.30$, the anisotropy below T_{comp} is much stronger (Fig. 2). When H is parallel to [100], H_{sat} is at most 4 kOe in the whole temperature range. On the contrary, when H is

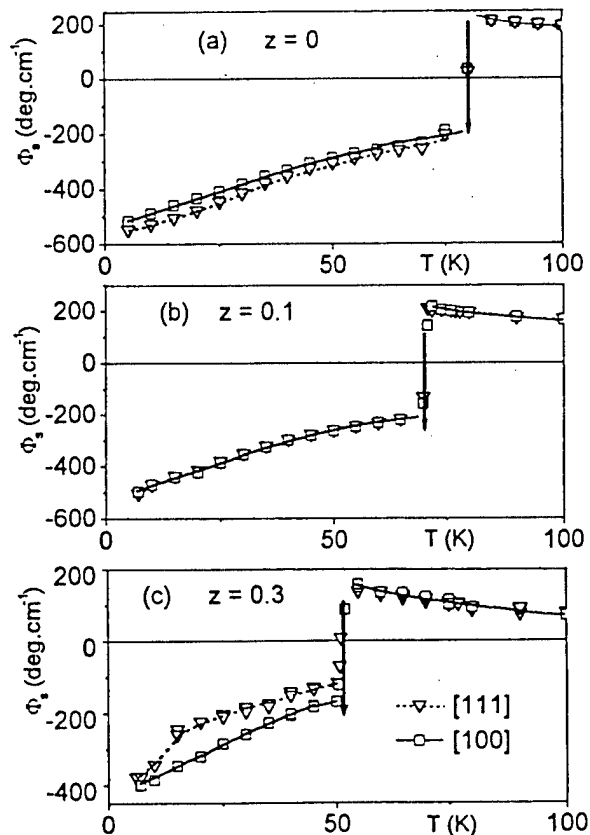


FIG. 3. Temperature variation of the spontaneous FR $\Phi_s(T)$ for (a) $z=0$, (b) $z=0.10$, (c) $z=0.30$ when H is parallel to [100] (\square) and when H is parallel to [111] (∇). The arrows indicate T_{comp} .

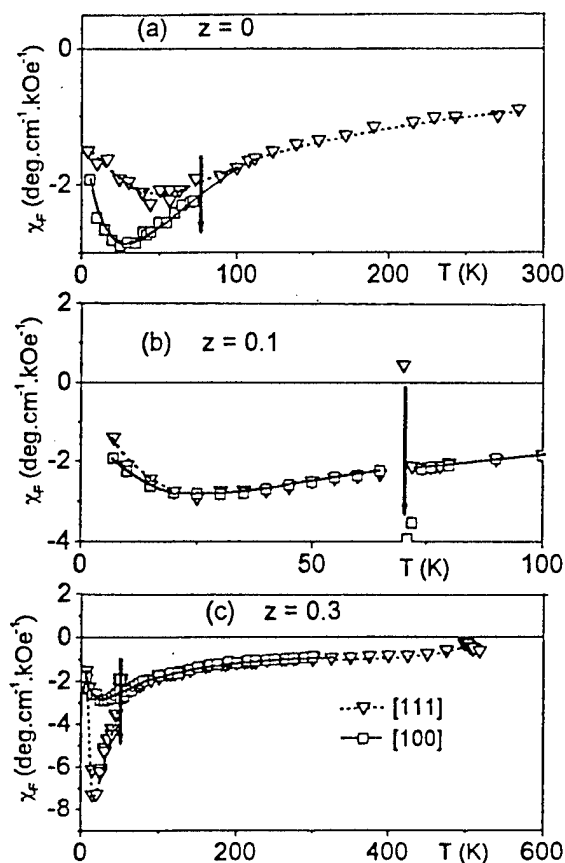


FIG. 4. Temperature variation of the FR susceptibility $\chi_F(T)$ for (a) $z=0$, (b) $z=0.10$, (c) $z=0.30$ when H is parallel to [100] (\square) and when H is parallel to [111] (∇). The arrows indicate T_{comp} .

parallel to [111], H_{sat} is strongly temperature dependent and the FRs are nonlinear in the 20 K– T_{comp} temperature zone. When $T > T_{\text{comp}}$ (Fig. 2), the anisotropy of the FR is no longer present and H_{sat} is of the order of 2 kOe for all concentrations and orientations.

The influence of the Sc concentration on the MO properties of the samples is best evidenced by the spontaneous FR $\Phi_s(T)$ presented in Fig. 3 for $z=0$, 0.10, and 0.30. Below T_{comp} , the FR anisotropy is present for $z=0$ and 0.30. The greater spontaneous absolute values are obtained when H parallel is to [111] for $z=0$ and H is parallel to [100] when $z=0.30$. The smallest values of H_{sat} are obtained for [100] and [111] when $z=0.30$ and 0, respectively. This indicates that in the experimental magnetic field range 0–20 kOe, the “easy” axis is shifted from [111] in pure ErIG garnet to [100] in ErIG:Sc with the greatest amount of Sc in the samples studied. This is confirmed by the behavior of the intermediate Sc concentration $z=0.10$. In this case, no FR anisotropy is observed within experimental accuracy. The only observed FR anisotropy concerns the “saturation” magnetic field which differs strongly as stated above.

This behavior is confirmed for the FR susceptibility, $\chi_F(T, z)$ (Fig. 4). In this case, the lowest χ_F values correspond to the easy axis as $|\chi| = |d\Phi/dH|$ is minimal at saturation. The easy axis is well shifted from [111] to [100] when z varies from 0 to 0.30. Note the discontinuity in the vicinity of T_{comp} .

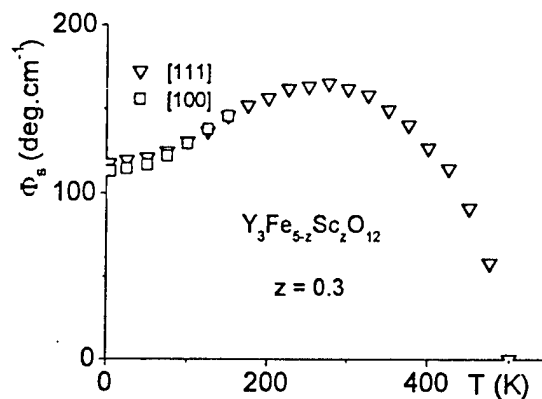


FIG. 5. Temperature variation of the spontaneous FR of $\text{Y}_3\text{Fe}_{5-z}\text{Sc}_z\text{O}_{12}$ ($z=0.30$) for H parallel to [100] and [111].

Within the framework of the one ion model,¹³ the FR of a three sublattice rare earth–iron–garnet is given by

$$\Phi_{\text{ErIG:Sc}} = \Phi_{\text{Er}} \mp \Phi_{\text{YIG:Sc}} = \pm (C_e + C_m) |M_c| \mp \Phi_{\text{YIG:Sc}}, \quad (1)$$

where $\Phi_{\text{Er}}(\lambda, T)$ is the Er^{3+} contribution to the spontaneous FR and the contributions from the Fe^{3+} [a] and (d) sublattices are represented experimentally by the FR at the same wavelength of the corresponding YIG garnet of the same composition.¹¹ Upper (lower) signs are valid for $T < T_{\text{comp}}$ ($T > T_{\text{comp}}$). $C_{e,m}(\lambda)$ are the respective MO electric “ e ” and magnetic “ m ” dipole coefficients of the $\{c\}$ sublattices with magnetizations $M_c(T)$.

We plotted in Fig. 5 the spontaneous FR of $\text{Y}_3\text{Fe}_{5-z}\text{Sc}_z\text{O}_{12}$ single crystals for $z=0.30$ with H parallel to [111] and [100]. Within experimental accuracy, no significant FR anisotropy is observed (maximum difference 4% at 6 K and less when T increases). For the magnetic anisotropy of YIG:Sc, the scandium substitution leads only to a variation of the K1 anisotropy constant smaller than 30% at 4.2 K when $z=0.30$.¹⁴ Therefore, the FR anisotropy observed in the ErIG:Sc single crystals is related to the Er sublattice.²

¹S. Geller, in *Physics of Magnetic Garnets*, edited by A. Paoletti (North-Holland, Amsterdam, 1978).

²M. Guillot, A. Marchand, F. Tch  ou, P. Feldmann, and H. Le Gall, *Z. Phys. B* **44**, 41 (1981).

³R. Hock, J. Baruchel, H. Fuess, B. Antonini, and P. Paroli, *J. Magn. Magn. Mater.* **104–107**, 453 (1992).

⁴M. Guillot, A. Marchand, H. Le Gall, P. Feldmann, and J. M. Desvignes, *J. Magn. Magn. Mater.* **15–18**, 835 (1980).

⁵P. Feldmann, H. Le Gall, J. M. Desvignes, M. Guillot, and A. Marchand, *J. Magn. Magn. Mater.* **21**, 280 (1980).

⁶P. Feldmann, J. Gouzerh, H. Le Gall, and M. Guillot, *J. Appl. Phys.* **53**, 8184 (1982).

⁷P. Feldmann, H. Le Gall, M. Guillot, and A. Marchand, *J. Appl. Phys.* **53**, 2486 (1982).

⁸N. M. Kolacheva, R. Z. Levitin, B. V. Mill’, and L. P. Shlyakhina, *Sov. Phys. Solid State* **21**, 604 (1979).

⁹M. Savosta, V. Doroshev, and V. Borodin, *J. Magn. Magn. Mater.* **157–158**, 523 (1996).

¹⁰P. R  schmann and P. Hansen, *J. Appl. Phys.* **52**, 6257 (1981).

¹¹J. Ostor  ro and M. Guillot, *J. Appl. Phys.* **81**, 4797 (1997).

¹²S. H  fner, *Optical Spectra of Transparent Rare Earth Compounds* (Academic, New York, 1978).

¹³W. A. Crossley, R. W. Cooper, J. L. Page, and R. P. Van Staple, *Phys. Rev.* **181**, 896 (1969).

¹⁴H. J. Van Hook, *IEEE Trans. Magn.* **MAG-7**, 770 (1971).

Crystal ion slicing of single-crystal magnetic garnet films

M. Levy^{a)} and R. M. Osgood, Jr.

Department of Applied Physics, Columbia University, New York, New York 10027

A. Kumar and H. Bakhru

Department of Physics, State University of New York at Albany, Albany, New York 12222

Epitaxial liftoff has been used for achieving heterogeneous integration of many III-V and elemental semiconductor systems. However, it has been heretofore impossible to integrate devices of many other important material systems. A good example of this problem has been the integration of single-crystal transition metal oxides on semiconductor platforms, a system needed for on-chip thin film optical isolators. We report here an implementation of epitaxial liftoff in magnetic garnets. Deep ion implantation is used to create a buried sacrificial layer in single-crystal yttrium iron garnet (YIG) and bismuth-substituted YIG (Bi-YIG) epitaxial layers grown on gadolinium gallium garnet (GGG). The damage generated by the implantation induces a large etch selectivity between the sacrificial layer and the rest of the garnet. Ten-micron-thick films have been lifted off from the original GGG substrates by etching in phosphoric acid. Millimeter-size pieces of excellent quality have been transferred to the silicon and gallium arsenide substrates. Study of the magnetic domain structure in the detached epilayers by Faraday contrast shows no changes in film anisotropy. Optical insertion loss measurements are also presented. © 1998 American Institute of Physics. [S0021-8979(98)31611-4]

The integration of magnetic garnet waveguides into silicon, gallium arsenide or indium-phosphite-based photonic integrated circuits (PICs) is of considerable technological importance. Optical isolators and circulators, which are essential components in the laser-source emitter end of the circuit, rely on the nonreciprocal properties of magnetic garnets for their operation. Bismuth-substituted yttrium iron garnet (Bi-YIG) and other rare-earth magnetic garnet films, used in the fabrication of these devices, are normally grown by liquid-phase or radio frequency sputter epitaxy on gadolinium gallium garnet (GGG) substrates. As a result it would be useful to develop viable techniques for on-chip integration of isolator materials. Despite several attempts, epitaxial growth of single-crystal magnetic garnets has not been realized on semiconductor substrates. As a result the integration of magneto-optic isolators and circulators into photonic circuits must rely on hybrid mounting techniques or wafer bonding and epitaxial liftoff.

The technology for epitaxial liftoff has been developed mostly in III-V semiconductors. It makes use of the large differential etch rate between a buried sacrificial layer and the epitaxial structure of interest to detach the latter from the substrate on which it has been grown. The technique was pioneered by Yablonovitch *et al.*¹ by relying on the high etch selectivity of AlAs over $\text{Al}_x\text{Ga}_{1-x}\text{As}$ in hydrofluoric acid. Subsequent work has demonstrated the liftoff of epitaxially grown layers in other III-V materials and the bonding of such layers on a variety of substrates. More recently Hunn *et al.*² have also demonstrated the separation of thin single-crystal diamond films from bulk diamond.

The work that we report here studies the technique of crystal ion slicing (CIS) for liftoff of a thin epitaxial layer. In

this technique buried sacrificial layers are formed in magnetic garnets, allowing the subsequent liftoff and bonding of $\sim 10\text{-}\mu\text{m}$ -thick films to semiconductor substrates. Deep ion implantation is used to generate a damage layer several microns beneath the sample surface. Since residual ion damage can, in principle, affect the top surface, techniques to minimize this damage should be examined in order to produce high quality films. For example, we have found that rapid thermal annealing eliminates this residual damage without jeopardizing the epitaxial liftoff process. Films of excellent quality are detached from the original substrate and van der Waals bonded to silicon and gallium arsenide. Faraday contrast examination of the magnetic domains in the samples shows that there is no noticeable change in the coercivity of the garnet as a result of the epitaxial liftoff process.

The samples used in this study are $10\text{-}\mu\text{m}$ and $95\text{-}\mu\text{m}$ -thick single-crystal films of YIG grown by liquid-phase epitaxy on a (111)-oriented GGG substrate. These epitaxial films have a formula unit of $\text{Y}_3\text{Fe}_5\text{O}_{12}$, with small amounts of lanthanum to improve lattice matching to the GGG substrate. Three- μm -thick Bi-YIG epitaxial films on GGG are also used to study the effect of ion implantation below the epilayer/substrate interface. The uniaxial growth anisotropy in these samples, typical of Bi-YIG films, results in the formation of magnetic domains with the magnetization directed normal to the sample surface. These domains can be easily observed via Faraday-contrast microscopy and their response to an applied magnetic field is used here to study the effect of ion implantation and epitaxial liftoff on the magnetic properties of the sample. The bismuth-substituted epilayers have a formula unit of $\text{Bi}_{0.6}\text{Y}_{2.4}\text{Fe}_5\text{O}_{12}$, with trace amounts of gallium.

Singly charged 3.8 MeV helium ions are implanted normal to the surface into the YIG and Bi-YIG epilayers, with-

^{a)}Electronic mail: MIGUEL@CUMSL.CTR.COLUMBIA.EDU

out any masking. The implant dose on all samples is 5×10^{16} ions/cm². The samples are mounted on a specially designed, 2 in. diam water-cooled target holder to ensure that the temperature of the substrate is below 400 °C. As an added precaution the beam current during the implant is kept low ($<0.25 \mu\text{A}/\text{cm}^2$). These precautions are necessary to avoid thermal modification of the optical absorptivity and magnetic anisotropy of the sample during implantation. The uniformity of the implantation is monitored by four Faraday cups outside the target holder.

Helium is chosen as the implantation species because of its light weight, yielding a deeply buried damage layer. Two dominant mechanisms for energy loss determine the implantation profile and the distribution of lattice damage in the crystal.³ The energy loss per unit trajectory length, known as the stopping power, is dominated by electronic scattering at high ionic energies. Energy loss for this process is adequately described by the Lindhard-Scharff-Schiott (LSS) theory,⁴ which predicts a stopping power proportional to $E^{1/2}$. Here E is the energy of the implanted ion along its trajectory. This process generates very little lattice damage.³ At low energies the stopping power is primarily due to Rutherford scattering with the host nuclei, and is inversely proportional to E^2 . This nonlinear dependence ensures that the majority of the ions are deposited in a relatively narrow spatial region of the sample.

Lattice defects are introduced by the transfer of energy to the target nuclei, and therefore form near the end of the ionic trajectories. Transport-of-ions-in-matter⁵ (TRIM) calculations for helium implanted at 3.8 MeV of energy into YIG show that the implantation profile is rather narrow and concentrated approximately $9.3 \mu\text{m}$ below the surface. Calculated profiles for the Bi-YIG samples exhibit an implantation depth of $8.8 \mu\text{m}$. Tests were also performed in the same materials for neon implantation, at the same energies and dosage as indicated above. Crystal ion slicing of the neon-implanted samples was unsuccessful due to the much higher level of near-surface damage generated by the heavier neon ions.

Insertion loss measurements in waveguided transmission were performed on the $3\text{-}\mu\text{m}$ -thick Bi-YIG epitaxial films. These tests compared the transmitted optical power of implanted and unimplanted samples at a wavelength of $1.55 \mu\text{m}$. In these samples the sacrificial layer due to the implantation forms about $6 \mu\text{m}$ below the waveguiding slab, in the GGG substrate. Figure 1 shows the total insertion loss relative to the optical fiber output power used to couple light into the waveguide by end-fire coupling. The data exhibit an excess loss of more than 5 dB in the ion-implanted material throughout the range of waveguide lengths studied. This excess loss is due to residual damage inflicted by the ion bombardment on the Bi-YIG epilayer during the implantation. It can be annealed out by rapid thermal annealing (RTA) without compromising the effectiveness of the epitaxial liftoff, as described below. Samples annealed after implantation exhibit no excess transmission loss relative to the unimplanted material, as shown in Fig. 1.

The samples are etched in commercial 85% dilution orthophosphoric acid, an etchant reported previously for lateral

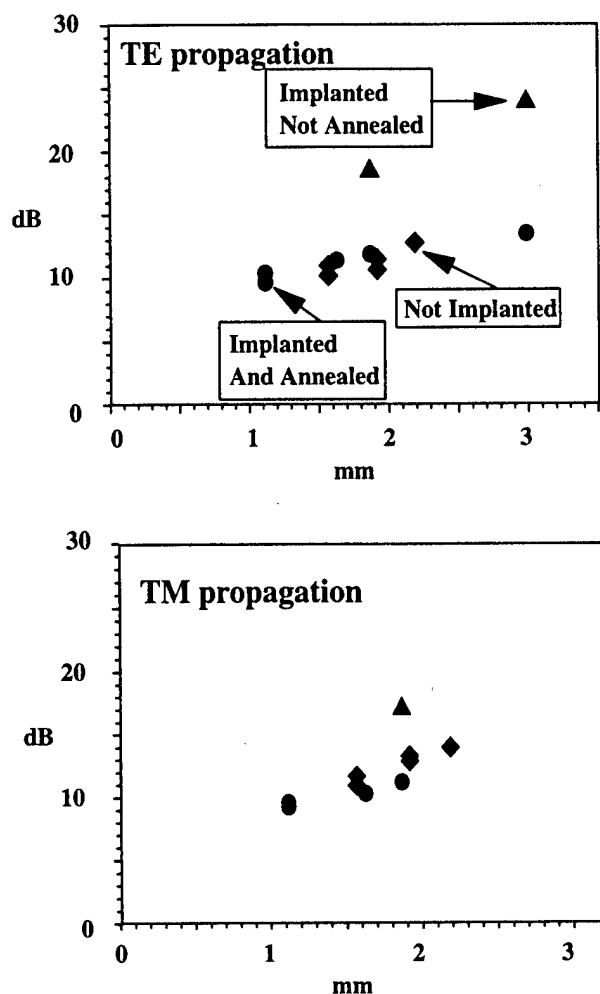


FIG. 1. Insertion loss vs slab waveguide length in Bi-YIG epilayers. The loss is measured relative to the input power. Triangles correspond to implanted material without annealing (RTA), circles to implanted and annealed samples, and rhombi to unimplanted material. The plot shows that there is degradation in insertion loss for ion-implanted waveguides after rapid thermal annealing, relative to the unimplanted material.

patterning of ion-implant waveguides in YIG.⁶ A deep undercut forms after several hours, centered about $9.5 \mu\text{m}$ below the top surface in the YIG and $9 \mu\text{m}$ in the Bi-YIG. The location of the undercut is in good agreement with the calculated implantation profile. Figure 2 is a micrographic side-view of the etched bismuth-substituted sample, showing the liftoff film still attached to its original substrate. Note that the Bi-YIG/GGG interface, located $3 \mu\text{m}$ below the top, appears visually unaffected by the ion implantation and subsequent etching. In particular, it exhibits no selective etching in spite of being traversed by the ionic trajectories during the implantation. The underside of the film, adjacent to the sacrificial layer, is also microscopically smooth.

If unprotected during etching, the top surface of the sample is roughened by exposure to the acid. This roughening is due to residual lattice damage near the top generated by the ion implantation, and correlates with the damage-induced excess loss in the optical measurements described before. Rapid thermal annealing before etching but after implantation repairs this residual damage without compromising the efficiency of the subsequent wet etching of the buried

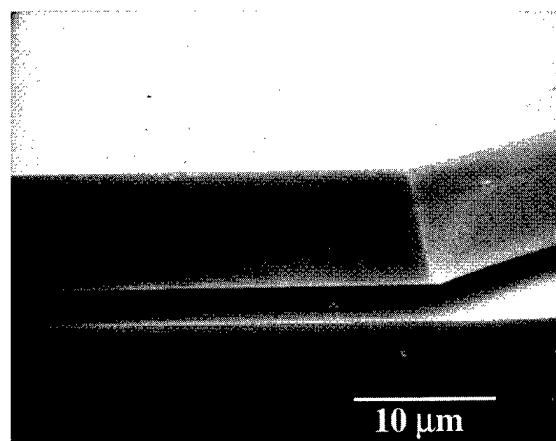


FIG. 2. Cross section of ion-implanted Bi-YIG showing the undercut as a result of wet etching in phosphoric acid. Note the smooth Bi-YIG/GGG interface $\sim 3 \mu\text{m}$ below the top surface.

layer. Specifically, tests show that a 20 s anneal (RTA) at 700°C in forming gas (5% hydrogen, 95% nitrogen) results in a smooth surface.⁷ The differential etch rate between the sacrificial layer and the rest of the sample is found by comparing the etch rate of the undercut to that of the top surface under the same conditions, and is measured to be in excess of 10^3 .

To fully detach a section of film of a square millimeter area from the substrate, the sample must be in the etchant for about 24 h. But contrary to the case of III-V materials, it is not necessary to rely on the stress created by any protective cover to allow the flow of reaction products away from the etching zone.¹ The films are then van der Waals bonded to silicon or GaAs. Figure 3 shows a YIG film bonded to GaAs. YIG films are quite brittle and must be handled carefully to avoid developing microfractures during the processing. We have been able to produce fracture-free films routinely, but have found that some protective encapsulation is needed to prevent cracks from developing.⁷ Initial tests indicate that this fracture formation is due to stress from bowing of the epilayer during the etching process.

The domain structure in YIG and Bi-YIG films after epitaxial liftoff was studied by Faraday contrast microscopy. The YIG samples used were (111) films with nearly planar anisotropy and some residual cubic anisotropy. Their magnetization was parallel to the [211] directions. The Bi-YIG films had uniaxial anisotropy. No change in anisotropy occurred as a result of the ion implantation and liftoff proce-

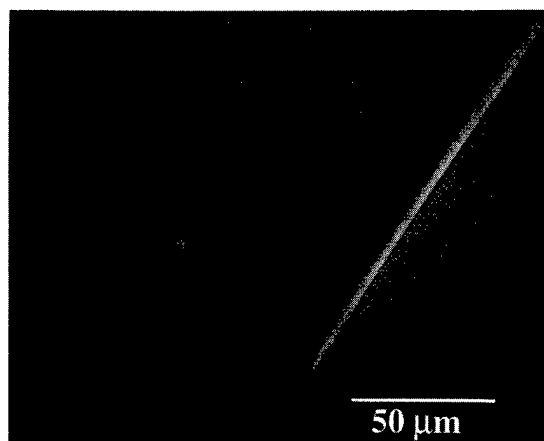


FIG. 3. Scanning electron micrograph of a fracture-free YIG film after epitaxial liftoff, onto a GaAs(100) wafer substrate.

dure. This contrasts with the effect of energetic heavy-ion implantation in garnets, where damage-generated changes are found in the domain structure.⁸ Electronic-dominated scattering is responsible for the stopping power in the YIG and Bi-YIG epilayer, causing little damage to the film except in and around the sacrificial layer. Comparison between the saturation magnetic field in the Bi-YIG crystal before and after implantation and liftoff shows no change within experimental uncertainty. Thus no significant degradation in the magnetic response results from damage-generated domain pinning during the crystal ion slicing.

The authors thank G. S. Cargill III, for illuminating discussions, and J. Kirtley and D. Petrov for magnetic domain imaging. M.L. and R.M.O. acknowledge support by MURI/DARPA under Contract No. F49620-96-1-0111.

¹Eli Yablonovitch, T. Gmitter, J. P. Harbison, and R. Bhat, *Appl. Phys. Lett.* **51**, 2222 (1987).

²J. D. Hunn, S. P. Withrow, C. W. White, R. E. Clausing, L. Heatherly, C. Paul Christensen, and N. R. Parikh, *Nucl. Instrum. Methods Phys. Res. B* **99**, 602 (1995).

³M. S. Dresselhaus and R. Kalish, *Ion Implantation in Diamond, Graphite and Related Materials* (Springer, Berlin, 1992).

⁴J. Lindhard, M. Scharff, and H. E. Schiott, *Mat. Fys. Medd. K. Dan. Vidensk. Selsk.* **33**, 14 (1963).

⁵J. P. Biersack and L. G. Haggermark, *Nucl. Instrum. Methods* **174**, 257 (1980).

⁶W. A. Johnson, J. C. North, and R. Wolfe, *J. Appl. Phys.* **44**, 4753 (1973).

⁷M. Levy, R. M. Osgood, Jr., A. Kumar, and H. Bakhru, *Appl. Phys. Lett.* **71**, (1997).

⁸P. Hansen, in *Proceedings of the International School of Physics Enrico Fermi*, edited by A. Paoletti (North-Holland, New York, 1978), p. 61.

Faraday rotation and magnetic properties of erbium gallium gallate under high magnetic field

M. Guillot,^{a)} T. Schmiedel,^{b)} and You Xu^{c)}

Laboratoire des Champs Magnétiques Intenses, CNRS/MPI 38042 Grenoble, France

Magnetization (M) and Faraday rotation (FR) have been measured in $\text{Er}_3\text{Ga}_5\text{O}_{12}$ single crystals in the 4.2–300 K temperature range under high dc magnetic field up to 300 kOe. Experimental data are reported for H applied parallel to the [111] and [100] directions at 633 and 550 nm wavelength. A strong anisotropy of both magneto-optical and magnetic properties is observed. At low temperature, FR and M are proportional only when the magnetization is weak (small magnetic field). In medium and high magnetic field, complex relationships between M and FR are found. The magnetization cannot account for the whole Faraday rotation anisotropy. These data are discussed taking into account the magnetic and magneto-optical properties of the isomorphous erbium iron garnet ferrite.

© 1998 American Institute of Physics. [S0021-8979(98)26111-1]

I. INTRODUCTION

There has been considerable interest in magneto-optical (MO) properties of magnetic ceramics over the last decades. This attention is particularly due to the promising technological applications of the Faraday rotation (FR) and of the Kerr effect (KE) in optical range devices since magnetization of the material can be read out using MO tools. Although numerous investigations of materials offering a maximum of figure of merit at a specific wavelength of laser diodes were conducted, the theoretical analysis of the MO properties are, however, scarce.^{1,2} Particularly the relationship between magnetization and MO effects was found to be more complex than simple models where the MO properties were supposed to scale proportionally to the magnetization.^{3–5} It should be noted that even inside one unique series of compounds, these studies are very delicate since many parameters like exchange splitting, spin-orbit coupling, lattice parameter cannot vary independently; furthermore they are usually performed at room temperature only where the energy schema are very complicated. One way to avoid this difficult task is to measure magnetic and MO properties on one unique crystal and under high magnetic field and that in a large temperature range.

An evident illustration of the complicated relationship between magnetization and MO properties is given, in the ferrimagnetic iron $\text{Er}_3\text{Fe}_5\text{O}_{12}$ garnet (ErIG), by the contribution to FR of the rare-earth sublattice; the rare-earth contribution vanishes near 75 K even the magnetic moment of the Er^{3+} ion is about of $5 \mu_B$.^{6,7} Recently using quantum theory, we have demonstrated that the rare-earth Fe superexchange interaction (SI) and the crystal field (CF) on the rare earth ion are crucial factors in the calculation of magnetic and MO properties. Furthermore when SI is large, the admixing of different ground term multiplets by the high-order perturbation of SI is important.⁸ Because in the ferrimagnetic garnet structure, SI corresponds to molecular fields in the range

100–300 kOe, we present, in this article, both magnetic and FR measurements in high dc magnetic field up to 300 kOe performed on the isomorphous paramagnetic $\text{Er}_3\text{Ga}_5\text{O}_{12}$ gallate (ErGaG) with special attention paid to the anisotropy of these properties. It is recalled that in ErGaG, the Néel point related to an antiferromagnetic long range ordering is below 1 K, the Er–Er superexchange interaction is negligible and the crystal is paramagnetic at 4.2 K.

II. EXPERIMENT

Faraday rotation (FR) and magnetization (M) measurements were performed on the same single crystals of composition $\text{Er}_3\text{Ga}_5\text{O}_{12}$ grown by the flux method. The FR measurements were realized at the National High Magnetic Field Laboratory (Florida State University Tallahassee USA); the M measurements, at the High Magnetic Field Laboratory (CNRS/MPI Grenoble). After the control of the single crystal quality by x-ray diffraction techniques, the crystal was x-ray oriented, cut, and polished to obtain two disks with respective planes of (111) and (100). The diameters were about 2 mm and the thickness were, respectively, 1.46 and 1.49 mm.

The external magnetic field attained was 300 kOe (FR measurements) and either 262 (at 4.2 K) or 200 kOe (M measurements), H being applied perpendicular to the major plane of each plate. In the first case, the high continuous magnetic field was produced by a 32 mm inner-bore water-cooled resistive magnet connected to a high powerful electrical power (12 MW) supply; in the second one, either a 50 mm inner-bore hybrid or a 50 mm inner-bore water-cooled resistive magnet was used. The magnetic measurements were carried out using the automatic magnetometer described in Ref. 9 leading to an experimental accuracy on M better than $\pm 2\%$.

MO properties like FR and KE have not been investigated much in high magnetic field. However, it was noted that one of the most important experimental difficulties is to separate the contribution of the sample from the contribution of the windows of the cryostat mainly because stray fields are always very large in high field setup.¹⁰ Our optical device will be described in detail in a forthcoming article.¹¹ However we would like to mention that, in contrast to optical

^{a)}Electronic mail: mguillot@labs.polycnrs-gre.fr

^{b)}Present address: National High Magnetic Field, Tallahassee Florida 32310.

^{c)}Present address: Department of Physics, Nanjing University, Nanjing 210008, China.

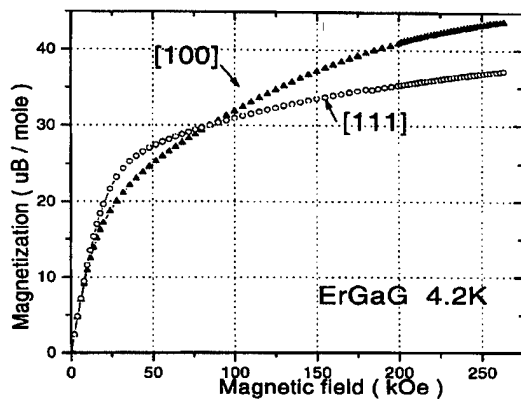


FIG. 1. Magnetization vs magnetic field applied parallel to the [111] and [100] crystallographic directions at 4.2 K in ErGaG.

system of Ref. 10, both the polarizer and the analyzer are located in the near vicinity of the sample in the low temperature chamber. Thin optical fibers were used to conduct the light from the source (lamp plus spectrometer) to the polarizer and from the analyzer to the detector. The polarizer and analyzer were crossed at room temperature in the presence of the sample. It is worth noting that without any sample, the plane of polarization of the emerging light from the analyzer was observed to be insensitive to the simultaneous presence of the high field and of low temperature. Furthermore the crossing of the polarizer and analyzer was observed to be insensitive to the presence of the high field. Finally, the experimental accuracy on FR may be estimated about $\pm 3\%$.

This article is limited to the data obtained at 633 ($15\,797\text{ cm}^{-1}$) and 550 ($18\,182\text{ cm}^{-1}$) nm wavelength. It is recalled that the ErGaG absorption spectrum consists of different sharp lines centered at 6775, 10 415, 12 496, 15 449, 18 525, 19 407, 20 717, 22 371, 22 701, and 24 893 cm^{-1} , respectively. These absorption peaks were attributed to transitions between the ground multiplet $^4I_{15/2}$ and different excited multiplets $^4I_{13/2}$, $^4I_{11/2}$, $^4I_{9/2}$, $^4F_{9/2}$, $^4S_{3/2}$, $^2H_{11/2}$, $^4F_{7/2}$, $^4F_{5/2}$, $^4F_{3/2}$, and $^2G_{9/2}$, respectively.¹²⁻¹⁵

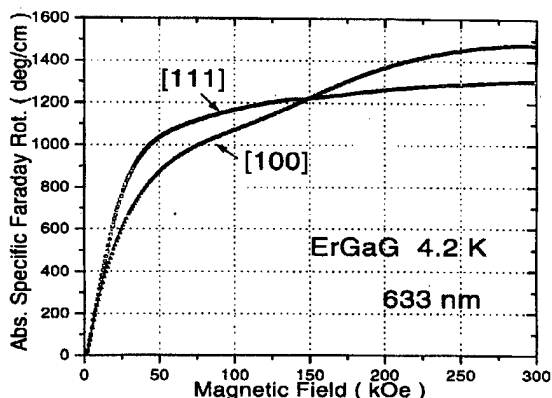


FIG. 2. Faraday rotation vs external field parallel to the [111] and [100] crystallographic directions at 4.2 K in ErGaG; experiments performed at 633 nm wavelength.

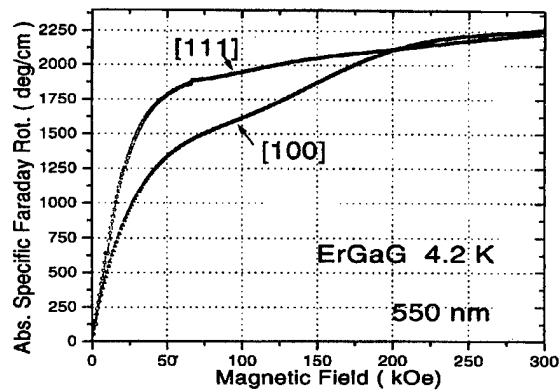


FIG. 3. Faraday rotation vs external field parallel to the [111] and [100] crystallographic directions at 4.2 K in ErGaG; experiments performed at 550 nm wavelength.

III. RESULTS AND DISCUSSION

An example of the magnetic behavior is given by Fig. 1 where the 4.2 K magnetization curves are given. It is noted that in the article, the M values are reported in Bohr magneton per mole where one mole is equal to $2(\text{Er}_3\text{Ga}_5\text{O}_{12})$ and that because there exist six magnetically inequivalent Er sites in the cubic crystallographic unit cell described by the $Ia\bar{3}d$ space group. The experimental data shown evidence of the following properties: (i) in H below about 25 kOe no anisotropy of the magnetization exists within our experimental accuracy ($\pm 2\%$); (ii) above 25 kOe, the field-induced anisotropy is observed between 4.2 and 50 K although at this last temperature, this anisotropy is becoming very weak; (iii) on each isothermal $M(H)$ curve, this anisotropic character is found to be increasing with H . But, the most important feature is the existence of a cross-over field H_{co} about 80 kOe; when $H > H_{co}$, the [100] magnetization is larger than the [111] one. It is clear that no saturation magnetization is observed and it is not possible to conclude unambiguously that [100] is, in the gallate, the easy direction of magnetization as it is in ErIG.¹⁶ However, because along the [100] direction, the relative change of M between 200 and 260 kOe is less than 12%, we deduce that, in this field region, the magnetic moment per Er^{3+} ion is about $7\mu_B$. Following this determination, two comments can be made: first, our value is in good agreement with the rare earth magnetic moment de-

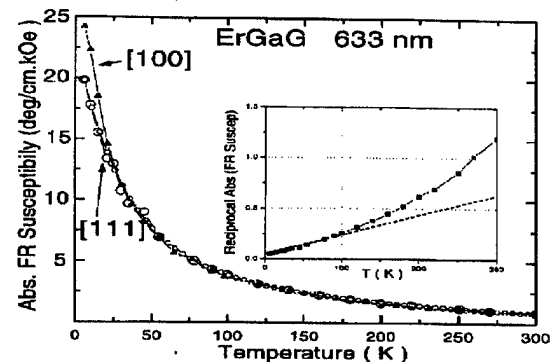


FIG. 4. Faraday rotation susceptibility vs temperature in ErGaG at 633 nm wavelength. (insert: reciprocal FR susceptibility).

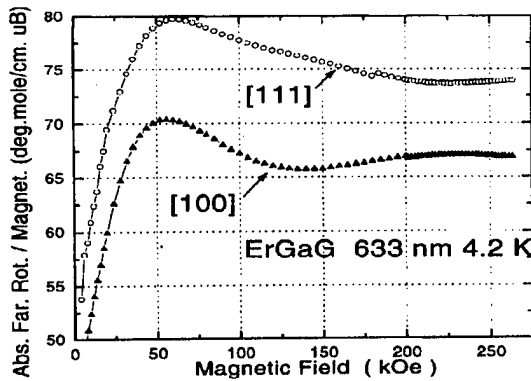


FIG. 5. Ratio of the Faraday rotation measured at 633 nm wavelength to the magnetization as a function of the applied field at 4.2 K for ErGaG.

duced in ErIG from direct magnetization measurements¹⁶ and from neutron diffraction study,^{17,18} second, it is confirmed that SI in the ferrite corresponds to external field in the 200–260 kOe range. Furthermore our data show unambiguously the strong quenching of the orbital moment by crystal field (CF) since, even at 4.2 K, the Er^{3+} magnetic moment remains less than the free-ion value corresponding to the ground multiplet $^4I_{15/2}$.

The high field variations of the FR are reported in Figs. 2 and 3 for H parallel to [111] and [100] at 4.2 K. The following remarks must be advanced: (i) the magnitudes of FR are very different for the two wavelengths; (ii) at 633 nm wavelength, a strong anisotropy of FR is evidenced whatever the field strength with the strongest FR observed above 150 kOe along [100]; note the MO cross-over field differs strongly from that found on the $M(H)$ curves (Fig. 1); (iii) at 550 nm wavelength, the FR anisotropy decreases rapidly above 200 kOe; below this field, the highest FR value corresponds to the [111] direction.

Because in low applied field, the FR is linear versus H the FR susceptibility (Verdet constant V) can be deduced; as expected a strong decrease of V with increase in temperature is obtained (Fig. 4). It is worthy to note that the anisotropy of V is present up to 25 K although no magnetic anisotropy was observed in low applied field as mentioned above. As shown in the inset of the Fig. 4, the reciprocal Verdet constant does not present a linear temperature dependence as found in some rare earth trifluorides.¹⁹

The comparison between the high magnetic dependencies of FR and M is illustrated by their ratio plotted in the Figs. 5 and 6 at 4.2 K. A strong anisotropy of this ratio is immediately remarked and it is clear that the relationship between the FR and M is complex. However for the two wavelengths, the ratio FR/ M is found to be field independent above 100 kOe at least for the [100] direction within an experimental accuracy estimated to be 5%. This conclusion may be considered as an experimental confirmation of the model proposed many years ago by Crossley *et al.*²⁰ where in the ferrimagnetic garnets, the contribution to FR of each sublattice is proportional to the sublattice magnetization.

Although MO effects in the visible region are mainly due to intraionic electric dipole transitions between the $4f^n$

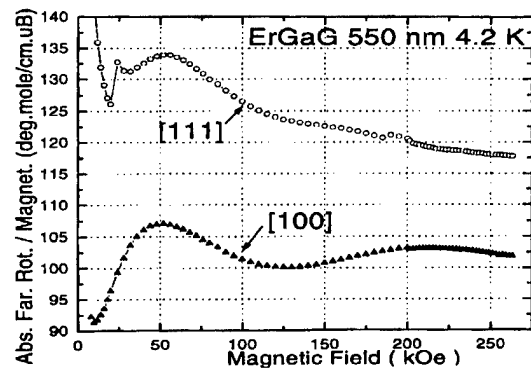


FIG. 6. Ratio of the Faraday rotation measured at 550 nm wavelength to the magnetization as a function of the applied field at 4.2 K for ErGaG.

and $4f^{n-1} 5d$ configurations, the strong difference between the data obtained at 633 and at 550 nm wavelength illustrates how the crystal field (CF) is the fundamental perturbation on the electronic states. The choice of the CF parameters is a crucial problem and only values obtained by Nekvasil *et al.*²¹ in SmIG and then corrected by the ratio of the radii of the rare earth ions allow a reasonable interpretation of the data in some light rare earth garnets (see Ref. 8 and references therein).

ACKNOWLEDGMENTS

The authors are indebted to J. M. Desvignes (CNRS Meudon Bellevue France) for the sample preparation. One (GM) of the authors is grateful to Jack E. Crow and to Bruce Brandt for the use of the high continuous field facilities of the NHMFL and for the helpful comments during the experiments performed at Tallahassee.

- ¹D. K. Misemer, J. Magn. Magn. Mater. **72**, 267 (1988).
- ²J. M. Oppeneer, J. Sticht, T. Maurer, and J. Kubler, Z. Phys. B **88**, 309 (1992).
- ³P. N. Argyres, Phys. Rev. **97**, 334 (1955).
- ⁴J. L. Erskine, and E. A. Stern, Phys. Rev. B **8**, 1239 (1973).
- ⁵M. Guillot, A. Marchand, H. Le Gall, P. Feldman, and J. M. Desvignes, J. Magn. Magn. Mater. **15–18**, 235 (1980).
- ⁶P. Feldman, H. Le Gall, M. Guillot, and A. Marchand, J. Appl. Phys. **53**, 2486 (1982).
- ⁷M. Guillot, F. Tcheou, A. Marchand, and P. Feldman, Z. Phys. B **44**, 53 (1981).
- ⁸J. Yang, Y. Xu, F. Zhang, and M. Guillot, Phys. Rev. B **56**, 11 119 (1997).
- ⁹J. C. Picoche, M. Guillot, and A. Marchand, Physica B **155**, 107 (1989).
- ¹⁰Y. Souche, A. Saadoui, and M. Guillot, Phys. E Sci. Instrum. **17**, 1108 (1984).
- ¹¹M. Guillot and T. Schmiedel (unpublished).
- ¹²G. B. Wybourne, J. Chem. Phys. **36**, 230 (1962).
- ¹³M. Veyssié-Cournillon, thesis, University Grenoble, 1966.
- ¹⁴R. I. Laming, S. B. Poole, and E. J. Tarbox, Opt. Lett. **13**, 1084 (1988).
- ¹⁵Y. Maeda, J. Appl. Phys. **72**, 3835 (1992).
- ¹⁶M. Guillot, A. Marchand, F. Tcheou, P. Feldman, and H. Le Gall, Z. Phys. **44**, 41 (1981).
- ¹⁷M. Guillot, F. Tcheou, A. Marchand, and P. Feldman, C.R. Acad. Sci. (Paris) Ser. B **291**, 227 (1980).
- ¹⁸R. Hock, H. Fuess, T. Vogt, and M. Bonnet, Z. Phys. B **82**, 283 (1991).
- ¹⁹C. Leycuras, H. Le Gall, M. Guillot, and A. Marchand, J. Appl. Phys. **55**, 2161 (1984).
- ²⁰W. A. Crossley, R. W. Cooper, J. L. Page, and R. P. Stapele, Phys. Rev. **181**, 896 (1969).
- ²¹V. Nekvasil, M. Guillot, A. Marchand, and F. Tcheou, J. Phys. C **18**, 3551 (1985).

On the origin of the magneto-optical effects in Li, Mg, Ni, and Co ferrite

W. F. J. Fontijn and P. J. van der Zaag^{a)}

Philips Research Laboratories, Prof. Holstlaan 4, 5656 AA Eindhoven, The Netherlands

R. Metselaar

Department of Chemistry, Eindhoven University of Technology, 5600 MB Eindhoven, The Netherlands

A reexamination of the magneto-optical (MO) spectra of $\text{Li}_{0.5}\text{Fe}_{2.5}\text{O}_4$, MgFe_2O_4 , NiFe_2O_4 , and CoFe_2O_4 is presented. Thus far the MO spectra of these compounds have been explained by either orbital promotion processes, oxygen to iron charge transfer transitions or crystal field transitions and, in the case of CoFe_2O_4 , a single intervalence charge transfer (IVCT) transition. For $\text{Li}_{0.5}\text{Fe}_{2.5}\text{O}_4$ and MgFe_2O_4 , the major transitions in the MO-Kerr spectra between 0.5 and 5.0 eV are assigned to intersublattice charge transfer (ISCT) transitions. The MO-Kerr spectrum of NiFe_2O_4 is more complex as in this case both Fe^{3+} and Ni^{2+} contribute to the spectrum. In NiFe_2O_4 an additional IVCT transition is observed at 2.9 eV. The complex MO spectrum of CoFe_2O_4 could be resolved using the dielectric tensors of $\text{Co}^{2+}\text{Al}_x^{3+}\text{Fe}_{2-x}^{3+}\text{O}_4$ ($x=0, 0.1, 0.6$, and 1) and rigorously fitting both the diagonal and the off-diagonal elements of the dielectric tensor with one set of transitions which was consistent for all degrees of Al^{3+} substitution. Thus, in these ferrites a consistent assignment of all the major transitions in the 2.0 to 5.0 eV energy range to either IVCT or ISCT transitions is made. © 1998 American Institute of Physics. [S0021-8979(98)22011-1]

I. INTRODUCTION

The identification and assignment of magneto-optical (MO) active transitions in spinel ferrites have been a subject of debate for many years. The identification of transitions is complex as in these compounds many bands overlap. In addition, the electronic structure of transition metal oxides such as ferrites is complex^{1,2} which has resulted in a variety of interpretations of the observed transitions. Recently, we have unraveled the MO-Kerr spectrum of Fe_3O_4 between 0.7 and 4.0 eV by rigorous fitting of all four elements of the dielectric tensor of Fe_3O_4 simultaneously, using the equations of the elements of the dielectric tensor which describe the basic line shapes of transitions in the microscopic theory (Lorentz-type lineshape). In addition, the complete dielectric tensors of Fe_3O_4 and of partially Mg^{2+} or Al^{3+} substituted Fe_3O_4 were fitted with only one set of parameters for all samples. The influence on the intensity of transitions of the gradual substitution of Fe^{2+} and/or Fe^{3+} provided evidence that the major transitions in Fe_3O_4 can be assigned to intervalence charge transfer and intersublattice charge transfer transitions (IVCT and ISCT, respectively).³ IVCT transitions are transitions in which an electron, through optical excitation, is transferred to a neighboring cation. IVCT transitions between Fe^{3+} ions on different crystallographic sites are traditionally called ISCT transitions.⁴ For reasons of clarity we will continue to refer to these transitions as ISCT transitions. (In our discussions parenthesis denote tetrahedral A sites and square brackets octahedral B sites.)

Thus far multiple interpretations have been reported for the ferrites $\text{Li}_{0.5}\text{Fe}_{2.5}\text{O}_4$, MgFe_2O_4 , NiFe_2O_4 , and CoFe_2O_4 . We will discuss them in chronological order. Krinchik *et al.* reported the off-diagonal element of the dielectric tensor of $\text{Li}_{0.5}\text{Fe}_{2.5}\text{O}_4$ between 2 and 5 eV.⁵ These authors reported

also the off-diagonal elements of NiFe_2O_4 , CoFe_2O_4 , CoCrFeO_4 between 1 and 5.4 eV and the equatorial Kerr effect of $(\text{Fe})[\text{NiCr}]_4\text{O}_4$.^{5,6} In addition to the transitions already identified in $\text{Li}_{0.5}\text{Fe}_{2.5}\text{O}_4$ and MgFe_2O_4 an additional broad band near 3 eV was identified in NiFe_2O_4 . This band was assigned to the CF transition ${}^3A_{2g}(\text{F}) \rightarrow {}^3T_{1g}(\text{P})$ of octahedrally coordinated Ni^{2+} . However, in this interpretation the disappearance of this transition in $(\text{Fe})[\text{NiCr}]_4\text{O}_4$ cannot be accounted for. From the observed influence of Al^{3+} and Cr^{3+} substitution on the equatorial Kerr spectra of NiFe_2O_4 and CoFe_2O_4 , Krinchik *et al.* conclude that the major transitions in $\text{Li}_{0.5}\text{Fe}_{2.5}\text{O}_4$ and MgFe_2O_4 are ISCT transitions.

Subsequently, Višnovsky *et al.* reported the diagonal and off-diagonal elements of the dielectric tensor of MgFe_2O_4 and reflectivity and polar Kerr spectra of $\text{Li}_{0.5}\text{Fe}_{2.5}\text{O}_4$ between 2 and 5.5 eV. These authors assigned the transitions identified to oxygen (2p) to iron (3d) charge transfer transitions.⁷ From the work of Bocquet *et al.*, however, it follows that this is an unlikely interpretation as the oxygen to iron charge transfer transitions are centered around 6 eV (Ref. 2) in agreement with previous reports.^{4,8} In 1983 Zhang *et al.* reported the diagonal (0.5–12 eV) and off-diagonal (0.5–5 eV) elements of the dielectric tensor of $\text{Li}_{0.5}\text{Fe}_{2.5}\text{O}_4$ and MgFe_2O_4 . The identified bands were assigned to $3d^n \rightarrow 3d^{n-1}4s$ orbital promotion transitions.⁸ However, these transitions are parity and partly spin forbidden and can, therefore, not account for the relatively large oscillator strength (10^{-3}) of the transitions observed in these ferrites. Finally, the MO-Kerr spectrum of CoFe_2O_4 has been extensively studied by Martens and co-workers.^{9,10} Two narrow diamagnetic transitions at 0.8 and 2.0 eV were identified and assigned to CF transitions [${}^4A_2 \rightarrow {}^4T_1(\text{F})$ and ${}^4A_2 \rightarrow {}^4T_1(\text{P})$] of tetrahedrally coordinated Co^{2+} . A broad paramagnetic band also at 2.0 eV was assigned to a $[\text{Co}^{2+}] \rightarrow [\text{Fe}^{3+}]$ IVCT transition. The broad diamagnetic band in the region above 3 eV remained unresolved.

^{a)} Author for correspondence.

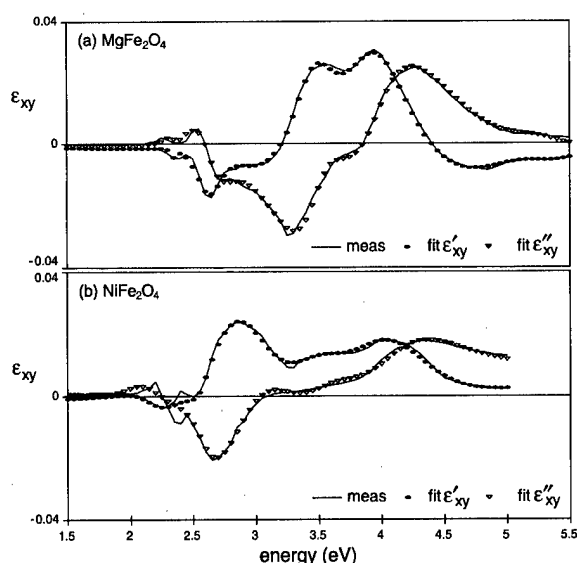


FIG. 1. (a) The measurement Ref. 7 and the fits of the real and imaginary part of the off-diagonal element of the dielectric tensor, ϵ'_{xy} and ϵ''_{xy} , of MgFe_2O_4 . (b) The measurement Ref. 5 and the fits of the real and imaginary part of the off-diagonal element of the dielectric tensor, ϵ'_{xy} and ϵ''_{xy} , of NiFe_2O_4 .

Here we report a study of the MO spectra of $\text{Li}_{0.5}\text{Fe}_{2.5}\text{O}_4$, MgFe_2O_4 , NiFe_2O_4 , and CoFe_2O_4 and identify the major transitions. For this purpose, we have taken the elements of the dielectric tensor of these compounds from literature and applied the same method used to resolve the MO spectrum of Fe_3O_4 .³

II. RESULTS AND DISCUSSION

First, we examine MgFe_2O_4 . We applied the method used to resolve the spectrum of Fe_3O_4 to the diagonal and off-diagonal element of the dielectric tensor of MgFe_2O_4 obtained from Refs. 8 and 7, respectively. The off-diagonal element and the fits are presented in Fig. 1(a). The set of transitions identified in MgFe_2O_4 is listed in Table I. To

assign these transitions, we compare them to the transitions found in Fe_3O_4 .³ The MO spectrum of Fe_3O_4 consists of two sets of transitions: IVCT transitions involving Fe^{2+} and Fe^{3+} and the ISCT involving two Fe^{3+} ions located on different crystallographic sites. Since the Fe^{2+} ions present in Fe_3O_4 are replaced by the nonmagnetic Mg^{2+} , the ISCT transitions should be the only remaining major transitions. Substitution of one ion with another may distort the lattice resulting in a shift in energy of the ISCT transitions. However, replacing Fe^{2+} with Mg^{2+} only has a small effect on the lattice since the lattice parameter of MgFe_2O_4 matches closely the lattice parameter of Fe_3O_4 . We conclude from our fit [Fig. 1(a)] that the MO-Kerr spectra of MgFe_2O_4 can be explained in a manner consistent with our interpretation of Fe_3O_4 , based on ISCT transitions, as suggested previously.¹¹

For $\text{Li}_{0.5}\text{Fe}_{2.5}\text{O}_4$ the elements of the dielectric tensor were obtained from Refs. 8 and 5. The set of transitions identified from our fits is listed in Table I. The same three major bands as in MgFe_2O_4 could be identified. The fact that the intensities in $\text{Li}_{0.5}\text{Fe}_{2.5}\text{O}_4$ are substantially higher than in MgFe_2O_4 is to be expected as this compound contains a larger amount of $[\text{Fe}^{3+}]$, which is one of the participating ions in the transition.⁵ Thus also the MO-Kerr spectra of $\text{Li}_{0.5}\text{Fe}_{2.5}\text{O}_4$ can be explained in a manner consistent with Fe_3O_4 based on ISCT transitions.

Only the off-diagonal element of the dielectric tensor of NiFe_2O_4 was available.⁵ The off-diagonal element and fit are presented in Fig. 1(b). The results of the fit are given in Table I. Again we observe the same set of ISCT transitions as in the previous samples. In addition, we observe an additional strong, relatively broad transition at 2.9 eV. This transition cannot be assigned to a CF transition. First of all, CF transitions of ions on octahedral sites are parity forbidden for any ion. Second, transitions of Ni^{2+} on tetrahedral sites cannot occur, as the NiFe_2O_4 sample used, is reported to be completely inverse, as expected for NiFe_2O_4 .¹² Third, CF transitions of Fe^{3+} on tetrahedral sites do not occur, as the term of a free Fe^{3+} ion is nondegenerate ($L=0$). Further-

TABLE I. The main MO-active transitions in MgFe_2O_4 , $\text{Li}_{0.5}\text{Fe}_{2.5}\text{O}_4$, NiFe_2O_4 , and CoFe_2O_4 , between 0.5 and 5.0 eV. Listed are transition energy, ω (eV), linewidth, Γ (eV), intensity, $(\epsilon_{xy})_{\text{max}}$, and assignment. Typical error bars for ω , Γ , and $(\epsilon_{xy})_{\text{max}}$ are ± 0.02 eV; ± 0.03 eV, and ± 0.002 , respectively. (Note that the parenthesis denote tetrahedral coordination and square brackets octahedral coordination.)

Sample		CF (Co^{2+}) $^4A_2 \rightarrow ^4T_1(\text{F})$	CF (Co^{2+}) $^4A_2 \rightarrow ^4T_1(\text{P})$	IVCT [M^{2+}] $\rightarrow [\text{Fe}^{2+}]t_{2g}$	ISCT (Fe^{3+}) t_2 $\rightarrow [\text{Fe}^{2+}]t_{2g}$	ISCT [Fe^{3+}] e_g $\rightarrow (\text{Fe}^{2+})t_2$	ISCT (Fe^{3+}) t_2 $\rightarrow [\text{Fe}^{2+}]e_g$
MgFe_2O_4	ω				2.64	3.47	3.95
	Γ				0.30	0.31	0.56
	$(\epsilon_{xy})_{\text{max}}$				-0.009	0.022	0.032
	shape				dia	dia	dia
$\text{Li}_{0.5}\text{Fe}_{2.5}\text{O}_4$	ω				2.63	3.46	4.09
	Γ				0.23	0.39	0.64
	$(\epsilon_{xy})_{\text{max}}$				-0.026	0.036	0.050
	shape				dia	dia	dia
NiFe_2O_4	ω			2.86	2.57	3.46	4.03
	Γ			0.53	0.22	0.54	0.67
	$(\epsilon_{xy})_{\text{max}}$			0.023	-0.007	0.011	0.017
	shape			dia	dia	dia	dia
CoFe_2O_4	ω	0.83	1.82	2.21	± 2.60	3.55	4.00
	Γ	0.10	0.18	0.25		0.29	0.50
	$(\epsilon_{xy})_{\text{max}}$	-0.056	-0.076	-0.054	<0.001	0.013	0.030
	shape	dia	para	para	dia	dia	dia

more, this additional transition cannot be due to an oxygen $2p$ to metal $3d$ charge transfer transition. Such a transition should occur at an energy of 6 eV (Ref. 1) and it would be both broader and more intense than the observed band. Therefore, we assign this transition to an IVCT transition between $[\text{Ni}^{2+}]$ and $[\text{Fe}^{3+}]$.¹³ This is consistent with the strength and width of similar transitions in Fe_3O_4 .³ Furthermore, the energy of an IVCT transition between two different cations is expected to be substantially higher than that between two identical cations which in Fe_3O_4 occurs at 0.55 eV.³

Evidence that the transition at 2.9 eV is indeed due to an IVCT transition between $[\text{Ni}^{2+}]$ and $[\text{Fe}^{3+}]$ comes from the equatorial Kerr spectrum of $(\text{Fe})[\text{NiCr}]\text{O}_4$ between 1 and 5.4 eV.⁶ No transitions whatsoever are found in this spectrum, ruling out that the transition at 2.9 eV in NiFe_2O_4 is due to a CF transition of Ni^{2+} . The absence of this transition is, however, in line with an IVCT involving $[\text{Fe}^{3+}]$. This also supports our assignment of the remaining transitions in NiFe_2O_4 to ISCT transitions. Another indication that all transitions in NiFe_2O_4 are similar transitions involving $[\text{Fe}^{3+}]$ is the influence of Al^{3+} substitution on the MO spectrum of $\text{NiAl}_x\text{Fe}_{2-x}\text{O}_4$ ($0 \leq x \leq 1.2$) which remains completely inverse up to $x = 1$.¹⁴ The entire spectrum remains unchanged up to $x = 0.3$, then the intensity of the entire spectrum decreases homogeneously.

The complete dielectric tensors of CoFe_2O_4 and $\text{CoAl}_x\text{Fe}_{2-x}\text{O}_4$ ($x = 0.1, 0.6, 1$) were taken from Martens *et al.*^{9,10} All four elements of the dielectric tensors of CoFe_2O_4 and $\text{CoAl}_x\text{Fe}_{2-x}\text{O}_4$ were fitted simultaneously with only one set of parameters for all spectra, thus allowing trends in intensity upon Al^{3+} substitution to be observed. The results of the fits for CoFe_2O_4 are shown in Table I. Our assignment of the first three transitions is identical to the assignment made previously.⁹ The first two are assigned to the CF transitions ${}^4A_2 \rightarrow {}^4T_1(\text{F})$ and ${}^4A_2 \rightarrow {}^4T_1(\text{P})$ (Co^{2+}) on A sites. These are the only two CF transitions which are allowed from the singlet 4A_2 ground state of (Co^{2+}) (note that CF transitions from octahedrally coordinated $[\text{Co}^{2+}]$ are parity forbidden). The third is assigned to a $[\text{Co}^{2+}] \rightarrow [\text{Fe}^{3+}]$ IVCT transition. The remaining two transitions are two of the three ISCT transitions observed in each of the three previous investigated compounds. The third ISCT near 2.6 eV, present in all other spinel ferrites discussed so far, is obscured in CoFe_2O_4 due to the intense band at 2.2 eV. To the evidence presented for the assignment of the CF transitions proposed by Martens *et al.*,⁹ one can add the observed changes in intensity as reported for $\text{CoAl}_x\text{Fe}_{2-x}\text{O}_4$.¹⁴ $\text{CoAl}_x\text{Fe}_{2-x}\text{O}_4$ changes from inverse to normal spinel between $x = 0$ to $x = 1.2$, i.e., Co^{2+} migrates to the tetrahedral site. The intensity of the transition at 1.9 eV increases for $x = 0.0$ to 0.8 then decreases for $x > 0.8$. The intensity of the transition at 2.2 eV slightly increases for $x = 0.3$ then decreases. This enhancement effect on IVCT transitions of a small amount of Al^{3+} , resulting from perturbation of the octahedral symmetry, was observed also in Fe_3O_4 containing a small amount of Al^{3+} .³ The bands between 3 and 5 eV

decrease steadily for $0 \leq x \leq 1.2$. The dependencies of the intensities of the IVCT transition (2.2 eV) and the ISCT transitions on the degree of Al^{3+} substitution tend, as expected, towards zero for CoAlFeO_4 in our fits. As discussed by Martens *et al.* the gradual decrease in intensity for the CF transitions of (Co^{2+}), however, is not straightforward. Their claim is that the sharp drop in Curie temperature for the series causes this. The fact that the energy of the IVCT transition is considerably larger than that of the first IVCT in Fe_3O_4 can be attributed to the fact that the IVCT is in this case between cations with different nuclei. The fact that the energy of this IVCT is smaller compared to the energy of the observed IVCT in NiFe_2O_4 is also not unexpected, if we take into account the relative energy position of the $3d$ bands.¹

III. CONCLUSIONS

The common feature of all spinel ferrites of the general type $\text{M}_x\text{Fe}_{3-x}\text{O}_4$ with Fe^{3+} ions on both tetrahedral and octahedral sites is a set of ISCT transitions at 2.6, 3.5, and 4.0 eV. This is evident from Table I for those spinel ferrites, where M is the nonmagnetic Mg^{2+} and Li^+ as well as for those where M is the magnetic Ni^{2+} and Co^{2+} . (This even applies to $\gamma\text{-Fe}_2\text{O}_3$, where M is in fact a vacancy.¹⁴) Whether these transitions dominate the spectrum depends on the presence of other contributing transitions. For $\text{M} = \text{Mg}$, Li , or other nonmagnetic ion (or vacancies), the set of ISCT transitions is the main feature. In Fe_3O_4 several IVCT transitions between $[\text{Fe}^{2+}]$ and Fe^{3+} are main contributors.³ In NiFe_2O_4 an IVCT between $[\text{Ni}^{2+}]$ and $[\text{Fe}^{3+}]$ at 2.9 eV is a main contributor. In CoFe_2O_4 CF transitions of tetrahedrally coordinated Co^{2+} and an IVCT transition between Co^{2+} and Fe^{3+} contribute significantly below 2.5 eV. These assignments are consistent with our interpretation of the MO spectra of Fe_3O_4 .

¹J. Zaanen and G. A. Sawatzky, J. Solid State Chem. **88**, 8 (1990).

²A. E. Bocquet, T. Mizokawa, T. Saitoh, H. Namatame, and A. Fujimori, Phys. Rev. B **46**, 3771 (1992).

³W. F. J. Fontijn, P. J. van der Zaag, M. A. C. Devillers, V. A. M. Brabers, and R. Metselaar, Phys. Rev. B **56**, 5432 (1997).

⁴G. B. Scott, D. E. Lacklison, H. I. Ralph, and J. L. Page, Phys. Rev. B **12**, 2562 (1975).

⁵G. S. Krinchik, K. M. Mukimov, Sh. M. Sharipov, A. P. Khrebtov, and E. M. Speranskaya, Sov. Phys. JETP **49**, 1074 (1979).

⁶G. S. Krinchik, A. P. Khrebtov, A. A. Askochenskii, E. M. Speranskaya, and S. A. Belyaev, Sov. Phys. JETP **45**, 366 (1977).

⁷Š. Višňovský, V. Prosser, R. Krishnan, V. Pařížek, K. Nitsch, and L. Svobodová, IEEE Trans. Magn. **MAG-17**, 3205 (1981).

⁸X. X. Zhang, J. Schoenes, W. Reim, and P. Wachter, J. Phys. C **16**, 6055 (1983).

⁹J. W. D. Martens, W. L. Peeters, H. M. van Noort, and M. Erman, J. Phys. Chem. Solids **46**, 411 (1985), and references therein.

¹⁰J. W. D. Martens, W. L. Peeters, P. Q. J. Nederpel, and M. Erman, J. Appl. Phys. **55**, 1100 (1984).

¹¹P. J. van der Zaag, W. F. J. Fontijn, P. Gaspard, R. M. Wolf, V. A. M. Brabers, R. J. M. van de Veerdonk, and P. A. A. van der Heijden, J. Appl. Phys. **79**, 5936 (1996).

¹²J. Smit and H. P. J. Wijn, Ferrites (Philips Technical Library, Eindhoven, 1959).

¹³Recently, a similar assignment for this peak was reached independently by M. Lenglet, F. Hochu, and J. Dürr (private communication).

¹⁴A. P. Khrebtov, A. A. Skochenskii, E. M. Speranskaya, and Kh. I. Turkmenov, Izv. Akad. Nauk SSSR **42**, 1652 (1978).

Magneto-optical properties of one-dimensional photonic crystals composed of magnetic and dielectric layers

Mitsuteru Inoue^{a)} and Ken'ichi Arai

Research Institute of Electrical Communication, Tohoku University, Katahira, Sendai 980-77, Japan

Toshitaka Fujii

*Department of Electrical and Electronic Engineering, Toyohashi University of Technology,
1-1 Hibari-Ga-Oka, Tempaku, Toyohashi 441, Japan*

Masanori Abe

Department of Physical Electronics, Tokyo Institute of Technology, Meguro-ku, Tokyo 152, Japan

The magneto-optical (MO) Faraday effect of one-dimensional photonic crystals (1D-PCs) composed of Bi-substituted yttrium-iron-garnet films and dielectric films such as SiO₂ and TiO₂ films were studied theoretically. Because of considerable localization of light, these media exhibit a very large MO effect. For instance, when the film structure is chosen to be appropriate for supporting the localization of light, the 1D-PC films can possess a huge Faraday rotation angle reaching to $-28 \text{ deg}/\mu\text{m}$ at $\lambda = 1.15 \mu\text{m}$. The analysis reveals that the MO characteristics of the 1D-PC films are almost governed by the degree of localization of light, which can be controlled by varying the number of reflection layers in the films. © 1998 American Institute of Physics.

[S0021-8979(98)44711-X]

I. INTRODUCTION

Recently, we have shown theoretically that a large magneto-optical (MO) Faraday effect takes place in bigyrotropic magnetic films with disordered multilayer structure¹⁻³ due to the weak localization of light;⁴ the films of interest are composed of Bi-substituted yttrium-iron-garnet (Bi:YIG) layers and SiO₂ layers which are piled up in a disordered sequence. These studies strongly indicate that films exhibiting a considerably large MO effect can be obtained if the film structure meets the so-called one-dimensional photonic crystal with a defect⁵ (1D-PC), or equivalently, optical microcavity,⁶ because the localization effect of light in these particular media is very large.

In this study, therefore, MO properties of films with 1D-PC structures have been investigated in detail so as to confirm the above consideration theoretically. First, the relation between the MO effect and the localization of light is explained to demonstrate the unique properties of the films. Then the key parameters governing the optical and MO properties of the films are elucidated. Based on these results, practical 1D-PC films with (SiO₂/TiO₂) $\times k$ /Bi:YIG/(TiO₂/SiO₂) $\times k$ structures are proposed.

II. MODEL AND THEORY

Since the procedure for analyzing the properties of films with multilayer structures has been described elsewhere in detail,¹⁻³ let us confine ourselves to an outline of the analysis by focusing on the expression of film structures and the matrix approach which enables us to handle various multilayer films systematically.

As shown in Fig. 1, we consider a magnetic multilayer film with N layers extending boundlessly in the X - Y plane.

The film is composed of Bi:YIG and SiO₂ layers which are generally stacked in an arbitrary sequence. The individual magnetic and dielectric single layers are assumed to have thicknesses d_M and d_S , respectively. Total thickness of film D is then expressed as $D = N_M d_M + N_S d_S$ with the numbers of magnetic and dielectric layers N_M and $N_S = N - N_M$, respectively. The film structure is designed by a binary number b^N with an N digit; for instance, $b^N = 101110...01$, where each digit of b^N corresponds to each layer of the film, and "1" and "0" are assigned to the magnetic and dielectric layers, respectively. When b^N and the density of magnetic material, $P_M = N_M d_M / D$, are given, the film structure is uniquely specified.

The properties of the films are clarified by solving Maxwell's equations with the bigyrotropic dielectric tensor for the magnetic layers under the electromagnetic boundary conditions imposed at all discontinuous planes. This is rather tedious, but is easily achieved by means of the matrix approach.¹ With this method, the state transition of light through one layer is expressed by a 4×4 complex matrix called the state matrix. Let Φ_M and Φ_S be the state matrices

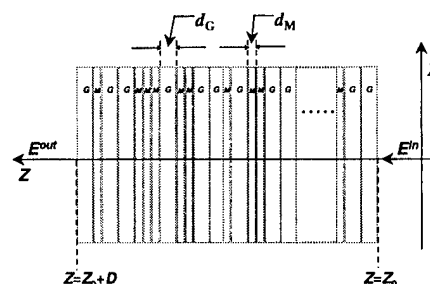


FIG. 1. Multilayer film composed of Bi:YIG and SiO₂ layers.

^{a)}Electronic mail: inouem@riec.tohoku.ac.jp

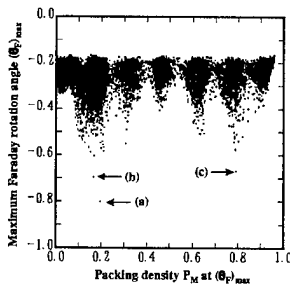


FIG. 2. Maximum Faraday rotation angle $(\theta_F)_{\max}$ vs packing density P_M at which $(\theta_F)_{\max}$ was obtained.

of the magnetic and dielectric layers; the state transition of light through the whole film is written as

$$\tau(Z_0 + D) = \Phi_M \cdot \Phi_S \cdot \Phi_S \cdot \dots \cdot \Phi_M \cdot \tau(Z_0) \equiv \Phi \cdot \tau(Z_0), \quad (1)$$

where $\tau = (E_X, E_Y, H_X, H_Y)$ with the tangential components of the electromagnetic field with respect to the discontinuous plane. Note that the multiple sequence of Φ_M and Φ_S in Eq. (1) corresponds to the sequence of 1 and 0 in b^N . For all the films, no matter what the stacking sequence and the stacking number are, the state of outgoing light $\tau(Z_0 + D)$ is obtained from the state of incident light $\tau(Z_0)$ multiplied from the left by Φ . Then, from the relation between $\tau(Z_0 + D)$ and $\tau(Z_0)$, optical and MO properties of the films, such as the transmissivity T and the Faraday rotation angle θ_F , are determined numerically.

The numerical calculations were performed using the typical values of dielectric tensors: for the Bi:YIG layers, $\epsilon_1 = 5.58$ and $\epsilon_2 = -1.98 \times 10^{-3}$ at $\lambda = 1.15 \mu\text{m}$ ($\theta_F \approx -0.1 \text{ deg}/\mu\text{m}$); for the SiO₂ layers $\epsilon_S = 2.5$ and for the TiO₂ layers $\epsilon_T = 4.7$.

III. MO EFFECT AND LOCALIZATION OF LIGHT

To demonstrate the unique MO properties of the films, we show in Fig. 2 the maximum Faraday rotation angles $(\theta_F)_{\max}$ of all 16 layer films ($b^{16} = 0000 \sim [FFFF]$, $P_M = 0.0 \sim 1.0$) as a function of the density P_M at which $(\theta_F)_{\max}$ was obtained. Among the films, three particular films, labeled (a), (b), and (c), exhibit considerably large Faraday rotation. The binary parameters of these films are (a) $b^{16} = 10101010101010101$, (b) 1010100111010101 , and (c) 1010101111101010 , where the strong correlation among the

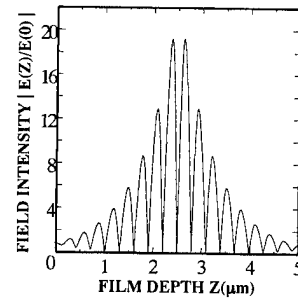


FIG. 4. Distribution of the light field in the film with $P_M = 0.4585$ in Fig. 3.

film structures exists: more than two Bi:YIG layers are sandwiched between the alternatively formed Bi:YIG and SiO₂ layers. This then indicates that the large MO effect of the films can be characterized by the film structures. In fact, films of this type exhibit very unique transmissivity T and Faraday rotation θ_F as shown in Fig. 3: at $P_M = 0.4585$, both T and θ_F of the film with $b^{34} = 101010101010101010101010101010101$ increase simultaneously and remarkably. In this case, θ_F of the film surprisingly exceeds $-16 \text{ deg}/\mu\text{m}$, the value of which is about 160 times larger than that of a Bi:YIG single layer film.

As shown in Fig. 4, light propagating in the film with $P_M = 0.4585$ in Fig. 3 is localized to a large extent at the center of the film, suggesting that the unique properties of the film originate from the localization effect of light. In Fig. 5, the transmission responses of the film to the independent incidences of lights with linear polarization and the right-hand and left-hand polarizations are shown. As is clearly seen in Fig. 5, the film structures (or P_M values) for which the circularly polarized lights are localized are slightly different from each other. This gives rise to the large rotation angle for the linearly polarized light, because the linearly polarized light decomposes into the circularly polarized lights as eigenmodes of lights in Bi:YIG layers.

IV. FILMS WITH 1D-PC STRUCTURES

The above results strongly indicate that the stronger the localization effect of light, the larger the MO effect of the

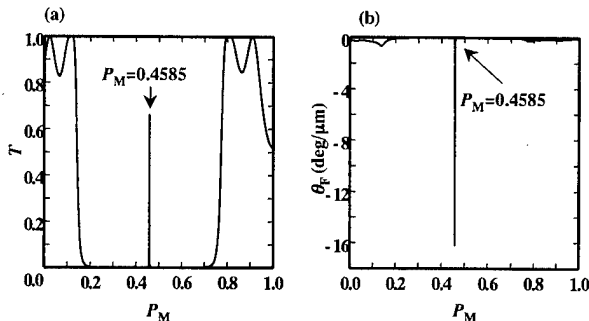


FIG. 3. Transmissivity T and Faraday rotation angle θ_F of the film with $b^{34} = 101010101010101010101010101010101$ vs density P_M at $\lambda = 1.15 \mu\text{m}$, where the film thickness D is $5 \mu\text{m}$.

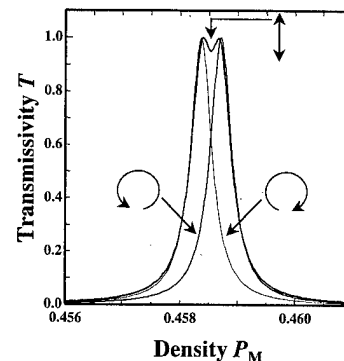
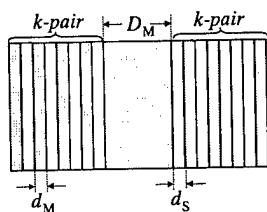
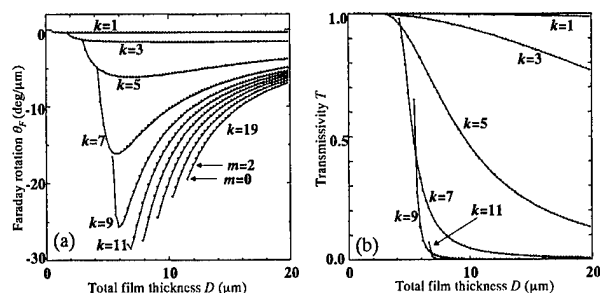
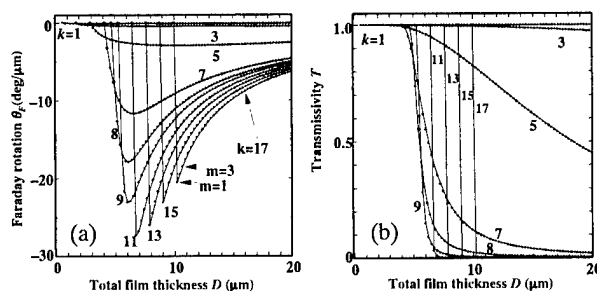


FIG. 5. Transmissivity of the film in Fig. 3 for three cases of incidence of lights with linear polarization and right-hand and left-hand circular polarizations.

FIG. 6. Bi:YIG/SiO₂ multilayer film with the 1D-PC structure.

films. In Fig. 3, the thicknesses of the Bi:YIG and SiO₂ layers of the film with $P_M=0.4585$ are evaluated as $d_M=0.127\ \mu\text{m}$ and $d_S=0.169\ \mu\text{m}$, respectively. These values are close to the one-fourth wavelength of light ($\lambda=1.15\ \mu\text{m}$) in each medium: for the Bi:YIG (SiO₂) layer, the diffraction index n_M (n_S) is about 2.36 (1.58) and the $\lambda/4n_M$ ($\lambda/4n_S$) is about $0.121\ \mu\text{m}$ ($0.182\ \mu\text{m}$). The structure of the film with $P_M=0.4585$ is then close to the 1D-PC structure, where the center cluster of Bi:YIG layers acts as an active layer while the other layers act as reflection layers of light.

With this respect, the optical and MO properties of the 1D-PC films were examined in detail by employing the film structure illustrated in Fig. 6: an active Bi:YIG layer with thickness of $D_M=m\lambda/2n_M$ ($m=0,1,2,\dots$) is sandwiched between two reflection layers which are composed of a k pair ($k=1,2,3,\dots$) of the Bi:YIG/SiO₂ layers related by $d_M n_M = d_S n_S = \lambda/4$. In Fig. 7, for cases of reflection layers composed of odd-pair layers, θ_F and T of the films are depicted as a function of the total film thickness D . The properties of the 1D-PC films are very sensitive to the values of k and m which determine the film structures. In general, by increasing the number of reflection layers, k , the transmissivity decreases while the Faraday rotation increases drastically. This is due to the fact that the localization of light is strengthened by increasing the value of k . The largest Faraday rotation in this system is $-28\ \text{deg}/\mu\text{m}$ when $k=11$ and $m=1$, and whose value is 280 times larger than that of a Bi:YIG single layer film. However, the transmissivity of this film is about 2%, and hence the use of this film in transmission mode is difficult. An appropriate choice of film structure then becomes necessary depending on the applications, where the

FIG. 7. Faraday rotation and transmissivity of the 1D-PC films with $(\text{Bi:YIG}/\text{SiO}_2) \times k/\text{Bi:YIG}/(\text{SiO}_2/\text{Bi:YIG}) \times k$ structure.FIG. 8. Faraday rotation and transmissivity of the 1D-PC films with $(\text{SiO}_2/\text{TiO}_2) \times k/\text{Bi:YIG}(\text{TiO}_2/\text{SiO}_2) \times k$ structure.

key parameters are the number of reflection layers, k , and the thickness of the center active layer which is governed by m . To achieve this, film design with a genetic algorithm is useful.⁷

To obtain the above 1D-PC films formation of many Bi:YIG layers, without losing their good MO properties, is needed. This is, however, rather troublesome, and 1D-PC films without this difficulty are favored. This is indeed fulfilled by the 1D-PC films with $(\text{SiO}_2/\text{TiO}_2) \times k/\text{Bi:YIG}/(\text{TiO}_2/\text{SiO}_2) \times k$ structures, where the thickness of the center Bi:YIG film is chosen to be $m\lambda/2n_M$ while the thicknesses of the TiO₂ and the SiO₂ layers, d_T and d_S , satisfy the relation $d_T n_T = d_S n_S = \lambda/4$ with the refractive index n_T of the TiO₂ layers. In these films, a Bi:YIG single-layer film is sandwiched between two dielectric multilayers acting as the reflection layers of light, and the MO interaction takes place in the center Bi:YIG film. Although the number of Bi:YIG layers in these 1D-PC films is greatly reduced in comparison with the previous 1D-PC films, these films exhibit almost comparable performance to that of the previous one. For instance, as shown in Fig. 8, the maximum Faraday rotation of the film reaches nearly $-28\ \text{deg}/\mu\text{m}$. This, in turn, indicates that the contribution by the Bi:YIG layers that comprise the reflection layers of light to the MO effect is considerably small, and that the MO effect of the 1D-PC film is governed by the degree of localization of light.

ACKNOWLEDGMENTS

The authors express their sincere thanks to Professor H. Nakatsuka of Tsukuba University for his valuable suggestions on the 1D-PC films. This work was supported in part by a Grand-In-Aid from the Ministry of Education, Science, Sports and Culture of Japan (Grant No. 09650356).

- ¹M. Inoue and T. Fujii, J. Appl. Phys. **81**, 5659 (1997).
- ²M. Inoue and T. Fujii, J. Magn. Soc. Jpn. **21**, 187 (1997).
- ³M. Inoue, K. I. Arai, T. Fujii, and M. Abe, J. Magn. Soc. Jpn. (in press).
- ⁴P. E. Wolf and G. Maret, Phys. Rev. Lett. **55**, 2696 (1985).
- ⁵T. Hattori, N. Tsurumachi, and H. Nakatsuka, J. Opt. Soc. Am. B **14**, 348 (1997).
- ⁶J. Faist, J.-D. Ganiere, Ph. Buffat, S. Sampson, and F.-K. Reinhart, J. Appl. Phys. **66**, 1023 (1989).
- ⁷M. Inoue, K. I. Arai, T. Fujii, and M. Abe, J. Magn. Soc. Jpn. (to be published).

Magneto-chromatic effects of tunable magnetic fluid grating

Chin-Yih Hong

Department of Mechanical Engineering, Da-Yeh University, Chang-Hwu 515, Taiwan

H. E. Horng,^{a)} I. J. Jang, J. M. Wu, and S. L. Lee

Department of Physics, National Taiwan Normal University, Taipei 117, Taiwan

Wai Bong Yeung

Institute of Physics, Academia Sinica, Taipei 115, Taiwan

H. C. Yang

Department of Physics, National Taiwan University, Taipei 106, Taiwan

The ordered structures in Fe_3O_4 kerosene-based magnetic fluid films were discovered and the magneto-chromatic effects were also observed under various magnetic fields. In this report, we studied the relationship between the ordered structures and the magneto-chromatic effects theoretically and experimentally. The nearly perfect hexagonal structures with the distance between two columns d in μm range for our magnetic fluid thin films offer a two-dimensional tunable magnetic fluid grating in the visible light region. By using a grating model, the diffraction patterns for visible lights at certain incident angle θ , wavelength λ , and column distance d , were calculated. Experimentally, it was found that the conditions of the observed light around the direction perpendicular to the plane of film coincide with the calculated results. Therefore, the magneto-chromatic effects resulting from the ordered structures of the tunable magnetic fluid grating were confined. © 1998 American Institute of Physics. [S0021-8979(98)22111-6]

I. INTRODUCTION

Due to its potential application, optical phenomena of magnetic fluids subjected to an external magnetic field were put under extensive study recently. Those works were concentrated on the optical transmission and optical scattering of magnetic fluid films, both with or without an external magnetic field. For the first area of research, it mainly utilized the character of the light absorption by magnetic fluid. The optical transmittance decreases with the increase of the film thickness as light passes through a magnetic fluid film. Several optical devices were developed including display devices^{1,2} and optical switches.³⁻⁵ Also, by varying the refractive index across a ferrofluid thin film resulting from a temperature gradient and/or a magnetic field, a diffraction ring can be altered.⁶ In contrast, for the second area of research, the nature of the one-dimensional (1D) ordered structure of magnetic fluid films under a parallel external magnetic field was used. When a magnetic fluid thin film is subjected to an external magnetic field parallel to the plane of film, the particles in the film start to agglomerate and form chains along the direction of field. Thus, the magnetic fluids become optically anisotropic.⁷ Reflection and Bragg diffraction may occur as a light ray incident obliquely on the thin film; birefringence and polarization may occur as light rays passing normally through the thin film. The light scatter intensity of these phenomena increases with an increase in both the magnetic field strength and particle concentration, and it tends to saturate at higher fields.⁸ By measuring the intensity as a function of magnetic field strength and time, the relaxation time and viscosity of the magnetic fluid drops

were calculated.⁹ Also, the spacings between 1D periodic chains formed from the droplets of magnetic emulsion under a parallel magnetic field were able to be measured because the chains gave rise to a strong Bragg diffraction, and the interaction forces between colloidal particles were determined based on the force-distance law.¹⁰ Moreover, they also reported that the thin film appeared colored in the back-scattering direction as the thin film was illuminated by a white light source.

In addition to the previous areas of research, other optical principles, such as light diffraction and interference, may also play an important role in the application if a 2D ordered structure in the magnetic thin film can be produced. In our past work,¹¹ 2D ordered structures in Fe_3O_4 kerosene-based magnetic fluid film were discovered. As a result, we had the magneto-chromatic effects observed under various magnetic fields.¹² In order to understand this consequence and to better manipulate the color from the grating, we study the relationship between the ordered structures and the magneto-chromatic effects theoretically and experimentally.

II. EXPERIMENTAL DETAILS

The magnetic fluid used in this work was a kerosene-based Fe_3O_4 ferrofluid prepared by the coprecipitation technique. The saturated magnetization of the sample is 10.58 emu/g and the particle size is around 100 Å.¹¹ The magnetic fluid was sealed in a 4 cm × 1 cm rectangular glass cell with a thickness of 6 μm to form a ferrofluid thin film. The experiment was performed at room temperature.

Throughout the experiment, the magnetic fields perpendicular to the film plane were generated by a pair of solenoids and were controlled by a personal computer. The applied field measured with a gaussmeter was uniform;

^{a)}Electronic mail: phyfv001@scn.tnu.edu.tw

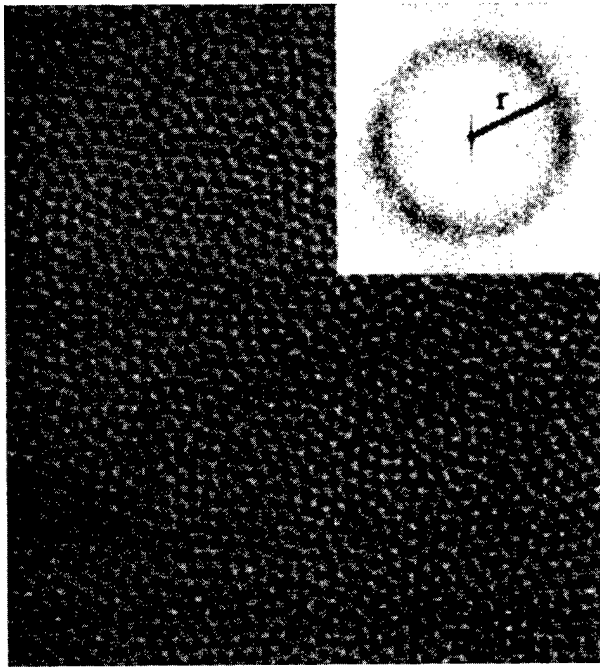


FIG. 1. A typical image of a hexagonal structure of magnetic fluid thin film and its FFT transformation. The column distance d_{FFT} can be calculated from $d_{\text{FFT}} = 2\pi/r$, where r is the radius of the FFT ring.

deviations of the field strength in the region of the film were found to be less than 1%. To generate white lights, a halogen lamp with Cokin 82B filter was used. The light ray was made near parallel by passing them through a telescope and a pair of optical lenses, and reflected by a mirror located beneath the thin film.

The images of the ordered hexagonal structures were taken by using a videoscope located above the thin film. They were used to calculate the column distances by fast Fourier transform (FFT) transformation. Figure 1 shows an example of an image of the hexagonal structure and its FFT transformation. For the measurement of the wavelength spectrum, an optical fiber located above the thin film in the direction perpendicular to the plane of the film was used to pick up the light that passed through the thin film and to feed the signal into a spectrometer for scanning the wavelength of the diffraction patterns. The scanned light signal was sensed by a photomultiplier, to which a program was used to change the voltage for the compensation of its sensing sensitivity.

III. RESULTS AND DISCUSSION

When an applied perpendicular magnetic field reaches a critical value H_h (80 Oe for the sample), a 2D column array is formed in a homogeneous magnetic fluid thin film. Figure 2 is a plot of the distance d between two columns as a function of the final magnetic field strength (H_f) and its ramping rate (dH/dt) with the initial magnetic field strength $H = 0$ Oe. It indicates that the distance decreases as both the magnetic field strength and the ramping rate increase. These distances d are in μm range. In this range, diffraction phenomena occur as a parallel white light ray passing through the film and a well saturated monocolored light can be observed. By varying the magnetic field strength and/or the

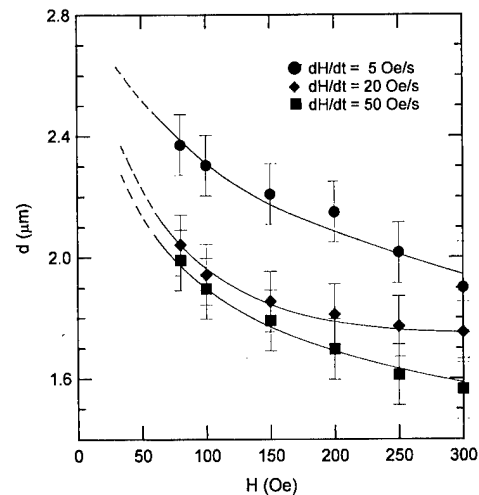


FIG. 2. The column distance d vs final magnetic field H_f with various ramping rate (dH/dt).

ramping rate resulting in a change of the distance d , the color of the film can be altered. In our laboratory, a large areal monocolored light over the entire visible light range can be produced and well manipulated. This phenomenon can be called the “magneto-chromatic effect.”

To analyze the transmitted lights, the wavelength spectrum of the transmitted light through the magnetic fluid film with zero field ($H_f = 0$ Oe) and the spectra of lights through the ordered structures of magnetic fluid film under the final field $H_f = 200$ Oe with various (dH/dt) were shown in Fig. 3. It reveals that each curve contains two peaks: the first one with wavelength shorter than 600 nm and the second one higher than 600 nm. These two peaks and their associated distributions move toward the shorter wavelength as (dH/dt) increases. The intensities of the first peak decrease as the ramping rate increases; contrarily the second peak has an opposite trend. At low ramping rate the color appeared is mainly due to the first peak, and as the ramping rate in-

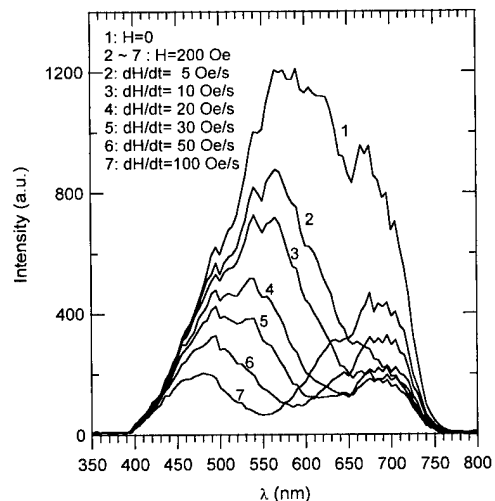


FIG. 3. The wavelength spectra at the final field $H_f = 200$ Oe with various (dH/dt). Curve 1 is the spectrum of the transmitted light through the magnetic fluid thin film without magnetic field.

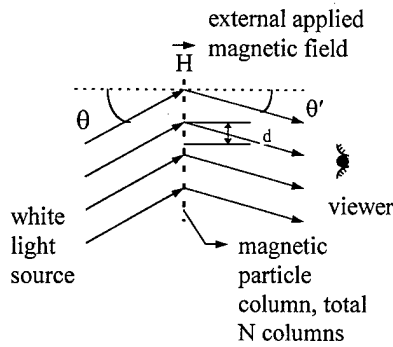


FIG. 4. Diagram for a grating model.

creases the color due to the second peak becomes more obvious.

To illustrate this magneto-chromatic phenomenon, a grating model was used as shown in Fig. 4. In this model, d is the separation distance between the adjacent slits with the distance between columns as defined above, θ is the angle formed between the incoming light ray and the direction perpendicular to the plane of the film, θ' is the angle formed between the diffracted rays and the direction perpendicular to the plane of the film, and N is the total number of magnetic particle columns diffracting the light. After diffraction, the intensity of the light, I , is

$$I \propto \frac{\sin^2(N\varphi/2)}{\sin^2(\varphi/2)},$$

where φ is the phase difference. The condition under which the light intensity I becomes maximum is the same as that under which the light becomes brightest after diffraction through the film. The condition is

$$\frac{\varphi}{2} = \frac{\pi}{\lambda} d(\sin \theta + \sin \theta') = \kappa\pi,$$

where κ is a non-negative integer and λ is the wavelength of light.

If the θ and θ' are not both equal to zero, the condition of $\kappa=0$ will never occur. Under the condition of $\kappa=1$, d will be related to λ by $d(\sin \theta + \sin \theta') = \lambda$. If λ is within the range of visible light, then the same d will allow only light with a wavelength of λ/κ for $\kappa=2,3,\dots$ to pass through the film. However, light with these wavelengths is outside the visible spectrum.

Based on the relationship of $d(\sin \theta + \sin \theta') = \lambda$, the wavelength becomes shorter as d decreases. When the (dH/dt) increases, the column distances decrease (as shown in Fig. 2) resulting in a shift of the wavelength of transmitted light toward shorter wavelength (as shown in Fig. 3) after light diffracted. As indicated before, the curves in this Fig. 3 contain two major peaks. Apparently, the first peak is the first-order maximum and the second peak may be contributed by a higher ordered effect which is due to the larger incident angle and viewing angle than those of the first-ordered effect. This higher order effect is mainly induced from the setup and can be improved by limiting only the light with a single incident angle and viewing angle in the experiment.

TABLE I. A list of curves 2–7 with various ramping rates (dH/dt) in Fig. 3 and their corresponding color, first-ordered peak wavelength λ_{peak} , column distance d_{FFT} calculated from FFT transformation, and that fitted from grating model d_{grating} .

Curve No. in Fig. 3	dH/dt ($H_f=200$ Oe)	Color	λ_{peak} (nm)	d_{FFT} (μm)	d_{grating} (μm)
2	$dH/dt=5$ Oe/s	yellow-green	565	2.15	2.17
3	$dH/dt=10$ Oe/s	green	545	1.97	1.99
4	$dH/dt=20$ Oe/s	blue	520	1.81	1.84
5	$dH/dt=30$ Oe/s	violet	500	1.73	1.76
6	$dH/dt=50$ Oe/s	violet-red ^a	485	1.70	1.72
7	$dH/dt=100$ Oe/s	red ^a	470	1.66	1.68

^aIn this case, the higher order red light becomes significant.

Also, the distance d between columns can be calculated by fitting the incident angle θ from data points and using the peak wavelength λ_{peak} that was obtained at $\theta' \approx 0^\circ$. Table I compares the distances $d_{\text{FFT}} (= 2\pi/r, r$ the radius of FFT ring) calculated from the FFT transformation of hexagonal structures and the distances $d_{\text{grating}} (= \lambda_{\text{peak}}/\sin \theta)$ from the first-ordered peak wavelength of the spectra, and they show a good agreement. Therefore, the magneto-chromatic effects resulting from the ordered structures of the tunable magnetic fluid grating were confined.

IV. CONCLUSION

As a 2D hexagonal structure formed in a magnetic thin film under a perpendicular magnetic field, the distances between particle columns can be altered by changing the field strength and/or the rate of change of field strength. The column distances are in μm range and are capable of diffracting the visible light. By changing the column distance, the color of light after interference can be varied. Thus, well saturated colors were observed and their corresponding wavelength spectra were measured. This phenomenon can be explained by a grating model theoretically. Our experiments have demonstrated the magneto-chromatic effects of magnetic fluid thin films by changing the rate of strength of the externally applied perpendicular magnetic field. This work exposed the possibility of using the magnetic fluid as an alternative material for optical devices.

¹R. E. Rosenweig, J. Resnick, L. Berger, H. Resnick, and P. Messina, U.S. Patents No. 3 648 269 (1972).

²L. T. Romankin, M. G. Slusarczuk, and D. A. Thompson, U.S. Patents No. 3 972 595 (1976).

³M. J. Brady, L. V. Gregor, and M. Johnson, U.S. Patents No. 4 384 761 (1983).

⁴J. M. Ginder, J. T. Remillard, and W. H. Weber, U.S. Patents No. 5 351 319 (1994).

⁵M. Saito, M. Takakuwa, and M. Miyagi, IEICE Trans. Electron. **E78-C**, 1465 (1995).

⁶T. Du, S. Yuan, and W. Luo, Appl. Phys. Lett. **65**, 1844 (1994).

⁷P. C. Sholten, IEEE Trans. Magn. **MAG-16**, 221 (1980).

⁸Z. Qi, W. Jianhua, and Z. Hesun, J. Mater. Sci. **31**, 4807 (1996).

⁹V. I. Drozdova and G. V. Shagrova, J. Magn. Magn. Mater. **85**, 93 (1990).

¹⁰F. Calderon, T. Stora, O. Monval, P. Poulin, and J. Bibette, Phys. Rev. Lett. **72**, 2959 (1994).

¹¹C.-Y. Hong, I. J. Jang, H. E. Horng, C. J. Hsu, Y. D. Yao, and H. C. Yang, J. Appl. Phys. **81**, 4275 (1997).

¹²H. E. Horng, C.-Y. Hong, W. B. Yeung, and H. C. Yang, Appl. Opt. (in press).

Superconductivity I

Tom Clinton, Chairman

Suppression of superconductivity by injection of spin-polarized current

Daniel Koller, M. S. Osofsky, D. B. Chrisey, J. S. Horwitz, R. J. Soulen, Jr.,
 R. M. Stroud, C. R. Eddy, J. Kim, R. C. Y. Auyeung, J. M. Byers, B. F. Woodfield,
 G. M. Daly, T. W. Clinton, and Mark Johnson
Naval Research Laboratory, Washington, DC 20375

A spin polarized current has been injected into high T_c superconductors resulting in a significant reduction in the superconductor's critical current. Such injection may serve as the basis of a new class of superconducting devices for control, switching and amplification. Preliminary results using both Permalloy and CMR materials as injectors are presented. © 1998 American Institute of Physics. [S0021-8979(98)42011-5]

I. INTRODUCTION

The superconductivity in thin films can be strongly influenced by the injection of a spin-polarized current from a magnetic material. The effect has been found to occur in both low T_c (Sn) and high T_c ($\text{YBa}_2\text{Cu}_3\text{O}_{7-\delta}$) superconductors when either a ferromagnetic material, permalloy ($\text{Ni}_{0.8}\text{Fe}_{0.2}$), or a colossal magnetic material LaSrMnO (LSMO) is used as the source of polarized quasiparticles. Control experiments showed that unpolarized current from a nonmagnetic metal had comparatively little effect. A phenomenological model in which the energy gap of the superconductor is strongly perturbed by the presence of excess spin polarized electrons is presented which is found to mimic the experimental results.

Nonequilibrium superconductivity has previously been studied by injecting a current from a *nonmagnetic* source. The influence of unpolarized, nonequilibrium quasiparticles (unpaired electrons) on the superconducting energy gap has been examined experimentally and theoretically.¹ Injection of unpolarized quasiparticles has also been used to make devices such as the CLINK and the QUITERON. Johnson and Silsbee first demonstrated² that a current injected from a ferromagnet into a nonmagnetic metal maintained a net spin polarization in the latter. It has also been shown that spin polarization persists into the interior of the low T_c superconductor, Nb.³ Evidence for spin injection from a ferromagnetic film into films of the high T_c superconductor YBCO was subsequently reported.⁴ While noting the inherently lower charge carrier densities in YBCO, the authors did not report the effect of the nonequilibrium spin population on the electronic transport properties of the superconducting film. Such effects are described in this article.

II. EXPERIMENTAL ARRANGEMENT

Figure 1 shows the typical experimental design. The top electrode (injector) is the source of the quasiparticles: If it is magnetic, the quasiparticles are polarized, whereas quasiparticles injected from a nonmagnetic film (control) are unpolarized.

The barrier can be either a metal film or low transmission tunnel barrier. The lower film is the superconductor. For some materials the sequence of the layers is reversed. A bias current I_{qp} generates an excess number density of quasiparticles, dn_{qp} , in the superconductor which suppresses the energy gap and diminishes the critical current of the film. The supercurrent flowing through the superconductor (I_T) is thus "pinched off" by the injected quasiparticle current, I_{qp} .

III. RESULTS FOR PERMALLOY

The first experiments proceeded with a gold metallic layer serving as a chemical barrier. The YBCO samples were 200 nm thick and 3 mm wide. The normal metal was 50 nm thick and 1 mm wide. The ferromagnetic film was permalloy, 100 nm thick and 1 mm wide. All films were produced by pulsed-laser deposition. Measurement of the modification of the superconducting order parameter by I_{qp} began with determination of the critical current I_c at 77 K in the absence of a bias current. This was achieved by measuring the current-voltage ($I-V$) curve of the YBCO stripe and choosing I_c at a voltage drop of 1 μV . $I-V$ curves were then taken as a function of I_{qp} injected through the Au/permalloy lead (po-

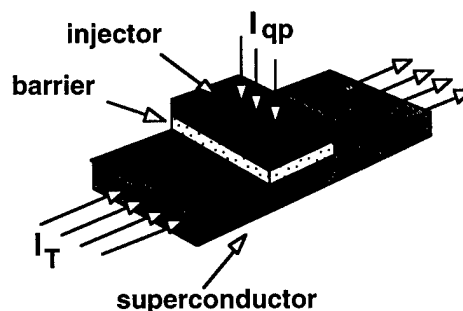


FIG. 1. Schematic representation of a spin injection device. Current I_{qp} passes from the magnetic film (upper) into the underlying superconducting film and decreases the supercurrent of the latter by decreasing the energy gap in the dark region.

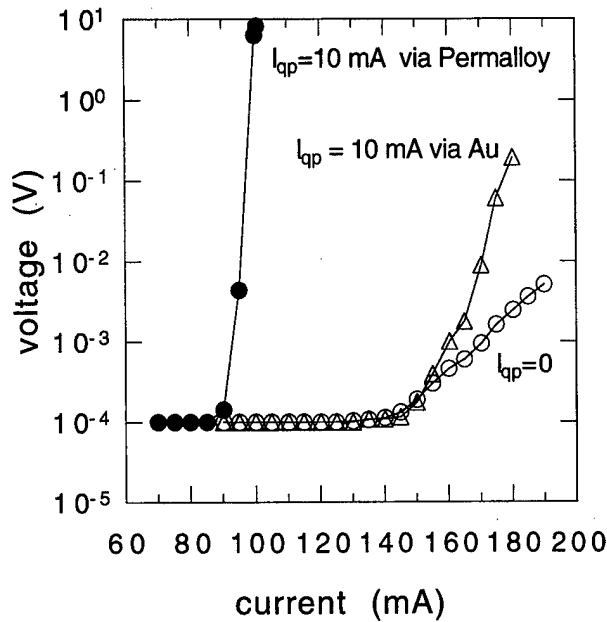


FIG. 2. Current-voltage curves observed for a Permalloy/Au/YBa₂Cu₃O₇ sample at 77 K. Open circles: curve in the absence of quasiparticle injection. Open triangles: curve with an unpolarized current of 10 mA. Solid circles: curve with a polarized current of 10 mA.

larized injection) or through the Au lead (unpolarized injection).⁵ In the latter case, the exclusively Au contact produced quasiparticle injection and served as a control. Permalloy was chosen as the ferromagnetic source because the conduction electrons involved in the transport current have a high degree (45%) of spin polarization.⁶

Differences in I_c between the runs were attributed to the differing effects of unpolarized versus polarized quasiparticle injection. Results are shown in Fig. 2 for our best sample. This figure demonstrates in a very striking way how a comparatively small amount of polarized quasiparticle current ($I_{qp} = 10$ mA) strongly depresses the transport current of the superconductor by depressing I_c to about 80 mA. By comparison, the same amount of unpolarized bias current has almost no effect on I_c . Similar behavior to that shown in Fig. 2 has been observed in other samples, but the differences in I_c between the Au and permalloy contacts were not as large.

IV. RESULTS FOR LSMO

Samples were made by first depositing an LaSrMnO film, then an insulating layer of SrTiO, and finally a layer of YBCO using pulsed laser deposition. No control film was deposited in these samples. 4-terminal resistance measurements indicate the YBCO had a transition temperature of 86 K with a width of about 5 K. The LSMO was also characterized resistively, and was found to have a peak temperature of approximately 260 K. All measurements were performed with the substrates emersed in liquid nitrogen to insure good thermal conductivity to the bath. The effect of the spin polarization, as shown in Fig. 3, was quite large. One way to

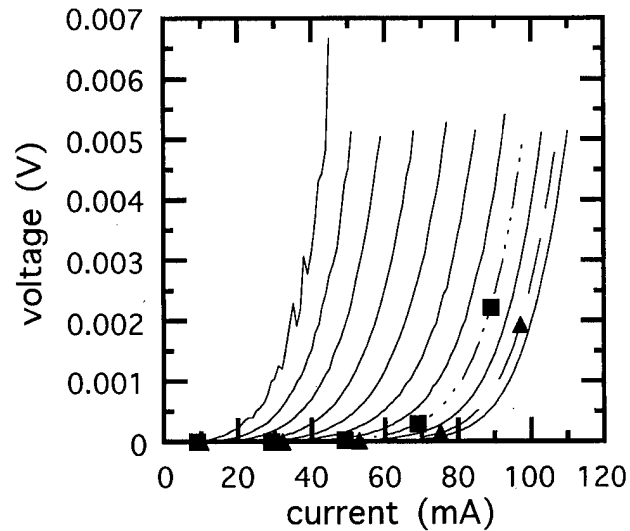


FIG. 3. Current-voltage curves observed for a LaSrMnO/SrTiO/YBa₂Cu₃O₇ sample at 77 K. Proceeding from left to right I_{qp} was: 2.0, 1.8, 1.6, 1.4, 1.2, 1.0, 0.8, 0.4 and 0.0 mA.

characterize the current gain is to plot I_c of the YBCO film as a function of I_{qp} . As shown in the inset to Fig. 4, the gain is roughly constant at 35.

A significant portion of the effect, however, may be due to heating. Slight suppression of I_c when current passed only through the LSMO was observed. In addition, the interface between the YBCO and LSMO was found to have a resistance of approximately 3 Kohm. At the highest currents shown in Fig. 3, some 22 mW was dissipated in the substrate. The relative importance of heating is being studied by varying the resistance of the magnetic stripe and by varying the resistance of the junction between it and the superconducting film. More recently, samples with improved materials have been fabricated. The T_c of the YBCO was increased to 90 K, with a transition width of only 2 K. The LSMO peak temperature increased to 300 K. Unfortunately, the devices so made show little or no gain. It is now clear that the characterization of the interface needs to be better addressed. Is the spin polarization maintained across the interface? What is the mechanism for transport across the interface? Is it tunneling of spins, or Ohmic conduction through resistive microshorts? These are the questions which are currently being investigated with samples of smaller geometries.

V. THEORY

The injection of excess quasiparticles into the superconductor weakens the pairing correlations, thereby reducing the superconducting energy gap Δ_k . The BCS gap equation, which is valid for both equilibrium and nonequilibrium situations, quantifies the energy gap reduction,

$$\Delta_k = \sum_{k'} V_{kk'} \frac{\Delta_{k'}}{2E_{k'}} [1 - f_{\uparrow}(E_{k'}) - f_{\downarrow}(E_{k'})], \quad (1)$$

where $E_k = (\epsilon_k^2 + \Delta_k^2)^{1/2}$ and $f_{\sigma}(E_k)$ is the spin-dependent

quasiparticle distribution function (QDF). The spin index σ identifies either the spin up (\uparrow) or down (\downarrow) orientation. For an isotropic gap Eq. (1) can be rewritten

$$-\ln \left[\frac{\Delta(T)}{\Delta_{\text{eq}}(0)} \right] = \int_{-\infty}^{\infty} d\epsilon \frac{f_{\uparrow}(E(\epsilon)) + f_{\downarrow}(E(\epsilon))}{2E(\epsilon)}, \quad (2)$$

where $E(\epsilon) = (\epsilon^2 + \Delta^2)^{1/2}$ and $\Delta_{\text{eq}}(0)$ is the zero-temperature equilibrium superconducting gap. The determination of the QDF's are vital for understanding the properties of a superconductor driven out of equilibrium. This can be difficult in general, but a useful ansatz is that the QDF has the form of a modified Fermi function

$$f_{\sigma}(E) = 1 / [\exp(E - \mu_{\sigma}^*) / k_B T + 1], \quad (3)$$

where $\sigma = (\uparrow, \downarrow)$ and the quantities μ_{σ}^* and T^* are used to parameterize the increased number of excess quasiparticles beyond the thermal equilibrium population. In equilibrium $\mu_{\uparrow}^* = \mu_{\downarrow}^* = 0$ and $T^* = T$. The number density of excess quasiparticle is given by

$$\delta n_{\sigma} = n_{\sigma} - n_{\text{eq}} = N(0) \int_{-\infty}^{+\infty} d\epsilon [f_{\sigma}(E(\epsilon)) - f_{\text{eq}}(E(\epsilon))], \quad (4)$$

where $N(0)$ is the single-spin density of states at the Fermi surface, n_{eq} and f_{eq} are the equilibrium single-spin quasiparticle density and distribution functions, respectively.

The QDF in Eq. (3) is a combination of two phenomenological models of nonequilibrium superconductivity: the μ^* and T^* models. Each is applicable in different circumstances. The μ^* model is a reasonable starting point when quasiparticles thermalize with low-energy phonons more often than they recombine into pairs and when the escape rate of phonons from the sample is large.⁸ In these limits the quasiparticles are in steady state at T but have an excess number denoted by the increased chemical potential μ^* . In the opposite limit, where recombination of quasiparticles is more likely than thermalization and the escape rate of phonons is small, the T^* model is applicable.⁹ The small escape rate causes the "phonon bottleneck" where recombining pairs emit a phonon of energy $\omega > 2\Delta$ but that phonon cannot easily leave the sample and, also, has sufficient energy to break a pair. The phonon bottleneck drives the phonons with energy $\omega > 2\Delta$ out of equilibrium to an effective temperature T^* . The excess quasiparticles acquire a steady-state distribution which is the same as equilibrium except that the temperature T^* is higher.

In the analysis of the CLINK device, the T^* model was used instead of the μ^* model since the phonon escape rate was considered small and, for tunnel injection of quasiparticles, recombination tends to dominate thermalization. However, spin-polarized injection of quasiparticle changes many of these considerations by introducing the spin-relaxation rate into the problem. Since it requires both up and down-spin quasiparticles to recombine into a pair, a spin-polarized population must first undergo spin relaxation then recombination. Spin relaxation has a relatively slow time scale compared to intrinsic recombination and thermalization times; thus, quasiparticles have the opportunity to thermalize to the ambient temperature T . With thermalization dominant,

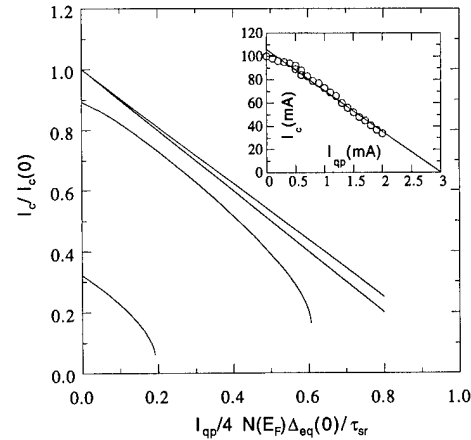


FIG. 4. The critical current I_c normalized by the critical current in the absence of I_{qp} as a function of I_{qp} . The quasiparticle current is normalized by the density of states and the gap at $T=0$, and by the spin relaxation, τ_{sr} . The upper curve is for a temperature $T=0$; the middle for $T=0.53 T_c$ and the lowest curve for $T=0.88 T_c$. Inset: Measured I_c of the YBCO sample as a function of spin polarized current I_{qp} .

the μ^* model becomes viable to the extent that the quasiparticle injection is spin-polarized. If the phonon escape rate is also large then the μ^* -model alone [$(T^*=T)$ in Eq. (3)] should be sufficient. In Fig. 4 we show the results of a calculation of the suppression of the critical current due to the injection of a 100% spin polarized current.

VI. CONCLUSION

A large depression of the supercurrent in YBCO films is observed when a current from a spin polarized film is introduced. Results from the most recent experiments indicate that heating may dominate the behavior of these devices. Work continues to determine what fraction of the effect is due to heating and what part due to spin polarized quasiparticle injection, and to study the effects of the interface on spin injection.

ACKNOWLEDGMENT

This work was supported in part by the Office of Naval Research under Contracts No. N0001496WX20507 and N0001495WX20270.

¹Nonequilibrium Superconductivity, edited by D. N. Langenberg and A. I. Larkin (North Holland, New York, 1986).

²M. Johnson and R. H. Silsbee, Phys. Rev. Lett. **55**, 1790 (1985); Phys. Rev. B **37**, 5312, 5326 (1988).

³P. M. Tedrow and R. Meservy, Phys. Rev. Lett. **26**, 192 (1971); **37**, 858 (1976).

⁴N. Hass, M. Covington, W. L. Feldmann, L. H. Greene, and M. Johnson, Physica C **235-240**, 1905 (1994).

⁵D. B. Chrisey, M. S. Osofsky, J. S. Horwitz, R. J. Soulen Jr., B. Woodfield, J. Byers, G. M. Daly, P. C. Dorsey, J. M. Pond, T. W. Clinton, and M. Johnson, IEEE Trans. Appl. Supercond. **7**, 2067 (1997).

⁶P. M. Tedrow and R. Meservy, Phys. Rev. B **7**, 318 (1973).

⁷R. M. Stroud, J. Kim, C. R. Eddy, D. B. Chrisey, J. S. Horwitz, D. Koller, M. S. Osofsky, and R. J. Soulen, Jr., "Fabrication of YBCO/STO/LSMO junctions for the control of supercurrent by spin-polarized quasiparticle current injection," Proceedings, 7th Joint MMM-Intermag Conference, J. Appl. Phys., these proceedings.

⁸C. S. Owen and D. J. Scalapino, Phys. Rev. Lett. **28**, 1559 (1972).

⁹W. H. Parker, Phys. Rev. B **12**, 3667 (1975).

Magnetoquenched superconducting valve

T. W. Clinton^{a)} and Mark Johnson

Naval Research Laboratory, Washington, DC 20375

A superconducting switch has been developed in a simple bilayer cross strip geometry using the magnetic fringe field of a ferromagnetic film to control the critical current in an underlying superconducting bridge. The magnetization of the ferromagnet is rotated in the plane of the film to vary the magnitude of the fringe field locally applied to the superconductor from negligible to substantial values. In the latter case, the magnetization is oriented such that the magnetic poles are along the edges of the cross strip directly above the superconductor. The large fringe field near the poles suppresses superconductivity over a length of order microns, giving rise to superconducting weak link behavior. A large modulation of the critical current is observed. The effect is demonstrated in the low T_c superconductors Pb ($T_c = 7.3$ K) and Sn ($T_c = 3.9$ K). Fabrication of the device involves minimal processing. Applications as a high speed switch, amplifier, nonvolatile storage cell, and controllable weak link are possible. © 1998 American Institute of Physics. [S0021-8979(98)15811-5]

There has been considerable effort over a period of decades to produce low power electronic devices using superconducting elements. In general, these devices are based on the principle of switching a superconducting component between its zero resistance state and its normal state with non-zero resistance. The superconducting field effect transistor (SuFET) was one of the first viable three terminal superconducting devices¹ and has had a recent revival with applications to the high T_c superconductors.² Its operation is based on modulating superconductivity with the application of an electric field via a gate voltage. Other three terminal devices, such as the controllable weak link (CLINK)³ and the quasiparticle injection tunneling effect (QUITERON)⁴ rely on quasiparticle injection to locally drive the superconductor out of equilibrium and suppress superconductivity. Both devices, developed in low T_c materials, showed current gain and the QUITERON was demonstrated to possess high switching speeds and power gain. These devices eventually lost favor because their gain was limited, though there is renewed interest in nonequilibrium effects generated by spin polarized quasiparticle injection in both low T_c (LTS) and high T_c (HTS) materials.⁵ Josephson junction based devices fabricated in LTS have found success as superconducting quantum interference device (SQUID) field sensors,⁶ and the rapid single flux quantum (RSFQ) logic circuitry has demonstrated fast switching and nonvolatile storage capabilities.⁷ Equivalent devices in HTS materials have not yet proven viable.

Recently we presented a novel superconducting switch in a bilayer thin film structure where the superconducting state of low T_c Sn ($T_c = 3.9$ K) was switched on or off by the magnetic fringe field of a ferromagnetic film.⁸ In this article, we present further results on Sn, as well as the first demonstration of the effect in Pb ($T_c = 7.3$ K). The critical current in a thin film of either Sn or Pb is controlled by the magnetic fringe field of a ferromagnetic film deposited as a cross strip

over the superconductor. The large fringe field near the poles of the ferromagnet depresses superconductivity over a length of order microns, creating superconducting weak links and a correspondingly lower critical current. A large modulation of the critical current is observed. A semiquantitative magneto-static model of the fringe fields and supporting data are presented.

The device geometry is depicted in Figs. 1(a) and 1(b). The superconductor (S) is Sn or Pb, the ferromagnet (F) is permalloy (Py), and the insulator, a native oxide layer of about 10-Å-thick SnO or PbO, respectively, inhibits a proximity effect between F and S. The magnetization \mathbf{M} of the thin Py film is constrained to the film plane. After \mathbf{M} has been saturated along the $\hat{x}(\hat{y})$ axis, the dipolar external field generated by the remanent magnetization \mathbf{M}_r can be characterized by magnetic poles at the edges of the film parallel to $\hat{y}(\hat{x})$. Typical field lines are sketched in Figs. 1(a) and 1(b). The field magnitude is large at positions near the poles and weak at remote positions. In Fig. 1(a), the magnetization of F is oriented along \hat{x} , the cross strip is extended beyond the width of the S bridge, and the magnetic field at S is weak and parallel to the film plane. In Fig. 1(b), the magnetization is oriented along \hat{y} , the magnetic poles are along the edges of the cross strip directly above the superconductor, and the field at S is perpendicular to the plane with substantial magnitude.

Figure 1(c) depicts a cross-sectional view of the device with \mathbf{M}_r of the F film along \hat{y} . The external field \mathbf{B} can be calculated from the distribution of magnetic poles and is represented by arrows and dotted field lines. To good approximation, the surface pole density of magnitude M poles/cm² can be represented as a line source located at the middle of the end surface and having line density $\lambda = d_F M$. The field magnitude in the vicinity of the line source varies inversely with distance r ,

$$B = \frac{4\pi M d_F}{2\pi r} = \frac{2M d_F}{r}. \quad (1)$$

^{a)}Electronic mail: clinton@anvil.nrl.navy.mil

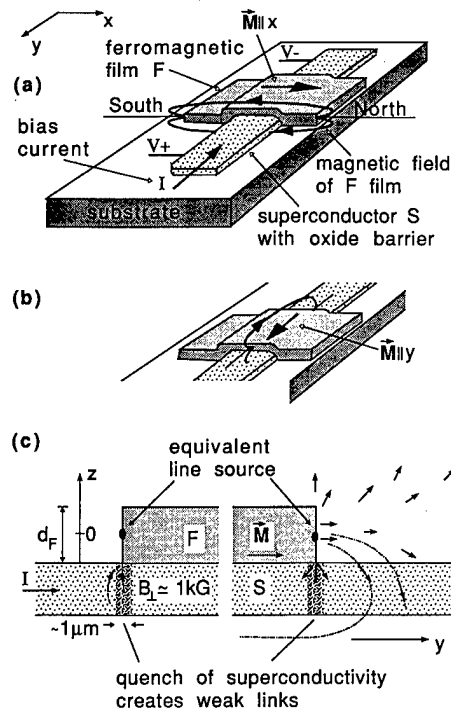


FIG. 1. (a) Prototype device geometry with F film remanent magnetization oriented along \hat{x} ; and (b) along \hat{y} . (c) Cross section of device geometry showing magnetic fringe field of F film and affect on underlying superconductor.

Typical dimensions in these structures are $d_F = 2000 \text{ \AA}$ for the F film thickness, $d_s = 400 \text{ \AA}$ for S, and the saturation magnetization of Py is $4\pi M_s \approx 11 \text{ kG}$, so the peak value of perpendicular field in the superconductor directly beneath one of the poles is of the order of a few kG and the decay width is less than a micron. In practice, the edges of our F films have some degree of roughness and the spatial extent of the fringe fields is expected to be broader, accompanied by a proportionately diminished value of peak magnitude. Nevertheless, a portion of S beneath an edge of F should be significantly affected by the relatively strong magnetic fringe fields when \mathbf{M} is along \hat{y} , and the short length scale of this magnetoquench should result in weak link behavior. Indeed, this "quench valve" can control the current flow in S, as is demonstrated below.

The Sn device consists of a 400-\AA -thick Sn film defined using a shadow mask to be 2 cm long and $400 \text{ }\mu\text{m}$ wide. The transition onset is $T_c \approx 3.9 \text{ K}$, the width is typically 100 mK or less, and the perpendicular upper critical field $H_{c2} \approx 850 \text{ Oe}$ ($T = 1.5 \text{ K}$). The F film layer is a cross strip of Py evaporated by e beam from a $\text{Ni}_{0.8}\text{Fe}_{0.2}$ source, with dimensions 2300 \AA thick, $400 \text{ }\mu\text{m}$ wide, and approximately $500 \text{ }\mu\text{m}$ long and extending about $50 \text{ }\mu\text{m}$ beyond the edge of the bridge on each side. The Pb device consists of a 350-\AA -thick Pb bridge ($T_c \approx 7.3 \text{ K}$, $\Delta T_c \leq 100 \text{ mK}$) defined photolithographically to be $100 \text{ }\mu\text{m}$ long and $5 \text{ }\mu\text{m}$ wide, with a 2150-\AA -thick Py cross strip. A native oxide layer ($\approx 10 \text{ \AA}$) is grown on the surfaces of Sn and Pb by glow discharge in oxygen before depositing the Py cross strip. SQUID magnetometer measurements determine the saturation magnetization of the Py to be $4\pi M_s = 11.5 \text{ kOe}$ at $T = 2.5 \text{ K}$. The co-

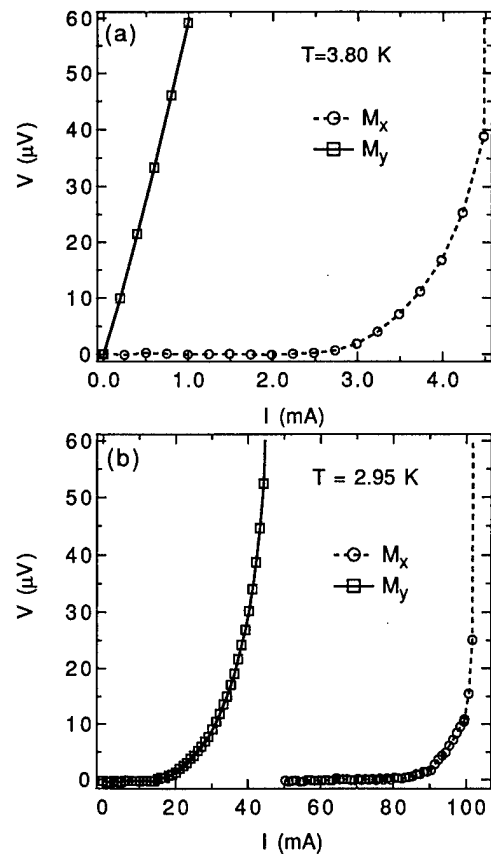


FIG. 2. (a) Sn-SnO-Py structure, voltage vs current at $T = 3.80 \text{ K}$ ($T_c = 3.9 \text{ K}$) for two remanent magnetization orientations M_y and M_x . (b) Voltage vs current at $T = 2.95 \text{ K}$ for two remanent magnetization orientations.

ercivity depends on several fabrication parameters and varies over all samples from $H_c \approx 2$ to 50 Oe . A field on the order of 100 Oe is applied along the chosen axis to orient \mathbf{M} , and is then reduced to zero prior to the transport measurement, unless noted otherwise. The data for the Pb device are measured in a cryostat with optical access to the sample as part of a magneto-optic Kerr effect photometer. Results similar to those presented in this article have been confirmed in more than ten samples.

The effect is demonstrated by the voltage versus current plot presented in Fig. 2 for a Sn-SnO-Py structure. In Fig. 2(a), the current-voltage (I - V) characteristics are plotted at $T = 3.80 \text{ K}$, just below T_c , where the righthand curve (M_x) was measured with \mathbf{M}_r oriented along \hat{x} as in Fig. 1(a); using a $1 \text{ }\mu\text{V}$ criterion the critical current is $I_{cx} = 3 \text{ mA}$. The lefthand curve (M_y) corresponds to \mathbf{M}_r along \hat{y} as in Fig. 1(b), and now the critical current is $I_{cy} = 0$. The I - V trace is linear for small voltages with a slope of $59 \text{ m}\Omega$. From the normal state resistance of the Sn bridge ($R_l \approx 27 \text{ }\Omega/\text{cm}$ just above T_c), $59 \text{ m}\Omega$ corresponds to a normal region about $20 \text{ }\mu\text{m}$ long, or a $10 \text{ }\mu\text{m}$ length under each edge of the F film. At lower temperatures as H_{c2} of Sn increases, these normal segments become narrower and should act like weak links in the superconducting bridge when they are comparable to the coherence length $\xi(T)$. Indeed, the data at lower temperatures are consistent with this. In Fig. 2(b) at $T = 2.95 \text{ K}$, well below T_c , we have $I_{cx} = 90 \text{ mA}$ (M_x) while $I_{cy} = 20 \text{ mA}$ (M_y),

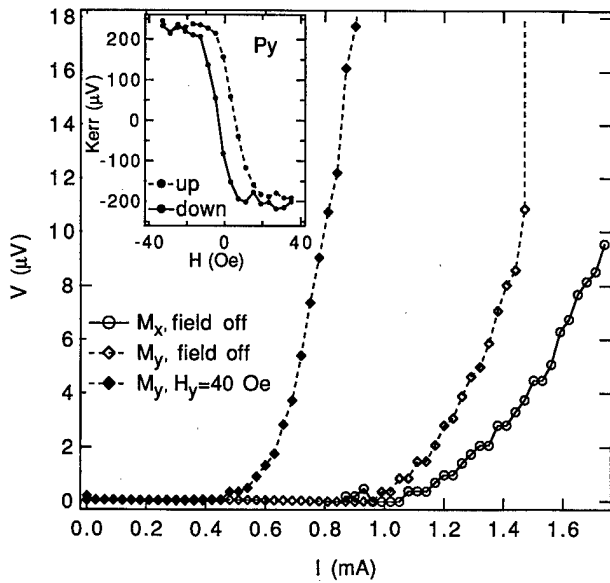


FIG. 3. Pb-PbO-Py structure, voltage vs current at $T = 6.2$ K ($T_c = 7.3$ K) for two remanent magnetization orientations M_x and M_y , as well as with an applied field $H_y = 40$ Oe to saturate Py magnetization, $M_y \approx M_s$. Inset: hysteresis loop of Py layer measured with magneto-optic Kerr effect photometer at room temperature. The Kerr rotation angle θ_K , and thus the Py magnetization M , is proportional to the photodiode voltage given in μV .

a 4.5-fold decrease. Thus, there is still a large suppression of I_c in switching magnetization states, but a nonzero I_{cy} indicates there is phase coherence across the quenched regions. Weak link behavior, such as Shapiro steps in the I - V characteristics as a function of rf power, and periodicity of I_c in applied magnetic flux, ϕ , have also been observed.⁹

Next, we turn to our Pb-PbO-Py structure. In Fig. 3, the voltage versus current characteristic at $T = 6.2$ K is plotted. The righthand curve (M_x) was measured with M_r oriented along \hat{x} as depicted in Fig. 1(a), while the middle curve (M_y) corresponds to M_r along \hat{y} as shown in Fig. 1(b). Consistent with the Sn data, I_c is suppressed when the remanent magnetization M_r is along \hat{y} (M_y). The inset of Fig. 3 is a hysteresis loop measured on the Py layer at room temperature with a magneto-optic Kerr photometer. The photodiode voltage is proportional to the Py magnetization M . The coercivity of the Py is roughly 5 Oe, and the magnetization is saturated by 40 Oe. At low temperatures, where the transport measurements are done, the loop is somewhat broader. It can also be seen from the figure that the remanent magnetization is only about half the saturation magnetization, $M_r \approx M_s/2$. From Eq. (1), the field at the Py film edge is proportional to M so the effect will be strongest with the magnetization saturated. The lefthand curve is measured with a small applied field along the y direction, $H_y = 40$ Oe, to saturate the magnetization. The applied field is parallel to the plane of the film and has no direct effect on the superconductivity at this temperature. However, I_c is suppressed even further as the Py magnetization is now saturated and the concomitant increase in perpendicular field at the edge of the film causes an

even greater quench of superconductivity in Pb, consistent with our magnetostatic model. Thus, it is desirable to produce ferromagnetic films with a square hysteresis loop, $M_r \approx M_s$, which is a tractable materials issue but not within the scope of this work.

The novel effect presented here has characteristics that make it promising for device applications. Since the switch requires zero quiescent power to maintain its state, the device is intrinsically a nonvolatile memory element. This coupled with its weak link nature puts it in a new class of Josephson-like devices: nonvolatile controllable weak links. Because the effect arises from the edge of a F film, a device can be made on a micron scale without degrading its performance. The speed of the device is set by magnetic domain switching times in the F film and flux relaxation in the superconductor. Domain switching imposes a limit between 1 GHz and 1 THz depending on material, while flux relaxation depends on the dimensions of the superconductor and for a micron scale device, these rates should be possible in a variety of materials.¹⁰ Small currents in a contiguous write wire can be used to switch the magnetization of the F film, and this integrated device should be capable of current, voltage, and power gain, and therefore capable of performing logic functions. Finally, fabrication of the device involves minimum processing. Since the effect does not involve transport, the nature of the F-S interface is not important and device fabrication is relatively simple.

In summary, we have demonstrated a novel superconducting switch using the magnetic fringe field of a ferromagnetic film to control the critical current in an underlying superconducting bridge. The effect is robust at temperatures well below the superconducting transition. The effect is modeled as the result of superconducting weak links being generated,⁹ and as such the switch is in a new class of Josephson-like devices. A semiquantitative magnetostatic model is in very good agreement with our results.⁸

This work is supported by ONR Contract No. N0001495WX20270.

¹R. E. Glover and M. D. Sherrill, Phys. Rev. Lett. **5**, 248 (1960).

²X. X. Xi, Q. Li, C. Doughty, C. Kwon, S. Bhattacharya, A. T. Findikoglu, and T. Venkatesan, Appl. Phys. Lett. **59**, 3470 (1991).

³Ting-wah Wong, J. T. C. Yeh, and D. N. Langenberg, Phys. Rev. Lett. **37**, 150 (1976).

⁴S. M. Faris, S. I. Raider, W. J. Gallagher, and R. E. Drake, IEEE Trans. Magn. **19**, 1293 (1983).

⁵Mark Johnson, Appl. Phys. Lett. **65**, 1460 (1994); V. A. Vas'ko, V. A. Larkin, P. A. Kraus, K. R. Nikolaev, D. E. Grupp, C. A. Nordman, and A. M. Goldman, Phys. Rev. Lett. **78**, 1134 (1997); Z. W. Dong *et al.*, Appl. Phys. Lett. **71**, 1718 (1997).

⁶See, for example, *Foundations of Applied Superconductivity*, edited by Terry P. Orlando and Kevin A. Delin (Addison-Wesley, Reading, MA, 1991).

⁷See, for example, K. K. Likharev and V. K. Semenov, IEEE Trans. Appl. Supercond. **1**, (1991).

⁸T. W. Clinton and Mark Johnson, Appl. Phys. Lett. **70**, 1170 (1997).

⁹T. W. Clinton and Mark Johnson (unpublished).

¹⁰See, for example, R. P. Huebener, L. G. Stafford, and F. E. Aspen, Phys. Rev. B **5**, 3581 (1972); M. R. Freeman, Phys. Rev. Lett. **69**, 1691 (1992).

Novel high- T_c transistors with manganite oxides

Z. W. Dong,^{a)} S. P. Pai, R. Ramesh, and T. Venkatesan

NSF MRSEC on Oxides, Department of Physics, University of Maryland, College Park, Maryland 20742

Mark Johnson

Naval Research Laboratory, Washington, D.C. 20375

Z. Y. Chen, A. Cavanaugh, Y. G. Zhao, X. L. Jiang, R. P. Sharma, S. Ogale,
and R. L. Greene

Center for Superconductivity Research, University of Maryland, College Park, Maryland 20742

One viable approach for transistor-like high- T_c three terminal devices is the quasiparticle injection device (QPID). We have fabricated $\text{Au/YBa}_2\text{Cu}_3\text{O}_7/\text{LaAlO}_3/\text{Nd}_{0.7}\text{Sr}_{0.3}\text{MnO}_3$ (NSMO) and $\text{Au/YBa}_2\text{Cu}_3\text{O}_7/\text{LaAlO}_3/\text{LaNiO}_3$ (LNO) heterostructures on (100) LaAlO_3 substrates by pulsed laser deposition for studies of quasiparticle injection effects in high- T_c superconducting thin films. The effect of the injection of spin-polarized quasiparticles from a ferromagnetic NSMO gate was compared to that of unpolarized quasiparticles from a nonmagnetic metallic LNO gate. A current gain greater than nine has been attained for spin-polarized QPIDs, which is an order of magnitude larger than the gain of spin unpolarized QPIDs. Such large effects could be useful in a variety of active high- T_c /colossal magnetoresistance heterostructure devices. © 1998 American Institute of Physics. [S0021-8979(98)42111-X]

I. INTRODUCTION

There has been significant research on the study of transistorlike superconducting three terminal devices such as flux-flow transistors,¹ electric field effect transistors,² anti-vortex Josephson junction transistors,³ and quasiparticle injection devices (QPIDs).^{4–10}

QPID is a nonequilibrium device. The injection of quasiparticles into a superconductor (S) creates a local nonequilibrium state which changes the quasiparticle spectrum and hence alters the superconducting order parameter.^{11,12} This usually causes a suppression in the critical current (I_c) density. QPIDs with low- T_c superconductors (LTS) have been extensively investigated using all kinds of injection sources to create the desired nonequilibrium transport for device applications.¹³ HTS, with their lower carrier densities, are more sensitive to quasiparticle injection. But the gain has been low. Nevertheless, these devices are attractive because their speed, which is limited by the effective quasiparticle relaxation time, may be of the order of 10–100 GHz.^{8,10} It should be noted that, in all the prior work, the quasiparticle injection sources are the free electrons and carry no spin polarization from the normal metal (N) gates through the insulating barriers (I).

However, quasiparticles can be spin-polarized. Tedrow and Meservey discovered that a ferromagnetic metal electrode (F) could inject spin-polarized quasiparticles into a superconductor.¹⁴ Johnson and Silsbee demonstrated that spin-polarized carriers injected into a normal metal diffuse over a distance δ_s , from the $F-N$ interface, and have a spin lifetime of T_1 (e.g., ~ 560 ps in Nb).¹⁵ Recently, an F metal layer of $\text{La}_{2/3}\text{Sr}_{1/3}\text{MnO}_3$ has been used as an injection source.¹⁶ The spin-polarized quasiparticles were indirectly

injected into a 600 Å thick $\text{DyBa}_2\text{Cu}_3\text{O}_7$ superconducting channel and a calculated current gain (G), defined as the ratio of critical current suppression to injection current ($G = \Delta I_c / I_{\text{inj}}$), of ~ 1 was achieved. Soon after, Dong *et al.*¹⁷ developed an *in situ* technique using pulsed laser deposition to fabricate $S-I-N$ and $S-I-F$ heterostructures for the studies of spin-polarized quasiparticle injection effects, where S is $\text{YBa}_2\text{Cu}_3\text{O}_7$ (YBCO), I is LaAlO_3 (LAO), F is $\text{Nd}_{2/3}\text{Sr}_{1/3}\text{MnO}_3$ (NSMO) and N is LaNiO_3 (LNO). The device geometry was designed for electronic applications with all quasiparticles directly injected into S . A current gain as large as five was attained for spin-polarized injection. This is 10 to 30 times larger than the gain of unpolarized injection devices. It strongly suggests that a new mechanism of pair breaking, associated with spin-polarized electrons, may be responsible for the suppression of I_c .

II. EXPERIMENTAL METHODS

The two structures used in this study are made on (100) LAO substrates by pulsed laser deposition. One is YBCO/LAO/NSMO ($S-I-F$) and the other is YBCO/LAO/LNO ($S-I-N$), where the NSMO is ferromagnetic below 170 K and acts as a spin-polarized injection source, while the LNO is metallic with quasiparticles carrying no spin polarization. The thickness of the LAO barrier layer is varied from 0–560 Å, and the other layers had the same thickness in both device structures: 1000 Å for the top YBCO layer and 2000 Å for the bottom NSMO or LNO layer. All thicknesses were determined and calibrated by Rutherford backscattering spectroscopy (RBS). The advantage of this comparison between the two types of structures, in contrast to comparing the manganite gate with a conventional metallic gate,¹⁶ is that the density of the carriers, the effect of lattice matching, the natural barrier of the interfaces, channel thickness, etc., are

^{a)}Currently at Read-Rite Corp., 44100 Osgood Road, Fremont, CA 94539.

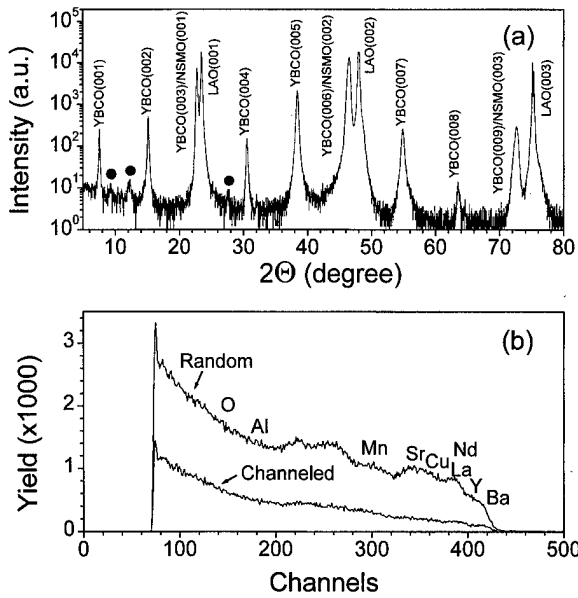


FIG. 1. (a) X-ray diffraction pattern of an *in situ* trilayer YBCO/LAO (400 Å)/NSMO. (b) Ion beam channeling and random Rutherford backscattering spectra with 3 MeV He^+ ion.

similar for both of our structures. This allows us to directly compare the injection effect of spin-polarized and unpolarized quasiparticles.

The laser energy density is 2 J/cm^2 for the deposition of NSMO and LAO and 1.5 J/cm^2 for YBCO.¹⁸ The substrate temperature is 600°C for LNO and 800°C for the other layers. During the deposition, the oxygen pressure is kept at 150 mTorr for YBCO and 400 mTorr for the other layers and is increased to 400 Torr during slow cooling of the samples. The x-ray diffraction pattern for the resulting *S-I-F* QPID is shown in Fig. 1(a). As can be seen, all layers are highly *c*-axis oriented. The YBCO is in the desired high- T_c 123 phase and the NSMO is in the cubic-type perovskite CMR phase, although there are three weak peaks which may arise from either (012) YBCO or BaCuO_2 . Figure 1(b) shows 3 MeV He^+ ion Rutherford random backscattering and channeling spectra which show a minimum yield of $\chi_{\min} \approx 16\%$ for the trilayer of *S-I-F*, indicating reasonably good crystallinity.

We have implemented a multilevel photolithography process involving image-reverse resist, selective wet etching, ion milling, thermal evaporation and lift-off procedure to integrate the devices on a small scale.^{17,18} The geometry of the devices allows the quasiparticles to be injected fully and directly into the *S* channel. Thus the effect can be studied quantitatively. The size of the devices is $20\text{--}250 \mu\text{m}$ wide and $220 \mu\text{m}$ long. The inset of Fig. 2 shows a schematic of our QPID configuration and a circuit for the injection measurements. The gate is biased with a Keithley 224 programmable current source. A standard four-probe technique is used for the electrical transport measurements of the *S* layer. In order to isolate the top Au from the bottom layer, a 2200 \AA thick rf-sputtered SiO_2 is deposited over the devices for passivation.

Figure 2 shows the temperature dependence of the resistivities of the individual layers in the devices: ferromagnetic

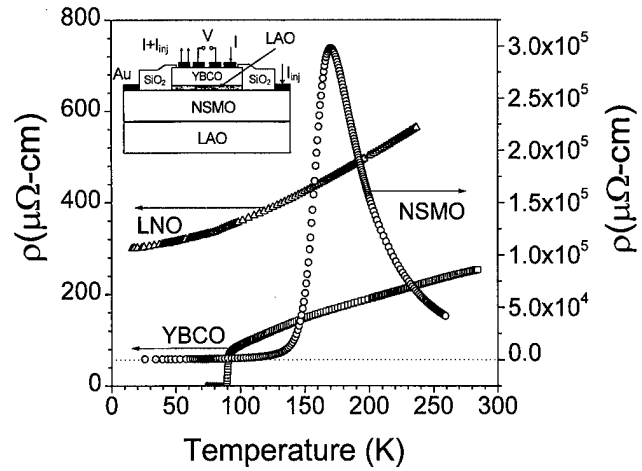


FIG. 2. R - T curves of YBCO (squares), NSMO (circles), and LNO (triangles) individual layers. YBCO has a T_c of 89 K, NSMO has a ferromagnetic transition at 170 K, and LNO is metallic. The inset is a schematic of a QPID.

NSMO, metallic LNO, and superconducting YBCO. The ferromagnetic transition occurs at 170 K for NSMO, confirmed by magnetization measurement. The resistivities of the NSMO and LNO layers are $\sim 1000 \mu\Omega \text{ cm}$ and $\sim 300 \mu\Omega \text{ cm}$ at 100 K, respectively, which are a little higher than that of the YBCO layer. The T_c of YBCO varies between 80 and 89 K in different devices. Vertical transport measurements show a contact resistance of order $10^{-4} \Omega \text{ cm}^2$ for a very thin LAO barrier layer.

III. RESULTS AND DISCUSSIONS

As described in Ref. 17, the I - V curves of all devices were found to be nonsymmetric. They exhibit a shift with respect to the zero current point in addition to showing a suppression in I_c . For each I - V curve there are two I_c values, positive critical current I_{cp} and negative critical current I_{cn} using a voltage criterion of $+2 \mu\text{V}$ or $-2 \mu\text{V}$, respectively. We defined the current shift (I_{shift}) in the I - V curves as $(I_{cp} + I_{cn})/2$ and I_c to be the half width of the zero voltage plateau, namely $I_c = (I_{cp} - I_{cn})/2$. This definition of I_c has thus taken into account the subtraction of the current from the shift caused by the injection current. Note that changing the direction of the injection current causes a shift in the opposite direction.

For all the devices we found a linear relationship between I_{inj} and I_{shift} , namely, $I_{\text{inj}} = -I_{\text{shift}}$, which is a consequence of the injection current totally participating in the current flow in the YBCO layer with zero resistance. In other words, if the injection current were parallel to the transport current in YBCO, the channel current would increase with increasing injection current. If the injection current flowed antiparallel to the channel current, the channel current would decrease since the injection current is subtracted from the transport current. If one takes the shift into account, the I - V curves are perfectly symmetric.

Figure 3 shows the I_c suppression versus injection current at different temperatures for both *S-I-F* and *S-I-N* QPIDs. In the *S-I-F* QPID [Fig. 3(a)], the I_c can be sup-

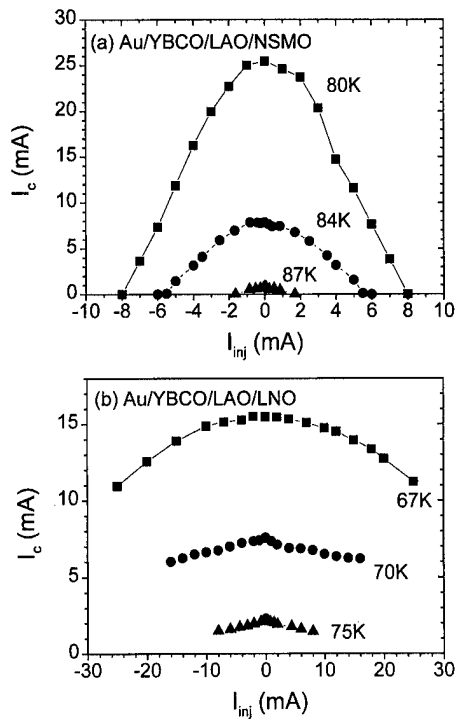


FIG. 3. Dependence of the critical current of both (a) Au/YBCO/LAO/NSMO ($S-I-F$) and (b) Au/YBCO/LAO/LNO ($S-I-N$) QPIDs, each with a 80 Å thick LAO barrier, on the injection current at different temperatures.

pressed to zero while in the $S-I-N$ QPID the I_c suppression is less than 30% even with injection currents in excess of 25 mA [Fig. 3(b)]. The current gain is 3.2 at 80 K for this particular $S-I-F$ QPID with an 80 Å thick LAO barrier. This is an order of magnitude larger than that for the $S-I-N$ spin-unpolarized QPID ($G \leq 0.3$) with the same LAO barrier thickness. In addition, we have systematically studied the effect as a function of the barrier thickness (details will be published elsewhere). A maximum gain of 9.3 was achieved at 84 K for an $S-I-F$ QPID with a 160 Å thick LAO barrier, which corresponds to a differential gain (dI_c/dI_{inj}) of 14. Typically, current gain is about 2–9 for barriers thinner than 200 Å. Upon increasing the barrier thickness beyond 200 Å, the current gain decreases very fast ($G \leq 1$). This shows that the optimal gain could be attained with a barrier thickness between 40–160 Å. The injection power density ($P_{inj} = J_{inj}^2 \times R_{area} \approx 1 \text{ W/cm}^2$) for $S-I-F$ QPIDs is even less than that for $S-I-N$ QPIDs. Based on these observations, the role of any significant thermal effect may be ruled out.

Since the sole difference between $S-I-N$ and $S-I-F$ QPIDs is spin-unpolarized injection in $S-I-N$ and spin-polarized injection in $S-I-F$, the observation of significantly larger gains for $S-I-F$ QPIDs suggests that spin-polarized quasiparticles generate a substantially larger nonequilibrium population. Although there is no formal theory describing nonequilibrium quasiparticle injection effect in HTS, let us do a semiquantitative analysis. The injected quasiparticle density is given by $\Delta n = J_{inj} \tau_r(T) / et$, where e is the electron charge and t is the thickness of YBCO.⁵ From experimental J_{inj} data and the estimation of

$\tau_r(T) \sim 10 \text{ ps}$, the maximum injected quasiparticle density is found to be of order 10^{17} cm^{-3} . We find that this density should be sufficiently large enough to suppress I_c ,^{6,17} giving a current gain of order 0.01–0.1 for $S-I-N$ QPIDs. However, the observed gain is of order 1 for $S-I-N$ QPIDs and the number of Cooper pairs in YBCO is a few orders of magnitude larger than the number of injected quasiparticles. This strongly indicates that the mechanism of pair breaking due to the injected spin-polarized quasiparticles could be very different from that of unpolarized quasiparticles in high- T_c oxides. We also found that lowering the temperature further increases the current gain, which is consistent with the measured temperature dependence of the quasiparticle relaxation time τ_r .¹⁹

ACKNOWLEDGMENTS

This work is supported by NSF Grant No. DMR9404579 and ONR Grants No. N00014-96-C-2008 and N00014-95-WX-20270, and the NFS MRSEC program at the University of Maryland.

- ¹J. Schneider, H. Kohlstedt, and R. Wordewer, *Appl. Phys. Lett.* **63**, 2426 (1993); L. Alff *et al.*, *J. Appl. Phys.* **75**, 1843 (1994).
- ²J. Mannhart, D. G. Schlom, J. G. Bednorz, and K. A. Muller, *Phys. Rev. Lett.* **67**, 2099 (1991); X. X. Xi, C. Doughty, A. Walkenhorst, C. Kwon, Q. Li, and T. Venkatesan, *ibid.* **68**, 1240 (1992).
- ³S. J. Berkowitz, Y. M. Zhang, W. H. Mallison, K. Char, E. Terzioglu, and M. B. Beasley, *Appl. Phys. Lett.* **69**, 3257 (1996).
- ⁴T. Kobayashi, K. Hashimoto, U. Kabasawa, and M. Tonouchi, *IEEE Trans. Magn.* **MAG-25**, 927 (1989).
- ⁵Yu. M. Bouguslavskij, K. Joosse, A. G. Sivakov, F. Roesthuis, G. J. Gerritsma, and H. Rogalla, *Physica C* **220**, 195 (1994).
- ⁶I. Iguchi, K. Nukui, and K. Lee, *Phys. Rev. B* **50**, 457 (1994).
- ⁷Q. Wang and I. Iguchi, *Physica C* **228**, 393 (1994). It should be noted that, in prior work (Refs. 1–6), gains were obtained without taking into account the I_{shift} .
- ⁸J. Mannhart, *Supercond. Sci. Technol.* **9**, 49 (1996).
- ⁹A. W. Kleinsasser and W. J. Gallagher, *Superconducting Devices*, edited by S. T. Ruggiero and D. A. Rudman (Academic, Boston, 1990), p. 325.
- ¹⁰Z. W. Dong, *High- T_c Superconducting Thin Film Devices* (Delft University Press, 2628 CN Delft, The Netherlands, 1995).
- ¹¹See, for example, J. J. Chang and D. J. Scalapino, *J. Low Temp. Phys.* **31**, 1 (1978).
- ¹²*Nonequilibrium Superconductivity, Phonons, and Kapitza Boundaries*, edited by K. E. Gray (Plenum, New York, 1981); K. E. Gray, *Appl. Phys. Lett.* **32**, 392 (1978).
- ¹³For a review see, for example, W. J. Gallagher, *IEEE Trans. Magn.* **MAG-21**, 709 (1985); R. A. Buhrman, *SQUIDS and their Applications*, edited by H. D. Halbohm and H. Lubbig (de Gruyter, Berlin, 1985), p. 171.
- ¹⁴P. M. Tedrow and R. Meserve, *Phys. Rev. B* **7**, 318 (1973); *Phys. Rev. Lett.* **37**, 858 (1976).
- ¹⁵M. Johnson and R. H. Silsbee, *Phys. Rev. Lett.* **55**, 1790 (1985); *Phys. Rev. B* **37**, 5326 (1988); M. Johnson, *Appl. Phys. Lett.* **65**, 1460 (1994).
- ¹⁶V. A. Vas'ko, V. A. Larkin, P. A. Kraus, K. R. Nikolaev, D. E. Grupp, C. A. Nordman, and A. M. Goldman, *Phys. Rev. Lett.* **78**, 1134 (1997).
- ¹⁷Z. W. Dong, R. Ramesh, T. Venkatesan, M. Johnson, Z. Y. Chen, S. P. Pai, P. R. Sharma, R. Shreekala, C. L. Lobb, and R. L. Greene, *Appl. Phys. Lett.* **71**, 1718 (1997).
- ¹⁸Z. W. Dong, T. Boettcher, C.-H. Chen, Z. Trajanovic, I. Takeuchi, V. Talyansky, R. P. Sharma, and T. Venkatesan, *Appl. Phys. Lett.* **69**, 3432 (1996).
- ¹⁹K. Krishna, J. M. Harris, and N. P. Ong, *Phys. Rev. Lett.* **75**, 3529 (1995). The authors studied HTS and observed an increase of $\tau_r(T)$ with decreasing temperature. Our observation of a large gain at lower temperature is consistent with $\Delta n(T) \propto \tau_r(T)$ being larger at lower T .

Extended x-ray absorption fine structure measurements of nonsuperconducting $\text{PrBa}_2\text{Cu}_3\text{O}_{6.9}$: Evidence against Ba site Pr substitution

V. G. Harris,^{a)} D. J. Fatemi, V. M. Browning, and M. S. Osofsky
Naval Research Laboratory, Washington, District of Columbia 20375

T. A. Vanderah
National Institute of Standards and Technology, Gaithersburg, Maryland

Extended x-ray absorption fine structure (EXAFS) measurements on nonsuperconducting $\text{PrBa}_2\text{Cu}_3\text{O}_{6.9}$ are reported. Theoretical Pr L_{II} EXAFS data, calculated for the case of Y-site and Ba-site occupation, were least-squares fit to the experimental Pr L_{II} EXAFS. Results indicate that the Pr ions overwhelmingly occupy the Y sites. These results present a serious challenge to models which rely on Ba-site Pr substitution as an explanation for the lack of superconductivity in $\text{PrBa}_2\text{Cu}_3\text{O}_{6.9}$. [S0021-8979(98)35711-4]

Despite more than a decade of intense research, the transport properties of the high temperature superconductors (HTS) are not well understood. Although the mechanism responsible for superconductivity is still under debate, most theories agree that the origin of superconductivity resides in the Cu–O planes which are common to all of the HTS. One exception is the oxygen or “charge reservoir” model proposed by Blackstead and Dow (BD).¹

In the $\text{RBa}_2\text{Cu}_3\text{O}_{7-\delta}$ ($R=Y$ and rare earths) or “123” compounds, the Cu–O chains serve as the charge reservoir. All of the 123 materials form metallic superconductors with the exception of $\text{PrBa}_2\text{Cu}_3\text{O}_{7-\delta}$ (PBCO) which, until recently, was reported to be insulating and nonsuperconducting. Nonsuperconducting PBCO presents a challenge to the BD model which predicts that this material should superconduct; therefore, recent reports of superconductivity in Pr materials which reportedly have the orthorhombic 123 structure have been touted as evidence in favor of BDs model.² However, these reports have yet to be independently verified, and the structure has yet to be confirmed by rigorous crystallography. Despite these results, it is still the general consensus that stoichiometric PBCO, when synthesized in a form isostructural with superconducting 123 materials, is both nonmetallic and nonsuperconducting.

In this article, we present extended x-ray absorption fine structure measurements of the nonsuperconducting compound $\text{PrBa}_2\text{Cu}_3\text{O}_{6.9}$ (PBCO). These results provide new insight regarding the structure of PBCO and confirm that Pr resides on the Y sites and is unlikely to occupy the Ba site in this material. This result is in conflict with assumptions made by several theories including the BD model.

A polycrystalline $\text{PrBa}_2\text{Cu}_3\text{O}_{6.9}$ powder was prepared by high-temperature solid-state reaction of reagent grade BaCO_3 , Pr_6O_{11} , and CuO in air within an alumina combustion boat. The starting materials were intimately mixed by grinding prior to each heating. As reported by others,³ a large number of reheatings, in this case 12, were required to obtain a single-phase sample for which all peaks in the powder

x-ray diffraction pattern could be accounted for. The mixture was heated first at 880 °C, twice at 925 °C, three times at 935 °C, and then six times at 945 °C. The final powder was pressed to ~1 g, 13 mm diameter disks that were sintered in air at 900 °C cooled at a rate of 75 °C/h to 500 °C, soaked at 500 °C for 15 days, and then furnace cooled to ambient temperature.

A sample disk was ground to a fine powder and subjected to x-ray powder diffraction analysis using $\text{Cu } K_\alpha$ radiation. All observable reflections in the x-ray powder pattern were used to refine the orthorhombic unit cell using a least-squares method.⁴ Compared with the single-crystal structural data reported for $\text{PrBa}_2\text{Cu}_3\text{O}_6$ and $\text{PrBa}_2\text{Cu}_3\text{O}_{6.9}$,⁵ the c parameter [11.712(1) Å] and unit cell volume [178.33(3) Å³] indicate an oxygen content of 6.9.

The x-ray absorption coefficient encompassing the Pr and Ba L absorption edges and the Cu K absorption edge was measured in transmission mode⁶ using the NRL beamline (X23B),⁷ at the National Synchrotron Light Source (Brookhaven National Laboratory, Upton, NY). Beamline X23B employs a double-crystal, fixed-exit monochromator with a pair of Si (111) crystals. Harmonic rejection is achieved by an upstream mirror that reflects only radiation of 10 keV or less. The extended x-ray absorption fine structure (EXAFS) data were collected when the storage ring energy was 2.5 GeV with a ring current between 110–250 mA. Because Pr K absorption occurs near 42 keV, too high an energy for most synchrotron EXAFS beamlines to operate, and the Pr L_{III} edge is contaminated by the Ba L_I edge fine structure, the Pr and Ba L_{II} absorption edges were used for EXAFS analysis.

The EXAFS analysis reported here involves the least-squares fitting of the phase and amplitude of experimental k -space data using a linear combination of simulated Pr(Y)-site and Pr(Ba)site L_{II} EXAFS data. The simulated L_{II} EXAFS data were generated using the multiple-scattering *ab initio* FEFF 6 codes of Rehr *et al.*,⁸ where the FEFF input files were generated using ATOM 4.2 codes of Ravel.⁹ These data

^{a)}Electronic mail: harris@zoltar.nrl.navy

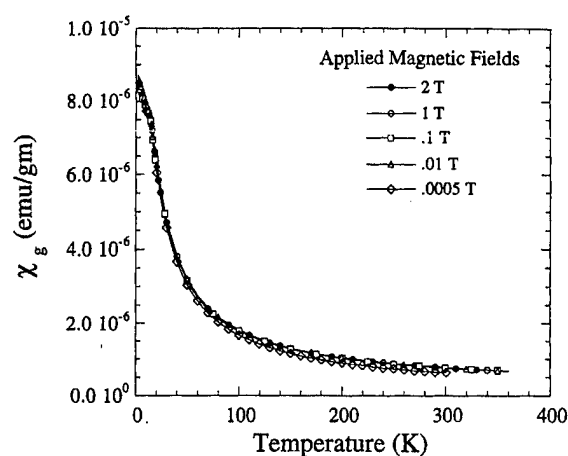


FIG. 1. Magnetic susceptibility of $\text{PrBa}_2\text{Cu}_3\text{O}_{6.9}$ sample as a function of temperature for several applied fields indicating lack of a superconducting state.

will henceforth be referred to as the FEFF data. The goodness-of-fit was determined numerically via the χ^2 fitting parameter.

The input parameters to FEFF codes were the lattice parameters determined by x-ray diffraction (XRD), the Debye temperature (Θ_D), and an amplitude reduction coefficient (S_0^2) of 1.0. The number of multiple scattering paths was set at six and applied to a cluster size of radius equal to 7.98 Å consisting of a total of 152 atoms. FEFF runs were repeated for Θ_D values ranging from 200 to 500 K at increments of 10 K. These data were then least-squares fit to the experimental data with one adjustable parameter, that being the relative occupancy of the Pr on the Ba- and Y-sites. A v_0 offset was systematically stepped through values ranging from ± 5 eV at a step-size of 0.25 eV to refine the value of E_0 , which had been arbitrarily assigned during refinement as the energy corresponding to the half height of the absorption step. The optimal value was determined by minimizing the χ^2 fitting parameter after which it was held fixed for the remainder of the analysis. Fitting was repeated for each combination of FEFF data as a function of Θ_D until, once again, χ^2 was minimized and a best fit was determined.

The temperature dependent magnetic susceptibility was measured in a SQUID susceptometer. The temperature sweeps were taken using applied magnetic fields of 2.0, 1.0, 0.1, 0.01, and 0.005 T. Except for the 0.005 T temperature sweep, data was taken while cooling the samples in field. In order to exclude pinning effects as a possible explanation for the suppression of any superconductivity, the 0.005 T temperature sweep was taken by first cooling the sample in zero field and then warming the sample in the applied field. The results are shown in Fig. 1, and indicate that the powder Pr sample is increasingly paramagnetic with decreasing temperature. A slight "kink" in the data near 12 K is consistent with observations of an antiferromagnetic ordering of the Pr sublattice which have been reported in numerous studies.^{10,11} The absence of any other features in the data is evidence for this material being a nonsuperconductor. The sensitivity of the system is such that a signal corresponding to as little as 0.05% bulk superconductivity would be detectable.

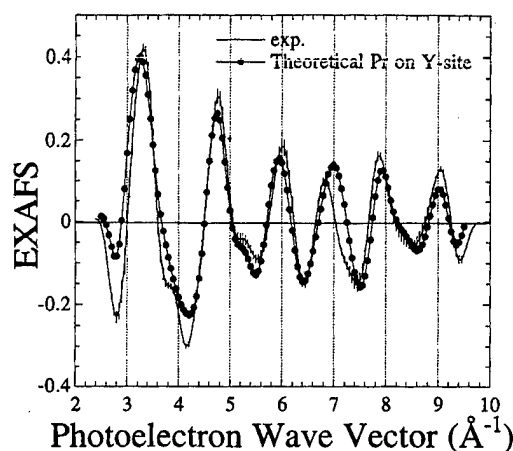


FIG. 2. Experimental $\text{Pr } L_{II}$ EXAFS after conversion to photoelectron wave vector space (k) with best fit data calculated using Y-site $\text{Pr } L_{II}$ FEFF data and Ba-site $\text{Pr } L_{II}$ FEFF data. See the text for discussion of calculated data. Least-squares fitting was performed using the relative fraction of site filling as the only adjustable parameter. The best fit reflects 100% occupation of Pr on the Y-sites.

The $\text{Pr } L_{II}$ EXAFS data was least-squares fit with FEFF data as described in Sec. II. The calculated best fit to the experimental EXAFS data are presented in Fig. 2. The best fit contains 0% Pr on the Ba-site. Again, the only adjustable parameter during fitting was the relative fraction of site occupation between the Y-site and the Ba-site. Figure 3 is a plot of the experimental $\text{Pr } L_{II}$ EXAFS with the Pr(Ba) -site L_{II} FEFF. Because the Pr(Ba) site L_{II} FEFF is nearly $\pi/2$ out of phase over a wide range of low- k values with respect to the Pr(Y) -site L_{II} FEFF (see Fig. 3), the least-squares fitting is acutely sensitive to even small amounts of Ba-site filling of Pr.

In Fig. 4 is plotted the χ^2 fitting parameter as a function of the percentage of Pr Ba-site filling. In these examples the percentage of Pr on the Ba-site was constrained to be a fixed percentage (1%–10%) and a least-squares best fit was calculated. In order to evaluate the sensitivity of these fitting analyses, an uncertainty limit of χ^2 values was defined by fitting the experimental mean \pm one standard deviation data with fit parameters fixed to those of the best fit. The standard

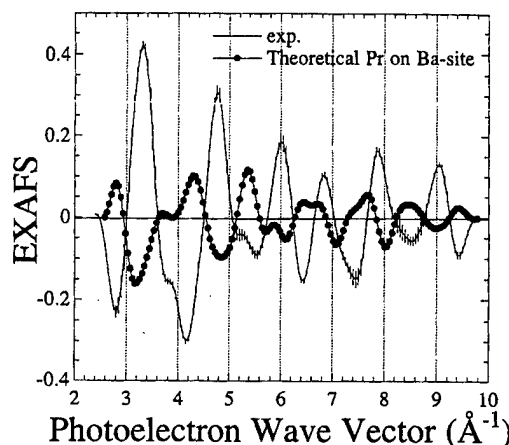


FIG. 3. Experimental $\text{Pr } L_{II}$ EXAFS after conversion to photoelectron wave vector space (k) with the Ba-site $\text{Pr } L_{II}$ FEFF data. Notice that the Pr(Ba) -site L_{II} FEFF is nearly $\pi/2$ out of phase over a wide range in k space.

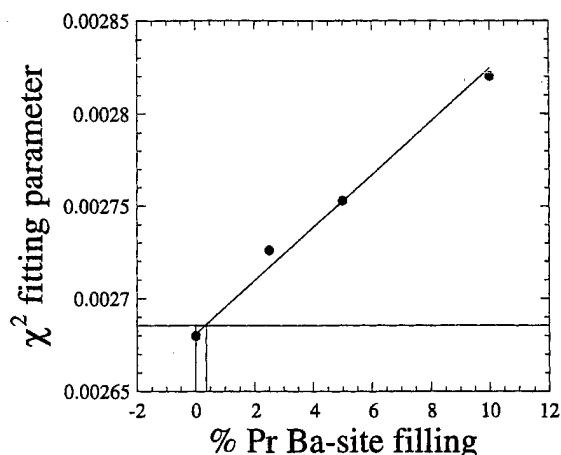


FIG. 4. χ^2 fitting parameter as a function of the percentage of Pr Ba-site filling. In these examples the percentage of Pr on the Ba-site was constrained to be a fixed percentage and a least-squares best fit was calculated. An uncertainty limit of χ^2 values is defined by fitting the experimental mean \pm one standard deviation data with fit parameters fixed to those of the best fit. (See the text for details.)

deviation is defined by both the statistical uncertainty (merging several data sets) and by the uncertainty introduced to the data set by the procedural steps leading to and including the Fourier transform. Fits which result in χ^2 values that fall outside of these limits indicate that the fit parameters are untenable.

The results presented in Fig. 4 reflect fits where the local environment of the Pr ions on the Ba-sites are not allowed to relax. This is a direct result of limiting the number of adjustable parameters to the fractional site filling. When one allows an additional degree of freedom, specifically, relaxation of the local environment surrounding these sites, then the uncertainty limits of permissible χ^2 values double allowing for approximately 1% of Pr ions on Ba sites.

Several mechanisms have been argued to be responsible for the absence of superconductivity in PBCO and/or its non-metallic transport. These mechanisms include magnetic pair breaking,¹² hole filling,^{13,14} hybridization effects,¹⁵ or some combination thereof. The most widely accepted theories are those which incorporate hybridization effects, since there exists an abundance of experimental evidence for hybridization of Pr 4*f* orbitals with Cu-3*d*/O-2*p* valence states.¹⁶⁻¹⁸ Fehrenbacher and Rice (FR)¹⁹ and Liechtenstein and Mazin (LM)²⁰ have proposed similar theories which argue that this hybridization results in the formation of a band which is competitive in energy to the normal conduction band responsible for transport in the superconducting 123 materials. In the FR model, this band is described as being very narrow resulting in localized states, in contrast, the LM model argues that this band is dispersive and attributes the observed nonmetallic transport to disorder arising from substitution of Pr on the Ba-site. Our results indicate that disorder due to Pr substitution for Ba cannot account for the nonmetallic transport as suggested by LM, suggesting that perhaps some other mechanism is responsible for disorder in the Cu-O planes or, as FR have suggested the nonmetallic transport is due to localized states in the Cu-O planes coupled with disorder in the Cu-O chains.

Blackstead and Dow present another argument suggesting that, when prepared using conventional techniques for producing superconducting 123 materials, PBCO is non-superconducting due to the tendency of Pr to sit on the Ba-site, where it acts as a "pair-breaker," thereby destroying superconductivity.²¹ It is hard to reconcile Ba-site Pr with extensive XRD studies by Lowe-Ma and Vanderah which indicate that PBCO is strictly isostructural with the superconducting 123 structures, except for a slight shortening of the apical Cu-O bond.⁵ However, the sensitivity of these techniques preclude ruling out small (<5%) amounts of Pr substitution on the Ba site. The site selectivity and local structure sensitivity afforded by the EXAFS technique allows us to conclude that Pr does not substitute for Ba in this compound in amounts greater than 1%. This result precludes the possibility of Ba-site Pr as a source of superconductivity suppression in PBCO. In light of this new evidence, we conclude that Ba-site substitution of Pr is not a valid explanation for the absence of superconductivity in PBCO. This must be viewed as a serious challenge for the charge reservoir model.

This research was carried out, in part, at the National Synchrotron Light Source (Brookhaven National Laboratories, Upton, NY) which is sponsored by the U.S. Department of Energy.

¹H. A. Blackstead and J. D. Dow, Phys. Lett. A **206**, 107 (1995).

²Z. Zou, K. Oka, T. Ito, and Y. Nishihara, Jpn. J. Appl. Phys., Part 2 **36**, L18 (1997).

³M. E. Lopez-Morales, D. Rios-Jara, J. Taguena, R. Escudero, S. LaPlaca, A. Bezing, V. Y. Lee, E. M. Engler, and P. M. Grant, Phys. Rev. B **41**, 655 (1990).

⁴C. K. Lowe-Ma, Report No. 8128, 1993 (unpublished).

⁵C. K. Lowe-Ma and T. A. Vanderah, Physica C **201**, 233 (1992).

⁶D. C. Koningsberger and R. Prins, *X-ray Absorption: Principles, Applications, Techniques of EXAFS, SEXAFS and XANES* (Wiley, New York, 1988), Vol. 92.

⁷R. A. Neiser, J. P. Kirkland, W. T. Elam, and S. Sampath, Nucl. Instrum. Methods Phys. Res. A **266**, 220 (1988).

⁸J. J. Rehr, S. I. Zabinsky, and R. C. Albers, Phys. Rev. Lett. **69**, 3397 (1992).

⁹B. Ravel, thesis, University of Washington, 1994 (unpublished).

¹⁰A. Kebede, C. S. Jee, J. Schwegler, J. E. Crow, T. Mihalism, G. H. Myer, R. E. Salomon, P. Schlottman, M. V. Kuric, S. H. Bloom, and R. P. Guertin, Phys. Rev. B **40**, 4454 (1989).

¹¹W. H. Li, J. W. Lynn, S. Skanthakumar, T. W. Clinton, A. Kebede, C. S. Jee, J. E. Crow, and T. Mihalism, Phys. Rev. B **40**, 5300 (1989).

¹²G. Y. Guo and W. M. Temmerman, Phys. Rev. B **41**, 6372 (1990).

¹³Y. Dalichaouch, M. S. Torikachvili, E. A. Early, B. W. Lee, C. L. Seaman, K. N. Yang, H. Zhou, and M. B. Maple, Solid State Commun. **65**, 1001 (1988).

¹⁴A. Matsuda, K. Kinoshita, T. Ishii, H. Shibata, W. Watanabe, and T. Yamada, Phys. Rev. B **38**, 2910 (1988).

¹⁵M. B. Maple, J. M. Ferreira, R. R. Hake, B. W. Lee, J. J. Neumeier, C. L. Seaman, K. N. Yang, and H. Zhou, J. Less-Common Met. **149**, 405 (1989).

¹⁶L. Soderholm, C. K. Loong, G. L. Goodman, and B. D. Dabrowski, Phys. Rev. B **43**, 7923 (1991).

¹⁷J. J. Neumeier, M. B. Maple, and M. S. Torkachvili, Physica C **156**, 574 (1988).

¹⁸J. S. Kang, J. W. Allen, Z. X. Shen, W. P. Ellis, J. J. Yeh, B. W. Lee, M. B. Maple, W. C. Spicer, and I. Lindau, J. Less-Common Met. **148**, 121 (1989).

¹⁹R. Fehrenbacher and T. M. Rice, Phys. Rev. Lett. **70**, 3471 (1993).

²⁰A. I. Liechtenstein and I. I. Mazin, Phys. Rev. Lett. **74**, 1000 (1995).

²¹P. Karen, H. Fjellvag, O. Braaten, A. Kjekshus, and H. Bratsberg, Acta Chem. Scand. **44**, 994 (1990).

Anisotropic thermal conductivity of c -axis aligned $\text{Bi}_2\text{Sr}_2\text{CaCu}_2\text{O}_x$ superconductor in high magnetic fields

S. C. Nakamae, J. Crow, J. Sarrao, and J. Schwartz

National High Magnetic Field Laboratory, Florida State University, Tallahassee, Florida 32310

The anomalous behavior of the thermal conductivity, κ , of high temperature superconductors (HTS) has been attributed to two conflicting theories (phonon domination and electron domination) since the discovery of HTS. Change in κ due to a magnetic field is a direct consequence of additional scattering processes between the phonons, the charge carriers, and the flux lines. The existing theories predict different scattering effects for the phonons and the electrons. Therefore, knowing magnetothermal conductivity can provide useful information for the nature of heat carriers in HTS and the understanding of the vortex dynamics. We have measured the in-plane thermal conductivity of a c -axis aligned $\text{Bi}_2\text{Sr}_2\text{CaCu}_2\text{O}_x$ superconductor in magnetic fields up to 17 T. The magnetic field was applied both parallel and perpendicular to the c axis and always perpendicular to the direction of heat flow. The results are compared to existing electronic and phononic models. It has been discovered that the electronic thermal conductivity, κ_e , calculated from the Wiedemann–Franz law, does not predict the measured behavior of the thermal conductivity. Rather, the phonon thermal conductivity, κ_{ph} , calculated from the extended BRT (Bardeen, Richayzen, and Tewordt) theory, reproduces the experimental results accurately. The anisotropy of the in-plane magnetothermal conductivity is also investigated. © 1998 American Institute of Physics. [S0021-8979(98)35811-9]

I. INTRODUCTION

Much work has been dedicated to the theoretical understanding of the thermal conductivity (κ) of HTS. Most of the existing theoretical models attribute the enhancement in κ below the transition temperature, T_c , to be of either the electronic origin^{1,2} or phononic origin.^{3–5} Furthermore, the crystal structure of HTS is highly anisotropic, causing anisotropy in κ . Consequently, the vortex structure in the mixed state of a layered HTS is strongly dependent on the field direction with respect to the c axis.⁶ The magnetothermal conductivity dependence on the field orientation reflects such vortex structure.

II. EXPERIMENT

A. Sample preparation and characterization

The crystals of $\text{Bi}_2\text{Sr}_2\text{CaCu}_2\text{O}_x$ were grown by a self-flux technique⁷ which produced shiny, micaceous crystals with a surface area of 1–3 mm². The sample used for the experiment was cut into a rectangular shape with dimensions 1.85 mm×1.7 mm×0.035 mm. SQUID and a Cantilever magnetometry were used to measure the magnetization and the transition temperature, T_c , of the sample. The Cantilever experiments were performed in the 20 T superconducting magnet (SCM). The upper critical field, H_{c2} was estimated from the magnetization data.

B. κ Measurements

The steady-state heat flow technique was used. The thermal conductivity, $\kappa(T)$, is calculated by

$$\kappa(T) = (Q \cdot l) / (A_x \cdot \Delta T), \quad (1)$$

where Q is the heat input for the sample (provided by a 100 Ω chip resistor), l ($=0.6 \pm 0.05$ mm) is the distance between the two thermocouples (Type E, 0.0005 in. diameter), A_x is the cross sectional area of the sample ($A_x = 1.7 \times 0.035 \pm 0.2$ mm²), and ΔT is the temperature difference between the two thermocouples. The schematic view of the experimental apparatus is presented in Fig. 1. The sample was mounted onto the Cu-heat sink with GE varnish with a thin sapphire plate in between for electrical insulation. A radiation shield can was placed around the sample area, then the sample space was evacuated to $<10^{-5}$ mbar. The sample temperature was monitored with a CERNOX temperature sensor. The sensor was placed on the Cu-heat sink underneath the base of the sample. The 20 T SCM was used for all thermal conductivity measurements. The field was applied both parallel and perpendicular to the c axis of the sample.

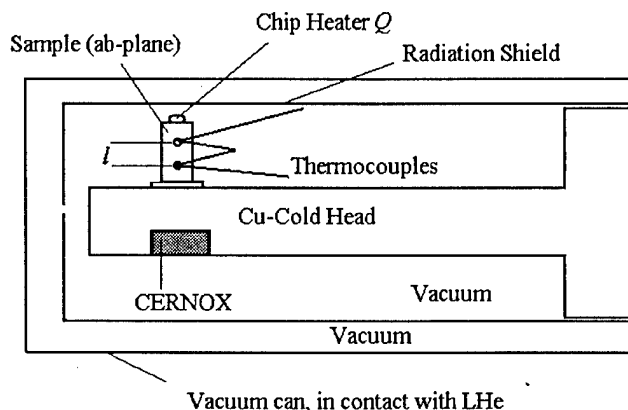


FIG. 1. Schematic view of the experimental apparatus.

III. THEORETICAL MODELS

A. κ_{ph} Models

Most of the theoretical models for the phonon thermal conductivity of superconductors available today are based on the BRT model⁸ which describes the κ_{ph} in zero magnetic field as

$$\kappa_{ph} = At^3 \int_0^\infty dx \frac{e^x x^4}{(e^x - 1)^2} (1 + \alpha t^4 x^4 + \beta t^2 x^2 + \delta t x + \gamma t x g(x, y))^{-1}, \quad (2)$$

where t , x , and y refer to reduced temperature (T/T_c), reduced phonon energy ($\hbar\omega/k_B T$), and the reduced energy gap ($\Delta/k_B T$), respectively. The coefficient A refers to the boundary scattering. The coefficients α , β , δ , and γ correspond to the relaxation rates for point-defects, sheetlike faults, dislocations and electron scattering. The exact form of $g(x, y)$ is found in Ref. 8.

In the presence of an applied magnetic field, H , the flux lines emerge, and thus an additional thermal resistance term appears, that is,

$$\Delta W(H, T) = \kappa^{-1}(H, T) - \kappa^{-1}(0, T) = \kappa_{ph-f}^{-1}(H, T). \quad (3)$$

For the in-field correction in the form of Eq. (2), we introduce an additional scattering term, $f(H/H_{c2})\gamma t x$, where $f(H/H_{c2})$ is a function of the reduced field. We have assumed that the relative area within the sample occupied by the flux lines is a function of the ratio between the applied field strength, H , and the upper critical field $H_{c2}(t)$. $f(H/H_{c2})$ must reach 1 (the maximum value) when the applied magnetic field exceeds $H_{c2}(t)$ of the sample at a given temperature. The flux lines are treated as line scattering sources. A similar analysis has been conducted by Mori *et al.* for the measurements on a $\text{Bi}_2\text{Sr}_2\text{Ca}_2\text{Cu}_3\text{O}_x$ polycrystalline sample.⁹ The simplified form of the $\Delta W(H, T)$ is

$$W(H, t) - W(0, t) = \left[At^3 \int_0^\infty dx \frac{e^x x^4}{(e^x - 1)^2} (f(H/H_{c2})\gamma' t x)^{-1} \right]^{-1}. \quad (4)$$

By integrating the above equation one obtains

$$\Delta W(H, t) = \frac{\gamma'}{At^2} f(H/H_{c2}). \quad (5)$$

Due to the highly anisotropic vortex structure of $\text{Bi}_2\text{Sr}_2\text{CaCu}_2\text{O}_x$, the form of $f(H/H_{c2})$ and the value of γ' are expected to be different for $H\parallel c$ and $H\perp c$ cases.

B. κ_e Models

In the electronic models, the main contribution to κ is believed to be the normal electrons in the Cu–O planes. Thus, we have used the Wiedemann–Franz law in conjunction with the experimental data on the microwave surface conductivity (σ) of a $\text{Bi}_2\text{Sr}_2\text{CaCu}_2\text{O}_x$ single crystal¹⁰ to estimate the electronic thermal conductivity in zero magnetic field. $\kappa_e = L\sigma T$, where L , Lorenz number, is taken to be $2.44 \times 10^{-8} \text{ W}\Omega/\text{K}^2$. Since the sample used in our experi-

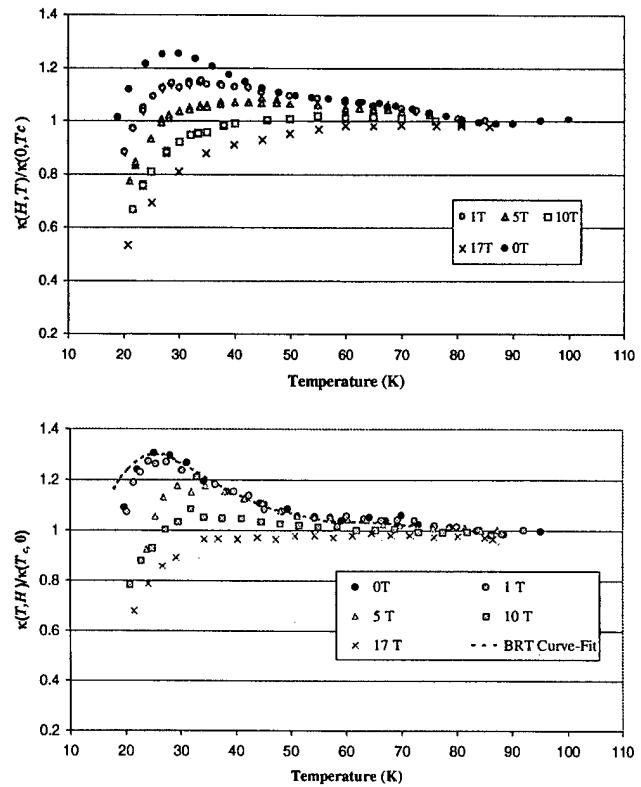


FIG. 2. (a) Normalized magnetothermal conductivity for $H\parallel c$ axis. (b) Normalized magnetothermal conductivity for $H\perp c$ axis.

ment contains more scattering sources than a single crystal, this value is considered to be the upper limit from the electronic contribution to the total thermal conductivity.

IV. RESULTS AND DISCUSSION

A. Magnetization results

From the magnetization measurements taken by SQUID and Cantilever magnetometry, the onset transition temperature is $85 \pm 1 \text{ K}$. From the Cantilever magnetization measurement results ($H\parallel c$), the upper critical field was observed to exceed 17 T immediately below T_c , and remains nearly constant for a wide temperature range for $75 \text{ K} > T > 35 \text{ K}$.¹¹ H_{c2} at $T=0 \text{ K}$ is estimated to be 80 T. For the procedure used to estimate H_{c2} , the readers should refer to Cho *et al.*¹¹ and Hao *et al.*¹²

B. κ Measurements and analysis

The normalized $\kappa(H, T)$ in applied magnetic fields up to 17 T for the two field orientations are presented in Figs. 2(a) and 2(b). The error analysis includes the heat leak through the gold wires, radiation loss between the sample and the radiation shield, and the voltage response change of the thermocouples in applied magnetic fields.¹³ The heat leak through the thermocouples was determined to be negligible compared to the other error sources.

First, the zero-field data is compared to the BRT model [see Fig. 2(b)]. The coefficients for the best fit are: $A = 57$, $\alpha = 44$, $\delta = 0.1$, $\delta = 2.0$ and $\gamma = 83$. The energy gap, $\Delta(0) = 8 \text{ meV}$, produces the correct $\kappa_{\max}(T)$ location,

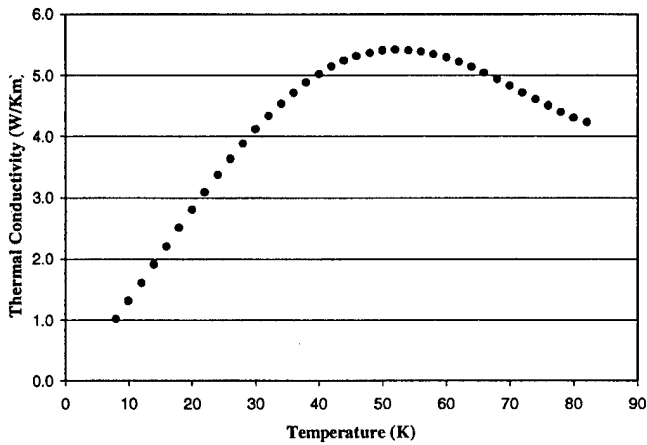


FIG. 3. Estimated maximum κ_e from microwave surface conductivity data and Wiedemann–Franz law.

though this value is lower than most of the values found in the literature.¹⁴ Next, the data is compared to the electronic model (Wiedemann–Franz law). We have found that if the electronic contribution dominates, the peak in κ must occur at a temperature between 55 and 60 K as shown in Fig. 3. Some of the reported κ data of $\text{Bi}_2\text{Sr}_2\text{CaCu}_2\text{O}_x$ superconductors^{15,16} show κ_{max} around 60 K, supporting the normal electron scenario; however, our measured peak of 32 K is approximately 25 K lower. This discrepancy is most likely due to the impurity scattering, which effectively reduces the electronic thermal conductivity. For this reason, we believe that in our $\text{Bi}_2\text{Sr}_2\text{CaCu}_2\text{O}_x$ superconductor, the thermal conductivity is dominated by phonons. Therefore, we have only utilized the phonon theory in the following in-field κ analysis.

C. $\kappa_{\text{ph}}(H, T)$ Analysis

The thermal resistance change (ΔW) in magnetic fields (due to flux lines) are compared to the theoretical values calculated from Eq. (5). The results are shown in Figs. 4(a) and 4(b). The dotted lines represent the theoretical curves with $f(H/H_{c2}) = (H/H_{c2})^{1/2}$ for $H \parallel c$ measurements and $f(H/H_{c2}) = H/H_{c2}$ for $H \perp c$ measurements. $H_{c2}(0 \text{ K}) = 80 \text{ T}$ was used for both calculations. The H_{c2} value is taken to be nearly constant for a wide temperature range as discussed previously and temperature dependent for $t < 0.4$. The agreement between the experimental data and the theoretical curves is within 10% for all field values.

V. SUMMARY

We have shown that the in-plane thermal conductivity of c -axis aligned $\text{Bi}_2\text{Sr}_2\text{CaCu}_2\text{O}_x$ crystals is strongly dependent on the phonon contribution, rather than the electronic contribution. The field dependence of κ , $f(H/H_{c2})$ is determined to be $(H/H_{c2})^{1/2}$ when $H \parallel c$ axis and H/H_{c2} when $H \perp c$ axis. The different forms of $f(H/H_{c2})$ may be explained by further theoretical studies on the anisotropic vortex-phonon

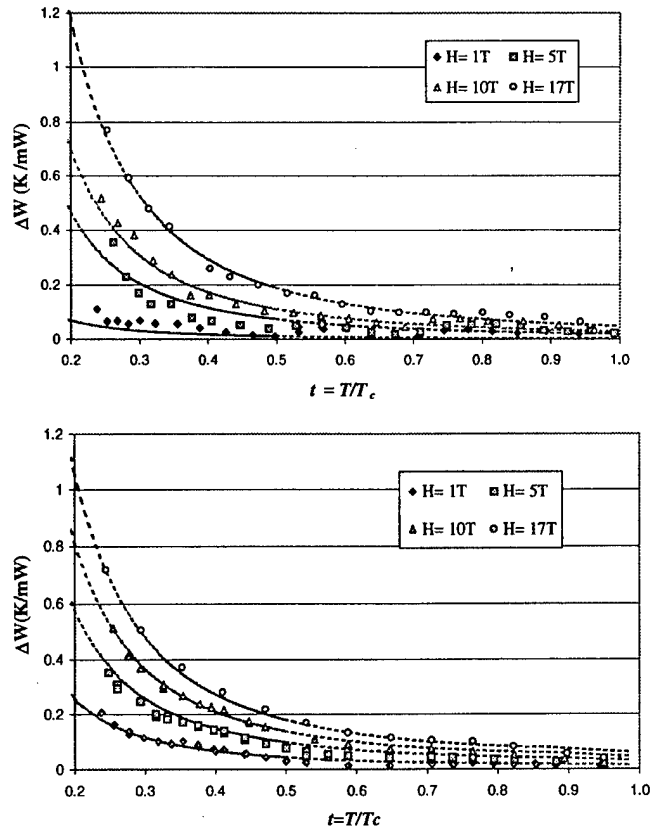


FIG. 4. (a) Thermal resistance change for $H \parallel c$ axis. (b) Thermal resistance change for $H \perp c$ axis.

scattering effects (vortex spacing, normal metal coherence length, and flux pinning strength). Although the theoretical calculations and the experimental results are in agreement, we have not considered the κ_e contribution. Therefore, the inclusion of κ_e to the data analysis may improve the theoretical model especially in the lower field range.

- ¹F. Yu, M. B. Salamon, J. P. Lu, and W. C. Lee, Phys. Rev. Lett. **69**, 1431 (1992).
- ²M. Houssa, Ph.D. thesis, Université de Liège, 1996.
- ³L. Tewordt and T. Wölkhausen, Solid State Commun. **70**, 839 (1989).
- ⁴C. Uher, J. Supercond. **3**, 337 (1990).
- ⁵L. Tewordt and T. Wölkhausen, Solid State Commun. **75**, 515 (1990).
- ⁶D. J. Bishop, P. L. Gammel, D. A. Huse, and C. A. Murray, Science **255**, 165 (1992).
- ⁷C. Kendziora *et al.*, Phys. Rev. B **45**, 13025 (1992).
- ⁸J. Bardeen, G. Richayzen, and L. Tewordt, Phys. Rev. **113**, 982 (1959).
- ⁹K. Mori, A. Tanaka, K. Nishimura, J. Sakurai, T. Sasaki, N. Kobayashi, Y. Tanaka, and M. Mimura, Physica C **235-240**, 1509 (1994).
- ¹⁰S. F. Lee, D. C. Morgan, R. J. Ormeno, D. M. Brount, R. A. Doyle, J. R. Waldram, and K. Kadowaki, Phys. Rev. Lett. **77**, 735 (1996).
- ¹¹J. H. Cho, Z. Hao, and D. C. Johnston, Phys. Rev. B **46**, 8679 (1992).
- ¹²Z. Hao, C. J. R., M. W. McElfresh, L. Civale, A. P. Malozemoff, and F. Holtzberg, Phys. Rev. B **43**, 2844 (1991).
- ¹³H. H. Sample, L. J. Neuringer, and L. G. Rubin, Rev. Sci. Instrum. **45**, 64 (1974).
- ¹⁴N. Hudáková, P. Samuely, P. Szabó, K. Knížek, V. Plecháček, and D. Sedmidubský, Physica B **218**, 217 (1996).
- ¹⁵G. Briceno, M. S. Fuhrer, and A. Zettl, Physica C **235-240**, 1505 (1994).
- ¹⁶P. B. Allen, X. Du, and L. Mihaly, Phys. Rev. B **49**, 9073 (1994).

Superconductivity in the new quaternary ruthenium borocarbide Y–Ru–B–C system

Y. Y. Hsu, H. C. Chiang, and H. C. Ku^{a)}

Department of Physics, National Tsing Hua University, Hsinchu, Taiwan 300, Republic of China

Two new quaternary borocarbide phases were discovered in the Y–Ru–B–C system: the (1111) YRuBC phase of the LuNiBC-type structure with tetragonal lattice parameters $a = 3.625\text{--}3.630\text{ \AA}$ and $c = 7.775\text{--}7.874\text{ \AA}$, and the (1221) YRu₂B₂C phase of the LuNi₂B₂C-type structure with tetragonal lattice parameters $a = 3.742\text{--}3.787\text{ \AA}$ and $c = 10.278\text{--}10.453\text{ \AA}$. Bulk superconductivity of 9.7 K was observed from transport and magnetic measurements for the annealed YRu₂B₂C sample with a short Ru–Ru bond length $d(\text{Ru–Ru}) = \sqrt{2} a/2 = 2.646\text{ \AA}$.

© 1998 American Institute of Physics. [S0021-8979(98)19211-3]

Superconductors with relatively high T_c up to 23 K have been reported in the quaternary borocarbides RT₂B₂C ($R = \text{Sc, Y, Th, U, or a rare earth; } T = \text{Ni, Pd, or Pt}$).^{1–13} The superconducting phases have been identified to be the LuNi₂B₂C-type (1221) body-centered tetragonal structure with space group $I4/mmm$. The structure is a three-dimensionally connected framework with LuC layers alternated with Ni₂B₂ layers where Ni is tetragonally coordinated by four boron atoms.⁴ Because of the great potential to find high T_c superconductors in this structure and other related structures, we investigate the Y–Ru–B–C system. In this article we report the discovery of two new quaternary borocarbides in the Y–Ru–B–C system. One is a high T_c compound YRu₂B₂C isostructural to LuNi₂B₂C.

All YRu_mB_mC ($m = 1, 2, 3, 4$) samples were prepared from high-purity elements (Y: 99.9%, Pd: 99.95%, B: 99.9995%, and C: 99.995%) with stoichiometric starting composition 1: m : m :1 ($m = 1\text{--}4$) under an argon atmosphere in a Zr-gettered arc furnace. The starting ingredients were slowly arc melted several times in order to ensure negligible weight loss and sample homogeneity. For annealing, the sample was wrapped in the Ta foil and sealed in a thick-wall (2 mm) quartz tube under Ar atmosphere, then annealed at 1200–1400 °C for one day. The crystallographic data were obtained with a Rigaku Rotaflex rotating anode x-ray diffractometer using Cu K_α radiation with a scanning rate of 1° in 2θ per minute. A Lazy Pulverix-PC program was employed for phase identification, lattice parameter calculation, and intensity calculation.

The magnetic susceptibility measurements were made with a μ -metal shielded Quantum Design MPMS₂ superconducting quantum interference device (SQUID) magnetometer down to 2 K in 10 G low magnetic field. The transport resistance data were obtained using the standard four-probe method with an ac (16 Hz) excitation current of 10 mA (rms) in the sample space chamber of the MPMS₂ down to 2 K.

For the as-melted YRuBC sample, powder x-ray diffraction data show a multiphase pattern with ~40% of the new LuNiBC-type (1111) phase (tetragonal lattice parameters $a = 3.635\text{ \AA}$, $c = 7.874\text{ \AA}$, and a unit volume $V = 104.0\text{ \AA}^3$),⁴

~40% of new LuNi₂B₂C-type (1221) phase (tetragonal $a = 3.787\text{ \AA}$, $c = 10.318\text{ \AA}$, and $V = 148.0\text{ \AA}^3$),⁴ and ~20% of unidentified impurity phases. Superconducting transition around 4 K was observed but with a very small (<1%) zero-field-cooled (ZFC) diamagnetic shielding signal of 9×10^{-6} emu (g G) at 2 K. This superconducting signal disappeared after the sample was annealed at 1200 °C for one day. The x-ray pattern for annealed sample indicates that after annealing, both the (1111) phase ($a = 3.620\text{ \AA}$, $c = 7.775\text{ \AA}$ and $V = 101.9\text{ \AA}^3$) and the (1221) phase ($a = 3.787\text{ \AA}$, $c = 10.314\text{ \AA}$, and $V = 147.9\text{ \AA}^3$) have a slightly reduced volume due to thermal diffusion and possible boron/carbon loss during annealing.

For the as-melted YRu₂B₂C sample, the powder x-ray diffraction data also show a multiphase pattern with ~70% of the new tetragonal (1221) phase ($a = 3.780\text{ \AA}$, $c = 10.278\text{ \AA}$, and $V = 146.9\text{ \AA}^3$), no new (1111) phase, and ~30% of unidentified impurity phases. No superconductivity was observed down to 2 K for the as-melted YRu₂B₂C sample. It is noted that the new (1221) phase unit cell volume of 146.9 \AA^3 in the as-melted YRu₂B₂C sample is smaller than $147.9\text{--}148.0\text{ \AA}^3$ observed from the multiphase YRuBC sample.

In order to enhance the effect of thermal diffusion and sample homogeneity through heat treatment, the YRu₂B₂C sample was annealed at a very high temperature of 1400 °C for one day in a thick-wall (2 mm) quartz tube. After the high temperature annealing, the x-ray diffraction pattern in Fig. 1 shows no improvement of the new (1221) phase concentration (~70%) but with a smaller unit cell volume ($a = 3.742\text{ \AA}$, $c = 10.453\text{ \AA}$, and $V = 146.4\text{ \AA}^3$). The calculated intensity using the atomic positions of the LuNi₂B₂C-type (1221) phase⁴ in YRu₂B₂C is shown in Fig. 2 for comparison. All unidentified impurity phases in as-melted sample disappeared after annealing, with the emergence of a new impurity phase of ternary YRu₄B₄ with tetragonal lattice parameter $a = 7.45\text{ \AA}$, $c = 14.99\text{ \AA}$.¹⁴ The variation of lattice parameters and unit cell volume for the new (1221) phase indicates that there is a homogeneity range YRu_{2–x}B_{2–y}C_{1–z} for the phase in the Y–Ru–B–C phase diagram.

The low temperature relative electrical resistance

^{a)}Electronic mail: hcku@phys.nthu.edu.tw

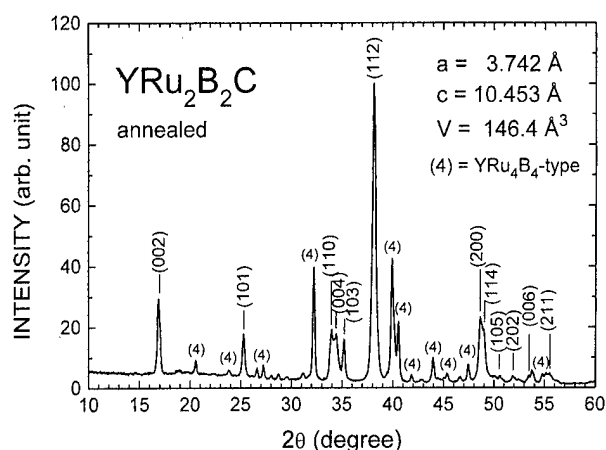


FIG. 1. Powder x-ray diffraction patterns of annealed $\text{YRu}_2\text{B}_2\text{C}$ sample. The new $\text{LuNi}_2\text{B}_2\text{C}$ -type (1221) tetragonal phase lines are indexed ($a=3.74 \text{ \AA}$, $c=10.453 \text{ \AA}$). Major impurity is the ternary tetragonal YRu_4B_4 (marked by (4), with $a=7.45 \text{ \AA}$, $c=14.99 \text{ \AA}$).

$R(T)/R(300 \text{ K})$ for the annealed $\text{YRu}_2\text{B}_2\text{C}$ sample is shown in Fig. 3. A sharp superconductivity transition with zero resistance $T_c(\text{zero})$ was observed at 9.6 K and a superconducting onset (1%) $T_c(\text{onset})$ around 10 K. The resistance decreases monotonically with decreasing temperature as expected for a metallic compound, with a large extrapolated residual resistance ratio $R(0)/R(300 \text{ K})$ of 0.73 due to the impurity scattering of the ternary YRu_4B_4 phase. Since the YRu_4B_4 impurity phase is a low T_c superconductor of 1.4 K¹⁴ and other ternary impurities YRuB_2 ($T_c=7.8 \text{ K}$), YRuB_4 ($T_c=1.4 \text{ K}$), and YRu_3B_2 (no T_c down to 1.2 K)^{15,16} were not observed, the new 10 K superconducting phase with narrow transition width of 0.4 K is probably due to the new (1221) phase having a shorter Ru-Ru bond length $d(\text{Ru-Ru})=\sqrt{2} a/2=2.646 \text{ \AA}$ as compared with $d=2.673 \text{ \AA}$ for the as-melted sample. In the isostructural non-magnetic $\text{RNi}_2\text{B}_2\text{C}$ system, similar T_c variation versus Ni-Ni bond length was observed with T_c of 17 K for $d(\text{Ni-Ni})=2.53 \text{ \AA}$, 4 K for 2.65 \AA , and below 1 K for 2.68 \AA .⁹ For the nonmagnetic $\text{RPd}_2\text{B}_2\text{C}$ system, T_c of 23 K for

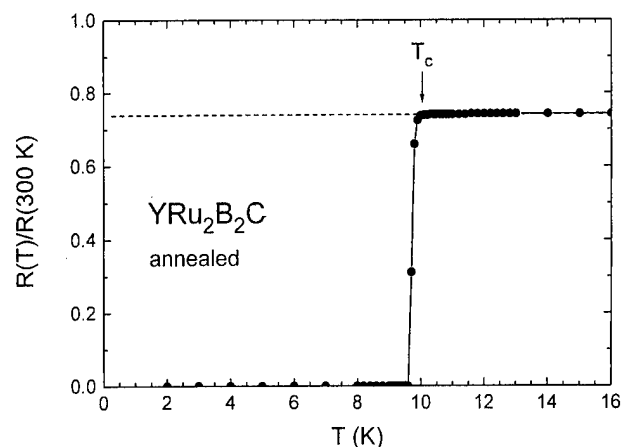


FIG. 3. Low temperature relative resistance $R(T)/R(300 \text{ K})$ of annealed $\text{YRu}_2\text{B}_2\text{C}$ sample, with $T_c(\text{onset})$ at 10 K, $T_c(\text{mid})$ at 9.7 K, and $T_c(\text{zero})$ at 9.6 K.

Pd-Pd bond length $d(\text{Pd-Pd})=2.53 \text{ \AA}$ and 2 K for $d=2.80 \text{ \AA}$ were observed.¹¹

The bulk nature of superconductivity can be checked through the magnetic measurement. The low temperature mass magnetic susceptibility $\chi_g(T)$ of the same sample is shown in Fig. 4 for both the zero-field-cooled (ZFC) and field-cooled (FC) measurements in a low applied field of 10 G. A diamagnetic superconducting transition signal was observed at 9.7 K, a value equal to the midpoint transition $T_c(\text{mid})$ of 9.7 K from the transport measurement. A large ZFC shielding signal of $-1.9 \times 10^{-2} \text{ emu/(g G)}$ at 2 K for the bulk sample indicates the bulk superconducting effect (using the calculated x-ray density of 7.12 g/cm^3). For the powder sample (200 mesh), smaller ZFC signal of $-3.4 \times 10^{-3} \text{ emu/(g G)}$ at 2 K was observed in Fig. 5, due to the multiphase nature of the sample. A large FC signal of $-2.0 \times 10^{-3} \text{ emu/(g G)}$ at 2 K for powder sample was observed as compared with smaller FC signal of $-2.9 \times 10^{-4} \text{ emu/(g G)}$ at 2 K for bulk sample to de-pinning in the powdering process.

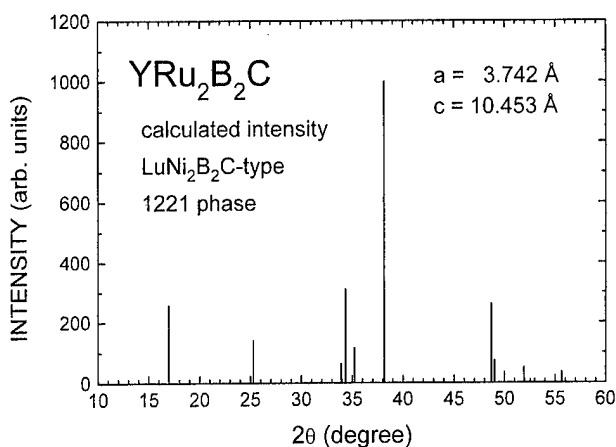


FIG. 2. Calculated intensity of $\text{LuNi}_2\text{B}_2\text{C}$ -type (1221) tetragonal phase in $\text{YRu}_2\text{B}_2\text{C}$.

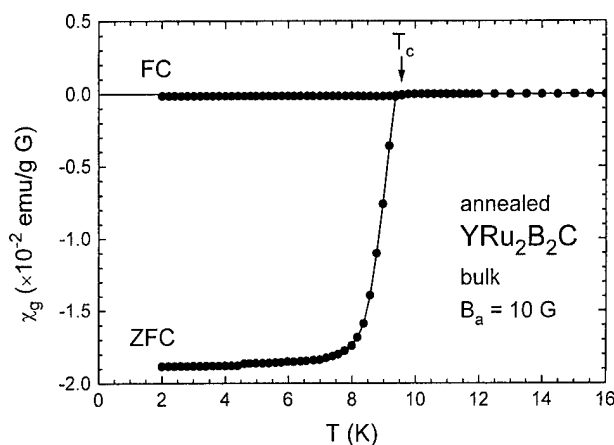


FIG. 4. Low temperature mass magnetic susceptibility χ_g of annealed $\text{YRu}_2\text{B}_2\text{C}$ bulk sample in field-cooled (FC) and in zero-field-cooled (ZFC) modes. The superconducting transition T_c at 9.7 K was observed.

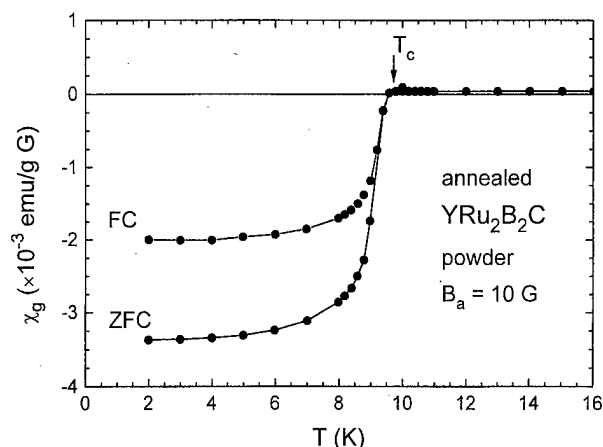


FIG. 5. Low temperature mass magnetic susceptibility χ_g of annealed $\text{YRu}_2\text{B}_2\text{C}$ powder sample (200 mesh).

To check the impurity superconductivity, two more samples were prepared. For the $\text{YRu}_3\text{B}_3\text{C}$ sample, the x-ray data showed mostly the YRu_4B_4 phase ($\sim 80\%$) for both as-melted and annealed samples. Two small superconducting transitions around 8 K ZFC diamagnetic signal of 1×10^{-5} emu/(g G) at 2 K and 4 K [ZFC diamagnetic signal of 2×10^{-4} emu/(g G) at 2 K] were observed. Since the orthorhombic ternary YRuB_2 phase has a T_c of 7.8 K,¹⁶ the 8 K transition is probably from the impurity YRuB_2 phase or the new $\text{YRu}_2\text{B}_2\text{C}$ phase. For the $\text{YRu}_4\text{B}_4\text{C}$ sample, the x-ray data show mostly the YRu_4B_4 phase ($>90\%$) for both as-melted and annealed samples. A small superconducting transition around 3 K was observed with the ZFC diamagnetic signal of 5×10^{-5} emu/(g G) at 2 K.

In conclusion, two new quaternary borocarbide phases were discovered in the Y–Ru–B–C system: the (1221) $\text{YRu}_2\text{B}_2\text{C}$ phase of the $\text{LuNi}_2\text{B}_2\text{C}$ -type structure and the (1111) YRuBC phase of the LuNiBC -type structure. Bulk

superconductivity of 9.7 K was observed for the annealed $\text{YRu}_2\text{B}_2\text{C}$ sample with the shortest Ru–Ru bond length. Impurity superconductivity of 3–4 K was also observed in the Y–Ru–B–C system.

This work was supported by the National Science Council of the Republic of China under Contract Nos. NSC86-2112-M007-007 and -025.

- ¹R. Nagarajan, C. Mazumdar, Z. Hossain, S. K. Dhar, K. V. Gopalakrishnan, L. C. Gupta, C. Godart, B. D. Badalia, and R. Vijayaraghavan, *Phys. Rev. Lett.* **72**, 274 (1994).
- ²R. J. Cava, H. Takagi, B. Batlogg, H. W. Zandbergen, J. J. Krajewski, W. F. Peck, Jr., R. B. van Dover, R. J. Felder, T. Siegrist, K. Mizuhashi, J. O. Lee, H. Eisaki, S. A. Carter, and S. Uchida, *Nature (London)* **367**, 146 (1994).
- ³R. J. Cava, H. Takagi, H. W. Zandbergen, J. J. Krajewski, W. F. Peck, Jr., T. Siegrist, B. Batlogg, R. B. van Dover, R. J. Felder, K. Mizuhashi, J. O. Lee, H. Eisaki, and S. Uchida, *Nature (London)* **367**, 252 (1994).
- ⁴T. Siegrist, H. W. Zandbergen, R. J. Cava, J. J. Krajewski, and W. F. Peck, Jr., *Nature (London)* **367**, 254 (1994).
- ⁵H. C. Ku, C. C. Lai, Y. B. You, J. H. Shieh, and W. Y. Guan, *Phys. Rev. B* **50**, 351 (1994).
- ⁶H. Eisaki, H. Takagi, R. J. Cava, B. Batlogg, J. J. Krajewski, W. F. Peck, Jr., K. Mizuhashi, J. O. Lee, and S. Uchida, *Phys. Rev. B* **50**, 647 (1994).
- ⁷J. L. Sarrao, M. C. de Andrade, J. Herrmann, S. H. Han, Z. Fisk, M. B. Maple, and R. J. Cava, *Physica C* **229**, 65 (1994).
- ⁸T. Takabatake, Y. Maeda, T. Konishi, and H. Fujii, *J. Phys. Soc. Jpn.* **63**, 2853 (1994).
- ⁹C. C. Lai, M. S. Lin, Y. B. You, and H. C. Ku, *Phys. Rev. B* **51**, 420 (1995).
- ¹⁰R. J. Cava, B. Batlogg, T. Siegrist, J. J. Krajewski, W. F. Peck, Jr., S. A. Carter, and R. J. Felder, *Phys. Rev. B* **49**, 12384 (1994).
- ¹¹P. J. Jiang, M. S. Lin, J. H. Shieh, Y. B. You, H. C. Ku, and J. C. Ho, *Phys. Rev. B* **51**, 16436 (1995).
- ¹²M. S. Lin, J. H. Shieh, Y. B. You, Y. Y. Hsu, J. W. Chen, S. H. Lin, Y. D. Yao, Y. Y. Chen, J. C. Ho, and H. C. Ku, *Physica C* **249**, 403 (1995).
- ¹³F. S. Jeng, Y. B. You, H. C. Ku, and J. C. Ho, *Phys. Rev. B* **53**, 6729 (1996).
- ¹⁴D. C. Johnston, *Solid State Commun.* **24**, 699 (1977).
- ¹⁵H. C. Ku and R. N. Shelton, *Mater. Res. Bull.* **15**, 1441 (1980).
- ¹⁶H. C. Ku, G. P. Meisner, F. Acker, and D. C. Johnston, *Solid State Commun.* **35**, 91 (1980).

Electron correlation in antiferromagnet and superconductor thiospinel Cu-Co-S₄

Kazuo Miyatani^{a)} and Toshiro Tanaka

Department of Materials Science and Engineering, Ehime University, Matsuyama 790-8577, Japan

Masayasu Ishikawa

Institute of Solid State Physics for Tokyo University, Roppongi, Tokyo 106, Japan

The Co-rich system (Co_{1-x}Cu_x)Co₂S₄ ($x=0-1$) and the Cu-rich system Cu[Cu_xCo_{2-x}]S₄ ($x=0-0.5$) were synthesized, and x-ray diffraction, magnetic susceptibility χ , and electrical resistivity ρ were studied. Curie-Weiss-type susceptibility with an antiferromagnetic structure with $T_N \approx 20$ K was observed for $x=0.3-1$ in the Co-rich system. This type of antiferromagnetism showed a similar behavior with those obtained previously for an antiferromagnetic and superconductive Cu-rich system. ρ showed a typical metallic-type temperature dependence and is proportional to T for the Co-rich system with antiferromagnetism and showed quadratic temperature dependence with the cross over temperature of 75 K for the Cu-rich system with antiferromagnetism and superconductivity. A 3d hole-electron correlation was observed to be concerned with Cu-S superconductivity. © 1998 American Institute of Physics. [S0021-8979(98)16811-1]

I. INTRODUCTION

In copper oxide high-temperature superconductors (HTS), the 3d hole carrier in the bonding orbits ($3d_{\gamma}-p_{\sigma}$) of the two-dimensional copper oxygen CuO₂ plane is responsible for the superconductivity, and the anisotropic properties result in complicated properties and physics. Among the various theoretical aspects for the origin of the superconductivity, the electron correlation is believed to take an important role.

From various exploring works on the copper sulfide superconductors by the present authors,^{1,2} the Cu-rich system Cu_{1+x}Co_{2-x}S₄ ($x=0-0.5$) was found to show an antiferromagnetic behavior on magnetic susceptibility with the Néel temperature $T_N \approx 20$ K ($x=0-0.5$) and to show superconductivity below $T_c = 4.0$ K depending on $x=0-0.5$. In the system, Cu-S bonding orbits are formed resulting in p -type conductivity like the case of Cu-O bonding in HTS. From a NMR study³ on Cu_{1.5}Co_{1.5}S₄ an enhancement of $(T_1T)^{-1}$ at T_N was observed.

In this work, a Co-rich cubic spinel system (Co_{1-x}Cu_x)Co₂S₄ ($x=0-1$) was developed and the crystallography, magnetic susceptibility, and electrical resistivity were studied to extend the understanding of the antiferromagnetism and superconductivity in the Cu-rich system.

II. EXPERIMENTS

The polycrystalline samples of the Co-rich system (Co_{1-x}Cu_x)Co₂S₄ ($x=0-1$) and the Cu-rich system Cu_{1+x}Co_{2-x}S₄ ($x=0-0.5$) were synthesized by a standard vacuum sealed quartz ampoule method. Starting materials of CuS, Co, and S were used, and the ampoule was heated at 500–800 °C for 20 h depending on the Cu composition. The system was synthesized well only when ~ 2 wt % moisture

was charged as a carrier gas. X-ray diffraction analysis showed these samples to be single phase and the Rietveld analysis showed that the whole system is a normal cubic spinel with the ionic distributions of (Co_{1-x}Cu_x)[Co₂]S₄ and Cu[Cu_xCo_{2-x}]S₄.

The lattice constant a and the u parameter, anion position, are shown in Fig. 1 over the entire range of Cu and Co concentrations, where starting from Co₃S₄ ($x=0$), $a(x)$ increases nonlinearly as Cu concentration increases, while the u parameter changes linearly within the experimental error and obeys the Begards law. The Cu locates in the tetrahedral site in the Co-rich system, and goes to the octahedral site also in the Cu-rich system.

The magnetic susceptibility of the Co-rich system (Co_{1-x}Cu_x)Co₂S₄ was measured above 2.8 K using a vibrating sample magnetometer. The low Cu doping range ($x=0-0.2$) basically showed a Pauli paramagnetism with a small temperature dependence. While Curie-Weiss-type susceptibility χ was observed for $x=0.3-1$, and an antiferromagnetic structure was observed below $T \approx 20$ K, which we assumed to be the Néel temperature. This antiferromagnetism continues to the superconductive Cu-rich system, which was observed previously.^{2,3} This antiferromagnetism is being studied by Sugita *et al.*⁴ of our working group using the NMR technique, and the $(T_1T)^{-1}$ enhancement was observed at ~ 55 and ~ 20 K for $x=0$ and 0.3, respectively, corresponding to the weak antiferromagnetic Néel temperature T_N .

The electrical resistivity ρ of the two systems was also measured above 10 K on the sintered and shaped bar samples by the conventional four-probe ac technique at 10 Hz using a helium refrigerator, and the results are shown in Figs. 2 and 3 for the Co- and Cu-rich systems, respectively. In the case of the Co-rich system in Fig. 2, ρ is, typically, metalliclike and is proportional to T except near Co₃S₄ ($x=0-0.15$). ρ of Co₃S₄ decreases rapidly below ~ 150 K and has a convex-

^{a)}Electronic mail: miyatani@enz.ehime-u.ac.jp

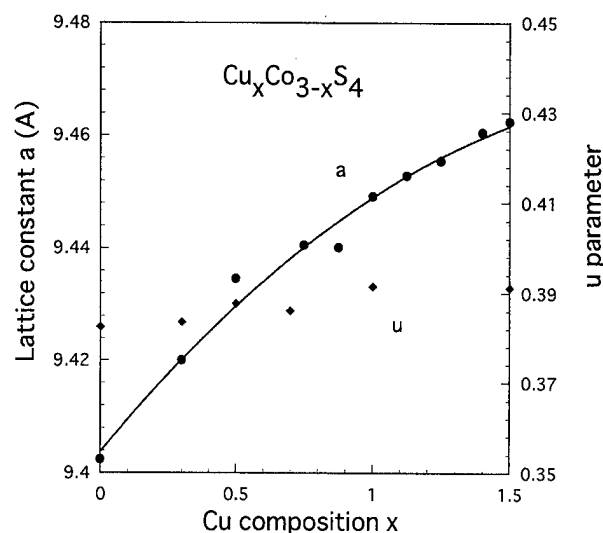


FIG. 1. The lattice constant a and u parameters of the Co and Cu systems $\text{Cu}_x\text{Co}_{3-x}\text{S}_4$ with cubic spinel structure.

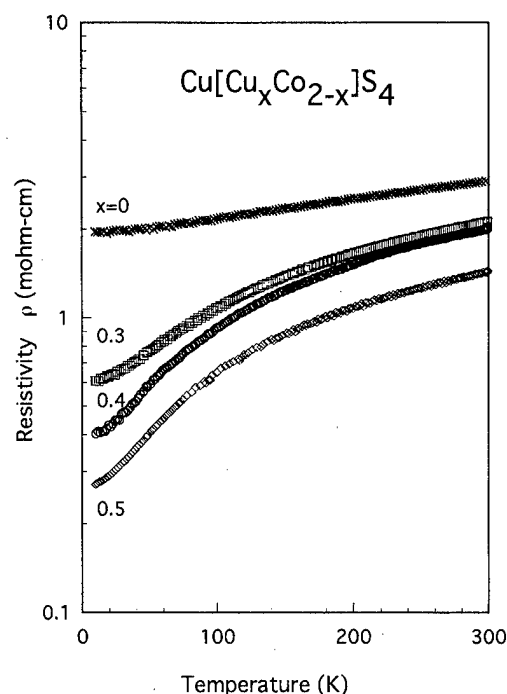


FIG. 3. The resistivity measured at ac (10 Hz) of the Cu-rich system $\text{Cu}[\text{Cu}_x\text{Co}_{2-x}]\text{S}_4$ ($x=0-0.5$) in the normal state.

type change. A small but broad structure was observed on the curve below ~ 60 K. It was also observed that the ρ of low-level Cu doping ($x \approx 0.05$) increases abruptly at low temperature, and a resistivity minimum appears at about 55 K, which corresponds to the T_N of Co_3S_4 . This resistivity minimum becomes less pronounced as the Cu concentration increases and disappears for the high-density Cu lattice $x > 0.2$.

ρ of the Cu-rich system with superconductivity showed a very large temperature dependence even in the normal state as is shown in Fig. 3. ρ of CuCo_2S_4 ($x=0$) is, typically, metalliclike and is proportional to T , however, ρ for $x=0.3, 0.4$, and 0.5 rapidly decreases as the temperature is lowered with a convex-type temperature dependence. The convexity is enhanced as x increases to 0.5 , and it becomes

superconductive in low temperature at $T_c=4.0$ K for $\text{Cu}_{1.5}\text{Co}_{1.5}\text{S}_4$ ($x=0.5$).

The self-consistent renormalization spin fluctuation theory⁵ and Fermi-liquid theory with a strong electron correlation⁶ suggest that the resistivity has a temperature dependence of

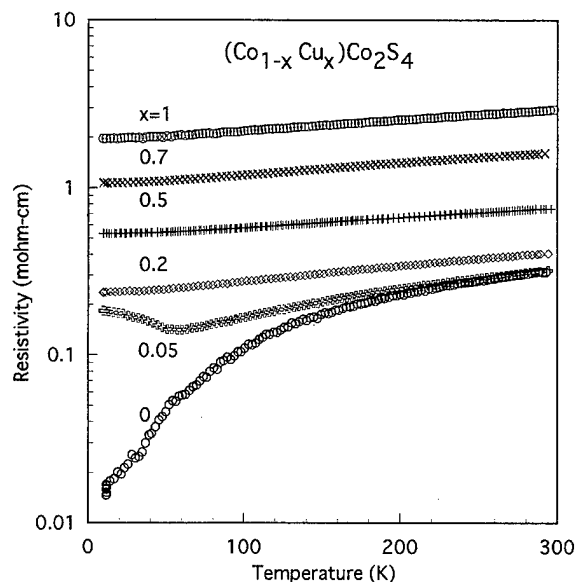


FIG. 2. The resistivity measured at ac (10 Hz) of the Co-rich system $(\text{Co}_{1-x}\text{Cu}_x)\text{Co}_2\text{S}_4$ ($x=0-1$) in the normal state.

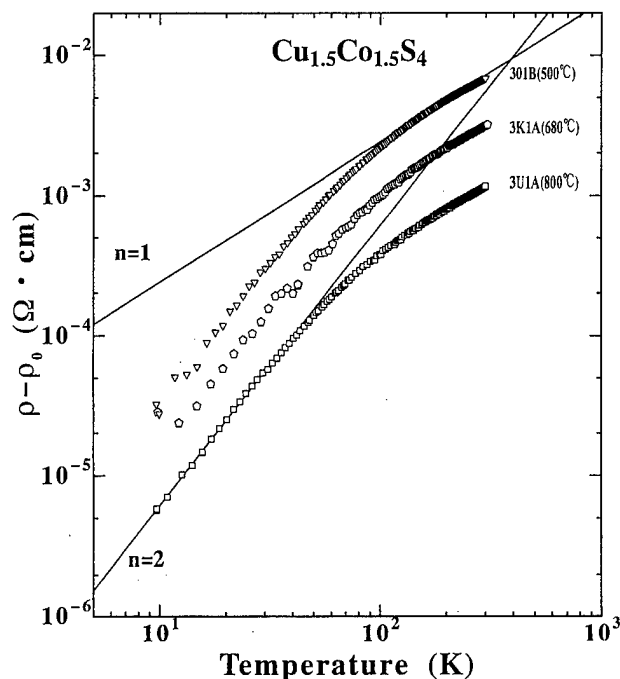


FIG. 4. The $\log(\rho - \rho_0)$ vs $\log T$ plots for the square law fitting in the normal state of the Cu-rich superconductive samples.

TABLE I. The quadratic term coefficient A and related parameters with typical heavy Fermion Kondo compounds and normal metals.

	Crystal structure	T_N (K)	T_c (K)	A ($\mu\Omega$ cm/K ²)	γ (mJ/mol K ²)	m^*/m
Cu _{1.5} Co _{1.5} S ₄	Cubic spinel	20	4.0 ^a	1.51~9.1
UPt ₃	Hexagonal	17	0.49–0.52	1.6($\perp c$), 0.7($\parallel c$)	450	180–230
URu ₂ Si ₂	Tetragonal	17.5	1.2	0.119	180	140
Pd	fcc	10 ⁻⁵	9.4	...
Ag	fcc	10 ⁻⁷	0.6	...

^aOur updated value is extended to 4.9 K.

$$\rho(T) = \rho_0 + AT^2/(T + T_l) = \rho_0 + A_l T^2$$

$$\text{for } T \ll T_l$$

$$= \rho_0 + A_h T \text{ for } T \gg T_l.$$

The electrical resistivity is, thus, expected to have a quadratic-type temperature dependence below the transformation temperature T_l and the linear temperature dependence above T_l .

ρ for the three samples of Cu_{1.5}Co_{1.5}S₄, synthesized at 500, 680, and 800 °C, are plotted in Fig. 4 to see the temperature dependence in terms of $\rho(T) = \rho_0 + AT^n$. It is shown that the resistivity fits relatively well with the quadratic term $n=2$ at low temperature and fits with a linear temperature term $n=1$ above the crossover temperature T_l .

The coefficient A is obtained from the quadratic term in Fig. 4 to be 1.5–9.1 $\mu\Omega$ cm/K² over all samples, and the crossover temperature T_l , which should correspond to the Debye temperature, to be ~ 75 K, respectively. It is interesting to compare A with those known as the typical Kondo compounds UPt₃ (0.7 $\parallel c$, $\mu\Omega$ cm/K²) (Ref. 7) and URu₂Si₂ (0.119 $\mu\Omega$ cm/K²) (Ref. 8) and those of typical metals Ag (10⁻⁷ $\mu\Omega$ cm/K²) and Pd (10⁻⁵ $\mu\Omega$ cm/K²). These values of A are listed in Table I with the Sommerfeld parameter γ and the effective mass ratio m^*/m . It is shown that the resistivity of Cu_{1.5}Co_{1.5}S₄ has a large quadratic term coefficient A comparable with those of the Kondo compounds known as the typical heavy Fermion.

III. DISCUSSION

The susceptibility shows an antiferromagnetic structure with $T_N \approx 20$ K for the Co-rich system ($x=0.3-1$), and the electrical resistivity rapidly changes from a quadratic-type to a metallic one by Cu doping ($x=0-0.2$), as is seen in Fig. 2. Cu doping also causes the resistivity minimum at ~ 55 K, which corresponds to the Néel temperature of weak antiferromagnetic Co₃S₄ ($x=0$).⁴ Thus, ρ seems to be sensitive with the spin state in the k space.

The coefficient A of the quadratic term given in Table I is proportional to the square of the Sommerfeld parameter γ .² The present result shows that A has the same order of

magnitude as the typical heavy Fermion compounds. This suggests that the superconductivity of the Cu-rich system is related to the large value of A , reflecting large γ , large effective mass m^* , a high density of state at the Fermi level, and a strong $3d$ hole correlation.

In the case of the TI-221 HTS Cu–O system,⁹ the resistivity shows the T linear type for the superconductive samples and shows the quadratic type for the nonsuperconductive sample depending on the oxygen concentrations. In contrast to this work, the present result for the Cu–S spinel system shows that the quadratic term is observed only for the Cu-rich superconductive compositions, but the linear term only for the Co-rich nonsuperconductor ($x=0.3-1$). We, thus, conclude that the present Cu–S system presents a typical example for the superconductivity concerned with the $3d$ hole electron correlation. Understanding of the spin correlation of antiferromagnetism with superconductivity is, however, still left to study in future work.

ACKNOWLEDGMENTS

This study was supported in part by Grant No. 06640481 from the Ministry of Education, Science and Culture in Japan. The authors are glad to express their cordial thanks to M. Fukuguchi and M. Miyamoto for experimental collaboration during their master thesis work.

¹K. Miyatani, M. Ishikawa, and T. Tanaka, Ferrites; Proceedings of the ICF6, Sixth International Conference on Ferrites, Tokyo (1992), p. 589.

²K. Miyatani, T. Tanaka, S. Sakita, M. Ishikawa, and N. Shirakawa, Jpn. J. Appl. Phys., Part 1 **32**, 448 (1993).

³Y. Furukawa, S. Wada, K. Miyatani, T. Tanaka, M. Fukuguchi, and M. Ishikawa, Phys. Rev. B **51**, 6159 (1995).

⁴H. Sugita, S. Wada, Y. Yamada, K. Miyatani, and T. Tanaka, J. Phys. Soc. Jpn. (to be published).

⁵T. Moriya, *Spin Fluctuations in Itinerant-Electron Magnetism* (Springer, Berlin, 1985); T. Moriya, Y. Takahashi, and K. Ueda, J. Phys. Soc. Jpn. **59**, 2905 (1990).

⁶K. Yamada and K. Yoshida, Prog. Theor. Phys. **76**, 621 (1986).

⁷U. Rauchschwalbe, Physica B & C **147**, 1 (1987); A. de Visser, J. J. M. Franse, and A. Menovsky, J. Magn. Magn. Mater. **43**, 43 (1984).

⁸A. LeR. Dawson, W. R. Datars, J. D. Garrett, and F. S. Razavi, J. Phys. **1**, 6817 (1989).

⁹Y. Kubo, Y. Shimakawa, T. Manoko, and H. Igarashi, Phys. Rev. B **43**, 7875 (1991).

Plausible d -wave cuprate superconductivity: Muon-spin-relaxation studies of $\text{RBa}_2\text{Cu}_3\text{O}_{7-\delta}$ vortex states

C. Boekema,^{a)} E. J. Ruiz, Z. C. Pobre, S. R. Punjabi, F. Kong, and O. Vera
Department of Physics, San Jose State University, San Jose, California 95192-0106

D. W. Cooke

Los Alamos National Laboratory, Los Alamos, New Mexico 87545

The rare-earth (R) magnetism and grain-size dependencies of magnetic field distributions in $\text{RBa}_2\text{Cu}_3\text{O}_{7-\delta}$ (RBCO) vortex states have been studied. A maximum-entropy technique has been applied to transverse field muon-spin-relaxation data of several polycrystalline cuprate superconductors. The main vortex signals for $R=\text{Er}$, Gd , and Ho reveal signs of two peaks in the field distribution below the applied field ($B_{\text{ext}}=1$ kOe) as predicted for d -wave superconductivity. For the RBCO ($R=\text{Er}$, Gd , Ho , Eu , Y) vortex states, we have confirmed low-field tails in the field distributions well below B_{ext} . The low-field tail may be caused by magnetic frustration in the vortex state or possible CuO -chain superconductivity below 25 K. Any interpretation of these (magnetic) vortex anomalies should comprise unconventional non-Bardeen-Cooper-Schrieffer-like fundamental properties of the cuprate vortex states. © 1998 American Institute of Physics. [S0021-8979(98)19311-8]

I. INTRODUCTION AND D -WAVE VORTEX STATES

Significant contributions toward understanding the vortex states of the cuprate superconductors are being made by magnetic resonance applications. Muon-spin-relaxation (μSR) studies of these mixed magnetic and superconducting states may provide direct answers to critical questions such as whether the magnetic field distribution shows the two distinct peaks in the main vortex part, as predicted by the Ginzburg-Landau (GL) theory.¹ The μSR studies² have indicated deviations from typical type II Abrikosov vortex behavior. Studying the interplay of magnetism and superconductivity can lead to a better understanding of the physical origin of cuprate superconductivity.

Although there is no general agreement on the fundamental mechanism of cuprate superconductivity, an excellent approach is the phenomenological (GL) theory. Application of the GL theory to *conventional* superconductors has revealed its ability to predict most of their vortex properties. The GL theory is based upon general concepts related to symmetries of the vortex system under investigation. With this approach, one adopts the basic assumption that "Cooper" pairs exist. Cooper pairs can be described by an "order parameter" $Y(r)$, and the "super-electron" density is given by $|Y(r)|^2$.

The GL theory (appropriate for d -wave symmetry) involves both d -wave and induced s -wave order parameters. Assuming type-II superconductivity, the magnetic field distribution in the d -wave vortex state can be predicted.¹ Characteristic of a d -wave superconductor, an oblique vortex lattice has been found; two distinct Van Hove-like singularities lead to the prediction of two distinct peaks in the magnetic field distribution of the vortex state.^{1(c),1(d)}

II. μSR RESEARCH AND DATA ANALYSIS

In our μSR research, we have investigated² the vortex states of ceramic cuprate superconducting $\text{RBa}_2\text{Cu}_3\text{O}_{7-\delta}$ RBCO samples which have T_c 's ranging from 66 to 94 K. R signifies a rare-earth (RE) element such as Er , Gd , Ho , Eu , or (the RE-like element) Y . The polycrystalline cuprate samples are high-quality single-phase ceramics prepared at Los Alamos National Laboratory. The samples were field cooled in 1 kOe transverse fields.

The μSR technique is similar to nuclear magnetic resonance (NMR) and the Mössbauer effect. In the transverse-field (TF) mode, the Larmor precession of the muon spin is proportional to the magnetic field at the muon-probe site. In μSR studies of magnetic field distributions, the recorded muon-decay time histograms are analyzed by the maximum-entropy (ME) method. Spectral densities found in the ME transform reflect directly the field distribution.^{2(a),3} ME has the advantage of producing in the frequency transform only structure for which sufficient statistical evidence in the time series is present. We analyze TF μSR data using an ME method based on the Burg algorithm for minimizing noise in the equation

$$S_i = \sum c_k S_{i-k} + n_i,$$

where S_i is the muon-spin polarization at time i , and n_i the assumed white noise term. The autoregressive coefficients c_k ($k=1,\dots,p$) are determined from the data, where p is the order of the model description. To maximize the ME- μSR signal-to-noise ratio, S_i can be weighted before ME transformation by an exponential or Gaussian filter function with a filter time T_f . Most ME analyses are performed using a Gaussian filter function, as μSR signals with Gaussian relaxation are expected below T_c . This reduces noise, but causes an expected $1/T_f$ broadening effect in the ME transformation.

^{a)}Electronic mail: boekemac@aol.com

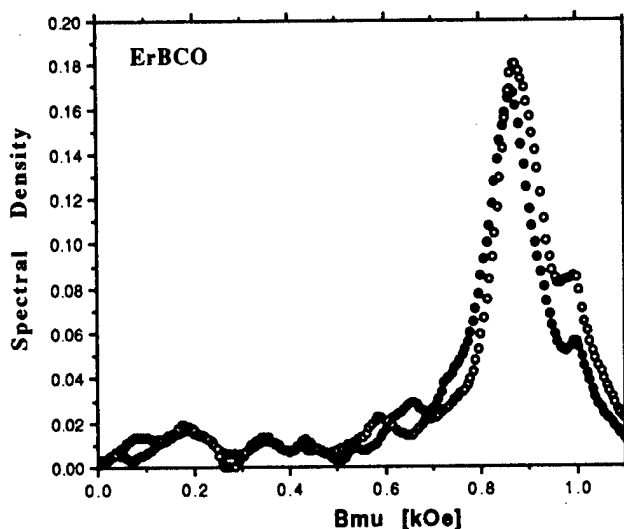


FIG. 1. ME transforms for ErBCO μ SR time-histogram data recorded at 1 kOe, and 4.5 K (●) and 5.5 K (○). Gaussian filtering ($T_f=0.7 \mu$ s) and background correction have been done. The falloff at 4.5 K (seen near 700 Oe) starts to disappear above 5 K; consequently, the main vortex and GB signals increase in intensity. The low-field tail stretches out to zero field; compare with the YBCO vortex (Fig. 3) result.

III. MAIN RESULTS and DISCUSSION

ME- μ SR analysis has shown the following features for RBCO vortex states: (0) A major vortex signal below the applied field of $B_{\text{ext}}=1$ kOe (see Fig. 1); (1) signs of the predicted twin peaks in the main vortex signal (suggesting d -wave symmetry, see Fig. 2); (2) a falloff below the applied field, when R is magnetic, and near 4 K; (3) a low-field tail below 25 K; (4) a peak near the applied field.

Likely, the major part corresponds to the vortex structure as observed by neutron scattering.⁴ Deviations 2 and 3 (see Fig. 1) indicate an unusual interplay between magnetism and superconductivity for the RBCO vortex states. As

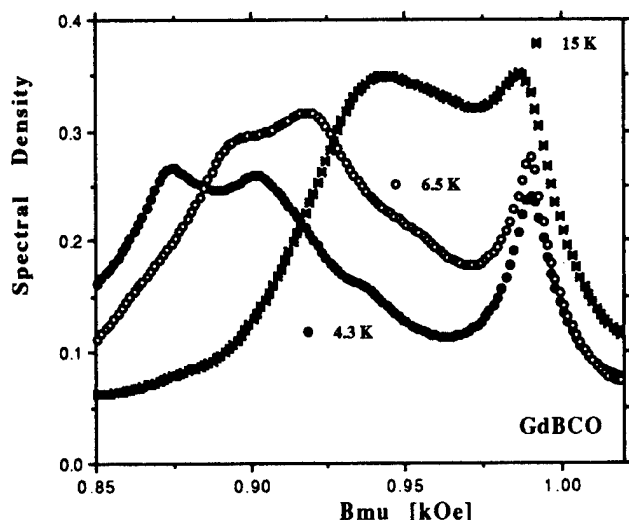


FIG. 2. ME transforms for GdBCO μ SR time-histogram data recorded at 1 kOe, and 4.3, 6.5, and 15 K. Gaussian filtering ($T_f=4.4 \mu$ s) and background correction have been done. The signals near the applied field are due to grain boundaries. A twin-peak signature can be seen developing below 10 K.

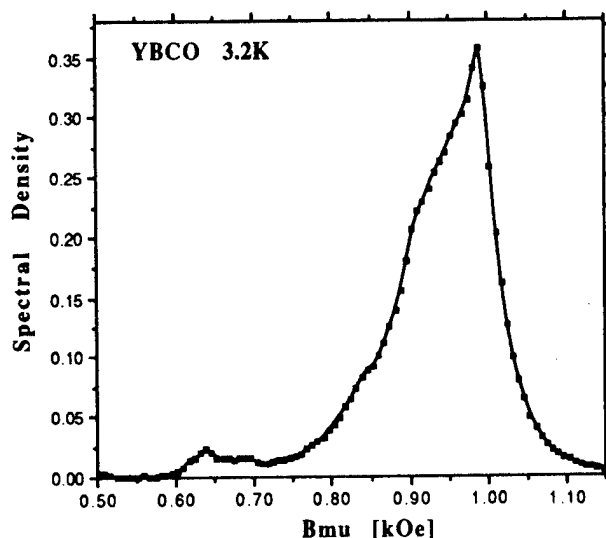


FIG. 3. ME transform for YBCO (large $70 \mu\text{m}$ grains) μ SR time-histogram data recorded at 1 kOe, and 3.2 K. Gaussian filtering ($T_f=1 \mu$ s) and background correction have been done. The low-field tail can clearly be seen. Below 600 Oe, the spectral density in the vortex field distribution is zero; compare with the ErBCO vortex (Fig. 1) results.

predicted^{1(c),1(d)} for d -wave superconductivity, the main vortex signals for $R=\text{Ho}$, Gd , and Er reveal signs of two peaks in the field distribution below the applied field below 10 K. Above 10 K, this signature disappears and is not present above 25 K. In Fig. 2, we show ME spectral density transforms for GdBCO (using 4.4μ Gaussian filtering) indicating signs of twin peaks, as predicted by the d -wave GL theory. Near 4 K, the main vortex signal with these peaks superimposed shifts to lower fields, as the magnitude of the R magnetic moment increases.

For the RBCO ($R=\text{Er}$, Gd , Ho , Eu , Y) vortex states, we also have observed low-field tails in the field distributions well below B_{ext} . The low-field tail is only present below 25 K. This tail is *not* seen in the *real* parts of the Fourier transforms (FT) because of sinc-wiggle and truncation effects.^{2(a),3} (The real FT part approximates the field distribution.) These non-Abrikosov tails in the YBCO vortex field distributions are slightly grain-size dependent.^{2(d)} In Fig. 3, a ME transform is shown for a YBCO sample having a large grain size ($\sim 70 \mu\text{m}$), with μ SR data recorded at 1 kOe and 3.2 K. The spectral density behavior and thus the field distribution at the muon-probe sites⁵ confirm the low-field tail (0.60–0.75 kOe) for RBCO vortex states with a nonmagnetic R ion.

The R -layer magnetism spreads the tail out to lower fields; for $R=\text{Er}$, this tail reaches as low as zero field (see Fig. 1). We speculate that the low-field tail is caused by magnetic frustration^{2(b)} in the vortex state or possible CuO chain superconductivity below 30 K. The latter possibility has been suggested by NMR evidence.⁶ Note also that the muon-probe sites are very near to the CuO chain layers.⁵ Furthermore, this tail does *not* show up in the vortex field distributions of the cuprates Bi2212 and Tl2223 (at 5 kOe).^{2(b)}

In ME transforms using an exponential filter time $T_f=4.4 \mu\text{s}$, the peak near the applied field clearly stands out, and its position is slightly T -dependent. This grain-boundary

TABLE I. Measured and predicted μ SR twin splittings for RBCO vortex field distributions.

R	T_c (K)	T (K)	D_{twin} (MHz)
Er	94	7.5	0.2
		5.0	0.4
Gd	93	6.5	0.3
		4.3	0.4
Ho	66	10	0.4
		6.2	0.6
a		0	0.1
b		0	0.2
μ SR simulation ^c			0.25

^aReference 1(c).^bReference 1(d).^cUsing a 0.2 MHz twin-splitting value.

(GB) peak originates from grain boundaries or other nonsuperconducting regions, where disorder in the chain layers exists at the atomic level. This particular μ SR signal is *not* seen in the vortex states of $\text{Pb}_{0.9}\text{In}_{0.1}$,^{2(c)} a prime example of a classical Bardeen–Cooper–Schrieffer (BCS) superconductor.

In Table I, we summarize the observed twin splittings and compare with the GL predictions. The ME estimates of the observed twin-peak splittings are about 2.5 times larger than predicted. Because of the large overlap of the GB peak and the main vortex signal for nonmagnetic R 's, no precise determination has been made in such cases, although weak indications do exist. To clearly resolve the predicted splitting, a μ SR time window of at least 5 μ s is required to see the “beat” pattern in the time histogram created by these twin peaks. Our μ SR time window is about 7.2 μ s (such a relative short time is the main reason a Fourier analysis will *fail* to show this twin-peak signature).

The main vortex signal is shifted from the GB signal as a result of the R -layer magnetism. However, this magnetic effect may also have enhanced the splitting. The *alternative*, that the second peak is caused by R magnetism, is less likely: the observed splitting appears to be independent of the R magnetic moment. In contrast, the falloff and low-field tail shift to lower fields with increasing R moment.² Note, R -layer magnetism in RBCO already has shown anomalous behavior: for instance, unusual high magnetic ordering temperatures (near 2 K for $R=\text{Er}$ and Gd).

The fact that the observed twin splitting is temperature dependent (see Fig. 2 and Table I) substantiates the likely existence of the twin-peak signature below 10 K. Preliminary ME transforms of *simulation* μ SR data using the twin-splitting prediction value^{1(d)} reveal a twin splitting enlarged by only 25% (see also Table I). Compared to the much larger observed splitting, this is not unexpected, and perhaps acceptable: namely, the cuprate vortex state is *not* typical type II (as is assumed for the d -wave vortex state).

IV. CONCLUSION

Maximum entropy is a sensitive method for examining μ SR vortex spectra. Not only has ME- μ SR analysis indicated magnetic anomalies in the vortex state, but is allowing for the current analysis of d -wave symmetry in cuprate superconductivity. Our ME- μ SR studies, especially the confirmation of the low-field vortex tail, indicate that cuprate superconductivity differs substantially from type II BCS-like behavior. Unusual characteristics like a falloff and low-field tail in the vortex field distributions do not conform to Abrikosov features of type II superconductors. The behavior of the cuprate vortex state indicates plausible d -wave symmetry, which could be an essential key ingredient in the understanding of the cuprate superconductivity mechanism.

ACKNOWLEDGMENTS

Research at San Jose State University is supported by NSF-REU and WiSE@SJSU. The authors also acknowledge the financial support of SJSU Graduate Studies and Research. Work at Los Alamos is supported by U.S.-DOE.

¹(a) C. Kallin and A. J. Berlinsky, *Hyperfine Interact.* **86**, 489 (1994); (b) D. L. Fedder and C. Kallin, *Phys. Rev. B* **55**, 559 (1997); (c) M. Franz et al., *ibid.* **53**, 5795 (1996); (d) I. Affleck et al., *ibid.* **55**, R704 (1997); (e) J.-H. Xu et al., *ibid.* **53**, R2991 (1996).

²(a) S. Alves et al., *Phys. Rev. B* **49**, 12396 (1994); *Hyperfine Interact.* **86**, 513 (1994) and references therein; (b) C. Boekema et al., *Phys. Rev.* **235–240**, 2633 (1994); *J. Phys. Chem. Solids* **56**, 1905 (1995); (c) C. Boekema, *Hyperfine Interact.* **86**, 487 (1994); (d) C. Boekema et al., *Physica C* **282–297**, 2069 (1997).

³D. S. Stephenson, *Prog. NMR Spectrosc.* **20**, 515 (1988).

⁴B. Keimer et al., *Phys. Rev. Lett.* **73**, 3459 (1994).

⁵W. K. Dawson et al., *J. Appl. Phys.* **64**, 5809 (1988).

⁶C. H. Recchia et al., *Phys. Rev. Lett.* (submitted); C. H. Pennington et al., *M2S-HTSC-V Conf. Proc.* **C282–297** (1997).

Flux patterns of multifilamentary Ag-sheathed $(\text{Pb,Bi})_2\text{Sr}_2\text{Ca}_2\text{Cu}_3\text{O}_{10+\delta}$ tapes

M. R. Koblishchka,^{a)} T. H. Johansen, and H. Bratsberg
Department of Physics, University of Oslo, Blindern, N-0316 Oslo, Norway

L. Püst
Department of Physics and Astronomy, Wayne State University, Detroit, Michigan 48202

A. Galkin, P. Nálevka, M. Maryško, and M. Jirsa
Institute of Physics, ASCR, Na Slovance 2, CZ-18040 Praha 8, Czech Republic

M. Bentzon, P. Bodin, P. Vase, and T. Freltoft
Nordic Superconductor Technologies A/S, Priorparken 878, DK-2605 Brøndby, Denmark

Flux patterns of multifilamentary Ag-sheathed $(\text{Pb,Bi})_2\text{Sr}_2\text{Ca}_2\text{Cu}_3\text{O}_{10+\delta}$ tapes comprising 19 filaments are visualized by means of magneto-optic imaging. In low fields, the shielding currents are seen to flow mainly in the outermost filaments. With increasing external magnetic field, the inner filaments also contribute to the current flow. To compare the local flux distribution with the integral magnetization values, magnetization loops are measured by a SQUID magnetometer on the same sample following the fields used in the magneto-optic imaging (± 120 mT) and covering fields up to ± 5 T at various temperatures. The magnetization loops also reveal that the multifilamentary tapes show the anomalous position of the central peak, but always less pronounced than in monofilamentary tapes. © 1998 American Institute of Physics. [S0021-8979(98)53111-8]

The Ag-sheathed multifilamentary tapes of $(\text{Pb,Bi})_2\text{Sr}_2\text{Ca}_2\text{Cu}_3\text{O}_{10+\delta}$ (Bi-2223) are an important development towards the practical use of high- T_c superconductors for power applications. These tapes show an improved mechanical stability and strain tolerance as compared to monofilamentary tapes.¹ For the development of Bi-2223 multifilamentary tapes in long lengths it is very important to control the defects introduced into the filaments during the deformation processes or during the formation of the superconducting phase, as defects within the filaments may alter or even impede the current flow.² Furthermore, magnetization measurements^{3–6} on tapes revealed an anomalous position of the low field or central peak, which is caused by stray fields at the grain circumferences.^{5,6} To understand the magnetic properties of such multifilamentary tapes, it is important to study in detail the flux entry, exit, and pinning within the various filaments. This task requires a *local* investigation technique, as the properties of a single filament are masked by the neighboring ones in an integral measurement. Here, we employ magneto-optic (MO) imaging,⁷ which can be carried out using an intact tape, i.e., the visualization of the flux structures is done *through* the silver sheath.^{8,9} In earlier work on Bi-2223 mono- and multifilamentary tapes using MO imaging, the flow of transport currents was visualized.^{2,10} The MO imaging technique is based on the Faraday effect in a magneto-optical active layer. Here, we have used a Bi-doped YIG film with in-plane anisotropy with a thickness of $4\text{ }\mu\text{m}$, half of which corresponds to the spatial resolution of our experiment. In order to obtain images with a relatively high contrast, an indicator film with a high field sensitivity (~ 0.1

mT) was used. The images are recorded using an 8-bit Kodak DCS 420 CCD digital camera and subsequently transferred to a computer for processing. In the MO apparatus the sample was mounted on the cold finger of an optical helium flow cryostat.¹¹ The magnetic field was applied perpendicular to the tape plane using a copper solenoid coil with a maximum field of ± 120 mT. The MO images presented here are maps of the z component of the local magnetic field, B_z .

The multifilamentary Bi-2223 tapes (19 filaments) were prepared by the “powder-in-tube” method with subsequent drawing and rolling.¹² One piece with dimensions $5 \times 3\text{ mm}^2$ cut from the tape was used for both the magnetization measurements and the MO imaging. The magnetization loops (MHLs) were recorded using a Quantum Design MPMS5 SQUID magnetometer (max. ± 5 T); with $B_{\text{ext}} \perp$ tape plane.

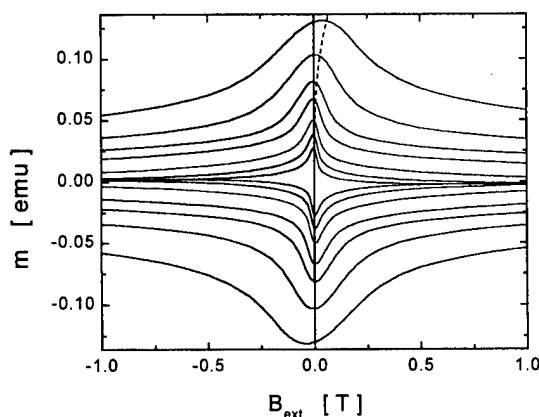


FIG. 1. MHLs measured on the multifilamentary tape at various temperatures 5 (outer loop), 10, 15, 20, 30, 40, and 50 K (inner loop). The anomalous position of the MHL maximum is indicated by a dashed line.

^{a)}Present address: SRL/ISTEC, 1-16-25 Shibaura, Minato-ku, Tokyo 105, Japan; electronic mail: koblishchka@istec.or.jp

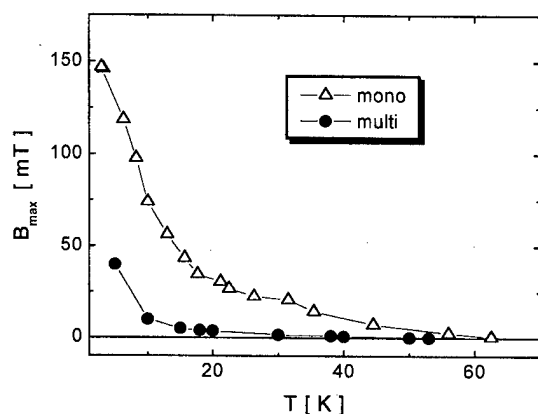


FIG. 2. The peak position, B_{\max} , as a function of temperature for the multifilamentary tape (●) and a monofilamentary tape (△, from Ref. 5).

In Fig. 1, MHLs are presented in the temperature range $5 \text{ K} \leq T \leq 50 \text{ K}$. It is also clearly visible that the multifilamentary Bi-2223 tapes exhibit the anomalous position of the central peak like monofilamentary tapes. The position of the maximum, B_{\max} , is plotted in Fig. 2 and compared to data of a monofilamentary tape. At low temperatures, the maximum position increases considerably, but is always found to be less pronounced than that of the monofilamentary tape.

Figure 3 presents a MHL measured at $T=18 \text{ K}$, using the same field steps as in the following MO experiment. For comparison, a full magnetization curve is shown. The positions, where the MO images are taken, are marked using open circles. In this way, a direct comparison of MHL data and the MO flux patterns becomes possible. In all MO images presented in this paper, flux is imaged as bright, whereas well-shielded areas stay dark.

Figure 4(a) shows a polarization image of a cross section of our tape. Flux patterns obtained in increasing external field after ZFC (virgin branch, I) are presented in Fig. 4. In Fig. 4(b), flux enters the sample like in a homogeneous sample (see, e.g., Ref. 7); the edges of the outermost cores are marked by arrows. Only the outermost filaments are contributing to the current flow. When increasing the field fur-

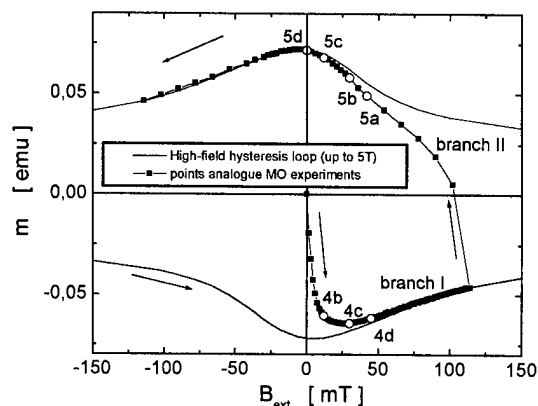


FIG. 3. MHLs measured at $T=18 \text{ K}$. The minor loop is obtained using the same field steps as in the MO experiment. The positions of the images shown in Figs. 4 and 5 are marked by open circles.

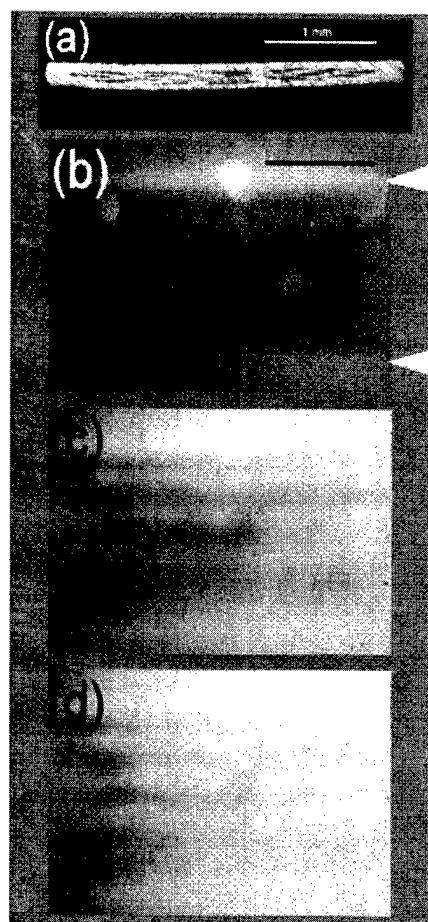


FIG. 4. Polarization image of the tape (a) and flux patterns of the virgin branch (I); (b) 12 mT, (c) 30 mT, and (d) 45 mT. The marker in (b) is 2 mm long.

ther (c),(d), more and more filaments contribute to the current flow. The filaments in our short sample are quite uniformly penetrated by the flux. Previous observations on longer sections of multifilamentary tapes have shown that when currents encounter a defect, they may switch into a neighboring filament, and after some distance, they may return to the original one.^{2,9} This shows that the filaments in the tape are magnetically coupled together.

In Fig. 5, we show flux patterns on the return branch (II). In Fig. 5(a), a nearly homogeneous flux pattern is obtained and individual filaments cannot be resolved. On further reduction of the field (b),(c), the filaments reappear and carry pinned flux.

In the remanent state Fig. 5(d), flux remains trapped in the center of each individual filament. However, no vortices of opposite polarity can be detected in the remanent state as in the case of monofilamentary tape.⁸ In the upper part of the sample, a broad dark stripe can be seen which is the result of field overlap between two different filaments as discussed in Ref. 9. The position of the maximum in the MHL corresponds to a flux pattern like the one presented in Fig. 5(c). This does not correspond to a minimum amount of flux in the sample, which is reached only when applying a small negative field. The flux distributions within a single filament are

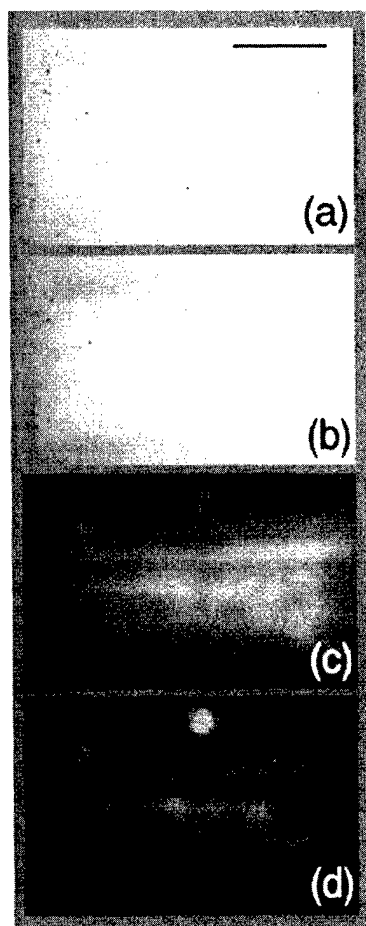


FIG. 5. Flux patterns of the return branch (II); (a) 45 mT, (b) 30 mT, (c) 12 mT, and (d) remanent state. The marker is 2 mm long.

found to be quite uniform. In contrast to this, most monofilamentary tapes show a “rough-looking” flux pattern at this low temperature, which is caused by a high intragranular current density; thus forcing the intergranular currents to flow around the well-shielded grains. This fact, and the large stray fields around such grains are probably responsible for

the anomalous position of the central peak in the MHL.⁵ As the grain coupling is improved along the silver sheath, this effect is not so strongly developed in the multifilamentary tapes. As a result, the peak is also shifted towards positive values, but much less pronounced as in the case of monofilamentary tapes.

In conclusion, we observed the anomalous central peak also in multifilamentary tapes, but always less pronounced than in monofilamentary tapes. Magneto-optic flux patterns reveal a quite uniform flux distribution within the filaments even at low temperatures which is a consequence of better grain growth and coupling along the silver sheath. This may be the reason for the less pronounced anomalous peak in multifilamentary tapes.

This work is supported by the Research Council of Norway; the work in Prague by Grant No. A1010512 of GA ASCR. L. P. acknowledges support from NATO under Grant No. 961357.

¹Z. Han, P. Skov-Hansen, and T. Freltoft, *Supercond. Sci. Technol.* **10**, 371 (1997).

²U. Welp, D. O. Gunter, G. W. Crabtree, W. Zhong, U. Balachandran, P. Haldar, R. S. Sokolowski, V. K. Vlasko-Vlasov, and V. I. Nikitenko, *Nature (London)* **276**, 44 (1996); U. Welp, D. O. Gunter, G. W. Crabtree, J. S. Luo, V. A. Maroni, W. L. Carter, V. K. Vlasko-Vlasov, and V. I. Nikitenko, *Appl. Phys. Lett.* **66**, 1270 (1995).

³M. R. Cimberle, C. Ferdeghini, R. Flükiger, E. Giannini, G. Grasso, D. Marrè, M. Putti, and A. S. Siri, *Physica C* **251**, 61 (1995).

⁴L. Půst, A. Galkin, and M. R. Koblischka, *Czech. J. Phys.* **46**, 1603 (1996).

⁵M. R. Koblischka, L. Půst, A. Galkin, and P. Nálezka, *Appl. Phys. Lett.* **70**, 514 (1997).

⁶K.-H. Müller, C. Andrikis, and Y. C. Guo, *Phys. Rev. B* **55**, 630 (1997).

⁷M. R. Koblischka and R. J. Wijngaarden, *Supercond. Sci. Technol.* **8**, 199 (1995).

⁸M. R. Koblischka, T. H. Johansen, and H. Bratsberg, *Supercond. Sci. Technol.* **10**, 693 (1997).

⁹M. R. Koblischka, T. H. Johansen, H. Bratsberg, and P. Vase, *Supercond. Sci. Technol.* (to be published).

¹⁰A. E. Pashitski, A. Polyanskii, A. Gurevich, J. A. Parrell, and D. C. Larbalestier, *Physica C* **246**, 133 (1995); *Appl. Phys. Lett.* **67**, 2720 (1995).

¹¹M. Baziljevich, T. H. Johansen, H. Bratsberg, Y. Shen, and P. Vase, *Appl. Phys. Lett.* **69**, 3590 (1996).

¹²P. Bodin, Z. Han, P. Vase, M. D. Bentzon, P. Skov-Hansen, R. Bruun, and J. Goul, *IOP Conf. Ser.* **158**, 1299 (1997).

Depth-dependent magnetism of layered superconductors: Nb/Si

S. M. Yusuf,^{a)} E. E. Fullerton,^{b)} R. M. Osgood II, and G. P. Felcher

Argonne National Laboratory, Argonne, Illinois 60439

We have studied magnetic field penetration and vortex line formation in a $[\text{Nb}(100 \text{ \AA})/\text{Si}(15 \text{ \AA})] \times 20$ multilayer by magnetization and polarized neutron reflection. With the magnetic field applied parallel to the surface, the magnetization revealed the presence of a kink above H_{cl} indicative of transitions between one row of fluxoids and two rows of fluxoids parallel to the surface. The spin dependence of neutron reflectivity below H_{cl} was consistent with a penetration depth of 1200 \AA , substantially larger than that of bulk Nb. In the mixed phase ($H_{ext} > H_{cl}$) the field was found to penetrate the surface, with a slope as found in the case of $H_{ext} < H_{cl}$. At $H_{ext} > H_{cl}$ vortices form inside the multilayer, in addition to there being surface penetration. A modulation of the vortex fields was found with the periodicity of the Nb/Si bilayers as evidenced by the spin dependence of the reflectivity at the first Bragg peak of the multilayer. © 1998 American Institute of Physics. [S0021-8979(98)19411-2]

The investigation of artificially layered superconductors has drawn much attention after the discovery of anisotropic high-temperature oxide superconductors. These artificial superlattices composed of alternating superconducting/nonsuperconducting layers have been found in recent years to exhibit novel magnetic properties. These layered superconductors have a coherence length shorter than the overall film thickness. When a magnetic field H_{ext} is applied parallel to such layered structures a series of maxima occurs in the magnetization measurements at specific field strengths H_N ($H_{C1} < H_N < H_{C2}$).^{1,2} These maxima in M_z have been explained in terms of transitions between specific multichain configurations of in plane vortices.² Above H_{cl} a first row of vortices is said to be formed close to the center of the film. An increase of the field causes a compression of this one-dimensional lattice until it becomes unstable, to be replaced by two rows of fluxoids with wider spacings. This process might be repeated for any transition from n rows of fluxoids to $n + 1$. This description is fundamentally different from that given by Bean for the distribution of magnetization in a layer of type II superconductor, where the fluxoids are trapped by impurity centers.

The scope of the present work is to attempt to observe vortex configuration by polarized neutron reflection, in a system—Nb/Si multilayers—whose magnetic properties closely resembled those of Nb/Cu multilayers.^{1,2}

The $[\text{Nb}(100 \text{ \AA})/\text{Si}(15 \text{ \AA})] \times 20$ multilayer was grown by reactive dc magnetron sputtering on a silicon (15 \AA) buffer layer and protected by a silicon cap (30 \AA). The films were deposited onto 1 in. silicon wafers. From these a small piece was cut for magnetization measurements, while the remaining surface was used for neutron reflectivity. The good layering of the material was confirmed by x-ray reflectivity measurements. Magnetization measurements as a function of

temperature (at a very low fixed applied field) indicated that the $[\text{Nb}(100)/\text{Si}(15)]_{20}$ system becomes superconducting below 7.5 K (T_C). Previous transport studies have found that for 15 \AA Si layers, Nb/Si behave as a coupled three-dimensional (3D) superconductor.³

Longitudinal magnetization (M_z) measurements were carried out using a superconducting quantum interference device (SQUID) magnetometer. The field was applied parallel to the layer planes in the zero field cooled (ZFC) condition. Figure 1 shows the magnetization M_z as a function of applied field at temperatures of 5, 3, and 2 K for the $[\text{Nb}(100)/\text{Si}(15)] \times 20$ multilayer. Two distinct features are present in Fig. 1. At low applied magnetic field a flux repulsion with a constant M_z/H_{ext} value (Meissner effect) is evident. At higher fields the flux expulsion is not complete. At 2 K, the first maximum occurs at $\sim 500 \text{ Oe}$; a second maximum at $\sim 900 \text{ Oe}$. In analogy with the interpretation of the Nb/Cu data we inferred that, at the lowest temperature, 300 Oe was below H_{cl} ; at 700 Oe one row of fluxoids was close to the

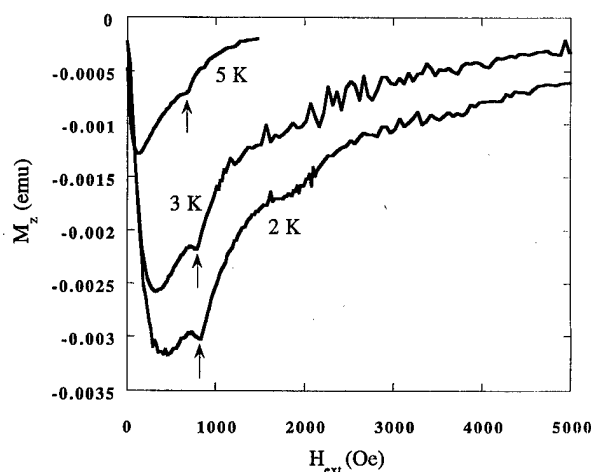


FIG. 1. Magnetization (M_z) as a function of magnetic field H_{ext} applied parallel to the surface of the multilayer at 2, 3, and 5 K. The first kink is shown by a vertical arrow.

^{a)}Electronic mail: yusuf@anlps.pns.anl.gov

^{b)}Present address: IBM Almaden Research Center, San Jose, CA 95120-6099.

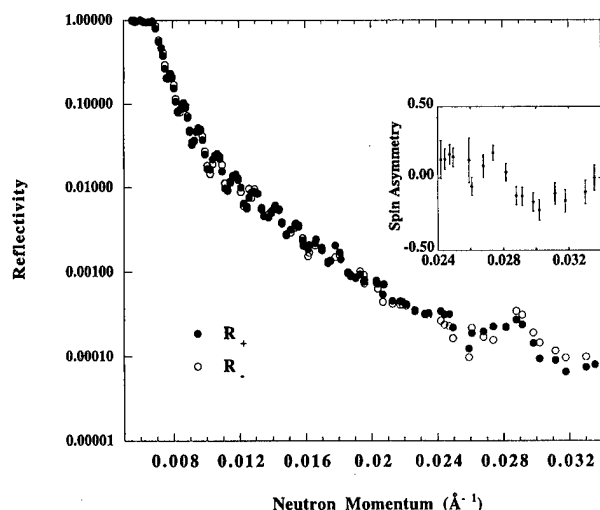


FIG. 2. Spin dependent reflectivities at 1.6 K and 700 Oe ZFC field. Solid dots indicate data for neutron spin parallel to the applied field (+); open circles for spins antiparallel to the field (-). In the inset: spin asymmetry $(R_+ - R_-)/(R_+ + R_-)$ in the region of the Bragg reflection.

film's center; at 1200 Oe the film contained two rows of fluxoids.

Polarized neutron reflectivity study gives information on the laterally averaged depth profile (both chemical and magnetic) as a function of the neutron momentum $Q = 2\pi \sin \theta / \lambda$, where λ is the neutron's wavelength and θ its angle of incidence with the surface.⁴ At large Q (large compared to the critical value at which the reflectivity is complete) the reflectance is the Fourier transform of the depth profile.

The instrument ("POSY I") used to record the polarized neutron reflection data is located at the Argonne Pulsed Neutron Source as described in Ref. 5. The sample temperature, in the experiments described here, was kept at 1.6 K. An electromagnet provides a vertical (perpendicular to the scattering plane) magnetic field up to 5 kOe parallel to the sample's surface. All measurements were taken in the ZFC condition.

Figure 2 depicts the R_+ and R_- as a function of Q measured at 1.6 K with $H_{\text{ext}} = 700$ Oe. Here R_+ and R_- represent, respectively, the reflectivities of neutrons with incident neutron spins parallel (+) and antiparallel (-) to the applied magnetic field on the sample. For small Q values a total reflection is observed up to the critical Q value. Beyond the critical Q value the reflectivities undergo several rapid oscillations which are due to the interference of reflections from the front and back surfaces of the multilayer. For yet larger Q values the presence of a Bragg peak is seen due to an existence of periodicity of Nb/Si layer structure with a period of 108 Å. The prominent feature of the reflectivities at and around the Bragg peak is the clear modulation of the spin asymmetry, $P = (R_+ - R_-)/(R_+ + R_-)$ (see inset of Fig. 2). This function is much more sensitive than the individual reflectivities to the magnetic depth profile. The spin asymmetry gives the most immediate signature of the magnetic character of the sample, being identically zero if the sample was nonmagnetic. The fact that nonzero P appears at the Bragg reflection indicates that the magnetic response is

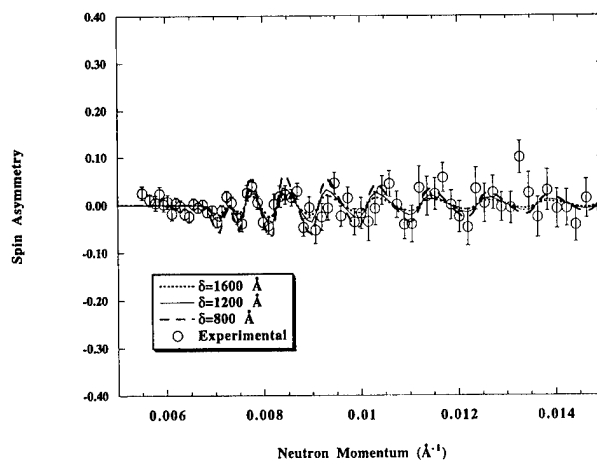


FIG. 3. The spin asymmetry $P = (R_+ - R_-)/(R_+ + R_-)$ as a function of neutron momentum transfer Q at 1.6 K and with 300 Oe ZFC field. The open circles show the measured values with their error bars. The spin asymmetry calculated from the model profile discussed in the text and a penetration depth of 1200 Å is shown by a solid curve. For comparison, the spin asymmetries are calculated for 800 Å (dashed line) and 1600 Å (dotted line) penetration depths.

modulated with the Nb/Si period. No such spin dependence was seen at the Bragg peak in 300 Oe applied field.

Open circles with error bars in Fig. 3 represent the spin asymmetry of reflected neutron beam as a function of neutron wave vector transfer Q measured at 1.6 K with $H_{\text{ext}} = 300$ Oe. The region of Q spanned here is that close to total reflection: this is the region most sensitive to the penetration depth of the external magnetic field in the superconductor.⁴ To calculate the reflectivities R_+ and R_- and hence P , a model profile for the chemical structure with the following parameters was used. The thicknesses of the Si and Nb layers are 15 and 93 Å, respectively. The scattering amplitude densities are $2.07 \times 10^{-6} \text{ Å}^{-2}$ and $3.96 \times 10^{-6} \text{ Å}^{-2}$, corresponding to the bulk values for Si and Nb, respectively. The solid line shows the polarization calculated assuming that the field penetration from both the surfaces of the multilayer has the exponential form $[B(x) = H_{\text{ext}} \exp(-x/\delta)]$, where x is the distance (depth) from the surface and δ is the penetration depth. The best-fitted penetration depth δ was found to be 1200 Å (with $\chi^2 = 1$); for comparison, the spin asymmetries for penetration depth of 800 and 1600 Å are also presented. It is to be mentioned that over this Q region a similar oscillation of P was observed with 700 Oe field (not shown).

To recap the findings, for $H_{\text{ext}} < H_{\text{cl}} (=500 \text{ Oe})$ the Meissner effect has been observed with a characteristic penetration depth of 1200 Å at 1.6 K. The value of the surface penetration depth is significantly larger than that of bulk Nb [(4.2 K) = 400 Å].⁶ When H_{ext} is increased to 700 Oe ($> H_{\text{cl}}$) we have observed a modulation of the magnetic field at the interior of the film in addition to the effect of surface penetration. The vortex field which causes the interior field has the periodicity of the Nb/Si layers. This does not necessarily rule out the longer wavelength modulations predicted for these multilayers. Those, if present, would give rise to further modulations of the spin asymmetry for which longer, more accurate measurements are required. What is worth noting is the detection of sizeable magnetic fluctuations over

spacings as low as ~ 100 Å. If, in a very naive picture the fluxoids are considered to be centered at the silicon layers, and their size is given in all direction, by the penetration depth (1200 Å—found for this material), the magnetic field should be practically uniform throughout the film.

This work was supported by U.S.-DOE, BES-MS Contract No. 31-109-ENG-38. The authors wish to thank Rick Goyette for his excellent technical assistance in carrying out the neutron reflection measurements.

- ¹J. Guimpel, L. Civale, F. de la Cruz, J. M. Murduck, and I. K. Schuller, *Phys. Rev. B* **38**, 2342 (1988).
- ²S. H. Brongersma, E. Verweij, N. J. Koeman, D. G. de Groot, R. Griessen, and B. I. Ivlev, *Phys. Rev. Lett.* **71**, 2319 (1993).
- ³J. D. Hettinger, B. R. Washburn, N. B. Remmes, D. G. Steel, K. E. Gray, E. E. Fullerton, and C. H. Sowers, *Phys. Rev. Lett.* **77**, 5280 (1996).
- ⁴G. P. Felcher, *Physica B* **192**, 137 (1993).
- ⁵G. P. Felcher, R. O. Hilleke, R. K. Crawford, J. Haumann, R. Kleb, and G. Ostrowski, *Rev. Sci. Instrum.* **58**, 609 (1987).
- ⁶J. Schelten, H. Ullmaier, and W. Schmatz, *Phys. Status Solidi B* **48**, 619 (1971).

Computation of the nonlinear magnetic response of a three dimensional anisotropic superconductor

Igor Žutić^{a)} and Oriol T. Valls^{b)}

School of Physics and Astronomy and Minnesota Supercomputer Institute, University of Minnesota, Minneapolis, Minnesota 55455-0149

Many problems in computational magnetism involve computation of fields which decay within a skin depth δ , much smaller than the sample size d . We discuss here a novel perturbation method which exploits the smallness of $\epsilon \equiv \delta/d$ and the asymptotic behavior of the solution in the exterior and interior of a sample. To illustrate this procedure we consider the computation of the magnetic dipole and quadrupole moments of an anisotropic, unconventional, three dimensional superconductor. The method significantly reduces the required numerical work and can be implemented in different numerical algorithms. © 1998 American Institute of Physics.

[S0021-8979(98)19511-7]

I. INTRODUCTION

In various problems of electrodynamics, field penetration is characterized by a skin depth, δ , much smaller than the actual sample size, d . For many purposes, the approximation of zero skin depth, or that eddy currents flow only as surface sheet currents, is not sufficiently accurate, as a detailed knowledge of the field penetration or accurate values of magnetic multipoles are required. It is then important to include the small corrections arising from finite skin depth.

In this article we examine the inclusion of skin depth corrections, focusing on the magnetic response of a high temperature superconductor (HTSC). For HTSCs, it is known¹⁻³ that examining the field penetration yields important information about the unconventional electronic pairing states in these materials and the still unknown nature of high temperature superconductivity.

Although we focus on this problem, our ideas have broad validity and applications. The magnetic response of a superconductor is related to that of an ordinary conductor in an harmonically applied field. The skin effect, with $\delta \ll d$, for a quasistatic regime where the frequency is restricted by $\omega \ll c/d$ (c is the speed of light), maps⁴ onto the problem of a superconductor of the same size and shape in a static applied magnetic field. The role of δ for a conductor is taken up by λ , the effective penetration depth of a superconductor ($\lambda \ll d$). Except for the simplest geometries where an analytic solution exists for the corresponding boundary value problem, obtaining small skin depth corrections can be computationally demanding. These difficulties arise from the non-trivial boundary conditions (including open boundary equations at infinity) and the requirement that the appropriate, generally nonlinear differential equations be solved very accurately within the narrow region where the skin effects are contained. Our method offers a way to resolve these difficulties.

We examine a superconductor in an applied uniform magnetic field, \mathbf{H}_a . The sample occupies a bounded region

$\Omega \subset \mathbf{R}^3$ and at its boundary, $\partial\Omega$, is surrounded by vacuum. For H_a smaller than a critical value, a superconductor is in the Meissner regime: the magnetic flux is expelled from the bulk of the sample. On $\mathbf{R}^3 \setminus \Omega$ the current is $\mathbf{j} \equiv 0$ and it is sufficient to find a magnetic scalar potential Φ , $\mathbf{H} = -\nabla\Phi$, which satisfies the Laplace equation. On Ω , the appropriate Maxwell equation is Ampère's law. For unconventional pairing states in HTSCs, the London relation⁵ $\mathbf{j} = \mathbf{j}(\mathbf{A})$ between current and vector potential⁶ \mathbf{A} , is nonlinear and nonanalytic.^{1,2,7} Thus it is advantageous to combine Ampère's law in terms of the vector potential with the relation $\mathbf{j}(\mathbf{A})$:

$$\nabla \times \nabla \times \mathbf{A} = \frac{4\pi}{c} \mathbf{j}(\mathbf{A}). \quad (1)$$

HTSCs in general have a highly anisotropic structure with different penetration depths, λ_i , along the various, $i = a, b, c$ crystallographic directions. We include this penetration depth anisotropy through the anisotropic, nonlinear, relation $\mathbf{j}(\mathbf{A})$ given in Ref. 7. By λ we shall denote the effective penetration depth (a function of λ_i), which plays the dominant role in the field decay studied. In the special case of an isotropic superconductor with a linear relation $\mathbf{j}(\mathbf{A})$, all the fields on Ω satisfy the vector Helmholtz equation $\nabla^2 \mathbf{F} = \mathbf{F}/\lambda^2$, where \mathbf{F} can be \mathbf{H} , \mathbf{j} , \mathbf{A} . The boundary conditions are $-\nabla\Phi = \mathbf{H}_a$, at infinity, while on $\partial\Omega$ \mathbf{H} is continuous⁵ and there is no normal component of current, $j_n|_{\partial\Omega} = 0$. From the open boundary condition at infinity combined with the continuity requirement it appears that to obtain the finite skin depth corrections, one would have to solve numerically the appropriate equations in all space.

II. PERTURBATION METHOD

To resolve these difficulties, we view the finite skin effects, i.e., for finite λ in a superconductor, as a small correction to the dominant perfect diamagnetic response at $\lambda = 0$. When skin effects are studied, one has to include these corrections, which are characterized by the small parameter $\epsilon \equiv \lambda/d \ll 1$. The boundary value problem in the $\epsilon = 0$ limit is

^{a)}Electronic mail: izutic@physics.spa.umn.edu

^{b)}Electronic mail: otvalls@maroon.tc.umn.edu

relatively simple, one has only to solve the Laplace equation for the scalar potential on $\mathbf{R}^3 \setminus \Omega$ with trivial Neumann boundary conditions on $\partial\Omega$. We assume that an accurate, either analytical or numerical, solution on $\mathbf{R}^3 \setminus \Omega$ in the $\epsilon=0$ limit is available.⁷ This will be the starting point from which we shall develop our perturbation method. The small skin effect is then treated as a perturbation from the $\epsilon=0$ solution.

To proceed with the perturbation calculation we consider the auxiliary problem consisting of Eq. (1) on Ω , the $\epsilon=0$ solution on $\mathbf{R}^3 \setminus \Omega$, and the boundary conditions on $\partial\Omega$, $j_n=0$ and continuity of the tangential component of \mathbf{H} (the continuity of H_n cannot be imposed, it vanishes for the external fields in the $\epsilon=0$ limit). This is computationally simple, as it decouples the solutions for the regions $\mathbf{R}^3 \setminus \Omega$ and Ω . From this auxiliary problem we can generate⁷ the skin corrections to leading order in ϵ , as we shall now see.

In this article we consider the magnetic moment of a superconductor for an arbitrary direction of \mathbf{H}_a in a sample without a rotational symmetry (this is an extension of Ref. 7), and the magnetic quadrupole moment. We match the asymptotic behavior of the solution on $\mathbf{R}^3 \setminus \Omega$ and that in Ω by employing integral identities for magnetic multipoles.⁷ At large distances from Ω , the multipole expansion of the fields can be considered and the asymptotic behavior is governed primarily by the lowest nonvanishing multipole term. There are two different ways to obtain the multipole moments: by examining the asymptotic behavior on $\mathbf{R}^3 \setminus \Omega$, and from the fields computed on Ω . By matching the asymptotic behavior we mean that the exact solution on $\mathbf{R}^3 \setminus \Omega$ is formally written in terms of the unknown multipole moments which must agree with those computed from the fields on Ω . We formulate integral identities to compute the magnetic multipoles from fields on Ω such that we can identify terms in these expressions which are of different orders in ϵ .

The magnetic moment⁸ is

$$\mathbf{m} = \frac{1}{2c} \int_{\Omega} d\Omega \mathbf{r}'' \times \mathbf{j}(\mathbf{r}''), \quad (2)$$

where \mathbf{r}'' is the position vector for a point in Ω and \mathbf{j} is found from Eq. (1). The components of \mathbf{m} can be written for $\epsilon \ll 1$ in the form $m_i = m_{0i}[1 - \alpha_i \epsilon + O(\epsilon^2)]$, $i=x,y,z$, where m_{0i} , denoting the i th component of the magnetic moment in the limit $\epsilon=0$, represents a perfect diamagnetic response. For an ellipsoid it is given by a demagnetization factor. The α_i describe small corrections to perfect diamagnetism due to current penetration. For a direction i , where $m_{0i}=0$ (it could vanish from symmetry arguments, for a particular direction of \mathbf{H}_a), one can still have $\alpha_i \neq 0$, because of the anisotropic and nonlinear relation $\mathbf{j}(\mathbf{A})$. The effects of nonlinearity $\mathbf{j}(\mathbf{A})$, absent for $\epsilon=0$, are typically small and can be thought of as field dependent corrections to α_i , linear in H_a .

To distinguish terms in Eq. (2) of various orders in ϵ , we use Ampère's law, identities from vector calculus, and Gauss' theorem to obtain⁷

$$\begin{aligned} \mathbf{m} &= \frac{1}{8\pi} \int_{\partial\Omega} dS [\mathbf{n}(\mathbf{r}'' \cdot \mathbf{H}) + \mathbf{n} \times (\mathbf{r}'' \times \mathbf{H})] + \frac{1}{8\pi} \int_{\Omega} d\Omega \mathbf{H} \\ &\equiv \mathbf{m}_1 + \mathbf{m}_2, \end{aligned} \quad (3)$$

where \mathbf{r}'' is the position vector for a point on $\partial\Omega$ and \mathbf{n} is the unit normal pointing outwards. The terms \mathbf{m}_1 and \mathbf{m}_2 are of different order in ϵ and the latter is small, i.e., of $O(\epsilon m_0)$. This can be seen from the expression for \mathbf{m}_2 . Since \mathbf{H} is confined to a "skin" layer of thickness λ , the integral over the whole volume of Ω is effectively only an integration over the region $\sim \lambda$ away from its surface. Thus \mathbf{m}_2 vanishes in the zero penetration limit ($\epsilon=0$) and $\mathbf{m}(\epsilon=0) \equiv \mathbf{m}_0 = \mathbf{m}_1$. In order to obtain \mathbf{m} to $O(\epsilon m_0)$ it is sufficient to compute \mathbf{m}_2 to leading (zeroth) order. The term \mathbf{m}_2 explicitly scales with ϵ and any first order corrections for the fields needed to compute it would only produce contributions of order $O(\epsilon^2 m_0)$.

A similar integral identity can be derived for the magnetic quadrupole moment, defined⁹ as a symmetric traceless tensor with components

$$Q_{ij} = \frac{1}{2c} \int_{\Omega} d\Omega [(\mathbf{r}'' \times \mathbf{j}) \mathbf{r}'' + \mathbf{r}'' (\mathbf{r}'' \times \mathbf{j})]_{ij}, \quad i, j = x, y, z. \quad (4)$$

Using the previously introduced notation for terms of different order in ϵ , $Q_{ij} \equiv Q_{1ij} + Q_{2ij}$ we can derive, employing integration by parts and standard identities

$$\begin{aligned} Q_{1ij} &= \frac{1}{8\pi} \int_{\partial\Omega} dS [(n_i r_j'' + n_j r_i'')(\mathbf{r}'' \cdot \mathbf{H}) - (r_i'' H_j + r_j'' H_i) \\ &\quad \times (\mathbf{n} \cdot \mathbf{r}'')], \end{aligned} \quad (5a)$$

$$Q_{2ij} = \frac{1}{8\pi} \int_{\Omega} d\Omega [3(r_i'' H_j + r_j'' H_i) - 2\delta_{ij}(\mathbf{r}'' \cdot \mathbf{H})], \quad (5b)$$

where δ_{ij} is the Kronecker symbol. If by $Q_{0ij} \neq 0$ we denote a particular component of the magnetic quadrupole tensor in the $\epsilon=0$ limit, then, as in the case of the magnetic moment, we conclude that Q_{1ij} is of $O(Q_{0ij})$ while Q_{2ij} is of $O(\epsilon Q_{0ij})$.

Using Eqs. (4) and (5) we can match the asymptotic behavior of solutions in regions $\mathbf{R}^3 \setminus \Omega$ and Ω . It is then possible to perturbatively obtain physical quantities to leading order in ϵ , using only the fields on Ω computed from the auxiliary problem. The fields and quantities evaluated from this problem are denoted by an overbar notation. We consider first the magnetic moment. On $\mathbf{R}^3 \setminus \Omega$, the scalar potential can be written as $\Phi = \Phi_a + \Phi_r$, where Φ_a is the potential due to the applied field and satisfies the open boundary condition at infinity, $-\nabla\Phi_a \rightarrow \mathbf{H}_a$, and Φ_r describes the presence of the superconductor. Since \mathbf{m}_2 , as we have shown, explicitly scales with ϵ , it can be accurately computed to first order in ϵ by obtaining its leading contribution. This is achieved by using the fields on Ω from the auxiliary problem, i.e., by writing $\bar{\Phi} = \bar{\Phi}_a + \bar{\Phi}_r$. The task of determining \mathbf{m} to $O(\epsilon m_0)$ is therefore reduced to that of correctly including the contribution of \mathbf{m}_1 to first order in ϵ . The exact solution for \mathbf{H} is continuous on $\partial\Omega$. To calculate m_{1i} , the i th component of \mathbf{m}_1 , we can use the external fields obtained from Φ . The part of Φ , which has a dipole character is characterized by the unknown vector \mathbf{m} , the correct value of the magnetic moment. The remaining part of Φ , has different

symmetry properties and does not contribute⁷ to m_i . Contributions to the i th component of \mathbf{m}_1 , $i=x,y,z$, (we take $m_{0i} \neq 0$) can be written as

$$m_{1i}(\mathbf{m}) = m_{1i}(\Phi_a) + m_{1i}(\Phi_r), \quad (6)$$

where $m_{1i}(\Phi_a)$, for Φ_a , which is known, can be simply calculated from Eq. (4). We define p_{ij} by $m_{1i}(\Phi_a) \equiv \sum_j p_{ij} m_{0j}$, $i, j=x,y,z$. The constants p_{ij} , which depend on the shape of Ω , can now be determined by solving for p_{ij} using the known values $m_{1i}(\Phi_a)$ and m_{0i} corresponding to \mathbf{H}_a applied along three independent directions. In the limit $\epsilon=0$, $m_{2i}=0$ and from Eq. (6) follows the identity

$$m_{0i} = \bar{m}_{1i} = \sum_j p_{ij} m_{0j} + \sum_j (\delta_{ij} - p_{ij}) m_{0j}, \quad (7)$$

where $m_{1i}(\Phi_r) = \sum_j (\delta_{ij} - p_{ij}) m_{0j}$. For $\epsilon \neq 0$, when the solution for Φ and \mathbf{H} is given in terms of a multipole expansion with unknown coefficients, $m_{1i}(\Phi_a)$ remains the same. The terms in Φ_r which contribute to the magnetic moment \mathbf{m} , will now have coefficients proportional to the correct unknown value of \mathbf{m} , slightly changed from the $\epsilon=0$ case. We can therefore write $m_{1i}(\Phi_r) = \sum_j (\delta_{ij} - p_{ij}) m_j$ and the correct value for m_{1i} satisfies $m_{1i} = \sum_j [m_{ij} - p_{ij}(m_{ij} - m_{0ij})]$. Employing the fact that m_{2i} and \bar{m}_{2i} agree to $O(\epsilon m_{0i})$ we can solve for m_i from $m_i = \sum_j [\delta_{ij} m_{ij} - p_{ij}(m_{ij} - m_{0ij})] + m_{2i}$, with the solution for m_i correct to $O(\epsilon)$:

$$m_i = m_{0i} + \sum_j p_{ij}^{-1} m_{2j} \approx m_{0i} + \sum_j p_{ij}^{-1} \bar{m}_{2j}. \quad (8)$$

Therefore the magnetic moment can be computed by only determining the lowest order contribution to m_2 .

Following an analogous procedure we can obtain a solution for the components of the quadrupole tensor Q_{ij} accurate to first order in ϵ . The resulting expression is similar to Eq. (8) with the constants p_{ij} replaced by the appropriate fourth rank tensor.

As a simpler example, it is instructive to consider an isotropic, linear superconducting sphere in an applied uni-

form magnetic field. Eq. (8) reduces¹⁰ to the analytical result⁵ $m = m_0(1 - 3\epsilon)$, where $m_0 = -H_a a^3/2$, $\epsilon \equiv \lambda/a$ and a is the sphere radius.

III. CONCLUSIONS

The ideas presented here can be used in problems in computational magnetics involving a small skin depth, by incorporating our perturbation procedure in the appropriate numerical algorithm. The integral identities for the magnetic multipoles are valid in the quasistatic regime and not restricted to the field of superconductivity.

We have addressed here the computation of small skin effects in a superconductor, using the perturbation method and matching the asymptotic behavior of a solution. We have shown how to accurately compute the nonlinear magnetic response of an anisotropic superconductor, by simplifying the boundary conditions and reducing the size of the computational domain.

ACKNOWLEDGMENTS

The authors thank Z. Škoda for discussion of our work and I.Ž. acknowledges support from the University of Minnesota Graduate School Doctoral Dissertation Fellowship.

¹D. Xu, S. K. Yip, and J. A. Sauls, Phys. Rev. B **51**, 16233 (1995).

²I. Žutić and O. T. Valls, Phys. Rev. B **54**, 15500 (1996).

³I. Žutić and O. T. Valls, Phys. Rev. B **56**, 11279 (1997).

⁴L. D. Landau and E. M. Lifshitz, *Electrodynamics of Continuous Media* (Pergamon, Oxford, 1960), p. 202.

⁵F. London, *Superfluids* (Wiley, New York, 1950), Vol. 1, pp. 29–37; T. P. Orlando and K. A. Delin, *Foundations of Applied Superconductivity* (Addison-Wesley, Reading, 1991), passim.

⁶In solving boundary value problems for superconductors one often considers instead of \mathbf{A} the gauge invariant velocity, $\mathbf{v}_s = \nabla\chi/2 + e/c\mathbf{A}$, where χ is the phase of the superconducting order parameter, and e the proton charge (with $\hbar = k_B = 1$).

⁷I. Žutić and O. T. Valls, J. Comput. Phys. **136**, 337 (1997), discusses in detail the perturbation method and possible limitations for the choice of Ω .

⁸J. D. Jackson, *Classical Electrodynamics* (Wiley, New York, 1975), p. 181.

⁹C. G. Gray, Am. J. Phys. **48**, 984 (1980).

¹⁰The derivation is given in detail in Ref. 7.

Temperature dependence of giant magnetoresistance properties of NiMn pinned spin valves

Sining Mao,^{a)} Nurul Amin, and Ed Murdock

Seagate Technology, 7801 Computer Avenue, Minneapolis, Minnesota 55435

The giant magnetoresistance response of NiMn pinned spin valves was studied at elevated temperature. Top spin valve films were made by ion beam sputtering and thermally treated to induce the strong unidirectional pinning field in the pinned layer. Both δR and $\delta R/R$ decrease linearly with temperature. The sheet resistance of the spin valves also increases linearly with temperature. The exchange coupling between pinned layer and free layer decreases slightly and the coercivity of the free layer increases slightly. The temperature dependence of the exchange pinning field is unique in NiMn spin valves. The pinning field has a weakly increasing temperature dependence up to 200 °C, then decreases to zero at the blocking temperature of 380 °C. Samples with different thickness NiMn layers show different temperature dependencies. However, the blocking temperature is unchanged. The pinning fields of NiMn, FeMn, IrMn, and NiO spin valves were also measured up to 200 °C; NiMn pinned spin valves show the least dependence of pinning field at elevated temperatures. © 1998 American Institute of Physics. [S0021-8979(98)27811-X]

INTRODUCTION

In spin valve recording heads, a sufficient pinning field [due to exchange coupling between an antiferromagnetic (AFM) pinning layer and a ferromagnetic (FM) pinned layer] is required to keep the pinned layer's magnetization unchanged during the operation of the spin valve (SV)/giant magnetoresistance (GMR) reader. So far various AFM materials, such as FeMn, NiO, NiMn, IrMn, PdPtMn, and TbCo, have been exploited as pinning layers in SV/GMR transducers.¹ NiMn has the strongest pinning strength (H_p) at high temperatures,^{2,3} while most AFM materials can be made with high H_p at room temperature but insufficient H_p for use of spin valve heads at elevated temperatures. In practice, MR-type recording heads operate at rather high internal temperatures. The stripe temperature can be as high as 200 °C. Moreover, thermal asperity events may temporarily create a much higher stripe temperature. The pinning must remain high at these temperatures.

In the as-grown phase the NiMn has a face-centered-cubic (fcc) structure which is not antiferromagnetic. A thermal treatment is needed to induce the fcc to face-centered-tetragonal (fct) phase transformation in the NiMn layer to provide the exchange field to the ferromagnetic layer through antiferromagnetic-ferromagnetic interaction. Such thermal annealing tends to damage the GMR properties of a spin valve. Careful film deposition and postannealing are needed to produce thermally stable NiMn spin valves (i.e., able to survive the aggressive NiMn annealing).² In this article, we present the temperature dependence of the pinning field and magnetoresistance of NiMn spin valves made by ion beam

deposition. In addition, a comparison between different pinning materials is also given.

EXPERIMENT

Spin valve films were deposited by a commercial multi-target ion beam sputtering apparatus, which has a base pressure of 1×10^{-8} Torr. A spin valve stack of a 80 Å Ta/ t Å NiMn/25 Å NiFe/15 Å Co/30 Å Cu/15 Å Co/55 Å NiFe/25 Å Ta substrate was sequentially deposited at deposition rates of 0.5–1 Å/s without breaking vacuum. Bilayers of the Ta/NiMn/NiFe/Ta substrate were made under the same conditions for a pinning field comparison. After deposition of the spin valves, a high temperature thermal anneal (~ 280 °C) in a static magnetic field for as long as 45 h was performed to further treat the films and to induce exchange coupling between NiMn and NiFe. The range of thickness t for the NiMn pinning layer is 80–500 Å. The pinned layer NiFe thickness was varied from 25 to 250 Å to study the pinning field variation. It shows a typical $1/t$ relationship with respect to the ferromagnetic layer thickness.³ The spin valves were characterized for structural properties using x-ray diffraction (XRD) (including a rocking curve scan). The films are highly (111) textured. High resolution cross-sectional transmission electron microscopy (TEM) images indicate the high quality of the interface microstructures.⁴ The magnetoresistance was measured by a dc four point probe method at different temperatures on a commercial GMR tester in air. Because of the use of the Ta cap layer no surface oxidation was observed during the measurement. A vibrating sample magnetometer (VSM) with a high temperature attachment was used for magnetization measurements on selected samples. Films with the same spin valve stack as NiMn were deposited us-

^{a)}Electronic mail: sining_mao@notes.seagate.com

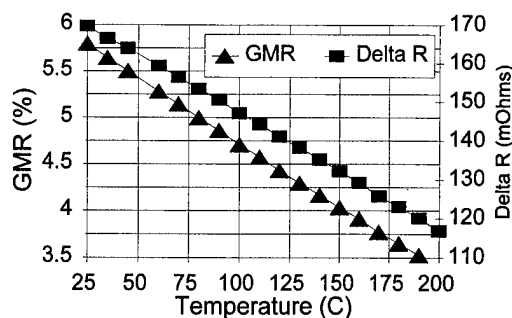


FIG. 1. Temperature dependence of the GMR ($\Delta R/R$) and ΔR for a NiMn spin valve.

ing IrMn, FeMn, and NiO pinning materials and measured between room temperature (RT) and 200 °C for comparison.

RESULTS AND DISCUSSION

Results of the GMR and ΔR from the high temperature GMR measurements of a spin valve are shown in Fig. 1. This is representative of all the NiMn spin valves with different thickness combinations. The GMR is defined by the resistance difference between the parallel state and the antiparallel state divided by the parallel state resistance. The R - H curves are similar to each other at different temperatures. The pinned layer has a very strong pinning field (typically >500 Oe) and is not switched up to 800 Oe.² The GMR response is inversely proportional to temperature between RT and 200 °C. The temperature coefficients of the GMR ratio and ΔR are $-0.36\%/^{\circ}\text{C}$ and $-0.23\%/^{\circ}\text{C}$, respectively. Low temperature GMR measurements confirmed the linear ΔR variation over a broader temperature range.⁵ This is consistent with our previous observation on FeMn spin valves but different from the bulklike T^n power law temperature dependence (where $n=1.5$), indicating a contribution from an intrachannel spin-mixing process in addition to the interchannel spin-mixing process.⁶

The reversible resistance increase of NiMn spin valves follows a simple linear relationship with temperature due to electron-phonon scattering. The increase of the normalized sheet resistance is plotted in Fig. 2 and is also compared with a MR film. The spin valve films have less increase in resis-

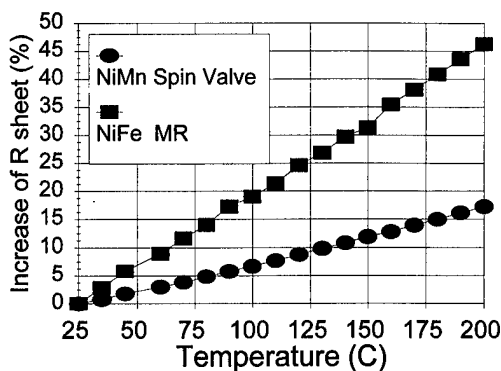


FIG. 2. Temperature dependence of the normalized resistance for a NiMn spin valve and a 225 Å NiFe MR film.

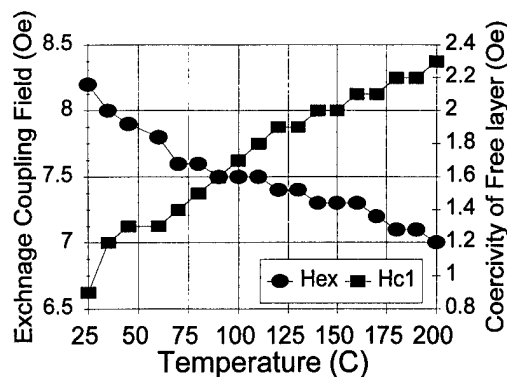


FIG. 3. Coercivity of the free layer and the exchange coupling field between the free layer and the pinned layer as a function of temperature.

tance than the AMR films. This will reduce the sensor self-heating effect and improve resistance to thermal spikes. The free layer magnetic properties are shown in Fig. 3. The coercivity of the free layer of Co/NiFe increases a little bit and the exchange field between the free layer and the pinned layer due to orange peel coupling decreases by 15% at 200 °C. The origin of the increase of free layer coercivity is unclear at this moment although it may be related to the magnetic interaction with the pinned layer.

Figure 4 is the pinning field dependence on the temperature in the range of RT~200 °C for NiMn, FeMn, IrMn, and NiO spin valves made at Seagate. Since the absolute value of the pinning field depends on the thickness of all the layers and their process details, only the normalized data are plotted to illustrate the temperature dependence. Figure 4 shows the dramatic difference between NiMn and the rest; NiMn spin valves retain their full pinning strength to nearly 200 °C. This is very important for practical recording heads whose active sensor operating environment is very hot. The blocking temperatures for FeMn, NiO, and IrMn are 150, 200, 220 °C, respectively. They are consistent with the published data.^{1,7} However, the blocking temperature of NiMn spin valves (380 °C, see Fig. 5) is much higher than that of all the other pinning materials. Furthermore the NiMn pinning field does not follow a $(1-1/T)$ relationship with temperature which is common among IrMn, FeMn, and NiO materials.⁷ The typical linear temperature dependence was shown by

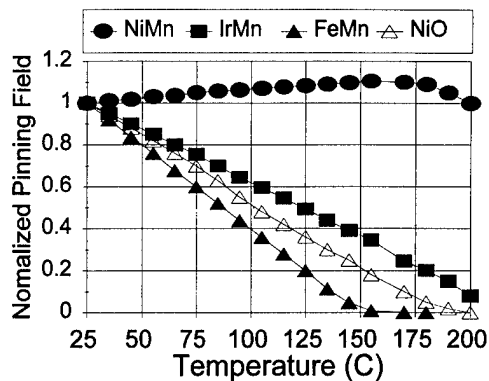


FIG. 4. Normalized pinning fields vs temperature for NiMn, FeMn, IrMn, and NiO spin valves.

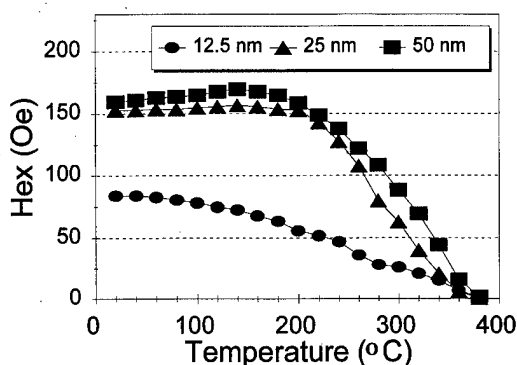


FIG. 5. Temperature dependence of the pinning field for NiFe/NiMn bilayers. The NiFe layer thickness is 250 Å and the NiMn layer thicknesses are 125, 250, and 500 Å, respectively. The grain sizes of the NiMn layers are 80, 190, and 260 Å, respectively.

Malozemoff based on thermal excitation⁸ and experimentally observed in various materials systems.^{9–11} The linear temperature dependence is also accompanied by a broader local blocking temperature distribution.^{7,11}

To further understand the unique temperature dependence of the pinning fields, we investigated the temperature dependence using a high temperature VSM on the NiMn/NiFe bilayers over a 500 °C range. The data are plotted in Fig. 5. It is very interesting to see that the temperature dependence of the NiMn depends upon the NiMn layer thickness and deviates from an inversely linear dependence. More important, the blocking temperature is the same for different layers thicknesses which again is quite different from other materials [like IrMn (Ref. 12) and NiO (Ref. 13)]. As pointed out by Lin *et al.*,⁷ the NiMn exchange coupling is through interaction of NiFe and NiMn antiferromagnetic clusters. The blocking temperature is primarily determined by the NiFe layer's ferromagnetic properties since the Néel temperature for NiMn is far above the blocking temperature, unlike the other materials which have much lower Néel temperatures.

The intrinsic antiferromagnetic crystalline anisotropy of the NiMn layer and the interfacial coupling strength are two dominant factors determining the pinning field.⁷ The temperature dependence of the pinning strength in NiMn films thicker than the critical thickness is mostly dominated by the uncompensated spin structures at the interface and the temperature dependence is similar to NiFe/CoO superlattice results.¹⁴ The microstructure of the NiMn will definitely influence the pinning strength and, further, the temperature dependence of the pinning field. To verify the hypothesis, we performed XRD and derived the grain size for the three samples, noted in the caption for Fig. 5. The smaller grains

in the thinner NiMn are more susceptible to thermal fluctuations and lose their AFM ordering easily, while the larger grain size helps to stabilize the AFM order against thermal energy and contributes to an insensitive temperature dependence. This implies that the blocking temperature distribution of the NiMn spin valves is also narrower. A complete study of the blocking temperature distribution is currently underway.

SUMMARY AND CONCLUSIONS

In summary, we have reported the magnetic and electrical responses of NiMn spin valves at elevated temperatures. The NiMn spin valves have a linear temperature response in terms of resistance, $\delta R/R$, δR , exchange field, and coercivity of the free layer. The temperature coefficient of resistance of NiMn spin valves is much smaller than conventional MR films. The pinning field is only weakly dependent on temperature (<200 °C) when the thickness of the NiMn pinning layer is sufficient (~250 Å). NiMn spin valves have the strongest pinning field at 200 °C of any AFM material published to date, and are very promising for spin valve head applications.

ACKNOWLEDGMENTS

The authors have benefited from stimulating discussions with Dr. G. Wang, Dr. C. Lai, Dr. S. Gangopadhyay, and Dr. R. Michel. They would like to thank Professor D. Lottis's group for low temperature GMR measurements and Professor J. Judy's group for high temperature VSM measurements.

¹ See, for example, Digests of Intermag '97, April, 1997, New Orleans, LA.

² S. Mao, S. Gangopadhyay, N. Amin, and E. Murdock, Appl. Phys. Lett. **69**, 3593 (1996).

³ T. Lin, D. Mauri, N. Staud, C. Hwang, J. K. Howard, and G. L. Gorman, Appl. Phys. Lett. **65**, 1183 (1994).

⁴ L. Tang, D. Laughlin, and S. Gangopadhyay, J. Appl. Phys. **81**, 4906 (1997).

⁵ D. Lottis (private communication).

⁶ J. Szucs, T. O'Brien, D. K. Lottis, S. Gangopadhyay, S. Mao, and E. Murdock, J. Appl. Phys. **81**, 4014 (1997).

⁷ T. Lin, C. Tsang, R. E. Fontana, and J. K. Howard, IEEE Trans. Magn. **31**, 2585 (1995).

⁸ A. P. Malozemoff, J. Appl. Phys. **63**, 3874 (1988).

⁹ M. J. Carey and A. E. Berkowitz, J. Appl. Phys. **73**, 6892 (1993).

¹⁰ P. J. Van der Zaag, A. R. Ball, L. F. Feiner, R. M. Wolf, and P. A. A. van der Heijden, J. Appl. Phys. **79**, 5103 (1996).

¹¹ C. H. Lai, T. J. Regan, B. L. White, and T. C. Anthony, J. Appl. Phys. **81**, 3989 (1997).

¹² H. N. Fuke, K. Saito, Y. Kamiguchi, H. Iwasaki, and M. Sahashi, J. Appl. Phys. **81**, 4004 (1997).

¹³ C. H. Lai, T. C. Anthony, E. Iwamura, and R. L. White, IEEE Trans. Magn. **32**, 3419 (1996).

¹⁴ K. Takano, R. H. Kodama, A. E. Berkowitz, W. Cao, and G. Thomas, Phys. Rev. Lett. (submitted).

Exchange biasing of permalloy films by $\text{Mn}_x\text{Pt}_{1-x}$: Role of composition and microstructure

Kannan M. Krishnan,^{a)} C. Nelson, and C. J. Echer

Materials Sciences Division, Lawrence Berkeley National Laboratory, Berkeley, California 94720

R. F. C. Farrow, R. F. Marks, and A. J. Kellock

IBM Research Division, Almaden Research Center, San Jose, California 95120-6099

The interfacial coupling energy, $\Delta\sigma$ for polycrystalline $\text{Ni}_{0.8}\text{Fe}_{0.2}$ (100 Å)/ $\text{Mn}_x\text{Pt}_{1-x}$ (t Å)/ SiO_2 bilayers, has been determined from wedge samples spanning a $\text{Mn}_x\text{Pt}_{1-x}$ composition range $0.42 < x < 0.76$ and $t \sim 350$ Å. $\Delta\sigma$ exhibits a sharp peak of 0.1 erg/cm^2 at 51% Mn. We compare the magnetic and microstructural properties of two bilayer films, which have the same compositions of permalloy and $\text{Mn}_x\text{Pt}_{1-x}$: [$\text{Ni}_{0.85}\text{Fe}_{0.15}$ (100 Å)/ $\text{Mn}_{0.49}\text{Pt}_{0.51}$ (t Å)]. In one case (normal structure), the epitaxial permalloy was grown first onto Pt/MgO(001), followed by 170 Å of $\text{Mn}_{0.49}\text{Pt}_{0.51}$. In the other structure (inverted), a 350 Å thick polycrystalline film of $\text{Mn}_{0.49}\text{Pt}_{0.51}$ was grown onto a SiO_2 substrate, followed by permalloy. The structures exhibited very different exchange bias fields (32 versus 86 Oe) and $\Delta\sigma$ values (0.021 versus 0.060 erg/cm^2), respectively. Significant differences in texture, grain size, and $\text{Mn}_{0.49}\text{Pt}_{0.51}$ layer thickness for the two samples are reported. © 1998 American Institute of Physics. [S0021-8979(98)47611-4]

The key to the performance¹ of spin valve structures is the pinning of a ferromagnetic layer, such as permalloy, by exchange biasing using an antiferromagnetic (AFM) layer.² Various AFM materials are being explored to achieve the desired pinning characteristics, temperature stability, and minimal postprocessing. These include NiMn and ternary $\text{Mn}_{1-x-y}\text{Pt}_x\text{Pd}_y$ alloys.^{3,4} $\text{Mn}_x\text{Pt}_{1-x}$ films not only show good promise as an exchange bias material but their high Néel temperature results in a high blocking temperature when they are exchange coupled with permalloy.⁵ In this paper we report on the exchange biasing in permalloy- $\text{Mn}_x\text{Pt}_{1-x}$ bilayer films, as a function of composition. Detailed electron microscopy investigation to elucidate the role of microstructure and composition in determining the strength of the interfacial coupling is also presented.

The films were grown by coevaporation in a molecular beam epitaxy system under ultrahigh vacuum ($\sim 10^{-10}$ mB). To determine the dependence of $\Delta\sigma$ on $\text{Mn}_x\text{Pt}_{1-x}$ layer composition, wedge samples were prepared, of the inverted type, comprised of $\text{Ni}_{0.85}\text{Fe}_{0.15}$ (100 Å)/ $\text{Mn}_x\text{Pt}_{1-x}$ (t Å)/ SiO_2 in which the composition x was graded spatially, covering the range $x = 0.42$ – 0.54 . The Py layer thickness and composition were constant across the wedge while the $\text{Mn}_x\text{Pt}_{1-x}$ thickness varied from 300 to 400 Å. This thickness variation was shown in separate experiments not to influence $\Delta\sigma$ significantly. The samples were grown in a dc magnetic field (~ 1 kOe, in the film plane, as for all the samples described in this article) and the substrate was held at 40 – 50°C . After growth, the samples were annealed (in the field) for 2 h at 180°C to achieve chemical ordering of the $\text{Mn}_x\text{Pt}_{1-x}$.

Two other samples (unwedged) were studied in this work. For these, the composition and thickness of the Py layer as well as the composition of the $\text{Mn}_x\text{Pt}_{1-x}$ layer were

kept constant and the same for both samples. The structures were: 10 Å Pt/170 Å $\text{Mn}_{0.49}\text{Pt}_{0.51}$ /100 Å $\text{Ni}_{0.85}\text{Fe}_{0.15}$ /10 Å Pt/MgO(001); referred to as SV1098 and 100 Å $\text{Ni}_{0.85}\text{Fe}_{0.15}$ /350 Å $\text{Mn}_{0.49}\text{Pt}_{0.51}$ / SiO_2 ; referred to as SV1171. The Pt seed layer was grown at 700°C and shown by *in situ* (reflection high-energy electron diffraction) (RHEED) analysis to be epitaxial, i.e., Pt(001)/MgO(001). The sample temperature was then reduced to 200°C for growth of Py and $\text{Mn}_{0.49}\text{Pt}_{0.51}$ films in a dc magnetic field. RHEED showed that the Py was epitaxial, i.e., Py(001)/Pt(001), but the $\text{Mn}_{0.49}\text{Pt}_{0.51}$ exhibited diffuse arcs indicating multiple orientations of this layer. In the case of SV1171, the entire structure was grown at $\sim 30^\circ\text{C}$ in a dc magnetic field and subjected to a subsequent anneal at $180^\circ\text{C}/2 \text{ h}$.

Following growth, samples SV1098 and SV1171 were characterized structurally, and their bulk compositions were determined by a combination of Rutherford backscattering spectroscopy and proton induced x-ray emission spectroscopy. In addition, local compositions were measured by x-ray emission spectroscopy in a transmission electron microscope (TEM) using a 100 Å probe and experimentally measured k factors.⁶ Energy-filtered images of the characteristic edges in electron energy-loss spectroscopy were obtained using a TEM equipped with a field-emission source and a commercial image filter. The interfaces were characterized by high-resolution electron microscopy.

Figure 1 shows the dependence of $\Delta\sigma$ on the composition (x) of $\text{Mn}_x\text{Pt}_{1-x}$ determined from point-by-point measurements, at room temperature, of the longitudinal Kerr loops of the wedge structure. $\Delta\sigma$ was determined from the exchange bias using the expression: $\Delta\sigma = H_e M_s t$ following Malozemoff.⁸ Here, H_e is the exchange bias field, and M_s and t are the saturation magnetization and thickness of the Py film, respectively. Data for individual inverted structures of compositions outside the wedge range are also included in Fig. 1. We note that for bulk $\text{Mn}_x\text{Pt}_{1-x}$ crystals the Néel

^{a)}Electronic mail: krishnan@lbl.gov

temperature (T_N) peaks near $x=0.50$.⁷ Similar composition dependence of T_N and $\Delta\sigma$ suggests a common origin, namely, as the crystal composition departs from the chemical-ordering composition ($x=0.5$), Mn either occupies sites outside the (001) sheets of antiferromagnetically aligned Mn (for $x>0.5$) or Pt occupies sites within the sheets (for $x<0.5$). In both cases, more Mn moments become uncompensated leading to diminished antiferromagnetic ordering. Kishi *et al.*³ report a similarly sharp peak near $x=0.5$ in H_e for exchange-coupled Py/MnPtPd structures.

The inset to Fig. 1 shows the longitudinal Kerr loops, recorded along the easy axis, for these samples. Both samples show a unidirectional shift in their hysteresis loops with exchange bias values of 32 Oe (SV1098) and 86 Oe (SV1171). The $\Delta\sigma$ values, calculated from these fields, are shown in Fig. 1. The value of $\Delta\sigma$ (0.060 erg/cm^2) for SV1171 is in good agreement with the wedge data for a sample of similar structure and composition. On the other hand, sample SV1098 has a much reduced value of $\Delta\sigma$ (0.022 erg/cm^2).

Specular ($\theta-2\theta$) x-ray diffraction scans for SV1098 confirmed a single orientation of Py: Py (001)/Pt,MgO(001). They also revealed multiple orientations of the $\text{Mn}_{0.49}\text{Pt}_{0.51}$ film, each having the chemically ordered tetragonal structure ($a=4.004 \text{ \AA}$, $c=3.664 \text{ \AA}$). The dominant orientation was $\text{Mn}_{0.49}\text{Pt}_{0.51}$ (100)/Py(001). For SV1171, the specular scan showed only a (111) peak for Py indicating a dominant (111) texture. All remaining peaks could be indexed on the basis of the chemically ordered, tetragonal phase of $\text{Mn}_{0.49}\text{Pt}_{0.51}$. Multiple peaks were present, indicating polycrystallinity with no preferred texture axis.

To understand the role of microstructure and composition, the two samples (SV1098, SV1171), were studied by electron microscopy. For sample SV1098, Fig. 2 shows a bright-field (BF) image (a), the corresponding selected area diffraction (SAD) pattern (b) and a dark-field image (c) using a portion of the Ni-Fe(112) ring (d). These images, taken from a thin ($t\sim 1000 \text{ \AA}$) area of the sample show that the grains with sizes $\sim 5 \text{ nm}$ have a significant in-plane rotation. The SAD pattern can be indexed to a combination of face-centered-cubic Ni-Fe ($a\sim 3.54 \text{ \AA}$), and Mn-Pt with an elementary tetragonal cell ($a\sim 2.82 \text{ \AA}$, $c\sim 3.69 \text{ \AA}$). The in-plane rotation of the grains is evident from the angular spread of both sets of spots in Figs. 2(b) and 2(d). Even though earlier $\theta-2\theta$ x-ray diffraction scans have confirmed good epitaxy, it appears that large-angle grain boundaries and significant mismatch in plane ($\sim 30^\circ$) between the grains abound. No evidence for the chemical ordering of $\text{Mn}_{0.49}\text{Pt}_{0.51}$ is readily discernible from these complicated SAD patterns. However, clear evidence for the ordering is seen in a microdiffraction pattern superstructure reflections [Fig. 2(e)], taken from a single grain using an 8 nm focused electron probe. A number of grains showed this feature but it is clear from this limited sampling that not all grains are chemically ordered. Similar analysis of sample SV1171 is shown in Figs. 2(f) (BF image) and 2(g) (SAD). Figure 2(f) shows a similar grain-size distribution to Fig. 2(a). The rings in the SAD pattern can be indexed to polycrystalline SiO_2 and $\text{Mn}_{0.49}\text{Pt}_{0.51}$ (grain size $\sim 5 \text{ nm}$). No evidence for NiFe is

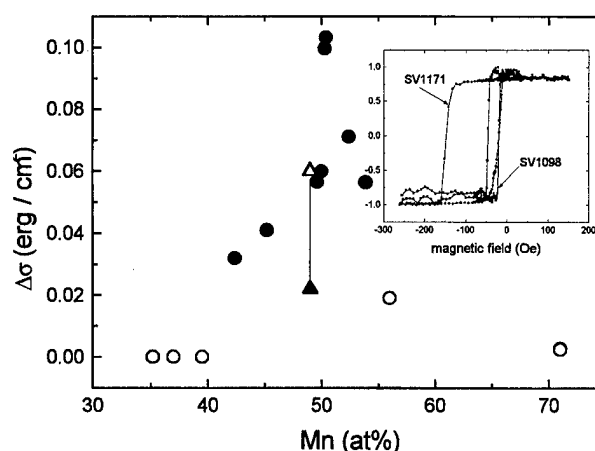


FIG. 1. Interfacial coupling energy density $\Delta\sigma$ as a function of composition for $\text{Ni}_{0.85}\text{Fe}_{0.15}$ (100 Å)/ $\text{Mn}_x\text{Pt}_{1-x}$ (300–400 Å)/ SiO_2 . The solid points are from a wedge sample, and open circles are from individual samples (error bars within data circles). The inset shows two representative longitudinal Kerr loops for samples SV1098 and SV1171, which have the same composition of $\text{Mn}_x\text{Pt}_{1-x}$ ($x=0.49$). The ordinate is the Kerr rotation on a normalized scale. The corresponding values of $\Delta\sigma$ for these samples are plotted as a filled (SV1098) and open (SV1171) triangles.

seen in the SAD pattern. There is only one weak shoulder on the side of the $\text{Mn}_{0.49}\text{Pt}_{0.51}$ (200) peak that shows up for Py in the electron diffraction pattern; perhaps this line was undetected or the thin layer was removed in the ion-milling process. Local compositions of the films were both $\text{Mn}_{0.49}\text{Pt}_{0.51}$ but the permalloy compositions were $\text{Ni}_{0.87}\text{Fe}_{0.13}$ and $\text{Ni}_{0.85}\text{Fe}_{0.15}$ for SV1098 and SV1171, respectively.

The nature of the interface and the chemical integrity of the various layers were studied by both energy-filtered imaging and high-resolution phase contrast imaging of cross-section samples. Using this technique, features in the characteristic energy-loss edges of the constituent elements can be measured both at high-energy ($\sim 1 \text{ eV}$) and spatial ($\sim 1-2 \text{ nm}$) resolution. Typically, in the electron microscope dipole selection rules, $\Delta l = \pm 1$ apply and the core edges of interest are the $1s \rightarrow p(K)$, $2p \rightarrow d(L)$, and $3d \rightarrow f(M)$ transitions. Specifically, for the elements of interest this would correspond to the K edges for oxygen (532 eV) and magnesium (1305 eV), L edges for manganese ($L_3 \sim 640 \text{ eV}$, $L_2 \sim 651 \text{ eV}$), iron ($L_3 \sim 708 \text{ eV}$, $L_2 \sim 721 \text{ eV}$), and nickel ($L_3 \sim 855 \text{ eV}$, $L_2 \sim 872 \text{ eV}$), and the $O_{2,3}$ edge for platinum (52 eV). Energy-filtered maps (using 10 eV windows) for cross-section samples of SV1098, after background subtraction and suitable correction to accommodate any thickness variations, along with a low-magnification image (a) and a high-resolution image of the interface (b) are shown in Fig. 3. The individual layers corresponding to MgO, NiFe, and Mn-Pt are clearly evident from the overlap of the images from their respective constituent elements. Within the resolution of this measurement the interfaces between the three layers are chemically sharp and are devoid of any pinholes. A similar result was also obtained for sample SV1171, but in the interest of brevity these energy-filtered images are not included in this article. Finally, the high-

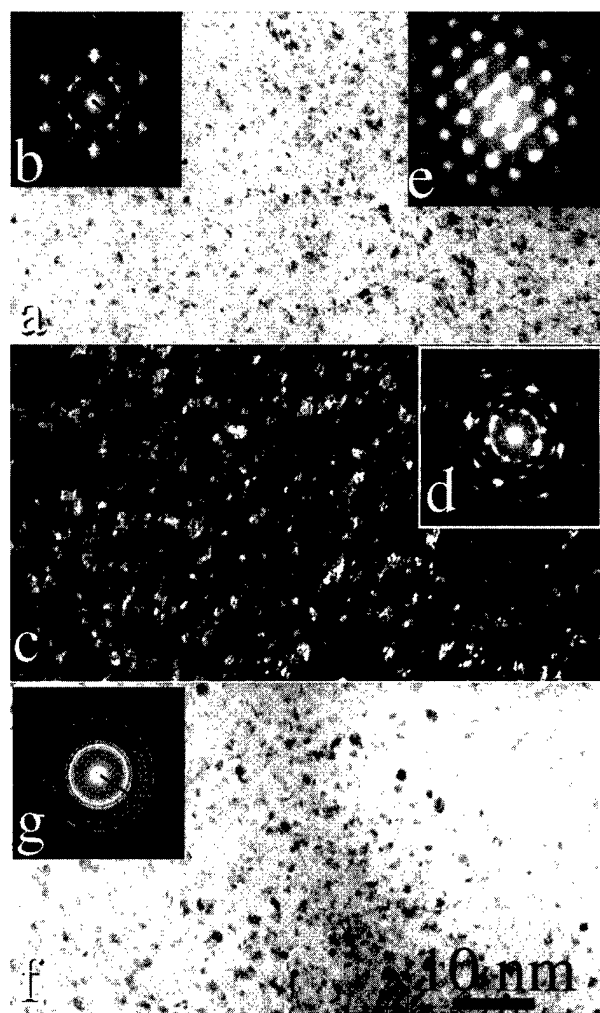


FIG. 2. Plan-view images and selected area diffraction for the two samples. Notice the reflection corresponding to chemical ordering in (e).

resolution electron microscope image reveals that the interface between the permalloy and Mn–Pt is structurally quite rough with significant strain.

The key result is that our data show a much reduced interfacial coupling for the epitaxial Py/Mn_{0.49}Pt_{0.51} sample (SV1098) in comparison with the inverted polycrystalline Py/Mn_{0.49}Pt_{0.51} sample (SV1171). Apart from the different crystallographic texture of the two structures, other differences include a small but significant difference in grain size and a large thickness difference of Mn_{0.49}Pt_{0.51}. Note that the model of Malozemoff⁸ does predict a linear dependence of $\Delta\sigma$ on the reciprocal of the domain size of the antiferromagnet. The smaller crystallographic grain size of SV1171 compared with SV1098 leads one to expect a smaller domain size, though this remains to be confirmed experimentally. Another difference between the samples may be that the degree of chemical ordering for sample SV1098 is less than for SV1171, leading to incomplete antiferromagnetic ordering in

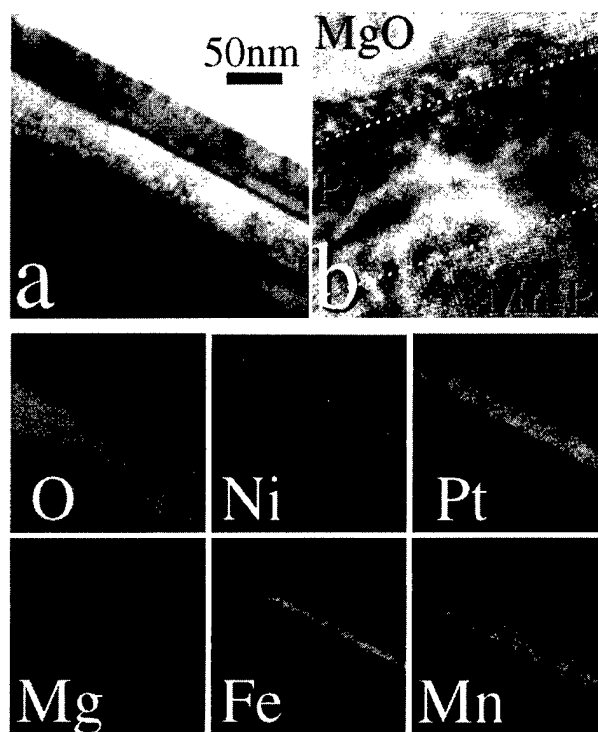


FIG. 3. Cross-sectional images and energy-filtered elemental images for sample SV1098.

this sample. The microdiffraction data for SV1098 do indicate incomplete and inhomogeneous ordering while the x-ray data for SV1171 are consistent with complete chemical ordering. A further structural difference between the samples is that in SV1098 the orientation of the interface plane of the antiferromagnet is predominantly (100), which is a plane of uncompensated Mn moments. Koon⁹ has predicted a smaller $\Delta\sigma$ value for such a plane compared with a compensated plane. However, we believe that the most likely explanation for the large difference in $\Delta\sigma$ in the present samples is that the thickness (170 Å) of Mn_{0.49}Pt_{0.51} in SV1098 may be approaching a critical thickness for exchange biasing.

This work was supported by U.S. Department of Energy under Contract No. DE-AC03-76SF00098.

¹J. C. S. Kools, IEEE Trans. Magn. **32**, 3165 (1996).

²W. H. Meiklejohn and C. P. Bean, Phys. Rev. B **102**, 1413 (1956).

³H. Kishi, Y. Kitadae, Y. Miyake, A. Tanaka, and K. Kobayashi, IEEE Trans. Magn. **32**, 3380 (1996).

⁴T. Lin, D. Mauri, N. Staud, C. Hwang, J. K. Howard, and G. L. Gorman, Appl. Phys. Lett. **65**, 1183 (1994).

⁵R. F. C. Farrow, R. F. Marks, S. Gider, A. C. Marley, and S. S. P. Parkin, J. Appl. Phys. **81**, 4986 (1997).

⁶K. M. Krishnan and C. J. Echer, in *Analytical Electron Microscopy*, edited by D. C. Joy (SF, 1987), p. 99.

⁷E. Kren, G. Kadar, L. Pal, J. Solyom, P. Szabo, and T. Tarnoczi, Phys. Rev. **171**, 574 (1968).

⁸X. Malozemoff, Phys. Rev. B **35**, 3679 (1987).

⁹N. C. Koon, preprint, 1996 Phys. Rev. Lett. (submitted).

Exchange coupling of NiFe/FeRh–Ir thin films

S. Yuasa,^{a)} M. Nývlt,^{b)} and T. Katayama

Electrotechnical Laboratory, 1-1-4 Umezono, Tsukuba, Ibaraki 305-8568, Japan

Y. Suzuki

JRCAT, National Institute for Advanced Interdisciplinary Research, Higashi, Tsukuba, Ibaraki 305-8562, Japan

We report unusually large room temperature coercive field H_c induced in $\text{Ni}_{0.81}\text{Fe}_{0.19}$ films grown on the (001) magnetically compensated surface of antiferromagnetic single crystal CsCl-type $\text{FeRh}_{0.95}\text{Ir}_{0.05}$ alloy thin layers on MgO (001) substrates. The specimens were prepared by conventional rf sputtering in Kr atmosphere, at 450–500 °C for FeRh–Ir and 20–200 °C for NiFe. The epitaxial growth of NiFe/FeRh–Ir and atomically flat terraces of FeRh–Ir were confirmed by x-ray reflectometry and scanning tunneling microscopy. For a NiFe(2.7 nm)/FeRh–Ir(22 nm) film, a maximum H_c of 810 Oe is observed. The $1/t_{\text{NiFe}}$ dependence of H_c for larger NiFe thicknesses indicates that the large coercive field originates from the magnetic interaction at NiFe/FeRh–Ir interface. The large H_c combined with high corrosion resistance make FeRh based alloys a promising candidate for application as pinning layers in spin-valve devices. © 1998 American Institute of Physics. [S0021-8979(98)29011-6]

I. INTRODUCTION

Thin antiferromagnetic films are currently attracting considerable attention of many researchers because they serve as pinning layers in spin valve structures. For the applications in spin valve based devices, it is essential to use the antiferromagnets with a high pinning force and a strong corrosion resistance. This is why we focused our interest on FeRh-based alloys.

FeRh alloys between 48 and 52 at. % of rhodium display an ordered CsCl (or B2) structure and are antiferromagnetic (AF) at room temperature. Under heating they exhibit a first order transition at a temperature $T_0 \sim 340$ K to a ferromagnetic (FM) state, as observed by Fallot and Hocart.¹ Extensive experimental and theoretical studies of structural and magnetic properties of these unusual materials were performed by several researchers. The AF–FM transformation is accompanied by a lattice expansion of about 0.3% while preserving the CsCl structure.²

Neutron diffraction experiments³ showed that iron atoms have an enhanced magnetic moment in the both AF and FM states [$\mu_{\text{Fe}}(\text{AF}) \sim 3.3 \mu_B$, $\mu_{\text{Fe}}(\text{FM}) \sim 3.1 \mu_B$]. Rhodium atoms have no appreciable moment in AF state while $\mu_{\text{Rh}}(\text{FM}) \sim 1.0 \mu_B$. These results are in a very good agreement with the conclusions of band structure calculations.^{4,5} In contrary to Mn-based antiferromagnets, the AF coupling in FeRh alloys takes place between successive ferromagnetically ordered (111) planes of Fe atoms.⁴

Preparation of the ordered FeRh alloy thin films is quite difficult since the structure and magnetic properties are very sensitive to the stoichiometry. We note that the CsCl ordering occurs for Rh content from 20 to 52 at. %, but the AF state is established only between 48 and 52 at. % of Rh.⁶

Lommel⁷ fabricated thin films of ordered FeRh alloy by several methods (alternate Fe and Rh deposition followed by diffusion anneal, codeposition and sputtering at 300 °C). More recently, other authors have tried cosputtering from Fe and Rh targets onto glass, followed by anneal at 600–1200 °C^{8,9} or by coevaporation.¹⁰ The common property of these films was a presence of paramagnetic disordered fcc phase, which appears probably due to an increased local concentration of Rh (on atomic scale) during the deposition and which reduces the growth of CsCl ordered structure.⁸ The retained fcc phase strongly affects the AF–FM transition, which is well manifested when measuring the magnetization as a function of temperature during heating cycles.^{7,8}

For practical applications as antiferromagnetic layers in spin valves operating at “usual” temperatures it is necessary to raise the transition temperature T_0 up to 450–500 K. This can be obtained by replacing about 5% of rhodium atoms with iridium.¹¹

As recently reported,¹² we can successfully grow $\text{FeRh}_{0.95}\text{Ir}_{0.05}$ ordered alloy (001) epitaxial films by sputtering from an alloy target on MgO (001) substrates heated above 300 °C. In this article, we present structural and magnetic properties of exchange coupled $\text{Ni}_{0.81}\text{Fe}_{0.19}/\text{FeRh}_{0.95}\text{Ir}_{0.05}$ epitaxial films on MgO (001) substrates.

II. SAMPLE PREPARATION AND CHARACTERIZATION

$\text{FeRh}_{0.95}\text{Ir}_{0.05}$ films were prepared by a conventional rf sputtering from alloy target (60 mm in diameter) on cleaved (001) surfaces of MgO substrates, heated up to 450–500 °C, under Kr pressure, $p(\text{Kr})$, of 8×10^{-3} Torr, at a rate of 0.05 nm/s. The film thickness ranged from 6 to 200 nm. After deposition, the films were annealed at the deposition temperature for 30–60 min.

A permalloy layer $\text{Ni}_{0.81}\text{Fe}_{0.19}$ was grown afterwards on each $\text{FeRh}_{0.95}\text{Ir}_{0.05}$ film, which was either water cooled or

^{a)}Electronic mail: yuasa@etl.go.jp

^{b)}Permanent address: Institute of Physics, Charles University, Ke Karlovu 5, 121 16 Praha 2, Czech Republic.

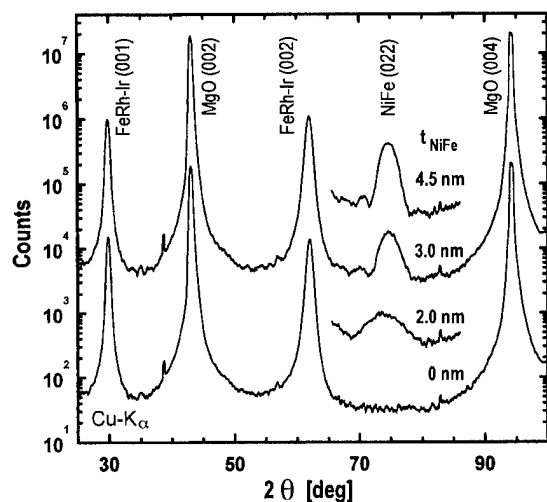


FIG. 1. X-ray diffraction θ - 2θ scans of $\text{NiFe}(t_{\text{NiFe}})/\text{FeRh-Ir}(22 \text{ nm})/\text{MgO}(001)$ samples for $25^\circ \leq 2\theta \leq 100^\circ$. The whole scans are shown for FeRh-Ir buffer without NiFe layer and for $t_{\text{NiFe}}=3 \text{ nm}$. For $t_{\text{NiFe}}=2$ and 4.5 nm , the most important parts of the scan with NiFe(022) diffraction peak are also included.

kept at temperatures up to 200°C . Permalloy was sputtered from an alloy target under $p(\text{Kr}) \sim 8 \times 10^{-3}$ Torr, at a rate of 0.05 nm/s .

X-ray diffraction (XRD) experiments, carried out in a symmetric θ - 2θ scan using $\text{Cu } K\alpha$ radiation, confirmed that the films are epitaxial with the ordered CsCl structure (Fig. 1). No peaks of the fcc disordered phase were detected. The average interplanar spacing agrees reasonably with the lattice constant $a=0.2985 \text{ nm}$, determined in bulk $\text{FeRh}_{0.95}\text{Ir}_{0.05}$ alloys.¹³ Only small differences were observed for the films thinner than 20 nm .

Surface morphology was studied by *ex situ* scanning tunneling microscopy (STM) using Nanoscope III equipment (Digital Instruments, Inc.) with a tungsten tip. These observations revealed that the FeRh-Ir surface consists of atomically flat (001) terraces of 100 nm average lateral size (Fig. 2). The terraces are separated by steps with a minimum height of approximately 0.3 nm , corresponding to the lattice parameter a of the CsCl structure, which indicates a layer-

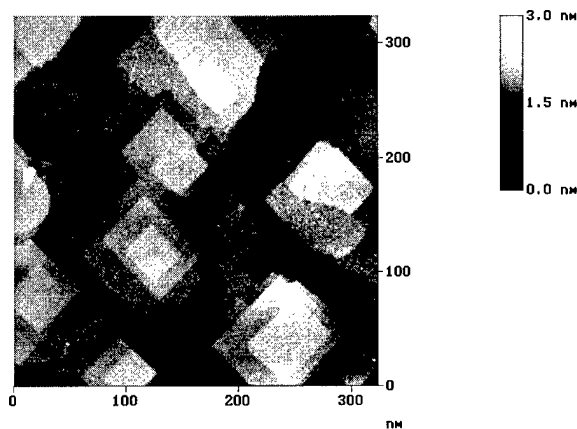


FIG. 2. Typical STM image of $324 \times 324 \text{ nm}^2$ surface of 200-nm -thick FeRh-Ir ordered alloy film on $\text{MgO}(001)$ substrate. The edges of the picture are parallel with $\text{MgO}[100]$ and $\text{MgO}[010]$ directions.

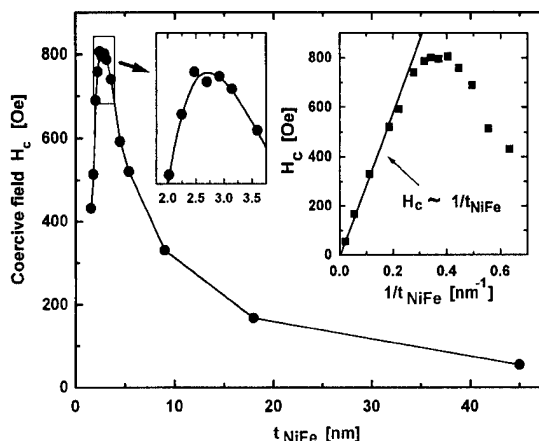


FIG. 3. Coercive field H_c in $\text{NiFe}(t_{\text{NiFe}})/\text{FeRh-Ir}(22 \text{ nm})/\text{MgO}(001)$ structure as a function of t_{NiFe} . The most interesting region, where H_c reaches its maximum, is magnified in the left inset. To justify the $1/t_{\text{NiFe}}$ behavior of H_c for thicker NiFe layers, we plotted H_c against $1/t_{\text{NiFe}}$ in the right inset.

by-layer growth process. The expected crystallographic relation between the alloy film and the MgO substrate is: $\text{FeRh-Ir}(001) \parallel \text{MgO}(001)$ and $\text{FeRh-Ir}[100] \parallel \text{MgO}[110]$, which means, that FeRh-Ir(001) layer grows epitaxially on MgO(001) with the unit cell rotated by 45° in the plane of the sample. Thus, the STM observations reveal, that the steps separating the FeRh-Ir terraces are parallel with FeRh-Ir $[100]$ and $[010]$ directions (Fig. 2).

XRD measurements showed that $\text{NiFe}(011)$ grows epitaxially on FeRh-Ir(001) plane (Fig. 1). The corresponding NiFe(022) XRD peak was observable for $t(\text{NiFe}) > 1.6 \text{ nm}$.

III. MAGNETIC PROPERTIES

Magnetic properties of FeRh-Ir and NiFe/FeRh-Ir systems were studied using a vibrating sample magnetometer, at temperatures ranging from 300 to 600 K . All measurements were performed with an in-plane geometry ($\mathbf{H} \parallel \text{MgO}[100]$, $\text{FeRh-Ir}[110]$).

At room temperature, we observed no appreciable FM behavior of the FeRh-Ir films. The AF-FM transition occurs in the temperature range from 400 to 500 K .¹² The magnetization change with temperature¹² is not steplike, typical for bulk alloys,^{11,14} however, it is much steeper than those reported earlier for FeRh films by other authors.⁷⁻⁹ This is true even for very thin (15 nm) FeRh-Ir layers.

Hysteresis loops of $\text{NiFe}(110)$ films grown on FeRh-Ir exhibit considerably large coercive field H_c . On the other hand, we detected no shift of the loop which is typical for FM layers exchange coupled with Mn-based antiferromagnets,¹⁵ even after field cooling from 600 K under $H=20 \text{ kOe}$. At a fixed NiFe thickness, the coercivity H_c is nearly constant for FeRh-Ir thicknesses $t_{\text{FeRh-Ir}} > 18 \text{ nm}$. Below this value, H_c is approximately proportional to $t_{\text{FeRh-Ir}}$. Results of STM observations show that this behavior is most probably related to the morphology changes (decrease of the terrace size and appearance of holes in the film) in the low FeRh-Ir thickness limit of continuous FeRh-Ir layer. Thus, for the following studies we have chosen

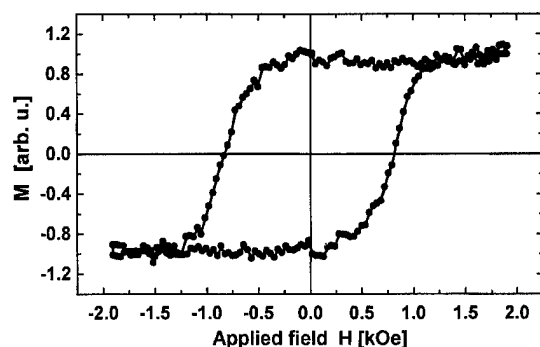


FIG. 4. Room temperature hysteresis loop in the NiFe(2.5 nm)/FeRh-Ir(22 nm)/MgO(001) structure.

$t_{\text{FeRh-Ir}}=22$ nm, which may be the optimum thickness for applications of these antiferromagnetic layers in spin valves.

We also studied the effect of permalloy layer thickness on H_c (Fig. 3). For ultrathin NiFe layers, H_c increases with t_{NiFe} and reaches a maximum of about 810 Oe at $t_{\text{NiFe}}=2.7$ nm. At and above this thickness, the NiFe layers exhibit square hysteresis loop (Fig. 4). For larger NiFe thicknesses, H_c decreases, obeying approximately the $H_c \sim 1/t_{\text{NiFe}}$ law (see inset of Fig. 3). Such a variation with t_{NiFe} suggests that the origin of the large coercive field occurs at the NiFe/FeRh-Ir interface. This explanation is also supported by the fact that samples with better FeRh-Ir surface morphology show larger H_c .

IV. CONCLUSIONS

We have prepared single crystal $\text{FeRh}_{0.95}\text{Ir}_{0.05}$ ordered alloy films with CsCl (B2) structure. $\text{Ni}_{0.81}\text{Fe}_{0.19}(011)$ layers were deposited on the atomically flat FeRh-Ir terraces. In-plane magnetization loops exhibit large coercive fields, H_c , which reached a maximum of 810 Oe for $t_{\text{FeRh-Ir}}=22$ nm and $t_{\text{NiFe}}=2.7$ nm. The observed H_c dependence on $(1/t_{\text{NiFe}})$ at

larger NiFe thickness suggests that those considerably large coercive fields originate from a magnetic interaction at NiFe/FeRh-Ir interface. The large H_c could be used as a pinning force in a spin valve structure. To understand the mechanism of the interface interaction and the effect of morphology on magnetic properties of these structures, further research is in progress.

ACKNOWLEDGMENTS

This study was supported by the Original Industrial Technology R&D Promotion Program from New Energy and Industrial Development Organization (NEDO) of Japan. One of the authors (M.N.) would like to express his thanks to the Electrotechnical Laboratory in Tsukuba for its kind hospitality during his stay and to NEDO for the opportunity to participate in this research.

- ¹M. Fallot and R. Hocart, *Rev. Sci.* **77**, 498 (1939).
- ²F. DeBergerin and L. Muldower, *C. R. Acad. Sci. (Paris)* **252**, 1347 (1961).
- ³G. Shirane, R. Nathans, and C. W. Chen, *Phys. Rev.* **134**, A1547 (1964).
- ⁴V. L. Morruzi and P. M. Marcus, *Phys. Rev. B* **46**, 2864 (1992).
- ⁵A. Szajek and J. A. Morkowski, *Physica B* **193**, 81 (1994).
- ⁶G. Shirane, C. W. Chen, P. A. Flinn, and R. Nathans, *Phys. Rev.* **131**, 183 (1963).
- ⁷J. M. Lommel, *J. Appl. Phys.* **37**, 1483 (1966).
- ⁸Y. Ohtani and I. Hatakeyama, *J. Appl. Phys.* **74**, 3328 (1993).
- ⁹Y. Ohtani and I. Hatakeyama, *J. Magn. Magn. Mater.* **131**, 339 (1994).
- ¹⁰J. van Driel, R. Coehoorn, F. R. de Boer, and G. Strijkers, paper C2-64 at International Conference on Magnetism 1997, 27.7.-1.8. 1997, Cairns, Australia (unpublished).
- ¹¹J. S. Kouvel, *J. Appl. Phys.* **37**, 1257 (1966).
- ¹²S. Yuasa, T. Katayama, K. Murata, M. Usukura, and Y. Suzuki, *J. Magn. Magn. Mater.* (to be published).
- ¹³S. Yuasa, Y. Otani, H. Miyajima, and A. Sakuma, *J. Magn. Soc. Jpn.* (in Japanese) **18**, 235 (1994); *IEEE Transl. J. Magn. Jpn.* **9**, 202 (1994).
- ¹⁴S. Yuasa, T. Akiyama, H. Miyajima, and Y. Otani, *J. Phys. Soc. Jpn.* **64**, 3978 (1995).
- ¹⁵see for example: B. Dieny, *J. Magn. Magn. Mater.* **136**, 335 (1994); J. C. S. Kools, *IEEE Trans. Magn.* **32**, 3165 (1996), and references therein.

Exchange anisotropy in $\text{Ni}_{82}\text{Fe}_{18}\text{O}\{100\}/\text{Ni}_{80}\text{Fe}_{20}$ bilayers

Chih-Huang Lai^{a)}

Read-Rite Corporation, 44100 Osgood Road, Fremont, California 94539

Robert L. White and Connie P. Wang

Department of Materials Science and Engineering, Stanford University, Stanford, California 94305

Thomas C. Anthony

Hewlett Packard Research Laboratories, 1501 Page Mill Road, Palo Alto, California 94304

$\text{Ni}_{0.82}\text{Fe}_{0.18}\text{O}\{100\}$ epitaxial films, ranging in thickness from 70 to 1200 Å, were grown by solid-source metal-organic chemical vapor deposition. The exchange field for 45 Å $\text{Ni}_{80}\text{Fe}_{20}$ on $\text{Ni}_{0.82}\text{Fe}_{0.18}\text{O}$ films reached 250 Oe at 200 Å $\text{Ni}_{0.82}\text{Fe}_{0.18}\text{O}$ and then stayed almost constant with increasing thickness of $\text{Ni}_{0.82}\text{Fe}_{0.18}\text{O}$. Furthermore, the coercivity for those films is only 55 Oe. The high exchange field and the low coercivity are attributable to the high in-plane anisotropy of $\text{Ni}_{0.82}\text{Fe}_{0.18}\text{O}\{100\}$ and the uncompensated spins in the interface of $\text{Ni}_{0.82}\text{Fe}_{0.18}\text{O}/\text{Ni}_{80}\text{Fe}_{20}$. The blocking temperature of these films is 180 °C, lower than that of $\text{NiO}/\text{Ni}_{80}\text{Fe}_{20}$ (~220 °C). The reduction of the blocking temperature may result from local Fe–O–Fe or Fe–O–Ni bonding, which loses the superexchange interaction at a lower temperature than the blocking temperature of NiO .

© 1998 American Institute of Physics. [S0021-8979(98)37211-4]

I. INTRODUCTION

The anisotropic exchange interaction between NiO and $\text{Ni}_{80}\text{Fe}_{20}$ has been extensively studied.^{1–3} Although NiO has shown potential as a biasing material, the low anisotropy of NiO , resulting in a relatively low exchange field (H_e) and a high coercivity (H_c) of $\text{NiO}/\text{Ni}_{80}\text{Fe}_{20}$ systems,² limits its use as a biasing layer in spin valves.³ To increase exchange fields, previous attempts were made to change the anisotropy of NiO by doping with cobalt (Co^{+2})¹ and strontium (Sr^{+2}).² In recent work,⁴ we demonstrated the growth of $\{111\}$ epitaxial and polycrystalline Fe-doped NiO by solid-source metal-organic chemical vapor deposition (MOCVD), and showed enhancement of H_e for the Fe content up to 18 at. %. Because the spin-compensated nature of $\text{NiO}\{100\}$ planes⁵ contrasts with the spin-uncompensated nature of $\{111\}$ planes, it would be interesting to examine the effect of Fe doping on the epitaxial $\text{NiO}\{100\}$ films. Because 18 at. % Fe doping showed maximum H_e in polycrystalline and $\{111\}$ Fe-doped NiO systems, we have deposited 18% Fe-doped $\text{NiO}\{100\}$ films of various thicknesses on $\text{MgO}\{100\}$, and report here the variation of the exchange field and the coercivity with the oxide thickness for the $\text{Ni}_{0.82}\text{Fe}_{0.18}\text{O}\{100\}/\text{Ni}_{80}\text{Fe}_{20}$ system.

II. EXPERIMENTAL PROCEDURES

Fe-doped NiO films ranging in thickness from 70 to 1200 Å were grown on $1\text{ cm} \times 1\text{ cm} \times 0.5\text{ mm}$ $\text{MgO}\{100\}$ substrates, using a solid-source MOCVD technique at a growth temperature of about 510 °C. The Fe content, fixed at 18 at. %, was controlled by the mixing ratio of solid-source $\text{Fe}(\text{TMHD})_3$ to $\text{Ni}(\text{TMHD})_2$ (TMHD: tetra-methyl-heptanedionate). $\text{Ni}_{80}\text{Fe}_{20}$ films 45 Å thick were deposited on the Fe-doped NiO films by dc magnetron sputtering in the pres-

ence of a magnetic field of 70 Oe. The surface of the oxide film was cleaned by ion beam bombardment before the deposition of $\text{Ni}_{80}\text{Fe}_{20}$, and 50 Å of Ta was used as a capping layer. The $\text{Ni}_{80}\text{Fe}_{20}$ and Ta films were deposited at room temperature. The microstructure and phases were identified by transmission electron microscopy (TEM). Since the anisotropic exchange is quite surface sensitive, we took the reflection high energy electron diffraction (RHEED) patterns on the oxide surface to examine the surface symmetry. Electron probe microanalysis (EPMA) was used to determine the average chemical compositions and the thicknesses of the films. The distribution of Fe dopants was measured by energy dispersive x-ray spectroscopy (EDX) attached to TEM. The valence states of Fe and Ni were determined by x-ray photoelectron spectroscopy (XPS). The surface roughness was estimated by atomic force microscopy (AFM). The hysteresis loops were taken using the magneto-optical Kerr effect (MOKE), and the exchange field was determined by the shift of the loops. High-temperature hysteresis loops were measured under pressures less than 2×10^{-6} Torr.

III. RESULTS

The atomic ratio of $\text{Fe}/(\text{Fe}+\text{Ni})$ was 18% measured with EPMA. In addition, the XPS chemical shifts of $\text{Ni}_{0.82}\text{Fe}_{0.18}\text{O}$ showed that the dominant valence state of Fe and Ni was +2. Figure 1 shows the high resolution cross-sectional TEM images of the sample $\text{MgO}\{100\}/950\text{ Å}\text{ Ni}_{0.82}\text{Fe}_{0.18}\text{O}/45\text{ Å}\text{ Ni}_{80}\text{Fe}_{20}/50\text{ Å}\text{ Ta}$. The continuous lattice fringes from MgO to $\text{Ni}_{0.82}\text{Fe}_{0.18}\text{O}$ indicated a high-quality epitaxial growth of $\text{Ni}_{0.82}\text{Fe}_{0.18}\text{O}\{100\}$ on $\text{MgO}\{100\}$. In addition, no extra spots found in the diffraction pattern indicated that no second phases formed, and that the majority of Fe dopants dissolved into the NiO matrix. From the line scan of EDX, we found the Fe dopants uniformly distributed into NiO matrix. The RHEED patterns of the $\text{Ni}_{0.82}\text{Fe}_{0.18}\text{O}$ surface consist of Kiku-

^{a)}Electronic mail: chih.lai@readrite.com



FIG. 1. The high resolution cross-sectional TEM image of MgO {100}/950 Å $\text{Ni}_{0.82}\text{Fe}_{0.18}\text{O}$ /45 Å $\text{Ni}_{80}\text{Fe}_{20}$ /50 Å Ta. The bottom-left corner is the lattice image of the interface between MgO {100} and $\text{Ni}_{0.82}\text{Fe}_{0.18}\text{O}$.

chi lines and intensity-modulated diffraction streaks, indicating that the $\text{Ni}_{0.82}\text{Fe}_{0.18}\text{O}$ film is single crystalline, however, not perfectly smooth. Thus, transmission-type diffraction patterns modulate the streaks and reveal the surface symmetry: fourfold and {100} aligned. The root-mean-square (rms) roughness on the surface of 450 Å $\text{Ni}_{0.82}\text{Fe}_{0.18}\text{O}$ was 8.5 Å, measured with AFM.

The hysteresis loop of 45 Å $\text{Ni}_{80}\text{Fe}_{20}$ on 450 Å $\text{Ni}_{0.82}\text{Fe}_{0.18}\text{O}$ {001} along the easy axis is shown in Fig. 2. The H_e and H_c are 255 and 55 Oe, respectively. Comparing with $\text{Ni}_{80}\text{Fe}_{20}$ on epitaxial MOCVD NiO {001},⁶ whose H_e and H_c are 40 and 250 Oe, 18% Fe doping in NiO {001} increases H_e as much as 6 times! This high ratio of H_e/H_c and high H_e are also different from the results reported in the pure polycrystalline NiO system,^{1,7} which typically has a H_e/H_c ratio of less than 2, and H_e smaller than 220 Oe. The interfacial coupling energy $K_e = H_e \times M_s \times t_f$ (M_s and t_f are the saturation magnetization and the thickness of $\text{Ni}_{80}\text{Fe}_{20}$, respectively) is ~ 0.09 erg/cm².

Figure 3 shows the changes in H_e and H_c (measured along the easy axis) of 45 Å $\text{Ni}_{80}\text{Fe}_{20}$ on $\text{Ni}_{0.82}\text{Fe}_{0.18}\text{O}$ {001} films as the thickness varies from 70 to 1200 Å. H_e appeared at oxide thickness $t_{af} = 140$ Å, reached to 250 Oe at $t_{af} = 200$ Å, and then H_e remained almost constant

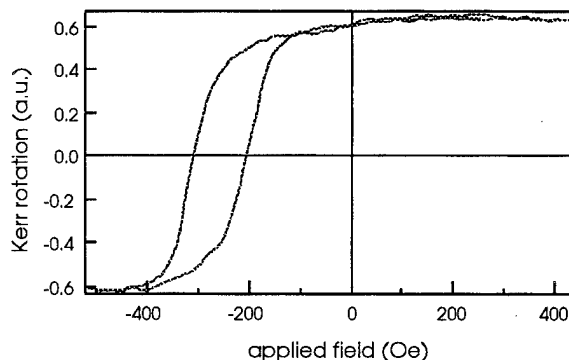


FIG. 2. Hysteresis loop of 45 Å $\text{Ni}_{80}\text{Fe}_{20}$ on 450 Å $\text{Ni}_{0.82}\text{Fe}_{0.18}\text{O}$ {001}. The field was applied along the easy axis.

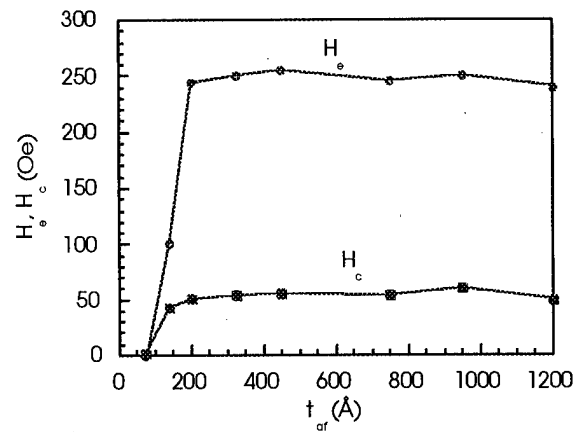


FIG. 3. AF thickness dependence (t_{af}) of the exchange field (H_e) and the coercivity (H_c) for 45 Å $\text{Ni}_{80}\text{Fe}_{20}$ on 450 Å $\text{Ni}_{0.82}\text{Fe}_{0.18}\text{O}$ {001} films.

(~ 250 Oe) with increasing thickness of $\text{Ni}_{0.82}\text{Fe}_{0.18}\text{O}$. The result is in contrast to that in the polycrystalline pure NiO systems,^{3,7} which show that a larger thickness ($t_{af} > 300$ Å) is needed to reach a saturated value of H_e ($H_e < 220$ Oe for 45 Å NiFe).

In spite of the enhancement of the exchange field in 18% Fe-doped {100} films, the blocking temperature T_b —the temperature at which H_e goes to zero—of these epitaxial {100} films was 180 °C, lower than that of pure NiO^{1,3} ($T_b \sim 200$ –220 °C). This result is similar to those of 18% Fe-doped polycrystalline and epitaxial {111} NiO films.⁴ The temperature dependence of H_e for 45 Å $\text{Ni}_{80}\text{Fe}_{20}$ on 450 Å $\text{Ni}_{0.82}\text{Fe}_{0.18}\text{O}$ {001} film is shown in Fig. 4. Note that the H_e is always larger than H_c until the temperature reaches T_b .

IV. DISCUSSION

At temperatures above $T_N = 523$ K, the Néel temperature of NiO, NiO is paramagnetic and crystal structure is cubic rock salt.⁵ Below T_N , the antiferromagnetic ordering results in a slight rhombohedral deformation of crystal, which consists of a contraction of the original unit cell along one of the {111} axes. The spins of NiO below T_N are arrayed in ferromagnetic sheets which are parallel to {111}, and the direction

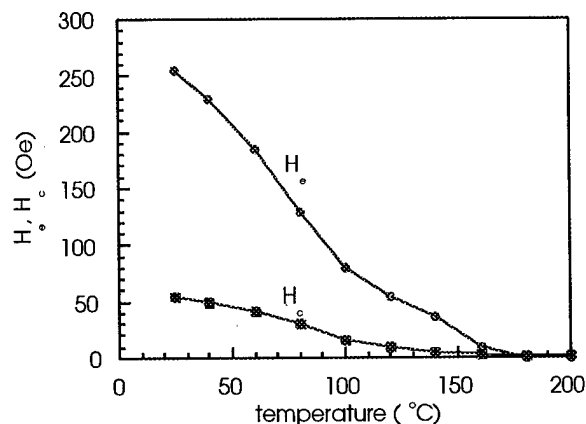


FIG. 4. Temperature dependence of the exchange field (H_e) and the coercivity (H_c) for 45 Å $\text{Ni}_{80}\text{Fe}_{20}$ on 450 Å $\text{Ni}_{0.82}\text{Fe}_{0.18}\text{O}$ {001} films.

of magnetization in neighboring planes is reversed;⁵ therefore, for {100} planes, spin compensation occurs since alternate spins are antiferromagnetically ordered in the planes. Ideally, if the $\text{Ni}_{80}\text{Fe}_{20}$ film coupled to a single-domain NiO {100} with an atomic flat interface, the exchange field should approach to zero. In reality, because of the interface roughness and finite-size multidomains, a nonzero H_e exists,^{2,8} but the value is smaller than that of $\text{Ni}_{80}\text{Fe}_{20}$ on polycrystalline NiO . In contrast to the NiO {100} case, $\text{Ni}_{80}\text{Fe}_{20}$ coupled to $\text{Ni}_{0.82}\text{Fe}_{0.18}\text{O}$ {100} shows high H_e . The surface roughness of MOCVD NiO and $\text{Ni}_{0.82}\text{Fe}_{0.18}\text{O}$ are similar, which eliminates the effect of interface roughness on H_e . From the results of EDX and XPS, we know that the Fe dopants distribute uniformly in the NiO matrix with valence state +2. Roth has done neutron diffraction to determine the magnetic structure of NiO and FeO ,⁵ and showed that the average moments per site of nickel and iron in NiO and FeO are $2\mu_B$ and $3.32\mu_B$, respectively. The uneven moments of Ni and Fe may increase the degree of uncompensation in the interface, which may contribute to the high nonzero value of H_e .

Two requirements are needed for achieving high exchange fields: an uncompensated interfacial spin configuration of an antiferromagnet (AF), and a large anisotropy of the AF to make the spins of the AF remain pinned during the magnetization reversal of ferromagnets. The most obvious way to have an uncompensated interface in NiO is to deposit ferromagnets on NiO {111}. In our previous work,^{4,6} we reported that the $\text{Ni}_{80}\text{Fe}_{20}$ on NiO {111} or on $\text{Ni}_x\text{Fe}_{1-x}\text{O}$ {111} showed large coercivities and relatively low exchange fields. We found that the contraction axis was perpendicular to interfaces,⁹ i.e., all spins lie within {111} planes parallel to the interface. Because in-plane anisotropy within those {111} planes is weak, the exchange field is low. On the other hand, NiO {100} planes have a compensated nature, but {100} planes are 54.7° away from the contraction axis; therefore, the field needed to rotate the spins within {100} planes is higher than that in {111}, resulting in a higher in-plane anisotropy. From the previous discussion, since Fe dopants may increase the degree of uncompensation, $\text{Ni}_{0.82}\text{Fe}_{0.18}\text{O}$ {100} satisfies both requirements for high H_e . Furthermore, FeO is known to have considerably higher magnetic anisotropy than NiO (Ref. 10) because the orbital degeneracy is not completely removed in FeO . The dissolved Fe atoms can participate in local Fe–O bonding and increase the anisotropy of NiO . In addition, high-quality epitaxial NiO films may form large magnetic domains, which may result in small H_e .¹¹ The Fe dopants can introduce stress and defects into NiO matrix and suppress the formation of large domains, and further enhance the H_e .

The high anisotropy of $\text{Ni}_{0.82}\text{Fe}_{0.18}\text{O}$ {100} is also reflected on a small thickness needed for high H_e and on a low coercivity of $\text{Ni}_{0.82}\text{Fe}_{0.18}\text{O}$ {100}/ $\text{Ni}_{80}\text{Fe}_{20}$. As the thickness of

$\text{Ni}_{0.82}\text{Fe}_{0.18}\text{O}$ increases, the volume anisotropy energy of $\text{Ni}_{0.82}\text{Fe}_{0.18}\text{O}$ ($K_{af} \times t_{af} \times \text{area of interface}$, K_{af} = anisotropy energy per unit volume of $\text{Ni}_{0.82}\text{Fe}_{0.18}\text{O}$) increases. The thickness needed for high H_e is the thickness at which the volume anisotropy energy of $\text{Ni}_{0.82}\text{Fe}_{0.18}\text{O}$ is large enough to pin its spins during the field reversal; therefore, larger anisotropy in the oxide (K_{af}) means smaller thickness (t_{af}) needed to reach high H_e . From our previous study,² we found that the main source of coercivity in the $\text{NiO}/\text{Ni}_{80}\text{Fe}_{20}$ system is the irreversible rotation of spins in NiO due to the low anisotropy of NiO . Consequently, when the anisotropy of NiO is increased by Fe doping, the coercivity is significantly reduced.

In spite of the enhancement of H_e , the blocking temperature of $\text{Ni}_{0.82}\text{Fe}_{0.18}\text{O}$ was reduced. This may be due to the local Fe–O–Fe or Fe–O–Ni bonding, which loses the superexchange interaction at a lower temperature than the Ni–O–Ni bonding does. This is consistent with the low Néel temperature (198 K) of FeO .

V. CONCLUSIONS

We have observed a high exchange field (250 Oe) and a low coercivity (55 Oe) for 45 Å $\text{Ni}_{80}\text{Fe}_{20}$ on the $\text{Ni}_{0.82}\text{Fe}_{0.18}\text{O}$ {100} films with thickness larger than 200 Å. The increase of H_e can be attributed to the high in-plane anisotropy of $\text{Ni}_{0.82}\text{Fe}_{0.18}\text{O}$ {100} and the uncompensated spin configuration in the interface due to the Fe doping. The high anisotropy of $\text{Ni}_{0.82}\text{Fe}_{0.18}\text{O}$ also results in a low coercivity and a small thickness needed to reach a high H_e . A reduction of the blocking temperature ($T_b = 180^\circ\text{C}$) of the $\text{Ni}_{0.82}\text{Fe}_{0.18}\text{O}/\text{Ni}_{80}\text{Fe}_{20}$ system possibly relates to the local Fe–O–Fe or Fe–O–Ni bonding, which loses the superexchange interaction at a temperature lower than the blocking temperature of NiO .

ACKNOWLEDGMENT

The authors are grateful to Professor R. S. Feigelson for MOCVD growth.

¹M. J. Carey and A. E. Berkowitz, Appl. Phys. Lett. **60**, 3060 (1992).

²C. H. Lai, H. Matsuyama, R. L. White, T. C. Anthony, and G. G. Bush, J. Appl. Phys. **79**, 6389 (1996).

³T. Lin, C. Tsang, R. E. Fontana, and J. K. Howard, IEEE Trans. Magn. **31**, 2585 (1995).

⁴C. H. Lai, W. E. Bailey, R. L. White, and T. C. Anthony, J. Appl. Phys. **81**, 4990 (1997).

⁵W. L. Roth, Phys. Rev. **110**, 1333 (1958).

⁶C. H. Lai, H. Matsuyama, R. L. White, and T. C. Anthony, IEEE Trans. Magn. **31**, 2609 (1995).

⁷S. Soeya, S. Tadokoro, T. Imagawa, M. Fuyama, and S. Narishige, J. Appl. Phys. **74**, 6297 (1993).

⁸R. P. Michel, A. Chaiken, C. T. Wang, and L. E. Johnson, Phys. Rev. B (to be published).

⁹C. H. Lai, Ph.D. thesis, Stanford University, 1997.

¹⁰J. Kanamori, Prog. Theor. Phys. **17**, 197 (1957).

¹¹A. P. Malozemoff, Phys. Rev. B **35**, 3679 (1987).

Temperature dependence of ferromagnetic resonance as induced by NiO pinning layers

P. Lubitz,^{a)} J. J. Krebs, M. M. Miller, and Shufan Cheng
Naval Research Laboratory, Washington, DC 20375

Ferromagnetic resonance (FMR) experiments have been conducted near 9.5 GHz on permalloy (Py) thin films which are components of spin valves and related structures. These so-called giant magnetoresistance structures often use antiferromagnetic NiO to achieve pinning of one magnetic layer. Magnetic anisotropies acting on these pinned layers were deduced by observing their resonances for fields perpendicular to and in the sample plane. We used data taken from 4 to 600 K to identify potential mechanisms of pinning, anisotropy, and linewidth. The anisotropic exchange pinning and an isotropic downward FMR shift vanish at a blocking temperature well below the bulk Néel temperature of NiO. The strong temperature dependencies of the isotropic shift and linewidth may reflect the presence of different spin pinning subsystems and the different time scales of the FMR and low frequency or static measurements. [S0021-8979(98)30211-X]

INTRODUCTION

Antiferromagnetic (AF) and spin glass systems in intimate contact with thin ferromagnetic films have been shown to produce large shifts in the position of the ferromagnetic resonance lines.¹ The ferromagnet is strongly exchange coupled to an ordered spin system with small net moment, and therefore experiences the constraints responsible for the ordering in that system—in effect, the ferromagnet gives us an external “handle” on the adjacent low moment system. Reported results¹ for FMR on such systems have shown a variety of temperature dependencies of the line shifts (e.g., $\alpha \exp(-T/T_0)$ for spin glasses but with more abrupt onsets for thin NiO and CoO). Also conspicuous is the nearly isotropic nature of the shifts, i.e., all directions appear “easy.” Such shifts apparently are independent not only of orientation but also of measurement frequency.^{1,2}

Using a system in wide use, Py (nominally 80 at. % Ni, 20% Fe) biased by NiO, we have conducted FMR measurements at about 9.5 GHz for temperatures from 4 to 600 K and for a variety of orientations. This system has been studied extensively by mostly static B–H loop, Kerr, and magnetoresistance measurements.³ Predictions of exchange coupling in FM/AF systems have been made⁴ but the results depend strongly on grain size and orientation, surface roughness, and magnetization process.

We determined the isotropic and anisotropic shifts and the linewidths. From their particular temperature dependencies, we make inferences as to the magnetic configurations which may be responsible for the phenomena observed.

EXPERIMENT

Spin valve structures and subcomponents were made by dc magnetron sputtering without cooling, i.e., at slightly above 300 K. For this paper, all Py and Cu layers were nominally 45 Å thick, NiO layers were 1000 Å, and all were polycrystalline. The structures were deposited on polished Si

wafers having a native oxide surface. After deposition of successive layers of Py, Cu, and Py again, in a magnetic field sufficient to align the Py layers, the NiO layer was formed by reactive sputtering of Ni. Separate films of Si/Py/Cu, Si/Cu/Py/NiO, and Si/Cu/Py/Cu were also made. All of these configurations have low roughness metal layers, a few angstroms rms, as determined by atomic force microscope and have low linewidths and coercivities for the unpinned magnetic layers.

FMR data were taken with a Bruker ECS9 system operating at about 9.46 GHz with temperature control provided by N₂ (100–600 K) or He (4–300 K) gas flow systems. Magnetoresistance and vibrating sample magnetometry data were also obtained on the samples at room temperature.

RESULTS

The as-made Py films with NiO overlayers have a static exchange bias field of about 100 Oe. Figure 1 shows in-plane FMR data illustrating several features: (a) low-field structure related to magnetoresistance changes, (b) a broad temperature sensitive absorption line arising from the Py layer adja-

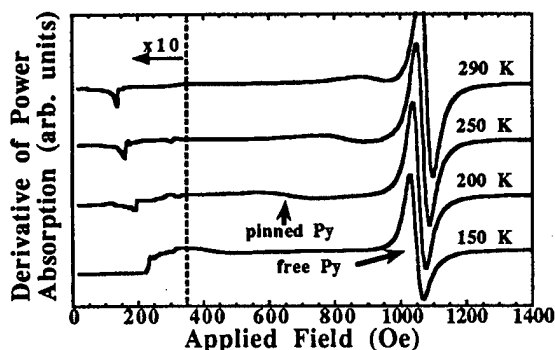


FIG. 1. FMR spectra of a spin valve with the applied field along the hard in-plane direction showing the switching of the pinned Py at low fields, and the pinned and free Py resonances (arrows).

^{a)}Electronic mail: lubitz@anvil.nrl.navy.mil

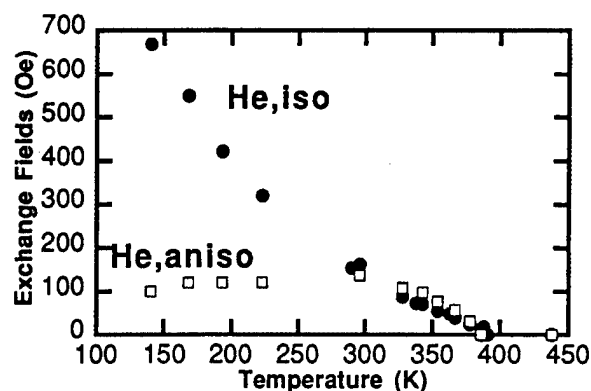


FIG. 2. $H_{e,iso}$ and $H_{e,aniso}$ as functions of temperature as derived from in-plane FMR data.

cent to NiO, and (c) a narrower line with weak angular and temperature dependence arising from the unpinned Py layer. The pinned Py resonance line moves downward rapidly in field position on cooling while the low field structures move upward more slowly, largely because the coercivity of the pinned layer increases.

It is difficult to determine the magnitude of exchange induced shifts absolutely. Films of the same thickness with different interface materials² generally have different moments. We considered use of the pinned line above the T_N of NiO (523 K) as a reference. However, its moment was found to change irreversibly near T_N because of diffusion of Cu into Py above 200 °C. Therefore we discuss only data up to 450 K and arbitrarily assign the position of the resonance at that temperature as a reference, H_{ref} .

We characterize the exchange effects for in-plane data by means of an anisotropic exchange field $H_{e,aniso}$ and an isotropic exchange shift $H_{e,iso}$. For the anisotropic effects, we take $H_{e,aniso} = H_r(\text{hard}) - H_r(\text{easy})$ so a reference is irrelevant. Here $H_r(\text{easy})$ is the resonance field when H is along the exchange bias favored direction established by the field during Py deposition while $H_r(\text{hard})$ is the corresponding field for H rotated by 180°. For the isotropic component, we take $H_{e,iso} = H_{ref} - [H_r(\text{easy}) + H_r(\text{hard})]/2$.

The $H_{e,iso}$ and $H_{e,aniso}$ data calculated in this way are shown in Fig. 2 as derived from in-plane FMR. For temperatures between 350 and 150 K, $H_{e,aniso}$ is essentially constant. At higher temperatures, this anisotropy disappears in a narrow temperature range, at essentially the same temperature at which the B-H loop shift (the usual exchange bias field) goes to zero. Since this is well below the bulk T_N , we ascribe this to the blocking transition as described by Carey *et al.*³ (only for the “as-deposited” condition did their exchange field disappear near 380 K; for samples which contain thin layers of CoO, they were able to increase the blocking temperature to near T_N by field cooling, which we are not able to duplicate).

Below about 150 K and for applied fields in the film plane, the pinned Py FMR lines fall below the field values necessary to saturate the Py (below zero field for the easy direction) and no easily interpreted spectra are seen. By taking data in the perpendicular orientation we were able to follow the increase in field shift down to 4 K. If we account

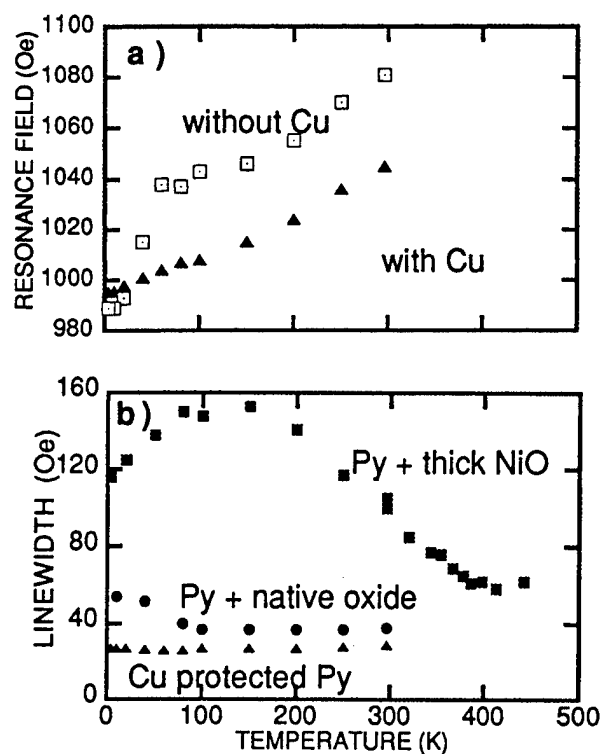


FIG. 3. (a) FMR fields for nominally unpinned Py with and without 45 Å Cu protective layers and (b) effect of Cu protective layers, native oxide, and thick NiO on temperature dependence of FMR linewidths of adjacent Py.

for the temperature dependence of M , the shift tracks that of the in-plane data over the common temperature region. This trend continues even down to 4 K if the sample is not reoriented during the cooling. However, below about 150 K, the spectra become hysteretic and additional lines appear which must be addressed in a later paper.

Near 300 K, linewidths of the pinned Py (Fig. 3) are about 100 Oe for all orientations and show a moderate increase to about 160 Oe near 150 K; for fields perpendicular to the film plane, the lines narrow to near 100 Oe at 4 K, if the sample is not reoriented. To determine what part of these effects is intrinsic to our Py, we also made and measured Py layers with Cu capped and native oxide surfaces. Py layers with native oxide surfaces have widths near 40 Oe at 300 K and these broaden at low temperatures (Patton⁵ reported somewhat similar results for oxidized Py). Cu protected Py has linewidths less than 30 Oe which narrow slightly with cooling.

In measuring nominally unpinned reference Py samples, we have found that they also generally show small isotropic (only downward) shifts, but these are significant only for temperatures below 50 K, see Fig. 3. The shift shows no freezing-in (i.e., it is the same after rotating 180° even at 4 K) and increases with decreasing temperature even near 4 K; the size of the shift varies inversely with Py thickness. These shifts bear a strong resemblance to those observed by Takano *et al.*⁴ We found that Py films having either a native oxide layer or deposited on the native oxide of Si have comparable shifts but Py films which have Cu on both surfaces show a much reduced effect.

DISCUSSION AND CONCLUSIONS

The temperature dependence of the Py FMR line shifts associated with NiO adjacent layers reveal a variety of distinctive phenomena. First, nominally static exchange fields $H_{e,\text{aniso}}$, which act like unidirectional fields and have the same magnitude as the exchange shifts of hysteresis loops³ (also reported² in FMR near room temperature), are clearly present. These have only a weak temperature dependence up to near the blocking temperature which in our samples is generally about 380 K (well below T_N), above which they become negligible. The linewidth decreases moderately with increasing temperature until above the blocking temperature, perhaps indicating that the mechanism responsible for the anisotropic shifts has spatial variations which broaden the line. In order to not be narrowed by the exchange interaction in the Py layer, these variations must have a scale of at least a few hundred angstroms, i.e., a Py "wall" width, $W = \sqrt{A/\Delta H_k M}$, where ΔH_k is a spatial variation of the exchange anisotropy, presumed to be about 100 Oe. The remaining width relative to unpinned Py may be related to the variable oxidation states of the surface species, which can allow additional relaxation mechanisms, especially since Fe is present.⁵ Note that the presence of even a thin native oxide on Py adds a significant width. (Our earlier work¹ showed that thin Cu or Ni surface layers on Fe polycrystalline films reduced the linewidths to the lowest values reported for metal films, 15 Oe., implicating the role of iron oxides in this line broadening.)

The origin of the isotropic and strongly temperature dependent fields $H_{e,\text{iso}}$ sensed by the FMR from about 150 K (and possibly much lower) up to the vicinity of T_N is much less certain. Earlier reports of isotropic shifts considered a spin-glass phase as the probable source.¹ It is tempting to postulate additional spin systems, e.g., small grain regions in the NiO at the interface with Py. Indeed, Chopra,⁶ using TEM, observed a fraction of small surface grains in his NiO biased spin valves. This conjecture is supported further by the absence of strong line broadening as $H_{e,\text{iso}}$ increases, implying that the mechanism arises from parts of the NiO with less than about 100 Å lateral extent.

The isotropic shifts indicate spin subsystems which can follow the external field rather than being frozen into the sample. One such shift [Fig. 3(a)], seen at low temperatures in nominally unpinned Py, can be attributed to a surface-oxide spin system since Cu capping eliminates it; this shift has the same temperature dependence and magnitude as a surface induced field reported by Takano *et al.*⁴ for CoO.

That effect has a frozen-in or remanent aspect which is much reduced for small applied fields. Since that field was not strongly frozen-in, even for CoO which has very strong single ion anisotropy, it is not surprising that our native oxide layers, which we presume to be mainly NiO with a much smaller local anisotropy, lack any memory at 4 K. The broadening accompanying this shift is likely to represent a true magnetic relaxation rather than a large scale inhomogeneity.⁵

Neél's analysis⁷ of the time dependence of the response of small magnetic particles predicts a response time $\tau = \tau_0 \exp(E/kT)$ where E is an energy barrier (e.g., magnetic anisotropy $K \times \text{volume}$) and τ_0 is a characteristic precession time (low microwave frequency). Hence, for small AF grains, the magnetic configuration can change rapidly for temperatures above E/k , but the configuration cannot evolve as fast as our microwave frequency. Thus, in the FMR experiment, the exchange anisotropy sensed, and thus the resonance field, are determined by a local energy minimum which appears static, but which easily follows reorientations of the Py moment and therefore does not appear as an anisotropic bias field. On cooling, a larger fraction of grains becomes aligned relative to the Py at any instant, giving a larger shift.

Much stronger exchange fields are sensed in FMR at low temperatures than are indicated by static experiments. Identification of a spin subsystem responsible for the large isotropic shifts will require more detailed analysis of the microstructure. Our data place strong constraints on the lateral size of the features, which impact the linewidth, on their anisotropy energy and volume, which determine freezing temperatures, and on the fraction of surface spins involved, which determines the size of the line shifts.⁴

¹P. Lubitz, M. Rubinstein, D. B. Chrisey, J. S. Horwitz, and P. R. Broussard, *J. Appl. Phys.* **75**, 5595 (1994); M. Rubinstein, P. Lubitz, W. E. Carlos, P. R. Broussard, D. B. Chrisey, J. Horwitz, and J. J. Krebs, *Phys. Rev. B* **47**, 15350 (1993); M. J. Park, S. M. Bhagat, M. A. Manheimer, and K. Moorjani, *J. Magn. Magn. Mater.* **54–57**, 109 (1986).

²R. D. McMichael, P. J. Chen, and W. F. Egelhoff (unpublished).

³M. J. Carey and A. E. Berkowitz, *J. Appl. Phys.* **73**, 6892 (1993).

⁴A. P. Malozemoff, *Phys. Rev. B* **35**, 3679 (1987); N. C. Koon, *Phys. Rev. Lett.* **78**, 4865 (1997); K. Takano, R. H. Kodama, A. E. Berkowitz, W. Cao, and G. Thomas, *Phys. Rev. Lett.* **79**, 1130 (1997).

⁵C. E. Patton, *J. Appl. Phys.* **39**, 3060 (1968).

⁶H. D. Chopra, B. J. Hockey, P. J. Chen, W. F. Egelhoff, Jr., M. Wuttig, and S. Z. Hua, *Phys. Rev. B* **55**, 8390 (1997).

⁷L. Neél, *Ann. Geophys. (C.N.R.S.)* **5**, 99 (1949); Y. Park, S. Adenwalla, G. P. Felcher, and S. D. Bader, *Phys. Rev. B* **52**, 12799 (1995).

Dependence of exchange coupling on antiferromagnetic layer thickness in NiFe/CoO bilayers

T. Ambrose^{a)} and C. L. Chien

Department of Physics and Astronomy, The Johns Hopkins University, Baltimore, Maryland 21218

A systematic study of the dependence of exchange coupling in NiFe/CoO bilayers on CoO layer thickness t_{AF} from 5 to 500 Å has been made. For large CoO thicknesses ($t_{AF} > 100$ Å), the exchange field varies as $1/t_{AF}$, whereas for small CoO thicknesses ($t_{AF} < 100$ Å), finite-size scaling of the Néel temperature T_N and also the blocking temperature T_B dominate. © 1998 American Institute of Physics. [S0021-8979(98)52811-3]

The exchange coupling between a ferromagnet (FM) and an antiferromagnet (AF) displays a rich variety of phenomena.¹ When a FM/AF bilayer thin film is field cooled across the AF Néel temperature (T_N), the hysteresis loop of the FM is now shifted or biased away from the origin. This shift, known as the exchange field (H_E), can be several hundreds Oe in size. The AF must possess sufficient anisotropy to withstand switching of the FM magnetization. The exchange field decreases with temperature and vanishes at a temperature termed the blocking temperature T_B , which is less than T_N of the AF layer. The anisotropy of the AF must decrease to zero at T_N . Near and below T_N , the anisotropy of the AF eventually becomes too weak to maintain its spin structure during the hysteresis cycle resulting in no exchange field.

Exchange biasing is important for applications in the spin-valve devices,² although the origin of this coupling remains unclear. Some of the important questions concerning exchange biasing include the relative spin orientation of the FM and AF layers, and the interaction between them. It has been well established that H_E varies inversely with the FM layer thickness.^{3,4} This demonstrates that the exchange coupling is transmitted across the FM/AF interface. It has been widely assumed that this exchange coupling is a short-range interaction occurring only at the interface, although some new results suggest otherwise.⁵ In this work, we address the dependence of exchange bias on the AF layer thickness.

There have been previous studies on the effect of the AF layer thickness on the exchange coupling strength in NiFe/FeMn^{6,7} in NiFe/NiO⁸ and in CoO/NiFe⁹ bilayers. In these works, both the exchange fields and blocking temperatures were observed to correlate with the AF layer thickness in some manner. Unfortunately, most of these measurements were not made at sufficiently low temperature to conclusively determine the dependence on the AF layer thickness. Recently, a study of the AF layer thickness dependence on H_E was made in Fe₃O₄/CoO bilayers,¹⁰ where the exchange field was measured to low temperatures. With the few samples, the values of H_E and the blocking temperature were observed to scale with the CoO thickness, but a clear relationship between the exchange field and the AF layer thickness was not determined.

In this work, we have determined the relationship between the AF layer thickness and the exchange bias using NiFe/CoO bilayers with a fixed NiFe layer and various CoO thicknesses from 5 to 500 Å. There are two qualitatively different behaviors of the dependence on the AF layer thickness t_{AF} . For $t_{AF} > 100$ Å, where T_N remains unchanged, H_E is found to vary as $1/t_{AF}$. For $t_{AF} < 100$ Å, the effect is due to finite-size scaling of T_N of very thin layers, and the results are in good agreement with the susceptibility measurements using CoO/SiO₂ multilayers.¹¹

To examine the AF layer thickness dependence on the exchange field, the NiFe/CoO system was chosen, involving a well-known AF insulator CoO with $T_N = 292$ K and permalloy (NiFe = Ni₈₁Fe₁₉) useful for many device applications. To carefully examine the AF layer thickness dependence, the bilayers in this study were taken from one large sample of a 300 Å film of NiFe grown on a wedge layer (5–500 Å) of CoO, which was grown on 300 Å Cu. The CoO wedge film allows many samples that were fabricated at the same time and under the same deposition conditions with CoO thickness being the only parameter. The NiFe was deposited in a magnetic field to induce an uniaxial anisotropy. We used the geometry of FM layer grown on top of the AF layer, so that the exchange field would saturate at low temperatures to reveal its dependence on the AF layer thickness.¹²

In Fig. 1(a), the temperature dependence of the exchange field of some representative samples with varying CoO layer thickness from 75 to 457 Å are shown. As expected, a plateau in the exchange field is observed at low temperatures whose value is intrinsic, for this bilayer geometry, to a specific AF layer thickness. The results for $t_{AF} > 100$ Å clearly show an increase in the exchange field as the CoO thickness is reduced. The values of H_E vanish essentially at 291 K, the Néel temperature of bulk CoO. As shown in Fig. 1(b), the coercivity (H_C) has a quasilinear temperature dependence, decreasing to the intrinsic H_C of permalloy at approximately 291 K. The exchange fields at low temperatures, represented by the values at 80 K are shown as a function of the CoO layer thickness in Fig. 2. The results can be best described by $1/t_{AF}$ shown as the dashed curve. It should be noted that this relation holds only at low temperature where H_E is not temperature dependent. At a high temperature, where H_E has a strong temperature dependence, the H_E values do not give

^{a)}Electronic mail: ambrose@jhvmvs.hcf.edu

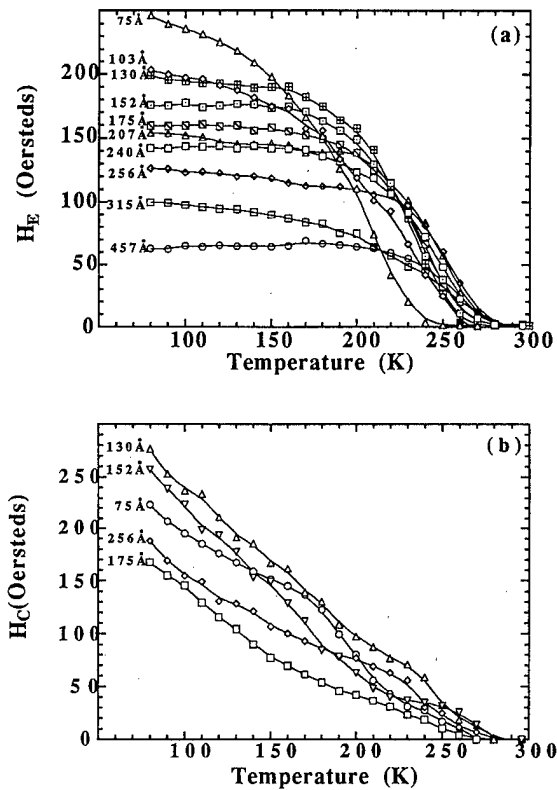


FIG. 1. Temperature dependence of (a) exchange field H_E and (b) coercivity H_C of representative samples of 300 Å NiFe/ x Å CoO/300 Å Cu with CoO thickness from 75 to 457 Å.

meaningful thickness dependence. For example, if one uses the exchange field values at 250 K, one would give a totally different thickness dependence from that at 80 K, as shown in Fig. 2. These results clearly demonstrate the dependence of exchange coupling on t_{AF} in the thickness range of $t_{AF} > 100$ Å, where T_N remains unchanged.

The results in Fig. 2 are rather unexpected and significant because it illustrates that the exchange coupling in a FM/AF bilayer involves more than just the interfacial spins in the FM and AF layers. To elaborate the argument, consider the ideal interface model as originally suggested by

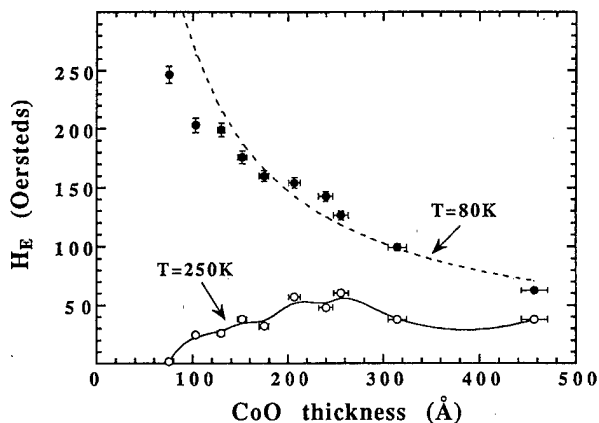


FIG. 2. The values of exchange field H_E measured at 80 and 250 K for 300 Å NiFe/ x Å CoO/300 Å Cu as a function of the CoO layer thickness. The dashed line for the data at 80 K is $1/t_{AF}$.

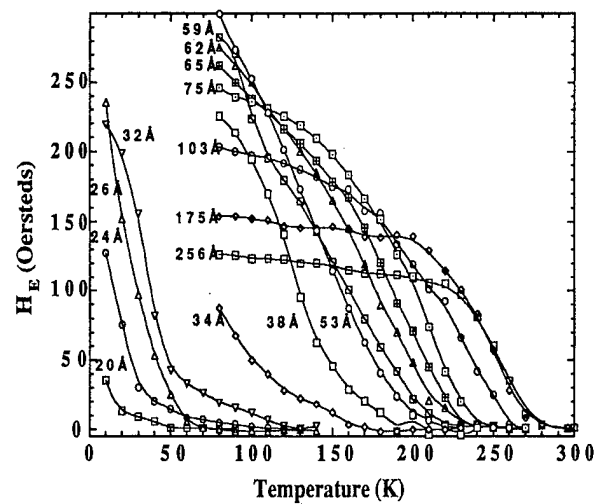


FIG. 3. Temperature dependence of exchange field H_E of 300 Å NiFe/ x Å CoO/300 Å Cu with CoO thickness from 20 to 256 Å.

Meiklejohn and Bean,¹ where the exchange coupling between neighboring spins at the FM/AF interface produces an exchange field of the form

$$H_E = \frac{nJS_{AF} \cdot S_{FM}}{M_{FM}t_{FM}}, \quad (1)$$

where S_{FM} and S_{AF} are the spins of the magnetic moments in the FM and AF layers at the interface, M_{FM} and t_{FM} are the magnetization and layer thickness of the FM, respectively, J is the spin-spin interaction strength between S_{FM} and S_{AF} and n is the number of interactions per unit area with strength J . Since only the interfacial FM and AF spins are assumed to be involved, the thickness of the AF layer does not appear at all. The very fact that H_E has a $1/t_{AF}$ dependence indicates that this simple model and Eq. (1) require modifications. The spin structure and the domain walls of the AF layer ultimately influence the exchange field as suggested by the recent micromagnetics calculations by Malozemoff,¹³ Mauri,¹⁴ and Koon.¹⁵

In Fig. 2, the values of H_E for AF layers smaller than 100 Å have not been included because these results are qualitatively different from those of the thicker layers, and also that their H_E values do not saturate at 80 K. These features are illustrated in Fig. 3 for CoO thicknesses spanning from 10 to 256 Å. While the blocking temperature T_B of samples with $t_{AF} > 100$ Å remains at the bulk value, T_B of the thinner samples progressively decreases with t_{AF} . As the layer thickness is reduced below 100 Å, one observes finite-size effects of T_N ,^{10,11} which is followed by T_B . It is interesting to compare the finite-size effects of T_B measured from exchange bias in NiFe/CoO bilayers, and the finite-size effects of T_N measured from dc susceptibility measurements using CoO/SiO₂ multilayers. In Fig. 4 the blocking temperatures T_B (solid squares) obtained from the exchange field temperature dependence in Fig. 3 are compared with the Néel temperatures T_N measured by susceptibility in CoO/SiO₂ multilayers.¹¹ Both sets of data are in excellent agreement. At each thickness, the blocking temperature T_B is slightly

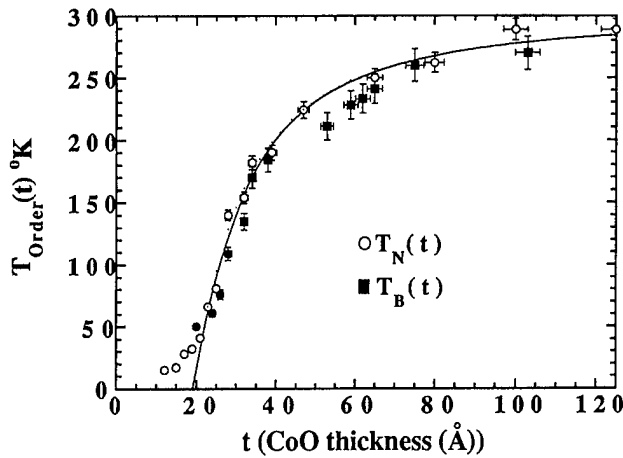


FIG. 4. Blocking temperature T_B (solid squares) of 300 Å NiFe/ x Å CoO/300 Å Cu and Néel temperature T_N (open circles) of CoO/SiO₂ multilayers, as a function of the CoO layer thickness. The solid line is the finite-size scaling relation taken from Ref. 11.

below T_N . This comparison also shows that the dependence of exchange bias in the thickness range of $t_{AF} < 100$ Å is largely effected by finite-size scaling of the AF Néel temperature.

To summarize, we have observed dependence of exchange bias on the antiferromagnetic layer thickness t_{AF} . For small values of t_{AF} (< 100 Å), this is mainly caused by the finite-size scaling of T_N , whose value always lies slightly higher than that of the blocking temperature T_B . For larger values of t_{AF} (> 100 Å), the exchange field has been

shown to scale inversely with t_{AF} . This suggests that the simple picture of interfacial coupling between the FM and AF spins be modified to include the spin structure and the domain structure within the AF layer.

This work has been supported under NSF MRSEC Program No. 96-32526 and Grant No. DMR-96-32526.

¹W. K. Meiklejohn and C. P. Bean, Phys. Rev. **102**, 1413 (1956).

²B. Dieny, V. S. Speriosu, S. S. P. Parkin, B. A. Gurney, D. R. Wilhoit, and D. Mauri, Phys. Rev. B **43**, 1297 (1991).

³C. Tsang, N. Heiman, and K. Lee, J. Appl. Phys. **52**, 2471 (1981).

⁴R. Jungblut, R. Coehoorn, M. T. Johnson, Ch. Sauer, P. J. van der Zaag, A. R. Ball, Th. G. S. M. Rijks, J. aan de Stegge, and A. Reinders, J. Magn. Mater. **148**, 300 (1995).

⁵N. Gokemeijer, T. Ambrose, and C. L. Chien, Phys. Rev. Lett. **79**, 4270 (1997).

⁶R. Jungblut, R. Coehoorn, M. T. Johnson, J. aan de Stegge, and A. Reinders, J. Appl. Phys. **75**, 6659 (1994).

⁷S. S. P. Parkin and V. S. Speriosu, *Magnetic Properties of Low Dimensional Systems II*, edited by L. Falicov, F. Meija-Lira, and J. L. Moran Lopez (Springer-Verlag, Berlin, 1990).

⁸K. Takano, R. Kodama, and A. E. Berkowitz, Phys. Rev. Lett. **79**, 1130 (1997).

⁹S. Soeya, S. Tadokoro, T. Imagawa, M. Fuyama, and S. Narishige, J. Appl. Phys. **74**, 6297 (1993).

¹⁰P. J. van der Zaag, A. R. Ball, L. F. Feiner, R. M. Wolf, and P. A. A. van der Heiden, J. Appl. Phys. **79**, 5103 (1996).

¹¹T. Ambrose and C. L. Chien, Phys. Rev. Lett. **76**, 1743 (1996).

¹²T. Ambrose, K. Leifer, K. J. Hemker, and C. L. Chien, J. Appl. Phys. **81**, 5007 (1997).

¹³A. P. Malozemoff, Phys. Rev. B **37**, 7673 (1988).

¹⁴D. Mauri, H. C. Siegmann, P. S. Bagus, and E. Kay, J. Appl. Phys. **62**, 3047 (1987).

¹⁵N. Koon, Phys. Rev. Lett. **78**, 4865 (1997).

Magnetic behavior of NiFe/NiO bilayers

Zhenghong Qian^{a)} and John M. Sivertsen

The Center for Micromagnetics and Information Technologies (MINT), Department of Chemical Engineering and Materials Science, University of Minnesota, Minneapolis, Minnesota 55455

Jack H. Judy

The Center for Micromagnetics and Information Technologies (MINT), Department of Electrical Engineering and Computer Science, University of Minnesota, Minneapolis, Minnesota 55455

In this study, the magnetic behavior of NiFe/NiO bilayers has been investigated. The relationship between the magnetic properties and interfacial interaction has been briefly discussed. Since magnetic properties of the bilayers are mainly determined by interfacial magnetic interaction, in this article, not only unidirectional interfacial anisotropy has been used to explain exchange field, H_{ex} ; also, for the first time, uniaxial interfacial anisotropy is introduced to describe interfacial interaction affecting the magnetic properties, especially coercivity H_c of the bilayers. In addition, a model is proposed to explain the magnetic behavior of the bilayers. The model has been tested by experiment. The experimental results are consistent with the model prediction, and this also confirms the assumption that the magnetization of the bilayer reverses by magnetic rotation. © 1998 American Institute of Physics. [S0021-8979(98)28411-8]

The exchange coupling between ferromagnetic (FM) and antiferromagnetic (AF) thin films has received increasing attention because it plays an important role in pinning the ferromagnetic layer in magnetoresistance (MR) heads or spin valves.¹ In recent years, although extensive works have been carried out to study various kinds of exchange coupled system,² the exchange coupling phenomenon is not yet fully understood. In particular, the simplest model predicts an exchange coupling H_{ex} typically 100 times greater than that observed in experiment. Recently, two models have been proposed by Mauri³ and Malozemoff⁴ to quantitatively explain this phenomenon. Both theoretical treatments of exchange coupling mechanism predict that the exchange field is proportional to $2(AK)^{1/2}$, where A and K are the exchange constant and anisotropy of the antiferromagnet, respectively. However, neither treatments can account for increased coercivities of the exchange coupled films. In this work, the relationship of magnetic properties with interfacial interaction has been explored, and a model for magnetic behavior of the FM/AF bilayers has been proposed and tested.

Magnetic behavior of the FM/AF bilayer is an interfacial phenomenon. It is believed that the magnetic properties of the bilayers are determined by interfacial interaction which is related to the spin distribution and arrangement at the interface. The interfacial magnetic interaction is strongly influenced by interfacial roughness and experimental conditions of depositing top FM layer.^{5,6} Interfacial roughness can provide more interfacial contact area and causes greater interfacial spin dispersion, leading to a higher coercivity of the bilayers.⁶ The interfacial interaction is also greatly dependent on experimental conditions.^{1,5} During sputtering, the incoming atoms with kinetic energy can disperse interfacial spins and promote interfacial interdiffusion. Lower sputtering pressure produces more incoming atoms with higher kinetic

energy which causes more atomic displacement and intermixing at the interface, which in turn enhances interfacial magnetic interaction, causing an increase of H_c . Similarly, substrate heating can promote interdiffusion which can enhance interfacial interaction, causing an increase of H_c . It is possible that, during sputtering deposition of NiFe on NiO, Fe atoms may replace some Ni atoms inside the NiO layer and on the interface, and O atoms in NiO may diffuse into NiFe layer to form a several Å thickness NiFeO interlayer and play a critical role in enhancing interfacial interaction between the NiO layer and NiFe layers. To verify this point, an interlayer of NiFeO was deposited by rf reactive sputtering of Ni_{0.80}Fe_{0.20} target to prepare a multilayer structure of NiFe(100 Å)/NiFeO(t)(400 Å)/Si. As shown in Table I, the 6 Å interlayer increases the interfacial magnetic interaction and causes a great increase of H_{ex} to 108 Oe and H_c to 58.5 Oe. However, with an increase of the NiFeO thickness, Both H_{ex} and H_c decrease. This is probably due to the larger thickness of NiFeO interlayer causing stronger dispersion of its spin configuration and reducing its antiferromagnetism. Furthermore, the evidence of interfacial magnetic interaction can also come from the fact that the magnetic properties of NiFe/NiO bilayers were observed measurement temperature dependent. H_{ex} decreases with increasing temperature and drops to zero at its blocking temperature T_B 175 °C.⁵ This is because, with an increase of temperature, the NiO spins are thermally fluctuating especially at the interface and reduce

TABLE I. Properties of NiFe(100 Å)/NiFeO(t)/NiO(400 Å) trilayers.

Sample number	NiFe(100 Å)/NiFeO(t)/NiO(400 Å)/Si	Exchange coupling field	Coercivity
Sample 1	$t=0$ Å	40 Oe	10 Oe
Sample 2	$t=6$ Å	108 Oe	58.5 Oe
Sample 3	$t=25$ Å	60 Oe	37 Oe
Sample 4	$t=50$ Å	40 Oe	20 Oe

^{a)}Electronic mail: qianx005@gold.tc.umn.edu

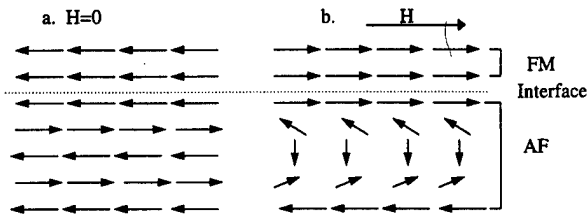


FIG. 1. Schematic view of possible domain wall formed by rotating interfacial spins at antiferromagnet together with spins at ferromagnet: (a) without applying field; (b) with an applying field, the domain wall formed.

its antiferromagnetism gradually along with its exchange coupling to the NiFe layer. Similarly, H_c greatly decreases to 1.6 Oe at T_B due to interfacial magnetic interaction (exchange coupling) disappearing at T_B .

Since interfacial magnetic interaction is so important in determination of magnetic behavior of the bilayer, for the first time, the uniaxial interfacial anisotropy is introduced into the following model to explain the magnetic behavior of NiFe/NiO bilayers.

This model is based on two assumptions: (1) the exchange interaction $-2J\mathbf{S}_F \cdot \mathbf{S}_A$ at the interface is so strong that it bonds interfacial spins together to pin any domain wall motion of FM layer so that magnetization reversal of NiFe layer can only occur through magnetic rotation and it rotates together with interfacial spin at the antiferromagnet. As shown in Fig. 1, to minimize the energy, a domain wall could be formed in the antiferromagnet, which causes an unidirectional interfacial anisotropy and plays the role of determining the exchange coupling field, H_{ex} . (2) The uniaxial interfacial anisotropy K_I (energy per unit interface area) is introduced by applied field during deposition and is the same as the uniaxial anisotropy K_u (energy per unit volume) of NiFe layer. K_I and K_u have the same easy axis which is induced by the same applied field during deposition of the FM layer on AF layer. Both K_I and K_u are key factors to control the coercivity, H_c . Thus, when a magnetic field is applied along the easy axis, the total energy of bilayer system is

$$E = 2(AK)^{1/2}(1 - \cos \theta) + (K_I + K_u t) \sin^2 \theta - HMt \cos \theta. \quad (1)$$

The first term is the energy of domain wall formed by rotating interfacial spin at the surface of antiferromagnet. The second term is due to uniaxial anisotropy K_u of FM layer and uniaxial interfacial anisotropy K_I . The third term is Zeeman energy term. t is the thickness of FM layer and θ is the angle of magnetization away from easy axis.

From Eq. (1), by $\partial E / \partial \theta = 0$ and $\partial^2 E / \partial \theta^2 \geq 0$, it is easy to find out that the possible stable angles θ for magnetization are at $\theta = 0^\circ$ and $\theta = 180^\circ$. Figure 2 is $E-\theta$ curve. As we can see, without applying field, only one energy well is formed at $\theta = 0^\circ$, which is stable position for magnetization M . However, after applying a negative field H , the energy well at $\theta = 0^\circ$ becomes shallow and another energy well is formed at $\theta = 180^\circ$. At a certain field called nucleation field, the energy well at $\theta = 0^\circ$ disappears, meaning $\theta = 0^\circ$ is no longer a stable angle for magnetization. Therefore, magneti-

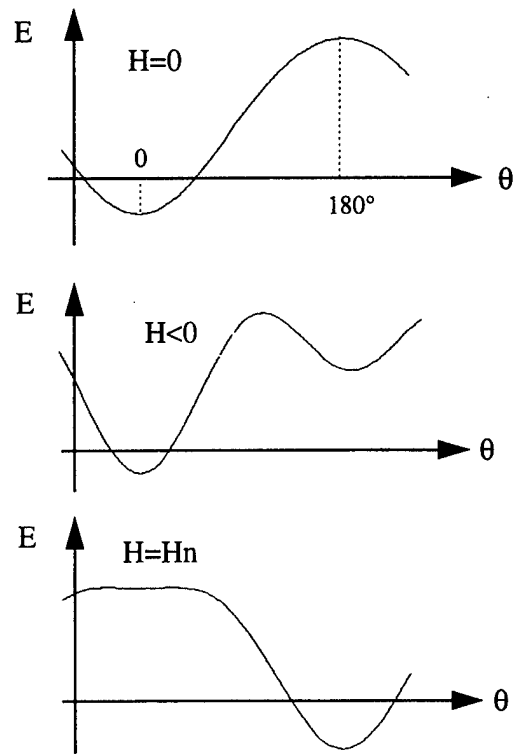


FIG. 2. $E-\theta$ curve (a) without applying field, $H=0$, only one energy well is formed at $\theta=0^\circ$, which is stable position for magnetization M ; (b) after applying a negative field H , the energy well at $\theta=0^\circ$ becomes shallow and another energy well is formed at $\theta=180^\circ$; (3) at a certain field called nucleation field, the energy well at $\theta=0^\circ$ disappears.

zation reversal should occur at the nucleation field, switching magnetization direction from $\theta=0^\circ$ to $\theta=180^\circ$, another energy stable position. Similarly, mathematically by $\partial E / \partial \theta = 0$ and $\partial^2 E / \partial \theta^2 = 0$, the nucleation field for magnetization reversal are given by

$$H_{0^\circ} = -2(AK)^{1/2}/Mt - 2(K_I + K_u t)/Mt, \quad (2)$$

$$H_{180^\circ} = 2(AK)^{1/2}/Mt - 2(K_I + K_u t)/Mt. \quad (3)$$

The above two formulas can be simplified as

$$H_{0^\circ} = -H_{ex} - H_c, \quad (4)$$

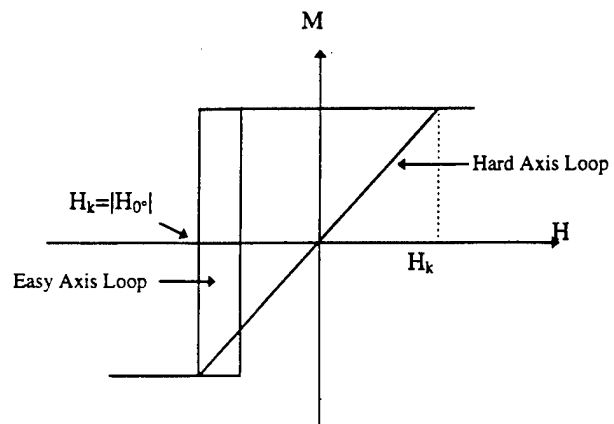


FIG. 3. Hysteresis loops of the bilayers constructed from the theoretical results of the model.

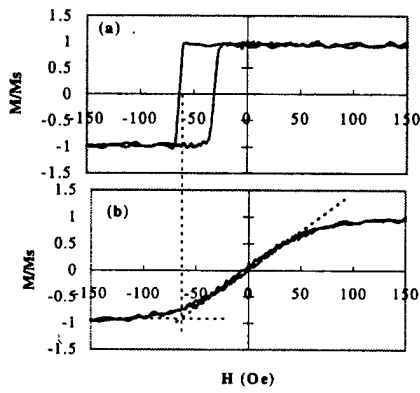


FIG. 4. Hysteresis loop of the NiFe(100 Å)/NiO(400 Å) bilayer where NiFe was deposited on NiO at RT: (a) H is parallel to easy axis; (b) H is perpendicular to easy axis.

$$H_{180^\circ} = H_{ex} - H_c, \quad (5)$$

where, $H_{ex} = 2(AK)^{1/2}/Mt$ is exchange coupling field; $H_c = |(H_{0^\circ} + H_{180^\circ})/2| = 2(K_I + K_u t)/Mt = 2K_I/Mt + H_k$ is coercivity. Here $H_k = 2k_u/M$ is the anisotropy field of the ferromagnetic layer. In this model, if we apply the field along hard axis, the model predicts that the coercivity $H_c = 0$, and the saturation field H_s , which is equal to the anisotropy field H_k , is equal to H_{0° : $H_s = H_k = H_{0^\circ}$. Thus, theoretical hysteresis loops of the bilayers can be constructed as shown in Fig. 3.

To test this model, NiFe(100 Å)/NiO(400 Å) bilayers were deposited on Si(100) substrates by rf sputtering and the magnetic properties of NiFe/NiO bilayers have been measured by vibrating sample magnetometer (VSM). The experimental data is in good agreement with modeling results. Either Fig. 4 or 5 shows that the anisotropy field H_k determined for hard axis hysteresis loop is approximately equal to the H_{0° . Table II is the magnetic data extricated from hysteresis loops of Figs. 4 and 5. As we can see, the H_k is almost equal to H_{0° , with an error less than 2%. Therefore, experimental data is consistent with model results, and

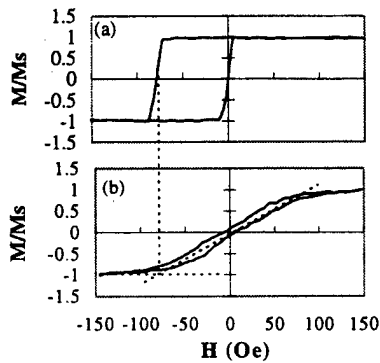


FIG. 5. Hysteresis loop of the NiFe(100 Å)/NiO(400 Å) bilayer where NiFe was deposited on NiO at a substrate temperature of 300 °C: (a) H is parallel to easy axis; (b) H is perpendicular to easy axis.

TABLE II. The data extricated from Figs. 4 and 5.

Sample	$ H_{\theta=0^\circ} $	$ H_{\theta=180^\circ} $	H_c	H_{ex}	H_k
Sample 1	63.7 Oe	30.8 Oe	16.5 Oe	47.3 Oe	65.0 Oe
Sample 2	78.3 Oe	0	39.2 Oe	39.2 Oe	78.5 Oe

thus also confirms our assumption that magnetization reversal of NiFe/NiO bilayers occurs through rotation. This is consistent with torque measurement conducted by Chih-Huang Lai⁷ which suggests that the magnetization process in the NiFe coupled to NiO is a pure rotation process. Since exchange coupling field H_{ex} is proportional to $2(AK)^{1/2}$, the induced domain wall formed in NiO layer by rotating its interfacial spins plays the decisive role in determining exchange coupling field, H_{ex} , of bilayers. It is reasonable, the wall thickness must be smaller than NiO layer thickness for the bilayer to have exchange coupling field H_{ex} . If the induced domain wall thickness is larger than NiO layer thickness, the spins of the NiO layer rotate irreversibly, causing an increase of H_c . Nevertheless, it cannot contribute exchange coupling field, H_{ex} . Obviously, only the induced domain wall thickness is smaller than NiO layer thickness, can the induced domain wall anchor, and couple to the bulk of the NiO layer, and play the role in determining H_{ex} . It is reported that the NiO layer thickness for NiFe/NiO bilayer having exchange coupling field is around 175 Å.⁷ In our model, the exchange coupling field H_{ex} is predicted to be $2(AK)^{1/2}/Mt$, depending on domain wall energy in the anti-ferromagnet and the thickness of ferromagnet. H_{ex} is predicted to decrease with an increase of the thickness of the ferromagnet, which is consistent with experimental results.⁸ Furthermore, since we have introduced uniaxial interfacial anisotropy K_I into the model, this model predicts that coercivity H_c is $2K_I/Mt + H_k$, decreasing with an increase of thickness of NiFe layer, which has also been confirmed by experiments.⁸ Also this model predicts the smallest H_c we can achieve is uniaxial anisotropy (H_k) of FM layer, which is around 4 to 5 Oe for NiFe films.

¹J. C. S. Kools, IEEE Trans. Magn. **32**, 3165 (1996).

²M. J. Carey and A. E. Berkowitz, Appl. Phys. Lett. **60**, 3096 (1996); S. Soeya, S. Tadokoro, T. Imagawa, M. Fuyama, and S. Narishige, J. Appl. Phys. **74**, 6297 (1993); T. Terashima and Y. Bando, Thin Solid Films **152**, 455 (1987); P. J. van del Zaag, R. M. Wolf, A. R. Ball, C. Bordel, L. F. Feiner, and R. Jungblut, J. Magn. Mater. **148**, 346 (1995); P. P. Freitas, J. L. Leal, T. S. Plaskett, and L. V. Melo, J. Appl. Phys. **75**, 6480 (1994).

³D. Mauri, H. C. Siegmann, P. S. Bagus, and E. Kay, J. Appl. Phys. **62**, 3047 (1987).

⁴A. P. Malozemoff, Phys. Rev. B **35**, 3679 (1987).

⁵Z. Qian, J. M. Sivertsen, and J. H. Judy, J. Magn. Soc. Jpn. **21**, 47 (1997).

⁶S. F. Cheng and J. P. Teter, J. Appl. Phys. **79**, 6234 (1996).

⁷C.-H. Lai, H. Matsuyama, and R. L. White, J. Appl. Phys. **79**, 6389 (1996).

⁸T. Lin, C. Tsang, R. E. Fontana, and J. K. Howard, IEEE Trans. Magn. **31**, 2585 (1995).

Direct experimental study of the magnetization reversal process in epitaxial and polycrystalline films with unidirectional anisotropy

V. I. Nikitenko, V. S. Gornakov, L. M. Dedukh, Yu. P. Kabanov, and A. F. Khapikov
*Institute of Solid State Physics, Russian Academy of Sciences, Chernogolovka,
Moscow District 142432, Russia*

A. J. Shapiro^{a)} and R. D. Shull
Metallurgy Division, National Institute of Standards and Technology, Gaithersburg, Maryland 20899

A. Chaiken^{b)} and R. P. Michel^{c)}
Materials Science and Technology Division, Lawrence Livermore National Lab, Livermore, California 94551

Direct observation of the magnetization reversal of epitaxial NiO/NiFe bilayers grown on (001) MgO and on polycrystalline Si substrates was performed by using the magneto-optical indicator film technique. It was shown that the unidirectional-axis magnetization reversal proceeds by domain nucleation and growth. A new phenomenon, an asymmetry in the activity of the domain nucleation centers, has been revealed. Remagnetization of the bilayer is shown to be governed by defect structures in the *antiferromagnetic* layer. © 1998 American Institute of Physics.
[S0021-8979(98)30311-4]

Since the discovery of unidirectional anisotropy¹ numerous investigations of this phenomenon have been carried out in ferromagnetic (FM) thin films deposited onto antiferromagnetic (AF) material.²⁻⁹ The simplest model, proposed by the authors who discovered this phenomenon, incorporates an exchange coupling across the flat interface between FM and AF spins. Because this model fails to describe the magnitude of the measured exchange anisotropy field, H_E , new models have been proposed, involving either planar¹⁰ or vertical¹¹ domain walls in the AF layer. At present, it is established that the exchange shift of the hysteresis loop of a thin exchange-biased FM film depends upon the behavior of ordered spins in the AF. However, the picture is still not entirely clear.

In particular, it is known that the magnitude of the coercive force, H_C , of AF/FM bilayers is much greater than the coercivity of corresponding "free" FM film.^{1,8,12} However, there is no model describing mechanisms responsible for this phenomenon. It is clear that the enhanced coercivity cannot be understood in terms of a spin coherent rotation model.¹ In this case the exchange anisotropy field, H_E , leads only to a shift in a hysteresis loop. The coercivity of the bilayer remains equal to the coercivity of the free FM layer. A model,¹⁰ taking into account the planar domain-wall formation in the AF, leads to the same value of H_C for both small and large interfacial exchange couplings, and even to lowered H_C for intermediate interfacial coupling magnitude.

The magnetization reversal of FM films could proceed by either domain wall nucleation and motion or by nonuniform spin rotation. These processes should have some features when the FM layer is exchange coupled to the AF substrate. These features can be revealed by direct visualization of the magnetization reversal.

In this paper, we study the magnetization reversal of epitaxial NiO/NiFe bilayers grown on both single crystal (001) MgO and polycrystalline Si substrates. In addition, the behavior of exchange-biased NiO/NiFe bilayers is compared with the reversal properties of unbiased NiFe films grown without an AF buffer.

In order to study the magnetization process in epitaxial NiO/NiFe bilayers we use the magneto-optical indicator film (MOIF) technique.¹³ The MOIF technique is based on the Faraday rotation of linearly polarized light in an indicator film, a Bi-substituted iron garnet film with in-plane anisotropy, which is placed on the sample. The polarized light passes through the indicator film and is reflected back by an Al underlayer covering the bottom surface of the film, which is adjacent to the sample surface. While the light is passing through the indicator film its polarization experiences a Faraday rotation through an angle proportional to the component of the local magnetic field parallel to the light propagation direction. The transmitted intensity of the reflected beam through an analyzing polarizer varies with the local field in the light path. The bright or dark variations of the image represent the variations of the perpendicular stray field component. The resulting real time Faraday portrait of the sample's stray magnetic fields presents the information about the static or dynamical domain structure as well as the defects of crystal structure which affect the spin distribution in the sample. The macroscopic hysteresis loops of the films were measured with a vibrating sample magnetometer. In addition, optical reflecting microscopy and a photoelasticity method¹⁴ were used to reveal defects in the thin films.

The NiO(500 Å)/NiFe(100 Å) bilayers were grown in a deposition system using ion beam sputtering onto the single crystal (001) MgO and polycrystalline Si substrates.¹² NiFe(500 Å) films grown onto (001) MgO or onto Si without NiO buffers were also prepared. Both uniaxial (in NiFe) and unidirectional (in NiO/NiFe) anisotropy were established during deposition by means of permanent magnets which produced a 300 Oe uniform bias field in the plane of the substrate.

^{a)}Electronic mail: shapiro@enh.nist.gov

^{b)}Present address: Hewlett-Packard, Mailstop 2U-20, 1501 Page Mill Rd., Palo Alto, CA 94304.

^{c)}Present address: Seagate Technology, 7801 Computer Ave., South, Minneapolis, MN 55435.

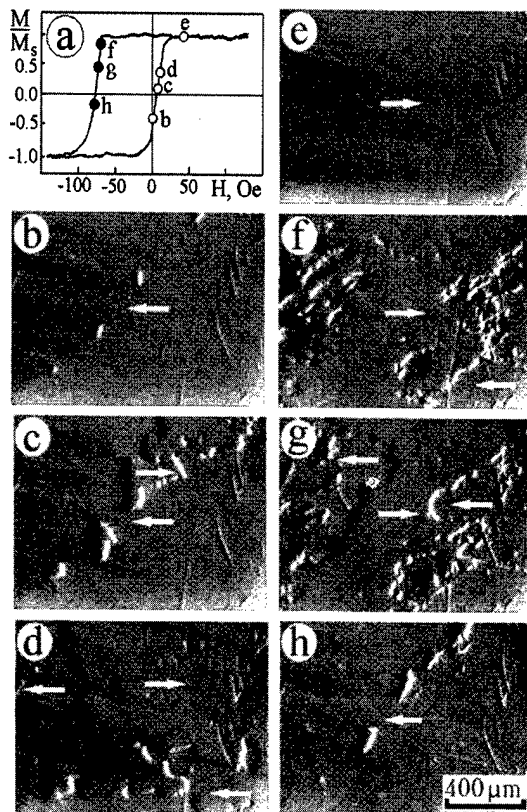


FIG. 1. Hysteresis loop (a) and MOIF images of domain structure (b)–(h) taken during magnetization reversal of a single-crystal NiO/NiFe bilayer along the $[110]$ unidirectional axis (b)–(e) and in the opposite direction (f)–(h). (b)–(h) are domain structures in the same exact area of the sample and correspond to the conditions indicated by the circles labeled by the same letters on the hysteresis loop in (a). Arrows indicate magnetization directions in domains.

The hysteresis loop and MOIF images of domain structure observed during the magnetization reversal of the NiO/NiFe bilayer grown on the (001) MgO substrate are shown in Fig. 1. The magnetic field was applied along the $[110]$ direction or along the reversed one. The $[110]$ direction coincides with the direction of a magnetic field applied during the bilayer growth. Letters on the hysteresis loop refer to the conditions of the corresponding MOIF patterns. The hysteresis loop exhibits an exchange shift ($H_E = 35$ Oe) and substantial coercivity ($H_C = 40$ Oe). The MOIF patterns display the magnetization reversal of the bilayer proceeds by nucleation and subsequent growth of domains with new magnetization orientations. Moreover, when the magnetic field is aligned along the unidirectional anisotropy axis, the nucleation of domains occurs in central regions of the field of view at some defects [Fig. 1(b)]. However, when the field is aligned in the opposite direction, the domain nucleation starts at other centers [Fig. 1(f)]. Former centers play no role in the nucleation and, moreover, the reversal is finished in their vicinity [Fig. 1(h)]. Thus, we demonstrate the existence of a new phenomenon, a field asymmetry in the activity of the domain nucleation centers.

In the above particular case we do not know what kind of defects play a role as domain nucleation centers. Therefore, we studied crystals of the NiFe and of the NiO/NiFe

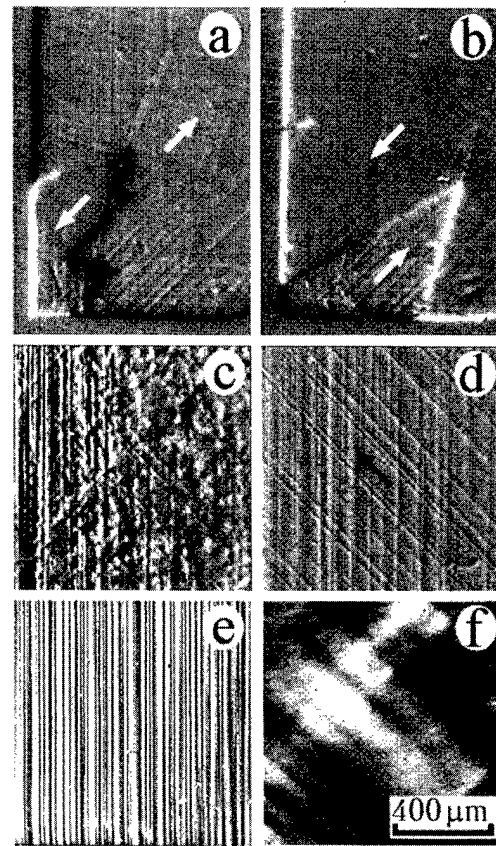


FIG. 2. (a), (b) MOIF images of domain structure in a deformed unbiased epitaxial NiFe(001) film created during remagnetization along the $[110]$ easy axis. H (applied field) = -2 Oe and $+2$ Oe in (a) and (b), respectively. Arrows indicate the magnetization directions in domains parallel and antiparallel to the applied field. (c), (d) Domain structure in the deformed part of the epitaxial NiO/NiFe(001) bilayer during the $[110]$ unidirectional-axis remagnetization (corresponds to the right-hand branch of the hysteresis loop in Fig. 1(a)). The arrow indicates the direction of the unidirectional axis and of the applied field. $H = +24$ Oe (c) and $+28$ Oe (d). (e) Surface steps associated with screw dislocation slip planes revealed in a reflected light at the NiFe surface in the NiO/NiFe bilayer. (f) Microstress fields caused by the slip planes of the edge dislocations revealed by a photoelasticity method (Ref. 14). All images are of the same magnification.

bilayers containing dislocations (Fig. 2). These films were grown onto the MgO substrates plastically deformed during cleaving into small pieces prior to the deposition. Figure 2(e) shows NiFe surface steps associated with the intersection of screw dislocation slip planes with the sample surface, are revealed in reflected light on the NiFe/NiO bilayer. Figure 2(f) shows contrast from microstresses surrounding edge dislocations in the same bilayer, as revealed by a photoelasticity method.¹⁴

The easy-axis hysteresis loop of free NiFe layer (grown on MgO without a NiO buffer) demonstrated no shift, and its coercive force was very small (~ 2 Oe). We did not observe any dislocation influence on the domain nucleation in these free NiFe films. This is due to almost zero permalloy magnetostrictive constants. There was also no field asymmetry in the domain nucleation. Domains nucleate and disappear at film edges for both field directions parallel to the easy axis due to the edge stray field. The magnetization reversal proceeds by means of motion of almost rectilinear domain walls

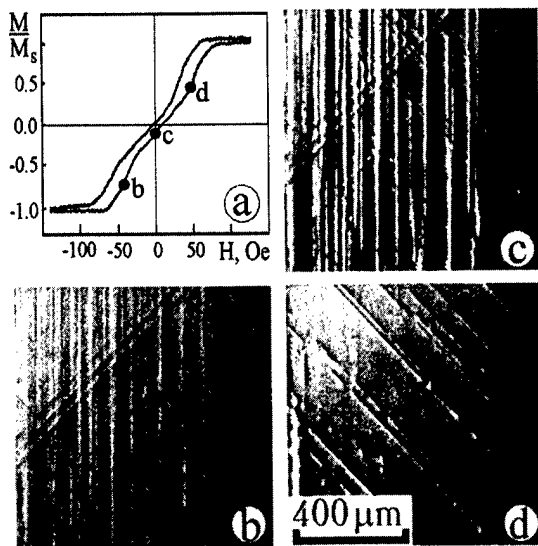


FIG. 3. Hysteresis loop (a) and MOIF patterns showing the domain structure (b)–(d) of the NiO/NiFe bilayer when it is remagnetized perpendicular to the $[110]$ unidirectional axis. The applied field direction is indicated by the arrow. All images are of the same exact sample area.

over the whole sample [Figs. 2(a) and 2(b)]. Though these particular patterns were obtained for the 500 Å thickness sample, such a behavior is typical for free FM films with different thicknesses.¹⁵

In contrast, a surprisingly strong influence of dislocations on the spin rotation and on the domain nucleation was revealed in NiO/NiFe bilayers [Figs. 2(c) and 2(d)]. It is important to note that domains nucleate not only around screw dislocation slip planes (which could create the NiFe magnetization frustrations at the NiO/NiFe interface steps), but also around edge dislocation slip planes. Actually, edge dislocations do not form steps on the interface boundary; their effect is only due to internal stress fields around the dislocation. These stress fields only affect the spin orientation in the antiferromagnet since the permalloy magnetostriction is extremely small.

A very important conclusion can be made from the analysis of the above data. Dislocations in the NiO/NiFe bilayer influence primarily the spin configuration of the AF layer. The spin behavior in the FM layer is affected only through its interaction with the AF layer.

Domain structures observed during the $[1\bar{1}0]$ hard-axis magnetization reversal of the plastically deformed NiO/NiFe bilayer are shown in Fig. 3. The hysteresis loop [Fig. 3(a)] has a symmetric shape and demonstrates a very small coercivity. In this case the magnetization reversal proceeds primarily by the incoherent rotation of magnetization vectors. However, an unusual nucleation of domains has also been revealed in the vicinity of dislocation slip lines. Figures 3(c) and 3(d) demonstrate how elongated domains arise along screw and edge dislocation slip planes.

For comparison, Fig. 4 shows typical domain structures for a polycrystalline NiO/NiFe bilayer (a) and for a polycrystalline free NiFe film (b) grown on Si. The magnetic field was applied along the unidirectional and along the easy axis,

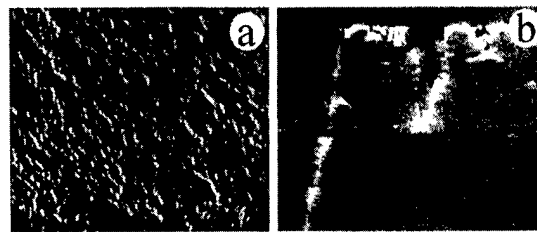


FIG. 4. Domain structure in a polycrystalline NiO/NiFe bilayer (a) and in a NiFe film (b) grown on Si. Both images are of the same magnification ($\times 45$). The magnetic field is applied along the unidirectional and easy axes, respectively. These directions are also, respectively, parallel to the vertical frame of the MOIF pattern.

respectively. Similar to the above results, imperfections in the NiO crucially affect the domain structure of the bilayer. As a result, the bilayer displays a complicated fine-scaled domain structure [Fig. 4(a)]. In contrast, in the polycrystalline NiFe film grown on Si without NiO buffer, the domain structure is simpler and the remagnetization proceeds by the motion of almost rectilinear domain walls with cross ties over large distances [Fig. 4(b)].

In conclusion, we have shown that the domain nucleation and propagation process is responsible for the magnetization reversal in thin-film NiO/NiFe bilayers. This implies that the model of the bilayer hysteresis behavior proposed in Ref. 2 should be extended by consideration of *two-dimensional* inhomogeneities in the AF spin distribution. Preliminary analysis shows that both exchange biasing and enhanced coercivity of the AF/FM bilayer as compared to a free FM layer can be explained in terms of the extended model in a unique manner. Calculations supporting the above suggested mechanism will be published elsewhere.

The Russian co-workers gratefully acknowledge a research grant from the Russian Foundation for Basic Research No. 97-02-16879.

- ¹W. H. Meiklejohn and C. P. Bean, *Phys. Rev.* **105**, 904 (1957).
- ²M. Takahashi, A. Yanai, S. Taguchi, and T. Suzuki, *Jpn. J. Appl. Phys.* **19**, 1093 (1980).
- ³C. Schlenker, S. S. P. Parkin, J. C. Scott, and K. Howard, *J. Magn. Magn. Mater.* **54–57**, 801 (1986).
- ⁴M. J. Carey and A. E. Berkowitz, *J. Appl. Phys.* **60**, 3060 (1992).
- ⁵A. Berger and H. Hopster, *Phys. Rev. Lett.* **73**, 193 (1994).
- ⁶R. Jungblut, R. Coehoorn, M. T. Johnson, J. aan de Stegge, and A. Reinders, *J. Appl. Phys.* **75**, 6659 (1994).
- ⁷T. J. Moran, J. M. Galego, and I. K. Schuller, *J. Appl. Phys.* **78**, 1887 (1995).
- ⁸D. V. Dimitrov, A. S. Murthy, G. C. Hadjipanayis, and C. P. Swann, *J. Appl. Phys.* **79**, 5106 (1996).
- ⁹R. F. C. Farrow, R. F. Marks, S. Gider, A. C. Marley, S. S. P. Parkin, and D. Mauri, *J. Appl. Phys.* **81**, 4986 (1997).
- ¹⁰D. Mauri, H. C. Siegmans, P. S. Bagus, and E. Kay, *J. Appl. Phys.* **62**, 3047 (1987).
- ¹¹A. P. Malozemoff, *Phys. Rev. B* **35**, 3679 (1987).
- ¹²R. P. Michel, A. Chaiken, C. T. Wang, and L. E. Johnson, *IEEE Trans. Magn.* **32**, 4651 (1996).
- ¹³V. S. Gornakov, V. I. Nikitenko, L. H. Bennett, H. J. Brown, M. J. Donahue, W. F. Egelhoff, R. D. McMichael, and A. J. Shapiro, *J. Appl. Phys.* **81**, 5215 (1997).
- ¹⁴V. I. Nikitenko and L. M. Dedukh, *Phys. Status Solidi A* **3**, 383 (1970).
- ¹⁵T. Miyazaki, T. Aljima, and F. Sato, *J. Magn. Magn. Mater.* **81**, 86 (1989).

Magnetic Microscopy and Imaging II

Paul Rice, Chairman

Spin-polarized tunneling by spin-polarized scanning tunneling microscopy

Hiroyoshi Kodama,^{a)} Takuya Uzumaki, and Mitsumasa Oshiki
Fujitsu Laboratories LTD., 10-1 Morinosato-Wakamiya, Atsugi 243-0197, Japan

Kazuhisa Sueoka
PRESTO, Faculty of Engineering, Hokkaido University N13, W8, Kita-ku, Sapporo 060-8628, Japan

Kōichi Mukasa
CREST-JST, Faculty of Engineering, Hokkaido University N13, W8, Kita-ku, Sapporo 060-8628, Japan

A spin-polarized scanning tunneling microscope (STM) using a GaAs tip has been studied to observe the magnetization with nanoscale resolution for a sample magnetized in the plane of the film. A STM image of Si(111) 7×7 surface reconstruction using the GaAs tip was observed clearly under ultra-high-vacuum conditions. We found that the cleaved GaAs tip has a capability of high atomic resolution. Next, circularly polarized light irradiated the GaAs tip, and the I - V characteristics were measured for magnetic $\text{Ni}_{80}\text{Fe}_{20}$ and nonmagnetic Au samples. Changes in the tunneling current, which is estimated to be approximately 7%, were observed only for the NiFe sample under the circularly polarized light irradiation. It suggests that the change in the tunneling current is due to the spin-polarized tunneling from the GaAs tip to the NiFe. © 1998 American Institute of Physics. [S0021-8979(98)47711-9]

I. INTRODUCTION

Magnetic recording densities are rapidly increasing. A technique for observing the actual magnetization is required to establish a higher density magnetic recording technique. A spin-polarized scanning tunneling microscope (SP-STM) offers the capability of measuring magnetization at the atomic scale, and has already been studied by some groups.¹⁻⁴ However, these previous studies used magnetic material tips, which might change the magnetization of the sample. We considered GaAs to be suitable for the tip of the SP-STM because of the polarized electron source by circularly polarized light⁵ and the nonmagnetic material. Recently, Prins *et al.*⁶ detected a spin-polarized tunneling current by using a GaAs tip and vertically magnetized Co film. They irradiated laser light to the GaAs tip through a thin Co film. This experimental system is suited for measuring vertically magnetized films. However, the sample condition is very severe, as it should be a thin, vertically magnetized film. We propose a SP-STM using a GaAs tip to observe the in-plane magnetized film. In our experimental system, the laser radiation irradiating the GaAs tip is transmitted parallel to the sample film surface. In this paper, we reported on our observation of STM images using the GaAs tip and we attempted to detect spin-polarized tunneling by measuring the I - V characteristics of the GaAs tip and the $\text{Ni}_{80}\text{Fe}_{20}$.

II. EXPERIMENT

An UHV-STM (JEOL:4500XT) system was used in our experiments. Figure 1 shows our experimental setup. An ul-

trahigh vacuum below the 10^{-8} Pa range was maintained inside the STM chamber. We used a semiconductor laser with a wavelength of 831 nm. Circularly polarized light was produced by combining this laser, a Pockels cell, and a $\lambda/4$ plate. The laser radiation was vertically irradiated to the tip through the viewing port. The laser power before passing through the viewing port was 16 mW. Since the semiconductor laser was invisible, we used a HeNe laser to accurately adjust the optical pass to the sample in parallel. In our UHV-STM system, the sample is biased positively with respect to the tip.

The GaAs tip was fabricated from a (100)-type oriented wafer doped with Zn ($7 \times 10^{17} \text{ cm}^{-3}$) by cleavage in air. Figure 2 shows scanning electron microscope (SEM) images

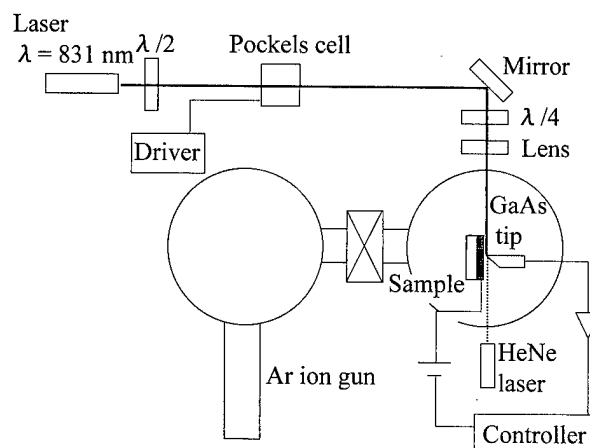


FIG. 1. Experimental setup.

^{a)}Electronic mail: hkodama@flab.fujitsu.co.jp

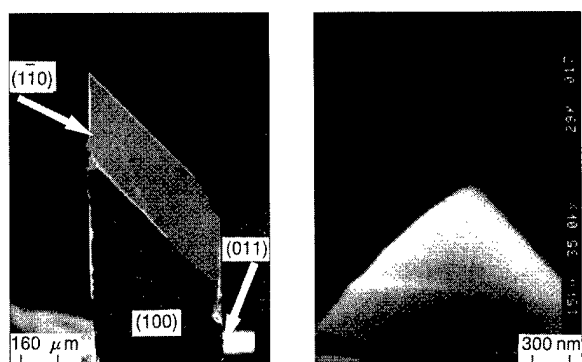


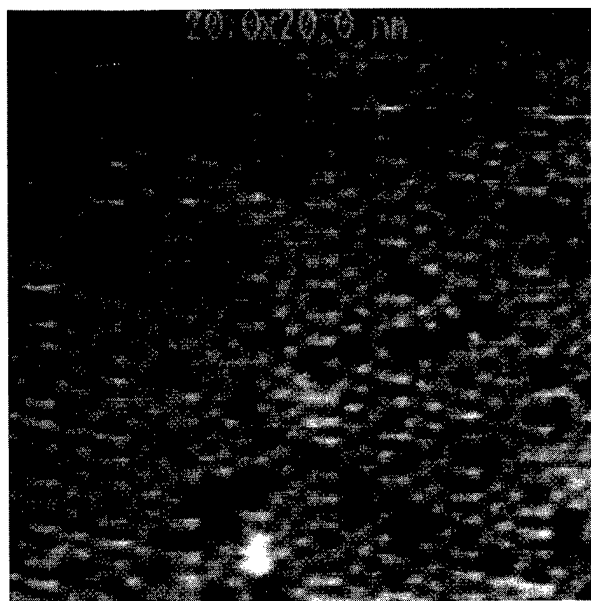
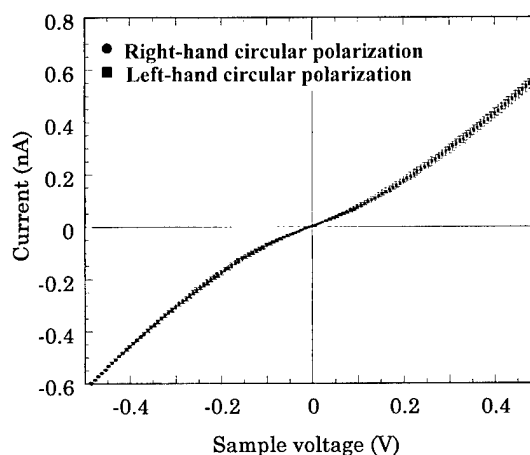
FIG. 2. (a) SEM image of GaAs tip. (b) Enlarged image.

of the GaAs tip. The wafer corner delimited by the (100), (011), and (110) planes was used as the tip. Circularly polarized light was vertically irradiated to the (100) plane. Figure 2(b) shows an expanded SEM image of the GaAs tip. After being cleaved, the tip was transferred to an UHV-STM chamber and the chamber was heated at 200 °C for 50 h.

A magnetic sample of a thin NiFe film (1000 Å) and a nonmagnetic sample of Au (300 Å) were deposited on a silicon substrate by ion-beam sputtering, which was not *in situ* with the STM. The samples were transferred into an UHV-STM chamber and cleaned by argon ion bombardment of 2 keV and 0.8 μA for 10 min in vacuum below 3.0×10^{-6} Pa. The STM observation showed that the NiFe film has grains about 30 nm wide and has 6 nm of corrugation. The sample magnetization was measured by using a vibrating sample magnetometer, and the coercivity H_C was 1 Oe.

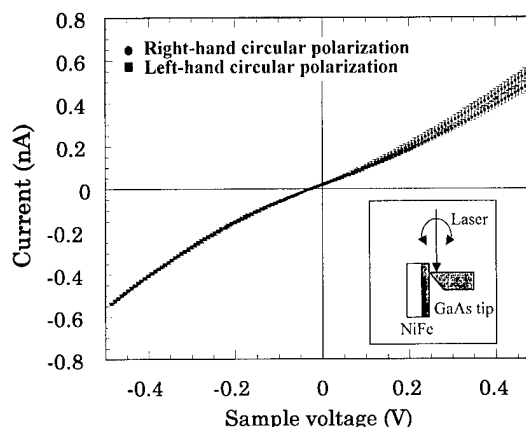
III. RESULTS AND DISCUSSION

Figure 3 shows an image of the Si(111) 7×7 surface reconstruction observed with the GaAs tip. The sample bias voltage was 1.0 V and tunneling current was 0.1 nA.

FIG. 3. Image of Si(111) 7×7 surface reconstruction observed using the GaAs tip. Sample bias voltage was 1.0 V and tunneling current was 0.1 nA.FIG. 4. I - V curves obtained with GaAs tip on Au thin film under irradiation by circularly polarized light. Set point current was -0.5 nA at -0.5 V for all curves.

voltage was 1.0 V and the tunneling current was 0.1 nA. The structure of the Si(111) 7×7 was clearly observed. We found that the cleaved GaAs tip has the capability of high atomic resolution.

First of all, we were concerned with the thermal expansion and the distance change of the sample to the tip when switching on the circular polarization light. We tried to estimate the effects of thermal expansion and distance changes by using Au as the sample. Figure 4 shows the I - V curves obtained with a GaAs tip on thin Au film under circularly polarized light irradiation. The I - V curves were measured continuously for five times, while irradiating with the left-hand circularly polarized light. After switching to the right hand, the circularly polarized light and the I - V curves were again measured continuously for five times. Switching back to the left-hand circularly polarized light, the I - V curves were once again measured continuously for five times. The set point current and voltage were at -0.5 nA and -0.5 V

FIG. 5. I - V curves obtained with GaAs tip on NiFe thin film under irradiation by circularly polarized light. Set point current was -0.5 nA at -0.5 V for all curves. The pumping configuration is shown in the inset. The curve of the upper side was irradiation by right-hand circularly polarized light. The curve of the lower side was irradiation by left-hand circularly polarized light.

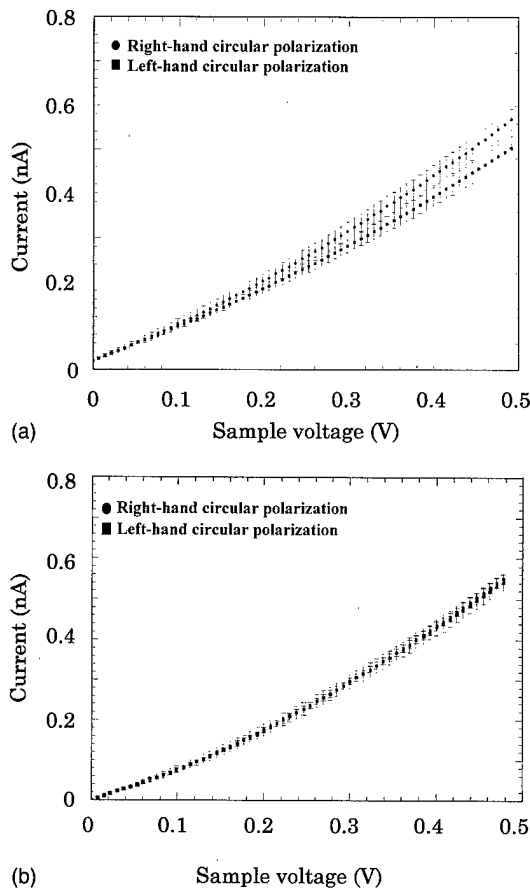


FIG. 6. Positive bias voltage area of I - V curve of the GaAs tip, NiFe sample, and the GaAs tip, Au sample. (a) NiFe-GaAs tip. (b) Au-GaAs tip.

for all curves. The results show that the effects of thermal expansion and distance changes in our system are very small.

Figure 5 shows the I - V curves obtained with a GaAs tip on thin NiFe film while irradiated with circularly polarized light. The procedure for this measurement was the same as in the Au measurement. In Fig. 5, the upper curve represents the case when irradiated by the right-hand circularly polarized light. The lower curve represents the case when irradiated by the left-hand circularly polarized light. Figure 6 shows the expansion chart of the positive bias area of Fig. 4 for the GaAs tip-Au sample, and Fig. 5 for the GaAs tip-NiFe sample. It clearly shows that a tunneling current change was observed only in the NiFe sample. The change in tunneling current at only the positive bias voltage area suggests the occurrence of spin-polarized tunneling, because the tunneling current was only observed with the NiFe sample.

We tried to estimate the current variation P_c from Fig. 6(a), as

$$P_c = \frac{I_R - I_L}{I_R + I_L}. \quad (1)$$

P_c was estimated to be about 7% from Eq. (1). Here, I_L is the tunneling current for the left-hand circularly polarized light irradiation, and I_R is the tunneling current for the right-hand circularly polarized light irradiation. The theoretical polarization of GaAs (P_{GaAs}) is 50%.⁵ The spin polarization of NiFe (P_{NiFe}) is about 30%.⁷ This value is measured by the spin-polarized tunneling technique using a thin-film Al-Al₂O₃-ferromagnetic-alloy tunnel junction. When this value is assumed, the theoretical maximum of variations in the current ratio ($P_{c \text{ max}}$) is defined as

$$P_{c \text{ max}} = P_{\text{GaAs}} \times P_{\text{NiFe}} = 0.5 \times 0.3 = 0.15, \quad (2)$$

and is about 15%. The P_c values in our experiment were about half the theoretical value. We consider that the variation current ratio of 7% is good for an initial attempt, because 15% is the ideal case. The difference between 15% and 7% shows the issue of the surface of GaAs and the spin-relaxation time of the carrier. Furthermore, we tried to increase the P_c value up to 15% using surface treatments and other techniques.

IV. CONCLUSION

This paper reports on observations of UHV-STM images using a GaAs tip. The structure of Si(111) 7×7 was clearly observed. We found that the cleaved GaAs tip has the capability of high atomic resolution. We proposed a SP-STM system that is suitable for observing in-plane magnetized film. An experimental system was developed in which the laser radiation for irradiating the GaAs tip is transmitted parallel to the film surface. Circularly polarized light irradiated the GaAs tip, and we measured the I - V characteristics of magnetic NiFe samples and of nonmagnetic Au samples. As a result, changes in the tunneling current were observed only when the sample was the magnetic NiFe material. This phenomenon suggests that spin-polarized tunneling was observed because the tunneling current change occurred only with the magnetic NiFe sample.

¹M. Johnson and J. Clarke, J. Appl. Phys. **67**, 6141 (1990).

²S. F. Alvarado and P. Renaud, Phys. Rev. Lett. **68**, 1387 (1992).

³K. Sueoka, K. Mukasa, and K. Hayakawa, Jpn. J. Appl. Phys., Part 1 **32**, 2989 (1993).

⁴R. Wiesendanger, H.-J. Güntherodt, G. Güntherodt, R. J. Gambino, and R. Ruf, Phys. Rev. Lett. **65**, 247 (1990).

⁵D. T. Pierce and F. Meier, Phys. Rev. B **13**, 5484 (1976).

⁶M. W. J. Prins, R. Jansen, and H. van Kempen, Phys. Rev. B **53**, 8105 (1996).

⁷D. Paraskevopoulos, R. Meserve, and P. M. Tedrow, Phys. Rev. B **16**, 4907 (1977).

Imaging of magnetic domains with scanning tunneling optical microscopy

P. Bertrand,^{a)} L. Conin, C. Hermann, G. Lampel, and J. Peretti

Laboratoire de Physique de la Matière Condensée (CNRS-URA D1254), Ecole Polytechnique, 91128 Palaiseau Cedex, France

V. I. Safarov

G.P.E.C. (CNRS-UMR 6631), Faculté des Sciences de Luminy, B.P. 901, Université de la Méditerranée, 13288 Marseille, France

Near field magneto-optical images of magnetic domains in ferromagnetic soft garnet films have been obtained with a scanning tunneling optical microscope working in total reflection geometry with shear-force control of the tip-to-sample distance. In this geometry a magneto-optical contrast is observed for the first time between domains of opposite magnetization without using modulation techniques. When applying a static or alternating external magnetic field, the magneto-optical images provide the location of domain wall pinning points. © 1998 American Institute of Physics. [S0021-8979(98)28511-2]

I. INTRODUCTION

Near-field optics promises to be a powerful technique for magnetic domain imaging with submicronic resolution. Nevertheless, only few experiments have demonstrated such capabilities¹⁻³ and in the total internal reflection geometry [the so-called scanning tunneling optical microscopy (STOM) configuration]⁴ domain visualization has been obtained only by indirect magneto-optical (MO) observation of domain wall motion in a soft ferromagnet.⁵

In the present article, we show that, thanks to the polarization properties of the optical fiber tips that we prepare (Sec. II), near-field MO contrast between domains of opposite magnetization may be obtained in the STOM configuration without using modulation techniques (Sec. III). The MO images presented here provide evidence for domain wall pinning by application of either static (Sec. III) or alternating (Sec. IV) external magnetic fields.

II. EXPERIMENTAL SETUP

A schematic view of the STOM setup that was constructed is drawn in Fig. 1. The sample is deposited on the external face of a semicylindrical prism illuminated by linearly *s*-polarized light (wavelength $\lambda = 647$ nm) at an incident angle beyond the limit of total internal reflection. The evanescent light is collected close to the sample surface by the tip of a tapered monomode optical fiber and guided to a photomultiplier tube (PMT) equipped with a polarization analyzer. The fiber is attached to a dither piezoelectric tube used for shear-force tip-to-sample separation control. The dither tube is in turn attached to a five-electrode piezo tube which allows fine *x*, *y*, and *z* motions of the tip while larger-scale motion of the microscope head is provided by a micrometric mechanical stage. A small coil surrounding the tip is used to apply an external magnetic field perpendicular to the film plane (i.e., parallel to the easy-magnetization axis of the sample) to change the magnetic structure of the sample.

The tip-to-sample separation is regulated by a novel shear-force detection technique. An ac voltage is applied to the dither piezo tube at a resonant vibration frequency of the fiber. The impedance variation of the piezo tube at this frequency is measured with a Wheatstone-type bridge via a lock-in amplifier. When the tip approaches the surface, the oscillation amplitude of the fiber decreases due to shear-force interactions and an impedance change of the piezo oscillator is detected. The related variation of the lock-in amplifier output signal is used in a feedback loop to control the tip-to-sample distance. This provides the topography of the surface independently and concurrently to the optical image, which is essential for the interpretation of the near-field optical contrast. Our shear-force measurement is comparable with several other electrical detection techniques recently proposed⁶⁻⁹ and provides many advantages when compared to standard optical detection techniques.^{10,11} It is easy and fast to set up as no tedious optics alignment is required. Scanning the tip over the surface does not change the measurement. The signal-to-noise ratio is high (better than 1000 in a 25 Hz bandwidth). The free space available around the tip is used to set the magnetic coil.

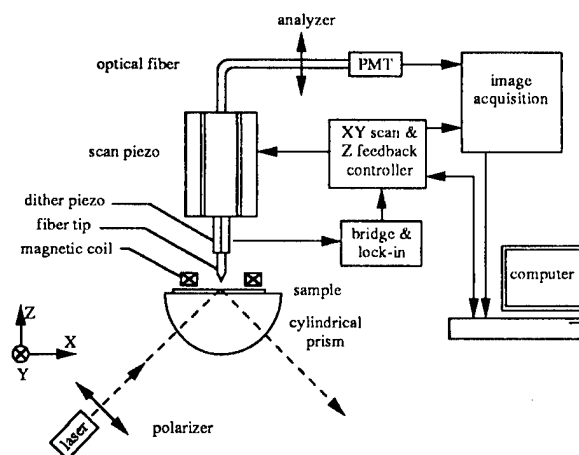


FIG. 1. Schematics of the scanning optical microscope setup.

^{a)}Electronic mail: pb@pmc.polytechnique.fr

Since the measurement of small MO effects requires a high degree of polarization sensitivity and a high collection efficiency, which both crucially depend on the tip condition, we have developed a fiber-pulling apparatus with a novel soft multiple-step procedure which strongly contrasts with the commonly used two-step fabrication process.¹² A weak pulling force is applied to the fiber during the whole process. A step-by-step taper of the fiber is provided by pulsed operation of a CO₂ laser (Synrad E-48-1) power stabilized by a homemade additional supply of the rf drive. The small elongation produced by each pulse is measured. This value is used to define the time width of the following laser shot. Between two subsequent pulses a time delay is provided to cool down the fiber. After about one hundred of these pulse-and-cool-down sequences, the diameter of the fiber taper neck is reduced (by about 1 μm steps) from 125 to nearly 8 μm . For the final tip formation a last laser shot is applied with only the weak pulling force previously mentioned and switched off when a specified fiber drawing speed is reached. This procedure permits control of the tip geometry and is used to create single-cone-shape tips with typical angles of 25°. This provides good mechanical properties for shear-force measurements and high light-collection efficiency. Shear-force and optical lateral resolutions better than 50 nm are achieved with these tips. From near-field optical measurements performed on a bare prism with polarized light, the tips exhibit characteristic collection properties of a dipolelike near-field probe.⁵ Collection efficiency in the surface plane is isotropic and extinction ratios as high as 1000:1 are reproducibly achieved for both *s*- and *p*-polarized light.

III. NEAR-FIELD MO IMAGING OF DOMAINS

The sample that we have studied is a 1- μm -thick single-crystal ferromagnetic garnet film grown on a garnet (GGG) substrate. Its magnetic properties are well known.¹³ This garnet is a soft ferromagnet with a saturation magnetic field H_s of a few Oe. The magnetic domain size is on the order of 4 μm and the easy-magnetization direction is perpendicular to the film plane. We denote φ as the angle between the analyzer and the incident light polarization. In the small Faraday rotation limit ($\tan(\theta_F) \approx \theta_F$) and assuming zero ellipticity, the intensity $I(\varphi)$ collected above the surface in near field is

$$I(\varphi) = I(0)[\cos^2(\varphi) + \theta_F^2 \sin^2(\varphi) + \theta_F \sin(2\varphi)]. \quad (1)$$

The sign of θ_F changes with the sign of the magnetization leading to a MO contrast between two domains of opposite magnetizations equal to $\Delta I(\varphi) = 2\theta_F \sin(2\varphi)I(0)$.

Figure 2(a) represents the shear-force topographic image of a 17 $\mu\text{m} \times 17 \mu\text{m}$ area of the sample surface. The surface roughness is a fraction of nanometer and the topographic image does not show any particular structure except a small defect of 400 nm lateral size and 10 nm height. Figure 2(b) shows the near-field MO image of the same area as Fig. 2(a), recorded simultaneously, and corresponding to $I(\varphi)$ for $\varphi \approx 85^\circ$. There is no external magnetic field and the scanning frequency is 4 Hz. A strong contrast between domains of opposite magnetizations is observed, which we checked to be reversible by inverting the polarization-analysis angle φ .

Figure 3(b) shows a 2.4 $\mu\text{m} \times 2.4 \mu\text{m}$ MO image re-

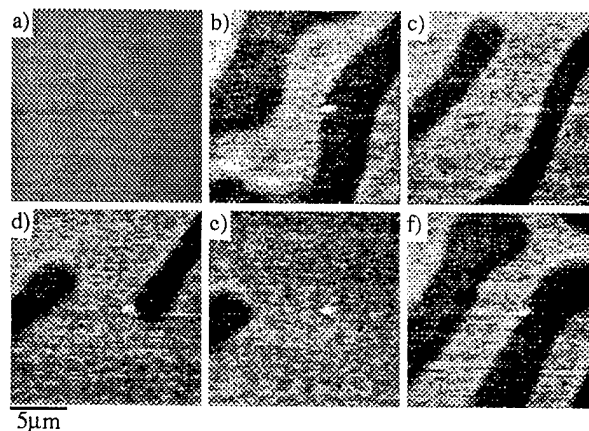


FIG. 2. Image (a) is a 17 $\mu\text{m} \times 17 \mu\text{m}$ shear-force topographic image of a garnet film surface. The other images are near-field MO images of the same sample area measured with a constant external magnetic field equal successively to (b) 0%, (c) 39%, (d) 47%, and (e) 55% of H_s . The last near-field MO image (f) is taken when the external magnetic field is reset to zero.

corded in the vicinity of a domain wall. The curve plotted in Fig. 3(a) corresponds to the profile of $I(\varphi)/I(0)$ along the horizontal line in Fig. 3(b) indicated by the arrow. As can be seen, the full grey scale of the image represents a few tenth of a percent of $I(0)$. The MO contrast of 2×10^{-3} , with a signal-to-noise ratio larger than 5, corresponds to a Faraday rotation $\theta_F \approx 0.3^\circ$. The apparent width of the domain wall is 0.3 μm . This value is somewhat larger than the ones usually quoted.¹³ This is possibly due to the thickness of our sample ($\approx 2 \mu\text{m}$). Finally, the domain wall shape does not appear to be uniform at the submicron scale.

When an external constant magnetic field is applied, the relative size and morphology of the magnetic domains change by motion of the domain walls. The size of the domains with magnetization parallel to the field (bright areas) increases while the size of the domains with opposite magnetization (dark areas) is reduced. This is illustrated in Figs. 2(c)–2(e) which have been obtained in external magnetic fields equal to 39%, 47%, and 55% of H_s , respectively. Two regimes are clearly identified during this process. The first occurs between Figs. 2(b) and 2(c), where magnetization reversal mainly changes the width of the domains without modifying the general domain configuration. The second regime is observed between Figs. 2(c) and 2(e). After the domain width has reached a minimum critical value measured

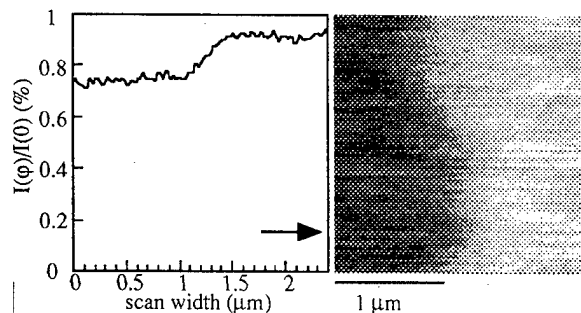


FIG. 3. The left-hand view is the profile of the near-field optical signal $I(\varphi)/I(0)$ corresponding to the line indicated by the black arrow of the 2.4 $\mu\text{m} \times 2.4 \mu\text{m}$ right-hand near-field MO image. Submicron structures along the domain wall are observed.

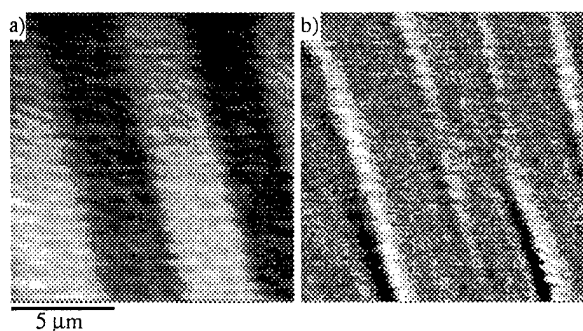


FIG. 4. The images (a) and (b) are obtained simultaneously on a $14\text{ }\mu\text{m}\times 14\text{ }\mu\text{m}$ area of the garnet film. They are recorded (a) without and (b) with an alternative external magnetic field. The contrasted lines in view (b) are related to the domain wall motion induced by the magnetic field modulation.

to be $1.3\text{ }\mu\text{m}$, the reversal of magnetization is mainly governed by domain shortening and/or collapse. The end of the black stripe domains appears in the image area before one domain is swept out of the scanned area.

Moreover one clearly sees that the defect observed in Fig. 2(a) pins a domain wall. Indeed, except in Fig. 2(e), i.e., close to the saturation of the sample magnetization, a domain wall is always near the defect. Images, not presented here, have been recorded at intermediate field values between those of Figs. 2(c) and 2(e). These additional images show that the end of the right-hand dark stripe domain moves with increasing magnetic field until it reaches the defect. From this stage, when the external magnetic field is increased from 47% to 53% of H_s , the left-hand dark domain termination still moves over $6\text{ }\mu\text{m}$ while the right-hand dark domain termination remains pinned on the defect. The right-hand dark domain jumps then out of the image for a very small additional increase of the magnetic field value from 53% to 57% of H_s . Finally, when the magnetic field is reset to zero as in Fig. 2(f), a new domain wall is again pinned on the same defect, although the domains configuration is different from the one existing before the large field application. This observation is reproducible with multiple magnetization cycles.

IV. NEAR-FIELD MO IMAGING OF DOMAIN WALLS

It has already been shown that applying an alternating magnetic field of amplitude much smaller than H_s causes a domain wall to oscillate around its location in zero external magnetic field.⁵ In the area where this motion takes place, the magnetization is periodically flipped and results in a MO modulation $\Delta I(\varphi)$ of $I(\varphi)$. Elsewhere, inside the domains, the magnetization is not modified and $I(\varphi)$ is constant [$\Delta I(\varphi)=0$]. Displaying $\Delta I(\varphi)$ through lock-in detection, images exhibit contrasted regions which correspond to the wall motion.

Figure 4 presents two images recorded on the same $14\text{ }\mu\text{m}\times 14\text{ }\mu\text{m}$ sample area. On Fig. 4(a), $I(85^\circ)$ is displayed without external magnetic field according to the static procedure described in Sec. III and Fig. 4(b) is obtained from $\Delta I(45^\circ)$ for an alternating field with an amplitude of a few percents of H_s . The magnetic field modulation frequency is

511 Hz. Several modulation frequencies from 80 Hz to 2 kHz have also been used without any change in the images. In both images the contrast of the MO signal can be reversed by changing the sign of φ . As expected, the contrasted areas in Fig. 4(b) coincide with the boundaries between domains of opposite magnetization in Fig. 4(a). However some of the domain walls in Fig. 4(b) exhibit discontinuities where $\Delta I(\varphi)=0$. These contrastless areas correspond to static points of the walls that we interpret as pinning points. It is very important to note that these points cannot be observed either in the zero magnetic field MO image of Fig. 4(a) or in the topographic image of the surface (which is not reproduced here).

V. CONCLUSION

In summary we have demonstrated in Sec. III the possibility to image magnetic domains in the STOM geometry with polarizer and analyzer almost crossed without using any modulation technique. A high MO contrast between domains of opposite magnetizations is obtained with quite large signal-to-noise ratio for Faraday rotations of about 0.3° . Fine features of the domain wall shape are shown. The MO images, obtained by application of static (Sec. III) or alternating (Sec. IV) external magnetic fields, allow to identify two types of domain wall pinning defects, respectively, correlated or uncorrelated with topographic structures. The results presented here are very promising for high resolution MO imaging of ultrathin (a few tens of nm) metallic magnetic multilayer films with similar Faraday rotations. Moreover the oblique incident angle in total reflection geometry should permit near-field MO imaging of domains not only in materials with perpendicular magnetic anisotropy but also with in-plane magnetization.

ACKNOWLEDGMENTS

We are grateful to A. Thiaville for providing us with garnet samples and fruitful discussions. P. Bertrand is a member of the Délégation Générale pour l'Armement.

- ¹E. Betzig, J. K. Trautman, R. Wolfe, E. M. Gyorgy, P. L. Finn, M. H. Kryder, and C. H. Chang, *Appl. Phys. Lett.* **61**, 142 (1992).
- ²T. J. Silva, S. Schultz, and D. Weller, *Appl. Phys. Lett.* **65**, 658 (1994); T. J. Silva and S. Schultz, *Rev. Sci. Instrum.* **67**, 715 (1996).
- ³C. Durkan, I. V. Shvets, and J. C. Lodder, *Appl. Phys. Lett.* **70**, 1323 (1997).
- ⁴D. Courlon, K. Sarayedine, and M. Spajar, *Opt. Commun.* **71**, 23 (1989); R. C. Reddick, R. J. Warmack, D. W. Chilcatt, S. L. Sharp, and T. L. Ferrel, *Rev. Sci. Instrum.* **61**, 3669 (1990).
- ⁵V. I. Safarov, V. A. Kosobukin, C. Hermann, G. Lampel, and J. Peretti, *Microsc. Microanal. Microstruct.* **5**, 381 (1994).
- ⁶K. Karrai and R. D. Grober, *Appl. Phys. Lett.* **66**, 1842 (1995).
- ⁷J. W. P. Hsu, M. Lee, and B. S. Deaver, *Rev. Sci. Instrum.* **66**, 3177 (1995); M. Lee, E. B. McDaniel, and J. W. P. Hsu, *ibid.* **67**, 1468 (1996).
- ⁸R. S. Decca, H. D. Drew, and K. L. Empson, *Rev. Sci. Instrum.* **68**, 1291 (1997).
- ⁹R. Brunner, A. Bietsch, O. Hollricher, and O. Marti, *Rev. Sci. Instrum.* **68**, 1769 (1997).
- ¹⁰E. Betzig, P. L. Finn, and J. S. Weiner, *Appl. Phys. Lett.* **60**, 2484 (1992).
- ¹¹R. Toledo-Crow, P. C. Yang, Y. Chen, and M. Vaez-Iravani, *Appl. Phys. Lett.* **60**, 2957 (1992).
- ¹²G. A. Valaskovic, M. Holton, and G. H. Morrison, *Appl. Opt.* **34**, 1215 (1995).
- ¹³A. Thiaville, F. Boileau, J. Miltat, and L. Arnaud, *J. Appl. Phys.* **63**, 3153 (1988).

Induction mapping of magnetostrictive materials

Jennifer Dooley

Jet Propulsion Laboratory, Pasadena, California 91109

Marc De Graef^{a)} and Michael E. McHenry

Department of Materials Science and Engineering, Carnegie Mellon, Pittsburgh, Pennsylvania 15213

An energy-filtered magnetic induction mapping technique has been implemented on a JEOL 4000EX equipped with a Gatan imaging filter. A study of the magnetic domain structure in Terfenol-D, a magnetostrictive actuator material, is presented as an example application of the technique. The method is equivalent to differential phase contrast microscopy by the reciprocity theorem. Image simulations of all stages of the induction mapping process are shown to support these observations. © 1998 American Institute of Physics. [S0021-8979(98)47811-3]

INTRODUCTION

There is a growing interest in both room-temperature and very-low-temperature magnetostrictive actuator materials. Terfenol-D, a rare-earth transition-metal magnet, possesses a room-temperature magnetostrictive strain of about 0.2%, the largest known.² Ni_2MnGa exhibits large magnetostrictive strains, which arise from a magnetically induced martensitic transformation in a temperature range near room temperature.³ Polycrystalline rare-earth low-temperature magnets have recently been shown to retain a significant fraction of the magnetostriction of the single crystals, and are considerably less expensive to produce.⁴ Determination of the fine scale magnetic structure is essential for prediction of, among other things, the bulk magnetostrictive strains. In addition, since virtually all engineering parameters of these materials are directly affected by microstructural features, the nature of these materials makes it necessary to closely combine the study of magnetic structure and microstructure. Lorentz microscopy, in particular, the Fresnel and Foucault observation modes,⁵ has for several decades been the dominant observation technique for qualitative magnetic domain observations.

The decreasing length scale of modern electronic and magnetic devices must be accompanied by improvements in the observation techniques used to study their micro- and nanostructures. The low-field sample environment and consequent increase in the focal length of the objective lens required for Lorentz microscopy results in a reduced final image magnification as compared to that of conventional transmission electron microscopy (TEM). This represents a serious limitation in the quantitative study of nanoscale magnetic structures. Furthermore, inelastic scattering in the sample contributes noise to the images, which further limits the attainable resolution of the standard Lorentz modes.

There are very few techniques capable of producing direct maps of the (in-plane) magnetic induction in a thin foil. Differential phase contrast (DPC) microscopy in a scanning TEM⁷ is perhaps the most successful method, but it requires the installation of descanning coils and a four-quadrant de-

tector, which are not accessible in the average research laboratory. For this method, the descanning coils are aligned such that any tilt of the beam arising from the scanning coils is compensated for at the plane of the quadrant detector so that any remaining shift of the beam over the detector is due to the Lorentz deflection. The magnitude of this deflection is measured as the difference signal from opposite quadrants of the detector and can be directly related to the components of the magnetic induction in two orthogonal directions $\pm U$ and $\pm V$. A technique equivalent to DPC by the reciprocity theorem for the TEM was proposed and implemented by Daykin and Petford-Long.⁸ This induction mapping technique has been adapted to the 4000EX+GIF (Gatan imaging filter) combination, the method has been applied to the Terfenol-D system, and simulation algorithms have been created for the mapping technique.

EXPERIMENTAL METHODS

This article presents a summary of energy-filtered Lorentz observations of the Terfenol-D system. A Lorentz microscopy setup, which combines a high-resolution top-entry JEOL 4000EX TEM with a postcolumn GIF, has been previously reported.⁶ With the main objective lens turned off, the sample is mounted in an essentially field-free region. The objective minilens, which sits below the plane of the specimen, provides sufficient field strength to focus the electrons into a diffraction pattern at the selected area aperture plane, thus providing Fresnel and Foucault observation modes. The energy filter provides an additional magnification of approximately $20\times$, and allows for the acquisition of zero-loss images, increasing the signal-to-noise ratio by at least an order of magnitude.⁶ The magnetic resolution of this system is better than 5 nm.

All images in this paper were obtained from a thin foil of Terfenol-D, or $\text{Tb}_{0.73}\text{Dy}_{0.27}\text{Fe}_{1.95}$, which has a cubic Laves phase structure ($a = 0.732$ nm).⁹ Single-crystal rods of Terfenol-D with $[211]$ growth direction were obtained from Etrema, Inc. These were oriented by reflection Laue diffraction and cut into disks with $[01\bar{1}]$ foil normal. Dimpled disks were then jet thinned in a chilled solution of 10% perchloric/90% acetic acid and ion milled for several hours with 4.5 kV

^{a)}Electronic mail: degraef@cmu.edu

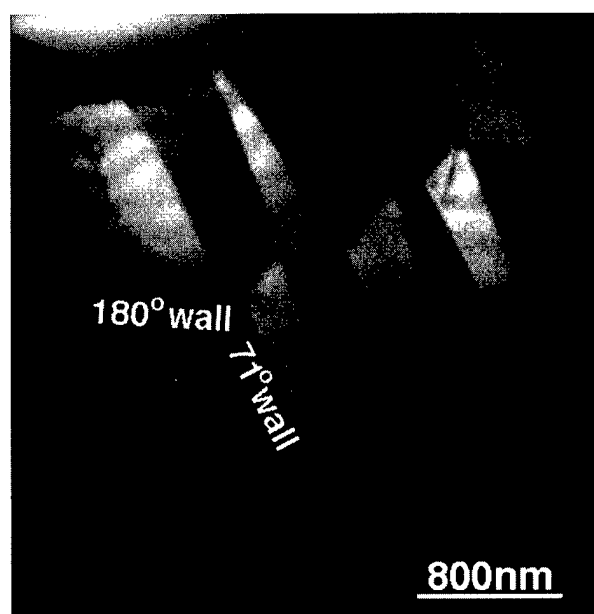


FIG. 1. Foucault image of a representative magnetic domain structure in Terfenol-D. This region is used in the induction maps of Fig. 2.

Ar^+ ions until electron transparent. For a detailed description of the microstructure of this material the reader is referred to Refs. 10, 11, and 6. Figure 1 shows a Foucault image of a characteristic lamellar domain arrangement. This area of the sample is used throughout the paper to illustrate the methods.

Magnetic induction mapping in the TEM was first introduced in Ref. 8 and adapted to the 4000EX+GIF combination in Ref. 6. A converged incident beam, with beam divergence angle θ_c , illuminates the region of interest on the sample. A small aperture truncates the transmitted beam in the back focal plane of the objective minilens and beam tilts are provided through the postspecimen image shift coils. The beam is tilted and images obtained with consecutive tilts are added together (approximating an integral with respect to beam tilt) and constitute the equivalent of the quadrant detector signals in DPC. For full details on the method the reader is referred to Ref. 12.

INDUCTION MAPPING RESULTS

Figure 2(a) shows four series of zero-loss Foucault images (slit width 15 eV), for two orthogonal tilt directions. The reader is referred to Ref. 12 for a description of the calibration of the tilt directions with respect to the microstructure. After aligning the Foucault images in each series they were summed on a per-pixel basis. The sums are shown in Fig. 2(b), along with the difference maps. Since the intensity in the difference map is proportional to the in-plane induction component in one of the two orthogonal directions, the difference maps can be represented as a single vector induction map, as shown in Fig. 2(c).

Using an image simulation algorithm developed by Mansuripur,¹³ a method similar to standard high-resolution simulations has been implemented for the computation of magnetic induction tilt series and difference maps for a given magnetic structure.¹² The results are shown in Fig. 3. The

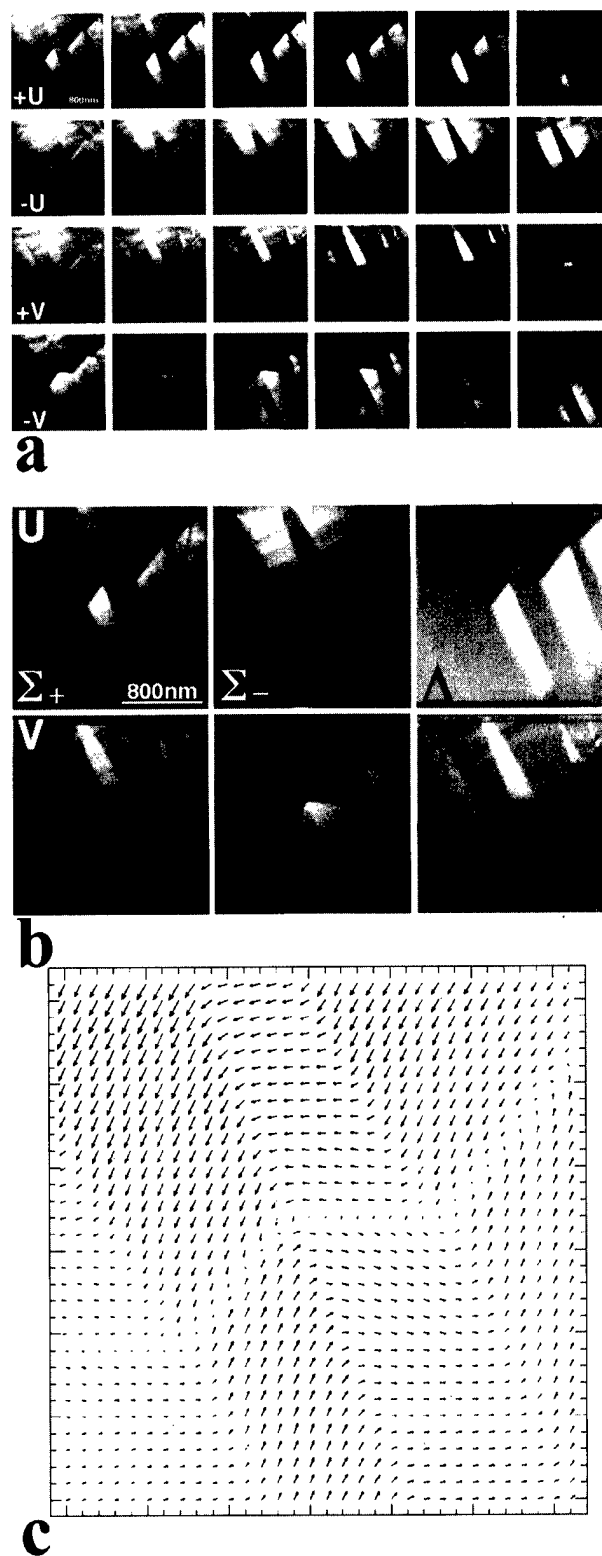


FIG. 2. (a) Foucault images as a function of postspecimen beam tilt for two orthogonal tilt directions. (b) Foucault sums and difference maps. (c) Vector induction map, created from the energy-filtered difference maps.

simulations were carried out for a 16 nm domain-wall width for the 180° Bloch-type wall, 10 nm for the 71° domain walls, a saturation magnetic induction of 1 T, foil thickness of 100 nm, beam divergence angle $\theta_c = 1$ mrad, a beam tilt increment of 3.5 μrad , aperture radius of 0.05 nm^{-1} , and an

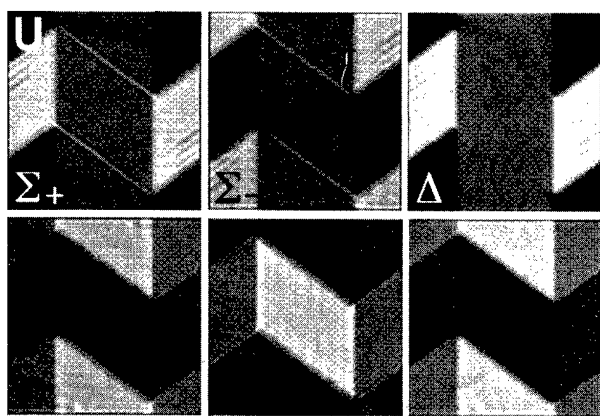


FIG. 3. Simulated summed tiltseries corresponding to Fig. 2(b); the top part of the simulated images is to be compared with the 180° domain-wall in Fig. 2(b).

incident beam energy of 400 kV. Tilt directions in the simulation were taken to be the same as in the experiment. The domain-wall profile from the filtered experimentally reconstructed map is shown in Fig. 4(a). The reconstructed 180° domain-wall width is estimated to be 83 nm, as each pixel corresponds to about 4.14 nm. For this case, one tilt direction was close to the normal of the domain wall. Figure 4(b) shows the simulated reconstructed map and the input profile.

Good qualitative agreement exists between these sets of images, including the presence of a faint bright fringe in the experimental $\pm U$ sums. The reconstructed vector map compares favorably with the experimental map in Fig. 2(b), as do the domain-wall profiles.

ACKNOWLEDGMENTS

The authors would like to thank N. T. Nuhfer for stimulating discussions, and N. Biery for providing the image

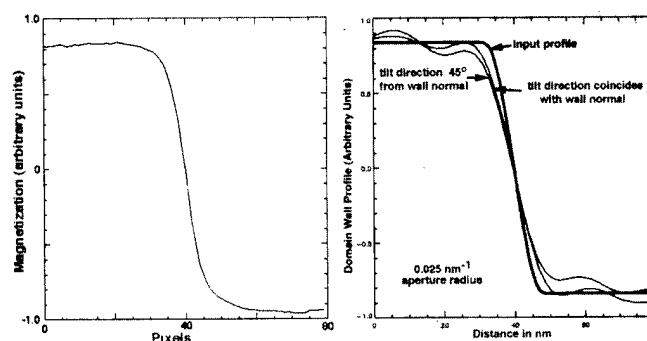


FIG. 4. (a) Line trace of the component of magnetic induction parallel to the domain wall averaged over 35 pixels and plotted over 80 pixels. (b) Comparison of the reconstructed magnetic induction component parallel to the 180° domain wall and the input profile.

alignment procedure used to compensate for image shifts during beam tilting. This work was supported in part by the National Science Foundation under Grant No. DMR 9403621 and by Rhône-Poulenc.

- ¹G. F. Clark, B. K. Tanner, and H. T. Savage, *Philos. Mag. B* **46**, 331 (1982).
- ²D. C. Jiles, *J. Phys. D* **27**, 1 (1994).
- ³K. Ullakko, J. K. Huang, C. Kantner, R. C. O'Handley, and V. V. Kokorin, *Appl. Phys. Lett.* **69**, 1966 (1996).
- ⁴M. Q. Huang, Y. Zheng, and W. E. Wallace, *J. Appl. Phys.* **75**, 6280 (1994).
- ⁵L. Reimer, *Transmission Electron Microscopy* (Springer, Berlin, 1993).
- ⁶J. Dooley and M. De Graef, *Ultramicroscopy* **67**, 113 (1997).
- ⁷J. N. Chapman, P. E. Batson, E. M. Waddell, and R. P. Ferrier, *Ultramicroscopy* **3**, 203 (1978).
- ⁸A. Daykin and A. Petford-Long, *Ultramicroscopy* **58**, 365 (1995).
- ⁹M. Al-Jiboory and D. Lord, *IEEE Trans. Magn.* **26**, 2583 (1990).
- ¹⁰D. Lord, H. Savage, and R. Rosemeier, *J. Magn. Magn. Mater.* **29**, 137 (1982).
- ¹¹R. James and D. Kinderlehrer, *Philos. Mag. B* **68**, 237 (1993).
- ¹²J. Dooley and M. De Graef, *Micron* (in press).
- ¹³M. Mansuripur, *J. Appl. Phys.* **69**, 2455 (1991).

Influence of current density on the magnetization process in active spin-valve elements

X. Portier^{a)} and A. K. Petford-Long

Department of Materials, University of Oxford, Oxford OX1 3PH, United Kingdom

T. C. Anthony and J. A. Brug

Hewlett-Packard Laboratories, 1501 Page Mill Road, Palo Alto, California 94304

Simultaneous magnetoresistance measurements and observation of magnetic domain structures have been performed on active spin-valve elements by means of *in situ* experiments in a Lorentz transmission electron microscope. Two different spin-valve structures with NiFe and NiFe/Co sense layers have been studied with two sizes of rectangular elements. The effect of different applied current values has been analyzed and the addition of a Co layer in the sense layer has a large influence on the spin-valve behavior and on the domain structure. Also, two different processes for magnetic domain growth and motion have been observed for low or high applied current densities.

© 1998 American Institute of Physics. [S0021-8979(98)17711-3]

INTRODUCTION

Numerous studies on spin-valves (SVs) have been performed over the past few years motivated by the promising use of SV structures in magnetoresistive storage systems.¹ A very good overview on SV structures and giant magnetoresistance (GMR) has recently been published.² For a better understanding of the micromagnetics of these materials, previous studies have been carried out on ferromagnetic (FM) thin films objects³ and on SV elements.⁴ In this article, we report on *in situ* experiments which enabled us to observe, by means of Lorentz electron microscopy,⁵ the magnetic domain evolution of active SV elements, namely, those through which different currents are being passed. The goal of this study is to analyze the behavior of active SV elements. We report results on the effect of the applied current value, the effect of the additional Co layer, and also that of the element size.

EXPERIMENTAL DETAILS

In situ experiments and observations in the Foucault mode of Lorentz microscopy were carried out using a modified JEOL 4000EX transmission electron microscope (TEM) operated at 400 kV and fitted with an AMG40 low-field objective lens pole piece. The SVs were deposited on a 40 nm alumina membrane by dc magnetron sputtering in a Sputtered Films, Inc. planetary deposition system. A 70 Oe field defined the easy axis during deposition. More details on the device configuration and fabrication are given elsewhere.⁶ The exchange anisotropy is about 500 Oe and the anisotropy field varies between 3 and 10 Oe depending on the sense layer structure and on the current value. Various currents were applied through the SV elements and, by monitoring the change in applied field (H_a), the GMR ratio of the sample could be plotted using $dR/R = (R - R_{\text{sat}})/R_{\text{sat}}$. The R_{sat} value corresponds to the parallel state of the magnetic

moments in the FM layers. The applied field, parallel to the easy axis and to the long axis of the elements, was changed by 1 Oe every 10 s in order to keep constant any time-dependent effects. This configuration has been preferred to the most commonly used one in recording applications (applied field along the hard axis) because the effects induced either by the sense layer structure or by the current density are more visible.

RESULTS AND DISCUSSION

The different configurations investigated are reported in Table I. For each of the samples, we have plotted the GMR curves for current values of 0.3, 2, and 3.5 mA during simultaneous observation of the magnetization reversal. Figure 1 shows the results obtained for samples 1 and 3 ($10 \mu\text{m} \times 30 \mu\text{m}$ elements with NiFe [Fig. 1(a)] and NiFe/Co [Fig. 1 (b)] sense layers). One can notice a shift of the curves with respect to remanence in both cases. This feature is most probably a result of FM coupling between the FM layers, mainly explained by roughness at the interfaces between the magnetic and nonmagnetic layers. According to the data in Table II, higher GMR ratios (in agreement with previous studies⁷), higher FM coupling, and higher coercivity (H_c) of the sense layer are observed for sample 3 than for sample 1 due to the presence of Co in the sense layer. With a higher current through the elements, there is a decrease in the GMR ratios, coercivities, and FM coupling in both cases and the slope of the GMR curves becomes more abrupt (more particularly for

TABLE I. Summary of the different configurations investigated.

Sample	Structure	Thicknesses (nm)	Sizes (μm)
1	NiFe/Cu/Co/NiFe/MnNi	8/3/2/6/25	10×30
2	NiFe/Cu/Co/NiFe/MnNi	8/3/2/6/25	4×10
3	NiFe/Co/Cu/Co/NiFe/MnNi	6/2/3/2/6/25	10×30
4	NiFe/Co/Cu/Co/NiFe/MnNi	6/2/3/2/6/25	4×10

^{a)}Electronic mail: xavier.portier@materials.ox.ac.uk

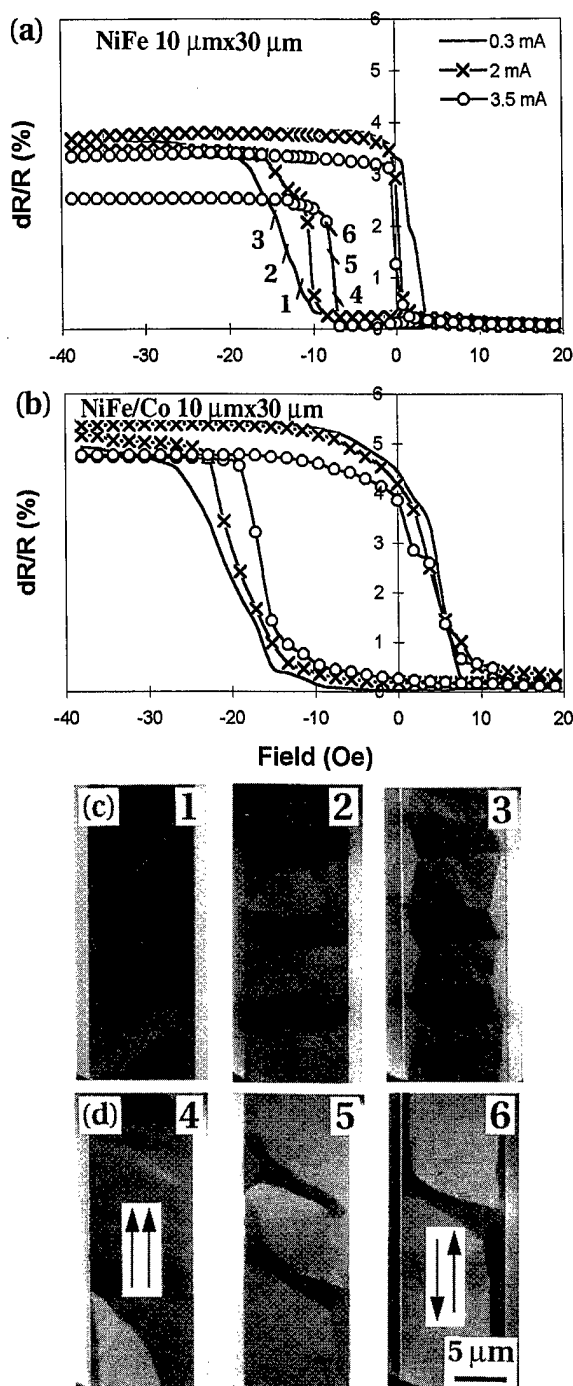


FIG. 1. (a), (b) Plots of GMR curves vs applied field for samples 1 and 3, respectively, and for current values of 0.3, 2, and 3.5 mA. The numbers in (a) refer to the Foucault images in (c) and (d) showing the evolution of the domain structure of sample 1 during the P-AP transition for current values of 0.3 and 3.5 mA, respectively. The applied field is pointing down vertically and the easy axis is in the opposite direction. Contacts are on the tops and bottoms of the images.

sample 1). Figures 1(c) and 1(d) show Foucault images of sample 1, corresponding to the transition from parallel (P) to antiparallel (AP) alignment of the magnetization in the FM layers for applied current values of 0.3 and 3.5 mA, respectively. The contrast shows the domain structure in the sense layer during the reversal assuming that the pinned-layer

magnetization is fixed and is parallel to the long axis of the element. The difference in slope observed in Fig. 1(a) is explained by a quicker reversal mechanism for the higher current values. For a low current, the magnetization direction of the sense layer gradually rotates within the domains (leading to an increase in ripple contrast) as the applied field changes [see images 2 and 3 in Fig. 1(c)]. The domain structure corresponding to the higher current value [see images 5 and 6 in Fig. 1(d)] shows larger domains with no ripple contrast. For sample 1, the limit of current value above which the SV element begins to be damaged by heating effects is around 4 mA. The GMR curve of sample 1 for the current value of 3.5 mA is not closed, meaning that some pinning effects between the two FM layers begin to affect the reversal mechanism. $R(I)$ and $R(T)$ measurements have been performed on sample 1 (not shown). For a current value of 3.5 mA, the resistance value has increased from 48Ω (at room temperature) up to 60Ω which corresponds to the resistance value obtained for a temperature of about 230°C . We therefore believe that the difference in reversal mechanism between Figs. 1(c) and 1(d) is a result of the increase in thermal energy provided by the 3.5 mA current value. For sample 3, the domain configuration (not shown) at 0.3 mA is identical to that of sample 1. At 3.5 mA, its domain structure is similar to that obtained for 0.3 mA but with much less ripple contrast.

Figures 2(a) and 2(b) show the GMR curves recorded for samples 2 and 4 ($4 \mu\text{m} \times 10 \mu\text{m}$ elements with NiFe and NiFe/Co sense layers, respectively) for applied current values of 0.3, 2, and 3.5 mA. Figures 2(c) and 2(d) are Foucault images of sample 2 taken during the P-AP transition for applied current values of 0.3 and 3.5 mA, respectively. The differences between NiFe and NiFe/Co SV properties as well as the evolution of the GMR ratio, coercivity, and FM coupling with the various current values are similar to the previous case. However, one can observe a much higher coercivity (see Table II). Such a result is the consequence of the shape anisotropy which increases as the stripe width is reduced ($H_c = 4\pi Mt/h$ where M is the saturation magnetization, t the thickness of the film, and h the stripe width). Also, the presence of pinning sites explained by corrosion and oxidation from the sides which occur during lithographic process could favor an increase in coercivity.⁸ Otherwise, the domain configurations shown in Figs. 2(c) and 2(d) are very similar to those corresponding to the previous section despite the lower size of the element. This feature allows us to think that the domain structure is more related to the *shape* of the element than to its size.

We want to emphasize that all these results and observations are very reproducible up to the limit of the current values given in Table II. These limits are more than one order of magnitude lower than that used in actual SV recording heads.⁹ The higher limit (4.5 mA) for samples 3 and 4 is consistent with the good thermal stability of Co in metallic multilayers.¹⁰

CONCLUSION

These results confirm clearly that the presence of a thin cobalt layer in the sense film increases the GMR ratio, the

TABLE II. Summary of the magnetic properties.

Sample	H_c sense layer	H_c sense layer	GMR ratio	GMR ratio	Limit ^a of	FM coupling	FM coupling
	0.3 mA (Oe)	3.5 mA (Oe)					
1	8	4	3.7	3	4	5	3.5
2	15	7	3.5	3	4	6	3
3	13	9	5.2	4	4.5	8	8
4	20	15	4.5	4	4.5	10	10

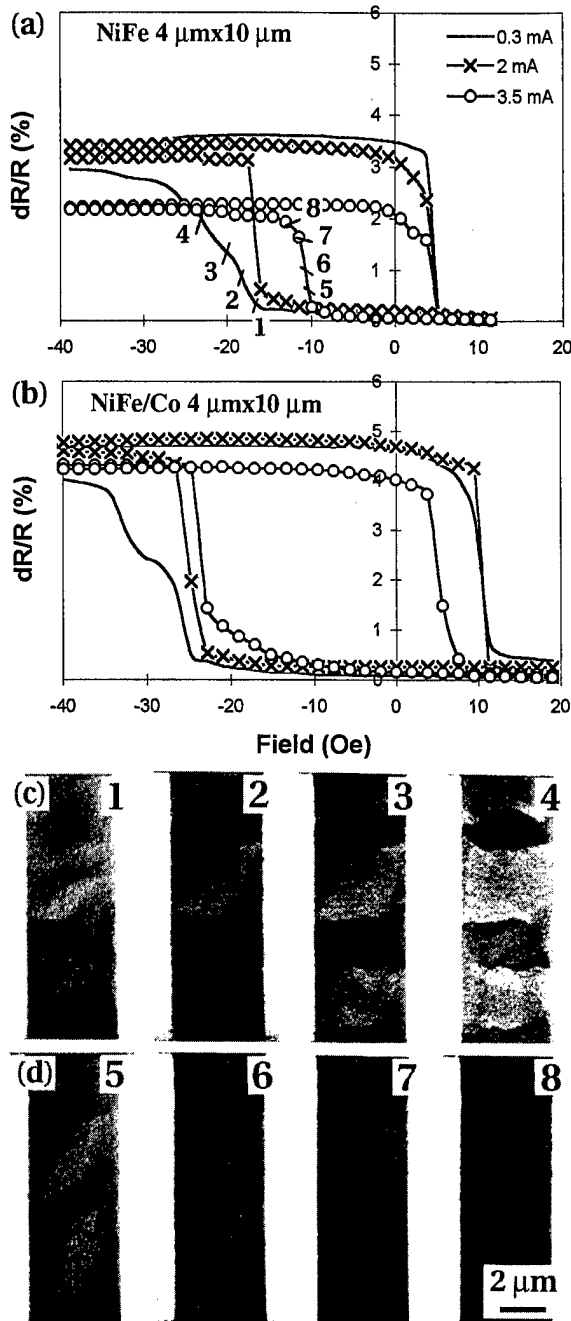
^aLimit above which irreversible heating damage to SVs occurs.

FIG. 2. (a), (b) GMR curves from samples 2 and 4. Numbers in (a) refer to the Foucault images in (c) and (d) which have been taken during the P-AP transition of sample 2 for current values of 0.3 and 3.5 mA, respectively.

coercivity, the FM coupling, and the thermal stability of the SV element. A decrease in the element size results in an increase in coercivity, probably due to the shape anisotropy, but it is worth noticing that the domain structure is very similar for the two sizes studied, indicating that the shape of the element is crucial for determining the domain configuration. An increase in the current density decreases the GMR ratio and the coercivity, and induces quicker transitions (lower anisotropy field) and larger domains for the reversal mechanism, these effects being more pronounced for the NiFe sense layer SV. As the contribution of the field induced by the sensing current is quite low for such a range of current values, the differences in domain structures between low and high current densities are mainly due to the increase in thermal energy of the element.

ACKNOWLEDGMENTS

This study has been supported by Hewlett-Packard Laboratories in Palo Alto through a collaboration with the Department of Materials in Oxford University (UK). A.K.P.L. also thanks the Royal Society for financial support.

¹B. Dieny, V. S. Speriosu, S. Metin, S. S. P. Parkin, B. A. Gurney, P. Baumgart, and D. R. Wilhoit, *J. Appl. Phys.* **69**, 4771 (1991).

²B. Dieny, *J. Magn. Magn. Mater.* **36**, 335 (1994).

³A. B. Johnston, J. N. Chapman, B. Khamsempour, and C. D. W. Wilkinson, *J. Phys. D* **29**, 1419 (1996).

⁴X. Portier, A. K. Petford-Long, R. C. Doole, J. A. Brug, and T. C. Anthony, *Appl. Phys. Lett.* **71**, 2032 (1997).

⁵J. P. Jakubovics, *Electron Microscopy in Materials Science*, edited by E. Ruedl and U. Valdre (Commission of the European Communities, Brussels, 1975), Vol. IV, p. 1303.

⁶X. Portier, A. K. Petford-Long, R. C. Doole, J. A. Brug, and T. C. Anthony, *IEEE Trans. Magn.* **33**, 3574 (1997).

⁷S. S. Parkin, *Phys. Rev. Lett.* **71**, 1641 (1993).

⁸J. Szucs, T. O'Brien, D. K. Lottis, S. Gangopadhyay, S. Mao, and E. Murdock, *J. Appl. Phys.* **81**, 4014 (1997).

⁹C. Tsang, R. E. Fontana, T. Lin, D. E. Heim, V. S. Speriosu, B. A. Gurney, and M. L. Williams, *IEEE Trans. Magn.* **30**, 3801 (1994).

¹⁰E. Y. Chen, S. Teharani, T. Zhu, M. Durlam, and H. Garonkin, *J. Appl. Phys.* **81**, 3992 (1997).

Magnetic domains of single-crystal $\text{Nd}_2\text{Fe}_{14}\text{B}$ imaged by unmodified scanning electron microscopy

L. H. Lewis and J.-Y. Wang^{a)}

Department of Applied Science, Brookhaven National Laboratory, Upton, New York 11973-5000

P. Canfield

Ames Laboratory and Department of Physics and Astronomy, Iowa State University, Ames, Iowa 50011

The stray flux manifestations of surface magnetic domains found in as-grown $\text{Nd}_2\text{Fe}_{14}\text{B}$ single crystals were observed, with a resolution in the range of $1\text{ }\mu\text{m}$, using conventional scanning electron microscopy (SEM) without instrumental modifications. A modified image-distortion mode was applied to image the three-dimensional stray flux emanating from the sample. The simplicity of the technique and the ready adaptability of the SEM to such modifications as *in situ* current and magnetic field application suggest that the results of this study may be extended to investigations of other materials of technological interest, such as perpendicular media disks. © 1998 American Institute of Physics. [S0021-8979(98)30411-9]

INTRODUCTION

The magnetic domain structure of magnetically ordered materials provides information of both fundamental and applied technological interest. Data concerning the micromagnetic state, the influence of inhomogeneities on the position of domain walls, and direct determinations of the domain size and behavior under dynamical conditions are useful for the determination of materials parameters as well as for the confirmation of modeling predictions. On the more practical side, magnetic domain imaging can be used as a quick way to ascertain the presence, character, and effects of defects in recording media, recording heads, and transformer alloys.

Magnetic domain images may be generated by a variety of techniques, each with its particular strengths and drawbacks.¹ Scanning electron microscopy (SEM) allows magnetic domains of bulk materials to be imaged by the deflection of a beam of incident electrons from the surface of a ferromagnetic material under the influence of $\mathbf{F}_{\text{Lorentz}}$. In this work, the applicability of SEM for imaging magnetic domains is demonstrated on a single-crystal specimen of $\text{Nd}_2\text{Fe}_{14}\text{B}$. It is hoped that a demonstration of the relative ease of this technique, combined with the adaptability of the SEM to such modifications as external field and current application as well as environment and temperature control, may prove to be helpful for researchers in both academia and industry.

EXPERIMENTAL DETAILS

Single crystals with the composition $\text{Nd}_2\text{Fe}_{14}\text{B}$ were grown out of a Nd-rich melt from high-purity elements placed in a tantalum crucible and cooled at $\sim 1\text{ }^\circ\text{C/h}$ from 1190 to 800 $^\circ\text{C}$. After cooling, well-formed prismatic crystals were removed from the excess flux. Room-temperature demagnetization curves indicate that the crystal possesses a coercivity under 1 Oe.

The magnetic domain observation was performed on a JEOL Model 6400 scanning electron microscope using a LaB_6 filament operated at 6 kV and 9 nA. The collector bias voltage was set at the factory to vary with the accelerating voltage, thus producing a high signal-to-noise ratio. The scanning electron microscope has not been modified or augmented in any way. Depending upon the domain characteristics of the material under investigation, either the type I or the type II contrast mode is available in SEM to image magnetic domains.² Type I contrast is applicable when the emitted secondary electrons possess a relatively low kinetic energy ($< 10\text{ eV}$) sensitive to deflection by the stray field emanating from the surface of the magnetic material. Type I contrast is operative on high anisotropy, uniaxial materials with surface stray fields unconfined by closure domains to remain within the material, which are characteristics of $\text{Nd}_2\text{Fe}_{14}\text{B}$. These surface stray fields reside above alternate domain walls and exert Lorentz forces $\mathbf{F}_{\text{Lorentz}}$ on the secondary electrons which are deflected in opposite directions, depending upon the polarity of the stray field. Magnetic contrast is produced when an unequal flux of secondary electrons reach the detector, positioned at an angle to the sample's surface. In this manner the intensity of domain contrast varies from a maximum to a minimum across a single domain.^{3,4} The domain contrast obtained by SEM is highly influenced by the surface morphology, because secondary electrons also give rise to a topographical image. In order to insure that the crystal surfaces were as smooth as possible, the specimen was mounted in a Gatan dual ion mill on a special sample holder to accommodate its thickness. The specimen surfaces were first ultrasonically cleaned in acetone and then ion milled in an Ar^+ beam for a total of 6 h at 3 kV and 0.5 mA. Metallic luster, in addition to a significant increase in the clarity of the domain images, was then obtained after this treatment. Experiments were conducted with the samples in the "as-is" condition except for the surface cleaning procedure described above. The initial working distance of the microscope was set at 39 mm, where it is ex-

^{a)}Present address: Applied Materials, 3050 Bowers Ave., Santa Clara, CA 95054; electronic mail: lhlewis@bnk.gov

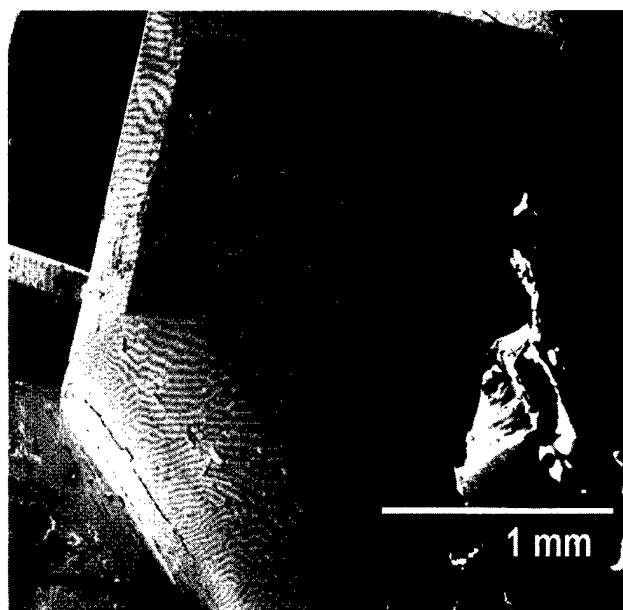


FIG. 1. Macroscopic view of the domain configuration on the (001) surface of the $\text{Nd}_2\text{Fe}_{14}\text{B}$ crystal.

pected that the external field from the objective lens would have little effect on the sample.⁵ Optical Kerr microscopy was also performed on same crystal at Rhône-Poulenc Inc. for image comparison.

RESULTS AND DISCUSSION

Figure 1 presents the familiar maze pattern of domains visible on the (001) plane of the $\text{Nd}_2\text{Fe}_{14}\text{B}$ single crystal. No change of the macroscopic domain structure of the $\text{Nd}_2\text{Fe}_{14}\text{B}$ crystal was observed with change in focusing strength, even at the shortest working distance allowed by the system (8 mm). Thus the magnetic field, due to objective lens, experienced by the sample is less than the coercivity of the crystal (1 G). Higher magnifications of the maze pattern reveal a fine structure which appears to consist of strings of neutral-grey beads separated by light and dark undulating lines. Figure 2(a) shows the magnetic domain images formed by electrons influenced by the Lorentz force $+F_{\text{Lorentz}}$. Features on the order of $1\ \mu\text{m}$ may be resolved. Each "bead" in the string is elliptical in shape, with the eccentricity increasing from round on the (100) surface to more elongated on other surfaces. The depth-of-field of the secondary electron imaging process produces a third dimension, causing the strings of beads to appear either concave-up or concave-down in alternate rows. By rotating the sample through an angle of 180° a change in the contrast is produced, because the Lorentz force changes in sign. This phenomenon is shown in Fig. 2(b), where the circled feature which possesses a concave-up appearance in the top portion of Fig. 2(b) possesses a concave-down appearance in the bottom portion of the figure. Kerr microscopy, Fig. 2(c), confirms that imaged "beads" are in reality spike domains, residing in rows of alternating magnetization between the larger stripe or "parallel plate" domains which extend through the bulk of the material. Spike domains are expected to form on the surfaces of uniaxial magnetic crystals with very high anisotropies,

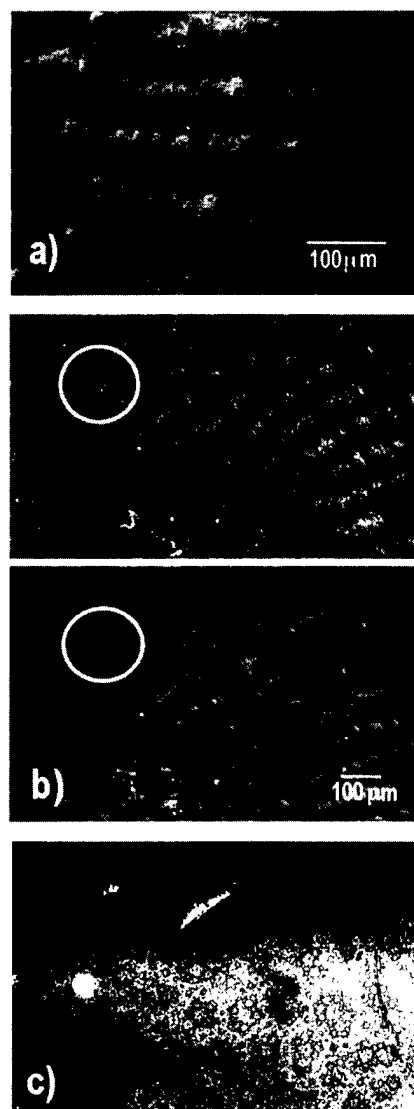


FIG. 2. (a) Higher-magnification image of the $\text{Nd}_2\text{Fe}_{14}\text{B}$ crystal, illustrating the fine structure of the domains. (b) Top: domain structures imaged at a rotation angle of 0° . Bottom: Specimen rotated by 180° relative to the original orientation. Circled regions indicate an inversion of the domain depth of field contrast. (c) Kerr micrograph of the same crystal surface imaged in (a) and (b).

such as $\text{Nd}_2\text{Fe}_{14}\text{B}$, that cannot easily form closure domains. The increased eccentricity of the spike domains found on surfaces oblique to the (001) surface may be understood as a manifestation of flux minimization for surfaces that contain only a component of the easy direction, as discussed by Goodenough.⁶ No domain contrast was observed on a surface that is parallel to an easy direction, such as a $(hk0)$ surface.

A novel feature of using secondary electrons to image magnetic materials is that the demagnetizing stray fields present at the material's surface can be viewed three dimensionally, as shown in Figs. 3(a)–3(c). The (001) surface of the sample is tilted such that there is a shallow angle with respect to the optical axis of the microscope. The fringing fields appear as parallel rows of hillocks separated by narrow troughs, suggesting that the origin of the stray fields are the parallel plate/maze domains that extend through the bulk of the crystal, not the surface spike domains.

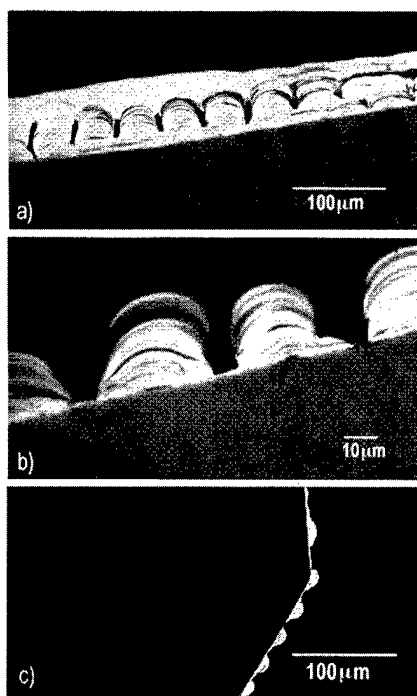


FIG. 3. (a) Image of the surface stray fields emanating from the crystal. (b) Enlargement of (a), illustrating the stray-field trough and hillock formations; (c) end-on view of surface flux from two crystallographic facets.

Generally, the image quality of magnetic contrast generated by F_{Lorentz} in SEM is generally poor. Both extensive theoretical⁷⁻⁹ and experimental¹⁰⁻¹² studies have been conducted to seek optimal parameters to improve the image quality. In most cases sample surface decoration^{13,14} or extensive image processing¹⁵ is still required. Recent work by others indicated that it was necessary to externally alter the detection system of the secondary electrons; Szmaja¹⁵ introduced an aperture in front of the secondary electron collector to act as an energy selector. Instead of having such an attachment inside the specimen chamber, the JEOL 6400 SEM is equipped, at the factory, with an automated bias adjustment circuitry to the collector which itself then acts as an energy filter. It should be borne in mind that this technique is most suitable for materials with a large, perpendicular magnetization vector because the resolution of the image is proportional to the Lorentz force of the excitation volume, as well as inversely proportional to the working distance between

the detector and the specimen. However, materials with smaller magnetizations relative to $\text{Nd}_2\text{Fe}_{14}\text{B}$ may be imaged, with comparable resolution, using a smaller electron accelerating voltage.

A high density of reversed spike domains are observed on all surfaces except the easy-plane (110) surface, with a resolution on the order of $1\text{ }\mu\text{m}$. This technique may prove to be useful for a quick and relatively simple characterization of a magnetic material surface condition and domain structure. It has the additional advantage over other magnetic domain imaging techniques in that a large area of material may be examined at one time. The simplicity of the technique and the ready adaptability of the SEM to such modifications as *in situ* current and magnetic field application may allow direct simulations and observations of a magnetic material operational performance.

ACKNOWLEDGMENTS

The authors thank Professor R. Gambino, Dr. W. McCallum, and Dr. B.-M. Ma of Rhône-Poulenc Inc. for helpful discussions and assistance. Research was performed under the auspices of the U.S. Department of Energy, Division of Materials Sciences, Office of Basic Energy Sciences under Contract No. DE-AC02-76CH0001. Ames Laboratory is operated by Iowa State University for the Department of Energy under Contract No. W-7405-ENG-82.

¹M. R. Scheinefein, J. Unguris, D. T. Pierce, and R. J. Celotta, *J. Appl. Phys.* **67**, 5932 (1990).

²J. P. Jakubovics, *Magnetism and Magnetic Materials*, 2nd ed. (University Press, Cambridge, 1994).

³D. C. Joy and J. P. Jakubovics, *Br. J. Appl. Phys. Ser. 2* **2**, 1367 (1969).

⁴T. Yamamoto and K. Tsuno, *Phys. Status Solidi A* **28**, 479 (1975).

⁵A. Gopinth, *Quantitative Scanning Electron Microscopy*, edited by D. B. Holt (Academic, New York, 1974).

⁶J. B. Goodenough, *Phys. Rev.* **102**, 356 (1956).

⁷D. J. Fathers, J. P. Jakubovics, D. C. Joy, D. E. Newbury, and H. Yakowitz, *Phys. Status Solidi A* **20**, 535 (1973).

⁸G. A. Jones, *Phys. Status Solidi A* **36**, 647 (1976).

⁹O. C. Wells, *J. Microsc.* **144**, RP-1 (1986).

¹⁰G. W. Kammlott, *J. Appl. Phys.* **42**, 5156 (1971).

¹¹D. J. Fathers, J. P. Jakubovics, D. C. Joy, D. E. Newbury, and H. Yakowitz, *Phys. Status Solidi A* **22**, 609 (1974).

¹²J. Fidler, H. Kirchmayr, and P. Skalicky, *Philos. Mag.* **35**, 1125 (1977).

¹³R. Gemperle, V. Kambersky, J. Simsova, L. Murtinová, L. Pust, P. Gommert, W. Schuppel, and R. Gerber, *J. Magn. Magn. Mater.* **118**, 295 (1993).

¹⁴R. Gemperle, L. Murtinová, and V. Kambersky, *Phys. Status Solidi A* **158**, 229 (1996).

¹⁵W. Szmaja, *J. Magn. Magn. Mater.* **153**, 215 (1996).

A flexible two-dimensional phase correction for interleaved echo-planar imaging reconstruction

Haiying Liu^{a)}

Department of Radiology, University of Minnesota, Minneapolis, Minnesota 55455

Interleaved echo-planar imaging (EPI) is a fast clinical magnetic resonance imaging (MRI) scheme that obtains multiple echoes with a proper phase encoding (PE) strategy to generate multiple k -space PE lines. Since these PE data lines are from different echoes that may carry different phase and amplitude errors originating from the static magnetic field inhomogeneity and nuclear spin relaxation, to form an image free of artifacts, both phase and amplitude errors need to be compensated properly. To address this issue, we have developed a general image reconstruction technique which is capable of accomplishing two-dimensional (2D) phase correction for image reconstruction of interleaved EPI data. In this technique we formulated the reconstruction as a problem of finding an optimal solution to a set of linear algebraic equations corresponding to an imaging measurement. The phase errors, as well as other constraints, can be incorporated into these equations. The final solution can be obtained by inverting the coefficient matrix of the equation via a complex singular value decomposition (SVD) procedure, free of k -space data gridding. 2D phase corrected images have been successfully reconstructed using a set of imaging data acquired on a clinical MRI scanner. The significance of the work is that it has demonstrated that the 2D spatial phase correction can be accomplished for a set of interleaved EPI acquisition. Also, this is a flexible image reconstruction method for further improving the resulting image quality. © 1998 American Institute of Physics. [S0021-8979(98)30511-3]

Interleaved echo-planar imaging (EPI) has already been widely used for many clinical magnetic resonance imaging (MRI) exams to achieve both short scan time and high spatial image resolution since it was first proposed by Rzedzian,¹ Farzaneh,² and Cho,³ then implemented by McKinnon⁴ and Butts⁵ in the early 1990's. The interleaved EPI technique obtains multiple echoes at different echo times (TE) for each repetition interval or each excitation with an oscillatory readout gradient waveform as shown in Fig. 1. This allows obtaining multiple k -space encoding lines per shot or per MR signal excitation (Fig. 2). Since in the technique the phase encoded data lines are coming from different echoes corresponding to different echo times due to main field inhomogeneity and spin relaxation, these different echoes may carry different errors in both amplitude and phase. To form an image free of artifacts, both phase and amplitude errors, as well as discontinuities, need to be compensated either by sliding the data sampling window³⁻⁵ or performing phase correction. It is known that the acquisition scheme using nonsliding data sampling window for the EPI acquisition using multiple shots suffers the same problems. However, such an approach for EPI with an appropriate phase correction scheme promises a relatively simple alternative in practice. Many phase correction methods have been developed for matching data of different k -space segments. Due to the intrinsic difficulty of the problem, most of them are only one dimensional in nature. Actual phase error due to susceptibility at a given echo time is often spatially two dimensional.

To obtain an image of an object, such as the human body, the object is placed in a very strong and uniform static magnetic field typically 1.5 T generated by a cylindrical shaped superconducting magnet, a sinc function modulated radio-frequency (rf) pulse is applied to the object from a rf antenna in concert with a slice select (SS) magnetic field gradient to excite proton nuclear spins within a thin slice of the object at a desired orientation. These excited spins are then spatially encoded according to their in-plane locations using two sets of magnetic field gradients varying linearly in space along two orthogonal orientations (Fig. 1). The corresponding spatially encoded MR signals are detected, amplified, demodulated, digitized, and transferred to a computer for storage, processing, and display. A digital image representation of the object is formed from these MR signals

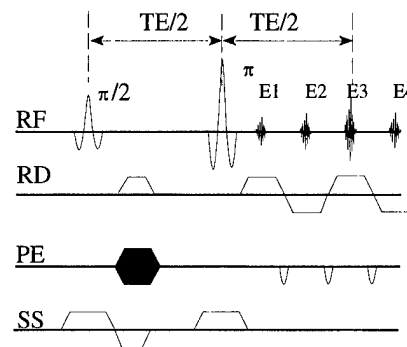


FIG. 1. The gradient and rf profiles for a four-echo interleaved EPI pulse sequence. E1, 2, 3, 4 denote four different MR gradient echoes of the imaging sequence, respectively.

^{a)}Electronic mail: Haiying.Liu-1@tc.umn.edu

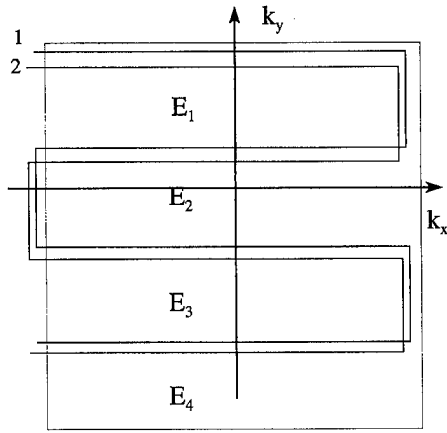


FIG. 2. Traversal of the four-echo interleaved EPI data acquisition in k -space. The rectangular k -space area is partitioned into four equal segments which are filled by different echoes, respectively. Index 1 and 2 denote the k -space trajectories of first and second excitation, respectively.

known as raw data that cover an area in 2D k space sufficiently large and dense for a required spatial resolution and field of view (FOV) using discrete Fourier transformation (DFT) or in most cases fast Fourier transformation (FFT). Although FFT based reconstruction is the most common method in MRI, it becomes less flexible for accomplishing a 2D phase correction. To address this problem, a 2D image reconstruction for the multiple shot EPI technique can be formulated as a numerical problem of finding a solution to an integral or linear equation as shown below:

$$\int_{-\infty}^{+\infty} \int_{-\infty}^{+\infty} [\rho(x,y) + n(x,y)] e^{i[\varphi_J(x,y) + k_x x + k_y y]} dx dy = s_J(k_x, k_y), \quad (1)$$

where $\rho(x,y)$ represents the unknown spin density function for a finite size object to be reconstructed, $n(x,y)$ denotes a noise contribution, $\varphi_J(x,y)$ is the 2D phase error induced by the static magnetic field inhomogeneity at the corresponding echo time indexed by J , and $s_J(k_x, k_y)$ denotes a measured raw data point corresponding to the k -space coordinate pairs of k_x, k_y commonly known as for the read, phase directions, respectively. In digital imaging, measured values for k_x, k_y are discrete and uniformly spaced. They can be related to the read $G_{rd}(t)$ and phase $G_{pe}(t)$ gradient profiles as follows:

$$k_x = \gamma \int_0^{TE} G_{rd}(t) dt, \quad (2)$$

$$k_y = \gamma \int_0^{TE} G_{pe}(t) dt,$$

where γ is the gyromagnetic ratio, and t denotes the sequence timing with the center of rf excitation as zero. For completely encoding an object in discrete digital image representation which consists of N row by N column pixels and covers a squared field of view of $L \times L$, the largest spacing Δk between neighboring points in k space is $2\pi/L$, and the maximum value k_{\max} is $N/2 \Delta k$. Furthermore, the noise term $[n(x,y)]$ can be assumed to be spatially and temporally uncorrelated. To seek an optimal solution for the density func-

tion $\rho(x,y)$ satisfying Eq. (1) we constructed a cost functional from a total squared error between a prediction and the measurement as follows:

$$E = \sum_{J,k \in K_J} |s_J(k_x, k_y) - \hat{s}_J(k_x, k_y)|^2, \quad (3)$$

where the integer number J denotes an echo index ($J = 0, 1, \dots, N_{\text{echo}} - 1$), k stands for $\{k_x, k_y\}$, K_J represents an area or a segment in the k space covered by the J th echo data, and “ \hat{s} hat” denotes a predicted k -space data point. Let us define this predicted k -space data point in the context of discrete image representation as

$$\begin{aligned} \hat{s}_J(k_x, k_y) &= \int_{-\infty}^{+\infty} \int_{-\infty}^{+\infty} \rho(x,y) e^{i(\varphi_J + k_x x + k_y y)} dx dy \\ &\approx \Delta x \Delta y \sum_{x=-L/2}^{+L/2} \sum_{y=-L/2}^{+L/2} \rho(x,y) e^{i(\varphi_J + k_x x + k_y y)}, \end{aligned} \quad (4)$$

where both x and y denote a set of discrete positional variables corresponding to each image pixel. Then we seek a solution for the spin density function that minimizes the cost functional. In this framework, a best estimation for the object spin density $\rho(x,y)$ was achieved through an optimization procedure in which the error functional was minimized with respect to the variation of $\rho(x,y)$. After some algebraic reductions, we derived a set of linear equations for the subsequent image reconstruction assuming that the size of image is L :

$$\begin{aligned} \sum_{y'} \rho(x, y') \sum_{J, k_y \in K_J^y} e^{i[\varphi_J(x, y') - \varphi_J(x, y)]} e^{ik_y(y - y')} \\ = \sum_{J, k_y \in K_J^y} e^{-i\varphi_J(x, y)} e^{-ik_y y} s_J(x, k_y), \end{aligned} \quad (5)$$

where y represents a set of discrete y coordinates within a finite range, the division of the y coordinate depends on the resolution limit, $s_J(x, k_y)$ is the data array $s_J(k_x, k_y)$ after performing a first discrete Fourier transformation with respect to k_x . For a fixed x coordinate, the system equation above for image reconstruction can be expressed in a form of matrix equation, $H\rho = f$, where H denotes a complex squared matrix whose elements are given by

$$H_{mn} = \sum_{J, k_y \in K_J^y} e^{i[\varphi_J(x, y_m) - \varphi_J(x, y_n)]} e^{ik_y(y_n - y_m)}. \quad (6)$$

ρ is the unknown column intensity vector for the image or spin density function of the object, whose m th element is defined as

$$\rho_m = \rho(x, y_m), \quad (7)$$

and f denotes an auxiliary complex column vector, whose n th element can be computed from the measured MR signal $S(x, k_y)$ as

$$f_n = \sum_{J, k_y \in K_J^y} e^{-i\varphi_J(x, y_n)} e^{-ik_y y_n} s_J(x, k_y). \quad (8)$$

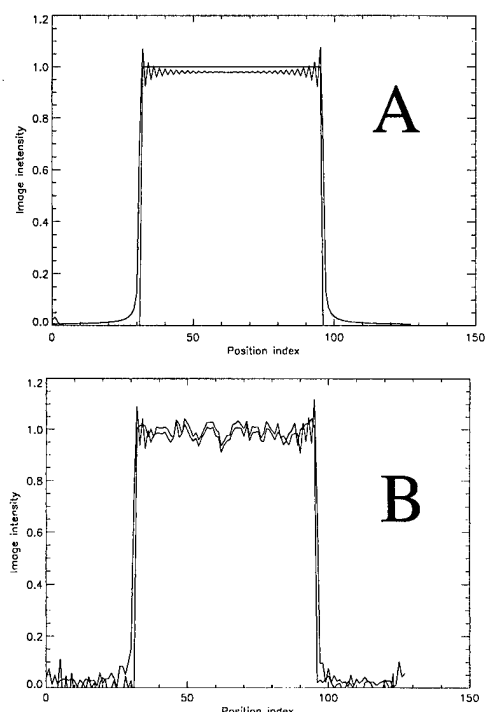


FIG. 3. Image of a 1D rectangular shaped object reconstructed using FFT and ART techniques. The profile showing ripples at the edges corresponds to the FFT technique. The almost perfect profile corresponds to the ART technique with 2D phase correction (A: without addition of noise; B: with noise).

The H matrix carries the information of a specific encoding strategy, as well as the phase and amplitude errors. Generally, for nonzero phase error, the matrix element $H_{m,n}$ is no longer shift invariant or only a function of parameter $(m-n)$. Therefore, a shift invariant point spread function does not exist for the problem. In practice, all the required phase error information can be estimated from a set of low spatial resolution image acquisitions for all echoes using the same imaging sequence except that all the phase encoding blips are modified. Since the typical phase errors at different echo times in MRI are low spatial resolution, this estimation for the phase error is often adequate. The optimal solution for the discrete image representation can be written symbolically as

$$\hat{\rho} = H^{-1}f, \quad (9)$$

where H^{-1} denotes an inverse of the complex H matrix, assuming that the inverse of H matrix does exist. In practice, this H matrix was first decomposed into a product of three matrices using a robust method known as complex singular value decomposition (SVD) as shown below:

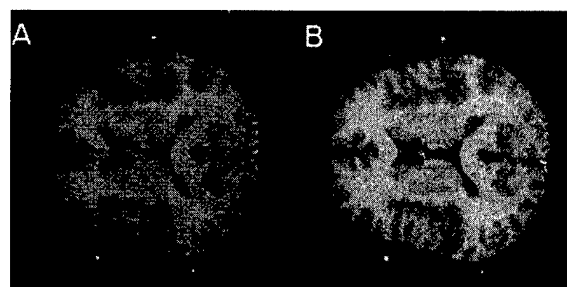


FIG. 4. A typical transverse MR-ART image of human brain (A) in comparison with that of DFT (B) at 1.5 T using an interleaved EPI sequence with an effective TE of 30 m.

$$H = UWV^T, \quad (10)$$

where U and V are two complex unitary matrixes, and W is a diagonal matrix. The inversion of the H matrix was easily obtained by carefully inverting the stable (or nonzero) elements of the diagonal W matrix.

Numerical simulations have been performed on a computer to validate the new 2D MR algebraic reconstruction technique (MR-ART). First, we numerically generated a set of testing data from a known 1D object function mimicking a four-echo multiple shot EPI technique. Furthermore, we incorporated a set of known, spatially dependent phase errors in these four echoes. Using the new image reconstruction method, the phase corrected image data were obtained and found to be identical to the known object data as shown in Fig. 3. When a noise was added, the resulting MR-ART image was sharper at various edges. Results showed that this method was robust in both image reconstruction and phase correction. We have successfully applied the new technique to interleaved spin echo (SE) EPI data obtained from a 1.5 T MRI system. This EPI sequence consists of four gradient echoes after a refocusing rf pulse. For a standard 2D imaging, four gradient echoes were phase encoded independently for covering four contiguous segments in k space corresponding to 256×256 matrix size. For 2D phase correction, four low spatial resolution (along phase encoding) data sets were obtained for all four echoes using a set of common phase encoding steps. Figure 4 displays a typical image from one of the human head imaging studies.

¹Rzedzian, Proc. 6th Soc. Magn. Reson. Imaging 26 (1988).

²F. Farzaneh and S. J. Riederer, Proc. 7th Soc. Magn. Reson. Imaging 70 (1989).

³Z. H. Cho *et al.*, Proc. 6th Soc. Magn. Reson. Med. 912 (1987).

⁴G. C. McKinnon, Magn. Reson. Med. **30**, 609 (1993).

⁵K. Butts *et al.*, Magn. Reson. Med. **31**, 67 (1994).

⁶H. Liu *et al.*, Int. Soc. SMagn. Reson. Med. 5th Annual Meeting **3**, 2013 (1997).

Metallic needle artifacts in magnetic resonance imaging

Haiying Liu^{a)}

University of Minnesota, 420 Delaware Street, SE, Minneapolis, Minnesota 55455

A better understanding of the appearance of a biopsy needle and its image artifacts as well as its interaction with various sequence parameters in magnetic resonance (MR) imaging is beneficial for its application in MR image guided surgical procedures. A standard analytical solution to an infinite long cylindrically shaped object immersed in a uniform magnetic field has been used to predict MR image artifacts. In a more practical setting, we investigated the characteristics of MR image artifacts associated with a finite length metallic needle, specifically at the tip of a biopsy needle when it is approximately parallel to the main magnetic field. The origin of the needle tip artifact, which is exhibited as a blooming ball, was studied using MR imaging techniques and numerical simulation employing finite element method. Satisfactory agreement between theory and experiment has been achieved. Results showed that the image artifacts associated with biopsy needle are present and dependent on MR imaging parameters, but the artifacts can be reduced if optimal imaging parameters were used. © 1998 American Institute of Physics. [S0021-8979(98)37311-9]

INTRODUCTION

The unprecedented interests in using MRI for guidance and monitoring of percutaneous minimally invasive interventions have been driven by magnetic resonance (MR) excellent soft tissue contrast, multiplanar capabilities and sensitivities to temperature, flow, susceptibility, etc.,¹⁻³ and also made practical by the recent advances in MR and related technologies. The possibility of an induced magnetic force and an image artifact of a biopsy needle during interventional MRI have long been two primary concerns for the safety of MR image guided surgical procedures and the quality of visualization and positional accuracy of the resulting images.^{1,2} Today, many of these obstacles have been overcome with the introduction of new materials such as titanium alloys and carbon fiber composites. Although metallic needles tend to have more severe image artifacts than those of carbon fiber, these metallic needles are often preferred because of clinical issues such as performance and visibility as well as practical issues such as machinability and production cost. As interventional MRI is steadily pushing itself to more delicate neurological surgical procedures where a much higher spatial precision is demanded, thus, any image artifact associated with the surgical instrument becomes an even more crucial problem. For interventional applications at high field (>1.0 T), the requirements for these MRI compatible devices (needles), are more stringent in terms of the need to control mechanical forces/torques and imaging artifacts. Suitable materials for these needles as well as other surgical devices are generally the nonferromagnetic, chemically inert, biocompatible, nontoxic materials such as titanium alloys, carbon fiber composites, copper, nonferromagnetic steel, etc.

THEORY

Disturbance of the uniform static magnetic field due to a cylindrically shaped object whose magnetic susceptibility

differs slightly from that of the surrounding can be predicted, and the resulting MR image distortion can be estimated. The image intensity artifacts and geometric distortion associated with a biopsy needle can to some extent be understood by modeling a biopsy needle as an infinitely long solid cylinder in a uniform static magnetic field. A general analytical expression for the resulting external field perturbation can be obtained by solving a simple static magnetics problem whose geometry is shown in Fig. 1:

$$\delta \mathbf{B}_{\text{ext}} = B_0 \frac{\mu_n - \mu_t}{\mu_n + \mu_t} \frac{a^2}{\rho^2} \sin \theta (\cos 2\psi \mathbf{e}_p + \sin 2\psi \mathbf{e}_q), \quad (1)$$

where θ is the angle between z axis and the long axis of the needle, the long axis of the needle is assumed to be in the $y-z$ plane, B_0 denotes the strength of the static uniform magnetic field whose direction is along the z direction as shown in Fig. 1, μ_n and μ_t represent the magnetic permeability of the needle material and surrounding tissue, respectively, a is the radius of the needle, p and q denote two axes orthogonal to the long axis of the needle, ρ is the radius of the observation point within the plane defined by p and q , ψ is the angle between the vector ρ and the p axis, and \mathbf{e}_p and \mathbf{e}_q are two unit vectors denoting the directions of p and q .

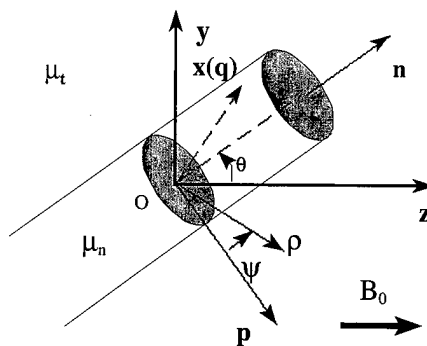


FIG. 1. Schematic of a solid metallic needle placed in an angle to the direction of the main magnetic field denoted by B_0 . The axis of the needle is assumed to be in the plane defined y and z axes.

^{a)}Electronic mail: haiying.liu-1@tc.umn.edu

axes. Inside the cylindrically shaped needle, the magnetic field error can be found analytically to be spatially uniform as given below:

$$\delta B_{in} = B_0 \left(\frac{\mu_n - \mu_t}{\mu_n + \mu_t} \sin \theta e_p + \frac{\mu_n - \mu_t}{\mu_t} \cos \theta e_l \right). \quad (2)$$

The magnetic susceptibility induced geometrical image distortion can be described as a pixel shift along the readout direction on the resulting MR image. This positional shift is inversely proportional to the readout gradient strength or the data sampling bandwidth for distorted coordinates which can be computed as follows:

$$\begin{aligned} X^d &= X + \frac{\delta B_{ext}}{G_{rd}}, \\ Y^d &= Y, \\ Z^d &= Z + \frac{\delta B_{ext}}{G_{sl}}, \end{aligned} \quad (3)$$

where X and Y denote the readout axis and phase axis of an image plane, respectively, Z is the slice axis, δB_{ext} is the static main magnetic field error, and G_{rd} and G_{sl} denotes the strength of the imaging readout gradient and slice select gradient, respectively. Due to the locally induced field inhomogeneity, the image intensity attenuation for a gradient echo sequence is determined by a transverse inhomogeneity induced intravoxel relaxation time constant denoted by τ which is proportional to the local field gradient ($\propto \nabla B$).

In the practical setting, these theoretical results for such an ideal case have severe limitations. For example, when a biopsy needle is placed parallel to the main static magnetic field, the resulting image artifact becomes minimal along the sheath of the needle, but exhibits a blooming ball shaped intensity void at its tip, which is not anticipated by the simple model. The immediate concern is that the visualization of the tip location may be obscured by this image artifact. In particular, the fact that a real needle is finite in length has not been fully considered in the model.

According to static magnetism theory, for a problem involving zero external macroscopic current, a magnetic scalar potential as well as magnetic charge can be introduced. The surface magnetic charge density (σ_m) for a rounded needle tip as well as the bulk charge density (ρ_m) can be computed from the magnetization M of the needle. Since the magnetization of the needle shaped object in a strong and uniform magnetic field is fairly uniform in the middle, there exists no bulk charge density inside the needle away from the ends. The charge exists predominantly on the surface and the ends. The bulk magnetization $M = \chi H$, where χ is the magnetic susceptibility [for titanium (Ti) 1.8×10^{-4} , water -0.88×10^{-5}] and H is the magnetic field intensity. At the end of the needle, H becomes spatially nonuniform due to the locally induced charges. Although the exact analytical solution for H is difficult to obtain, its numerical solution can be relatively easily obtained using a finite element method (FEM). By integrating the effect of both the surface charge over the surface area of the needle and the bulk charge over the volume of the needle, the total perturbation on the mag-

netic scalar potential in the vicinity of the tip of the needle can be obtained numerically for arbitrarily complex geometries:

$$\Phi(\mathbf{r}) = \frac{1}{4\pi} \int \frac{\sigma_m(\mathbf{r}')}{|\mathbf{r}' - \mathbf{r}|} dS' + \frac{1}{4\pi} \int \frac{\rho_m(\mathbf{r}')}{|\mathbf{r}' - \mathbf{r}|} dV', \quad (4)$$

where \mathbf{r} denotes the coordinates for an observation point and \mathbf{r}' denotes the source coordinates. The perturbation on the magnetic flux density external to the needle can be obtained by taking the gradient of the resultant magnetic scalar potential. An axisymmetric FEM model with a set of proper boundary conditions has been constructed for simulating the static magnetic behavior of a needle in a uniform magnetic field. From this model, using FEA software, we obtained the values for the internal and external H field from which the bulk magnetization (M) was derived. From M , both bulk and the surface magnetic charge densities can be determined. The overall magnetic flux density disturbance can be obtained at arbitrarily high spatial resolution by integration using the expression shown above. Starting from the resulting field perturbation of the static uniform main magnetic field, various MR image artifacts, such as an image intensity void and an image geometric distortion, can be numerically simulated and predicted for different imaging techniques.

MATERIALS AND RESULTS

A nonferromagnetic stainless steel needle with a flat tip was used in our imaging experiments. All imaging experiments were conducted on a Philips 1.5T clinical whole body MR scanner (ACS-NT, Best, Netherlands). An imaging phantom, which contained the needle and a nonmagnetic grid structure immersed in water, has been constructed for studying the image artifact associated with a biopsy needle. For better signal to noise ratio, a receive-only head coil was used for the imaging experiments. The high resolution 3D field-echo (FE) and spin-echo (SE) images at multiple data sampling bandwidth were obtained with a FOV of 20 cm and data sampling matrix size of 256×256 .

When the needle was placed perpendicular and parallel to the direction of the main magnetic field, an arrowhead and

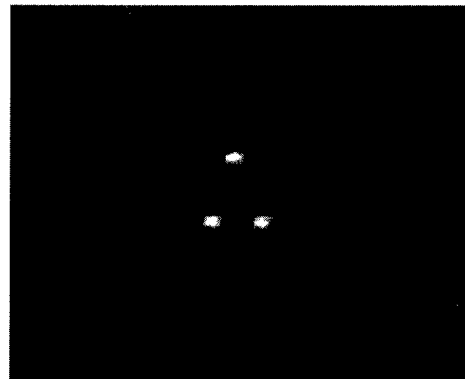


FIG. 2. A coronal 2D spin echo image of a MR compatible stainless steel needle with the readout gradient placed vertically. The main magnetic field direction is vertical. Imaging parameters are: FOV=10 cm, slice thickness=5 mm, TR/TE=550/9.5 ms, flip 90, image matrix size 128×128 .

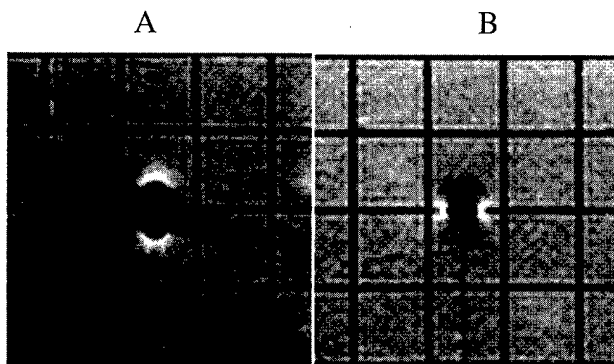


FIG. 3. Two coronal 2D spin echo images at the exact same slice position through the needle with the readout gradient polarity vertically up (left-hand side) and vertically down (right-hand side). The main static magnetic field direction is vertical.

ball-shaped image artifact appeared on the resulting MR images of 3D field-echo technique as shown in Figs. 2 and 3, respectively (readout is along the main field direction). For the perpendicular case, the expected arrow shaped appearance due to the geometric distortion around the needle stem could be simulated.³ In the case where the needle is parallel to the main field, the image artifact in the direction normal to the axis of the needle becomes minimal in the middle of the needle stem, but the size of the intensity void at the tip of the needle appears significantly larger than the diameter of the needle. The actual location of the needle tip was at the center of the reference square grid, whose dimension was 15 mm×15 mm. Generally, we found that the center of the artifact coincided with the true needle tip location. Furthermore, as the readout gradient is inverted, the appearance of the artifact is quite different [Fig. 3(B)]. The resulting image artifact tends to collapse to a small perpendicular line at a level corresponding to the tip of the needle. As the readout gradient was tilted with respect to the needle, the resulting artifact shape followed the readout direction. For example when the needle was placed at a 40° angle with respect to the

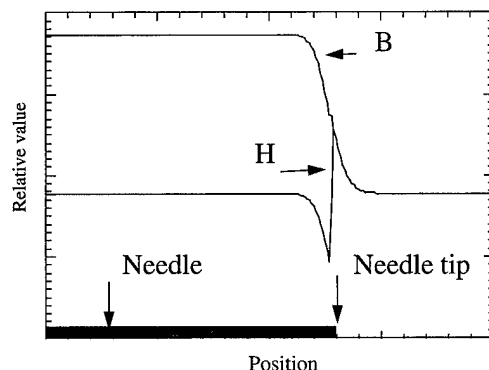


FIG. 4. Magnetic field intensity (H) and flux density along a metallic needle axis at 1.5 T. Only one end of the needle is shown.

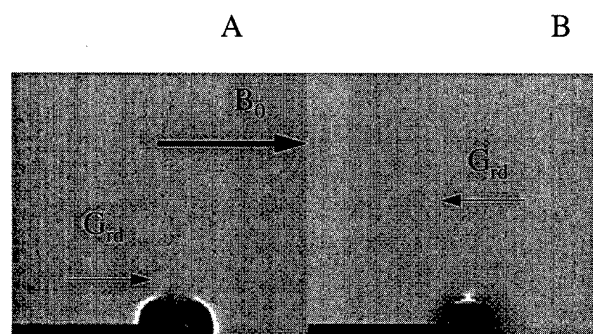


FIG. 5. Two numerically simulated coronal 2D spin echo images through the MR compatible stainless steel needle with the readout gradient polarity indicated. The main magnetic field direction is horizontal.

z axis while keeping readout parallel to the main field, we observed that the needle stem appeared wider as the angle increased. In addition, there still existed the same tip artifact along the readout direction. When the phase encoding gradient was set to be perpendicular to the needle, the size of the artifact was reduced. The magnetization and field were numerically simulated, the field intensity H and flux density B along the needle long axis are shown in Fig. 4. Using the needle magnetization as an input, the field perturbation external to the needle was computed at high spatial resolution. Based on the calculated error field, an imaging experiment can be simulated assuming everything else is perfect. Simulated images qualitatively reproduced the observed image artifact as shown in Fig. 5. Figure 4 shows that the error magnetic field intensity (ΔH) above and below the tip are pointing in opposite directions. This is consistent with the fact that the magnetic charge is mostly localized at the surface of the tip. At 1.5 T, based on a rough estimation assuming the needle is uniformly magnetized, the resulting field perturbation on the surface of a nonferromagnetic metallic needle tip can be as large as 6 kHz.

CONCLUSION

We have shown the overall appearance of the MR image artifacts associated with the tip of a biopsy needle for various relevant imaging parameters, and demonstrated that these image artifacts originate from both rf off resonance effects and geometric distortion. A theoretical explanation has been introduced and validated using the MR imaging results. Practical experience indicates that moderating image artifacts to some extent enhances the visibility of the needle. Understanding the characteristics of the needle artifact and interaction with imaging parameters can help in not only optimizing the imaging parameter and technique to reduce the potential image artifact but also in interpreting the artifact properly.

¹P. R. Mueller, D. D. Stark, J. F. Simeone, S. Saini, R. J. Butch, R. R. Edelman, J. Wittenberg, and J. T. Ferrucci, *Radiology* **161**, 605 (1986).

²R. B. Lufkin, L. Teresi, and W. N. Hanafey, *AJR* **149**, 380 (1987).

³M. E. Ladd, P. Erhart, J. F. Debatin, B. J. Romanoski, P. Boesiger, and G. C. McKinnon, *Magn. Reson. Med.* **36**, 646 (1996).

Magnetic properties of MnZnTi and NiZn ferrite films deposited by laser ablation

M. M. Amado,^{a)} M. S. Rogalski, L. Guimarães, and J. B. Sousa
IFIMUP and Physics Department, University of Porto, 4150 Porto, Portugal

I. Bibicu
Institute of Atomic Physics, P.O. Box MG-06, Bucharest, Romania

R. G. Welch and S. B. Palmer
University of Warwick, Coventry CV4 7AL, United Kingdom

The magnetic behavior of MnZnTi and NiZn ferrite films, deposited by laser ablation, is studied comparatively to that of the bulk material, using a vibrating-sample magnetometer (VSM), transmission, and conversion electron Mössbauer measurements. Both the VSM and Mössbauer analysis show that the films exhibit the single phase pattern of the target material. Mössbauer hyperfine field values for films are close to those found for the bulk, and this accounts for the same saturation magnetization values determined by VSM. Laser ablated films exhibit a higher coercive field, which is explained in terms of the crystallite size distribution, with average values of 300–600 nm, as estimated from the Mössbauer line broadening. © 1998 American Institute of Physics. [S0021-8979(98)48911-4]

I. INTRODUCTION

MnZnTi and NiZn ferrite films have been deposited by laser ablation with stoichiometries close to the target^{1–4} and, most importantly, without postdeposition heat treatments to form the spinel structure, as required by other synthesis processes such as rf or dc sputtering. As laser ablation deposition is a “dry-processing” technique, compatible with other approaches currently used in modern technology, of continuing interest for producing ferrite films, the magnetic properties of the films must be understood within the context of the requirements for potential applications. However, there have been few, if any, systematic studies that correlate the magnetic quality of the ferrite films with the spinel microstructure. In this article we correlate the saturation magnetization and the coercive field for the MnZnTi and NiZn ferrite films with the hyperfine parameters of their conversion electron Mössbauer spectra (CEMS). We also compare the magnetic properties of the laser ablated films with those of the bulk material.

II. EXPERIMENTAL PROCEDURE

The MnZnTi and NiZn ferrite targets were prepared by conventional powder ceramic techniques⁵ with nominal compositions $\text{Mn}_{0.66}\text{Zn}_{0.26}\text{Ti}_{0.02}\text{Fe}_{2.06}\text{O}_4$ and $\text{Ni}_{0.35}\text{Zn}_{0.65}\text{Fe}_2\text{O}_4$. Laser ablation was performed, as described elsewhere,^{1–4} inside a stainless-steel vacuum chamber, with a base pressure of 10^{-5} mbar, using an excimer laser source Lambda Physik model LPX 100, operated with XeCl* active mixture ($\lambda = 308$ nm), giving 30 ns, 65–75 mJ pulses, at a repetition

rate of 21 Hz. A high repetition rate was desirable from the standpoint of minimizing the concentration of background impurities in the films. The target was rotated at a frequency of 0.2 Hz for uniform target wear and to minimize droplets on the substrate, which was located at a distance of 4 cm from the target surface and parallel to its surface. The ferrite films were deposited onto high silicon content glass substrates, at substrate temperatures of 850 °C and at oxygen pressures of 0.15–0.2 mbar. This substrate temperature ensures high atomic mobility, so improving film crystallinity. After deposition, the films were cooled slowly to room temperature by turning off the power to the substrate heater and raising the pressure in the vacuum chamber to 2 mbar of oxygen.

The relative elemental concentrations were used to estimate the atomic composition of the deposited films, by considering their values normalized to the nominal composition of the targets. We have found an average composition $\text{Mn}_{1-x-y-d}\text{Zn}_x\text{Ti}_d\text{Fe}_{2+y}\text{O}_4$ with $x=0.2\text{--}0.22$, $y=0.13\text{--}0.15$, $d\sim 0.01$, and respectively, $\text{Ni}_{1-x-y}\text{Zn}_x\text{Fe}_{2+y}\text{O}_4$ with $x=0.58\text{--}0.64$ and $y=0.08\text{--}0.1$. As the error in the determination of the areas of the peaks in the x-ray energy spectrum exceeds the Ti content in the bulk material, the average composition of the films may be assumed to be satisfactorily stoichiometric with respect to the targets. The Mn, Ni, Zn, and Fe concentrations of our films remained almost constant irrespective of the deposition conditions, within the error of the energy dispersive spectroscopy (EDS) system, although the data suggest a slight deficiency of Zn (a few atomic percents) in the films as compared with the original targets.

The magnetization curves were measured for the target material and the films, at room temperature, by a vibrating

^{a)}Electronic mail: amado@fisf.fc.up.pt

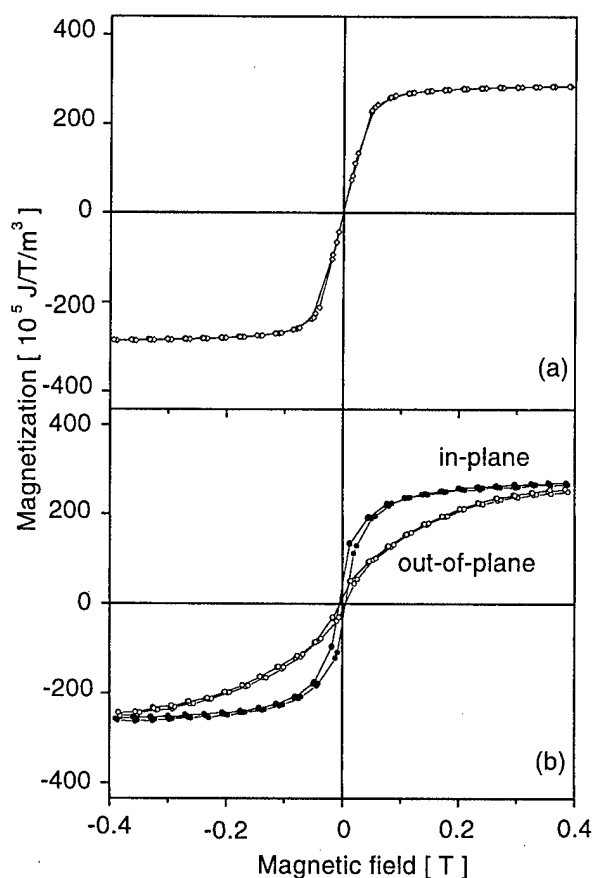


FIG. 1. VSM magnetization loops of MnZnTi ferrite target (a) and film (b), measured in-plane and out-of-plane.

sample magnetometer (VSM). Transmission Mössbauer spectra has been obtained from the powdered target material, on a constant acceleration spectrometer with a $^{57}\text{Co}/\text{Rh}$ source. The CEMS spectra were recorded from the films using a room temperature detector.⁶ The integrated Mosswin program⁷ has been employed to calculate the spectral parameters and the crystallite size distribution for the films.

III. RESULTS AND DISCUSSION

Typical in-plane and out-of-plane magnetization curves are shown Fig. 1 for the MnZnTi ferrite target and films. The saturation magnetization was determined for films to be within a few percent of the value for the bulk material, namely in the range $(220\text{--}280) \times 10^5 \text{ J/T/m}^3$ ($220\text{--}280 \text{ emu/cm}^3$), and this is consistent with stoichiometric ferrites. However, the coercive field H_c for the films, with values in the range of 6400 to 14300 A/m (20 to 45 Oe), is obviously larger than that found for the targets. This suggests a strong influence from the film microstructure, and is likely to indicate the presence of crystallite shape anisotropy.⁸

The room temperature transmission and CEMS spectra for the MnZnTi target material and film, respectively, are plotted in Fig. 2. The computed spectrum of the bulk material contains one sextet for the tetrahedral (A) iron, which has the highest effective fields $H(A) = 40.9 \text{ T}$, another sextet for the octahedral (B) iron, $H(B) = 38.1 \text{ T}$, and an additional subspectrum ($H = 34.3 \text{ T}$) assigned to $\text{Ti}^{4+}\text{Fe}^{2+}$ pairs, formed by fast electron transfer between multivalent iron and

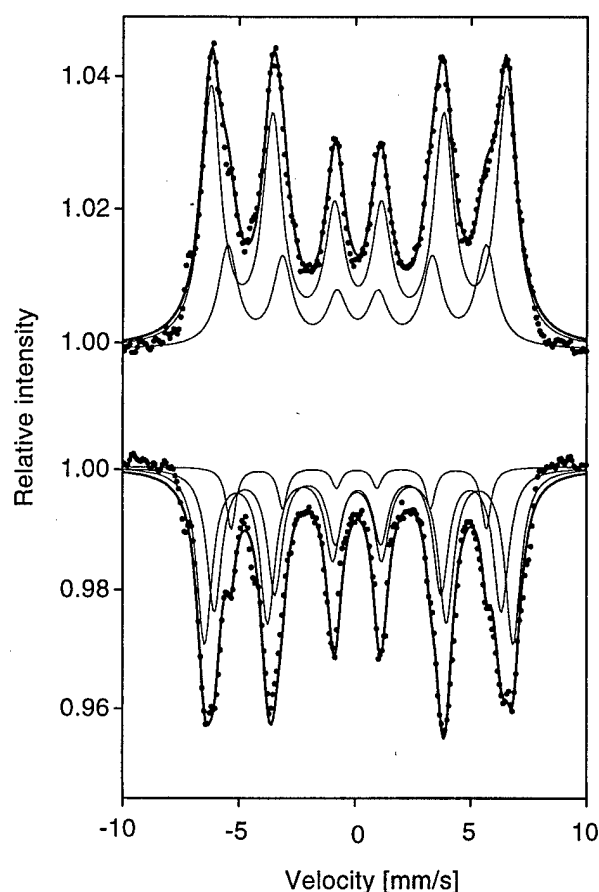


FIG. 2. Room temperature transmission Mössbauer spectrum from the MnZnTi target and CEMS spectrum from the laser ablated film.

titanium ions.⁵ The CEMS spectra from the film indicate slightly smaller values of the magnetic fields at the two sites, $H(A) = 39.5 \text{ T}$ and $H(B) = 36.2 \text{ T}$, which is consistent with the magnetization behavior [see Figs. 1(a) and 1(b)]. The relative iron concentration at the octahedral site decreases upon ablation, and this is likely to be related to the Zn deficiency, as indicated by elemental analysis. There is a line-width increase in the CEMS spectra with respect to the transmission data, which allows an estimate of the crystallite size distribution, as described before.⁹ The average crystallite size is found to be in the range of 300–600 nm, in agreement with the atomic force microscope (AFM) image analysis.³ This crystallite size is smaller than in the bulk material, and results in increasing the number of low angle grain boundaries, which act as pinning sites for domain walls and are responsible for larger H_c values.⁸

From the magnetization curves of NiZn ferrite, shown in Fig. 3, the film saturation magnetization was found to be $660 \times 10^5 \text{ J/T/m}^3$ (660 emu/cm^3), which is close to the value for the bulk material, as expected from stoichiometric NiZn ferrite. The coercive field of about 25.5 kA/m (80 Oe), is larger than the values found for the target, and this can be also attributed to a decrease in the crystallite size. This conclusion is supported by the Mössbauer data analysis.

The transmission spectrum from the NiZn target material shows typical relaxation features, which appear as two sextets, $H(A) = 36.4 \text{ T}$ and $H(B) = 30.6 \text{ T}$, and a quadrupole split doublet ($\Delta E_Q = 1.31 \text{ mm/s}$, $IS = 0.35 \text{ mm/s}$), indicating

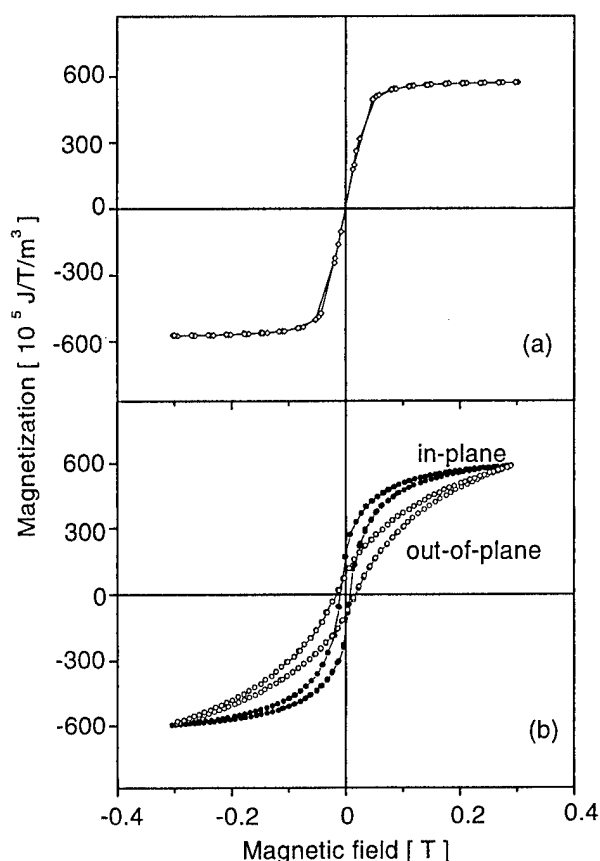


FIG. 3. VSM magnetization loops of NiZn ferrite target (a) and film (b), measured in-plane and out-of-plane.

thermally excited domain wall oscillations.¹⁰ These parameters are close to those previously reported¹¹ for the same range of Zn concentration ($x=0.65$). The corresponding (CEMS) parameters of the film, $H(A)=35.7 \text{ T}$ and $H(B)=30.3 \text{ T}$, are consistent with the saturation magnetization data obtained by VSM. The smaller concentration of the quadrupole doublet in the CEMS spectrum, corresponding to almost the same x , can be explained on account of a lower density of the film material¹⁰ (Fig. 4). In other words, our film should be regarded as having some concentration of vacancies and voids, yielding a lower average density. Although such free spaces are expected to result in high-temperature quenched samples, the morphology analysis⁴ indicates that we are not dealing with macroporosities that unfold on the surface. This result is also consistent with the increased coercive field values found for the films (see Fig. 3).

IV. CONCLUSION

The VSM and Mössbauer analysis of the MnZnTi and NiZn ferrite targets and laser ablated films indicate that the films exhibit the single phase pattern of the bulk material. The hyperfine field values for films are close to those found for the targets, and this accounts for the similar range, determined by VSM, for the saturation magnetization values. The higher coercivity of laser ablated films is consistent with the

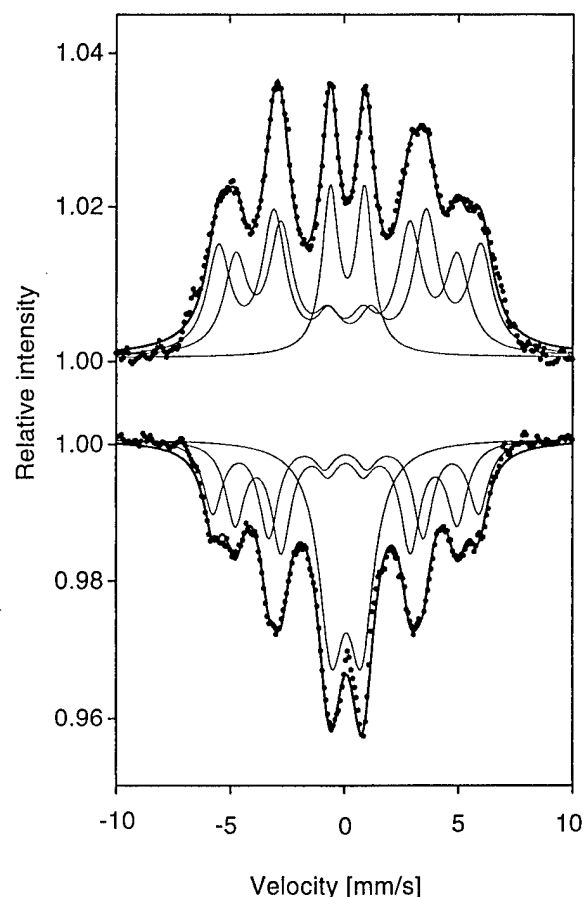


FIG. 4. Room temperature transmission Mössbauer spectrum from NiZn target and CEMS spectrum from the laser ablated film.

crystallite size distribution, with average values of 300–600 nm, as estimated from the spectral line broadening. A satisfactorily qualitative explanation of the magnetic properties is obtained on taking proper account of both the intrinsic properties, such as stoichiometry, of which the saturation magnetization and hyperfine fields are mainly dependent, and the extrinsic properties, like the crystallite size, with direct influence on the coercive field and the line broadening of CEMS spectra.

¹ C. A. Carosella, D. B. Chrisey, P. Lubitz, and J. S. Horwitz, *J. Appl. Phys.* **71**, 5107 (1992).

² C. Vittoria, U.S. Patent 5, 227, 204 (1993).

³ R. G. Welch, J. Neamtu, M. S. Rogalski, and S. B. Palmer, *Solid State Commun.* **97**, 355 (1996).

⁴ R. G. Welch, J. Neamtu, M. S. Rogalski, and S. B. Palmer, *Mater. Lett.* **29**, 199 (1996).

⁵ J. Neamtu, V. Spinu, and G. Filoti, *J. Magn. Magn. Mater.* **133**, 481 (1994).

⁶ I. Bibicu and M. S. Rogalski, *Meas. Sci. Technol.* **7**, 113 (1996).

⁷ M. M. P. Azevedo, M. S. Rogalski, and J. B. Sousa, *Meas. Sci. Technol.* **8**, 941 (1997).

⁸ C. M. Williams, D. B. Chrisey, P. Lubitz, K. S. Grabowski, and C. M. Cotell, *J. Appl. Phys.* **75**, 1676 (1994).

⁹ M. S. Rogalski, M. M. P. Azevedo, and J. B. Sousa, *J. Magn. Magn. Mater.* **163**, L257 (1996).

¹⁰ C. M. Srivastava, S. N. Shringi, and R. G. Srivastava, *Phys. Rev. B* **14**, 2041 (1976).

¹¹ D. C. Dobson, J. W. Linnett, and M. M. Rahman, *J. Phys. Chem. Solids* **31**, 2727 (1970).

Structure and soft magnetic properties of sputter deposited MnZn-ferrite films

M. F. Gillies,^{a)} R. Coehoorn, and J. B. A. van Zon
Philips Research, Prof. Holstlaan 4, 5656 AA Eindhoven, The Netherlands

D. Alders
Department of Physics, Eindhoven University of Technology, P.O. Box 513, 5600 MB Eindhoven, The Netherlands

In this paper we report the soft magnetic properties of thin films of sputtered MnZn ferrite deposited on thermally oxidized Si substrates. A high deposition temperature, 600 °C, together with the addition of water vapor to the sputtering gas was found to improve the initial ac permeability, μ . The highest value obtained was approximately 30. For MnZn-ferrite films with much larger grain sizes, as obtained by deposition on a polycrystalline Zn-ferrite substrate, a μ of 100 was obtained. The results are discussed in terms of the so-called nonmagnetic grain boundary model. © 1998 American Institute of Physics. [S0021-8979(98)53211-2]

I. INTRODUCTION

The growth of thin layers of magnetically soft ferrites such as MnZn or NiZn ferrite has been studied recently by various groups.¹⁻³ This interest is motivated by potential applications such as magnetic thin-film read heads,⁴ cladding layers for thin film inductors,⁵ and microwave acoustic devices.² For most applications, two of the most important parameters are the resistivity of the layer and the ac permeability, μ . While the resistivity is similar to that of the bulk the permeability of the thin ferrite films, on which many authors do not report explicitly, appears to be significantly less. This may be deduced from previously published M vs H loops² where, even when grown epitaxially, the films lack the true softness which characterizes the bulk material.

It has been shown by other authors that the addition of oxygen during deposition can have the effect of improving the softness of a thin film MnZn ferrite.¹ We however, found that this can easily lead to an undesired oxygen rich ferrite. In the case of Fe_3O_4 it was found that the exact oxidation state of sputtered films could be more accurately controlled using H_2O .⁶ In this paper we report the effects on the soft magnetic properties of MnZn ferrite when a small amount of water vapor is added to the sputtering gas.

II. EXPERIMENT

The films were deposited in a Perkin Elmer 2400-8L rf diode sputter system, using Ar at a constant pressure of 0.29 Pa (2.2 mTorr). The background pressure was approximately 1.3×10^{-4} Pa. The substrate temperature during deposition was monitored by a thermocouple inserted into the substrate table and silver paste was used to ensure a good thermal contact. The films were sputtered from a 10 cm diameter $\text{Mn}_{0.51}\text{Zn}_{0.42}\text{Fe}_{2.03}\text{O}_4$ polycrystalline ferrite target which has a bulk μ of approximately 4000. The deposition rate was 0.2 $\mu\text{m/h}$, with a rf power of 250 W, and the films, which were grown on Si substrates with a 0.5 μm pregrown thermal SiO_2

layer, were approximately 0.9 μm thick. The initial ac permeability was measured⁷ using an HP4129A analyzer with an applied ac field of 2.5 A/m.

III. MAGNETIC PROPERTIES

The magnetic properties were studied as a function of two deposition parameters: additional water vapor in the sputtering chamber and substrate temperature. The effect of the presence of an additional amount of water vapor on the soft magnetic properties is shown, for three different substrate temperatures, T_s , in Figs. 1(a)–1(c). In the case of no additional added water vapor, [$p(\text{H}_2\text{O}) = 1.3 \times 10^{-4}$ Pa] an increase in T_s does have an effect on μ , though the maximum value attained was only 16. Upon increasing $p(\text{H}_2\text{O})$ the coercivity H_c [Fig. 1(a)] is reduced, and for a T_s of 550 or 600 °C H_c is approximately 1.6 kA/m with the addition of 0.13 Pa of H_2O . For $T_s = 500$ °C the minimum H_c is approximately 2.8 kA/m.

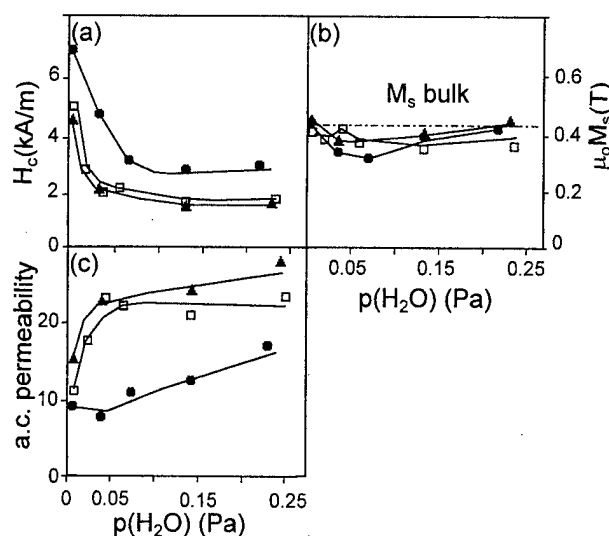


FIG. 1. The effect of the partial water-vapor pressure during sputtering on (a) the coercive field, (b) the saturation magnetization, and (c) the ac permeability of thin ferrite films. Deposited at 500 °C (circles), 550 °C (squares), and 600 °C (triangles).

^{a)}Electronic mail: gillies@natlab.research.phillips.com

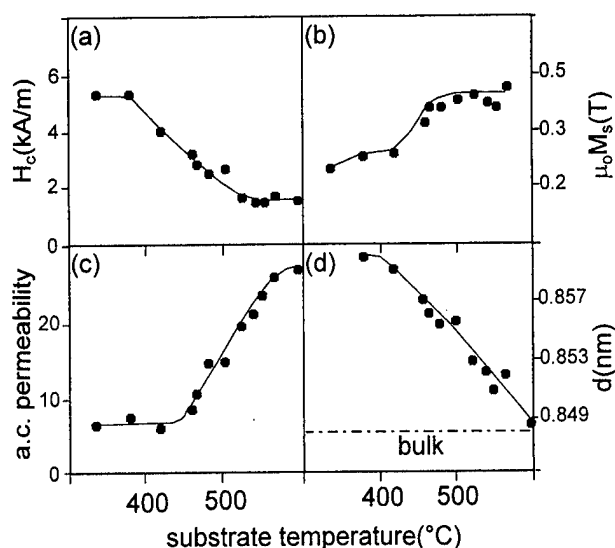


FIG. 2. The effect of a variation in substrate temperature at $p(\text{H}_2\text{O})=0.13$ Pa on (a) the coercive field, (b) the saturation magnetization, (c) the ac permeability, and (d) the lattice parameter of a $0.9\text{ }\mu\text{m}$ MnZn-ferrite film.

The room temperature saturation magnetization, $\mu_0 M_s$, of the sputtered films, Fig. 1(b), is only slightly lower than that of the bulk material (0.44 T).

The ac permeability did not show any rolloff in the 1–13 MHz frequency range and the average value of permeability over this frequency range is what is given in Fig. 1(c). For the different T_s the trend is similar: an increasing $p(\text{H}_2\text{O})$ leads to a higher μ , with the maximum, $\mu \approx 27$, being achieved with a T_s of 600°C and a $p(\text{H}_2\text{O})$ of 0.23 Pa.

While the trends in magnetic properties are independent of T_s the actual values of H_c and μ are not. The magnetic and structural properties (Sec. IV) of the sputtered ferrite were therefore measured for a new series of films where T_s was varied while holding the $p(\text{H}_2\text{O})$ constant at 0.13 Pa. Figure 2(a) shows the influence of temperature on H_c which falls to approximately 1.4 kA/m for T_s higher than 560°C . An increase in T_s also leads to an increase in the $\mu_0 M_s$, Fig. 2(b). Substrate temperatures which are less than 450°C , result in a μ below 10, Fig. 2(c). Above 450°C μ increases rapidly with increasing temperature and at 600°C μ is approximately 27.

IV. STRUCTURAL PROPERTIES

The structural properties of the ferrite were also studied both as a function of $p(\text{H}_2\text{O})$ and T_s . The width and position of the strongest peak, (400), in the θ - 2θ Cu $K\alpha$ x-ray spectra did not show any relation to $p(\text{H}_2\text{O})$ (while T_s was fixed). The stoichiometry of these films, together with those deposited with various substrate temperatures, was checked using x-ray fluorescence, XRF, and electron probe microanalysis, EPMA. For depositions at T_s less than 500°C the composition did not appear to be influenced by $p(\text{H}_2\text{O})$ and was, within experimental error, the same as the target material. For depositions at higher T_s films showed Zn deficiency if deposited without H_2O . The fact that this did not occur in the presence of H_2O may be due to the oxidation of metallic Zn on the surface of the film which would slow

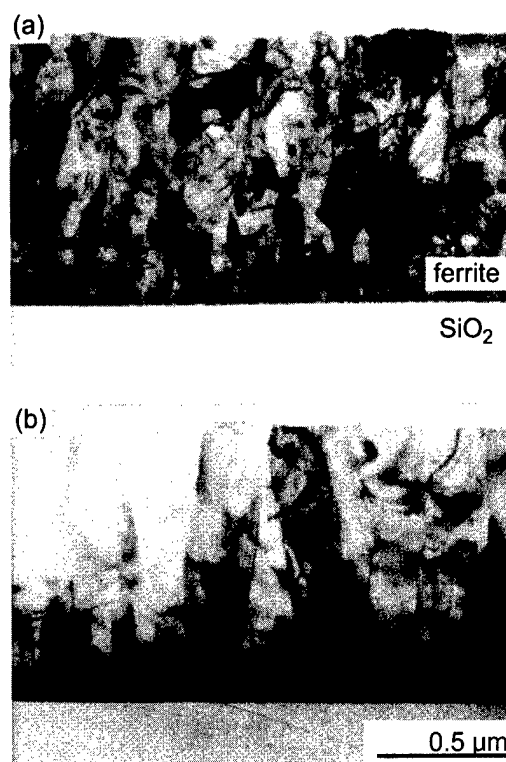


FIG. 3. TEM cross sections of films deposited at (a) 523°C and (b) 604°C .

down any evaporation. For films with a reasonably high μ , such as those deposited at $550^\circ\text{C}/0.13$ Pa water vapor, the stoichiometry was, within experimental error, the same as the target.

From the (400) x-ray diffraction peak positions the lattice parameter perpendicular to the film was determined for films deposited at different T_s , Fig. 2(d). The bulk (target) lattice parameter was 0.848 nm. These experiments, as well as x-ray measurements with a varying direction of the scattering vector and mechanical stress measurements, reveal a reduction in stress for increasing T_s . Due to the strain present in the ferrite films it is not possible to accurately determine the average crystal size via the analysis of x-ray peak widths. This was therefore determined via transmission electron microscopy (TEM) cross sections for films deposited at $T_s = 523, 565$, and 604°C . [The cross sections shown here are only for films deposited at 523 and 604°C (Figs. 3(a) and 3(b), respectively).] While it is possible to discern a columnar structure within all the films it is clear that for a higher deposition temperature the columnar structure is more clearly defined. For the film deposited at $T_s = 523^\circ\text{C}$ there exist imperfections throughout the whole thickness of the film. This is in contrast to films deposited at a higher T_s where the formation of small crystallites only occurs during the initial stage of growth. In the later stages of growth a very distinct columnar structure appears. From the TEM cross sections the estimated average grain sizes for the depositions at 523, 565, and 604°C were 90, 110, and 175 nm, respectively.

V. FILMS GROWN ON A Zn-FERRITE SUBSTRATE

In Sec. IV the values for the approximate grain size of the ferrite films, as determined through TEM, were reported.

From the nonmagnetic grain boundary model⁸ (NMGB model) the relationship between the effective initial permeability, μ_e , the average grain size, D , and the intrinsic permeability, μ_i , of the ferrite within a grain is given by

$$\mu_e = \frac{\mu_i D}{\mu_i \delta + D}, \quad (1)$$

where δ is the width of the nonmagnetic grain boundary zone. Equation (1) implies that for fixed values of δ and μ_i , μ_e can be increased by increasing the grain size. We therefore increased the in-plane grain size of the MnZn-ferrite films by growing on a mechanically polished polycrystalline Zn-ferrite (ZnFe_2O_4) substrate with a grain size of approximately 15 μm . Since the lattice parameter mismatch is less than 0.5% and the thermal expansion coefficients are similar,⁹ Zn ferrite is an ideal substrate on which to grow MnZn ferrite. On account of the substrate being paramagnetic at room temperature the magnetic properties of a MnZn-ferrite film can be measured without a contribution from the substrate. Figure 4 shows a scanning electron microscope photograph of a 0.9 μm thick MnZn-ferrite film, deposited with $p(\text{H}_2\text{O})=0.13$ Pa and $T_s=560$ °C. As can be seen the in-plane grain size is around 15 μm . The film had a H_c of less than 0.1 kA/m and was therefore much softer than those deposited on the Si/SiO₂ substrates ($H_c \approx 1.4$ kA/m for films deposited under identical conditions on Si/SiO₂). The ac permeability of the films deposited on Zn ferrite was 100 ± 5 .

VI. DISCUSSION AND CONCLUSIONS

The improvement in soft magnetic properties by adding water vapor to the sputtering gas was an unexpected result, for which we do not yet have an explanation. We did, however, consider the possibility that the presence of H₂O affects the oxidation state of either the Fe or Mn ions in the ferrite. Using a wet chemical technique it was found that the fraction of Fe²⁺ and Mn³⁺ ions in the films, with and without water vapor, were very similar to that of the target. It could, however, still be possible that the concentration of either Fe²⁺ or Mn³⁺ ions at the grain boundaries is not as in the bulk material and, since these ions can give rise to a large single ion anisotropy in the presence of a crystal field, this could result in grain boundaries with a high anisotropy. The effect of high anisotropy grain boundaries was considered by Pankert¹⁰ and leads to a reduction in permeability.

The effect of the substrate temperature on the soft magnetic properties, which was also observed for films grown on the Zn ferrite, must be related to the increased mobility of the atoms when they arrive at the surface. This has the obvious effect of increasing the grain size which, according to the NMGB model, leads to a magnetically softer film. A higher temperature would also reduce the density of dislocations and other imperfections in the bulk of the grains and could reduce the thickness of the nonmagnetic grain boundary, thereby improving the softness of the ferrite.

The reduction in lattice parameter for increasing T_s , Fig. 2(d), is indicative of a lowering in the total stress which is present in these films (this was also checked using mechani-

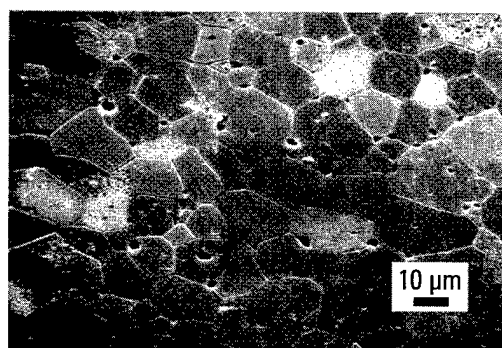


FIG. 4. SEM photograph of 0.9 μm MnZn-ferrite film deposited on a Zn-ferrite substrate.

cal stress measurements). Taking the sign of the thermal mismatch between the substrate and the film into account such a behavior cannot be explained in terms of a thermal mismatch alone and there must exist excessive stress within the ferrite film itself. A shift in the lattice parameter, with respect to that of the bulk, is also observed for the MnZn-ferrite film deposited on Zn ferrite. A lowering of total stress for higher deposition temperatures may be responsible, at least in part, for the higher permeability achieved with these temperatures.

As would be expected from the NMGB model the choice of Zn ferrite as a substrate and the consequently larger grain size of the MnZn-ferrite film lead to a higher permeability. If, however, one substitutes into Eq. (1) the average grain size of the film shown in Fig. 4, together with a nonmagnetic grain-boundary thickness of a few nanometers (for the bulk a value of 1.4 nm has been determined⁸) then $\mu_i \approx \mu_e$, where μ_e has been found to be approximately 100. Such a low value of μ_i may be caused by the presence of residual stress in the films though it is important to realize that the cation distribution was not checked in these sputtered layers and that a deviation from the desired distribution could also result in a low μ .

A permeability of 30, as obtained for thin films on Si/SiO₂ is sufficient to utilize these layers as cladding layers for thin film inductors. As a flux guide material in yoke-type thin film read heads⁴ a permeability of 30 is not quite sufficient. Further effort is therefore needed to realize a higher permeability and a lower deposition temperature.

ACKNOWLEDGMENTS

The authors would like to thank J. Daams, J. Donkers, M. A. Verheijen, and K. van de Aker for their x-ray and TEM work.

¹C. M. Williams, D. B. Chrisey, P. Lubitz, K. S. Grabowski, and C. M. Cotell, *J. Appl. Phys.* **75**, 1676 (1994).

²Y. Suzuki *et al.*, *Appl. Phys. Lett.* **68**, 714 (1996).

³H. Mikami, Y. Nishikawa, and Y. Omata, *Conf. Proc. Int. Conf. Ferrites* **7**, 126 (1996).

⁴P. J. van der Zaag, J. M. M. Ruigrok, and M. F. Gillies, *Philips J. Res.* **51** (1998).

⁵W. A. Roshen, *IEEE Trans. Magn.* **26**, 2880 (1990).

⁶Z. Zhou *et al.*, *J. Magn. Magn. Mater.* **115**, 87 (1992).

⁷J. P. C. Bernards, *IEEE Trans. Magn.* **30**, 4881 (1994).

⁸P. J. van der Zaag, *J. Appl. Phys.* **74**, 4085 (1993).

⁹K. Venkata Sivakumar, *J. Mater. Sci. Lett.* **10**, 61 (1990).

¹⁰J. Pankert, *J. Magn. Magn. Mater.* **138**, 45 (1994).

Emission studies of Ba-hexaferrite plume produced by a KrF excimer laser

P. Papakonstantinou,^{a)} M. C. O'Neill,^{b)} R. Atkinson,^{c)} R. Al-Wazzan, T. Morrow,
and I. W. Salter

Department of Pure and Applied Physics, The Queen's University of Belfast, BT7 1NN, North Ireland,
United Kingdom

Optical emission measurements and intensified charge coupled detector images of a plasma generated by the interaction of a KrF excimer laser with a Ba-ferrite target have been used to study the laser ablation deposition of Ba ferrite thin films. Time integrated spectra were collected as a function of distance above the target surface and as a function of oxygen pressure. Temporal profiles showed that close to the target the plume is insensitive to ambient oxygen pressure and at greater distances a much more pronounced influence is observed. Time resolved images of the overall optical plasma emission clearly demonstrated how the presence of oxygen confines the plasma and enhances its emission. © 1998 American Institute of Physics. [S0021-8979(98)29711-8]

I. INTRODUCTION

The *M*-type hexaferrites are an important class of materials for microwave, high-density magnetic and magneto-optical (MO) recording technologies. *M*-type Ba and Sr-hexaferrite with perpendicular magnetic anisotropy have been previously grown *in situ* on (001) oriented single crystal substrates of Al₂O₃,¹ yttria stabilized zirconia (YSZ), and Si², using pulsed laser deposition (PLD). Our earlier studies revealed that hexaferrite films prepared from stoichiometric targets at 840 °C, and 0.1 mbar for a target substrate distance of 30 mm exhibited the highest degree of crystalline quality and nearly bulk magnetic and magneto-optical properties. At reduced oxygen pressures (<0.1 mbar) the films, which were grown at 840 °C, displayed an enhanced fraction of in plane oriented (*c*_{||}) crystallites while at increased oxygen pressures

(>0.1 mbar) the surface was populated with outgrowths which also contributed negatively to the perpendicular anisotropy and made the surface rough.

We describe the propagation of excimer laser ablated plasma into background oxygen pressures, used for film growth, as observed by emission spectroscopy and intensified charged coupled detector array (ICCD) photography. The emission characteristics of the plume were correlated with the quality of the Ba-hexaferrite films synthesized by PLD. First, we report on temporally integrated, spatially resolved emission spectra from plasmas along the direction perpendicular to the target surface. The data were collected for plasmas propagating both in vacuum and in an ambient oxygen, from which the composition and state of ionization of the emitting species could be deduced. We have also investigated the effect of oxygen pressure on the spatial and temporal behavior of a number of atomic and ionic species in the plume. Effective species velocities were derived from the time dependent profiles and plasma temperatures were esti-

mated from the integrated line intensity ratios of ionic species. Furthermore, the expansion of the plasma in vacuum and oxygen ambient has been photographed with a gated, intensified CCD array camera system.

II. EXPERIMENTAL PROCEDURES

The apparatus used in the present experiments has been described previously.³ All measurements were carried out on plasmas produced following KrF excimer laser ($\lambda = 248$ nm, full width at half maximum (FWHM)=20 ns) ablation, in vacuum and oxygen pressures up to 0.5 mbar, at a laser fluence of 2 J/cm², with the laser beam incident at 45° to the rotating BaFe₁₂O₁₉ target. Temporally integrated emission spectra were recorded by imaging, at a 1:1 magnification, the luminescent plume onto the entrance slit (25 μ m wide, 3.7 mm high) of a compact spectrograph (Oriol Multispec) fitted with a 1024 element photodiode array (Oriol Intaspec). The plasma was viewed perpendicular to its main expansion direction, *z*. The compact spectrograph/diode array assembly was mounted on a micrometer driven transverse slide enabling the spectrograph slit to select light from sections of the plasma adjacent to the target (*z*<0.5 mm) to sections 30 mm along the *z* axis. The detection system provided wavelength coverage from 350–700 nm at a spectral resolution of ~ 1 nm. All recorded spectra were integrated over 100 consecutive laser pulses, accumulated at a repetition rate of 10 Hz.

For temporally resolved measurements a gated intensified 1024 photodiode array and a digital delay generator (DDG) was employed. This detection system had a temporal resolution of ~ 100 ns and a spectral resolution of ~ 1 nm. All spectra data were corrected for a wavelength variation of the intensified photodiode array system.

Temporally resolved two-dimensional (2D) imaging of the total laser-induced plasma emission of a BaFe₁₂O₁₉ target was performed using a fast gated, ICCD camera system.

III. RESULTS AND DISCUSSION

Figure 1 presents a typical spectrum of the temporally integrated plasma emissions observed 2 mm from the target

^{a)}Current address: FORTH, Institute of Electronic Structure & Laser, GR-711 10 Heraklion, Greece.

^{b)}Current address: Seagate Technology, Disc Drive, Springtown, Londonderry, N. Ireland, United Kingdom.

^{c)}Electronic mail: Ronald.Atkinson@QUB.AC.UK

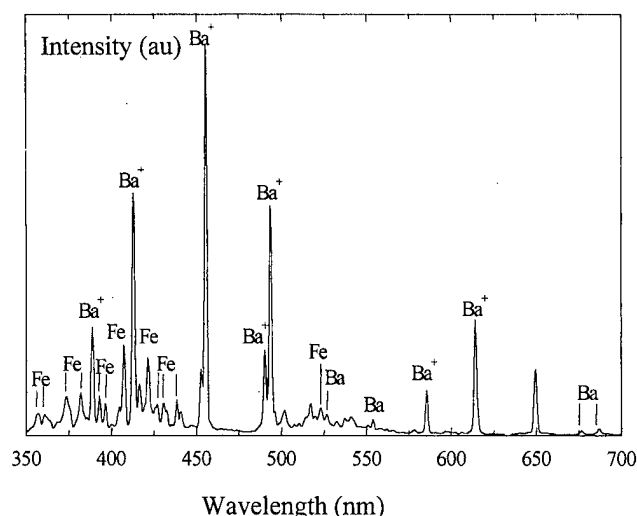


FIG. 1. Temporally integrated emission spectrum recorded at 2 mm from a $\text{BaFe}_{12}\text{O}_{19}$ target at a base pressure of 10^{-5} mbar.

surface at a base pressure of 10^{-5} mbar. Only emission lines from Ba and Fe neutrals and singly ionized Ba species were observed. Note that no lines could be assigned to ionized Fe species in this highly ionized region. This is not surprising since Fe^+ does not have any strong emission lines in the studied wavelength range; presumably its presence is obscured by strong overlapping emissions emanating from other species.

Furthermore, no bands attributable to diatomic oxide molecules such as BaO and FeO could be detected either in vacuum or under oxygen atmospheres along the plasma expansion axis. The reaction of Ba with O_2 to form ground-state BaO is exothermic by 0.55 eV for low energy Ba atoms and would occur readily for more energetic Ba atoms within the plume.⁴ The BaO formed may undergo collisional excitation but its weak extended emission band system over the range of 450–750 nm renders identification difficult. The absence of any identifiable strong BaO in the emission spectra is not therefore unexpected.

Conversely, the formation of excited FeO from oxidation reactions of atomic Fe species at the plume oxygen interface is considered unlikely. The reaction of Fe with O_2 is endothermic by 0.92 eV and does not occur for normal collision energies. Some gas phase oxidation might be expected during the earlier energetic phases of plume expansion but the FeO formed could dissociate rapidly (dissociation energy of FeO is 4.18 eV) by collisions with energetic electrons in the high temperature plasma or by single laser photon absorption. It is therefore likely that the ultimate Fe content in the laser deposited films is mainly incident on the growing film in the form of atomic Fe and that appreciable oxidation occurs on the surface.

In the neighborhood of the target surface ($z < 0.5$ mm), Stark broadened ionic and atomic lines were superimposed on a continuum background. The continuous emission, produced from a hot dense core has been reported⁵ during ablation of several materials.

In vacuum the intensities of all species fell off by a factor greater than 10, over the first 10 mm. The decline is

attributed to a reduction in electron impact excitation of the plasma species as the ion and electron number densities decrease due to free expansion into vacuum.

Introduction of oxygen caused a marked enhancement of the emission at all wavelengths. This is due to confinement of the plasma material within a smaller volume by the higher ambient oxygen pressure, hence enhancing the rate of collisional excitation and the corresponding visible emission. A continuous increase in emission with oxygen pressure was observed in the $0 \leq z < 20$ mm region. However, for distances of 20 to 30 mm, the radiated emission increased and reached a maximum at 0.1 mbar above which it fell off. Having previously recognized, that the best quality hexaferrite films are obtained at 30 mm and 0.1 mbar, it can be insinuated that the excited state species provide the necessary surface mobility to promote perpendicularly (c_{\perp}) oriented growth.

It is interesting to examine the nature of the emitting species and effective plasma temperatures along the axis of the plume at 0.1 mbar. Beginning at 2 mm, the main spectral characteristics were similar to those found in vacuum (Fig. 1) i.e., predominant radiation from Ba^+ with less prominent emissions from neutral Ba and Fe. However, at distances further away from the target, this dominance of Ba^+ transitions slowly receded and stronger emissions from Ba and Fe neutrals emerged as a result of collisional recombination processes. Assuming local thermodynamic equilibrium conditions, the effective temperature of the plasma, as estimated from the temporally integrated Ba^+ emission line intensity ratios decreased over the range 1.4–0.8 eV as the contact front of the plume expanded from 2 to 30 mm. The high temperatures (9500 K) of the species incident on the growing film are thought to facilitate film crystallization and oriented growth.

Further insight into the ablation process was gained by recording the temporal evolution of the Ba (553.5 nm), Fe (438.3 nm), and Ba^+ (614.2 nm) emissions at positions 5, 10, and 20 mm from the target, in different oxygen pressures. The delay time, at which peak radiation was attained, yielded straightforwardly the most probable front axial velocity v_z . The results indicated that at small distances from the target surface ($z = 5$ mm), the Ba^+ species outnumbered the Ba and Fe neutral population in agreement with the time integrated data. Moreover, the intense ion emission front was observed in advance of the corresponding neutral front by 10%–20%. Increasing the oxygen pressure up to 0.5 mbar caused an increase in the emission intensities and a minor shift in the corresponding temporal profiles towards greater delay times. It appears, that the dense plasma expands virtually unhindered by the background oxygen at this region. The explanation for the nondependence of the species velocity on the oxygen pressure is to be found on the mass of the ablated products which is large compared to that of the background gas, set in motion by the plume.⁶

Increase in oxygen pressure had a more pronounced influence on the temporal profiles at greater distances from the target. Figure 2 shows the Fe (438.3 nm) time traces at 20 mm. Evidently the emission maximum is increasingly delayed by an increase in oxygen pressure which implies that the plasma expansion is slowed by the higher oxygen pres-

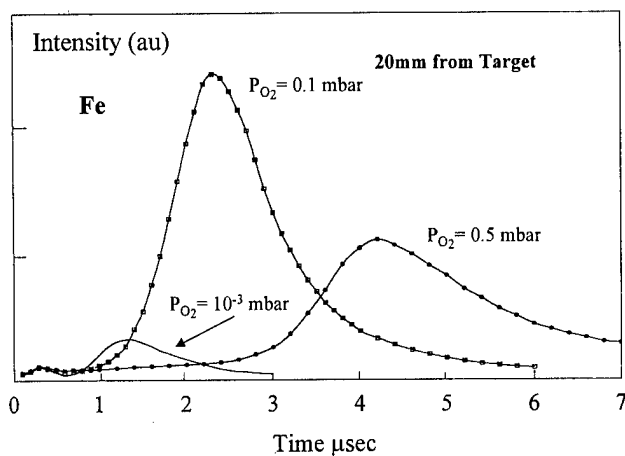


FIG. 2. Temporally resolved emission profiles of Fe recorded 20 mm from the target, in 10^{-5} , 0.1, and 0.5 mbar oxygen.

sures. Moreover, comparable maximum velocities (v_z) were obtained for the emission fronts of all the species ($\sim 8.4 \times 10^5$ cm/s at 0.1 mbar and $\sim 4.6 \times 10^5$ cm/s at 0.5 mbar). A closer inspection of the temporal profiles recorded at 20 mm revealed a fast and slow component, the latter being eminently intensified with oxygen pressure.

At 0.5 mbar the plasma front was cooled to such an extent that a decrease in the peak emission was observed at the location of 20 mm (Fig. 2). It is apparent that a further decrease in the peak emission is expected at the longer distance of 30 mm for the same oxygen pressure. At 0.5 mbar the luminous plume length is smaller than the target-substrate distance of 30 mm and mainly thermalized nonluminous species, transported by diffusion, reach the substrate. The low kinetic energies of the species, together with changes from the stoichiometric arrival cation ratio, are responsible for the presence of misaligned grains and/or foreign phase in the films grown at pressures much higher than 0.1 mbar.¹ Nevertheless, optimum crystalline and morphological properties could be obtained for a target substrate distance of about 30 mm at a pressure of 0.1 mbar, i.e., for a substrate position within the end of the fully expanded plume.

In Fig. 3 are shown 2D images depicting expanding visible Ba ferrite plume in vacuum and 0.1 mbar 1 and 2 μ s after the laser impact. It is clearly shown that the background oxygen pressure confines the plasma slows its expansion and enhances the emission particularly at its expansion front. The bright luminance at the expansion front, is correlated principally with the delayed intense peaks of Fig. 2.

A qualitative picture of the plasma plume dynamics emerges from these spectroscopic results. In vacuum fast "hot" highly ionized material expands rapidly in essentially a free collisionless expansion, strongly forward directed ($v_z \sim 6.6 \times 10^6$ cm/s), leaving behind it, cooler, slower, mainly neutral material. In an oxygen atmosphere, the fast components at the contact front are progressively slowed down re-

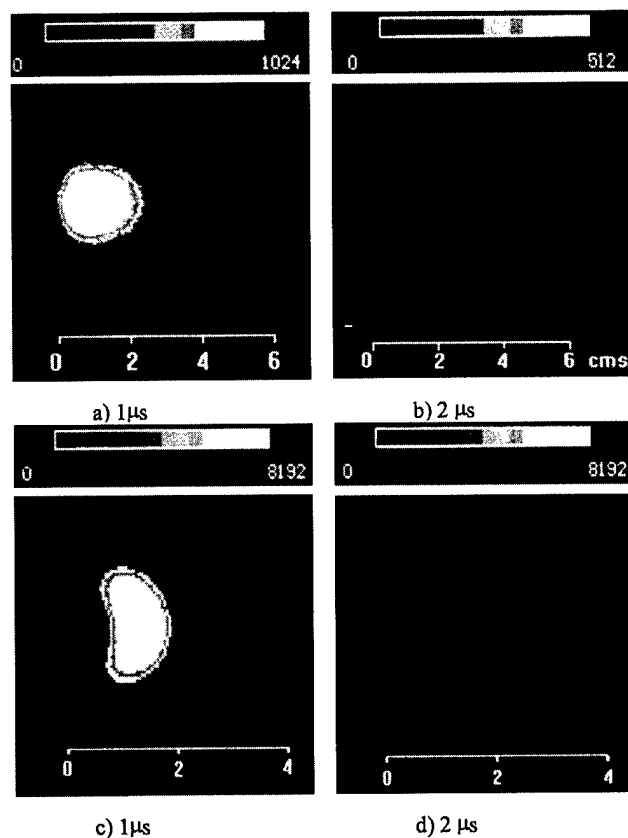


FIG. 3. ICCD images of the visible plasma emission recorded 1 and 2 μ s after laser impact upon a $\text{BaFe}_{12}\text{O}_{19}$ target in an oxygen pressure of 10^{-5} (a) and (b) and 0.1 (c) and (d) mbar.

sulting in collisional redistribution of high z directed velocities into x and y directions⁷ producing a more homogeneous plasma with an equilibrated temperature smaller than 1 eV.

IV. CONCLUSIONS

Temporal emission profiles and time resolved ICCD optical images of the plasma clearly demonstrate, how increasing the oxygen pressure confines the plasma, slows its expansion and enhances the emission particularly at its expanding front. It is concluded that the role of oxygen pressure is not only to supply the oxygen constituent to the film but also to slow down the highly energetic species which otherwise will cause damage to the deposited layer.

¹P. Papakonstantinou, M. O'Neill, R. Atkinson, I. W. Salter, and R. Gerber, *J. Magn. Magn. Mater.* **152**, 401 (1996).

²P. Papakonstantinou, R. Atkinson, I. W. Salter, and R. Gerber, *J. Magn. Soc. Jpn.* **19**, 177 (1995).

³A. H. El-Astal, S. Ikram, T. Morrow, W. G. Graham, and D. G. Walmsley, *J. Appl. Phys.* **77**, 6572 (1995).

⁴A. H. El-Astal, T. Morrow, W. G. Graham, and D. G. Walmsley, *Supercond. Sci. Technol.* **8**, 529 (1995).

⁵W. A. Weimer, *Appl. Phys. Lett.* **52**, 2171 (1988).

⁶D. B. Geohegan, in *Pulsed Laser Deposition of Thin films*, edited D. B. Chrisey and G. K. Hubler (Wiley, New York, 1994), p. 115.

⁷R. A. Al-Wazzan, J. M. Hendron, and T. Morrow, *Appl. Surf. Sci.* **96-98**, 170 (1996).

Fine grained Mn–Zn ferrite for high frequency driving

K. Takadate,^{a)} Y. Yamamoto, and A. Makino

Central Laboratory, Alps Electric Company, Ltd., 1-3-5 Higashitakami, Nagaoka, Niigata 940, Japan

T. Yamaguchi

Faculty of Engineering, Kyushu Sangyo University, 2-3-1 Matsukadai, Higashi-ku, Fukuoka 813, Japan

I. Sasada

Department of Electronics, Kyushu University, 6-10-1 Hakozaki, Higashi-ku, Fukuoka 812-81, Japan

A Mn–Zn ferrite with a grain size of about 2 μm has been developed for the transformer driven at around 1 MHz. The developed ferrite exhibits considerably lower core losses than a conventional Mn–Zn ferrite with a grain size of about 10 μm at a frequency of 0.5 to 2 MHz. The thin-type transformer using the developed ferrite driven at 1 MHz shows a high efficiency of more than 95% at an output power of 10 to 17 W and a much lower surface temperature rise than the transformer using the conventional ferrite. © 1998 American Institute of Physics. [S0021-8979(98)42211-4]

I. INTRODUCTION

Low-profile transformers are necessary to miniaturize the power supplies because the transformers are one of the largest components of a power converter. Miniaturization of the transformers has been investigated in high frequency driving up to the MHz range. Therefore, the core materials used in the low profile transformer are desired to have low core losses at the MHz range. Thus, we have developed a fine grained Mn–Zn ferrite^{1,2} for high frequency driving at the MHz range. Moreover the low-profile transformer should have the structure, in which uniform flux density in the core and current density in the conductor are achieved, to reduce the core and copper loss. A conductor-embedded-type transformer has been suggested to meet the needs of the transformer design.^{3,4} In this article, we report on the performance of the fine grained Mn–Zn ferrite and a thin-type transformer with the conductor-embedded-type structure using the developed ferrite.

II. EXPERIMENT

Mn–Zn ferrite with a fine grain was prepared by a conventional powder metallurgical process. The raw materials are hydrothermally precipitated ferrite powder and additives, 0.01 wt %SiO₂, 0.021 wt %CaCO₃, 0.038 wt %Ta₂O₅, and 0.034 wt %TiO₂. The composition and the particle size of the hydrothermal ferrite powder are Fe_{2.08}Mn_{0.73}Zn_{0.19}O₄ and about 0.13 μm , respectively. The hydrothermal ferrite powder and the additives were uniformly mixed with a planetary ball mill and calcined at 1173 K in pure nitrogen. The calcined powder was then pressed into a disk shape and sintered at 1348 K for 4 h in the reduced atmosphere of about 30 Pa.

Core losses of the developed ferrite were compared with those of a conventional Mn–Zn ferrite, which is widely used as a core material for the driving frequency at less than 500 kHz. The core losses were measured on the condition of $B_m \times f = 25\,000$ [T \times Hz] at a frequency from 100 kHz to 2 MHz and $B_m = 15$ to 75 mT at 1 MHz, where B_m is a peak

value of the induced flux density and f is driving frequency. Dimensions of the samples are an outer diameter of 8 mm, an inner diameter of 4 mm, and a thickness of 2 mm. The conductor-embedded-type transformers³ were constructed using the developed ferrite and the conventional ferrite. A ratio of the primary and secondary windings is 2:1. These windings were made of a copper foil and separated by a polyimido insulator. Efficiency and a temperature rise of the transformers were measured on a condition of an input voltage of 30 V under a sinusoidal wave at 1 MHz varying the current by changing the load resistance.

III. RESULTS AND DISCUSSION

A. Core loss of fine grained Mn–Zn ferrite

Figure 1 shows the microstructures of the developed fine grained Mn–Zn ferrite and the conventional Mn–Zn ferrite. The grain size of the developed ferrite is about 2 μm , which is much smaller than the 10 μm of the conventional ferrite. Figure 2 shows the frequency dependence of the core losses (P_{cv}) for the developed ferrite and the conventional ferrite. The developed ferrite exhibits low P_{cv} compared with the conventional ferrite at a frequency range from 0.5 to 2 MHz. Especially at 1 MHz, P_{cv} of the fine grained ferrite is about 25% that of the conventional ferrite. Table I shows computationally separated loss components of P_{cv} ,⁵ which are the eddy current loss (P_e), the equivalent dielectric loss (P_d)

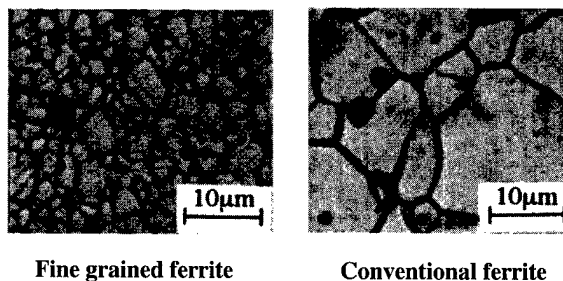


FIG. 1. Microstructures of the fine grained ferrite and the conventional ferrite.

^{a)}Electronic mail: takadate@alps.co.jp

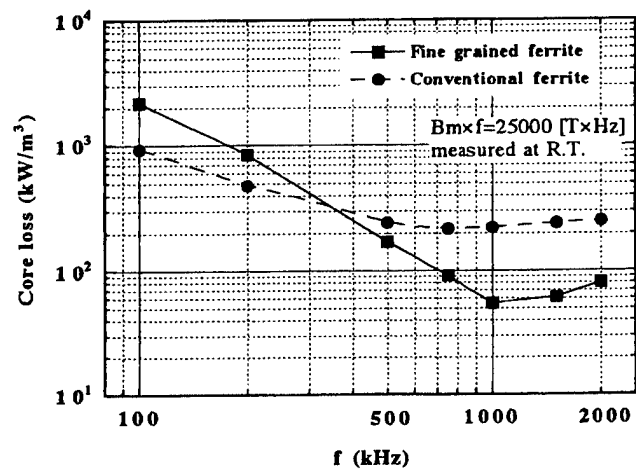


FIG. 2. Core losses as a function of frequency for the fine grained ferrite and the conventional ferrite.

due to displacement currents, the hysteresis loss (P_h), and the residual loss (P_r), for the developed ferrite and the conventional ferrite at 1 MHz. P_r of each ferrite occupies a large part of the P_{cv} , the ratio of P_r on P_{cv} in the developed ferrite and the conventional ferrites are 54% and 87%, respectively. P_r of the developed ferrite is about 85% lower than that of the conventional ferrite. P_{cv} of the developed ferrite, therefore, is lower than that of the conventional one. It has been reported that the core losses of ferrites in the MHz range are reduced with a decreasing of the grain size.⁶⁻⁹ Although not understood sufficiently, the cause of this effect is supposed that any magnetic resonance would be suppressed. For example, the suppression of natural resonance can be considered. It is known that the domain of ferrites is subdivided with a decreasing of the grain size.¹⁰ With the decrease of the domain size, the number of domain walls per volume increase; therefore, the amplitude of vibration in each domain wall is reduced in the same B_m . In other words, the switching frequency of the spin inside the domain wall (fs) is reduced. The low P_r of the developed ferrite is presumably caused by the suppression of the natural resonance for the spin inside the domain wall¹¹ at 1 MHz owing to low fs .

In power supplies the input capacity (P_{in}) is an elemental property. P_{in} is expressed by the following equation:¹²

$$P_{in} = 4.44 \times f \times B_m \times N \times I \times A_{ce}, \quad [W], \quad (1)$$

where f is switching frequency, B_m is maximum flux density, N is turn number of windings, I is input current, and A_{ce} is effective core cross sectional area. It is clear from the Eq. (1) that P_{in} is determined by $f \times B_m$ and allowable $f \times B_m$ is limited by the core losses. Figure 3 shows the core losses as a function of B_m for the developed ferrite and the conven-

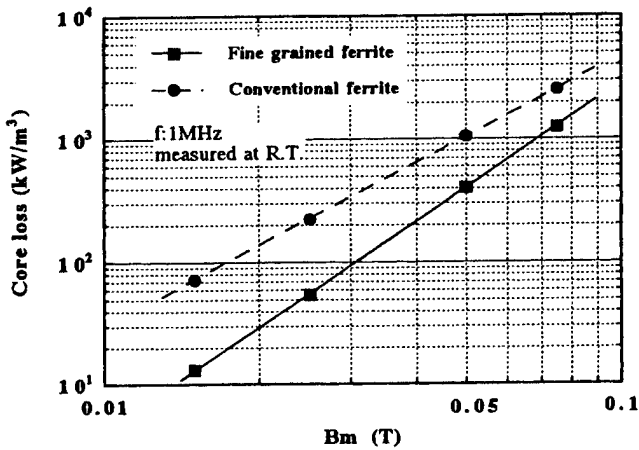


FIG. 3. Core losses as a function of B_m for the fine grained ferrite and the conventional ferrite.

tional ferrite at 1 MHz. At the same level of the core loss, B_m of the developed ferrite is larger than that of the conventional ferrite. For instance, B_m of the developed ferrite is about 1.6 times larger than that of the conventional ferrite at 400 kW/m³. Therefore, the transformer using the developed ferrite is expected to achieve a higher P_{in} when compared with the transformer using the conventional ferrite in the same transformer configuration. In other words, it is possible to miniaturize the transformer by using the developed ferrite in the same P_{in} because N or A_{ce} can be reduced owing to the large B_m .

B. Performance of conductor-embedded-type transformer using fine grained ferrite

We made a conductor-embedded-type transformer³ using the developed ferrite and the conventional ferrite to confirm the performance of the developed ferrite as a thin-type transformer for a high frequency converter. Figure 4 shows the structure of the transformer. In the conductor-embedded-type transformer, the primary and secondary coils were arranged in the ferrite core and the height of the transformer is only 3 mm. Moreover, minimized flux leakage, uniform flux density, and current density are achieved by having an en-

TABLE I. Each loss component at a frequency of 1 MHz, B_m of 25 mT for the developed ferrite and the conventional ferrite.

Sample	P_{cv}	P_e	P_d	P_h	P_r
Developed ferrite	54.8	1.2	0.1	24.0	29.5
Conventional ferrite	218	0.2	0.5	26.3	191

unit: kW/m³

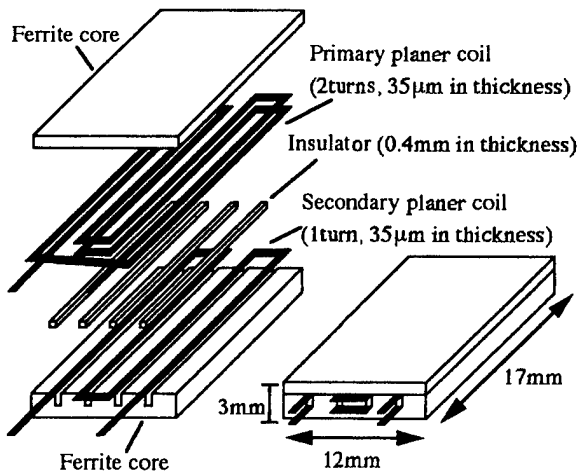


FIG. 4. Structure of conductor-embedded-type transformer.

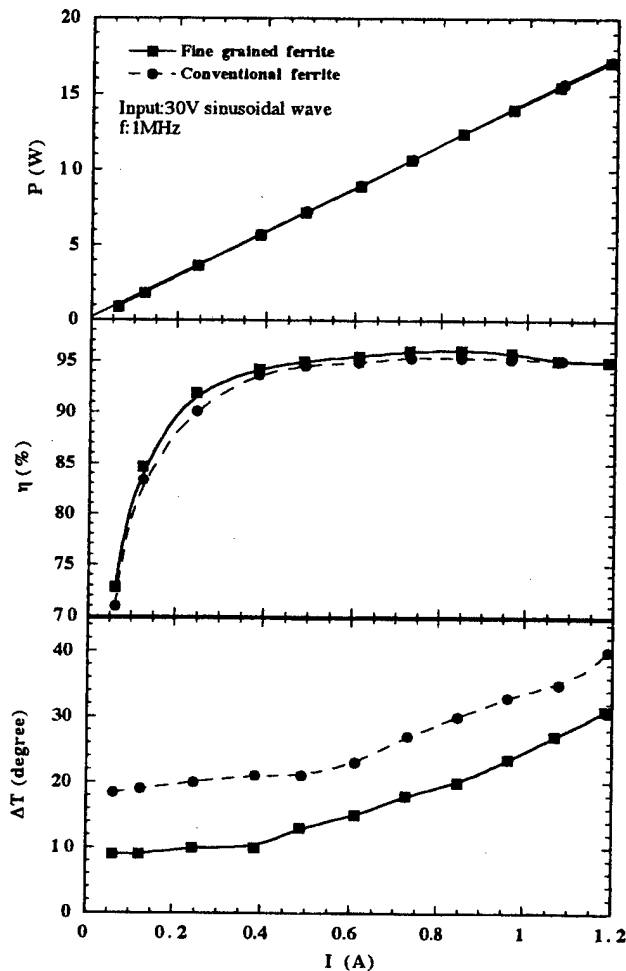


FIG. 5. Output power (P), efficiency (η), and surface temperature rise (ΔT) on the conductor-embedded-type transformers as a function of output current (I).

closed conductor within the ferrite.^{3,4} Figure 5 shows the output power (P), efficiency (η), and surface temperature rise (ΔT) of the transformers as a function of the output current (I). The transformers exhibit a high η of more than 95% at an output power of 10 to 17 W. High efficiencies are presumably associated with the structural characteristics, as mentioned above. ΔT of each transformer increases with increasing I , because the copper losses increase. The transformer using the developed ferrite shows a high η and a low ΔT as compared with that of the conventional ferrite. A clear difference between the two transformers can be seen in ΔT . ΔT of the transformer using the developed ferrite is about 10 °C lower than that of the conventional ferrite irrespective

of I . The low ΔT is caused by the low core loss of the developed ferrite at 1 MHz. For the safe operation of transformers, ΔT is limited in the transformer design.¹³ In the limited ΔT , the maximum power capacity of the transformer using the developed ferrite is higher than that of the conventional ferrite. For instance, at the same level of ΔT , 30 °C, the power capacity of the transformer using the developed ferrite is 40% larger than that of the conventional ferrite. Therefore, the fine grained ferrite is expected to be useful as the core material for the transformers driven at a high frequency around 1 MHz and the conductor-embedded-type transformer using the fine grained ferrite is effective in realizing the low profile and high-density switching converter.

IV. CONCLUSION

We have developed the fine grained Mn-Zn ferrite with a grain size of 2 μm . The developed ferrite exhibited low core losses as compared with the conventional Mn-Zn ferrite at a frequency range from 0.5 to 2 MHz. Therefore, at the same level of core loss, it is possible for the developed ferrite to drive in a high flux density at a high frequency. The thin-type transformer, the conductor-embedded type, using the developed ferrite shows high efficiencies and low surface temperature rises at the driving frequency of 1 MHz when compared with the transformer using the conventional ferrite. It is concluded that the fine grained Mn-Zn ferrite is suitable for high frequency driving and effective in achieving the transformers with a low profile and high power density.

- ¹ Y. Yamamoto and A. Makino, *J. Magn. Magn. Mater.* **133**, 500 (1994).
- ² Akihiro Makino and Yutaka Yamamoto, *Advances in Science and Technology 4, New Horizons for Materials*, edited by P. Vincenzini (Techna Srl, 1995), p. 361.
- ³ T. Yamaguchi, I. Sasada, and K. Harada, *J. Magn. Soc. Jpn.* **16**, 445 (1992).
- ⁴ I. Sasada, T. Yamaguchi, K. Harada, and Y. Notohara, *IEEE Trans. Magn.* **29**, 323 (1993).
- ⁵ H. Saotome and Y. Sakaki, *IEEE Trans. Magn.* **33**, 728 (1997).
- ⁶ P. J. van der Zaag, P. J. van der Valk, and M. Th. Rekveldt, *Appl. Phys. Lett.* **69**, 4 (1996).
- ⁷ T. Nakano, N. Sato, and T. Nomura, *J. Magn. Soc. Jpn.* **20**, 501 (1996).
- ⁸ K. Takadate, Y. Yamamoto, and A. Makino, *Proceedings of International Symposium on Ferrites in Asia 1997* (unpublished).
- ⁹ H. Kobiki, A. Fujita, and S. Gotoh, *Proceedings of the 7th International Conference on Ferrites: J. Phys. (Paris), Colloq.* **7**, C1-103 (1996).
- ¹⁰ P. J. van der Zaag, A. Noordermeer, J. J. M. Ruigrok, P. T. Por, M. Th. Rekveldt, D. M. Donnet, and J. N. Chapman, *Proceedings of the 6th International Conference on Ferrites*, 1992, p. 819.
- ¹¹ S. Yamada and E. Otsuki, *J. Appl. Phys.* **81**, 15 (1997).
- ¹² R. E. Steven, *Electrical Machines and Power Electronics* (Van Nostrand Reinhold, London, 1983), p. 175.
- ¹³ N. Yamashita, N. Murakami, and T. Yachi, *Proceedings of IEEE 10th Applied Power Electronics Conference*, 1995, p. 297.

Particle size dependence of rotational responses in Ni–Zn ferrite

P. S. Anil Kumar

*Centre for Advanced Studies in Material Science and Solid State Physics, Department of Physics,
University of Pune, Pune 411 007, India*

S. R. Sainkar, J. J. Shrotri, S. D. Kulkarni, C. E. Deshpande, and S. K. Date^{a)}

Physical Chemistry Division, National Chemical Laboratory, Pune 411 008, India

Active powders of Ni–Zn ferrite were synthesized by soft chemical approaches and were processed with varying concentrations of Bi₂O₃. The sintered products were characterized extensively using a vibrating sample magnetometer, scanning electron microscopy, and resistivity techniques. The loss factor and the permeability have been evaluated. At an optimum concentration of Bi₂O₃ doping the loss factor has been reduced by 20%. The rotational responses are found to be strongly dependent on particle size. © 1998 American Institute of Physics. [S0021-8979(98)19611-1]

I. INTRODUCTION

High electrical resistivity and low magnetic coercivity make Ni–Zn ferrite a technologically important material for applications in the megahertz frequency region.^{1,2} The performance characteristics of these ferrites in this frequency region are being improved by following a variety of synthetic approaches and selective grain and grain-boundary doping.³ The main focus is to reduce the loss factor at the operational frequency and to improve the rotational responses. As the main loss mechanism in the megahertz frequency region is due to an eddy current, efforts are being made to increase the resistivity of this material further so as to considerably reduce the loss. Within the same chemical composition of the material under consideration, the performance characteristics are determined by the microstructural features, viz., size, shape, and orientation of individual particles.³ To tailor these materials, a new concept of microstructural engineering has been evolved in the scientific literature. Recently we have been able to reveal a useful microstructure–magnetic permeability correlation in Ni–Zn ferrite.⁴ It is shown that the initial permeability of this material and the frequency at which the loss factor gives a minimum strongly depend on the microstructural features of this material.

In the present work, we have followed soft chemical approaches to synthesize fine particles of Ni–Zn ferrite (<50 nm) as the conventional ceramic method yielded particles of bigger size (>1 μ m). High resistivity Bi₂O₃ is doped at the grain boundary in different proportions. The choice of Bi₂O₃ is based on the fact that it is nonmagnetic, it has a low melting temperature, and it is a nonferrite forming oxide. The loss factor has been reduced substantially at optimal doping of 2 wt % Bi₂O₃. We have been successful in showing a clear correlation between rotational responses and the microstructure in Ni–Zn ferrite.

II. EXPERIMENT

Active powders of Ni–Zn ferrite, (a representative composition Ni_{0.8}Zn_{0.2}Fe₂O₄) have been synthesized by a soft

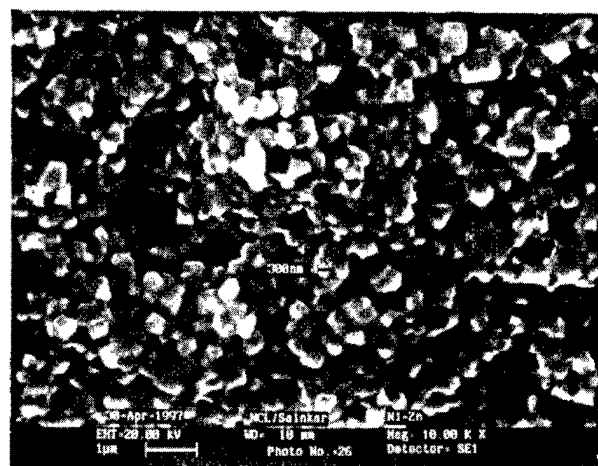
chemical method at a temperature as low as 80 °C with a saturation magnetization of 45 emu/g and particle size <50 nm. Details of the synthesis are described elsewhere.⁵ This active powder is divided into five batches and they were mixed with 0, 1, 2, 4, and 6 wt % Bi₂O₃ (the samples are labeled as B0, B1, B2, B4, and B6, respectively). This mixture was mixed with 2 wt % PVA and pressed into toroid and pellet forms. The toroids and pellets were then sintered in air at 1100 °C for 1 h.

The microstructural features of all the samples were obtained using a (Leica–Cambridge 440) scanning electron microscope (SEM). The sintered pellets were fractured to expose the inside portion and mounted onto a specimen mounting stub. The samples were coated by a thin layer of gold to prevent charging of the specimen. The porosity of the material is calculated from the density of the material and the theoretical density. For the theoretical density calculation it is assumed that the doped Bi₂O₃ exists as such. The initial permeability (μ_i) and the loss factor ($\tan \delta \mu_i$) of all the toroids were evaluated using a Q meter (HP 4192) in the frequency range 1–40 MHz. The two probe dc resistivity of all the samples was measured using an Impedance bridge (General Radio 1608A). Both surfaces of the pellets were coated with conducting silver paste before being sandwiched between the two electrodes of the sample holder for improved electrical contact. The Curie temperature (T_c) and the saturation magnetization at room temperature for all the samples were measured using a vibrating sample magnetometer (EG&G PAR 4500). The room temperature saturation magnetization was obtained from the hysteresis loop measurement in a field range of ± 15 kOe. The (T_c) was obtained from the temperature dependence of magnetization.

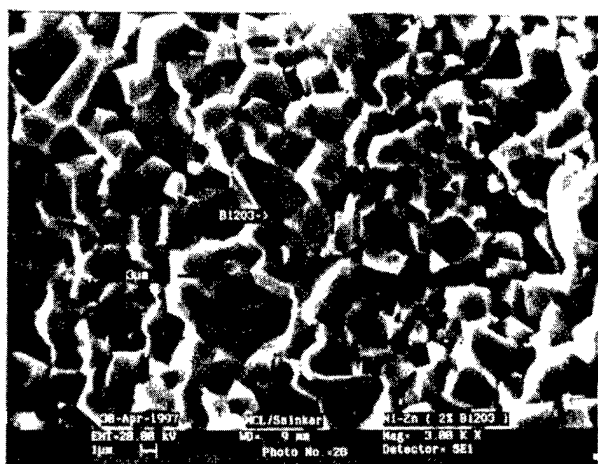
III. RESULTS AND DISCUSSION

Figures 1(a) and (b) show the scanning electron micrographs of samples B0 and B2, respectively. It is clearly seen from the micrographs that the undoped sample, B0, has an average particle size of ~ 300 nm. With 2 wt % Bi₂O₃ doping the grains have grown substantially to ~ 3 μ m. The particle sizes obtained from the scanning electron micrographs of all the samples (B0, B1, B2, B4, and B6) are given in Table I. It

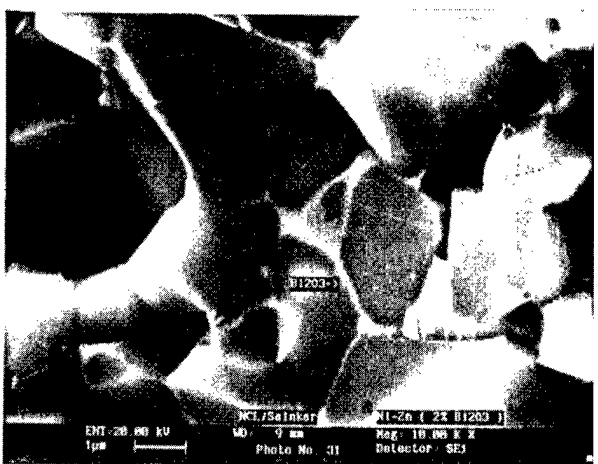
^{a)}Electronic mail: skdate@ems.ncl.res.in



(a)



(b)



(c)

FIG. 1. The SEM of (a) B0 and (b) B2. The micrograph shown in (c) is an enlarged version of (b).

Bi_2O_3 at the grain boundary. This is clearly shown in Fig. 1(c) which is an enlarged micrograph of Fig. 1(b).

Figure 2 shows the temperature dependence of the magnetization for samples B0, B1, and B6. It may be seen from Fig. 2 that the $T_c \sim 485^\circ\text{C}$ for all the samples. The (T_c) for the undoped as well as for the Bi_2O_3 doped samples is the same, indicating that the doped Bi_2O_3 has not altered the cation distribution or the chemical composition of the ferrite phase. Hence it is concluded from the magnetic measurements and SEM micrographs that the doped Bi_2O_3 has been trapped in the grain boundaries. The inset in Fig. 2 shows the hysteresis loop for B0 and B6. The magnetization at 15 kOe is less for B6 compared to that of B0. This is due to the presence of nonmagnetic Bi_2O_3 along with the ferrite phase.

In Table I, the room temperature electrical resistivity, the porosity, and the initial permeability (μ_i) measured at 5 MHz of all the samples are given along with the particle size. The resistivity of B0 is of the order of $10^6 \Omega \text{ cm}$. For Bi_2O_3 doped samples the resistivity is considerably increased by two orders of magnitude ($\sim 10^8 \Omega \text{ cm}$). It has been shown that the resistivity of Ni-Zn is comprised of grain and grain-boundary resistivities.⁶ Hence the increase in resistivity for the doped samples is assigned to the increase in the intergranular resistivity due to the presence of high resistivity⁷ Bi_2O_3 at the grain boundary. The porosity of the samples decreased with an increase in the % of Bi_2O_3 of doping. This is because of the filling of the voids by the doped Bi_2O_3 .

The initial permeability of the undoped sample is ~ 37 . It is known that the permeability of a polycrystalline sample is described as the superposition of two magnetization mechanisms, i.e., spin rotation and domain-wall motion^{8,9} so that

$$\mu_i = 1 + \chi_{\text{spin}} + \chi_{\text{dw}},$$

where χ_{spin} and χ_{dw} are magnetic susceptibility due to spin rotation and domain-wall motion, respectively. For single domain particles the contribution to permeability from domain-wall motion is absent. B0 possesses submicron par-

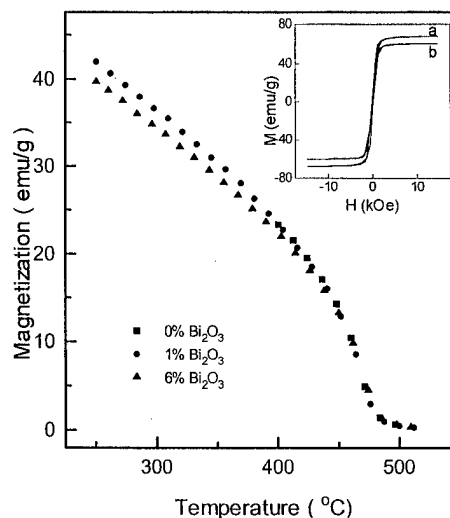


FIG. 2. The temperature variation of magnetization of $\text{Ni}_{0.8}\text{Zn}_{0.2}\text{Fe}_2\text{O}_4$ with different amounts of Bi_2O_3 doping. Data for the undoped sample are not shown below 390 K for clarity. Inset: Hysteresis loops for (a) undoped and (b) 6 wt % Bi_2O_3 doping.

is clearly seen from Table I that the particle size remains unchanged for different degrees of Bi_2O_3 . For the Bi_2O_3 doped samples, the presence of an additional phase is seen at the grain boundaries and is assigned to the presence of doped

TABLE I. Average particle size, room temperature electrical resistivity, porosity, and initial permeability of $\text{Ni}_{0.8}\text{Zn}_{0.2}\text{Fe}_2\text{O}_4$ with different Bi_2O_3 doping levels.

Sample	B0	B1	B2	B4	B6
Percentage of Bi_2O_3 doping	0	1	2	4	6
Average particle size	~ 300 nm	~ 3 μm	~ 3 μm	~ 3 μm	~ 3 μm
Resistivity Ω cm	3.5×10^6	6.7×10^8	5.2×10^8	4×10^8	3.5×10^8
Porosity (%)	13	9.7	6.5	5.8	5.4
Initial permeability μ_i 5 MHz	37	75	70	64	48

ticles which are single domain particles. For B1 the permeability is ~ 75 and the particle size is ~ 3 μm . van der Zaag *et al.*¹⁰ have earlier shown that particles with sizes ≥ 3 μm are multidomain. Hence the contribution from the domain-wall motion enhances the initial permeability of B1. For Bi_2O_3 doped samples the particle size remains unchanged; however the permeability decreases as the % of Bi_2O_3 increases. This is likely to be due to the incorporation of excess nonmagnetic material between the grains.

Figure 3 shows the loss factor V_s frequency curves of all the samples. The loss factor has been substantially reduced by 20% up to 2 wt % Bi_2O_3 doping compared to the undoped sample. A further increase in the Bi_2O_3 concentration increases the loss factor. The frequency at which the loss factor gave a minimum (f_{lossmin}) shifted to low frequency for the Bi_2O_3 doped samples. For the undoped sample $f_{\text{lossmin}} \sim 25$ MHz whereas for the Bi_2O_3 doped samples $f_{\text{lossmin}} \sim 5$ MHz. This is due to the increase in grain size for the doped samples. Although the porosity of the samples is progressively decreasing, f_{lossmin} remains unchanged for the doped samples. The interesting observation that (i) the grains grow substantially with Bi_2O_3 doping, (ii) the grain size of the

sintered ferrites, however, remains same for different degrees of Bi_2O_3 doping, (iii) f_{lossmin} shifts from ~ 25 to ~ 5 MHz on doping, (iv) f_{lossmin} remains unchanged from B1 to B6, and (v) the initial permeability is increased substantially for B1 compared to B0, suggesting that the rotational responses are particle size dependent.

IV. CONCLUSION

Fine particles of Ni-Zn ferrite were synthesized and processed with varying concentrations of Bi_2O_3 and the doped Bi_2O_3 is distributed in the grain boundaries as evidenced by scanning electron micrographs and the (T_c) measurements. The resistivity of the material is increased considerably due to the presence of high resistivity Bi_2O_3 at the grain boundaries. The Bi_2O_3 doping has increased the particle size of the material considerably. It is observed that the rotational responses are particle size dependent rather than porosity. With optimal doping of 2 wt % Bi_2O_3 we could reduce the loss factor considerably (20% reduction). We have developed a low power-loss material and demonstrated the dependence of rotational response to particle size in Ni-Zn ferrite.

ACKNOWLEDGMENTS

One of the authors (P.S.A.K.) is grateful to University Grants Commission India for financial support and to Professor D.S. Joag for constant encouragement.

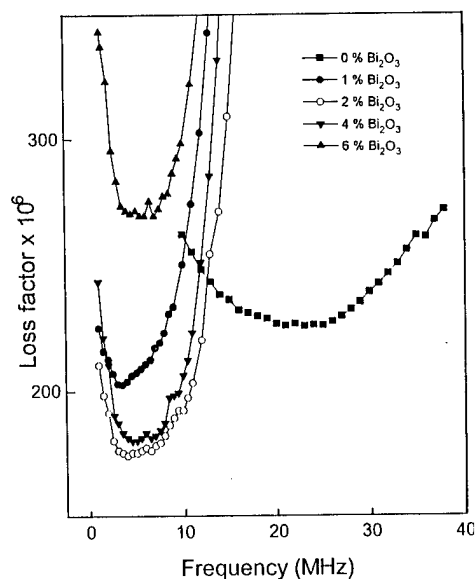


FIG. 3. The frequency dependence of the loss factor for different samples.

- ¹ P. I. Slick, in *Ferromagnetic Materials*, edited by E. P. Wohlfarth (North-Holland, Amsterdam, 1980), Vol. 2, p. 196, and references therein.
- ² U. Enz, in *Ferromagnetic Materials*, edited by E. P. Wohlfarth (North-Holland, Amsterdam, 1987), Vol. 3, p. 1.
- ³ A. Goldman, *Modern Ferrite Technology* (Van Nostrand Reinhold, New York, 1990), p. 157, and references therein.
- ⁴ P. S. Anil Kumar, J. J. Shrotri, C. E. Deshpande, and S. K. Date, *J. Appl. Phys.* **81**, 4788 (1997).
- ⁵ P. S. Anil Kumar, J. J. Shrotri, C. E. Deshpande, S. D. Kulkarni, and S. K. Date, *Mater. Lett.* **27**, 293 (1996).
- ⁶ C. G. Koops, *Phys. Rev.* **83**, 121 (1951).
- ⁷ T. K. Gupta, *J. Am. Ceram. Soc.* **73**, 1817 (1990).
- ⁸ G. T. Rado, *Rev. Mod. Phys.* **25**, 81 (1953).
- ⁹ T. Tsutaoka, M. Ueshima, T. Tokunaga, T. Nakamura, and K. Hatakeyama, *J. Appl. Phys.* **78**, 3983 (1995).
- ¹⁰ P. J. van der Zaag, P. J. van der Valk, and M. Th. Rekveldt, *Appl. Phys. Lett.* **69**, 2927 (1996).

Processing and cation redistribution of MnZn ferrites via high-energy ball milling

D. J. Fatemi,^{a)} V. G. Harris, and V. M. Browning
U.S. Naval Research Laboratory, Washington, District of Columbia 20375

J. P. Kirkland
SFA Inc., Landover, Maryland 20785

We have produced MnZn ferrites via high-energy ball milling (HEBM) of elemental oxides MnO, ZnO, and Fe₂O₃. X-ray diffraction (XRD) indicates a pure phase spinel forms after 21 h of HEBM. Extended x-ray absorption fine structure (EXAFS) analysis shows a nonequilibrium cation distribution, with an unusually high population of Zn cations on the octahedral sublattice. We then used EXAFS modeling to study cation site occupancy in an equilibrium MnZn-ferrite standard subjected to HEBM. We found that HEBM produces an increased preference for octahedral-site occupation among all cations for milling durations up to 300 min. After an initial improvement in magnetic properties, the magnetization diminishes steadily throughout this interval. With further increases in milling duration these structural and magnetic trends reverse, possibly due to annealing effects evidenced by XRD. © 1998 American Institute of Physics. [S0021-8979(98)42311-9]

The technique of high-energy ball milling (HEBM) has been the subject of great interest in recent years due to its promise for producing improved and/or novel materials through mechanical attrition or alloying.¹ Spinel ferrites are particularly attractive candidates for such processing studies due to their importance both in solid-state microwave devices and in soft magnet applications where loss minimization is critical.² Despite these motivations, there have been few investigations of ferrite production via ball milling.

In an early work, Lefelshtel *et al.*³ attempted to alloy ZnO and Fe₂O₃ in a ball mill, achieving partial conversion to ZnFe₂O₄ according to x-ray diffraction (XRD). Peaks associated with the elemental oxides were still dominant. More recently, Kosmac and Courtney⁴ subjected ZnO and Fe₂O₃ to HEBM and found that Zn ferrite became the dominant phase after 2.5 h. However, no trace of the spinel phase was seen by XRD after another 2.5 h milling. Similar results were achieved in the alloying of Ni ferrite from NiO and Fe₂O₃. Subsequently, Jovalekic *et al.*⁵ combined NiO and Fe₂O₃ and attributed all peaks in the XRD pattern to the spinel phase after milling 35 h, with little change in the XRD pattern upon subsequent milling. In a different application of ball milling, Hamdeh *et al.*⁶ subjected partially inverted ZnFe₂O₄ to HEBM for 10 h, increasing the inversion parameter and the magnetization.

In this article, we report the formation of MnZn ferrite from HEBM of MnO, ZnO, and Fe₂O₃. We find these milled ferrites have low temperature magnetization and coercivity equal to those processed via traditional ceramic processing techniques. We provide structural analysis of the product through both XRD and extended x-ray absorption fine structure (EXAFS) studies. Multiple scattering EXAFS analysis⁷ shows the milled ferrites to have a higher inversion param-

eter than a standard ferrite of similar stoichiometry, with an unusually high population of Zn ions on the octahedral sublattice.

Modification of the MnZn ferrite standard by HEBM was also performed. EXAFS analysis reveals that HEBM increases octahedral-site occupation among all cations for times up to 5 h. Superconducting quantum interference device (SQUID) magnetometry indicates improved magnetic properties in samples milled for short durations, followed by diminished magnetization with increased milling. With milling durations greater than 5 h the structural and magnetic trends reverse, possibly due to annealing effects.

Processing of MnZn ferrite was accomplished by combining MnO, ZnO, and Fe₂O₃, totaling 5 g, with the molar ratio 1:1:2 in the steel vial of the SPEX 8000 high-energy shaker mill. The vial was loaded with two stainless steel 8 g balls and two 1 g balls in air and shaken at about 1200 Hz. In order to maintain an equal ball:powder mass ratio for all samples, the vial was cleaned and reloaded with 5 g of new material for each milling trial.

Modification of a standard MnZn ferrite, prepared by traditional fire-and-grinding techniques, was achieved by subjecting 2.6 g samples of the standard to HEBM for periods ranging from 0.5 to 9 h.

Samples were characterized for their structural properties using XRD and EXAFS, and for their magnetic properties using SQUID magnetometry. θ - 2θ XRD scans were performed using a Philips XRG 3100 x-ray generator and Cu $K\alpha$ radiation. Refinement analysis leading to calculation of the lattice parameter was performed using the Philips APD™ software package.

EXAFS data were collected using beamlines X23B and X23A2 of the National Synchrotron Light Source at Brookhaven National Laboratory. The beamlines use double-crystal, fixed-exit monochromators, with Si (111) crystals in X23B and Si (311) crystals in X23A2. All spectra reported here were collected using the transmission technique.⁸ The storage ring current and energy at the time of data collection

^{a)}Electronic mail: dfatemi@anvil.nrl.navy.mil

were 200–350 mA and 2.5 GeV, respectively. Samples consisted of powders spread uniformly onto adhesive tape with several layers of powdered tape constituting a single sample. The number of layers was chosen empirically to provide nearly one absorption length at the absorption edge being measured.

EXAFS analysis followed established procedures⁹ leading to the Fourier transformation of EXAFS data to radial coordinate space (Å). Quantitative analysis of the cation distribution followed the approach previously employed by Harris *et al.*⁷ which included the least-squares fitting of multiple-scattering simulated XAFS data generated using the codes of Rehr *et al.*¹⁰

Portions of XRD patterns for the starting material, the sample ball-milled 21 h, and a standard $\text{Mn}_{0.5}\text{Zn}_{0.5}\text{Fe}_2\text{O}_4$, prepared by conventional ceramic techniques, are shown in Fig. 1. The calculated lattice parameter for the standard is 8.431 Å.

The XRD scan for the starting material contains peaks characteristic of MnO, ZnO, and Fe_2O_3 phases. However, after 21 h milling, peaks only attributable to the MnZn ferrite phase are observed, with even the most intense peaks in the starting material's data (see, for example, $2\theta = 33.5^\circ$, 50° , and 54.5°) no longer visible. XRD features for the milled samples have broadened and have reduced amplitudes coinciding to the formation of fine-grained strained particles which are characteristic of the HEBM technique. The calculated lattice parameters for the 21 h and 40 h milled ferrites are 8.422 and 8.429 Å, respectively.

Hysteresis loops, i.e., M vs H curves, collected using a SQUID magnetometer at 10 K reveal that the MnZn ferrite processed through ball milling is equal in magnetization and coercivity to that of the standard. These data are collected at low temperatures to overcome the superparamagnetic contribution of the milled sample.

Fourier transformed (FT) EXAFS data collected from Fe, Mn, and Zn K absorption are shown in Fig. 2. Transforms for the 40 h ball-milled sample are compared with similar data collected from the standard. The positions of the Fourier peaks typically correspond to bond distances (uncorrected for electron phase shifts) between the absorber and the backscatterers, while the amplitudes arise predominantly from the coordination and the atomic order of atom shells at that distance. The Fourier peaks seen in Fig. 2 have been assigned to atom pair correlations within the ferrite unit cell.¹¹ The appearance of Fourier peaks of significant amplitude over the full range of r space indicates that the ferrite forms with both short-range and long-range ordering.

In Fig. 2 the data sets in each panel are plotted on different y-axis scales. The reason for this is the reduced Fourier peak amplitudes characteristic of the large atomic disorder created by the ballistic nature of HEBM processing. It is interesting to note that the near neighbor oxygen peaks do not experience large disorder, whereas the cation–cation and next near neighbor oxygen correlations are strongly affected. We postulate that the strong ionic character of the metal–oxygen bond maintains the structural integrity of the polyhedra subunits and defines the cleavage planes to occur between polyhedra joined at edges and corners.

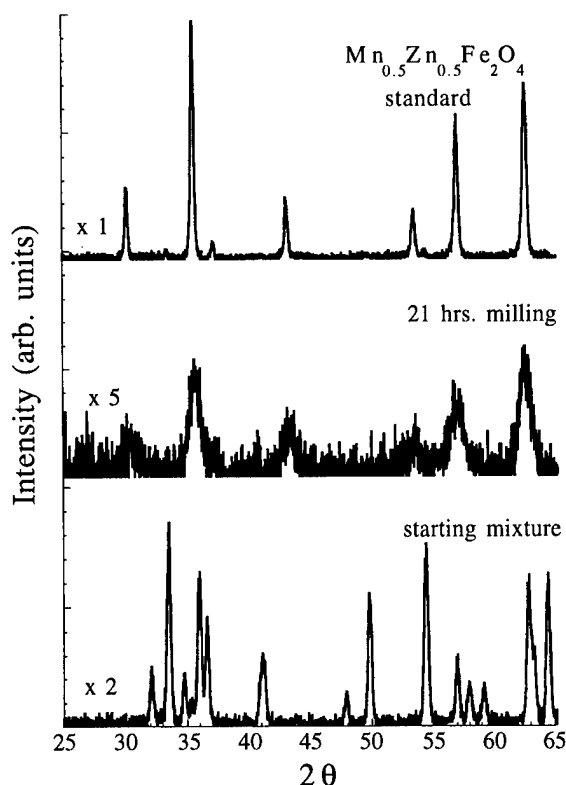


FIG. 1. Partial θ – 2θ x-ray diffraction scans illustrating ferrite formation from the ball milling of elemental oxides (radiation used was $\text{Cu } K_\alpha$).

The chief feature in the Fourier transform which signifies tetrahedral-site (A-site) occupancy for the absorber is the peak near 3.1 Å [denoted A on panel (a)]. The peak's amplitude predominantly arises from the scattering of 12 B-site cations and 12 anions centered near 3.48 Å. The octahedral-site (B-site) absorber is similarly fingerprinted by a peak near 2.6 Å [denoted B on panel (a)]. The amplitude arises solely from the scattering of six B-site cations and six anions centered near 2.97 Å (both Fourier peaks are shifted to small r due to electron phase shifts). The amplitudes of these peaks reflect qualitatively the distribution of absorbing cations on the A and B sites.

In comparing the B:A peak ratios of the sample milled 40 h to the standard, one infers that the milled sample possesses a higher fraction of Fe and Mn cations on the A sublattice, while an unusually high population of Zn cations resides on the B sublattice. Numerous studies have established that Fe and Mn cations may occupy both A- and B- sites depending upon the type and amount of other cations present. Zn cations, in contrast, do not typically occupy B sites. However, recent work by Hamdeh *et al.*⁶ suggests that ball milling of partially inverted Zn ferrite aerogels increases B-site filling by Zn cations.

Stabilization of nonequilibrium cation distributions was subsequently investigated through HEBM of the MnZn ferrite standard. FT Mn EXAFS data for the standard and samples ball milled between 45 and 540 m are shown in Fig. 3. All of the features to be discussed in this report are also seen in Fe and Zn EXAFS.

The inset in Fig. 3 shows the ratio of the amplitudes of the B and A peaks as a function of milling time. Up to 5 h, all cations show increased B-site occupation with milling

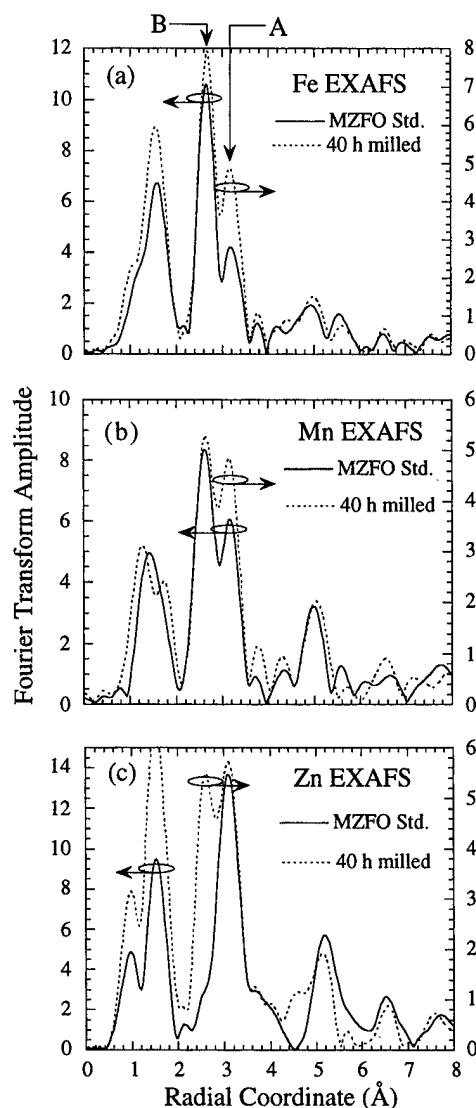


FIG. 2. Fourier transformed (a) Fe, (b) Mn, and (c) Zn EXAFS data from MnZn ferrite formed after 40 h of milling and from the standard (k weighting for all data is k^3 with k ranges of (a) 2.85–13.4, (b) 3.1–11.7, and (c) 2.5–12.6 \AA^{-1}).

duration. However, this trend reverses after 5 h for all cations, with the distribution returning to near equilibrium for Fe and Mn cations after 9 h milling.

Particle size analysis was performed using the Scherrer method. Though the technique is not definitive as it ignores line broadening in the XRD pattern due to strain, it is interesting that this analysis indicates a trend of decreasing particle size for durations between 0.75 and 5 h, with the thickness dropping from 16.6 to 11.2 nm. This trend then reverses, yielding a crystallite diameter of 13.6 nm after 9 h milling. The direct correlation between particle size measurements and B-site occupation by cations suggests that the altered site distribution may be due to a modified surface structure, possibly arising from oxidation of cations near the surface. This is consistent with recently reported models by Chen *et al.*¹² and van der Zaag *et al.*¹³ Charge conservation is provided by the creation of additional vacancies on the A sublattice, as seen by the reduced A peak in the FT EXAFS data.

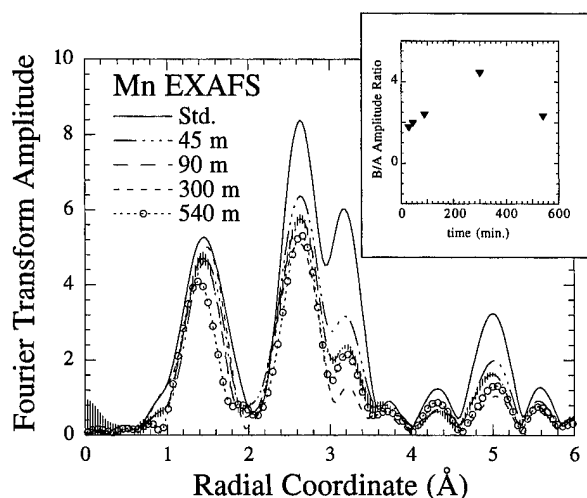


FIG. 3. Fourier transformed Mn EXAFS data for milled samples and starting material. Data are k^3 weighted with k range of 3–11.7 \AA^{-1} .

SQUID magnetometry shows that after 0.5 h milling, samples possess increased low-temperature saturation magnetization and reduced anisotropy fields. These improvements may be due to enhanced imbalance between sublattice moments resulting from segregation of Mn^{III} ions to the B sublattice. However, upon further milling, magnetization diminishes rapidly until after 5 h, when improvement again occurs, yielding a magnetization in the sample milled 9 h that is similar to the standard. XRD measurements indicate that some dissociation occurs and increases with milling duration, peaking near 5 h, after which this trend reverses. This suggests that the reduced magnetization may arise from the presence of secondary phases.

D.J.F. was supported as a National Research Council research associate at the time of this research. This work was performed in part at the National Synchrotron Light Source which is sponsored by the U.S. Department of Energy.

¹C. C. Koch, *Annu. Rev. Mater. Sci.* **19**, 121 (1989).

²A. Goldman, *Modern Ferrite Technology* (Van Nostrand Reinhold, New York, 1990).

³N. Lefelshtel, S. Nadiv, I. J. Lin, and Y. Zimmels, *Powder Technol.* **20**, 211 (1978).

⁴T. Kosmac and T. H. Courtney, *J. Mater. Res.* **7**, 1519 (1992).

⁵C. Jovalekic, M. Zdujic, A. Radakovic, and M. Mitric, *Mater. Lett.* **24**, 365 (1995).

⁶H. H. Hamdeh, J. C. Ho, S. A. Oliver, R. J. Willey, G. Oliveri, and G. Busca, *J. Appl. Phys.* **81**, 1851 (1997).

⁷V. G. Harris, N. C. Koon, C. M. Williams, Q. Zhang, M. Abe, and J. P. Kirkland, *Appl. Phys. Lett.* **68**, 2082 (1996).

⁸S. M. Heald, in *X-Ray Absorption: Principles, Applications, Techniques of EXAFS, SEXAFS, and XANES*, edited by D. C. Koningsberger and R. Prins (Wiley, New York, 1988).

⁹D. E. Sayers and B. A. Bunker, in *X-Ray Absorption Principles, Applications, Techniques of EXAFS, SEXAFS, and XANES*, edited by D. C. Koningsberger and R. Prins (Wiley, New York, 1988).

¹⁰J. J. Rehr, S. I. Zabinsky, and R. C. Albers, *Phys. Rev. Lett.* **69**, 3397 (1992).

¹¹V. G. Harris, N. C. Koon, C. M. Williams, Q. Zhang, M. Abe, J. P. Kirkland, and D. A. McKeown, *IEEE Trans. Magn.* **31**, 3473 (1995).

¹²J. P. Chen, C. M. Sorensen, K. J. Klabunde, G. C. Hadjipanayis, E. Devlin, and A. Kostikas, *Phys. Rev. B* **54**, 9288 (1996).

¹³P. J. van der Zaag, V. A. M. Brabers, M. T. Johnson, A. Noordermeer, and P. F. Bongers, *Phys. Rev. B* **51**, 12 009 (1995).

The effect of intragranular domain walls in MgMnZn-ferrite

P. J. van der Zaag^{a)}

Philips Research Laboratories, Professor Holstlaan 4, 5656 AA Eindhoven, The Netherlands

M. Kolenbrander

Philips Components, Central Innovation Magnetic Products, 5600 MD Eindhoven, The Netherlands

M. Th. Rekveldt

Interfacultair Reactor Instituut, Delft University of Technology, 2629 JB Delft, The Netherlands

The effect of grain size, D , on the intragranular domain state and initial permeability, μ_i , of polycrystalline MgMnZn ferrites has been investigated. The intragranular domain state is found to change from mono- to two domain at $D=2.9\pm0.2\ \mu\text{m}$. Despite this change, μ_i follows a continuous dependence on D , which can be described by the nonmagnetic grain boundary model. The results show that in spinel ferrites with an anisotropy of $72\ \text{J/m}^3$, μ_i is still due to rotation of magnetization. © 1998 American Institute of Physics. [S0021-8979(98)19711-6]

I. INTRODUCTION

It is well known that the initial permeability, μ_i , of polycrystalline soft ferrites depends on grain size, D . The traditional domain wall size (DWS) model by Globus and co-workers considers this grain size dependence to be due to bulging of a domain wall spanning each ferrite grain.¹ Recently, a different model has been proposed.²⁻⁴ In this nonmagnetic grain boundary (NMGB) model, μ_i of polycrystalline ferrites is considered to be influenced by a "non"-magnetic grain boundary. In this model rotation of magnetization is the dominant mechanism for μ_i .

We have shown by neutron depolarization⁵ that in MnZn ferrites with grain size $D<3.8\ \mu\text{m}$, the grains are monodomain and intragranular domain walls are absent.^{6,7} (The occurrence of a monodomain state in these fine-grained MnZn ferrites has been confirmed by magnetic force microscopy.⁸) Since intragranular domain walls are absent at $D<3.8\ \mu\text{m}$, μ_i must be due to rotation of magnetization in these MnZn ferrites. Moreover, up to $D=16\ \mu\text{m}$, the D dependence of μ_i could be described by the NMGB model, without a discontinuity at the transition from the mono- to two-domain state.⁷ This also shows for two-domain MnZn ferrites, which contain an intragranular domain wall, that μ_i is due to rotation. The MnZn ferrites considered thus far have a low anisotropy, K , of $32\ \text{J/m}^3$.⁷ One might wonder to which extent the results obtained apply to ferrites with a higher anisotropy. For this purpose the intragranular domain state as well as μ_i of a series of MgMnZn ferrites with constant composition but varying grain size were studied.

II. EXPERIMENTAL PROCEDURES

Ferrites with composition $\text{Mg}_{0.8}\text{Zn}_{0.2}\text{Mn}_{0.1}\text{Fe}_{1.85}\text{O}_{3.925}$ were prepared by conventional ceramic processing. MgMnZn ferrites of this composition have a Curie temperature, T_C , of $220\ ^\circ\text{C}$ and spontaneous magnetization, $\mu_0 M_s$, of $0.32\pm0.01\ \text{T}$ at $20\ ^\circ\text{C}$. By using different milling proce-

dures and adjusting the sinter temperature between 1100 and $1350\ ^\circ\text{C}$, polycrystalline ferrites with a grain size between 0.5 and $8.0\ \mu\text{m}$ were prepared. The mean linear intercept, D , is taken as a measure of the grain size, because it gives an unequivocal definition of grain size independent of the grain shape. D was determined from micrographs, depending on the grain size, either taken by a scanning electron microscope (Philips, SEM 515) or an optical microscope. Sample porosities varied between 2% and 10% . The magnetic domain size in the thermally demagnetized state was determined at room temperature by neutron depolarization.⁵ The initial permeability, μ_i , was determined between -50 and $250\ ^\circ\text{C}$, at a frequency of $10\ \text{kHz}$ and an induction level $B\approx0.04\ \text{mT}$.

III. RESULTS AND DISCUSSION

Figure 1(a) shows a SEM micrograph of the finest-grained MgMnZn ferrite used in this study with $D=0.51\pm0.05\ \mu\text{m}$. Figure 1(b) shows an optical micrograph of the coarsest-grained ferrite in this study with $D=8.0\pm0.8\ \mu\text{m}$.

Figure 2 gives the results of a neutron depolarization (ND) study at zero magnetic field of the domain size, Δ , versus the grain size, D , for $\text{Mg}_{0.8}\text{Zn}_{0.2}\text{Mn}_{0.1}\text{Fe}_{1.85}\text{O}_{3.925}$. It is important to note that ND determines the average domain size *within the bulk* of a magnetic material. As neutrons traverse the grains in a bulk material on random chords, Δ determined by ND also corresponds to a mean linear intercept value. Figure 2 shows similarly to the observations in other ferrites,^{6,7,9} that at low D values the domain size is equal to the grain size as can be seen by comparison to the solid line for which $\Delta/D=1$. At $D>2.9\ \mu\text{m}$ the data points follow the dashed line. This line corresponds to the ratio $\Delta/D=0.63$ calculated for the two-domain state⁶ and confirmed in previous experiments on MnZn ferrite^{7,8} and NiZn ferrite.⁹ Hence, for $D>2.9\ \mu\text{m}$ a domain wall appears to be present in these MgMnZn ferrites. This difference in intragranular domain state is reflected in the MHz dissipation, as has been demonstrated and discussed in more detail previously.⁹ Figure 3 displays the loss factor $\tan\delta\mu$ at $5\ \text{MHz}$ vs D for the MgMnZn ferrites. A reduction of the loss

^{a)} Author to whom correspondence should be addressed; electronic mail: zaag@natlab.research.philips.com

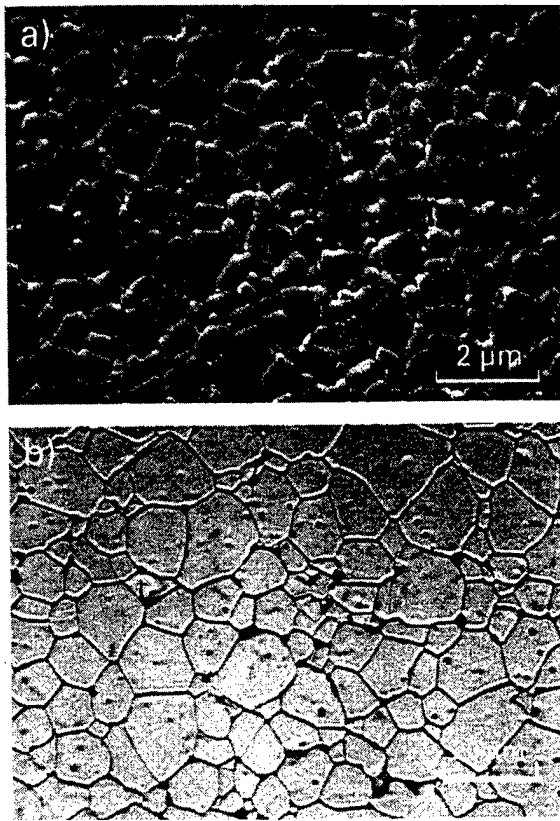


FIG. 1. Micrographs of the microstructure of two representative MgMnZn ferrites: (a) the finest-grained sample, grain size $D = 0.51 \pm 0.05 \mu\text{m}$, (b) the coarsest-grained sample, $D = 8.0 \pm 0.8 \mu\text{m}$.

factor at the grain size at which the MgMnZn ferrites become monodomain is observed.¹⁰

Theoretically with decreasing grain size a transition from a two- to a monodomain state is expected for an *isolated* particle, because the domain wall energy scales with the domain wall area as $\propto D^2$, whereas the magnetostatic energy decreases more rapidly with D^3 .¹¹ A complication in the case discussed here is that the situation of an isolated

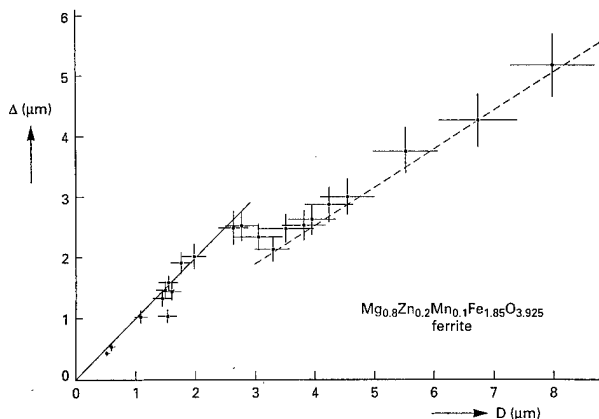


FIG. 2. The domain size Δ as a function of grain size D for $\text{Mg}_{0.8}\text{Zn}_{0.2}\text{Mn}_{0.1}\text{Fe}_{1.85}\text{O}_{3.925}$. The solid line corresponds to $\Delta/D = 1$, the ratio corresponding to monodomain grains; the dashed line corresponds to $\Delta/D = 0.63$, the ratio corresponding to grains in the two-domain state.

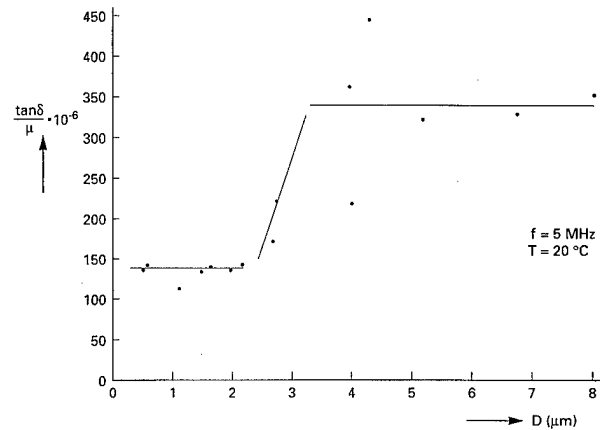


FIG. 3. The loss angle $\tan(\delta)/\mu_i$ at 5 MHz vs grain size for the same MgMnZn ferrite composition.

particle is not met in densely sintered ferrites. Hence, in the calculation of the critical grain size, D_C , at which this transition occurs, the reduction of the magnetostatic energy by the soft-magnetic environment has to be taken into account. In a first approximation,⁹ this can be done by using the isotropic permeability correction proposed earlier for the calculation of D_C (mean intercept value).⁷ Applying this correction to the rigorous, analytical expressions derived by Brown¹² for the upper and lower grain size limits at which an isolated particle becomes monodomain yields:

$$D_{C_{\text{lower}}} = 3.6 \sqrt{\frac{A \frac{2}{3} \mu_{ic}}{\frac{1}{2} \mu_0 M_S^2}} \quad (1)$$

$$D_{C_{\text{upper}}} = 28 \sqrt{\frac{A \frac{2}{3} \mu_{ic}}{\frac{1}{2} \mu_0 M_S^2}} \sqrt{\pi + \frac{K \frac{2}{3} \mu_{ic}}{\frac{1}{2} \mu_0 M_S^2}} \quad (2)$$

with A the exchange constant and μ_{ic} the initial permeability at D_C . Using the numerical values for the MgMnZn ferrite studied here: $A = 3.4 \times 10^{-12} \text{ J/m}$, $\mu_{ic} \approx 150$ (see below), $K \approx 72 \text{ J/m}^3$ and $\mu_0 M_S = 0.32 \text{ T}$ yields $0.32 \mu\text{m}$ as a lower limit and $4.7 \mu\text{m}$ as an upper limit for D_C . In view of the approximations made to account for the soft-magnetic environment, the experimentally found $D_C = 2.9 \pm 0.2 \mu\text{m}$ seems reasonable. Micromagnetic theory is being developed which will deal more accurately with the soft-magnetic environment and interparticle interactions.¹³

For $D < 2.9 \mu\text{m}$ intragranular domain walls are absent. Thus in this range the domain wall size (DWS) model¹ cannot hold. It is therefore of interest to investigate the μ_i of these MgMnZn ferrites in this range and just above D_C , where an intragranular domain wall is present. The results of such a study are presented in Fig. 4. Figure 4 gives μ_i at room temperature versus D for the same MgMnZn ferrite composition for which Δ has been determined. The μ_i data were corrected for variations in porosity, p , using the expression²:

$$\mu_i^{\text{corr}} = \mu_i \frac{1 + p/2}{1 - p}. \quad (3)$$

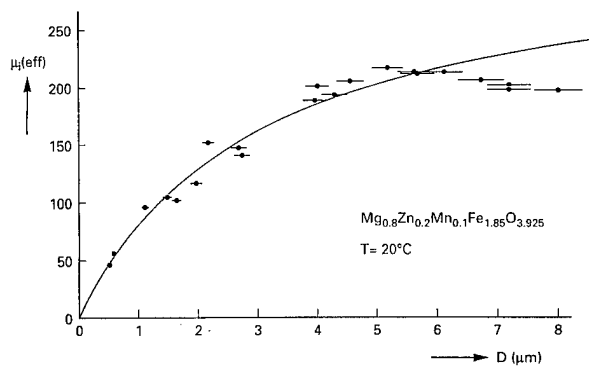


FIG. 4. The initial permeability $\mu_i(\text{eff})$ vs grain size. The curve traced through the data is a fit to the nonmagnetic grain boundary model for μ_i .

The curve in Fig. 4 is a least-squares fit to the NMGB model²⁻⁴:

$$\mu_i(\text{eff}) = \frac{\mu_i D}{\mu_i \delta + D} \quad (4)$$

in which μ_i is the bulk intrinsic initial permeability and δ the nonmagnetic grain boundary thickness. The best fit given in Fig. 4, was obtained with $\mu_i = 329 \pm 31$ and $\delta = 9.4 \pm 0.7$ nm. For $D > 6 \mu\text{m}$, the fit to the NMGB model deviates from the data. Further analysis showed that this is due to *intragranular* porosity, which only occurs in samples with $D > 6 \mu\text{m}$ [compare Figs. 1(a) and 1(b)]. This is the result of the higher sinter temperature (1350 °C) used. Due to increased grain growth at these temperatures, pores can no longer follow the moving grain boundaries during the sintering. Consequently, they become locked within the grains.¹⁴ The interesting aspect of Fig. 4 is that while intragranular domain walls are present at $D > 2.9 \mu\text{m}$ no extra contribution to μ_i is observed. The NMGB model can describe the D dependence of μ_i both in the mono- and two-domain regime. This also implies that in these MgMnZn ferrites the initial permeability is of rotational origin. A similar conclusion has been derived for low anisotropy ($K = 32 \text{ J/m}^3$) MnZn ferrites.⁷ Apparently, at the higher K of this MgMnZn ferrite ($K \approx 72 \text{ J/m}^3$), the initial permeability is of rotational origin also when intragranular domain walls are present within the grains.

Finally, we investigated the effect of temperature on the values found for δ . The results are given in Fig. 5 and were obtained from fits of Eq. (1) of μ_i vs D at various temperatures. Only data for which $D < 6 \mu\text{m}$ were used to avoid the problem of intragranular porosity mentioned above. Interestingly, in the case of MgMnZn ferrite, δ is found to be temperature dependent. This shows that δ cannot be considered nonmagnetic, and is better considered a "hard" magnetic

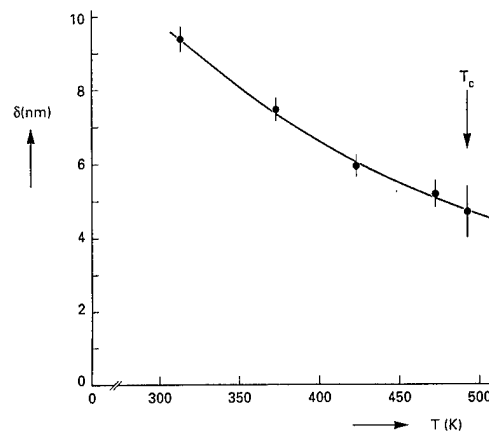


FIG. 5. The width of the nonmagnetic grain boundary δ vs temperature T for $\text{Mg}_{0.8}\text{Zn}_{0.2}\text{Mo}_{0.1}\text{Fe}_{1.85}\text{O}_{3.925}$. The term δ was determined from fits as shown in Fig. 4. Note that δ depends on T .

grain boundary,⁷ i.e., having a high anisotropy due to spin canting as found for ultrafine ferrite particles.¹⁵

IV. CONCLUSION

We have shown by neutron depolarization that the transition from the mono- to two-domain state occurs at $D = 2.9 \pm 0.2 \mu\text{m}$ in polycrystalline $\text{Mg}_{0.8}\text{Zn}_{0.2}\text{Mn}_{0.1}\text{Fe}_{1.85}\text{O}_{3.925}$. Despite this change in intragranular domain state the NMGB model describes the grain size dependence of the initial permeability, μ_i , well for these ferrites both below and above D_C . This shows that also for ferrites with an anisotropy constant $K = 72 \text{ J/m}^3$ the initial permeability is rotational in origin.

¹A. Globus, J. Phys. (Paris), Colloq. **C1**, 1 (1977); M. Guyot and V. Cagan, J. Magn. Magn. Mater. **27**, 202 (1982).

²H. Rikukawa, IEEE Trans. Magn. **MAG-18**, 1535 (1982).

³J. Smit, Adv. Ceram. **16**, 1 (1986).

⁴E. G. Visser and M. T. Johnson, J. Magn. Magn. Mater. **101**, 143 (1991).

⁵R. Rosman and M. Th. Rekveldt, Z. Phys. B **79**, 61 (1990); R. Rosman, H. Fredrikze, and M. Th. Rekveldt, *ibid.* **81**, 149 (1990).

⁶P. J. van der Zaag, M. T. Johnson, A. Noordermeer, P. T. Por, and M. Th. Rekveldt, J. Magn. Magn. Mater. **99**, L1 (1991).

⁷P. J. van der Zaag, J. J. M. Ruigrok, A. Noordermeer, M. H. W. M van Delden, P. T. Por, M. Th. Rekveldt, D. M. Donnet, and J. N. Chapman, J. Appl. Phys. **74**, 4085 (1993).

⁸I. Abu Shiekah, J. Aarts, and P. J. van der Zaag (submitted).

⁹P. J. van der Zaag, P. J. van der Valk, and M. Th. Rekveldt, Appl. Phys. Lett. **69**, 2927 (1996).

¹⁰The ferromagnetic resonance frequency of all these ferrites is $\geq 30 \text{ MHz}$.

¹¹C. Kittel, Phys. Rev. **70**, 965 (1946).

¹²W. F. Brown, Jr., J. Appl. Phys. **39**, 993 (1968).

¹³A. Aharoni and J. P. Jakubovics, J. Phys. (Paris) Colloq. (1998) (in press).

¹⁴See, for example, P. J. L. Reijnen, Ph.D. thesis, Delft University of Technology, 1969.

¹⁵J. M. D. Coey, Phys. Rev. Lett. **27**, 1140 (1971).

Line width of manganese–zinc ferrite polycrystals with oxygen partial pressure

Soon Cheon Byeon^{a)} and Kug Sun Hong

School of Materials Science & Engineering, College of Engineering, Seoul National University, Seoul 151-742, Korea

In-Tae Kim

Division of Ceramics, Korea Institute of Science and Technology, P.O. Box 131, Cheongryang, Seoul, Korea

A systematic variation in line width at X band (9.78 GHz) with oxygen partial pressure was observed in $\text{Mn}_{0.47}\text{Zn}_{0.47}\text{Fe}_{2.06}\text{O}_4$ polycrystalline samples. The linewidth of the samples increased from 105 to 188 Oe with decreasing atmospheric parameters from 8.4 to 6.4. It was found that contribution of anisotropy and porosity to the linewidth was small compared to the variation in linewidth with oxygen partial pressure. Estimation of the Fe^{2+} concentration of samples by measuring their thermoelectric power revealed that an increase in the concentration from 1.88 to 2.44 wt % was accompanied by decreasing oxygen partial pressure. As the resistivity of grain does not vary with oxygen partial pressure, the contribution of eddy current will be the same irrespective of the oxygen partial pressure. Therefore, the systematic increase in linewidth observed in our present study was attributed to the increase in Fe^{2+} concentration with decreasing oxygen partial pressure. © 1998 American Institute of Physics. [S0021-8979(98)49011-X]

I. INTRODUCTION

Iron-excess manganese–zinc ferrites are widely used in high frequency circuit components such as transformers, noise filters, and magnetic recording heads because both of their electrical resistivities and initial permeabilities are much higher than those of metals at high frequencies (up to 200 MHz). Recently, applications are being extended to include components being used to shield the electromagnetic interference (EMI).^{1,2}

The ferromagnetic resonance (FMR) of ferrites is important to investigate their magnetic properties at high frequency because the resonance originates from the interaction between spin and electromagnetic waves. For instance, the loss of ferrites at microwave frequency largely depends on their line width of FMR. The broader the line width, the more lossy the sample is due to higher dispersion.

Recently, a lot of research has been focused on microwave applications of yttrium iron garnet (YIG) because it has very low loss. In order to reduce the cost, polycrystalline YIG, instead of single crystals, is preferred. In the case of polycrystalline ferrites, it is known that anisotropy as well as porosity contribute to the line broadening of FMR.³ These contributions can be estimated quantitatively. However, there are contributions that can hardly be quantified. One of those is the eddy current loss which represents the conduction of electrons in response to the magnetic field of electromagnetic waves.^{4,5} Since the conduction mechanism of ferrites is known to be a small polaron hopping of electrons between Fe^{2+} and Fe^{3+} ions, the Fe^{2+} concentration should be measured in order to quantify the contribution of eddy current loss. In the case of YIG, however, this is very diffi-

cult because the Fe^{2+} concentration is very low. (As a matter of fact this is the reason that YIG has very low loss.)

Manganese–zinc ferrite has interesting features. Its crystal structure is mixed spinel and it has high Fe^{2+} concentration in octahedral sites. Furthermore, its Fe^{2+} concentration can be easily manipulated by varying oxygen partial pressure during heat treatment. Therefore, the objective of our present study is to investigate the effects of Fe^{2+} concentration of manganese–zinc ferrites on their line width of FMR.

II. EXPERIMENTAL PROCEDURE

Manganese–zinc ferrite of the composition $\text{Mn}_{0.47}\text{Zn}_{0.47}\text{Fe}_{2.06}\text{O}_4$ was prepared using the conventional mixed oxide method. Experimental details were described elsewhere.⁶ The specimens were sintered at 1350 °C for 5 h in an air atmosphere. During cooling, the oxygen partial pressure was controlled using the following equation which was suggested by Morineau and Paulus,⁷

$$\log P_{\text{O}_2} = a - \frac{14540}{T(K)}, \quad (1)$$

where a is atmospheric parameter which represents an oxidation potential. In our present study, the atmospheric parameter was kept constant during the cooling process. In more detail, manganese–zinc ferrite samples with $a = 6.44, 7.07, 7.56, 7.96$, and 8.44 were prepared in order to investigate the effect of oxidation on their line width.

Electrical resistivity was measured at room temperature using impedance spectroscopy. Impedance was measured in the frequency range of 100 Hz to 40 MHz using an impedance/gain phase analyzer (Hewlett Packard, Model HP 4194A). Thermoelectric power was measured at room tem-

^{a)}Electronic mail: byeon@plaza.snu.ac.kr

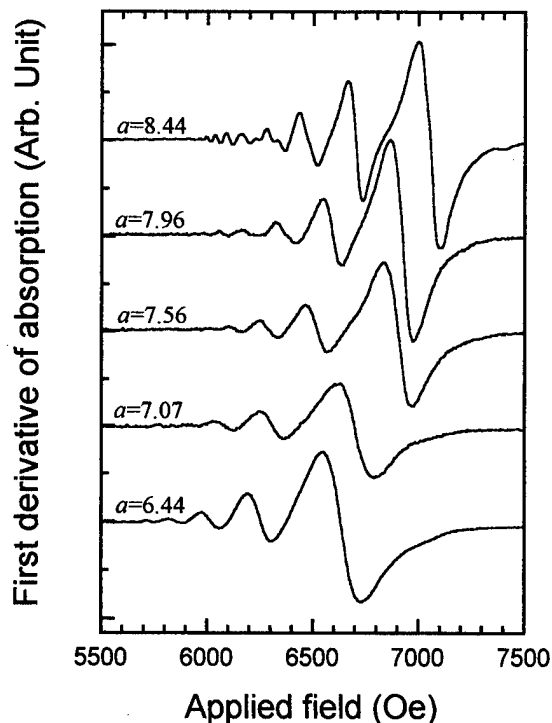


FIG. 1. Ferromagnetic resonance spectra of manganese-zinc ferrite samples with various oxygen partial pressures.

perature using the dc method. From these data, the Fe^{2+} concentration was calculated. Please refer to our previous work for details.⁶

Porosity was calculated from the bulk density of the sample which was determined by Arkimedes' method.

Ferromagnetic resonance (FMR) spectra were recorded at 300 K using an X-band (9.78 GHz) spectrometer (Bruker, Model ER 301). Samples were cut and polished to a thin plate with a dimension of $0.5 \text{ mm} \times 0.5 \text{ mm} \times 0.01 \text{ mm}$ and were placed at the center of a cavity oscillating in the rectangular TE_{102} mode. The sample can be rotated on a dielectric post inserted through the wall of the cavity. A conventional field modulation technique was used.

III. RESULTS

Figure 1 shows FMR spectra of manganese-zinc ferrite samples measured at 9.78 GHz. The dc magnetic field was applied perpendicular to the thin plate. The spectra were recorded as a first derivative of the absorption. An increase in resonance field and intensity were observed with increasing oxygen partial pressure. The g values were calculated from the resonance field in different orientations with respect to

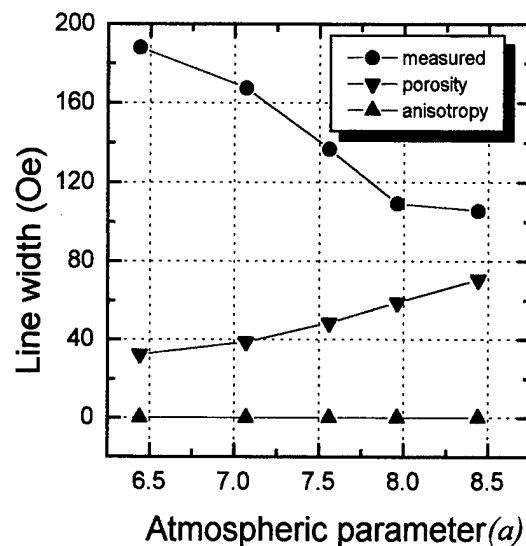


FIG. 2. Linewidth as a function of oxygen partial pressure.

the applied field. The g values decreased from 1.95 to 1.90 with increasing atmospheric parameter. Yager *et al.* reported that the g values of a stoichiometric manganese-zinc ferrite is 2.05.^{8,9} In this experiment, the g values are slightly smaller than that of the stoichiometric manganese-zinc ferrite as the composition is iron-excess manganese-zinc ferrite. Yager *et al.* reported that iron-excess ferrites give slightly reduced g values.⁴

It is also noteworthy that there are many subsidiary resonances at a lower field besides the main resonance. These resonances seem to be standing magnetostatic modes.

Figure 2 shows the linewidth as a function of the oxygen partial pressure used in the cooling process. Here the absolute value of the linewidth was of the order of 10^2 Oe and the variation in the linewidth was about 80 Oe. The linewidth decreased almost linearly with increasing oxygen partial pressure.

Table I summarizes the Fe^{2+} ion concentration, resistivity of the grain and the grain boundary, and saturated magnetization ($4\pi M_s$) of the manganese-zinc ferrite samples reported in our previous work.^{6,10} Porosity of the samples is also listed in Table I.

IV. DISCUSSION

A. Quantitative estimation of change in linewidth with Fe^{2+} concentration

As mentioned previously, the linewidth of the FMR of polycrystalline ferrites is a sum of various contributions of

TABLE I. Oxygen partial pressure dependence of grain boundary and grain resistivity, saturation magnetization, and porosity.

Atmospheric parameter (a)	6.44	7.07	7.56	7.96	8.44
Fe^{2+} ion concentration (wt %)	2.44	2.38	2.32	1.94	1.88
Grain boundary resistivity ($\Omega \text{ m}$)	0.019	0.057	0.230	0.357	0.366
Grain resistivity ($\Omega \text{ m}$)	0.009	0.012	0.010	0.008	0.009
Saturation magnetization (G)	4319	4324	4319	4366	4280
Porosity	0.005	0.006	0.008	0.009	0.012

anisotropy, porosity, and eddy current loss. Therefore, the linewidth, ΔH of manganese–zinc ferrite polycrystals can be given as follows,¹¹

$$\begin{aligned}\Delta H &= \Delta H_{\text{anisotropy}} + \Delta H_{\text{porosity}} + \Delta H_{\text{eddy}} + \Delta H_{\text{others}} \\ &= \frac{8\pi\sqrt{3}}{21} \frac{H_A^2}{4\pi M_s} + \frac{8}{\sqrt{3}\pi} 4\pi M_s \frac{P_{\text{eff}}}{1+P_{\text{eff}}} + \Delta H_{\text{eddy}} \\ &\quad + \Delta H_{\text{others}},\end{aligned}\quad (2)$$

where H_A is anisotropy field, $4\pi M_s$ saturation magnetization, and P_{eff} is effective porosity.

In order to calculate the contribution of the anisotropy term, the anisotropy field in Eq. (2) should be known. The cubic anisotropy field ($H_A = 4K_1/3M_s$) was calculated using anisotropy constants reported by Hoekstra *et al.*¹² and the saturation magnetization in Table I. Hoekstra *et al.* reported that the anisotropy constant decreased from 1500 to 100 erg/cm³ with an increasing oxygen partial pressure. The anisotropy field calculated using these values decreased from 6 to 0.4 Oe with increasing oxygen partial pressure. These anisotropy fields contribute to a linewidth smaller than 0.1 Oe. So the contribution of the anisotropy field to the linewidth was negligible.

In Fig. 2, the contributions of anisotropy and porosity to the linewidth calculated using Eq. (2) are illustrated. The porosity term increased by 40 Oe with increasing oxygen partial pressure. Since the measured linewidth decreased 80 Oe with increasing oxygen partial pressure, the contribution of the ΔH_{eddy} term should be -120 Oe. Compared to the linewidth of the sample prepared under the lowest oxygen partial pressure, the magnitude of the ΔH_{eddy} term is larger than 60%. In Table I, the Fe^{2+} concentration decreased by 0.6 wt % with increasing oxygen partial pressure. Therefore, it can be suggested that the 0.6 wt % decrease in Fe^{2+} concentration of manganese–zinc ferrite polycrystalline sample was accompanied by a 60% decrease in their linewidth.

B. Linewidth versus eddy current loss

It is well known that eddy current loss is correlated with conductivity.⁵ In Table I, the change in grain boundary resistivity with oxygen partial pressure was 1 order of magnitude and thus appears to be responsible for the large contribution of the ΔH_{eddy} term. In our previous work, however, it was demonstrated that the change in grain boundary resistivity originated mainly from the change in grain boundary thickness. Furthermore, the capacitive grain boundary will be shorted at high frequency and thus will not contribute to the eddy current loss.

In Table I, the change in resistivity of grains with oxygen partial pressure is negligible. Since the eddy current loss

increases almost linearly with increasing conductivity we must address another mechanism for the broadening of linewidth. According to Galt and Clogston, the presence of Fe^{2+} ions in octahedral sites of spinel ferrites can cause a broadening of linewidth due to relaxation.^{13–15} For the sake of convenience, ferromagnetic resonance can be illustrated as precession of spins along the direction of the applied dc magnetic field. In other words, the magnetization direction is changing with time. Since Fe^{2+} and Fe^{3+} ions have different magnetic moments they tend to align themselves in order to minimize the free energy of the system. This rearrangement takes finite time and thus phase lag results in a line broadening.

V. CONCLUSIONS

It was suggested that the linewidth of manganese–zinc ferrite polycrystals decreased by 80 Oe with increasing oxygen partial pressure. The calculation of contributions of anisotropy and porosity to the linewidth revealed that the eddy current loss term was -120 Oe. It was suggested that 0.6 wt % decrease in Fe^{2+} concentration with increasing oxygen partial pressure was accompanied by a 60% decrease in the linewidth.

Since the decrease in the grain resistivity of the manganese–zinc ferrite was negligible, a relaxation mechanism was suggested to be responsible for the 60% decrease in the linewidth.

ACKNOWLEDGMENT

This study was supported by Korea Ministry of Education Research Fund for Advanced Materials in 1997.

- ¹P. I. Slick, in *Ferromagnetic Materials*, edited by E. P. Wohlfarth (North-Holland, New York, 1980), Vol. 2, pp. 189–241.
- ²E. C. Snelling, *Soft Ferrites, Properties and Applications*, 2nd ed. (Butterworth, London, 1988), pp. 1–135.
- ³C. E. Patton, in *Magnetic Oxides, Part 2*, edited by D. J. Craik (Wiley, New York, 1975), pp. 575–648.
- ⁴W. A. Yager, J. K. Galt, and F. R. Merritt, *Phys. Rev.* **99**, 1203 (1955).
- ⁵M. Sparks, *Ferromagnetic Relaxation Theory* (McGraw-Hill, New York, 1964), pp. 157–160.
- ⁶S. C. Byeon, K. S. Hong, J. G. Park, and W. N. Kang, *J. Appl. Phys.* **81**, 7835 (1997).
- ⁷R. Morineau and M. Paulus, *Phys. Status Solidi A* **20**, 373 (1973).
- ⁸W. A. Yager, F. R. Merritt, and C. Guillaud, *Phys. Rev.* **81**, 477 (1951).
- ⁹W. H. von Aulock, *Handbook of Microwave Ferrite Materials* (Academic, New York, 1965), p. 345.
- ¹⁰S. C. Byeon, K. S. Hong, and H. J. Je, *Mater. Res. Bull.* **32**, 579 (1997).
- ¹¹E. Schlomann, *J. Phys. Chem. Solids* **6**, 242 (1958).
- ¹²B. Hoekstra, E. M. Gyorgy, P. K. Gallagher, D. W. Johnson, Jr., G. Zydzik, and L. G. van Uitert, *J. Appl. Phys.* **49**, 4902 (1978).
- ¹³J. K. Galt, *Bell Syst. Tech. J.* **33**, 1023 (1954).
- ¹⁴J. K. Galt, W. A. Yager, and F. R. Merritt, *Phys. Rev.* **93**, 1119 (1954).
- ¹⁵A. M. Clogston, *Bell Syst. Tech. J.* **34**, 739 (1955).

The diffusion of tracer oxygen atoms in Ni ferrites

V. B. Fetisov and G. A. Kozhina^{a)}

Ural State Economic University, 62, 8th March str., 620219 Ekaterinburg, Russia

A. Ya. Fishman

Institute of Metallurgy, UrO RAN, 101, Amundsen str., 620016 Ekaterinburg, Russia

T. E. Kurennykh and V. B. Vykhodets

Institute of Physics of Metals, UrO RAN, 18 Kovalevskaya str., 620219 Ekaterinburg, Russia

Oxygen tracer diffusion in polycrystalline nickel ferrites $\text{Ni}_{(1-x)}\text{Fe}_{(2+x)}\text{O}_{(4)}$ ($x=0.1; 0.2; 0.4$) at temperatures of 450–700 °C was studied. The number of ^{18}O atoms diffusing to the sample was determined using the $^{18}\text{O}(p,\alpha)^{15}\text{N}$ nuclear reaction at the energy of the primary beam particles equal to 762 keV. The nuclear physical experiments were performed on a 2 MV Van de Graaff accelerator. It has been established the oxygen diffusion is characterized by relatively small activation energy (0.89 eV for $x=0.2$) and low pre-exponential factors ($\sim 10^{-13} \text{ cm}^2/\text{s}$ for $x=0.2$). These results suggest that oxygen diffusion in the ferrites under consideration occurs by means of structural vacancies with their concentration about 10^{-9} – 10^{-11} . © 1998 American Institute of Physics. [S0021-8979(98)22511-4]

I. INTRODUCTION

This study has been performed to derive data on the oxygen tracer diffusion in ferrites, the parameters of the corresponding energy barriers, and the diffusion mechanism. The lack of information about the oxygen diffusion in ferrites has been the main reason for launching these investigations. In addition, the diffusion information may be helpful in analyzing the structural defects in the oxygen sublattice and straightforward determination of the limiting stage in the kinetics of the redox processes in ferrites. Thus, this study into diffusion may reinforce or demolish the existing concept on the fast (compared to anions) diffusion of cations (cation vacancies), which limits the kinetics of the redox processes in ferrites. One more important result may consist in ascertaining the presence of structural vacancies in the anion sublattice of ferrites and determining their concentration. This issue has long been debated. These and other findings relating to the oxygen diffusion kinetics are important for understanding the processes, which take place during the ferrite synthesis, thermal and thermomagnetic treatments, and operation of ferrites.

II. EXPERIMENT

To measure the diffusion coefficients of ^{18}O tracers, the samples underwent isothermal annealing in an ^{18}O -enriched oxygen atmosphere. Subsequently the concentration of the ^{18}O isotope was determined using the nuclear microanalysis method. By this method the concentration profiles $c(x)$ of ^{18}O atoms can be measured down to the depth of several microns without breaking the sample. Usually the diffusion coefficients are determined by solving Fick's second law for $c(x)$ taking the initial and boundary conditions of the diffusion problem realized in the experiment. In our case the preliminary experiments showed that the depth resolution of

the nuclear microanalysis method was insufficient for correct measurements of the $c(x)$ profiles. Therefore, in the nuclear physical experiments we determined the number of ^{18}O atoms per unit surface area Q of the annealed sample as a function of the annealing time t . The data were processed allowing for the presence of a certain number of ^{18}O atoms in the initial samples. It was also measured during the nuclear physical experiments. In terms of this approach, the diffusion coefficients D were calculated from the equation of Fick's second law for the function $Q(t)$. For the diffusion from a constant surface concentration source to a semi-infinite sample the solution of this equation is

$$Q = \frac{C_0}{\sqrt{\pi}} 2\sqrt{Dt}, \quad (1)$$

where C_0 is the concentration of the ^{18}O isotope on the surface of the sample. The value of C_0 was calculated using the expression

$$C_0 = \gamma C^0, \quad (2)$$

where γ is the degree of enrichment of oxygen with the ^{18}O isotope. In our experiments $\gamma=0.8$; C^0 is the oxygen concentration of the samples under study, which represented metastable cation-deficient spinels—analogs of the $\gamma\text{-Fe}_2\text{O}_3$ phase. As has been mentioned in the foregoing, the profiles $c(x)$ and the concentrations C_0 were not determined experimentally and therefore the only criterion confirming fulfillment of the boundary conditions of the diffusion problem was fulfillment of the dependence (1). Although this dependence was met quite well (as will be shown below), in the future we are going to obtain additional data, which would permit estimating more reliably the fulfillment of the boundary conditions of the diffusion problem. These data may include experimental measurements of the concentration profiles $c(x)$ allowing for an adequate depth resolution, or the concentration of ^{18}O atoms on the surface of the sample, C_0 ,

^{a)}Electronic mail: uinh@uinh.rcupi.e-burg.su

or the dependence $Q(t)$ analyzed for a wider interval of time than the interval used in this study. The experimental data reported in this article do not eliminate completely the systematic errors in measured D .

The ferrite samples, $\text{Ni}_{1-x}\text{Fe}_{2+x}\text{O}_4$, $x=0.1$, $x=0.2$ (samples No. 1 and No. 2), and $x=0.4$, were prepared by standard ceramic method using A. R. grade NiO , Fe_2O_3 . The powders of these oxides were mixed in desired proportions and were ground in an automatic agate mortar under ethanol for 35 h. The dried powders were mixed with polyvinyl alcohol and water and were pressed into 1.3 cm diameter pellets. These samples were fired at 900 °C for 15 h, then they were ground again and were formed into pellets in the same manner. Final sintering was done in a furnace at 1250 °C for 10 h. The completion of the solid state reaction was checked by the x-ray diffraction studies. It has been established from radiography and microstructural data that all samples were single phase spinels with the following crystal lattice parameters: 0.8342(9) nm ($x=0.1$); 0.8346(6) nm ($x=0.2$); and 0.8355(2) nm ($x=0.4$). The mean crystallite size was about 10 μm . Samples No. 1 and No. 2 were synthesized from different starting materials and had the same chemical composition. Prior to diffusion annealing in the ^{18}O atmosphere at a preset temperature, the samples were annealed in the ^{16}O atmosphere at the same temperature until its mass was constant. As a result, the samples were oxidized up to saturation through the formation of metastable cation-deficient spinels. It was confirmed by an x-ray examination.¹ The aim of this treatment was to separate the oxygen self-diffusion process and the oxidation process, which leads to an increase in the number of oxygen atoms in the lattice. According to the x-ray data, ferrites with $x=0.4$ have two phases if they are annealed at a temperature of 550 °C or higher. The samples with more than one phase in the structure were excluded from consideration.

The oxide samples had a flat surface 5×5 mm in size and were several millimeters thick. Diffusion annealings were performed at the oxygen pressure of 0.21 atm. The volume of the quartz tube was sufficiently large to rule out a marked change in the isotope composition of the gas during annealing. This was confirmed by special experiments where oxygen was and was not replaced in the quartz tube during annealings and then the concentrations of ^{18}O and ^{16}O isotopes were measured in the samples. Subsequent to isothermal annealing, the samples were cooled to room temperature and the concentration of ^{18}O atoms was determined in the samples. One and the same sample was used to study the dependence $Q(t)$ at each temperature, i.e., every sample was heated repeatedly to the preset annealing temperature and then was cooled to room temperature. The nuclear physical measurements were made after every heating/cooling cycle. The time required to reach a constant temperature was less than 10 min, while the cooling time was approximately 1 min. The temperature was measured with an accuracy of ± 1 °C using a chromel–alumel thermocouple. The quartz tube was placed in a massive metal cylinder during annealings. This arrangement eliminated a temperature gradient at the samples within the said accuracy limits.

The number of ^{18}O atoms diffusing to the sample was

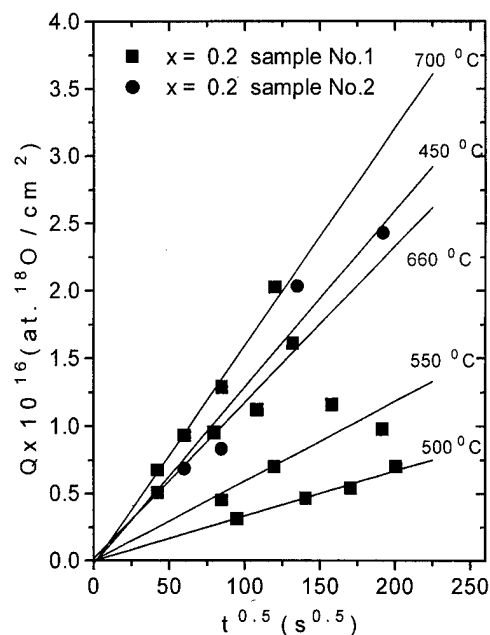


FIG. 1. The number of ^{18}O atoms per unit surface area of samples $\text{Ni}_{1-x}\text{Fe}_{2+x}\text{O}_4$ vs annealing time.

determined using the $^{18}\text{O}(p, \alpha)^{15}\text{N}$ nuclear reaction at the energy of the primary beam particles equal to 762 keV. The nuclear physical experiments were performed on a 2 MV Van de Graaff accelerator. The proton beam diameter was 1 mm, i.e., the measured Q was averaged over a large number of crystallites. The test flat surface of the samples was placed perpendicular to the axis of the primary beam. The nuclear reaction products were registered at an angle of 160°. The energy spectrum of these products was measured by a silicon surface-barrier detector about 1 cm in diameter. The standard deviation of the measured Q was less than 5%. The nondestructive measurements were made down to a depth of about 2 μm . The ^{18}O atoms were found to penetrate to the samples for not more than 0.2 μm .

As has been mentioned in the foregoing, Q was determined several times at random places on every sample. According to the preliminary experiments, the distribution inhomogeneity of the ^{18}O atoms on the test surface of the samples could be as high as 15%.

III. RESULTS AND DISCUSSION

Figure 1 shows the dependence $Q(t)$ for ferrite samples having different compositions at several temperatures of diffusion annealing. One may see that in all the instances the dependences, which correspond to the solution (1) of Fick's second law, are reasonably fulfilled over a wide interval of time. The deviation of Q from the linear dependences does not exceed the experimental errors. These errors are due mainly to different rates at which ^{18}O atoms arrive to various areas of the samples, i.e., to their inhomogeneity in terms of diffusion. The accuracy of the nuclear physical measurements makes a smaller contribution to the experimental errors.

The measured diffusion coefficients are presented in Fig. 2. Note first that in all the instances the diffusion coefficients

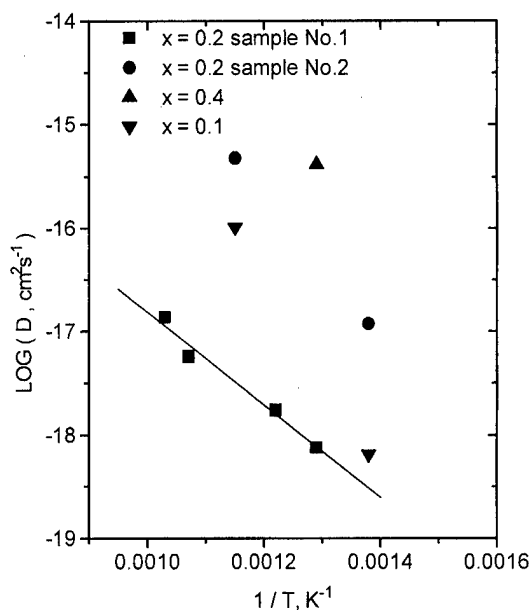


FIG. 2. Temperature dependence of diffusion coefficients of oxide ions in $\text{Ni}_{1-x}\text{Fe}_{2+x}\text{O}_4$ ceramics.

of the ^{18}O atoms measured by us proved to be much lower than those reported in literature^{2,3} for iron atoms in spinels of the analogous composition, which were measured at similar temperatures or extrapolated to the temperature interval of 500–700 °C. This fact suggests that the limiting stage in oxidation or reduction of spinel-like magnetites is the diffusion of oxygen cations rather than anions. It supports the conjectures on the mechanism of the redox reactions.² Let it be noted that the low values of the oxygen diffusion coefficients are due to a very small pre-exponential factor D_0 in the temperature dependence $D = D_0 \exp(-E/kT)$. In the case of the sample having the composition $\text{Ni}_{0.8}\text{Fe}_{2.2}\text{O}_4$ (sample No. 1) $D_0 = 4.68 \times 10^{-13} \text{ cm}^2/\text{s}$, whereas for cations D_0 is of the order of $10^{-4} \text{ cm}^2/\text{s}$.²

One more important conclusion may be drawn from the analysis of D_0 and the diffusion activation energy E determined in this study. They adduce a unique evidence that in the samples at hand oxygen atoms diffuse through structural vacancies rather than thermal equilibrium vacancies in the oxygen sublattice. This inference is supported, first, by a low diffusion activation energy $E = (0.89 \pm 0.1) \text{ eV}$. When thermal equilibrium vacancies are involved in diffusion, the diffusion activation energy is equal to the sum of the oxygen atom migration energy E_m and the vacancy formation energy E_f : $E = E_m + E_f$. However, E_f usually exceeds 1 eV.⁴ On the other hand, if diffusion involves thermal equilibrium and structural vacancies, the order of the pre-exponential factor D_0 is roughly determined by the respective expressions⁵

$$D_0 \sim a^2 \nu \quad \text{and} \quad D_0 \sim a^2 \nu n_v, \quad (3)$$

where $a \sim 10^{-8} \text{ cm}$ is the lattice constant; $\nu \sim 10^{12} \text{ s}^{-1}$ is the vibration frequency of oxygen atoms in the lattice; n_v is the concentration of structural vacancies. Taking into account the value of D_0 found in this study, the order of the concentration of structural vacancies may be estimated at $10^{-9} - 10^{-11}$ (this range allows for some uncertainty in the values of ν and more complicated expressions for D_0 , which contain other parameters⁵). It has been mentioned in the Introduction that the presence of structural vacancies in the oxygen subsystem of ferrites is questionable. Therefore this result may be treated as the first attempt (to the best of our knowledge) to measure directly the concentration of structural oxygen vacancies in these compounds. Note that such small concentrations of structural vacancies can hardly be measured by other techniques.

One more challenge of this study was to analyze the effect of the chemical composition of the cation sublattice of the ferrite on the diffusion coefficient of oxygen tracers. But we have failed to meet this challenge because of uncontrolled factors. From Fig. 2 it is seen that in samples synthesized from different starting materials and having the same chemical composition the oxygen diffusion coefficients differ by two orders of magnitude. A probable cause for this large difference in the diffusion coefficients in the samples No. 1 and No. 2 is the doping of the cation sublattice with impurities, which was not controlled in our experiments. The most probable uncontrolled impurities in the samples studied may be Ca, Se, Cu, and V. For example, doping of the cation sublattice of ZnO with impurities at the level of 0.3 at. % was shown⁶ to change the diffusion coefficient of ^{18}O tracers by one or two orders of magnitude. Clearly these large uncontrolled changes in the diffusion coefficient made it impossible to derive reliable information concerning the effect of the nickel content on the oxygen diffusion coefficient in nickel ferrites.

One more point is worth noting. A very low value of the oxygen diffusion activation energy (0.89 eV) and the corresponding high mobility of structural oxygen vacancies indicate that oxygen vacancies may participate in the local rearrangement of the structure during the processes that determine the thermomagnetic properties of ferrites.

This work was supported by the Russian Fund For Fundamental Investigation (Project No. 96-03-32106a).

¹V. B. Fetisov, G. A. Kozhina, A. V. Fetisov, U. P. Vorobyov, and E. A. Pastukhov, Dokl. Akad. Nauk **350**, 789 (1996).

²B. Gillot, Ann. Chim. (Paris) **3**, 209 (1978).

³R. Linder and A. Akerstrom, Z. Phys. Chem. (Leipzig) **6**, 163 (1956).

⁴E. G. Moya, D. Juve, and C. Grattapain, Defect Diffus. Forum **143–147**, 1207 (1997).

⁵E. E. Maller and L. Wang, Defect Diffus. Forum **143–147**, 1067 (1997).

⁶H. Haneda, I. Sakaguchi, A. Watanabe, and J. Tanaka, Defect Diffus. Forum **143–147**, 1219 (1997).

Conversion electron Mössbauer studies on strontium ferrite films with in-plane and perpendicular anisotropies

Antony Ajan,^{a)} B. Ramamurthy Acharya,^{b)} Shiva Prasad, and S. N. Shringi
Department of Physics, Indian Institute of Technology, Bombay-400 076, India

N. Venkataramani

ACRE, Indian Institute of Technology, Bombay-400 076, India

Hexagonal strontium ferrite thin films with in-plane and perpendicular magnetic anisotropies have been studied using conversion electron Mössbauer spectroscopy. The hyperfine parameters of the films were found to be similar to the one obtained for bulk strontium ferrite. However, the intensity ratios of the first and second lines of the Mössbauer spectra were found to be different for films deposited at different rf powers. This indicated a change in the anisotropy of the deposited film. The resultant change in the magnetization direction and crystallization texture was compared to other measurements. © 1998 American Institute of Physics. [S0021-8979(98)20111-3]

I. INTRODUCTION

Recently a number of materials has been investigated for application as thin film media for high density recording. Hexagonal ferrite ($\text{BaFe}_{12}\text{O}_{19}$ and $\text{SrFe}_{12}\text{O}_{19}$) thin films are investigated due to their possible application in longitudinal and perpendicular recording media.¹⁻⁴ In addition to their chemical stability and mechanical hardness, hexagonal ferrite media in both particulate and thin film mode have been shown to exhibit lower recording noise.¹⁻³ In thin film form it is important to control the crystallographic texture, microstructure, and magnetic properties for such applications. The properties of these thin films can be significantly varied by changing the deposition conditions.

Mössbauer studies have been used in past to give information about the magnetic ordering, cation distribution, valence levels, impurity, etc. in ferrites. Mössbauer studies on bulk polycrystalline strontium ferrite has also been reported.⁵⁻⁷ In strontium ferrite, Fe^{3+} is located at five different types of sites which are denoted in literature as $12k$, $4f_1$, $4f_2$, $2a$, and $2b$.⁵⁻⁷ Since Fe^{3+} in different sites has different hyperfine parameters, the resultant Mössbauer spectrum is a superposition of five subspectra corresponding to five different Fe^{3+} sites. The ratio of the area under the subspectra gives the ratio of occupation of these sites. In the case of the reported bulk Mössbauer spectra only four six-line Mössbauer patterns have been resolved. The hyperfine parameters of $4f_1$ and $2a$ are close to each other and hence not resolved for polycrystalline materials. In this article we report on the conversion electron Mössbauer spectroscopy (CEMS) study of strontium ferrite films deposited by rf sputtering under various conditions. The results obtained were compared with the Mössbauer studies on bulk.

II. EXPERIMENTAL DETAILS

The strontium ferrite films were deposited by rf sputtering using a Leybold Z400 sputtering unit. The films were

deposited at two different rf powers of $P=60$ and 330 W (power densities of 1.3 and 7.5 W/cm², respectively) and two different O_2/Ar gas ratios of $R=1.5\%$ and 15% . These films were prepared on 2 in. diam Si(111) wafers, and were enriched with ^{57}Fe by placing a small quantity of enriched Fe_2O_3 on the strontium ferrite target. The use of films with larger areas and with enrichment by ^{57}Fe is for enhancement of the signal to noise ratio in the Mössbauer spectra. The distance between the target and the substrate was maintained at 50 mm. At $P=60$ W, the deposition rates were 13 and 10 Å/s for $R=1.5\%$ and 15% , while for $P=330$ W, they were 40 and 37 Å/s respectively. The films were prepared at ambient temperatures and were then annealed at 800°C for 3 h in air. Films of ≈ 240 nm thickness were used in this study.

The Mössbauer spectra for the target material were recorded in transmission mode by taking a small portion of the material from the target used for sputtering. Mössbauer spectra of the thin films were recorded using the scattering mode (CEMS). A 10 mci ^{57}Co source on a Rh matrix was used as the Mössbauer source.

III. RESULTS AND DISCUSSIONS

In Fig. 1 a Mössbauer spectrum for the bulk target material is shown. The hyperfine parameters were obtained from the least square fit method. The hyperfine parameters ob-

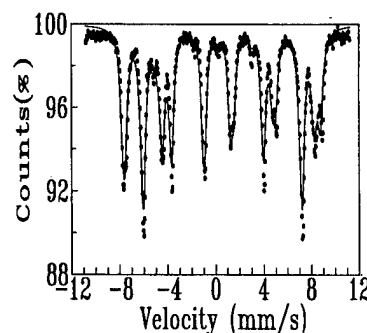


FIG. 1. Transmission Mössbauer spectrum for the bulk strontium ferrite powder. The fitted spectra are shown as solid lines.

^{a)}Electronic-mail: antony@phy.iitb.ernet.in

^{b)}Present address: Toyota Technological Institute, 2-12-1 Hisakata, Tempaku-ku, Nagoya 468, Japan

TABLE I. The results of Mössbauer analysis of the strontium ferrite bulk sample and thin films.

Sample	Site	Field (kOe)	IS (mm/s)	QS (mm/s)	Intensity ratio, b	Relat. intensity
Bulk	12k	412	0.37	0.42	2.0	48.6
	4f ₁ , 2a	491	0.27	0.16		27.5
	4f ₂	512	0.40	0.29		19.7
	2b	422	0.32	2.47		4.2
Film A 60 W, 1.5%	12k	409	0.37	0.42	1.2	50.1
	4f ₁ , 2a	487	0.27	0.21		30.6
	4f ₂	512	0.39	0.29		15.0
	2b	432	0.36	2.60		4.3
Film B 60 W, 15%	12k	409	0.37	0.42	0.9	49.4
	4f ₁ , 2a	487	0.27	0.21		31.8
	4f ₂	517	0.39	0.29		16.6
	2b	427	0.32	2.68		2.2
Film C 330 W, 1.5%	12k	409	0.37	0.472	2.2	51.1
	4f ₁ , 2a	487	0.27	0.21		29.7
	4f ₂	512	0.39	0.29		15.6
	2b	432	0.23	2.42		3.6
Film D 330 W, 15%	12k	411	0.37	0.46	2.8	51.1
	4f ₁ , 2a	487	0.27	0.21		26.8
	4f ₂	513	0.39	0.29		19.3
	2b	432	0.40	2.60		2.8

tained for the bulk sample are listed in Table I. The hyperfine parameters obtained agree well with the reported values for bulk strontium ferrite.

The Mössbauer spectrum for one of the as-deposited films is shown in Fig. 2. The as-deposited films show a paramagnetic doublet spectrum. Magnetization data on as-deposited samples show a similar result.⁸ Mössbauer spectra of the crystallized films deposited at different rf powers and different O₂/Ar ratios are shown in Fig. 3. All the spectra look identical except the second and fifth peaks which are positioned at ≈ -4 and $+4$ mm/s, respectively. The intensities of the second and fifth lines are comparatively high for the film which is deposited at higher power, i.e., 300 W compared to the film deposited at a lower power (60 W).

The hyperfine parameters were obtained from the least square fit method by fitting Lorentzian lines. The values of different parameters like hyperfine field, isomer shift, quadrupole splitting, and the intensity ratios of the first and sec-

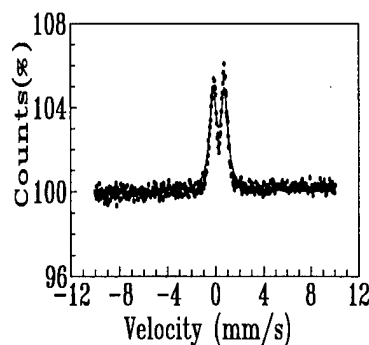


FIG. 2. Conversion electron Mössbauer spectrum for the as-deposited strontium ferrite film on Si(111), deposited at rf power = 60 W and on O₂/Ar ratio of 15%.

ond lines of subspectra (b) were iterated to obtain the best fit. The intensity of the second and fifth lines, (b), was taken to be the same for all the subspectra. This is because of the spin structure of SrFe₁₂O₁₉, where spins of Fe³⁺ at different sites are parallel to the *c* axis. The various parameters of the fitted Mössbauer spectra are listed in Table I. A comparison of these parameters with the bulk strontium ferrite values shows that the ratios of the area under different subspectra match well with bulk values within an error of $\pm 4\%$. This shows that the strontium ferrite films have a nearly stoichiometric composition and a cationic distribution like that of the bulk. The presence of any second phase would have led to a modification in the spectra from the bulk. Hyperfine field values obtained for all the samples agree well with the bulk sample. The isomer shift (IS) as well as the quadrupole shift (QS) values are also found to agree within the experimental error

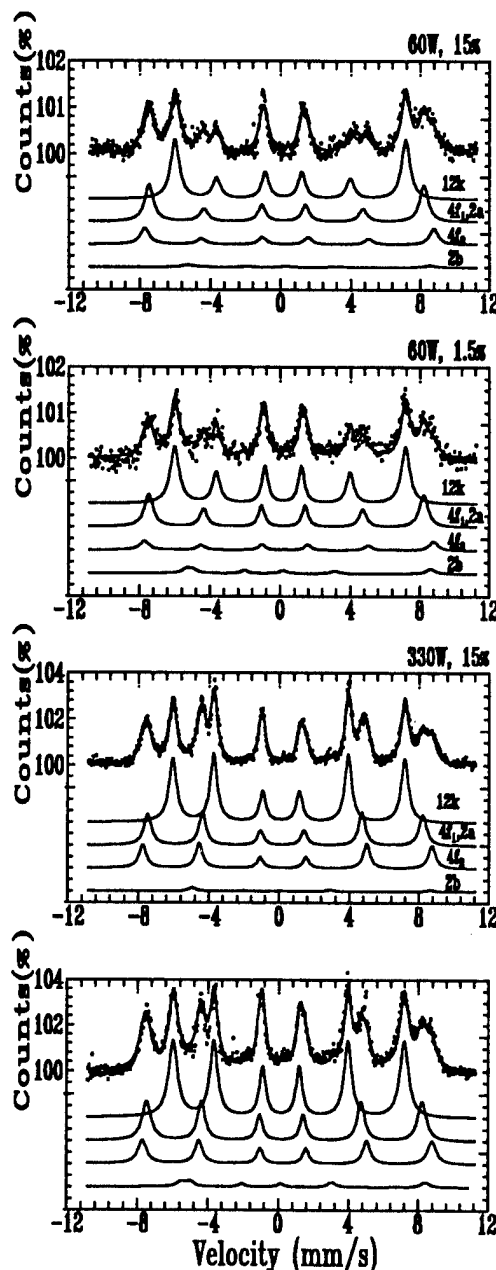


FIG. 3. Conversion electron Mössbauer spectra for strontium ferrite films on Si(111) with different powers and O₂/Ar ratios.

TABLE II. Magnetic properties of strontium ferrite thin films deposited under different conditions.

Sample	Power (W)	O ₂ /Ar (%)	H _c (kOe)		M _s (emu/cc)	M _r /M _s	
				⊥			⊥
A	60	1.5	3.9	4.1	240	0.50	0.94
B	60	15	3.1	3.4	270	0.45	0.98
C	330	1.5	3.9	3.7	280	0.60	0.55
D	330	15	3.6	3.5	275	0.70	0.61

(± 0.04 mm/s). indicates the chemical as well as the structural environments in thin film form are identical with the bulk strontium ferrite.

The **b** value, which indicates the local magnetic moment direction with respect to the incident γ ray direction, was found to vary significantly with the rf power and the O₂/Ar ratio. For film deposited at the 60 W the **b** value decreases from 1.2 to 0.9 as the O₂/Ar ratio increases from 1.5% to 15%. This **b** value, lower than 2, indicates that the magnetic moment direction tends to lie perpendicular to the plane of the film. The orientation is better for a higher O₂/Ar ratio. For a film deposited at 330 W the **b** value increases from 2.2 to 2.8 as the O₂/Ar ratio increases from 1.5% to 15%. This **b** value, higher than 2, indicates that the magnetic moment direction tends to lie in the plane of the film. Again the orientation is better for a higher O₂/Ar ratio. Thus our results indicate that for the same rf power the orientation improves with a higher O₂/Ar ratio. A value of **b**=2 indicates that a random orientation was found from fitting the bulk polycrystalline powder sample. The x-ray diffraction (XRD) studies⁸ carried out on Sr ferrite films deposited at 60 W and at different O₂/Ar ratio show a predominant *c*-axis orientation perpendicular to the film plane. The sample deposited at higher power ($P=330$, W) and with a different O₂/Ar ratio had a predominant *c*-axis orientation in the film plane. The easy axis was randomly distributed within the film plane.

The magnetic properties of the films used in this study are listed in Table II.

The coercivity (H_c) values decrease from 4.1 kOe for the sample deposited at 60 W with a 1.5% O₂/Ar ratio to 3.4

kOe for the sample deposited at 60 W with a 15% O₂/Ar ratio. Similarly, the H_c values decrease from 3.7 kOe for the sample deposited at 330 W with a 1.5% O₂/Ar ratio to 3.4 kOe for the sample deposited at 330 W with a 15% O₂/Ar ratio. Other properties such as M_r/M_s , etc. also show a considerable change with the change in the O₂/Ar ratio, as is evident from Table II. Large M_r/M_s confirms that samples with 60 W power have a perpendicular orientation.

It is interesting to note that even though the orientation is better for a higher O₂/Ar ratio the coercivity is comparatively small. A study by Acharya *et al.*⁹ on these samples indicated that intergranular interaction increases with the O₂/Ar ratio. This intergranular interaction could be the cause for the reduced coercivity in these films even though the orientation has improved with increasing O₂/Ar ratio.

IV. CONCLUSION

Hyperfine parameters obtained from Mössbauer analysis were found to be similar in bulk and in thin film samples. The **b** value, on the other hand, is found to be different from the bulk and was also dependent on power and the O₂/Ar ratio. This indicates textured growth in these films which was confirmed by XRD studies.⁹ These studies indicate that by varying the deposition condition we could achieve films with either the easy axis parallel to or perpendicular to the plane of the film. This information can be very useful for longitudinal and transverse magnetic recording.

¹X. Sui, A. Singh, Y. Chen, D. N. Lambeth, and M. H. Kryder, IEEE Trans. Magn. **31**, 2776 (1995).

²T. L. Hylton, M. A. Parker, M. Ullah, K. R. Coffey, U. Umphress, and J. K. Howard, J. Appl. Phys. **75**, 5960 (1994).

³J. Li, R. Sinclair, S. S. Rosenblum, and H. Hayashi, J. Magn. Magn. Mater. **153**, 246 (1996).

⁴Y. Hoshi, Y. Kubota, and M. Naoe, IEEE Trans. Magn. **31**, 2782 (1995).

⁵R. H. Vogel and B. J. Evans, J. Appl. Phys. **49**, 1570 (1978).

⁶V. F. Belov, T. A. Khimich, M. N. Shipko, I. S. Zheludev, E. V. Korneev, and N. S. Ovanesyan, Sov. Phys. JETP **37**, 1089 (1973).

⁷G. K. Thomson and B. J. Evans, J. Appl. Phys. **73**, 6295 (1993).

⁸B. R. Acharya, S. Prasad, N. Venkataramani, S. N. Shringi, and R. Krishnan, J. Appl. Phys. **79**, 478 (1996).

⁹B. R. Acharya, S. Prasad, N. Venkataramani, E. Abarra, and T. Suzuki, IEEE Trans. Magn. **33**, 3640 (1997).

Symposium on Exchange Biasing

William H. Meiklejohn, Chairman

Role of the antiferromagnet in exchange-biased $\text{Fe}_3\text{O}_4/\text{CoO}$ superlattices (invited)

Y. Ijiri, J. A. Borchers, R. W. Erwin, and S.-H. Lee

NIST Center for Neutron Research, National Institute of Standards and Technology, Gaithersburg, Maryland 20899

P. J. van der Zaag and R. M. Wolf

Philips Research Laboratories, Prof. Holstlaan 4, 5656 AA Eindhoven, The Netherlands

Using neutron diffraction techniques, we have directly characterized the antiferromagnetic spin structure of CoO in exchange-biased $\text{Fe}_3\text{O}_4/\text{CoO}$ (001) superlattices. The CoO antiferromagnetic order is long-range and extends coherently across intervening ferrimagnetic Fe_3O_4 layers. The ordering is influenced significantly by not only epitaxial growth constraints but also by coupling to the Fe_3O_4 layers. The antiferromagnetic order in these $\text{Fe}_3\text{O}_4/\text{CoO}$ (001) samples exhibits significant dependence on field cooling preparations. The CoO spins show a strong tendency to align perpendicular to the net ferrimagnetic moment with some changes in the average domain size associated with field cooling. The CoO spin structure in the exchange-biased state illustrates important aspects of recent biasing theories but with unusually large domain sizes. © 1998 American Institute of Physics. [S0021-8979(98)17811-8]

I. INTRODUCTION

Recently, there has been a renewed interest in studying magnetic systems exhibiting exchange anisotropy or exchange biasing.¹⁻⁷ First discovered in the 1950s,⁸ these systems typically consist of ferromagnetic (FM) materials in contact with antiferromagnetic (AFM) materials. Due to exchange-coupling between the FM and AFM layers, a host of unusual magnetic behavior is observed, including a field shift or *bias* in the FM hysteresis loop after field cooling through the AFM ordering temperature (T_N). Despite over 40 years of experimental and theoretical effort, there is still considerable debate about the mechanisms for this exchange-biasing effect. In particular, recent theories have concentrated on the detailed role of AFM domain wall formation as an essential element to understanding the exchange anisotropy.⁹⁻¹¹ The nature of the AFM and FM coupling at the interface is also under discussion, as well as the ideal AFM spin configuration for maximal biasing effect. In most experiments, the interfacial behavior of the antiferromagnet is usually inferred from bulk measurements or from the FM response.^{6,7} In contrast, elastic neutron diffraction provides a method to determine directly the nature of the AFM order in such systems.¹²

In this article, we discuss neutron diffraction results that directly focus on the CoO AFM behavior in exchange-biased $\text{Fe}_3\text{O}_4/\text{CoO}$ (001) superlattices. The growth of crystalline superlattices is possible because the spinel Fe_3O_4 and rock salt CoO structures have similar bulk lattice parameters ($a_{\text{Fe}_3\text{O}_4} = 8.398 \text{ \AA}$ and $2a_{\text{CoO}} = 8.508 \text{ \AA}$) and have complementary oxygen sublattices in the (001) plane.^{4,13} By growing superlattices with thin layers and multiple repeats, we can highlight the interfacial region which is of interest for exchange-

biasing. In addition, the bulk properties of both CoO and Fe_3O_4 have been studied extensively.^{14,15} Bulk CoO orders antiferromagnetically below $\sim 291 \text{ K}$ in ferromagnetic sheets that alternate sign along $\langle 111 \rangle$ "propagation" directions, leading to distinct $\{111\}$ domains. Bulk Fe_3O_4 orders ferrimagnetically below $\sim 858 \text{ K}$ with a net moment of $4.2 \mu_B$ per unit cell. As demonstrated previously, the $\text{Fe}_3\text{O}_4/\text{CoO}$ (001) system exhibits substantial exchange-biasing, despite the fact that the CoO (001) *interface* is expected to be compensated with no net moment.⁴ Thus, the $\text{Fe}_3\text{O}_4/\text{CoO}$ system is a good model to study the role of the antiferromagnet in producing biasing.

For superlattices of this system, we find that the CoO AFM ordering is long-range and propagates coherently through intervening Fe_3O_4 layers. The Co moment directions are constrained by sample epitaxy and influenced as well by perpendicular coupling to the ferrimagnetic Fe_3O_4 layers. Upon field cooling and field cycling, subtle changes in the AFM domain sizes are observed. These features are illustrative of the complex role of the antiferromagnet in exchange-biased systems.

II. EXPERIMENTAL DETAILS

Two $\text{Fe}_3\text{O}_4/\text{CoO}$ superlattices, $[\text{Fe}_3\text{O}_4 (100 \text{ \AA})/\text{CoO} (30 \text{ \AA})]_{50}$ and $[\text{Fe}_3\text{O}_4 (100 \text{ \AA})/\text{CoO} (100 \text{ \AA})]_{50}$, were grown by oxidic molecular beam epitaxy (MBE) onto 1.6 cm diameter [001] MgO substrates. Reflection high energy electron diffraction and x-ray scattering measurements show that the deposition results in epitaxial [001] superlattices with rocking curve full widths at half maximum (FWHM) of $\sim 0.2^\circ$ and interfacial widths of $\sim 2 \text{ \AA} \pm 1 \text{ \AA}$. For comparison, a third

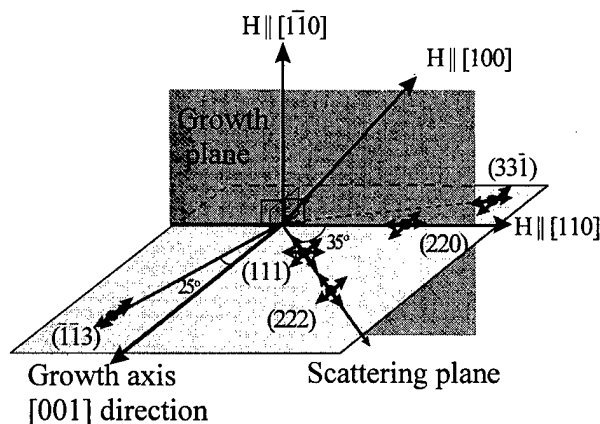


FIG. 1. Schematic showing the reciprocal space reflections discussed in the text as well as the directions in which the samples were field cooled. The scan directions through each peak are designated with small arrows.

superlattice with nonmagnetic MgO as spacer layers $[\text{MgO} (30 \text{ \AA})/\text{CoO} (30 \text{ \AA})]_{333}$ was also grown by MBE onto an [001] MgO substrate.

After preliminary characterization by x-ray analysis, neutron diffraction data were obtained on three triple-axis spectrometers (BT-2, BT-9, and SPINS) at the National Institute of Standards and Technology. For unpolarized measurements (BT-2 and BT-9), a pyrolytic graphite (PG) monochromator and analyzer were used to select elastically scattered neutrons of energy 14.8 meV. Typical collimation of $40' - 48' - 48'$ resulted in resolution in the growth direction of ~ 0.012 to 0.030 \AA^{-1} for all of the reflections of interest. For polarized measurements (SPINS), a supermirror polarizer and an Al coil spin flipper were positioned before and after the sample to select all four neutron spin cross sections, $[(++)$, $(--)$, $(+-)$, and $(-+)$], with polarization efficiencies greater than 91%.¹⁶ The + and - signs denote the neutron polarization before or after scattering from the sample.

For these experiments, the samples were oriented vertically with the [110] in-plane axis and [001] growth direction defining the scattering plane as shown in Fig. 1. The superlattices were cooled in a 14 kOe field applied in several directions within the sample growth plane. The specific reflections studied and the directions of the scans are also illustrated in Fig. 1.¹⁷ In these superlattices and consistent with bulk structure factor calculations,^{12,14} the {111} class of reflections have the strongest contribution from the CoO AFM order. The (331) and (113) reflections provide additional information about the CoO magnetic ordering, whereas the (222) reflection has only a structural contribution from the CoO. The Fe_3O_4 structural and magnetic order contributes to all these reflections and is solely responsible for the (220) reflection. For the three superlattices, the (222) satellite reflections were nearly resolution limited in the growth axis direction, indicating that the structural coherence is long range.

III. RESULTS AND DISCUSSION

A. Zero field characterization

The AFM order of the superlattices was first characterized in zero field. Figure 2(a) shows typical neutron diffrac-

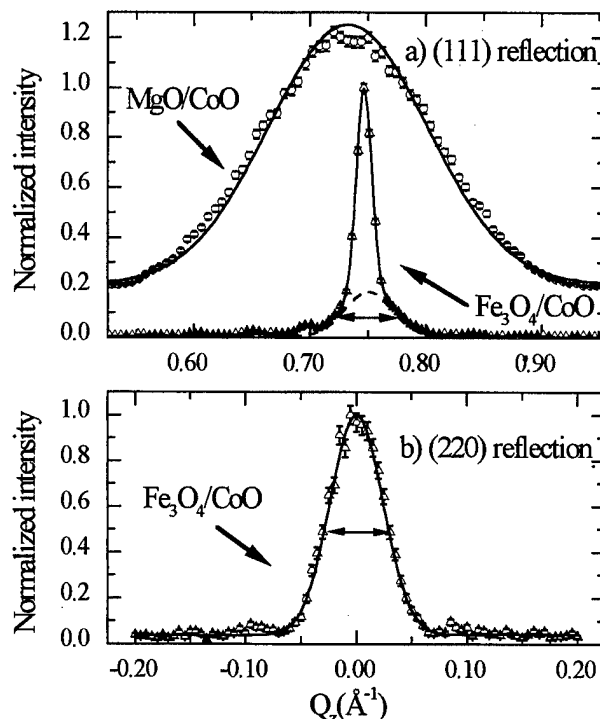


FIG. 2. Neutron diffraction scans along the [001] Q_z direction through the (a) (111) and (b) (220) reflection. The circles (\circ) refer to the $[\text{MgO} (30 \text{ \AA})/\text{CoO} (30 \text{ \AA})]_{333}$ at 15 K, and the triangles (Δ) refer to the $[\text{Fe}_3\text{O}_4 (100 \text{ \AA})/\text{CoO} (30 \text{ \AA})]_{50}$ superlattice at 28 K, both normalized to the peak values. The MgO/CoO data has been displaced from the origin by a factor of 0.2 for clarity. Solid lines denote fits to Gaussians. The dashed lines in the (111) scan show the broad Gaussians associated with the Fe_3O_4 component. The double-headed arrows indicate the width of the broad features in the $[\text{Fe}_3\text{O}_4 (100 \text{ \AA})/\text{CoO} (30 \text{ \AA})]_{50}$ reflection.

tion scans of the (111) reflection along the [001] direction. As illustrated in the figure, the line shapes differ quite significantly for the MgO/CoO sample as compared to the exchange-biased $\text{Fe}_3\text{O}_4/\text{CoO}$ samples.

For the unbiased MgO/CoO superlattice, the (111) structural reflection is forbidden such that the diffracted intensity originates entirely from the AFM CoO ordering. The broad line shape in this case indicates that the magnetic order has limited coherence along the growth axis direction. Considering the full width at half maximum and the instrumental resolution, we find that the magnetic coherence length is $\sim 35 \pm 5 \text{ \AA}$ and is thus restricted to a single CoO layer. This result is not surprising given that the MgO spacers are nonmagnetic and that the superexchange interaction in bulk CoO is short range.¹⁴ The temperature dependence of the AFM ordering is also consistent with bulk CoO, as the intensity of the (111) reflection decreases to zero at $T_N = 300 \pm 10 \text{ K}$, as compared with the bulk AFM CoO $T_N \sim 291 \text{ K}$.

In contrast, for the two $\text{Fe}_3\text{O}_4/\text{CoO}$ superlattices, the (111) reflection senses the CoO AFM order as well as the structural and magnetic ordering of the Fe_3O_4 . In these samples, the scattering contributions from the two oxides can be distinguished by the differences in line shape and temperature dependence. As illustrated in Fig. 2(a) for the $\text{Fe}_3\text{O}_4 (100 \text{ \AA})/\text{CoO} (30 \text{ \AA})$ sample, the $\text{Fe}_3\text{O}_4/\text{CoO}$ (111) reflection in the growth direction shows a two-component line shape with a broad and narrow contribution.

The magnitude of the broad component is not sensitive to temperature for the range of $T = 10$ to 600 K which is well below the ordering temperature of bulk Fe_3O_4 (858 K). As shown in Fig. 2(b), the (220) reflection, which is solely due to the Fe_3O_4 layers, is also quite broad. For both samples, these broad peak widths give coherence lengths of ~ 100 Å along the growth axis direction which correspond to the width of a single Fe_3O_4 layer. These data indicate that the registry of the Fe_3O_4 spinel lattice is not retained across the intervening CoO interlayers. This lack of coherence is not surprising due to the nonunique alignment of the Fe tetrahedral sites in the spinel relative to the rock salt CoO template at each Fe_3O_4 /CoO interface. Thus, the differences in the two crystal structures is expected to result in some type of structural disorder.¹⁸ In particular, the existence of stacking faults in the Fe_3O_4 layers has been observed and modeled extensively in Fe_3O_4 /NiO superlattices.¹² These structural faults thus lead to the broadened peak widths observed in Fig. 2. Note that these reflections have both a magnetic and structural component from the Fe_3O_4 layers. Due to the broadening from structural features, the magnetic coherence length of the Fe_3O_4 is masked and may in fact still be long range.

As the broad component of the (111) reflection tracks the Fe_3O_4 structural and magnetic order, the narrow component measures the CoO AFM order. We note that the magnitude of the narrow component is sensitive to temperature. Upon heating, this intensity decays smoothly to zero at temperatures near or above the bulk CoO T_N value of 291 K. Specifically, the AFM ordering temperatures as determined by this method are 450 ± 15 K for the $[\text{Fe}_3\text{O}_4(100 \text{ Å})/\text{CoO}(30 \text{ Å})]_{50}$ superlattice and 325 ± 15 K for the $[\text{Fe}_3\text{O}_4(100 \text{ Å})/\text{CoO}(100 \text{ Å})]_{50}$ superlattice. The apparent increase in the AFM ordering temperature with increasing relative Fe_3O_4 thickness is consistent with observations in a series of Fe_3O_4 /CoO superlattices as well as for Fe_3O_4 /NiO and NiO/CoO samples.^{12,19,20} These changes are in agreement with mean-field simulations of the exchange coupling between the Co and Fe spins at the superlattice interfaces.¹² In addition to alterations in the CoO ordering temperature, we note that the CoO line width is much more narrow than for the MgO/CoO superlattice [Fig. 2(a)]. Thus, in both Fe_3O_4 /CoO samples, the AFM order is long range along the growth axis direction. Considering the full width at half maximum (FWHM) deconvoluted by the instrumental resolution, we find that the magnetic coherence lengths are always greater than 300 Å and in some cases greater than 800 Å. This long-range order may result from local exchange coupling to the Fe_3O_4 at the superlattice interfaces. Apparently, the alternation of the Fe_3O_4 moments preserves the phase of the CoO AFM order from one layer to the next. Scanning in the growth plane, we find that the CoO AFM order is also long range.

B. Moment direction determination

To determine the AFM moment directions within each {111} domain, we examined the three superlattices with polarized neutron diffraction. Figures 3(a)–3(c) shows typical polarized neutron diffraction data of the (111) reflection scanned in the [001] direction for the three samples taken at

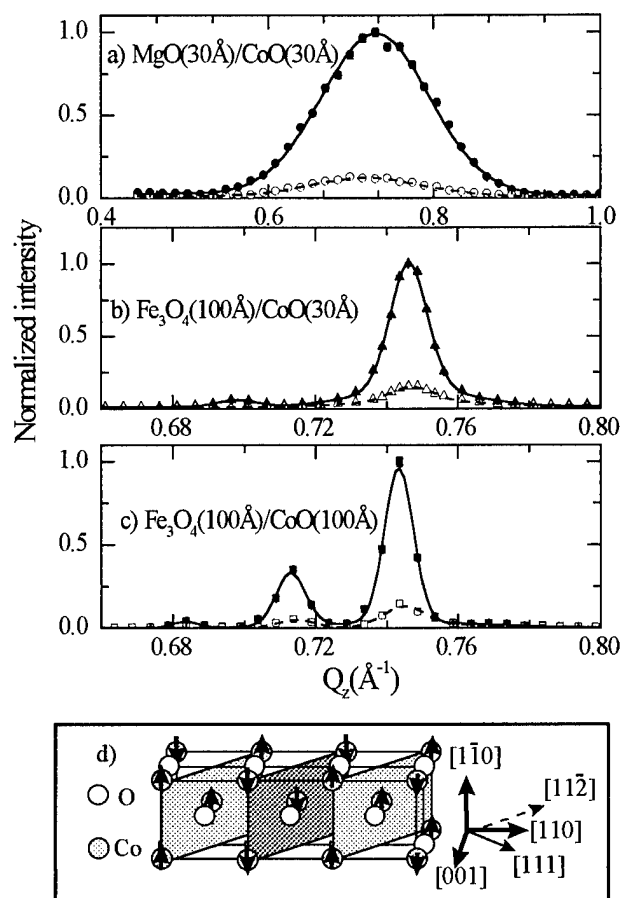


FIG. 3. Polarized neutron diffraction scans of the (111) reflection along the [001] direction for the (a) \circ $[\text{MgO}(30 \text{ Å})/\text{CoO}(30 \text{ Å})]_{333}$, (b) \triangle $[\text{Fe}_3\text{O}_4(100 \text{ Å})/\text{CoO}(30 \text{ Å})]_{50}$, and (c) \square $[\text{Fe}_3\text{O}_4(100 \text{ Å})/\text{CoO}(100 \text{ Å})]_{50}$ superlattices after cooling in a 14 kOe along the [110] direction to 78 K. The closed symbols denote the nonspin flip scattering which is sensitive to the CoO moment along [110]. The open symbols denote the spin flip scattering which is sensitive to the CoO moments along the [112] direction. (d) Illustration of the spin structure as determined from the above diffraction data.

78 K. In these measurements with the sample orientation as in Fig. 1, the nonspin flip $[(++)$ and $(--)]$ intensities are sensitive to the AFM CoO moment contribution parallel to the [110], while the spin flip $[(+-)$ and $(-+)]$ intensities are sensitive to the AFM CoO moment component parallel to the [112] direction. As illustrated in the figure, for all three superlattices, the non-spin flip contribution dominates the spin flip, indicating that the AFM moments associated with the (111) reflection lie along the [110] direction. The small amount of CoO spin flip scattering detectable is at the efficiency limit of the polarizing elements. Thus to within $\pm 2^\circ$, nearly all the Co spins within the alternating ferromagnetic sheets point in the $\pm[110]$ direction for the (111) domain, as illustrated in Fig. 3(d).²¹ This moment orientation persists to the AFM ordering temperature and did not change as a function of field cooling in three different directions within the growth plane, namely in the [110], [110], and [100] directions. The intensities observed for the (331) and (113) antiferromagnetic reflections confirm that the AFM moments are essentially confined to the (111) plane.

For this (111) domain, the alignment of the Co moments along this single [110] direction within the sample growth

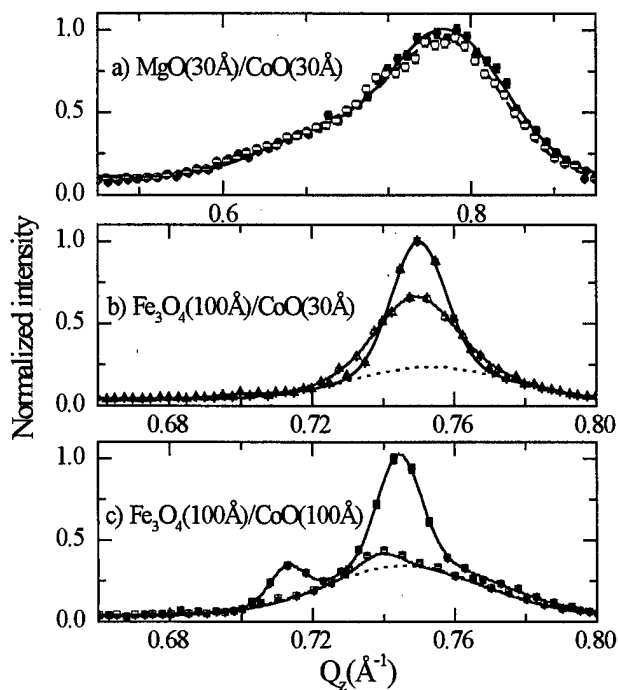


FIG. 4. Neutron diffraction scans along the $[001] Q_z$ direction through the (111) reflection after zero field cooling and field cooling in 14 kOe field along the $[\bar{1}\bar{1}0]$ direction to 78 K. Data are normalized to the zero field cooled data. The circles (\circ and \bullet), squares (\square and \blacksquare), and triangles (\triangle and \blacktriangle) refer to the $[\text{MgO}(30\text{ \AA})/\text{CoO}(30\text{ \AA})]_{333}$, $[\text{Fe}_3\text{O}_4(100\text{ \AA})/\text{CoO}(30\text{ \AA})]_{50}$, and $[\text{Fe}_3\text{O}_4(100\text{ \AA})/\text{CoO}(100\text{ \AA})]_{50}$ superlattices, respectively. Open symbols refer to the zero field cooled data, and closed symbols refer to the field cooled data. Dashed lines indicate the broad Fe_3O_4 contribution.

plane contrasts with the behavior of bulk CoO, which has three different moment directions ($[\bar{1}\bar{1}3]$, $[\bar{1}\bar{3}\bar{1}]$, and $[3\bar{1}\bar{1}]$) canted out of the (111) plane by 8° .¹⁴ These data suggest that the CoO spin structure in these superlattices is altered as a consequence of epitaxial growth constraints. We note that the bulk lattice parameter of CoO differs from that of Fe_3O_4 and that of the substrate MgO by $\sim 1.0\%$ – 1.5% .

C. Field-dependent domain characteristics

While the antiferromagnetic moment *directions* are influenced by structural features, the *number* of spins aligned in these directions is determined by the nature of the interfacial coupling as revealed by field-dependent measurements. Figure 4 shows the results at remanence after cooling the three superlattices from 320 to 78 K in a 14 kOe field applied in the $[\bar{1}\bar{1}0]$ direction. The data are scaled against similar data obtained after cooling to 78 K in zero applied field.

For the MgO/CoO superlattice, the field cooling treatment leads to little change in the intensity of the (111) reflection relative to the zero field cooled state. The applied magnetic field appears to have little effect on the AFM CoO order. This lack of a field response is not surprising in that the applied field of 14 kOe is roughly an order of magnitude less than the typical fields in which many antiferromagnets undergo a spin flop transition and align mostly perpendicular to the applied field.²²

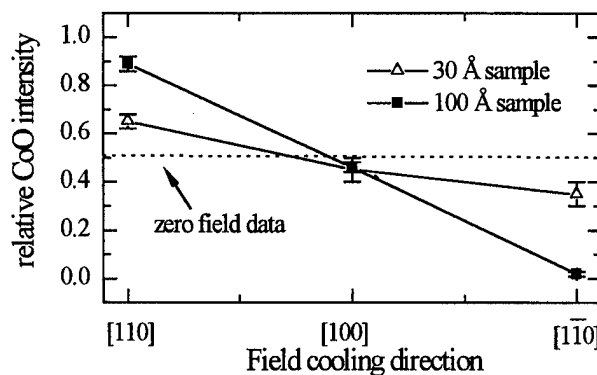


FIG. 5. The relative integrated intensity of the CoO contribution to the (111) reflection scanned along the $[001]$ direction after cooling from 320 K to 78 K in a 14 kOe field applied in different directions within the sample growth plane. The triangles (\triangle) refer to the $[\text{Fe}_3\text{O}_4(100\text{ \AA})/\text{CoO}(30\text{ \AA})]_{50}$ and the squares (\blacksquare) to the $[\text{Fe}_3\text{O}_4(100\text{ \AA})/\text{CoO}(100\text{ \AA})]_{50}$ superlattices. The data are normalized to data obtained after zero field cooling to 78 K as indicated by the solid line. For the 100 Å sample, the zero field data was obtained after randomizing the Fe_3O_4 magnetization by successively decreasing cycles of the field at 350 K. Lines between points are a guide to the eye.

In contrast, both of the $\text{Fe}_3\text{O}_4/\text{CoO}$ superlattices [Figs. 4(b)–4(c)] show a significant decrease in the (111) intensity upon field cooling in the $[\bar{1}\bar{1}0]$ direction, as CoO spins are driven out of this (111) domain. Note that this change is associated with the narrow CoO contribution and not the broader Fe_3O_4 component. This field effect is large relative to that observed for nonmagnetic MgO spacers and indicates the importance of the coupling of the AFM CoO moments to the Fe_3O_4 layers.

The nature of this coupling is apparent when considering the effect of field cooling in different directions within the sample growth plane. Figure 5 shows the integrated CoO intensity at the (111) reflection in remanence after field cooling along the $[110]$, $[100]$, and $[\bar{1}\bar{1}0]$ directions. The field cooling data have been normalized against comparable zero field cooled data which has been set to 0.5. For both $\text{Fe}_3\text{O}_4/\text{CoO}$ samples, the AFM (111) intensity is *highest* upon field cooling in the $[110]$ direction, as CoO spins are driven *into* the (111) domain. From the polarized beam data discussed in the previous section, we have determined that the AFM spins in the (111) domain are lined up along the $\pm[\bar{1}\bar{1}0]$ direction irrespective of field treatment. Thus, the preferred orientation of the AFM spins in the (111) domain is *perpendicular* to the net ferrimagnetic moment, which is aligned along the $[110]$ applied field direction. The extent to which this perpendicular arrangement is preferred is different for the two samples, as the field cooling effect is more pronounced for the $[\text{Fe}_3\text{O}_4(100\text{ \AA})/\text{CoO}(100\text{ \AA})]_{50}$ superlattice than for the $[\text{Fe}_3\text{O}_4(100\text{ \AA})/\text{CoO}(30\text{ \AA})]_{50}$ sample. This difference is also consistent with magnetization measurements on these samples. The $[\text{Fe}_3\text{O}_4(100\text{ \AA})/\text{CoO}(100\text{ \AA})]_{50}$ superlattice showed a much larger field shift for the hysteresis loop at 78 K as compared to the $[\text{Fe}_3\text{O}_4(100\text{ \AA})/\text{CoO}(30\text{ \AA})]_{50}$ sample (1300 ± 100 Oe vs 550 ± 50 Oe).²⁰

The direct observation of field-cooling dependent changes in the AFM (111) intensity agrees with most current models of exchange-biasing, to the degree that the nature of

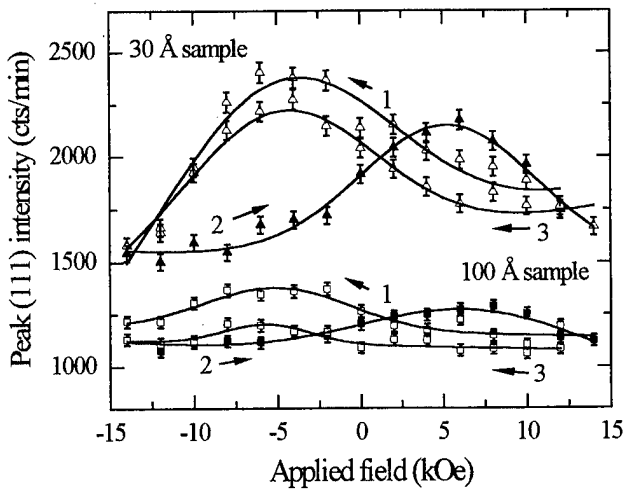


FIG. 6. Changes in the (111) peak intensity upon field cycling in the $\pm[1\bar{1}0]$ direction after field cooling to 78 K in +14 kOe along the $[110]$ direction. The triangles (Δ) refer to the $[\text{Fe}_3\text{O}_4(100\text{ Å})/\text{CoO}(30\text{ Å})]_{50}$ and the squares (\square) to the $[\text{Fe}_3\text{O}_4(100\text{ Å})/\text{CoO}(100\text{ Å})]_{50}$ superlattices. The numbers and arrows refer to the order and direction of the field cycling. Solid lines are guides to the eye.

the antiferromagnet is essential to the effect. In particular, the observed perpendicular coupling between the antiferromagnetic CoO and ferrimagnetic Fe_3O_4 moments has been predicted previously by Hinchey and Mills²³ and connected to exchange-biasing more recently by Koon.¹¹ The coupling contrasts with most models of exchange-biasing which assume that the antiferromagnet always couples collinearly with the ferromagnet.⁷⁻¹⁰

Upon field cycling after field cooling in the $[1\bar{1}0]$ direction, we also observe some changes in the (111) peak intensity, as shown in Fig. 6. While field cooling in 14 kOe in the $[110]$ direction drives CoO spins out of the (111) domain (Fig. 4), the AFM spin structure is not completely frozen for both samples (Fig. 6). The partial return of the AFM spins into the (111) domain occurs at field values which are similar in magnitude to the coercive fields of the two samples [$H_c \sim 6000 \pm 100$ Oe for $\text{Fe}_3\text{O}_4(100\text{ Å})/\text{CoO}(30\text{ Å})$ and $\sim 3200 \pm 100$ Oe for $\text{Fe}_3\text{O}_4(100\text{ Å})/\text{CoO}(100\text{ Å})$ at 78 K]. As evident in Fig. 6, the $[\text{Fe}_3\text{O}_4(100\text{ Å})/\text{CoO}(100\text{ Å})]_{50}$ superlattice shows less recovery upon field cycling than the $[\text{Fe}_3\text{O}_4(100\text{ Å})/\text{CoO}(30\text{ Å})]_{50}$ sample and is hence more effectively “frozen” into a spin configuration. We note that in contrast to the 30 Å sample, for the 100 Å CoO superlattice, memory of the field cooled direction is retained upon heating and cooling above the AFM ordering temperature, indicating again the coupling to the Fe_3O_4 layers. To the degree to which this AFM response tracks the biasing, these differences are also consistent with the larger exchange-biasing fields and higher temperatures for the onset of biasing for the $[\text{Fe}_3\text{O}_4(100\text{ Å})/\text{CoO}(100\text{ Å})]_{50}$ sample.^{5,20}

However, the domain formation in these $\text{Fe}_3\text{O}_4/\text{CoO}$ superlattices is more subtle than that proposed by many of these models. Figure 7 shows the full widths at half maximum for the narrow CoO (111) reflection in remanence after field cooling in different directions within the sample growth plane. For both samples the widths for zero field cooling match within error those obtained after field cooling in the

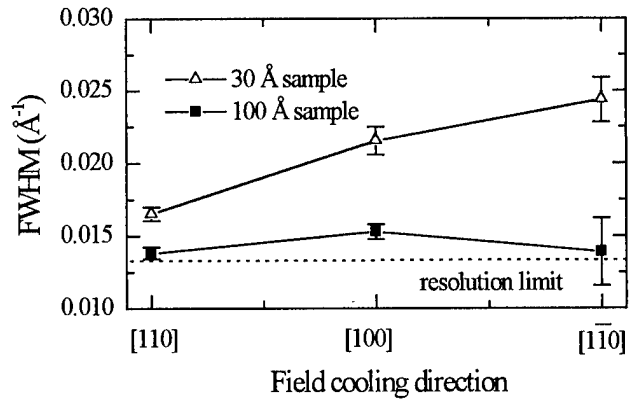


FIG. 7. The full width at half maximum (FWHM) for the (111) CoO contributions scanned along the $[001]$ direction after cooling to 78 K in a 14 kOe field applied in different directions within the sample growth plane. The triangles (Δ) refer to the $[\text{Fe}_3\text{O}_4(100\text{ Å})/\text{CoO}(30\text{ Å})]_{50}$ and the squares (\blacksquare) to the $[\text{Fe}_3\text{O}_4(100\text{ Å})/\text{CoO}(100\text{ Å})]_{50}$ superlattices. The dashed line indicates the instrumental resolution limit. Lines between points are a guide to the eye.

$[110]$ direction. The larger errors associated with the widths for the $[1\bar{1}0]$ orientation reflect the decrease in CoO (111) intensity for these scans. After deconvolution with the instrumental resolution, the FWHM is inversely proportional to the AFM domain size along the growth axis direction. For the $\text{Fe}_3\text{O}_4(100\text{ Å})/\text{CoO}(30\text{ Å})$ sample, the average coherence length in the growth axis direction varies from $\sim 310 \pm 20$ Å for field cooling in the unpreferred $[1\bar{1}0]$ direction to $\sim 700 \pm 100$ Å for field cooling in the preferred $[110]$ direction. Field cooling thus leads to changes in the average domain size. However, in the case of the 100 Å sample, the widths are nearly resolution limited for all field directions with growth axis coherence lengths of greater than 800 Å. Thus, in both samples, domain walls do not occur at every superlattice interface. Scanning the (111) reflection along the $[110]$ direction in the growth plane, we find similarly large domain sizes across the sample plane.

In addition, upon field cycling, we observe changes in the average domain size of less than a few percent for the $[\text{Fe}_3\text{O}_4(100\text{ Å})/\text{CoO}(100\text{ Å})]_{50}$ sample which has larger exchange-biasing fields.^{5,20} This contrasts with most recent models of exchange biasing in that we do not observe domain walls forming in the antiferromagnet near each $\text{Fe}_3\text{O}_4/\text{CoO}$ interface upon field reversal. However, small twists or incomplete domain walls may form in the antiferromagnet which are not within the sensitivity of our measurement technique. Alternatively, the ferrimagnetic Fe_3O_4 may exhibit domain wall formation upon field cycling. In $\text{Fe}_3\text{O}_4/\text{NiO}$ multilayers, polarized neutron reflectivity experiments showed different magnetization depth profiles for the Fe_3O_4 layers before and after field reversal, suggesting such domain wall formation.²⁴ Further experiments are underway to explore this possibility for these $\text{Fe}_3\text{O}_4/\text{CoO}$ superlattices.

IV. SUMMARY/CONCLUSION

We have demonstrated the complex nature of the AFM spin structure in $\text{Fe}_3\text{O}_4/\text{CoO}$ superlattices. The spin arrangement of the CoO is influenced by both growth constraints

and a preferred perpendicular coupling to the net Fe_3O_4 moments. In general, the CoO domains are long range and extend coherently across intervening Fe_3O_4 layers. Upon field cooling, the AFM spins "freeze" into large domains which do not change size substantially upon field cycling. These results illustrate the importance of the details of the AFM spin structure in exchange-biased systems.

ACKNOWLEDGMENT

This work is based upon activities supported by the National Science Foundation under Agreement #DMR-9423101.

- ¹M. J. Carey and A. E. Berkowitz, Appl. Phys. Lett. **60**, 3060 (1992).
- ²R. Jungblut, R. Coehoorn, M. T. Johnson, J. aan de Stegge, and A. Reinders, J. Appl. Phys. **75**, 6659 (1994); R. Jungblut, R. Coehoorn, M. T. Johnson, Ch. Sauer, P. J. van der Zaag, A. R. Ball, Th.G.S.M. Rijks, J. aan de Stegge, and A. Reinders, J. Magn. Magn. Mater. **148**, 300 (1995).
- ³J. Nogues, D. Lederman, T. J. Moran, I. K. Schuller, and K. V. Rao, Appl. Phys. Lett. **68**, 3186 (1996); J. Nogues, D. Lederman, T. J. Moran, and I. K. Schuller, Phys. Rev. Lett. **76**, 4624 (1996).
- ⁴P. J. van der Zaag, A. R. Ball, L. F. Feiner, R. M. Wolf, and P. A. A. van der Heijden, J. Appl. Phys. **79**, 5103 (1996).
- ⁵Y. Ijiri, J. A. Borchers, R. W. Erwin, S.-H. Lee, P. J. van der Zaag, and R. M. Wolf, Phys. Rev. Lett. **80**, 608 (1998).
- ⁶T. J. Moran and I. K. Schuller, J. Appl. Phys. **79**, 5109 (1996).
- ⁷K. Takano, R. H. Kodama, A. E. Berkowitz, W. Cao, and G. Thomas, Phys. Rev. Lett. **79**, 1130 (1997).
- ⁸W. H. Meiklejohn and C. P. Bean, Phys. Rev. **102**, 1413 (1956); **105**, 904 (1957).
- ⁹D. Mauri, H. C. Siegmann, P. S. Bagus, and E. Kay, J. Appl. Phys. **62**, 3047 (1987).
- ¹⁰A. P. Malozemoff, J. Appl. Phys. **63**, 3874 (1988).
- ¹¹N. C. Koon, Phys. Rev. Lett. **78**, 4865 (1997).
- ¹²J. A. Borchers, R. M. Erwin, S. D. Berry, D. M. Lind, J. F. Ankner, E. Lochner, K. A. Shaw, and D. Hilton, Phys. Rev. B **51**, 8276 (1995).
- ¹³R. M. Wolf, A. E. M. De Veirman, P. van der Sluis, P. J. van der Zaag, and J. B. F. aan de Stegge, Mater. Res. Soc. Symp. Proc. **341**, 23 (1994).
- ¹⁴W. L. Roth, Phys. Rev. **110**, 1333 (1958); B. van Laar, Phys. Rev. **138**, A584 (1963); D. Herrmann-Ronzau, P. Burlet, and J. Rossat-Mignod, J. Phys. C **11**, 2123 (1978).
- ¹⁵J. Smit and H. P. J. Wijn, *Ferrites* (Wiley, New York, 1959).
- ¹⁶c.f. W. G. Williams, *Polarized Neutrons* (Oxford University Press, New York, 1988).
- ¹⁷All reflections are indexed relative to the Fe_3O_4 spinel unit cell and the CoO magnetic unit cell.
- ¹⁸T. Terashima and Y. Bando, Thin Solid Films **152**, 455 (1987).
- ¹⁹J. A. Borchers, M. J. Carey, R. W. Erwin, C. F. Majkrzak, and A. E. Berkowitz, Phys. Rev. Lett. **70**, 1878 (1993).
- ²⁰P. J. van der Zaag, L. F. Feiner, J. M. Gaines, R. M. Wolf, P. A. A. van der Heijden, J. A. Borchers, R. W. Erwin, and Y. Ijiri (unpublished).
- ²¹We note that these measurements are sensitive to the *average* direction of CoO AFM spins. While a small number of CoO spins in different directions would not be detected, it would be expected that a number of the nearby CoO spins should display a sizeable twisting toward the average direction, leading to an increase the spin-flip scattering beyond that observed.
- ²²L. Néel, Compt. Rend. **5**, 232 (1936); I. S. Jacobs, J. Appl. Phys. **32**, 61S (1961).
- ²³L. L. Hinchey and D. L. Mills, Phys. Rev. B **34**, 1689 (1986).
- ²⁴A. R. Ball, A. J. G. Leenaers, P. J. van der Zaag, K. A. Shaw, B. Singer, D. M. Lind, H. Fredrikze, and M. Th. Rekveldt, Appl. Phys. Lett. **69**, 1489 (1996).

Role of interfacial uncompensated antiferromagnetic spins in unidirectional anisotropy in $\text{Ni}_{81}\text{Fe}_{19}/\text{CoO}$ bilayers (invited)

Kentaro Takano, R. H. Kodama,^{a)} and A. E. Berkowitz

Department of Physics and Center for Magnetic Recording Research, University of California, San Diego, La Jolla, California 92093

W. Cao^{b)} and G. Thomas

Department of Materials Science and Mineral Engineering, University of California, Berkeley, California 94720

The uncompensated spins on the surfaces of antiferromagnetic CoO films exhibit a thermoremanent magnetization after field cooling from $T > T_N$ that has the same temperature dependence as the exchange field of $\text{Ni}_{81}\text{Fe}_{19}/\text{CoO}$ bilayers after field cooling. This suggests that these interfacial uncompensated spins are responsible for unidirectional anisotropy. A model based on a calculation of the density of these interfacial uncompensated spins predicts the correct magnitude of the exchange field, as well as the observed inverse dependence on average interfacial grain size.

© 1998 American Institute of Physics. [S0021-8979(98)37411-3]

I. INTRODUCTION

Exchange anisotropy¹ refers to the exchange interactions at an interface between ferromagnetic (FM) and antiferromagnetic (AFM) materials. Cooling a FM/AFM thin film bilayer from $T_C(\text{FM}) > T > T_N(\text{AFM})$ in a saturating magnetic field produces a unidirectional anisotropy that is manifested as a $\sin \theta$ component in the torque curve and a hysteresis loop displaced along the field axis. The loop shift is called the exchange field H_E . Recently, the technological application of AFM thin films to bias magnetoresistive devices² important to the magnetic recording industry has revived the interest in exchange anisotropy. Despite extensive experimental and theoretical investigations in the past 40 years, the basic details of the mechanism of this phenomenon remained unclear.

Assuming Heisenberg exchange across an epitaxial atomically smooth FM/AFM interface,

$$H_E = \frac{J_{\text{ex}} S_{\text{FM}} S_{\text{AFM}}}{a^2 M_{\text{FM}} t_{\text{FM}}}, \quad (1)$$

where J_{ex} is the exchange parameter, S_{FM} and S_{AFM} are the spins of the interfacial atoms, a is the cubic lattice parameter, and M_{FM} and t_{FM} are the magnetization and thickness of the FM layer, respectively. Observed exchange fields, however, are typically less than a few percent of the values predicted by this idealized model. A quantitatively satisfactory model for a specific exchange coupled system has not been reported until recently.³

Our measurements of thermoremanent magnetization (TRM) in CoO/MgO multilayers show that the spins responsible for this moment are interfacial and constitute $\sim 1\%$ of the spins in a monoatomic layer of CoO. The TRM exhibited the same features and temperature dependence as the ex-

change field of $\text{Ni}_{81}\text{Fe}_{19}/\text{CoO}$ bilayers. Since the TRM originates from the uncompensated interfacial AFM spins, they appear to be the spins responsible for unidirectional anisotropy. A model is presented which predicts the observed exchange field. It is based on a calculation of the density of interfacial uncompensated spins, and accounts for grain size, orientation, and interfacial roughness.

II. EXPERIMENTAL PROCEDURES

CoO has a Néel temperature, $T_N = 293$ K. The AFM ordering is characterized by FM aligned (111) planes with adjacent antiparallel (111) planes. The AFM alignment results from the superexchange coupling of the cobalt cation atoms via the p orbitals of the oxygen atoms. CoO/MgO multilayers were used to determine the magnetic properties of uncoupled CoO films since MgO is nonmagnetic. CoO and MgO share the fcc NaCl structure with bulk cubic lattice parameters which differ by only 1.1%. The structural similarity permits interlayer coherent growth. A series of $\text{CoO}(t_{\text{CoO}} \text{ \AA})/\text{MgO}(t_{\text{MgO}} \text{ \AA})$ multilayers were deposited with CoO thicknesses t_{CoO} ranging from 16 to 103 Å, and MgO thicknesses $t_{\text{MgO}} \sim 20$ Å. The structural characterization and heat capacity measurements of these multilayers are discussed in detail elsewhere.⁴ Thin film bilayers of CoO and permalloy ($\text{Ni}_{81}\text{Fe}_{19}$) were used to determine the role of AFM thickness on the interfacial exchange properties. A series of films was deposited with CoO thicknesses ranging from 100 to 3000 Å; the permalloy layer thickness was fixed at 300 Å. An Ag capping layer was deposited as an oxidation barrier.

The CoO⁵ and MgO films were reactively sputtered from a metal target. The permalloy was deposited by dc sputtering from an alloy target. The substrates were backed by Alnico magnets to apply a bias field during deposition to induce an easy axis in the permalloy. The films were deposited at 373 K with a rotating substrate table (~ 0.6 Hz) heated by a quartz lamp. The deposition rates were ~ 27 Å/min for the oxides and ~ 15 Å/min for the permalloy. Film thicknesses

^{a)}Current address: Naval Research Laboratory, Code 6342, 4555 Overlook Ave. SW, Washington, DC 20375-5320.

^{b)}Current address: Komag Inc, 1704 Automation Pkwy., San Jose, CA 95131.

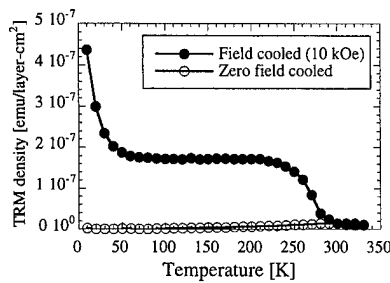


FIG. 1. FC and ZFC moment densities vs temperature of the $[\text{CoO}(103 \text{ Å})/\text{MgO}(30 \text{ Å})]_{15}$ multilayer.

were established from rate checks. The substrates were Si(100) wafers with a native amorphous oxide layer ($\sim 30 \text{ Å}$). The films were polycrystalline as determined by x-ray diffraction and transmission electron microscopy (TEM). No evidence for any phase other than CoO was detected. The cubic lattice parameter derived from the (111) peak position is 4.27 Å which is slightly expanded (0.2%) from the bulk parameter (4.260 Å).

Magnetic measurements of the CoO/MgO multilayers and permalloy/CoO bilayer films were taken using a superconducting quantum interference device (SQUID) magnetometer. From a series of hysteresis loops measured at temperatures ranging from 10 to 320 K, the temperature dependences of the exchange fields were obtained for field cooled (FC) permalloy/CoO bilayer films. The permalloy easy axis (induced by the Alnico magnet) was aligned parallel to the measurement field.

III. RESULTS

The CoO/MgO multilayers were cooled from 350 to 10 K in zero field (ZFC) and in $+10 \text{ kOe}$ (FC). Magnetization measurements were made in a 100 Oe field. Field cooling resulted in a stable magnetization—i.e., a TRM. Figure 1 shows the FC and ZFC measurements for the $[\text{CoO}(103 \text{ Å})/\text{MgO}(30 \text{ Å})]_{15}$ multilayer. The interfacial TRM density exhibits two features: (i) an intermediate temperature region ($200 \text{ K} \geq T \geq 50 \text{ K}$) where the magnetization is independent of temperature (a “plateau”) and (ii) a low temperature increase ($T \leq 50 \text{ K}$). The magnitudes of these two features scale closely with the number of CoO layers and have no dependence on the net CoO thickness in the multilayers. Therefore the uncompensated moment of both features is an interfacial effect and not a bulk effect. Neutron data⁶ give $3.8 \mu_B$ for the magnetic moment of Co^{2+} in CoO. Thus the measured interfacial uncompensated moment represents $\sim 1\%$ of the spins in a monoatomic layer of CoO.

If the CoO/MgO multilayer is field cooled to 100 K and then zero field cooled from 100 to 10 K, the low temperature increase feature is absent from the TRM. Hence, the spins responsible for the low temperature increase require a moderate cooling field below 100 K to align them and will be referred to as the low freezing temperature (LFT) spins. For $T < 100 \text{ K}$, we observed relaxation and hysteresis. The LFT magnetization and irreversibility disappear above 100 K which is considerably lower than T_N , so we infer that the LFT spins are weakly coupled to the spins in the core of the

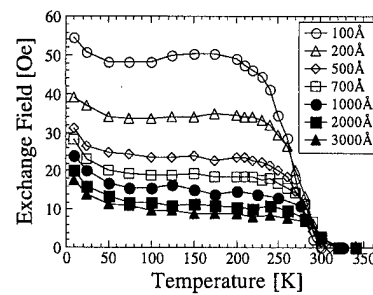


FIG. 2. Temperature dependence of H_E for permalloy (300 Å)/CoO bilayers with CoO thicknesses of 100–3000 Å.

CoO layers. These spins may be a small fraction of surface spins that are frustrated. Similar magnetic behavior was observed in disordered surface spins in NiFe_2O_4 nanoparticles⁷ and in isolated spin clusters in powders of randomly diluted fcc $\text{Co}_x\text{Mg}_{1-x}\text{O}$.⁸

In Fig. 1, the bifurcation of the FC and ZFC susceptibilities occurs at $295 \pm 5 \text{ K}$ (the bulk T_N of CoO). This suggests that the spins responsible for the plateau feature are magnetically coupled to the spins in the core of the CoO layers. For $100 < T < 200 \text{ K}$, the spins responsible for the plateau have anisotropy fields much larger than the LFT spins since (i) no magnetization reversal was observed in fields as large as -55 kOe and (ii) the $M-H$ loops exhibited a vertical displacement along the moment axis equal to the contribution due to the TRM. The TRM temperature dependence (for $T > 50 \text{ K}$) was similar to the temperature dependence of the sublattice magnetization for CoO as determined by neutron diffraction.⁹ This correlation further suggests a strong coupling of these interfacial spins to the core spins of the CoO film.

The permalloy/CoO bilayers were cooled from 350 K ($> T_N + 50 \text{ K}$) to 10 K in a $+10 \text{ kOe}$ field. Figure 2 shows $H_E(T)$ for some of the CoO thicknesses. $H_E(T)$ of permalloy/CoO films exhibit the plateau and low temperature increase features in identical temperature regions as the TRM of the CoO/MgO multilayers. In Fig. 3, the TRM of the $[\text{CoO}(103 \text{ Å})/\text{MgO}(30 \text{ Å})]_{15}$ multilayer and the $H_E(T)$ of the permalloy/CoO(100 Å) bilayer have been normalized at 70 K. The curves overlap at all temperatures except for the lowest temperature region $T < 50 \text{ K}$. Due to the distribution of lower anisotropy fields exhibited by the LFT spins, only a

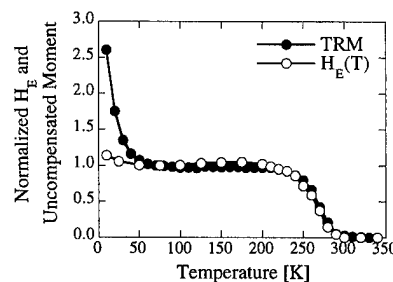


FIG. 3. $H_E(T)$ (○) of the permalloy/CoO(100 Å) bilayer and the TRM (●) of the $[\text{CoO}(103 \text{ Å})/\text{MgO}(30 \text{ Å})]_{15}$ multilayer normalized at 70 K. The overlap for $T > 50 \text{ K}$ strongly suggests that the interfacial uncompensated spins responsible for the TRM plays an important role in the exchange field mechanism.

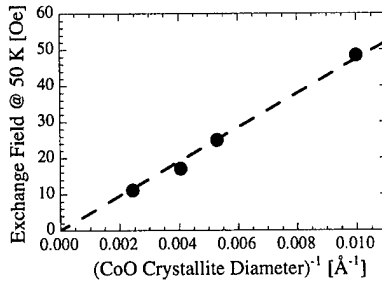


FIG. 4. Linear relationship between the plateau value of $H_E(T=50\text{ K})$ of the permalloy/CoO bilayers and the inverse of the CoO crystallite diameter.

small fraction of the LFT spins have sufficient anisotropy to effectively pin the permalloy layer. The correlation above 50 K strongly suggests that the interfacial uncompensated spins which are responsible for the TRM play an important role in the exchange field mechanism. The correlation also suggests that the temperature dependence of H_E is consistent with strong *net* unidirectional interfacial Heisenberg exchange that is proportional to the spin density of the uncompensated interfacial AFM spins. This proportionality, however, will only be observed for AFM grains with high magnetocrystalline anisotropy energy. This condition is not likely to be satisfied (i) in lower anisotropy AFM materials such as NiO and (ii) in small AFM grains since the magnetic energy scales with the grain volume. The observation that $\sim 1\%$ of the interfacial AFM spins are uncompensated is consistent with measured permalloy/CoO exchange fields of $\sim 1\%$ of the interfacial Heisenberg exchange model [Eq. (1)].

The H_E dependence with the CoO thickness suggests a structural origin for the density of uncompensated spins. Cross-sectional TEM showed a columnar structure for all thicknesses. The sizes of the CoO crystallites at the permalloy/CoO interface were examined by TEM plan views of CoO films without any capping layers. The average CoO crystallite diameter for thicknesses of 100, 500, 1000, and 3000 Å were determined by an analysis of the dark and bright field images. Figure 4 shows the linear relationship between $H_E(50\text{ K})$, which is representative of the plateau value, and the inverse of the CoO crystallite diameter.

IV. MODELING

The correlation between the temperature dependence of the TRM of the CoO/MgO multilayers and the exchange field of the permalloy/CoO bilayers suggests a direct relationship between the interfacial density of uncompensated spins and the strength of the exchange field. We present a model for H_E which demonstrates its connection with the interfacial density of uncompensated spins, and predicts the inverse relationship between H_E and the grain diameter. We assume that each CoO crystallite is a single AFM domain. We define the normal to the FM aligned (111)-type spin plane as $\hat{\mathbf{p}}$, and define the probability of finding a crystallite with that orientation at the AFM film surface as $f(\hat{\mathbf{p}})d\Omega_{\hat{\mathbf{p}}}$. We define the easy axis (known to be near the tetragonal axis in bulk CoO⁶) for a crystallite as $\hat{\mathbf{e}}$, and the probability of finding a crystallite with that easy axis as $g(\hat{\mathbf{e}})d\Omega_{\hat{\mathbf{e}}}$ (the sign of $\hat{\mathbf{e}}$ will be specified below). The FM aligned spin planes

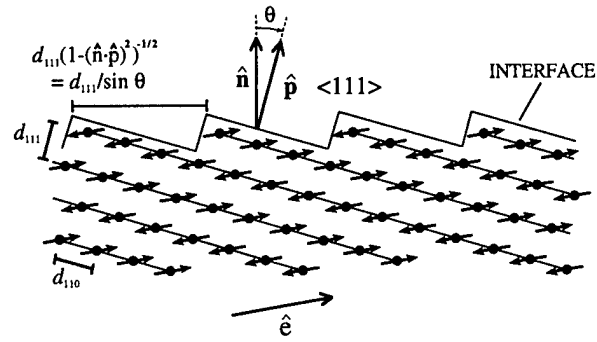


FIG. 5. Schematic of interface cross section. Film normal is $\hat{\mathbf{n}}$, $\hat{\mathbf{p}}$ is the normal to the parallel spin plane (111) of the AFM, and $\hat{\mathbf{e}}$ is the AFM spin axis (in this case $N_{\text{rows}}=4$).

will intersect the interface in a series of atomic steps with spacing $d_{111}(1-(\hat{\mathbf{n}}\cdot\hat{\mathbf{p}})^2)^{-1/2} (=d_{111}/\sin\theta)$, where $d_{111}(=a\sqrt{3}/3=0.577a)$ is the spacing of (111) planes, and $\hat{\mathbf{n}}$ is the film normal, as indicated in Fig. 5. The interfacial layer of spins of each crystallite will consist of alternate rows of antiparallel spins pointing in the $\pm\hat{\mathbf{e}}$ directions. If $\hat{\mathbf{p}}$ is close to $\hat{\mathbf{n}}$, there may be two or more rows of parallel spins from each (111) spin plane at the interface. The number of adjacent rows of parallel spins may be estimated as

$$N_{\text{rows}} = \text{trunc} \left\{ \frac{d_{111}}{d_{110}} [1 - (\hat{\mathbf{n}}\cdot\hat{\mathbf{p}})^2]^{-1/2} \right\}, \quad (2)$$

where “trunc” gives the largest integer less than the argument and d_{110} represents the in-plane spacing. The interfacial exchange energy for crystallite i is

$$U_i = - \sum_{j=1}^N J_{\text{ex}} \mathbf{S}_{\text{FM},j} \cdot \mathbf{S}_{\text{AFM},j}.$$

If the ferromagnetic layer is in a single domain state,

$$\begin{aligned} U_i &= -\mathbf{S}_{\text{FM}} \cdot \left[\sum_{j=1}^N J_{\text{ex}} \mathbf{S}_{\text{AFM},j} \right] \\ &= -\mathbf{S}_{\text{FM}} \cdot [J_{\text{ex}}(N_{+,i} - N_{-,i})\mathbf{S}_{\text{AFM}}\hat{\mathbf{e}}], \end{aligned}$$

where N_{\pm} is the number of interfacial spins pointing in the $\pm\hat{\mathbf{e}}$ direction, and we define the sign of $\hat{\mathbf{e}}$ such that $J_{\text{ex}}(N_{+,i} - N_{-,i}) \equiv J_{\text{ex}}\Delta N_i$ is positive. As indicated in Fig. 6, if the AFM film is cooled below T_N in zero field, the uncompensated moment of the AFM domains are randomly oriented but collinear with the Néel axes of the AFM grains. If the AFM film is field cooled below T_N , the uncompensated moment of the AFM domain will orient itself such that $+\hat{\mathbf{e}}$ has a component in the direction of the adjacent FM spins (i.e., $\hat{\mathbf{H}}_{\text{cool}}$). Therefore

$$U_i^{\text{FC}} = -|J_{\text{ex}}|S_{\text{AFM}}S_{\text{FM}}\Delta N_i|\hat{\mathbf{e}}\cdot\hat{\mathbf{H}}_{\text{cool}}|.$$

The total interfacial energy is then

$$\begin{aligned} U_{\text{tot}}^{\text{FC}} &= -|J_{\text{ex}}|S_{\text{AFM}}S_{\text{FM}}N_c \left[\int d\Omega_{\hat{\mathbf{p}}} f(\hat{\mathbf{p}})\Delta N_i \right] \\ &\quad \times \left[\int d\Omega_{\hat{\mathbf{e}}} g(\hat{\mathbf{e}})|\hat{\mathbf{e}}\cdot\hat{\mathbf{H}}_{\text{cool}}| \right], \end{aligned}$$

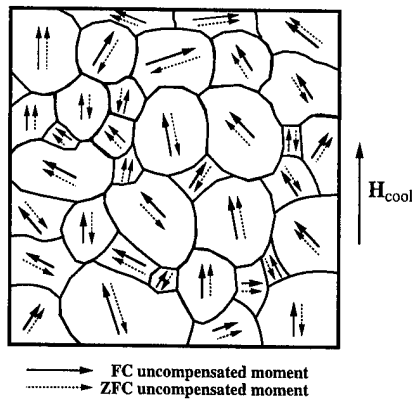


FIG. 6. Schematic of uncompensated spin moment of uniaxial AFM grains. The uncompensated AFM spins are collinear with the Néel axes of the core of the AFM grains. The uncompensated AFM moments are randomly aligned in the zero field cooled case; whereas in the field cooled case, the uncompensated AFM moments are aligned along the uniaxial direction with a component in the cooling field direction.

where $N_c = \text{area}/L^2 = \text{total number of crystallites at the interface}$. If we assume that the AFM spins are frozen below T_N , and that $g(\hat{\mathbf{e}})$ is azimuthally symmetric, we find that the interfacial energy as a function of $\hat{\mathbf{S}}_{\text{FM}}$ is

$$\frac{U_{\text{tot}}^{\text{FC}}(\hat{\mathbf{S}}_{\text{FM}})}{\text{area}} = -(1/L^2)|J_{\text{ex}}|S_{\text{AFM}}S_{\text{FM}}(\hat{\mathbf{H}}_{\text{cool}} \cdot \hat{\mathbf{S}}_{\text{FM}}) \times \left[\int d\Omega_{\hat{\mathbf{p}}} f(\hat{\mathbf{p}}) \Delta N_i \right] \times \left[\int d\Omega_{\hat{\mathbf{e}}} g(\hat{\mathbf{e}}) |\hat{\mathbf{e}} \cdot \hat{\mathbf{H}}_{\text{cool}}| \right]. \quad (3)$$

Finally, following Malozemoff,¹⁰ we have

$$H_E = \frac{[U_{\text{tot}}^{\text{FC}}(-\hat{\mathbf{S}}_{\text{FM}}) - U_{\text{tot}}^{\text{FC}}(\hat{\mathbf{S}}_{\text{FM}})]/\text{area}}{2M_{\text{FM}}t_{\text{FM}}},$$

where M_{FM} and t_{FM} are the magnetization and thickness of the FM layer.

To compute the first integral in Eq. (3), we numerically calculated the average number of uncompensated spins for elliptical crystallites as a function of N_{rows} , which is related to the orientation $\hat{\mathbf{p}}$ by Eq. (2). We incorporated interfacial roughness as specified by the average lateral dimension of interfacial topographic features. We first mapped the interfacial plane onto a square lattice for computational convenience (this mapping slightly changes the shape of the model crystallites, but this is not significant). As shown in Fig. 7(a), the interfacial plane consists of a periodic pattern of N_{rows} rows of spins in the $+\hat{\mathbf{e}}$ direction, followed by N_{rows} rows of spins in the $-\hat{\mathbf{e}}$ direction. To simulate roughness, we superimposed elliptical “islands” of monoatomic thickness on the spin map. Figure 7(b) depicts the effect of adding one atomic layer as reversing the direction of the spin at each site covered by the island, since successive layers of CoO spins have opposite direction. The major axis of these islands was kept fixed (denoted “feature diameter”), while the position, orientation of the major axes, and aspect ratio (from 1:1 to 1:1.5) were varied. Islands were superimposed sequentially, allow-

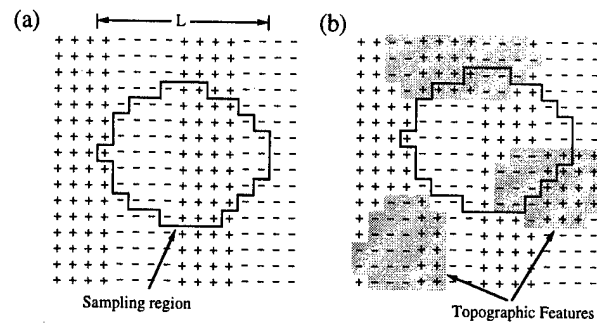


FIG. 7. Topographical representation of the interfacial plane. (a) Periodic pattern of $N_{\text{rows}} = 4$ (as in Fig. 5) with a sample region representing a model crystallite. (b) Elliptical islands of a monoatomic layer thickness were superimposed on the spin map to simulate roughness. Note that adding one atomic layer reverses the direction of the underlying spin.

ing overlap between them, until the total area of the islands equaled the total area of the spin map. Figure 8 is a representative topographical map containing overlapping islands with a feature diameter of 20 lattice parameters and coverage equal to the total area of the map. The varying shades of gray represent the degree of interfacial elevation above the base spin pattern consisting of a periodic pattern of N_{rows} rows of antiparallel spins [see Fig. 7(a)]. To compute the number of uncompensated spins for a model crystallite, ΔN_i , we simply added the total number of spins in each direction within an elliptical region, having major axis equal to L , on the spin map. We created a spin map which was several times larger than L , so a statistical average could be taken by varying the position, orientation of the major axis, and aspect ratio of the model crystallite (similar to the above procedure for generating roughness). Averages were taken by computing ΔN_i for 10^6 model crystallites. Although the base layer of the spin maps represents fully compensated spin planes (excluding perfect $\langle 111 \rangle$ orientation), the uncompensated moment originates from the finite dimensions imposed by the boundaries of the model crystallites and the density of roughness terraces.

The results of these calculations are summarized as follows: (1) a perfectly regular interface, with equally spaced

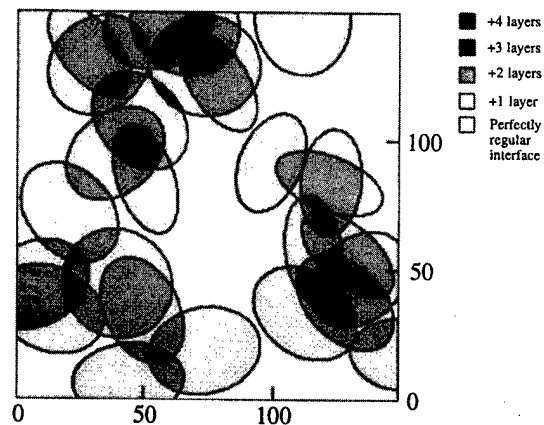


FIG. 8. Topographical map containing overlapping islands. The islands have a feature diameter of 20 lattice parameters and coverage equal to the total area of the map. The legend correlates the different shades of gray with the height of interfacial elevation above the base spin pattern [see Fig. 7(a)].

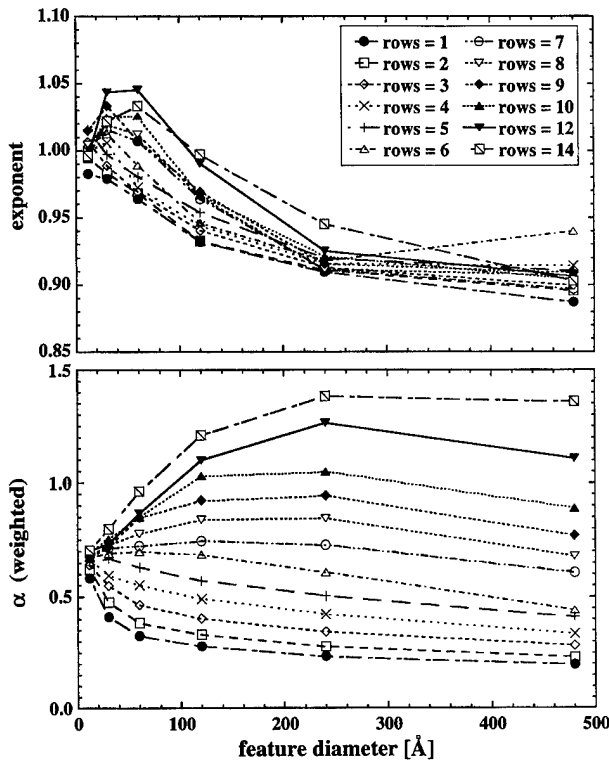


FIG. 9. Calculated values of the prefactor α and the exponent in power-law fits of $\langle \Delta N \rangle$ vs feature diameter and N_{rows} . $N_{\text{rows}}=1$ corresponds to $\theta > 24.1^\circ$ and $N_{\text{rows}}=14$ corresponds to $3.3^\circ > \theta > 3.1^\circ$. Prefactor α is weighted based on equal population of domains with the four different (111)-type parallel spin planes.

atomic terraces, results in $\langle \Delta N \rangle = \alpha(L/d_{110})^{0.5}$, (2) the addition of roughness results in $\langle \Delta N \rangle \approx \alpha(L/d_{110})^{0.90 \sim 1.04}$, (3) for small values of feature diameter $\langle \Delta N \rangle = 0.6(L/d_{110})$, independent of N_{rows} , and (4) the prefactor α increases as N_{rows} increases. These results are shown in Fig. 9. Since the result of Eq. (3) is proportional to $\langle \Delta N \rangle / L^2$, the rough case gives $H_E \sim L^{-1}$, in agreement with the experimental results of Fig. 4.

As an example, we calculate H_E for the 100 Å thick sample as follows. Recent work by the authors suggests,¹¹ via a mean field analysis of exchange coupled bilayers having different FM layers, that the interfacial exchange is a direct exchange between the metal ions. Following this approach, we estimate that the constant $J_{\text{ex}} S_{\text{AFM}} S_{\text{FM}} = \bar{T}_C / 8$

$= 143$ K, where \bar{T}_C is the Curie temperature of the interfacial alloy $(\text{Ni}_{81}\text{Fe}_{19})_{0.5}\text{Co}_{0.5}$.¹² X-ray diffraction rocking curves of the CoO (222) peak are nearly flat, indicating the absence of a strong crystallographic texture. Therefore, we assume uniform distributions of crystallite orientations (i.e., $f(\hat{\mathbf{p}})$ and $g(\hat{\mathbf{e}})$ are constant). With these parameters, we calculate exchange fields of 107, 80, 63, 50, 40, and 31 Oe for topographic feature diameters of 12, 30, 60, 120, 240, and 480 Å, respectively. The experimental result of 48 Oe is consistent with a topographic feature diameter of approximately 120 Å. This result is consistent with interfacial roughness of only a few “extra” atomic steps across the face of each crystallite.

V. SUMMARY

We measured the interfacial uncompensated moment on an AFM surface as a TRM of a field-cooled CoO/MgO multilayer. The temperature dependence of the interfacial uncompensated AFM moment parallels that of the exchange field of permalloy/CoO bilayers. A model for unidirectional anisotropy correctly predicts the inverse dependence of the uncompensated spins on grain size and the correct magnitude of H_E .

ACKNOWLEDGMENTS

This work was supported in part by the MRSEC Program of the NSF under Award No. DMR-9400439 and by the ATP Heads Program administered by NSIC.

¹W. H. Meiklejohn and C. P. Bean, Phys. Rev. **102**, 1413 (1956); **105**, 904 (1957).

²B. Dieny *et al.*, Phys. Rev. B **43**, 1297 (1991).

³K. Takano *et al.*, Phys. Rev. Lett. **79**, 1130 (1997).

⁴E. N. Abarra *et al.*, Phys. Rev. Lett. **77**, 3451 (1996).

⁵W. Cao *et al.*, Scr. Metall. Mater. **25**, 2633 (1991).

⁶W. L. Roth, Phys. Rev. **110**, 1333 (1958).

⁷R. H. Kodama *et al.*, Phys. Rev. Lett. **77**, 394 (1996).

⁸R. Kannan and M. S. Seehra, Phys. Rev. B **35**, 6847 (1987).

⁹D. C. Khan and R. A. Erickson, J. Phys. Chem. Solids **29**, 2087 (1968).

¹⁰A. P. Malozemoff, Phys. Rev. B **35**, 3679 (1987).

¹¹K. Takano (unpublished).

¹²For a homogeneous FM, molecular field theory (see Ref. 13) gives $J_{\text{ex}} = 3k_B T_C / [2zS(S+1)]$ where z is the coordination (12 for fcc). Treating the spins classically, we replace $S(S+1)$ with S^2 . The exchange parameter for the interfacial alloy $\text{FM}_{0.5}\text{Co}_{0.5}$ is $J_{\text{ex}} = 3k_B \bar{T}_C / (2z\langle S_{\text{FM}} S_{\text{AFM}} \rangle)$.

¹³B. D. Cullity, *Introduction to Magnetic Material* (Addison-Wesley, 1972), p. 135.

Measurements of the ferromagnetic/antiferromagnetic interfacial exchange energy in Co/CoO and Fe/FeF₂ layers (invited)

E. Dan Dahlberg,^{a)} Brad Miller, and Bradford Hill

Physics Department and Magnetic Microscopy Center, University of Minnesota, Minneapolis, Minnesota 55455

B. J. Jonsson, Valter Strom, and K. V. Rao

Department of Condensed Matter Physics, Royal Institute of Stockholm, Stockholm, Sweden

Josep Nogues and Ivan K. Schuller

Department of Physics, University of California, San Diego, La Jolla, California

Two measurement techniques, both relying on reversible rotations of the magnetization, have been used to determine the magnitude of the interfacial exchange energy (IEE) between ferromagnetic and antiferromagnetic (F/AF) layers. One technique is to use the anisotropic magnetoresistance to determine rotations of the magnetization away from the unidirectional easy axis, where the rotation is accomplished by applying external magnetic fields less than the effective F/AF exchange field. The second technique uses measurements of the ac susceptibility as a function of the angle between the ac field and the unidirectional exchange field. Both of the reversible process techniques result in values of the IEE larger (by as much as a factor of 10 in Co/CoO bilayers) than the traditional irreversible technique of measuring a shift in the hysteresis loop. The ac susceptibility technique was also used to measure one Fe/FeF₂ bilayer. For this sample, the IEE values obtained by reversible and irreversible methods are equivalent. © 1998 American Institute of Physics. [S0021-8979(98)53611-0]

Meikeljohn and Bean^{1,2} discovered an interfacial exchange energy between ferromagnets and antiferromagnets which could generate a unidirectional easy axis for the ferromagnet. This unidirectional anisotropy is generated by field cooling the system from above the Néel temperature to below. Although this discovery occurred almost 40 years ago, we have not yet developed a fundamental understanding of this phenomena. Briefly, the first model to attempt to describe the observed behavior assumed that the ferromagnet was uniformly coupled to one sublattice of the antiferromagnet. However simple calculations with this model gave interfacial exchange energies (IEE) approximately a factor of 100 times larger than the values reported by experiments. Due to this discrepancy alternate models of the IEE were developed, however, none of these appear to completely explain the observed data.³ Our lack of understanding of the IEE may arise, not from a lack of theoretical understanding but instead from an inherent error in the experimental determination of the IEE.

Historically the experimental determinations of the IEE phenomenon have been almost exclusively from measurements of the shift or offset in the hysteresis loops of direct exchange coupled ferromagnet/antiferromagnet systems. This measurement technique is intrinsically irreversible, and is actually a measure of the nucleation and propagation of domain walls during the reversal process. As such its relation to the exchange bias energy is not necessarily simple. An-

other difficulty with this technique is the common observation that cycling through multiple hysteresis loops results in decreasing values of the shift in the loops.

We have recently used two different experimental techniques which involve only reversible rotations of the magnetization to determine the interfacial exchange energy in Co/CoO bilayers.^{4,5} These measurements produce values of the energy which are consistently larger than those determined by hysteresis loop measures on the same films. Although these reversible measures are larger than the irreversible measures, they are still less than the original predictions based on a direct coupling between the ferromagnet surface and a single sublattice of the antiferromagnet.

In what follows, we will briefly summarize both the techniques and results from the above mentioned two works. In both, the samples consisted of sputtered Co films (thicknesses from 2 to 30 nm) with a native oxide coating formed upon removal from the sputtering system (thus forming bilayers of Co/CoO). As the CoO has a Néel temperature slightly below room temperature, the exchange bias direction was easily controlled by field cooling the bilayers from room temperature to low temperature. In addition to the Co/CoO work, we will mention one study of another system, Fe exchange coupled to epitaxially grown antiferromagnetic FeF₂. At the end are a series of conclusions which can be drawn from this work.

Our first reversible measurement of the IEE relied on the anisotropic magnetoresistance (AMR) to determine the direction of the magnetization in thin films.⁴ In this work, the resistance of Co/CoO bilayers were measured as a function of the angle between an in-plane applied magnetic field and the exchange bias direction. The applied magnetic fields

^{a)}Electronic mail: dand@physics.spa.umn.edu

were as large as 40% of the effective field of the IEE. Using the relationship for the resistance of a ferromagnet with an angle between the current and the magnetization,⁶ we were able to fit the resistance of the films as a function of the applied field direction with one adjustable parameter, the average exchange biasing energy. As shown in this work, the applied magnetic field could be rotated through a full 2π twice obtaining the same angle dependent resistance data indicating the reversible nature of the measurement technique.

In order to prove a difference between the reversible and irreversible measurements, the maximum possible value for the hysteresis loop measured exchange anisotropy was used, the value of the magnetic field when the magnetization reversed. Thus, this determination included half the width of the hysteresis loop in the shift, i.e., the reported values for the hysteresis loop determination of the exchange bias were the exchange bias field plus the coercivity (this was not clearly stated in this work). This is certainly an overestimate of the exchange bias but even so, it was still smaller than that determined by the reversible AMR technique. In general, when correcting for the coercivity, the AMR determined IEE was about a factor of 4 times larger than the hysteresis loop measurement for films on the order of 4 nm thick.

Another interesting feature found in this work was that the magnetization rotation through the ferromagnetic film was not uniform in the AMR or reversible measurements. Although this was not observed in the hysteresis measurement, it is rather obvious it should be present as shown in the following. The exchange pinning of the ferromagnet occurs at the interface between the Co and the CoO. In a thick Co film, say on the order of 10 nm or more, the spins at the free surface, opposite the interface, are only weakly pinned (the bias must propagate through the film via the direct exchange of the Co from one layer to the next). In this case if a magnetic field is applied at a large angle to the biasing direction, the spins on the free surface rotate towards the field more than those at the pinning interface. Thus, in progressing through the film thickness, the rotation varies from a maximum amount (on the free surface) to a minimum (at the pinning interface). This situation is not dissimilar to having a domain wall or a partial wall form through the thickness of the film.

The second reversible technique we used to measure the IEE was the ac susceptibility. In this case the ac susceptibility was measured as a function of the angle between the exchange bias direction and the ac magnetic field with ac magnetic fields as small as 0.1% of the effective exchange bias field. A simple understanding of how this was used to determine the IEE is to consider the analogy with the susceptibility of an antiferromagnet.⁷ The measured susceptibility of an antiferromagnet depends upon the orientation of the magnetic field to the spins in the sublattices, with the collinear susceptibility smaller than the perpendicular susceptibility. The difference between these susceptibilities is related to the exchange energy between the two sublattices.

The ac susceptibility measurements were performed as a function of temperature revealing a linear temperature dependence of the exchange biasing magnitude (the AMR study was performed only at 4 K). The results from this

second study were in agreement with the AMR study, in that this reversible measurement of the IEE was larger than that determined by the irreversible hysteresis loop technique. However, it found energies larger by as much as a factor of 10 than the hysteresis loop measurements (recall a factor of 4 was observed in the AMR studies). It is important to note that the two reversible studies were made on different sets of samples so it is not clear if this difference in the factor is due to the smaller field used in the ac susceptibility study or sample differences.

An interesting feature of note in the susceptibility study came from two Co samples of the same thickness. One was partially capped with Ag prior to oxidation to prevent the formation of the CoO over some fraction of the surface while the other did not have the oxide inhibiting Ag coating. Surprisingly, the hysteresis loop measurement of the sample with the partial Ag overcoat indicated an IEE larger than the sample with the full oxide. This was contradicted by the ac susceptibility measurements on the same two samples which indicated a reduction in the IEE for the sample with the smaller ferromagnetic antiferromagnetic interface area as one would expect. Although this comparison was between only these two samples, it does suggest that there may be difficulties in trying to determine even the systematics of the interfacial exchange energy by hysteresis loop measurements.

Another system we have recently investigated by the ac susceptibility method is Fe deposited on epitaxially grown FeF_2 .⁸ This system is rather unique for two reasons; it does not exhibit a decay or alteration of the ferromagnetic antiferromagnetic IEE upon repeated hysteresis loop cycles at low temperatures and the determination of the exchange energy from the loop shifts agree with that determined by the reversible techniques. That the loops are preserved upon repeated cycles is probably the result of two things. The crystalline anisotropy energy of the FeF_2 is high and the epitaxial growth with twinning results in the FeF_2 film being large single crystals. Thus the FeF_2 sublattice orientations are well fixed and the applied magnetic field and the exchange from the iron film is insufficient to reorient the sublattice orientations. This might be sufficient to assume the two techniques would give the same value for the IEE, however this means that either the energy and dynamics for domain wall formation (which is localized to the wall width) is identical to the uniform rotation of the magnetization at the interface, or the hysteresis loop reversal mechanism is not by wall formation but instead of coherent rotation.

In ending, a number of conclusions and questions can be drawn from these studies.

First, in general, reversible measurements of the interfacial exchange coupling energy are more accurate than measures relying on irreversible processes. A cautionary note however arises upon considering the anisotropy energy of the antiferromagnet. If the crystalline anisotropy or the crystallite size of the antiferromagnet is small compared to exchange bias energy, then pinning of the ferromagnet is not only by the interfacial exchange coupling but instead will be a mixture of the exchange energy and the anisotropy energy.

Thus in this case, even reversible measurements do not provide an accurate determination of the interfacial exchange energy.

Next, there is the question of what the hysteresis loop measures. The irreversible techniques are almost certainly measurements of some combination of domain wall nucleation energies in the ferromagnetic film where the lowest interfacial energy occurs and domain wall pinning. For this reason, even systematic studies of the IEE where grain size or some other parameter is varied is suspect unless their effect on the wall nucleation and pinning are well known.

It is interesting that the Fe/FeF₂ system reveals equivalent results for the IEE using both reversible and irreversible measures. This preliminary result is interesting for the following reasons. The robust nature of the loop shift upon repeated magnetic reversals may be an indicator when the hysteresis loop technique is accurate for determining the IEE. However, when the details are considered, it is surprising that the energetics of wall formation and propagation are the same as the as small rotations of the magnetization. However, as stated, only one sample was investigated and certainly more must be studied before any conclusions are drawn.

Finally there are the apparent differences in the measured values of the energy for the AMR (factor of 4 times

larger than the hysteresis determined value) and ac susceptibility (as much as a factor of 10 times larger) techniques. One possibility is this may be due to the differences in the field of measurement as the minimum ac susceptibility magnetic field is approximately 0.01 that of the AMR technique. However, it is important to note that these measurements were not performed on the same set of samples. This clearly warrants a study of the exchange bias energies determined by the ac susceptibility, AMR, and hysteresis loop techniques on the same samples.

Research was supported by ONR Grant No. N/N00014-95-1-0799 and DOE.

¹W. H. Meiklejohn and C. P. Bean, *Phys. Rev.* **102**, 1413 (1956).

²W. H. Meiklejohn and C. P. Bean, *Phys. Rev.* **105**, 904 (1957).

³A. P. Malozemoff, *J. Appl. Phys.* **63**, 3874 (1988).

⁴B. H. Miller and E. D. Dahlberg, *Appl. Phys. Lett.* **69**, 3932 (1996).

⁵V. Strom, B. J. Jonsson, K. V. Rao, and D. Dahlberg, *J. Appl. Phys.* **81**, 5003 (1997).

⁶T. R. McGuire and R. I. Potter, *IEEE Trans. Magn.* **MAG-11**, 1018 (1975).

⁷C. Kittel, *Introduction to Solid State Physics*, 7th ed. (Wiley, New York, 1996).

⁸J. Nogues, D. Lederman, T. J. Moran, I. K. Schuller, and K. V. Rao, *Appl. Phys. Lett.* **68**, 3186 (1996); J. Nogues, D. Lederman, T. J. Moran, and I. K. Schuller, *Phys. Rev. Lett.* **76**, 4624 (1996).

Rare Earth Nitride and Carbide Hard Magnets

L. H. Lewis, Chairman

Immobilization diffusion in R_2Fe_{17} nitrides

R. Skomski and S. Wirth^{a)}

Max-Planck-Institut für Mikrostrukturphysik, Weinberg 2, 06120 Halle, Germany

The diffusion of nitrogen in R_2Fe_{17} intermetallics is investigated by an approach which reconciles the solid-solution and immobilization theories of nitrogen diffusion. It turns out that two-sublattice diffusions may yield sharp concentration profiles but leave the phase structure of the nitride unchanged. Beside the reaction time and a local relaxation time there exists a global relaxation time which governs the smoothing of concentration gradients. Due to the large number of unknown energy parameters involved it is difficult to make quantitative predictions, but in general the diffusion behavior depends on factors such as the use of N_2 or NH_3 as a nitrogen source. © 1998 American Institute of Physics. [S0021-8979(98)42411-3]

I. INTRODUCTION

Since the discovery of interstitial permanent magnets such as $Sm_2Fe_{17}N_3$,¹ the diffusion of nitrogen and carbon in R_2Fe_{17} intermetallics has attracted much attention.²⁻¹² The knowledge of the diffusion mechanism is necessary to predict the extrinsic properties of the interstitial magnets. A particular problem is that soft regions associated with incomplete nitrogenation destroy coercivity by acting as nucleation centers, so that the nitrogen concentration in the material has to be homogeneous.^{2,3}

In recent years, there has been considerable controversy about the phase structure of interstitial nitrides. According to the solid-solution theory, the reaction of molecular nitrogen with Sm_2Fe_{17} yields homogeneous solid solutions $Sm_2Fe_{17}N_x$ with intermediate nitrogen contents.^{2,3,5,8,10,13} By contrast, the two-phase theory states that the nitrides $R_2Fe_{17}N_x$ are a mixture of nitrated ($x \approx 3$) and unnitrated ($x \approx 0$) phases without intermediate nitrogen contents.^{6,11,12} Figure 1 illustrates the difference between solid solutions and compounds.

It is important to note that phase segregation is caused by *attractive interactions* between interstitial atoms, whereas the on-site interaction between the interstitial atoms and the host lattice changes leaves the phase structure unchanged.^{8,10,14} In fact, phase transitions of gases in metals are caused by long-range elastic interactions, which yield a critical temperature T_0 below which phase segregation occurs. By contrast, electronic interactions in metals are short ranged and largely repulsive.^{8,10,14}

The nitrogen atoms diffuse inwards from the surface of the R_2Fe_{17} particles, which has given rise to the qualitative concept of core-shell diffusion.¹⁵ A key question is whether the nitrogen concentration profiles $0 \leq c(r,t) \leq 1$ of partly

nitrated particles are smooth or steplike (Fig. 2). The one-sublattice diffusion equation $\partial c / \partial t = D \nabla^2 c$, where $D = D_0 \times \exp(-E_a/k_B T)$, yields smooth nitrogen profiles.^{2,8,10} Based on this model, an activation energy $E_a = 133$ kJ/mole was obtained from thermopiezic measurements on Sm_2Fe_{17} in N_2 . Both this activation energy and the diffusion parameter $D_0 = 1.02$ mm²/s are typical for $2p$ atoms in transition metals.^{2,3,8,10} Note that experimental diffusion constants vary between from 59 to 163 kJ/mole.^{4,7,8,16}

In the two-phase regime the diffusion constant depends on c and T . The mean-field result $D = D_0 \exp(-E_a/k_B T) \times [1 - 4c(1-c)T_0/T]$ shows that there exist negative diffusion constants below T_0 , which describe the creation of sharp phase boundaries.¹⁰ Note the width of the “sharp” transition regions is as large as about $1 \mu m$,¹² which can hardly be interpreted as critical fluctuations in the vicinity of the unknown critical temperature T_0 .

Most of the evidence available for $Sm_2Fe_{17}N_x$ produced from N_2 gas favors a gas-solid solution at typical nitrogenation temperatures of about $500^\circ C$. In particular, intermediate lattice parameters have been observed by x-ray diffraction analysis,³ samples with intermediate nitrogen contents ex-

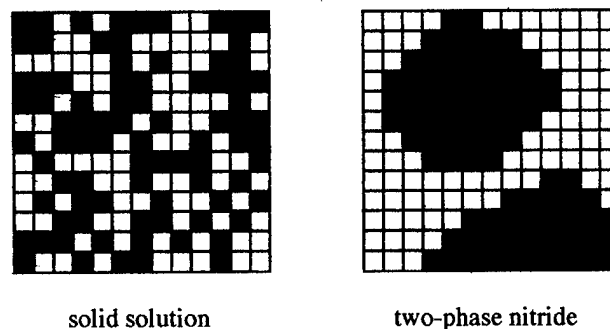


FIG. 1. Interstitial modification of a square lattice of interstitial sites. Black and white squares denote filled and empty interstitial sites, respectively.

^{a)}Also at: MARTECH, Florida State University, Keen Bldg. 318, Tallahassee, Florida 32306.

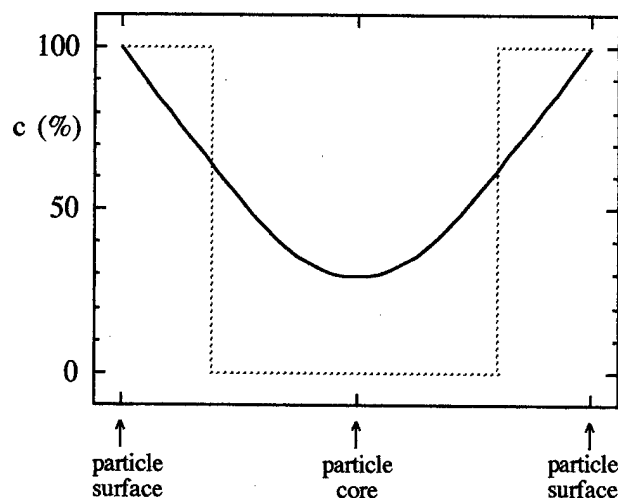


FIG. 2. Nitrogen concentration profiles for spherical particles: (solid line) ideal one-sublattice diffusion and (dotted line) sharp interface.

hibit intermediate Curie temperatures,⁵ homogenization of partly nitrated grains yields intermediate nitrogen concentrations,¹³ electron micrographs show smoothly varying nitrogen concentrations,⁹ and domain-size observations¹⁷ can be explained by intermediate anisotropy constants only.

However, in practice it is difficult to distinguish solid solutions from two-phase nitrides,^{10,18} and the solid-solution character of $R_2Fe_{17}N_x$ has been questioned by several authors.^{6,11,12} Zhang *et al.* have argued that nitrogen diffusion in R_2Fe_{17} compounds is realized by more than two sublattices of interstitial sites.^{11,12} Starting from the known crystal structure, they postulated the existence of trapping (t) and free (f) sites. It is assumed that the f -sites act as an easy diffusion pathway for the nitrogen atoms, which immobilize on the t sites. In the limit of ideal immobilization, where the on-site energy U_t goes to minus infinity, the immobilization mechanism yields sharp diffusion boundaries.¹⁹ However, this limit amounts to an infinite heat of reaction, whereas experimental reaction energies U_t are merely of order -57 kJ/mole.²

In this theoretical study, we investigate the possibility of immobilization diffusion and relate the diffusion behavior to the site and saddle-point energies of the nitrogen atoms. In particular, we answer the question whether immobilization diffusion leads to phase segregation.

II. IMMOBILIZATION DIFFUSION

As a rule, R_2Fe_{17} intermetallics containing light rare earths crystallize in the rhombohedral Th_2Zn_{17} structure, whereas heavy rare earths tend to form the hexagonal Th_2Ni_{17} structure. The two structures derive from the $CaCu_5$ structure but differ by the stacking of the $CaCu_5$ -type layers. In the rhombohedral structure, the majority of the nitrogen atoms occupies the large octahedral $9e$ sites (t sites), whereas the equilibrium occupancy of the $18g$ or $3b$ sites (f sites) is small.^{1,2,10,20} Since there are three t sites per formula unit, the nominal composition of the nitrides is often written as $R_2Fe_{17}N_3$.

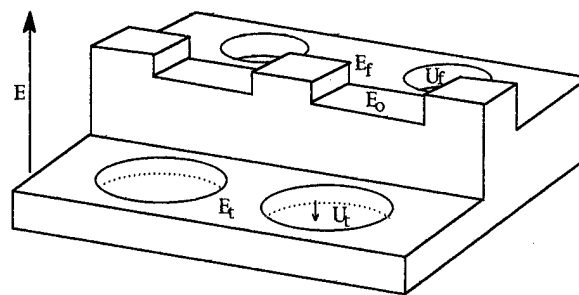


FIG. 3. Schematic energy landscape of the two-sublattice diffusion model. Note that E_0 is not necessarily larger than E_f and E_t .

In the limit of strong immobilization, the nitrogen uptake is determined by the differential equation $dL/dt \approx D_f \langle c_f \rangle / \langle c_t \rangle L$, where L is the thickness of the fully nitrated shell and D_f is the diffusion constant of the f -type nitrogen atoms. The averages $\langle c_t \rangle \approx 1$ and $\langle c_f \rangle \ll 1$ are the equilibrium nitrogen concentrations on the respective sites. The solution of this equation, $L = \sqrt{2D_f \langle c_f \rangle t / c_0}$, is reminiscent of the diffusion length $L_0 = \sqrt{Dt}$ and yields the reaction time $t_R \approx R^2 / D \langle c_f \rangle$.

In reality, U_t is finite and we have to start from the two-sublattice diffusion equation

$$\frac{\partial c_t}{\partial t} = D_t \nabla^2 c_t - W_{ft} c_t + W_{tf} c_f, \quad (1a)$$

$$\frac{\partial c_f}{\partial t} = D_f \nabla^2 c_f - W_{tf} c_f + W_{ft} c_t, \quad (1b)$$

where the intrasublattice diffusion constants D_i ($i=f, t$) are

$$D_i = D_0 \exp\left(\frac{U_i}{k_B T} - \frac{E_i}{k_B T}\right). \quad (2)$$

The intersublattice transition rates $W_{ft} = W(t \rightarrow f)$ and $W_{tf} = W(f \rightarrow t)$ are given by

$$W_{ft} = \Gamma_0 \exp\left(\frac{U_t}{k_B T} - \frac{E_0}{k_B T}\right), \quad (3a)$$

$$W_{tf} = \Gamma_0 \exp\left(\frac{U_f}{k_B T} - \frac{E_0}{k_B T}\right). \quad (3b)$$

In Eqs. (1) and (2), U_f and U_t are the nitrogen on-site energies, E_f and E_t are intrasublattice saddle-point energies, and E_0 is the energy of the intersublattice saddle point connecting neighboring f and t sites (Fig. 3). In a fair approximation, $\Gamma_0 = D_0 / a_{\text{eff}}$, where $a_{\text{eff}} \approx 3 \text{ \AA}$ is an effective jumping distance.

Since Eq. (1) is difficult to solve, we use the approximate ansatz

$$c_i(x, t) = c_{i0} \exp(-t/\tau) \cos(2\pi x/L), \quad (4)$$

which transforms Eq. (1) into a quadratic secular equation. The diagonalization of the matrix yields two relaxation modes (Fig. 4). The local relaxation time t_L ,

$$t_L = \frac{a_{\text{eff}}^2}{D_0} \exp\left(\frac{E_0 - U_f}{k_B T}\right), \quad (5)$$

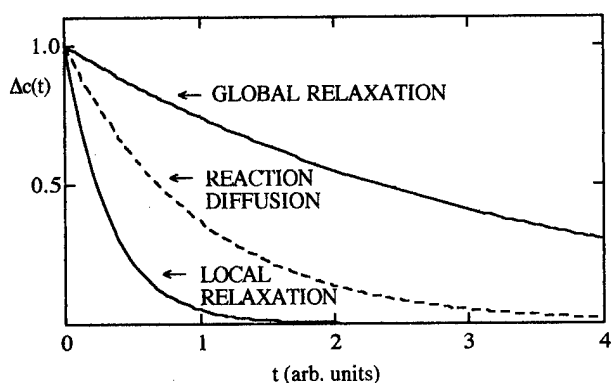


FIG. 4. Splitting of relaxation modes due to immobilization diffusion (schematic). Δc is the deviation from equilibrium.

describes transitions from the f sublattice to the t sublattice and is comparatively small. Note that the local character of t_L is seen from the absence of the "particle size" L in Eq. (5).

The global relaxation time

$$t_G = \frac{L^2}{4\pi^2} \frac{\exp(-U_i/k_B T)}{\exp(-E_i/k_B T) + \exp(-E_f/k_B T)} \quad (6)$$

describes the approach towards macroscopic equilibrium and equals the time necessary to homogenize an originally step-like concentration profile. For one-sublattice solid-solution diffusion $t_G \approx t_R$, whereas immobilization diffusion is characterized by $t_G > t_R$. Since the homogenization leads to smooth nitrogen concentration profiles, the existence of sharp boundaries during immobilization diffusion does not establish a separate nitride phase. By comparison, interatomic interaction yields sharp equilibrium phase boundaries below T_0 .^{2,3,8,10,14}

III. DISCUSSION AND CONCLUSIONS

Since Eq. (1) involves five energy values, it is not possible to predict the diffusion behavior from the known $\text{Sm}_2\text{Fe}_{17}\text{N}_x$ values U_i and $E_a = E_i - U_i$. Magnetic after effect measurements¹⁶ yield a third experimental value, $Q = E_0 - E_f/2 - E_i/2 = 62$ kJ/mole for $\text{Nd}_2\text{Fe}_{17}\text{N}_x$.

A possible explanation for the steplike profiles observed for $\text{Sm}_2\text{Fe}_{17}$ heated in ammonia is that the high effective nitrogen pressure associated with the presence of NH_3 enhances the concentration $\langle c_f \rangle$ and therefore reduces t_R .^{8,9,21} Note, however, that NMR experiments on $\text{Sm}_2\text{Fe}_{17}$ nitrided in ammonia show a large number of defects,^{8,22} which complicates the interpretation of the experimental results.

In general, we expect some dependence of the energy parameters on the rare earth's atomic number. A particularly difficult situation is found in intermetallics which may occur

in either of the 2:17 structures, such as Y_2Fe_{17} . Variable²³ nitrogen environments observed by NMR indicate a considerable volume fraction of intermediate material, which is contradictory to the absence of intermediate nitrogen concentrations in $\text{Y}_2\text{Fe}_{17}\text{N}_x$. This does not exclude, however, that $\text{Y}_2\text{Fe}_{17}\text{N}_x$ is more difficult to homogenize than $\text{Sm}_2\text{Fe}_{17}\text{N}_x$.

In conclusion, we have shown that intersublattice diffusion involving nonequivalent sites leads to local and global relaxation modes. In general, both relaxation times differ from the reaction time. Depending on the site and saddle-point energies involved, smooth or steplike nitrogen concentration profiles are obtained, but the phase structure of the nitride is not affected by immobilization.

¹J. M. D. Coey and H. Sun, J. Magn. Magn. Mater. **87**, L251 (1990).

²R. Skomski and J. M. D. Coey, J. Appl. Phys. **73**, 7602 (1993).

³J. M. D. Coey, R. Skomski, and S. Wirth, IEEE Trans. Magn. **28**, 2332 (1992).

⁴J. M. D. Coey, J. F. Lawler, H. Sun, and J. E. M. Allan, J. Appl. Phys. **69**, 3007 (1991).

⁵M. Katter, J. Wecker, C. Kuhrt, L. Schultz, and R. Grössinger, J. Magn. Magn. Mater. **117**, 419 (1992).

⁶C. C. Colucci, S. Gama, and F. A. O. Cabral, IEEE Trans. Magn. **28**, 2578 (1992).

⁷C. N. Christodoulou and N. Komada, J. Alloys Compd. **206**, 1 (1994).

⁸R. Skomski, S. Brennan, and S. Wirth, in *Interstitial Intermetallic Alloys*, edited by F. Grandjean, G. J. Long, and K. H. J. Buschow (Kluwer, Dordrecht, 1995), p. 371.

⁹R. Skomski, K. Kobayashi, S. Brennan, and J. M. D. Coey, J. Magn. Magn. Mater. **140-144**, 1079 (1995).

¹⁰R. Skomski, in *Rare-Earth-Iron Permanent Magnets*, edited by J. M. D. Coey (University Press, Oxford, 1996), p. 178.

¹¹Y. D. Zhang, J. I. Budnick, and W. A. Hines, Appl. Phys. Lett. **67**, 208 (1995).

¹²Y. D. Zhang, J. I. Budnick, W. A. Hines, and D. P. Yang, J. Appl. Phys. **79**, 4596 (1996).

¹³T. Mukai and T. Fujimoto, J. Magn. Magn. Mater. **103**, 165 (1992).

¹⁴H. Wagner and H. Horner, Adv. Phys. **23**, 587 (1974).

¹⁵J. M. D. Coey and D. P. F. Hurley, J. Magn. Magn. Mater. **104-107**, 1098 (1992).

¹⁶M. L. Sartorelli, H. Kronmüller, and B. P. Hu, Proceedings of the 9th International Symposium on Magnetism Anisotropy and Coercivity in RE-TM Alloys, São Paulo 1996 (unpublished), p. 107.

¹⁷K.-H. Müller, P. A. P. Wendhausen, D. Eckert, and A. Handstein, Proceedings of the 7th International Symposium on Magnetism Anisotropy and Coercivity in RE-TM Alloys, Canberra 1992 (unpublished), p. 34.

¹⁸For example, both sharp and smooth concentration profiles yield double-peak x-ray diffraction patterns for intermediate concentrations (Fig. 6 in Ref. 2).

¹⁹J. Crank, *The Mathematics of Diffusion* (University Press, Oxford, 1975).

²⁰O. Isnard, S. Miraglia, J. L. Soubeyrou, J. Pannetier, and D. Fruchart, Phys. Rev. B **45**, 2920 (1992).

²¹R. Skomski, S. Brennan, and J. M. D. Coey, Phys. Status Solidi A **139**, K11 (1993).

²²Cz. Kapusta, P. C. Riedi, G. J. Tomka, W. Kocemba, S. Brennan, and J. M. D. Coey, Proceedings of the 9th International Symposium on Magnetism Anisotropy and Coercivity in RE-TM Alloys, São Paulo 1996 (unpublished), p. 217.

²³Cz. Kapusta and P. C. Riedi, in *Interstitial Intermetallic Alloys*, edited by F. Grandjean, G. J. Long, and K. H. J. Buschow (Kluwer, Dordrecht, 1995), p. 497.

Magnetic anisotropy of $R_2Fe_{17}N_x$ compounds

X. C. Kou^{a)} and F. R. de Boer

Van der Waals-Zeeman Institute, University of Amsterdam, 1108 XE, Amsterdam, The Netherlands

G. Chouteau

Grenoble High Field Magnet Laboratory, 38042 Grenoble, France

A nearly perfect magnetic alignment of $R_2Fe_{17}N_x$ powders ($<20\text{ }\mu\text{m}$) with respect to the c axis was obtained by using the sample-rotation magnetic-alignment technique. The magnetization from 4.2 to 300 K was measured on the magnetically aligned samples by means of the sample-extraction method in a static field up to 23 T. The Fe-sublattice anisotropy was determined by analyzing the magnetization curves of $R_2Fe_{17}N_x$ with $R=Y, Ce, Gd$, and Lu . Compared to corresponding R_2Fe_{17} compounds, the Fe-sublattice anisotropy of $R_2Fe_{17}N_x$ is substantially lower. For $R_2Fe_{17}N_x$ with $R=Pr, Nd, Sm, Tb$, and Er , the magnetization curves in the $[001]$ direction show no anomaly whereas a first-order magnetization process (FOMP) was detected in corresponding R_2Fe_{17} compounds, suggesting that the FOMP transition in R_2Fe_{17} is suppressed upon nitrogeation.

© 1998 American Institute of Physics. [S0021-8979(98)15911-X]

I. INTRODUCTION AND MOTIVATION

The easy magnetization direction (EMD) of $R_2Fe_{17}N_x$ for all rare earths (R) except that for $R=Sm$ is within the basal plane. A detailed study of the magnetic anisotropy of these compounds is still lacking. This is because, on one hand, single crystals of $R_2Fe_{17}N_x$ are not possible to be grown by the conventional method since the compounds decompose above about 800 K. On the other hand, the powdered particles of $R_2Fe_{17}N_x$ compounds exhibit basal-plane anisotropy and can therefore not be well aligned magnetically by using the static-field-alignment technique. In the present investigation, a sample-rotation magnetic-alignment technique was used to align fine single-crystalline powder of $R_2Fe_{17}N_x$ compounds in an optimal way so that the magnetic anisotropy of the whole series of compounds can be systematically studied. This method has been applied by Wang *et al.*¹ to $Y_2Co_{14}B$ and Er_2Co_{17} , by Kou *et al.* to $Er_2Fe_{14}B^2$ and to the whole R_2Fe_{17} series,^{3,4} by Téllez-Blanco *et al.*⁵ to $Y_3(Fe,Ti)_{29}$, and by Zhang *et al.*⁶ to Sm_2Fe_{17} .

II. EXPERIMENTAL DETAILS

Polycrystalline ingots of R_2Fe_{17} compounds with $R=Y, Ce, Pr, Nd, Sm, Gd, Tb, Dy, Ho, Er, Tm$, and Lu were prepared by induction melting appropriate amounts of the constituent metals having a purity better than 99.99 wt %. X-ray diffraction was used to check the phase purity and to determine the lattice constants of the annealed samples, and also to determine the degree of magnetic alignment of the aligned samples. The $R_2Fe_{17}N_x$ compounds were obtained by flowing purified nitrogen gas N_2 over finely powdered R_2Fe_{17} ($<20\text{ }\mu\text{m}$) in a quartz tube at 773 K for 10 h. The particle size of R_2Fe_{17} is not expected to change during the nitrogeation process. It is therefore reasonable to assume that the $R_2Fe_{17}N_x$ powder particles have the same size distribution as the R_2Fe_{17} powder. The $R_2Fe_{17}N_x$ particles were

mixed with epoxy resin and embedded into a teflon tube of cylindrical shape. The teflon tube was connected with a motor that enables the tube to be spun in a static field of about 1 T with the cylinder axis perpendicular to the field direction until the epoxy resin has solidified. This process ensures that the basal planes, perpendicular to the c axis, are aligned parallel to each other and that the c axis will be parallel to the cylinder axis. The details including a schematic illustration of the sample-rotation magnetic-alignment method can be found in Ref. 3. X-ray diffraction performed on magnetically aligned samples with the sample surface parallel and perpendicular to the cylinder axis (i.e., to the c axis), indicates perfect magnetic alignment with respect to the c axis.

The magnetization parallel to the c axis, the magnetic hard direction for all $R_2Fe_{17}N_x$ compounds except for $R=Sm$, was measured from 5 to 300 K by means of the sample-extraction method in the 23 T resistive magnet at the Grenoble High Magnetic Field Laboratory. For calibration, the magnetization of the $R_2Fe_{17}N_x$ compounds was determined in a superconducting quantum interference device

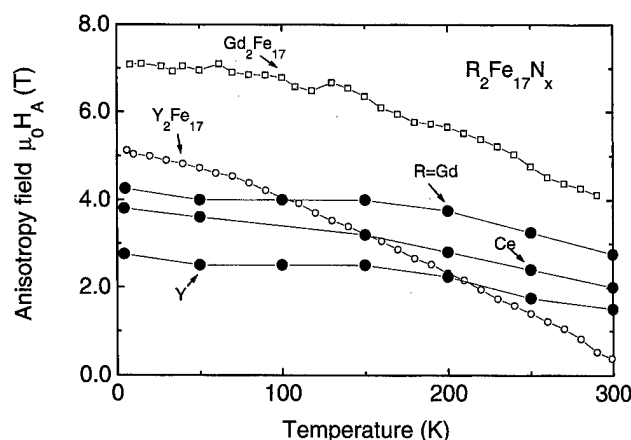


FIG. 1. Temperature dependence of the anisotropy field of $R_2Fe_{17}N_x$ compounds with $R=Y, Ce$, and Gd . The data for Y_2Fe_{17} and Gd_2Fe_{17} , taken from Ref. 3, are presented for comparison.

^{a)}Author to whom correspondence should be addressed; electronic mail: kou@phys.uva.nl

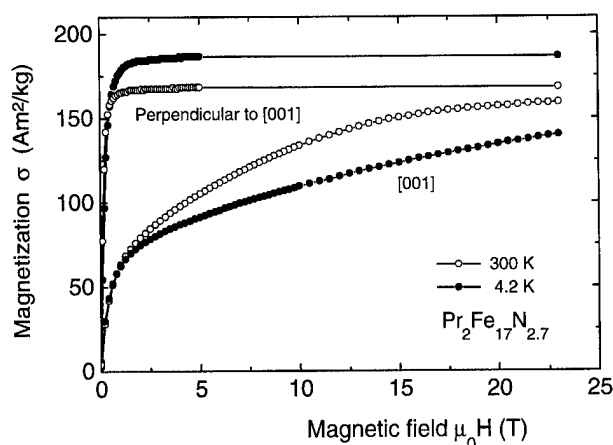


FIG. 2. The magnetization measured on magnetically aligned $\text{Pr}_2\text{Fe}_{17}\text{N}_{2.7}$ with the field applied in the [001] direction, the magnetic hard direction. The magnetization data in the easy direction has been obtained in a SQUID magnetometer in fields up to 5 T on fine powder consisting of small single crystals ($<20\ \mu\text{m}$) which were loosely loaded in the sample holder. The data at 23 T was taken as the same as at 5 T with the purpose to demonstrate the magnetic anisotropy.

(SQUID) magnetometer in field strengths up to 5 T on finely powdered single crystallites ($<20\ \mu\text{m}$) which were loaded loosely in the sample holder so that they could be oriented by the applied field. During the measurements, the EMD of the single crystallites is always parallel to the field direction which ensures that the saturation magnetization is measured.

III. RESULTS AND DISCUSSION

X-ray diffraction shows that the $\text{R}_2\text{Fe}_{17}\text{N}_x$ compounds with $\text{R}=\text{Ce}$, Pr , Nd , and Sm have a rhombohedral structure, with $\text{R}=\text{Y}$, Ho , Er , Tm , and Lu a hexagonal structure and with $\text{R}=\text{Gd}$, Tb , Dy these two structures are coexisting. This is similar to their R_2Fe_{17} parent compounds. The Fe-sublattice anisotropy in $\text{R}_2\text{Fe}_{17}\text{N}_x$ compounds can be estimated from a study of compounds in which the R-sublattice

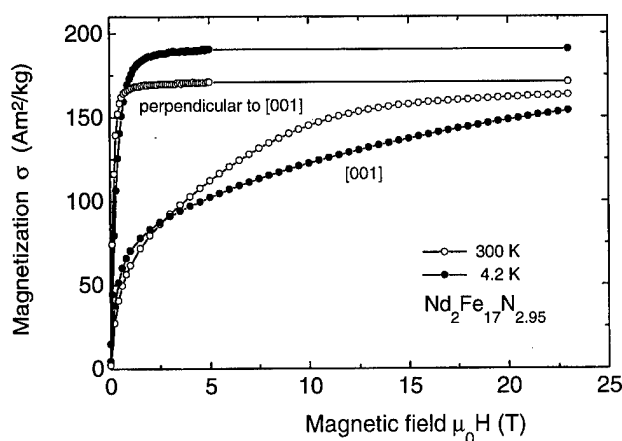


FIG. 3. The magnetization measured on magnetically aligned $\text{Nd}_2\text{Fe}_{17}\text{N}_{2.95}$ with the field in the [001] direction, the magnetic hard direction. The magnetization data in the easy direction has been obtained in a SQUID magnetometer in fields up to 5 T on fine powder consisting of small single crystals ($<20\ \mu\text{m}$) which were loaded loosely in the sample holder. The data at 23 T was taken as the same as at 5 T with the purpose to demonstrate the magnetic anisotropy.

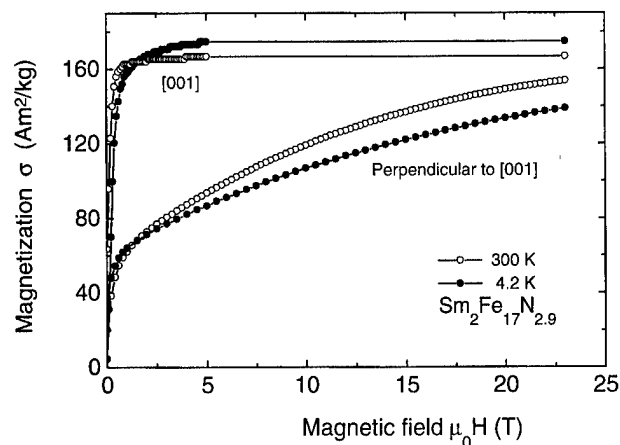


FIG. 4. The magnetization measured on magnetically aligned $\text{Sm}_2\text{Fe}_{17}\text{N}_{2.9}$ with the measuring field applied perpendicular to the [001] direction. The magnetization data in the [001] direction has been obtained in a SQUID magnetometer in fields up to 5 T on fine powder consisting of small single crystals ($<20\ \mu\text{m}$) which were loaded loosely in the sample holder. The data at 23 T was taken as the same as at 5 T with the purpose to demonstrate the magnetic anisotropy.

anisotropy is absent. This is the case for $\text{R}=\text{Y}$, Gd , and Lu . Y and Lu are nonmagnetic, and Gd is an S-state R element which in principle does not contribute to the anisotropy in $\text{Gd}_2\text{Fe}_{17}\text{N}_x$. Due to the tetra-valent state Ce , the Fe-sublattice anisotropy can be also evaluated by studying $\text{Ce}_2\text{Fe}_{17}\text{N}_x$. Figure 1 shows the temperature dependence of the anisotropy field H_A of $\text{R}_2\text{Fe}_{17}\text{N}_x$ compounds with $\text{R}=\text{Y}$, Gd , and Ce , obtained by analyzing the magnetization curves. The values of H_A were determined to be the field where a singularity appears in the curve of d^2M/dH^2 versus H . This is basically the idea of the singular-point-detection (SPD) method which has been widely used to determine the anisotropy field directly on polycrystalline magnetic materials.⁷ The values of H_A of Y_2Fe_{17} and $\text{Gd}_2\text{Fe}_{17}$ obtained from a previous study³ are presented for comparison. It is evident that at low temperature the anisotropy field of $\text{Y}_2\text{Fe}_{17}\text{N}_x$ and $\text{Gd}_2\text{Fe}_{17}\text{N}_x$ is much lower than that of Y_2Fe_{17} and $\text{Gd}_2\text{Fe}_{17}$. For the Fe sublattice, the magnetic anisotropy energy E_a equals $0.5 H_A M_s$ where H_A is the anisotropy field and M_s the spontaneous magnetization. The M_s values of R_2Fe_{17} are only slightly changed upon nitrogenation. It can therefore be concluded that at low temperatures the Fe-sublattice anisotropy in $\text{R}_2\text{Fe}_{17}\text{N}_x$ compounds is lower than that in the corresponding R_2Fe_{17} compounds. Compared to the Fe-sublattice anisotropy, the R-sublattice anisotropy is, in most cases, dominating at low temperatures. The Sm-, Er-, and Tm-sublattice anisotropy favor an EMD parallel to the c axis both in R_2Fe_{17} and in $\text{R}_2\text{Fe}_{17}\text{N}_x$ compounds. $\text{Tm}_2\text{Fe}_{17}$ is the only compound in the whole R_2Fe_{17} series which shows a spin-reorientation transition at about 72 K.⁸ This transition is caused by competition between the planar Fe sublattice and the uniaxial Tm sublattice. Partly due to the lowering of the Fe-sublattice anisotropy in $\text{R}_2\text{Fe}_{17}\text{N}_x$ compounds, a spin-reorientation transition at 146 K is also induced in $\text{Er}_2\text{Fe}_{17}\text{N}_{3.0}$.⁹ Very exciting is that the $\text{Sm}_2\text{Fe}_{17}\text{N}_x$ becomes

easy-axis materials over the whole temperature range of magnetic ordering, which makes it a very promising candidate for permanent magnets fabrication.

In a previous study,⁴ a pronounced first-order magnetization process (FOMP) in $\text{Pr}_2\text{Fe}_{17}$ with the field applied in the [001] direction has been reported. The EMD of the $\text{Pr}_2\text{Fe}_{17}$ is not changed upon nitrogenation. Therefore, it is interesting to study whether the FOMP is still present in $\text{Pr}_2\text{Fe}_{17}\text{N}_x$. The magnetization at various temperatures from 4.2 to 300 K of magnetically aligned $\text{Pr}_2\text{Fe}_{17}\text{N}_x$ was measured with the field applied in the [001] direction. In Fig. 2, the measurements at 4.2 and 300 K are shown. No indication of an anomaly is found in the magnetization curve in the [001] direction, suggesting that the FOMP found in $\text{Pr}_2\text{Fe}_{17}$ is suppressed after nitrogenation. The absence of any anomaly in the magnetization curve of $\text{Pr}_2\text{Fe}_{17}\text{N}_x$ has also been reported by Isnard *et al.*¹⁰ The FOMP is a field-induced magnetic phase transition¹¹ which is strongly related to the magnetic anisotropy. In $\text{R}_2\text{Fe}_{17}\text{N}_x$ compounds containing a magnetic R ion, both the R- and the Fe-sublattice contribute to the total magnetic anisotropy. The Fe-sublattice anisotropy does not show any anomaly in the temperature dependence. It can therefore be concluded that, in general, the crystalline electric field acting on the magnetic R^{3+} ions cause the FOMP transitions. Figure 3 shows the magnetization curves measured on magnetically aligned $\text{Nd}_2\text{Fe}_{17}\text{N}_{2.95}$. Similar to what was found in $\text{Pr}_2\text{Fe}_{17}\text{N}_{2.7}$, no FOMP transition is detected for $\text{Nd}_2\text{Fe}_{17}\text{N}_{2.95}$ in [001] direction where a FOMP exists in the corresponding $\text{Nd}_2\text{Fe}_{17}$. The same is true for $\text{Tb}_2\text{Fe}_{17}\text{N}_2$.

As discussed above, $\text{Sm}_2\text{Fe}_{17}$ is the only compound of the whole R_2Fe_{17} series having the EMD changed from basal plane in $\text{Sm}_2\text{Fe}_{17}$ to c axis in $\text{Sm}_2\text{Fe}_{17}\text{N}_x$. The magnetic alignment of fine particles of $\text{Sm}_2\text{Fe}_{17}\text{N}_{7.9}$ was made by us-

ing the conventional static-field-alignment method. In Fig. 4, the magnetization measured on magnetically aligned $\text{Sm}_2\text{Fe}_{17}\text{N}_{2.9}$ is shown. It is evident that the magnetic anisotropy of $\text{Sm}_2\text{Fe}_{17}\text{N}_{2.9}$ is huge. At 300 K, a field strength of 23 T in hard direction is not yet enough to get the magnetization saturated. Liu *et al.*¹² reported that, at 4.2 K, the magnetization in the hard direction is not saturated at a field strength of 38 T.

ACKNOWLEDGMENT

One of the authors (X.C.K.) would like to thank the European Commission for a grant in the TMR Program.

- ¹ Wang Qun, Zhao Zhi-gang, Liu Wei, X. K. Sun, Y. C. Chuang, and F. R. de Boer, J. Magn. Magn. Mater. **109**, 59 (1992).
- ² X. C. Kou, E. C. H. P. Sinnecker, and R. Grössinger, J. Magn. Magn. Mater. **147**, L231 (1995).
- ³ X. C. Kou, E. C. H. P. Sinnecker, and R. Grössinger, J. Phys.: Condens. Matter **8**, 1557 (1996).
- ⁴ X. C. Kou, F. R. de Boer, R. Grössinger, G. Wiesinger, H. Suzuki, H. Kitazawa, T. Takamasu, and G. Kido, J. Magn. Magn. Mater. (in press).
- ⁵ J. C. Téllez-Blanco, X. C. Kou, and R. Grössinger, J. Magn. Magn. Mater. **164**, L1 (1996).
- ⁶ Y. D. Zhang, J. I. Budnick, and W. A. Hines, J. Appl. Phys. **81**, 5647 (1997).
- ⁷ G. Asti, in *Handbook of Ferromagnetic Materials*, edited by K. H. J. Buschow and E. P. Wohlfarth (North-Holland, Amsterdam, 1990), Vol. 5, p. 398.
- ⁸ R. Grössinger, X. C. Kou, T. H. Jacobs, and K. H. J. Buschow, J. Appl. Phys. **69**, 5596 (1991).
- ⁹ X. C. Kou, R. Grössinger, M. Katter, J. Wecker, L. Schultz, T. H. Jacobs, and K. H. J. Buschow, J. Appl. Phys. **70**, 2272 (1991).
- ¹⁰ O. Isnard, M. Guillot, S. Miraglia, and D. Fruchart, J. Appl. Phys. **79**, 4608 (1996).
- ¹¹ M. Yamada, H. Kato, H. Yamamoto, and Y. Nakagawa, Phys. Rev. B **38**, 620 (1988).
- ¹² J. P. Liu, K. Bakker, F. R. De Boer, T. H. Jacobs, D. B. De Mooij, and K. H. J. Buschow, J. Less-Common Met. **170**, 109 (1991).

Coercive $\text{Sm}_2\text{Fe}_{17}\text{N}_3$: A model pinning system created by heavy ion irradiation

N. M. Dempsey,^{a)} X. L. Rao, and J. M. D. Coey
Department of Physics, Trinity College Dublin, Dublin 2, Ireland

J. P. Nozières
Laboratoire Louis Néel, CNRS, Grenoble, France

M. Ghidini
Clarendon Laboratory, Parks Road, Oxford, United Kingdom

B. Gervais
CIRIL, Caen Cedex, France

Swift high energy (5 GeV) Pb ion irradiation has been employed to create defects in the high performance permanent magnet material $\text{Sm}_2\text{Fe}_{17}\text{N}_3$. Total ion fluences in the range from 10^{11} to 2×10^{13} ions/cm² were studied. In Mössbauer spectra at 26 and 300 K, both a paramagnetic doublet and a broad ferromagnetic contribution characteristic of an amorphous or strongly disordered phase are found to be induced by irradiation. Magnetization reversal was studied and coercivity is found to increase upon irradiation, up to fivefold at 5 K ($\mu_0 H_c = 1.5$ T) for the highest ion fluence. Initial magnetization curves of the irradiated samples are characteristic of material with a pinning type coercivity mechanism with a maximum initial depinning field of 0.4 T for the highest fluence. Magnetization measurements made parallel and perpendicular to the ion beam direction suggest that the defects created are highly anisotropic in shape. The temperature dependence of the coercivity has been analyzed within the framework of the Gaunt model of domain wall pinning. © 1998 American Institute of Physics. [S0021-8979(98)19811-0]

I. INTRODUCTION

Magnetization reversal in hard magnetic materials with magnetocrystalline anisotropy is generally described within the framework of a nucleation/propagation model. Magnetization reversal is a three step process: first nucleation of a small volume of reverse magnetization at defects such as inclusions, precipitates, or grain boundaries with the formation of a domain wall at the defect-matrix boundary; then transfer of this domain wall to within the hard matrix phase and finally its propagation through the whole grain in order to achieve full reversal. Depending on which of these stages dominates, one talks of nucleation or pinning-type coercivity. As most permanent magnets are of the nucleation type, a considerable amount of experimental and numerical work has been devoted to magnetization processes in such systems.¹ Given the complexity of the microstructure in real magnets, recent attempts have focused on model systems formed either by diluting the matrix phase in a nonmagnetic phase or by patterning thin films into arrays of identical, noninteracting particles.^{2,3} So far much less attention has been devoted to pinning-type systems. One-dimensional calculations predict the pinning force to be maximum when the defect size is comparable to the domain wall width δ_w .⁴ As high performance metallic permanent magnets are generally intermetallic $3d-4f$ compounds, the magnetocrystalline anisotropy is very large, thus leading to domain wall widths of a few nanometers.⁵ An increase in coercivity may therefore

be expected for nanometer-scale defects. Swift heavy ions are known to create nanometer sized defects in some metallic targets.⁶ Latent tracks have been observed in metals when the energy deposited by electronic excitations is above a threshold value.⁷ The configuration of the latent tracks gradually changes from strings of small separated damaged droplets to more or less homogeneously damaged cylinders as the electronic stopping power is increased above this threshold.

Pinning has already been observed in ion-irradiated garnets, where the domain walls are wide, after appropriate chemical etching of the damage tracks.⁸ In this article, we report on the direct development of pinning type coercivity by the controlled creation of defects by swift heavy ion irradiation. The material studied is $\text{Sm}_2\text{Fe}_{17}\text{N}_3$ ($\delta_w = 3.4$ nm), an intermetallic $3d-4f$ compound which exhibits much potential as a permanent magnet material, e.g., large magnetization, large uniaxial anisotropy, and high Curie temperature.⁹

II. EXPERIMENTAL DETAILS

$\text{Sm}_2\text{Fe}_{17}$ powder with a particle size of 20–65 μm was nitrided in a flowing mixed gas ($\text{NH}_3 + \text{H}_2$) system. Traces of a Sm rich phase were found in the parent material. To prepare samples for ion irradiation, the powder was mixed with epoxy resin (2:1 by wt) and sandwiched between two 15 μm sheets of Al foil. The thickness of the powder and epoxy mixture was then reduced to 50 μm by lamination in a roller mill. Several square sections (16 mm²) were then cut from the same sheet and irradiated with a 5 GeV Pb^{56+} ion beam at the GANIL accelerator in Caen, France. The total fluence

^{a)}Electronic mail: ndempsey@vax1.tcd.ie

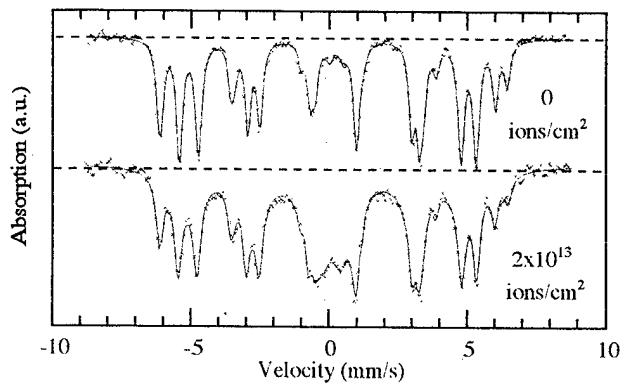


FIG. 1. Mössbauer spectra of a nonirradiated reference sample ($\Phi = 0$ ions/cm²) and the sample irradiated with highest fluence ($\Phi = 2 \times 10^{13}$ ions/cm²) at room temperature.

ranged from 10^{11} to 2×10^{13} ions/cm². The penetration depth of the ions in the magnetic material was estimated from the TRIM code¹⁰ to be of the order of 100 μm . Mössbauer spectroscopy was carried out at 26 K and at room temperature with a ⁵⁷Co source in a rhodium matrix. Magnetic measurements were performed between 5 K and room temperature on an 8 T vibrating sample magnetometer (VSM) and a 10 T extraction magnetometer.

III. RESULTS AND DISCUSSION

Mössbauer analysis was used to evaluate the total amount and magnetic nature of the defect induced by irradiation. The room temperature Mössbauer spectra of a reference sample and of the sample irradiated at the highest fluence are given (Fig. 1). In the reference sample, about 3% of a paramagnetic phase is detected. This may be attributed to the decomposition products of the Sm rich trace phase during the $\text{NH}_3 + \text{H}_2$ heat treatments.¹¹ The spectrum of the irradiated sample has an additional paramagnetic doublet centered about zero velocity and a broad ferromagnetic contribution characteristic of an amorphous or strongly disordered phase. The total paramagnetic contribution accounts for about 17% of the Fe atoms. The quantity of the additional broad ferromagnetic contribution is estimated to be about 35%. The ratio of the additional paramagnetic to ferromagnetic phases decreases from 1:2 at room temperature to 1:3.5 at 26 K. These results indicate that the defects created are not of a uniform magnetic nature. This is not surprising as it is known that in Fe-based intermetallic alloys the magnetic configuration is very dependent on the Fe-Fe interatomic distances as well as on their coordination number. A core and shell defect of a different magnetic structure may thus be envisaged.

The fraction of the total surface damaged, p , may be expressed as a function of the total fluence, Φ , and the area of a latent track of radius r ,

$$p(\Phi, r) = 1 - \exp(-\pi r^2 \Phi). \quad (1)$$

Assuming a minimum defect radius of about 1.5 nm, based on the results from other metals (Ref. 7), we expect about

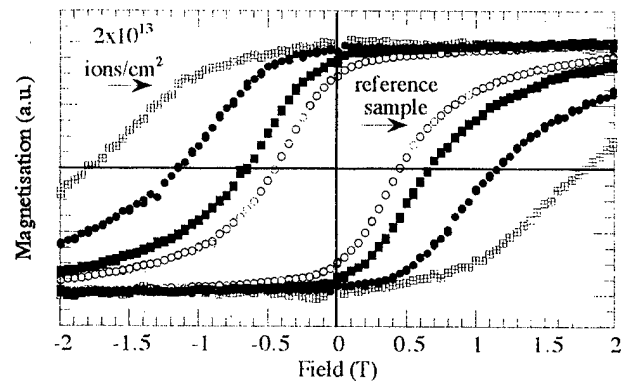


FIG. 2. Hysteresis loops of a reference sample (nonirradiated) together with those of the samples irradiated at 10^{12} (solid square), 5×10^{12} (solid circles), and 2×10^{13} ions/cm², measured at 5 K.

75% of the sample to be damaged at a fluence of 2×10^{13} ions/cm² if the defects are continuous tracks. As Mössbauer measurements indicate a maximum of 52% damage, at this fluence discontinuous tracks are most likely.

The hysteresis loops of some irradiated samples, measured at 5 K, are compared with that of a reference nonirradiated sample (Fig. 2). The coercive field is defined as the field at which the irreversible susceptibility is maximum. It increases upon irradiation, up to fivefold for the highest fluence of 2×10^{13} ions/cm², where we have made the approximation that $(\chi_{\text{irr}}) \approx (dM/dH)$. The initial magnetization curves of the reference sample and the two samples of highest fluence are given (Fig. 3). In the reference sample, the initial susceptibility is large which indicates free motion of the domain walls, as expected for large multidomain particles. In the irradiated samples, the initial susceptibility is practically zero until a critical field is reached. Such a behavior is generally ascribed either to single domain particles or to domain wall pinning in multidomain particles. As the size of the ferromagnetic particles is many times the critical single-domain particle size ($d_c = 0.3 \mu\text{m}$), the former is irrelevant. This critical field, H_p , thus corresponds to the minimum field required to depin the domain walls from the irradiation induced defects. The coercive and depinning

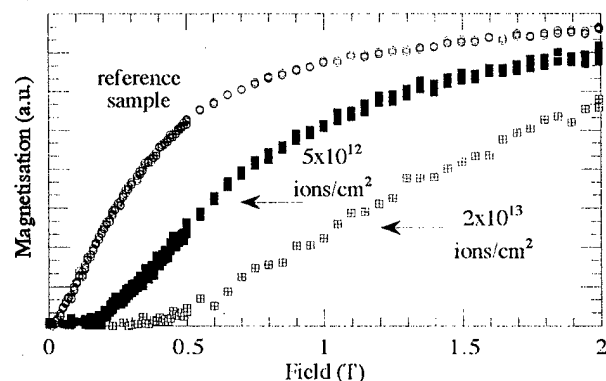


FIG. 3. Virgin magnetization curve of a reference sample (nonirradiated) together with those of the samples irradiated with 5×10^{12} and 2×10^{13} ions/cm², measured at 5 K.

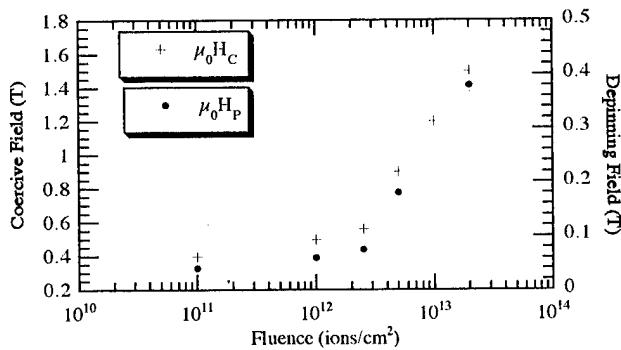


FIG. 4. Coercive and initial depinning fields as a function of ion fluence measured at 5 K.

fields measured at 5 K are plotted as a function of the ion fluence (Fig. 4).

Magnetization measurements made in-plane and out-of-plane, i.e., perpendicular and parallel to the direction of the ion beam, are reported for a total ion fluence of 1×10^{13} ions/cm² (Fig. 5). The out-of-plane coercivity is significantly higher than the in-plane coercivity. However, no difference is observed in a reference sample. The pinning of a domain wall by spherical defects within a ferromagnetic grain should be independent of the orientation of the domain wall. This is not the case for cylindrical defects, a wall which is parallel to and travelling towards the defect should be pinned when it meets the defects as it is then in a minimum energy position [Fig. 5 inset (a)]. However, a wall which lies perpendicular to the defect and is travelling along its axis will not be pinned, as it will always be at the same energy [Fig. 5 inset (b)]. In an isotropic sample, the domain walls, which align with the easy axis of the grain, are randomly oriented. Grains which have their easy axis parallel to the applied field contribute most to the $M(H)$ curve near H_c as it

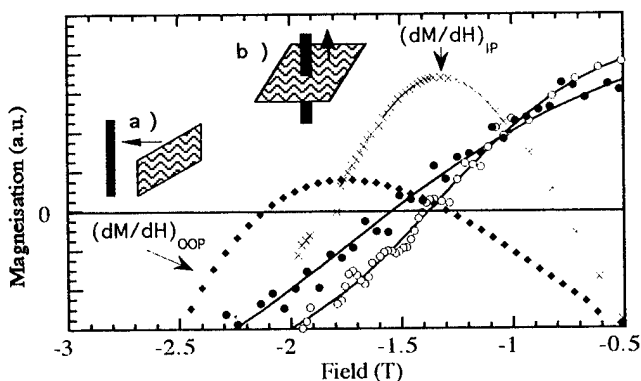


FIG. 5. Demagnetization curves of an ion irradiated sample (10^{13} ions/cm²) measured out-of-plane [(OOP), full circle] and in-plane [(IP), empty circles]. The derivatives of the fitted magnetization data which indicate values of coercivity of 1.8 and 1.3 T for the OOP and IP measurements, respectively, are also given. Schematic diagrams of a domain wall travelling (a) parallel and towards and (b) perpendicular and along a cylindrical defect are included.

is the projection of M along H which is measured. Therefore, a difference in the value of coercivity measured out-of-plane and in-plane for an isotropic sample reflects a difference in the coercivity of grains with domain walls travelling parallel and towards the ion path compared with grains where the domain walls are travelling perpendicular and along the ion path. These results support the evidence for extended defects, though we can conclude the tracks are discontinuous or continuous.

Gaunt has studied the pinning of domain walls in ferromagnetic materials.¹² If the unpinning process involves breakaway from a single defect, and the volume swept out by the wall contains, on average, one replacement pin then we are dealing with "strong pinning." "Weak pinning" involves the cooperative breakaway from many pinning sites and pinning is due to a fluctuation in the pinning site density. The predicted temperature dependence of coercivity is different for each regime. The temperature dependence of the coercivity of the sample irradiated with highest fluence has been analyzed and the observed result may be accounted for by weak pinning.¹³

IV. CONCLUSION

It has been established that significant increases in coercivity may be induced in coarse grained multidomain $\text{Sm}_2\text{Fe}_{17}\text{N}_3$ by irradiation with swift high energy heavy ions. Initial magnetization curves of the irradiated samples are characteristic of material with a pinning type coercivity mechanism. Mössbauer analysis reveals that the irradiation induced defects have both paramagnetic and ferromagnetic contributions, a core-shell structured defect is suggested. Quantitative analysis of the spectra as well as magnetization measurements indicate that the defects are highly anisotropic in shape and discontinuous. The temperature dependence of the coercivity may be explained within the framework of the Gaunt model of weak pinning.

¹For a review, see D. Givord and M. F. Rossignol, in *Rare-Earth Iron Permanent Magnets*, Monographs on The Physics and Chemistry of Materials, edited by J. M. D. Coey (Oxford University Press, Oxford, 1996), Vol. 5, Chap. 5.

²M. Hehn, K. Ounadjela, J. P. Bucher, F. Rousseaux, D. Decanini, B. Bartenlian, and C. Chappert, *Science* **272**, 1782 (1996).

³O. Fruchart, J. P. Nozieres, B. Kevorkian, J. C. Toussaint, D. Givord, F. Rousseaux, D. Decanini, and F. Carcenac, *Phys. Rev. B* (to be published).

⁴B. D. Cullity, *Introduction to Magnetic Materials* (Addison-Wesley, Reading, MA, 1972).

⁵J. M. D. Coey, in *Rare-Earth Iron Permanent Magnets*, Monographs on The Physics and Chemistry of Materials, edited by J. M. D. Coey (Oxford University Press, Oxford, 1996), Vol. 54, Chap. 1.

⁶A. Barbu, H. Dammak, A. Dunlop, and D. Lesueur, *MRS Bull.* **20**, 29 (1995).

⁷A. Barbu, A. Dunlop, D. Lesueur, and R. S. Averback, *Europhys. Lett.* **15**, 37 (1991).

⁸H. Heitmann, P. Hansen, K. Witter, and R. Spohr, *J. Magn. Magn. Mater.* **10**, 97 (1979).

⁹J. M. D. Coey and H. Sun, *J. Magn. Magn. Mater.* **87**, 251 (1990).

¹⁰J. F. Ziegler and J. P. Bierzack, *The Stopping Range of Ions in Solids* (Pergamon, New York, 1985).

¹¹N. M. Dempsey (unpublished).

¹²P. Gaunt, *Philos. Mag. B* **48**, 261 (1983).

¹³N. M. Dempsey, Thesis Trinity College Dublin, 1998.

Hydrogenation and disproportionation of $\text{Sm}_2\text{Fe}_{17-x}\text{Ga}_x$ at high hydrogen pressures

M. Kubis,^{a)} K.-H. Müller, and L. Schutz

IFW Dresden, Institut für Metallische Werkstoffe, D-01171 Dresden, Germany

O. Gutfleisch and I. R. Harris

School of Metallurgy and Materials, University of Birmingham, Birmingham, B15 2TT, United Kingdom

In order to apply the hydrogenation-disproportionation-desorption-recombination process for the preparation of highly coercive $\text{Sm}_2\text{Fe}_{15}\text{Ga}_2\text{C}_y$, which exhibits excellent magnetic properties together with a high thermal stability, the disproportionation of $\text{Sm}_2\text{Fe}_{17-x}\text{Ga}_x$ was investigated. A systematic study of the hydrogen absorption behavior of $\text{Sm}_2\text{Fe}_{17-x}\text{Ga}_x$ ($x=0, 0.5, 1$, and 2) at hydrogen pressures between 0.5 and 8 bar by means of hydrogen differential thermal analysis (HDTA) showed that increased hydrogen pressures promote the disproportionation of the stabilized $2:17$ phase. X-ray diffraction investigations of the HDTA samples showed a decreasing content of the $2:17$ phase for increasing hydrogen pressures. It was possible to achieve a nearly full disproportionation even for the most stable compound $\text{Sm}_2\text{Fe}_{15}\text{Ga}_2$ by applying a pressure of 8 bar. Microstructural changes within the disproportionated mixture as a result of the applied pressure have been documented in detail by high resolution scanning electron microscopy. © 1998 American Institute of Physics. [S0021-8979(98)22611-9]

Highly stable and coercive $\text{Sm}_2\text{Fe}_{17-x}\text{Ga}_x\text{C}_y$ materials ($1 \leq x, y \leq 3$) produced by melt spinning¹ or mechanical alloying² are candidates for a new class of permanent magnets. The hydrogenation-disproportionation-desorption-recombination (HDDR) process is another, very effective method for the production of highly coercive $\text{Sm}_2\text{Fe}_{17}\text{N}_y/\text{C}_y$ powders.³⁻⁵ In this process, coarse grained $\text{Sm}_2\text{Fe}_{17}$ disproportionates into an intimate mixture of SmH_z ($1.9 \leq z \leq 2.8$) and $\alpha\text{-Fe}$. In the second step, the hydrogen is desorbed and the constituents recombine into a fine grained microstructure. This material exhibits a high coercivity after subsequent nitrogeneration or carburization.⁶ However, the partial substitution of Fe by Ga in $\text{Sm}_2\text{Fe}_{17}$ stabilizes the $2:17$ phase against disproportionation by hydrogen. Therefore it is impossible to complete the HDDR process for a Ga content $x > 0.5$ under standard conditions.⁷ In this work the hydrogenation and disproportionation step was carried out under increased hydrogen pressure, using pressures up to 8 bar in order to achieve complete disproportionation of $\text{Sm}_2\text{Fe}_{17-x}\text{Ga}_x$ with $x=1$ and 2 into SmH_z and $\alpha\text{-(Fe,Ga)}$.

Elemental Sm, Fe, and Ga (purities 99.9%) were arc melted to form prealloys. The prealloys were melted together with additional Fe in an induction furnace. A Sm excess of 30% was used to compensate for evaporation losses and to reach nominal compositions of $\text{Sm}_2\text{Fe}_{17-x}\text{Ga}_x$ with $x=0, 0.5, 1$, and 2 . The samples were homogenized in an inert gas atmosphere at 1050°C for 72 h. The resulting material was crushed into particles with diameters below $100\text{ }\mu\text{m}$.

The hydrogen absorption behavior was investigated by hydrogen differential thermal analysis (HDTA). For each experiment about 180 mg samples were heated in hydrogen at pressures between 0.5 and 8 bar with a heating rate of 5

K/min. After heating up to 950°C the samples were cooled down in hydrogen atmosphere. Phase changes during disproportionation were observed by x-ray diffraction (XRD) using $\text{Cu K}\alpha$ radiation. Microstructural changes were investigated by means of high resolution scanning electron microscopy (HRSEM Hitachi S-4000 FE) in the backscattered mode.

HDTA experiments at hydrogen pressures of $0.5, 1, 2, 4$, and 8 bar were carried out for all samples. The HDTA curves in Fig. 1 show the temperature difference ΔT between sample pan and reference pan for $\text{Sm}_2\text{Fe}_{16}\text{Ga}$ during heating in hydrogen atmosphere. The ΔT peaks between 550 and 800°C are related to an exothermic reaction which can be attributed to the disproportionation of $\text{Sm}_2\text{Fe}_{16}\text{Ga}$. For increasing hydrogen pressures the temperature, at which the

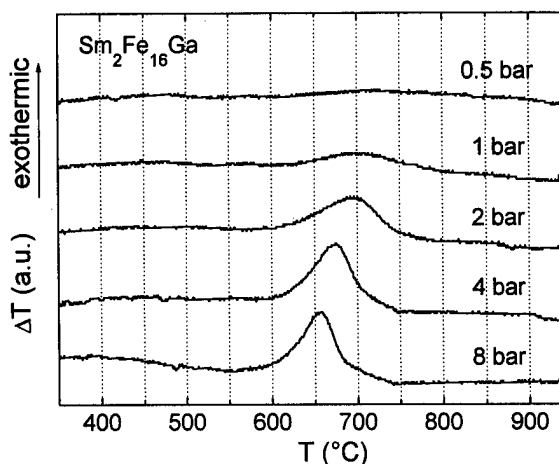


FIG. 1. HDTA curves of $\text{Sm}_2\text{Fe}_{16}\text{Ga}$ for different hydrogen pressures. The exothermic peaks are related to the disproportionation of $\text{Sm}_2\text{Fe}_{16}\text{Ga}$ into SmH_z and $\alpha\text{-(Fe,Ga)}$ and it can be seen that an increased hydrogen pressure promotes the disproportionation reaction.

^{a)} Author to whom correspondence should be addressed; electronic mail: Kubis@ifw-dresden.de

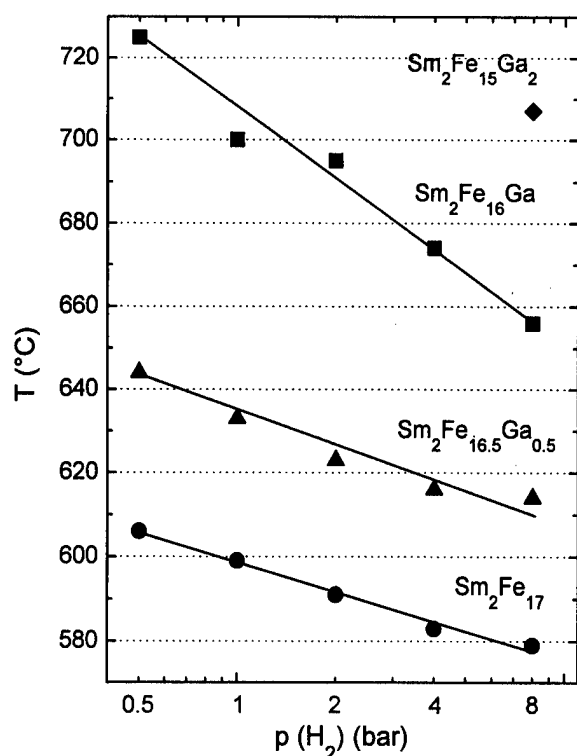


FIG. 2. Disproportionation temperatures of $\text{Sm}_2\text{Fe}_{17-x}\text{Ga}_x$ ($x=0, 0.5, 1$, and 2) for different pressures; plotted in the form T against $\log p$, reasonably linear relationships are obtained.

disproportionation peak occurs, decreases. This decrease can be explained in terms of a decrease of the free enthalpy of samarium hydride with increasing hydrogen pressure, which promotes the disproportionation reaction and increases the kinetics of this reaction. The effect of hydrogen pressure in this case is very similar to that found for the disproportionation of $\text{Nd}_2\text{Fe}_{14}\text{B}$.⁸ The same behavior was observed for all $\text{Sm}_2\text{Fe}_{17-x}\text{Ga}_x$ samples with $x=0, 0.5, 1$, and 2 . The temperatures, at which the disproportionation peaks occur, are given in Fig. 2 for all samples and pressures. For $\text{Sm}_2\text{Fe}_{15}\text{Ga}_2$, it was only possible to detect one peak, connected to the disproportionation at the highest pressure. For hydrogen pressures below 8 bar, the disproportionation reaction of this material was too sluggish to result in a defined exothermic peak. With increasing Ga content, the disproportionation occurs at increasing temperatures due to the enhanced stability of the 2:17 structure against the disproportionation by hydrogen. A similar effect was observed for the disproportionation of Ga-containing $\text{Nd}_2\text{Fe}_{14}\text{B}$ alloys.⁹ The fact that the Ga addition to the $\text{Nd}_2\text{Fe}_{14}\text{B}$ phase increases the stability against disproportionation was reported earlier.^{10,11} Thermodynamic model calculations showed that an increased stability of the $\text{Nd}_2(\text{Fe}, \text{Ga})_{14}\text{B}$ phase is caused by the substitution of Fe by Ga because of a less negative hydride formation enthalpy compared to that of the ternary $\text{Nd}_2\text{Fe}_{14}\text{B}$ compound.¹² The partial substitution of Fe by Ga in $\text{Sm}_2\text{Fe}_{17}$ seems to have a similar effect.

The HDTA samples were also investigated by XRD and HRSEM. The XRD patterns of the HDTA treated $\text{Sm}_2\text{Fe}_{16}\text{Ga}$ samples corresponding to Fig. 1 are presented in

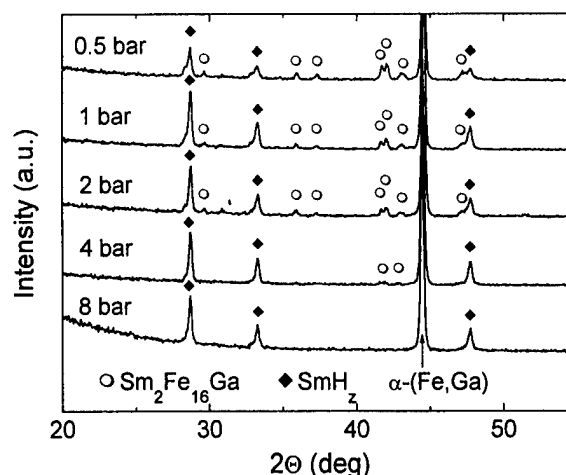


FIG. 3. XRD patterns of $\text{Sm}_2\text{Fe}_{16}\text{Ga}$ after hydrogen treatment at different pressures (corresponding to Fig. 1). Main reflections originate from α -(Fe,Ga) and SmH_2 ; remaining reflections of the nondisproportionated 2:17 phase disappear with increasing hydrogen pressures.

Fig. 3. Although there was only a very weak exothermic peak of the disproportionation at a pressure of 0.5 bar (see Fig. 1), the XRD patterns are dominated by the α -(Fe,Ga) and SmH_2 reflections, even for this relatively low pressure. The HRSEM images in Figs. 4(a) and 4(b) show the partially disproportionated structure of the $\text{Sm}_2\text{Fe}_{16}\text{Ga}$ sample after HDTA at 0.5 bar. Figure 4(a) shows a detail of the reaction front between the gray region of nondisproportionated 2:17 phase in the upper left corner and the disproportionated mixture of SmH_2 (bright) and α -(Fe,Ga) (dark). In the vicinity of the nondisproportionated phase, the disproportionated mixture has a lamellae-like appearance. Okada *et al.*¹³ characterized the microstructural changes during the HDDR reactions of $\text{Sm}_2\text{Fe}_{17}$ by transmission electron microscopy. They observed a similar disproportionated microstructure which was described as rodlike or spherical SmH_2 particles embedded in an α -Fe matrix. A similar microstructure consisting of NdH_2 rods in an α -Fe matrix has been observed in disproportionated NdFeB -type material.¹⁴ According to these references, we suggest that the lamellae-like structures in Fig. 4(a) are in fact SmH_2 rods embedded in α -Fe. The very fine SmH_2 rods with diameters of about 20 nm are formed during the eutectoid-type disproportionation reaction. This initial stage of the disproportionation reaction is very well observable due to the extremely slow reaction speed under the applied conditions. With increasing distance from the reaction front, i.e., with increasing disproportionation time, the SmH_2 rods increase in diameter to about 150 nm and their shape transforms into a more irregular three-dimensional one. Similar coarsening processes had been observed for disproportionated $\text{Sm}_2\text{Fe}_{17}$ and NdFeB -type alloys.^{13,15} Figure 4(b) shows an image with lower magnification in order to give an overview of the partially disproportionated structure in the sample. The intensities of the reflections of the nondisproportionated 2:17 phase in the XRD patterns in Fig. 3 decrease with increasing pressure and the reflections disappear completely after the HDTA treatment at 8 bar. The fully

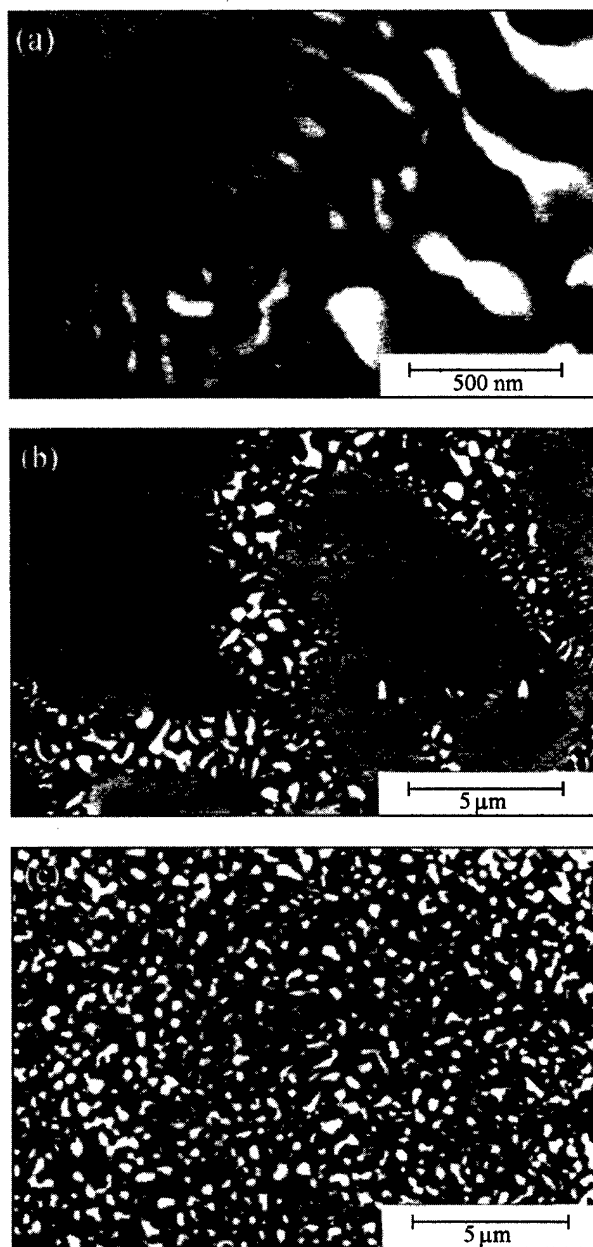


FIG. 4. HRSEM images of $\text{Sm}_2\text{Fe}_{16}\text{Ga}$ after HDTA. Figure 4(a) shows a detail of the reaction front between nondisproportionated 2:17 phase (gray, upper left corner) and the disproportionated mixture of SmH_2 (white) and $\alpha\text{-Fe}$ (black). A coarsening of the SmH_2 phase with increasing distance from the reaction front is observable. Figures 4(b) and 4(c) show the different degrees of disproportionation of $\text{Sm}_2\text{Fe}_{16}\text{Ga}$ after HDTA at 0.5 and 8 bar, respectively.

disproportionated $\text{Sm}_2\text{Fe}_{16}\text{Ga}$ material is shown in the HRSEM image in Fig. 4(c). The fine grained mixture of SmH_2 and $\alpha\text{-(Fe,Ga)}$ extends over the entire sample and remains of nondisproportionated 2:17 phase cannot be found. Again, very fine and somewhat coarser regions can be observed within the disproportionated mixture.

The results of the XRD investigation of $\text{Sm}_2\text{Fe}_{15}\text{Ga}_2$ after HDTA at different pressures are in good agreement with the results obtained for $\text{Sm}_2\text{Fe}_{16}\text{Ga}$. The intensity of the remaining 2:17 reflections of $\text{Sm}_2\text{Fe}_{15}\text{Ga}_2$ (not shown) is larger due to the higher stability of the Ga richer compound against the disproportionation. However, the reflections associated with the 2:17 structure have almost disappeared after the HDTA treatment at 8 bar.

In order to develop a submicron-grained hard magnet via the HDDR route, the disproportionated alloy has to recombine into the original 2:17-type phase. However, one possibility is that the alloy recombines into the disordered TbCu_7 -type structure.⁴ An investigation of HDDR processes in $\text{Sm}_2\text{Fe}_{17-x}\text{Ga}_x$ by means of reactive grinding showed that the Ga substitution stabilizes the 1:7 structure.¹⁶ Desorption and recombination experiments on alloys studied in the present work, which were disproportionated by means of high hydrogen pressures, are still in progress.

In summary, an enhanced hydrogen pressure has a favorable effect on the disproportionation of $\text{Sm}_2\text{Fe}_{17-x}\text{Ga}_x$. The complete disproportionation of the samples with high Ga content under increased hydrogen pressures is very promising for an application of the HDDR process for the preparation of highly stable and coercive gas carbonated $\text{Sm}_2\text{Fe}_{17-x}\text{Ga}_x\text{C}_y$ powders, which could be used for the production of fully dense permanent magnets by hot compaction.

The work of M. Kubis was supported by Sächsisches Ministerium für Wissenschaft und Kunst.

- ¹B. G. Shen, L. S. Kong, F. W. Wang, and L. Cao, *Appl. Phys. Lett.* **63**, 2288 (1993).
- ²J. Ding, P. G. McCormick, and R. Street, *Proceedings of the 13th Workshop on RE Magnets and their Applications*, Birmingham, England, 1994 (unpublished) p. 787.
- ³H. Nakamura, S. Sugimoto, M. Okada, and M. Homma, *Mater. Chem. Phys.* **32**, 280 (1992).
- ⁴C. N. Christodoulou and T. Takeshita, *J. Alloys Compd.* **196**, 155 (1993).
- ⁵P. A. P. Wendhausen, B. Gebel, N. M. Dempsey, K.-H. Müller, and J. M. D. Coey, in *Ref. 2*, p. 831.
- ⁶N. M. Dempsey, P. A. P. Wendhausen, B. Gebel, K.-H. Müller, and J. M. D. Coey, *Proceedings of the 14th Workshop on RE Magnets and their Applications*, Sao Paulo, Brazil, 1996 (unpublished), p. 349.
- ⁷M. Kubis, L. Cao, A. Handstein, B. Gebel, K.-H. Müller, and L. Schultz, *J. Appl. Phys.* **81**, 6485 (1997).
- ⁸D. Book and I. R. Harris, *J. Alloys Compd.* **221**, 187 (1995).
- ⁹S. Sugimoto, O. Gutfleisch, and I. R. Harris, *J. Alloys Compd.* **260**, 284 (1997).
- ¹⁰M. Uehara, H. Tomizawa, and S. Hirohara, *IEEE Trans. Magn.* **29**, 2770 (1993).
- ¹¹T. Tomida, P. Choi, Y. Machara, M. Uehara, H. Tomizawa, and S. Hirohara, *J. Alloys Compd.* **242**, 129 (1996).
- ¹²K. H. J. Buschow, *IEEE Trans. Magn.* **30**, 565 (1994).
- ¹³M. Okada, K. Saito, H. Nakamura, S. Sugimoto, and M. Homma, *J. Alloys Compd.* **231**, 60 (1995).
- ¹⁴O. Gutfleisch, M. Matzinger, J. Fidler, and I. R. Harris, *J. Magn. Mater.* **147**, 320 (1995).
- ¹⁵O. Gutfleisch, N. Martinez, M. Verdier, and I. R. Harris, *J. Alloys Compd.* **215**, 227 (1994).
- ¹⁶M. Kubis, L. Cao, K.-H. Müller, and L. Schultz, *J. Phys. D* **30**, L51 (1997).

Electron microscopy studies of high coercive melt-spun $\text{Sm}_{2+\delta}\text{Fe}_{15}\text{Ga}_2\text{C}_2$ permanent magnets

J. van Lier,^{a)} A. Zern, H. Labitzke, J. Thomas, M. Seeger, and H. Kronmüller
Max-Planck-Institut für Metallforschung, Heisenbergstr. 1, D-70569 Stuttgart, Germany

The influence of over-stoichiometric Sm contents on the magnetic properties of melt-spun Ga stabilized $\text{Sm}_2\text{Fe}_{17}$ carbides has been investigated. For optimum heat treated $\text{Sm}_{2+\delta}\text{Fe}_{15}\text{Ga}_2\text{C}_2$ ribbon flakes an increase of the room temperature coercivity could be observed from $\mu_0 H_C = 1.5$ T for stoichiometric samples to $\mu_0 H_C = 2.2$ T for $\delta = 0.15$. This effect is very interesting because of the improved temperature stability. At 500 K a maximum energy density of $(BH)_{\text{max}} = 31.4$ kJ/m³ for $\delta = 0.09$ can be observed. It is assumed that a Sm-rich nonmagnetic intergranular phase decouples the grains magnetically and is consequently the origin of the high coercivities of these samples. Electron microscopy studies of these melt-spun $\text{Sm}_{2+\delta}\text{Fe}_{15}\text{Ga}_2\text{C}_2$ samples with different Sm contents have been performed by scanning electron microscopy (SEM) and transmission electron microscopy (TEM). A broad grain size distribution (50–250 nm) is observed in the SEM, but there is no difference among samples with different Sm contents. TEM studies show no change in grain shape with variation of the δ value. High resolution TEM (HRTEM) studies indicate the existence of a very thin intergranular phase for samples with an excess of Sm which was proved using high resolution energy dispersive x-ray analysis (EDX) studies with a scanning TEM. These investigations show a significant increase of the Sm content at the grain boundaries for these highly coercive samples. © 1998 American Institute of Physics. [S0021-8979(98)16011-5]

I. INTRODUCTION

The magnetic properties of the binary alloy $\text{Sm}_2\text{Fe}_{17}$ can be changed drastically by interstitial modifications of the rhombohedral $\text{Th}_2\text{Zn}_{17}$ structure. The planar anisotropy can be altered by carburation or nitrogenation to a uniaxial one with high anisotropy fields and a simultaneous increase of the Curie temperature by more than 250 K.¹ For example, for $\text{Sm}_2\text{Fe}_{17}\text{C}_2$ values of $\mu_0 H_A \approx 16$ T and $T_C \approx 670$ K are observed.² Full-potential linear-muffin-tin-orbital calculations have shown that the volume expansion favorably influences the magnetic properties of the hexagonal and rhombohedral $\text{RE}_2\text{Fe}_{17}$ alloys whereas the chemical effect of the interstitial atoms detracts from them.^{3,4} But these $\text{Sm}_2\text{Fe}_{17}(\text{N,C})_y$ alloys decompose at $T = 600\text{--}700$ °C into $\text{Sm}(\text{N,C})$ and $\alpha\text{-Fe}$. In the case of carbides, the decomposition can be suppressed to temperatures up to $T \approx 1000$ °C by substituting Ga for Fe.⁵

II. SAMPLE PREPARATION

We have prepared several $\text{Sm}_{2+\delta}\text{Fe}_{15}\text{Ga}_2\text{C}_y$ samples with different Sm contents by remelting a Fe_{15}C_3 prealloy in an arc furnace together with elementary Sm and Ga for several different times under argon atmosphere. The purity of the elements was at least 99.9%. The best magnetic properties could be reached for all compositions by melt spinning the ingots into mainly amorphous ribbons followed by a subsequent crystallization treatment at 775 °C for 15 min under high vacuum. Both Sm and C evaporate during this proce-

dures. Chemical analyses determined Sm contents of $-0.05 \leq \delta \leq 0.19$ and a carbon content of $y = 2.18 \pm 0.05$ for all samples.

For the microstructural observations in the scanning electron microscope (SEM) the ribbon flakes were broken so that the cross sections of the ribbon flakes could be investigated. The plan-view transmission electron microscope (TEM) samples were prepared by electrochemical polishing followed by Ar-ion-beam milling. To suppress changes of the microstructure during ion milling the samples were cooled with liquid N₂.

III. RESULTS AND DISCUSSION

The magnetic measurements were performed in a PAR vibrating sample magnetometer (VSM). The $\text{Sm}_{2+\delta}\text{Fe}_{15}\text{Ga}_2\text{C}_2$ samples exhibit a well squared hysteresis loop and only a small field range in which the demagnetization takes place.⁶ The coercivity of the samples is nearly independent of Sm content with values of $\mu_0 H_C \approx 1.5$ T ($T = 300$ K) for $\delta \leq 0.03$ as shown in Fig. 1. These values are in good agreement with recent results for stoichiometric mechanical alloyed, intense ball milled and melt-spun $\text{Sm}_2\text{Fe}_{17-x}\text{Ga}_x\text{C}_y$ samples.⁷⁻⁹ But for higher Sm contents the coercivity is drastically enhanced with a saturation-like behavior at $\mu_0 H_C \approx 2.2$ T for $\delta \geq 0.09$. The demagnetization curve of the sample with $\delta = 0.19$ exhibits two steps with two different critical fields ($\mu_0 H_{\text{crit}}^1 \approx 0.7$ T, $\mu_0 H_{\text{crit}}^2 \approx 2.2$ T) leading to a lower coercivity. We assume that this is affected by a small amount of a second hard magnetic phase occurring for high Sm contents. The vertical dotted line in Fig. 1 indicates the end of the stability range of the 2:17 phase.

As the maximum energy density $(BH)_{\text{max}}$ at elevated temperatures is governed by irreversible demagnetization

^{a)}Electronic mail: vanlier@vaxph.mpi-stuttgart.mpg.de

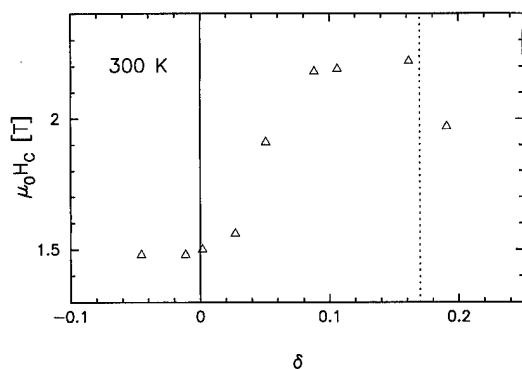


FIG. 1. Coercive field $\mu_0 H_c$ vs Sm excess δ at room temperature for samples of the $\text{Sm}_{2+\delta}\text{Fe}_{15}\text{Ga}_2\text{C}_2$. The vertical dotted line indicates the end of the stability range of the left phase.

processes, the enhanced coercivities improve the temperature stability of the magnets. At $T=500$ K the maximum energy density is enlarged from $(BH)_{\text{max}}^{500\text{ K}} = 25 \text{ kJ/m}^3$ for stoichiometric compounds to $(BH)_{\text{max}}^{500\text{ K}} = 31.4 \text{ kJ/m}^3$ for $\delta=0.09$.

The drastic effect of δ on the extrinsic property $\mu_0 H_c$ which was found in the whole ferromagnetic temperature range could not be correlated to a change of intrinsic magnetic properties. The intrinsic properties especially the anisotropy constants K_1 and K_2 , which were determined in the temperature range from $T=80$ K to $T=570$ K for three samples with different Sm contents ($\delta = 0.03, 0.05, 0.09$),⁶ are independent of the Sm content. Also, the Curie temperature T_C is not affected by δ . A detailed analysis of temperature dependent hysteresis measurements within the nucleation model^{10,11} shows that over-stoichiometric Sm in $\text{Sm}_{2+\delta}\text{Fe}_{15}\text{Ga}_2\text{C}_2$ magnets reduces the effect of internal

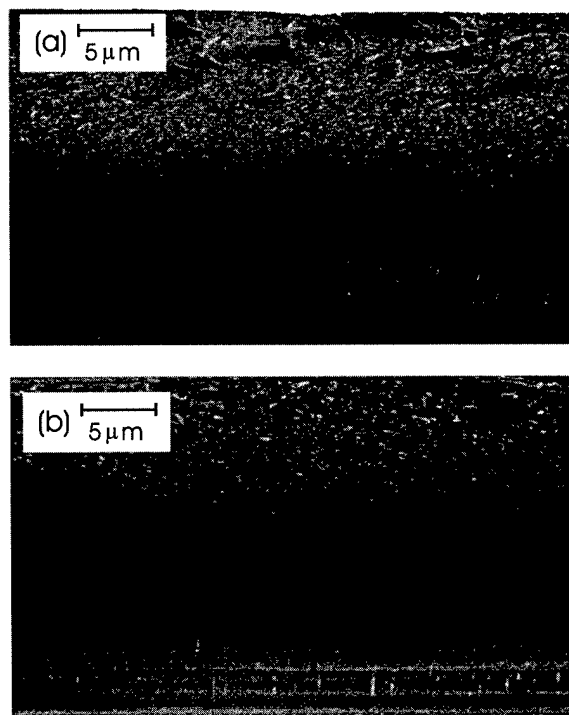


FIG. 2. SEM micrographs of $\text{Sm}_{2+\delta}\text{Fe}_{15}\text{Ga}_2\text{C}_2$ samples with $\delta=-0.05$ (a) and $\delta=0.19$ (b).

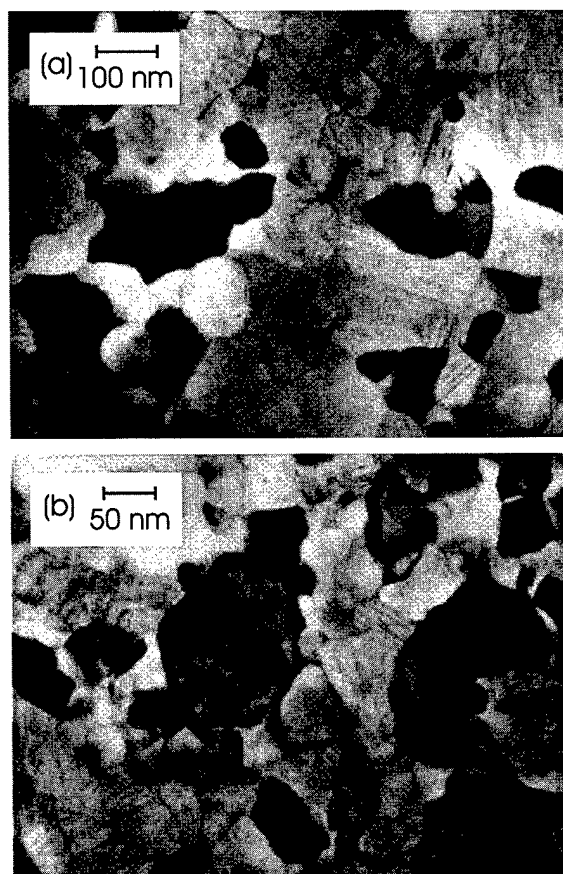


FIG. 3. TEM micrographs of $\text{Sm}_{2+\delta}\text{Fe}_{15}\text{Ga}_2\text{C}_2$ samples with $\delta=0.00$ (a) and $\delta=0.11$ (b).

stray fields on the coercivity.¹² Combining this information leads to the assumption that the change of the coercivity is forced by a Sm-rich nonmagnetic intergranular phase which decouples the grains magnetically comparable to Nd-rich $\text{Nd}_2\text{Fe}_{14}\text{B}$ permanent magnets.^{13,14} To prove this and to exclude the influence of other changes in the microstructure we performed different electron microscopy studies.

A high resolution field emission SEM DSM 982 GEMINI (Zeiss) was used to investigate the grain size of the annealed ribbon flakes. Figures 2(a) and 2(b) shows the micrographs of the cross sections for two samples with $\delta=-0.05$ and $\delta=0.19$, respectively. A broad grain size distribution can be observed for both samples, with comparable fractions of coarse and fine grains. At a higher magnification the grain sizes can be estimated to be $d \approx 50$ nm in the finely grained regions at the wheel side of the ribbon and $d \approx 250$ nm in the coarsely grained regions on the gas side. But there is no difference for samples with different Sm contents.

Conventional TEM and high resolution TEM (HRTEM) studies were performed in a JEOL JEM 4000 FX electron microscope at an acceleration voltage of 400 kV. No significant differences between samples with different Sm contents could be observed considering the shape of the grains as shown in the TEM micrographs of Fig. 3 in the case of $\delta=0.00$ [Fig. 3(a)] and $\delta=0.11$ [Fig. 3(b)]. The grains of both samples are very irregular and have very sharp edges and bent surfaces, leading to large stray fields and consequently to relatively low coercivities compared to the theo-

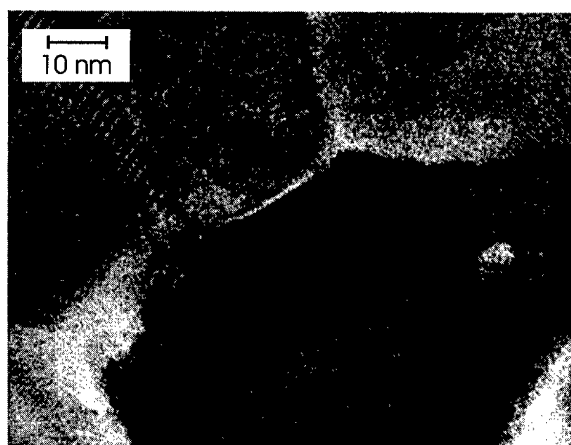


FIG. 4. HRTEM micrograph of a $\text{Sm}_{2+\delta}\text{Fe}_{15}\text{Ga}_2\text{C}_2$ sample with $\delta=0.11$.

retical upper limit $H_N^{\min} \approx 5.3$ T for isotropic magnets. The minimum nucleation field for misoriented grains H_N^{\min} is deduced from the nucleation model.

HRTEM investigations indicate the existence of a very thin intergranular phase for over-stoichiometric samples. This is shown in Fig. 4 for $\delta=0.11$ where this phase has a width of $b \approx 0.7$ nm. It should be mentioned that the average value of b is smaller and that this phase is often not visible because of canted orientations of the grain boundaries. This boundary phase was not found in stoichiometric samples.

To prove the existence of this intergranular phase we performed high resolution energy dispersive x-ray (EDX) analyses with a so called "dedicated scanning TEM (STEM)." The electron source of this STEM, dedicated for high resolution chemical analyses, is a cold field emission source with a beam diameter of 1 nm at a beam current of 1 nA and an energy bandwidth of less than 0.5 eV. The acceleration voltage was 100 kV and the EDX analyses were performed on a reduced area of $3 \text{ nm} \times 4 \text{ nm}$. The EDX spectra measured with a Noran HP Ge detector (high purity germanium) can only be analyzed qualitatively. We investigated several regions of the samples by a relative comparison of the compositions in the grain boundary phase and within the grains. The sample with $\delta=0.11$ exhibits an enhanced value of the Sm content in the grain boundaries. The difference of the average values measured for the Sm content in the grain

boundaries (13.1 at. %) and in the grains (12.2 at. %) is $\Delta\text{Sm} = 0.9$ at. %. As the width of the intergranular phase is only $b \approx 0.5$ nm, this phase has a contribution of only approximately 15% to the EDX measurement over the investigated area of $3 \text{ nm} \times 4 \text{ nm}$. This leads to a corrected change of the Sm content of $\Delta\text{Sm} \approx 5$ at. % which corresponds to a significant enhancement of the Sm content in the boundary phase of about 40%. In contrast to this, we found no differences in the compositions of grains and grain boundaries in the sample with $\delta=0.00$.

IV. CONCLUSION

We have reported a strong influence of the Sm content on the coercive field of melt-spun $\text{Sm}_{2+\delta}\text{Fe}_{15}\text{Ga}_2\text{C}_2$ permanent magnets which is not forced due to changes of the intrinsic properties. Furthermore, it was shown that neither the grain size nor the grain shape is affected by the Sm content. A Sm-enriched boundary phase could be observed in samples with over-stoichiometric Sm contents. This intergranular phase decouples the grains magnetically and is the reason for the enhanced coercivities and the improved magnetic properties at elevated temperatures.

- ¹X. P. Zhong, R. J. Radwanski, F. R. de Boer, T. H. Jacobs, and K. H. J. Buschow, *J. Magn. Magn. Mater.* **86**, 333 (1990).
- ²H. Sun, Y. Otani, and J. M. D. Coey, *J. Magn. Magn. Mater.* **104–107**, 1439 (1992).
- ³T. Beuerle and M. Fähnle, *Phys. Status Solidi B* **174**, 257 (1992).
- ⁴P. Uebele, K. Hummler, and M. Fähnle, *Phys. Rev. B* **53**, 3296 (1996).
- ⁵B. G. Shen, L. S. Kong, F. W. Wang, and L. Cao, *Appl. Phys. Lett.* **63**, 2288 (1993).
- ⁶J. van Lier, M. Seeger, and H. Kronmüller, *J. Magn. Magn. Mater.* **167**, 43 (1997).
- ⁷J. Ding, P. G. McCormick, and R. Street, in *Proceedings of the 13th International Workshop on RE Magnets and their Applications*, Birmingham, 1994, edited by R. Harris, p. 787.
- ⁸L. Cao, A. Handstein, W. Grünberger, J. Edelman, L. Schultz, and K.-H. Müller, *Appl. Phys. Lett.* **68**, 129 (1996).
- ⁹B. G. Shen, H. Y. Gong, Z. H. Cheng, L. S. Kong, F. W. Wang, B. Liang, J. X. Zhang, H. Q. Guo, and J. G. Zhao, *J. Magn. Magn. Mater.* **153**, 332 (1996).
- ¹⁰H. Kronmüller, *Phys. Status Solidi B* **144**, 385 (1987).
- ¹¹G. Martinek and H. Kronmüller, *J. Magn. Magn. Mater.* **86**, 177 (1990).
- ¹²J. van Lier, M. Seeger, and H. Kronmüller, *J. Appl. Phys.* **82**, 2453 (1997).
- ¹³J. Fidler, *IEEE Trans. Magn.* **MAG-21**, 1955 (1985); J. Fidler and K. G. Knoch, *J. Magn. Magn. Mater.* **80**, 48 (1989).
- ¹⁴A. Zern, M. Seeger, J. Bauer, and H. Kronmüller, *Magnetic Hysteresis in Novel Magnetic Materials*, edited by G. C. Hadjipanayis (Kluwer Academic, Norwell, MA, 1997), p. 631.

Pressure induced reversal of the volume expansion caused by interstitial nitrogen in Nd₂Fe₁₇N₃

G. K. Marasinghe, W. J. James, and P. C. Ezekwenna

Department of Physics, Department of Chemistry, and the Graduate Center for Materials Research, University of Missouri-Rolla, Rolla, Missouri 65409

H. Luo and W. B. Yelon

University of Missouri Research Reactor, Columbia, Missouri 65211

Y. Zhao and R. B. Von Dreele

Manual Lujan, Jr. Neutron Scattering Center, Los Alamos National Laboratory, Los Alamos, New Mexico 87545

M. Ellouze and Ph. l'Héritier

LMGP, ENS Physique de Grenoble, 38402 St Martin d'Heres, France

Crystallographic properties of Nd₂Fe₁₇N₃ have been investigated using powder neutron diffraction techniques at pressures up to 7.3 GPa. With increasing pressure, the unit cell volume of Nd₂Fe₁₇N₃ decreases almost linearly at a rate of 6.1 Å³/GPa without undergoing a phase transformation or expelling the interstitial nitrogen atoms. The observed rate of contraction corresponds to a bulk modulus of 1.4×10^{11} N/m² for Nd₂Fe₁₇N₃. The unit cell volume of Nd₂Fe₁₇N₃ at 7.3 GPa is approximately equal to that of Nd₂Fe₁₇ at atmospheric pressure. Even though the unit cell of Nd₂Fe₁₇ expands anisotropically due to nitrogenation, contraction of the Nd₂Fe₁₇N₃ unit cell under pressure appears to be isotropic with lattice parameters *a* and *c* decreasing by approximately 1.8% as the sample pressure increases from ambient to 7.3 GPa. © 1998 American Institute of Physics. [S0021-8979(98)35911-3]

I. INTRODUCTION

The increase in Curie temperature which accompanies the interstitial nitrogenation¹ of R₂Fe₁₇ (R=rare earth) type intermetallics is generally attributed to the resulting longer near neighbor iron-iron distances. However, it has been pointed out^{2,3} that the relationships between near neighbor iron-iron distances and magnetic properties, especially the Curie temperature, of rare earth iron intermetallics are complex and not well understood.

Measuring the crystallographic and magnetic properties of a given sample under different pressures would enable one to study the direct correlation between the interatomic distances and magnetic interactions. High pressure magnetic properties, especially the Curie temperature, of several rare earth transition metal intermetallics have been reported by several workers,⁴⁻⁹ see Table I. Unfortunately, studies on structure-pressure relationships are less common and limited to measuring compressibility^{8,9} at different pressures and temperatures. However, more detailed information on structure-pressure relationships (dependence of the lattice parameters and interatomic distances on sample pressure) is necessary for a better understanding of the role played by interatomic distances in determining magnetic properties. Herein we report the preliminary results from a neutron diffraction study of Nd₂Fe₁₇N₃ at pressures up to 7.3 GPa.

II. EXPERIMENTAL METHODS

Nd₂Fe₁₇ samples were prepared from elements of purity 99.9% at. % or better by induction melting followed by annealing at 1000 °C for 72 h. Nd₂Fe₁₇N₃ was synthesized by

gas phase insertion of nitrogen into finely ground (maximum particle size was 50 μ) Nd₂Fe₁₇ at 450 °C and 10 MPa. The phase purity of the samples was checked by x-ray diffraction on a Guinier Hägg camera using Cu K_α radiation. The nitrogen content, lattice parameters, and atomic positions for the Nd₂Fe₁₇N₃ sample were determined from a powder neutron diffraction pattern obtained at 23 °C and atmospheric pressure at the University of Missouri Research Reactor (MURR) using 1.4766 Å neutrons. Neutron diffraction data obtained at MURR were refined using the FULLPROF code¹⁰ on the basis of the Th₂Zn₁₇-type structure.

Time of flight neutron diffraction patterns at high pressure were obtained at 23 °C on the high intensity powder diffractometer (HIPD) at the Manual Lujan, Jr. Neutron Scattering Center (MLNSCE), Los Alamos National Laboratory. The sample used was a wet mixture of approximately 90 mg of Nd₂Fe₁₇N₃ powder, 160 mg of NaCl powder, and Florinert

TABLE I. Structural and magnetic properties of several rare earth transition metal intermetallics at high pressure.

Material	Max pressure (GPa)	Compressibility (GPa ⁻¹)	dT_c/dP (K GPa ⁻¹)	Ref.
Nd ₂ Fe ₁₇ N ₃	7.3	7×10^{-3a}	...	This work
Ce ₂ Fe ₁₇ H ₃	1	...	-58	7
Nd ₂ Fe ₁₄ B	4	...	-26	5
Nd ₂ Fe ₁₇	1.4	...	-36	6
Nd(FeTi) ₁₂	0.9	...	-27	8
Nd ₃ Fe ₂₉	1	7×10^{-3b}	-28	9

^aReciprocal of the bulk modulus calculated from neutron diffraction data.

^bCalculated from linear thermal expansion data as described in Ref. 9.

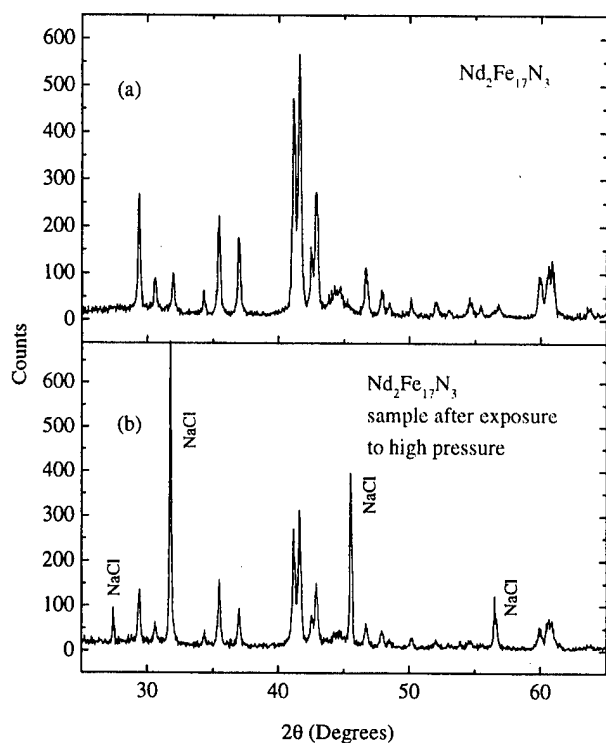


FIG. 1. X-ray diffraction patterns measured at 23 °C and atmospheric pressure of $\text{Nd}_2\text{Fe}_{17}\text{N}_3$ (a) before and (b) after the high pressure experiment. Diffraction pattern (b) contains lines due to NaCl which was added to the $\text{Nd}_2\text{Fe}_{17}\text{N}_3$ sample as a pressure sensor during the high pressure experiment.

FC-70.¹¹ Diffraction lines from NaCl were used to monitor sample pressure.¹² The purpose of using Fluorinert was to provide a hydrostatic pressure medium. Approximately 100 mm³ of the slurried sample were loaded into a Paris-Edinburgh pressure cell¹³ with tungsten carbide anvils. Ti-Zr gaskets were used to contain the sample. Each data set was collected in two detector banks centered at $\pm 90^\circ$ for about 10 h at an average proton current of approximately 70 μA on the spallation source. Six data sets were collected at 0.27, 1.44, 2.21, 3.55, 5.54, and 7.30 GPa. Time of flight neutron diffraction data were analyzed using the GSAS code.¹⁴ An x-ray diffraction pattern of the sample used for

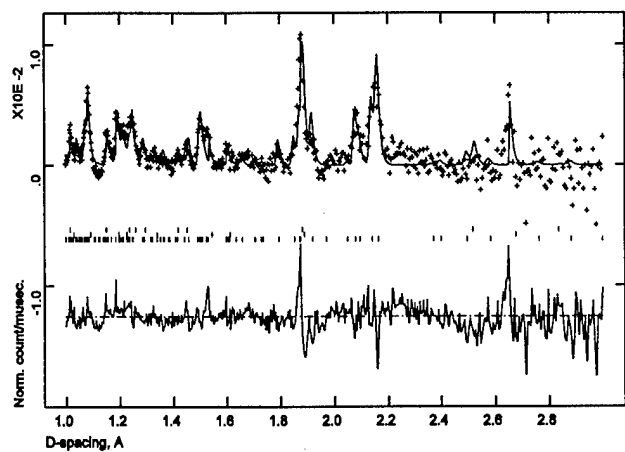


FIG. 2. Time of flight neutron diffraction data collected at 7.3 GPa on detector bank No. 3 for $\text{Nd}_2\text{Fe}_{17}\text{N}_3$. A preliminary fit used to obtain lattice parameters is also shown.

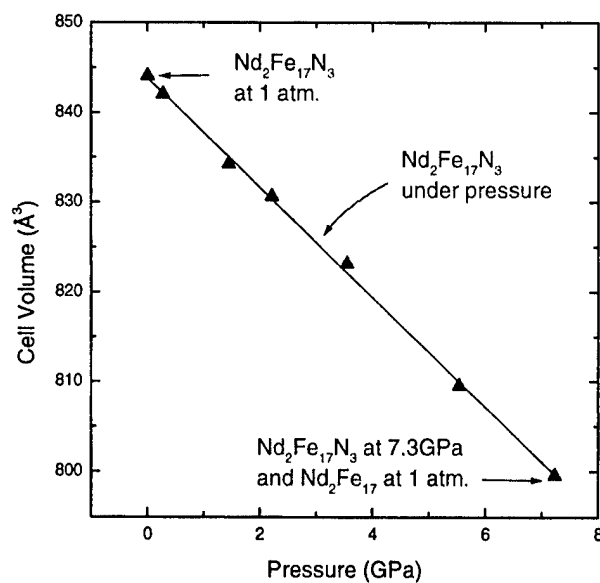


FIG. 3. Dependence of the unit cell volume of $\text{Nd}_2\text{Fe}_{17}\text{N}_3$ on sample pressure.

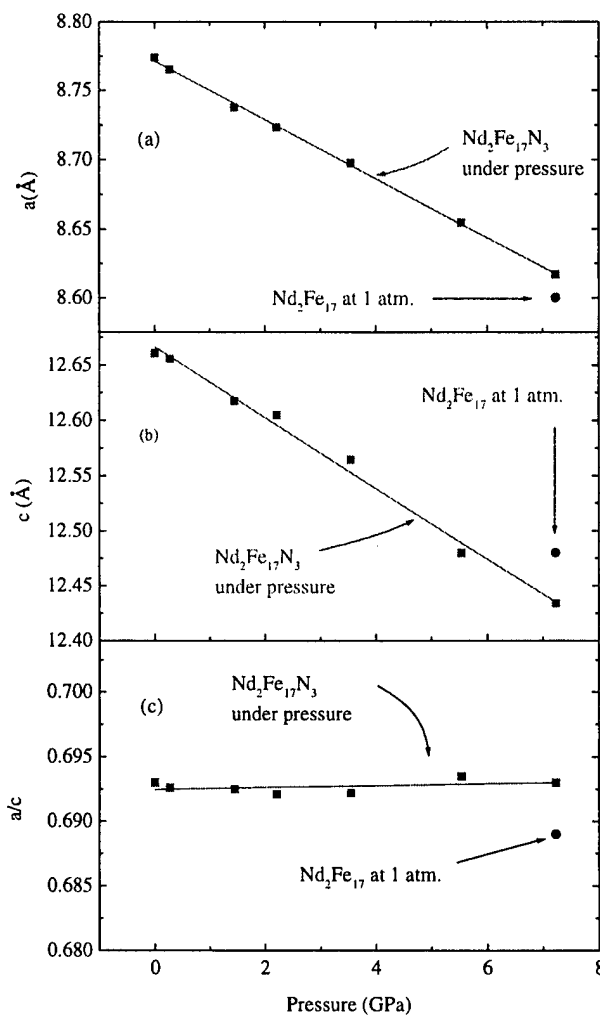


FIG. 4. Dependence of lattice parameters (a) a , (b) c , and (c) a/c of $\text{Nd}_2\text{Fe}_{17}\text{N}_3$ on sample pressure. Ambient pressure lattice parameters a , c , and a/c of $\text{Nd}_2\text{Fe}_{17}$ are also shown.

TABLE II. Lattice parameters of $\text{Nd}_2\text{Fe}_{17}\text{N}_3$ obtained by refining time of flight neutron diffraction patterns measured at 23 °C.

Pressure (GPa)	Lattice parameter			
	<i>a</i> (Å)	<i>c</i> (Å)	Vol. (Å ³)	<i>a/c</i>
0 ^a	8.7740	12.6605	844.07	0.6930
0.27	8.7652	12.6557	842.06	0.6926
1.44	8.7378	12.6172	834.25	0.6925
2.21	8.7232	12.6047	830.64	0.6921
3.55	8.6976	12.5646	823.15	0.6922
5.54	8.6546	12.4799	809.54	0.6935
7.23	8.6170	12.4339	799.56	0.6930

^aFrom neutron diffraction data obtained at MURR.

the high pressure experiment was obtained at atmospheric pressure on a Philips PW 1800/10 x-ray diffractometer using Cu K_α radiation. This x-ray diffraction pattern was analyzed using the FULLPROF code.¹⁰

III. RESULTS AND DISCUSSION

X-ray diffraction patterns of $\text{Nd}_2\text{Fe}_{17}\text{N}_3$ measured before the high pressure experiment, see Fig. 1(a), indicate that the sample is single phase except for a small amount of α -Fe. Analysis of the neutron diffraction pattern obtained at ambient pressure for $\text{Nd}_2\text{Fe}_{17}\text{N}_3$ at MURR confirmed the nitrogen content to be three per formula unit. All time-of-flight neutron diffraction data, see Fig. 2, could be fit based on the $\text{Nd}_2\text{Fe}_{17}\text{N}_3$ structure indicating that the sample did not undergo a phase transformation during exposure to high pressure.

Dependence of the lattice parameters and the unit cell volume of $\text{Nd}_2\text{Fe}_{17}\text{N}_3$ on sample pressure, see Table II, is shown in Figs. 3 and 4, respectively. The unit cell of $\text{Nd}_2\text{Fe}_{17}\text{N}_3$ contracts with increasing pressure at a rate of 6.1 Å³/GPa. This rate corresponds to a compressibility of 7×10^{-3} GPa⁻¹ or a bulk modulus of 14×10^{11} Nm⁻². The unit cell volume of $\text{Nd}_2\text{Fe}_{17}\text{N}_3$ at 7.3 GPa is approximately equal to that of $\text{Nd}_2\text{Fe}_{17}$ at atmospheric pressure. Even though the unit cell of $\text{Nd}_2\text{Fe}_{17}$ expands anisotropically when nitrogenated, contraction of the $\text{Nd}_2\text{Fe}_{17}\text{N}_3$ unit cell under pressure appears to be isotropic with both *a* and *c* lattice parameters decreasing by approximately 1.8% as the sample pressure increases from ambient to 7.3 GPa, see Table III.

The similarity of the lattice parameters and unit cell volume, obtained by refining the x-ray diffraction patterns shown in Fig. 1, of $\text{Nd}_2\text{Fe}_{17}\text{N}_3$ before and after the high pressure experiment, see Table III, strongly suggests that the interstitial nitrogen atoms were not expelled during exposure to high pressure even though the unit cell of $\text{Nd}_2\text{Fe}_{17}\text{N}_3$ was compressed down to the size of $\text{Nd}_2\text{Fe}_{17}$. The stability of $\text{Nd}_2\text{Fe}_{17}\text{N}_3$ under high pressure is in sharp contrast to its

TABLE III. The lattice parameters of $\text{Nd}_2\text{Fe}_{17}$ at ambient pressure, $\text{Nd}_2\text{Fe}_{17}\text{N}_3$ at ambient pressure before and after the high pressure experiment, and $\text{Nd}_2\text{Fe}_{17}\text{N}_3$ at 7.3 GPa.

	<i>a</i> (Å)	<i>c</i> (Å)	Vol. (Å ³)	<i>a/c</i>
$\text{Nd}_2\text{Fe}_{17}$ at 1 atm	8.600(1)	12.483(2)	799.7	0.689
$\text{Nd}_2\text{Fe}_{17}\text{N}_3$ at 1 atm	8.774(3)	12.660(2)	844.1	0.693
% change $\text{Nd}_2\text{Fe}_{17}$ to $\text{Nd}_2\text{Fe}_{17}\text{N}_3$	2.02	1.42	5.6	0.6
$\text{Nd}_2\text{Fe}_{17}\text{N}_3$ at 7.3 GPa	8.617(6)	12.433(8)	799.6	0.693
$\text{Nd}_2\text{Fe}_{17}\text{N}_3$ % change ambient to 7.3 GPa	-1.8	-1.8	-5.6	0.0
$\text{Nd}_2\text{Fe}_{17}\text{N}_3$ at 1 atm after high pressure experiment	8.768(2)	12.652(3)	842.5	0.693
$\text{Nd}_2\text{Fe}_{17}\text{N}_3$ at 1 atm % change after high pressure experiment	0.07	0.07	0.2	0.0

thermal instability which leads to expulsion of nitrogen by decomposition when heated beyond 550 °C.¹⁵

Results discussed herein have established the need to measure the Curie temperature of $\text{Nd}_2\text{Fe}_{17}\text{N}_3$ at comparable pressures. Such an experiment is now in the design stage.

ACKNOWLEDGMENTS

The authors wish to thank the Division of Materials Research of the U.S. National Science Foundation for Grant No. DMR-9614596, the staff at the Manuel Lujan, Jr. Neutron Scattering Center (MLNSCE) and Los Alamos Neutron Science Center (LANSCE), and the Office of Basic Sciences, Department of Energy, which funds MLNSCE and LANSCE.

- ¹J. M. D. Coey and H. Sun, J. Magn. Magn. Mater. **87**, L251 (1990).
- ²G. K. Marasinghe, P. C. Ezekwenna, W. J. James, Z. Hu, and W. B. Yelon, J. Appl. Phys. **81**, 5103 (1997).
- ³Gary J. Long, O. A. Pringle, F. Grandjean, and K. H. J. Buschow, J. Appl. Phys. **72**, 4854 (1992).
- ⁴M. Brouha and K. H. J. Buschow, J. Appl. Phys. **44**, 1813 (1973).
- ⁵J. Kamarád, Z. Arnold, and Schneider, J. Magn. Magn. Mater. **67**, 29 (1987).
- ⁶Z. Arnold, J. Kamarád, P. A. Algarabel, B. Garcia-Landa, and M. R. Ibarra, IEEE Trans. Magn. **30**, 619 (1994).
- ⁷O. Isnard, R. Zach, S. Niziol, M. Bacmann, S. Miraglia, J.-L. Soubeyrou, and D. Fruchart, J. Magn. Magn. Mater. **140-144**, 1073 (1995).
- ⁸Z. Arnold, J. Kamarád, L. Morellon, and M. R. Ibarra, J. Appl. Phys. **81**, 5693 (1997).
- ⁹J. Kamarád, M. R. Ibarra, L. Morellon, P. A. Algarabel, and Z. Arnold, J. Magn. Magn. Mater. **157/158**, 381 (1996).
- ¹⁰FULLPROF code developed by J. Rodriguez Carjaval, Institute Laue Langevin, Grenoble, France.
- ¹¹Product of 3M Company, St. Paul, MN, USA.
- ¹²D. L. Decker, J. Appl. Phys. **42**, 3239 (1971).
- ¹³J. M. Besson, R. J. Nemes, G. Hamel, G. S. Loveday, G. Weill, and S. Hull, Physica B **180/181**, 907 (1992).
- ¹⁴A. C. Larson and R. B. Von Dreele, Los Alamos National Laboratory Report LAUR 86-748.
- ¹⁵P. C. Ezekwenna, Ph.D. thesis, INPG, Grenoble, France, 1993.

A neutron diffraction structural study of $R_2Fe_{17-x}Al_x(C)$ ($R=Tb, Ho$) alloys

W. B. Yelon,^{a)} H. Luo, and M. Chen

Research Reactor Center, University of Missouri-Columbia, Columbia, Missouri 65211

W. C. Chang and S. H. Tsai

Department of Physics, National Chung Cheng University, Ming-Hsiung, Chia-Yi, Taiwan, Republic of China

The title compounds were confirmed to have the Th_2Zn_{17} type rhombohedral structure (space group $R\bar{3}m$) except for $Ho_2Fe_{16}Al$ and $Ho_2Fe_{15}Al_2$ which have the Th_2Ni_{17} type hexagonal structure (space group $P6_3/mmc$) while $Ho_2Fe_{13}Al_3$ is a mixture of the two phases with the hexagonal phase dominant. A larger unit cell favors the formation of an ordered rhombohedral phase rather than a disordered hexagonal phase. Both the substitution of Fe by Al and the insertion of C can expand the cell and lead to the formation of an ordered rhombohedral phase. The site preferences of Al are somewhat different with and without C. In both series, C is mainly found at the $9e$ interstitial site.

© 1998 American Institute of Physics. [S0021-8979(98)20211-8]

I. INTRODUCTION

It is well known that both the insertion of C and N^{1-3} and the substitution of Fe by Al, Ga, Si^{4-8} can lead to a great enhancement in the magnetic properties of the rare-earth transition metal compounds. One advantage of the carbides over the nitrides is that C atoms cannot only be introduced into the compounds from gas phase reaction but can also be introduced directly from melting, leading to better thermodynamic stability. The upper limit for C concentration by gas phase insertion is near 3 C atoms per formula unit with a fully filled octahedral $9e$ site. However, it is hard to introduce more than one C atom/f.u. from the melt. It was found that with certain substituents for Fe, such as Ga and Al, higher C concentration (>2 C atoms/f.u.) can be achieved in some 2-17 carbides.⁹⁻¹¹ As part of a comprehensive study on the effect of combined substitutional-interstitial modification on the structure and magnetic properties of the rare-earth $(RE)_2Fe_{17}$ compounds, especially with a higher substituent concentration, $Tb_2Fe_{17-x}Al_xC$, $Ho_2Fe_{17-x}Al_x$, and $Ho_2Fe_{17-x}Al_xC$ ($x=1-4$) have been studied by neutron diffraction and magnetic measurements. The magnetic properties of the carbided samples were reported elsewhere.¹² Here we report the structural details of these samples.

II. EXPERIMENT

All samples were prepared by arc melting of the constituent elements of purity at least 99.9% in a high purity argon atmosphere at the National Chung Cheng University in Taiwan. For the carbided specimens, a master alloy of Fe_3C is first melted in a vacuum induction furnace from pure Fe metal and graphite. The samples were remelted several times and then homogenized at 1100 °C for 24 h. Neutron diffraction data were collected on less than 1g of powdered samples at the University of Missouri Research Reactor using the high resolution position-sensitive detector (PSD) diffractometer. The samples were contained in thin wall V cans

and were measured at room temperature. The neutron wavelength used was 1.7675 Å. The data were accumulated in 24 h with 2θ ranging from 5° to 105° in 0.05° steps. The neutron diffraction powder patterns were analyzed by the Rietveld method¹³ using the FULLPROF program for multi-phase refinement, including magnetic structure refinement. T_c was measured by thermogravimetric analysis (TGA).

III. RESULTS AND DISCUSSION

$Tb_2Fe_{17-x}Al_xC$, $Ho_2Fe_{17-x}Al_xC$, and $Ho_2Fe_{13}Al_4$ were confirmed to have the Th_2Zn_{17} type rhombohedral structure (space group $R\bar{3}m$) while $Ho_2Fe_{16}Al$ and $Ho_2Fe_{15}Al_2$ have the Th_2Ni_{17} type hexagonal structure (space group $P6_3/mmc$), and $Ho_2Fe_{14}Al_3$ is a mixture of the two phases with the hexagonal phase dominant (67 wt %). The refinement results for $Tb_2Fe_{17-x}Al_xC$ and $Tb_2Fe_{17-x}Al_x$ (data from Ref. 14) are shown in Table I and those for the Ho specimens are shown in Table II. All samples are almost free of α -Fe (<0.5 wt %).

From Tables I and II, it can be seen that the hexagonal Ho samples have the smallest unit cells. This indicates that the size of the unit cell is a determinant factor in forming either an ordered rhombohedral phase or a disordered hexagonal phase. The substitution of Fe with bigger Al atoms and/or the insertion of C atoms expand the cell and resemble the bonding for light (and larger) rare-earths which crystallize in the ordered rhombohedral structure. The unit cell volume increases about $2 \text{ Å}^3/\text{f.u.}/\text{Al atom}$, with or without C. A small deviation is found with $Ho_2Fe_{13}Al_4$, which may reflect the discontinuity from the phase transition. In the carbided samples, the effect of different C contents has been taken into consideration.

The Al site occupancies for $Tb_2Fe_{17-x}Al_xC$ and $Tb_2Fe_{17-x}Al_x$ are shown in Fig. 1. Compared with the data for $Tb_2Fe_{17-x}Al_x$, Al still prefers the Fe(18h) site and totally avoids Fe(9d) (not shown in the figure) in the carbided samples. The Al occupancies in the carbided samples at 18h are higher than that in samples without C. In $Tb_2Fe_{15}Al_2C$, Al has a lower occupancy at the Fe(6c) as compared to

^{a)}Electronic mail: yelon@reactor.murr.missouri.edu

TABLE I. The refinement results and T_c for $\text{Tb}_2\text{Fe}_{17-x}\text{Al}_x\text{C}$ and $\text{Tb}_2\text{Fe}_{17-x}\text{Al}_x$. Data for $\text{Tb}_2\text{Fe}_{17-x}\text{Al}_x$ are from Ref. 14. Numbers in parentheses are uncertainties.

Compound	$\text{Tb}_2\text{Fe}_{16}\text{Al}_1\text{C}$	$\text{Tb}_2\text{Fe}_{15}\text{Al}_2\text{C}$	$\text{Tb}_2\text{Fe}_{14}\text{Al}_3\text{C}$	$\text{Tb}_2\text{Fe}_{13}\text{Al}_4\text{C}$	$\text{Tb}_2\text{Fe}_{15}\text{Al}_2$	$\text{Tb}_2\text{Fe}_{14}\text{Al}_3$	$\text{Tb}_2\text{Fe}_{13}\text{Al}_4$
$x(\text{Al})$, refined	1.01	2.09	2.82	3.94	1.98	3.14	4.08
$y(\text{C})$, refined	0.96	1.07	0.97	1.06	—	—	—
a , Å	8.6189(1)	8.6343(2)	8.6581(1)	8.6826(1)	8.5768(2)	8.6011(2)	8.6212(1)
c , Å	12.4697(3)	12.4919(3)	12.5316(3)	12.5814(3)	12.5191(4)	12.5549(3)	12.5872(2)
$V/\text{f.u.}$, Å ³	267.40	268.84	271.18	273.802	265.8	268.1	270.1
Tb, 6c z	0.3425(4)	0.3430(4)	0.3424(3)	0.3424(4)	0.3413(4)	0.3408(3)	0.3406(3)
Fe, 6c z	0.0957(5)	0.0953(3)	0.0956(2)	0.0963(3)	0.0958(3)	0.0957(2)	0.0941(2)
Fe, 18f x	0.2878(4)	0.2878(2)	0.2865(2)	0.2860(2)	0.2964(2)	0.2947(1)	0.2896(1)
Fe, 18h x	0.1688(3)	0.1695(2)	0.1698(2)	0.1698(2)	0.1676(1)	0.1684(10)	0.1690(1)
Fe, 18h z	0.4881(4)	0.4885(2)	0.4879(2)	0.4876(2)	0.4921(2)	0.4920(10)	0.4895(1)
μ , Tb 6c	-6.0(3)	-5.4(1)	-5.1(2)	-4.5(2)	-4.5(1)	-4.3(1)	-4.1(1)
μ , Fe 6c	2.7(4)	2.7(1)	2.6(2)	2.7(4)	2.7(2)	3.0(1)	3.1(1)
μ , Fe 9d	1.9(3)	1.8(1)	1.7(2)	1.4(2)	1.9(1)	1.9(1)	2.0(1)
μ , Fe 18f	1.4(3)	1.4(1)	1.2(2)	1.1(3)	1.9(1)	2.0(1)	2.1(1)
μ , Fe 18h	1.3(2)	1.4(1)	1.1(2)	1.0(5)	1.5(1)	1.8(1)	1.6(1)
χ^2	1.93	2.66	1.73	1.32	2.57	2.49	2.56
R factor	4.85	5.10	4.43	4.59	5.88	5.24	5.26
R_w factor	6.28	6.51	5.72	5.85	6.80	6.10	5.95
R_{mag} factor	8.47	8.92	10.8	10.5	10.1	8.23	5.07
T_c , K	529	529	516	475	^a	^a	^a

^aNo T_c data from Ref. 14.

$\text{Tb}_2\text{Fe}_{15}\text{Al}_2$, but the Al atoms fill up the 6c site more rapidly at a higher concentration which results in a higher 6c occupancy in $\text{Tb}_2\text{Fe}_{13}\text{Al}_4\text{C}$ than in $\text{Tb}_2\text{Fe}_{13}\text{Al}_4$. The behavior at the Fe(18f) site at higher concentration is just the opposite. C is found at the octahedral 9e site.

The behavior of the Al occupancies in $\text{Ho}_2\text{Fe}_{17-x}\text{Al}_x\text{C}$ (Fig. 2) is similar to that in the Tb carbides, namely Al atoms prefer the 18h site and fill up the 6c site more rapidly at higher concentration. C is only found at the 9e site. Because of the similarity in site environment between the hexagonal structure and the rhombohedral structure, the Al site occupancies shown in Table II for the hexagonal phase in

$\text{Ho}_2\text{Fe}_{17-x}\text{Al}_x$ ($x=1-3$) are those of equivalent sites in the rhombohedral structure. For the hexagonal structure, it is straightforward to figure out the Al occupancies at 6g, 12k, and 12j (equivalently 9d, 18h, and 18h in the rhombohedral structure, respectively) because there is no reason to believe these sites are not fully filled. The Al occupancies at the dumb bell 4e/4f sites can also be determined with the assumption that every possible dumb bell site is fully occupied by either a dumbbell or a rare-earth atom, that is, the occupancy of the rare-earth 2b site and that of the Fe 4e site add up to 1 and so do the rare-earth 2c and Fe 4f. Thus, the hexagonal structure can be fully modelled and refinement

TABLE II. The cell parameters, T_c , Al site occupancies for $\text{Ho}_2\text{Fe}_{17-x}\text{Al}_x\text{C}$ and $\text{Ho}_2\text{Fe}_{17-x}\text{Al}_x$. For the hexagonal phase in $\text{Ho}_2\text{Fe}_{17-x}\text{Al}_x$ ($x=1-3$), the Al site occupancies shown are those at equivalent sites of the rhombohedral structure. Numbers in parentheses are uncertainties.

Compound	$\text{Ho}_2\text{Fe}_{16}\text{Al}_1\text{C}$	$\text{Ho}_2\text{Fe}_{15}\text{Al}_2\text{C}$	$\text{Ho}_2\text{Fe}_{14}\text{Al}_3\text{C}$	$\text{Ho}_2\text{Fe}_{13}\text{Al}_4\text{C}$	$\text{Ho}_2\text{Fe}_{16}\text{Al}_1$	$\text{Ho}_2\text{Fe}_{15}\text{Al}_2$	$\text{Ho}_2\text{Fe}_{14}\text{Al}_3$	$\text{Ho}_2\text{Fe}_{13}\text{Al}_4$
$x(\text{Al})$, refined	0.98	2.23	3.01	4.02	1.40	2.12	3.11	3.94
$y(\text{C})$, refined	0.78	1.04	0.76	0.83	—	—	—	—
a , Å	8.5840(2)	8.6092(2)	8.6312(2)	8.6539(2)	8.4961(3)	8.5226(3)	8.5506(4)	8.5949(6)
c , Å	12.4531(3)	12.4819(4)	12.5173(4)	12.5600(3)	8.3145(4)	8.3278(4)	8.3468(4)	12.5650(9)
$V/\text{f.u.}$, Å ³	264.89	267.07	269.19	271.54	259.88	261.93	264.251	267.95
Al%, 6c	5.4(6)	10(1)	22(1)	32(1)	3(1)	15(2)	17(3)	30(2)
Al%, 9d	0.0	0.0	0.0	0.0	7(1)	11(2)	8(2)	0.0
Al%, 18f	4.0(6)	11(1)	11(1)	18(1)	10(1)	11(1)	19(3)	23(2)
Al%, 18h	10.6(6)	22(1)	30(1)	38(1)	10(1)	12(1)	21(3)	33(2)
μ , Ho 6c	-4.2(1)	-3.9(1)	-3.2(2)	-2.4(2)	-4.2(1)	-3.7(1)	^a	-4.3(3)
μ , Fe 6c	2.5(1)	2.2(2)	2.4(2)	2.5(2)	1.0	1.1	^a	1.6(5)
μ , Fe 9d	1.7(1)	1.7(1)	1.5(2)	1.3(1)	1.0	1.1	^a	0.9(3)
μ , Fe 18f	1.2(1)	1.2(1)	1.2(2)	1.2(2)	1.0	1.1	^a	0.6(4)
μ , Fe 18h	1.3(1)	1.2(1)	1.1(2)	1.2(2)	1.0	1.1	^a	0.6(4)
χ^2	2.02	3.51	2.51	2.00	2.02	2.24	3.65	1.98
R factor	4.63	5.69	4.74	4.77	4.95	4.76	6.18	6.21
R_w factor	5.95	7.48	6.09	6.17	6.22	6.07	8.19	7.78
R_{mag} factor	15.0	15.3	10.9	11.5	15.6	13.4	...	15.1
T_c , K	486	501	484	442	379	405	417	408

^aMoments not refined.

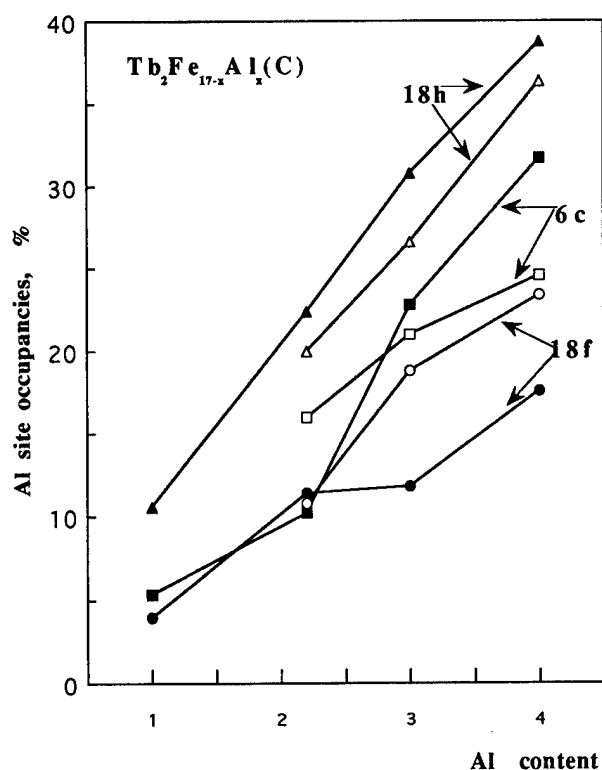


FIG. 1. Al site occupancies as a function of the Al contents in $Tb_2Fe_{17-x}Al_xC$ (closed symbols) and $Tb_2Fe_{17-x}Al_x$ (open symbols). Squares represent the site occupancies at the Fe(6c), circles for Fe(18f), and triangles for Fe(18h).

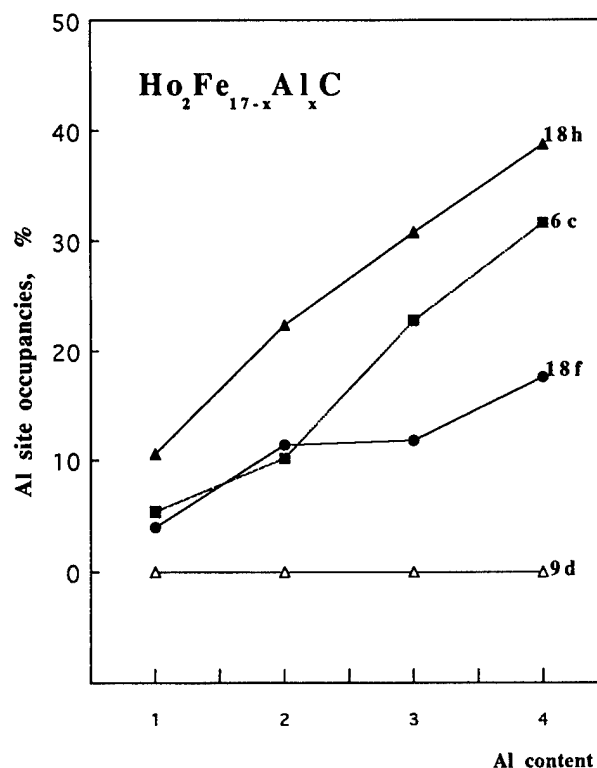


FIG. 2. Al site occupancies as a function of the Al contents in $Ho_2Fe_{17-x}Al_xC$.

results are shown in Table II. The Al 6g occupancy in the hexagonal structure is surprising since no Al is found at the cognate 9d site in the rhombohedral structure as in $Ho_2Fe_{17-x}Al_xC$ and $Ho_2Fe_{13}Al_4$.

From the TGA results, the Curie temperatures of the carbides are much higher than those of their uncarbided counterparts. However, within the same series, even though the unit cell volume increases almost linearly with the Al concentration, T_c reaches a maximum between $x=1$ and 2 for $R_2Fe_{17-x}Al_xC$ (Tables I and II), while for $Tb_2Fe_{17-x}Al_x$ (data not yet published) and $Ho_2Fe_{17-x}Al_x$, T_c peaks around $x=3$. Longer bond lengths resulting from the Al substitution and/or C insertion favor the ferromagnetic exchange and thus increase the T_c of the compound. However, as more Al atoms are introduced into the compound, magnetic exchange will be lost. That is why T_c declines with higher Al content. The shifting of the peak of T_c towards the lower Al concentration region with C may be caused by the change in Al site occupancies after the introduction of C or by bond lengths longer than optimum.

Magnetic refinements show that the moments for both the rare-earth and Fe atoms are along the basal plane in samples with and without C. The moments for Tb and Ho atoms couple antiferromagnetically to the Fe sublattice, as expected. The Fe 6c moments have the highest refined values in the Fe sublattice.

ACKNOWLEDGMENTS

This work was supported by the National Science Foundation (Grant No. DMR 9614596), US and the National Science Council (Contract No. NSC-85-2112-M194-002), Taiwan.

- ¹D. B. de Mooij and K. H. J. Buschow, *J. Less-Common Met.* **142**, 349 (1988).
- ²J. M. D. Coey and H. Sun, *J. Magn. Magn. Mater.* **87**, 1251 (1990).
- ³R. B. Helmholdt and K. H. J. Buschow, *J. Less-Common Met.* **155**, 15 (1989).
- ⁴W. B. Yelon, H. Xie, G. J. Long, O. A. Pringle, F. Grandjean, and K. H. J. Buschow, *J. Appl. Phys.* **73**, 6029 (1993).
- ⁵G. J. Long, G. K. Marasinghe, S. Mishra, O. A. Pringle, Z. Hu, W. B. Yelon, D. P. Middleton, K. H. J. Buschow, and F. Grandjean, *J. Appl. Phys.* **76**, 5383 (1994).
- ⁶Z. Hu, W. B. Yelon, S. Mishra, G. J. Long, O. A. Pringle, D. P. Middleton, K. H. J. Buschow, and F. Grandjean, *J. Appl. Phys.* **76**, 443 (1994).
- ⁷R. van Mens, *J. Magn. Magn. Mater.* **61**, 24 (1986).
- ⁸G. J. Long, G. K. Marasinghe, S. Mishra, O. A. Pringle, F. Grandjean, K. H. J. Buschow, D. P. Middleton, W. B. Yelon, F. Pourarian, and O. Isnard, *Solid State Commun.* **88**, 761 (1993).
- ⁹B. Shen, F. Wang, L. Kong, L. Cao, and H. Guo, *J. Magn. Magn. Mater.* **127**, L267 (1993).
- ¹⁰Z. H. Cheng, B. G. Shen, F. W. Wang, J. X. Zhang, H. Y. Gong, and W. S. Zhan, *J. Phys., Condens. Matter* **7**, 3195 (1995).
- ¹¹W. B. Yelon, Z. Hu, W. C. Chang, and S. L. Lu, *IEEE Trans. Magn.* **32**, 4410 (1996).
- ¹²W. C. Chang, S. H. Tsai, L. J. Chao, H. Luo, Z. Hu, and W. B. Yelon, *J. Magn. Magn. Mater.* **172**, 277 (1997).
- ¹³H. M. Rietveld, *J. Appl. Crystallogr.* **2**, 65 (1969).
- ¹⁴G. K. Marasinghe, S. Mishra, O. A. Pringle, G. J. Long, Z. Hu, W. B. Yelon, F. Grandjean, D. P. Middleton, and K. H. J. Buschow, *J. Appl. Phys.* **76**, 6731 (1994).

High remanence (Sm, Zr)Fe₇N_x + α -Fe nanocomposite magnets through exchange coupling

T. Hidaka, T. Yamamoto, H. Nakamura, and A. Fukuno^{a)}

Materials Research Center, TDK Co., 570-2 Matsugasaki, Minami-Hatori, Narita-shi 286-8588, Japan

We have investigated the influence of α -Fe content on the magnetic properties of (Sm, Zr)Fe₇N_x + α -Fe nanocomposite permanent magnet materials. As α -Fe content increases, the saturation magnetization and the remanence increase while the coercivity decreases monotonously. Also we confirmed the influence of microstructure on magnetic properties. Uniform and fine grain sizes of around 20 nm realized high remanence and high squareness of demagnetizing curve such as $B_r = 9.9$ kG, $H_cJ = 9.1$ kOe, $H_k/H_cJ = 29.9\%$, and $(BH)_{\max} = 17.8$ MGOe. These experimental results agree well with micromagnetic calculations by other researchers. Compaction-molded bonded magnet was prepared by magnetic powders with magnetic properties of $B_r = 9.9$ kG, $H_cJ = 8.2$ kOe, $(BH)_{\max} = 17.5$ MGOe and 2 wt% of epoxy resin. Bonded magnet with a density of 5.91 g/cm³ showed high magnetic properties as follows: $B_r = 7.6$ kG, $H_cJ = 8.4$ kOe, and $(BH)_{\max} = 12.0$ MGOe. © 1998 American Institute of Physics. [S0021-8979(98)22711-3]

I. INTRODUCTION

These days, nanocomposite magnets, which consist of magnetically hard and soft phases, have gained much attention because of their high remanence and maximum energy products. So many theoretical and experimental investigations of these magnets have been reported.¹⁻⁸

Isotropic (Sm, Zr)Fe₇N_x + α -Fe nanocomposite magnet, which was developed by the authors through a rapidly quenching method including heat treatment and nitrogeneration, showed magnetic properties high enough for practical use.⁹⁻¹² Also this nanocomposite magnet has shown small deterioration of magnetic properties during pulverization and stable magnetic properties for long time aging at elevated temperature compared with isotropic Nd₂Fe₁₄B single phase-type magnetic powders.¹⁰

In this article we focused on the influence of α -Fe content and also microstructure on the magnetic properties of (Sm, Zr)Fe₇N_x + α -Fe nanocomposite magnets. We also verified the agreement between experimental results and theoretical calculations for nanocomposite magnets.

II. EXPERIMENT

The Sm-Zr-Fe-Co alloys were rapidly solidified by melt spinning onto a Be-Cu roller at a substrate velocity of $V_s = 75$ m/s, under an argon atmosphere. As-quenched flakes were pulverized into particle size of less than 106 μ m. The heat treatment in order to form nanoscaled (Sm, Zr)Fe₇ and α -Fe mixture was carried out over the temperature range of 700–750 °C for 1 h on the overquenched powder samples in an argon atmosphere. After heat treatment, powders were nitrogenated at around 450 °C for 20 h in a nitrogen gas flow atmosphere. The composition of powder samples was checked by fluorescence x-ray method. The nitrogen contents were measured by mass analysis of gas evolved from high-temperature molten alloys. X-ray diffraction analysis

was performed with Cu $K\alpha$ radiation. Transmission electron microscopy (TEM) observation was made with a JOEL JEM-2000FX electron microscope operating at 200 kV. Magnetic properties of powders were measured by using a vibrating sample magnetometer (VSM) with the applied field of 20 kOe after pulse magnetization of 50 kOe. No demagnetization correction has been applied. Resin bonded magnets were fabricated with 2 wt% epoxy resin at a die press pressure of 12 ton/cm² without magnetic field. Magnetic properties of bonded magnets were measured by using a B - H tracer with the applied field of 30 kOe.

III. RESULTS AND DISCUSSION

A. Influence of α -Fe content

In order to investigate the influence of α -Fe content on the magnetic properties of (Sm, Zr)Fe₇N_x + α -Fe nanocomposite magnet, magnetic powder samples with various Sm content were prepared. Their composition is shown in Table I. Nitrogen contents of samples were in a range of 3.7–4.0 wt%. We calculated the α -Fe content for these samples. We did not discriminate Co from Fe, however Co ratio to Fe is around 0.05. A composition of Sm_{10.4}Zr_{3.5}(Fe, Co)_{86.1} has been used for (Sm, Zr)Fe₇ phase with TbCu₇ structure. This compositional analyzed value was obtained by TEM-energy dispersive spectroscopy (EDS) analyses on fine hard phase grains individually.¹² The calculations were performed in the

TABLE I. Composition of magnetic powder samples and calculated phase existence ratio of Fe.

	Sm (at. %)	Zr (at. %)	Fe+Co (at. %)	α -Fe (wt%)	Fe ₈ Zr (wt%)	SmFe ₇ (wt%)
Powder A	8.16	3.40	88.44	16.33	1.68	81.99
Powder B	7.82	3.41	88.77	18.81	2.03	79.16
Powder C	7.79	3.42	88.79	19.00	2.08	78.92
Powder D	7.70	3.42	88.88	19.64	2.16	78.20
Powder E	7.42	3.46	89.12	21.64	2.51	75.85

^{a)}Electronic mail: afukuno@mb1.tdk.co.jp

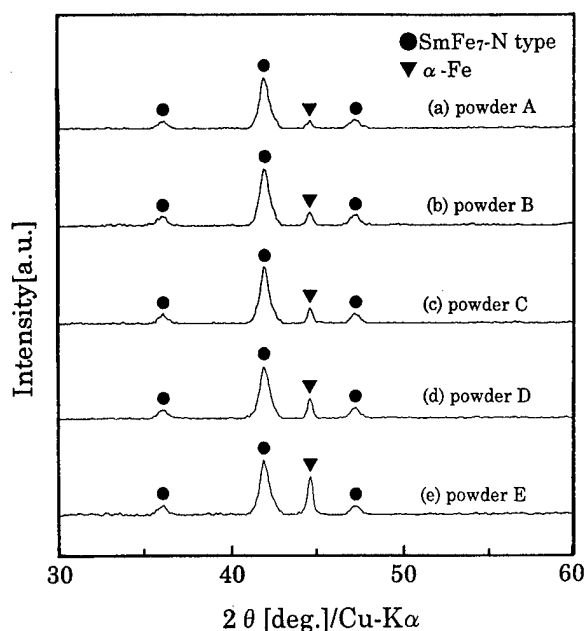


FIG. 1. X-ray diffraction patterns of magnetic powder samples with various contents of Sm, which were summarized in Table I.

following sequences. First, all of the Sm metal could form (Sm, Zr)Fe₇ phase. Second, the rest of the Zr metal forms Fe₃Zr.¹¹ Finally, the rest of the Fe metal exists as α -Fe phase. The results are given in Table I. X-ray diffraction patterns of these powders are shown in Fig. 1. The peak intensity of α -Fe increased with calculated value of α -Fe content. Dependence of the magnetic properties of these powders on α -Fe content is shown in Fig. 2. As α -Fe content increases, the saturation magnetization and the remanence increase while the coercivity decreases. These phenomena were reported theoretically^{6,7} and experimentally.⁸ Since almost all the micromagnetic calculations applied for the Nd₂Fe₁₄B/Fe₃B or Nd₂Fe₁₄B/ α -Fe system, the calculated value does not coincide, but the tendency agrees well with these results. It was pointed out by Bauer *et al.* that the squareness of the demagnetization curve deteriorated with increasing α -Fe content.⁸ In our research, $(BH)_{\max}$ reached a peak at around 19 wt% of α -Fe, because the same heat treatment condition, including nitrogenation, was applied for sample powders A–E. However, optimization of the heat treatment condition will enable higher magnetic properties, especially for sample powder E.

B. Influence of microstructure

Figure 3 shows bright-field TEM micrographs of powder samples. Figure 3(a) shows uniform and fine grains, which size around 20 nm. Figure 3(b) shows less uniform grains including grain sizes of 60 nm compared with Fig. 3(a). Each magnetic powder showed magnetic properties as follows: (a) $Br=9.9$ kG, $HcJ=9.1$ kOe, $Hk/HcJ=29.9\%$, $(BH)_{\max}=17.8$ MGOe and (b) $Br=9.5$ kG, $HcJ=9.8$ kOe, $Hk/HcJ=22.7\%$, $(BH)_{\max}=15.5$ MGOe, respectively.

We confirmed that fine and uniform microstructure realized higher remanence and Hk/HcJ ratio.

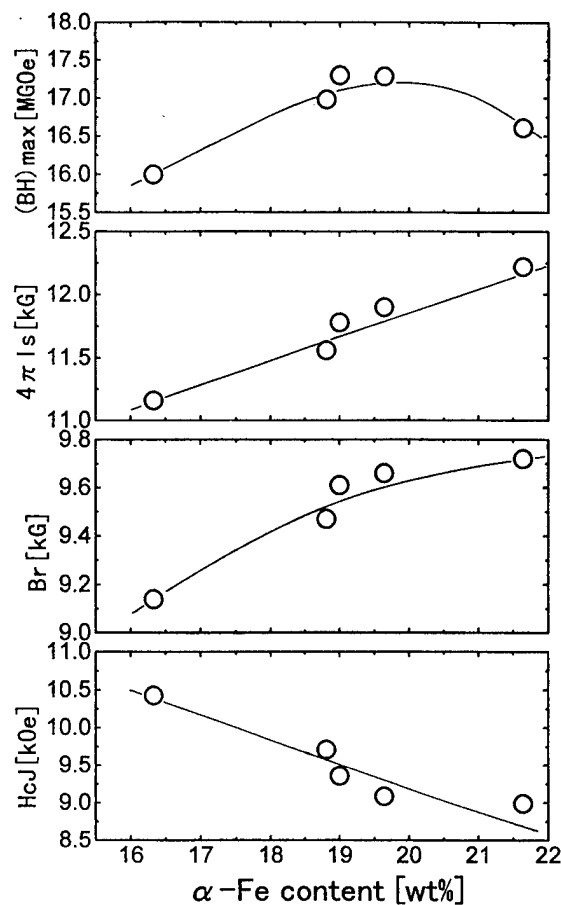


FIG. 2. Dependence of the magnetic properties on α -Fe content.

Theory also predicts^{6,7} that the smaller and more uniform microstructures are essential for higher remanence, especially the Hk/HcJ ratio. The theoretical calculation on the influence of microstructure such as grain sizes and uniformity on magnetic properties agreed well with our experimental results.

C. Magnetic properties of bonded magnet

Compaction-molded bonded magnet made by mixing with a 2 wt% epoxy resin was prepared with magnetic powders with magnetic properties as follows: $Br=9.9$ kG, $HcJ=8.2$ kOe, and $(BH)_{\max}=17.5$ MGOe. The density of bonded magnet made with die press pressure 12 ton/cm² was 5.91 g/cm³. This value was 77% of the powder's density.⁹ Demagnetization curve of bonded magnet is shown in Fig. 4. The bonded magnet showed excellent magnetic properties as follows: $Br=7.6$ kG, $HcJ=8.4$ kOe, and $(BH)_{\max}=12.0$ MGOe. These values are superior to commercially available isotropic Nd₂Fe₁₄B single-phase-type bonded magnet.

IV. CONCLUSIONS

We have investigated the magnetic properties and the microstructures of (Sm, Zr)Fe₇N_x + α -Fe nanocomposite magnets. Observed behavior agreed with theoretical calculations.

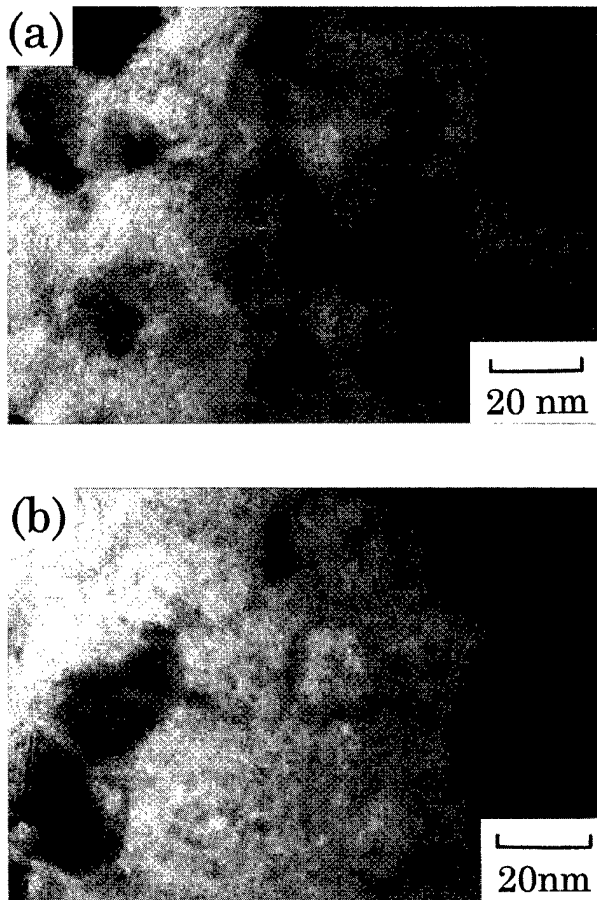


FIG. 3. TEM micrographs of magnetic powder samples of magnetic properties as follows: (a) $B_r=9.9$ kG, $H_{cJ}=9.1$ kOe, $H_k/H_{cJ}=29.9\%$, $(BH)_{\max}=17.8$ MGOe and (b) $B_r=9.5$ kG, $H_{cJ}=9.8$ kOe, $H_k/H_{cJ}=22.7\%$, $(BH)_{\max}=15.5$ MGOe.

- (1) When α -Fe content is in the range of 16–22 wt%, increasing α -Fe content, the saturation magnetization, the remanence increase, and the $(BH)_{\max}$ reach a peak while the coercivity decreases monotonously.
- (2) As the microstructure of grains became smaller and more uniform, the magnetic properties of this magnet improved, especially the H_k/H_{cJ} ratio. We also made bonded magnet and evaluated magnetic properties.

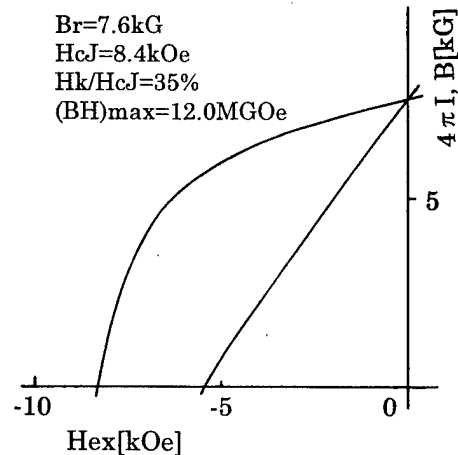


FIG. 4. Demagnetization curve of a $(\text{Sm}, \text{Zr})(\text{Fe}, \text{Co})_7\text{N}_x + \alpha\text{-Fe}$ bonded magnet.

- (3) Compaction-molded bonded magnet showed excellent magnetic properties as follows: $B_r=7.6$ kG, $H_{cJ}=8.4$ kOe, and $(BH)_{\max}=12.0$ MGOe.

¹E. F. Kneller and R. Hawig, IEEE Trans. Magn. **27**, 3588 (1991).

²J. Ding, P. G. McCormick, and R. Street, J. Magn. Magn. Mater. **124**, 1 (1993).

³A. Manaf, R. A. Buckley, and H. A. Davies, J. Magn. Magn. Mater. **128**, 302 (1993).

⁴S. Hirosawa, H. Kanekiyo, and M. Uehara, J. Appl. Phys. **73**, 6488 (1993).

⁵A. Inoue, A. Takeuchi, A. Makino, and T. Masumoto, Mater. Trans., Jpn. Inst. Metals **36**, 676 (1995).

⁶R. Fischer, T. Schrefl, H. Kronmüller, and J. Fidler, J. Magn. Magn. Mater. **150**, 329 (1995).

⁷H. Fukunaga, N. Kitajima, and Y. Kanai, Mater. Trans. Jpn. Inst. Metals **37**, 846 (1996).

⁸J. Bauer, M. Seeger, A. Zern, and H. Kronmüller, J. Appl. Phys. **80**, 1667 (1996).

⁹T. Yoneyama, T. Yamamoto, and T. Hidaka, Appl. Phys. Lett. **67**, 3197 (1995).

¹⁰T. Yamamoto, T. Hidaka, T. Yoneyama, H. Nishio, and A. Fukuno, Mater. Trans. Jpn. Inst. Metals **37**, 1232 (1996).

¹¹T. Hidaka, N. Uchida, T. Yamamoto, H. Nakamura, M. Iwasaki, G. Nishizawa, and A. Fukuno, J. Magn. Soc. Jpn. **21**, 373 (1997) (in Japanese).

¹²A. Fukuno, T. Yamamoto, T. Hidaka, and H. Nakamura, J. Jpn. Soc. Powder and Powder Metallurgy **44**, 833 (1997) (in Japanese).

Effect of Al substitution on the local environments and magnetic properties of partially nitrogenated $(\text{Er}_{0.5}\text{Pr}_{0.5})_2\text{Fe}_{17}$ permanent magnets

V. G. Harris and D. J. Fatemi

U.S. Naval Research Laboratory, Washington, D.C. 20375

K. G. Suresh and K. V. S. Rama Rao

Department of Physics, Indian Institute of Technology, Madras-600 036, India

Extended x-ray absorption fine structure measurements of the Fe K, and Pr and Er L_{III} absorption edges, were carried out to elucidate the relationship between the local structure and magnetism in Al substituted, partially nitrogenated $(\text{Er}_{0.5}\text{Pr}_{0.5})_2\text{Fe}_{17}$ permanent magnets. We find that the nitrogenation acts to dilate both the Fe-Fe and the (Pr,Er)-Fe bonds, thus raising the T_C via a magnetovolume effect. However, nitrogenation of Al-substituted samples acts to decrease the average Fe-Fe bond distance, thus reducing the exchange on the Fe sublattice and lowering T_C relative to the nitrogenated parent compound. This is opposite to the trend measured in systems when N is absent. © 1998 American Institute of Physics. [S0021-8979(98)36011-9]

I. INTRODUCTION

In recent years the magnetovolume enhancement of the magnetic properties in the R_2T_{17} (R : rare earths) permanent magnet compounds has been the subject of much activity. This trend has been spurred largely by the discovery that nitrogenation of these compounds expands the transition metal sublattice and results in a significant increase in the Curie temperature (T_C).¹⁻³ Following in this vein, others have experimented with the substitution of Al and Ga with mixed results.⁴⁻⁸ For example, combining neutron diffraction (ND) and Mossbauer effect (ME) measurements, Long *et al.*⁴ and Yelon *et al.*⁵ have reported compressive studies of the structure and magnetic properties of Al substituted $\text{Nd}_2\text{Fe}_{17}$. This group of researchers have also reported similar styled investigations of the effects of nitrogenation on $\text{Nd}_2\text{Fe}_{17}$ ⁹ and $\text{Pr}_2\text{Fe}_{17}$,¹⁰ and the effects of Ga substitution in the $\text{Nd}_2\text{Fe}_{17}$ system.⁶ Suresh and Rama Rao (SRR) have reported on the magnetic, structural and transport properties of the $(\text{Er}_y\text{Pr}_{1-y})_2\text{Fe}_{17}$ compounds,^{11,12} as well as the effects of Al substitution,⁸ nitrogenation,¹² and the combined use of Al substitution and nitrogenation on these properties.^{7,13}

In the case of $\text{Nd}_2\text{Fe}_{17-x}\text{Al}_x$, Long and Yelon report a near-linear increase in lattice parameters and unit cell volumes with increasing x . A similar result was found by Suresh and Rama Rao in the $(\text{Er}_y\text{Pr}_{1-y})_2\text{Fe}_{17-x}\text{Al}_x$ system. The T_C is reported to increase with increasing Al content for the $\text{Nd}_2\text{Fe}_{17-x}\text{Al}_x$ samples, reaching a maximum near $x=3.5$. For the $(\text{Er}_y\text{Pr}_{1-y})_2\text{Fe}_{17-x}\text{Al}_x$ samples, T_C reaches a maximum for $x=3$, then drops precipitously for $x>4$. The agreement between these results and those of Long *et al.*^{4,9,10} and Yelon *et al.*⁵ suggest that the choice of R plays a minor role in the effect of both Al substitution and nitrogenation.

When Al substitution and nitrogenation are used in conjunction these trends appear to be violated. Taking the case of $(\text{Er}_{0.5}\text{Pr}_{0.5})_2\text{Fe}_{17-x}\text{Al}_x\text{N}_y$, where $y=1$ and $x=0-5$, T_C decreases from the nitrided parent compound with increasing x , ultimately having no effect on the T_C for $x>4$. This result appears to be closely related to the degree of nitrogenation achievable when the parent compound contains Al substituted for Fe. Suresh and Rama Rao report, in agreement with

Buschow *et al.*, the amount of nitrogen one can incorporate into the 2:17 structure is inversely proportional to the amount of Al, with y decreasing with increasing x until $y=0$ for $x=6$.⁷

In this article, we explore the effects of Al substitution on the local structure and magnetism of the permanent magnet, $(\text{Er}_{0.5}\text{Pr}_{0.5})_2\text{Fe}_{17-x}\text{Al}_x\text{N}_y$.

II. EXPERIMENT

The compounds were prepared by arc melting elements of 99.9% purity for Pr and Er and 99.99% purity for Fe and Al under dynamic positive pressure of Ar gas. The melted ingots were then homogenized at 900 °C for 7 days. The nitrogenation was carried out using a high pressure apparatus that was specifically designed for this purpose. The degree of nitrogenation was measured by monitoring the pressure drop in the reactor due to absorption by the sample. This apparatus is described in detail in Ref. 12.

Powder x-ray diffraction, using a fixed anode Co target, verified that all samples were nearly pure phase, with some having trace amounts of α -Fe. For the range of Al substitution that we study here, $0 \leq x \leq 3$, the a and c parameters are measured to increase $\sim 1\%$.

Magnetization measurements were carried out using a PAR vibrating sample magnetometer in the temperature range of 28–800 K, and Mossbauer effect (ME) measurements using a conventional fixed acceleration spectrometer with a 20 mCi ^{57}Co source embedded in a Rh matrix over a temperature range of 18–700 K. We direct the reader to Refs. 7 and 13 for details of the long-range-structure and magnetic properties of these samples.

In preparation of x-ray absorption measurements the powder samples were spread onto 3M Scotch Magic Tape™. Multiple layers of these powdered tapes were stacked in order to tailor the amount of absorption by the sample at the absorption edge being measured. This was done so as to optimize the signal to noise and to improve the uniformity of the sample exposed to the radiation. The x-ray absorption coefficient, in the range of the Fe K and Pr and Er L_{III} ab-

sorption edges, were measured in transmission mode using the X23B beamline¹⁴ at the National Synchrotron Light Source (Brookhaven National Laboratory).

Following the procedural steps outlined in Ref. 15, the extended fine structure above the absorption edge was isolated, normalized to the edge energy and step height, and converted to photoelectron wave vector space (k). In k space, a cubic spline background was fit and removed from the data to minimize the nonoscillatory atomic background curvature. These data were then Fourier transformed (FT) to radial coordinates for examination of the local environments around the absorbing atoms. In this form the FT peaks are offset from their true bond distances by an electronic phase shift.

Quantitative analysis of the local environment around Fe, Pr, and Er was performed by Fourier-filtering the NN peak in the FT EXAFS spectra and least squares fitting these data with simulated single-scattering EXAFS data generated using the FEFF (vs 6) codes of Rehr *et al.*¹⁶ This type analysis provides a quantitative measure of the nearest neighbor (NN) distance (i.e., bond lengths), Debye-Waller coefficients (DWCs) (i.e., thermal and static atomic disorder), and the coordination number, i.e., the total number of atoms contributing to the local coordination sphere around the absorbing atoms.

III. RESULTS AND DISCUSSION

We are limited by space considerations and provide only EXAFS analysis of the Fe K and Pr L_{III} EXAFS. The Er L_{III} analysis is omitted here and will be presented elsewhere.

Figure 1 is a plot of the FT Fe EXAFS collected from the Al-substituted and nitrided samples, together with data for the parent compound. These data have been analyzed using identical background removal procedures and FT parameters, and are plotted on the same axes to allow for direct comparison. The x axis is limited to $1.0 \text{ \AA} < r < 5.0 \text{ \AA}$ to allow a clear inspection of the NN region. Samples having $x=0, y=1$; $x=0, y=0$; and $x=3, y=1$; are plotted with error bars that were calculated to reflect both the statistical uncertainty and the error introduced to the data from the procedural steps prior to and including the Fourier transformation. The inset panel depicts a plot of the average Fe-Fe/Al bond distance (henceforth denoted $\langle r \rangle_{\text{Fe-Fe/Al}}$) and the average Fe-Fe/Al DWC (henceforth denoted $\langle \text{DWC} \rangle_{\text{Fe-Fe/Al}}$) calculated for the atoms contributing to the NN peak as a function of x . Values coinciding to the parent compound are to provide a reference baseline.

In the FT data of Fig. 1 we see that significant structural change occurs around the Fe atoms with the substitution of Al. These are most visible as changes in the Fourier peak amplitudes appearing over $2 \text{ \AA} < r < 5 \text{ \AA}$ and a shift in the position of the NN Peak. Because the NN peak of Fe is dominated by other Fe and Al atoms that are distributed on 4 inequivalent sites (i.e., 6c, 9d, 18f, 18h) we opt to describe the environment as an average Fe-Fe/Al bond unless otherwise specified. This simplification reduces the number of adjustable parameters in our fitting analysis from as many as 12 to no more than 3.

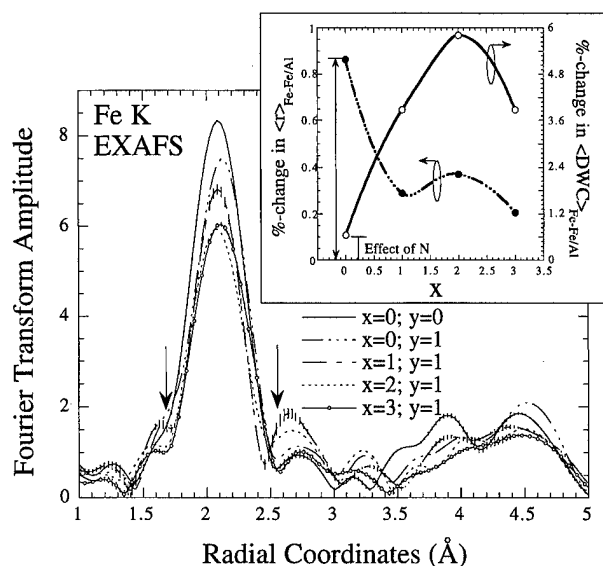


FIG. 1. Fourier transformed Fe K EXAFS for $(\text{Er}_{0.5}\text{Pr}_{0.5})_2\text{Fe}_{17-x}\text{Al}_x\text{N}_y$ where $x=0, 1, 2$ and 3 and $y=0, 1$. A k^3 -weighting was applied to a k -range of 2.3 – 13.25 \AA^{-1} . The inset panel depicts a plot of the percent change in the calculated average Fe-Fe/Al bond distance and the Debye-Waller coefficient for the Fe coordination sphere relative to the same in the parent compound. These data were deduced from a least-squares fitting of a FF r range indicated by the arrows.

Upon nitrogenation the $\langle r \rangle_{\text{Fe-Fe/Al}}$ increases 0.9% from that of the parent compound. This result is a direct measurement of the dilation of the Fe coordination sphere which reflects the expansion of the Fe sublattice and accounts for the widely reported increase in Curie temperature experienced when the 2:17s are nitrided. With the substitution of Al we observe that $\langle r \rangle_{\text{Fe-Fe/Al}}$ decreases abruptly (-0.6%), plateaus, and then continues its decrease. Although, others have reported a unit cell volume increase with the substitution of small amounts of Al ($x < 4$) (sans N),^{4,8} we observe that in partially nitrided samples, the Al acts to contract the Fe coordination sphere relative to the nitrided baseline. This contraction is no doubt responsible for the measured decrease in Curie temperature in these compounds, and is consistent with the ME results of Suresh and Rama Rao¹³ who found that the T_C and the HFF of all Fe sites reduce with increased Al content for these samples.

The $\langle \text{DWC} \rangle_{\text{Fe-Fe/Al}}$ increases with increased Al content for $0 < x < 2$, and experiences a relative decrease for $x=3$. Because it is reasonable for one to assume that the thermal component to the DWC does not change appreciably with x , this trend largely reflects the static displacements of atoms about their mean bond distance. The abrupt reversal in the DWC for $x=3$, and the corresponding reduction in the $\langle r \rangle_{\text{Fe-Fe/Al}}$, signals increased ordering and a closer packing of atoms around the Fe atoms for $x=3$.

In separate fitting analyses, the Fe-Al correlations were fit simultaneously with the Fe-Fe correlations in the same manner as described in Sec. II B. These fitting results (not shown) indicate that the Fe-Al bond undergoes an abrupt decrease for $x=3$. The most plausible explanation of this result and the behavior of the average Fe environment is a

redistribution of Al atoms to sites having a closer NN distance.

Long *et al.*⁴ report that Al atoms preferentially reside in the 18h site for low x (i.e., $x < 4$), and prefer the 6c and 18f sites for higher x (i.e., $x > 6$). Because the 18h sites have a NN distance of ~ 2.576 Å, while the 6c sites have a longer average NN distance of ~ 2.675 Å, one would expect a slight dilation of the Fe coordination sphere.¹⁷ Instead we measure a distinct contraction of the Fe coordination sphere, suggesting that the behavior of the Al site filling is significantly effected by the presence of the N ions. Our measured contraction is more consistent with a redistribution of Al atoms to the 9d sites although we cannot rule out some other electronic interaction which might facilitate a contracted bond distance without the need for redistribution of sites.

Figure 2 is plots of FT Pr L_{III} EXAFS data for all samples. Because of the onset of the Fe K transition at 7112 eV, the Pr L_{III} extended fine structure is terminated at approximately 11 Å^{-1} . Data for samples $x=0, y=0$; $x=0, y=1$; and $x=3, y=1$ are plotted with error bars. Like the Fe data of Fig. 1, we see that nitrogenation acts to increase the radius of the Pr coordination sphere by 1.7%. The $\langle \text{DWC} \rangle_{\text{Pr-Fe/Al}}$ increases 24%, compared to the modest increases of $<1\%$ for the Fe environment. This effect is fully consistent with what one would expect if the N ions were to occupy sites in close proximity to the R sites creating static strain fields between the R and Fe/Al NN atoms. This observation is consistent with the results of Capehart, Mishra, and Pinkerton who performed EXAFS studies to determine the site occupation of the N interstitials, and concluded that they reside on the 9e sites.¹⁸

With Al substitution, the Pr environment experiences a steady increase in the atomic disorder as evidenced by the increase in $\langle \text{DWC} \rangle_{\text{Pr-Fe/Al}}$. In addition, the $\langle r \rangle_{\text{Pr-Fe/Al}}$ increases 1.0% for the range $1 < x < 3$, then experiences a small dip for $x=3$. However, the FT of the $x=3$ data clearly shows a large asymmetry in the NN environment indicating at least a bimodal distribution of bonds. Because we fit this range of data with a single "average" bond length a physical interpretation of the fitting results may not be tenable. Alternatively, the appearance of this high- r asymmetry in the NN region is consistent with a preferential filling of Al on the 9d sites which have the largest Pr-Fe/Al bond distance, 3.342 Å. This result alone would not be compelling save for the trend in the Fe EXAFS data which supports a redistribution of Al atoms to the 9d sites as a source of the measured contraction of the Fe coordination sphere.

In summary, we find the act of nitriding the $(\text{Er}_{0.5}\text{Pr}_{0.5})_2\text{Fe}_{17}$ structure is to dilate both the Fe and Pr coordination spheres leading to an increase in the T_C via a positive magnetovolume effect on the Fe sublattice. Second, we report that in the concurrent use of Al substitution and partial nitrogenation acts to reduce the radius of the Fe coordination sphere thus reducing the Fe-Fe exchange and lowering T_C .

We observe local structural changes around Fe and Pr with Al substitution that suggest either a preferential redistribution of Al atoms to the 9d sites for $x \geq 3$, or an electronic interaction that facilitates a contracted bonding ar-

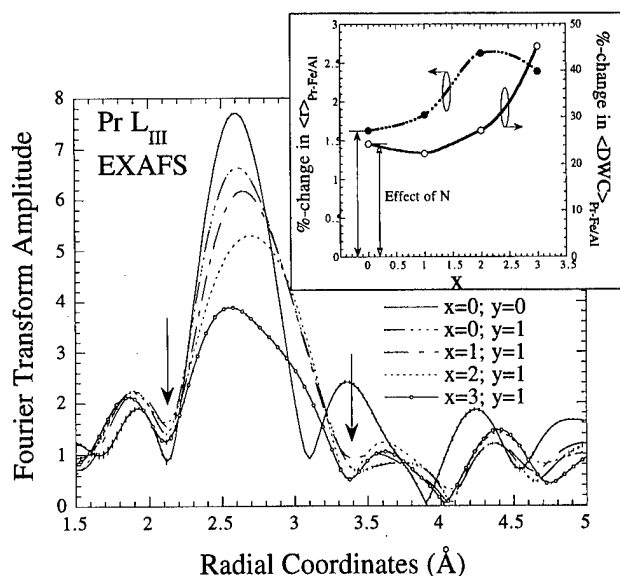


FIG. 2. Fourier transformed Pr L_{III} EXAFS for $(\text{Er}_{0.5}\text{Pr}_{0.5})_2\text{Fe}_{17-x}\text{Al}_x\text{N}_y$, where $x=0, 1, 2$ and 3 and $y=0, 1$. A k^3 -weighting was applied to a k range of 2.3 – 10.9 Å^{-1} . The inset panel depicts a plot of the calculated average Pr-Fe/Al bond distance and the Debye-Waller coefficient for the Pr coordination sphere relative to the same in the parent compound. These data were deduced from a least-squares fitting of a FF r range indicated by the arrows.

range for Fe and a dilated bonding arrangement for Pr. This result suggest that the presence of N in the unit cell alters the site filling characteristics of Al in this compound.

ACKNOWLEDGMENT

This work was performed in part at the National Synchrotron Light Source at Brookhaven National Laboratory (Upton, NY), which is supported by the U.S. Department of Energy.

- ¹J. M. D. Corey and H. Sung, J. Magn. Magn. Mater. **87**, L251 (1990).
- ²H. Sung *et al.*, J. Phys.: Condens. Matter **2**, 6565 (1990).
- ³K. H. J. Buschow *et al.*, J. Magn. Magn. Mater. **92**, L35 (1990).
- ⁴G. J. Long *et al.*, J. Appl. Phys. **76**, 5383 (1994).
- ⁵W. B. Yelon *et al.*, J. Appl. Phys. **73**, 6029 (1993).
- ⁶Z. Hu *et al.*, J. Appl. Phys. **76**, 443 (1994).
- ⁷K. G. Suresh and K. V. S. Rama Rao, in *International Symposium on Magnetic Anisotropy and Coercivity in Rare Earth - Transition Metal Alloys*, Sao Paulo, 1996 (World Scientific, Singapore, 1996), p. 391.
- ⁸K. G. Suresh and K. V. S. Rama Rao, J. Appl. Phys. **79**, 345 (1996).
- ⁹G. J. Long *et al.*, J. Appl. Phys. **72**, 4845 (1992).
- ¹⁰G. J. Long *et al.*, J. Appl. Phys. **74**, 504 (1993).
- ¹¹K. G. Suresh and K. V. S. Rama Rao, J. Less-Common Met. **238**, 90 (1996).
- ¹²K. G. Suresh and K. V. S. Rama Rao, IEEE Trans. Magn. **31**, 3722 (1995).
- ¹³K. G. Suresh and K. V. S. Rama Rao, Phys. Rev. B **55**, 15060 (1997).
- ¹⁴R. A. Neiser *et al.*, Nucl. Instrum. Methods Phys. Res. A **266**, 220 (1988).
- ¹⁵D. C. Koningsberger and R. Prins, *X-ray Absorption: Principles, Applications, Techniques of EXAFS, SEXAFS and XANES*, Vol. 92 (Wiley, New York, 1988).
- ¹⁶J. J. Rehr, S. I. Zabinsky, and R. C. Albers, Phys. Rev. Lett. **69**, 3397 (1992).
- ¹⁷The NN bond distances are calculated using lattice parameters of $a = 8.621 \text{ Å}$ and $c = 12.518 \text{ Å}$.
- ¹⁸T. W. Capehart, R. K. Mishra, and F. E. Pinkerton, Appl. Phys. Lett. **58**, 1395 (1991).

^{57}Fe Mössbauer study of the interstitial nitrogen atom effects of $\text{NdFe}_{10.5}\text{V}_{1.5}\text{N}_x$

Jinbo Yang,^{a)} Weihua Mao, and Yingchang Yang

Department of Physics, Peking University, Beijing 100871, People's Republic of China

Zhenjie Zhao and Fashen Li

Department of Physics, Lanzhou University, Lanzhou Gansu 730000, People's Republic of China

Magnetic and ^{57}Fe Mössbauer spectra measurements were carried out to study the interstitial nitrogen atom effects in the $\text{NdFe}_{10.5}\text{V}_{1.5}\text{N}_x$ ($0 \leq x \leq 2.1$) compounds. It is found that saturation magnetization, magnetocrystalline anisotropy, hyperfine fields, and isomer shifts of $\text{NdFe}_{10.5}\text{V}_{1.5}\text{N}_x$ are strongly enhanced upon nitrogenation, due to magneto-volume effects and chemical bonding effects of nitrogen atoms. On the basis of the variation of isomer shifts and hyperfine fields as a function of nitrogen concentration, and by using a set of phenomenological formulas, the contributions of magneto-volume effect and the chemical bonding effect to the hyperfine parameters are successfully separated. The pure magneto-volume effect and the chemical bonding effect of the nitrogen atoms will give a positive contribution to the average hyperfine fields and isomer shifts of the Fe atoms in the $\text{NdFe}_{10.5}\text{V}_{1.5}\text{N}_x$ nitrides. © 1998 American Institute of Physics. [S0021-8979(98)18511-0]

I. INTRODUCTION

Magnetic properties of ThMn_{12} -type Fe-rich ternary intermetallic compounds $\text{RFe}_{12-x}\text{M}_x$, in which R is rare earth and M is Ti, V, Cr, Mo, Si, Mn, W and Al, can be considerably improved by introducing C or N atoms in the interstitial sites.^{1,2} Due to the interstitial nitrogen atom effect, $\text{NdFe}_{12-x}\text{M}_x\text{N}_y$ nitrides are considered as a candidate for permanent magnetic applications. The magnetic properties of the $\text{NdFe}_{12-x}\text{M}_x\text{N}_y$ vary with the third element M . Among them, $\text{NdFe}_{12-x}\text{V}_x\text{N}_y$ possesses a higher Curie temperature and a larger saturation magnetization (M_s). Therefore, the effects of the interstitial atoms on the magnetic properties of $\text{RFe}_{12-x}\text{V}_x\text{N}_y$ compounds are a topic of great interest from the point of view of theoretical studies or in the technical applications.

The effects of C or N atoms in the interstitial sites could be decomposed into two parts: magneto-volume effect and chemical bonding effect. The theoretical effort to distinguish the influences of these two effects on the Fe moments has been made on the basis of calculations of local magnetic moments for different Fe sites in $\text{YFe}_{11}\text{TiN}^{3,4}$ and $\text{R}_2\text{Fe}_{17}\text{Z}_3$ ($R = \text{Y, Gd}, Z = \text{C, N}$)^{5,6} by means of the local spin density approximation and linear muffin tin orbital theory. However, up to date, experimental investigations on them are rarely found in literature. Li *et al.* have investigated, by high pressure Mössbauer effect, the interstitial atoms effects in $\text{Gd}_2\text{Fe}_{17}\text{C}_x$.⁷ Since the high pressure Mössbauer measurements are not easy to carry out, herein we try to experimentally separate these two effects from conventional Mössbauer measurements. For this purpose, Mössbauer spectra of $\text{NdFe}_{10.5}\text{V}_{1.5}\text{N}_x$ with various nitrogen concentration were measured. And by using a set of phenomenological formulas, the contributions of magneto-volume effect and the chemical

bonding effect to the hyperfine parameters are successfully separated.

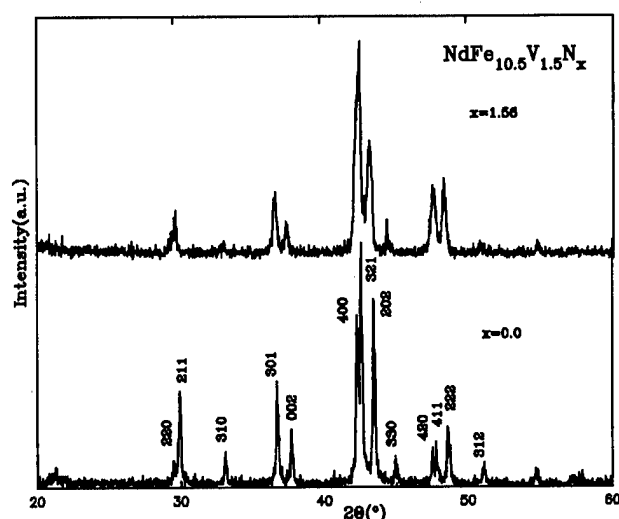
II. EXPERIMENTAL METHODS

Parent alloys were prepared by arc melting of 99.9% pure metals in an argon atmosphere, followed by a heat treatment at 900 °C for three days. The homogenized ingots were pulverized into fine powders with an average size of about 15 μm . Nitrogenation was performed by heating powders in purified nitrogen gas at atmospheric pressure at 500–600 °C for 1–8 h. X-ray diffraction (XRD) and chemical analysis were made to determine the structure and the nitrogen content. The samples of cylindrical shape ($\phi 3 \times 4$ mm) were aligned in a magnetic field of 10 kOe and fixed in epoxy resin. The magnetization curves of aligned samples were measured by a vibrating sample magnetometer with a field of up to 20 kOe at room temperature. ^{57}Fe Mössbauer spectra were collected using a conventional constant acceleration spectrometer with a 20 m Ci source of ^{57}Co in rhodium at room temperature.

III. RESULTS AND DISCUSSIONS

Figure 1 shows the $\text{CuK}\alpha$ XRD patterns of the $\text{NdFe}_{10.5}\text{V}_{1.5}$ and $\text{NdFe}_{10.5}\text{V}_{1.5}\text{N}_x$. The XRD patterns show that alloys before and after nitrogenation are of ThMn_{12} -type tetragonal structure. It is evident that the diffraction peaks of $\text{NdFe}_{10.5}\text{V}_{1.5}\text{N}_x$ shift to lower angle, indicating that the lattice expands after nitrogenation and the nitrogen atoms mainly occupy interstitial sites. The unit cell volumes V and relative change in unit cell volume upon nitrogenation, $\delta V/V$, are summarized in Table I. It can be seen from the table that the unit cell volume of $\text{NdFe}_{10.5}\text{V}_{1.5}\text{N}_x$ increases with nitrogen content. This indicates that the higher nitrogenation concentration it is, the more nitrogen atoms it will enter into the interstitial sites. A number of neutron diffraction studies on

^{a)}Electronic mail: jbyang@ibm320h.phy.pku.edu.cn

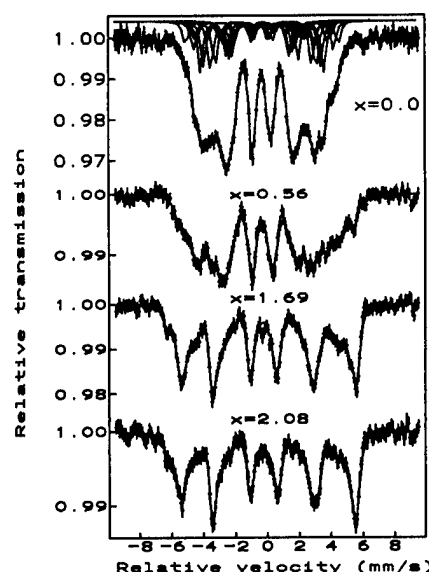
FIG. 1. X-ray diffraction patterns of the $\text{NdFe}_{10.5}\text{V}_{1.5}\text{N}_x$ and $\text{NdFe}_{10.5}\text{V}_{1.5}\text{N}_x$.

$\text{YTiFe}_{11}\text{N}_x$, $\text{YFe}_{10}\text{V}_2\text{N}_x$, and $\text{YFe}_{10}\text{Mo}_2\text{N}_x$ or $\text{YFe}_{11}\text{MoN}_x$ have been made.^{8,9} All these studies lead to the same conclusion that nitrogen atoms were found to occupy the octahedral $2b$ interstitial sites. Accordingly, full occupation of these $2b$ sites in the case of $\text{NdFe}_{10.5}\text{V}_{1.5}$ nitrides leads to a composition as $\text{NdFe}_{10.5}\text{V}_{1.5}\text{N}_{1.0}$. However, the experimentally estimated nitrogen content x ranges from 0 to as large as 2.1, which is much more than the theoretical value of one nitrogen atom per formula unit. This fact suggests that the nominal nitrogen content is much larger than the nitrogen occupancy number on the $2b$ site. A neutron diffraction study to detect the location of additional nitrogen atoms in these compounds is on course.

The measured values of saturation magnetization and anisotropy fields H_a of $\text{NdFe}_{10.5}\text{V}_{1.5}\text{N}_x$ are summarized in Table I. It is evident that a significant dependence of nitrogen content on saturation magnetization and magnetocrystalline anisotropy of $\text{NdFe}_{10.5}\text{V}_{1.5}\text{N}_x$ is observed. The increase of the saturation magnetization is a result of the magneto-volume effect and the chemical bonding effect, which increases the Fe magnetic moments upon nitrogenation. It is clearly that the chemical bonding effect between N and Nd changes the sign of the second-order crystal field parameter of Nd and results in c -axis anisotropy in the nitrides.¹⁰ However, it is difficult to experimentally separate the influences of magneto-volume effect and chemical bonding effect on the Fe mag-

TABLE I. The unit cell volume V , relative changes in unit cell volume $\delta V/V$, and intrinsic magnetic properties of $\text{NdFe}_{10.5}\text{V}_{1.5}\text{N}_x$. The data errors were given in parenthesis.

x	$V(\text{\AA}^3)$	$\delta V/V(\%)$	$M_s(\text{emu/g})$ RT	$H_a(\text{T})$ RT
0.00	344.4(3)	0.0	114.1(5)	0.5(4)
0.56	349.2	1.4(2)	121.1	4.1
1.03	353.7	2.7	124.8	6.2
1.56	358.9	4.2	127.0	9.5
1.69	360.0	4.8	129.2	9.9
2.08	362.0	5.1	131.9	10.3

FIG. 2. Mössbauer spectra of $\text{NdFe}_{10.5}\text{V}_{1.5}\text{N}_x$ at room temperature.

netic moments in the nitrides. Accordingly, a Mössbauer study on these compounds was carried out.

Representative Mössbauer spectra of $\text{NdFe}_{10.5}\text{V}_{1.5}\text{N}_x$ measured at room temperature are shown in Fig. 2. The Mössbauer spectra of the $\text{NdFe}_{10.5}\text{V}_{1.5}$ and their nitrides have been fitted to eleven subspectra with relative intensities calculated by Denissen *et al.*¹¹ and Sinnemann *et al.*¹² for similar compounds with the ThMn_{12} structure. By assuming the V goes randomly to the $8i$ sites, the probability $P_n(m)$ of finding m vanadium atoms in a shell of n $8i$ nearest neighbors is given by the binomial distribution

$$P_n(m) = \frac{n!}{m!(n-m)!} x^m (1-x)^{n-m}, \quad (1)$$

where x is the concentration of vanadium atom. The relative intensities of the subspectra were given in Table II. On the basis of these probabilities, the subspectra with intensities less than 3% were neglected. This led to a maximum of 11 subspectra for fitting a whole Mössbauer spectrum. The hyperfine fields (B_{hf}) at three Fe sites take the order $B_{\text{hf}}(8i) > B_{\text{hf}}(8j) > B_{\text{hf}}(8f)$, according to the analyses and opinions.¹¹⁻¹⁵

The fitted hyperfine parameters are listed in Table III. The average hyperfine field ($\overline{B_{\text{hf}}}$) increases monotonously with nitrogen content. This is due to the magneto-volume effect and chemical bonding effect of nitrogen atoms. The average isomer shift (IS) of $\text{NdFe}_{10.5}\text{V}_{1.5}\text{N}_x$ also steadily increases with the nitrogen content x .

TABLE II. Calculated intensities, (%) for the different subspectra of $\text{NdFe}_{10.5}\text{V}_{1.5}\text{N}_x$.

Fe sites	Fe nearest neighbors							
	13	12	11	10	9	8	7	6
$8i$	2.3	6.8	8.2	4.9	1.5	0.2		
$8j$				5.8	14.0	12.6	5.0	0.8
$8f$				5.8	14.0	12.6	5.0	0.8

TABLE III. The hyperfine parameters of NdFe_{10.5}V_{1.5}N_x at room temperature. The isomer shifts are relative to α -Fe at room temperature. The data errors were given in parentheses.

x	$\overline{B}_{\text{hf}}(\text{T})$	$\overline{\text{IS}}(\text{mm/s})$
0.00	22.8(5)	-0.123(3)
0.56	25.1	-0.008
1.03	27.9	0.044
1.56	29.1	0.073
1.69	32.5	0.081
2.08	33.4	0.095

The following two effects are responsible for the changes of the hyperfine parameters upon nitrogenation: (1) the magneto-volume effect due to the increase of the unit cell volume upon nitrogenation, (2) the chemical effect mainly due to charge transfer and hybridization between the interstitial atoms and the neighboring Fe atoms. According to the suggestion of Wagner and Wortmann for the metal hydrides,¹⁶ these two effects can be separated with a sets of phenomenological equations

$$\frac{d \ln \overline{B}_{\text{hf}}}{dn} = \left(\frac{\partial \ln \overline{B}_{\text{hf}}}{\partial \ln V} \right)_n \frac{d(\ln V)}{dn} + \left(\frac{\partial \ln \overline{B}_{\text{hf}}}{\partial n} \right)_V, \quad (2)$$

$$\frac{d \overline{\text{IS}}}{dn} = \left(\frac{\partial \overline{\text{IS}}}{\partial \ln V} \right)_n \frac{d(\ln V)}{dn} + \left(\frac{\partial \overline{\text{IS}}}{\partial n} \right)_V, \quad (3)$$

where the \overline{B}_{hf} and $\overline{\text{IS}}$ are the average hyperfine fields and isomer shifts of Fe atoms in the RFe_{10.5}V_{1.5}N_x, V is the unit cell volume of NdFe_{10.5}V_{1.5}N_x, and n is a ratio of nitrogen atoms to the other metal atoms in a formula unit. In Eqs. (2) and (3), the first term gives the contribution of the magneto-volume effect and the last term is the contribution of the chemical bonding effect.

Generally, $(\partial \ln \overline{B}_{\text{hf}} / \partial \ln V)_n$ and $(\partial \overline{\text{IS}} / \partial \ln V)_n$ are derived from the high pressure Mössbauer measurements. In spite of nonlinear dependence of the IS and B_{hf} at Fe sites on V and n , in the first order of approximation, we supposed that $(\partial \ln \overline{B}_{\text{hf}} / \partial \ln V)_n = A$, $(\partial \ln \overline{B}_{\text{hf}} / \partial n)_V = B$, $(\partial \overline{\text{IS}} / \partial \ln V)_n = C$, and $(\partial \overline{\text{IS}} / \partial n)_V = D$ are constant in these compounds, and quantitatively estimate the magneto-volume effect and chemical bonding effect. Then Eqs. (2) and (3) can be written as

$$d \ln \overline{B}_{\text{hf}} = A * d(\ln V) + B * dn, \quad (4)$$

$$d \overline{\text{IS}} = C * d(\ln V) + D * dn. \quad (5)$$

Because we have prepared a series of samples with various nitrogen concentration and unit cell volume, the values of A , B , C , and D can be obtained through solving Eqs. (4) and (5). The values of $d \ln V / dV$ can be obtained from the x-ray diffraction measurements. By using values of the $d \ln \overline{B}_{\text{hf}}$, $d \overline{\text{IS}}$, $d \ln V$, and dn calculated from Table III and Table I, and solving the Eqs. (4) and (5) by using least-

squares method, one derives the values of $A=6.8$ T and $B=0.7$ T, $C=1.80$ mm/s, and $D=0.04$ mm/s, respectively.

It is noticed from the values of A and B that both magneto-volume effect and chemical bonding effect will increase the hyperfine field. This is in good agreement with the conclusion of the band calculation³ that nitrogen atoms will enhance the Fe moments not only through lattice expansion but also by changing the electronic bonding nature. The increase of the hyperfine field through magneto-volume effect is due to a decrease in Fe-Fe overlap. The formation of tight covalent bonding between neodymium and nitrogen atoms releases the Fe atoms from the bonding with neodymium atoms and then promotes the exchange splitting of the Fe atoms, which will further increase the magnetic moments and hyperfine fields of Fe atoms due to chemical bonding effect. The results of isomer shifts indicate that chemical bonding effect and magneto-volume effect will give rise to an increase of isomer shifts. It is easy to understand that the volume expansion will decrease s electron density in the nuclear sites which gives an increase to the isomer shifts. The value $(\partial \overline{\text{IS}} / \partial \ln V) = 1.80$ mm/s is closed to that of NdFe_{12-x}Mo_xN_{0.9} (2.0 mm/s).¹⁴ The chemical bonding effect of the nitrogen atoms promotes the mobility of the electrons, and then in turn decreases the s -like charge density at Fe nucleus, so that isomer shifts at Fe sites increase.

ACKNOWLEDGMENTS

This work was supported by the National Natural Science Foundation and the National Target Basic Research Project.

- ¹Y. C. Yang, X. D. Zhang, S. L. Ge, Q. Pan, Y. T. Hou, S. Huang, and L. Yang, in *Proceeding of the Sixth International Symposium on Magnetic Anisotropy and Coercivity in Rare-Earth-Transition-Metal Alloys*, edited by S. G. Sanker (Carnegie Mellon University, Pittsburgh, PA, 1990), p. 190.
- ²Y. C. Yang, X. D. Zhang, S. Z. Dong, and Q. Pan, *J. Appl. Phys.* **74**, 6847 (1993).
- ³A. Sakuma, *J. Phys. Soc. Jpn.* **61**, 4119 (1992).
- ⁴Y. P. Li and J. M. D. Coey, *Solid State Commun.* **81**, 447 (1992).
- ⁵T. Beuerle and M. Fähnle, *Phys. Status Solidi B* **174**, 257 (1992).
- ⁶P. Uebele, K. Hummler, and M. Fähnle, *Phys. Rev. B* **53**, 3296 (1996).
- ⁷F. S. Li, J. J. Sun, C. L. Yang, R. J. Zhou, B. G. Shen, H. Micklitz, and M. Abd-Elmeguid, *Hyperfine Interact.* **94**, 1959 (1994).
- ⁸W. B. Yelon and G. C. Hadjipanayis, *IEEE Trans. Magn.* **MAG-28**, 2316 (1992).
- ⁹H. Sun, Y. Morij, H. Fujii, M. Akayama, and S. Funahashi, *Phys. Rev. B* **48**, 13 333 (1993).
- ¹⁰Y. C. Yang, X. D. Pei, H. L. Li, X. D. Zhang, L. S. Kong, Q. Pan, and M. H. Zhang, *J. Appl. Phys.* **70**, 6574 (1991).
- ¹¹C. J. M. Denissen, R. Coehoorn, and K. H. J. Buschow, *J. Magn. Magn. Mater.* **87**, 52 (1990).
- ¹²Th. Sinnemann, M. Rosenberg, and K. H. J. Buschow, *J. Less-Common Met.* **146**, 223 (1989).
- ¹³R. Coehoorn, *Phys. Rev. B* **41**, 11 790 (1990).
- ¹⁴Q. N. Qi, B. P. Hu, and J. M. D. Coey, *J. Appl. Phys.* **75**, 6235 (1994).
- ¹⁵I. A. Al-Omari, S. S. Jaswal, A. S. Fernando, D. J. Sellmyer, and H. H. Hamdeh, *Phys. Rev. B* **50**, 12 665 (1994).
- ¹⁶F. E. Wagner and G. Wortmann, in *Hydrogen in Metals I*, edited by G. Alefeld and J. Volkl (Springer, Berlin, 1977).

A study of nitrogenation of a $\text{NdFe}_{12-x}\text{Mo}_x$ compound by *in situ* neutron powder diffraction

C.-K. Loong^{a)} and S. M. Short

Argonne National Laboratory, Argonne, Illinois 60439

J. Lin and Y. Ding

Department of Materials Chemistry, Peking University, Beijing 100871, China

The effects on the crystal lattice of a $\text{NdFe}_{12-x}\text{Mo}_x$ ($x \approx 1.7$) during controlled nitrogenation over the 25–600 °C temperature range were studied by neutron powder diffraction. Prior to nitrogenation the sample contained a major phase of $\text{NdFe}_{10.3}\text{Mo}_{1.7}$ and a minor phase (~ 12 vol %) of bcc-Fe. The sample inside the furnace was connected to a closed volume of ultrapure nitrogen gas while neutron data were collected over regular time intervals during sequential heating. Substantial nitrogen absorption occurred between 500 and 600 °C. During the nitrogenation process the $\text{NdFe}_{12-x}\text{Mo}_x\text{N}_y$ lattice expanded while the bcc-Fe lattice contracted. An increasing decomposition of the compound into bcc-Fe at 600 °C was observed. The average size of the $\text{NdFe}_{12-x}\text{Mo}_x\text{N}_y$ crystalline grains decreased starting at ~ 300 °C, reaching a minimum at ~ 500 °C and then increased markedly at higher temperatures. The development of lattice strains, on the other hand, showed an opposite trend, i.e., a maximum at 500 °C. © 1998 American Institute of Physics. [S0021-8979(98)29811-2]

I. INTRODUCTION

Interstitial introduction of nonmetallic atoms such as N, C, or B into rare-earth (R) transition-metal (TM) compounds is one of the effective methods for fabricating new hard magnetic materials with improved properties. The method of gas-phase interstitial modification (GIM) has been applied to two families of R-TM intermetallics, the 2:17 and the 1:12 systems, with $\text{Sm}_2\text{Fe}_{17}\text{N}_y$ and $\text{NdFe}_{12-x}\text{Mo}_x\text{N}_y$ being the leading targeted materials. Depending on the dissociation energy of the gas molecules, the strain-stress conditions of the lattice, and the nature of the gas-lattice interaction, these metastable phases of nitrides are formed within a relatively narrow temperature window. A considerable amount of investigations of the reaction mechanism and phase formation have been carried out for the $\text{Sm}_2\text{Fe}_{17}\text{N}_y$ compounds using the GIM method.^{1–5} The corresponding behavior of the $\text{NdFe}_{12-x}\text{Mo}_x\text{N}_y$ system, on the other hand, has not been well characterized.

The crystal structure of the parent compounds of the 1:12 family, $\text{RFe}_{12-x}\text{M}_x$ ($\text{M}=\text{Mo}, \text{Ti}, \text{V}, \text{Cr}, \text{W}, \text{or Si}$) is based on the ThMn_{12} -type body-centered tetragonal structure (space group $I4/mmm$, 2 formula units per cell).⁶ The inclusion of M atoms is essential to the stabilization of the ThMn_{12} structure. In the case of $\text{RFe}_{10}\text{Mo}_2$, the R, and Fe atoms occupy the $2a$ and $(8i, 8j, 8f)$ sites, respectively, and the Mo atoms preferably occupy the $8i$ site. Upon nitrogenation the lattice expands, causing a narrowing of the Fe $3d$ band and thereby a larger saturation moment and higher Curie temperature.⁷ Since the N atoms occupy the $2b$ site which is in close proximity to the R atoms, the crystalline electric fields surrounding the R atoms are modified significantly.⁸ In $\text{RFe}_{12-x}\text{Mo}_x\text{N}_y$ the magnetic anisotropy changes from planar

(for $y=0$) to uniaxial along the c direction. The magnetic properties of $\text{RFe}_{12-x}\text{Mo}_x$ and its $\text{RFe}_{12-x}\text{Mo}_x\text{N}_y$ ($y < 0 \leq 1$) have been investigated by many workers.^{8–17}

As the formation of $\text{RFe}_{12-x}\text{M}_x\text{N}_y$ occurs within a rather limited composition range ($1.5 < x < 2.5$ and $0 < y < 1$), many authors reported the observation of impurity phases, most often α -Fe, in the parent and/or nitrogenated materials.^{9–14,16,17} This difficulty has prompted an attempt in synthesizing $\text{NdFe}_{10}\text{Mo}_2$ using a polymer-network gel process.¹⁸ Concerns about the stability of the 2:17 compounds have led to numerous investigations of the MIG process.^{1–5,19} During the nitrogenation of $\text{Sm}_2\text{Fe}_{17}$, the diffusion of nitrogen into the bulk of particles via extended defects on the surfaces, the development of lattice strains, and the decomposition of the materials at high temperatures were studied by several workers.^{1,3,5} Similar studies of the $\text{NdFe}_{12-x}\text{Mo}_x\text{N}_y$ system, to the best of our knowledge, have not been reported. In this article, we present the results of an *in situ* neutron-diffraction study of the nitrogenation process of a $\text{NdFe}_{10.3}\text{Mo}_{1.7}$ compound.

II. EXPERIMENTAL DETAILS: RESULTS AND DISCUSSION

The $\text{NdFe}_{10.3}\text{Mo}_{1.7}$ sample was prepared by arc melting under a purified argon atmosphere from the elemental materials of at least 99% purity, followed by vacuum annealing at 950 °C for a week. After cooling, the sample was ground into a powder with particle size, examined by optical microscopy, about 20–30 μm . X-ray diffraction analysis, carried out on a Rigaku D/Max-2000 diffractometer, showed the ThMn_{12} -type structure of the $\text{NdFe}_{10.3}\text{Mo}_{1.7}$ compound and a small amount of bcc α -Fe.

The neutron diffraction experiment was performed using a time-of-flight powder diffractometer (SEPD) at the Intense

^{a)}Electronic mail: ckloong@anl.gov

Pulsed Neutron Source of Argonne National Laboratory. The powder (~ 20 g) was held inside a cylindrical, thin-wall vanadium tube. Four layers of very fine stainless-steel screens were laid at the open bottom and vent holes were left at the top of the tube to allow permeation of N_2 gas. The sample tube was placed inside an insert of the furnace which was connected to a manifold of a gas handling apparatus filled with 1 ℓ 99.999% pure nitrogen gas at 1 atm pressure and room temperature. After repeated purging, the nitrogen gas was expanded into the furnace insert, and the pressure was monitored throughout the experiment. The data were collected by detectors situated at mean scattering angles of $\pm 90^\circ$ for which a resolution of $\Delta d/d = 0.5\%$ can be achieved (d is the atomic plane spacing). By virtue of the highly collimated neutron entrance and exit in a 90° -scattering geometry and the negligible neutron coherent scattering amplitude of vanadium, Bragg-scattering intensity solely from the sample was recorded. The sample temperature, monitored by thermocouples above and below the sample, were controlled at a selected temperature to within 10°C in all runs. The diffraction data were collected for 1 h at a constant temperature as the temperature was raised stepwise from room temperature to $\sim 600^\circ\text{C}$. At about 450, 500, 550, and 600°C several 1 h runs were made in order to study the kinetics of N_2 absorption. No attempt was made to wait until the saturated absorption before raising to the next temperature. Each data set analyzed by the Rietveld refinement technique using the generalized structural analysis system (GSAS) computer code,^{20,21} therefore represents the lattice response averaged over the 1 h period at a temperature during nitrogenation.

In order to obtain information about the thermal expansion of the un-nitrogenated sample, measurements were also performed on a fresh powder from room temperatures to 600°C under a vacuum environment.

Figure 1 shows a portion of the diffraction pattern typical of runs at 134 and 596°C . The fresh sample prior to nitrogenation contains a major phase of $\text{NdFe}_{10.3}\text{Mo}_{1.7}$ and a minor phase (~ 12 vol %) of bcc α -Fe. As the temperature increases from 24 to $\sim 450^\circ\text{C}$, the unit-cell volume of both phases increase at a normal rate as expected from thermal expansion. At $\sim 500^\circ\text{C}$, however, the salient drop of the nitrogen gas pressure in conjunction with a shift of the d spacing and the intensities of the Bragg reflections indicate clearly the formation of nitride $\text{NdFe}_{10.3}\text{Mo}_{1.7}\text{N}_y$. The weighted R factors of the two-phase structural refinements varies from $\sim 8\%$ at room temperature to $\sim 12\%$ at 600°C . Figure 2 shows the unit-cell volume of the nitride and α -Fe phases as well as the $2b$ site occupancy of nitrogen and the α -Fe volume fraction as a function of temperature. By comparing with the unit-cell volumes of the un-nitrogenated phases [Fig. 2(a)], it can be seen that over a 7 h period at 500°C the unit cell of $\text{NdFe}_{10.3}\text{Mo}_{1.7}\text{N}_y$ expands continuously as more N atoms diffuse into the lattice whereas the bcc unit cell of the α -Fe lattice contracts. Furthermore, since the $2b$ site is located at the midpoint of two R atoms along the c axis, the unit-cell expansion of the nitride is highly anisotropic, i.e., larger in the c direction. The same behavior occurs at 500 and 600°C . Meanwhile, as y increases, the

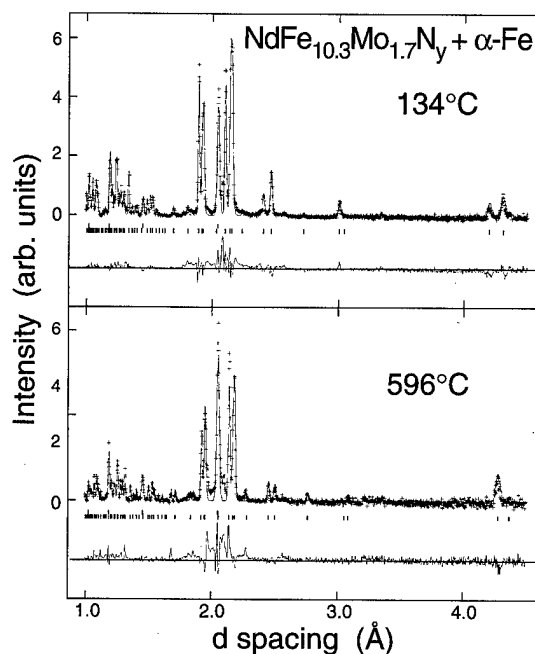


FIG. 1. The Rietveld profile fits of diffraction data for the $\text{NdFe}_{10.3}\text{Mo}_{1.7}\text{N}_y$ (+ α -Fe) sample at 134 and 596°C . The dots are the observed, background-subtracted intensities. The solid lines represent the calculated intensities. Tick marks of top and bottom rows indicate the positions of the Bragg reflections for α -Fe and $\text{NdFe}_{10.3}\text{Mo}_{1.7}\text{N}_y$ phases, respectively. Differences between the observed and calculated intensities are shown at the bottom of each panel.

volume fraction of α -Fe also increases from 15% at 400°C to 25% in the last run at 600°C . Therefore, as more N atoms are incorporated into the Nd-Fe-Mo compound, the lattice expands and exerts compressive stresses on the α -Fe domains in the sample. At increasing temperatures the material becomes less stable, as can be seen from the accelerated precipitation of α -Fe phase.

Information regarding the average crystalline grain size and the lattice microstrains of the nitride can be obtained from the Rietveld refinements of the diffraction data.²⁰ As shown in Fig. 3 the size and strains of the Nd-Fe-Mo domains do not change significantly up to about 300°C . Above $\sim 300^\circ\text{C}$ the coherency of the crystalline domains decreases rapidly, as indicated by the reduction of average grain size and the rise of lattice strains. These effects are largest at about 500°C where nitrogen diffusion rate is near a maximum (see Fig. 2), and the behavior reverses precipitously, i.e., increasing grain size and reducing strains, between 500 and 600°C . The signals from the α -Fe phase are too weak to warrant similar grain-size and strain analysis. These results enable us to speculate the following scenario. Below 300°C nitrogen diffusion into the sample is minimal, perhaps lacking the thermal and gas-solid interaction energies to activate the dissociation of nitrogen molecules. At $\sim 300^\circ\text{C}$ N atoms begin to diffuse and interact with the atoms on the intergranular boundaries of the $\text{NdFe}_{10.3}\text{Mo}_{1.7}$ particles. It is not until about 400°C when N atoms interact with the Fe (and Nd) atoms in the bulk of the particles, forming chemical bonds through hybridization of the N-2p and Fe-3d states.²² Presumably N diffuses into the bulk through defect structures extended inward from the surface while imposing ex-

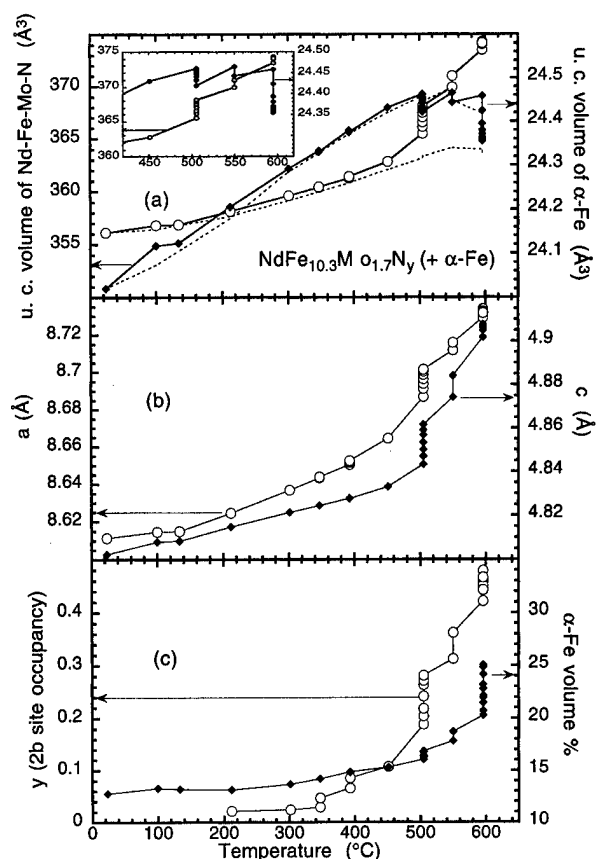


FIG. 2. The unit-cell volumes of the $\text{NdFe}_{10.3}\text{Mo}_{1.7}$ and $\alpha\text{-Fe}$ lattices (symbols) (a), the lattice parameters of the nitride phase (b), the nitrogen occupancy of the $2b$ site in $\text{NdFe}_{10.3}\text{Mo}_{1.7}\text{N}_y$, and the volume fraction of $\alpha\text{-Fe}$ (c) as a function of temperature during nitrogenation. The solid lines connect the data points each of which represents 1 h of data collection. There are 7, 2, and 9 data points at 500, 550, and 600 °C, respectively, some of which are overlapping. Typical uncertainties of the parameters are comparable to the size of the symbols. In (a) the temperature dependence of the unit-cell volumes of the $\text{NdFe}_{10.3}\text{Mo}_{1.7}$ and $\alpha\text{-Fe}$ lattices without nitrogenation is given by the dashed lines. For clarity, the high-temperature data in (a) are reproduced in the inset.

pansive pressure. Consequently, the homogeneity of the long-range atomic order is degraded and increasing microstrains are generated within crystalline domains in the temperature interval of 400–500 °C. Above 500 °C the nitrogenated domains are annealed to form larger and more relaxed crystalline grains. Concurrent with these processes the $\alpha\text{-Fe}$ particles are under compressive stress from the neighboring nitride domains and more $\alpha\text{-Fe}$ phase is nucleated in the sample.

Investigations of nitrogenation of $\text{Sm}_2\text{Fe}_{17}$ have been studied by Christodoulou and Takeshita⁵ using x-ray diffraction and thermomagnetic analysis (TMA), and by Colucci and co-workers³ using TMA and electron probe microanalysis. Electronic band calculations of model compounds within the $\text{RFe}_{12-x}\text{Mo}_x\text{N}_y$ system have been reported by several research teams.^{12,22–24} Our results agree qualitatively with the observations of these workers. Clearly, more studies, both experimental and theoretical, are needed to elucidate the atomic organization and microscopic phenomena associated with the GIM process in rare-earth transition-metal compounds.

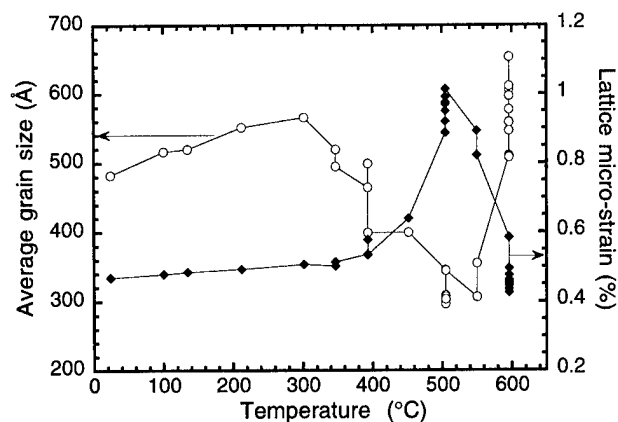


FIG. 3. The average crystalline grain size and lattice microstrain of $\text{NdFe}_{10.3}\text{Mo}_{1.7}\text{N}_y$ as a function of temperature during nitrogenation.

ACKNOWLEDGMENT

Work performed at Argonne is supported by the U.S. DOE-BES under Contract No. W-31-109-ENG-38.

- ¹J. M. D. Coey, J. F. Lawler, H. Sun, and J. E. M. Allan, *J. Appl. Phys.* **69**, 3007 (1991).
- ²J. M. D. Coey, R. Skomski, and S. Wirth, *IEEE Trans. Magn.* **28**, 2332 (1992).
- ³C. C. Colucci, S. Gama, and C. A. Ribeiro, *J. Alloys Compd.* **194**, 181 (1993).
- ⁴M. Katter, J. Wecker, C. Kuhrt, and L. Schultz, *J. Magn. Magn. Mater.* **117**, 419 (1992).
- ⁵C. N. Christodoulou and T. Takeshita, *J. Alloys Compd.* **202**, 171 (1993).
- ⁶D. B. De Mooij and K. H. J. Buschow, *J. Less-Common Met.* **136**, 207 (1988).
- ⁷S. S. Jaswal, W. B. Yelon, G. C. Hadjipanayis, Y. Z. Wan, and D. J. Sellmyer, *Phys. Rev. Lett.* **67**, 644 (1991).
- ⁸E. Tomey, M. Bacmann, D. Fruchart, D. Gignoux, and J. L. Soubeyroux, *J. Magn. Magn. Mater.* **157&158**, 115 (1996).
- ⁹M. Anagnostou, C. Christides, M. Pissas, and D. Niarchos, *J. Appl. Phys.* **70**, 6012 (1991).
- ¹⁰W. B. Yelon and G. C. Hadjipanayis, *IEEE Trans. Magn.* **28**, 2316 (1992).
- ¹¹M. Endoh, K. Nakamura, and H. Mikami, *IEEE Trans. Magn.* **28**, 2560 (1992).
- ¹²H. Sun, Y. Mori, H. Fujii, M. Akayama, and S. Funahashi, *Phys. Rev. B* **48**, 13 333 (1993).
- ¹³X. Chen, L. X. Liao, Z. Altounian, D. H. Ryan, and J. O. Ström-Olsen, *J. Magn. Magn. Mater.* **111**, 130 (1992).
- ¹⁴B.-P. Hu, H.-S. Li, J. P. Gavigan, and J. M. D. Coey, *J. Phys.: Condens. Matter* **1**, 755 (1989).
- ¹⁵W. E. Wallace and M. Q. Huang, *IEEE Trans. Magn.* **28**, 2312 (1992).
- ¹⁶Y. Z. Wang, G. C. Hadjipanayis, Z. X. Tang, W. B. Yelon, V. Papaefthymiou, A. Moukarika, and D. J. Sellmyer, *J. Magn. Magn. Mater.* **119**, 41 (1993).
- ¹⁷Y.-C. Yang, Q. Pan, X.-D. Zhang, M.-H. Zhang, C.-L. Yang, Y. Li, S.-L. Ge, and B.-F. Zhang, *J. Appl. Phys.* **74**, 4066 (1993).
- ¹⁸S. F. Liu, J. H. Lin, X. L. Qian, J. M. Bai, and M. Z. Su, *Chem. Mater.* **8**, 2545 (1996).
- ¹⁹O. Isnard, J. L. Soubeyroux, S. Miraglia, D. Fruchart, L. M. Garcia, and J. Bartolomé, *Physica B* **180&181**, 624 (1992).
- ²⁰A. C. Larson and R. B. Von Dreele, Los Alamos Report LAUR 86-748, 1987.
- ²¹H. W. Rietveld, *J. Appl. Crystallogr.* **2**, 65 (1968).
- ²²S. Asano, S. Ishida, and S. Fujii, *Physica B* **190**, 155 (1993).
- ²³S. S. Jaswal, Y. G. Ren, and D. J. Sellmyer, *J. Appl. Phys.* **67**, 4564 (1990).
- ²⁴R. Coehoorn, K. H. J. Buschow, M. W. Dirken, and R. C. Thiel, *Phys. Rev. B* **42**, 4645 (1990).

Crystallization and Mössbauer studies of melt-spun $\text{NdFe}_{10.7}\text{TiB}_{0.3}\text{N}_\delta$ alloys

Chul Sung Kim,^{a)} Sung Yong An, and Young Rang Uhm
Department of Physics, Kookmin University, Seoul 136-702, Korea

Seung Wha Lee

School of Electrical and Electronics Engineering, Chungbuk National University, Cheongju 360-763, Korea

Y. B. Kim and C. S. Kim

Korea Research Institute of Standards Science, Taejon 305-606, Korea

Magnetic properties of melt-spun $\text{NdFe}_{10.7}\text{TiB}_{0.3}\text{N}_\delta$ ribbons have been investigated as functions of quenching rate and nitriding period. $\text{NdFe}_{10.7}\text{TiB}_{0.3}$ were prepared with substrate velocity $v_s \leq 18$ m/s and were nitrogenated at 500 °C for 15 min. The $\text{NdFe}_{10.7}\text{TiB}_{0.3}\text{N}_\delta$ retains the ThMn_{12} -type tetragonal structure with lattice constants $a_0 = 8.640$ Å and $c_0 = 4.811$ Å, but with an increase in the unit cell volume. The $\text{NdFe}_{10.7}\text{TiB}_{0.3}\text{N}_\delta$ was confirmed to have uniaxial anisotropy by x-ray diffraction. Mössbauer spectra were taken at various temperatures ranging from 13 to 855 K. The Curie and Debye temperatures are determined to be $T_c = 833$ K and $\Theta = 390$ K, respectively. Each spectrum below T_c was fitted with six subspectra of Fe sites ($8i_1$, $8i_2$, $8j_2$, $8j_1$, $8f$, and $\alpha\text{-Fe}$). The area fraction of the subspectra at 13 K are 10.2%, 8.2%, 16.5%, 17.5%, 44.3%, and 3.3%, respectively. The magnetic hyperfine fields for the Fe sites decrease in the order, $H_{\text{hf}}(8i) > H_{\text{hf}}(8j) > H_{\text{hf}}(8f)$. © 1998 American Institute of Physics. [S0021-8979(98)22811-8]

I. INTRODUCTION

Since the discovery by Yang *et al.*¹ that nitrogen absorption can enhance the Curie temperature T_c , saturation magnetization M_s , and magnetocrystalline anisotropy of RFe_{11}Ti (R=rare earth) compounds, nitrided $\text{R}(\text{Fe}, \text{M})_{12}$ (R=Sm, Nd, Gd, La, Ce, Tb, Dy, Ho, Y, or Er; M=Ti, V, Cr, Mo, Mn, W, Co, Al, or Si phases).²⁻⁵ Phases characterized by the tetragonal ThMn_{12} structure have become of interest from the perspective of permanent magnet applications. We concentrate our studies on the $\text{Nd}(\text{Fe}, \text{M})_{12}$ compound because the cost of Nd is much lower than that of Sm. The $\text{NdFe}_{11}\text{Ti}$ nitride is known to have a higher anisotropy field and Curie temperature than those of $\text{Nd}_2\text{Fe}_{14}\text{B}$.⁶

In this study, we prepared $\text{NdFe}_{10.7}\text{TiB}_{0.3}\text{N}_\delta$ compounds by substituting B for Ti. The crystallographic and magnetic properties of the compounds were studied using x-ray diffraction, vibrating sample magnetometry, and Mössbauer spectroscopy.

II. EXPERIMENTAL PROCEDURES

Alloys of $\text{NdFe}_{10.7}\text{TiB}_{0.3}$ were prepared by arc melting under an argon gas atmosphere. Each ingot was melt spun, again under argon, by ejecting molten alloy through an orifice in a quartz crucible onto the surface of a copper disk. The quench rate was varied by changing the surface velocity v_s of the disk, with v_s in the range 7–40 m/s. From the x-ray analysis we found that the $\text{NdFe}_{10.7}\text{TiB}_{0.3}$ starting composition yielded essentially single-phase ribbons, but only for quench rates in the $v_s \leq 18$ m/s range.

Nitriding was carried out on ground (<40 μm diam) powders of the melt-spun ribbons under a static 120 kPa pressure of N_2 gas. All samples in this work were nitrided at

773 K for 15 min. The nitrogen content in $\text{NdFe}_{10.7}\text{TiB}_{0.3}\text{N}_\delta$ alloys measuring by a thermopiezic analyzer is about 0.9.

A Mössbauer spectrometer of the electromechanical type⁷ was used in the constant-acceleration mode. A ^{57}Co single-line source in a rhodium matrix was used at room temperature.

III. RESULTS AND DISCUSSION

X-ray diffraction patterns show that the structure remains unchanged but that there are changes in lattice parameters as listed in Table I. The peaks in the pattern for $\text{NdFe}_{10.7}\text{TiB}_{0.3}$ can be indexed on the basis of the tetragonal ThMn_{12} -type unit cell. The $\text{NdFe}_{10.7}\text{TiB}_{0.3}\text{N}_\delta$ alloy exhibits a ThMn_{12} structure with unit cell constants of $a_0 = 8.640$ Å and $c_0 = 4.811$ Å, in addition to a small amount of $\alpha\text{-Fe}$. As shown in Table I, the lattice constants, a_0 and c_0 , increase markedly as nitrogen is introduced into the 1:12 structure. The relative increase in the unit-cell volume was found to be nearly constant at 1.7%. X-ray diffraction from a $\text{NdFe}_{10.7}\text{TiB}_{0.3}\text{N}_\delta$ powder oriented in a magnetic field perpendicular to the plane of diffraction showed a drastic increase of the intensity of the (002) peak. This result suggests that the c axis remains the easy magnetization axis.

Figure 1 shows some of the Mössbauer spectra of $\text{NdFe}_{10.7}\text{TiB}_{0.3}\text{N}_\delta$ measured at various absorber temperatures from 13 to 800 K. Using a least-squares computer program, six sets of six Lorentzian lines corresponding to the $8i_1$, $8i_2$, $8j_2$, $8j_1$, $8f$, and $\alpha\text{-Fe}$ sites were fitted to the Mössbauer spectra below the Curie temperature, T_c , under the following well-known restraints,⁸ which are valid when the quadrupole interaction is much weaker than the magnetic hyperfine interaction.

X-ray diffraction and the neutron diffraction data⁹ show that in $\text{Nd}(\text{Fe}, \text{M})_{12}\text{N}_\delta$ the nitrogen atoms occupy the 2b

^{a)}Electronic mail: cskim@phys.kookmin.ac.kr

TABLE I. Lattice parameters a_0 and c_0 , unit cell volume V , relative change in unit cell volume upon nitrogenation $\Delta V/V$, Curie temperature T_c , and saturation magnetization M_s of $\text{NdFe}_{10.7}\text{TiB}_{0.3}$ and $\text{NdFe}_{10.7}\text{TiB}_{0.3}\text{N}_\delta$.

Compound	$a_0(\text{\AA})$	$c_0(\text{\AA})$	$V(\text{\AA}^3)$	$\Delta V/V(\%)$	$T_c(\text{K})$	$M_s(\text{emu/g})$	
						$T=77\text{ K}$	$T=295\text{ K}$
$\text{NdFe}_{10.7}\text{TiB}_{0.3}$	8.587	4.788	353.05		570	124.2	113.5
$\text{NdFe}_{10.7}\text{TiB}_{0.3}\text{N}_\delta$	8.640	4.811	359.14	1.7	833	118.4	110.7

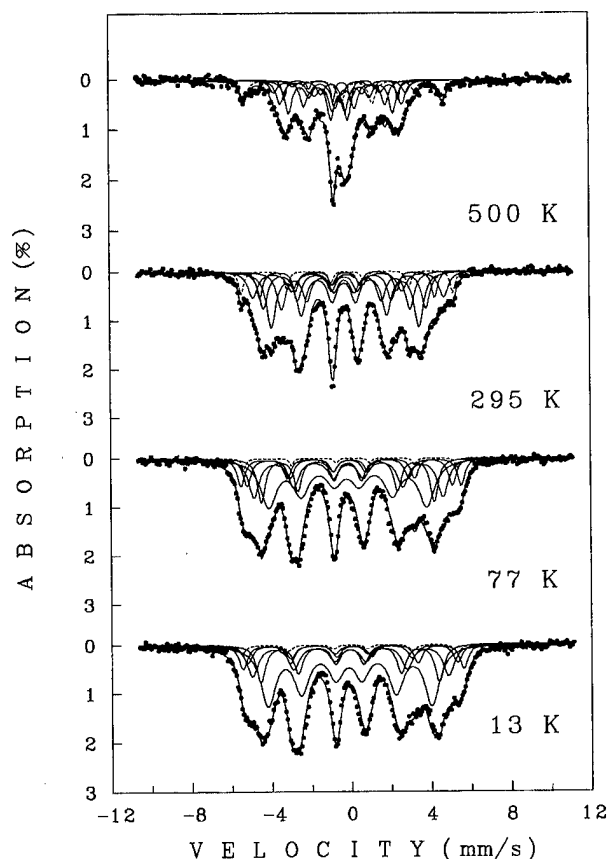


FIG. 1. Mössbauer spectra of $\text{NdFe}_{10.7}\text{TiB}_{0.3}\text{N}_\delta$ at various temperatures.

sites, whereas the iron atoms occupy the $8j$ and $8f$ sites preferentially, and M atoms reside only on the $8i$ sites. In the $\text{Nd}(\text{Fe}, \text{M})_{12}\text{N}_\delta$ structure, the distribution of M atoms may cause a distribution of Fe nearest neighbors in each Fe site, which results in quite broad outer lines in the Mössbauer spectra due to a distribution of hyperfine fields.

Using the neutron diffraction data, an acceptable fit of the Mössbauer spectra of $\text{NdFe}_{10.7}\text{TiB}_{0.3}\text{N}_\delta$ was performed using five sites ($8i_1$, $8i_2$, $8j_2$, $8j_1$, and $8f$). The resulting areas of the subspectra $8i_1$, $8i_2$, $8j_2$, $8j_1$, $8f$, and $\alpha\text{-Fe}$ at 13 K were 10.2, 8.2, 16.5, 17.5, 44.2, 3.3%, respectively. The $\alpha\text{-Fe}$ content of the parent compounds was less than 0.5%, so it was not included in the fits, but there was about 3% $\alpha\text{-Fe}$ in the nitride spectra. The dashed lines in Fig. 1 indicate the spectrum of $\alpha\text{-Fe}$. The Mössbauer parameters of the absorbers obtained are listed in Table II. The temperature dependence of the isomer shifts relative to $\alpha\text{-Fe}$ at room temperature, for each $8i$, $8j$, and $8f$ site increase with decreasing temperature, consistent with the second-order Doppler shift.

Figure 2 shows the temperature dependence of the magnetic hyperfine field for $\text{NdFe}_{10.7}\text{TiB}_{0.3}\text{N}_\delta$. The magnetic hyperfine fields for the Fe sites decrease in the order $H_{\text{hf}}(8i) > H_{\text{hf}}(8j) > H_{\text{hf}}(8f)$. The fractional change of the average magnetic hyperfine field, $[H_{\text{hf}}(T) - H_{\text{hf}}(0)]/H_{\text{hf}}(0)$, as a function of temperature is shown in Fig. 3. The average magnetic hyperfine field decreases with increasing temperature according to¹⁰ $[H_{\text{hf}}(T) - H_{\text{hf}}(0)]/H_{\text{hf}}(0) = -0.52(T/T_c)^{3/2} - 0.43(T/T_c)^{5/2}$ for $T/T_c < 0.7$. This value of

TABLE II. Mössbauer parameters for $\text{NdFe}_{10.7}\text{TiB}_{0.3}$ and $\text{NdFe}_{10.7}\text{TiB}_{0.3}\text{N}_\delta$. H_{hf} is the magnetic hyperfine field in units of kOe, ΔE_Q is the quadrupole splitting, and δ is the isomer shift relative to metallic iron at room temperature in units of mm/s.

Compound	$T(\text{K})$	Mössbauer parameters	Sites					Mean
			$8i_1$	$8i_2$	$8j_2$	$8j_1$	$8f$	
$\text{NdFe}_{10.7}\text{TiB}_{0.3}$	13	H_{hf}	359	339	313	287	264	312
		ΔE_Q	0.02	-0.03	-0.01	0.03	0.05	
		δ	0.16	0.08	-0.08	-0.04	-0.08	0.01
$\text{NdFe}_{10.7}\text{TiB}_{0.3}\text{N}_\delta$	13	H_{hf}	342	327	304	295	253	304
		ΔE_Q	-0.01	0.01	0.01	0.00	0.03	
		δ	0.11	0.05	-0.07	-0.10	-0.13	-0.03
$\text{NdFe}_{10.7}\text{TiB}_{0.3}$	295	H_{hf}	298	275	262	238	209	256
		ΔE_Q	0.06	0.06	0.03	0.05	0.03	
		δ	-0.06	-0.13	-0.19	-0.23	-0.18	-0.16
$\text{NdFe}_{10.7}\text{TiB}_{0.3}\text{N}_\delta$	295	H_{hf}	301	273	253	230	201	252
		ΔE_Q	0.04	0.04	0.02	0.01	0.03	
		δ	-0.08	-0.08	-0.23	-0.24	-0.21	-0.17

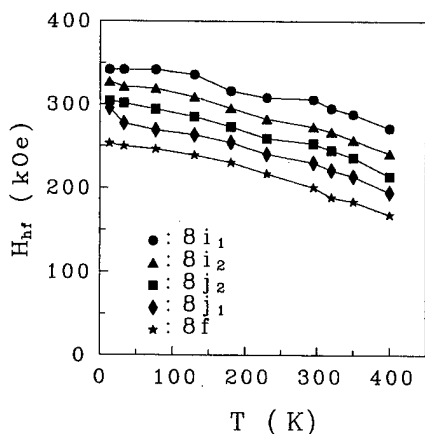


FIG. 2. Temperature dependence of magnetic hyperfine field, H_{hf} in $\text{NdFe}_{10.7}\text{TiB}_{0.3}\text{N}_\delta$.

$\text{NdFe}_{10.7}\text{TiB}_{0.3}\text{N}_\delta$ is much larger than that of the parent alloy ($B_{3/2}=0.48$ and $C_{5/2}=0.22$).⁷ Hence, it seems that spin waves having long wavelengths are excited in the nitride alloy rather than in the parent alloy.

Table I shows the VSM data before and after nitrogenation for $\text{NdFe}_{10.7}\text{TiB}_{0.3}$. The values of the Curie temperature T_c and anisotropy field H_A are estimated to be 833 K and 8 T at 295 K. It is clearly seen that nitrogenation enhances the Curie temperature of the nitrides remarkably. As Ti is replaced with B for nitrated $\text{NdFe}_{10.7}\text{TiB}_{0.3}\text{N}_\delta$ it is found that B is very effective for the increase Curie temperature ($T_c = 833$ K) and magnetization ($M_s = 110.7$ emu/g), which are by about 19% and 22%, respectively, larger than those of $\text{NdFe}_{10.7}\text{Ti}_{1.3}\text{N}_\delta$. In addition, considerable amounts of the α -Fe phase are formed, having higher Curie temperatures. The increase in the 1:12 Curie temperature is attributed to the increase in the Fe-Fe distance with the expansion of the unit cell volume. Above the Curie temperature, the VSM data show that the magnetic moment increases again. The

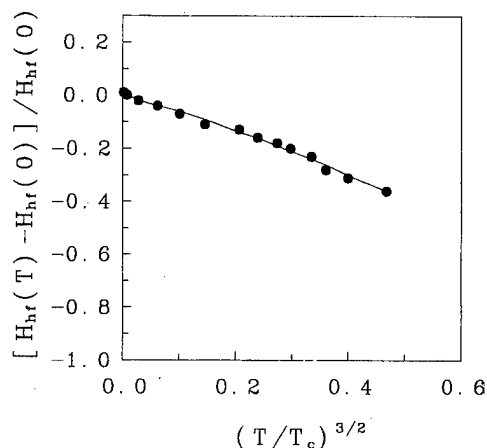


FIG. 3. Fractional change of the average magnetic hyperfine field, H_{hf} , as a function of $(T/T_c)^{3/2}$.

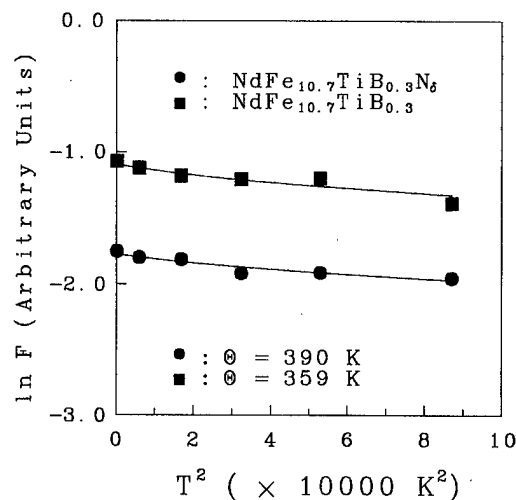


FIG. 4. Natural logarithm of the absorption area F vs T^2 for $\text{NdFe}_{10.7}\text{TiB}_{0.3}\text{N}_\delta$.

formation of α -Fe is the main reason for the increasing magnetic moment. It is worth nothing that the saturation magnetization M_s and magnetic hyperfine field H_{hf} of the nitride at 295 and at 77 K is lower than that of the parent alloy. This phenomenon was also found in $\text{NdFe}_{12-x}\text{Mo}_x\text{N}_{1-\delta}$ ² and in $\text{NdFeV}_3\text{N}_{1-\delta}$.¹¹ Although $\text{NdFe}_{10.7}\text{TiB}_{0.3}\text{N}_\delta$ has a lower saturation magnetization than other nitride compounds, it can very likely be used for permanent magnet in applications requiring medium or small energy products.

Figure 4 shows $\ln F$ versus T^2 for $\text{NdFe}_{10.7}\text{TiB}_{0.3}\text{N}_\delta$ and $\text{NdFe}_{10.7}\text{TiB}_{0.3}$, where F stands for the total resonance absorption to the recoil-free fraction f . From the temperature variation of the total Mössbauer absorption areas, we obtained the Debye temperatures of $\text{NdFe}_{10.7}\text{TiB}_{0.3}\text{N}_\delta$ and $\text{NdFe}_{10.7}\text{TiB}_{0.3}$ which are 390 ± 5 and 359 ± 5 K, respectively.

ACKNOWLEDGMENTS

This work was supported by the Korea Science and Engineering Foundation (961-0210-065-2) and BSRI (97-2424), Ministry of Education.

- ¹Y. Yang, X. Zhang, S. Ge, Q. Pan, L. Kong, H. Li, J. Yang, B. Zhang, Y. Ding, and C. Ye, J. Appl. Phys. **70**, 6001 (1991).
- ²Y. Z. Wang, B. P. Hu, X. L. Rao, G. C. Liu, L. Yin, W. Y. Lai, W. Gong, and G. C. Hadjipanayis, J. Appl. Phys. **73**, 6251 (1993).
- ³Q. Qi, B. Hu, and J. M. D. Coey, J. Appl. Phys. **75**, 6235 (1994).
- ⁴M. Anagnostou, C. Christides, M. Pissas, and D. Niarchos, J. Appl. Phys. **70**, 6012 (1991).
- ⁵F. E. Pinkerton, C. D. Fuerst, and J. F. Herbst, J. Appl. Phys. **75**, 6015 (1994).
- ⁶Y. B. Kim, H. T. Kim, K. W. Lee, C. S. Kim, and T. K. Kim, IEEE Trans. Magn. **28**, 2566 (1992).
- ⁷C. S. Kim, Y. J. Lee, S. W. Lee, Y. B. Kim, and C. S. Kim, J. Appl. Phys. **79**, 5516 (1996).
- ⁸H. N. Ok, K. S. Baek, E. C. Kim, and C. S. Kim, Phys. Rev. B **48**, 3212 (1993).
- ⁹Y. C. Yang, X. D. Zhang, L. S. Kong, Q. Pan, S. L. Ge, J. L. Yang, Y. F. Ding, B. S. Zhang, and C. T. Ye, Solid State Commun. **78**, 313 (1991).
- ¹⁰C. L. Chien and R. Hasegawa, Phys. Rev. B **16**, 2115 (1997).
- ¹¹B. P. Hu, H. S. Li, and J. M. D. Coey, J. Appl. Phys. **67**, 4838 (1990); R. S. Wei, Z. Z. Wu, and L. Ying, J. Magn. Magn. Mater. **139**, 175 (1995).

A Mössbauer study of plasma nitrided iron

F. A. O. Cabral and J. H. de Araujo

Departamento de Física Teórica e Experimental-UFRN, C.P. 1641, 59072-970, Natal-RN-Brazil

R. C. Araujo and S. Gama

Instituto de Física Gleb Wataghin Universidade Estadual de Campinas-UNICAMP, C.P. 6165, 13083-970, Campinas-SP-Brazil

Iron powder has been nitrided in a glow discharge plasma of a mixture of nitrogen and hydrogen, in order to verify the existence of a metastable iron nitrogen solid solution, previously observed from the $\text{Sm}_2\text{Fe}_{17}\text{N}_3$ phase decomposition process. Our results show that, for short nitridation times, we obtain a mixture of Fe_4N , a small amount of $\alpha\text{-Fe}$ and an iron nitrogen solid solution the amount of which increases after heat-treatment at 610°C . This iron nitrogen solid solution is characterized by Mössbauer spectroscopy which shows a typical $\alpha\text{-Fe}$ spectrum, but with lower hyperfine field and broader linewidth. TMA measurements show that the Curie temperature is similar to that of $\alpha\text{-Fe}$. © 1998 American Institute of Physics. [S0021-8979(98)36111-3]

I. INTRODUCTION

The Fe-N binary system is of significant technological and scientific importance. Ferromagnetic iron nitride has attracted much attention because of its high magnetic flux and good corrosion and wear resistance. These properties of iron nitride are of technological interest for potential high magnetic flux density applications in severe working conditions.

Iron and nitrogen form Fe_4N , Fe_2N (Fe_3N) and Fe_8N (Fe_{16}N) phases.¹ The γ -phase austenite is stable above 590°C . The maximum solubility of nitrogen in $\alpha\text{-Fe}$ is 0.1 wt % at 590°C which decreases to ≈ 0.004 wt % when the temperature decreases to 200°C . The α -iron nitrogen solid solution has a lattice parameter and magnetic properties practically similar to those of $\alpha\text{-Fe}$. However, a recent study of the ternary $\text{Sm}_2\text{Fe}_{17}\text{N}_3$ nitride decomposition process² showed the formation of a metastable iron nitrogen solid solution with Curie temperatures lower than that for $\alpha\text{-Fe}$, ranging from 700 to 770°C . The purpose of this investigation is to verify the existence of this metastable iron nitrogen solid solution independently from the decomposition mechanism for the $\text{Sm}_2\text{Fe}_{17}$ nitride. We synthesized $\gamma'\text{-Fe}_4\text{N}$ in a glow discharge plasma and then carried out heat treatments under vacuum to promote Fe_4N decomposition.

II. EXPERIMENT

The samples were prepared by nitriding high purity (99.99%) iron powder having a particle size of about $30\text{--}50\ \mu\text{m}$. The iron powder was nitrided at 500°C in a glow discharge plasma of a mixture of N_2 and H_2 in the proportion 1:9, during periods of time ranging from 3 to 12 h. The sample temperature was monitored by a type K sheathed thermocouple. Heat treatment of the samples was carried out at 610°C under rotary pump vacuum. The samples were subsequently quenched in water. We also performed TMA measurements in order to determine both the magnetic behavior of the Fe_4N samples under decomposition and the Curie temperature of the resulting decomposition phases. The Curie temperatures were determined from the maximum

in the derivative of the susceptibility curve. The Mössbauer spectra were obtained with a conventional constant acceleration spectrometer in triangular velocity mode with a ^{57}Co source in a rhodium matrix at room temperature. The spectrometer was calibrated with a $25\ \mu\text{m}$ thick $\alpha\text{-Fe}$ foil. The density of the absorber was $2\ \text{mg Fe/cm}^2$.

III. RESULTS AND DISCUSSION

Figure 1 shows the Mössbauer spectra of as-nitrided and heat treated samples. For the as-nitrided sample the Mössbauer spectrum is basically composed of a mixture of the Fe_4N subspectrum and two $\alpha\text{-Fe}$ subspectra. The low inten-

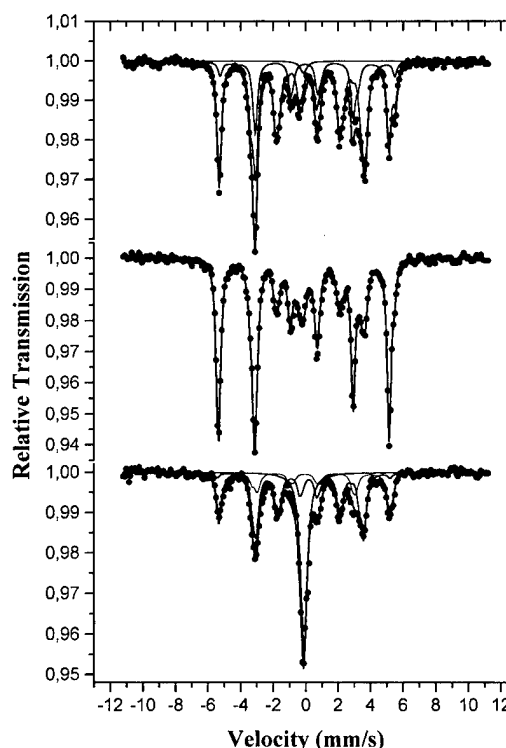


FIG. 1. Mössbauer spectra for the as nitrided and heat treated samples.

TABLE I. Mössbauer parameters for the as nitrated and heat treated samples. The isomer shift values are quoted relative to the center of the α -Fe calibration spectrum.

Samples	Phases	Area (%)	H (kOe)	ΔE_Q (mm/s)	δ (mm/s)
as-nitrated	α -Fe	12.1	334	-0.01	-0.10
	ss	25.9	323	0.02	-0.07
	γ -Fe	1.5	0	0.00	-0.15
	Fe_4N	60.5	208	0.08	0.21
			210	-0.18	0.18
15 min	α -Fe	3.9	330	0.03	-0.10
			325	0.06	0.08
	γ -Fe	7.3	0	0.00	-0.15
	Fe_4N	35.0	207	0.09	0.21
			211	-0.15	0.16
	α -Fe	3.7	332	0.01	-0.09
			320	-0.02	-0.05
30 min	γ -Fe	27.9	0	0.00	-0.12
	Fe_4N	47.3	201	0.07	0.18
			203	-0.16	0.16
	α -Fe	3.7	332	0.01	-0.09
			320	-0.02	-0.05
	γ -Fe	7.3	0	0.00	-0.15
	Fe_4N	47.3	203	-0.16	0.16

sity singlets in the center of the spectrum are assigned to the austenite phase. The Fe_4N phase subspectrum is composed of three sextets (Table I). The two lower hyperfine field sextets are assigned to FeII sites (faces) A and B and the higher one is assigned to FeI sites (corner).³ The α -Fe subspectrum is composed of two sextets. The one with hyperfine field around 330 kOe is assigned to pure α -Fe and the other sextet with hyperfine field around 325 kOe and larger linewidth ($\Gamma=0.40$ mm/s) is assigned to an iron nitrogen solid solution and is ascribed to the Fe atoms whose first and second nearest octahedral interstitial sites are occupied by nitrogen atoms in the martensite phase.^{4,5} After heat treatment at 610 °C for 15 min there is a large increase of the solid solution at the expense of the Fe_4N phase. The spectrum of the sample heat

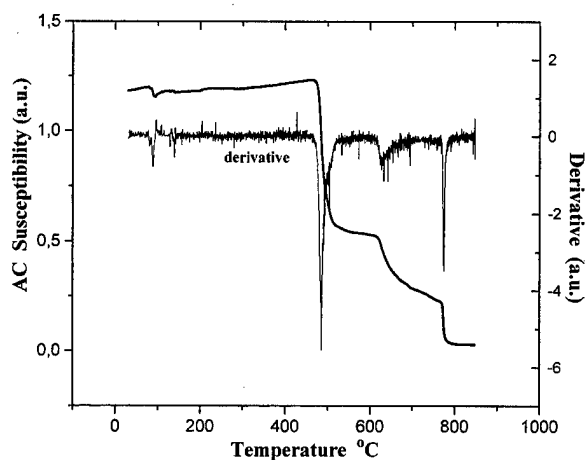


FIG. 2. TMA curve for the as nitrated sample (1st run).

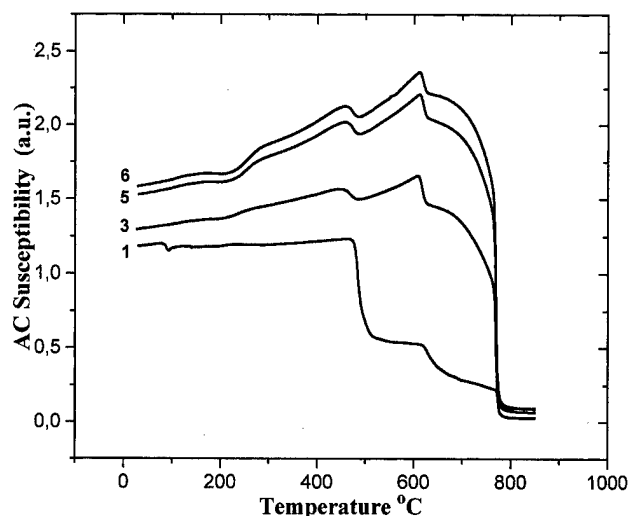


FIG. 3. Sequential TMA's for the as nitrated sample.

treated at 610 °C for 30 min shows a very large increase in the austenite phase at the expense of the Fe_4N phase.

We performed a sequence of TMA measurements up to 850 °C. Figure 2 shows the TMA heating curve of the first run, for the as-nitrated sample. We observe the magnetic transition of the Fe_4N phase at around 480 °C, the signal associated with the $\gamma \leftrightarrow \alpha\text{-Fe} + \text{Fe}_4\text{N}$ transition at around 600 °C, and the magnetic transition of the α -Fe and/or the iron nitrogen solid solution at 770 °C. The following runs, up to 850 °C, reproduce the form of the heating curve of the first run. However, the Fe_4N magnetic signal decreases and the curves (Fig. 3) show a far higher value of the susceptibility. We do not observe any variation of the Curie temperature of the iron nitrogen solid solution.

IV. CONCLUSIONS

Iron nitrogen solid solution can be formed in the iron samples nitrated in a glow discharge of mixture of a nitrogen and hydrogen. The Mössbauer spectrum of the iron nitrogen solid solution is typical of α -Fe, but with a lower hyperfine field around 325 kOe and a larger linewidth of $\Gamma=0.40$ mm/s. The Curie temperature observed is similar to that for α -Fe. This contrasts with the case of the metastable iron nitrogen solid solution resulting from the $\text{Sm}_2\text{Fe}_{17}$ nitride decomposition process which showed a different Curie temperature.

¹ Binary Alloy Phase Diagrams, 2nd ed., edited by T. B. Massalski (American Society for Metals, Cleveland, 1990), p. 1729.

² F. A. O. Cabral, S. Gama, E. de Moraes, N. L. Sanjurjo, C. A. Ribeiro, and C. C. Colucci, IEEE Trans. Magn. **32**, 4365 (1996).

³ A. J. Nozik, J. C. Wood, Jr., and G. Haacke, Solid State Commun. **7**, 1677 (1969).

⁴ I. Fall, D. N. C. Uwakweh, and J. M. R. Genin, Hyperfine Interact. **69**, 517 (1991).

⁵ V. G. Gavriljuk, V. M. Nadutov, and K. Ullakko, Scr. Metall. Mater. **25**, 905 (1991).

Macroscopic Quantum Tunneling and Spin Dynamics

Bruce Harmon, Chairman

Experimental evidence of macroscopic resonant tunneling of magnetization in antiferromagnetic ferritin

E. del Barco,^{a)} F. Luis, J. Tejada, X. X. Zhang, J. Bartolomé, and J. M. Hernandez
Departamento de Física Fundamental, Universidad de Barcelona, Diagonal 647, Barcelona 08028, Spain

E. M. Chudnovsky
Physics Department, Lehman College, The City University of New York, Bronx, New York 10468-1589

Macroscopic resonant quantum tunneling of magnetization has been observed in antiferromagnetic ferritin particles. The dependence of magnetic viscosity on the applied magnetic field has been systematically investigated in the temperature range 1.8–10 K. The zero maximum in field dependence of viscosity and the maximum in the field dependent blocking temperature are interpreted to be due to the resonant spin tunneling between matching spin levels. © 1998 American Institute of Physics. [S0021-8979(98)53311-7]

Since the discovery of the resonant quantum tunneling in high-spin molecules,^{1–4} we have been working in order to observe the same phenomena in mesoscopic particles with much higher spin values. The main problem when using mesoscopic particles is that they are not identical. In a typical sample of magnetic nanoparticles there is a distribution of spin values and a random orientation of the easy axis. These facts make it difficult to observe fine behaviors like the resonant quantum tunneling of magnetization. However, as we have recently published,⁵ it is possible to detect this effect in ferritin molecules because: (a) the magnetic core of these molecules is antiferromagnetic therefore having higher crossover temperature between the classical and quantum regime than ferromagnetic particles, (b) the net spin is small and the anisotropy barrier height is large making experimentally possible the observance of the discrete orientation of the magnetic moment, and (c) the molecules are independent between them, which very much simplifies the explanation.

The quantum dynamics of magnetization in ferritin have received much attention since Awschalom and co-workers reported a resonance in the absorption spectrum of ferritin in the range of milliKelvin, which they attributed to the macroscopic quantum coherence.⁶ This hypothesis establishes an important paradox:⁷ while the Kelvin range experiments indicate that the magnetic moments of the particles are frozen below a few Kelvin (the blocking temperature of ferritin is about 13 K),⁸ the resonance experiments in the milliKelvin range were interpreted as the quantum tunneling of spin with a rate of 10^6 – 10^7 s^{−1}. The explanation to this paradox could be the following: resonant quantum tunneling only occurs when the levels of the opposite orientation of the spin coincide at both wells. If this is true, we should be able to observe an increase of the relaxation rate around zero magnetic field. We report that this is what exactly occurs in ferritin.

In our experiments we have used a dilute sample of natural ferritin with about 10^{14} molecules. The ferritin has a spherical cavity of 8 nm which contains mineral ferrihydrite with phosphate. Its core is equivalent to a magnetic particle with a diameter between 3 and 7.5 nm. The ferritin core contains about 4500 Fe³⁺ ions. However, the spin of the particle is small (around 100). This is due to the antiferromagnetic magnetic order between the two sublattices of the Fe³⁺ ions. Only about 15 noncompensated surface spins contribute to the magnetic moment of the particle, which coincides with the theoretical estimation of $(4500)^{1/3} \approx 16$. This noncompensated spin locks in one of the two directions along the anisotropy axis of the particle. The interactions between particles can be neglected as both the ac and dc magnetic susceptibility experiments on samples with different dilution degree indicate. Above 13 K the particles are superparamagnetic,⁸ as it has been proved by ac and dc susceptibility measurements, that is, their magnetic moments frequently jump between the two opposite orientations over the anisotropy barrier. Below 13 K the particles are essentially frozen and the transition from s to $-s$ can occur only due to quantum tunneling: in the absence of the magnetic field and in the limit of weak dissipation, sublattices should interchange in a coherent manner.⁹

Gider¹⁰ and Friedman¹¹ brought to light a nonmonotonic behavior of the field dependence to the blocking temperature, T_B . The variation of T_B with the applied field deduced from our experiments of the zero field cooled (ZFC) magnetization are shown in Fig. 1. We can observe a nonmonotonic dependence of the blocking temperature as a function of magnetic field. Contrary to what is expected in this kind of system, the blocking temperature increases when the magnetic field increases. This anomalous behavior is observed up to 2.5 kOe, where it reaches its maximum and then decreases at higher fields following the expected behavior.

The measurements of the ZFC magnetization have been

^{a)}Electronic mail: edb@ffn.ub.es

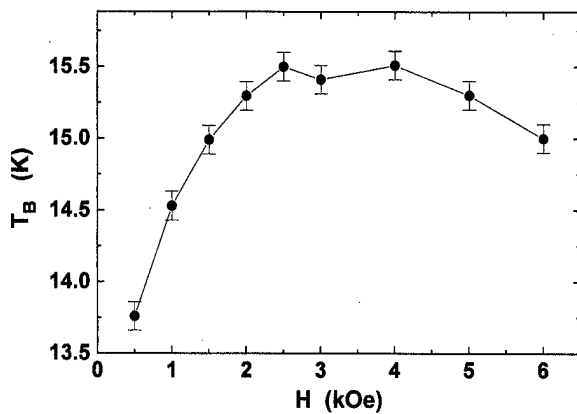


FIG. 1. Zero field cooled magnetization curves obtained by cooling the sample in zero field and then heating it at different applied field. The inset shows the field dependence of the blocking temperature.

obtained by cooling the sample down to 2 K without applied field. Then a magnetic field is applied. Afterwards, the magnetization is measured while the temperature increases. The process is repeated at different magnetic fields. At low temperature, the magnetization of the system is small because the particles are frozen and they cannot jump over the anisotropy barrier and solely the smallest particles can arrange its magnetic moment along the applied field. As the temperature increases, every time bigger particles rotate their magnetic moments contribute to increase the magnetization. The blocking temperature, T_B , is defined as the temperature at which the majority of the particles become unfrozen, at the time scale of the experiment. T_B is therefore proportional to the anisotropy energy barrier $U = KV$, where K is the anisotropy energy constant and V is the volume of the particle. At temperatures over T_B , $M(T)$ follows the Curie law of the superparamagnetism.

Another way to verify the acceleration of the magnetic relaxation towards the equilibrium state at zero field is the magnetic hysteresis measurement. The field derivative of the magnetic hysteresis loops explains how fast the system reaches the equilibrium. The peaks observed in both the hysteresis loops of the Mn_{12} -Ac molecules were the key elements in the discovery of the resonant spin tunneling. In the hysteresis loops of ferritin we observe⁵ a clear peak at zero magnetic field (Fig. 2). The peaks at non-zero-magnetic field values are not detectable because of the impossibility to orient the ferritin molecules with their easy axis parallel to the applied magnetic field.

Finally we confirmed the acceleration of the magnetic relaxation at $H=0$ by measuring directly the relaxation rate as a function of the applied magnetic field.⁵ The method is the following: the sample is cooled from 50 K down to the measurement temperature. Then a magnetic field is applied and the magnetization is measured during the relaxation to the equilibrium state. The relaxation behavior is, with high accuracy, logarithmic in time during four decades (Fig. 3). This is a typical behavior in a system with broad distribution of energy barriers. The control parameter of the relaxation is the magnetic viscosity defined as

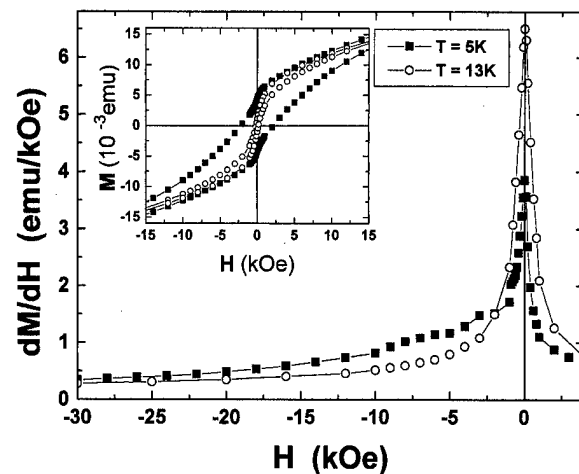


FIG. 2. Field derivative of the magnetization at a constant sweep rate. Inset shows hysteresis loops from which dM/dT has been obtained (Ref. 5).

$$S = \frac{1}{M_{eq}(H,T)} \frac{dM(H,T,t)}{d \ln(t)}, \quad (1)$$

where $M_{eq}(H,T)$ is the equilibrium magnetization of the system at fixed temperature and field. The latter was deduced from the field cooled magnetization measurements.

The magnetic viscosity as a function of the applied magnetic field at different temperatures is shown in Fig. 4.⁵ At 2.4 and 3 K the viscosity increases with the magnetic field. In the range from 4.2 to 8 K the viscosity first decreases when the applied magnetic field increases, reaches its minimum at one value of the applied field which depends on the temperature, and then increases at higher fields. Over 8 K the viscosity always decreases monotonically.

This unusual behavior of the magnetic relaxation in ferritin can be explained if one takes into account quantization of spin levels of the particle. The lower spin levels should be separated by the energy of the antiferromagnetic resonance, $\Delta E = (2\epsilon_{an}\epsilon_{ex})^{1/2}$, where $\epsilon_{an} = g\beta H_{an}$ is the anisotropy energy and $\epsilon_{ex} = JS$, where J is the exchange constant and S is the sublattice spin. This energy is much bigger than the one

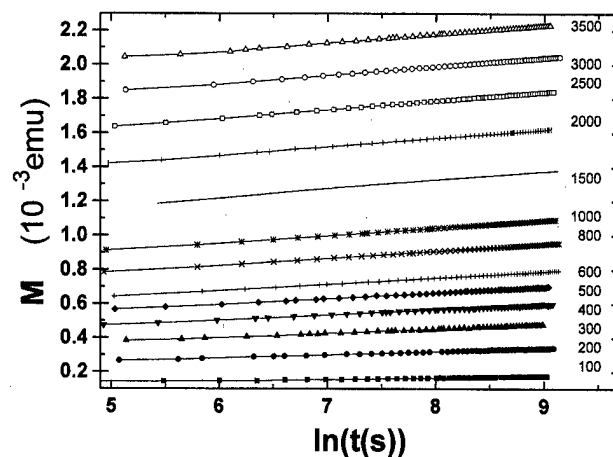


FIG. 3. Time dependence of the magnetization at different applied fields at 6.5 K. The numbers near the data are the values of the applied magnetic field in Oe.

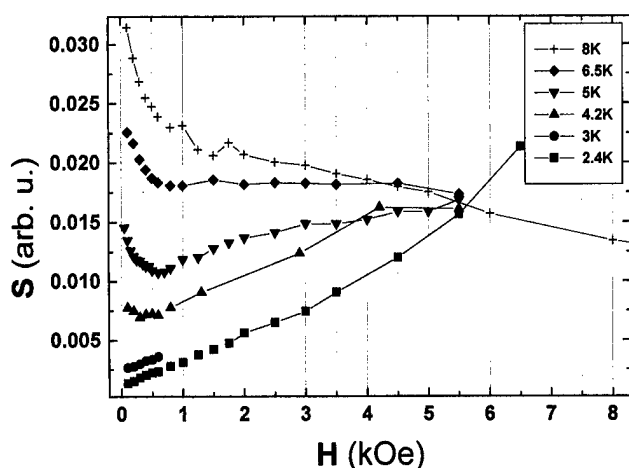


FIG. 4. Magnetic viscosity as a function of the magnetic field at different temperatures (Ref. 5).

corresponding to ferromagnetic particle with the same size. In ferritin, this energy is about 10 K which is comparable to the separation of the lower levels in Mn_{12} molecules.

The resonant quantum tunneling between the matching spin levels occurs when $2g\beta Hs = n\Delta E$, where $n=0,1,2,\dots$. All the corresponding values of the magnetic field are separated by

$$\Delta H = \frac{H_{\text{an}}}{2s} \left(\frac{2\epsilon_{\text{ex}}}{\epsilon_{\text{an}}} \right)^2. \quad (2)$$

For a ferromagnetic particle, the separation between the low levels can be estimated around 0.1 Oe. This value is smaller than the splitting of the levels and the resonance will not be observable. However, this value for the same particle of spin S with antiferromagnetic order is a factor $(S/s) (\epsilon_{\text{ex}}/\epsilon_{\text{an}})^{1/2}$ bigger, which in ferritin is a factor 10^4 . Consequently, the field spacing between resonances in ferritin must be of order of kOe, that is, comparable to that in Mn_{12} . However, due to the different orientation and magnitude of the noncompensated spin, contrary to the case of a Mn_{12} crystal, only the $H=0$ resonance occurs simultaneously in all ferritin particles. To see high order resonances one must have a sample with oriented ferritin particles having a single s value.

As in $\text{Mn}_{12}\text{-Ac}$, in ferritin the tunneling in our temperature range must be thermally assisted, this is, it occurs from excited spin states as well as from the ground state. The spin states are characterized by the projection of s on the anisotropy axis, $s_z|m\rangle = m|m\rangle$. At $H=0$ the states corresponding to m and $-m$ are degenerated and the resonant tunneling between these states takes place. At low temperature (below

3 K) only the lowest levels $m = \pm s$ are occupied. The tunneling splitting of these levels is given by

$$\Delta_S \propto T_c \exp \left[-S \left(\frac{\epsilon_{\text{an}}}{\epsilon_{\text{ex}}} \right)^{1/2} \right], \quad (3)$$

where T_c is the crossover temperature, which in ferritin is about 3.2 K. This tunneling splitting determines the width of the resonance with the magnetic field. Since tunneling is weak this width is extremely small. According to Ref. 6 where measurements were performed in the mK range, the width of this resonance is about 10^{-4} Oe. This should explain why we do not see the $H=0$ peak in the viscosity at low temperature. As the temperature increases above 3 K, higher m levels become thermally populated and tunneling between them dominates the relaxation. The width of these levels must be large due to their finite lifetime with respect to the decay down to the ground state levels $m = \pm s$. Consequently, the width of the resonance on the magnetic field becomes large enough to observe the $H=0$ maximum in the viscosity. As the temperature continues to increase towards the blocking temperature, the system enters the superparamagnetic regime dominated by thermal overbarrier transitions. In this regime the viscosity monotonically decreases with the field, reflecting the progressive disappearance of the metastability.

In conclusion, we have presented data on the magnetic relaxation in ferritin which show strong departure from the conventional behavior. A plausible explanation to all data is given within the model of thermally assisted resonant tunneling between spin levels.

J.T. acknowledges support from CICYT No. IN96-0027 and CIRIT No. 1996 PIRB 00050 Projects. The work of E.M.C. has been supported by the U.S. National Science Foundation Grant No. DMR-9024250. E.D.B. acknowledges support from the University of Barcelona.

¹J. R. Friedman, M. P. Sarachik, J. Tejada, and R. F. Ziolo, Phys. Rev. Lett. **76**, 3830 (1996).

²J. M. Hernández *et al.*, Europhys. Lett. **35**, 301 (1996).

³L. Thomas *et al.*, Nature (London) **383**, 145 (1996).

⁴M. A. Novak and R. Sessoli, in *Quantum Tunneling of Magnetization*, edited by L. Gunther and B. Barbara (Kluwer, Dordrecht, 1995), p. 171.

⁵J. Tejada *et al.*, Phys. Rev. Lett. **79**, 1754 (1997).

⁶D. D. Awschalom *et al.*, Phys. Rev. Lett. **68**, 3092 (1992).

⁷J. Tejada, Science **272**, 424 (1996); A. Garg, *ibid.* **272**, 424 (1996); S. Gider, D. D. Awschalom, D. P. Divincenzo, and D. Loss, *ibid.* **272**, 425 (1996).

⁸J. Tejada and X. X. Zhang, J. Phys.: Condens. Matter **6**, 263 (1994).

⁹B. Barbara and E. M. Chudnovsky, Phys. Lett. A **145**, 205 (1990).

¹⁰S. Gider *et al.*, Science **268**, 77 (1995).

¹¹J. R. Friedman *et al.*, Phys. Rev. B (to be published).

Field-tuned quantum tunneling of the magnetization

D. García-Pablos^{a)} and N. García

Laboratorio de Física de Sistemas Pequeños y Nanotecnología, Consejo Superior de Investigaciones Científicas, Serrano 144, E-28006-Madrid, Spain

H. De Raedt

Institute for Theoretical Physics and Materials Science Centre, University of Groningen, Nijenborgh 4, NL-9747 AG Groningen, The Netherlands

The response of the magnetization to a time-dependent applied magnetic field in single-spin models for uniaxial magnets is studied. We present staircase magnetization curves obtained from the numerically exact solution of the time-dependent Schrödinger equation. Steps are shown to correspond to field-tuned quantum tunneling between different pairs of nearly degenerate energy levels. We investigate the role played by different terms that allow for tunneling processes: transverse fields and second-order and fourth-order transverse anisotropies. Magnetization curves for nonsaturated initial states and for excited initial states showing steps when the field decreases in absolute value are also presented. These results are discussed in relation to recent experiments on high-spin compounds. © 1998 American Institute of Physics. [S0021-8979(98)16111-X]

Magnetic molecules containing high-spin clusters¹ such as Mn_{12} or Fe_8 provide physical systems by which to study quantum tunneling of the magnetization (QTM).^{2,3} Recent experiments on these systems^{4,5} have reported the appearance of steps in the hysteresis loops at low temperature which have been attributed to thermally assisted resonant tunneling between quantum states. This interpretation is based on a single-spin $S=10$ model with strong uniaxial anisotropy ($\mathcal{H} = -DS_z^2 - g\mu_B \mathbf{S}\mathbf{H}$, where D is the uniaxial anisotropy energy) for which energy levels ($|Sm\rangle$ for $\mathbf{H} \parallel \hat{z}$, where $S_z|Sm\rangle = m|Sm\rangle$) cross at fields $g\mu_B H_n = nD$. At these fields, the relaxation time of the magnetization shows minima. For QTM to occur, this model has to be extended to include symmetry breaking terms such as those originating from dipolar interaction, interaction with nuclear spins or phonons, etc.⁵⁻⁷ The detailed mechanism by means of which QTM occurs in hysteresis experiments on uniaxial magnets is investigated in this article. Previously, magnetization tunneling in mesoscopic systems has been semiclassically studied by several authors⁸⁻¹⁰ and, more recently, quantum dynamical calculations for several models of nanomagnets such as the Heisenberg model¹¹ and the single-spin quantum model¹² have shown the occurrence of resonant coherent QTM at zero temperature. The staircase structure in the magnetization curves for a time-dependent field has been recently shown¹³ to be well described by successive Landau-Zener (LZ) transitions.^{14,15} In addition, recent theoretical works have also studied the problem of spin tunneling in a swept magnetic field.^{16,17}

The most general Hamiltonian for a single quantum spin including a transverse field (which might have a hyperfine or dipolar origin), second-order and fourth-order transverse anisotropies, and a time-dependent applied magnetic field is

$$\mathcal{H} = -K_x S_x^2 - K_y S_y^2 - K_z S_z^2 - C_x S_x^4 - C_y S_y^4 - C_z S_z^4 - \Gamma S_x - \mathbf{H}(t)\mathbf{S}, \quad (1)$$

where K_z , K_x and K_y are the anisotropy constants along the easy, medium, and hard axes, respectively, $\mathbf{S} = (S_x, S_y, S_z)$ is the vector representing the magnetization, C_x , C_y , and C_z are the fourth-order anisotropy constants, Γ is the transverse field, and $\mathbf{H}(t) = H(t)(\sin \theta, 0, \cos \theta)$ denotes the applied field.

The time evolution of the magnetization at $T=0$ is obtained from the exact numerical solution of the time-dependent Schrödinger equation (TDSE), $i\hbar \partial |\Psi(t)\rangle / \partial t = \mathcal{H} |\Psi(t)\rangle$, where $|\Psi(t)\rangle$ denotes the wave function of the spin system at time t . We study the following situation: First we set the applied magnetic field to its minimum value $H(t=0) = -H_0$ and put the system in the corresponding ground state, i.e., $|\Psi(0)\rangle = |\Phi_0(0)\rangle$ where $\mathcal{H}(-H_0)|\Phi_0(0)\rangle = E_0(-H_0)|\Phi_0(0)\rangle$. The time evolution of the wave function is then calculated by means of $|\Psi(t+\tau)\rangle = \exp(-i\tau\mathcal{H})|\Psi(t)\rangle$, where τ is the time step used to integrate the TDSE. During the integration of the TDSE, the applied field changes from $-H_0$ to H_0 with a given speed, which is defined by the field step ΔH between two consecutive field values and the amount of time τ_H the system feels each constant field. The temporal evolution of the α th ($\alpha = x, y, z$) component of the spin can be calculated from $\langle S_\alpha(t) \rangle = \langle \Psi(t) | S_\alpha | \Psi(t) \rangle$. For each constant field value we compute the expectation value of S_α averaged over time $\bar{S}_\alpha = 1/\tau_H \int_0^{\tau_H} dt \langle S_\alpha(t) \rangle$. In the following we will refer to $M = \bar{S}_z/S$ as the magnetization. The energy of the system is given by $E[H(t)] = \langle \Psi(t) | \mathcal{H} | \Psi(t) \rangle$.

In order to understand the origin of the steps in the magnetization curves, we first consider the simplest case of (1), namely, a single spin 1/2 system described by the Hamiltonian $\mathcal{H} = -\Gamma \sigma_x - H(t)\sigma_z$, where σ_x and σ_z are the Pauli-spin matrices, and we study the response of the magnetization to the time-dependent applied field $H(t)$. Γ sets the scale of the splitting at $H=0$ between the two energy levels (see inset of Fig. 1). Figure 1 presents the magnetization curves for several field sweep rates for the ground state as the initial state, showing steps of different sizes at $H=0$.

^{a)}Electronic mail: danielgp@fsp.csic.es

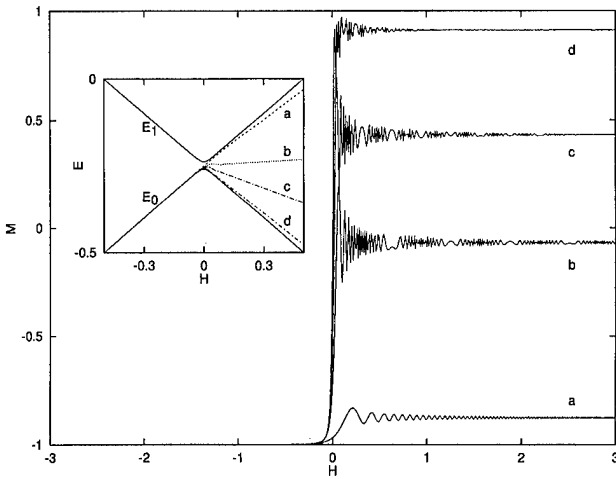


FIG. 1. M vs H for model (1) with $S=1/2$, $K_z=1.0$, and $\Gamma=0.02$ for several field sweep rates $\Delta H/\tau_H$: $\Delta H=0.001$ and (a) $\tau_H=0.1$, (b) $\tau_H=1$, (c) $\tau_H=2$, and (d) $\tau_H=5$. Initial state: Φ_0 . The inset shows the levels crossing and the system energy for cases (a)–(d).

According to the adiabatic theorem, a slowly changing external perturbation will keep the system in the eigenstate it started from (Φ_0) unless this eigenstate comes closer to another eigenstate (Φ_1). Then the adiabatic approximation might break down, allowing the system to escape from Φ_0 and tunnel to Φ_1 via the Landau–Zener tunneling mechanism.¹⁴ The probability of staying in the same eigenstate Φ_0 (which has opposite magnetization after the crossing) when the field is swept is given by $p=1-\exp[-\pi\Delta E^2/(2\Delta H/\tau_H)]$, which depends on the energy splitting and the field sweep rate $\Delta H/\tau_H$. The final state is then a linear combination of both eigenstates with weights p and $1-p$ and the size of the step at $H=0$ is proportional to p , i.e., $\Delta M=pM_0^{\text{final}}+(1-p)M_1^{\text{final}}-M_0^{\text{initial}}$, where the superscripts initial and final refer to before and after the crossing. Curve (d) is the closest to adiabatic behavior ($p\approx 1$, large step); curve (a) corresponds to a fast sweep and the scattering is almost complete ($p\approx 0$, small step). The appearance of steps in the magnetization curves is a general feature for many models of uniaxial magnets and follows naturally from the occurrence of field-tuned tunneling transitions between nearly degenerate eigenstates of the Hamiltonian. The size of the step depends on the energy-level splitting of the participating levels, the weight of the corresponding eigenstates in the current state of the system, the field sweep speed, and the value of the magnetization itself.

In Fig. 2 we present magnetization curves for the Hamiltonian most commonly assumed^{4,5} in the attempt to explain recent experimental data ($\mathcal{H}=-K_z S_z^2-\mathbf{H}(t)\mathbf{S}$, with $\mathbf{H}\parallel\hat{z}$ and $S=10$), supplemented by terms that break the rotational symmetry about the z axis, i.e., those in model (1). These terms allow for the occurrence of field-tuned QTM and the corresponding steps in the magnetization. All these cases have in common that, for some specific fields H_n , pairs of energy levels become almost degenerate. If $\Phi_0(-H_0)$ is the initial state, the levels involved in the crossing at H_n are E_n and E_{n+1} .

Curves (a), (b), and (c) correspond to the case including

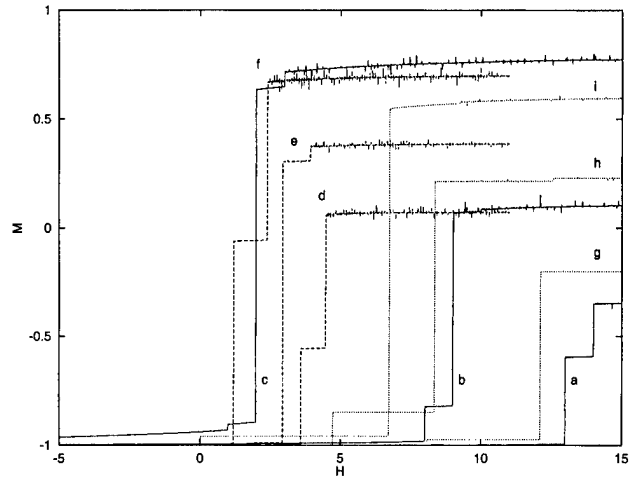


FIG. 2. M vs H for model (1) with $S=10$, $K_z=1$, and $\theta=0^\circ$ supplemented by a transverse field term for Γ equal to (a) 0.5, (b) 2, and (c) 6.5; second-order anisotropy terms with $K_x=0.6$ and K_y equal to (d) 0.5, (e) 0.4, and (f) 0.1; and fourth-order anisotropy terms with $C=C_x=C_y=C_z$ equal to (g) 0.0005, (h) 0.0025, and (i) 0.01. Field sweep parameters for (a), (b), (c): $\Delta H=3\times 10^{-5}$, $\tau_H=1200$; for (d), (e), (f): $\Delta H=2\times 10^{-5}$, $\tau_H=800$; for (g), (h), (i): $\Delta H=3\times 10^{-5}$, and $\tau_H=900$.

a transverse field. Γ allows all transitions $\Delta m=\pm 1$. At resonance $H_n=nK_z=n$, and the values of n for which steps appear depend on Γ . Thus, for (a) $\Gamma=0.5K_z=0.5$ we find $n=12,13,14$; for (b) $\Gamma=2$, $n=8,9$; and for (c) $\Gamma=6.5$, $n=1,2,3$.

Curves (d), (e), and (f) show that the presence of second-order transverse anisotropy terms can also induce QTM. They correspond to $K_z=1$, $K_x=0.6$, and several values of K_y . For $K_y=K_x$, the energy and S_z commute and no tunneling occurs. These transverse anisotropy terms change the spacing between resonant fields although they remain regularly spaced as in case the case of a transverse field Γ . These terms allow transitions that obey the selection rule $\Delta m=\pm 2$. For (d) $K_y=0.5$, $n=8,10$; for (e) $K_y=0.4$, $n=4,6,8$; and for (f) $K_y=0.1$, $n=2,4$.

Fourth-order anisotropy terms [curves (g), (h), and (i)] allow the occurrence of field-tuned tunneling between levels satisfying $\Delta m=\pm 4$. In this case, the fields at which pairs of energy levels cross are not equally spaced. Results are shown for different values of $C_x=C_y=C_z=C$. For (g) $C=0.0005K_z=0.0005$, $n=8,12$; for (h) $C=0.0025$, $n=4,8,12$; and for (i) $C=0.01$, $n=0,4,8$.

None of the curves in Fig. 2 presents steps when $|\mathbf{H}|$ decreases. This can be easily understood since the system starts from the ground state Φ_0 and the energy level scheme as a function of the field is such that E_0 only crosses another level at zero field. Another feature of these curves is that the magnetization does not reach the saturation value (unless the system stays in the ground state when crossing $H=0$ in which case there is one big step from $M=-1$ to $M=1$) even for $H\rightarrow\infty$. The explanation comes from the fact that the system can only gain or lose energy through the time-dependent field but not through interaction with the environment.

The field sweep rate ($\Delta H/\tau_H$) is a crucial parameter in this problem. As was shown for the simple case of a single

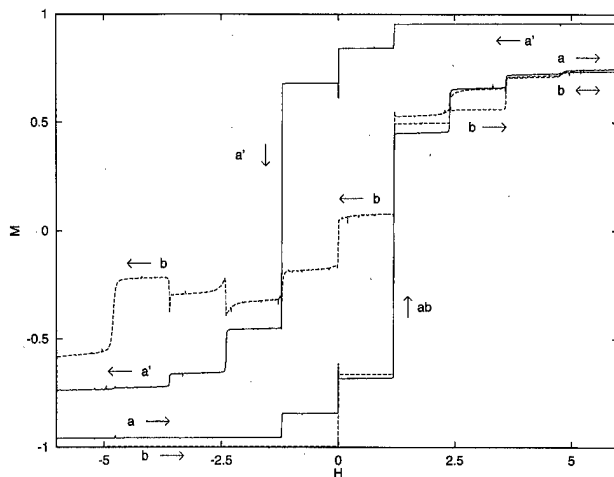


FIG. 3. M vs H for model (1) with $S=10$, $K_x=0.6$, $K_y=0.1$, $K_z=1.0$, $C=\Gamma=0$, and $\theta=0^\circ$. Curves (a) and (a'): The field goes (a) from $-H_0$ to H_0 and (a') from H_0 to $-H_0$ for $H_0=10.0$, starting from the initial states: $\Psi_{(a)}^{(a')}(0)=c_0\Phi_0(\mp H_0)+c_1\Phi_1(\mp H_0)+c_2\Phi_2(\mp H_0)$, respectively, where $c_0=0.7$, $c_1=0.22$, and $c_2=0.08$. Field sweep parameters: $\Delta H=0.0025$, $\tau_H=10^5$. Curve (b): The initial state is $\Phi_0(-H_0)$ and the field goes from $-H_0$ to H_0 and then, before reaching saturation, back to $-H_0$ for $H_0=10.0$. At $H=H_0$, where the field is reversed, $\Psi(H_0)=\sum_n c_{2n}\Phi_{2n}(H_0)$, where $c_0=0.168$, $c_2=0.653$, $c_4=0.038$, $c_6=0.111$, $c_8=0.027$, and $c_{10}=0.002$.

spin $1/2$, the probability of QTM depends on it. In general, the lower the sweep rate, the larger the size of the step. However, also relevant is the smoothness of the field swept: If ΔH is too large, the size of the steps depends in a non-trivial way on ΔH , τ_H , and ΔE , and LZ theory does not apply.

In Fig. 3 we consider the case of an initial state which is not the ground state but a linear combination of several eigenstates. Unlike the ground state, the excited levels can become nearly degenerate with other levels for $H \neq 0$, and therefore there is a nonzero probability of finding steps when $|H|$ decreases, as illustrated by curves (a) and (a'). Moreover, if the field is reversed after one sweep from $-H_0$ to H_0 [curve (b)], the system restarts from a linear combination of several eigenstates (corresponding to a nonsaturated state in an experiment) and the situation is similar to that of curves (a) and (a'). As shown by curve (b), there is some probability of finding steps when $|H|$ decreases and of getting both negative and positive steps. The same reasoning applies to QTM from thermally populated excited levels. Although the tunneling probability increases with the excitation level, and smaller off-diagonal terms are required to induce field-tuned QTM, the fact that the tunneling processes involve excited levels implies that some probability of finding steps when $|H|$ decreases exists, at variance with the experimental results. Moreover, preliminary experimental results in which the field is reversed before saturation is reached show that steps can appear when $|H|$ decreases,¹⁸ in qualitative agreement with our findings.

We have shown that $T=0$ field-tuned QTM leads to staircase magnetization curves. The following might be relevant when comparing to experiments^{4,5} on Mn_{12} : A trans-

verse field Γ allows $\Delta m = \pm 1$ transitions and yields equally spaced steps, in agreement with experiments. However, the theoretical magnetization curves [with Γ as the only off-diagonal term and $\Phi_0(-H_0)$ as the initial state] look similar to the experimental ones (steps at the first energy level crossings $g\mu_B H_n = nD$, n small) for much larger values ($\Gamma \sim 1-5D \equiv 0.44-2.2T$) than those estimated for dipolar ($\sim 0.01T$) or hyperfine ($\sim 0.05T$) interactions.¹⁹ Second-order transverse anisotropy terms are often discarded due to Mn_{12} tetragonal symmetry, although local symmetries could affect the structure of the spectrum. These terms are relevant for other systems such as Fe_8 .²⁰ Fourth-order anisotropy terms cannot account for all the steps observed and they lead to nonequally spaced steps. They can be responsible for small deviations from $\Delta m = \pm 1$ transitions and equally spaced steps. However, the single-spin model proposed for the Mn_{12} molecule may be too simple to mimic the actual energy spectrum: The single-spin $S=10$ system is described by 21 eigenstates whereas a proper description of the magnetic state of the Mn_{12} molecule requires 10^8 states. A better understanding of the situation when the field is not swept smoothly enough and the Landau-Zener picture does not apply is also needed, especially since this appears to be the experimental case. Finally, further experimental work investigating the possibility of obtaining steps for decreasing $|H|$ and observing negative (opposite to the field sweep) steps may clarify the effect of thermal activation, which in principle allows the appearance of these steps.

This work was partially supported by Spanish and European research contracts.

- ¹D. Gatteschi *et al.*, Science **265**, 1054 (1994).
- ²D. D. Awschalom, D. P. DiVincenzo, and J. F. Smyth, Science **258**, 414 (1992).
- ³Quantum Tunneling of the Magnetization-QTM'94, edited by B. Barbara and L. Gunther, NATO ASI Series E (Vol. 301 Kluwer Academic, Dordrecht, 1995).
- ⁴J. R. Friedman, M. P. Sarachik, J. Tejada, and R. Ziolo, Phys. Rev. Lett. **76**, 3830 (1996).
- ⁵L. Thomas, F. Lioni, R. Ballou, D. Gatteschi, R. Sessoli, and B. Barbara, Nature (London) **383**, 145 (1996).
- ⁶P. Politi, A. Rettori, F. Hartmann-Boutron, and J. Villain, Phys. Rev. Lett. **75**, 537 (1995).
- ⁷A. Burin, N. V. Prokof'ev, and P. C. E. Stamp, Phys. Rev. Lett. **76**, 3040 (1995).
- ⁸J. L. van Hemmen and A. Sütö, Europhys. Lett. **1**, 481 (1986); Physica **141B**, 37 (1986).
- ⁹M. Enz and R. Schilling, J. Phys. C **19**, 1765 (1986); **19**, L711 (1986).
- ¹⁰E. M. Chudnovsky and L. Gunther, Phys. Rev. Lett. **60**, 661 (1988).
- ¹¹D. García-Pablos, N. García, P. A. Serena, and H. De Raedt, Phys. Rev. B **53**, 741 (1996); D. García-Pablos, N. García, and H. De Raedt, *ibid.* **55**, 931 (1997).
- ¹²D. García-Pablos, N. García, and H. De Raedt, Phys. Rev. B **55**, 937 (1997).
- ¹³H. De Raedt, S. Miyashita, K. Saito, D. García-Pablos, and N. García, Phys. Rev. B **56**, 11 761 (1997).
- ¹⁴C. Zener, Proc. R. Soc. London, Ser. A **137**, 696 (1932).
- ¹⁵S. Miyashita, J. Phys. Soc. Jpn. **64**, 3207 (1995).
- ¹⁶V. V. Dobrovitski and A. K. Zvezdin, Europhys. Lett. **38**, 377 (1997).
- ¹⁷L. Gunther, Europhys. Lett. **39**, 1 (1997).
- ¹⁸B. Barbara (private communication).
- ¹⁹F. Hartmann-Boutron, P. Politi, and J. Villain, Int. J. Mod. Phys. B **10**, 2577 (1996).
- ²⁰C. Sangregorio, T. Ohm, C. Paulsen, R. Sessoli, and D. Gatteschi, Phys. Rev. Lett. **78**, 4645 (1997).

Resonant magnetic quantum tunneling through thermally activated states

J. F. Fernández, J. Bartolomé, and F. Luis^{a)}

Instituto de Ciencia de Materiales de Aragón, C.S.I.C.-Universidad de Zaragoza, 50009- Zaragoza, Spain

A theory of the magnetic relaxation of a large spin ($S=10$) having a large uniaxial magnetocrystalline anisotropy is outlined. The theory explains magnetic relaxation observed in Mn_{12} acetate. The *joint* action of local fields and a fourth order distortion of the magnetocrystalline anisotropy is necessary to account for the tunneling that is observed, between the $m=-4$ and $m=4$ unperturbed states. Even in resonance, tunneling takes place mainly incoherently in Mn_{12} acetate. It proceeds through the lowest energy state doublet which is not blocked by longitudinal local fields. The relaxation rate Γ has been calculated using a master equation. The model gives magnetization hysteresis loops and ac magnetic susceptibility curves which are in quantitative agreement with experimental results. For temperatures below 0.5 K approximately, nonresonant tunneling from the ground state becomes the dominant relaxation mechanism. © 1998 American Institute of Physics. [S0021-8979(98)18611-5]

We present a theory of quantum tunneling through thermally activated states of a large quantum spin. Ours differs from other theories which have been presented recently^{1,2} in two respects: (1) our master equation involves eigenstates of the exact Hamiltonian for the spin, whereas eigenstates of S_z are used in Refs. 1 and 2; (2) the spin Hamiltonian of Ref. 1 contains only off diagonal terms which are linear in S_x (or S_y), arising from random internal fields, whereas we show below that only the joint action of linear and quartic (result of the anisotropy) spin terms can give an account of the tunneling observed experimentally in Mn_{12} acetate.² The main purpose of this contribution is to give numerical results, that follow from our theory, which can be compared to experiments in Mn_{12} acetate.³

I. SPIN HAMILTONIAN: RESONANCE CONDITION

Our model is based on the following spin Hamiltonian:⁴

$$\mathcal{H} = -DS_z^2 + \mathcal{H}'_1 + \mathcal{H}'_2, \quad (1a)$$

where

$$\mathcal{H}'_1 = -A_4 S_z^4 - g\mu_B H_z S_z \quad (1b)$$

and

$$\mathcal{H}'_2 = C(S_+^4 + S_-^4) - g\mu_B H_x S_x. \quad (1c)$$

The first term in \mathcal{H} favors the spin alignment along the z direction (c crystallographic axis of Mn_{12} acetate). The two local energy minima are separated by an energy barrier $U = DS^2 + A_4 S^4$ (≈ 70 K in Mn_{12} acetate⁵). \mathcal{H}'_1 and \mathcal{H}'_2 are stationary perturbations. They include higher order anisotropy terms and the interaction with the local magnetic field \mathbf{H} . In Mn_{12} acetate, this local field is a superposition of an external applied field \mathbf{H}^0 and an internal field \mathbf{H}_d , where the effect of dipolar and hyperfine interactions are included.⁴

Unperturbed states $|m\rangle$ and $|-m\rangle$ are degenerate. The diagonal perturbation \mathcal{H}'_1 upsets this resonance condition. New resonance conditions for $|m\rangle$ and $|-m-n\rangle$ are

achieved if $H_z = H_{nm}$, where $H_{nm} = n(1 + \alpha_{nm})D/g\mu_B$, $\alpha_{nm} = (A_4/D)[m^2 + (m+n)^2]$, and $n=0,1,2,\dots$

In resonance, the off diagonal terms induce tunneling between these degenerate unperturbed states and lift the degeneracy by $\Delta\hat{E}_{l,l+1}$. Index l labels eigenstates $|\Psi_l\rangle$ of \mathcal{H} in increasing order of energy. Consider large deviations from the resonance condition above. More specifically, if $g\mu_B(2m+n)|H_{nm} - H_z| \gg \Delta\hat{E}_{l,l+1}$ the eigenfunctions of \mathcal{H} become localized on either side of the energy barrier, and quantum tunneling becomes blocked. In resonance only random dipolar fields contribute to $H_{nm} - H_z$. Then, the above inequality is *not* fulfilled for upper energy levels, through which tunneling proceeds freely.

Both terms in Eq. (1c) are necessary in order to explain the magnetic relaxation observed experimentally in Mn_{12} acetate.⁶ For $H_z = nH_1$, and n odd, the fourth order spin term alone would give $\Delta\hat{E} = 0$ for all energy levels, whereas quantum tunneling is observed for such field values. Therefore, it is necessary to consider the interaction with the internal field. However, this perturbation, by itself, is not sufficient. For Mn_{12} acetate, $H_{dx} \approx (\sqrt{2})H_{dz} \approx 6 \times 10^{-2} H_1$.³ Using this value, it follows that $\Delta\hat{E}_{l,l+1} \ll 2g\mu_B m H_{dz}$ for states $m=4, -4$ ($l=13$). This would be in disagreement with tunneling experiments in Mn_{12} acetate.⁷ We find that joint action of both interactions leads to good agreement with experiments^{7,8} using $D=0.60$ K, $A_4/D=1.7 \times 10^{-3}$, $C/D=5.1 \times 10^{-5}$, and $H_{dx}=6.4 \times 10^{-2} H_1$. These parameters are, within given errors, the ones obtained from high field electron paramagnetic resonance (EPR) experiments.⁵

II. QUANTUM TUNNELING THROUGH THERMALLY ACTIVATED STATES

In Mn_{12} acetate above 2 K, tunneling occurs through excited states.^{3,7} Consider a spin interacting with a thermal bath. Assume an initial state $|\Psi_i\rangle$ with low energy E_i , which is localized on the left-hand side of the energy barrier and that no field is applied. Phonon induced transitions involving a large change in the magnetic number m have a negligible

^{a)}Electronic mail: fluis@posta.unizar.es

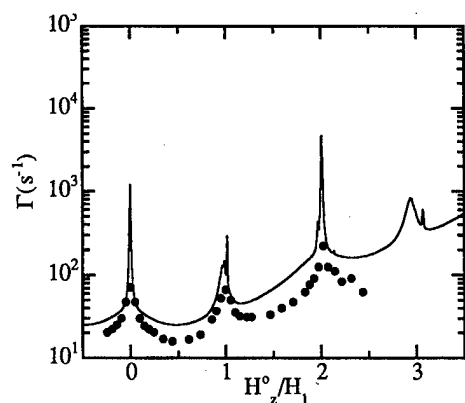


FIG. 1. Calculated (continuous line) and experimental (points) relaxation rate at $T=5$ K as a function of the longitudinal applied field. H_1 is, in every case, the smallest nonzero field where Γ peaks.

probability. Therefore, absorption of a phonon brings the system to a higher energy state, localized on the same side of the barrier. The final state is a coherent superposition of two energy eigenstates $|\Psi_l\rangle$ and $|\Psi_{l+1}\rangle$, that differ in energy by $\Delta E_{l,l+1}$, if $g\mu_B(2m+n)|H_z - H_{nm}| > \Delta E_{l,l+1}$. Energy conservation does not allow such *coherent* superposition to last for times much longer than $\hbar/\Delta E_{l,l+1}$. On the other hand, $g\mu_B H_{dz} \gg \hbar/\tau_0$, where $\tau_0 \approx 10^{-7}$ s is a typical lifetime of an excited state, holds for Mn_{12} . It follows then that $\tau_0 \gg \hbar/\Delta E_{l,l+1}$. Consequently, the system is in an *incoherent* superposition of energy eigenstates most of the time before it decays into states localized on the other side of the energy barrier. There is a nonvanishing probability to decay on the opposite side of the energy barrier, because these excited energy eigenfunctions extend over both positive and negative m values. When the local field deviates from its resonant value, states become more localized, and, consequently, the total relaxation rate decreases. This scheme explains qualitatively the resonance observed experimentally at every crossing field. A more quantitative account follows.

Since incoherence prevails, the time evolution of $\langle S_z \rangle$, can be calculated with Pauli's master equation. Transition

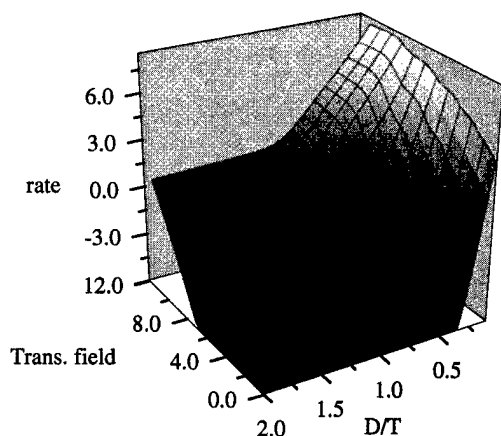


FIG. 2. Relaxation rate (in logarithmic scale) as a function of the inverse temperature at several values of the transverse local field (in units of $D/g\mu_B$) and fixed $H_z = 10^{-3} D/g\mu_B$.

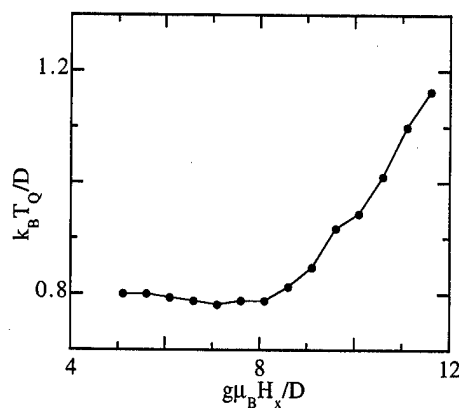


FIG. 3. Crossover temperature (see the text) for $H_z = 10^{-3} D/g\mu_B$ as a function of the transverse local field.

probabilities between numerically exact energy eigenstates l and l' have been calculated using Fermi's Golden Rule, as in Ref. 9, which gives

$$W_{l' \leftarrow l} = q |E_l - E_{l'}|^3 |\langle E_{l'} | B(S) | E_l \rangle|^2 A_{l,l'}, \quad (2)$$

where $A_{l,l'} = n_{l,l'}$ and $A_{l,l'} = 1 + n_{l,l'}$ for upward and downward transitions, respectively. Here, $n_{l,l'} = 1/[\exp(\Delta E_{l,l'}/k_B T) - 1]$ is the average number of phonons of energy $\Delta E_{l,l'}$. We have chosen the simplest operator $V = [S_x, S_z]_+ + [S_y, S_z]_+$ which is Hermitian and time reversal invariant. The term q is a parameter which measures the strength of the spin-phonon interaction. We chose its magnitude to give best agreement between the calculated ac susceptibility and experimental data obtained at $T=5$ K. Results from our calculations are compared to experimental results in the following section.

III. RESULTS

Numerical calculations show⁶ that $\langle S_z \rangle_l$ relaxes exponentially to equilibrium, except for a very short initial time interval (of the order of τ_0). The relaxation rate Γ equals the absolute value of the largest nonzero eigenvalue of the transition matrix W . Γ for $T=5$ K is plotted as a function of the applied field in Fig. 1. As expected (see Sec. II) maxima of Γ appear at crossing field values, in good agreement with experiments.⁸

When $H_x = H_{dx}$, that is, if no transverse field is applied, Γ follows Arrhenius law $\Gamma = \Gamma_0 \exp(U_{ef}/k_B T)$, at least in the temperature range $0.1 < D/k_B T < 0.35$ for all values of the longitudinal field. This means that there is only one relaxation channel in this temperature range.

As the magnitude of the transverse field increases, lower lying tunneling state pairs may become unblocked. Consequently, U_{ef} decreases, as inferred from the slope of the Γ vs $1/T$ curves in Fig. 2. Below a crossover temperature T_Q , thermal population of the excited states becomes so small that the spin reversal can only take place by nonresonant tunneling from the ground state.⁴ Thus, Γ is temperature independent below T_Q (see Fig. 2). As H_x increases, the probability for this tunneling mechanism increases. Consequently, T_Q becomes larger (see Fig. 3). If $H_x > 12 H_1$, the

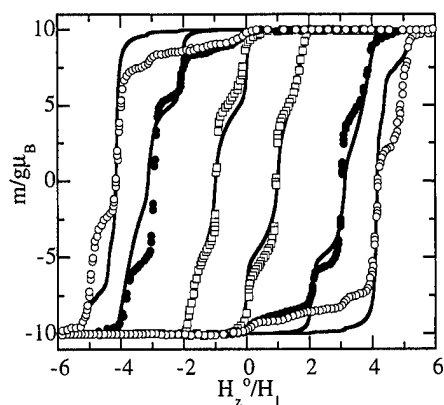


FIG. 4. Magnetization, in units of $g\mu_B$, as a function of the longitudinal applied field. Points represent experimental data at different temperatures; \circ , 1.77 K; \bullet , 2.1 K; \square , 2.64 K. Continuous lines stand for the results of our numerical calculations.

ground state is not blocked by H_{dz} and coherent tunneling can proceed, unassisted, through the ground state doublet.

Knowledge of Γ enables us to calculate magnetization hysteresis loops. Internal fields vary almost randomly between different molecules. In order to compare the results of our calculations to experiments, all physical magnitudes have been broadened using a Lorentzian distribution of local fields, with standard deviation $\sigma = 4 \times 10^{-2} H_1$. Figure 4 shows hysteresis loops calculated at three different temperatures, which are in reasonable agreement with the experiments.³ The field is changed in steps of $10^{-2} H_1$ and the best fit is obtained if it is kept constant for 15 s.

Our calculations show that, to a good approximation, only the smallest eigenvalue of the transition matrix is relevant to magnetic relaxation. Therefore, ac magnetic susceptibility, for a given local field, has been calculated using Debye's formula

$$\chi - \chi_{hf} = \frac{\chi_{eq} - \chi_{hf}}{1 + i\omega/\Gamma}, \quad (3)$$

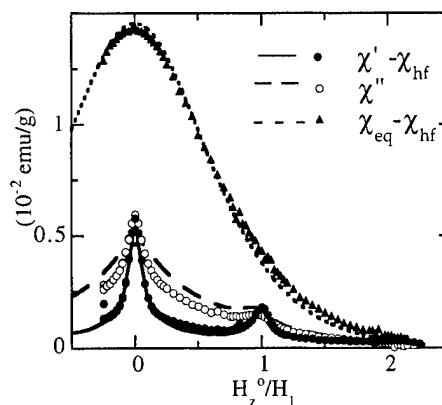


FIG. 5. Magnetic susceptibility for $\omega/2\pi = 15$ Hz and $T = 5$ K as a function of the longitudinal applied field. Data points represent experimental results for a single crystal of Mn_{12} acetate (see Ref. 8), lines are the theoretical values. The high frequency component χ_{hf} has been subtracted from the experimental data because it vanishes in our calculations.

where χ_{eq} is the equilibrium susceptibility, and then broadened with a distribution of local fields. The calculated susceptibility is compared in Fig. 5 to some experimental data. The quantitative agreement is gratifying.

- ¹D. A. Garanin and E. M. Chudnovsky, Phys. Rev. B **56**, 11102 (1997).
- ²A. Fort, A. Rettori, J. Villain, D. Gatteschi, and R. Sessoli, Phys. Rev. Lett. **80**, 612 (1998).
- ³J. R. Friedman, M. P. Sarachik, J. Tejada, and R. Ziolo, Phys. Rev. Lett. **76**, 3830 (1996); J. M. Hernández, X. X. Zhang, F. Luis, J. Bartolomé, J. Tejada, and R. Ziolo, Europhys. Lett. **35**, 301 (1996); L. Thomas, F. Lioni, R. Ballou, D. Gatteschi, R. Sessoli, and B. Barbara, Nature **383**, 145 (1996).
- ⁴P. Politi, A. Rettori, F. Hartmann-Boutron, and J. Villain, Phys. Rev. Lett. **75**, 537 (1995); F. Hartmann-Boutron, P. Politi, and J. Villain, Int. J. Mod. Phys. B **10**, 2577 (1996).
- ⁵A. Caneschi, D. Gatteschi, and R. Sessoli, J. Am. Chem. Soc. **113**, 5873 (1991); A. L. Barra, D. Gatteschi, and R. Sessoli, Phys. Rev. B **56**, 8192 (1997).
- ⁶F. Luis, J. Bartolomé, and J. F. Fernández, Phys. Rev. B **57**, 505 (1998).
- ⁷F. Luis, J. Bartolomé, J. F. Fernández, J. Tejada, J. M. Hernández, X. X. Zhang, and R. Ziolo, Phys. Rev. B **55**, 11448 (1997).
- ⁸J. Tejada *et al.* (unpublished).
- ⁹J. Villain, F. Hartmann-Boutron, R. Sessoli, and A. Rettori, Europhys. Lett. **27**, 159 (1994).

Unusual properties of the molecular nanomagnet Mn_{12}ac

M. A. Novak,^{a)} A. M. Gomes, and R. E. Rapp

*Instituto de Física, Universidade Federal do Rio de Janeiro,
C.P. 68528, Rio de Janeiro, RJ 21944-007, Brazil*

The magnetic properties of the Mn_{12}ac molecular cluster were studied by complex susceptibility and specific heat measurements. Extensive ac susceptibility measurements done under a magnetic field on good quality single crystals and zero field powder sample specific heat results indicate that the usual uniaxial Hamiltonian, as well as the recently proposed fourth order corrections, are not enough to account for all the observations. Very low temperature specific heat data indicate the presence of zero field splitting of the ground state which is much larger than expected. Finally, specific heat measurements done under a magnetic field permitted us to observe and measure the lattice spin relaxation by calorimetric methods with time constants that are in agreement with the magnetic relaxation measurements. © 1998 American Institute of Physics. [S0021-8979(98)49111-4]

INTRODUCTION

Molecular crystals containing isolated magnetic clusters have recently renewed the attention to the relaxation properties of small magnetic particles,^{1,2} because they permit the macroscopic observation of single nanomagnetic particle properties, avoiding complications due to size and orientation distribution existing in traditional small magnetic particle systems. In particular, for the most studied one, Mn_{12}ac , it was possible to observe unusual magnetic quantum phenomena at the nanoscopic scale: thermally assisted quantum tunneling and field tuned resonant tunneling.³⁻⁵ These ferromagnetic clusters formed by 12 Mn atoms coupled by antiferromagnetic superexchange interaction are embedded in large molecules with the formula $[\text{Mn}_{12}(\text{CH}_3\text{COO})_{16}(\text{H}_2\text{O})_4\text{O}_{12}]$, being well isolated from each other.⁶ A $S=10$ spin configuration is stabilized below 20 K with a high anisotropy³ responsible for the slow superparamagnetic relaxation of the magnetization observed below 4 K.⁷ The high uniaxial crystalline anisotropy splits the $S=10$ levels in 10 doublets with $m_s = \pm 10$ lowest in energy. The simplest spin Hamiltonian in zero field may be written as

$$H = -DS_z^2 - g\mu_B \mathbf{S} \cdot \mathbf{B} \quad (1)$$

with the splitting parameter D first determined by electron paramagnetic resonance (EPR) spectroscopy⁸ to be $D/k_B = 0.86$ K, so the total anisotropy energy barrier is $\Delta E/k_B = 86$ K. At very low temperatures, each cluster of this system can be considered as blocked in one of the two "macroscopic" degenerated states $|m_s = \pm 10\rangle$. Classically, the switching between those states occurs only by a thermal activation process over the barrier. The magnetic relaxation time was found to follow an Arrhenius Law:⁷

$$\tau = \tau_0 e^{\Delta E/k_B T} \quad (2)$$

with $\Delta E/k_B = 64$ K and the prefactor $\tau_0 = 2.4 \times 10^{-7}$ s. Below 2 K, the relaxation time deviates from the Arrhenius law, becoming temperature independent⁹ and being attrib-

uted to quantum tunneling of magnetization (QTM). Other evidence of QTM came from the unusual increase of the relaxation time for small fields.³ More recently, magnetization curves in oriented powder⁴ and single crystal⁵ showing steps at regular field intervals were interpreted, using the Hamiltonian Eq. (1), as thermally assisted resonant quantum tunneling at fields where the energy of opposite spin orientation crossed. Recently, we showed that the expected specific heat Schottky contributions from Eq. (1) were not in agreement with the experimental results above 3 K.¹⁰ Better agreement was obtained using a Hamiltonian including fourth order terms in spin operators, proposed recently by Barra *et al.*¹¹ Still a considerable linear term, as well as a low temperature specific heat contribution, remained to be explained and will be addressed by this article from extended specific heat measurements down to 0.1 K.

EXPERIMENTAL RESULTS AND DISCUSSION

We will now present new ac susceptibility measurements as function of temperature and external field at various frequencies (from 1 Hz to 10 kHz). The temperature dependence of the relaxation data, obtained from the maxima of

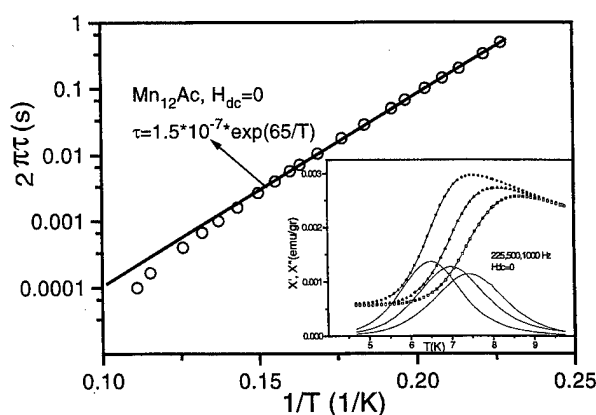


FIG. 1. Arrhenius fit for the relaxation time for the Mn_{12}ac in zero field. Inset shows real (line with symbol) and imaginary susceptibility at selected frequencies.

^{a)}Electronic mail: mnovak@if.ufrj.br.

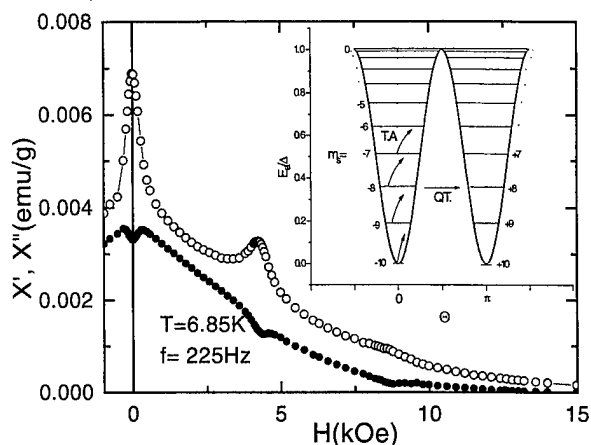


FIG. 2. Susceptibility as function of external field along c axis. Inset shows a sketch of the anisotropy energy barrier as function of orientation of the spin with the c axis.

the imaginary part of the susceptibility,³ is shown in Fig. 1. The total effective energy barrier obtained by fitting Eq. (2), $\Delta E/k_B = 65$ K, and $\tau_0 = 1.5 \times 10^{-7}$ s depend slightly on the temperature range considered due to the small downward curvature. The slope of this plot, $d \ln \tau/d(1/T)$, may be considered as an effective energy barrier (E_{ef}) which changes with T . In the high frequency (and temperature) range, E_{ef} reaches 95 K and τ_0 about 10^{-10} s, closer to the usual attempt frequency of traditional superparamagnets. This reflects the decreasing importance that thermally activated quantum tunneling (TAQT) between the middle of the barrier states have as the temperature is raised. Around 10 K most of the spins switch by classical over barrier thermal activation which is much faster than TAQT.

In Fig. 2 we show typical curves of ac susceptibility data obtained under an external field along the easy c axis which permitted us to determine the resonant field at which level crossing occurs. From several curves done from 4.3 up to 10 K and using various frequencies we were able to determine up to four resonances with values of the applied field $H = 0.0, 4.3, 8.8$, and 12.9 kOe, and independent of temperature. Those fields are close to the ones found at lower temperatures in magnetization measurements^{5,12} but have a much narrower width. χ' shows a maximum with a Lorentzian shape, whereas χ'' shows either a maximum or a local minimum at the resonant fields, depending if the temperature is below of above the blocking temperature for the measurement frequency. The main resonance occurs at a zero field and has a half width around 600 Oe. This is much larger than the expected linewidth for tunneling resonance,¹³ and reflects the presence of a distribution of local fields of different origins: hyperfine, dipolar, and demagnetizing.

The specific heat measurements were done using the semiadiabatic method from 1.4 up to 25 K in a home made cryostat and from 0.1 to 1.5 K in another calorimeter attached to the mixing chamber of a dilution refrigerator. Each data was collected using a 1 min heat pulse and monitoring the temperature drift for several minutes before and after the heat pulse with automated data acquisition systems. Three different contributions to the total specific heat are expected:

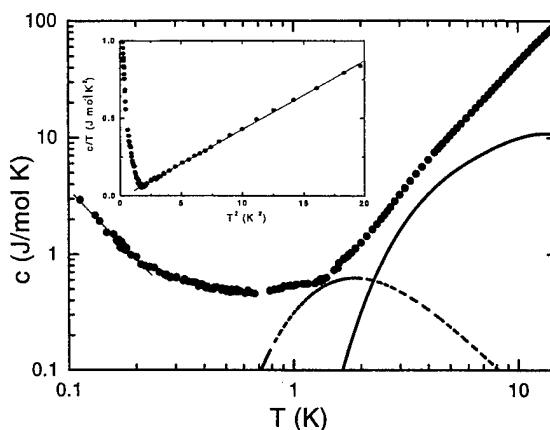


FIG. 3. Specific heat data in zero field in the whole temperature range. Calculated Schottky contribution using energy levels given by Eq. (4) (full line). The splitting of the $m_s = \pm 10$ ground state is represented by the broken line. The straight line at lowest T is the hyperfine T^{-2} fit. Inset shows the resultant c/T T^2 plot after subtracting the two Schottky contributions, showing a negligible linear term.

lattice c_l , hyperfine c_h , and magnetic Schottky c_s :

$$c = c_l + c_h + c_s. \quad (3)$$

The hyperfine contribution is negligible above 3 K. We analyze the data above this temperature by calculating the magnetic Schottky contribution due to the zero field splitted energy levels given by the recently proposed Hamiltonian and parameters of Ref. 10:

$$H = DS_z^2 + AS_z^4 + B(S_+^4 + S_-^4). \quad (4)$$

The contributions that are left are c_l and an extra one below 3 K which cannot be attributed to pure hyperfine interactions within the Mn atoms. In Fig. 3 we show the experimental results and the calculated Schottky specific heat as the full line. A T^3 Debye term could be extracted above 3 K, leaving a considerable linear contribution with a small rounded maximum at 1.89 K. This is not expected by Eq. (4), which gives a ground state splitting too small to explain this contribution. Recent neutron scattering experiments¹⁴ which agree with this last Hamiltonian reported the existence of a distinct energy level around 0.2 THz which would correspond to a ground state splitting of about 5 K. Our data below 3 K can be explained if we invoke a 4.5 K splitting of the ground state and assuming that only 17% of the total clusters contribute to this anomaly. This also eliminates the unexplained apparent linear term in the specific heat above 3 K,¹⁰ as shown in the inset of Fig. 3. At the lowest temperature the line is the expected T^{-2} contribution due to the Mn nuclear hyperfine interaction. The 17% factor may be related to a fast relaxation process present in this system also corresponding to a fraction of the total magnetization. In fact, recent ac susceptibility measurements show that this second relaxation process follows roughly an Arrhenius behavior down to 2 K with relaxation time extrapolated to 1 K of the order of 50 s. The origin of this splitting cannot be related to a combination of hyperfine and dipolar fields, as it corresponds to an equivalent field of 3.3 kOe. Estimates of this local field add up to about 0.5 kOe and have a distribution

which depends on the magnetization of the sample. This is in agreement with the ac susceptibility resonance at a zero field in Fig. 2. The local fields are also responsible for the non-negligible specific heat between 0.3 and 0.8 K, unaccounted by pure Mn hyperfine interactions or by the ground state splitting. Another possibility for the ground state splitting may be due to canting of individual Mn spins within each cluster occurring at a temperature above 2 K, a process which is not cooperative, thus not giving rise to any sharp anomaly in the specific heat.

Finally, we consider the effect of an external magnetic field, leading to a field dependent Schottky anomaly. For simplicity we use the simple Hamiltonian in Eq. (1). Although the system is not in equilibrium, one may consider in quasiequilibrium and count only the states that are accessible in the measuring time. The system may be regarded as two sets of spins with the same energy level spacing, one with the $+m_s$ or down states and the other with the $-m_s$ or up states separated by the anisotropy barrier. In the zero field, the thermal excitations take place within each side of the double well and from one side to the other with a smaller probability due to tunneling. At a low enough temperature, when the switching time is much longer than the typical measuring time (at 3 K the time for spin reversal is 300 s), the two sets of energy levels become independent from each other, reducing the number of the accessible states to about one half. In the presence of a small magnetic field, as long as the two sets of levels continue being independent, the specific heat should be almost the same as the field produces small changes in the level spacing within each well. Figure 4 shows the specific heat data in a field of 3 kOe as well as in zero field. An excess contribution due to the field becomes apparent above 3 K, which corresponds to the blocking temperature for the experimental time window. At lower temperatures the relaxation time is much longer than the time scale of our measurements, so each cluster spin remains blocked in either side of the barrier, and the specific heat remains almost the same as in the zero field. As the temperature is increased and the relaxation time becomes comparable to the experimental time, the states in both sides become progressively accessible as the spins unblock and the specific heat increases. In fact, in the temperature evolution after each heat pulse an extra exponential time dependence appears from which we could determine what we call the lattice-spin relaxation time, having a fair agreement with the magnetic relaxation time constant as can be seen in the inset of Fig. 4.

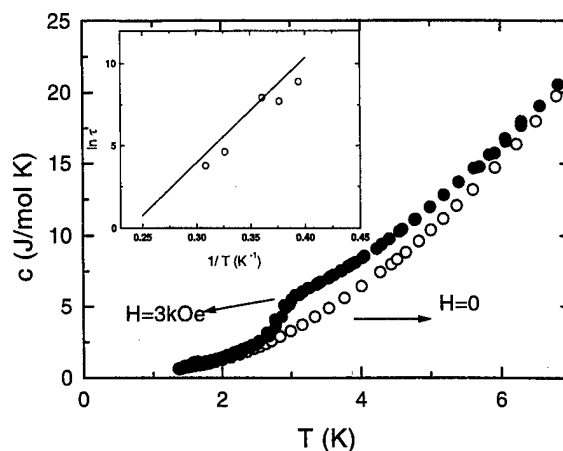


FIG. 4. Specific heat of Mn_{12}ac powder in 0.3 kOe and a zero applied field. Inset shows lattice spin relaxation time data and spin lattice relaxation from magnetic measurements as straight line.

In conclusion, low temperature specific heat measurements on Mn_{12}ac clusters show clearly a splitting of the ground state and also allowed the observation of lattice spin relaxation.

ACKNOWLEDGMENTS

The authors would like to acknowledge A. Caneschi for supplying us with samples, R. Sessoli, C. Paulsen, and P. Stamp for fruitful discussions, and the financial support from FINEP, CNPq, and FUJB (Brazil).

- ¹D. D. Awschalom and D. P. DiVincenzo, *Phys. Today* **48**, 43 (1995).
- ²D. Gatteschi, A. Caneschi, L. Pardi, and R. Sessoli, *Science* **265**, 1054 (1994).
- ³M. A. Novak and R. Sessoli, in *Quantum Tunneling of Magnetization-QTM'94*, edited by L. Gunther and B. Barbara, NATO ASI Series E (Kluwer, Dordrecht, 1995), Vol. 301, p. 171.
- ⁴J. R. Friedman, M. P. Sarachik, J. Tejada, and R. Ziolo, *Phys. Rev. Lett.* **76**, 20 (1996).
- ⁵L. Thomas *et al.*, *Nature (London)* **145**, 383 (1996).
- ⁶T. Lis, *Acta Crystallogr., Sect. B: Struct. Crystallogr. Cryst. Chem.* **36**, 2042 (1980).
- ⁷R. Sessoli, D. Gatteschi, A. Caneschi, and M. A. Novak, *Nature (London)* **365**, 141 (1993).
- ⁸R. Sessoli *et al.*, *J. Am. Chem. Soc.* **115**, 1804 (1993).
- ⁹C. Paulsen and J. G. Park, in *Quantum Tunneling of Magnetization-QTM'94*, edited by L. Gunther and B. Barbara, NATO ASI Series E (Kluwer, Dordrecht, 1995), Vol. 301, p. 189.
- ¹⁰A. M. Gomes *et al.*, *Phys. Rev. B* **57**, 5021 (1998).
- ¹¹A. L. Barra, D. Gatteschi, and R. Sessoli, *Phys. Rev. B* **56**, 1 (1997).
- ¹²F. Lioni *et al.*, *J. Appl. Phys.* **81**, 4608 (1997).
- ¹³N. V. Prokof'ev and P. C. Stamp, *J. Low Temp. Phys.* **104**, 143 (1996).
- ¹⁴M. Hennen *et al.*, *Phys. Rev. B* **56**, 8819 (1997).

Comparison of the spin dynamics in different types of molecular magnetic rings from ^1H NMR

A. Lascialfari^{a)}

Department of Chemistry, University of Florence, Firenze, Italy

Z. H. Jang and F. Borsa^{a),b)}

Ames Laboratory and Department of Physics and Astronomy, Iowa State University, Ames, Iowa 50011

D. Gatteschi

Department of Chemistry, University of Florence, Firenze, Italy

A. Cornia

Department of Chemistry, University of Modena, Modena, Italy

Proton spin-lattice relaxation (NSLR) measurements have been performed in two molecular copper magnetic rings containing 6 and 8 spins ($S = 1/2$), respectively, in an almost coplanar arrangement in order to probe the spin dynamics of the spins in the ring. The NSLR results obtained in the Cu6 and Cu8 rings as a function of temperature and of applied magnetic field are compared with previous results of NSLR of ^1H in the iron(III) rings Fe6 and Fe10 ($S = 5/2$). At room temperature, common features are found in the spin dynamics while at low temperature, when correlation effects become important, important differences are observed in the rings depending on the kind of coupling between magnetic spins (ferromagnetic or antiferromagnetic) and on the spin value S .

© 1998 American Institute of Physics. [S0021-8979(98)19911-5]

I. INTRODUCTION

The recent successes in synthesizing solid lattices of weakly coupled magnetic molecular building blocks has opened up the possibility of studying experimentally magnetism at the mesoscopic scale.¹ The study of molecules is of particular interest, where strongly interacting spins are arranged in almost coplanar ring configurations, a situation which can be easily modeled theoretically.²

Molecular clusters containing 6 and 10 iron(III) spins ($S = 5/2$) in almost coplanar ring configuration have been recently investigated by magnetic susceptibility³ and proton NMR.⁴ We present here ^1H NMR results in a new set of rings containing 6 and 8 copper ions, respectively, also in almost coplanar configuration. The copper ions have $S = 1/2$ and thus these rings represent mesoscopic scale "quantum" spin rings. The comparison of the ^1H NMR in the quantum copper rings with the ^1H NMR in iron(III) ($S = 5/2$) "classical" rings appears particularly interesting. The two new Cu rings investigated here are the cluster $[(\text{PhSiO}_2)_6\text{Cu}_6(\text{O}_2\text{SiPh})_6] \cdot 6\text{EtOH}$ which will be denoted as Cu6⁵ and the cluster $[\text{Cu}_8(\text{dmpz})_8(\text{OH})_8] \cdot 2\text{C}_6\text{H}_5\text{NO}_2$ which will be denoted as Cu8.⁶ In the Cu6 ring, the coupling between nearest neighbor Cu^{2+} spins is ferromagnetic (FM) with coupling constant $|J|/k_B = 60.5$ K and the ground state configuration is magnetic with total spin $S = 3$.⁵ In the Cu8 ring, on the other hand, the coupling is antiferromagnetic (AM) with a large $|J|/k_B$ value ($\cong 800$ K) and the ground state is a $S = 0$ nonmagnetic singlet.⁷

II. RESULTS AND DISCUSSION

The NMR measurements were performed on polycrystalline powder samples synthesized as described in Refs. 5 and 6. The proton nuclear spin-lattice relaxation rate (NSLR) T_1^{-1} was measured with a standard Fourier transform pulse NMR spectrometer by monitoring the recovery of the nuclear magnetization following a short sequence of saturating radio frequency pulses.^{4,8} The recovery was nonexponential due to the presence of many inequivalent protons in the irradiated NMR line. The NSLR reported here was obtained from the initial decay of the magnetization. T_1^{-1} is thus a weighted average over all protons.⁴

The protons in the molecules are coupled to the Cu^{2+} spins via nuclear-electron dipolar interactions. The fluctuations of the Cu^{2+} spins generate a time dependent hyperfine field at the proton site which induces nuclear spin-lattice relaxation. Thus, measurements of NSLR allow one to probe the spin dynamics of the spins in the ring.

The general expression for the NSLR due to the coupling of the protons to the fluctuating Fe or Cu spins is^{9,10}

$$\frac{1}{T_1} = \frac{(\hbar \gamma_n \gamma_e)^2}{(4 \pi g^2 \mu_B^2)} k_B T \left[\frac{1}{4} \sum_q A^\pm(q) \chi^\pm(q) f_q^\pm(\omega_e) + \sum_q A^z(q) \chi^z(q) f_q^z(\omega_n) \right], \quad (1)$$

where $\omega_n = \gamma_n H$ and $\omega_e = \gamma_e H$ are the Larmor frequencies of the proton and of the free electron, respectively, g is the Lande's factor, μ_B is the Bohr magneton, k_B is the Boltzman constant, $\chi(q)$ is the generalized q -dependent spin susceptibility, and $f_q(\omega)$ is the spectral density of the collective spin fluctuations.⁹ The coefficients $A^\pm(q)$ and $A^z(q)$ are the Fourier transforms of the spherical components of the product of

^{a)}Also at: Department of Physics "A. Volta," Unita INFM di Pavia, Via Bassi 6 I27100 Pavia, Italy

^{b)}Electronic mail: borsa@ameslab.gov

two dipole-interaction tensors⁹ describing the hyperfine coupling of a given proton to the Cu magnetic moments. The symbol \pm and z refer to the components of the Cu spins transverse and longitudinal with respect to the quantization direction which is here the external magnetic field.

In the high temperature approximation, Eq. (1) can be approximated as

$$\frac{1}{T_1} = \frac{(\hbar \gamma_n \gamma_e)^2}{(4\pi g^2 \mu_B^2)} k_B T \chi(q=0) \left[\frac{1}{2} A^\pm \Phi^\pm(\omega_e) + A^z \Phi^z(\omega_n) \right], \quad (2)$$

where $\Phi^\alpha(\omega) = \sum_q f_q^\alpha(\omega)$ are the Fourier transforms of the auto-correlation functions (CF) of the transverse ($\alpha = \pm$) and longitudinal ($\alpha = z$) components, respectively, of the local Cu spin. The enhancement of T_1^{-1} at low fields is similar to what is observed in one dimensional paramagnetic chains where it results from the diffusive behavior at a long time of the correlation function in 1D Heisenberg systems.⁹ In a finite size ring, one expects that the spin auto-correlation function has an initial fast decay with correlation frequency $\Gamma_D \propto |J|/\hbar$ followed by a much slower decay due to the cyclic boundary conditions of the ring, terminating with a cut-off frequency Γ_A which depends on anisotropic terms in the spin hamiltonian.^{8,9,11} Thus we write⁸

$$\frac{1}{T_1} = \frac{(\hbar \gamma_n \gamma_e)^2}{(4\pi g^2 \mu_B^2)} k_B T \chi(q=0) \left[\frac{1}{2} A^\pm \frac{\Gamma_A}{(\omega_e^2 + \Gamma_A^2)} + \frac{1}{2} \frac{A^\pm}{\Gamma_D} + A^z \left(\frac{1}{\Gamma_D} + \frac{1}{\Gamma_A} \right) \right] = \frac{A}{B + H^2} + C. \quad (3)$$

The experimental results about the dependence of the NSLR on the external magnetic field at room temperature in Fig. 1 were fitted by using the second part of Eq. (3) with H measured in Tesla and $1/T_1$ in ms^{-1} (see curves in Fig. 1). For Fe6, we have not done a fit of the data due to the large experimental uncertainty. However, as can be seen in Fig. 1(a), the data for Fe6 can be accounted for by the same theoretical curve which fits the Fe10 data.

Since the exchange coupling J is much greater than the anisotropy, one expects $\Gamma_D \gg \Gamma_A$. Thus from the fitting parameters in Eq. (3), we can estimate values for Γ_A , A^\pm , and A^z from experiments with the assumption that A^\pm and A^z are of the same order of the magnitude. The estimated values are shown in Table I together with the values of Γ_D calculated from the spin diffusion model, i.e., $\Gamma_D = (2\pi J/\hbar)[S(S+1)]^{-1/2}$.⁸ The calculated values of Γ_D support the assumption $\Gamma_D \gg \Gamma_A$. The value of Γ_A for Fe10 (Fe6) corresponds to $\hbar\Gamma_A/k_B = 0.6$ K very close to the anisotropy energy deduced from Fe6 susceptibility measurements.³ The values of Γ_A in Table I do not change appreciably for the different rings indicating that the anisotropy is small for all the Heisenberg rings. Finally the values of the hyperfine coupling constants are of the correct order of structure data. In fact, A^\pm and A^z are products of two dipolar interaction tensor components and thus of the order of r^{-6} where r is the distance between a proton and a Cu (Fe) electron spin. We conclude that the main feature of the high temperature spin

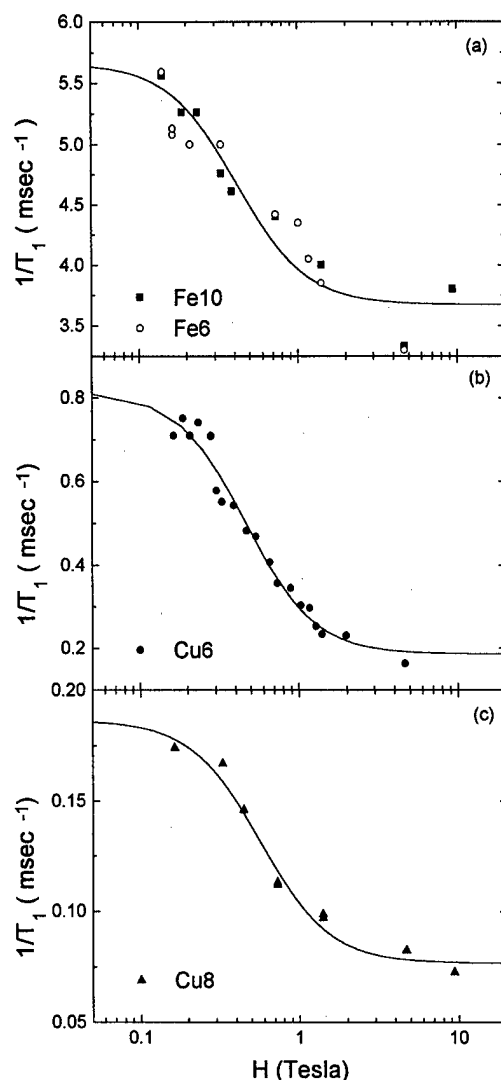


FIG. 1. Proton average nuclear spin-lattice relaxation rate (NSLR) vs applied magnetic field at room temperature for the two classical iron(III) rings (a) and for the two quantum copper rings (b) and (c). The curves are the results of the fit to Eq. (3) with the parameters in Table I.

dynamics is the persistence at long times of the spin-spin correlation function due to the periodic boundary conditions in the ring. This feature seems to be common to all rings.

The temperature dependence of the NSLR is a sensitive probe of correlation effects of the spins in the ring and/or the presence of the gap from the ground state to the first excited state due to the finite size of the spin system. Contrary to the high temperature case, the low temperature spin dynamics displays a variety of behaviors according to the type of ring. We present here preliminary results with a qualitative discussion. A complete study including ^{63}Cu NMR results will be published elsewhere.⁷

The temperature dependence of the ^1H NSLR is shown in Fig. 2. The temperature dependence of the classical AF ring Fe6 from Ref. 4 is reported in Fig. 2(c) for the purpose of comparison. In comparing the data for the AF rings in Figs. 2(b) and 2(c), it is noted that in both cases the NSLR displays an exponential drop at low temperature due to the condensation of the system in its $S=0$ nonmagnetic ground state separated by a gap Δ/k_B from the first excited triplet

TABLE I.

Ring	Γ_D (10^{12} rad/s) (calc.)	Γ_A (10^{10} rad/s)	A^\pm (10^{45} cm $^{-6}$)	A^z (10^{45} cm $^{-6}$)	J/k_B (K)	$T_\chi(q=0)$ ($T=300$ K) (emu/mole of magnetic ion)
Fe10 (Fe6)	5.33 (11.05)	7.5 ± 1.5	5.3 ± 2	5 ± 0.5	13.8 (28.6)	3.2 ± 0.2 (2.5 ± 0.2)
Cu6	6.86	8.2 ± 0.7	13 ± 3	2 ± 0.4	60.5	0.47 ± 0.03
Cu8	90.6	9.9 ± 3	15 ± 4	5.2 ± 1	~ 800	0.085 ± 0.01

state. For Fe6, the gap, derived from susceptibility measurements, is $\Delta/k_B = 20$ K³ while for Cu8, $\Delta/k_B \cong 600$ K.⁷ These values are consistent with the NSLR results although somewhat different values for the gap are derived from NSLR.^{4,7} For Fe6, one observes an enhancement of $1/T_1$ at low T which is not present in the susceptibility data [see Fig. 2(c) and inset] and is thus arising from a slowing down of the

spin fluctuations as the system becomes more correlated, i.e., a decrease of Γ_D in Eq. (3). For Cu8, it is not possible to say if the enhancement of $1/T_1$ is present since one should extend the measurement at higher temperature where the system decomposes.

Another comparison can be made between the FM ring Cu6 and the AF ring Fe6 in Figs. 2(a) and 2(c). In the temperature range of 300–50 K, the NSLR increases in the FM case and it decreases in the AF case indicating that the spin dynamics is dominated by the behavior of the static response function $T\chi(q=0)$ in Eq. (3). In both cases, the NSLR has a critical divergence for T approaching the short range “ordering” temperature $|J|/k_B$ as shown in Fig. 2. (For Cu6, $|J|/k_B = 60.5$ K⁵ while for Fe6 $|J|/k_B = 28.8$ K.^{3,4} Finally, although in both Fe6 and Cu6 the NSLR drops as $T \rightarrow 0$ due to the gap, in the case of the Cu6 FM ring, there remains sizeable nuclear relaxation due to the degeneracy of the $S=3$ ground state. A quantitative analysis of the low temperature nuclear relaxation should give information about the excitations in the $S=3$ ground state.

ACKNOWLEDGMENTS

We thank M. Luban for helpful discussions. This work was supported by funds from Ministero per L'Universita' e la Ricerca Scientifica e Tecnologica and Consiglio Nazionale delle Ricerche. Ames Laboratory is operated for U.S. Department of energy by Iowa State University under Contract No. W-7405-Eng-82. This work at Ames Laboratory was supported by the Director for Energy Research, Office of Basic Energy Sciences.

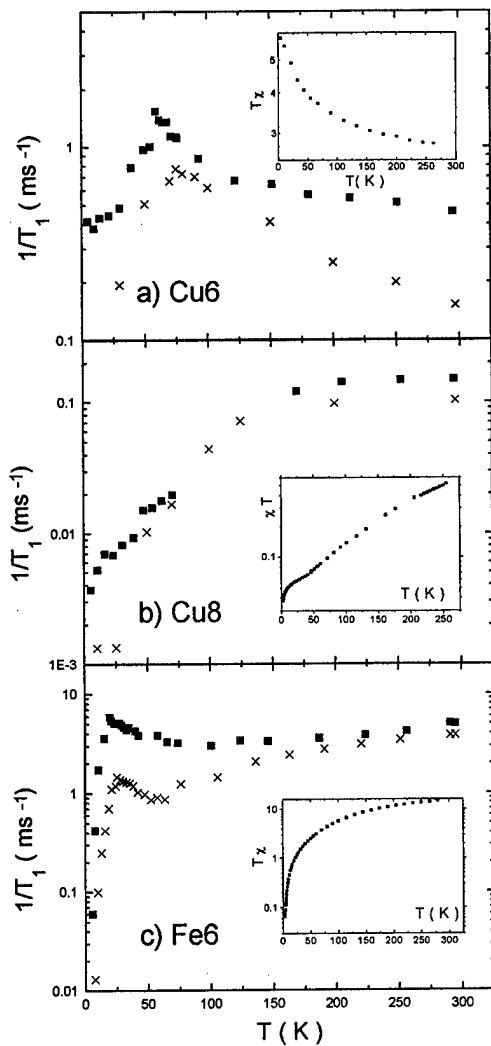


FIG. 2. Proton average NSLR vs temperature (a) for Cu6 ring: (■) 7 MHz; (×) 60 MHz. The inset shows the behavior of $T\chi$ (emu/mol) from Ref. 5. (b) for Cu8 ring: (■) 7 MHz; (×) 62 MHz. In the inset $T\chi$ (emu/mol) from Ref. 7. (c) for Fe6 ring: (■) 7 MHz; (×) 60 MHz. In the inset $T\chi$ (emu/mol) from Ref. 3.

¹D. Gatteschi, A. Caneschi, L. Pardi, and R. Sessoli, *Science* **265**, 1055 (1994).

²J. C. Bonner and M. E. Fisher, *Phys. Rev.* **135**, A640 (1964).

³[Fe10] K. L. Taft and S. J. Lippard, *J. Am. Chem. Soc.* **112**, 9629 (1990); [Fe6] A. Caneschi, A. Cornia, A. C. Fabretti, S. Foner, D. Gatteschi, R. Grandi, and L. Schenetti, *Chem. Eur. J.* **12**, 1379 (1996).

⁴A. Lascialfari, D. Gatteschi, F. Borsa, and A. Cornia, *Phys. Rev. B* **55**, 14 341 (1997).

⁵E. Rentschler, D. Gatteschi, A. Cornia, A. C. Fabretti, A. L. Barra, O. I. Shchegolikhina, and A. A. Zhdanov, *Inorg. Chem.* **35**, 4427 (1996).

⁶G. A. Ardizzoia, M. A. Angaroni, G. La Monica, F. Cariati, S. Cenini, M. Moret, and N. Masciocchi, *Inorg. Chem.* **30**, 4347 (1991).

⁷A. Lascialfari *et al.* (unpublished).

⁸A. Lascialfari, D. Gatteschi, F. Borsa, A. Shastri, Z. H. Jang, and P. Carretta, *Phys. Rev. B* **57**, 514 (1998).

⁹F. Borsa and M. Mali, *Phys. Rev. B* **9**, 2215 (1974); D. Hone, C. Scherer, and F. Borsa, *Phys. Rev. B* **9**, 965 (1974).

¹⁰T. Moriya, *Prog. Theor. Phys.* **28**, 371 (1962).

¹¹J. H. Luscombe and M. Luban, *J. Phys.: Condens. Matter* **9**, 6913 (1997).

Analysis of electron paramagnetic resonance experiments in colossal magnetoresistance materials

D. L. Huber

Department of Physics, University of Wisconsin-Madison, Madison, Wisconsin 53706

An analysis is given of recent electron paramagnetic resonance (EPR) experiments in manganite materials displaying colossal magnetoresistance behavior. These experiments have established that in highly homogeneous samples characterized by a single resonance line, the EPR linewidths above the critical region associated with the paramagnetic-ferromagnetic transition are inversely proportional to $T\chi(T)$, where χ denotes the susceptibility. This behavior indicates that the linewidth does not reflect a coupling to the lattice vibrations but rather is caused by a spin-only mechanism. The possibility that the linewidth arises from the dipolar interaction is assessed using an effective interaction model. On the basis of the model calculation, it is concluded that the dipolar interaction is probably too weak to account for the observed broadening and that the linewidth most likely arises from tetragonal and orthorhombic distortions of the octahedral crystal field at the sites of the Mn ions. The EPR linewidth in samples with very low concentrations of Mn^{4+} ions is expected to vary with temperature as $[T\chi_{\text{sp}}(T)]^{-1}$, where $\chi_{\text{sp}}(T)$ is the susceptibility of the ferromagnetically coupled spin polaron. By measuring the temperature dependence of the linewidth, one may be able to determine the temperature dependence of the polaron susceptibility. © 1998 American Institute of Physics. [S0021-8979(98)16911-6]

I. INTRODUCTION

Understanding the behavior of Mn-based materials showing colossal magnetoresistance (CMR) properties is a challenge for both experimentalists and theorists. Although most of the attention has been focused on the effect of applied magnetic field and temperature on the conductivity, there is much to be learned from studies of the spin-dependent properties through measurements of the static and dynamic spin susceptibilities. This is a consequence of the fact that the dominant magnetic interaction is the double exchange (DE) coupling, which is associated with the "hopping" of electrons between Mn ions. In the simple picture, it is these mobile electrons that are the source of the anomalous transport.

Experimental studies of CMR materials have been hampered by the difficulty of obtaining high-quality samples. This has been a particular problem for electron paramagnetic resonance (EPR) measurements, which are unusually sensitive to sample inhomogeneities. Recently, the results of a series of EPR measurements have been reported by Granado *et al.*¹ that provide direct evidence of the effect of sample homogeneity on the EPR spectra. The results of similar measurements on high-quality samples of $\text{La}_{1-x}\text{Sr}_x\text{MnO}_3$ have been also been reported by Lofland *et al.*² Of particular interest here are the measurements of the EPR linewidth of a highly homogeneous, ceramic sample of $\text{La}_{2/3}\text{Ca}_{1/3}\text{MnO}_3$ presented in Ref. 1. The authors found that the linewidth varied as $A/T\chi(T)$, where χ denotes the susceptibility and A is a temperature-dependent parameter $\approx 7200 \text{ Oe K}$. This behavior was observed over the range $300 \text{ K} \leq T \leq 900 \text{ K}$ ($T_c = 270 \text{ K}$). The absence of a temperature dependence to the linewidth beyond that associated with the product $T\chi(T)$ was interpreted as indicating that the linewidth arose from a spin-only mechanism, in contrast to earlier results where the

linewidth was attributed to a spin-phonon mechanism.³⁻⁵ Such an interpretation was based on measurements which found the parameter A to be a linear function of the temperature indicative of a one-phonon mechanism.⁶

It is beyond the scope of this paper, and probably premature, to characterize EPR measurements that do *not* show a linewidth varying with temperature as $[T\chi(T)]^{-1}$ as being influenced by sample inhomogeneity. Rather, we take the point of view that measurements that *do* find that A approaches a constant value at high temperatures are directly probing a spin-only relaxation mechanism for the total spin. In this paper, we will discuss possible microscopic spin-only mechanisms for the relaxation of the moment in CMR materials. We will also comment briefly on the importance of EPR measurements on samples with very low concentrations of Mn^{4+} ions.

II. ANALYSIS

Due to the role of the double exchange mechanism, a quantitative analysis of the EPR linewidth even in the high-temperature limit is a formidable problem. Since we are mainly interested in a qualitative analysis of the linewidth in the $\text{La}_{2/3}\text{Ca}_{1/3}\text{MnO}_3$ sample described in Ref. 1, we will approximate the DE interaction by a nearest-neighbor Heisenberg interaction, with an effective spin determined by the weighted averages of the spins of the Mn^{3+} and Mn^{4+} ions and an exchange integral inferred from the paramagnetic Curie temperature, $T_{\text{cp}} \approx 370 \text{ K}$. Support for such an approximation comes from inelastic neutron scattering studies in $\text{La}_{0.7}\text{Pb}_{0.3}\text{MnO}_3$, where the magnon dispersion curves over much of the Brillouin zone were fit with the corresponding Heisenberg spin-wave dispersion relation obtained from an exchange interaction with an effective spin equal to 1.85 and a nearest-neighbor coupling J equal to 27.6 K .⁷

In a similar spirit, we equate the paramagnetic Curie temperature of $\text{La}_{2/3}\text{Ca}_{1/3}\text{MnO}_3$ to the standard expression

$$k_B T_{cp} = (2/3) z J S_{\text{eff}} (S_{\text{eff}} + 1), \quad (1)$$

where $z (=6)$ is the number of nearest neighbors and S_{eff} is an effective spin defined to ensure that the effective Curie constant $(1/3)g^2\mu_B^2 S_{\text{eff}}(S_{\text{eff}}+1)$ is equal to the weighted average of the Curie constants of the Mn^{3+} and Mn^{4+} ions, $(1/3)g^2\mu_B^2\{6(1-x) + (15/4)x\}$. Using this expression with $x=1/3$, one obtains $S_{\text{eff}}(S_{\text{eff}}+1)=5.25$ and an effective nearest-neighbor Heisenberg interaction J equal to 17.6 K. Since the $\text{La}_{0.7}\text{Pb}_{0.3}\text{MnO}_3$ sample had a Curie temperature of 355 K, whereas the measured Curie temperature of the $\text{La}_{2/3}\text{Ca}_{1/3}\text{MnO}_3$ sample was 270 K, our value for J , when scaled by the ratio $(355/270)$, is equal to 23.1 K, which is reasonably close to the value inferred for the Pb sample, 27.6 K, indicating a measure of consistency between the high- and low-temperature analyses. A more stringent test of the analysis is provided by a calculation of the zero-temperature spin stiffness D . For a Heisenberg ferromagnet with nearest-neighbor interactions, one has $D=2JSd^2$, where d is the nearest-neighbor separation 3.9 Å. Replacing S by the average spin, $S_{\text{av}}=2(1-x) + (3/2)x=11/6$ ($x=1/3$), one obtains $D=85 \text{ meV Å}^2$. This value is within a factor of 2 of the stiffness obtained from inelastic neutron scattering studies of $\text{La}_{0.67}\text{Ca}_{0.33}\text{MnO}_3$, where it was found that $D=155 \text{ meV Å}^2$ for a sample with $T_c=250 \text{ K}$.⁸

With the parameters of the effective nearest-neighbor Heisenberg Hamiltonian in hand, one can proceed to calculate the high-temperature limit of the EPR linewidth using the well-known technique of spectral moments.⁹ We first consider the dipolar mechanism. In the exchange narrowed limit, the Lorentzian linewidth (half width at half height) δ is expressed approximately as $(\pi/2)^{1/2}(M_2)^{3/2}(M_4)^{-1/2}$,¹⁰ where M_2 and M_4 denote the second and fourth moments of the line-shape function. Integrating over angles and specializing to a simple cubic lattice with nearest-neighbor interactions, we obtain the result

$$\delta \approx 1.5g^4\mu_B^4[S_{\text{eff}}(S_{\text{eff}}+1)]^{1/2}d^{-6}J^{-1}, \quad (2)$$

where d , as before, is the distance between nearest-neighbor Mn ions. With the values given previously for J and S_{eff} one has $\delta \approx 3 \text{ Oe}$. This value is to be compared with the high-temperature limit of the linewidth in $\text{La}_{2/3}\text{Ca}_{1/3}\text{MnO}_3$ inferred from the ΔH_{pp} data in Ref. 1 and the corresponding paramagnetic Curie temperature, 370 K. One finds $\delta \approx 1800 \text{ Oe}$. Although the theoretical estimate for δ was obtained from an effective Heisenberg Hamiltonian, we believe that the discrepancy of a factor of 600 between the two values of δ is too large to be attributed to the approximations and can be explained only by the existence of an alternative relaxation mechanism. This will be discussed in the following section.

III. DISCUSSION

As noted above, the estimate of the dipolar contribution to the high-temperature limit of the EPR linewidth is too small by a factor of 600, indicating the need to consider

alternative mechanisms. A possible clue to the origin of the linewidth lies in the failure so far to observe a resonance signal in stoichiometric LaMnO_3 . Stoichiometric LaMnO_3 has orthorhombic symmetry at room temperature,¹¹ whereas at room temperature, oxygen-annealed $\text{La}_{1-x}\text{Ca}_x\text{MnO}_3$ can have cubic symmetry for $x>0.2$.¹² Since the high-temperature limit of the dipolar linewidth in LaMnO_3 is calculated to be on the order of 10 Oe (the Néel temperature in orthorhombic LaMnO_3 is 140 K and $S=2$, so the corresponding value for the nearest-neighbor Heisenberg exchange integral in the mean-field approximation is 6 K), the absence of a resonance in LaMnO_3 is attributed to the presence of second-order [i.e., DS_z^2 and $E(S_x^2 - S_y^2)$] anisotropy terms in the spin Hamiltonian for the Mn^{3+} ions that come from the interplay of spin-orbit coupling and the noncubic components of the crystal field. Such terms are not invariant under rotation of the total spin. As a consequence, they can lead to the fast relaxation of the spin moment giving rise to a resonance that is too broad to be detected. [The cubic components of the crystal field are thought not to play an important role since the ten energy levels of the lowest manifold of the Mn^{3+} (d^4) ion in an octahedral field are degenerate to first order in the spin-orbit interaction.¹³] Even in the case of the cubic phases of $\text{La}_{1-x}\text{Ca}_x\text{MnO}_3$, we expect local departures from octahedral symmetry due to the presence of Mn^{3+} , which is a Jahn-Teller ion. We hypothesize that it is the noncubic crystal symmetry or the local Jahn-Teller distortions (dynamic and static) from cubic symmetry that is responsible for the anomalously large high-temperature linewidth in $\text{La}_{1-x}\text{Ca}_x\text{MnO}_3$ and other Mn-based CMR materials.¹⁴ Nevertheless, the single-ion mechanism is weaker than it is in the stoichiometric material presumably because of an enhanced effectiveness of the DE relative to Heisenberg superexchange interaction in producing an exchange narrowed linewidth, a point that will be addressed in a separate publication. The effectiveness of the DE is also consistent with the presence of only a very weak (and thus, presumably, not intrinsic) resonance in the cubic Mn^{4+} compound CaMnO_3 .¹⁵ Only when there are substantial concentrations of both Mn^{4+} and Mn^{3+} ions is there an intense resonance signal. Also, we note that while we have emphasized the importance of single-ion mechanisms, one cannot yet rule out anisotropic exchange couplings as a contributor to the relaxation.

The discussion in the preceding paragraph points to the importance of measurements of the EPR linewidth in samples with very small concentrations of Mn^{4+} ions.¹⁴ In such systems, we expect that a spin-polaron picture will be appropriate. We predict that at high temperatures, the linewidths in these materials will vary as $A'/T\chi_{\text{sp}}(T)$, where $\chi_{\text{sp}}(T)$ denotes the susceptibility of the spin polaron, which we expect to be proportional to $(T-T_{\text{sp}})^{-1}$, where T_{sp} denotes an effective spin-polaron paramagnetic Curie temperature reflecting the strength of the ferromagnetic correlations. In contrast, the parameter A' should have about the same magnitude it has in $\text{La}_{2/3}\text{Ca}_{1/3}\text{MnO}_3$, assuming a similar microscopic relaxation mechanism. It is also possible that the random motion of the spin polaron can play a role in the relaxation of the moment of the cluster. If this is the case,

one might expect a motionally narrowed linewidth with a temperature dependence proportional to $\exp[E_a/k_B T]$, where E_a denotes a thermal activation energy for the polaron hopping.

Finally, we would like to stress that although the dipolar interaction does not appear to make a significant contribution to the EPR linewidth at high temperatures, it can be important near the ferromagnetic critical temperature, where short-range anisotropic terms become relatively less important.¹⁶ Should this be the case (which would require that the transition be second order, or at least weakly first order), one would expect that the product $T\chi(T)\Delta H$ would increase as $T \rightarrow T_c$ from the paramagnetic side. Because of the pronounced effect of the applied field on the phase transition, definitive measurements of dynamical critical effects should be made in zero field.

ACKNOWLEDGMENTS

The authors would like to thank S. M. Bhagat, J. W. Lynn, S. B. Oseroff, M. Rzechowski, and M. S. Seehra for helpful comments and communications. The authors would also like to thank the authors of Ref. 1 for a preprint of their work.

¹E. Granado *et al.*, *Proceedings of the Vth International Workshop on Non-Crystalline Solids, Santiago de Compostela, Spain (1997)*, edited by J.

Rivas (World Scientific) (to be published). Similar results are reported in M. Tovar *et al.*, these proceedings.

²S. E. Lofland *et al.*, *Phys. Lett. A* **233**, 476 (1997), and references therein.

³A. Shengelaya, G.-M. Zhao, H. Keller, and K. A. Muller, *Phys. Rev. Lett.* **77**, 5296 (1996).

⁴C. Rettori *et al.*, *Phys. Rev. B* **55**, 3083 (1997).

⁵M. S. Seehra, M. M. Ibrahim, V. Suresh Babu, and G. Srinivasan, *J. Phys.: Condens. Matter* **8**, 11 283 (1996).

⁶D. L. Huber and M. S. Seehra, *J. Phys. Chem. Solids* **36**, 723 (1975), and references therein; see also M. S. Seehra and D. L. Huber, *AIP Conf. Proc.* **24**, 261 (1975).

⁷T. G. Perring *et al.*, *Phys. Rev. Lett.* **77**, 711 (1996).

⁸J. W. Lynn *et al.*, *J. Appl. Phys.* **81**, 5488 (1997).

⁹J. H. Van Vleck, *Phys. Rev.* **74**, 1168 (1948).

¹⁰A. Abragam, *The Principles of Nuclear Magnetism* (Clarendon, Oxford, 1961), pp. 435–440.

¹¹Q. Huang *et al.*, *Phys. Rev. B* **55**, 14 987 (1997).

¹²G.-Q. Gong *et al.*, *Appl. Phys. Lett.* **67**, 1783 (1995).

¹³W. Low, *Paramagnetic Resonance in Solids* (Academic, New York, 1960), pp. 84–85.

¹⁴The issue of static versus zero-point dynamic Jahn–Teller distortions depends on the time scale. The EPR linewidth is proportional to the time integral of the correlation function $\langle [S_x^T, H_{\text{anis}}](t)[H_{\text{anis}}, S_x^T](0) \rangle$, where S_x^T denotes the x component of the total spin and H_{anis} is the anisotropic part of the Hamiltonian. If this correlation function decays at a rate that is rapid in comparison with the characteristic frequencies of the dynamic Jahn–Teller effect, then the distinction between the static and dynamic linewidth mechanisms disappears. Such would appear to be the case for the DE interaction in the manganites where the characteristic time scale of the correlation function is set by the hole bandwidth.

¹⁵S. B. Oseroff *et al.*, *Phys. Rev. B* **53**, 6521 (1996).

¹⁶D. L. Huber, *Solid State Commun.* **48**, 831 (1983).

A novel method for quantitative study of domain reversal behavior

Sug-Bong Choe and Sung-Chul Shin^{a)}

Department of Physics, Korea Advanced Institute of Science and Technology, Taejeon 305-701, Korea

A novel method to quantitatively analyze the domain reversal behavior has been adopted to understand the total-thickness-dependent domain reversal behavior in Co/Pd multilayers. The wall-motion speed and the nucleation rate were simultaneously determined by analyzing serial domain images observed using a real-time domain observation system. Using this method, sensitive decrement of the wall-motion speed with increasing total multilayer thickness has been found to be responsible for the contrasting reversal behavior in Co/Pd multilayers. © 1998 American Institute of Physics. [S0021-8979(98)49211-9]

I. INTRODUCTION

Magnetization reversal in magnetic thin films is of interest for applications as well as fundamental understanding of magnetism. The contrasting reversal behaviors in numerous systems have been reported to occur by either the nucleation dominant process or the wall-motion dominant one.¹⁻⁴ Interestingly, the reversal phenomena were found to be very strongly dependent on the total film thickness.^{5,6} These reversal behaviors have been analyzed by the thermally activated relaxation model based on the magnetization viscosity curve⁷ and also, compared with the theoretical predictions using micromagnetic simulations.⁸ Recently, we have developed a novel method to quantitatively analyze the magnetization reversal behavior by considering both the nucleation and wall-motion processes based on the time-dependent domain patterns.⁹ In this article, we have applied the novel method to investigate the contrasting magnetization reversal behavior in Co/Pd multilayers with varying the total multilayer thickness.

II. DESCRIPTION OF THE PRESENT METHOD

Details of the model have been described elsewhere.⁹ Briefly, the model of magnetization reversal is proposed by using the time-dependent domain patterns based on circular domains. In the model, the reversed domains expand at all domain boundaries by the wall-motion speed V and simultaneously, new domains are formed by the nucleation rate R per unit time and unit area during the magnetization reversal from the initially saturated state. Then, the expansion of the reversed domain area da in time dt is given by

$$da = lVdt + \pi r_0^2 R(s-a)dt, \quad (1)$$

where l is the domain boundary length, r_0 is the characteristic radius of nucleation, s is the total area under examination, and a is the area of reversed domains. Similarly, the increment of the domain boundary length dl in time dt becomes

$$dl = 2\pi Vdt + 2\pi r_0 R(s-a)dt. \quad (2)$$

Then, the wall-motion speed V and the nucleation rate R are explicitly given by

$$\left. \begin{aligned} V &= (a' - r_0 l' / 2) / (l - \pi r_0) \\ R &= (l l' / 2\pi - a') / (l - \pi r_0) r_0 (s - a) \end{aligned} \right\}, \quad (3)$$

where a' and l' denote the first derivation of a and l , respectively. Thus, the wall-motion speed V and the nucleation rate R can be simultaneously determined by measuring the reversed domain area $a(t)$ and the domain boundary length $l(t)$.

A real-time domain observation system has been adopted to measure the reversed domain area and the domain boundary length during the magnetization reversal. Serial domain images of 256 frames with 10 frames per second were obtained using a modified magneto-optic Kerr microscope capable of $\times 1000$ magnification with an objective of 0.9 N.A. and equipped with advanced digital video processing. The image, composed of 200×160 pixels with the unit size of 164×164 nm, was initially obtained in 256 gray levels and then, intensified by noise filtering and black-and-white image extraction processes. Then, the reversed domain area $a(t)$ and the domain boundary length $l(t)$ were determined by counting black and white cells, and by edge determining algorithms, respectively, for each image at the corresponding time t . The measurement error due to the geometric difference between the theory based on circular domains and the observation based on square cells is decreased with increasing domain radius, and does not exceed 50% for the single pixel domain of 82 nm radius.

The magnetization reversal behavior of Co/Pd multilayered system has been investigated. Samples of $(2 \text{ \AA} \text{ Co} / 11 \text{ \AA} \text{ Pd})_n$ with varying the number of repeats n , were prepared on glass substrates by e -beam evaporation under the base pressure of 1.0×10^{-6} Torr at the ambient temperature. The multilayered structure was achieved by alternatively exposing the substrate to the two e -beam sources with typical deposition rates of 0.3 $\text{\AA}/\text{s}$ for Co and 0.5 $\text{\AA}/\text{s}$ for Pd. The layer thickness was controlled within a 4% accuracy by the thickness-control technique using real-time thickness measurement.¹⁰

III. RESULTS AND DISCUSSION

All samples in this study had perpendicular magnetic anisotropy and showed Kerr hysteresis loops of unit squareness. Figure 1 shows the hysteresis loops of Kerr rotational angles measured at the wavelength of 4000 \AA for the type I

^{a)}Electronic mail: scshin@sorak.kaist.ac.kr

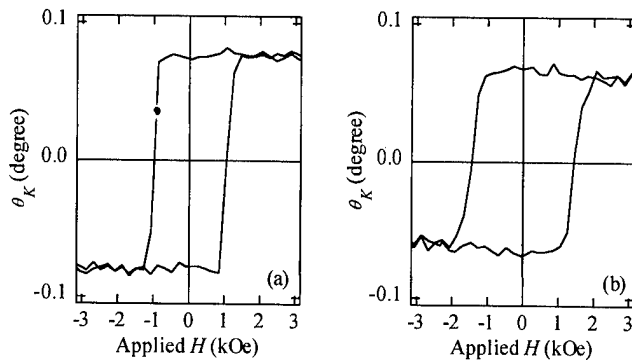


FIG. 1. Hysteresis loops of Kerr rotational angle measured at 4000 Å of (a) the type I sample of $(2 \text{ Å Co}/4 \text{ Å Pd})_{10}$ and (b) the type II sample of $(2 \text{ Å Co}/4 \text{ Å Pd})_{23}$. Coercivities, H_c , are 1.0 and 1.5 kOe, respectively.

sample of $(2 \text{ Å Co}/11 \text{ Å Pd})_{10}$ and the type II sample of $(2 \text{ Å Co}/11 \text{ Å Pd})_{23}$. The samples have coercivities, H_c , of 1.0 and 1.5 kOe, respectively.

In Fig. 2, we show the magnetization viscosity curves of types I and II samples under various reversing applied fields as denoted in the figures. The curves were measured by averaging the intensity of the images observed by the microscope at low magnification and normalizing by the intensities between the initially saturated state and the completely reversed state. The abscissa axis is also normalized by the half relaxation time τ which is sensitively dependent on the strength of an applied field. The normalized curves for a given sample are completely coincident with each other, but the curves between the samples are quite contrasting. The viscosity curve of the type I sample shown in Fig. 2(a) exhibits initially a slow decay, with accelerated reversal with time. This curve has a typical shape of thermally activated relaxation, with low nucleation rate and fast domain-wall speed.⁷ In contrast, the type II sample shown in Fig. 2(b) exhibits initially a fast decay and then, slow down to an equilibrium state. This shape can be interpreted as a typical behavior of thermally activated relaxation with large nucleation rate and slow domain-wall speed.

Serial domain images of magnetization reversal were taken by the real-time observation system under an applied field of $0.8 H_c$ for each sample. Figure 3 shows the typical

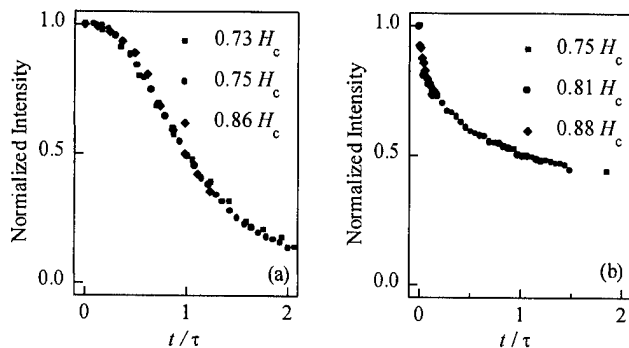


FIG. 2. Viscosity curves under several reversing applied fields for (a) the type I sample and (b) the type II sample. The curves were normalized by the maximum Kerr intensity and the half relaxation time τ .

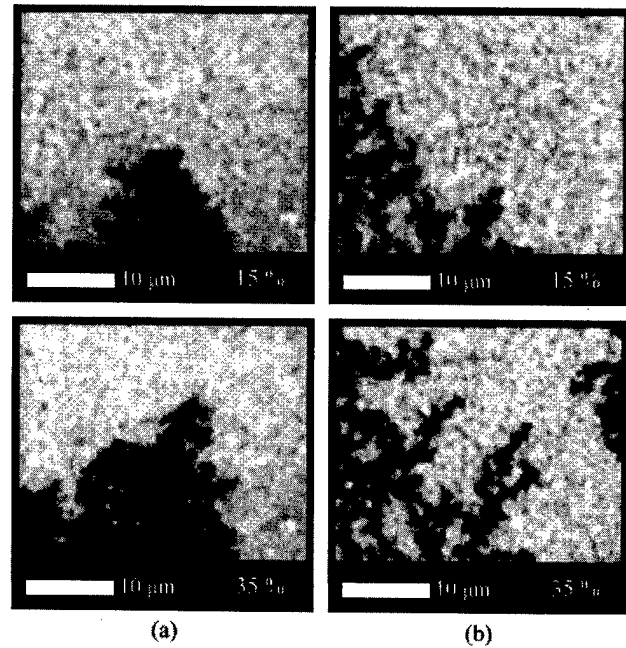


FIG. 3. Typical domain patterns during magnetization reversal of (a) the type I sample and (b) the type II sample under reversing applied fields of $0.8 H_c$ for the corresponding samples. The number of percent denoted at the bottom of each frame is the areal fraction of the reversed domain.

domain reversal patterns of types I and II samples having the same areal fractions of reversed domains. The areal expansion by the wall-motion process is clearly observed in the type I sample as shown in Fig. 3(a), while the stripe growth by the nucleation process is seen in the type II sample as shown in Fig. 3(b).

Quantitative analysis on the contrasting reversal behaviors of these samples were carried out. The reversed domain area $a(t)$ and the domain boundary length $l(t)$ measured from the domain reversal patterns of types I and II samples, are plotted in Fig. 4. The lines with squared symbols in each plot of Fig. 4 show the reversed domain area $a(t)$ and they are very consistent with the magnetization viscosity curves shown in Fig. 2.

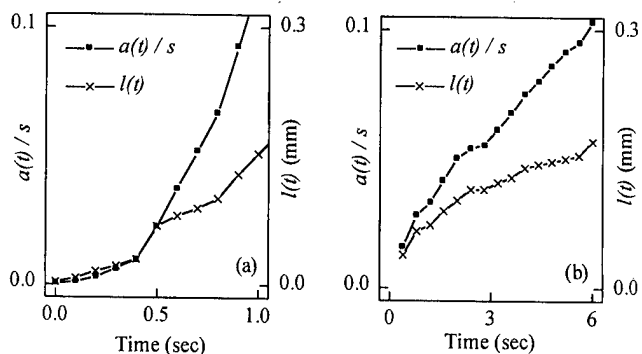


FIG. 4. Plots of the fractional area of reversed domain $a(t)/s$ and the domain boundary length $l(t)$, with respect to time t , measured from the domain images during the magnetization reversal under the applied field of $0.8 H_c$ for (a) the type I sample and (b) the type II sample.

TABLE I. The mean values of the wall-motion speed V , the nucleation rate R , and the ratio V/R of the first 20% of reversal under an applied field of $0.8 H_c$ for types I and II samples.

Sample ID	V ($\mu\text{m s}^{-1}$)	R ($\mu\text{m}^{-2} \text{s}^{-1}$)	V/R (μm^3)
Type I	1.34	0.41	3.27
Type II	0.06	0.08	0.74

The wall-motion speed V and the nucleation rate R of each sample were determined by using the present method. The first derivatives $a'(t)$ and $l'(t)$ in Eq. (3) were obtained by the finite-difference method¹¹ and the characteristic radius r_0 was set to 82 nm corresponding to the pixel size of our observation. The values of wall-motion speed V , the nucleation rate R , and the ratio V/R of types I and II samples, are listed in Table I. It is quite understandable that the wall-motion speed of the wall-motion dominant sample of type I is larger than that of the nucleation dominant sample of type II, but it is unexpected that the nucleation rate of the type I sample is found to be also larger than that of the type II sample. However, the reversal behavior is determined by a counterbalance between the wall-motion process and the nucleation process, and the change in the wall-motion speed between the samples is quite a bit larger than the change in the nucleation rate: the wall-motion speed decreases more than a factor of 20, while the nucleation rate decreases only a factor of 5. Thus, the type I sample shows wall-motion dominant reversal with a large ratio of 3.27 between the wall-motion speed and the nucleation speed, while the type II sample exhibits nucleation dominant reversal with a small ratio of 0.74. Therefore, one might conclude that the contrasting reversal behavior in this system is caused by the sensitive change in the wall-motion speed overcoming the nucleation rate.

It is worthwhile to note that the present result is quite contrastive compared with the previous one in Ref. 9: the contrasting reversal behavior in Co/Pd multilayers having a different thickness of the Co sublayers with a fixed number

of repeats was caused by the change in the nucleation rate. The previous result was understood to be caused by the change in the magnetic properties among the samples of different Co-sublayer thickness, but the present result is probably dominated by the change in the wall-pinning effect due to the different structural irregularities between the samples of different total multilayer thickness.

IV. CONCLUSION

A novel method to quantitatively analyze the magnetization reversal behaviors of magnetic films has been adopted to investigate the reversal behavior of Co/Pd multilayered films. The wall-motion speed and the nucleation rate were simultaneously determined from serial domain images captured by a real-time domain observation system. With increasing total thickness in the Co/Pd multilayered system, the wall-motion speed was much more sensitively decreased than the nucleation rate. Thus, it could be concluded that the contrasting reversal behavior observed in this system is mainly caused by the variation in the wall-motion speed.

ACKNOWLEDGMENT

This work was supported by the Ministry of Science and Technology of Korea.

- ¹J. Pommier, P. Meyer, G. Pónissard, J. Ferré, P. Bruno, and D. Renard, *Phys. Rev. Lett.* **65**, 2054 (1990).
- ²R. D. Kirby, J. X. Shen, Z. S. Shan, and D. J. Sellmyer, *J. Appl. Phys.* **70**, 6200 (1991).
- ³S.-B. Choe and S.-C. Shin, *J. Appl. Phys.* **81**, 5743 (1997).
- ⁴S.-B. Choe and S.-C. Shin, *Phys. Rev. B* **57**, 1085 (1998).
- ⁵J. X. Shen, R. D. Kirby, Z. S. Shan, D. J. Sellmyer, and T. Suzuki, *J. Appl. Phys.* **73**, 6418 (1993).
- ⁶T. G. Pokhil and E. N. Nikolaev, *IEEE Trans. Magn.* **MAG-29**, 2536 (1993).
- ⁷M. Labrune, S. Andrieu, F. Rio, and P. Bernstein, *J. Magn. Magn. Mater.* **80**, 211 (1989).
- ⁸R. D. Kirby, J. X. Shen, R. J. Hardy, and D. J. Sellmyer, *Phys. Rev. B* **49**, 10 810 (1994).
- ⁹S.-B. Choe and S.-C. Shin, *Appl. Phys. Lett.* **70**, 3612 (1997).
- ¹⁰S.-B. Choe and S.-C. Shin, *Korean Appl. Phys.* **9**, 674 (1996).
- ¹¹W. H. Press, S. A. Teukolsky, W. T. Vetterling, and B. P. Flannery, *Numerical Recipes in C*, 2nd ed. (Cambridge University Press, Cambridge, 1992), Chap. 19.

Surface spin waves in metamagnets with nonuniaxial single-ion anisotropy

D. H. A. L. Anselmo and E. L. Albuquerque^{a)}

Departamento de Física, Universidade Federal do Rio Grande do Norte, Natal, RN 59072-970, Brazil

M. G. Cottam

Department of Physics and Astronomy, University of Western Ontario, London, Ontario N6A 3K7, Canada

A microscopic theory is employed to investigate the spin wave spectra in metamagnetic materials that consist of ferromagnetically ordered layers, with the intralayer ferromagnetic exchange interactions being much stronger than the weak antiferromagnetic interaction between adjacent layers. © 1998 American Institute of Physics. [S0021-8979(98)29911-7]

Theoretical and experimental studies of surface spin waves in ordered magnetic materials have been the focus of considerable interest for many years. Many of these works have been concerned with the spin wave properties, at the low-temperature regime, of Heisenberg ferromagnets and antiferromagnets, mainly in terms of their dispersion relations, thermodynamics, and Green functions (for a review see Refs. 1–3). Besides, as a result of recent advances in fabrication techniques, spin wave excitations in magnetic superlattices of impressive quality have been also extensively studied by considering the nature of the solutions for the appropriate wave field in each film. They are then linked together through appropriate boundary conditions and with the assistance of Bloch's theorem. The surfaces and interfaces in these layered structures play an important role in the properties of the entire system and, indeed, most of the interesting properties of these excitations are due to the surface and interface effects.^{4–7}

In this article we extend previous studies in this subject by considering the propagation of surface spin waves in metamagnets which present nonuniaxial anisotropy. The metamagnetic materials consist of ferromagnetically ordered layers, with the intralayer ferromagnetic exchange interactions being much stronger than the weak antiferromagnetic interaction between adjacent layers. We consider also the presence of a weak external magnetic field \mathbf{H} applied perpendicular to the layers. In the regime of low temperatures and for small values of an external magnetic field \mathbf{H} the adjacent layers of the metamagnet material order are antiparallel to one another, giving the antiferromagnetic (AFM) phase. On the other hand, for larger \mathbf{H} , enough to overcome the interlayer antiferromagnetic coupling, the overall ordering is ferromagnetic (FM phase). The spin wave analysis is more straightforward in this case since the direction of net spin alignment is the same on both sublattices (this case is not treated here).

We consider that the metamagnet has single-ion anisotropic energy. This is a fine structure energy of an ion under the influence of the crystalline electrical field, to which the spin-orbit coupling and intraatomic magnetic interactions among the spins contribute. The forms of the anisotropic spin Hamiltonian is determined from the point symmetry

around the ion, and is assumed to be a function of the direction cosines of the magnetization vector \mathbf{M} with respect to the crystallographic axes. In the absence of an external magnetic field, \mathbf{M} lies in the direction in which the free energy is minimal. This direction is called the axis of “easy” magnetization, and usually we call the related anisotropic field as uniaxial (“easy-axis”) single-ion anisotropy. When an external magnetic field is applied, the magnetization vector deviates to a new direction at which the torque exerted by the external magnetic field balances the torque originating in the anisotropic energy. Thus a nonuniaxial (“easy-plane”) single-ion anisotropy component appears. We take into account in this article both types of anisotropic field.

Rather than using a “continuum” approximation, as was done in a recent paper⁸ dealing with some nonuniaxial effects in magnetic superlattices, we develop here a microscopic theory, taking into account surface effects in a semi-infinite metamagnet that has a (001) surface and occupies the half space $z > 0$. The method of calculation is the same as the one presented in previous papers.^{9,10}

The spin Hamiltonian for nonuniaxial metamagnets can be written as:^{10,11}

$$H = \sum_{i,j} J_{ij} (\mathbf{S}_i \cdot \mathbf{S}_j + \sigma S_i^z S_j^z) - \frac{1}{2} \sum_{i,i'} J'_{ii'} (\mathbf{S}_i \cdot \mathbf{S}_{i'} + \sigma' S_i^z S_{i'}^z) - \frac{1}{2} \sum_{j,j'} J'_{jj'} (\mathbf{S}_j \cdot \mathbf{S}_{j'} + \sigma' S_j^z S_{j'}^z) + H_z + H_A, \quad (1)$$

where the Zeeman Hamiltonian is given by

$$H_z = -g \mu_B H \left(\sum_i S_i^z + \sum_j S_j^z \right), \quad (2)$$

and the anisotropic Hamiltonian is expressed by

$$H_A = -D \left(\sum_i (S_i^x)^2 + \sum_j (S_j^x)^2 \right) - F \left(\sum_i (S_i^x)^2 - (S_i^y)^2 \right) - F' \left(\sum_j (S_j^x)^2 - (S_j^y)^2 \right). \quad (3)$$

We suppose plane-wave solutions of the type $S_i^+ = s_n(k_{\parallel}) \exp[i(\mathbf{k}_{\parallel} \cdot \boldsymbol{\rho} - \omega t)]$ and $S_i^- = r_n(k_{\parallel}) \exp[i(\mathbf{k}_{\parallel} \cdot \boldsymbol{\rho} - \omega t)]$ where n stands for the layer index. Using these assumptions

^{a)}Electronic mail: ela@dfte.ufrn.br

in the Heisenberg equation for the spin operator S_i^+ , with $\hbar=1$, we get the following set of coupled equations for the spin wave amplitudes:

for $n=1$:

$$[E_- + (1 + \sigma)Sv(0)]s_1 - Sv(k_{\parallel})s_2 + 2FS\eta^{1/2}r_1 = 0, \quad (4)$$

$$[E_- + (1 + \sigma)Sv(0) - 2\omega]r_1 - Sv(k_{\parallel})r_2 + 2FS\eta^{1/2}s_1 = 0; \quad (5)$$

for $n=2m+1$; $l=i$:

$$E_-s_{2m+1} - Sv(k_{\parallel})s_{2m+2} - Sv(-k_{\parallel})s_{2m} + 2FS\eta^{1/2}r_{2m+1} = 0, \quad (6)$$

$$(E_- - 2\omega)s_{2m+1} - Sv(k_{\parallel})s_{2m+2} - Sv(-k_{\parallel})s_{2m} + 2FS\eta^{1/2}r_{2m+1} = 0; \quad (7)$$

for $n=2m$; $l=j$:

$$E_+s_{2m} - Sv(k_{\parallel})s_{2m+1} - Sv(-k_{\parallel})s_{2m-1} - 2F'S\eta^{1/2}r_{2m} = 0, \quad (8)$$

$$[E_+ - 2\omega]r_{2m} - Sv(k_{\parallel})r_{2m+1} - Sv(-k_{\parallel})r_{2m-1} + 2FS\eta^{1/2}s_{2m} = 0, \quad (9)$$

where $E_{\pm} = \omega - g\mu_B H \pm E_0 \pm 2(1 + \sigma)Sv(0)$, $E_0 = E_0(k_{\parallel}) = g\mu_B H_A + (1 + \sigma')Su(0) - Su(k_{\parallel})$, and we have defined the Fourier transforms of the intralayer bulk exchange interaction by

$$u(k_{\parallel}) = \sum_i J'_{ii'} \exp[i\mathbf{k}_{\parallel} \cdot (\mathbf{r}_i - \mathbf{r}_{i'})] \\ = \sum_j J'_{jj'} \exp[i\mathbf{k}_{\parallel} \cdot (\mathbf{r}_j - \mathbf{r}_{j'})], \quad (10)$$

while for the interlayer exchange interaction we consider

$$v(k_{\parallel}) = \sum_{\delta} J_{ij} \exp(i\mathbf{k}_{\parallel} \cdot \delta), \quad (11)$$

where δ is a vector joining the i sites in layer n to that j sites in layer $n+1$. After a tedious algebraic manipulation of these equations, we get the following matrix set of equations:

$$(A + \Delta_1)F = \Theta G, \quad (12)$$

$$(A^* + \Delta_1^*)G = \Theta^* F. \quad (13)$$

Here F and G are infinite-dimensional column matrices, whose elements are specified by $F_m = s_{2m}$ and $G_m = r_{2m}$. Also, A is a trigonal matrix given by

$$A = \begin{bmatrix} d & -\tau^{-1} & 0 & 0 & \cdots \\ -\tau & d & -\tau^{-1} & 0 & \cdots \\ 0 & -\tau & d & -\tau^{-1} & \cdots \\ 0 & 0 & -\tau & d & \cdots \\ \vdots & \vdots & \vdots & \vdots & \ddots \end{bmatrix}, \quad (14)$$

while the matrix $\Theta = \delta I + \Delta_2$ ($\Theta^* = \delta^* I + \Delta_2^*$), where I is the identity matrix. The matrix Δ_i ($i=1$ or 2) describes the perturbing effect of the surface, and is expressed by

$$(\Delta_i)_{m,m'} = \Delta_i \delta_{m,1} \delta_{m',1}; \quad i=1,2. \quad (15)$$

The surface spin wave equation corresponds to

$$\det(I - \Theta^* A_1^* \Theta^{-1} A_1) = 0, \quad (16)$$

where

$$A_1 = A + \Delta_1; \quad A_1^* = A^* + \Delta_1^*, \quad (17)$$

whose solutions are

$$[(\xi_1 - t\xi_3)(\Gamma + \beta) - \xi_2\xi_4 + (s - ht)\xi_3\xi_4 + \xi_5 \\ - gt\xi_1(\Gamma - gt)] \cdot \bar{M} = 0, \quad (18)$$

where

$$s = -\tau b; \quad t = \tau^2 a, \\ h = -\tau^{-1} b; \quad g = \tau^{-2} a, \quad (19) \\ \Gamma = 1 - 2a - c; \quad \beta = \Delta_2 a / (\delta + \Delta_2).$$

In all these matrix equations, the terms d , τ , δ , δ^* , Δ_i , Δ_i^* ($i=1$ or 2), and ξ_j ($j=1-5$) are complicated expressions involving the physical parameters of the metamagnet materials. Their full algebraic expressions can be found elsewhere.¹² Also, \bar{M} is the determinant:

$$\bar{M} = \begin{vmatrix} \Gamma & h & g & 0 & 0 & 0 & \cdots \\ s & \Gamma & h & g & 0 & 0 & \cdots \\ t & s & \Gamma & h & g & 0 & \cdots \\ 0 & t & s & \Gamma & h & g & \cdots \\ 0 & 0 & t & s & \Gamma & h & \cdots \\ \vdots & \vdots & \vdots & \vdots & \vdots & \vdots & \ddots \end{vmatrix}. \quad (20)$$

If we choose $\bar{M} \neq 0$, the surface spin-wave dispersion relation is then given by the first term of Eq. (18).

On the other hand, the bulk spin-wave dispersion relation can be found using the ansatz $M \cdot u = 0$, where u is a column matrix with elements $u(n)$ representing a mode amplitude. Then,

$$tu_{n-2} + su_{n-1} + \Gamma u_n + hu_{n+1} + gu_{n+2} = 0. \quad (21)$$

By choosing the solutions such that $u(n) = \alpha x^n$ (for x unknown), using the definitions of a , b , and τ , and denoting $y = \tau x$, we get

$$a(y^2 + y^{-2}) - b(y + y^{-1}) = -\Gamma. \quad (22)$$

This is a fourth-degree equation for y . The roots of this equation, together with the assumption that $x = \exp(2ik_z c_0)$, where $2c_0$ is the distance between even (or odd) adjacent layers, yield the following bulk dispersion relations:

$$\cos(2k_z c_0) = \frac{1}{2\tau} \left(\pm \sqrt{(d + d^*)^2 + 4(dd^* - \delta\delta^*) + 16} \right. \\ \left. + (d + d^*) \right). \quad (23)$$

Equation (23) is an implicit dispersion relation. It can be obtained by supposing that the roots of Eq. (22) occur at pairs, and that the pairs are complex conjugate one of the other. In compact form they can be written as

$$[\tau \cos(2k_z c_0)]^2 - (d + d^*)\tau \cos(2k_z c_0) - (dd^* - \delta\delta^*) - 4 \\ = 0. \quad (24)$$

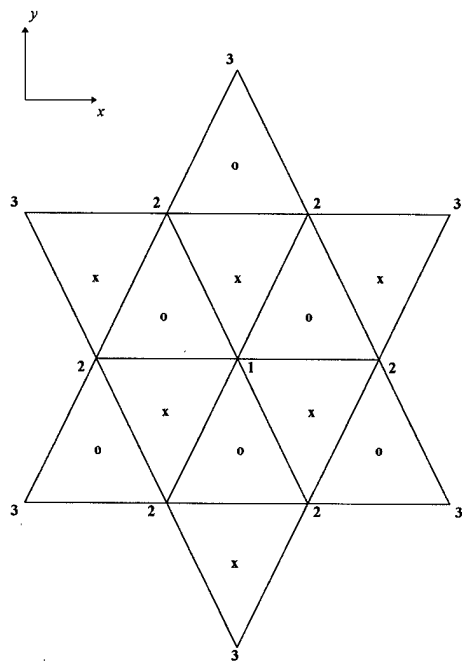


FIG. 1. Crystallographic arrangements of Fe^{2+} ions (solid circles) in the ferromagnetically ordered layers for FeBr_2 and FeCl_2 . The nearest and next-nearest intralayer neighbors to the ion labeled 1 are those labeled 2 and 3, respectively. The crosses and open circles represent the positions of the ions in the adjacent layers above and below the planes for FeCl_2 .

The solutions of the above expression give the bulk modes for the spin waves, and they are valid in the antiferromagnetic phase.

We now apply the surface and bulk (for completeness) dispersion equations to determine the spin-wave spectra for the specific cases of FeBr_2 and FeCl_2 . They have their crystallographic arrangements of magnetic ions as depicted in Fig. 1. Both materials have the same trigonal arrangements of magnetic Fe^{2+} ions within each ferromagnetically ordered layer. They differ, however, in the stacking arrangements of the layers. In FeBr_2 , the Fe^{2+} ions in one layer are vertically situated above and below those in the adjacent layers, although in FeCl_2 the layers are staggered with respect to one another. The crosses and open circles in Fig. 1 represent the positions of the ions in the adjacent layers above and below the planes.

Figure 2 shows the dispersion relation for bulk and surface spin waves in FeBr_2 in the AFM phase. We take as the applied magnetic field $g\mu_B H = 1.6 \text{ cm}^{-1}$. We plot the frequency ω (in units of 10 cm^{-1}) against $k_x a$ (here we consider $k_{\parallel} = k_x$). The physical parameters used here are those described in Ref. 10, with the nonuniaxial anisotropic field $F = F' = 2 \text{ cm}^{-1}$. Comparison of this spectrum with those in which there is no nonuniaxial component of the anisotropic field (Fig. 2 in Ref. 10) shows that the bulk band is now split, giving rise to two separated bands limited by the curves $k_z a = 0$ and $k_z a = \pi$. Besides, there are also two well defined surface modes (shown by the dashed lines) below and between these bulk bands. The inset gives a better insight into this situation (observe that the bulk bands are shown as shaded).

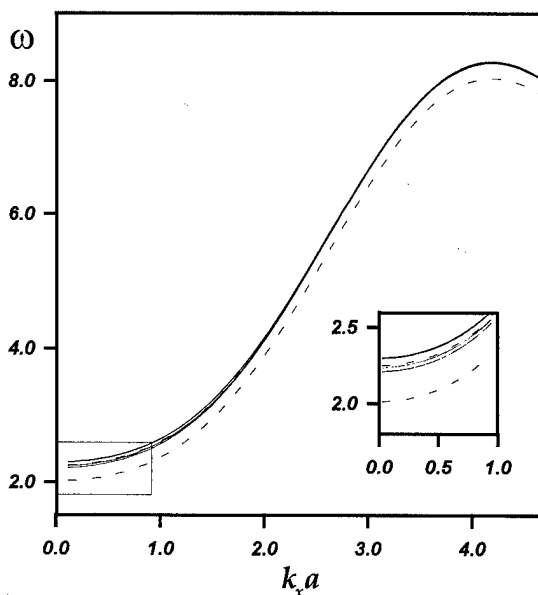


FIG. 2. Dispersion relations of bulk (shaded areas) and surface (dashed lines) spin waves in FeBr_2 in the AFM phase as a function of the in-plane wave vector $k_x a$ for the applied magnetic field $g\mu_B H = 1.6 \text{ cm}^{-1}$.

The spin-wave spectra for the FeCl_2 metamagnet (not shown here) is qualitatively quite the same of that for FeBr_2 , but the low-frequency surface branch is very close to the first bulk band. This fact, which is due to their different crystal structure, presents an additional difficulty in probing this mode experimentally.

Appropriated experimental techniques for studying the spin-wave spectrum in metamagnets would include light scattering spectroscopy of the Raman and Brillouin types and magnetic resonance. For FeBr_2 , the light scattering technique may be more suitable, since our theoretical predictions indicate that at least one branch (the low-frequency one) of the surface spin waves is well separated in frequency (even in the absence of the nonuniaxial anisotropic field) from the bulk modes.

- ¹M. G. Cottam and A. A. Maradudin, in *Surface Excitations*, edited by V. M. Agranovich and R. Loudon (North-Holland, Amsterdam, 1984).
- ²M. G. Cottam and D. J. Lockwood, *Light Scattering in Magnetic Solids* (Wiley, New York, 1986).
- ³M. G. Cottam and D. R. Tilley, *Introduction to Surface and Superlattice Excitations* (Cambridge University Press, Cambridge, 1989).
- ⁴E. L. Albuquerque, P. Fulco, E. F. Sarmiento, and D. R. Tilley, *Solid State Commun.* **58**, 41 (1986).
- ⁵R. E. Camley and M. G. Cottam, *Phys. Rev. B* **35**, 189 (1987); R. E. Camley, M. G. Cottam, and D. R. Tilley, *Solid State Commun.* **81**, 571 (1992).
- ⁶J. Barnas, *J. Phys. C* **21**, 1021 (1988); **21**, 4097 (1988).
- ⁷C. A. Ramos, D. Lederman, A. R. King, and V. Jaccarino, *Phys. Rev. Lett.* **65**, 2913 (1990).
- ⁸E. L. Albuquerque and M. G. Cottam, *Phys. Rev. B* **46**, 14 543 (1992).
- ⁹S. Gopalan and M. G. Cottam, *Phys. Rev. B* **42**, 624 (1990).
- ¹⁰J. H. Baskay and M. G. Cottam, *Phys. Rev. B* **42**, 4304 (1990).
- ¹¹D. H. A. L. Anselmo and E. L. Albuquerque, *Phys. Status Solidi B* **198**, 827 (1996).
- ¹²D. H. A. L. Anselmo, E. L. Albuquerque, and M. G. Cottam (unpublished).

Exchange narrowing effects in the EPR linewidth of Gd diluted in Ce compounds

Pablo A. Venegas^{a)}

Physics Department, University of California, Santa Cruz, California 95064

Paulo R. S. Netto

Departamento de Física, Universidade Estadual Paulista, Caixa Postal 473, 17033-360, Bauru-SP, Brazil

Anomalous thermal behavior on the EPR linewidths of Gd impurities diluted in Ce compounds has been observed. In metals, the local magnetic moment EPR linewidth, ΔH , is expected to increase linearly with the temperature. In contrast, in $\text{Ce}_x\text{La}_{1-x}\text{Os}_2$ the Gd EPR spectra show a nonlinear increase. In this work, the mechanisms that are responsible for the thermal behavior of the EPR lines in $\text{Ce}_x\text{La}_{1-x}\text{Os}_2$ are examined. We show that the exchange interaction between the local magnetic moments and the conduction electrons are responsible for the narrowing of the spectra at low temperatures. At high temperatures, the contribution to the linewidth of the exchange interaction between the local magnetic moments and the Ce ions has an exponential dependence on the excitation energy of the intermediate valent ions. A complete fitting of the EPR spectra for powdered samples is obtained. © 1998 American Institute of Physics. [S0021-8979(98)39911-9]

I. INTRODUCTION

During the last two decades Ce compounds have been extensively studied and many of them show anomalies typical of intermediate valence systems.¹ Electron paramagnetic resonance (EPR) spectra of magnetic ions diluted in Ce compounds allow us to study locally the influence of the intermediate valent Ce ions. In normal metals, the thermal behavior of the local moments EPR linewidth, ΔH , is linear and described by the Korringa mechanism.² In contrast, in $\text{Ce}_x\text{A}_{1-x}\text{Pd}_3$ ($\text{A}=\text{Ag}, \text{Y}$) and $\text{Ce}_x\text{La}_{1-x}\text{Os}_2$ the Gd spectra shows a nonlinear increase of ΔH in the temperature range $4.2 < T < 300$ K, and a strong dependence on the Ce concentration.^{3,4} At low temperatures (T) the slope $d(\Delta H)/dT$ is smaller than in the isostructural non-IV compounds MPd_3 ($\text{M}=\text{Sc}, \text{Y}, \text{La}$)⁵ and LaOs_2 ,⁴ however, at high temperatures the resonance line is strongly broadened and the slope asymptotically approaches the value measured on them. Then, to describe this abnormal behavior of linewidth other mechanisms different from the Korringa are necessary.

It was demonstrated⁶ that at high temperatures, the indirect exchange interaction between the local magnetic and the Ce $4f$ electrons has an appreciable contribution to the linewidth of the magnetic impurities at high temperature. The Ce interconfigurational fluctuations are transferred via the Ruderman-Kittel-Kasuya-Yosida (RKKY) interaction to the Gd site as an effective alternating magnetic field, which relaxes the Gd spins. However, this mechanism is not sufficient to describe the low temperature behavior of the Gd linewidth. It is well known^{7,8} that the Gd EPR spectra shows a resolved fine structure at low T , which is narrowed due to

the exchange interaction between local magnetic moments and conduction electron when the temperature is increased. Then, for the correct description of the thermal behavior of the Gd spectra it is necessary to include not only the intermediate valence effects but also the narrowing mechanism. The goal of this work is to calculate the EPR spectra of Gd diluted in $\text{Ce}_x\text{La}_{1-x}\text{Os}_2$ including the both mechanisms.

II. THEORETICAL ANALYSIS

To obtain the EPR absorption, the transverse dynamic susceptibility of the local magnetic moments coupled to the conduction electrons is necessary. The susceptibility, including the crystal field interaction, can be obtained using the projector formalism in the Liouville space.⁹ Normally the EPR experiments are performed at a concentration that the conduction electrons static susceptibility is much smaller than those of the local moments, then, in this approximation, the susceptibility for the system in the nonbottleneck regime can be written as follows

$$\chi^+(\omega) \approx 1 - \omega_0 \left[\sum_{M,M'} P_M(\Omega^{-1})_{M,M'} \right], \quad (1)$$

where $\Omega_{M,M'}^{-1}$ is the transition matrix, the quantum numbers M and M' describe the various Zeeman states ($M, M' = -S, -S+1, \dots, S-1$) associated to the $S=7/2$ Gd spin and P_M are transition probabilities associated to the $M \leftrightarrow M+1$ transition and can be written as:

$$P_M = C_M \exp^{M\hbar\omega_0/kT} / \sum_M C_M \exp^{M'\hbar\omega_0/kT}, \quad (2)$$

where $C_M = S(S+1) - M(M+1)$ and k is the Boltzmann constant. The elements of the transition matrix for kT large compared to $\hbar\omega_0$ are expressed by the formula

^{a)}On leave from Departamento de Física, Universidade Estadual Paulista, Av. Engenheiro Luiz E. Coube S/N, 17033-360 Bauru-SP, Brazil.

$$\begin{aligned}\Omega_{M,M'} = & (\hbar\omega_0/g\mu_B - H - H_M)\delta_{M,M'} - i\Delta H_{res}\delta_{M,M'} \\ & - i\frac{1}{2}bC_{M'}(2\delta_{M,M'} - \delta_{M,M'}) \\ & - \delta_{M,M'+1} - \delta_{M,M'-1},\end{aligned}\quad (3)$$

where ω_0 is the microwave frequency, H is the variable external magnetic field, ΔH_{res} is the temperature independent residual linewidth of the various fine structure lines, b is the Korringa parameter, μ_B is the Bohr magneton, and H_M is the resonance field of the Gd $M \rightarrow M+1$ transition. As we can see, the transition matrix is a tridiagonal matrix where the diagonal elements contain the linewidth of each resonance line and the resonance field. The upper and lower diagonals terms represent the fluctuation rates of the local moment between two consecutive resonance frequencies.

In a cubic environment the fine structure spectra is given by

$$\begin{aligned}H(\pm\frac{7}{2} \leftrightarrow \pm\frac{5}{2}) &= H_0 \mp (1-5\phi)b_4, \\ H(\pm\frac{5}{2} \leftrightarrow \pm\frac{3}{2}) &= H_0 \pm (1-5\phi)b_4, \\ H(\pm\frac{3}{2} \leftrightarrow \pm\frac{1}{2}) &= H_0 \pm (1-5\phi)b_4, \\ H(+\frac{1}{2} \leftrightarrow -\frac{1}{2}) &= H_0,\end{aligned}\quad (4)$$

where b_4 is the crystal field parameter for the Gd ion, ϕ is given by

$$\phi = \sin^2 \theta \cos^2 \theta + \sin^4 \theta \cos^2 \varphi \sin^2 \theta \quad (5)$$

and θ and φ are spherical coordinates of the applied magnetic field H with respect to the axes of the crystal.

As it was shown previously,^{7,8} for the LaSb:Gd and CePd₃:Gd, the spin-spin interaction between Gd ions has an important role in the calculation of the resonance spectra. In both cases was found that when the spin-spin interaction is not taken into account the narrowing in the theoretical spectra occurs at higher temperatures than in the experiment, the transition $1/2 \leftrightarrow 1/2$ does not appear in the theoretical spectra in the intermediate temperature range, however, it appears in the experiment, and the experimental linewidth of the single line at high temperatures is smaller than the calculated one. The discrepancies between theory and experiment can be overcome by introducing this interaction. Unfortunately, no theoretical calculation which takes spin-spin interaction into account exists at present. We shall introduce the spin-spin interaction in a phenomenological way.^{7,8} This can be done by adding to the transition matrix elements the term:

$$\Omega_{M,M'}^{ex} = i\frac{H_{ex}}{P_M}(1 - \delta_{M,M'}) - i\frac{6H_{ex}}{P_M}\delta_{M,M'}, \quad (6)$$

where H_{ex} is the exchange-field parameter. The transition matrix has some properties that must be satisfied for this additional term. First, $P_M \text{Im}(\Omega_{M,M'})$ are the elements of a negative-definite symmetric matrix. This guarantees a positive energy absorption. Second, as the total spin commutes with the exchange Hamiltonian, the relation $\sum_M \Omega_{M,M'} = 0$ must hold. Since these two requirements are satisfied, we can believe that the additional term for the transition matrix describes the main effects of the spin-spin interaction. Because of the random distribution of the Gd ions, it is realistic to assume a distribution of H_{ex} . For the present calculations we

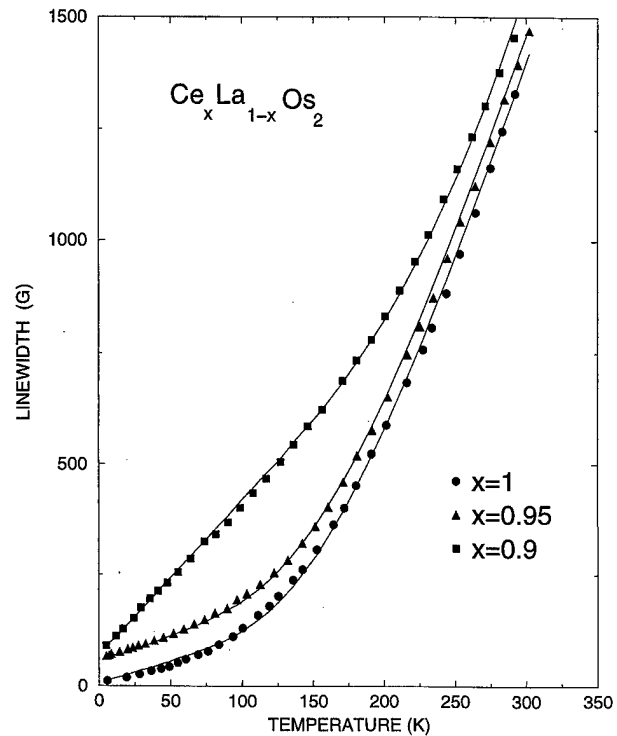


FIG. 1. Temperature dependence of the Gd linewidth for selected values of concentration x in $\text{Ce}_x\text{La}_{1-x}\text{Os}_2$. The full lines represent the theoretical results. The residual linewidths are not realistic and the data has been shifted to avoid curve overlap.

use a slightly modified Lorentzian distribution for the exchange field with a maximum at $H_{ex}=0$. The mean exchange field amounts to about 95 G and the distribution function was cut off at 1500 G.

III. THE LINEWIDTH

In our metallic host the impurity EPR linewidth calculations must consider the energy transfer between the impurity spin S , the spin of the host rare earth ions (Ce), the spins of the conduction electrons as well as the lattice, in the presence of static external magnetic field and a small alternating field. In the present work we shall assume that the system is in the unbottlenecked regime, i.e., the conduction electrons and the host magnetic ions are in equilibrium with the lattice. In addition we shall assume that the transverse susceptibility associated with the impurity at the impurity resonance frequency is much larger than those of the other spin systems at the same frequency. In this limit one can consider only the transverse magnetization, M_x , of the impurities and neglect the interaction of the rf field with the magnetic host ions and the conduction electrons. In other words, the magnetic host ions and the conduction electrons are "passive dissipative

TABLE I. Obtained parameters b, b_4, A, E_{ex} that fit the linewidth thermal behavior for Gd diluted in $\text{Ce}_x\text{La}_{1-x}\text{Os}_2$. E_{ex} (expt.) is the experimental value of E_{ex} to be taken as a comparison.

x	b [G/K]	b_4 [G]	A [G]	E_{ex} (theor.)	E_{ex} (expt.)
1.0	1.07	4.8	10 200	670	500
0.95	1.32	10.6	10 150	684	
0.9	3.5	9.0	9800	1243	

systems.” With these assumptions the impurity linewidth can be expressed as:

$$\Delta H = \Delta H_{res} + bT + \Delta_{IF}, \quad (7)$$

where ΔH_{res} is the residual linewidth, b is the usual Korringa contribution, originated from the impurity-conduction-electron exchange interaction, and Δ_{IF} is the impurity linewidth due to the exchange interaction with the Ce host ions.⁶ The last contribution arises from the RKKY coupling between the Ce and Gd ions, which transfers the Ce fluctuations to the Gd site. Ce ions fluctuate between the $4f^0$ and the $4f^1$ configurations. If we assume the $4f^0$ configuration as the ground state (with $J_z = 0$), the contribution of the excited $4f^1$ configuration to the impurity linewidth can be written as:

$$\Delta_{IF} = A e^{-E_{ex}/T}, \quad (8)$$

where E_{ex} is the energy required to delocalize a single electron from the Ce $4f^1$ configuration and A is an adjustable parameter defined in Ref. 6.

The resonance absorption P is calculated using the relation $P = [\text{Re}(\chi^+(\omega)) - \text{Im}(\chi^+(\omega))]$. To obtain the EPR linewidth of the powdered samples we have to integrate the absorption over all directions of the magnetic field.

IV. RESULTS AND DISCUSSION

Using the results above we calculate the total linewidth of the Gd resonance. Figure 1 shows the calculated and experimental linewidth of a $\text{Ce}_x\text{La}_{1-x}\text{Os}_2$ powdered sample, as a function of temperature for selected concentrations of Ce. The residual linewidth is sample dependent and it was not considered in the plot. To fit the data we adjust the parameters b , b_4 , A , and E_{ex} using the Monte Carlo simulated annealing. With this technique it is possible to obtain more accurate results than previous calculations with conventional methods.⁶⁻⁸ Comparing our theoretical results with the experimental data we can see that in all of the cases we got an excellent fit. According to our model, at low T the main contribution to the linewidth is originated in the usual Korringa mechanism and the exchange narrowing effects. At high temperatures the population of the excited Ce $4f^1$ configuration is increased, and the exponential contribution given by Δ_{IF} is the most important. The parameters used to fit the experimental data are shown in Table I. The analysis *a priori* of the exchange narrowing effects in this system is not easy because there do not exist a single crystal spectra to obtain by a direct measure the crystal field parameter, however, if we look for the spectra of $\text{Ce}_{0.8}\text{La}_{0.2}\text{Os}_2$ in Fig. 1(a) of Ref. 4 we can see clearly that the Dysonian type line does not fit the experimental result. The experimental spectra shows the typical broadening at low T due to the fine structure contribution, and these effects tend to be more important in higher Ce concentrations.⁸ If we compare the exchange narrowing effects for the present case with that in CePd_3 (Ref. 8) certainly the exchange narrowing effects are less important in the former one, due to the smaller crystal field parameter. Otherwise, its contribution is more important at lower temperatures than in CePd_3 because the higher Korringa parameter values collapse the spectra at lower tempera-

tures. It is necessary to point out that the minimization results show clearly a nonzero value for the crystal field parameter which reflects the importance of this mechanism. On the other hand, looking for the intermediate valence mechanism, the effect of the Ce concentration at high temperature seems clear. The increase in the excitation energy value when the Ce concentration is reduced agree with the interconfigurational fluctuation model.¹⁰⁻¹³ This model predicts an increasing on the excitation energy when we cross from the intermediate valence to the magnetic regime. On the other hand, the A value depends on the strength of the Ce fluctuation spectra and we can expect an increase with the Ce concentration. The small values of b obtained for high Ce concentrations (when compared with those of LaOs_2) agree with the experimental results of Ref. 4 at low T , with the prediction of the ‘‘hybridization hole’’ model³ for Gd diluted in CePd_3 powdered sample and with that obtained in Ref. 8 for the monocrystalline spectra of the same compound. This result agrees also with that obtained by Hirst¹² for low T , but not with the result obtained in Ref. 14, which predicts a higher value for b . However, the thermal behavior of the linewidth obtained by the latter authors agrees, at least qualitatively, with that obtained here. It is important to observe that in contrast to the hybridization hole model, here we have supposed a constant density of states as in a normal metal. The nonlinear contribution to the linewidth, at high T , according with the present model, is originated in the exchange interaction of the magnetic impurities with the Ce ions.

In conclusion, our calculations using the intermediate valence and exchange narrowing mechanism permit a quantitative description of the thermal behavior of Gd linewidths. Note that the values obtained for the excitation energy are, within the experimental error, close to that founded by Sereni *et al.*¹⁵ The agreement with experimental results supports our interpretation.

ACKNOWLEDGMENTS

P.A.V. thanks the Brazilian Agency Capes for partial financial support and P.R.S.N. thanks the Brazilian agency CNPQ for financial support.

- ¹J. M. Robinson, Phys. Rep. **51**, 1 (1979).
- ²J. Korringa, Physica (Amsterdam) **16**, 601 (1950).
- ³H. Schaeffer and B. Elschner, Z. Phys. B Condensed Matter **53**, 109 (1983).
- ⁴M. Schlott, H. Schaeffer, and B. Elschner, Z. Phys. B Condensed Matter **63**, 427 (1986).
- ⁵T. Gambke, B. Elschner, R. Kremer, and M. Schanz, J. Magn. Magn. Mater. **36**, 124 (1983).
- ⁶P. A. Venegas and G. E. Barberis, Phys. Rev. B **46**, 911 (1992).
- ⁷P. Urban, D. Davidov, B. Elschner, T. Plefka, and G. Sperlich, Phys. Rev. B **12**, 72 (1975).
- ⁸P. A. Venegas and G. E. Barberis, Solid State Commun. **58**, 447 (1986).
- ⁹T. Plefka, Phys. Status Solidi B **55**, 129 (1973).
- ¹⁰L. L. Hirst, Phys. Kondens. Mater. **11**, 255 (1970).
- ¹¹L. L. Hirst, AIP Conf. Proc. **24**, 11 (1975).
- ¹²L. L. Hirst, in Valence Instabilities and Narrow Band Phenomena, edited by R. D. Parks (1977), p. 3.
- ¹³T. Gambke, B. Elschner, and L. L. Hirst, Phys. Rev. Lett. **40**, 1290 (1978).
- ¹⁴M. M. Ochi and O. L. T. de Meneses, Solid State Commun. **75**, 355 (1990).
- ¹⁵J. G. Sereni, G. L. Olcese, and C. Rizzuto, J. Phys. C **5**, 337 (1979).

High field magnetic properties in single crystal Nd₃Co

Izuru Umehara, Ying Lu, Qing Feng Lu, Yoshiya Adachi, Masato Endo, and Kiyoo Sato^{a)}
*Division of Physics, Faculty of Engineering, Yokohama National University, Tokiwadai 79-5,
 Hodogaya-ward, Yokohama City 240, Japan*

Michael Bartashevich and Tsuneaki Goto
Institute of Solid State Physics, University of Tokyo, Roppongi Tokyo, Japan

Magnetization as a function of field was measured in pulsed fields of up to 40 T at various temperatures along the principal axes of single crystal Nd₃Co. Along the *a* axis we observed metamagnetic transitions at fields of 1.9 and 4.5 T at 4.2 K. We also observed a sharp increase in the magnetic moment in applied fields between 9.5 and 14 T. Along the *b* axis a metamagnetic transition was observed at a field of 1.5 T at 4.2 K. Along the *c* axis we observed ferromagnetic behavior. The *H*-*T* (magnetic field and temperature) phase diagram was obtained using a superconducting quantum interference device magnetometer. © 1998 American Institute of Physics. [S0021-8979(98)51411-9]

I. INTRODUCTION

The intermetallic compounds, R₃Co (R: rare earth metals except Ce), crystallize in the orthorhombic Fe₃C-type structure (space group Pnma) in which R occupies two non-equivalent very low symmetry crystallographic sites, i.e., 4*c* (point group *m*) and 8*d* (point group 1).¹⁻⁵ In our previous study⁶ (of electrical resistivity, magnetic susceptibility and specific heat measurements), it was reported that Nd₃Co has three magnetic transitions at low temperatures (spin reorientation temperatures T_{R1} =8 K and T_{R2} =13 K, and Néel temperature T_N =25 K). We also reported two field induced metamagnetic transitions along the *a* axis (transition fields of H_{a1} =1.8 T and H_{a2} =4.5 T) and one transition along the *b* axis (transition field H_b =1.9 T) below 7 T at 1.5 K. We proposed a canted magnetic structure to explain the complex magnetization process in Nd₃Co.⁶ However, a field of 7 T is not enough to achieve the saturation moment. Thus we have measured the high field magnetization in a pulsed magnetic field of up to 40 T at various temperatures. Since there are many magnetic phases in Nd₃Co, we aim to determine a magnetic phase diagram for the *a* axis in applied magnetic fields of up to 5 T and for temperatures down to 5 K. In this article we report the saturation moments and the magnetic phase diagram.

II. EXPERIMENT

A single crystal of Nd₃Co was obtained by the Bridgman method with an alumina crucible in a high vacuum quartz tube. Details of the sample preparation are described in Ref. 7. The magnetization curves were obtained in pulsed magnetic fields of up to 40 T at 4.2, 12, 19, and 30 K along the principal axes of the orthorhombic structure. The magnetization curves in fields up to 5 T were measured by a superconducting quantum interference device (SQUID) magnetometer

at various temperatures. The temperature dependencies of the magnetic susceptibilities were measured by means of vibrating sample magnetometer (VSM).

III. RESULTS AND DISCUSSIONS

We measured the temperature dependence of the magnetic susceptibility along the *a*, *b*, and *c* axes in the temperature range from 4.2 to 300 K under a constant field of 1 T. Figure 1 shows a part of the susceptibilities. Above 150 K the susceptibilities obey the Curie-Weiss law and the paramagnetic Curie temperatures θ_a , θ_b , and θ_c along the *a*, *b*, and *c* axes were estimated to be 39.4, 28.7, and 34.6 K, respectively. The effective magnetic moments along the *a*, *b*, and *c* axes are 3.64, 3.60 and 3.60 μ_B , respectively. These values are in good agreement with the expected values 3.62 μ_B from the trivalent Nd ion. This suggests that the cobalt has no magnetic moment. It is difficult to determine the crystalline field parameters from the anisotropy in magnetic susceptibility because there are too many parameters

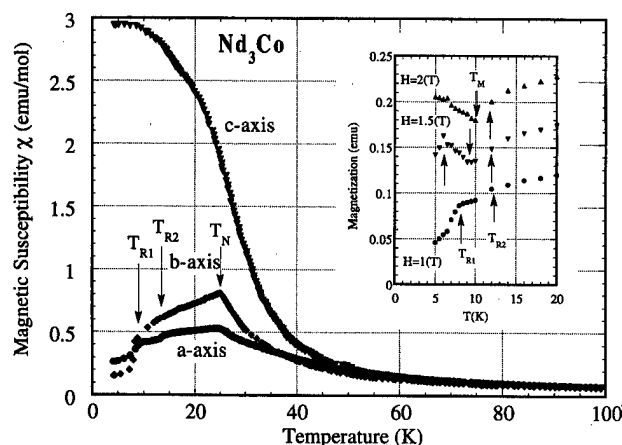


FIG. 1. Temperature dependence of the magnetic susceptibility of Nd₃Co in an external field of 1 T over the temperature range 4.2–100 K. The inset shows the temperature dependence of the magnetization at various magnetic fields obtained using a SQUID.

^{a)}Electronic mail: sato@physics.sci.ynu.ac.jp

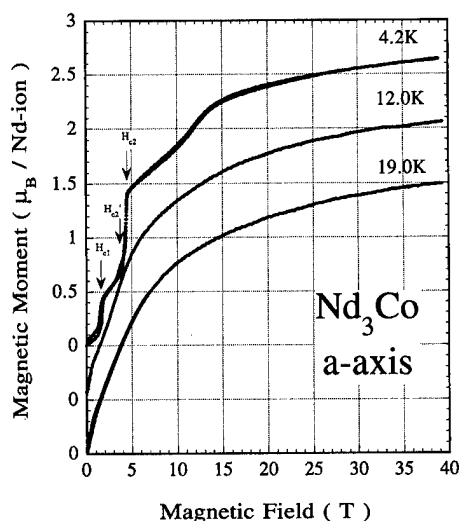


FIG. 2. Magnetization curve along the *a* axis in fields up to 40 T at 4.2, 12, and 19 K in Nd₃Co.

related to the low symmetry sites denoted by monoclinic *m* and triclinic *l* point symmetry. The reciprocal susceptibility deviates from the Curie–Weiss law below 150 K. This deviation may be due to higher order crystalline electric field parameters in the Hamiltonian.⁸ The inset shows in detail the temperature dependence of the magnetization at various magnetic fields. T_{R1} , T_{R2} , and T_M are the critical points in the thermomagnetic curves.

Figure 2 shows the magnetization curves along the *a* axis at various temperatures. Metamagnetic transitions with hysteresis are seen in fields of 1.9 and 4.5 T at 4.2 K. These transitions are due to the reversals of antiferromagnetic components along the *a* axis of the canted moments in the 4*c* and 8*d* sites. We also observe a sharp increase in magnetization in the field range from 9.5 to 14 T at 4.2 K. The increase in moment is $0.4 \mu_B/\text{Nd ion}$. This is not due to a metamagnetic transition. This phenomenon originates from the sign of the second and fourth order anisotropic constants such as is seen in the magnetization along the $\langle 111 \rangle$ direction in Fe metal or along the hard axis in Tb metal.⁹ At 12 K, we found that a metamagnetic transition shifts to about 3 T, as well as 1 T at 19 K. The saturated moments, M_s , at 4.2, 12, and 19 K are estimated to be 2.82, 2.73, and $2.66 \mu_B/\text{Nd ion}$, respectively. The value of saturation magnetization M_s extrapolated to 0 K is $2.87 \mu_B/\text{Nd ion}$, which is obtained by means of the $1/H^2$ law. This value is 88% of the free ion value of $3.27 \mu_B/\text{Nd ion}$. This is a result of the strong magnetic anisotropy due to the crystalline electric field effect in this compound.

Figure 3 shows the magnetization curves along the *b* axis at various temperatures. A metamagnetic transition with hysteresis occurs at 1.9 T at 4.2 K. This transition is most likely due to reversal of the antiferromagnetic component along the *b* axis of the Nd ion in the 8*d* site. The transition fields decrease with increasing temperature. The saturated moments at 4.2, 12, 19, and 30 K are estimated to be 2.57, 2.52, 2.49, and $2.32 \mu_B/\text{Nd ion}$, respectively. The value of saturation magnetization along the *b* axis extrapolated to 0 K

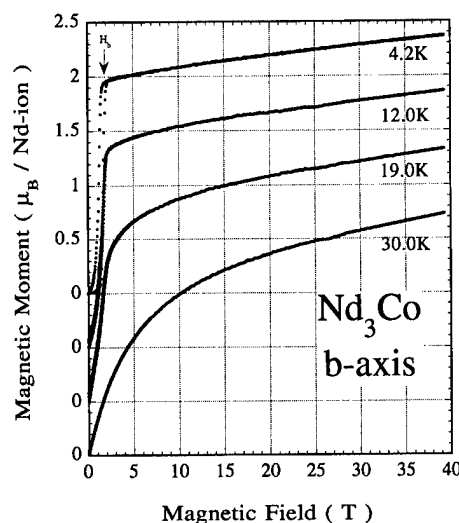


FIG. 3. Magnetization curve along the *b* axis in fields up to 40 T at 4.2, 12, 19, and 30 K in Nd₃Co.

is about $2.57 \mu_B/\text{Nd ion}$. This value is 78% of the free ion value $3.27 \mu_B/\text{Nd ion}$.

Figure 4 shows the magnetization curves along the *c* axis at various temperatures. These magnetization curves suggest that the resultant magnetic moment along the *c* axis is the ferromagnetic. The Nd moments on both the 4*c* and 8*d* sites have ferromagnetic components in this direction. The saturated moments M_s at 4.2, 12, 19, and 30 K are estimated to be 2.34, 2.34, 2.32, and $2.27 \mu_B/\text{Nd ion}$, respectively. The value of saturation magnetization along the *c* axis extrapolated to 0 K is $2.34 \mu_B/\text{Nd ion}$. This value is 71% of the free ion value. This value is the most suppressed one among those of the three principal axes. This suppression of the saturation moment on all three axes indicates the easy axis of this crystal is not one of the principal axes on either of the two nonequivalent sites.

In order to determine a magnetic phase diagram, for the

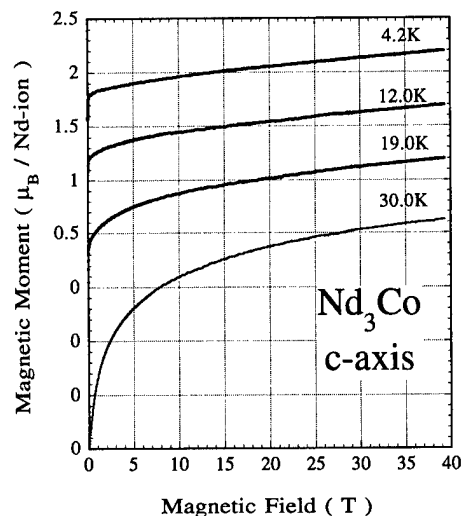


FIG. 4. Magnetization curve along the *c* axis in fields up to 40 T at 4.2, 19, and 30 K in Nd₃Co.

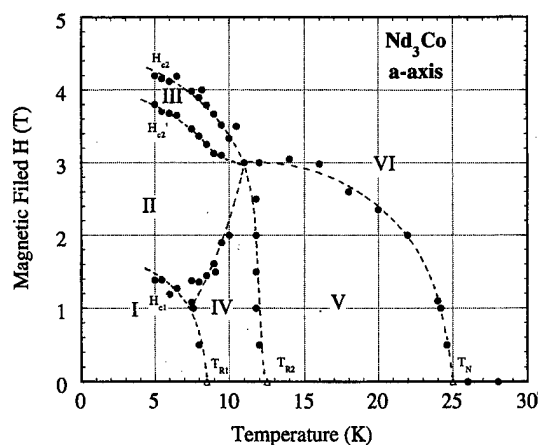


FIG. 5. Phase diagram of the magnetic field H and temperature T along the a axis in Nd_3Co .

field of up to 5 T by SQUID magnetometer. Figure 5 shows the H - T phase diagram along the a axis, which obtained from the critical temperatures denoted T_{R1} , T_{R2} , and T_M in the inset of Fig. 1 and the critical fields H_{c1} , H_{c2} , and H'_{c2} in Fig. 2, respectively. The three transitions made by means of the specific heat measurement⁶ in zero magnetic field mentioned above are denoted as triangles in Fig. 5. In phase I, there is a ferromagnetic component along the c axis and antiferromagnetic components along the a and b axes, respectively. Above H_{c1} the metamagnetic transition occurs. Above H'_{c2} and H_{c2} , the second and third metamagnetic transitions occur along the a axis, denoted as phases II and

III, respectively. Phase II is a state in which ferromagnetic and antiferromagnetic components coexist along the a axis. The states of phases III and IV are unknown. Phase V is also a state in which ferromagnetic and antiferromagnetic components coexist along the a axis, however it is different from phase II. Phase VI is a field induced ferromagnetic state. Neutron diffraction measurements in a magnetic field are needed to clarify each magnetic state and we are currently undertaking such a study.

ACKNOWLEDGMENTS

This work was supported by Grant-in-Aid for Scientific Research from the Ministry of Education, Science and Culture of Japan and also partly supported by a project of the Venture Business Laboratory at Yokohama National University.

- ¹J. L. Feron, D. Gignoux, R. Lemaire, and D. Paccard, *Terres* **2**, 75 (1970).
- ²N. V. Baranov, P. E. Markin, A. I. Kozlov, and E. V. Sinitsyn, *J. Alloys Compd.* **200**, 43 (1993).
- ³N. V. Baranov, A. V. Pirogov, and A. E. Teplykh, *J. Alloys Compd.* **226**, 70 (1995).
- ⁴D. Gignoux, J. C. Gomez-Sal, and D. Paccard, *Solid State Commun.* **44**, 695 (1982).
- ⁵Q. F. Lu, I. Umehara, Y. Adachi, M. Endo, and K. Sato, *J. Appl. Phys.* **66**, 1480 (1997).
- ⁶I. Umehara *et al.*, *J. Phys. Soc. Jpn.* (submitted).
- ⁷Q. F. Lu, I. Umehara, Y. Adachi, and K. Sato, *Trans. Jpn. Inst. Met.* **38**, 1 (1997).
- ⁸Y. Aoki, H. Sato, H. Sugawara, P. Svoboda, R. Settai, Y. Onuki, and K. Sugiyama, *J. Magn. Magn. Mater.* **150**, 151 (1995).
- ⁹S. Chikazumi, *Physics of Ferromagnetism*, 2nd ed. (1997), p. 275.

Evolution of magnetism in $\text{Nd}(\text{Co}_{1-x}\text{Si}_x)_2$ and $\text{Ho}(\text{Co}_{1-x}\text{Si}_x)_2$

T. D. Cuong, L. Havela, and V. Sechovský

Department of Metal Physics, Charles University, Ke Karlovu 5, CZ-121 16 Praha 2, The Czech Republic

Z. Arnold and J. Kamarád

Institute of Physics, Academy of Sciences of the Czech Republic, Cukrovarnická 10, CZ-162 00 Praha 6, The Czech Republic

We report on a comparative study of the effects of Si doping and of external pressure on magnetism and related phenomena in $\text{Nd}(\text{Co}_{1-x}\text{Si}_x)_2$ and $\text{Ho}(\text{Co}_{1-x}\text{Si}_x)_2$ compounds. The lattice volume in the Ho system is almost composition invariable for x up to 0.1, whereas an increase of $\approx 6\%$ is observed in the Nd system. Si substitutions for Co cause a dramatic increase of T_C in the Ho system for $x \leq 0.075$ and a gradual reduction of T_C in Nd analogs, whereas the Co moment becomes suppressed for $x > 0.05$ in both cases. Negative pressure effects both on T_C and the Co magnetic moment, although quantitatively different, are found in both systems. Expected changes of electronic structure and their influence on the hierarchy of exchange interactions and formation of the Co moment are discussed. © 1998 American Institute of Physics. [S0021-8979(98)40011-2]

Co magnetism in RECo_2 (RE=rare-earth element) compounds is frequently studied with respect to the itinerant electron metamagnetism.¹⁻³ Materials with rare-earth atoms without 4*f* electrons, YCo_2 or LuCo_2 serve as archetypes of spin-fluctuation systems with a high T_{sf} and a nonmagnetic ground state. Magnetic fields above 60 T induce in these two compounds a metamagnetic state due to a sudden field-induced splitting of the Co majority and minority 3*d* subbands. The Co metamagnetic state may be induced in DyCo_2 , HoCo_2 , and ErCo_2 in zero external field employing a large exchange field due to ferromagnetically ordered 4*f* magnetic moments at T_C . This first-order phase transition is accompanied by a pronounced drop of the electrical resistivity,⁴ and a sudden volume expansion due to Co moment formation.

The larger lattice volume of light rare-earth counterparts like PrCo_2 or NdCo_2 allows less delocalized Co 3*d* states and the Co moment to form. The second-order phase transition at T_C is accompanied by resistivity and volume anomalies usual for metallic ferromagnets.⁴

The nearness of ferromagnetism in YCo_2 and LuCo_2 is manifest also by the substitutions of some *p* atoms, like Al, for Co driving these compounds towards ferromagnetism. The $\text{RE}(\text{Co}_{1-x}\text{Al}_x)_2$ were subjected by papers focused on spin-fluctuation^{2,5-7} and magnetovolume phenomena.^{3,8,9} Although the lattice volume in $\text{Y}(\text{Co}_{1-x}\text{Si}_x)_2$ and $\text{Lu}(\text{Co}_{1-x}\text{Si}_x)_2$ compounds is altered only slightly with increasing x up to 0.10, one also observes suppression of T_{sf} , enhancement of the low-temperature susceptibility, and reduction of the critical metamagnetic field. Ferromagnetism is, however, not reached.¹⁰⁻¹³ Various aspects of magnetism in $\text{RE}(\text{Co}_{1-x}\text{Si}_x)_2$ compounds with RE=Gd, Tb, Dy, Ho, and Er were studied as well.^{12,14,15} Strong enhancement of T_C with Si doping has been observed for the latter three cases. Negative pressure effects on T_C in the heavy-rare-earth RECo_2 compounds are reported.¹⁷ Here we report on effects of Si doping and of external pressure on magnetism in the $\text{Nd}(\text{Co}_{1-x}\text{Si}_x)_2$ and $\text{Ho}(\text{Co}_{1-x}\text{Si}_x)_2$ systems.

The $\text{Nd}(\text{Co}_{1-x}\text{Si}_x)_2$ and $\text{Ho}(\text{Co}_{1-x}\text{Si}_x)_2$ polycrystalline samples for $x \leq 0.15$ were produced by melting stoichiometric mixtures of pure metals under argon atmosphere and annealed at 950 °C for 50 h in vacuum. The x-ray diffraction revealed only the expected cubic C15 structure. The lattice volume in the Ho system is almost composition invariable but an increase of about 6% is observed in $\text{Nd}(\text{Co}_{1-x}\text{Si}_x)_2$ for x between 0 and 0.10.

The resistivity was studied on bar-shaped samples (size $\approx 1 \times 1 \times 7 \text{ mm}^3$) using the ac four-terminal technique. The compressibility and the thermal expansion were measured using microstrain gauges (Micro-Measurements Inc., SK-350) fixed on a plane sample surface. The strain gauges were calibrated using the relevant reference data on Cu and Fe. The pressure experiments were performed in a CuBe cell silica fixed hydrostatic pressure up to 9 kbar cooled in the He closed-cycle refrigerator. The pressure was measured *in situ* using a manganin pressure sensor.

The first-order magnetic phase transition at T_C in the Ho compounds is reflected in a resistivity drop $\Delta\rho$ (see Fig. 1) and an abrupt expansion of the lattice (Fig. 2). Usual "second-order-type" resistivity (Fig. 3) and thermal-expansion (Fig. 4) anomalies are exhibited by the Nd counterparts. The additional resistivity and expansion anomalies at T_R (≈ 17 and 42 K in HoCo_2 and NdCo_2 , respectively) are attributed to the reorientation of the easy-magnetization axis.^{16,17}

The resistivity in Ho compounds above T_C is strongly affected by a spin-disorder scattering on RE moments and by a conduction electron scattering on 3*d* spin fluctuations.¹⁸ When the 4*f* moments order ferromagnetically at T_C they produce a strong exchange field acting on the Co 3*d* states. Consequently, the 3*d* majority and minority subbands split, spin fluctuations at the Co sites quench and a metamagnetic state is induced by a first-order transition. The consequent reconstruction of the Fermi surface and the drastically suppressed conduction-electron scattering yield the huge resis-

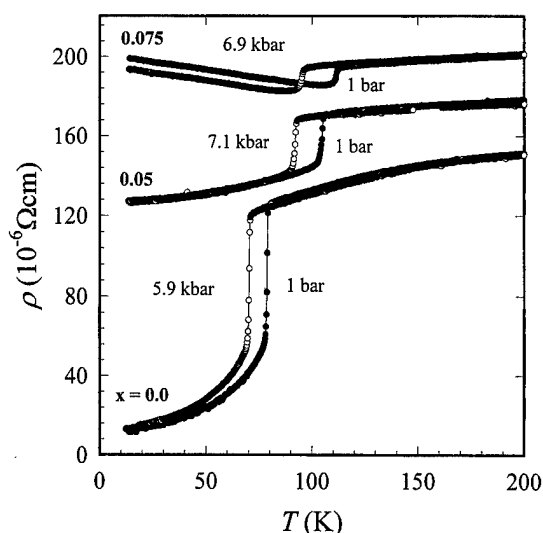


FIG. 1. Temperature dependence of resistivity of $\text{Ho}(\text{Co}_{1-x}\text{Si}_x)_2$ for $x=0$ (in 1 and 5.9 kbar), 0.05 (in 1 and 7.1 kbar), and 0.075 (in 1 and 6.9 kbar).

tivity drop. The abrupt lattice expansion observed at T_C (Fig. 2) is attributed to the positive magnetovolume effect of the Co moment formation.

The metamagnetism is obviously absent in NdCo_2 in which the Co moment exists already in the paramagnetic range and just the ferromagnetic ordering of the Co and Nd moments takes place at T_C by a second-order magnetic phase transition. This is reflected in a change of slope of the $\rho(T)$ and $\Delta L/L(T)$ curves (see Figs. 3 and 4), respectively. Qualitatively comparable magnetovolume effects are observed at low temperatures both in Ho and Nd compounds, however.

Si substitutions for Co have a strikingly different impact on T_C in the two systems (see Figs. 1–4 and also Fig. 5). The slow decrease of T_C of Nd compounds with increasing x seems to reflect the dilution of a “magnetic” element (Co) by a “nonmagnetic” one (Si) but T_C increases rapidly in $\text{Ho}(\text{Co}_{1-x}\text{Si}_x)_2$ for x up to 0.075 followed by a slow decrease at a similar rate as for the Nd counterparts and the

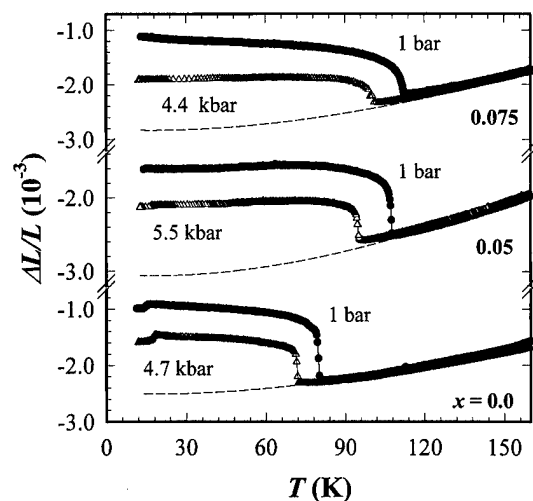


FIG. 2. Temperature dependence of thermal expansion of $\text{Ho}(\text{Co}_{1-x}\text{Si}_x)_2$ for $x=0$ (in 1 and 4.7 kbar), 0.05 (in 1 and 5.5 kbar), and 0.075 (in 1 and 4.4 kbar).

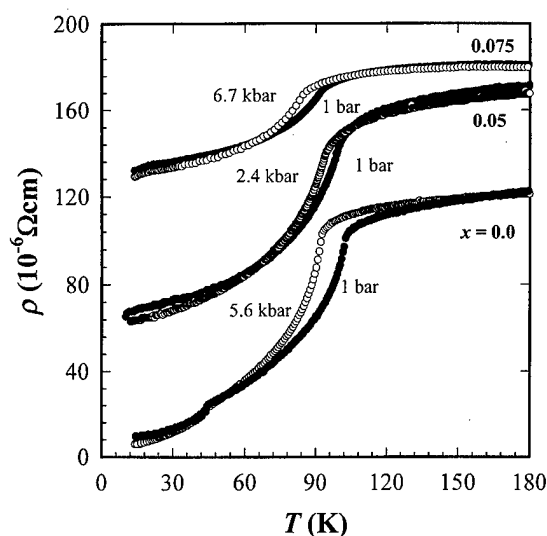


FIG. 3. Temperature dependence of resistivity of $\text{Nd}(\text{Co}_{1-x}\text{Si}_x)_2$ for $x=0$ (in 1 and 5.6 kbar), 0.05 (in 1 and 2.4 kbar), and 0.075 (in 1 and 6.7 kbar).

relevant magnetization, resistivity, and volume anomalies associated with magnetic ordering become progressively broadened. Besides a more extended dilution of the Co sublattice, the effects of the increasing substitutional disorder on the Co sites on exchange interactions are considered as a possible source of this development. Note that the weak decreasing trend of the T_C vs x for the Nd system also becomes more pronounced for $x > 0.05$. The spin-reorientation temperature T_R is gradually lowered with increasing x both in the Nd and Ho systems.

The resistivity drop $\Delta\rho$ at T_C in $\text{Ho}(\text{Co}_{1-x}\text{Si}_x)_2$ is gradually reduced with increasing Si content and vanishes for $x > 0.075$. For $x \leq 0.05$, the resistivity decreases monotonously with further lowering temperature and tends to saturate in the low-temperature limit. For $x > 0.05$ the low-temperature behavior is modified and the resistivity increases with decreasing temperature. Discussion of this effect which

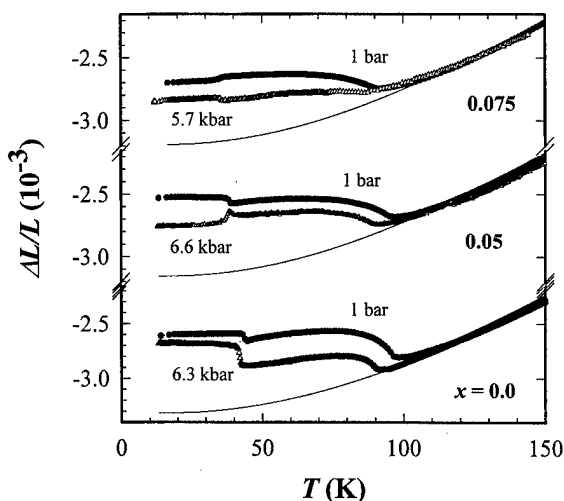


FIG. 4. Temperature dependence of thermal expansion of $\text{Nd}(\text{Co}_{1-x}\text{Si}_x)_2$ for $x=0$ (in 1 and 6.3 kbar), 0.05 (in 1 and 6.6 kbar) and 0.075 (in 1 and 5.7 kbar).

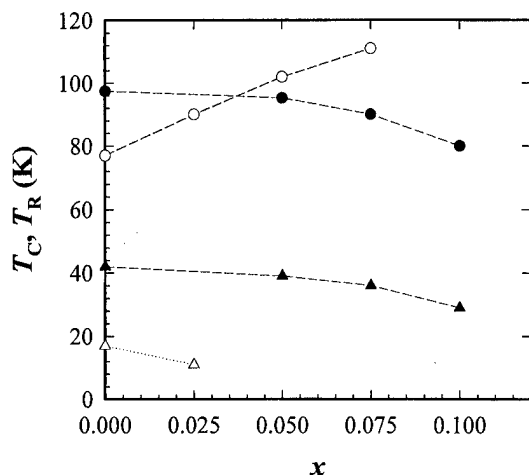


FIG. 5. Concentration dependence of T_C and T_R in $\text{Nd}(\text{Co}_{1-x}\text{Si}_x)_2$ (● and ▲) and $\text{Ho}(\text{Co}_{1-x}\text{Si}_x)_2$ (○ and △) for $x \leq 0.075$.

develops with further increasing x is beyond the scope of this paper. Similar effects were reported also for $\text{Er}(\text{Co}_{1-x}\text{Si}_x)_2$ (Ref. 14) and $\text{Ho}(\text{Co}_{1-x}\text{Al}_x)_2$ (Ref. 17) but are lacking in the $\text{Nd}(\text{Co}_{1-x}\text{Si}_x)_2$ compounds.

Magnetovolume data for $\text{Y}(\text{Co}_{1-x}\text{Al}_x)_2$ (Ref. 19) allow an assumption that the Co sublattice plays the dominant role in the magnetovolume phenomena in RECo_2 compounds. Then we may estimate the Co moment from the formula: $\omega_s \approx C\mu_{\text{Co}}^2$ (C is the magnetoelastic coupling constant). Ho compounds show an initial increase by about 10% for $x \leq 0.025$ followed by a monotonous decrease upon further increasing x . The Co expansion $\Delta V/V = 3\Delta L/L$ at T_C also vanishes for $x > 0.075$ where the Co metamagnetism disappears. The value of ω_s in $\text{Ho}(\text{Co}_{0.9}\text{Si}_{0.1})_2$ points to a considerable residual Co moment which, however, is not a result of any metamagnetism at T_C but may be tentatively attributed to a stable Co moment similar to NdCo_2 .

Application of pressure reduces T_C both in the Nd and Ho systems with almost composition invariant (for $x \leq 0.075$) values of $\partial \ln T_C / \partial p \approx -15$ and -23 Mbar^{-1} pointing to extrapolated critical pressures for the disappearance of ferromagnetism $p_c \approx 67$ and 43 kbar , respectively. The compressibility of the $\text{Ho}(\text{Co}_{1-x}\text{Si}_x)_2$ compounds which is $\kappa_p \approx 0.98 \text{ Mbar}^{-1}$ at room temperature increases drastically below T_C , where $\kappa_f = (\kappa_p + \kappa_m) = 1.4 \text{ Mbar}^{-1}$ for HoCo_2 , and κ_m is the magnetic contribution to the compressibility. This softening is intimately connected with the reduction of the spontaneous magnetostriction (see Fig. 2) due to pressure-induced suppression of the Co moment.

A rough estimation of the relevant softening of compressibility in the $\text{Nd}(\text{Co}_{1-x}\text{Si}_x)_2$ compounds gives a value, $\omega_s/p_c \approx 0.02 \text{ Mbar}^{-1}$, which is smaller by more than one order in comparison with the Ho compounds and well comparable with very small magnetostriction of all the ferromagnetic Co-rich alloys.

The results document that the Si substitutions for Co in the RECo_2 compounds are not only a simple dilution of the

Co sublattice, but besides the effective reduction of the overlap integral of $3d$ wave functions between Co-Co nearest neighbors (which may lead to a narrowing of the Co $3d$ band) and the variation of the count of Co $3d$ electrons in the system, a considerable involvement of the Si- $3p$ states in the electronic structure of the system has to be considered, namely their hybridization with the Co $3d$ states⁸ and the RE $5d$ states. The leading component of the exchange interaction coupling the RE magnetic moments and determining the ordering temperature in the heavy rare-earth RECo_2 materials without stable Co moments like in HoCo_2 is born from the hybridization of the RE $5d$ -electron states with the Co $3d$ states. The strong enhancement of the exchange interaction deduced from the increasing T_C in the heavy-rare-earth systems can be tentatively attributed to an additional contribution to the exchange interaction which arises from the $5d$ - $3p$ (Si) hybridization. In NdCo_2 and the other RECo_2 compounds with a stable Co magnetic moment the direct Co-Co ($3d$ - $3d$) exchange interaction also contributes substantially, acting as a leading term and yields considerably larger T_C values. Since the Co moment is instantly reduced with increasing Si content in the $\text{Nd}(\text{Co}_{1-x}\text{Si}_x)_2$ compounds, the Co-Co exchange interaction weakens reducing T_C as a direct consequence. The effects of the $3d(\text{Co})$ - $3p(\text{Si})$ hybridization involving both the Co moment and the exchange interaction within the Co sublattice cannot be omitted.

This work was supported by the Ministry of Education of the Czech Republic (Project No. ES011) and by the Grant Agency of the Charles University (No. 40-97/B-FYZ/MFF).

¹E. P. Wohlfarth and P. Rhodes, *Philos. Mag.* **7**, 1917 (1962).

²T. Goto, H. Aruga Katori, T. Sakakibara, H. Mitamura, K. Fukamichi, and K. Murata, *J. Appl. Phys.* **76**, 6682 (1994), and references therein.

³N. H. Duc, T. D. Hien, P. E. Brommer, and J. J. M. Franse, *J. Magn. Magn. Mater.* **104-107**, 1252 (1992), and references therein.

⁴J. M. Fournier and E. Gratz, in *Handbook on the Physics and Chemistry of Rare Earths*, edited by K. A. Gschneidner, Jr., L. Eyring, G. R. Choppin, and G. H. Lander (North-Holland, Amsterdam, 1993), Vol. 17, p. 409, and references therein.

⁵N. Pillmayr, G. Hilscher, M. Forshuber, and K. Yoshimura, *J. Magn. Magn. Mater.* **90-91**, 964 (1990).

⁶N. H. Duc, *J. Magn. Magn. Mater.* **131**, 224 (1994).

⁷N. H. Duc, P. E. Brommer, X. Li, F. R. de Boer, and J. J. M. Franse, *Physica B* **212**, 83 (1995).

⁸J. G. M. Armitage, R. G. Graham, P. C. Riedi, and J. S. Abell, *J. Phys.: Condens. Matter* **2**, 8779 (1990).

⁹N. H. Duc, J. Voiron, S. Holtmeier, P. Haen, and X. Li, *J. Magn. Magn. Mater.* **125**, 323 (1993).

¹⁰M. Aoki and H. Yamada, *Physica B* **177**, 259 (1992).

¹¹K. Murata, K. Fukamichi, T. Goto, K. Suzuki, and T. Sakakibara, *J. Phys.: Condens. Matter* **2**, 6659 (1994).

¹²N. H. Duc, *J. Magn. Magn. Mater.* **152**, 219 (1996).

¹³D. Michels, J. Timlin, and T. Mihalisin, *J. Appl. Phys.* **67**, 5289 (1990).

¹⁴T. D. Cuong, L. Havela, V. Sechovský, A. V. Andreev, Z. Arnold, J. Kamarád, and N. H. Duc, *J. Appl. Phys.* **81**, 4221 (1997).

¹⁵N. H. Duc and N. K. Oanh, *J. Phys.: Condens. Matter* **9**, 1585 (1997).

¹⁶W. Steiner, E. Gratz, H. Ortbauer, and H. W. Camen, *J. Phys. F* **8**, 1525 (1978).

¹⁷E. W. Lee and F. Pourarian, *Phys. Status Solidi A* **33**, 483 (1976).

¹⁸N. H. Duc, T. D. Hien, R. Z. Levitin, A. S. Markosyan, P. E. Brommer, and J. J. M. Franse, *Physica B* **176**, 232 (1992).

¹⁹H. Wada, K. Yoshimura, G. Kido, M. Sigha, M. Mekata, and Y. Nakamura, *Solid State Commun.* **65**, 23 (1988).

On the nature of the magnetic phase transition of the HoCo₂ intermetallic

P. J. von Ranke^{a)}

Ames Laboratory, Iowa State University, Ames, Iowa 50011

N. A. de Oliveira^{b)}

Universidade do Estado do Rio de Janeiro, Rua São Francisco Xavier 524, Rio de Janeiro, RJ 20550-013, Brazil

In this work we calculate the itinerant and localized magnetization curves of the Laves phase intermetallic compound HoCo₂ and discuss the nature of its magnetic phase transition. The numerical results were calculated from the self-consistent solution of magnetic coupled equations obtained through the combination of functional integral methods with molecular field approximation. © 1998 American Institute of Physics. [S0021-8979(98)24711-6]

An interesting feature presented by rare-earth cobalt intermetallic compounds RCo₂ (R=Er, Dy, Ho), is the existence of a first-order magnetic phase transition,¹⁻⁹ which has been discussed in the literature in terms of the instability of the Landau free energy around the critical temperature.³ However, as far as we know, there are no explicit calculations of the effects of the temperature on the magnetization curve of these intermetallics. This kind of calculation is very important, not only to determine the order of the magnetic phase transition but also to determine the possible change of easy magnetization direction and to find any anomalies along the magnetization curve.

The main goal of this article is to calculate in a quantitative way the temperature dependence of the itinerant and localized parts of the magnetization of the Laves phase intermetallic compound HoCo₂ and to discuss the nature of its magnetic phase transition. In the formulation of the problem we start from the following two-sublattice model Hamiltonian including localized spins and itinerant electrons, in the approximation of five identical *d* subbands:¹⁰

$$H = \sum_l \epsilon_0^{\text{Ho}} a_{l\sigma}^+ a_{l\sigma} + \sum_{ll'} T_{ll'}^{\text{HoHo}} a_{l\sigma}^+ a_{l'\sigma} + \sum_j \epsilon_0^{\text{Co}} a_{j\sigma}^+ a_{j\sigma} + \sum_{jj'} T_{jj'}^{\text{CoCo}} a_{j\sigma}^+ a_{j'\sigma} + \sum_{lj} T_{lj}^{\text{HoCo}} (a_{l\sigma}^+ a_{j\sigma} + a_{j\sigma}^+ a_{l\sigma}) + U^{\text{Ho}} \sum_l n_{l\uparrow} n_{l\downarrow} + U^{\text{Co}} \sum_j n_{j\uparrow} n_{j\downarrow} - J_{df} \sum_l J_l^f S_l^d. \quad (1)$$

Here ϵ_0^{Ho} is the center of *d*-energy band at Ho sublattice; ϵ_0^{Co} is the corresponding term of the Co sublattice; the terms $T_{ll'}^{\text{HoHo}}$ and $T_{jj'}^{\text{CoCo}}$ represent the hopping between sites of the same sublattice, and T_{lj}^{HoCo} is the intersublattice hopping. U^{Ho} (U^{Co}) is the Coulomb interaction parameter between itinerant electrons at Ho (Co) site; J_{df} is the exchange integral interaction parameter between localized 4*f* spins and itinerant electrons and J^f is the total angular momentum of Ho⁺³ ions.

Using the functional integral method in the static approximation to treat the electron-electron interaction,¹⁰ we decouple the total Hamiltonian (1) into two new effective ones:

$$\bar{H}_f = -J_{df} \sum_l \langle S_l^d \rangle \cdot J_l^f - \sum_{ll'} J_l^f \left[\frac{1}{2} \left(\frac{J_{df}}{g_e \mu_B} \right)^2 \cdot \chi_{ll'}^d \right] \cdot J_{l'}^f, \quad (2)$$

$$\begin{aligned} \bar{H}_d = & \sum_l \epsilon_{l\sigma}^{\text{Ho}} a_{l\sigma}^+ a_{l\sigma} + \sum_{ll'} T_{ll'}^{\text{HoHo}} a_{l\sigma}^+ a_{l'\sigma} + \sum_j \epsilon_{j\sigma}^{\text{Co}} a_{j\sigma}^+ a_{j\sigma} \\ & + \sum_{jj'} T_{jj'}^{\text{CoCo}} a_{j\sigma}^+ a_{j'\sigma} + \sum_{lj} T_{lj}^{\text{HoCo}} (a_{l\sigma}^+ a_{j\sigma} + a_{j\sigma}^+ a_{l\sigma}) \\ & - J_{df} \sum_l J_l^f S_l^d, \end{aligned} \quad (3)$$

where μ_B is the Bohr magneton and g_e is the Landé factor of the itinerant electrons. The effective Hamiltonian (\bar{H}_f) de-

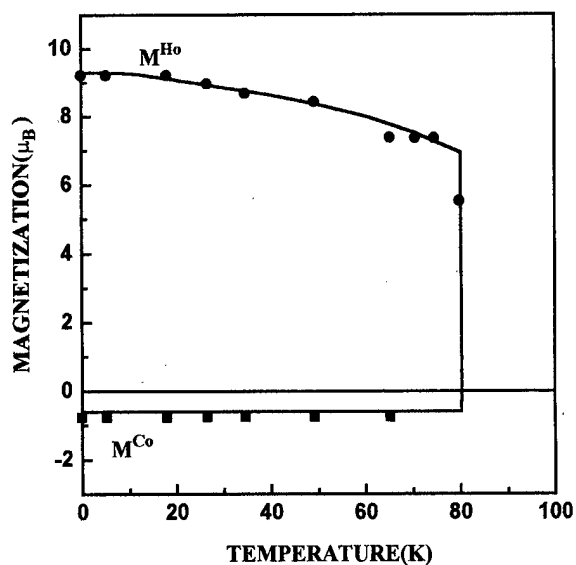


FIG. 1. Temperature dependence of the itinerant (M^{Co}) and localized (M^{Ho}) magnetization of HoCo₂ (in units of μ_B). The full lines are the theoretical calculations and the circles (squares) are experimental data for Ho (Co) (see Ref. 9).

^{a)}Permanent address: Universidade do Estado do Rio de Janeiro.

^{b)}Electronic mail: nilson@uerj.br

scribes a subsystem of the localized $4f$ spins coupled to itinerant electrons via the itinerant magnetization $\langle s_l^d \rangle$ and via the electronic magnetic susceptibility $\chi_{ll'}^d$. The term in brackets in (\bar{H}_f) , which depends on the magnetic susceptibility of itinerant electrons, defines an effective exchange interaction between localized $4f$ spins.¹⁰ This effective exchange interaction establishes a connection between the localized magnetization at Ho sites and the electronic structure of the Co sublattice and plays an important role in the appearance of local magnetization at Ho sublattice. Using the molecular field approximation, the temperature dependence of localized magnetization (M^{Ho}) of the Ho sublattice, is obtained in a standard way in terms of Brillouin function.

$$M^{\text{Co}} = \langle \xi \rangle = \frac{\int d\xi d\nu \xi e^{-\beta\{U^{\text{Co}}/4(\xi^2 + \nu^2) + 1/\pi \int dz f(z) \text{Im} \sum_{\sigma} \ln[1 - V^{\text{Co}}(\xi\nu) F_{\sigma}^{\text{Co}}(z)]\}}}{\int d\xi d\nu e^{-\beta\{U^{\text{Co}}/4(\xi^2 + \nu^2) + 1/\pi \int dz f(z) \text{Im} \sum_{\sigma} \ln[1 - V^{\text{Co}}(\xi\nu) F_{\sigma}^{\text{Co}}(z)]\}}}, \quad (4)$$

where $f(z)$ is the Fermi function; $z = \epsilon + i\delta$, $\delta \rightarrow 0$; V^{Co} is a local potential at the Co sublattice that comes from the CPA treatment of the disordered Hamiltonian and F^{Co} is the local Green's function of the Co sublattice.¹⁰

The magnetization curve of the HoCo_2 intermetallic was calculated using a standard model d density of states extracted from *ab initio* calculation¹¹ and the following fixed parameters: $U^{\text{Ho}} = 0.5$ eV, $U^{\text{Co}} = 1.0$ eV, and $J_{df} = 0.065$ eV. The calculated temperature dependence of the itinerant and localized magnetizations of the HoCo_2 intermetallic, Fig. 1, shows a first-order magnetic phase transition at $T_c = 80$ K. In this intermetallic, the first-order magnetic phase transition is associated with the abrupt enhancement of the effective exchange interaction between localized spins near the critical temperature. This abrupt enhancement can be explained in the following way: due to the position of the Fermi level in a deep region near a sharp peak in the d density of states, a small value of the localized magnetization at the rare-earth sublattice induces a metamagnetic transition at the Co sublattice, yielding an abrupt enhancement of the electronic magnetic susceptibility and consequently in the effective exchange interaction parameter between localized spins. This self-consistent process gives rise to a large value of the magnetic moment at Ho sites, thus producing a discontinuity in the magnetization curve at the critical temperature.

This model can be straightforwardly extended to calculate the temperature and concentration dependence of the magnetization of $\text{R}(\text{Co}_{1-x}\text{T}_x)_2$ pseudobinaries,^{12,13} where (R=Er, Dy, Ho) and T is sp or d -transition element. In

The effective Hamiltonian (\bar{H}_d) describes a two-sublattice itinerant electron system without electron-electron interaction and under the action of an effective magnetic field generated by the localized $4f$ spins. In this Hamiltonian the effective energies $\epsilon_{l\sigma}^{\text{Ho}}$ and $\epsilon_{j\sigma}^{\text{Co}}$ incorporate fluctuating charge (ν) and spin (ξ) fields defining a very complicated disorder problem. In order to simplify the numerical calculations, we use the homothetic band approach to treat the two sublattices of the intermetallic and use the coherent potential approximation (CPA) to deal with the intrinsic disorder introduced by the functional integral method.¹⁰ Within these approximations, the temperature dependence of the itinerant magnetization on the Co sublattice (M^{Co}) is given self-consistently by the mean value of the spin fluctuating field:¹⁰

these pseudobinaries, increasing T concentration smears out the electronic density of states near the Fermi level in a such way that the effective exchange interaction parameter between localized spins increases smoothly with temperature, changing the nature of the magnetic phase transition from first to second order.

The authors are greatly indebted with Professor Affonso Gomes for his help in the development of the theoretical formulation presented in this article. This work was partially supported by CNPq (Brazilian agency of funds).

¹K. H. J. Buschow, Rep. Prog. Phys. **40**, 1179 (1977), and references therein.

²D. Gignoux, F. Givord, and R. Lemaire, Phys. Rev. B **12**, 3878 (1975).

³D. Bolch, D. M. Edwards, M. Shimizu, and J. Voiron, J. Phys. F **5**, 1217 (1975).

⁴D. Gignoux, F. Givord, and W. C. Koehler, Physica B & C **86-88**, 165 (1977).

⁵D. Gignoux, F. Givord, and J. Schweizer, J. Phys. F **7**, 1823 (1977).

⁶S. Hirose and Y. Nakamura, J. Phys. Soc. Jpn. **51**, 2819 (1982).

⁷A. P. Guimarães, K. M. B. Alves, N. Alves, and E. Gratz, J. Appl. Phys. **61**, 3995 (1987).

⁸L. Nordström, M. S. S. Brooks, and B. Johansson, J. Magn. Magn. Mater. **104-107**, 1378 (1992).

⁹P. Hendy and E. W. Lee, Phys. Status Solidi A **50**, 101 (1978).

¹⁰N. A. de Oliveira and A. A. Gomes, J. Magn. Magn. Mater. **117**, 175 (1992).

¹¹H. Yamada, J. Inoue, and M. Shimizu, J. Phys. F **15**, 169 (1985).

¹²S. W. Zochowski, S. A. Creiger, and A. Taiu, J. Magn. Magn. Mater. **140**, 839 (1995).

¹³T. D. Cuong, L. Havela, V. Sechovsky, A. V. Andeev, Z. Arnold, J. Kamarad, and N. H. Duc, J. Appl. Phys. **81**, 4221 (1997).

Recovery of ErCo₂ Fermi level by substitution of Co by Ni and Fe

F. Garcia,^{a)} H. dos Santos, M. R. Soares, A. Y. Takeuchi, and S. F. da Cunha

Centro Brasileiro de Pesquisas Físicas, 22290-180, Rio de Janeiro, Brazil

Magnetic and electrical resistivity measurements performed in Er(Co_{1-x}Ni_x)₂ have shown that the critical concentration for the first-order magnetic phase transition is near to $x_c = 0.10$. For higher Ni concentration the results suggest that Co is no longer magnetic. Experimental results presented here for Er(Co_{0.8}Ni_{0.2x}Fe_{0.2(1-x)})₂ and Er(Co_{0.9}Ni_{0.1x}Fe_{0.1(1-x)})₂ systems, show that when Co is replaced by Fe, the 3d band is filled up, whereas for Ni substitution that band is depleted. The saturation moment obtained from isothermal magnetization measurements indicates that Co recovers its moment and couples parallel to the Fe moment and antiparallel to the Er moment. Characteristics of spin fluctuation are also observed. These results show that with a suitable combination of Co, Ni, and Fe we can recover the original density of the states of the ErCo₂ compound. © 1998 American Institute of Physics. [S0021-8979(98)24811-0]

I. INTRODUCTION

Within the series of R-3d (R=heavy rare earth) intermetallics the RCo₂ Laves phases show interesting magnetic properties.¹ In contrast to RFe₂, where the Fe moments are practically independent, whether the R ions bear a magnetic moment or not, the existence of a Co moment is intimately connected with the existence of a moment on the R sites. On the other hand, in RNi₂, where the Fermi-level E_F lies in the flat low density of states $N(E)$ region, Ni is never magnetic in this system, even in compounds with magnetic R ions. From band-structure calculations² it has been concluded that most of the outstanding features observed in the family of the RCo₂ compounds can, at least qualitatively, be understood by considering the Fermi-level position E_F , which is situated near a local peak. The high value together with a special shape of the density of states $N(E)$ curves in the vicinity of the Fermi level give rise to spin fluctuations in the d band and they are also responsible for the occurrence of itinerant metamagnetism.

In the present work, electrical resistivity and magnetization measurements in some selected samples of Er(Co, M)₂ (M=Fe and Ni) compounds were performed in order to get further information to support the band picture for the observed behaviors. A small amount of Co is replaced by 3d transition metals Fe and Ni in ErCo₂. As Fe substitution shifts the Fermi level toward lower energy, while Ni substitution shifts it toward higher energy, we might obtain the characteristic of the original density of states of the ErCo₂ compound by suitable combination of Co, Ni, and Fe.

II. EXPERIMENTAL PROCEDURE

The samples were prepared by arc melting the constituent elements in an argon atmosphere. To avoid the appearance of spurious phases, a 6 wt % excess of rare earth over the stoichiometric composition was necessary. The ingots were then annealed in evacuated sealed quartz tubes for a period of one week at $T = 800^\circ\text{C}$. The crystal structure and

the lattice parameter were determined at room temperature by x-ray powder diffraction. All the samples are single phase cubic MgCu₂ type.

Electrical resistivity measurements were performed using a standard dc four-point method; magnetization measurements were carried out using a vibrating sample magnetometer and magnetic ac susceptibility (χ_{AC}) measurements were performed using a lock-in amplifier ($f = 125\text{ Hz}$).

III. RESULTS AND DISCUSSION

The temperature dependence of the magnetization (in $H_{app} = 100\text{ Oe}$) in all samples shows a difference between field-cooled and zero-field-cooled measurements, for $T < T_C$. This difference disappears under higher applied fields (5 kOe). This thermal irreversibility is related to domain-wall motion in the crystal. The saturation moments per formula unit μ_{sat}/fu of these compounds were obtained by extrapolation of the magnetization to infinite field, from M vs $1/H$ curves performed at 4.2 K, in fields up to 80 kOe.

Figure 1 shows the electrical resistivity ρ versus temperature of the Er(Co, M)₂ (M=Fe, Ni) system. The residual resistivity has been subtracted in these plots. The $\rho(T)$ curves for ErCo₂ and Er(Co_{0.90}Ni_{0.10})₂ (Ref. 3) show a discontinuous change at T_C , characteristic of a first-order transition. At high temperatures (basically, $T > T_C$) these curves present a clear tendency towards saturation and huge values, if compared to the De Gennes–Friedel spin-disorder resistivity. This additional contribution to the resistivity was well explained by Baranov *et al.*⁴ as spin-fluctuation scattering of the 3d band.

For Er(Co_{0.80}Ni_{0.20})₂, apart from the peak at low temperatures, the temperature dependence of the electrical resistivity $\rho(T)$ is typically of metallic ferromagnets (see ErNi₂) and shows an anomaly at $T = T_C$. The pronounced curvature of $\rho(T)$ curves (characteristic for the spin-fluctuation system) that is observed in ErCo₂ above T_C is suppressed for more than 20 at. % Ni and the temperature dependence becomes almost constant. On the other hand, the saturation moments per formula unit μ_{sat}/fu for ErNi₂ and Er(Co_{0.80}Ni_{0.20})₂ compounds are $7.2\mu_B$ and $7.1\mu_B$, respec-

^{a)}Electronic mail: flavio@cat.cbpf.br

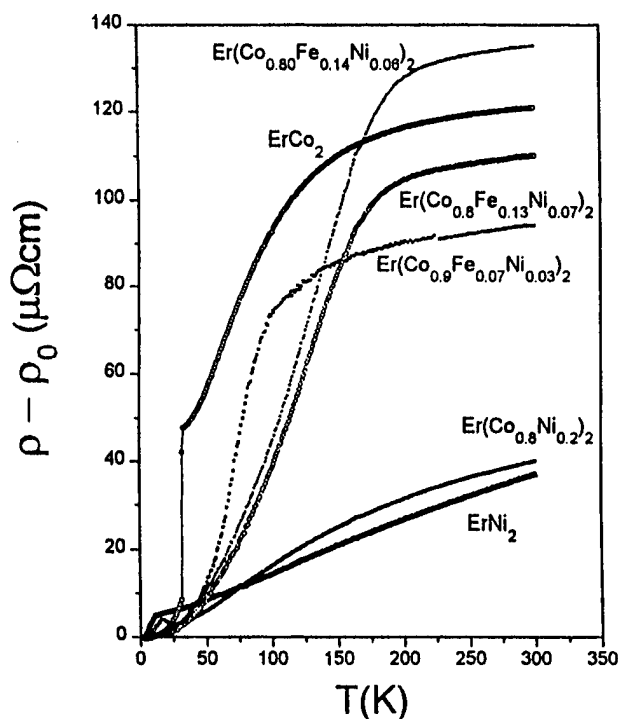


FIG. 1. Temperature dependence of the electrical resistivity for $\text{Er}(\text{Co}, \text{M})_2$ ($\text{M}=\text{Fe}$ and Ni).

tively. These properties suggest that in alloys containing more than about 20 at. % Ni, the Co is no longer magnetic.

Bearing in mind that the main purpose of this work is to recover the original ErCo_2 Fermi-level position, we performed measurements in $\text{Er}(\text{Co}_{0.80}\text{Fe}_{0.14}\text{Ni}_{0.06})_2$ and $\text{Er}(\text{Co}_{0.80}\text{Fe}_{0.13}\text{Ni}_{0.07})_2$ compounds. Indeed, results of $\rho(T)$ curves show behavior similar to that of ErCo_2 , i.e., saturation tendency above T_C indicating that spin-fluctuation scattering is present. As the spin-fluctuation scattering produces an additional contribution to the electrical resistivity at high tem-

peratures, we estimated the total variation of the resistivity $\Delta\rho = \rho(300\text{ K}) - \rho(1.5\text{ K})$. For ErCo_2 we found $\Delta\rho = 121\text{ }\mu\Omega\text{ cm}$ and for ErNi_2 and $\text{Er}(\text{Co}_{0.80}\text{Ni}_{0.20})_2$, 37 and $40\text{ }\mu\Omega\text{ cm}$, respectively. However, in $\text{Er}(\text{Co}_{0.80}\text{Fe}_{0.13}\text{Ni}_{0.07})_2$ and $\text{Er}(\text{Co}_{0.80}\text{Fe}_{0.14}\text{Ni}_{0.06})_2$, $\Delta\rho$ reaches values of 94 and $135\text{ }\mu\Omega\text{ cm}$, respectively. These results show clearly that spin-fluctuation effects are present in these compounds.

Around T_C , the resistivity curves show a sharp increase. However, they are not a conclusive indication of a first-order transition.⁵ To try to elucidate this point we have measured a sample of $\text{Er}(\text{Co}_{0.90}\text{Fe}_{0.07}\text{Ni}_{0.03})_2$. Results show a larger variation of ρ at T_C , but it is not yet conclusive about the order of the phase transition, in contrast to the situation for $\text{Er}(\text{Co}_{0.90}\text{Ni}_{0.10})_2$,³ which presents a clearly first-order phase transition. This behavior is not unexpected, considering that there is a large chemical disorder (Fe, Co, and Ni) in the crystal. This disorder can produce a distribution of first-order transition phase temperatures.

IV. CONCLUSIONS

We have successfully reproduced in substituted compounds the Fermi level of ErCo_2 . This conclusion is of use in theoretical models where parameters largely depend on the detailed form of the band structure. Moreover, the electrical resistivity results are also important to a better understanding of the saturation and spin-fluctuations effects. The first-order transition cannot be clearly confirmed, but there is a strong indication of its presence.

¹D. Givord, F. Givord, and R. Lemaire, J. Phys. Colloq. **32**, C1-668 (1971).

²E. A. Skrabek and W. E. Wallace, J. Appl. Phys. **34**, 1356 (1963).

³M. R. Soares, F. Garcia, M. El Massalami, A. Y. Takeuchi, and S. F. da Cunha (unpublished).

⁴N. V. Baranov, E. Bauer, E. Gratz, R. Hauser, A. Markosyan, and R. Resel, *Proceedings of the 4th International Conference on the Physics of Transition Metals*, Vol. 1, edited by P. M. Oppeneer and J. Kübler (World Scientific, Singapore, 1993), p. 370.

⁵J. J. Franse, T. D. Hien, N. H. Kngan, and N. H. Duc, J. Magn. Magn. Mater. **39**, 275 (1987).

Theoretical study of hyperfine fields at impurity nuclei in GdX (X=Zn,Cd) compounds: A two-center model

A. L. de Oliveira, V. P. Ramunni, and M. V. Tovar Costa

Centro Brasileiro de Pesquisas Físicas, Rua Dr. Xavier Sigaud, 150, Rio de Janeiro, 22290-180, RJ, Brazil

N. A. de Oliveira

Instituto de Física, Universidade do Estado do Rio de Janeiro, Rua São Francisco Xavier, 524, Rio de Janeiro, 20550-013, RJ, Brazil

A. Troper

Centro Brasileiro de Pesquisas Físicas, Rua Dr. Xavier Sigaud, 150, Rio de Janeiro, 22290-180, RJ, Brazil and Instituto de Física, Universidade do Estado do Rio de Janeiro, Rua São Francisco Xavier, 524, Rio de Janeiro, 20550-013, RJ, Brazil

We theoretically discuss the local moment formation and the hyperfine field behavior of nonmagnetic ($s-p$ and noble) impurities diluted in ferromagnetic rare-earth compounds GdX (X=Zn, Cd). It is experimentally observed in these systems that all impurities enter substitutionally at the "nonmagnetic" X lattice site, creating a strong local charge perturbation. In our simplified model, one calculates the local magnetic moment in the perturbed conduction band at the origin (a charge perturbed X site). The polarization of the conduction band arises from the Gd 4f moments and the conduction electron polarization produced by the host magnetic moment at the origin is treated within the Born approximation. The general trend of the experimental hyperfine field data is well reproduced by our self-consistent calculations. © 1998 American Institute of Physics. [S0021-8979(98)40111-7]

In recent years, a systematic experimental study was made in order to obtain the magnetic hyperfine field at nonmagnetic ($s-p$ and noble) impurities diluted in the intermetallic compounds GdZn and GdCd.¹ These compounds have the CsCl type structure with lattice parameter $a=3.60$ and 3.75 Å and are ferromagnetic below $T_c=270$ and 265 K, respectively. The saturation magnetic moment of GdZn is $7.50\mu_B$, the excess moment of $0.5\mu_B$ being ascribed to $5d$ conduction electrons. Similarly, one has an excess moment of about $0.4\mu_B$ in the case of GdCd. The hyperfine field at an impurity in GdZn was found to be nearly the same to that in GdCd; moreover, the experimental data showed that the behavior of the hyperfine fields at nonmagnetic impurities in GdX (X=Zn, Cd) are quite similar to those in Gd metal, i.e., one always has negative hyperfine fields along a $s-p$ series.

As far as ferromagnetic Gd host is concerned, the experimental results can be compared with the calculation of Leal *et al.*,² which is an extension of the Daniel-Friedel model.³ More recently, de Oliveira *et al.*⁴ have discussed the problem of nonmagnetic impurities in Gd and Ni hosts, using a formulation due to Speier *et al.*,⁵ which takes into account neighbor effects arising from the translational symmetry breaking. The model described in Ref. 4 was also used to describe intermetallic compounds GdX (X=Zn, Cd).⁶ In that work, an effective one-site host model was adopted, where the intermetallic compound was described by a single lattice constituted by the same "effective atoms," namely Gd-like elements, which create a host exchange splitting proportional to the excess of magnetization verified in the GdX (X=Zn, Cd) compounds. A weakness of the model⁶ is that it is experimentally known that the nonmagnetic impurities enter at the X site.¹ Moreover, the polarization of the conduction

electron gas is created by the Gd 4f spins, located at the Gd sublattice sites which interact with the $5d$ -conduction electrons of the compound, thus originating also the indirect interaction between the Gd moments.

In order to partially restore the two sublattice character of the GdX compounds, we would like to discuss here a theoretical approach to study the systematics of hyperfine fields at nonmagnetic impurities placed in GdZn and GdCd compounds. This approach is based on a two-center model introduced by Blandin and Campbell⁷ to discuss hyperfine fields at $s-p$ sites (Y) in Heusler alloys X_2MnY . We hope to bring out in this formulation the effect of charge screening at the nonmagnetic impurity site, on the polarization at that site. In this sense, our present calculation can be seen as an extension of the Ruderman-Kittel-Kasuya-Yosida (RKKY) approach to an electron gas with a strong local charge perturbation.

The unperturbed conduction electrons within a tight binding formulation are described by the propagator:

$$g_{ij}(E) = \sum_k \frac{e^{i\mathbf{k} \cdot (\mathbf{R}_i - \mathbf{R}_j)}}{E - \epsilon_k}, \quad (1)$$

where ϵ_k is the dispersion relation for the conduction band.

A nonmagnetic impurity at the origin introduces a spin-independent local potential V_0 , originated from the charge difference between impurity and host conduction electrons. The spin-dependent potential, introduced by a polarized 4f spin located at \mathbf{R}_n is given by $V_n^\sigma = \sigma J \langle S_Z \rangle$. So, the general Dyson equation defining the two-center scattering problem is

$$G_{ij}^\sigma(E) = g_{ij}(E) + \sum_{l,m} g_{il}(E) V_{lm}^\sigma G_{mj}^\sigma(E), \quad (2)$$

with

$$V_{lm}^{\sigma} = V_0 \delta_{lm} + V_n^{\sigma} \delta_{lm} \delta_{mn}. \quad (3)$$

In order to get the spin polarization at the origin, let us define

$$G_{ij}^{\sigma}(E) = g_{ij}(E) + \delta G_{ij}^{\sigma}(E). \quad (4)$$

The *exact* solution of the scattering problem defined by (2)–(4) leads to

$$\begin{aligned} \delta G_{00}^{\sigma}(E; \mathbf{R}_n) &= \frac{g_{0n}(E)g_{n0}(E)}{[1 - V_0 g_{00}(E)]^2} \\ &\times \left\{ \frac{V_n^{\sigma}}{1 - V_n^{\sigma} [g_{00}(E) + g_{n0}(E)T_0(E)g_{0n}(E)]} \right\} \end{aligned} \quad (5)$$

and therefore

$$\begin{aligned} \sum_{\sigma} \sigma \delta G_{00}^{\sigma}(E; \mathbf{R}_n) &= \frac{2J\langle S_Z \rangle g_{0n}(E)g_{n0}(E)}{[1 - V_0 g_{00}(E)]^2} \\ &\times \left\{ \frac{1}{1 - J\langle S_Z \rangle [g_{00}(E) + g_{n0}(E)T_0(E)g_{0n}(E)]} \right\}, \end{aligned} \quad (6)$$

with

$$T_0(E) = \frac{V_0}{1 - V_0 g_{00}(E)}. \quad (7)$$

The spin-dependent potential V_n^{σ} is small as compared to the strong local charge potential perturbation V_0 ; so it can be treated in the Born approximation, yielding:

$$\begin{aligned} \delta G_{00}^{\uparrow}(E; \mathbf{R}_n) - \delta G_{00}^{\downarrow}(E; \mathbf{R}_n) &= \frac{2J\langle S_Z \rangle}{[1 - V_0 g_{00}(E)]^2} g_{0n}(E)g_{n0}(E) + \mathcal{O}(J\langle S_Z \rangle)^3. \end{aligned} \quad (8)$$

Since we are interested in the hyperfine field at the origin, we calculate the local magnetization $\tilde{m}(0)$ arising from the *sum* of contributions over neighboring magnetic sites. So

$$\begin{aligned} \tilde{m}(0) &= -\frac{1}{\pi} \int_{-\infty}^{E_F} \text{Im} \frac{2J\langle S_Z \rangle}{[1 - V_0 g_{00}(E)]^2} \\ &\times \sum_n g_{0n}(E)g_{n0}(E) dE \\ &= \frac{1}{\pi} \int_{-\infty}^{E_F} \frac{2J\langle S_Z \rangle}{[1 - V_0 g_{00}(E)]^2} \left[Z \frac{\partial g_{00}(E)}{\partial E} \right. \\ &\quad \left. + g_{00}^2(E) \right] dE, \end{aligned} \quad (9)$$

where Z represents the number of neighboring magnetic impurities. In the present case, each X site is surrounded by 8 Gd neighbors and therefore $Z=8$.

Notice that if one introduces the effect of a nonlocal charge potential due to the impurity symmetry breaking, it is

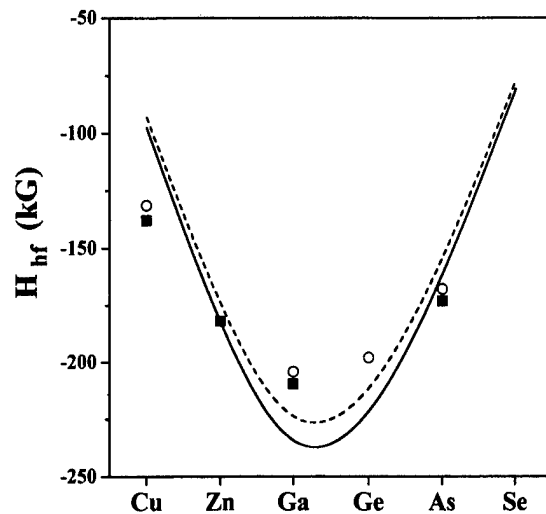


FIG. 1. Calculated hyperfine fields for 4s-p impurities in GdZn (full line) and GdCd (dashed line) compounds. The experimental data (squares for GdZn and open circles for GdCd) were collected from Ref. 1.

easily shown that at the lowest approximation the local potential V_0 can be replaced by the effective nonlocal potential^{4,5}

$$V_{\text{eff}} = V_0 + (\alpha^2 - 1)E, \quad (10)$$

where α is a proportionality factor associated to the radii of the impurity and host atomic wave functions and V_{eff} is self-consistently obtained via an extended Friedel sum rule.⁸ Then, one obtains the conduction electron polarization (CEP) hyperfine field

$$H_{\text{hf}} = A(Z_{\text{imp}})\tilde{m}(0), \quad (11)$$

where $A(Z_{\text{imp}})$ is the Fermi–Segrè coupling estimated by Campbell.⁹ In our self-consistent numerical calculations, we adopted a density of states similar to that calculated by Postnikov *et al.*¹⁰ Figure 1 illustrates the self-consistently calculated CEP hyperfine field at 4s-p impurities in GdX intermetallics. In Fig. 2 the case of 5s-p impurities is exhibited

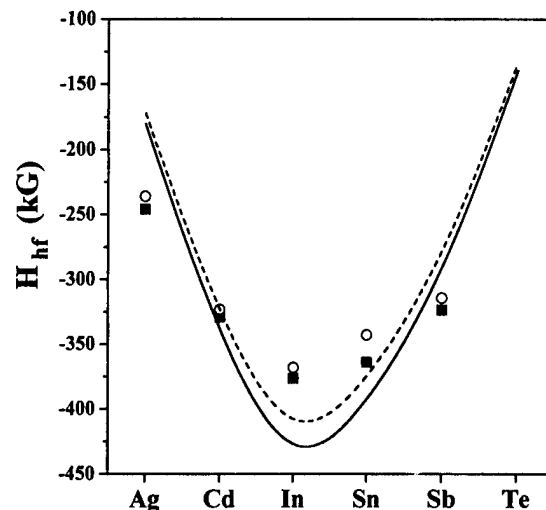


FIG. 2. Calculated hyperfine fields for 5s-p impurities in GdZn (full line) and GdCd (dashed line) compounds. The experimental data (squares for GdZn and open circles for GdCd) were collected from Ref. 1.

and one observes a quite similar behavior, i.e., all hyperfine fields are negative and the corresponding negative local moments are very small. Similarly to our previous Daniel–Friedel type calculation,⁶ discrepancies are systematically observed in the case of isoelectronic noble impurities Cu, Ag, and Au. This is because the impurity nd^{10} filled shell creates at the strongly charge perturbed local density of states at the origin, an Anderson–Moriya d -hump.¹¹ The Friedel–Anderson-like d resonance generates a local d moment, which turns out to be of the order of $0.25\mu_B$, thereby originating a core polarization contribution to the hyperfine field. Full details about this calculation will be given elsewhere.¹²

We would like to thank Conselho Nacional de Desenvolvimento Científico e Tecnológico-CNPq-Brazil and Fundação de Amparo a Pesquisa do Estado do Rio de Janeiro-FAPERJ, for partial financial support.

- ¹Y. Kasamatsu, K. Kojima, and T. Hihara, *Hyperfine Interact.* **51**, 841 (1989); *J. Phys. Soc. Jpn.* **63**, 1508 (1994).
- ²C. E. Leal, O. L. T. de Menezes, and A. Troper, *Solid State Commun.* **50**, 619 (1984); C. E. Leal and A. Troper, *ibid.* **61**, 317 (1987).
- ³E. Daniel and J. Friedel, *J. Phys. Chem. Solids* **24**, 1601 (1963).
- ⁴A. L. de Oliveira, M. V. Tovar Costa, N. A. de Oliveira, and A. Troper, *J. Appl. Phys.* **81**, 4215 (1997).
- ⁵W. Speier, J. F. van Acker, and R. Zeller, *Phys. Rev. B* **41**, 2753 (1990); J. F. van Acker, W. Speier, J. C. Fuggle, and R. Zeller, *ibid.* **43**, 13916 (1991).
- ⁶A. L. de Oliveira, M. V. Tovar Costa, N. A. de Oliveira, and A. Troper, *J. Magn. Magn. Mater.* **177–181**, 1091 (1998).
- ⁷A. Blandin and I. A. Campbell, *Phys. Rev. Lett.* **31**, 51 (1973); I. A. Campbell and A. Blandin, *J. Magn. Magn. Mater.* **1**, 1 (1975).
- ⁸N. A. de Oliveira, A. A. Gomes, and A. Troper, *Phys. Rev. B* **52**, 9137 (1995).
- ⁹I. A. Campbell, *J. Phys. C* **2**, 1338 (1969).
- ¹⁰A. V. Postnikov, V. P. Antropov, and O. Jepsen, *J. Phys.: Condens. Matter* **4**, 2475 (1992).
- ¹¹A. Troper, O. L. T. de Menezes, P. Lederer, and A. A. Gomes, *Phys. Rev. B* **18**, 3709 (1978).
- ¹²A. L. de Oliveira, V. P. Ramunni, M. V. Tovar Costa, N. A. de Oliveira, and A. Troper (to be published).

Magnetic transitions in $\text{Tb}_{0.7}\text{Nd}_{0.3}\text{Mn}_2\text{Ge}_2$ compound

Shibaji Saha and Naushad Ali

Department of Physics and Molecular Science Program, Southern Illinois University at Carbondale, Carbondale, Illinois 62901

Sunil Labroo and Dale Zych

Department of Physics, State University of New York, Oswego, New York 13126

In this article we report a new compound, $\text{Tb}_{0.7}\text{Nd}_{0.3}\text{Mn}_2\text{Ge}_2$, which behaves like SmMn_2Ge_2 , a compound with reentrant ferromagnetic order. Magnetization and thermal expansion measurements have been performed to study polycrystalline $\text{Tb}_{0.7}\text{Nd}_{0.3}\text{Mn}_2\text{Ge}_2$. Temperature dependent magnetization data shows that from 800 to 426 K the sample behaves like a paramagnet. A Néel transition is observed at 426 K (T_4) and the antiferromagnetic phase persists until 334 K (T_3). From 334 K (T_3) to 277 K (T_2) the sample exists in a ferromagnetic state. At 277 K (T_2) the sample transforms into an antiferromagnetic phase. Interestingly, at 117 K (T_1) the sample enters into a ferromagnetic-like phase. Thermal expansion study shows a sharp change in the sample dimension around T_1 (125 K). This change in the dimension most likely triggers the reentrant magnetic transition (T_1) observed in the magnetization measurement. The sharp change in thermal expansion suggests this transition at T_1 to be of first order. The relatively small and shallow dimensional change around T_2 (275 K) implies a weak first order transition. The dimensional changes found at the two transitions strongly suggest that Mn–Mn intralayer distance plays an important role in the multiple magnetic phases in $\text{Tb}_{0.7}\text{Nd}_{0.3}\text{Mn}_2\text{Ge}_2$. © 1998 American Institute of Physics.

[S0021-8979(98)33511-2]

The rare-earth-intermetallic compounds RMn_2X_2 (R =rare-earth, X =Ge, Si) have been studied^{1,2} intensively for more than 15 years. The various compounds with different R and X combinations show a wide variety of magnetic behavior. All the RMn_2X_2 compounds have tetragonal ThCr_2Si_2 crystal structure, where each element resides in a square plane of their own and these planes are then stacked along the c axis with the sequence ... $\text{R}-\text{X}-\text{Mn}-\text{Mn}-\text{X}-\text{R}$... the easy axis of magnetization being along the c axis.

Among all the RMn_2X_2 compounds, SmMn_2Ge_2 possesses the most intriguing magnetic behavior.³ With the lowering of temperature from 400 to 2 K it shows four distinct magnetic states: from 400 to ~ 340 K (T_3) it is paramagnetic; from 340 to ~ 150 K (T_2) it is ferromagnetic; from 150 to ~ 100 K (T_1) it is antiferromagnetic; and finally, it reenters another ferromagnetic phase below 100 K and this is sustained until 2 K, the lowest temperature of measurement. Temperature dependence of lattice constants⁴ shows that the ferro- to antiferromagnetic (T_2) and antiferromagnetic to ferromagnetic (T_1) transitions are enhanced by magnetostriction. More importantly, these interesting transitions in SmMn_2Ge_2 and also the magnetic behavior of the whole family of RMn_2X_2 compounds is strongly correlated to the Mn–Mn intralayer distance $R_{\text{Mn}-\text{Mn}}^a$.^{3–5} This critical dependence has been investigated in RMn_2Ge_2 and in particular in SmMn_2Ge_2 by external pressure^{6,7} and by chemical pressure.^{8–10} NMR study¹¹ has been done on SmMn_2Ge_2 to understand reentrant ferromagnetism. A magnetoresistance study¹² on SmMn_2Ge_2 indicates a new transition around 30 K and it has been attributed to Sm.

Due to very high neutron absorption coefficient of Sm, it has not been possible to subject SmMn_2Ge_2 to neutron dif-

fraction experiments. Therefore, the suggestions on the magnetic structure of SmMn_2Ge_2 were largely made on the basis of the pressure and temperature-dependent magnetization studies of SmMn_2Ge_2 and those of the other members of the RMn_2X_2 compounds.^{3,4,7} It was thought that magnetic moments of Mn are always arranged parallel (giving ferromagnetic order) within the (001) plane and depending on temperature the moments on two successive planes could be either directed parallel or antiparallel. This view has recently been revised¹³ due to the understanding of the Mn-sublattice ordering from the neutron diffraction studies on RMn_2Ge_2 (La–Nd), LaMn_2Si_2 , and $\text{La}_{0.3}\text{Y}_{0.7}\text{Mn}_2\text{Ge}_2$ compounds.^{14–16} According to these studies, the Mn moments in many RMn_2X_2 compounds possess both ferromagnetic and antiferromagnetic components giving a canted arrangement. Having found the magnetic structure of RMn_2X_2 compounds, Venturini *et al.*¹³ synthesized a SmMn_2Ge_2 -like compound, $\text{Nd}_{0.35}\text{La}_{0.65}\text{Mn}_2\text{Si}_2$, and they have studied it by magnetization and neutron diffraction measurements. The magnetic structure found for $\text{Nd}_{0.35}\text{La}_{0.65}\text{Mn}_2\text{Si}_2$ is thought to be valid for SmMn_2Ge_2 . In this article we report on a new compound, $\text{Tb}_{0.7}\text{Nd}_{0.3}\text{Mn}_2\text{Ge}_2$, which also shows SmMn_2Ge_2 -like behavior. This compound can provide us understanding of the reentrant magnetic behavior in SmMn_2Ge_2 and in other similar compounds.

Samples were synthesized by arc melting in Ar atmosphere of the proper amounts of the constituent elements. The purity of the elements were 99.9% for Tb and Nd, 99.99% for Mn, and 99.999% for Ge. Samples were then annealed under vacuum at 1173 K for ten days. Magnetization measurements were carried out by means of a SQUID magnetometer. The magnetization measurements above 400

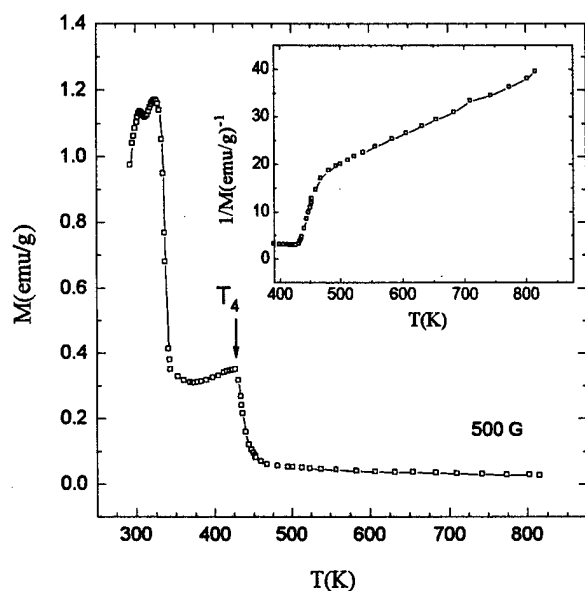


FIG. 1. High-temperature magnetization data of the $\text{Tb}_{0.7}\text{Nd}_{0.3}\text{Mn}_2\text{Ge}_2$ sample at an applied field of 500 G. The inset shows inverse magnetization as a function of temperature.

K were carried out with a vibrating sample magnetometer. Thermal expansion measurements were made by using a capacitance dilatometer. X-ray data reflect the presence of a main phase with ThCr_2Si_2 -type tetragonal structure. It also shows the presence of a minor amount of impurity phase.

Figure 1 shows the high-temperature magnetization of $\text{Tb}_{0.7}\text{Nd}_{0.3}\text{Mn}_2\text{Ge}_2$ at a constant applied field of 500 G. From 800 K down to about 470 K the inverse magnetization (inset) shows a good linear dependence on temperature indicating that the moments are paramagnetic. The cusp at 426 K (T_4) indicates a Néel transition and the antiferromagnetic phase (AFI) persists down to 335 K (T_3). It is important to note that in $\text{Nd}_x\text{Tb}_{1-x}\text{Mn}_2\text{Ge}_2$ compound⁸ the Néel transition was not observed. A comparison between the magnetic orderings of the Mn moments in TbMn_2Ge_2 (Ref. 17) [where Mn mo-

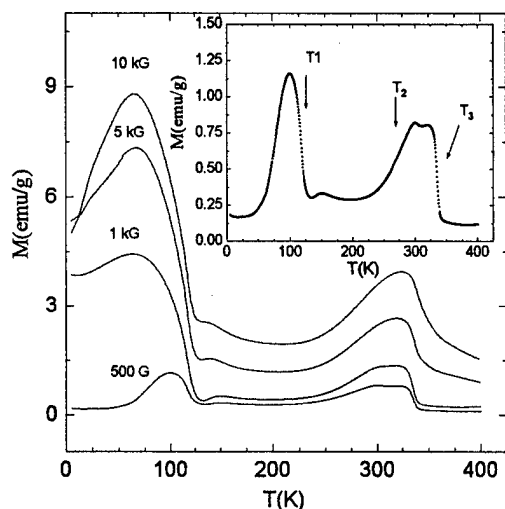


FIG. 2. Temperature dependence of magnetization of $\text{Tb}_{0.7}\text{Nd}_{0.3}\text{Mn}_2\text{Ge}_2$ at different magnetic fields ranging from 500 G to 10 kG. The inset shows a magnified view of the magnetization vs temperature data at 500 G.

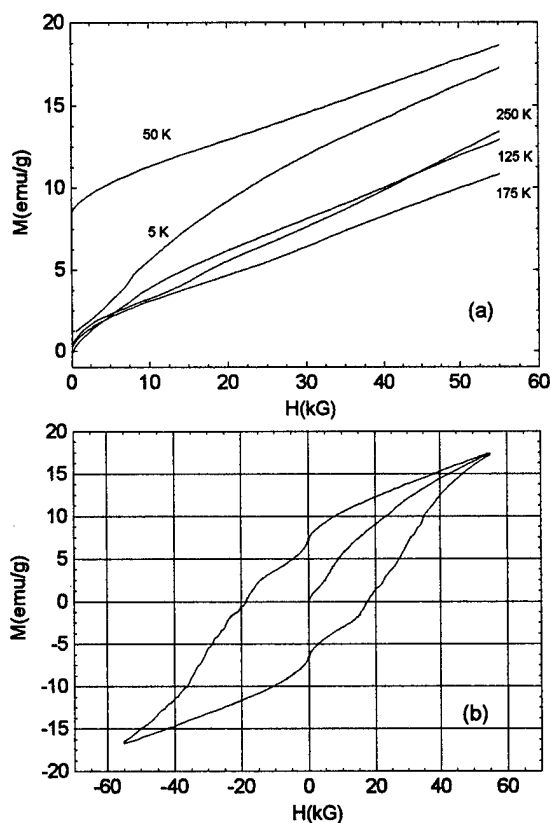


FIG. 3. (a) Magnetization of $\text{Tb}_{0.7}\text{Nd}_{0.3}\text{Mn}_2\text{Ge}_2$ as a function of applied magnetic field at different temperatures. (b) Magnetic hysteresis curve of $\text{Tb}_{0.7}\text{Nd}_{0.3}\text{Mn}_2\text{Ge}_2$ at 5 K.

ments are arranged ferromagnetically along the (001) planes] and in NdMn_2Ge_2 (Ref. 13) [where Mn moments have both ferromagnetic and antiferromagnetic components along the (001) planes] suggest that Mn moments might have an antiferromagnetic ordering in $\text{Tb}_{0.7}\text{Nd}_{0.3}\text{Mn}_2\text{Ge}_2$ in the temperature range of 426 to 335 K. However, further investigation in this temperature range is necessary for a definitive conclusion. Figure 1 also shows that the sample is transformed into a ferromagnetic phase (FMI) below 335 K. Inset of Fig. 2 shows the temperature-dependent magnetization data of the $\text{Tb}_{0.7}\text{Nd}_{0.3}\text{Mn}_2\text{Ge}_2$ sample at temperatures below 400 K and at a constant applied field of 500 G. Below 335 K the sample is transformed into a ferromagnetic phase (FMI). This ferromagnetic ordering most likely is coming from the ferromagnetic coupling among the Mn moments in the adjacent Mn planes.¹³ This ferromagnetic phase is retained down to 277 K (T_2) where the sample transforms to an antiferromagnetic phase (AFII). The AFII phase extends down to 117 K (T_1). As the temperature is decreased further, the sample transforms into the apparent ferromagnetic phase. The magnetization data in the inset of Fig. 2 thus suggests that $\text{Tb}_{0.7}\text{Nd}_{0.3}\text{Mn}_2\text{Ge}_2$ behaves very similar to SmMn_2Ge_2 . The low-temperature magnetic ordering in $\text{Tb}_{0.7}\text{Nd}_{0.3}\text{Mn}_2\text{Ge}_2$ is most likely due to the ordering of Tb and Nd moments as well as Mn moments. To better understand the magnetic behavior of the sample, especially below 100 K, we performed several temperature-dependent measurements at different magnetic fields. This result is shown in Fig. 2. The data

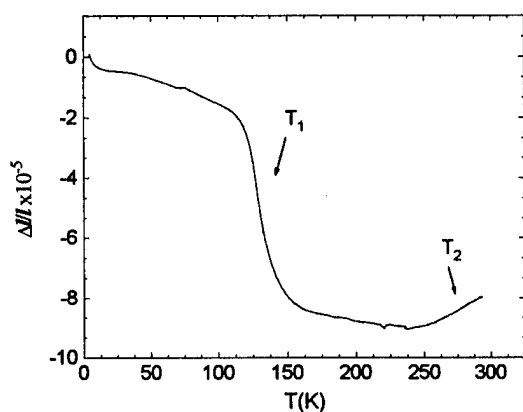


FIG. 4. Relative thermal expansivity $\Delta l/l$ of $\text{Tb}_{0.7}\text{Nd}_{0.3}\text{Mn}_2\text{Ge}_2$ as a function of temperature.

below 50 K for 1 kG field show that the sample approaches the saturation value. Surprisingly, this indication of saturation reverses for high field measurements at 5 and 10 kG. This may suggest that the rare-earth sublattice in $\text{Tb}_{0.7}\text{Nd}_{0.3}\text{Mn}_2\text{Ge}_2$ has a complicated magnetic structure due to the competition between the Tb–Mn, Nd–Mn, and Tb–Nd couplings. This complicated magnetic behavior is also indicated from the neutron study⁸ on the two closest compounds, namely, $\text{Tb}_{0.6}\text{Nd}_{0.4}\text{Mn}_2\text{Ge}_2$ and $\text{Tb}_{0.8}\text{Nd}_{0.2}\text{Mn}_2\text{Ge}_2$. At low temperature $\text{Tb}_{0.8}\text{Nd}_{0.2}\text{Mn}_2\text{Ge}_2$ shows a ferrimagnetic structure of the Mn and R magnetic moments along the *c* axis. On the other hand, at low temperature $\text{Tb}_{0.6}\text{Nd}_{0.4}\text{Mn}_2\text{Ge}_2$ has a ferromagnetic component along the *c* axis and an antiferromagnetic one along the *a* axis.

Figure 3(a) shows isothermal magnetization data with the variation of applied field. At 50 K magnetization increases relatively faster at low fields (up to 5 kG) and increases with the increase of the field but never saturates, even at 55 kG, the maximum applied field. At 5 K magnetization increases slowly up to 7.5 kG. The curvature becomes positive for fields higher than 7.5 kG. Again, at 5 K magnetization does not saturate at 55 kG. The steady increase in the magnetization for high fields at 50 and 5 K indicates that at low temperatures there may be an antiferromagnetic component present in the magnetic ordering of the rare-earth elements in $\text{Tb}_{0.7}\text{Nd}_{0.3}\text{Mn}_2\text{Ge}_2$ and the overall magnetic ordering is not simple collinear ferromagnetic or ferrimagnetic. Figure 3(b) shows the magnetic hysteresis curve of $\text{Tb}_{0.7}\text{Nd}_{0.3}\text{Mn}_2\text{Ge}_2$ at 5 K. The hysteresis, with rather high coercivity, at least shows that at low temperature $\text{Tb}_{0.7}\text{Nd}_{0.3}\text{Mn}_2\text{Ge}_2$ has either ferromagnetic or ferrimagnetic order in it.

In RMn_2Ge_2 compounds, especially in SmMn_2Ge_2 , the FM–AF and AF–FM transitions accompany magnetostric-

tion. To verify any possible dimensional change in the $\text{Tb}_{0.7}\text{Nd}_{0.3}\text{Mn}_2\text{Ge}_2$, we measured its relative thermal expansivity from 5 K to room temperature. This result is presented in Fig. 4. At 120 K a sharp change in the sample dimension occurs. This transition temperature corresponds to the reentrant magnetic transition (T_1) found in the magnetization measurement (inset of Fig. 2). The sharp dimensional change clearly indicates that the order of the transition is of first order. Thermal expansion data also indicate a small and shallow dimensional change around 275 K. This dimensional change corresponds to the AFI–FMI transition (T_2) observed in the magnetization measurement. Considering the magnetization and thermal expansion data we suggest this transition at T_2 to be of weak first-order type. The dimensional change observed at T_1 and T_2 strongly suggest that Mn–Mn intralayer distance plays an important role in the magnetic behavior of $\text{Tb}_{0.7}\text{Nd}_{0.3}\text{Mn}_2\text{Ge}_2$.

A neutron diffraction study would be necessary to determine the magnetic structure of $\text{Tb}_{0.7}\text{Nd}_{0.3}\text{Mn}_2\text{Ge}_2$ and it would provide a more complete understanding of the magnetic behavior of this as well as other compounds with reentrant magnetic behavior.

This work was supported in part by a grant from Consortium for Advanced Radiation Source, University of Chicago, Illinois.

- ¹A. Szytula and J. Leciejewicz, *Handbook Phys. Chem. Rare Earths* **12**, 133 (1989).
- ²A. Szytula, *J. Alloys Compd.* **178**, 1 (1992).
- ³H. Fujii, R. Okamoto, T. Shigeoka, and N. Iwata, *Solid State Commun.* **53**, 715 (1985).
- ⁴M. Duraj, R. Duraj, A. Szytula, and Z. Tomkowicz, *J. Magn. Magn. Mater.* **73**, 240 (1988).
- ⁵A. Szytula and S. Siek, *J. Magn. Magn. Mater.* **27**, 49 (1982).
- ⁶M. Duraj, R. Duraj, and A. Szytula, *J. Magn. Magn. Mater.* **82**, 319 (1989).
- ⁷R. Duraj, M. Duraj, and A. Szytula, *J. Magn. Magn. Mater.* **132**, 67 (1994).
- ⁸L. Morellon, P. A. Algarabel, M. R. Ibarra, and C. Ritter, *Phys. Rev. B* **55**, 12363 (1997).
- ⁹S. Saha and N. Ali, *J. Appl. Phys.* **79**, 5233 (1996).
- ¹⁰S. Saha and N. Ali, *J. Alloys Compd.* **250**, 651 (1997).
- ¹¹J. S. Lord, P. C. Riedi, G. S. Tomka, Cz. Kapusta, and K. H. J. Buschow, *Phys. Rev. B* **53**, 283 (1996).
- ¹²E. V. Sampathkumaran, P. L. Paulose, and R. Mallik, *Phys. Rev. B* **54**, R3710 (1996).
- ¹³G. Venturini, R. Welter, E. Rossouche, and B. Malaman, *J. Magn. Magn. Mater.* **150**, 197 (1995).
- ¹⁴R. Welter, G. Venturini, E. Rossouche, and B. Malaman, *J. Alloys Compd.* **218**, 204 (1995).
- ¹⁵G. Venturini, R. Welter, E. Rossouche, and B. Malaman, *J. Alloys Compd.* **210**, 213 (1995).
- ¹⁶G. Venturini, R. Welter, E. Rossouche, and B. Malaman, *J. Alloys Compd.* **223**, 101 (1995).
- ¹⁷G. Venturini, B. Malaman, and E. Rossouche, *J. Alloys Compd.* **240**, 139 (1996).

Magnetic moment, thermal and electrical transport in the inverse Mott systems $\text{BaCo}_{0.9}\text{Ni}_{0.1}\text{S}_{2-y}$ and CuIr_2S_4

H. Kang, P. Mandal,^{a)} I. V. Medvedeva,^{b)} J. Liebe, G. H. Rao,^{c)} and K. Bärner

4. Phys. Institut der Universität Göttingen, Bunsenstr. 13-15, D-37073 Göttingen, Germany

A. Poddar^{a)} and E. Gmelin

Max-Planck-Institut für Festkörperforschung, Heisenbergstr. 1, D-70569 Stuttgart, Germany

The antiferromagnetic $\text{BaCo}_{0.9}\text{Ni}_{0.1}\text{S}_{2-y}$ and the paramagnetic CuIr_2S_4 Mott systems show an inverse conductivity behavior, i.e., the metallic phase occurs at low or high temperatures, respectively, which also suggests inverse behavior in other transport properties. In this contribution we present magnetization data, conductivity, thermal conductivity, and Seebeck effect in the temperature range $4.2 \text{ K} < T < 350 \text{ K}$ and in particular through the metal-insulator transition at T_{MI} . We recover the anomalies in $\chi(T)$, $\sigma(T)$, which are discussed using Jahn-Teller and anti-Jahn-Teller models; also, we compare the anomalies in $\sigma(T)$, $S(T)$, and of the heat conductivity $\kappa(T)$ at T_{MI} . In particular, for $\text{BaCo}_{0.9}\text{Ni}_{0.1}\text{S}_{1.95}$, we find a step in κ of almost one order of magnitude (times 6) and a large pressure shift, $\leq -24 \text{ K/kbar}$, which makes this material a potential pressure activated heat switch, while CuIr_2S_4 shows a small step of κ (times 1.2) and a pressure shift of $+2.8 \text{ K/kbar}$. © 1998 American Institute of Physics. [S0021-8979(98)40211-1]

I. INTRODUCTION

In the search for nongaseous cooling devices, pure solid state cooling has gathered renewed interest. With thermodynamic cycles, however, heat switches which connect and disconnect heat reservoirs have to be used. Solid state nonmechanical thermal switches at higher temperatures might be provided by metal-insulator MI transitions, as in metals the heat is often carried by electrons (Wiedemann-Franz law), while by phonons in insulators. Therefore, we have investigated the thermal conductivity of two recently found metal-insulator transitions, i.e., $\text{BaCo}_{0.9}\text{Ni}_{0.1}\text{S}_{2-y}$ and CuIr_2S_4 . For the first compound the metallic phase is at low temperatures; κ shows a step of times 6 at T_{MI} and T_{MI} has a large negative pressure shift, -24 K/kbar .¹ For the second compound the metallic phase is at high temperatures; κ changes by a factor of 1.2 at T_{MI} and T_{MI} shows a small positive pressure shift $+2.0 \text{ K/kbar}$.² Inverse behavior is also suggested by the specific heat capacity: the entropy change for CuIr_2S_4 is very high, 14 J/molK , suggesting an addition of electronic and lattice contribution and significantly lower for $\text{BaCo}_{0.9}\text{Ni}_{0.1}\text{S}_{2-y}$, 2.6 J/molK , suggesting a subtraction in this case.³ This means that the lattice entropy increases at T_{MI} in both cases while the electronic contribution is inverse, as expected.

II. EXPERIMENT AND RESULTS

The sample preparation and the experimental apparatus used are described in detail elsewhere.³⁻⁵ For the susceptibility measurements we have used the Faraday method and in some cases a superconducting quantum interference de-

vice (SQUID) magnetometer. The electrical conductivity and the Hall effect are measured using the four- and five-point method, respectively, while both the thermoelectric power and the heat diffusivity are taken from the initial amplitude and decay time of the transient thermoelectricity (TTE). The specific heat capacity data were obtained using a Perkin-Elmer DSC 2.

The temperature-independent susceptibility χ of nonmagnetic metals and insulators is usually written as the sum of Larmor (l), Landau, and Pauli (p) susceptibilities. For CuIr_2S_4 , the valence mixed configuration $(\text{Cu}^+\text{Ir}^{3+}\text{Ir}^{4+}\text{S}_4^{2-})$ gives $\chi l = -3.9 \times 10^{-7} \text{ emu/g}$ while $(\text{Cu}^+\text{Ir}_2^{3+}\text{S}_3^{-2})$ would give $\chi l = -3.8 \times 10^{-7} \text{ emu/g}$.³ Our experimental value, $\chi = -2.9 \times 10^{-7} \text{ emu/g}$ thus slightly favors a configuration of the second type. At low temperatures a Curie-type contribution of different magnitude⁶ always appears to be superimposed on χl , (Fig. 1) suggesting an impurity content of about 10^{-4} , which is close to the starting element purity. The constant positive Pauli-susceptibility χp in the metallic state, $T > T_{\text{MI}}$, has been used to estimate the density of states at the Fermi level. Our $\chi p = 8 \times 55 \times 10^{-7} \text{ emu/g}$ gives $N(E_F) = 1.66 \text{ states/eV atom}$ (literature value: 0.67 in these units⁶).

In the case of $\text{BaCo}_{0.9}\text{Ni}_{0.1}\text{S}_{2-y}$ a shallow maximum appears close to $T_N \approx 250 \text{ K}$, suggesting quasi-two-dimensional antiferromagnetic order.^{7,8} A spin compensated magnetic state also exists below T_{MI} , however long range magnetic order has not been found.⁹ Some random magnetic component is also suggested by the difference of $M(T)$ under zero field cooled (ZFC) and field cooled (FC) conditions (Fig. 1). Here, the field cooled magnetization curve for $T < T_{\text{MI}}$ differs slightly from the field warmed magnetization curve, but only when previously cooled in zero field.

In the metallic state of CuIr_2S_4 (compound I, Fig. 2), phonon scattering of the conduction carriers plus scattering on impurities (residual resistance, originating from impurities, vacancies, etc.), suffices to describe $\sigma = 1/\rho(T)$. In the

^{a)}Permanent address: Saha Institute of Nuclear Physics, 1/AF Bidhannagar, 700064 Calcutta, India.

^{b)}Permanent address: Institute for Metal Physics, S. Kovalevskaya Str. 18, 620219 Ekaterinburg, Russia.

^{c)}Permanent address: Institute of Physics, Chinese Academy of Sciences, Beijing 100080, P.R. China.

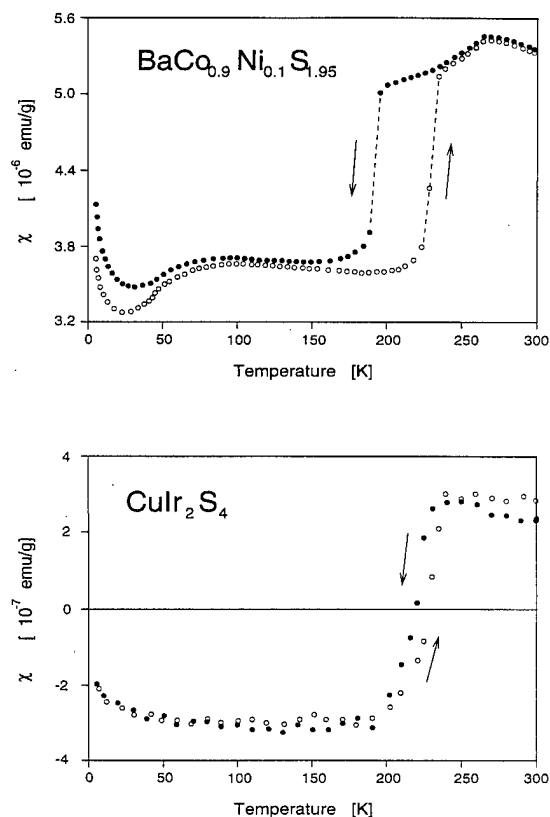


FIG. 1. Magnetic susceptibilities of CuIr_2S_4 and $\text{BaCo}_{0.9}\text{Ni}_{0.1}\text{S}_{2-y}$ vs temperature.

insulating state, activated behavior occurs. It is unclear, however, whether an Arrhenius law, $\ln(\rho/\rho_0) = -\Delta E/kT$, or a Mott law, $\ln(\rho/\rho_0) = -(T_0/T)^{1/4}$, better describes the resistivity in the insulating state, as the effective activation energy ΔE (or kT_0) changes strongly with the temperature (Fig. 2). Apparently, other CuIr_2S_4 samples can come closer to an Arrhenius law,⁶ suggesting a variable random component, most probably a sulfur deficit S_{4-y} .

The heat conductivity $\kappa(T)$ of CuIr_2S_4 (Fig. 2) shows only a small anomaly at the transition between the high temperature metallic state and the low temperature activated (semiconducting) state. This suggests a compensating effect. For nonmagnetic materials, the heat conductivity is usually written as a sum:¹⁰ $\kappa = \kappa_{\text{ph}} + \kappa_e$. As there is a structural change at T_{MI} , a phonon part κ_{ph} could indeed counteract an electronic part κ_e (Fig. 3). The ascending slope of κ below T_{MI} follows the general trend in insulators, $\kappa \sim 1/T^2$.¹⁰ An almost constant κ as observed in the metallic phase at high temperatures is typical for technical metals, i.e., suggests a large number of defects.

The linear dependence of S in the metallic phase suggests diffusion thermopower S_d ; from that $E_F \approx 1$ eV has been estimated.³ For the semiconducting phase, the thermal activation of the carriers determines S , e.g., $S = (k/e) \times (\Delta E/kT + \text{const.})$; assuming an Arrhenius law or, alternatively, $S \sim \sqrt{T}$ for a variable range hopping (VRH) regime.¹¹ VRH thus would explain the curved ascending part of $S(T)$ for $T < T_{\text{MI}}$.

Activated behavior occurs in the insulating phase of $\text{BaCo}_{0.9}\text{Ni}_{0.1}\text{S}_{2-y}$ (compound II), while $\sigma(T)$ is nearly con-

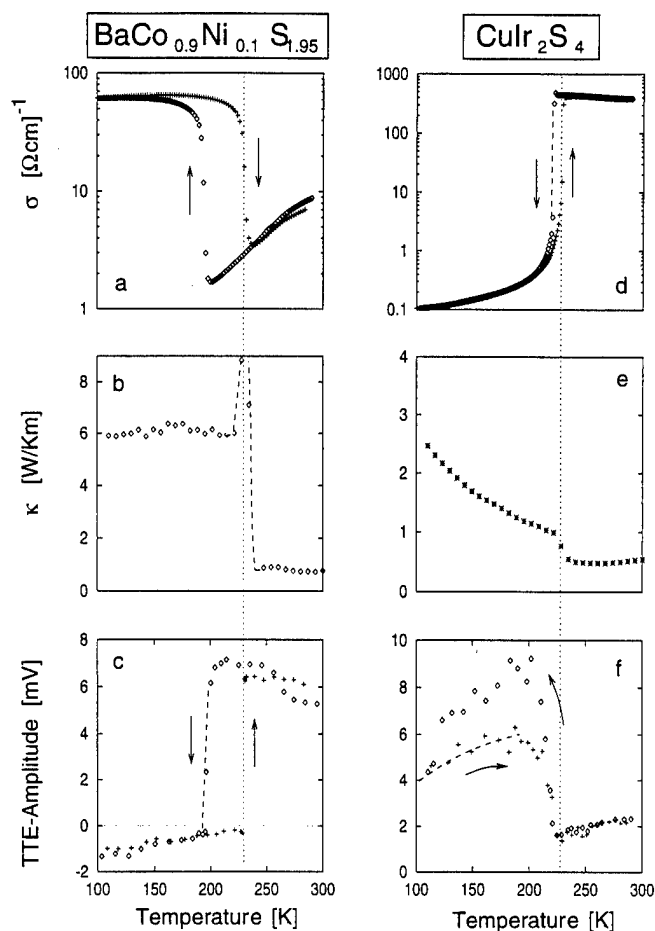


FIG. 2. Electrical and heat conductivities of CuIr_2S_4 and $\text{BaCo}_{0.9}\text{Ni}_{0.1}\text{S}_{2-y}$ vs temperature and the TTE amplitudes.

stant in the metallic state, again suggesting a large number of structural and/or spin defects.

The activation energy in the insulating state decreases with the pressure, -8 meV/kbar,¹ and increases with y , $+4.5$ meV/at. %.⁷ The y -dependence of the resistivity in the metallic state is stronger¹ as is the pressure dependence.^{1,7} This is probably due to increasing nonstoichiometry hole doping in the one case (y), while under pressure the carrier concentration would remain constant.

The conductivity κ is nearly constant, in the metallic state of $\text{BaCo}_{0.9}\text{Ni}_{0.1}\text{S}_{2-y}$, although for metals we expect

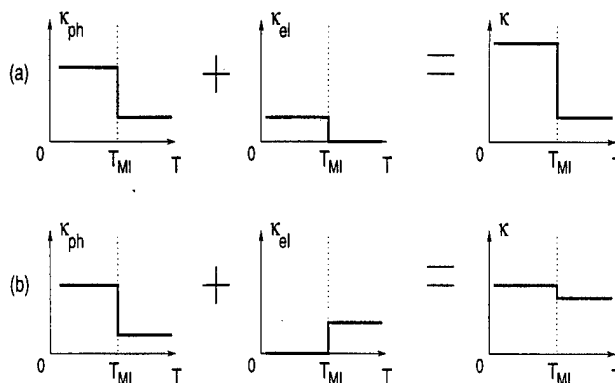


FIG. 3. Reconstruction of the step in heat conductivity at T_{MI} of CuIr_2S_4 and $\text{BaCo}_{0.9}\text{Ni}_{0.1}\text{S}_{2-y}$

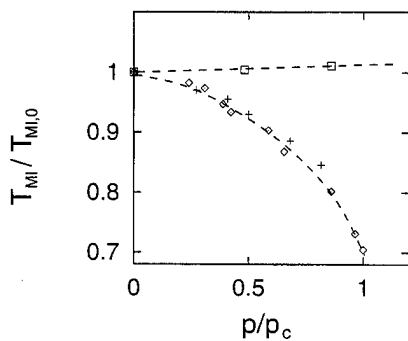


FIG. 4. P - T phase diagram in reduced scales $\text{BaCo}_{0.9}\text{Ni}_{0.1}\text{S}_{2-y}$: $T_{M0} = 205, 230$ K, +, o : $P_c = 2$ and 2.9 kbar CuIr_2S_4 : $T_{M0} = 228$ K, $P_c = 2.9$ kbar.

$\kappa \sim 1/T$.¹² For the insulating phase, κ is almost constant, too, i.e., a $1/T^2$ law is not observed. A small structure appears close to the Néel point $T_N \approx 250$ K, suggesting a magnetic contribution, κ_m , which is numerically small. We observe a significant step in both κ and D_T at T_{MI} , with the higher heat conductivity in the metallic state, as expected. Either both κ_{ph} and κ_m are small, or change in the same direction as κ_e . For both compounds, the low temperature state has the lower symmetry^{6,9} and thus the step in κ_{ph} should run parallel to the step in κ_e in one case (II) and opposite in the other case (I), i.e., $\Delta\kappa_{ph}$ is not small and adds to $\Delta\kappa_e$ for compound II, while it subtracts for compound I (Fig. 3).

$S(T)$ of $\text{BaCo}_{0.9}\text{Ni}_{0.1}\text{S}_{2-y}$ changes abruptly at $T_{MI} = 230$ K. The zero crossing suggests two types of carriers and a two-band model. $S(T)$ of $y = 0.05$ indeed shows activated behavior in the semiconducting phase—a fit yields $\Delta E = 0.03$ eV as compared to 0.09 eV from $\rho(T)$.

In the metallic and magnetic state one should find two contributions for S : a magnetic, S_m , and an electron diffusion part, i.e., $S = S_m + S_d$.¹³ While the smaller negative values of S below T_{MI} are consistent with a metallic regime and electrons, the small ascending slope below T_{MI} is not consistent with electron diffusion and thus suggests magnon or phonon drag.

With increasing pressure, the MI transition of $\text{BaCo}_{0.9}\text{Ni}_{0.1}\text{S}_{2-y}$ shifts to low temperatures, and the resistivity step at the transition increases. The critical pressure P_c at which the MI transition does not occur anymore (Fig. 2), is higher for higher $T_{MI} = T_c$, that is for larger y . In Fig. 4, the similarity of the P - T diagrams for two compounds with different y has been demonstrated by using reduced variables T/T_c and P/P_c . The compounds with smaller y can thus be regarded as a “precompressed” compounds in relation to the highest sulfur deficit $y \leq 0.15$, i.e., we may consider an effective lattice contraction as a result of the action of the internal (structural or chemical) and external pressure, with a conversion ratio of about 1.5 at. %/kbar. With T and P critical but numerically different for various y , the concept of a critical volume at which the transition always occurs has been put forward.⁵

III. PHASE TRANSITION MODELS

The idea of a critical volume in $\text{BaCo}_{0.9}\text{Ni}_{0.1}\text{S}_{2-y}$ is consistent with the microscopic model of this MI transition as

proposed by Philips.^{15,16} here, it is proposed that the high temperature semiconducting state is stabilized through screening of the electrostatic charges by thermally activated carriers. At low temperatures the carriers freeze out, increasing the electrostatic energy of the crystal and a new (better screening, i.e., metallic) ground state may be installed. The introduction of many electronic states close to the Fermi-level of the metallic phase via the distortion would further stabilize the metallic phase (Fermi-level pinning/anti-Jahn-Teller effect¹⁶). Several observations are consistent with this approach: for example, applying pressure reduces the energy gap, -8 meV/kbar,¹ thus prolonging the activated carrier screening and indeed the insulating state is stabilized under pressure.

The nature of the transition in CuIr_2S_4 is still unclear. A valence mixture of iridium, say $\text{Ir}^{+3}/\text{Ir}^{+4}$, which might drive the change of state in a Verwey-type of transition, has been ruled out.⁶ Because of the cubic-tetragonal lattice distortion at T_{MI} the transition has been classified as Jahn-Teller-like. The $(t_{2g})^4$ orbital of Ir in octahedral configuration is twofold degenerate and could be split by distortion. However, as the observed distortion is rather small and as a Jahn-Teller effect has not been observed directly, the distortion might not be the driving force but a secondary or coupled order parameter. Thus, alternatively, a condensation of quasiparticles (e.g., Jahn-Teller-polarons) into a gap state has been discussed.¹⁴

ACKNOWLEDGMENTS

The authors thank the Deutsche Forschungsgemeinschaft for continuous support and L. Haupt and U. Sondermann for helpful discussions and some of the experiments.

¹C. Looney, J. S. Schilling, L. S. Martinson, and J. W. Schweitzer, Phys. Rev. Lett. **76**, 4789 (1996).

²T. Furubayashi, T. Matsumoto, T. Hagino, and S. Nagata, J. Phys. Soc. Jpn. **63**, 3333 (1994).

³H. Kang, P. Mandal, I. V. Medvedeva, K. Bärner, A. Poddar, and E. Gmelin, Phys. Status Solidi A **163**, 465 (1997).

⁴H. Kang, diploma thesis, University of Göttingen, Göttingen 1997.

⁵H. Kang, I. V. Medvedeva, K. Bärner, and U. Sondermann, Physica B **245**, 20 (1998).

⁶T. Hagino, T. Tojo, T. Atake, and S. Nagata, Philos. Mag. B **71**, 8811 (1995).

⁷L. S. Martinson, J. W. Schweitzer, and N. C. Baenziger, Phys. Rev. Lett. **71**, 125 (1993).

⁸S. A. M. Mentink, T. E. Mason, B. Fisher, J. Genossar, L. Patlagan, A. Kanigel, M. D. Lumsden, and B. D. Gaulin, Phys. Rev. B **55**, 12375 (1997).

⁹I. Felner, J. Gersten, S. Litvin, U. Asaf, and T. Kröner, Phys. Rev. B **52**, 10097 (1995).

¹⁰S. Welzel-Gerth, B. Franz, H. W. Gronert, and E. F. Wassermann, J. Magn. Magn. Mater. **101**, 37 (1991).

¹¹M. Jaime, M. B. Salamon, K. Pettit, M. Rubinstein, R. E. Treece, J. S. Horowitz, and D. B. Chrisez, Appl. Phys. Lett. **68**, 1576 (1996).

¹²J. M. Ziman, *Prinzipien der Festkörpertheorie* (Deutsch, Frankfurt, 1975), pp. 224 and 233.

¹³T. Gron, K. Bärner, Ch. Kleeberg, and I. Okonska-Kozłowska, Physica B **225**, 191 (1996).

¹⁴H. Kang, K. Bärner, I. V. Medvedeva, P. Mandal, A. Poddar, and E. Gmelin, J. Alloys Compd. (in press).

¹⁵J. C. Philips, Phys. Rev. B **47**, 11615 (1993).

¹⁶J. C. Philips, Phys. Rev. B **40**, 8774 (1989).

Magnetocrystalline anisotropy of $(\text{Fe}_{1-x}\text{Co}_x)_3\text{P}$

A. Broddefalk,^{a)} P. Granberg, and P. Nordblad

Department of Materials Science, Uppsala University, Box 534, S-751 21 Uppsala, Sweden

Hui-ping Liu and Y. Andersson

Department of Inorganic Chemistry, Uppsala University, Box 538, S-751 21 Uppsala, Sweden

The magnetocrystalline anisotropy energy (MAE) of $(\text{Fe}_{1-x}\text{Co}_x)_3\text{P}$ ($x=0, 0.1, 0.2, 0.33$) has been studied in the temperature range 5 K–300 K. The compound crystallizes in a tetragonal structure with three non-equivalent metal sites and shows an easy planar behavior with the magnetic moments aligned in the ab plane and the c axis as the hard direction. The MAE of Fe_3P was investigated using magnetization measurements on a single crystalline sample. The anisotropy constants were found to be $K_1 \approx -851 \text{ kJ/m}^3$ and $K_2 \approx 9 \text{ kJ/m}^3$ at 5 K and $K_1 \approx -648 \text{ kJ/m}^3$ and $K_2 \approx 11 \text{ kJ/m}^3$ at 300 K. The MAE of the cobalt substituted systems was investigated on sintered samples formed into spheres. K_1 for these samples was calculated from a fit of the magnetization versus internal field strength using the law of approach to saturation. © 1998 American Institute of Physics. [S0021-8979(98)51511-3]

I. INTRODUCTION

Among the T_3X compounds ($\text{T}=3\text{d}$ element and $\text{X}=\text{nonmetal element}$), ordered magnetic structures are only found for $\text{X}=\text{P}$ and group IV elements.¹ The phosphides crystallize in a tetragonal system where Fe_3P is ferromagnetic, Mn_3P is antiferromagnetic and Ni_3P and Cr_3P are Pauli paramagnetic.^{2,3} The Co_3P phase does not exist in the binary Co-P system.⁴ In previous studies of the magnetic properties of $(\text{Fe}_{1-x}\text{M}_x)_3\text{P}$ ($\text{M}=\text{Cr, Mn, Co, Ni}$) no information about the magnetocrystalline anisotropy can be found.^{2,3}

$(\text{Fe}_{1-x}\text{Co}_x)_3\text{P}$ ($x<0.37$) crystallizes in the tetragonal Fe_3P structure (see Fig. 1). In a previous report,⁵ structural and magnetic properties, such as the individual moments of each magnetic atom and the Curie temperature, were described. The total magnetic moment, the critical temperature as well as the cell parameters were found to decrease with increasing cobalt concentration. Neutron diffraction experiments on samples with compositions $x=0.1$ and $x=0.33$ showed that the Co distribution is approximately 20% on position M(1) and 40% on both M(2) and M(3) (see Fig. 1). From magnetization measurements on oriented grains, performed by Meyer and Cadeville,⁶ the anisotropy constants of Fe_3P were found to be $K_1 = -530 \text{ kJ/m}^3$ and $K_2 = 240 \text{ kJ/m}^3$. Magnetization measurements on single crystal Fe_3P made by Lisher *et al.*⁷ showed an easy-planar behavior with an anisotropy in the basal plane of 2 kJ/m^3 .

Close to saturation, the magnetization process is governed by the magnetocrystalline anisotropy energy (MAE) and the magnetostatic energy. In a uniaxial crystal, the MAE may be expressed as $E_a = K_1 \sin^2 \theta + K_2 \sin^4 \theta + \dots$ where θ is the angle of the magnetization with respect to the unique axis. For the easy-axis case, $K_1 > 0$, while for the easy-planar case, $K_1 < 0$. For the easy-planar case, with an applied field H_a parallel to the unique axis, the magnetization at equilibrium is given by

$$H_a = \left[\frac{-(2K_1 + 4K_2)}{\mu_0 M_s^2} + N \right] M + \frac{4K_2}{\mu_0 M_s^4} M^3, \quad (1)$$

where N is the demagnetization factor and M_s the saturation magnetization. In the polycrystalline case, one has to take an average over all possible orientations. Provided that $|K_1| \gg |K_2|$, an expansion of M up to the third-order term leads to^{8,9}

$$M = M_s \left[1 - \frac{1}{15} \left(\frac{2K_1}{\mu_0 M_s} \right)^2 \frac{1}{H^2} - \frac{2}{105} \left(\frac{2K_1}{\mu_0 M_s} \right)^3 \frac{1}{H^3} \right], \quad (2)$$

where H is the internal magnetic field. K_1 can thus be obtained from a fit of the magnetization according to

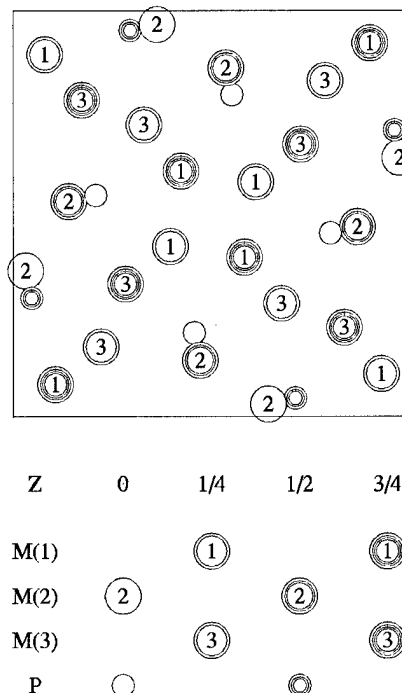


FIG. 1. The crystal structure of Fe_3P projected on the (001) plane.

^{a)}Electronic mail: arvid.broddefalk@material.uu.se

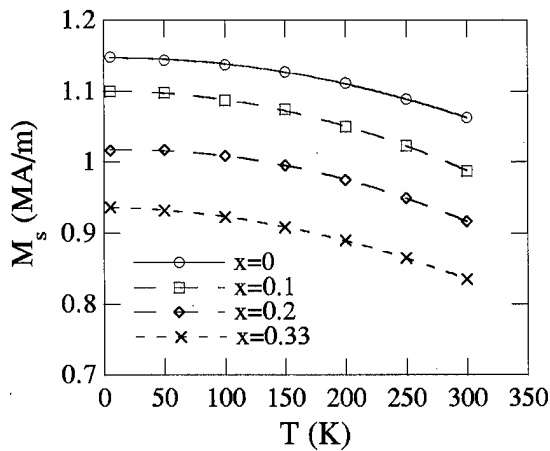


FIG. 2. Saturation magnetization vs temperature for $(\text{Fe}_{1-x}\text{Co}_x)_3\text{P}$. M_s is derived from fits of the experimental magnetization curves to the law of approach to saturation.

$$M = M_s \left(1 - \frac{b}{H^2} - \frac{c}{H^3} \right). \quad (3)$$

This equation is called the law of approach to saturation. The determination of K_1 using this method has some drawbacks. The magnetization rotation is not the only process involved. Local fields due to inhomogeneities and field induced increased spontaneous magnetization complicate the M vs H behavior. Instead of Eq. (3), the law of approach to saturation obtained by experiment is

$$M = M_s \left(1 - \frac{a}{H} - \frac{b}{H^2} - \frac{c}{H^3} \right) + \chi H, \quad (4)$$

where a is an inhomogeneity parameter and χ is the susceptibility, which also takes care of a dia- or paramagnetic contribution from the sample holder.

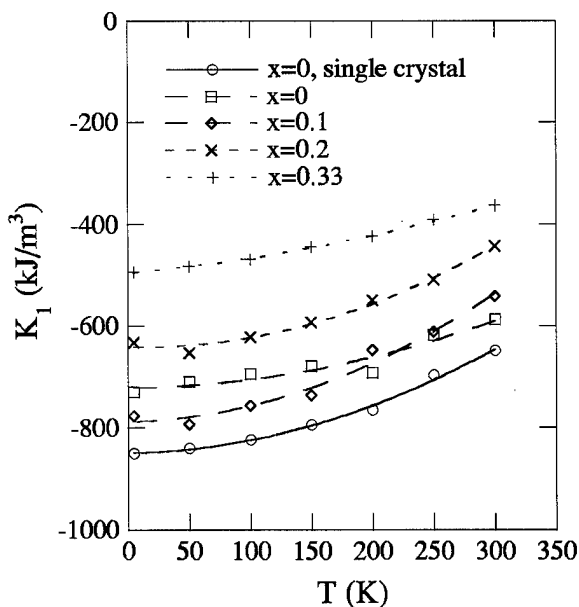


FIG. 3. K_1 vs T for $(\text{Fe}_{1-x}\text{Co}_x)_3\text{P}$. The estimated error in the data points due to scatter in the raw data and an uncertainty in the fitting procedure are about 40 kJ/m^3 for $x=0, 0.2$ and 0.33 and about 60 kJ/m^3 for $x=0.1$. The difference is due to a difference in the sample masses.

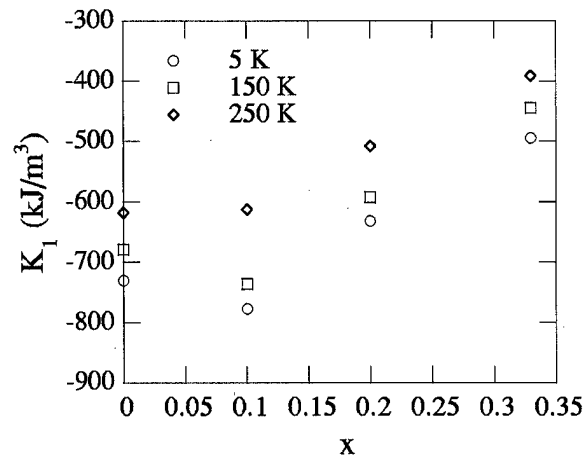


FIG. 4. K_1 at three different temperatures vs x .

II. EXPERIMENTS AND RESULTS

A single crystal disc of Fe_3P with the c axis in the disc plane was measured in a Quantum Design MPMS 5.5 T superconducting quantum interference device (SQUID) magnetometer. The magnetocrystalline anisotropy constants K_1 and K_2 were obtained by fitting H_a vs M data to Eq. (1). K_2 was found to be small and positive ($K_2 < 20 \text{ kJ/m}^3 \ll |K_1|$). Magnetization measurements on spherical sintered samples of $(\text{Fe}_{1-x}\text{Co}_x)_3\text{P}$ were carried out in a 5 T LakeShore magnetometer. The M vs H curves were analyzed using Eqs. (2) and (4). An easy planar behavior with $K_2 \ll |K_1|$ has thus been assumed for all temperatures and for all Co concentrations. For all the samples, the a/H term was omitted since the curve fits were not improved by it. In Fig. 2 the temperature dependence of the saturation magnetization is shown. The anisotropy constants of the different samples is plotted versus temperature in Fig. 3. In this region of Co concentration, the critical temperature decreases almost linearly from 692 K for $x=0$ to 646 K for $x=0.33$.⁵

The systematic difference in magnitude of K_1 for Fe_3P as derived from measurements on the single crystal compared to the results from the polycrystalline sample is probably due to some inadequacy in the derivation of K_1 from Eq. (4) using a limited field interval (9 kOe–50 kOe). The relative variation of K_1 with temperature and Co concentration should however be adequately captured. $|K_1|$ decreases quite regularly with temperature for all the samples. It is noticeable however that there is an increase of $|K_1|$ with x at low Co concentrations followed by a clear decrease at large values of x (see Fig. 4). First principles calculations of the MAE of $(\text{Fe}_{1-x}\text{Co}_x)_3\text{P}$ (Ref. 10) are now in progress.

ACKNOWLEDGMENT

Financial support from the Swedish Natural Science Research Council (NFR) is acknowledged.

¹O. Beckman and L. Lundgren, *Handbook of Magnetic Materials*, edited by K. H. J. Buschow (North-Holland, Amsterdam, 1991), Vol. 6.

²R. J. Gambino, T. R. McGuire, and Y. Nakamura, *J. Appl. Phys.* **38**, 1253 (1967).

³M. Goto, H. Tange, T. Tokunaga, H. Fujii, and T. Okamoto, *Jpn. J. Appl. Phys.* **16**, 2175 (1977).

- ⁴S. Rundqvist, Y. Andersson, and S. Pramatus, *J. Solid State Chem.* **28**, 41 (1979).
- ⁵Hui-Ping Liu, P. James, A. Broddefalk, P. Granberg, Y. Andersson and O. Eriksson (unpublished).
- ⁶A. J. P. Meyer and M.-C. Cadeville, *J. Phys. Soc. Jpn.* **17**, 223 (1962).
- ⁷E. J. Lisher, C. Wilkinson, T. Eriksson, L. Häggström, L. Lundgren, and R. Wäppling, *J. Phys. C* **7**, 1344 (1974).
- ⁸R. Grössinger, *Phys. Status Solidi A* **66**, 665 (1981).
- ⁹S.-C. Zhu, H.-Y. Chen, and F.-P. Wen, *IEEE Trans. Magn.* **30**, 6 (1994).
- ¹⁰O. Eriksson and P. James (private communication).

Magnetic moment and hyperfine field on Fe sites in $R\text{Fe}_6\text{Sn}_6$ compounds

Xiao-lei Rao,^{a)} J. Cullen, V. Skumryev, and J. M. D. Coey

Department of Physics, Trinity College Dublin, Dublin 2, Ireland

Electronic structure and hyperfine fields are calculated for antiferromagnetic YFe_6Sn_6 using the linear muffin-tin orbital method. The results show that Fe atoms have a strong ferromagnetic character with a full majority-spin band. The Fe moment is $2.2 \mu_B$ while the Fermi contact term contributes a hyperfine field of 20 T at the natural lattice parameters. The hyperfine field is close to the experimental value of 22 T measured at low temperature. The calculation shows that the core s electrons contribute 24 T to the hyperfine field, but the $4s$ electron contributes 4 T in the opposite direction. Calculations using different unit cell volumes reveal that only the core electron contributions to the hyperfine field are proportional to the Fe magnetic moment with a conversion factor of $11.8 \text{ T}/\mu_B$; the $4s$ contribution is not. The large local Fe moment and small hyperfine field are similar to those found in Fe_2P and FeO . © 1998 American Institute of Physics. [S0021-8979(98)51611-8]

I. INTRODUCTION

Fe-based heavy rare earth stannides of chemical formula $R\text{Fe}_6\text{Sn}_6$ with HfFe_6Ge_6 -derived crystal structures were first reported by Malaman *et al.*¹ and by Wang *et al.*² The rare-earth atoms and Sn–Sn dumbbell pairs in $R\text{Fe}_6\text{Sn}_6$ occupy a single crystallographic site in the HfFe_6Ge_6 -type unit cell in a complex way which makes otherwise equivalent Fe sites distinguishable. The nearest Fe–Fe distances are around 2.68 Å, 5% larger than in $\alpha\text{-Fe}$. The well-separated Fe atoms lead to strong ferromagnetism with a large magnetic moment. Recently we reported the results of a ^{57}Fe Mössbauer study of $R\text{Fe}_6\text{Sn}_6$ ($R=\text{Y}$, Gd, Tb, Dy, Ho, Er, and Tm) at room temperature and at 25 K.³ The spectra show a single sextet even though there are several Fe inequivalent iron sites in the unit cell. Hyperfine fields are almost the same for all R elements. At 25 K the values are around 22 T which would imply an average Fe moment of $1.5 \mu_B$ with the usual conversion factor of $15 \text{ T}/\mu_B$ found in many R–Fe compounds,⁴ $0.7 \mu_B$ less than $\alpha\text{-Fe}$. Because of the antiferromagnetism, the value of the Fe moment is difficult to obtain from magnetization measurements without a very high field.

Here we study the electronic structure and hyperfine fields of YFe_6Sn_6 using the linear muffin-tin orbital (LMTO) method in order to examine the relation between magnetic moment and hyperfine field on Fe sites. Calculations were made on expanded and contracted unit cells as well as at the natural cell volume.

II. BAND CALCULATION METHOD

The crystal structure of YFe_6Sn_6 is derived from the HfFe_6Ge_6 -type unit cell (Fig. 1) described by space group $P6/mmm$ where Fe 6i sites form planar layers. Ideally, the Y atoms occupy the Hf-1b site while Sn atoms enter into Ge-2c and Ge-2d sites and dumbbell Ge-2e sites. However real YFe_6Sn_6 crystallizes in a far more complex structure defined by the space group $Cmcm$ with 208 atoms and 9

inequivalent Fe sites in each unit cell. This complexity comes from the distribution of Y atoms and Sn–Sn 2e dumbbell pairs among the Hf-1b sites. Since the Mössbauer spectrum of the compound did not differentiate the Fe sites, an approximation is made to simplify the complex structure: we used the HfFe_6Ge_6 -type structure to define the unit cell and to assign the atomic positions according to the HfFe_6Ge_6 -type TmFe_6Sn_6 .⁵ Detailed information is shown in Table I. The lattice parameters of YFe_6Sn_6 , $a=5.371 \text{ Å}$ and $c=8.894 \text{ Å}$, are taken from the experimental x-ray diffraction pattern based on the HfFe_6Ge_6 -type structure. The ratio of c/a is kept constant for calculating the band structures for varied unit cell volumes. Concerning the magnetic structure, we assume a ferromagnetic coupling within the Fe layer and an antiferromagnetic coupling between the layers within one unit cell. Because of this antiferromagnetic coupling, the unit cell has to be doubled along the c direction to allow for the crystallographic and magnetic symmetry.

The LMTO⁶ has been employed within the atomic spheres approximation (ASA). Exchange and correlation interactions were treated with the local spin density functional (LSDF) approximation, using the form given by von Barth

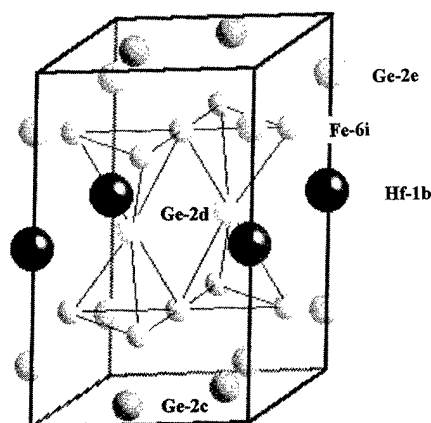


FIG. 1. The unit cell of HfFe_6Ge_6 .

^{a)}Electronic mail: huanlab@aphy02.iphy.ac.cn

TABLE I. Crystallographic data used for the YFe_6Sn_6 band calculations.

Compounds	Structure type	Space group	Atomic position		
YFe_6Sn_6	HfFe_6Ge_6	hP13 ($P6/mmm$, No. 191)	Fe	6i	(1/2, 0, 0.251)
			Sn1	2e	(0, 0, 0.162)
			Sn2	2d	(1/3, 2/3, 1/2)
			Sn3	2c	(1/3, 2/3, 0)
			Y	1b	(0, 0, 1/2)

and Hedin⁷ and by the parameters used by Janak.⁸ The scalar-relativistic approximation was used without considering the spin-orbit coupling.⁹ In the ASA, in most cases there is a reasonable region for choosing the ratio of the Wigner-Seitz sphere radii for different elements which only results in a variation of calculated moments of $0.05 \mu_B$ per magnetic atom, even smaller than the neglected orbital contribution. In the calculations reported here, the ratio $r_Y:r_{\text{Fe}}:r_{\text{Sn}}$ of 1.35:1:1.1 was chosen. With the experimental lattice parameters, the maximum overlap of the atomic spheres is less than 25%, which ensures a reliable convergence of the self-consistent calculations. The basis set of valence states is $4s$, $4p$, and $3d$ for Fe and $5s$, $5p$, and $4d$ for Y and Sn. The number of k points in the irreducible part of the Brillouin zone on which the calculation of the self-consistent potential was based was chosen to be 84. The total energy converged to within 10^{-4} Ry.

III. RESULTS AND DISCUSSION

The density of states (DOS) of the Fe $3d$ band in YFe_6Sn_6 with the natural lattice parameters and at 12.5% volume expansion or contraction are shown in Fig. 2. In all cases the majority and minority $3d$ bands are well split, with the Fermi level above the majority band, a typical feature for a strong ferromagnet. This is the result of the large Fe-Fe nearest-neighbor distance in YFe_6Sn_6 . The trend was clearly demonstrated on α -Fe band structures with different lattice parameters: its magnetic state at the natural lattice parameter $a=2.86 \text{ \AA}$ is a weak ferromagnet. At larger lattice parameters, the $3d$ electrons become more localized. The bandwidth decreases and the Fermi level shifts towards the top of the spin-up subband. When the lattice parameter reaches 2.96 \AA (the Fe-Fe distance is 2.56 \AA), the $3d$ spin-up band is full. The ferromagnetic state now has a strong ferromagnetic character. Since there are no other electrons available, the increased states in the spin-up band of α -Fe can only be filled by its spin-down $3d$ electrons. The net magnetic moment increases until strong ferromagnetism is realized. In comparison, the Fe-Fe distance in YFe_6Sn_6 is 2.68 \AA . A strong ferromagnetic feature is expected when the lattice parameter dependence is similar to that of α -Fe. The long tail with energy below -0.3 Ry is due to the Sn hybridization, which can be recognized by the Sn- $2e$ band (inset in Fig. 2).

The calculated magnetic moment of Fe, which is $2.2 \mu_B$ at the experimental lattice parameters, is much higher than the value estimated from Mössbauer spectra but lower than the moment in α -Fe with the same Fe-Fe distance. Charge transfer and hybridization of neighboring Sn electrons reduce

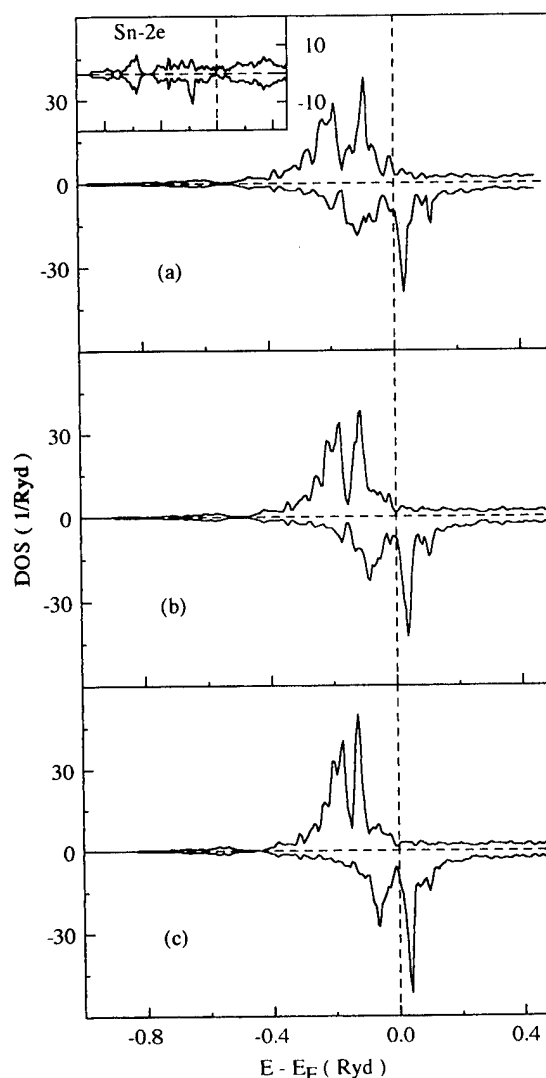


FIG. 2. The density of states at iron sites in YFe_6Sn_6 with (a) 12.5% volume contraction, (b) natural unit cell volume, and (c) 12.5% expansion. Inset is the DOS of the Sn- $2e$ site.

the value of the moment. The corresponding hyperfine field is -20 T . As the lattice parameters vary, both the magnetic moments [Fig. 3(a)] and the absolute value of hyperfine fields [Fig. 3(b)] increase with enlarged unit cell volumes. The $4s$ contribution to the hyperfine field which increases linearly with the unit cell volume is opposite to the core contributions in direction. The latter feature is quite different from most of the R-T intermetallics where both contributions are in the same direction, resulting in larger total hyperfine fields. The reason is that the $4s$ valence electrons are polarized in the same direction as the Fe $3d$ moment. In many other R-Fe compounds, where the Fe $3d$ bands have a weak ferromagnetic character because the average Fe-Fe distance is only about 2.55 \AA , the $4s$ - $3d$ hybridization then pushes the $4s$ majority weight above the Fermi level and leads to less $4s$ majority occupation. The opposite phenomenon occurs for the minority band. This results in a negatively polarized $4s$ shell, whose contribution to the hyperfine field is in the opposite direction to the Fe $3d$ moment but in the same direction as the core s electron hyperfine field. However in the strong magnetic state as in YFe_6Sn_6 , the

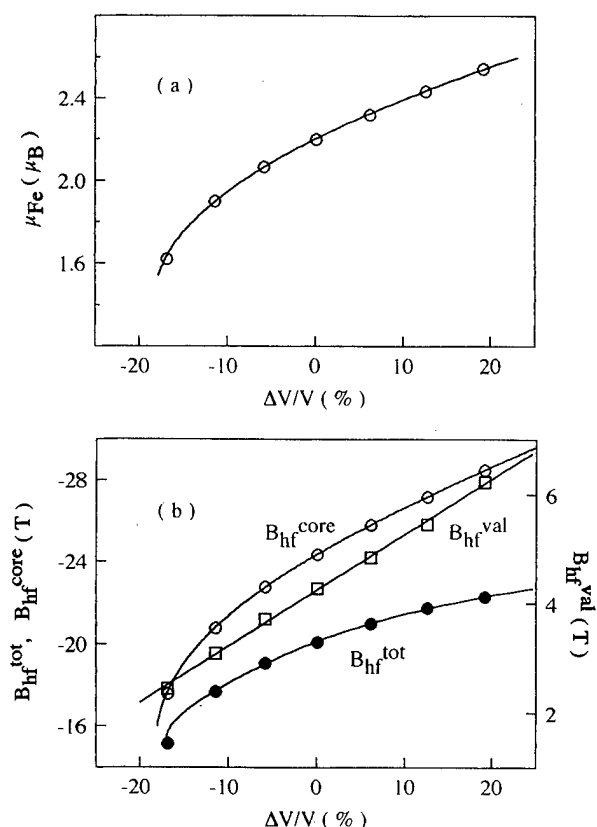


FIG. 3. Unit cell volume dependence of (a) Fe magnetic moments and (b) Fe hyperfine fields in YFe_6Sn_6 .

majority 3d band is full. Direct ferromagnetic 4s mixing into the majority band dominates the above antiferromagnetic hybridization. The hyperfine field of the 4s electrons is in the same direction as Fe moment. Similar behavior was reported by Eriksson *et al.* for the Fe_2P and FeO hyperfine interactions¹⁰ because in both cases the Fe atoms are strongly ferromagnetic.

Upon plotting the hyperfine fields against magnetic moments on Fe sites for different unit cell volumes, as shown in Fig. 4, only the contribution of core electrons to the hyperfine field increases linearly with the local moment. The non-linear relation between the valence 4s electron term in the hyperfine field makes the relation between the magnetic moment and the total hyperfine field deviate from linearity. The slope of the core electron contribution is 11.3 T/ μ_B , just at the lower limit of the data observed experimentally. The total hyperfine field at the natural cell volume is 20 T, 10% lower than the experimental value measured at 25 K. This may be attributed to an overestimate of the valence contributions since the DOS already shows that the covalent tendency is

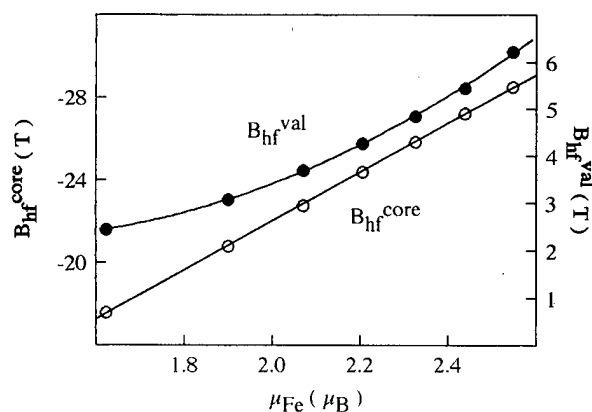


FIG. 4. The hyperfine fields as a function of magnetic moments on Fe sites in YFe_6Sn_6 with different unit cell volumes.

relatively strong for the $\text{Fe}6i\text{-Sn}2e$ neighbors. The LMTO method has limited power in handling less itinerant systems.

IV. CONCLUSION

Because of the strong ferromagnetic character of the Fe electronic structure due to the large Fe-Fe nearest-neighbor distance and because of the electron transfer from neighboring Sn atoms, the Fe atoms in YFe_6Sn_6 bear a large magnetic moment of 2.2 μ_B but show a relatively small hyperfine field of only 20 T. Proportionality of hyperfine fields and magnetic moments on the Fe sites only holds for the core electron contribution or when the valence electron contribution to the hyperfine field is negligible.

ACKNOWLEDGMENTS

The authors are grateful to Dr. M. Fähnle of the Max-Planck-Institut für Festkörperforschung in Stuttgart for providing the original code for the LMTO-ASA calculations. They are indebted to Dr. Qi-nian Qi for adapting the code for the present calculations.

- ¹B. Malaman, G. Venturini, and B. Roques, *Mater. Res. Bull.* **23**, 1629 (1988).
- ²Y. B. Wang, D. Wiarda, D. H. Ryan, and J. M. Cadogan, *IEEE Trans. Magn.* **30**, 4951 (1994).
- ³X.-L. Rao and J. M. D. Coey, *J. Appl. Phys.* **81**, 5181 (1997).
- ⁴P. C. M. Gubbens, J. H. F. van Apeldoorn, A. M. van der Kraan, and K. H. J. Buschow, *J. Phys. F* **4**, 921 (1975).
- ⁵B. Chafik El Idrissi, G. Venturini, and B. Malaman, *Mater. Res. Bull.* **26**, 1331 (1991).
- ⁶O. K. Andersen, *Phys. Rev. B* **12**, 3060 (1975).
- ⁷U. von Barth and L. Hedin, *J. Phys. C* **5**, 1629 (1972).
- ⁸J. F. Janak, *Solid State Commun.* **25**, 53 (1978).
- ⁹D. D. Koelling and B. N. Harmon, *J. Phys. C* **10**, 3107 (1977).
- ¹⁰O. Eriksson, J. Sjöström, B. Johansson, L. Häggström, and H. L. Skriver, *J. Magn. Magn. Mater.* **74**, 347 (1988).

Hydrogen-induced changes in TbNiAl

H. N. Bordallo, H. Nakotte,^{a)} and J. Eckert

MLNSC, Los Alamos National Laboratory, Los Alamos, New Mexico 87545

A. V. Kolomiets and L. Havela

Department of Metal Physics, Charles University, 12116 Prague 2, The Czech Republic

A. V. Andreev

Academy of Sciences of the Czech Republic, 18040 Prague 8, The Czech Republic

H. Drulis and W. Iwasieczko

Polish Academy of Sciences, 50-950 Wroclaw, Poland

Neutron diffraction was used to determine the deuterium sites in TbNiAlD_{1.28} and TbNiAlD_{0.8}. Both samples were found to crystallize in the orthorhombic Amm2 space group. Our analysis reveals that deuterium in TbNiAlD_{1.28} occupies positions at $x=0$ and $x=1/2$ only, while TbNiAlD_{0.8} shows the formation of two different phases. For TbNiAlD_{1.28}, additional magnetic reflections are observed below 16 K indicating antiferromagnetic order. On the other hand, at 10 K, only one of the TbNiAlD_{0.8} phases was found to be magnetic. In addition, our study of the localized vibrations of hydrogen in TbNiAlH_{1.39} and in its non-magnetic analog YNiAlH_{1.35} using inelastic neutron scattering supports the existence of two different hydrogen sites in the saturated hydrides. © 1998 American Institute of Physics. [S0021-8979(98)33611-7]

Although hydrides of intermetallic compounds are used extensively as hydrogen-storage media,¹ little is known about the exact nature of metal-hydrogen interactions. However, this knowledge is of essential importance for the understanding of thermodynamic and other properties.

Magnetic order in intermetallic TbNiAl is based on well-defined $4f$ moments, which are coupled by indirect exchange interaction of *RKKY* type. Ehlers and Maletta² found that this compound undergoes two magnetic phase transitions around 23 and 47 K, forming complex magnetic structure. They reported, based on neutron-diffraction data, that magnetic ordering occurs in two Tb sublattices, described by two different propagation vectors, i.e., $\mathbf{q}=(1/2,1/2,1/2)$ and $\mathbf{q}=(1/2,0,1/2)$. Recently, it was shown that introduction of hydrogen (deuterium) into TbNiAl can lead to drastic alterations of its magnetic properties.³ Furthermore, x-ray studies revealed that hydrogenation (deuteration) is accompanied by orthorhombic distortion of the hexagonal ZrNiAl-type structure,⁴ adopted by pure TbNiAl, but the location of H(D) atoms in the crystal lattice remained unknown.

Here we report on some properties (crystal and magnetic structures, lattice vibration) of TbNiAl hydrides and deuterides studied by means of neutron diffraction and inelastic neutron scattering.

Samples were prepared by arc melting. Several remeltings were done in order to achieve high homogeneity. Crystal structure of the obtained compound had been checked by x-ray analysis, which confirmed that it was a single-phase TbNiAl polycrystal. Hydrides (deuterides) were obtained as follows: first, the intermetallic compound was crushed and activated in the high vacuum of $\sim 10^{-6}$ Torr at 350 °C for 1

h, afterwards it was cooled down to room temperature and exposed to H(D) at 10 atm pressure. Amount of absorbed H was determined by monitoring decrease of pressure in the calibrated volume. In order to obtain the lower deuteride, the saturated sample was heated up to 155 °C and kept at this temperature until pressure has stabilized. Then the reaction chamber was disconnected from the hydrogenation system and cooled down to the room temperature. X-ray analysis was used to check to quality of the resulting compounds.

For the neutron-diffraction experiments, powder samples of TbNiAlD_{1.28} and TbNiAlD_{0.8} were ground and sealed in vanadium tubes under helium atmosphere. Diffraction data were taken at various temperatures between 5 and 300 K using the powder diffractometers NPD and HIPD at the Lujan Center. NPD is a high-resolution diffractometer, used for crystal-structure refinements, with four detector banks covering d -spacings up to 4 Å, while HIPD is a high-intensity diffractometer, well suited for magnetic-structure refinements, with eight detector banks covering a range up to 20 Å. The data were analyzed by using the Rietveld-refinement program package GSAS.⁵

For the inelastic-neutron-scattering studies, hydrogenated samples of YNiAlH_{1.35} and TbNiAlH_{1.39} were sealed under helium atmosphere in aluminum cans. Measurements were performed at low temperatures using the filter difference spectrometer (FDS) at the Lujan Center. The spectra shown in Fig. 3 are obtained by numerical deconvolution of the instrumental function from the raw data.⁶

Our Rietveld refinements on TbNiAlD_{1.28} and TbNiAlD_{0.8} indicate that both compounds form in the base-centered orthorhombic space group Amm2, with structural parameters as given in Tables I and II, respectively. Using an orthorhombic notation, a hexagonal unit cell can be described by the parameters a , b , c , and $b=a\sqrt{3}$. If the hexagonal structure is distorted, we get $a/b \neq \sqrt{3}$. Here we cho-

^{a)}Permanent address: Department of Physics, New Mexico State University, Las Cruces, New Mexico 88003.

TABLE I. Refined structural parameters for TbNiAlD_{1.28} at 300 K.

Atom	Site	x	y	z	% occupancy
Tb(1)	4e	0.5	0.2096 (2)	0.0434 (3)	100
Tb(2)	2b	0.5	0	0.6550 (4)	100
Ni(1)	4d	0	0.3319 (2)	0.2751 (3)	100
Ni(2)	2b	0.5	0	0.2481 (3)	100
Al(1)	4d	0	0.1179 (4)	0.3339 (6)	100
Al(2)	2a	0	0	0	100
D(1)	4e	0.5	0.3330 (3)	0.2628 (6)	98±1
D(2)	4d	0	0.3834 (3)	0.07775 (4)	94±1

$a=3.73422(7)$ Å, $b=12.3667(3)$ Å, $c=7.627775(2)$ Å; R factors: $R_{wp}=4.8\%$; $R_p=3.5\%$; Reduced $\chi^2=1.7$.

sed to use the standard notation of the space group Amm2, defined for this structure. Therefore, in the present article the coordinates a and c are interchanged, comparing to the notation mentioned above.

Atom fractions of Tb, Ni, and Al were found to be very close to the exact 1:1:1 stoichiometry, and we subsequently refined only the D fractions in the two samples.

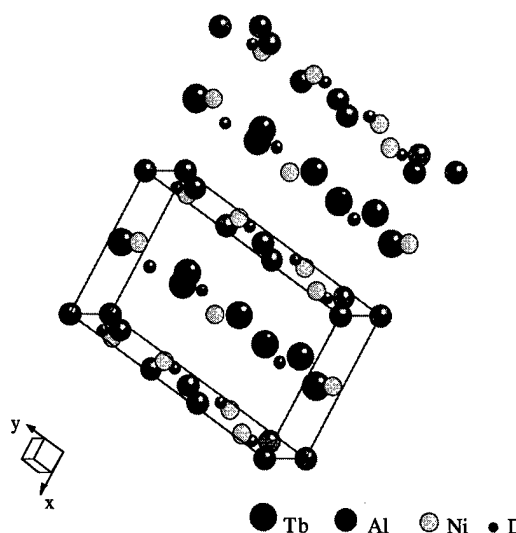
The room-temperature refinement on TbNiAlD_{1.28} clearly indicates that only two different fourfold interstitial positions are occupied by D atoms (Table I) (which seems to be in contradiction to four different D positions in TbNiAlD_{1.04}, recently reported by Yartys *et al.*⁷). The resulting structure is shown in Fig. 1.

The diffraction data on the second sample (which had a nominal composition of about TbNiAlD_{0.8}) indicate the formation of two phases with quite different lattice parameters. The GSAS software package allows the parallel refinement of multiple phases, and our best fit yielded two phases: a main phase of TbNiAlD_{0.81} and an "impurity phase" of TbNiAlD_{0.83} with volume fractions of about 70% and 30%, respectively. The structure of the main phase is found to be closely related to those of TbNiAlD_{1.28} (Table II) with the D occupying positions in the $x=0$ and $x=1/2$ planes only. For

TABLE II. Refined structural parameters of TbNiAlD_{0.8}, main (phase 1) and impurity (phase 2) phases, at room temperature.

Phase	Atom	Site	x	y	z	% occupancy
1	Tb(1)	4e	0.5	0.211 (4)	0.027 (2)	100
	Tb(2)	2b	0.5	0	0.636 (2)	100
	Ni(1)	4d	0	0.3286 (4)	0.205 (2)	100
	Ni(2)	2b	0.5	0	0.231 (2)	100
	Al(1)	4d	0	0.125 (1)	0.335 (3)	100
	Al(2)	2a	0	0	0	100
	D(1)	4e	0.5	0.322 (1)	0.217 (3)	81±1
	D(2)	4d	0	0.346 (1)	0.015 (3)	44±2
2	Tb(1)	4e	0.5	0.2069 (4)	0.052 (4)	100
	Tb(2)	2b	0.5	0	0.659 (4)	100
	Ni(1)	4d	0	0.3339 (7)	0.249 (3)	100
	Ni(2)	2b	0.5	0	0.247 (3)	100
	Al(1)	4d	0	0.117 (3)	0.353 (1)	100
	Al(2)	2a	0	0	0	100
	D(1)	8f				44.0±0.4
	D(2)	8f				16.7±0.7

Phase 1: $a=3.8396(1)$ Å, $b=12.4571(6)$ Å, $c=7.2877(4)$ Å; Phase 2: $a=3.91174(8)$ Å, $b=12.3524(8)$ Å, $c=7.1206(4)$ Å; R factors: $R_{wp}=10\%$; $R_p=7\%$; reduced $\chi^2=12$.

FIG. 1. Crystal structure at room temperature of TbNiAlD_{1.28} and TbNiAlD_{0.8} (main phase).

the impurity phase, on the other hand, we have indications that the D atoms are located between those planes. However, data on a single-phase sample are needed in order to determine their exact positions. The structure of the main phase (TbNiAlD_{0.81}) is the same as the one shown in Fig. 1. For both phases, we find that only a fraction of the D positions are occupied (see Table II).

For both samples, magnetic ordering sets in at low temperatures. In TbNiAlD_{1.28}, the HIPD data revealed two extra peaks at 7.21 and 12.90 Å, which occur below 16 K [Fig. 2(a)]. These reflections are magnetic in origin and can be indexed in the Amm2 cell with doubled a and b axis, indicating a magnetic propagation vector of $\mathbf{q}=(1/2,1/2,0)$. Similarly, in the biphasic sample (TbNiAlD_{0.8}), magnetic reflections are seen at the 20 K NPD data, which are absent at room temperature [Fig. 2(b)]. Closer inspection reveals that some magnetic contributions can be indexed assuming a cell doubling of a and b axis of the main phase, where the D atoms occupy $x=0$ and $x=1/2$ positions.

These findings provide evidence that D may occupy different positions in the crystal lattice, and magnetic properties of the material are strongly dependent on the location of those atoms. The location of D (H) in these materials seems to be extremely sensitive to small differences in such conditions, as sample preparation, aging, etc. This may explain recent bulk magnetic results, where different behavior was reported for some TbNiAl deuterides and hydrides with equal nominal compositions.³ Furthermore, our neutron results indicate a ratio between main and impurity phases of TbNiAlD_{0.8} of about 3:1, while x rays performed some few months earlier indicated a phase ratio of 10:1 only.⁸ This may indicate that (some of) the phases are not stable enough and decomposition or phase transformation may influence the properties in addition. A detailed study of samples with different history is required in order to confirm this.

Hydrogen vibrations in metals can be observed only by inelastic neutron scattering, which selectively probes hydrogen motions because of the large neutron scattering cross

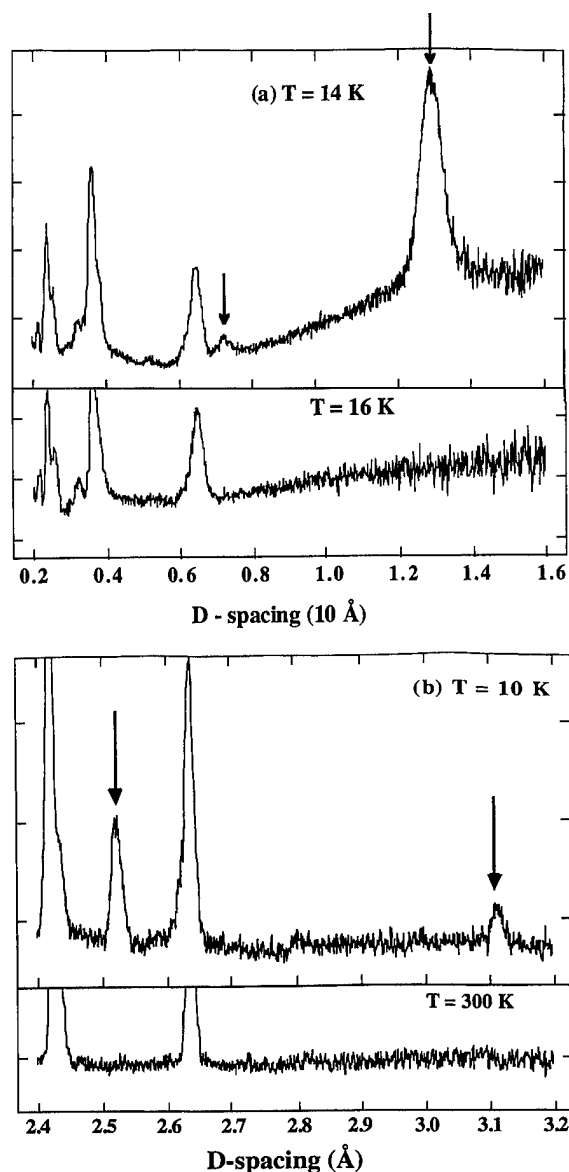


FIG. 2. Portion of the powder patterns for (a) TbNiAlD_{1.28} taken at 14 and 16 K on HPD, and (b) TbNiAlD_{0.8} taken at 10 K and at room temperature on NPD. Magnetic reflections seen at low temperature in the upper panels are marked by arrows.

section of hydrogen. The vibrational spectra of hydrogen for TbNiAlH_{1.39} and its nonmagnetic⁹ analog, YNiAlH_{1.35}, measured at 40 and 20 K, respectively, are displayed in Fig. 3. The deconvoluted spectra were fitted using a Gaussian line shape for the peaks. The results are shown as solid lines in Fig. 3.

The YNiAlH_{1.35} spectrum shows three main bands at about 430, 937, and 1200 cm⁻¹. In addition, shoulders at 540, 832, and 1055 cm⁻¹ can be distinguished. The results are very similar to those obtained on LaNi₅H_{0.15}.¹⁰ In that work, the existence of two H sites was assumed, because, in absence of any degeneracy, each H site gives rise to three vibrations modes. NMR measurements on YNiAlH_x by Bandyopadhyay *et al.*¹¹ also indicate that H occupies two different interstitial sites, with different degrees of mobility.

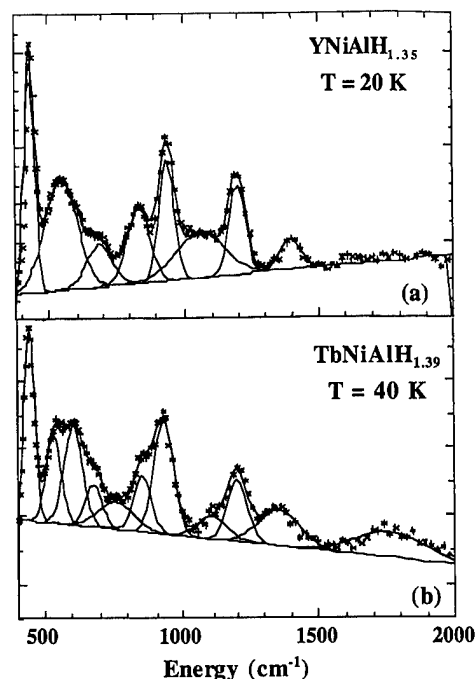


FIG. 3. Inelastic-neutron-scattering results of (a) YNiAlH_{1.35} at 20 K and (b) TbNiAlH_{1.39} at 40 K. The gaussian fits represent the localized hydrogen vibrations.

Therefore, we may assume a similar assignment of the modes observed in YNiAlH_{1.35}: the strong bands are characteristic for the first hydrogen site, while the shoulders may be assigned to the second site.

Our spectrum of TbNiAlH_{1.39} is similar to the spectrum of YNiAlH_{1.35}: main vibrational bands observed at 449, 935 (with shoulder at 857 cm⁻¹), and 1203 cm⁻¹ (with shoulder at 1110 cm⁻¹). However, the scattering intensity around 540 cm⁻¹ is now split into two peaks, which are located at 535 and 606 cm⁻¹, respectively.

In conclusion, we propose an assignment of the vibrational modes YNiAlH_{1.35} and TbNiAlH_{1.39} to specific H sites. Nevertheless, a reliable assignment of the modes is possible only with the aid of calculations. For this purpose, we have initiated a vibrational analysis for these systems.

The authors thank R. A. Robinson for helpful discussions. Work at the Lujan Center was supported by the Department of Energy, Basic Energy Sciences under Contract No. W-7405-ENG-36 and the Grant Agency of the Czech Republic, Grant No. 106/98/0507.

¹Hydrogen in Intermetallic Compounds, edited by L. Schlapbach (Springer, Berlin, 1988).

²G. Ehlers and H. Maletta, Z. Phys. B **99**, 145 (1996).

³A. V. Kolomiets *et al.*, J. Alloys Comp. **253-254**, 343 (1997).

⁴I. Jacob, Z. Hadari, and J. J. Reilly, J. Less-Common Met. **103**, 123 (1984).

⁵A. C. Larson and R. B. Von Dreele, Los Alamos National Laboratory Report L-UR-86-748.

⁶D. S. Sivia *et al.*, Nucl. Instrum. Methods Phys. Res. A **290**, 492 (1990).

⁷V. A. Yartys *et al.*, J. Alloys Comp. (to be published).

⁸A. V. Kolomiets (private communication) (1997).

⁹B. Bandyopadhyay *et al.*, Phys. Rev. B **38**, 8455 (1988).

¹⁰R. Hempelmann *et al.*, J. Less-Common Met. **104**, 1 (1984).

¹¹B. Bandyopadhyay *et al.*, J. Phys.: Condens. Matter **2**, 1253 (1990).

Thermal transport in $\text{Sr}_{1-x}\text{Ca}_x\text{RuO}_3$

M. Shepard, P. F. Henning,^{a)} G. Cao, and J. E. Crow

National High Magnetic Field Laboratory, 1800 E. Paul Dirac Drive, Tallahassee, Florida 32306

We have studied the thermal conductivity $K(T, B)$ ($6 < T < 250$ K, $0 < B < 15$ T) of single crystals of SrRuO_3 , a ferromagnet with $T_c = 160$ K, and isostructural but paramagnetic CaRuO_3 , as well as the intermediate crystals $(\text{Sr}, \text{Ca})\text{RuO}_3$ for the purpose of probing charge carrier (K_e), phonon (K_p), and magnon (K_m) excitations in these systems. The contributions of electron and phonon scattering processes to the thermal conductivities have been estimated using a Wiedemann-Franz relationship to estimate K_e and thus obtain K_p at higher temperatures. Roughly 50% of the thermal conductivity is estimated to be phononic near room temperature. Amorphous behavior is observed in the doped samples, and no break in the thermal conductivity is seen at the ferromagnetic onset. A comparison of magnetothermal conductivity and magnetoresistivity measurements at lower temperatures in SrRuO_3 and CaRuO_3 reveals that additional scattering mechanisms have become important. These investigations argue for the importance of phonon and magnon contributions, in addition to electronic contributions, to the magnetic behavior in $\text{Sr}_{1-x}\text{Ca}_x\text{RuO}_3$. Results will be discussed in relation to recent theoretical work on these systems and measurements on related systems. © 1998 American Institute of Physics. [S0021-8979(98)33711-1]

I. INTRODUCTION

SrRuO_3 and CaRuO_3 along with the mixed crystals, i.e., $(\text{Sr}, \text{Ca})\text{RuO}_3$ are interesting systems where electron correlations and lattice distortions may have a profound impact on their ground state electronic and magnetic properties.¹ Although SrRuO_3 and CaRuO_3 are isostructural, crystallizing in a distorted perovskite structure with similar lattice parameters, SrRuO_3 is an itinerant ferromagnet with $T_c = 160$ K, while CaRuO_3 remains paramagnetic to 30 mK apparently due to a slightly more distorted structure, due to Ca's smaller ionic radius ($\text{Sr} = 1.18$ Å vs $\text{Ca} = 1.00$ Å). The stark contrast between SrRuO_3 and CaRuO_3 is surprising because the s -like character of Sr and Ca do not have a density of states at the Fermi surface and therefore should not be a driving force for the ground states of these two compounds.² This lack of sensitivity of the magnetic ground state to Sr and Ca suggest that lattice distortions may play a dominant role in determining their ground states. The sensitivity of the magnetic ordering to small structural changes is similar to the behavior seen in ferromagnetic lanthanum manganite perovskites,³ where the Mn-O-Mn bond angle is important to the magnetic ground state and magnetic ordering temperature. Recently, work presented on the magnetic and transport properties of $\text{Sr}_{1-x}\text{Ca}_x\text{RuO}_3$ single crystals indicates a steady decrease in the ferromagnetic transition temperature as the Ca concentration is increased, with signs of magnetic ordering appearing at as low a concentration as $x = 0.99$, i.e., 1% Sr in CaRuO_3 .⁴ In addition, the easy axis for magnetization within the ferromagnetic state of SrRuO_3 is in the ab plane and rotates out of the ab plane with increasing Ca doping. The magnetic hysteresis also appears to increase with increasing x for the mixed crystals. Since local lattice distortions appear to drive the magnetic ground state behavior of

the $(\text{Sr}, \text{Ca})\text{RuO}_3$ system, thermal conductivity measurements may be a useful probe of coupling of the lattice, i.e., phonons, to the magnetic and electronic excitations.

Recent studies of the thermal conductivity in the lanthanum manganites indicate a large lattice contribution to the thermal conductivity, as well as a strong link between the lattice and the magnetic properties.^{5,6} The field dependence of the thermal conductivity of SrRuO_3 has been recently reported and evidence for magnons below the ordering temperature and coupling of the lattice to the magnons is demonstrated.⁷ In this article, the behavior of the thermal conductivity in $\text{Sr}_{1-x}\text{Ca}_x\text{RuO}_3$ will be presented and discussed in the framework of the contributions of electrons and phonons to the total thermal conductivity, as well as to the nature of the ferromagnetism.

II. EXPERIMENTAL RESULTS AND DISCUSSION

Single crystals of SrRuO_3 and CaRuO_3 were grown by a flux growth technique described previously.⁴ The thermal conductivity was measured by a standard steady-state one heater, two thermometer technique. The thermometers used were $12.5\ \mu\text{m}$ type E differential thermocouples; magnetic field dependences of the thermocouples were corrected.⁸ The heater was a $100\ \Omega$ RuO_2 chip heater with little temperature variation of the resistance over the temperature range of interest. The base temperature was monitored with a Cernox thermometer. Field was parallel to the c axis and the heat flow was applied along the a - b plane. Resistivity measurements were made using a standard four-probe dc technique, with field applied parallel to the c axis and current flow applied in the ab plane. Errors in the absolute values of the measurements are limited by the size of the samples, typically $0.4\ \text{mm} \times 0.4\ \text{mm} \times 0.1\ \text{mm}$, with an error from size calculations determined to be $< 10\%$.

In Fig. 1 is shown the thermal conductivity $K(T)$ versus temperature measured for several $\text{Sr}_{1-x}\text{Ca}_x\text{RuO}_3$ crystals.

^{a)}Present address: Department of Physics, Brookhaven National Laboratory, Upton, NY.

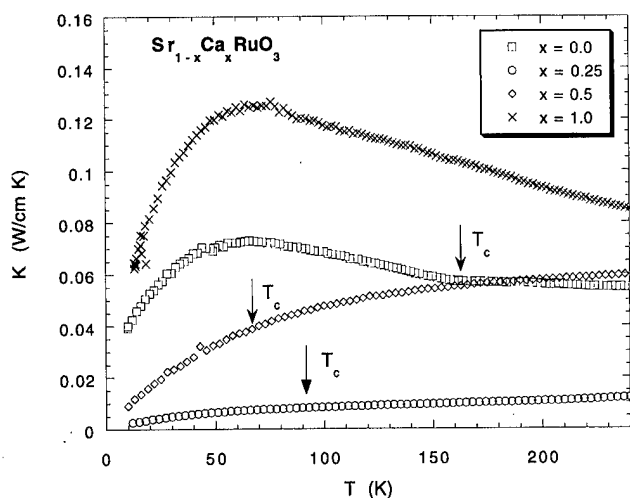


FIG. 1. Thermal conductivity vs temperature for $\text{Sr}_{1-x}\text{Ca}_x\text{RuO}_3$. The ferromagnetic Curie temperatures T_c are indicated by arrows.

The magnitudes of $K(T)$ at 250 K, ranging from 8 to 1 W/m K are comparable to values reported for LaMnO_3 (Refs. 5, 6) as well as YBCO.⁹ In comparison, the thermal conductivity of a good metal is much larger, e.g., Cu at room temperature is on the order of 400 W/m K. Shown in Fig. 2 is the temperature dependence of the resistivity for $(\text{Sr}, \text{Ca})\text{RuO}_3$; like the high-temperature superconducting compounds, the resistivity at and above room temperature varies linearly with T . For SrRuO_3 , the calculated mean free path is on the order of the lattice spacing, typical of “bad metals.”¹⁰ As shown in Fig. 2, a clear anomaly is seen in the resistivity at the Curie temperature, T_c .

The thermal conductivities of both SrRuO_3 and CaRuO_3 increase as the temperature decreases ($dK/dT < 0$) at higher temperatures. An Umklapp-limited peak occurs as lattice impurities dominate over phonon processes at approximately the same temperature, 60 K, followed by a drop in the thermal conductivity at low temperatures. For an electronic system, low-temperature thermal resistivity typically follows a power law given by

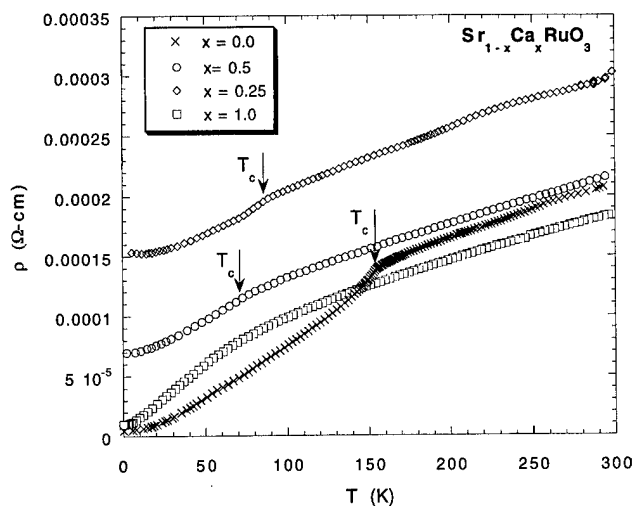


FIG. 2. Electrical resistivity vs temperature for $\text{Sr}_{1-x}\text{Ca}_x\text{RuO}_3$. The ferromagnetic Curie temperatures T_c are indicated by arrows.

$$W(e) = \frac{a}{T} + bT^2, \quad (1)$$

where $W(e) = 1/K(e)$, a/T represents impurity scattering, and bT^2 is due to electron-phonon scattering. At sufficiently low temperatures, the thermal conductivity then usually drops off as T . In addition, SrRuO_3 has a slope change in the thermal conductivity at the ferromagnetic ordering T_c for both the electrical and thermal conductivities. In contrast, the crystals with $x=0.25$ and $x=0.5$ do not display any anomalies in $K(T)$ at T_c even though a clear anomaly is observed in the resistivity. At high temperatures, $K(T)$ for $x=0.25$ and 0.50 behave similar to amorphous materials ($dK/dT > 0$). The Umklapp-limiting peak is not present. This is similar to behavior seen in thermal conductivities measured for certain dopings of LaMnO_3 .^{5,6} The amorphous-like behavior of the thermal conductivity reflects a reduction in the mean free path of the carriers as increasing lattice impurities or distortions decrease the electron and phonon scattering lifetimes. This is puzzling since these are high quality single crystals.

Resistivity data from $\text{Sr}_{1-x}\text{Ca}_x\text{RuO}_3$ can be used to estimate the electronic thermal conductivity using the Wiedemann-Franz law $K(e) = L_0 T / \rho$, where $L_0 = 2.4 \times 10^{-8} \text{ W}/\Omega \text{ K}^2$ is the ideal Lorenz number, and ρ is the resistivity. Using data obtained from Fig. 2, and assuming that in this region $K(\text{tot}) = K(e) + K(\text{ph})$, the phonons account for $\sim 50\%$ of the thermal conductivity. By comparison, in a good metal like Cu the phonon portion will be on the order of 5%. An estimate of the Lorenz number for SrRuO_3 has been obtained assuming the anomaly in both $\rho(T)$ and $K(T)$ is solely driven by critical scattering of the electron transport. In Fig. 3, an expanded view of $K(T)$ and $\rho(T)$ above and below T_c are shown. Assuming that contributions to the magnetic critical scattering in the vicinity of T_c are electronic in nature and the phonons only contribute a smooth temperature dependence to $K(T)$, we can estimate the Lorenz number from the following expressions:

$$K(\text{tot}) = K(\text{ph}) + \frac{LT}{\rho}, \quad (2)$$

$$\frac{dK}{dT} = \frac{dK(\text{ph})}{dT} + \frac{L}{\rho} + \frac{LT}{\rho^2} \frac{d\rho}{dT}. \quad (3)$$

Taking the limits as $T \rightarrow T_c$ from both sides, the Lorenz number for SrRuO_3 is determined to be $L = 1.63 \times 10^{-8} \text{ W}/\Omega \text{ K}^2$. This is smaller than the ideal Lorenz number, $L = 2.4 \times 10^{-8} \text{ W}/\Omega \text{ K}^2$.

To better understand the relative importance of electrons and phonons to $K(T)$, the magnetic field dependences of $K(T)$ and $\rho(T)$ have been measured. Measurements of thermal and electrical magnetoresistivities are summarized for SrRuO_3 and CaRuO_3 in Fig. 4, where $[\rho(B) - \rho(0)]/\rho(0)$ and $[W(B) - W(0)]/W(0)$ with $W = 1/K$ are shown. For SrRuO_3 , the field dependences of the electrical and thermal resistivities are both negative at higher temperatures, as the resistance is decreased due to a reduction in electronic scattering processes. As the temperature is reduced, the electrical magnetoresistivity decreases, displaying a maximum near the

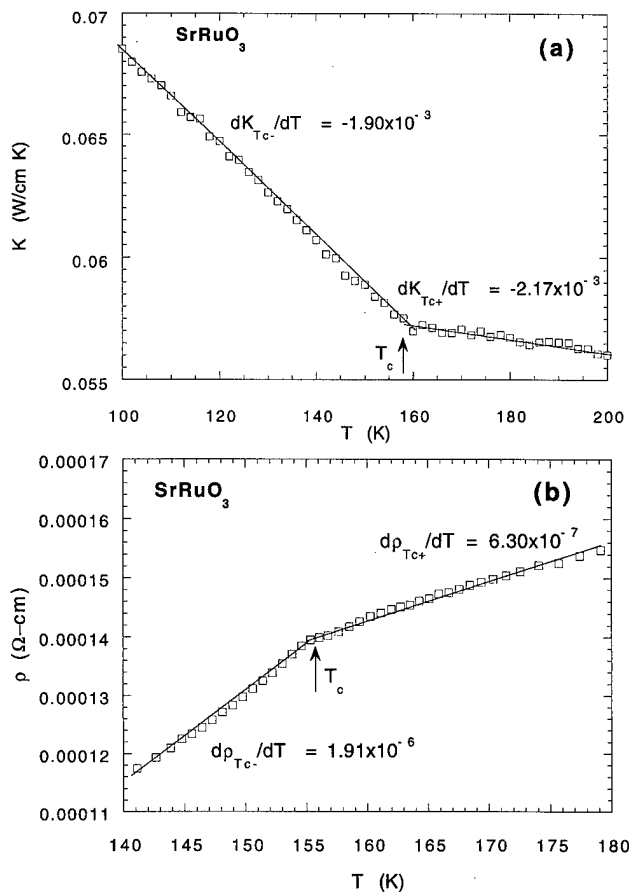


FIG. 3. (a) The slopes of K vs T above and below T_c . (b) The slopes of ρ vs T above and below T_c . These values are used to estimate a Lorenz number of $L = 1.63 \times 10^{-8}$ W/ Ω K² in SrRuO₃.

ferromagnetic transition. Such behavior is characteristic of ferromagnetic systems where the damping of the ferromagnetic fluctuations in the vicinity of T_c leads to a negative magnetoresistance peaking around T_c . However, the thermal magnetoresistance has a maximum value near the Umklapp-limiting peak, before decreasing and changing signs at lower temperatures. In CaRuO₃, the electrical magnetoresistance is small (<2%) at all temperatures, but the magnetothermal resistivity has a substantial contribution at temperatures below 60 K. This field dependence is unexpected, since there is no magnetic ordering in CaRuO₃. However, a very small percentage of doping ($\sim 1\%$) does lead to magnetic tendencies in this compound. High field magnetization data, as well as a large Pauli susceptibility term, indicate that CaRuO₃ is a strongly exchange-enhanced paramagnet, which points to the possibility of spin fluctuations contributing to scattering processes at lower temperatures.

In summary, the thermal conductivities for Sr_{1-x}Ca_xRuO₃ have been investigated as a function of field and temperature. Using the Wiedemann-Franz Law and measured resistivity, 50% of the thermal conductivity is estimated to be phononic near room temperature. An estimate of the Lorenz number has been obtained for SrRuO₃ assuming that the anomaly seen in both $\rho(T)$ and $K(T)$ is due to critical scattering of the electrons. A value smaller than the

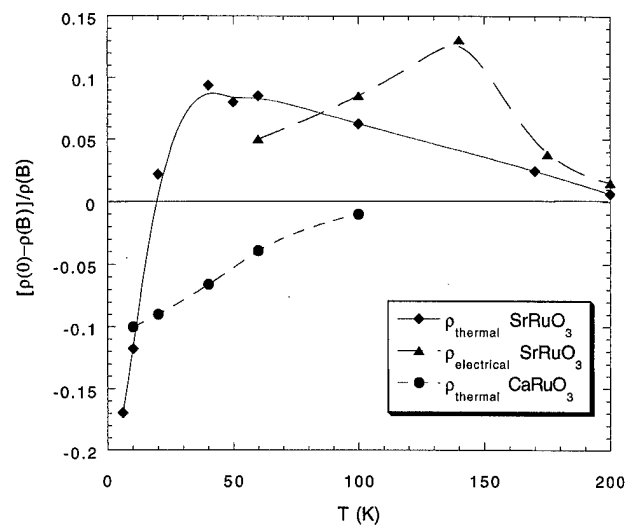


FIG. 4. Plots of magnetoresistivity and magnetothermal resistivity at $H = 10$ T as a function of temperature. Shown are the electrical resistivity of SrRuO₃ (triangles), thermal resistivity of SrRuO₃ (diamonds) and thermal resistivity of CaRuO₃ (circles).

ideal Lorenz number is obtained, $L = 1.63$ W/ Ω K². Amorphous behavior is observed in the doped samples, and no break in the thermal conductivity is seen at the ferromagnetic onset even though a clear anomaly is seen in $\rho(T)$. Also, field dependences of the thermal resistivities of SrRuO₃ and CaRuO₃ are not consistent with the electrical resistivities, which points to an additional contribution to the magnetic behaviors in addition to electronic scattering. Evidence for magnon-phonon scattering has been investigated for SrRuO₃, and the magnetic thermal conductivity of CaRuO₃ is similar to behavior noted in other nearly magnetic systems.¹¹ Research is continuing on these systems to better determine the role of phonon, electrons, and magnons to the transport properties of these interesting systems.

ACKNOWLEDGMENT

This research was supported by NSF Cooperative Agreement DMR95-27035 and the State of Florida.

¹ See, for example, P. A. Cox, *Transition Metal Oxides: An Introduction to Their Electronic Structure and Properties* (Clarendon, Oxford, 1995), and references within.

² I. I. Mazin and D. J. Singh, Phys. Rev. B **56**, 2556 (1997).

³ H. Y. Hwang, S. W. Cheong, P. G. Radaelli, M. Marezio, and B. Batlogg, Phys. Rev. Lett. **75**, 914 (1995).

⁴ G. Cao, S. McCall, M. Shepard, J. E. Crow, and R. P. Guertin, Phys. Rev. B **56**, 321 (1997).

⁵ J. L. Cohn, J. J. Neumeier, C. P. Popoviciu, K. J. McClellan, and Th. Leventouri, Phys. Rev. B **56**, R8495 (1997).

⁶ D. W. Visser, A. P. Ramirez, and M. A. Subramanian, Phys. Rev. Lett. **78**, 3947 (1997).

⁷ P. Henning, M. Shepard, G. Cao, J. E. Crow, S. McCall, J. Bolivar, and R. P. Guertin, Phys. Rev. B (to be published).

⁸ H. H. Sample, L. J. Neuringer, and L. G. Rubin, Rev. Sci. Instrum. **45**, 64 (1974).

⁹ C. Uher, in *Thermal Conductivity of High-Temperature Superconductors*, edited by D. Ginsberg, Physical Properties of High Temperature Superconductors IV (1994).

¹⁰ P. B. Allen, H. Berger, O. Chauver, L. Forro, T. Jarlborg, A. Junod, B. Revaz, and G. Santi, Phys. Rev. B **53**, 4393 (1996).

¹¹ K. Ueda and T. Moriya, J. Phys. Soc. Jpn. **39**, 605 (1975).

Magnetic transitions and oxygen content of $\text{Ca}_3\text{Ru}_2\text{O}_7$

S. McCall, G. Cao, and J. E. Crow

National High Magnetic Field Laboratory, 1800 East Dirac Drive, Tallahassee, Florida 32306

R. P. Guertin

Department of Physics, Tufts University, Medford, Massachusetts 02155

Magnetization and magnetoresistivity of as-grown, oxygenated, and argon annealed single crystals of $\text{Ca}_3\text{Ru}_2\text{O}_7$ are presented for $5 < T < 300$ K and $0 < H < 7$ T. As-grown $\text{Ca}_3\text{Ru}_2\text{O}_7$ has been shown to have an antiferromagnetic metallic phase for $48 < T < 56$ K and $0 < H < 4$ T, located between the high-temperature paramagnetic metallic and the low-temperature antiferromagnetic insulating phase. Details of the field dependence of the magnetoresistance of as-grown $\text{Ca}_3\text{Ru}_2\text{O}_7$ show slight variations between the H - T metal-insulator and paramagnetic-antiferromagnetic phase boundaries as determined from magnetization and from magnetoresistance measurements, but well-characterized samples with oxygen addition or deletion show much more extensive variations. Oxygenation lowers the electrical resistivity and sustains the 6 T first-order field-induced magnetic transition for $T \ll T_M$. However, magnetization is linear through the same field region, and argon annealed samples, with decreased oxygen content, show the same linearity of the magnetization. The results underscore the importance of oxygen content in the ruthenates, in analogy with the role of oxygen content in the cuprates. © 1998 American Institute of Physics. [S0021-8979(98)33811-6]

Transition metal oxide systems with extended d -shell orbitals, particularly those of the $4d$ and $5d$ transition elements, generally show metallic conductivity and a weak non-localized magnetic moment. Transition metal oxide systems with more localized d -shell orbitals, in particular those of the $3d$ elements, tend to be more highly correlated and are often insulators with highly localized magnetic moments. Many of the transition metal oxide systems currently under intense scrutiny are exceptions to these rather general assertions, and they show anomalous properties because the electrons responsible for the moment are degenerate or nearly so with those responsible for charge transport. The transition metal oxides of ruthenium fall into this category, and at least in the material studied most extensively, SrRuO_3 , the d -electrons which give rise to localized-like magnetism are also responsible for the electrical transport, there being essentially no s -like contribution to the density of states at the Fermi surface.¹

Of the ruthenate materials studied to date, the anisotropic bilayered compound $\text{Ca}_3\text{Ru}_2\text{O}_7$ possesses the most extensive and varied array of properties.² The high-temperature effective paramagnetic moment, $2.42\mu_B/\text{Ru}$, is close to that expected for the low spin state ($S=1$) of the $4d^4$ Ru configuration, $2.83\mu_B/\text{Ru}$. To date all work has been reported on as-grown single crystals of $\text{Ca}_3\text{Ru}_2\text{O}_7$,² and this report focuses on more detailed measurements of the magnetic and transport properties of as-grown $\text{Ca}_3\text{Ru}_2\text{O}_7$ but also reports preliminary data for oxygen annealed (oxygen-rich) and argon annealed (oxygen-poor) samples. Details of sample preparation of the as-grown single crystals are given elsewhere.² Some of the materials in this study were annealed in high purity oxygen for periods of up to two days to increase the oxygen content and others in high purity argon for the same period in order to deplete the oxygen content. In

all the samples studied the Ca/Ru ratio was maintained according to analysis determined with a scanning electron microscope using electron dispersive energy analysis. Annealing times in excess of two days caused the samples to lose their as-grown shiny appearance and gave spurious electrical conductivity.

In Ref. 2, we presented the magnetic and transport properties of as-grown single crystal $\text{Ca}_3\text{Ru}_2\text{O}_7$ for the purpose of describing an antiferromagnetic metallic (AFM) phase which spans the temperature range, $48 \leq T \leq 56$ K, between the high temperature, $T > T_N = 56$ K, paramagnetic metallic (PMM), and low temperature, $T < T_M = 48$ K, antiferromagnetic insulating (AFI) phase. The transition from PMM to AFM is second order, the transition from AFM to AFI being first order. Detailed electrical resistivity versus temperature data, $\rho(T)$, showing both transitions is shown in Fig. 1 for several values of the applied magnetic field, where the field is along the "easy" magnetocrystalline axis $[110]$. The inset shows $\rho(T)$ for $H=0$ over a more extensive temperature range. Several features of the data of Fig. 1 and the inset should be noted: (1) The resistivity is "metallic," i.e., $d\rho/dT > 0$, for all $T > T_M$ but it has a very large magnitude, even in well-characterized single-crystal samples. This alone probably puts $\text{Ca}_3\text{Ru}_2\text{O}_7$ in the "bad metal" category, namely, $k_F\lambda \approx O(1)$, where λ is the quasiparticle mean free path calculated if Boltzmann transport were to apply.³ (2) A puzzling aspect of $\rho(T)$ for $T > T_M$ is the isotropy: there is practically no detectable variation in the $\rho(T)$ for layered $\text{Ca}_3\text{Ru}_2\text{O}_7$ for current along the $[100]$, $[010]$, or $[001]$ directions, though there are large variations in the paramagnetic regime of a sister compound, $\text{Sr}_3\text{Ru}_3\text{O}_7$,⁴ which undergoes ferromagnetic transitions below about 105 K. (3) At $T = T_M$, $\rho(T)$ rises abruptly (and with slight thermal hysteresis) but does not attain large values as in the case of the canonical metal in-

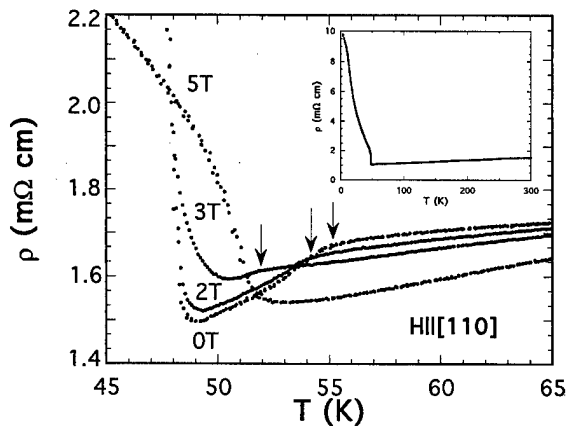


FIG. 1. Detail of the electrical resistivity vs temperature in the region of the two magnetic transitions in $\text{Ca}_3\text{Ru}_2\text{O}_7$ taken at several external magnetic fields along the "easy" magnetocrystalline axis, $[110]$. The arrows denote the Neel temperature for the various fields. The inset shows electrical resistivity at zero field over an extended temperature range.

sulator transition material, V_2O_3 .⁵ For $T < T_M$, $\rho(T)$ of $\text{Ca}_3\text{Ru}_2\text{O}_7$ shows large anisotropy (factors of $O(2)$ between current parallel to $[100]$ vs $[001]$), which suggests a structural change or perhaps a shift in the conductivity to lower dimensionality at T_M .

One feature common to all as-grown samples of $\text{Ca}_3\text{Ru}_2\text{O}_7$ is the very close coupling of spin and charge system at low temperatures as evidenced by their respective behavior at the several zero and high field transitions. Most recently, data taken in pulsed magnetic fields demonstrated a AFI to PMM transition for $H||[001]$, the "hard" magnetocrystalline axis: Both isothermal $M(H)$ and $\rho(H)$ for $T \ll T_M$ show a first-order-like transition at $H = 37$ T.⁶ For $H||[110]$, the "easy" axis (see data of Fig. 1), the transition occurs at much lower fields, 6 T. The pulsed field data demonstrate this close spin-charge coupling persists even in fields to 37 T.

The data of Fig. 1 show for the first time the magnetic field dependence of the AFM transition determined from $\rho(H, T)$ with $H||[110]$. The break in the resistivity curve at $T_N = 56$ K is apparent in this figure. Normally, this decrease could be associated with a Fisher-Langer⁷ type anomaly, i.e., spin flip scattering decreases for $T < T_N$, thereby decreasing $\rho(T)$. However, that theory addresses s -wave scattering at localized magnetic sites, which does not at all resemble the situation in the ruthenates because of the absence of s -electrons at the Fermi surface. Nevertheless, the resistive anomaly is consistent with the loss of spin flip scattering. The $M-I$ transition becomes more rounded with increasing field, and the PMM-AFM transition is initially suppressed with field and then becomes more rounded. The field appears to have no effect on the $M-I$ transition up to 4 T, although there is some broadening of the onset, and the line of $M-I$ transitions terminates at a critical point at $H = 4$ T and $T = 48$ K. (The data of Fig. 1 are from a different sample than presented in Ref. 2.) The apparent transition at about 52 K for $H = 5$ T may reflect some combination of field-induced magnetic and structural changes over a wider temperature range.

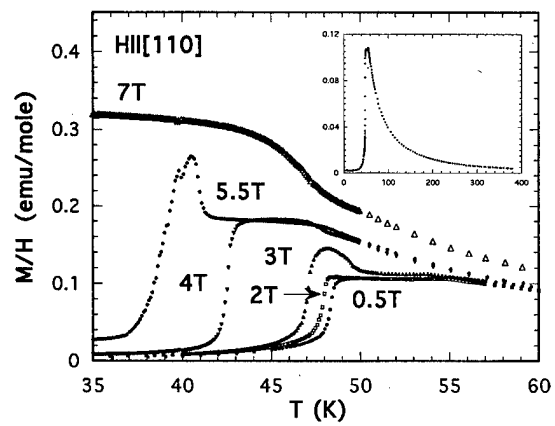


FIG. 2. Magnetization divided by applied field for $\text{Ca}_3\text{Ru}_2\text{O}_7$ along $[110]$ vs temperature in the vicinity of two magnetic transitions. The inset shows an expanded temperature range for 0.5 T applied field.

In Fig. 2 we show the temperature dependence of the magnetization, $M(H, T)$, for several applied fields with $H||[110]$, and as in Fig. 1, the data are shown for the vicinity of the PMM-AFM and AFM-AFI transitions. The inset shows the low field susceptibility data over a much wider temperature range, showing the magnetic ordering temperature and the subsequent reduction of the magnetization below the $M-I$ transition. The Neel temperature, T_N , de-

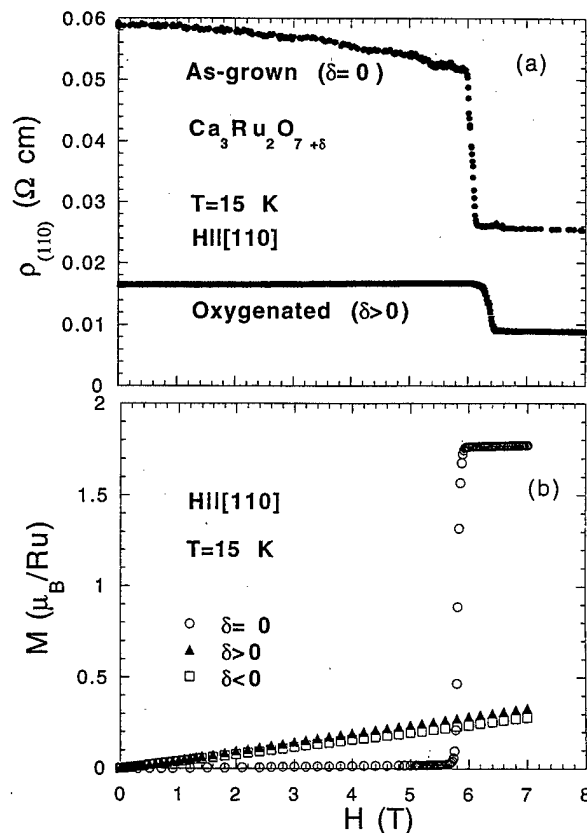


FIG. 3. (a) Electrical resistivity vs field along the easy axis for as-grown and oxygenated single crystals of $\text{Ca}_3\text{Ru}_2\text{O}_7$ showing transition from the antiferromagnetic insulating to the paramagnetic metallic phase. (b) Magnetization vs field for as-grown, oxygenated, and oxygen depleted samples in the vicinity of the field-induced phase transition of (a).

creases uniformly with field, in accordance with the resistivity data of Fig. 1. At low temperatures, the field-induced $M-I$ transition is tightly coupled to the metamagnetic transition, indicating the charge and spin mechanisms are intimately related. This field-induced metamagnetic transition results from strong anisotropic forces dominating the exchange forces, but near T_N the anisotropic forces weaken, and a two-step metamagnetism appears.² The $M-I$ transition temperature, as measured by the sharp $M(H, T_M)$ drop, decreases with increasing field and becomes more rounded. This is further evidence for a weakening of the anisotropic forces near T_N . Yet, the $\rho(H, T)$ measurements of Fig. 1 indicate the $M-I$ transition appears to be field independent, contrary to Fig. 2, thus suggesting that the charges and spins decouple in the vicinity of T_N .

Figure 3 illustrates some rather dramatic differences in magnetization and transport data obtained from as-grown samples vs. annealed samples. The as-grown data shown are the same as those in Ref. 2, but many other measurements on as-grown single crystals show nearly identical field-induced transitions. All data were taken at $T=15\text{ K} \ll T_M$ and illustrate the first-order character of the transition from the AFI to the PMM phase. Whereas the field-induced metamagnetic transition at $H=6\text{ T}$ can be seen from both resistivity and magnetization data for the as-grown crystals, the latter is absent entirely from the oxygen-rich and oxygen-depleted crystals. The drop in $\rho(T, H=6\text{ T})$ is as precipitous at the transition field as in the as-grown crystal, decreasing to about 50% of the zero field value.

The data of Fig. 3 suggest a decoupling of the magnetic and transport properties in $\text{Ca}_3\text{Ru}_2\text{O}_7$ with altered oxygen content. Preliminary measurements indicate the following consistencies: (1) The $M-I$ transition temperature never varies from $T_M=48\text{ K}$, as determined from $\rho(T)$ measurements, regardless of the type of annealing procedure (except for highly oxygenated but not well characterized samples).

(2) Oxygen-rich samples show generally higher conductivity, perhaps due to hole-like carrier doping, and oxygen-poor samples (argon annealed) show lower (sometimes nonmetallic) conductivity than as-grown crystals. (3) For both cases shown in Fig. 3 the field-induced metamagnetic transition is seen for resistive measurements but not magnetic measurements, at least to 7 T. The data suggest the "easy" axis may have shifted from $[110]$, though the evidence from resistivity measurements suggests it has not. It is interesting that the susceptibility represented by M/H for non as-grown samples is the same as the susceptibility of as-grown samples for the field along the "hard" $[001]$ axis, suggesting a major shift of the easy axis as a result of oxygen content (A shift in the easy axis of magnetization was found in $\text{Sr}_{1-x}\text{Ca}_x\text{RuO}_3$ for $0.2 < x < 0.5$).⁸)

Future high field experiments will attempt to quantify the role of oxygen content in magnetocrystalline anisotropy in the ruthenates. In general, we believe that for the ruthenates, oxygen content will be as important parameter in predicting the physical properties as it is for the cuprates.

This work was supported by the National Science Foundation under Cooperative Agreement No. DMR95-27035 with the State of Florida.

¹D. Singh and I. Mazin (unpublished).

²G. Cao, S. McCall, J. E. Crow, and R. P. Guertin, Phys. Rev. Lett. **78**, 1751 (1997).

³V. J. Emery and S. A. Kivelson, Phys. Rev. Lett. **74**, 3253 (1995).

⁴G. Cao, S. McCall, and J. E. Crow, Phys. Rev. B **55**, R672 (1997).

⁵For example, see D. B. McWhan, J. P. Remeika, T. M. Rice, W. F. Brinkman, J. P. Maita, and A. Menth, Phys. Rev. Lett. **27**, 941 (1971).

⁶S. McCall, G. Cao, J. E. Crow, H. Harrison, C. Mielke, A. Lacerda, and R. P. Guertin, Proceedings of 5th International Conference on Research in High Magnetic Fields, Physica B (to be published).

⁷M. E. Fisher and J. S. Langer, Phys. Rev. Lett. **13**, 665 (1968).

⁸G. Cao, S. McCall, M. Shepard, J. E. Crow, and R. P. Guertin, Phys. Rev. B **56**, 321 (1997).

Anisotropic Magnetoresistance and Granular GMR

Thomas McGuire, Chairman

Anisotropic magnetotransport properties of epitaxial thin films of conductive ferromagnetic oxide SrRuO_3

R. A. Rao, D. B. Kacedon, and C. B. Eom^{a)}

Department of Mechanical Engineering and Materials Science, Duke University, Durham, North Carolina 27708

We have studied the crystallographic domain structure dependent anisotropy in the magnetotransport properties of epitaxial thin films of the conductive ferromagnetic oxide SrRuO_3 . Single domain SrRuO_3 thin films on miscut (001) SrTiO_3 substrates exhibit a strong anisotropy in magnetization and magnetoresistance that reflects the inherent magnetocrystalline anisotropy of the material. In contrast, the SrRuO_3 thin film on (001) LaAlO_3 substrate shows identical magnetization and magnetotransport properties in two orthogonal directions on the film due to the presence of 90° domains in the plane. For both films, large negative magnetoresistance effects ($\sim 10\%$) are observed when the applied magnetic field is parallel to the current due to the suppression of spin fluctuations near T_c and the anisotropic magnetoresistance effect at low temperatures. © 1998 American Institute of Physics. [S0021-8979(98)31711-9]

Since the discovery of colossal magnetoresistance (CMR) in doped perovskite manganite thin films,¹ there has been a great deal of interest in the magnetoresistance of perovskite magnetic oxide thin films. Among the many perovskite magnetic oxides SrRuO_3 is especially attractive, since it is a rare case of $4d$ itinerant ferromagnetism ($T_c \sim 160$ K) with a GdFeO_3 -type pseudocubic perovskite structure and a bulk lattice parameter of 3.93 \AA .^{2,3} This material exhibits strong magnetocrystalline anisotropy in single crystal bulk³ and single domain thin film⁴ samples. It is also structurally and chemically similar to the LaMnO_3 -based CMR materials. As in CMR materials, magnetic ordering decreases electrical resistivity in SrRuO_3 rendering it attractive for magnetotransport studies.⁵

The successful growth of single crystal SrRuO_3 thin films on miscut SrTiO_3 substrates⁶ allows us to study the intrinsic anisotropic magnetotransport properties of SrRuO_3 . Recently, we have controlled the growth mechanisms⁷ and domain structure⁸ of SrRuO_3 thin films by using miscut substrates. In this article, we report on the magnetization and magnetotransport properties of epitaxial SrRuO_3 thin films with different crystallographic domain structures.

The SrRuO_3 thin films were deposited from a 2 in. diam stoichiometric composite target using a 90° off-axis sputtering technique^{9,10} on a vicinal (001) SrTiO_3 substrate miscut by 2° towards the in-plane [010] axis and an exact (001) LaAlO_3 substrate. The thickness of the films is about 3000 \AA .

The film on 2° miscut (001) SrTiO_3 substrate grew by step flow due to the presence of a periodic step structure on the substrate.⁷ This film has a purely (110) texture normal to the substrate. All the crystallographic planes and direc-

tions for SrRuO_3 referred to in this work are based on the orthorhombic unit cell. As the miscut direction is close to the [010] direction of the substrate, the one directional step flow leads to a single domain film with an in-plane epitaxial arrangement of $\text{SrRuO}_3[\bar{1}10]/\text{SrTiO}_3[010]$ and $\text{SrRuO}_3[001]/\text{SrTiO}_3[100]$.⁸ Furthermore, due to the small lattice mismatch between SrRuO_3 and SrTiO_3 this film has a coherent growth resulting in a strained lattice with in-plane and out-of-plane lattice parameters of 3.90 and 3.96 \AA , respectively.

The film on LaAlO_3 substrate has a three dimensional island growth mechanism⁷ due to the large lattice mismatch with the substrate. Therefore, this film has a strain-free lattice with both in-plane and out-of-plane lattice parameters the same as that of the bulk material (3.93 \AA). The out-of-plane film texture is a mixture of (110) and (001) normal to the substrate.

The influence of the domain structure on the magnetization of the films was studied with a superconducting quantum interference device (SQUID) magnetometer. The samples were cooled in a magnetic field of 0.05 T applied parallel to the film surface. Magnetization measurements on the single domain film showed an anisotropic behavior with the in-plane $[\bar{1}10]$ direction being the easier axis for magnetization compared to the [001] direction, which is in agreement with previously reported results. Accordingly, this film showed a fully saturated magnetization at low temperatures ($\sim 5 \text{ K}$), when the field is applied along the $[\bar{1}10]$ direction, as shown in Fig. 1(a). However, an unsaturated and lower magnetization ($\sim 65\%$ of the value in the $[\bar{1}10]$ direction) is obtained when the field is in the [001] direction. In contrast, the film on LaAlO_3 shows identical unsaturated magnetization when the field is applied along any of the two orthogonal directions on the film surface due the presence of 90° domains in the plane of the film, as shown in Fig. 1(b).

^{a)}Electronic mail: eom@acpub.duke.edu

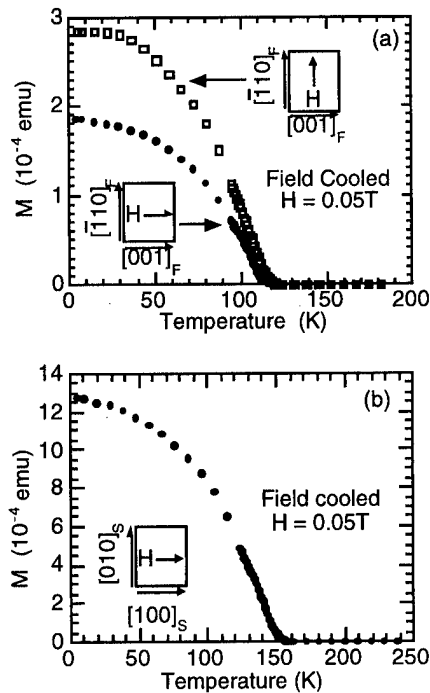


FIG. 1. Temperature dependence of magnetization of (a) single domain SrRuO₃ thin film on miscut SrTiO₃ and (b) multidomain SrRuO₃ film on (001) LaAlO₃ substrate. The inset shows the field direction with respect to the crystallographic directions of the film and substrate denoted by the subscripts *F* and *S*, respectively.

Magnetoresistance (MR) measurements were performed on these films using an Oxford Instruments MAGLAB 2000™ materials characterization system. For the single domain SrRuO₃ thin film, the resistivity was measured in four orientations of the *J* (current density) and *H* (applied field) directions with respect to the in-plane $\bar{1}10$ and 001 directions of the film (i.e., $J \parallel H \parallel \bar{1}10$; $J \parallel H \parallel 001$; $J \perp H$, $J \parallel 001$; and $J \parallel \bar{1}10$). In contrast, for the film on an exact (001) LaAlO₃ substrate, the resistivity was measured along the 010 and 100 directions of the LaAlO₃ substrate in two orientations ($J \parallel H$ and $J \perp H$) because of the equivalence of the two orthogonal directions. The temperature dependence of resistivity was measured by zero-field cooling (ZFC) and field warming.

The temperature dependence of resistivity for both the films in zero applied field shows the characteristic change of slope at the Curie temperature (*T_c*) signifying a ferromagnetic phase transition. Above *T_c* the resistivity increases linearly with temperature and is expected to continue without saturation.¹¹ The *T_c* of the film on SrTiO₃ (~120 K) is also significantly lower than that for the film on LaAlO₃ substrate (*T_c* ~ 155 K). This *T_c* suppression in the films on SrTiO₃ substrate is believed to be due partly to the coherent growth induced lattice strain in these films.¹² Furthermore, it is believed that this film might be a little deficient in Ru, which could also contribute to the *T_c* suppression.

The magnetoresistance was calculated as: $MR = [\rho(H) - \rho(0)]/\rho(0)$, where $\rho(H)$ and $\rho(0)$ are the resistivity at a field *H* and at zero field, respectively. The largest MR among all four combinations of *J* and *H* directions is observed at low temperatures, when the current and field are parallel to

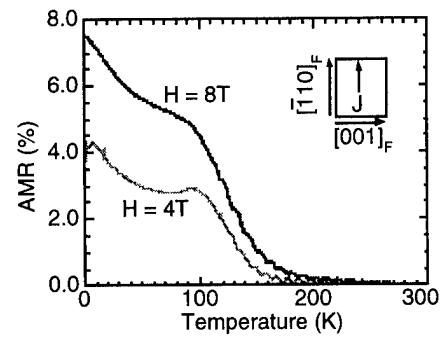


FIG. 2. The negative AMR vs temperature for a single domain SrRuO₃ film on 2° miscut (001) SrTiO₃ substrate toward the 010 direction at applied fields of 4 and 8 T with $J \parallel \bar{1}10$.

the $\bar{1}10$ direction.¹³ We believe that this is due to the $\bar{1}10$ direction being the easier axis for magnetization compared to the 001 direction. The spins are more easily aligned in the $\bar{1}10$ direction which accounts for the larger change in resistivity due to the magnetic field.

A large negative MR is observed at temperatures just below *T_c* in all orientations of the current and field which has already been attributed to the suppression of spin fluctuations.¹⁴ Furthermore, the negative MR is larger when the applied field is parallel to the current, especially at low temperatures. This is due to the anisotropic magnetoresistance (AMR) effect. The AMR effect is the change in angle between the magnetization and current because of magnetization rotation observed at high fields that are smaller than the anisotropy field. Such an AMR effect has been observed in single domain SrRuO₃ thin films at a field of 6 T and is found to increase as the temperature is lowered below *T_c*.¹⁵

Figure 2 shows the negative AMR as a function of temperature at two different values of applied field for the single domain film with current along the miscut direction. The AMR is measured as the ratio of change in resistivity to the average resistivity as shown below:

$$\frac{\Delta \rho}{\rho_{av}} = \frac{3(\rho_{\parallel} - \rho_{\perp})}{(\rho_{\parallel} + 2\rho_{\perp})}, \quad (1)$$

where ρ_{\parallel} and ρ_{\perp} are resistivities with *H* parallel and perpendicular to the current direction. The AMR is unusual in sign since usually ρ_{\perp} is less than ρ_{\parallel} . The magnitude of the AMR is ~8% at low temperatures and high fields. Clearly, the AMR increases as the field is increased and the temperature is lowered. As the easy axis of SrRuO₃ lies in the (001) plane making an angle of 30°–45° with respect to the $\bar{1}10$ direction,⁴ complete orientation of *M* along the applied field direction does not take place when the field is applied in the (110) plane. Therefore, as the field is increased the angle between *M* and the current changes leading to the AMR effect. It has been shown that the Lorentz force component for $H \perp J$ in these films is negligible.¹⁴ Furthermore, if Lorentz force were to dominate, a positive MR should have been seen above *T_c* for $H \perp J$. However, all films show negligible MR above *T_c* which suggests that the difference between $H \parallel J$ and $H \perp J$ is primarily due to the AMR effect.

The field dependence of the magnetoresistance was also measured in the four combinations of *J* and *H* directions.

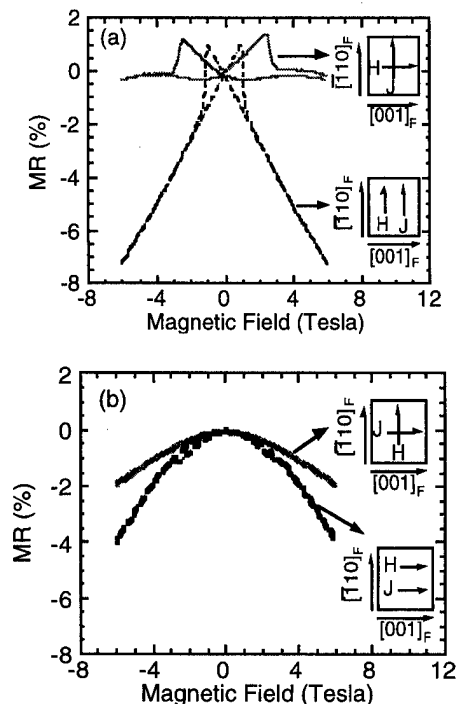


FIG. 3. MR vs field of a SrRuO₃ film on a 2° miscut SrTiO₃ substrate with (a) $J \parallel [110]$ and (b) $J \parallel [001]$.

The samples were heated to above T_c in zero field between successive MR versus field measurements, in order to erase any hysteresis effects. Figures 3(a) and 3(b) compare the hysteresis in the MR versus field data at 5 K for the single domain SrRuO₃ thin film with the current along the $[110]$ and $[001]$ direction. As the film is single domain, the magnetocrystalline anisotropy of SrRuO₃, which is attributed to the large spin-orbit coupling of Ru, contributes to a strong anisotropy in the MR behavior seen in Fig. 3. The hysteresis effect itself is related to the magnetization hysteresis. The peak in the MR hysteresis corresponds to the coercive field and the point of overlap between the forward and backward sweeps of the field corresponds to the saturation field. As the applied field is increased beyond saturation, the magnetization of the sample does not change significantly, but magnetization rotation occurs contributing to a larger negative MR when $J \parallel H$ due to the AMR effect.

The magnetoresistance properties of the multi domain film on LaAlO₃ were also measured. In contrast to the single domain film, the resistivity of this film has an additional contribution from the crystallographic domain boundaries due to the incoherent three dimensional island growth. The temperature dependence of MR for the film on LaAlO₃ showed features similar to that of single domain film on miscut SrTiO₃. A sharp increase in MR at T_c and larger MR at low temperatures are observed when the field and current are parallel.

The field dependence of MR shows some differences compared to the single domain film, as seen in Fig. 4. The MR at 5 K is shown in two orthogonal directions with $J \parallel H$ and $J \perp H$. When the sample was rotated by 90° the MR behavior obtained was identical due to the equivalence of the two orthogonal directions within the plane. The grain size of

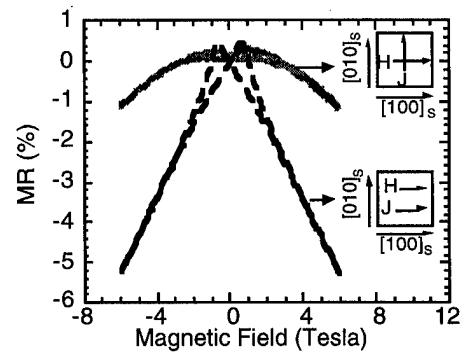


FIG. 4. MR vs field of a SrRuO₃ film on an exact (001) LaAlO₃ substrate with $J \parallel H$ and $J \perp H$.

these films, as observed from scanning tunneling microscopy images⁷ and the magnetic domain wall spacing of similar films observed by Lorentz microscopy imaging,¹⁶ are comparable (~ 2000 Å). Therefore, it is believed that the film on LaAlO₃ does not have any magnetic domain walls. The crystallographic domain boundaries in this film act as magnetic boundaries as well and the change in relative orientation of the magnetization of adjacent crystallographic domains contributes to the hysteresis.

The authors would like to thank M. L. Stutzman for patterning the samples, M. Lee for SQUID measurements, and L. Klein and Q. Gan for helpful discussions. This work was supported by ONR Grant No. N00014-95-1-0513, and NSF Grant No. DMR 9421947, a NSF Young Investigator Award (CBE), and a David and Lucile Packard Fellowship (CBE).

- ¹ S. Jin, T. H. Tiefel, M. McCormack, R. A. Fastnacht, R. Ramesh, and L. H. Chen, *Science* **246**, 413 (1994).
- ² A. Callaghan, C. W. Moeller, and R. Ward, *Inorg. Chem.* **5**, 1572 (1966); J. M. Longo, P. M. Raccach, and J. B. Goodenough, *J. Appl. Phys.* **39**, 1327 (1968).
- ³ A. Kanbayashi, *J. Appl. Phys.* **41**, 1879 (1976); G. Cao, S. McCall, M. Shepard, and J. E. Crow, *Phys. Rev. B* **56**, 321 (1997).
- ⁴ L. Klein, J. S. Dodge, C. H. Ahn, J. W. Reiner, L. Mieville, T. H. Geballe, M. R. Beasley, and A. Kapitulnik, *J. Phys.: Condens. Matter* **8**, 10111 (1996).
- ⁵ L. Klein, J. S. Dodge, C. H. Ahn, G. J. Snyder, T. H. Geballe, M. R. Beasley, and A. Kapitulnik, *Phys. Rev. Lett.* **77**, 2774 (1996).
- ⁶ C. B. Eom, R. J. Cava, R. M. Fleming, J. M. Phillips, R. B. van Dover, J. H. Marshall, J. W. P. Hsu, J. J. Krajewski, and W. F. Peck, *Science* **258**, 1766 (1992).
- ⁷ R. A. Rao, Q. Gan, and C. B. Eom, *Appl. Phys. Lett.* **71**, 1171 (1997).
- ⁸ Q. Gan, R. A. Rao, and C. B. Eom, *Appl. Phys. Lett.* **70**, 1962 (1997).
- ⁹ C. B. Eom, J. Z. Sun, K. Yamamoto, A. F. Marshall, K. E. Luther, S. S. Laderman, and T. H. Geballe, *Appl. Phys. Lett.* **55**, 595 (1989).
- ¹⁰ C. B. Eom, J. Z. Sun, S. K. Streiffer, A. F. Marshall, K. Yamamoto, B. M. Lairson, S. M. Anlage, J. C. Bravman, T. H. Geballe, S. S. Laderman, and R. C. Taber, *Physica C* **171**, 351 (1990).
- ¹¹ P. B. Allen, H. Berger, O. Chauvet, L. Forro, T. Jarlborg, A. Junod, B. Revaz, and G. Santi, *Phys. Rev. B* **53**, 4393 (1996).
- ¹² Q. Gan *et al.* (unpublished).
- ¹³ D. B. Kacedon, R. A. Rao, and C. B. Eom, *Appl. Phys. Lett.* **71**, 1724 (1997).
- ¹⁴ S. C. Gausepohl, M. Lee, K. Char, R. A. Rao, and C. B. Eom, *Phys. Rev. B* **52**, 3459 (1995).
- ¹⁵ L. Klein, A. F. Marshall, J. W. Rainer, C. H. Ahn, T. H. Geballe, M. R. Beasley, and A. Kapitulnik, preprint (1997).
- ¹⁶ A. F. Marshall, *Epitaxial Oxide Thin Film Symposium*, presented at the Mater. Res. Soc. Symp. Proc. 1997 Spring Meeting.

Giant spontaneous Hall effect and magnetoresistance in $\text{La}_{1-x}\text{Ca}_x\text{CoO}_3$ ($0.1 \leq x \leq 0.5$)

A. V. Samoilov,^{a)} G. Beach, C. C. Fu, and N.-C. Yeh

Department of Physics 114-36, California Institute of Technology, Pasadena, California 91125

R. P. Vasquez

Center for Space Microelectronics Technology, Jet Propulsion Laboratory, California Institute of Technology, Pasadena, California 91109

Results of resistivity and Hall effect measurements in $\text{La}_{1-x}\text{Ca}_x\text{CoO}_3$ ($0.1 \leq x \leq 0.5$) epitaxial films and ceramics are presented. The spontaneous Hall effect in $\text{La}_{1-x}\text{Ca}_x\text{CoO}_3$ (LCCO) is observed for ferromagnetic samples with $x \geq 0.2$. The Hall effect is largest near the magnetic percolation threshold $x = 0.2$. For $x = 0.2$, the low-field slope of the Hall resistivity, $\rho_{xy}/(\mu_0 H)$, attains a large value of $2 \times 10^{-6} \text{ m}^3/\text{C}$ below the Curie temperature T_c , which may be applied to sensitive low-field detection. Except near the magnetic percolation threshold, the longitudinal resistivity of LCCO decreases with increasing field at all temperatures. Anomalous temperature-dependent magnetoresistance occurs in the sample with $x = 0.2$, which may be associated with the spin-state transition in LCCO. © 1998 American Institute of Physics. [S0021-8979(98)26211-6]

I. INTRODUCTION

The perovskite cobaltite oxide $\text{La}_{1-x}\text{Ca}_x\text{CoO}_3$ (LCCO) is ferromagnetic for $x > 0.15$, with the Curie temperature increasing up to $T_c \approx 180 \text{ K}$ for $x = 0.3$ – 0.5 ¹ (see Fig. 1, upper inset). Substitution of divalent Ca for trivalent La in the parent compound LaCoO_3 results in mixed valency of Co ions ($\text{Co}^{3+}/\text{Co}^{4+}$), and chemically doped holes induce ferromagnetism via the double-exchange interaction.^{2–4} Both the trivalent and tetravalent cobalt ions are known to exist in multiple spin configurations. For instance, low- and high-spin states for trivalent cobalt ions have the electronic configurations of $t_{2g}^6 e_g^0$ (Co^{III}) and $t_{2g}^4 e_g^2$ (Co^{3+}), with spin $S = 0$ and 2, correspondingly.^{5,6} In LaCoO_3 , the crystal-field splitting energy is larger than the Hund's energy, and the trivalent Co ions are in the low-spin state at low temperatures. Divalent Ca ions in $\text{La}_{1-x}\text{Ca}_x\text{CoO}_3$ polarize the oxygen p electrons and stabilize the high-spin configuration of trivalent Co ions because of the reduced crystal-field effect. As a result, magnetic clusters are formed near each divalent atom. With the increasing doping concentration, the clusters reach magnetic and conducting percolation threshold. A similar system, $\text{La}_{1-x}\text{Sr}_x\text{CoO}_3$, is found to have metallic electrical conduction for $0.3 \leq x \leq 0.5$, with "hole-poor", lower-spin matrix interpenetrating the metallic "hole-rich", higher-spin regions.^{5,6} In this work, we report the observations of a giant ferromagnetic Hall effect and magnetoresistance in LCCO. The possible physical origin of these phenomena is discussed in the context of magnetic clusters and spin transitions due to the multiple spin configurations of the cobaltites.

II. EXPERIMENT

The transport properties are studied in LCCO epitaxial films ($x = 0.2, 0.3$, and 0.5) and in a LCCO $x = 0.1$ ceramic

sample. The films, $(2\text{--}5) \text{ mm} \times (2\text{--}5) \text{ mm} \times (100\text{--}300) \text{ nm}$ in size, are grown by pulsed laser deposition using stoichiometric targets of LCCO, in 100 mTorr of oxygen. The temperature of the LaAlO_3 substrates is 700°C . The growth is followed by annealing in 1 atm oxygen at 900°C for 10 h, and the epitaxy of the films is confirmed by x-ray rocking curves. The results for the $x = 0.5$ samples⁷ are very similar to those for the $x = 0.3$ sample and are not shown here. The ceramic sample, $6.1 \text{ mm} \times 2.8 \text{ mm} \times 1.7 \text{ mm}$ in size, is cut from the LCCO target with $x = 0.1$. The magnetic field is applied perpendicular to the plane of the largest dimensions. Details of transport measurements are given in Ref. 7.

III. RESULTS

Figure 1 shows the temperature (T) dependence of the electrical resistivity ρ in zero magnetic field. The sample

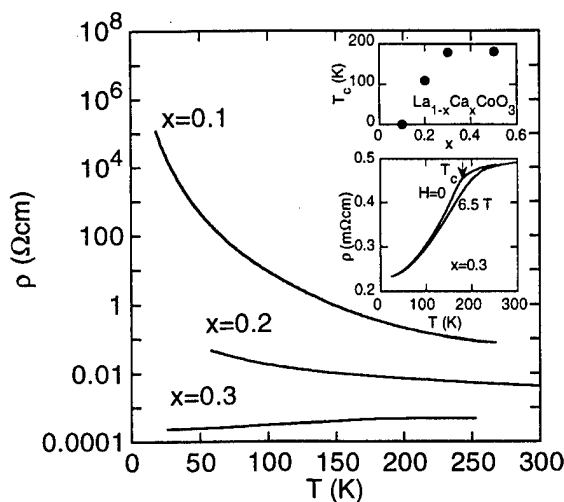


FIG. 1. (Upper panel) The resistivity vs temperature for the $x = 0.1$ ceramic sample and for the two epitaxial films (with $x = 0.2$ and 0.3). Upper inset: the doping dependence of the transition temperature $T_c(x)$ in $\text{La}_{1-x}\text{Ca}_x\text{CoO}_3$. Lower inset: $\rho(T)$ dependence for $\text{La}_{0.7}\text{Ca}_{0.3}\text{CoO}_3$ in magnetic fields 0 and 6.5 T.

^{a)}Electronic mail: samoilov@cco.caltech.edu

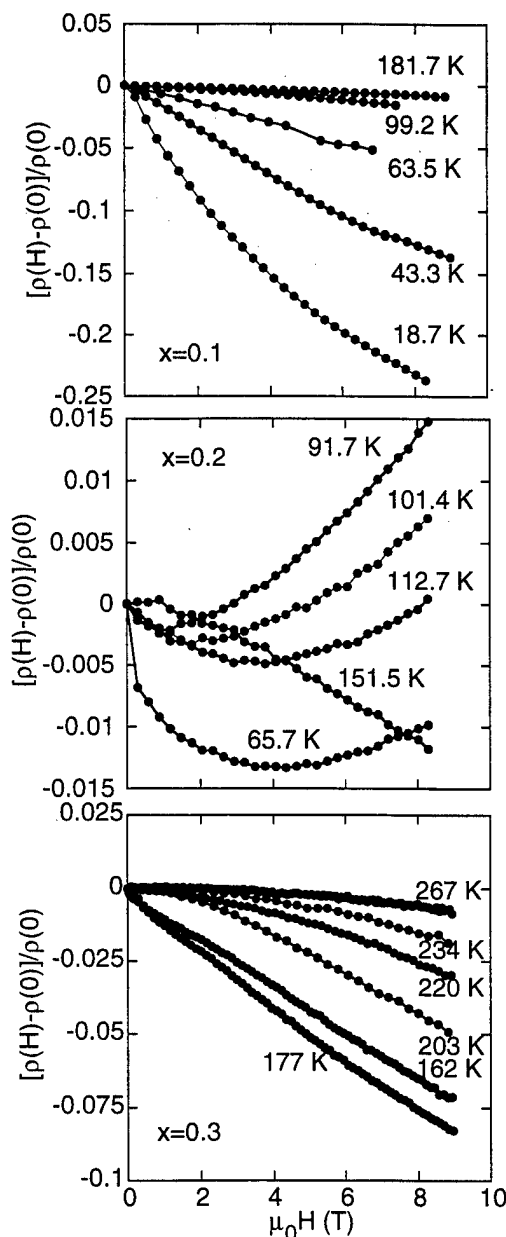


FIG. 2. (Upper panel) The magnetic field dependences of the longitudinal resistivity for $x=0.1$, 0.2 , and 0.3 . The temperature is indicated near each curve. Solid lines are guides to the eye.

with $x=0.3$ exhibits metalliclike resistivity. Below T_c , increasing magnetic order with decreasing temperature decreases carrier scattering and therefore results in a large decrease in the resistivity on cooling through T_c (Fig. 1, lower inset). The resistivity of the samples with $x=0.2$ and 0.1 has semiconductinglike behavior (Fig. 1, main panel), which has been attributed to trapping of holes at the divalent doping ions.⁵

The magnetic field (H) dependence of the resistivity is depicted in Fig. 2. The origin of the negative magnetoresistance for $x=0.3$ can be understood in terms of conventional behavior for metallic ferromagnets, where the magnetoresistivity is due to the suppression of the spin-disorder scattering, which is strongest near the transition temperature, see Fig. 2, bottom panel.

For the ceramic $x=0.1$ sample (Fig. 2, top panel), the magnetoresistance is also negative, and at low temperatures attains relatively larger values (up to 25%) than those of the metallic samples. Unlike samples with high concentration of the Ca atoms, which demonstrate bulk ferromagnetism, the $x=0.1$ sample consists of isolated clusters containing Co^{3+} and tetravalent cobalt ions. These clusters are localized at the Ca ions at low temperatures. The electrical conduction occurs via the hopping motion of holes in the insulating matrix of low-spin, trivalent Co^{III} ions. Each hopping process consists of transferring the tetravalent configuration $[\text{Co}^{\text{IV}} (S=1/2) \text{ or } \text{Co}^{4+} (S=5/2)]$ from one Co ion to another, accompanied by transforming of the neighboring Co^{III} ions into Co^{3+} ions.⁵ With increasing temperature, the ratio of Co^{3+} to Co^{III} ions in the matrix increases, facilitating the hopping process and increasing the conductivity. On the other hand, the presence of an external magnetic field helps aligning the spins of Co^{3+} and $\text{Co}^{4+}(\text{Co}^{\text{IV}})$ ions, thereby increasing the hopping rate and resulting in negative magnetoresistivity. With increasing temperature, the correlations between the spins of Co^{3+} and $\text{Co}^{4+}(\text{Co}^{\text{IV}})$ ions become weaker, therefore larger fields are required to align the spins, and the magnetoresistance decreases (Fig. 2, top panel). We note that the magnetoresistance data on LCCO with $x=0.1$ and 0.3 are consistent with those on $\text{La}_{1-x}\text{Sr}_x\text{CoO}_3$ with the same doping levels.⁸

On the other hand, the LCCO sample with $x=0.2$ exhibits an anomalous magnetoresistance behavior (Fig. 2, middle panel), which has not been seen in $\text{La}_{1-x}\text{Sr}_x\text{CoO}_3$. The relative change of the resistivity with the magnetic field $[\rho(H) - \rho(0)]/\rho(0)$ in LCCO with $x=0.2$ is of the order of 1%, smaller than that for $x=0.3$ (Fig. 2, bottom panel). At high temperatures ($T \gtrsim 120$ K), the magnetoresistance is negative over the whole field range. At lower temperatures, the resistivity as a function of the increasing magnetic field exhibits a nonmonotonic behavior (Fig. 2, middle panel): the initial decrease at small fields is followed by an increase at larger fields. This positive upturn contribution to the resistivity at high fields increases as the temperature is lowered (compare the isotherms at $T=112.7$, 101.4 , and 91.7 K in Fig. 2, middle panel). However, when the temperature decreases further, the negative contribution grows substantially, and the positive upturn in the ρ -vs- H curves becomes less pronounced. (See the isotherm at $T=65.7$ K in Fig. 2, middle panel.) The complexity of the magnetoresistivity behavior in LCCO with $x=0.2$ may be related to the closeness of T_c to the temperature where the $\text{Co}^{3+}/\text{Co}^{\text{III}}$ ratio in the intercluster matrix reaches 50:50 (≈ 110 K, according to Ref. 5). This novel behavior in the magnetoresistance of LCCO awaits further theoretical investigations. We also note that the occurrence of the nonmonotonic field dependence of the resistivity coincides with the temperature interval in which the giant spontaneous Hall effect is observed. (See Ref. 7, Fig. 3, and the discussion below.)

Figure 3 is a representative result of the Hall effect measurements on LCCO with $x=0.2$. In our previous work,⁷ we have demonstrated that the Hall resistivity in LCCO for $0.2 \leq x \leq 0.5$ is proportional to the magnetization M : $\rho_{xy}(H, T) = R_s(T)[\mu_0 M(H, T)]$, where R_s is the spontaneous Hall co-

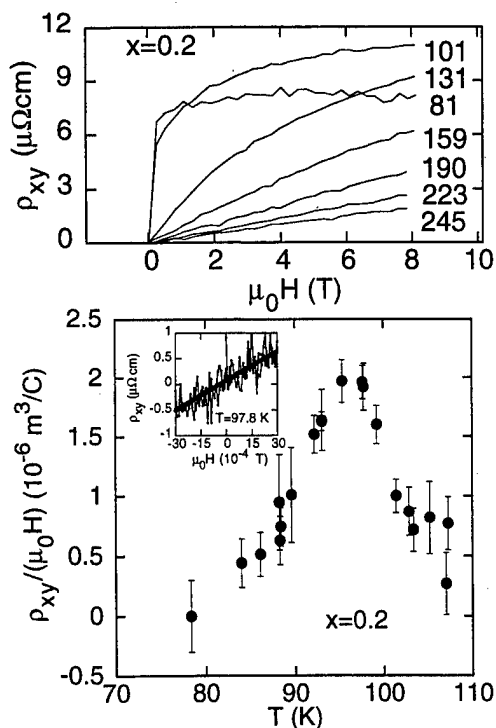


FIG. 3. Top panel: The Hall resistivity vs magnetic field for a $x=0.2$ epitaxial film sample. The temperature is indicated near each curve in Kelvins. Note a very steep rise of ρ_{xy} at low fields and at $T < T_c \approx 110 \text{ K}$. Bottom panel: The initial slope of the ρ_{xy} -vs- H curves as a function of temperature below $T_c \approx 110 \text{ K}$ for a $x=0.2$ epitaxial film sample. Inset: ρ_{xy} -vs- H at low fields for the same sample at $T=97.8 \text{ K}$.

efficient, and μ_0 is the permeability of vacuum. The spontaneous Hall coefficient in LCCO peaks nearest the transition temperature, with $R_s(T_c) \approx 0.25 \times 10^{-6} \text{ m}^3/\text{C}$ for $x=0.3$ and 0.5 and $1.35 \times 10^{-6} \text{ m}^3/\text{C}$ for $x=0.2$. The latter value is the largest for known ferromagnetic metals.⁷ For $x=0.1$, no Hall effect signal can be detected within our instrumental resolution. As illustrated in Fig. 3, the ρ_{xy} -vs- H curves for $x=0.2$ becomes progressively more nonlinear as the temperature is decreased in the paramagnetic state above $T_c \approx 110 \text{ K}$. In the ferromagnetic state, the Hall resistivity as a function of H is found to be hysteretic.⁷ If the sample is cooled in $H=0$, the Hall resistivity at $T < T_c$ shows a very sharp rise with increasing magnetic field, consistent with alignment of magnetic domains. We investigate this initial increase of $\rho_{xy}(H)$ by using a small copper coil to supply small fields up to $\pm 30 \times 10^{-4} \text{ T}$ (Fig. 3, bottom panel, inset). Within this magnetic field range, the Hall resistivity is linear with field and is reversible. The temperature dependence of the slope $\rho_{xy}/(\mu_0 H)$ is shown in the main panel of Fig. 3. (We note that $\rho_{xy}/(\mu_0 H)$ should not be confused with R_s : $\rho_{xy}/(\mu_0 H) = R_s M/H = R_s \chi$, where χ is the susceptibility.) The slope increases with the increasing temperature,

passes through a maximum $\rho_{xy}/(\mu_0 H) \approx 2 \times 10^{-6} \text{ m}^3/\text{C}$ at $T \approx 97 \text{ K}$ and drops to $5 \times 10^{-8} \text{ m}^3/\text{C}$ at $T=110 \text{ K}$. (The latter value is inferred from measurements over a larger field range.) The peaking behavior of $\rho_{xy}/(\mu_0 H)$ -vs- T in the ferromagnetic state is due to the decreasing susceptibility and increasing spontaneous Hall coefficient R_s with the increasing temperature.

In order to appreciate the large magnitude of the slope $\rho_{xy}/(\mu_0 H)$ in LCCO with $x=0.2$, we estimate the "effective" carrier density n , had the Hall effect in LCCO been entirely due to the Lorentz force rather than the magnetization. Using $\rho_{xy}/(\mu_0 H) = 1/(ne)$, where e is the electron charge, we obtain a small value $n = 3 \times 10^{24} \text{ m}^{-3}$, comparable to that in sensitive semiconducting Hall-effect magnetometers.

The spontaneous Hall effect in magnetic materials is generally associated with the spin-orbit interaction.^{9,10} In LCCO, the spin-orbit interaction in the ferromagnetic state may be further enhanced at the boundaries between the low-spin, low-conduction and the high-spin, high-conduction regions.

In summary, the $\text{La}_{1-x}\text{Ca}_x\text{CoO}_3$ system exhibits novel behavior in the magnetoresistance for $x=0.2$ and a very large spontaneous Hall effect at $x \geq 0.2$. These phenomena may be attributed to a magnetism associated with the coexistence of multiple spin configurations in the cobaltites. On the practical side, our finding of the giant Hall effect in these cobaltites appears promising for applications to sensitive low-field magnetometers.

ACKNOWLEDGMENTS

The research at Caltech is jointly supported by the National Aeronautics and Space Administration, Office of Space Science (NASA/OSS), Caltech President's Fund, and the Packard Foundation. Part of the research was performed at the Center for Space Microelectronics Technology, Jet Propulsion Laboratory, Caltech, and was sponsored by NASA/OSS. A.V.S. is a Millikan Senior Research Fellow in Physics.

¹H. Taguchi, M. Shimada, and M. Koizumi, *J. Solid State Chem.* **41**, 329 (1982).

²G. H. Jonker and J. van Santen, *Physica (Amsterdam)* **16**, 337 (1950).

³C. Zener, *Phys. Rev.* **82**, 403 (1960).

⁴P.-G. de Gennes, *Phys. Rev.* **118**, 141 (1960).

⁵M. A. Se  ar  s-Rodr  guez and J. B. Goodenough, *J. Solid State Chem.* **118**, 323 (1995).

⁶M. Itoh *et al.*, *J. Phys. Soc. Jpn.* **63**, 1486 (1994).

⁷A. V. Samoilov, N.-C. Yeh, and R. P. Vasquez, *Mater. Res. Soc. Symp. Proc.* **474**, 247 (1997); A. V. Samoilov *et al.* (to be published).

⁸R. Mahendiran and A. K. Raychaudhuri, *Phys. Rev. B* **54**, 16 044 (1996).

⁹C. M. Hurd, *The Hall Effect in Metals and Alloys* (Plenum, New York, 1972).

¹⁰A. Fert and D. K. Lottis, in *Concise Encyclopedia of Magnetic and Superconducting Materials* (Oxford University, New York, 1992), p. 287.

Giant magnetoresistance in granular CuFeNi alloys

C. S. Martins, H. R. Rechenberg, and F. P. Missell^{a)}

Instituto de Física, Universidade de São Paulo, C.P. 66318, 05315-970 São Paulo, S. P., Brazil

Giant magnetoresistance (MR) was studied in alloys of composition $\text{Cu}_{80}\text{Fe}_{10}\text{Ni}_{10}$, $\text{Cu}_{80}\text{Fe}_{15}\text{Ni}_5$, $\text{Cu}_{80}\text{Fe}_5\text{Ni}_{15}$, and $\text{Cu}_{80}\text{Fe}_{20}$, produced by melt spinning and annealed in the temperature range 300–600 °C. Materials were characterized by Mössbauer spectroscopy at several temperatures. At both 78 and 300 K, spectra for all CuFeNi compositions showed a singlet associated with superparamagnetic Fe nanoparticles, but at 4.2 K the sextet characteristic of ferromagnetic Fe was visible. From the hyperfine field reduction we estimated the radius of the Fe particles. Magnetization data for $\text{Cu}_{80}\text{Fe}_{10}\text{Ni}_{10}$ at 300 K were compared with a model which features a log-normal distribution of noninteracting superparamagnetic particles. Thus the mean magnetic moment and the particle density were determined. The magnetoresistance ratio MR was compared to a model which considers bulk and interface scattering. © 1998 American Institute of Physics.

[S0021-8979(98)26311-0]

I. INTRODUCTION

After the discovery of giant magnetoresistance (GMR) in granular solids,^{1,2} it has become increasingly clear that the size distribution of the magnetic nanoparticles plays an important role in the phenomenon. For a random distribution of noninteracting moments of the same magnitude, the magnetoresistance ratio $\text{MR} = [\rho(H) - \rho(H=0)]/\rho(H=0)$ should be a quadratic function³ of the relative magnetization M/M_s . However, many granular systems do not follow the expected quadratic behavior and various explanations have been proposed for this. Some consider the role of magnetic interactions, while others refer to the distribution of magnetic particles. In any case, a careful consideration of this problem should furnish important insights into magnetotransport in granular solids.⁴

In the present paper we determined GMR in granular $\text{Cu}_{80}(\text{Fe}, \text{Ni})_{20}$ alloys.^{5–7} The magnetoresistance ratio MR and the relative magnetization M/M_s were studied in terms of a model which employs a log-normal distribution of noninteracting superparamagnetic particles. Mössbauer spectroscopy furnished additional information about the size of the magnetic nanoparticles.

II. EXPERIMENT

Alloys of composition $\text{Cu}_{80}\text{Fe}_{10}\text{Ni}_{10}$, $\text{Cu}_{80}\text{Fe}_{15}\text{Ni}_5$, $\text{Cu}_{80}\text{Fe}_5\text{Ni}_{15}$, and $\text{Cu}_{80}\text{Fe}_{20}$ were melt spun on a copper wheel in a He atmosphere at wheel speeds ≈ 40 m/s. Compositions reported here are in atomic percent, in contrast with Refs. 5–7 where weight percent was used. The resulting ribbons, about 1 mm wide and 30 μm thick, were then annealed in an Ar atmosphere at various temperatures in the range 300–600 °C to maximize the magnetoresistance.

Magnetization measurements were made with a vibrating sample magnetometer (VSM) mounted on a 90 kOe superconducting solenoid. Magnetoresistance was measured with an ac bridge with the magnetic field applied in the rib-

bon plane. Some measurements of the anisotropic magnetoresistance (AMR) were made in fields up to 20 kOe. For $\text{Cu}_{80}\text{Fe}_{10}\text{Ni}_{10}$, the AMR was found to be on the order of 0.5% at 300 K. A standard, constant acceleration spectrometer with a $^{57}\text{CoRh}$ source was used for the Mössbauer spectroscopy.

III. GMR AND MÖSSBAUER RESULTS

Of the four alloys studied, $\text{Cu}_{80}\text{Fe}_{10}\text{Ni}_{10}$ showed the largest values of the magnetoresistance ratio $\text{MR} = [\rho(H) - \rho(H=0)]/\rho(H=0)$. In Fig. 1, we show MR as a function of the applied magnetic field at 4.2 K for $\text{Cu}_{80}\text{Fe}_{10}\text{Ni}_{10}$ ribbons annealed for two hours at the indicated temperatures. Our largest value of $\text{MR} \approx -17\%$ was obtained for an annealing temperature of 400 °C, in agreement with Ref. 7. However, our value of MR is smaller than that reported in Ref. 7, in part, because those authors chose a different normalization for this quantity. For the higher annealing temperatures, the field dependence of MR appears to be nearly linear at high fields.

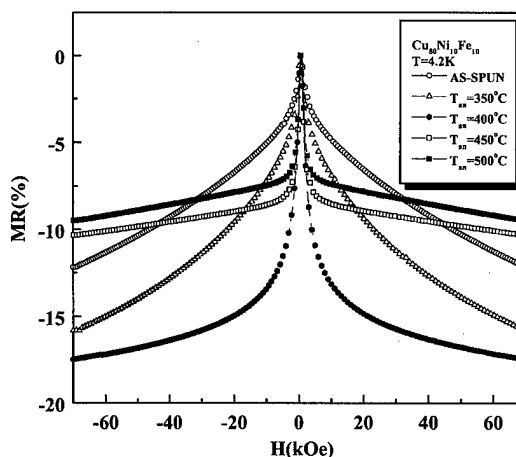


FIG. 1. Magnetoresistance ratio MR vs magnetic field H for $\text{Cu}_{80}\text{Fe}_{10}\text{Ni}_{10}$ at 4.2 K for different annealing temperatures.

^{a)}Electronic mail: fmissell@macbeth.if.usp.br

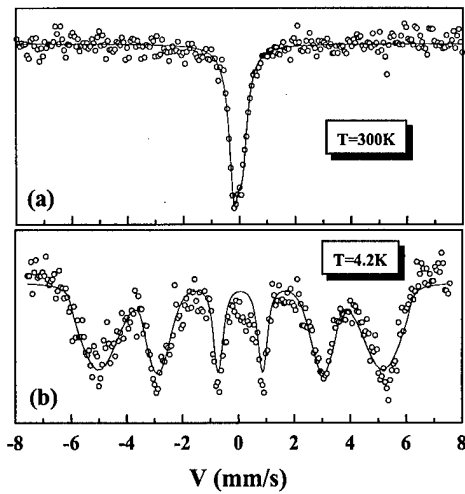


FIG. 2. Mössbauer spectrum for $\text{Cu}_{80}\text{Fe}_{10}\text{Ni}_{10}$ ribbon annealed at 400°C for two hours. Measurements at (a) 300 and (b) 4.2 K.

To characterize the magnetic state of the nanoparticles in these ribbons, all samples were characterized by Mössbauer spectroscopy. At both 78 and 300 K, Mössbauer spectra for all CuFeNi ribbons, both as-cast and annealed, showed a singlet associated with superparamagnetic Fe. The 300 K spectrum for $\text{Cu}_{80}\text{Fe}_{10}\text{Ni}_{10}$ is shown in Fig. 2(a). At 4.2 K, however, the temperature is below the blocking temperature for the Fe nanoparticles and the characteristic Fe sextet appears as shown in Fig. 2(b). The solid curve superimposed on the data of Fig. 2(b) corresponds to a fit made using a Gaussian distribution of hyperfine fields. The Gaussian was centered at 314 kOe and had a width of 82 kOe. For comparison, we note that $\alpha\text{-Fe}$ has a hyperfine field of about 340 kOe at 4.2 K. As we discuss below, magnetization measurements at 300 K on $\text{Cu}_{80}\text{Fe}_{10}\text{Ni}_{10}$ allowed us to estimate $2.1 \mu_B/\text{Fe}$ for this material, characteristic of $\alpha\text{-Fe}$. Thus, both magnetization and Mössbauer measurements indicate the presence of nanoparticles with composition close to that of $\alpha\text{-Fe}$.

The observed hyperfine field reduction can be explained by the collective oscillation model for small particles.⁸ From the expression $H_{\text{part}}/H_{\text{bulk}} = 1 - kT/2KV$, we obtained an estimate for the anisotropy energy barrier $KV/k = 26$ K. This value yields a Mössbauer blocking temperature of order 15 K, which is consistent with our experiments. Assuming $K \approx 4.8 \times 10^4 \text{ J/m}^3$, we obtain a mean radius 1.2 nm for the Fe nanoparticles. This is at least an order of magnitude smaller than the value reported⁹ for Fe nanoparticles in splat-cooled and annealed $\text{Cu}_{75}\text{Fe}_{25}$. To understand this discrepancy, we prepared a sample of $\text{Cu}_{80}\text{Fe}_{20}$ by melt spinning. The Mössbauer spectrum of the as-cast sample at 300 K showed a singlet superimposed upon a well-defined sextet, indicating the presence of many large Fe particles with blocking temperatures above 300 K. Apparently the presence of Ni in the alloy facilitates the formation of a solid solution and results in a greater dispersion of the Fe in the Cu matrix.

IV. GMR VS. MAGNETIZATION

As mentioned in the introduction, a study of the dependence of MR on the reduced magnetization can furnish a

useful characterization of the material as well as important insights into the mechanisms responsible for this effect. This article follows a treatment developed in Ref. 4, which, in first approximation, neglects interactions between particles, but considers a log-normal distribution of magnetic moments associated with the superparamagnetic particles. When the magnetic moment distribution function is used to fit the magnetization curve, one obtains two parameters associated with the distribution curve, which can then be used to calculate the mean magnetic moment and the particle density. Using the same distribution function in a model¹⁰ for the MR provides information on electron scattering within the magnetic grains and at magnetic-nonmagnetic interfaces.

Thus our first task is to determine the normalized curves of magnetization and MR. For this study, we considered $\text{Cu}_{80}\text{Fe}_{10}\text{Ni}_{10}$ because the MR was largest for this sample. However, we considered $T = 300$ K, since the ferromagnetic hysteretic contribution to M was very small at this temperature and it was straightforward to determine the anhysteretic magnetization curve. Since the magnetization had not saturated at 70 kOe, data were fitted to the expression $M = M_s(1 - a/H)$ in order to obtain the saturation magnetization M_s . We obtained $M_s = 19 \text{ emu/g}$ ($2.1 \mu_B/\text{Fe}$), as mentioned above. The MR data were also fitted to a similar expression to determine the saturation magnetoresistance MR_s : $\text{MR} = \text{MR}_s(1 - b/H)$. If $\text{MR} \sim (M/M_s)^2$, then the constant b should equal $2a$. In fact, we obtained $\text{MR}_s = -5.5\%$ and $b = 2a$. The normalized magnetoresistance $\text{MR}_n = \text{MR}/\text{MR}_s$ was plotted as a function of the normalized magnetization M/M_s and the result is nearly a parabola. Deviations from the parabolic form are subtle and must be characterized with care.⁴

The normalized magnetization data up to 70 kOe were then compared with an expression⁴ wherein the magnetization of a distribution of superparamagnetic grains is given in terms of the Langevin function $L(x) = \coth x - 1/x$

$$M(H, T) = \int_0^\infty \mu L\left(\frac{\mu H}{kT}\right) f(\mu) d\mu. \quad (1)$$

The magnetic moment distribution function $f(\mu)$ is a log-normal function divided by μ

$$f(\mu) = \frac{N}{\sqrt{2\pi}\sigma} \frac{1}{\mu} \exp\left[-\frac{\ln^2(\mu/\mu_0)}{2\sigma^2}\right]. \quad (2)$$

This distribution function has a peak near μ_0 and has width σ . In Fig. 3 we show experimental data for $\text{Cu}_{80}\text{Fe}_{10}\text{Ni}_{10}$ annealed at 400°C . The data agree well with the model below 20 kOe and deviate only slightly above that field. We determined the parameters of $f(\mu)$, $\mu_0 = 450 \mu_B$ and $\sigma = 0.93$, and then calculated the mean magnetic moment per grain $\langle\mu\rangle = 693 \mu_B$ and the number of magnetic grains per gram of material: $N = 3 \times 10^{18}/\text{g}$ for our $\text{Cu}_{80}\text{Fe}_{10}\text{Ni}_{10}$ at 300 K. Using the above value of the mean moment $\langle\mu\rangle$ and a value of $2.1 \mu_B/\text{atom}$ for $\alpha\text{-Fe}$, we estimated the mean radius of a magnetic particle to be $r = 1.6$ nm, in good agreement with the radii of magnetic particles encountered in CuCo ⁴ and consistent with our Mössbauer results presented above.

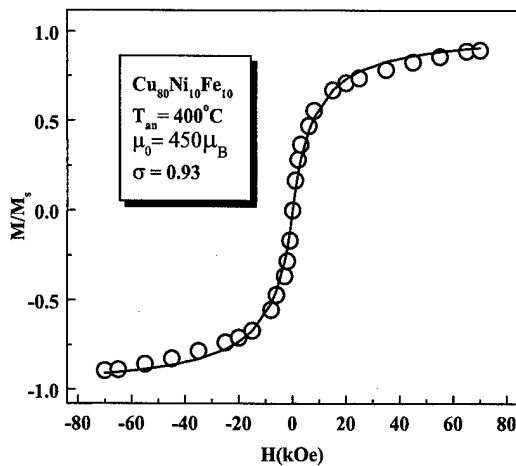


FIG. 3. Magnetization data for $\text{Cu}_{80}\text{Fe}_{10}\text{Ni}_{10}$ ribbon annealed at 400 °C (circles) compared with model which assumes lognormal distribution of noninteracting superparamagnetic particles.

In Ref. 4, the distribution of magnetic moments was used in a model proposed by Zhang and Levy¹⁰ for granular films based upon the formalism for the magnetoresistance in layered structures. Both bulk and interface scattering contribute to the magnetoresistance by means of the factor $\mu + \alpha \mu^{2/3}$, where the parameter α is proportional to the ratio between the interface and bulk scattering cross sections and has been given in Eq. (9) of Ref. 4. We tried fitting our MR data to this model, using the values of μ_0 and σ determined from the magnetization, and treating α as an adjustable parameter. We used

$$\text{MR}(H, T) = -\frac{A}{N^2} \left[\int_0^\infty (\mu + \alpha \mu^{2/3}) L\left(\frac{\mu H}{kT}\right) f(\mu) d\mu \right]^2, \quad (3)$$

where both A and α are coefficients which do not depend upon H and N is the number of grains per unit volume. The result is shown in Fig. 4. There is good agreement for magnetic fields below about 15 kOe, after which the agreement is somewhat worse. Larger values of α do not bring the calculated (dashed) curve into better agreement with the data. In Ref. 4, the MR data in $\text{Cu}_{90}\text{Co}_{10}$ were in good agreement with the model for fields up to 20 kOe. The authors of Ref. 4 have defined two parameters f and g which measure the flatness of the parabolic relation between MR and M/M_s . Calculating these parameters, we find that their values correspond to the limit of the validity of the model. Therefore, it seems that a further discussion of the relationship between MR and M/M_s in $\text{Cu}_{80}\text{Fe}_{10}\text{Ni}_{10}$ will require an extension of the model of Ref. 4.

V. CONCLUSIONS

Both magnetization and Mössbauer measurements indicate the presence of nanoparticles in $\text{Cu}_{80}\text{Fe}_{10}\text{Ni}_{10}$ with com-

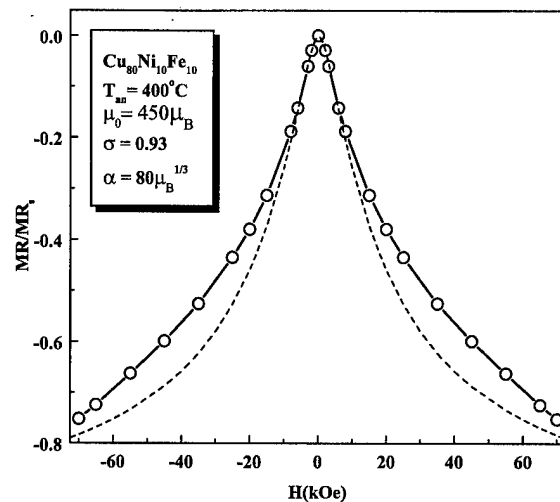


FIG. 4. Normalized magnetoresistance for $\text{Cu}_{80}\text{Fe}_{10}\text{Ni}_{10}$ ribbon annealed at 400 °C (circles) compared with curve calculated using Eq. (3) (dashed curve).

position close to that of α -Fe and effective radius slightly larger than 1 nm. This size is considerably smaller than that found for Fe particles in splat-cooled⁹ $\text{Cu}_{75}\text{Fe}_{25}$, but is comparable to values encountered in $\text{Cu}_{90}\text{Co}_{10}$. Thus $\text{Cu}_{80}\text{Fe}_{10}\text{Ni}_{10}$ and $\text{Cu}_{90}\text{Co}_{10}$ seem to be physically comparable and it is interesting to compare MR results in these materials. The magnetization data for $\text{Cu}_{80}\text{Fe}_{10}\text{Ni}_{10}$ at 300 K were found to be in good agreement with curves calculated assuming a distribution of noninteracting superparamagnetic Fe particles. However, the MR data agreed with the proposed model only for low fields.

ACKNOWLEDGMENTS

FAPESP, CNPq, CAPES, and FINEP provided financial support. The authors wish to thank M. Knobel and S. Jonen for useful discussions and S. A. Romero for the melt-spun ribbons.

- ¹A. E. Berkowitz, J. R. Mitchell, M. J. Carey, A. P. Young, S. Zhang, F. E. Spada, F. T. Parker, A. Hutten, and G. Thomas, *Phys. Rev. Lett.* **68**, 3745 (1992).
- ²J. Q. Xiao, J. S. Jiang, and C. L. Chien, *Phys. Rev. Lett.* **68**, 3749 (1992).
- ³J. I. Gittleman, Y. Goldstein, and S. Bozowski, *Phys. Rev. B* **5**, 3609 (1972).
- ⁴E. F. Ferrari, F. C. S. da Silva, and M. Knobel, *Phys. Rev. B* **56**, 6086 (1997).
- ⁵L. H. Chen, S. Jin, T. H. Tiefel, S. H. Chang, M. Eibschutz, and R. Ramesh, *Phys. Rev. B* **49**, 9194 (1994).
- ⁶L. H. Chen, Y. K. Yang, and Y. H. Chang, *IEEE Trans. Magn.* **31**, 4012 (1995).
- ⁷L. H. Chen, S. Jin, T. H. Tiefel, S. Y. Liao, and Y. D. Yao, *J. Appl. Phys.* **79**, 5599 (1996).
- ⁸S. Mørup, H. Topsøe, and J. Lipka, *J. Phys. (France)* **37**, C6-287 (1976).
- ⁹M. S. Rogalski, M. M. Pereira de Azevedo, and J. B. Sousa, *J. Magn. Mater.* **163**, L257 (1996).
- ¹⁰S. Zhang and P. M. Levy, *J. Appl. Phys.* **73**, 5315 (1993).

Microstructure and giant magnetoresistance of Co–Cu granular films fabricated under the extremely clean sputtering process

Masakiyo Tsunoda,^{a)} Kentaro Okuyama, Makoto Ooba, and Migaku Takahashi
Department of Electronic Engineering, Tohoku University, Sendai 980-77, Japan

In order to clarify the influence of the impurities in the sputtering atmosphere on the microstructure and the giant magnetoresistance (GMR) properties of nanogranular thin films, Co–Cu alloy films were prepared on quartz substrates at room temperature under the different purity of the sputtering atmosphere by changing the base pressure, 10^{-11} Torr extremely clean process (XC) and 10^{-7} Torr lower grade process (LG). The correlation between the microstructure and the GMR of films after an annealing procedure is discussed. As results, we found that; (1) A Co-rich phase combined with oxygen was formed at grain boundary in the films as deposited under the LG process; (2) the gradual progress of the grain growth of precipitates with increasing annealing temperature was observed in the XC-processed films, while the coarse grain growth of the matrix phase, resulting in the abrupt change of magnetoresistance occurred in the LG-processed films. We conclude that regulated impurity concentration in the films is an essential parameter to control the precipitation process from the supersaturated solid solution and to realize the desirable microstructure of the nanogranular GMR thin films. © 1998 American Institute of Physics. [S0021-8979(98)26411-5]

I. INTRODUCTION

The origin of giant magnetoresistance (GMR) observed in nanogranular thin films is a spin-dependent scattering of conduction electrons which occurs at the interface between a nonmagnetic matrix and magnetic fine particles of precipitate.^{1,2} In the case of sputter deposited Co–Cu granular films, supersaturated solid solution and fine particles are generally formed as deposited, and the magnetic fine particles grow by postannealing.^{3,4} Since the precipitating process from the supersaturated solid solution is strongly affected by defects and dissolved oxygen in the films, one can expect the drastic change of the microstructure and the GMR properties of nanogranular films with decreasing impurity concentration in the films. In the present study, in order to clarify the influence of the contaminating impurities obtained during the deposition process, we prepared Co–Cu alloy films by changing the purity of the sputtering atmosphere and investigated the correlation between the microstructure and the GMR of them through heat treatment.

II. EXPERIMENTAL PROCEDURE

$\text{Co}_x\text{Cu}_{1-x}$ (x =atom fraction Co) films 300 nm thick were prepared onto fused quartz substrates at room temperature by using a specialized dc magnetron sputtering machine which enables pumping down to 8×10^{-12} Torr. For the process gas, ultraclean Ar gas (UC-Ar), whose moisture level is less than 1 ppb, was used.⁵ In order to make two different residual impurity levels in the sputtering atmosphere, the base pressure of 3×10^{-11} Torr (extremely clean process: XC process) and 3×10^{-7} Torr (lower grade process: LG process) were prepared respectively by changing the pumping time after venting the chamber with air. The flow rate of the UC-Ar gas during sputtering was 100 sccm to make the

pressure 5 mTorr. The impurity levels of the sputtering atmosphere were calculated as 0.01 ppm for the XC process and 1 ppm for the LG process, respectively.⁵ Annealing was performed in vacuum on a same sample subsequently from 150 to 450 °C for 1 h at each temperature. Microstructure of films was examined by x-ray diffraction (XRD) and transmission electron microscope (TEM). Magnetoresistance was measured at room temperature in the film plane by a dc four probe method with maximum applied field of 14 kOe.

III. RESULTS AND DISCUSSION

A. Microstructure

Figure 1 shows TEM images of $x=0.17$ samples as deposited under the XC and the LG processes, respectively. The characteristic grain diameter of the XC-processed film (≈ 30 nm) is larger than that of the LG-processed film (≈ 20 nm). It is noteworthy that a different phase with bright contrast distinguished from grains is observed at triple points of the grain boundary in the LG-processed film. In order to identify the phase with bright contrast, energy dispersion x-ray spectroscopy (EDS) analysis was performed on the LG-

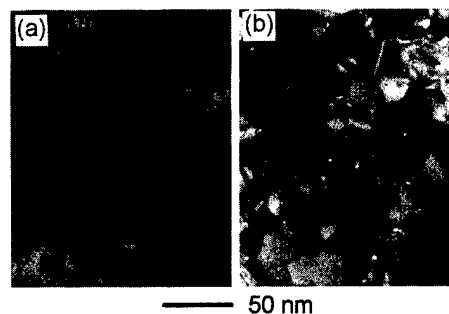


FIG. 1. TEM images of $\text{Co}_{0.17}\text{Cu}_{0.83}$ alloy films as deposited under the XC process (a) and the LG process (b).

^{a)}Electronic mail: wacky06@ec.ecei.tohoku.ac.jp

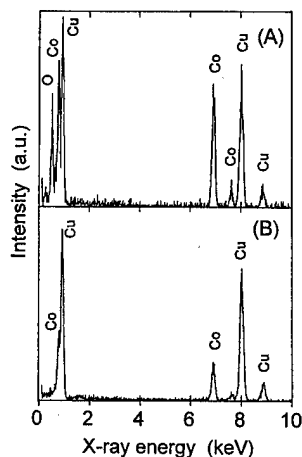


FIG. 2. Characteristic x-ray profiles from the grain boundary phase (A) and the grain (B) of a $\text{Co}_{0.17}\text{Cu}_{0.83}$ alloy film as deposited under the LG process.

processed film. Figure 2 shows the characteristic x-ray profiles obtained when 1-nm-diam electron beam was focused on the grain boundary phase (A) and on the grain (B), respectively. By comparing these profiles, we can say that the phase at triple points in the LG-processed film has higher concentration of Co than the grains. In addition, oxygen, which is not appeared in the grains, is clearly detected in the grain boundary phase. On the other hand, in the XC-processed film, no intergranular phase is observed in Fig. 1(a), indicating the homogeneous distribution of Co in the whole film. It seems reasonable to suppose that the major impurity element, H_2O in the LG-processed atmosphere is the most probable species affecting the change of the microstructure of the as-deposited films. Namely, H_2O unites preferentially with Co adatoms arrived at the substrate and immobilizes them to be nuclei for the condensation of Co adatoms. In the XC process, because of the lack of this nucleation, grains of homogeneous supersaturated solid solution can grow large.

Figure 3 shows the changes of peak intensity and width of major diffraction line from (111) crystal plane in the XRD profile as functions of annealing temperatures, T_a for $x=0.17$ samples. In the case of XC-processed film, the dif-

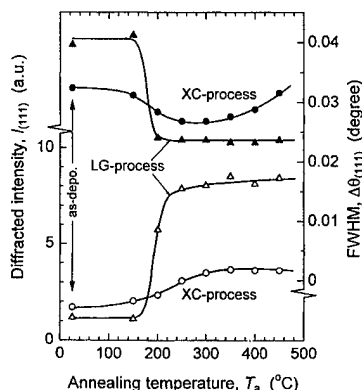


FIG. 3. Changes of XRD profiles of $\text{Co}_{0.17}\text{Cu}_{0.83}$ films of the XC process and the LG process, as deposited and after annealed at various temperatures, T_a . Peak intensity (open figures) and width (filled figures) for (111) diffraction line are plotted.

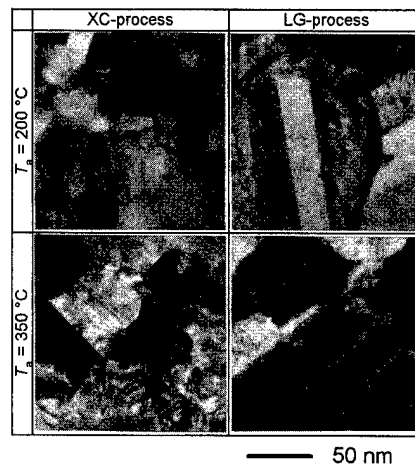


FIG. 4. TEM images of $\text{Co}_{0.17}\text{Cu}_{0.83}$ alloy films of the XC process and the LG process, after annealed at $T_a=200$ and 350°C , respectively.

fracted lines gradually become large and sharp up to 300°C , and turn to become broad above 350°C . On the other hand, in the case of LG-processed film, abrupt increase of intensity and sharpening of diffraction line are observed at 200°C , which suggests a coarse grain growth. Figure 4 shows TEM images of $x=0.17$ films in the both processes after annealed at 200 and 350°C , respectively. In the XC-processed film, corresponding with the changes of XRD profile, the gradual grain growth with increasing T_a is observed. Also we can see the obscure lattice image of grains with increasing T_a , which is suggesting the decomposition of supersaturated solid solution. In contrast, in the LG-processed film, we can see the coarse grain growth at 200°C . The characteristic grain size was larger than several hundred nm. The Co-rich phase which existed at the grain boundary as seen in the as-deposited film with bright contrast [Fig. 1(b)] is cut apart and dispersed in the coarsened matrix grains as fine particles.

B. GMR and magnetic properties

Figure 5 shows the changes of ρ_s and $\Delta\rho (= \rho_0 - \rho_s)$ as a function of the annealing temperature, T_a , for the films with $x=0.13$, 0.17 , and 0.25 fabricated under the XC and the LG processes. ρ_0 and ρ_s are defined as the resistivity measured without and with applied field of 14 kOe, respectively. ρ_s gives a scale of the resistivity when the magnetization of the film is saturated, though 14 kOe was not large enough especially in the films as-deposited and after annealed at lower temperature. We attend to the $x=0.17$ as a typical example. In the XC-processed film, ρ_s which was $52 \mu\Omega \text{ cm}$ as-deposited gradually decreases, with increasing T_a . $\Delta\rho$ which was $1.8 \mu\Omega \text{ cm}$ as-deposited gradually increases and reaches maximum value of $2 \mu\Omega \text{ cm}$ at $T_a=150^\circ\text{C}$, then decreases with increasing T_a . The increase of $\Delta\rho$ below 150°C can be explained by the increasing volume and heightening the Co concentration of the Co-rich phase by precipitation from the supersaturated solid solution. Namely, the enlarging magnetization of Co-rich phase makes film easy to saturate even at 14 kOe and enhances the difference of spin-dependent scattering between zero and maximum applied field. Above 200°C , the decrease of $\Delta\rho$ is explained by

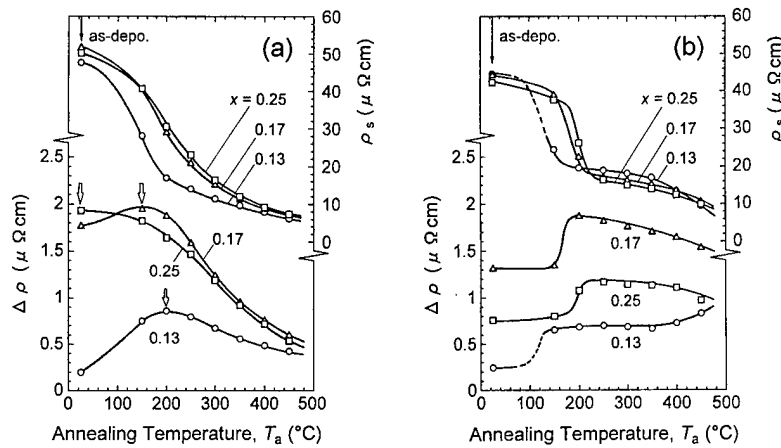


FIG. 5. Changes of resistivity ρ_s and magnetoresistance $\Delta\rho$ as functions of annealing temperature for $\text{Co}_x\text{Cu}_{1-x}$ films of the XC process (a) and the LG process (b).

grain growth of Co-rich phase leading to lower their surface/volume ratio. Here, we should notice the annealing temperature where $\Delta\rho$ reaches maximum (indicated as open arrows in the figure) becomes lower with increasing Co content. This means that highly supersaturated Co are easy to precipitate and to make large grains of Co-rich phase at relatively lower temperature. These experimental facts support the grain growth discussed above. On the other hand, in the LG-processed films, abrupt drop of ρ_s is observed at $T_a = 200^\circ\text{C}$ in $x = 0.17$ case. Corresponding to this change, $\Delta\rho$ steeply increases from 1.3 to 1.9 $\mu\Omega\text{cm}$ at $T_a = 200^\circ\text{C}$. By taking into account the structural change as previously shown in Figs. 3 and 4, one can say that the physical origin of the abrupt changes of ρ_s and $\Delta\rho$ at $T_a = 200^\circ\text{C}$ is the decrease of grain boundary scattering and the randomizing direction of the magnetization of particulate Co-rich phase at zero field. In addition, from the slight decrease of $\Delta\rho$ above 200°C , we can conclude that the grain growth of Co-rich phase resulting from the decomposition of the supersaturated solid solution is not significant in the LG-processed film up to 450°C , contrary to the XC-processed one.

Figure 6 shows the changes of $M_{10\text{ kOe}}$, which is the magnetization measured under applied field of 10 kOe, and

the coercivity, H_c of $x = 0.17$ samples as a function of T_a . Measurement was performed at room temperature. In the XC-processed film, $M_{10\text{ kOe}}$ gradually increases with increasing T_a . H_c arises from $T_a = 200^\circ\text{C}$ and also increases gradually, indicating that magnetic stability against thermal agitation is induced by grain growth of the Co-rich phase. On the other hand, in the LG-processed film, $M_{10\text{ kOe}}$, which is 190 emu/cc as-deposited and larger than that of the film in the XC process, slowly increases and becomes smaller than the XC process above 350°C . H_c also increases fairly slightly up to 450°C . These changes well correspond with the changes of microstructure and the GMR discussed above.

IV. CONCLUSION

Co-Cu alloy films were fabricated under the different purity of the sputtering atmosphere by changing the base pressure, 10^{-11} Torr (XC process) and 10^{-7} Torr (LG process). The correlation between the microstructure and the giant magnetoresistance of Co-Cu alloy films was examined. As results, we found that: (1) A Co-rich phase combined with oxygen was formed at grain boundary in the as-deposited films in the LG process; (2) the gradual progress of the grain growth of Co-rich phase with increasing annealing temperature, accompanying a gradual change of magnetoresistance, were observed in the XC-processed films; (3) in the LG-processed films, the coarse grain growth of the matrix phase resulted in abrupt change of magnetoresistance.

We conclude that the regulated impurity concentration in the films is an essential parameter to control the precipitation process from supersaturated solid solution and to realize the desirable microstructure of the nanogranular GMR thin films.

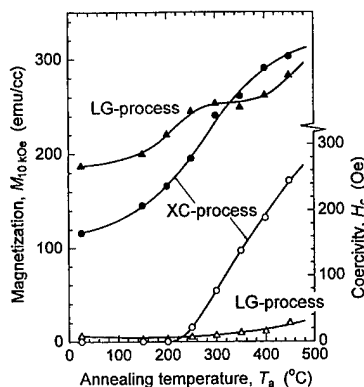


FIG. 6. Changes of magnetization under $H = 10\text{ kOe}$ (filled figures) and coercivity (open figures) as functions of annealing temperature for $\text{Co}_{0.17}\text{Cu}_{0.83}$ films of the XC process and the LG process.

¹S. Zhang, Appl. Phys. Lett. **61**, 1855 (1992).

²S. Zhang and P. M. Levy, J. Appl. Phys. **73**, 5315 (1993).

³A. E. Berkowitz, M. J. Carey, J. R. Michell, A. P. Young, S. Zhang, F. E. Spada, F. T. Parker, A. Hutten, and G. Thomas, Phys. Rev. Lett. **68**, 3745 (1992).

⁴J. Q. Xiao, J. S. Jiang, and C. L. Chien, Phys. Rev. Lett. **68**, 3749 (1992).

⁵K. Okuyama, T. Shimatsu, S. Kuji, and M. Takahashi, IEEE Trans. Magn. **31**, 3838 (1995).

Giant magnetoresistance and remanence in granular CoCu codeposited films

A. D. C. Viegas,^{a)} J. Geshev, and J. E. Schmidt

Instituto de Física-UFRGS, C.P. 15051, 91501-970, Porto Alegre, RS, Brazil

E. F. Ferrari

Instituto de Física "Gleb Wataghin", UNICAMP, C.P. 6165, 13083-970, Campinas, SP, Brazil

We present experimental magnetoresistance, magnetization, and remanence data for CoCu granular films obtained by electron beam codeposition, subsequently submitted to a thermal treatment. The magnetization measurements show coexistence of superparamagnetic and ferromagnetic (or blocked superparamagnetic) Co grains. By modeling the experimental magnetization curves, the distribution function of the superparamagnetic particle size, the volume fraction of the blocked part of the Co particles, and their saturation magnetization are obtained. δM plots are constructed using the remanence curves. A correlation between the changes of the δM parameters and those of the giant magnetoresistance, caused by the annealing, is discussed. © 1998 American Institute of Physics. [S0021-8979(98)46811-7]

I. INTRODUCTION

The so-called granular ferromagnetics are composites of two materials, one of which consists of nanosized ferromagnetic particles (e.g., Fe, Co) dispersed in nonmagnetic metallic matrix (e.g., Ag, Cu, Au). Since the discovery of the effect of giant magnetoresistance (GMR) in such systems,^{1,2} they have been widely investigated due to their potential for practical applications and because they can be easily produced (usually sputtering, coevaporation, melt spinning, mechanical alloying, or electrodeposition), and their microstructure can be modified by suitable thermal treatment. The GMR in these granular systems is comparable to the ones found in multilayers. Extensive studies have been made to link the GMR response to the structural properties (e.g., interface, particle shape, size and density, intergranular distances, etc.).^{3,4}

The GMR effect in these systems is believed to be a manifestation of the conduction electron spin-dependent scattering on the local magnetic configuration. Qualitatively, it is assumed that the scattering probability is proportional to the correlation degree of the moments of adjacent pair of granules $\langle \mu_i \cdot \mu_j \rangle$.^{5,6} The resistance of the heterogeneous alloys is maximum in the case of random distribution, i.e., low correlation of magnetic moments at zero field. The applied field aligns the magnetic moments (high correlation) thus decreasing the resistance of the system.³

The magnetoresistive behavior of an homogeneous superparamagnetic (SPM) system has a relatively simple interpretation based on a description by the Langevin function. In this case it is given by $[L(\mu H/k_B T)]^2$, where H is the applied field, k_B the Boltzman's constant, and T the temperature. All the theories that use this description predict a dependence of the fractional magnetoresistance on the square of the reduced magnetization. However, this relation fails in some granular systems.⁷ Interparticle interactions⁸ and de-

pendence of the scattering process on cluster size⁹⁻¹¹ are the mechanisms that have been introduced to explain this discrepancy.

The effect of interactions on GMR of granular solids has been investigated,¹² using a model that obtain the moment configuration in the presence of dipolar magnetic fields. The GMR effect is found to be lowered by these interactions, and connected to low-range correlation of the magnetic moments. In this case, a deviation from the parabolic law is also observed. In the present work, the influence of the thermal treatment on the microstructure, magnetoresistance, and magnetic properties of CoCu codeposited films is investigated. The latter, along with the fact that the GMR for our samples do not saturate for the maximum magnetic field available, do not allowed us to use the deviations from the parabolic law to estimate the interaction effects. We used the technique based on the δM^{dc} plot, which has been extensively used recently, because it proved to be very sensitive to small changes in the remanence produced by interaction between the magnetic regions of the system.

II. EXPERIMENT

The 5000-Å-thick Co-Cu films with different compositions were codeposited by means of electron beam gun on Si (111) substrate. The nominal compositions are 10%, 20%, and 30% of cobalt. Thermal treatment was performed in a rapid annealing furnace under Ar atmosphere between 100 and 350 °C for 1 h. The magnetization and remanence curves were measured at room temperature using an alternating gradient magnetometer with the field applied parallel to the sample's plane. The magnetoresistance curves were measured in fields up to 6 kOe using the standard four points method.

III. RESULTS AND DISCUSSION

The conventional x-ray diffraction shows a pure fcc Cu structure, no traces of hcp Co are observed. Due to the small

^{a)}Electronic mail: dcviegas@if.ufrgs.br

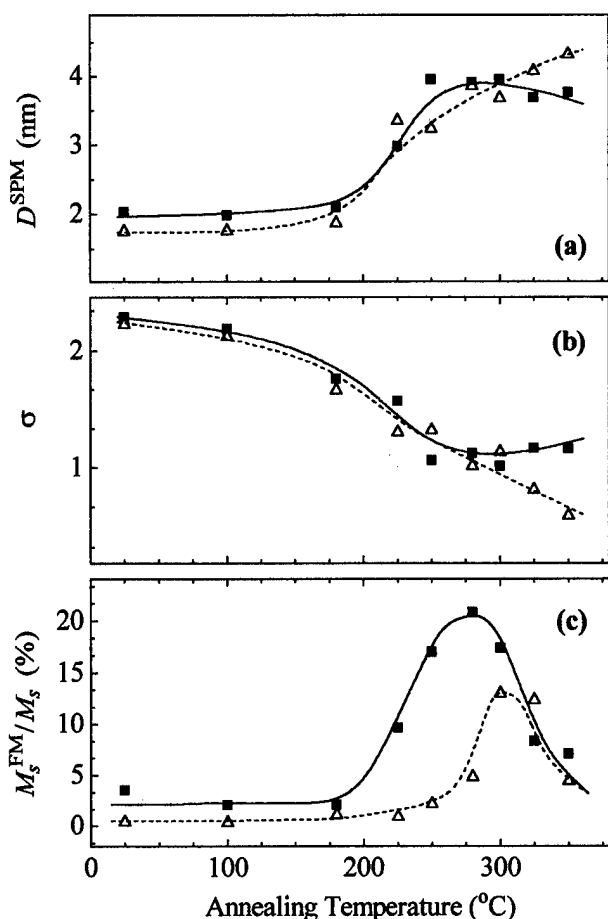


FIG. 1. (a) D^{SPM} and (b) σ vs. T_{ann} obtained from the SPM fit of the experimental magnetization curves for the samples with 10% and 20% Co concentrations; (c) The ratio between FM component and total magnetization; squares: 10% Co, and triangles: 20% Co. The lines are guide to the eye.

size of the Co particles and the high lattice coherency between the fcc Co phase and the Cu matrix, this Co phase cannot be distinguished.

The experimental magnetization curves show hysteresis. Here, as in our previous work,¹³ we consider the samples as consisting of two magnetic Co phases: (i) noninteracting SPM particles and (ii) “blocked” [interacting and/or larger ferromagnetics (FM)] grains. The sample magnetization can be written as $M(H) = M^{\text{FM}}(H) + M^{\text{SPM}}(H)$. The M^{SPM} term is a weighted superposition of Langevin functions assuming the following magnetic moment distribution function¹⁴

$$f(\mu) = \frac{N}{\sqrt{2\pi}} \frac{1}{\mu} \exp\left[-\frac{\ln^2(\mu/\mu_0)}{2\sigma^2}\right], \quad (1)$$

where N is the volumetric SPM particle density, μ_0 the particle magnetic moment, and σ the width of the distribution which differs from the log-normal one by the factor $1/\mu$. The mean value of μ is defined as $\langle\mu\rangle = \mu_0 \exp(\sigma^2/2)$.

In Figs. 1(a) and 1(b) the values of the mean SPM particle size, D^{SPM} , and σ used to fit the SPM components of the experimental magnetization curves are displayed as a function of the annealing temperatures, T_{ann} for the samples with 10% and 20% Co concentrations. Due to the low SPM

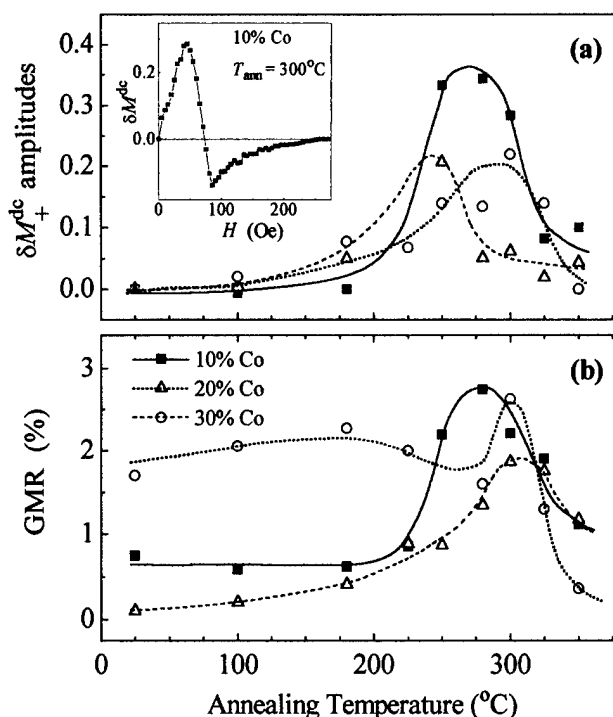


FIG. 2. (a) δM^{dc}_+ vs. T_{ann} constructed from the remanent magnetization curves; the inset in this figure is a representative δM^{dc} plot for the sample with 10% Co, annealed at 300 °C. (b) GMR vs. T_{ann} for samples with different Co concentration. The lines are guide to the eye.

contribution to the total magnetization of the 30% Co sample, it was not possible to fit its SPM component. The dependence of the FM fraction, defined as M_s^{FM}/M_s , on T_{ann} is shown in Fig. 1(c) (the method of estimation of M_s^{FM} is described elsewhere).¹³

When the particles are sufficiently close to each other, the magnetic interactions can induce correlation between the adjacent moments, which may be both Ruderman–Kittel–Kasuya–Yosida (RKKY) and/or dipolar in nature. We tried to estimate this effect by using the maxima of the δM^{dc} plots, defined in our recent works.^{13,15} The positive amplitude values, δM^{dc}_+ vs T_{ann} are represented in Fig. 2(a) (the negative ones almost do not change as a function of T_{ann} having values of ≈ 0.2). The inset in Fig. 2(a) shows a representative δM^{dc} plot (10% Co, $T_{\text{ann}} = 300$ °C). The reduced GMR values, defined as $[R(H) - R(H=0)]/R(H=0)$, obtained for $H_{\text{max}} = 6$ kOe, are shown in Fig. 2(b).

$T_{\text{ann}} \leq 200$ °C does not change significantly the morphology, magnetic, and magnetotransport properties of the samples. Figure 1(c) shows that in this T_{ann} range, the samples contain mostly SPM particles, with $D^{\text{SPM}} \approx 2$ nm. M_s values are rather smaller than M_s^{Co} for bulk Co, indicating that there is a large number of Co atoms dissolved in the Cu matrix.

Annealing at higher temperatures up to approximately 300 °C, results in a gradual increase of D^{SPM} and a decrease of σ , i.e., the SPM particles become larger and more uniform in size. Their number increases as well, as the total M_s values increase for all samples at the expense of the atomically diluted Co in the Cu matrix. GMR is enhanced, reaching its maximum for $T_{\text{ann}} \approx 300$ °C for all samples (for H_{max}

=6 kOe). This increase could be explained, assuming that the main contribution to the GMR comes from the random orientation of the SPM Co magnetic moments:² annealing at higher temperatures increases the number of SPM particles, changes their size, and the mean distance between them. The latter would become comparable to the mean free path of the conduction electrons, and more selective scattering would occur, thus increasing GMR. Although the FM fraction increases with increasing T_{ann} , it remains relatively small and does not influence the GMR, as observed from the magnetoresistance curves, which do not show rapid response at low fields and do not saturate at 6 kOe.

GMR of the samples annealed at $T_{\text{ann}} > 300^\circ\text{C}$ decreases, despite that the D^{SPM} and σ do not change significantly. However, a decrease of the total M_s is observed for all samples, which can be explained by the decrease of the number of the SPM particles, as well as the increase of the distance between them, so the scattering event becomes infrequent and far apart, thus GMR is small. The decrease of M_s is not very clear, but we suggest that some Co is redissolved in the Cu matrix,¹⁶ which is expected to be present at high temperature.

All δM^{dc} plots are characterized by positive peaks in low fields and a relatively shallow minima in higher fields. There are two cases to be considered.

(i) the FM particles are mainly fcc Co, and weak positive (ferromagnetic, magnetizing) interactions present. This suggestion is supported by the similarity of the shape of the experimental δM^{dc} plots to that calculated for a disordered system of noninteracting cubic anisotropy particles with four easy magnetization axes,¹³ as well as by the statement of Kimoto *et al.*¹⁷ and Anno,¹⁸ that small Co particles have a fcc structure. In this case, the increase of δM^{dc} by increasing T_{ann} means that the interactions favoring parallel alignment weaken, and δM^{dc} tends to reach the value of ≈ 0.5 of that calculated for the noninteracting case plot.¹³ Thus, the maximum of the GMR, which is in the same T_{ann} range where δM^{dc} is maximum, can be associated with the weaker interactions, even that the FM fraction is not very large, having its maximum of $\approx 20\%$ for 10% and 20% Co.

(ii) The samples consist of hcp (uniaxial) Co. In such cases, positive deviations from the noninteracting zero line¹⁹ are attributed to strong FM interactions between the adjacent grains. The increase of δM^{dc} by increasing T_{ann} suggests increase of these interactions, and as result, GMR should be depressed, on the contrary of what is observed here. Therefore, we believe that the data support the first suggestion—the Co is mainly in fcc phase.

The reduction of δM^{dc} for the higher T_{ann} can be attributed not to an increase of the negative interactions, but mainly to an extinction of the FM phase, as indicated in Fig. 1(c).

IV. CONCLUSION

Experimental magnetoresistance and magnetization data for thermally treated CoCu codeposited films were reported. It was obtained that the GMR has maximum of $\approx 3\%$ (for $H_{\text{max}} = 6$ kOe) when the SPM particles have a specific size range and their size distribution width is relatively narrow. Assuming that the Co particles are mainly fcc, a correlation between the changes of the δM parameters and of GMR is observed. However, as the relative FM fraction is rather low in our samples, one should not assume that the magnetic interactions are the main, determining factor for the GMR changes.

ACKNOWLEDGMENTS

Research supported by CNPq, FAPERGS, and FINEP.

- ¹A. E. Berkovitz, J. R. Mitchell, M. J. Carey, A. P. Young, S. Zhang, F. E. Spada, F. T. Parker, A. Hutten, and G. Thomas, *Phys. Rev. Lett.* **68**, 3745 (1992).
- ²J. Q. Xiao, J. S. Jiang, and C. L. Chien, *Phys. Rev. Lett.* **68**, 3749 (1992).
- ³S. Zhang and P. Levy, *J. Appl. Phys.* **73**, 5315 (1993).
- ⁴S. Zhang, *Appl. Phys. Lett.* **61**, 1855 (1992).
- ⁵J. I. Gitelman, Y. Goldstein, and S. Bozowski, *Phys. Rev. B* **9**, 3609 (1972).
- ⁶M. R. Parker, J. A. Barnard, D. Seale, and A. Waknis, *J. Appl. Phys.* **73**, 5512 (1993).
- ⁷C. Bellouard, B. George, and G. Marchal, *J. Phys.: Condens. Matter* **6**, 7239 (1994).
- ⁸J. F. Greg, S. M. Thompson, S. J. Dawson, K. Ounadjela, C. R. Staddon, J. Hamman, C. Fermon, G. Saux, and K. O'Grady, *Phys. Rev. B* **49**, 1064 (1994).
- ⁹V. Madurga, R. J. Ortega, V. N. Korenivsky, H. Medelius, and K. V. Rao, *J. Magn. Magn. Mater.* **140**, 465 (1995).
- ¹⁰N. Wiser, *J. Magn. Magn. Mater.* **147**, 253 (1995).
- ¹¹J. Vergara, R. J. Ortega, V. Madurga, and K. V. Rao, *J. Appl. Phys.* **81**, 4596 (1997).
- ¹²M. El-Hilo, K. O'Grady, and R. W. Chantrell, *J. Appl. Phys.* **76**, 6811 (1994).
- ¹³A. D. C. Viegas, J. Geshev, L. S. Dorneles, J. E. Schmidt, and M. Knobel, *J. Appl. Phys.* **82**, 3047 (1997).
- ¹⁴E. F. Ferrari, F. C. S. da Silva, and M. Knobel, *Phys. Rev. B* **56**, 6086 (1997).
- ¹⁵A. D. C. Viegas, J. Geshev, L. F. Schelp, and J. E. Schmidt, *J. Appl. Phys.* **82**, 2466 (1997).
- ¹⁶J. Wecker, R. von Helmolt, L. Schultz, and K. Samwer, *IEEE Trans. Magn.* **29**, 3087 (1993).
- ¹⁷K. Kimoto, Y. Kamiya, M. Nonoyama, and R. Uyada, *Jpn. J. Appl. Phys.* **2**, 702 (1963).
- ¹⁸E. Anno, *Phys. Rev. B* **50**, 17 502 (1994).
- ¹⁹P. E. Kelly, K. O'Grady, P. I. Mayo, and R. W. Chantrell, *IEEE Trans. Magn.* **2**, 3881 (1989).

Thin Films: Structure and Magnetism

Robin Farrow, Chairman

Structural and magnetic properties of "expanded" Mn

Ilya L. Grigorov^{a)} and J. C. Walker*Department of Physics and Astronomy, The Johns Hopkins University, Baltimore, Maryland 21218*

M. E. Hawley and G. W. Brown

Materials Science and Technology Division, Los Alamos National Laboratory, Los Alamos, New Mexico 87545

M. Lütt and M. R. Fitzsimmons

Manuel Lujan Jr. Neutron Scattering Center, Los Alamos National Laboratory, Los Alamos, New Mexico 87545

Structural and magnetic properties of "expanded" Mn deposited on (111) oriented fcc noble metals were studied with single-crystal x-ray diffraction and exchange bias measurements. A single peak corresponding to this phase was found at momentum transfer $q=2.86 \text{ \AA}^{-1}$ along six equivalent [112] directions of the noble metal substrate. Magnetic hysteresis of the field cooled Fe/Mn bilayers exhibited a characteristic shift along the field axis, indicating antiferromagnetic order in the expanded Mn with $T_N \geq 20 \text{ K}$. The magnetic and structural data are consistent with understanding the expanded phase as trigonally distorted α -Mn. © 1998 American Institute of Physics. [S0021-8979(98)37511-8]

I. INTRODUCTION

The properties of Mn epitaxially grown on close-packed surfaces has recently generated much interest. Deposited on these surfaces, Mn first assumes a close-packed structure with a lattice parameter close to that of fcc Mn. When the layer exceeds a critical thickness, which ranges between 2 and 12 Å, depending on the substrate material, Mn undergoes a $\sqrt{3} \times \sqrt{3}$ reconstruction. This new structure is called the "expanded" phase.¹⁻⁴ Based on the well-known ability of Mn to form crystals with ions of different sizes, Arrott *et al.*¹ developed a model in which expanded Mn was treated as a Lave phase of Mn with itself. Specifically, hexagonal-close-packed (hcp) MgZn₂ and fcc MgCu₂ alloys were proposed as possible prototypes for the expanded phase. Three-dimensional reflection high energy electron diffraction (RHEED) analysis of Mn grown on hcp Co (0001) suggested that the structure of expanded Mn was closest to (111) oriented MgCu₂.³ This is in contradiction to the results of recent extended x-ray absorption fine structure (EXAFS) measurements of Mn grown on Ir(111).⁵ In fact, the best fit to the experimental EXAFS spectra was achieved when expanded Mn was treated as a 50%–50% mixture of γ -Mn (fcc) and ground state α -Mn. Attempts to determine the magnetic properties of expanded Mn resulted in a similar controversy. The results of all studies agreed on the antiferromagnetic nature of this phase, but ordering temperatures ranging from 30 to above 320 K were reported.^{4,6}

Determination of the structure of expanded Mn is complicated by the fact that this phase does not have clearly identifiable x-ray Bragg peaks with the momentum transfer

in the growth direction. In addition, the magnetic susceptibility of expanded Mn is small,⁴ so the minor changes in magnetic background obscure the results of susceptibility measurements. In this study, experimental techniques have been chosen to bypass these complications. Grazing incidence x-ray diffraction (GID)⁷ has been used to analyze the scattering from expanded Mn in the plane of the film. The magnetic properties of Mn have been tested in an exchange-bias experiment (similar to the one used in Ref. 6), which is capable of distinguishing between paramagnetic and antiferromagnetic order in a material via its interaction with an adjacent ferromagnetic layer.

II. SAMPLE PREPARATION

Expanded Mn was grown on Cu(111) and Ag(111) base layers predeposited on epi-polished MgO(111) single-crystal substrates covered with a 15 Å thick seed layer of Mn. The temperature of the substrate was maintained at 200 °C during the growth of the seed and base layers. After deposition of the base, the substrate was cooled to 0 °C and further growth proceeded at temperatures between 0 and 25 °C. The surface crystallinity was monitored via *in situ* RHEED. The samples used for structural analysis [Fig. 1(b) inset] consisted of a single layer of Mn on the base. The samples for magnetic characterization [Fig. 2(b) inset] contained a layer of Fe on top of the Mn.

The difference between Cu and Ag cubic lattice parameters is 13%, which yields diffraction peaks well separated in reciprocal space. The choice of these materials for Mn growth insured that weak reflection(s) from Mn would not be overshadowed by diffraction from the base in at least one of the samples. The epitaxy of Mn on either of these substrates has not yet been studied. The lattice parameter of the close-packed (111) Cu surface is within the range of the lattice

^{a)}Currently at Superconductivity Technology Center, Los Alamos National Laboratory, Los Alamos, NM 87545.

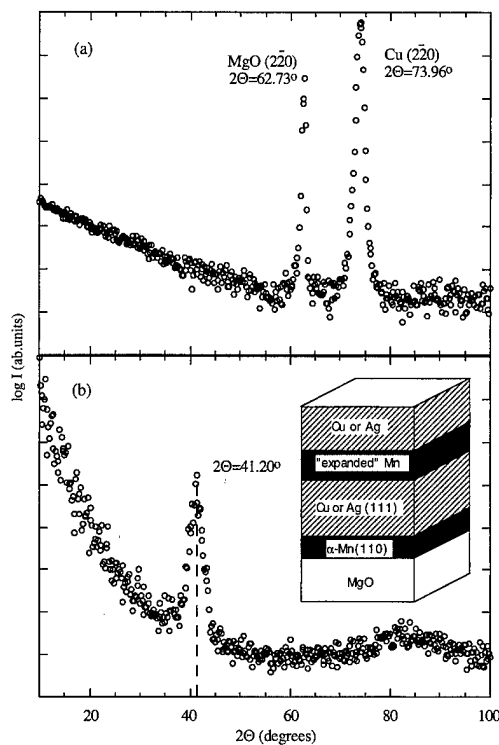


FIG. 1. GID Θ — 2Θ scan for Cu-based sample. (a) $q||$ MgO $[1\bar{1}0]$. (b) $q||$ MgO $[112]$. Inset: sample for the GID experiment.

parameters of the surfaces on which the growth of the expanded Mn has been observed; the lattice parameter of Ag is well outside this range. Indeed, the growth of Mn proceeded differently on each base. On Cu, formation of the expanded phase followed the growth of 2–3 Å of close-packed Mn, while on Ag, the intermediate close-packed phase did not form at all and Mn grew in the expanded phase from the onset. With increasing thickness, the RHEED streaks broadened and diffuse background increased, suggesting increasing roughness of the Mn surface. This deterioration was greater in films grown on Ag(111).

III. STRUCTURAL CHARACTERIZATION

Diffraction spectra for the sample containing an 80 Å Mn layer on Cu(111) are shown in Fig. 1. Along the $[1\bar{1}0]$ direction (upper plot) two peaks correspond to MgO (220) and Cu (220) Bragg reflections. These are the only in-plane reflections expected from (111) oriented fcc Cu and MgO for the x-ray wavelength $\lambda = 1.54$ Å. Diffraction with q along the $[112]$ direction (lower plot) produced a single peak at $2\Theta = 41.20^\circ$ ($|q| = 2.86$ Å $^{-1}$). This peak was found to be sixfold symmetric with respect to sample rotation around the film normal. Identical measurements performed on the sample containing a 55 Å thick Mn layer on Ag(111) produced similar spectra, with the Ag(220) peak replacing the Cu peak in Fig. 1. The in-plane diffraction spectra of a reference sample (Cu base on MgO(111)) showed no peaks in the $[112]$ direction. This result and the sixfold symmetry of the $q_{112} = 2.86$ Å $^{-1}$ peak imply that it arises from expanded Mn.

Two finer points are also worth mentioning in this re-

gard: (a) an extremely weak peak at $q_{111} = 2.94$ Å $^{-1}$ was observed in out-of-plane diffraction spectra of the samples grown on Ag, but not on Cu (an identical peak was also reported in Ref. 5); (b) the x-ray momentum transfer in $[112]$ direction does not match the surface reciprocal lattice vector in the same direction (2.69 Å $^{-1}$) obtained by *in situ* RHEED.

Diffraction peaks obtained from expanded Mn are inconsistent with either fcc or Lave phase structures. The discrepancy between the surface and bulk momentum transfer indicates a difference between bulk and surface periodicities. This suggests a rather complicated atomic arrangement in expanded Mn. We observed a similar discrepancy in α -Mn(110) grown at elevated temperature on MgO(111). A qualitative analysis of the atomic arrangement in α -Mn(110) suggests that the symmetry and size of the surface unit cell observed in the expanded phase may be achieved from α -Mn by a combination of a strain along the $[110]$ direction and a shear along the $[001]$ direction. Such a distortion would reduce the symmetry of the crystal to trigonal. To explain the x-ray data one has to invoke an additional lattice expansion in the plane of the film.

IV. MAGNETIC CHARACTERIZATION

The magnetic properties of expanded Mn were investigated by coating it with a 10–30 Å thick Fe film and measuring the exchange bias induced across the Fe/Mn interface. Initial growth of Fe on Mn was characterized by a gradual decrease in the intensity of Mn RHEED streaks. Upon deposition of approximately 12 Å of Fe, a sharp RHEED pattern, corresponding to multidomain bcc Fe (110), was observed. Nevertheless, in samples containing more than 10 Å of Mn on Ag(111) and more than 20 Å of Mn on Cu(111), weak and fuzzy RHEED reflections from Mn were observed along with the Fe diffraction pattern even for an Fe thickness of 30 Å. The absence of the Fe RHEED pattern for low coverages and the coexistence of the RHEED patterns at higher coverages indicate significant short-scale roughness of the Fe/Mn interface. Mössbauer spectroscopy of the Fe layer suggests that the microscopic interdiffusion of Fe and Mn was confined to the first 1–2 ML (at least in the smoothest samples) while the remainder of the Fe layer showed properties close to that of bulk bcc Fe.

Exchange bias in Fe/Mn bilayers was measured by field cooling the sample in 5 kG applied in the plane of the film and recording the hysteresis curve of the ferromagnetic layer. The measurements were performed in a superconducting quantum interference device (SQUID) magnetometer with a typical offset field of ≈ 4 Oe. The magnitude of the exchange field H_E (shift of the center of the hysteresis from $H = 0$) was studied as a function of temperature. In a system where an antiferromagnet and a ferromagnet have a common interface, H_E is nonzero below the blocking temperature T_B , somewhat lower than the Néel temperature of the antiferromagnet.⁸ The value of T_B may thus be used to place a lower limit on T_N .

The temperature dependencies of the exchange field in Fe/Mn bilayers grown on Ag and Cu bases are shown in Fig. 2. In all samples, a nonzero exchange bias at temperatures

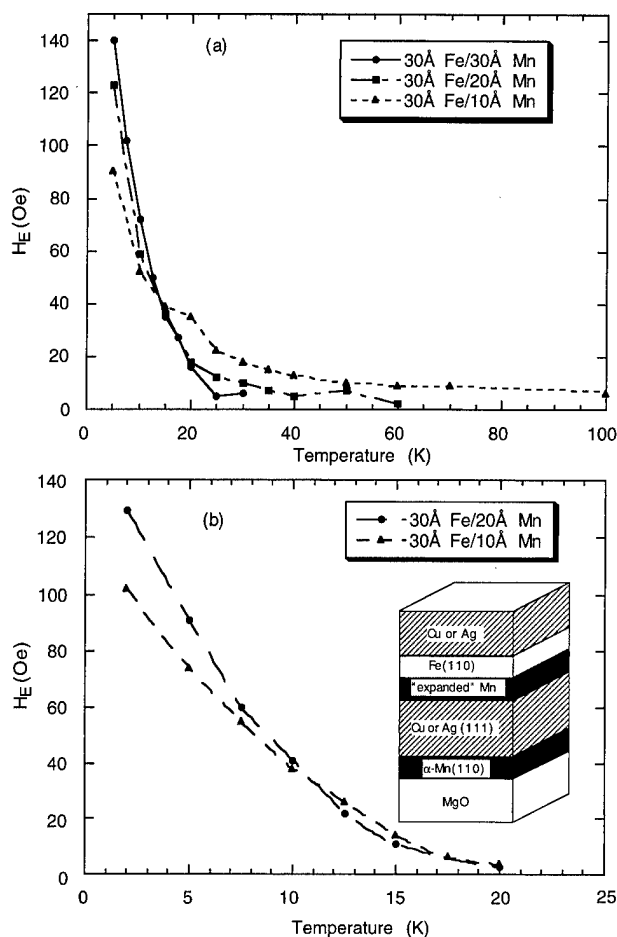


FIG. 2. Exchange field as a function of temperature in the bilayers grown on (a) Cu(111) and (b) Ag(111). Inset: sample for magnetic characterization.

below 20 K indicated antiferromagnetic order in expanded Mn. The temperature dependence of the bias in the films with different Mn thickness was noticeably different, depending on the base. In samples grown on Ag, the blocking temperature showed no dependence on Mn thickness. On Cu, decreasing the thickness of the Mn layer resulted in the region of nonzero $H_E(T)$ extending to higher temperatures [Fig. 2(a)].

V. DISCUSSION

The exchange bias effect originates from the spin interactions across the ferromagnet–antiferromagnet interface and therefore may be affected by the roughness of the interface. In Fe/Mn bilayers, the roughness is due to the roughness of the bare Mn layer which increased with increasing thickness, most rapidly when grown on Ag. Since all Ag based samples exhibited the same $T_B \approx 20$ K, independent of Mn thickness, roughness can be eliminated as a reason for the drop in T_B with increasing Mn thickness in samples grown on Cu.

Alternatively, the observed behavior of T_B in samples of different composition may be explained if the fraction of γ -Mn grains in the layer is taken into account. The γ -Mn is antiferromagnetic with a Néel temperature of 540 K, so the presence of this phase should alter the magnetic properties of the Mn layer and specifically the blocking temperature mea-

sured in the exchange-bias experiment. The presence of γ -Mn grains in Mn layers grown on hexagonal surfaces has been suggested before, in reference to Mn/Co³ and Mn/Ir⁵ multilayers, although the spatial distribution of this phase across the layer remains unknown.

It is reasonable to assume that different substrates promote γ -Mn growth to a different degree. The major indication of this dependency comes from the different Mn layer thicknesses at which $\sqrt{3} \times \sqrt{3}$ reconstruction of the RHEED pattern occurs in different systems. Among the samples analyzed in this study, the epitaxial growth of γ -Mn occurred in Cu-based samples (lattice mismatch 3%) and not in Ag-based samples (lattice mismatch –9%). The RHEED observations discussed in Sec. II suggest that even in the most favorable case (Cu base), the γ -Mn is confined to a few monolayers closest to the substrate.

Because of this confinement, increasing the Mn thickness on Cu-based samples leads to a decreasing fraction of γ -Mn in the layer. Our data correlates this decrease with the drop in T_B . On Ag, the Mn layer consists of the pure expanded phase and samples with different layer thickness show the same $T_B \approx 20$ K. Roughly the same value of T_B is observed in the sample containing the thickest Mn layer grown on Cu (30 Å). This interpretation also helps explain the high value of $T_B \approx 320$ K observed in Co/Mn multilayers where the presence of fcc grains was more apparent.³

Finally, the small value of T_B in the expanded Mn is also consistent with this phase being a distorted α -Mn ($T_N = 95$ K). If the $(3\bar{3}0)$ reflection of α -Mn is taken as a reference point ($|q| = 2.99 \text{ \AA}^{-1}$), expanded Mn results from 5% expansion within the (110) plane. Based on the out-of-plane peak observed in Ag-based samples, 2% expansion in that direction may be argued. An increase in atomic volume can result in the decrease of the absolute value of the exchange between magnetic ions which would lead to a suppression in T_N .

In conclusion, the structural data obtained in this study suggest that the atomic arrangement in the expanded phase of Mn is similar to that of trigonally distorted α -Mn. Pure expanded Mn is antiferromagnetic with a Néel temperature likely equal to or below that of α -Mn, which is also consistent with the proposed distortion. Higher values of T_B , also seen in previous studies, may be attributed to the presence of fcc grains.

ACKNOWLEDGMENTS

Portions of this study were supported by NSF Grant No. 9410148 and the U.S. Department of Energy BES-DMS under Contract No. W-7405-Eng-36.

¹A. S. Arrott, B. Hienrich, S. T. Purcell, J. F. Cochran, and K. B. Urquhart, J. Appl. Phys. **61**, 3721 (1987).

²V. L. O'Brien and B. P. Tonner, J. Vac. Sci. Technol. A **13**, 1544 (1995).

³K. Ounadjela, P. Vennegues, Y. Henry, A. Michael, V. Pierrin-Bohnes, and J. Arabski, Phys. Rev. B **49**, 8561 (1994).

⁴I. L. Grigorov, and J. C. Walker, J. Appl. Phys. **81**, 3907 (1997).

⁵S. Andrieu, H. M. Fisher, A. Piecuch, A. Traverse, and J. Mimault, Phys. Rev. B **54**, 2822 (1996).

⁶Y. Henry and K. Ounadjela, Phys. Rev. Lett. **76**, 1994 (1996).

⁷H. Dosch, Phys. Rev. B **35**, 2137 (1987).

⁸C. Tsang and K. Lee, J. Appl. Phys. **53**, 2606 (1982).

Growth and magnetism of one Mn monolayer on Ag(100)

O. Elmouhssine,^{a)} G. Morañtis, J. C. Parlebas, and C. Demangeat
*Groupe d'Etude des Matériaux Métalliques, IPCMS, UMR46-CNRS, 23, rue du Loess,
 67037 Strasbourg Cedex, France*

P. Schieffer, M. C. Hanf, C. Krembel, and G. Gewinner
*Laboratoire de Physique et de Spectroscopie Electronique, 4, rue des Frères Lumière,
 68093 Mulhouse, France*

Structural properties of Mn films, with a thickness of one monolayer (ML), deposited on a Ag(100) substrate have been investigated both experimentally (photoemission and ion scattering spectroscopies) and theoretically (tight-binding linear muffin-tin orbital method). The magnetic structure of the films and the effect of magnetism on their relative stability have been investigated *ab initio*. We find that after Mn evaporation [at room temperature (RT)], a superficial MnAg alloy is formed. Mild annealing gives rise to the formation of an (almost) inverted Mn monolayer covered by a Ag plane, i.e., the second atomic plane of the sample is mainly constituted by Mn atoms, whereas the first atomic layer is almost a pure Ag plane. A complete inversion of the Mn ML can be obtained by direct sequential deposition of Mn and Ag at 80 K. Our calculations on the energetic stability of 1 ML of Mn on top of Ag(100) versus 1 ML of Mn covered by one Ag atomic plane, show that the second situation is energetically preferred. This is also true when this situation is compared to the formation of a 2-ML-thick MnAg alloy on Ag(100). We find that the inverted Mn monolayer tends to be ferromagnetic and that magnetism acts against interdiffusion. © 1998 American Institute of Physics. [S0021-8979(98)29111-0]

Much work has been devoted in the last years to the growth and magnetic properties of thin transition metal films deposited on noble metals.^{1,2} Interesting magnetic effects are expected when a species grows on a substrate with a crystallographic structure that is different from its bulk one. In this respect, we have grown Mn ultrathin films on a Ag(100) substrate and analyzed the resulting overlayers by ion scattering spectroscopy (ISS) and x-ray photoelectron diffraction (XPD). We show that deposition of 1 monolayer (ML) of Mn on Ag(100) at room temperature (RT) gives rise to a pseudomorphic superficial alloy where the Mn atoms are confined within the first and the second (but not in deeper) atomic layers. Annealing the film or depositing the Mn at a higher temperature (however <350 K) causes the Mn atoms, initially in the first layer, to occupy sites in the second layer. To complete this structural study we have performed *ab initio* electronic band structure calculations. The experimental and theoretical results are in good agreement and show evidence of an inverted Mn ML, i.e., 1 ML of Mn covered by one Ag plane. Experimentally, this inverted monolayer is found to be stable up to ≈ 350 K, with Ag atoms substituted by Mn atoms in deeper layers above this temperature.

The experiments were conducted in an ultrahigh vacuum chamber equipped with photoemission, low energy electron diffraction (LEED), and ISS techniques. The Mn was deposited at a low rate, typically 0.2 ML/min, onto Ag(100) substrate which had been prepared *ex situ* by mechanical and chemical polishing and cleaned *in situ* by sputtering and annealing. The Mn coverage was determined by a quartz microbalance as well as core level photoemission. The base

pressure was below 4×10^{-10} Torr, even during evaporation, and contamination levels were below the detection limit. Figure 1 shows typical Mn $2p_{3/2}$ XPD profiles, obtained in the [001] high symmetry plane of the Ag substrate, for 0.9 ML of Mn deposited at 80 K and 300 K. As can be seen, the relevant data do not show any modulations when growth takes place at 80 K, i.e., the Mn must lie flat on top of the Ag substrate. If bilayer formation or alloying were to take place, one should observe strong forward scattering of the photoelectrons emitted by Mn in the second or deeper atomic layers. Such a strong forward scattering peak becomes apparent indeed in the [001] plane at a polar angle $\theta=45^\circ$ when the Mn is deposited at RT. In the [110] plane, however, the profiles (not shown) remain quite isotropic for all structures considered here. This can be simply interpreted in terms of formation of a surface alloy involving the two topmost atomic layers, which are mixed MnAg layers.³⁻⁵ This surface alloy keeps the Ag face-centered-cubic (fcc) lattice, with the same parallel and perpendicular parameters, and exhibits a composition close to $\text{Mn}_{0.5}\text{Ag}_{0.5}$, as well as a $c(2 \times 2)$ superstructure immediately after deposition. Moreover, it appears to be unstable upon annealing at RT³ or above. The effect of mild annealing at 330 K is summarized in Table I. On one hand, the composition of the topmost layer as determined by ISS evolves from $\approx 40\%$ of Mn for a sample left about 100 min after deposition at RT, to 27% of Mn after annealing at 330 K. On the other hand, Mn enrichment of the second atomic layer shows up in a marked increase of the 45° forward scattering peak: The anisotropy $A = [I(45^\circ) - I(30^\circ)] / [I(45^\circ) + I(30^\circ)]$ increases from 20% to 24%. This is because only Mn atoms in the second layer contribute to the forward scattering peak. Actually, a

^{a)}Electronic mail: omar@nantos.u-strasb.fr

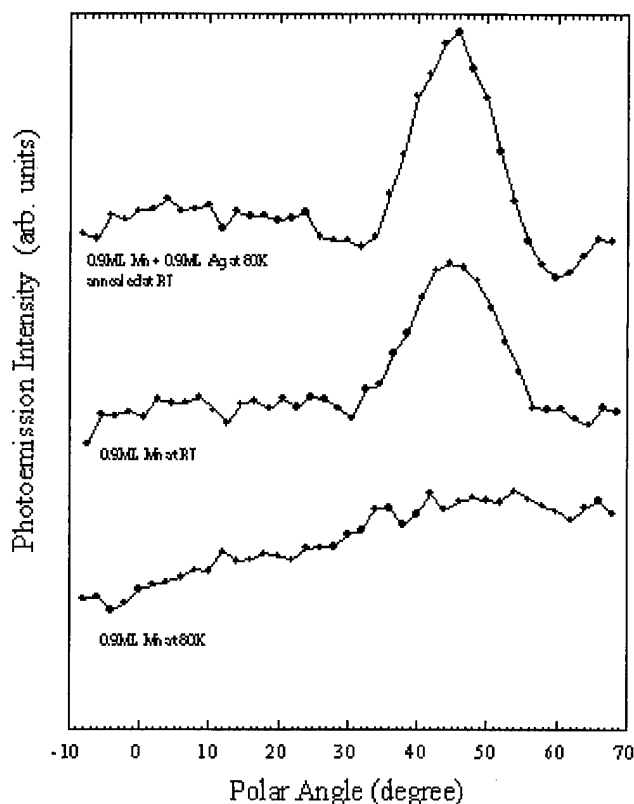


FIG. 1. Angular distributions of the Mn $2p_{3/2}$ core level intensity in the [001] plane for 0.9 ML of Mn after deposition at 80 K (bottom) and at RT (middle), and for 0.9 ML of Mn+0.9 ML of Ag deposited at 80 K and annealed at RT (top). The photon energy is 1486.6 eV Al K_{α} and the kinetic energy of the Mn $2p_{3/2}$ photoelectrons is about 849 eV. The polar angle θ is referred to as the surface normal.

nearly complete inversion of the Mn monolayer can be obtained by direct sequential deposition of 0.9 ML Mn and Ag at 80 K and subsequent annealing at 300 K to improve atomic order. As can be seen in Figure 1, the relevant XPD profile closely resembles the one obtained upon deposition at RT. Yet the anisotropy A is now as large as 32% and the surface composition close to a pure Ag layer. Hence, a nearly perfect Ag/Mn/Ag(100) structure is grown in this way. This structure shows a sharp $p(1 \times 1)$ LEED pattern and, according to XPD, remains stable up to ≈ 350 K. At higher temperature the Mn atoms tend to move into deeper atomic layers of the Ag(100) substrate.

To gain more insight into the stability of Mn/Ag(100) films, we have performed *ab initio* calculations for the following systems: (1) Mn (1 ML)/Ag(100), (2) Ag (1 ML)/Mn(1 ML)/Ag(100), and (3) $\text{Mn}_{0.5}\text{Ag}_{0.5}$ (2 ML)/Ag(100). These calculations simulate the experimental process of the

TABLE II. Energy differences between the three structural situations in mRy/Mn atom [(1) Mn (1 ML)/Ag(100), (2) Ag (1 ML)/Mn (1 ML)/Ag(100), (3) MnAg (2 ML)-alloy/Ag(100)], for the NM, FM, and AFM states.

	$\Delta E_{(2)-(1)}$ (mRy/Mn atom)	$\Delta E_{(3)-(1)}$ (mRy/Mn atom)	$\Delta E_{(2)-(3)}$ (mRy/Mn atom)
NM	-45.75	-8.50	-37.25
FM	-23.25	-10.50	-12.75
AFM	-19.00	-7.75	-11.25

Mn growth on Ag(100), if the Mn film evolves from an on-top ML on Ag(100) to an inverted ML covered by a Ag plane, through a MnAg alloy formation. In the case of a MnAg alloy, we consider the simple case where one has a 2-ML-thick epitaxial MnAg alloy with a $c(2 \times 2)$ structure, which keeps the fcc lattice of Ag(100) substrate. We apply the tight-binding linear muffin-tin^{6,7} method in the atomic-sphere approximation, together with the local spin-density approximation of von Barth and Hedin.⁸ The ultrathin films for situations (1), (2), and (3) are, respectively, modeled by $\text{Mn}_1/\text{Ag}_7/\text{Mn}_1$, $\text{Ag}_1/\text{Mn}_1/\text{Ag}_5/\text{Mn}_1/\text{Ag}_1$ and $[\text{Mn}_{0.5}\text{Ag}_{0.5}]_2/\text{Ag}_5/[\text{Mn}_{0.5}\text{Ag}_{0.5}]_2$ slabs, using the supercell technique. All nonmagnetic and magnetic calculations are performed taking into account the $c(2 \times 2)$ unit cell containing two atoms per layer and using the experimental lattice constant of Ag ($a_{\text{Ag}}^{\text{exp}} = 7.73$ a.u.). For the k -space integration, we use the tetrahedron method^{9,10} and an increasing number of k points, until convergence is obtained. Total energy convergence is assumed with an accuracy better than 10^{-5} Ry.

In order to investigate the energetic stability of an on-top Mn ML against the formation of an inverted Mn ML, we compare the total energy $E_{(1)}$ of 1 ML of Mn deposited on Ag(100), with the total energy $E_{(2)}$ of a Mn ML covered by a Ag layer. The energy differences $\Delta E_{(2)-(1)} = E_{(2)} - E_{(1)}$ for nonmagnetic (NM), ferromagnetic (FM), and antiferromagnetic (AFM) Mn films are reported in Table II. Regardless of the magnetic state of the Mn films, we find that $\Delta E_{(2)-(1)}$ has negative values, which means that the situation (2), where Mn atoms form an inverted ML, is the energetically preferred state. The role which magnetism plays in modifying the stability of Mn films is elucidated by comparing the magnetic (FM and AFM) calculations with the NM one. The effect of magnetism appears with a large reduction ($\approx 50\%$) of $\Delta E_{(2)-(1)}$, which means that magnetism acts against interdiffusion and tends to stabilize the Mn ML film on the Ag(100) substrate. Of course, it should be kept in mind that the usual driving forces for layer inversion and interdiffusion such as atomic size mismatch, relative heteroatomic and homoatomic bond strengths¹¹ play a major role in this system too. Yet we find that the Mn case is a special one where magnetism makes a large unusual contribution to the total energy of surface atomic configurations. The magnetic energy gain for the FM state (22.5 mRy/Mn atom) is lower than for the AFM one (26.75 mRy/Mn atom), indicating that the long range magnetic order of the Mn films contributes to the strength of the magnetism effect on the stability of the magnetic films. The main effect, however, remains the for-

TABLE I. XPD anisotropy (A) and Mn fraction in the second atomic layer for 0.9 ML Mn deposited at RT (a) before and (b) after annealing 5 h at 330 K, and (c) for 0.9 ML Mn+0.9 ML Ag deposited sequentially at 80 K and annealed at RT for 5 min.

	a	b	c
Anisotropy A (%)	20	24	32
Mn in 2nd layer	0.60	0.73	0.97

TABLE III. Ferromagnetic (FM) and antiferromagnetic (AFM) spin moments (in units of μ_B) and the energy differences between the FM and AFM states (in units of mRy/Mn atom) in the three structural situations. For situation (3), surface and interface Mn moments are given. $\Delta E_{(FM)-(AFM)} < 0$ means that the FM configuration is the most stable state.

	(1)	(2)	(3)
μ_{FM}	4.04	3.79	4.15/3.85
μ_{AFM}	± 4.11	± 3.93	4.26/-3.95
$\Delta E_{(FM)-(AFM)}$	1.00	-3.50	-1.75

mation of large local magnetic moments on Mn atoms, roughly $4 \mu_B$ for all structures (see Table III).

As to the magnetic structure of the Mn film, we compare the total energy $E_{(FM)}$ of the FM film with the total energy $E_{(AFM)}$ of the AFM one in the two structural situations. The energy differences $\Delta E_{(FM)-(AFM)} = E_{(FM)} - E_{(AFM)}$, together with the Mn magnetic moments, are reported in Table III. Interestingly, we find that the magnetic structure of Mn ML film depends on the coordination number of its constituent atoms with respect to Ag atoms. While it is known from previous works,¹² as well as the present one, that a Mn ML film on Ag(100) is predicted to be $c(2 \times 2)$ AFM, the inverted Mn ML prefers the $p(1 \times 1)$ FM structure. Experimentally, we generally observe a sharp $p(1 \times 1)$ LEED pattern in 20–400 eV range but with a weak $c(2 \times 2)$ superstructure, at primary energies below 100 eV, for the flat Mn ML on Ag(100) obtained by deposition at 80 K. This superstructure is attributed to inplane AFM order and found to be definitely absent for the inverted ML in the 80–350 K range.¹³ These observations are consistent with the present calculations but cannot rule out the possibility that the inverted layer is still inplane AFM below 80 K, i.e., coating with a Ag top layer merely reduces the Néel temperature below 80 K.

We have also investigated the case of MnAg-alloy formation for a better understanding of the growth mode of Mn films on the Ag(100) substrate. The MnAg alloy is modeled by a 2-ML-thick $c(2 \times 2)$ MnAg alloy on top of Ag(100), where every second Mn atom is substituted by a Ag atom in a checkerboard type monolayer. In Table II, we report the results of the energy differences $\Delta E_{(3)-(1)}$ and $\Delta E_{(2)-(3)}$, respectively, between the total energy $E_{(3)}$ of the MnAg alloy on Ag(100) and the total energies of the two other structural configurations, $E_{(1)}$ and $E_{(2)}$, respectively. The negative values of these energy differences means that MnAg-alloy formation is energetically preferred to 1 ML of Mn

deposited on top of Ag(100), and energetically prohibited to the formation of an inverted Mn ML. This is in agreement with the experimental observation of the alloy formation in the two topmost layers of the sample, immediately after Mn deposition, and the further Mn/Ag atoms exchange, increasing the Mn concentration in the second atomic plane of the sample.

To summarize, we have shown that Mn monolayer on top of Ag(100) is unstable at RT. A MnAg superficial alloy is formed in the two topmost atomic layers, immediately after Mn deposition. Moreover, the Mn incorporation in the second plane is thermally activated, and an inverted Mn layer tends to be formed by mild annealing. Eventually, the completely inverted ML remains stable up to 350 K. These experimental findings are in line with our electronic band structure calculations, which show that the inverted Mn layer constitutes the energetically preferred state as compared to a MnAg alloy formation or to a Mn monolayer on top of Ag(100). Moreover, the calculations show that magnetism acts against interdiffusion and tends to stabilize the Mn monolayer film on top of Ag(100), but not to the extent to prevent the formation of an inverted Mn layer at RT or above. As to the magnetic structure of the inverted Mn ML, we find that the $p(1 \times 1)$ FM order is energetically preferred to the $c(2 \times 2)$ AFM one.

This work was partly supported by NATO Grant No. CRG 960975 and by the European Community Human Capital and Mobility Program through Contract No. CHRX-CT93-0369.

¹S. Blügel, Phys. Rev. Lett. **68**, 851 (1992).

²J. A. C. Bland and B. Heinrich, *Ultrathin Magnetic Structures* (Springer, Berlin, 1994).

³P. Schieffer, C. Krembel, M. C. Hanf, and G. Gewinner, Phys. Rev. B **55**, 13 884 (1997).

⁴P. Schieffer, C. Krembel, M. C. Hanf, D. Bolmont, and G. Gewinner, Solid State Commun. **97**, 757 (1996).

⁵P. Schieffer, M. C. Hanf, C. Krembel, M. H. Tuilier, G. Gewinner, and D. Chandesris, Surf. Rev. Lett. (in press, 1997).

⁶O. K. Andersen and O. Jepsen, Phys. Rev. Lett. **53**, 2571 (1984).

⁷O. K. Andersen, Z. Pawlowska, and O. Jepsen, Phys. Rev. B **34**, 5253 (1986).

⁸U. von Barth and L. Hedin, J. Phys. C **5**, 1629 (1972).

⁹O. Jepsen and O. K. Andersen, Solid State Commun. **9**, 1763 (1971).

¹⁰G. Lehman and M. Taut, Phys. Status Solidi B **54**, 469 (1972).

¹¹J. M. Roussel, A. Saul, and G. Treglia, Phys. Rev. B **55**, 10 931 (1997).

¹²S. Blügel, B. Drittler, R. Zeller, and P. H. Dederichs, Appl. Phys. A **49**, 547 (1989); S. Blügel, and P. H. Dederichs, Europhys. Lett. **9**, 597 (1989).

¹³P. Schieffer, C. Krembel, M. C. Hanf, and G. Gewinner, Phys. Rev. B **57**, 1141 (1998).

Structural stability, magnetism, and surface magneto-optic Kerr effect spectra of MnAg(001) surface alloys

Soon C. Hong^{a)}

Department of Physics, University of Ulsan, Ulsan 680-749, Korea

Miyoung Kim and A. J. Freeman

Department of Physics and Astronomy, Northwestern University, Evanston, Illinois 60208-3112

The stability of a MnAg surface alloy was investigated employing the total energy and atomic force full-potential linearized augmented plane wave method based on the local density approximation for: (i) a clean Ag(001), (ii) 1 ML Mn overlayer [1 Mn/Ag(001)], (iii) 1 and 2 ML MnAg alloys as overlayers on Ag(001) [1(MnAg)/Ag(001) and 2(MnAg)/Ag(001)], and (iv) 1 ML Mn diffused into Ag(001) substrate [Ag/1 Mn/Ag(001)]. Results obtained show that 2(MnAg)/Ag(001) is much more stable than 1 Mn/Ag(001) (by a large energy difference of 150 meV), whereas 1(MnAg)/Ag(001) is marginally more stable (by a slight energy difference of 8 meV) compared to a separate phase of Ag and Mn atoms. Surface Mn and subsurface Mn atoms in 2(MnAg)/Ag(001) were found to be coupled antiferromagnetically with magnetic moments of 3.96 and $-3.55 \mu_B$, respectively. The surface corrugation ($\Delta z = 0.05$ a.u.) of 2(MnAg)/Ag(001) was found to be much smaller than that ($\Delta z = 0.5$ a.u.) of another magnetically stabilized surface alloy system, MnCu/Cu(001). No significant magneto-optical effects for antiferromagnetic Ag/Mn/Ag(001) were found due to the small off-diagonal elements of the optical conductivity. © 1998 American Institute of Physics. [S0021-8979(98)47911-8]

I. INTRODUCTION

It has been known that an alloy could have a different chemical composition at a surface from that of its bulk, with new physical properties which cannot be seen in bulk. In addition to alloy surfaces, surface alloys can be synthesized by depositing one material on the surface of a second metal and subsequent annealing.¹ Further, surface alloys phases may not be found in bulk and so may provide new desirable physical properties not seen in a bulk.

While different surface alloys could be stabilized by different mechanisms, it has been reported that the enhanced ferromagnetic magnetic moment ($\sim 3.65 \mu_B$) at the surface plays an important role in stabilizing the surface alloy of MnCu on Cu(001).²

Recently, some very interesting results were also obtained for Mn atoms grown on an Ag(001) surface. A prominent $c(2 \times 2)$ low-energy electron diffraction (LEED) pattern was observed when one monolayer (ML) dosage of Mn atoms is deposited on Ag(001) at room temperature, whereas only a diffuse $c(2 \times 2)$ LEED pattern was observed for a half-ML dosage. The prominent LEED pattern was confirmed with LEED current-voltage ($I-V$) analysis to be best fitted to a 2 ML MnAg surface alloy on an Ag(001) substrate [2(MnAg)/Ag(001)].³

We report on first principles calculations done to give some physical informations on the formation of a MnAg surface alloy. Employing the full-potential linearized augmented plane wave (FLAPW) method,⁴ the atomic structure of the MnAg surface alloy was determined from total energy and atomic force calculations for clean Ag(001), 1(MnAg)/

Ag(001), 1 Mn/Ag(001), Ag/1 Mn/Ag(001), and 2(MnAg)/Ag(001). In addition to the magnetic moments, we also calculated the optical conductivity tensor and the polar Kerr angles for Ag/1 Mn/Ag(001) (which turns out to be energetically the most stable system) and also for a free standing Mn monolayer and a Mn bulk with Ag lattice constants.

II. METHOD

To investigate the atomic structure of Mn atoms grown on Ag(001), we calculated total energies and atomic forces⁵ of the system, employing the FLAPW method. Single slabs composed of seven layers in total were employed and the two dimensional unit cell was taken with two atom types per layer to accommodate the $c(2 \times 2)$ structure observed in LEED.³

The local density Kohn-Sham equations⁶ are solved self-consistently using the FLAPW method with about 1400 basis functions and 15 special k points within the irreducible 2D Brillouin zone. Self-consistency is assumed when the average root mean square differences between input and output charge and spin densities are less than $1 \times 10^{-4} e/(a.u.)^3$ and the total energy is stable to within 0.02 mRy. The lattice constant ($a = 7.58$ a.u.) obtained from calculations for bulk Ag with the same method is adopted for the 2D lattice constant of the Ag substrate. A relaxed structure is assumed to be found if the atomic forces are less than 1.5 mRy/a.u.

For the polar surface magneto-optical Kerr effect (SMOKE) calculation, we treated the spin-orbit coupling (SOC) in a second variational method⁷ without spin-flip contributions by neglecting the off-diagonal elements of the SOC matrix. For the optical conductivity tensor the interband transitions were calculated with linear response theory.⁸ We

^{a)}Electronic mail: schong@uou.ulsan.ac.kr

TABLE I. Total energies (eV) of 1 Mn/Ag(001), 2(MnAg)/Ag(001), and Ag/1 Mn/Ag(001) in paramagnetic (PM), ferromagnetic (FM), and antiferromagnetic (AFM) phases referred to that of 1 Mn/Ag(001) in the PM state.

System	Total energy (eV)		
	PM	FM	AFM
1 Mn/Ag(001)	0.0	-1.53	-1.60
2(MnAg)/Ag(001)	-0.25	-1.64	-1.75
Ag/1 Mn/Ag(001)	-0.72	-1.94	-1.96

did not include the intraband contribution (which contributes in the low energy region below 2 eV)⁹ which is usually done by adding the Drude term to the diagonal conductivity elements, due to the difficulty of finding the Drude lifetime and conductivity for the various environments used. We introduced finite lifetime broadening effects by using a Lorentzian corresponding to a life time parameter, τ (taken as 0.41 eV), to calculate the optical conductivity elements. Then the complex Kerr angle is obtained by Fresnel's law.¹⁰

III. RESULTS

A. Atomic structure: Total energy and atomic force calculations

Relaxed structures of our systems were determined from minimization of the total energy and absolute values of the atomic forces. To determine the stability of the MnAg surface alloy, we first calculated the total energies of the fully relaxed Ag(001), 1 Mn/Ag(001), and 1(MnAg)/Ag(001) and compared the total energy ($TE_{1 \text{ (MnAg)/Ag}}$) of ML MnAg surface alloy to the average of the total energies of a clean Ag(001) (TE_{Ag}) and ML Mn on Ag(001) ($TE_{1 \text{ Mn/Ag}}$). The difference, $TE_{1 \text{ MnAg/Ag}} - \frac{1}{2}(TE_{\text{Ag}} + TE_{1 \text{ Mn/Ag}})$, was found to be small, about -8 meV. This indicates that the ordered MnAg surface alloy ML is energetically slightly more stable compared to a separate existence of Ag and Mn layers, but this may not be observable at room temperature, and may explain why the distinct $c(2 \times 2)$ LEED pattern was not observed in the experiment when a half-ML of Mn atoms was deposited on Ag(001).

Table I shows the total energies of 1 Mn/Ag(001), 2(MnAg)/Ag(001), and Ag/1 Mn/Ag(001) in different magnetic states, i.e., paramagnetic (PM), ferromagnetic (FM), and antiferromagnetic (AFM), referred to that of 1 Mn/Ag(001) in the PM state. In these calculations, the average interlayer spacing of bulk Ag and Mn were used for those of Mn-Ag and MnAg-Ag with no allowance for relaxation. Since the relaxation energy is of order 10 meV and the energy differences among magnetic states and atomic structures are of order 100 meV, any conclusions from these calculations should not be changed by including relaxation. As shown in Table I, AFM states are found to be the most stable compared to PM and FM states for all three systems: 2(MnAg)/Ag(001) is much more stable compared to 1 Mn/Ag(001), by 150 meV, which is the reason why a prominent $c(2 \times 2)$ LEED pattern was observed in the experiment when the dosage of Mn atoms is 1 ML.³ Furthermore, Ag/1 Mn/Ag(001) is the most stable among the three systems so that

TABLE II. Magnetic moments (μ_B) of Mn atoms in 1 Mn/Ag(001), Ag/1 Mn/Ag(001), 1(MnAg)/Ag(001), and 2(MnAg)/Ag(001).

System	Magnetic moments (μ_B)	
AFM 1 Mn/Ag(001)	3.94	
AFM Ag/1 Mn/Ag(001)	3.73	
FM 1 (MnAg)/Ag(001)	4.16	
AFM 2(MnAg)/Ag(001)	S	3.96
	S-1	-3.55

Ag surface segregation would occur when the system is annealed. This also agrees with experiment where an analysis of the LEED $I-V$ curve indicated diffusion of Mn into the Ag substrate with annealing.³

For 1(MnAg)/Ag(001), surface corrugation ($\Delta z_S = z_{\text{Ag}} - z_{\text{Mn}} \approx 0.02$ a.u.) in the FM phase was found to be negligible whereas a significant corrugation ($\Delta z_S \approx +0.4$ a.u.) was found in the PM phase. By comparison, the results for 1(MnCu)/Cu(001)² show corrugation (Δz_S) to be -0.5 a.u. and almost zero for the FM and PM phases, respectively. Our results come from the 13% larger atomic radius of Ag compared to that of Cu. As found from total energy calculations for 1 Mn/Ag(001),¹¹ AFM coupling results in a larger interlayer spacing (by 0.03 a.u.) compared to FM coupling. Even though we did not calculate which magnetic state would be more stable in 1(MnAg)/Ag(001) (since allowing AFM coupling requires four atom types per layer and much more computing time), AFM coupling between Mn atoms might result in further reduced corrugation. Noting that the atomic radius of Mn is much smaller than that of Ag, this result is very interesting and may be explained by magnetic pressure due to the greatly enhanced magnetic moment ($4.16 \mu_B$) of Mn in the surface alloy compared to those (1.84 or $1.75 \mu_B$, depending on atom type)¹² of bulk Mn.

For 2(MnAg)/Ag(001) in the AFM ground state, somewhat larger corrugations ($\Delta z_S = +0.05$ and $\Delta z_{S-1} = -0.098$ a.u.) were calculated.

B. Magnetism

Magnetic moments of Mn atoms in relaxed AFM 1 Mn/Ag(001), Ag/1 Mn/Ag(001), 2(MnAg)/Ag(001), and FM 1(MnAg)/Ag(001) are presented in Table II. As mentioned in the previous section, AFM couplings between neighboring Mn atoms in 1 Mn/Ag(001), Ag/1 Mn/Ag(001), and 2(MnAg)/Ag(001) are found to be more stable compared to the FM couplings. The magnetic moments are calculated to be 3.94, 3.73, and $4.16 \mu_B$ for Mn atoms in 1 Mn/Ag(001), Ag/1 Mn/Ag(001), and 1(MnAg)/Ag(001), and 3.96 and $-3.55 \mu_B$ for Mn(S) and Mn(S-1) atoms in 2(MnAg)/Ag(001), respectively. The magnetic moments are much more enhanced compared to experimental values in bulk Mn.¹³ The magnetic moment ($4.16 \mu_B$) of the monolayer MnAg surface alloy [1(MnAg)/Ag(001)] is gigantic, corresponding to the almost fully magnetized value due to the large distance between Mn atoms and the small band hybridization between Mn and Ag atoms. This value is larger than those (3.75 and $3.5 \mu_B$, respectively)² of 1 MnCu/Cu(001) and 1 MnNi/Ni(001) by 11% and 19%, respectively.

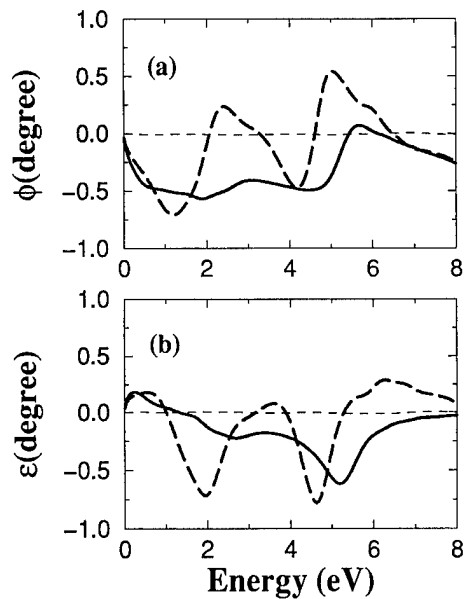


FIG. 1. Complex Kerr angles, (a) rotation ϕ and (b) ellipticity ϵ for: FM Mn bulk (thick solid), FM (thick dashed) Mn free standing monolayer, and AFM Ag/Mn/Ag(001) (thin dotted). All systems have the Ag lattice constant. In the AFM Mn free standing ML case the results are so small [essentially zero as in the AFM Ag/Mn/Ag(001) case] to not show up in these plots.

C. Smoke

We calculated the MOKE for (i) AFM Ag/1 Mn/Ag(001) which is the most stable system compared to 1 Mn/Ag(001) or 2(MnAg)/Ag(001), (ii) FM and AFM Mn free standing ML, and (iii) FM Mn bulk with the same (Ag) lattice constant. The results are shown in Fig. 1. For AFM systems we obtained negligible MOKE angles compared to those of FM systems, due to their small off-diagonal conductivity elements, σ_{xy} . The finite value of σ_{xy} which is crucial for the magneto-optical effects results from the spin-orbit coupling and the exchange splitting. As pointed out by Erskine and Stern,¹⁴ the imaginary part of the off-diagonal conductivity elements, $\sigma_{xy}^{(2)}$, which measures the difference in absorption of the right and left circularly polarized light, vanishes if either the spin-orbit coupling or the exchange coupling is switched off since the spin up and spin down contributions cancel each other. This cancellation will also occur in AFM from the contribution of atoms with opposite magnetic moments and, as a result, the off-diagonal elements of conductivity are negligibly small compared to the diagonal elements.

Figure 1 shows that there is a significant surface effect on MOKE; the MOKE angles for FM ML Mn and for bulk Mn are totally different. We found that the surface effect mainly influences σ_{xy} and this influence is reflected in MOKE; the peak positions exhibited in the MOKE angles in Fig. 1 coincide well with those that occur in σ_{xy} . However, the diagonal conductivity, σ_{xx} , shows similar behavior for both ML and bulk Mn (except for different magnitudes).

We also found that different peak positions in the absorptive part of the diagonal conductivity, $\sigma_{xx}^{(1)}$, are well explained by the change of density of states (DOS) for d

bands due to different environment and magnetic ordering. For example, a large absorption peak was observed around the energy region of 2 eV (3 eV) for AFM Ag/Mn/3 Ag (AFM ML) in which the extremely narrow spin down d bands lying around 2 to 3 eV (3 to 4 eV) below E_F gives a large peak in the density of states (DOS).

IV. CONCLUSIONS

The bilayer MnAg surface alloy on Ag(001) is much more stable energetically compared to a Mn monolayer on Ag(001) by about 150 meV whereas the monolayer MnAg surface alloy is slightly more stable compared to the separation of Mn and Ag atoms at the surface. These facts are consistent with recent experiments which observed bright $c(2 \times 2)$ LEED spots for a bilayer MnAg surface alloy and dim LEED spots for the monolayer. The surface corrugations (0.02 and 0.05 a.u.) of 1(MnAg)/Ag(001) and 2(MnAg)/Ag(001) was found to be much smaller than that (0.5 a.u.) of a MnCu surface alloy on Cu(001)—also in agreement with experiment. The magnetic moments were calculated to be 4.16, 3.96, and 3.55 μ_B for Mn(S) in MnAg(001), and Mn(S) and Mn(S-1) in 2(MnAg)/Ag(001).

We found no significant magneto-optical effects for AFM Ag/1 Mn/Ag(001) due to the small off-diagonal elements of the optical conductivity compared to the diagonal elements. The conductivity elements were largely influenced by the change of the d band density of states caused by surface effects and different magnetic ordering.

ACKNOWLEDGMENTS

Work at UOU was supported by KOSEF excellence program through ASSRC at Yonsei Univ. and the BSRI (97-2440) program. Work at N.U. supported by the Office of Naval Research (Grant No. N00014-94-1-0030) and by grants of computer time at the Pittsburgh Supercomputing Center (supported by the NSF Division of Advanced Scientific Computing) and the Arctic Region Supercomputing Center.

¹U. Bardi, Rep. Prog. Phys. **57**, 939 (1994).

²O. Rader, W. Gudat, C. Carbone, E. Vescove, S. Blügel, R. Kläsger, W. Eberhardt, M. Wuttig, J. Redinger, and F. J. Himpsel, Phys. Rev. B **55**, 5404 (1997).

³W. Kim, J. Seo, J.-S. Kim, H.-G. Min, W. Kim, S.-J. Oh, and Soon C. Hong, Phys. Rev. B (in press).

⁴E. Wimmer, H. Krakauer, M. Weinert, and A. J. Freeman, Phys. Rev. B **24**, 864 (1981).

⁵R. Yu, D. Singh, and H. Krakauer, Phys. Rev. B **45**, 8671 (1991).

⁶W. Kohn and L. J. Sham, Phys. Rev. **140**, A1133 (1965).

⁷H. McDonald, W. E. Pickett, and D. D. Koelling, J. Phys. C **13**, 2675 (1980).

⁸C. S. Wang and J. Callaway, Phys. Rev. B **9**, 4897 (1974).

⁹K. H. J. Buschow, *Ferromagnetic Materials*, Vol. IV, edited by E. P. Wohlfarth and K. H. J. Buschow (Elsevier Science, New York, 1988), p. 493.

¹⁰P. M. Oppeneer, T. Maurer, J. Sticht, and J. Kübler, Phys. Rev. B **45**, 10 924 (1992).

¹¹S. C. Hong, M. Kim, and A. J. Freeman (unpublished).

¹²*Magnetic Properties of Metals*, edited by H. P. J. Wijn (Springer, Berlin, 1991), pp. 4 and 5.

¹³H. Yamagata and K. Asayama, J. Phys. Soc. Jpn. **33**, 400 (1972).

¹⁴J. L. Erskine and E. A. Stern, Phys. Rev. Lett. **39**, 1329 (1973).

Artificial FeCu(100) epitaxial ordered alloy films: Element-selective magnetic properties

W. Kuch,^{a)} M. Salvietti, Xingyu Gao, M. Klaua, J. Barthel, Ch. V. Mohan, and J. Kirschner

Max-Planck-Institut für Mikrostrukturphysik, Weinberg 2, D-06120 Halle, Germany

Epitaxial artificial FeCu alloy thin films in the fcc $L1_0$ ordered phase were prepared by pulsed laser deposition on Cu(100). Magnetic circular dichroism in x-ray absorption at the Fe and Cu $L_{2,3}$ edges was used to study the electronic and magnetic properties of the normally immiscible FeCu(100) alloy films. The Fe exhibits magnetic moments comparable to that of fcc Fe films, ruling out the occurrence of nonmagnetic fcc Fe. The ratio between orbital and spin contribution to the Fe d moments is significantly enhanced in FeCu with respect to Fe/Cu(100), and amounts to ≈ 0.12 . An induced magnetic moment of the Cu atoms is observed, which carries about 7% of the total d -band moment of the FeCu film. © 1998 American Institute of Physics. [S0021-8979(98)48011-3]

Magnetic artificial alloys have not yet been subject to investigations concerning their element-selective magnetic properties. Artificial alloys of the otherwise immiscible elements Fe and Cu have been synthesized mechanically in the bulk by ball milling techniques^{1,2} as well as by sputtering.^{3,4} It was reported that for Fe concentrations below $\approx 70\%$ the fcc structure is assumed, and for higher Fe concentrations the bcc structure.^{2,3} In contrast to these techniques we use pulsed laser deposition to stabilize the fcc phase of epitaxial artificial FeCu alloy thin films on Cu(100). The films grow in a layer-by-layer mode already starting with the first layer, as judged by reflection high energy electron diffraction during growth.⁵ Subsequent deposition of monoatomic layers of Fe and Cu results in the $L1_0$ ordered phase of FeCu. These films exhibit an easy axis of magnetization in the film plane.⁵ Scanning tunneling microscopy investigations show a degree of layer perfection better than 98% per deposited FeCu bilayer.⁵ Spin-resolved valence band photoemission measurements revealed bands which are present due to the reduced size of the alloy Brillouin zone perpendicular to the film plane.⁶ This reflects the doubling of the unit cell in the ordered alloy with respect to pure Cu or Fe, and additionally proves the structural quality of our stacked samples.

In this contribution we report results of magnetic circular dichroism in soft x-ray absorption (XMCD) measurements of these fcc FeCu alloy films. XMCD probes the spin asymmetry of the unoccupied part of the band structure just above the Fermi level. The dichroism, i.e., the difference in absorption cross section upon reversal of the magnetization direction, depends on the transition probability for spin-up and spin-down electrons into the mainly minority type unoccupied bands, and constitutes an element selective measure of magnetic and electronic properties.⁷ Sum rules^{8,9} allow under some assumptions to extract the elementally resolved spin and orbital magnetic moments from the experimental absorption spectra.

Films of 10 atomic layers (monolayers, ML), alternately consisting of Fe and Cu, were deposited by pulsed laser

deposition at room temperature on a Cu(001) substrate. A cap layer of 3 ML Au was evaporated on top for protection against residual gases. After preparation of the samples, which was done at the laboratory in Halle, the samples were transferred under ultrahigh vacuum (UHV) conditions to the Berlin synchrotron radiation source (BESSY). During the transport a pressure of about 4×10^{-8} Pa was maintained in the transfer chamber. The typical time interval for transfer and transport elapsed between the preparation of the samples and the beginning of the measurements at BESSY was about 4 h.

XMCD measurements were performed at a sample temperature of 120 K. The sample was remanently magnetized along the in-plane [110] direction by ramping the current through a coil. The magnetization procedure was monitored by magneto-optical Kerr effect, as was the presence of the remanence before and after each scan of data acquisition.

Absorption spectra were taken at the PM-3 beamline at BESSY. The photon energy resolution was ≈ 1.5 eV in the region of the Fe and Cu L edges. Circularly polarized x rays were obtained by selecting light from 0.3 mrad below the ring orbit. Measurements of Co reference films yielded an estimate of about 40% for the degree of circular polarization in that configuration. The total electron yield was recorded by measuring the sample drain current with a bias voltage of -27 V applied. The sample magnetization was reversed after each energy scan. The 8 or 10 scans at the Fe L edge, and between 40 and 60 at the Cu L edge were summed up. The spectra were normalized to the current of a gold grid monitor located just behind the exit slit of the monochromator, and corrected for the angle of light incidence of 45° and the estimated degree of circular polarization. The analysis of the Fe $L_{2,3}$ absorption spectra was done as outlined in Ref. 10 or 11. In particular, the spectra were normalized to unity edge jump, and two step functions of 0.5 eV width and $2/3(1/3)$ height at the $L_3(L_2)$ absorption maxima were subtracted. A constant number of Fe $3d$ holes of 3.34 was assumed.¹² The Cu $L_{2,3}$ spectra were analyzed by comparing them to the spectra of Ref. 13, taking into account the different angle of incidence and the different degree of light polarization in our

^{a)}Electronic mail: kuch@port.exp.bessy.de

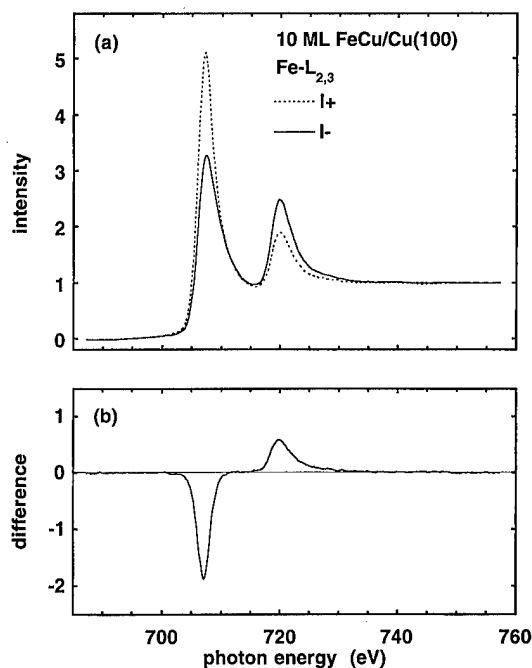


FIG. 1. (a) Absorption spectra at the Fe $L_{2,3}$ edge of a 10 ML FeCu film for parallel (dotted line) and antiparallel alignment of magnetization direction and light helicity (solid line). (b) Difference between the spectra of (a).

experiment. In this way the value for the ratio of white line intensity to number of d holes for Cu of Ref. 13 is used, and it is not necessary to integrate the Cu absorption intensity.

Absorption spectra at the Fe- $L_{2,3}$ edge are shown in Fig. 1(a). Spectra for parallel and antiparallel alignment of magnetization direction and light helicity are reproduced by dotted and solid lines, respectively. The difference between the two spectra is plotted in Fig. 1(b). A strong dichroism is observed with negative (positive) peaks at the L_3 (L_2) edges. The sum rule analysis of the data yields a spin moment of $1.8 \pm 0.06 \mu_B$, and a ratio of orbital to spin moment of 0.12 ± 0.03 .

Measurements under identical experimental conditions of 3.5 ML fcc Fe/5 ML Co/Cu(100) films, which are entirely ferromagnetically ordered,¹⁴ resulted in a similar spin moment of $1.9 \pm 0.1 \mu_B$, and also in a similar (within 5%) white line intensity.⁶ The cited errors represent the accuracy and reproducibility of the measurements, and do not include systematic errors due to uncertainties in the exact degree of circular polarization, the number of $3d$ holes, or the details of the steplike background subtracted for white line integration. They are, however, appropriate for comparing results obtained from different samples under identical experimental conditions. Comparing the results from the FeCu alloy and the Fe/Co reference film, we conclude that all of the Fe atoms in the FeCu alloy film carry a moment close to that of fcc Fe. In the sum-rule analysis the contribution of the magnetic dipole term⁹ to the spin moment is usually neglected, a variation of which may introduce an additional error of up to 10%.¹⁵ The ratio μ_L/μ_S between the orbital and spin moment, nevertheless, is significantly enhanced in the FeCu film, being about a factor of 3 larger than in the 3.5 ML Fe film (0.04 ± 0.01).⁶ Increased orbital moments have been ob-

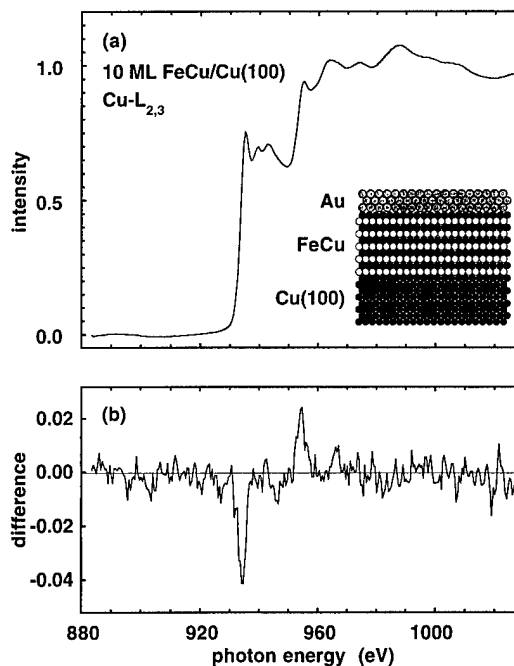


FIG. 2. (a) Absorption spectrum at the Cu $L_{2,3}$ edge of a 10 ML FeCu film, averaged over antiparallel and parallel alignment of magnetization direction and light helicity. The inset shows a sketch of the film architecture. (b) Absorption difference between antiparallel and parallel alignment of magnetization direction and light helicity at the Cu $L_{2,3}$ edge. Note the different vertical scale with respect to (a).

served previously in films of decreasing thickness,¹⁶ and have been discussed in terms of higher density of states at the Fermi level,^{16,17} and magnetic anisotropy.^{15,18} We tentatively conclude the observed orbital moments as a consequence of the ordered layer stacking, reflecting the electronic structure of the FeCu films.

Figure 2(a) shows the absorption spectrum of FeCu at the Cu $L_{2,3}$ edge. Here, the average absorption for both magnetization directions is reproduced rather than the individual curves, because the difference between these is much smaller than at the Fe $L_{2,3}$ edge, and would not be reproduced clearly on the scale of Fig. 2(a). This is seen from Fig. 2(b), where analogously to Fig. 1(b) the difference in absorption between antiparallel and parallel alignment of magnetization direction and light helicity at the Cu $L_{2,3}$ edge, corrected for the angle of light incidence and the estimated degree of circular polarization, is reported. Note the vertical scale, which is blown up by an (arbitrary) factor of 10 with respect to Fig. 2(a). A small but distinct dichroism at the energetic positions of the Cu L_3 and L_2 edges with the same sign as at the respective Fe edges is observed. It amounts to about -4% and $+2\%$ of the Cu edge jump height. A magnetic moment is thus present at the Cu atoms, introduced by the presence of the Fe atoms.

Applying the sum rules to the spectra of Fig. 2 yields Cu atomic spin moments of $0.05 \pm 0.005 \mu_B$. Before comparing this value to other systems, it has to be considered though that by measuring the absorption by the total electron yield there is still a significant contribution from the Cu(100) substrate to the Cu absorption signal at the thickness of the FeCu films (10 ML). For a mean free path of 11 ML ($\approx 20 \text{ \AA}$) the Cu signal stems to about 55% from the substrate. Assuming

that the substrate atoms do not show any magnetic dichroism, $\mu_S = 0.12 \pm 0.01 \mu_B$ is obtained for the Cu atoms in the FeCu film. Comparing that to the Fe atomic moment it is found that about 7% of the *d*-band magnetic moment of the FeCu film is carried by the Cu atoms.

The induced Cu magnetic moments are higher than those observed in Co/Cu multilayers ($0.05 \mu_B$)^{13,19} or Fe/Cu multilayers (up to $0.09 \mu_B$, depending on the Cu layer thickness),¹⁹ but comparable to Co₉₀Cu₁₀ films ($0.13 \mu_B$).^{13,19} Theoretical calculations for Cu induced moments in Fe/Cu multilayers yielded values of 0.07,²⁰ 0.05,²¹ and $0.06 \mu_B$.²² For a layered FeCu alloy similar to the one investigated here the resulting theoretical moment was $0.08 \mu_B$.²² This is slightly lower than what we observe experimentally, but has the right order of magnitude. It is conceivable that details in which the geometric structure assumed for the calculations differs from the structure realized in the FeCu samples may account for the differences between theory and experiment.

In conclusion, we have investigated ultrathin epitaxial fcc FeCu ordered alloy films on Cu(100). Element selective electronic and magnetic properties were obtained by XMCD at the Fe and Cu *L*_{2,3} edges. Induced moments of the Cu atoms, which amount to about 6% of that of the Fe moments, and increased Fe orbital moments were found. The findings are attributed to the modification of the electronic structure due to hybridization between Fe and Cu derived states, the reduced symmetry along the surface normal, and altered dimensionality in the layered alloys.

We thank the BESSY staff and B. Zada for technical support. Funding by the BMBF under Contract No. 05 621EFA 0 is gratefully acknowledged. M.S. thanks the European Union for a stipend.

¹A. R. Yavari, P. J. Desré, and T. Benamer, Phys. Rev. Lett. **68**, 2235 (1992); J. Eckert, J. C. Holzer, I. C. E. Krill, and W. L. Johnson, J. Mater. Res. **7**, 1908 (1992); P. Crespo, A. Hernando, R. Yavari, O. Drbohlav, A. García Escorial, J. M. Barandiarán, and I. Orúe, Phys. Rev. B **48**, 7134 (1993); V. G. Harris, K. M. Kemner, B. N. Das, N. C. Koon, A. E. Ehrlich, J. P. Kirkland, J. C. Woicik, P. Crespo, A. Hernando, and A.

García Escorial, *ibid.* **54**, 6929 (1996); P. J. Schilling, J.-H. He, J. Cheng, and E. Ma, Appl. Phys. Lett. **68**, 767 (1996).

²K. Uenishi, K. F. Kobayashi, S. Nasu, H. Hatano, K. N. Ishihara, and P. H. Shingu, Z. Metallkd. **83** (2), 132 (1992).

³C. L. Chien, S. H. Liou, D. Kofalt, W. Yu, T. Egami, and T. R. McGuire, Phys. Rev. B **33**, 3247 (1986).

⁴K. Sumiyama, T. Yoshitake, and Y. Nakamura, Acta Metall. **33**, 1791 (1983).

⁵S. Sundar Manoharan, J. Shen, H. Jenniches, M. Klaua, and J. Kirschner, J. Appl. Phys. **81**, 3768 (1997); S. Sundar Manoharan, M. Klaua, J. Shen, J. Barthel, Ch. V. Mohan, and J. Kirschner (unpublished).

⁶W. Kuch, M. Salviati, Xingyu Gao, M.-T. Lin, M. Klaua, J. Barthel, Ch. V. Mohan, and J. Kirschner (unpublished).

⁷J. L. Erskine and E. A. Stern, Phys. Rev. B **12**, 5016 (1975); G. Schütz, W. Wagner, W. Wilhelm, R. Kienle, R. Zeller, R. Frahm, and G. Materlik, Phys. Rev. Lett. **58**, 737 (1987).

⁸B. T. Thole, P. Carra, F. Sette, and G. van der Laan, Phys. Rev. Lett. **68**, 1943 (1992).

⁹P. Carra, B. T. Thole, M. Altarelli, and X. Wang, Phys. Rev. Lett. **70**, 694 (1993).

¹⁰C. T. Chen, Y. U. Idzerda, H.-J. Lin, N. V. Smith, G. Meigs, E. Chaban, G. H. Ho, E. Pellegrin, and F. Sette, Phys. Rev. Lett. **75**, 152 (1995).

¹¹J. Stöhr, J. Electron Spectrosc. Relat. Phenom. **75**, 253 (1995).

¹²R. Wu and A. J. Freeman, Phys. Rev. Lett. **73**, 1994 (1994).

¹³M. G. Samant, J. Stöhr, S. S. P. Parkin, G. A. Held, B. D. Hermsmeier, F. Herman, M. van Schilfgaarde, L.-C. Duda, D. C. Mancini, N. Wassdahl, and R. Nakajima, Phys. Rev. Lett. **72**, 1112 (1994).

¹⁴W. L. O'Brien and B. P. Tonner, Phys. Rev. B **52**, 15 332 (1995); J. Appl. Phys. **79**, 5629 (1996); E. J. Escorcia-Aparicio, R. K. Kawakami, and Z. Q. Qiu, *ibid.* **79**, 4964 (1996).

¹⁵D. Weller, J. Stöhr, R. Nakajima, A. Carl, M. G. Samant, C. Chappert, R. Mégy, P. Beauvillain, P. Veillet, and G. A. Held, Phys. Rev. Lett. **75**, 3752 (1995).

¹⁶M. Tischer, O. Hjortstam, D. Arvanitis, J. H. Dunn, F. May, K. Baberschke, J. Trygg, J. M. Wills, B. Johansson, and O. Eriksson, Phys. Rev. Lett. **75**, 1602 (1995).

¹⁷O. Eriksson, L. Nordström, A. Pohl, L. Severin, A. M. Boring, and B. Johansson, Phys. Rev. B **41**, 11 807 (1990); H. Ebert, R. Zeller, B. Drittler, and P. H. Dederichs, J. Appl. Phys. **67**, 4576 (1990).

¹⁸P. Bruno, Phys. Rev. B **39**, 865 (1989); J. Stöhr and H. König, Phys. Rev. Lett. **75**, 3748 (1995).

¹⁹G. A. Held, M. G. Samant, J. Stöhr, S. S. P. Parkin, B. D. Hermsmeier, M. van Schilfgaarde, and R. Nakajima, Z. Phys. B **100**, 335 (1996).

²⁰G. Y. Guo, H. Ebert, W. M. Temmermann, and P. J. Durham, Phys. Rev. B **50**, 3861 (1994).

²¹O. Hjortstam, J. Trygg, J. M. Wills, B. Johansson, and O. Eriksson, Phys. Rev. B **53**, 9204 (1996).

²²Y. Zhou, L. Zhong, W. Zhang, and D.-S. Wang, J. Appl. Phys. **81**, 4472 (1997).

Orbital magnetic moment enhancement at surfaces and interfaces within the framework of the local density approximation+ U method

A. B. Shick and A. J. Freeman

Department of Physics and Astronomy, Northwestern University, Evanston, Illinois 60208-3112

A. I. Liechtenstein

IFF Forschungszentrum Jülich, Jülich D-52428, Germany

Stimulated by MCXD measurements, the determination of orbital magnetic moments, M_L , at surfaces and interfaces has become a subject of strong interest. We combine the rotationally invariant local density approximation (LDA)+ U total energy functional with a relativistic self-consistent spin-polarized version of the total energy full-potential linearized augmented plane wave method in order to determine M_L at surfaces and interfaces. As illustration, the method is applied to Co overlayers on Cu(001). We find an enhancement of the Co orbital magnetic moment in LDA+ U calculations in comparison with local spin density functional approximation (LSDA) results. M_L as a function of magnetic Co-film thickness is analyzed. The M_L/M_S ratio is calculated to be different for different Co layers (i.e., interface, surface, or remaining Co layers) in Co/Cu(001), and is shown to be dependent on the Co overlayer thickness. Finally, the use of LDA+ U is shown to give M_L/M_S in better agreement with MCXD data than does LSDA. © 1998 American Institute of Physics. [S0021-8979(98)37611-2]

First principles electronic structure calculations of transition metal surfaces and ultrathin films¹ show that there is a significant enhancement of spin and orbital magnetic moments at the surface in comparison to their bulk values. The enhancement of the spin moment, which is caused by reduced coordination of the surface atom due to symmetry lowering, is accompanied by an enhancement of the orbital magnetic moment. However, calculations¹ which are based on the local spin density functional approximation (LSDA) do not provide a complete description for orbital magnetic moments even for the case of bulk transition metal ferromagnets.² Now, within LSDA spin-orbit coupling (SOC) is the only effect considered responsible for orbital magnetization and other sources, namely noncentral field contributions to the electron–electron interaction³ and orbital current polarization,⁴ are neglected.

We examine the influence of electron–electron interactions on M_L . It was shown very recently,³ that Hubbard mean-field exchange energy contributes to the orbital polarization (OP) differently than the so-called orbital polarization correction of Brooks (OPB).⁵ The latter is based on the intuitive analogy with atomic theory⁶ and does not take into account the Coulomb contribution U to the OP. Moreover, whereas spin and orbital polarization effects are coupled³ via the common set of Slater integrals (which are used to represent the electron–electron interaction⁷), they are treated independently in OPB.

We start from the rotationally invariant local density approximation (LDA)+ U total energy functional of the form⁷

$$E^{\text{tot}}(\rho^\sigma(\mathbf{r}), \hat{n}^\sigma) = E^{\text{LSDA}}(\rho^\sigma(\mathbf{r})) + E^{\text{ee}}(\hat{n}^\sigma) - E^{\text{dc}}(\hat{n}^\sigma), \quad (1)$$

where, E^{LSDA} is the LSDA total energy functional of spin density $\rho^{\uparrow,\downarrow}$, E^{ee} is the electron–electron interaction energy in the Hartree-Fock approximation (which depends on the

site-occupation matrix \hat{n} for the set of correlated electrons and can be obtained by projection of the electron eigen functions on a site-centered angular momentum basis set), and E^{dc} is the “double-counting” term⁷ to compensate the electron–electron energy which is included in E^{LSDA} . Further, only the d -electron contributions to E^{ee} and E^{dc} are considered, and we approximate the site-occupation matrix by its MT part only (this is a reasonable approximation for 3d-electron systems since almost all of the d -electron spin density is located within the MT sphere). Applying the variational principle then yields a set of single-particle Kohn–Sham equations, where, in addition to the usual Kohn–Sham spin-dependent potential there is a projection operator of the form $\sum_{m,m'} V_{mm'}^\sigma |Y_{lm}\rangle \langle Y_{lm'}|$ acting on the d electrons. The $V_{mm'}^\sigma$ depend on the site-occupation matrix $\hat{n}_{mm'}^\sigma$, angular matrix elements of the on-site electron–electron interaction, and a set of Slater integrals $F^{2k}(k=0,1)$ (the explicit form of $V_{mm'}^\sigma$ is given by Eq. (5) of Ref. 7).

We have combined the rotationally invariant LDA+ U and the relativistic version of the full-potential linearized augmented plane wave (FLAPW) method by making use of a second variation procedure:⁹ first, scalar-relativistic wave functions are determined within the conventional FLAPW method with the LSDA effective potential (first variation); then the LDA+ U Kohn–Sham equations are solved in the orthogonal basis of these wave functions (only the MT contributions in the LDA+ U Hamiltonian are considered); finally new second variation eigen functions are used to solve the relativistic Kohn–Sham–Dirac equations (with spin-orbit coupling included)¹⁰ and the self-consistent ground state charge and spin densities and site-occupation matrices are obtained.

TABLE I. Layer by layer resolved spin M_S and orbital M_L magnetic moments and their ratio, $R_{LS}=M_L/M_S$, for the Co_n ($n=1,2,3$) overlayers (labeled from the top layer) for different values of U (eV) and $J=1$ eV in comparison with the LSDA results.

Layer		LSDA	$U=1$	$U=1.5$	$U=2$
Co/Cu₅					
Co ₁	$M_S(M_L)$	1.827 (0.129)	1.828 (0.162)	1.853 (0.177)	1.874 (0.195)
Co ₁	R_{LS}	0.071	0.089	0.096	0.104
Co₂/Cu₅					
Co ₁	$M_S(M_L)$	1.821 (0.115)	1.823 (0.138)	1.857 (0.150)	1.879 (0.157)
Co ₂	$M_S(M_L)$	1.594 (0.089)	1.596 (0.105)	1.642 (0.115)	1.687 (0.127)
Co ₁	R_{LS}	0.063	0.076	0.081	0.084
Co ₂	R_{LS}	0.056	0.066	0.070	0.075
Co₃/Cu₅					
Co ₁	$M_S(M_L)$	1.882 (0.112)	1.882 (0.136)	1.895 (0.148)	1.920 (0.156)
Co ₂	$M_S(M_L)$	1.680 (0.077)	1.681 (0.091)	1.697 (0.10)	1.733 (0.111)
Co ₃	$M_S(M_L)$	1.618 (0.088)	1.629 (0.107)	1.652 (0.118)	1.689 (0.128)
Co ₁	R_{LS}	0.060	0.072	0.078	0.081
Co ₂	R_{LS}	0.046	0.054	0.059	0.064
Co ₃	R_{LS}	0.054	0.066	0.071	0.076

As an illustrative example, we used a slab model consisting of five Cu substrate layers covered by n ($n=1,2,3$) Co overlayers on each side. The ideal fcc structure with a bulk Cu lattice constant ($a=6.83$ a.u.) is assumed. The special k -points method is used for the two-dimensional Brillouin zone (2DBZ) integrations and 55 k points in the irreducible part of the BZ are employed for the self-consistent calculations with the magnetization assumed to be perpendicular to the film and a Gaussian broadening is used for weighting the eigen states. Lattice harmonics with angular momentum l up to eight are used to expand the charge and spin densities and wave functions within the muffin-tin sphere. More than 70 plane waves per atom/spin are used as the first variational basis set to solve the scalar-relativistic Kohn-Sham equations; all occupied and empty states up to 1 Ry above E_F are used as a second variational basis set.¹¹ Self-consistency is achieved to within $5 \times 10^{-5} e/(\text{a.u.})^3$ for charge and spin densities.

The total Coulomb interaction matrix for d electrons is defined by F^0 , F^2 , and F^4 Slater integrals. In principle, they could be linked to the Coulomb (U) and exchange parameters (J) obtained from the LSDA.¹² The F^2 and F^4 were obtained from the value of the intra-atomic exchange $J=(F^2+F^4)/14$ which is assumed to be equal to the LSDA Stoner exchange, and the ratio $F^4/F^2=0.625$ for 3d elements.¹³ For a metallic system there is an additional problem related to dynamical screening of the U by itinerant d electrons. Therefore we choose $J=I_{\text{LSDA}}=1$ eV¹⁴ and varied $F^0(=U)$ from 1 to 2 eV.

The calculated M_L and M_S magnetic moments and their ratio, R_{LS} , for Co_n ($n=1,2,3$) overlayers on Cu for different values of U (from 1 to 2 eV) and with $J=1$ eV are presented in Table I.¹⁵ As seen from these data: (i) M_S , M_L , and R_{LS} depend on the location of the Co layer in the overlayer and on the overlayer thickness; (ii) for $U=J=1$ eV, there is practically no increase of M_S (due to the fact that $I=(U+4J)/5$ is equal to I_{LSDA} for $U=J$) but M_L is bigger in LDA+ U than in LSDA calculations and yields an enhancement of R_{LS} by orbital polarization; (iii) there is an increase

of both M_S and M_L with an increase of U , resulting in an increase of R_{LS} .

Very recent MCXD experiments¹⁶ show quite a pronounced enhancement of R_{LS} in the ultrathin Co overlayers on fcc Cu(001). In order to compare our results with experiment, we took into account the decay in intensity of the MCXD signal from Co layers lying under the surface layer.¹⁶ Then, the effective ratio is taken as¹⁶

$$R_{LS}^{\text{eff}} = \left[A(D)e^{-\mu(D-1)} + \sum_{n=3,D} B(D,n)e^{-\mu(n-2)} + C(D) \right] / \sum_{n=0,D-1} e^{-\mu n} \quad (2)$$

with $\mu=d/\lambda$, where d is the Co-Co interlayer distance, D is the Co-overlayer thickness, and $\lambda=32.14$ a.u. is the effective electron escape depth. The parameters $A(D)$, $B(D,n)$, $C(D)$ represent R_{LS} for interface, intermediate, and surface layers, respectively. In contrast to Ref. 16, we keep an explicit dependence of A , B , and C parameters on the overlayer thickness and layer position (n). The calculated values of R_{LS}^{eff} for LSDA and LDA+ U with $U=2$ eV and $J=1$ eV are given in Table II. Whereas the LSDA results deviate significantly from experiment, the LDA+ U values provide much improved quantitative agreement. The use of an overlayer thickness independent set of A , B , and C parameters in

TABLE II. The effective R_{LS} ratio for the ($n=1,2,3$) Co_n/Cu_5 as a result of LDA+ U calculations with $U=2$ eV and $J=1$ eV in comparison with the LSDA results, FP-LMTO^{a,b} calculations and experiment.^a

Layer	LDA+U	OPB ^{a,b}	LSDA	Exp. ^a
Co/Cu ₅	0.104	0.141	0.071 0.065 ^b	
Co ₂ /Cu ₅	0.080		0.060	0.105
Co ₃ /Cu ₅	0.075		0.055	0.100

^aReference 16 (an accuracy of experimental data is estimated as ± 0.005).^bReference 17.

the ultrathin film limit, as in Ref. 16, is in disagreement with the results of the present calculations (cf., Table I). Thus, there is a significant overestimation of the M_L enhancement in Ref. 16 for the ultrathin film limit which is a consequence of an oversimplified interpretation of the experimental data.

The present LSDA results for M_S and M_L for Co/Cu(001) agree quite well with the results of first principle-linear muffin-tin orbital (FP-LMTO) calculations.¹⁷ However, the LDA+ U yields an enhancement of both M_S and M_L with increase of U while OPB¹⁷ acts on M_L only. This is one of the reasons why R_{LS} in LDA+ U is smaller than in OPB. Another possible reason is that values of M_L in OPB strongly depend on the values of the Racah parameters.⁵ The spin-polarized radial wave functions are used in Refs. 16 and 17 to calculate the Slater integrals F^2 and F^4 and Racah parameters, $B=9F^2-5F^4/441$. The values of F^2 and F^4 should be consistent with the values of the Stoner exchange I (this is not shown in Refs. 16 and 17) and their overestimation may lead to an artificial enhancement of M_L .

Finally, as seen from Table I, the spin (M_S) and especially the orbital (M_L) polarizations depend significantly on U . The use of LDA+ U ⁷ instead of LSDA for calculations of M_L/M_S improves significantly the quantitative agreement with experimental data (cf. Table II) for the Co overlayers on Cu(001).

This work was supported by the U.S. Office of Naval Research (Grant No. N00014-94-1-0030) and by a grant of

computing time at the Arctic Region Supercomputing Center and at the Pittsburgh Supercomputing Center.

- ¹R. Wu, D.-S. Wang, and A. J. Freeman, *J. Magn. Magn. Mater.* **132**, 103 (1994).
- ²J. Trygg *et al.*, *Phys. Rev. Lett.* **75**, 2871 (1995).
- ³I. V. Solov'yev, A. I. Liechtenstein, and K. Terakura (unpublished).
- ⁴K. Capelle and E. K. U. Gross, *Phys. Rev. Lett.* **78**, 1872 (1997).
- ⁵O. Eriksson, M. S. S. Brooks, and B. Johanson, *Phys. Rev. B* **41**, 7311 (1990) and references therein.
- ⁶J. S. Griffith, *The Theory of Transition Metal Ions* (Cambridge University Press, Cambridge, 1971).
- ⁷A. I. Liechtenstein, V. I. Anisimov, and J. Zaanen, *Phys. Rev. B* **52**, R5468 (1995).
- ⁸E. Wimmer, H. Krakauer, M. Weinert, and A. J. Freeman, *Phys. Rev. B* **24**, 864 (1981).
- ⁹C. Li, A. J. Freeman, H. J. F. Jansen, and C. L. Fu, *Phys. Rev. B* **42**, 5433 (1990).
- ¹⁰A. B. Shick, D. L. Novikov, and A. J. Freeman, *Phys. Rev. B* **56**, R14259 (1997).
- ¹¹The use of such a "low" energy cutoff for the LDA+ U second variation part is because only the d -state contributions to the LDA+ U Hamiltonian were considered and states more than 1 Ry above E_F do not have d character.
- ¹²V. I. Anisimov and O. Gunnarsson, *Phys. Rev. B* **43**, 7570 (1991).
- ¹³F. M. F. de Groot *et al.*, *Phys. Rev. B* **42**, 5459 (1990).
- ¹⁴J. F. Janak, *Phys. Rev. B* **16**, 255 (1977).
- ¹⁵The induced M_S in the interface Cu layer is not negligible but small (0.03 μ_B and less) while all other Cu-substrate layers are almost nonmagnetic and M_L for the Cu layers is close to 0.
- ¹⁶M. Tischer *et al.*, *Phys. Rev. Lett.* **75**, 1602 (1995).
- ¹⁷O. Hjortstam *et al.*, *Phys. Rev. B* **53**, 9204 (1996).

Magnetic extended x-ray absorption fine structure at the $L_{3,2}$ edges of Fe and Co on Cu(001)

P. Srivastava,^{a)} L. Lemke, H. Wende, R. Chauvistré, N. Haack, and K. Baberschke
Institut für Experimentalphysik, Freie Universität Berlin, Arnimallee 14, D-14195 Berlin-Dahlem, Germany

J. Hunter-Dunn, D. Arvanitis, and N. Mårtensson
Department of Physics, Uppsala University, Box 530, S-75121 Uppsala, Sweden

A. Ankudinov and J. J. Rehr
Department of Physics, University of Washington, Seattle, Washington 98175

We report magnetic extended x-ray absorption fine structure (EXAFS) measurements on 30 monolayer Fe and Co films on Cu(001) substrates at $L_{3,2}$ edges. For 3d transition metals, the magnetic EXAFS at the L edges is of great interest since it probes final d states which mainly contribute to magnetism. Magnetic EXAFS oscillations were detected up to 500 eV above the edge corresponding to 11.5 \AA^{-1} in k space. Over such a large range, the long wavelength wiggles from the Fe and Co nearest neighbor backscattering and previously observed fast oscillations are clearly seen. It is shown that without using any deconvolution procedure a meaningful analysis can be performed despite an interference of L_3 and L_2 edges. In the case of Fe, experimental data are compared with multiple-scattering calculations. © 1998 American Institute of Physics. [S0021-8979(98)50211-3]

I. INTRODUCTION

The extended x-ray absorption fine structure (EXAFS) technique has contributed a great deal to determine the local atomic structure and the dynamics of adsorbates on metal surfaces.¹ The availability of circularly polarized synchrotron radiation has enabled one to add magnetic selectivity to EXAFS. The difference in spin-polarized EXAFS, i.e., magnetic EXAFS (MEXAFS), can be determined by measuring the spin-dependent absorption in the EXAFS energy range. MEXAFS has opened up a new possibility for investigating static and dynamic magnetic phenomena from a site selective point of view.²⁻¹⁴ Earlier MEXAFS experiments on the 3d transition metal K edge^{5,8-13} and on 4f rare-earth L edges^{3,5,10-13} have shown that with this technique it is possible to study magnetic short range ordering and get useful information regarding magnetic spin moments of neighboring atoms. In the case of pure 3d metals (Fe, Co, Ni), it was found that K -edge MEXAFS oscillations are primarily due to scattering from magnetic nearest neighbors.^{5,9,10,12,13} Therefore, one can distinguish between magnetic and nonmagnetic neighbors by comparing EXAFS and MEXAFS Fourier transforms. Studies at K edges, probing final p states, which are very common in EXAFS, have some disadvantages in MEXAFS. For example, in the case of 3d transition metals, MEXAFS studies at K edges provide no information about the d states which mainly contribute to magnetism and also result in a lower MEXAFS signal. However, L -edge EXAFS and MEXAFS analyses probing d states in the case of 3d transition metals may be difficult due to smaller spin-orbit splitting [13 eV (Fe), 15 eV (Co), 17 eV (Ni)] between the

L_3 and L_2 edges. This leads to an additive overlap of the (M) EXAFS spectra of the two edges, which, in the case of MEXAFS may also partly cancel the signal as the dichroic effects have the same profiles but opposite signs.

We report EXAFS and MEXAFS measurements on 30 monolayer (ML) Fe and Co films on Cu(001) substrates up to 500 eV above the $L_{3,2}$ edges. In the case of Fe, the experimental data are compared with multiple-scattering (MS) calculations.

II. EXPERIMENTAL AND DATA ANALYSIS DETAILS

Thin Fe and Co films of 30 ML thickness were grown at room temperature on Cu(001) substrates in ultrahigh vacuum (UHV) conditions and characterized by means of *in situ* low energy electron diffraction (LEED). The L -edge spectra were recorded in quasitotal electron yield mode at grazing (20°) x-ray incidence at 75 K using circularly polarized light on SX 700 monochromator beamlines at the BESSY synchrotron facility in Berlin.¹⁵

In the analysis of EXAFS, it is a well established technique to put a spline simulating the atomic background μ_0 in rough $\mu(E)$ data. Using the circularly polarized light the total absorption coefficient $\mu(E)$ in normal EXAFS can be defined as $\mu(E) = [\mu^+(E) + \mu^-(E)]/2$. Theoretically, the measured linear absorption coefficient $\mu(E)$ can be related to the fine structure $\chi(E)$ by $\mu(E) = \mu_0(E)[1 + \chi(E)]$. For the magnetic case one gets $\mu^\pm(E) = \mu_0(E)[1 + \chi(E) \pm \chi_M(E)/2]$. However, to extract magnetic information it can be derived as $\mu_M(E) = \mu^+(E) - \mu^-(E)$ and $\chi_M = \mu_M/\mu_0 = (\mu^+ - \mu^-)/\mu_0$. Throughout the text the modulations in EXAFS and MEXAFS signals are shown as χ and χ_M , respectively. Taking the difference between the right and the left polarization for MEXAFS, one may think at first glance that the background (transmission function, etc.) is

^{a)}Corresponding author. Permanent address: Department of Physics, University of Rajasthan, Jaipur 302 004, India; electronic mail: babgroup@physik.fu-berlin.de

automatically subtracted. However, it was found in the present experiments that this did not work satisfactorily because of small changes in the background. The best way found was to take the ratio deriving χ_M from μ^+/μ^- . A Taylor expansion of μ^+/μ^- around $\chi_M=0$ in first order results in $\mu^+/\mu^-|_{\chi_M=0} \approx 1 + \chi_M(1/1 + \chi)$. An approximation $(1/1 + \chi) \approx 1$ produces an error of less than 5% in the magnitude of χ_M provided $\mu^+ + \mu^- \gg \mu^+ - \mu^-$. Therefore, $1 + \chi_M \approx \mu^+/\mu^-$.

The oscillations in the extended energy regions of both EXAFS and MEXAFS of the $L_{3,2}$ edge is a combination of both edges offset by the energy separation of L_3 and L_2 edges. In k space, modulations in the EXAFS/MEXAFS signals can be expressed as $\chi(k) = \chi_{L_3}(k) + \alpha\chi_{L_3}(k + \Delta k)$. With $\chi_{L_2} = \alpha\chi_{L_3}$, $\alpha = 1/2$ for EXAFS and $\alpha = -1$ for MEXAFS. That is to say, for ferromagnets, both $\chi(k)$ and $\chi_M(k)$ oscillations contain the same basic information [nearest neighbor distances, $A(k)$, etc.]. The value of Δk steadily decreases as a function of k . For very large and very small spin-orbit splittings, α cannot be treated simply as a constant. Therefore, care has to be taken when analyzing other systems. Before starting to analyze the experimental data we checked if the superposition of the two edges hinders the analysis. This was done using *ab initio* curved wave calculations with the FEFF7S code.¹⁶ It has been shown recently¹⁷ that the superposed signal of the two edges (L_{3+2}) has a small phase shift compared to the L_3 edge. This superposition of the two edges only results in the change of intensity of various features in the Fourier transforms; their positions remain almost the same. Therefore, an analysis can be carried out on the experimental spectra containing the superposed signal of L_3 and L_2 edges. Similar results were found for EXAFS data.¹⁷ However, it was found that the effect of the superposition of L_3 and L_2 edges is more dramatic in the magnetic case. For a specific analysis of the phase relation between $\chi(k)$ and $\chi_M(k)$ it is more convenient to deconvolute L_3 and L_2 contributions. This is addressed separately.¹⁸

III. RESULTS AND DISCUSSION

Figures 1 and 2 show $k \cdot \chi(k)$ and $k \cdot \chi_M(k)$ oscillations for Fe and Co films and their corresponding Fourier transforms. Magnetic signals are normalized to $P_c = 1$ and 0° grazing incidence. Here, we would like to point out that intensities of MEXAFS signals for Fe and Co cannot be compared directly as both films have different structures. Nevertheless the ratio MEXAFS/EXAFS for the n.n. peak is higher for Fe (1:34) as compared to Co (1:40). In the case of Fe, for MEXAFS it can be seen from Fig. 1(a) that, apart from the higher frequency components, the χ_M profiles clearly show slow oscillations at intermediate and high k values. For Co the $\chi_M(k)$ profile is different. Here, the oscillations at lower k values contain information mostly from the nearest neighbor shell. This is clear if one compares the $\chi(k)$ and $\chi_M(k)$ lower k values which contain information mostly from the nearest neighbor shell. This is also clear if one compares $\chi(k)$ and $\chi_M(k)$ and their corresponding Fourier transforms (Fig. 2). At large k values higher frequency contributions can be seen. Differences in the $\chi_M(k)$ of Fe

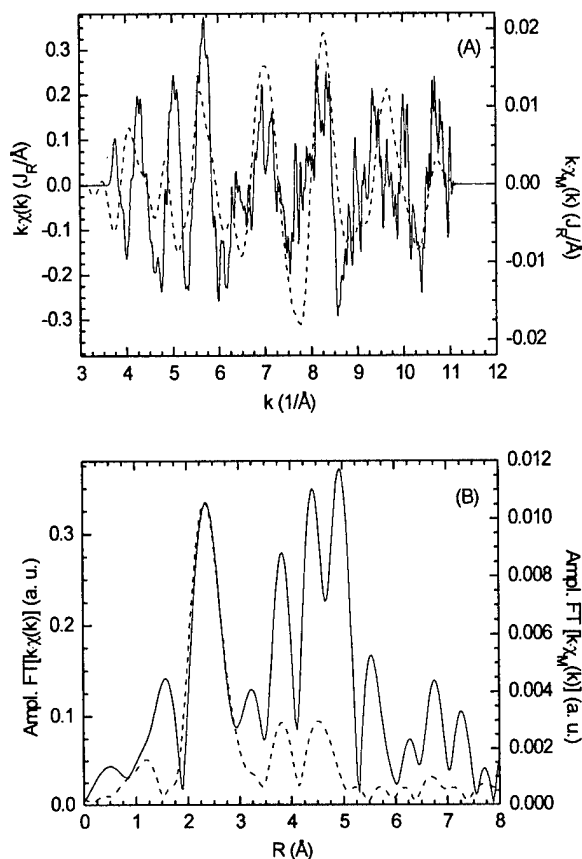


FIG. 1. (a) The normalized EXAFS [$k \cdot \chi(k)$] (dashed line) and MEXAFS [$k \cdot \chi_M(k)$] (solid line) signals and (b) their corresponding Fourier transforms of 30 ML Fe film on Cu(001) measured at grazing x-ray incidence at 75 K.

and Co can originate from the different structures of the films and spin-orbit splitting [$\Delta E_{L_{2,3}} = 13$ eV(Fe), 15 eV(Co)]. Further analysis is in progress to draw some quantitative results.

The Fourier transforms of Fe and Co [Figs. 1(b) and 2(b)] also show distinct differences in R space. The positions of the main peaks of both elements for MEXAFS and EXAFS are not at the same distances. This is not surprising as the peak positions in the Fourier transform do not appear at the real distances but are shifted because of (M) EXAFS phase shifts which are not expected to be identical. For both elements, the MEXAFS Fourier transforms show an enhancement in the features above the main peak especially in the region between 3.5 and 5 Å. It is interesting since all neighbors probed in the magnetic and normal scattering processes are ferromagnetic. As this enhancement was more pronounced in the case of Fe, a theoretical simulation with a bcc unit cell using FEFF7S was performed. It is shown with the Fourier transform of the experimental spectrum in Fig. 3. The structure analysis of the film from the EXAFS data is discussed in detail elsewhere.¹⁷ The dashed line in the spectrum shows the simulation taking into account both single and multiple-scattering paths. It is in qualitative agreement with the experimental Fourier transform. Also, a simulation (dotted line) considering only the single-scattering (SS) paths is shown. The peak at 2.49 Å was scaled to the experiment. The main peak is a superposition of two peaks, A and

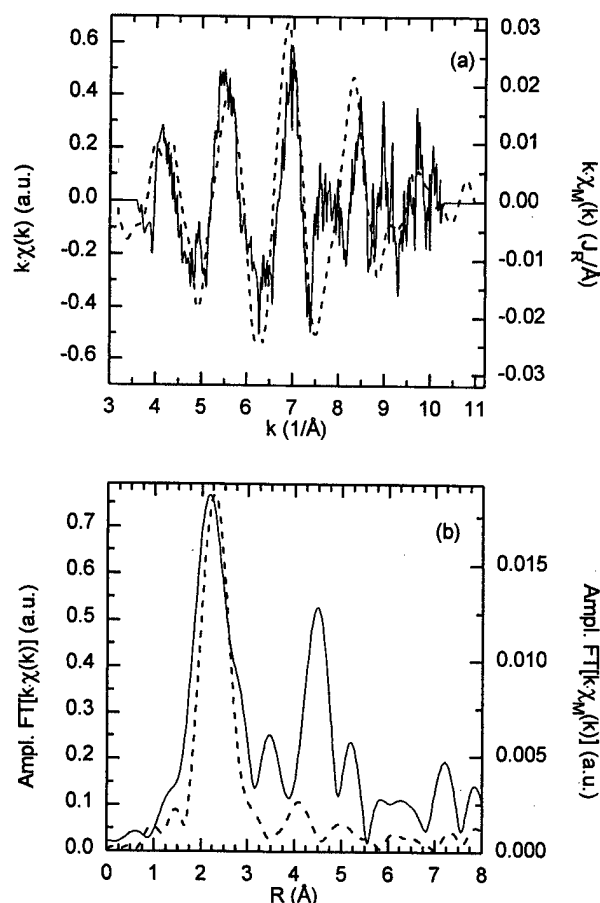


FIG. 2. (a) The normalized EXAFS [$k \cdot \chi(k)$] (dashed line) and MEXAFS [$k \cdot \chi_M(k)$] (solid line) signals and (b) their corresponding Fourier transforms of 30 ML Co film on Cu(001) measured at grazing x-ray incidence at 75 K.

B. The nearest neighbor peak A at 2.49 Å is ascribed to the SS path between atoms 1 and 2 (see the inset). Peaks B and C at 2.87 and 4.06 Å are due to SS paths between atoms 1 ↔ 3 and 1 ↔ 4, respectively. Feature D at 4.76 Å is ascribed to SS paths 1 ↔ 5. As discussed previously,¹⁷ various features between 3.5 and 5 Å in the Fourier transform of Fe showing enhancement in intensity are due to “fast” oscillations as is shown in Fig. 1(a). Therefore, the present theoretical analysis suggests that these high frequency contributions do contain appreciable amounts of SS and MS path lengths implying that the magnetic character of both single and multiple-scattering path lengths increases. However, one cannot neglect the contribution of the overlapping of the L_3 and L_2 edges in the enhancement of these features. In the case of Co, a detailed structural analysis is in progress.

A combination of a MEXAFS *ab initio* calculations with experiments leads to qualitative determination of major contributions to nearest shells from single- and multiple-scattering path lengths. Furthermore, our results show that the ratio of normal/magnetic EXAFS is at least one order of magnitude larger than previous results at K edges, i.e., approximately 34/1 and 40/1 for Fe and Co, respectively. Within the error of the experiment and theoretical models it also agrees with the different magnetic moments for the two elements.

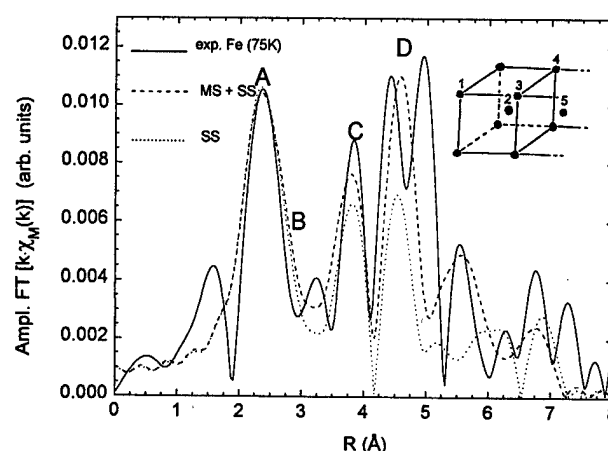


FIG. 3. Simulated Fourier transforms taking into account both multiple- and single-scattering (dashed line) paths and only single-scattering paths (dotted line) for a bcc cluster (shown in the inset) along with the experimental (solid line) MEXAFS data of 30 ML Fe film on Cu(001) recorded at grazing x-ray incidence at 75 K.

The L -edge MEXAFS as pioneered in Refs. 6 and 7 may therefore be the method of choice to study magnetic structure and dynamics from a local point of view.

ACKNOWLEDGMENT

This work was supported by DFG SFB 290 and BMBF (05621 KEA5) grants. One of the authors (P.S.) is grateful to the Alexander von Humboldt (AvH) foundation for financial support.

- ¹ See, for example, B. K. Teo, *EXAFS: Basic Principles and Data Analysis* (Springer, Berlin, 1986); D. Arvanitis and K. Baberschke, *J. Electron Spectrosc. Relat. Phenom.* **75**, 149 (1995), and references therein.
- ² G. Schütz, W. Wagner, W. Wilhelm, P. Kienle, R. Zeller, R. Frahm, and G. Materik, *Phys. Rev. Lett.* **58**, 737 (1987).
- ³ G. Schütz, R. Frahm, P. Mautner, R. Wienke, W. Wagner, W. Wilhelm, and P. Kienle, *Phys. Rev. Lett.* **62**, 2620 (1989).
- ⁴ G. Schütz, M. Knülle, and H. Ebert, *Phys. Scr.* **T49**, 302 (1993).
- ⁵ G. Schütz and D. Ahlers, *Lecture Notes in Physics*, Herrsching Proceedings, edited by H. Ebert and G. Schütz (Springer, Berlin, 1995) p. 229.
- ⁶ V. Chakarian, Y. U. Idzerda, K. M. Kemner, J.-H. Park, G. Meigs, and C. T. Chen, *J. Appl. Phys.* **79**, 6493 (1996).
- ⁷ Y. U. Idzerda, V. Chakarian, and J. W. Freeland, *Synchrotron Radiat. News* **10**, 6 (1997).
- ⁸ O. Isnard, S. Miraglia, D. Fruchart, C. Giorgetti, S. Pizzini, E. Dartyge, G. Krill, and J. P. Kappler, *Phys. Rev. B* **49**, 15 692 (1994).
- ⁹ K. Kobayashi, H. Maruyama, H. Maeda, T. Iwazumi, H. Kawata, and H. Yamazaki, *Physica B* **208–209**, 779 (1995).
- ¹⁰ E. Dartyge, F. Baudelet, C. Brouder, A. Fontaine, J. P. Kappler, G. Krill, C. Giorgetti, M. F. Lopez, and S. Pizzini, *Physica B* **208–209**, 751 (1995).
- ¹¹ G. Schütz, P. Fischer, K. Attenkofer, M. Knülle, D. Ahlers, S. Stähler, C. Detlefs, H. Ebert, and F. de Groot, *J. Appl. Phys.* **76**, 6453 (1994).
- ¹² M. Knülle, D. Ahlers, and G. Schütz, *Solid State Commun.* **94**, 267 (1995).
- ¹³ G. Schütz, P. Fischer, E. Goering, K. Attenkofer, D. Ahlers, and W. Rössl, *Synchrotron Radiat. News* **4**, 13 (1997).
- ¹⁴ C. Brouder and M. Hikam, *Phys. Rev. B* **43**, 3809 (1991).
- ¹⁵ J. Hunter-Dunn, D. Arvanitis, N. Mårtensson, M. Tischer, F. May, M. Russo, and K. Baberschke, *J. Phys. C* **7**, 1111 (1995).
- ¹⁶ A. Ankudinov and J. J. Rehr, *Phys. Rev. B* **52**, 10 214 (1996); **56**, R1712 (1996).
- ¹⁷ L. Lemke, H. Wende, P. Srivastava, R. Chauvistré, N. Haack, K. Baberschke, J. Hunter-Dunn, D. Arvanitis, N. Mårtensson, A. Ankudinov, and J. J. Rehr, *J. Phys. Condens. Matter* **10**, 1917 (1998).
- ¹⁸ H. Wende, J. W. Freeland, V. Chakarian, Y. U. Idzerda, L. Lemke, and K. Baberschke, *J. Appl. Phys.* (these proceedings).

Probing local magnetic disorder by investigating spin dependent photoelectron scattering

H. Wende,^{a)} J. W. Freeland, V. Chakarian, and Y. U. Idzerda^{b)}
Naval Research Laboratory, Code 6345, Washington, D.C. 20375

L. Lemke and K. Baberschke

Institut für Experimentalphysik, Freie Universität Berlin, Arnimallee 14, D-14195 Berlin-Dahlem, Germany

We present here systematic temperature dependent magnetic extended x-ray absorption spectroscopy (MEXAFS) measurements. This fine structure can be explained by the spin dependent scattering of the photoelectron and yields information about the local magnetic surroundings of the absorbing atom. We find a strong temperature dependence at temperatures far below the Curie temperature. This shows that the intensity of the MEXAFS signal is not only determined by the value of the magnetic moment but also by the relative vibrations of the backscattering atom to the absorbing atom. © 1998 American Institute of Physics. [S0021-8979(98)50311-8]

Temperature dependent extended x-ray absorption fine structure spectroscopy (EXAFS) is a well established technique to obtain local structure and bond dynamics.¹ Recently it was shown in experimental works²⁻⁵ and in theoretical works⁶⁻⁹ that magnetic EXAFS (MEXAFS) experiments performed with circularly polarized light give insight into the spin dependent scattering of the photoelectron for ferromagnetic and anti-ferromagnetic samples. This scattering information yields the distances to the magnetic neighbors and results in a picture of the local magnetic structure which can be directly related to the local atomic structure. By probing the temperature dependence of the local magnetic disorder using magnetic EXAFS we can get a more complete picture of the magnetic behavior. This work presents a systematic investigation of the temperature dependence of the MEXAFS. We chose a polycrystalline Fe thin film of 500 Å as a model system as it is known that the Debye model describes the temperature dependence of the spin averaged EXAFS reasonably well¹⁰ although measuring at temperatures far below the Curie temperature of Fe we find an even stronger temperature dependence for the MEXAFS compared to the EXAFS. This shows that the temperature dependence of the MEXAFS is not only determined by the temperature dependence of the magnetic moment which should be constant in the temperature region investigated (70–400 K) but also by the thermal vibrations of the absorbing atom to the backscattering atom.

The helicity dependent transmission measurements in the soft x-ray regime at the $L_{3,2}$ edges had been done at the Naval Research Laboratory (NRL) facility located at the U4B beamline of the National Synchrotron Light Source (NSLS). The experimental details are reported elsewhere.^{11,12} Because of the small separation of the two edges ($\Delta E = 13.1$ eV) due to spin-orbit splitting, the recorded data represent the sum of the two edges. We show that this is not a further complication as we can model the

overlapped contributions quite well using the ab initio FEFF7 code.¹³ We measured the helicity dependent absorption coefficients $\mu^+(E)$ and $\mu^-(E)$ for right and left circularly polarized light, respectively. The spin averaged absorption defined as $\mu(E) = [\mu^+(E) + \mu^-(E)]/2$ exhibits the regular EXAFS. The EXAFS is defined by $\chi = (\mu - \mu_0)/\mu_0$ where μ is the x-ray absorption coefficient and μ_0 is the atomic x-ray absorption coefficient. Generally speaking, one has to take $p \rightarrow d$ and $p \rightarrow s$ transitions for the $L_{3,2}$ edges into account. But the $p \rightarrow s$ transitions are weak and can be neglected for our system.¹ Therefore the same analysis as is known for K edge EXAFS can be performed at the $L_{3,2}$ edges here. The magnetic signal is described by the helicity dependent absorption coefficients which exhibit a difference $\mu_m(E) = \mu^+(E) - \mu^-(E)$ which is known as magnetic circular x-ray dichroism (MCXD) for the near edge region. This difference shows a small oscillatory fine structure $\chi_m = (\mu^+ - \mu^-)/\mu_0$ in the extended energy region—the MEXAFS.

The EXAFS was analyzed in the conventional way by extracting the oscillations with a spline and normalizing the data to the edge jump. In addition to the removal of the atomic background $\mu_0(E)$ of the combined $L_{3,2}$ edges the spline function had to remove the L_1 edge. The L_1 edge jump was found to be 10% of the combined $L_{3,2}$ edge jump and has no pronounced features. The experimental data for the combined edges for the lowest temperature of 70 K are shown in Fig. 1. In order to understand the effect of the overlap of the two edges we compared the experimental EXAFS data to a FEFF7 simulation of the combined edges. For this simulation we calculated $\mu_{L_3}(E)$ and $\mu_{L_2}(E)$ and added the contributions taking edge jump ratios of $J_{L_3}:J_{L_2} = 2:1$ into account. The best agreement between theory and experiment was achieved with a bulk bcc structure for Fe with a Debye temperature of $\theta_D = 520$ K. The good agreement shown in Fig. 1 indicates that the data can be described by simply adding the L_2 contribution to the L_3 contribution. With the help of the ab initio simulation every peak in the Fourier transform of the data [shown in Fig. 1(b)] can be related to specific scattering paths. The main contribution of

^{a)}Permanent address: Institut für Experimentalphysik, Freie Universität Berlin, Arnimallee 14, D-14195 Berlin-Dahlem, Germany.

^{b)}Electronic mail: idzerda@nrl.navy.mil

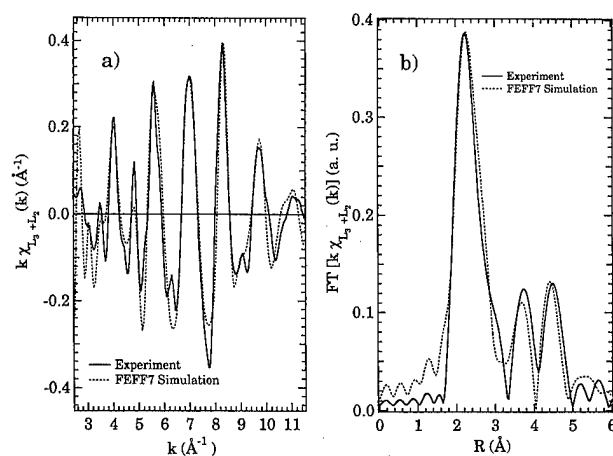


FIG. 1. Comparison of the FEFF7 simulation (dotted line) to experimental EXAFS data (solid line) for the combined L_3 and L_2 edges. (a) The k weighted EXAFS oscillations $k \cdot \chi_{L_3+L_2}(k)$ are well reproduced by the simulation in phase as well as in amplitude. (b) The Fourier transform (FT) $[k \cdot \chi_{L_3+L_2}(k)]$.

the Fourier transform contains two single scattering paths (nearest and next nearest neighbor). The contributions in Fourier transform for higher distances ($R > 3.6$ Å) are also described well by the simulation. A more detailed analysis of the scattering paths of the higher shells shows that one finds a complicated interference of single and multiple scattering paths in this range. Therefore the temperature dependence of the main peak only will be investigated here.

We will later analyze the data of the L_3 edge only since the L_3 edge interferes destructively with the L_2 edge for the MEXAFS case. Therefore we separated the contributions of the L_3 and L_2 edges by using an iterative Van Cittert deconvolution method in energy space.¹⁴ To test the performance of this method we deconvoluted the EXAFS simulation of the combined edges and compared the result to the initial simulation of the L_3 edge. Having found perfect agreement we can establish this method as a standard tool for these kinds of investigations. As we have to analyze the temperature dependence of the MEXAFS for the L_3 edge only we will discuss the temperature dependence of the EXAFS for the L_3 edge as well. However, we find the same structural and dynamic results for the EXAFS for the dataset of the combined edges as for the deconvoluted dataset of one edge. The deconvoluted experimental EXAFS data of the L_3 edge are shown in Figs. 2(a) and 2(b). It turns out that the peak positions in the Fourier transform $FT[k \cdot \chi_{L_3}(k)]$ [Fig. 2(b)] of the L_3 edge are the same as those of the combined edges $FT[k \cdot \chi_{L_3+L_2}(k)]$.

As the main peak in the Fourier transform contains the nearest and the next nearest neighbor distance contributions, we had to perform a least square fit using FEFFIT¹⁵ for the analysis of the temperature dependence of the main peak. This code modifies the Debye temperature of the two scattering paths calculated with FEFF7 to get the best fit to the experimental data. As the Fourier transform of the experimental data exhibits a small temperature dependence on the main peak position, indicating the presence of small anharmonicity of the absorber-backscatterer pair potential, a tem-

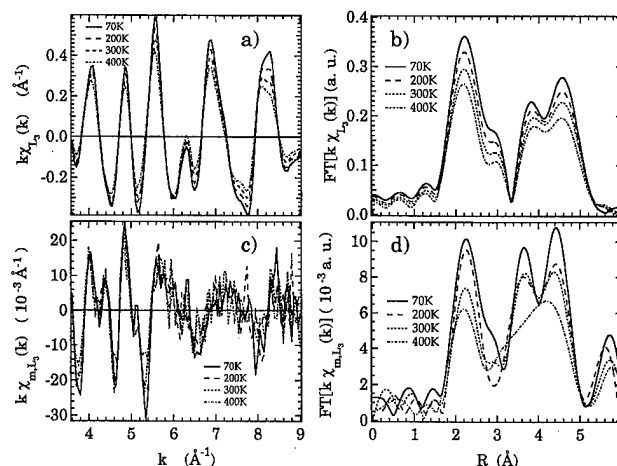


FIG. 2. The temperature dependent deconvoluted L_3 EXAFS data (a), (b) in comparison to the deconvoluted L_3 MEXAFS (c), (d) data. Although the data have been taken at a longer k range, the data are shown in a smaller k range because the MEXAFS noise level became too high for an appropriate fit above $k > 9.0$ Å⁻¹. Note that the EXAFS Fourier transform (a) is different from that in Fig. 1(b) due to interference effects of the L_3 edge by the L_2 edge. A similar difference is observed in the MEXAFS data (d) compared to the EXAFS data (b) since the magnetic and the spin averaged damping must not be the same. The temperature dependent damping can clearly be seen in the Fourier transform (b), (d). Note the stronger damping for the MEXAFS data.

perature dependent third cumulant $c_3(T)$ calculated from the linear expansion coefficient for Fe was included in the fit.¹ The clear temperature dependence of the experimental EXAFS data was fitted with the correlated Debye model¹⁶ yielding a Debye temperature of $\theta_D = (520 \pm 40)$ K (see Fig. 3) in good agreement with calorimetric measurements for the bulk system [θ_D (calorimetric) = 470 K].¹⁷ The damping of the EXAFS oscillations is described by the mean square relative displacement $\sigma_{\text{tot}}^2(T) = \sigma_{\text{dyn}}^2(T) + \sigma_{\text{stat}}^2$ where $\sigma_{\text{dyn}}^2(T)$ describes the dynamic disorder due to thermal vibrations and σ_{stat}^2 is a measure of the static disorder. As the amplitude of the fit agrees quite well with the experiment, no additional static disorder (σ_{stat}^2) had to be introduced for the spin averaged EXAFS. This shows that the polycrystalline films are well ordered ($\sigma_{\text{stat}}^2 \leq 2 \times 10^{-3}$ Å²) from a local point of view and must therefore consist of large crystallites. The MEXAFS analysis is not as straightforward as that for the EX-

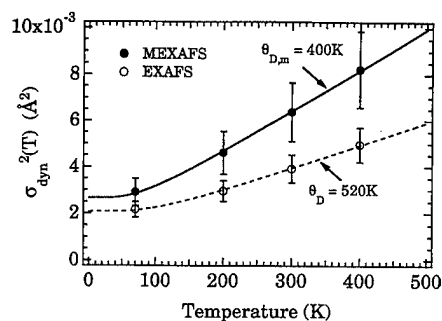


FIG. 3. The temperature dependence of the dynamic part of the MSD $\sigma_{\text{dyn}}^2(T)$ for the nearest neighbor distance (R_1) for the EXAFS data (closed circles) and for the MEXAFS data (open circles). The solid line and the dotted line depict the temperature dependence of the MSD calculated by the Debye model.

AFS. The reason is the different way in which the L_3 edge interferes with the L_2 edge in the helicity dependent investigation. The EXAFS/MEXAFS signal of the combined edges can be explained as

$$\chi_{L_3+L_2}(E) = \frac{2}{3}[\chi_{L_3}(E) + \alpha \cdot \chi_{L_3}(E + \Delta E)], \quad (1)$$

with $\chi_{L_2}(E) = \alpha \cdot \chi_{L_3}(E + \Delta E)$ and $\alpha = \frac{1}{2}$ for EXAFS (quantum degeneracy for L_3 and L_2 edge jumps 2:1) and $\alpha = -1$ for MEXAFS (phase relation for MCXD -1:1). The prefactor $2/3$ takes into account the fact that the edge jump of the combined $L_{3,2}$ edges is 1.5 times larger than the μ_{L_3} edge jump. The negative sign of α for the MEXAFS case leads to destructive interference in the MEXAFS of the combined edges. Due to this interference a deconvolution of the MEXAFS data is necessary. An additional cross check of the deconvolution method is the comparison of the phase shift of the Fourier backtransformed main peak of the Fourier transform for MEXAFS compared to that for EXAFS. We find a phase shift of exactly $\pi/2$ for MEXAFS compared to that for EXAFS as predicted.⁷

The deconvoluted MEXAFS data are shown in Figs. 2(c) and 2(d). A qualitative comparison of the MEXAFS data to EXAFS data shows that the peak positions of the Fourier transforms [Figs. 2(b) and 2(d)] of the main peak are the same for both cases. Also, the temperature dependent damping is comparable. The quantitative FEFFIT yields the same structural results of the Fe bulk bcc structure as we found in the EXAFS analysis. The Debye model analysis of the MEXAFS temperature dependence results in a value for the "magnetic" Debye temperature of $\theta_{D,m} = (400 \pm 40)$ K, showing that the temperature dependence of the MEXAFS data is even stronger than that of the EXAFS. This means that the mean square relative displacement $\sigma^2(T)$ reveals a stronger increase with temperature for the MEXAFS compared to the EXAFS as shown in Fig. 3. This result is surprising at first since the Curie temperature of bulk Fe is $T_C = 1050$ K and therefore a temperature range of 70–400 K results in a reduced temperature range [$t = (T_C - T)/T_C$] of 0.9–0.6. In this temperature range one does not expect a strong temperature dependence of the magnetic signal. Nevertheless one can understand our findings by the scattering of the photoelectron. The MEXAFS signal is determined by the difference in scattering potential for the spin up electron and

the spin down electron. Although the magnetic behavior of the Fe sample is determined by the 3d bands, the difference in scattering potential has the same form as the spin averaged potential.⁷ Therefore any deviation from equilibrium due to thermal vibrations still affects the MEXAFS signal. This explains why the dynamic part of mean square relative displacement $\sigma_{\text{dyn}}^2(T)$ shows about the same increase with higher temperatures that we find for MEXAFS as compared to EXAFS. As magnetic fluctuations are also present in the reduced temperature range of 0.9–0.6, we can understand the even stronger temperature dependence for the spin-dependent MEXAFS compared to the spin averaged EXAFS.

To summarize, we have found that the temperature dependence of the MEXAFS is not only determined by the temperature dependence of the magnetic moment (which is probed in the near edge MCXD technique) but also by atomic thermal vibrations. Since we find an even stronger temperature dependence in the MEXAFS compared to the EXAFS, we find additional local magnetic disorder which maybe can be explained by magnetic fluctuations.

This work was supported by the DFG SFB 290, by BMBF Project No. 05 621 KEA 5 and by the Office of Naval Research. The authors want to thank J. J. Rehr for helpful discussions. One of the authors (H.W.) wants to thank the Freie Universität Berlin and the Naval Research Laboratory for support during his stay at Brookhaven National Laboratory.

¹B. K. Theo, *EXAFS: Basic Principles and Data Analysis* (Springer, Berlin, 1986).

²G. Schütz *et al.*, Phys. Rev. Lett. **58**, 737 (1987).

³O. Isnard *et al.*, Phys. Rev. B **49**, 15 692 (1994).

⁴K. Kobayashi *et al.*, Physica B **208-209**, 779 (1995).

⁵E. Dartyge *et al.*, Physica B **208-209**, 751 (1995).

⁶C. Brouder *et al.*, Phys. Rev. B **43**, 3809 (1991).

⁷A. Ankudinov *et al.*, Phys. Rev. B **52**, 10 214 (1995).

⁸C. Brouder *et al.*, Phys. Rev. B **54**, 7334 (1996).

⁹A. Ankudinov *et al.*, Phys. Rev. B **56**, R1712 (1997).

¹⁰L. Tröger *et al.*, Phys. Rev. B **49**, 888 (1994).

¹¹C. T. Chen *et al.*, Phys. Rev. Lett. **75**, 152 (1995).

¹²W. T. Elam *et al.*, Phys. Rev. B **38**, 26 (1988).

¹³S. I. Zabinsky *et al.*, Phys. Rev. B **52**, 2995 (1995).

¹⁴A. F. Jones *et al.*, Gen. Phys. **3**, 462 (1970).

¹⁵E. A. Stern *et al.*, Physica B **208-209**, 117 (1995).

¹⁶E. D. Crozier, J. J. Rehr, and R. Ingalls, in *X-Ray Absorption*, edited by D. C. Koningsberger and R. Prins (Wiley-Interscience, New York, 1988).

¹⁷C. Kittel, *Introduction to Solid State Physics* (Wiley, New York, 1986).

Magnetoresistance in single Fe(001) ultrathin films

S. Yuasa,^{a)} T. Katayama, M. Nývlt, and Y. Suzuki
Electrotechnical Laboratory, Umezono, Tsukuba 305-8568, Japan

T. Yori

College of Science and Technology, Nihon University, Funabashi 274-8501, Japan

Magnetoresistance in Au(001)-sandwiched Fe(001) ultrathin films was investigated at $T=1.6$ K. Effects of both the Fe layer and the Au cap layer were investigated using wedge-shaped Fe and Au cap layers. The total thicknesses of the films were kept much thinner than the mean free path of the conduction electrons in order to enhance the magnetoresistance by electron channeling between the surface and the substrate. The Fe wedge-shaped films in the range $d_{\text{Fe}}=0-4$ Å showed a granular-type giant magnetoresistance (GMR) because of a discontinuity in the Fe layer. The films with $d_{\text{Fe}}=4-25$ Å also showed that the GMR component through the Fe layer is continuous. In the Au cap wedge-shaped films, the GMR component nearly vanished at $d_{\text{Au cap}}=0$. The MR ratio increased linearly with $d_{\text{Au cap}}$ in the range $d_{\text{Au cap}}=0-50$ Å and saturated at $d_{\text{Au cap}}\sim 130$ Å. Moreover, the CuO overlayer on the Au cap wedge-shaped film resulted in a 25% decrease in the MR ratio in the whole $d_{\text{Au cap}}$ range. These phenomena can be interpreted as differences in spin flip probability for electron reflections on the surface and at the interfaces. © 1998 American Institute of Physics. [S0021-8979(98)50411-2]

The giant magnetoresistance (GMR) effect in magnetic multilayers is mainly caused by spin-dependent scattering of conduction electrons through ferromagnetic layers with parallel or antiparallel magnetization configurations. In metallic multilayers with two ferromagnetic layers so-called spin-valve films, reflections of conduction electrons at the free surface and at the interface between the buffer layer and the substrate, are considered to have a larger influence on GMR compared to multilayers with many ferromagnetic layers. It has recently been reported that the MR ratio in spin-valve films changes with various kinds of cap layers,¹ showing the importance of electron scattering at the surface and at the interface. This effect has been attributed to the change in specularity of the reflection, but details of it are still unclear.

In order to investigate the effect of surface reflection on magnetoresistance, multilayered films with small numbers of ferromagnetic layers are suitable. For this reason, we focused on a single ferromagnetic ultrathin layer with a buffer layer and a cap layer of nonmagnetic metal. The magnetoresistance in the single ultrathin ferromagnetic layer had been studied in Au/Co/Au system earlier by Kolb *et al.*² They deposited a Co(0001) wedge-shaped ultrathin layer ($d_{\text{Co}}=0-8$ Å) sandwiched between a buffer layer (230 Å) and a cap layer (230 Å) of Au(111) onto a glass substrate, and observed GMR up to 5% at low temperature. The MR ratio reaches a maximum value at $d_{\text{Co}}\sim 3$ Å which corresponds to a crossover from a discontinuous (i.e., granular) to a continuous Co layer. Above $d_{\text{Co}}=6$ Å, where the Co layer is continuous,³ the GMR component still appears because of the small magnetic domain sizes.^{2,3} Even taking into account the granular character and the fine domain structure of the Co layer, the MR ratio is quite large for a single ultrathin ferromagnetic layer with much thicker nonmagnetic buffer and

cap layers. The MR is considered to be enhanced by electron channeling and a high specular reflection at the free surface and/or at the interface between the buffer layer and the substrate. If the total thickness of the film is much smaller than the mean free path of the conduction electrons, the current is mainly dominated by electron channeling. This increases the chances of spin-dependent scattering which occurs when electrons go across the ferromagnetic ultrathin layer. An increase of specular reflection enhances the MR ratio by lowering the resistivity of the film. Besides the specularity of the reflection, spin flip scattering at the surface and at the interface may also influence the magnetoresistance. However, this effect is unclear at the present stage.

In order to investigate the effect of electron reflections at the surface and at the interface between the buffer layer and the substrate, we measured the magnetoresistance in a Au(001)/Fe(001)/Au(001) system in which we had been studying quantum well oscillations of the magneto-optical Kerr effect.^{4,5} We selected this system because layer-by-layer growth and lattice matching are better than those in the Au(111)/Co(0001)/Au(111) system.

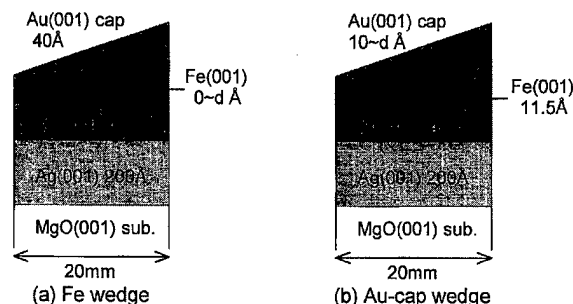


FIG. 1. Schematic cross sections of (a) a Fe wedge-shaped film and (b) an Au cap wedge-shaped film.

^{a)}Electronic mail: yuasa@etl.go.jp

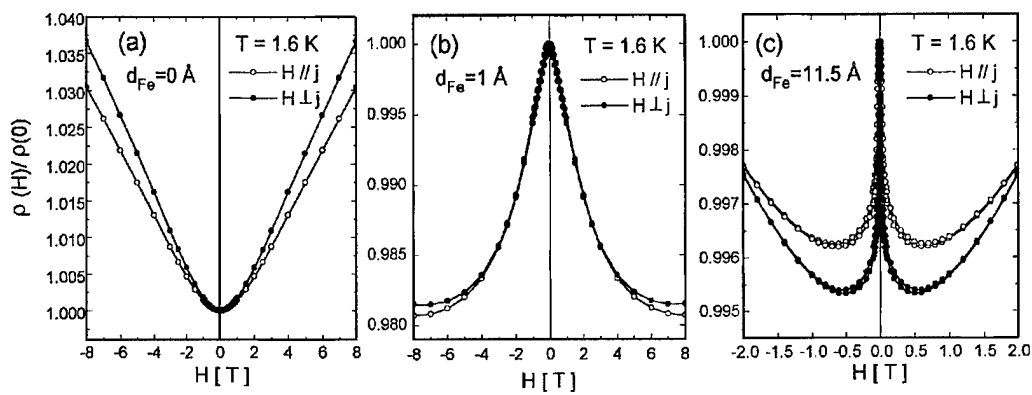


FIG. 2. Typical MR curves in the Fe wedge-shaped samples at 1.6 K for various Fe thicknesses (a) $d_{\text{Fe}}=0$, (b) $d_{\text{Fe}}=1$, (c) $d_{\text{Fe}}=11.5$.

The samples were prepared by the molecular beam epitaxy (MBE) deposition technique under pressure in the 10^{-10} Torr range. Polished MgO(001) single crystals were used as the substrates. The deposition process was observed and controlled by quartz thickness monitors and by reflection high energy diffraction (RHEED). For electric transport measurements, samples with relatively thin buffer layers were prepared as shown in Fig. 1. After thermal flashing the substrate at 850 °C for 10 min, a Ag buffer layer of 200 Å and a Au buffer layer of 40 Å were both deposited at room temperature. To prevent mixing of the Au and Fe, an ultra-thin Fe layer and a Au cap layer were deposited at room temperature. After deposition of the Au(001) buffer and cap layers, a 1×5 RHEED, reconstruction pattern was clearly observed. Wedge-shaped layers were prepared by continuously moving a shutter over the sample during the deposition.

The samples were either Fe wedge shaped [Fig. 1(a)] or Au cap wedge shaped [Fig. 1(b)]. Two Fe wedge-shaped samples were prepared, one with Fe thickness d_{Fe} varying from 0 to 18 Å and the other with d_{Fe} from 0 to 200 Å. For the Au cap wedge, two samples were prepared with d_{Au} ranging from 10 to 50 Å, and from 10 to 250 Å. The minimum thickness of the Au cap layer was set at 10 Å, because below this thickness the Fe layer is oxidized in air.

Quantum well oscillations of the polar Kerr effect were measured as a function of Fe and Au cap layer thickness at room temperature in order to check the quality of the samples by comparing them with those with thicker buffer layers that were studied previously by Kerr effect measurements.^{4,5} The surface morphology and the magnetic domain structure were observed by atomic force microscopy (AFM) and by magnetic force microscopy (MFM), respectively. The electric resistivity was measured by a dc four-probe method at 1.6 K in a magnetic field up to 9 T.

The AFM observation showed that the Au(001) surface in all the samples has a gentle wavy structure with an average period of 1000 Å and an average amplitude of 10 Å. No change of the surface morphology was observed by varying the thicknesses of the Fe and Au cap layers. Clear quantum well oscillations of polar Kerr ellipticity were observed in the Fe wedges with $d_{\text{Fe}} > 4$ Å, indicating good quality of the Fe layer. Ferromagnetic hysteresis curves were also observed for $d_{\text{Fe}} > 4$ Å by a longitudinal Kerr measurement. On the

other hand, no Kerr ellipticity signal was detected for $d_{\text{Fe}} < 4$ Å. This indicates that the Fe layer with $d_{\text{Fe}} < 4$ Å is discontinuous and superparamagnetic at room temperature. The Au cap wedge-shaped films also showed quantum well oscillation of the polar Kerr effect, indicating that there is no oxidation of the Fe layer when $d_{\text{Au cap}} \geq 10$ Å.

Figures 2 and 3 show typical MR curves for various Fe thicknesses in the Fe wedge-shaped films and a MR ratio, $\Delta\rho(H)/\rho(H=0)$, as a function of Fe thickness, respectively. The magnetoresistance of the Fe wedge can be classified into four parts depending on the Fe thickness as follows.

- (1) $d_{\text{Fe}}=0$ [Fig. 2(a)]: The film with no Fe layer simply shows the magnetoresistance of Ag and Au, which arises from the Lorentz force acting on conduction electrons.⁶
- (2) $d_{\text{Fe}}=0.3\text{--}4$ Å [Fig. 2(b)]: The film shows typical granular-type GMR because of the discontinuity of the Fe layer. The MR ratio reaches a maximum in this range as seen in Fig. 3(a).
- (3) $d_{\text{Fe}}=4\text{--}30$ Å [Fig. 2(c)]: The film shows a finite GMR component although the Fe layer is continuous in this range. The difference in the MR ratio in the two field directions ($H \parallel j$ and $H \perp j$) is due to anisotropic MR (AMR) in the Fe layer. The GMR in this range is considered to originate from a fine domain structure although the magnetic domains were not observed by MFM maybe because of too small a stray field. In this

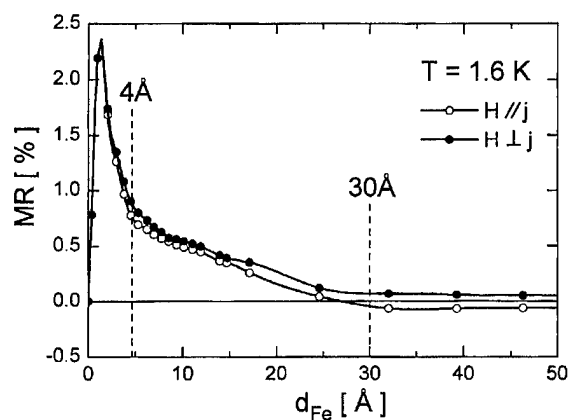


FIG. 3. MR ratio $[\rho(0) - \rho(H)]/\rho(0)$ in the Fe wedge-shaped samples at 1.6 K as a function of Fe thickness, d_{Fe} .

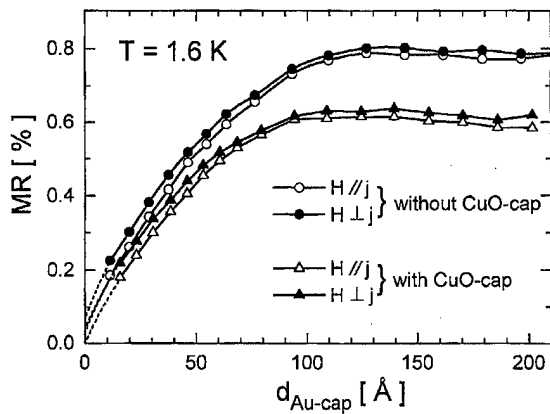


FIG. 4. MR, ratio $[\rho(0) - \rho(H)]/\rho(0)$ in the Au cap wedge-shaped samples at 1.6 K as a function of Au cap thickness, $d_{\text{Au cap}}$.

range, the MR ratio gradually decreases with d_{Fe} (see Fig. 3), which can be attributed to an increase of magnetic domain size, as is also observed in Co(0001) ultrathin films.³

- (4) $d_{\text{Fe}} > 30 \text{ Å}$: The film shows only AMR, with no GMR component. In this range, magnetic domains with average sizes larger than $10 \mu\text{m}$ were observed by MFM. The disappearance of the GMR is consistent with the macroscopic domain size in which there is very little chance for conduction electrons to go from one domain to neighboring domains.

Figure 4 shows the MR ratio $[\rho(0) - \rho(H)]/\rho(0)$ in the Au cap wedge-shaped samples as a function of Au cap thickness, $d_{\text{Au cap}}$. When extrapolating $d_{\text{Au cap}}$ to 0, the GMR component almost vanishes. The MR ratio increases approximately in proportion to $d_{\text{Au cap}}$ when $d_{\text{Au cap}} < 50 \text{ Å}$, and saturates at $d_{\text{Au cap}} \sim 130 \text{ Å}$ above which it slightly decreases with $d_{\text{Au cap}}$. This behavior can be understood as follows. The mean free path of conduction electrons in the Ag and Au layers was roughly estimated to be about $3\text{--}5 \mu\text{m}$ at 1.6 K using the same method as in Ref. 7. Since the total thickness of the film ($260\text{--}500 \text{ Å}$) is much smaller than the mean free path, the current flows mainly by electron channeling (Fig. 5). In the film with no Au cap layer [Fig. 5(a)], conduction electrons with a spin antiparallel to the magnetization of a domain in the Fe layer are reflected on an interface between the Fe and the buffer layers because of spin-dependent scattering, while the electrons with a spin parallel to the magnetization go into the Fe layer and are reflected on the surface.

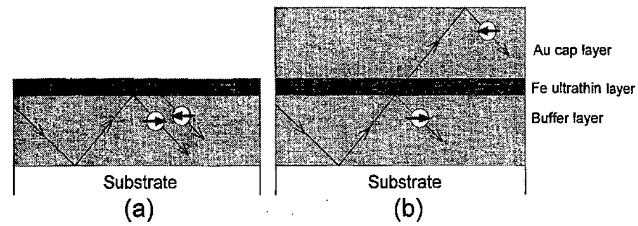


FIG. 5. Schematic illustrations for the paths of conduction electrons in the films (a) without a Au cap layer and (b) with a Au cap layer.

Because the Fe layer is ultrathin, the spin-dependent scattering on the interface barely changes the mean free path of electrons. Therefore, GMR does not appear when there is no cap layer. On the other hand, in the film with Au cap layer, spin-dependent scattering in the Fe layer changes the mean free path of conduction electrons [Fig. 5(b)]. Thus, GMR appears with an increase of the cap layer thickness. The saturation of MR ratio at $d_{\text{Au cap}} \sim 130 \text{ Å}$ can be interpreted as a shunting effect in the cap layer.

Moreover, we have studied the effect of an oxide overlayer on the Au cap wedge-shaped sample. A 30-Å -thick Cu layer was deposited on the Au cap wedge and oxidized in air for one day. The CuO capping increased the film resistivity by 6%. This can be understood by a lower specular reflectivity at the interface between Au and CuO than that at the free surface of Au. On the other hand, MR ratio decreased by 25% as a result of CuO capping (Fig. 4). The large decrease of MR ratio cannot be explained only by the change of a specular reflectivity. This indicates that probability of spin flip scattering during surface reflection is increased by the CuO capping.

This study was supported by the Original Industrial Technology R&D Promotion Program from the New Energy and Industrial Technology Development Organization (NEDO) of Japan.

¹H. Sakakima, Y. Kawawake, and E. Hirota, Abstract of the 15th International Colloquium on Magnetic Films and Surfaces, No. 7–15, 1997.

²E. Kolb *et al.*, J. Magn. Magn. Mater. **147**, 315 (1995).

³R. Allenspach, M. Stampanoni, and A. Bischof, Phys. Rev. B **65**, 3344 (1990).

⁴T. Katayama, Y. Suzuki, M. Hayashi, and A. Thiaville, J. Magn. Magn. Mater. **126**, 527 (1993).

⁵W. Geerts, Y. Suzuki, T. Katayama, K. Taninaka, K. Ando, and Y. Yoshida, Phys. Rev. B **50**, 12 581 (1994).

⁶I. Campbell and A. Fert, *Ferromagnetic Materials*, edited by E. P. Wohlfarth (North-Holland, Amsterdam, 1982), Vol. 3.

⁷D. C. Larson and B. T. Botko, Appl. Phys. Lett. **5**, 155 (1964).

Magnetic properties of very thin single and multilayer NiFeCo and CoFe films deposited by sputtering

D. Wang and J. M. Daughton

Nonvolatile Electronics Inc., 11409 Valley View Road, Eden Prairie, Minnesota 55344

K. Bussmann and G. A. Prinz

Naval Research Laboratory, 4555 Overlook Ave. S. W., Washington, D.C. 20375

As the size of the giant magneto resistive (GMR) devices continues to decrease into submicrometer regime, the demagnetizing field from the magnetic layers will increase to very high values, prohibiting switching with a reasonably small current. The most feasible way to reduce it is to make the magnetic layers thinner. Single layers of NiFeCo and CoFe films as well as multilayers consisting of these with various underlayers have been deposited by rf diode sputtering in a magnetic field. NiFeCo becomes nonmagnetic at 15, 10, and 6 Å when using Ta, Si₃N₄, and Cu underlayers, respectively. The magnetization of NiFeCo films sandwiched with Cu decreases as the films become thinner, indicating that about one atomic layer loses its magnetic moment at each interface with Cu. The induced magnetic anisotropy is a strong function of the NiFeCo film thickness, changing from 7 Oe for 20 Å to 17 Oe for 100 Å. CoFe films lose very little magnetic moment at the interfaces with Cu. Multilayers of [NiFeCo/Cu/CoFe/Cu] with different Cu underlayer thickness have been made and the magnetic and GMR properties show a strong dependence on the Cu buffer layer thickness due to different interface roughnesses. With proper designing of the interfaces, these very thin magnetic films have high potential for ultrahigh-density magnetic memory and other applications. © 1998 American Institute of Physics.

[S0021-8979(98)37711-7]

For future ultrahigh-density giant magneto resistive (GMR) magnetic random access memory (MRAM) and other applications, the size of the devices will continue to decrease to submicrometer and beyond. Accordingly, the demagnetizing field will increase as the size gets smaller,¹ leading to a prohibitively high switching field which needs to be surpassed by a current in the device. In order to reduce this demagnetizing field the most feasible way is to use very thin magnetic layers. Though other means such as molecular beam epitaxy (MBE) are capable of making very thin magnetic layers,² sputtering remains the most practical technique for manufacturing. The objectives of this study are to identify how thin a magnetic layer can be made with sputtering, to find out if they are compatible with other materials which have to be in contact with them, and to determine their magnetic properties. NiFeCo and CoFe films are chosen because of their excellent magnetic properties in bulk form and extensive usage in practical film applications.³

Films were deposited by rf diode sputtering in a PE2400 system equipped with four 8 in. targets, a single wafer load lock, and a water cooling wafer chuck.⁴ The deposition parameters are 175 W power, 750 V target bias voltage, 20 mTorr ultrapure Ar, and a target-substrate spacing of 1.5 in. The substrates are 4 in. Si(100) wafers coated with 2000 Å of Si₃N₄ by low pressure chemical vapor deposition (LPCVD). The base pressure was better than 1.5×10^{-7} Torr before deposition. A magnetic field of 1.6 kA/m (20 Oe) was applied during magnetic layer deposition to induce an easy magnetic axis. The entire deposition process was computer controlled.

Magnetic properties were measured using a vibrating

sample magnetometer (VSM) and an alternating gradient force magnetometer (AGM). Magneto-transport properties were measured using a computer controlled four-point probe.

NiFeCo films of varying thickness are deposited on different buffer layers of Ta, Si₃N₄, and Cu. NiFeCo films become nonmagnetic at a thickness of 15, 10, and 6 Å on Ta, Si₃N₄, and Cu buffer layers, and with Ta, Ta, and Cu over coatings, respectively. Among these three buffer layers, Cu is the best in retaining the magnetization of NiFeCo. On Cu buffer layers the NiFeCo magnetization decreases as the film becomes thinner, as shown in Fig. 1. It is estimated that there is a magnetically dead layer of about 2 Å at each interface of NiFeCo with Cu, except at 6 Å nominal thickness where the magnetization becomes zero. The magnetization of 100 Å NiFeCo is about 1100 emu/cc, similar to the bulk value at this stoichiometry.⁵ Figure 1(b) shows the thickness dependence of the induced anisotropy field H_k . H_k is about 17 Oe at 100 Å, decreases when the film is thinner, is about 7 Oe at 20 Å, and becomes negligibly small when the film is much thinner than 20 Å. When the Co concentration in NiFeCo is increased from 20 at. % to 40 at. %, H_k increases to 23 Oe for a 100 Å film and 11 Oe for a 20 Å film, as shown in Fig. 1(b).

Figure 2 shows the CoFe thickness dependence of the magnetization with Cu buffer and over coats. These CoFe films have little moment loss (~ 0.5 Å at each interface) with a magnetization of about 1450 emu/cc, similar to its bulk value at this stoichiometry.⁵ The difference in their magnetization reductions for CoFe and NiFeCo is likely due to the fact that Ni is metallurgically miscible with Cu, and Co and Fe are not.

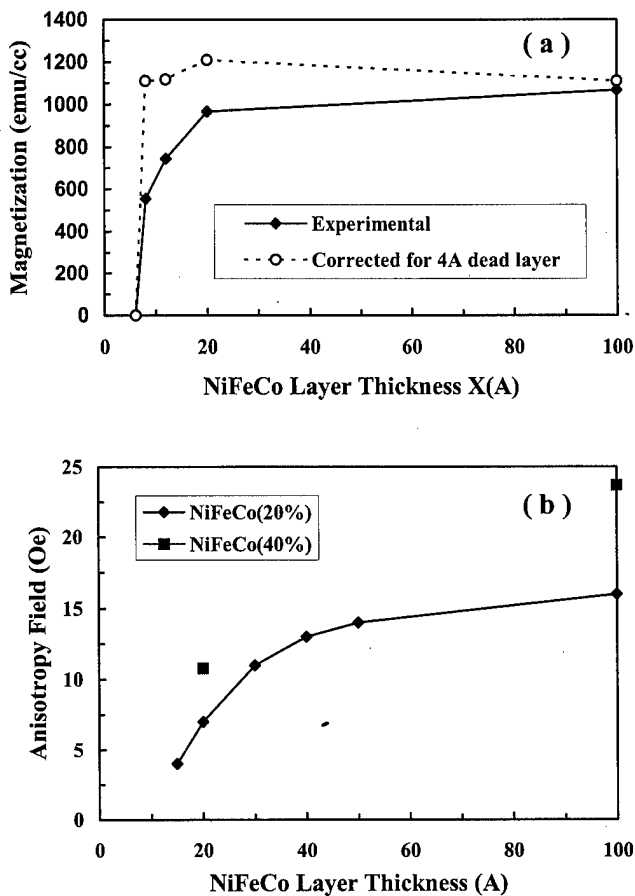


FIG. 1. Thickness dependence of magnetization (a) and anisotropy field H_K (b) for NiFeCo single layers of varying thickness sandwiched between Cu buffers and over coats.

Figure 3 shows the hysteresis loops of a 100 Å NiFeCo film with (a) and without (b) a Cu buffer layer of 1500 Å. A thick Cu underlayer will be necessary in vertical GMR MRAM as the bottom conductor. The thick Cu underlayer increases the coercivity of the NiFeCo layer dramatically, to

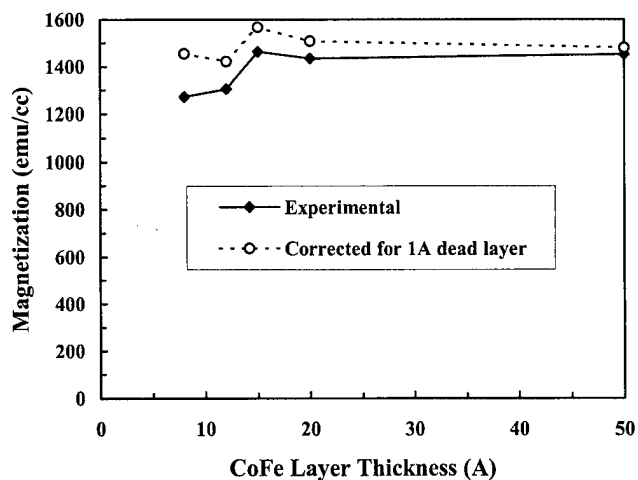


FIG. 2. Thickness dependence of the magnetization of CoFe single layers sandwiched between a Cu underlayer and over coat.

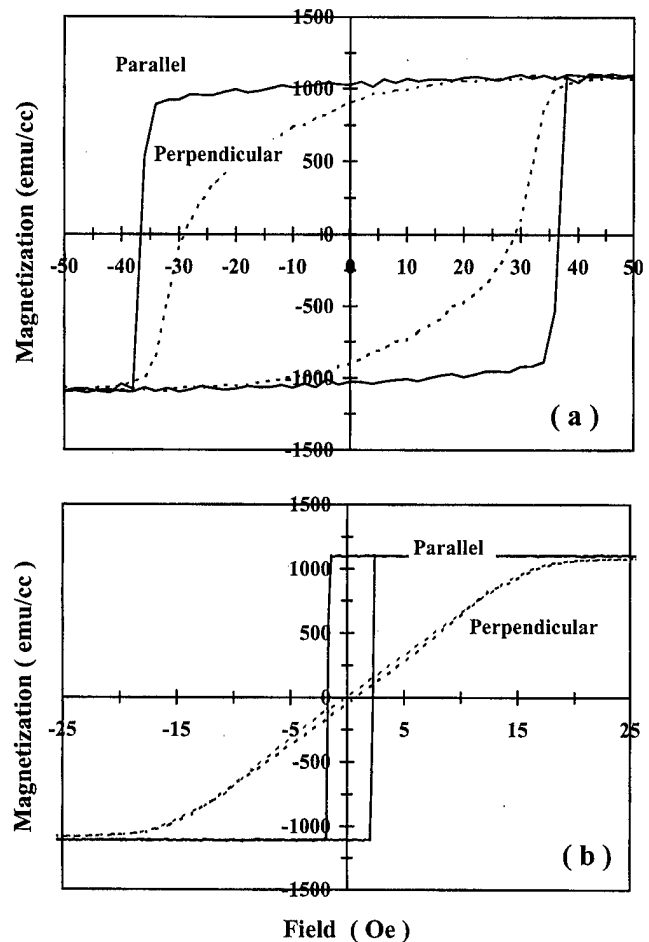


FIG. 3. Hysteresis loops of 100 Å NiFeCo films with (a) and without (b) a 1500 Å buffer layer, with applied field parallel and perpendicular to the induced easy axes. Notice the difference in field scales.

37 Oe at 1500 Å Cu from 2 Oe with no Cu. This coercivity value is about twice as much as the intrinsic induced anisotropy field.

In order to search for the origin of the high coercivity with thick Cu underlayers, atomic force microscopy (AFM) images were taken with tapping mode on Si_3N_4 and Cu 1500 Å, as shown in Fig. 4. Cu 1500 Å has much larger grains and rougher surface than Si_3N_4 . The rms roughnesses are 15 and 2 Å for Cu 1500 Å and Si_3N_4 , respectively. It is clear that the rougher surface of the Cu causes the increase in coercivity of NiFeCo. Similarly, a CoFe single layer has a coercivity of 13 Oe with a 40 Å Cu buffer layer and 50 Oe with a 1500 Å Cu buffer layer.

Figure 5 shows the hysteresis loops of dual bilayers of $-\text{XCu}[\text{12NiFeCo}/\text{75Cu}/\text{11CoFe}/\text{75Cu}]_2$ with a varying Cu buffer layer thickness X . The switching fields for both the soft NiFeCo layers and the hard CoFe layers increase as the Cu buffer layer becomes thicker, because the interface becomes rougher. The thick Cu spacer of 75 Å is required to totally eliminate the exchange coupling between the magnetic layers. The antiparallel state is only realized due to the difference in the coercivities of the NiFeCo and CoFe layers.

Figure 6 gives current-in-plane (CIP) GMR plots for the dual bilayers with a 40 Å Cu buffer layer (a) and a 1500 Å buffer layer (b). Due to the thick Cu spacers as well as the

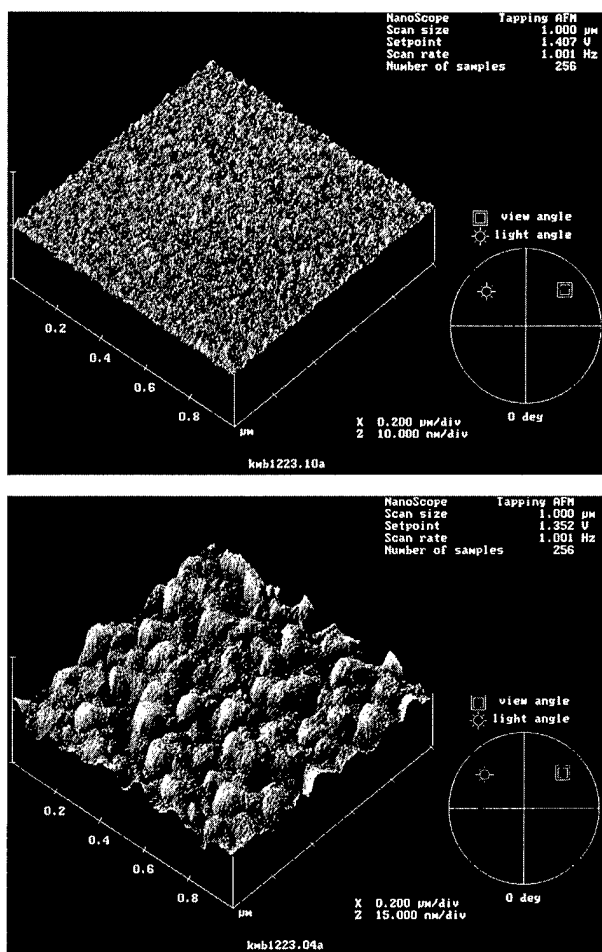


FIG. 4. AFM surface images of Si(100)/Si₃N₄ 2000 Å (a) and Si(100)/Si₃N₄ 2000 Å/Cu 1500 Å (b) using tapping mode. The rms roughnesses are 15.0 and 2.0 Å, respectively, with and without Cu. The vertical scale z is 10 nm for (a) and 15 nm for (b).

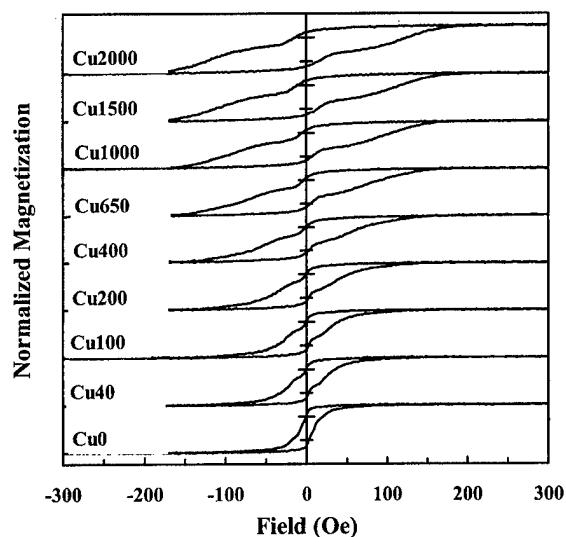


FIG. 5. Hysteresis loops of dual bilayers of $-XCu-[12NiFeCo/75Cu/11CoFe/75Cu]_2$ with varying Cu buffer layer thickness X . All numbers are in angstroms.

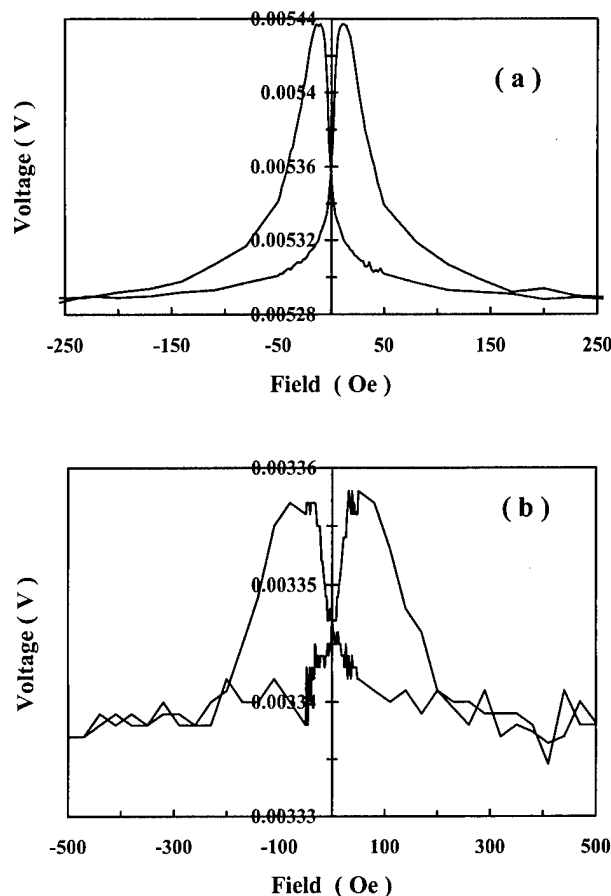


FIG. 6. Magneto resistive traces of $-[12NiFeCo/75Cu/11CoFe/75Cu] \times 2$ with 40 Å Cu (a) and 1500 Å Cu (b) buffer layer. Notice the difference in field scales.

thick Cu buffer layer the CIP GMR is only a few percent to a fraction of a percent. Current perpendicular to plane (CPP) GMR on patterned devices is about 16%, with a high switching field around 200 Oe mainly from the rough surface.⁶ In order to make the device work at a reasonably low switching field, the starting surface has to be made smoother through either improved sputtering or a polishing technique such as chemical-mechanical polishing (CMP).

The authors appreciate helpful discussions with Dr. Jimmy Zhu, Dr. Mark Tondra, Dr. ShuFan Cheng, Dr. Jim Krebs, and Dr. Peter Lubitz. The authors also thank Mike Jackson from RIM and Professor Jack Judy from MINT, both at the University of Minnesota, for their help in VSM measurements. This work was supported by NRL.

¹W. Vavra, S. F. Cheng, A. Fink, J. J. Krebs, and G. A. Prinz, Appl. Phys. Lett. **66**, 2579 (1995).

²R. K. Kawakami, E. J. Escorcia-Aparicio, and Z. Q. Qiu, J. Appl. Phys. **79**, 4532 (1996).

³J. M. Daughton and Y. J. Chen, J. Appl. Phys. **29**, 2705 (1993).

⁴D. Wang, J. Anderson, and J. M. Daughton, IEEE Trans. Magn. **33**, 3520 (1997).

⁵R. M. Bozorth, *Ferromagnetism*, edited by W. Perkins (IEEE, New York, 1993).

⁶K. Bussmann, S. F. Cheng, G. A. Prinz, Y. Hu, D. Wang, and R. Beech (these proceedings).

Ferromagnetic resonance linewidth in thin films coupled to NiO

R. D. McMichael,^{a)} M. D. Stiles, P. J. Chen, and W. F. Egelhoff, Jr.
National Institute of Standards and Technology, Gaithersburg, Maryland 20899

The out-of-plane angular dependence of the ferromagnetic resonance linewidth, ΔH , has been measured for thin magnetic films coupled to NiO and for uncoupled control films. In the control films, ΔH is described by nearly angle-independent damping parameters. In the NiO-coupled films, however, the damping was found to depend strongly on magnetization orientation, with linewidth values comparable to the control samples at normal orientation, but several times larger when the magnetization lies in plane. The additional linewidth in the NiO-coupled films follows the angular dependence of the number of nearly degenerate spin wave modes, in agreement with the predictions of a two-magnon scattering model of damping which incorporates a spin wave dispersion relation suitable for ultrathin films. © 1998 American Institute of Physics. [S0021-8979(98)37811-1]

I. INTRODUCTION

Increased ferromagnetic resonance linewidth^{1,2} is a part of the complex phenomenology of exchange anisotropy that includes shifted hysteresis loops,³ rotational hysteresis,⁴ shifts in the Brillouin scattering frequency,⁵ and ferromagnetic resonance (FMR) field.^{1,2,6} Explanations of the increased linewidth in ferromagnet/antiferromagnet bilayers have been based on a dispersion of resonance fields due to dispersion of the exchange bias.^{1,2} This article presents, for the first time, measurements of the FMR linewidth, ΔH , as a function of the magnetization orientation from in-plane to film normal. These results are compared with the predictions of a two-magnon model of FMR damping.

II. EXPERIMENT

The samples in this study were deposited by dc magnetron sputtering in 0.25 Pa (2 mTorr) Ar. The base pressure before depositing a film was approximately 10^{-6} Pa (10^{-8} Torr) of which 90% was hydrogen. The films consisted of Ni₈₀Fe₂₀, Co, and Co₃₀Ni₃₅Fe₃₅ deposited on 50 nm NiO and capped with Au or Ta, and the magnetic film thickness ranged from 4.0 to 10.0 nm. These films were deposited in a field which set the direction of the exchange anisotropy field, \mathbf{H}_{ex} . The corresponding control films were deposited with 2.0 nm layers of Ta separating the magnetic films from the NiO.

Ferromagnetic resonance spectra were taken using an x-band spectrometer operating at 9.78 GHz. The samples were mounted on the side of a quartz rod passing through the center of the TE₁₀₂ microwave cavity, and sample orientation was controlled by a goniometer with a precision of $\pm 0.12^\circ$. Samples were mounted with \mathbf{H}_{ex} directed parallel to the rotation axis, along the z direction (see Fig. 1) so that the applied field, \mathbf{H} was always perpendicular to \mathbf{H}_{ex} . Resonance fields and peak-to-peak field linewidths of 10 nm thick Ni₈₀Fe₂₀ films on NiO and on Ta are shown in Fig. 2.

The free energy, \mathcal{F} , of the magnetization is modeled by

$$\mathcal{F} = K_u \sin^2 \theta \sin^2 \phi + K_a \sin^2 \theta \cos^2 \phi - \mu_0 \mathbf{M} \cdot \mathbf{H} - \mu_0 \mathbf{M} \cdot \mathbf{H}_{\text{ex}} - \mu_0 \mathbf{M} \cdot \mathbf{H}_{\text{ra}}, \quad (1)$$

where K_u and K_a are uniaxial anisotropies with hard axes directed along the y and x directions, respectively. \mathbf{H} is the applied field and \mathbf{H}_{ra} is a rotatable anisotropy field, $\mathbf{H}_{\text{ra}} \parallel \mathbf{M}$, included to model an isotropic negative resonance field shift.⁶ The angles are defined in Fig. 1. The resonance condition is given by

$$(\omega/\gamma)^2 = (M^2 \sin^2 \theta)^{-1} [\mathcal{F}_{\theta\theta} \mathcal{F}_{\phi\phi} - \mathcal{F}_{\theta\phi}^2], \quad (2)$$

where the subscripts indicate partial derivatives, evaluated at values of θ and ϕ which minimize \mathcal{F} , and $\gamma = g\mu_B/\hbar \approx 1.76 \times 10^{11} \text{ T}^{-1} \text{ s}^{-1}$.

The H_{res} data was fit using an orthogonal least-squares algorithm⁷ to obtain values for the parameters in Eq. (1). The fit parameters are then used to calculate ϕ and values of $d\omega/dH$ corresponding to each data point.

While the measurements were made by sweeping H at fixed ω , theoretical linewidth calculations are simpler at fixed H . To make comparisons with theoretical results, values for $\Delta\omega$ are obtained from the ΔH data using $\Delta\omega = (d\omega/dH)\Delta H$ where $d\omega/dH$ is calculated numerically using parameters obtained from the H_{res} fit described above. Plots of $\Delta\omega/\gamma$ vs ϕ for the 10 nm thick Ni₈₀Fe₂₀ samples are shown in Fig. 3. There is a smooth increase in $\Delta\omega$ in the NiO coupled film as \mathbf{M} is rotated from the sample normal (90°) to in-plane (0°). In contrast, $\Delta\omega$ does not depend strongly on ϕ for the Ni₈₀Fe₂₀ film on Ta. Other films with different thick-

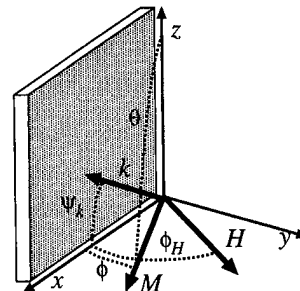


FIG. 1. Coordinate system used in to describe the orientation of \mathbf{M} , \mathbf{H} , and \mathbf{k} with respect to the film.

^{a)}Electronic mail: robert.mcmichael@nist.gov

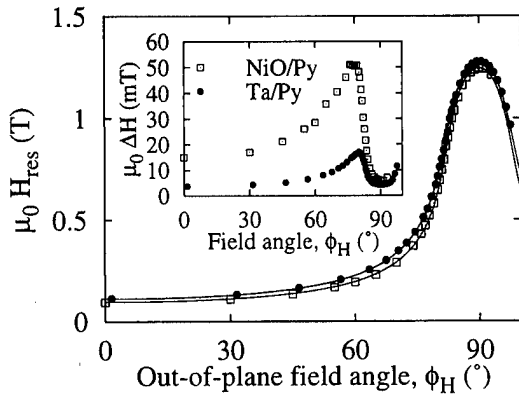


FIG. 2. Resonance fields and linewidths (inset) for 10 nm thick films of $\text{Ni}_{80}\text{Fe}_{20}$ on NiO and on Ta. The solid lines are fits to the H_{res} data.

nesses and compositions described above were measured, and the results show very similar linewidth behavior.

III. TWO-MAGNON THEORY

The ferromagnetic film is modeled as a $N_x \times N_y \times N_z$ rectangular array of spins with lattice parameter a . The thickness of the film, d , is given by $d = N_y a$. The coordinate system used to describe the orientation of \mathbf{M} , \mathbf{H} , and the spin wave propagation vector, \mathbf{k} , is shown in Fig. 1.

In a uniform film, the normal modes can be described as a uniform precession mode, which couples to the microwave excitation field, and a manifold of spin wave modes which are not directly excited. Nonuniformities will induce coupling between the normal modes, leading to a broadening of the resonance.

The two-magnon model of FMR damping⁸⁻¹⁰ treats nonuniformities as perturbations. The scattering rate, $\lambda_{0,k \rightarrow \lambda}$, of uniform precession, or $k=0$, magnons into other, $k \neq 0$ spin wave mode is

$$\lambda_{0,k \rightarrow \lambda} = \frac{2\pi}{\hbar} \sum_k |A_k|^2 \delta(\hbar\omega_0 - \hbar\omega_k), \quad (3)$$

where A_k is the coefficient of the perturbation Hamiltonian term which couples the uniform precession and spin wave modes. As λ represents the rate of decay of a population of

$k=0$ magnons, it also represents a contribution to the frequency linewidth, $\Delta\omega = \lambda + \delta\omega_0$, of continuously driven uniform precession.

If the inhomogeneity is restricted to the interface, the perturbation Hamiltonian can be modeled as an exchange bias or anisotropy field, $H_p(\mathbf{r})$, acting on the first layer of atoms in the ferromagnet. This field varies randomly from grain to grain along the interface, but is correlated over a distance, ξ , corresponding to a grain size. When the expectation value of $|A_k|^2$ is calculated using $A_k = \gamma\hbar\mu_0/\sqrt{N}H_p(\mathbf{k})^9$ under the assumption that $\langle H_p(\mathbf{r})H_p(\mathbf{r}') \rangle \approx \langle H_p^2 \rangle \exp[-|\mathbf{r}-\mathbf{r}'|/\xi]$,

$$\lambda = \frac{2\pi\gamma^2\mu_0^2\langle H_p^2 \rangle}{N_x N_z d^2} \sum_k \frac{2\pi\xi^2}{[1-(k\xi)^2]^{3/2}} \frac{\delta\omega_k/\pi}{[\delta\omega_k^2 + (\omega_0 - \omega_k)^2]}. \quad (4)$$

In this expression, the δ function in Eq. (3) has been replaced by a Lorentzian with $\delta\omega_k$ chosen to represent the intrinsic spin wave linewidth.

The spin wave dispersion relation, $\omega_k = \omega(k, \psi_k, H, \phi_h, M, \phi, d)$, is the source of angular dependence in Eq. (4). It is derived assuming uniform precession through the thickness of the film because in the thickness range of interest, spin waves with components of \mathbf{k} perpendicular to the plane of the film will have $\omega_k > \omega_0$ and will not count in the sum. Starting with $d\mathbf{M}/dt = -|\gamma|\mathbf{M} \times \mathbf{H}$ and using magnetostatic fields given by

$$H_y^D(\mathbf{k}) = -NkM_y(\mathbf{k}), \quad (5)$$

$$H_{x,z}^D(\mathbf{k}) = -\mathbf{k}[M_x(\mathbf{k})k_x + M_z(\mathbf{k})k_z](1 - N_k)/|k|^2, \quad (6)$$

where $N_k = [1 - \exp(-kd)]/kd$,¹¹ the resulting dispersion relation is

$$\begin{aligned} (\omega_k/\mu_0\gamma)^2 = & [H_i + Dk^2 + M(1 - N_k)\sin^2 \psi_k] \\ & \times [H_i + Dk^2 + MN_k \cos^2 \phi \\ & + M(1 - N_k)\sin^2 \phi \cos^2 \psi_k] \\ & - [M(1 - N_k)\cos \psi_k \sin \psi_k \sin \phi]^2, \end{aligned} \quad (7)$$

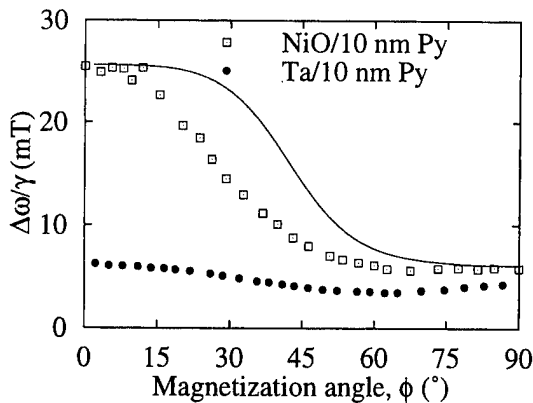


FIG. 3. Frequency linewidth, $\Delta\omega/\gamma$ for 10 nm thick $\text{Ni}_{80}\text{Fe}_{20}$ films on NiO and Ta plotted as a function of magnetization orientation. The solid line is the prediction of the two-magnon model.

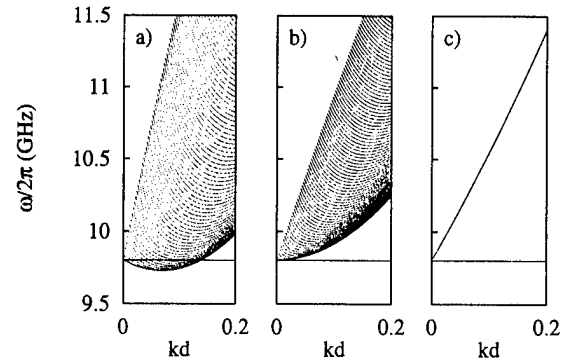


FIG. 4. Spin wave manifolds calculated for a 10 nm thick $\text{Ni}_{80}\text{Fe}_{20}$ film with (a) \mathbf{M} oriented in the plane of the film, (b) at $\phi=45^\circ$, and (c) normal to the film. The applied field is set to give $\omega_0/2\pi = 9.8$ GHz in each case.

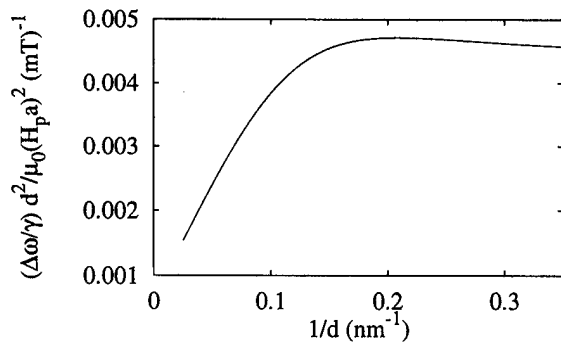


FIG. 5. Thickness dependence of the number of degenerate spin waves calculated for a $\text{Ni}_{80}\text{Fe}_{20}$ film at 34 GHz, using $\mu_0 \delta \omega_k / \gamma = 10$ mT and $\xi = 40$ nm.

where H_i is the internal static magnetic field, D is the spin wave dispersion constant, and the angles are defined in Fig. 1. Spin wave manifolds calculated from Eq. (7) are shown in Fig. 4.

The solid line in Fig. 3 is the result of the two-magnon theory for a 10 nm film of $\text{Ni}_{80}\text{Fe}_{20}$ assuming that $\xi = 40$ nm, which is a typical grain size for these films. To match the experimental data at 0° and 90° , the value of $\mu_0 H_p a / d$ was adjusted to 35 mT and an intrinsic linewidth $\delta \omega_0 = \delta \omega_k = 5$ mT was used.

It is helpful to think about the result in Eq. (4) in terms of two parts: the terms outside the summation having to do with the strength of the scattering of spin waves, and the summation over magnon wavevectors which is essentially a weighted count of the number of spin wave modes having wave vectors matching the spatial fluctuations of the perturbing field and with frequencies close enough to ω_0 to accept the scattered energy. The angular dependence of $\Delta \omega$ is contained entirely within the mode counting terms through ω_k , and the thickness dependence is shared by the mode counting and the scattering strength terms.

The quantity $\Delta \omega d^2 / (H_p^2 a^2)$ contains only the thickness dependence of the mode counting, with the explicit $1/d^2$ thickness dependence of the scattering strength factored out. This quantity is plotted in Fig. 5 as a function of inverse film thickness for $\text{Ni}_{80}\text{Fe}_{20}$ films with \mathbf{M} in plane ($\phi = 0$).

The thickness dependence of the two-magnon model, with an explicit $1/d^2$ dependence in the scattering strength and a $1/d$ thickness dependence in the mode counting does

not agree well with published results^{1,2} which show the linewidth increasing linearly with $1/d$ for $d > 10$ nm and decreasing for a thinner sample. The $1/d^2$ dependence of the scattering strength can be eliminated if the perturbing field is assumed to act on spins throughout the thickness of the sample, rather than on the surface spins. It is interesting to note that the thickness dependence of the mode counting part alone, without the implicit thickness dependence of the scattering strength, is very similar to that of previously published results (see Ref. 2, Fig. 5).

IV. CONCLUSIONS

The experimental results show consistently that for magnetic films deposited on NiO, the FMR linewidth is several times larger for \mathbf{M} in plane than for \mathbf{M} normal to the film, and that the frequency linewidth changes smoothly as a function of magnetization orientation. In agreement with the two-magnon model, these results are consistent with a proportionality between the frequency linewidth and the number of nearly degenerate spin wave modes.

If the perturbation is restricted to the interface, the two-magnon model predicts an explicit $1/d^2$ dependence multiplying the $\sim 1/d$ dependence of the mode counting. This result is not supported by previous experimental data.^{1,2} However, if the perturbation is allowed to act throughout the thickness of the film, there is no explicit thickness dependence and the agreement with experiment is quite good.

¹V. S. Speriosu, S. S. P. Parkin, and C. H. Wilts, *IEEE Trans. Magn.* **23**, 2999 (1987).

²W. Stoecklein, S. S. P. Parkin, and J. C. Scott, *Phys. Rev. B* **38**, 6847 (1988).

³W. H. Mielkejohn and C. P. Bean, *Phys. Rev.* **102**, 1413 (1956).

⁴D. Paccard, C. Schlenker, O. Massenet, R. Montmory, and A. Yelon, *Phys. Status Solidi* **16**, 301 (1966).

⁵A. Ercole, T. Fujimoto, M. Patel, C. Daboo, R. J. Hicken, and J. A. C. Bland, *J. Magn. Magn. Mater.* **156**, 121 (1996).

⁶R. D. McMichael, M. D. Stiles, P. J. Chen, and W. F. Egelhoff, Jr. (unpublished).

⁷P. T. Boggs and J. E. Rogers, *Contemporary Mathematics* **112**, 183 (1990).

⁸M. Sparks, R. Loudon, and C. Kittel, *Phys. Rev.* **122**, 791 (1961).

⁹H. B. Callen, *Fluctuation, Relaxation and Resonance in Magnetic Systems*, edited by D. Ter Haar (Plenum, New York, 1961), p. 69; C. Warren Haas and H. B. Callen, *Magnetism*, edited by G. T. Rado and H. Suhl (Academic, New York, 1963), Vol. 1, p. 449.

¹⁰M. J. Hurben, D. R. Franklin, and C. E. Patton, *J. Appl. Phys.* **81**, 7458 (1997).

¹¹K. J. Harte, *J. Appl. Phys.* **39**, 1503 (1968).

Magnetic ordering in Co films on stepped Cu(100) surfaces

S. T. Coyle and M. R. Scheinfein

Dept. of Physics and Astronomy, PSF 470 Box 871504, Arizona State University, Tempe, Arizona 85287

Ultrathin films of Co were grown on Cu(100) and characterized by nanometer resolution secondary electron microscopy, Auger electron spectroscopy, and the surface magneto-optic Kerr effect. An unexpected out-of-plane remanence was detected in many films. The anisotropy of atoms near defects along the Co/vacuum interface calculated via the Néel model indicates that atoms at the bottom corner of a step edge are canted out-of-plane. Full three-dimensional micromagnetics simulations which incorporate site specific anisotropy (including step edges, kinks, and voids) have been performed. Simulations with unidirectional arrays of $[1\bar{1}0]$ steps, such as vicinal surfaces, do not exhibit out-of-plane remanence. Simulations with facets consisting of connected $[110]$ and $[1\bar{1}0]$ steps exhibit out-of-plane remanence of 0.03. This is lower than the experimental value of 0.11. © 1998 American Institute of Physics. [S0021-8979(98)37911-6]

I. INTRODUCTION

Magnetic surface anisotropies play a key role in determining the magnetic properties of thin films and multilayers.¹ Recently the anisotropy of steps has been found to be important in understanding the magnetic behavior of some systems.²⁻⁴ Since the roughness of the Co/Cu interface plays a key role in determining GMR properties,⁵ characterizing the Co/Cu interface including the effect of defects is important. Ultrathin films of Co were grown on Cu(100) in order to study the morphology and the resulting magnetic properties at early stages of growth. The films were characterized by nanometer resolution secondary electron microscopy, Auger electron spectroscopy, and the surface magneto-optic Kerr effect (SMOKE).⁶ An unexpected out-of-plane remanence was detected in many films.

The cause of this out-of-plane component of the magnetization could be related to film morphology at the early stages of growth. One possible mechanism which may produce out-of-plane magnetization is defect related anisotropy on imperfect surfaces. The anisotropy of atoms near defects along the Co/vacuum interface has been calculated. Atoms along the bottom corner of a $\langle 110 \rangle$ step which have strong uniaxial anisotropy canted out-of-plane, may couple to the spins of nearby atoms. A significant out-of-plane component to the magnetization may occur for some critical density of these sites. This short article will address the feasibility of this mechanism for the origin of the perpendicular component to the observed magnetization.

Co grown on substrates with high defect densities resulted in dramatic faceting of step edges and the creation of rectangular pits.⁶ The anisotropy of atoms of low coordination created by this morphology may significantly affect the magnetization of the film, and may thus affect the GMR properties of multilayers. To evaluate the equilibrium magnetic microstructure in such films, and to determine if the anisotropy at sites with low symmetry may be responsible for the observed out-of-plane remanence, full three-dimensional micromagnetics simulations were performed incorporating the calculated site specific anisotropies.

II. EXPERIMENTAL RESULTS

Morphological characterization with concurrent magnetization measurements was obtained from Co grown on bulk single crystal Cu(100) samples.⁶ Cu substrates were cleaned by repeated Ar^+ ion sputter and anneal (600 C) cycles. Co was grown by electron-beam evaporation at rates between 0.05 ML/min and 0.2 ML/min at pressures $< 5 \times 10^{-10}$ mbar (1 ML = 1.53×10^{15} atoms/cm²). Samples were transferred *in situ* into the SMOKE chamber for magnetic characterization, then transferred *in situ* into an ultrahigh vacuum scanning transmission electron microscope for nanometer resolution secondary electron (SE) imaging.⁷ SE micrographs revealed complex growth morphologies which varied between different films. Many films contained high densities of steps, kinks, and facets.

Co/Cu(100) films in this study became ferromagnetic at room temperature at about 1.7 ML. Zero field susceptibility in the paramagnetic regime and remanence in the ferromagnetic regime generally increased with coverage. In many films a second magnetic phase was detected with out-of-plane remanence and a coercivity 5–10 times the in-plane value which increased with Co coverage. Figure 1 contains such Kerr hysteresis loops taken in the longitudinal [Fig. 1(a)] and polar [Fig. 1(b)] geometries⁷ from a 2 ML thick film. As a result of the 45° incident scattering angle, polar signals were five times stronger than the longitudinal signals.⁸ The out-of-plane component of the magnetization in the film in Fig. 1 is therefore ~ 0.11 .

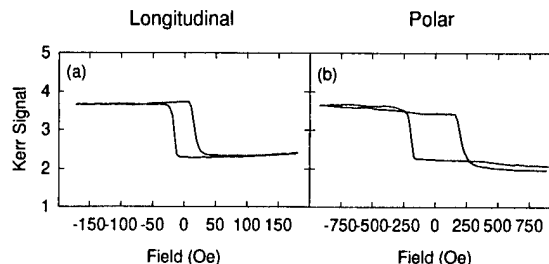


FIG. 1. Kerr hysteresis loops from a sample exhibiting out-of-plane remanence. Part (a) was taken in the longitudinal geometry and (b) was taken in the polar geometry. The Kerr signal is given in arbitrary units, and the scales in (a) and (b) are the same.

III. MICROMAGNETICS SIMULATIONS

The anisotropy of face centered cubic atoms has been calculated for reduced symmetry structures such as steps and kinks following the Néel model of anisotropy,⁹ and including the effects of strain.¹⁰ In agreement with Chuang *et al.*,¹¹ the anisotropy of atoms along the bottom corner of a step edge (step corner) was found to be uniaxial and canted out-of-plane, while the anisotropy of atoms along the top corner of a step (step edge) was uniaxial in-plane along the step direction. The anisotropy of bulk atoms and surface atoms was biaxial in-plane along $\langle 110 \rangle$. The anisotropy of kink edge atoms was biaxial in-plane along $\langle 110 \rangle$ and that of kink corner atoms was uniaxial in-plane along the kink direction. A summary of these results is given in Table I, and a schematic of a Co surface identifying individual sites is presented in Fig. 2. Strain due to the misfit of face-centered-cubic (fcc) Co and fcc Cu has been included in all anisotropy calculations except when noted.

The anisotropy terms (Table I) proportional to $\cos^2 \theta$ extract a high penalty for magnetization out of the plane. Of the remaining terms, those proportional to $L(r_0)$ are larger by a factor of 10^2 than terms containing e_0 or $Q(r)$. The step corner, kink-in corner and kink-out corner sites hold promise for out-of-plane magnetization due to the term proportional to $\sin \theta \cos \theta$. The step corner has an energy minimum which is out-of-plane, while the kink-in corner and kink-out corner sites have energy minima which are in-plane.

These atomic, site specific anisotropy energies have been incorporated into micromagnetics simulations¹² of Co on stepped Cu(100). The simulation searches for solutions to the Landau-Lifshitz-Gilbert equation. The following energies were included: exchange energy, site-specific anisotropy energy, magnetostatic self-energy, and external magnetostatic field energy. The saturation magnetization, exchange stiffness, gyromagnetic frequency gamma, and damping con-

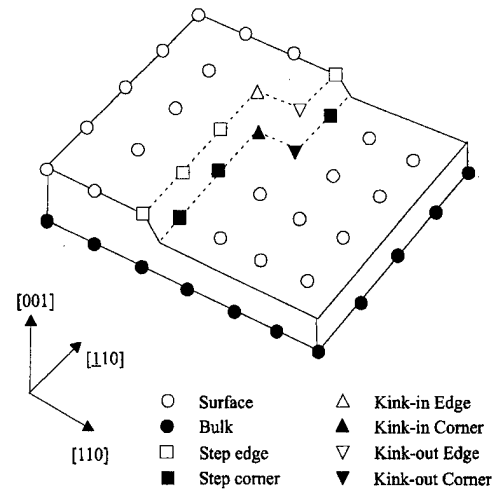


FIG. 2. Schematic representation of atomic sites in the vicinity of a kinked $\langle 110 \rangle$ step. The anisotropy of these sites is given in Table I.

stant alpha were set to the bulk values for Co. This is a continuum model which has been discretized at atomic length scales.

The micromagnetic structure of two monolayer (ML) films has been simulated where the top layer consists of a terrace one half the width of the bottom layer. The two step edges in the top layer were aligned along $[1\bar{1}0]$ or $[100]$. In some simulations kinks were inserted into the step edges at regular intervals and the terrace widths were varied. The simulations used periodic boundary conditions in both in-plane directions. The system was discretized into cells with sides of length $a_0/\sqrt{2}$ on a simple cubic lattice, where a_0 is 0.361 nm. This insured that the volume of the region with

TABLE I. Anisotropy energies for fcc (100) sites described in the text and shown schematically in Fig. 2. Derivations of anisotropy energy and the value of the constants have been given in Ref. 9. Note r , θ , and ϕ have been defined in the usual way. The step direction is $[1\bar{1}0]$. For $[110]$ steps, change ϕ to $\tau - \phi$.

Site/constant	Anisotropy energy
Bulk unstrained (E_{bu})	$Q(r)/4(\sin^2 2\theta + \sin^2 2\phi \sin^4 \theta)$
Bulk strained	$(-6e_0L(r_0) - e_0\partial L/\partial r r_0)\cos^2 \theta + E_{bu}$
Surface	$(-1/2L(r_0) - 3e_0L(r_0) - e_0\partial L/\partial r r_0)\cos^2 \theta + E_{bu}$
Step edge	$(-1/4L(r_0) - 3e_0L(r_0) - 3/4e_0\partial L/\partial r r_0)\cos^2 \theta$ $+ (-1/2L(r_0) - 1/2e_0\partial L/\partial r r_0)\sin^2 \theta \sin \phi \cos \phi + E_{bu}$
Step corner	$(-1/4L(r_0) - 9/2e_0L(r_0) - e_0\partial L/\partial r r_0)\cos^2 \theta$ $- 1/2L(r_0)\sin \theta \cos \theta (\sin \phi + \cos \phi) + E_{bu}$
Kink-in edge	$(-1/2L(r_0) - 3e_0L(r_0) - e_0\partial L/\partial r r_0)\cos^2 \theta + E_{bu}$
Kink-out edge	$(-3e_0L(r_0) - 1/2e_0\partial L/\partial r r_0)\cos^2 \theta + E_{bu}$
Kink-in corner	$(-1/4L(r_0) - 11/2e_0L(r_0) - e_0\partial L/\partial r r_0)\cos^2 \theta$ $+ (-1/4L(r_0) - 1/2e_0L(r_0))\sin^2 \theta \cos^2 \phi$ $- 1/2L(r_0)\sin \theta \cos \theta \cos \phi + E_{bu}$
Kink-out corner	$(-1/4L(r_0) - 7/2e_0L(r_0) - e_0\partial L/\partial r r_0)\cos^2 \theta$ $+ (1/4L(r_0) + 1/2e_0L(r_0))\sin^2 \theta \cos^2 \phi$ $- 1/2L(r_0)\sin \theta \cos \theta \cos \phi + E_{bu}$
$Q(r_0)$	$-1.2 \times 10^6 \text{ erg/cm}^3$
$L(r_0)$	$-1.5 \times 10^8 \text{ erg/cm}^3$
$\partial L/\partial r r_0$	$5.5 \times 10^8 \text{ erg/cm}^3$
e_0	0.019

step anisotropy matched the volume occupied by a step oriented along $\langle 110 \rangle$. The system was allowed to relax with no applied field in order to determine the equilibrium magnetization distribution in the film.

No significant out-of-plane ($\langle M_z \rangle > 0.01$) component of the magnetization was present in the equilibrium magnetization distribution. The spins of the step corner atoms were expected to couple to the spins in the terraces and perhaps cause them to be somewhat canted out-of-plane. This did not occur as a result of the balance between the anisotropy energies of neighboring atoms and the exchange energy which couples them. The out-of-plane anisotropy of the step corner site occurs via the term proportional to $\cos \theta (\sin \theta \sin \varphi + \sin \theta \cos \varphi)$ [i.e., $m_z(m_x + m_y)$]. The minimum energy occurs when $-m_z = m_x + m_y$. This equals zero for $\varphi = 3\pi/4$ ($[1\bar{1}0]$), which is the uniaxial anisotropy axis for the step edge site. Although the anisotropy energy of the step edge and step corner sites are about equal, the coupling via exchange to nearby surface and bulk sites (biaxial $\langle 110 \rangle$) ensures that the step edge site is dominant. For any initial condition on the magnetization the final minimized energy configuration has the spins aligned along the step direction, and the out-of-plane component vanishes with $(\sin \varphi + \cos \varphi)$.

The magnetization configuration is somewhat different for faceted steps and square islands. At the corner joining a $[110]$ step to a $[1\bar{1}0]$ step, the magnetization of each step will be forced away from $\langle 110 \rangle$ by the field due to the other step, resulting in a nonzero out-of-plane component. If the density of facets is large enough or the size of islands small enough a significant out-of-plane remanence will exist. This configuration has been simulated via a square island ($3\text{ nm} \times 3\text{ nm}$) on a $5\text{ nm} \times 5\text{ nm}$ square layer with periodic boundary conditions. The length of the sides of the island was chosen to approximate the length of facets observed in films which exhibited out-of-plane remanence. The out-of-plane component of the calculated average equilibrium magnetization was ~ 0.03 . This was significantly less than the results from Kerr loops shown in Fig. 1.

IV. CONCLUSION

It is apparent from these micromagnetics simulations that the anisotropy of step atoms can not be responsible for

the out-of-plane remanence we observed experimentally. For surfaces with a high density of $\langle 110 \rangle$ facets, this anisotropy may be a contributing factor. This micromagnetics result from semi-infinite parallel $\langle 110 \rangle$ steps agrees with the experimental results from Co deposits on vicinal Cu(1 1 13) surfaces.⁴ The anisotropy switches to biaxial in-plane at increased temperatures.¹³ This may be due to Cu atoms decorating the step edges,¹⁴ or to restructuring of the step edges with rectangular protrusions perpendicular to the original step.¹⁵ In the latter case, micromagnetics simulations reported here predict a small ($\sim 3\%$) out-of-plane component to the magnetization.

ACKNOWLEDGMENTS

The authors would like to acknowledge Dr. G. G. Hembree for collaboration in the experimental work. This work is supported by ONR under Grant No. N00014-93-1-0099.

¹U. Gradmann, J. Magn. Magn. Mater. **54/57**, 733 (1986).

²M. E. Buckley, F. O. Shumann, and J. A. C. Bland, J. Phys. **8**, L147 (1996).

³M. Albrecht, T. Furubayashi, M. Przybylski, J. Korecki, and U. Gradmann, J. Magn. Magn. Mater. **113**, 207 (1992).

⁴A. Berger, U. Linke, and H. P. Oepen, Phys. Rev. Lett. **68**, 839 (1992).

⁵W. F. Egelhoff, Jr., P. J. Chen, R. D. K. Misra, T. Ha, Y. Kadmon, C. J. Powell, M. D. Stiles, R. D. McMichael, C.-L. Lin, J. M. Sivertsen, and J. H. Judy, J. Appl. Phys. **79**, 282 (1996).

⁶S. T. Coyle, G. G. Hembree, and M. R. Scheinfein, J. Vac. Sci. Technol. A **15**, 1785 (1997); S. T. Coyle, J. L. Blue, and M. R. Scheinfein, J. Vac. Sci. Technol. A (in press); S. T. Coyle and M. R. Scheinfein, Appl. Phys. Lett. (in press).

⁷K. R. Heim, S. D. Healy, Z. J. Yang, J. S. Drucker, G. G. Hembree, and M. R. Scheinfein, J. Appl. Phys. **74**, 7422 (1993).

⁸Z. J. Yang and M. R. Scheinfein, J. Appl. Phys. **74**, 6810 (1993).

⁹L. Néel, J. Phys. Radium **15**, 225 (1959).

¹⁰H. Fujiwara, H. Kadomatsu, and T. Tokaunaga, J. Magn. Magn. Mater. **31-34**, 809 (1983).

¹¹D. S. Chuang, C. A. Ballentine, and R. C. O'Handley, Phys. Rev. B **49**, 15 084 (1994).

¹²M. R. Scheinfein (LLG Micromagnetics Simulator, © 1997).

¹³W. Wulfhekkel, S. Knappmann, B. Gehring, and H. P. Oepen, Phys. Rev. B **50**, 16 074 (1994).

¹⁴W. Weber, C. H. Back, A. Bischof, D. Pescia, and R. Allenspach, Nature (London) **374**, 788 (1995).

¹⁵M. Giesen, F. Schmitz, and H. Ibach, Surf. Sci. **336**, 269 (1995).

Overpotential driven perpendicular magnetization of electrodeposited ultrathin cobalt films

J. L. Bubendorff, E. Beaurepaire, C. Mény, and J. P. Bucher

Institut de Physique et de Chimie des Matériaux de Strasbourg, UMR 46 CNRS, 23 rue du Loess, F-67037 STRASBOURG Cedex, France

Depending on the overpotential applied during electrodeposition of ultrathin cobalt films ($\eta = 0.1$ – 2.2 V), either in-plane or out-of-plane magnetization can be stabilized. The regime of high supersaturation in particular allows to engineer electrodeposited cobalt films on Au(111) that show perpendicular magnetization (in the thickness range from 2 to 8 atomic layers) exactly like their ultrahigh vacuum grown counterparts. The film topography depends on the overpotential as shown by atomic force microscopy: continuous films are obtained at low overpotential whereas high overpotential leads to the formation of islands. The perpendicular magnetization results from a subtle thickness dependent competition between the shape and the interface anisotropy. © 1998 American Institute of Physics. [S0021-8979(98)48111-8]

Adsorption of atoms on a substrate is a nonequilibrium process, the system is temporarily supersaturated and tries to restore equilibrium by forming islands. Nucleation and growth compete to restore equilibrium.¹ Therefore, magnetic properties of growing islands may strongly differ from those of a continuous film and the system becomes truly two dimensional only after the islands have coalesced.²

Compared to physical vapor deposition techniques which rely on costly equipment operating under ultrahigh vacuum (UHV) electrochemical deposition techniques are cheap, versatile, and allow a wide range of parameters to be adjusted for giant magnetoresistance applications^{3,4} and in nanostructured magnetic needles and multilayers with high aspect ratios.^{5,6} Furthermore, high values of supersaturation (which are necessary to precipitate clusters) can be achieved that are ideally adapted to the engineering of nanostructured advanced materials.

In this work, we show how the magnetic anisotropy (the tendency of the magnetization to align along a given direction) of ultrathin, electrodeposited, and Cu covered cobalt films on Au(111) can be tuned continuously from in-plane to out-of-plane by carefully controlling the overpotential $\eta = |U_{\text{applied}} - U_{\text{Co/Co}^{2+}}|$ during deposition in a beaker. We found $U_{\text{Co/Co}^{2+}} = -1.02$ V/mercury sulfate electrode (MSE) (potential quoted versus the mercury sulfate electrode) and the Co deposition starts at $\eta = 0.13$ V.⁷ The configuration with perpendicular magnetization has been stabilized previously only on ultrathin epitaxial films grown in UHV^{8–13} and is of considerable interest for technological applications, in particular magneto-optic data storage.

Gold substrates were prepared by vacuum evaporation of 100-nm-thick gold films onto freshly cleaved mica substrate. Each sample was then flame annealed leading to (111) textured gold films with terraces 100 to 200 nm wide as verified by scanning tunnel microscopy (STM).¹⁴ Electrochemical measurements were conducted in a three electrode cell under potentiostatic mode, with a mercury sulfate electrode (MSE) as a reference and a Pt counter electrode. Solutions of 4×10^{-2} M CoSO_4 and 9×10^{-3} M CoCl_2 , were prepared with reagent grade chemicals in bidistilled water. No additives (such as saccharine¹⁵ or benzotriazole¹⁶) have been

used and pH=4 is achieved by adding H_3BO_4 to the solution. Under the conditions of our experiment, (see Ref. 17 for details) deposits with purity comparable to MBE can be achieved.¹⁸

Bulk deposition of cobalt is performed only after a high quality gold Au(111) electrode has been identified by its characteristic $\sqrt{3} \times 22$ reconstruction and dereconstruction peaks in the cyclic voltammograms (cyclic current–voltage curves).¹⁹ In order to induce widely different growth modes, a set of samples of thicknesses comprised between 1 and 100 AL have been grown at overpotentials between $\eta = 0.18$ and 2.2 V corresponding to deposition rates between 0.15 and 50 AL/s. Cobalt films have been covered *in situ* by an additional 30-AL-thick Cu film after addition of CuSO_4 solution to the base solution, at $\eta = 0$ V (Cu^{2+} ion concentration 5×10^{-4} M deposition rate 0.3 AL/s). The Cu/Co/Au films have finally been emerged from the solution and tested (*ex situ*) for their magnetic and structural properties.

Figure 1 compares the topography of two Co films, 1.5 nm thick, without Cu protection, prepared at $\eta = 0.18$ (a) and 0.68 V (b). After emersion under potentiostatic control ($\eta = 0$ V), the films are directly observed using tapping mode AFM. The deposit made at $\eta = 0.68$ V consists of connected islands with a lateral extension of about 30 nm and average height of 2 to 3 nm. The islands are found to be disconnected for equivalent thicknesses below 1 nm and coalesce with increasing Co thickness, similar to what was observed for UHV grown films.²⁰ For $\eta = 0.18$ V, the Co film is quite continuous since growth is probably initiated at step edges and defects and the Co film follows the topography of the underlying gold substrate.

The local crystallographic structure of the buried Co films has been studied elsewhere²¹ by zero field NMR. At pH=4 and $\eta = 0.68$ V, the films are made of up to 84% hcp cobalt with the *c* axis perpendicular to the Au(111) plane. The remaining 16% are cobalt atoms in a cfc environment. For $\eta = 0.18$ V, the concentration of hcp-Co drops to 77% mainly due to the presence of stacking faults in the hcp phase (11%). The Co/Au interface is found to be very sharp.²¹ In particular, it always involves one complete plane of atomic Co and no intermixing, like in Co/Cu multilayers,²² occurs.

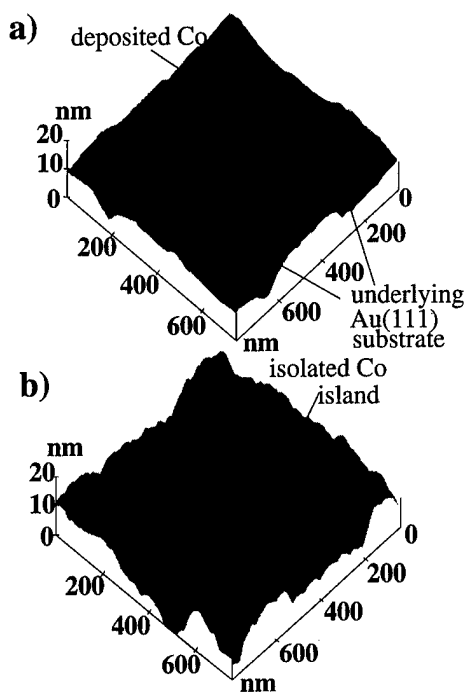


FIG. 1. AFM images of an uncovered 1.5-nm-thick cobalt film as a function of overpotential. (a) $\eta = 0.18$ V, (b) 0.68 V. Clearly seen in the pictures are the flat gold patches, about 500 nm wide, on mica (note dilated z scale) which are covered either by a smooth film of cobalt at low overpotential or granular islands of cobalt at high overpotential.

Magnetic hysteresis loops, in the configuration with the magnetic field perpendicular and parallel to the film plane, have been measured by magneto-optic Kerr effect. Figure 2 shows the hysteresis loops for 3.6-AL-thick Co films, obtained at overpotentials of 0.18 and 0.68 V. At $\eta = 0.18$ V the component of the magnetization is strongest along a direction parallel to the film plane whereas at $\eta = 0.68$ V, the easy direction of the magnetization is perpendicular to the film plane (rectangular shape of the hysteresis loop). The saturation magnetizations $M_s(\eta = 0.18 \text{ V}) = 1250 \pm 180 \text{ G}$ and $M_s(\eta = 0.68 \text{ V}) = 1395 \pm 200 \text{ G}$ as measured by alternating field gradient and superconducting quantum interference device (SQUID) magnetometry are in good agreement with the bulk value $M_s = 1420 \text{ G}$.^{8,9}

The ratio of the remnant magnetization [$M_r = M(H = 0)$] in the perpendicular direction over the saturation magnetization M_s , provides a good measure of the tendency of the system to stabilize the out-of-plane configuration. Figure 3(a) shows M_r/M_s as a function of the film thickness t_{Co} for

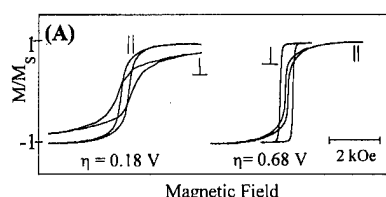


FIG. 2. Hysteresis loops recorded by magneto-optical Kerr effect on a 3.6-AL-thick cobalt film. The magnetic field is applied perpendicular (\perp) and parallel (\parallel) to plane. Overpotentials during electrodeposition were $\eta = 0.18$ and 0.68 V, respectively.

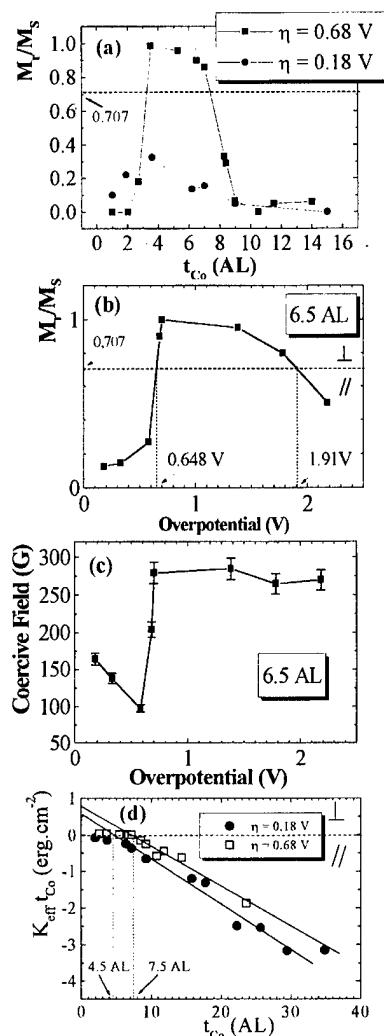


FIG. 3. (a) Ratio of remnant magnetization M_r over saturation magnetization M_s in the perpendicular configuration as a function of film thickness for $\eta = 0.18$ and 0.68 V. (b) M_r/M_s and (c) polar coercive field H_C as a function of η for cobalt films 6.5 AL thick. The continuous increase of M_r/M_s shows the evolution towards fully out-of-plane magnetization $H_C = 280 \text{ G}$ at overpotentials $\eta \geq 0.68 \text{ V}$. (d) Product of the effective anisotropy (K_{eff}) and the film thickness (t_{Co}) as a function of t_{Co} for $\eta = 0.18$ and 0.68 V. The slopes of the curves lead to K_u while K_s is the intercept at $t_{\text{Co}} = 0$.

two widely different deposition rates. The ability of high growth rates to stabilize the out-of-plane configuration for $3 \text{ AL} < t_{\text{Co}} < 7 \text{ AL}$ (M_r/M_s is close to 1) appears clearly while the out-of-plane magnetization is never stable in films deposited at low deposition rates at room temperature. The drop of M_r/M_s at large t_{Co} is attributed to the fact that shape anisotropy, which tends to align the magnetization in the film plane, overcomes the surface and magnetocrystalline anisotropy. The significant role of the overpotential η applied during deposition on the magnetic properties is evidenced in Fig. 3(b) (case of 6.5 AL film). After a steep increase for $\eta > 0.6 \text{ V}$, M_r/M_s reaches a value of 1 and the magnetization remains perpendicular for $0.65 < \eta < 1.9 \text{ V}$. The coercive field H_C [Fig. 3(c)] reached a saturation value of 280 G at $\eta = 0.68 \text{ V}$, close to the values obtained for films grown under UHV.⁸⁻¹³ Further optimization in the sample preparation process (ion concentration, gold surface preparation

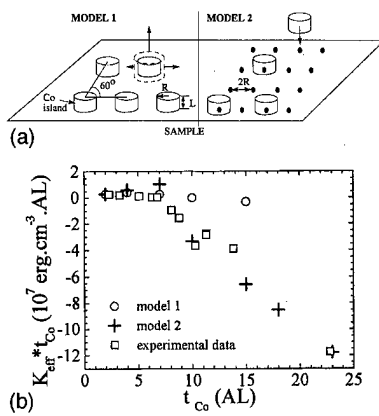


FIG. 4. (a) Models 1 and 2 for the growth of Co films at $\eta=0.68$ V. (b) Comparison between experimental data and the calculated values of $K_{\text{eff}}t_{\text{Co}}$ vs t_{Co} .

prior to deposition) may contribute to an increase in H_C , and make these films attractive for magneto-optical data-storage applications.

To obtain quantitative information about the magnetic anisotropy, we first assume flat, continuous, cobalt structures with uniaxial anisotropy, and express the total energy as $E = -\mathbf{M} \cdot \mathbf{H} + K_{\text{eff}} \sin^2 \vartheta$, where K_{eff} is an effective anisotropy term and ϑ is the angle between the magnetization and the normal to the film plane. The effective anisotropy can be quantified by calculating the area between perpendicular and parallel magnetization curves (first order approximation)²³ and may be written as the sum of three terms:⁷ $K_{\text{eff}} = K_v + \beta K_s/t_{\text{Co}} - 2\pi\alpha M_s^2$, where K_v is a volume, K_s an interface contribution (accounting for Co/Cu and Co/Au interfaces), $2\pi\alpha M_s^2$ the shape anisotropy, and α and β two parameters depending on the film topography. When the film is continuous and planar, α and β are strictly equal to 1. A thickness dependent competition between the volume and interface term and the shape anisotropy occurs leading to perpendicular (respectively, in-plane) magnetization when K_{eff} is positive (respectively, negative). Figure 3(d) represents $K_{\text{eff}}t_{\text{Co}}$ versus t_{Co} for films prepared at $\eta=0.18$ and 0.68 V. At $\eta=0.68$ V, the slope of the curve in Fig. 3(d) (in the regime $t_{\text{Co}} > 8$ AL) leads to $K_v = 670$ kJ/m³ and $K_s = 0.8$ mJ/m². The slope of the curve changes abruptly at $t_{\text{Co}} = 7$ AL and K_{eff} turns positive below 7 AL, leading to perpendicular magnetization. For deposits made at $\eta=0.18$ V, ($K_v = 370$ kJ/m³ and $K_s = 0.6$ mJ/m²), on the contrary, K_{eff} goes smoothly to zero but remains always negative. Our value of K_v and K_s are in good agreement with known values obtained by the same analysis for MBE grown films.^{10,12,13}

At low coverages when the films are discontinuous, β is different from 1 and decreases with the increasing proportion of uncovered gold surface. β can be taken as the proportion of covered gold surface while α depends on the shape of cobalt islands. On the basis of AFM images for $\eta=0.68$ V, and in order to get numerical inputs for the expression of K_{eff} we now assume cylindrical islands of height L and radius R that are distributed on a hexagonal lattice [see Fig. 4(a)]. Expressions of α have been given as a function of $L/2R$.²⁴ For $t_{\text{Co}} = 2$ AL, the AFM images lead to a density $D = 15$ nucleation centers per μm^2 , average values of L and R are,

respectively, 1.7 and 7 nm. In the following, two models are considered corresponding respectively to instantaneous and progressive nucleation [Fig. 4(a)]. *Model 1* considers that the cylindrical islands grow laterally and vertically, in such a way that the ratio $L/2R$ and the number of islands remains constant (instantaneous nucleation). α takes the value 0.65 and β changes as a function of Co coverage. At coalescence, α becomes equal to 1, therefore the shape anisotropy dominates K_{eff} at high coverage. *Model 2* describes in a simplified way the progressive nucleation. Cobalt islands are added stepwise on a hexagonal lattice [see Fig. 4(a)]. The nucleation rate and the ratio $L/2R$ are constant. The islands grow until they reach a thickness $L = 7.5$ AL. As shown on Fig. 4(b), both models reproduce correctly the positive value of $K_{\text{eff}}t_{\text{Co}}$ at low Co coverage as well as the slope change of $K_{\text{eff}}t_{\text{Co}}$ versus t_{Co} when islands coalesce. The progressive nucleation however seems to fit the data better at higher coverage.

In the case of Co deposited at $\eta=0.18$ V, the best approximation consists in taking $\alpha=1$ (since the deposits are flat and laterally extended), while β is allowed to change with the Co coverage. Since β is small at low coverage, the in-plane shape anisotropy remains dominant at any thickness. It is mainly the topographic difference between films prepared at $\eta=0.18$ and 0.68 V that leads to different t_{Co} dependent variations of the shape and interface anisotropy. In this respect, our model could also be applied to UHV grown films where "3D" islands formed in the first growth stage.²⁰

This work has been supported by the Centre National de la Recherche Scientifique (CNRS-ULTIMATECH program).

- ¹H. Roeder, E. Hahn, H. Brune, J. P. Bucher, and K. Kern, *Nature (London)* **366**, 141 (1993).
- ²H. J. Elmers et al., *Phys. Rev. Lett.* **73**, 898 (1994).
- ³M. Alper et al., *J. Appl. Phys.* **75**, 6543 (1994).
- ⁴S. K. J. Lenczowski, C. Schoenenberger, M. A. M. Gijs, and W. J. M. de Jonge, *J. Magn. Magn. Mater.* **148**, 455 (1995).
- ⁵A. Blondel et al., *Appl. Phys. Lett.* **65**, 3019 (1994).
- ⁶L. Piraux et al., *Appl. Phys. Lett.* **65**, 2484 (1994).
- ⁷J. L. Bubendorff, Thesis, Université Louis Pasteur, 1997 (unpublished).
- ⁸C. Chappert et al., *J. Magn. Magn. Mater.* **54**, 795 (1986).
- ⁹C. Chappert and P. Bruno, *J. Appl. Phys.* **64**, 5736 (1988).
- ¹⁰P. Beauvillain et al., *J. Magn. Magn. Mater.* **121**, 503 (1993).
- ¹¹J. Ferré et al., *Appl. Phys. Lett.* **56**, 1586 (1990).
- ¹²R. Allenspach, M. Stampanoni, and A. Bischof, *Phys. Rev. Lett.* **65**, 3344 (1990).
- ¹³M. Speckmann, H. P. Oepen, and H. Ibach, *Phys. Rev. Lett.* **75**, 2035 (1995).
- ¹⁴J. P. Bucher, L. Santesson, and K. Kern, *Langmuir* **10**, 979 (1994).
- ¹⁵R. D. Fischer, *J. Electrochem. Soc.* **106**, 479 (1962).
- ¹⁶M. J. Armstrong and R. H. Muller, *J. Electrochem. Soc.* **138**, 2303 (1991).
- ¹⁷J. L. Bubendorff, E. Beaupaire, C. Meny, P. Panissod, and J. P. Bucher, *Phys. Rev. B* (to be published).
- ¹⁸W. Schindler and J. Kirschner, *Phys. Rev. B* **55**, R1989 (1997).
- ¹⁹G. J. Edens, X. Gao, and J. Weaver, *J. Electroanal. Chem.* **375**, 357 (1994).
- ²⁰B. Woigtlander, G. Meyer, and N. M. Amer, *Phys. Rev. B* **44**, 10 354 (1991); T. H. Gentner, T. Detzel, F. Scheurer, and J. P. Bucher, *Thin Solid Films* **275**, 58 (1996).
- ²¹J. L. Bubendorff, E. Beaupaire, C. Meny, P. Panissod, and J. P. Bucher, *Phys. Rev. B* **56**, R7120 (1997).
- ²²P. Panissod, J. P. Jay, C. Meny, M. Wojcik, and E. Jedryka, *Hyperfine Interact.* **97/98**, 75 (1996).
- ²³J. R. Childress et al., *Phys. Rev. B* **45**, 2855 (1992).
- ²⁴G. W. Crabtree, *Phys. Rev. B* **16**, 1117 (1977).

Magnetic and structural characterizations of HCP permalloy films grown by molecular beam epitaxy

J. C. A. Huang,^{a)} Y. M. Hu, and C. C. Yu

Physics Department, National Cheng-Kung University, Tainan, Taiwan 70101, Republic of China

An hcp metastable phase of $\text{Ni}_{80}\text{Fe}_{20}$ ($1\bar{1}00$) structure has been grown as high-quality epitaxial films on $\text{Co}(1\bar{1}00)$ and $\text{Cr}(211)$ planes. The epilayers of $\text{Ni}_{80}\text{Fe}_{20}$ grow as hcp structure up to a critical thickness of ~ 100 Å, and the further layers transform to twinned fcc structure. Magneto-optical Kerr effect study indicates that the hcp $\text{Ni}_{80}\text{Fe}_{20}$ ($1\bar{1}00$) layers exhibit strong crystalline induced uniaxial magnetic anisotropy with easy axis along the hcp[0001] direction. The subsequent fcc $\text{Ni}_{80}\text{Fe}_{20}$ layers show decreasing coercive fields as the film thickness increased. For the thick fcc film, interestingly, the magnetic easy axis shifts 90° with respect to that of the underlying hcp layers. The result is explained by the shape anisotropy effect due to the formation of quasi-1D columnar islands directed perpendicular to the hcp[0001] direction. © 1998 American Institute of Physics. [S0021-8979(98)53711-5]

Surface magnetism has attracted much attention in recent years because of fundamental research and advanced technological applications. The orientation of magnetization for a ferromagnetic thin film can often be determined by the competition between magnetocrystalline anisotropy, shape anisotropy, and surface or interface anisotropy, etc.¹ There has also been an increasing interest in understanding the relationship between the magnetic anisotropies and the crystal structures. It has been demonstrated that the crystal structure and magnetic anisotropy (MA) of the magnetic thin films may depend strongly on the underlying substrates or buffer layers.^{2,3}

In a previous work, the authors reported the magnetic properties of Co/Cr films and multilayers.⁴⁻⁷ In this investigation we study the novel fabrication and structural transformation (hcp to fcc) of metastable hcp $\text{Ni}_{80}\text{Fe}_{20}$ ($1\bar{1}00$) films grown on $\text{Co}(1\bar{1}00)$ and $\text{Cr}(211)$. We demonstrate here the control of crystal structure and MA of $\text{Ni}_{80}\text{Fe}_{20}$ films by selecting suitable buffer layers and by varying the film thickness. Presently, we assess the degree to which any of the results is predictable.

The crystal growth was carried out in a vacuum product made molecular beam epitaxial (MBE) chamber equipped with four *e*-beam sources. This MBE chamber allowed sample transfer under ultrahigh vacuum (UHV) condition to an analysis chamber for morphological and magnetic characterizations by AFM and MOKE. Details of the MBE chamber in which epitaxial growth and surface characterization took place were described elsewhere.⁸ The $\text{Co}(1\bar{1}00)$ was prepared on $\text{Cr}(211)/\text{Mo}(211)$ seeding layers using epitaxial grade $\text{Al}_2\text{O}_3(1\bar{1}00)$ or $\text{MgO}(110)$ substrates.⁴⁻⁷ The initial $\text{Mo}(211)$ and $\text{Cr}(211)$ buffer layers of ~ 100 Å were grown at 900 and 350 °C, respectively, followed by $\text{Co}(1\bar{1}00)$ layers ~ 100 Å thick at 300–350 °C. The hcp $\text{Ni}_{80}\text{Fe}_{20}(1\bar{1}00)$ films

were grown on the fresh $\text{Co}(1\bar{1}00)$ [or directly on $\text{Cr}(211)$] plane at the optimal growth temperatures which ranged from 100 to 300 °C.

The crystal structure and quality were characterized by reflection high energy electron diffraction (RHEED) and x-ray diffraction (XRD). The correlation between the structural and magnetic properties was investigated by magneto-optical Kerr effect (MOKE) technique. Longitudinal (LMOKE) and polar (PMOKE) configurations of MOKE were employed to determine the in-plane and out-of-plane magnetization loops of the samples. Note that the penetration depth⁵ of the He–Ne laser for the MOKE experiment is about 150 Å, surface layers can be conveniently probed by MOKE during epitaxial growth.

By RHEED and XRD studies we have determined the following orientation relations:

$$\begin{aligned} &\text{Ni}_{80}\text{Fe}_{20}(211) \parallel \text{Ni}_{80}\text{Fe}_{20}(1\bar{1}00) \parallel \text{Co}(1\bar{1}00) \parallel \text{Cr}(211) \parallel \text{Mo}(211) \parallel \\ &\text{Al}_2\text{O}_3(1\bar{1}00); \\ &\text{Ni}_{80}\text{Fe}_{20}[0\bar{1}1] \parallel \text{Ni}_{80}\text{Fe}_{20}[11\bar{2}0] \parallel \text{Co}[11\bar{2}0] \parallel \text{Cr}[\bar{1}11] \parallel \text{Mo}[\bar{1}11] \parallel \\ &\text{Al}_2\text{O}_3[0001]; \\ &\text{Ni}_{80}\text{Fe}_{20}[\bar{1}11] \parallel \text{Ni}_{80}\text{Fe}_{20}[0001] \parallel \text{Co}[0001] \parallel \text{Cr}[0\bar{1}1] \parallel \text{Mo}[0\bar{1}1] \parallel \\ &\text{Al}_2\text{O}_3[1120]. \end{aligned}$$

The crystal structure and magnetic property of $\text{Co}(1\bar{1}00)$ on $\text{Cr}(211)$ had been described elsewhere.⁴⁻⁷ Schematic diagrams of the epitaxial relations and lattice geometry between hcp $\text{Ni}_{80}\text{Fe}_{20}(1\bar{1}00)$ and fcc $\text{Ni}_{80}\text{Fe}_{20}(211)$ are provided in Fig. 1.

On the $\text{Co}(1\bar{1}00)$ surface, RHEED studies show that hcp $\text{Ni}_{80}\text{Fe}_{20}(1\bar{1}00)$ film can be stabilized up to a critical thickness (t_c) of ~ 100 Å, and the further epilayers transform to fcc structure, as shown in Figs. 2(b)–2(d). The RHEED image of the $\text{Co}(1\bar{1}00)$ plane is shown in Fig. 2(a) for comparison. Detailed RHEED measurements (for all principle azimuths) indicate that the hcp $\text{Ni}_{80}\text{Fe}_{20}(1\bar{1}00)$ and $\text{Co}(1\bar{1}00)$ films possess much alike crystal symmetry and lattice parameters. With increasing fcc $\text{Ni}_{80}\text{Fe}_{20}$ layer thickness to about 500 Å, the RHEED patterns remained almost unchanged for the beam directed along the $\text{Ni}_{80}\text{Fe}_{20}[\bar{1}11]$ azimuth. How-

^{a)}Electronic mail: jcahuang@mail.ncku.edu.tw

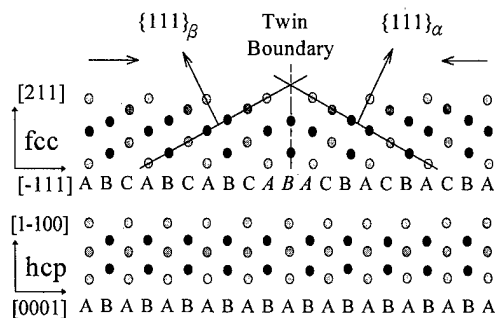


FIG. 1. Schematic diagrams showing the epitaxial relations, lattice geometry, and the stacking sequence for both hcp(1100) and subsequent fcc(211) layers (after phase transformation) along the close-packed direction. A twin boundary in fcc layers is shown as a consequence of stacking fault.

ever, for the beam directed along the $\text{Ni}_{80}\text{Fe}_{20}[\bar{0}11]$ azimuth the RHEED pattern developed into two sets of angled streaks [shown in Fig. 2(f)], indicating the faceting growth of twinned $\{111\}$ planes (indexed as $\{111\}_\alpha$ and $\{111\}_\beta$ in Fig. 1). Accordingly, the surface morphology changed from the isotropiclike characteristic into a clear quasi-1D feature with columns quite uniformly directed along the $\text{fcc}[\bar{0}11]$, as displayed in Figs. 4(a) and 4(b), respectively. The growth of the twinned $\text{fcc}\{111\}$ plane is more favorable than that of (211) surface owing to the reduction of surface energy. Note that the angle of the RHEED streaks is consistent with a $\{111\}$ facet of a (211) surface.

Note that hcp $\text{Ni}_{80}\text{Fe}_{20}(1\bar{1}00)$ films can also be stabilized up to ~ 100 Å on Cr(211) plane. Tilt XRD scans on 100 Å $\text{Ni}_{80}\text{Fe}_{20}$ on Cr(211) samples [Fig. 3(a)] reveal that the lattice spacings of hcp $\text{Ni}_{80}\text{Fe}_{20}$ are $a = 2.50$ Å, $c = 4.07$ Å, very close to those of the hcp Co ($a = 2.51$ Å, $c = 4.07$ Å) and those for the unit cell of Cr(211) plane (2.49 Å \times 4.07 Å). The growth of metastable hcp $\text{Ni}_{80}\text{Fe}_{20}$ could be

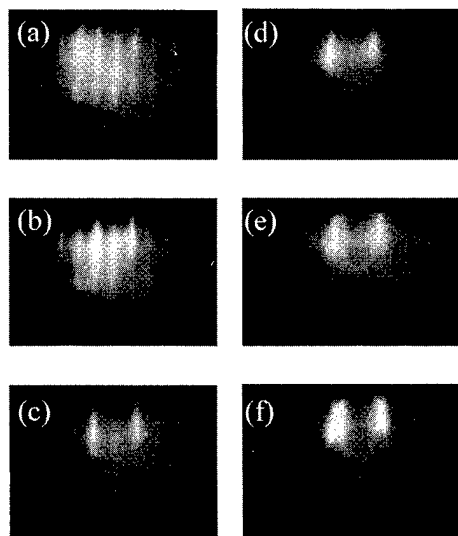


FIG. 2. RHEED patterns for (a) 100 Å Co($\bar{1}100$), and the subsequent $\text{Ni}_{80}\text{Fe}_{20}$ layers of (b) 50 Å, (c) 100 Å, (d) 150 Å, (e) 200 Å, and (f) 500 Å thick. The RHEED beam was directed parallel to the $\text{Co}[1\bar{1}20]$ ($\parallel\text{Ni}_{80}\text{Fe}_{20}[1\bar{1}20]\parallel\text{Ni}_{80}\text{Fe}_{20}[0\bar{1}1]$) azimuth.

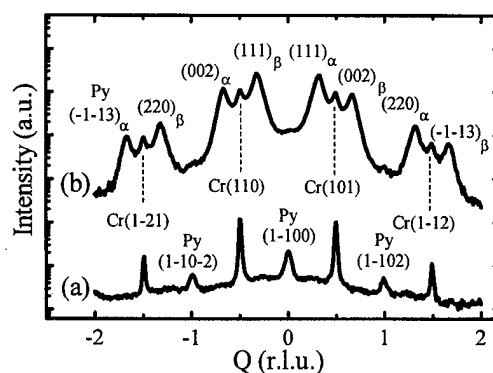


FIG. 3. Tilt (h, k, l) x-ray diffraction spectra scanned from $h = -2.5$ to $h = 2.5$ [$k = 0$, $l = (1\bar{1}00)$] for $\text{Ni}_{80}\text{Fe}_{20}(\text{Py})$ films grown on Cr(211) seed layers: (a) $\text{Py} = 100 \text{ \AA}$ and (b) $\text{Py} = 1000 \text{ \AA}$.

due to the smallness of the energy difference between the fcc and hcp phases for most 3d transition metals.⁹ In addition, we point out that similar phase transformation process was also observed in Ni₈₀Fe₂₀ films grown on Cr(211), though the growth of twinned {111} planes occurred at higher thickness of ~ 700 Å due to the surface roughness of the Cr(211). The twinned fcc(211) structure for thick Ni₈₀Fe₂₀ layers was confirmed by the tilt XRD spectrum shown in Fig. 3(b). These results suggest a general pathway for structure and morphology transformations from hcp(1100) to fcc(211). It is noted that Harp¹⁰ *et al.* reported a fcc \rightarrow hcp phase transition mechanism in Co where transformation occurs by the

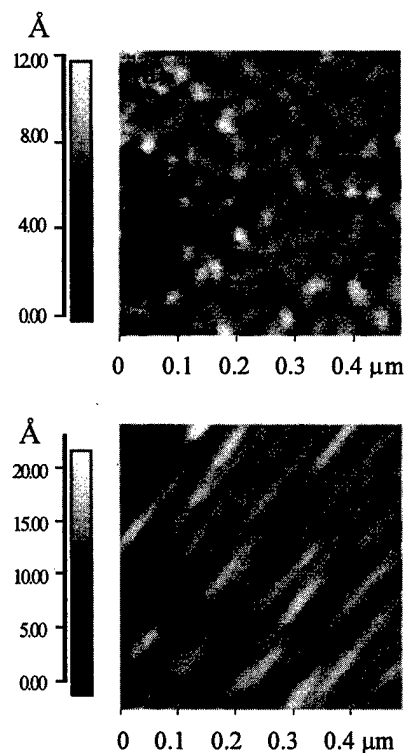


FIG. 4. The AFM image of (a) 100 Å and (b) 500 Å thick $\text{Ni}_{80}\text{Fe}_{20}$ layers grown on $\text{Co}(1\bar{1}00)$, the columnar direction of the quasi-1D-like islands in (b) is determined as parallel to $\text{fcc Ni}_{80}\text{Fe}_{20}[0\bar{1}1]$.

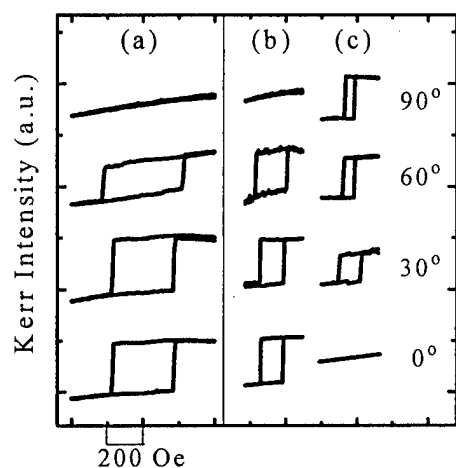


FIG. 5. The angular dependent LMOKE hysteresis loops for (a) 100 Å Co(1100) and the subsequent $\text{Ni}_{80}\text{Fe}_{20}$ layers of (b) 100 Å and (c) 500 Å thick. The applied magnetic field is along $\text{Co}[11\bar{2}0]$ ($\parallel \text{hcpNi}_{80}\text{Fe}_{20}[11\bar{2}0] \parallel \text{fccNi}_{80}\text{Fe}_{20}[011]$) direction for 90° azimuth, and along $\text{Co}[0001]$ ($\parallel \text{Ni}_{80}\text{Fe}_{20}[0001] \parallel \text{Ni}_{80}\text{Fe}_{20}[\bar{1}11]$) direction for 0° azimuth.

slipping of $\{111\}$ planes along a $\langle 11\bar{2} \rangle$ direction, which is essentially a reverse process of the case discussed here.

Figures 5(a)–5(b) display the angular dependent LMOKE hysteresis loops of 100 Å Co (1100) and subsequent 100 Å $\text{Ni}_{80}\text{Fe}_{20}$ (1100) (hcp), respectively. Both magnetic layers are difficult to be magnetized along the out-of-plane directions because no PMOKE signal was observed. LMOKE measurements show that the hcp $\text{Ni}_{80}\text{Fe}_{20}$ layers exhibit uniaxial MA with large coercive field ($H_c > 80$ Oe) and easy axis along the $\text{hcp}[0001]$, much like the underlying hcp Co layers because large coercive fields and MA constants ($K_{u1} \sim 10^5$ ergs/cm³) were measured in hcp $\text{Ni}_{80}\text{Fe}_{20}$ on Cr(211).¹¹ Thus we believe that the strong MA in hcp $\text{Ni}_{80}\text{Fe}_{20}$ layers [on Co(1100)] could be partly resulted from the magnetocrystalline effect in addition to the exchange coupling effect to the underlying Co layers.

With increasing the $\text{Ni}_{80}\text{Fe}_{20}$ layer thickness above 100 Å, the H_c gradually decreases to ~ 20 –25 Oe though the direction of the easy axis remains unchanged ($\parallel \text{fcc}[\bar{1}11] \parallel \text{hcp}[0001]$). Interestingly, the magnetic easy axis shifts to $\text{fcc}[011]$ (perpendicular to $\text{fcc}[\bar{1}11]$ and $\text{hcp}[0001]$) for $\text{Ni}_{80}\text{Fe}_{20}$ layers of about 500 Å thick, as shown in Fig. 5(c). Note that the shift of the magnetic easy axis in the thick fcc layers coincides with the faceting growth of $\{111\}$ twins [see Fig. 2(f)] and the formation of quasi-1D-like columnar structure [Fig. 4(b)]. Therefore, we believe that the change of magnetic easy axis in the thick fcc $\text{Ni}_{80}\text{Fe}_{20}$ layers are induced by the strong shape anisotropy effect.

The authors are grateful for the financial support by the ROC NSC under Grant Nos. 87-2112-M-006-014 and 87-2732-M-006-001.

¹ See, for example, *Ultrathin Magnetic Structure I*, edited by J. A. C. Bland and B. Heinrich (Springer, Berlin, 1994).

² J. M. Florczak, E. Dan Dahlberg, J. N. Kuznia, A. M. Wowchak, and P. I. Cohen, *J. Appl. Phys.* **69**, 4997 (1991).

³ N. Metoki, Th. Zeidler, A. Stierle, K. Brohl, and H. Zabel, *J. Magn. Magn. Mater.* **118**, 57 (1993).

⁴ J. C. A. Huang, Y. Liou, Y. D. Yao, W. T. Yang, C. P. Chang, S. Y. Liao, and Y. M. Hu, *Phys. Rev. B* **52**, R13110 (1995).

⁵ J. C. A. Huang, F. C. Tang, W. W. Fang, R. L. Liu, Y. M. Hu, C. K. Lo, Y. Liou, Y. D. Yao, W. T. Yang, C. P. Chang, and S. Y. Liao, *J. Appl. Phys.* **79**, 4790 (1996).

⁶ Y. Liou, J. C. A. Huang, Y. D. Yao, C. H. Lee, K. T. Wu, C. L. Lu, S. Y. Liao, Y. Y. Chen, N. T. Liang, W. T. Yang, C. Y. Chen, and B. C. Hu, *J. Appl. Phys.* **79**, 6516 (1996).

⁷ C. K. Lo, Y. Liou, C. P. Chang, I. Klik, Y. D. Yao, and J. C. A. Huang, *Appl. Phys. Lett.* **68**, 2155 (1996).

⁸ J. C. A. Huang, T. E. Wang, C. C. Yu, Y. M. Hu, P. B. Lee, and M. S. Yang, *J. Cryst. Growth* **171**, 442 (1997).

⁹ H. L. Skriver, *Phys. Rev. B* **31**, 1909 (1985); A. T. Paxson, *ibid.* **41**, 8127 (1990).

¹⁰ G. R. Harp, R. F. C. Farrow, D. Weller, T. A. Rabedeau, and R. F. Marks, *Phys. Rev. B* **48**, 17538 (1993).

¹¹ J. C. A. Huang, Y. M. Hu, C. C. Yu, and C. H. Lee (unpublished).

CMR Materials and Their Properties

R. B. Van Dover and A. Gupta, Chairmen

Transport and magnetic properties of epitaxial and polycrystalline magnetite thin films

X. W. Li

Department of Physics, Brown University, Providence, Rhode Island 02912

A. Gupta

IBM T. J. Watson Research Center, Yorktown Heights, New York 10598

Gang Xiao and G. Q. Gong

Department of Physics, Brown University, Providence, Rhode Island 02912

The transport and magnetic properties of magnetite (Fe_3O_4) thin films grown epitaxially on single crystal $\text{MgO}(100)$ and $\text{SrTiO}_3(100)$ substrates, and with multiple grain orientations on polycrystalline SrTiO_3 substrates, have been investigated. The films are grown using pulsed laser deposition and their epitaxial quality determined using ion channeling measurements. Transport and magnetic studies of Fe_3O_4 films as a function of thickness and morphology suggest that epitaxial strain and growth defects affect the width and temperature of the Verwey transition. In addition, these factors also significantly influence the magnetic coercivity of the films. The low-field magnetoresistance (MR) behaviors of epitaxial and polycrystalline films as a function of temperature have been compared and they were found to be quite similar, suggesting very small contribution to the MR from grain boundaries. © 1998 American Institute of Physics. [S0021-8979(98)17911-2]

I. INTRODUCTION

Magnetite (Fe_3O_4) has the so-called cubic inverse spinel structure in which the Fe cations occupy interstices of a face-centered-cubic (fcc) close packed frame of oxygen ions. The eight tetrahedral (*A*) sites are solely occupied by Fe^{3+} , while the 16 octahedral (*B*) sites are equally shared by Fe^{3+} and Fe^{2+} ions. Rapid hopping of electrons between Fe^{2+} and Fe^{3+} ions in the *B* sites results in good room-temperature conductivity. Upon cooling, bulk Fe_3O_4 undergoes a metal-insulator transition (Verwey transition) at a temperature $T_v \sim 120$ K, where the electron hopping is frozen and the conductivity decreases by about two orders of magnitude.¹ Although it is generally accepted that the transition is due to the ordering of the Fe^{3+} and Fe^{2+} ions,^{1,2} the mechanism governing the transport and magnetic properties of this material above and below the transition is not yet well understood.

A number of differences has been observed in the transport and magnetic properties of thin films as compared to bulk magnetite. In particular, the Verwey transition is broadened and shifted to lower temperatures in the case of the former. This has been ascribed to the interaction between the film and the substrate, resulting in stress and rigid structural coupling of the film.^{3,4} Differences in the saturation magnetization and coercivity of thin films and bulk samples have also been reported.^{5,6} In this work, we have determined the crystallinity of Fe_3O_4 films grown on different substrates using ion channeling, and subsequently studied their temperature-dependent transport, magnetic, and magnetoresistance properties as a function of film thickness and morphology.

II. EXPERIMENT

The magnetite films have been grown on (100)-oriented MgO and SrTiO_3 single crystals and on polycrystalline SrTiO_3 substrates using the pulsed laser deposition technique. The polycrystalline SrTiO_3 substrates, with 3 μm average grain size, are obtained by cutting and optically polishing sintered pellets (97%–98% density) of the material.⁷ The Fe_3O_4 target used for the ablation has been prepared by a standard solid-state reaction method. A focused KrF excimer laser (248 nm) beam has been used for ablation, with a repetition rate of 4 Hz and fluence of ~ 2 – 3 J/cm² at the target. Prior to deposition, the substrates are heated to 750 °C and the surface cleaned using a 100 eV Ar ion beam. The films are then grown at a temperature of 350 °C in vacuum ($\sim 10^{-6}$ Torr). Following growth, the films are cooled down to room temperature at a rate of 15 °C/min. Some of the films have also been deposited using a frequency-tripled Nd:YAG laser (355 nm) and have been found to exhibit very similar transport and magnetic properties to those grown using the KrF laser.⁶ The film thicknesses, after deposition, have been determined using Rutherford backscattering spectroscopy (RBS). The standard four-probe dc method has been used for the resistivity measurements, while the magnetic measurements have been carried out using a superconducting quantum interference device (SQUID) magnetometer.

III. RESULTS AND DISCUSSION

We have investigated the crystalline quality of the Fe_3O_4 films grown on single crystal MgO and SrTiO_3 substrates by

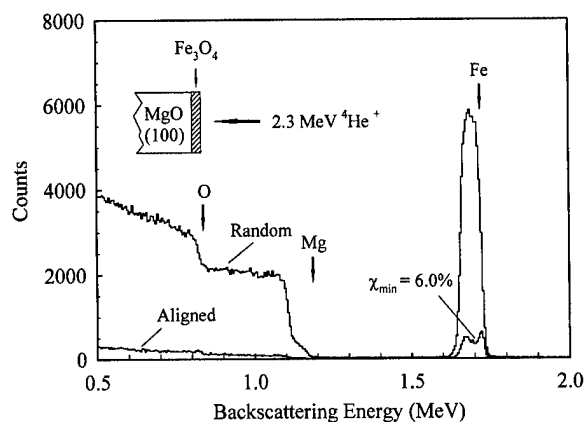


FIG. 1. Rutherford backscattering spectrum showing counts vs backscattering energy for both channeling and random 2.3 MeV $^4\text{He}^+$ ions backscattered from a Fe_3O_4 film on a $\text{MgO}(100)$ substrate.

ion channeling spectroscopy. Figure 1 shows the $\langle 100 \rangle$ aligned and random RBS spectra (2.3 MeV $^4\text{He}^+$ ions) for a Fe_3O_4 film on $\text{MgO}(100)$. The ratio (χ_{\min}) of the backscattered yield along $\langle 100 \rangle$ to that in a random direction is 6.0%. Previous transmission electron microscopy measurements of Fe_3O_4 films grown on $\text{MgO}(100)$ have also confirmed epitaxial growth of the film, with the $\langle 100 \rangle$ and $\langle 010 \rangle$ axes aligned with the respective cubic axes of the substrate.⁶ For the film grown on the $\text{SrTiO}_3(100)$ substrate, χ_{\min} has been measured to be 17.4%, suggesting that it has a lower crystalline quality than the film grown on MgO .

Figure 2 displays the resistance (R) as a function of temperature for Fe_3O_4 films grown on $\text{MgO}(100)$ substrates with different thicknesses. Overall, the films exhibit a broadened Verwey transition as compared to measurements reported for bulk samples. The transition is the sharpest for the 6600 Å thick film, with a transition temperature (T_v) of about 121 K. This is determined from the maximum in the slope of the Arrhenius plot for thermally activated hopping transport [$\ln(R/T)$ vs $1/T$]. The resistance change at the transition decreases in magnitude and the transition gets broader with decreasing film thickness, and is not noticeable for the thinnest films. The transition temperature, as determined from the Arrhenius plot, is plotted as a function of film thickness and shown as an inset in Fig. 2. T_v increases quite rapidly with the initial increase in film thickness and then

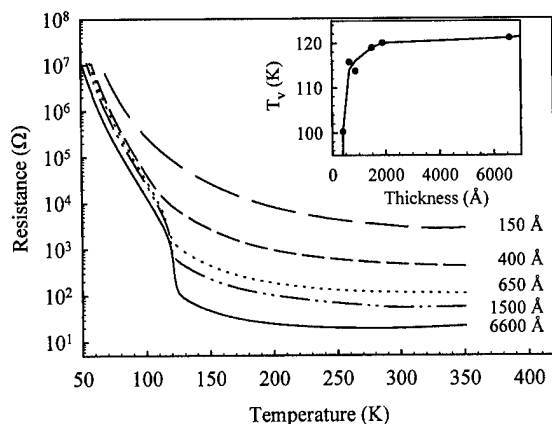


FIG. 2. Resistance as a function of temperature for Fe_3O_4 films with different thicknesses. The Verwey transition temperature (T_v) determined from Arrhenius plots as a function of film thickness is shown in the inset.

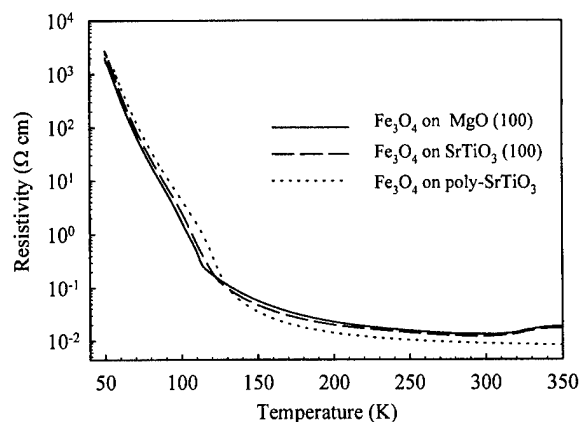


FIG. 3. Resistivity as a function of temperature for ~ 850 Å thick Fe_3O_4 films grown on $\text{MgO}(100)$, $\text{SrTiO}_3(100)$, and polycrystalline (3 μm average grain size) substrates.

gradually levels off at a value close to the bulk. The broadening and reduction in T_v for the thinner films is possibly caused by the residual strain in the films resulting from the lattice mismatch with the substrate. The growth of Fe_3O_4 , which has a slightly smaller lattice parameter than that of the MgO substrate, results in an in-plane expansion of the Fe_3O_4 lattice accompanied by Poisson compression in the perpendicular direction. A similar behavior has been observed in Fe_3O_4 films grown by molecular beam epitaxy (MBE) and reactive sputter deposition.^{4,5} Besides substrate-induced stress, Van De Veerdonk *et al.* have suggested that the rigid structural coupling between the magnetite film and the cubic lattice of the substrate also suppresses the orthorhombic deformation accompanying the Verwey transition leading to a depressed T_v .⁴

We have also investigated the influence of film morphology on the resistivity behavior of Fe_3O_4 . For this purpose, we have compared the transport and magnetic properties of ~ 850 Å thick film of Fe_3O_4 grown on (100)-oriented MgO and SrTiO_3 single crystals and on polycrystalline SrTiO_3 substrates. The resistivity (ρ) as a function of temperature for the three films is plotted in Fig. 3. It is interesting to note that the value of ρ is comparable over the measured temperature range for the three films. Nonetheless, the epitaxial film on MgO exhibits the sharpest transition, although with a T_v lower than those for the epitaxial and polycrystalline films grown on SrTiO_3 . The higher T_v for the films on SrTiO_3 can be understood based on the lattice mismatch between the film and the substrate. Because of the close lattice match between Fe_3O_4 and MgO (lattice mismatch, $\eta = 3.3 \times 10^{-3}$), the film grows coherently until a critical thickness (t_c) is reached. Based on the shear modulus and elastic modulus, Van De Veerdonk *et al.* have estimated t_c to be about 200 Å for film growth on MgO .⁴ Above t_c , the growth becomes incoherent, with partial or complete relaxation of the strain by formation of misfit dislocations. The lattice mismatch is significantly larger ($\eta = -70 \times 10^{-3}$) for growth on SrTiO_3 , resulting in incoherent growth without any strain for any film thickness. The lower T_v for growth on MgO could be interpreted as resulting from some residual strain in the film, even when it is above the critical thickness. Although the films on SrTiO_3 are unstrained and have higher T_v , the higher con-

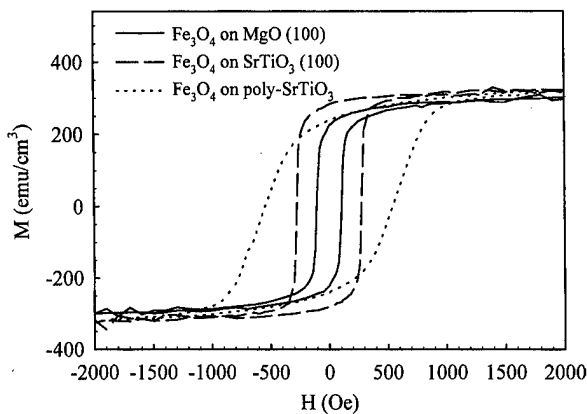


FIG. 4. Magnetization hysteresis loops at 300 K for the three films whose resistivity plots are shown in Fig. 3.

centration of defects in the films results in a broadened transition, particularly for the polycrystalline film.

Figure 4 plots the in-plane magnetic hysteresis loops measured at room temperature for the three films discussed above. The field is applied along the $\langle 100 \rangle$ direction for the films on single crystal substrates. It is interesting to note that the film on $\text{SrTiO}_3(100)$ exhibits a higher coercivity (H_c) than the film on $\text{MgO}(100)$. The polycrystalline film has even higher H_c and displays a much more gradual and rounded hysteresis loop than the epitaxial films. This would be expected for the average of a random orientation of grains. We speculate that the higher H_c of the films on SrTiO_3 as compared to MgO is related to the absence of strain in the case of the former.

We finally briefly discuss the low-field magnetoresistance (MR) properties of the epitaxial Fe_3O_4 film grown on MgO and the polycrystalline film grown on the polycrystalline SrTiO_3 substrate. Figure 5 shows the MR ratio at 1500 Oe as a function of temperature for the two films. The resistance hysteresis loop for the polycrystalline film at 123 K is shown as an inset. The MR ratio is defined according to $\Delta R/R = (R_p - R_{1500})/R_{1500}$, where R_p is the peak resistance which occurs at the coercive field, and R_{1500} is the resistance at 1500 Oe. The MR behavior for the two films is quite similar, with a peak occurring close to T_v , as has also been previously observed.^{6,8} Consistent with the transport and magnetic data, the MR peak occurs at a slightly higher temperature and is somewhat broader for the polycrystalline film on SrTiO_3 than for the epitaxial film on MgO . Interestingly, there is very small MR associated with the grain boundaries in the polycrystalline film. This is unlike the behavior of manganite films, where a relatively large low-field MR has been observed below the Curie temperature.⁷ The low-field MR in the manganites has been attributed to spin-dependent transport of polarized electrons at the grain boundaries which serve as pinning centers for the magnetic domain walls. A similar behavior would have been expected for Fe_3O_4 based on the half-metallic behavior of its conduction electrons. However, unlike manganites, the grain boundary resistance in Fe_3O_4 is quite insignificant as evidenced from Fig. 3, thereby possibly resulting in a stronger coupling between the grains. Additional work is needed to further clarify the role of grain boundaries in the MR behavior of Fe_3O_4 and other half-metallic systems.

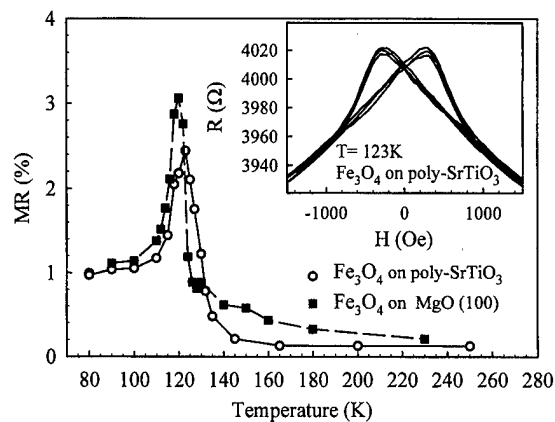


FIG. 5. Magnetoresistance at $H=1500$ Oe as a function of temperature for a polycrystalline (850 Å thick) and an epitaxial (1500 Å thick) Fe_3O_4 film. The resistance hysteresis as a function of magnetic field for the polycrystalline film at 123 K is shown in the inset.

IV. SUMMARY

In summary, we have measured the crystallinity of Fe_3O_4 films grown on (100)-oriented MgO and SrTiO_3 substrates using ion channeling spectroscopy. The results show that the films grow epitaxially on both substrates, with those grown on MgO exhibiting better crystallinity because of the smaller lattice mismatch. Polycrystalline films with multiple grain orientations have also been grown on intentionally fabricated polycrystalline SrTiO_3 substrates. The Verwey transition and the magnetic coercivity are strongly influenced by the thickness and morphology of the films, which we primarily attribute to the residual strain in the films. The low-field magnetoresistance behavior of the epitaxial and polycrystalline films has also been studied, and the MR magnitude has been found to be quite small ($\sim 2\%$ – 3% at 1500 Oe) for both the films, with very little contribution resulting from grain boundary transport.

ACKNOWLEDGMENTS

The authors thank T. R. McGuire, W. J. Gallagher, and J. Slonczewski for useful discussions, P. R. Duncombe for preparation of the ablation target, and G. Coleman for the RBS measurements. This work was supported in part by NSF Grant Nos. DMR-9414160 and DMR-9258306.

¹ *Ferromagnetic Materials*, edited by E. P. Wohlfarth (North-Holland, Amsterdam, 1982), Vol. 3, pp. 260–268.

² J. M. Zuo, J. C. H. Spence, and W. Petuskey, *Phys. Rev. B* **42**, 8451 (1990).

³ J. S.-Y. Feng, R. D. Pashley, and M.-A. Nicolet, *J. Phys. C* **8**, 1010 (1975).

⁴ R. J. M. Van De Veerdonk, M. A. M. Gijs, P. A. A. Van Der Heijden, R. M. Wolf, and W. J. M. De Jonge, *Mater. Res. Soc. Symp. Proc.* **401**, 455 (1996).

⁵ D. T. Margulies, F. T. Parker, F. E. Spada, R. S. Goldman, J. Li, R. Sinclair, and A. E. Berkowitz, *Phys. Rev. B* **53**, 9175 (1996).

⁶ G. Q. Gong, A. Gupta, G. Xiao, W. Qian, and V. P. Dravid, *Phys. Rev. B* **56**, 5096 (1997); W. Qian, V. P. Dravid, A. Gupta, G. Q. Gong, and G. Xiao, *J. Mater. Sci.* (in press).

⁷ X. W. Li, A. Gupta, G. Xiao, and G. Q. Gong, *Appl. Phys. Lett.* **71**, 1124 (1997).

⁸ V. V. Gridin, G. R. Hearne, and J. M. Honig, *Phys. Rev. B* **53**, 15518 (1996).

Observation of spin-dependent transport and large magnetoresistance in $\text{La}_{0.7}\text{Sr}_{0.3}\text{MnO}_3/\text{SrTiO}_3/\text{La}_{0.7}\text{Sr}_{0.3}\text{MnO}_3$ ramp-edge junctions

C. Kwon,^{a)} Q. X. Jia, Y. Fan, M. F. Hundley, and D. W. Reagor

Materials Science and Technology Division, Mail Stop K763, Los Alamos National Laboratory, Los Alamos, New Mexico 87545

We have fabricated ferromagnet-insulator-ferromagnet junctions using a ramp-edge geometry based on $(\text{La}_{0.7}\text{Sr}_{0.3})\text{MnO}_3$ ferromagnetic electrodes and a SrTiO_3 insulator. Pulsed laser deposition was used to deposit the multilayer thin films and the devices were patterned using photolithography and ion milling. As expected from the spin-dependent tunneling, the junction magnetoresistance is dependent on the relative orientation of the magnetization in the electrodes. A junction magnetoresistance (JMR) as large as 30% is observed at low temperatures and low fields. In addition, we have found that JMR is reduced at high temperatures ($T > 100$ K) and decreases monotonically with increasing field at high fields ($0.5 \text{ T} < H < 1 \text{ T}$). Possible causes for these are also discussed. © 1998 American Institute of Physics. [S0021-8979(98)20411-7]

There has been a great deal of interest in magnetic tunnel junctions based on conventional ferromagnetic metals due to the large junction magnetoresistance (JMR) observed at room temperature.¹ Due to the uneven spin distribution of conduction electrons at the Fermi level in the ferromagnets, one can expect tunneling probability to be dependent on the relative magnetization orientation of the ferromagnet electrodes. By assuming that spin is conserved in the tunneling process and tunneling current is dependent on the density of states at Fermi level of two electrodes, Jullier showed the maximum change in the tunneling resistance (ΔR) as²

$$\Delta R/R_A = (R_A - R_P)/R_A = 2P_1P_2/(1 + P_1P_2),$$

where R_A and R_P are the junction resistances when the magnetizations are antiparallel and parallel, respectively, and P_1 and P_2 are the spin polarizations of the two electrodes.

Recently, doped manganites, $(\text{R}_{0.7}\text{M}_{0.3})\text{MnO}_3$ where R is a rare earth element such as La, Pr, and Nd, and M is a divalent element such as Ba, Sr, and Ca, have been rediscovered due to the large magnetoresistance near the metal-insulator transition temperature.³ One of the most intriguing facts of the doped manganites is the half-metallic nature predicted by the strong Hund's coupling and a relatively narrow carrier conduction band.⁴ A half-metallic ferromagnet has 100% spin polarization for conduction electrons, and thus it offers potential as a ferromagnetic metal electrode in devices based on spin-dependent transport effects. Hence, compared to the tunneling junctions based on the conventional ferromagnetic metal electrodes, MR in the tunneling junctions made of the manganites is expected to be larger. Sun *et al.* have demonstrated the existence of large magnetoresistance at low fields and low temperatures in the trilayer sandwich junctions using doped manganites.⁵

We report on the fabrication and characterization of ramp-edge ferromagnet-insulator-ferromagnet junction devices using $(\text{La}_{0.7}\text{Sr}_{0.3})\text{MnO}_3$ (LSMO) and SrTiO_3 (STO) as

the ferromagnet and insulator layers, respectively. A large junction magnetoresistance ($\text{JMR} = [(R_j(H) - R_j(1000 \text{ Oe})) / R_j(1000 \text{ Oe})]$) of 30% is obtained at low temperatures in fields of 200 Oe. The junction magnetoresistance is observed to be dependent on the relative orientation of the magnetization in the electrodes as expected from the spin-dependent tunneling. Various possibilities to affect the device performance are discussed such as the changes in the magnetization process and the reduction of the spin polarizability in the electrodes.

A schematic diagram of a ramp-edge junction device structure is shown in Fig. 1. At first, a multilayer including a buffer layer (STO), a bottom electrode (LSMO), and a thick insulation layer (STO) was deposited *in situ* on LaAlO_3 substrate using pulsed laser deposition (PLD). The oxygen background pressure was 400 mTorr and the heater block temperature was 700 °C. The device was defined using conventional photolithography and the ramp edge was created by ion milling with Ar ions. The ramp-angle measured using atomic force microscope (AFM) after the Ar ion milling was 12°–14°. After removing the photoresist, a thin insulating barrier of STO and a top electrode of LSMO were deposited *in situ* under 400 mTorr oxygen and at 700 °C. The insulating barrier and the top electrode were patterned to form a junction and counter electrode as shown in Fig. 1. Finally, gold was sputtered for contact pads. The thicknesses of top and bottom electrodes are 900 and 1100 Å. The thickness of the insulating STO barrier is about 10–20 Å. The junction width is determined by the tap width as shown in Fig. 1(a) which was 5 μm. A detailed description of the ramp-edge device fabrication process can be found in an earlier publication.⁶

As-grown LSMO films under the above growth conditions have a Curie temperature, T_c , of 350 K and a metal-to-metal transition at the same temperature (LSMO has a paramagnetic metal-to-ferromagnetic metal transition near T_c).⁷ The resistive transitions of both top and bottom LSMO electrodes were measured after the device fabrication process and showed the same temperature dependence, suggesting

^{a)}Electronic mail: chuhee@lanl.gov

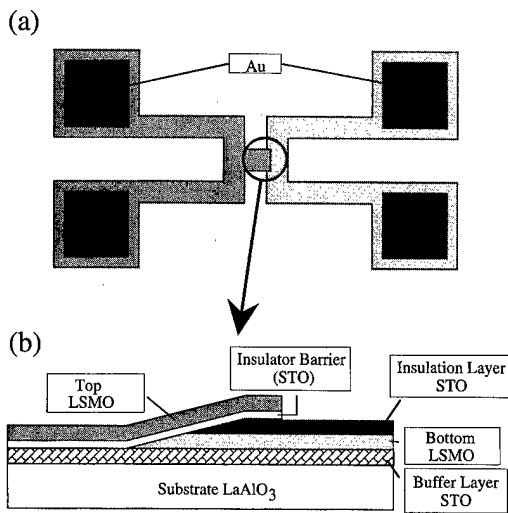


FIG. 1. Schematic diagram of a ramp-edge LSMO/STO/LSMO junction device. (a) Top view, (b) cross section of the junction area.

minimal damage from the patterning process. The JMR was measured with a four-terminal ac resistance bridge and a dc current source in fields up to ± 1 T in the temperature range of 16–300 K. The current was flowing across the insulating barrier layer similar to the current-perpendicular-to-plane (CPP) geometry in a trilayer sandwich junction.⁵ The magnetic field was applied in the plane either parallel or perpendicular to the current. No significant difference was observed in the field dependence of JMR. Also these junctions withstood temperature cycling and were stable in the ambient conditions.

The field dependent junction resistance, $R_j(H)$, and JMR, $\Delta R_j/R_j(1000 \text{ Oe})$ of a device at 15.7 K is shown in Fig. 2. JMR values as large as 30% are observed at low fields (between 180 and 220 Oe). The shape of JMR versus field is similar to that of metal-electrode-based tunnel junctions.¹ At high fields, the junction resistance is low because the magnetization in both electrodes is parallel. When H is between the coercive fields of the top and bottom electrodes (i.e., the electrode magnetization vectors are antiparallel), the junction resistance reaches a maximum value. Generally the JMR in-

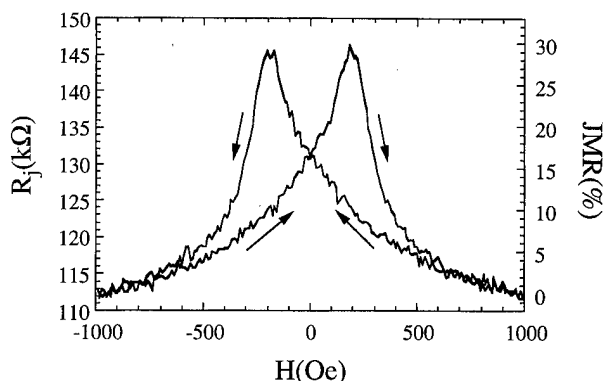


FIG. 2. The junction resistance and magnetoresistance of the ramp-edge junction taken at 15.7 K. JMR is defined by $[(R_j(H) - R_j(1000 \text{ Oe})) / R_j(1000 \text{ Oe})]$. The arrows indicate the direction of magnetic field sweep.

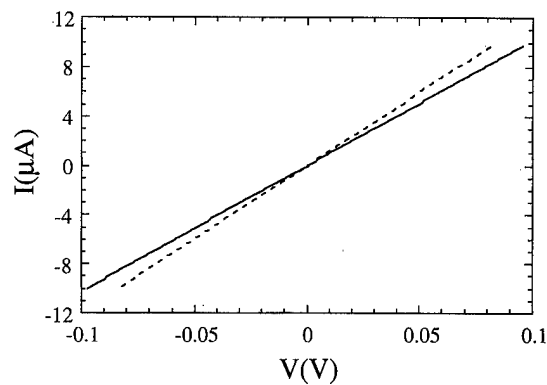


FIG. 3. I - V characteristics of a junction at $T = 16.1$ K with $H = 5000$ (dotted line) and 200 Oe (solid line).

creases nearly linearly with decreasing temperature and saturates at values as large as 30% below 100 K. Large JMR ($> 10\%$) was observed in junctions with R_j ranging from 5 to 200 $\text{k}\Omega$.

The current-voltage (I - V) characteristics of a different junction measured at 16.1 K in $H = 5000$ (dotted line) and 200 Oe (solid line) are depicted in Fig. 3. As seen from Fig. 2, the magnetization in the electrodes is parallel (antiparallel) at $H = 5000$ Oe (200 Oe). At small bias voltages (± 0.1 V), the I - V characteristics show a linear behavior as expected for the tunneling junction with a high energy barrier.^{1,8} Since polycrystalline films⁹ and powder samples⁴ have the field dependent MR similar to Fig. 2 and linear I - V , there is a question whether these characteristics in the ramp-edge junctions are originated not from spin-dependent tunneling but from the granularity in electrodes. In some devices with a poor quality insulator barrier where the transport through microshorts is dominating, we observed a small JMR ($< 1\%$; similar to MR from epitaxial films) at low temperatures indicating the lack of polycrystalline and grain boundary effects across electrodes. This result establishes that the large JMR is from spin-dependent tunnelinglike transports. Unlike the conventional spin-dependent tunneling devices,¹ JMR in the ramp-edge devices does not depend on the dc bias voltage up to the measured range.

The high field JMR, $\Delta R_j(H)/R_j(1 \text{ T})$, at room temperature (solid line) and 20 K (dotted line) for a ramp-edge junc-

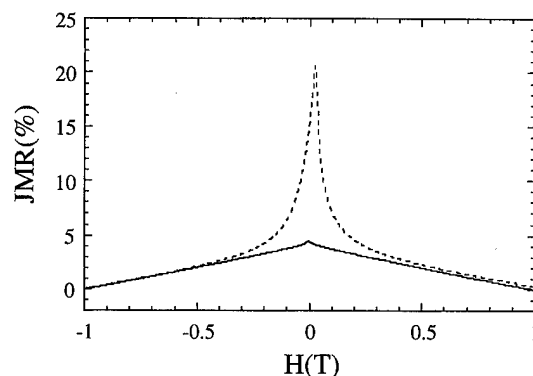


FIG. 4. The high field JMR, $\Delta R_j(H)/R_j(1 \text{ T})$, at room temperature (solid line) and 20 K (dotted line).

tion are presented in Fig. 4. As expected, the low field MR has a maximum in both cases suggesting that the spin-dependent tunneling can be observed even at room temperature. However, there are two questions arising from the results: (1) Why does R_j not saturate, but rather continues to decrease with increasing field up to ± 1 T; and (2) why is the JMR at room temperature so small compared with that at low temperature, even though the spin polarizability in LSMO changes less than 30% if estimated from the bulk magnetization?⁷ The similar results have been reported in the sandwich tunnel junctions⁵ and grain boundary devices¹⁰ using the doped manganites. The second question is especially important for device applications.

The value and the field dependence of JMR strongly depend on the magnetization process and the spin polarizability of the electrodes particularly near the junction. Even though the doped manganites do not have strong crystalline and magnetic anisotropies as a single crystal, magnetic anisotropies induced by the epitaxial growth and the film thickness^{11,12} have been observed in LSMO thin films. Domain pinning due to defects at the interfaces can also hamper the magnetization process. The magnetic anisotropy and domain pinning increase the field required to reach the saturation magnetization, hence, affecting JMR and its field dependence. There was a report on the reduced spin polarizability at the surface of a LSMO film,¹³ which can significantly reduce JMR at high temperatures. Also the surface degradation during the patterning process using ion milling can reduce the spin polarizability at the junction electrodes. The defect mediated scattering in the insulator and at the interfaces is another possible reason to reduce JMR.⁵

In summary, we have successfully fabricated LSMO/STO/LSMO junction devices using a ramp-edge geometry. A junction magnetoresistance of 30% in fields around 200 Oe was observed at $T=15.7$ K. A linear $I-V$ characteristic has been observed at low bias (± 0.1 V) and JMR does not

depend on the junction bias up to 0.1 V. The reduced JMR at high temperature and the field dependence of JMR at high fields can be caused by the magnetization process and the reduced spin polarizability at the junction electrodes.

We would like to thank Dr. M. E. Hawley for AFM support and Dr. Y. Gim for critical reading of the manuscript. This work was performed under the auspices of the United States Department of Energy.

- ¹J. S. Moodera, L. R. Kinder, T. M. Wong, and R. Meservey, *Phys. Rev. Lett.* **74**, 3273 (1995); J. S. Moodera and L. R. Kinder, *J. Appl. Phys.* **79**, 4724 (1996).
- ²M. Juliere, *Phys. Lett. A* **54**, 225 (1975).
- ³J. Volger, *Physica (Utrecht)* **20**, 49 (1954); K. Chahara, T. Ohno, M. Kasai, and Y. Kozono, *Appl. Phys. Lett.* **63**, 1990 (1993); R. von Helmolt, J. Wecker, B. Holzapfel, L. Schultz, and K. Samwer, *Phys. Rev. Lett.* **71**, 2331 (1993).
- ⁴H. Y. Hwang, S.-W. Cheong, N. P. Ong, and B. Batlogg, *Phys. Rev. Lett.* **77**, 2041 (1996), and reference therein.
- ⁵J. Z. Sun, W. J. Gallagher, P. R. Duncombe, L. Krusin-Elbaum, R. A. Altman, A. Gupta, Y. Lu, G. Q. Gong, and G. Xiao, *Appl. Phys. Lett.* **69**, 3266 (1996); J. Z. Sun, L. Krusin-Elbaum, P. R. Duncombe, A. Gupta, and R. B. Laibowitz, *Appl. Phys. Lett.* **70**, 1769 (1997).
- ⁶Q. X. Jia, D. Reagor, H. Kung, M. Hawley, C. Mombourquette, S. R. Foltyn, X. D. Wu, and D. E. Peterson, *Supercond. Sci. Technol.* **9**, 985 (1996); D. Reagor, R. Houlton, K. Springer, M. Hawley, Q. X. Jia, C. Mombourquette, F. Garzon, and X. D. Wu, *Appl. Phys. Lett.* **66**, 2280 (1995).
- ⁷A. Urushibara, Y. Moritomo, T. Arima, A. Asamitsu, G. Kido, and Y. Tokura, *Phys. Rev. B* **51**, 14 103 (1995).
- ⁸R. Meservey and P. M. Tedrow, *Phys. Rep.* **238**, 174 (1994).
- ⁹X. W. Li, A. Gupta, G. Xiao, and G. Q. Gong, *Appl. Phys. Lett.* **71**, 1124 (1997).
- ¹⁰N. D. Mathur, G. Burnell, S. P. Isaac, T. J. Jackson, B.-S. Teo, J. L. MacManus-Driscoll, L. F. Cohen, J. E. Evetts, and M. G. Blamire, *Nature (London)* **387**, 266 (1997).
- ¹¹C. Kwon, S. E. Lofland, S. M. Bhagat, M. Rajeswari, T. Venkatesan, R. Ramesh, A. R. Kratz, and R. D. Gomez, *IEEE Trans. Magn.* **33**, 3964 (1997).
- ¹²Y. Suzuki, H. Y. Hwang, S.-W. Cheong, and R. B. van Dover, *Appl. Phys. Lett.* **71**, 140 (1997).
- ¹³J.-H. Park (private communication).

Grain boundary effects on transport in metalorganic chemical vapor deposition-grown, Ca-doped lanthanum manganites

J. J. Heremans, S. Watts, S. Wirth, X. Yu, E. S. Gillman,
K. H. Dahmen, and S. von Molnár^{a)}

MARTECH, Florida State University, Tallahassee, Florida 32306-4000

The transport properties of metalorganic chemical vapor deposited films of lanthanum manganite grown on various substrates are investigated. The more disordered films show a magnetoresistance that is both large and relatively temperature independent over a wide temperature range. At low magnetic fields, a linear field dependence is observed and is attributed to spin-polarized intergrain tunneling. In addition, at low fields a hysteretic dependence of resistivity on the magnetic field has been observed. This effect has been attributed to the scattering of spin-polarized carriers at the grain boundary. © 1998 American Institute of Physics. [S0021-8979(98)18011-8]

INTRODUCTION

Because of their large magnetoresistance (MR), doped perovskite manganites show promise for magnetoresistive sensor applications. However, for a single crystal sample, the resistivity and MR are strongly temperature dependent, peaking sharply near the Curie temperature T_C , and the sensitivity to low fields remains small.¹ These characteristics limit the usefulness of the materials for technical applications. Yet in some recent experiments²⁻⁶ it has been shown that the existence of grain boundaries can drastically alter the temperature and low field behavior.

Our own efforts have focused on controlling the crystallite alignment (or texture) of the films via the choice of substrate; large lattice mismatches and other interface effects between the film and the substrate can lead to varying degrees of disorder in crystallite alignment. In this article, the temperature dependence and low field transport properties are examined for two highly disordered (low texture) $\text{La}_{0.59}\text{Ca}_{0.41}\text{MnO}_3$ films grown by liquid delivery metalorganic chemical vapor deposition (LD-MOCVD) on single crystal sapphire (SAP) and yttrium-stabilized zirconia (YSZ) substrates. Throughout, a comparison is drawn with a highly textured film of the same composition grown on LaAlO_3 (LAO).

EXPERIMENT

Details on the fabrication of the films by LD-MOCVD are reported elsewhere.⁷ The samples were not postannealed. The average orientation of the crystallites within the film was characterized with pole figures.

Van der Pauw⁸ transport measurements were performed in an ac four-probe configuration at magnetic fields up to 60 kOe. The three samples were mounted with the conducting plane parallel to the field (there is no demagnetization field in this configuration) and always measured simultaneously with a current of 0.1–1 μA . For large field sweeps, the rate was 2 kOe/min in both directions while for low field sweeps the rate was 200 Oe/min. In both cases, the measured field

values were corrected for sweep rate errors. For low field sweeps, the measurements were augmented with static field measurements in which the field was held constant for 10–30 min (relevant because of a time dependent hysteresis, discussed below).

Magnetic measurements were performed in a commercial superconducting quantum interference device (SQUID) magnetometer (Quantum Design). The samples were mounted with the film plane perpendicular to the field in order to measure the magnetization in emu/cm^3 directly without requiring knowledge of the film volume.

RESULTS

Pole figures were used to characterize the crystallite orientation of the samples; the results are shown in Fig. 1. They indicate that the LAO film is highly textured; the crystallites are well aligned with respect to the normal of the (001) surface as well as in the plane of the surface. The YSZ and

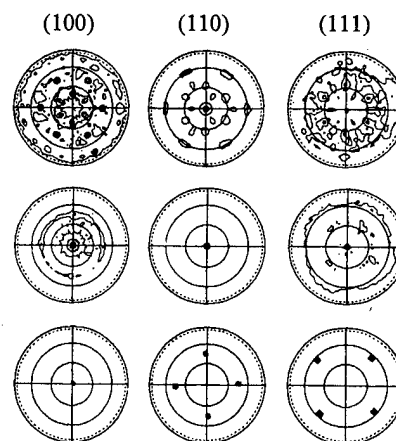


FIG. 1. Pole figures of the $\text{La}_{0.59}\text{Ca}_{0.41}\text{MnO}_3$ films grown on different substrates. The crystallites of the film on the (001) oriented LAO substrate (bottom) are very well aligned normal to the surface as well as within the surface plane. The crystallites on the (001) oriented YSZ (middle) are well aligned with their (110) direction normal to the surface, but randomly oriented otherwise. The least texture is developed in the film on the (0001) oriented SAP (top), faintly resembling the sixfold symmetry of the substrate.

^{a)}Electronic mail: molnar@phy.fsu.edu

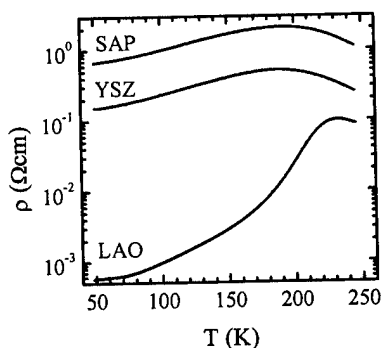


FIG. 2. Zero-field resistivity vs temperature for the films grown on sapphire (SAP, top curve), yttrium-stabilized Zr_2O_3 (YSZ, middle curve), and LaAlO_3 (LAO, lower curve). The relative change of resistivity with varying temperature is small for the more disordered films.

SAP films are less textured with a preferentially oriented (011) surface direction. The crystallite alignment is more pronounced in the YSZ than in the SAP film.

The magnetization data in an applied magnetic field of 6500 Oe are comparable for all three samples, and reach a value of approximately 500 emu/cm^3 . This is below the maximum theoretical magnetization of about 570 emu/cm^3 . Magnetization versus temperature at 5 kOe (not shown) is similar for the three samples, as also found in Ref. 4. The data indicate $T_C \sim 230 \text{ K}$ for the films.

Figure 2 shows a plot of the logarithm of resistivity ρ versus temperature for the three films. Resistivity was calculated assuming an average thickness of $\sim 1000 \text{ \AA}$ for all three samples. The SAP and YSZ films have the same temperature dependence, with a difference only in magnitude. They are, however, quite different from the LAO film. The resistivity of the LAO film decreases by about two orders of magnitude between the temperature T_m of the resistivity peak and 50 K. While the SAP and YSZ films are much more resistive than the LAO film, they are much less sensitive to temperature, changing only by a factor of 3 in the same temperature range. The data resemble those³ for films grown on single crystal and polycrystalline SrTiO_3 .

A detailed study of the dependence of the resistivity ratio $\rho/\rho(H=0)$ on field and temperature is presented in Fig. 3 (the YSZ sample is not shown, but is similar to the SAP sample). For $T < T_m$, the YSZ and SAP films behave quite differently than the LAO film, featuring a steep low field slope that, around 2 kOe, breaks to a much more gradual dependence, nearly linear up to 30 kOe. In similar data for sintered bulk materials⁴ such features are attributed to spin-polarized intergrain tunneling. Close examination of our LAO sample also reveals these features, but at low temperatures (at 10 and 50 K), and over a much smaller resistivity scale. In fact, in the LAO sample the apparent contribution of intergrain tunneling leads to a more pronounced magnetoresistance at 50 K than at 100 K.

All three films also display a low field hysteretic resistivity peak, particularly prominent at low temperatures, as shown in Fig. 4 for $T = 10 \text{ K}$. Such hysteresis was not observed in Refs. 2–4 and 9. It has been demonstrated,^{5,6} however, that a low field hysteresis is a hallmark of grain boundary magnetoresistance caused by scattering of spin-polarized

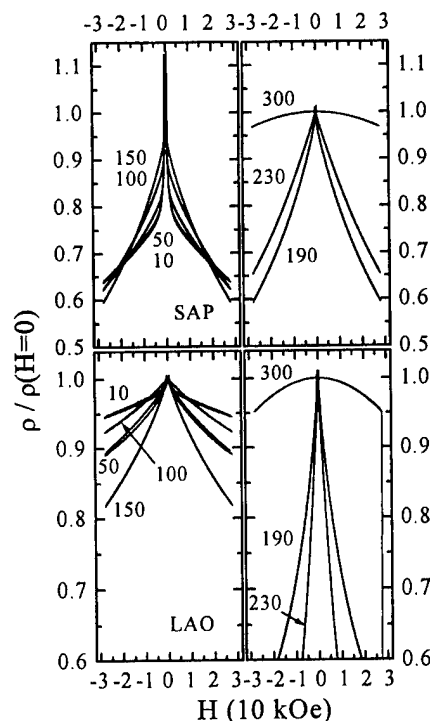


FIG. 3. Resistivity ratio $\rho/\rho(H=0)$ vs magnetic field H (parallel to the film plane) for various temperatures. Data are shown for field sweeps in both directions. The top panels refer to the SAP sample; the bottom panels refer to the LAO sample. The left panels contain data for temperatures of 10, 50, 100, and 150 K. The right panels contain data for temperatures of 190, 230, and 300 K.

carriers at the interface. We emphasize that the relative magnitude of this effect remains much smaller for the LAO sample than for the YSZ and SAP samples, consistent with their differences in texture.

Finally, we observe a ubiquitous time-dependent hysteresis evident in fields as high as 60 kOe, common to some degree to all of our film samples (see, e.g., the high field, low

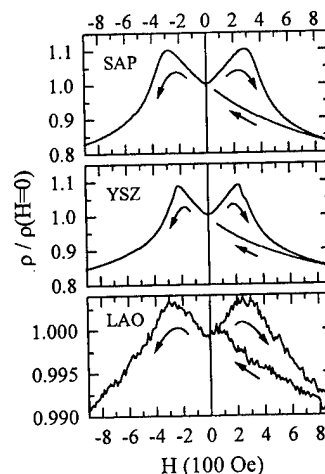


FIG. 4. The low field hysteresis in the resistivity ratio $\rho/\rho(H=0)$ vs magnetic field at 10 K for the SAP (top), YSZ (middle), and LAO (bottom) samples. Shown are data from a 0 to -2 kOe sweep (after first sweeping to 30 kOe and back), a 0 to 1 kOe sweep (after having continued the sweep from -2 to 30 kOe and then back to 0), and the return sweep to 0. Data were also acquired at static field points over long time periods (10–30 min) to verify the accuracy of the swept data.

temperature data in Fig. 3). This effect is clearly unconnected to the low field hysteresis (Fig. 4), which does not depend on time.

CONCLUSIONS

The substrate on which the $\text{La}_{1-x}\text{Ca}_x\text{MnO}_3$ thin films are deposited strongly influences the film texture, which in turn has dramatic consequences on the film's magnetoresistive properties. A film grown on LAO is highly textured and shows many of the features observed in single crystals (such as resistivity and magnetoresistance sharply peaked near T_C). On the other hand, growths on YSZ and SAP substrates result in much more disordered films, and both the resistivity and MR remain substantial over a wider temperature range. Furthermore, the MR of the latter films show a large, linear field dependence at low fields up to 2 kOe, which has been attributed to spin-polarized intergrain tunneling. A low field hysteresis is also observed due to scattering of spin-polarized carriers at the interface. This effect was not observed in earlier studies of films on similar substrates.

The data show a clear correlation between transport properties and film texture. In other works,²⁻⁶ the transport properties characteristic of our disordered films have been attributed to grain boundary effects. These effects may be due to either (1) the number of grain boundaries (i.e., the size of the grains) or (2) the relative orientation of the grains.¹⁰ The pole figure measurements indicate that the grains are misaligned, so the latter mechanism should be prominent in the less textured films. However, we have been unable to

determine conclusively which of the two mechanisms contributes more to grain boundary effects in our samples.

The above observations point to the importance of film morphology in developing useful magnetoresistive devices from the lanthanum manganites.

ACKNOWLEDGMENTS

The author gratefully acknowledge E. Lochner, T. Fellers, and J. M. D. Coey for their assistance and helpful discussions. This work was supported by Office of Naval Research Grant No. ONR N00014-96-1-0767.

- ¹J. M. D. Coey, M. Viret, and S. von Molnár (unpublished).
- ²R. Mahesh, R. Mahendiran, A. K. Raychaudhuri, C. N. R. Rao, *Appl. Phys. Lett.* **68**, 2291 (1996).
- ³A. Gupta, G. Q. Gong, G. Xiao, P. R. Duncombe, P. Lecoeur, P. Trouiloud, Y. Y. Wang, V. P. Dravid, and J. Z. Sun, *Phys. Rev. B* **54**, R15 629 (1996).
- ⁴H. Y. Hwang, S.-W. Cheong, N. P. Ong, and B. Batlogg, *Phys. Rev. Lett.* **77**, 2041 (1996).
- ⁵K. Steenbeck, T. Eick, K. Kirsch, K. O'Donnell, and E. Steinbeiss, *Appl. Phys. Lett.* **71**, 968 (1997).
- ⁶N. D. Mathur, G. Burnell, S. P. Isaac, T. J. Jackson, B.-S. Teo, J. L. MacManus-Driscoll, L. F. Cohen, J. E. Evetts, and M. G. Blamire, *Nature (London)* **387**, 266 (1997).
- ⁷E. S. Gillman *et al.* (unpublished).
- ⁸L. J. van der Pauw, *Philips Tech. Rev.* **20**, 220 (1958).
- ⁹R. Shreekala, M. Rajeswari, K. Ghosh, A. Goyal, J. Y. Gu, C. Kwon, Z. Trajanowic, T. Boettcher, R. L. Greene, R. Ramesh, and T. Venkatesan, *Appl. Phys. Lett.* **71**, 282 (1997).
- ¹⁰K. H. Kim, J. Y. Gu, H. S. Choi, D. J. Eom, J. H. Jung, and T. W. Noh, *Phys. Rev. B* **55**, 4023 (1997).

Magnetic anisotropy and spin diffusion through spin disordered interfaces in magnetoresistive manganites

B. Martínez,^{a)} Ll. Balcells, J. Fontcuberta, and X. Obradors

ICMAB-CSIC. Campus Universitat Autònoma de Barcelona, E-08193 Bellaterra, Spain

C. H. Cohenca and R. F. Jardim

Instituto de Física, Universidade de São Paulo, 05315-970 São Paulo, Brazil

The magnetoresistance and the magnetization of ceramic $\text{La}_{2/3}\text{A}_{1/3}\text{MnO}_3$ ($\text{A} = \text{Sr}, \text{Ca}$) oxides have been studied as a function of the grain size. It is found that these ceramics become magnetically harder when reducing the particle size exhibiting a large magnetic anisotropy that increases when reducing the grain size. In concomitance with this enhancement of the magnetic hardness, a gradual increase of the low-field magnetoresistance is also detected, signaling the relevance of the surface and interfaces contribution to the magnetic and transport properties. We suggest that both phenomena could be closely related and associated to the existence of some degree of spin disorder at the grain boundaries. We propose that these features are fingerprints of quenched spin disorder at interfaces that can be tuned through bandwidth modulation of the magnetic frustration. © 1998 American Institute of Physics. [S0021-8979(98)29211-5]

I. INTRODUCTION

The huge magnetoresistance (MR) of manganese perovskites (up to $10^7\%$) has a serious drawback on the need for large magnetic fields to obtain such large changes of the resistance. This fact was an important handicap since many of their potential applications require a good response in the low field regime. In this sense, the discovery of two well separated MR contributions in ceramic $\text{La}_{2/3}\text{A}_{1/3}\text{MnO}_3$ ($\text{A} = \text{Ca}, \text{Sr}$) samples, one attributed to an intrinsic intragranular component and the other to a nonintrinsic intergranular effects,² could be of a major importance for technological applications.

Even the actual mechanism laying behind the low field magnetoresistive response is still obscure, two different interpretations have been given, namely, spin-polarized intergrain tunnelling² and spin-dependent scattering at the grain boundaries.³ It is therefore evident that, whatever the mechanism, a strong influence of the surface magnetic disorder on the conduction process should be expected. The relevance of surface spin disorder in the later mechanism is evident by itself. On the other hand, according to the current understanding of the spin tunnelling mechanism, the MR should be proportional to the intergrain exchange coupling,⁴ that can be tuned by appropriate tailoring of both bulk and surface magnetic interactions.⁵⁻⁷ Therefore, reducing the particle size of the ceramics would imply an increase of the number of junctions and the low-field MR should be significantly enhanced. Nevertheless, since both the scattering³ and tunnelling⁴ models predict a quadratic dependence on the magnetization M [$\text{MR} \approx (M/M_s)^2$], it is not possible to distinguish between them on this aspect alone.

On the other hand, it has been shown that the degree of spin disorder can be controlled via the $\sigma^{1-x}(e_g)$ bandwidth, by the appropriate choice of the lanthanide^{6,7} or via the rela-

tive strength of the (F/AF) interactions by the choice of the alkaline earth.⁵ At the grain surface of a ceramic sample, charge carrier mobility should be severely dampened, the relative strength F/AF reduced, and therefore, the competition of interactions reinforced. At the same time, charge carriers in manganites are fully polarized and in a transport experiment, a current of carriers should travel from grain to grain. Thus, surface spin disorder should severely affect the intergrain resistivity, in a very sensitive way. In this article, we will explore the influence of both particle size and magnetic disorder on the low field magnetoresistive response of ceramic manganites.

II. EXPERIMENTAL AND RESULTS

Ceramic samples of $\text{La}_{2/3}\text{Sr}_{1/3}\text{MnO}_3$ were prepared by conventional solid-state techniques in oxygen atmosphere,^{5,6} while $\text{La}_{2/3-x}\text{Y}_x\text{Ca}_{1/3}\text{MnO}_3$ ($x = 0-0.25$) samples were prepared by a sol-gel method.⁸ The particle size effects were studied in a series of four samples (A-D) of $\text{La}_{2/3}\text{Sr}_{1/3}\text{MnO}_3$ with particle sizes of $A \approx 0.5-1 \mu\text{m}$, $B \approx 2-5 \mu\text{m}$, $C \approx 10-20 \mu\text{m}$, and $D \approx 50-100 \mu\text{m}$ prepared by using different methods (mechanical attrition and different sinterization temperatures) in order to control particle size.⁹ The influence of the magnetic disorder was explored in $\text{La}_{2/3-x}\text{Y}_x\text{Ca}_{1/3}\text{MnO}_3$ ($x = 0-0.25$) samples. Magnetization measurements were done using a superconducting quantum interference device (QD) (SQUID) system up to 5 T. Transport measurements were performed, using the standard four probe method, on samples of about $0.5 \times 1 \times 5 \text{ mm}^3$ with the current applied perpendicular to the magnetic field.

In Fig. 1 we show the $\rho(T)$ curves for samples A-D. The electrical resistivity has essentially the very same form and steadily increases, in all the temperature range, from sample D to A reflecting grain size reduction and degradation of the grain connectivity. A sort of maximum of the resistivity exists at $T \approx 365 \text{ K}$ for all the samples, thus showing that the oxygen stoichiometry is essentially the same.

^{a)}Electronic mail: Ben.Martinez@icmab.es

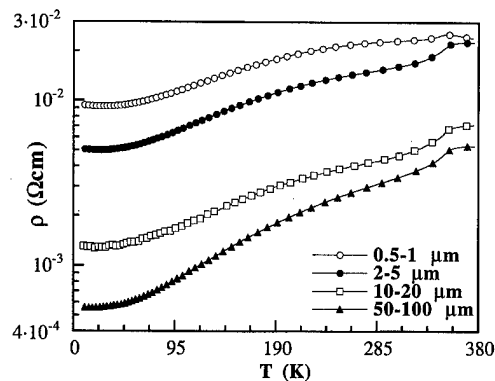


FIG. 1. Thermal dependence of the electrical resistivity of the $\text{La}_{2/3}\text{Sr}_{1/3}\text{MnO}_3$ samples as a function of the particle size.

As already observed in ceramic samples,² the magnetoresistance (MR) of samples A–D, as a function of field, displays two well defined regimes.⁹ In the low-field regime extending only a few kOe, a sharp decrease is found, with variations of MR up to 30% at low temperatures, but decreasing when T increases. On the contrary, in the high field regime the variation of MR is almost linear with a slope $S = dR(H)/dH$ very much smaller than for low fields.

The low field MR may be evaluated by extrapolating back to $H=0$ the almost linear behavior of the normalized resistance $[R(H)/R(0)]$ observed above 5 kOe. Subtracting the intercept with the y axis from 1 we have the variation of the MR in the low field regime, the so-called low field magnetoresistance (LFMR) depicted in Fig. 2. The key point in this figure is that LFMR not only decreases with T but, also clearly depends on the particle size, becoming smaller as the particle size increases. It is also worth mentioning that the MR does not show the expected quadratic dependence on the magnetization at any temperature (see inset of Fig. 2).

Our results also show that the slope $S = dR(H)/dH$ of the high field linear portion of $R(H)$ becomes progressively reduced when increasing the particle size.⁹ Thus, even the high field region of $R(H)$ is affected by grain boundary effects. Nevertheless, a significant difference does exist be-

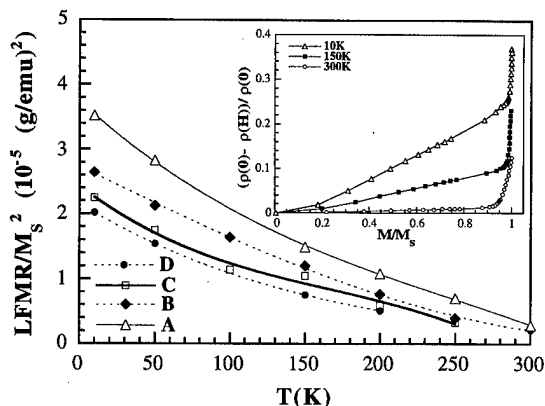


FIG. 2. Low-field magnetoresistance as defined in the text vs temperature as a function of the particle size (A=0.5–1 μm , B=2–5 μm , C=10–20 μm , and D=50–100 μm .) Inset: MR vs normalized magnetization, the absence of the expected quadratic dependence on M/M_s is evidenced.

tween the low and the high field regimes: whereas in the first case, the normalized LFMR, strongly depends on the particle size, the high field magnetoresistance dependence is very smooth.

On the other hand, the isothermal field dependence of the magnetization in ferromagnets can be described in terms of the so-called “law of approximation to saturation” (LAS):

$$M(H) = M_s [1 - a/H - b/H^2] + \chi_d H, \quad (1)$$

where M_s is the saturation magnetization, χ_d is the high field differential susceptibility, and a and b are fitting parameters. In order to get an estimate of the magnetic anisotropy energy in these samples we assume, in a first approximation, the expression of K_1 for uniaxial systems:

$$K_1 = [(105/8)bM_s^2]^{1/2}. \quad (2)$$

The obtained values of K_1 are around 10^7 erg/cm³. These values of the magnetic anisotropy are surprisingly large for a transition metal oxide and raises several questions about its origin. Nevertheless, they should be considered just as an upper limit for the magnetic anisotropy since, at the maximum field applied (55 kOe) samples may be far from saturation and other contributions (canting, frustration, etc.) may affect the values determined in this way. In any case, it is evident that decreasing the particles size implies an increment of the magnetic hardness that is reflected also in the increase of the LFMR. Whether the origin of this hardness is an increase of the surface anisotropy or an increase of the magnetic frustration is still an open question. We think that it may be closely related with the existence of a magnetically disordered surface layer, as already observed in magnetic nanoparticles,¹⁰ whose contribution increases as particle size decreases and is specially relevant for transport experiments since electrons have to cross through this surface layer from one grain to another.

In order to check this idea we have modified the spin disorder in ceramic samples of $\text{La}_{2/3-x}\text{Y}_x\text{Ca}_{1/3}\text{MnO}_3$ ($x=0-0.25$), with essentially the same particle size, by changing the Y content. As already mentioned in the introduction, the competition between F and AF interactions can be tuned via the $\sigma^{1-x}(e_g)$ bandwidth,^{6,7} or by the choice of the alkaline earth.⁵

The $\rho(H)$ and $M(H)$ loops for samples with $x=0, 0.15$, and 0.25 are shown in Fig. 3. It is found that both coercive fields, H_c , and anisotropy fields, H_a , increase gradually with x showing no other contributions to the irreversibility than those coming from domain rotation. Nevertheless, (ZFC-FC) measurements at high fields do show irreversible behavior below about 40 K (see Fig. 4) and, as expected, the irreversibility becomes broader as x increases. The existence of magnetic irreversibility at such high fields is attributed to the freezing of a part of the spin system into a metastable spin-glass-like state, in close similarity with what is observed in magnetic nanoparticles.¹⁰

As shown in Fig. 3, the electrical resistivity displays strongly enhanced hysteresis as compared to the magnetization and it is more evident as x increases. Notice, for in-

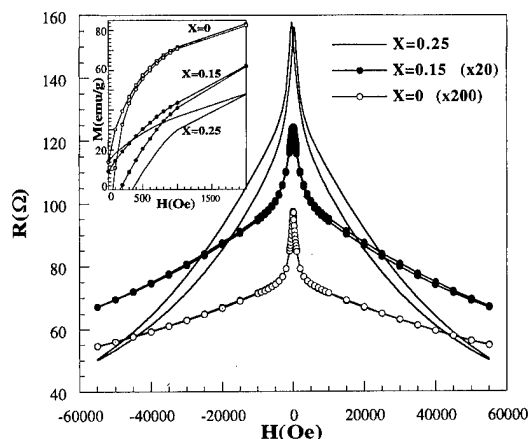


FIG. 3. $R(H)$ loops for the three samples of $\text{La}_{2/3-x}\text{Y}_x\text{Ca}_{1/3}\text{MnO}_3$ as a function of the doping rate ($x=0, 0.15$, and 0.25). Inset: Detail of the positive quadrant of the hysteresis loops for the same three samples.

stance, that for $x=0.25$, at 5 K, $\rho(H)$ is irreversible up to 55 kOe whereas the $M(H)$ is closed at about 2 kOe.

In short, irreversibility in the resistivity appears to be more prominent than in the magnetization. This observation is extremely significant because it clearly shows that even if a small fraction of the spins are frozen in a disordered configuration [the $M(H)$ loops are closed], the resistivity is still hysteretic. The obvious explanation of this remarkable result is that electrical resistivity measurements sense the surface spin state at the grain boundaries. It is thus clear that any effect modifying the surface magnetization should change $\Delta\rho$. Therefore, the irreversibility in $\rho(T, H)$ reveals a quenched surface spin disorder. It also means that the surface glassiness displays significant magnetoresistance. It is clear that in our micrometric particles, the surface spins contribution to the magnetization should be necessarily only a minor fraction of the bulk magnetization. For instance, from the $\Delta M(10 \text{ K}, 5 \text{ kOe})$ value one can estimate a nonmagnetic layer of about 10 nm, that is only of about 1% of the particle radius.

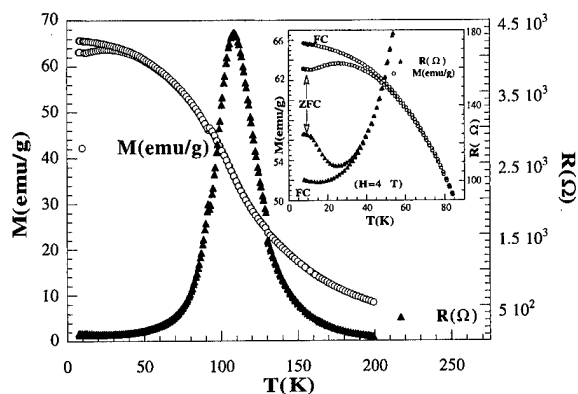


FIG. 4. ZFC-FC curves of both magnetization and resistance for the sample of $\text{La}_{2/3-x}\text{Y}_x\text{Ca}_{1/3}\text{MnO}_3$ with $x=0.25$ in a field of 40 kOe. Inset: Detail of the low temperature region showing the irreversibility in both $M(T)$ and $R(T)$.

The resistivity measured after ZFC-FC processes also displays low-temperature hysteretic behavior and, as expected, the FC resistivity is always lower than the ZFC one. In Fig. 4 we include the $\rho(T, 50 \text{ kOe})$ data for the $x=0.25$ sample. We note again the more pronounced irreversible character $\rho(T)$ when compared to $M(T)$: i.e., for $x=0.25$, the difference in $\rho(T)$ ZFC/FC is of about 20% while $\Delta M \approx 3\%$. Therefore, the available experimental data, particularly the observation of open hysteresis loops $\rho(H)$ up to fields well above (at least one order of magnitude) H_a can be well understood as a result of the existence of a significant spin disorder at the grain boundaries. The persistence of hysteresis on the resistivity when magnetization loops are almost reversible is a key observation which, essentially reveals the surface nature of the spin disorder. This hysteresis is more pronounced in the Y rich samples; an effect which is consistent with an enhanced magnetic frustration and the softer interatomic magnetic coupling.^{6,7} The observation of higher coercive fields for $x=0.25$ than for $x=0$ (Fig. 3) also fits into this picture.

III. CONCLUSION

In summary, we have shown that the MR of ceramic samples displays a clear dependence on the particle size specially in the low field regime. The magnetic behavior gives clues in the sense that the system becomes magnetically harder as particle size decreases, whether it is due to an increase of magnetic surface anisotropy or an increase of the magnetic frustration is still an open question. In this sense, we have shown that spin disorder seems to be increased at grain surface. Low-field magnetoresistance, could thus originate from the field suppressed magnetic disorder at the particle surface layer. The relevance of these observations for the spin polarized devices, where magnetic and electrical interfaces are at the heart, is thus as clear as polarization and can be seriously reduced.

ACKNOWLEDGMENTS

The authors would like to acknowledge the CiCYT (MAT97-0699), the GRQ-95-8029, and the OXSEN-CEE Projects for financial support.

- ¹S. Jin *et al.*, *Science* **264**, 463 (1994).
- ²H. Y. Hwang, S.-W. Cheong, N. P. Ong, and B. Batlogg, *Phys. Rev. Lett.* **77**, 2041 (1996).
- ³X. W. Li, A. Gupta, Gang Xiao, and G. Q. Gong, *Appl. Phys. Lett.* **71**, 1124 (1997).
- ⁴J. S. Helman and B. Abeles, *Phys. Rev. Lett.* **37**, 1429 (1976).
- ⁵J. L. García-Muñoz, J. Fontcuberta, B. Martínez, A. Seffar, S. Piñol, and X. Obradors, *Phys. Rev. B* **55**, R668 (1997).
- ⁶J. Fontcuberta, B. Martínez, A. Seffar, S. Piñol, J. L. García-Muñoz, and X. Obradors, *Phys. Rev. Lett.* **76**, 1123 (1996); J. Fontcuberta, B. Martínez, A. Seffar, S. Piñol, J. L. García-Muñoz, and X. Obradors, *Europhys. Lett.* **34**, 379 (1996).
- ⁷H. Y. Hwang *et al.*, *Phys. Rev. Lett.* **75**, 914 (1995); Y. Tokura *et al.*, *ibid.* **76**, 3184 (1996).
- ⁸P. A. Suzuki and R. Jardim, *Physica C* **267**, 153 (1996).
- ⁹L. Balcells, J. Fontcuberta, B. Martínez and X. Obradors, *J. Phys.: Condens. Matter* **10**, 1883 (1998).
- ¹⁰R. H. Kodama, A. E. Berkowitz, E. J. McNiff, Jr., and S. Foner, *Phys. Rev. Lett.* **77**, 394 (1996).

Scanning magnetoresistance microscopy of $\text{La}_{0.67}\text{Sr}_{0.33}\text{MnO}_3$ films

D. K. Petrov,^{a)} A. Gupta, J. R. Kirtley, and L. Krusin-Elbaum

IBM Research Division, T. J. Watson Research Center, Yorktown Heights, New York 10598

H. S. Gill

IBM Corporation, N17/142, 5600 Cottle Road, San Jose, California 95193

We have developed a magnetic imaging scheme using the magnetoresistive spin valve head in a dc bias mode as a sensing element. By scanning the head in contact with the sample we obtain a submicron spatial resolution map of the normal component of the magnetic field in the temperature range 4.2–300 K. The writing element of the sensor can be used to alter the local magnetic structure in a controlled way. This technique was applied to image the magnetic domain structure down to 77 K in patterned thin films of $\text{La}_{0.67}\text{Sr}_{0.33}\text{MnO}_3$, known for their colossal magnetoresistance. A reorientation of single or multiple domains in the films was accomplished by applying a local magnetic field with the writing element, while the effect on magnetotransport was monitored with the simultaneous measurement of current–voltage characteristics. © 1998 American Institute of Physics. [S0021-8979(98)27911-4]

The drive toward high areal densities in magnetic recording has led to significant advances in developing high spatial resolution read/write magnetic sensors. Presently, the state-of-the-art sensors in the recording industry are magnetoresistive spin valve heads (MRSVs).¹ With excellent (submicron) spatial resolution (at least in one direction) and high field sensitivity of nearly $30 \mu\text{V/G}$, these sensors deliver a capability beyond the magnetic storage media, for which they were originally designed. Integrated into a suitable scanning system, they offer a uniquely robust scheme to image surface magnetic fields on a submicron scale in materials of both scientific and technological interest.

The past several years have witnessed growing development and use of a variety of magnetic imaging techniques. Among these techniques are magnetic force microscopy (MFM),² scanning superconducting quantum interference device (SQUID) microscopy,³ Lorentz transmission electron microscopy (LTEM),⁴ Kerr microscopy,⁵ scanning micro-Hall probe microscopy (SHPM),⁶ and others. All of these techniques record the magnetic structure at the surface of the material by sensing a vertical component of the surface stray magnetic fields. The techniques vary in their limits of applicability. A SQUID microscope, for example, has the highest field sensitivity. It can resolve $10^{-6} \Phi_0/\text{Hz}^{1/2}$ at a noise level of $4 \times 10^{-7} \text{ G/Hz}^{1/2}$. However, since it uses a superconducting device, the temperature window is limited to below the transition temperature T_c and the spatial resolution is at best a few microns, limited by its pickup loop area. MFM, on the other hand, has an excellent spatial resolution ($\sim 50 \text{ nm}$), but it requires a separate knowledge of surface topography and is difficult to quantify since it responds to field gradients. LTEM has been used to image magnetic domain boundaries with remarkable detail, but at a price of hardware complexity and cost.

We set out to develop a simple and robust magnetic sensing scheme using the leading edge technology magnetoresistive spin valve heads—the scheme closest to the scan-

ning Hall technique, but less costly and with less material complexity.⁶ The unique feature of MRSV heads—in addition to their noninvasive “read” function—is their “write” capability. They can be used to locally apply a field and thus provides an additional tool to control and probe a local magnetic environment on the surface. MR heads were used previously to image and manipulate bits on magnetic storage disks⁷ using ac mechanical modulation and in dc mode to image and record bits on magnetic disks and image magneto-optic and perpendicular media, magnetic tape, and magnetic particles at room temperature.⁸ The sensitivity of our MRSVs allows us to use them in a dc mode and also at cryogenic temperatures, thus expanding the applicability range.

The spin valve is a layered structure which consists of magnetic layers weakly coupled across a thin copper layer. While the magnetization in one magnetic (pinned) layer is fixed, the other (free) layer can change its magnetization depending on the local magnetic environment. The field sensitive component of the resistance of the structure depends on the cosine of the relative angle between the magnetization vectors in the two magnetic films, making the spin valves attractive as simple and efficient sensors for low field applications.¹ The technique we describe involves raster scanning a MRSV sensor in physical contact with the imaged surface. A schematic of the instrument is shown in Fig. 1. The MRSV head is attached to a flexible cantilever, which adjusts to variations in surface topography. The sample is mounted on a high-precision, x – y – z positioning stage driven by a mechanical micromotor. The x – y component of the stage is used for raster scanning. Approach to the sample is made by using a micrometer screw, while at the same time monitoring the output signal of the device. The scan dimensions range from 20 to $400 \mu\text{m}$ at 77 K, with a nominal scan step of 500 nm. The action of the mechanical motor (with a $0.5 \mu\text{m}$ step) is further reduced with a lever.³ The spatial resolution of the images is limited by the size of the gap between the shields ($0.25 \mu\text{m}$ in our case). A dc current bias in the range of 3–4.5 mA is supplied to the MRSV element

^{a)}Electronic mail: petrov@us.ibm.com

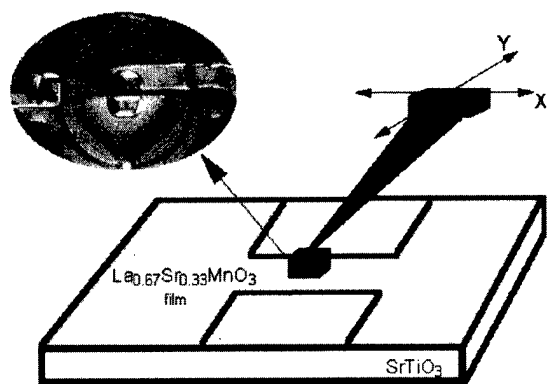


FIG. 1. A schematic of the experimental setup with an expanded view of the inductive coil of the “write” element and the outer shield in the upper left corner. The MR head (not drawn to scale) is scanned in contact with the sample. The “read” element is $2\ \mu\text{m}$ behind the “write” element.

by a constant current source and the magnetoresistive response is recorded in a Wheatstone bridge configuration. The sensitivity at these current levels is $\sim 30\ \mu\text{V/G}$. The “write” function of the head is accomplished with currents of ± 20 – $40\ \text{mA}$ through the “write” element, corresponding to fields up to $80\ \text{G}$ at the surface. The system is configured so that the magnetic surface imaging can be recorded simultaneously with the dynamic resistance (dV/dI) and the current–voltage (I – V) characteristics of the sample under study using a standard ac modulation technique. The entire stage is placed in a liquid helium cryostat where, by means of helium exchange gas, the temperature is controlled in the range 4.2 – $300\ \text{K}$.

We demonstrate the capability of this technique by using it in a study of colossal MR (CMR) manganite perovskite thin films⁹ grown on periodically grooved single crystal, a (100) oriented single crystal, and a polycrystalline SrTiO_3 substrate as described previously.¹⁰ CMR materials have received a great deal of attention because of their potential for sensor and memory applications.^{10–14} A large low-field MR component has been observed in polycrystalline thin films and bulk manganite samples.^{10,11} While the exact mechanism for this low-field MR is not yet completely understood (magnetotunneling^{11,14} versus spin scattering at the grain boundaries¹⁰), the degree of alignment of the magnetization in adjacent grains is crucial for the magnetotransport. By using the read/write MR head we can directly probe the effect of changes in the intragranular domain structure on magnetotransport.

An illustrative example of a MRSV image is shown in Fig. 2. This image is of a $\text{La}_{0.67}\text{Sr}_{0.33}\text{MnO}_3$ film deposited on a patterned substrate with regularly spaced grooves. The thickness of the magnetic layer follows the morphology of the corrugated surface. The domain structure is controlled by the step-edge weak links appearing as a result of sharp steps in the topography of the substrate. The spatial periodicity here is about $5\ \mu\text{m}$, but we can resolve single magnetic domains of submicron size, well visible along the washboard pattern. This image was obtained after the film was cooled down to $77\ \text{K}$ in the remnant field.

The “write” capability of the MRSV element is illus-

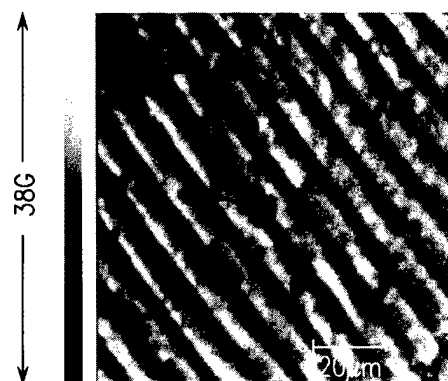


FIG. 2. An image of a $\text{La}_{0.67}\text{Sr}_{0.33}\text{MnO}_3$ film deposited on a periodically grooved substrate. The full gray scale corresponds to a field variation of $38\ \text{G}$. Black corresponds to a negative field (\downarrow) and white to positive field (\uparrow).

trated in Fig. 3, which shows an image of a $\text{La}_{0.67}\text{Sr}_{0.33}\text{MnO}_3$ epitaxial film deposited on a 24° bicrystal SrTiO_3 substrate. Cooling the sample down to $77\ \text{K}$ in an in-plane homogeneous external field of $100\ \text{G}$ [above the coercive field $H_c(77\ \text{K})=30\ \text{Oe}$] allows us to image the bicrystalline grain boundary because the local disorder along the boundary nucleates a domain structure on the scale of the physical width of the boundary ($\sim 10\ \text{\AA}$). The magnetic width of the boundary is $\sim 2\ \mu\text{m}$, wider due to spreading of the return field lines at the surface. We search for the anisotropy induced effects by writing five domains, two on each side of the boundary and one directly on the boundary. The domains are nucleated by a $30\ \text{mA}$ pulse through the inductive coil of the “write” element. The images of the domains in Fig. 3 show vertical (\uparrow and \downarrow) components of the field at the edges of the domains. The effect of the crystallographic mismatch produces domains of different shapes on the two sides of the boundary. This effect can be imaged due to the elongated shape of the “write” element.

Now we illustrate the joint “read,” “write,” and magnetotransport measurement capabilities of our MRSV microscope using patterned polycrystalline manganite films, which exhibit a low-field MR effect.¹⁰ The task here is to switch the individual grains in the “write” mode, to image them in the “read” mode, and to correlate these images with the magnetotransport across the grain boundaries. We pattern a $10\ \mu\text{m}$ wide bridge structure in films with an average grain size of $\sim 14\ \mu\text{m}$. Thus, we have a single grain across the bridge width and a few grains along its length. The image in Fig.

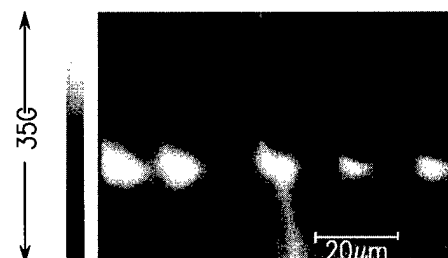


FIG. 3. Domains written on a $\text{La}_{0.67}\text{Sr}_{0.33}\text{MnO}_3$ epitaxial film deposited on a bicrystal substrate. The grain boundary appears as a faint line. The black and white spots correspond to the poles of the written domains.

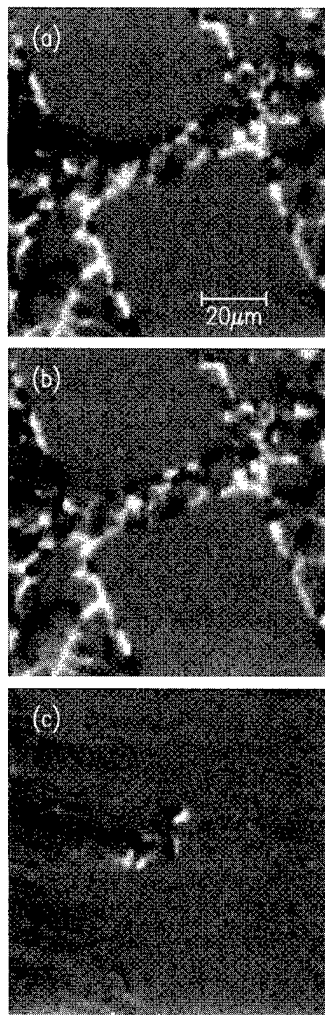


FIG. 4. Images of $\text{La}_{0.67}\text{Sr}_{0.33}\text{MnO}_3$ polycrystalline films (a) before and (b) after using the “write” element over the center of the bridge. (c) The difference between the images (a) and (b) shows the switched domains only.

4(a) shows well resolved individual grains with randomly oriented in-plane magnetization. Curve 2 in Fig. 5 shows simultaneously obtained dV/dI of this domain configuration, measured across the entire length of the bridge. We modify the domain configuration by writing with a 40 mA pulse at the center of the bridge [Fig. 4(b)]. The difference image in Fig. 4(c) clearly indicates the local action of the “write” element—only domains in the center of the bridge are altered, and the corresponding dV/dI vs V (curve 3) reflects this switch. Switching different grains along the bridge length produces a variety of dV/dI 's (curves 1, 4, and 5), depending on the local grain configuration and on the writing current. The curves represent averaging over several grains on the bridge. The resistance change across the grain boundaries, produced by the rotation of magnetic moment in adjacent grains, is about $50\ \Omega$. An indirect indication of this process was reported in Refs. 10, 12, and 13. The parabolic shape of dV/dI vs V in Fig. 5 can be produced either by tunneling¹⁵ or by spin scattering¹⁰ at the boundary. A detailed temperature dependence of the transport across a single grain will enable to distinguish between the two processes.

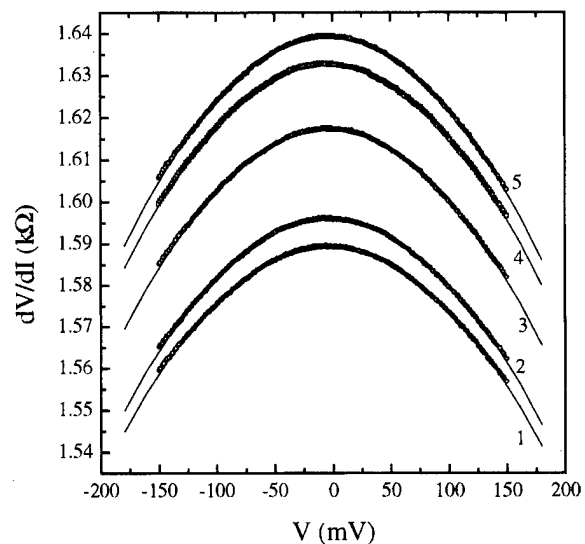


FIG. 5. Dynamic resistivity vs voltage curves of a polycrystalline bridge with different domain configurations. Parabolic fits to the data are shown as solid lines. Curves 2 and 3 correspond to the configuration imaged in Figs. 4(a) and 4(b), respectively.

This work was supported in part by NSF GOALI Grant No. DMR-9510731.

- ¹B. Dieny, J. Magn. Magn. Mater. **136**, 335 (1994); D. E. Heim, R. E. Fontana, Jr., C. Tsang, V. S. Speriosu, B. A. Gurney, and M. L. Williams, IEEE Trans. Magn. **30**, 316 (1994).
- ²D. Rugar, H. J. Maimin, P. Guethner, S. E. Lambert, J. E. Stern, I. McFadyen, and T. Yogi, J. Appl. Phys. **68**, 1169 (1990).
- ³J. R. Kirtley, M. V. Ketchen, K. G. Stawiasz, J. Z. Sun, W. J. Gallagher, S. H. Blanton, and S. J. Wind, Appl. Phys. Lett. **66**, 1138 (1994).
- ⁴J. N. Chapman, A. B. Johnston, and L. J. Heyderman, J. Appl. Phys. **76**, 5349 (1995).
- ⁵B. E. Argile, B. Petek, and D. A. Herman, Jr., J. Appl. Phys. **61**, 4303 (1987).
- ⁶A. M. Chang, H. D. Hallen, L. Harriot, H. F. Hess, H. L. Kao, J. Kwo, R. E. Miller, R. Wolfe, J. van der Ziel, and T. Y. Chang, Appl. Phys. Lett. **61**, 1974 (1992); A. Oral, J. Bending, and M. Henini, *ibid.* **69**, 1324 (1996).
- ⁷R. O'Barr, M. Lederman, and S. Schultz, J. Appl. Phys. **79**, 6067 (1996).
- ⁸S. Y. Yamamoto, D. C. Vier, and S. Schultz, IEEE Trans. Magn. **32**, 3410 (1996); S. Y. Yamamoto and S. Schultz, Appl. Phys. Lett. **69**, 3263 (1996); S. Y. Yamamoto, S. Schultz, Y. Zhang, and H. N. Bertran, IEEE Trans. Magn. **33**, 891 (1997); S. Y. Yamamoto and S. Schultz, Appl. Phys. Lett. **81**, 4696 (1997); S. Y. Yamamoto, R. O'Barr, S. Schultz, and A. Scherer, IEEE Trans. Magn. **33**, 3016 (1997).
- ⁹R. von Helmling, J. Wecker, B. Holzapfel, L. Schulz, and K. Samwer, Phys. Rev. Lett. **71**, 2331 (1993); S. Jin, H. Tiefel, M. McCormack, R. A. Fatuacht, R. Ramesh, and L. H. Chen, Science **264**, 413 (1994).
- ¹⁰A. Gupta, G. Q. Gong, G. Xiao, P. R. Duncombe, P. Lecouer, P. Trouiloud, Y. Y. Wang, V. P. Dravid, and J. Z. Sun, Phys. Rev. B **54**, R15 629 (1996).
- ¹¹H. Y. Hwang, S.-W. Cheong, N. P. Ong, and B. Batlogg, Phys. Rev. Lett. **77**, 2041 (1996).
- ¹²D. N. Mathur, G. Burnell, S. P. Isaac, T. J. Jackson, B.-S. Teo, J. L. MacManus-Driscoll, L. F. Cohen, J. E. Evetts, and M. G. Blamire, Nature (London) **387**, 266 (1997).
- ¹³K. Steenbeck, T. Eick, K. O'Donnell, and E. Steinbess, Appl. Phys. Lett. **71**, 968 (1997).
- ¹⁴J. Z. Sun, W. J. Gallagher, P. R. Duncombe, L. Krusin-Elbaum, R. A. Altman, A. Gupta, Y. Lu, G. Q. Gong, and G. Xiao, Appl. Phys. Lett. **69**, 3266 (1996).
- ¹⁵E. L. Wolf, *Principles of Electron Tunneling Spectroscopy* (Oxford University Press, Oxford, 1985).

Magnetic anisotropy of doped manganite thin films and crystals

Y. Suzuki^{a)}

Department of Materials Science & Engineering, Cornell University, Ithaca, New York 14853

H. Y. Hwang, S-W. Cheong, T. Siegrist, and R. B. van Dover

Bell Laboratories, Lucent Technologies, Murray Hill, New Jersey 07974

A. Asamitsu and Y. Tokura

JRCAT/NAIR, Tsukuba 305, Japan

Magnetic anisotropy of $\text{La}_{0.7}\text{Sr}_{0.3}\text{MnO}_3$ thin films and single crystals has been measured using vibrating sample and torque magnetometry. The magnetic anisotropy of thin films is dominated by strain anisotropy due to the lattice mismatch between the film and SrTiO_3 substrate. The two and fourfold symmetries in the (110) and (001) films, respectively, can only be explained by stress anisotropy contributions ($K_{\text{stress}} \sim 8.4 \times 10^4 \text{ ergs/cm}^3$). Magnetic anisotropy of $\text{La}_{0.7}\text{Sr}_{0.3}\text{MnO}_3$ single crystals, subject to no external stress, reveals a uniaxial anisotropy in the (100) plane of $K_1 \sim 1.8 \times 10^4 \text{ ergs/cm}^3$ that can be attributed to magnetocrystalline effects. © 1998 American Institute of Physics. [S0021-8979(98)20511-1]

The doped manganites materials $\text{RE}_{1-x}\text{AE}_x\text{MnO}_3$ (for trivalent rare earth ions RE and divalent alkaline earth ions AE) have received much interest due to the “colossal” changes in resistance in response to an applied field.¹⁻⁵ Bulk studies of the manganite materials have revealed dramatic changes in magnetic properties, including magnetoresistance and Curie temperature, in response to lattice distortions imposed by chemical or hydrostatic pressure.^{6,7} In the absence of external stresses, magnetocrystalline anisotropy should be easily deduced from appropriately oriented single crystal samples. In epitaxial films, the substrate imposes a strain on the film which affects not only Curie temperature and magnetoresistance properties but also the magnetic anisotropy. Jin *et al.* and Kwon *et al.* have demonstrated the effects of strain on the magnetoresistive properties of epitaxial manganite films.^{8,9} Lecoer *et al.* have studied the magnetic anisotropy of $\text{La}_{0.7}\text{Sr}_{0.3}\text{MnO}_3$ (LSMO) thin films by using Kerr microscopy.¹⁰

In this article, we present magnetic anisotropy results on both films and single crystals of LSMO as measured by torque magnetometry. Detailed studies of the magnetic anisotropy of (001) and (110) LSMO films on (001) and (110) SrTiO_3 (STO) substrates indicate the dominant effect of strain due to the lattice mismatch between the film and substrate.¹¹ Single crystal samples shed light on the magnetocrystalline anisotropy in this material that is masked by the strain anisotropy in epitaxial films.

We studied several different types of LSMO samples: epitaxial films of (001) and (110) orientation and single crystal disks with a (100) axis of rotation. The films of LSMO were grown on (001) and (110) STO ($a=b=c=3.911 \text{ Å}$) substrates using pulsed laser deposition. In this article, we will describe the orientation of the manganite films in terms of the pseudocubic lattices parameters $a'_{\text{bulk}}=b'_{\text{bulk}}=c'_{\text{bulk}}=3.87 \text{ Å}$. The single crystals have a cubic perovskite structure with a rhombohedral distortion and a rhombohedral lat-

tice constant of 7.78 Å . The single crystal orientation will be described in terms of the rhombohedral lattice parameters. Deposition conditions, structural characterization, and the magnetoresistive properties have been described in another publication.^{11,12} Films with thicknesses varying from 500 to 3000 Å were fabricated. The single crystals were grown by the float zone method.¹³ The resulting single crystal rod has the [100] direction at 17° away from its rotational axis as measured by Laue diffraction. A disk sample (2.83 mm radius and 0.57 mm thick) with a (100) axis of rotation was then cut from the rod. Structural characterization indicates excellent crystallinity for the films and crystals and smooth surface morphology for the films.¹¹⁻¹³

Measurements of the magnetic anisotropy of the films and crystals were performed using vibrating sample and torque magnetometry with the magnetic field in the plane of the film and single crystal disk. A Lakeshore vibrating sample magnetometer 7307 was used to make the magnetization measurements and a custom-built torque magnetometer was used to measure the torque as a function of angle on both the epitaxial films and single crystals.

We present here results on the magnetic anisotropy of epitaxial films and single crystals of LSMO. While the magnetic anisotropy of epitaxial films is dominated by strain effects due to the lattice mismatch between the film and the substrate, the single crystals exhibit an anisotropy indicative of the crystal lattice. We measured the magnetic anisotropy of the films on both the torque magnetometer and vibrating sample magnetometer (VSM). In order to measure the anisotropy on the VSM, we first saturate the film to ensure that the sample is initially in a single domain state. Then the magnetization is measured as the field is lowered. We measured the magnetization at various angles that the applied field makes with respect to the crystal axes in the plane of the film. Figure 1 shows a typical plot of a (001) LSMO film. At $H=1 \text{ kOe}$, there is no evidence of angular dependence of the magnetization, thus indicating that the sample is in the saturated state (Fig. 1). Below 900 Oe, which we call the anisotropy field, the sample is no longer saturated in the direction

^{a)}Electronic mail: suzuki@msc.cornell.edu

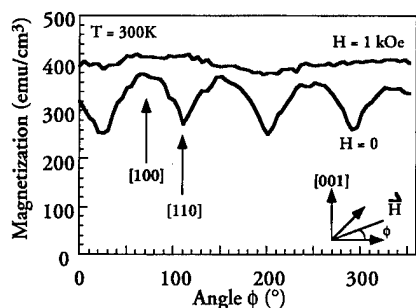


FIG. 1. Magnetization vs angle ϕ of a (001) LSMO film on (001) STO at room temperature. The field is applied in the plane of the film as a function of angle ϕ as shown in the inset. The sample was initially poled positive and then the magnetization measurements were made at 1 kOe and zero field.

of the applied field as observed in the angular dependence of the magnetization. The angular dependence indicates that [100] and [110] directions are easy and hard, respectively. The fourfold symmetry of Fig. 1 can be explained by either cubic magnetocrystalline or stress anisotropy but not rhombohedral magnetocrystalline anisotropy. In order to distinguish between the two factors, we studied the magnetic anisotropy of (110) oriented films. In these films, the [001], [110], and [111] directions are all in the plane of the film. We observe uniaxial anisotropy in the plane of these films with the easy direction along the [001] direction and the hard direction along the [110] direction. The anisotropy field of $H_K = 840$ Oe determined from magnetization measurements of (110) films is consistent with that of the (001) films.

Torque magnetometer measurements of (110) LSMO films also reveal a uniaxial anisotropy in the (110) plane (Fig. 2). There are three possible explanations for this behavior: cubic or rhombohedral magnetocrystalline or stress anisotropy. If cubic magnetocrystalline anisotropy were to explain the result, the torque L can be expressed as a function of angle θ between the applied field and the [001] direction in the following way: $L = (K_1/4 + K_2/64)\sin 2\theta + (3K_1/8 + K_2/16)\sin 4\theta - (3K_2/64)\sin 6\theta$ where K_1 and K_2 are the first and second order magnetocrystalline anisotropy constants.¹⁴ When we fit the torque curve with the above expression, we obtain K_1 and K_2 from fitting the fourfold and sixfold terms. Now cubic magnetocrystalline would predict a twofold term of $K_1/4 + K_2/64 \sim 7.5 \times 10^3$ ergs/cm³. In fact, we observe a twofold or uniaxial anisotropy contribution of -8.4×10^4 ergs/cm³. This large twofold contribution

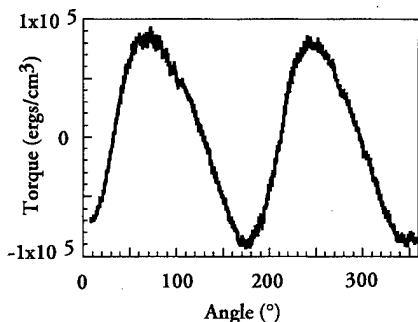


FIG. 2. Torque curve of a (110) LSMO film on (110) STO at room temperature in a 2.8 kOe field. The field is applied in the plane of the film as a function of angle θ between the applied field and the [001] direction.

cannot be explained by cubic magnetocrystalline anisotropy or sample misalignment and indicates that there is an additional anisotropy contribution with a hard [110] direction. Furthermore rhombohedral magnetocrystalline anisotropy would predict a uniaxial anisotropy in both the (110) and (100) planes and none in the (001) plane. These predictions are inconsistent with our film results.

Although the symmetry of the magnetic anisotropy of the films are the same when measured by VSM or torque magnetometry, the anisotropy constants derived from the VSM measurements are much larger than those measured by the torque magnetometer. If the anisotropy constant is not constant throughout the sample, it is not surprising that anisotropy constants deduced from anisotropy fields (measured on the VSM) tend to overestimate the average anisotropy constant measured in the torque curves. In fact, Kwon *et al.*⁹ also have observed wide in-plane ferromagnetic resonance lines indicative of a distribution of anisotropies in our films. $H_{ex} = Ms/(dM/dH)|_{H=0}$ is a more appropriate value for the anisotropy field than H_{sat} (the field when M reaches M_s) to estimate an anisotropy constant consistent with torque measurements.¹¹ For example, for the 2500 Å LSMO film, $H_{ex} = 410$ Oe obtained from the magnetization data is consistent with the anisotropy constant $K = 8.4 \times 10^4$ ergs/cm³ deduced from the torque magnetometer data.

Therefore magnetic anisotropy data from epitaxial films on STO indicate that lattice mismatch between the film and substrate induces a strain anisotropy of the order of $K = 8.4 \times 10^4$ ergs/cm³. Further studies of the magnetic anisotropy as a function of film thickness have confirmed the effect of strain especially on thinner films.¹¹ However in single crystals the magnetic anisotropy should be indicative of magnetocrystalline anisotropy. Magnetocrystalline anisotropy includes the effects of lattice distortions that have been the focus of recent scrutiny. To our knowledge, there has been very little work in understanding the magnetocrystalline anisotropy of the doped manganite material. Perekalina *et al.*¹⁵ have observed a uniaxial magnetocrystalline anisotropy of single crystal (La, Sr, Pb)MnO₃ in the (100) and (110) planes and no anisotropy in the (001) planes. They describe the symmetries of their magnetic anisotropy in terms of a rhombohedral magnetocrystalline anisotropy with $K_1 \sim 2 \times 10^4$ ergs/cm³ and $K_2 = 0$.

We have measured the magnetic anisotropy of (100) LSMO single crystal disks grown by the float-zone method in contrast to the Pb flux method used by Perekalina *et al.* We observe a predominantly uniaxial anisotropy with easy and hard directions along the [001]/[010]. Measurement of the magnetic anisotropy from the angular dependence of the magnetization is precluded in such bulk samples where there are significant effects from shape anisotropy. The finite thickness of the disk (0.57 mm in contrast to the 2000 Å of the film) adds a shape anisotropy contribution to such measurements. By contrast, torque measurements of a saturated sample preclude these shape effects. Figure 3 shows the torque curves for a single crystal sample in fields from 0.4 to 1.8 kOe. As soon as we reach a field of 600 Oe, we obtain a saturated torque curve. The torque curve is predominantly twofold with an anisotropy constant of 1.8×10^4 ergs/cm³

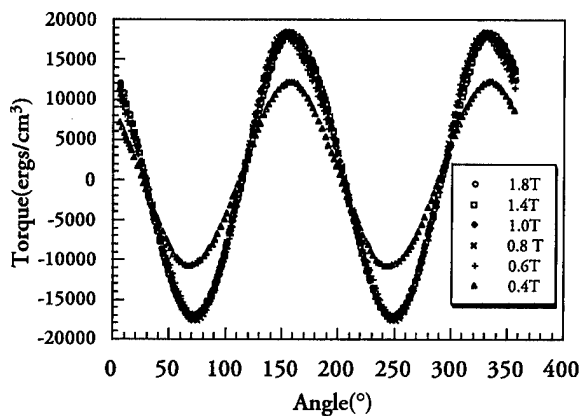


FIG. 3. Torque curves of a (100) LSMO single crystal disk, at room temperature and at a variety of fields in the plane of the disk, shows that 600 Oe is required to saturate the sample.

and a fourfold component that is 4% of the twofold contribution. Torque curves measured with clockwise and counterclockwise field rotation are identical, thus showing no evidence of rotational hysteresis (Fig. 4).

In our crystal samples, we obtain an anisotropy constant of $K = 1.8 \times 10^4$ ergs/cm³ in the (100) plane. The discrepancy in anisotropy values compared to those of Perekalina ($K_1 = 2 \times 10^4$ ergs/cm³) may be attributed to the presence of Pb in their samples which may result in structural distortions that affect the magnetic anisotropy.

For a cubic crystal, one would expect fourfold symmetry in the torque curve of the (100) plane which is not what we observe. For a rhombohedral crystal, one would expect twofold magnetocrystalline anisotropy for an untwinned crystal. X-ray diffraction of our single crystal samples indicate that there is significant twinning in the single crystal. While a rhombohedral crystal with all four different kinds of twin domains should exhibit fourfold symmetry in the (100) plane, twinning of two types of domains may not necessarily change the underlying twofold symmetry of the crystal structure. Therefore the observed twofold anisotropy is not inconsistent with rhombohedral magnetocrystalline anisotropy.

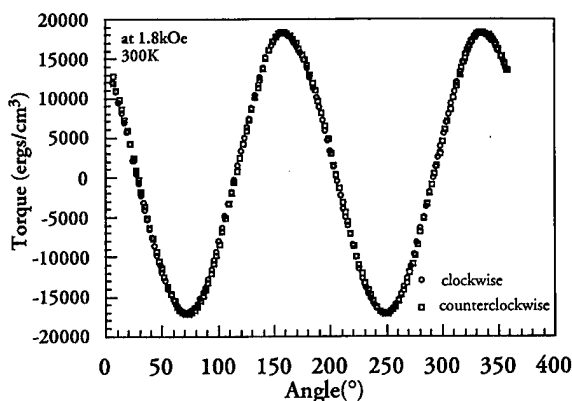


FIG. 4. Torque curves of a (100) LSMO single crystal disk measured with the field rotated clockwise and counterclockwise indicate no effects due to rotational hysteresis.

We consider some possible origins of the observed twofold symmetry. Site ordering has been observed in the garnet and TbFe systems to give rise to an anisotropy.¹⁶⁻¹⁸ Our uniaxial anisotropy cannot be explained by growth induced anisotropy due to site ordering since growth induced anisotropy would result in a perpendicular anisotropy in our single crystal disk samples. Our uniaxial anisotropy cannot be explained by misalignment of the (100) axis with the axis of rotation due to cleaving uncertainties or misalignment of the sample holder. The misalignment is to within 3°. The total energy density of a disk sample would be $E = K_{mc} \cos^2 \theta + K_{shape} \sin^2 \theta$ where K_{mc} and K_{shape} are the magnetocrystalline and shape anisotropy, respectively. If the twofold contribution is due to the misalignment, then the second term in the above expression should be equal to 1.8×10^4 ergs/cm³. Given the dimensions of our disk sample, the calculated shape anisotropy is 4.5×10^5 ergs/cm³. Even if our misalignment were 3°, the shape anisotropy term in the above energy density expression would be only 1224 ergs/cm³ and not be able to account for the entire 1.8×10^4 ergs/cm³. We have eliminated some of the possible origins of the strong twofold anisotropy in the (100) plane of the crystal. These observations lead us to conclude that the twofold symmetry that we observe in the (100) plane can be attributed to the rhombohedral magnetocrystalline anisotropy of the LSMO crystal.

We acknowledge Maura Weathers for her help in x-ray diffraction. This project is supported by the NSF through a CAREER award and the Materials Science Center at Cornell University.

- ¹ R. V. Helmolt, J. Wecker, B. Holzapfel, L. Schultz, and K. Samwer, *Phys. Rev. Lett.* **71**, 2331 (1993).
- ² S. Jin, T. H. Tiefel, M. McCormack, R. A. Fastnacht, R. Ramesh, and L. H. Chen, *Science* **264**, 413 (1994).
- ³ H. L. Ju, C. Kwon, Qi Li, R. L. Greene, and T. Venkatesan, *Appl. Phys. Lett.* **65**, 2108 (1994).
- ⁴ J. Z. Liu, I. C. Chang, S. Irons, P. Klavins, R. N. Shelton, K. Song, and S. R. Wasserman, *Appl. Phys. Lett.* **66**, 3218 (1995).
- ⁵ M. E. Hawley, X. D. Wu, P. N. Arendt, C. D. Adams, M. F. Hundley, and R. H. Heffner, *Mater. Res. Soc. Symp. Proc.* **401**, 531 (1995).
- ⁶ H. Y. Hwang, T. T. M. Palstra, S.-W. Cheong, and B. Batlogg, *Phys. Rev. B* **52**, 15 046 (1995).
- ⁷ M. R. Ibarra, P. A. Algarabel, C. Marquina, J. Basco, and J. Garcia, *Phys. Rev. Lett.* **75**, 3541 (1995).
- ⁸ S. Jin, T. H. Tiefel, M. McCormack, H. M. O'Bryan, L. H. Chen, R. Ramesh, and D. Schurig, *Appl. Phys. Lett.* **67**, 557 (1995).
- ⁹ C. Kwon, K.-C. Kim, M. C. Robson, S. E. Lofland, S. M. Bhagat, T. Venkatesan, R. Ramesh, and R. D. Gomez, *J. Magn. Magn. Mater.* **172**, 229 (1997).
- ¹⁰ P. Lecoeur, P. L. Trouillard, G. Xiao, A. Gupta, G. Q. Ging, X. W. Li, J. Appl. Phys. **82**, 3934 (1997).
- ¹¹ Y. Suzuki, H. Y. Hwang, S.-W. Cheong, and R. B. van Dover, *Appl. Phys. Lett.* **71**, 140 (1997).
- ¹² Y. Suzuki, C. Tsai, H. Y. Hwang, S.-W. Cheong, and R. B. Van Dover, *Mater. Res. Soc. Symp. Proc.* (to be published).
- ¹³ A. Urushibara, Y. Moritomo, T. Arima, A. Asamitsu, G. Kido, and Y. Tokura, *Phys. Rev. B* **51**, 14 103 (1995).
- ¹⁴ R. M. Bozorth, *Ferromagnetism* (IEEE, New York, 1993), p. 582.
- ¹⁵ T. M. Perekalina, I. E. Lipinski, V. A. Timofeva, and S. A. Cherkezyan, *Sov. Phys. Solid State* **32**, 1827 (1990).
- ¹⁶ E. M. Gyorgy, M. D. Sturge, L. G. Van Uitert, E. J. Heilner, and W. H. Grodkiewicz, *J. Appl. Phys.* **44**, 438 (1973).
- ¹⁷ A. Rosenzweig, W. J. Tabor, and R. D. Pierce, *Phys. Rev. Lett.* **26**, 779 (1971).
- ¹⁸ F. Hellman, E. M. Gyorgy, and R. C. Dynes, *Phys. Rev. Lett.* **68**, 1391 (1992).

Investigation of granular films composed of interdispersed $\text{La}_{1/3}\text{Ca}_{2/3}\text{MnO}_3$ particles and metallic Au particles

Mark Rubinstein,^{a)} P. R. Broussard, L. H. Allen, Kristl B. Hathaway,
and Michael M. Miller

Naval Research Laboratory, Washington D.C. 20375

Jonathan Z. Sun

IBM T. J. Watson Research Center, Yorktown Heights, New York 10598

We have carried out a study of composite, granular films made by depositing LCMO (a colossal magnetoresistive perovskite) and pure, metallic Au onto MgO and LaAlO_3 substrates. Elevated temperature caused the Au to segregate into small, micron-sized granules. The films were studied by atomic force microscopy, magnetoresistivity, superconducting quantum interference device magnetization measurements, and magnetically modulated microwave absorption. © 1998 American Institute of Physics. [S0021-8979(98)28011-X]

I. INTRODUCTION AND MOTIVATION

A deposition process, recently described by Allen and Cukauskas,¹ was used to grow composite superconducting thin films composed of adjacent YBCO and metallic gold granules. Although scanning electron microscopy micrographs showed a well segregated region of Au and YBCO with large, micron-sized Au grains, transport measurements of these films indicated the existence of Josephson tunneling between YBCO grains, with the separations between grains of the order of only tens of angstroms. The above-mentioned authors concluded that Au diffuses into the grain boundaries, weakening the coupling between YBCO grains, thereby creating granular films with interesting microscopic properties.

Since LCMO ($\text{La}_{1/3}\text{Ca}_{2/3}\text{MnO}_3$) and YBCO are both ceramic perovskites, we expected that a granular Au/LCMO composite can be grown with the same techniques that Allen and Cukauskas used to deposit Au/YBCO films. This expectation proved to be true.

Section II describes the deposition technique and the morphology of the resulting films, while Sec. III summarizes the magnetic and transport measurements. Section IV summarizes the microwave absorption experiments. We are led to conclude that films containing small LCMO granules with diameters of the order of 500 Å can be easily made.

II. FILM PREPARATION AND MORPHOLOGY

First, a Au layer was evaporated onto a cleaned MgO substrate at ambient temperatures and then heated to 800 °C in order to coalesce the Au film into discrete islands on the substrate surface. Next, the sample was silver pasted onto a substrate holder and heated for the LCMO deposition. The LCMO was deposited over the sample using off-axis sputtering as previously described by Broussard *et al.*² The sputtered LCMO filled in the regions between the Au islands but did not stick to the gold, yielding a composite film consisting of micron-sized "islands" of Au protruding from an

"ocean" of LCMO. The relative thickness of the deposited layers determines the filling factor, i.e., the ratio of perovskite to gold.

The morphology of the composite Au/LCMO films was studied using atomic force microscopy (AFM) and scanning electron microscopy (SEM). Figure 1 presents a comparison between the AFM images for a sample with 200 Å of Au and one with 600 Å of Au. For both samples the amount of LCMO deposited is the same (1000 Å). For the 200 Å sample [Fig. 1(a)], we see that the Au has coalesced into islands of $\approx 1.5 \mu\text{m}$ in diameter and $0.5 \mu\text{m}$ in height, which occupy $\approx 28\%$ of the film surface, with the LCMO film occupying the area in between the Au islands. For the 600 Å sample [Fig. 1(b)], we see that the Au islands have begun to coalesce, forming structures up to $7 \mu\text{m}$ in length, which occupy now only $\approx 24\%$ of the film surface. What most distinguishes the two samples is the appearance of smaller islands only $\approx 400 \text{ Å}$ in height above the LCMO film and $\approx 0.5 \mu\text{m}$ in diameter in Fig. 1(b). These smaller islands occupy 16% of the film surface. SEM microscopy was unable to resolve the smaller islands, however energy dispersive analysis by x ray (EDAX) does indicate the presence of Au in the regions between the large Au islands. So it is conceivable that these small islands are due to Au droplets that did not coalesce into the large islands during the annealing stage.

III. MAGNETISM AND TRANSPORT

In Fig. 2(a) we display a plot of the percent of magnetoresistance versus temperature for sputtered LCMO films with three different thicknesses of Au: 200, 400, and 600 Å. Each film contains 1000 Å LCMO. In this case, the percent of magnetoresistance is defined as $[R(1) - R(0)]/R(0)$, where $R(0)$ is the resistance at zero applied field and $R(1)$ is the resistance at 1 T. LCMO is a magnetic perovskite with a Curie temperature $T_c = 250 \text{ K}$, in the vicinity of which a very large, "colossal" magnetoresistance has been discovered.³ A pure LCMO film has a single negative magnetoresistance peak at $\approx 250 \text{ K}$. As the gold granules occupy an increasing

^{a)}Electronic mail: rubinstein@anvil.nrl.navy.mil

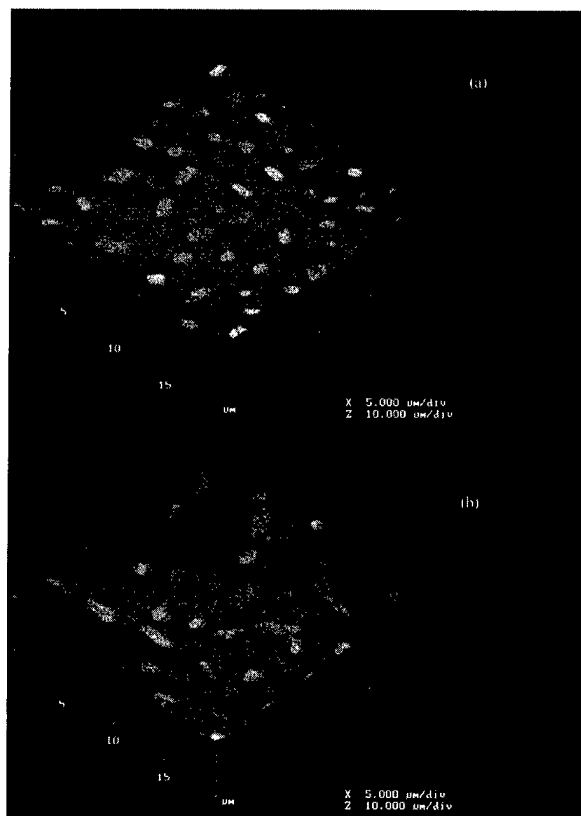


FIG. 1. Atomic force micrographs of the surface for (a) the 200 Å Au/1000 Å LCMO and (b) the 600 Å Au/1000 Å LCMO composite films.

percentage of the total film surface, the primary 250 K peak decreases in intensity, and a secondary peak appears at 190 K. At even larger gold concentrations, the secondary peak merges with the main peak to form a tail.

In Fig. 2(b) we display a plot of percent of magnetoresistance versus temperature for two Au/LCMO granular films which have been manufactured by laser ablation. The ablated sample containing 200 Å Au/1000 Å LCMO displays what appears to be two negative peaks at ≈ 220 and ≈ 180 K. A broad transition at ≈ 165 K appears in the 200 Å Au/200 Å LCMO ablated film, no doubt of inhomogeneous origin. In both Figs. 2(a) and 2(b), the percent of magnetoresistance does not exceed 40%; increasing the gold concentration tends to decrease the magnetoresistance from its bulk value.

It is not unexpected that some broadening of the transition temperature occurs when the LCMO samples become increasingly granular. There are several physical models, some granular and others continuum, which can explain this phenomenon. Because the magnetoresistance can display two negative peaks [e.g., Fig. 2(a)], we are tempted to employ a mean field theory first utilized by Gittleman *et al.*⁴ and others,⁵ which attributes the high temperature peak at T_{c0} to the magnetic ordering of the individual granules, and the low temperature peak at T_c to the ordering of the granules with respect to each other. Such an explanation for the temperature dependence of the magnetic transition in granular Au/LCMO parallels the explanation of the superconducting transition in granular Au/YBCO.¹ (In these granular su-

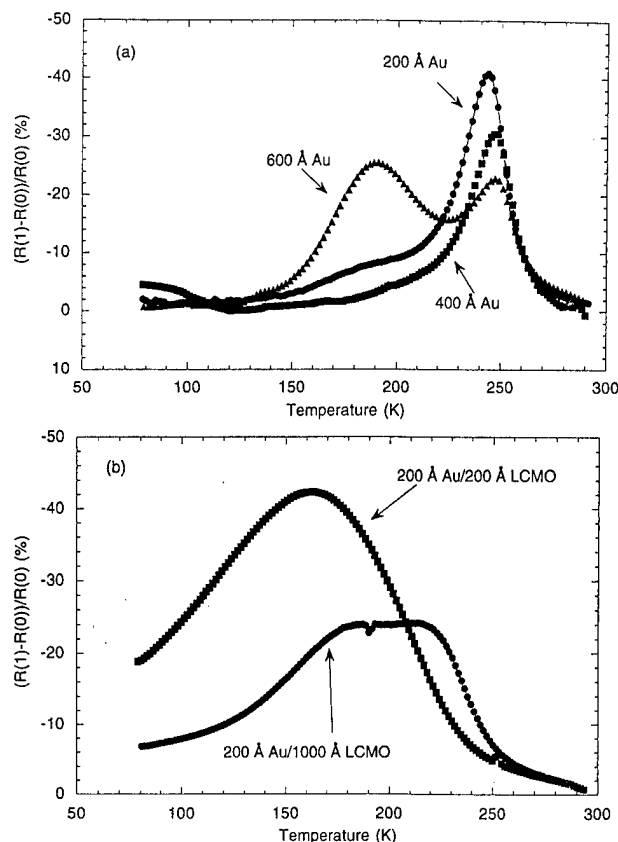


FIG. 2. (a) Percent of magnetoresistance $\{[R(T) - R(0T)]/R(0T)\} \times 100\}$ vs temperature for granular films composed of 200 Å Au/1000 Å LCMO (diamonds), 400 Å Au/1000 Å LCMO (squares), 600 Å Au/1000 Å LCMO (circles). The LCMO layer was deposited by sputtering. (b) Percent of magnetoresistance $\{[R(T) - R(0T)]/R(0T)\} \times 100\}$ vs temperature for granular films composed of 200 Å Au/200 Å LCMO (circles), and 200 Å Au/1000 Å LCMO (squares). The LCMO layer was deposited by laser ablation.

perconductors, the resistivity starts to drop at the transition temperature T_{c0} of the individual superconducting grains. Finally, at a lower temperature, T_c , the Josephson coupling energy between adjacent grains, causes their phases to lock together, and the sample becomes completely superconducting.)

However, a more likely scenario to that presented above is to attribute T_{c0} to the transition temperature of the very large, "infinite" clusters, and to attribute the low temperature transition (or the "tail" of the primary transition) to smaller grains of LCMO whose transition temperature is depressed by surface interactions. This picture neglects the interaction between the grains.

Turning from resistivity measurements to magnetization measurements, we have measured the zero-field-cooled (ZFC) and field-cooled (FC) magnetization in sputtered Au/LCMO with volumetric ratios of 0.2, 0.4, and 0.6. The results are shown in Fig. 3. The arrows indicate the temperatures of the susceptibility peak of the ZFC susceptibilities. A small measuring field is used (30 G) to minimize the hysteresis of the granules themselves. The superparamagnetic blocking temperature T_B has been variously identified as the temperature at the peak of the ZFC magnetization or the temperature at which the ZFC and FC magnetizations meet.

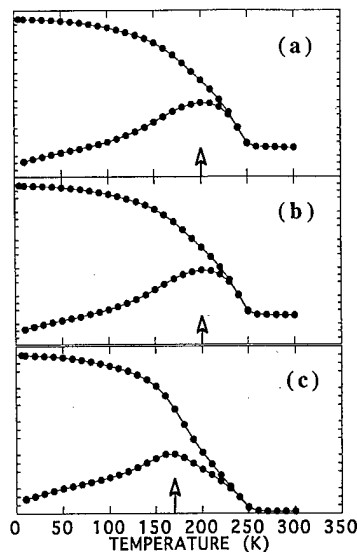


FIG. 3. ZFC and FC magnetization vs temperature for (a) 200 Å Au/1000 Å LCMO, (b) 400 Å Au/1000 Å LCMO, and (c) 600 Å Au/1000 Å LCMO (circles). The LCMO layer was deposited by sputtering. The arrows indicate the blocking temperature in the ZFC data.

Assuming that the magnetic anisotropy energy exceeds the interparticle interaction, the volume of an average grain in a static magnetization experiment can be estimated by the relation⁶

$$(1/2)KV \approx 25k_B T_B. \quad (1)$$

Here, V is the volume of the grain, and K is the dominant anisotropy energy. Utilizing ferromagnetic resonance techniques, Ramachandran *et al.*⁷ found the demagnetizing field, $H_D = 4\pi M \approx 5000$ G, and a negligible crystalline anisotropy field, $H_A \approx 0$, for LCMO. Using the dipolar shape anisotropy $2\pi M_s^2$ as the dominant dipolar anisotropy energy in Eq. (1), and also using $T_B = 200$ K as appropriate for the 600 Å Au/1000 Å LCMO sample shown in Fig. 3(c), we obtain a value of 400 Å as an estimate for the grain diameter based on the magnetization studies. This is the correct magnitude for the fine structure visible in the micrographs of Fig. 1(b), and absent in Fig. 1(a) with less Au, from which we conclude that the metallic Au may serve to separate LCMO grains by diffusing into the grain boundaries. Similar tentative conclusions have been reached by Allen and Cukauskas in their studies of superconducting Au/YBCO composites.¹

Each of the three Au/LCMO magnetization curves shown in Fig. 3 represents a different concentration of Au. It can be seen that the temperature of the susceptibility peak moves to lower temperatures as the Au content increases. We can attempt to explain this fact using Eq. (1), and assuming that increasing Au content causes the average volume V of the grains to decrease, thereby decreasing T_B .

IV. MICROWAVE ABSORPTION

Magnetically modulated microwave absorption (MAMMA) is a microwave absorption technique which uti-

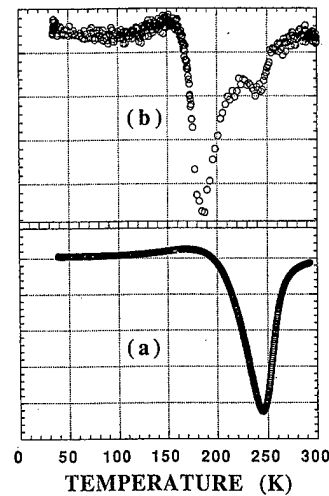


FIG. 4. MAMMA spectra as a function of temperature of (a) a pure LCMO film and (b) a 600 Å Au/1000 Å LCMO granular film. The LCMO layer was deposited by sputtering.

lizes magnetic field modulation and a temperature sweep.⁸ The absorption is monitored using the conventional electron spin resonance (ESR) spectroscopic methodology, which involves field modulation and phase sensitive detection at the modulation frequency. The difference is that one scans along the temperature axis at a fixed magnetic field value rather than scans along the magnetic field at a fixed temperature.

In Figs. 4(a) and 4(b) we display the MAMMA response (the field-modulated microwave absorption curve as a function of temperature) at an applied field of ≈ 10 kG for a thin film of pure LCMO and a granular film of 600 Å Au/1000 Å LCMO. The response is characterized by a derivativelike peak occurring at a temperature corresponding to the peak in the magnetoresistance.

Figure 4(a) exhibits a single peak at ~ 250 K, the Curie temperature of LCMO, as expected. Figure 4(b) exhibits two peaks: a smaller peak near the Curie temperature of the individual grains (~ 250 K) and a larger peak near a temperature we have identified as either the ordering temperature of the grains with respect to one another or as the ordering temperature of the very small grains. The microwave absorption serves to verify the two-peaked nature of the magnetoresistance.

¹L. H. Allen and E. J. Cukauskas, IEEE Trans. Appl. Supercond. **5**, 1218 (1995); L. H. Allen, E. J. Cukauskas, and M. A. Fisher, *ibid.* **5**, 1218 (1995).

²P. R. Broussard, S. B. Qadri, V. Browning, and V. C. Cestone, Appl. Surf. Sci. **115**, 80 (1997).

³J. S. Tiefel, T. H. McCormack, M. Fastnacht, R. A. Ramesh, and L. H. Chen, Science **264**, 413 (1994).

⁴J. L. Gittleman, Y. Goldstein, and S. Bozowski, Phys. Rev. B **5**, 3609 (1972).

⁵S. Morup and G. Christiansen, J. Appl. Phys. **73**, 6955 (1993); J. S. Helman and B. Abeles, Phys. Rev. Lett. **37**, 1429 (1976).

⁶A. H. Morrish, *The Physical Principles of Magnetism* (Wiley, New York, 1965), p. 362.

⁷J. S. Rachachandran, S. M. Bhagat, J. L. Peng, and M. Rubinstein, Solid State Commun. **96**, 127 (1995).

⁸B. F. Kim, J. Bohandy, K. Moorjani, and F. J. Adrian, J. Appl. Phys. **63**, 2029 (1988).

Magnetic and transport properties of radiation damaged $\text{La}_{0.7}\text{Ca}_{0.3}\text{MnO}_{3.0}$ thin films

V. M. Browning,^{a)} R. M. Stroud, W. W. Fuller-Mora, J. M. Byers, M. S. Osofsky, D. L. Knies, K. S. Grabowski, D. Koller, J. Kim, D. B. Chrisey, and J. S. Horwitz
Naval Research Laboratory, Washington, District of Columbia 20375

Magnetization and resistivity measurements are reported for a series of radiation damaged $\text{La}_{0.7}\text{Ca}_{0.3}\text{MnO}_3$ pulsed laser deposited thin films. When plotted as a function of activation energy, trends in the electrical transport properties are similar to those exhibited in the magnetic properties. A sharp drop in both T_c and T_p in samples with activation energies greater than ~ 110 meV suggests a "decoupling" of the magnetic and transport properties. The results suggest the magnetic order is no longer sufficient to delocalize the system of the extra disorder induced by the radiation damage.
 [S0021-8979(98)38011-1]

I. INTRODUCTION

The mixed valent metal-oxide perovskite $\text{La}_{0.7}\text{Ca}_{0.3}\text{MnO}_{3.0}$ (LCMO) is known to exhibit "colossal" magnetoresistance¹ (CMR) near a transition from insulating to metallic behavior. This transition occurs at a temperature, T_p , at which the resistivity reaches its maximum value and which is nearly coincident with the onset of ferromagnetic ordering of the Mn spins at the Curie temperature, T_c . Although the ferromagnetism in these materials is attributed to a double exchange mechanism mediated by the $\text{Mn}^{3+}-\text{O}-\text{Mn}^{4+}$ bond,² the origin of the metal-insulator transition in these materials remains a subject of considerable debate. In particular, the high temperature activated behavior, although generally believed to be some form of hopping mechanism, is not well understood. Since a prerequisite for hopping transport is the formation of spatially localized states, it has been speculated that magnetic disorder above the Curie temperature may be the source of localization in the CMR materials. However, Millis *et al.*,³ have argued that the double exchange mechanism alone is not sufficient to account for a disorder driven metal-insulator transition in this system and conclude that lattice distortions play a necessary and crucial role in the observation of a metal-insulator transition and the resulting CMR effect. Experimental results to date have yet to yield a definitive conclusion regarding the role of structure and magnetism in the CMR materials.

In an effort to better understand the relationship between structure, magnetism, and transport in the CMR materials we have looked at the evolution of both the magnetic and transport properties in radiation damaged pulsed laser deposited LCMO thin films. It has previously been demonstrated that ion beam irradiation can be used to "tune" both the magnetic and transport properties in the CMR materials.⁴ We have used this technique to produce a series of LCMO thin films with varying amounts of radiation damage. Our results reveal that both the Curie temperature and peak temperature exhibit a sharp drop in magnitude in samples with activation energies larger than ~ 110 meV, thereby establishing a rela-

tionship between transport and magnetism in this system. Further study of this relationship may lead to a more clear understanding of how the two phenomena are coupled in the CMR materials.

II. EXPERIMENT

The LCMO films were grown by pulsed laser deposition on single crystal (100) LaAlO_3 substrates. Complete details of the deposition procedure can be found elsewhere.⁵ A post-deposition anneal at 1000°C in an oxygen atmosphere was performed to oxygenate the as-deposited films and to minimize extrinsic structural defects. After annealing, the films were irradiated with 10 MeV I ions in order to introduce a controlled quantity of structural defects. The flux of incident ions ranged from 5.0×10^{12} ions/cm² to 20.0×10^{12} ions/cm² and were estimated by TRIM simulations⁶ to result in displacement damage of between 0.006 and 0.021 displacements per atom (d.p.a.). The incident ion energy was chosen to produce uniform damage and implantation of the incident ions into the substrate, in contrast with an earlier study of Ar irradiation in which TRIM simulations indicated nonuniform damage and implantation of the ions in the films.⁴

The transport properties of the films were characterized by measuring the temperature dependence of the resistivity while cooling the films in a closed cycle refrigerator. The resistivities of the samples were measured using a standard four-probe technique. The measuring currents ranged from 10 nA to 100 μA depending on the magnitude of the resistivity being measured.

The magnetic measurements were taken using a superconducting quantum interference device (SQUID) magnetometer. Hysteresis curves, which allowed measurement of the saturation magnetization and coercivity, were taken by sweeping field at fixed temperature ($T=10$ K), while the temperature dependent magnetization measurements, which allowed measurement of the Curie temperature, T_c , were taken by cooling the sample in an applied field ($H=1000$ Oe). All of the magnetization measurements were corrected for the diamagnetic signal of the substrate as determined from a series of measurements on blank LaAlO_3

^{a)}Electronic mail: browning@anvil.nrl.navy.mil

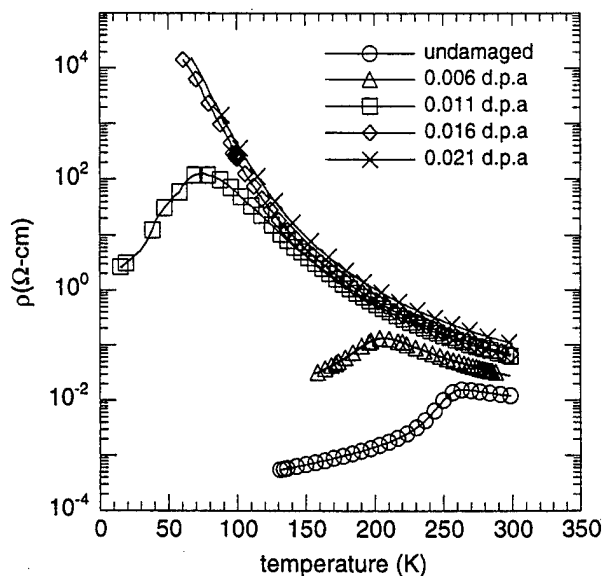


FIG. 1. Resistivity vs temperature data for radiation damaged pulsed laser deposited LCMO thin films.

substrates. There is an estimated 10% uncertainty in the absolute magnitude of the magnetization values due to the uncertainty in calculating the sample volume.

III. RESULTS AND DISCUSSION

Figure 1 shows the resistivity versus temperature curves for the LCMO films. The effect of the radiation damage manifests itself as an increase in the resistivity as well as a reduction in T_p . For the most heavily irradiated samples, no peak in resistivity was observed down to ~ 40 K where the resistance became too large to measure in our apparatus. These two films were further studied at low temperatures by using an electrometer to confirm that the resistivity of the films at 4.2 K was greater than $10^4 \Omega\text{-cm}$.

The exact mechanism which dominates transport at temperatures above T_p remains unclear. In a simple thermally activated semiconducting system, the resistivity is expected to exhibit a temperature dependence with $\rho = \rho_0 \exp(\Delta/k_B T)$. If the conduction is by small polarons, as suggested by Millis *et al.*,³ then the resistivity should exhibit a temperature dependence $\rho = \rho_0(T) \exp(\Delta/k_B T)$ where $\rho_0(T) \sim T$ for adiabatic polarons and $\rho_0(T) \sim T^{3/2}$ for non-adiabatic polarons. It has also been suggested that the activated behavior may be due to variable range hopping (v.r.h.)⁷ which results in a temperature dependent resistivity $\rho = \rho_0 \exp(T_0/T)^{1/4}$. In general, with limited temperature range, it is difficult to discriminate between these models. In the present study, it was found that all of the models could be equally well fit to the data. The activation energies ($\Delta = k_B T_0$) obtained using a semiconducting fit are 57.0 meV for the undamaged sample and 100.9, 111.5, 117.5, and 117.9 meV for the samples irradiated with 5.0×10^{12} , 10.0×10^{12} , 15.0×10^{12} , and 20.0×10^{12} I ions/cm², respectively. In order to confirm that the error in the extracted activation energy using the data near T_p for the low damage samples was minimal ($< 5\%$), the temperature range of the undam-

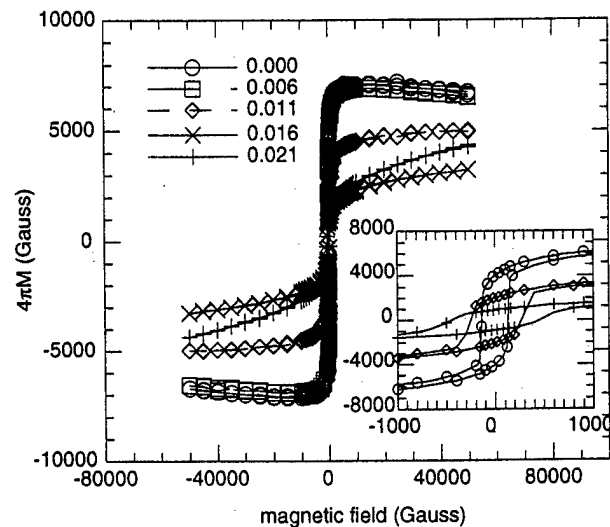


FIG. 2. Field dependence of the magnetization ($4\pi M$) of radiation damaged pulsed laser deposited LCMO thin films. The inset shows the low field behavior for the undamaged, 0.006 d.p.a. and 0.021 d.p.a. films.

aged sample was increased by measuring its resistivity up to 400 K (data not shown in Fig. 1) and the fit was reapplied over the entire data range.

Hysteresis loops taken on the various samples are shown in Fig. 2. Of note is the sharp decline in the saturation magnetization and the significant increase in the coercive field with increasing damage (see Fig. 2 inset). It is also interesting to note that the most heavily damaged samples continue to exhibit a residual paramagnetism above the saturation field. This observation is consistent with what one expects to see in a ferromagnetic system that is becoming increasingly disordered and/or frustrated. Further evidence for this can be seen in the temperature dependence of the magnetization as plotted in Fig. 3. These data show a reduction in T_c with

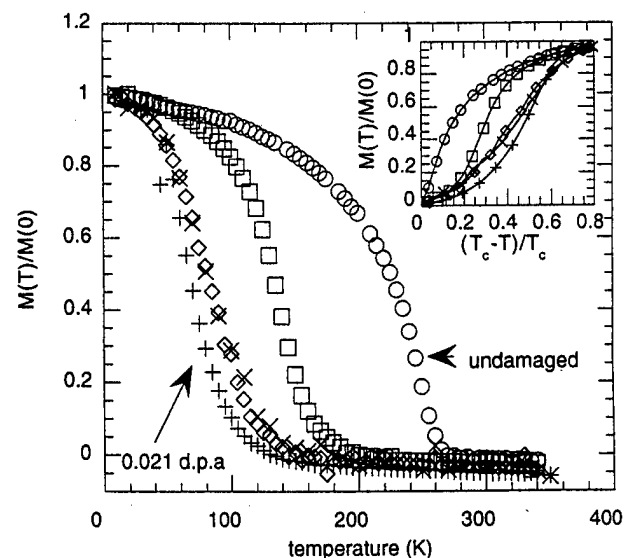


FIG. 3. Temperature dependence of the normalized magnetization of a series of pulsed laser deposited LCMO films with damage levels ranging from: 0.000 d.p.a. (○), 0.006 d.p.a. (□), 0.011 d.p.a. (◇), 0.016 d.p.a. (×), and 0.021 (+). The inset shows the data plotted as a function of reduced temperature, $(T_c - T)/T_c$.

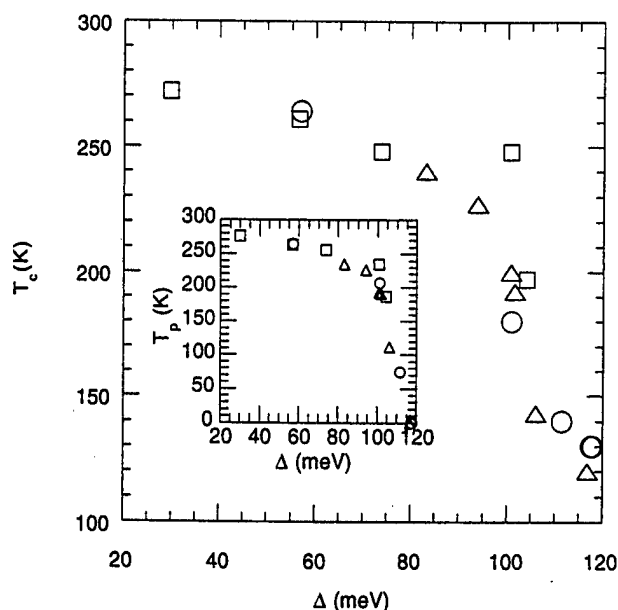


FIG. 4. Curie temperature, T_c , plotted against activation energy, Δ , for several series of radiation damaged LCMO thin films. The circles represent data for the series of samples which are the focus of the current study. Additional data points come from oxygen deficient LCMO films irradiated with Si ions (triangles) and LCMO films irradiated with I ions grown from a Mn-rich target (squares). The inset shows the corresponding data for the T_p values as a function of Δ .

increased damage and when plotted versus reduced temperature, $(T_c - T)/T_c$, significant broadening of the transition region is evident (see Fig. 3 inset). These results are interpreted as indicative of a weakening and broadening of the magnetic exchange distribution both of which are attributed to the increased disorder resulting from the radiation damage.

The reduced $4\pi M$ and T_c values, the increased coercivity, and the observation of paramagnetism at high fields below T_c , are all features consistent with the behavior seen in both superparamagnetic and spin-glass systems. Although it is impossible based upon the current experimental results to distinguish between the two effects, considering the length scale (~ 20 – 50 Å) and homogeneity associated with the atomic displacements, we consider it more likely that the results are a result of spin-glass formation. Further study of the temperature dependent magnetization as a function of field-cooled and zero-field cooled initial conditions as well as measurements at higher fields will help to clarify this issue. However, it has recently been reported by Cai *et al.*⁸ that spin-glass behavior can be induced via spin disorder in Fe-doped LCMO. Therefore it is likely that the spin disorder introduced by the radiation damage in the current study, and by Fe substitution in Cai *et al.*'s samples, result in similar effects.

Figure 4 plots the T_c values versus activation energy obtained from the samples reported on in this study together with values obtained from two other series of radiation damaged pulsed laser deposited LCMO films. The additional data sets come from one series of oxygen deficient LCMO films that were irradiated with Si ions and a series of I irradiated

LCMO films that were prepared from a Mn-rich target. The inset to Fig. 4 shows the dependence of T_p as a function of activation energy. Both curves exhibit a sharp drop near 110 meV, beyond which the metal-insulator transition is completely suppressed despite the existence of a ferromagnetic transition. This result does not change qualitatively when using values for activation energies obtained using the other model dependent expressions for resistivity discussed earlier and suggests that the increasing disorder results in a decoupling of the magnetic and electronic transport properties. This implies that in samples which exhibit activated behavior with $\Delta > 110$ meV (as determined using a semiconducting expression for the resistivity), the magnetic ordering is no longer sufficient to delocalize the system. The fact that this trend is seen in samples obtained from several series prepared under different processing conditions suggests that this behavior may be universal in the LCMO system.

IV. CONCLUSION

In summary, resistivity and magnetization data presented for radiation-damaged LCMO thin films show similar trends when examined as a function of radiation damage. These results show, in agreement with previous reports, that the ion irradiation has a deleterious effect on both the magnetic and transport properties and that the radiation damage results in spin disorder which likely is responsible for the observation of behavior similar to that observed in spin-glass systems. An examination of the trends in the magnetic and transport properties as a function of radiation damage has established a relationship between the onset of magnetic ordering (Curie temperature) and the activation energy as determined from the high temperature resistivity measurements.

ACKNOWLEDGMENTS

The authors would like to acknowledge helpful discussions with Dr. Jim Krebs concerning the magnetization results. In addition, R. M. Stroud and J. M. Byers gratefully acknowledge support from the NRC/NRL Cooperative Research Associateship program.

- ¹S. Jin, T. H. Tiefel, M. McCormack, Jr., A. Fastnacht, R. Ramesh, and L. H. Chen, *Science* **264**, 413 (1994).
- ²C. Zener, *Phys. Rev.* **82**, 403 (1951); P. W. Anderson and H. Hasegawa, *Phys. Rev.* **100**, 675 (1955); P. G. DeGennes, *Phys. Rev.* **118**, 141 (1960).
- ³A. J. Millis, P. B. Littlewood, and B. I. Shraiman, *Phys. Rev. Lett.* **74**, 5144 (1995).
- ⁴C.-H. Chen, V. Talyansky, C. Kwon, M. Rajeswari, R. P. Sharma, R. Ramesh, T. Venkatesan, J. Melngailis, Z. Zhang, and W. K. Chu, *Appl. Phys. Lett.* **69**, 3089 (1996).
- ⁵R. M. Stroud, V. M. Browning, J. M. Byers, D. B. Chrisey, W. W. Fuller-Mora, K. S. Grabowski, J. S. Horwitz, J. Kim, D. L. Knies, and M. S. Osofsky, *Proc. Mater. Res. Soc. Symp. in Epitaxial Oxide Thin Films III*, edited by C. Foster, J. S. Speck, D. Schlom, C.-E. Eom, and M. E. Hawley (1997), p. 474.
- ⁶J. F. Ziegler, J. P. Biersack, and U. Littmark, *The Stopping and Range of Ions in Solids* (Pergamon, New York, 1985).
- ⁷M. Jaime, M. B. Salamon, K. Pettit, M. Rubinstein, R. E. Treece, J. S. Horwitz, and D. B. Chrisey, *Appl. Phys. Lett.* **68**, 1576 (1996).
- ⁸J.-W. Cai, C. Wang, B.-G. Shen, J.-G. Zhao, and W. S. Zhan, *Appl. Phys. Lett.* **71**, 1727 (1997).

Evolution of strain-dependent transport properties in ultrathin $\text{La}_{0.67}\text{Sr}_{0.33}\text{MnO}_3$ films

H. L. Ju^{a)} and Kannan M. Krishnan^{b)}

Materials Sciences Division, Lawrence Berkeley National Laboratory, Berkeley, California 94720

D. Lederman

West Virginia University, Physics Department, Morgan Town, West Virginia 26506

We report on a systematic investigation of strain-induced lattice distortion effects on the crystal structure and transport properties of as-grown and postannealed ultrathin $\text{La}_{0.67}\text{Sr}_{0.33}\text{MnO}_3$ epitaxial films grown on LaAlO_3 (001) substrates by pulsed laser deposition. The resistivity of the as-grown films is critically dependent on the thickness, i.e., 100 Å thick films show insulating behavior, 300 Å thick films show metal-insulator transitions, and 500 Å thick films show metallic behavior. However, all the annealed films show identical metallic behavior. Conventional θ - 2θ x-ray scans with momentum transfer (q) along the [001] direction, and θ - 2θ scans of the (103) and (113) peaks, with q having a component perpendicular to the growth direction, were used to measure the out-of-plane and in-plane lattice parameters of the sample. Φ scans of the (103) and (113) peaks revealed a fourfold symmetry which is consistent with a tetragonal unit cell. These data conclusively show that significantly elongated tetragonal structures ($c/a = 1.02$ – 1.04) are insulating whilst films with cubic unit cells, relaxed either due to annealing or as a function of thickness, have metallic characteristics. © 1998 American Institute of Physics. [S0021-8979(98)52911-8]

The transport properties of manganite perovskites $\text{R}_{1-x}\text{A}_x\text{MnO}_3$ ($\text{R}=\text{La, Pr, Nd}$, $\text{A}=\text{Ca, Sr, Ba}$) in the double exchange formalism¹ is sensitive to both the Mn–O bond distance ($d_{\text{Mn-O}}$) and the Mn–O–Mn bond angle (θ). Slight changes in $d_{\text{Mn-O}}$ or θ affect the on-site coulomb correlation energy and/or bandwidth and may lead to a metal–insulator transition. Note $d_{\text{Mn-O}}$ and θ can be altered either by substitutions,^{2,3} external pressure,⁴ or, in a controlled fashion, by strain due to epitaxial growth on lattice-mismatched substrates.^{5–7} In the latter case, the strain is also a function of the thickness, annealing conditions, and mechanisms of strain relaxation. Although there exist numerous studies of the effect of lattice changes, induced by chemical substitutions and external pressure, on the transport and structure of manganite perovskites, there has been little investigation on the effect of lattice distortion induced by substrate strain on the transport and structure. In addition, the reports were focused on relatively thick films (thickness ≥ 1000 Å) most of which were post annealed at high temperature (for example, 900 °C) at which significant lattice relaxation can occur making the films unsuitable for strain study. Hence, we have chosen to study lattice distortion, strain, and its influence on the transport properties in the $\text{La}_{0.67}\text{Sr}_{0.33}\text{MnO}_3$ (LSMO) system, which is a metallic and ferromagnetic compound with a high transition temperature of 370 K.² Epitaxially grown LSMO[001] \parallel LaAlO_3 [001] films are expected to be under compressive strain since $d_{\text{LSMO}}(3.88 \text{ Å}) > d_{\text{LAO}}(3.78 \text{ Å})$. In this article, we report on the critical thickness and annealing (strain relaxation) dependence of the transport and structural properties of such ultrathin [001]LSMO/[001]LAO films.

LSMO films with thickness ranging from 100 to

500 Å, were deposited from a target of composition $\text{La}_{0.67}\text{Sr}_{0.33}\text{MnO}_3$ by pulsed laser deposition on LaAlO_3 (001) substrates at 640 °C/300 mTorr O_2 ; a condition that gives optimal quality of 100 Å thick films (low resistivity, high transition temperature, large residual ratio). After the deposition the films were cooled down to room temperature at 10 °C/min in an oxygen pressure of 400 Torr. Each wafer was cut into two pieces—one half was left as grown and the other half was annealed at 900 °C 1 bar O_2 /10 h. The temperature dependence of the dc resistivity in a field, H ($=1 \text{ T}$) and zero field, was measured using a standard four-probe technique. The field was applied in a direction perpendicular to the film surface and the current direction.

X-ray diffraction data were obtained using an 18 kW rotating Cu anode generator equipped with a four-circle sample goniometer. The samples were scanned with the momentum transfer vector \mathbf{q} having components both parallel and perpendicular to the growth direction of the samples. The interplanar distance along the [001] direction, assuming a perovskite unit cell, was determined from θ - 2θ scans with \mathbf{q} along the growth direction. The in-plane lattice parameters were determined from θ - 2θ scans of the (103) and (113) peaks, with \mathbf{q} having a component perpendicular to the growth direction of the sample. For all samples, Φ scans of the (103) and (113) peaks revealed a fourfold symmetry consistent with a tetragonal unit cell (i.e., $a=b \neq c$, where c is (001) lattice parameter). The [100] direction of the sample and the LaAlO_3 substrate (assuming a pseudoperovskite unit cell) coincided with one another.

Figure 1 shows representative x-ray data from both annealed and as-grown 100 Å thick samples. Similar results were obtained from the 300 and 500 Å samples, although the peaks in the thicker samples were generally narrower and more intense. The data in Fig. 1(a) were obtained with \mathbf{q}

^{a)}Electronic mail: hiju@lbl.gov

^{b)}Author to whom correspondence should be addressed.

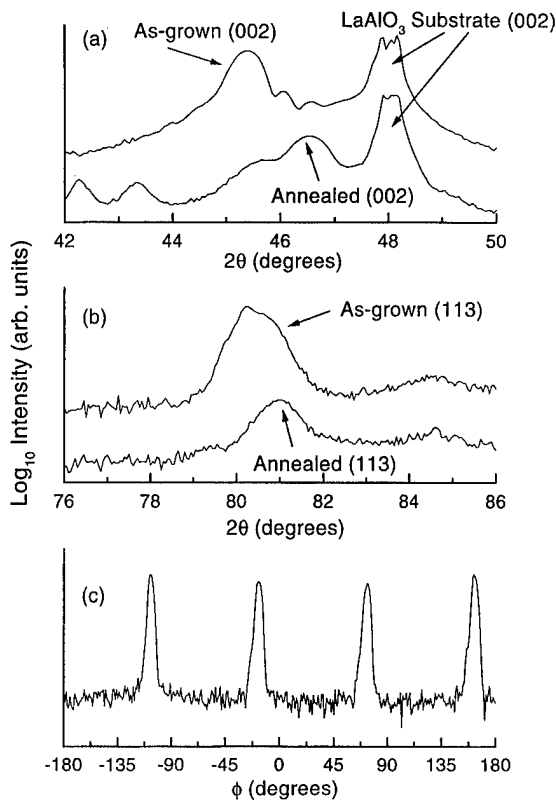


FIG. 1. θ - 2θ scans with q along the [001] growth direction (a) and the [113] direction (b) for both annealed and as-grown 100 Å thick samples (top and bottom scans, respectively). The scans from the annealed and as-grown samples were displaced from one another in graphs (a) and (b) for greater clarity. The peaks due to the LaAlO_3 substrate, indexed using a pseudoperovskite unit cell, are also indicated. Note (c) is a Φ scan of the (103) reflection of the annealed sample, which shows a fourfold symmetry characteristic of the pseudoperovskite structure. All samples in this study had the same fourfold symmetry, with the [100] direction coinciding with that of the LaAlO_3 substrate.

along the [001] direction, so that the sample peaks correspond to the (002) reflection. In both of these scans, the peak near $2\theta=48^\circ$ is a substrate peak. The top scan, measured in the as-grown sample, shows a single peak at approximately $2\theta=45.5^\circ$, while the other, smaller peaks result from the finite thickness of the film. The bottom scan in Fig. 1(a), obtained from the annealed sample, shows several peaks, the strongest of which appears near $2\theta=46.5^\circ$. The other

TABLE I. Lattice parameters of $\text{La}_{0.67}\text{Sr}_{0.33}\text{MnO}_3/\text{LaAlO}_3$ thin film samples determined from x-ray diffraction data. The c axis represents the lattice parameter along the growth [001] direction, while the a axis represents the [010] and [100] directions. The corresponding Mn-O-Mn bond angles (θ) and the Mn-O bond distances, both in-plane and out-of-plane are also shown.

Sample	c (Å)	a (Å)	d_{out} (Å)	θ_{out}	d_{in} (Å)	θ_{in}
100 Å as-grown	3.99	3.82	2.00	180°	1.96	151°
100 Å annealed	3.91	3.87	1.96	171°	1.96	160°
300 Å as-grown	3.98	3.85	1.99	180°	1.96	156°
300 Å annealed	3.90	3.88	1.95	167°	1.96	162°
500 Å as-grown	3.91	3.82	1.96	171°	1.96	151°
500 Å annealed	3.88	3.87	1.96	162°	1.96	160°
bulk	3.88	3.88	1.96	162°	1.96	162°

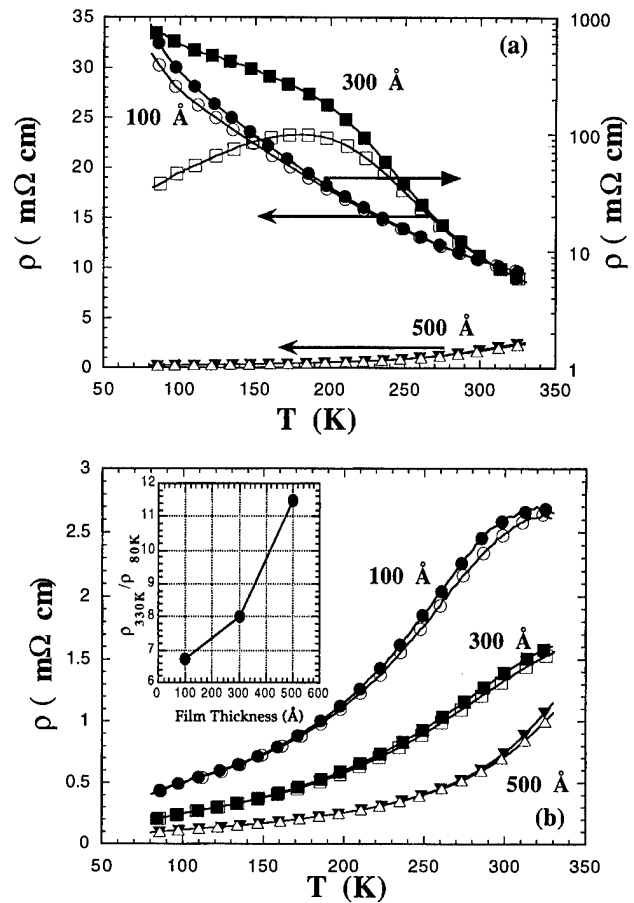


FIG. 2. Temperature dependence of the resistivity of $\text{La}_{0.67}\text{Sr}_{0.33}\text{MnO}_3$ films with thickness from 100, 300, 500 Å thick as-grown (a) and annealed films (b) without field (full symbol) and with an applied field of 1 T (empty symbol). Inset shows the resistivity ratio $\rho_{330\text{K}}/\rho_{80\text{K}}$ as a function of thickness.

weaker peaks could be due to different phases formed during the annealing process. Clearly, the effect of annealing is to shift the peaks to higher angles, which means that the (001) interplanar distance contracts. The scans in Fig. 1(b) were obtained with q along the [113] direction. The top scan again represents the as-grown sample, while the bottom scan represents the annealed sample. The effect of annealing in this case is to shift the peak to higher angles. Figure 1(c) is a Φ scan of the (103) reflection of the annealed 100 Å sample, showing the fourfold symmetry characteristic of the tetragonal crystal structure. All samples showed the same fourfold symmetry. From scans such as those shown in Figs. 1(a) and 1(b), the in-plane and out-of-plane lattice parameters were calculated assuming that the [100] and [010] in-plane directions are equivalent, and that the unit cell is tetragonal. Similar scans of the (103) reflection were used to confirm the results. The results are shown in Table I. It is clear that annealing causes the c axis (along the growth direction) to contract while the a axis (in the plane) expands.

The temperature dependence of the resistivity for the as-grown and annealed films is shown in Fig. 2. The resistivity of the as-grown films [Fig. 2(a)] shows a critical dependence on thickness (t). For $t=100$ Å, it is completely insulating over the entire temperature range investigated with a significant magnetoresistance (MR) effect observed below

200 K. MR increases with a decrease in temperature and reaches $\sim 50\%$ at 1 T and 80 K. However, the absolute magnitude of the resistivity at 80 K is $\sim 1000 \text{ m}\Omega \text{ cm}$ (or $\sim 1 \Omega \text{ cm}$) and rather small compared to that of insulating bulk samples ($> 10^3 \Omega \text{ cm}$).² For $t=300 \text{ \AA}$, the zero-field resistivity is also insulating (with the magnitude of the resistivity smaller than that for $t=100 \text{ \AA}$), but when a field of 1 T is applied the resistivity, $\rho_{H=1\text{T}}(T)$ is suppressed below 270 K and shows a peak around 180 K, with metal-like behavior at lower temperatures. The MR for $t=300 \text{ \AA}$ was found to increase with decreasing temperature. Unlike the above two cases, for $t=500 \text{ \AA}$ a metallic behavior with a room temperature resistivity of $\sim 2 \text{ m}\Omega \text{ cm}$, along with a large MR effect near and above room temperature, but with insignificant MR at low temperature, is observed.

Contrary to the critical thickness dependence of resistivity and MR for the as-grown films, the annealed films [Fig. 2(b)] uniformly show a metallic behavior with significant MR above room temperature. However, the magnitude of the resistivity decreases with an increase in film thickness. For example, the resistivity at 330 K, $\rho_{330\text{K}}$ is $2.7 \text{ m}\Omega \text{ cm}$ for 100 \AA , $1.6 \text{ m}\Omega \text{ cm}$ for 300 \AA , $1.2 \text{ m}\Omega \text{ cm}$ for 500 \AA . The resistivity ratio $\rho_{330\text{K}}/\rho_{80\text{K}}$ increases with increasing film thickness— $\rho_{330\text{K}}/\rho_{80\text{K}} \sim 6, \sim 8, \sim 12$ for 100 \AA , 300 \AA , and 500 \AA thick films, respectively. Moreover, the thicker the film the higher the resistivity peak temperature. The temperature dependence of resistivity reveals that the 100 \AA thick film exhibits a resistivity peak at 320 K, 300 \AA thick film exhibits a resistivity approaching a peak, and the 500 \AA thick film exhibits resistivity with a sharp increase.

Changes in lattice constants of perovskites determine two key structural parameters that impact on their transport properties: Mn–O–Mn bond angle (θ) and bond distance ($d_{\text{Mn-O}}$). (Note: both in-plane and out-of-plane values are shown in Table I). However, it has been shown that for $\text{R}_{0.67}\text{A}_{0.33}\text{MnO}_3$ ($\text{R}=\text{La, Pr, Nd, Y}$; $\text{A}=\text{Ca, Sr, Ba}$), changes in (R , A) site ionic size only affect θ , with $d_{\text{Mn-O}}$ remaining unchanged ($d_{\text{Mn-O}}=1.96 \text{ \AA}$).⁸ This corresponds to a maximum lattice parameter of 3.92 \AA . Hence, it is reasonable to assume that larger values of the lattice parameter imply stretching of $d_{\text{Mn-O}}$ (θ fixed at 180°) and smaller lattice parameters imply a contraction of θ ($d_{\text{Mn-O}}$ fixed at 1.96 \AA). In the as-grown films, a is $\sim 3.82\text{--}3.85 \text{ \AA}$ but c depends on film thickness, i.e., $c=3.99 \text{ \AA}$ for $t=100 \text{ \AA}$ and $c=3.91 \text{ \AA}$ for $t=500 \text{ \AA}$. Thus, the thickness dependence of the resistivity as a function of temperature of as-grown LSMO thin films may be related to changes in the c parameter. For bulk $\text{La}_{0.67}\text{Sr}_{0.33}\text{MnO}_3$, where $d_{\text{Mn-O}}=1.96 \text{ \AA}$ and $a=c=3.88 \text{ \AA}$,² θ is found to be $\sim 162^\circ$. For tetragonally distorted LSMO thin films θ and $d_{\text{Mn-O}}$ are, in principle, different along the a (in-plane) and c (out-of-plane) axis directions. For the as-grown films, the in-plane Mn–O–Mn bond angle, θ_{in} is $\sim 151^\circ\text{--}156^\circ$ and this decrease in the bond angle (with respect to the bulk) may significantly reduce the double exchange interaction. However, θ_{in} and d_{in} are independent of thickness and may not explain the thickness dependence of the resistivity. On the other hand, the out-of-plane Mn–O–Mn angle, θ_{out} for the as-grown films is $\sim 180^\circ$ and the

out-of-plane Mn–O distance, d_{out} is significantly stretched (Table I). Note d_{out} for the insulating, $t=100 \text{ \AA}$, as-grown film is greater than that for metallic $t=500 \text{ \AA}$ film by 0.04 \AA . The influence of the bond distance $d_{\text{Ti-O}}$ (distance between Ti and O) on the transport properties has been reported⁹ for the bulk, cubic perovskite ($\theta=180^\circ$ between Ti–O–Ti) compound $\text{Nd}_{1-x}\text{Ba}_x\text{TiO}_3$ (NBTO) where a small increase in $d_{\text{Ti-O}}$ ($\sim 0.02 \text{ \AA}$) is responsible for a change from metallic to insulating behavior for $0.7 \leq x \leq 0.9$. The change in $d_{\text{Mn-O}}$ in LSMO thin films, particularly in the out-of-plane direction, is greater than the change in $d_{\text{Ti-O}}$ of NBTO and may be responsible for its insulating behavior. However, there are important differences in the electronic transport between LSMO and NBTO. Whilst the conduction pathway in bulk NBTO is three dimensional, in LSMO thin films the conduction pathway is quasi-two dimensional. Thus, the difference in c for the as-grown films may be responsible for the critical dependence of the resistivity on the film thickness for as-grown films. The quasi-two-dimensional conduction path in ultrathin films of LSMO may be responsible for the observed correlation between the c -axis lattice parameter and the resistivity, pending future investigation.

Preliminary transmission electron microscope measurements¹⁰ show that the 100 \AA thick film relaxes upon annealing by forming a dislocation network with a periodicity determined by the lattice mismatch between the substrate ($d=3.78 \text{ \AA}$) and the film ($d=3.88 \text{ \AA}$). For all films, after annealing, the c axis contracts and the a axis expands resulting in a cubic structure with $a=c \sim 3.88 \text{ \AA}$. There is neither change in a , c , nor the temperature dependence of the resistivity as a function of thickness. The minor differences, i.e., the magnitude of the resistivity and ratio $\rho_{300\text{K}}/\rho_{80\text{K}}$, may be due to variations in the dislocation network created to accommodate the strain. Detailed electron microscopy work to further understand the role of the microstructure, interdiffusion at interface, and strain relaxation mechanism are in progress.

This work was supported by the Director, Office of Energy Research, Office of Basic Energy Sciences, Materials Sciences Division of the U.S. Department of Energy under Contract No. DE-AC03-76SF00098.

¹P. G. de Gennes, Phys. Rev. **118**, 141 (1960).

²H. Y. Hwang, S.-W. Cheong, P. G. Radaelli, M. Marezio, and B. Batlogg, Phys. Rev. Lett. **75**, 914 (1995).

³H. L. Ju, J. Gopalakrishnan, J. L. Peng, Q. Li, G. C. Xiong, T. Venkatesan, and R. L. Greene, Phys. Rev. B **51**, 6143 (1995).

⁴K. Khazeni, Y. X. Jia, L. Lu, V. H. Crespi, M. L. Cohen, and A. Zettl, Phys. Rev. Lett. **76**, 295 (1996).

⁵S. Jin, T. H. Tiefel, M. McCormack, H. M. O'Bryan, L. H. Chen, R. Ramesh, and R. D. Schurig, Appl. Phys. Lett. **67**, 557 (1995).

⁶N.-C. Yeh, R. P. Vasquez, D. A. Beam, C.-C. Fu, J. Huynh, and G. Beach, J. Phys.: Condens. Matter **9**, 3713 (1997).

⁷T. Y. Koo, S. H. Park, K.-B. Lee, and Y. H. Jeong, Appl. Phys. Lett. **71**, 977 (1997).

⁸J. L. García-Muñoz, J. Fontcuberta, B. Martínez, A. Seffar, S. Piñol, and X. Obradors, Phys. Rev. B **55**, R668 (1997).

⁹C. Eylem, H. L. Ju, B. W. Eichhorn, and R. L. Greene, J. Solid State Chem. **114**, 164 (1995).

¹⁰K. M. Krishnan, K. Verbist, and H. L. Ju (unpublished).

Contrasting magnetic and structural properties of two La manganites with the same doping levels

T. R. McGuire,^{a)} P. R. Duncombe, G. Q. Gong,^{b)} A. Gupta, and X. W. Li^{b)}
 IBM T. J. Watson Research Center, Yorktown Heights, New York 10598

S. J. Pickart and M. L. Crow

Department of Physics, University of Rhode Island, Kingston, Rhode Island 02881

Powder and sintered samples of $\text{La}_{0.9}\text{MnO}_3$ (LMO) and $\text{La}_{0.62}\text{Y}_{0.07}\text{Ca}_{0.31}\text{MnO}_3$ (LYCMO) are used in this study. The two initial calcined in air powders have almost identical ferromagnetic properties with $T_c \approx 250$ K, and saturation magnetization of $\sigma \approx 90$ emu/gm corresponding to $\text{Mn}^{4+}(0.3)/\text{Mn}^{3+}(0.7)$. Heating the calcined powders in argon to high temperatures lowers T_c to ≈ 120 K; however, subsequent oxygen annealing brings back the high T_c form. The LYCMO remains ferromagnetic with $\sigma \approx 90$ emu/gm in both heat treatments but only has a colossal magnetoresistance (MR) for $T_c \approx 120$ K. In contrast the LMO with $T_c \approx 120$ K has σ reduced to one-half its ferromagnetic value and the MR is almost zero. Neutron diffraction shows only the ferromagnetic structure below T_c for LYCMO but the low magnetization of LMO is best interpreted as a mixed ferro-antiferromagnetic structure rather than a canted one. © 1998 American Institute of Physics. [S0021-8979(98)20611-6]

Our previous studies of a self-doped $\text{La}_{1-x}\square_x\text{MnO}_{3-\delta}$ perovskite vacancy (\square) structure showed different magnetic and magnetoresistance properties between films and bulk samples.¹ Preparation and annealing procedures also caused significant changes in the bulk properties. In this article we look at the changes induced in bulk $\text{La}_{0.9}\square_{0.1}\text{MnO}_{3-\delta}$ (LMO) systematically and compare it to $\text{La}_{0.62}\text{Y}_{0.07}\text{Ca}_{0.31}\text{MnO}_{3-\delta}$ (LYCMO) which has a "colossal" magnetoresistance (CMR) discovered by Jin *et al.*² and by Chen *et al.*³ The two compositions LMO and LYCMO are chosen because they have the same mixed valency of Mn and comparison should help our understanding about magnetic and transport properties in these oxides.

To facilitate the presentation Table I lists the various samples studied, their preparation, and structure data. The initial powders are obtained by the reaction of high purity ($\text{La}_2\text{O}_3, \text{MnO}, \text{CaCO}_3$) component oxides or carbonates heated in air at 1050°C . These are designated as calcined in Table I. Subsequent oxygen annealing did not change the calcined powder sample magnetic properties. To cause changes it is necessary to heat the sample in argon to reduce the oxygen content of the powder. Sintered bar samples are prepared from the calcined powders at temperatures of $1550\text{--}1600^\circ\text{C}$ for 16 h at which temperatures there is evidently a loss of oxygen. It is necessary to reanneal in oxygen to obtain magnetic properties for the bars similar to the original calcined powders.

Magnetic data for the two calcined powders are plotted in Fig. 1(a) for LMO and in Fig. 2(a) for LYCMO. Since these samples were adjusted to have the same valency distribution of Mn, it is not surprising that they have about the same Curie temperature (T_c) and the same saturation magnetization σ_s . Assuming O_3 per formula unit (i.e., $\delta=0$)

both compositions have the ratio $\text{Mn}^{4+}(0.3)/\text{Mn}^{3+}(0.7)$. Using spin only of Mn^{4+} and Mn^{3+} as $3n_B$ and $4n_B$ Bohr magnetons, respectively, with ferromagnetic alignment we calculate $\sigma_s = 90.7$ emu/gm for LMO and $\sigma_s = 99.6$ emu/gm for LYCMO. The measured values estimated for $1/H \rightarrow 0$ are 90 emu/gm for LMO and 94.5 emu/gm for LYCMO and the measured σ_s are in reasonable agreement with the calculated values. Curie temperatures estimated from low field magnetization are illustrated in Fig. 1(a) for $H = 150$ Oe. The θ intercept is obtained from the linear portion of the reciprocal susceptibility ($1/\chi_M$) projected to the horizontal axis as given by the Curie-Weiss law $\chi_M = C_M/(T - \theta)$. The molar Curie constant C_M is proportional to the square of the average effective moment $(\mu_{\text{eff}})^2 = g^2 S(S+1)$ of the Mn ions with spin S and $n_B = gS$. To obtain μ_{eff} the relation $8C_M = (\mu_{\text{eff}})^2$ can be used. Reciprocal susceptibilities are plotted for each of the samples studied. These plots are useful not only to obtain μ_{eff} but the departure of $1/\chi_M$ from linearity is a measure of the short range order or cluster formation⁴ of the Mn magnetic moments above T_c . From molecular field theory the θ temperature intercept is a measure of the sign and strength of the exchange interactions between neighboring Mn ions. Where short range order is strong, the Curie temperature is depressed and $\theta > T_c$. In the two calcined samples, Figs. 1(a) and 2(a) $\theta \approx T_c$, indicating very little short range order.

In Figs. 1–4 values of C_M are marked for each $1/\chi_M$ linear plot. These values are all larger than expected and give Mn atomic moments of $4\text{--}5 n_B$ as compared to the $3.7 n_B$ expected for $\text{Mn}^{4+}(0.3)/\text{Mn}^{3+}(0.7)$ ratio. The high values of C_M are evidently due to a small amount of short range order which persists up to 400 K. Magnetic data for the calcined powder heated in argon are shown in Figs. 1(b) and 2(b). For LMO there is a decrease in T_c , θ , and σ_s , but for LYCMO, although a large decrease in T_c is obtained, θ and σ_s change very little. In addition, the reciprocal susceptibility for LY-

^{a)}Electronic mail: mcguire@watson.ibm.com

^{b)}Department of Physics, Brown University, Providence, RI 02912.

TABLE I. Preparation and structure for powder^a LMO and LYCMO.

Figure	Preparation	X ray (room T)	Neutron diffraction
1(a) LMO	Calcined in air 16 hrs, 1050 °C	Rhombohedral Perovskite	
1(b) LMO	1(a) in argon 1 h, 1050 °C	Orthorhombic	Canted or mixed $<T_c$ No structure $>T_c$
2(a) LYCMO	Calcined in air 16 h, 1050 °C	Cubic	
2(b) LYCMO	2(a) in argon 1 hr, 1350 °C	Cubic	Ferro structure $<T_c$ No structure $>T_c$

^aThe bar samples Figs. 3–6 are sintered and subsequently oxygen annealed.

CMO [Fig 2(b)] now shows a significant departure from linearity indicating short range order or clusters of Mn moments, an effect also found in films.⁵ The change in LMO due to argon annealing shows $\theta < T_c$, meaning that negative exchange interactions are now present. Such interactions cause partial antiferromagnetic alignment of the Mn moments. As we can note from Table I, neutron diffraction measurements have peaks indicating that there is a canted or mixed magnetic structure⁶ composed of ferro- and antiferromagnetic regions. The most probable magnetic structure for LMO can be obtained by comparing the transverse (AF) and parallel (F) spin components from neutron diffraction peaks with estimates of AF/F from magnetization data. We find very poor agreement for a canted structure, but for a mixed phase the volume ratio AF/F is in better agreement for the two sets of measurements if we use the high field magnetization data. We also note that there is a change in crystal structure⁷ for LMO going from a rhombohedral cell for the calcined powder to an orthorhombic cell for the argon anneal. This may be also a reason for the decrease in T_c and σ_S and the mixed magnetic structure. As we shall discuss, this sample has lost its electrical conductivity and is now a semiconductor. As seen in Table I, the powder LYCMO remains

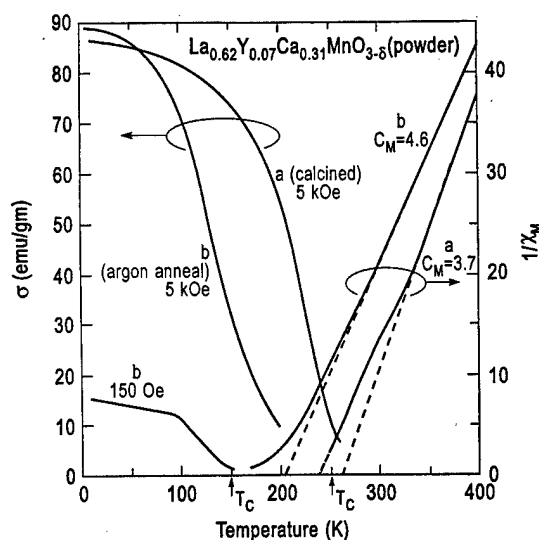


FIG. 2. (a) Plots of σ and $1/\chi_M$ for LYCMO powder after the initial calcine. Note the similarity to calcined LMO in Fig. 1(a). (b) Magnetic data for LYCMO powder after annealing in argon.

the same cubic perovskite for both the calcined and the argon anneal. The neutron diffraction measurement did not indicate any magnetic structure above T_c in the region of short range order, nor was it possible to establish that clusters of aligned Mn magnetic moments exist because of statistical uncertainty in the data. Below T_c a ferromagnetic structure is observed.

Our second group of measurements is on sintered samples. Bars are cut approximately $10 \times 3 \times 1 \text{ mm}^3$ for both the magnetic (Figs. 3 and 4) and the magnetoresistance studies (Figs. 5 and 6). The high temperature sintering causes a loss of oxygen and the magnetic properties of the sintered bars are similar to the powder argon annealed samples in Figs. 1(b) and 2(b). To make the sintered samples similar to the calcined powder ones we heat the sintered samples in O_2 for 60 h at 800–950 °C. Let us consider first the LMO in Fig. 3 where the conversion by oxygen anneal in Fig. 3(b) is only

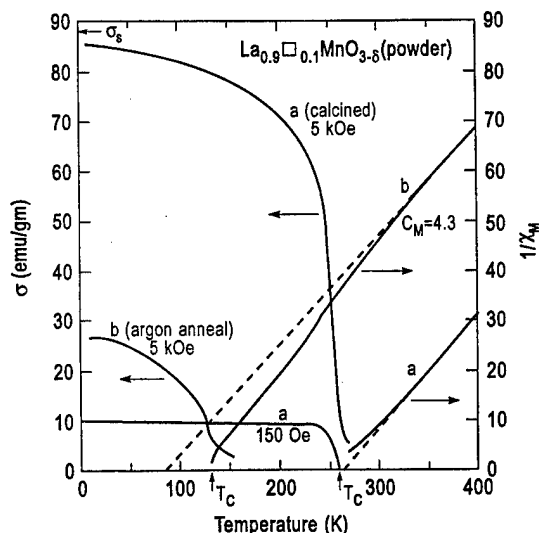


FIG. 1. (a) Plots of magnetization σ (emu/gm) and reciprocal molar susceptibility $1/\chi_M$ vs T for (LMO) calcined powder. (b) Data for LMO after annealing in argon.

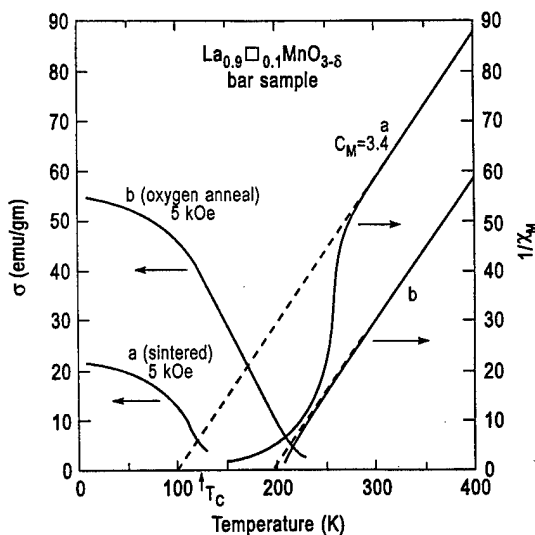


FIG. 3. (a) Magnetic data for the sintered bar sample of LMO. (b) Magnetic data for the oxygen annealed bar sample of LMO.

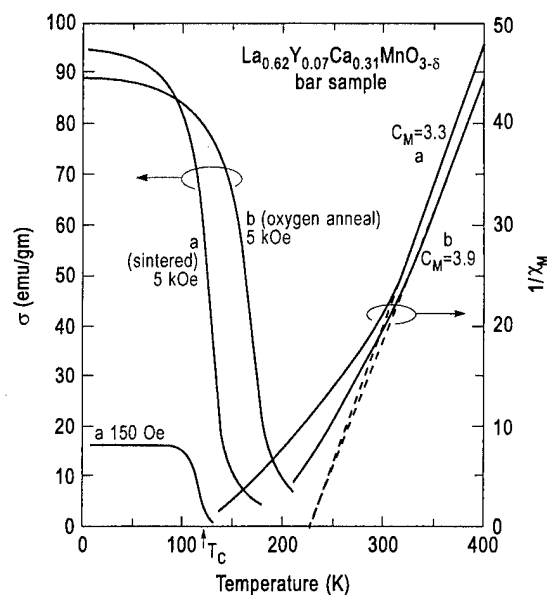


FIG. 4. (a) Magnetic data for the sintered bar sample of LYCMO. (b) Magnetic data for the oxygen annealed sample of LYCMO.

partly successful. In addition, the sharp drop in the $1/\chi_M$ at 250 K in the original sintered sample is probably due to a low percent inhomogeneous oxygen content. The CMR plots of the two LMO samples are shown in Fig. 5. The sintered sample in Fig. 5(a) has a very small response to an applied field of $H=40$ kOe and exhibits a large nonmetallic resistivity. Figure 5(b) shows LMO after the O_2 anneal. Now the

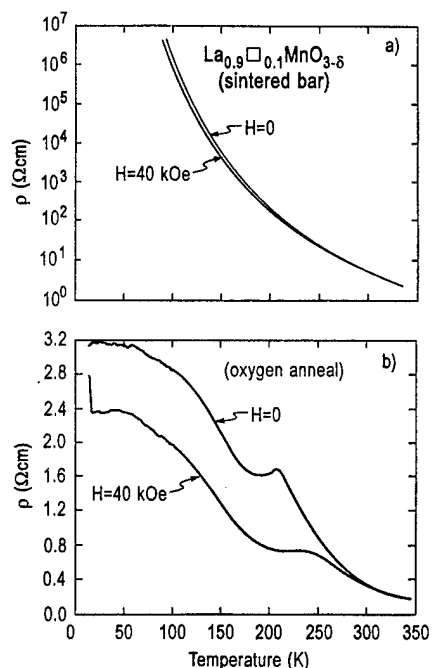


FIG. 5. (a) Resistivity as a function of T at $H=0$ and $H=40$ kOe for the sintered LMO bar in Fig. 3(a). The percentage change in magnetoresistance at 100 K is about 5%. (b) Resistivity vs T at $H=0$ and $H=40$ kOe for oxygen annealed LMO in Fig. 3(b). The CMR maximum for $T=200$ K is 100%. The CMR can be calculated from ρ ($\rho_{H=0} - \rho_{H=40 \text{ kOe}} / \rho_{H=40 \text{ kOe}}$). The CMR extended down to low temperature is probably due to a canted or mixed magnetic structure that remains after annealing.

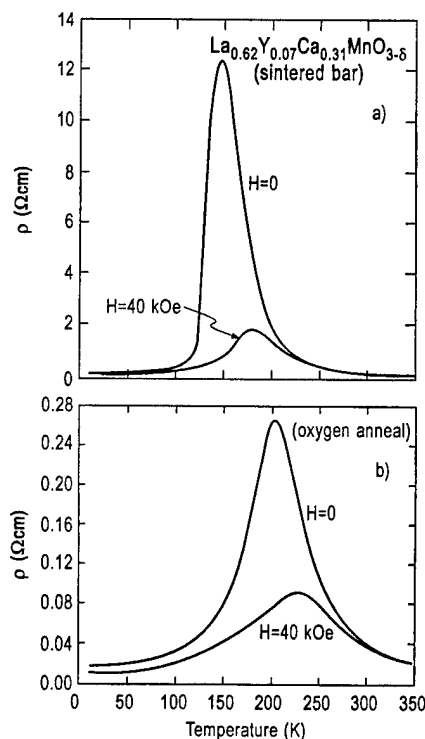


FIG. 6. (a) Resistivity vs T for sintered LYCMO at $H=0$ and $H=40$ kOe in Fig. 4(a). The CMR is about 2500% at 150. (b) Resistivity vs T for oxygen annealed LYCMO at $H=0$ and $H=40$ kOe in Fig. 4(b). The CMR is about 300% at 2.

resistivity has dropped to $2 \Omega \text{ cm}$ at 100 K compared to $10^6 \Omega \text{ cm}$ before the O_2 anneal. The maximum CMR for the annealed LMO is about a 100% change at $T_c \approx 200$ K. The CMR measurements for LYCMO are given in Figs. 6(a) and 6(b) where the CMR is 2400% at 150 K for the sintered sample and 300% after the O_2 anneal. If the CMR depends on short range order clusters⁴ with polaron formation⁸ or hopping,⁹ the raising of T_c decreases these effects.

¹ A. Gupta, T. R. McGuire, P. R. Duncombe, M. Rupp, J. Z. Sun, W. J. Gallagher, and G. Xiao, Appl. Phys. Lett. **67**, 3494 (1995); J. Appl. Phys. **79**, 4549 (1996).

² S. Jin, H. M. O'Bryan, T. H. Tiefel, M. McCormack, and W. W. Rhodes, Appl. Phys. Lett. **66**, 382 (1995).

³ L. H. Chen, T. H. Tiefel, T. T. M. Palstra, R. Ramesh, and C. Koon, IEEE Trans. Magn. **32**, 4692 (1966).

⁴ J. S. Smart, *Effective Field Theories of Magnetism* (Saunders, Philadelphia, 1996), pp. 45–52.

⁵ J. Z. Sun, L. Krusin-Elbaum, A. Gupta, G. Xiao, and S. S. P. Parkin, Appl. Phys. Lett. **67**, 2726 (1995); **69**, 1002 (1996).

⁶ E. O. Wollan and W. C. Koehler, Phys. Rev. **100**, 545 (1955).

⁷ A. Maignan, C. Michel, M. Herveu, and B. Raveau, Solid State Commun. **101**, 53 (1997).

⁸ S. S. L. Billinge, R. G. DiFrancesco, G. H. Kwei, J. J. Neumier, and J. D. Thompson, Phys. Rev. Lett. **77**, 715 (1996).

⁹ M. Viret, L. Rann, and J. M. D. Coey, J. Appl. Phys. **81**, 4964 (1997).

Magnetoresistance effects of $\text{La}_{0.7}\text{M}_{0.3}\text{MnO}_{3-\delta}$ far below the Curie temperature ($\text{M}=\text{Ca}, \text{Pb}$)

K. Dörr and K.-H. Müller

Institute for Solid State and Material Research Dresden, D-01171 Dresden, Germany

E. S. Vlahov

Institute of Solid State Physics, Sofia 1784, Bulgaria

R. A. Chakalov and R. I. Chakalova

Institute of Electronics, Sofia 1784, Bulgaria

K. A. Nenkov,^{a)} A. Handstein, B. Holzapfel, and L. Schultz

Institute for Solid State and Material Research Dresden, D-01171 Dresden, Germany

Single-crystalline and nontextured polycrystalline thin films of $\text{La}_{0.7}\text{Pb}_{0.3}\text{MnO}_{3-\delta}$ (LPMO) and $\text{La}_{0.7}\text{Ca}_{0.3}\text{MnO}_{3-\delta}$ (LCMO) have been prepared by pulsed laser deposition and by magnetron sputtering, respectively. The oxygen deficiency δ of the samples was controlled by heat treatments under defined oxygen pressure. For $\delta \approx 0$, the polycrystalline as well as the single-crystalline films are ferromagnetic metals with Curie temperatures T_c of 220–270 K. At low temperatures $T \ll T_c$, the polycrystalline LCMO films show a negative magnetoresistance ratio (MR) at $T=20, 77$, and 180 K of -30% , -20% , and -8% , respectively, for a field of 1.5 kOe. At 20 K, around 200 Oe, the field sensitivity is as high as $-0.5\% (\text{Oe})^{-1}$. A possible mechanism for this phenomenon is the spin-polarized tunneling through grain boundaries. For the single-crystalline films, the change of δ from 0 to about 0.1 has a similar effect as changing the doping level x from 0.3 to 0.1, namely, a transition from a ferromagnetic metal to a ferromagnetic insulator. By variation of δ , the low-temperature resistivity of these samples can be controlled within many orders of magnitude. The negative MR of oxygen-deficient single-crystalline LPMO and LCMO films was found to be as large as -20% at $T=0.2T_c$. © 1998 American Institute of Physics. [S0021-8979(98)38111-6]

Manganese oxides $(\text{R}^{3+})_{(1-x)}(\text{A}^{2+})_x\text{MnO}_3$ ($\text{R}=\text{La}$ or rare earth metals, $\text{A}=\text{Ca}, \text{Sr}, \text{Ba}, \text{Pb}$, $x=0.2-0.4$) have been intensively studied as a colossal magnetoresistance effect (CMR) is observed near the ferromagnetic ordering of the Mn spins.¹ The Curie temperature (T_c) is associated with a metal-insulator transition. Recently, polycrystalline samples were found to exhibit large magnetoresistance in a temperature range $T < T_c$, that appears in low magnetic fields and therefore is a step towards practical application of these materials.² The transport process of carriers through the structurally and magnetically disordered grain boundary is under investigation.³⁻⁵

The properties of these manganese oxides with perovskite structure strongly depend on the oxygen content that influences the carrier density and the magnetic ordering. Spin-glass behavior has been reported for oxygen deficient samples.⁶ There is, however, a lack of systematic investigations elucidating the dependence of the magnetic and transport properties on the oxygen content.

The aim of our work was to investigate the low-field MR effect in polycrystalline thin films at $T < T_c$. A further intention was to study the influence of oxygen deficiency on the magnetotransport at low temperatures.

Single-crystalline films of $\text{La}_{0.7}\text{M}_{0.3}\text{MnO}_{3-\delta}$ ($\text{M}=\text{Ca}, \text{Pb}$) were prepared on LaAlO_3 (100) substrates by pulsed

laser deposition and by radio-frequency magnetron sputtering, respectively. Nontextured polycrystalline films were grown on MgO and Y-stabilized ZrO_2 (YSZ) substrates by magnetron sputtering. The oxygen deficiency δ was controlled by heat treatments at 300–900 °C under an oxygen pressure of 10^{-3} – 10^{-2} Pa. The structure of the films was investigated by x-ray diffraction including pole figure measurements. Magnetic and magnetotransport measurements were carried out in a Lake Shore susceptometer and in a superconducting quantum interference device magnetometer. The resistance R of the samples was measured in dependence on temperature and magnetic field H , up to 70 kOe, by the usual four-probe technique. The magnetoresistance ratio is determined as $\text{MR}=[R(H)-R(0)]/R(0)$.

In contrast to single crystals and single-crystalline films of stoichiometric $\text{La}_{0.7}\text{M}_{0.3}\text{MnO}_3$ ($\text{M}=\text{Sr}, \text{Ca}, \text{Ba}, \text{Pb}$), polycrystalline films^{5,7} and ceramic samples² exhibit considerable magnetoresistance at temperatures far below T_c . This effect occurs in low magnetic fields and increases with decreasing temperature as shown in Fig. 1 for a polycrystalline $\text{La}_{0.7}\text{Ca}_{0.3}\text{MnO}_3$ film grown on YSZ. The most pronounced resistance drop appears in small fields $H < 500$ Oe (inset of Fig. 1). The coercive field of this film is about 100 Oe. The increased slope of MR vs H for the 160 K curve, compared with that of the low temperature curves, for fields $H > 10$ kOe is attributed to the suppression of thermally activated spin fluctuations (i.e., the CMR effect near T_c).

The charge transport in polycrystalline manganites is af-

^{a)}Also at International Laboratory for High Magnetic Fields and Low Temperatures, 53-529 Wrocław, Poland.

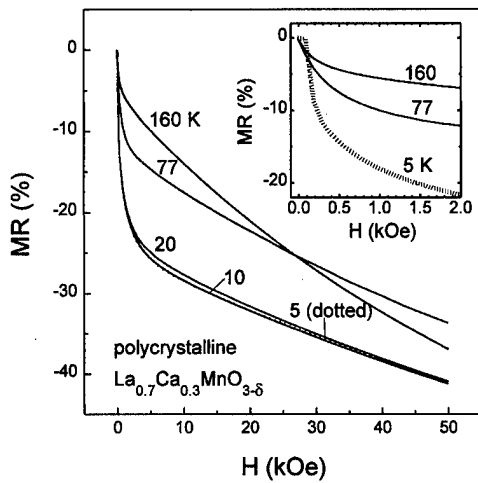


FIG. 1. Magnetoresistance ratio vs magnetic field for a polycrystalline $\text{La}_{0.7}\text{Ca}_{0.3}\text{MnO}_{3-\delta}$ film measured at various temperatures. Inset: low-field range $H < 2$ kOe, expanded.

ected by grain boundaries because of their structural and magnetic disorder. As a possible transport mechanism, spin-polarized tunneling (SPT) of electrons through the grain boundaries was proposed.² The spin-polarization factor of the density of states at the Fermi level should be very high in these compounds.^{8,9} The tunneling probability will be restricted by a nonparallel orientation of the magnetization of adjacent grains. Gupta *et al.*⁵ have shown by Kerr microscopy that grains of several microns in size often coincide with the magnetic domains and are characterized by their individual switching field in the magnetization process. Our films show a nearly complete saturation of magnetization at fields of 3–5 kOe for $T \ll T_c$. Therefore, the main part of the resistance drop in $H < 2$ kOe (Fig. 1) is attributed to SPT. Magnetic scattering by magnetic disorder in the grain-boundary region could be responsible for the further decrease of resistance observed in an increasing magnetic field $H > 5$ kOe (Fig. 1). This decrease is much stronger than that found for single-crystalline samples.

One aim was to check if the observed MR behavior in low magnetic fields is compatible with spin-polarized tunneling. In some field interval $0 < H < H_1$, a linear dependence of the MR on the square of the normalized magnetization was found for several polycrystalline films: $\text{MR}(H) = a + b [M(H)/M(50 \text{ kOe})]^2$ (Fig. 2). For the sample of Fig. 2, we find $H_1 = 1.2$ kOe, $a \approx 0$, and $b = -0.21$. This is consistent with the first term in the high temperature expansion of the MR for SPT given by Hwang,²

$$\text{MR}(H, T) = -JP/(4kT)[m(H, T)^2 - m(0, T)^2], \quad (1)$$

where J is the intergrain exchange constant, P is the spin-polarization factor, and m is the magnetization normalized to the saturation value.

In order to examine the temperature dependence of the low-field contribution, MR^* , to the magnetoresistance, we extrapolated the $\text{MR}(H)$ curve from $H > 10$ kOe to zero field using a polynomial fit. The intersection point at the vertical axis ($H=0$) gives the value of MR^* . At low temperatures, $T < 0.1T_c$, a saturation of MR^* is found. With increasing

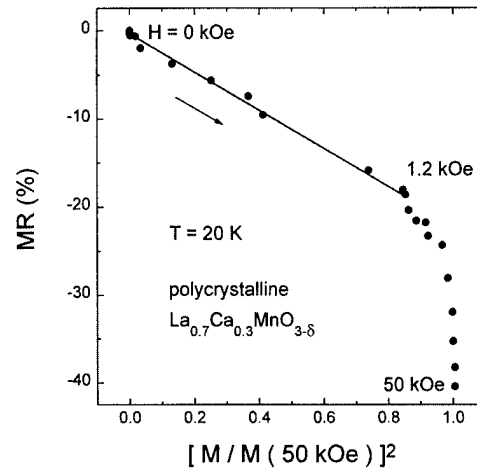


FIG. 2. Magnetoresistance ratio vs square of magnetization normalized to the value measured at $H = 50$ kOe, for the sample of Fig. 1.

temperature, MR^* drops rapidly. MR^* proportional to T^{-1} , according to Eq. (1), is only observed for a small temperature interval around $1/2T_c$.

If the magnetic field is increased above technical saturation, the MR grows continuously without a significant increase of magnetization (Fig. 2). [Because of a not exactly known diamagnetic contribution of our substrates, small changes of film magnetization in high fields ($< 10\%$) cannot be detected.] This increase in MR is ascribed to an ordering of the spins in the grain-boundary region by the high field. Such an ordering should influence the resistance of the grain boundary via the double-exchange mechanism,⁵ but it has a small effect on the total magnetization.

A considerable low-temperature MR arises in single-crystalline films of $\text{La}_{0.7}\text{Ca}_{0.3}\text{MnO}_{3-\delta}$ and $\text{La}_{0.7}\text{Pb}_{0.3}\text{MnO}_{3-\delta}$ after the oxygen content has been reduced ($\delta > 0$) by annealing. This low-temperature MR is small in low magnetic fields and does not saturate in magnetic fields up to 50 kOe (Fig. 3, for a LPMO sample). In the inset of Fig. 3, three $\text{La}_{0.7}\text{Pb}_{0.3}\text{MnO}_{3-\delta}$ films with reduced oxygen content [$\delta(A) < \delta(B1) < \delta(B2)$, prepared from one original sample] are characterized by their temperature dependence of resistance. The curves resemble those of $\text{La}_{1-x}\text{Sr}_x\text{MnO}_3$ samples with a doping level of $x = 0.1-0.3$.¹⁰ This should be expected because the oxygen deficiency reduces the Mn^{4+} -to- Mn^{3+} concentration ratio. The insulating behavior of the oxygen-deficient samples at low temperatures can be qualitatively discussed using the magnetic localization model of Viret *et al.*¹¹ Recently, these authors suggested a random magnetic potential

$$kT_0 = 171\alpha^3 U_m [1 - (M/M_s)^2] v \quad (2)$$

to be responsible for charge carrier localization, where α is the inverse localization length, U_m the Hund's rule splitting energy, v the cell volume, and M_s the collinear saturation magnetization. In this model, the occurrence of spin canting should lead to insulating behavior at low temperatures when M/M_s has a constant value smaller than one. Under the assumption that spin canting is the only reason for the reduced saturation magnetization measured for our oxygen-deficient

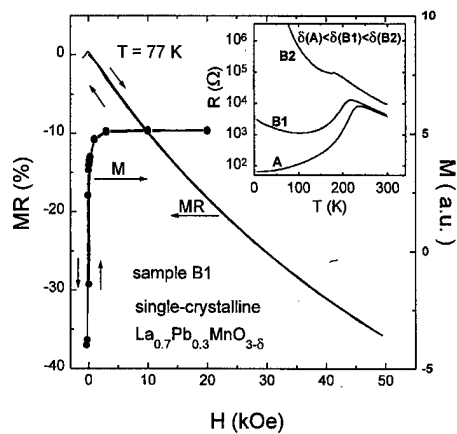


FIG. 3. Magnetoresistance ratio and magnetization vs field for an oxygen-deficient single-crystalline $\text{La}_{0.7}\text{Pb}_{0.3}\text{MnO}_{3-\delta}$ film ($T_c=200$ K) at $T=77$ K. Inset: resistance vs temperature of three pieces, A, B1, and B2, of an original $\text{La}_{0.7}\text{Pb}_{0.3}\text{MnO}_3$ sample, annealed in different oxygen atmospheres resulting in $\delta(A)<\delta(B1)<\delta(B2)$.

films, we estimate $M/M_s(5\text{ K})\approx 0.85$ for sample B2 from the values of saturation magnetization measured before and after the desoxygenation. However, it cannot be excluded that magnetic inhomogeneity in the sense of a mixture of ferromagnetic and nonferromagnetic regions leads to the reduced saturation magnetization and the insulating low-temperature behavior of our oxygen deficient samples. The resistance data for the low-temperature insulating state of B1 and B2 can be well fitted to $R(T)=R_\infty \exp(T_0/T)$. This does not agree with the variable range hopping (VRH) mechanism of Ref. 11. But the idea of magnetic localization should not be restricted to this special kind of hopping mechanism and therefore is expected to apply to our data.

In Fig. 4, the temperature dependence of the MR of several oxygen-deficient samples is shown. The MR peak near T_c broadens substantially for the $\text{La}_{0.7}\text{Pb}_{0.3}\text{MnO}_{3-\delta}$ samples B1 and B2 which therefore exhibit a considerable MR far below T_c . In the inset of Fig. 4, the curves of two $\text{La}_{0.7}\text{Ca}_{0.3}\text{MnO}_{3-\delta}$ samples [$\delta(S)\approx 0$, $\delta(S1)\approx 0.07$] are shown for comparison. The MR of the oxygen deficient sample S1 has a second maximum of MR at a temperature $T_1<T_c$. It is possible that for B1 and B2 this low-temperature maximum of the MR is there, but it overlaps the main peak around T_c . The estimated peak temperature T_1 for B1 and S1 nearly equals that of the minimum of R vs T . Further work should clarify if the low temperature maximum of the MR at T_1 is associated with a canted spin structure or with magnetic inhomogeneity.

In summary, we have examined the magnetoresistance and the magnetization of single-crystalline and polycrystalline films of $\text{La}_{0.7}\text{M}_{0.3}\text{MnO}_{3-\delta}$ ($M=\text{Ca}, \text{Pb}$) in the ferromagnetic state. For the polycrystalline samples, the value of the large negative low-field MR was found to saturate at low temperatures and then to drop rapidly with increasing temperature. A quadratic correlation with the magnetization, MR

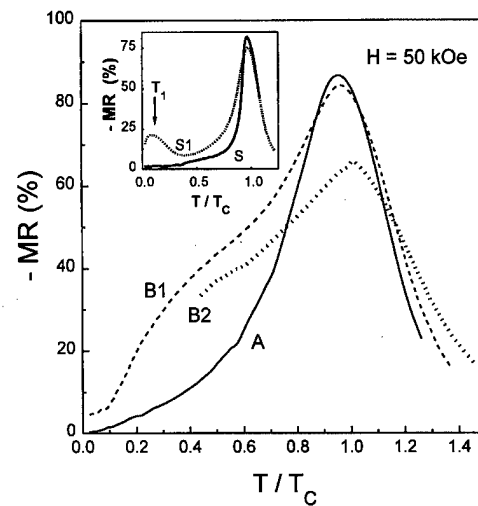


FIG. 4. Magnetoresistance ratio vs temperature for the three single-crystalline $\text{La}_{0.7}\text{Pb}_{0.3}\text{MnO}_{3-\delta}$ films from Fig. 3. Inset: magnetoresistance ratio vs temperature for two single-crystalline $\text{La}_{0.7}\text{Ca}_{0.3}\text{MnO}_{3-\delta}$ films with $\delta(S)\approx 0$, $\delta(S1)\approx 0.07$.

proportional to $(M/M_s)^2$, was observed in a field range $0<H<H_1$, a field value near the saturation field of magnetization. Single-crystalline films undergo a second metal-to-insulator transition at low temperatures, after their oxygen content has been reduced by an annealing procedure. They show a large negative MR at $T\ll T_c$, that does not saturate up to $H=50$ kOe. This MR effect due to oxygen deficiency may be important for the understanding of the MR of oxygen-deficient polycrystalline material.

The authors thank D. Eckert for doing some measurements and for helpful discussions. The authors E. V., K. N., and K. D. thank the DFG, Contract No. 436BUL112/5/97, the SMWK, Contract No. 4-7531.50-04-IFW/702, and the SMWK, scholarship of HSP3 program, respectively, for financial support of this work.

¹ J. M. D. Coey, M. Viret, and S. von Molnár, Adv. Phys. (to be published).

² H. Y. Hwang, S.-W. Cheong, N. P. Ong, and B. Batlogg, Phys. Rev. Lett. **77**, 2041 (1996).

³ N. D. Mathur, G. Burnell, S. P. Isaac, T. J. Jackson, B.-S. Teo, J. L. MacManus-Driscoll, L. F. Cohen, J. E. Evetts, and M. G. Blamire, Nature (London) **387**, 266 (1997).

⁴ K. Steenbeck, T. Eick, K. Kirsch, K. O'Donnell, and E. Steinbeiss, Appl. Phys. Lett. **71**, 968 (1997).

⁵ A. Gupta, G. Q. Gong, G. Xiao, P. R. Duncombe, P. Lecoeur, P. Trouilloud, Y. Y. Wang, V. P. Dravid, and J. Z. Sun, Phys. Rev. B **54**, R15 629 (1996).

⁶ H. L. Ju and H. Sohn, J. Magn. Magn. Mater. **167**, 200 (1997).

⁷ E. S. Vlahov, R. A. Chakalov, R. I. Chakalova, K. A. Nenkov, K. Dörr, A. Handstein, and K.-H. Müller, J. Appl. Phys. **83**, 2152 (1998).

⁸ J. Z. Sun, L. Krusin-Elbaum, P. R. Duncombe, A. Gupta, and R. B. Laibowitz, Appl. Phys. Lett. **70**, 1769 (1997).

⁹ J.-H. Park, C. T. Chen, S.-W. Cheong, W. Bao, G. Meigs, V. Chakarian, and Y. U. Idzerda, Phys. Rev. Lett. **76**, 4215 (1996).

¹⁰ A. Urushibara, Y. Moritomo, T. Arima, A. Asamitsu, G. Kido, and Y. Tokura, Phys. Rev. B **51**, 14 103 (1995).

¹¹ M. Viret, L. Ranno, and J. M. D. Coey, J. Appl. Phys. **81**, 4964 (1997).

Fully relativistic theory for the magnetic extended x-ray absorption fine structure

D. Ahlers^{a)} and G. Schütz

Lehrstuhl für Experimentalphysik II, Universität Augsburg, Memmingerstrasse 6, D-86135 Augsburg, Germany

V. Popescu and H. Ebert

Institut für Physikalische Chemie, Universität München, Theresienstrasse 37, D-80333 München, Germany

A fully relativistic theoretical description of the magnetic extended x-ray absorption fine structure (MEXAFS) is presented that has been set up within the framework of relativistic multiple scattering theory on the basis of the Dirac equation for spin-polarized, magnetic solids. The multiple scattering processes in the final state are treated using the scattering path expansion technique for finite atomic clusters. Results of the approach for the Fe *K* and the Gd *L* edges are presented and are compared with experiment. An analysis of the theoretical spectra clearly shows that the MEXAFS spectra can be interpreted on the basis of the so-called sum rules in a way completely analogous to the case of near-edge x-ray magnetic circular dichroism. This means that the *K*- and *L*₁-edge spectra directly reflect the orbital polarization of the final states with *p* character. The *L*_{2,3}-edge spectra, on the other hand, give, after suitable superposition, access to the spin and orbital polarization of the *d* states.

© 1998 American Institute of Physics. [S0021-8979(98)51711-2]

I. INTRODUCTION

The magnetic extended x-ray absorption fine structure (MEXAFS), the analogon to normal EXAFS when using circularly polarized radiation, has become an interesting technique to study the magnetic short range order around the absorbing atom in an element selective manner.¹ As for x-ray magnetic circular dichroism (XMCD) in the near-edge region, the MEXAFS originates from the interplay of spin-polarization and spin-orbit coupling. On this basis a phenomenological model for MEXAFS has been developed by Schütz and Ahlers by introducing a spin-dependent back-scattering term to conventional EXAFS.² A more profound treatment of MEXAFS using nonrelativistic multiple scattering theory for a finite cluster of atoms has been developed by Brouder and co-workers^{3,4} as well as by Ankudinov and Rehr.^{5,6} In both cases, however, spin-orbit coupling and/or spin polarization are considered only in an approximate way. We present results from a fully relativistic description of MEXAFS based on relativistic multiple scattering theory for magnetic systems.⁷ These spectra are discussed on the basis of the so-called sum rules.

II. THEORETICAL FRAMEWORK

The basis for the calculation of the x-ray absorption coefficient $\mu^\lambda(\omega)$ presented below is the conventional expression⁸

$$\mu^{\lambda}(\omega) \propto \sum_{iocc} \langle \Phi_i | X_{q\lambda}^\times \mathcal{T} G^+(E_i + \hbar\omega) X_{q\lambda} | \Phi_i \rangle \Theta(E_i + \hbar\omega - E_F). \quad (1)$$

Here the wave function Φ_i of the involved initial core states are solutions to the Dirac equation for a spin-dependent potential.⁹ The electron photon interaction operator $X_{q\lambda}$ describes the coupling of the electronic current density operator to the vector potential $\mathbf{A}_{q\lambda}$ of light with wave vector \mathbf{q} , frequency ω , and polarization λ . The final states are represented by the Green's function:⁸

$$G^+(\mathbf{r}_n, \mathbf{r}_n, E) = \sum_{\Lambda\Lambda'} Z_\Lambda(\mathbf{r}_n, E) \tau_{\Lambda\Lambda'}^{nn} Z_{\Lambda'}^\times(\mathbf{r}_n, E) - \sum_{\Lambda} Z_\Lambda(\mathbf{r}_n, E) J_\times(\mathbf{r}_n, E), \quad (2)$$

with the wave functions Z_Λ and J_Λ [$\Lambda = (\mu, \kappa)$] being the regular and irregular, respectively, solutions to the Dirac equation. Finally, the quantity $\tau_{\Lambda\Lambda'}^{nm}$ is the so-called scattering path operator that consistently represents all multiple scattering events within a solid and has to fulfill the self-consistency condition:

$$\underline{T}^{nm} = \underline{t}^n \delta_{nm} + \underline{t}^n \sum_{k \neq n} \underline{G}^{nk} \underline{T}^{km}, \quad (3)$$

where \underline{t}^n is the single site *t* matrix for site *n* and \underline{G}^{nk} is the free electron propagator connecting sites *k* and *n*. For the EXAFS region it is sufficient to account only for multiple

^{a)}Electronic mail: ahlers@physik.uni-wuerzburg.de

scattering paths within the vicinity of the absorbing atom. Therefore it is possible to reduce the problem to a cluster of limited size. In that case Eq. (3) can be inserted repeatedly into itself, yielding for $\tau_{\Lambda\Lambda}^n$ in Eq. (2) a series of scattering paths with increasing complexities.

From these considerations it is obvious that there is no fundamental difference for the x-ray absorption in the near edge and EXAFS regions. Therefore the question arises as to whether the interpretation of the XMCD spectra with the so-called sum rules also holds for the EXAFS region. As derived by Igarashi and Hirai,¹⁰ Carra *et al.*¹¹ and Thole *et al.*,¹² the sum rules can be expressed as

$$\frac{\int \mu_c(K)/E dE}{\int \mu_0(K)/E dE} = \frac{3}{N_{hp}} \langle l_z \rangle_p, \quad (4a)$$

$$\int [\mu_c(L_3) - \mu_c(L_2)] dE = \frac{3N}{4N_{hd}} (\langle \sigma_z \rangle_d + 7 \langle T_z \rangle_d), \quad (4b)$$

$$\int [2\mu_c(L_3) + \mu_c(L_2)] dE = \frac{3N}{2N_{hd}} \langle l_z \rangle_d. \quad (4c)$$

Here $\mu_c(X)$ ($X=K, L_2, L_3$) are the circular dichroism spectra, i.e., they give the difference in absorption for left and right circularly polarized radiation at the various edges. N is the sum of the energy integrals for all partial absorption spectra and N_{h1} is the number of holes for angular momentum character 1. The expectation values $\langle \sigma_z \rangle$ and $\langle l_z \rangle$ give the spin and angular momentum of the absorber atom and $\langle T_z \rangle$ is a measure for the asphericity of the spin magnetization that can be neglected in most cases.

III. EXPERIMENTAL DETAILS

The experiments were performed at the R6Mo II station at the HASYLAB in Hamburg using the two beam transmission mode. The estimated intensity of the beam monochromatized by a Si(111) double crystal was 10^7 – 10^8 photons/s eV with a circular polarization of 60%–70%. The spectra were sampled alternating the external magnetic field every second at each energy point. A magnetic field of $B_0 = 0.2$ T was applied and the Gd sample was cooled to 150 K.

The measured quantities of the experiment are the spin-averaged absorption coefficient $\mu_0(E) = \frac{1}{2}[\mu^+(E) + \mu^-(E)]$ and the corresponding dichroic signal $\mu_c(E) = \frac{1}{2}[\mu^+(E) - \mu^-(E)]$ for parallel (+) and antiparallel (–) orientation of the photon “spin” to the spin of the majority-like electrons in the sample. The spin-averaged EXAFS spectra $\chi_0(E) = [\mu_0(E) - \mu_{\text{atom}}(E)]/\mu_{\text{atom}}(E)$ have been deduced in the conventional way by subtracting the free atom absorption μ_{atom} . The MEXAFS spectra are denoted as the difference $\chi_c(E) = [\mu_c(E)/\mu_{\text{atom}}(E)]/(P_c \cdot M_z)$. They are rescaled for full circular polarization $P_c = 1$ and complete alignment of the sample magnetization along the photon k vector $M_z = 1$.

IV. APPLICATION TO Fe AND Gd

In Fig. 1 we compare the results of our theoretical calculations and the experimental spectra for the Fe K edge in body-centered-cubic (bcc) Fe. The top panel gives the con-

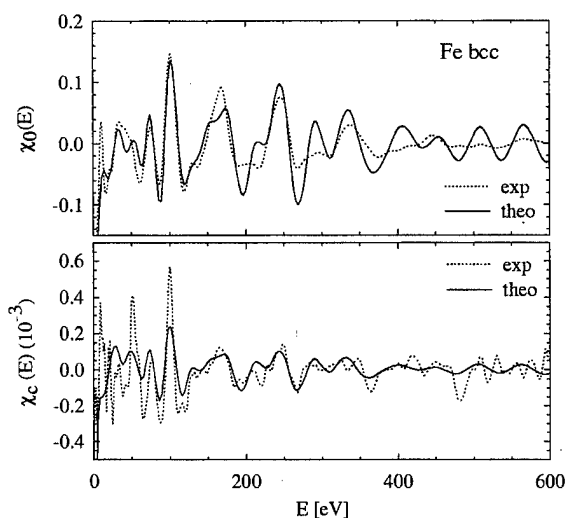


FIG. 1. X-ray absorption spectra at the K edge of Fe. Top: absorption for unpolarized radiation $\chi_0(E)$. Bottom: dichroic signal $\chi_c(E)$.

ventional EXAFS $\chi_0(E)$ with the characteristic oscillations in the high energy region. In the lower panel the magnetic EXAFS signal $\chi_c(E)$ is shown. The dichroic signal is about three orders of magnitude smaller than the normal EXAFS and therefore even less pronounced than in the XANES region. For the calculations a cluster of eight neighboring shells with 113 atoms and a radius of 6.4 Å was used. The path expansion considered paths with up to two scattering centers and a total length of 7.5 Å. The orbital momentum expansion was carried to $l_{\text{max}} = 7$. In both cases the overall agreement with the experimental data is very satisfying. All significant features of the spectra are reproduced by the theoretical calculations in a correct way. Here one has to note that $\chi_c(E)$ is obtained in quantitative agreement without any adjustable parameter. The overestimation of the magnitude of the oscillations at very high energies in the normal EXAFS can be explained by the fact that lattice vibrations are not yet incorporated into our model. The smaller dichroic signal at low energies is caused by the limited size of the cluster used. In particular longer and high order scattering paths contribute to the signal in this region.

In Fig. 2 the results at the Gd L edges in hexagonal-close-packed (hcp) Gd are compared with experiment. While the left panel shows the conventional EXAFS, the dichroic signal is given in the right. The amplitude of the dichroic signal at the L edges is only one order of magnitude smaller than the normal EXAFS and hence much larger than at K edges. A cluster of six shells with 38 atoms was used in the calculation considering all paths with up to two scattering centers and a total length of 7 Å. The orbital momentum was again limited to $l_{\text{max}} = 7$. There is a small underestimation of the EXAFS oscillations in the calculated results at energies below 130 eV. Also the dichroic signal at the L_1 edge is larger in the experiment than was predicted by the calculation. Nevertheless all features in the spectra are reproduced in a very satisfying way. The pronounced features at about 150 eV are attributed to so-called magnetic multiple electron excitations (MMEEs)¹³ and can obviously not be reproduced by our model.

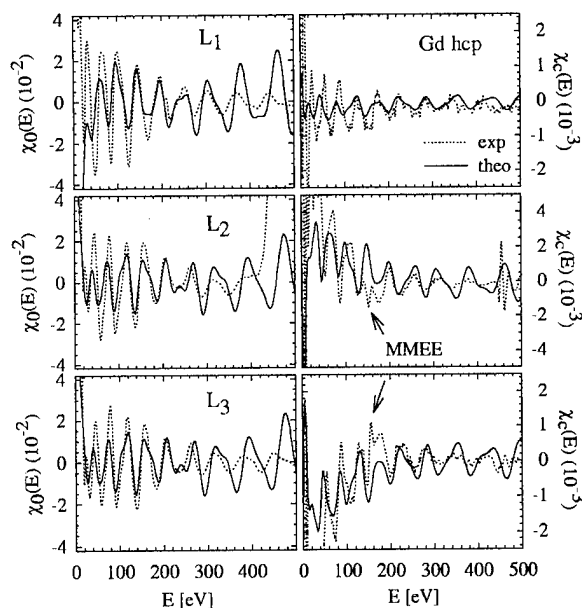


FIG. 2. X-ray absorption spectra at the $L_{2,3}$ edge of Gd. Left: absorption for unpolarized radiation $\chi_0(E)$. Right: dichroic signal $\chi_c(E)$.

The theoretical approach presented above opens the way for a very detailed interpretation and analysis of the MEXAFS spectra. Thinking of the absorption as a local process at the absorbing atom the primary physical information to be read from these spectra can be obtained on the basis of the sum rules. As was demonstrated for the XANES region by various authors,^{14,15} the differential form of the sum rules for the K and L_1 edges allows one to connect $\chi_c(E)$ to the orbital polarization $d\langle l_z \rangle_p/dE$ of the p states.

In Fig. 3 the orbital polarization is shown together with the experimental data for the Fe K and the Gd L_1 edges. It is obvious that all the prominent features of the spectra can be

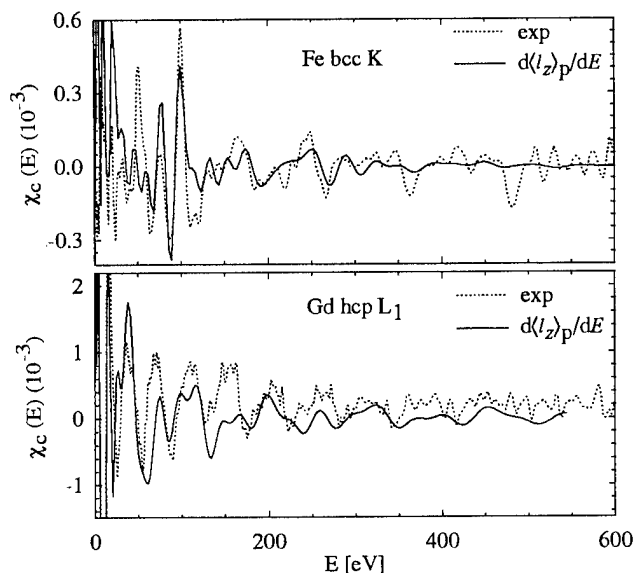


FIG. 3. Orbital- $d\langle l_z \rangle_p/dE$ polarization for the p states of Fe and Gd compared with the dichroic signal.

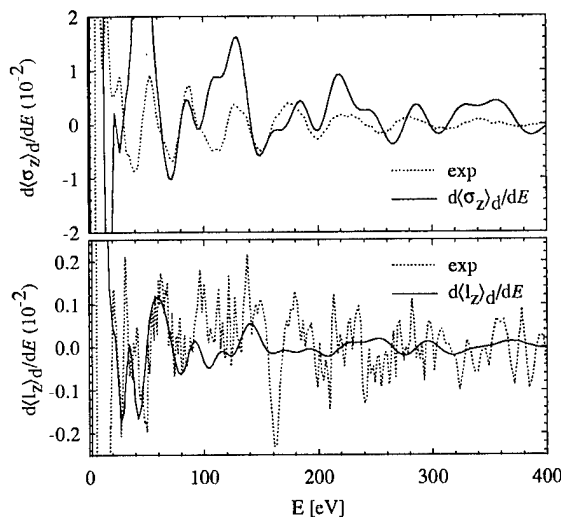


FIG. 4. Spin- $d\langle \sigma_z \rangle_d/dE$ and orbital- $d\langle l_z \rangle_d/dE$ polarization for the d states of hcp Gd compared with those extracted from the experimental data using Eq. (4).

related to the structure of the orbital polarization. This gives strong evidence for the applicability of the K - and L_1 -edge sum rule even up to very high energies.

In Fig. 4 the theoretical spin and orbital polarizations as extracted by Eq. (4) are compared with the same quantity determined from the experimental data. The strong peak in $d\langle l_z \rangle_d/dE$ is related to the MMEE mentioned above. Due to the spectroscopic ground state $^8S_{7/2}$ an orbital polarization of the $5d$ states is introduced only by spin-orbit and exchange effects and adds $\approx 0.25\mu_B$ to the total magnetic moment of $7.64\mu_B$.¹⁶ Accordingly, the spin polarization is about 10 times as large as the orbital contribution. Apart from the deviation in the spin polarization at about 120 eV the agreement is satisfactory. In spite of the uncertainty for the orbital polarization because of the limited experimental resolution these results give a clear indication that the sum rules are not limited to the circular dichroism in the XANES region.

ACKNOWLEDGMENTS

This work was supported by the German Federal Ministry of Education and Research and by the Deutsche Forschungsgemeinschaft.

- ¹G. Schütz et al., Phys. Rev. Lett. **62**, 2620 (1989).
- ²G. Schütz and D. Ahlers, in *Spin-Orbit Influenced Spectroscopies of Magnetic Solids*, Lecture Notes in Physics, Vol. 466, edited by H. Ebert and G. Schütz (Springer, Heidelberg, 1996), p. 229.
- ³E. Dartyge et al., Physica B **208-209**, 751 (1995).
- ⁴C. Brouder et al., in Ref. 2, p. 259.
- ⁵A. Ankudinov and J. J. Rehr, Phys. Rev. B (in press).
- ⁶A. Ankudinov and J. J. Rehr, Phys. Rev. B **52**, 10 214 (1995).
- ⁷H. Ebert, V. Popescu, and D. Ahlers, J. Phys. (Paris), Colloq. **7**, C2 (1997).
- ⁸H. Ebert, Rep. Prog. Phys. **59**, 1665 (1996).
- ⁹H. Ebert, J. Phys.: Condens. Matter **1**, 9111 (1989).
- ¹⁰J. Igarashi and K. Hirai, Phys. Rev. B **50**, 17 820 (1994).
- ¹¹P. Carra et al., Phys. Rev. Lett. **70**, 694 (1993).
- ¹²B. T. Thole et al., Phys. Rev. Lett. **68**, 1943 (1992).
- ¹³E. Dartyge et al., Phys. Rev. B **46**, 3155 (1992).
- ¹⁴H. J. Gotsis and P. Stange, J. Phys.: Condens. Matter **6**, 1409 (1994).
- ¹⁵M. S. S. Brooks et al., in Ref. 2, p. 211.
- ¹⁶J. Sticht et al., Solid State Commun. **53**, 529 (1985).

Spin-dependent extended x-ray absorption fine structure in magnetic oxides

D. Ahlers^{a)}

Universität Augsburg, Institut für Experimentalphysik II, Memmingerstrasse 6, D 86135 Augsburg, Germany

K. Attenkofer and G. Schütz

Universität Würzburg, Institut für Experimentalphysik IV, Am Hubland, D 97074 Würzburg, Germany

The spin-dependent extended x-ray absorption fine-structure (EXAFS), i.e., the magnetic counterpart to the conventional EXAFS when using circularly polarized light in a ferro(i)magnet, was measured at the $L_{2,3}$ edges of Eu in $\text{Eu}_3\text{Fe}_5\text{O}_{12}$ and EuO and at the K edge of CrO_2 . Complementary near-edge x-ray magnetic circular dichroism measurements at the O K edge were made to directly access the oxygen magnetization. It is shown that there is an influence of the nearly nonmagnetic oxygen atoms on the magnetic EXAFS depending on the local symmetry of the crystal as well as on the relative direction of the magnetic moments of neighboring atoms. The observed influences at distances corresponding to the oxygen neighbors in EuO are interpreted as the harmonic focusing effect, i.e., over-next magnetic neighbors behind the oxygen are responsible for the observed contributions. © 1998 American Institute of Physics. [S0021-8979(98)51811-7]

I. INTRODUCTION

Since the first observation of a magnetic contribution to the extended x-ray absorption fine structure (EXAFS),¹ spin-dependent EXAFS (SPEXAFS), this new spectroscopic method has evolved to provide new attractive possibilities to study the magnetic short range order in ferro(i)magnetic materials.² From a variety of systematic studies the relative amplitude of the dichroic contribution is found to be directly proportional to (a) the spin polarization $\langle\sigma_z\rangle$ of the photoelectron ejected after absorption of a circularly polarized photon and (b) the average spin moment of the neighboring coordination shells. Since the spin polarizations $\langle\sigma_z\rangle(L_3) = 0.25$ and $\langle\sigma_z\rangle(L_2) = -0.50$ are related by a factor of -2 , the ratio between the $L_{2,3}$ -edge dichroic signals can be used to test the polarization dependence of the SPEXAFS model. At the K edge the spin polarization $\langle\sigma_z\rangle(K) \sim 0.03$ is very small since there is no spin-orbit coupling in the initial state. The correlation of the SPEXAFS to the spin moment can be expressed in terms of the amplitude maxima of the Fourier transform (FT).³

$$\frac{1}{\langle\sigma_z\rangle} \frac{\max\{\text{FT}[\chi_c(k)]\}}{\max\{\text{FT}[\chi_0(k)]\}} = +2.4(2)\% \mu_S(\mu_B), \quad (1)$$

where μ_S is the average spin moment of the neighboring shell. In this article we report on new precise measurements of the $L_{2,3}$ edges of Eu in EuO and $\text{Eu}_3\text{Fe}_5\text{O}_{12}$ and the K edge of Cr in CrO_2 focusing on the role of the oxygen next neighbors in the SPEXAFS signal.

II. EXPERIMENTAL DETAILS

The experiments in the hard x-ray regime were performed at the RöMo II station at the HASYLAB in Hamburg using the two beam transmission mode. For EuO a magnetic field of $B_0 = 0.5$ T was applied and the sample was cooled to 10 K. $\text{Eu}_3\text{Fe}_5\text{O}_{12}$ and CrO_2 were measured at room tempera-

ture with $B_0 = 0.25$ T. The O K edges of $\text{Eu}_3\text{Fe}_5\text{O}_{12}$ and CrO_2 were recorded at the SX700/III station at BESSY using the total electron yield technique. The same mode was used for the O K edge of EuO at the Dragon beamline at the ESRF. The sample conditions were identical to those of the hard x-ray experiments. In the experiment the measured quantities were the spin-averaged absorption coefficient $\mu_0(E) = \frac{1}{2}[\mu^+(E) + \mu^-(E)]$ and the corresponding dichroic signal $\mu_c(E) = \frac{1}{2}[\mu^+(E) - \mu^-(E)]$ for parallel (+) and antiparallel (−) orientations of the photon “spin” to the spin of the majoritylike electrons in the sample. The spin-averaged EXAFS spectra $\chi_0(k) = [\mu_0(k) - \mu_{\text{atom}}(k)]/\mu_{\text{atom}}(k)$ were deduced with the free atom absorption μ_{atom} . The SPEXAFS spectra are denoted as the difference $\chi_c(k) = [\mu_c(k)/\mu_{\text{atom}}(k)]/[P_c \cdot M_z]$. They are rescaled for full circular polarization $P_c = 1$ and complete alignment of the magnetization $M_z = 1$. For the Fourier transformation all spectra were weighted with k^1 and folded with a Kaiser-Bessel window.

III. RESULTS AND DISCUSSION

A. The garnet $\text{Eu}_3\text{Fe}_5\text{O}_{12}$

Garnets form an overall cubic lattice [space group $Ia\bar{3}d(O_h^{12})$]. The metallic ions are distributed over three different lattice sites: two octahedral sites A (Fe^{3+}), three tetrahedral sites D (Fe^{3+}), and then three dodecahedral sites C (Eu^{3+}). All ions are coupled by superexchange via oxygen atoms in general positions H . The A and D lattices are coupled strongly antiparallel, whereas the A and C lattices are weakly parallel. In the upper panel of Fig. 1 the spin-averaged $\chi_0(k)$ and the spin-dependent $\chi_c(k)$ signals are presented. Since the Eu L_3 edge at 6977 eV is followed by the Fe K edge at 7111 eV, the usable range of the L_3 edge $\chi_0(k)$ is very short. The ratio of -2 is conserved in the SPEXAFS, indicating that the orbital moment does not contribute to the magnetic scattering. One immediately notices that the normal and magnetic signals differ drastically in the

^{a)}Electronic mail: ahlers@physik.uni-wuerzburg.de

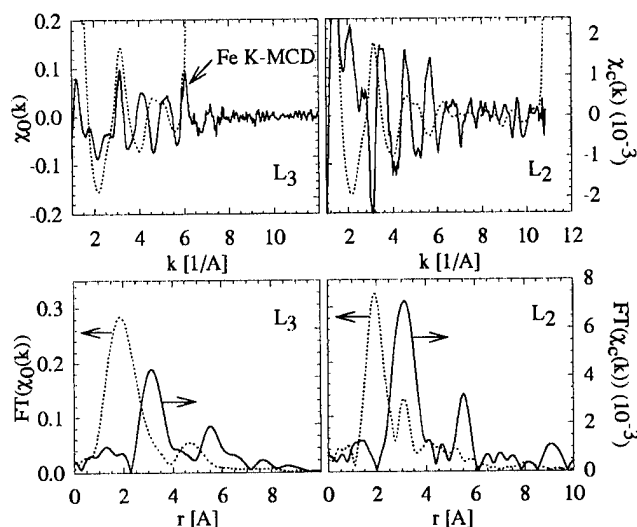


FIG. 1. Top: The $\chi_0(k)$ (dotted line) and $\chi_c(k)$ (solid line) spectra of Eu at the $L_{2,3}$ edges. Bottom: The FT [$\chi_0(k)$] (dotted line) and FT [$\chi_c(k)$] (solid line) spectra. Due to the interference of the Fe K edge the transformation interval for χ_0 is very short. Since the photoelectron polarization at the K edges is small, one can neglect this influence when transforming χ_c .

frequency of their oscillation. Looking at the Fourier transforms in Fig. 1 this observation becomes more clear. Typical for oxides, the FT of $\chi_0(k)$ is dominated by the strong first maximum resulting from the next oxygen neighbors. The second peak, due to the limited resolution at the L_3 edge that is only visible in the L_2 FT, indicates the positions of three next-neighbor shells occupied by 2 Fe on D , 4 Fe on A , 4 Fe on D , and 4 Eu on C sites, respectively. All peaks appear at slightly smaller distances as is expected from the crystal structure. In the EXAFS analysis such a shift is connected with the k dependence of the scattering phase and is normally in the order of 0.3–0.5 Å. The FT spectra have not been corrected for this shift since such a correction for the SPEXAFS would be arbitrary. In the FT of the $L_{2,3}$ SPEXAFS the prominent oxygen peaks have vanished due to an increase in the maxima at 3.3 and 5.7 Å. By forming the ratio of the FT lines at 3.1 Å, applying the formalism of Eq. (1), one obtains an estimation of the average spin-moment buildup in the three unresolvable shells of $\mu_{sp} = 4.9\mu_B$. This is somewhat larger than the theoretical sum of the individual moments of $4.1\mu_B$, but can be explained by the differences in the distance of these shells. Nevertheless the results presented indicate that the strength of the SPEXAFS is correlated to the magnetic moment of the backscattering atoms.

B. The half-metal CrO_2

Chromium dioxide belongs to a class of transition-metal dioxides with a rutile structure and a predicted half-metallic character.⁴ Ferromagnetic ordering sets in at $T_c = 392$ K, the coupling mediated by the O^{2+} ions via superexchange. The left panels of Fig. 2 show the spin-averaged $\chi_0(k)$ and spin-dependent $\chi_c(k)$ measurements at the Cr K edge. Note that due to the small photoelectron polarization $\langle\sigma_z\rangle \sim 1.2\%$ the dichroic signal is extremely small. As for the garnet, two different frequencies of oscillation are observed which is confirmed in the FT spectra in the right hand panels of Fig. 2. The spin-averaged spatial distribution FT[$\chi_0(k)$] is domi-

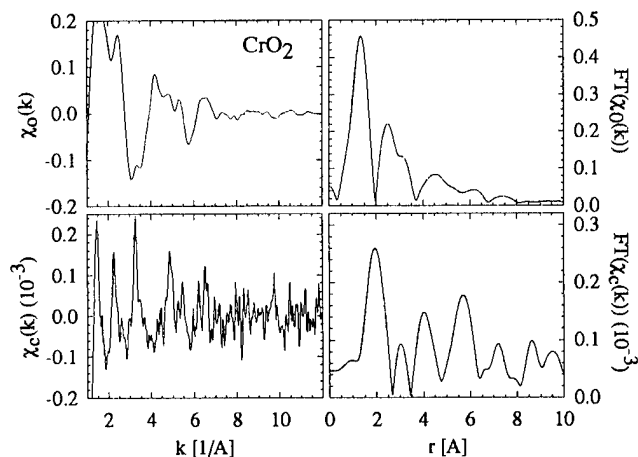


FIG. 2. The spin-averaged (top) and the dichroic signal (bottom) at the Cr K edge in CrO_2 (left). The corresponding Fourier transforms are shown at the right.

nated by three peaks originating from 6 O (1.4 Å), from 6 Cr (2.5 Å), and from 16 O (3.2 Å) neighbors, respectively. In the spin-dependent distribution FT[$\chi_c(k)$] only one major peak is visible at 2 Å, and it is shifted by almost 0.5 Å towards smaller distances than is the Cr peak in the EXAFS. That only one peak remains clearly indicates that this peak must be attributed to the Cr shell. Applying Eq. (1) to these Cr lines gives a magnetic moment of $2.0\mu_B$, in good agreement with theoretical predictions.⁴ The reason for the large shift, at this size it has not been seen before in a comparison between EXAFS and SPEXAFS might be due to the band-like character of the magnetism of CrO_2 . The strong delocalization of the magnetic electrons is surely influencing the spatial distribution of the SPEXAFS.

C. The chalcogenide EuO

The divalent europium chalcogenides are very representative of simple isotropic Heisenberg magnets. In these semiconductors the magnetic Eu^{2+} ions (ground state $^8S_{7/2}$) form simple face-centered-cubic (fcc) lattices. Two coupling mechanisms are considered for EuO: the direct interaction between the Eu neighbors and the coupling of the Eu ions via superexchange of the oxygen. The extracted spin-averaged $\chi_0(k)$ (dotted line) and the spin-dependent $\chi_c(k)$ signal (solid line) are presented in the top panel of Fig. 3. Looking at the frequency of the oscillations, a difference is not seen here. The FT for EuO, displayed in the bottom panel of Fig. 3, supports this finding. Since the spectra were recorded at 10 K, damping by the Debye–Waller factor, representing lattice vibrations, is almost negligible, thus extending the L_3 EXAFS far into the L_2 -edge region. This effect becomes visible at the L_2 -edge FT in the large unexpected peak at about 1.6 Å. The first line at 2.2 Å corresponds to the first oxygen coordination shell. The second line at 3.4 Å represents the next Eu neighbors. An approximation of the average moment of the neighboring Eu shell using Eq. (1) yields $6.2\mu_B$. The same procedure for the oxygen peak, however, leads to the unrealistic value of $5.9\mu_B$. We believe that the contributions at the oxygen sites are caused by a focusing effect. In EXAFS analysis this well known phenomenon de-

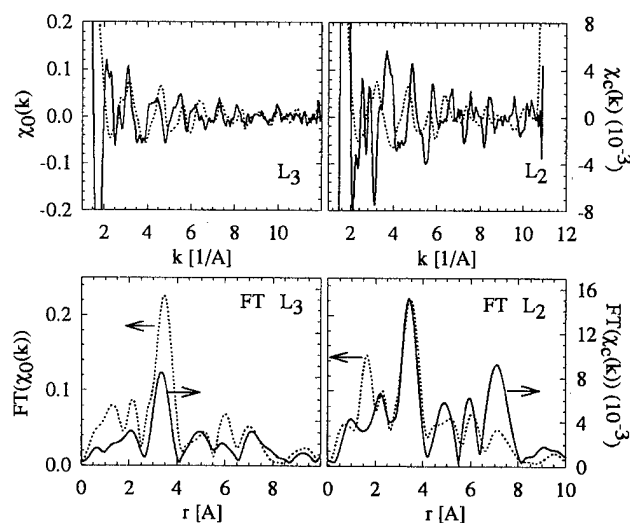


FIG. 3. Top: The $\chi_0(k)$ (dotted line) and $\chi_c(k)$ (solid line) spectra of Eu at the $L_{2,3}$ edges. Bottom: The FT [$\chi_0(k)$] (dotted line) and FT [$\chi_c(k)$] (solid line) spectra. The unexpected lines at 1.6 Å in the L_2 -edge FT are tails from the EXAFS at the L_3 edge.

scribes the fact that those shells directly behind closer neighbors appear stronger in the Fourier analysis than that estimated by their simple distance.⁵ The outgoing photoelectron wave experiences the potential of the first neighbor as a kind of a lens, focusing it on the over next neighbor. This way the effective amplitude is enhanced. In the case of EuO we have a higher harmonic of this effect. A wave corresponding to the oxygen distance effectively interferes also when scattered at the Eu neighbor behind the oxygen, the distance being twice as large. So if one imagines the wave with a knot at the oxygen site, one sees the full spin moment of the Eu atom in the SPEXAFS at the oxygen position.

D. The oxygen measurements

Figure 4 shows the near-edge x-ray magnetic circular dichroism (XMCD) spectra of the oxygen K edge in $\text{Eu}_3\text{Fe}_5\text{O}_{12}$, EuO , and CrO_2 . The spin-averaged absorption $\mu_0(E)$ (left) is characterized by the typical narrow first peak and a broad second peak which for the garnet is almost twice as high as that for EuO . The absorption profile for CrO_2 is even more complex. Since CrO_2 is not stable, there is a surface contamination with Cr_2O_3 . The characteristic line at 531 eV, however, is only visible for CrO_2 and can be used to estimate the concentration. The amplitude of the spin-dependent signal $\mu_c(E)$ (right) is in all cases very small. In the Eu compounds the dichroic oxygen signal displays a very complex structure with effects of the order of only 0.5%. There are two dispersive structures visible at 530 and 536 eV, the former with the same sign as that for $\text{Eu}_3\text{Fe}_5\text{O}_{12}$ and EuO , the latter, however, with the opposite sign. Possibly this is an effect of the ferrimagnet $\text{Eu}_3\text{Fe}_5\text{O}_{12}$, where the magnetic moments neighboring the oxygen cite are coupled antiparallel. The oxygen K -edge dichroism in CrO_2 is much simpler and amounts to 1%. Only one dispersive structure is found, indicating that the coupling mechanism is less complex. Although a final interpretation of the oxygen spectra is still to be made, there is no hint about a particular large moment in the case of EuO .

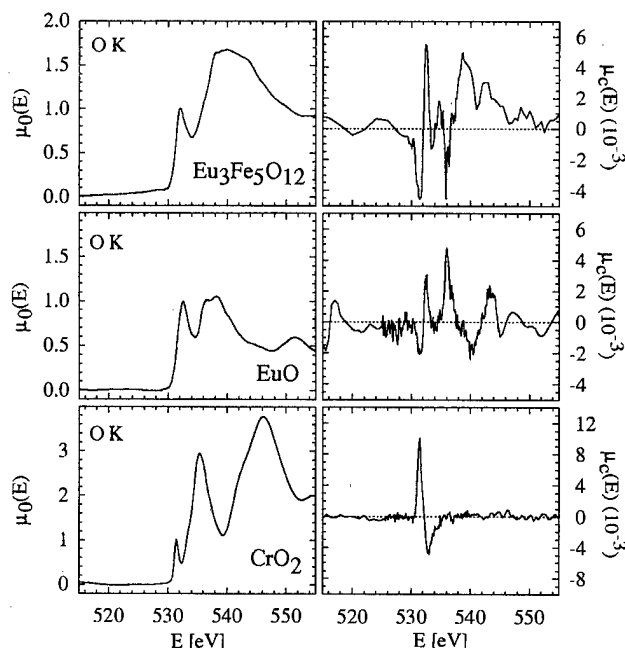


FIG. 4. The spin-averaged (left) and the dichroic signal (right) at the O K edge in $\text{Eu}_3\text{Fe}_5\text{O}_{12}$ (top), EuO (center), and CrO_2 (bottom). The spectra are normalized to 1 for the first peak in the spin-averaged absorption. The structure of the dichroic signal is extremely complex.

IV. CONCLUSION

New results of magnetic EXAFS measurements on magnetic oxides were presented. The contribution of the oxygen to the dichroic signal was thereby very different for the different compounds. In $\text{Eu}_3\text{Fe}_5\text{O}_{12}$ there was no contribution by the oxygen to the SPEXAFS at all. In the half-metal CrO_2 the next magnetic neighbor shell was shifted twice as much towards smaller distances than the corresponding electronic shell, indicating an influence particular on the magnetic scattering phase. In EuO a strong peak occurs at the oxygen position, which cannot be explained by oxygen magnetization. We believe that we have shown that the focusing effect, well known in EXAFS analysis, gives a reasonable explanation of the observed phenomenon. Further experiments using Compton and neutron scattering to accurately determine spin and orbital moment distributions and theoretical calculations are needed to clarify the specific details of these phenomena.

ACKNOWLEDGMENTS

The authors thank S. Fischer of the Forschungszentrum Jülich for providing the EuO sample. This work was supported by the German Federal Minister of Education and Research and the Deutsche Forschungsgemeinschaft.

¹G. Schütz *et al.*, Phys. Rev. Lett. **58**, 737 (1987).

²G. Schütz *et al.*, Phys. Rev. Lett. **62**, 2620 (1989).

³G. Schütz and D. Ahlers, in *Spin-Orbit Influenced Spectroscopies*, Lecture Notes in Physics, Vol. 466, edited by H. Ebert and G. Schütz (Springer, Heidelberg, 1996).

⁴P. A. Cox, *Transition Metal Oxides* (Oxford University Press, Oxford).

⁵B. K. Teo, *EXAFS: Basic Principles and Data Analysis* (Springer, Berlin, 1986).

Probing the magnetic microstructure of an amorphous GdFe system with magnetic anomalous small angle x-ray scattering

P. Fischer^{a)}

Institute for Physics, EP II, University of Augsburg, Memmingerstr. 6, D 86135 Augsburg, Germany

R. Zeller and G. Schütz

Institute for Experimental Physics IV, University of Würzburg, Am Hubland, D 97074 Würzburg, Germany

G. Goerigk and H.-G. Haubold

Forschungszentrum Jülich GmbH, IFF, D 52425 Jülich, Germany

K. Pruegl and G. Bayreuther

Institute for Experimental and Applied Physics, University of Regensburg, Universitätsstr. 31, D 93053 Regensburg, Germany

The combination of x-ray magnetic circular dichroism (X-MCD) with anomalous small angle x-ray scattering (ASAXS) allows to determine size distributions and correlations lengths in the nanometer range of magnetic precipitates in granular systems. Results on an amorphous GdFe system with a pronounced perpendicular magnetic anisotropy are reported. Standard ASAXS measurements taken at the Fe *K* edge provide information on the electronic structure yielding a correlation maximum at 75 Å and an average particle radius of 6 Å. The magnetic scattering curves (MASAXS) were obtained at the corresponding Gd *L*_{3,2} edges. Their intensities can be explained by magnetic contributions to the anomalous scattering factors *f'* and *f''*. A change of sign in the MASAXS is observed between profiles taken at the *L*₃ and the *L*₂ edge and with the change of circular polarization as expected from X-MCD. © 1998 American Institute of Physics. [S0021-8979(98)24911-5]

I. INTRODUCTION

A fundamental understanding of magnetic microstructures is an outstanding challenge both in current research of magnetism and its technological applications. Thereby reliable information on the electronic and magnetic structure on a typical length scale of 1–100 nm is mandatory. Among other recent observations of novel phenomena like the occurrence of the GMR, quantum oscillations or the magnetic interface anisotropy in magnetic thin films or multilayered systems, the origin of the perpendicular magnetic anisotropy in granular thin GdFe films is in particular still an open problem.

An established technique to study size distributions and correlations of particles in the nm range is the small angle x-ray scattering (SAXS). Using tunable x rays with high brilliance being available at synchrotron sources the mode of contrast enhancement (anomalous SAXS=ASAXS) can be engaged, i.e., involving the element-specific anomalous scattering amplitude *f'*(*E*), which varies with energy by about 20% in the vicinity of absorption edges, thus providing more detailed structural information on multicomponent systems.

In a two-phase model the scattering contrast Δc in SAXS is given by $(n_1 \cdot f_1 - n_2 \cdot f_2)$ with *n_i*, *f_i* being the density and atomic scattering amplitudes of phase *i*. The cross section $d\sigma/d\Omega$ is proportional to Δc^2 which in the case of anomalous scattering can be related to $(n_1 = n_2)$

$$\frac{d\sigma}{d\Omega} \approx |f(E, Z)|^2 = |f_0 + f'(E) + if''(E)|^2, \quad (1)$$

with the atomic form factor $f_0 = Z$ (atomic number) and *f'* and *f''* being the additional anomalous contributions. *f'* and *f''* are connected to each other via a Kramers–Kronig relation, whence *f''* can be related to the absorption coefficient $\mu(E)$ via the optical theorem

$$f''(E) = \frac{mc}{4\pi e^2} \frac{E}{h} \mu(E). \quad (2)$$

The effect of x-ray magnetic circular dichroism (X-MCD), i.e., the dependence of the absorption of circular polarized x rays on the projection of the magnetization onto the photon propagation direction (\hat{e}_z) in ferromagnetic samples¹ occurs in the vicinity of inner-core absorption edges. Due to angular momentum conservation in the absorption process the photoelectron acquires both an expectation value of the spin $\langle \sigma_z \rangle$ and the orbital $\langle l_z \rangle$ momentum projected onto \hat{e}_z . It can therefore serve as a local probe for the spin and orbital polarization of the absorbing atom according to the principle of Pauli. $\langle \sigma_z \rangle$ amounts to –50% and +25% at the *L*₂ and *L*₃ edges, while $\langle l_z \rangle = +75\%$ at both *L*_{2,3} edges. X-MCD has become a powerful tool for the element-specific and symmetry-selective investigation of the local magnetic structure on an atomic scale. Applying magneto-optical sum rules,² it is possible to determine in certain cases spin and orbital moments separately. Beyond this local magnetic structure a spin-dependent contribution has been manifested in the extended x-ray absorption fine structure (EXAFS)

^{a)}Electronic mail: fischer@physik.uni-augsburg.de

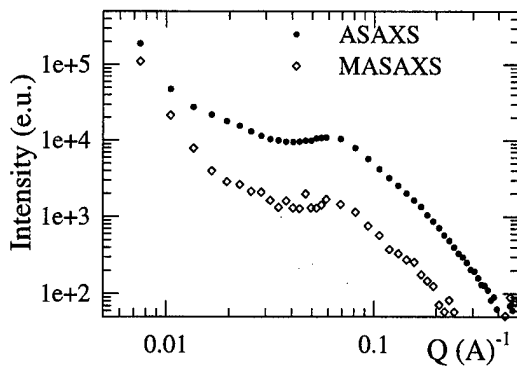


FIG. 1. ASAXS (●) and MASAXS (◇) scattering profiles of the amorphous GdFe system taken at the Fe K -edge and the Gd L_3 edge.

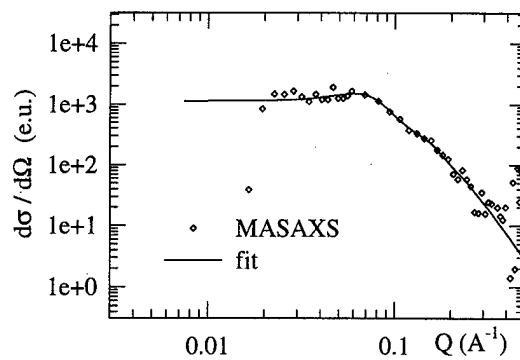


FIG. 2. MASAXS (◇) at the Gd L_3 edge with a Q^{-4} background subtracted for small Q values and results from a fit (—) taking into account a log-normal distribution including correlation.

range (magnetic EXAFS=MEXAFS), too, which allows to study the magnetic short-range order in multicomponent systems even on a larger size scale up to 20 Å.

The potential of X-MCD, however, is not restricted to the study of absorption profiles. In principle every method used in spectroscopy or crystallography, where the absorption coefficient is involved, can be extended to its magnetic counterpart. Thus the basic idea of magnetic anomalous small angle x-ray scattering (MASAXS) is to achieve the contrast enhancement via the effect of X-MCD. As the dichroic signal depends on the projection of the local magnetization of the absorbing atoms onto \hat{e}_z the magnetic scattering curves reflect the size distribution and correlation lengths of the magnetic scattering precipitates. Given the magnetic absorption coefficient for parallel/antiparallel alignment of magnetic electrons relative to \hat{e}_z by $\mu^\pm(E) = \mu_0(E) \pm \mu_c(E)$ the corresponding scattering amplitudes $f'^\pm(E)$ and $f''^\pm(E)$ both acquire magnetic contributions $f'_c(E)$ and $f''_c(E)$, namely,

$$f'^\pm(E) = f'(E) \pm f'_c, \quad (3)$$

$$f''^\pm(E) = f''(E) \pm f''_c. \quad (4)$$

Inserting Eqs. (3) and (4) into Eq. (1) the magnetic cross section, i.e., the difference in scattered intensities for parallel and antiparallel orientation is given by

$$\left(\frac{d\sigma}{d\Omega}\right)^+ - \left(\frac{d\sigma}{d\Omega}\right)^- \approx 4(f_0 + f')f'_c + 4f''f''_c. \quad (5)$$

II. EXPERIMENTAL DETAILS

The experiments were performed at the JUSIFA beamline at HASYLAB/Hamburg (FRG). The setup for the ASAXS measurements, described in detail in Ref. 3, was modified slightly for the magnetic measurements. In order to illuminate the sample with circular polarized x rays, the inclined view method was used. The beam position control monitor was set to an asymmetric position 2.5 mm above/below the orbital plane with a slit height of 1.4 mm. The beam height position was checked by recording the beam profile after each scan. The calculated degree of circular polarization amounts to $\approx 70\%$. A small solenoid provided

magnetic flux densities up to 60 mT with its field direction pointing parallel/antiparallel to the photon beam direction sufficient to saturate the sample.

The magnetic contrast scattering curve was then obtained according to Eq. (5) by recording two scattering profiles with parallel/antiparallel orientation of the magnetization relative to \hat{e}_z and fixed circular degree of polarization at an incident photon energy where the maximum dichroic effect is expected. The results reported here were obtained with a binary Gd₂₈Fe₇₂ system. The amorphous film was prepared by coevaporation from two electron-gun sources in a high vacuum system onto a 15 μm Mylar^R foil. For chemical protection, the Gd-Fe films of thickness $h = 105\text{--}115$ nm were covered with 20–22 nm Al layers on both sides of the Gd-Fe layer. A stack of 12 foils was enough to achieve a transmission of 0.5. A strong magnetic anisotropy perpendicular to the surface was verified by vibrating sample magnetometer (VSM) measurements and Faraday effect results

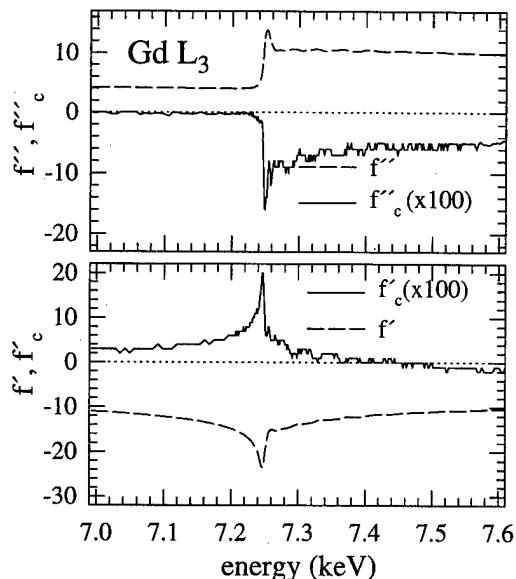


FIG. 3. Anomalous scattering factors f' and f'' (---) and the corresponding magnetic contributions f'_c and f''_c (—) calculated from highly accurate MEXAFS results at the Gd L_3 edge in Gd metal. The magnetic values are multiplied by a factor 100.

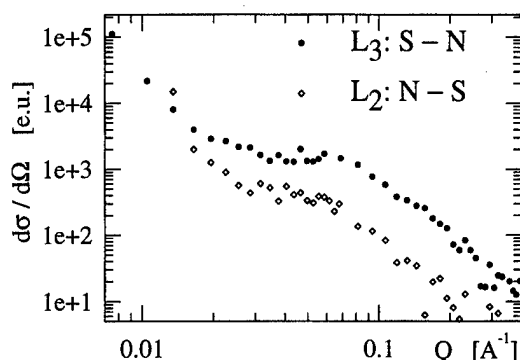


FIG. 4. MASAXS obtained at the Gd L_3 (●) and L_2 (◇) edge indicating the change of sign of the profile for the different edges.

exhibiting a rectangular hysteresis loop with a magnetic coercive field of ≈ 20 mT.

III. RESULTS AND DISCUSSIONS

In Fig. 1 the magnetic scattering curve intensity obtained in that way versus momentum transfer Q measured at the Gd L_3 edge ($E=7243$ eV) is presented in comparison with the ASAXS profile obtained at the corresponding Fe K edge indicating the gross similarity of the electronic and magnetic structure. The profile can be interpreted as due to two size distributions, where the Q^{-4} behavior at small Q values can be attributed to large particles. After a pronounced maximum at $Q \sim 0.06 \text{ \AA}^{-1}$, which can be interpreted as a correlation maximum, the tail of a size distribution of smaller particles can be observed.

Fit procedures taking into account a log-normal distribution to the experimental data including a correlation yielded a correlation length of 74.9 \AA and size of the particle radius of 5.3 \AA with slightly enhanced values for the magnetic case (76.6 \AA and 5.8 \AA , respectively). The results are shown in Fig. 2, where the Q^{-4} tail of the large particles had been subtracted. Corresponding EXAFS and MEXAFS studies indicate no wide range ordering compared to pure bcc Fe.⁴ This points to a rather complex structure of the system studied. Although the crystal structure seems to be amorphous, there is to some extent an ordered chemical structure, which is consistent with the assumption that column-like structures are formed in that magneto-optical films. Furthermore, the observed magnetic anisotropy could also be related to those columns. On the other hand, the magnetic correlation observed in the MASAXS would then originate from a chemical inhomogeneity.

The intensity of the MASAXS profile can be related to accurate experimental measurements of MEXAFS in a wide range around the Gd L_3 edge with the help of the optical theorem [Eq. (2)] and a Kramers–Kronig relation. The obtained results in a pure Gd system for f' , f'_c and f'' , f''_c , respectively, as function of energy are shown in Fig. 3. From these data the contrast ratio between ASAXS and MASAXS observed in Fig. 1 can be directly deduced. It is interesting that this ratio is larger than the dichroic effect at $E = 7243$ eV observed in absorption due to the large contribu-

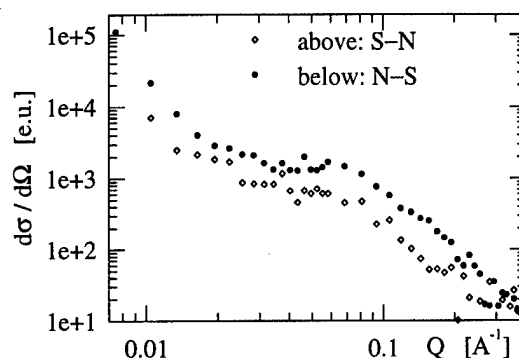


FIG. 5. MASAXS obtained at the Gd L_3 edge above (◇) and below (●) the orbital plane indicating the change of sign of the profile with circular degree of polarization.

tion of f'_c . However, similar enhanced effects have also been observed in magnetic resonant scattering in Ni.⁵

Characteristic features of X-MCD can be manifested by performing the MASAXS at the corresponding spin-orbit split L_2 edge of Gd. Taking into account the different values for $\langle \sigma_z \rangle$ at the $L_{3,2}$ edges their should be a change in sign of the scattering profile comparing the results at the $L_{3,2}$ edges. The MASAXS profiles shown in Fig. 4 exactly follow this feature as the direction of magnetization (N and S) has to be reversed (S–N) at the L_2 edge in order to yield the same sign of the profile compared to the L_3 edge (N–S) and the scattering intensity at the L_2 edge is decreased compared to the L_3 edge as expected. As the dichroic signal depends on the relative orientation of the circular polarization photons and the magnetization of the sample MASAXS spectra taken with reversed photon helicity, i.e., above and below the orbital plane (see Fig. 5) proof again a change of sign as expected.

IV. OUTLOOK AND CONCLUSION

Magnetic small angle x-ray scattering is a new technique, which allows valuable insights into structural characteristics of magnetic particles in granular systems and diluted alloys on a nm scale. Additional support to establish reliable models of the magnetic structures will be provided by magnetic imaging techniques allowing a quantitative information on the local magnetization with high resolution.⁶

ACKNOWLEDGMENT

This work was supported by the German federal ministry of education, science, research and technology (BMBF) Project No. 05-621-WAA-6.

¹G. Schütz, W. Wagner, W. Wilhelm, P. Kienle, R. Zeller, R. Frahm, and G. Materlik, *Phys. Rev. Lett.* **58**, 737 (1987).

²B. T. Thole, P. Carra, F. Sette, and G. van der Laan, *Phys. Rev. Lett.* **68**, 1943 (1992); P. Carra, B. T. Thole, M. Altarelli, and X. Wang, *ibid.* **70**, 694 (1993).

³H.-G. Haubold *et al.*, *Rev. Sci. Instrum.* **60**, 1943 (1989).

⁴H. Nizam, diploma thesis, University of Augsburg, Germany (1996).

⁵J. Hunecke, diploma thesis, University of Munich, Germany (1990).

⁶P. Fischer, G. Schütz, G. Schmahl, P. Guttman, and D. Raasch, *Z. f. Phys.* **101**, 313 (1996).

Magnetic x-ray investigation at the $L_{2,3}$ edges of Nd in $\text{Nd}_2\text{Fe}_{14}\text{B}$

F. Bartolomé, J. M. Tonnerre, L. Sève, D. Raoux, and J. E. Lorenzo
Laboratoire de Cristallographie, CNRS. BP 166 38042 Grenoble Cedex 9, France

J. Chaboy, L. M. García, and J. Bartolomé
ICMA, CSIC-Universidad de Zaragoza, Facultad de Ciencias, 50009 Zaragoza, Spain

M. Krisch and A. Rogalev
European Synchrotron Radiation Facility, B.P. 220, 38043 Grenoble Cedex, France

R. Serimaa
Physics Department, University of Helsinki, Finland

C-C. Kao
National Synchrotron Light Source, Brookhaven National Laboratory, Upton, New York 11973

G. Cibin and A. Marcelli
LNF, INFN, Frascati, Italy

A systematic study of x-ray magnetic circular dichroism, x-ray resonant magnetic scattering, and resonant inelastic x-ray scattering at the $L_{2,3}$ edges of Nd on $\text{Nd}_2\text{Fe}_{14}\text{B}$ is presented. The combined information allows to assign a dipolar or quadrupolar origin to different features appearing in the experimental spectra and to study the thermal dependence of the Nd moment orientation below the spin reorientation transition which takes place at $T_{\text{SRT}}=135$ K. © 1998 American Institute of Physics. [S0021-8979(98)25011-0]

The possibility offered by near-edge x-ray magnetic techniques of separately probing a given element in a material containing several magnetic species can be used to disentangle a wide set of problems on the magnetism of materials, as, for example, rare-earth (R)-transition metal (TM) intermetallics. However, the interpretation of x-ray magnetic circular dichroism (XMCD) and resonant magnetic scattering (XRMS) at the $L_{2,3}$ edges of R ions ($2p \rightarrow 5d$ transitions) has been a controversial subject since the first experimental results were obtained. It has been pointed out that, to properly describe the observed signals, several aspects had to be included in the analysis, among others the contribution from $2p \rightarrow 4f$ quadrupolar excitation channels in the pre-edge region.¹ In this article, we report on a combined study of XMCD, XRMS, and resonant inelastic x-ray scattering (RIXS) which allows to assign a multipolar origin to the different features appearing in the experimental spectra at the Nd $L_{2,3}$ edges, and to apply this information to the study of the thermal dependence of the orientation of the Nd magnetic moments upon the spin reorientation transition (SRT) taking place on $\text{Nd}_2\text{Fe}_{14}\text{B}$. Below $T_{\text{SRT}} \approx 135$ K, the easy axis magnetization direction (EMD) continuously rotates from the [001] axes (high- T phase) towards the [110] axis. Although the behavior of the bulk magnetization has been well determined, the evolution of the magnetic moments on the microscopic scale is less understood. It has been proposed that the Nd and Fe moments can be considerably noncollinear in the low-temperature phase.^{2,3} Different macro- and microscopic techniques have been applied to study the SRT, but no general agreement on the mutual orientation of the R and Fe moments in the low temperature phase has been reached so far.⁴

To directly study the reorientation angles of Nd atoms on the SRT, we measured temperature-dependent XMCD at the $L_{2,3}$ edges of Nd in a single crystal of $\text{Nd}_2\text{Fe}_{14}\text{B}$. The chosen geometry was as follows: the incident photon wave vector, \mathbf{k}_i , the [001] and the [110] axes of the plate-shaped single crystal lied in the horizontal plane, both [001] and [110] axes forming an angle of 45° with \mathbf{k}_i . A magnetic field of 1 T was applied parallel to \mathbf{k}_i . In the dipolar approximation ($2p \rightarrow 5d$ transitions), XMCD is proportional to $\cos(\alpha)$, where α is the angle between the Nd atomic magnetic moment, $\bar{\mu}_{\text{Nd}}$, and \mathbf{k}_i . Below T_{SRT} , $\bar{\mu}_{\text{Nd}}$ rotates from the [001] axes by an angle $\theta_{\text{Nd}}(T)$. Consequently, the described XMCD experiment is sensible to both, $\theta_{\text{Nd}}(T)$ (through $\alpha(T) = 45^\circ - \theta_{\text{Nd}}(T)$) and $\mu_{\text{Nd}}(T)$.

Figure 1 shows five representative XMCD spectra at the $L_{2,3}$ edges of Nd in $\text{Nd}_2\text{Fe}_{14}\text{B}$ recorded at different temperatures in the vicinity of SRT, as indicated in the figure. Two

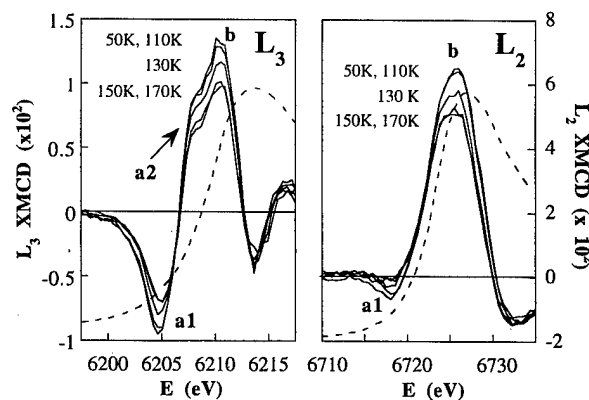


FIG. 1. Normalized XMCD spectra recorded at different temperatures at the L_3 (left panel) and L_2 (right panel) edges of Nd in $\text{Nd}_2\text{Fe}_{14}\text{B}$. The spin averaged absorption ($T=150$ K) is also shown (a.u., dashed line).

^aElectronic mail: bartolom@polycnrs-gre.fr

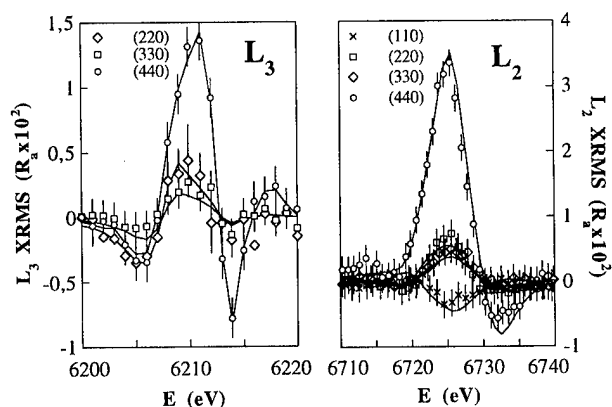


FIG. 2. XRMS asymmetry ratios for several ($hh0$) Bragg reflections at the L_3 (left panel) and L_2 (right panel) absorption edges of Nd in $\text{Nd}_2\text{Fe}_{14}\text{B}$. Lines are the results of a regularisation analysis fitting including a quadrupolar origin for a1 and a2 features (see Fig. 1).

main features (labeled “a1” and “b”) are observed in the edge and pre-edge region, while a smaller shoulder (labeled “a2”) is only observed at the L_3 edge. 170 and 150 K XMCD curves are very similar at both edges, indicating the magnetic saturation of the sample in this range of temperature, above T_{SRT} and well below $T_c \approx 600$ K. The XMCD spectra recorded at 150, 130, and 110 K present a noticeable enhancement coincident with T_{SRT} . Below 110 K, XMCD remains again almost independent of temperature, showing no differences between 110 and 50 K. These experimental results reflect the sensibility of the technique to the SRT occurring below 135 K. However, the interpretation of the observed thermal variations is not simple: the spectra recorded at different temperatures do not scale, as it should be the case if the whole signal would have a single dipolar (E1) origin and the only differences would be originated by $\theta_{\text{Nd}}(T)$. This is more evident at the L_2 edge, where the a1 feature is only observed below T_{SRT} . It has been theoretically pointed out^{1,5} and experimentally confirmed⁶ that the pre-edge features in $L_{2,3}$ dichroic spectra in rare earth ions have its origin in quadrupolar (E2) $2p \rightarrow 4f$ transitions.

XRMS is the scattering counterpart of XMCD.⁷ It allows to discriminate the multipolar origin of the observed magnetic signals by studying different Bragg reflections, as dipolar and quadrupolar contributions have different angular dependence. We performed room-temperature XRMS on $\text{Nd}_2\text{Fe}_{14}\text{B}$ on several ($hh0$) reflections at the $L_{2,3}$ edges of Nd. ($hh0$) Bragg reflections were selected because the two nonequivalent crystallographic sites occupied by Nd ions, 4f and 4g, contribute very differently to the structure factor for different h values. This fact, although it is not the objective of the present study, allow to deconvolute the resonant magnetic signal created by Nd ions occupying 4f and 4g sites.

The experimental results are shown in Fig. 2. Their spectral shape reflects roughly that of XMCD and, within the experimental errors, the same features are present at both edges (a1 feature is visible even at room temperature in (220) and (330) reflections at the L_2 edge). Full lines in Fig. 2 are the results of a fitting procedure based on the standard interpretation of XRMS⁷ by means of a regularization technique analysis. A proper fitting of the whole data set was only

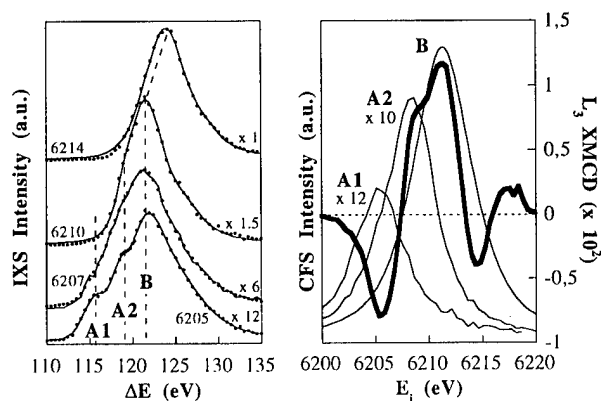


FIG. 3. RIXS intensity at four incident energies (left panel) and CFS scans (right panel, thin lines) together with XMCD (thick line) at Nd L_3 edge on $\text{Nd}_2\text{Fe}_{14}\text{B}$. RIXS data are scaled as indicated in both panels.

possible by allowing for a E2 origin for a1 and a2 features, with an intensity which at the L_3 edge is comparable to that of the E1 one (b and higher energy features).

Standard absorption measurements at the $L_{2,3}$ edges of rare-earth ions cannot separate the two E1 and E2 excitation channels due to the $2p$ core-hole lifetime broadening. However, it has been shown that such a separation can be achieved by means of resonant inelastic x-ray scattering (RIXS) experiments.⁸ In Nd, this can be realized by studying the resonance behavior of the $4d^9 4f^4 5d^0$ and the $4d^9 4f^3 5d^1$ final state multiplets as the incident photon energy is tuned through the $2p^5 4f^4 5d^0$ and $2p^5 4f^3 5d^1$ intermediate state excitation energies, monitoring the $4d_{5/2,3/2} \rightarrow 2p_{3/2}$ radiative decay channel $L\beta_{2,15}$ of Nd. In Fig. 3 (left panel), we present as a function of the energy transfer, ΔE , four representative RIXS spectra obtained at different fixed incident energies, E_i , (indicated in the figure) in the vicinity of the Nd L_3 edge. The spectrum recorded at $E_i = 6210$ eV $\approx E_{L_3}$ corresponds to the largest incident energy at which the maximum of the central feature, labeled “B,” remains at $\Delta E \approx 121.6$ eV, indicating that the photoelectron has been excited to a $5d$ localized intermediate state without acquiring extra kinetic energy. At higher incident energies (upper curve), this feature moves towards higher ΔE as the photoelectron acquires extra kinetic energy when promoted to the $5d$ band. The two lower spectra were recorded with E_i in the pre-edge region. Two extra channels, labeled “A1” and “A2” appear as distinct shoulders in the RIXS spectra at $\Delta E \approx 115.5$ and 118.5 eV. Previous experimental results⁸ and theoretical calculations⁹ allow an unambiguous assignment of features A1, A2, and B. Feature B is assigned to the $4d^9 4f^3 5d^1$ final state multiplet, resonantly enhanced at the $2p^5 4f^3 5d^1$ intermediate state excitation energies, corresponding to the strong dipolar $2p \rightarrow 5d$ channel. Features A1 and A2 are ascribed to the $4d^9 4f^4 5d^0$ final state multiplets which are resonantly enhanced at the $2p^5 4f^4 5d^0$ intermediate state excitation energies, corresponding to the weak quadrupolar $2p \rightarrow 4f$ excitation channel. Features A1 and A2 are observed at lower ΔE values than feature B, i.e., at smaller intermediate state excitation energies. This is consistent with the strength of the Coulomb interaction between the pro-

moted electron and the $4d$ core hole resulting in a $4d^9 4f^4 5d^0$ final state more strongly bound than the $4d^9 4f^3 5d^1$ or $4d^9 4f^3 5d^1 \epsilon^*$ states.

To directly compare the inelastic scattering spectra with the XMCD, the evolution of the peak intensities of features A1, A2, and B is monitored by scanning the incident and scattered photon energy together, thus keeping ΔE constant and fixed to the values corresponding to the excitation energies of features A1, A2, and B, respectively. These constant-final-state (CFS) spectra are reported in Fig. 3 (right panel, thin line) together with the corresponding L_3 edge XMCD (thick line) measured on the same sample.

It is evident that features A1, A2, and B correspond to three different resonances, reaching their maximum intensity at different incident photon energies and that their correspondence with the XMCD features below and at the edge is rather evident. The energy position around which the dipolar B resonance is centered corresponds to the strongest feature in the XMCD spectra. This observation is in agreement with the commonly accepted interpretation of the XMCD signal at the absorption threshold. More importantly, A1 and A2 features resonate at two different energies, in coincidence with the a1-a2 structure in the Nd L_3 XMCD.

Once the origin of a1, a2, and b features of the XMCD spectra at the L_3 edge has been determined, we can properly treat the temperature variation of the dichroic signals, obtaining information about $\theta_{\text{Nd}}(T)$. Although the strong differences in the relative E2/E1 intensity between the two absorption edges remain to be fully explained, there have been theoretical efforts¹⁰ which qualitatively describe the observation, predicting an up-to-now never observed quadrupolar contribution to the XMCD at the L_2 edge of rare-earth ions. It is well known¹¹ that the intensity of a dichroic E1 contribution depends linearly on $(W_{1,1} - W_{1,-1})\cos\alpha$, while a E2 one is proportional to $((W_{2,1} - W_{2,-1})\cos 2\alpha + (W_{2,2} - W_{2,-2})\sin^2\alpha)\cos\alpha$, where $W_{L,M}$ are the matrix elements the 2^L pole transitions. Given the order of magnitude of the involved transition energies, $W_{L,M}$ will be treated as temperature independent in the range of interest of our study. By integration of the dichroic intensities, the $W_{L,M}$'s remain in the equations as constant factors. We have studied the temperature dependence of the E2/E1 intensity ratio at both edges. The temperature dependence of XMCD through $\mu_{\text{Nd}}(T)$ is overcome by studying the ratio between two dichroic signals which depend on the same way on $\mu_{\text{Nd}}(T)$. The experimental ratio values obtained at both edges are shown in Fig. 4. Furthermore, we have fitted the temperature dependence of the E2/E1 ratio to the theoretical angular dependence calculated by using the $\theta_{\text{SR}}^{\text{Nd}}(T)$ values corresponding to the strongly noncollinear arrangement in the low-temperature phase conjectured by Onoedera² from ^{57}Fe Mössbauer spectroscopy data. The remarkable agreement of the fit to the experimental E2/E1 ratio strongly supports Onoedera's prediction, with an average value of $\theta_{\text{Nd}} \approx 57^\circ$ to

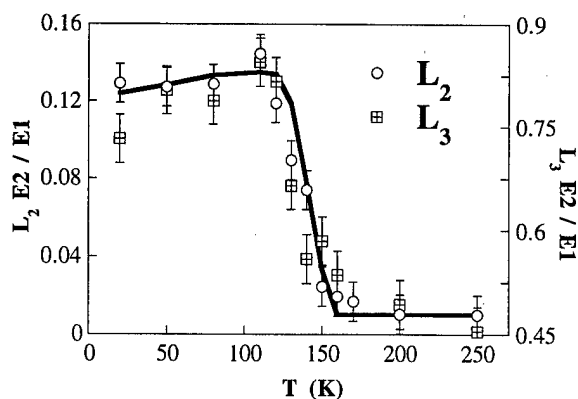


FIG. 4. Temperature dependence of the E2/E1 ratio of the XMCD spectra at the L_2 (open symbols) and L_3 (crossed squares) absorption edges. The thick line corresponds to the expected behaviour for the predicted noncollinear configuration between Fe and Nd ions in Ref. 2 for a dipolar b and quadrupolar a1 and a2 features.

compare with $\theta_{\text{Fe}} \approx 27^\circ$ at the lowest temperatures. The observed angular behavior of E2/E1 at the L_2 edge (coincident with that from L_3) is, to the authors knowledge, the first experimental evidence of a quadrupolar contribution to the dichroism of a rare-earth ion at the L_2 edge.

In summary, our combined XMCD, XRMS, and RIXS study at the Nd $L_{2,3}$ edges in the $\text{Nd}_2\text{Fe}_{14}\text{B}$ has allowed to separately observe the E1 and E2 absorption channels, evidencing the E2 origin of the magnetic pre-edge features at both edges in XMCD and XRMS and showing how this different spectroscopic origin provides new information on the magnetic properties of materials.

This work has been partly financed by Spanish CICYT, project MAT96/448. XMCD and XRMS experiments were performed at ID12A and BM32 beamlines at the ESRF, respectively. RIXS experiments were performed at X21 at NSLS. The authors highly acknowledge the staff of both facilities for the kind support received.

¹P. Carra and M. Altarelli, Phys. Rev. Lett. **64**, 1286 (1990).

²H. Onoedera, A. Fujita, H. Yamamoto, M. Sagawa, and Y. Matsuura, J. Magn. Magn. Mater. **68**, 6 (1987); **68**, 15 (1987).

³A. Koizumi, K. Namikawa, H. Maruyama, K. Mori, and H. Yamazaki, Jpn. J. Appl. Phys., Part 1 **32**, 332 (1993).

⁴J. F. Herbst, Rev. Mod. Phys. **63**, 819 (1991), and references therein.

⁵X. Wang, T. C. Leung, B. N. Harmon, and P. Carra, Phys. Rev. B **47**, 9087 (1993).

⁶J. C. Lang, G. Srajer, C. Detlefs, A. I. Goldman, H. König, X. Wang, B. N. Harmon, and R. W. McCallum, Phys. Rev. Lett. **74**, 4935 (1995).

⁷J. P. Hannon, G. T. Trammell, M. Blume, and D. Gibbs, Phys. Rev. Lett. **10**, 1245 (1988).

⁸M. Krisch, C. C. Kao, F. Sette, W. A. Caliebe, K. Hämmäläinen, and J. B. Hastings, Phys. Rev. Lett. **74**, 4931 (1995).

⁹M. van Veenendaal and R. Benoist, Phys. Rev. B (in press).

¹⁰M. van Veenendaal, J. B. Goedkoop, and B. T. Thole, Phys. Rev. Lett. **78**, 1162 (1997).

¹¹P. Carra, H. König, B. T. Thole, and M. Altarelli, Physica B **192**, 182 (1993).

Epitaxial $\text{Fe}_{100-x}\text{Co}_x/\text{Ag}(001)$ alloy films: Structure and element-specific magnetic moments from magnetic linear dichroism

E. Kisker, A. Faust, R. Schellenberg, A. Fanelisa, and F. U. Hillebrecht
Heinrich-Heine-Universität Düsseldorf, Universitätsstrasse 1, 40225 Düsseldorf, Germany

The structure and element-specific local magnetic moments in $\text{Fe}_{100-x}\text{Co}_x/\text{Ag}(001)$ ($16 < x < 70$) epitaxial ultrathin alloy films have been determined by photoelectron diffraction (PED) and related magnetic linear dichroism in angle-resolved core-level photoemission, using a laboratory x-ray source. The PED peaks of the Fe and Co $2p$ core levels for any of the alloy compositions are at emission angles as expected for a bcc lattice. The dichroism increases for the Fe $2p_{3/2}$ core level with increasing x , whereas that of the Co $2p_{3/2}$ dichroism is virtually independent on the alloy composition. The dichroism of both the Fe and the Co core levels scales well with the calculated dependence of the local magnetic moment on the alloy composition rather than with the average saturation magnetization. © 1998 American Institute of Physics. [S0021-8979(98)40311-6]

I. INTRODUCTION

We have shown recently that the photoemission intensity in angle-resolved core level photoemission with linearly (p)-polarized radiation depends on the direction of the magnetization.¹ Subsequently it was shown² that this effect persists when using unpolarized radiation from standard laboratory x-ray sources (e.g., Mg or Al K_α), due to the presence of the p -polarized component. Consequently, this experimentally relatively easily accessible effect can be used for element-specific magnetometry. Within a purely atomic picture, the dichroism at a fixed energy is proportional to $M \cdot (k \times E) \cdot (k \cdot E)$.³ In dealing with a crystalline solid, the emission angle α of the photoelectrons with respect to the crystal lattice is an additional variable. Changing α gives rise to well-known photoelectron diffraction patterns, characterized by dominant forward scattering peaks along low-index crystallographic directions at photoelectron energies exceeding about 400 eV. The emission angle dependence of the dichroism is strongly affected by photoelectron diffraction, the latter being an independent source for an intensity asymmetry upon a change in magnetization direction.^{4,5} Accordingly, information on the geometric structure and on magnetic properties is obtained from the dichroism data. Here we will apply this method for the first time to element-specifically determine the magnetic moment in epitaxial $\text{Fe}_{100-x}\text{Co}_x$ alloy thin films.

II. EXPERIMENT

Figure 1 shows the experimental geometry. We used a standard x-ray photoelectron spectrometer (CLASS 150, VSW) and a Mg K_α x-ray source. The spectrometer and the x-ray source make an angle of 45° with respect to each other, the electron emission direction is in the incidence plane. The emission angle (α) of the photoelectrons with respect to the crystal lattice is varied by rotating the sample around an axis perpendicular to the plane of incidence. The sample surface was a (100) plane of the bcc lattice, which prevailed for all alloy concentrations, and the axis of rotation coincided with a (100) direction in the plane of the surface. Consequently,

the scanned emission directions were also in a (100) plane. The samples are remanently magnetized by a short field pulse of about 80 Oe prior to performing an energy scan at a preset value of α . The geometrical conditions between \mathbf{M} , \mathbf{k} , and \mathbf{E} remain constant when α is changed. A wide range in α was spanned to obtain the PED and the intensity asymmetry pattern. The films, obtained by coevaporation of Fe and Co onto an Ag(001) substrate at room temperature from e -beam heated rods, were 20 ML thick.

III. DATA EVALUATION

The dichroism is quantified by its asymmetry value, $A = (I^\uparrow - I^\downarrow)/(I^\uparrow + I^\downarrow)$, where I^\uparrow, \downarrow are the intensities for the two magnetization directions. When the alloy composition is changed, the line-to-background ratio changes. Since we are concerned with determining the intensity asymmetry of core level lines from different alloy compositions, background subtraction is mandatory. Here we subtract constant backgrounds as determined by the intensities at the onset of the $2p_{3/2}$ core level spectra prior to calculating the dichroism. In

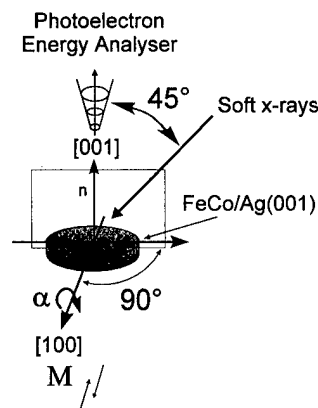


FIG. 1. The experimental geometry. The unmonochromatized Mg K_α radiation and the acceptance cone of the photoelectron spectrometer are at an angle of 45° . The sample is rotated about its [100] direction to vary the angle (α) between the surface normal (\mathbf{n}) and the photoelectron collection direction.

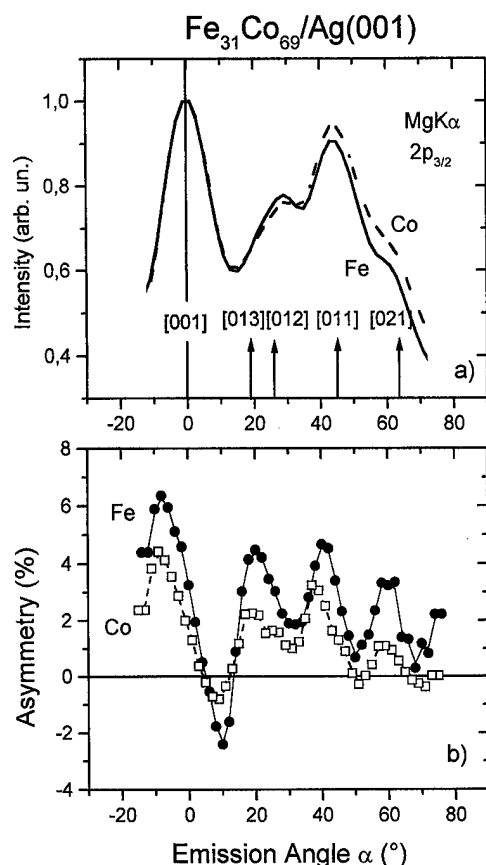


FIG. 2. Angular dependences of the photoelectron intensities (a) and asymmetries (b) as obtained from the $2p_{3/2}$ core levels of an epitaxial $\text{Fe}_{31}\text{Co}_{69}/\text{Ag}(001)$ alloy film. Full line and filled circles are for Fe, dashed line and empty squares for Co. Vertical bars indicate the emission angles corresponding to low-index crystallographic directions.

plots showing angular dependences the asymmetry is plotted. Since the asymmetry tends to diverge where the background subtracted intensity becomes very small, we plot the intensity difference normalized to the maximum in $(I^\uparrow + I^\downarrow)$ in plots showing binding energy dependences. This so-called normalized intensity difference is equal to the asymmetry at that binding energy where $(I^\uparrow + I^\downarrow)$ has its maximum value.

The intensity asymmetry caused by PED is large and easy to measure in a conventional XPS spectrometer. However, extracting the full amount of information on the structural and magnetic properties requires one to fit the dichroism data by a PED theory since no simple quantitative interpretation of the angular dependence of the intensity asymmetry on structural and magnetic properties has been given so far. We therefore chose to average out the PED oscillations in the dichroism data by integrating over the emission angle. Since the dichroism oscillations are not symmetric with respect to zero dichroism, the angular averaged asymmetry curve is different from zero. We have shown recently that such angular integrated data obtained from $\text{Fe}(001)$ compare well with data from an amorphous Fe containing metallic glass where PED effects are absent.⁵ The PED intensity diffraction pattern still provides the opportunity to simultaneously get information on the crystal structure.

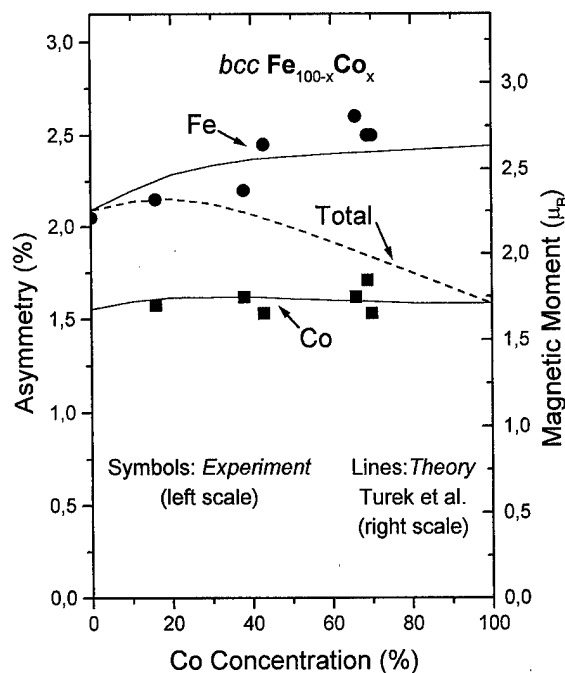


FIG. 3. Dependence of the linear magnetic dichroism, obtained with unpolarized light, on alloy composition (left scale) for Fe (circles) and Co (squares). The curves show results calculated by Turek *et al.* (Ref. 6, right scale) for the local moments of Fe (upper) and Co (lower), as well as the concentration-weighted average (dashed).

IV. RESULTS

Energy distribution curves have been measured for the Fe and Co $2p_{3/2}$ and $2p_{1/2}$ core levels for emission angles ranging from -20° to 70° . For any of the alloy compositions studied, we observe well-defined photoelectron diffraction peaks for each of the Fe $2p_{3/2}$, Fe $2p_{1/2}$, Co $2p_{3/2}$, and Co $2p_{1/2}$ peaks. Because of their higher intensities, the $j=3/2$ sublevels are evaluated here. Figure 2(a) shows the angular distributions of the photoelectron intensities for the peak energies of the Fe and Co $2p_{3/2}$ photoemission lines, and Fig. 2(b) shows the angular distribution of the associated intensity asymmetries for an epitaxial $\text{Fe}_{31}\text{Co}_{69}/\text{Ag}(001)$ alloy film. Well-defined peaks in the intensity are observed at emission angles corresponding to the $\langle 001 \rangle$ (0°), $\langle 012 \rangle$ (18.4°), $\langle 013 \rangle$ (26.6°), $\langle 011 \rangle$ (45°), and $\langle 021 \rangle$ (63.4°) forward-scattering directions. The peaks corresponding to the $\langle 013 \rangle$ and $\langle 012 \rangle$ directions merge into one broader peak. The asymmetry changes sign in going from $\alpha = -10^\circ$ towards $\alpha = +10^\circ$ and oscillates further with increasing angle. The pattern can be viewed as a virtually symmetrical oscillation offset from zero by about 2%. The oscillations at larger angles are reduced in amplitude from that centered at normal emission ($\alpha = 0$). The angular dependences are virtually independent on the alloy composition and compare well with those observed in pure $\text{Fe}/\text{Ag}(001)$ films.

The concentration dependence of the element-specific dichroism is shown in Fig. 3. When changing the alloy composition from 16% to about 70% Co concentration, a slight increase of the dichroism is observed for the Fe $2p_{3/2}$ core level, whereas the dichroism of the Co $2p_{3/2}$ is essentially independent on the composition. These findings compare

well with the calculated dependence of the magnetic moments for bulk random bcc $\text{Fe}_{100-x}\text{Co}_x$ alloys.^{6,7} It is worthwhile to mention that the Fe and the Co dichroism as a function of the Co concentration does not follow the dependency of the average moment which decreases by 20% in going from $x=16$ to $x=70$ as a result of the smaller magnetic moment of the Co as compared to that of the Fe. This shows that the magnetic linear dichroism probes the element-specific local magnetic moments.

V. CONCLUSIONS

We have shown that structural and magnetic properties of a composite material can be determined by photoelectron diffraction and the related magnetic linear dichroism in angle-resolved core level photoemission, using an unpolarized laboratory x-ray source. The dependence of the element-specific $2p_{3/2}$ core level dichroism of Fe and Co in epitaxial $\text{Fe}_{100-x}\text{Co}_x/\text{Ag}(001)$ alloy films compares well the calculated dependences of the local magnetic moments on the alloy composition.

ACKNOWLEDGMENTS

This work was supported by the Deutsche Forschungsgemeinschaft (SFB 166) and the Ministerium für Wissenschaft und Forschung, NRW. One of us (E.K.) is also grateful for a grant from the Volkswagenstiftung and for the hospitality extended to him during a sabbatical stay at the Lawrence Berkeley Laboratory and the Naval Research Laboratory. Helpful discussions with Professor C.S. Fadley and Dr. J. Menchero on the interpretation of the PED effects on the intensity asymmetry are gratefully acknowledged.

¹C. Roth, F. U. Hillebrecht, H. B. Rose, and E. Kisker, Phys. Rev. Lett. **70**, 3479 (1993).

²F. U. Hillebrecht and W.-D. Herberg, Z. Phys. B (Condensed Matter) **93**, 299 (1994).

³G. van der Laan and B. T. Thole, Solid State Commun. **92**, 427 (1994).

⁴A. Fanelisa *et al.*, Phys. Rev. B **54**, 17 962 (1996).

⁵R. Schellenberg *et al.*, Phys. Rev. B (in press).

⁶I. Turek, J. Kudrnovsky, V. Drchal, and P. Weinberger, Phys. Rev. B **49**, 3352 (1994).

⁷H. Ebert and M. Battocletti, Solid State Commun. **98**, 785 (1996).

Magnetic anisotropies of Ni–Pt and Co–Pt alloys

S. S. A. Razee and J. B. Staunton

Department of Physics, University of Warwick, Coventry CV4 7AL, United Kingdom

F. J. Pinski

Department of Physics, University of Cincinnati, Ohio 45221

B. Ginatempo and E. Bruno

Dipartimento di Fisica and Unità INFM, Università di Messina Salita Sperone 31, I-98166, Italy

We present the magnetocrystalline anisotropy of disordered $\text{Ni}_{1-x}\text{Pt}_x$ and disordered fcc $\text{Co}_{1-x}\text{Pt}_x$ alloys using the spin-polarized relativistic Korringa–Kohn–Rostoker coherent-potential approximation in which the spin-orbit coupling and magnetism are treated on an equal footing. In both the pure fcc ferromagnetic elements (Ni as well as Co), the magnetic easy axis is along the [111] direction of the crystal. Addition of Pt to Ni changes the magnetic easy axis to the [001] direction, in agreement with the experimental observations, although the magnitudes of the calculated magnetocrystalline anisotropy energies for different compositions are somewhat different from the corresponding experimental values. In contrast, addition of Pt to Co does not alter the magnetic easy axis, only the magnitude of the magnetocrystalline anisotropy energy is affected. The origin of this contrasting behavior may lie in the larger size of the magnetic moment of Co (as compared to Ni). © 1998 American Institute of Physics. [S0021-8979(98)33911-0]

Magnetocrystalline anisotropy of a ferromagnetic material is a consequence of the coupling of the spin of the electron with its orbital motion. This so-called spin-orbit coupling (SOC), though very small compared to the exchange energy responsible for the magnetism, determines the equilibrium or “easy” axis of magnetisation in most solids. Clearly, SOC is a relativistic phenomenon and can only be adequately described in a fully relativistic formalism in which magnetism and SOC are treated on an equal footing. In a recent publication,¹ we presented a scheme to calculate the magnetocrystalline anisotropy energy (MAE) of a disordered alloy within the spin-polarized relativistic Korringa–Kohn–Rostoker coherent-potential approximation (SPR-KKR-CPA).² This theory is based on the relativistic spin-polarized density functional theory derived by MacDonald and Vosko³ and others. Within this formalism, the MAE of a system is expressed as

$$\begin{aligned} \Delta E = & -\frac{1}{\pi} \text{Im} \int^{E_F} d\epsilon \left[\frac{1}{\Omega_{BZ}} \int d\mathbf{k} \ln \|I + [t_c^{-1}(\mathbf{e}_2) \right. \\ & - t_c^{-1}(\mathbf{e}_1)] \tau_c(\mathbf{k}; \mathbf{e}_1) \| + x \{ \ln \|D_A(\mathbf{e}_1)\| \\ & - \ln \|D_A(\mathbf{e}_2)\| \} + (1-x) \{ \ln \|D_B(\mathbf{e}_1)\| \\ & - \ln \|D_B(\mathbf{e}_2)\| \} \Big] - \frac{1}{2} n(E_{F_2}; \mathbf{e}_2) (E_{F_1} - E_{F_2})^2 \\ & + \mathcal{O}(E_{F_1} - E_{F_2})^3. \end{aligned} \quad (1)$$

In Eq. (1), $t_c(\mathbf{e}_1)$ and $t_c(\mathbf{e}_2)$ are the SPR-KKR-CPA t -matrices for magnetization along \mathbf{e}_1 and \mathbf{e}_2 directions, respectively, and $\tau_c(\mathbf{k}; \mathbf{e}_1)$ is the path-operator matrix in the \mathbf{k} -space,

$$\tau_c(\mathbf{k}; \mathbf{e}_1) = [t_c^{-1}(\mathbf{e}_1) - g(\mathbf{k})]^{-1} \quad (2)$$

and

$$D_A(\mathbf{e}_1) = [I - \tau_c^{00}(\mathbf{e}_1) \{t_c^{-1}(\mathbf{e}_1) - t_A^{-1}(\mathbf{e}_1)\}]^{-1} \quad (3)$$

with similar expressions for $D_A(\mathbf{e}_2)$, $D_B(\mathbf{e}_1)$, and $D_B(\mathbf{e}_2)$.

The striking feature of Eq. (1) is that the MAE can be calculated directly. This is in contrast with some other approaches which involve the subtraction of the total energies of the system for two magnetization directions calculated separately. Therefore, the use of Eq. (1) guarantees against many possible numerical instabilities.⁴ In particular, Eq. (1) is derived by algebraically canceling many terms in the total energy, e.g., all core contributions. Remember that the energy difference is only a tiny fraction ($\sim 10^{-10}$) of the total energy, and thus impossible to extract as the difference in the total energies except when the total energies are calculated with the utmost precision. The use of Eq. (1) also reduces the systematic error by ensuring that the same integration grids are used for both magnetization directions (this is not guaranteed when the two total energies are calculated separately). Additionally, in most cases, the second term of Eq. (1) is expected to be quite small compared to ΔE , and in such cases we need to know the Fermi energy corresponding to only one magnetization direction. The first term which contains the predominant contribution to ΔE needs to be evaluated accurately. The Brillouin zone integration involved in the above equation is the most time-consuming part of the calculation. Owing to the preferred direction of magnetization, the symmetry in the Brillouin zone is reduced and it is necessary to perform the Brillouin zone integration in the 1/16 of the zone when the magnetization is along the [001] direction and in the 1/4 of the zone when it is along the [111] direction (as opposed to 1/48 in the nonrelativistic case) for cubic systems. Also, if the k -points are not sampled properly, it may take as many as 500 000 k -points to get a converged result as has been demonstrated in earlier studies.⁵

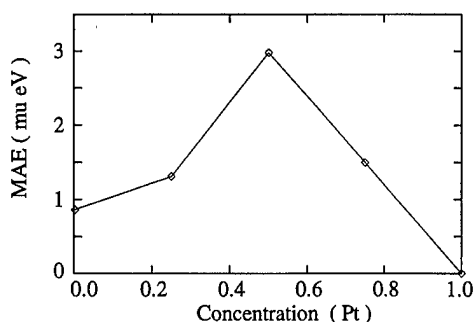


FIG. 1. Magnetocrystalline anisotropy energy (MAE) defined as $E(001) - E(111)$ for $\text{Co}_{1-x}\text{Pt}_x$ alloys as a function of Pt concentration. The solid line is a guide to the eye.

Our method and its computational aspects have been discussed in detail elsewhere.¹ In what follows, we briefly describe the important points relevant to the present study. We start with the self-consistent potentials obtained by the spin-polarized scalar relativistic KKR-CPA. The SPR-KKR-CPA equations are solved for two magnetization directions separately to a high degree of precision (10^{-9}). The energy integration is performed around a complex contour in order to obtain an accurate integration with comparably fewer points.⁶ The Brillouin zone integration is performed by the recently proposed hybrid adaptive quadrature scheme.⁷ In our earlier study¹ we had used the prism method⁸ and we needed $\sim 100\,000$ k -points to achieve a good convergence in MAE. The advantage of the hybrid method is that it puts more points only where needed and therefore the number of k -points is greatly reduced. In our calculations we have found that, when the energy is near the real axis, we have to put $\sim 25\,000$ points for a good convergence whereas far from the real axis we need much less number of k -points (For example, when the imaginary part of the energy is 0.5 Ry, we need only 100 points to achieve same level of convergence.)

In this article, we present the MAE of disordered fcc $\text{Co}_{1-x}\text{Pt}_x$ and $\text{Ni}_{1-x}\text{Pt}_x$ alloys. We note that in both fcc Co as well as fcc Ni the easy magnetic axis is along the [111] direction of the crystal and the theoretical calculations also predict the same.¹ In Fig. 1 we show the results of our calculations for these alloys. We note that the MAE for $\text{Co}_{1-x}\text{Pt}_x$ alloys, defined as $E(001) - E(111)$ remains positive throughout the whole concentration range implying that the magnetic easy axis remains unchanged at [111]. The MAE is maximum around the equiatomic composition. To our knowledge there are no experimental results on the bulk disordered fcc $\text{Co}_{1-x}\text{Pt}_x$ alloys. However, the experimental results for the ordered Co-Pt alloy are very different from our calculated results for disordered alloys; both the magnitude of the MAE as well as the magnetic easy axis are different ($\text{MAE} \sim 400 \mu\text{eV}$). The reason for this could lie in either the compositional ordering or in the tetragonal distortion or in a combination of the two. We are working on this aspect and we defer it to a later publication.

Experimental results on ferromagnetic $\text{Ni}_{1-x}\text{Pt}_x$ alloys (which are disordered and fcc) reveal that the easy axis of magnetisation changes to [001] with the addition of Pt with

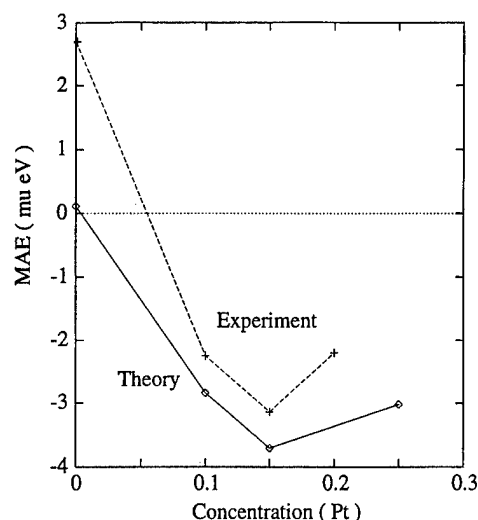


FIG. 2. Experimental and theoretical values of magnetocrystalline anisotropy energy (MAE) defined as $E(001) - E(111)$ for $\text{Ni}_{1-x}\text{Pt}_x$ alloys as a function of Pt concentration. The lines are guide to the eye.

the magnitude of MAE being largest around 15% Pt.⁹ In Fig. 2 we show our calculations and the experimental results; both show similar trends, although the magnitudes of MAE differ. Also, the minima around 15% Pt is less pronounced than that in the experimental results. Nevertheless, we reproduce the experimental observations that addition of Pt to Ni alters the easy magnetic axis. Further calculations and measurements are needed to examine the extent of the agreement. However, it is important to realize that, although both fcc Ni and fcc Co have their magnetization vectors pointing along the [111] direction, addition of Pt to Ni changes the magnetic easy axis. Whereas when Pt is added to Co, the easy axis is not affected; only the magnitude of the MAE is changed. Both the size of the magnetic moment as well as the SOC are important factors that determine the magnetocrystalline anisotropy of a material. In the present alloy systems, the SOC are similar in strength. Thus, it seems possible that this contrasting behavior originates in the size of the magnetic moment. The larger moment of cobalt (compared to nickel) seems to stabilize the direction of the easy axis, although other mechanisms are also possible, e.g., sensitivity to the position of the Fermi level.⁵

In summary, we have presented calculations of MAE of $\text{Co}_{1-x}\text{Pt}_x$ and $\text{Ni}_{1-x}\text{Pt}_x$ alloys within the SPR-KKR-CPA scheme. Our results show that, besides the known SOC effect, the size of the magnetic moment also plays a role in determining the magnetocrystalline anisotropy of a material. We end by pointing out the need of a more comprehensive approach to the calculation of the magnetocrystalline anisotropy energy which should include the effects of atomic short-range order and loss of cubic symmetry.

This research is supported by the Engineering and Physical Sciences Research Council (UK) and National Science Foundation (USA), Grant No. DMR95-31223.

- ¹S. S. A. Razee, J. B. Staunton, and F. J. Pinski, Phys. Rev. B **56**, 8082 (1997).
- ²H. Ebert, B. Drittler, and H. Akai, J. Magn. Magn. Mater. **104**, 733 (1992).
- ³A. H. MacDonald and S. Vosko, J. Phys. C **12**, 2977 (1979).
- ⁴J. B. Staunton, M. Matsumoto, and P. Strange, in *Applications of Multiple Scattering Theory to Materials Science*, edited by W. H. Butler, P. H. Dederichs, A. Gonis, and R. L. Weaver, MRS Symposia Proceedings No. 253 (Materials Research Society, Pittsburgh, 1992), p. 309.
- ⁵G. H. O. Daalderop, P. J. Kelly, and M. F. H. Schuurmans, Phys. Rev. B **41**, 11919 (1990).
- ⁶R. Zeller, J. Deutz, and P. H. Dederichs, Solid State Commun. **44**, 993 (1982).
- ⁷E. Bruno and B. Ginatempo, Phys. Rev. B **55**, 12946 (1997).
- ⁸G. M. Stocks, W. M. Temmerman, and H. Winter, in *Electrons in Disordered Metals and at Metallic Surfaces*, edited by P. Phariseau, B. L. Gyorffy, and L. Scheire, NATO ASI Series B, Vol. 42 (Plenum, New York, 1979).
- ⁹H. Kadomatsu, T. Tokunaga, and H. Fujiwara, J. Phys. Soc. Jpn. **50**, 3 (1981).

Ground state properties of a high-spin $\text{Mn}_{12}\text{O}_{12}$ molecule in an organic compound

S. Y. Wang^{a)}

Institute of Solid State Physics, Academia Sinica, 230031-Hefei, People's Republic of China

Liang-Jian Zou

Center for Theoretical Physics, Chinese Center of Advanced Science and Technology (World Laboratory), Box 8730, Beijing, People's Republic of China and Institute of Solid State Physics, Academia Sinica, 230031-Hefei, People's Republic of China

X. G. Gong and Q. Q. Zheng

Institute of Solid State Physics, Academia Sinica, 230031-Hefei, People's Republic of China

H. Q. Lin

Department of Physics, The Chinese University of Hong Kong, Shatin New Territory, Hong Kong

The electronic structure and the magnetism of a $\text{Mn}_{12}\text{O}_{12}$ molecule at ground state have been studied by density functional theory with a local spin density approximation. We have found that the magnetic moments of Mn ions in the tetrahedron and those of Mn ions in the crown of the $\text{Mn}_{12}\text{O}_{12}$ molecule align antiferromagnetically. The average moment per Mn ion is about $3.07\mu_B$ in the tetrahedron and $4.07\mu_B$ in the crown. The total spin amounts to $20.0\mu_B$ which is in agreement with recent experimental results. The significant difference of magnetic moments between Mn ions at two sites is attributed to the different exchange splitting of $3d$ orbitals. However, the charge difference between the two kinds of Mn ions is as small as 0.22 electrons. The charge density and the spin density exhibit strong directional dependence, which indicates the strong anisotropy in this molecule. © 1998 American Institute of Physics. [S0021-8979(98)40411-0]

The study of large molecular clusters of metal ions is a very important area of interest which is expanding rapidly.¹ Very recently, many new phenomena such as the quantum tunneling of magnetization, gigantic relaxation time and magnetic bistability²⁻⁸ were discovered in a so-called high-spin molecular organic compound— $\text{Mn}_{12}\text{O}_{12}$ acetate.^{9,10} These new observations have further enhanced the interest because of its suitability for the investigation of magnetic properties on nanoscale or mesoscopic dimensions, and its promise of use in data storage devices.

$\text{Mn}_{12}\text{O}_{12}$ acetate has a well-defined crystal structure which can be described as a $\text{Mn}_{12}\text{O}_{12}$ molecule surrounded by some organic ligands.^{9,10} The molecule contains two kinds of manganese ions bridged by oxygen. The inner four ions form a tetrahedron in the center of cluster (denoted by Mn_t) and the outer eight form a crown (denoted by Mn_c). A recent experiment¹¹ shows that the molecule has a large net spin $S=10$, which is always oriented along the easy axis S_4 . Although a strong interplay could exist in the $\text{Mn}_{12}\text{O}_{12}$ molecule, the interaction between the molecules themselves is still weak because of the large distance. Many experiments^{2-8,10} have shown that at low temperature, the $\text{Mn}_{12}\text{O}_{12}$ molecule acts just like a high-spin magnet with clean discrete quantum numbers ($m_s = -10, \dots, +10$). So, unlike many other nanomagnetic materials, the magnetic behavior of $\text{Mn}_{12}\text{O}_{12}$ acetate should be mainly determined by the $\text{Mn}_{12}\text{O}_{12}$ molecule.

So far, in spite of some experimental observations²⁻¹³

having been made, there is still a lack of many theoretical studies^{14,15} for such an interesting material, especially studies of the electronic structure and the magnetism on a microscopic level. In this article, we report our results of first principle studies on the $\text{Mn}_{12}\text{O}_{12}$ molecule. We have employed the discrete variational method (DVM)^{16,17} based on density functional theory (DFT) with a local spin density approximation (LSDA)¹⁸ to study the ground state properties of the $\text{Mn}_{12}\text{O}_{12}$ molecule. In DVM, the Kohn-Sham equation (in atomic units),

$$(-\nabla^2/2 + V_C + V_{XC})\phi_{i\sigma} = \epsilon_{i\sigma}\phi_{i\sigma}, \quad (1)$$

with charge density $\rho_\sigma(\mathbf{r})$,

$$\rho_\sigma(\mathbf{r}) = \sum_i n_{i\sigma} |\phi_{i\sigma}(\mathbf{r})|^2 \quad (2)$$

is solved self-consistently where $\phi_{i\sigma}$ is the single particle wave function for the molecule with occupation $n_{i\sigma}$, V_C is the Coulomb potential of the nuclei and electrons, and V_{XC} is the exchange-correlation potential under LSDA. In the present calculation, the numerical atomic orbitals obtained by self-consistent LDA calculations for a single atom are used as the variational bases to expand the one particle wave functions. The discrete summation method of pseudo-random points in the three dimensional space and group theory are adopted to simplify the solution of the eigenvalue equations. The Coulomb potential is obtained by means of fitting charge density to a multipolar expansion which ensures that the DVM gives more precise results.¹⁷ In our calculation, the order of the multipolar expansion functions has

^{a)}Electronic mail: wang@isp.hfcas.ac.cn

TABLE I. The magnetic moments (m), Mulliken orbital occupation numbers (Occ.) and charges for the Mn cations in the $\text{Mn}_{12}\text{O}_{12}$ molecule. Symbols \uparrow and \downarrow indicate the spin-up and the spin-down states, respectively.

	Occ. (\uparrow)	Occ. (\downarrow)	Total Occ.	$m(\mu_B)$
Mn _i cations				
3d	3.62	0.55	4.17	+3.07
4s	0.01	0.01	0.02	0.00
			Charge +2.82	Total +3.07
Mn _c cations				
3d	0.14	4.22	4.36	-4.07
4s	0.02	0.02	0.04	0.00
			Charge +2.60	Total -4.07

been chosen up to 2. The density of states (DOS) is obtained by using the Lorentzian broadening scheme, and the partial DOS (PDOS) is defined as:

$$D_{nl\sigma}^q = \sum_i P_{nl\sigma}^q \frac{\delta/\pi}{(\epsilon - \epsilon_{i\sigma})^2 + \delta^2}, \quad (3)$$

where $P_{nl\sigma}^q$ is the Mulliken population¹⁹ of the atomic orbital χ_{nl} of atom q in the molecular spin orbital $\phi_{i\sigma}$. The DOS of atom q with spin σ is obtained by a sum of n , l and i , and the total DOS of spin σ is given by the sum of all the atoms. To check the reliability of our method on the Mn-O system, we first study antiferromagnetically coupled MnO. We found magnetic moment of about $4.98\mu_B$ for the Mn cation, which is in agreement with experimental result.²⁰

For calculation of the $\text{Mn}_{12}\text{O}_{12}$ molecule, we adopted the experimental atomic distance,⁹ and put the z axis parallel to the easy axis. In Table I, we have presented magnetic moments, Mulliken orbital occupation numbers and charges for the Mn cations. From Table I, it can be seen the magnetic moment of the Mn_i cation is about $3.07\mu_B$ and that of the Mn_c cation is about $-4.07\mu_B$, which suggests that the two kinds of manganese ions are antiferromagnetically coupled. Considering the small contribution from the O anion, we get a total net spin amounting to $20.0\mu_B$ for the $\text{Mn}_{12}\text{O}_{12}$ molecule, which is exactly the same as the data derived from the experiment.¹¹ At the same time, we note that there is a large difference in Mulliken occupation numbers for the Mn 3d orbitals with spin up and with spin down. For the Mn_i cation, the electron occupation number in the 3d orbital with spin up is about 3.62, but it is only 0.55 in 3d orbital with spin down while, for the Mn_c cation, the electron occupation numbers of the 3d orbital with spin up and spin down are 0.14 and 4.22, respectively. In addition, for all the Mn ions, there are nearly no electrons in the 4s orbital, most of them have been transferred to oxygen atoms. The different occupation numbers show that the exchange splitting might have a significant difference for both kinds of Mn ions. In order to see this difference more clearly, we have presented the 3d PDOS of Mn cations as well as the total DOS of the $\text{Mn}_{12}\text{O}_{12}$ molecule in Fig. 1 and Fig. 2, respectively. From Fig. 1, the very large exchange splitting in the Mn 3d orbitals can be clearly observed, and both the spin-up and the spin-down PDOS have similar distribution. From PDOS, we can get the average value of the calculated exchange splitting, which is about 4.5

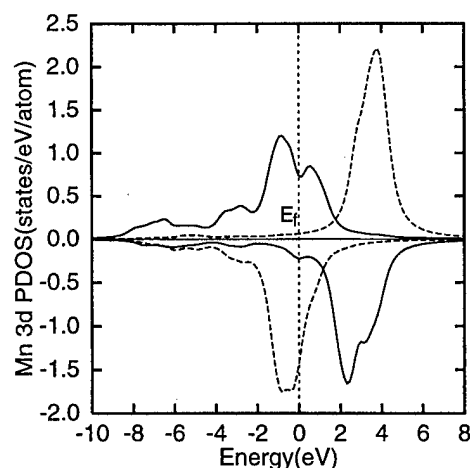


FIG. 1. The 3d PDOS for spin-up (upper panel) and spin down (lower panel) of the Mn_i cation (solid lines) and of the Mn_c cation (dashed lines). The Fermi level is shifted to zero.

eV for Mn_i cations and 3.0 eV for Mn_c cations. The large difference of exchange splitting between Mn_c and Mn_i ions leads to the large difference of magnetic moments, although the total occupation numbers in 3d orbitals are almost the same. From the total DOS shown in Fig. 2, the large net spin resulting from the large orbital exchange splitting in the $\text{Mn}_{12}\text{O}_{12}$ molecule can be observed. The charges for the two kinds of Mn ions are different, but their difference is small, only about 0.22.

To check the dependence of magnetic moment on the atomic distance, we have performed the calculations with the atomic distance 15% larger or smaller than the experimental result. We found that the total magnetic moment of the $\text{Mn}_{12}\text{O}_{12}$ molecule remains the same. For each Mn ion, the magnetic moment changes only a few percent. These results indicate that the magnetic properties of the $\text{Mn}_{12}\text{O}_{12}$ molecule are insensitive to the atomic distance.

In Fig. 3 and Fig. 4, we have presented the charge density as well as the corresponding spin density contour plots on the plane perpendicular to the S_4 axis (denoted by σ_h) and the plane including the S_4 axis and that perpendicular to

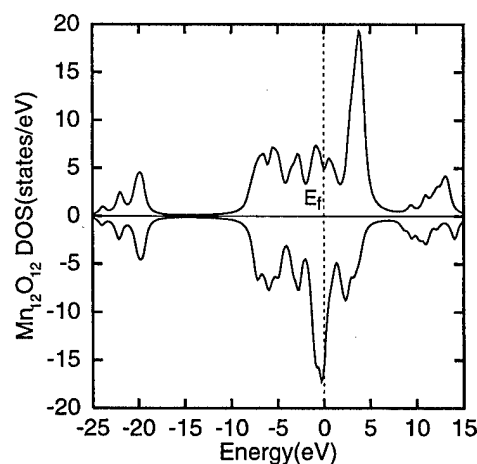


FIG. 2. The total DOS for spin up (upper panel) and spin down (lower panel) of the $\text{Mn}_{12}\text{O}_{12}$ molecule.

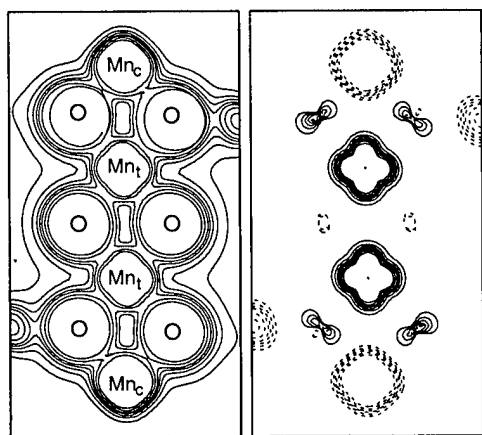


FIG. 3. Charge density (left panel) and spin density (right panel) contours of the $\text{Mn}_{12}\text{O}_{12}$ molecule on the plane perpendicular to the S_4 axis. The solid line stands for the positive value, and dashed line stands for the negative value.

σ_h (denoted by σ_v). On plane σ_h , it is obvious that, other than being spherical-like, the distribution of the charge density and the spin density for all Mn cations exhibits extremely strong directional dependence. However, on plane σ_v , the charge density and the spin density for Mn_c cations are spherically distributed, and those for Mn_t cations are only somewhat distorted from a spherical distribution. The strong directional dependence of the charge density and the spin density shows the large anisotropy of charge density and spin density in the $\text{Mn}_{12}\text{O}_{12}$ molecule which are mainly due to the distinction of neighboring atoms for Mn cations. So, it can

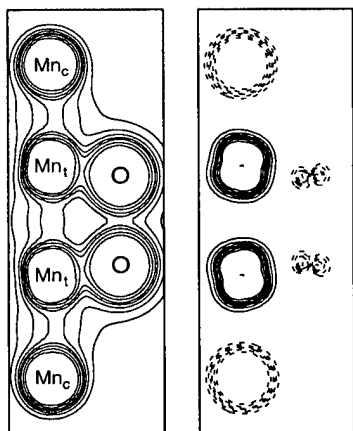


FIG. 4. Charge density (left panel) and spin density (right panel) contours of the $\text{Mn}_{12}\text{O}_{12}$ molecule on the plane including the S_4 axis. The solid line stands for the positive value, and the dashed line stands for the negative value.

be expected that there exists great magnetic anisotropy in $\text{Mn}_{12}\text{O}_{12}$ acetate.

In summary, the electronic and the magnetic properties of the $\text{Mn}_{12}\text{O}_{12}$ molecule at ground state have been investigated by the DVM with LSDA. We have found that the magnetic moments in the inner shell and the outer shell are antiferromagnetically aligned. The calculated total magnetic moment $20.0\mu_B$ for the $\text{Mn}_{12}\text{O}_{12}$ molecule is in good agreement with recent experimental data.¹¹ However, we did not find a significant difference in the occupation numbers for Mn_c and Mn_t . We attribute the large difference of magnetic moment for Mn_c and Mn_t ions to the different exchange splitting of $3d$ orbitals. The experimental observation of the strong anisotropy of $\text{Mn}_{12}\text{O}_{12}$ acetate^{10,12} has been confirmed by the strong anisotropy of the charge density and the spin density.

The authors are greatly indebted to Z. Zeng for her valuable suggestions. One of the authors (S.Y.W.) would like to express his gratitude to M. Z. Li, D. Y. Sun, M. C. Qian, and H. Wu for their valuable help. This work was supported by NNSF Grant No. 19574057 and by the PanDeng Project (95-YU-41).

- ¹D. Gatteschi, A. Caneschi, L. Pardi, and R. Sessoli, *Science* **265**, 1054 (1994).
- ²C. Paulsen, J.-G. Park, B. Barbara, R. Sessoli, and A. Caneschi, *J. Magn. Magn. Mater.* **140-144**, 379 (1995).
- ³B. Barbara, W. Wernsdorfer, L. C. Sampaio, J. G. Park, C. Paulsen, M. A. Novak, R. Ferré, D. Mailly, R. Sessoli, A. Caneschi, K. Hasselbach, A. Benoit, and L. Thomas, *J. Magn. Magn. Mater.* **140-144**, 1825 (1995).
- ⁴J. R. Friedman, M. P. Sarachik, J. Tejada, and R. Ziolo, *Phys. Rev. Lett.* **76**, 3830 (1996).
- ⁵E. M. Chudnovsky, *Science* **274**, 938 (1996).
- ⁶R. Sessoli, D. Gatteschi, A. Caneschi, and M. A. Novak, *Nature (London)* **365**, 141 (1993).
- ⁷L. Thomas, F. Lioni, R. Ballou, D. Gatteschi, R. Sessoli, and B. Barbara, *Nature (London)* **383**, 145 (1996).
- ⁸J. M. Hernández, X. X. Zhang, F. Luis, J. Bartolomé, J. Tejada, and R. Ziolo, *Europhys. Lett.* **35**, 301 (1996).
- ⁹L. Lis, *Acta Crystallogr., Sect. B: Struct. Crystallogr. Cryst. Chem.* **36**, 2042 (1980).
- ¹⁰R. Sessoli, H.-L. Tsai, A. R. Schake, S. Wang, J. B. Vincent, K. Folting, D. Gatteschi, G. Christou, and D. N. Hendrickson, *J. Am. Chem. Soc.* **115**, 1804 (1993).
- ¹¹A. Caneschi, D. Gatteschi, and R. Sessoli, *J. Am. Chem. Soc.* **113**, 5873 (1991).
- ¹²M. A. Novak, R. Sessoli, A. Caneschi, and D. Gatteschi, *J. Magn. Magn. Mater.* **146**, 211 (1995).
- ¹³C. Paulsen, J.-G. Park, B. Barbara, R. Sessoli, and A. Caneschi, *J. Magn. Magn. Mater.* **140-144**, 1891 (1995).
- ¹⁴J. Villain, F. Hartmann-Boutron, R. Sessoli, and A. Rettori, *Europhys. Lett.* **27**, 159 (1994).
- ¹⁵P. Politi, A. Rettori, F. Hartmann-Boutron, and J. Villain, *Phys. Rev. Lett.* **75**, 537 (1995).
- ¹⁶D. E. Ellis and G. S. Painter, *Phys. Rev. B* **2**, 2887 (1970).
- ¹⁷B. Delly and D. E. Ellis, *J. Chem. Phys.* **76**, 1949 (1982).
- ¹⁸P. Hohenberg and W. Kohn, *Phys. Rev. B* **136**, 864 (1964).
- ¹⁹R. S. Mulliken, *J. Chem. Phys.* **23**, 1841 (1955).
- ²⁰D. Adler, in *Solid State Physics*, edited by F. Seitz, D. Turnbull, and H. Ehrenreich (Academic, New York, 1968), Vol. 21.

A comparison between a two-material and three-material magnetic current limiter

S. Young and F. P. Dawson^{a)}

Department of Electrical and Computer Engineering, University of Toronto, Toronto, Ontario M5S-3G4, Canada

M. Iwahara and S. Yamada

Department of Electrical and Computer Engineering, Kanazawa University, Kodatsuno 2-40-20, Kanazawa 920, Japan

This paper investigates the inductance versus current characteristics of a two-material and a three-material magnetic current limiter. The two-material device consists of a NdFeB permanent magnet, a high saturation flux density magnetic material, and a high saturation flux density magnetic pole piece placed on both sides of the magnet. The three-material device consists of a NdFeB permanent magnet, a high saturation flux density magnetic material, and a low saturation flux density material. Finite-element results for the three-material device agree with the results obtained using design equations. In contrast, the results obtained for the two-material device show that the transition current is overestimated and that the ratio of the maximum safe current and transition current, as well as the unsaturated inductance is underestimated. Extending the magnet beyond the adjoining surfaces improves the sharpness of the transition characteristics when the ratio of the core length to the core width is large. © 1998 American Institute of Physics. [S0021-8979(98)16211-4]

I. INTRODUCTION

Power systems especially in city centers are becoming increasingly interconnected in an effort to increase the reliability of the electric supply. This increasing interconnectivity results in raised short circuit levels, which traditional circuit breakers are straining to limit. A number of current limiting approaches such as tuned impedances, switched impedances, superconductors, series arc devices, and thermistorlike devices have been proposed in the past to address this problem.^{1,2} Unfortunately, these approaches all have reliability problems. Recently, a passive current limiting device consisting of three magnetic materials was proposed.³ The device should be reliable but would be expensive to produce. Two of these devices connected in series and in magnetic opposition to each other would provide bipolar current limiting.

This paper proposes two simplified structures, which address the concern over cost. The inductance versus current characteristic of each device is investigated. Finally, the optimal two-material and three-material device designs are compared.

II. SIMPLIFIED CURRENT LIMITER CONFIGURATIONS

The structure shown in Fig. 1(a) consists of a NdFeB permanent magnet sandwiched between the central pole faces of two high permeability, high saturation, flux density grain oriented *E* cores. The enlarged core section on either

side of the magnet is designed to confine the magnet's flux to the central core area. Most of this core section can be designed to operate out of saturation by choosing its height to be greater than a specified minimum value. The core sections with the reduced area have a coil wrapped around them. Core saturation exists when no coil current is applied. An unsaturated condition occurs if the coil current exceeds a critical value.

The second structure shown in Fig. 1(b) consists of two high permeability, high saturation, flux density *C* cores placed pole to pole. An additional structure consisting of an extended NdFeB permanent magnet sandwiched between two equally sized blocks of low saturation, flux density moderate permeability materials is centrally placed between the two *C* cores and has a coil wrapped around it.

III. DESIGN CRITERIA AND ASSUMPTIONS

The major design criteria for a current limiter are shown in Fig. 2. The objective is to maximize the ratio between the unsaturated (L_{unsat}) and saturated (L_{sat}) inductance subject to cost constraints, to extend the current range over which the unsaturated inductance value is maintained, and to maintain a uniform flux distribution in the saturated region. A uniform distribution provides a sharper transition region, at I_{knee} , between the saturated and unsaturated state.

The magnetic devices are assumed to be infinitely long in the *z* direction so as to allow a comparison between the two 2d devices and to minimize the effects of leakage flux in the *z* direction. The inductance versus current characteristics

^{a)}Electronic mail: dawson@ecf.utoronto.cu

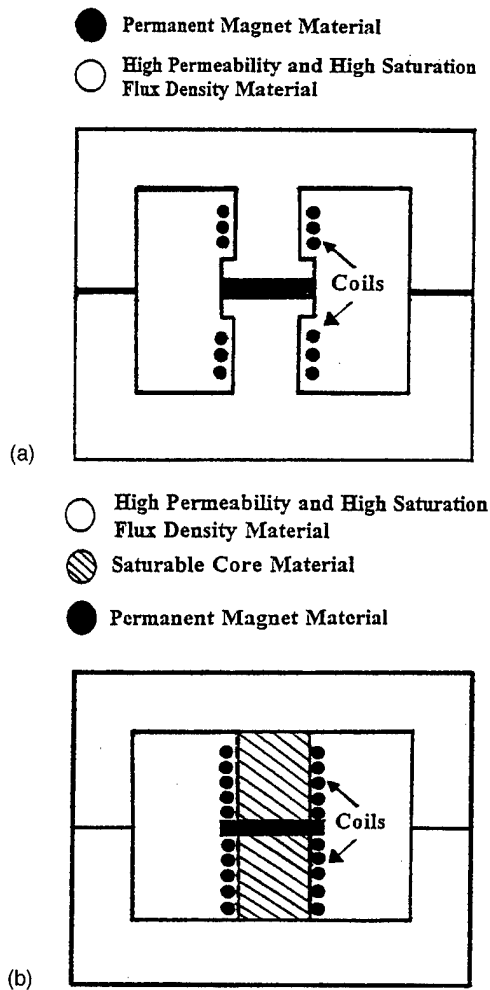


FIG. 1. Unipolar current limiters: (a) two material and (b) three material.

are obtained using Infolytica's MAGNET 5.2 finite-element analysis software package.

The two-material and three-material designs are based on the following specifications and the design equations.⁴ Functional: knee current $I_{knee}=50$ A, $I_{max}/I_{knee}=2.1$, $L_{unsat}=14$ mH, and number of turns $N=100$. Magnet parameters: remnant flux density $B_m=1.144$ T, recoil line slope $\mu_m=1.1$, and magnet length $l_{mag}=1$ cm. Central core parameters: $B_c^* A_{core}/A_{mag}=0.4$ T where B_c represents the saturation flux density of the saturable core material and A_{core} is the saturable core area. A_{mag} represents the magnet area for the two-material device and is equal to A_{core} for the three-material device. (Note: selecting a value higher/lower than

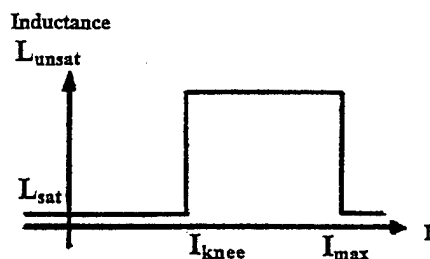


FIG. 2. Design criteria for a magnetic current limiter.

Core width = 16.5 cm Magnet width = 40 cm
 Region A, F TR66 $l_{core}=16.5$ cm
 Region B, G air; E (coil region) air
 U1 Rectangular focusing blocks: C,D are TR66.
 material $\mu=20,000$
 U2 Trapezoidal focusing blocks: C is TR66; D is air.
 U3 Rectangular focusing blocks: C,D are MU3 a linear core
 material $\mu=1000$.
 U4 Trapezoidal focusing blocks: C is MU3; D is air.
 U5 Rectangular focusing blocks: C,D are MU4 a linear core
 material $\mu=10,000$.
 U6 Trapezoidal focusing blocks: C is MU4; D is air.

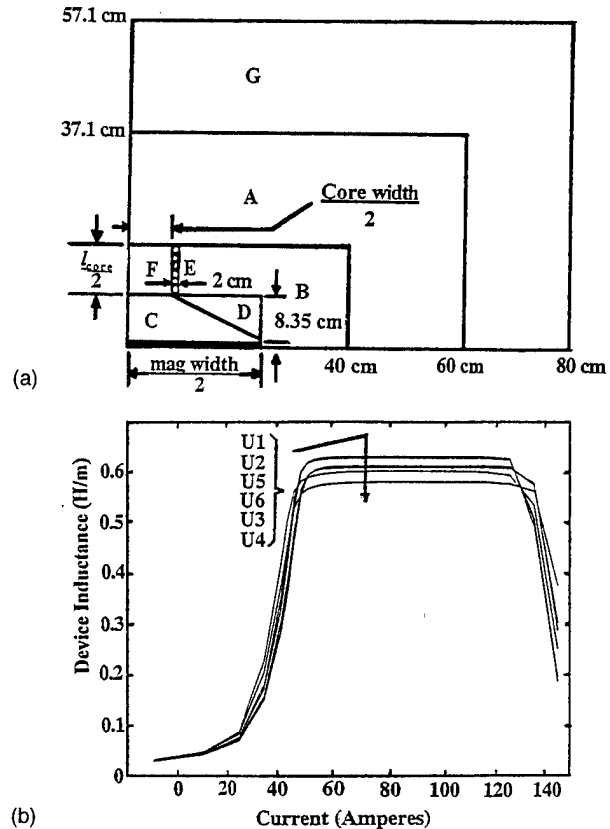


FIG. 3. Two-material current limiter; (a) geometry of one quarter of the device, and (b) inductance vs current characteristics.

0.4 T results in a higher/lower I_{max}/I_{knee} ratio but a larger/smaller magnet volume.) The choice of 0.4 T, approximately half of B_m , is a compromise. B_c for the two-material design is 1.77 T (i.e., TR66 core material). B_c for the three-material design is 0.4 T.

IV. SIMULATED INDUCTANCE VERSUS CURRENT CHARACTERISTICS

A. Two-material device

Figure 3(a) shows one quarter of the device and the tests which were performed. The purpose of these tests was to investigate the effect of the core pole face material and shape on the inductance versus current profile. Figure 3(b) shows the finite-element results for the inductance versus current characteristics. A larger leakage flux is observed with the higher permeability material, therefore, L_{unsat} is high. Tapering of the extended area section reduces the leakage flux, thus lowering the unsaturated inductance. Low permeability material does not contain the magnet flux very well. There-

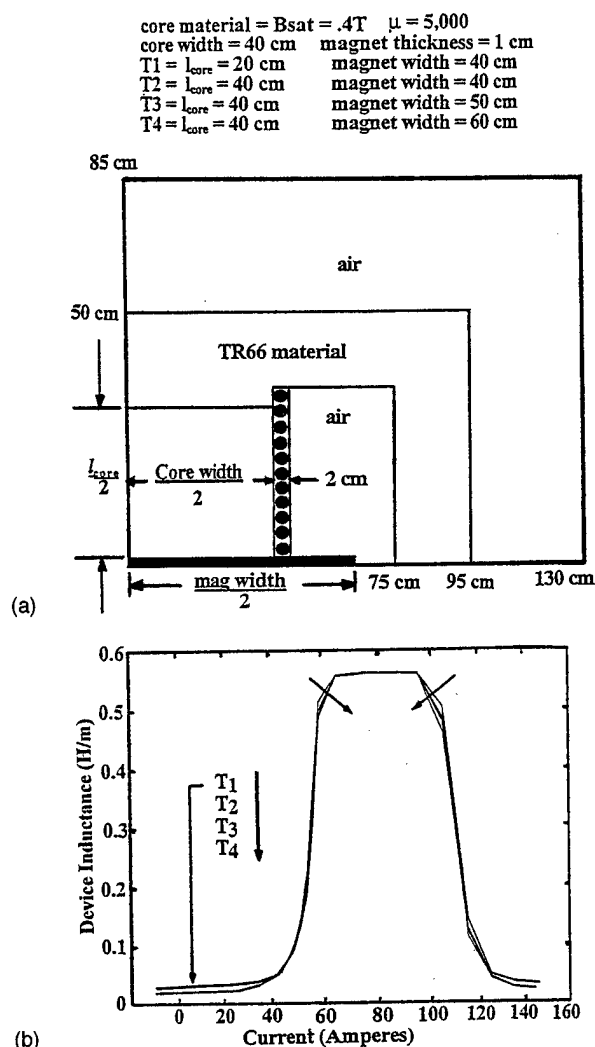


FIG. 4. Three-material current limiter: (a) geometry of one quarter of the device, and (b) inductance vs current characteristics.

fore, the saturated-to-unsaturated transition occurs at a lower knee current and is less well defined. The ratio $I_{\text{max}}/I_{\text{knee}}$ increases due to the reduced flux confinement.

B. Three-material device

Figure 4(a) shows one quarter of the device and the tests which were performed. The purpose of these tests was to determine the effect of the core length and magnet extension on the inductance versus current profile. Figure 4(b) shows the finite-element results for the inductance versus current characteristics. The core length influences only the saturated inductance value. The magnet extension improves the sharpness of the transition from the saturated to the unsaturated state, especially if the core length to core width ratio is large.

C. Comparison of the two-material and three-material current limiter

Both devices were designed according to the specifications in Sec. III and the stipulation that $L_{\text{unsat}}/L_{\text{sat}} = 40$. TR66 material is used for the E core on the two-material device. The extended area section is trapezoidal in shape so as to

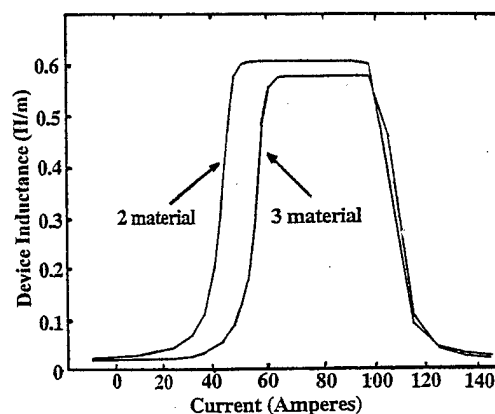


FIG. 5. Comparison of a two-material and three-material inductance vs current characteristics.

reduce the leakage inductance. This improves the sharpness of the transition at I_{knee} and increases the $L_{\text{unsat}}/L_{\text{sat}}$ ratio.

The width and thickness of the magnet in contact with the core material for both designs is 40 and 1 cm, respectively. In the three-material case, the magnet extends an additional 5 cm away from the outside surface of the core material. The core length and core width are 40 cm for the three-material device and 10 cm for the two-material device. The height of the extended area sections for the two-material device is 29 cm.

Figure 5 shows the inductance versus current characteristics for the two-material and three-material device. The results of the design equations for the three-material device are in agreement with finite-element results shown in Fig. 5. In contrast, the results of the design equations for the two-material device show that I_{knee} is overestimated, the ratio $I_{\text{max}}/I_{\text{knee}}$ is underestimated, and L_{unsat} is underestimated. Also, the transition characteristic for the two-material device is poorly defined. Thus, under normal ac operating conditions, the flux density in the core of the two-material device cycles between an unsaturated value and a saturated value. This results in a large minor hysteresis loop area, and consequently, high operating losses.

V. CONCLUSIONS

Finite-element results for the three-material current limiting device agree with the results obtained using design equations. In contrast, the results obtained for the two-material current limiting device show that the transition current is overestimated, and that the ratio of the maximum safe current, and the transition current, as well as the unsaturated inductance are underestimated. Extending the magnet beyond the adjoining surfaces improves the sharpness of the transition characteristics when the ratio of the core length to the core width is large.

¹E. Leung, IEEE Spectr., 26 (1997).

²R. A. Dougal, IEEE Trans. Power Electron 11, 304 (1996).

³S. Young, F. P. Dawson, and A. Kondrad, J. Appl. Phys. 76, 6871 (1994).

⁴S. Young, F. P. Dawson, S. Yamada, and M. Iwahara, IEEE Ind. Applic. Soc. 2, 1159 (1997).

Reversible and irreversible components of tensor magnetization and magnetostriction

F. Liorzou, Y. Yu, and D. L. Atherton^{a)}

Department of Physics, Queen's University, Kingston, Ontario K7L 3N6, Canada

Tensor magnetostriction and magnetization hysteresis loops for a 25 mm ferrite magnet cube were measured. These describe the magnetization properties and reflect the anisotropy of the system. The sample investigated allowed the magnetization to be interpreted in terms of a magnetization vector rotation process and described by the Stoner–Wohlfarth model. The reversible and irreversible components were extracted for both the magnetostriction and magnetization tensors. Up to now, very few direct measurements of these reversible changes in strain have been reported. The different magnitudes of reversible magnetization and magnetostriction are analyzed and explained qualitatively by a representation involving both magnetization and magnetostriction processes. The magnetostrictive effect is taken into account quite simply by considering a demagnetized sphere distorted into an ellipsoid of revolution when saturated. The ellipsoid will rotate as the magnetization vector according to the Stoner–Wohlfarth model. Two cases are illustrated depending on the easy axes location. These explain the experimental results obtained with the ferrite sample.

© 1998 American Institute of Physics. [S0021-8979(98)16311-9]

I. INTRODUCTION

Magnetostrictive effects in polycrystalline samples are closely associated with changes of magnetization, and depend on the direction of the bulk easy axis, on the magnetization mechanisms (domain wall motion, magnetization vector rotation), and also on the reversible or irreversible processes. Here the influence of some of those parameters is reported.

- (1) Nine element tensor magnetic hysteresis loops and magnetostriction loops were measured on a ferrite permanent magnet cube. Previous articles^{1–3} have already shown the significance of obtaining tensor measurements which also define the sample bulk easy axes.
- (2) Our specimen contains highly oriented fine Ba particles. The grain size is small enough to assume that the whole magnetization is provided by moment rotation.
- (3) Reversible magnetization and also magnetostriction were separated experimentally using incremental field reversals. The different magnitudes of the reversible magnetization and magnetostriction tensor elements are analyzed and explained qualitatively.

II. EXPERIMENTS

The sample investigated is an Indiana Indox 5 ferrite permanent magnet cube (25.5 mm size) with nominal composition $\text{BaO}_6\text{Fe}_2\text{O}_3$. The cube sample was placed between the closed pole pieces of a variable gap electromagnet. Three 20-turn flux coils, as well as a strain gauge, were installed on the cube to measure magnetization and magnetostriction, respectively (Fig. 1). This method ensures that the results are comparable. The experimental apparatus and measurement technique have been described previously.^{1–3} In order to es-

timate the contribution of reversible and irreversible processes, small field reversals of dH are made every three points while the magnetization and magnetostriction major loops are described. Those small incremental reversible changes are then summed to give the reversible component. This operation is very sensitive to noise and requires accurately measured experimental loops. The irreversible parts are then deduced by subtracting the reversible components from the total.

A. Magnetization, reversible, and irreversible components

Only the diagonal components of the magnetization tensor are reported presently (the off diagonal components are much smaller).³ Figure 2 shows the reversible and irreversible magnetization components. It has been shown previously^{1,3} that the tensor enables the sample's easy axis to be located close to the z axis (as represented schematically in Fig. 1). This gives rise to the measurement of a very square zZ magnetization loop with the largest irreversible process.

B. Magnetostriction, reversible, and irreversible components

Because dimensional change in one direction is accompanied by a comparable change in the transverse direction, the magnetostriction is also measured in the x , y , and z directions, for each direction of the applied field. The result is then presented in the form of a 3×3 matrix in Fig. 3, which represents the complete magnetostriction tensor. As mentioned previously, this sample, composed mainly of single domain grains, gives the magnetostriction component of rotational magnetization.

Separation of reversible and irreversible magnetostriction components has been achieved by the method described above. This is depicted in Fig. 4.

^{a)}Electronic mail: Atherton@physics.queensu.ca

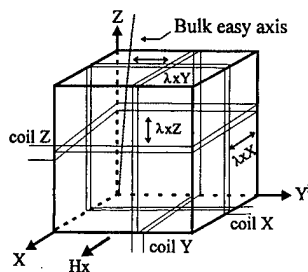


FIG. 1. Schematic showing 25 mm ferrite cube and associated X , Y , and Z coordinate system. For field applied in the x direction, λ_{xX} , λ_{xY} , and λ_{xZ} represent the three components of magnetostriction. The coils X , Y , and Z allow measurement of magnetization in each direction.

The tensor magnetostriction loops also reflect dependence on the easy axis of the sample. In particular, the zZ element shows a sudden variation of magnetostriction at the coercive field, as evident in Fig. 4. This phenomenon is purely irreversible. This sudden irreversible rotation is also observed in the corresponding zZ element of magnetization. Such behavior is not observed in the other elements.

Generally speaking, one can note the high rate of reversible compared to irreversible events involved in magnetostriction. At first glance, this result is surprising in view of the corresponding reversible and irreversible magnetization rates.

III. INTERPRETATION

The classical model used to explain rotational magnetization is the Stoner–Wohlfarth model.⁴ This model states that, due to the anisotropy energy (here the magnetocrystalline energy), moment rotation under positive to negative field variations consists of reversible and irreversible portions. The latter corresponds to switching of magnetization due to the presence of metastable energy states. The sudden change of magnetostriction observed in the zZ element can then be interpreted as irreversible switching of moments, which is, again according to the model, particularly significant when the applied field and easy axes directions are close to each other. So this confirms the correctness of the sample's bulk easy axis direction determined elsewhere.

It was noted that reversible magnetostriction comprises the main magnetostriction component. Irreversible switching of moments does not provide such a high rate of magnetostriction as magnetization. This feature can be interpreted as follows: Assume that under the action of the magnetostric-

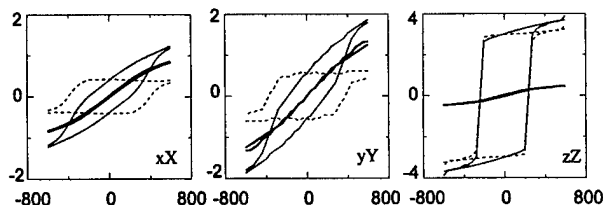


FIG. 2. Total, reversible (thick line) and irreversible (dotted line) component of tensor magnetization diagonal elements. The field is applied respectively in the three orthogonal directions (x, y, z). The horizontal axis is the magnetic field in kA/m, the vertical axis the magnetization in A/m (10^{-5}).

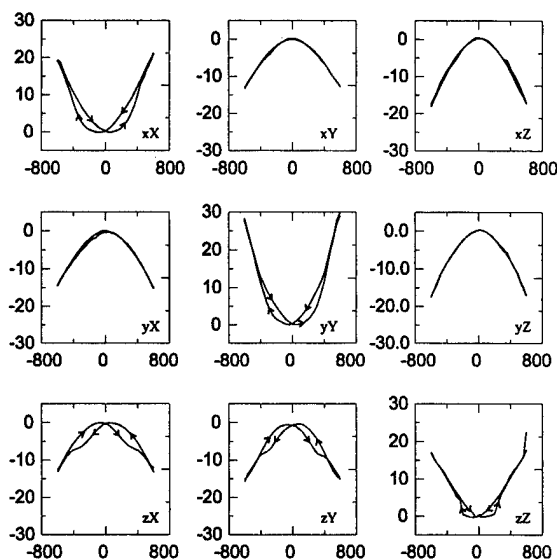


FIG. 3. Measured tensor magnetostriction for the Indox 5 cube. Labels xX , xY , and xZ represent magnetostriction components measured along the x , y , and z directions with magnetic field in the x direction, and so on. In each figure, the horizontal axis is the magnetic field in kA/m and the vertical the magnetostriction in microstrain (10^{-6}).

tive effect, the particles that compose the sample spherical in shape when demagnetized, become elongated in the direction of magnetization after magnetization. The ellipse so defined rotates according to the angle between the magnetization and the varying applied field. The magnetostriction is then deduced by calculating the change of length in a specific direction.

Two completely different cases are examined corresponding to the experimental situation:

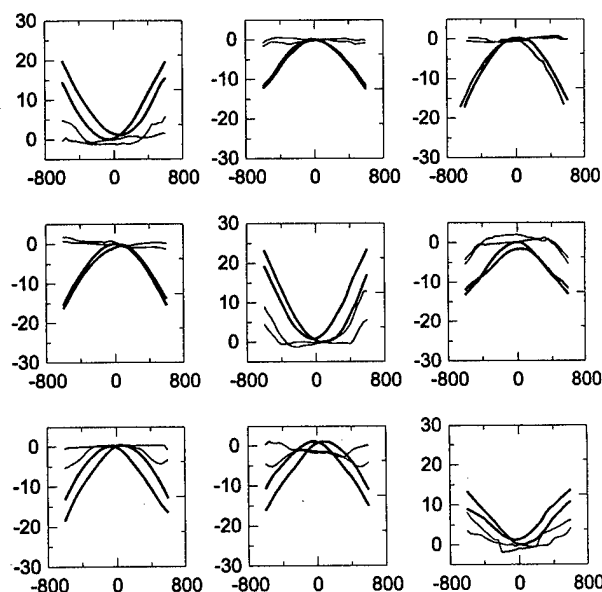


FIG. 4. Reversible (thick line) and irreversible (thin line) component of tensor magnetostriction elements. In each figure, the horizontal axis is the magnetic field in kA/m and the vertical axis is the magnetostriction in microstrain (10^{-6}).

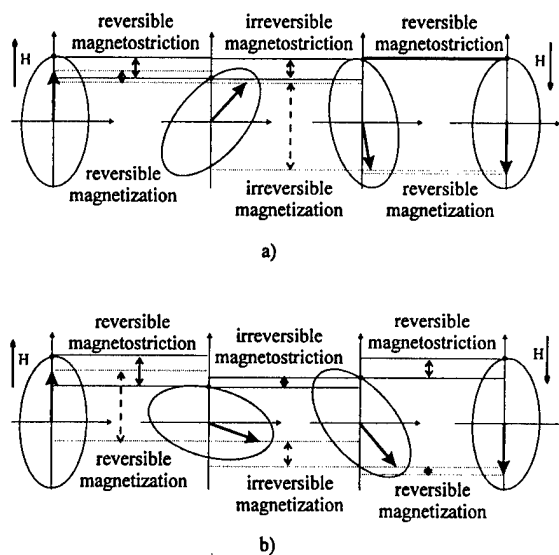


FIG. 5. (a) Magnetization and magnetostriction processes when the easy axis is close to the field direction. The magnetostrictive effect is illustrated simply by considering a demagnetized sphere distorted into an ellipsoid when saturated. The ellipsoid will rotate as the magnetization vector (symbolized by an arrow). (b) Magnetization and magnetostriction processes when the easy axis is nearly perpendicular to the field direction.

- (1) when the easy axis is close to the field direction (i.e., in the z direction in the ferrite sample);
- (2) when the easy axis is nearly perpendicular to the magnetic field direction (i.e., in the x or y direction).

Let us first examine the first case [Fig. 5(a)]. Depending on the magnitude of the field (positive to negative values), different stages of the magnetization process provided by the Stoner–Wohlfarth model are shown. The arrows indicate the magnetization direction calculated by the model while the ellipse represents the magnetostrictive effect hypothesized to elongate the spherical particle in the direction of magnetization (the actual elongation is proportionally much smaller than represented). The figure shows clearly the different rates of both reversible and irreversible magnetostriction and magnetization events. A gradual reversible rotation of the mo-

ment takes place first and, at a certain critical field, an irreversible jump occurs. This discontinuity is observed clearly in the zZ element of magnetization and in smaller amount in the zZ element of magnetostriction. So, during the process (which describes a half loop), the magnetostriction shows a comparable rate of reversible and irreversible events, while the irreversible rate of magnetization is much higher than the reversible one. These features are observed in the experimental data for this situation (all the labelled z elements of magnetostriction and magnetization).

In the case where the easy axis is nearly perpendicular to the field direction, illustrated in Fig. 5(b), the irreversible magnetostriction becomes very small. For the magnetization, the reversible events also become dominant, the irreversible part, however, is still present. Again, the experimental loops show this behavior (the labelled x , and y subfigures in the magnetostriction tensor and the x and y magnetization loops).

IV. CONCLUSION

Both tensor magnetization and magnetostriction have been measured in a ferrite cube sample. The magnetization mechanism is a Stoner–Wohlfarth type vector rotation.

Reversible and irreversible components of magnetization and magnetostriction have been extracted. The different magnitudes of these components have been analyzed and explained qualitatively by a representation involving both magnetization and magnetostriction processes. The rotating ellipse, used to represent the magnetostrictive effect in a particle during magnetization, seems to be appropriate and helpful for interpreting the experimental results.

ACKNOWLEDGMENT

Research supported by Natural Sciences and Engineering Research Council of Canada.

¹Y. Yu, T. W. Krause, P. Weyman, and D. L. Atherton, *J. Magn. Magn. Mater.* **169**, 207 (1997).

²Y. Yu, L. Clapham, D. L. Atherton, and T. W. Krause, *J. Magn. Magn. Mater.* (in press).

³Y. Yu and D. L. Atherton, *J. Magn. Magn. Mater.* **169**, 199 (1997).

⁴E. C. Stoner and E. P. Wohlfarth, *IEEE Trans. Magn.* **27**, 3475 (1948).

Fundamental study for rosary-shaped magnetic actuators

H. Saotome^{a)} and K. Sakaguchi

Faculty of Engineering, Chiba University, Inage, Chiba 263, Japan

Rosary-shaped magnetic actuators are proposed. The actuators consist of multiple permanent magnet cubes connected in a queue or in a circle. By applying the magnetic field to the magnet cubes, the actuators are supposed to move in liquid and convey medicine in a human body. For the first stage, this article shows the fundamental analysis and experimental results of controlling one-magnet motions. We studied motions of a magnet of two poles, put in water, where the magnet was equipped with a float. The floating magnet was column shaped with a 10 mm diam and 6 mm height. We have succeeded in independently fixing the position and angle of the magnet by controlling the currents flowing in two separate coils. © 1998 American Institute of Physics. [S0021-8979(98)16411-3]

I. INTRODUCTION

Magnets made of Nd-Fe-B material have a large energy product. With the development of these strong magnets, various types of magnetic actuators can be produced. We propose magnetic actuators with magnet cubes connected in a queue or in a circle, as shown in Fig. 1. The actuators are driven by the controlled magnetic field. The size of each magnet element can be reduced to millimeter range and more, therefore, it is possible that the actuators may work in a human body, such as in the digestive and circulatory systems. The driving field is generated by the coil currents outside the body.

In order to realize the actuators in Fig. 1, for the first step, we studied how to control the position and angle of one magnet by the currents flowing in two separate coils. Its method and experimental results are shown in this article.

II. MOTION OF A MAGNET

A. Position and angle fixation

Assuming a magnet whose magnetic moment is \mathbf{M} , the force \mathbf{F} and the torque \mathbf{T} of the magnet, generated by the magnetic field \mathbf{H} , are given by

$$\mathbf{F} = (\mathbf{M} \cdot \text{grad}) \mathbf{H} \quad (1)$$

and

$$\mathbf{T} = \mathbf{M} \times \mathbf{H}, \quad (2)$$

respectively.^{1,2} The magnet moves toward the position where the magnetic field is maximum and faces the direction of the magnetic field. The torque is proportional to the magnetic field while the force is proportional to its gradient. From Eqs. (1) and (2) it is found that the force and torque on the magnet can be independently controlled by the magnetic field distribution around the magnet.

We assumed x - y coordinates and put a magnet on the x axis, as shown in Fig. 2. The magnetic field is generated by two separate coils shown in Fig. 3. Figure 4 shows calculated magnetic field distributions on the x axis, given by control-

ling the currents I_1 and I_2 of the coils. The values of the currents are shown by $[I_1, I_2]$ in Fig. 4. The depicted magnetic field $H(x)$ is of the x direction and calculated by

$$H(x) = \frac{nI_1 a^2}{2\{a^2 + (x+d)^2\}^{3/2}} + \frac{nI_2 a^2}{2\{a^2 + (x-d)^2\}^{3/2}}, \quad (3)$$

where n is the number of turns of the coils.

Because the angle (θ) of the magnet with respect to the x axis is not controlled by $H(x)$ only, we used the geomagnetic field as the field of the y direction, i.e., $H(x)$ is perpendicular to the geomagnetic field H_g , which is uniformly distributed in the space around the magnet. As a result, θ is determined by

$$\theta = \tan^{-1} \left\{ \frac{H_g}{H(x)} \right\}, \quad (4)$$

i.e., the fixation of θ is carried out by controlling the magnitude of $H(x)$. On the other hand, the force of the x direction is given by

$$F = M \cos \theta \frac{\partial H(x)}{\partial x}. \quad (5)$$

By the force, the magnet moves to the position where

$$\frac{\partial H(x)}{\partial x} = 0. \quad (6)$$

From Eqs. (4), (5), and (6), it is found that the position and angle of the magnet can be controlled by the $H(x)$ distribution, which is generated by I_1 and I_2 .

When we want to carry out the fixation of the position and angle of the magnet, the values of I_1 and I_2 , corresponding to the goal, are not analytically obtained with Eqs. (3), (4), and (6). However, it is observed from Fig. 4 that the peak position of the magnetic field is approximately determined by the ratio

$$r = \frac{I_1}{I_1 + I_2}, \quad (7)$$

^{a)}Electronic mail: saotome@cute.te.chiba-u.ac.jp

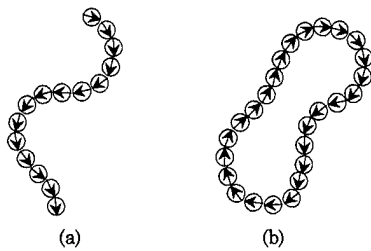


FIG. 1. Proposed magnetic actuators. (a) Queue-shaped type and (b) circular type.

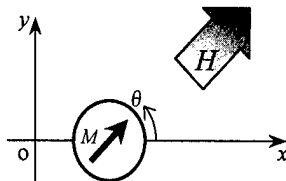


FIG. 2. A magnet put on the x - y coordinates.

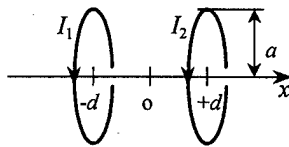


FIG. 3. Two separate coils for generating magnetic field distribution.

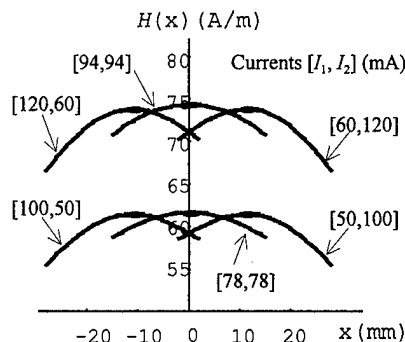


FIG. 4. Calculated magnetic field distributions on the x axis. The number of turns of the coils, $n=50$ (turns), the radius of the coils, $a=53$ (mm), and the distance between the coils, $d=19$ (mm).

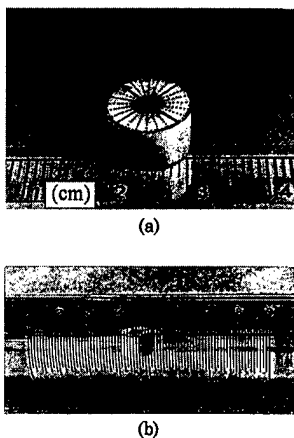


FIG. 5. (a) A floating magnet of two poles. (b) The magnet is put in a pipe and floating on water.

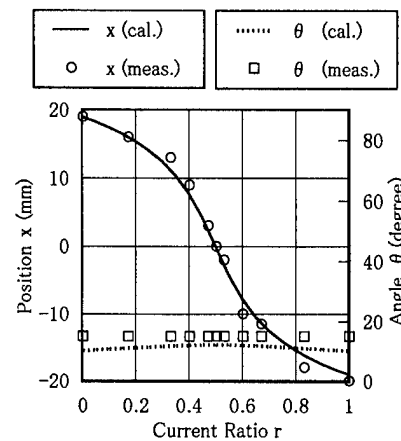


FIG. 6. Position control by the current ratio.

and the magnitude of the magnetic field is proportional to the total current

$$I_t = I_1 + I_2. \quad (8)$$

This result implies that we can control x and θ by r and I_t , respectively.

B. Implementation

In order to demonstrate the control of the position and angle by experiments, a magnet of two poles, equipped with a float, was made, as shown in Fig. 5(a). The magnet is column shaped with a 10 mm diam and 6 mm height. The magnet is put in a transparent pipe and floating on water, as shown in Fig. 5(b). The pipe is put in perpendicular to the geomagnetic field, i.e., it is set on the x axis in Fig. 3. We made the radius of the coils, $a=53$ (mm), and the distance of the coils, $2d=38$ (mm).

Figure 6 shows the calculated and experimental results of x and θ when the current ratio r has been changed and the total current is kept at $I_t=300$ (mA). The calculated and experimental results almost coincide with each other. It is also found from Fig. 6 that the position x has been controlled by the current ratio r , while the angle θ is almost kept at a constant value.

Figure 7 shows the calculated and experimental results of x and θ when the total current I_t has been changed and the

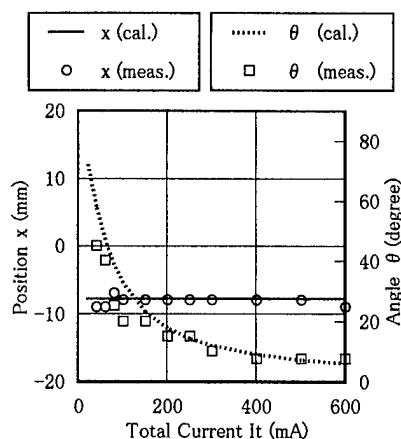


FIG. 7. Angle control by the total current.

current ratio is kept at $r=0.6$. The calculated and experimental results almost coincide with each other. It is also found from Fig. 7 that the angle θ has been controlled by the total current I_t , while the position x is almost kept at a constant value.

III. CONCLUSION

As shown above, we have succeeded in independently controlling the position and the angle of a two-pole magnet

by the current ratio and the total current of two separate coils, respectively. This technique will be the basis of controlling the proposed actuators in Fig. 1.

¹K. Ohta, *Zikikougaku no kiso I* (Kyoritsu, Tokyo, 1973), Chap. 1, in Japanese.

²M. Matsumoto, *Denzikigaku* (Kyoritsu, Tokyo, 1985), Chap. 12, in Japanese.

The design and analysis of axial field multipole impulse magnetizing fixtures

C. D. Riley

Magnetic Systems Technology Ltd., Sheffield Technology Park, 60 Shirland Lane, Sheffield, S9 3SP United Kingdom

G. W. Jewell and D. Howe

Department of Electronic and Electrical Engineering, The University of Sheffield, Mappin St. Sheffield, S1 3JD United Kingdom

A methodology for the design of fixtures for the multipole magnetization of axially magnetized permanent magnet rings is presented. The methodology, which is based on three-dimensional analytical field calculation techniques, embraces the calculation of the fixture electrical parameters, the electrical simulation of the fixture performance and the calculation of the level of saturation achieved in the permanent magnet. The methodology is validated by means of an experimental case study on a 6 pole isotropic NdFeB magnet ring. © 1998 American Institute of Physics. [S0021-8979(98)36211-8]

INTRODUCTION

Axially magnetized multipole permanent magnet rings are widely used in devices such as axial-field machines for radiator cooling fans, electric wheel chair motors, office equipment and automotive electric window mechanisms.^{1,2} This paper addresses a key stage during the device manufacture, viz. the multipole magnetization of the magnet ring by means of capacitor discharge impulse magnetization. Schematics of the typical forms of single and double sided, axial field multipole magnetizing fixtures are shown in Fig. 1. Two-dimensional magnetic field calculation techniques have been employed in the design of axial field multipole magnetizing fixtures with some degree of success by a number of authors.^{3,4} However, in many cases, particularly those involving magnet rings with a relatively large ratio of outer to inner diameter, and fixtures in which the end-windings are located in close proximity to the outer edge of the magnet ring, recourse to three-dimensional analysis is necessary.

The design methodology presented in this paper is applicable to a wide range isotropic and anisotropic permanent magnet materials. However, the focus in this paper is on isotropic NdFeB bonded magnets since they are particularly difficult to multipole magnetize, both in terms of the high magnetizing field strengths required to ensure saturation (typically 2500 kA/m), and the isotropic behavior which dictates that the magnetizing field distribution must conform to the desired orientation of the final remanent magnetization.

DESIGN METHODOLOGY

The design methodology is based on a scanning approach in which the relative merits of a large number of candidate fixture designs are compared. A given axial field fixture/magnetizer system can be fully described by a relatively small number of parameters, viz. the basic topology (i.e., single or double sided), the number of conductors per pole, the arrangement of the conductors at each pole, the conductor diameter, the radial overhang of the conductors, and the magnetizer capacitance and

initial voltage. The performance of a particular combination of parameters is predicted in a number of stages:

- (i) Calculation of fixture inductance and initial resistance.
- (ii) Calculation of the peak current and temperature rise during the impulse period.
- (iii) Calculation of the localized magnetizing field at a number of points within the magnet volume.
- (iv) Calculation of the level of saturation and degree of alignment achieved in the magnet.

The cornerstone of the design methodology is the calculation of the three-dimensional magnetizing field distribution produced by a given design of magnetizing fixture. This is the basis for determining both the fixture inductance and the level of saturation achieved in the magnet. An analytical field calculation technique is employed, since air-cored magnetizing fixtures generally represent a good approximation to a linear problem domain.⁴ The field calculation technique is based on the superposition of the field produced by the individual straight and curved conductors segments from which a multipole fixture is composed. The coordinate systems used in the calculation of the flux density at a general point P due to straight conductors and arc segments are shown in

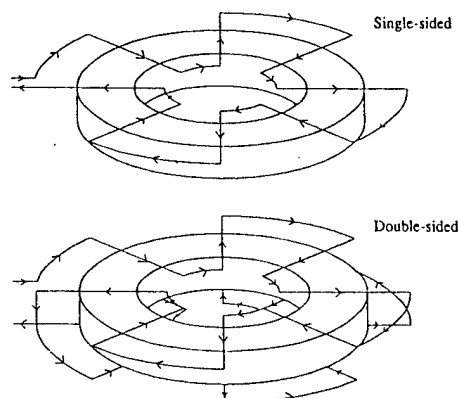


FIG. 1. Schematic representations of single and double-sided axial field multipole magnetizing fixtures.

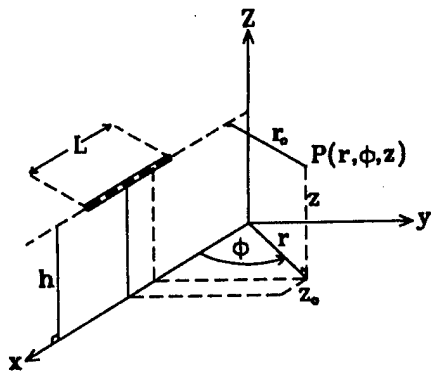


FIG. 2. Three-dimensional coordinate system for the calculation of flux density at the general point P due to a finite length straight conductor.

Figs. 2 and 3, respectively. The components of flux density produced by the conductor segments at the general point P when carrying a current I , are given by Eqs. (1) and (2), respectively,

$$\begin{aligned} B_r &= B_m \frac{(h-z)}{r_0} \sin \phi, \\ B_\phi &= B_m \frac{(h-z)}{r_0} \cos \phi, \\ B_z &= B_m \frac{r \sin \phi}{r_0}, \end{aligned} \quad (1)$$

where

$$\begin{aligned} B_m &= \frac{\mu_0 I}{4\pi r_0} \left[\frac{(z_0 + (L/2))}{[r_0^2 + (z_0 + (L/2))^2]^{1/2}} - \frac{(z_0 - (L/2))}{[r_0^2 + (z_0 - (L/2))^2]^{1/2}} \right], \\ B_r &= \frac{\mu_0 I a z}{4\pi} \int_{\Psi_1}^{\Psi_2} \frac{\cos(\Psi - \phi)}{\bar{R}^3} d\Psi, \\ B_\phi &= \frac{\mu_0 I a z}{4\pi} \int_{\Psi_1}^{\Psi_2} \frac{\sin(\Psi - \phi)}{\bar{R}^3} d\Psi, \\ B_z &= \frac{\mu_0 I a}{4\pi} \int_{\Psi_1}^{\Psi_2} \frac{a - r \cos(\Psi - \phi)}{\bar{R}^3} d\Psi, \end{aligned} \quad (2)$$

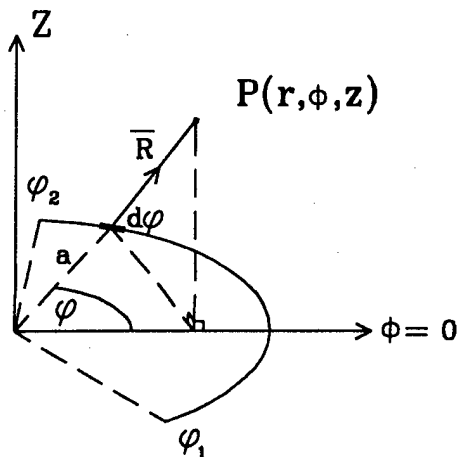


FIG. 3. Three-dimensional coordinate system for the calculation of flux density at the general point P due to a finite length arc segment conductor.

where

$$\bar{R} = [a^2 + r^2 + z^2 - 2ar \cos(\Psi - \phi)]^{1/2}.$$

The integral terms in each of the above expressions are evaluated numerically by means of a second order integration. The net resultant field at a given point can be calculated by a summation of the contributions of each elemental conductor, with due account of the individual current polarities.

The overall fixture inductance is calculated from a summation of the flux linkage of each winding layer. This in turn, is evaluated by integrating the analytically calculated axial component of flux density over at a number of discrete points on a surface which covers one pole and is located at the same axial position as the winding layer under consideration. To ensure that an adequate number of discrete points are used, an algorithm is employed which automatically increases the number of summation points until the fractional change in the predicted value of inductance falls below a prespecified tolerance. The fixture resistance is given by

$$R_{\text{fix}} = \frac{\left[\sum_{j=1}^N p \left(2l_{rj} + \frac{2\pi}{p} (r_{oj} + r_{ij}) \right) \right] \rho_{\text{Cu}}}{A_c},$$

where N =number of coils per pole, p =number of poles, l_{rj} =length of radial conductors, r_{ij}, r_{oj} =inner, outer end-winding radii, A_c =cross sectional area of conductor, ρ_{Cu} =electrical resistivity of copper.

The peak current and temperature rise of a given fixture/magnetizer combination is predicted by an electrical simulation previously developed for the design and analysis of multipole radial magnetizing fixtures, in which due account is taken of the change in fixture resistance caused by heating during the impulse period.³

The three-dimensional analytical field calculation technique can be used to determine the magnitude and orientation of the applied magnetizing field strength at a large number of points within the magnet. Whereas neglecting the nonlinearity in calculating the level of applied field is valid in a large number of cases, due account of the self-demagnetizing effect must be taken in calculating the net magnetizing field strength to which a region of the magnet is exposed. This is achieved by using an established technique previously proposed by the authors.³

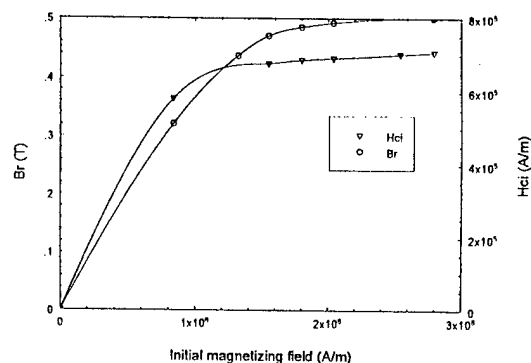


FIG. 4. Measured dependency of the remanence and intrinsic coercivity of Plastiform 2004D isotropic NdFeB on the magnitude of the initial magnetizing field strength.

TABLE I. Fixture design parameters and measured performance.

Conductors per pole	6	Predicted time to peak	258 μ s
Conductor diameter	2.0 mm	Measured peak current	23.6 kA
Capacitor voltage	2.8 kV	Measured time to peak	255 μ s
Volume saturation	97.2%	Predicted resistance	34.1 m Ω
Orientation	97.3%	Predicted inductance	15.4 μ H
Temperature	135 $^{\circ}$ C	Measured resistance	36.0 m Ω
Predicted peak current	23.1 kA	Measured inductance (at 1 kHz)	14.8 μ H

Having established the distribution and orientation of the localized net magnetizing field, the level of saturation can be calculated from material characteristics such as those in Fig. 4 which shows the measured dependency of the remanence and intrinsic coercivity on the magnitude of the magnetizing field strength. A useful global figure of merit for comparing different fixture designs is the percentage volume saturation, which is defined as the integral over the magnet volume of the products of the remanence and coercivity achieved at each discrete point as a percentage of the maximum obtainable values in a fully saturated magnet.⁵ In order to quantitatively compare the degree of axial orientation of the magnetization, a further figure of merit can be employed, viz. the percentage axial alignment, which is a weighted average of the degree of alignment at each discrete point.

CASE STUDY

In order to validate the various constituent calculation techniques, and to demonstrate the utility of the overall design methodology, a fixture to magnetize a 6-pole isotropic NdFeB magnet ring was designed and constructed. The magnet ring (inner diameter 40 mm, outer diameter 120 mm), comprised 5 layers of 1 mm thick Arnold Engineering Plastiform 2004D flexible bonded NdFeB sheet, the characteristics of which were shown previously in Fig. 4. The fixture was designed to operate with an existing 10 kJ capacitor discharge magnetizer (0–3 kV continuously variable, 0–2200 μ F in 445 μ F increments), with a rated maximum current of 45 000 A.

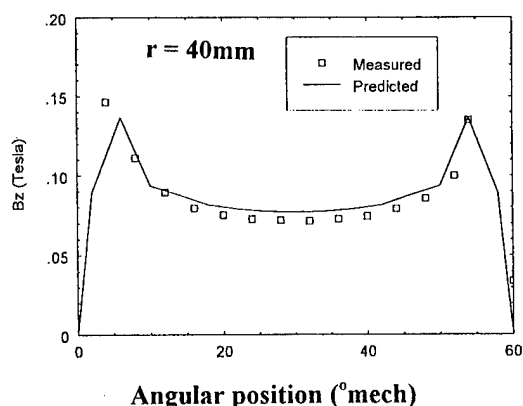


FIG. 5. Measured and predicted profiles of the normal component of flux density 0.5 mm above the magnet surface (circumferential profile at a radius of 40 mm).

In order to produce as near an ideal axial orientation of magnetization within the isotropic magnet ring, a double-sided fixture was selected since this topology of fixture inherently produces a better axially aligned magnetizing field than a single-sided fixture. An axial clearance of 1 mm was specified between the leading conductors and the surface of the magnet in order to provide sufficient containment for the winding, while a maximum conductor temperature of 200 $^{\circ}$ C (from a 20 $^{\circ}$ C starting ambient) was specified.

Following extensive scanning of the fixture parameters, the fixture design whose parameters are shown in Table I was identified as being the most suitable.

The measured inductance and resistance of the fixture were in good agreement with the predicted values, as shown in Table I.

Following the magnetization of the magnet ring, the normal component of flux density at a distance of 0.5 mm from the magnet surface was measured using a Hall effect gaussmeter equipped with a probe with an element of diameter 0.2 mm. In order to confirm that the measured flux density profiles correspond to a fully saturated magnet with the desired orientation, a three-dimensional magnetostatic finite element calculation of the field produced by an idealized magnet with same demagnetization characteristic was performed, i.e., a magnet which is fully saturated throughout its volume with an entirely axial direction of magnetization. The finite element calculation was performed using MEGA.⁶ Figure 5 shows the excellent correlation between the measured and predicted flux density along a circumferential profile spanning one pole at a radial distance of 40 mm from the center of the magnet ring. This demonstrates, that as predicted during the design synthesis, the selected fixture does indeed produce a very close approximation to a fully saturated, fully axially orientated 6 pole magnet ring. This demonstrates albeit on a rather large magnet ring, that by careful design of the fixture, the properties of a multipole magnetized ring can often show negligible departure from those which can be achieved with individually magnetized segments. However, it is likely that this departure from an idealized orientation will inevitably become more pronounced as the magnet size is reduced.

¹J. G. W. West, *Automotive and Aerospace Applications of NdFeB*, Proceedings Gorham/Intertech NdFeB 95 Conference, San Diego, California.

²P. Campbell, *Electrical Rev.* 8th March (1974).

³J. K. Lee and E. Furlani, *J. Appl. Phys.* **67**, 1570 (1990).

⁴G. W. Jewell, Ph.D. thesis, The University of Sheffield, 1992.

⁵G. W. Jewell, C. D. Riley, and D. Howe, *IEEE Trans. Magn.* **33**, 708 (1997).

⁶*MEGA Reference Manual* (The Applied Electromagnetics Research Centre, The University of Bath, UK).

Fabrication of a micromotor driven by electromagnetic vibration

T. Honda^{a)} and J. Yamasaki

Kyushu Institute of Technology, 1-1 Sensuichou, Tobata-ku, Kitakyushu 804, Japan

A new electromagnetic rotary mechanism utilizing a friction drive is proposed. An electromagnetic vibration excited on a permanent magnet is converted to a rotary movement through a frictional force. A trial motor, composed of a magnet rotor with inclined legs and an excitation coil, was fabricated and successfully operated. A no-load revolution speed up to 400 rpm and a reversible rotation were achieved. © 1998 American Institute of Physics. [S0021-8979(98)49311-3]

I. INTRODUCTION

During the last decade there has been much work towards realizing micromotors for the microelectromechanical systems. Most of these efforts focused mainly on electrostatic side-drive micromotors and variable reluctance magnetic ones, which, however, face a serious problem. Their very high revolution speed over 10^4 rpm and poor torque are unacceptable for practical applications.

To solve this problem and realize the practical micromotor, two rotary mechanisms with large torque at a low revolution speed have so far been proposed. One is a wobble mechanism,^{1,2} in which a cylinder rotor rolls inside a stator with either electrostatic or electromagnetic forces. The other is a friction drive mechanism, which converts a mechanical vibration to a rotary movement through a frictional force. Several kinds of ultrasonic micromotors based on a piezoelectric vibration have been proposed,^{3,4} but only a few attempts have been made at the other friction drive motors.

In this study, we proposed a new magnetic micromotor utilizing the friction drive mechanism, which can convert the electromagnetic vibration to the rotary movement. In this article, the structure, principle, and no-load characteristics of the trial motor are described.

II. DEVICE STRUCTURE

Figure 1(a) shows a side view of a trial-fabricated friction drive motor. It consists of a cylinder rotor, 5 mm in diameter and 3 mm in height, and a small solenoid coil. The rotor is a NdFeB magnet, magnetized along the height direction, and has four elastic legs on the base. The legs, made of a polyethylene terephthalate (PET) film with a thickness of 0.1 mm, are inclined at a certain angle, θ , arranged equally round the perimeter of the rotor base, as shown in Fig. 1(b). The size of the legs is 1.5 mm long and 1.25 mm wide. In this study, we examined two different inclined angles: $\theta = 50^\circ$ and 85° . The rotor is laid on a cover glass fixed on the end of the coil. In order to vibrate the rotor by using the attractive force, an ac current biased with a dc current is applied to the coil. The value of the dc current is the same as the amplitude of the ac current. Thus the rotor is magnetically fixed on the coil end without any external mechanical preload.

III. OPERATION PRINCIPLE

Let the z axis be the vertical direction in Fig. 1. The vertical force, F_z , acting on the magnet with magnetization, M_z , and volume, V , is given by

$$F_z = M_z \cdot \int dH_z/dz \cdot dV, \quad (1)$$

where H_z is the z component of the magnetic field produced by the solenoid coil. The attractive force by the sinusoidal current biased with the dc current can be represented by

$$F_z(t) = -F_0 z (1 + \sin 2\pi f t)/2, \quad (2)$$

where $F_0 z$ is the maximum attractive force in the z direction and f is the excitation frequency. Since the legs act as elastic springs, the rotor vibrates downward and upward according to the attractive force. At the same time an angular movement occurs due to the frictional force of the tip of the legs.

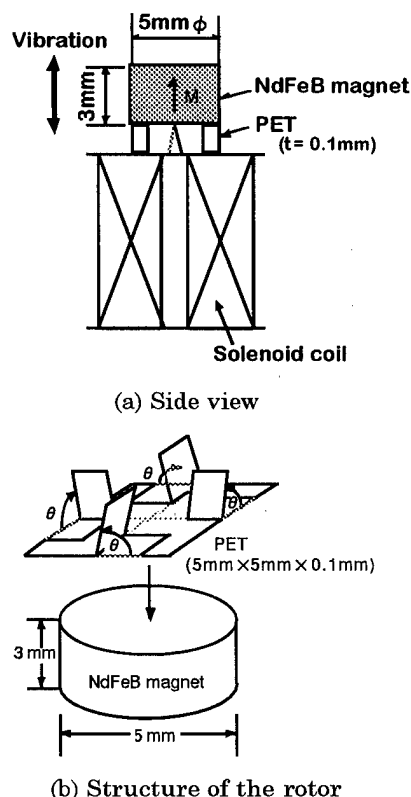


FIG. 1. Schematic view of the trial motor.

^{a)}Electronic mail: honda@mag.ele.kyutech.ac.jp

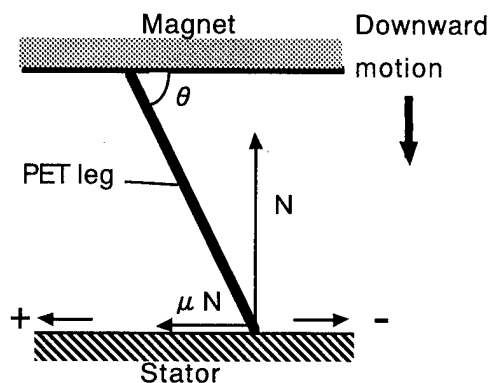


FIG. 2. Relation between the normal reaction and the frictional force.

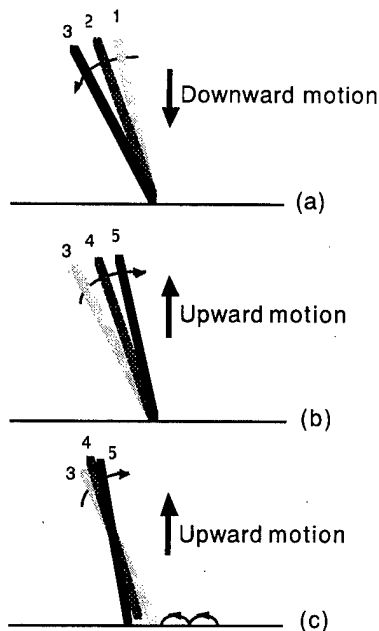
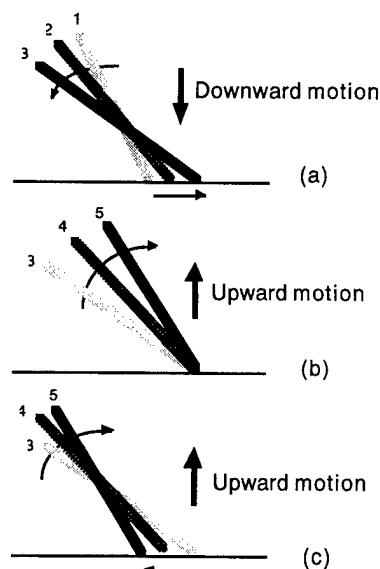
Before turning to a closer consideration about the angular movement, we must describe the sliding condition of the leg during the downward motion. Figure 2 shows the relation between the normal reaction, N , and the frictional force, μN , at the tip of the leg when the rotor starts displacing downward. Here μ is the frictional coefficient. Taking account of the moment equilibrium about the hinge, the following relation is found:

$$\theta = \tan^{-1}(1/\mu). \quad (3)$$

If $\theta \geq \tan^{-1}(1/\mu)$, the tip of the leg is self-locked and cannot slide during the downward motion. On the other hand, if $\theta < \tan^{-1}(1/\mu)$, the tip slides in the right-hand direction. In general, μ is 0.2–0.5 and, therefore, the angle that satisfies Eq. (3) may be 60° – 80° . We will consider the predicted behavior of the rotor in the following two cases.

A. $\theta \geq \tan^{-1}(1/\mu)$

Figure 3 illustrates the predicted behavior for $\theta \geq \tan^{-1}(1/\mu)$. At a low frequency range, the rotor vibrates

FIG. 3. Predicted behavior of the leg for $\theta \geq \tan^{-1}(1/\mu)$.FIG. 4. Predicted behavior of the leg for $\theta < \tan^{-1}(1/\mu)$.

around the contact point without sliding and remains at the original position, as shown in Figs. 3(a) and 3(b). At higher frequencies, however, the tip slides in the left-hand direction during the upward motion because the increase in the z component of the acceleration of the vibration decreases the normal reaction and hence reduces the frictional force. If the z component of the acceleration is larger than that of the gravity, the tip may take off from the stator and touch down to the left side, as shown in Fig. 3(c). Thus, the rotor moves in the left-hand direction at higher frequencies.

B. $\theta < \tan^{-1}(1/\mu)$

Figure 4 illustrates the predicted behavior for $\theta < \tan^{-1}(1/\mu)$. During the downward motion, the leg slides in the right-hand direction, as shown in Fig. 4(a). During the upward motion, on the other hand, two different behaviors are possible, depending on the frequency, as shown in Figs. 4(b) and 4(c). At a low frequency range, the tip is pushed against the stator and the rotor stands up around the tip without sliding. Thus the motor moves in the right-hand direction. At a high frequency range, the tip moves in the left-hand direction for the same reason as in Fig. 3(c). In this case, the rotational direction depends on the difference of the sliding distance between upward and downward motions.

IV. RESULTS AND DISCUSSION

In this study, we examined the no-load revolution speed when $F_0 z$ was approximately 120 mN. Figure 5 shows the revolution speed for $\theta = 50^\circ$ and 85° as a function of the excitation frequency. The sign of the revolution speed means the rotational direction, in case of a plus sign, rotates in the left-hand direction in Fig. 2.

First, we focus on the result for $\theta = 85^\circ$. The motor hardly rotated below 600 Hz though the slight rotation in the negative direction was observed around 200 Hz. The rotation in the positive direction suddenly occurred at 600 Hz and

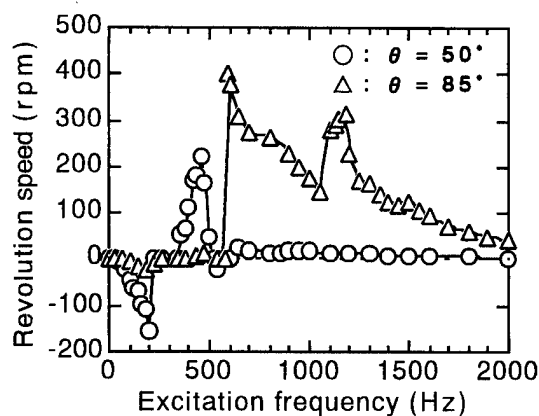


FIG. 5. Revolution speed as a function of the excitation frequency.

reached a peak of 400 rpm at the same time. This sudden rotation was caused by the mechanical resonance in the z direction. Afterwards the revolution speed decreased with increasing the frequency and then exhibited a second peak around 1.2 kHz, which may be due to the resonance in the angular direction.

On the other hand, the result for $\theta = 50^\circ$ showed a reversible rotation. At lower frequencies below 200 Hz, the motor rotated in the negative direction, as expected, and the revolution speed increased with increasing the frequency. The maximum revolution speed of 160 rpm was obtained at 200 Hz. But the rotation stopped at the range 200–300 Hz because the amplitude of the vibration in the z direction was too large to rotate stably. Afterwards, the rotational direction

changed to the positive direction with the increasing the frequency and reached a peak of 230 rpm at 480 Hz. The rotation in the positive direction at higher frequencies suggests that the sliding distance is larger during the upward motion than during the downward motion.

Finally, we must remark on the torque of the motor. The torque measured was only the order of 10^{-5} Nm. Of course, the torque can be improved by increasing the electromagnetic attractive force. One promising method would be to insert the core into the driving coil. This point is currently under investigation.

V. CONCLUSIONS

We have proposed a new type of rotary micromechanism which can convert the electromagnetic vibration to the rotary movement through the frictional force of the inclined legs. The trial motor based on this mechanism successfully rotated and exhibited unique characteristics depending on the inclined angle of the legs. The unique characteristics obtained suggest that the mechanism is useful as a driving principle of a micromotor.

¹S. C. Jacobsen, R. H. Price, J. E. Wood, T. H. Rytting, and M. Rafaelef, *Sens. Actuators* **20**, 1 (1989).

²W. Trimmer and R. Jebens, *Sens. Actuators* **20**, 17 (1989).

³K. R. Udayakumar, S. F. Bart, A. M. Flynn, J. Chen, L. S. Tavrow, L. E. Cross, R. A. Brooks, and D. J. Ehrlich, *Proc. IEEE MEMS'91 Workshop*, 109 (1991).

⁴T. Uchiki, T. Nakazawa, K. Nakamura, M. Kurosawa, and S. Ueha, *Jpn. J. Appl. Phys.* **30**, 2289 (1991).

New permanent magnet couplings for screwing devices

L. Quéllec, V. Lemarquand, and G. Lemarquand

Laboratoire d'Electrotechnique et de Magnétisme de Brest, IUT, Rue de Kergoat, 29287 Brest, France

The use of permanent magnet coaxial synchronous couplings in screwing devices allows one to adjust the screwing torque very precisely, but the symmetrical behavior of classical systems always leads to a partial unscrewing. This article shows that the dissymmetry of this behavior can be enhanced only by the modification of the shape of the magnets stuck on the rotors. The consideration of some basic geometrical parameters (number and length of poles) and the application of rules to reach the dissymmetry lead to improved couplings for screwing devices.

© 1998 American Institute of Physics. [S0021-8979(98)17011-1]

I. INTRODUCTION

The permanent magnet couplings¹ allow transmitting forces and torques without any contact between interacting parts. The use of distance attraction forces between magnets makes it possible to obtain total watertightness, by means of a nonmagnetic wall in the airgap between the rotors. The autonomy and the absence of servicing for these couplings also explain their use in high security and pumping devices, as well as in mixing devices in farm-produce or pharmaceutical industries. This article first studies classical permanent magnet coaxial synchronous couplings (Fig. 1) with jointive, identical in shape poles (jointive poles have radial sides in contact); manufactured magnets (called poles of the coupling), alternatively north (whose magnetization is oriented towards the airgap) and south magnetized, are stuck on the inside and outside magnetic rotors.

Section II of this article describes optimization^{2,3} of these structures. Section III deals with new coupling structures that are designed and optimized to solve some problems of screwing devices. It shows that the unscrewing that occurs after the synchronism is broken can be avoided by reshaping the magnets. All the calculations are done with a two-dimensional finite elements program⁴ (FLUX2D). The three-dimensional (3D) phenomena are avoided since all the couplings considered here are 1 m long; they also all have a 2 mm wide airgap and a 50 mm average radius in the airgap. The magnet material is $\text{Sm}_2\text{Co}_{17}$, which is defined with a remanence of 1 T and a magnetic permeability of 1. Its high coercive field (900 kA/m) allows regarding all sorts of magnet shapes with a very low risk of demagnetization.

II. OPTIMIZATION OF CLASSICAL COUPLINGS

The synchronous driving is created by a tangential attraction between opposite magnetized poles, due to the angular deviation between the driving and the driven rotor. The transmitted torque increases with the deviation up to a pull-out value, which is the maximum torque the coupling can transmit. Then, an additional angular deviation breaks the synchronism, and the rotors begin to slip. The knowledge and the control of this pull-out torque allow one to design precise screwing devices, since the screwing stops when this value of torque is reached.

A. Number of poles

At a given distance of a magnet, the level of magnetic induction depends on the outer surface of the magnet (Fig.

2). Moreover, the torque transmitted by a magnetic coupling quadratically depends on the average level of magnetic induction in the airgap. The study of the transmitted torque versus the number of pairs of poles shows that an optimum angular width of the magnets exists for an imposed width of airgap (Fig. 3), since the width of jointive poles is a direct function of the number of poles. This optimum is displaced in Fig. 3, to the left (respectively right) when the airgap is widened (respectively narrowed). For a very large number of poles, the dead zones (parts of magnets where the field lines directly close up on the neighbor pole) cover the whole magnets, and the pull-out torque value tends towards zero.

B. Length of magnets

Two face to face magnets in a coupling are submitted to a primary force due to the magnetic masses⁵ of their airgap surfaces and an opposite secondary force due to the interaction of their posterior face magnetic masses with the airgap face of the other magnet. The increase of their length L (Fig. 1) moves their posterior face away and reduces the strength of the secondary force. The total force is hence increased, and the pull-out torque tends towards an asymptotical value (Fig. 4). The induction level in the magnets, for systems whose length of magnets places them at the bending of the curve on Fig. 4 is the half of the remanent induction level. If the demagnetization characteristic is linear,² this implies that their magnets work at their highest level (point of $-BH_{\text{max}}$), which is of course economically favorable.

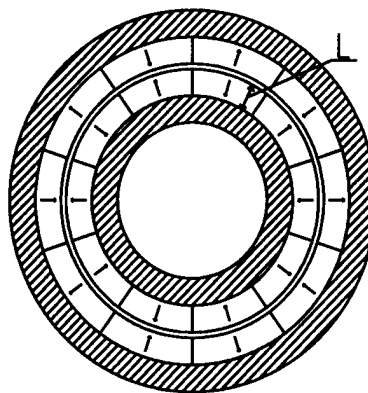


FIG. 1. Classical type of a permanent magnet coaxial synchronous coupling.

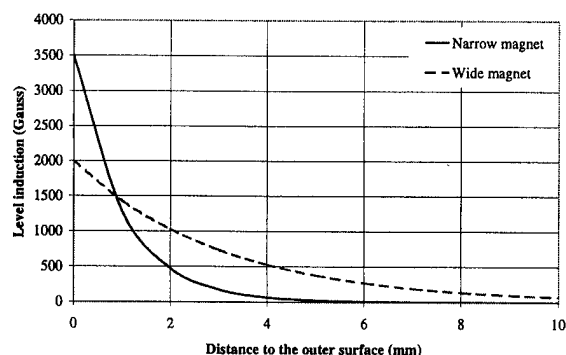


FIG. 2. Level of induction measured as a function of the distance to the surface, for a wide and a narrow magnet, which have the same length.

C. Conclusion

The goal of the maximum possible pull-out torque necessitates the optimization of both number of poles and length of magnets. This conclusion is subjected to a compromise according to economical criteria, since magnet materials and manufacturing are both expensive. It sometimes appears to be cheaper to add some length of magnets (if the system size allows it), instead of increasing the number of poles.

III. IMPROVEMENT OF COUPLINGS FOR SCREWING DEVICES

The curve linking the transmitted torque to the angular deviation between the rotors is sinusoidal for a classical type of permanent magnet coaxial synchronous couplings (Fig. 5). This symmetrical shape means that after the synchronous screwing—up to the pull-out torque—the lead rotor is submitted to an unscrewing torque that has the same value as the screwing one. The goal of this study is to modify the shape of the poles to reach systems whose torque-deviation curve is as dissymmetrical as possible: negative and positive maximum values of torque and angular ranges for screwing and unscrewing should be as different as possible.

A. Influence of the cyclic ratio

The decrease of the cyclic ratio (ratio of the angular width of the north-magnetized poles on the polar pitch, which is the angular size of two consecutive poles) implies narrower and more angularly spaced out peaks for the curve (Fig. 5). This type of coupling does not have the same angular stiffness depending on the direction of rotation: the slope of the curve is not the same whether it is considered on one side of a peak or on the other side.

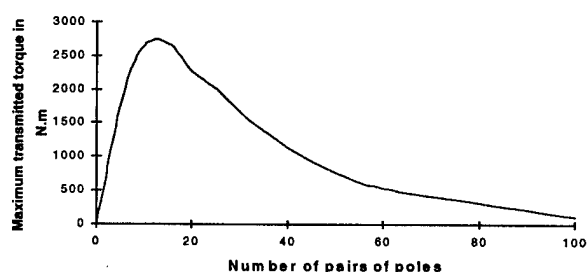


FIG. 3. Pull-out torque as a function of the number of pairs of poles.

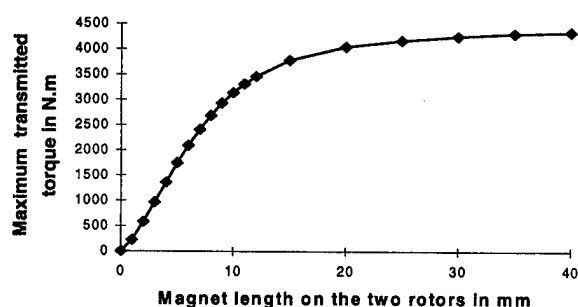


FIG. 4. Pull-out torque as a function of the length of magnets for a system fitted out with five pairs of poles.

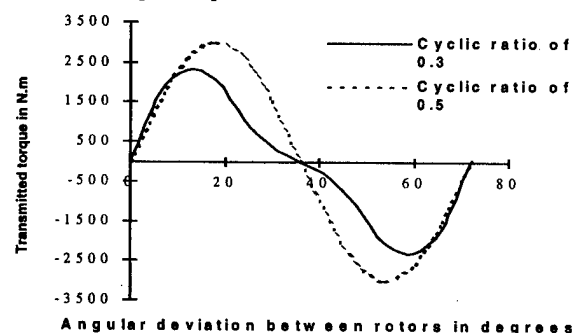


FIG. 5. Transmitted torque versus angular deviation of rotors for two cyclic ratios in the case of a five pairs of poles system.

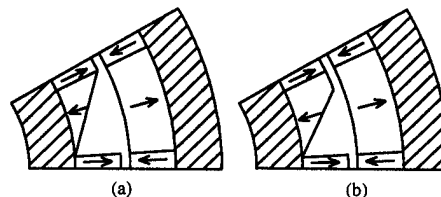


FIG. 6. Geometry of permanent magnet coupling with inclined plane (a) and inclined plane-plateau (b) south-magnetized poles on inside rotor.

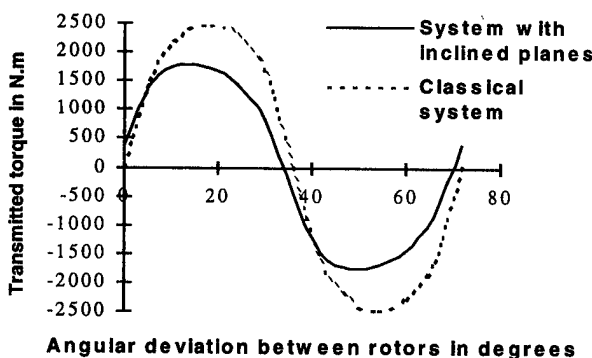


FIG. 7. Comparison of a classical system and a system with inclined planes poles, with five pairs of poles.

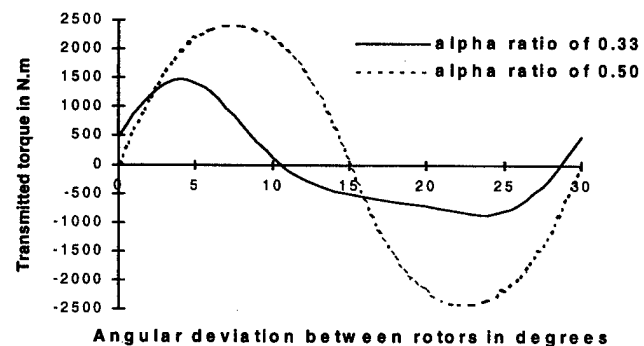


FIG. 8. Transmitted torque vs the deviation angle between rotors, for a plateau/pole ratio of 0.33 and a cyclic ratio of 0.25, compared to a classical system (12 pairs of poles).

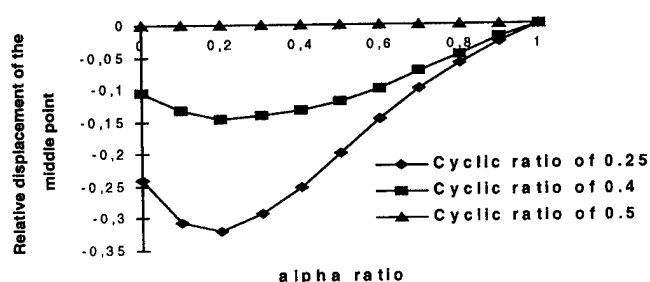


FIG. 9. Displacement of the middle point of the curve vs the α ratio (12 pairs of poles).

B. Dissymmetrical poles

To have a dissymmetrical behavior of the coupling, the field lines have to be concentrated in the airgap at the positive maximum torque position, but not at the negative maximum torque position. This is why poles that are not invariant by rotation are introduced as poles with inclined planes, for example [Fig. 6(a)]. The whole curve and the angular position of the maximum torque values in the peaks are displaced in the same direction (Fig. 7). The forces are functions of $(1/r^2)$, where r is the distance between magnets. As r is not the same on both sides of the south poles, the resultant force is no longer equal to zero for no deviation. The increase of the slope of the inclined plane emphasizes this phenomenon, and reduces the torque level (the average distance between face to face poles is increased). A plateau made on the south magnets [Fig. 6(b)] allows one to reach higher torque values.

C. Cyclic ratio different from 0.5 and dissymmetrical south-magnetized poles

All the couplings studied at the end of this article are fitted out with 12 pairs of poles. By combining the distance between peaks (due to the decrease of the cyclic ratio, and the displacement of the curve, due to one rotor with south-magnetized poles fitted out with a plateau and an inclined plane) the torque-deviation curves become dissymmetrical (Fig. 8). The relative size of the plateau on the south poles of one rotor, measured by the α ratio of the angular size of the plateau to the angular width of the south poles, has an influence on the dissymmetry of the curve (Fig. 9). This dissymmetry is measured by two parameters: the "Minmax ratio" of the difference between the values of positive and negative maximum torques on the absolute value of the higher maximum (Fig. 10) and the relative displacement of the "middle point" of the curve (M point on Fig. 8). The most interesting

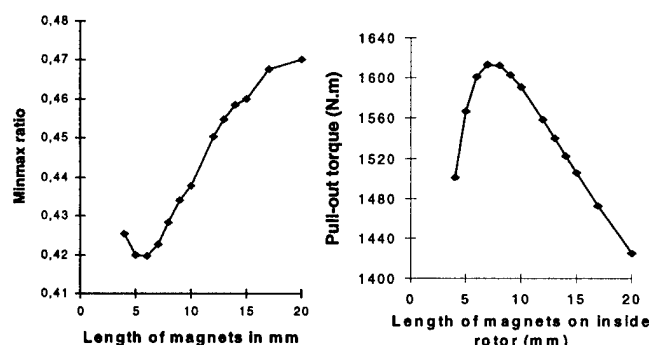


FIG. 11. Minmax ratio and maximum transmitted torque as functions of the length of magnets on the inside rotor (12 pairs of poles).

system with regard to the dissymmetry is thus fitted out with a cyclic ratio of 0.25 and an α ratio of 0.2, for which the unscrewing torque is almost half of the screwing one. This configuration of coupling is considered in the next section. The "perfect case" would be a screwing torque higher than the unscrewing one and a screwing range for rotors angular deviation greater than the unscrewing one, this seems impossible because of the conservation of energy.

D. Influence of the length of asymmetrical magnets

The introduction of dissymmetrical poles implies a loss of torque level. The increase of the magnet length on the dissymmetrical rotor can then be considered. As this increases the imbalance distance between airgap surfaces, the dissymmetry is enhanced (Fig. 11). However, the slope of the inclined plane increases as well, and from a limit value of length, the field lines close up more easily on the neighbor magnet, and do not take part in the airgap induction level. That is why the pull-out torque level does not follow the increase of length (Fig. 11). A compromise will consequently have to be chosen once more, depending on the wanted levels of pull-out torque and dissymmetry.

IV. CONCLUSION

The number of poles and the length of the magnets stuck on the rotors are parameters that allow one to optimize classical permanent magnet coaxial synchronous couplings. It is possible to minimize the volume of magnet for a given torque or to maximize the torque for a given volume. Moreover, new structures of couplings are presented. They are adapted to screwing devices and allow one to avoid the unscrewing which occurs after the end of the synchronous driving and screwing. Original shapes of the magnets give a screwing torque value almost two times higher than the unscrewing one, and therefore solve the problem.

¹W. Baran and M. Knorr, "Synchronous Couplings with SmCo5 Magnets," Second International Workshop on Rare Earth-Cobalt Permanent Magnets and their Applications, paper No. II-7.

²M. H. Nagrial, *Electric Machines Power Sys.* **21**, 115 (1993).

³J. P. Yonnet, "Calculation of Permanent Magnet Couplings," 12th International Workshop on RE Magnets and their Applications.

⁴C. Sabonnadière, *La CAO en Electrotechnique* (Dunod, France).

⁵P. Brissonneau, *Magnétisme et Matériaux Magnétiques pour l'Electrotechnique* (Hermès, France, 1997).

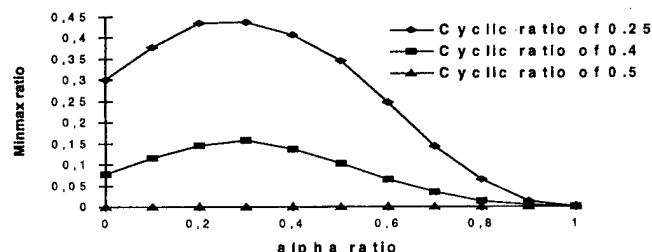


FIG. 10. Minmax ratio as a function of the plateau/pole ratio (24 poles).

A comparative analysis of permanent magnet-type bearingless synchronous motors for fully magnetically levitated rotors

J. F. Charpentier and G. Lemarquand^{a)}

Université de Bretagne Occidentale, LEMB-IUT de Brest, rue de kergoat, 29287 Brest, France

Radial instability of synchronous motors is important data to design magnetic bearings. Moreover, original motor structures must be proposed to decrease the instability. In this article, four structures with a permanent magnet rotor, six poles, and the same main mechanical dimensions are analyzed and compared. The first concerns a rotor with six tiles of permanent magnets radially magnetized and adhered to an iron core. The second is a rotor with six axial permanent magnets tangentially magnetized and separated by iron pole pieces, where the shaft is amagnetic. The third design proposes a rotor with six contiguous tiles of permanent magnets tangentially magnetized and an amagnetic shaft. In the fourth structure each north pole is made up of two contiguous tiles of permanent magnets tangentially magnetized in opposite direction and each south pole is made up of an iron pole piece. The shaft of this structure is amagnetic. The stator structure and the currents in stator windings produce a six poles flux distribution. A finite element method program is employed to study the forces and the torques. The four structures are designed to provide the same motor performance (torque). The radial instability is modeled by outcentering the rotor. The relationships between the radial force and the type of structure are analyzed. The result is that the third structure is the best solution for fully magnetically levitated rotors. It has a small instability and does not generate any disturbing force whose frequency is the double of the rotation frequency. This structure also has good properties to be used as a radial magnetic bearing. © 1998 American Institute of Physics. [S0021-8979(98)17111-6]

I. INTRODUCTION

Some studies,¹⁻³ showed an interest in bearingless motors. Most of them consider asynchronous machines that fulfill the double function of a motor and a radial bearing. If there are losses in the rotor, the corresponding calories are hardly evacuated from this body that rotates contactless in vacuum. Furthermore some studies⁴ have shown an interest in the synchronous motor compared to an asynchronous motor in term of stability. These are two good reasons to justify the use of permanent magnet synchronous machines. Section III of the article studies and compares four structures of rotors for permanent magnet synchronous machines from a destabilization point of view. Section IV shows that a permanent magnet synchronous machine with three pairs of poles is able to assume the function of a radial bearing. Each phase is constituted by three windings. These windings are not serial or parallel connected, as usually done, but they have separate feedings. The radial forces are obtained via the unbalance of the currents in the windings of a same phase.

II. STRUCTURES PRESENTATION

The aim of this work is to study the influence of the rotor structure of a permanent magnet motor without bearings on the instability and on the radial forces obtained when the windings are unbalanced. Four different structures of six pole three phase motors are presented and evaluated.

A. Choice of the structure of the stator

The structure of the stator is the same for the four different machines. We made the choice of a slotless armature to minimize the influence of the stator parameters in this study. The main dimensions of the stator are:

- (i) armature diameter: 128 mm,
- (ii) coil thickness: 3 mm,
- (iii) mechanic air gap: 2 mm.

The maximum current density in each coil is 6 A/mm². This value corresponds to a suitable temperature rise in the motor under normal conditions of work. The stator structure is described in Fig. 1.

B. Description of the structures of the rotor

Four structures of permanent magnet rotors are considered. They have been designed to deliver the same torque when two phases are fed by the same current. Neodymium iron boron magnets with a remanence of 1 T are used in these structures.

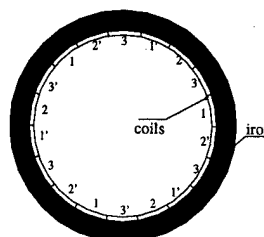


FIG. 1. Stator structure.

^{a)}Electronic mail: lemb@univ-brest.fr

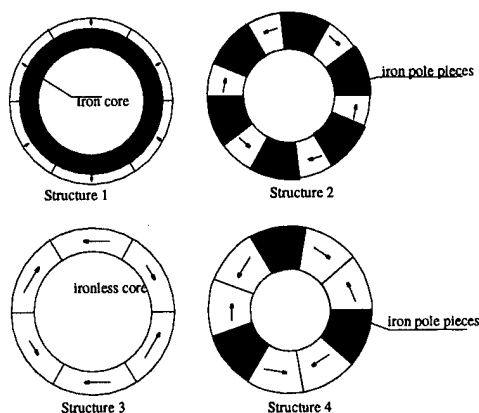


FIG. 2. Rotor structures.

The structures are described in Fig. 2. The first design is a classical design of a PM motor. The magnets are oriented radially and stuck in a cylindrical iron core. In the second structure iron pole pieces sandwich PM segments tangentially magnetized. In the third structure, six opposite tangential permanent magnets are assembled in an ironless rotor. In the fourth structure the south poles are made up of iron pole pieces and the north poles of two opposite tangential permanent magnets.

These structures are studied using a two-dimensional (2D) finite element field calculation code. All the simulation results are given for 1 m long structures.

Figure 3 shows the torque calculated for each motor versus the rotor position when two phases (phases 1 and 3) are fed by the same current. The origin for the rotor position is the position of maximum torque. We can see that the torques developed by these machines are quite similar. Nevertheless the magnet volume is more important in structures 3 and 4 because the magnetic airgap is very large in these types of structures.

III. STUDY OF RADIAL INSTABILITY

A criterion of choice for a motor is not necessarily the performance with regard to the weight, but the fact that it does not destabilize the whole rotating device. When the device is levitated, the stiffness of the bearings has to be higher than the antistiffness of the motor. The presented structures have to be characterized from this point of view.

To study the radial instability of the motors we have simulated the behavior of the structures when the rotor is

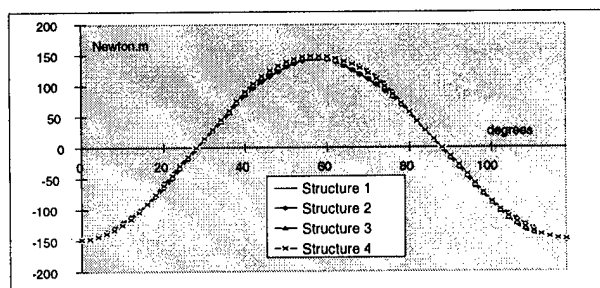


FIG. 3. Torque vs angular position of the rotor.

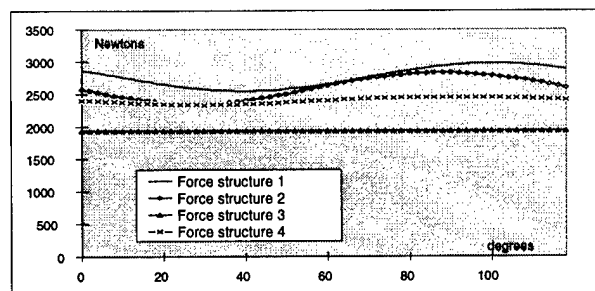


FIG. 4. Forces amplitude versus angular position of the outcentred rotor (outcentering value is 0.8 mm).

outcentered at 0.8 mm. The outcentering is generally due to the unbalance of the rotor. Figure 4 shows the amplitude of the radial forces exercised on the outcentered rotor versus the rotor position for each machine when two phases fed by the same dc current. This radial force is always oriented in the direction of the radial displacement of the rotor. The maximal values of these forces are quite comparable to the values of the tangential forces which contribute to create the torque.

For the third structure, the value of the force created on the outcentered rotor does not vary with the angular position of the rotor. In this structure this radial force is only produced by the influence of the magnets on the iron of the stator.

In structures 1, 2, and 3 the force amplitude varies with the angular position of the rotor. This variation is due to the influence of the windings on the rotor iron. The first two structures present a large variation of the radial forces with the angular position of the rotor. For the fourth structure this variation is less important.

We also note that the values of the forces are more important in the case of structures 1, 2, and 4 than in the case of the third structure.

The radial displacement of the rotor is created by its unbalance and the unbalance has the same angular speed as the rotor. Let us call N the point of the rotor that is the nearest from the stator at every moment. This point is moving with an angular speed ω_n . Let ω_r be the angular velocity of the rotor. When the radial displacement of a magnetically levitated machine corresponds to a direct mode, the movement of the N point is in the same direction as the rotor movement. Thus the angular velocity of the N point with regard to the stator is zero. Point N is always the same point. If this point varies, this will induce movements with a very low frequency: the motor antistiffness is either constant or very slowly variable, which is not a problem dynamically.⁵ On the contrary, when the radial displacement of the machine corresponds to a retrograde mode, the movement of the N point is in the opposite direction as the rotor one. Its movement with regard to the stator has an angular velocity of $\omega_n = -2\omega_r$. As the radial force depends on the rotor position, this implies that the force is modulated with a frequency $2f_r$. As a consequence, this generates an excitation at the frequency $2f_r$, which is a source of the instability of the machines. This explains the presence of second harmonics in the machine's movements and the obligation to damp movements which have this frequency. The more dependent

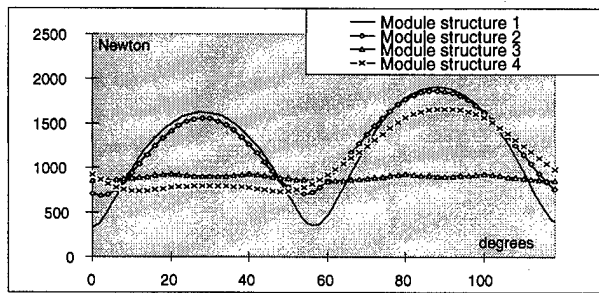


FIG. 5. Forces amplitude vs angular position of the rotor with unbalanced currents.

on the rotor position the radial force is, the more important the movement at the $2f_r$ frequency is, and the more unstable the machine is. For this reason, structures 1 and 2 are not interesting at all. Structure 4 is acceptable, as the force is modulated slightly by the rotor position. Although not optimum with regard to the volume of magnet, the third structure is dynamically the most interesting because its radial force is independent from the rotor position. Its radial antistiffness (ratio of the radial force over the radial displacement of the rotor) is also the smallest of the four structures and therefore the easier to compensate by the bearings.

IV. STUDY OF RADIAL FORCES OBTAINED WITH UNBALANCED CURRENTS

The rotor is now centered and the currents in the stator are unbalanced to create radial forces. The idea is now to study whether the structures can be also used as magnetic bearings. In Figs. 5 and 6 the force amplitude and orientation are presented versus the rotor position when two phases are fed and unbalanced. One of the three coils of each active phases (1 and 3) is crossed by a 12 A/mm^2 current density

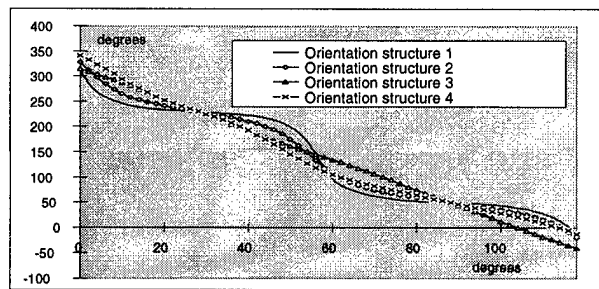


FIG. 6. Forces orientation vs the angular position of the rotor with unbalanced currents.

and the two other coils of these phases by a 3 A/mm^2 current density. Figure 5 shows that structures 1 and 2 create radial forces with a high mean value, but with an important modulation with the rotor position. Furthermore, Fig. 6 shows that the direction of the forces also depends on the rotor position. For the fourth structure, the radial force is very important when the coils are facing the iron of the rotor, and less important when facing the magnets. The modulation is still important. Finally, the third structure creates a force of almost constant amplitude without regard to the angular position of the rotor. The direction of the force varies linearly with the angular position of the rotor. The force is oriented in the direction of the axis of the coil which has the maximum current (50° or 230°) when a pole is facing this axis, and oriented perpendicular to this axis (-40° or 140°) when a pole is facing the current. This means that this configuration is suitable for use as a radial bearing.

V. CONCLUSION

Among the four proposed and studied structures that generate the same torque, some of them are optimized with regard to the volume of magnet that is used to create this torque. But other differences appear when they are studied from two other points of view: that of radial instability and that of the bearing function. Indeed, the destabilizing effect of the motor is an important thing for levitated devices, as the motor should destabilize the rotating system as less as possible. Furthermore, it is interesting to have an actuator that could also fulfill the function of a bearing. It then appears from our study that the third presented structure (although difficult to realize with tangential magnetized magnets, and not optimum with regard to the volume of the magnets) is dynamically the most interesting one. Indeed, it has very good characteristics, when considering its radial instability, especially with regard to the creation of a disturbing force at a frequency that is double the rotation frequency. This structure is also easy to control as a radial magnetic bearing.

¹R. Bosch, "Development of a bearingless electrical motor," Proceedings of ICEM'88, edited by G. Schweitzer (vdl Hochschulverlag AG an der ETH, Zurich, 1988), pp. 331-335.

²M. Oshima, IEEE Trans. Ind. Appl. **32**, 363 (1996).

³R. Schob and J. Bischel, "Vector control of the bearingless motor," 4th International Symposium on Magnetics Bearings, edited by G. Schweitzer (vdl Hochschulverlag AG an der ETH, Zurich, 1994).

⁴M. Oshima, A. Chiba, T. Fukao, and A. Rahman, IEEE Trans. Ind. Electron. **43**, 292 (1996).

⁵M. Fumagalli, B. Feeny, and G. Schweitzer, "Dynamics of rigid rotors in retainer bearings," 3rd International Symposium on Magnetics Bearings, Alexandria, VA, edited by P. E. Allaire (Technomic Publishing Company, Lancaster, PA, 1992).

Spin reorientation in (Pr,RE)–(Co,TM)–B magnets (RE=Tb, TM=Fe,Cr,Mn)

D. H. Kim and G. Hadjipanayis

Department of Physics and Astronomy, University of Delaware, Newark, Delaware 19716-2570

Small substitutions of Pr with Tb and Co with Fe, Cr, Mn were used to increase the spin reorientation temperature of the $\text{Pr}_2\text{Co}_{14}\text{B}$ compound which is around 395 °C. Spin reorientation temperatures were obtained by measuring magnetization vs temperature curves at temperatures up to 750 °C. Several ribbons with high spin reorientation temperature were fabricated by melt-spinning and they were annealed in the temperature at 600–700 °C to obtain the optimum coercivity. Our results show that spin reorientation temperature is sharply increased with Fe substitution and reaches a maximum (575 °C) in the sample with 25% Fe substituted for Co. Small amounts of Tb, Cr, and Mn are effective in increasing the spin reorientation temperature. The optimum coercivities of ribbons are in the range of 7–10.5 kOe and ribbons with high spin reorientation temperature show an improved temperature dependence of coercivity. © 1998 American Institute of Physics. [S0021-8979(98)36311-2]

I. INTRODUCTION

$\text{Nd}_2\text{Co}_{14}\text{B}$ and $\text{Pr}_2\text{Co}_{14}\text{B}$ magnet alloys exhibit high Curie temperatures, which make them the possibility for high temperature application.^{1–3} Among them, the anisotropy field of $\text{Nd}_2\text{Co}_{14}\text{B}$ is significantly lower and makes this Co-substituted alloy a poor candidate to become permanent magnet. In the case of $\text{Pr}_2\text{Co}_{14}\text{B}$, an opposite behavior is observed with the anisotropy field of $\text{Pr}_2\text{Co}_{14}\text{B}$ being much higher than that of $\text{Pr}_2\text{Fe}_{14}\text{B}$. Several studies have reported that high coercivities with value up to 25 kOe in sintered magnets⁴ and melt-spun $\text{Pr}_2\text{Co}_{14}\text{B}$ ribbons could be obtained.^{5,6} However, the $\text{Pr}_2\text{Co}_{14}\text{B}$ magnet has a spin reorientation temperature at around 395 °C⁷ where its anisotropy is changed from uniaxial to planar, this puts an upper temperature limit on the application of these magnets.

In this study we tried to prepare Pr(Tb)–Co(Fe,Cr,Mn)–B-based magnets with higher spin reorientation temperature. As is well known, no spin reorientation is observed in $\text{Pr}_2\text{Fe}_{14}\text{B}$ and the spin reorientation temperature of $\text{Tb}_2\text{Co}_{14}\text{B}$ is much higher than that of $\text{Pr}_2\text{Co}_{14}\text{B}$.

II. EXPERIMENT

All the alloys with $(\text{Pr,RE})_{13}(\text{Co,TM})_{80}\text{B}_7$ (RE=Tb, TM=Fe, Cr, Mn) were prepared by arc-melting, followed by homogenization at 1000 °C for 24 h under Ar atmosphere. Spin reorientation temperature was obtained by measuring magnetization vs temperature curves at temperatures up to 750 °C. Several ribbons with high spin reorientation temperature were fabricated by melt-spinning at a wheel speed of 50 m/s. The as-spun ribbons were confirmed to be almost amorphous within the resolution of x-ray diffraction experiment. The ribbons were studied using differential scanning calorimetry (DSC) for the identification of possible phase transformation. The coercivity of samples was optimized through annealing at the temperature range of 600–700 °C for 2.5–40 min. Magnetic properties were measured by a vibrating sample magnetometer (VSM) with a maximum field of 20 kOe and the temperature dependence of coercivity was measured up to 450 °C.

III. RESULTS AND DISCUSSION

The temperature dependence of magnetization curves for $\text{Pr}_{13}(\text{Co}_{1-x}\text{Fe}_x)_{80}\text{B}_7$ ($x=0.1, 0.25, 0.6$) alloys are shown in Fig. 1. The curves were measured in a low applied magnetic field of 200 Oe to show clearly the effects of magnetic transitions. As one can see, the magnetization increases as the temperature increases due to the decline of magnetocrystalline anisotropy field with temperature, and all curves exhibit an unusual curvature at the temperature where its anisotropy is changed from uniaxial to planar. The spin reorientation temperature is determined from the inflection point of this curve. Using the same method, the spin reorientation temperatures for $\text{Pr}_{13}(\text{Co}_{1-x}\text{Fe}_x)_{80}\text{B}_7$ ($0 \leq x \leq 0.6$) were obtained as shown in Fig. 2. It is found that spin reorientation temperature is sharply increased with Fe substitution because there is no spin reorientation in the $\text{Pr}_2\text{Fe}_{14}\text{B}$, and reaches a maximum (575 °C) in the sample with 25% Fe substitution for Co. But for higher Fe substitution, the spin reorientation temperature is dropped down to around 300 °C. In the $\text{Pr}_2(\text{Fe,Co})_{14}\text{B}$ system, the magnetocrystalline anisotropy is strongly dependent on the Fe content and shows a minimum at the composition with 25% Fe content.³ Therefore, at this composition, a confusion of magnetocrystalline anisotropy may be existed and cause a drop of the spin reorientation temperature, which originates from the competition between the 3d and 4f sublattice anisotropy.³ On the other hand, the Curie temperature of the sample is continuously decreased as the Fe content increases.

Figure 3 shows the temperature dependence of magnetization curves for $\text{Pr}_{13}(\text{Co}_{0.4}\text{Fe}_{0.6})_{79}\text{M}_1\text{B}_7$ ($\text{M}=\text{Cr, Mn}$). The results indicate that samples with a small amount of Cr and Mn do not show spin reorientation phenomena up to the Curie temperature. In the case of $(\text{Pr}_{1-z}\text{Tb}_z)_{13}(\text{Co}_{0.4}\text{Fe}_{0.6})_{80}\text{B}_7$ ($z=0.2, 0.5$), as shown in Fig. 4, Tb substitution is effective in increasing both the spin reorientation temperature, with 1 °C/1% Tb ratio, and the Curie temperature.

X-ray diffraction showed that all the as-spun ribbons were almost amorphous in structure. Calorimetric DSC studies showed that all the samples have an exothermic peak at

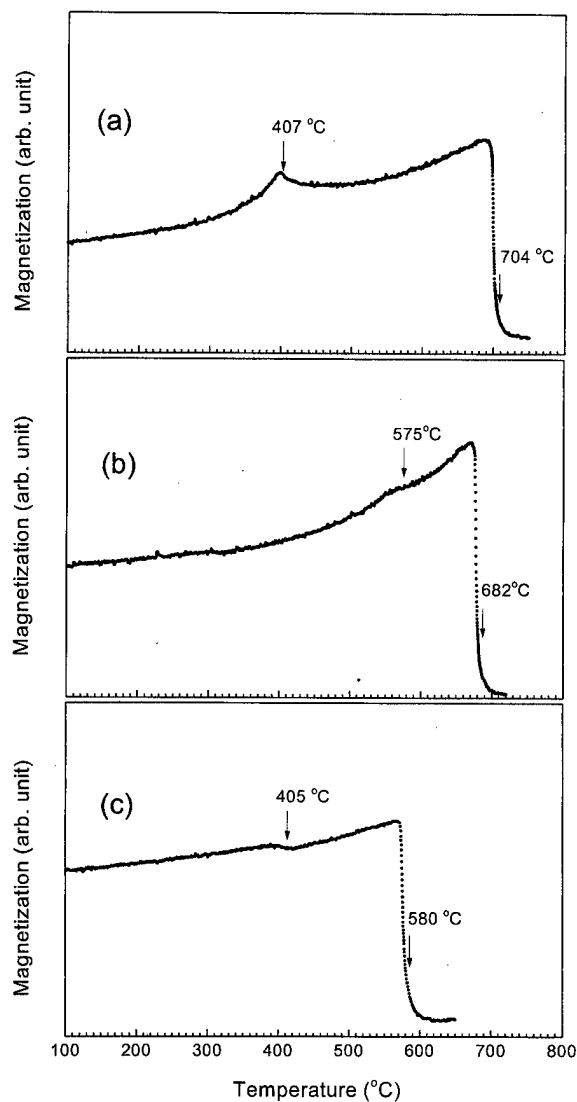


FIG. 1. Temperature dependence of magnetization for (a) $\text{Pr}_{13}(\text{Co}_{0.9}\text{Fe}_{0.1})_{80}\text{B}_7$, (b) $\text{Pr}_{13}(\text{Co}_{0.75}\text{Fe}_{0.25})_{80}\text{B}_7$, and (c) $\text{Pr}_{13}(\text{Co}_{0.4}\text{Fe}_{0.6})_{80}\text{B}_7$.

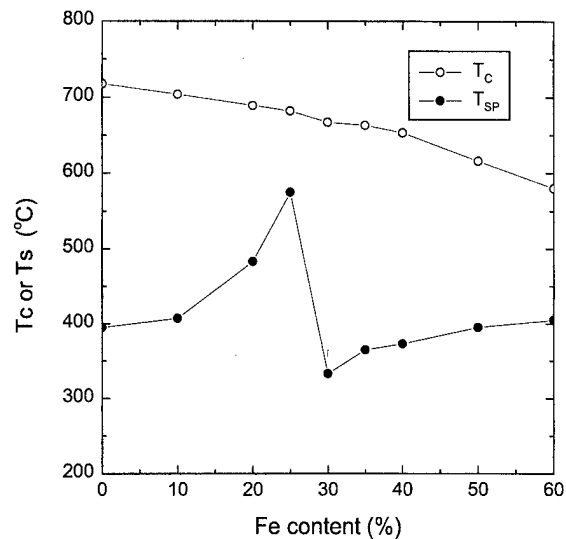


FIG. 2. Spin reorientation temperature as a function of Fe content in $\text{Pr}_{13}(\text{Co}_{1-x}\text{Fe}_x)_{80}\text{B}_7$.

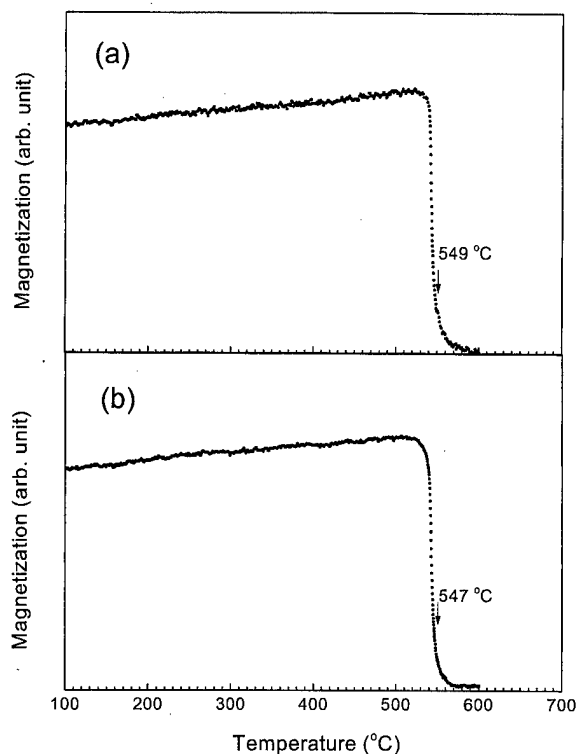


FIG. 3. Temperature dependence of magnetization for (a) $\text{Pr}_{13}(\text{Co}_{0.4}\text{Fe}_{0.6})_{79}\text{Cr}_1\text{B}_7$ and (b) $\text{Pr}_{13}(\text{Co}_{0.4}\text{Fe}_{0.6})_{79}\text{Mn}_1\text{B}_7$.

around 550 °C where the amorphous phase transforms into the 2:14:1 phase.

Figure 5 shows the coercivity change as a function of aging time at 600–700 °C for $\text{Pr}_{13}(\text{Co}_{0.5}\text{Fe}_{0.5})_{80}\text{B}_7$ ribbons. To develop a high coercivity, an annealing temperature over

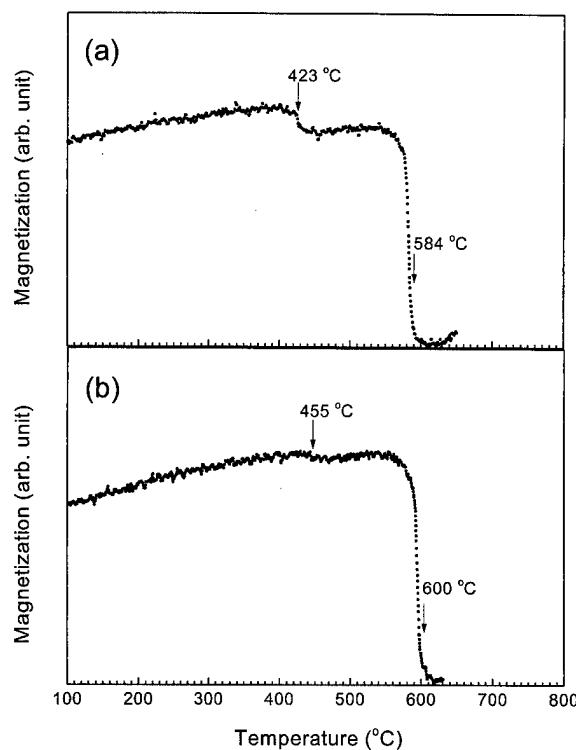


FIG. 4. Temperature dependence of magnetization for (a) $(\text{Pr}_{0.8}\text{Tb}_{0.2})_{13}(\text{Co}_{0.4}\text{Fe}_{0.6})_{80}\text{B}_7$ and (b) $(\text{Pr}_{0.5}\text{Tb}_{0.5})_{13}(\text{Co}_{0.4}\text{Fe}_{0.6})_{80}\text{B}_7$.

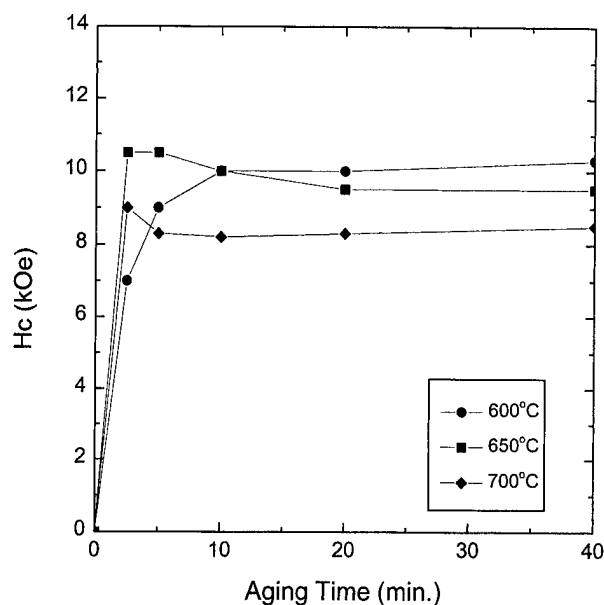


FIG. 5. Coercivity change as a function of aging time at temperatures in the range of 600–700 °C for $\text{Pr}_{13}(\text{Co}_{0.5}\text{Fe}_{0.5})_{80}\text{B}_7$.

600 °C is required and the optimum coercivity is 10.5 kOe after annealing at 650 °C for 2.5 min. The other samples show a similar trend and optimum coercivities are in the range of 7–10.5 kOe as listed in Table I. The lowest coercivity is obtained in the sample with 25% Fe substitution where the maximum spin reorientation temperature was obtained. This is because the magnetocrystalline anisotropy is a minimum at the composition with maximum spin reorientation temperature. In the Cr and Mn cases, the substitutions were not effective to improve the coercivity.

Figure 6 shows the temperature dependence of coercivity for $\text{Pr}_{13}(\text{Co}_{1-x}\text{Fe}_x)_{80}\text{B}_7$ ($x=0.2, 0.25$, and 0.5) ribbons having different spin reorientation temperature. Samples with $x=0.2$ and 0.25 which have higher spin reorientation temperature (480 and 575 °C, respectively) show a low coercivity at room temperature because of their lower magnetocrystalline anisotropy field. However, as the temperature increases the decline of coercivity is smaller than the other sample with $x=0.5$ which has a lower spin reorientation temperature (395 °C). In order to be shown this tendency more clearly, the ratio of coercivity decrease (H_c/H_c at room temperature) as a function of temperature is shown in Fig. 6(b).

TABLE I. Optimum coercivities in $\text{Pr}_{13}(\text{Co,TM})_{80}\text{B}_7$ ribbons.

Sample	T_{sp} (°C)	H_c (kOe)	Annealing condition
$\text{Pr}_{13}(\text{Co}_{0.8}\text{Fe}_{0.2})_{80}\text{B}_7$	480	7.0	650 °C, 5 min
$\text{Pr}_{13}(\text{Co}_{0.75}\text{Fe}_{0.25})_{80}\text{B}_7$	575	7.4	650 °C, 5 min
$\text{Pr}_{13}(\text{Co}_{0.5}\text{Fe}_{0.5})_{80}\text{B}_7$	395	10.5	650 °C, 2.5 min
$\text{Pr}_{13}(\text{Co}_{0.4}\text{Fe}_{0.6})_{79}\text{Cr}_1\text{B}_7$	-	9.1	650 °C, 5 min

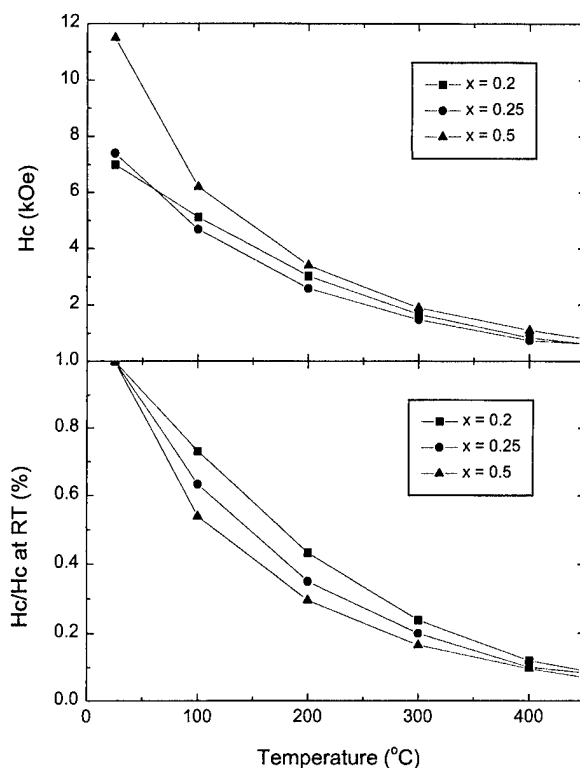


FIG. 6. Temperature dependence of coercivity for $\text{Pr}_{13}(\text{Co}_{1-x}\text{Fe}_x)_{80}\text{B}_7$ ($x=0.2, 0.25$, and 0.5) having different spin reorientation temperature.

IV. CONCLUSIONS

High spin reorientation temperatures of 575 °C have been obtained in $\text{Pr}_{13}(\text{Co}_{0.75}\text{Fe}_{0.25})_{80}\text{B}_7$ with relatively small decline of Curie temperature. Samples with a small amount of Cr and Mn do not show spin reorientation phenomena up to their Curie temperature, which is found to decrease with substitution. Tb substitution is effective in increasing both the spin reorientation temperature, with 1 °C/1% Tb ratio, and the Curie temperature. Samples with higher spin reorientation temperature show an improved temperature dependence of coercivity.

ACKNOWLEDGMENT

Work supported by AFOSR MURI Grant No. F49620-96-1-0434.

¹K. H. J. Buschow, D. B. de Mooij, S. Sinnema, R. J. Radwanski, and J. J. M. Franse, *J. Magn. Magn. Mater.* **51**, 211 (1985).

²H. Fujii, W. E. Wallace, and E. B. Boltich, *J. Magn. Magn. Mater.* **61**, 251 (1986).

³K. H. J. Buschow, *Ferromagnetic Materials*, Vol. 4, edited by E. P. Wohlfarth and K. H. J. Buschow (Elsevier Science, New York, 1988).

⁴C. N. Christodoulou, W. E. Wallace, and T. B. Massalski, *J. Appl. Phys.* **66**, 2749 (1989).

⁵C. N. Christodoulou, T. B. Massalski, and W. E. Wallace, *J. Magn. Magn. Mater.* **125**, 177 (1993).

⁶C. D. Fuerst, J. F. Herbst, and F. E. Pinkerton, *J. Appl. Phys.* **64**, 5556 (1988).

⁷E. B. Boltich, A. T. Pedziwiatr, and W. E. Wallace, *J. Magn. Magn. Mater.* **66**, 317 (1987).

Magnetization processes in hybrid magnets

M. Emura, A. C. Neiva, and F. P. Missell^{a)}

Instituto de Física, Universidade de São Paulo, C. P. 66318, 05315-970 São Paulo, S.P., Brazil

K. L. Babcock

Digital Instruments, Santa Barbara, California 93103

J. Ormerod and S. Constantinides

The Arnold Engineering Company, Marengo, Illinois 60152

Injection-molded, oriented hybrid magnets consisting of mixtures of $\text{BaO} \cdot 6\text{Fe}_2\text{O}_3$ and MQP-Q (exchange-coupled $\text{Nd}_2\text{Fe}_{14}\text{B} + \alpha\text{-Fe}$) are compared to bonded magnets made only from ferrite or MQP-Q. The magnetic fractions of the hybrid magnets consist of 80, 60, or 40 wt % ferrite blended with 20, 40, or 60 wt % MQP-Q. The microstructure was investigated by x-ray diffraction, scanning electron microscopy, atomic force microscopy, and magnetic force microscopy. Atomic and magnetic force microscopy images indicated differences between the physical and magnetic microstructures. Magnetic interactions were studied via isothermal remanence (IRM) and dc-demagnetization (DCD) remanence curves and Henkel plots. In contrast to what is observed in exchange spring magnets, the IRM and DCD susceptibilities of all magnets present peaks of nearly the same width, centered at roughly the same value of the magnetic field, consistent with weak dipolar interactions between magnetic particles. The IRM susceptibilities show structure associated with magnetic inhomogeneities in the samples. © 1998 American Institute of Physics. [S0021-8979(98)17211-0]

Bonded magnets constitute the fastest growing segment of the permanent magnet market.^{1,2} These materials are produced by encapsulating a magnetic powder in a resin or polymer and then compacting or molding the material to the final part shape. The commercially important bonded magnets are based primarily upon ferrite or NdFeB . However, low-neodymium, exchange-coupled alloys are also interesting for bonded magnets because of their good corrosion resistance and low saturation fields. The Magnequench alloy MQP-Q ($\text{Nd}_2\text{Fe}_{14}\text{B} + \alpha\text{-Fe}$) has recently been used with barium ferrite to produce hybrid magnets with interesting coercive properties.² For a bonded magnet whose magnetic fraction consists of 20 wt % MQP-Q and 80 wt % ferrite, the reversible temperature coefficient of coercivity is approximately zero around and above room temperature. Furthermore, at 100 °C, the coercive field H_c of the hybrid is larger than that of either the bonded ferrite or the bonded MQP-Q. Enhanced hysteresis characteristics due to anisotropic dipole interactions have been observed³ in composite mixtures $\text{Sm}_2\text{Co}_{17}/\text{Sm}_2\text{Fe}_{17}\text{N}_3$ and $\text{Sm}_2\text{Co}_{17}/\text{Fe}$.

In this article, we investigate magnetic interactions in several hybrid magnets and present data on their magnetic and structural properties. The bonded magnets present an ideal opportunity to study systems in which dipole interactions should be the predominant form of interaction between particles.

Five commercial bonded magnet compositions were considered in this work. Three anisotropic hybrid magnets, produced by injection molding, had magnetic fractions consisting of 80, 60, or 40 wt % Ba ferrite blended with 20, 40, or 60 wt % of MQP-Q melt-spun ribbons and a binder of

Nylon 12. These have been designated as samples 2401, 2402, and 2403, respectively. An anisotropic magnet consisting only of Ba ferrite is designated as 1060, while an isotropic magnet whose magnetic fraction is MQP-Q is identified as 2203. For the latter two magnets, polyamide was used as a binder. The saturating field requirements as well as the temperature dependence of the coercivity for these magnets have been published previously.² For all magnets, we were able to reproduce the catalog density by assuming the volume fraction of the magnetic material to be 60%.

The alignment of these magnets was characterized with a Philips MDP 1880 powder diffractometer using $\text{Cu } K\alpha$ radiation. The microstructure was examined with an optical microscope as well as with a Leica Cambridge F440 scanning electron microscope (SEM). Magnetization M measurements between 4.2 and 300 K were made with a vibrating sample magnetometer mounted in a 9 T superconducting coil, while measurements above 300 K were made in a furnace mounted on a 2 T electromagnet. In all cases, M versus H was corrected using an appropriate demagnetization factor.

Images were also obtained using a Digital Instruments D3000 scanning probe microscope. The device allows simultaneous collection of topography data, by Tapping ModeTM atomic force microscopy (AFM), and magnetic stray field data, by LiftModeTM magnetic force microscopy (MFM).⁴ The topographical information from each raster line is used to maintain a constant height above the sample surface during collection of the magnetic information to minimize the effect which topological features have on the stray field distribution. In the topological images, light areas are higher than the average and dark areas are lower than the average.

^{a)}Electronic mail: fmissell@macbeth.if.usp.br

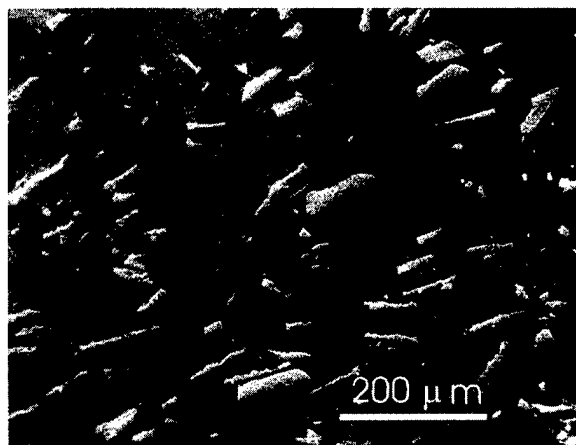


FIG. 1. SEM image of sample 2401 showing inhomogeneous distribution of MQP-Q ribbons.

In the magnetic images, light areas correspond to tip-sample interactions producing a negative force gradient, while positive gradients correspond to dark areas.⁴

In the hybrid magnets, the Ba ferrite grains present a high degree of alignment as can be verified by x-ray diffractograms in which the (00 k) peaks of this phase are prominent. Optical metallography and SEM observations show the ribbons of MQP-Q to be randomly dispersed in the ferrite-Nylon 12 matrix. In Fig. 1, a low magnification SEM image of sample 2401 is presented where the random orientation of the MQP-Q ribbons can be seen. A useful way to quantify the degree of alignment of these samples is in terms of the ratio M_r/M_s , where M_r is the measured remanence and M_s is the saturation magnetization, obtained by extrapolating high-field M values to infinite fields using $M=M_s(1-a/H)$. Values of M_r/M_s are presented in Table I. This ratio is seen to decrease as the ferrite fraction of the magnet decreases. Values of $M_r/M_s=0.8-0.9$ are commonly encountered in aligned sintered magnets, while $M_r/M_s=0.5$ is the value expected for noninteracting single-domain particles.

A group of Ba ferrite grains in an unmagnetized sample of 2401 can be clearly seen in Fig. 2(a), which was obtained by AFM. Note the presence of a large ferrite grain in the center of the figure. The magnetic stray fields for the same region of the sample, obtained by MFM, are shown in Fig. 2(b). The magnetic stray fields associated with the large ferrite grain in the center of the figure are very nonuniform over the grain, indicating the presence of two domains in this grain. Furthermore, the stray fields of several small neighboring grains have the same orientation as one of the do-

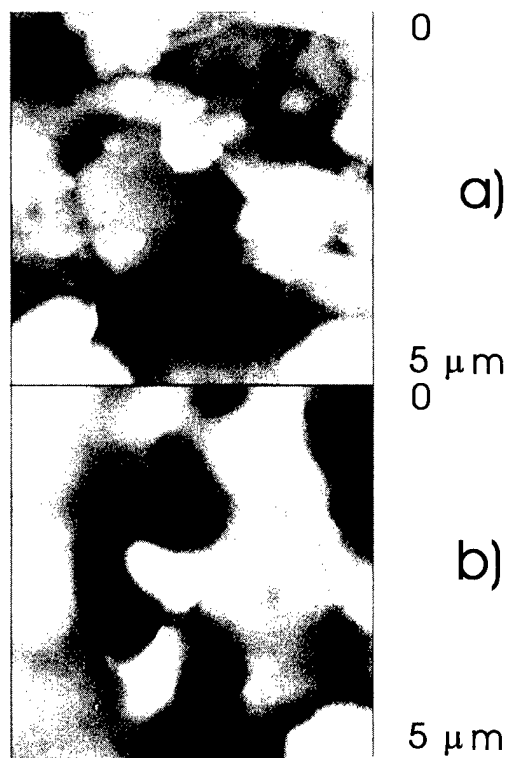


FIG. 2. (a) AFM image of the $5\text{ }\mu\text{m}\times 5\text{ }\mu\text{m}$ region of Ba ferrite in sample 2401. (b) MFM image of the same $5\text{ }\mu\text{m}\times 5\text{ }\mu\text{m}$ region showing stray magnetic fields present in the sample. Note that the magnetic domain structure does not coincide with the grain structure.

main in the large central grain. In general, we can see that the stray field distribution does not coincide with the grain structure of the sample. It is known that magnetic interactions between neighboring grains can lead to collective phenomena, known as interaction domains. The details of inter-grain interactions will depend upon exchange, anisotropy, magnetic moment, grain size, and grain misorientation, all of which will affect the stray fields. Interaction domains have been observed in many kinds of magnets, including exchange-coupled nanostructured rare-earth magnets.⁵ In the present case, the existence of interaction domains is evidence for locally inhomogeneous magnetization states in the hybrid magnets.

A magnetic evaluation of magnetostatic interactions was made using the so-called IRM and DCD remanence curves and Henkel plots. The isothermal remanence (IRM) curve $M_r(H)$ started from an ac-demagnetized state, with the remanent magnetization being measured as a function of increasing positive applied field until positive saturation was obtained. The dc-demagnetization (DCD) curve $M_d(H)$ was measured from a positive saturation condition, with the remanence measured as a function of increasing negative field, until negative saturation was reached. For any system of single-domain noninteracting particles, Wohlfarth showed that $M_d(H)=M_r(\infty)-2M_r(H)$.

In Fig. 3, we show the IRM and DCD susceptibilities, $\chi_r=dM_r/dH$ and $\chi_d=dM_d/dH$, for the five magnets studied. For noninteracting systems, the two curves should be of the same width, should have maxima at the same values of

TABLE I. Magnetic characteristics of the bonded magnets.

Sample	M_r/M_s	$H'_r(\text{kOe})$	$H_r(\text{kOe})$	$\Delta'_r(\text{kOe})$	$\Delta_r(\text{kOe})$
1060	0.91	3.8	3.9	2.5	2.4
2401	0.75	4.2	4.2	4.0	2.7
2402	0.68	4.9	4.8	4.0	2.9
2403	0.59	4.7	4.3	4.3	3.4
2203	0.54	5.9	5.1	4.1	3.4

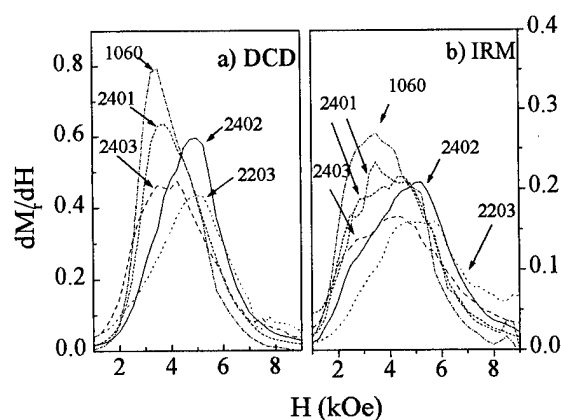


FIG. 3. IRM and DCD susceptibilities of the bonded magnets studied. For magnet 2401, the two IRM curves are for different samples and show different structure.

the magnetic field, and the amplitudes should differ by a factor of 2, as can be seen by differentiating the Wohlfarth relation. Values of the widths and centers of the IRM (Δ_r, H_r) and DCD (Δ_d, H_d) curves are given in Table I. It is most remarkable that these predictions are roughly obeyed for the five magnets studied, even though four of them contain varying amounts of exchange-coupled MQP-Q. A recent study⁶ of several exchange-coupled NdFeB alloys showed that the amplitude of χ_d was up to 50 times greater than that of χ_r , while the width of the former was about ten times less than the latter. On the other hand, CoNiCr thin films⁷ approached the ideal behavior for large values of the Cr underlayer thickness, consistent with a reduction in exchange coupling between grains with increasing Cr underlayer.

In Fig. 3, two χ_r curves are shown for magnet 2401, corresponding to different samples. Each curve presents some structure, not unlike, but smaller than that reported in Ref. 6. However, the structure observed on the two curves corresponding to sample 2401 in Fig. 3 is different from curve to curve. Since our samples clearly present inhomogeneities (see Fig. 1) in the distribution and orientation of the MQP-Q ribbons, we believe this to be the probable cause of the structure observed in χ_r .

Finally, in Fig. 4 we present Henkel plots [$m_d = M_d(H)/M_r(\infty)$ versus $m_r = M_r(H)/M_r(\infty)$] for the five magnets studied in this paper. The diagonal line corresponds to the Wohlfarth line mentioned above. Points above this line correspond to magnetizing interactions, while points below this line are indicative of demagnetizing interactions. In Fig. 4 there is a clear progression in the behavior of the data as the fraction of MQP-Q is increased (fraction of ferrite is decreased). Sample 1060 shows strong magnetizing interactions at low fields. Data for sample 2401 present an s-shaped behavior, which has been seen frequently in exchange-coupled magnets.⁸ This s-shaped curve has been discussed via the Preisach model in terms of a competition between

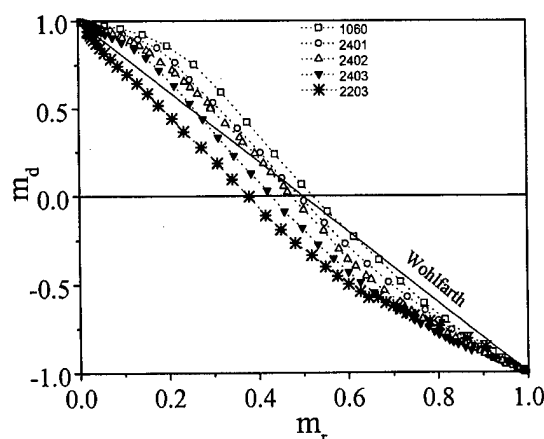


FIG. 4. Henkel plots for all samples, in which the reduced DCD remanence is given as a function of the reduced IRM remanence.

mean-field effects and random interactions.⁸ Finally, for sample 2203, whose magnetic fraction is only MQP-Q, all points are in the demagnetizing region of the Henkel plot.

Henkel plots can be discussed in terms of the Preisach model,⁹ where one can invoke random interactions and magnetizing or demagnetizing mean-field interactions to explain behavior such as that seen in Fig. 4. Here, we will limit our comments to a comparison with comparable fully dense magnets. For example, the Henkel plot of a fully dense Ba ferrite magnet shows much stronger magnetizing interactions, with nearly all of the data points lying above the Wohlfarth line. For the bonded magnet (1060) shown here, the magnetizing mean-field contributions seem to have been reduced considerably. Similarly, exchange-coupled magnets show an s-shaped Henkel plot, which has been discussed using the Preisach model in terms of a competition between mean-field effects and random interactions.⁸ In the present case, sample 2203 appears to have greatly reduced or negative mean-field interactions. Thus, the effect of the binder may be to reduce the mean-field effects in these bonded magnets.

FAPESP, CNPq, CAPES, and FINEP provided financial support. X-ray diffraction and SEM work were performed at the Laboratório de Caracterização Tecnológica-EPUSP.

¹J. J. Croat, J. Appl. Phys. **81**, 4804 (1997).

²J. Ormerod and S. Constantinides, J. Appl. Phys. **81**, 4816 (1997).

³J. O'Sullivan, X. L. Rao, and J. M. D. Coey, J. Appl. Phys. **81**, 5124 (1997).

⁴K. Babcock, M. Dugas, S. Manalis, and V. Elings, Mater. Res. Soc. Symp. Proc. **355**, 311 (1995).

⁵W. Rave, D. Eckert, B. Gebel, A. Handstein, R. Schäfer, and K.-H. Müller, *Magnetic Anisotropy and Coercivity in Rare-Earth Transition Metal Alloys* (World Scientific, Singapore, 1996), pp. 297–306.

⁶L. H. Lewis, D. O. Welch, and V. Panchanathan, J. Appl. Phys. **81**, 4422 (1997).

⁷P. I. Mayo, K. O'Grady, P. E. Kelly, J. Cambridge, I. L. Sanders, T. Yogi, and R. W. Chantrell, J. Appl. Phys. **69**, 4733 (1991).

⁸See, for example, D. R. Cornejo, M. Lo Bue, V. Basso, G. Bertotti, and F. P. Missell, J. Appl. Phys. **81**, 5588 (1997), and references therein.

⁹V. Basso and G. Bertotti, IEEE Trans. Magn. **30**, 64 (1994).

Mechanical strength of the solid-HDDR treated Nd-Fe-B-type materials

H. W. Kwon^{a)} and S. J. Kang

Department of Materials Science and Engineering, The Pukyong National University, Nam-Gu, Pusan, South Korea 608-737

The hydrogenation, disproportionation, desorption, recombination (HDDR) is known as a unique process through which a noncoercive cast Nd-Fe-B-type material can be easily converted into a coercive one. Although the conventional HDDR process generally leads to a powderlike material, a solid-HDDR material can be realized if the HDDR process is properly modified (solid-HDDR). In the present study, the change of mechanical strength (compressive strength) of the Nd-Fe-B-type material during the solid-HDDR has been investigated using a sintered magnet with composition $\text{Nd}_{13.8}\text{Dy}_{0.7}\text{Fe}_{78.25}\text{Si}_{0.15}\text{Mn}_{0.6}\text{B}_{6.5}$. It has been found that the low strength of the hydrided material was improved by the subsequent disproportionation. The restoration of the strength was explained by the eutectoidlike disproportionation structure containing fine neodymium hydride rod embedded in tough iron matrix. The high strength of disproportionated material was reduced radically in an earlier stage of recombination, and this was explained by the reduction of the disproportionated phase. The reduced strength was, however, recovered by further recombination, and this was explained by the fact that as the recombination continues the recombined grains become continuous and adhere together. The optimally HDDR processed material has a comparable or even higher strength with respect to the initial sintered material prior to the solid-HDDR. The present study suggested that the mechanical strength of Nd-Fe-B-type material could be retained even after the solid-HDDR. © 1998 American Institute of Physics. [S0021-8979(98)17311-5]

I. INTRODUCTION

The hydrogenation, disproportionation, desorption, recombination (HDDR) is known as a unique process through which a noncoercive cast Nd-Fe-B-type material can be easily converted into a coercive one, and the HDDR process generally leads to a powderlike material.¹⁻⁴ It has been reported, however, that material in a solid form can be obtained by the HDDR process if it is properly modified (solid-HDDR).^{5,6} Noncoercive Nd-Fe-B-type cast ingot material can, therefore, be converted into a magnet with high coercivity in solid form using the solid-HDDR process, and a successful attempt has been reported by another group.⁵ In order that the solid-HDDR treated material can be utilized as a magnet, the material has to exhibit not only a high coercivity but also a sufficient mechanical strength. It is, therefore, of great interest to well understand the change of mechanical strength of the Nd-Fe-B-type material during the solid-HDDR.

II. EXPERIMENT

In order to assess correctly the mechanical strength of HDDR treated material, it is important to use a compositionally and structurally homogeneous material. Since an ordinary Nd-Fe-B-type ingot material has a variety of inhomogeneity and structural flaws, the cast ingot material is considered to be unsuitable for assessing the change of mechanical strength during the HDDR. In the present study, therefore, a sintered magnet rather than a cast ingot material was used because the sintered magnet could be considered to be more homogeneous in terms of composition and structure.

The magnet used was anisotropic with a chemical composition of $\text{Nd}_{13.8}\text{Dy}_{0.7}\text{Fe}_{78.25}\text{Si}_{0.15}\text{Mn}_{0.6}\text{B}_{6.5}$. A disk-shaped (13 mm ϕ , 3 mm thick) sample was subjected to a solid-HDDR process. The sample was heated under vacuum up to around 650 °C, at which hydrogen gas was introduced. After introducing the hydrogen gas, the sample was heated rapidly (50 °C/min) toward the disproportionation temperature. The sample disproportionated for a given period was subsequently subjected to the desorption and recombination treatment under vacuum. The samples at each step were rapidly cooled down to room temperature to stop further process and then removed from the HDDR reactor. The compressive strength of the materials under various conditions was measured using a universal testing machine. The dimensions of the specimen used for the measurement of the compressive strength were 5×5×3 mm³. Compression was performed along the direction parallel to the aligning direction of the anisotropic sintered magnet with a strain rate of 2.7×10⁻³/s.

III. RESULTS AND DISCUSSION

The hydrogenated sample showed very friable character and no appreciable strength was measured. The low strength of the hydrided material was enhanced by disproportionation. Variation of the compressive strength as a function of the disproportionation temperature for the samples disproportionated for 2 h at each temperature was examined and the result is shown in Fig. 1. It appears that the compressive strength of the sample disproportionated at low temperature (650 °C) appears to be very low compared to the initial strength (85 kgf/mm²) prior to the HDDR, and it increases with increasing the disproportionation temperature up to 800 °C, above which it levels off. Of particular interest is

^{a)}Electronic mail: hwkwon@dolphin.pknu.ac.kr

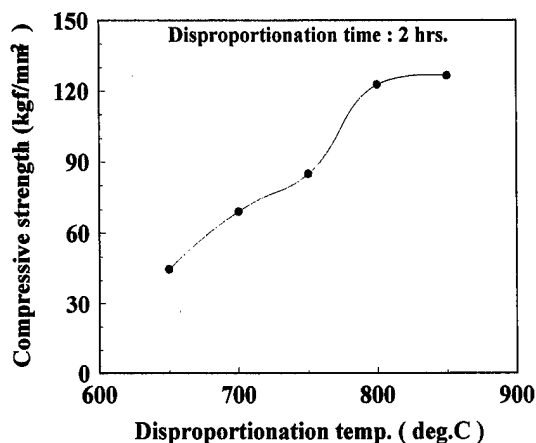


FIG. 1. Variation of the compressive strength as a function of disproportionation temperature for the hydrogenated magnet.

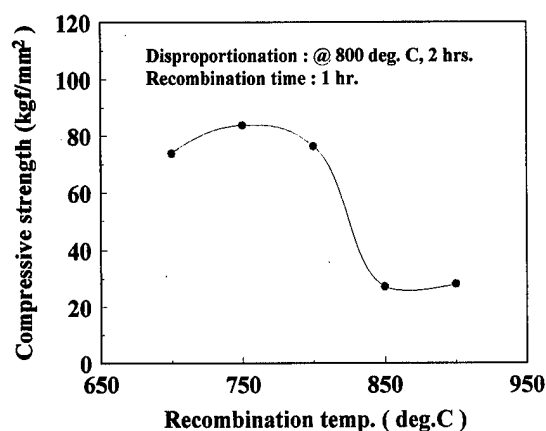


FIG. 3. Variation of the compressive strength as a function of recombination temperature for the fully disproportionated material.

that the compressive strength of the fully disproportionated material has been found, unexpectedly, to be higher than that of the initial sintered magnet before HDDR. The low strength of the sample disproportionated at the lower temperatures may be explained by the presence of a significant amount of brittle hydride phase which has not been disproportionated. As the disproportionation temperature increases, more disproportionation reaction may proceed for the given period and the remaining hydride may be lessened. It has been reported^{6,7} that the disproportionation of the $\text{Nd}_2\text{Fe}_{14}\text{BH}_x$ and the $\text{NdFe}_4\text{B}_4\text{H}_x$ phases leads to a particular eutectoidlike microstructure consisting of fine neodymium hydride rods embedded in a tough iron matrix. The disproportionated phases are, therefore, expected to have a considerable mechanical strength because of the particular structure containing plenty of tough iron. The gradual increase in the compressive strength with increasing the temperature may, thus, probably be explained by the gradual increase in the amount of disproportionated phases.

Variation of the compressive strength as a function of disproportionation time for the samples at fixed temperature was examined and the results are shown in Fig. 2. It is apparent that the compressive strength at each temperature in-

creases as the disproportionation time increases and then levels off. For the sample disproportionated at low temperature, the strength has not reached the peak value within the period used in the present study and still increases. The gradual increase in the compressive strength is due, needless to say, to the increase in the amount of the disproportionated phase as the time goes on.

It should be interesting to know whether the high compressive strength observed from the fully disproportionated sample can be maintained when it is subjected to a subsequent recombination. The fully disproportionated sample (disproportionated at 800 °C for 2 h) was subjected to recombination under vacuum at various temperatures for 1 h. The variation of the strength as a function of the recombination temperature is shown in Fig. 3. It appears that the compressive strength of the samples recombined at temperatures lower than 800 °C still shows relatively high strength over 70 kgf/mm². On the other hand, the samples recombined at higher temperature above 850 °C have significantly low strength around 30 kgf/mm². The high strength observed in the samples recombined at lower temperature may be due to the presence of a significant amount of the tough disproportion-

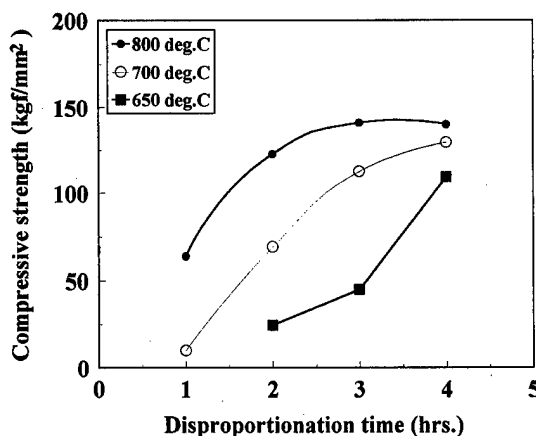


FIG. 2. Variations of the compressive strength as a function of disproportionation time at various temperatures for the hydrogenated magnet.

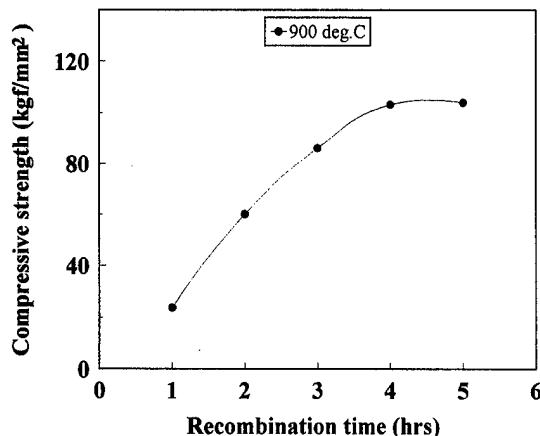


FIG. 4. Variation of the compressive strength as a function of recombination time at 900 °C for the fully disproportionated material.

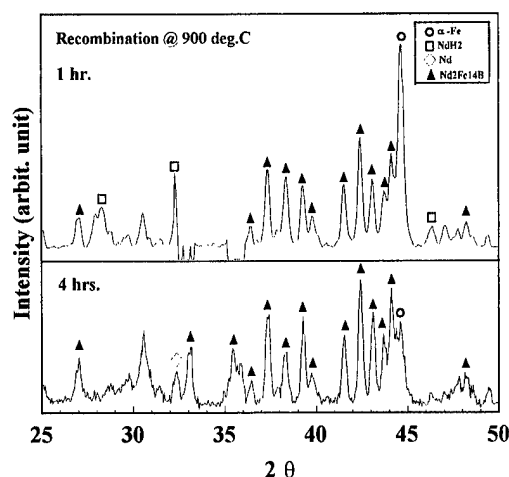


FIG. 5. X-ray diffraction spectrum of the materials recombined at 900 °C for different periods.

tionated phases which have not been recombined. As the temperature increases the recombination reaction may proceed more rapidly, and a greater amount of the recombined grains may be formed. The lower strength of the samples recombined at higher temperature may, therefore, be attributed to the reduction of the tough disproportionated phases. It should be noted that this sample may certainly have a significant amount of recombined phase. The recombined grains may, however, be distributed discontinuously throughout the sample and no significant adhesion between the grains may have been achieved. This may possibly explain the low strength observed from the samples recombined at higher temperatures.

It should be interesting to see whether the low strength of the sample recombined at higher temperatures observed in the previous result can be enhanced by a further recombination. The change of compressive strength with the recombination time at 900 °C was examined and the result is shown in Fig. 4. It is apparent that the strength increases as the recombination time increases, and then levels off after 4 h. As discussed earlier, the low strength observed from the samples recombined for shorter periods may be attributed to the reduction of tough disproportionated phases (see Fig. 5). As the time increases the recombination may continue, thus resulting in further reduction of the disproportionated phases and leading to a greater formation of the recombined $\text{Nd}_2\text{Fe}_{14}\text{B}$ phase (see Fig. 5). It should be emphasized here that the recombined grains may begin to distribute more continuously throughout the sample and adhere together. The strength of the sample may, therefore, be recovered, and this explains the gradual increase in the strength with recombina-

tion time. The saturation of the strength enhancement observed from the samples recombined longer than 4 h may be due to the completion of the recombination. It is worth noting that, as can be seen in the Fig. 4, the fully recombined sample has a comparable or even higher strength with respect to the initial sintered material prior to the solid HDDR. The present study thus indicates clearly that a properly controlled solid-HDDR process can lead to a material in a solid form with a sufficient mechanical strength. It should be noted that the development of magnetic properties with the solid-HDDR step has not been studied in the present work. Further work is presently under way to investigate the magnetic properties using a cast ingot material.

IV. CONCLUSIONS

The compressive strength of the solid-HDDR material was measured for the sintered magnet under various HDDR conditions, and it has been found that the low strength of the hydrided material was improved by the subsequent disproportionation. The restoration of the strength was explained by the eutectoidlike disproportionation structure containing fine neodymium hydride rod embedded in tough iron matrix. The high strength of disproportionated material was reduced radically in an earlier stage of recombination, and this was explained by the reduction of the disproportionated phase. The reduced strength was, however, recovered by further recombination, and this was explained by the fact that, as the recombination continues, the recombined grains become continuous and adhere together. The optimally HDDR processed material has a comparable or even higher strength with respect to the initial sintered material prior to the solid-HDDR. The present study suggested that the mechanical strength of Nd-Fe-B-type material could be retained even after the solid-HDDR.

ACKNOWLEDGMENT

The authors would like to acknowledge that the present work was supported by the Korea Science and Engineering Foundation under Grant No. 961-0806-041-2.

¹I. R. Harris, Proceedings of the 12th International Workshop on RE Magnets and Application, Canberra, Amsterdam, 1992 (unpublished), p. 347.

²T. Takeshita, J. Alloys Compd. **193**, 231 (1993).

³H. W. Kwon, IEEE Trans. Magn. **32**, 4398 (1996).

⁴H. W. Kwon, IEEE Trans. Magn. **33**, 3826 (1997).

⁵X. J. Zhang, P. J. McGuinness, and I. R. Harris, J. Appl. Phys. **69**, 5838 (1991).

⁶N. Martinez, D. G. R. Jones, and O. Gutfleisch, J. Appl. Phys. **76**, 6825 (1994).

⁷O. Gutfleisch, N. Martinez, and I. R. Harris, Proceedings of the 8th International Symposium on Magnetic Anisotropy and Coercivity in RE-TM alloys, Sao Paulo, Brazil, 1996 (unpublished), p. 243.

Thermal expansion of compounds $R_{n+1}\text{Co}_{3n+5}\text{B}_{2n}$ ($R=\text{Y}$ and Gd ; $n=1, 2, 3$, and ∞)

H. Ido, Y. Suzuki, and T. Suzuki

Department of Applied Physics, Tohoku Gakuin University, Tagajo 985, Japan

Thermal expansions of the lattice parameters a and c of the system in the title have been measured by x-ray diffraction technique to investigate the nature of magnetic interactions as well as chemical bond in these systems. Our data reveals that a spontaneous magnetostriction caused by the Co-Co intrasublattice interaction in YCo_4B ($n=1$) occurs in the c plane unlike YCo_5 whose magnetostriction occurs only along the c axis. It is also found that the positive spontaneous magnetostriction of GdCo_4B in the c plane can be divided into three contributions due to the Co-Co, Co-Gd, and Gd-Gd interactions in the crystal. Thermal expansion coefficients in the c plane in the paramagnetic temperature region strongly decrease with increasing n in the Gd system. This implies a significant covalent bonding in the R-B layer in the present compounds. These results are discussed on the basis of the results of energy band calculation together with the previous magnetic data. © 1998 American Institute of Physics. [S0021-8979(98)36411-7]

I. INTRODUCTION

The compound systems expressed by the general formula $R_{n+1}\text{Co}_{3n+5}\text{B}_{2n}$ (R : rare earth; $n=0, 1, 2, 3$, and ∞) are known to have interesting crystallographic regularity as shown in Fig. 1.^{1,2} Recently energy band calculations were performed³ for YCo_4B and YCo_3B_2 compounds, and the magnetic moment of the Co atoms at the different crystallographic sites (see Fig. 1) were also evaluated and found to be in qualitative agreement with experimental data. These results reflect the crystallographic regularity. In this work, thermal expansions along the a and c axis were measured by x-ray diffraction for the systems in the title to obtain spontaneous magnetostrictions in the ferrimagnetic ($R=\text{Gd}$) or ferromagnetic ($R=\text{Y}$) temperature region and thermal expansion coefficients in the paramagnetic temperature region. The former provides an information about the nature of exchange interactions and the latter the nature of chemical bonds in the present compound systems. Experimental data are discussed by taking into account the crystallographic regularity shown in Fig. 1.

II. EXPERIMENTAL METHOD AND RESULTS

To determine the temperature variations of the lattice parameters a and c , x-ray ($\text{CuK}\alpha$) diffraction angles of (200)

and some (00 l) lines for powdered samples were measured as function of temperature. The results are shown in Figs. 2 to 6.

Curie temperatures determined by magnetization measurements are also shown by arrows in Figs. 2 to 6. Spin reorientation from axial to planar anisotropy with decreasing temperature was found only for YCo_4B ² at around T_{SR} shown in Fig. 3. A small anomaly was found for the a axis near T_{SR} , which was also found in the work by Hong *et al.*⁴ From the data shown in Figs. 2 to 6, we obtained the following main results; (1) the spontaneous magnetostriction occurs only for the a axis, (2) the spontaneous magnetostriction of the Gd system is larger than that of the Y system (see Figs. 2 and 3), which seems to decrease with increasing n because there are no clear anomaly at the Curie temperatures (see Fig. 5), and (3) a linear thermal expansion coefficients α_a ($=1/ada/dT$) and α_c ($=1/cdc/dT$) in the paramagnetic temperature region showing a clear contrast, namely, α_a and α_c decreases and increases significantly with increasing n , respectively, as illustrated in Fig. 7. The above results (1) and (2) correlate with the nature of magnetic interactions in the present compound systems, and the result (3) shows the

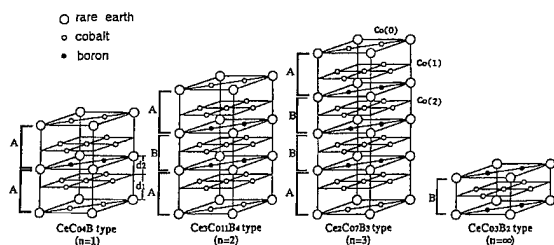


FIG. 1. Crystal structure of $R_{n+1}\text{Co}_{3n+5}\text{B}_{2n}$ compound system. The crystallographic units A and B, and three different Co atoms, Co(0), Co(1), and Co(2) are explained and used in the text.

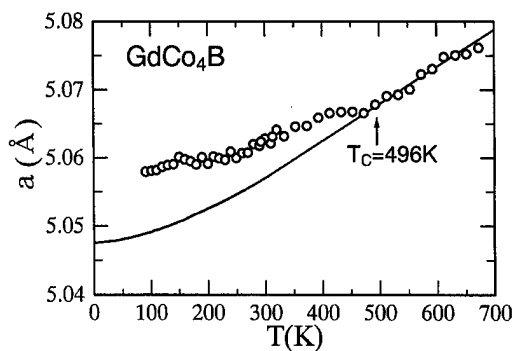


FIG. 2. Temperature dependence of a axis for GdCo_4B . T_C means Curie temperature. The solid line is drawn on the basis of the normal thermal expansion of nonmagnetic compound YNi_4B (Ref. 4).

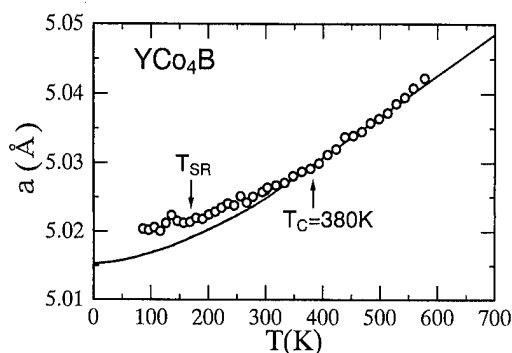


FIG. 3. Temperature dependence of a axis for YCo_4B . T_{SR} means spin reorientation temperature. The solid line is drawn on the basis of the normal thermal expansion of nonmagnetic compound YNi_4B (Ref. 4).

nature of the chemical bond in the present systems having the crystallographic regularity shown in Fig. 1.

III. DISCUSSION OF EXPERIMENTAL RESULTS

A. Thermal expansion in the paramagnetic temperature region

It is convenient to discuss first the results (3) mentioned above. It is very interesting that α_a decreases significantly as n (or B content) increases and reaches $0.87 \times 10^{-6} \text{ deg}^{-1}$ at $n = \infty$ (or GdCo_3B_2). This value is even smaller than the linear thermal expansion coefficient of diamond⁵ ($= 1.0 \times 10^{-6} \text{ deg}^{-1}$), which implies that a strong covalent bond is formed in the R-B layer. The n -dependence of α_a can be explained by the fact that the number of R-B layer in the crystals of $\text{R}_{n+1}\text{Co}_{3n+5}\text{B}_{2n}$ increase as n increases as seen in Fig. 1. It is also noted² that the a axis of $\text{R}_{n+1}\text{Co}_{3n+5}\text{B}_{2n}$ expands significantly as n changes from $n=0$, where there is no R-B layer, to $n=1$ though the atomic radius of B is smaller than that of the Co atom. This fact also may suggest the existence of the strong covalent bond in the R-B layer mentioned above.

Before discussing the n -dependence of α_c , we will discuss the magnetic moments of the Co atoms in $\text{R}_{n+1}\text{Co}_{3n+5}\text{B}_{2n}$. As seen in Fig. 1, there are three kinds of Co atoms expressed by Co(0), Co(1), and Co(2) which oc-

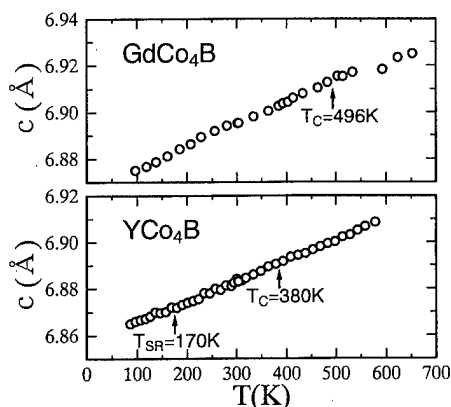


FIG. 4. Temperature dependence of c axis for GdCo_4B and YCo_4B . No spontaneous magnetostriction is observed.

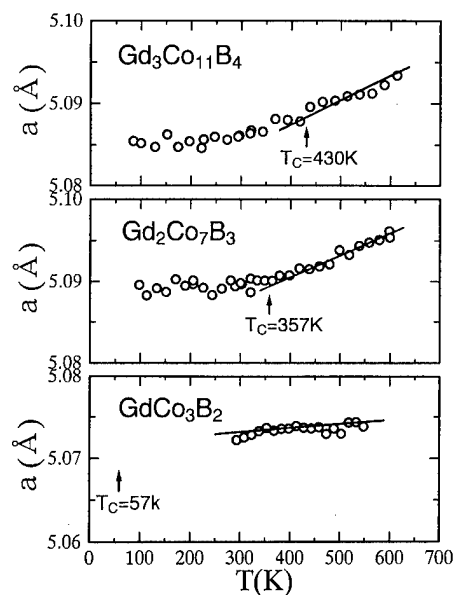


FIG. 5. Temperature dependence of a axis for $\text{Gd}_{n+1}\text{Co}_{3n+5}\text{B}_{2n}$ with $n = 2, 3$, and ∞ .

cupy the different crystallographic sites. Co(N), where N is 0, 1 or 2, means the Co atom having N -neighboring R-B layer(s). If the magnetic moment of Co(N) is expressed by $\mu_{\text{Co}}(N)$ and is assumed to be constant throughout the $\text{Y}_{n+1}\text{Co}_{3n+5}\text{B}_{2n}$ system, the averaged Co moment $\mu_{\text{Co}}(n)$ is expressed by the following equation for n :

$$\mu_{\text{Co}}(n) = (2\mu_{\text{Co}}(0) + 6\mu_{\text{Co}}(1) + 3(n-1)\mu_{\text{Co}}(2)) / (3n+5). \quad (1)$$

YCo_3B_2 which includes only Co(2) was found to be Pauli paramagnetic with a susceptibility of $\chi = 1.9 \times 10^{-6} \text{ emu/g}$, therefore $\mu_{\text{Co}}(2) = 0$. Our previous experimental data $\mu_{\text{Co}}(1) = 0.632 \mu_B$, and $\mu_{\text{Co}}(2) = 0.465 \mu_B$ were measured. We obtain $\mu_{\text{Co}}(0) + 3\mu_{\text{Co}}(1) = 2.53 \mu_B$ and $2.56 \mu_B$ by put-

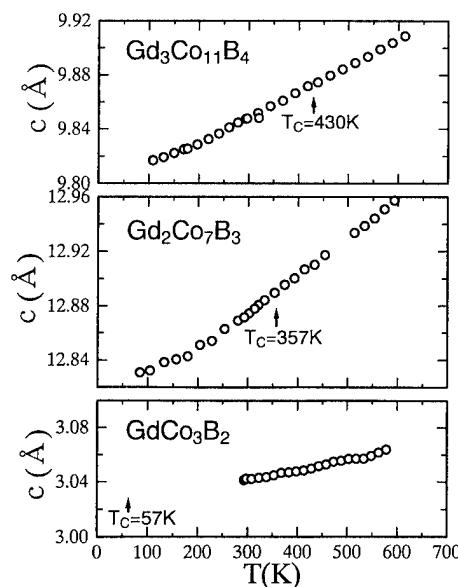


FIG. 6. Temperature dependence of c axis for $\text{Gd}_{n+1}\text{Co}_{3n+5}\text{B}_{2n}$ with $n = 2, 3$, and ∞ .

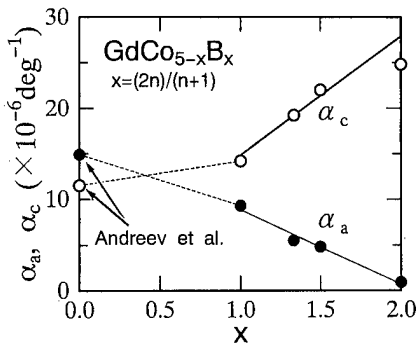


FIG. 7. Boron composition dependence of thermal expansion coefficients α_a and α_c . The data for $n=0$ are taken from Ref. 8.

ting the values of $\mu_{Co}(1)$ and $\mu_{Co}(2)$ mentioned above into Eq. (1), respectively. The obtained values of 2.53 and 2.56 are very close to each other, which means Eq. (1) is a good approximation. If $\mu_{Co}(0)$ is approximated by the Co moment of YCo_5 , $(1.55 \pm 0.10)\mu_B$ averaged over the five different data obtained in the previous work,⁷ we obtain $\mu_{Co}(1) = 0.33\mu_B$. The values of $\mu_{Co}(0) = 1.55\mu_B$, $\mu_{Co}(1) = 0.33\mu_B$ and $\mu_{Co}(2) = 0\mu_B$ are qualitatively supported by the energy band calculation³ for YCo_4B and YCo_3B_2 ; $\mu_{Co}(0) = 1.75\mu_B$, $\mu_{Co}(1) = 0.55\mu_B$ and $\mu_{Co}(2) = 0\mu_B$. To confirm if the above values are valid or not, neutron diffraction measurement will be performed. Equation (1) is based on the assumption that all crystallographic units A and B shown in Fig. 1 have approximately the same electronic state, respectively. Therefore all units A and B shown in Fig. 1 are considered to have the same thermal expansion coefficients $\alpha_c(A)$ and $\alpha_c(B)$ along the c axis, respectively. If $\alpha_c(A) = 15 \times 10^{-6} \text{ deg}^{-1}$ and $\alpha_c(B) = 28 \times 10^{-6} \text{ deg}^{-1}$ are assumed, the n -dependence of thermal expansion coefficient $\alpha_c(n)$ is calculated as shown by the bold solid line in Fig. 7. Agreement between the solid line and the observed values is good, which supports the assumption of Eq. (1). It is also noted that α_c and α_a for $GdCo_3B_2$ shows a clear contrast like the case of graphite⁵ whose linear thermal expansion coefficients at room temperature are $\alpha_c = 25.9 \times 10^{-6} \text{ deg}^{-1}$ and $\alpha_{\perp c} = -1.2 \times 10^{-6} \text{ deg}^{-1}$.

B. Spontaneous magnetostriction

It is noted that the spontaneous magnetostriction in Figs. 2 and 3 occurs only along the a axis (or in the c plane), which contrasts with the case of YCo_5 whose striction occurs only along the c axis.⁸ For this fact, the R-B layer(s) must play an important role, namely the strong covalent bond in the R-B layer disconnects the exchange interaction along the c axis. This is supported also by the drastic change of T_c between YCo_5 ($T_c = 980 \text{ K}$)⁷ and YCo_4B ($T_c = 380 \text{ K}$). The spontaneous magnetostriction of $GdCo_4B$ in Fig. 2 comes from the inter- and intrasublattice exchange interactions with exchange parameters J_{Gd-Co} , J_{Co-Co} , and J_{Gd-Gd} , while that of YCo_4B from intrasublattice interaction J_{Co-Co} only. The spontaneous magnetostriction $\omega_a (= \Delta a/a)$ can be expressed by the mean field model,⁹

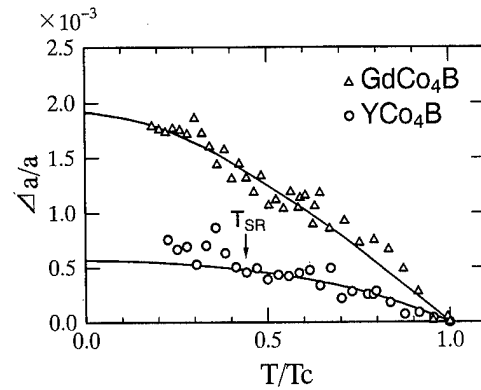


FIG. 8. Spontaneous magnetostrictions for $GdCo_4B$ and YCo_4B obtained from Figs. 2 and 3. The solid lines are the calculated ones (see the text).

$$\omega_a = A_{Co-Co} M_{Co}^2 + B_{Co-Gd} M_{Co} M_{Gd} + C_{Gd-Gd} M_{Gd}^2, \quad (2)$$

where M_{Co} and M_{Gd} are the sublattice spontaneous magnetizations in the unit of $\mu_B/f.u.$, where $f.u.$ means RCo_4B , and A_{Co-Co} , etc., are constants proportional to products of $(c_{11} + c_{12})^{-1}$, and $\partial J_{Co-Co}/\partial a$, $\partial |J_{Gd-Co}|/\partial a$ and $\partial J_{Gd-Gd}/\partial a$, respectively, where c_{ij} is the elastic constant.⁹ Since temperature dependences of M_{Co} and M_{Gd} of $GdCo_4B$ and YCo_4B have been obtained,⁶ we can calculate ω_a for RCo_4B ($R=Gd$ and Y) as shown by the solid lines in Fig. 8. In this calculation, we take $A_{Co-Co} = 9.0 \times 10^{-5} \mu_B^{-2}$, $B_{Gd-Co} = 11.0 \times 10^{-5} \mu_B^{-2}$, and $C_{Gd-Gd} = -1.2 \times 10^{-5} \mu_B^{-2}$. The spontaneous magnetostrictions seem to be well expressed by Eq. (2). Since the values of M_{Co} and M_{Gd} at $T=0 \text{ K}$ were taken to be $2.53 \mu_B/f.u.$ and $7.0 \mu_B/f.u.$, the main contribution to the spontaneous magnetostriction is found to be the second term in Eq. (2). Since $B_{Gd-Co} \propto (c_{11} + c_{12})^{-1} (\partial |J_{Gd-Co}|/\partial a)$, the absolute value of J_{Gd-Co} increases with the a -axis expansion. The spontaneous magnetostriction of the Gd system with $n=2$ and $n=3$ are not clearly observed, as seen in Fig. 5. This fact can be explained by the increase of c_{ij} caused by the strong covalent bond in the R-B layer(s).

¹ P. Rogl, in *Handbook on the Physics and Chemistry of Rare Earths*, edited by K. A. Gschneider and L. Eyring (North-Holland, Amsterdam, 1984), Vol. 6, p. 335.

² H. Ogata, H. Ido, and H. Yamauchi, *J. Appl. Phys.* **73**, 591 (1993).

³ H. Yamada, K. Terao, H. Nakazawa, I. Kitagawa, N. Suzuki, and H. Ido, *J. Magn. Magn. Mater.* **183**, 94 (1998).

⁴ N. M. Hong *et al.* (private communication).

⁵ *Table of Constants in Physics* (in Japanese), edited by Iida (Asakura Shoten, Tokyo, 1969), p. 124.

⁶ Y. Suzuki, T. Ito, T. Uchida, O. Nashima, N. M. Hong, and H. Ido, *J. Appl. Phys.* **81**, 5141 (1997).

⁷ *Landolt-Bornstein, New Series III*, edited by H. R. Kirchmayr and E. Burzo (Springer, Berlin, 1990), p. 269.

⁸ A. V. Andreev, in *Handbook of Magnetic Materials*, edited by K. H. Buschows (Elsevier, Amsterdam, 1995), Vol. 8, p. 74.

⁹ H. Ido, T. Suzuki, and I. Iguchi, *J. Magn. Magn. Mater.* **31-34**, 159 (1983).

Specific-heat studies of RCu_4Al_8 compounds ($\text{R}=\text{Er}, \text{Y}$)

I. H. Hagmusa, F. E. Kayzel, E. Brück, and K. H. J. Buschow^{a)}

Van der Waals-Zeeman Institute, University of Amsterdam, Valckenierstraat 65, 1018 XE Amsterdam, The Netherlands

Specific-heat measurements have been performed on the tetragonal ThMn_{12} -type compound ErCu_4Al_8 and YCu_4Al_8 in the temperature range 1.5–200 K. A sharp peak in the specific heat, signals the antiferromagnetic transitions at $T_N = 5.18$ K. In order to separate out the effect of the Er sublattice we have also performed measurements on the YCu_4Al_8 compound in the same temperature range. From the temperature dependence of the magnetic contribution to the specific heat of ErCu_4Al_8 we obtained the temperature dependence on the magnetic entropy and discuss our results in terms of the crystal field level scheme proposed earlier from inelastic neutron scattering.

© 1998 American Institute of Physics. [S0021-8979(98)53411-1]

INTRODUCTION

Ternary-rare-earth compounds of the type RT_4Al_8 crystallize in the ThMn_{12} -type crystal structure in which rare-earth atoms occupy the $2a$ position, transition metal (T) the $8f$, and aluminum the $8i$ and $8j$ positions.^{1,2} They exist for several $3d$ transition elements including $\text{T}=\text{Cr}, \text{Mn}, \text{Fe}$, and Cu . The magnetic properties of these compounds depend strongly on the T component and vary between no magnetic ordering above 1.6 K for $\text{T}=\text{Mn}$ and magnetic-ordering temperatures well above 100 K for $\text{T}=\text{Fe}$. Much higher-ordering temperatures can be realized with the same structure type for compounds of compositions around $\text{RFe}_{10}\text{M}_2$ where $\text{M}=\text{Si}, \text{Ti}, \text{V}, \text{W}$, and Mo .³ Several of the latter compounds are considered as candidates for permanent-magnet materials and owe most of their magnetocrystalline anisotropy to the crystal-field induced R sublattice anisotropy. This crystal-field induced anisotropy is fairly complicated because it seems to be dominated by the contribution of higher-order-crystal-field parameters. The high-ordering temperatures of the $\text{RFe}_{10}\text{M}_2$ compounds prevent a thorough study of the crystal-field interaction in ThMn_{12} compounds. For this reason crystal-field studies have mainly concentrated on RT_4Al_8 representatives in which magnetic ordering occurs at very low temperatures or is absent altogether. In view of the many parameters involved, experimental information obtained by a technique complementary to the inelastic neutron scattering⁴ is desirable.

In the present investigation we report on specific-heat measurements performed in zero magnetic field on the ErCu_4Al_8 and YCu_4Al_8 compounds in the temperature range 1.5–200 K. The results are discussed in terms of the crystal-field-level scheme presently available from INS spectroscopy.⁴

EXPERIMENTAL DETAILS

The samples of the ErCu_4Al_8 and YCu_4Al_8 compounds were prepared in polycrystalline form by melting stoichiometric amounts of the elements (of at least 99.9% purity) in

an arc furnace under a reduced argon atmosphere. Vacuum annealing was performed at 800 °C for 6 weeks. Selected specimens of each sample were subsequently characterized by x-ray diffraction and were shown to be single phase with all Bragg peaks consistent with ThMn_{12} structure.

We have measured the specific heat in zero field in the temperature range from 1.5 to 200 K. About 200–400 mg of each compound were mounted on a sapphire plate in a thermal frame by using apiezone. This setup comprises the possibilities for measurements using the standard adiabatic method.

RESULTS AND DISCUSSION

The specific heat of the ErCu_4Al_8 and YCu_4Al_8 compounds has been measured at zero-magnetic field as a function of temperature. Plots of c/T vs T at zero field are given in Fig. 1. The data shown for ErCu_4Al_8 are characterized by

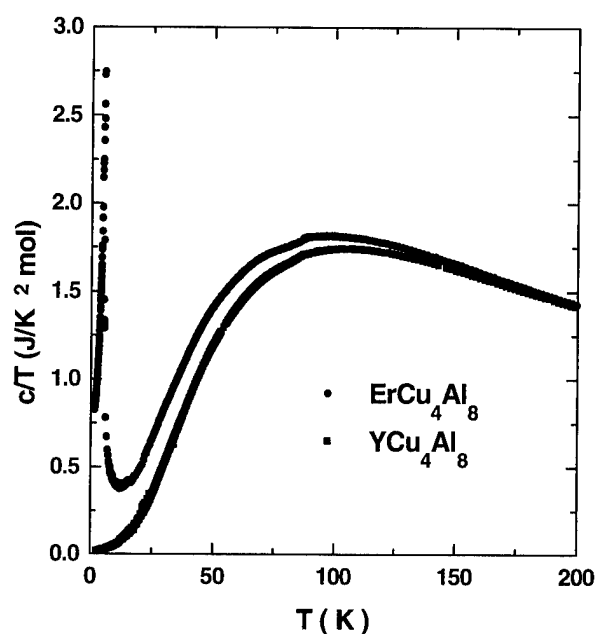


FIG. 1. Temperature dependence of the specific heat (c/T) of the ErCu_4Al_8 and YCu_4Al_8 compounds.

^{a)}Electronic mail: buschow@phys.uva.nl

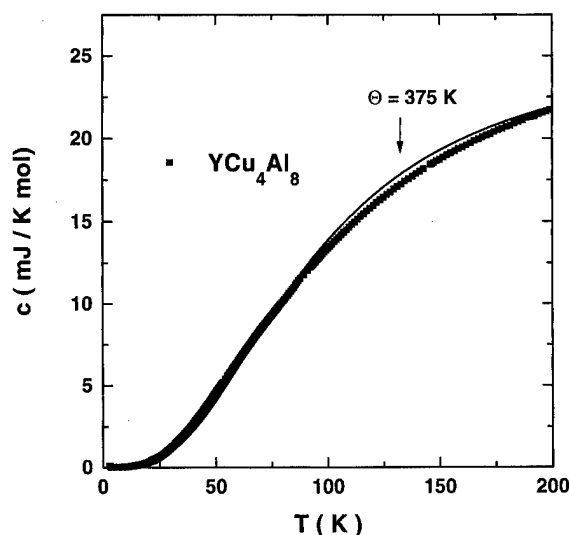


FIG. 2. Temperature dependence of the specific heat (c) of YCu_4Al_8 . The thin solid curve represents a fit to the data points made on the basis of Eq. (1).

a sharp anomaly at 5.18 K. This anomaly is attributed to antiferromagnetic ordering. A Néel type transition at $T_N = 6$ K has also been observed by magnetic measurements,⁵ and the antiferromagnetic nature of the magnetic ordering has been confirmed by neutron diffraction experiment performed by Baio *et al.*⁶

As seen in Fig. 1, no peak is observable in the same temperature range for YCu_4Al_8 . The specific-heat data of this compound have been analyzed by using the formula

$$c = \gamma T + 9Nk_B(T/\Theta_D) \int_0^{\Theta_D/T} \frac{x^4 e^x dx}{(e^x - 1)^2} \quad (1)$$

where γ is the electronic specific-heat coefficient and Θ_D the Debye temperature. From a plot of c/T vs T^2 of the low-temperature data, we have determined γ to be equal to $0.02 \text{ J/K}^2\text{mol}$. From fitting the specific heat curve over the whole temperature range considered we derived $\Theta_D = 375 \text{ K}$. The experimental data and the calculated curve are compared in Fig. 2. These data were subsequently used to separate out the magnetic contribution to the specific heat of the Er sublattice.

In Fig. 3 we have plotted the temperature dependence of c_m/T , where c_m is the magnetic specific heat for the ErCu_4Al_8 compound, obtained by subtracting the nonmagnetic part from the observed specific heat. These data have been used, in turn, to obtain the temperature dependence of S_m/R , where S_m is the magnetic entropy. The temperature dependence of S_m/R is also shown in Fig. 3.

The crystal field splitting in the ErCu_4Al_8 compound was studied earlier by inelastic neutron scattering (INS) experiments.⁴ These experiments had led to propose a level scheme in which the ground state is a doublet state, particularly rich in $|J_z = \pm 7/2\rangle$. The first excited level, lying at about 42 K from the ground state, is a doublet dominated by the $|J_z = \pm 9/2\rangle$ wave function. The overall crystal field splitting is about 313 K. The magnetic ordering at about 5.2 K involves therefore mainly the isolated ground state doublet.

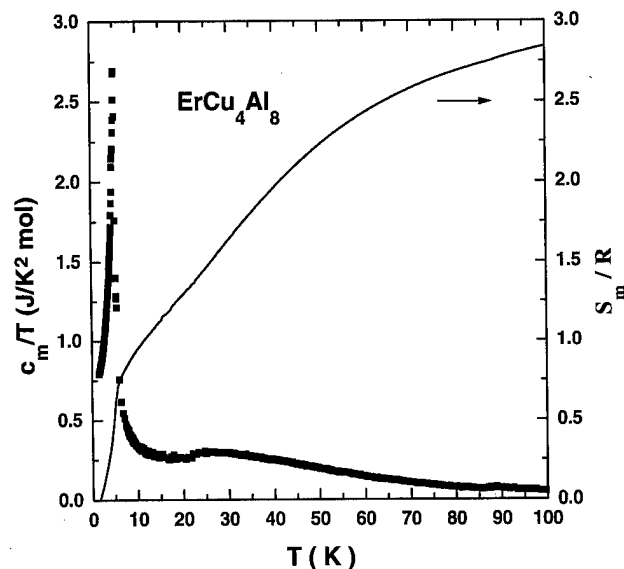


FIG. 3. Temperature dependence of the magnetic contribution to the specific heat (c_m/T) of ErCu_4Al_8 (left scale). The thin solid curve represents the temperature dependence of the magnetic entropy (right scale).

The entropy reached at the magnetic transition is expected to be equal to $R \ln 2 = 0.7$, which is in satisfactory agreement with the data shown in Fig. 3. It can furthermore be seen in Fig. 3 that in the paramagnetic regime a small Schottky anomaly is found, leading to a shallow maximum in the specific heat curve at about 25 K. It is well known that Schottky anomalies of this type are generally observed at temperatures roughly halfway in temperature between the ground state and the first excited state. The specific heat data are therefore in reasonable agreement with the level separation of 42 K mentioned above. Finally, at high temperatures, the entropy is expected to reach its maximum value $R \ln(2J+1)$. For Er with $J = 15/2$ this maximum value corresponds to $S_m/R = \ln(16) = 2.77$. This value is seen in Fig. 3 to be reached at 100 K. We previously mentioned that the INS measurements had indicated an overall crystal field splitting of 313 K and from the corresponding level scheme it can be derived that at 100 K only about half of the levels will be populated. At first sight this seems to be in conflict with the entropy data presented in Fig. 3. However, one has to bear in mind that the magnetic contribution to the specific heat of ErCu_4Al_8 has been obtained by using the YCu_4Al_8 data for estimating the phonon contribution. In view of the large difference in atomic weight between Er and Y, the phonon contribution based on the YCu_4Al_8 data very likely is underestimated. It means that the magnetic contribution of ErCu_4Al_8 is somewhat too large, in particular in the high-temperature regime. This, in turn, leads to an overestimation of S_m/R in the high-temperature part and causes the apparent discrepancy with the INS data. An extension of our specific heat measurements to more compounds of this series is planned in the near future.

- ¹O. Moze, R. M. Ibberson, and K. H. J. Buschow, *J. Phys.: Condens. Matter* **2**, 1677 (1990).
- ²T. Kamimori, W. L. Liu, H. Kadomatsu, M. Goto, and H. Fujiwara, *J. Phys. C* **8**, Suppl. 49, 381 (1988).
- ³H. S. Li and J. M. D. Coey, in *Magnetic Materials*, edited by K. H. J. Buschow (Elsevier Science, Amsterdam, 1991), Vol. 6.
- ⁴R. Caciuffo, G. Amoretti, K. H. J. Buschow, O. Moze, A. P. Murani, and B. Paci, *J. Phys.: Condens. Matter* **7**, 7981 (1995).
- ⁵I. Felner and I. Nowik, *J. Phys. Chem. Solids* **40**, 1035 (1979).
- ⁶G. Baio, O. Moze, G. Amoretti, R. Sonntag, N. Stüsser, and K. H. J. Buschow, *Z. Phys. B* **102**, 449 (1997).

Magnetic and structural properties of commercial $\text{Sm}_2(\text{Co,Fe,Cu,Zr})_{17}$ -based magnets

X. Chen, J. F. Liu, C. Ni, and G. Hadjipanayis^{a)}

Department of Physics and Astronomy, University of Delaware, Newark, Delaware 19716-2570

A. Kim

YBM MAGNEX, Inc., 110 Terry Drive, Newtown, Pennsylvania 18940

A newly developed $\text{Sm}(\text{Co,Fe,Cu,Zr})_z$ magnet, with $z \approx 7$, has a lower temperature coefficient of coercivity β , as compared with other commercial magnets with $z \approx 7.7$. It was found that the initial magnetization curve for the newly developed magnet is typical of pure uniform domain wall pinning, while for the commercial magnets nucleation and domain wall pinning occur simultaneously, although domain wall pinning is still the dominant mechanism. It was also found that the magnetic viscosity parameter S_v has similar temperature dependence with the coercivity. Transmission electron microscope studies showed that the smaller cell size contributes to the low temperature coefficient of coercivity. © 1998 American Institute of Physics.

[S0021-8979(98)20011-9]

I. INTRODUCTION

In permanent magnets, the coercivity and remanence decrease with increasing temperature with rates, known as temperature coefficients, given by $\beta = dH_c/dT$ and $\alpha = dM_r/dT$, respectively. $\text{Sm}_2(\text{Co,Fe,Cu,Zr})_{17}$ magnets so far have the lowest temperature coefficient among rare-earth permanent magnets, and hence, they are very promising candidates for high temperature applications. The coercivity temperature coefficient β ($\sim 0.3\%/^\circ\text{C}$) is much higher than the remanence temperature coefficient α ($\sim 0.03\%/^\circ\text{C}$), and because of this, the coercivity is reduced more rapidly with increasing temperature than the remanence. The low coercivities at high temperatures lead to a very low energy product and limit the high temperature applications of these magnets.

The coefficient β is strongly dependent on the magnetization reversal mechanism, which is sensitive to the magnet composition, processing parameters, microstructure, and microchemistry of the phases present. Earlier studies showed that SmCo_5 , SmTM_7 , and $\text{SmTM}_{7.43}$ magnets have different high temperature behavior.¹ Recent studies showed that the high temperature performance of $\text{Sm}_2(\text{Co,Fe,Cu,Zr})_{17}$ -based magnets is very sensitive to the iron content. High iron content resulted in a greater irreversible loss.² A $\text{Sm}(\text{Co,Fe,Cu,M})_7$ magnet, where M is at least one or a combination of Zr, Hf, Ti, Mn, Nb, V, Mo, and W, was found to effectively reduce the temperature coefficient of coercivity with a moderately high room temperature coercivity (~ 20 kOe) and good loop squareness.³ But it is not yet clear why their high temperature behavior is different. A systematic investigation of magnetic and structural properties of $\text{Sm}_2(\text{Co,Fe,Cu,Zr})_{17}$ -based magnets is needed in order to understand their high temperature behavior and find a way to improve their performance at temperatures above 400°C .

II. EXPERIMENT

Several $\text{Sm}_2(\text{Co,Fe,Cu,Zr})_{17}$ -based magnets from Crucible, EEC, and Arnold were used to study and understand the temperature dependence of magnetic properties up to 600°C . The crystallographic structure was studied using a Philips x-ray diffractometer. The magnetic properties at and below room temperature were tested using a superconducting quantum interference device (SQUID) magnetometer with a maximum applied field of 55 kOe. High temperature magnetic properties were measured using a vibrating sample magnetometer (VSM). Microstructure analysis was carried out using a JEOL JEM-2000FX transmission electron microscope (TEM). Magnetic viscosity measurements were carried out using the VSM.

III. RESULTS AND DISCUSSION

A. Temperature dependence of magnetic properties

All the as-received magnets had the $\text{Th}_2\text{Zn}_{17}$ rhombohedral structure. A typical x-ray diffraction pattern is shown in Fig. 1. The commercial $\text{Sm}(\text{Co, Fe, Cu, Zr})_z$ magnets with $z \approx 7.7$ received from different companies were designated as C1, C2, C3, and C4, the Crucible newly developed magnet with $z \approx 7$ was designated as N1. The Curie temperature, saturation magnetization at 55 kOe, intrinsic coercivity $H_{ci}(\text{RT})$ and $H_{ci}(450^\circ\text{C})$, and temperature coefficient of co-

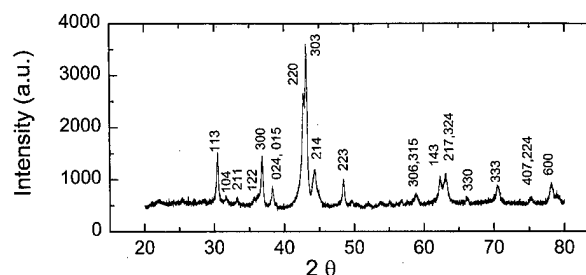


FIG. 1. Typical x-ray pattern of $\text{Sm}_2(\text{Co,Fe,Cu,Zr})_{17}$ magnets.

^{a)}Electronic mail: hadji@udel.edu

TABLE I. Curie temperature T_c , saturation magnetization M_s at 55 kOe, intrinsic coercivity H_{ci} at room temperature and 450 °C, and the temperature coefficient of coercivity β for $\text{Sm}(\text{Co}, \text{Fe}, \text{Cu}, \text{Zr})_z$ magnets.

Sample	T_c (°C)	M_s (emu/g)	H_{ci} (RT) (kOe)	H_{ci} (450 °C) (kOe)	β (%/°C) (RT-450 °C)
C1	810	104	22.6	3.5	-0.20
C2	811	104	23.1	2.9	-0.20
C3	818	112	34.3	3.2	-0.21
C4	815	103	27.7	2.6	-0.21
N1	810	93	19.6	6.2	-0.16

ercivity $\beta(\text{RT}-450^\circ\text{C})$ for all the received magnets were measured and listed in Table I. The temperature coefficient of coercivity ($\text{RT}-T_1$) is calculated using the following formula: $\beta(\text{RT}-T_1) = \{[H_{ci}(\text{RT}) - H_{ci}(T_1)]/[H_{ci}(\text{RT}) \times (\text{RT} - T_1)]\} \times 100\%$, where T_1 is the operation temperature. The Curie temperature for all the samples is above 800 °C with small differences of less than 10 °C. A single value of Curie temperature for each sample was identified during measurements. Sample N1 has the highest coercivity at 450 °C and lowest temperature coefficient of H_{ci} . The temperature dependence of coercivities for all the samples is shown in Fig. 2. It is interesting to note that sample N1, with a H_{ci} of 6.2 kOe at 450 °C, has the lowest coercivity at room temperature, while sample C3, with a H_{ci} of only 3.15 kOe at 450 °C, has the highest coercivity at room temperature. Therefore, high room temperature coercivity does not necessarily mean high coercivity at higher temperatures.

B. Initial magnetization curves

Figure 3 shows the normalized initial magnetization curves at room temperature. Samples N1, which has the highest coercivity above 400 °C, and C1 to C4, which have very low coercivity above 400 °C, show a strong pinning dominated initial magnetization curve, but if we take a closer look at the initial curves, they are different. The initial curve for N1 is typical of pure uniform strong domain wall pinning, while the initial curve for sample C3 is typical of mixed pinning and nucleation mechanisms. Nucleation and domain wall movement occurs at very low applied fields and then the domain wall is pinned by strong pinning sites. For samples C1, C2, and C4, local nucleation and domain wall

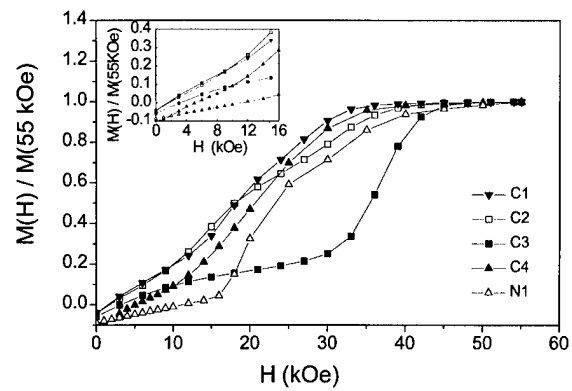


FIG. 3. Normalized initial magnetization curves at room temperature.

pinning processes occur simultaneously, although, in general, it is still dominated by a strong domain wall pinning mechanism.

We believe that pure and uniform strong domain wall pinning is a critical factor for high coercivity at high temperatures for $\text{Sm}(\text{Co}, \text{Fe}, \text{Cu}, \text{Zr})_z$ magnets.

C. Magnetic viscosity analysis

Magnetic viscosity analysis is another way to understand the behavior of magnetization reversal. From the logarithmic dependence of magnetization, the magnetic viscosity coefficient $S = -dM/d \ln(t)$ can be obtained. S is related to the magnetic viscosity parameter (S_v) through the equation $S_v = S/\chi^{\text{irr}}$, where χ^{irr} is the irreversible susceptibility.⁴ Magnetic viscosity measurements were carried out for two typical samples. The detailed measurement method was described elsewhere.⁵ Figure 4 shows the temperature dependence of magnetic viscosity parameter S_v .

The magnetic viscosity parameter S_v for sample N1, which has the highest coercivity at 450 °C, is less temperature dependent, as compared to the C4 sample, which has the lowest coercivity at 450 °C. This result indicates that the magnetic viscosity parameter S_v and coercivity H_{ci} have a similar temperature dependence.

D. Microstructure comparison

TEM analysis showed a similar microstructure for all the 2:17 magnet samples, consisting of a mixture of cellular and

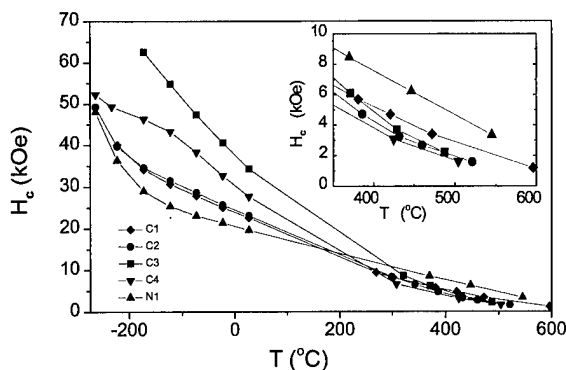


FIG. 2. Temperature dependence of coercivity.

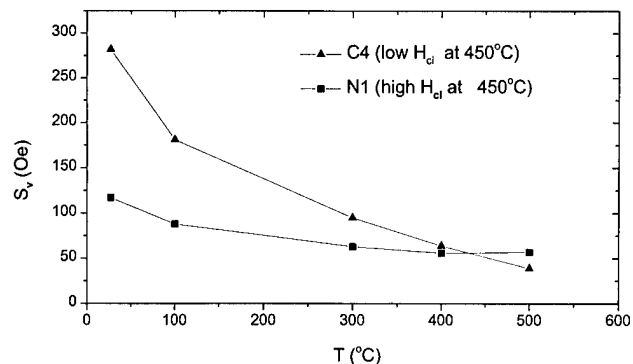


FIG. 4. Temperature dependence of the magnetic viscosity parameter S_v .

TABLE II. Comparison of microscopic features.

Sample	Phases identified	Cell size (nm)	Wall thickness (nm)	Density of lamella
N1	2:17 & 1:5	43	6–15	Low
C1	2:17 & 1:5	63	5–20	High
C2	2:17 & 1:5	75	10–40	High
C4	2:17 & 1:5	80	2–12	High

lamellae structure. A statistical analysis was performed on the cellular and lamellae structure. Table II shows the cell size, the cell boundary thickness, and the density of the lamella phase for all the samples. The microstructure of samples N1 and C2 is shown in Fig. 5. Sample N1, which

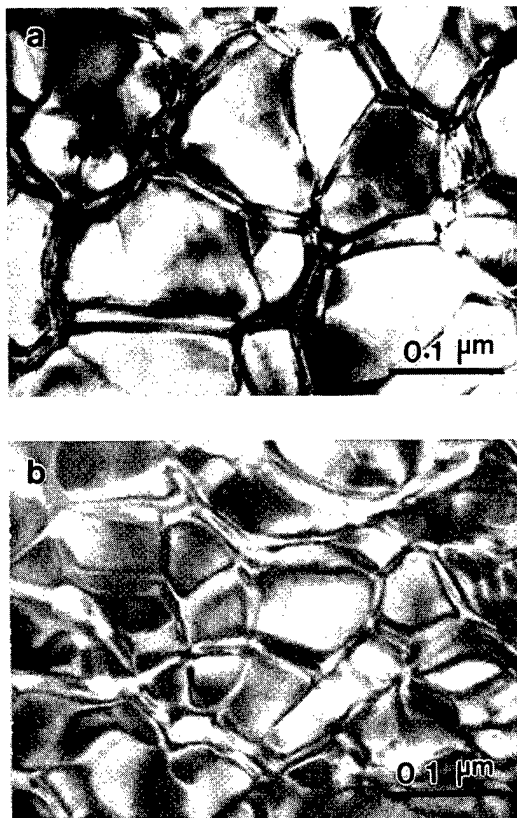


FIG. 5. Microstructure of samples (a) C2 and (b) N1.

has the highest coercivity at 450 °C and lowest temperature coefficient of coercivity β , has the smallest cell size. It should be noted that sample N1 has relatively higher Sm content than all the other samples, and this would help to form more 1:5 cell boundaries according to the phase diagram. Therefore, smaller cells could be expected after a suitable heat treatment. Smaller cell size contributes to a high coercivity at high temperatures. The smaller the cell, the stronger and more uniform the domain wall pinning, and this is confirmed by their initial magnetization curves. All the samples with high density of lamella precipitates have higher coercivity at room temperature. The density of lamella phase can increase the room temperature coercivity but has little contribution to the coercivity at high temperatures, indicating that the pinning force of this lamella phase decreases rapidly as the temperature increases. Smaller cell size is another key feature for the magnets with high temperature performance.

IV. CONCLUSION

The temperature coefficient of coercivity β is a very important factor for the high temperature performance of commercial $\text{Sm}_2(\text{Co}, \text{Fe}, \text{Cu}, \text{Zr})_{17}$ -based magnets. Commercial samples with $z \approx 7.7$ showed a $\beta(\text{RT} - 450^\circ\text{C}) = -0.2\%/^\circ\text{C}$, which resulted in a H_{ci} of about 3 kOe at 450 °C. However, magnet N1 with $z \approx 7$ gave a $\beta(\text{RT} - 450^\circ\text{C})$ of $-0.16\%/^\circ\text{C}$, resulting in a H_{ci} of about 6.2 kOe at the same temperature. It was found that the initial magnetization curve for the magnet with high coercivity at 450 °C is typical of pure strong uniform domain wall pinning, while for the magnet with a low coercivity at 450 °C is typical of mixed mechanism although it is still dominated by domain wall pinning. It was also found that the magnetic viscosity parameter S_v is less temperature dependent for the magnets with a higher coercivity at high temperatures. TEM studies showed that smaller cell sizes have a contribution to high coercivity at high temperatures, while a higher density of the lamella phase leads to higher coercivity at low temperatures.

ACKNOWLEDGMENT

This work is supported by Air Force Office of Scientific Research under Grant No. MURI F49620-96-1-0434.

¹S. Liu, H. F. Mildrum, and K. J. Strnat, J. Appl. Phys. **53**, 2383 (1982).

²S. Liu and E. P. Hoffman, IEEE Trans. Magn. **33**, 3859 (1997).

³A. S. Kim, J. Appl. Phys. **81**, 5609 (1997).

⁴P. Guant, Philos. Mag. **34**, 775 (1976).

⁵J. F. Liu, H. L. Luo, and J. Wan, J. Phys. D **25**, 838 (1992).

The magnetization study of melt-spun ribbons of B containing TbFe₂ alloys

K. S. Kim and S. C. Yu^{a)}

Department of Physics, Chungbuk National University, Cheongju 361-763, Korea

S. R. Kim and S. H. Lim

Thin Film Technology Center, Korea Institute of Science & Technology, Seoul, 130-650, Korea

We have carried out the magnetization study of melt-spun ribbons of $(\text{Tb}_{0.33}\text{Fe}_{0.67})_{1-x}\text{B}_x$ ($x=0, 0.02, 0.05, 0.1, \text{ and } 0.15$) alloys. The temperature dependence of magnetization was measured using a superconducting quantum interference device and a vibrating-sample magnetometer during heating from 5 to 800 K, with an applied field of either 10 or 50 kOe. The present study shows the existence of noncollinear magnetic structures. From an analysis of the approach to saturation magnetization, the average magnetic moment μ_a , random anisotropy field H_r , and local random anisotropy constant K_L have been extracted. It is found that μ_a decreases from 1.68 ($x=0$) to 1.33 μ_B ($x=0.15$) and K_L increases with increasing B concentration. This result suggests that the addition of B seems to increase the random anisotropy and hence to decrease the magnetic order, resulting a sperimagnet with large spread angle. © 1998 American Institute of Physics.

[S0021-8979(98)49411-8]

I. INTRODUCTION

Cubic Laves phase TbFe₂ compound is known to exhibit the largest magnetostriction at room temperature.¹ Nanocrystalline grain structure in TbFe₂-B alloys was by crystallization a melt-spun amorphous phase² and the alloy with nanocrystalline grain structure was found to exhibit better magnetostrictive characteristics at low magnetic fields than for bulk TbFe₂ alloy. Recently, it was shown for giant magnetostrictive RE-Fe [(RE) rare earths] based alloys that homogeneous and ultrafine grains were obtained even in the as-spun state.³ This was made possible at a suitable quenching rate, together with the addition of a suitable amount of B to RE-Fe alloys. We therefore find it appropriate to investigate in detail the magnetic properties of melt-spun $(\text{Tb}_{0.33}\text{Fe}_{0.67})_{1-x}\text{B}_x$ ($x=0, 0.02, 0.05, 0.1, \text{ and } 0.15$) alloys. Abnormal behavior in the temperature dependence of magnetization measured at 10 kOe is observed in all the specimens. Magnetization is very small at low temperatures and it initially increases with increasing temperature, reaches a maximum, and then decreases with the further increase of temperature. This result may be explained by strong random anisotropy at low temperatures. In the framework of the two sublattice model, the abnormal magnetization behavior can be explained in terms of the existence of the conical spin structure which is caused by the noncollinear magnetic couplings between Fe atoms, and between Tb atoms due to the structural disorder. It is noted that the spins from Tb and Fe atoms couple antiferromagnetically. In this article, in order to obtain intrinsic magnetic properties we analyzed the temperature and field dependence of magnetization of melt-spun ribbons of B containing TbFe₂ alloys.

II. EXPERIMENT

The Tb-Fe-B alloys were arc melted in an Ar atmosphere and, in some cases, the alloy ingots were also ob-

tained by induction melting. Subsequent melt spinning was carried out in an Ar atmosphere with a surface velocity of 50 m/s. The melt temperature was maintained at just above the melting point. The ribbons obtained were 20 μm thick and about 1 to 2 mm wide. The structure of the samples was examined by x-ray diffraction using Cu $K\alpha$ radiation and also by transmission electron microscopy (TEM). The formation of an amorphous phase was observed more clearly from TEM. A previously TEM study³ showed that the melt-spun ribbons consists of nanocrystalline grains and an amorphous phase. The magnetization measurements were performed by using a superconducting quantum interference device (SQUID) and a vibrating-sample magnetometer (VSM) during heating from 5 to 800 K, with an applied field of either 10 or 50 kOe.

III. RESULTS AND DISCUSSION

A. Temperature dependence of magnetization

Figure 1 shows the temperature dependence of magnetization for the melt-spun $(\text{Tb}_{0.33}\text{Fe}_{0.67})_{1-x}\text{B}_x$ ($x=0, 0.02, 0.05, 0.1, \text{ and } 0.15$) alloys at 10 kOe. It can be seen in all the curves that the magnetization increases with increasing temperature and reaches a maximum at a temperature T_{max} , above which the magnetization starts to decrease, as expected, upon approaching the Curie temperature T_c . It seems that the applied field of 10 kOe is not enough to magnetize the specimens at low temperatures. With increasing B content, the magnetization at T_{max} decreases from 90 ($x=0$) to 72 emu/g ($x=0.15$). In the framework of the two sublattice model, the abnormal behavior of these magnetization curves can be explained in terms of the existence of noncollinear magnetic structures. Figure 1 shows the temperature dependence of magnetization for the same samples at a higher magnetic field of 50 kOe. As can be seen in Fig. 2, the temperature dependence of magnetization at an applied magnetic field of 50 kOe becomes similar to that observed in normal ferromagnets or ferrimagnets.

^{a)}Electronic mail: scyu@cbucc.chungbuk.ac.kr

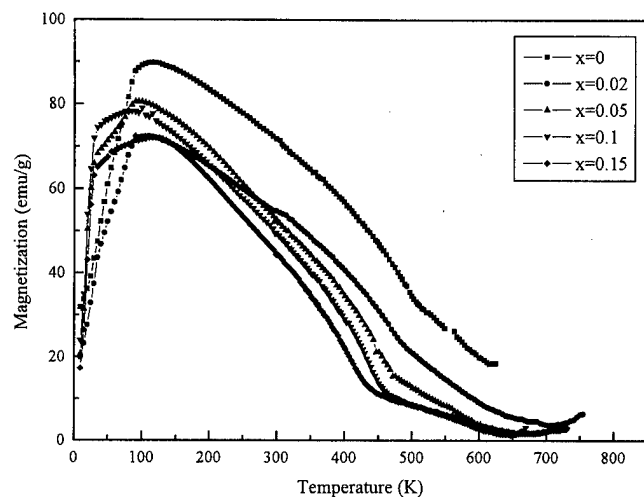


FIG. 1. The temperature dependence of magnetization for the melt-spun ribbons of $(\text{Tb}_{0.33}\text{Fe}_{0.67})_{1-x}\text{B}_x$ ($x=0, 0.02, 0.05, 0.1$, and 0.15) alloys at an applied magnetic field of 10 kOe.

Figure 3 represents the magnetization at 5 K with an applied field of 50 kOe and the Curie temperature as a function of B concentration. It is seen from Fig. 3 that the magnitude of magnetization decreases monotonically with the increase of B. At low temperatures, the magnetization $M(T)$ is well described in terms of the Bloch's $T^{3/2}$ law. The Bloch coefficients B , which is the thermal average of the total contribution arising from spin waves of all wavelengths, is related to the spin wave stiffness D , through the expression⁴

$$D = \zeta(3/2)^{2/3} [g \mu_B / M(0) B]^{2/3} (k_B / 4\pi), \quad (1)$$

where $\zeta(3/2)$ is the Riemann zeta function and g is the spectroscopic splitting g factor. The values of D were determined from a fit to the SQUID magnetic data measured at 50 kOe in the temperature range 5–200 K. It is found that the value of D decreases from 126.8 to 65.1 meV \AA^2 with increasing B concentration from $x=0$ to $x=0.15$. This may be due to the increasing proportion of negative Fe–Fe interactions at short interatomic separations and the decrease of average

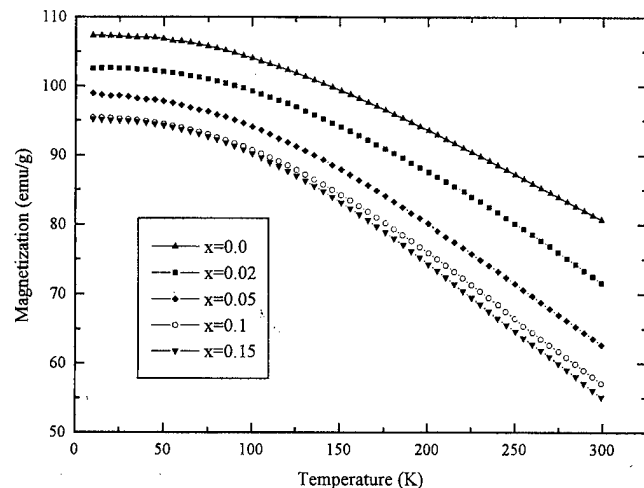


FIG. 2. The temperature dependence of magnetization for the melt-spun ribbons of $(\text{Tb}_{0.33}\text{Fe}_{0.67})_{1-x}\text{B}_x$ ($x=0, 0.02, 0.05, 0.1$, and 0.15) alloys at an applied magnetic field of 50 kOe.

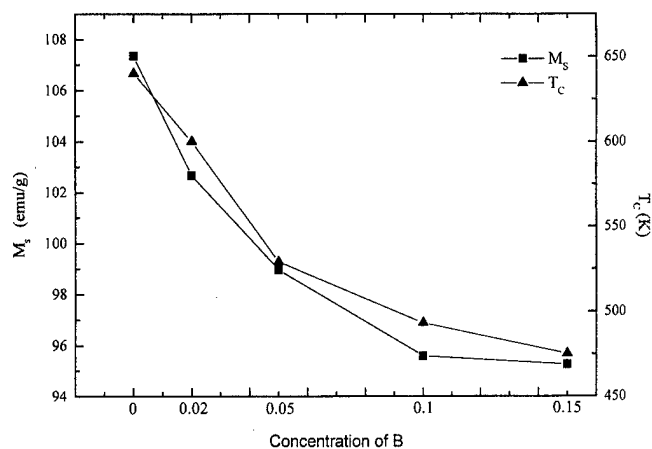


FIG. 3. The magnetization measured at the temperature of 5 K and at the field of 50 kOe, and the Curie temperature as a function of B concentration.

iron moment. In order to clarify this behavior, we estimated the exchange stiffness A and the average moment of the samples. The value of A can be obtained from the mean field model and from the Curie temperature.^{5,6} One can drive the following relation

$$A = (C S_{\text{Fe}} k_B T_c) / 4(S_{\text{Fe}} + 1) r_{\text{Fe-Fe}} \quad (2)$$

where C is the concentration of Fe in atomic percent, S_{Fe} is the spin moment of Fe and $r_{\text{Fe-Fe}}$ is the nearest neighbor distance. We can calculate S_{Fe} , from the relation of $M(\mu_B) = 2x_{\text{Fe}} S_{\text{Fe}} \mu_B$, where $M(\mu_B)$ and x_{Fe} are the magnetic moment of sample and the concentration of Fe, respectively. The magnetic moment arises from the contribution of the moments of Fe (μ_{Fe}) and Tb (μ_{Tb}), which are aligned antiferromagnetically. It is known that the transition metal (TM) moment is reduced when RE is alloyed. This is due to the hybridization of the $3d$ orbitals of TM with the $5d$ ones of RE. We found $\mu_{\text{Tb}} = 0.64 \mu_B$ in $\text{Tb}_{0.33}\text{Fe}_{0.67}$ alloy. This value is lower than the theoretical value expected for the free ion Tb ($9.0 \mu_B$). This suggests that the spin structure of Tb is not collinear but conical. This is to be expected for the rare earth with a strong spin-orbit coupling and hence strong random local anisotropy. An independent estimate of exchange integral J is provided by the expression for the Curie temperature in the molecular field approximation. It is known that the exchange integral between two Fe atoms depends sensitively on the relation between their interatomic separation and the range of their $3d$ orbitals. Exchange integral J is described in terms of the Curie temperature

$$T_c = 2 \langle Z \rangle J_{\text{Fe-Fe}} S_{\text{Fe}} (S_{\text{Fe}} + 1) / 3k_B. \quad (3)$$

Figure 4 shows the exchange constant and exchange integral as a function of the B content. It is seen from Fig. 4 that both the exchange stiffness constant and the exchange integral decrease with increasing B concentration. This result can be expected from the suppression of the magnetic random anisotropy in the B-free sample, thus the random magnetic anisotropy seems to be minimized. In order to clarify this behavior, we analyzed the field dependence of magnetization.

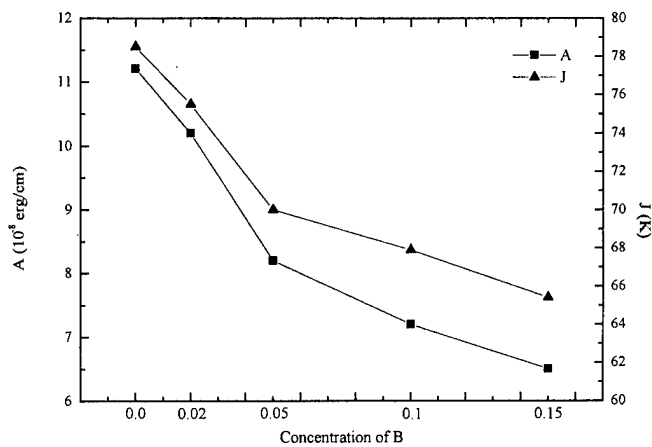


FIG. 4. The exchange stiffness constant and the exchange integral as a function of B concentration.

B. Field dependence of magnetization

According to the Chudnovsky model,^{7,8} for applied fields less than the exchange field H_{ex} , magnetization shows a linear dependence on $H^{1/2}$. It is known that magnetization can be written phenomenologically as

$$M = M_s(1 - a_1/H^{1/2} - a_2/H - a_3/H^2) + \chi_{hf}H. \quad (4)$$

The terms involving a_1 and a_2 result from the fluctuations of the local orientation of the easy axis and structural inhomogeneities, respectively. The term a_3/H^2 is ignored in our calculations, because in our case the applied field is not so high. χ_{hf} is the high field magnetic susceptibility. The magnetization curves for all samples are found to fit Eq. (4) as shown in Fig. 5. From the fit, one can deduce the field H_s , where $H_s = H_r/H_{ex}^3$. The random anisotropy field H_r and the local random anisotropy constant K_L are related as $H_r = 2K_L/M_0$. The exchange field can also be expressed as $H_{ex} = 2A/M_0(R_a)^2$, where R_a is the atomic correlation

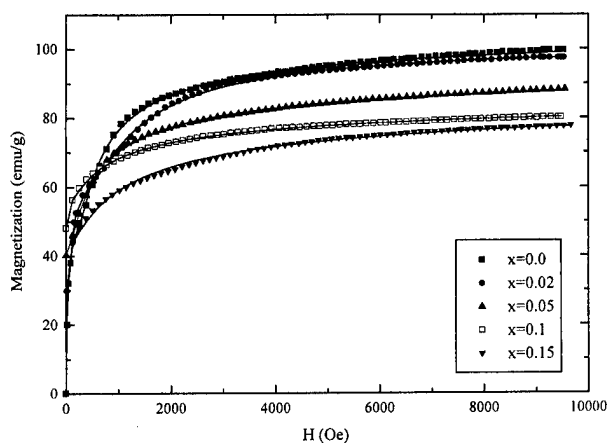


FIG. 5. The field dependence of magnetization at 5 K for the melt-spun ribbons of $(\text{Tb}_{0.33}\text{Fe}_{0.67})_{1-x}\text{B}_x$ ($x=0, 0.02, 0.05, 0.1$, and 0.15) alloys. The solid lines represent the fit of the data to Eq. (4).

TABLE I. The values of average magnetic moment (μ_a), average half cone angle (θ) of the iron subnetwork, exchange field (H_{ex}), anisotropy field (H_r), and random anisotropy constant (K_L) for the melt-spun ribbons of $(\text{Tb}_{0.33}\text{Fe}_{0.67})_{1-x}\text{B}_x$ ($x=0, 0.02, 0.05, 0.1$, and 0.15) alloys.

$(\text{Tb}_{0.33}\text{Fe}_{0.67})_{1-x}\text{B}_x$	μ_a (μ_B)	θ ($^\circ$)	H_{ex} (T)	H_r (T)	K_L (10^6 erg/cm ³)
$x=0$	1.68	58	2.6	0.4	2.1
$x=0.02$	1.62	62	2.5	0.6	3.1
$x=0.05$	1.52	68	2.1	1.0	5.0
$x=0.1$	1.40	74	2.0	1.1	5.3
$x=0.15$	1.33	78	1.9	1.3	6.2

length, taken generally as 10 \AA in the case of an amorphous phase.⁹ The values of H_{ex} and μ_a decrease with increasing B concentration. This indicates that the magnetic structure of these alloys changes with the addition of B. The decrease of H_{ex} and the increase of H_r with increasing B concentration can be explained by the conical magnetic structure with larger spread angle at higher B content. The present result shows that the random magnetic anisotropy increases with increasing B content. Indeed, it is seen in Table I that the average magnetic moment decreases from 1.68 to $1.33 \mu_B$ and the local random magnetic anisotropy constant K_L increases with increasing B content. Using the relation¹⁰

$$\mu_{Fe} = \mu_{Fe}(\text{free ion})(1 + \cos \theta)/2 \quad (5)$$

the average half cone angle is estimated to be 58° for the iron subnetwork in the B-free sample. This indicates that the Fe moments have a conical spin structure due to strong random anisotropy. The reduction in the Fe moment arises from the random local anisotropy which tends to align the Fe moment along random directions. In particular, one observes that the spread angle increases with increasing B content. This result is consistent with the observation that the local random magnetic anisotropy increases with increasing B content. It would be of interest to compare the present results with those reported previously³ where magnetostriction decreases with increasing B content.

The research was supported by the Korean Science and Engineering Foundation under Grant No. 96-0702-05-01-3.

¹A. E. Clark, in *Ferromagnetic Materials*, edited by E. P. Wohlfarth (North-Holland, Amsterdam, 1980), Vol. 1, Chap. 7.

²S. Kikuchi, T. Tanaka, S. Sugimoto, M. Okada, M. Homma, and K. Arai, *J. Magn. Soc. Jpn.* **17**, 267 (1993).

³S. H. Lim, T. H. Noh, I. K. Kang, S. R. Kim, and S. R. Lee, *J. Appl. Phys.* **76**, 267 (1994).

⁴F. Keffer, in *Encyclopedia of Physics* (Springer, Berlin, 1966), Vol. XVII-2.

⁵R. Hasegawa, *J. Appl. Phys.* **45**, 3109 (1974).

⁶N. Heiman, K. Lee, and R. Potter, *J. Appl. Phys.* **47**, 2634 (1976).

⁷E. M. Chudnovsky, W. M. Saslow, and R. A. Serota, *Phys. Rev. B* **33**, 251 (1986).

⁸E. M. Chudnovsky, *J. Appl. Phys.* **64**, 5770 (1988).

⁹C. D. Graham, Jr. and M. R. J. Gibbs, *IEEE Trans. Magn.* **29**, 3457 (1993).

¹⁰J. M. D. Coey, J. Chappert, J. P. Rebouillat, and T. S. Wang, *Phys. Rev. Lett.* **61**, 1061 (1976).

Alternating current susceptibility study of $\text{Dy}_2\text{Fe}_{17-x}\text{Ga}_x$ compounds

V. Skumryev, Xiao-lei Rao, and J. M. D. Coey^{a)}

Department of Physics, Trinity College, Dublin 2, Ireland

N. Sheludko

Faculty of Physics, Sofia University, Sofia-1126, Bulgaria

The effect of Ga substitution for Fe in $\text{Dy}_2\text{Fe}_{17-x}\text{Ga}_x$ on the low field ac susceptibility is reported. The easy magnetization direction is along the c axis for $x > 6.3$ while for $x < 6$ it is within the basal plane. With decreasing temperature a spin reorientation from an easy axis to an easy cone takes place when $6 \leq x \leq 6.3$. Two other anomalies have been found in the susceptibility of easy plane materials when the field is applied in the plane: (i) at T near room temperature, both χ' and χ'' depend on the frequency and χ'' shows a maximum which shifts to higher temperatures with increasing frequency; (ii) at low temperatures an increase in χ' is accompanied by time varying effects. While the latter is related to the domain structure reconstruction due to a change of the in-plane anisotropy, the former is caused by thermally activated domain wall pinning and depinning. The Ga substitution strongly affects the low temperature anomaly which disappears when $x > 2$, whereas it has little effect on the high temperature one. © 1998 American Institute of Physics. [S0021-8979(98)30011-0]

INTRODUCTION

Substitution of some Ga for Fe in R_2Fe_{17} can effectively increase the Curie temperature and induce room temperature uniaxial anisotropy.¹⁻⁵ However, the reasons for these changes are not quite clear. Temperature dependence of anisotropy constants is one among many studies which may help to understand the origin of the change of anisotropy type. When such changes take place upon substitution, a temperature-induced spin reorientation transition (SRT) can be expected for certain compositions.

Owing to the direct relation between domain-magnetization-rotation (DMR) susceptibility, and the anisotropy constants \mathbf{K}_i and spontaneous magnetization \mathbf{M}_s , the low-field ac-susceptibility technique is often used to detect SRT caused by change in the anisotropy energy. However, there can also be a contribution to the ac susceptibility from domain-wall displacement (DWD), which makes the analysis complicated, since factors other than the intrinsic parameters \mathbf{M}_s and \mathbf{K}_i will play a role. Thus different types of anomalous temperature dependence could arise, which cannot be directly related to \mathbf{K}_i and explained by the classical technical magnetization theories for DWD. Susceptibility anomalies have been found in a number of rare earth-transition metal based alloys and have received different, sometimes controversial, explanations in the literature.⁶⁻⁹

Here we present the results from an ac-susceptibility search for spin reorientation transitions in $\text{Dy}_2\text{Fe}_{17-x}\text{Ga}_x$ in which an anomalous temperature dependence of χ_{ac} was also found and studied.

EXPERIMENTAL METHODS

The real χ' and imaginary χ'' components of the ac susceptibility ($\chi = \chi' - j\chi''$) have been measured at an ac-

field amplitude of $H_m = 8$ A/m and fixed frequencies f between 10 and 1000 Hz using a mutual impedance bridge. Measurements were taken while warming the samples at a constant rate from 4.2 K (for some samples from 77 K) after zero field cooling. Measurements above room temperature on bulk polycrystalline samples have been taken only at $f = 100$ Hz with a setup different from the one used at low temperatures.

Oriented samples with a cylindrical shape ($l = 10$ mm, $d = 3$ mm) have been prepared by mixing 10%–15% fine powder (particle size under $15 \mu\text{m}$) with epoxy resin, followed by alignment in a 1 T magnetic field in two different ways depending on the type of the room temperature magnetic anisotropy. For alignment of easy axis materials ($x \geq 6$) a static magnetic field was applied, while for the easy plane materials ($x < 6$) a rotating field was used¹⁰ to insure that the magnetically hard c axis of all crystallites is collinear.

For calculating χ_{ac} , the sample volume was determined by the mass-density technique using the net mass and x-ray density. No demagnetizing corrections were performed (the demagnetizing factors are smaller than 0.05).

RESULTS AND DISCUSSION

Above room temperature, χ_{ac} for all samples changes smoothly without any indication of SRT up to the Curie temperature, at which temperature a Hopkinson type maximum occurs. This shows that the room temperature anisotropy type is maintained. The measured T_c are in good agreement with those reported by Shen *et al.*²

Below room temperature, depending on the Ga concentration, four different types of behavior were found.

- (1) For all samples with Ga above $x = 6.3$ (i.e., $x = 6.8$; 7 and 8) χ' is very small (less than 0.1) and changes smoothly without any peculiarities, regardless of the direction of

^{a)}Electronic mail: jcoey@tcd.ie

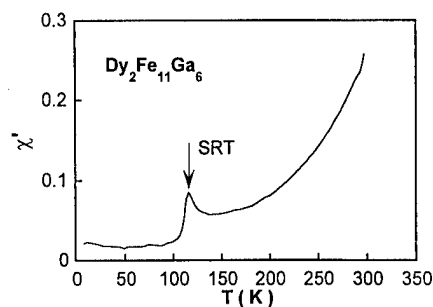


FIG. 1. χ'' as a function of temperature measured at $H_m = 8$ A/m. The field is applied perpendicular to the easy c axis.

the applied field. The easy magnetization direction is along the c axis for all temperatures. The small value of χ' reflects the uniaxial character of the anisotropy and the reduced value of M_s , due to the combined effects of Ga dilution and antiparallel coupling of the rare earth and Fe sublattices.

- (2) For $x=6$ and 6.3 a sharp peak on transverse χ' appears at temperatures of 116 and 110 K, respectively; see Fig. 1. The peak position and the susceptibility itself are frequency independent. It is natural to attribute this peak to a SRT, at which deviation of the moments from the easy c axis takes place with decreasing temperature. This attribution is supported by the magnetization and Mössbauer data obtained on oriented samples, suggesting that below the SRT the magnetic moments are along an easy cone. It is worth noting that the change of the anisotropy type in $\text{Dy}_2\text{Fe}_{17-x}\text{Ga}_x$ takes place at a lower Ga concentration than in $\text{Y}_2\text{Fe}_{17-x}\text{Ga}_x$, where \mathbf{K}_1 of the Fe sublattice has been found⁵ to change sign slightly above $x = 6.5$.
- (3) For easy plane samples with Ga above $x=2$, χ_{ac} measured with the field applied in the easy plane is an order of magnitude higher than that for easy axis materials, Fig. 2(c). With increasing temperature χ' increases. At low T all the curves measured at different frequencies coincide, while above about 230 K they depend strongly on f but tend to merge again when approaching room temperature. In the latter region χ'' starts to increase from a negligible value and forms a peak, Fig. 3(c). Both the χ'' peak and the χ' curve shift to higher T for higher f .
- (4) For $\text{Dy}_2\text{Fe}_{17}$ and for samples with $x=1$ and 2 (all of them with easy plane anisotropy) another anomaly appears between 145 and 155 K, where the parallel χ' forms a dip (for the Ga-free sample) or shoulder (for $x = 1$ and 2). In this temperature region χ' depends on the warming rate and it also decays with time.

If the field is applied perpendicular to the easy plane materials, χ_{ac} for all of them is much smaller, Fig. 2(b), and it changes smoothly without any anomaly.

Similar anomalous behavior has already been observed in $\text{Sm}_2\text{Fe}_{17}$ and discussed extensively in the literature.⁶⁻⁹ In a recent publication⁹ Chen, Skumryev, and Coey emphasized the difference between the high and low temperature anomalies. They suggested that the latter is related to domain struc-

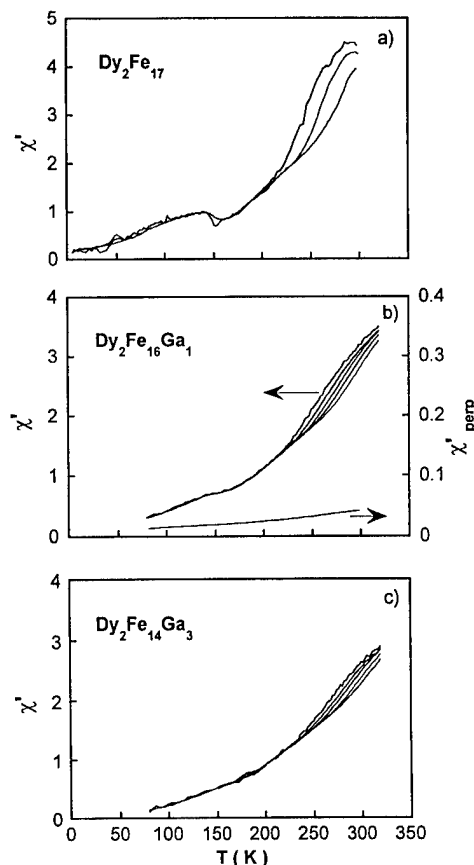


FIG. 2. χ' as a function of temperature at $H_m = 8$ A/m, applied along ab plane, for different frequencies: (a) $f = 10, 100$ and 1000 Hz; (b) and (c) $f = 10, 30, 100, 300$, and 1000 Hz. The curves shift to higher T at greater f . On the right-hand y axis of (b) χ' measured with field along the hard c axis is plotted.

ture reconstruction accompanied by thermally hysteretic pseudostatic wall pinning and depinning, whereas the former is caused by thermally activated dynamic domain wall pinning and depinning due to local directional ordering around domain walls.

In order to trigger the low temperature anomaly a sudden change in the domain structure is required. For easy plane anisotropy materials, where most domain walls lie in the ab plane, such a change could arise if the in-plane anisotropy constant \mathbf{K}_3 changes rapidly. Indeed, for a $\text{Dy}_2\text{Co}_{17}$ single crystal a drop in χ' was observed at temperatures where \mathbf{K}_3 vanishes.⁷ For $\text{Dy}_2\text{Fe}_{17-x}\text{Ga}_x$ easy plane materials we found that \mathbf{K}_1 and \mathbf{K}_2 decrease with Ga substitution. Although it was not possible to determine \mathbf{K}_3 for our polycrystalline samples, we can expect that Ga substitution would also affect the in-plane anisotropy constant and hence the low temperature anomaly. Indeed, as we see from Fig. 2, the anomaly is strongly affected by Ga substitution and disappears above $x=2$.

The high temperature anomaly could be caused by thermally activated local directional ordering of Fe atoms or a small amount of hydrogen in the sample,⁹ and it has no direct relation to the change in the anisotropy energy affected by Ga. Indeed, as can be seen from Figs. 2 and 3, Ga substitution has little effect on it. The anomaly was observed for all samples with an easy plane anisotropy. Using the set of data

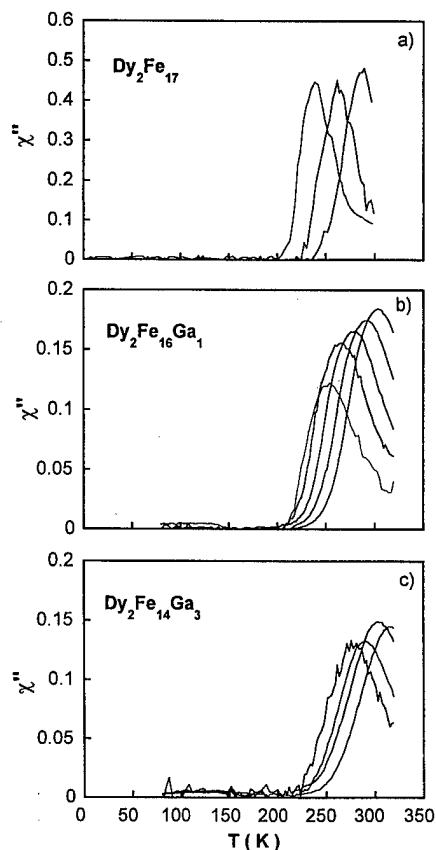


FIG. 3. χ'' as a function of temperature at $H_m = 8$ A/m, applied along ab plane, for different frequencies: (a) $f = 10$, 100 and 1000 Hz; (b) $f = 10$, 30, 100, 300, and 1000 Hz; (c) $f = 30$, 100, 300, and 1000 Hz. The curves shift to higher T at greater f .

for χ' and χ'' measured on $\text{Dy}_2\text{Fe}_{16}\text{Ga}_1$ [Figs. 2(b) and 3(b)] and following the procedure described in Ref. 9 χ'' vs χ' plots were obtained for fixed temperatures between 250 and 290 K. Most points fits on a semicircle, which suggests the existence of single relaxation time τ for a thermally activated process at a given temperature. The relaxation time obeys an

Arrhenius law with an activation energy $Q \approx 0.5$ eV and a pre-exponential factor $\tau_0 \approx 2 \times 10^{-13}$, which is characteristic of a Debye process.

CONCLUSION

It has been found that for all temperatures below T_c the easy magnetization direction is along the c axis for Ga substitution $x > 6.3$ while for $x < 6$ it is within the basal plane. With decreasing temperature a spin reorientation from an easy axis to an easy cone takes place in a narrow compositional range between $x = 6$ and $x = 6.3$. Two other anomalies in the susceptibility of easy plane materials have been found when it is measured in a field within the plane. The Ga substitution strongly affects the low temperature anomaly which disappears above $\text{Ga} = 2$, whereas it has little effect on the high temperature one.

ACKNOWLEDGMENTS

The authors are grateful to Ll. Martines for help with data processing and to R. Borges for helping with the preparation of the manuscript.

- ¹Z. Wang and R. A. Dunlap, *Philos. Mag.* **69**, 103 (1994).
- ²B. G. Shen, Z. H. Cheng, H. Y. Gong, B. Liang, Q. W. Yan, and W. S. Zhan, *Solid State Commun.* **95**, 813 (1995).
- ³W. Z. Li, N. Tang, J. L. Wang, F. M. Yang, Y. W. Zeng, J. J. Zhu, and F. R. de Boer, *J. Appl. Phys.* **76**, 6740 (1994).
- ⁴Z. Hu, W. B. Yelon, S. Mishra, G. J. Long, O. A. Pringle, D. P. Midlon, K. H. J. Bushow, and F. Grandjean, *J. Appl. Phys.* **76**, 443 (1994).
- ⁵Ll. Martines, J. Muñoz, V. Skumryev, N. Sheludko, B.-g. Shen, X.-l. Rao, and J. M. D. Coey, *J. Phys.: Condens. Matter* **10**, 4035 (1998).
- ⁶J. Bartolomé, L. M. García, F. J. Lazaro, Y. Grincourt, L. G. de la Fuente, C. de Francisco, J. M. Muñoz, and D. Fruchart, *IEEE Trans. Magn.* **30**, 577 (1994).
- ⁷X. C. Kou, T. S. Zhao, R. Grössinger, and F. R. de Boer, *Phys. Rev. B* **46**, 6225 (1992).
- ⁸M. L. Sartorelli, L. Kleinschroth, and H. Kronmüller, *J. Magn. Magn. Mater.* **140-144**, 997 (1995).
- ⁹D.-X. Chen, V. Skumryev, and J. M. D. Coey, *Phys. Rev. B* **53**, 15 014 (1996).
- ¹⁰S. Brennan, R. Skomski, O. Cugat, and J. M. D. Coey, *J. Magn. Magn. Mater.* **140-144**, 971 (1995).

Heat diffusivity of $\text{Nd}_{1-x}\text{Sr}_x\text{MnO}_{3-\delta}$ and $\text{La}_{1-x}\text{Ca}_x\text{MnO}_{3-\delta}$ compounds

J. Liebe, H. Kang, L. Haupt, P. Mandal,^{a)} I. V. Medvedeva,^{b)} G. H. Rao,^{c)} and K. Bärner

4. Phys. Institut der Universität Göttingen, Bunsenstr. 11-15, D-37073 Göttingen, Germany

A. Poddar, P. Muruguraj, R. Fischer, and E. Gmelin

Max-Planck-Institut für Festkörperforschung, Heisenbergstr. 1, 70569 Stuttgart, Germany

E. Gommert, R. v. Helmolt, and J. Wecker

Siemens AG, P.O. Box 3220, 91050 Erlangen, Germany

The thermal diffusivity of bulk and epitaxial layer samples of the giant magnetoresistance compounds $\text{Nd}_{0.67}\text{Sr}_{0.33}\text{MnO}_{3-\delta}$ and $\text{La}_{0.67}\text{Ca}_{0.33}\text{MnO}_{3-\delta}$ is investigated in a comparative study for temperatures between 35 and 350 K in order to detect preparational differences and to correlate the thermal transport with magnetization M and resistivity ρ . We find for Nd–Sr an anomaly of the heat diffusivity D near 145 K (80 K La–Ca) which we attribute to a temperature-induced canted metal to AFM insulator transition and a second anomaly in $D(T)$ near 250 K (300 K) which we assign to the transition to paramagnetism. The low-temperature anomaly can be a step of up to five times in the heat conductivity, which makes these compounds potential magnetic field activated heat switches, as this transition can also be induced by a magnetic field. © 1998 American Institute of Physics. [S0021-8979(98)44811-4]

I. INTRODUCTION

The magnetic and transport properties of $\text{RE}_{1-x}\text{EA}_x\text{MnO}_{3-\delta}$ compounds close to $x=1/3$ and $x=1/2$ are very sensitive to oxygen stoichiometry, way of preparation, annealing procedure, and atmosphere. In this contribution, we concentrate on the discussion of heat conductivity κ of Nd–Sr and La–Ca samples close to $x=1/3$, but of different make. Here, too, we observe a strong dependence on preparational conditions. As for example the oxygen content and interfacial stresses are difficult to determine with epitaxial layers, while with ceramics, defects and grain boundaries are often unspecified, we use a secondary characterization via other structure sensitive properties, e.g., electrical resistivity and magnetization. This way, at least a rough classification of the samples and a correlation of the different physical quantities can be achieved.

II. SAMPLE PREPARATION AND EXPERIMENT

The epitaxial thin films of thickness of $150\text{ nm} < d < 500\text{ nm}$ were deposited on SrTiO_3 substrates by laser ablation of polycrystalline targets. Substrate temperatures between 600 and 900 °C were used at a deposition pressure of 0.4 mbar oxygen. The x-ray diffraction patterns showed no other reflections than those consistent with a cubic unit cell. More details are given in the figure captions.

The “bulk” Nd–Sr sample is prepared by conventional solid state reaction. Stoichiometric proportions of high purity

starting materials, Nd_2O_3 , SrCO_3 , MnO_2 , are weighed and wet mixed for two hours in a planetary mill. The slurry is dried and further calcined in a recrystallized alumina crucible at 1200 °C for 24 h in air with three intermediate dry mixing/milling (carbide jar and ball) steps. Subsequently, the powder is cooled to room temperature, finely ground in a vibromill, and uniaxially pressed to pellets. The pellets are then sintered at 1500 °C for 5 h, cooled to 1300 °C at a rate of 30 K/h, and held there for 15 h. After that, it was cooled to room temperature at a rate of 120 K/h. X-ray powder diffraction confirmed a single phase with a pseudocubic structure ($a_0=3.852\text{ Å}$). The composition was tested using wet chemical analysis (ICP technique) and the weight in composition was confirmed within 3%. The “ceramic” sample, prepared from oxides and carbonates as above, was reacted in air at 1300 °C for several days with intermediate grindings. Pellets were pressed from the powders, sintered in air at 1250 °C for 10 h and cooled slowly to room temperature. The annealing procedure was repeated once. The x-ray peaks could be fitted to a cubic structure with lattice parameter $a_0=3.854\text{ Å}$.

The experimental setup used and the data reduction procedure is described in detail elsewhere.^{1,2} In order to measure κ we have chosen the transient thermoelectric effect (TTE), which primarily measures the heat diffusivity D , however, once D is known, the thermal conductivity κ can be calculated using specific heat capacity data, as $c_p \approx c_v$, $D = \kappa / c_v \rho_0$ (ρ_0 : density). We try to characterize each sample by its δ value and measurements of several physical quantities, taken on the same sample. Generally, with increasing δ both the magnetic moment and the conductivity are reduced.¹⁻⁶ From that, the oxygen content can be estimated; this has been done here by comparing the shifts and resistivity peaks obtained for different substrate temperatures of

^{a)}Permanent address: SINP, A-1F Bidhannagar, Calcutta 7000064, India.

^{b)}Permanent address: Institute for Metal Physics, S. Kovalevskaya 18, 62021 Ekaterinburg, Russia.

^{c)}Permanent address: Institute of Physics, Chinese Academy of Sciences, Beijing 100080, People's Republic of China.

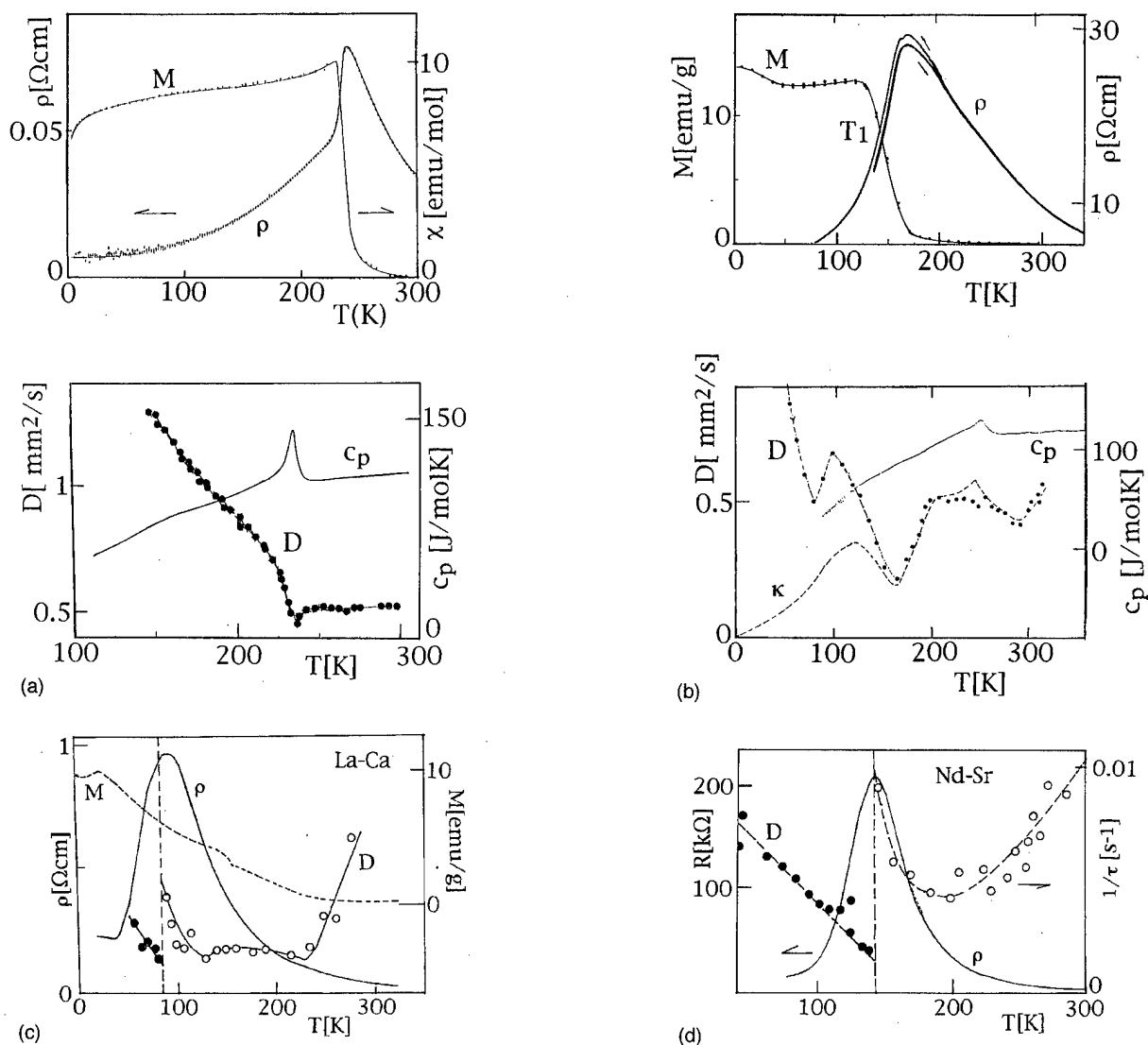


FIG. 1. Heat diffusivity D , specific heat capacity c_p , resistivity ρ , and magnetic moment M at $B = 100$ G of two bulk samples of $\text{RE}_{0.67}\text{EA}_{0.33}\text{MnO}_{3-\delta}$ vs temperature. (a) Bulk Nd-Sr $\delta \leq 0.04$, (b) ceramic Nd-Sr, $\delta \leq 0.14$. (c) Two epitaxial samples: laser ablation, SrTiO_3 substrate, 0.4 mbar O_2 Nd-Sr: $\delta \leq 0.1$, $T_s = 600^\circ\text{C}$, thickness: $d \approx 500$ nm and La-Ca: $\delta \leq 0.13$, $T_s = 800^\circ\text{C}$, $d \leq 150$ nm.

oxygen deficient Nd-Sr epitaxial layers⁷ with those of oxygen deficient La-Ca epitaxial layers and both of these with results obtained on oxygen deficient La-Ba ceramic samples, whose oxygen content had been chemically determined.⁶ Generally, an increasing oxygen deficit δ shifts all transitions to lower temperatures and simultaneously increases the spin randomness.¹⁻⁷

III. RESULTS

The magnetization of sample 1 is too low for collinear Mn-based ferromagnetism; therefore, $M(T)$ shows a canted order-disorder transition ($T_c = 240$ K). The spin disorder for $T > T_c$ could be paramagnetism or spin-glass like. The low resistivity for $T < T_c$ shows the correlation between metallic conductivity and (canted) ferromagnetism. The shape of $\rho(T)$ for $T < T_c$ suggests spin disorder scattering in particular, while activated behavior, i.e., a Mott or Arrhenius law is observed for $T > T_c$, suggesting a gap opening at T_c . The

heat diffusivity curve, $D(T)$, also shows T_c as a dip, while the low value of D for $T > T_c$, $0.5 \text{ mm}^2 \text{ s}^{-1}$, indeed suggests spin disorder.

While for sample 1 long-range magnetic order is introduced at 240 K, sample 2 shows a significant rise of magnetic moment $M(T)$ only at 150 K, which is again accompanied by a sharp drop in resistivity and is tentatively designated T_1 . The specific heat capacity $c_p(T)$, however, shows a peak around 240 K, suggesting a spin-compensated but mainly coherent magnetic structure for $150 \text{ K} < T < 240$ K and an incoherent, i.e., thermal or topological spin random structure for $T > 240$ K. The resistivity versus temperature curve $\rho(T)$ shows a weak shoulder at 240 K, suggesting a convoluted (double) resistivity peak and with it two different activated regimes. The absolute values of D and κ are comparable to those found for $\text{LaMnO}_{3-\delta}$.⁸ The dip in D close to 300 K could mark a final transition to paramagnetism, while the low value of D again suggests spin randomness. Close to T_1 , a peak of D is observed (see also Ref. 2). The epitaxial layers, samples 3 and 4, both show a broad

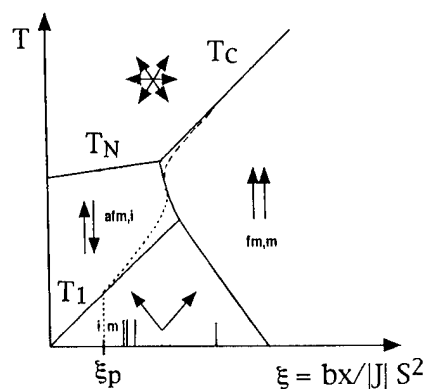


FIG. 2. Tentative phase diagram and placement of the samples 1–4; temperature scale might be slightly different for each sample.

resistivity peak like sample 2 which thus also might be a convolution. A step up to a factor of 5 is observed close to T_1 , which is accompanied by a sign change of the thermoelectric power in both cases; filled and open circles are used to demonstrate this. Again we observe the lowest value of D in the intermediate regime, $150\text{ K} < T < 250\text{ K}$. As the magnetic moment of La–Ca [Fig. 1(c)] is rather low, spin disorder is suggested, like in sample 2.

IV. DISCUSSION

The strong correlation of transport and magnetization is generally ascribed to the double exchange mechanism: here, metallic conductivity should occur together with ferromagnetisms through spindependent transfer of the extra electrons of the valence mixture. This correlation is indeed observed very often. The large variety of phenomena like GMR, field-induced metal-insulator transitions, mixed valence ordering, etc. are thought to occur mainly because of a competition of this double exchange mechanism and conventional superexchange of comparable strength, while a (spin) random component may be introduced through the oxygen deficit. In addition, large magnetovolume effects occur⁴ and point to a strong mutual influence between lattice and spin system, e.g., the idea of a rigid lattice has to be abandoned in general and polarons and Jahn–Teller like effects should be found. Although a phase diagram resulting from the competitive exchange has only been considered in connection with a rigid lattice and band filling scheme by deGennes, for an overview this diagram (Fig. 2) is still suitable. However, to the original diagram a few modifications have to be added:

- (1) The quadrupel point should be split by some additional (spin-orbit) interaction.
- (2) The randomness of the system introduces a percolation threshold for the conduction at which the carrier concentration is finite, x_p ; this is simultaneously a metal-insulator ($m-i$) boundary.
- (3) The paramagnetic region might be split into a spin-glass-like and a pm state because of the random elements.
- (4) The antiferromagnetic and paramagnetic phases might be insulating for $x > x_p^5$; i.e., the $m-i$ boundary runs probably first along T_1 and then along T_c .
- (5) Instead of a fixed carrier concentration as independent variable one should use the original ξ variable, i.e., the

ratio of maximal double exchange and superexchange energies $\xi = bx/|J|S^2$.

This way pressure effects and mechanical strains can be implemented to first order through the distance dependences of the transfer and exchange integrals $b(r)$, $J(r)$. If we tentatively place our samples 1–4 into that diagram, we assume that with increasing δ we have increasing nonstoichiometry hole doping and simultaneously an increase of spin randomness.^{1–5}

Figure 1 shows several anomalies in D and κ . First, with broad resistivity peaks one always finds a peak or a step close to the transition between the low-temperature metallic state and the high-temperature activated (semiconducting) region (at T_1). For magnetic materials, the heat conductivity is usually written as a sum of three terms,⁹ $\kappa = \kappa_{ph} + \kappa_{el} + \kappa_m$. As there are no structural changes in this temperature region, the phonon part κ_{ph} should be constant through this transition, while both the electronic κ_{el} and magnetic parts κ_m might be subject to change. This would also mean a higher sum $\kappa_{el} + \kappa_m$ in the thermally activated states. The flat region of the $\kappa(T)$ dependence for La–Ca and $T > 100\text{ K}$ might be due to blocked heat conduction in a spin-glass-like state and thus the increase in κ at higher temperatures, $T \geq 350\text{ K}$, could be connected with the onset of the paramagnetic regime.¹⁰

Magnetization measurements have shown that while stoichiometric $\text{La}_{0.67}\text{Ca}_{0.33}\text{MnO}_3$ is a double exchange ferromagnet, oxygen deficient samples, e.g., $\text{La}_{0.67}\text{Ca}_{0.33}\text{MnO}_{3-\delta}$, $0 < \delta \leq 0.3$ are more complicated. At lower δ values and close to T_c a spin-polaron peak is often superimposed to the spin disorder scattering.⁵ However, with high $\delta > 0.1$ a change in character, i.e., an order-order transition has been proposed.^{1–5} In particular, a whole sequence of different magnetically ordered phases with decreasing temperature, i.e., paramagnetic (pm), spin glass like (sg), antiferromagnetic (afm), and canted has been proposed.^{1–5}

ACKNOWLEDGMENTS

The authors thank the Deutsche Forschungsgemeinschaft for continuous support. They are also indebted to the Alexander von Humboldt foundation.

¹J. Liebe, E. Kraus, L. Haupt, P. Mandal, K. Bärner, and R. v. Helmolt, Appl. Phys. Lett. **68**, 2343 (1996).

²J. Liebe, H. Kang, L. Haupt, P. Mandal, I. V. Medvedeva, K. Bärner, A. Poddar, and E. Gmelin, Physica B **239**, 322 (1997).

³R. v. Helmolt, J. Wecker, K. Samwer, and K. Bärner, J. Magn. Magn. Mater. **151**, 411 (1995).

⁴I. V. Medvedeva, Yu. S. Bersenev, K. Bärner, L. Haupt, P. Mandal, and A. Poddar, Physica B **229**, 194 (1997).

⁵K. Bärner, L. Haupt, and R. v. Helmolt, Phys. Status Solidi B **187**, K61 (1995).

⁶H. L. Ju, J. Gopalakrishnan, J. L. Peng, Qi Li, G. C. Xiong, T. Venkatesan, and R. L. Greene, Phys. Rev. B **51**, 6143 (1995).

⁷H. L. Ju, C. Kwon, Qi Li, R. L. Greene, and T. Venkatesan, Appl. Phys. Lett. **65**, 2108 (1994).

⁸M. Kobayashi, H. Satoh, N. Kamegashira, and K. Inoue, J. Alloys Compd. **192**, 93 (1993).

⁹S. Welzel-Gerth, B. Franz, H. W. Gronert, and E. F. Wassermann, J. Magn. Magn. Mater. **101**, 37 (1991).

¹⁰J. Liebe, E. Kraus, L. Haupt, K. Bärner, P. Mandal, I. V. Medvedeva, R. v. Helmolt, and E. Gmelin, J. Phys. IV, France **7**, C1-635 (1997).

Magnetic properties of (Pr(Ca, Sr))MnO₃ studied by nuclear magnetic resonance

G. J. Tomka,^{a)} P. C. Riedi, and Cz. Kapusta^{b)}

Department of Physics and Astronomy, University of St. Andrews, St. Andrews, Fife KY16 9SS, United Kingdom

G. Balakrishnan, D. McK. Paul, M. R. Lees, and J. Barratt

Physics Department, University of Warwick, Coventry, CV4 7AL, United Kingdom

The valence state of Mn in magnetoresistive perovskites has been widely related to the level of alkaline metal substitution of the rare earth, by assuming that the Mn exists in 3+ or 4+ valence states. Measurements have been made on a series of samples in the system Pr_{1-(x+y)}Ca_xSr_yMnO₃. ⁵⁵Mn nuclear magnetic resonance (NMR) zero field spin echo measurements on a single crystal with $x=0.1$ and $y=0$ show distinct resonances around 310 MHz (Mn⁴⁺) and 400 MHz (Mn³⁺) but also at 590 MHz (Mn²⁺). An increase in the Mn²⁺ resonance frequency in an applied field implies that the Mn²⁺ moment is antiferromagnetically coupled to the net magnetization. Spectra from powder samples are much broader. The resonance frequencies increase as the Pr content is reduced. For systems with $x+y=0.4$, there is little change in the NMR spectrum as the proportions of Ca and Sr are altered. © 1998 American Institute of Physics. [S0021-8979(98)26511-X]

In recent years the large family of magnetic materials known as perovskites have been the subject of intensive research. They exhibit properties such as high temperature superconductivity and extremely high magnetoresistance.^{1-3,8} The renewed interest follows theoretical and experimental studies dating back to the 1950's.⁴⁻⁷

The cubic crystal structure of simple perovskites is distorted orthorhombically for many systems, such as Pr_{1-x}Ca_xMnO₃. It is the distorted perovskite manganese oxides of the form R³⁺A²⁺MnO₃ which exhibit the large negative magnetoresistance.⁸ The magnetoresistive response is thought to arise from the relationship between the level of A²⁺ dopant and the Mn valence affecting carrier mobility. The carriers hop preferentially between ions with a parallel spin configuration, stabilizing ferromagnetism (FM). The valence state v of the Mn ^{v +} has been widely related to the concentration x of the dopant by the formula

$$R_{1-x}^{3+}A_x^{2+}Mn_{1-x}^{3+}Mn_x^{4+}O_3^{2-}.$$

Transport measurements¹ made across a wide range of temperatures, however, indicate that there is some disproportionation of the 3+ state into 2+ and 4+ states. Here we present spin echo nuclear magnetic resonance (NMR) data on Pr_{1-(x+y)}Ca_xSr_yMnO₃. For $x=0.4$ and $y>0.1$, the system has the characteristics of a ferromagnetic conductor,³ as described below. The system was studied using an automated swept frequency spectrometer,⁹ in two regimes:

The first regime, $y=0$, exhibits² a number of different antiferromagnetic (AFM) structures for $x>0.5$, and mixed ferromagnetic (FM) and AFM characteristics for $x<0.5$. It is found to remain insulating for all compositions, though for $x=0.3$ a metamagnetic transition to a ferromagnetic conduc-

tor has been observed.¹⁰ At 4.2 K both the Mn and Pr sublattices are magnetically ordered. In this investigation the most detailed measurements have been made from 1.7 to 15 K on a single crystal with $x=0.1$ and $y=0$ in fields from 0 to 8 T. For this system the Curie temperature is 100 K, with a spin reorientation at around 70 K. The Pr sublattice orders at around 30 K, and the low temperature structure consists of moments FM coupled in plane with AFM coupling between planes.

In the second regime the total dopant level, $x+y$, is kept at 0.4 for a range of x and y . It has been found that despite the constant level of alkaline earth doping, there are changes in the magnetic properties of the system at 4.2 K as x/y is varied.³ For $y=0$, the system is AFM at low temperatures ($T_N=170$ K), but the introduction of Sr results in a mixed AFM/FM magnetic system. Above $y=0.1$ the material shows FM behavior with a decrease of resistivity, suggesting an increase in the stability of the ferromagnetic state.³ The magnetic and electronic properties are related to lattice distortions, introduced by a combination of size mismatch of the alkaline earth atom and the Jahn-Teller effect, with FM becoming increasingly dominant as the proportion of the Sr is increased.

NMR measurements were made on two samples with composition Pr_{0.9}Ca_{0.1}MnO₃; sample A was a single crystal produced by the floating zone method, using an infrared image furnace. The quality of crystals produced by this method is detailed by Balakrishnan *et al.*¹¹ Sample B was a powder produced, as described by Lees *et al.*¹²

The ⁵⁵Mn NMR zero field spin-echo spectrum of sample A in Fig. 1 shows three distinct resonances around 310, 400, and 590 MHz. These data have been obtained at 4.2 K in a carefully tuned and matched coil, and have been corrected for transverse relaxation (T_2) and the frequency squared signal dependence. No change in the resonant frequencies was observed in the range 1.7 to 15 K, but the drop in the relax-

^{a)}Electronic mail: gt2@st-and.ac.uk

^{b)}Also at Dept. of Solid State Physics, University of Mining and Metallurgy, 30-059 Cracow, Poland.

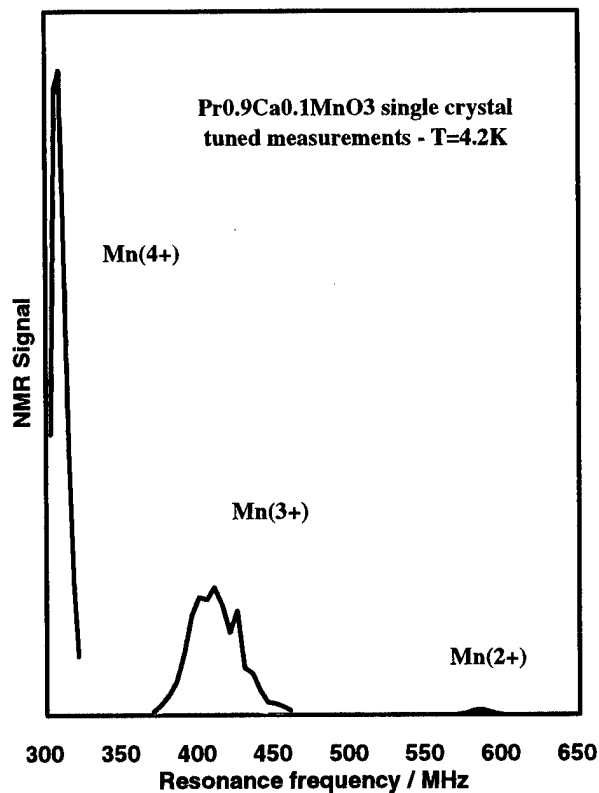


FIG. 1. ^{55}Mn NMR spin-echo spectrum of $\text{Pr}_{0.9}\text{Ca}_{0.1}\text{MnO}_3$ single crystal at 4.2 K. Measurements are corrected for transverse relaxation effects and the "frequency squared" response effect.

ation time T_2 of the signals with temperature meant that no data were obtainable above 15 K.

The lines around 310 and 400 MHz were ascribed to Mn^{4+} and Mn^{3+} , respectively. The ^{55}Mn NMR resonance at 590 MHz is commonly ascribed to Mn in its $2+$ valence state and has been observed in a number of related systems such as spinel-type oxides¹³ and manganese ferrites,¹⁴ though it is interesting that no Mn^{2+} is observed in the La based perovskites by photoemission studies.¹⁵

The NMR data provide the first direct evidence for the presence of Mn in the $2+$ valence state in the $\text{R}^{3+}\text{A}^{2+}\text{MnO}_3$ systems, though indirect evidence of the inadequacy of the nominal $3+/4+$ valence approach has been obtained from thermoelectric power measurements across a wide range of temperatures.¹ Although it has been shown that layered manganese systems containing only Mn^{2+} and Mn^{3+} can be prepared, these have only been formed under highly reducing conditions.¹⁶ Since our data were obtained from a single crystal it is unlikely that the Mn^{2+} signal arises from any such spurious phase, though the large size difference may make Mn^{2+} difficult to accommodate in the lattice, and its association with lattice defects or an impurity phase cannot be ruled out. However, it should be noted that a large Mn^{2+} signal is not exhibited in the powder systems, as detailed below. Furthermore, the crystal was checked with x-ray Laue back reflection, which showed clear diffraction spots comparable to those shown in earlier work.¹¹

The data obtained at 4.2 K show that the apparent populations of the magnetically ordered Mn states, as detected by NMR are in the ratio 0.545:0.45:0.005 for the $4+$, $3+$, and

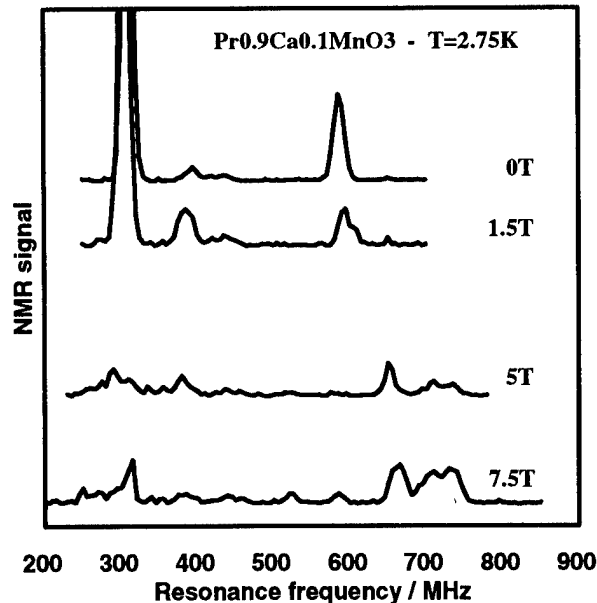


FIG. 2. ^{55}Mn NMR spin echo spectrum of $\text{Pr}_{0.9}\text{Ca}_{0.1}\text{MnO}_3$ single crystal at 2.75 K, with a range of applied fields.

$2+$ states, respectively. The nominal valence model would give an expected ratio of 0.1:0.9:0. The discrepancy is indicative of a large NMR enhancement of the Mn^{4+} signal, which may be due to domain wall enhancement arising from a preferential pinning of domain walls at the neighboring Ca dopant sites or may reflect the electron hopping dynamics. The rapid drop of the intensity of the Mn^{4+} line with applied field, as shown in Fig. 2, is consistent with removal of domain wall enhancement effects. The greater spread of hyperfine fields for the Mn^{3+} resonance compared with that of the Mn^{4+} line, shown in Fig. 2, is consistent with the presence of Jahn-Teller distortion about the Mn^{3+} ion.^{6,8}

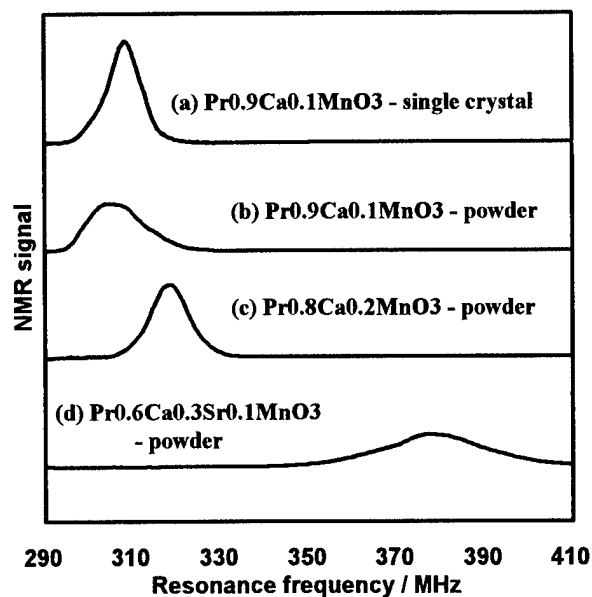


FIG. 3. ^{55}Mn NMR spin echo spectra at 4.2 K of Mn^{4+} for $\text{Pr}_{1-(x+y)}\text{Ca}_x\text{Sr}_y\text{MnO}_3$ with $y=0$ for (a) single crystal $x=0.1$, (b) powder $x=0.1$, (c) powder $x=0.2$, and (d) spectrum of Mn^{4+} for $\text{Pr}_{0.6}\text{Ca}_{0.3}\text{Sr}_{0.1}\text{MnO}_3$ powder.

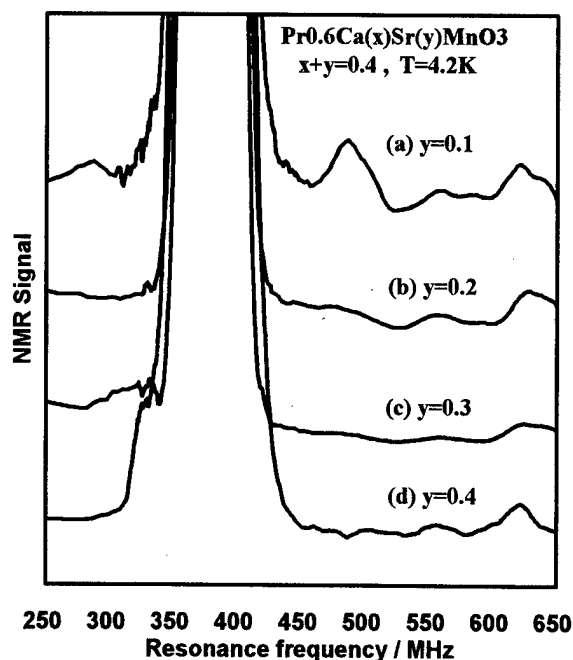


FIG. 4. Low intensity part of ^{55}Mn NMR spin echo spectra at 4.2 K for $\text{Pr}_{1-(x+y)}\text{Ca}_x\text{Sr}_y\text{MnO}_3$ with $x+y=0.4$ for (a) $y=0.1$, (b) $y=0.2$, (c) $y=0.3$, and (d) $y=0.4$.

A single $\text{Mn}^{3+}/\text{Mn}^{4+}$ mixed-state line at around 380 MHz has been observed in a range of other systems.¹⁷ This line arises from fast carrier hopping between the two Mn ions and therefore provides information about the ferromagnetic double-exchange mechanism. The absence of this line for $\text{Pr}_{0.9}\text{Ca}_{0.1}\text{MnO}_3$ suggests that if a double-exchange process is responsible for the ferromagnetism in this system, the hopping time must be greater than the period of the Larmor precession of the Mn nuclear spins ($\sim 10^{-9}$ s). The unusual absence of this line is consistent with the low conductivity of the ferromagnetic ground state, and suggests that the ferromagnetic ordering of the Pr sublattice ($T_c = 30$ K) may play a role in determining the low temperature magnetic structure of this system.

In Fig. 2, it can be seen that the resonance frequencies of the Mn^{3+} and the Mn^{4+} decrease with applied field, whereas the resonance frequency of the Mn^{2+} increases. Mn^{2+} is an S-state ion, so the hyperfine field at the nucleus is dominated by the contact interaction due to the host electron spin, i.e., the hyperfine field is antiparallel to the Mn^{2+} moment. The increase in the Mn^{2+} resonance frequency in an applied field implies that the Mn^{2+} moment is antiferromagnetically coupled to the net magnetization.

Figure 3 shows the Mn^{4+} spectrum, (a) from single crystal sample A, (b) from the powder sample B, and (c) from a powder sample $\text{Pr}_{0.8}\text{Ca}_{0.2}\text{MnO}_3$. A powder sample of

$\text{Pr}_{0.6}\text{Ca}_{0.3}\text{Sr}_{0.1}\text{MnO}_3$, in Fig. 3(d) is also shown for comparison. It can be seen that the peak frequency of samples A and B is similar, though the line B is broader because of the greater inhomogeneity in the powder system. We were unable to detect any clear higher frequency resonance peaks from these powder samples, presumably because of this increased inhomogeneity. The shift in the peak indicates an increase in the magnitude of the field at the Mn nucleus as the Pr concentration is decreased, and may reflect an increase in mobility of the double exchange carrier between the Mn^{3+} and Mn^{4+} sites. The peak positions for the $\text{Pr}_{1-(x+y)}\text{Ca}_x\text{Sr}_y\text{MnO}_3$ samples with $x+y=0.4$, produced as described by Lees *et al.*,³ Figs. 3(d) and 4, are all around 380 MHz. This corresponds to an increase in the magnitude of the hyperfine field of about 3 T. As described above, the 380 MHz signal can be ascribed to a mixed $\text{Mn}^{3+}/\text{Mn}^{4+}$ state where the carrier hopping time is shorter than $\sim 10^{-9}$ s.

Despite the changes in the physical properties of $\text{Pr}_{1-(x+y)}\text{Ca}_x\text{Sr}_y\text{MnO}_3$ observed by Lees *et al.*,³ there is little change in the spectrum as the proportions of Ca and Sr are changed. Figure 4 shows the positions of the resonance lines for the Sr doped samples. Small peaks are observable at around 430 and 620 MHz, and are most well defined for the sample with the lowest Sr doping. The signals are extremely broad compared with the single crystal sample, and a distinct spin echo signal was observable across the whole range of frequencies shown in Fig. 4.

The authors acknowledge the support of the EPSRC and thank A. M. Portis and members of OXSEN for ideas and advice.

- ¹M. F. Hundley and J. J. Neumeier, *Phys. Rev. B* **55**, 11 511 (1997).
- ²Z. Jirak, S. Krupicka, Z. Simasa, M. Dlouha, and S. Vratilava, *J. Magn. Mater.* **53**, 153 (1985).
- ³M. R. Lees, L. J. Chang, J. Barratt, G. Balakrishnan, C. V. Tommy, D. McK. Paul, C. D. Dewhurst, and C. Ritter, *Physica B* **230**, 313 (1997).
- ⁴C. Zener, *Phys. Rev.* **81**, 440 (1951).
- ⁵E. O. Wollan and W. C. Koehler, *Phys. Rev.* **100**, 545 (1955).
- ⁶J. B. Goodenough, *Phys. Rev.* **100**, 564 (1955).
- ⁷P. G. De Gennes, *Phys. Rev.* **118**, 141 (1960).
- ⁸A. P. Ramirez, *J. Phys.: Condens. Matter* **9**, 8171 (1997).
- ⁹J. S. Lord and P. C. Riedi, *Meas. Sci. Technol.* **6**, 149 (1995).
- ¹⁰H. Yoshizawa, H. Kawano, Y. Tomioka, and Y. Tokura, *Phys. Rev. B* **52**, R13 145 (1995).
- ¹¹G. Balakrishnan, M. R. Lees, and D. McK. Paul, *J. Phys.: Condens. Matter* **9**, L471 (1997).
- ¹²M. R. Lees, G. Balakrishnan, J. Barratt, D. McK. Paul, and C. D. Dewhurst, *J. Phys.: Condens. Matter* **8**, 2967 (1996).
- ¹³M. Mizoguchi and A. Tasaki, *J. Phys. Soc. Jpn.* **29**, 1382 (1970).
- ¹⁴T. Kubo, A. Hirai, and H. Abe, *J. Phys. Soc. Jpn.* **26**, 1094 (1969).
- ¹⁵J. H. Park, C. T. Chen, S.-W. Cheong, W. Bao, G. Meigs, V. Chakarian, and Y. U. Idzerda, *Phys. Rev. Lett.* **76**, 4215 (1996).
- ¹⁶J. P. Chapman, J. P. Attfield, M. Molg, C. M. Friend, and T. P. Beals, *Angew. Chem.* **35**, 2482 (1996).
- ¹⁷Cz. Kapusta, P. C. Riedi, G. J. Tomka, W. Kocemba, M. R. Ibarra, J. M. De Theresa, M. Viret, and J. M. D. Coey (unpublished).

Anomalous low-field magnetization in $\text{La}_{2/3}\text{Ca}_{1/3}\text{MnO}_3$ near the critical point: Stable clusters?

V. S. Amaral,^{a)} J. P. Araújo, Yu. G. Pogorelov, and J. B. Sousa

IFIMUP, Departamento de Física, Faculdade de Ciências da Universidade do Porto, Rua do Campo Alegre 687, 4150 Porto, Portugal

P. B. Tavares and J. M. Vieira

Departamento de Engenharia Cerâmica e do Vidro, Universidade de Aveiro, 3800 Aveiro, Portugal

J. M. B. Lopes dos Santos

Centro de Física do Porto, Departamento de Física, Universidade do Porto, Rua do Campo Alegre 687, 4150 Porto, Portugal

A. A. C. S. Lourenço

INESC, Rua do Campo Alegre 687, 4150 Porto and Departamento de Física, Universidade de Aveiro, 3800 Aveiro, Portugal

P. A. Algarabel

Departamento de Física de la Materia Condensada, Instituto de Ciencia de Materiales, Universidad de Zaragoza-CSIC, 50009 Zaragoza, Spain

The magnetic behavior of bulk $\text{La}_{2/3}\text{Ca}_{1/3}\text{MnO}_3$ ($T_C=267$ K) at low fields in the paramagnetic phase was studied. Near T_C ($T-T_C<30$ K) we find a sequence of steplike features in the effective Curie constant $C(T)=M(T-T_C)/H$ at well defined temperatures and intermediate plateaus, accompanied by temperature hysteresis. On approaching T_C , the C values at each plateau follow a geometrical progression, with the effective spin S doubled at each step. The first plateau gives $S=5.5$, corresponding to a cluster of three Mn^{3+} ions sharing one extra hole. This suggests that close to T_C short range magnetic order at low fields develops hierarchically through a series of most stable cluster states. © 1998 American Institute of Physics. [S0021-8979(98)52311-0]

I. INTRODUCTION

The doped manganites $\text{Ln}_{1-x}\text{A}_x\text{MnO}_3$ (where Ln and A are trivalent lanthanide and divalent alkali-earth, respectively) are of great interest now due to the colossal magnetoresistance effect (CMR).¹ Although the basic mechanism for the onset of uniform ferromagnetism, the Zener's double exchange (DE) interaction, was recognized long ago,² it does not provide a satisfactory description of the magnetic state close to the transition temperature T_C .³ It was already noted in the previous authors' work⁴ that certain features observed in the critical behavior of MR disagree with the classical concept of electron spin scattering by thermodynamic fluctuations of localized Mn spins. A possible explanation was proposed through coexistence of thermodynamic and static fluctuations, the latter being due to spontaneous formation of spin clusters by local DE in the random potential of chaotically distributed dopants. Also it was evidenced⁵ that in these materials the magnetization per manganese atom $M(T)$ at higher temperatures T (up to about three times T_C) and applied field H does not follow the classical Curie-Weiss law $M_{\text{CW}}=C\mu_B^2 H/k_B(T-T_C)$. In particular, the apparent Curie constant (for $T-T_C$ up to ~ 100 K), obtained from the data of Ref. 5 on $\text{La}_{2/3}\text{Ca}_{1/3}\text{MnO}_3$, is $C\approx 11.4$, much higher than the simple weighted sum $\bar{C}=xC_{3/2}+(1-x)C_2$ of Brillouin contributions $C_S=4/3S(S+1)$ from Mn^{4+} ($S=3/2$) and Mn^{3+} ($S=2$); for $x=1/3$ we have $\bar{C}=7$. There is a general

consensus about the relation of this effect to the formation of composite cluster spins,^{6,7} for instance, a spin-coupled pair of Mn^{4+} and Mn^{3+} will contribute $C_{7/2}=21$ which is ≈ 1.6 times greater than the sum $C_{3/2}+C_2$ for two uncoupled spins, and such enhancement must be even stronger for greater clusters. The same data show that at sufficiently high temperatures the Curie-Weiss law with $C\approx\bar{C}$ is restored (but with modified $T'_C>T_C$). This suggests that cluster formation is favored closer to the transition temperature. But, like the usual ferromagnetic transition, a strong enough external field will suppress the critical spin fluctuations and spontaneous cluster structure can be smeared. In the present work we study the deviations from uniform paramagnetic behavior of $\text{La}_{2/3}\text{Ca}_{1/3}\text{MnO}_3$ with approaching T_C , at as low applied fields as possible. Besides confirming the difference between the Curie constants close and far from T_C at fields ranging above some kOe, we found some essentially new effects close to T_C at fields below ~ 50 Oe. Particularly, a sequence of steplike features observed at well-defined temperatures and accompanied by temperature hysteresis suggests a discontinuous dynamics of spin clustering with possible hierarchical structure.

II. EXPERIMENT

A bulk ceramic sample of composition $\text{La}_{0.67}\text{Ca}_{0.33}\text{MnO}_3$ was prepared by standard solid-state methods from oxides and carbonates, with three intermediate grindings and final sintering at 1300°C for 50 h and very slow cooling to room

^{a)}Electronic mail: vbamaral@fc.up.pt

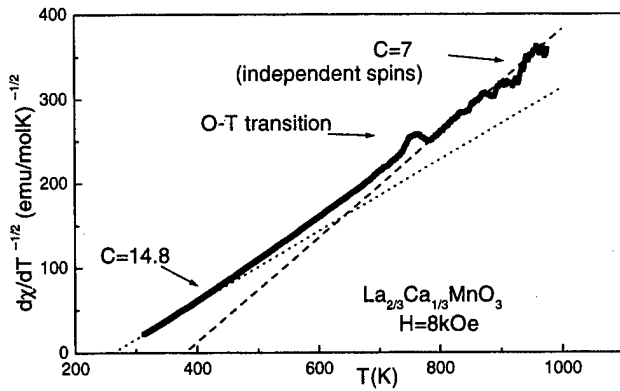


FIG. 1. $(dM/dT)^{-1/2}$ from high temperature measurements at field 8 kOe. The arrow indicates the orthorhombic-trigonal structural transition at $T_{O-T} \approx 750$ K.

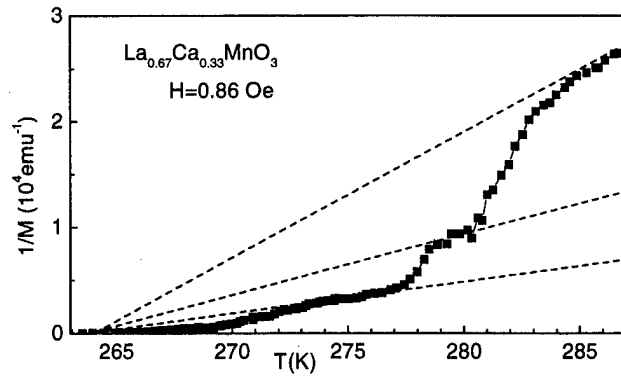


FIG. 2. Inverse magnetization close to T_C . Instead of a continuous decrease, we find a sequence of steps and intermediate regions where a Curie-like type of dependence seems valid (lines).

temperature within 20 h. Powder diffraction showed a single phase orthorhombic structure (P_{bnm}), and scanning electron microscopy revealed that the samples have very small porosity and 10 μm average grain size. High resolution electrical resistivity and magnetoresistance measurements confirmed the characteristic behavior of these ferromagnetic ceramics.⁸

The low field magnetization of the sample was measured with a Quantum Design superconducting quantum interference device (SQUID) magnetometer. In order to reduce the effect of frozen magnetic fields in the superconducting coil and ensure a better field homogeneity, prior to these measurements the coil was heated to room temperature. During the measurement of these low field data, the maximum magnetic field did not exceed 30 Oe. The measurements at constant magnetic field were taken on cooling the sample from high temperatures (320–380 K), down to 20 K and then on heating back to the initial temperature. On the first run, at 1.36 Oe, a zero-field cooled curve was also measured. High temperature (300–1000 K) magnetic measurements were taken in an Oxford Instruments vibrating sample magnetometer (VSM) with a constant applied field of 8 kOe.

III. RESULTS AND DISCUSSION

Well above T_C where the sample magnetization $M(T)$ is small, we separated the paramagnetic term from the diamagnetic background by means of the derivative dM/dT to evaluate the function $1/\sqrt{dM/dT}$. For $M=M_{CW}$ it should be linear in temperature: $(T-T_C)/\mu_B\sqrt{CH/k_B}$, but from our measurements up to 1000 K this function is slightly nonlinear (Fig. 1). Hence, either C or T_C (or both) are not exactly constants, and therefore the effective cluster spin $S_{\text{eff}} = 3C/4\bar{S} - 1$ (note that C is defined per one Mn spin, and the mean spin value $\bar{S} = x3/2 + (1-x)2 = 11/6$ provides $C\bar{S} \approx \bar{C}$) and its coupling to neighbor spins (clusters) $J_{\text{eff}} \approx 4T_C/C$ are temperature dependent. We found the experimental value of the Curie “function” $C(T)$ to increase from $\approx \bar{C}$ at $T > 800$ K to ≈ 14.8 at 300–350 K (from the two linear asymptotes far and close to T_C), in agreement with known data.^{6–8} The same $C(T)$ value at 300 K is obtained with SQUID and VSM measurements. The hump at the orthorhombic-trigonal structural transition $T_{O-T} \approx 750$ K

(shown in Fig. 1), can be explained by the increase of exchange at shrinking lattice parameters. To our knowledge, this is the first report of the $O-T$ transition through magnetic measurements. Resistivity measurements showing a kink at T_{O-T} were reported in literature.⁹

To understand the high-temperature behavior of $C(T)$, we calculated the spectrum of spin states for the simplest cluster model of two Mn^{3+} atoms, sharing one extra hole with hopping amplitude t . Apart from the splitting between bonding and antibonding states, known already from the semiclassical approach,² the spectrum is characterized by equal separation $t/4$ between levels which is not exactly equivalent to isotropic Heisenberg exchange. With decreasing temperature the calculated Curie function rapidly grows from the asymptotic value $C_{3/2} + C_{3/2} + C_{1/2}$, for fully independent components, to the limit $C_{7/2}$ for the fully aligned cluster spin.

Closer to T_C , where the diamagnetic contribution can be neglected, $C(T)$ can be defined directly as $M k_B (T - T_C)/\mu_B^2 H$ where $T_C = 263.5$ K fits best. For magnetic fields above 50 Oe, $C(T)$ displays even faster growth, which can be associated with a rapid continuous increase of effective cluster spin S_{eff} . Similar behavior for $(\text{La}_{1-x}\text{Tb}_x)_{2/3}\text{Ca}_{1/3}\text{MnO}_3$ was already reported.¹⁰ In addition to this, in lowest fields (< 50 Oe) some discrete steplike features appear in the magnetization data. In Fig. 2 we show the inverse magnetization as a function of temperature. It is seen that between steps a Curie-like behavior is observed (lines). The Curie function $C(T)$ is represented in Fig. 3 for several fields. Here these anomalies are more clear, with steps at well-defined temperatures and intermediate plateaus, and lower is the field better resolved are these features. This effect is new and it shows that intrinsic short range magnetic order in the considered material develops through a series of more or less stable intermediate states (clusters). We plotted the logarithms of plateau heights of $C(T)$ at different fixed fields and found them to grow almost linearly with the plateau number ($n=0,1,2,\dots$) (Fig. 4). The case $n=0$ is taken as the limiting value for independent spins measured at high temperatures: $\log C_{\text{step}}(n) \approx \log \bar{C} + \gamma n$, with $\gamma \approx \log(2.1 \pm 0.1)$. This can be interpreted as if the typical cluster spin S_{eff} is doubled each time as the corresponding temperature

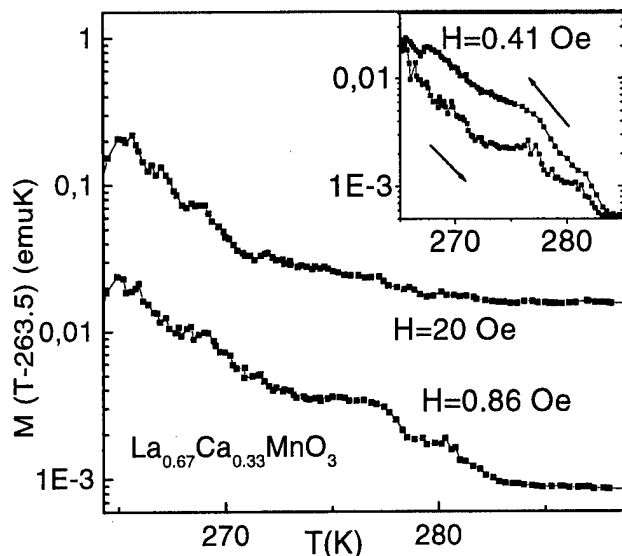


FIG. 3. Steplike behavior of the Curie function at low magnetic fields close to T_C . Inset: Temperature irreversibility effects.

T_n is reached. The first plateau around $T_1 \approx 290$ K with $C_1 \approx 15$ relates to $S_{\text{eff}} \approx 5.5$, which fits to a cluster of three Mn^{3+} ions sharing one extra hole, in coherence with the stoichiometric $\text{Mn}^{3+}/\text{Mn}^{4+}$ ratio. The consecutive plateaus around $T_2 \approx 280$ K, $T_3 \approx 276$ K, $T_4 \approx 269$ K, and $T_5 \approx 266$ K (observed in fields down to 0.5 Oe) can correspond to condensation of clusters with $S_{\text{eff}} \approx 11, 22, 44, 88$.

It is noteworthy that neither the temperature intervals between the steps nor their stability against the applied field are equal. For instance, the feature at $T_3 \approx 276$ K (supposedly 12 Mn^{3+} ions coupled by four extra holes) looks particularly stable. Also a considerable temperature hysteresis of magnetization $M(T)$, confined just to the range of steplike behav-

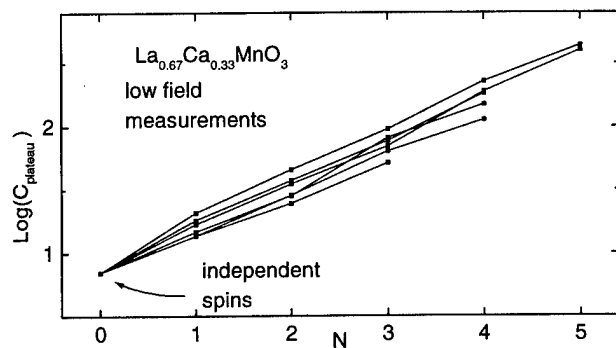


FIG. 4. Approximate linearity of logarithms of the plateau C values vs plateau number, indicating that these follow a geometrical progression, with the effective spin S doubled each time as a step occurs. The point for plateau 0 is obtained at high temperatures.

ior, suggests that the steps can be compared to a series of first kind phase transitions in the spin subsystem (inset to Fig. 3).

The sequence of cluster states for this sample can consist of: a triplet of Mn^{3+} ions sharing one extra hole, in line, six Mn^{3+} ions sharing two extra holes, possibly in a 2×3 rectangle, twelve Mn^{3+} ions sharing three extra holes possibly in a $2 \times 2 \times 3$ parallelepiped (two cubes) and so on. The calculation of the lowest energy level for clusters in a cubic lattice containing three Mn^{3+} ions for each hole in the double exchange Hamiltonian gives the following values: $E/t = -1.41, -1.71, -1.89, -2.06, -2.08$, and -2.20 for the cases of 1, 2, 3, 4, 6, and 9 holes in a cluster. Some of these values were recently reported by Gehring and Coombes.¹¹ It can be seen that the formation of clusters with more than four holes (12 ions) does not lead to a considerable energy reduction, while loosing in entropy. This may serve as an explanation for the above-indicated stability of the feature at $T_3 \approx 276$ K.

For comparison, the same measurements were also done on a less doped sample of $\text{La}_{0.75}\text{Ca}_{0.25}\text{MnO}_3$. Here the effect of strong enhancement of the Curie constant and hysteresis at low fields are also observed close to the transition temperature ≈ 232 K, however, no clear fine structure was seen even at lowest fields.

ACKNOWLEDGMENTS

This work is partially supported by JNICT under the contract PBIC/C/CTM/1967/95 and by PRODEP 3/94 from UTAD-Vila Real. J. P. Araújo acknowledges a scholarship from JNICT and Yu. G. Pogorelov from PRAXIS XXI BCC/6428/95. We thank M. A. Sá for assistance in VSM measurements.

- ¹R. M. Kusters, J. Singleton, D. A. Keen, R. Mc Greevy, and W. Hayes, *Physica B* **155**, 362 (1989).
- ²P. W. Anderson and H. Hasegawa, *Phys. Rev.* **100**, 675 (1955).
- ³A. J. Millis, P. B. Littlewood, and B. I. Shraiman, *Phys. Rev. Lett.* **74**, 5144 (1995).
- ⁴J. B. Sousa, V. S. Amaral, Yu. G. Pogorelov, A. L. Guimarães, J. P. Araújo, M. E. Braga, J. A. Mendes, M. R. Ibarra, P. Algarabel, J. Blasco, J. García, C. Marquina, A. del Moral, and J. M. de Teresa, *J. Appl. Phys.* **81**, 5760 (1997).
- ⁵S. B. Oseroff, M. Torikachvili, J. Singley, S. Ali, S. W. Cheong, and S. Schultz, *Phys. Rev. B* **53**, 6521 (1996).
- ⁶J. M. de Teresa, M. R. Ibarra, P. A. Algarabel, C. Ritter, C. Marquina, J. Blasco, J. García, A. del Moral, and Z. Arnold, *Nature (London)* **386**, 256 (1997); J. M. de Teresa, C. Ritter, M. R. Ibarra, P. A. Algarabel, J. L. García-Muñoz, J. Blasco, J. García, and C. Marquina, *Phys. Rev. B* **56**, 3317 (1997).
- ⁷J. Tanaka, H. Nozaki, S. Horiuchi, and M. Tsukioka, *J. Phys. Lett.* **44**, L129 (1983).
- ⁸J. P. Araújo, P. B. Tavares, V. S. Amaral, A. A. C. S. Lourenço, J. B. Sousa, and J. M. Vieira, *Key Engineering Materials* **132-136**, 1412 (1997).
- ⁹P. G. Radaelli, M. Marezzi, H. Y. Hwang, S.-W. Cheong, and B. Batlogg, *Phys. Rev. B* **54**, 8992 (1996).
- ¹⁰J. Blasco, J. García, J. M. de Teresa, M. R. Ibarra, P. A. Algarabel, and C. Marquina, *J. Phys.: Condens. Matter* **8**, 7427 (1996).
- ¹¹G. A. Gehring and D. J. Coombes, *J. Magn. Magn. Mater.* **177-181**, 873 (1998).

Low field magnetotransport in $\text{La}_{0.7}\text{Sr}_{0.3}\text{MnO}_3$ films

B. S. Teo,^{a)} N. D. Mathur, S. P. Isaac, J. E. Evetts, and M. G. Blamire

Department of Materials Science, University of Cambridge, Pembroke Street, Cambridge CB2 3QZ, United Kingdom

We have observed a strong correlation between the degree of epitaxy and the low field resistance versus field $R(H)$ behavior in highly textured $\text{La}_{0.7}\text{Sr}_{0.3}\text{MnO}_3$ films grown by pulsed laser deposition on SrTiO_3 substrates. Highly epitaxial films show a small temperature dependent low field hysteretic $R(H)$ peak near the magnetic ordering temperature (T_c), when the applied field is parallel to the transport current ($J\parallel H$). In contrast, films with reduced epitaxy show a much larger low field hysteretic $R(H)$ behavior with a pronounced in-plane angular dependence. The magnitude of this response grows with decreasing temperature below T_c . Our data and analysis suggest that even low angle grain boundaries play a fundamental role in transport properties in colossal magnetoresistive materials. © 1998 American Institute of Physics. [S0021-8979(98)26611-4]

I. INTRODUCTION

In recent years, much effort has concentrated on understanding the magnetotransport properties of alkaline earth substituted perovskite manganese oxide $\text{La}_{1-x}\text{A}_x\text{MnO}_3$ ($\text{A}=\text{Ba}, \text{Sr}, \text{Ca}, \text{Pb}$, or vacancies).^{1,2} These doped lanthanum manganites with a perovskite structure exhibiting colossal magnetoresistance (CMR) in the vicinity of the ferromagnetic ordering temperature (T_c) with a large applied magnetic field of the order of few Tesla. More recently, there have been a number of reports of a sensitive low field response in polycrystalline materials,^{3,4} heterostructures,⁵ and artificial grain boundaries.⁶ Resistance as a function of applied field [$R(H)$] plots for these systems share the common features of a hysteretic low field peak structure, which is reminiscent of metallic spin valve or spin tunnel devices. It has been noted recently that similar, though smaller, low field peaks can also be observed in epitaxial thin films near the ferromagnetic ordering temperature T_c .⁷

In this article, we report the results of careful measurements on batches of films with varying degrees of epitaxy. At low temperatures, we observe an angular and field dependent resistance hysteresis in the samples with the lowest degree of epitaxy. This behavior is absent in the films with higher crystalline order. We attribute the phenomenon to the low angle grain boundaries in the material. We demonstrate that a recently developed model for grain boundary behavior is consistent with the results.

II. EXPERIMENTAL DETAILS

$\text{La}_{0.7}\text{Sr}_{0.3}\text{MnO}_3$ (LSMO) thin films were grown on (001) SrTiO_3 (STO) substrates by pulsed laser deposition at growth temperatures between 900 and 600 °C in an oxygen ambient of 15 Pa, and annealed *in situ* at the growth temperature in 50 kPa of oxygen for 1 h. All films showed a single (001) growth direction and texture scans showed that in each case the film was aligned with the substrate crystal axes. X-ray rocking curves (θ scans) showed that films grown above

700 °C (designated type I films) had a full width at half maximum (FWHM) of 0.2–0.5°. In contrast, a broad FWHM of $\approx 2^\circ$ was shown by the films grown at 600 °C (type II), indicating a significantly lower crystalline quality, implying the presence of a high density of low angle grain boundaries. The magnetization of the films was measured against temperature and field using a vibrating sample magnetometer (VSM) at temperatures down to 77 K. The low field transport properties of the samples were measured as a function of temperature, magnetic field, and in-plane angle between transport current and the applied magnetic field (θ) using a standard four-point probe. The contacts to the film were made using spring-loaded “pogo” pins without patterning the sample so that subsequent magnetization measurement could be made to obtain meaningful comparisons of electrical and magnetic properties.

III. RESULTS

$R(H)$ measurements of type II films (Fig. 1) show a large resistance hysteresis which is especially pronounced at low temperature, and diminishes as the temperature increases towards T_c . At higher fields, these samples show a highly linear variation of resistance with applied field which is a characteristic feature of data from both polycrystalline samples,⁴ and artificial grain boundaries.⁶ The large negative magnetoresistance (MR) [defined as $\text{MR}=(R_{\text{res}}-R_{\text{max}})/R_{\text{max}}$, where R_{max} is the maximum resistance and R_{res} is the resistance at $H=0$ extrapolated from high field slope] decreases as temperature increases. By comparison type I films showed a small resistance hysteresis only near T_c . At 77 K, not only is the absolute resistance two orders of magnitude lower than for type II films, but the samples display an extremely small positive MR when $J\perp H$ ($\theta=90^\circ$) as opposed to a negative MR in the $\theta=0$ configuration (see inset to Fig. 1).

We show in Fig. 2 the angular dependence of the resistance for type II films as a function of θ at various applied fields at 77 K, as measured during a series of field sweeps. While the resistances measured at $H=0$ and $H=H_c$ do not show a significant angular dependence, at an applied field of

^{a)}Electronic mail: bst21@cus.cam.ac.uk

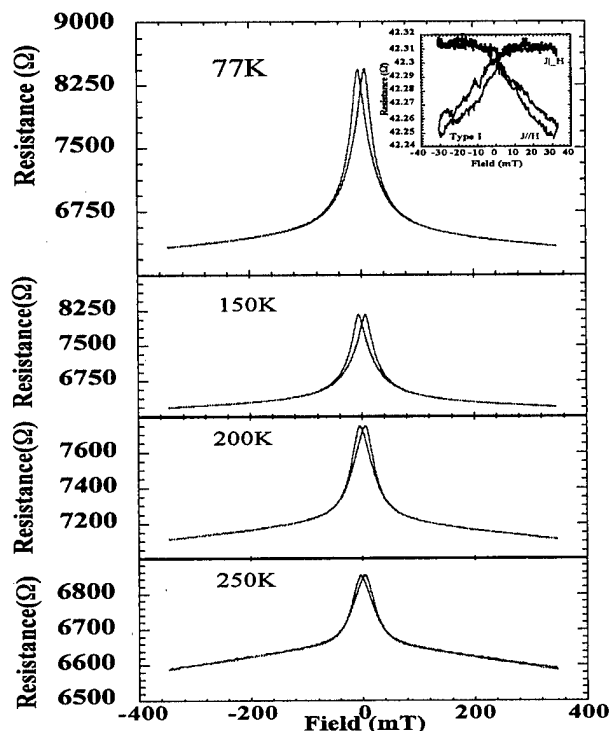


FIG. 1. Resistance (R) vs in-plane applied field (H) at a series of temperatures for type II films. Inset shows the corresponding $R(H)$ curve with the current parallel and perpendicular to the applied field for a type I film at 77 K.

50 or 250 mT the resistance gradually increases with θ , reaching a maximum at 90° before decreasing back to a minimum at 180° . We have confirmed that this is not a simple demagnetization effect caused by the shape of the chip by repeating the measurement with the current at 90° to the original direction.

Figure 3 shows the in-plane magnetization loop for both types I and II samples. The high field magnetization of the type II sample is both lower than in the case of the type I sample, and less square. This data appears to contradict that of Gupta *et al.*³ in which the high field magnetization for polycrystalline samples was found to be higher than for epitaxial films. However, in our measurements the high field

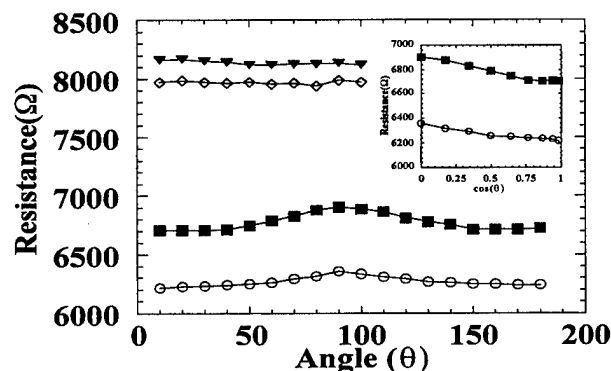


FIG. 2. Resistance vs angle (θ) between current and field direction for a type II films at a series of applied fields at 77 K: \blacktriangledown peak maximum, \diamond 0 mT, \blacksquare 50 mT, and \circ 250 mT. The inset show the data for 50 and 250 mT replotted vs $\cos(\theta)$.

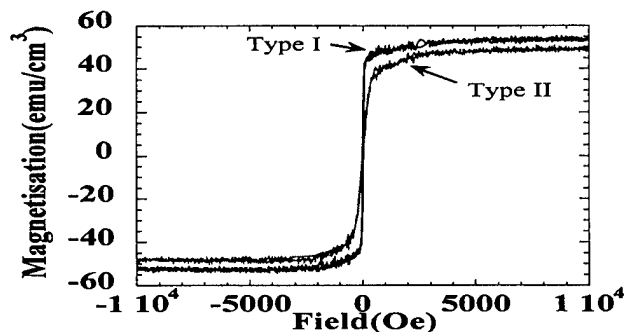


FIG. 3. Magnetic hysteresis loops measured at room temperature for types I and II films.

differential susceptibility for the type II material is higher than it is for the type I samples which is consistent with a reduced magnetic order associated with the grain boundaries.

IV. DISCUSSION

The possibility that the low field MR can be an intrinsic effect due to domain wall scattering can be ruled out, since single crystal materials (like our type I samples) show an MR which vanishes as the temperature tends to zero. The finite MR at low temperature shown by type II samples is similar to that for truly polycrystalline films reported by Li *et al.*⁸ and Steenbeck *et al.*,⁹ and the linear high field response is similar to that reported by Hwang *et al.*⁴ The implication is therefore that even low angle grain boundaries can dramatically modify the transport properties of the CMR manganites. In our previous studies of bicrystal grain boundary devices,⁶ a phenomenological model¹⁰ based on the existence of a region of depressed magnetic order induced by grain boundary was proposed to explain both the high field and the low field MR behavior. In this model the low temperature MR behavior in isolated grain boundaries is attributed to structural disorder and strain at the grain boundaries, thus depressing the local magnetic order and so greatly reducing carrier mobility.

Direct evidence for a reduction in magnetic order in type II samples is provided by the measured difference in the magnetization data between the two film types; the lowest high field magnetization is measured in the type II samples which contain the highest proportion of grain boundary material. This confirms that the spontaneous magnetization in the grain boundary regions is lower than it is within grains. The reduced squareness of the magnetization loop taken for the type II sample is consistent with the onset of the high field regime occurring at higher fields than it does during measurements of the type I samples. This finding is consistent with the existence of a magnetocrystalline anisotropy which has been reported to play a measurable role at low fields.⁷

The main result of the model described in Ref. 10 is that the magnetoresistance of polycrystalline films can be approximated as

$$\Delta R_{gb}/R_0 = -\gamma(M_0^2 + 2M_0\chi_{gb}fM_e + 2M_0\chi_{gb}H), \quad (1)$$

TABLE I. Summary of the data for a type II sample at four different measurement temperatures. R_{90} and R_0 are the resistance of the films for $\theta=90^\circ$ and 0° , respectively, dR/dH is the high field change in resistance with applied field, M_e is the magnetization deduced from Eq. (1) used the analysis in the text, and M_{spont} is the measured magnetization of the same film.

Temperature (K)	$R_{90}(\Omega)$	$R_0(\Omega)$	$R_{\text{max}}(\Omega)$	$dR/dH(\Omega \text{ mT}^{-1})$	M_e	$M_{\text{spont}}(\text{mT})$
77	6275	6173	8163	0.670	152	148
150	7014	6937	8062	0.517	149	140
200	7161	7111	7751	0.357	140	124
250	6654	6630	6893	0.239	100	113
300	5530	5523	5603	0.132	53	81

where M_e is the saturation magnetization of the intragranular material, f is the fraction of M_e applied to the grain boundary region (usually, but not necessarily the cosine of the angle between the direction of M_e and the normal to the grain boundary), M_0 is the spontaneous grain boundary magnetization, and χ_{gb} is the differential susceptibility of the grain boundary. This model correctly predicts the linear high field magnetoresistance observed in both artificial grain boundary devices and polycrystalline material (see Fig. 1).

The angular dependence observed in Fig. 3 is accounted for in this model by the variable f . In our films we expect a range of grain boundary orientations to be present; however, it is only grain boundaries which lie perpendicular to the current flow which are likely to contribute significantly to the resistivity, and consequently we can replace the angle between the induced magnetization and the normal to the significant grain boundaries $\arccos(f)$ by the angle between the current and field (θ). The inset of Fig. 2 shows that a plot of R at fixed field versus $\cos(\theta)$ is linear as predicted by Eq. (1).

On the basis that $f=\cos(\theta)$, the difference in MR between the $\theta=0^\circ$ and 90° field configurations should be equal to $2\gamma M_0 \chi_{\text{gb}} M_e$. The ratio between this quantity and the high field slope (dR/dH) should then be equal to M_e . Table I shows data obtained from a type II film at a number of temperatures. The excellent agreement between the measured magnetization and that inferred from the model provides considerable support for this model.

V. CONCLUSIONS

The results presented here demonstrate that even highly textured CMR thin films can have magnetotransport proper-

ties which are identical to fully polycrystalline samples. This highlights the significance of low angle grain boundaries in manganite perovskites, and places strict requirements for the growth of ideal CMR material on nonideal substrates. More positively, it demonstrates that control of the sample microstructure allows the development of technologically desirable low field properties in simple single layer films.

ACKNOWLEDGMENT

This work was supported by the UK Engineering and Physical Sciences Research Council under the Advanced Magnetism Programme.

- ¹M. McCormack, S. Jin, T. H. Tiefel, R. M. Fleming, J. M. Phillips, and R. Ramesh, Appl. Phys. Lett. **64**, 3045 (1994).
- ²S. Jin, T. H. Tiefel, M. McCormack, R. A. Fastnacht, R. Ramesh, and L. H. Chen, Science **264**, 413 (1994).
- ³A. Gupta, G. Q. Gong, G. Xiao, P. R. Duncombe, P. Lecoeur, P. Trouiloud, Y. Y. Wang, V. P. Dravid, and J. Z. Sun, Phys. Rev. B **54**, 15 629 (1996).
- ⁴H. Y. Hwang, S. W. Cheong, N. P. Ong, and B. Batlogg, Phys. Rev. Lett. **77**, 2041 (1996).
- ⁵J. Z. Sun, L. Krusin-Elbaum, P. R. Duncombe, A. Gupta, and R. B. Laibowitz, Appl. Phys. Lett. **69**, 3266 (1996).
- ⁶N. D. Mathur, S. P. Isaac, G. Burnell, B.-S. Teo, L. F. Cohen, J. L. MacManus-Driscoll, J. E. Evetts, and M. G. Blamire, Nature (London) **387**, 266 (1997).
- ⁷J. O'Donnell, M. Onellion, M. S. Rzchowski, J. N. Eckstein, and I. Bozovic, Phys. Rev. B **55**, 5873 (1997).
- ⁸X. W. Li, A. Gupta, G. Xiao, and G. Q. Gong, Appl. Phys. Lett. **71**, 1124 (1997).
- ⁹K. Steenbeck, T. Eick, K. Kirsch, K. O'Donnell, and E. Steinbeiss, Appl. Phys. Lett. **71**, 968 (1997).
- ¹⁰J. E. Evetts, N. D. Mathur, S. P. Isaac, B. S. Teo, L. F. Cohen, J. L. MacManus-Driscoll, and M. G. Blamire, Philos. Trans. R. Soc. London, Ser. A 356 (in press).

Magnetostriction and field induced transitions in $\text{La}_{1-x}\text{Sr}_x\text{MnO}_3$ in pulsed magnetic fields

Yu. F. Popov,^{a)} A. M. Kadomtseva, and G. P. Vorob'ev
Moscow State University, Moscow 119899, Russia

V. Yu. Ivanov, A. A. Mukhin, and A. K. Zvezdin
General Physics Institute of the Russian Academy of Science, 38 Vavilov St., Moscow 117942, Russia

A. M. Balbashov
Moscow Power Engineering Institute, 14 Krasnokazarmennaya St., Moscow 105835, Russia

Magnetostriction $\lambda_{||}(H)$ and field-induced phase transitions were studied in the single crystal of $\text{La}_{1-x}\text{Sr}_x\text{MnO}_3$ ($x=0, 0.05, 0.1$, and 0.175) in the pulsed magnetic fields up to 230 kOe. Anomalies in the $\lambda_{||}(H)$ curves were revealed at 200 kOe in the LaMnO_3 , which were identified with the spin-reorientation $A_yF_z \rightarrow A_zF_y$ in the magnetic field $H \parallel b$ axis. A complicated magnetostriction behavior was observed in $\text{La}_{0.875}\text{Sr}_{0.125}\text{MnO}_3$, related to the field-induced transition between orthorhombic and rhombohedral crystal structures. © 1998 American Institute of Physics. [S0021-8979(98)47011-7]

Lanthanum manganites doped by the divalent ions Sr (Ca) attract a considerable recent attention due to an observation of various interesting phenomena such as a giant negative magnetoresistance, magnetic, structural and metal-insulator phase transitions, a charge ordering.¹⁻⁴ Various field induced magnetic and structural phase transitions are expected in these compounds. Magnetostriction may serve as a sensitive indicator of the change of magnetic and crystal structures. The recent finding of the field induced structural phase transition in $\text{La}_{0.83}\text{Sr}_{0.17}\text{MnO}_3$ ^{3,5} indicates a strong coupling between the magnetic and crystal subsystems in these compounds. In this article we report on the magnetoelastic properties and field induced transitions in $\text{La}_{1-x}\text{Sr}_x\text{MnO}_3$ in pulsed magnetic fields.

Single crystals of $\text{La}_{1-x}\text{Sr}_x\text{MnO}_3$ ($x=0, 0.05, 0.1$, and 0.175) were grown by the floating zone method with radiation heating in an air atmosphere. X-ray powder diffraction measurements showed that grown crystals were of single phase; however, they had a twin structure.

The magnetostriction was measured by a quartz sensor, stuck on the samples, in pulsed magnetic fields up to 230 kOe at temperatures of 10–300 K. Magnetization $M(T, H)$, ac magnetic susceptibility $\chi_{ac}(T)$ and resistance $\rho(T)$ measurements were performed in the static magnetic fields $H \leq 12$ kOe at $T=4.2$ –300 K.

LaMnO_3 : It is known that $\text{La}_{1-x}\text{Sr}_x\text{MnO}_3$ manganites have a distorted perovskite crystal structure, which undergoes a structural phase transition between a low-temperature orthorhombic phase and a high-temperature rhombohedral one.^{2,3,5,6} In the pure LaMnO_3 Mn^{3+} spins are ordered antiferromagnetically at $T_N \approx 140$ K along b axis of the orthorhombic $Pbmn$ crystal and a small spin canting takes place along c axis (magnetic layer structure of the A_yF_z type).⁷⁻⁹

Our magnetic measurements have shown that there are four easy directions of a spontaneous magnetic moment in

the studied LaMnO_3 crystals due to an existence of the twin structure in the samples. The easy axes lie approximately in the (110) and (1-10) planes of the orthorhombic crystal. There are six types of the twins with c axis along the $\langle 100 \rangle$ directions corresponding to the high temperature cubic cell.⁹ Estimated values of the spontaneous magnetic moment and transverse susceptibility for the nontwin crystal at $T=78$ K are $m_0 = 4.2 \pm 0.5$ emu/g and $\chi_{\perp} = (1.8 \pm 0.3) 10^{-4}$ cm³/g, respectively.

The measurements of the longitudinal magnetostriction $\lambda_{||}$ were carried out in the magnetic field H oriented along the b axis in one of the twins. The example of the $\lambda_{||}(H)$ curve for LaMnO_3 at $T=29$ K is shown in Fig. 1, where the apparent jump is observed at $H \sim 200$ kOe on the background of the smooth increasing of the magnetostriction. We identified this anomaly with the spin-reorientation phase transition from A_yF_z to A_zF_y magnetic configuration induced by the $H \parallel b$ axis in one of the twins. Recently an anomaly in the magnetization behavior of the LaMnO_3 was observed near the same magnetic field ($H \approx 210$ kOe) applied along b axis.¹⁰ The threshold field H_c of this transition may be determined analogously, to the corresponding transitions in orthoferrites:¹¹

$$H_c = -H_D + (H_D^2 + 2H_A H_E)^{1/2}, \quad (1)$$

where $H_E = M_0/2\chi_{\perp} \approx 330$ kOe, $H_D = m_0/\chi_{\perp} \approx 23$ kOe (at $T=78$ K) are the isotropic and antisymmetric exchange fields, respectively, $H_A = K_{cb}/M_0$ is the effective anisotropy field in the bc plane and K_{cb} is the corresponding anisotropy constant, $M_0/2$ is the sublattice magnetization. Using the value of the antiferromagnetic resonance frequency for LaMnO_3 ^{9,12} $\hbar\omega = g\mu_B(2H_A H_E)^{1/2} \approx 17$ –19 cm⁻¹ at the $T < 50$ K, where μ_B is the Bohr magneton and $g \approx 2$ is a g tensor, we have estimated H_c as 180–200 kOe that is in good agreement with our experiment. We note the small contribu-

^{a)}Electronic mail: popov@plm1.phys.msu.su

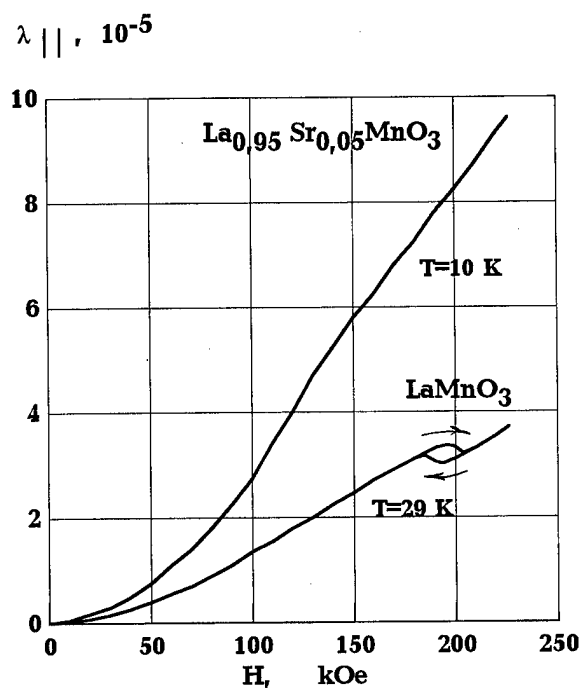


FIG. 1. Magnetic field dependence of the magnetostriction in LaMnO_3 and $\text{La}_{0.95}\text{Sr}_{0.05}\text{MnO}_3$.

tion of the antisymmetric exchange to the threshold field $H_c[H_D \ll (2H_A H_E)^{1/2}]$ allows to consider the observed spin reorientation as a simple spin-flop transition.

$\text{La}_{0.95}\text{Sr}_{0.05}\text{MnO}_3$: In the case of small substitutions of the La^{3+} ions by the Sr^{2+} the magnetic structure remains of the $A_y F_z$ type is evidenced by neutron scattering and magnetic study of the $\text{La}_{0.96}\text{Sr}_{0.04}\text{MnO}_3$.¹³ Our study of the practically nontwin single crystal of the $\text{La}_{0.95}\text{Sr}_{0.05}\text{MnO}_3$ confirms this conclusion. The corresponding magnetization curves presented in Fig. 2 show that the spontaneous magnetic moment is along the c axis, the magnetic susceptibilities along a and c axes are practically equal to each other

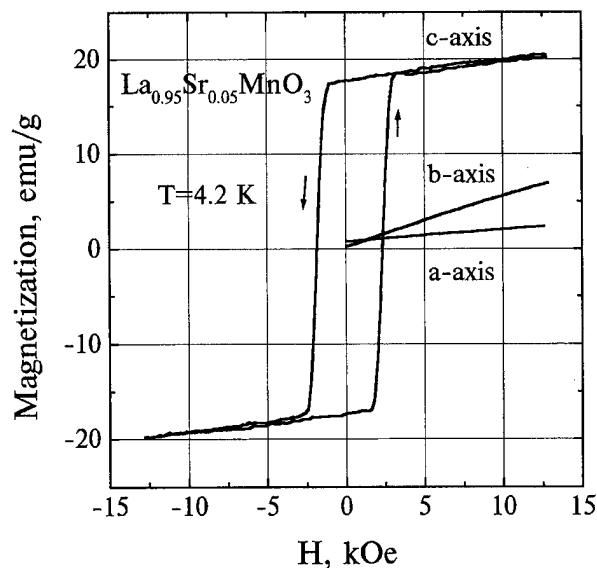


FIG. 2. Magnetization curves in $\text{La}_{0.95}\text{Sr}_{0.05}\text{MnO}_3$ along different crystallographic axes ($T=4.2$ K).

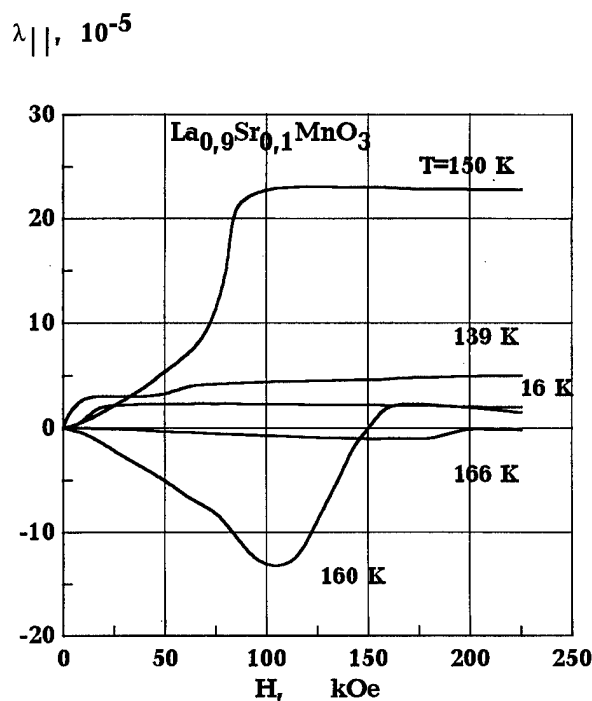


FIG. 3. Magnetic field dependence of the magnetostriction in $\text{La}_{0.9}\text{Sr}_{0.1}\text{MnO}_3$.

and determine the transverse susceptibility ($\chi_a \approx \chi_c = \chi_\perp$), and the susceptibility along b axis, determined by the rotation susceptibility ($\chi_b \approx \chi_{\text{rot}} = m_0^2 / K_{cb}$), is much greater than $\chi_{a,c}$. The large value of the χ_{rot} is consistent with the noticeable increase (about 4 times) of the canting angle and decrease of the anisotropy constant K_{cb} as compare with the pure LaMnO_3 . It implies also the decrease of the threshold field induced the spin-reorientation $A_y F_z \rightarrow A_z F_y$, whose value is estimated as 35 kOe using Eq. (1).

However, our measurements of the longitudinal magnetostriction along b axis $\lambda_\parallel \equiv \lambda_{bb}$ in the $\text{La}_{0.95}\text{Sr}_{0.05}\text{MnO}_3$ (Fig. 1) do not exhibit any anomaly in the $\lambda_\parallel(H)$ curve near of the expected threshold magnetic field (~ 35 kOe) besides a weak bend observed at 100–150 kOe. The absence of the apparent anomaly in the $\lambda_\parallel(H)$ curve of the $\text{La}_{0.95}\text{Sr}_{0.05}\text{MnO}_3$ may be due to a smooth character of the $A_y F_z \rightarrow A_z F_y$ spin reorientation which occurs through the angular $A_y A_z F_z F_y$ phase in contrast to the practically abrupt transition in pure LaMnO_3 . In this case we cannot exclude a more crucial role of the twin structure in a mask of the smooth spin reorientation in the $\text{La}_{0.95}\text{Sr}_{0.05}\text{MnO}_3$ sample, destined for the magnetostriction measurements.

$\text{La}_{0.9}\text{Sr}_{0.1}\text{MnO}_3$: For the $\text{La}_{0.9}\text{Sr}_{0.1}\text{MnO}_3$ composition, which already exhibits the ferromagnetic ordering ($T_C \approx 165$ – 170 K), we observed unusual behavior of the longitudinal magnetostriction near T_C (Fig. 3). The magnetostriction had no anomalies at the low temperatures (10–130 K) and reached only the saturation value about $(2-3) \times 10^{-5}$. However, a weak jump aroused near 50 kOe at $T=139$ K, which was transformed at 150 K to the strong anomaly near 80 kOe accompanied by increasing the magnetostriction up to one order of the magnitude. With the further temperature increasing, the magnetostriction changed a sign in the weak

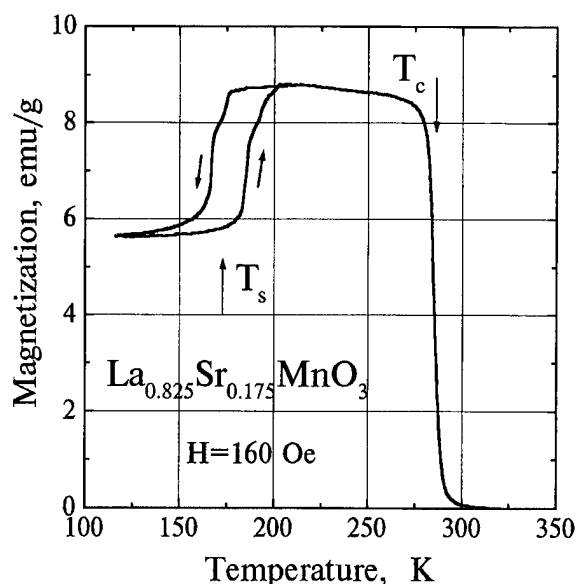


FIG. 4. Temperature dependence of the magnetization in $\text{La}_{0.825}\text{Sr}_{0.175}\text{MnO}_3$ at $H = 160$ Oe.

magnetic fields, but the positive jump in the higher field remained up to T_C despite its amplitude being reduced (see curves at 160 and 166 K at Fig. 3).

Such complicated behavior of the magnetostriction near T_C may be associated with field induced magnetic and structural phase transitions. According to the neutron scattering studies^{14,15} an antiferromagnetic ordering as well as a structural transition related to a polaron ordering takes place in $\text{La}_{0.9}\text{Sr}_{0.1}\text{MnO}_3$ below T_C which implies a possibility of the magnetic field effect on these transitions.

$\text{La}_{0.825}\text{Sr}_{0.175}\text{MnO}_3$: The strong effect of magnetic field on the phase transitions between orthorhombic and rhombohedral crystal structures was observed in the $\text{La}_{0.83}\text{Sr}_{0.17}\text{MnO}_3$, where the structural transition temperature T_S , close to T_C , was decreased from 280 K at $H = 0$ down to 220 K at $H = 70$ kOe.^{3,5} However, in the case of $x = 0.16$ and 0.18 the T_S 's remained almost unchanged since there was a considerable difference between corresponding T_S and T_C .⁵ The mechanism of the transition is connected with a lower value of the magnetization in the orthorhombic phase than in the rhombohedral one.

We studied the composition with $x = 0.175$, where, according to our magnetic measurements (Fig. 4), $T_C \approx 285$ and $T_S \approx 160$ –190 K. Figure 5 shows the dependence of the longitudinal magnetostriction versus the magnetic field at several temperatures. At the low temperatures ($T < 182$ K) the magnetostriction behaved in ordinary manner without anomalies (curve at 150 K), while near the T_S the magnetostriction increased rapidly after reaching a threshold value (curves at 182 and 194 K), which we identify with field-induced structural transition. We note the strong hysteretic phenomena accompanying the transition, so that the crystal does not remain in the initial state after removing the magnetic field. We cannot exclude additional relaxation effects in the related phenomena considering the measurements in the pulsed magnetic fields.

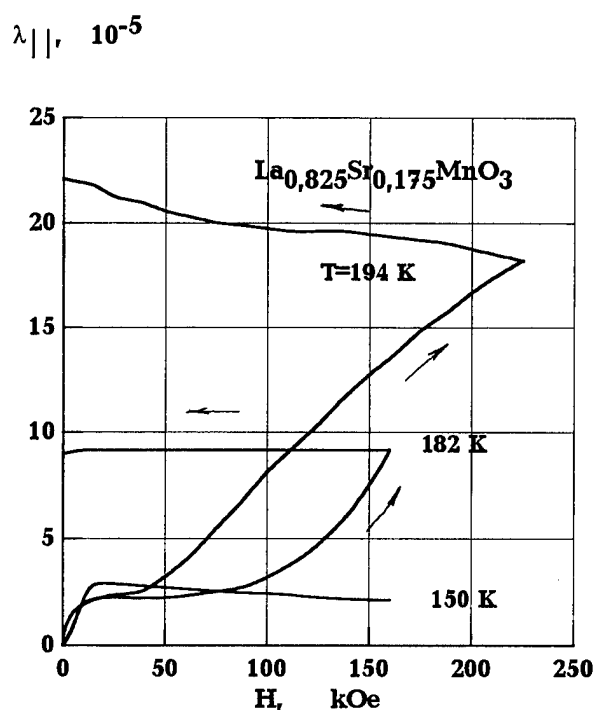


FIG. 5. Magnetic field dependence of the magnetostriction in $\text{La}_{0.825}\text{Sr}_{0.175}\text{MnO}_3$.

In conclusion, we have studied the magnetostriction in $\text{La}_{1-x}\text{Sr}_x\text{MnO}_3$ in the strong pulsed magnetic fields and demonstrated its sensitivity to the field induced spin reorientation and structural phase transition, observed in LaMnO_3 and $\text{La}_{0.825}\text{Sr}_{0.175}\text{MnO}_3$, respectively.

This work was supported in part by the Russian Foundation for Basic Researches (Grant 97-02-17325).

- ¹R. von Helmholt, J. Wecker, B. Holzapfel, L. Schultz, and K. Samwer, *Phys. Rev. Lett.* **71**, 2331 (1993).
- ²A. Urushibara, Y. Moritomo, T. Arima, A. Asamitsu, G. Kido, and Y. Tokura, *Phys. Rev. B* **51**, 14 103 (1995).
- ³A. Asamitsu, Y. Moritomo, Y. Tomioka, T. Arima, and Y. Tokura, *Nature (London)* **373**, 407 (1995).
- ⁴Y. Tomioka, A. Asamitsu, H. Kuwahara, Y. Moritomo, and Y. Tokura, *Phys. Rev. B* **53**, R1689 (1996).
- ⁵A. Asamitsu, Y. Moritomo, R. Kumai, Y. Tomioka, and Y. Tokura, *Phys. Rev. B* **54**, 1716 (1996).
- ⁶A. Wold and R. J. Arnett, *J. Phys. Chem. Solids* **9**, 176 (1959).
- ⁷E. O. Wollan and W. C. Koehler, *Phys. Rev.* **100**, 545 (1955).
- ⁸G. Matsumoto, *J. Phys. Soc. Jpn.* **29**, 606 (1970).
- ⁹F. Moussa, M. Hennion, J. Rodriguez-Carvajal, H. Moudén, L. Pinsard, and A. Revcolevschi, *Phys. Rev. B* **54**, 15 149 (1996).
- ¹⁰S. Mitsudo, K. Hirano, H. Nojiri, M. Motokawa, K. Hirota, A. Nishizawa, N. Kaneko, and Y. Endoh, Abstract of the International Conference on Magnetism, Cairns, Australia, 1997 (unpublished), Q3-19.
- ¹¹J. S. Jacobs, H. Burns, and L. M. Levinson, *J. Appl. Phys.* **92**, 1631 (1971).
- ¹²V. Yu. Ivanov, V. D. Travkin, A. A. Mukhin, S. P. Lebedev, A. A. Volkov, A. Pimenov, A. Loidl, A. M. Balbashov, and A. V. Mozhaev, *J. Appl. Phys.* **83** (1998), these proceedings.
- ¹³H. Kawano, R. Kajimoto, M. Kubota, and H. Yoshizawa, *Phys. Rev. B* **53**, 2202 (1996).
- ¹⁴Y. Yamada, O. Hino, S. Nohdo, R. Kanao, T. Inami, and S. Katano, *Phys. Rev. Lett.* **77**, 904 (1996).
- ¹⁵H. Kawano, R. Kajimoto, M. Kubota, and H. Yoshizawa, *Phys. Rev. B* **53**, R14 709 (1996).

Magnetic properties, resistivity, and heat capacity of EuMnO_3 and $\text{Eu}_{0.7}\text{A}_{0.3}\text{MnO}_3$ ($\text{A}=\text{Ca}, \text{Sr}$) compounds

Y. M. Mukovskii

Moscow Steel and Alloys Institute, 075, Leninskii.prosp. 4, Moscow 117936, Russia

G. Hilscher and H. Michor^{a)}

Institut für Experimentalphysik, Technische Universität Wien, Wiedner Hauptstrasse 8-10, A-1040 Wien, Austria

A. M. Ionov

Institute for Solid State Physics, Chernogolovka, Moscow Region 142432, Russia

We present magnetic-, resistivity-, and specific-heat measurements of the title compounds and found that in $\text{Eu}_{0.7}\text{Sr}_{0.3}\text{MnO}_3$ an insulator-metal transition can be induced by an external field below 60 K while $\text{Eu}_{0.7}\text{Ca}_{0.3}\text{MnO}_3$ remains insulating. EuMnO_3 exhibits two magnetic transitions at 35 and 47 K which are associated with the appearance of a weak ferromagnetic component and antiferromagnetic ordering. With respect to the parent compound, Ca and Sr substitution enhance the ferromagnetic component significantly, however, for low fields and after zero-field cooling the antiferromagnetic ground state is preserved to a large extent. © 1998 American Institute of Physics. [S0021-8979(98)26711-9]

I. INTRODUCTION

Rare earth manganite perovskites $\text{R}_{1-x}\text{A}_x\text{MnO}_{3+\delta}$ ($\text{R}=\text{rare earth elements}, \text{A}=\text{Ca}, \text{Sr}, \text{Ba}, \text{Pb}$) show colossal magnetoresistance and attracted renewed attention not only due to their potential applications but also because of their rich physical properties (for a review see, e.g., Ramirez¹ and references therein). Since most of the works were devoted to La and Pr based manganites it is the aim of this article to study the properties of $\text{Eu}_{0.7}\text{A}_{0.3}\text{MnO}_3$ where Eu is suggested to be trivalent and thus exhibits a nonmagnetic groundstate ($J=0$) and a smaller ionic radius than La^{+3} .

II. EXPERIMENTAL DETAILS AND STRUCTURAL CHARACTERIZATION

Ceramic samples of the title compounds were synthesized from Eu_2O_3 , MnO_2 , SrCO_3 and CaCO_3 of high purity by sintering at temperatures 900–1100 °C for 24 h. The resulting powders were reground and annealed in air at 1300 °C for 12 h. As follows from x-ray analysis the samples have distorted perovskite structure and contained less than 5% impurity phases. Resistivity was measured by four-point technique by a Keithley-182 nanovoltmeter with 10 G Ω input impedance; contacts were made by ultrasonic soldering

with indium. ac susceptibility and dc magnetization were measured by a conventional lock-in technique and by a superconducting quantum interferometer device (SQUID) magnetometer, respectively. Heat capacity measurements were carried out by a quasiadiabatic step heating technique in fields up to 11 T. The valence state of Eu ions at room temperature was estimated by x-ray photoelectron spectroscopy (XPS) using the ESCALAB-5 electron spectrometer and twin anode Al/Mg source. Clean surfaces of EuMnO_3 were obtained by cleavage *in situ* in UHV and/or by ion bombardment. Electronic structure and binding energies of the Eu 4*f* spectra of EuMnO_3 were compared with divalent and trivalent oxides of Eu and found to be very close to the trivalent oxide Eu_2O_3 . The lattice parameters and structural data are collected in Table I.

III. RESULTS AND DISCUSSION

Shown in Fig. 1(a), *b* is the specific heat and ac susceptibility of EuMnO_3 and the substituted compounds. For the parent EuMnO_3 compound both measurements exhibit a double peak at 47 and 35 K. The former corresponds to the antiferromagnetic (AF) ordering while the anomaly at 35 K is attributed to the evolution of a weak ferromagnetic (FM) component which we derive from the dc magnetization at various external fields in Fig. 2. For clarity we present in

TABLE I. The structures and lattice parameters of the title compounds. The error is given in brackets.

	Structure	<i>a</i> (Å)	<i>b</i> (Å)	<i>c</i> (Å)	γ	<i>V</i> (Å ³)
EuMnO_3	Orthorhombic	5.336(2)	5.833(2)	7.456(3)	90.0	232.1(3)
$\text{Eu}_{0.7}\text{Sr}_{0.3}\text{MnO}_3$	Orthorhombic	5.436(3)	5.458(3)	7.666(2)	90.0	227.5(3)
$\text{Eu}_{0.7}\text{Ca}_{0.3}\text{MnO}_3$	Monoclinic	5.376(2)	5.516(3)	7.553(2)	89.71(3)	224.0(3)

^{a)}Electronic mail: herwig@xphys.tuwien.ac.at

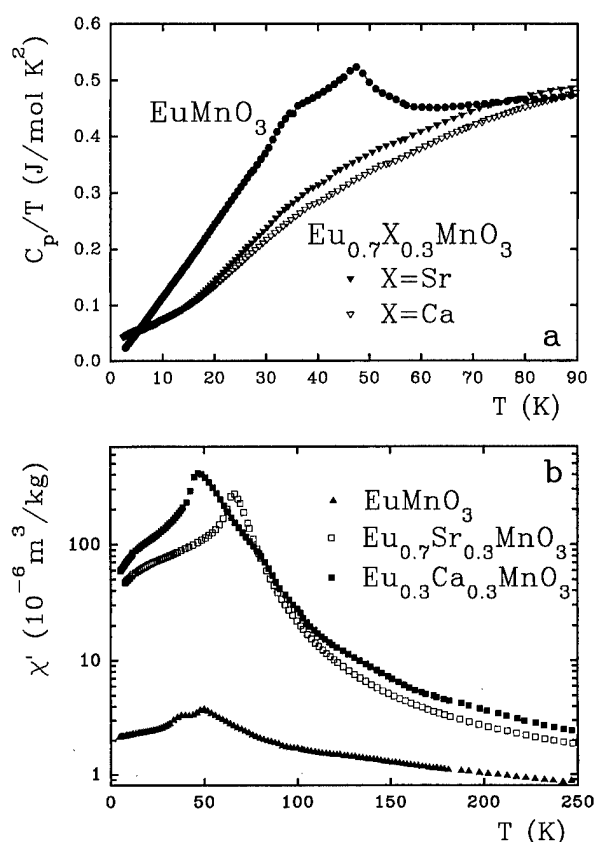


FIG. 1. The specific heat, C_p/T vs T , (a) and the real part of the ac susceptibility in a semilogarithmic scale (b) of EuMnO_3 , $\text{Eu}_{0.7}\text{Sr}_{0.3}\text{MnO}_3$, and $\text{Eu}_{0.7}\text{Ca}_{0.3}\text{MnO}_3$.

Fig. 2 only the magnetization measurement after zero-field cooling (ZFC) for $\mu_0 H \geq 0.1$ T but both the field cooled (FC) and ZFC magnetization for 10 mT. The AF ordering temperature is in agreement with the early report on EuMnO_3 by Pauthenet and Veyret² (45 K) and that of Troyanchuk *et al.*³ for $\text{EuMnO}_{3.02}$ (40 K) who also showed that with growing oxygen deficiency T_N moves to higher temperatures. In the dc magnetization T_N is not as clearly seen as in the specific heat and ac susceptibility data but coincides with the disappearance of the irreversibility between the ZFC and FC

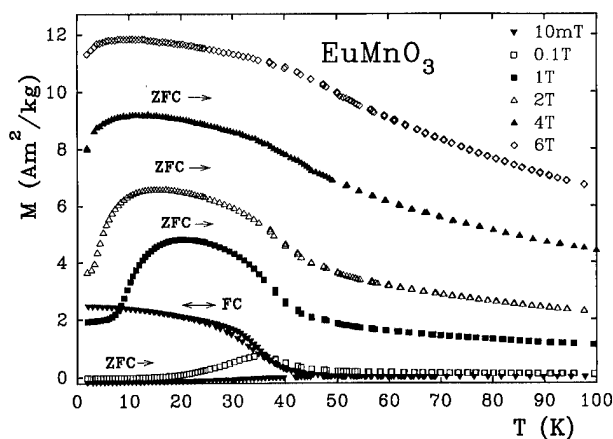


FIG. 2. The temperature-dependent magnetization of EuMnO_3 measured after zero-field cooling (ZFC) for $\mu_0 H \geq 0.1$ T and both the field cooled (FC) and ZFC magnetization data for 10 mT.

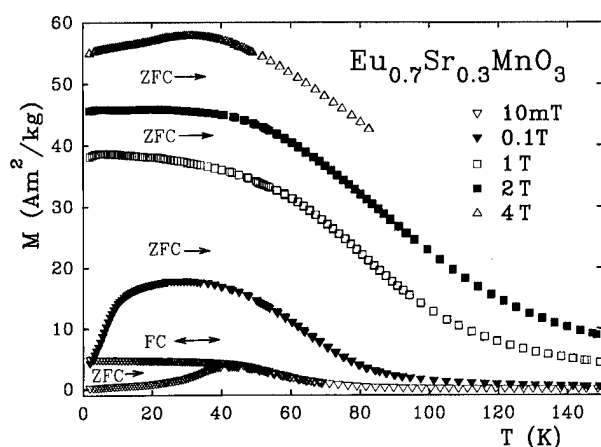


FIG. 3. The temperature-dependent magnetization of $\text{Eu}_{0.7}\text{Sr}_{0.3}\text{MnO}_3$ measured after zero-field cooling (ZFC) for $\mu_0 H \geq 0.1$ T and both the field cooled (FC) and ZFC magnetization data for 10 mT.

branch of the magnetization. The occurrence of a weak FM component is associated with a thermal hysteresis of the field cooled magnetization for cooling and warming. In the ZFC magnetization a maximum occurs at 35 K which is broadened and washed out with growing external fields. This is consistent with the specific heat data where the AF ordering temperature remains nearly unchanged while the 35 K anomaly is washed out and entropy is transferred to higher temperatures as the external field is raised. Furthermore a metamagnetic transition into a weak FM state is observed at about 3 T at 2 K concomitant with the occurrence of a remanent magnetization of about 3 Am²/kg after a linear decrease of $M(H)$ from a value of 11.9 Am²/kg at 6 T. This together with the above findings indicates a more complex AF ordering than in LaMnO_3 where FM sheets are coupled antiferromagnetically. Nevertheless, we assume for EuMnO_3 basically a similar AF coupling since in the low temperature specific heat a dominant T^2 term is present over a wide temperature range and is clearly seen as the linear temperature dependence in the C_p/T versus T plot in Fig. 1(a). The heat capacity of EuMnO_3 can well be described in the temperature regime from 2 to 20 K with the Debye function (yielding a Debye temperature $\Theta_D = 470$ K) and a T^2 term with a coefficient of 10 mJ/mol K⁴ but without the necessity to include a γT term. The T^2 term is also observed in the layered antiferromagnet LaMnO_3 and is supposed to arise from a linear and quadratic spin wave dispersion corresponding to linear AF and planar FM excitations.⁴

For the Sr and Ca substituted samples a FM contribution, which is far from the full Mn moment, dominates the magnetization process but for low fields and for zero-field cooling the AF coupling is preserved to a large extent. As shown in Fig. 3 the shape of the $M(T)$ curves for ZFC and FC is similar to that of the parent compound. However, the “spontaneous moment” extrapolated from high fields of the Arrott plots in Fig. 4 is 1.45 $\mu_B/\text{f.u.}$ (1.55 $\mu_B/\text{f.u.}$) and the moment at 6 T and 2 K amounts to 2.17 $\mu_B/\text{f.u.}$ (2.7 $\mu_B/\text{f.u.}$) for $\text{Eu}_{0.7}\text{Ca}_{0.3}\text{MnO}_3$ ($\text{Eu}_{0.7}\text{Sr}_{0.3}\text{MnO}_3$). A metamagnetic transition is clearly visible in the Arrott plot for 2 K at a field of 0.2 T which is reduced with rising temperatures. Both the

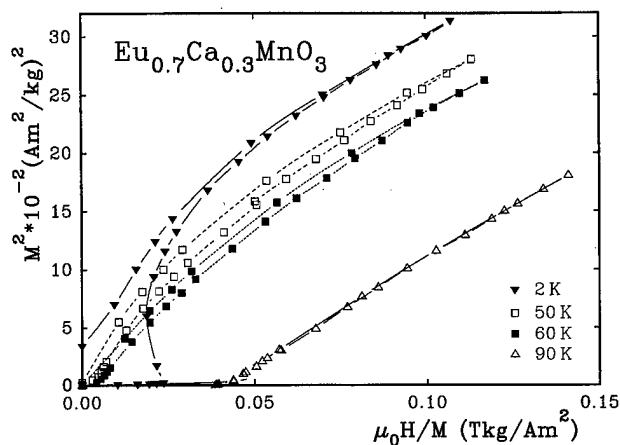


FIG. 4. Isothermal magnetization measurements on $\text{Eu}_{0.7}\text{Ca}_{0.3}\text{MnO}_3$ for various temperatures displayed as Arrott plot, M^2 vs $\mu_0 H/M$.

small value of the ZFC magnetization in low fields and the metamagnetic transition provide strong indication of the basically AF ground state of the Sr and Ca doped compounds with $x=0.3$ at low fields. The FM ordering temperature deduced from the high field regime of the Arrott plot is 74 and 62 K for $\text{Eu}_{0.7}\text{Ca}_{0.3}\text{MnO}_3$ and $\text{Eu}_{0.7}\text{Sr}_{0.3}\text{MnO}_3$, respectively. Note the low field data of the isotherm at 60 K indicate already paramagnetism although a hysteresis opens at higher fields yielding a small but finite remanent magnetization. T_C of the Sr doped sample coincides with the maximum of the ac susceptibility (63 K) while for the Ca doped sample the shoulder of $\chi_{ac}(T)$ at about 75 K can be correlated with T_C but a maximum of $\chi_{ac}(T)$ occurs at significantly lower temperatures (47 K). While the absence of a specific heat anomaly at T_C remains unresolved for the Ca and Sr substituted samples the significant change of the low temperature heat capacity is obvious. A broad Schottky anomaly which presumably arises from higher multiplets of Eu^{+3} makes it impossible to disentangle the lattice contribution from a possibly small γT term, however, the dominant spin-wave T^2 term of the parent compound is diminished upon Ca or Sr substitution. The appearance of a broad Schottky term is in line with an increase of the effective moment deduced from the high temperature susceptibility: EuMnO_3 $\mu_{\text{eff}} = 5.3 \mu_B/\text{f.u.}$; $\text{Eu}_{0.7}\text{Ca}_{0.3}\text{MnO}_3$ $\mu_{\text{eff}} = 5.9 \mu_B/\text{f.u.}$; $\text{Eu}_{0.7}\text{Sr}_{0.3}\text{MnO}_3$ $\mu_{\text{eff}} = 6.8 \mu_B/\text{f.u.}$

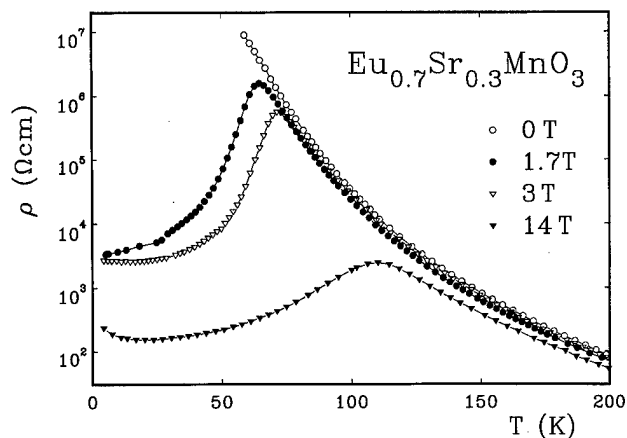


FIG. 5. The resistivity, $\rho(T)$, of $\text{Eu}_{0.7}\text{Sr}_{0.3}\text{MnO}_3$ for various fields as labeled.

Both the Ca and Sr doped samples remain insulating in zero-field down to 50 K where the resistance exceeds the value to be measured with the present set up. However, with an external field the metal insulator transition can be induced for $\text{Eu}_{0.7}\text{Sr}_{0.3}\text{MnO}_3$ below 60 K (see Fig. 5) while for $\text{Eu}_{0.7}\text{Ca}_{0.3}\text{MnO}_3$ a field of 11 T is not sufficient to induce the metallic state. This is in line with the magnetic data showing that even the doped compounds with $x=0.3$ exhibit basically an AF ground state and ferromagnetism can be induced by an external field. Thus, these samples fit to the general phase diagram proposed by Hwang *et al.*⁵ where $\text{Eu}_{0.7}\text{Sr}_{0.3}\text{MnO}_3$ is situated on the verge of the FM insulator to a FM metal while $\text{Eu}_{0.7}\text{Ca}_{0.3}\text{MnO}_3$ with the smaller tolerance factor remains insulating.

ACKNOWLEDGMENTS

The work was partly supported by the Grant in Fundamental Sciences N95-0-7.4-142 of the Education Ministry, Russia and Grant SAS N 95-1.4 of the Science Ministry, Russia.

¹A. P. Ramirez, J. Phys.: Condens. Matter **9**, 8171 (1997).

²R. Pauthenet and C. Veyret, J. Phys. (France) **31**, 65 (1970).

³I. O. Troyanchuk, H. Szymczak, N. V. Samsonenko, and A. Nabialek, Phys. Status Solidi A **157**, 167 (1996).

⁴B. F. Woodfield, M. L. Wilson, and J. M. Byers, Phys. Rev. Lett. **78**, 3201 (1997).

⁵H. Y. Hwang, S-W. Cheong, P. G. Radaelli, M. Marezio, and B. Batlogg, Phys. Rev. Lett. **75**, 914 (1995).

Evidence for a gap in the excitation spectrum of CrO₂

A. Barry^{a)} and J. M. D. Coey

Department of Physics, Trinity College, Dublin 2, Ireland

L. Ranno

Laboratoire Louis Néel, CNRS, Grenoble, France

K. Ounadjela

Institut de Physique et Chimie des Matériaux, Strasbourg, France

Magnetization and resistivity of CrO₂ powders and oriented CrO₂ films on different TiO₂ single-crystal substrates are reported, and the low-temperature specific heat is measured on powders. The $M(T)$ data follow a Bloch $T^{3/2}$ law, with no sign of a spin-wave gap. The residual resistivity depends strongly on film texture, but a T^2 temperature dependence of the resistivity is found in all samples above a cut-off temperature of the order of 70 K. The behavior is attributed to electron-magnon spin-flip scattering which is suppressed at low temperature in a half-metallic ferromagnet. © 1998 American Institute of Physics. [S0021-8979(98)44911-9]

I. INTRODUCTION

CrO₂ is a unique ferromagnet. It is a metallic oxide which crystallizes in the rutile (TiO₂) structure. The Cr ions, which are octahedrally coordinated by oxygen, have a formal 4+ valence state and an electronic configuration [Ar]3d². The two d electrons occupy spin split t_{2g} subbands. Numerous electronic band structure calculations predict "half-metallic" ferromagnetism with complete spin polarization of the 3d electrons at and below the Fermi level.¹⁻⁴ One t_{2g} ↑ electron is localized in a narrow xy band while the other is itinerant in a half-filled band of $yz+zx$ character. The Fermi level falls in a deep dip in the density of states at the center of this band; the empty ↓ states are ≈1 eV higher in energy.^{3,4} The tendency toward gap formation has been confirmed by photoemission measurements.⁵ The dip in the density of states in the middle of the half-filled band suggests that CrO₂ is close to a Mott-Hubbard transition. Like mixed-valence manganates having the perovskite structure, the ferromagnetic order of CrO₂ is mainly due to itinerant d electrons moving among localized ion cores⁴ ($S=1/2$ for CrO₂, $S=3/2$ for manganites).

Here we discuss magnetic, thermal, and transport properties of CrO₂ and present evidence for a gap in the excitation spectrum for spin-flip electron scattering.

II. EXPERIMENTAL METHODS AND RESULTS

CrO₂ films, 0.5–2 μm in thickness, have been prepared by the thermal decomposition of CrO₃ under high oxygen pressure onto oriented TiO₂ substrates.⁶ X-ray diffraction showed that the films are single phase, and grazing incidence diffraction indicated that they grow epitaxially. Atomic force microscopy (AFM) pictures reveal that CrO₂ films on TiO₂(100) and (110) have an acicular (needlelike) structure with grains of ≈50 μm length oriented with their axes in the plane of the substrate. On TiO₂(001), the textured CrO₂

films have the needle axis normal to the plane, resulting in the appearance of grains with circular cross sections of 1–5 μm in diameter (Fig. 1).

The resistivity of CrO₂ films having a (100), (110), or (001) texture have been measured in the temperature range 5–300 K using a four-probe technique. The results are shown in Fig. 2. The residual resistivity is quite different for the three samples. The film with its c axis perpendicular to the plane of the film has the highest residual resistivity, due to the greater number of grain boundaries compared to those films with their c axis in plane. The grain boundary resistivity for the (001) film is estimated from the size of the crystals (≈3 μm) to be $r_{gb} \approx 5 \times 10^{-10} \Omega \text{ m}^2$, which is similar to the value found in manganites.⁷ The (001) film shows a low-field magnetoresistance similar to that of CrO₂ powder compacts⁸ and two-phase films⁹ as well as polycrystalline manganite films¹⁰ and ceramics.¹¹ Consistent fits to the resistivity could not be obtained with a normal expression in powers of T that

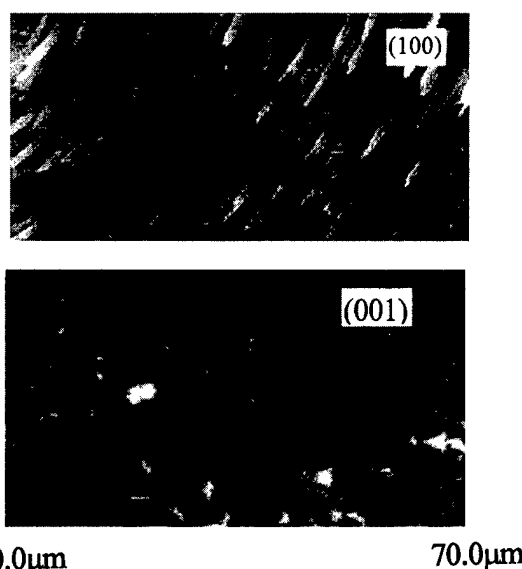


FIG. 1. AFM pictures of CrO₂ films on TiO₂ (a) (100) and (b) (001).

^{a)}Electronic mail: barrya@tcd.ie

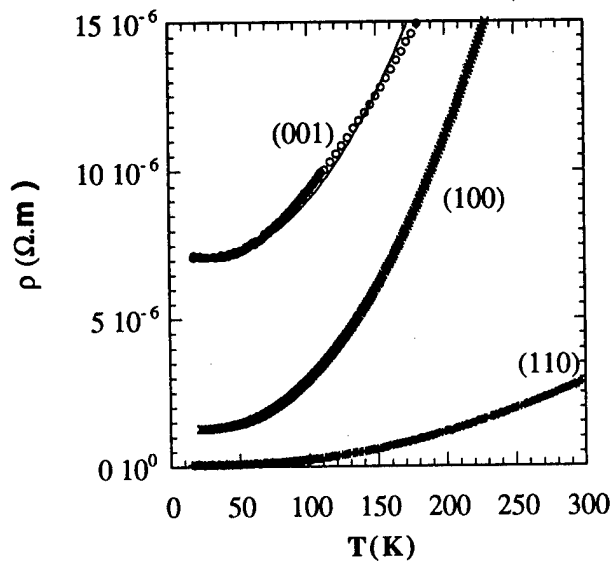


FIG. 2. Resistivity curves for CrO₂ films grown on TiO₂(100), (110), and (001). The solid lines are the fits to Eq. (1).

was used in Ref. 6. Superior fits over the full range of temperature were obtained with

$$\rho(T) = \rho_0 + \alpha T^2 \exp(-\Delta/T), \quad (1)$$

parameters ρ_0 , α , and Δ are listed in Table I. At low temperatures, the films with few grain boundaries are fairly good metals, with a residual resistivity below 10 $\mu\Omega$ cm, which barely changes up to about 70 K. However, at room temperature and above, CrO₂ becomes a poor metal, with a resistivity that exceeds the Ioffe–Regel limit.^{3,12} A change in the slope of $\rho(T)$ occurs at T_c but the derivative $d\rho/dT$ remains positive.⁶

Magnetic measurements were carried out using extraction or vibrating sample magnetometers on commercial acicular powder and on a CrO₂ powder obtained by decomposing CrO₃ in a high-pressure reactor vessel. The latter contained Cr₂O₅ impurities. Arrott plots in the temperature range 300–520 K gave a Curie temperature of 396(6) K. The magnetization measured in a field of 1 T was found to follow the Bloch $T^{3/2}$ law (Fig. 3):

$$M(T) = M(0)(1 - BT^{3/2}), \quad (2)$$

with $B = 3.4 \times 10^{-5} \text{ K}^{-3/2}$. The spin-wave stiffness constant D estimated from B is approximately 150 meV \AA^2 .¹³ Any gap in the ferromagnetic dispersion relation is estimated from the data of Fig. 4 to be less than 5 K. Measurements of magnetocrystalline anisotropy¹⁴ show it is of the order of 0.1 K.

TABLE I. Parameters from fits of the resistivity of CrO₂ films to Eq. (1).

Resistivity	ρ_0 ($\mu\Omega$ m)	α ($\Omega \mu\text{K}^{-2}$)	Δ (K)
100	1.23	359×10^{-12}	73
110	0.07	41×10^{-12}	80
001	7.07	480×10^{-12}	73

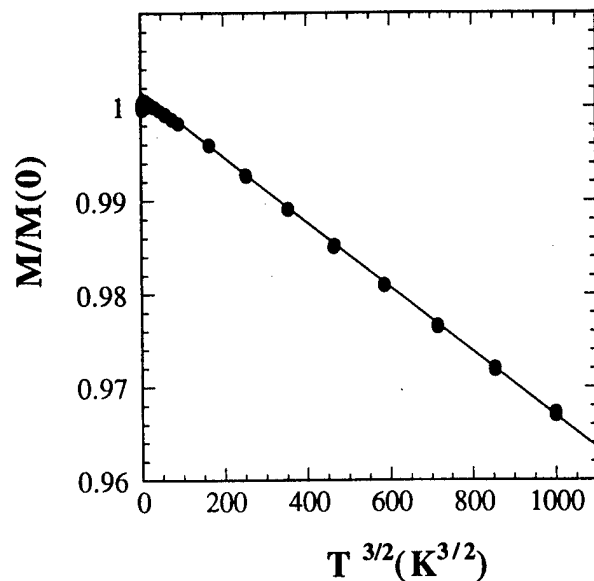


FIG. 3. $M(T)$ for a CrO₂ powder showing $T^{3/2}$ behavior.

Specific heat as a function of temperature has been measured on the commercial powder in the range 2–40 K (Fig. 4). We fit the data below 15 K to the expression

$$C = \gamma T + \beta T^3 + \alpha T^{5/2}, \quad (3)$$

where the electronic specific heat coefficient $\gamma = 5.1(9) \text{ mJ/mol K}^2$ corresponds to a density of states at the Fermi level of 2.2 states/eV. This may be compared with a calculated value of 0.69 states/eV.³ The value of β , 0.028 mJ/mol K⁴, corresponds to a Debye temperature of 593 K. The third term is associated with spin-wave excitations. The value of α , 1.9 mJ/mol K^{5/2} corresponds to $D = 60 \text{ meV } \text{\AA}^2$.

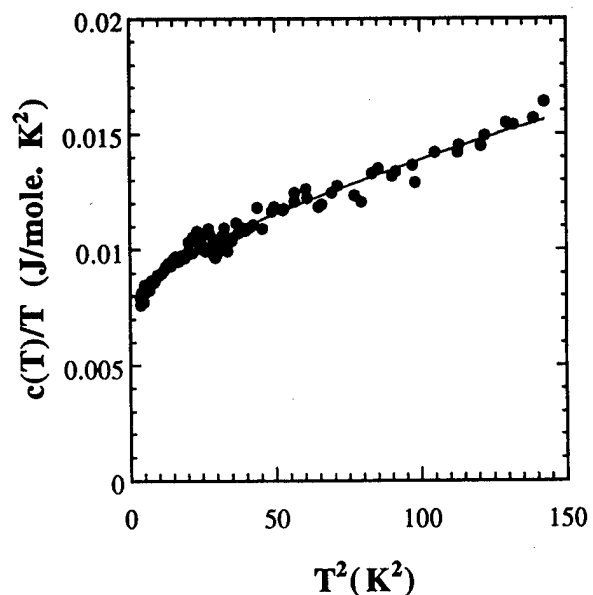


FIG. 4. C/T vs T^2 for pressed CrO₂ powder. The solid line is the fit to Eq. (3).

III. DISCUSSION

At temperatures below about 100 K, we have seen that CrO_2 is intrinsically a fairly good metal, with a residual resistivity of a few $\mu\Omega$ cm. The films with resistivity considerably higher than this have a distinct granular structure. The value of the electronic specific heat coefficient γ is similar to that of iron (which has approximately two holes in the $3d$ band), but the difference between the density of states at the Fermi level inferred from γ and the value calculated by Lewis *et al.*³ shows that the effective mass in the oxide $m^* = 3.2 m$. The calculations also show that the Fermi surface area in CrO_2 is small, which is to be expected if it is just on the metallic side of the Mott transition.

It is remarkable to see how the good metal changes into a poor one on approaching T_c . The temperature dependence of the resistivity is characteristic of spin-disorder scattering. Although there are several other possible origins of a T^2 temperature dependence, electron-magnon scattering is the most likely in the present case since the compound is a ferromagnet. Electron-magnon scattering has recently been established as the dominant scattering process in ferromagnetic manganites.¹⁵ The ineffectiveness of the scattering mechanism below 100 K is not related to any gap in the magnon spectrum, since neither magnetization, specific heat, nor anisotropy show any evidence of a gap of this magnitude. It must, rather, be associated with the electronic structure of CrO_2 . Electron-magnon scattering is a spin-flip process, and spin-flip scattering is impossible at low temperature in a half-metallic ferromagnet because the nearest available \downarrow states to scatter into are well above the Fermi level.¹⁶ The problem is how to relate the spin-polarized density of states to spin disorder. In fact, spin polarization must persist on a local scale even at temperatures above T_c since the susceptibility follows a Curie-Weiss law.¹⁴ The relation $kT = Dq_T^2 = 4\pi^2 D/\lambda_T^2$ defines the minimum wavelength λ_T of magnons excited at a temperature T . The significance of the gap $\Delta = 80$ K may be that $\lambda_\Delta \approx 30 \text{ \AA}$ is the critical wavelength where spin-flip scattering becomes important. An electron which travels this distance finds \downarrow states available on sites where there is locally a maximum spin deviation associated with the spin wave, and it can therefore undergo a spin-flip scattering process there with absorption or emission of a magnon. The distance λ_Δ is determined by the nonspin-flip scattering processes. This concept is illustrated in Fig. 5.

The poor metal at room temperature and above, where the mean free path is comparable to the interatomic spacing, may be understood in terms of Mott-Hubbard localization in the half-metallic system. This arises when the bandwidth $W = 2zt < U$, where z is the coordination number, t the interatomic transfer integral, and U the on-site Coulomb repulsion. At temperatures near and above T_c , any site will have a fluctuating number z' of neighbors with reversed spins to

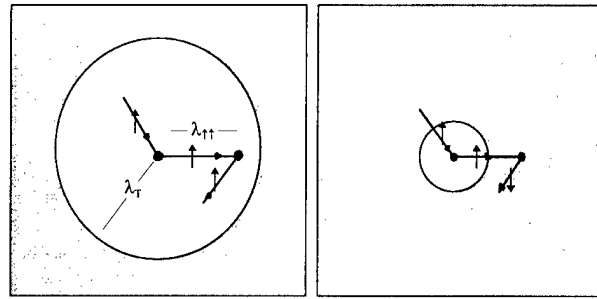


FIG. 5. Spin-flip scattering in a half-metallic ferromagnet is ineffective at temperatures where the nonspin-flip mean free path $\lambda_{\uparrow\uparrow}$ is less than the shortest magnon wavelength λ_T (left), but it is dominant when $\lambda_{\uparrow\uparrow} > \lambda_T$.

which transfer is forbidden, so the effective bandwidth is reduced by a factor $(z - z')/z$. Conduction is possible only when a local fluctuation of the spins of an atom relative to its neighbors to all parallel makes the system locally metallic. At any instant, the number of $3d$ electrons which are delocalized and available to conduct is reduced to a fraction of the number of sites. Since spin-disorder resistivity is inversely proportional to the electron density, values well in excess of the typical Ioffe-Regel limit, $150 \mu\Omega$ cm, can arise.

ACKNOWLEDGMENTS

This work forms part of the OXSEN program, supported by the European Union (EU). The authors are grateful to A. E. Berkowitz for the CrO_2 powder and to P. Lambour for his assistance with the specific heat measurements. One of the authors L.R. acknowledges a TMR fellowship from the EU. Many thanks to F. Ott for helpful discussions.

- ¹K. Schwarz, J. Phys. F **16**, L211 (1986).
- ²S. Matar, G. Demazeau, J. Sticht, V. Eyert, and J. Kübler, J. Phys. I **2**, 315 (1992).
- ³S. P. Lewis, P. B. Allen, and T. Sasaki, Phys. Rev. B **55**, 10 253 (1997).
- ⁴M. A. Korotin, V. I. Anisimov, D. I. Khomskii, and G. A. Sawatzky (unpublished).
- ⁵T. Tadjika, T. Mizokawa, J. Okamoto, A. Fujimori, M. Nohara, H. Takagi, Y. Yamaura, and M. Takano (unpublished).
- ⁶L. Ranno, A. Barry, and J. M. D. Coey, J. Appl. Phys. **81**, 5774 (1997).
- ⁷K. Steenbeck, T. Eick, K. Kirsch, K. O'Donnell, and E. Steinbeiss, Appl. Phys. Lett. **71**, 968 (1997).
- ⁸J. M. D. Coey, A. E. Berkowitz, L. I. Balcells, F. F. Putris, and A. Barry (unpublished).
- ⁹H. Y. Hwang and S.-W. Cheong, Science **278**, 1607 (1997).
- ¹⁰X. W. Li, A. Gupta, G. Xiao, and C. Q. Gong, Appl. Phys. Lett. **71**, 1124 (1997).
- ¹¹H. Y. Hwang, S. W. Cheong, N. P. Ong, and B. Batlogg, Phys. Rev. Lett. **77**, 2041 (1996).
- ¹²N. F. Mott, *Metal-Insulator Transitions*, 2nd ed. (Taylor and Francis, London, 1990).
- ¹³A. H. Morrish, *The Physical Principles of Magnetism* (Wiley, New York, 1965).
- ¹⁴B. L. Chamberland, Mater. Res. Bull. **2**, 827 (1967).
- ¹⁵M. Jaime, P. Lin, M. B. Salamon, and P. D. Han (unpublished).
- ¹⁶K. Kubo and N. Ohata, J. Phys. Soc. Jpn. **33**, 21 (1972).

Effect of low Fe doping in $\text{La}_{0.8}\text{Sr}_{0.2}\text{MnO}_3$

Antony Ajan^{a)}

Department of Physics, Indian Institute of Technology, Powai, Bombay 400 076, India

N. Venkataramani

ACRE (Advanced Center for Research in Electronics), Indian Institute of Technology, Powai, Bombay 400 076, India

Shiva Prasad and S. N. Shringi

Department of Physics, Indian Institute of Technology, Powai, Bombay 400 076, India

A. K. Nigam and R. Pinto

Tata Institute of Fundamental Research, Homi Bhabha Road, Bombay 400 005, India

The effect of low Fe substitution in Mn sites of $\text{La}_{0.8}\text{Sr}_{0.2}\text{MnO}_3$ is presented. We report the electrical and magnetic properties of these materials in the Fe concentration range $x=0$ to $x=0.1$. The metal-insulator transition temperature is found to vary significantly with very small Fe doping. The metal to insulator transition temperature increases slightly when a very small amount of Fe is doped ($<1\%$) and then it decreases significantly with further doping of Fe. The magnetic moment of $\text{La}_{0.8}\text{Sr}_{0.2}\text{MnO}_3$ decreases almost linearly with Fe doping at room temperature. © 1998 American Institute of Physics. [S0021-8979(98)26811-3]

I. INTRODUCTION

Giant magnetoresistance (GMR) effect shown on the perovskite oxide materials has attracted a lot of research interest. The metal-insulating transition temperature (T_{tr}) is known to be dependent on the Mn–O–Mn bond angle and bond length. Double exchange^{1–3} has been used to explain qualitatively the transport phenomena as well the magnetic ordering observed in these perovskite oxides. The insulating material LaMnO_3 when doped with divalent ions such as Ca, Sr, Ba, Pb, etc. causes a conversion of proportional number of Mn^{3+} to Mn^{4+} . The electron hopping between the mixed Mn valence states then causes ferromagnetic ordering and metallic conduction in these systems.²

Up to date, much exploration of the GMR perovskite materials has been done through doping of La sites with rare earths (Y, Nd, Pr, etc.) of different sizes, which brings strong lattice effects thus influencing the double exchange.^{4,5} However, very few studies have been carried^{6–8} out to observe the effects of transition metal ion doping on Mn sites, which will bring out the changes in electronic structure thus influencing double exchange. Effect of large doping of Fe ($>10\%$) on $\text{La}_{0.8}\text{A}_x\text{MnO}_3$ (where $\text{A}=\text{Sr}, \text{Ca}, \text{Ba}, \text{Pb}$) systems and its magnetic ordering has been reported earlier by Banks *et al.*⁹ However, the effect of lower Fe doping ($<10\%$) has not been reported on a systematic study. In this article we report the effect of low Fe ($<10\%$) doping on Mn sites of $\text{La}_{0.8}\text{Sr}_{0.2}\text{MnO}_3$ system.

II. EXPERIMENTAL DETAILS

The samples were prepared by the conventional solid state technique by taking Fe_2O_3 , MnCO_4 , SrCO_3 , and La_2O_3 in appropriate stoichiometric proportion as the starting material. These powders were milled and calcined at 900°C .

The calcined powder was remilled and the compacts were sintered at 1300°C in air for 6 h. The fired samples were characterized by x-ray diffraction, with $\alpha\text{-Al}_2\text{O}_3$ used as the internal standard. Resistivity studies were carried out on 2-mm-thick rectangular samples. Resistivity measurements were carried out for all the samples in the temperature range from 15 to 473 K by conventional four-probes method. In the range 15–300 K a closed cycle refrigerator was employed to cool the sample and for high temperature studies (room temperature to 473 K) a variable temperature oil bath was used. Room temperature magnetization studies were carried out by using a vibrating sample magnetometer (VSM) setup with a maximum field of 0.4 T.

III. RESULTS AND DISCUSSION

The x-ray diffraction (XRD) spectra of samples with extreme concentration of Fe ($x=0, 0.1$) are shown in Fig. 1. It is clearly seen from the figure that both the samples show similar XRD pattern. XRD spectra for all the other samples between these concentrations are also found to be similar. The XRD spectra were indexed by assuming a pseudocubic structure. The lattice constants were found to be 3.8790 and 3.8811 Å for $x=0$ and $x=0.1$, respectively. The studies of Fe doping on Ca containing LaMnO_3 systems ($>10\%$)⁷ also does not show any changes in the lattice parameter. Studies by Jian *et al.*⁸ also showed that the lattice parameter of $\text{La}_{0.67}\text{Ca}_{0.33}\text{Mn}_{1-x}\text{Fe}_x\text{O}_3$ remains nearly identical, i.e., 3.8571 Å for $x=0.0$ and 3.8561 Å for $x=0.1$. This indicates that the doping of Fe has hardly any influence on lattice parameter. This could be because of the identical ionic sizes¹⁰ of Fe^{3+} and Mn^{3+} .

In Fig. 2 the variation of normalized resistance with temperature is shown. All the samples show a metal-insulator transition temperature. At low temperature, for all the samples, the resistance curve tends to flatten out. Transition

^{a)}Electronic mail: antony@niharika.phy.iitb.ernet.in

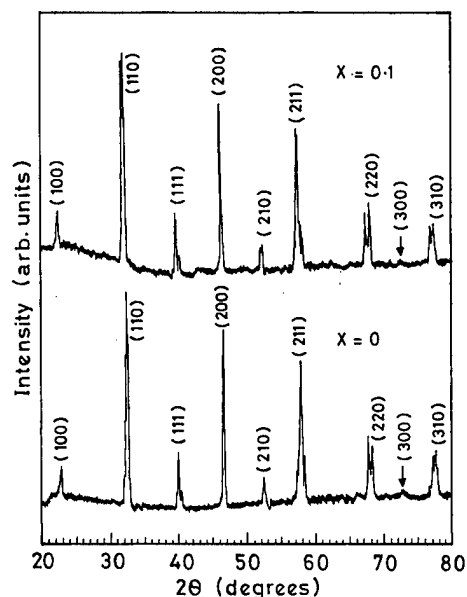


FIG. 1. XRD spectra for the samples $\text{La}_{0.8}\text{Sr}_{0.2}\text{Mn}_{1-x}\text{Fe}_x\text{O}_3$ with $x=0$ and 0.1 .

temperature is found to be strongly dependent of the Fe doping even at low concentrations.

For the parent sample, i.e., $\text{La}_{0.8}\text{Sr}_{0.2}\text{MnO}_3$ the transition temperature is found to be 350 K which is agreeing with the reported values for the Sr composition 0.2.¹¹ Transition temperature T_{tr} increases when doped with small amount of Fe (≈ 0.005) and then it decreases systematically with the addition of Fe content and for $x=0.1$, transition temperature was found to be ≈ 260 K. Recently Ahn *et al.*⁷ showed that in the Ca containing LaMnO_3 system both in the ferromagnetic as well as the antiferromagnetic region the transition temperature is varying with respect to the Fe doping ($>10\%$). In the ferromagnetic region transition temperature decreases with increase in Fe concentration. The decrease in the transition temperature with Fe doping could be due to the

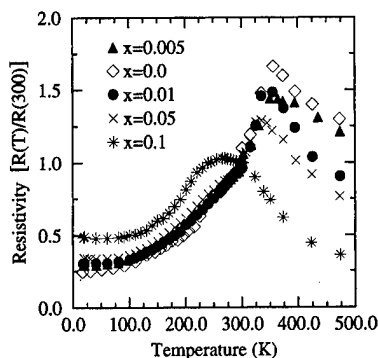


FIG. 2. Temperature dependence of normalized resistance for Fe doped samples $\text{La}_{0.8}\text{Sr}_{0.2}\text{Mn}_{1-x}\text{Fe}_x\text{O}_3$, $0 < x < 0.1$.

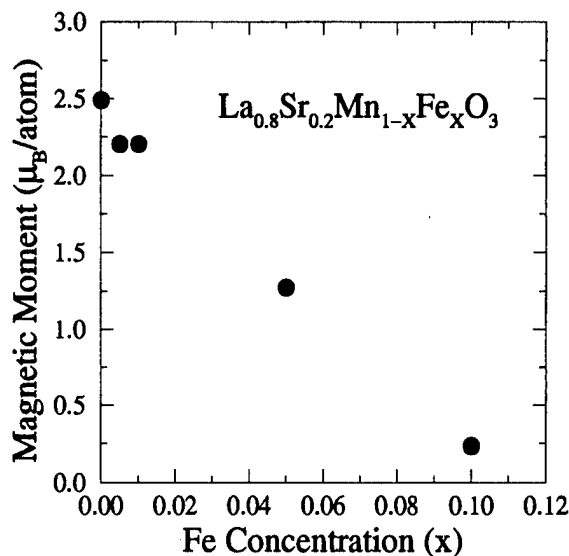


FIG. 3. Variation of magnetic moment with different concentration of Fe in $\text{La}_{0.8}\text{Sr}_{0.2}\text{Mn}_{1-x}\text{Fe}_x\text{O}_3$, $0 < x < 0.1$.

replacement of Fe^{3+} on Mn^{3+} thus reducing the double exchange interaction.

Magnetization studies on these systems indicates the ferromagnetic nature of the samples. The variation of magnetic moment of the sample with Fe concentration at room temperature is shown in Fig. 3. With the Fe doping the magnetic moment of the sample decreases. The magnetic moment decreases almost linearly with the Fe doping. Magnetic moment decreased from 2.52 to $0.2 \mu_B$ for $x=0$ and $x=0.1$, respectively. In the case of Ca containing systems⁷ the decrease of magnetic moment is found to be from 3.2 to $2 \mu_B$ for $x=0$ to $x=0.1$ at 5 K.

IV. CONCLUSION

The lattice parameter of $\text{La}_{0.8}\text{Sr}_{0.2}\text{MnO}_3$ does not change with Fe concentration. Metal-insulator transition temperature was found to increase at a very low concentration of Fe ($<1\%$) and decreases with further addition of Fe. Magnetic moment of the samples decreases sharply even at very low concentration of Fe.

¹C. Zener, Phys. Rev. **82**, 403 (1951).

²P. W. Anderson and H. Hasegawa, Phys. Rev. **100**, 675 (1955).

³P.-G. De Gennes, Phys. Rev. **118**, 141 (1960).

⁴H. Y. Hwang, S. W. Cheong, P. G. Radaelli, M. Marezio, and B. Batlogg, Phys. Rev. Lett. **75**, 914 (1995).

⁵J. Fontcuberta, B. Martinez, A. Seffar, S. Pinol, A. Roig, E. Molins, X. Obradors, J. Alonso, and J. M. Gonzalez-Calbet, J. Appl. Phys. **79**, 5182 (1996).

⁶G. H. Jonker, Physica (Utrecht) **22**, 707 (1956).

⁷K. H. Ahn, X. W. Wu, K. Liu, and C. L. Chien, J. Appl. Phys. **81**, 5505 (1997).

⁸J.-W. Cai, C. Wang, B.-G. Shen, J.-G. Zhao, and W.-S. Zhan, Appl. Phys. Lett. **71**, 1727 (1997).

⁹E. Banks and N. Tashima, J. Appl. Phys. **41**, 1186 (1986).

¹⁰R. D. Shannon, Acta Crystallogr., Sect. A **32**, 751 (1976).

¹¹A. Urushibara, Phys. Rev. B **51**, 14 103 (1995).

Magnetic and transport properties of Pb perovskites and Fe containing giant magnetoresistance perovskites

J. Gutiérrez and J. M. Barandiarán

Departamento de Electricidad y Electrónica, Universidad del País Vasco/EHU, P.O. Box 644, E-48080 Bilbao, Spain

M. Insausti, L. Lezama, A. Peña, J. J. Blanco, and T. Rojo

Departamento de Química Inorgánica, Universidad del País Vasco/EHU, P.O. Box 644, E-48080 Bilbao, Spain

The magnetic and magnetoresistive properties of the $\text{Ln}_{0.7}\text{Pb}_{0.3}\text{Mn}_{1-x}\text{Fe}_x\text{O}_3$ ($\text{Ln}=\text{La}$, Nd , and $x=0, 0.1$) perovskites, prepared by the sol-gel low temperature method, have been studied. In all cases the exact stoichiometry is different from the nominal one probably due to the presence of cation vacancies. All the phases exhibit ferromagnetic behavior with T_c values ranging from 345 K observed for $\text{La}_{0.7}\text{Pb}_{0.3}\text{MnO}_3$ to 75 K for $\text{Nd}_{0.7}\text{Pb}_{0.3}\text{Mn}_{0.9}\text{Fe}_{0.1}\text{O}_3$. The 10% Fe contribution lowers the T_c by about 130 K in the La compound and 90 K in the Nd one. These results can be interpreted in terms of antiferromagnetic coupling between Mn and Fe. However, the influence of the Nd ions is not well known although it seems not ordered down to 10 K. The magnetoresistance [$\text{MR} = \Delta R/R(0)$] measured at 6 T in pellets of pressed powder reaches values of about 80% around the magnetic transition. © 1998 American Institute of Physics. [S0021-8979(98)52411-5]

I. INTRODUCTION

During the last years the hole-doped perovskite $\text{A}_{1-x}\text{A}'_x\text{MnO}_3$ type compounds ($\text{A}=\text{La}^{3+}$, Sm^{3+} , Pr^{3+} , Nd^{3+} , ..., $\text{A}'=\text{Ca}^{2+}$, Pb^{2+} , Sr^{2+} , Ba^{2+} , Cd^{2+}) have attracted the attention of scientific community due to the observation of colossal magnetoresistance (MR) phenomenon.¹⁻³ The magnetic behavior and transport properties of these samples are determined by several factors such as the percentage of the divalent ions, the ionic radii of the metal ions, the method used in the preparation of the samples, etc. The distortion of the perovskite structure has a direct influence not only on the Mn–O distance, but also on the angle of the $\text{Mn}^{3+}\text{–O–Mn}^{4+}$ bond. It has been also observed that ferromagnetic coupling and metal–insulator transition temperature are very sensitive to the change of these parameters.² On the other hand, the substitution of the Mn ions by other transition metal ions can give rise to important modifications in the magnetic and transport properties.⁴

In this work we report the magnetic and magnetoresistive properties of $\text{Ln}_{0.7}\text{Pb}_{0.3}\text{Mn}_{1-x}\text{Fe}_x\text{O}_3$ ($\text{Ln}=\text{La}$, Nd and $x=0, 0.1$), which have been prepared by the sol-gel low temperature method. This method presents the advantage of using low-temperature synthesis, that results not only in smaller grains but also produces high purity and homogeneous powders.⁵ We compare structural, magnetic, and magnetoresistance measurements with the aim to reach a better understanding of the effect caused by the presence of different lanthanide elements and the substitution of Mn by Fe ions in the samples.

II. EXPERIMENT

Mixed oxides of compositions $\text{Ln}_{0.7}\text{Pb}_{0.3}\text{Mn}_{1-x}\text{Fe}_x\text{O}_3$ ($\text{Ln}=\text{La}$, Nd and $x=0, 0.1$) were prepared by the sol-gel method with the required quantities of La_2O_3 , $\text{Pb}(\text{NO}_3)_2$,

$\text{Mn}(\text{C}_2\text{H}_3\text{O}_2)_2 \cdot 4\text{H}_2\text{O}$, and $\text{Fe}(\text{NO}_3)_3 \cdot 9\text{H}_2\text{O}$ as starting materials. Citric acid and ethyleneglycol were used as gelling agents for the La and Mn ions in a nitrate solution. After drying in a sand bath, the obtained gel was subjected to successive heat treatments at different temperatures: 773, 973, and 1073 K, respectively, each of them for 10 h. The microcrystalline powder thus obtained was pelletized and sintered at 1173 K for 10 h in flowing oxygen. In the following, the prepared compounds will be labeled as LaPb, LaPbFe, NdPb, and NdPbFe.

The $\text{Mn}^{3+}/\text{Mn}^{4+}$ content of each sample was determined by redox titration using an excess of FeSO_4 (0.025 M) solution and back titration with 0.5 M permanganate. In all cases we observed a greater content of Mn^{4+} to that corresponding to the nominal composition (see Table I). These deviations from theoretical stoichiometries could be due to an excess in the oxygen concentration or more probably to the presence of cation vacancies.⁶

TABLE I. % Mn^{4+} , Goldschmidt's tolerance factor, t [$t=(r_A+r_O)/\sqrt{2}(r_B+r_O)$], and crystallographic data for the studied compounds.

Sample	% Mn^{4+}	t	Space group	Lattice parameters
$\text{La}_{0.7}\text{Pb}_{0.3}\text{MnO}_3$	65	0.9915	$R\bar{3}c$	$a=b=5.514 \text{ \AA}$ $c=13.405 \text{ \AA}$ $\beta=119.99^\circ$
$\text{La}_{0.7}\text{Pb}_{0.3}\text{Mn}_{0.9}\text{Fe}_{0.1}\text{O}_3$	53	0.9915	$R\bar{3}c$	$a=b=5.519 \text{ \AA}$ $c=13.340 \text{ \AA}$ $\beta=119.97^\circ$
$\text{Nd}_{0.7}\text{Pb}_{0.3}\text{MnO}_3$	56	0.9688	Pnma	$a=5.480 \text{ \AA}$ $b=7.720 \text{ \AA}$ $c=5.456 \text{ \AA}$
$\text{Nd}_{0.7}\text{Pb}_{0.3}\text{Mn}_{0.9}\text{Fe}_{0.1}\text{O}_3$	57	0.9688	Pnma	$a=5.484 \text{ \AA}$ $b=7.728 \text{ \AA}$ $c=5.467 \text{ \AA}$

X-ray diffractograms were recorded on a Philips X'PERT diffractometer using Cu K_α radiation. The space group and lattice parameters, determined by the Rietveld method using the FULLPROF program,⁷ are shown in Table I. The diffraction maxima of the La phases were indexed in a rhombohedral space group ($R\bar{3}c$) while Nd ones exhibit an orthorhombic symmetry (Pnma). This result is in good agreement with the higher distortion exhibited by the neodymium perovskitelike compounds. In this way, the Goldschmidt's tolerance factors t of these phases are lower than those obtained for the La compounds (see Table I). However, the t values are greater than 0.968 in all cases, hinting for a good stability of the structure.

Magnetic and resistance measurements were performed in a quantum design MPMS-7 superconducting quantum interference device magnetometer. The zero field cooling (ZFC) and field cooling (FC) curves were performed under an applied field of 8 kA/m. $M(T)$ curves at 1 T applied field and hysteresis loops at 10 K and up to 7 T were also obtained. The resistance and MR versus temperature measurements were carried out using a dc four-probe system with the current parallel to the applied field.

III. RESULTS AND DISCUSSION

The temperature dependence of the resistance measured under zero and 6 T applied fields for all samples is shown in Fig. 1. In absence of applied field a resistance maximum, characteristic of a semiconductor-metal transition, is observed. For the LaPb composition the transition temperature is $T_{SC-M} \approx 270$ K, which is into the range of values observed for La manganites doped with alkaline-earth ions (235–330 K).⁸ However, the change of La by Nd in the perovskite composition gives as a result a drastic decreasing in the value of this T_{SC-M} , being now ≈ 140 K. These transition temperatures decrease when adding Fe to the compositions (see Table II).

When applying a 6 T magnetic field the value of the resistance decreases in all the temperature range. In all samples a change in the MR behavior occurs around the semiconductor-metal transition temperature. The relative magnetoresistance defined as: $[R(6T) - R(0T)]/R(0T)$,⁹ is higher in the samples containing Fe, reaching values of around 65% and 80% for the La and Nd phases, respectively.

The magnetic behavior observed from ZFC and FC curves corresponds to a magnetic inhomogeneous system¹⁰ where ferromagnetic grains or clusters are embedded in a nonferromagnetic matrix. The ZFC and FC measurements have been carried out under applied field of 8 kA/m, lower than the value of coercivity measured at 10 K for all samples. The results are shown in Fig. 2. All compositions, except NdPbFe, show an extraordinary similarity, hinting for the same magnetization process at low applied field. The ZFC curves show a maximum at a given temperature and fall at higher temperature due to the ferro-paramagnetic transition. For temperatures below that maximum, the decrease in the magnetization value is probably due to noncollinear effects. In all samples the Curie temperature is very close to the blocking temperature, T_b , of the largest clusters in the

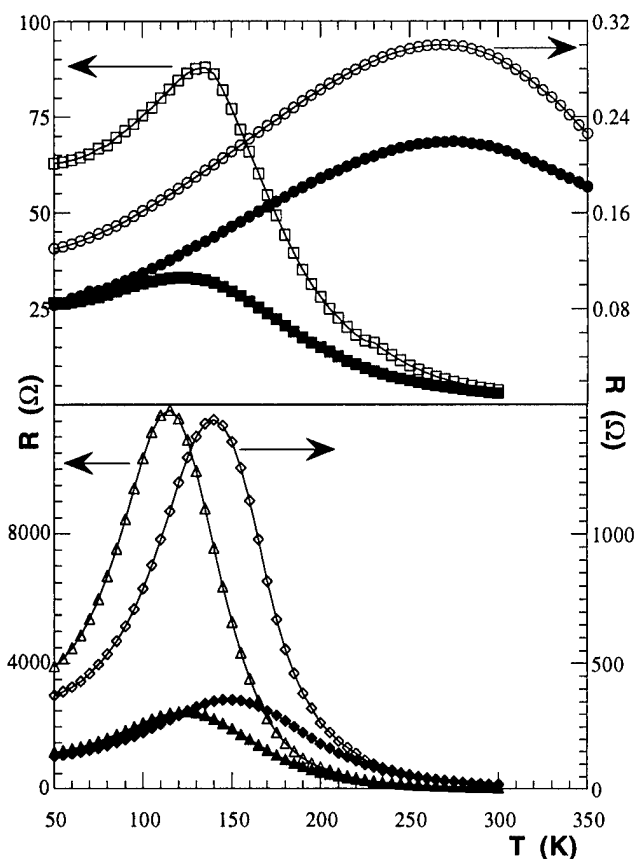


FIG. 1. Resistance vs temperature curves for the LaPb(\circ), LaPbFe(\square), NdPb(\diamond), and NdPbFe(\triangle) samples obtained under 0 (open symbol) and 6 T (full symbol) applied magnetic fields.

assembly.¹¹ At this temperature, bifurcation between ZFC and FC curves occurs losing the magnetization process its reversibility. The observed T_c values are clearly higher for the La phases than for the Nd ones. The introduction of iron in the samples causes an important decrease in the temperature of the ferromagnetic ordering (see Table II) following the same behavior observed for the semiconductor-metal transition.

The thermal evolution of the magnetization under 1 T applied field for all compounds is reported in Fig. 3(a). The observed behavior is essentially similar, but important differences on the magnetic moments are observed. The values of these moments are higher for the La phases than for the Nd ones, as was also observed for the T_c values. The influence on the magnetic moment values when introducing Fe is drastic, as was observed for $\text{La}_{0.7}\text{Ca}_{0.3}\text{Mn}_{1-x}\text{Fe}_x\text{O}_3$.¹² In this

TABLE II. Values of Curie temperatures, T_c , magnetization per magnetic ion, $M/N\mu_B$ at 10 K and 7 T, and transition temperature in the resistance behavior, T_{SC-M} , for the studied samples.

Sample	T_c (K)	$M/N\mu_B$	T_{SC-M} (K)
$\text{La}_{0.7}\text{Pb}_{0.3}\text{MnO}_3$	345(5)	3.28(10)	270(5)
$\text{La}_{0.7}\text{Pb}_{0.3}\text{Mn}_{0.9}\text{Fe}_{0.1}\text{O}_3$	215(5)	2.79(10)	135(5)
$\text{Nd}_{0.7}\text{Pb}_{0.3}\text{MnO}_3$	165(5)	3.30(10)	140(5)
$\text{Nd}_{0.7}\text{Pb}_{0.3}\text{Mn}_{0.9}\text{Fe}_{0.1}\text{O}_3$	75(5)	2.52(10)	115(5)

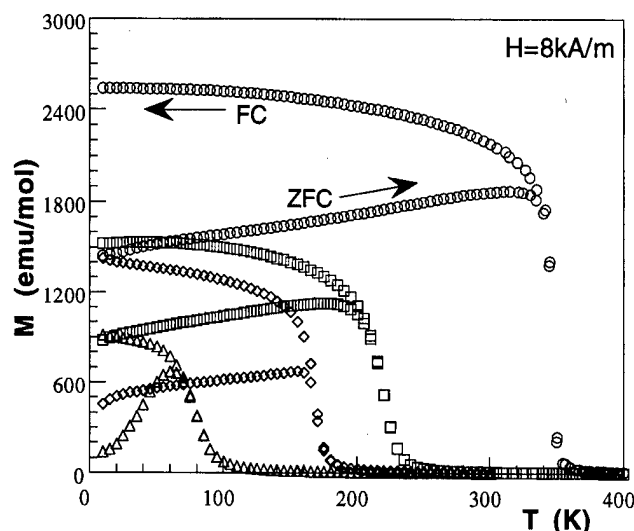


FIG. 2. Zero field cooling (ZFC, increasing temperature arrow) and field cooling (FC, decreasing temperature arrow) magnetization vs temperature curves for the studied samples, measured at $H_{app}=8$ kA/m.

way, decreases of a 49% for the NdPb and a 15% for the LaPb compositions have been measured at 10 K.

Values of the magnetization per magnetic ion at 10 K and up to 7 T applied field for all compositions are summarized in Table II. LaPb and LaPbFe compositions show the same features reaching quickly the magnetic saturation and keeping constant the difference in the magnetic moment found at 1 T applied field [see Fig. 3(b)]. The observed saturation moment for the LaPb phase agrees well with that expected for the volumetrically determined Mn^{3+}/Mn^{4+} composition. For the LaPbFe compound the magnetic moment is clearly lower than that calculated by adding Mn and Fe magnetic moments, but not so low as correspond to a fully antiparallel ordering of the Fe^{3+} ions. This fact suggests the presence of canted spins in the antiferromagnetic couplings induced by the iron ions.

For NdPb and NdPbFe the spins are not fully aligned under the applied maximum fields (7 T). The magnetic moment of the Fe phase is considerably lower. However, the slow evolution of the magnetization curve indicates that lower differences in the values of the magnetic moments should be probably measured at higher applied fields. These results together with the whole appearance of the ZFC curves suggest the presence of antiferromagnetic interactions Fe–O–Mn and that the Nd ions are not magnetically ordered even at 10 K.

Finally, it is to note that both the T_c and T_{SM-M} values are lower for the Nd phases than for the La ones. This fact is in good agreement with the lower ionic radii of the Nd^{3+} ions and the corresponding larger distortion of its perovskite-type structures. Besides, the introduction of Pb ions causes a similar effect that the Sr ones on the critical temperatures because of its similar ionic radii. These values correspond to

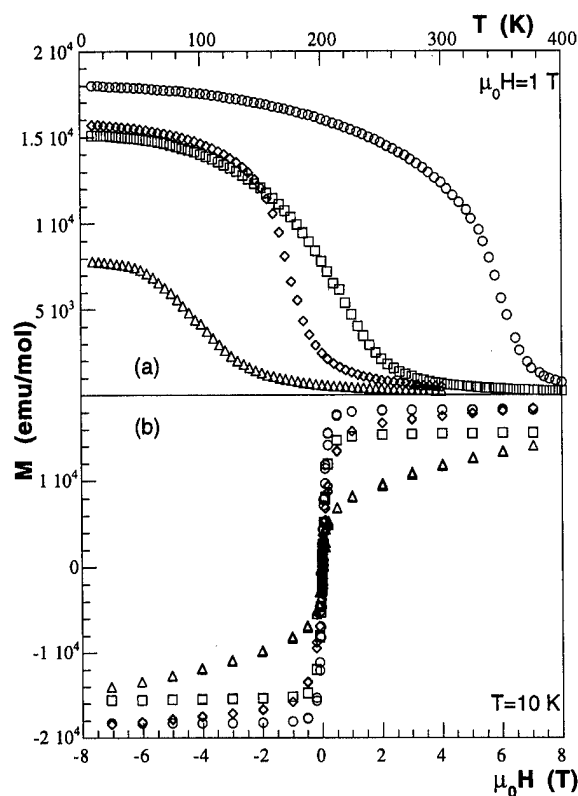


FIG. 3. (a) Magnetization vs temperature curves, $M(T)$, measured at $H_{app}=1$ T, and (b) hysteresis loops measured at 10 K for the studied samples.

the less distorted structures and give rise to the greater T_c and T_{SM-M} values observed in these type of compounds.⁸

ACKNOWLEDGMENT

This work was financially supported by the Basque Government under Project No. PGV 96/94.

- ¹G. H. Jonker and J. H. van Santen, *Physica (Utrecht)* **XVI**, 337 (1950).
- ²H. Y. Hwang, S.-W. Cheong, P. G. Radaelli, M. Marezio, and B. Batlogg, *Phys. Rev. Lett.* **75**, 914 (1995).
- ³P. Schiffer, A. P. Ramirez, W. Bao, and S.-W. Cheong, *Phys. Rev. Lett.* **75**, 3336 (1995).
- ⁴A. Maignan, F. Damay, C. Martin, and B. Raveau, *Mater. Res. Bull.* **32**, 965 (1997).
- ⁵C. J. Brinker and G. R. Scherer, *Sol-Gel Science, The Physics and Chemistry of Sol-Gel Processing* (Academic, New York, 1990).
- ⁶C. N. R. Rao, A. K. Cheetham, and R. Mahesh, *Chem. Mater.* **8**, 2421 (1996).
- ⁷J. Rodríguez-Carvajal, *FULLPROF Program Rietveld Pattern Matching Analysis of Powder Patterns* (ILL, Grenoble, 1990).
- ⁸(a) R. Mahesh, R. Mahendiran, A. K. Raychandhuri, and C. N. Rao, *Solid State Chem.* **120**, 204 (1995); (b) R. Mahendiran, R. Mahesh, A. K. Raychandhuri, and C. N. Rao, *Solid State Commun.* **7**, 515 (1995).
- ⁹K. Chahara, T. Ohno, M. Kasai, and Y. Kozono, *Appl. Phys. Lett.* **63**, 1990 (1993).
- ¹⁰H. L. Ju and H. Sohn, *J. Magn. Magn. Mater.* **167**, 200 (1997), and references therein.
- ¹¹T. J. Jackson, S. B. Palmer, H. J. Blythe, and A. S. Halim, *J. Magn. Magn. Mater.* **159**, 269 (1996).
- ¹²L. Righi, P. Gorria, M. Insausti, J. Gutiérrez, and J. M. Barandiarán, *J. Appl. Phys.* **81**, 5767 (1997).

90 MeV ^{16}O ion irradiation effects on transport and magnetization in epitaxial thin films of $\text{La}_{0.75}\text{Ca}_{0.25}\text{MnO}_3$

Ravi Bathe,^{a)} S. K. Date,^{b)} S. R. Shinde,^{c)} L. V. Saraf,^{c)} S. B. Ogale,^{c)} and S. I. Patil
Department of Physics, University of Pune, Pune 411007, India

Ravi Kumar, S. K. Arora, and G. K. Mehta
Nuclear Science Center, New Delhi, India

The influence of 90 MeV ^{16}O ion irradiation on the electric and magnetic properties of epitaxial thin films of $\text{La}_{0.75}\text{Ca}_{0.25}\text{MnO}_3$ is studied. These films were deposited on $\text{LaAlO}_3(100)$ substrates by the pulsed excimer laser deposition technique. The thickness of each film was about 3000 Å. The high quality of the films was ensured by x-ray diffraction and transport measurements. The films were irradiated with 90 MeV oxygen ions at different doses (10^{11} – 10^{14} ions/cm²). It is observed that at a low dose of 10^{11} ions/cm² the resistivity peak temperature (T_p) and the Curie temperature (T_c) increase, however as the dose is increased further, the T_p and T_c decrease. At the higher dose of 10^{14} ions/cm², the film becomes insulating and does not show any peak in the resistivity–temperature curve down to 60 K. These results are discussed in terms of the effects of ion induced compositional inhomogeneity and strain on the film properties. © 1998 American Institute of Physics. [S0021-8979(98)45011-4]

INTRODUCTION

Interest in the transport properties of doped perovskite oxides of the type $\text{A}_{1-x}\text{B}_x\text{MnO}_{3+y}$ ($\text{A}=\text{La}, \text{Nd}, \text{Y}; \text{B}=\text{Ca}, \text{Ba}, \text{Sr}$) has grown rather sharply during the past few years since the discovery of colossal magnetoresistance (CMR) behavior in these compounds.^{1–4} A prominent feature of these materials is the occurrence of a peak in resistivity (T_p) close to the ferromagnetic transition temperature (T_c) and a spectacular (up to a thousandfold) reduction in the resistivity upon application of a magnetic field of several tesla.^{4,5} Earlier studies have shown that the transport in these oxides is strongly influenced by the $\text{Mn}^{+3}/\text{Mn}^{+4}$ ratio (i.e., the amount of doping).^{6,7} It has also been established that the transport and magnetization in these oxides is primarily controlled by the $\text{Mn}^{+3}\text{--O--Mn}^{+4}$ network. The transport is considered to occur by the so called Zener double exchange model,⁸ although the validity of this model has increasingly been questioned in recent years.⁹ As the oxygen content in these materials decreases, the resistivity increases and the magnetic transition temperature shifts to lower temperature.¹⁰ The presence of grain boundaries modifies the magneto-transport behavior completely.¹¹ External pressure has also been shown to influence the semiconductor (paramagnetic)–metal (ferromagnetic) transition.¹² Thus, it appears that the magneto-transport properties of doped manganese oxides are very sensitive to lattice strain and disorder. The strain can influence the $\text{Mn}^{+3}\text{--O--Mn}^{+4}$ bond angle as well as bond distances while other forms of disorder could additionally influence the charge imbalance.

It is well known that irradiation of solids with energetic particles leads to creation of a wide variety of defect states

therein.¹³ In particular, damage by energetic ion beams has been well studied over the past decades. At medium ion energies (keV range), the damage is caused by the nuclear loss, whereas at higher energies (MeV–GeV range) it is caused by the electronic loss mechanism. Since irradiation can lead to a controlled introduction of defect states in the material system, it has been and is being beneficially used to control the material properties. Since the magnetic properties are also affected significantly by defects, irradiation can be used to control such properties as the coercivity and the retentivity of the materials, which are important in different applications.

In this work, we have examined the effects of 90 MeV ^{16}O irradiation on the structural, magnetic, and transport properties of $\text{La}_{0.75}\text{Ca}_{0.25}\text{MnO}_3$ (LCMO) thin films. The results are presented in terms of the observed shift in the ferromagnetic transition temperature, changes in the resistivity behavior and the activation energy, structural modifications, and change in the magnetization of the films, as a function of the irradiation dose.

EXPERIMENT

The LCMO target used for the deposition of the thin films was prepared by solid state reaction starting from the respective elemental oxides following a standard ceramic route. The LCMO thin films, having thicknesses of about 3000 Å, were grown on $\text{LaAlO}_3(100)$ single-crystal substrates by the pulsed laser deposition technique. A KrF excimer laser ($\lambda = 248$ nm, $t_p = 20$ ns) was employed and ablation was performed at a laser energy density of 2 J/cm². The substrate temperature was maintained at 700 °C while the oxygen partial pressure was 200 mTorr during deposition. The deposited films were cooled to room temperature in 500 Torr oxygen ambient. The irradiations of epitaxial thin films of LCMO were performed on the pelletron accelerator with 90 MeV oxygen ions at different doses, e.g., 10^{11} , 10^{12} , 10^{13} ,

^{a)}Electronic mail: rmb@physics.unipune.ernet.in

^{b)}Also at the National Chemical Laboratory, Pashan, Pune 411 008, India.

^{c)}Presently at the Department of Materials and Nuclear Engineering, University of Maryland, College Park, MD 20740.

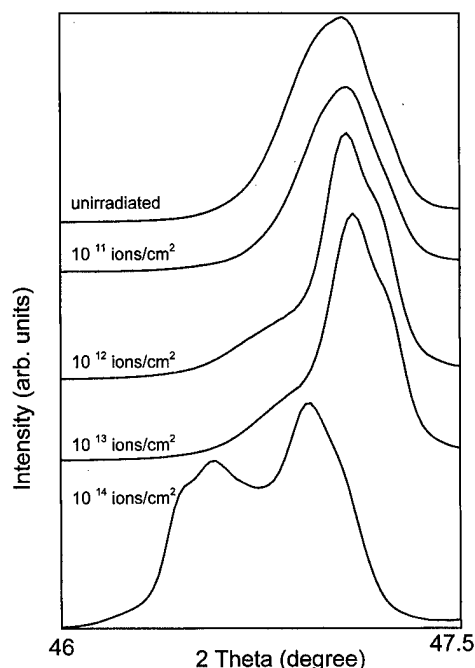


FIG. 1. X-ray diffraction patterns for the as-deposited film and for the films irradiated at different doses of 1×10^{11} , 1×10^{12} , 1×10^{13} , and 1×10^{14} ions/cm².

and 10^{14} ions/cm². The irradiated samples were characterized for structural quality by x-ray diffraction. The resistivity of each sample was measured using a standard four probe technique. The magnetization curves as a function of temperature from 300 to 80 K were obtained using a vibrating sample magnetometer (VSM).

RESULTS AND DISCUSSIONS

The electronic and nuclear energy loss values for 90 MeV ^{16}O ions in LCMO, calculated using the TRIM code simulation program are 2.5 MeV cm²/mg and 1.44 keV cm²/mg, respectively. Also, the range of ions used in our experiments is about 39 μm , indicating that the entire passage of ions in the film is dominated by the electronic energy loss. It is well known that in this regime of energy loss continuous columns of amorphous/defected material are created after irradiation if the loss is more than a threshold value.¹⁴ Using Szenes's model¹⁴ one can calculate the threshold value of electronic energy loss for the formation of columnar defects. For LCMO, this value comes out to be about 20 MeV cm²/mg, which is much larger than the energy loss in our experiments. Therefore, the possibility of formation of columnar defects is ruled out and it is quite likely that small chaplets¹⁵ of defected regions are formed in the LCMO lattice in our experiments. Indeed, our x-ray diffraction (XRD) data showed that amorphization does not occur in the system, however, stoichiometry defects are introduced with increasing ion dose. We highlight this aspect by focusing on the (004) XRD peak for LCMO (Fig. 1). In the sample irradiated at the low dose of 10^{11} ions/cm² however, no discernable change in the line shape is seen. The peak is, however, seen to shift slightly towards higher theta value, indicating a decrease in the d value, which implies modification of strain.

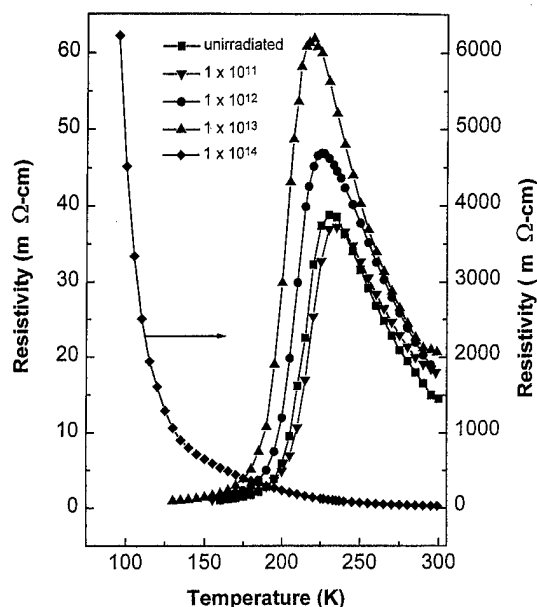


FIG. 2. Resistivity vs temperature curves for the as-deposited film and films irradiated at different ion doses.

It can be seen that for dose values of 10^{12} and 10^{13} ions/cm² shoulders appear on the XRD peak and they grow with the dose. At a dose of 10^{14} ions/cm² phase disproportion is apparent.

Figure 2 shows the resistivity (ρ) as a function of temperature for the as-deposited and irradiated films. At a dose of 10^{14} ions/cm² the film does not show any transition from the insulating state to the metallic state, at least down to 60 K. The plot of T_p versus irradiation dose is shown in Fig. 3. Initially at a lower dose of 10^{11} ions/cm², the T_p increases and then starts decreasing for a dose of 10^{12} ions/cm² and above. Figure 3 also shows the variation of activation en-

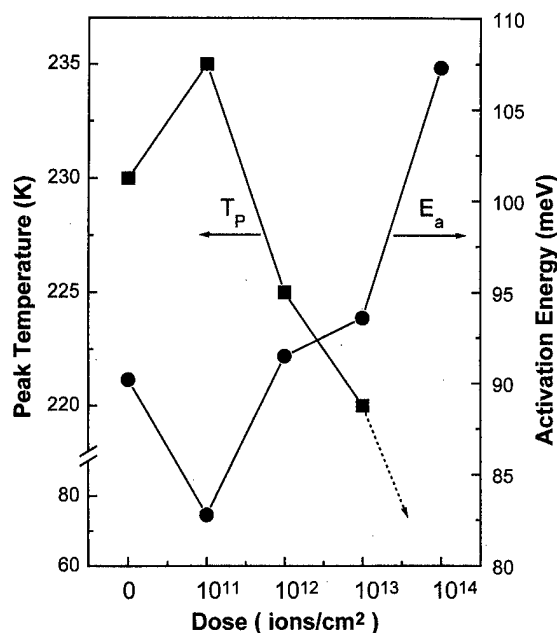


FIG. 3. Dependence of the resistivity peak temperature (T_p) and the activation energy (E_a) as a function of irradiation dose.

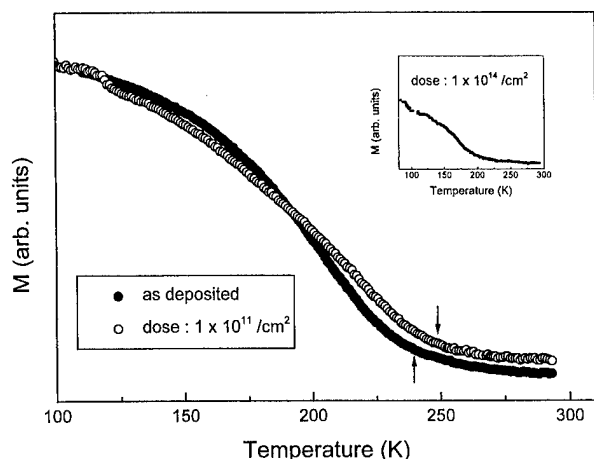


FIG. 4. Magnetization vs temperature curves for the as-deposited film and the film irradiated at a dose of 1×10^{11} ions/cm². The arrows show T_c 's. The inset shows the data for the film irradiated at a dose of 1×10^{14} ions/cm².

ergy, E_a , for hopping transport in the semiconducting region ($T > T_p$) with the irradiation dose. These values were obtained from $\ln(\rho)$ vs $1/T$ plots. The lower value of activation energy for the dose of 10^{11} ions/cm² again suggests release of deposition induced microscopic strains. The increase in the activation energy with irradiation dose can be attributed to the strain developed in the LCMO lattice due to irradiation induced stoichiometry defects revealed by the XRD data.

The magnetization curves as a function of temperature for the as-deposited film and the film irradiated at the lowest dose of 1×10^{11} ions/cm² are compared in Fig. 4. The arrows show the Curie temperature (T_c). It clearly shows that T_c for the film irradiated at 1×10^{11} ions/cm² is more than that of the unirradiated film, establishing a T_c - T_p correlation. At higher doses this transition temperature decreases below that of the unirradiated film. This behavior of T_c with the irradiation dose is also consistent with that of T_p . It can be seen from the inset of Fig. 4 that the magnetization curve for the film irradiated at 1×10^{14} ions/cm² shows no well defined transition from the paramagnetic to the ferromagnetic state as we decrease the temperature. This can be explained if one visualizes the formation of small chaplets of amorphous and/or inhomogeneities uniformly distributed throughout the film. Evidence for this is obtained from the XRD data dis-

cussed earlier. Such type of defects is capable of affecting the angle and length of the $\text{Mn}^{+3}\text{-O-Mn}^{+4}$ bond, which in turn affects the double-exchange interaction.

In conclusion we have explained the effects of 90 MeV ^{16}O ion irradiation on the epitaxial $\text{La}_{0.75}\text{Ca}_{0.25}\text{MnO}_3$ thin films grown by pulsed laser deposition. The electrical and magnetic measurements show that the resistivity peak temperature (T_p) and ferromagnetic transition temperature, i.e., Curie temperature (T_c), shift towards lower value with irradiation dose, except for the case of a low dose of 1×10^{11} ions/cm². The lower dose apparently relaxes the LCMO lattice, releasing deposition induced microscopic strain present in the as-deposited films, causing an increase in T_p and T_c and a decrease in the activation energy. At high doses, irradiation induced disorder introduces compositional inhomogeneity and related strain in the films which apparently affect the angle and length of the $\text{Mn}^{+3}\text{-O-Mn}^{+4}$ bond, and hence the exchange interaction between the cations.

- ¹K. Chahara, T. Ohno, M. Kasai, and Y. Kosono, *Appl. Phys. Lett.* **63**, 1990 (1993).
- ²R. Von Helmolt, J. Wecker, B. Holzapfel, L. Schultz, and K. Samwer, *Phys. Rev. Lett.* **71**, 2331 (1993).
- ³H. L. Ju, C. Kwon, Qi Li, R. L. Greene, and T. Venkatesan, *Appl. Phys. Lett.* **65**, 2108 (1994).
- ⁴S. Jin, T. H. Tiefel, M. McCromack, R. A. Fastnacht, R. Ramesh, and L. H. Chen, *Science* **264**, 413 (1994).
- ⁵M. McCormack, S. Jin, T. H. Tiefel, R. M. Fleming, J. M. Phillips, and R. Ramesh, *Appl. Phys. Lett.* **64**, 3045 (1994).
- ⁶G. H. Jonker and J. H. Van Santen, *Physica (Amsterdam)* **16**, 337 (1950).
- ⁷J. B. Goodenough, *Phys. Rev.* **100**, 564 (1955).
- ⁸C. Zener, *Phys. Rev.* **82**, 403 (1951).
- ⁹M. F. Hundley, M. Hawley, R. H. Heffner, Q. X. Jia, J. J. Neumeier, and J. Tesmer, *Appl. Phys. Lett.* **67**, 860 (1995); A. J. Millis, P. B. Littlewood, and B. I. Shraiman, *Phys. Rev. Lett.* **74**, 514 (1995).
- ¹⁰H. L. Ju, J. Gopalakrishnan, J. L. Peng, Q. Li, G. C. Xiang, T. Venkatesan, and R. L. Greene, *Phys. Rev. B* **51**, 6143 (1995).
- ¹¹R. Shreekala, M. Rajeshwari, K. Ghosh, J. Y. Gu, C. Kwon, Z. Trajanovic, T. Boettcher, R. L. Green, R. Ramesh, and T. Venkatesan, *Appl. Phys. Lett.* **71**, 282 (1997).
- ¹²J. J. Neumeier, M. F. Hundley, J. D. Thompson, and R. H. Heffner, *Phys. Rev. B* **52**, R7006 (1995).
- ¹³M. W. Thomson, *Defects and Radiation Damage in Metals* (Cambridge University Press, Cambridge, 1969).
- ¹⁴G. Szenes, *Phys. Rev. B* **51**, 8026 (1995).
- ¹⁵F. Thibaudau, J. Cousty, E. Salanzat, and S. Bouffard, *Phys. Rev. Lett.* **67**, 1582 (1991).

Colossal magnetoresistance in $\text{La}_{1-x}\text{Li}_x\text{MnO}_3$

X. L. Wang^{a)}

Centre for Superconducting and Electronic Materials, University of Wollongong, Wollongong, NSW 2522, Australia

S. J. Kennedy

Neutron Scattering Group, ANSTO, NSW, 2234, Australia

Peter Gehringer and Wolfgang Lang

Ludwig Boltzmann Institut fuer Festkoerperphysik, Kopernikusgasse 15, A-1060 Wien, Austria

H. K. Liu

Centre for Superconducting and Electronic Materials, University of Wollongong, Wollongong, NSW 2522, Australia

S. X. Dou

Centre for Superconducting and Electronic Materials, University of Wollongong, Wollongong, NSW 2522, Australia

$\text{La}_{1-x}\text{Li}_x\text{MnO}_3$ ($x=0, 0.1, 0.2$, and 0.3) were synthesized by using conventional solid state reaction and partial melting technique. The compounds were determined to be of rhombohedral structure by x-ray powder diffraction. For the $x=0.2$ and $x=0.3$ samples, room temperature neutron powder diffraction patterns were collected and analyzed with the Rietveld method. The analysis showed that the Li substitutes onto the La site in the rhombohedral perovskite lattice. Resistivities were measured between 4.2 K and room temperature in the magnetic fields of 0, 1, 2, 4, 8, and 13 T. A wide semiconductor-metal transition at temperatures between 160 and 210 K or between 200–230 K were observed for both samples with $x=0.2$ and 0.3 , respectively. Large magnetoresistances above 20%–80% were achieved at fields from null to 13 T over a wide temperature range from the ferromagnetic transitions down to 4.2 K. However, the $x=0$ and 0.1 samples show a semiconducting behavior in resistivity measured between 77 and 300 K. © 1998 American Institute of Physics. [S0021-8979(98)45111-9]

I. INTRODUCTION

Recent discovery of colossal magnetoresistance (CMR) phenomenon in doped LaMnO_3 perovskite (LMO)^{1–4} which exhibit a field-induced change in electrical conductivity by many orders of magnitude, has stimulated much research worldwide because of its importance both for fundamental research in solid state physics and for practical application in magnetoelectronics. Upon doping La^{3+} by divalent ions, both Mn^{3+} and Mn^{4+} ions are present. Electron hopping occurs via the double-exchange (DE) mechanism.^{5–7} Up to now, substitution of La^{3+} by divalent ions such as Ca, Sr, Ba, Pb, or Cd have been widely studied in order to achieve mixture valences of Mn^{3+} and Mn^{4+} . It was found that the geometry of the Mn–O–Mn bond plays a crucial role since the oxygen ion mediates the DE. Distortion of the crystal structure leads to the buckling of octahedral network,⁸ and changes the interatomic distance and bond angle, hence influencing the electron hopping and DE interaction. The value of MR above 10^5 was achieved in doped LMO thin films with optimized straining of the lattice.⁹ This reflects that the lattice distortion favors the CMR. The DE will be enhanced if the Mn–O distance decreased. To decrease Mn–O distance, studies have been done on substitution of La^{3+} by smaller $3+$ ions, (eg, Pr, Y, Nd) or substitution Ca by Y.^{10,11}

With decreasing average ionic radius of the La site, MR increases dramatically.¹⁰ Films of $\text{La}_{0.6}\text{Y}_{0.07}\text{Ca}_{0.33}\text{MnO}_3$ on LaAlO_3 substrate give a much higher MR value (10^9) than the undoped La–Ca–Mn–O films.⁹ From a practical viewpoint, large MR over a wide temperature range is highly desirable. However, MR was widely observed to be restricted to a narrow temperature range around ferromagnetic transition (FT) in single crystals and epitaxial thin films of doped LMO. Although polycrystalline thin films showed MR at a relative wide temperature range, the resistivity is much higher than that of epitaxial thin films.^{12–14} The large resistivity would give high levels of electrical noise. For the occurrence of DE, the amount of Mn^{4+} should be sufficient enough in the LMO and $x=0.3$ was found to be optimum doping level in $\text{La}_{1-x}\text{M}_x\text{MnO}_3$ ($\text{M}=\text{Ca}, \text{Sr}, \text{Ba}, \dots$) which corresponds to 30% Mn^{4+} . Compared with substitution of La by the $2+$ ions, substitution by $1+$ ions, such as H^+ , Li^+ , Na^+ , K^+ , or Rb^+ , will be easy to achieve a high percentage of Mn^{4+} with the same doping level as that by $2+$ ions substitution. For every ion with $1+$ valence substitution for trivalent lanthanum ion, two Mn^{3+} need to be oxidized to Mn^{4+} . H^+ radius is so small that it is expected to distribute in atomic gaps instead of occupying La sites. While Na and K are not stable, they evaporate significantly at high temperatures.¹⁵ In this article, we report our studies on LMO with Li^+ partially substituted for La instead of using a divalent ion for doping into La site. The optimum Li-doped LMO

^{a)}Corresponding author: Electronic mail: xlw01@uow.edu.au

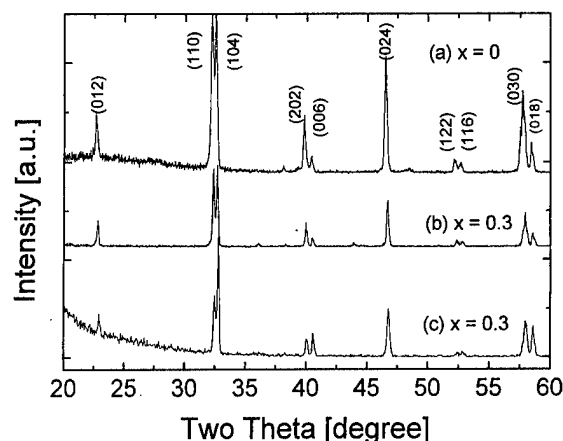


FIG. 1. XRD patterns of powdered $\text{La}_{1-x}\text{Li}_x\text{MnO}_3$ (a) and (b) and surface of samples prepared by partial melting (c).

shows a ferromagnetic transition at 230 K which is the same as that in Ca-doped LMO and a nearly constant magnetoresistance $\Delta\rho/\rho_0=20\%-80\%$ with the application of magnetic fields from 1 up to 13 T over a very wide temperature range between 230 and 4.2 K.

II. EXPERIMENT

The Li-doped LMO samples were synthesized by conventional solid state reaction and partial melting technique. High purity powders of La_2O_3 , LiCO_3 , and MnCO_3 were weighed according to nominal composition of $\text{La}_{1-x}\text{Li}_x\text{MnO}_3$ ($x=0, 0.1, 0.2$, and 0.3). After mixing them well, these powders were pressed into pellets 10 mm in diameter. The pellets were first sintered at a temperature of 1100 °C for 24 h (referred to as sintered samples). After grinding and pressing, the pellets were then partially melted at a temperature of 1500 °C for 10 min and rapidly cooled down to 900 °C and quenched in air (referred to as partially melted samples). A post annealing in O_2 at 700 °C was carried out for some samples. Bar samples were cut from the as-prepared bulks for a standard four-probe resistance-temperature (R-T) measurement. The resistivity of the samples were measured as a function of temperature between 300–77 K at null field and 4.2–300 K at fields from null up to 13 T. X-ray diffraction (XRD) neutron powder diffraction, and scanning electron microscopy (SEM) were carried out for characterization of the samples.

III. RESULTS AND DISCUSSIONS

The compounds were determined to be of rhombohedral structure by x-ray powder diffraction as shown in Fig. 1 and contain a small amount of unknown impurity phase for as-sintering samples [Figs. 1(a) and 1(b)]. The amount of impurity phase was found to gradually increase with an increasing Li doping level. Room-temperature neutron powder diffraction patterns of the $x=0.2$ and $x=0.3$ as-sintered samples were analyzed with the Rietveld method. The patterns were fitted with space group $R3c$ and Bragg R factor of 2.3% and 5.0%, respectively. A neutron powder diffraction pattern of the $x=0.2$ sample is shown in Fig. 2 with the fit to

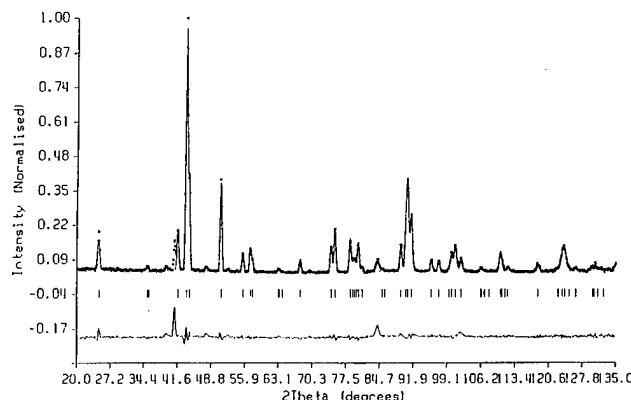


FIG. 2. Room-temperature neutron powder diffraction pattern for as-sintered sample ($x=0.2$) and Rietveld refinement of pattern.

the data. Most of the peaks are well fitted by a rhombohedral perovskite structure. The analysis showed Mn and O are fully occupied and concentrations of La are 0.884 and 0.832 for samples with $x=0.2$ and 0.3 , respectively, indicating that the Li substitutes onto the La site in the rhombohedral perovskite lattice. However, the exact doping level of Li is much lower than that in nominal compositions. The as-sintered samples reveal very porous morphologies by scanning electron microscopy and have a high resistance at room temperature due to a large amount of grain boundaries. As-partially melted samples are of high density with lower resistance at room temperature and contains less impurities than as-sintered samples as shown in Fig. 1(c). The intensity ratios of (104)/(110), (006)/(202), and (018)/(030) reflections of the partially melted samples are higher than those of the as-sintered samples with the same Li doping level. This reveals that the partially melted samples have a (001) orientation tendency when compared with as-sintered one. The temperature dependencies of resistivity at a temperature range between 77 and 300 K is shown in Fig. 3 for both $x=0.2$ and 0.3 as-partially melted samples annealed in O_2 . These two samples exhibit a semiconductive-metallic transition between 200–230 K and 160–210 K, respectively. However, samples with $x=0$ and 0.1 are semiconductive without

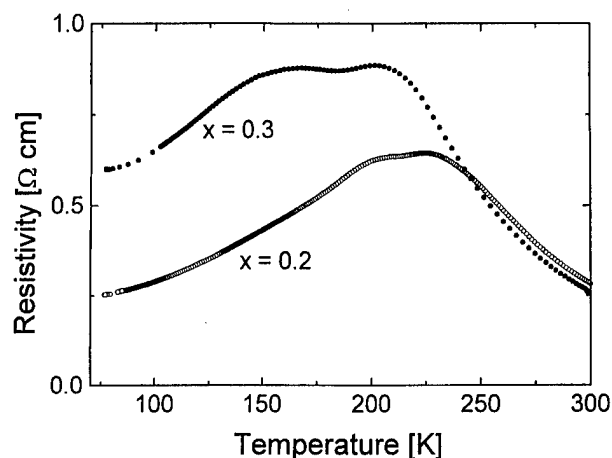


FIG. 3. Resistivity-temperature of Li-doped LMO samples partially melted and annealed in O_2 between 77 and 300 K at null field.

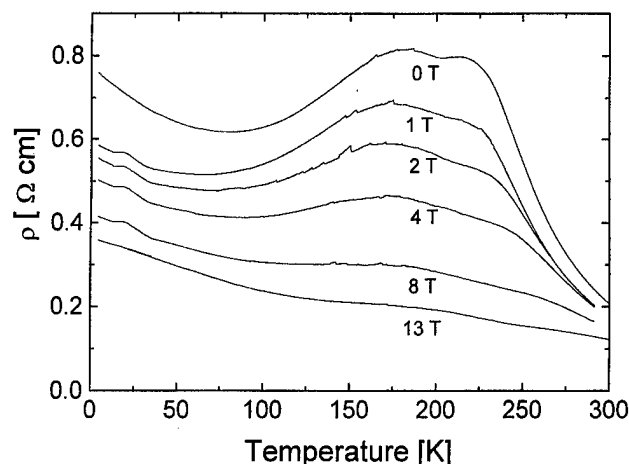


FIG. 4. Resistivity-temperature of as-partially melted sample with $x=0.2$ between 4.2 and 300 K in different fields.

any transition above 77 K. Figure 4 shows a temperature dependence of the resistance for an as-partially melted sample ($x=0.2$) at field of 0, 1, 2, 4, 8, and 13 T. At zero field, the resistance increases with decreasing temperature until 230 K at which a ferromagnetic transition (FT) takes place. Below 230 K, the resistance remains constant between 230 and 170 K which is wider than that annealed in O_2 (Fig. 3) and reduces slowly with further cooling down to 77 K and then increasing with a further decrease of temperature. With increasing magnetic fields, the FT was gradually increased up to 270 K. Meanwhile, the room-temperature resistance decreases, indicative of a typical ferromagnetic transition behavior and paramagnetism above FT. Magnetoresistance, $\Delta\rho/\rho_0 = [\rho_0 - \rho_H]/\rho_0$, shows a nearly constant values of 17%–20%, 22%–30%, 30%–48%, 45%–65%, and 52%–80% for fields of 1, 2, 4, 8, and 13 T, respectively, over a very wide temperature range between 4.2 and 230 K as shown in Fig. 5. Such a large MR over a wide temperature range achieved in the Li-doped $LaMnO_3$ is the same as that

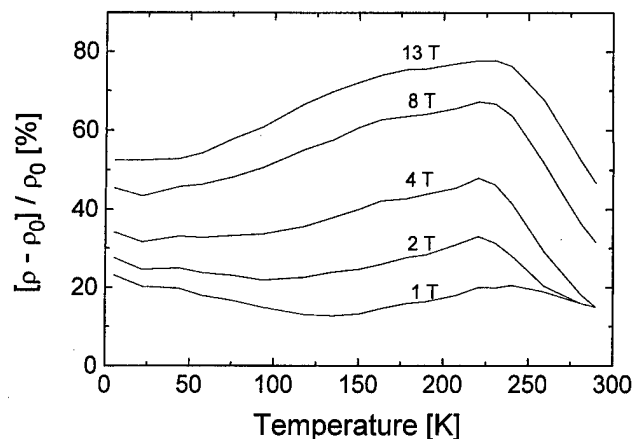


FIG. 5. Magnetoresistance of an as-partially melted sample with $x=0.2$ between 4.2 and 300 K in different fields.

observed in polycrystalline thin films of Ca-doped $LaMnO_3$ with a field of 5 T¹⁴ and wider than Na^{1+} doped LMO bulks and thin films.¹²

The magnetic moment versus temperature ($m-T$) for an as-partially melted sample with $x=0.2$ measured at 50 Oe shows a typical ferromagnetic transition at 230 K which is in accord with the onset of transition in the resistance-temperature curve (Fig. 4). However, the ferromagnetic transition width derived from $m-T$ is narrow (215–230 K) which could not account for the constant value of resistance in a wide temperature range between 230 and 170 K. The SEM morphologies of the Li and Ca doped $LaMnO_3$ show that the partially melted samples are very dense and no clear grain boundaries can be seen. Grain sizes are much larger than that of polycrystalline bulk samples synthesized by a conventional solid state reaction (as-sintered samples). Since both Li and Ca doped LMO samples prepared by the partial melting technique are polycrystalline and without any preferred orientation as seen from their XRD, the possible effect of grain boundaries on the MR over a wide temperature range seems unclear for the Li-doped $LaMnO_3$.^{11,16} In addition, the radius of the Li^{1+} is much smaller (0.78 Å) than La^{3+} . Distortion of the lattice due to the Li substitution for La will be larger than that of Ca, Sr, and other 2+ ions and Na^{1+} doped $LaMnO_3$ and induce large amount of crystal defects, nonuniform substitutions, and oxygen deficiencies which may lead to the broadening in the resistance-temperature curve and hence cause the large MR over a broad temperature range. The real origin of the broadening of resistance in the R-T curve is unclear and needs further study. From a practical viewpoint, the large MR over such a wide temperature range is beneficial for the application of magnetoelectronic devices fabricated by the CMR magnanites. To achieve a larger and constant MR near room temperature, fabrication of thin films of the Li doped $LaMnO_3$ and optimization of oxygen are necessary.

¹S. Jin *et al.*, Science **264**, 413 (1994).

²R. von Helmolt, J. Wecker, B. Holszapfel, L. Schultz, and K. Samwer, Phys. Rev. Lett. **71**, 2331 (1993).

³M. A. Subramanian *et al.*, Science **273**, 81 (1996).

⁴A. P. Ramirez, R. J. Cava, and J. Krajewski, Nature (London) **386**, 156 (1997).

⁵C. Zener, Phys. Rev. **81**, 403 (1951).

⁶P.-G. de Gennes, Phys. Rev. **118**, 141 (1960).

⁷P. W. Anderson and H. Hasegawa, Phys. Rev. **100**, 675 (1955).

⁸J. B. Torrance, P. Lacorre, and A. I. Nazzari, Phys. Rev. B **45**, 8209 (1992).

⁹Review article, S. Jin, JOM, March, 1997 (unpublished), p. 61.

¹⁰H. Y. Hwang, S.-W. Cheong, P. G. Radaelli, M. Marezio, and B. Batlogg, Phys. Rev. Lett. **75**, 941 (1995).

¹¹S. Jin *et al.*, Appl. Phys. Lett. **66**, 382 (1995).

¹²A. Gupta, G. Q. Gong, G. Xiao, P. R. Duncombe, P. Lecoeur, P. Trouilloud, Y. Y. Wang, and V. P. Dravid, Phys. Rev. B **54**, R15 629 (1996).

¹³R. Shreekala, M. Rajeswari, K. Ghosh, A. Goyal, J. Y. Gu, C. Kwon, Z. Trajanovic, T. Boettcher, R. L. Greene, R. Ramesh, and T. Venkatesan, Appl. Phys. Lett. **71**, 282 (1997).

¹⁴R. Mahesh, R. Mahendiran, A. K. Raychaudhuri, and C. N. R. Rao, Appl. Phys. Lett. **68**, 2291 (1996).

¹⁵M. Sahana *et al.*, Appl. Phys. Lett. **70**, 2909 (1997).

¹⁶H. Y. Hwang, S.-W. Cheong, N. P. Ong, and B. Batlogg, Phys. Rev. Lett. **77**, 2041 (1996).

Magnetic, dielectric, and transport properties of $\text{La}_{1-x}\text{Sr}_x\text{MnO}_3$ at submillimeter wavelengths

V. Yu. Ivanov, V. D. Travkin, A. A. Mukhin,^{a)} S. P. Lebedev, and A. A. Volkov
General Physics Institute of the Russian Academy of Science, 38 Vavilov Street, 117942 Moscow, Russia

A. Pimenov and A. Loidl
Experimentalphysik V, Universität Augsburg, D-86159 Augsburg, Germany

A. M. Balbashov and A. V. Mozhaev
Moscow Power Engineering Institute, 14 Krasnokazarmennaya Street, 105835 Moscow, Russia

Antiferromagnetic resonance (AFMR), dynamic conductivity, and dielectric permittivity have been studied in the $\text{La}_{1-x}\text{Sr}_x\text{MnO}_3$ perovskites at a frequency range of $\nu = 3\text{--}33\text{ cm}^{-1}$ by the use of a quasi-optical backward-wave-oscillator technique. Two AFMR modes have been observed in LaMnO_3 and $\text{La}_{0.95}\text{Sr}_{0.05}\text{MnO}_3$. Temperature dependencies of their resonance frequencies, linewidths, and mode contributions to a static magnetic permeability have been obtained and corresponding parameters of magnetic interactions have been extracted. A jump in the dielectric permittivity $\epsilon'(T)$ was found at $T = 100\text{--}120\text{ K}$ in $\text{La}_{0.9}\text{Sr}_{0.1}\text{MnO}_3$, which indicates the existence of an additional phase transition (probably, a polaron ordering) besides the ferromagnetic transition at 170 K. A sharp increase of the dynamic conductivity $\sigma'(\nu, T)$ was observed near Curie temperature (285 K) at a metal–semiconductor transition in $\text{La}_{0.825}\text{Sr}_{0.175}\text{MnO}_3$, which was slightly smaller than its static value. © 1998 American Institute of Physics. [S0021-8979(98)31811-3]

The recent observation of the colossal negative magnetoresistance in doped perovskites $\text{R}_{1-x}\text{A}_x\text{MnO}_3$, where R is a trivalent rare-earth ion and A is a divalent ion such as Ca or Sr,¹ has attracted considerable interest in these compounds. Their magnetic, electronic transport, structural, and optical properties exhibit a remarkable variation with the doping level.^{2–4}

The parent compound LaMnO_3 (Mott-type insulator) has a canted antiferromagnetic layer (A_yF_z) structure with a Neel temperature $T_N \approx 140\text{ K}$.^{5–7} Manganese ions Mn^{3+} have a $3d^4$ electronic configuration with a total spin $S = 2$, where three electrons occupying t_{2g} orbitals may be considered as a local spin of $S = 3/2$, while the remaining electron occupies an e_g orbital hybridized with oxygen $2p$ states. The spins of the t_{2g} and e_g electrons are parallel aligned due to on-site Hund coupling. The substitution of the rare-earth ions by Sr (or Ca) ions results in doping of holes to the e_g orbitals and a transition from a canted antiferromagnetic insulating state to a ferromagnetic metallic state,^{1,2,8} which is stabilized due to a double exchange.⁹

Recent spectroscopic investigations of the doped lanthanum manganites indicate that their dynamic properties change drastically through the phase transitions and are very sensitive to the doping level. An infrared study of the optical conductivity of $\text{La}_{1-x}\text{Sr}_x\text{MnO}_3$ has shown a large variation of the electronic structure in a wide frequency range ($\sim 2\text{ eV}$) with the spin polarization of the conduction carriers⁴ and a shift of phonon frequencies at the ferromagnetic metal–insulator transition.¹⁰ Inelastic neutron scattering experiments have revealed spin excitations in pure LaMnO_3 ,^{7,11} and these dramatically change with doping level.¹² In this work we performed investigations of antifer-

romagnetic resonance (AFMR), dynamic conductivity, and dielectric permittivity of $\text{La}_{1-x}\text{Sr}_x\text{MnO}_3$ manganites in the submillimeter frequency range by means of a quasi-optical backward-wave-oscillator technique.^{13,14}

Single crystals of $\text{La}_{1-x}\text{Sr}_x\text{MnO}_3$ ($x = 0, 0.05, 0.1, 0.15$, and 0.175) were grown by the floating zone method with radiation heating in an air atmosphere. X-ray powder diffraction measurements showed that grown materials were of single phase. However, x-ray topography has revealed a twin structure in the crystals.

Resistance, $\rho(T)$, was measured using the four-probe method at $T = 4.2\text{--}400\text{ K}$ in magnetic fields H up to 12 kOe. Magnetization $M(T, H)$ and ac magnetic susceptibility $\chi_{ac}(T)$ measurements were performed in magnetic fields $H \leq 12\text{ kOe}$ at $T = 4.2\text{--}400\text{ K}$.

The transmission $T(\nu)$ and phase shift $\Delta\varphi(\nu)$ spectra of thin plane-parallel plates were measured using a quasi-optical submillimeter backward-wave-oscillator spectrometer^{13,14} in the frequency range $\nu = 3\text{--}33\text{ cm}^{-1}$ at temperatures of $5\text{--}300\text{ K}$. The complex dielectric permittivity $\epsilon(\nu, T) = \epsilon' + i\epsilon''$ as well as the dynamic conductivity $\sigma(\nu, T)$ were determined from the $T(\nu)$ and $\Delta\varphi(\nu)$ spectra using Fresnel's formulas for the transmission and phase shift of the plane-parallel plate.¹⁵ In order to take into account the AFMR mode contribution we used a harmonic oscillator model for a permeability dispersion:

$$\mu = 1 + \sum_i \Delta\mu_i \nu_i^2 / (\nu_i^2 - \nu^2 + j\nu\Delta\nu_i), \quad (1)$$

where ν_i , $\Delta\nu_i$, and $\Delta\mu_i$ are the resonance frequency, linewidth, and mode contribution to the static permeability of the i th mode, respectively, $j = \sqrt{-1}$.

LaMnO_3 : In the transmission spectra of the pure LaMnO_3 we observed two lines close together, which appeared at $T < T_N = 140\text{ K}$. We have identified the lines with

^{a)}Electronic mail: mukhin@ss.gpi.ru

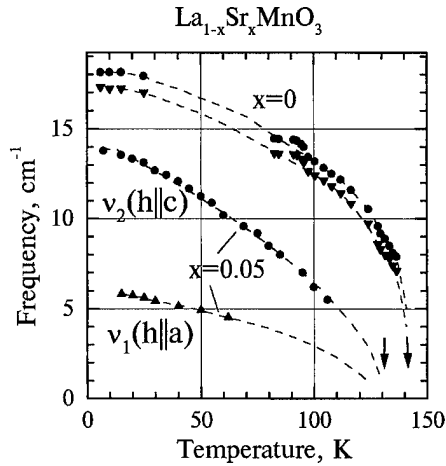


FIG. 1. Temperature dependence of the AFMR frequencies in $\text{LaMn}_{1-x}\text{Sr}_x\text{O}_3$ for $x=0$ and 0.05. Arrows indicate the corresponding Neel temperatures.

two AFMR modes and have fitted $T(\nu)$ spectra using Fresnel's formulas and Eq. (1) for the permeability. The temperature dependence of the AFMR frequencies is shown in Fig. 1. The values of the linewidth, mode contribution, and complex dielectric permittivity are equal to $\Delta\nu_{1,2} \approx 0.5 \text{ cm}^{-1}$, $\Delta\mu_{1,2} \approx 0.035$, and $\epsilon' \approx 20.5$, $\epsilon'' \approx 0.1$, respectively, at $T=80 \text{ K}$. An inelastic neutron scattering study of LaMnO_3 gives the gap for the spin waves at about 19.8 cm^{-1} at 20 K (Ref. 7) and 19.4 cm^{-1} at 8 K ,¹¹ in agreement with our resonance frequency values of 18.1 and 17.3 cm^{-1} at 4.2 K (Fig. 1).

According to Refs. 6 and 7 the antiferromagnetic spin axis in LaMnO_3 is along the b axis of the orthorhombic Pbm crystal and a small spin canting takes place along the c axis (magnetic structure of the A_yF_z type). There are two AFMR modes in the crystal whose frequencies are determined by¹⁴

$$\nu_1 = \gamma(2H_E H_A^{cb})^{1/2}, \quad \nu_2 = \gamma(2H_E H_A^{ab} + H_D^2)^{1/2}, \quad (2)$$

where $H_A^{cb} = K_{cb}/M_0$, $H_A^{ab} = K_{ab}/M_0$, and $K_{cb,ab}$ are anisotropy constants for the cb and ab crystallographic planes, respectively, H_E and H_D are isotropic and antisymmetric exchange fields, respectively, $M_0/2$ is a sublattice magnetization, and γ is a gyromagnetic ratio. The first (quasiferromagnetic) mode is excited by $h||a$ and b axes, while the second (quasiantiferromagnetic) mode is excited by $h||c$ axis. The corresponding mode contributions are: $\Delta\mu_1^a = 4\pi\rho\chi_\perp$, $\Delta\mu_1^b = 4\pi\rho\chi_{\text{rot}}$ for mode 1 and $\Delta\mu_2^c = 4\pi\rho\chi_\perp$ for mode 2, where $\chi_\perp = M_0/2H_E$ and $\chi_{\text{rot}} = m_0^2/K_{cb}$ are transverse and rotation susceptibilities, respectively, $m_0 = \chi_\perp H_D$ is the weak ferromagnetic moment and $\rho \approx 6.5 \text{ g/cm}^3$ is the crystal density. Due to the twin structure of the investigated LaMnO_3 crystals both modes were observed simultaneously with nearly equal mode contributions at various polarization of radiation. Assuming equal volume for all six kinds of the twins and their even distribution in the sample we obtain $\Delta\mu_1 = 1/3(\Delta\mu_1^a + \Delta\mu_1^b)$ and $\Delta\mu_2 = 1/3\Delta\mu_2^c$ and then we may estimate $\chi_\perp \approx (1.4 \pm 0.2) \times 10^{-4} \text{ cm}^3/\text{g}$ and the corresponding exchange field $H_E \approx 3.3 \times 10^5 \text{ Oe}$. This value of the χ_\perp is in a reasonable agreement with the $\chi_\perp = (1.8 \pm 0.3)$

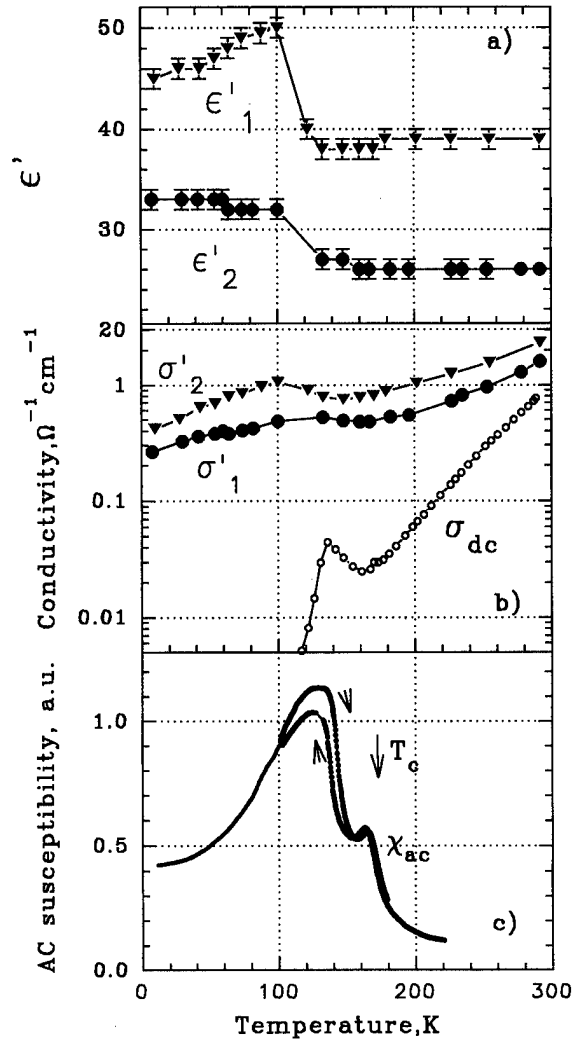


FIG. 2. Temperature dependence of the dielectric permittivity $\epsilon'_{1,2}(7.5 \text{ cm}^{-1})$ (a), dynamic $[\sigma'_{1,2}(7.5 \text{ cm}^{-1})]$ and static (σ_{dc}) conductivity (b) and ac magnetic susceptibility χ_{ac} (c) of $\text{La}_{0.9}\text{Sr}_{0.1}\text{MnO}_3$. Indices 1,2 correspond to the two crystallographic directions: 1— $[-110]$ and 2— $[-11-2]$.

$\times 10^{-4} \text{ cm}^3/\text{g}$ deduced from our static measurements. Using the interplane exchange constant obtained from an inelastic neutron scattering study of the spin waves in LaMnO_3 ,^{7,11} we can determine $H_E \approx 4 \times 10^5 \text{ Oe}$ that is close to our data. Using the value of the weak ferromagnetic moment for a single domain $m_0(T=78 \text{ K}) = 4.2 \pm 0.5 \text{ emu/g}$ deduced from our static measurements and anisotropy constant $K_{cb}(T=78 \text{ K}) \approx 3 \times 10^6 \text{ erg/g}$ ($\approx 6 \text{ cm}^{-1}/\text{ion}$) determined from the AFMR frequency we may estimate $\chi_{\text{rot}} = 6 \times 10^{-6} \text{ cm}^3/\text{g}$. The small value of the χ_{rot} , i.e., $\chi_{\text{rot}} \ll \chi_\perp$, explains the nearly equal mode contributions ($\Delta\mu_1 \approx \Delta\mu_2$) observed in our experiment. We note also the small contribution of the antisymmetric exchange field H_D into the AFMR frequency and nearly equal values of the anisotropy constants in different crystallographic planes that permit the use of a simple model of an uniaxial antiferromagnet to describe the spin waves in LaMnO_3 .^{7,11}

$\text{La}_{0.95}\text{Sr}_{0.05}\text{MnO}_3$: Two AFMR modes were revealed for this composition, which in contrast to the pure LaMnO_3 , had significantly different frequencies (Fig. 1). What's more, the

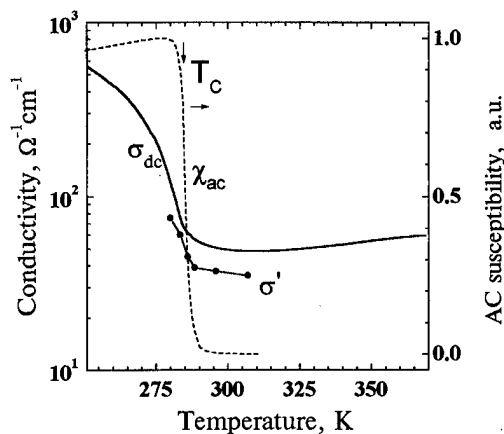


FIG. 3. Temperature dependence of the dynamic $\sigma'_{1,2}$ (at $7-20 \text{ cm}^{-1}$) and static (σ_{dc}) conductivity and ac magnetic susceptibility (χ_{ac}) of $\text{La}_{0.825}\text{Sr}_{0.175}\text{MnO}_3$.

samples (*b*-cut plane parallel plates) practically did not contain twins and we were able to determine excitation conditions and identify the modes: the low frequency mode (ν_1) observed at the $h\parallel a$ axis was identified as a quasiferromagnetic mode, while the high frequency mode (ν_2) excited by the $h\parallel c$ axis was identified as a quasiantiferromagnetic one. The values of the mode contributions and linewidths are ($T = 10 \text{ K}$): $\Delta\mu_1 = 0.016 \pm 0.003$, $\Delta\mu_2 = 0.015 \pm 0.003$, $\Delta\nu_{1,2} \approx 2 \text{ cm}^{-1}$.

We assumed above that the magnetic structure is of the A_2F_z type. This conclusion is confirmed by the neutron scattering and magnetic study of the $\text{La}_{0.96}\text{Sr}_{0.04}\text{MnO}_3$,¹⁶ where the magnetic structure remains similar to that of pure LaMnO_3 , however, with increased value of a canting angle. According to our static measurements of $\text{La}_{0.95}\text{Sr}_{0.05}\text{MnO}_3$ the magnetic susceptibilities $\chi_a \approx \chi_c = (1.3-1.9) \times 10^{-4} \text{ cm}^3/\text{g}$, $\chi_b = (5.3 \pm 0.5) \times 10^{-4}$, and spontaneous moment along the *c* axis $m_0 = 18 \pm 4 \text{ emu/g}$ are in agreement with the A_2F_z magnetic structure. However, we note a noticeable increase (about four times) of the canting angle and significant decrease of the anisotropy constant in the *cb* plane. The estimated values of the K_{cb} are: $(0.7 \pm 0.2) \times 10^6 \text{ cm}^3/\text{g}$ from the AFMR data and $(0.6 \pm 0.2) \times 10^6 \text{ cm}^3/\text{g}$ from the rotation susceptibility (χ_b).

The dielectric properties of $\text{La}_{0.95}\text{Sr}_{0.05}\text{MnO}_3$ are similar to LaMnO_3 , however we note their anisotropy and higher dielectric losses, in particular, $\epsilon'_a \approx 24$, $\epsilon''_a = 0.6-0.7$, and $\epsilon'_c \approx 20$, $\epsilon''_c \approx 0.2-0.3$ for $\nu = 5-13 \text{ cm}^{-1}$ and $T = 80 \text{ K}$.

$\text{La}_{0.9}\text{Sr}_{0.1}\text{MnO}_3$: Magnetic, dielectric, and transport properties of this composition suffer significant changes as compared with previous ones. We did not observe magnetic modes in the range $5-20 \text{ cm}^{-1}$ since the magnetic ordering at $T < T_C \approx 170 \text{ K}$ is of the ferromagnetic type and a ferromagnetic resonance is expected at much lower frequencies. However, apparent anomalies were observed in the temperature dependence of the dielectric permittivity and conductivity (Fig. 2). A pronounced jumplike behavior for $\epsilon'(T)$ and a maximum for $\sigma'(T)$ between 100 and 120 K indicate the existence of an additional phase transition besides the magnetic transition at T_C . The anomalous behavior of the ac magnetic susceptibility at $T < T_C$ [Fig. 2(c)] confirms this

conclusion. One possible origin of this transition may be related to a polaron ordering connected with a freezing of holes on the lattice sites.¹⁷

We note also an anisotropy of the ϵ' and σ' for different crystallographic directions [Figs. 2(a) and 2(b)]. The dynamic conductivity $\sigma'(T)$ is considerably greater than the static one, $\sigma_{dc}(T)$ [Fig. 2(b)]. This indicates that not only free charge carriers contribute to the dynamic σ' but also contributions from the localized carriers and crystal lattice are of importance at the submillimeter wavelengths.

$\text{La}_{0.825}\text{Sr}_{0.175}\text{MnO}_3$: For the high conducting composition ($x = 0.175$) a considerable decrease of the transmission $T(\nu)$ for the 0.026 mm plate on lowering the temperature was observed near the ferromagnetic phase transition at $T_C \approx 285 \text{ K}$, accompanied by a metal-semiconductor transition. In particular, T decreases from 2×10^{-3} at 300 K to 10^{-4} at 280 K . The extracted dynamic conductivity $\sigma'(\nu, T)$ is slightly smaller than its static value $\sigma_{dc}(T)$ and exhibits a sharp increase at the phase transition (Fig. 3). The main contribution to $\sigma'(\nu, T)$ is Drude-like, practically without frequency dispersion. The real part of the dielectric permittivity amounts to $\epsilon'(T = 295 \text{ K}) = 37$ and shows no frequency dispersion.

In conclusion, this study of the submillimeter properties of the $\text{La}_{1-x}\text{Sr}_x\text{MnO}_3$ perovskites shows the intimate relations between their magnetic excitations, charge carriers, and crystal lattice dynamics and gives insight into the origin of their unusual magnetic, electronic, and structural properties.

This work was supported in part by the Russian Foundation for Basic Research (Grant Nos. 97-02-17325 and 96-02-18091) and the Ministry of Science and Technical Policy of the Russian Federation.

- ¹R. von Helmholt, J. Wecker, B. Holzapfel, L. Schultz, and K. Samwer, Phys. Rev. Lett. **71**, 2331 (1993).
- ²A. Urushibura, Y. Moritomo, T. Arima, A. Asamitsu, G. Kido, and Y. Tokura, Phys. Rev. B **51**, 14103 (1995).
- ³Y. Okimoto, T. Katsufuji, T. Ishikawa, A. Urushibura, T. Arima, and Y. Tokura, Phys. Rev. Lett. **75**, 109 (1995).
- ⁴Y. Okimoto, T. Katsufuji, T. Ishikawa, T. Arima, and Y. Tokura, Phys. Rev. B **55**, 4206 (1997).
- ⁵E. O. Wollan and W. C. Koehler, Phys. Rev. **100**, 545 (1955).
- ⁶G. Matsumoto, J. Phys. Soc. Jpn. **29**, 606 (1970).
- ⁷F. Moussa, M. Hennion, J. Rodriguez-Carvajal, H. Moudden, L. Pinsard, and A. Revcolevschi, Phys. Rev. B **54**, 15149 (1996).
- ⁸G. H. Jonker and J. H. van Santen, Physica (Utrecht) **16**, 337 (1950).
- ⁹C. Zener, Phys. Rev. **81**, 440 (1951); **82**, 403 (1951).
- ¹⁰K. H. Kim, J. Y. Gu, H. S. Choi, G. W. Park, and T. W. Noh, Phys. Rev. Lett. **77**, 1877 (1996).
- ¹¹K. Hirota, N. Kaneko, A. Nishizawa, and Y. Endoh, J. Phys. Soc. Jpn. **65**, 3736 (1996).
- ¹²M. Hennion, F. Moussa, J. Rodriguez-Carvajal, H. Moudden, L. Pinsard, and A. Revcolevschi, Physica B **234-236**, 851 (1997).
- ¹³A. A. Volkov, Yu. G. Goncharov, G. V. Kozlov, S. P. Lebedev, and A. M. Prokhorov, Infrared Phys. **25**, 369 (1985).
- ¹⁴A. M. Balbashov, G. V. Kozlov, A. A. Mukhin, and A. S. Prokhorov, in *High Frequency Processes in Magnetic Materials*, edited by G. Srinivasan and A. Slavin (World Scientific, Singapore, 1995), Chap. 2, pp. 56-98.
- ¹⁵M. Born and E. Wolf, *Principles of Optics*, 4th ed. (Pergamon, Oxford, 1980).
- ¹⁶H. Kawano, R. Kajimoto, M. Kubota, and H. Yoshizawa, Phys. Rev. B **53**, 2202 (1996).
- ¹⁷Y. Yamada, O. Hino, S. Nohdo, R. Kanao, T. Inami, and S. Katano, Phys. Rev. Lett. **77**, 904 (1996).

Unusual substitutional properties of Ru in the $\text{La}_{0.7}\text{Sr}_{0.3}\text{Mn}_{1-x}\text{Ru}_x\text{O}_3$ system

S. Sundar Manoharan,^{a)} H. L. Ju, and Kannan M. Krishnan^{b)}

Lawrence Berkeley National Laboratory, Materials Sciences Division, 72-150, Berkeley, California 94720

$\text{La}_{0.7}\text{Sr}_{0.3}\text{Mn}_{1-x}\text{Ru}_x\text{O}_3$, $0 \leq x \leq 0.2$ samples were prepared both in bulk and thin film formed using pulsed laser deposition. Magnetization measurements of bulk samples indicate a marginal decrease in T_c from 366 to 335 K up to 15% Ru substitution in Mn site. X-ray diffraction of the $\langle 100 \rangle$ oriented epitaxial films indicate a monotonic increase in the lattice parameter with Ru doping. The magnetoresistive behavior of the Ru substituted films are comparable with the parent $\text{La}_{0.7}\text{Sr}_{0.3}\text{MnO}_3$ films. Unlike other elemental substitution in Mn sites, the effect of Ru to stabilize magnetic ordering at elevated temperatures is exceptional. © 1998 American Institute of Physics. [S0021-8979(98)26911-8]

Hole-doped manganese oxides exhibit a very large negative magnetoresistance at temperatures close to their paramagnetic to ferromagnetic transition.¹⁻³ The magnetic interaction is mediated by the double exchange interaction between the Mn^{3+} and Mn^{4+} ions. It is now understood that at least three factors govern the insulator to metal (I-M) transition in these materials:^{4,5} the average size of the cations (A, Ln, in $\text{Ln}_{1-x}\text{A}_x\text{MnO}_3$) where A is a divalent dopant and Ln is a lanthanide element, the mixed valence state of manganese (hole carrier density) and the size mismatch between the A and Ln cations. However, preliminary studies of the substitution of metallic elements for manganese in such perovskite manganites has shown that it is possible to dramatically modify their magnetic and transport properties. For example,⁶ $\text{Pr}_{1-x}\text{Ca}_x\text{MnO}_3$ can be driven from insulator to a metal by doping with Cr and Co in Mn sites. In all these attempts it has been observed that any substitution which alters the Zener pairs ($\text{Mn}^{3+}/\text{Mn}^{4+}$) drastically reduces the Curie temperature. The prospects for realizing practical application of these materials largely depends on their low field response and achieving a Curie temperature, T_c above room temperature. Of all the materials reported so far, Ba, Sr, and Pb^{7} substituted $\text{La}_{1-x}\text{A}_x\text{MnO}_3$ shows T_c above 300 K. On the other hand, all substitutions including those on Mn sites drastically reduce T_c . Despite this background, we attempted to evaluate the effect of Ru substitution for three reasons: (i) 4d orbitals of Ru are more delocalized compared to the 3d transition metals; (ii) SrRuO_3 is a well known ferromagnet and a highly conducting perovskite oxide by virtue of Ru:4d-O:2p exchange interactions, and (iii) it is now fairly well understood that the conductivity in manganites is proportional to the ferromagnetic ordering and therefore we could expect better exchange interactions between Mn and Ru in a mixed perovskite. In this article, we present the synthesis of both bulk and thin films of $\text{La}_{0.7}\text{Sr}_{0.3}\text{Mn}_{1-x}\text{Ru}_x\text{O}_3$ (where $0.0 \leq x \leq 0.2$). We document

for the first time that Ru doping upto 15 at. % in Mn site does not lower the ferromagnetic ordering as observed for other transition metals.

The Ru doped manganites, $\text{La}_{0.7}\text{Sr}_{0.3}\text{Mn}_{1-x}\text{Ru}_x\text{O}_3$ were prepared in the form of pellets by calcining mixtures of oxides of La_2O_3 , SrCO_3 , MnCO_3 , and RuO_2 initially at 1100 °C and at 1400 °C after intermittent grinding. Thin films were grown on LaAlO_3 substrates at 300 mTorr oxygen partial pressure and at a substrate temperature of 680 °C by pulsed laser deposition (PLD). The KrF excimer laser employed for the deposition was operated with a pulse energy density of 2 J/cm² and 5 Hz pulse rate. After deposition the films were cooled to room temperature in 200 Torr of O_2 pressure. The bulk polycrystalline samples of the parent $\text{La}_{0.7}\text{Sr}_{0.3}\text{MnO}_3$ and the Ru substituted compounds are both single phase with orthorhombic symmetry. However, their films grown on LaAlO_3 $\langle 100 \rangle$ shows cubic symmetry. The (002) peak shows a monotonic increase in lattice parameter from 3.87 to 3.94 Å with increasing Ru doping. The x-ray pattern (Fig. 1) shows epitaxial growth of Ru-substituted films on the LaAlO_3 substrates.

Magnetization curves for bulk $\text{La}_{0.7}\text{Sr}_{0.3}\text{Mn}_{1-x}\text{Ru}_x\text{O}_3$ are

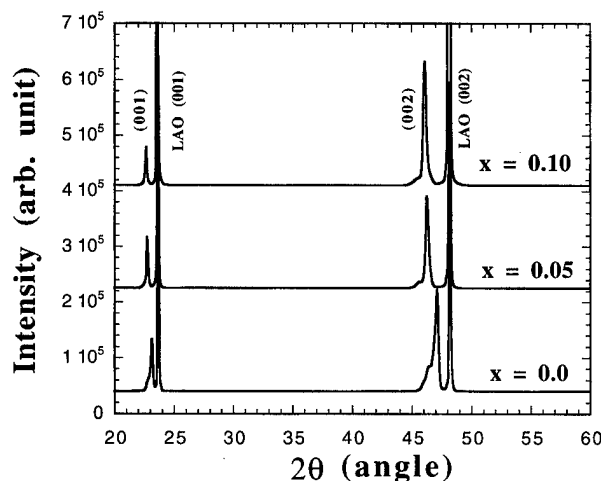


FIG. 1. X-ray diffraction of $\text{La}_{0.7}\text{Sr}_{0.3}\text{Mn}_{1-x}\text{Ru}_x\text{O}_3$ for $x = 0, 0.05$, and 0.1 thin films grown by PLD on LaAlO_3 $\langle 100 \rangle$ substrates. Note the systematic increase in c parameter (002 reflection) with increasing Ru doping.

^{a)}On summer leave from Dept. of Chemistry, Indian Inst. of Technology, Kanpur 208 016, India; electronic mail: ssundar@iitk.ernet.in

^{b)}Author to whom all future correspondence should be addressed; electronic mail: krishnan@lbl.gov

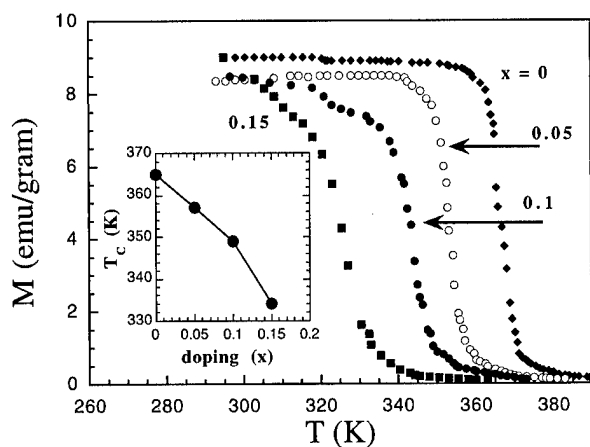


FIG. 2. Temperature dependence of the magnetization (at $H=200$ Oe) of $\text{La}_{0.7}\text{Sr}_{0.3}\text{Mn}_{1-x}\text{Ru}_x\text{O}_3$ above room temperature in the doping range $0 \leq x \leq 0.15$.

shown in Fig. 2. The M vs T curves indicate a monotonic decrease in T_c , from 365 K for $\text{La}_{0.7}\text{Sr}_{0.3}\text{MnO}_3$ (LSMO) to 335 K for $\text{La}_{0.7}\text{Sr}_{0.3}\text{Mn}_{0.85}\text{Ru}_{0.15}\text{O}_3$ (For $x=0.1$ and 0.15 , a shoulder was seen in M vs T curve.) This is possibly due to instrumental error and not due to phase separation since our x-ray results show single phase without any impurity phase within the x-ray resolution of about 2%. The Curie temperature for the parent LSMO agrees well with the reported T_c values. Note the unusual doping effect of Ru which shows a very marginal decrease in T_c for doping upto 15% of Ru (ΔT_c is only around 35 K which is marginal). A large decrease in T_c in other cases, for example; doping of Al^{3+} , Fe^{3+} , and Ti^{4+} has been argued to have direct effect on the magnetic ordering. The positive influence of Ru doping on magnetic ordering could be interpreted based on the mixed valence states of Ru, as RuO_2 , RuO_3 , Ru_2O_3 etc. Although similar effects due to variable states has been observed recently by Raveau *et al.* on Cr and Co doping in $\text{Pr}_{0.5}\text{Ca}_{0.5}\text{MnO}_3$ it should be noted that Cr and Co ions aid only in the insulator metal transition and not in the charge transfer mechanism. A rapid disappearance of the charge ordering has been observed for doping as small as $x > 0.02$ for Cr and Co. Ru substitution on the other hand stabilizes magnetic ordering upto 15%. This can be attributed to the $4d$ metal character of Ru. It is now fairly well understood that the $3d$ electrons are more localized compared to $4d$ electrons. Therefore exchange interaction between Mn–O–Ru could be favored much more than any other transition metals. The presence of variable oxidation state of Ru is evident from the x-ray photoelectron spectrum (Fig. 3) of the Ru substituted bulk samples. The peaks corresponding to 483.0 and 486.2 eV suggests the presence of a possible redox couple involving $\text{Ru}^{3+}/\text{Ru}^{4+}$. This further suggests that an interplay of a mixed Zener pair such as $\text{Mn}^{3+}/\text{Mn}^{4+}$ – $\text{Ru}^{3+}/\text{Ru}^{4+}$ could be decisive in the charge ordering.

Figure 4 shows resistivity versus temperature plot for the parent $\text{La}_{0.7}\text{Sr}_{0.3}\text{MnO}_3$ film and the Ru substituted film, $\text{La}_{0.7}\text{Sr}_{0.3}\text{Mn}_{0.9}\text{Ru}_{0.1}\text{O}_3$. Although ferromagnetic ordering occurs well above the room temperature, R vs T plot for the bulk samples show a very broad transition and the metal-

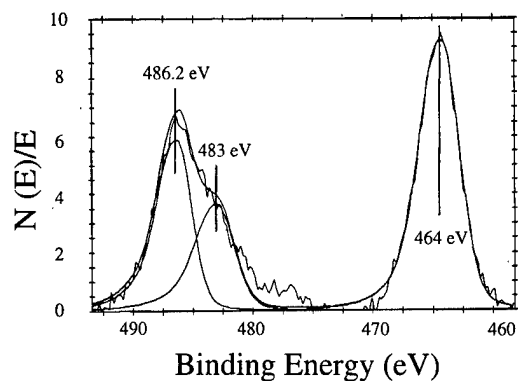


FIG. 3. X-ray photoemission spectroscopy (XPS) spectrum showing variable oxidation state for the Ru ($x=0.1$) bulk samples. The peaks corresponding to 483.0 and 486.2 eV suggests the presence of a possible redox couple involving $\text{Ru}^{3+}/\text{Ru}^{4+}$.

insulator transition occurs below 300 K. This is attributed to the role of the grain boundaries. However, upon subsequent annealing at elevated temperatures, well sintered pellets do show a M–I transition in accordance with the magnetic ordering temperature. The as-grown films of LSMO and Ru substituted films also show the same semiconducting behavior. In order to overcome this discrepancy, which could occur either from the enhanced role of grain boundaries or from loss of oxygen, the laser targets were sintered with 3% Ag_2O , to promote O_2 saturation of oxygen in the films during growth and annealing. Silver gets oxidized to AgO during laser ablation and during film growth AgO dissociates yielding its oxygen to the $\text{La}_{0.7}\text{Sr}_{0.3}\text{Mn}_{1-x}\text{Ru}_x\text{O}_3$ films. It is well known that addition of Ag_2O to bulk $\text{YBa}_2\text{Cu}_3\text{O}_7$ and self doped $\text{La}_{1-x}\text{MnO}_3$ increases the oxygen content in the

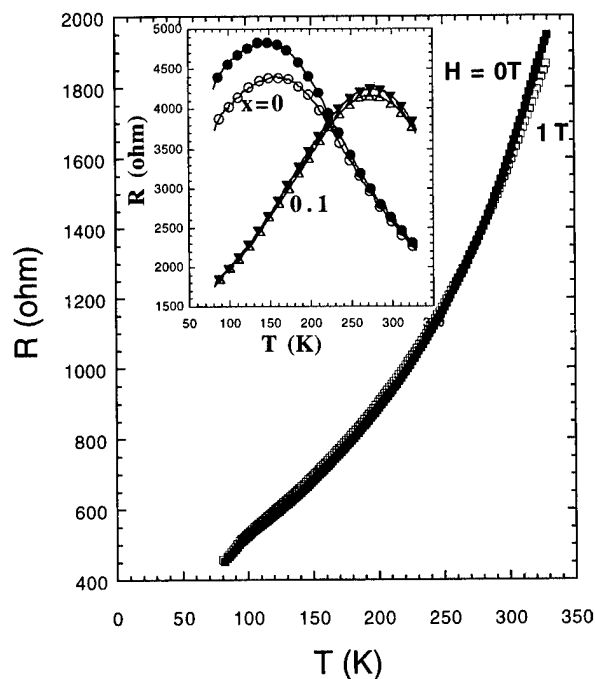


FIG. 4. Temperature dependence of the resistivity at $H=0$ and 1 T of 3% Ag doped $\text{La}_{0.7}\text{Sr}_{0.3}\text{Mn}_{1-x}\text{Ru}_x\text{O}_3$ ($x=0.1$) film. Inset shows the temperature dependence of the resistivity at $H=0$ and $H=1$ T for parent $x=0$ and $x=0.1$ without Ag doping (full symbol: $H=0$, empty symbol: $H=1$ T).

YBCO and $\text{La}_{0.7}\text{MnO}_3$ film, respectively.^{8,9} Consequently, 3% Ag containing LSMO and Ru substituted LSMO films showed a metal-insulator transition corresponding to the ferromagnetic ordering. In summary we have shown for the first time the exceptional ability of Ru to stabilize magnetic ordering in the $\text{La}_{0.7}\text{Sr}_{0.3}\text{Mn}_{1-x}\text{Ru}_x\text{O}_3$. It should be possible to apply such an effect to other perovskite manganites to evaluate the actual role played by Ru in ferromagnetism and to understand double exchange mechanism in mixed Zener pairs like $\text{Mn}^{3+/4+}$ - $\text{Ru}^{3+/4+}$.

ACKNOWLEDGMENTS

The authors thank Dr. Frank Ogeltree for recording the XPS data. This work was supported by the Director, Office

of Energy Research, Office of Basic Energy Sciences, Materials Sciences Division of the U.S. Department of Energy under Contract No. DE-AC03-76SF00098.

¹R. M. Kusters *et al.*, *Physica B* **155**, 362 (1989).

²R. Von Helmolt *et al.*, *Phys. Rev. Lett.* **71**, 2331 (1993).

³H. L. Ju *et al.*, *Appl. Phys. Lett.* **65**, 2108 (1994).

⁴C. Martin *et al.*, *J. Mater. Chem.* **6**, 1245 (1996).

⁵A. Maignan *et al.*, *Z. Phys. B* **102**, 19 (1997).

⁶B. Raveau *et al.*, *J. Solid State Chem.* **130**, 162 (1997).

⁷S. Sundar Manoharan *et al.*, *J. Appl. Phys.* **76**, 3923 (1994).

⁸D. Kumar *et al.*, *Appl. Phys. Lett.* **62**, 3522 (1993).

⁹S. Sundar Manoharan *et al.*, *J. Solid State Chem.* **117**, 420 (1995).

Angle-resolved magnetic and transport properties of $\text{Pr}_{0.7}\text{Sr}_{0.3}\text{MnO}_3$ thin films

J. Wolfman,^{a)} W. Prellier, Ch. Simon, and B. Mercey

Laboratoire Crismat, UMR CNRS 6508, ISMRA, Bd du Juin 14050, Caen cedex, France

In this communication, the variation of the resistance and of the magnetization with respect to the angle between the applied magnetic field and the substrate normal is discussed for a $\text{Pr}_{0.7}\text{Sr}_{0.3}\text{MnO}_3$ thin film at 30 K. An angular hysteresis is observed for these properties and this behavior is correlated with the magnetic domain wall motion. It is shown that the number of domain walls is controlled through the rotation of the applied magnetic field, and that these domain walls play an important part in the colossal magnetoresistance behavior of these films. Furthermore, a model describing the reversal of the magnetization with the rotation of the magnetic field has been developed. This model enables one to extract the dependence of the resistance upon the direction of the magnetization with respect to the crystalline axis. © 1998 American Institute of Physics. [S0021-8979(98)52511-X]

Manganese perovskites exhibiting colossal magnetoresistance (CMR) have drawn large interest these last few years, particularly for the realization of thin films with technological applicability.^{1,2} However, the microscopic mechanism of CMR is not clearly established. The double exchange (DE) interaction,³ which has been classically involved to explain CMR, relates the hopping rate of an e_g hole between two Mn sites to the angle between the respective moments of these Mn sites. Yet this interaction does not consider the direction of the moments with respect to the hopping direction (i.e., the local current direction) nor to the crystalline direction. Eckstein *et al.* have shown⁴ that the resistivity of a $\text{La}_{0.66}\text{Ca}_{0.33}\text{MnO}_3$ thin film depends upon the angle between the in-plane applied magnetic field and the current direction. They have compared this effect to the anomalous magnetoresistance (AMR) observed in metal thin films. However, this resistivity variation could also be related to the direction of the Mn moments with respect to the crystalline axis. In order to investigate this possibility, we have carried out magnetic and transport measurements on a $\text{Pr}_{0.7}\text{Sr}_{0.3}\text{MnO}_3$ thin film, while varying the direction of the applied magnetic field, \mathbf{B} , with respect to the crystalline axis, and keeping \mathbf{B} perpendicular to the current direction.

In situ annealed $\text{Pr}_{0.7}\text{Sr}_{0.3}\text{MnO}_3$ thin films were grown on LaAlO_3 substrates by pulsed laser deposition. The microstructure has been investigated by x-ray diffraction and transmission electron microscopy (TEM), and is discussed, with respect to the growth conditions, in details elsewhere.⁵ TEM has evidenced that the films crystallize epitaxially and with the space group Pbnm. The growth axis is in the $[110]$ direction ($a \approx b \approx \sqrt{2} a_p$) and the c axis is in the plane of the film ($c \approx 2a_p$). The pseudocubic structure of this material, identical to that obtained by rf sputtering,⁶ gives rise to the coexistence of domains with perpendicular c axis. The thickness of the films was determined to be 7000 Å (mechanical probe measurement).

Electrical measurements, registered by the four-probe method along the $[100]$ direction of LaAlO_3 , evidence a transition from an activated state ($E_a = 108$ meV) to a metallic state at $T = 240$ K as the temperature is decreased. This transition is correlated with the onset of ferromagnetic ordering at $T_c = 252$ K. These temperatures are comparable to those observed in bulk materials ($T_c = 259$ K).⁷ A magnetic field of 70 kG, applied in the plane of the film and perpendicular to the current I , gives rise to a CMR ($R_0/R_{70\text{ kG}}$) of 400% at $T = 200$ K. The spontaneous magnetization of this composition has been reported to be 564 emu/cm³ at 5 K (neutron diffraction⁷), i.e., locally, the magnetic moments are almost completely polarized. The maximum magnetization measured was 426 emu/cm³ in a magnetic field of 17 kG at 5 K, evidencing the existence of magnetic domains.

Magnetic and transport measurements presented below, were made at a constant field modulus B and at 30 K. The direction of \mathbf{B} was varied inside a plane containing the substrate $[010]$ direction and the substrate normal ($\mathbf{B} \perp \mathbf{I}$). Θ_B , defined as the angle between the \mathbf{B} direction and the substrate normal, was varied from -90° to $+90^\circ$. Furthermore, transport measurements were made as Θ_B was varied back to -90° .

The Θ_B dependence of the resistance and of the magnetization are given in Figs. 1 and 2, respectively, and will be discussed together. It should be noted that the measured magnetic moment, herein called M_{\parallel} (see Fig. 2), is the component of the global moment \mathbf{M} along the \mathbf{B} direction. Thus, if Θ_M is defined as the angle between \mathbf{M} and the substrate normal, $M_{\parallel} = M \cos(\Theta_M - \Theta_B)$. The observed decrease of M_{\parallel} at low fields [Fig. 2(b)] results from two effects. First, as \mathbf{M} rotates out of the plane of the film, the internal field H_i decreases due to the increase of the demagnetizing field H_d [$H_d = 4\pi M \cos(\Theta_M)$], leading to a decrease of M . Second, as \mathbf{B} rotates out of the plane, \mathbf{M} tends to follow \mathbf{B} , but is delayed with respect to \mathbf{B} owing to H_d , increasing $\Theta_M - \Theta_B$. At 600 G [Fig. 1(a)], the resistance presents a large hysteresis and two maximum. For $B = 2500$ G the hysteresis tends to be restricted around $\Theta_B = 0^\circ$. For a further B in-

^{a)} Author to whom correspondence should be addressed; electronic mail: wolfman@crismat.ismra.fr

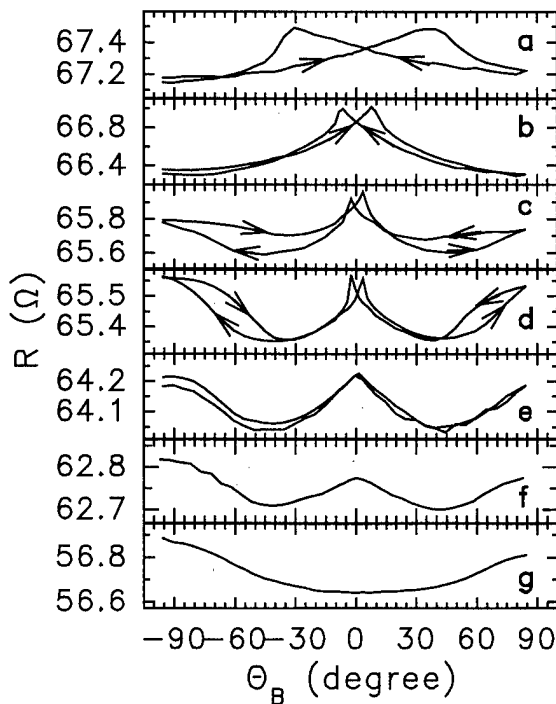


FIG. 1. Θ_B dependence of the resistance in an applied magnetic field equal to (a) 600 G, (b) 2.5 kG, (c) 4.5 kG, (d) 5.5 kG, (e) 12.5 kG, (f) 20 kG, and (g) 60 kG.

crease [Figs. 1(c) and 1(d)], a hysteresis develops for higher Θ_B , the resistance maximum moving toward $\Theta_B=0$. The maximum of resistance are expected to arise as \mathbf{M} is perpendicular to the substrate (maximum H_d). The fact that they do not appear for $\Theta_B=0$ denotes that \mathbf{M} is delayed with respect to \mathbf{B} . A decrease of the resistance is also observed for $B \geq 4500$ G around $\Theta_B=45^\circ$ and 0° . For $B > 7000$ G, the resistance is reversible with respect to Θ_B . The reversibility (or the irreversibility) of $R(\Theta_B)$ upon \mathbf{B} can be accounted for by the magnetic domain wall motion. The $M(B)$ curve at 30 K with $\mathbf{B} \parallel$ to the film (not shown) indeed presents hysteresis of the magnetization for $B < 3500$ G. This hysteresis, due to domain wall motion, is thus reversible (irreversible) for $B > 3500$ G ($B < 3500$ G). In the out-of-plane magnetic field

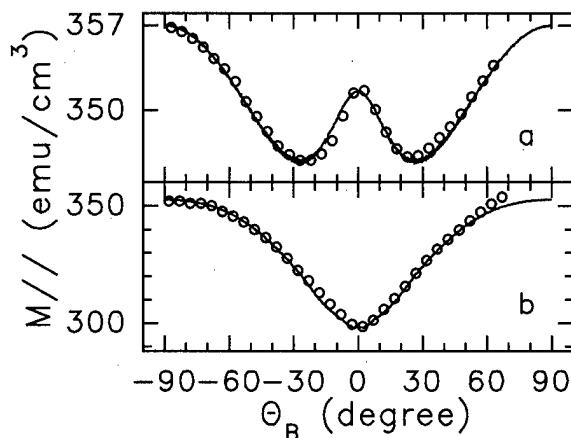


FIG. 2. Θ_B dependence of $M \parallel$ (see text) for $B=20$ kG (a) and $B=7.5$ kG (b) (circles) accompanied by the correspondent fits (solid lines) from the model (see text).

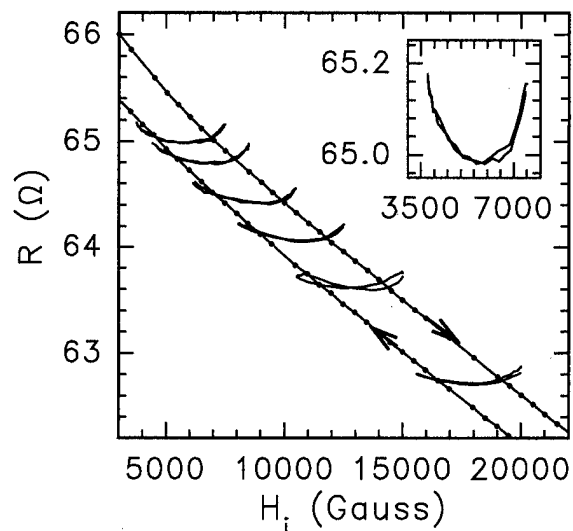


FIG. 3. H_i dependence of the resistance extracted from the $R(\Theta_B)$ curves (solid lines) in an applied \mathbf{B} of (from bottom to top): 20 kG, 15 kG, 12.5 kG, 10.5 kG, 8.5 kG, 7.5 kG. In insert, $B=7.5$ kG. Also shown in $R(H)$ while H is ramped from 0 G to 70 kG and back to 0 G (lines with dots) in the plane of the film.

set up described above, H_d is about 4000 G for $B=7500$ G and $\Theta_M=0$ [see Fig. 2(b) for $\Theta_B=-90^\circ$], leading to an internal field of about 3500 G.

To establish the correlation between Θ_M and Θ_B at a fixed applied field, we have developed a model describing $\mathbf{M}(\Theta_B)$, which takes into account the applied field \mathbf{B} , the demagnetizing field \mathbf{H}_d , and the magnetocrystalline energy. The magnetization was assumed to be homogeneous to define H_d . Furthermore, we assumed that \mathbf{M} is pointing in the direction of the internal field \mathbf{H}_i ($\mathbf{H}_i = \mathbf{B} + \mathbf{H}_d$). The total energy is minimized in a step-by-step calculation, varying Θ_B . This model does not account for hysteresis behavior, and was then used for $B > 7000$ G. A detailed description of the model will be published elsewhere. The calculations result in a good quantitative agreement as exemplified by that displayed in Fig. 2 (solid lines). Thus, the variation of Θ_M and H_i as functions of Θ_B can be calculated by this model.

We have represented the variation of the resistance extracted from the $R(\Theta_B)$ curves as a function of H_i in Fig. 3 (the minimum H_i is for $\Theta_B=0$ and corresponds to the maximum H_d). Figure 3 also displays the variation of the resistance upon a magnetic field \mathbf{H} [$R(H)$], while the latter is applied along the [010] direction of the substrate (i.e., $\mathbf{H}_i = \mathbf{H}$), and ramped from 0 to 70 kG and back to 0 G. It appears that the resistance extracted from the $R(\Theta_B)$ curves are much less sensitive to H_i than is $R(H)$. $R(H)$ is hysteretic, resulting from a different magnetic state before and after the application of a 70 kG field: the number of magnetic domains can be assumed to be different, giving rise to an increase (decrease) of the scattering rate of the carriers as the number of domain walls increases (decreases). The $R(H_i)$ curves deduced from the $R(\Theta_B)$ curves are reversible and join the two branches of the $R(H)$ curve as H_i varies. This indicates a nucleation of magnetic domains as \mathbf{M} rotates from $\Theta_M=0$ to $\Theta_M=90^\circ$. The dependence of the resistance upon H_i (see the inset of Fig. 3) results from the onset of two

antagonist effects. As \mathbf{M} rotates from $\Theta_M = 90$ to $\Theta_M = 0$, \mathbf{H}_i decreases, giving rise to a slight decrease of \mathbf{M} . From the DE point of view, decreasing \mathbf{M} leads to a decrease of the hopping rate, i.e., an increase of the resistance. However, it has been shown that, during the same rotation ($\Theta_M = 90 - \Theta_M = 0$), the number of domain walls decreases, tending to decrease the resistance. The competition between the decrease of both \mathbf{M} and the number of domain walls explains the not monotonous variation of R upon \mathbf{H}_i . The $R(\Theta_B = \pm 90)$ values are systematically higher than the $R(H)$ values from the upper branch (field increasing) and can be accounted for by the existence of a larger number of magnetic domain walls, since the $R(\Theta_B)$ curves were registered one after the other, increasing \mathbf{B} . Since R is not monotonous in \mathbf{H}_i , it appears that \mathbf{H}_i is not the primary factor in determining $R(\Theta_B)$.

To investigate the Θ_M dependence of the resistance, we have plotted in Fig. 4 the normalized $R(\Theta_M)$ curves for four different \mathbf{B} . These curves are field independent for $\Theta_M \geq 60^\circ$ and diverge for lower Θ_M values. Because of the co-existence of magnetic domains, there is some deviation of the local magnetic moment direction (Θ_m) with respect to the global moment direction (Θ_M); Θ_M is then the spatial average value of the Θ_m . In a plot displaying the total energy as a function of Θ_M for a fixed Θ_B , there appears two local minima with a difference energy ΔE . The probability of a local moment direction to shift from one local minimum to the other is related to ΔE : the lower ΔE is, the more easily Θ_m shifts (ΔE has to be compared to the energy cost E_n of a domain nucleation). The calculation shows that as Θ_B decreases, ΔE decreases and minimizes for $\Theta_B = 0$. Local magnetic direction fluctuations are then favored by a decrease of Θ_B (which implies a decrease of Θ_M). For a fixed Θ_B , ΔE depends also upon \mathbf{B} : the higher \mathbf{B} is, the higher ΔE is. In the field independent part of the $R(\Theta_M)$ curves, the deviations of Θ_m around Θ_M are negligible, which implies that ΔE is large compared to E_n . For $\Theta_B < 60^\circ$, the $R(\Theta_M)$ curves separate, and their different shapes are thus due to different ΔE (for a fixed Θ_B and Θ_M) owing to the different applied magnetic fields. If we assume that deviations of Θ_m around Θ_M are negligible for $\mathbf{B} = 60$ kG (i.e., $\Theta_M \cong \Theta_m \cong \Theta_B$), we can describe the real dependence of the resistance

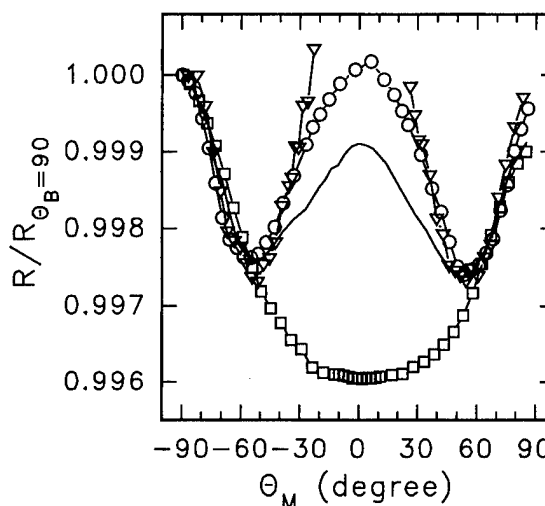


FIG. 4. Θ_M dependence of the resistance extracted from the $R(\Theta_B)$ curves, normalized to $R(\Theta_B = -90^\circ)$, in an applied \mathbf{B} of: 7.5 kG (triangles), 12.5 kG (circles), 20 kG (solid line) and 60 kG (squares).

upon \mathbf{M} as follows: the resistance is maximum when \mathbf{M} is in the film plane and is minimum when \mathbf{M} is perpendicular to the film. At lower fields, the fluctuations of Θ_m around Θ_M imply the creation of magnetic domain walls which take part in the observed increase of the resistance around $\Theta_B = 0$ (inset of Fig. 3). Finally, it has been shown that AMR is not the only anisotropic effect involved in CMR thin films; the resistance also depends upon the direction of the magnetization with respect to the crystalline axis.

¹R. M. Kusters, J. Singleton, D. A. Keon, R. M. Greedy, and W. Hayes, *Physica B* **155**, 362 (1989).

²S. Jin, H. M. O'Bryan, T. H. Tiefel, M. Mc Cormack, and W. W. Rhodes, *Appl. Phys. Lett.* **66**, 382 (1995).

³P. D. De Gennes, *Phys. Rev.* **118**, 141 (1960).

⁴I. Bozovic, J. N. Eckstein, J. O'Donnell, M. Onellion, and M. S. Rzechowski, *Appl. Phys. Lett.* **69**, 9 (1996).

⁵J. Wolfman, W. Prellier, B. Mercey, and Ch. Simon (unpublished).

⁶B. Mercey, Ph. Lecoeur, M. Hervieu, J. Wolfman, Ch. Simon, H. Murray, and B. Raveau, *Chem. Mater.* **9**, 1177 (1997).

⁷K. Knirzeck, Z. Jirak, E. Pollert, and F. Zounova, *J. Solid State Chem.* **100**, 292 (1992).

Fabrication of $\text{YBa}_2\text{Cu}_3\text{O}_{7-\delta}/\text{SrTiO}_3/\text{La}_{0.7}\text{Sr}_{0.3}\text{MnO}_{3-\delta}$ junctions for the control of supercurrent by spin-polarized quasiparticle current injection

R. M. Stroud,^{a)} J. Kim, C. R. Eddy, D. B. Chrisey, J. S. Horwitz, D. Koller, M. S. Osofsky, and R. J. Soulen, Jr.

Naval Research Laboratory, Washington, DC 20375

R. C. Y. Auyeung

S. F. A. Inc., Largo, Maryland 20774

Supercurrent suppression by the injection of spin-polarized quasiparticle current from a ferromagnet into a superconductor is demonstrated in $\text{YBa}_2\text{Cu}_3\text{O}_{7-\delta}/\text{SrTiO}_3/\text{La}_{0.7}\text{Sr}_{0.3}\text{MnO}_{3-\delta}$ junctions at 77 K. Negative current gains as large as 35 have been observed. The magnitude of the effect depends on the net polarization of the injection current, film resistivities, barrier microstructure, and injection geometry. Fabrication of the junctions is discussed in terms of optimizing these parameters for maximum supercurrent suppression. © 1998 American Institute of Physics.

[S0021-8979(98)31911-8]

I. INTRODUCTION

Trilayer ferromagnet-chemical barrier-high temperature superconductor junctions, called spin injection devices, are a new direction in superconducting transistors. The spin injection devices operate by the disruption of Cooper pair formation in the superconductor film due to the injection excess spin state quasiparticles from the ferromagnetic film. A small injection current can suppress a large supercurrent, producing a large negative current gain.

The spin injection device is the natural extension of earlier work on injection of spin-polarized currents into normal metals¹ and low temperature superconductors,² and unpolarized quasiparticle injection into superconductors.³ However, the possibility of transistorlike devices based on spin-polarized quasiparticle injection was only recently investigated in a study of permalloy/Au/ $\text{YBa}_2\text{Cu}_3\text{O}_{7-\delta}$ junctions.⁴ All-oxide spin injection devices consisting of $\text{La}_{0.67}\text{Sr}_{0.33}\text{MnO}_3/\text{La}_2\text{CuO}_4/\text{DyBa}_2\text{Cu}_3\text{O}_7$ (Ref. 5) and $\text{La}_{0.7}\text{Sr}_{0.3}\text{MnO}_{3-\delta}/\text{SrTiO}_3/\text{YBa}_2\text{Cu}_3\text{O}_{7-\delta}$ (Ref. 6) junctions have since been investigated.

The potential advantages of superconducting transistors have inspired many different types of devices.⁷ None has yet to exhibit all of the necessary characteristics for bridging the gap between research tool and useful application. Each fails in either reproducible fabrication, gain, power handling, or speed. Spin injection devices offer the potential for increased speed and gain compared to existing devices.

Spin injection devices are also an exciting system in which to study nonequilibrium superconductivity and spin dynamics. It should be possible to measure the spin diffusion length of a superconductor simply by varying the film thickness in these devices. Devices with film thickness greater than the spin diffusion length would exhibit less supercurrent suppression because spin flip scattering would decrease the net polarization of the injected quasiparticles. For anisotropic

superconductors such as $\text{YBa}_2\text{Cu}_3\text{O}_{7-\delta}$, the spin diffusion length could be measured along each axis independently by changing the injection direction.

The suppression of supercurrent by spin injection must be unambiguously demonstrated before spin injection devices can become either useful superconducting transistors or an arena for the investigation of nonequilibrium superconductivity. In this article, supercurrent suppression in a $\text{YBa}_2\text{Cu}_3\text{O}_{7-\delta}/\text{SrTiO}_3/\text{La}_{0.7}\text{Sr}_{0.3}\text{MnO}_{3-\delta}$ trilayer junction is demonstrated, and the fabrication and material issues necessary for producing the optimum spin injection effect are outlined.

II. PROCEDURE

$\text{La}_{0.7}\text{Sr}_{0.3}\text{MnO}_{3-\delta}$ (LSMO) films were deposited on (100) SrTiO_3 single crystal substrates by pulsed laser deposition (PLD). Typical deposition conditions were: a 750 °C substrate temperature, a 200 mT O_2 atmosphere, and 2 J/cm² laser fluence. The resultant 1000 Å thick films were patterned into 100–150 μm wide microbridges. The patterning was performed using wet-etch photolithography, with a 100% HCl etch solution. After patterning, the LSMO films were annealed at 800 °C to remove surface impurities and lower the contact resistance.

The insulating barrier and superconducting films were deposited sequentially through a rectangular shadow mask by PLD. The barrier was either SrTiO_3 (STO) or CeO_2 , 50–400 Å thick, deposited at 750 °C in 300 mT O_2 . The superconductor was $\text{YBa}_2\text{Cu}_3\text{O}_{7-\delta}$ (YBCO), 500–1000 Å thick, deposited at 790 °C in 320 mT O_2 . The YBCO was patterned into a microbridge by wet-etch photolithography, to produce a YBCO-LSMO cross with a square junction area of 10⁴ μm². A schematic of the device is shown in Fig. 1.

The suppression of YBCO supercurrent was determined by measuring the transport critical current at 77 K as a function of current through the junction.

^{a)}Electronic mail: rms@ccf.nrl.navy.mil

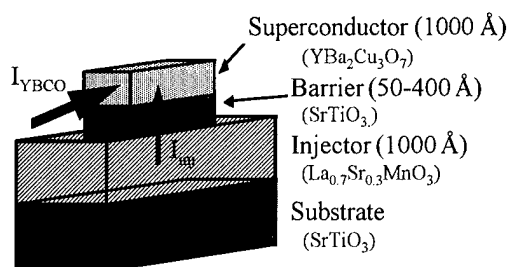


FIG. 1. Junction schematic.

III. RESULTS

The suppression of critical current in a YBCO/400 Å STO/LSMO device is shown in Fig. 2. For an injection current (I_{inj}) of 2 mA, the critical current of the YBCO (I_c) is reduced from 97 to 27 mA.

The current gain of the device is obtained from the slope of the plot of critical current versus injection current (Fig. 3), $\Delta I_c / \Delta I_{inj}$. For the 400 Å barrier device, the gain was -35 . In comparison, the suppression of critical current by resistive heating due to a current along the axis of the microbridge in the LSMO film, i.e., no injection, results in a gain of -6 .

IV. DISCUSSION

The key issue for operation of the spin-polarized quasiparticle injection devices is the delivery of highly polarized injection current into a narrow region of the superconductor. This provides the greatest density of excess spin state quasiparticles to suppress the superconductivity. Suppression of the superconductivity by dynamical effects not related to spin-polarized injection, such as resistive heating, must be minimized or eliminated to obtain a clear interpretation of the spin injection effect. As shown in Fig. 2, however, both spin-polarized injection and resistive heating contribute to

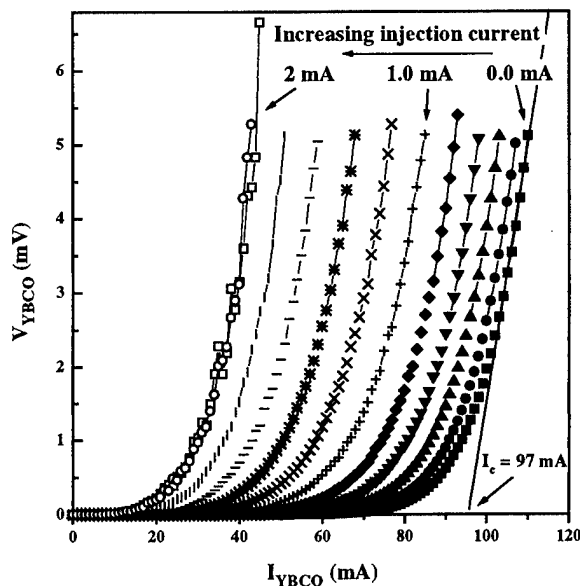


FIG. 2. Voltage vs $\text{YBa}_2\text{Cu}_3\text{O}_{7-\delta}$ supercurrent. The critical current decreases from 97 mA for no injection current to 27 mA for an injection current of 2 mA.

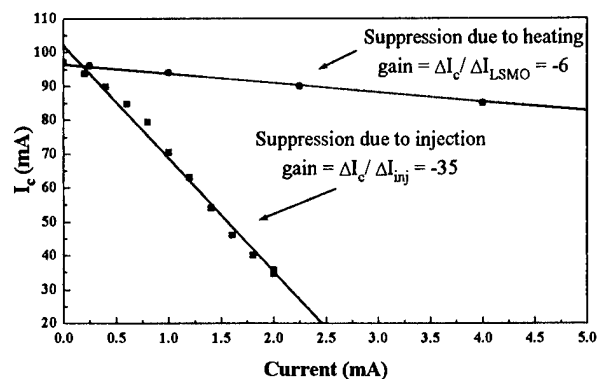


FIG. 3. Critical current vs injection current.

the observed negative current gain (Fig. 3). Careful consideration of the materials processing and device design parameters is needed so that the spin injection effect may be quantified, understood, and optimized.

There are several ways in which the spin-polarized current can be injected. Depending on the particular insulating barrier thickness and microstructure, the injection will occur by tunneling, capacitive coupling, defect mediated processes such as pin holes or conduction at grain boundaries, or some combination of these processes. Only tunneling, pin holes, or grain boundary current will preserve a high degree of spin polarization; capacitive coupling does not preserve the polarization because no current flows from the ferromagnet to the superconductor. For thick barriers (100 Å), tunneling is not significant, so the spin-polarized injection current must be defect-mediated transport. For very thin barriers (<100 Å), there may be both pin hole injection current and tunneling injection current. For the 400 Å thick barrier device, the asymmetric s -shape of the barrier current-voltage (I - V) curve (Fig. 4) indicates that the transport is defect-mediated, possibly due to pin holes and interface defects.

The maximum suppression will occur when the current density of the spin-polarized quasiparticles is highest. High injection current densities relative to the YBCO supercurrent can be achieved by minimizing the width of the LSMO microbridge relative to the YBCO microbridge width. Increasing the injection current to obtain high current density is not desirable, because Joule heating from a large current could raise the temperature of the superconductor, and lower the critical current. For this reason we have adopted the YBCO/STO/LSMO cross-stripe sandwich geometry. The junction is

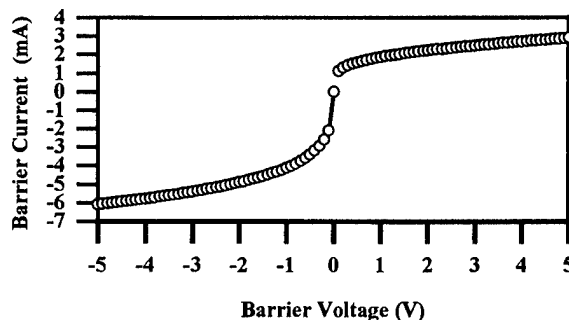


FIG. 4. Current vs voltage for the trilayer junction.

constrained to a rectangle defined by the overlap of the LSMO and YBCO microbridges. No other contact is made between the LSMO and YBCO, except potentially along the LSMO step edges, if the barrier does not provide uniform coverage. The step edges must be very gradual to provide uniform coverage with very thin barriers. The slope of the wet-etched LSMO edge measured by profilometry was $0.1 \mu\text{m}/10 \mu\text{m} = 0.01$, sufficiently gradual to uniform coverage by the barrier.

The insulating barrier has two functions—to chemically protect the superconductor and to spread the injection current so that it can suppress the conductivity uniformly. If the superconductor itself is nonuniform, suppression will occur preferentially along weak links. Only an insulating barrier can ensure that the injection current reaches the weak links; a metallic barrier would allow the injection current to find the path of least resistance around the weak links. It is possible for the device to operate by injection through a distribution of pin holes in the barrier into a network of weak links, and because the area of the pinholes is small compared to the junction area the current density could be further increased.

The maximum current gain due to spin injection will occur in devices with 100% spin-polarized injection, but 100% spin-polarized injection current is not required in order to observe a spin injection effect.⁴ No disruption of the superconductivity will result from minority spin state quasiparticles, assuming they form Cooper pairs with majority spin state quasiparticles and the energy released in pair formation is removed from the superconductor in the form of phonons. The remaining excess majority spin state quasiparticles will continue to suppress the superconductivity. In this case, a larger injection current would be required to observe the suppression because a reduced fraction of the quasiparticles would be available to suppress the superconductivity.

The net polarization of the injection current in the superconductor depends on the net polarization at the ferromagnet and the number of spin flip scattering events that occur between the ferromagnet and superconductor. Complete polarization of the injection current is only possible if the injection source is 100% polarized, and no spin flip scattering events occur in the barrier, or at the LSMO-STO and STO-YBCO interfaces. Even if the injection current is 100% polarized at the source, a reduction in the spin polarization could occur at the film interfaces as a result of spin glass formation due to interdiffusion or oxygen vacancies. Spin flip events at bulk defects in the barrier are also possible.

Because spin scattering cannot be completely eliminated in the barrier and at interfaces the injection current in the

superconductor will never have 100% net polarization. However the polarization is maximized through the use of a highly polarized injector, such as LSMO, and a thin chemical barrier. In earlier spin injection experiments, the injection source was permalloy, which provided a maximum polarization of 40%, which was sufficient to observe supercurrent suppression. Half metallic ferromagnets, such as CrO_2 or LSMO and other rare earth manganites, are ideal choices for injectors because they carry 100% spin-polarized current, and they are more compatible for growth and processing with YBCO than traditional metal ferromagnets because of their oxide structures.

A major obstacle to quantifying the suppressive effect of the spin polarization of the injected current is the similar suppression produced by simple resistive heating. From the current gain plotted in Fig. 3, it is clear that heating is a significant effect in the junction with a 400 \AA thick barrier, even when the current is restricted to the LSMO. To lower the heating, the input power must be lowered. This can be achieved by decreasing resistances of the barrier, the injector, and the interfaces. The input power could also be lowered by decreasing the injector microbridge width, producing higher current density at lower injection currents.

V. SUMMARY

The control of superconductivity in $\text{YBa}_2\text{Cu}_3\text{O}_{7-\delta}$ by injection of spin-polarized quasiparticle current offers the possibility of a new type of superconducting transistor. Supercurrent suppression has been demonstrated in $\text{YBa}_2\text{Cu}_3\text{O}_{7-\delta}/\text{SrTiO}_3/\text{La}_{0.7}\text{Sr}_{0.3}\text{MnO}_{3-\delta}$ junctions. Current gains as large as -35 have been observed. The materials and fabrication issues that affect the size of the observed gain, including the mode of current injection, the polarization of the injection current, the structure of the barrier, device geometry, and resistive heating have been investigated.

¹M. Johnson and R. H. Silsbee, Phys. Rev. B **37**, 5326 (1988).

²M. Johnson, Appl. Phys. Lett. **65**, 1460 (1994).

³T. Wong, J. T. C. Yeh, and D. N. Langenberg, Phys. Rev. Lett. **37**, 150 (1976).

⁴D. B. Chrisey, M. S. Osofsky, J. S. Horwitz, R. J. Soulen, Jr., B. Woodfield, J. Byers, G. M. Daly, P. C. Dorsey, J. M. Pond, T. W. Clinton, and M. Johnson, IEEE Trans. Appl. Supercond. **7**, 2067 (1997).

⁵V. A. Was'ko, V. A. Larkin, P. A. Kraus, K. R. Nikolaev, D. E. Grup, C. A. Nordman, and A. M. Goldman, Phys. Rev. Lett. **78**, 1134 (1997).

⁶R. J. Soulen, M. S. Osofsky, D. B. Chrisey, J. S. Horwitz, R. Stroud, J. M. Byers, B. F. Woodfield, G. M. Daly, T. W. Clinton, M. Johnson, and R. C. Y Auyeung, Proceedings of 1997 European Conference on Superconductors (in press).

⁷J. Mannhart, Semicond. Sci. Technol. **9**, 92 (1996).

Magnetism and colossal magnetoresistance in the compound $\text{Sr}_{14}\text{MnSb}_{11}$

D. J. Webb,^{a)} R. Cohen, P. Klavins, and R. N. Shelton

Department of Physics, University of California, One Shields Avenue, Davis, California 95616

J. Y. Chan and S. M. Kauzlarich

Department of Chemistry, University of California, One Shields Avenue, Davis, California 95616

The magnetization and resistivity of single crystals of the ferromagnetic compound $\text{Sr}_{14}\text{MnSb}_{11}$ are measured as functions of magnetic field, temperature, and crystal orientation. The uniform magnetic susceptibility is used to identify $T_C = 39$ K. The ferromagnetic state is found to have a hard axis (c axis) anisotropy. The resistivity data place the compound in the class of colossal magnetoresistance (CMR) materials such as Ca-doped LaMnO_3 . The data are also compared to the related CMR material $\text{Eu}_{14}\text{MnSb}_{11}$. © 1998 American Institute of Physics.

[S0021-8979(98)45211-3]

I. INTRODUCTION

Recently, we have shown that the compounds $\text{Eu}_{14}\text{MnSb}_{11}$ ¹ and $\text{Eu}_{14}\text{MnBi}_{11}$ ² can be classified as colossal magnetoresistance (CMR) materials.³ In CMR materials, the magnetoresistance is much larger than for simple metallic ferromagnets, such as Fe and Ni, and is largest in a region of temperature where there are large ferromagnetic spin fluctuations and T_C appears to mark a metal-insulator transition. These two compounds are part of a large set of isostructural compounds with the formula $\text{A}_{14}\text{MPn}_{11}$ ($\text{A} = \text{Ca}, \text{Sr}, \text{Ba}, \text{Eu},$ or Yb , $\text{M} = \text{Al}, \text{Ga}, \text{In},$ or Mn , and $\text{Pn} = \text{P}, \text{As}, \text{Sb},$ and Bi).⁴ They crystallize in the space group $I4_1/acd$ and have a tetragonal unit cell with eight formula units in the cell. This series of compounds with $\text{M} = \text{Al}, \text{Ga},$ or In belong to the class of Zintl compounds.⁵ Zintl phases are composed of electropositive ions which donate electrons to the more electronegative components forming covalent bonding networks or closed shell anions. Because Zintl compounds are salts, the main group Zintl phases are all expected to be insulators (possibly with small band gaps); in particular, the main group compounds isostructural to $\text{Sr}_{14}\text{MnSb}_{11}$ are all known⁶ to be semiconducting. Since all of these phases are isostructural, one might expect the Mn compounds to be semiconductors with local moments on the Mn. However, most of the compounds containing the transition metal Mn are conducting, have ferromagnetic exchange coupling, and display an intimate connection between the conductivity and the magnetism. The conductivity is unexpected because the materials are salts made up of isolated cations and isolated anion complexes and conducting paths are not apparent. In addition, the high magnetic transition temperatures are unexpected because the Mn^{3+} ions, which are tetrahedrally coordinated with four Pns, are quite isolated from their neighboring Mn ions, about 11 Å interionic spacing for the Mn.

The importance of the Mn to both the magnetism and the conductivity is illustrated in an examination of the gross properties of the series, of which the alkaline earth contain-

ing compounds have been studied^{7,8} in the greatest detail. There is a metal-insulator (M-I) boundary between the $\text{Pn} = \text{As}$ compounds [semiconductors with resistivity $\rho(T = 300 \text{ K}) > \text{few thousand } \mu\Omega \text{ cm}$ and negative $d\rho/dT$] and the $\text{Pn} = \text{Sb}$ compounds [semimetals with $\rho(T = 300 \text{ K})$ of order $1000 \mu\Omega \text{ cm}$ but $d\rho/dT$, still slightly negative at high T]. The $\text{Pn} = \text{Bi}$ compounds are the most conducting [$\rho(T = 300 \text{ K})$ of order $100 \mu\Omega \text{ cm}$ and $d\rho/dT$, positive] of all but can still be considered to be near a M-I boundary. Near neighbor Mn spins in the conducting compounds all have fairly strong ferromagnetic exchange coupling and order at temperatures between 10 and 100 K. The Mn spins in the semiconducting As compounds have an exchange coupling which is quite weak (Curie-Weiss $\theta < 0.5 \text{ K}$); however, under hydrostatic pressure even these As compounds have Mn moments coupled ferromagnetically⁹ with ($-\theta > 10 \text{ K}$). In this article we examine the magnetization and resistivity of one of these compounds, $\text{Sr}_{14}\text{MnSb}_{11}$, and compare with $\text{Eu}_{14}\text{MnSb}_{11}$.

II. DETAILS OF THE EXPERIMENTS

The measurements were performed on needlelike ($0.1 \text{ mm} \times 0.1 \text{ mm} \times 1 \text{ mm}$) single crystals with the needle long axis coincident with the tetragonal c axis. These needles were grown from the elements by loading stoichiometric quantities of the elements into Ta tubes in a drybox. The tubes are welded shut and then sealed in quartz tubes under vacuum. The sample is then placed in a zone furnace in a temperature gradient of about 10°C/cm at an average $T = 1000\text{--}1250^\circ\text{C}$ for several days. The sample was examined in a drybox and appropriate needles were removed for measurement.

The magnetization data were acquired with a quantum design superconducting quantum interference device (SQUID) magnetometer with a temperature range of $2 \text{ K} < T < 300 \text{ K}$ and a magnetic field range of $-5 \text{ T} < H < 5 \text{ T}$. A single needle shaped crystal was mounted at the center of an Al rod about 12 cm long which is then sealed under vacuum inside a thin quartz tube. The needle axis was oriented either parallel to the applied magnetic field (H_{para}) or perpendicular (H_{perp}). The absolute value of the magnetiza-

^{a)}Electronic mail: webb@physics.ucdavis.edu

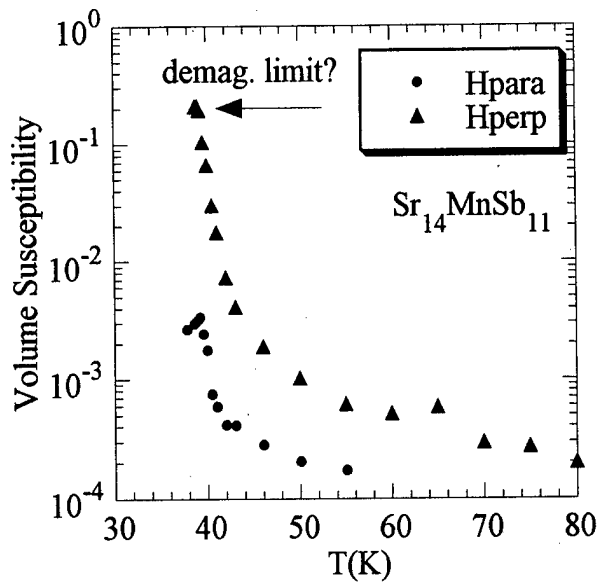


FIG. 1. Volume magnetic susceptibility (emu/cm^3) of a single crystal of $\text{Sr}_{14}\text{MnSb}_{11}$ as a function of the temperature for two orientations of the applied field in relation to the c axis of the crystal.

tion is determined by the volume of the crystal which is a quantity we cannot measure well. Given this problem we have chosen to normalize the magnetization data so that the saturation magnetization, M_s , at the lowest T is appropriate for the $4 \mu_B$ present on the Mn^{+3} ion. This is consistent with M_s for the powder samples we have measured^{6,7} in the past. The electrical resistivity measurements were performed in the same instrument in the same orientation of the crystal with the same ranges of temperature and field. Four leads were attached along the length of the crystal with silver paint for the resistivity measurements. Because of the geometry of the crystal the current, I , is always applied along the c axis of the tetragonal cell but magnetic field may be applied either parallel or perpendicular to I .

III. DC MAGNETIZATION AND SUSCEPTIBILITY

In Fig. 1 we show χ as a function of T both for H_{para} to the c axis and H_{perp} . We will call these χ_{para} and χ_{perp} , respectively. The data with H_{para} do not need a demagnetization correction and the data for H_{perp} have not been corrected for demagnetization because the cross-sectional area is not simple and is not constant over the length of the sample. One sees that there is a very strong anisotropy with the c axis being a magnetic hard axis. Note that this crystal-line anisotropy dominates the shape anisotropy of the needle. This is in contrast to $\text{Eu}_{14}\text{MnSb}_{11}$ for which the c axis was an easy axis. One can identify $T_C = 39$ K, from these data, as the temperature where there is a kink in the measured $\chi_{\text{perp}}(T)$. If the assumption is made that χ_{perp} is demagnetization limited below T_C then the demagnetization factor is 0.2 which is probably reasonable but slightly larger than the expected value of 0.16 for the thin wire geometry. The irregular shape of the crystal, the large demagnetization factor, and the scatter in the magnetic moment data on these very tiny single crystals make a detailed analysis of critical phe-

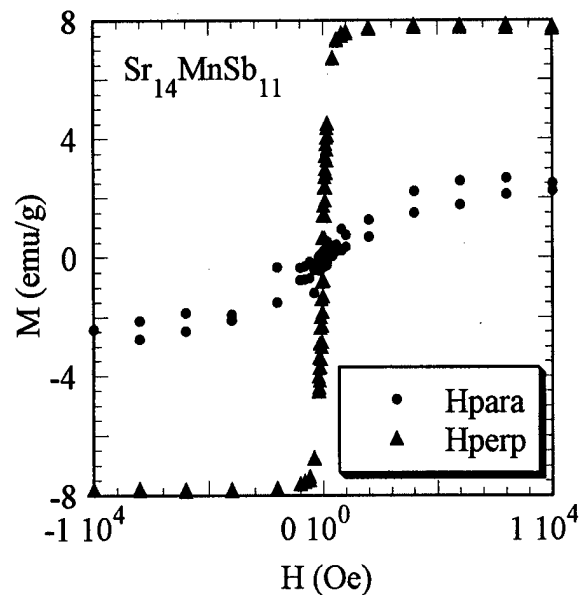


FIG. 2. Magnetic hysteresis loops at $T = 5$ K for two orientations of a single crystal of $\text{Sr}_{14}\text{MnSb}_{11}$.

nomena in these samples problematic and we do not attempt it here. In Fig. 2 we show the hysteresis loops for H_{para} and H_{perp} . Again, one sees the results of the magnetically hard c axis.

IV. ELECTRICAL RESISTIVITY

Figure 3 shows the measured resistivity as a function of T and H applied perpendicular to the c axis, that is, H is applied along an easy direction. The zero field resistivity rises as T is decreased then drops at or near T_C in a manner which is roughly similar to many other CMR materials³ including $\text{Eu}_{14}\text{MnSb}_{11}$. This behavior is generally characterized as a semiconductor to metal transition which occurs at or near T_C . This characterization is made clearer in Fig. 4

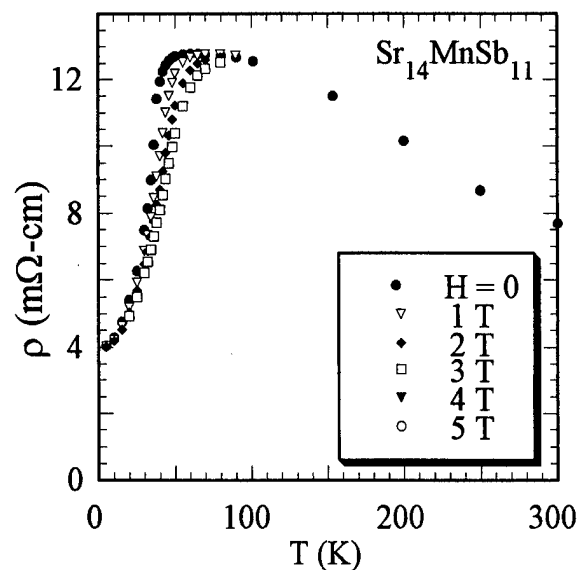


FIG. 3. Resistivity of $\text{Sr}_{14}\text{MnSb}_{11}$ as a function of temperature for six values of magnetic field applied in the easy direction (H_{perp}).

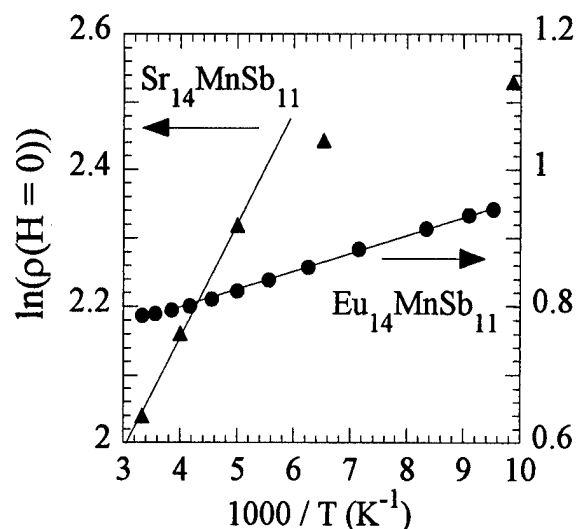


FIG. 4. Natural logarithm of the resistivity of single crystals of $\text{Sr}_{14}\text{MnSb}_{11}$ and $\text{Eu}_{14}\text{MnSb}_{11}$ as a function of $1000/T$. Each of these compounds has an activated conductivity at high temperatures.

which shows that the high temperature zero field resistivity of $\text{Sr}_{14}\text{MnSb}_{11}$ follows, at highest T , the simple form for activated conduction. This figure also shows the data for $\text{Eu}_{14}\text{MnSb}_{11}$ which obey the simple form for T nearly to T_C . We note that the values of the activation energy one gets from Fig. 4 are quite small (few meV). It seems likely that these are not band gap energies but the results of electron-electron correlations as in coulomb gap materials and/or Kondo insulators. In any case, this form is inconsistent with variable range hopping conductivity⁴ seen in the La manganites. Variable range hopping is not expected in this family of Zintl compounds because they are ordered stoichiometric compounds.

V. SUMMARY

We have shown that the compound, $\text{Sr}_{14}\text{MnSb}_{11}$, has a very large negative magnetoresistance in the vicinity of the Curie temperature. In addition, there appears to be a change from semiconductorlike behavior in the electron transport at high T to metallic behavior at low T to metallic behavior at low T . For these reasons, we place this compound in the class of CMR materials.

ACKNOWLEDGMENTS

This research was supported by the National Science Foundation under Grant Nos. DMR-95-05565 (J.Y.C. and S.M.K.) and DMR-97-01735 (P.K. and R.N.S.) and by the Campus Laboratory Collaborations Program of the University of California (S.M.K. and D.I.W.).

¹J. Y. Chan, S. M. Kauzlarich, P. Klavins, R. N. Shelton, and D. J. Webb, *Chem. Mater.* **9**, 3132 (1997).

²J. Y. Chan, S. M. Kauzlarich, P. Klavins, R. N. Shelton, and D. J. Webb, *Phys. Rev. B* (in press).

³For a review and selected references see; A. P. Ramirez, *J. Phys.: Condens. Matter* **9**, 8171 (1997).

⁴For a review see; S. M. Kauzlarich, in *Chemistry, Structure, and Bonding of Zintl Phases and Ions*, edited by S. M. Kauzlarich (VCH, New York, 1996), p. 245.

⁵H. Schäfer, *Annu. Rev. Mater. Sci.* **15**, 1 (1985).

⁶S. M. Kauzlarich, M. M. Thomas, D. A. Odink, and M. M. Olmstead, *J. Am. Chem. Soc.* **113**, 7205 (1991); S. L. Brock, L. J. Weston, M. M. Olmstead, and S. M. Kauzlarich, *J. Solid State Chem.* **107**, 513 (1993).

⁷T. Y. Kuromoto, S. M. Kauzlarich, and D. J. Webb, *Chem. Mater.* **4**, 435 (1992).

⁸A. Rehr, T. Y. Kuromoto, S. M. Kauzlarich, J. Del Castillo, and D. J. Webb, *Chem. Mater.* **6**, 93 (1994).

⁹J. Del Castillo, D. J. Webb, S. M. Kauzlarich, and T. Y. Kuromoto, *Phys. Rev. B* **47**, 4849 (1993).

Polycrystalline and laminated $\text{La}_{0.7}\text{Sr}_{0.3}\text{MnO}_3$ films made by pulsed laser deposition

F. J. Cadieu,^{a)} R. Rani, X. R. Qian, C. F. Cadieu, and Li Chen
Physics Department, Queens College of CUNY, Flushing, New York 11367

W. Mendoza and S. A. Shaheen
MARTECH, Florida State University, Tallahassee, Florida 32306

Highly smooth and particulate free relatively thick polycrystalline $\text{La}_{0.7}\text{Sr}_{0.3}\text{MnO}_3$ films out to 6 μm thick have been grown by shadowed pulse laser deposition at 30 Hz (248 nm, 500 mJ). Such films exhibited a low field and high field magnetoresistance as previously reported by a number of groups. Multilayer films made with alternating 8-nm-thick barium ferrite and 16-nm-thick $\text{La}_{0.7}\text{Sr}_{0.3}\text{MnO}_3$ laminations exhibited the same high field response, but did not exhibit the low field magnetoresistance component. This is consistent with the low field component arising from intergrain scattering. Patterned films have been simultaneously deposited onto *R*-plane, *C*-plane, and polycrystalline alumina substrates. The films were postannealed at 750 K in 200 Torr O_2 for 45 min. The low field magnetoresistance was most pronounced for the single layer films made onto *C*-plane sapphire and then polycrystalline alumina substrates. The films exhibited a broad maximum in resistivity versus temperature at 162, 210, and 218 K for films grown onto *R*-plane sapphire, *C*-plane sapphire, and alumina substrates, respectively. Restricted grain size films made with $\text{La}_{0.7}\text{Sr}_{0.3}\text{MnO}_3$ and barium ferrite laminations exhibited a single linear magnetoresistance response of $-0.43\%/k\text{Oe}$ for in plane applied fields of $\pm 10 k\text{Oe}$. © 1998 American Institute of Physics. [S0021-8979(98)45311-8]

I. INTRODUCTION

Although La-manganite bulk samples exhibit a large magnetoresistance at relatively low temperatures,¹ the narrowness of the transition region as a function of temperature, and the high multi-Tesla magnetic field values required for saturating the magnetoresistance have precluded applications. Over the last several years a number of groups have reported broadened transitions for polycrystalline films with enhanced low field magnetoresistance.²⁻⁵ The enhanced low field magnetoresistance in polycrystalline films has been attributed to either intergrain spin polarized tunneling,³ or to spin-dependent scattering of polarized electrons at the grain boundaries.⁵ An important attribute of the polycrystalline samples is that magnetoresistive response extends over a wide temperature range. Such a wide temperature response of the magnetoresistance is critical to the development of the La manganites for technological devices. The Sr substituted $\text{La}_{0.7}\text{Sr}_{0.3}\text{MnO}_3$ for polycrystalline samples exhibits a broad transition with appreciable magnetoresistance in the vicinity of room temperature and consequently is attractive for magnetic sensor applications. For device applications it is also necessary that other materials such as soft magnetic films be deposited which exhibit compatible processing properties with the La manganites. This presents processing problems since oxide materials generally require relatively high processing temperatures compared to metallic magnetic films. In this article we demonstrate two things necessary for La-manganite device applications. One is that the low magnetic field response of $\text{La}_{0.7}\text{Sr}_{0.3}\text{MnO}_3$ films can be controlled, and

linearized by using layered film strips. The low field magnetoresistance was made linear without changing the temperature of the resistance maximum by laminating the $\text{La}_{0.7}\text{Sr}_{0.3}\text{MnO}_3$ deposit with highly resistive barium hexaferrite film layers. The second is that high magnetization and highly corrosion resistant $\text{Fe}_{0.8}\text{Co}_{0.2}$ films can be deposited in conjunction with the La manganites to provide magnetic flux paths as well as electrical contacts. In previous studies polycrystalline versus epitaxial films have been studied.⁴ In this study polycrystalline samples have been studied in which the intergrain coupling has been changed by laminating with resistive barium ferrite layers to isolate the grains. Single and multilayer films were made by pulsed laser deposition (PLD) that exhibit large differences in the temperature of the resistance maximum as well as different low field magnetoresistive responses.

II. EXPERIMENT

PLD utilizing a Lambda Physik 305Fi excimer laser has been used to deposit La-manganite films from a set of bulk compound targets. In addition, a multitarget carousel has been used in some cases to allow the alternate deposition of barium hexaferrite films in conjunction with La-manganite film layers. The films were deposited using a wavelength of 248 nm, pulse energy of 500 mJ, at 30 Hz, with an estimated pulse width of 15 ns. A shadow mask has been used to shield part of the substrate during the PLD process. In this manner the number of particulates reaching the substrate in and out of the shadow region could be observed. Very fine grained, $<300 \text{ \AA}$, highly (130) textured films were grown in 120 mTorr O_2 behind a shadow plate at an average rate of 6 $\text{\AA}/\text{s}$

^{a)}Electronic mail: fred_cadieu@qc.edu

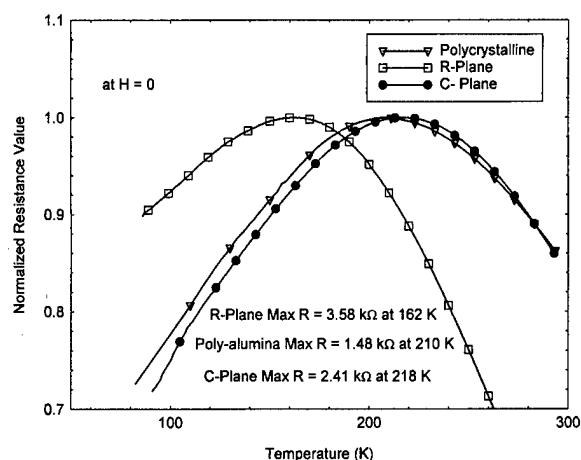


FIG. 1. The normalized resistances measured in zero field for a set of $\text{La}_{0.7}\text{Sr}_{0.3}\text{MnO}_3$ films simultaneously made onto *R*-plane sapphire, *C*-plane sapphire, and polycrystalline alumina substrates are shown as a function of temperature.

simultaneously onto *C*-plane, *R*-plane sapphire, and polycrystalline alumina substrates. The films discussed here were deposited using a substrate temperature of 750 °C in 120 mTorr of flowing oxygen. Low field magnetoresistance measurements were made using a standard four-terminal technique, and in other cases using FeCo sputtered film magnetic flux paths which also acted as the electrical connections to the La-manganite film strips. During the PLD deposition patterned La-manganite films have been directly deposited by using alumina contact masks to only expose a strip of the substrates. Film thicknesses, grain sizes, and the presence of particulates has been studied using a scanning electron microscope (SEM). Film compositions were determined by electron excited x-ray spectroscopy in the SEM. Magnetization measurements were made using a vibrating sample magnetometer.

As a means of making electrical as well as magnetic field circuit connections to La-manganite films, sputtered films of $\text{Fe}_{0.8}\text{Co}_{0.2}$ have been used in most cases. The sputtered $\text{Fe}_{0.8}\text{Co}_{0.2}$ films exhibited an in plane intrinsic coercivity of 18 Oe and a saturation flux density of 24 kG as determined by extrapolating the perpendicular to the plane measurements to the in plane saturation flux density. The FeCo films were diode sputter deposited in 17 mTorr Ar at 150 °C. A key feature of these FeCo sputtered films was their corrosion resistance which made it possible to reoxygenate La-manganite films without changing the electrical, magnetic, and appearance properties of the in-plane FeCo sputtered films.

III. RESULTS AND DISCUSSION

Figure 1 shows the resistance of strips of $\text{La}_{0.7}\text{Sr}_{0.3}\text{MnO}_3$ films that were simultaneously deposited as masked strips onto *R*-plane sapphire, *C*-plane sapphire, and polished polycrystalline alumina substrates. The films were deposited at substrate temperatures of 750 °C in 120 mTorr O_2 using a stainless steel shadow between the target and substrates. The films were thus relatively particulate free and highly smooth. The resistances shown in the figure are normalized to the

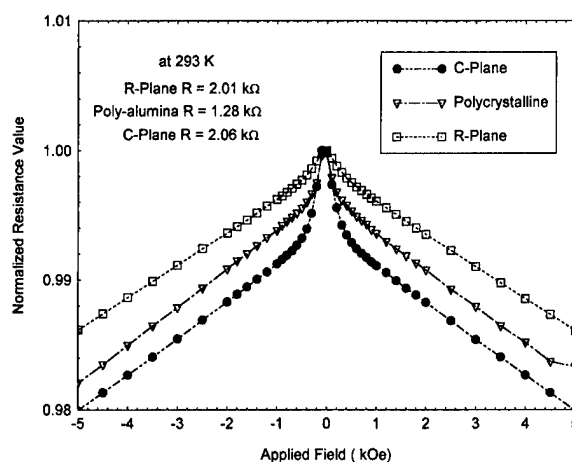


FIG. 2. The normalized resistances measured at 293 K are shown as a function of in-plane applied magnetic field for the same set of substrates as shown in Fig. 1.

maximum value at the resistance maximum. The temperature of the resistance maximum and strip resistance at the maximum were for *R*-plane sapphire 162 K and 3.58 kΩ, for *C*-plane sapphire 218 K and 2.41 kΩ, and for polycrystalline alumina 210 K and 1.48 kΩ. The resistance maximum for the films deposited onto *C*-plane and polycrystalline alumina occurs at a temperature of 56 and 48 K higher, respectively, than that for the *R*-plane substrate. Figure 2 shows the low field in plane magnetoresistance of these films as measured at 293 K. The resistances are shown normalized to the zero field response to illustrate the contrasting behavior of the *R*-plane sapphire, *C*-plane sapphire, and alumina substrates. The strip resistances at 293 K, respectively for *R*-plane sapphire, *C*-plane sapphire, and polycrystalline alumina were 2.01, 2.06, and 1.28 kΩ. The film deposited onto the polycrystalline alumina substrate exhibited a resistance of only 62% of that of the *C*-plane sapphire substrate sample. The low field response of the inexpensive polycrystalline alumina substrate sample is comparable to that of the *C*-plane sapphire substrate sample. No evidence for any hysteresis in the magnetoresistance was observed for any of these samples in

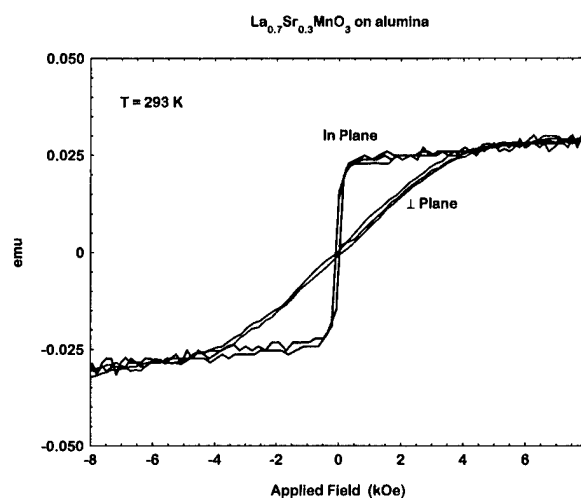


FIG. 3. Room temperature hysteresis loops are shown for a polycrystalline $\text{La}_{0.7}\text{Sr}_{0.3}\text{MnO}_3$ film deposited onto an alumina substrate.

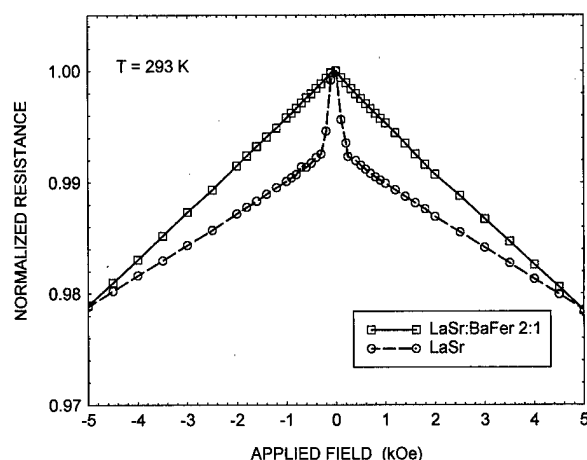


FIG. 4. Normalized resistances as measured at 293 K for $\text{La}_{0.7}\text{Sr}_{0.3}\text{MnO}_3$ films made with and without barium ferrite laminations, 2:1 thickness ratio, are shown.

this temperature range. Low field magnetoresistance at room temperature, 20 °C, exhibited an enhanced $(1/R)(\Delta R/\Delta H)$ of $-2.2\%/k\text{Oe}$ for $H < 0.25/k\text{Oe}$, and an overall $(1/R) \times (\Delta R/\Delta H) = -0.24\%/k\text{Oe}$ up to 20 kOe. The low field magnetoresistance was least for the R -plane sapphire sample. Room temperature hysteresis loops for a $\text{La}_{0.7}\text{Sr}_{0.3}\text{MnO}_3$ film made onto an alumina substrate are shown in Fig. 3. The in plane coercivity was ≈ 40 Oe. The room temperature $4\pi M_s$ was indicated to be 3.9 kG by the joining of the perpendicular loop to the in-plane loop.

It has been possible to eliminate the low magnetic field peaked magnetoresistance by restricting the size of the $\text{La}_{0.7}\text{Sr}_{0.3}\text{MnO}_3$ grains and by restricting intergrain coupling. This was accomplished by making thin $\text{La}_{0.7}\text{Sr}_{0.3}\text{MnO}_3$ film layers alternated with intervening layers of barium ferrite. Barium ferrite was chosen since it exhibits a very high resistivity compared to the $\text{La}_{0.7}\text{Sr}_{0.3}\text{MnO}_3$ films, and because it offers compatible film processing conditions. Figure 4 shows the room temperature normalized magnetoresistance response for $\text{La}_{0.7}\text{Sr}_{0.3}\text{MnO}_3$ films made with and without barium ferrite laminations in a 2:1 thickness ratio. The effective resistivity of the laminated film was approximately twice the resistivity for low temperature processed polycrystalline $\text{La}_{0.7}\text{Sr}_{0.3}\text{MnO}_3$ samples.³ These films were made under the same conditions onto polycrystalline alumina substrates. The laminated film had a total thickness of $1.4 \mu\text{m}$ and from average deposition per pulse calculations, consisted of 60 layers of 16-nm-thick $\text{La}_{0.7}\text{Sr}_{0.3}\text{MnO}_3$ alternated with 59 layers of 8-nm-thick barium ferrite such that the first and last layers were $\text{La}_{0.7}\text{Sr}_{0.3}\text{MnO}_3$. The thickness of the layers was determined by SEM measurements of average thickness per laser pulse for separate films of $\text{La}_{0.7}\text{Sr}_{0.3}\text{MnO}_3$ and barium ferrite made under the same conditions. The layered film samples were made without shadowing by sequentially switching between targets with a motorized carousel. The substrate temperature in each case was 750 °C in 120 mTorr O_2 followed by 45 min at 750 °C in 200 Torr O_2 . The intergrain coupling was sufficient to maintain electrical conduction, but it has not been possible to directly observe distinct

layers under SEM examination. The average $\text{La}_{0.7}\text{Sr}_{0.3}\text{MnO}_3$ grain size is thus set equal to the average indicated thickness of 16 nm. The film made with barium ferrite laminations exhibited a linear magnetoresistance of $-0.43\%/k\text{Oe}$ from 0 to ± 5 kOe, while the $\text{La}_{0.7}\text{Sr}_{0.3}\text{MnO}_3$ film exhibited the usual low field enhanced magnetoresistance. The barium ferrite layers for the deposition conditions used did not exhibit appreciable magnetic properties. Room temperature hysteresis loops for the layered film were similar to Fig. 3 in shape and exhibited a similar coercivity as for the $\text{La}_{0.7}\text{Sr}_{0.3}\text{MnO}_3$ film only. The perpendicular to the film plane loop joined the in-plane loop at 2.0 kOe indicating an effective $4\pi M_s$ for the composite structure of 2.0 kG. The barium ferrite layers as deposited are thus mainly acting as nonmagnetic resistive layers.

IV. CONCLUSIONS

It has been shown that $\text{La}_{0.7}\text{Sr}_{0.3}\text{MnO}_3$ polycrystalline films, in which the grain size and intergrain coupling have been restricted to an average size of 16 nm by layering with resistive barium ferrite, exhibit the usual maximum in resistivity characteristic of polycrystalline $\text{La}_{0.7}\text{Sr}_{0.3}\text{MnO}_3$ films. A principal difference was that only a single linear magnetoresistive response was exhibited from 0 to ± 5 kOe. This response was measured at 293 K. This temperature was 83 K above the temperature of the resistance maximum for polycrystalline $\text{La}_{0.7}\text{Sr}_{0.3}\text{MnO}_3$ films deposited onto alumina substrates. Reference 3 attributes the low field enhanced magnetoresistance to spin-polarized tunneling between grains in polycrystalline samples. Tunneling is expected to contribute an increased resistivity with increasing temperature⁵ that is not observed for these samples and is not expected to be dominant at room temperature. Between grain spin dependent transport is expected to be restricted in the laminated samples. That the low field response is suppressed is thus consistent with the cause of the low field magnetoresistance as depicted in Ref. 5, spin-dependent scattering of polarized electrons at grain boundaries.

ACKNOWLEDGMENTS

The PLD system was purchased with NSF-ARI Grant No. STI-9512308, and with partial support from the NYS Graduate Research Initiative. This work was supported through a subcontract from Florida State University as a part of an Office of Naval Research Grant No. ONR N00014-96-1-0767 and in part by a PSC-CUNY Faculty Research Award Grant.

¹Y. Tokura, J. Phys. Soc. Jpn. **63**, 3931 (1994).

²A. Gupta, G. Q. Gong, G. Xiao, P. R. Duncombe, P. Lecouer, P. Trouiloud, Y. Y. Wang, V. P. Dravid, and J. Z. Sun, Phys. Rev. B **54**, R15 629 (1996).

³H. Y. Hwang, S.-W. Cheong, N. P. Ong, and B. Batlogg, Phys. Rev. Lett. **77**, 2041 (1996).

⁴R. Shreekala, M. Rajeswari, K. Ghosh, A. Goyal, J. Y. Gu, C. Kwon, Z. Trajanovic, T. Boettcher, R. L. Greene, R. Ramesh, and T. Venkatesan, Appl. Phys. Lett. **71**, 282 (1997).

⁵X. W. Li, A. Gupta, Gang Xiao, and G. Q. Gong, Appl. Phys. Lett. **71**, 1124 (1997).

Colossal magnetoresistance and Mössbauer studies of the manganites

$\text{La}_{1-x}\text{Sn}_x\text{Mn}_{0.985}\text{Fe}_{0.015}\text{O}_{3+\delta}$

Z. W. Li, A. H. Morrish,^{a)} and X. Z. Zhou

Department of Physics, University of Manitoba, Winnipeg R3T 2N2, Canada

S. Dai

Institute of Physics, Chinese Academy of Science, Beijing 100080, People's Republic of China

Colossal magnetoresistance (CMR), Mössbauer spectra, and phase compositions of the iron-doped manganites, $\text{La}_{1-x}\text{Sn}_x\text{Mn}_{0.985}\text{Fe}_{0.015}\text{O}_{3+\delta}$ ($x=0.3$ and 0.5), have been studied. A small amount of iron doping modifies the CMR and other magnetic properties of the manganites. $\text{La}_{0.7}\text{Sn}_{0.3}\text{Mn}_{0.985}\text{Fe}_{0.015}\text{O}_{3+\delta}$ exhibits CMR; the magnetoresistance coefficient with $H=20$ kOe and $T=225$ K is about 80%. $\text{La}_{0.7}\text{Sn}_{0.3}\text{Mn}_{0.985}\text{Fe}_{0.015}\text{O}_{3+\delta}$ consists of two phases, $(\text{LaSn}^{2+})\text{MnO}_3$, or ABO_3 , and $(\text{LaSn}^{4+})_2\text{Mn}_2\text{O}_7$, or $\text{A}_2\text{B}_2\text{O}_7$. The ABO_3 phase has a transition from paramagnetism to ferromagnetism at $T=225$ K. The CMR has its origin in the ABO_3 phase. © 1998 American Institute of Physics. [S0021-8979(98)27011-3]

I. INTRODUCTION

The colossal magnetoresistance (CMR) in the manganites has attracted much attention. These manganites can be classified into two categories. One is the perovskite-type compound (ABO_3) with a chemical formula $(\text{R}_{1-x}^{3+}\text{D}^{2+}) \times (\text{Mn}_{1-x}^{3+}\text{Mn}_x^{4+})\text{O}_3$ ($\text{R}=\text{rare-earth}$ and $\text{D}=\text{Ca, Sr, Ba, Pb, and Cd, all divalent}$).¹ The other is the pyrochlore-type compound ($\text{A}_2\text{B}_2\text{O}_7$) with the formula $\text{Ti}_2^{3+}\text{Mn}_2^{4+}\text{O}_7$.^{2,3}

Recently, it has been discovered that $\text{La}_{0.7}\text{Sn}_{0.3}\text{MnO}_{3+\delta}$ exhibits CMR near room temperature (250 K).⁴ Its magnetoresistivity coefficient (classical) is as high as 74% in $H=70$ kOe. Further investigation shows that the iron doping modifies the CMR and other magnetic properties of the manganites. In this article, studies of CMR, Mössbauer spectrum, x-ray diffraction, and ac susceptibility for the iron-doped manganites $\text{La}_{1-x}\text{Sn}_x\text{Mn}_{0.985}\text{Fe}_{0.015}\text{O}_{3+\delta}$ ($x=0.3$ and 0.5) are reported.

II. EXPERIMENT

Samples of $\text{La}_{1-x}\text{Sn}_x\text{Mn}_{0.985}\text{Fe}_{0.015}\text{O}_{3+\delta}$ ($x=0.3$ and 0.5) as well as $\text{La}_{0.7}\text{Sn}_{0.3}\text{MnO}_{3+\delta}$ were synthesized using conventional ceramic techniques. A mixture of the oxides (La_2O_3 , SnO_2 , MnO_2 , and $^{57}\text{Fe}_2\text{O}_3$) of stoichiometric composition was shaped by pressure and presintered at 800 °C for 10 h. Then the samples were sintered at 1200 °C for 20 h in air.

X-ray diffraction (XRD) was performed with a Philips diffractometer using $\text{Cu } K\alpha$ radiation. The ac susceptibilities were measured at 2.4 kHz in a driving field of 30 mOe rms from 4.2 to 300 K. The magnetoresistances were examined at 4.2–300 K with zero field and a 20 kOe applied field using the standard four-probe method. Mössbauer spectra were taken between 4.2 K and room temperature with a conventional constant-acceleration spectrometer. The γ -ray source was ^{57}Co in a Rh matrix. Calibration was made using an α -Fe spectrum.

^{a)}Electronic mail: physics@umanitoba.ca

III. RESULTS AND DISCUSSION

A. Magnetoresistance

The iron-doped sample, $\text{La}_{0.7}\text{Sn}_{0.3}\text{Mn}_{0.985}\text{Fe}_{0.015}\text{O}_{3+\delta}$ exhibits a colossal magnetoresistance. The resistances of this compound in zero and in an applied magnetic field of 20 kOe are shown as a function of temperature in Fig. 1(a). A small amount of iron doping modifies the magnetoresistance effect for $\text{La}_{0.7}\text{Sn}_{0.3}\text{MnO}_{3+\delta}$. Figure 1(b) shows the temperature dependences of the magnetoresistance coefficient, $\text{MR} = -\Delta\rho/\rho(0,T) \times 100\%$, in $H=20$ kOe for $\text{La}_{0.7}\text{Sn}_{0.3}\text{MnO}_{3+\delta}$ and the iron-doped sample. The maximum MR is as high as 80% for $\text{La}_{0.7}\text{Sn}_{0.3}\text{Mn}_{0.985}\text{Fe}_{0.015}\text{O}_{3+\delta}$, but only 40% for $\text{La}_{0.7}\text{Sn}_{0.3}\text{MnO}_{3+\delta}$. In addition, our previous work⁴ has shown that the resistivity, with increasing mag-

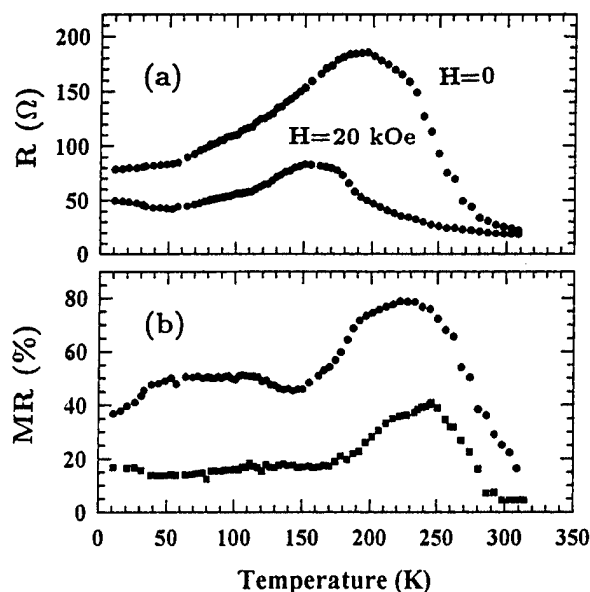


FIG. 1. (a) Resistance-temperature curves in zero and a 20 kOe applied magnetic field for $\text{La}_{0.7}\text{Sn}_{0.3}\text{Mn}_{0.985}\text{Fe}_{0.015}\text{O}_{3+\delta}$; (b) the magnetoresistance coefficient-temperature curve (circles) and also that for $\text{La}_{0.7}\text{Sn}_{0.3}\text{MnO}_{3+\delta}$ (squares).

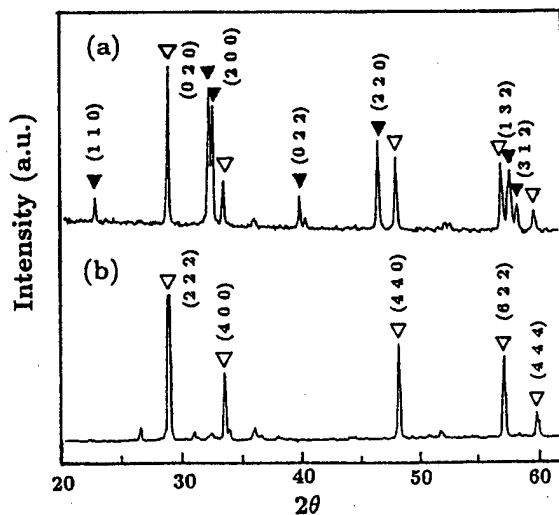


FIG. 2. X-ray diffraction patterns for (a) $\text{La}_{0.7}\text{Sn}_{0.3}\text{Mn}_{0.985}\text{Fe}_{0.015}\text{O}_{3+\delta}$ and (b) $\text{La}_{0.5}\text{Sn}_{0.5}\text{Mn}_{0.985}\text{Fe}_{0.015}\text{O}_{3+\delta}$. The black and white triangles represent the ABO_3 and $\text{A}_2\text{B}_2\text{O}_7$ phases, respectively.

netic fields, decreases more rapidly for $\text{La}_{0.7}\text{Sn}_{0.3}\text{Mn}_{0.985}\text{Fe}_{0.015}\text{O}_{3+\delta}$ than for $\text{La}_{0.7}\text{Sn}_{0.3}\text{MnO}_{3+\delta}$; however, in the high field of 70 kOe, the MR is almost the same for both. Thus, the iron-doped sample has a larger MR in the lower fields. However, the temperature corresponding to the maximum MR is shifted toward a lower temperature, from 250 K for $\text{La}_{0.7}\text{Sn}_{0.3}\text{MnO}_{3+\delta}$ to 225 K for the Fe-doped sample.

B. Phase analyses

The x-ray diffraction patterns for $\text{La}_{1-x}\text{Sn}_x\text{Mn}_{0.985}\text{Fe}_{0.015}\text{O}_{3+\delta}$ with $x=0.3$ and 0.5 are shown in Figs. 2(a) and 2(b), respectively. For $\text{La}_{0.7}\text{Sn}_{0.3}\text{Mn}_{0.985}\text{Fe}_{0.015}\text{O}_{3+\delta}$ the XRD lines can be divided into two sets, denoted by the open and closed triangles in Fig. 2(a). The positions and relative intensities indicated by the closed triangles agree well with those for $\text{La}_{0.8}\text{Sr}_{0.2}\text{MnO}_3$. Therefore, this phase is identified as ABO_3 . On the other hand, the positions and relative intensities of the remaining lines are almost the same to those for $\text{La}_{0.5}\text{Sn}_{0.5}\text{Mn}_{0.985}\text{Fe}_{0.015}\text{O}_{3+\delta}$.

For $\text{La}_{0.5}\text{Sn}_{0.5}\text{Mn}_{0.985}\text{Fe}_{0.015}\text{O}_{3+\delta}$, the positions and relative intensities of the XRD lines are similar to those for $\text{La}_2\text{Sn}_2\text{O}_7$ and $\text{Ti}_2\text{Mn}_2\text{O}_7$. Hence, $\text{La}_{0.5}\text{Sn}_{0.5}\text{Mn}_{0.985}\text{Fe}_{0.015}\text{O}_{3+\delta}$ appears to be single phase $\text{A}_2\text{B}_2\text{O}_7$ and $\text{La}_{0.7}\text{Sn}_{0.3}\text{Mn}_{0.985}\text{Fe}_{0.015}\text{O}_{3+\delta}$ is a mixture of the two phases, ABO_3 and $\text{A}_2\text{B}_2\text{O}_7$.

C. Susceptibility

The ac susceptibilities for $\text{La}_{1-x}\text{Sn}_x\text{Mn}_{0.985}\text{Fe}_{0.015}\text{O}_{3+\delta}$ with $x=0.3$ and 0.5 are shown in Fig. 3. For the sample with $x=0.5$, a transition from paramagnetism to ferromagnetism is not observed between room temperature and 4.2 K. Only small peaks appear at 50 and 65 K; this may imply a spin-glass transition as described by Blasco *et al.*⁵ or an antiferromagnetic transition. Their origin is as yet unsolved.

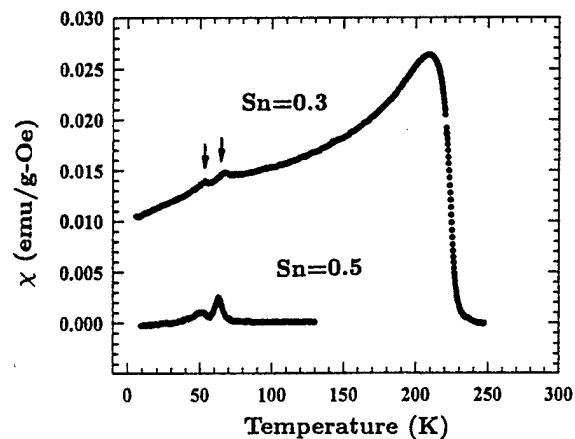


FIG. 3. Susceptibility-temperature curves for $\text{La}_{0.7}\text{Sn}_{0.3}\text{Mn}_{0.985}\text{Fe}_{0.015}\text{O}_{3+\delta}$ and for $\text{La}_{0.5}\text{Sn}_{0.5}\text{Mn}_{0.985}\text{Fe}_{0.015}\text{O}_{3+\delta}$.

$\text{La}_{0.7}\text{Sn}_{0.3}\text{Mn}_{0.985}\text{Fe}_{0.015}\text{O}_{3+\delta}$ has two magnetic transitions. One is a transition from paramagnetism to ferromagnetism. Based on the maximum slope in dM/dH , the Curie temperature is 225 K. The other transition, indicated by the arrows in the figure, occurs at 50–65 K, the same as the transition temperature for the sample with $x=0.5$. Thus, it is concluded that the transitions observed at 225 K and at low temperature are associated with the ABO_3 and $\text{A}_2\text{B}_2\text{O}_7$ phases, respectively.

D. Mössbauer spectra

The Mössbauer spectra of $\text{La}_{1-x}\text{Sn}_x\text{Mn}_{0.985}\text{Fe}_{0.015}\text{O}_{3+\delta}$ with $x=0.3$ and 0.5 from 300 to 4.2 K together with computer-fitted subspectra are shown in Fig. 4. The fitted Mössbauer parameters at $T=4.2$ K are listed in Table I. The isomer shifts are about 0.34–0.37 mm/s at room temperature and about 0.50 mm/s at 4.2 K for both the ABO_3 and $\text{A}_2\text{B}_2\text{O}_7$ phases. This implies that all Fe ions have ferric valency (Fe^{3+}).

The Mössbauer spectra of the sample with $x=0.5$ ($\text{A}_2\text{B}_2\text{O}_7$) are a paramagnetic doublet from room temperature to 65 K. The doublet starts to disappear and become a sextet between 65 and 50 K. The Mössbauer spectrum of the sample with $x=0.3$ has two paramagnetic doublets at room temperature. The inner doublet is associated with the ABO_3 phase and the outer doublet with the $\text{A}_2\text{B}_2\text{O}_7$ phase. The inner doublet starts to become a sextet below 230 K. However, the outer doublet remains until $T=65$ K. Only below 65 K does the outer doublet disappear; the spectra thus consist of two sextets, consistent with the previous results.⁶

The Mössbauer spectrum of the sample with $x=0.3$ with $T=4.2$ K and an applied longitudinal field of 50 kOe is shown in Fig. 4(e). The hyperfine field, $H_{\text{hf}}(H_a)$, in the presence of the applied magnetic field, H_a , is given by

$$H_{\text{hf}}(H_a) = [H_{\text{hf}}(0)^2 + H_a^2 + 2H_{\text{hf}}(0)H_a \cos \theta]^{1/2}, \quad (1)$$

where $H_{\text{hf}}(0)$ is the hyperfine field in zero applied field and θ is the angle between $H_{\text{hf}}(0)$ and H_a . The angle θ can also be obtained from the ratio of the 2nd plus 5th to the 3rd plus 4th line areas by

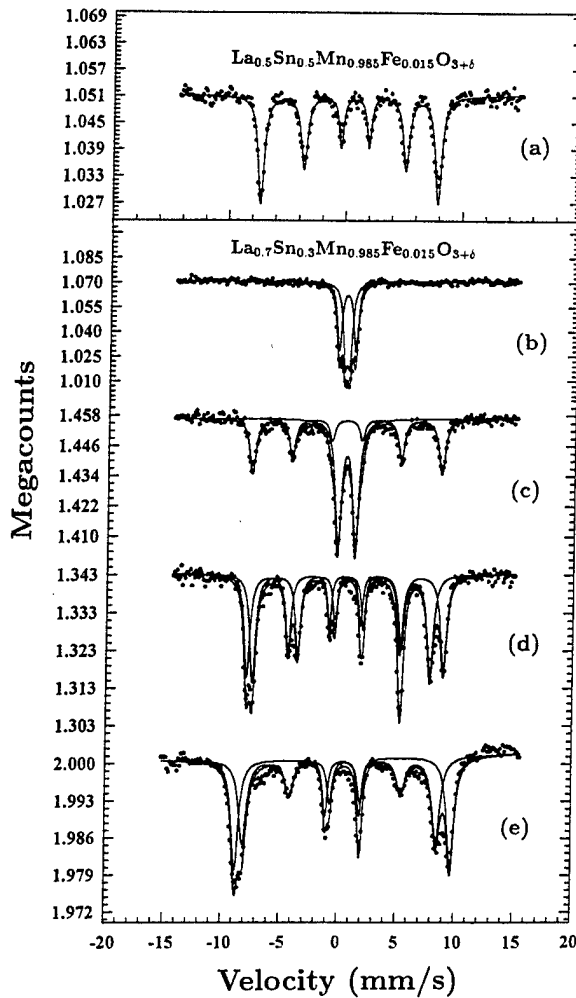


FIG. 4. Mössbauer spectra of (a) $\text{La}_{0.5}\text{Sn}_{0.5}\text{Mn}_{0.985}\text{Fe}_{0.015}\text{O}_{3+\delta}$ at $T=4.2$ K, and of $\text{La}_{0.7}\text{Sn}_{0.3}\text{Mn}_{0.985}\text{Fe}_{0.015}\text{O}_{3+\delta}$ at (b) $T=300$ K, (c) $T=77$ K, (d) $T=4.2$ K, in zero field, and (e) at $T=4.2$ K in a longitudinal applied field of 50 kOe.

$$\theta = \cos^{-1} \sqrt{\frac{4 - A_{2,5}/A_{3,4}}{4 + A_{2,5}/A_{3,4}}} \quad (2)$$

For the ABO_3 phase, $H_{\text{hf}}(H_a)$ is just equal to a sum of $H_{\text{hf}}(0)$ and H_a . Hence, $\theta=0$ obtained from Eq. (1) is consistent with the disappearance of the 2nd and 5th lines. These results show that all Fe moments are collinear but antiparallel with the applied field. Further, since ABO_3 is ferromagnetic, the Fe ions are antiparallel to the Mn ions, which have a ferromagnetic structure. The antiferromagnetic Fe–O–Mn superexchange interaction can weaken the double exchange interaction between Mn^{3+} and Mn^{4+} ions, as described by Leung *et al.*⁷ As a result, the Curie temperature is reduced for the Fe-doped sample.

TABLE I. Mössbauer parameters of $\text{La}_{1-x}\text{Sn}_x\text{Mn}_{0.985}\text{Fe}_{0.015}\text{O}_{3+\delta}$ ($x=0.3$ and 0.5) in zero and a 50 kOe applied field, H_a , at $T=4.2$ K. Here, δ is the isomer shift with respect to $\alpha\text{-Fe}$, ϵ is the quadrupole splitting, H_{hf} is the hyperfine field, and b is the ratio of the 2nd plus 5th to the 3rd plus 4th.

Sample	Phase	δ (mm/s)	$H_a=0$ kOe ϵ (mm/s)	H_{hf} (kOe)	b
$x=0.5$	$\text{A}_2\text{B}_2\text{O}_7$	0.50(3)	-0.46(3)	474(3)	2.0
$x=0.3$	$\text{A}_2\text{B}_2\text{O}_7$	0.51	-0.64	474	2.0
	ABO_3	0.50	0.03	525	2.0
$x=0.3$	$\text{A}_2\text{B}_2\text{O}_7$	0.47(3)	$H_a=50$ kOe -0.41(3)	514(3)	1.30
	ABO_3	0.56	0.04	576	0.0

For the $\text{A}_2\text{B}_2\text{O}_7$ phase, the Mössbauer subspectrum is still a sextet in an applied field of 50 kOe; therefore the antiferromagnetic coupling between the Fe moments is excluded. The nonzero 2nd and 5th lines imply that the Fe moments are noncollinear. The average angle $\langle\theta\rangle$ is estimated to be about 36° from Eq. (1) and about 44° from Eq. (2). Therefore, the Fe moments in the $\text{A}_2\text{B}_2\text{O}_7$ phase may be either canted with ferromagnetic coupling or be in a spin-glass state.

IV. CONCLUSIONS

A small amount of iron doping modifies the CMR and other magnetic properties of the manganites. $\text{La}_{0.7}\text{Sn}_{0.3}\text{Mn}_{0.985}\text{Fe}_{0.015}\text{O}_{3+\delta}$ exhibits CMR; the magnetoresistance coefficient in $H=20$ kOe and at $T=225$ K is about 80%. $\text{La}_{0.5}\text{Sn}_{0.5}\text{Mn}_{0.985}\text{Fe}_{0.015}\text{O}_{3+\delta}$ is a single phase with the $\text{A}_2\text{B}_2\text{O}_7$ structure and $\text{La}_{0.7}\text{Sn}_{0.3}\text{Mn}_{0.985}\text{Fe}_{0.015}\text{O}_{3+\delta}$ is a mixture of the ABO_3 and $\text{A}_2\text{B}_2\text{O}_7$ phases. The ABO_3 phase is associated with a transition from paramagnetism to ferromagnetism at $T=225$ K and the $\text{A}_2\text{B}_2\text{O}_7$ phase with another transition between 50 and 60 K. Hence, the CMR has its origin in the ABO_3 phase.

ACKNOWLEDGMENTS

The financial support of the Natural Sciences and Engineering Research Council of Canada is acknowledged. The authors thank Mr. J.H. Zhao for assistance with the ac susceptibility measurements.

- ¹S. Jin, H. M. O'Bryan, T. H. Tiefel, M. McCormack, and W. W. Rhodes, Appl. Phys. Lett. **66**, 382 (1995).
- ²Y. Shimakawa, Y. Kubo, and T. Manako, Nature (London) **379**, 53 (1996).
- ³M. A. Subramanian, B. H. Toby, A. P. Ramirez, W. J. Marshall, A. W. Sleight, and G. H. Kwei, Science **273**, 81 (1996).
- ⁴S. Dai, Z. W. Li, A. H. Morrish, X. Z. Zhou, J. G. Zhao, and X. M. Xiong, Phys. Rev. B **55**, 14125 (1997).
- ⁵J. Blasco, J. Garcia, J. M. Teresa, M. R. Ibarra, P. A. Algarabel, and C. Marquina, J. Phys.: Condens. Matter **8**, 7427 (1996).
- ⁶A. H. Morrish, Z. W. Li, S. Dai, X. Z. Zhou, J. G. Zhao, and X. M. Xiong, Hyperfine Interactions (in press).
- ⁷L. K. Leung, A. H. Morrish, and B. J. Evans, Phys. Rev. B **13**, 4069 (1976).

Electron spin resonance and magnetization in perovskite and pyrochlore manganites

M. Tovar,^{a)} M. T. Causa, G. Ibañez, C. A. Ramos, A. Butera, F. Rivadulla, and B. Alascio
*Centro Atómico Bariloche and Instituto Balseiro, Comisión Nacional de Energía Atómica
 and Universidad Nacional de Cuyo, 8400 San Carlos de Bariloche, Río Negro, Argentina*

S. B. Oseroff

San Diego State University, San Diego, California 92182

S-W. Cheong

AT&T Bell Laboratories, New Jersey 07974

X. Obradors and S. Piñol

Instituto de Ciencia de Materiales de Barcelona, 08193 Bellaterra, Spain

We have performed electron spin resonance (ESR) and dc susceptibility, $\chi_{dc}(T)$, measurements in $\text{La}_{0.7}\text{Ca}_{0.3}\text{MnO}_3$ perovskite up to 1000 K. This is adequately described in the paramagnetic regime in the constant coupling approximation assuming an effective Heisenberg-like pair interaction. The ESR linewidth is given by $\Delta H_{pp}(T) = \Delta H_{pp}(\infty)[C/T\chi(T)]$. The ESR intensity follows the T dependence of $\chi_{dc}(T)$. We conclude that the relaxation mechanism is essentially the same for the whole studied paramagnetic range. The observed behavior reflects the progressive importance of magnetic clustering on approaching T_c . We have found similar T dependence for $\text{La}_{0.7}\text{Sr}_{0.3}\text{MnO}_3$ and $\text{La}_{0.7}\text{Pb}_{0.3}\text{MnO}_3$ perovskites, and also for the pyrochlore $\text{In}_2\text{Mn}_2\text{O}_7$. © 1998 American Institute of Physics. [S0021-8979(98)27111-8]

The discovery of “colossal” magnetoresistance (CMR) in manganese oxides has renewed the interest in this kind of material. Perovskites $\text{A}_{1-x}\text{A}'_x\text{MnO}_3$ ($\text{A}=\text{La}, \dots; \text{A}'=\text{Ca}, \text{Sr}, \dots$) with $x \approx 0.3$ exhibit CMR effects near the paramagnetic (PM) to ferromagnetic (FM) transition temperature, T_c . These oxides show electron spin resonance (ESR) lines in the PM phase with large variations as a function of T and a large increase in intensity near T_c reflecting the dependence of the static susceptibility.¹⁻³ However the agreement between the measured intensities and a Curie-Weiss (CW) law was not satisfactory above 500 K. Simultaneously a change in the slope of the linewidth, ΔH_{pp} vs T was observed. It was suggested¹ that these effects may be due to the formation of $\text{Mn}^{3+}-\text{Mn}^{4+}$ spin clusters when T_c is approached from above. On the other hand, a possible mechanism related to a crossover from a bottlenecked regime where Mn^{3+} and Mn^{4+} are strongly coupled to an isothermal one where a decrease of the ESR intensity may be expected has been discussed.³ Studies in an extended temperature range were required^{2,3} in order to correlate these observations with theoretical models for CMR involving double exchange and electron-phonon interactions. We have performed ESR and magnetization measurements up to 1000 K, including the pyrochlore $\text{In}_2\text{Mn}_2\text{O}_7$ to compare the properties of ferromagnetic Mn oxides with different crystalline structures.

Ceramic samples of $\text{La}_{0.67}\text{Ca}_{0.33}\text{MnO}_3$ were prepared from the oxides by standard methods. Structure and phase purity were checked by powder x-ray diffraction. A single crystal of $\text{La}_{0.67}\text{Pb}_{0.33}\text{MnO}_3$ was also measured. Pyrochlore $\text{In}_2\text{Mn}_2\text{O}_7$ was prepared through solid state reactions under a

pressure of ≈ 35 kbar as described in Ref. 4. The dc magnetic susceptibility, $\chi_{dc}(T)$, was measured using a Faraday balance and a SQUID magnetometer. ESR measurements were performed at $\omega=1.2, 9.4$, and 34 GHz with an ESP-300 Bruker Spectrometer from 100 to 300 K. For 9.4 GHz the measurements were extended up to 1000 K.

At high temperatures $\chi_{dc}(T)$ follows a CW dependence, $\chi_{dc}(T) = C/(T - \Theta)$. For temperatures below $\approx 1.5 \Theta$, the curve for the inverse susceptibility vs T shows a positive curvature (see Fig. 1) and $\chi_{dc}(T)$ diverges at $T_c < \Theta$. Both temperatures are given in Table I.

The double exchange interaction is used to describe the FM interaction between Mn ions in CMR perovskites. A simplified model for this interaction⁵ indicates that the hop-

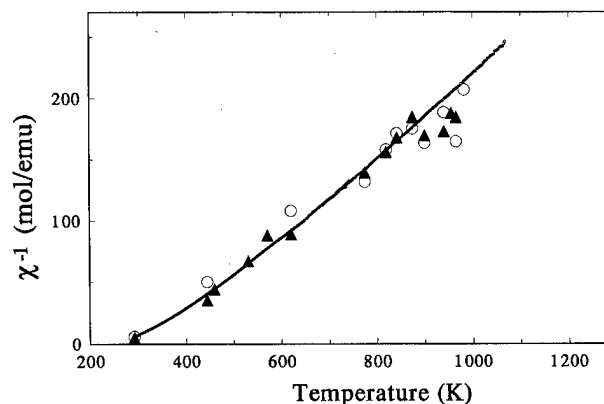


FIG. 1. Inverse susceptibility vs T for $\text{La}_{0.67}\text{Ca}_{0.33}\text{MnO}_3$. Small circles correspond to $\chi_{dc}(T)$, large circles to $\chi_{ESR}(T)$ from $(\Delta H_{pp})^2/h_{pp}$ and triangles to $\chi_{ESR}(T)$ from numerical integration.

^{a)}Electronic mail: tovar@cab.cnea.edu.ar

TABLE I. Values for the Curie constant, Curie-Weiss and critical temperatures, and exchange constant obtained from susceptibility measurements.

Compound	C emu K mol	Θ (K)	T_c (K)	T_c/Θ	J/k_B
$\text{La}_{0.67}\text{Ca}_{0.33}\text{MnO}_3$	2.8(1)	368	260	0.69	49
$\text{In}_2\text{Mn}_2\text{O}_7$	2.4(1)	145	130	0.89	10

ping of electrons between Mn^{4+} ions couples them forming high spin magnetic clusters. The effective FM coupling for Mn ions that results from this model may be described by an isotropic Heisenberg like interaction between Mn^{3+} ($3d^4$) and Mn^{4+} ($3d^3$) pairs.

$$\mathcal{H} = -2J \sum_{\langle i,j \rangle} S_1^i \cdot S_2^j, \quad (1)$$

where S_1 and S_2 identify the spin of Mn^{4+} and Mn^{3+} species, respectively, with $S_1 = 3/2$ and $S_2 = 2$.

In the Weiss mean field approximation (WMFA), the high-temperature behavior associated with this Hamiltonian, is given by a CW law with $C = N_A g^2 \mu_B^2 (f_1 + f_2) / 3k_B$ and $k_B \Theta / J = 4z f_1 f_2 / 3(f_1 + f_2)$, where z is the number of nearest neighbors and $f_1 = x S_1(S_1 + 1)$, $f_2 = (1-x) S_2(S_2 + 1)$. For $x = 0.33$, the calculated value is $C = 2.64$ emu K mol, which is compared with the experimental results of Table I. We have derived values for J from the measured Θ , also listed in Table I.

The main assumption of the WMFA model is the statistical independence of the spins, neglecting the short range order, which produces the curvature in $\chi_{dc}^{-1}(T)$. Small clusters models,⁶ such as the constant coupling approximation (CCA) takes into account the correlation between neighboring spins. The magnetic system is considered as an ensemble of spin pairs interacting through an effective Hamiltonian,

$$\mathcal{H} = -2JS_1 \cdot S_2 + g\mu_B(S_1 + S_2) \cdot [H + H_e], \quad (2)$$

where H_e is an effective field acting on the pair, determined by consistency requirements.⁶ A consequence of treating in more detail the formation of magnetic clusters (pairs in the CCA) is the appearance of short range order above T_c with a simultaneous reduction of $H_e(T)$, as compared to the values derived in the WMFA. Thus, the long range order is achieved at a temperature $T_c < \Theta$ and the calculated susceptibility adequately describes the positive curvature shown in Fig. 1. The experimental values for the ratio T_c/Θ (see Table I) are consistent with the values calculated⁶ in the CCA for either $S = 3/2$ or 2 ($T_c/\Theta = 0.77$ and 0.79, respectively).

In the case of pyrochlore $\text{In}_2\text{Mn}_2\text{O}_7$, the mechanisms for electrical conduction and magnetism are related⁷ to the intermediate valence arising from a hybridization of Mn $3d$ electrons with the conduction bands of In. In this case the magnetic interactions occurs between Mn^{4+} ($S = 3/2$) ions. Our susceptibility data, in coincidence with previous reports,⁸ shows the same positive curvature present in the perovskites.

The paramagnetic ESR spectrum of powdered samples consists of a single lorentzian line with a g value of 1.992(3), which is constant and independent of the microwave frequency at high temperatures. Since the ESR signals are in-

tense near T_c , the measured linewidth, ΔH_{pp} , is dependent on sample mass due to "overloading" of the cavity.⁹ In order to avoid these effects we repeated the experiments at each temperature with different amounts of material extrapolating to zero mass.

As a function of T , the ESR linewidth showed a behavior similar to that described in previous reports^{1,3}: When T approaches T_c from above, $\Delta H_{pp}(T)$ decreases and goes through a minimum at $T_{\min} > T_c$. The value of T_{\min} and the rate of increase of the linewidth below this temperature are dependent on the microwave frequency. Variations of the g factor were also observed for $T_c < T < T_{\min}$. Above T_{\min} the g factor is constant and $\Delta H_{pp}(T)$ independent of frequency.

The intensity of the ESR spectrum, $I(T)$, is an important parameter to identify the nature of the resonant species^{1-3,10} through the temperature dependence of χ_{ESR} , corresponding to the resonant species. There are several experimental difficulties in the determination of $I(T)$ because the linewidth increases by ≈ 10 from T_{\min} to high temperatures and the peak-to-peak amplitude of the measured derivative signal, h_{pp} , decreases up to three orders of magnitude in the same T range. This is a probable cause for the disagreement between recently reported results.^{1-3,10} Since the differences led the authors to different interpretations we have made a careful determination of $I(T)$ for $\text{La}_{0.67}\text{Ca}_{0.33}\text{MnO}_3$, up to 1000 K, that may shed some light on this controversial subject. $I(T)$ was determined by numerical double integration of the spectra and also approximating the area by $\Delta H_{pp}^2 h_{pp}$. In order to obtain $\chi_{\text{ESR}}(T)$, shown in Fig. 1, we have renormalized the measured $I(T)$ using values of Q_L determined at each temperature. We found that the temperature dependence is the same for both χ_{ESR} and χ_{dc} . Between T_c and T_{\min} significant line-broadening and g shifts, both dependent on microwave frequency, were observed. Since these effects, related¹⁰ to the proximity of T_c , may confuse the analysis of the results in the paramagnetic regime we have not included this temperature region in the analysis.

The temperature dependence of $\Delta H_{pp}(T)$ above T_{\min} was originally found¹ to be almost linear with T for $\text{La}_{0.67}\text{Ca}_{0.33}\text{MnO}_3$ up to 700 K and similar results were recently reported¹⁰ up to 600 K for $\text{La}_{1-x}\text{Sr}_x\text{MnO}_3$. A small tendency to saturation was found later^{2,3} above $T \approx 600$ K. Up to this temperature, our results for $\text{La}_{0.67}\text{Ca}_{0.33}\text{MnO}_3$, $\text{La}_{0.67}\text{Sr}_{0.33}\text{MnO}_3$, and $\text{La}_{0.67}\text{Pb}_{0.33}\text{MnO}_3$ present the same quasilinear behavior. In the case of $\text{La}_{0.67}\text{Ca}_{0.33}\text{MnO}_3$, we have extended the measurements up to ≈ 1000 K and found significant deviations from linearity at high temperatures, as shown in Fig. 2(a). For $\text{In}_2\text{Mn}_2\text{O}_7$, see Fig. 2(b), a similar T dependence was observed.

In treating the T dependence of ΔH_{pp} of magnetic compounds in the PM region, Dormann and Jaccarino¹¹ argued, following Huber's¹² approach, that the main variation is given by the expression

$$\Delta H_{pp}(T) = [\chi_s(T)/\chi_{\text{ESR}}(T)] \Delta H_{pp}(\infty), \quad (3)$$

where $\chi_s(T) = C/T$ is the single ion susceptibility and $\chi_{\text{ESR}}(T)$ corresponds to the paramagnetic behavior of the coupled system. The continuous line in Fig. 2, drawn with $\chi_{dc}(T)$ data, shows an excellent agreement with the experi-

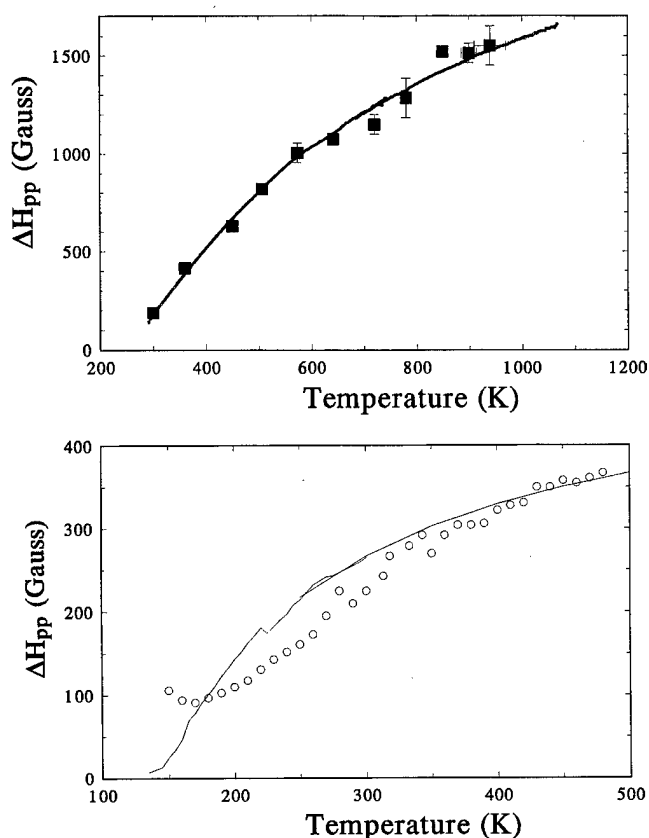


FIG. 2. ΔH_{pp} vs T taken at X band for (a) $\text{La}_{0.67}\text{Ca}_{0.33}\text{MnO}_3$ and (b) $\text{In}_2\text{Mn}_2\text{O}_7$. Solid lines correspond to Eq. (3).

mental $\Delta H_{pp}(T)$, including not only the quasilinear behavior near T_c , but also the saturation at higher temperatures. For $\text{In}_2\text{Mn}_2\text{O}_7$, the T dependence is also well described, although with small systematic departures near T_c , that may be related to spin-glass-like behavior.⁸

The limiting values $\Delta H_{pp}(\infty) = 2500$ and 500 G, determined for $\text{La}_{0.67}\text{Ca}_{0.33}\text{MnO}_3$ and $\text{In}_2\text{Mn}_2\text{O}_7$, respectively, corresponds to spin-spin interactions.¹² If the only anisotropic contributions were of dipolar origin, exchange narrowed lines would be expected. Using the J values of Table

I calculated values for $\Delta H_{pp}(\infty)$ are of the correct magnitude for $\text{In}_2\text{Mn}_2\text{O}_7$, but about an order of magnitude smaller for $\text{La}_{0.67}\text{Ca}_{0.33}\text{MnO}_3$. Therefore, other anisotropic interactions must be considered in order to explain our results.¹³

In conclusion, we have analyzed in detail the temperature dependence of the dc susceptibility and ESR line parameters in the PM regime of FM manganites. We found that: (a) The static magnetic susceptibility $\chi_{dc}(T)$ is well described in a mean field approximation of the small cluster type, although the ratio T_c/Θ calculated in the CCA is slightly different than that calculated for either $S = 3/2$ or $S = 2$. (b) The temperature dependence of the ESR of the system, independently of the exact nature of the resonant species, may be described by a common curve, whose temperature scale is determined by T_c and the infinite temperature linewidth kept as an adjustable parameter related to spin-spin interactions.

The authors acknowledge partial support from CEE-DGXII, NSF, and CONICET (Argentina). One of the authors (F. R.) acknowledges a fellowship from Ministerio de Educación y Ciencia de España.

¹ S. B. Oseroff, M. Torikachvili, J. Singley, S. Ali, S-W. Cheong, and S. Schultz, Phys. Rev. B **53**, 6521 (1996).

² C. Rettori, D. Rao, J. Singley, D. Kidwell, S. B. Oseroff, M. T. Causa, J. J. Neumeier, K. J. McClellan, S-W. Cheong, and S. Schultz, Phys. Rev. B **55**, 3083 (1997).

³ A. Shengelaya, Guo-meng Zhao, H. Keller, and K. A. Müller, Phys. Rev. Lett. **77**, 5296 (1996).

⁴ S-W. Cheong, H. Y. Hwang, B. Batlog, and L. W. Rupp, Jr., Solid State Commun. **98**, 63 (1996).

⁵ J. Briático, B. Alascio, R. Allub, A. Butera, A. Caneiro, M. T. Causa, and M. Tovar, Phys. Rev. B **53**, 14020 (1996); R. Allub and B. Alascio, *ibid.* **55**, 14113 (1997).

⁶ S. Smart, *Effective Field Theories of Magnetism* (W. B. Saunders Company, London, 1966).

⁷ C. Ventura and B. Alascio, Phys. Rev. B **56**, 14533 (1997).

⁸ N. P. Raju, J. E. Greedan, and M. A. Subramanian, Phys. Rev. B **49**, 1086 (1994).

⁹ M. S. Seehra, Rev. Sci. Instrum. **39**, 1044 (1968).

¹⁰ S. E. Lofland, P. Kim, P. Dahiroc, S. M. Baghat, S. D. Tyagi, S. G. Karabashev, D. A. Shulyatev, A. A. Arsenov, and Y. Mukovskii, Phys. Lett. A **233**, 476 (1997).

¹¹ E. Dormann and V. Jaccarino, Phys. Lett. A **48**, 81 (1974).

¹² D. L. Huber, J. Phys. Chem. Solids **32**, 2145 (1971).

¹³ M. T. Causa and M. C. G. Passeggi, Phys. Lett. A **98**, 291 (1983).

Thermal conductivity and magnetic transitions in $\text{Mn}^{3+}/\text{Mn}^{4+}$ manganites

J. Hejtmánek, Z. Jiráček, Z. Arnold, M. Maryško, and S. Krupička

Institute of Physics of ASCR, Cukrovarnická 10, 16200 Prague 6, Czech Republic

C. Martin and F. Damay

Laboratoire CRISMAT, URA CNRS 1318, ISMRa, Boulevard du Maréchal Juin, 14050 Caen Cedex, France

We report on a comparative study of three manganites: $\text{Pr}_{0.5}\text{Sr}_{0.5}\text{MnO}_3$, $\text{Pr}_{0.5}\text{Ca}_{0.5}\text{MnO}_3$, and $\text{Pr}_{0.5}\text{Sr}_{0.3}\text{Ca}_{0.2}\text{MnO}_3$, which all exhibit the same $\text{Mn}^{3+}/\text{Mn}^{4+} = 1:1$ concentration but show a very distinct magnetic behavior. The $\text{Pr}_{0.5}\text{Sr}_{0.5}\text{MnO}_3$ sample is a ferromagnet (FM) below $T_C = 265$ K and becomes the A-type antiferromagnet at $T_N = 140$ K. In $\text{Pr}_{0.5}\text{Ca}_{0.5}\text{MnO}_3$ the charge order develops at $T_{CO} = 245$ K and the CE-type antiferromagnetism occurs below $T_N = 175$ K. The $\text{Pr}_{0.5}\text{Sr}_{0.3}\text{Ca}_{0.2}\text{MnO}_3$ sample exhibits the FM transition at $T_C = 225$ K and the CE type antiferromagnetism and charge ordering occur simultaneously at $T_N = T_{CO} = 160$ K (185 K) upon cooling (heating), respectively. The study is complemented by the data on two systems of 30% Mn^{4+} , the ferromagnetic metal $\text{Pr}_{0.7}\text{Sr}_{0.1}\text{Ca}_{0.2}\text{MnO}_3$, and insulator $\text{Pr}_{0.85}\text{K}_{0.15}\text{MnO}_3$, both with similar Curie temperature $T_C \sim 140$ K. The electrical resistivity, thermoelectric power, thermal conductivity, and volume thermal expansion data are analyzed with respect to observed magnetic transitions and reveal the significantly distinct ground state of the A-type and CE-type antiferromagnets. We suppose that phonons and charge carriers are coupled via the Jahn–Teller effect and the CMR effect observed in manganites originates thus from a mutual interplay of a strong electron–phonon interaction and spin order. © 1998 American Institute of Physics.

[S0021-8979(98)32011-3]

Ferromagnetic perovskites $\text{Ln}_{1-x}\text{A}_x\text{MnO}_3$ with a high concentration of formally tetravalent manganese have become a subject of numerous studies. The competing ferromagnetic and antiferromagnetic interactions for the samples with nominal $\text{Mn}^{3+}/\text{Mn}^{4+} \sim 1:1$ concentration have been shown to lead to fascinating transport anomalies below room temperature. The magnetic and transport properties of these perovskites are in some sense predetermined by the crystal structure, which is principally controlled by the interlayer mismatch expressed as Goldschmidt's tolerance factor. A number of important additional factors, both cooperative [Jahn–Teller (J-T) distortion, orbital, and charge ordering] and local (ion size mismatch) critically influence, however, the thermodynamic stability of the competing phases. Besides, the role of dynamic J-T modes coupled with carriers and the existence of magnetic polarons was recently underlined.^{1,2} One of the feasible methods used to probe complexly these interactions is the investigation of thermal properties in comparison to magnetic, structural, and electrical data. In this article we report on the thermal conductivity, thermal expansion, thermoelectric power, and electrical resistivity measurements on praseodymium based samples with 30% and 50% Mn^{4+} concentration.

Ceramic samples were prepared using a solid state reaction from appropriate amounts of respective oxides and carbonates as described elsewhere.^{3,4} Structural characterization of the 50% samples has been done by the neutron diffraction. The thermal expansion was calculated using the refined lattice parameters, whereas for the 30% samples, this quantity was measured using the strain gauge method. All the thermal conductivity and transport data were measured using the

steady state four point technique from 12 to 300 K. The results of the thermal conductivity and electrical resistivity were corrected for the sample porosity.

The neutron diffraction on the 50% samples showed that $\text{Pr}_{0.5}\text{Sr}_{0.5}\text{MnO}_3$ is ferromagnet below $T_C = 265$ K and upon further cooling it exhibits an antiferromagnetic transition at $T_N = 140$ K. The observed A (planar) type of the antiferromagnetism is not compatible with any $\text{Mn}^{3+}/\text{Mn}^{4+}$ order; the lattice distortion below T_N shows, however, that the partially occupied manganese $3d_{\gamma}$ orbitals are oriented at the transition into the MnO_2 planes. A different situation is encountered in $\text{Pr}_{0.5}\text{Ca}_{0.5}\text{MnO}_3$. The $\text{Mn}^{3+}/\text{Mn}^{4+}$ (1:1) order occurs at $T_{CO} = 245$ K and an antiferromagnetism of a complex kind (CE type) develops below $T_N = 175$ K. The third compound under investigation $\text{Pr}_{0.5}\text{Sr}_{0.3}\text{Ca}_{0.2}\text{MnO}_3$ exhibits the ferromagnetic transition at $T_C = 225$ K and, contrary to pure Sr or pure Ca doped samples, the CE type antiferromagnetism and charge ordering occur simultaneously at $T_N = T_{CO} = 160$ K (185 K) upon cooling (heating), respectively.

The transport properties of the studied samples below the room temperature are shown in Figs. 1 and 2 where the temperature dependences of electrical resistivity and thermoelectric power are displayed. In $\text{Pr}_{0.5}\text{Sr}_{0.5}\text{MnO}_3$ the ferromagnetic transition at 265 K is accompanied by a small decrease of electrical resistivity, which is followed by an increase at the antiferromagnetic transition at 140 K. Even at the lowest temperatures the conductivity remains high which suggests that the $3d_{\gamma}$ electrons in the MnO_2 planes are delocalized. Both in $\text{Pr}_{0.5}\text{Ca}_{0.5}\text{MnO}_3$ and $\text{Pr}_{0.5}\text{Sr}_{0.3}\text{Ca}_{0.2}\text{MnO}_3$, the conduction is strongly activated with a pronounced anomaly at the charge ordering temperatures while the ferromagnetic

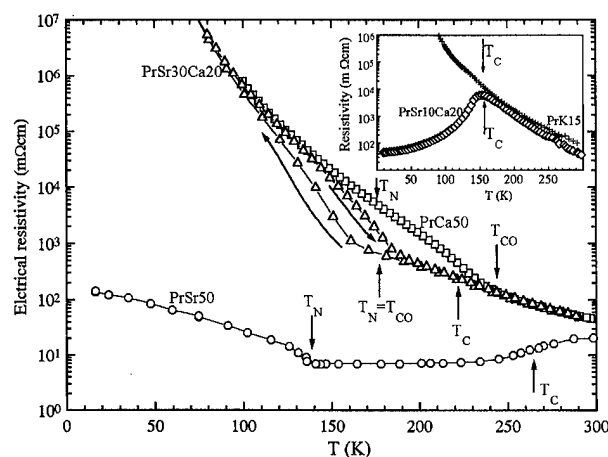


FIG. 1. Temperature dependence of the electrical resistivity for $\text{Pr}_{0.5}\text{Sr}_{0.5}\text{MnO}_3$ (\circ), $\text{Pr}_{0.5}\text{Ca}_{0.5}\text{MnO}_3$ (\square), and $\text{Pr}_{0.5}\text{Sr}_{0.3}\text{Ca}_{0.2}\text{MnO}_3$ (\triangle). In the inset the data for $\text{Pr}_{0.7}\text{Sr}_{0.1}\text{Ca}_{0.2}\text{MnO}_3$ (\diamond) and $\text{Pr}_{0.85}\text{K}_{0.15}\text{MnO}_3$ ($+$) are displayed. The arrows denote the ferromagnetic (T_C), antiferromagnetic (T_N), and charge order (T_{CO}) transition temperatures.

transition in $\text{Pr}_{0.5}\text{Sr}_{0.3}\text{Ca}_{0.2}\text{MnO}_3$ at 225 K is nearly invisible. For a comparison, the coincidence of the ferromagnetic and I - M transition in the CMR compound $\text{Pr}_{0.7}\text{Sr}_{0.1}\text{Ca}_{0.2}\text{MnO}_3$ with $R(0\text{ T})/R(5\text{ T})=20$ at T_C is exemplified in the inset while no metallic transition occurs in another 30% sample $\text{Pr}_{0.85}\text{K}_{0.15}\text{MnO}_3$ where dissimilar size of the substituent leads to a localization of carriers.³

The temperature independent and negative thermoelectric power in the paramagnetic state of the 50% samples is in general agreement with previously published results and can be understood if polaronic carriers strongly interact with the spin background. The thermopower is then dominated by the configurational entropy term where both the spin and orbital degeneracy should be considered.⁵ A detailed analysis is, however, out of the scope of this work. The ferromagnetic transition, if present, is always accompanied by a decrease of the absolute value of thermopower. The barely metallic states could be thus indicated also in $\text{Pr}_{0.5}\text{Sr}_{0.3}\text{Ca}_{0.2}\text{MnO}_3$ and

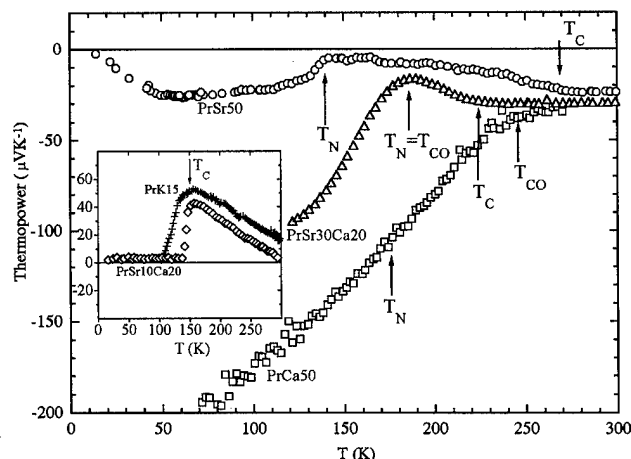


FIG. 2. temperature dependence of the thermoelectric power for $\text{Pr}_{0.5}\text{Sr}_{0.5}\text{MnO}_3$ (\circ), $\text{Pr}_{0.5}\text{Ca}_{0.5}\text{MnO}_3$ (\square), and $\text{Pr}_{0.5}\text{Sr}_{0.3}\text{Ca}_{0.2}\text{MnO}_3$ (\triangle). In the inset the data for $\text{Pr}_{0.7}\text{Sr}_{0.1}\text{Ca}_{0.2}\text{MnO}_3$ (\diamond) and $\text{Pr}_{0.85}\text{K}_{0.15}\text{MnO}_3$ ($+$) are displayed.

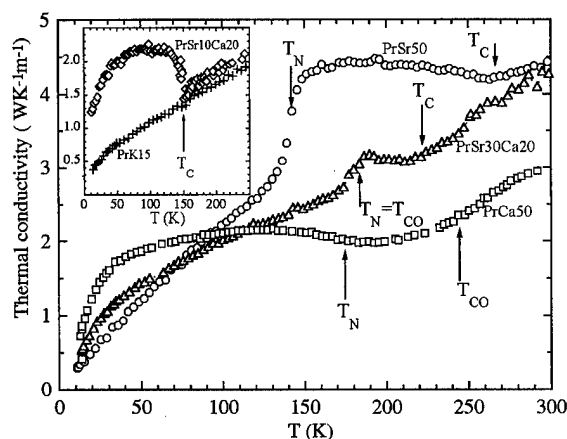


FIG. 3. Temperature dependence of the thermal conductivity for $\text{Pr}_{0.5}\text{Sr}_{0.5}\text{MnO}_3$ (\circ), $\text{Pr}_{0.5}\text{Ca}_{0.5}\text{MnO}_3$ (\square), and $\text{Pr}_{0.5}\text{Sr}_{0.3}\text{Ca}_{0.2}\text{MnO}_3$ (\triangle). In the inset the data for $\text{Pr}_{0.7}\text{Sr}_{0.1}\text{Ca}_{0.2}\text{MnO}_3$ (\diamond) and $\text{Pr}_{0.85}\text{K}_{0.15}\text{MnO}_3$ ($+$) are displayed.

$\text{Pr}_{0.85}\text{K}_{0.15}\text{MnO}_3$ samples despite their increasing resistivity below T_C . The charge ordering transition in $\text{Pr}_{0.5}\text{Ca}_{0.5}\text{MnO}_3$ and $\text{Pr}_{0.5}\text{Sr}_{0.3}\text{Ca}_{0.2}\text{MnO}_3$ is characterized by a divergence of the thermopower to large negative values while the onset of antiferromagnetic order in $\text{Pr}_{0.5}\text{Sr}_{0.5}\text{MnO}_3$ is evidenced only by a small drop down to $\sim 25\text{ }\mu\text{V K}^{-1}$, followed by a thermodynamical return to zero.

In order to visualize the interrelation of the transport and lattice effects, the thermal conductivity and the volume thermal expansion data are displayed in Figs. 3 and 4. For samples $\text{Pr}_{0.5}\text{Ca}_{0.5}\text{MnO}_3$ and $\text{Pr}_{0.5}\text{Sr}_{0.3}\text{Ca}_{0.2}\text{MnO}_3$, the temperature dependence of lattice parameters is included in the lower panel of Fig. 4. It should be noted that an analysis of observed electrical and thermal conductivities on the basis of the Wiedemann-Franz law, which enables one to estimate the upper limit of the electronic part of the thermal conductivity using the Lorenz number, excludes any appreciable electronic contribution to the heat transport even in the metallic samples. So the thermal conductivity is confined essentially to phonons and their scattering processes. In agreement with previously published data on the $\text{Mn}^{3+}/\text{Mn}^{4+}$ perovskites^{6,7} the measured values of thermal conductivity are extremely low and comparable with glassy materials. As a possible explanation one can consider large static disorder due to localized Mn^{4+} defects (in Mn^{3+} concentrated systems with strong J-T effects), the electron and/or spin density fluctuations observed as static objects (coherent length of tens Å) at low doping and present presumably as itinerant magnetic polarons at higher doping of carriers and, finally, the presence of anomalous acoustic phonons. These anomalous phonons may arise due to coupling with soft optical modes which have locally character of octahedra tiltings or vibrations of the J-T type. In the paramagnetic region of perovskites with 30%–50% Mn^{4+} the low thermal conductivity (actual mean free path of phonons $\sim 10\text{ Å}$) can be associated with magnetic polarons and/or vibronic interactions of Mn^{3+} ions (the dynamic Jahn-Teller modes). The latter possibility seems to be more relevant since the thermal conduction is essentially low even in the ferromagnetic state where magnetic polarons should vanish.

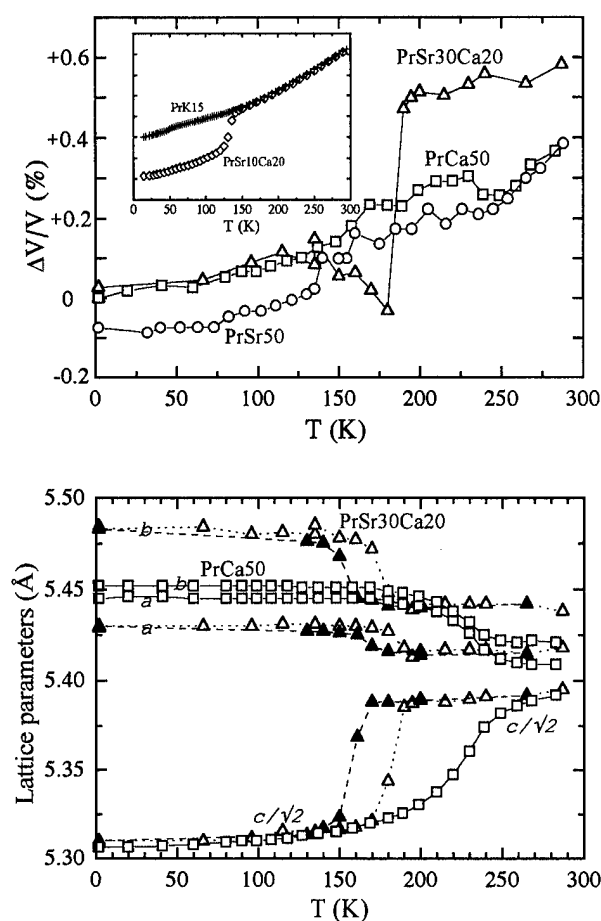


FIG. 4. Upper panel: the volume thermal expansion for $\text{Pr}_{0.5}\text{Sr}_{0.5}\text{MnO}_3$ (\circ), $\text{Pr}_{0.5}\text{Ca}_{0.5}\text{MnO}_3$ (\square), and $\text{Pr}_{0.5}\text{Sr}_{0.3}\text{Ca}_{0.2}\text{MnO}_3$ (\triangle), $\text{Pr}_{0.7}\text{Sr}_{0.1}\text{Ca}_{0.2}\text{MnO}_3$ (\diamond), and $\text{Pr}_{0.85}\text{K}_{0.15}\text{MnO}_3$ ($+$). Lower panel: the temperature dependence of the lattice parameters for $\text{Pr}_{0.5}\text{Ca}_{0.5}\text{MnO}_3$ (\square) and $\text{Pr}_{0.5}\text{Sr}_{0.3}\text{Ca}_{0.2}\text{MnO}_3$ (\triangle). Open symbols represent the temperature increase, full symbols the temperature decrease. The data are normalized with respect to two ground states (metallic and insulating) which differ in volume of $\sim 0.15\%$. (See Ref. 8).

The insets of Figs. 3 and 4 show the thermal behavior for 30% Mn^{3+} . In the case of the $\text{Pr}_{0.7}\text{Sr}_{0.1}\text{Ca}_{0.2}\text{MnO}_3$ sample, the simultaneous magnetic and I - M transition is accompanied by a sharp increase of the thermal conductivity below T_C , while for the insulating $\text{Pr}_{0.85}\text{K}_{0.15}\text{MnO}_3$ no enhancement is observed. The sharp decrease of the unit cell volume of about $\sim 0.15\%$ in $\text{Pr}_{0.7}\text{Sr}_{0.1}\text{Ca}_{0.2}\text{MnO}_3$ and the absence of this anomaly in $\text{Pr}_{0.85}\text{K}_{0.15}\text{MnO}_3$ points out the first order character of the I - M transition and underlines the different ground state of the two samples. Moreover, these results indicate that the enhancement of thermal conductivity cannot be linked to the ferromagnetism alone and is rather due to an electronic transition which suppresses significantly the amplitude of dynamic J-T modes. This supports the previous hypothesis that the J-T modes are the principle scatterers of phonons in manganese perovskites.

Enhancement of the thermal conductivity below T_C is observed also in the 50% Mn^{4+} samples $\text{Pr}_{0.5}\text{Sr}_{0.5}\text{MnO}_3$ and $\text{Pr}_{0.5}\text{Sr}_{0.3}\text{Ca}_{0.2}\text{MnO}_3$. The volume anomaly is absent, however, suggesting that the transition is not of the first order. With further cooling the thermal conductivity is suppressed

at the antiferromagnetic temperature T_N and recovers its value extrapolated from the paramagnetic domain. The depression of the thermal conductivity in $\text{Pr}_{0.5}\text{Sr}_{0.3}\text{Ca}_{0.2}\text{MnO}_3$ is accompanied by a sharp and exceptionally large decrease of the unit cell volume which makes about -0.5% . This effect is related to a specific arrangement of octahedral tilts in this compound at elevated temperatures, which are suddenly reorganized with the charge ordering at $T_N = T_{CO}$. The large drop of volume is followed by a smaller and gradual increase between 185 and 150 K. This is a common effect of orbital ordering, associated with increasing size of the Mn^{3+}O_6 octahedra with the J-T distortion.

In the case of $\text{Pr}_{0.5}\text{Ca}_{0.5}\text{MnO}_3$ the orbital ordering at $T_{CO} = 245$ K is characterized by a small increase of the unit cell volume, but the transition is not accompanied by any marked anomaly in the thermal conductivity. The thermal conductivity shows, however, a minimum at 180 K and a broad enhancement at lower temperatures. Below 100 K it surpasses significantly the thermal conductivity of the $\text{Pr}_{0.5}\text{Sr}_{0.5}\text{MnO}_3$ sample. The minimum of thermal conductivity is likely associated with a small decrease of the unit cell volume at 170 K. The occurrence of the anomaly close to $T_N = 175$ K instead of T_{CO} could be related to the fact that the transition from the high temperature disordered state to the ordered one is diffusive—see the lower panel of Fig. 4.

In summary, we have studied the magnetic, transport, thermal, and structural properties of several praseodymium based manganites. It appears that the CE- and A-type antiferromagnetic phases exhibit quite distinct transport properties, their ground state is insulating in the former and conducting (2-dim) in the latter one; the itinerant behavior being restricted to the ferromagnetically coupled MnO_2 layers in which the $\text{Mn}^{3+}/\text{Mn}^{4+}$ ordering is in fact absent. In all systems the thermal conductivity is low. We associate this observation with phonon scattering processes which involve the dynamics of d_γ states. These active J-T modes are often partially frozen and can be then evidenced by diffraction methods as small, ordered, or disordered distortions. The thermal conductivity is enhanced only when the electronically homogeneous state (metallic or insulating) is formed. In that case the dynamic J-T modes are suppressed or a complete (static) J-T ordering develops.

The authors acknowledge the financial support of the Grant Agency of the Academy of Sciences of the Czech Republic (Grant No. A1010610/1996).

- ¹A. J. Millis, B. I. Shraiman, and R. Mueller, *Phys. Rev. Lett.* **77**, 175 (1996).
- ²J. M. De Teresa, M. R. Ibarra, P. A. Algarabel, C. Ritter, C. Marquina, J. Blasco, J. García, A. del Moral, and Z. Arnold, *Nature (London)* **386**, 256 (1997).
- ³Z. Jirák, J. Hejtmánek, K. Knížek, and R. Sonntag, *J. Solid State Chem.* **132**, 98 (1997).
- ⁴V. Caignaert, E. Suard, A. Maignan, Ch. Simon, and B. Raveau, *J. Magn. Magn. Mater.* **53**, 153 (1996).
- ⁵D. B. Marsh and P. E. Parris, *Phys. Rev. B* **54**, 16 602 (1996).
- ⁶J. Hejtmánek, Z. Jirák, S. Krupička, C. Martin, Ch. Simon, A. Maignan, B. Raveau, E. Grivei, and J. P. Issi, *J. Appl. Phys.* **81**, 4975 (1997).
- ⁷D. W. Visser, A. P. Ramirez, and M. A. Subramanian, *Phys. Rev. Lett.* **78**, 3947 (1997).
- ⁸M. R. Ibarra (private communication).

Influences on relaxation of exchange biasing in NiO/Ni₆₆Co₁₈Fe₁₆ bilayersP. A. A. van der Heijden^{a)} and T. F. M. M. MaasDepartment of Physics, Interuniversity Research Institute COBRA,
Eindhoven University of Technology (EUT), 5600 MB Eindhoven, The NetherlandsJ. C. S. Kools,^{b)} F. Roozeboom, and P. J. van der Zaag

Philips Research Laboratories, Prof. Holstlaan 4, 5656 AA Eindhoven, The Netherlands

W. J. M. de Jonge

Department of Physics, Interuniversity Research School COBRA,
Eindhoven University of Technology (EUT), 5600 MB Eindhoven, The Netherlands

The stability of the exchange biasing field, H_{eb} , has been studied for NiO/Ni₆₆Co₁₈Fe₁₆ bilayers. A forced antiparallel alignment of the ferromagnetic magnetization to H_{eb} results in a gradual decrease and even a reversal of H_{eb} . The decrease of H_{eb} increases with temperature and is independent of the external field and NiO layer thickness. This decrease can be interpreted by a thermally assisted relaxation process. A new effect of the relaxation process on H_{eb} is demonstrated by using different cooling rates. © 1998 American Institute of Physics. [S0021-8979(98)18111-2]

I. INTRODUCTION

Direct exchange coupling at the interface between a ferromagnetic (F) layer and an antiferromagnetic (AF) layer may result in exchange biasing,¹ which induces a unidirectional anisotropy of the F layer. The unidirectional anisotropy gives rise to a shift of the hysteresis loop of the F layer along the field axis, which is equal to the exchange biasing field, H_{eb} . The magnitude of H_{eb} depends on temperature and becomes zero at a temperature called the blocking temperature, T_B . It is known that directing the external field (and thereby the magnetization of the F layer) antiparallel to H_{eb} while cooling at temperatures below T_B results in a decrease of H_{eb} .^{2,3}

Recently, we have shown that an antiparallel alignment of the magnetization of the F layer to H_{eb} at a constant temperature results in a gradual decrease and even a reversal of H_{eb} .⁴ The observed behavior of H_{eb} is interpreted by a macroscopic two-level model. The two-level model can result from an AF layer consisting of AF domains with uniaxial anisotropy, which are laterally decoupled and exchange-coupled to the F layer following Fulcomer and Charap.⁵ This results in an absolute and a local energy minimum for the sublattice (staggered) magnetization direction of an AF domain, see insets of Fig. 1. After cooling the sample in an applied magnetic field from above T_B to a certain temperature below T_B , the staggered magnetization directions of the AF domains are assumed to be distributed over the two energy minima according to the Boltzmann distribution function. This situation (at $t=0$) gives rise to the observed ex-

change biasing field and is shown in the inset (a) of Fig. 1. The forced antiparallel alignment of H_{eb} and the magnetization of the F layer after $t=0$ results in an interchange of the two energy minima. Subsequently, a thermally assisted redistribution of the now nonequilibrium distribution of the staggered magnetization directions of the AF domains occurs [see inset (b) of Fig. 1] and, therefore, a relaxation of H_{eb} . Among others, the relaxation time of an AF monodomain

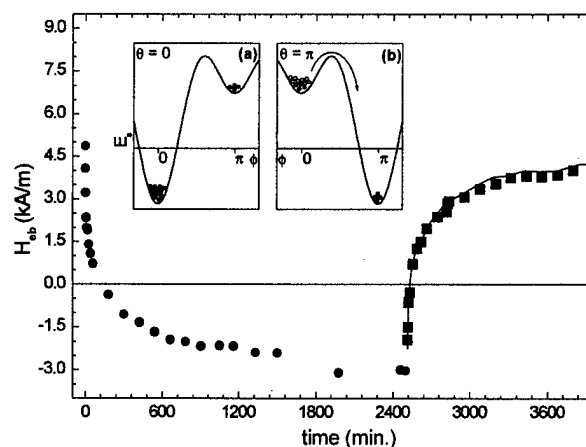


FIG. 1. The time dependence of H_{eb} at 425 K for Si(100)/40 nm NiO/5 nm Ni₆₆Co₁₈Fe₁₆/5 nm Ta. At $t=0$ the external field is reversed, forcing an antiparallel alignment of the magnetization of the F layer and H_{eb} (circles). After 42 h (2520 min.), the direction of the external field and thereby the magnetization of the F layer is reversed again (squares). The line after $t=2520$ min. represents the inverted data for H_{eb} after $t=0$. The insets show a schematic representation of dependence of the energy per unit area, E_s , on the angle ϕ of the staggered magnetization of an AF domain with uniaxial anisotropy, which is exchange coupled to a F layer with the magnetization directed along $\theta=0$ (a) and π (b). The circles represent the distribution over the two minima at thermal equilibrium, $t=0$ (a) and just after the reversal of the magnetization of the F layer (b).

^{a)}Present address: AMC, 75 Robin Hill Road, Goleta, CA 93117.

^{b)}Present address: CVC Products, 3100 Laurelview Court (Bldg. H), Fremont, CA 94538.

increases with thickness, which is assumed to be correlated to the grain size.

Here, we report to which extent the Fulcomer-Charap model provides an at least qualitative description of the observed decrease of H_{eb} after reversing the applied field (and thereby the magnetization direction of the F layer) at $t=0$. The implications of the model for the observed $H_{eb}(t)$ are demonstrated by experiments using different cooling rates from above T_B to room temperature.

II. EXPERIMENTAL DETAILS

Samples consisting of Si(100)/40 or 60 nm NiO/5 nm $\text{Ni}_{66}\text{Co}_{18}\text{Fe}_{16}$ /5 nm Ta were grown at room temperature in an applied field of 10–15 kA/m by a multisource sputter apparatus. Pressure prior to deposition was typically 10^{-8} Torr. The metallic layers were deposited by dc-magnetron sputtering at a pressure of 5 mTorr Ar and the NiO layers were deposited by rf-magnetron sputtering from a NiO target in an Ar pressure of 1 mTorr. After deposition, the samples were annealed up to 500 K after which the samples were field-cooled down to room temperature in about 10 h in order to improve the exchange biasing.

The experiments were carried out using a variable temperature Magneto-Optical Kerr Effect (MOKE) apparatus. The sample was heated from room temperature to the desired temperature in an external field, which was applied parallel to H_{eb} . Subsequently, H_{eb} was measured as a function of time at a constant temperature and external field. Note, that H_{eb} was obtained from a hysteresis loop measurement during which the direction of the applied field (and the magnetization of the F layer) was varied. This implies that relaxation contributions to H_{eb} faster than half the hysteresis loop time of 12 s cannot be observed.

III. RESULTS AND DISCUSSION

The blocking temperature for the NiO/ $\text{Ni}_{66}\text{Co}_{18}\text{Fe}_{16}$ bilayers is 480 K, as determined from the temperature dependence of H_{eb} ,⁴ which is similar to the results obtained by others.³ Figure 1 shows H_{eb} as function of time at 425 K for Si(100)/40 nm NiO/5 nm $\text{Ni}_{66}\text{Co}_{18}\text{Fe}_{16}$ /5 nm Ta. At $t=0$ an external field is applied, which forces an antiparallel alignment of the magnetization of the F layer and H_{eb} . A gradual decrease of H_{eb} is observed resulting in zero exchange biasing within 2 h after which H_{eb} changes sign and becomes negative. After 42 h the external field and thereby the magnetization direction of the F layer is reversed, which results in an increase of H_{eb} . The increase of H_{eb} as a function of time is identical to the inverted behavior of H_{eb} observed after $t=0$. The reversibility of the time dependence of H_{eb} upon the reversal of the external applied field (and thereby the magnetization direction of the F layer) implies a magnetic origin and not some structural cause for the change in H_{eb} .

Within the Fulcomer-Charap model the relaxation of H_{eb} arises from the redistribution of the staggered magnetization directions of the AF domains due to the exchange coupling between the AF domains and the F layer. However, the magnetization directions of the AF domains may also be

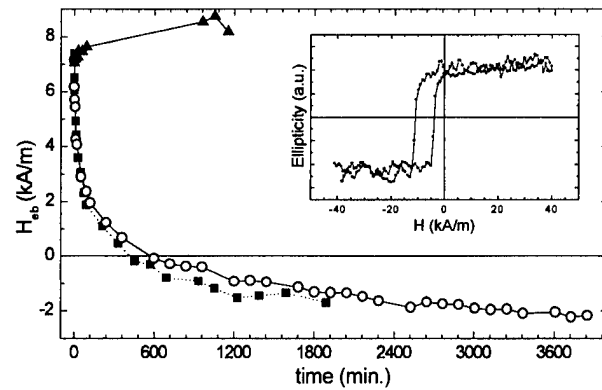


FIG. 2. The time dependence of H_{eb} at 425 K for Si(100)/40 nm NiO/5 nm $\text{Ni}_{66}\text{Co}_{18}\text{Fe}_{16}$ /5 nm Ta applying different magnitudes of the external field antiparallel to H_{eb} . The magnetization of the F layer is directed parallel to H_{eb} for an external field of -6 kA/m (up triangles) and antiparallel to H_{eb} for external fields of -45 kA/m (squares) and -125 kA/m (circles). The inset shows the hysteresis loop measurement at $t=0$.

influenced by an external applied field, e.g., if an AF domain possess a small magnetic moment due to finite size effects^{6,7} and the exchange coupling energy at the AF and F interface is smaller than the Zeeman coupling energy of the AF domain.⁸ Figure 2 shows the time dependence of H_{eb} for different magnitudes of the external field applied antiparallel to H_{eb} . The figure shows that a decrease of H_{eb} is only observed if the magnetization direction of the F layer is antiparallel to H_{eb} , but is independent of the magnitude of the (small) external field.

Figure 3 shows the normalized exchange biasing fields as a function of time during an antiparallel alignment of H_{eb} and the magnetization of the F layer at different temperatures for samples consisting of a 40 to 60 nm NiO layer. The exchange biasing fields are normalized to the initial value at $t=0$. The gradual decrease of H_{eb} increases with temperature, which is discussed elsewhere.⁴ Apart from the curves at 375 K, the decrease of H_{eb} is independent of the AF-layer thickness, which is inconsistent with the assumption that the AF grains are monodomain throughout the entire AF-layer.

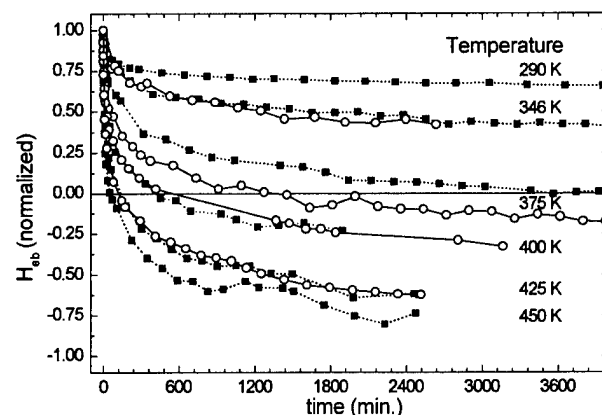


FIG. 3. The exchange biasing field, H_{eb} as function of time at different temperatures during a forced antiparallel alignment of the magnetization of the F layer and H_{eb} . The squares and circles represent the data of samples consisting 40 and 60 nm NiO/5 nm $\text{Ni}_{66}\text{Co}_{18}\text{Fe}_{16}$ /5 nm Ta grown on Si(100), respectively. The values of H_{eb} are normalized to the initial value $t=0$.

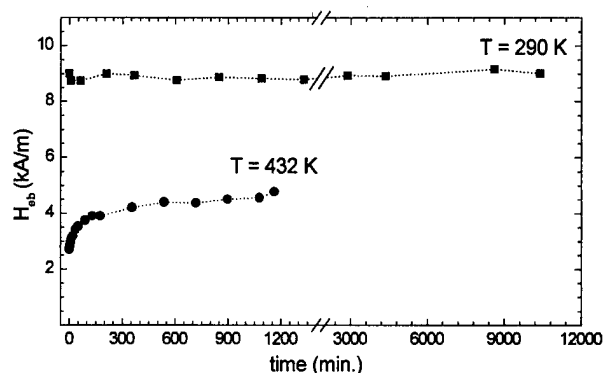


FIG. 4. The figure shows H_{eb} as function of time at 290 K after field cooling from 550 K down to 290 K in 2 min for Si(100)/40 nm NiO/5 nm $\text{Ni}_{66}\text{Co}_{18}\text{Fe}_{16}$ /5 nm Ta. Subsequently, the sample is heated up to 432 K in 20 min after which again the time dependence of H_{eb} is measured. During these experiments the magnetization of the F layer is directed parallel to H_{eb} . Note the break in the time axis.

thickness. In that case the relaxation rate of H_{eb} would be expected to reduce with increasing AF-layer thickness for columnar grown AF layers. Columnar growth has been observed for these NiO layers by transmission electron microscopy experiments.

Interestingly, the distribution of the AF domains over the two energy minima is not only influenced by the magnetization direction of the F layer, but also by a change in temperature. Decreasing the temperature results in a new equilibrium distribution, which will only be attained if the relaxation rate is faster than the cooling rate. This implies that the magnitude of H_{eb} is not only influenced by the direction of the magnetization of the F layer during cooling below T_B , which is already demonstrated by others,^{2,3} but also by the cooling rate. The effect of varying the cooling rate has been investigated by field cooling from above T_B to 290 K in 2 min instead of our standard 10 h. This results in a decreased H_{eb} of 9 kA/m, at $t=0$, instead of 12 kA/m. Figure 4 shows the subsequent variation of H_{eb} as a function of time for a *parallel* alignment of the magnetization of the F layer and H_{eb} after cooling in 2 min. The time dependence of H_{eb} at 290 K shows a constant value for H_{eb} indicating that the thermal energy is too small to relax the nonequilibrium distribution of the AF domains. However, after increasing the temperature to 432 K in 20 min, a relaxation of H_{eb} is observed from 2.7 kA/m to about 4.8 kA/m (see Fig. 4). Subsequent slow cooling to 290 K in about 7 h results in an increased value for H_{eb} of 13 kA/m.

IV. CONCLUSIONS

We have shown that the gradual decrease of H_{eb} during a forced antiparallel alignment of the magnetization of the F

layer to H_{eb} results from the exchange coupling at the F and AF interface and is independent of the (small) external field. The decrease of H_{eb} as a function of time increases with temperature indicating a thermally assisted relaxation process. These three observations are consistent with the model proposed by Fulcomer and Charap in which the decrease of H_{eb} is described by a thermally assisted relaxation process of AF domains, which are mutually decoupled and exchange-coupled to the F layer. However, the similar behavior of H_{eb} for the 40 and 60 nm NiO layers is inconsistent with the assumption that the AF grains are monodomain. This suggests that the mechanism of exchange biasing is more complex than described by the Fulcomer–Charap model, e.g., by the formation of AF domain walls in the AF grains as proposed by more recent models.^{9–11} We note, however, that the detailed nature of the exchange biasing mechanism is not important for the general assumptions on which the macroscopic two-level relaxation model is based.

An new effect of the relaxation process is demonstrated by field cooling from above T_B to 290 K in 2 min instead of 10 h, which results in a decrease of H_{eb} from 12 to 9 kA/m. This effect does not only support the relaxation model, but also shows the importance of using a sufficiently low cooling rate to obtain exchange biasing in spin valve devices when using a magnetic anneal treatment.

ACKNOWLEDGMENTS

Part of this work was supported by the Dutch Technology Foundation (STW) and the EC-ESPRIT project on Novel Magnetic Nanodevices of artificially layered Materials (NM).²

¹W. H. Meiklejohn and C. P. Bean, Phys. Rev. **102**, 1413 (1956); *ibid.* **105**, 904 (1957).

²V. S. Speriosu, D. A. Herman, Jr., I. L. Sanders, and T. Yogi, IBM J. Res. Dev. **34**, 884 (1990).

³S. Soeya, T. Imagawa, K. Mitsuoka, and S. Narishige, J. Appl. Phys. **76**, 5356 (1994).

⁴P. A. A. van der Heijden, T. F. M. M. Maas, W. J. M. de Jonge, J. C. S. Kools, F. Roozeboom, and P. J. van der Zaag, Appl. Phys. Lett. **72**, 492 (1998).

⁵E. Fulcomer and S. H. Charap, J. Appl. Phys. **43**, 4190 (1972).

⁶J. T. Richardson, D. I. Yiagas, B. Turk, K. Forster, and M. V. Twigg, J. Appl. Phys. **70**, 6977 (1991).

⁷R. H. Kodama, S. A. Makhlof, and A. E. Berkowitz, Phys. Rev. Lett. **79**, 1393 (1997).

⁸J. Nogues, D. Lederman, T. J. Moran, and I. K. Schuller, Phys. Rev. Lett. **76**, 4624 (1996).

⁹D. Mauri, H. C. Siegmann, P. S. Bagus, and E. Kay, J. Appl. Phys. **62**, 3047 (1987).

¹⁰A. P. Malozemoff, J. Appl. Phys. **63**, 3874 (1988).

¹¹N. C. Koon, Phys. Rev. Lett. **78**, 4865 (1997).

Thermal fluctuation aftereffect of exchange coupled films for spin valve devices

Junichi Fujikata,^{a)} Kazuhiko Hayashi, Hidefumi Yamamoto, and Masafumi Nakada
Functional Devices Research Laboratories, NEC Corporation, 1-10 Nisshin-cho, Fuchu-city, Tokyo 183,
Japan

The annealing-time-dependent change in the unidirectional anisotropy field for exchange coupled films with FeMn, PdPtMn, NiMn, and NiO, which are generally used for spin valve, was investigated after thermal annealing below their blocking temperatures. It was shown that the distribution of local blocking temperature was similar for each exchange coupled film. The annealing-time-dependent change in the unidirectional anisotropy was explained by the use of thermal fluctuation aftereffect model, and the relaxation time for the anisotropy change was found to be much larger for FeMn than for PdPtMn, NiMn, and NiO, when normalizing annealing temperature by their blocking temperatures. From the viewpoint of device application, however, NiMn was proven to be the most promising antiferromagnet in terms of thermal stability because of its highest blocking temperature. © 1998 American Institute of Physics. [S0021-8979(98)48211-2]

I. INTRODUCTION

Thermal stability of unidirectional anisotropy of pinned layers for spin valve films is very important for magnetoresistive head application, and studying the annealing-time-dependent change in unidirectional anisotropy is very useful for estimating device lifetime. With respect to the thermal stability of the exchange coupled films, the temperature dependence of exchange coupling field (H_{ex}) has been reported, and Fulcomer and Charap have explained this dependence based on thermal fluctuation theory.¹ Tsang, Speriosu *et al.*, and Soeya *et al.* have reported that FeMn/NiFe and NiO/NiFe films have a variety of exchange paths, and that local exchange anisotropy rotates at local blocking temperature.²⁻⁴ Nishioka *et al.* investigated how the grain size of antiferromagnets affects temperature dependence of exchange coupling for a FeMn/NiFe system, based on thermal fluctuation theory.⁵

In this study, exchange coupled films with FeMn, PdPtMn,⁶ NiMn, and NiO, which are generally used for spin valves, were annealed below the blocking temperatures (T_B), and their annealing-time-dependent change in exchange anisotropy was investigated. Experimental results were compared with those obtained in a thermal fluctuation after effect model.

II. EXPERIMENT

Ferromagnetic/antiferromagnetic bilayer films of $\text{Ni}_{81}\text{Fe}_{19}$ (15nm)/ $\text{Ni}_{50}\text{Mn}_{50}$ (30 nm), $\text{Ni}_{81}\text{Fe}_{19}$ (10 nm)/ $\text{Pd}_{17}\text{Pt}_{32}\text{Mn}_{51}$ (30 nm), $\text{Ni}_{81}\text{Fe}_{19}$ (6 nm)/ $\text{Fe}_{50}\text{Mn}_{50}$ (15 nm), and NiO (50 nm)/ $\text{Ni}_{81}\text{Fe}_{19}$ (6 nm) were prepared on glass substrates by rf and dc magnetron sputtering. The argon sputtering pressure was 3.0×10^{-1} Pa. To prevent oxidation, 10 nm of Ta capping layers were deposited for each film. They were annealed at 270 °C for 15 h for NiFe/NiMn, 270 °C for 5 h for NiFe/PdPtMn, and 200 °C for 1 h for

NiFe/FeMn under pressures of less than 2.0×10^{-4} Pa with a dc applied magnetic field of 500 Oe to induce unidirectional anisotropy.

The thermal stability of exchange coupled films with the antiferromagnets, NiMn, PdPtMn, FeMn, and NiO was studied by measuring the exchange anisotropy field (H_{ex}) at room temperature (RT) after thermal annealing below their blocking temperatures with a magnetic field of 500 Oe applied, antiparallel to their easy axes. Magnetization was obtained using a vibrating sample magnetometer (VSM). The crystalline structure and grain size of exchange coupled films was analyzed by x-ray diffraction (XRD) and cross sectional TEM.

III. RESULTS AND DISCUSSION

A. Exchange anisotropy rotation

Figures 1(a)–1(d) show H_{ex} dependence on temperature. T_B of NiFe/FeMn, NiFe/PdPtMn, NiFe/NiMn, and NiO/NiFe is about 160, 330, 360, and 200 °C. The exchange coupling energy for each system is 0.14, 0.18, 0.13, and 0.07 mJ/m² at RT, which are comparable to those reported by other groups.^{6,7} The average grain size for each manganese antiferromagnet is about 7 to 8 nm, and for NiO it is about 10 nm with columnar structures. The dotted lines show the exchange anisotropy change below the blocking temperature when exchange coupled films are annealed with a magnetic field of 500 Oe applied, antiparallel to the easy axes. The local exchange anisotropy of all exchange coupled films rotates below the blocking temperature, which shows they have a broad distribution of local blocking temperature, and the spin directions of antiferromagnetic grains rotate at the local blocking temperature.^{3,4}

Figure 2(a) shows H_{ex} dependence on annealing temperature. H_{ex} is normalized by the value at RT. H_{ex} decreases gradually with increasing annealing temperature, indicating that the local blocking temperature is distributed below the blocking temperatures for each exchange coupled film. Fig-

^{a)}Electronic mail: fujikata@memsub.cl.nec.co.jp

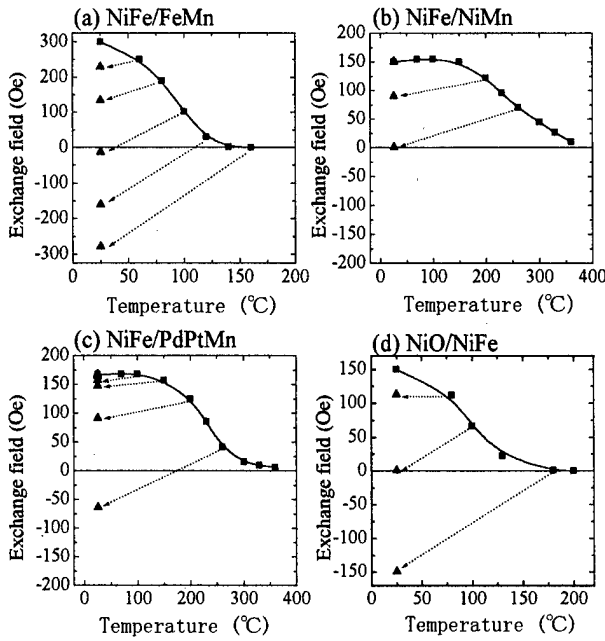


FIG. 1. Exchange field dependence on temperature for (a) NiFe/FeMn, (b) NiFe/NiMn, (c) NiFe/PdPtMn, and (d) NiO/NiFe. The dotted lines shows exchange field change by thermal annealing below the blocking temperature.

ure 2(b) shows H_{ex} dependence on annealing temperature normalized by the respective blocking temperatures. H_{ex} dependence on normalized annealing temperature is very similar for each exchange coupled film, which shows that the distribution of local blocking temperatures is similar for each exchange coupled film, under the assumption that the distri-

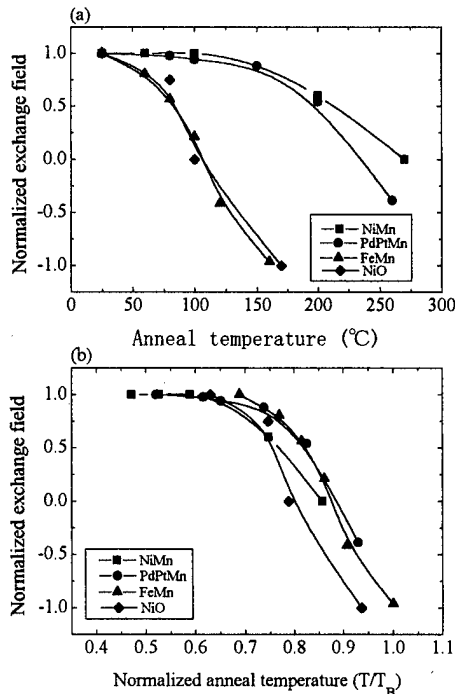


FIG. 2. (a) Normalized exchange field dependence on annealing temperature. (b) Normalized exchange field dependence on normalized annealing temperature (T/T_B).

bution of local blocking temperature corresponds to the distribution of exchange coupling energy.

B. Annealing-time-dependent change model for H_{ex}

We studied the annealing-time-dependent change in H_{ex} for exchange coupled films. A thermal fluctuation aftereffect model is assumed^{1,5} and results obtained with it are compared with experimental results. For simplicity, both ferromagnet and antiferromagnet are assumed to have uniaxial anisotropies with their easy axes, parallel to the X direction. The total energy of the antiferromagnetic layer is expressed by

$$U = \sum S_i [K_u D_i \sin^2 \theta_i - J_{ex} \cos(\theta_i - \varphi)]. \quad (1)$$

Here, K_u is the magnetic anisotropy constant of the antiferromagnetic grain, and J_{ex} is the exchange coupling constant. S_i and D_i are the interface area and the height of the antiferromagnetic grain. θ_i is the angle between the $+X$ direction and the interface magnetic moment of the i th antiferromagnetic grain, and φ is the angle between the $+X$ direction and the ferromagnetic moment.

E_{exi} and H_{ai} are introduced by

$$E_{exi} = J_{ex} S_i, \quad (2)$$

$$H_{ai} = K_u S_i D_i. \quad (3)$$

In this study, the ferromagnetic moment is antiparallel to the easy axis, and substituting φ for π , the energy of i th antiferromagnetic grain (U_i) is expressed by

$$U_i = H_{ai} \sin^2 \theta_i + E_{exi} \cos \theta_i, \quad (4)$$

$$\begin{aligned} dU_i/d\theta_i &= 2H_{ai} \sin \theta_i \cos \theta_i - E_{exi} \sin \theta_i \\ &= 2H_{ai} \sin \theta_i (\cos \theta_i - E_{exi}/2H_{ai}). \end{aligned} \quad (5)$$

When H_{ai} is larger than $E_{exi}/2$, the energy profile shows two local minimums at $\theta=0$ and π , respectively. The energy of the barrier is written as

$$E_{bi} = H_{ai} [1 + (E_{exi}/H_{ai})^2/4]. \quad (6)$$

Therefore, $p_{i+}(t)$ and $p_{i-}(t)$ are determined by their initial values and thermal excitation of the particles. [p_{i+} : the probability of the i th grain at higher minimum energy ($\theta=0$), p_{i-} : the probability of the i th grain at lower minimum energy ($\theta=\pi$)]. The main equations to determine them may be written as follows:

$$\begin{aligned} dp_{i-}/dt &= \nu_0 \{ p_{i+} \exp[-(E_{bi} - E_{exi})/(kT)] \\ &\quad - p_{i-} \exp(-E_{bi} + E_{exi})/(kT) \} \end{aligned} \quad (7)$$

$$p_{i+} + p_{i-} = 1 \quad (8)$$

(ν_0 : trial number per second to overcome the barrier).

Solving Eqs. (7) and (8), we get

$$p_{i-}(t) = p_L^{\text{inf}} [1 - \exp(-t/\tau_i)] + (1 - p_{0+}) \exp(-t/\tau_i). \quad (9)$$

Here, $p_L^{\text{inf}} = p_{i-}(t=\infty)$, the probability of the i th grain at the lower minimum energy at equilibrium, and τ_i , the relaxation time, are expressed by

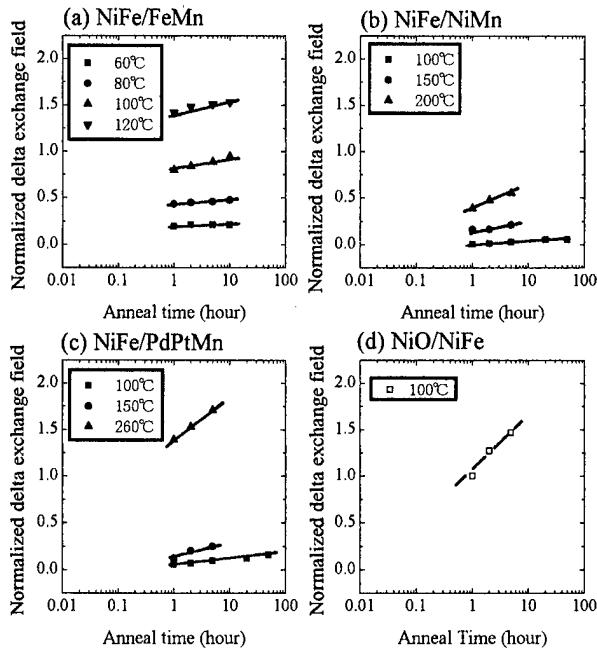


FIG. 3. Dependence of normalized exchange field change on annealing time for (a) NiFe/FeMn, (b) NiFe/NiMn, (c) NiFe/PdPtMn, and (d) NiO/NiFe.

$$p_L^{\text{inf}} = 1 / \{1 + \exp[-2E_{\text{ex}} / (kT)]\} \quad (10)$$

$$1/\tau_i = \nu_0 \{ \exp[-(E_{\text{bi}} - E_{\text{exi}}) / (kT)] + \exp[-(E_{\text{bi}} + E_{\text{exi}}) / (kT)] \}. \quad (11)$$

In this study, the initial value of p_{0+} is nearly equal to 1 and p_L^{inf} is nearly equal to 1 at equilibrium. Therefore, Eq. (9) is expressed by

$$p_{i-}(t) = 1 - \exp(-t/\tau_i). \quad (12)$$

Here, we introduce the distribution of the relaxation time for spin rotation, which arises from the distribution of grain size in the antiferromagnetic layer. The distribution function is assumed to be expressed by

$$\int g(\tau) / \tau d\tau = 1. \quad (13)$$

When $g(\tau)$ is assumed to be uniform between τ_{min} and τ_{max} (that is, the distribution of grain size in the antiferromagnetic layer is assumed to be uniform between maximum grain size and minimum grain size), the annealing-time-dependent change of H_{ex} is expressed by⁸

$$\begin{aligned} \Delta H_{\text{ex}} &= 2 \sum E_{\text{exi}} p_{i-} / M_s V_m \\ &\doteq 2 H_{\text{ex0}} \left\{ 1 - \int [g(\tau) / \tau] e^{-t/\tau} d\tau \right\} \\ &= 2 H_{\text{ex0}} [1 + (-\ln \tau_{\text{max}} + 0.577 + \ln t) / \ln(\tau_{\text{max}} / \tau_{\text{min}})] \end{aligned} \quad (14)$$

(M_s , V_m : saturation magnetization and volume of the ferromagnet). Therefore, the annealing-time-dependent change in H_{ex} is expressed by

$$\Delta H_{\text{ex}} / H_{\text{ex0}} = h + K \ln(t) \quad (15)$$

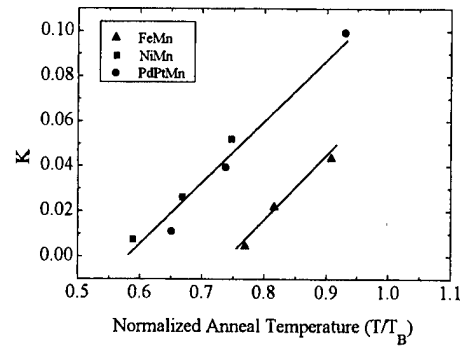


FIG. 4. Coefficient K dependence on normalized annealing temperature (T/T_B).

(ΔH_{ex} : change in exchange field, H_{ex0} : initial exchange field, h : rapid decrease term of H_{ex} caused by the distribution of local blocking temperature, K : coefficient for annealing-time-dependent change in H_{ex}).

That is, the annealing-time-dependent change in H_{ex} is explained by thermal fluctuation aftereffect and is proportional to the logarithm of annealing time.

C. Experimental results for annealing-time-dependent change in H_{ex}

Figures 3(a)–3(d) shows the change rate of the H_{ex} dependence on annealing time. Experimental results agree well with those obtained with the thermal fluctuation aftereffect model, and the annealing-time-dependent change in H_{ex} is proportional to the logarithm of annealing time. The slope versus logarithm of annealing time (coefficient K) increases with an increase in annealing temperature, because exchange anisotropy rotation arises from thermal fluctuation. For NiO/NiFe films, H_{ex} change rate dependence on annealing time is strong. Figure 4 shows coefficient K dependence on annealing temperature. In Fig. 4, annealing temperature is normalized by T_B . Coefficient K increases with increasing annealing temperature, and different antiferromagnets have different K values. It is shown that K is much smaller for FeMn than for NiMn, PdPtMn, and NiO. That is, the energy barrier for anisotropy rotation is larger for FeMn than that for NiMn, PdPtMn, and NiO, when annealing temperature is normalized by the respective blocking temperatures of the materials. Taking these blocking temperatures into account, however, the rate of decrease in H_{ex} for NiMn/NiFe is estimated to be no more than 20% after 10^5 hours of annealing at 100 °C, while for FeMn/NiFe it is 150%. From the viewpoint of device application, therefore, NiMn is proven to be the most promising antiferromagnet in terms of thermal stability.

¹E. Fulcomer and S. H. Charap, J. Appl. Phys. **43**, 4190 (1972).

²C. Tsang and K. Lee, J. Appl. Phys. **53**, 2605 (1982).

³V. S. Speriosu *et al.*, IBM J. Res. Dev. **34**, 884 (1990).

⁴S. Soeya *et al.*, J. Appl. Phys. **76**, 5356 (1994).

⁵K. Nishioka *et al.*, J. Appl. Phys. **80**, 4528 (1996).

⁶H. Kishi *et al.*, IEEE Trans. Magn. **32**, 3380 (1996).

⁷T. Lin *et al.*, IEEE Trans. Magn. **31**, 2585 (1995).

⁸L. Néel, Rev. Mod. Phys. **25**, 293 (1953).

Effect of buffer layer on antiferromagnetic grain size and exchange-coupling field of $\text{Cr}_{70}\text{Al}_{30}/\text{Fe}_{19}\text{Ni}_{81}$ bilayers

K. Ikarashi, Y. Otani, and K. Fukamichi

Department of Materials Science, Graduate School of Engineering, Tohoku University, Sendai 980-77, Japan

O. Kitakami and Y. Shimada

Research Institute of Scientific Measurements, Tohoku University, Sendai 980-77, Japan

J. Echigoya

Department of Materials Science, Faculty of Engineering, Iwate University, Morioka 020, Japan

H. Uyama

Magnetic Devices Division, Alps Electric Co., Ltd., 1-3-5 Higashi-Takami, Nagaoka 940, Japan

A. Makino

Central Research Laboratory, Alps Electric Co., Ltd., 1-3-5 Higashi-Takami, Nagaoka 940, Japan

$\text{MgO}/\text{Cr}_{70}\text{Al}_{30}/\text{Fe}_{19}\text{Ni}_{81}$ and $\text{ZnO}/\text{Cr}_{70}\text{Al}_{30}/\text{Fe}_{19}\text{Ni}_{81}$ layered films with different buffer layer thicknesses were prepared on (100)Si substrates in order to investigate the relationship among the exchange-coupling field, the grain size, and the lattice constant of the antiferromagnetic layer. The exchange-coupling field was found to consist of the intragrain exchange coupling and the intergrain coupling fields. The former field is inversely proportional to the product of the lattice constant and the grain size. The latter field is constant and changes its sign in association with the increase of the buffer layer thickness. [S0021-8979(98)48311-7] © 1998 American Institute of Physics.

I. INTRODUCTION

Unidirectional anisotropy induced by the exchange coupling between ferromagnetic and antiferromagnetic layers is useful for stabilizing ferromagnetic domain structures in magnetoresistive sensors and spin valve heads. For these applications, a variety of antiferromagnetic/ferromagnetic bilayers such as $\text{MnFe}/\text{Fe-Ni}$, $\text{NiMn}/\text{Fe-Ni}$, $\text{NiO}/\text{Fe-Ni}$, and $\text{CrMnPt}/\text{Fe-Ni}$ have been intensively investigated.¹⁻⁵

Recently we have found that $\text{Cr}_{70}\text{Al}_{30}$ alloy is promising as an antiferromagnetic layer for the exchange-coupled bilayer because of its high Néel temperature of 900 K,⁶ high corrosion resistance, and high electrical resistivity of 1300 $\mu\Omega\text{ cm}$ at room temperature. Our previous studies showed that the exchange-coupling field of $\text{Cr}_{70}\text{Al}_{30}/\text{Fe}_{19}\text{Ni}_{81}$ bilayers ranges about 100 Oe and is inversely proportional to the product of the antiferromagnetic grain size and the lattice constant.^{7,8}

In the present study, MgO (or ZnO)/ $\text{Cr}_{70}\text{Al}_{30}/\text{Fe}_{19}\text{Ni}_{81}$ layered films with different buffer layer thicknesses were prepared to alter the crystallographic states in the antiferromagnetic layer such as the grain size and the lattice constant. The effects of the crystallographic states on the exchange-coupling field are discussed in terms of the intergrain coupling.

II. EXPERIMENT

MgO (or ZnO)/ $\text{Cr}_{70}\text{Al}_{30}/\text{Fe}_{19}\text{Ni}_{81}$ layered films were deposited on (100)Si substrates by a magnetron sputter deposition method. The MgO or ZnO buffer layer was first deposited with a rf power of 200 W, and then $\text{Cr}_{70}\text{Al}_{30}/\text{Fe}_{19}\text{Ni}_{81}$ bilayers were deposited with a dc power of 30 W. The MgO

buffer layer thickness was varied from 0 to 1000 Å, while the ZnO buffer layer thickness was varied from 0 to 500 Å. The base pressure before the deposition was 4×10^{-7} Torr. Argon pressure during the deposition was 4×10^{-3} Torr for the buffer layers and the following bilayers. A magnetic field of 300 Oe was applied during the deposition. No postannealing was carried out.

Magnetization measurements were performed by a vibrating sample magnetometer (VSM). The exchange-coupling field H_{ex} was defined as the shift of the hysteresis loop along the applied field axis. The crystal structure, the grain size, and the lattice constant were examined by x-ray ($\text{Cu K}\alpha$) diffractometry.

III. RESULTS AND DISCUSSION

The exchange-coupling field H_{ex} appears when the $\text{Cr}_{70}\text{Al}_{30}$ layer thickness reaches about 300 Å. This critical thickness is much thicker than that for MnFe (~ 50 Å),³ suggesting that the magnetocrystalline anisotropy of the $\text{Cr}_{70}\text{Al}_{30}$ layer is relatively small, and the $\text{Cr}_{70}\text{Al}_{30}$ layer cannot sustain a single antiferromagnetic domain structure. The exchange-coupling field H_{ex} is thus considered to appear when the antiferromagnetic layer is thick enough to accommodate an antiferromagnetic domain wall parallel to the film surface. In other words, the antiferromagnetic/ferromagnetic interfacial exchange coupling energy arises from the formation of the antiferromagnetic domain wall. Therefore we fixed the antiferromagnetic $\text{Cr}_{70}\text{Al}_{30}$ layer thickness at 1000 Å, and varied the MgO or ZnO buffer layer thickness in order to change the grain size and the lattice constant of the $\text{Cr}_{70}\text{Al}_{30}$ layer. The x-ray diffraction analyses show that the

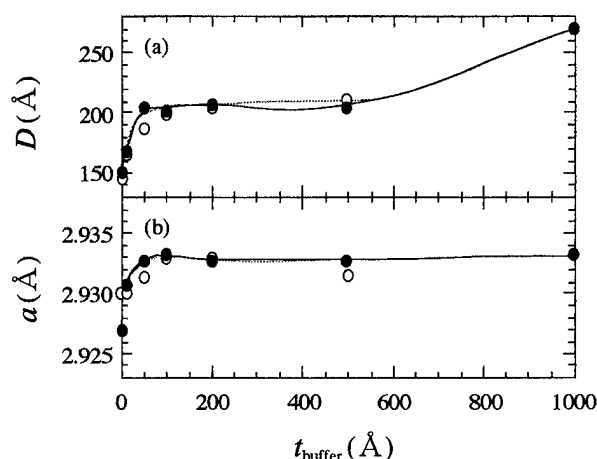


FIG. 1. (a) The grain size D and (b) the lattice constant a as a function of buffer layer thickness t_{buffer} for the antiferromagnetic $\text{Cr}_{70}\text{Al}_{30}$ layer in MgO (●) [or ZnO (○)]/ $\text{Cr}_{70}\text{Al}_{30}$ / $\text{Fe}_{19}\text{Ni}_{81}$ layered films.

$\text{Cr}_{70}\text{Al}_{30}$ layer has a bcc structure and that no clear preferential orientation is obtained for all the thicknesses of the buffer layers.

Figures 1(a) and 1(b) show the grain size D and the lattice constant a of the antiferromagnetic $\text{Cr}_{70}\text{Al}_{30}$ layer as a function of buffer layer thickness t_{buffer} . The grain size D was evaluated by Scherrer's equation. For both MgO and ZnO buffer layers, the values of D sharply increase with t_{buffer} and are almost saturated at around $t_{\text{buffer}} \approx 100$ Å. In the case of the MgO buffer layer, the value of D again increases gradually above $t_{\text{buffer}} \approx 500$ Å. On the other hand, the values of a for both MgO and ZnO buffer layers seem saturated above $t_{\text{buffer}} \approx 100$ Å, indicating that the lattice strain at the interface between the buffer layer and the $\text{Cr}_{70}\text{Al}_{30}$ layer is released with increasing t_{buffer} .

These variations clearly reflect on the exchange-coupling field H_{ex} and the coercive field H_c as shown in Figs. 2(a) and 2(b). The variations of H_{ex} and H_c are quite similar. For the films with the MgO buffer layer, both H_{ex} and H_c decrease remarkably up to $t_{\text{buffer}} \approx 100$ Å followed by gradual increase

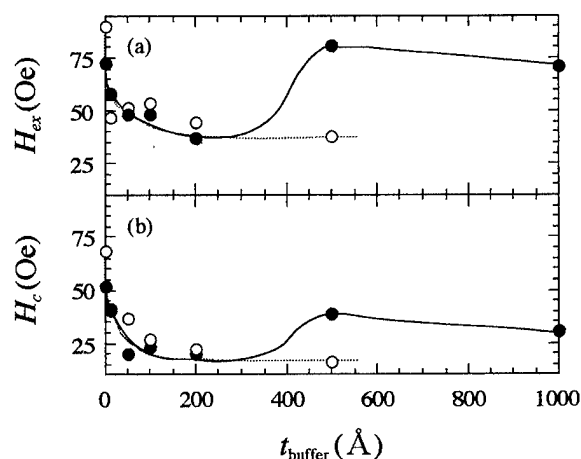


FIG. 2. (a) The exchange-coupling field H_{ex} and (b) the coercive field H_c as a function of buffer layer thickness t_{buffer} for MgO (●) [or ZnO (○)]/ $\text{Cr}_{70}\text{Al}_{30}$ / $\text{Fe}_{19}\text{Ni}_{81}$ layered films.

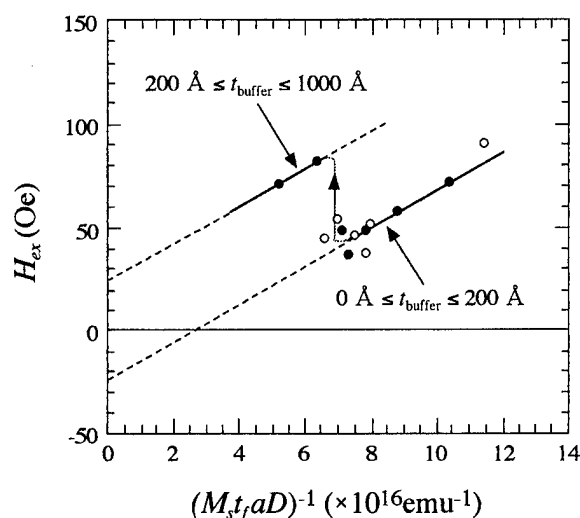


FIG. 3. H_{ex} vs $(M_s t_f a D)^{-1}$ plot for MgO (●) [or ZnO (○)]/ $\text{Cr}_{70}\text{Al}_{30}$ / $\text{Fe}_{19}\text{Ni}_{81}$ layered films with different buffer layer thickness t_{buffer} .

at around $t_{\text{buffer}} \approx 500$ Å. For the ZnO buffer layer, no gradual increase at $t_{\text{buffer}} \approx 500$ Å was observed.

In our previous study,⁸ we have shown that the exchange-coupling field is given by the sum of the intrinsic intragrain exchange-coupling field $H_{\text{ex}}^{\text{in}}$ and the extrinsic intergrain coupling field H_g . Since the $\text{Cr}_{70}\text{Al}_{30}$ layer is polycrystalline solid solution, the random field approximation⁹ was applied to evaluate the intrinsic exchange-coupling field $H_{\text{ex}}^{\text{in}}$ from the microscopic exchange energy at the interface J_i . Taking the grain size D as a characteristic length of the exchange-coupling area, the effective exchange-coupling energy J_{eff} is given by $J_{\text{eff}} = f_i J_i / \sqrt{N} = f_i a J_i / D$, where N is the number of exchange coupled spin pairs at the interface plane, f_i is the structural parameter of order unity, and a is the lattice constant of the antiferromagnetic layer. The intrinsic exchange-coupling field $H_{\text{ex}}^{\text{in}}$ is thus given by $H_{\text{ex}}^{\text{in}} = f_i J_i / M_s t_f a D$, where M_s is the saturation magnetization of the ferromagnetic layer and t_f is the thickness of the ferromagnetic layer. This shows that $H_{\text{ex}}^{\text{in}}$ is inversely proportional to $M_s t_f a D$. On the other hand, the extrinsic intergrain coupling field H_g is caused by the intergrain coupling which arises from the coupling between the antiferromagnetic grains through the grain boundaries or the ferromagnetic layer.

Using the obtained values of D and a , H_{ex} was plotted against $(M_s t_f a D)^{-1}$ in Fig. 3. All the values of H_{ex} are categorized into two lines with the same inclination which gives a reasonable magnitude of the microscopic exchange energy $J_i = 9.3 \times 10^{-16}$ erg. This value is in good agreement with the exchange energy evaluated from the Néel temperature of $\text{Cr}_{70}\text{Al}_{30}$. The value of H_g is negative (-20 ± 1 Oe) when the thickness t_{buffer} is lower than 200 Å, whereas it is positive ($+21 \pm 1$ Oe) when the thickness t_{buffer} is in the range from 200 to 1000 Å. This behavior is purely originated from the crystallographic states of the $\text{Cr}_{70}\text{Al}_{30}$ layer, because the same tendencies were observed, regardless of the kind of buffer layer. As mentioned above, therefore, the origin of H_g is the intergrain coupling through the antiferro-

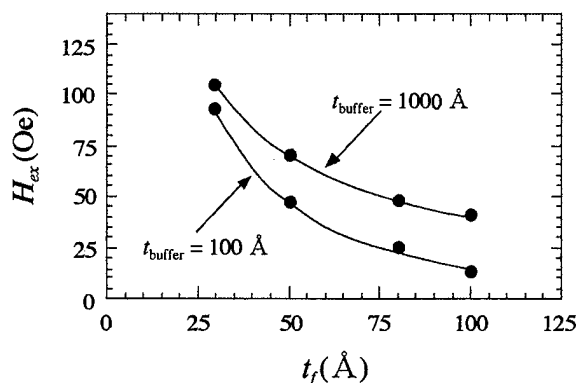


FIG. 4. The exchange-coupling field H_{ex} as a function of ferromagnetic layer thickness t_f for MgO/Cr₇₀Al₃₀/Fe₁₉Ni₈₁ layered films with different buffer layer thickness t_{buffer} .

magnetic grain boundaries or through the ferromagnetic layer.

In order to make this point clearer, Cr₇₀Al₃₀/Fe₁₉Ni₈₁ bilayers with different Fe₁₉Ni₈₁ thicknesses ($t_f = 30, 50, 80$, and 100 Å) were prepared on MgO buffer layers of 1000 or 100 Å. As shown in Fig. 4, the value of H_{ex} varies inversely proportional to the thickness t_f in keeping with the relationship that the exchange-coupling field H_{ex} for the thicker MgO buffer layer is larger than that for the thinner one by $2H_g$. By using the data in Fig. 4, $M_s H_{ex} t_f$ vs $M_s t_f$ plot was then carried out in Fig. 5. Since the relationship between the intrinsic and extrinsic exchange energies is given by $M_s H_{ex} t_f = f_i J_i / aD + M_s H_g t_f$, the value and sign of H_g can be determined as slopes from the $M_s H_{ex} t_f$ vs $M_s t_f$ plot. It should be noted that the first intrinsic energy term is constant

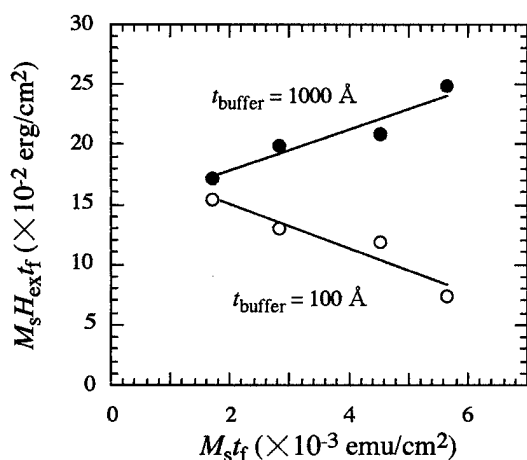


FIG. 5. $M_s H_{ex} t_f$ vs $M_s t_f$ plots for MgO(1000 Å)/Cr₇₀Al₃₀(1000 Å)/Fe₁₉Ni₈₁(50 Å) layered films (●), and MgO(100 Å)/Cr₇₀Al₃₀(1000 Å)/Fe₁₉Ni₈₁(100 Å) layered films (○).

for the fixed buffer layer thickness since the antiferromagnetic grain size and the lattice constant are the same. The values of $f_i J_i / aD$ are 15×10^{-2} erg/cm² for $t_{buffer} = 1000$ Å and 18×10^{-3} erg/cm² for $t_{buffer} = 100$ Å. Two linear lines are clearly observed with positive ($+19$ Oe) and negative (-18 Oe) slopes, indicating that the transition from the negative H_g to the positive H_g occurs with increasing the antiferromagnetic grain size D . This implies that when the MgO buffer layer is thin, the antiferromagnetic Cr₇₀Al₃₀ grains weakly couple through the grain boundaries, suppressing the formation of the antiferromagnetic domain wall. On the contrary, the antiferromagnetic grain growth associated with the increase of the buffer layer thickness t_{buffer} leads to a magnetically separated antiferromagnetic configuration, encouraging the formation of the antiferromagnetic domain wall during the magnetization reversal. Although the above explanation describes the trend of the transition, it is difficult to explain the origin of the positive H_g . This requires further study.

In conclusion, the exchange-coupling mechanism of the MgO (or ZnO)/Cr₇₀Al₃₀/Fe₁₉Ni₈₁ layered films with different buffer layer thicknesses was investigated in connection with the crystallographic states in the antiferromagnetic layer. The grain size and the lattice constant of the Cr₇₀Al₃₀ layer were significantly varied with the thickness of the buffer layer. The exchange-coupling field was found to consist of the intragrain intrinsic exchange-coupling field and the intergrain exchange-coupling field. The former is inversely proportional to the product of the lattice constant and the grain size. The latter changes its sign from negative to positive when the thickness of the buffer layer exceeds 200 Å.

ACKNOWLEDGMENTS

This work is partly supported by the New Energy and Industrial Technology Development Organization (NEDO), RFTF of the Japan Society for the Promotion of Science, and the Grant-in-Aid for Scientific Research from the Ministry of Education, Science, Sports and Culture in Japan.

¹C. Tsang, IEEE Trans. Magn. **MAG-25**, 3692 (1989).

²B. Dieny, V. S. Speriosu, S. S. Parkin, B. A. Gurney, D. R. Wilhoit, and D. Mauri, Phys. Rev. B **43**, 1297 (1991).

³T. Lin, D. Mauri, N. Stand, C. Hwang, J. K. Howard, and G. L. Gorman, Appl. Phys. Lett. **65**, 1183 (1994).

⁴S. Soeya, T. Imagawa, K. Mitsuoka, and S. Narishige, J. Appl. Phys. **76**, 5356 (1994).

⁵S. Soeya, H. Hoshiya, M. Fuyama, and S. Tadokoro, J. Appl. Phys. **80**, 1006 (1996).

⁶E. Koser, E. Wachtel, and K. Grube, Z. Metallkd. **54**, 393 (1963).

⁷H. Uyama, Y. Otani, K. Fukamichi, O. Kitakami, Y. Shimada, and J. Echigoya, J. Magn. Soc. Jpn. **21**, 911 (1997) (in Japanese).

⁸H. Uyama, Y. Otani, K. Fukamichi, O. Kitakami, Y. Shimada, and J. Echigoya, Appl. Phys. Lett. **71**, 1258 (1997).

⁹A. P. Malozemoff, Phys. Rev. B **35**, 3679 (1987).

Magnetic, temperature, and corrosion properties of the NiFe/IrMn exchange couple

A. J. Devasahayam, P. J. Sides, and M. H. Kryder

Data Storage Systems Center, Carnegie Mellon University, Pittsburgh, Pennsylvania 15213

Exchange biasing properties of the NiFe/IrMn exchange couple were investigated by varying the IrMn composition and sputtering conditions. At a composition of Ir₂₀Mn₈₀ an exchange field of ~ 60 Oe and a coercivity of 8 Oe were obtained for the structure Si/Ta-75 Å/NiFe-250 Å/IrMn-500 Å. The maximum exchange field obtained was similar for rf diode, rf magnetron, and dc magnetron sputtering of the IrMn. X-ray diffraction measurements showed that the crystalline texture was (111) for both the NiFe and IrMn, but a strong crystalline texture did not necessarily correspond to a large exchange field. The interfacial exchange energy, J_k , was evaluated to be 0.145 erg/cm² and the minimum thickness of IrMn needed to support an exchange field was 75 Å. The blocking temperature was measured to be a function of the IrMn thickness and was in the range of 220–250 °C for thicknesses >200 Å. Below this, the blocking temperature rapidly decreased to a value of 130 °C at 75 Å of IrMn. Corrosion testing was done in a Battelle Class II type corrosive environment. Using the exchange field as a figure of merit, it was found that the IrMn corrosion properties were only slightly better than FeMn, and significantly worse than NiMn and CoNiO. We were also able to successfully fabricate NiFe based spin-valves pinned with IrMn and they show good magnetic properties. Our results show that IrMn is a good alternative to FeMn. © 1998 American Institute of Physics. [S0021-8979(98)18211-7]

I. INTRODUCTION

FeMn and NiO are the most commonly used antiferromagnetic exchange biasing materials.^{1,2} However, neither of them are ideal. FeMn has both poor corrosion resistance and poor temperature stability with a blocking temperature of 150 °C. NiO fares much better in these two areas, but has a low interfacial exchange energy of 0.059 erg/cm² which renders it unsuitable for high density, narrow track width applications. IrMn is a possible alternative material which was reported to have a good combination of exchange fields, corrosion resistance and temperature stability when coupled with Co₉₀Fe₁₀.³

In this article, the magnetic properties of IrMn when exchange coupled to NiFe are examined as a function of composition and sputtering parameters. The temperature stability was also investigated with respect to IrMn thickness. Corrosion properties were measured in an environmental chamber and compared with FeMn, CoNiO, and NiMn. Finally, NiFe based spin-valve structures were fabricated with IrMn as the exchange pinning material, and these showed good magnetic properties.

II. EXPERIMENTAL PROCEDURE

IrMn was deposited from a Mn target with Ir chips bonded to it. The number of Ir chips attached was adjusted in order to obtain optimum magnetic properties. These properties were characterized with a $B-H$ loop tracer and vibrating sample magnetometer. Rf diode sputtered films were deposited in a unidirectional field of 35 Oe to define the pinning direction. Magnetron sputtered films had no external fields applied. Crystallographic properties were measured with a x-ray diffractometer and compositional information was obtained with an Energy Dispersive X-ray Fluorescence ma-

chine. Corrosion measurements were done in a Battelle Class II environmental chamber previously described.⁴

III. RESULTS AND DISCUSSION

A. Magnetic properties

Good exchange biasing properties of the NiFe/IrMn couple were obtained when the IrMn films deposited were in the antiferromagnetic phase. This corresponds to an Ir content in the range of 16–32 at. %. The Ir₂₀Mn₈₀ composition had the highest exchange fields as shown in Fig. 1(a).

The biasing properties were further optimized by varying the sputtering conditions. In all these experiments, the NiFe thickness was kept constant at 250 Å. A strong (111) texture for NiFe and IrMn was observed as is plotted in the x-ray scan in Fig. 1(b). The (111) peak of IrMn occurs at an angle $2\theta=41.52^\circ$, which corresponds to a lattice constant, a , of 3.76 Å.

The effect of varying the deposition pressure while keeping the power constant at 250 W is shown in Fig. 2. Also plotted in that figure is the (111) peak intensity, in counts, of the IrMn layer, which indicates the strength of this texture.

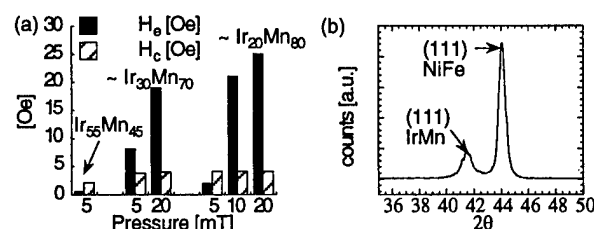


FIG. 1. (a) H_e and H_c for samples with different compositions sputtered at 250 W rf power and (b) a typical x-ray scan of a NiFe/Ir₂₀Mn₈₀ sample.

The plot shows that the exchange field (H_e) increases with increasing sputtering pressure to a maximum of 37 Oe at 30 mT of pressure. The (111) peak intensity of IrMn does not show a clear correlation with the exchange field. It does appear that a poor (111) texture corresponds to a large exchange field. Substrate bias is undesirable for good exchange properties, since zero bias yields the largest exchange field as shown in Fig. 3. Also, poor (111) crystalline texture of the IrMn is seen at zero bias. The exchange field increases as the sputtering power decreases and reaches a maximum of 55 Oe at 50 W of power as illustrated in Fig. 4. The IrMn (111) peak intensity seems to generally follow the opposite trend, increasing in intensity with increasing power. It can be concluded that low power, high pressure and zero substrate bias are desirable for good exchange fields, while strong (111) texture for IrMn does not correspond to good biasing fields. These samples also had coercivities of 4–12 Oe.

The effect of using magnetron sputtering instead of the previously used rf diode sputtering was studied with samples of the same structure. Optimizing the sputtering conditions for both rf and dc magnetron sputtering yielded a maximum exchange field of 57 and 62 Oe, respectively. These values are similar to those obtained with rf diode sputtering.

A minimum thickness of 75 Å of IrMn is needed for a large exchange field to be observed as shown in Fig. 5(a). Above this value, the exchange field reaches a peak of about 58 Oe with 200 Å and then gradually decreases on increasing the IrMn thickness. This is a commonly observed trend with exchange biasing materials. The exchange fields also follow the usual inverse relationship with the thickness of NiFe as illustrated in Fig. 5(b). By fitting a $1/t$ curve to the data, an interfacial exchange energy, J_k , of 0.145 erg/cm² is calculated. This value is larger than that of NiO, CoNiO, and NiMn as-deposited, but lower than that obtained when NiMn is annealed.

B. Temperature properties

The blocking temperature was measured for several samples, with different IrMn thicknesses and these results are plotted in Fig. 6(a). In this figure, the exchange field for each sample is normalized to the original exchange field obtained at room temperature. This value decreases monotonically for all the samples. For thicknesses of 200 Å and above, the plotted lines are virtually the same leading to a blocking temperature in the range of 200–250 °C. Below this thickness of IrMn, the blocking temperature falls off and is about 130 °C for a 75 Å IrMn film. This trend is plotted in Fig. 6(b) and can be explained in terms of a “finite size effect.” The phenomenon arises out of the finite size of the system which bounds the correlation length⁵ and can be described by a simple scaling law shown in Eq. (1). In this equation, T_B is the blocking temperature, t is the thickness of IrMn, C_0 is the correlation length at $T=0$ K, and λ is the shift exponent for finite size scaling:⁶

$$\frac{T_B(\infty) - T_B(t)}{T_B(\infty)} = \left(\frac{C_0}{t} \right)^\lambda. \quad (1)$$

Assuming $T_B(\infty) = 523$ K (250 °C), $[1 - T_B/T_B(\infty)]$ is plot-

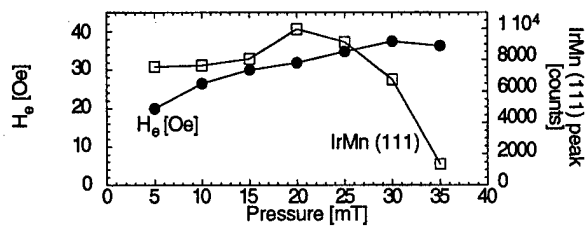


FIG. 2. H_e and IrMn (111) peak intensities vs sputtering pressure at 250 W rf power for NiFe-250 Å/IrMn-500 Å samples.

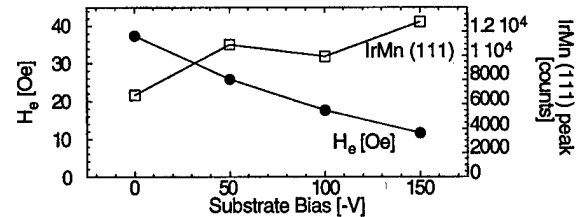


FIG. 3. H_e and IrMn (111) peak intensities vs substrate bias at 250 W rf power and 30 mT pressure for NiFe-250 Å/IrMn-500 Å samples.

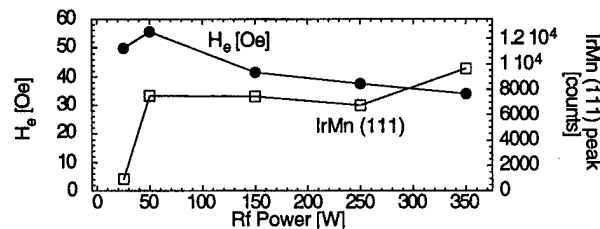


FIG. 4. H_e and IrMn (111) peak intensities vs power at a sputtering pressure of 30 mT for NiFe-250 Å/IrMn-500 Å samples.

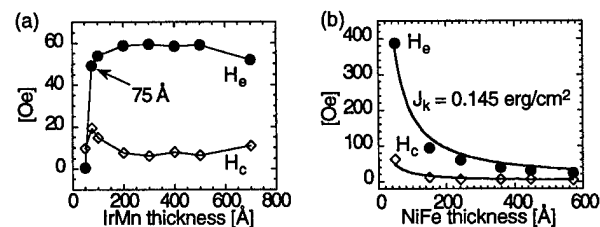


FIG. 5. H_e vs (a) the thickness of IrMn and (b) the thickness of NiFe, keeping NiFe constant at 250 Å and IrMn constant at 500 Å, respectively.

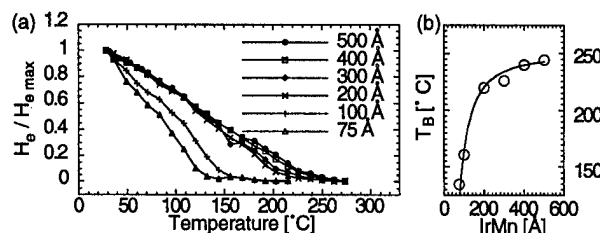


FIG. 6. (a) Normalized H_e vs temperature for Si/Ta/NiFe-250 Å/IrMn-X Å with IrMn thickness as a parameter and (b) blocking temperature vs IrMn thickness.

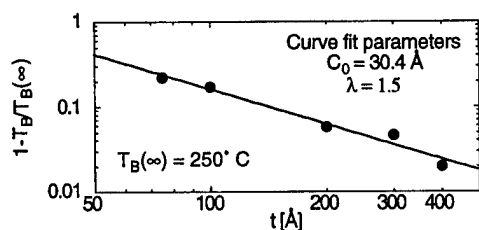


FIG. 7. Log-log plot of $1 - T_B/T_B(\infty)$ vs IrMn layer thickness assuming $T_B(\infty) = 250^\circ\text{C}$.

ted versus the IrMn layer thickness in a log-log plot shown in Fig. 7. The linear curve fit yields a value of 1.5 for λ , which is close to the theoretical value.⁶

C. Corrosion measurements

The corrosion resistance measurements were done in a Battelle Class II type of environment. The samples were exposed to the pollutants in an impinging jet configuration which was designed to have good uniformity of exposure of the sample surface to the pollutants. The parameters of the experiment are noted in the table inset of Fig. 8. Samples were cut into equal sizes to minimize any skewing of the data due to size effects. The exchange field was used as the figure of merit and was measured after successive exposures in the chamber. The sample structure used was: substrate/NiFe-250 Å/exchange material-500 Å. The exchange materials tested were FeMn, NiMn, CoNiO, and IrMn. The normalized exchange field vs exposure time is shown in Fig. 8. From the figure, it can be seen that CoNiO has the best corrosion properties, showing no degradation over the entire exposure time of 140 h. NiMn is second best, showing very little deterioration of the exchange field up to 40 h of exposure at which point the IrMn and FeMn provide almost no exchange bias. Between 15 and 40 h of exposure, the IrMn out performs the FeMn. As a comparison, metal-evaporated tape has a similar corrosion resistance, in terms of magnetic moment reduction over time, as does NiMn.⁴

D. NiFe based IrMn pinned spin-valves

NiFe based spin valves with an IrMn pinning layer were fabricated with and without Co to enhance the GMR effect. The large pinning field of IrMn is illustrated in the hysteresis loop of a NiFe spin valve shown in Fig. 9(a). In this case, a pinning field of 650 Oe was obtained for 29 Å of NiFe. The

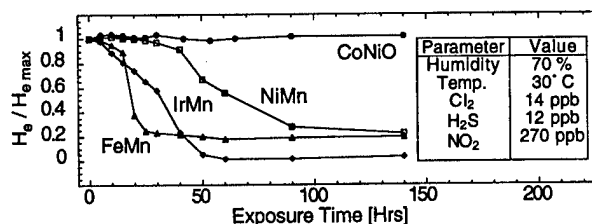


FIG. 8. Normalized H_e vs exposure time for several exchange couples with the structure substrate/NiFe-250 Å/exchange material-500 Å.

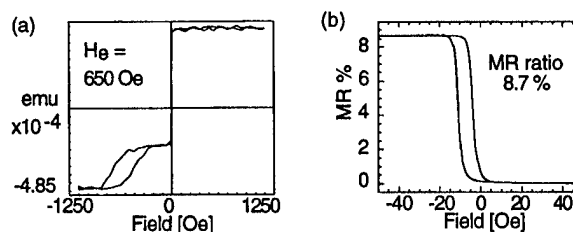


FIG. 9. (a) MH Loop of a spin valve with the structure Ta/NiFe-67 Å/Cu-27 Å/NiFe-29 Å/IrMn-125 Å. (b) MR loop of the free layer of a Co enhanced spin valve with the structure Ta/NiFe-47 Å/Co-17 Å/Cu-24 Å/Co-13 Å/NiFe-22 Å/IrMn-200 Å.

MR response of a Co enhanced spin valve is shown in Fig. 9(b). The maximum MR value in this case, with Co on both Cu interfaces is 8.7%. NiFe only spin-valves and Co on the pinned layer/Cu interface spin-valves had MR ratios of 4.9% and 7.4%, respectively.

IV. SUMMARY

By varying the IrMn alloy composition and sputtering conditions, an exchange field of 60 Oe was obtained when $\text{Ir}_{20}\text{Mn}_{80}$ was coupled with 250 Å of NiFe. This corresponds to an interfacial exchange energy of 0.145 erg/cm². A minimum thickness of 75 Å of IrMn was needed in order to provide a large exchange. The blocking temperature was found to be a function of IrMn thickness and, this was explained in terms of a finite size effect. At thicknesses of IrMn > 200 Å, the blocking temperature was in the range of 220–250 °C. Corrosion measurements showed that IrMn was slightly less corrosive than FeMn, but worse than CoNiO and NiMn. NiFe based spin-valves fabricated with IrMn had an MR ratio as high as 8.7%. These spin-valves had a pinning field of 650 Oe for 29 Å of NiFe.

Our results show that IrMn has significantly superior temperature stability and exchange biasing properties when compared to FeMn. However, it has only marginally better corrosion resistance than FeMn. We have also found a dependence of the blocking temperature on the thickness of IrMn. Considering all these properties, IrMn appears to be a good alternative to FeMn for providing domain stabilization for MR heads and a pinning layer for spin-valve heads.

ACKNOWLEDGMENTS

This work is supported in part by Storage Tek and by the National Science Foundation under Grant No. ECD-8907068. The United States Government has certain rights in this material.

¹ M. F. Toney, C. Tsang, and J. K. Howard, J. Appl. Phys. **70**, 6227 (1991).

² J. X. Shen and M. T. Kief, J. Appl. Phys. **79**, 5008 (1996).

³ H. N. Fuke, K. Saito, Y. Kamiguchi, H. Iwasaki, and M. Sahashi, J. Appl. Phys. **81**, 4004 (1997).

⁴ J. P. Kampf, P. J. Sides, and G. W. D. Spratt, J. Elect. Chem. Soc. **142**, 3550 (1995).

⁵ S. S. Parkin and V. S. Speriosu, Magnetic Properties of Low-Dimensional Systems **50**, 110 (1990).

⁶ T. Ambrose and C. L. Chien, J. Appl. Phys. **79**, 5920 (1996).

Spin-flop tendencies in exchange-biased Co/CoO thin films

J. A. Borchers,^{a)} Y. Ijiri, S.-H. Lee, and C. F. Majkrzak

National Institute of Standards and Technology, Gaithersburg, Maryland 20899

G. P. Felcher

Argonne National Laboratory, Argonne, Illinois 60439

K. Takano, R. H. Kodama, and A. E. Berkowitz

Center for Magnetic Recording Research, University of California at San Diego, La Jolla, California 94720

In order to study the antiferromagnetic (AFM) spin structure near the interface of exchange-biased bilayers, polarized neutron diffraction measurements were performed on a series of (111) Co (7.5 nm)/CoO (X nm) and CoO (X nm) thin films where $X=20, 40$, and 100 nm. In these samples, field cooling through the Néel temperature of the AFM increases the component of the CoO moment perpendicular to the applied field, relative to the parallel component. The subsequent application of a 500 Oe field perpendicular to the cooling direction rotates both the Co and CoO moments. Experiments on CoO films without Co showed a smaller difference between the parallel and perpendicular CoO moments in response to cooling and applied fields. Exchange coupling between the Co and CoO layers is apparently responsible for the increased projection of the AFM moments perpendicular to the cooling field. © 1998 American Institute of Physics. [S0021-8979(98)53011-3]

The term “exchange biasing” describes a phenomenon associated with interfacial coupling between ferromagnetic (FM) and antiferromagnetic (AFM) materials. In particular, a shift of the magnetic hysteresis loop along the field axis is observed after field cooling these composites through the Néel temperature of the AFM. Since its discovery over 40 years ago in oxidized Co particles,¹ a number of experimental studies^{2–6} have focused on layered systems because of their potential applications in magnetic sensors.⁷ Still unresolved, however, is the link between exchange biasing and the microscopic orientation of the spins in the AFM layer. Early theories^{1,8,9} assumed that the AFM spins at the interface couple collinearly to the FM layer. Alternately, Koon¹⁰ has suggested that the AFM and FM spins can align perpendicular depending on the interfacial structure. Takano *et al.*⁵ observed a correlation between the thermoremanent moment of polycrystalline CoO/MgO multilayers and the exchange biasing field of CoO/permalloy bilayers. This result suggested that uncompensated interfacial spins are the principal origin of exchange biasing in that system. Unfortunately, it is difficult to determine the AFM spin structures involved in exchange biasing because few experimental techniques can probe AFM order in buried and interfacial layers.

The scope of the present experiment is to determine the orientation of the AFM moments relative to the FM spins in (111) Co (7.5 nm)/CoO (X nm) thin films ($X=20, 40$, and 100 nm) using polarized neutron diffraction methods. After field cooling our epitaxial samples, we find that the percentage of CoO spins perpendicular to the field exceeds the percentage of parallel spins. The difference between the parallel and perpendicular AFM moment projections in the Co/CoO bilayers appears to be induced by proximity to the FM layer.

This behavior may arise from perpendicular coupling between the Co and CoO spins, as predicted by Koon.¹⁰

For this study, the CoO films were reactively sputtered at 100°C in 2 mTorr, of Ar and a small partial pressure of oxygen (0.09 mTorr) onto 1 in-diam (0001) Al_2O_3 substrates. We examined five single-layer and bilayer samples with differing compositions, SiO_2 (10 nm)/CoO (X)/ Al_2O_3 ($X=40$ and 100 nm) and SiO_2 (10 nm)/Co (7.5 nm)/CoO (X)/ Al_2O_3 ($X=20, 40$, and 100 nm). In order to induce exchange biasing and uniaxial anisotropy in the FM layer, the Co/CoO bilayers were deposited in a 300 Oe field applied along the [1120] Al_2O_3 in-plane axis. High-angle x-ray diffraction confirms that the CoO layers are epitaxial with (111) preferred orientation and are twinned in the growth plane.¹¹ Fits to x-ray reflectivity data for the Co/CoO (40 nm) bilayer indicate that the width of the Co/CoO interface is approximately 1.0 nm due to roughness or interdiffusion.

Magnetization measurements, performed in a superconducting quantum interference device (SQUID) magnetometer, reveal that exchange biasing is observed for a comparable epitaxial Co/CoO (100 nm) bilayer grown under similar conditions on a smaller substrate. Figures 1(a) and 1(b) show hysteresis loops at 10 and 200 K respectively after cooling in a 10 kOe field applied along the same direction as the growth field. Both the coercive field and the exchange-biasing field, H_{eb} , change as a function of temperature, as shown in Fig. 1. These field values are expected to differ for bilayers with thinner CoO and may depend on the film structure as determined by the substrate characteristics.

For these and related biased layers,¹² the temperature marking the onset of biasing is nearly equal to the Néel temperature, T_N , of the AFM component. Bulk CoO orders as a collinear antiferromagnet below $T_N=291$ K. The spins are ferromagnetically aligned in (111) sheets and are nearly perpendicular to a $\langle 111 \rangle$ axis. The moment direction alternates

^{a)}Electronic mail: borchers@rdstrad.nist.gov

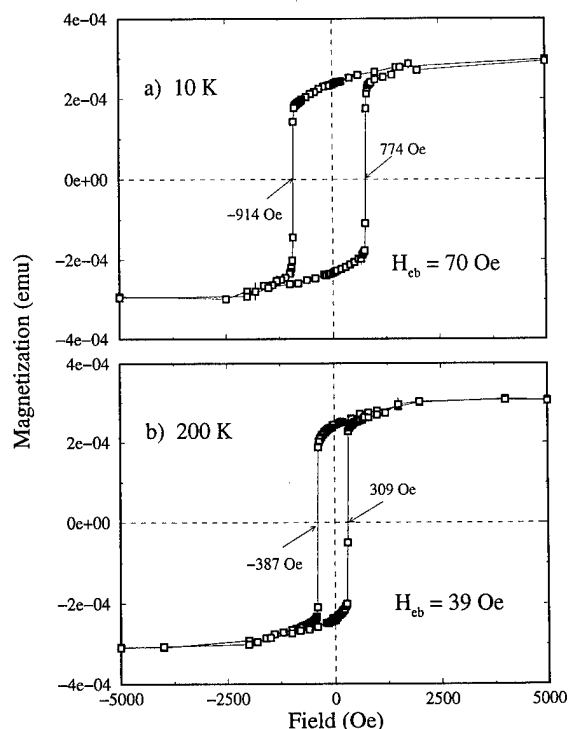


FIG. 1. Magnetization as a function of field for a Co/CoO (100 nm) bilayer at (a) 10 K and (b) 200 K after field cooling from room temperature in a 10 kOe field applied along the in-plane easy axis.

in neighboring (111) planes.¹³ The CoO spins can thus align in any of four equivalent {111} domains. For our thin films, the [111] “propagation axis” of one of these domains is parallel to the growth directions. Due to twinning, however, there are six additional propagation axes tilted 70.5° from the [111] growth direction. Complementary neutron diffraction studies¹⁴ revealed that a large portion of the CoO spins reside in these six off-axis domains. We restricted our study to the characterization of those spins in the (111) growth-axis domain, which give rise to a $(1/2\ 1/2\ 1/2)$ magnetic reflection in our neutron data.

To characterize the AFM structure associated with the biased state in the Co/CoO bilayers, we performed polarized neutron diffraction measurements on these samples using the spin-polarized triple-axis spectrometer (SPINS) at the NIST Research Reactor. An electromagnet provided fields ranging from 50 to 2400 Oe. Since the maximum field is limited, we examined our samples at 200 K, rather than 10 K, in order to ensure saturation of the Co layer upon field cooling (Fig. 1). On the SPINS spectrometer, polarizing elements were positioned before and after the sample to select the spin direction of the incident and scattered neutrons. The polarization efficiencies were approximately 92%. For all scans through the $(1/2\ 1/2\ 1/2)$ CoO reflection, we measured both the non-spin-flip (NSF) and spin-flip (SF) scattered intensities. The NSF intensity is proportional to the square of the average CoO moment projection parallel to the vertical applied field, while the SF intensity is proportional to the square of the average moment projection perpendicular to the field.¹⁵ These moment projections may belong to the same or to different (111) domains.

Figure 2 shows typical scans through the $(1/2\ 1/2\ 1/2)$

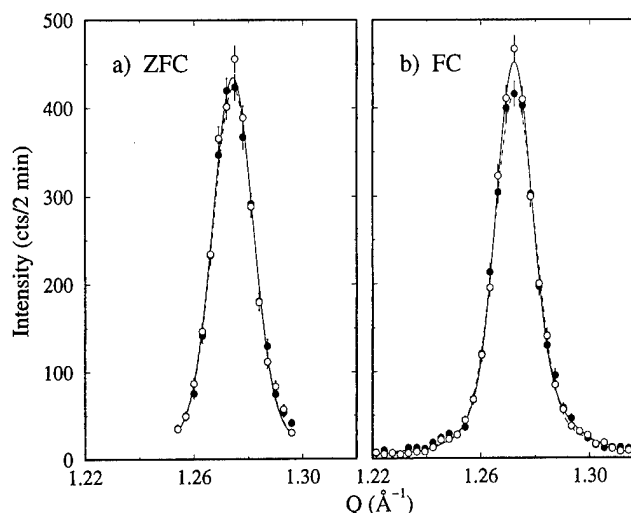


FIG. 2. Polarized neutron diffraction scan through the $(1/2\ 1/2\ 1/2)$ reflection for a Co/CoO (100 nm) bilayer at 200 K. The wave vector Q is defined as $Q = (4\pi/\lambda)\sin\theta$ where the neutron wavelength $\lambda = 0.417$ nm and θ is the scattering angle. The shaded circles represent the NSF intensity and the open circles mark the SF intensity. The data in (a) were obtained after demagnetizing the sample and then cooling in zero field. The data in (b) were obtained in a 2200 Oe field after field cooling in -2200 Oe from room temperature. These data have not been corrected for the efficiencies of the polarizing elements.

reflection for the Co/CoO (100 nm) bilayer at 200 K. After cooling the sample in zero field, the NSF and SF intensities are approximately equal [Fig. 2 (a)]. These results are consistent with random orientation of the CoO spins within the growth plane. Upon cooling in a -2200 Oe field and measuring in a 2200 Oe field, the SF intensity increases slightly relative to the NSF as shown in Fig. 2(b). To determine if this difference is significant, we counted the NSF and SF intensities at the center of the $(1/2\ 1/2\ 1/2)$ reflection for extended times. Upon demagnetizing and zero field cooling, the ratio of the NSF to SF intensity is 1.001 ± 0.011 , compared to a ratio of 0.941 ± 0.017 for the same field preparation as in Fig. 2(b). However, a single-layer CoO (100 nm) film also gives a NSF/SF ratio of 0.94 ± 0.012 upon field cooling in 2400 Oe (Fig. 3). The AFM spins in the Co/CoO (100 nm) bilayer do not clearly show any effects from coupling to the FM Co layer. Since the data in Fig. 2 represent the CoO spin configuration averaged both along the growth axis and across the growth plane, the direction of the CoO moments near the Co/CoO interface cannot be directly distinguished from the direction of those moments in the remainder of the 100 nm layer. Any local deviations of the CoO spin direction at the Co/CoO interface may be masked by the bulk behavior of the thick AFM layer.

To determine if the perpendicular AFM spins are close to the interface, we measured the $(1/2\ 1/2\ 1/2)$ NSF and SF peak intensities for Co/CoO samples with thinner CoO layers. Initially cooling in zero field, the Co/CoO (40 nm) bilayer shows a tendency for perpendicular spin alignment (NSF/SF = 0.933 ± 0.01). Upon field cooling and measuring in 2400 Oe, the NSF/SF ratio of 0.873 ± 0.01 is significantly smaller than that for the Co/CoO (100 nm) sample, as shown in Fig. 3. This ratio varies only slightly up to 0.895 ± 0.011

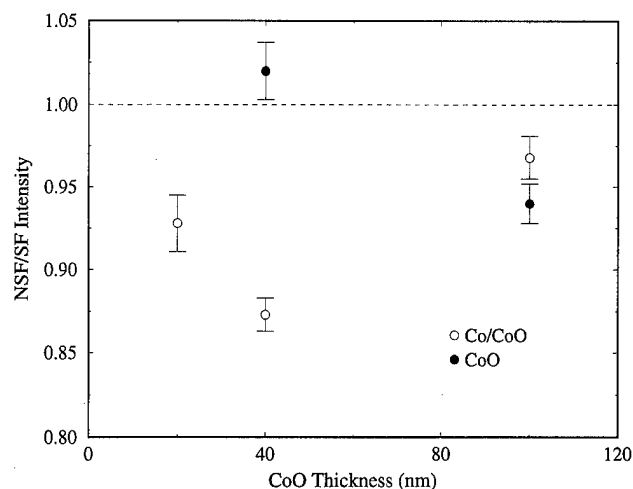


FIG. 3. Ratio of the NSF to SF peak intensities for the $(1/2\ 1/2\ 1/2)$ CoO magnetic reflection as a function of CoO layer thickness for several Co/CoO and CoO samples, as marked. The samples were cooled to 200 K in a 2200–2400 Oe field and then measured in the same field. These data have not been corrected for background contributions or for the efficiencies of the polarizing elements. Background corrections would increase the ratio for the thinnest samples with the weakest intensities.

when the field is lowered to 150 Oe. Thus this spin configuration appears to “freeze in” upon field cooling. The average perpendicular projection of the CoO moment is at least 3% larger than the parallel projection. For the Co/CoO (20 nm) bilayer, a NSF/SF ratio of 0.928 ± 0.017 was measured in 2300 Oe after field cooling. This value is comparable to that for the Co/CoO (40 nm) bilayer. As shown in Fig. 3, the Co/CoO (20 nm) and Co/CoO (40 nm) films have a larger fraction of perpendicular spins than the Co/CoO (100 nm) film. This result may indicate that the canted spins are confined primarily to a finite region near the Co/CoO interface. For a more careful check of this hypothesis, the NSF/SF ratio should be accurately measured over the entire Q range of the Bragg reflection (e.g., Fig. 2).

Overall, these data suggest that the CoO spins in the biased bilayers prefer a perpendicular orientation relative to the cooling field. However, this alignment could either be a consequence of the Co/CoO interlayer coupling or a direct response to the cooling field. To distinguish between these two effects, we performed field-dependent diffraction measurements on a CoO (40 nm) film. Upon field cooling and measuring the sample in a 2300 Oe field, the ratio of the NSF to SF intensities for the $(1/2\ 1/2\ 1/2)$ reflection is 1.02 ± 0.017 , which is significantly greater than the value measured for the corresponding Co/CoO (40 nm) bilayer (Fig. 3). The random orientation of the AFM spins is unperturbed by cooling fields up to 2300 Oe. The preferred perpendicular orientation observed in Co/CoO bilayers thus appears to result from interlayer coupling. The following measurement for the Co/CoO (40 nm) bilayer further supports this conclusion. We first cooled the sample to 200 K in a 2400 Oe field applied in-plane parallel to the Co growth field direction. We lowered the field to zero and then applied an in-plane field of 500 Oe at an angle of 90° relative to the field cooling direc-

tion while maintaining a temperature of 200 K. The resultant NSF/SF ratio is 1.02 ± 0.011 , which is larger than the 0.873 ± 0.01 ratio obtained in a 2400 Oe field after initially field cooling along the easy axis (Fig. 3). The “frozen” CoO spins thus try to align perpendicular to the reoriented Co layer moment. Since the 500 Oe field is too small to rotate the CoO spins, the moment reorientation is a direct response to the change in the Co magnetization direction.

In conclusion, we observe a preferential orientation of the CoO moments away from the Co magnetization direction in (111) Co/CoO bilayers. Within the (111) growth-axis domain, the perpendicular projection of the CoO moment relative to the field direction is larger than the parallel projection for the three bilayers considered. This result is consistent with Koon’s model,¹⁰ which predicts 90° coupling between the FM and AFM layers. The preferred perpendicular orientation of the AFM develops when the Co/CoO bilayer is field cooled through the AFM T_N into the biased state. Thus the CoO spin reorientation appears to be a direct consequence of exchange coupling between the Co and CoO layers. Unfortunately, we cannot as yet determine if the perpendicular spins reside in the interfacial region, or if the spins in the off-axis {111} domains play an important role. By controlling the AFM spin population in the growth-axis and off-axis domains, future diffraction studies of related CoO films may indeed provide a complete understanding of the physical origin of exchange biasing.

This work is based upon activities supported by the National Science Foundation under Agreement No. DMR-9423101. The work of G.P.F. was supported by USDOE-BES under Contract No. W 31-109-ENG-38. We appreciate helpful discussions with R. W. Erwin.

- ¹W. H. Meiklejohn and C. P. Bean, Phys. Rev. **102**, 1413 (1956); **105**, 904 (1957).
- ²M. J. Carey and A. E. Berkowitz, Appl. Phys. Lett. **60**, 3060 (1992).
- ³R. Jungblut, R. Coehoorn, M. T. Johnson, J. ann de Stegge, and A. Reinders, J. Appl. Phys. **75**, 6659 (1994).
- ⁴J. Nogues, D. Lederman, T. J. Moran, I. K. Schuller, and K. V. Rao, Appl. Phys. Lett. **68**, 3186 (1996); J. Nogues, D. Lederman, T. J. Moran, and I. K. Schuller, Phys. Rev. Lett. **76**, 4624 (1996).
- ⁵K. Takano, R. H. Kodama, A. E. Berkowitz, W. Cao, and G. Thomas, Phys. Rev. Lett. **79**, 1130 (1997).
- ⁶Y. Ijiri, J. A. Borchers, R. W. Erwin, S.-H. Lee, P. J. van der Zaag, and R. M. Wolf, Phys. Rev. Lett. **80**, 608 (1998); J. Appl. Phys. (these proceedings).
- ⁷B. Dieny, V. S. Speriosu, S. S. P. Parkin, B. A. Gurney, D. R. Willhout, and D. Mauri, Phys. Rev. B **43**, 1297 (1991).
- ⁸D. Mauri, H. C. Siegmann, P. S. Bagus, and E. Kay, J. Appl. Phys. **62**, 3047 (1987).
- ⁹A. P. Malozemoff, Phys. Rev. B **37**, 7673 (1988); J. Appl. Phys. **63**, 3874 (1988).
- ¹⁰N. C. Koon, Phys. Rev. Lett. **78**, 4865 (1997).
- ¹¹M. J. Carey, F. E. Spada, A. E. Berkowitz, W. Cao, and G. Thomas, J. Mater. Res. **6**, 2680 (1991).
- ¹²M. J. Carey, A. E. Berkowitz, J. A. Borchers, and R. W. Erwin, Phys. Rev. B **47**, 9952 (1993).
- ¹³W. L. Roth, Phys. Rev. **110**, 1333 (1958); D. Herrmann-Ronzaud, P. Burllet, and J. Rossat-Mignod, J. Phys. C **11**, 2123 (1978).
- ¹⁴J. A. Borchers, M. J. Carey, R. W. Erwin, C. F. Majkrzak, and A. E. Berkowitz, Phys. Rev. Lett. **70**, 1878 (1993).
- ¹⁵R. M. Moon, T. Riste, and W. C. Koehler, Phys. Rev. **181**, 920 (1969).

Dependence of exchange field and coercivity on cooling field in NiFe/CoO bilayers

T. Ambrose^{a)} and C. L. Chien

Department of Physics and Astronomy, The Johns Hopkins University, Baltimore, Maryland 21218

The effects of different cooling fields (H_{FC}) on both the exchange field and coercivity in a NiFe/CoO bilayer have been investigated. The exchange field is strongly effected by H_{FC} at low field values and levels off at high values, whereas the coercivity is only weakly influenced. © 1998 American Institute of Physics. [S0021-8979(98)48411-1]

I. INTRODUCTION

When a ferromagnet/antiferromagnet (FM/AF) bilayer is field cooled across the AF Néel temperature T_N , an exchange coupling is established.¹ As a result, the hysteresis loop at $T < T_N$ is now shifted away from zero field. In addition to this shift, known as the exchange field (H_E), the coercivity (H_C) also increases. The exchange coupling disappears as the bilayer is brought above T_N of the AF layer. It is thought that the magnetic field applied to the FM/AF bilayer during field cooling plays an important role in establishing a strong unidirectional anisotropy due to the exchange coupling. Since the FM layer already orders at $T > T_N$, some form of exchange coupling will result even without cooling in an external field. For example, previous work in FeMn/NiFe bilayers, with the deposition of the AF layer on top of a magnetized FM layer, has shown a displaced hysteresis loop without the necessity of field cooling.² The values of both H_E and H_C , however, are less for the bilayer films without field cooling as compared to those of the field cooled bilayers. In the NiFe/NiO system, the as-deposited samples showed a shifted hysteresis loop at room temperature.³ The values of H_E and H_C at room temperature in fact decreased after the samples were field cooled through the $T_N = 525$ K of NiO. However, heating the sample at elevated temperatures might have degraded the NiFe/NiO interface resulting in lesser exchange coupling values.

It should be also noted that during the fabrication of the FM/AF bilayers, an *in situ* magnetic field in the deposition chamber is often used. In such cases, the as-prepared bilayers have already experienced field cooling. For *ex situ* field cooling, large cooling fields, 10 kOe or more are typically used.¹⁻⁵ There have been no systematic studies of the effects of the value of the cooling field.

In this work, we investigate the importance of the cooling field in the exchange coupling of NiFe/CoO bilayers. The magnitude of the cooling field H_{FC} , has a significant effect on the resultant exchange coupling. The value of H_E increases with H_{FC} before saturation, whereas H_C increases marginally with H_{FC} but decreases slightly at high H_{FC} .

II. EXPERIMENT

For the present studies, a large bilayer sample of 300-Å-thick NiFe (NiFe = Ni₈₁Fe₁₉) was deposited in a field of 200

Oe on top of a [111] oriented CoO layer of 300 Å. The [111] orientation is obtained by growing CoO on a 300 Å Cu buffer layer on a Si [100] substrate. The sample was cut into many squares of a few mm each in size. Every field cooling study was made on a fresh sample at 80 K in either a vibrating sample magnetometer (VSM) or a superconducting quantum interference device (SQUID) magnetometer with a specific cooling field H_{FC} .

III. RESULTS AND DISCUSSIONS

At 298 K, which is above the $T_N = 292$ K of CoO, one obtains a narrow and square hysteresis loop, as shown in Fig. 1(a), with $H_E = 0$ and $H_C = 3$ Oe. Cooling the sample with $H_{FC} = 0$ Oe to 80 K yields a large hysteresis loop with

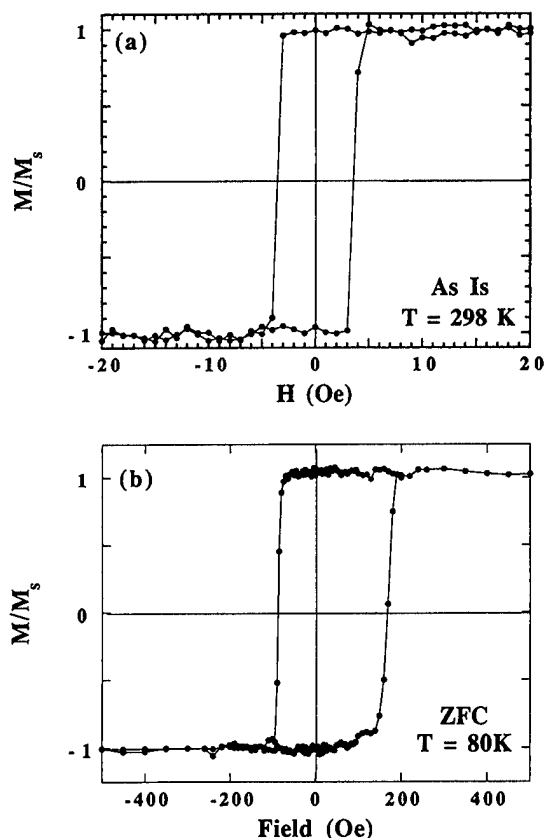


FIG. 1. Hysteresis curves for the 300 Å NiFe/300 Å CoO bilayer film at (a) room temperature and at (b) 80 K after zero field cooling.

^{a)}Electronic mail: ambrose@huvms.hcf.jhu.edu

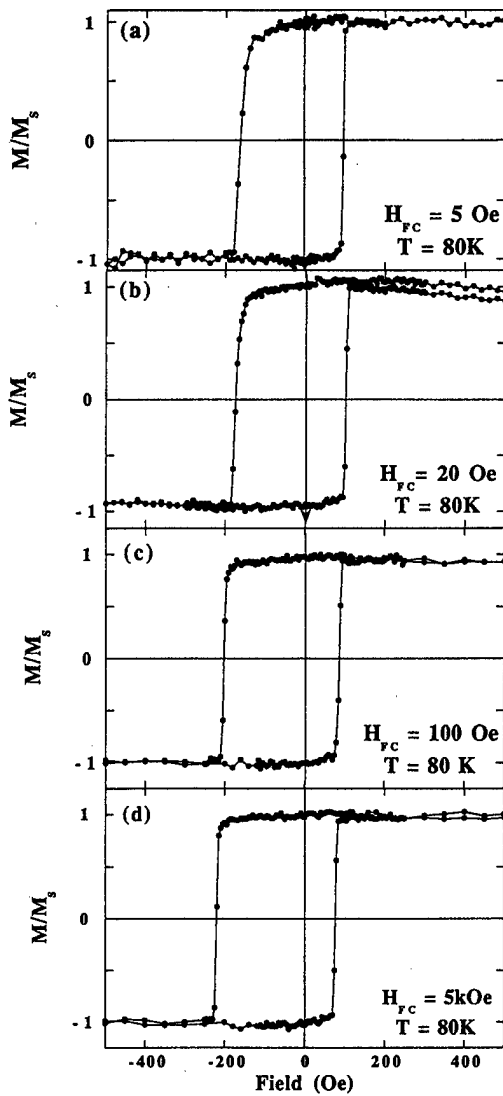


FIG. 2. Representative hysteresis loops measured at 80 K of the 300 Å NiFe/300 Å CoO bilayers for cooling field H_{FC} of (a) 5, (b) 20, (c) 100, and (d) 5000 Oe.

$H_C = 129$ Oe as shown in Fig. 1(b), vividly revealing the exchange coupling. Since the bilayer sample was deposited in a field, exchange coupling has been locked in when the sample was cooled in $H_{FC} = 0$. We have purposely placed the sample, so that the deposition field is in the negative H direction of the VSM, such that the loop in Fig. 1(b) is shifted to the right, instead of to the left of $H = 0$.

In Fig. 2 some representative hysteresis loops are shown for various cooling field H_{FC} values. As expected, the loops are now shifted to the left due to H_{FC} . Even a small H_{FC} (e.g., 5 Oe) can shift the loop from the positive side [Fig. 1(b)] to negative side [Fig. 2(a)]. As the value of H_{FC} increases both the shift in the loop (i.e., H_E) and the loop width (i.e., H_C) are observed to increase.

The values of the exchange field H_E and the coercivity H_C are shown in Fig. 3 as a function of the cooling field H_{FC} . The values of H_E and H_C are determined from two fields (H_{left} and H_{right}) of the hysteresis loop where the magnetization is zero by the relations of $H_E = -(H_{left} + H_{right})/2$ and $H_C = -(H_{left} - H_{right})/2$. In this convention a

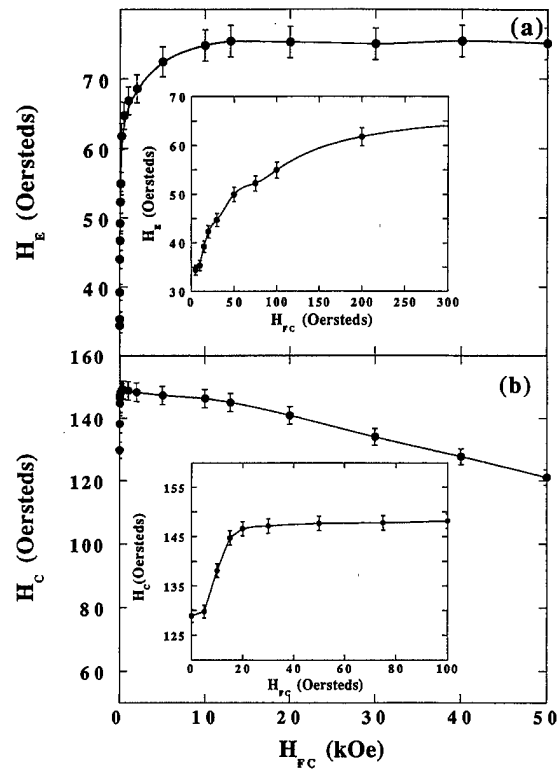


FIG. 3. (a) Exchange field and (b) coercivity at 80 K as a function of the field cooling H_{FC} magnitude. The inset in (a) shows the increase in H_E for small H_{FC} and the inset in (b) shows the increase in H_C for small H_{FC} .

hysteresis loop that is shifted to the left of $H = 0$ is defined as having a positive exchange field and H_C is always positive. As shown in Fig. 3(a), H_E increases monotonically with H_{FC} until it levels off at about $H_{FC} = 8$ kOe. The rapid rise of H_E for small values of H_{FC} is shown in the inset of Fig. 3(a). Beyond $H_{FC} = 10$ kOe, H_E is essentially independent of H_{FC} . For the coercivity H_C , there is a lesser effect due to H_{FC} . The value of H_C rises from 129 Oe at $H_{FC} = 0$ to 142 Oe at $H_{FC} = 20$ Oe and remains essentially unchanged. Only at $H_{FC} = 10$ kOe, H_C begins to decrease slightly to 120 Oe at $H_{FC} = 50$ kOe. One notes that for small H_{FC} (< 100 Oe), the hysteresis loops are not as square as those for larger H_{FC} as shown in Fig. 2. It should be mentioned that every data point in Fig. 3 has been obtained by measuring a fresh and different sample. All of these samples have been cut from a large bilayer. The consistency of the results is remarkable.

In the present case of NiFe/CoO bilayers, even at $H_{FC} = 50$ kOe, the hysteresis loop is always shifted to the left of $H = 0$. In contrast, Fe/FeF₂ bilayers are the only case that the loop can be shifted to the right of $H = 0$ under a very large H_{FC} ,⁴ probably because FeF₂ has a weaker anisotropy as compared to CoO.

It has recently been shown that the FM/AF exchange coupling involves unidirectional (UD) anisotropy and uniaxial (UA) anisotropy, giving rise to H_E and H_C , respectively, both of which are integral parts of the exchange coupling.⁶ The results in Fig. 3 show that the UA anisotropy and H_C are weakly effected by the cooling field H_{FC} . The value of H_{FC} exerts the most influence on the UD anisotropy and H_E , particularly at small H_{FC} values.

Although uncoupled NiFe has a small H_C as shown in Fig. 1(a), the zero field cooled exchange-coupled NiFe at 80 K shown in Fig. 1(b), has much larger H_C value of about 130 Oe. During field cooling, the cooling field H_{FC} must be larger than 130 Oe to maintain the single domain state of NiFe. With H_{FC} less than 130 Oe, the values of H_E will be compromised. Indeed, the field range of $0 < H_{FC} < 130$ Oe causes the most changes in H_E . At $H_{FC} = 300$ Oe, H_E essentially reaches the terminal value. Once NiFe is aligned in the single domain state by a sufficiently large H_{FC} , any further effects on the FM magnetization and the AF spin structure are minimal.

The results shown in Fig. 3 have been taken at 80 K. Since both H_C and H_E have distinct temperature dependencies, we comment on the effect due to measurements at different temperature. Using the film geometry of FM layer on top of the AF layer, H_E saturates to a value at temperatures sufficiently below T_N while H_C increases linearly with decreasing temperature.⁷ If the measurement had been taken at a temperature lower than 80 K, the value of H_C increases but the value of H_E remains unchanged. Both the zero field cooled and the field cooled samples will have a larger H_C at temperatures below 80 K. The results shown in Fig. 3 will be somewhat modified to reflect the lower measuring temperature. A larger cooling field is also required to achieve the ultimate value of H_E because the zero field cooled bilayer has a larger coercivity.

Finally, in NiFe/CoO bilayers, the exchange coupling causes a shifted hysteresis loop and a very large enhancement of the coercivity by about 50 times. Both H_E and H_C are tell-tale signs of exchange coupling. As shown in this work, while the value of H_E can be varied to a large extent, the value of H_C remains essentially unchanged.

IV. CONCLUSION

In conclusion, the magnitude of the cooling field in establishing FM/AF exchange coupling has a strong influence on the value of the resultant exchange field H_E , whereas the coercivity H_C is much less effected. A cooling field in excess of the coercivity of the zero field cooled exchange-coupled FM layer is required in order to reach the ultimate value of H_E .

ACKNOWLEDGMENT

This work has been supported by NSF MRSEC Program No. 96-32526.

¹W. K. Meiklejohn and C. P. Bean, Phys. Rev. **102**, 1413 (1956).

²C. Tsang, N. Heiman, and K. Lee, J. Appl. Phys. **52**, 2471 (1981).

³M. J. Carey and A. E. Berkowitz, Appl. Phys. Lett. **60**, 3060 (1992).

⁴J. Nogues, D. Lederman, T. J. Moran, and I. Schuller, Phys. Rev. Lett. **76**, 4624 (1996).

⁵T. J. Moran and I. Schuller, J. Appl. Phys. **79**, 5109 (1996).

⁶T. Ambrose, R. L. Sommer, and C. L. Chien, Phys. Rev. B **56**, 83 (1997).

⁷T. Ambrose and C. L. Chien, J. Appl. Phys. **81**, 5007 (1997).

First-principles exchange interactions between ferromagnetic and antiferromagnetic films: Co on NiMn, a case study

T. C. Schulthess^{a)} and W. H. Butler

Metals and Ceramics Division, Oak Ridge National Laboratory, Oak Ridge, Tennessee 37831-6114

Heisenberg exchange parameters at the interface of antiferromagnetic NiMn with ferromagnetic Co are calculated from first principles. We use a layer version of the Korringa-Kohn-Rostocker multiple-scattering approach and an expression, which is based on the expansion of the band energy, to calculate the exchange parameters from the underlying electronic structure. For bulk systems, the parameter sets yield Curie temperatures that are in good agreement with experimental values. In the interface region, the interlayer interactions in NiMn change significantly compared to the bulk while the intralayer interactions are almost unchanged. © 1998 American Institute of Physics.

[S0021-8979(98)48511-6]

I. INTRODUCTION

Exchange interactions between ferromagnetic and antiferromagnetic films are of considerable interest since their understanding is closely related to the effect known as exchange anisotropy (or exchange bias). Even though this effect has been known since the late 1950s¹ and has important technological applications, its understanding from a microscopic point of view is not established. A simple model that postulates exchange interactions between the antiferromagnet (AF) and the ferromagnet (FM) was introduced by Mauri *et al.*² and explains the effect by a domain wall which is pushed into the AF when the magnetization in the FM is reversed. Malozemoff³ explained the exchange interaction with a random field that is attributed to the interface roughness. However experiments by Nogués *et al.*⁴ showed that exchange anisotropy for Fe/FeF₂ is present with perfectly smooth interfaces and that the roughness actually reduces the bias field. Recently Koon⁵ used a Heisenberg model with nearest neighbor interactions to show that frustration effects near the interface favor the FM to orient perpendicular to the easy axis of the AF. In order to explain exchange anisotropy, the moments have to be confined to the plane parallel to the interface and there is no apparent physical justifications for this restriction.⁶ The major unknowns in the model are the exchange interactions between the AF and the FM. It is the purpose this work to provide such a set of exchange parameters for an AF-FM system which should yield exchange anisotropy. If for example the AF-FM exchange interactions are very large compared to corresponding quantities in the AF, one could expect the net moment induced in the AF layer next to the interface to be large enough such that in-plane motion of the moments is forced by the magnetostatic interactions.

In the present work we follow an approach proposed by Liechtenstein *et al.*⁷ in which Heisenberg exchange parameters can be determined directly from first principles electronic structure calculations. The system that we investigate is chosen to give the best compromise between relevance to

real applications and the possibilities of state of the art electronic structure methods. Usually Ni-Fe is used as a FM on AF NiMn substrates.⁸ In order to simplify the calculations we replace the random Ni-Fe alloy by a pure FM. Since no FM fits naturally onto NiMn we chose Co because it has magnetic properties which are fairly robust with respect to structural distortions and can thus be viewed as a good representative of a FM material to interface with NiMn.

II. METHOD

Our aim is to map the rather complex spin dependent part of the energy functional of density functional theory within the local density approximation onto a simple Heisenberg Hamiltonian,

$$E = - \sum_{ij, i \neq j} J_{ij} \hat{\mathbf{s}}_i \cdot \hat{\mathbf{s}}_j, \quad (1)$$

which is the sum over all exchange interaction, J_{ij} , between moments of fixed magnitude, located on sites labeled by i and represented by a vector of unit length $\hat{\mathbf{s}}_i$. For the description of the electronic structure, multiple scattering theory (MST) provides a natural starting point, since it expands the Green function in a localized basis around every site. The key operator used in this context is the scattering-path operator (SPO), $[\tau_{ij}(\epsilon)]_{Ls, L's'}$, from which the one-particle Green function and hence the charge and moment density may be calculated. It gives, at energy ϵ , the scattered spherical wave of angular momentum $L' = (l', m')$ and spin s' from site j resulting from an incident wave of angular momentum L and spin s at site i . An expression for the exchange parameters in terms of these SPOs, which is based on an expansion of the band energy, was first given for the ferromagnetic case by Liechtenstein *et al.*,⁷ and later extended to the case of arbitrary orientation of the atomic moments by Antropov *et al.*⁹ who wrote the pair exchange parameter as

$$[J_{ij}]_{\alpha\beta} = - \frac{1}{4\pi} \text{Im} \int_{-\infty}^{\epsilon_F} \text{Tr}_L (\Delta_i \tau_{ij}^\alpha \Delta_j \tau_{ji}^\beta - \Delta_i \tau_{ij}^0 \Delta_j \tau_{ji}^0) d\epsilon. \quad (2)$$

^{a)}Electronic mail: schulth@mst.ms.ornl.gov

In this expression $\Delta_i = 1/2 \sum_{\nu=1,3} \text{Tr}_s(t_i^{-1} \sigma^\nu)$ and $\tau_{ij}^\nu = 1/2 \text{Tr}_s(\tau_{ij} \sigma^\nu)$ where t_i is the single site scattering matrix, σ^0 is the 2×2 unit matrix, and $\sigma^{\nu=1,3}$ are the three Pauli matrices. In the present case we will be concerned with collinear ferro and antiferromagnetically aligned atomic moments which we take to be parallel to the z axis.¹⁰ Thus the exchange interactions reduce to

$$J_{ij} = -\frac{1}{4\pi} \text{Im} \int_{-\infty}^{\epsilon_F} \text{Tr}_L(\tilde{\Delta}_i \tau_{ij}^\dagger \tilde{\Delta}_j \tau_{ji}^\dagger) d\epsilon, \quad (3)$$

with $\tilde{\Delta}_i = (t_{i\uparrow}^{-1} - t_{i\downarrow}^{-1}) \text{sgn}(\hat{\mathbf{z}} \cdot \hat{\mathbf{s}}_i)$, and (\uparrow, \downarrow) denote the actual spin channel. There exists an important sum rule,^{7,9} which for collinear spins can be written as

$$J_i = \sum_{j \neq i} J_{ij} \text{sgn}(\hat{\mathbf{s}}_i \cdot \hat{\mathbf{s}}_j) = -\frac{1}{4\pi} \text{Im} \int_{-\infty}^{\epsilon_F} \text{Tr}_L(\tilde{\Delta}_i [\tau_{ii}^\dagger - \tau_{ii}^\dagger] + \tilde{\Delta}_i \tau_{ii}^\dagger \tilde{\Delta}_i \tau_{ii}^\dagger) d\epsilon. \quad (4)$$

This last expression will be used to check the convergence of the calculated exchange interactions.

In order to comply with the symmetry requirement in thin films and planar interfaces, we consider the solid as a superposition of 2D-periodic atomic layers. We use the layer version of the Korring-Kohn-Rostocker (LKRR) method¹¹ to calculate the electronic structure and the approach outlined in Ref. 12 to determine the SPOs that enter the application of Eq. (3) to the layered geometry. The potentials are treated in the atomic sphere approximation (ASA).

III. RESULTS

NiMn crystallizes in a face centered tetragonal structure in which Ni and Mn-layers alternate in the (001) direction. Our calculations¹³ are performed at the experimental lattice constant for thin films,⁸ $a = 3.697 \text{ \AA}$ with a c/a ratio of 0.9573. In accordance with the experimental magnetic structure,¹⁴ we find Ni to be nonmagnetic and the Mn layers to consist of two square sublattices that have opposite magnetic moments. The magnitude of the Mn moment is $3.2 \mu_{\text{Bohr}}$, which is slightly smaller than the experimental value of $3.8 \pm 0.3 \mu_{\text{Bohr}}$. The crystal structure of Co is assumed to match that of NiMn, i.e., it is fct with the same basal lattice constant as NiMn but with a c/a ratio chosen to conserve the experimental atomic volume of hexagonal Co. This approximation is imposed by the requirement of the LKRR method that there has to be an overall 2D periodicity of the system under consideration. However, the robustness of the magnetic structure of Co with respect to changes in the crystal structure allows us to assume that this structural approximation will not significantly alter the magnetic properties of the Co film and the exchange parameters between the NiMn and Co. The magnetic moment of Co in this artificial fct structure is $1.60 \mu_{\text{Bohr}}$ which is similar to $1.63 \mu_{\text{Bohr}}$, the value calculated for hcp Co.

In Table I the exchange interactions of bulk Co and NiMn are compiled. The cutoff is chosen in order that the agreement between the sum over calculated J_{ij} and the value determined directly from Eq. (4) is better than one percent. The results clearly indicate that in Co not only the magnitude

TABLE I. Calculated values for J_i (first row) and J_{ij} (remaining rows) in meV for bulk Co and MnNi. Values for Co are given for the fct and the fcc structure.

Co	fct	fcc	Mn	fct
J_i	179.6	177.8	J_i	153.4
(0.5, 0, 0.5)	14.1	12.4	(0.5, 0.5, 0)	-27.1
(0.5, 0.5, 0)	8.1	12.4	(0, 0, 1)	16.1
(0, 0, 1)	1.2	0.4	(1, 0, 0)	6.7
(0, 1, 0)	0.7	0.4	(0.5, 0.5, 1)	1.8
(0.5, 0.5, 1)	1.2	1.5	(0, 1, 1)	-2.3
(1, 0.5, 0.5)	2.0	1.5	(1, 1, 1)	4.7

but also the coupling between the magnetic moments on different sites are robust with respect to the change of the structure. The Curie temperature that corresponds to the set of exchange interactions can be estimated within a mean field consideration from⁷ $T_C = 2/(3k_B) J_i$ and is found to be 1375 K for fcc Co, which is in good agreement with the experimental value of 1388 K. Similarly, the Neel temperature of NiMn is estimated to 1187 K which is slightly higher than the experimental value of 1070 ± 40 K given by Pál *et al.*¹⁴ Note that the nearest neighbor Mn interactions are remarkably large.

Since not very much is known about the details of the interface between NiMn and a ferromagnetic material, we consider the two possibilities of perfect interfaces, i.e., the cases where Co is next to Ni and Mn, respectively. In the calculations the electronic charge was relaxed self-consistently in 12 atomic layers consisting of 6 Co layers and three repeat units of NiMn. On the AF side of the interface the potentials were fixed to the bulk values and on the other side we used potentials that were converged for Co with the Fermi energy fixed to the value of NiMn. This assures that the electrochemical potential is the same on both side of the interface. We have explicitly checked the effect of this shift in the Fermi energy on the magnetic moments and the exchange interaction in Co and found that it is negligible. The relative size of the atomic spheres of Ni and Mn was chosen such that in the bulk every site is charge neutral.

Even though the method applied here is not limited to the case of collinear atomic moments, the magnetization in Co is chosen to be aligned with the moments of one of the two Mn sublattices. This particular (but arbitrary) choice of the relative magnetization directions provides an important check of the transferability of the exchange parameters. Breaking the symmetry by introducing the NiMn-Co interface with collinear magnetic moments introduces two types of Co-Mn interactions which are equivalent from a geometrical point of view but inequivalent with respect to the relative directions of the moments. The difference between the two gives an estimate of the error introduced when one assumes that the exchange interactions are scalars instead of tensors as actually required by Eq. (2). The results for the exchange interactions of the two types of interfaces are given in Fig. 1. Only values that differ from the corresponding bulk values are shown. Whenever the values between the two sub-

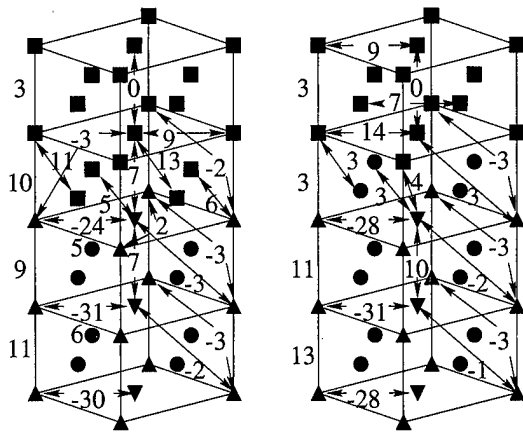


FIG. 1. Exchange interaction in meV for Co-MnNi (left panel) and Co-NiMn (right panel). Squares, circles, up and down triangles represent respectively, Co, Ni, up and down Mn.

sets mentioned previously differ, they are both shown, and it can be seen that the agreement between the sets is reasonable.

All interactions converge rapidly to their bulk values inside Co, but convergence is much slower on the NiMn side. Despite this interface effect on NiMn, the intralayer interactions remain similar to their bulk values. The most significant influence of the interface is between next nearest out of plane Mn neighbors, where the interactions reverse sign and further enforce the antiferromagnetic alignment of the moments. The values for nearest out of plane neighbors are reduced by about 30% but remain strong. In the case where Co layers border with Mn, the Co-Mn coupling between next nearest neighbors is almost the same as between corresponding Mn sites and consequently one order of magnitude larger than the equivalent interactions in Co. The interactions between nearest Co-Mn neighbors however roughly correspond to the average value between the interactions in Co and NiMn. For the other interface, where Ni is next to Co, the coupling between Co and Mn is much smaller, but the Ni layer at the interface has a nonvanishing moment of $0.30 \mu_{\text{Bohr}}$ which leads to finite interactions between Ni and its nearest Co and Mn neighbors.

IV. CONCLUSIONS

The electronic structure and the exchange interactions obtained in the present calculations yield magnetic moments

and critical temperatures that are in good agreement with experimental values. While the Co-Mn interactions at the interface are much larger than the averaged bulk values, they are still smaller than the intralayer interactions in NiMn, which are found to be very large. Since the latter are an intrinsic property of the AF system, we do not expect any qualitative changes in the ratio of interfacial AF-FM and bulk AF-AF interactions for other FM interfaced with NiMn. Thus, following the argumentation mentioned in the introduction, we are lead to the conclusion¹⁵ that a Heisenberg model with perfect interfaces will not yield exchange anisotropy for the NiMn-FM system and therefore more realistic interface structures have to be considered.

ACKNOWLEDGMENT

Research sponsored by the Division of Materials Sciences, U.S. Department of Energy under Contract No. DE-AC05-96OR22464 with Lockheed Martin Energy Research Corporation.

¹W. H. Meiklejohn and C. P. Bean, Phys. Rev. **105**, 904 (1957).

²D. Mauri, H. C. Siegmann, P. S. Bagus, and E. Kay, J. Appl. Phys. **62**, 3047 (1987).

³A. P. Malozemoff, J. Appl. Phys. **63**, 3874 (1988).

⁴J. Nogués, D. Lederman, T. J. Moran, I. K. Schuller, and K. V. Rao, Appl. Phys. Lett. **68**, 3186 (1996).

⁵N. C. Koon, Phys. Rev. Lett. **78**, 4865 (1997).

⁶T. C. Schulthess and W. H. Butler (unpublished).

⁷A. I. Liechtenstein, M. I. Kastelson, V. P. Antropov, and V. A. Gubanov, J. Magn. Magn. Mater. **67**, 65 (1987).

⁸T. Lin, D. Mauri, N. Staud, C. Hwang, and G. L. Gorman, Appl. Phys. Lett. **65**, 1183 (1994).

⁹V. P. Antropov, M. I. Kastelson, B. N. Harmon, M. van Shilfgaarde, and A. I. Liechtenstein (unpublished).

¹⁰Since spin-orbit coupling is not included in the present calculations the spin direction can be chosen independently of the lattice.

¹¹J. M. MacLaren, S. Crampin, D. D. Vvedensky, and J. B. Pendry, Phys. Rev. B **40**, 12 164 (1989).

¹²T. C. Schulthess, R. Monnier, and S. Crampin, Phys. Rev. B **50**, 18 564 (1994).

¹³We have used *s*, *p*, and *d* partial waves, 16 energy points on a semicircular contour in the complex energy plane, 36 special *k* points in the 1/8th section of the 2D Brillouin zone, and 37 plane waves for the interlayer scattering.

¹⁴L. Pál, E. Krén, G. Kádár, P. Szabó, and T. Tarnóczy, J. Appl. Phys. **39**, 538 (1968).

¹⁵Preliminary micromagnetic calculation confirm this conclusion. A more detailed study will be published elsewhere.

Critical Phenomena and Phase Transitions

D. L. Huber, Chairman

Local and global demagnetization process: Is there any self-organized critical behavior?

O. A. Chubykalo and J. M. González

Instituto de Ciencia de Materiales de Madrid, CSIC, Cantoblanco, 28049 Madrid, Spain

The behavior of local and global demagnetization processes (avalanches and Barkhausen jumps) is analyzed in terms of a micromagnetic model. Our study of the statistics of these events as a function of exchange correlation length parameter, system size, and system driving rate shows the absence of self-organized critical behavior if a realistic model of a magnetic system is considered. © 1998 American Institute of Physics. [S0021-8979(98)34011-6]

Systems exhibiting self-organized critical (SOC) behavior react to an external perturbation through collective events (avalanches) having size and duration distribution functions which are system size scaleable.¹ The concept of SOC has been brought to magnetic systems on the basis of the occurrence of collective events during the demagnetization process. In the magnetic systems context, the basic experimental evidence of the occurrence of SOC-like behavior is considered to be the observation of the $1/f^\alpha$ frequency dependence of the power spectrum of the Barkhausen jumps (BJ)^{2,3} (a BJ is identified with the sudden changes of the magnetization of a specimen under the action of a slowly varying external field). The experiments showing this behavior were carried out by using a wide range of the system driving rates without any further system parameters tuning. Also, from theoretical point of view, it has been shown that even in the one-dimensional (1D) case with a single propagating domain wall, the presence of dipolar interactions can originate a SOC-like behavior.² We should, nevertheless, point up here that the actual observation of SOC in magnetic systems is still an open question. For instance, up to now, there is not agreement in the literature about the concrete frequency dependence of the power spectrum associated to SOC. Moreover, the latest experiments on Barkhausen noise have revealed the absence of the common indications of SOC.⁴ Beside this, it has been proposed that the observed behavior could be the consequence of system sweeping of instabilities rather than of a real SOC dynamic.⁵ Finally, most of the theoretical investigations of the SOC behavior are based on the random-field Ising models^{2,6} and consider an equilibrium-type dynamics which is only valid in the limit of zero temperature and infinitely small field sweeping rate.

To try to clarify the above introduced point, we have performed micromagnetic calculations using a model⁷ system describing a textured polycrystal with exchange coupled grains. Our model is of the 1D-type (a chain of magnetic moments, representing atomic planes, and allowed to oriented in 3D). The model considered explicitly anisotropy,

Zeeman, exchange, and magnetostatic energy contributions. The moments were organized in grains, each one having its own easy axis orientation (the easy axes orientations were distributed in a cone having a 20° apex angle whose axis coincided with the applied demagnetizing field direction). The parameters of the system included intrinsic magnetic properties (the exchange-to-anisotropy ratio, a , and the magnetostatic-to-anisotropy ratio, m), system size parameters (the system size, S , measured in number of grains and the grain size, N_1 , measured in number of moments), and driving rate parameters (the field increment Δh , and the duration of the relaxation stage at constant field, ΔMCS , measured in number of Monte Carlo steps). We have considered three models having different intergranular exchange characteristics: (A) ferromagnetic-type interactions with an effective intergranular exchange constant equal to that considered inside each grain, (B) ferromagnetic-type interactions with uniformly distributed effective intergranular exchange couplings, and (C) both ferro- and antiferromagnetic-type coupling with uniformly distributed intensities. The three models differ by the strengths of the coupling between the propagating domain walls and the grain boundaries which act as pinning centers: the pinning is weaker in the model A case and stronger in that of model C. The evolution of the system was followed by using a Monte Carlo algorithm at constant temperature. The dynamics of the magnetic moments was much more realistic than that used in the Ising models. It reproduced adequately real magnetic materials properties: the occurrence of multiple metastable states, the coexistence of temperature- and field-induced nucleation events, the observation of time dependent effects (viscosity), etc. Also, and unlike the Ising-model dynamics, we considered a finite field sweeping rate.

The crucial property of our model is the observation, even for slowly driven systems, of several coexisting propagating domain walls. Thus, we should distinguish between an avalanche (a local event related to the nucleation and consequent propagation, possibly during several field steps,

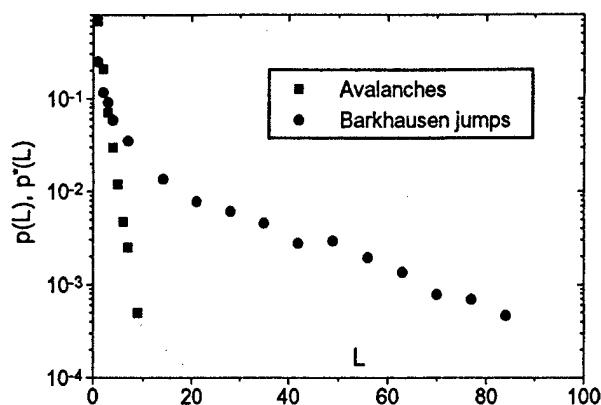


FIG. 1. Avalanche and BJ size distribution functions for model C. The simulation parameter values are: $a=0.1$, $m=0.3$, $N_1=10$, $S=100$, $\Delta h=0.01$, $\Delta MCS=500$.

of the domain walls limiting a reversed region⁷) and a Barkhausen jump (a global change of the magnetization of the system). Typically, the statistics of these two events are different (see Fig. 1) which is explained by the coexistence of several avalanches in the system. If the avalanche size distribution function, $p(L)$, decreases exponentially, the BJ size distribution function, $p^*(L)$, spans a large fraction of the system size. This is a typical situation in models B and C and takes place in model A when the exchange parameter is small enough (see Fig. 10 of Ref. 7). On the contrary, scaleable avalanche size distribution functions are observed (only for the case of model A, see Fig. 12 of Ref. 7), when the avalanches starting at different points of the system cluster in one unique BJ. One of the necessary conditions of the occurrence of SOC is the observation of system-size scaleable avalanche size distribution functions. The multiple nucleation sites and the occurrence of simultaneously propagating domain walls led, in the case of strong pinning centers (models B and C), to avalanche size distribution functions exponentially decreasing and system-size independent (see Fig. 2). In the weak pinning centers case (model A), the avalanche size distributions can be system-size dependent but this happens for small-size systems only (see Fig. 3 and Fig. 8 of Ref. 7). On the contrary, the BJ size distribution func-

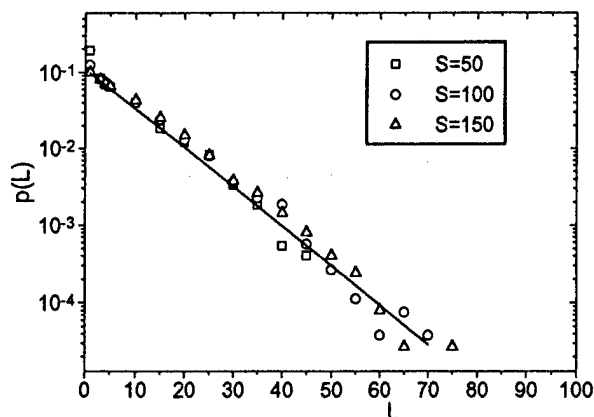


FIG. 2. Avalanche size distribution functions for different size systems (model B). The system parameter values are: $a=5$, $m=0.3$, $N_1=3$, $\Delta h=0.01$, $\Delta MCS=500$.

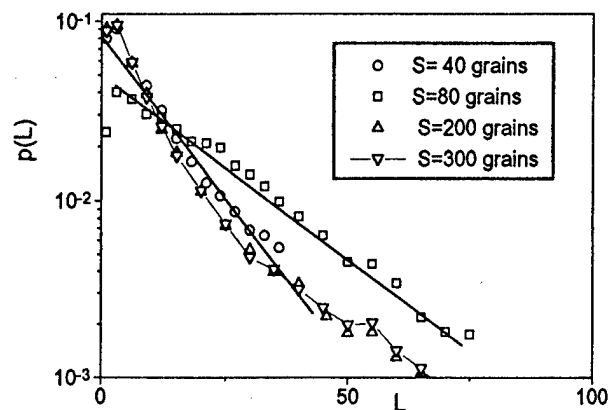


FIG. 3. Avalanches size distribution functions for different size systems (model A). The system parameter values are: $a=2.0$, $m=0.3$, $N_1=3$, $\Delta h=0.001$, $\Delta MCS=150$.

tions are always system-size dependent (see Fig. 4). The increase of the system size leads to the appearance of additional nucleation centers which originate larger BJ's and even a nonmonotonous behavior for sufficiently large system sizes. In this case, by changing the system driving rate, one can again have statistics similar to those characterizing SOC behavior, i.e., having power distribution functions for the BJ sizes. The observation of such behavior has nothing to do with the occurrence of real SOC since in this case BJ's consist of several uncorrelated events (avalanches started in different parts of the system).

It is commonly accepted that, in order to observe the self-organized criticality, the existence of two time scales (rapid avalanches and large intervals between these events) are necessary (see, e.g., Ref. 8). Under these circumstances, the dynamics of the system is close to that of the sandpile and Ising models. In our model, by varying the system driving rate, the avalanche size and BJ size distributions can coincide, but only for very special values of the driving rate parameters which requires very fine tuning. In general, the decrease of the system driving rate does not make our system to behave similarly to a sandpile system due to the properties present in real systems (and absent in the Ising model), such as viscosity. Indeed, the reduction of the field step leads to

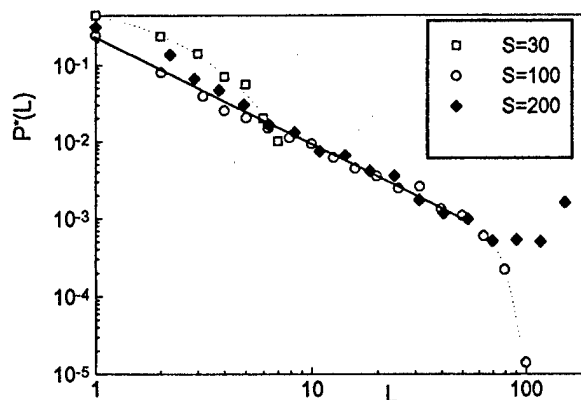


FIG. 4. Barkhausen jump size distribution functions for different size systems (model C). The system parameter values are: $a=0.1$, $m=0.3$, $N_1=10$, $\Delta h=0.01$, $\Delta MCS=500$.

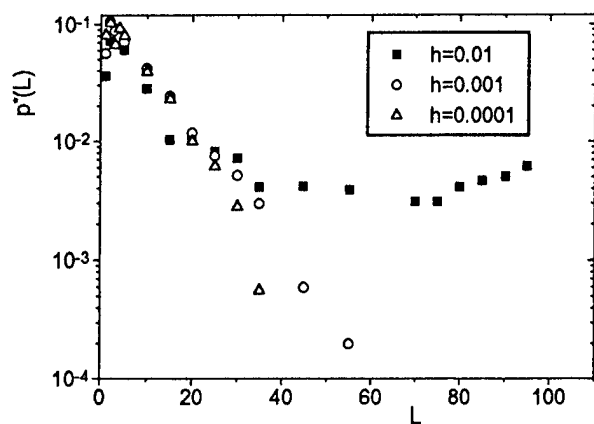


FIG. 5. Barkhausen jumps size distributions functions for different driving rates in model B. The system parameter values are: $a=5$, $m=0.3$, $N_1=3$, $S=100$, $\Delta h=0.01$, $\Delta MCS=500$.

the following effects: (i) decrease of the nucleation rate per constant field stage, (ii) increase of the efficiency of the grain boundaries as pinning centers, and (iii) increase of the relaxational effects. The resulting behavior is a complex interplay between all these mechanism and, for instance, in the BJs case (Fig. 5) the field sweeping rate reduction leads to more rapidly decreasing BJ size distribution functions. (Similar effect is observed for the avalanche statistics.)

In the case of the Ising models, domain walls always consist of two magnetic moments. In our case (as in real situations) domain walls have internal structure and interact with grain boundaries. Thus, the important parameter is the ratio between the exchange correlation length (determining the domain wall size) and the structural correlation length of the system (the grain size N_1). In Ref. 7 it has been shown that in the case of model A, by changing this ratio, the system undergoes a transition from subcritical state (small avalanches only) to supercritical (all avalanches of the system size) via the state of critically (avalanches spanning a considerable part of the system size). In model C (strong pinning centers) the influence of the exchange-to-anisotropy param-

eter on the dynamics of the system is different (see Ref. 9). In this case the antiferromagnetically coupled grain boundaries have a very strong associated pinning effect, which is more relevant in the case of narrow walls (small a values). Grain boundaries also act as very effective nucleation centers (in this case the energy required to partially invert the set of moments forming a wall is sufficiently reduced by the antiferromagnetic coupling). Thus, in the case of model C and unlike the case of model A, presented in Ref. 7, the increase of the exchange-to-anisotropy parameter leads to the reduction of average avalanche size. This parameter also changes the BJs statistics. Therefore, in order to observe critical avalanche and BJ distribution functions, the tuning of the correlation exchange length parameter is necessary. The latter excludes the occurrence of SOC.

In conclusion, our micromagnetic calculations with finite temperature and finite field sweeping rate showed the absence of SOC: (i) The criticality of the avalanche size distribution functions is destroyed by the occurrence of simultaneously propagating domain walls. (ii) The observation of scaleable size distributions (in small size systems exclusively) requires the tuning of the exchange correlation length. (iii) The fact that the BJ size distribution shows, without any parameter tuning, scaleable behavior is not an evidence for the occurrence of SOC because, as we have shown, BJs are sum of simultaneously occurring smaller size events which we believe are uncorrelated.

¹P. Bak, C. Tang, and K. Wiesenfeld, Phys. Rev. Lett. **59**, 381 (1987).

²O. Geoffroy and J. L. Porteseil, J. Magn. Magn. Mater. **133**, 1 (1994).

³J. S. Urbach, R. C. Madison, and J. T. Markert, Phys. Rev. Lett. **75**, 4694 (1995).

⁴J. R. Petta, M. B. Weissman, and K. P. O'Brien, Phys. Rev. E **54**, R1029 (1996).

⁵D. Sornette, J. Phys. I **4**, 209 (1994).

⁶P. Sethna, K. Dahmen, S. Kartha, J. Krumhansl, B. W. Roberts, and J. D. Shore, Phys. Rev. Lett. **70**, 3347 (1993).

⁷J. M. Gonzalez, O. A. Chubykalo, and J. Gonzalez, Phys. Rev. B **55**, 921 (1997).

⁸B. Drossel, Phys. Rev. Lett. **78**, 1392 (1997).

⁹O. A. Chubykalo, J. M. González, and J. González, J. Magn. Magn. Mater. (to be published).

Non-Heisenberg couplings and ferromagnetic instability in a random antiferromagnetic spin-1 chain

R. N. Bhatt

Department of Electrical Engineering, Princeton University, Princeton, New Jersey 08544

Kun Yang^{a)}

Condensed Matter Physics 114-36, California Institute of Technology, Pasadena, California 91125

A random antiferromagnetic spin-1 chain with both Heisenberg and biquadratic nearest neighbor couplings is found to exhibit a novel ferromagnetic-like instability at low energies, if there is competition between the Heisenberg and biquadratic couplings, *even though each individual nearest neighbor coupling is such as to produce a singlet ground state for the isolated pair*. This instability leads to the generation of ferromagnetic couplings, and thus to the formation of weakly coupled large moments at low temperatures. A perturbative calculation (up to 4th order) is performed to investigate whether such a situation is physically realizable in spin-1 systems. © 1998 American Institute of Physics. [S0021-8979(98)25111-5]

Great interest in quantum spin chains was triggered by Haldane's famous conjecture¹ that integer and half integer Heisenberg antiferromagnetic (AF) chains have qualitatively different behavior. Recently, there has also been much work on random spin chains,²⁻⁷ and considerable progress has been made.

In the past, most theoretical studies of magnetic systems have focused on the Heisenberg model, when the system is isotropic or invariant under spin rotation:

$$H = \sum_{ij} H_{ij} = \sum_{ij} J_{ij} \mathbf{S}_i \cdot \mathbf{S}_j, \quad (1)$$

where \mathbf{S}_i is the spin operator on site i , and J_{ij} is the coupling between sites i and j . The coupling is ferromagnetic (F) when $J_{ij} < 0$, and AF otherwise. In the case of spin-one-half system ($S = 1/2$), rotational invariance uniquely constrains the coupling to be of the Heisenberg form (1). In systems with higher spins ($S \geq 1$), however, one may have higher order couplings between spins, and the most general form of the coupling between spins i and j that respects rotational invariance is

$$H_{ij} = \sum_{n=1}^{2S} J_{ij,n} (\mathbf{S}_i \cdot \mathbf{S}_j)^n. \quad (2)$$

It is known that the existence of higher order couplings between spins may change the physics of the system dramatically. For example, in a uniform spin-1 chain with nearest neighbor couplings only ($J_{i,i+1;1} = J$, $J_{i,i+1;2} = D$ and all others zero), besides the usual ferromagnetic phase and the Haldane gapped phase,¹ represented by the ferromagnetic and antiferromagnetic Heisenberg models respectively, the system also supports a spontaneously dimerized phase⁸ and a disordered gapless phase⁹ when biquadratic couplings (D) between neighboring spins are sizable; for special ratios between these couplings, the system is critical and becomes exactly soluble.

When both Heisenberg and biquadratic couplings are present, in principle they may be of opposite nature, i.e., one being AF and favoring a singlet $S_{\text{tot}} = 0$ ground state, and the other being ferromagnetic, favoring a $S_{\text{tot}} = 2$ ground state. In a pure spin-1 chain, the ground state is a singlet as long as the ground state of an individual bond is not the quintuplet (i.e., $S_{\text{tot}} = 2$), and the ferromagnetic tendency (if present) is overwhelmed by AF couplings; thus, no large moments can form. The situation, however, becomes qualitatively different in the presence of *strong randomness*. In this case a powerful method to study the problem is an asymptotically exact real space renormalization group (RG) scheme,² using which we find effective *ferromagnetic* couplings get generated at low energies even if all original couplings are AF overall (i.e., such that the ground state of every nearest neighbor pair taken in isolation is a singlet). A detailed analysis of this effect will be given in a separate publication;¹⁰ however, the basic physical picture is quite simple and summarized below.

In the presence of strong randomness, the energy scales (given by the couplings) become well separated, and low- and high-energy subspaces of the entire Hilbert space get decoupled perturbatively. An efficient way to study the low-energy physics of the system is to focus on the low-energy subspace and perturbatively project the original couplings into this subspace; in this projection process the couplings get renormalized. Due to the different nature of the Heisenberg and biquadratic couplings, they are renormalized by different amounts. In particular, if originally the net coupling is overall AF, after renormalization, the dominant (AF) coupling may get suppressed and a small ferromagnetic coupling (if present) can become dominant, leading to *effective* ferromagnetic bonds.

As an example, we consider a pure AF Heisenberg spin-1 chain, and replace some bonds by very weak impurity bonds (weak compared to the bulk Haldane gap) with both Heisenberg and biquadratic couplings. Consider a bond of this type between spins labeled i and j (Figure 1 shows two such pairs $i, j : 1, 2$ and $3, 4$), with the net coupling $H_{ij} = J_{ij} \mathbf{S}_i \cdot \mathbf{S}_j + D_{ij} (\mathbf{S}_i \cdot \mathbf{S}_j)^2$. In this case, the original pure

^{a)}Electronic mail: kunyang@cco.caltech.edu

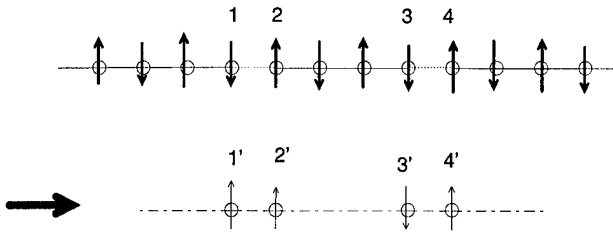


FIG. 1. Illustration of effective spin-1/2 edge spins (thick arrows) appearing at the edges of a segment with regular coupling (solid lines). The thick arrows are original spin-1's and thin arrows are effective edge spin-1/2's. The solid lines are original pure Heisenberg couplings; the dotted lines are the original impurity bonds; the dashed (dot-dashed) lines are effective couplings between spin-1/2's of different (same) segment, which are random and can be either F or AF.

chain is chopped into weakly coupled segments of the AF Heisenberg spin-1 chain, and the low-energy degrees of freedom (below the bulk Haldane gap) are due to spin-1/2's (s_i) living at the ends of the segments (see Fig. 1).⁷ The impurity bond between i and j (where i, j could be 1, 2 or 3, 4) couples the two spin-1/2s living on sites i and j (now labeled as i' and j' , and spin operators with lower case, because of the change of spin from spin-1 to spin-1/2), by the Heisenberg form (guaranteed by rotational invariance and special properties of spin-1/2)

$$\tilde{H}_{i'j'} = \tilde{J}_{i'j'} \mathbf{s}_{i'} \cdot \mathbf{s}_{j'} + C_{i'2'}. \quad (3)$$

It is straight forward to show that $\tilde{J}_{i'j'} = \alpha^2 (J_{ij} - D_{ij}/2)$, where α is a projection constant of order 1. Thus the coupling is *ferromagnetic* if

$$J_{ij} - D_{ij}/2 < 0, \quad (4)$$

while the original bond between i and j may be AF under the same condition (i.e., the ground state of H_{ij} is a singlet). The couplings through the Haldane chain may also be either ferromagnetic or antiferromagnetic, as has been discussed earlier.⁷ Thus in the system that we are considering, the low energy effective model is a spin-1/2 chain with random F and AF Heisenberg couplings.

Westerberg *et al.*⁴ have studied the spin-1/2 chain with random F and AF Heisenberg couplings and demonstrated that in such a system at low temperatures active spins form large moments that are weakly coupled. Interesting thermodynamic properties, e.g., a Curie-like susceptibility, follows. Our results here show that such novel behavior can occur in a random spin-1 chain even if all the bare couplings are AF.

In order for the novel effects discussed above to become possible, one needs to have a biquadratic coupling that is of opposite nature to the Heisenberg coupling, with a comparable coupling constant. In the rest of this article we address the issue how non-Heisenberg coupling may be generated in nature and under what conditions they become important, and for convenience focus on systems with $S=1$. If the coupling between two spin-1 objects is rotationally invariant, it must take the form: $H_{ij} = J \mathbf{S}_i \cdot \mathbf{S}_j + D (\mathbf{S}_i \cdot \mathbf{S}_j)^2$, and the biquadratic coupling is ferromagnetic when $D > 0$, and antiferromagnetic otherwise (opposite to the case of Heisenberg coupling J). We model a spin-1 object by putting two spin-1/2 electrons in a open shell with N orbitals of an atom, and

assume Hund's rule coupling forces them to occupy different orbitals and form a total spin-1 (i.e., they have parallel spins).¹¹ We also assume crystal field breaks the degeneracy of the orbitals, and the electrons stay in orbitals 1 and 2 in the ground state; and the energy cost for taking an electron from orbitals 1 or 2 to other orbitals in the same atom without changing its spin is V . This crystal field splitting V , however, may be small compared to the scale of Coulomb interaction U between the electrons (which gives rise to the Hund's rule), and other energy scales involved.

The coupling between two neighboring such spin-1 objects (i and j) comes from hopping of electrons from one site to the other, described by the following hopping Hamiltonian:

$$H' = - \sum_{a,b=1}^N t_{ab} \sum_{\sigma=\uparrow,\downarrow} (c_{ia\sigma}^\dagger c_{jb\sigma} + h.c.), \quad (5)$$

where $c_{ia\sigma}^\dagger$ is the creation operator of an electron in orbital a of site i with spin σ , and t_{ab} is the hopping matrix element which is small compared to the scale of Coulomb interaction U , so the electrons are mostly localized on one site or the other, and the virtual hopping processes give rise to the coupling between the spins. We assume $t_{ab} = t$ for $a=b$, and $t_{ab} = t'$ for $a \neq b$.¹² Since the t_{ab} is spin independent, H' is invariant under spin rotation, and will give rise to rotationally invariant spin couplings. In the following we calculate the strength of such couplings, using standard nondegenerate perturbation theory.

The leading order contribution is of second order in t , which comes from the virtual process where an electron hops from one site to the other, and hops back. We find the energy gain from such processes depends on the total spin of the system:

$$\Delta E_0^{(2)} = - \frac{4t'^2}{U_a} (N-2) - \frac{6(t^2 + t'^2)}{U_a}, \quad (6)$$

$$\Delta E_1^{(2)} = \left[- \frac{4t'^2}{3U_p} - \frac{8t'^2}{3U_a} \right] (N-2) - \frac{4(t^2 + t'^2)}{U_a}, \quad (7)$$

$$\Delta E_2^{(2)} = - \frac{4t'^2}{U_p} (N-2). \quad (8)$$

Here $\Delta E_S^{(2)}$ stands for the energy difference (compared to the unperturbed ground state with $t_{ab}=0$) of states with total spin S to the second order in t ; U_p and U_a are the energy cost for taking one electron from one site to the other, and form a total spin 3/2 (parallel) or 1/2 (antiparallel) with the original spin-1. Hund's rule suggests $U_p < U_a$. We have neglected the crystal field splitting, assuming it is small compared to the U 's.

These spacings between levels with different total spins can be described by a Heisenberg coupling between the two spin-1's with

$$J^{(2)} = \frac{4t'^2}{3} \left(- \frac{N-2}{U_p} + \frac{N-1/2}{U_a} \right) + \frac{2t^2}{U_a}, \quad (9)$$

plus an unimportant constant, and *no* biquadratic coupling, i.e., $D^{(2)}=0$. This is not surprising because second-order processes involve only one electron exchange; since the spin

of the electron is one-half, Heisenberg coupling is the only possibility that respects rotational invariance. Since $J^{(2)}$ involves the difference of terms, it may have either sign: the energy denominator favors parallel spins, while antiparallel spins have greater phase space due to the Pauli principle, and there exists the possibility that the magnitude of $J^{(2)}$ can be small, if the two opposite terms in (9) are close in magnitude.

Biquadratic couplings can arise from higher order hopping or exchange processes, involving hopping of two or more electrons, and will be of order $O(t^4)$ or higher. Naively, one would expect this to be much smaller than J because in most cases the additional t 's lead to additional energy denominators, of order U , will introduce at least two more factors of t/U , which is small. We point out, however, that there is a special class of two-electron hopping processes that can partially avoid the additional factors of $1/U$, and potentially make sizable contribution at order t^4 (which could be comparable to J under favorable circumstances). These are processes where one electron hops from site i to site j , and another electron hops from site j to site i , and in the intermediate state where there are two electrons on each site, the spins arrange themselves to form a triplet on each site. The energy of such an intermediate state is not of the Coulomb energy scale U , but of the crystal field splitting of the orbitals V , which may be quite small. The fourth-order perturbation calculation of the contribution of these processes is quite involved; the results are

$$\Delta E_0^{(4)} = -\frac{2t'^4}{VU_a^2}(N-2)^2, \quad (10)$$

$$\Delta E_1^{(4)} = -\frac{8t'^4}{9V}\left(\frac{1}{U_p} - \frac{1}{U_a}\right)^2(N-2)^2, \quad (11)$$

$$\Delta E_2^{(4)} = -\frac{8t'^4}{VU_p^2}(N-2)^2. \quad (12)$$

From this we obtain the contributions to J and D from the fourth order processes discussed above to be

$$J^{(4)} = -\frac{8t'^4}{9V}\left(\frac{2}{U_p^2} - \frac{1}{U_a^2} + \frac{1}{U_a U_p}\right)(N-2)^2, \quad (13)$$

$$D^{(4)} = -\frac{2t'^4}{9V}\left(\frac{4}{U_p^2} + \frac{1}{U_a^2} - \frac{4}{U_a U_p}\right)(N-2)^2. \quad (14)$$

From the above expressions, we see that the biquadratic coupling D may be comparable to the usual Heisenberg coupling J if (a) V is small,¹³ (b) the orbital degeneracy N is

large, and (c) if there is a cancellation due to opposing terms in Eq. (9). In addition to the factors considered above, some other physical effects not included in our model may also enhance D . One possibility is that the hopping matrix element may depend on the ionic state, e.g., it may be larger for a second particle hop, because of the ion's bigger size. This will further enhance the contribution of the fourth-order term, and therefore the biquadratic coupling.

In summary, we have shown that there exists in a random *antiferromagnetic* spin-1 chain with nearest neighbor isotropic couplings, consisting of both Heisenberg and biquadratic exchange, the possibility of a *ferromagnetic-like* instability. This causes the formation of arbitrarily large effective spins at low temperatures, leading to a pure Curie behavior for the magnetic susceptibility. We have also discussed how non-Heisenberg coupling between spins are generated for $S > 1/2$, and under what conditions they become comparable to the Heisenberg coupling. We argue that these conditions may be realizable in real systems.

This work was supported by NSF Grant DMR-9400362 (at Princeton), and a Sherman Fairchild fellowship (at Caltech). Part of this work was performed while the authors were at Aspen Center for Physics, and part while one of the authors (R.N.B.) was visiting the Institute for Theoretical Physics at Santa Barbara.

¹ F. D. M. Haldane, Phys. Lett. **93A**, 464 (1983).

² C. Dasgupta and S. K. Ma, Phys. Rev. B **22**, 1305 (1980).

³ D. S. Fisher, Phys. Rev. B **50**, 3799 (1994).

⁴ E. Westerberg, A. Furusaki, M. Sigrist, and P. A. Lee, Phys. Rev. Lett. **75**, 4032 (1995).

⁵ R. A. Hyman, K. Yang, R. N. Bhatt, and S. M. Girvin, Phys. Rev. Lett. **76**, 839 (1996).

⁶ K. Yang, R. A. Hyman, R. N. Bhatt, and S. M. Girvin, J. Appl. Phys. **79**, 5096 (1996).

⁷ R. A. Hyman and K. Yang, Phys. Rev. Lett. **78**, 1783 (1997).

⁸ A. Klumper, Europhys. Lett. **9**, 815 (1989); M. T. Batchelor and M. N. Barber, Phys. Rev. B **40**, 4621 (1989).

⁹ C. Itoi and M.-H. Kato, Phys. Rev. B **55**, 8295 (1997).

¹⁰ K. Yang and R. N. Bhatt, preprint cond-mat/9712252.

¹¹ In some real systems, like, e.g., Ni^{2+} , we have two holes instead of two electrons in the $3d$ shell, but the physics should be the same.

¹² In real systems the hopping matrix element depends on the specific orbitals involved and may be zero for certain pairs of orbitals due to symmetry. To simplify the algebra, we assume it is t for hopping between the same orbitals and t' for different orbitals; these may be taken to be the average values of the two. The results are not altered qualitatively by this simplification.

¹³ In principle, when V is small compared to t , the straightforward nondegenerate perturbation expansion needs to be modified. However, the final answer will be of the same order of magnitude as that obtained from the perturbation calculation.

Universal magnetic fluctuations in the two-dimensional XY model

P. Archambault

*Laboratoire de Physique, Ecole Normale Supérieure, 46 Allée d'Italie,
F-69364 Lyon Cedex 07, France*

S. T. Bramwell

Department of Chemistry, University College London, 20 Gordon Street, London, United Kingdom

J.-Y. Fortin, P. C. W. Holdsworth,^{a)} S. Peysson, and J.-F. Pinton

*Laboratoire de Physique, Ecole Normale Supérieure, 46 Allée d'Italie,
F-69364 Lyon Cedex 07, France*

We discuss the probability distribution function for the magnetic order parameter M , in the low temperature phase of the two-dimensional XY model. In this phase the system is critical over the whole range of temperature. The thermally averaged value of the order parameter $\langle M \rangle$, which is zero in the thermodynamic limit, has abnormally large finite size corrections. An exact result, within a spin wave calculation gives $\langle M \rangle = (1/2N)^{T/8\pi J}$, where J is the magnetic exchange constant and N the number of spins. We show, using Monte Carlo simulation, that the distribution function, $Q(y - \langle y \rangle)$, $y = T^{-1} L^{T/4\pi J} M$, is an asymmetric universal function. Using a diagrammatic technique, we show that the asymmetry comes from three-spin and higher correlations. If only two-spin correlations are considered, the distribution is Gaussian. However, as there are contributions from two-spin terms separated by all distances, the distribution remains broad and is consistent with a divergent susceptibility. © 1998 American Institute of Physics. [S0021-8979(98)51911-1]

The long-ranged correlations that characterize a critical point mean that at this special point finite size effects are much more important than the $1/\sqrt{N}$ corrections given by the central limit theorem.¹ For example scaling arguments give, for the magnetization, $\langle M \rangle$, at a critical point² $\langle M \rangle \sim L^{-\beta/\nu}$, with β and ν the critical exponents for the magnetization and the correlation length. For strong fluctuations β is small and ν is large, leaving the finite size magnetization measurable right into the physical domain. This is nowhere better observed than in the low temperature phase of the two-dimensional XY model, where the system is critical over a whole range of temperature. In fact it is an ideal system in which to study finite size fluctuations near a critical point as it shows critical behavior over a range of temperatures below the Kosterlitz–Thouless transition temperature T_{KT} ,³ it is extremely accessible to analytic techniques and is of broad experimental relevance.⁴

The model is defined with the Hamiltonian

$$H = -J \sum_{\langle i,j \rangle} \cos(\theta_i - \theta_j), \quad (1)$$

where J is the ferromagnetic coupling constant and θ_i the angle of orientation of spin vector S_i , constrained to lie in a plane. The summation is over nearest neighbors and we take the spins to be on the sites of a square lattice with periodic boundary conditions. We use a system of units with Boltzmann's constant k_B equal to unity throughout. We simplify this to what we refer to as the harmonic XY or HXY model.⁵ Its Hamiltonian is

$$H = -J \sum_{\langle i,j \rangle} \left[1 - \frac{1}{2} (\theta_i - \theta_j - 2\pi n)^2 \right], \quad (2)$$

where $n=0, \pm 1$ is an integer chosen so that $(\theta_i - \theta_j - 2\pi n)$ lies between $\pm \pi$. This model is almost the Villain model,⁶ but is more practical from a numerical point of view, as the vortex variable n is not a thermodynamic variable, but is constrained to the values $n=0, \pm 1$.⁷ We concentrate, in this article, on the temperature regime well below T_{KT} where the vortex density is exponentially small and the HXY reduces to a model of harmonic spin waves, which can be solved exactly.⁸

We define an instantaneous scalar order parameter M :

$$M = \frac{1}{N} \sqrt{\left(\sum_{i=1,N} S_i \right) \cdot \left(\sum_{i=1,N} S_i \right)}. \quad (3)$$

Within the spin wave approximation one can derive the following result for the equilibrium magnetization $\langle M \rangle$, exact to leading order in N :⁸

$$\langle M \rangle = \left(\frac{1}{2N} \right)^{T/8\pi J}. \quad (4)$$

$\langle M \rangle$ falls to zero in the thermodynamic limit, which confirms the Mermin–Wagner theorem⁹ that the thermodynamic magnetization is zero at all finite temperature. However, putting in numbers for $T \sim O(J)$ one can easily convince oneself that $\langle M \rangle$ is measurable throughout the physical domain.

The susceptibility per spin, defined as

^{a)}Electronic mail: pcwh@enslapp.ens-lyon.fr

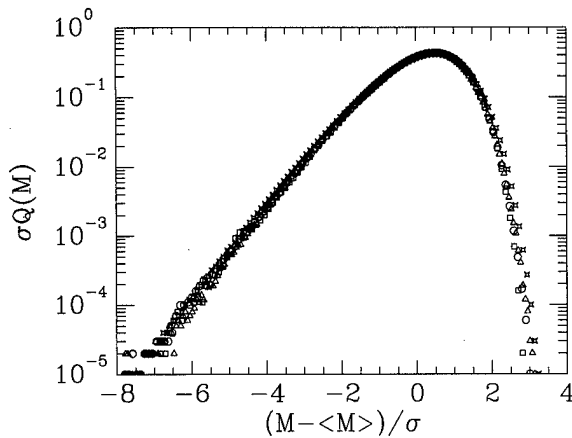


FIG. 1. $\log[\sigma Q(M)]$ vs $(M - \langle M \rangle)/\sigma$ for $T/J=0.5$ for $N=100$ (stars), $N=1024$ (circles), $N=10\,000$ (squares), and for $T/J=1.0$ for $N=1024$ (triangles).

$$\chi = \frac{N}{T} (\langle M^2 \rangle - \langle M \rangle^2), \quad (5)$$

is given by the expression

$$\chi = \frac{\langle M \rangle^2}{T} \sum_r \left\{ \exp \left[\frac{T}{J} \times G(r) \right] - 1 \right\}, \quad (6)$$

where $G(r)$ is the lattice Green's function for a square lattice

$$G(r) = \frac{1}{N} \sum_{q \neq 0} \frac{e^{i\mathbf{q} \cdot \mathbf{r}}}{\gamma_q}, \quad (7)$$

$$\gamma_q = 4 - 2 \cos(q_x) - 2 \cos(q_y).$$

To an excellent approximation one finds

$$\chi = \frac{1}{2a_{2D}} \frac{N \langle M \rangle^2 T}{J^2}, \quad a_{2D} = 258.6, \quad (8)$$

with the susceptibility per spin therefore diverging as $\chi \sim N^{1-T/4\pi J}$.

From Eq. (8) we see that the prefactor of the "divergent" susceptibility is small and goes to zero as T goes to zero. The normalized standard deviation of the distribution,

$$\frac{\sigma}{\langle M \rangle} = \sqrt{\frac{\langle M^2 \rangle - \langle M \rangle^2}{\langle M \rangle^2}} = \frac{\sqrt{N\chi T}}{N \langle M \rangle}, \quad (9)$$

has a numerical value of only ≈ 0.04 T, but is independent of system size. In a noncritical system, with finite correlation length one expects $\sigma/\langle M \rangle$ to go to zero as $N^{-1/2}$ in the large N limit. The scalar magnetization therefore appears to be a well-defined quantity despite its fluctuations, as measured by the susceptibility, being divergent in the thermodynamic limit, as shown above.

We are interested here in the probability distribution function $Q(M)$. The distribution function for the magnetization at a critical point has been discussed by several authors.^{2,10} Binder² argues, using the example of an Ising system with distribution $P_L(M)$, that within the critical region

$$P_L(M) = L^{\beta/\nu} P(L/\xi, ML^{\beta/\nu}), \quad (10)$$

where ξ is the correlation length. ξ is the length scale at which one can expect a cross over to a noncritical regime with Gaussian fluctuations. Very close to the critical point the correlation length of the infinite system would be much bigger than the system size L . In this situation one expects self-similar behavior in the system, with L being the only important scale above the microscopic length. P_L should therefore depend on the single variable $ML^{\beta/\nu}$.

For the two-dimensional XY model, despite the fact that β and ν do not exist in a conventional sense,⁵ their ratio, x , is perfectly well defined through Eq. (4) for all temperatures $T \leq T_{KT}$. Within the spin wave approximation one finds $x = T/4\pi J$. Near T_{KT} the scaling relation

$$x = \beta/\nu = \frac{d}{\delta+1} = \frac{1}{8} \quad (11)$$

is satisfied by putting $T/J \approx \pi/2$, which is the mean field approximation for T_{KT} .³ More precisely, we have shown⁵ that the renormalization of the temperature due to vortices is taken into account correctly by replacing T/J with the effective temperature $(T/J)_{\text{eff}} = \pi/2$ at a temperature $T^*(L) \approx T_{KT}$, in which case the scaling relation is satisfied exactly. We therefore expect universal finite size scaling in the same manner. However, in our case we have a line of critical points for all temperatures less than T_{KT} with temperature dependent exponent x . It is therefore by no means obvious that we should find the same scaling functions for different temperatures.

In Fig. 1 we plot Monte Carlo data for $\log[\sigma Q(M)]$ versus $(M - \langle M \rangle)/\sigma$ for $N=10^2$, 10^3 , and 10^4 spins at $T/J=0.5$ as well as for $N=10^3$ spins at $T/J=1.0$. The run length was typically 10^7 Monte Carlo steps per spin. The data clearly fall on a universal curve over five orders of magnitude. We can effectively define a reduced variable $y = M/\sigma \sim T^{-1} ML^{T/4\pi}$, with $\bar{y} = \langle M \rangle/\sigma \sim T^{-1}$ which is independent of L . Our universal function is therefore of the form $Q(y - \bar{y})$ and we do indeed find a single universal function for all temperatures and all system sizes. We observe corrections to universality for systems containing less than 100 spins.

The function is clearly not Gaussian and shows an asymmetry, with an enhanced probability for fluctuations towards a smaller magnetization. This corresponds to the fact that the long wavelength spin waves, with amplitude diverging with N , provide the possibility of large scale fluctuations below the average value, at zero cost in free energy. Indeed the logarithm of $Q(M)$ corresponds to the effective free energy at the critical point, or fixed point function, discussed in detail during the pioneering days of critical phenomena.¹¹

From a mathematical point of view the spin wave model studied here offers the opportunity to calculate the distribution function analytically. We present here some analytic results as a first step towards the calculation of $Q(M)$.

We consider the moments of the distribution

$$\langle z^n \rangle = \left\langle \left(\frac{M - \langle M \rangle}{\sigma} \right)^n \right\rangle, \quad (12)$$

and are interested, initially in their leading N and T dependence. After some work one can write for $\langle M^n \rangle$ (Ref. 12),

$$\langle M^n \rangle = \left(\frac{\langle M \rangle}{2N} \right)^n \text{Tr} \prod_{i \neq j}^n e^{-\epsilon_i \epsilon_j (T/2J) G(\mathbf{r}_i - \mathbf{r}_j)}, \quad (13)$$

where the trace is over the variables $\epsilon_i = \pm 1$ and over the sites \mathbf{r}_i . For the n th moment the product contains n exponential terms. $G(\mathbf{r}_i - \mathbf{r}_j)$ is the lattice Green's function joining points i and j .

This is the starting point for a diagrammatic expansion: the exponential is expanded and the trace taken. The sites are represented by vertices and the Green's functions $G(\mathbf{r}_i - \mathbf{r}_j)$ by a line joining the points i and j . Numerically we find that the graphs making the leading contribution consist of simply connected single loops. Further, in calculating the moment $\langle z^n \rangle$ we find that the only single loop graphs that count are those of length n . The contribution of such a graph to $\langle M^n \rangle$ is then

$$\frac{1}{n!} \left(\frac{-T\langle M \rangle}{2NJ} \right)^n G(r_{12})G(r_{23})\dots G(r_{n-1n})G(r_{n1}), \quad (14)$$

and passing into Fourier space the graph finally reduces to

$$\left(-\frac{T\langle M \rangle}{2NJ} \right)^n \sum_{\mathbf{q} \neq 0} \frac{1}{\gamma_{\mathbf{q}}^n}. \quad (15)$$

One can see that the leading N dependence of the sum over $\gamma_{\mathbf{q}}^{-n}$ is N^n and we find numerically that higher order corrections disappear rapidly with increasing N . Given that $\sigma \sim T\langle M \rangle$, we therefore find that to an excellent approximation the moments $\langle z^k \rangle$ are independent of N and T , in agreement with our numerical simulations.

Although this result is specific to the Gaussian model we have used, it is interesting to note that it shows, explicitly and without recourse to a scaling hypothesis or to phenomenology of any kind, the existence of a universal non-Gaussian finite size scaling function $\sigma Q((M - \langle M \rangle)/\sigma)$.

Finally, and after some rather tedious manipulation, we are able to write the distribution Q in the form

$$Q(M) = \int_{-\infty}^{\infty} \frac{dt}{2\pi\sigma} \exp -it \left(\frac{M - \langle M \rangle}{\sigma} \right) + \sum_{k \geq 2} \frac{a_k}{2k} \left(-it \sqrt{\frac{2}{a_2}} \right)^k, \quad (16)$$

where

$$a_k = \frac{1}{N^k} \sum_{\mathbf{q} \neq 0} \frac{1}{\gamma_{\mathbf{q}}^k}. \quad (17)$$

From this expression one can see clearly the origin of the non-Gaussian element in the distribution. Including the term $k=2$ only, we find a Gaussian function. This comes explicitly from the sum of contributions from two-vertex loops, or two-particle correlations only. Just keeping these terms, which corresponds to a Hartree approximation, results in a wide distribution with a correctly diverging susceptibility; but the distribution remains Gaussian. The non-Gaussian be-

havior therefore comes from graphs of three and higher order, with the asymmetry coming from the odd terms.

The low temperature, or spin wave region yields itself extremely well to analytical work and to numerical work. At a critical point, in order to enter into the universal regime one must exceed a transient length scale over which microscopic details disappear.¹¹ Within the Gaussian approximation, the transient effects are exceedingly small with the result that the probability distribution fits onto the universal curve with as little as 100 spins.

There is a considerable literature on universal finite size scaling behavior, with Ising systems being predominantly considered.^{13,14} In addition, models similar to ours occur in problems of the growth of interfaces between two phases.¹⁵ We have shown here, in this work that the two-dimensional XY model is an ideal system in which to further the study of critical fluctuations in a finite system.

Our result that the universal function is independent of the critical exponents is not what one would expect in general. Rather, one expects the form of the function to depend on the universality class and hence on the exponents. It will be interesting to try to quantify this universality class dependence in other models, where n -spin correlators are not simple functions of two-spin correlators.

In conclusion we have shown that the critical finite size corrections to the thermodynamic limit spill over into the physical domain. This being the case experiments on a large class of systems should be possible in which order parameter distribution function analogous to $Q(M)$ can be measured directly.

It is a pleasure to thank J. L. Cardy, J. T. Chalker, Z. Rač, and T. Ziman for useful discussions.

¹ L. D. Landau and E. M. Lifshitz, *Statistical Physics* (Pergamon, Oxford, 1980), Vol. 1.

² See, for example, K. Binder, *Computational Methods in Field Theory*, edited by H. Gauslever and C. B. Lang (Springer, Berlin, 1992).

³ J. M. Kosterlitz and D. J. Thouless, *J. Phys. C* **6**, 1181 (1973).

⁴ H.-J. Elmers, *Int. J. Mod. Phys. B* **9**, 3115 (1995); F. Huang, M. T. Kief, G. J. Mankey, and R. F. Willis, *Phys. Rev. B* **49**, 3962 (1994); S. T. Bramwell and P. C. W. Holdsworth, *J. Appl. Phys.* **73**, 6096 (1993); W. J. Nuttall, D. Y. Wells, B. O. Noh, and R. J. Birgeneau, *J. Phys.: Condens. Matter* **7**, 4337 (1995).

⁵ S. T. Bramwell and P. C. W. Holdsworth, *J. Phys.: Condens. Matter* **5**, L53 (1993); *Phys. Rev. B* **49**, 8811 (1994).

⁶ J. Villain, *J. Phys. (France)* **36**, 581 (1975).

⁷ J. V. José, L. P. Kadanoff, S. Kirkpatrick, and D. R. Nelson, *Phys. Rev. B* **16**, 1217 (1977).

⁸ P. Archambault, S. T. Bramwell, and P. C. W. Holdsworth, *J. Phys. A* **30**, 8363 (1997).

⁹ N. D. Mermin and H. Wagner, *Phys. Rev. Lett.* **17**, 1133 (1966).

¹⁰ J.-P. Bouchaud and A. Georges, *Phys. Rep.* **195**, 127 (1990).

¹¹ K. G. Wilson and J. Kogut, *Phys. Rep.*, *Phys. Lett.* **12C**, 77 (1974).

¹² S. Peysson, Rapport de stage de D.E.A. de Physique Théorique Rhône-Alpin 1997 (unpublished).

¹³ A. D. Bruce, *J. Phys. C* **14**, 3667 (1981).

¹⁴ K. Binder, *Z. Phys. B* **43**, 119 (1981).

¹⁵ G. Foltin, *Phys. Rev. E* **50**, R639 (1994); Z. Rac and M. Plischke, *J. Phys. E* **50**, 3530 (1994); M. Plischke, Z. Rac, and R. K. P. Zia, *Phys. Rev. E* **50**, 3589 (1994).

Semiquantitative analysis of magnetic phase transitions in the $\text{MnFeP}_{1-x}\text{As}_x$ series of compounds

R. Zach^{a)}

Institute of Physics, Technical University of Cracow, 1 St. Podchorążych, 30 084 Cracow, Poland

M. Guillot

Laboratoire Magnetiques Champs Intenses-Max Planck Institute, CNRS, BP-166X, 38 042 Grenoble, France

J. Toboła

Faculty of Physics and Nuclear Techniques, The University of Mining and Metallurgy, Mickiewicza 30, 30 059 Cracow, Poland

On the basis of the relation $T(\sigma, H)$ derived within the framework of the Bean-Rodbell model a semiquantitative analysis of (B, T) magnetic phase diagrams in the hexagonal region of the $\text{MnFeP}_{1-x}\text{As}_x$ ($0.15 \leq x \leq 0.66$) series of compounds was carried out. It was found that the first order transition line in the (B, T) plane is terminated by the isolated critical point for $x=0.33$ and $x=0.5$ contents. The positive value of dB_C/dT and the saturation of the magnetization was found to be in agreement with the experiment. Thus the Bean-Rodbell model and the molecular field approximation can be applied to describe the discontinuous Ferro-Para magnetoelastic phase transition. Semiquantitative agreement between the theoretical and the experimental (B, T) magnetic phase diagrams was obtained. For the $\text{MnFeP}_{0.67}\text{As}_{0.33}$ compound the electronic structure calculations were performed by the Korringa-Kohn-Rostoker with the coherent potential approximation method. The density of states (DOS) curve calculated in the nonmagnetic state shows that the Fermi level falls in a deep minimum of DOS. It indicates that the metamagnetic B -field induced phase transition between the paramagnetic and the ferromagnetic states may be observed (metamagnetism of itinerant electrons) which remains in good agreement with our experimental results. © 1998 American Institute of Physics. [S0021-8979(98)52011-7]

INTRODUCTION

The $\text{MnFeP}_{1-x}\text{As}_x$ series of compounds in the hexagonal region (Fe_2P type) considered in this article exhibit very peculiar magnetic properties. In zero magnetic field, for investigated ranges of temperature and composition, the metamagnetic magnetoelastic phase transition was pointed out.^{1,2} Moreover, the influence of dc magnetic field, pressure, and temperature on magnetoelastic phase transitions of these compounds were also established.¹⁻³ For $0.2 \leq x \leq 0.275$ the (B, T) phase diagrams show the existence of the critical end point while for $x=0.33$ and $x=0.5$ contents the isolated critical point (ICP) was confirmed. For $\text{MnFeP}_{0.67}\text{As}_{0.33}$ and $\text{MnFeP}_{0.5}\text{As}_{0.5}$ the metamagnetic field induced phase transition between the paramagnetic (disordered) state and the ferromagnetic one was observed.^{1,2,4,5} In this article we present a semiquantitative analysis of (B, T) magnetic phase diagrams for $x=0.33$ and $x=0.5$ contents based both on the molecular field approximation (the Bean-Rodbell model⁶) and on the itinerant electron model of phase transitions.⁷⁻⁹ In the latter the ground state density of states (DOS) electronic structure of $\text{MnFeP}_{0.67}\text{As}_{0.33}$ was calculated using the Korringa-Kohn-Rostocker (KKR) with the coherent potential approximation (CPA) method.^{10,11} The spin polarized electronic structure computations were presented for Fe_2P

and $\text{MnFeP}_{0.7}\text{As}_{0.3}$ in an earlier paper.¹² The calculated magnetic moments were found to be in close agreement with diffraction neutron measurements.¹²

RESULTS AND DISCUSSION

The critical behavior of the magnetic system will be analyzed on the basis of the generalized Gibbs free energy in the form as follows:⁶

$$G_j(\sigma, T) = G_{\text{ex}} + G_H + G_{\text{dist}} + G_{\text{entr}} + G_{\text{press}}, \quad (1)$$

where G_{ex} , G_H , G_{dist} , G_{entr} , and G_{press} are the exchange energy calculated on the basis of the molecular field model, the Zeeman energy, the elastic energy, the entropy term, and the pressure term, respectively. Furthermore, the thermodynamical analysis of the (B, T) magnetic phase diagrams will be limited to the diagrams where the ICP was experimentally found. Minimizing the free energy G [Eq. (1)] with respect to volume in the case of lack of external pressure ($G_{\text{press}} = 0$) we obtain

$$\begin{aligned} \frac{G_{\text{min}}}{Nk} = & -\frac{3j}{2(j+1)} T_0 \sigma^2 - \frac{9}{20} \frac{[(2j+1)^4 - 1]}{[2(j+1)]^4} T_0 \eta_j \sigma^4 \\ & - \frac{g \mu_B j H \sigma}{k} - TS_j(\sigma), \end{aligned} \quad (2)$$

where

^{a)}Corresponding author; electronic mail: puzach@cyf-kr.edu.pl

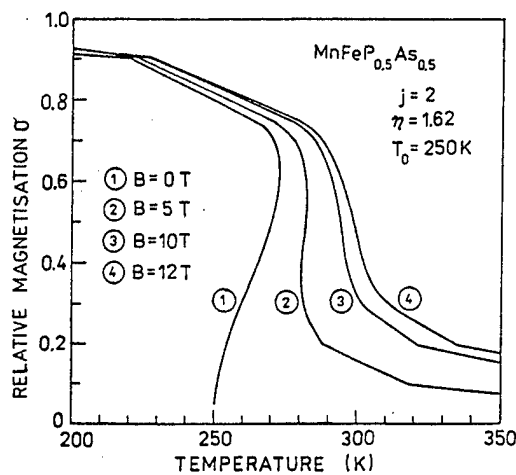


FIG. 1. Calculated magnetization $\sigma_H(T)$ for $\text{MnFeP}_{0.5}\text{As}_{0.5}$ ($j=2$, $\eta=1.62$, $T_0=250$ K).

$$\eta_j = \frac{5}{2} \frac{[4j(j+1)]^2}{[(2j+1)^4 - 1]} Nk\kappa T_0 \beta^2,$$

N is number of magnetic atoms per unit volume; T_0 is the Curie temperature for assuming incompressible lattice; S_j is magnetic entropy, k is the Boltzmann constant; g is the Landé factor; κ is the coefficient of compressibility, and j is total angular momentum.

When minimizing G_{\min} [Eq. (2)] with respect to σ in the presence of external magnetic field, we obtain an implicit expression of temperature T dependent relative magnetization σ :

$$T(\sigma, H) = \frac{\left[aT_0\sigma + bT_0\sigma^3 + \frac{g\mu_B j}{k} H \right]}{B_j^{-1}(\sigma)}, \quad (3)$$

where

$$a = \frac{3j}{j+1}; \quad b = \frac{9}{5} \frac{(2j+1)^4 - 1}{[2(j+1)]^4} \eta_j; \quad B_j^{-1}(\sigma) = \frac{\partial S_j}{\partial \sigma}.$$

From Eq. (3) the magnetization plots at constant magnetic field can be derived from the isofield magnetization $\sigma_H(T)$ curves.

The magnetization measurements in the low temperature range show that the saturation magnetization is about $\sim 4 \mu_B/\text{fu}$ so we conclude that the angular momentum is $j=2$ (it was assumed that $g=2$). Also, the magnetic moment of $3.9 \mu_B/\text{fu}$ was found from the KKR-CPA calculations. In the external magnetic field up to 28 T the ICP was unambiguously experimentally confirmed only in the case of two As contents. So the samples $\text{MnFeP}_{0.5}\text{As}_{0.5}$ and $\text{MnFeP}_{0.67}\text{As}_{0.33}$ were chosen for detailed numerical analysis. The magnetization versus temperature plots $\sigma_H(T)$ for selected external magnetic field values are presented in Fig. 1. They were obtained using the following model parameters: $j=2$, $\eta=1.62$, and $T_0=250$ K. In this case the best agreement with the experimental results measured in $\text{MnFeP}_{0.5}\text{As}_{0.5}$ was achieved.⁴ In the magnetic fields $B=0$ and 5 T the first order transition still exist (lines 1 and 2 in Fig. 1). However, for the fields $B=10$ and 12 T the first

order transition is not shown. It means that the first order discontinuous phase transition is terminated above $B \sim 10$ T. It allows one to conclude, that in the vicinity of $T_{\text{cr}} \sim 300$ K and $B_{\text{cr}} \sim 11$ T, the ICP is reached. Such a phenomenon was experimentally observed for $\text{MnFeP}_{0.5}\text{As}_{0.5}$.^{1,4} Similar dependencies of magnetization versus temperature $\sigma_H(T)$ at selected magnetic fields for $\text{MnFeP}_{0.67}\text{As}_{0.33}$ were also calculated. For magnetic field $B=0$, 10, and 20 T the discontinuous phase transition occurs. However, for field $B \sim 25$ T this type of transition is not found. It is concluded that in the vicinity of $T_{\text{cr}} \sim 250$ K and $B_{\text{cr}} \sim 25$ T the ICP is established. In the case of this compound ($x=0.33$) the best agreement with experimental results was obtained for $j=2$, $\eta=2.7$, and $T_0=155$ K.

It is interesting to examine the free energy in more detail. Let us return to the minimal Gibbs free energy expressed by Eq. (2). We expand the entropy into a power series of σ and after collecting terms in like powers of σ the $(G_{\min} - G_0)/Nk$ can be written as follows:⁴

$$\begin{aligned} \frac{G_{\min} - G_0}{Nk} = & \left(\frac{3j}{j+1} \right) [T - T_0] \frac{\sigma^2}{2} + \frac{9}{5} \frac{[(2j+1)^4 - 1]}{[2(j+1)]^4} \\ & \times (T - \eta_j T_0) \frac{\sigma^4}{4} + 6c_j T \frac{\sigma^6}{6} - \frac{g\mu_B j H}{k} \sigma. \end{aligned} \quad (4)$$

The coefficient c_j of the magnetic entropy term can be calculated on the basis of the power series expansion of the magnetic entropy expression into powers of σ (up to sixth order). Thus c_j is determined as

$$c_j = \frac{1}{2} \frac{j}{(j+1)^5} \left(\frac{99}{175} j^4 + \frac{198}{175} j^3 + \frac{63}{50} j^2 + \frac{243}{350} j + \frac{243}{1400} \right). \quad (5)$$

To illustrate some features of the free energy at the first order transition, the free energy isotherms in the vicinity of the temperature corresponding to ICP are reported in Fig. 2. For this the model parameters $j=2$, $\eta=1.62$, $T_0=250$ K,

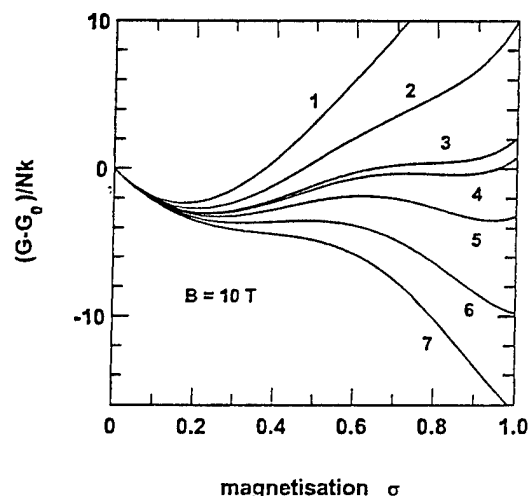


FIG. 2. The free energy $(G_{\min} - G_0)/Nk$ isotherms vs σ in the vicinity of the ICP as calculated on the basis of Landau expansion [Eq. (4)] for $j=2$; $\eta=1.62$; $T_0=250$ K and $B=10$ T. (1) $T=330$, (2) 320, (3) 314, (4) 313, (5) 310, (6) 305, and (7) 300 K.

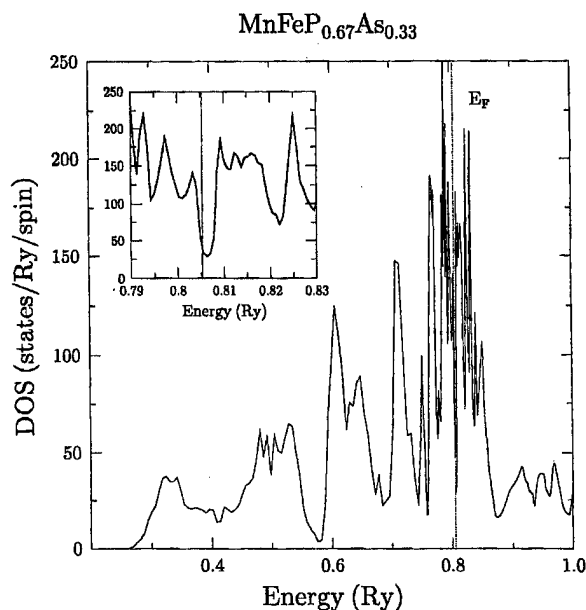


FIG. 3. Total DOS for $\text{MnFeP}_{0.67}\text{As}_{0.33}$ in the nonmagnetic ground state. The inset shows the DOS in the vicinity of E_F .

and $B = 10$ T were chosen for calculations of $(G_{\min} - G_0)/Nk$. The free energy minima which determine the spontaneous magnetization were found to be strongly dependent on temperature. The free energy minima ($B = 10$ T) become less and less pronounced and shift towards higher values of σ when the temperature decreases.

Now we will discuss the itinerant electron paramagnetism, which was observed in several 3d-metal compounds [i.e., YCo_2 , TiBe_2 , FePt_3 , $\text{Co}(\text{Se}_{1-x}\text{S}_x)_2$, RCO_5]⁷ under magnetic fields in the range 10–50 T where different types of transitions either from paramagnetism to ferromagnetism or from antiferromagnetism to ferromagnetism were observed. This first order type of transition, characteristic of itinerant paramagnets in the magnetic field, is strongly related to a shape of the density of states near the Fermi level. The magnetic properties of paramagnets with the DOS close to the Stoner criterion may be significantly modified by magnetic field if the DOS strongly varies in the vicinity of E_F .^{8,9}

In Fig. 3 the total DOS curve for $\text{MnFeP}_{0.67}\text{As}_{0.33}$ in the nonmagnetic state is presented. A more detailed analysis of the DOS curve near the Fermi level showed that E_F is located in the vicinity of the deep DOS minimum (Fig. 3). The semiquantitative computations of the DOS derivative in the neighborhood of the Fermi energy demonstrate that the second derivative of DOS calculated at E_F for $\text{MnFeP}_{0.67}\text{As}_{0.33}$ is positive. We conclude that the field induced metamagnetic transition from the paramagnetic (nonmagnetic in KKR-CPA computations) to the magnetically ordered phase is explained theoretically in this compound, in agreement with the experiment. A specific manifestation of the itinerant nature of the metamagnetic transition is the strong field dependence of the susceptibility of the paramagnet. This property was experimentally observed in the case of $\text{MnFeP}_{0.67}\text{As}_{0.33}$ and

$\text{MnFeP}_{0.5}\text{As}_{0.5}$.^{1,2,4} Quantitative analysis of such a type of phase transition is possible if the temperature dependence of the molecular field coefficient λ is known. Note that for Fe λ strongly depends on the temperature but for Mn this dependence was not found.⁹

As a comparison, the electronic band structure calculations for Fe_2P in the paramagnetic (nonmagnetic) state were performed by KKR method, which showed a very profound minimum of the density of states in the vicinity of the Fermi level. The Fermi energy E_F is in the region where the first derivative of the density of states is very large. This is in agreement with the strong sensitivity of the magnetic properties of Fe_2P on such parameters as external pressure, magnetic field, and composition. Moreover, the second derivative of the DOS curve calculated at the Fermi level is also positive. Note that an isolated critical point, similar to that in the $\text{MnFeP}_{1-x}\text{As}_x$ series, was found experimentally in this compound. However, in the latter the value of the critical field was found to be much smaller than that in the former.¹³

CONCLUSIONS

Semiquantitative analysis of magnetic phase diagrams exhibiting the ICP for the $\text{MnFeP}_{1-x}\text{As}_x$ series of compounds led to conclusions that can be summed up as follows.

- (1) The Bean–Rodbell model was successfully applied to describe the discontinuous Ferro–Para magnetoelastic phase transition.
- (2) A semiquantitative agreement between the theoretical and the experimental (B, T) magnetic phase diagrams was obtained. The discontinuous transition line in the (B, T) plane is terminated by the ICP.
- (3) For the nonmagnetic $\text{MnFeP}_{0.67}\text{As}_{0.33}$ compound KKR–CPA ground state electronic structure calculations were performed. They showed that the Fermi level is in the vicinity of the deep minimum of the DOS curve.

¹R. Zach, M. Guillot, and R. Fruchart, *J. Magn. Magn. Mater.* **89**, 221 (1990).

²R. Zach, M. Guillot, J. C. Picoche, and R. Fruchart, *IEEE Trans. Magn.* **29**, 3252 (1993).

³R. Zach, M. Guillot, J. C. Picoche, and R. Fruchart, *J. Magn. Magn. Mater.* **140–144**, 1541 (1995).

⁴R. Zach, Thesis of habilitation, *Zeszyty Naukowe Politechniki Karkowskiej* z. 21, No. 2 (1997).

⁵R. Zach, M. Bacmann, D. Fruchart, M. Guillot, S. Kaprzyk, S. Nizioł, and J. Toboła, *J. Alloys. Compd.* **262–263**, 508 (1997).

⁶C. P. Bean and D. S. Rodbell, *Phys. Rev.* **126**, 104 (1962).

⁷M. Cyrot and M. Lavagna, *J. Phys. (France)* **40**, 763 (1979).

⁸R. Z. Levitin and A. S. Markosyan, *Sov. Phys. Usp.* **31**, 730 (1988) [*Usp. Fiz. Nauk* **155**, 623 (1988)].

⁹M. Shimizu, *J. Phys. (France)* **43**, 155 (1982); M. Shimizu, *Rep. Prog. Phys.* **44**, 329 (1981).

¹⁰S. Kaprzyk, *Acta Phys. Pol. A* **91**, 135 (1997).

¹¹A. Bansil, S. Kaprzyk, and J. Toboła, *Mater. Res. Soc. Symp. Proc.* **253**, 505 (1992).

¹²J. Toboła, M. Bacmann, D. Fruchart, S. Kaprzyk, A. Koumina, S. Nizioł, J. L. Soubeyroux, P. Wolfers, and R. Zach, *J. Magn. Magn. Mater.* **157–158**, 708 (1996).

¹³L. Lundgren, G. Tarmohamed, O. Beckmen, B. Carlsson, and S. Rundqvist, *Phys. Scr.* **17**, 39 (1978).

Magnetic behavior of the low-dimensional compounds $\text{Ba}_2\text{Cu}_3\text{O}_4\text{Cl}_2$ and $\text{Ba}_3\text{Cu}_2\text{O}_4\text{Cl}_2$

D. Eckert, K. Ruck, M. Wolf, G. Krabbes, and K.-H. Müller^{a)}

IFW Dresden, P.O. Box 270016, 01171 Dresden, Germany

Orthorhombic $\text{Ba}_3\text{Cu}_2\text{O}_4\text{Cl}_2$ contains folded Cu_2O_4 chains along the crystallographic a direction with two different Cu sites. In single crystals of this compound the magnetization measured for a field applied parallel to the a axis shows a spin-flop transition at a threshold field of 2.6 T for temperatures below $T_N \approx 20$ K. Above T_N a Curie–Weiss behavior is found with a paramagnetic moment of $2.0 \mu_B$ per Cu atom. Parallel to the b or c axis the magnetization increases linearly with the field strength, and no metamagnetic transition was detected for these directions. It is concluded that $\text{Ba}_3\text{Cu}_2\text{O}_4\text{Cl}_2$ has localized magnetic moments which, at low temperatures, order antiferromagnetically parallel to the a axis. The bulklike magnetic behavior of this compound is probably caused by a strong coupling between the Cu_2O_4 chains. Tetragonal $\text{Ba}_2\text{Cu}_3\text{O}_4\text{Cl}_2$ is built up of Cu_3O_4 planes, also with two types of copper atoms (Cu_A, Cu_B). Its magnetization increases nearly linearly with the field. Below $T_{NA} = 337$ K single-crystalline $\text{Ba}_2\text{Cu}_3\text{O}_4\text{Cl}_2$ shows a spontaneous magnetization and ferromagnetic hysteresis for fields applied parallel to the tetragonal $[100]$ or $[110]$ directions. For $T < T_{NB} \approx 33$ K, the coercive field is more than one order of magnitude larger compared to that measured in the temperature range $T_{NB} < T < T_{NA}$. The spontaneous magnetization observed in $T_{NB} < T < T_{NA}$ may be attributed to weak ferromagnetism of the Dzyaloshinsky–Moriya type. The behavior of $\text{Ba}_2\text{Cu}_3\text{O}_4\text{Cl}_2$ at lower temperatures, $T \leq T_{NB}$, is not yet understood. © 1998 American Institute of Physics. [S0021-8979(98)25211-X]

Compounds containing copper oxide layers or chains and related oxychlorides are of interest because they may become superconductors when doped. Moreover, they show nearly two-dimensional quantum antiferromagnetic^{1,2} or even quasi-one-dimensional behavior.^{1,3,4} Tetragonal $\text{Ba}_2\text{Cu}_3\text{O}_4\text{Cl}_2$ is built up of Cu_3O_4 planes with two types of copper atoms (Cu_A, Cu_B),⁵ whereas the orthorhombic $\text{Ba}_3\text{Cu}_2\text{O}_4\text{Cl}_2$ contains folded Cu_2O_4 chains along $[100]$, also with two different Cu sites.⁶ The magnetic properties of $\text{Ba}_3\text{Cu}_2\text{O}_4\text{Cl}_2$, to the best of our knowledge, have not been investigated so far. On the other hand, it is well known that in $\text{Ba}_2\text{Cu}_3\text{O}_4\text{Cl}_2$ as well as $\text{Sr}_2\text{Cu}_3\text{O}_4\text{Cl}_2$ the moments of the Cu_A and Cu_B atoms order antiferromagnetically at different temperatures $T_{NA} \approx 300, \dots, 380$ K and $T_{NB} \approx 30, \dots, 40$ K, respectively.^{7–9} A small spontaneous magnetization M_0 within the basal plane of the tetragonal lattice has been reported.^{8,9} The presence of this spontaneous magnetization in the temperature range $T_{NB} < T < T_{NA}$ is contradictorily discussed in the literature. The Dzyaloshinsky¹⁰–Moriya¹¹-type interaction leading to weak ferromagnetism has been quoted in Ref. 8. This has been questioned referring to the high degree of crystal symmetry.⁹ Only little is known on the ferromagnetic hysteresis of these materials. Here, we will present some novel results on (i) the magnetic properties of $\text{Ba}_3\text{Cu}_2\text{O}_4\text{Cl}_2$ and $\text{Ba}_2\text{Cu}_3\text{O}_4\text{Cl}_2$ and (ii) their relation to the lattice structure of these compounds.

Single crystals of $\text{Ba}_3\text{Cu}_2\text{O}_4\text{Cl}_2$ were prepared by flux methods. $\text{Ba}_2\text{Cu}_3\text{O}_4\text{Cl}_2$ single crystals were grown directly from the stoichiometric melt. The crystals of both compounds were grown up to a size of $20 \times 10 \times 0.1 \text{ mm}^3$. The

characterization with x-ray methods confirmed the reported structure.^{5,6} The magnetic measurements on the single-crystalline samples were performed in a Quantum Design superconducting quantum interference device magnetometer with a maximum field of 5 T and a temperature range from 1.7 to 400 K.

The field dependence of the magnetization M of $\text{Ba}_3\text{Cu}_2\text{O}_4\text{Cl}_2$, measured along the crystallographic a axis for various temperatures is presented in Fig. 1. Below 20 K these curves show a metamagnetic behavior,¹² i.e., an upward curvature in a limited range of H . At a threshold field H_t of 2.6 T the M versus H curve measured at low temperatures jumps between two straight lines. Above the jump, the slope is considerably larger than below. No metamagnetic behavior has been found for $H \parallel b$ or c , i.e., the M versus H curves (not shown in Fig. 1) are straight lines that, for all temperatures, nearly coincide with the straight line measured for $H \parallel a$, above the threshold field. These observations indicate a spin-flop transition,¹³ i.e., a transition from a collinear antiferromagnetic structure with localized moments aligned along the a axis to a configuration perpendicular to the field. Above the spin-flop transition the moments progressively rotate towards the field direction. The most prominent example of compounds with Cu^{++} magnetic moments that undergo a spin-flop transition is $\text{CuCl}_2 \cdot 2\text{H}_2\text{O}$.^{14,15} The temperature dependence of the susceptibility χ , shown in Fig. 2, is consistent with the concept of spin flopping. For sufficiently high temperatures the $\chi(T)$ curves are well described by the Curie–Weiss law $\chi = C/(T - \theta)$, with the two fitting parameters C (Curie constant) and θ (paramagnetic Curie temperature). The positive value of θ manifests that the Cu^{++} moments experience, in addition to the dominating

^{a)}Electronic mail: khm@ifw-dresden.de

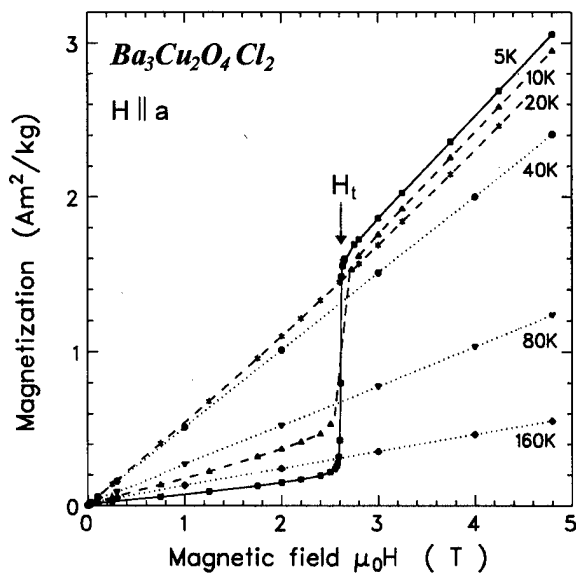


FIG. 1. Field dependence of the specific magnetization of a $\text{Ba}_3\text{Cu}_2\text{O}_4\text{Cl}_2$ single crystal, measured for different temperatures parallel to the crystallographic a axis. Below the Néel temperature $T_N \approx 20$ K a spin-flop transition is observed at the threshold field of $\mu_0 H_t = 2.6$ T.

antiferromagnetic coupling, a ferromagnetic exchange interaction. A mean paramagnetic moment of $2.0 \mu_B$ per Cu^{++} ion has been determined from the fitted value of C . For $T < \theta \approx T_N$ and $H < H_t$, the susceptibility χ increases linearly with T for $H \parallel a$ but it remains nearly constant for $H \parallel b$ or c . Obviously, the magnetic coupling between the Cu_2O_4 chains in $\text{Ba}_3\text{Cu}_2\text{O}_4\text{Cl}_2$ is strong enough to allow a three-dimensional antiferromagnetic behavior connected with a spin-flop transition.

Figure 3 shows the magnetization curves of $\text{Ba}_2\text{Cu}_3\text{O}_4\text{Cl}_2$ measured for three crystallographic directions at 40 K, i.e., at a temperature between the two reported an-

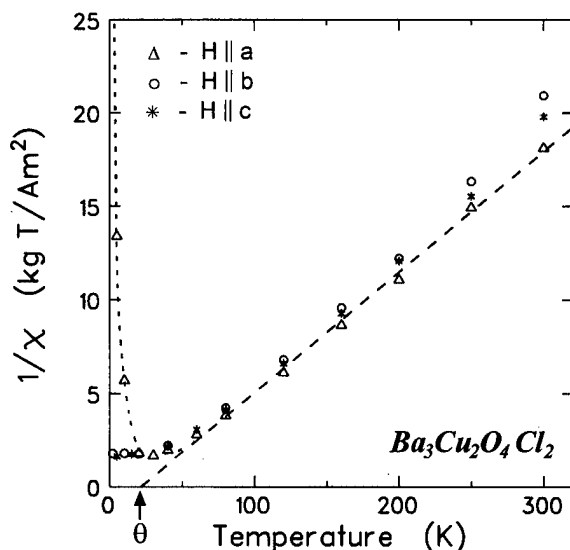


FIG. 2. Temperature dependence of the reciprocal dc susceptibility $1/\chi$, indicating a paramagnetic Curie temperature, $\theta \approx 21$ K. For H parallel to the a direction, temperatures below T_N and $H < H_t$ (see Fig. 1), $1/\chi$ strongly increases with decreasing temperature, but it is nearly constant for $H \parallel b$ or c .

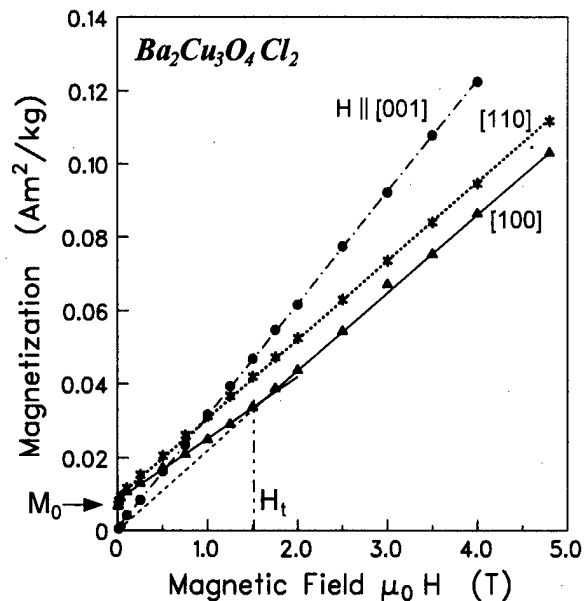


FIG. 3. Field dependence of the specific magnetization of a $\text{Ba}_2\text{Cu}_3\text{O}_4\text{Cl}_2$ single crystal, measured at $T = 40$ K with the magnetic field H applied parallel to different crystallographic directions. For H parallel to $[110]$ or $[100]$ the extrapolation to $H = 0$ gives a finite magnetization $M_0 > 0$.

tiferromagnetic ordering temperatures T_{NA} and T_{NB} . The straight line measured along $[001]$ indicates that this direction is perpendicular to the antiferromagnetically ordered Cu_A^{++} moments. On the other hand, the finite magnetization M_0 measured for $H \rightarrow 0$ in both directions in the basal plane, $[100]$ and $[110]$, indicates the presence of a small spontaneous magnetization as reported in Ref. 8. Furthermore, some metamagnetic behavior at a threshold field H_t is found for $H \parallel [100]$. The temperature dependence of the residual magnetization M_0 , measured for $H \parallel [100]$ and $H \parallel [110]$, is given in Fig. 4. The value of M_0 is not much different for both directions and it vanishes at $T \approx 337$ K, which is close to the reported⁸ upper Néel temperature T_{NA} . Significantly smaller values of M_0 are observed for $H \parallel [100]$, only below the

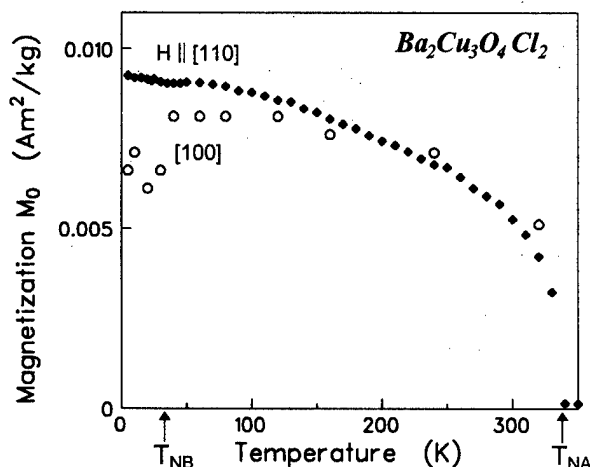


FIG. 4. Temperature dependence of the residual magnetization M_0 according to Fig. 3, for two directions in the basal plane. M_0 vanishes at $T_{NA} \approx 337$ K, the upper of the two Néel temperatures. $T_{NB} \approx 33$ K is the lower Néel temperature determined from the minimum of the susceptibility.

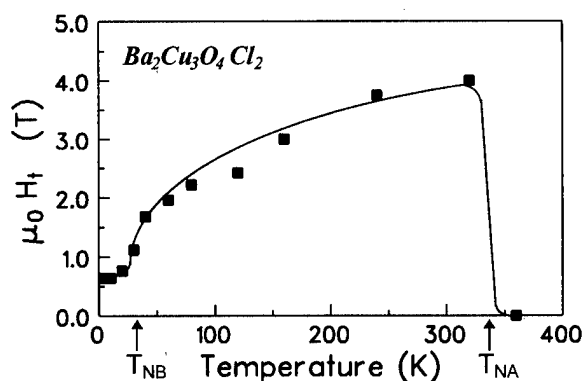


FIG. 5. Temperature dependence of the threshold field H_t for $H||[100]$ (as defined in Fig. 3).

lower of the two Néel temperatures, $T_{NB} \approx 33$ K, which has been obtained from the singularities of the temperature dependence of the inverse magnetic susceptibility $1/\chi$, not presented in a figure. As shown in Fig. 5, the threshold field H_t increases with increasing temperature, almost in the whole range $T_{NB} < T < T_{NA}$. Contrary to the results of Ref. 8 where ferromagnetic hysteresis was found for $H||[110]$ but not for $H||[100]$, we observed similar types of hysteresis curves for both directions. This is not surprising in view of the square symmetry in the tetragonal basal plane. Typical hysteresis loops measured for $H||[100]$ are presented in Fig. 6. Above the lower Néel temperature T_{NB} the coercive field H_c is more than one order of magnitude smaller than below. Between T_{NB} and T_{NA} , $\mu_0 H_c$ is only about 0.5 mT, for both directions $[110]$ and $[100]$, and does not much depend on temperature. The microscopic mechanism for the magnetic properties of $\text{Ba}_2\text{Cu}_3\text{O}_4\text{Cl}_2$, as presented in Figs. 3–6 and reported in Ref. 8, remains to be clarified. At higher fields the demagnetization curve measured for $H||[100]$ (cf. Fig. 3) approaches a straight line passing through the origin. A similar behavior is observed for certain ferrimagnetic compounds that exhibit field-induced spin canting,¹⁶ which is to some extent comparable to the spin-flop transition discussed for $\text{Ba}_3\text{Cu}_2\text{O}_4\text{Cl}_2$. In the temperature range of $T_{NB} - T_{NA}$, however, ferrimagnetism can be excluded to interpret Fig. 3 because only one type of magnetic ions, Cu_A^{++} , is reported to take part in the ordered magnetic structure.⁷ The anisotropic pseudodipolar interaction between the antiferromagnetically ordered Cu_A and the paramagnetic Cu_B moments has been successfully proposed⁹ to explain, for temperatures above T_{NB} , the presence of a spontaneous magnetization and the metamagnetic behavior of $\text{Sr}_2\text{Cu}_3\text{O}_4\text{Cl}_2$, which has the same structure as $\text{Ba}_2\text{Cu}_3\text{O}_4\text{Cl}_2$. The weak point of this scenario is that it does not work below T_{NB} where both types of Cu moments are antiferromagnetically ordered but a spontaneous magnetization is still present. Weak ferromagnetism of the Dzyaloshinsky–Moriya (DM) type^{10,11} has also been quoted to be the relevant mechanism.⁸ This has been questioned referring to the “perfectly tetragonal structure.”⁹ However, this argument though being valid for $\text{Sr}_2\text{CuO}_2\text{Cl}_2$

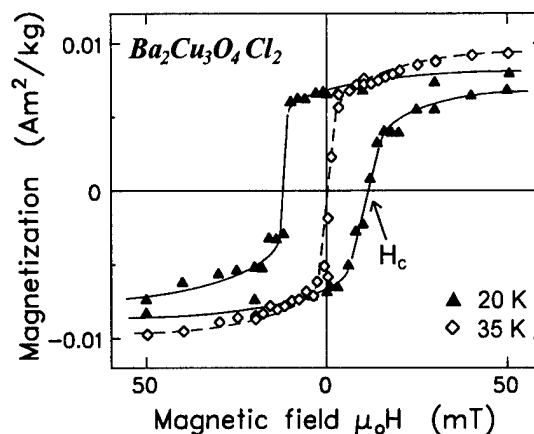


FIG. 6. The hysteresis loop of $\text{Ba}_2\text{Cu}_3\text{O}_4\text{Cl}_2$, measured below $T_{NB} \approx 33$ K for $H||[100]$, is characterized by a coercive field $\mu_0 H_c$ of about 15 mT. Above T_{NB} the coercive field is more than one order of magnitude smaller.

does not hold for $\text{Sr}_2\text{Cu}_3\text{O}_4\text{Cl}_2$ in the temperature range above T_{NB} , where in terms of symmetry the Cu_B atoms can be considered to be nonmagnetic. Although both compounds have the same tetragonal space group, weak ferromagnetism is not forbidden for $\text{Sr}_2\text{Cu}_3\text{O}_4\text{Cl}_2$ and $\text{Ba}_2\text{Cu}_3\text{O}_4\text{Cl}_2$ because not only the crystal symmetry has to be taken into account but also the symmetry of the zero-order collinear antiferromagnetic order. The problem is, however, that below T_{NB} where two different types of Cu^{++} ions are antiferromagnetically ordered, the DM scenario cannot be used without modification. Thus, the intrinsic magnetic properties of $\text{Ba}_2\text{Cu}_3\text{O}_4\text{Cl}_2$ observed below T_{NB} is not yet understood at all.

The authors are grateful to M. S. Golden for stimulating discussions.

- ¹D. C. Johnston, in *Handbook of Magnetic Materials*, Vol. 10, edited by K. H. J. Buschow (North-Holland, Amsterdam, 1997), p. 1.
- ²M. Greven, R. J. Birgeneau, Y. Endoh, M. A. Kastner, M. Matsuda, and G. Shirane, *Z. Phys. B* **96**, 465 (1995).
- ³M. Matsuda, K. Katsumata, K. M. Kojima, M. Larkin, G. M. Luke, J. Merrin, B. Nachumi, Y. J. Uemura, H. Eisaki, N. Motoyama, S. Uchida, and G. Shirane, *Phys. Rev. B* **55**, R11 953 (1997).
- ⁴M. Troyer, M. E. Zhitomirsky, and K. Ueda, *Phys. Rev. B* **55**, R6117 (1997).
- ⁵R. Kipka and Hk. Müller-Buschbaum, *Z. Anorg. Allg. Chem.* **419**, 58 (1976).
- ⁶R. Kipka and Hk. Müller-Buschbaum, *Z. Anorg. Allg. Chem.* **422**, 231 (1976).
- ⁷K. Yamada, N. Suzuki, and Y. Akimitsu, *Physica B* **213&214**, 191 (1995).
- ⁸T. Ito, H. Yamaguchi, and K. Oka, *Phys. Rev. B* **55**, R684 (1997).
- ⁹F. C. Chou, A. Aharony, R. J. Birgeneau, O. Entin-Wohlman, M. Greven, A. B. Harris, M. A. Kastner, Y. J. Kim, D. S. Kleinberg, Y. S. Lee, and Q. Zhu, *Phys. Rev. Lett.* **78**, 535 (1997).
- ¹⁰I. J. Dzyaloshinsky, *Phys. Chem. Solids* **4**, 241 (1958).
- ¹¹T. Moriya, *Phys. Rev.* **120**, 91 (1960).
- ¹²D. Gignoux and D. Schmitt, *J. Alloys Compd.* **225**, 423 (1995).
- ¹³L. Néel, *Ann. Phys. (Paris)* **5**, 232 (1936).
- ¹⁴N. J. Poulis, J. v. d. Handel, J. Ubbink, J. A. Poulis, and C. J. Gorter, *Phys. Rev.* **82**, 552 (1951).
- ¹⁵K. L. Dudko, V. V. Eremenko, N. V. Gapon, V. N. Savitskii, and V. V. Soloviev, *J. Phys. Colloq.* **49**, C8 (1988).
- ¹⁶J. J. M. Franse and R. J. Radwanski, in *Handbook of Magnetic Materials*, Vol. 7, edited by K. H. J. Buschow (North-Holland, Amsterdam, 1993), p. 307.

Magnetic, electrical, and structural studies on the metal-insulator transition in $\text{CuIr}_2\text{S}_{4-x}\text{Se}_x$ ($0 \leq x \leq 4$)

P. Somasundaram, D. Kim, and J. M. Honig

Department of Chemistry, Purdue University, West Lafayette, Indiana 47907

T. M. Pekarek

Department of Natural Sciences, University of North Florida, Jacksonville, Florida 32224

T. Gu and A. I. Goldman

Department of Physics, Iowa State University, Ames, Iowa 50011

Magnetic transitions and structural transformations have been investigated in $\text{CuIr}_2\text{S}_{4-x}\text{Se}_x$ ($0 \leq x \leq 4$). It is found from magnetic, resistivity, and thermopower studies that the transition temperature decreases as the Se concentration is increased. The change in magnetization occurs over a 10–15 K range at lower Se concentration, while it broadens to 30 K for an Se concentration of $x=0.5$. Low-temperature studies proved that beyond the composition corresponding to $x=0.5$ the cubic structure is stabilized. The metal-insulator transition beyond the $x=0.5$ composition arises from the electronic rather than from the lattice contribution. © 1998 American Institute of Physics. [S0021-8979(98)40511-5]

I. INTRODUCTION

Chalcogenide spinel compounds have been studied extensively from a variety of viewpoints such as crystal structure, magnetism, superconductivity, and giant magnetoresistance. The thiospinel compound, CuIr_2S_4 , displays a metal-insulator transition around 230 K.¹ The magnetization changes from paramagnetism at high temperatures to diamagnetism at low temperatures and exhibits hysteresis on heating and cooling. Earlier studies have indicated² that the formal valence of Cu and Ir changes as one varies the sulfur composition in $\text{CuIr}_2\text{S}_{4+x}$ ($x=0, 0.1$, and -0.1). We have investigated the magnetic transition and structural transformations in $\text{CuIr}_2\text{S}_{4-x}\text{Se}_x$ ($0 \leq x \leq 4$). It is found that the transition temperature decreases as the Se concentration is increased. The magnetic, thermopower, and x-ray diffraction studies prove that beyond the composition corresponding to $x=0.5$ the cubic structure is stabilized; the broadened metal-insulator transition beyond this composition is attributed to electronic effects.

II. EXPERIMENTAL METHODS

Stoichiometrically mixed powders of Cu, Ir, S, and Se were fired at 850 °C in sealed quartz ampoules for 8 days. After regrinding, the powders were pelletized and sintered at 850 °C for 4 days. During sintering the ampoules were provided with additional powder of the same composition to minimize the escape of S and Se from the pellet. Powder x-ray diffraction was performed on a diffractometer with a low-temperature attachment. Sintered samples were employed for magnetization studies using a Cryogenic Consultants Limited SQUID magnetometer. Magnetization data were taken at 5 to 324 K in fields up to 6 T. Electrical resistivity was carried out by means of the standard four-

probe technique. Measurements of Seebeck coefficients were performed in an automated thermopower setup.³

III. RESULTS AND DISCUSSION

Powder x-ray diffraction of different compositions at 300 K confirmed that all the samples were monophasic and

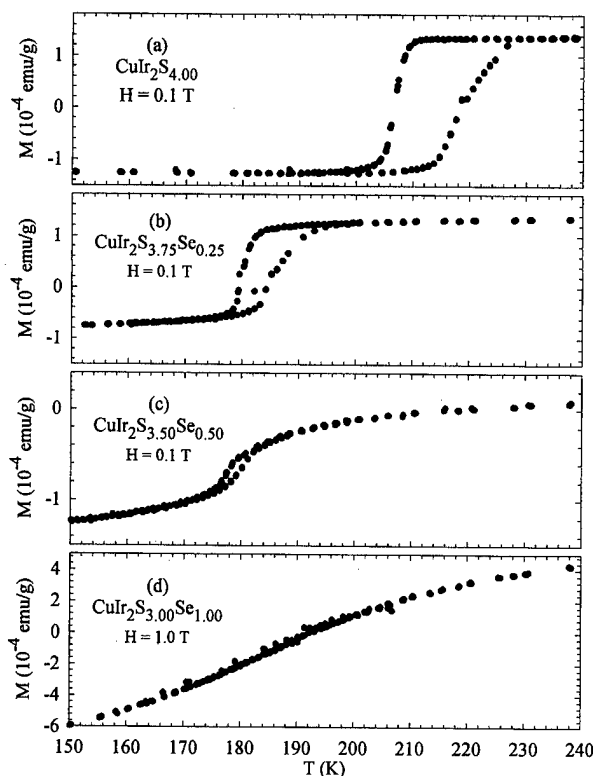


FIG. 1. (a)–(d) Warming and cooling magnetization versus temperature data indicating a shift in the metal to insulator transitions of $\text{CuIr}_2\text{S}_{4-x}\text{Se}_x$ for $x=0, 0.25, 0.5$, and 1.0 .

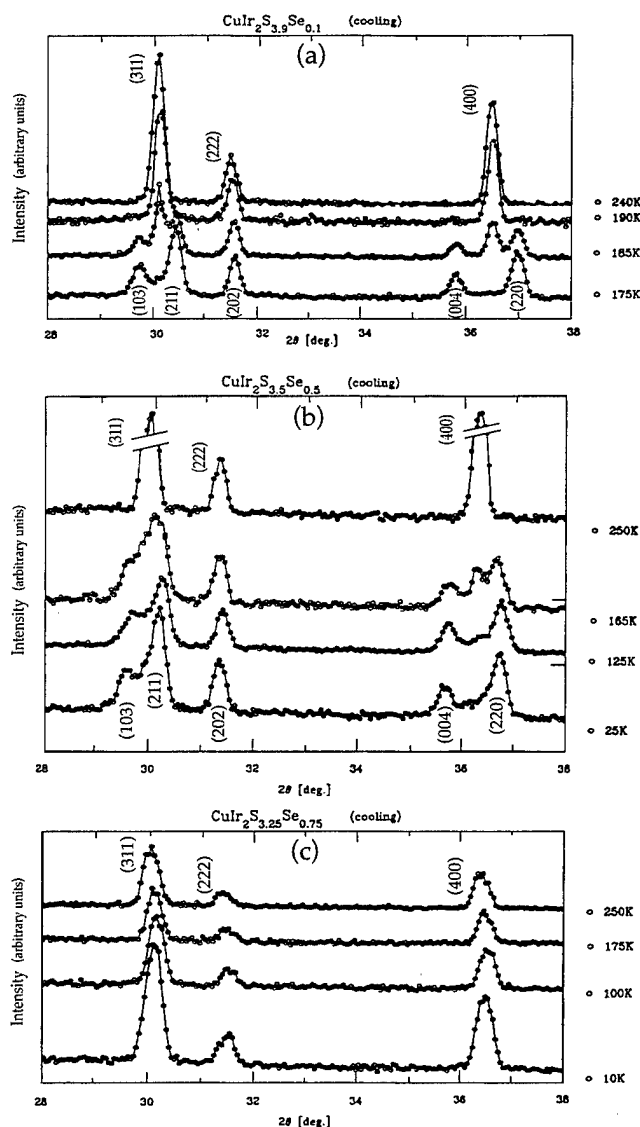


FIG. 2. X-ray diffraction pattern near the transition for $x=0.1$ (a), 0.5 (b), and 0.75 (c).

cubic in structure at the limit of detection. The variation of magnetization as a function of temperature is given in Figs. 1(a)–1(d) for the compositions $x=0, 0.25, 0.5$, and 1.0 . As can be seen, a change in magnetization occurs over a 10–15 K range at the lower Se concentrations of $x=0$ and 0.25 , while for the composition $x=0.5$ the transition is spread over a region of 30 K. The mean temperature of the transition diminishes as x is increased. The hysteresis on cooling and heating is progressively reduced as the Se concentration is increased. This hysteresis in magnetization is associated with the cubic to tetragonal transition and with the concomitant volume change.

Figure 2 shows the x-ray diffraction pattern obtained while cooling the samples. The transformation from the cubic structure to the tetragonal structure is clearly seen to occur close to the transition temperature for $x=0.1$, while for $x=0.5$ the peaks are also broadened close to the transition because of the lattice strain introduced by the Se substitution. Beyond this composition the cubic structure appears to be stabilized. This trend is also confirmed from the variation of

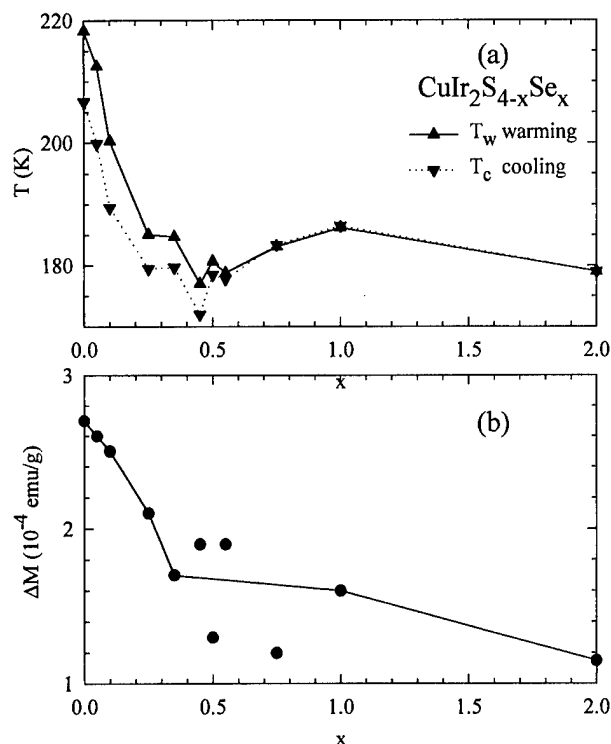


FIG. 3. (a) Variation of transition temperature as a function of composition in $\text{CuIr}_2\text{S}_{4-x}\text{Se}_x$ ($x=0-2.0$). (b) Variation of the change in magnetization curve as a function of composition in $\text{CuIr}_2\text{S}_{4-x}\text{Se}_x$ ($x=0-2.0$).

transition temperature T_c as a function of composition, as shown in Fig. 3(a). As can be seen, the hysteresis in magnetization disappears for $x>0.5$, the points beyond that composition are read off from the midpoint of very broad transitions. The irregularities in T_c for $0.3<x<0.5$ arise because of the difficulties in estimating T_c values from the spread-out transition range. From the magnitude of the change in magnetization (between the dia- and para-magnetic states) as shown in Fig. 3(b), it is clear that the number of carriers available for transition is reduced as the Se concentration increases. From resistivity measurements shown in Fig. 4(b), it is found that beyond the $x=0.5$ composition $\text{CuIr}_2\text{S}_{4-x}\text{Se}_x$ becomes less semiconducting; for $x=4.0$ the material is metallic. For the $x=0.75$ composition, the cubic phase is the stable phase at and below room temperature [see Fig. 2(c)]. The metal-insulator transition beyond the $x=0.5$ composition arises mainly from the electronic rather than from the lattice contribution. This is confirmed from the thermopower and resistivity measurements on selected samples. As can be seen from Figs. 4(a) and 4(b) the transition is broadened for $x=0.55$ and $x=0.75$. The $x=0.75$ sample still undergoes a gradual changeover to a metal, even though it remains cubic. At high temperatures, the Seebeck coefficient approaches a constant value of $-40 \mu\text{V}/\text{deg}$ for all the compositions studied. The variation of Seebeck coefficient is sharpest for $x=0.45$; this coincides with the higher value of resistivity for this sample. At this composition both cubic and tetragonal phases coexist over a 10 K range encompassed by the hysteresis.

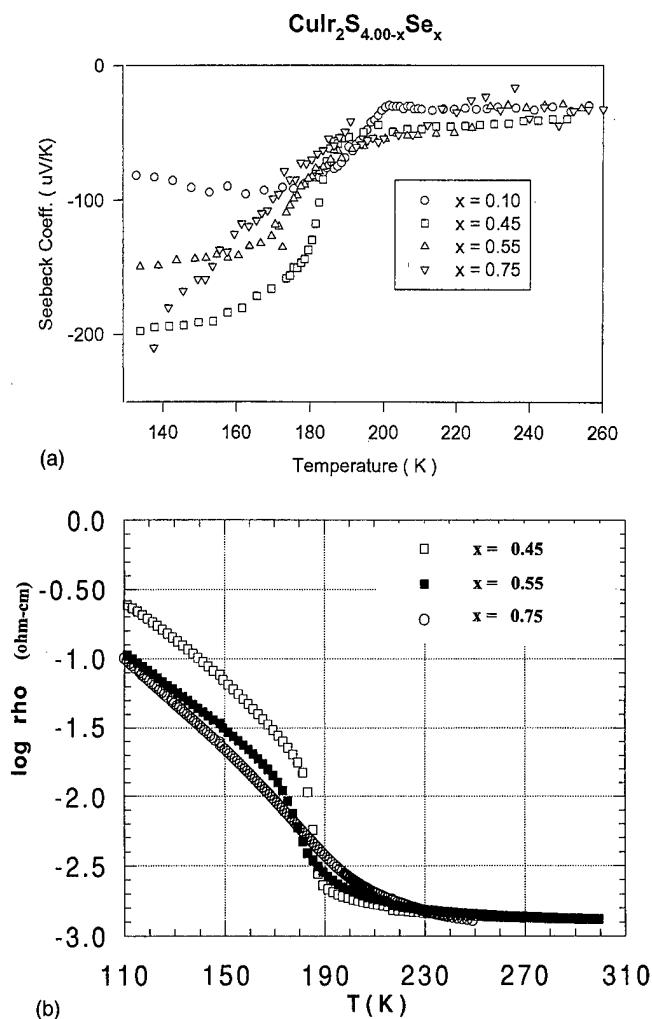


FIG. 4. (a) Measured Seebeck coefficients versus temperature for $\text{CuIr}_2\text{S}_{4-x}\text{Se}_x$ ($x = 0.1, 0.45, 0.55$, and 0.75). (b) Variation of resistivity as a function of temperature for $x = 0.45, 0.55$, and 0.75 .

The metal-insulator transition at higher Se compositions could be driven by change in bond angles. Since Se is larger than S, a higher Se concentration stabilizes the larger volume of the cubic structure. The octahedral interstices containing

the Ir atoms increase in size when S atoms are substituted by the larger Se atoms. The transition to the insulating phase can then be attributed to the positional ordering of Ir^{3+} and Ir^{4+} ions at compositions with low Se concentration, similar to the Verwey transition of Fe_3O_4 .^{4,5} This approach is based on the assumption that charge transport involves an activated hopping process of carriers among nearest neighbors of the octahedrally coordinated cationic interstices. Normally, for materials undergoing metal-insulator transitions the switching process in the absence of electronic effects is thermally activated.⁶ However, in the case of $\text{CuIr}_2\text{S}_{4-x}\text{Se}_x$, the switching process could be due to the type of electrothermal effects discussed by Chudnovskii *et al.*⁷ Further studies on the electronic structure are essential to determine the precise origin of the metal-insulator transition in $\text{CuIr}_2\text{S}_{4-x}\text{Se}_x$.

IV. CONCLUSION

We have found that the Se substitution decreases the transition temperature and changes the magnetic properties of $\text{CuIr}_2\text{S}_{4-x}\text{Se}_x$. The cubic structure is stabilized for compositions beyond $x = 0.5$; the metal-insulator crossover at higher Se concentrations in the cubic phase is attributed to electronic effects.

ACKNOWLEDGMENT

This research was supported in part by NSF Grant No. DMR-96-12130.

¹T. Furubayashi, T. Matsumoto, T. Hagino, and S. Nagata, J. Phys. Soc. Jpn. **63**, 3333 (1994).

²P. Somasundaram, D. Kim, J. M. Honig, and T. M. Pekarek, J. Appl. Phys. **81**, 4618 (1997).

³D. Kim and J. M. Honig, Phys. Rev. B **49**, 4438 (1994).

⁴J. M. Honig and J. Spalek, J. Less-Common Met. **156**, 423 (1989).

⁵N. F. Mott, in *Metal-Insulator Transitions*, 2nd ed. (Taylor and Francis, London, 1990).

⁶J. L. Jackson and M. P. Shaw, J. Solid State Chem. **12**, 408 (1975).

⁷F. A. Chudnovskii, A. L. Pergament, G. B. Stefanovich, P. Somasundaram, and J. M. Honig, Phys. Status Solidi **162**, 601 (1997).

Finite size scaling in the thin film limit

C. Waldfried, D. Welipitiya, T. McAvoy, and P. A. Dowben

*Department of Physics & Astronomy and the Center for Materials Research and Analysis,
University of Nebraska-Lincoln, Lincoln, Nebraska 68588-0111*

E. Vescovo

National Synchrotron Light Source, Brookhaven National Laboratory, Upton, New York 11973

The thickness dependent spin-polarized electronic structure of strained thin and ultrathin films of Gd is characterized by a distinct change in the critical exponent λ in the formalism of finite size scaling. The reduced critical exponent in the ultrathin films can be correlated to the increased dominance of the surface magnetic structure and the increasing paramagnetic-like behavior of the bulk. © 1998 American Institute of Physics. [S0021-8979(98)34111-0]

With decreasing film thickness the surface may become increasingly more important for the magnetic ordering of ultrathin films. The surface and bulk electronic structure may adopt the role of “actor” or “spectator” in a ferromagnetic thin film.¹ Electronic structure and its influence will depend in any case, upon electron wave vector² and the film thickness.³

The distinct magnetic properties of the surface as well as the bulk will have significant effects on the finite size scaling behavior of thin films and deviations from the expected finite size scaling behavior⁴

$$\frac{T_C(\infty) - T_C(d)}{T_C(\infty)} = C \cdot d^{-\lambda} \quad (1)$$

can be expected.³ If surface magnetism has a prominent “active” role in the magnetic ordering of ultrathin films it will influence the critical exponent λ . There have been a few examples of deviations in the critical exponent λ in the thin film limit to date.⁵

We studied the finite size scaling behavior for increasingly thinner films of strained Gd^{6,7} with spin-polarized photoemission as described elsewhere.^{2,3} The spin-polarized valence-band photoemission spectra of the strained Gd films have distinct features attributable to the surface and the bulk.^{2,3,8} This permits one to characterize the magnetic behavior of the surface and the bulk separately,^{2,3} as has been done for “unstrained” Gd(0001).⁹ Strained films of gadolinium with an increased lattice constant of approximately 4% have been obtained by growing Gd on a Mo(112) substrate. The half filled 4f shell of gadolinium results in highly localized moments which couple via “RKKY-like” interactions through itinerant valence electron states. The magnetic structure of the system is strongly influenced by the intra-atomic 4f–(5d,6s) wave function overlap and 5d,6s valence electron itinerancy.¹⁰ The electronic valence-band structure, hybridization, and electron itinerancy are all very sensitive to the lattice configuration. Expansive strain of 4% within the hexagonal closed-packed system substantially alters the electronic and magnetic valence-band structure.^{2,3,6} The strain results in increased electron localization of the itinerant valence electrons and therefore enhances local moment ferromagnetism.

The thickness dependent Curie temperature of strained Gd, as determined from spin-polarized photoemission, exhibits a decrease with decreasing film thickness, characteristic of finite size scaling behavior. Figure 1 shows the reduced Curie temperature $[T_C(\infty) - T_C(d)]/T_C(\infty)$ as a function of film thickness d in a logarithmic plot. The data points displayed are for the strained Gd surface (○) [$T_C(\infty) = 370$ K] and the strained Gd bulk (■) [$T_C(\infty) = 340$ K]. Each data point has been determined from the temperature-dependent exchange splitting and spin polarization of the corresponding spin-polarized photoemission features. While there is a wave vector dependence of the exchange splitting and spin polarization,² the Curie temperatures have been deduced from the valence-band spectra with maximum exchange splitting, which is at the Brillouin zone edge.² This Brillouin zone point provides the best indicator of T_C . For comparison, the data for unstrained Gd(0001) (●) [$T_C(\infty) = 293$ K] is shown, which has been extracted from magnetic susceptibility measurements by Farle and co-workers for Gd/W(110).¹¹ In this logarithmic plot the slope of the displayed data points marks the critical exponent λ of the finite size scaling description of the correlation length, as denoted in Eq. (1).

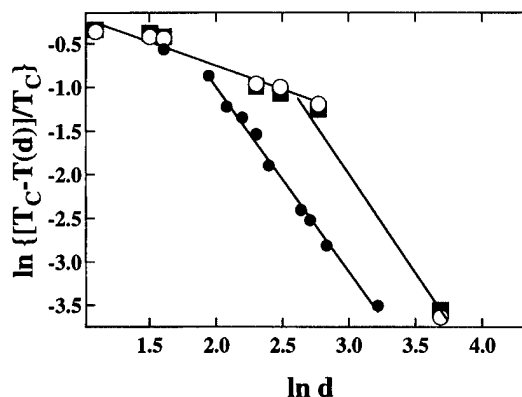


FIG. 1. The reduced Curie temperature $[T_C(\infty) - T_C(d)]/T_C(\infty)$ as a function of film thickness d in a logarithmic plot. The data points displayed are for the strained Gd surface (○) [$T_C(\infty) = 370$ K], the strained Gd bulk (■) [$T_C(\infty) = 340$ K], and the unstrained Gd (●) [$T_C(\infty) = 293$ K]. The latter data are adapted from Ref. 11.

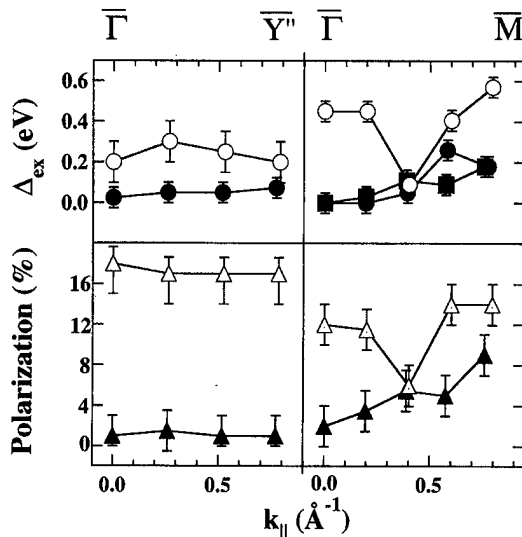


FIG. 2. The exchange splitting (top) and spin asymmetry above background (bottom) of the surface (open symbols) and bulk (filled symbols) spin subbands as a function of wave vector. Data are shown for a 4 ML thick (left) and a 40 ML thick (right) strained Gd film. The data points have been extracted from spin-polarized photoemission spectra.

Clearly the thickness dependence of the reduced Curie temperature for strained thin films of Gd does not follow the expected fixed exponential. A variation of the critical exponent with film thickness is indicated. For film thicknesses of more than approximately 15 monolayers (ML), the critical exponent λ is comparable to the one of the unstrained Gd films, as determined by the similar slope. For the ultrathin films ($d \leq 15$ ML), the slope for strained Gd is reduced by a factor of approximately 4, reflecting a reduced critical exponent λ and decreased sensitivity to finite size scaling. A variation of the critical exponent similar to the one evident for strained Gd is possibly indicated for the unstrained Gd films at thicknesses of less than approximately 8 ML (Fig. 1). The limited data points for the ultrathin films ($d < 10$ ML) that are presented in Ref. 11 make this postulate, however, rather weak. A deviation from the expected finite size scaling behavior is also apparent in Gd/W multilayers for Gd interlayer thickness of less than approximately 15 ML.¹² A crossover from three- to two-dimensionality is possible,^{5,13} but generally dimensionality crossover should result in an increase in the critical exponent¹⁴—not a decrease as observed here.

Concomitant with the variation of the critical exponent for decreasing film thicknesses, the bulk bands of the strained Gd films become paramagnetic-like over an increasingly larger volume in k -space.³ The dominance of the surface magnetic ordering in the ultrathin films is indicated in Fig. 2. Figure 2 plots the exchange splitting (top) and spin asymmetry (bottom) of surface (open symbols) and bulk (filled symbols) spin subbands as a function of wave vector for a 4 ML thick film (left) and a 40 ML thick film (right). While the magnitude of the measured exchange splitting is an indirect indication of the $5d$ moment,¹⁵ the polarization (above background) provides insight into the extent of the magnetic activity, Stoner-like magnetism and/or rigid band ferromagnetism.

The exchange splitting of the bulk bands of the 4 ML thick strained Gd films is small throughout the surface Brillouin zone and exceeds the experimental resolution of 0.05 eV only near the zone edge ($\Delta_{ex} \approx 0.07$ eV), indicative of minimal Stoner-like ferromagnetism, away from the vicinity of the zone edge \bar{Y}'' . There is also no significant polarization (above background) in the region of the Gd bulk bands well away from the Fermi level for any wave vector. The bulk bands of the 4 ML thick Gd films exhibit the paramagnetic-like behavior expected with direct contact to a ferromagnet. For the 40 ML thick films, the magnetic ordering of the bulk bands follows a distinct wave vector dependence with negligible exchange splitting at the zone center $\bar{\Gamma}$ and substantial exchange splitting of approximately 0.25 eV near the zone edge \bar{M} . The spin asymmetry behaves similarly with minimal asymmetry at $\bar{\Gamma}$ and large polarization at \bar{M} . The wave vector dependent exchange splitting of the thicker strained Gd films suggests a change from paramagnetic-like behavior at the Brillouin zone center to Stoner-like magnetism at the zone edge.

The magnetic ordering of the surface behaves differently from that of the bulk. The exchange splitting of the surface state of the 4 ML thick Gd films is of the order of 0.25 eV with little variation for different wave vectors. The spin polarization in the region of the surface sensitive states approaches approximately 17% (above background). The large spin asymmetry and relatively small exchange splitting is indicative of predominantly rigid band magnetism with some Stoner-like ferromagnetic contributions, largely independent of wave vector. This is in contrast to the strong wave vector dependence of the magnetic behavior of the thicker films (40 ML). The surface state exchange splitting is large at the Brillouin zone center ($\Delta_{ex} \approx 0.45$ eV) and at the Brillouin zone edge ($\Delta_{ex} \approx 0.57$ eV). The minimum in the exchange splitting of the surface feature at the Brillouin zone interior ($\Delta_{ex} \approx 0.10$ eV) has been attributed to a wave vector dependent change from a surface state (zone center and zone edge) to a surface resonance (zone interior).² This dip of the surface exchange splitting is reflected in the spin asymmetry, which reduces to 4% in the Brillouin zone interior as compared to 10% at the zone center and 12% at the zone edge.

With decreasing film thickness the region of the Brillouin zone in which the bulk bands are paramagnetic becomes increasingly larger and the surface magnetic ordering increasingly dominant, characterized by diminishing Stoner-like magnetism and strengthened rigid band magnetism. At the same time the bandstructure of the strained Gd films changes significantly. The bulk bands of the thicker films are dispersive with a bandwidth w of approximately 1.6 eV, in contrast to the ultrathin films which appear nearly dispersionless ($w \leq 0.15$ eV). This has substantial consequences for the coherence length which can be estimated as $l \approx \sqrt{w/k_B T_C} a$.¹⁶ Considering that there is a change in the bandwidth w of a factor of approximately 10 with decreasing film thickness, the bulk electron coherence length in the ultrathin films is expected to be much shorter as compared to the thicker films. The surface state electrons of the strained Gd films are considerably more localized as compared to

those of the bulk bands, which is reflected in the narrow bandwidth of $w \leq 0.2$ eV, which is even smaller for the thinner film thicknesses. As a result, the magnetic structure of the increasingly thinner strained Gd films are governed by an *RKKY* interaction that is of increasingly shorter electron coherence length. Finite size effects may become less influential for decreased electron coherence lengths well away from T_C . In any case, the surface state exchange splitting is large at the Brillouin zone center where the band structure is most sensitive to long range order. Some bulk bands exhibit the smallest exchange splitting at zone center. This indicates that the surface may increasingly dominate the thin film magnetism. A deviation from finite size scaling in terms of a reduced critical exponent is expected and consistent with our thickness dependent critical temperature data (Fig. 1). For the limit of $5d$ valence electrons that are highly localized, polarized only by the local $4f$ moments (which themselves do not have to be aligned, due to spin wave excitations), the electron coherence length becomes negligible and a vanishing critical exponent ($\lambda \rightarrow 0$) is expected for the thin film limit ($d \rightarrow 1$), a change distinct from dimensionality effects.

The reduced critical exponent for the ultrathin films is consistent with the magnetic behavior observed in free Gd clusters by Douglass *et al.*^{17,18} Gd clusters of different sizes exhibit very similar magnetic moments per atom (although substantially reduced from that of the bulk gadolinium value). More importantly the Curie temperatures of these small Gd_N clusters ($N=10-92$) are even larger than that of bulk gadolinium. Clearly, finite size scaling behavior fails in the physical world of small clusters and a trend of $\lambda \rightarrow 0$ as $N \rightarrow 1$ is indicated. Indeed ferromagnetic monolayers at finite temperature are known and routinely observed in the thin film limit of ultrathin films. Cluster studies indicate that the atomic coordination number may have significant influence on the magnetic behavior, and are an example of a catastrophic failure of finite size scaling behavior.

In the thin film limit, the apportionment of relative roles in the magnetic ordering of surface and bulk becomes very important for the description of the finite size scaling behav-

ior. For strained Gd films, the short electron coherence length of the *RKKY* interaction is dominating the magnetic behavior of the ultrathin films, with the result of a substantially reduced critical exponent λ . There is no a priori reason why this behavior should be restricted to the strained Gd films grown on a Mo(112) substrate. In fact a similar behavior is anticipated in the "relatively unstrained" Gd(0001) ultra-thin films grown on W(110), although experimental confirmation does not as yet exist.

This work was supported by NSF through Grant Nos. DMR-92-21655 and DMR-94-96131. The experiments were carried out at the National Synchrotron Light Source which is funded by the DOE.

- ¹M. Donath, in *Electronic Surface and Interface States on Metallic Systems*, edited by E. Bertel and M. Donath (World Scientific, Singapore, 1995), p. 233 ff.
- ²C. Waldfried, T. McAvoy, D. Welipitiya, P. A. Dowben, and E. Vescovo, Phys. Rev. B (submitted).
- ³C. Waldfried, T. McAvoy, D. Welipitiya, E. Vescovo, and P. A. Dowben, Europhys. Lett. (submitted).
- ⁴M. E. Fisher and M. N. Barber, Phys. Rev. Lett. **28**, 1516 (1972).
- ⁵A. Aspelmeier, F. Gerhardter, and K. Baberschke, J. Magn. Magn. Mater. **132**, 22 (1994); J. T. Ou, F. Wang, and D. L. Lin, Phys. Rev. E **56**, 2805 (1997).
- ⁶C. Waldfried, D. N. McIlroy, and P. A. Dowben, J. Phys.: Condens. Matter **9**, 10615 (1997).
- ⁷C. Waldfried, D. N. McIlroy, and P. A. Dowben, Phys. Rev. B **54**, 16460 (1996); **56**, 9973 (1997).
- ⁸C. Waldfried, D. N. McIlroy, D. Welipitiya, T. McAvoy, E. Vescovo, and P. A. Dowben, J. Appl. Phys. **83** (1998).
- ⁹D. Li, J. Pearson, S. D. Bader, D. N. McIlroy, C. Waldfried, and P. A. Dowben, Phys. Rev. B **51**, 13895 (1995).
- ¹⁰W. Nolting, T. Dambeck, and G. Borstel, Z. Phys. B **94**, 409 (1994).
- ¹¹M. Farle *et al.*, Phys. Rev. B **47**, 11571 (1993).
- ¹²J. S. Jiang and C. L. Chien, J. Appl. Phys. **79**, 5615 (1996).
- ¹³Yi Li and K. Baberschke, Phys. Rev. Lett. **68**, 1208 (1992).
- ¹⁴K. Binder and P. C. Hohenberg, Phys. Rev. B **9**, 2194 (1973); T. Kaneyoshi, *Introduction to Surface Magnetism* (CRC, Boca Raton, FL, 1991).
- ¹⁵F. J. Himpsel, J. Magn. Magn. Mater. **102**, 261 (1991).
- ¹⁶H. Capellmann and V. Vieira, Solid State Commun. **43**, 747 (1982).
- ¹⁷D. C. Douglass, J. P. Bucher, and L. A. Bloomfield, Phys. Rev. Lett. **68**, 1774 (1992).
- ¹⁸D. C. Douglass, A. J. Cox, J. P. Bucher, and L. A. Bloomfield, Phys. Rev. B **47**, 12874 (1992).

Phase diagram of a highly diluted, disordered Ising system: The Al-rich, Al-Fe system

J. Restrepo^{a)} and G. A. Pérez Alcázar

Departamento de Física, Universidad del Valle, A.A. 25360, Cali, Colombia

J. M. González

Instituto de Ciencia de Materiales de Madrid-CSIC, Cantoblanco 28049, Madrid, Spain

Disordered solid solutions containing a highly diluted magnetic element in which competitive exchange interactions are present can allow the observation of magnetic ordering (ferromagnetism, antiferromagnetism, and spin-glass behavior) at dilutor element contents different from those corresponding to ordered alloys. In this work we present a simulational study of the magnetic properties of the Al-rich, Al-Fe disordered alloy system, which meets the above mentioned requirements and is therefore a good candidate to show differences between the magnetic phase diagrams corresponding to the ordered and disordered states. Our simulations were carried out on the basis of a randomly site-diluted Ising model, using the Monte Carlo method as energy minimization tool. In our model, the spins of the Fe atoms are assumed to be coupled by a direct nearest-neighbor ferromagnetic exchange J (depending on the Al concentration), and by an Al-mediated antiferromagnetic superexchange interaction $-\alpha J$. Our results suggest the presence of ferromagnetic order for Al concentrations higher than those for which that order disappears in ordered alloys and the occurrence, for Fe atomic percentages between 10% and 25%, of a re-entrant spin glass phase whose freezing temperature decreases with the degree of dilution. © 1998 American Institute of Physics. [S0021-8979(98)34211-5]

I. INTRODUCTION

Most of the work on the Al-Fe alloys in the literature,^{1,2} focuses on systems where the atoms have well defined ordered positions into the crystalline structure. These works, which cover exclusively the Fe-rich region of the phase diagram (Fe contents above 50 at. % Fe), show that, in the vicinity of 30 at. % Al and in the temperature region between 90 and 170 K, there is a multicritical point in the magnetic phase diagram where the paramagnetic, ferromagnetic, and spin-glass phases meet. In contrast with the magnetic behavior of these ordered systems, the disordered alloys, in which the atoms are randomly distributed in the crystalline lattice, still exhibit³ ferromagnetism at 50 at. % Al. Further theoretical work,⁴ suggests that this ferromagnetic phase could be even present at higher Al concentrations. Very recently, a Monte Carlo study⁵ of the magnetic properties of Fe-rich, Al-Fe disordered alloys, based on a site-diluted Ising model, in which an explanation of why the Ising model can be appropriate is given, has predicted, in agreement with experimental data,³ a smooth decrease of the Curie temperature with the increase of the Al content. That decrease goes beyond 30 at. % Al, the concentration for which the ordered alloys loose their long range magnetic order.¹ In the present work we report simulation studies of the magnetic phase diagram of Al-Fe disordered alloys with Al contents higher than 50 at. %. We simulate the magnetic properties of these alloys in the framework of a random-site diluted Ising model with ferromagnetic and antiferromagnetic bonds for the first and second coordination shells, respectively. The tempera-

ture evolution of the magnetization, the Edwards-Anderson parameter, the magnetic susceptibility and, the magnetic specific heat are presented and discussed.

II. DESCRIPTION OF THE MODEL

In order to study the magnetic properties of Al-Fe disordered alloys we have considered a diluted and random site Ising model with nearest-neighbors (nn) and next-nearest-neighbors (nnn) interactions. The zero-field Hamiltonian of this model can be written as

$$H = - \sum_{\langle i,j \rangle} J_{ij} \sigma_i \sigma_j - \sum_{\langle i,j \rangle} J_{ij}^* \sigma_i \sigma_j, \quad (1)$$

(nn) (nnn)

where $J_{ij} > 0$ is the ferromagnetic exchange parameter corresponding to (nn) Fe-Fe pairs, $J_{ij}^* = -\alpha J_{ij} < 0$ is the antiferromagnetic superexchange parameter corresponding to (nnn) Fe-Fe pairs (which are separated by an Al atom), α is the competition parameter taken to be 0.05,⁴ and $\sigma_i = \pm 1$ or 0, depending on the occupation of the i th site by an Fe atom or an Al one, respectively. In order to consider site dilution the following probability distribution was simulated,

$$P(\epsilon_i) = p \delta(\epsilon_i - 1) + q \delta(\epsilon_i), \quad (2)$$

where p and q are the percent concentration of magnetic and nonmagnetic sites ($p + q = 1$) and $\epsilon_i = 1$ or 0, depending on the i th site occupation by a magnetic or nonmagnetic atom, respectively. The (nn) and (nnn) bonds are determined according to $J_{ij} = \epsilon_i \epsilon_j J$ and $J_{ij}^* = -\alpha \epsilon_i \epsilon_j J$, respectively.

As it has been already shown,³ the increase of the Al content produces an increase of the lattice parameter, due to the large atomic size of the Al atoms. Therefore, the Fe-Fe

^{a)}Electronic mail: johans@calima.univalle.edu.co

exchange integral should depend on the Al concentration q . Here, it was taken to vary from 50 up to 90 at. % Al according to³

$$J(q) = J_1 - J_0 q, \quad (3)$$

where $J_1 = 12.85$ meV and $J_0 = 0.95J_1$ according to previous works,^{3,4} for which a good agreement with experimental data was obtained.

In the case of (nn) interactions, $J_{ij} = 0$ for the diluted Fe–Al and Al–Al bonds and J_{ij} is given by Eq. (3) for ferromagnetic Fe–Fe bonds. For (nnn) interactions, $J_{ij} = -\alpha J$ only for those Fe atoms which are separated by an Al one, and $J_{ij} = 0$ otherwise.

In agreement with the known crystalline structure of these alloys series, our simulated system consists on a three-dimensional (3D) bcc structure ($11 \times 11 \times 11$ atoms) with periodic boundary conditions. In order to minimize Eq. (1), we have used the standard Monte Carlo method implemented with the Metropolis dynamics. Each Monte Carlo step (MCS) involves the evaluation of the spin-flip probability at all the different magnetic sites in the lattice. The maximum number of Monte Carlo steps was taken to be 10 000 MCS. The magnetization, the magnetic energy, the magnetic susceptibility taken from the fluctuations in the magnetization, and the Edwards–Anderson (EA)⁶ parameter, were evaluated. MCS averages of these quantities, were considered in order to give thermodynamic equilibrium values for each particular system (atomic distribution) realization. We have repeated the relaxation process for different system realizations (corresponding to the same q value and having different random Fe and Al atomic distributions) and carried out configurational averages. All the different runs were performed, simulating a typical zero field cooling (ZFC) measurement, by applying, during the heating process and data collection, a 100 Oe field. The critical temperature T_c values, linked to a ferroparamagnetic transition, for each considered q value, were determined from the maximum observed in the temperature dependence of the susceptibility and the magnetic specific heat.⁷ The freezing temperatures associated to the spin glass transition are obtained from the temperature dependence of the Edwards–Anderson parameter q_{EA} .^{8,9}

III. RESULTS AND DISCUSSION

Figure 1 shows (for q ranging from 0.60 up to 0.90) the temperature dependences of the magnetic specific heat C_m , and the magnetic susceptibility χ . From the maximum of these curves, an estimation of the T_c value was obtained. It is remarkable in Fig. 1 the rounded broad maximum present in the C_m vs T curves corresponding to high Al contents, which is possibly associated to a large negative critical exponent.¹⁰ This behavior is characteristic of a spin glass¹⁰ phase. In order to compare the T_c values obtained from C_m and χ , we have defined the β parameter, given by $\beta = T_c[C_m]/T_c[\chi]$. In the range 50–70 at. % Al, the β value was 1.0. For higher Al contents, the obtained β values are given in Table I. For 75 at. % Al and higher Al contents, a shift between the cusps of the C_m vs T and χ vs T curves, increasing with the dilution increase is observed. Such behavior has already been

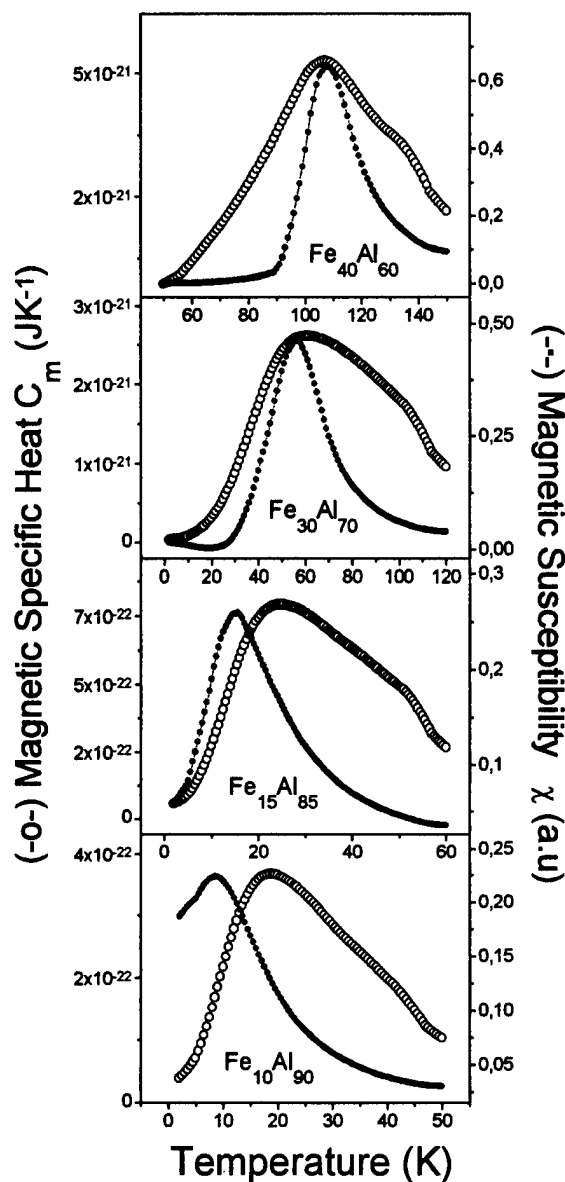


FIG. 1. Magnetic specific heat C_m (open circles) and susceptibility χ (solid circles), dependences on the temperature for different q values.

observed in magnetic specific heat $C_m(T)$ measurements obtained in spin glasses,¹⁰ where the maxima temperatures range between 1.3 and 1.8 T_f (T_f = freezing temperature obtained by susceptibility measurements).

In order to obtain the freezing temperature, an extrapolation to the temperature axis^{8,9} of the q_{EA} data correspond-

TABLE I. Compositional dependence of $\beta = T_c[C_m]/T_c[\chi]$ in the at. % Al range in which different temperatures are measured for the C_m and χ maxima.

q	β
0.75	1.2
0.80	1.3
0.825	1.4
0.85	1.5
0.875	1.8
0.90	2.0

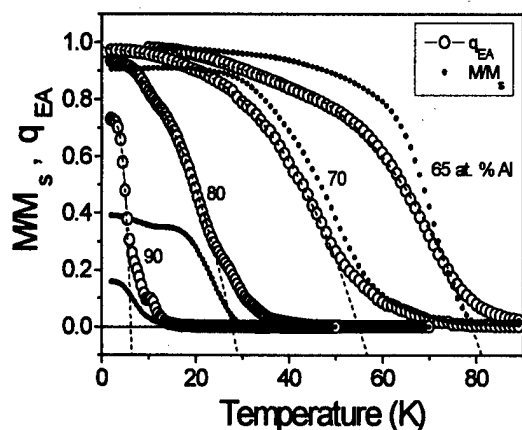


FIG. 2. Temperature dependences of the Edwards-Anderson parameter and the magnetization (this one normalized to the 0 K spontaneous magnetization value) for different Al contents. The dashed lines correspond to the polynomial, through which and by extrapolation, the freezing temperatures were obtained.

ing to temperatures below the inflection point by means of a third order polynomial, was performed as it is shown in Fig. 2. This figure shows the q_{EA} parameter and magnetization dependences on the temperature for different q values. Up to 75 at. % Al, the system becomes saturable and the thermal evolutions of M/M_s and q_{EA} agree with a ferromagnetic behavior. Also, the C_m and χ peaks are practically coincident, as expected for a well defined ferroparamagnetic transition. In contrast with this behavior, for Al contents higher than 75 at. % Al, the magnetization does not reach its saturation value, as it can be observed for 80 and 90 at. % Al in Fig. 2. The observed differences (see Table I), in this Al concentration range, between the C_m and χ peak temperatures, are, as already indicated, in agreement with the typical experimental results obtained in spin glasses. On the other hand, the difference between the T_f values, obtained by extrapolation from the q_{EA} vs T curves, and those corresponding to T_c and obtained from the χ vs T curves, define, in the high Al content region, two clearly distinguishable phases.

In Fig. 3 we show the proposed magnetic phase diagram summarizing the results of the present study. We would like to stress that the data shown in this figure exhibit two remarkable features. First, in contrast to the behavior of the ordered alloys, a pure ferromagnetic phase can be identified for Al concentrations of up to 75 at. %. Arguably results from the disorder, due to which the probability of finding

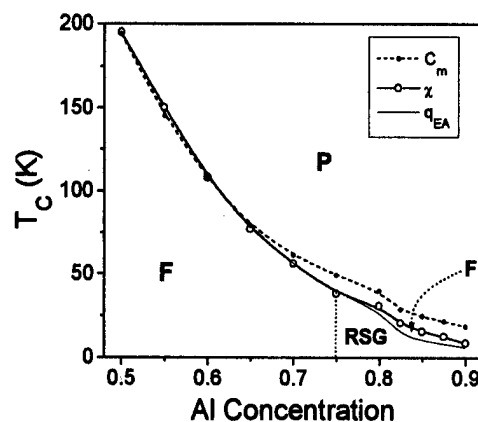


FIG. 3. Disordered Al-rich, Al-Fe magnetic phase diagram proposed in the present work.

two Fe atoms into the first and second coordination shell of a given Fe atom (forming a sort of Fe cluster) is nonzero even for large Al contents (this can be readily shown by considering a binomial atomic distribution). Second, the data strongly suggest the occurrence of a re-entrant spin glass phase for Al contents higher than 75 at. % Al. This can be attributed both to the disorder and to the competition between the ferro and antiferromagnetic exchange couplings, which plays a relevant role in this range of Al concentrations and temperature.

ACKNOWLEDGMENT

This work was supported by Universidad del Valle and COLCIENCIAS, Colombian Agency for the Scientific Research Funding.

¹P. Shukla and M. Wortis, Phys. Rev. B **21**, 159 (1980).

²G. S. Grest, Phys. Rev. B **21**, 165 (1980).

³G. A. Pérez Alcázar, J. A. Plascak, and E. Galvao da Silva, Phys. Rev. B **34**, 1940 (1986).

⁴E. Mina, A. Bohórquez, L. E. Zamora, and G. A. Pérez Alcázar, Phys. Rev. B **47**, 7925 (1993).

⁵J. Restrepo, J. M. González, and G. A. Pérez Alcázar, J. Appl. Phys. **81**, 5270 (1997).

⁶S. F. Edwards and P. W. Anderson, J. Phys. F **5**, 965 (1975).

⁷K. Binder and D. W. Heermann, *Monte Carlo Simulation in Statistical Physics: An Introduction*, edited by H. K. V. Lotsch (Springer, Germany, 1988), Chap. 2.

⁸K. Binder and K. Schröder, Phys. Rev. B **14**, 2142 (1976).

⁹K. Binder and D. Stauffer, *Topics in Current Physics: Monte Carlo Methods in Statistical Physics*, edited by K. Binder (Springer, Berlin, 1986), Chap. 8.

¹⁰J. A. Mydosh, *Spin Glasses: An Experimental Introduction* (Taylor & Francis, London, 1993), pp. 51, 77, and 99.

Processing effects on the magnetostrictive and physical properties of SmFe_2 /metal composites

F. E. Pinkerton,^{a)} T. W. Capehart, J. F. Herbst, E. G. Brewer, and C. B. Murphy
*Physics and Physical Chemistry Department, General Motors Research and Development Center,
30500 Mound Road, Warren, Michigan 48090-9055*

Hot pressed SmFe_2/Fe and SmFe_2/Al composites combine the large magnetostriction of SmFe_2 with the mechanical robustness of the Fe or Al matrix. Here we report the dependence of the magnetostriction, density, and mechanical hardness on processing parameters, specifically on the SmFe_2 volume fill fraction and the consolidation temperature. The magnetostriction increases monotonically with increasing SmFe_2 content, but both the density and hardness decrease; low fill fraction composites are within 10% of theoretical density and have hardnesses of 40–85 Rockwell *B*, whereas hot pressed SmFe_2 powder alone has high porosity (exceeding 30%) and is too soft to register on the Rockwell *B* hardness scale. The best combination of properties lies in the range of 40%–60% SmFe_2 . Similar competition between magnetostriction and physical properties is observed as a function of the temperature used to consolidate the samples. The magnetostriction falls slowly as the hot press temperature increases, probably as a result of chemical reaction between the SmFe_2 phase and the matrix metal. On the other hand, higher temperature improves the consolidation, resulting in higher density and hardness. These results demonstrate that the magnetostrictive and physical properties of SmFe_2 composites can be tailored by adjusting the fill fraction and processing temperature. © 1998 American Institute of Physics.
[S0021-8979(98)34311-X]

I. INTRODUCTION

Magnetostrictive materials show considerable promise as the active elements in automotive force and torque sensors (see, e.g., Ref. 1). We have recently reported the development of hot pressed magnetostrictive composites comprised of the magnetostrictively active compound SmFe_2 embedded in an Fe or Al matrix.² We use SmFe_2 , with saturation magnetostriction $\lambda_s = -1560$ ppm,³ because of its reduced cost compared to TbFe_2 -based compositions; we expect that similar results would be obtained with TbFe_2 and $(\text{Tb}, \text{Dy})\text{Fe}_2$. Our preliminary work concentrated on composites made with 50% SmFe_2 powder by volume in which we achieved saturation magnetostrictions $|\lambda_s| = 280$ –440 ppm. These values are roughly an order of magnitude larger than those of magnetostrictive steels such as T250 maraging steel ($\lambda_s = 29$ ppm), and the composites offer mechanical integrity considerably superior to that of pure SmFe_2 . The SmFe_2 component was obtained either from single-phased annealed SmFe_2 ingot or from melt-spun and crystallized SmFe_2 ribbons. In the latter case the composites were good permanent magnets in addition to being highly magnetostrictive.

This article examines the composite's magnetostriction as the fill fraction of SmFe_2 powder is varied from 20% to 100% by volume. We also report on changes in magnetostriction as the hot press temperature is varied between 530 and 730 °C (Fe) or between 500 and 620 °C (Al). We additionally monitor two important physical properties of the composite, namely the physical density ρ , which is a mea-

sure of the porosity of the sample, and the Rockwell hardness, which we use as a relative indication of the mechanical integrity of the composite.

II. EXPERIMENTAL PROCEDURES

This work considers composites made from annealed single-phased SmFe_2 ingot; we expect that similar results would be obtained for our ribbon-based composites. Composites were prepared as detailed previously.² Starting ingots having the $\text{Sm}_{0.333}\text{Fe}_{0.667}$ stoichiometry were cast by induction melting, then annealed for either 100 or 270 h at 700 °C to obtain single-phased ingots of SmFe_2 . The 100 h anneal was sufficient to produce pure SmFe_2 material, and no further benefit was derived from annealing for the longer time; both anneals generated identical SmFe_2 ingots as determined by x-ray diffraction analysis. The ingots were high energy ball milled for 5 mins in a SPEX 8000 mixer/mill to obtain SmFe_2 powder. The powder was mixed with either Fe or Al powder and hot pressed at 95 MPa to obtain a composite cylinder 12.7 mm in diameter and about 7 mm high. A series of composites was hot pressed at 610 (Fe) or 540 °C (Al) in which the volume fraction of SmFe_2 was varied between 20% and 100%. A second series of composites was fabricated in which the SmFe_2 fraction was fixed at 50% by volume while the hot press temperature was varied between 530 and 730 °C for Fe, and between 500 and 620 °C for Al.⁴

The magnetostrictive strain λ as a function of the applied magnetic field H was measured using constantan strain gauges in a half-bridge configuration, mounted on the flat face of the cylindrical sample. In this arrangement two strain

^{a)}Electronic mail: fpinkert@gmr.com

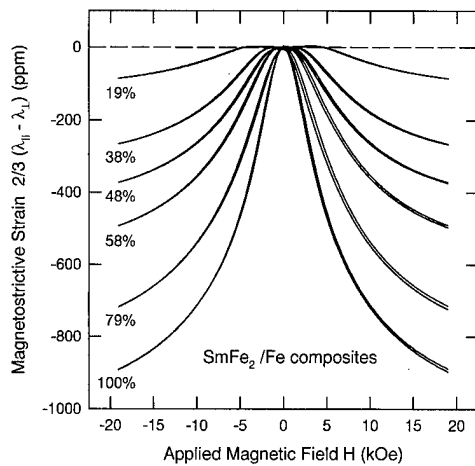


FIG. 1. Magnetostriction $2/3(\lambda_{||} - \lambda_{\perp})$ as a function of applied magnetic field H for hot pressed SmFe_2/Fe composites made at various SmFe_2 fill fractions.

gauges simultaneously measure the strain $\lambda_{||}$ parallel to the direction of H and the strain λ_{\perp} in the direction perpendicular to H , providing a direct measurement of the difference $(\lambda_{||} - \lambda_{\perp})$. For an isotropic magnetostrictor (as is often assumed to be the case for randomly oriented polycrystalline materials such as these composites) and in a magnetic field large enough to saturate the magnetostrictive response this difference is proportional to the saturation magnetostriction λ_s :

$$\lambda_s = \frac{2}{3} (\lambda_{||} - \lambda_{\perp}).$$

Magnetostrictive strains were measured in magnetic fields up to ± 19 kOe.

The physical density ρ was determined from the sample dimensions and weight. The hardness was obtained using a standard hardness tester on the Rockwell B scale.

III. RESULTS AND DISCUSSION

The magnetostrictive strains $\lambda = 2/3(\lambda_{||} - \lambda_{\perp})$ as functions of the applied magnetic field H are shown for various SmFe_2 fill fractions in Fig. 1 for composites made with Fe. A similar set of curves is generated for composites with Al. As expected, composites with larger SmFe_2 fill fractions show higher magnetostrictive strains. Recently a mathematical model of magnetostriction in composite materials was developed which describes the observed fill fraction dependence rather well.⁵

None of the magnetostriction curves in Fig. 1 reach saturation in the maximum applied field of 19 kOe (the same is true for composites with Al). Somewhat surprisingly, it is easier to saturate the magnetostriction as the SmFe_2 content increases, with the pure SmFe_2 sample having the most nearly saturated appearance. The origin of this effect is not understood. To quantify this observation, the saturation magnetostriction λ_s was estimated by performing a least squares fit of each magnetostriction curve to the empirically chosen formula

$$\lambda(H) = \lambda_s [1 - e^{-(H-h_c)/h_0}],$$

where $\lambda_s = 2/3(\lambda_{||} - \lambda_{\perp})(H \rightarrow \infty)$ and h_c and h_0 are fitting parameters. By comparing the magnetostriction at 19 kOe,

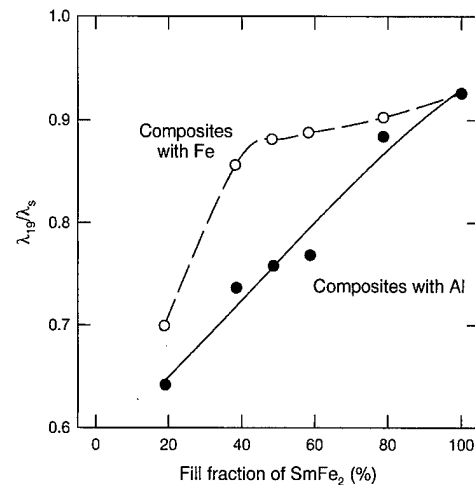


FIG. 2. Ratio λ_{19}/λ_s of the magnetostriction $\lambda_{19} = 2/3(\lambda_{||} - \lambda_{\perp})$ measured at the maximum applied field of $H = 19$ kOe to the extrapolated saturation magnetostriction $\lambda_s = 2/3(\lambda_{||} - \lambda_{\perp})$ in the limit of very large field. The lines are guides to the eye.

$\lambda_{19} = 2/3(\lambda_{||} - \lambda_{\perp})(H = 19 \text{ kOe})$, to λ_s the relative degree of saturation can be assessed. The ratios λ_{19}/λ_s are shown in Fig. 2 for Fe (open circles) and Al (filled circles) composites. While composites at high SmFe_2 fill fraction are close to saturation ($\lambda_{19}/\lambda_s \approx 1$), at low fill fractions they are far from saturation, especially with Al.

The dependence of $2/3(\lambda_{||} - \lambda_{\perp})$ at 19 kOe on the SmFe_2 fill fraction is shown in Fig. 3 for the composites made with Fe. Also shown is the physical density ρ normalized to its theoretical value $\rho_{\text{theoretical}}$ calculated from the volume fraction of the two constituents and the known densities of the SmFe_2 and Fe components. The value of $\rho_{\text{theoretical}}$ is only approximate since it does not take into account any chemical reaction between the two constituents, which would form additional phases having different densities. Nevertheless, the ratio $\rho/\rho_{\text{theoretical}}$ serves as a rough measure of the porosity of the sample. The porosity at SmFe_2 fill fractions up to 50% is less than 15%, and decreases as the SmFe_2 fraction drops. At high fill fractions the porosity is quite large, reaching a value exceeding 30% in a sample comprised of pure

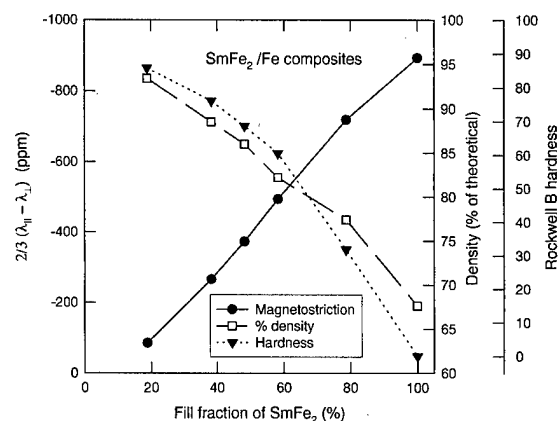


FIG. 3. Dependence of the magnetostriction $2/3(\lambda_{||} - \lambda_{\perp})$ at $H = 19$ kOe (●), the density ρ normalized to the theoretical density $\rho_{\text{theoretical}}$ (□), and the hardness (▼) on the volume fraction of SmFe_2 in hot pressed composites made with an Fe matrix.

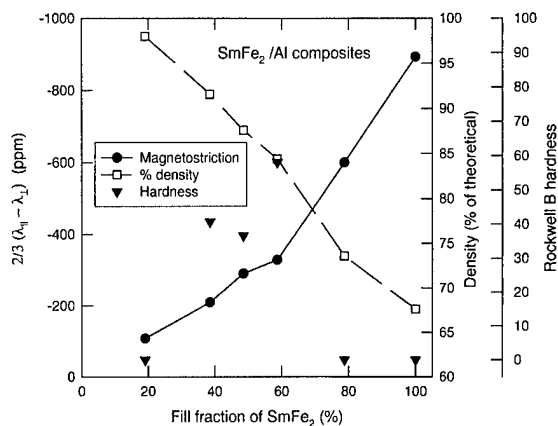


FIG. 4. Dependence of the magnetostriction $2/3(\lambda_{||} - \lambda_{\perp})$ at $H = 19$ kOe (●), the density ρ normalized to the theoretical density $\rho_{\text{theoretical}}$ (□), and the hardness (▼) on the volume fraction of SmFe₂ in hot pressed composites with Al.

hot pressed SmFe₂ powder. Finally, the hardness is shown on Fig. 3 as the filled inverted triangles. The pure SmFe₂ sample is too soft to register on the Rockwell *B* scale, but the hardness increases steadily as the SmFe₂ fraction decreases, reaching nearly 90 Rockwell *B* at low fill fraction.

Figure 4 shows similar data for composites made with Al. The trends in magnetostriction and density are very similar to those observed in the Fe composites. The density ratios of the Al composites tend to be slightly higher than those of the corresponding Fe composites, probably because of the greater malleability of Al. The hardness is substantially reduced in the Al composites and is also quite variable. This can be associated with the mechanical softness of annealed Al, and suggests that the hardness of the Al composites is quite sensitive to the details of the hot press, in ways which are currently not fully controlled.

The variation of these properties with hot press temperature is shown in Figs. 5 and 6 for composites made at 50 vol % SmFe₂ with Fe and Al, respectively. In both cases the magnetostriction decreases slowly with increasing hot press temperature. We ascribe this loss to chemical reaction between the SmFe₂ and Fe or Al matrix at elevated tempera-

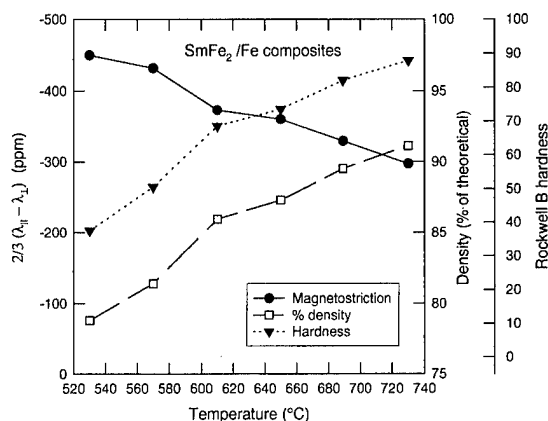


FIG. 5. Dependence of the magnetostriction $2/3(\lambda_{||} - \lambda_{\perp})$ at $H = 19$ kOe (●), the density ρ normalized to the theoretical density $\rho_{\text{theoretical}}$ (□), and the hardness (▼) on the hot press temperature in 50 vol % SmFe₂ composites with Fe.

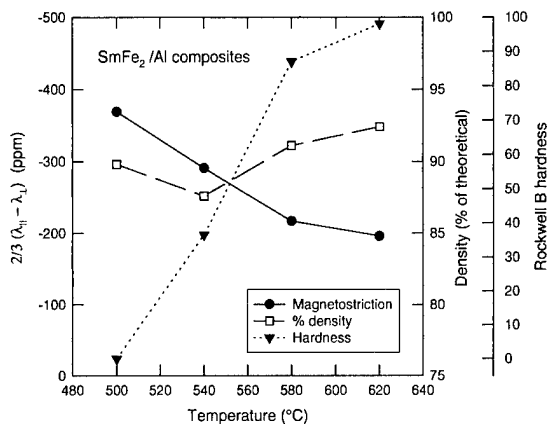


FIG. 6. Dependence of the magnetostriction $2/3(\lambda_{||} - \lambda_{\perp})$ at $H = 19$ kOe (●), the density ρ normalized to the theoretical density $\rho_{\text{theoretical}}$ (□), and the hardness (▼) on the hot press temperature in 50 vol % SmFe₂ composites with Al.

ture, which converts part of the material at the particle interfaces into additional, low magnetostrictive rare earth-Fe or rare earth-Al phases. On the other hand, higher hot press temperatures substantially improve the consolidation, resulting in better density and hardness values.

In conclusion, the magnetostriction of SmFe₂/metal composites scales in the expected fashion with the magnetostrictive SmFe₂ content. The best mechanical properties are found at relatively low fill fractions (20%–40%), where the porosity is around 10% and the hardness exceeds 40 (Al) or 80 (Fe) Rockwell *B*. The consolidation temperature also strongly influences the properties; with higher hot press temperature giving reduced magnetostriction but improved consolidation. These results indicate that some tailoring of the materials properties can be done if some of the high magnetostriction can be sacrificed in favor of mechanical properties. Taken as a whole, these results begin to establish limits on the SmFe₂ fill fraction and the hot press temperature which simultaneously provide significant magnetostriction and reasonable mechanical properties.

ACKNOWLEDGMENTS

The authors wish to thank S. Gillman, M. Colosky, and A. Badawy of Delphi Saginaw Steering Systems for their support and encouragement. They are grateful to Tom Perry for many valuable discussions and Martin Meyer for his assistance with this project.

¹I. J. Garshelis, IEEE Trans. Magn. **28**, 2202 (1992).

²F. E. Pinkerton, T. W. Capehart, J. F. Herbst, E. G. Brewer, and C. B. Murphy, Appl. Phys. Lett. **70**, 2601 (1997).

³A. E. Clark, in *Ferromagnetic Materials*, Vol. 1, edited by E. P. Wohlfarth (North-Holland, Amsterdam, 1980), pp. 531–589.

⁴We have no reason to expect that uniaxial hot pressing introduces significant texture. Orientation during hot pressing is known to occur in Nd-Fe-B due to a combination of diffusion slip and stress-assisted preferential grain growth during deformation of the tetragonal Nd₂Fe₁₄B phase [see, e.g., R. K. Mishra, J. Appl. Phys. **62**, 967 (1987)]. Even so, Nd-Fe-B magnets develop a texture of no more than 10% during hot pressing; full orientation requires an additional die upsetting step. We have no evidence that any similar mechanism is operative in the cubic RFe₂ phase.

⁵J. F. Herbst, T. W. Capehart, and F. E. Pinkerton, Appl. Phys. Lett. **70**, 3041 (1997).

Magnetomechanical coupling and elastic moduli of polymer-bonded Terfenol composites

J. Hudson, S. C. Busbridge, and A. R. Piercy^{a)}

Department of Mechanical and Manufacturing Engineering, University of Brighton,
Brighton BN2 4GJ, United Kingdom

The dependence of coupling coefficient (k) and elastic moduli (E_H and E_B) on particle size and volume fraction of Terfenol powder in polymer-bonded composites has been investigated. Materials were prepared with powder in five size ranges between 106 and 710 μm and in three volume fractions (V_F). The moduli show a ΔE effect, which is negative for small bias fields and positive for larger fields. E_H is found to be independent of particle size and to vary with V_F in agreement with model predictions. The maximum value of k , for each sample, is found to be independent of both particle size and V_F and a simple model is presented which predicts this behavior and indicates that the low values of k_{max} arise mainly from the low modulus of the epoxy binder. © 1998 American Institute of Physics. [S0021-8979(98)25311-4]

INTRODUCTION

Polymer-bonded Terfenol powder composite materials are the focus of increasing attention¹⁻⁴ for applications at higher frequencies than are possible with bulk Terfenol. There does not, however, appear to be any published work aimed at investigating the dependence of the magnetomechanical properties of these materials on composition parameters. The present work, which forms part of a program designed to elucidate the variation of properties with particle size and volume fraction, reports results for the magnetomechanical coupling coefficient (k) and elastic moduli at constant H and constant B (E_H and E_B , respectively).

EXPERIMENT

The composite samples were prepared from Terfenol powder in five particle-size ranges (106–150, 150–212, 212–300, 300–500, and 500–710 μm) each in three volume fractions (nominally, 55%, 62% and 70%) with epoxy (Araldite AY103/HY951) as the binding material. For each composition, two rectangular samples, of size 50×10×7 mm, were prepared using a cold compression-moulding technique under pressures of 20–150 MPa applied to the largest-area face of the samples. The range of volume fractions used was limited by the difficulty of maintaining uniformity for lower concentrations and of avoiding porosity for higher concentrations.

Static and dynamic magnetomechanical properties were measured at room temperature, with zero stress bias. The bias field, which was provided by an electromagnet, was applied along the long axis of the sample, which was also the direction of measurement. E_H and E_B were determined from the resonance and antiresonance frequencies (f_{max} and f_{min}), respectively, which were obtained from the frequency dependence of the magnitude of the electrical impedance of a 70-turn coil around the sample.

The coupling coefficient k was evaluated by three methods:

(a) from f_{max} and f_{min} using

$$k = \sqrt{1 - \frac{f_{\text{max}}^2}{f_{\text{min}}^2}}, \quad (1)$$

(b) from analysis of the complex impedance loop,
(c) by the “three-parameter method” using

$$k = \sqrt{\frac{d_{\sigma}^2 E_H}{\mu_{\sigma}}}, \quad (2)$$

where d_{σ} and μ_{σ} are the dynamic d coefficient and permeability, respectively, and E_H , was obtained from f_{max} . All the properties were determined as functions of the bias field.

RESULTS AND DISCUSSION

The variation of E_H and E_B with the bias field and the associated k dependence [from Eq. (1)] are shown in Figs. 1 and 2, respectively, for the sample having a particle size of 300–500 μm and 64% volume fraction. This bias-field dependence, in which E_H decreases to a minimum value at the

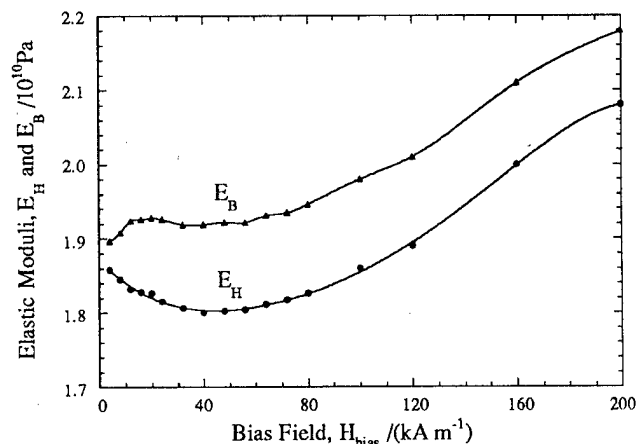
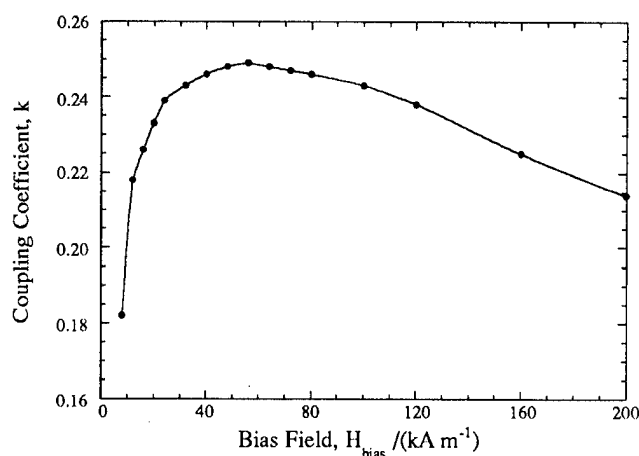


FIG. 1. Typical variation of E_H and E_B with bias field.

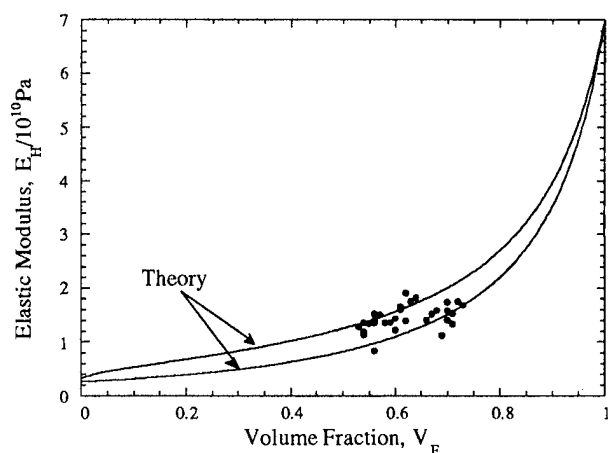
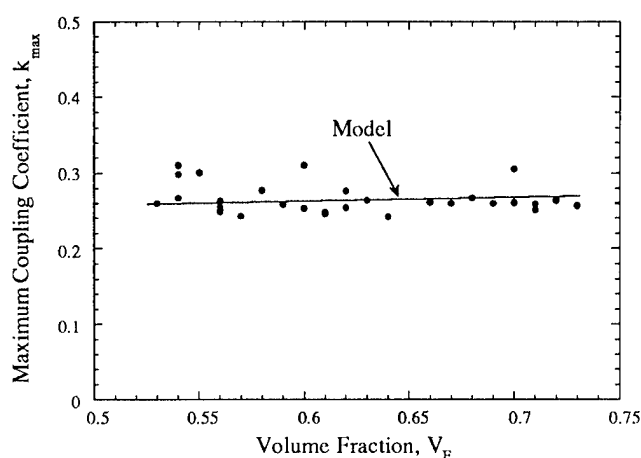
^{a)}Electronic mail: a.r.piercy@bton.ac.uk

FIG. 2. Typical variation of k with bias field.

bias field corresponding to maximum k and then increases, was typical of all samples. The values of E_H found here are similar to those obtained by Sandlund *et al.*¹ The negative ΔE effect was also observed in earlier work,^{1,3} although the positive ΔE at higher bias fields was not reported and Ruiz de Angulo *et al.*³ also observed a much more flat dependence of k on the bias field. The form of behavior found here, apart from the negative ΔE region, is more reminiscent of that for bulk Terfenol.

A more detailed comparison between the present work and the earlier publications is difficult because information on particle size is not given in Sandlund *et al.*¹ and in Ruiz de Angulo *et al.*³ it was "less than 125 μm ." It is likely that a wider range of particle size, in each sample, was used in the earlier work. Furthermore, the volume fractions employed here are probably lower than in the earlier work and it is not possible to compare the properties of the binders used.

The dependence of E_H (at the bias field for maximum k) on volume fraction (V_F) is given in Fig. 3 where the solid lines represent the limiting theoretical values of the modulus given by the models of Ravichandran,⁵ calculated using the manufacturer's value of 2.7–3.3 GPa for the modulus of the epoxy and 70 GPa for bulk Terfenol. Although the dependence of E_H on V_F is weak, it is clear that within experimen-

FIG. 3. The variation of E_H with volume fraction for all samples.FIG. 4. The variation of k_{max} with volume fraction for all samples.

tal uncertainty there is good agreement with the model, which gives values very different from a linear interpolation. No systematic dependence of E_H on particle size was found.

Figure 4 shows the dependence of the maximum value of k (which occurs at a bias field of about 60 kA m^{-1} for each sample) on V_F and clearly, within the experimental uncertainty, k_{max} is independent of V_F . Similarly, no systematic dependence on particle size was observed.

The average value for k_{max} obtained using Eq. (1) was 0.26, while Eq. (2) and the complex impedance loop, which we believe generally provide the more accurate measures of k , gave an average value of 0.15. This value for k is considerably smaller than that reported by Sandlund *et al.*¹ although it is not clear, in the latter case, whether a dynamic value for the d coefficient was used, as in our work, with Eq. (2). Our measurements show that incremental d coefficients, obtained from static magnetostriction curves, are at least a factor of 2 greater than the dynamic values obtained by alternating excitation.

In modeling the dependence of k on V_F we consider the V_F dependence of the three parameters in Eq. 2. Our measurements of static properties indicate that the saturation magnetostriction is independent of V_F in the range used and that the magnetization varies in proportion to V_F . We, therefore, take the dynamic susceptibility χ to be proportional to V_F and this is confirmed by our experimental measurements.⁷ The ratio d/χ is a function of the magnetization process and λ_{sat}/M_s only⁶ and we assume that the magnetization process does not vary with V_F . This leads, with the above assumptions, to the prediction that d is independent of V_F , which is again confirmed by our measurements.⁷

Equation (2) then leads to

$$k^2 = k_1^2 \left(\frac{E}{E_1} \right) \frac{(1 + \chi_1)}{(1 + \chi_1 V_F)}, \quad (3)$$

where the subscript "1" refers to the values for a composite with $V_F = 1$, which we note will not be the values measured for bulk Terfenol, but rather for a hypothetical 100% dense, randomly orientated powder material. Our measurements⁷ of dynamic susceptibility give an extrapolated value of $\chi_1 = 1.4$ and taking (E/E_1) from Fig. 3 into Eq. (3) with k_1

$=0.5$ leads to a predicted dependence for k shown by the solid line in Fig. 4. The model, therefore, predicts that k_{\max} is virtually independent of V_F in the range used, in agreement with the experimental results within experimental uncertainties.

The low value of k_{\max} measured (and predicted) for our materials can be seen from Eq. (3) to be due principally to the low modulus ratio (E/E_1) which, in turn, arises from the low elastic modulus of the epoxy. Use of a higher-modulus binder should, therefore, lead to an increase in k_{\max} as well as an increase in the forces generated by the material.¹ On the other hand, if the considerations which lead to Eq. (3) are valid, then increase in V_F (within practical constraints) would not lead to a significant increase in k .

The not-inconsiderable variations observed (Figs. 3 and 4) in the measured properties for similar volume fractions and particle sizes arise, we believe, from two main sources: variations in the elastic modulus of the epoxy, due to the small quantities used in mixing the two components; and variations in the orientation of the magnetic particles.

CONCLUSION

It has been shown both experimentally and theoretically that the magnetomechanical coupling coefficient in these

composites is essentially independent of both particle size and volume fraction and the relatively low value of the coupling coefficient has been shown to arise mainly from the low modulus of the epoxy binder. The elastic moduli are shown to be independent of particle size and to follow the model dependence on volume fraction.

ACKNOWLEDGMENT

This work has been carried out with the support of B&W Loudspeakers Ltd., Steyning, U.K.

¹L. Sandlund, M. Fahlander, T. Cedell, A. E. Clark, J. B. Restorff, and M. Wun-Fogle, *J. Appl. Phys.* **75**, 5656 (1994).

²D. Kendall and A. R. Piercy, *Ferroelectrics* **187**, 153 (1996).

³L. Ruiz de Angulo, J. S. Abell, and I. R. Harris, *J. Magn. Magn. Mater.* **157/158**, 508 (1996).

⁴K. W. Dennis, M. R. Govindaraju, D. C. Jiles, M. Linde, and R. W. McCallum, *J. Appl. Phys.* **81**, 5423 (1997).

⁵K. S. Ravichandran, *J. Am. Ceram. Soc.* **77**, 1178 (1994).

⁶A. R. Piercy, S. C. Busbridge, and D. Kendall, *J. Appl. Phys.* **76**, 7006 (1994).

⁷J. Hudson (unpublished).

First-principles theory of magnetoelastic coupling and magnetic anisotropy strain dependence in ultrathin Co films on Cu(001)

A. B. Shick, D. L. Novikov, and A. J. Freeman

Department of Physics and Astronomy, Northwestern University, Evanston, Illinois 60208-3112

The magnetoelastic coupling and magnetic anisotropy energy (MAE) of (i) an uncovered and (ii) a Cu-capped Co overlayer on Cu(001) are determined employing a self-consistent relativistic spin-polarized version of the total-energy full-potential linearized augmented plane-wave (FLAPW) method and the magnetic torque method. Layer-resolved contributions to the magnetoelastic coupling and MAE are obtained. We find surface magnetoelastic coupling coefficients to be positive for the Co layer and negative for the Cu substrate and cap layers. A substantial difference of magnetoelastic coupling coefficients for thin films as opposed to bulk is demonstrated, which causes a negative magnetostriction coefficient (λ_{001}) for uncovered Co overlayer and a positive λ_{001} for the Cu-capped Co overlayer on Cu(001). © 1998 American Institute of Physics.

[S0021-8979(98)40611-X]

Recent experimental investigations of ultrathin Co films on Cu(001) demonstrate the existence of a magnetoelastic coupling contribution to the magnetic anisotropy energy (MAE) due to tetragonal strain.¹ Chappert and Bruno² considered a magnetoelastic strain relaxation contribution to the surface MAE due to interfacial dislocations, and pointed out that homogeneous strain does not contribute to the surface MAE. However, O'Handley and co-workers³ found a magnetoelastic homogeneous strain contribution to the surface MAE which is caused by a substantial difference between magnetoelastic coupling constants for bulk and surface. The Néel pair-interaction model analysis⁴ and general group symmetry considerations⁵ both show that in addition to bulk magnetoelastic coupling coefficients, surface magnetoelastic coupling coefficients must be introduced to describe true ultrathin film magnetoelastic coupling.

Here we report results for first-principles calculations of the surface magnetoelastic coupling constant and the magnetostriction coefficient for an uncovered and a Cu-capped Co overlayer on Cu(001) in order to investigate quantitatively this reverse magnetostriction effect. The full-potential linear-augmented plane-wave (FLAPW) method⁶ is used to obtain self-consistent solutions of the Kohn–Sham–Dirac equations in terms of a second variation for SOC;⁷ the total-energy and MAE dependence on surface strain are employed to determine the surface magnetoelastic coupling constant and magnetostriction coefficients. We used a symmetric slab model consisting of (i) five Cu substrate layers and a pseudomorphic Co overlayer on each side (Co/5Cu) for a Co overlayer on Cu and (ii) three Cu substrate layers and Cu-capped Co overlayers on each side (Cu/Co/3Cu) for the Cu-capped Co overlayer on Cu. The ideal fcc structure with a lattice constant $a=6.83$ a.u. is assumed for the Cu substrate layers while the vertical Co–Cu distance is varied as a parameter.

The 55 special k points mesh in the irreducible part of the two-dimensional Brillouin zone (2D BZ) is used for the self-consistent calculations for the perpendicular spin quantization axis. Lattice harmonics with angular momentum l up to eight are used to expand the charge and spin densities and

wave functions within the muffin-tin sphere. Self-consistency is achieved to within $1 \times 10^{-5} e/(a.u.)^3$ for charge and spin densities.

The MAE is obtained by applying the “local force” theorem for spin-quantization axis rotation in the (110) plane and using the Hellman–Feynman theorem to calculate a magnetic torque $T(\theta)$ (Ref. 8) at $\theta=\pi/4$ (where θ is the angle between the spin-quantization direction and the surface normal) with 400 special k points in the 1/4 of the 2D BZ.⁹ The use of magnetic torque allows us to calculate layer-resolved contributions to the total MAE. For comparison with earlier calculations, the calculated MAE (total and layer resolved) for Co/5Cu and Cu/Co/3Cu for the Cu(001) interlayer distance (3.415 a.u.) is shown in Table I. The results obtained are in fairly good agreement with our previous calculations⁷ based on the “local force” theorem for spin-quantization axis rotation, with results of relativistic screened Korringa–Kohn–Rostoker (KKR) calculations^{10,11} and with state-tracking calculations.¹²

The strain tensor for Co/5Cu and Cu/Co/3Cu is assumed³ diagonal with in-plane strain $e_0=e_{xx}=e_{yy}=(a_{Cu}-a_{Co})/a_{Co}$ and perpendicular strain $e_z=(l_{Co-Cu}-l_{Co-Co})/l_{Co-Co}$, where a and l are the lattice constant and interplanar distance, respectively. For a given in-plane strain, say $e_0=1.9\%$, the calculated ground-state relativistic total energy (E_{tot}) and MAE versus e_z are shown in Fig. 1 for Co/5Cu and in Fig. 2 for Cu/Co/3Cu.

For Co/5Cu the results indicate a good linear dependence of the MAE on e_z (cf., Fig. 1), in agreement with previous non-self-consistent SOC-second-variation calculations.¹³ As follows from the layer-by-layer “MAE” decomposition (cf., Fig. 1), the Co-layer contribution to the total MAE (e_z) is dominant compared with the Cu substrate contribution. For Cu/Co/3Cu the results again show that the MAE (e_z) (cf., Fig. 2) is well approximated by a linear dependence. The deviation from linearity is less than 0.05 meV and does not allow us to perform a rigorous quantitative treatment of nonlinear magnetoelastic effects. There is an increase in the absolute value of MAE with an increase of

TABLE I. The uniaxial surface MAE (meV/atom) for Co/5Cu and Cu/Co/3Cu (total and Co, Cu ML resolved) with the unrelaxed Cu(001) interlayer distance (3.415 a.u.) calculated by the magnetic torque method (T) in comparison with results of "local force" (LF) theorem for spin-quantization axis rotation and "state-tracking" (ST) method.

	T	LF ^a	LF ^{b,c}	ST ^d
Co/5Cu				
E_{MC}^{tot}	-0.395	-0.46	-0.38 ^b	-0.38
E_{MC}^{Co}	-0.44		-0.42 ^c	
E_{MC}^{Cu}	0.045			
Cu/Co/3Cu				
E_{MC}^{tot}	0.70		0.83 ^b	
E_{MC}^{Cu}	0.02		0.08	
E_{MC}^{Co}	0.68		0.67	
$E_{MC}^{Cap Cu}$	0.0		0.08	

^aReference 7.

^bReference 10.

^cReference 11.

^dReference 12.

strain $|e_z|$ for the Cu/Co/3Cu case which is mainly due to the Co-layer contribution (cf., Fig. 2) while for Co/5Cu the absolute value of MAE decreases with an increase of $|e_z|$ (cf., Fig. 1). The Co-layer contributions to the MAE (e_z) for Co/5Cu and Cu/Co/3Cu are calculated to be dominant (cf., Figs. 1 and 2).

The uniaxial MAE of strained Co/5Cu and Cu/Co/3Cu is given by,³

$$E = -B_1^v(e_\perp - e_0) - \frac{B_1^s}{t}(e_\perp - e_0) + \frac{2K_2}{t}, \quad (1)$$

where B_1^v and B_1^s are volume and surface components of the magnetoelastic coupling coefficient,³ K_2 is the uniaxial surface magnetocrystalline anisotropy constant, and t is the magnetic layer thickness. Then, K_2 , volume (E_{ME}^v) and surface (E_{ME}^s) magnetoelastic energy contributions, and the total surface MAE (E^s) (cf., Table II) are calculated using the

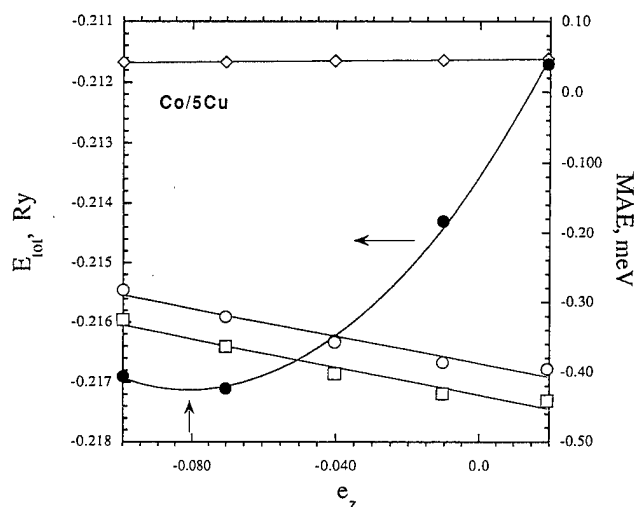


FIG. 1. Ground-state all-electron total energy (left scale) and the MAE [total (circle), Co (square), Cu (diamond)] (right scale), as a function of perpendicular strain e_z for Co/5Cu.

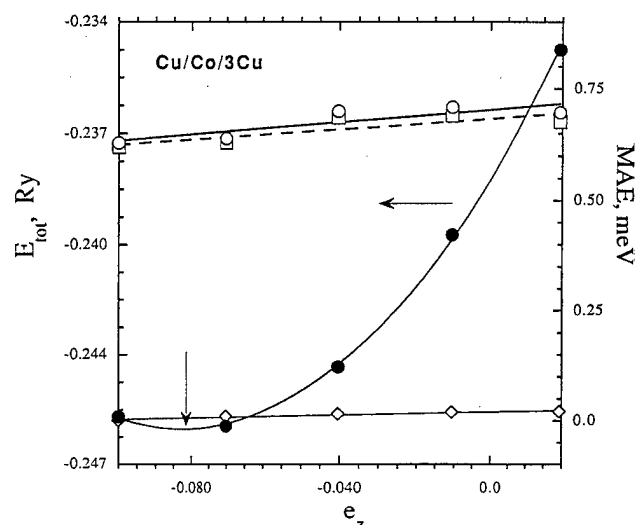


FIG. 2. Ground-state all-electron total energy (left scale) and the MAE [total (circle), Co (square), Cu (diamond)] (right scale), as a function of perpendicular strain e_z for Cu/Co/3Cu.

MAE dependence on e_\perp , the equilibrium e_\perp (cf., Figs. 1 and 2), and the experimental value of B_1^v for fcc-Co (-1.12 meV/atom).¹⁴

As given in Table II for the total MAE there is fairly good agreement with the results of Ref. 15 for the Co/5Cu case and only qualitative agreement for the Cu/Co/3Cu case. The substantial disagreement between our results and those of Ref. 15 arises from the lack of a volume uniaxial MAE contribution in Ref. 15. As pointed out in Ref. 1, the absence of this contribution contrasts with the experimentally observed tetragonal distortion in Co films.

For the Cu/Co/3Cu we found MAE to be positive, in disagreement with the negative MAE measured in Ref. 16 for ultrathin Co/Cu(001) films (with more than 3 Co layers) covered by ten overlayers of Cu (cf., Table II). This dis-

TABLE II. The equilibrium perpendicular strain (e_z , %), total and Co and Cu layer-resolved surface magnetoelastic coupling coefficients (B_1^s , meV/atom), the uniaxial surface MCA's ($2K_2$, meV/atom), volume magnetoelastic energies (E_{ME}^v , meV/atom), surface magnetoelastic energies (E_{ME}^s , meV/atom), total surface magnetic anisotropy energies (E^s , meV/atom), and MAE at the equilibrium e_z .

e_\perp	B_1^s	$2K_2$	E_{ME}^v	E_{ME}^s	E^s	MAE
Co/5Cu						
-8.09	2.10	-0.41	-0.11	0.21	-0.20	-0.32
	2.13(Co)	-0.45	-0.11	0.215	-0.235	
	-0.04(Cu)	0.045		0.00	0.045	
Ref. ^a		-0.375	0.00		-0.375	-0.375
Cu/Co/3Cu						
-8.23	0.44	0.70	-0.11	0.045	0.745	0.635
	0.54(Co)	0.68	-0.11	0.055	0.735	
	-0.17(Cu)	0.02		-0.02	0.00	
Ref. ^a		0.12	0.00		0.12	0.12
Ref. ^b			-0.07		-0.20	-0.27
Ref. ^c						-0.01

^aExperiment (Ref. 15).

^bExperiment (Ref. 16).

^cState-tracking results for 2Cu/Co/2Cu slab (Ref. 12).

agreement may be due to the recently demonstrated results¹¹ that there are strong oscillations in MAE (from positive to negative) for the unrelaxed Cu/Co/Cu(001) system as a function of the number of Co overlayers in the ultrathin film limit, and MAE is positive for one Co layer.

The surface magnetoelastic coefficients (cf., Table II) are calculated to be positive for both Co/5Cu and Cu/Co/3Cu and we found a surface magnetoelastic contribution to MAE from the Co layer to be significantly smaller for Cu/Co/3Cu than for Co/5Cu. Surprisingly, the surface magnetoelastic anisotropy estimated in Ref. 4 on the basis of the strain-dependent Néel model (0.07 meV/atom) and experimental data¹⁶ is in quite reasonable agreement with the result of our calculation (0.045 meV/atom). The magnetostriction coefficients, λ_{001} , were calculated by making use of magnetoelastic theory (with e_0 fixed by the substrate), and are -4.4×10^{-5} for Co/5Cu and 1.5×10^{-5} for Cu/Co/3Cu, respectively. Both of the calculated values of λ_{001} differ from the bulk value for fcc-Co [1.3×10^{-4} Ref. 14] due to surface contributions to magnetoelastic coupling coefficients.

Finally, in addition to the uniaxial surface MCA contribution [i.e., the $2K_2/t$ term in Eq. (1)], the magnetoelastic surface contribution to the uniaxial surface MAE has to be considered. The linear MAE dependence on perpendicular strain (e_z) (cf., Figs. 1 and 2) yields a qualitative similarity between first-principles theory and the phenomenological strain-dependent Néel model.⁴ The calculated values of the surface magnetoelastic coupling coefficient B_1^s for Co/Cu(001) and Cu/Co/Cu(001) are positive (cf., Table II) and cause the difference between ultrathin film effective magnetoelastic coefficient and its value for bulk fcc-Co.

We thank K. Hathaway, D. S. Wang, and R. Q. Wu for helpful discussion and M. Kowalewski, B. Heinrich, and L. Szunyogh for providing information in advance of publication. Work supported by the U.S. Office of Naval Research (Grant No. N00014-94-1-0030) and by a grant of computing time at the Arctic Region Supercomputing Center and at the Pittsburgh Supercomputing Center.

¹B. Heinrich and J. F. Cochan, *Adv. Phys.* **42**, 523 (1993).

²C. Chappert and P. Bruno, *J. Appl. Phys.* **64**, 5736 (1988).

³O. Song, C. A. Ballentine, and R. C. O'Handley, *Appl. Phys. Lett.* **64**, 2593 (1994); G. Bochi, O. Song, and R. C. O'Handley, *Phys. Rev. B* **50**, 2043 (1994).

⁴B. Heinrich, J. F. Cochan, and M. Kowalewski (unpublished).

⁵E. du Tremolet de Lacheisserie, *Phys. Rev. B* **51**, 15925 (1995).

⁶E. Wimmer, H. Krakauer, M. Weinert, and A. J. Freeman, *Phys. Rev. B* **24**, 864 (1981) and references therein.

⁷A. B. Shick, D. L. Novikov, and A. J. Freeman, *Phys. Rev. B* **56**, 14259 (1997).

⁸X. Wang, R. Wu, D.-S. Wang, and A. J. Freeman, *Phys. Rev. B* **54**, 61 (1996).

⁹The fourfold volume and in-plane surface MAE is then neglected.

¹⁰L. Szunyogh, B. Újfalussy, C. Blaas, U. Pustogowa, C. Sommers, and P. Weinberger (unpublished).

¹¹L. Szunyogh, B. Újfalussy, U. Pustogowa, and P. Weinberger, *Phys. Rev. B* **56**, 14036 (1997).

¹²D. S. Wang, R. Q. Wu, and A. J. Freeman, *J. Magn. Magn. Mater.* **129**, 327 (1994).

¹³R. Q. Wu, L. Chen, and A. J. Freeman, *J. Magn. Magn. Mater.* **170**, 103 (1997).

¹⁴H. Fujiwara, H. Kadomatsu, and T. Tokaunaga, *J. Magn. Magn. Mater.* **31-34**, 809 (1983).

¹⁵P. Krams, F. Lauks, R. L. Stamps, B. Hillebrands, and G. Güntherodt, *Phys. Rev. Lett.* **69**, 3674 (1992).

¹⁶M. Kowalewski, C. M. Schneiner, and B. Heinrich, *Phys. Rev. B* **47**, 8748 (1993).

Effects of heteroepitaxial strain on Laves phases TbFe_2 and DyFe_2

M. Huth^{a)} and C. P. Flynn

Department of Physics and Materials Research Laboratory, University of Illinois at Urbana-Champaign,
1110 West Green Street, Urbana, Illinois 61801

(110) oriented growth was observed for thin films of the highly magnetostrictive Laves phases TbFe_2 and DyFe_2 on Ta (110). On Nb (111), TbFe_2 nucleates in the (111) orientation. Depending on the substrate temperature during growth, varying degrees of residual tensile strain were observed in the films. For TbFe_2 grown on Ta (110) at 680 °C, x-ray diffraction revealed a splitting of the (220) Bragg reflection into a strain free component structurally coherent with the template, and a component with 0.5% biaxial tensile strain at room temperature. This strained component can be attributed to the difference in thermal expansion between the sapphire substrate and the TbFe_2 film. Magnetic hysteresis measurements revealed that the axis of easy magnetization lies in the film plane for both (110) and (111) oriented samples. © 1998 American Institute of Physics.
[S0021-8979(98)25411-9]

Cubic Laves phase compounds of the type RFe_2 (R: rare earth) offer several materials of interest in both applied and basic research. An example with possible applications is highly magnetostrictive TbFe_2 , epitaxially grown on a piezoelectric substrate, which holds promise for delay lines in surface acoustic wave devices.¹ These cubic compounds possess highly symmetric structures with 24 atoms in the conventional unit cell. Therefore they represent valuable model systems for the study of thin film growth applied to systems of moderate complexity. The ability to tailor specific aspects of the film properties, like the magnetic anisotropy by choice of specific growth conditions is the critical requirement for serious attempts to optimize these systems for specific applications.

Here we report investigations of the structural properties of thin epitaxial TbFe_2 and DyFe_2 films grown under various conditions and the influence of structure on their magnetic properties, with the main emphasis on TbFe_2 . The film growth was performed in a Perkin Elmer 430 molecular beam epitaxy (MBE) system with a base pressure of 6×10^{-11} Torr. Sapphire substrates in (11 $\bar{2}$ 0) *a*-plane or (0001) *c*-plane orientations were cleaned with basic and organic solvents and then annealed for one hour in vacuum at 1000 °C. Buffer layers of bcc refractory metals were then deposited by electron beam evaporation onto the heated substrates. Ta(110) was grown on the sapphire *a*-plane at 1000 °C, and Nb (111) was grown on *c*-plane sapphire at 750 °C. The growth rates were kept in the range 0.2 Å/s to 0.3 Å/s for a typical thickness of 400 Å. During this buffer layer growth the pressure increased to about 2×10^{-9} Torr.

The samples were next cooled to the range 450–680 °C for deposition of TbFe_2 or DyFe_2 at a growth rate of 0.2 Å/s for a film thickness of 400 Å to 1000 Å in a background pressure of about 8×10^{-11} Torr. TbFe_2 and DyFe_2 were grown in (110) orientation by using a Ta (110) buffer layer as template for nucleation of the desired orientation. On Nb (111), TbFe_2 nucleated in the (111) orientation. The Fe and

Tb were sublimed from high temperature effusion cells using high purity alumina and tantalum liners, respectively. With its higher vapor pressure, Dy allowed the use of a conventional effusion cell with BN liner. The Fe to Tb/Dy rate ratio was monitored using a quadrupole mass spectrometer and kept constant within $\pm 3\%$ of the nominal stoichiometry of 2:1. This mass spectrometer was calibrated by an independent measurement of film stoichiometry by Rutherford backscattering (RBS) with 2 MeV ^4He at an incidence of 15° with respect to the film normal. The film structure was investigated *in situ* by reflection high-energy electron diffraction (RHEED) and *ex situ* by x-ray diffraction on a two-circle diffractometer in the Bragg–Brentano geometry using Cu K_α radiation.

Oderno *et al.*² have shown that DyFe_2 and TbFe_2 (110) can be grown on Nb (110) buffer layers. In their work, the best results were obtained by preparing a 10–30 Å thick Fe seed layer, prior to the deposition of the Laves phase. The initial nucleation was described as three-dimensional suggested by RHEED investigations. Mosaicity could not be reduced below 1° for the (220) Bragg reflection.² Our RHEED investigations of the direct growth of DyFe_2 (110) on Ta (110) suggest two-dimensional nucleation, evolving into a rough three-dimensional surface after two to three monolayers and smooth again after a continuous film forms. Here we report that a mosaic spread as low as 0.04° could be observed without the use of an Fe seed layer. This corresponds to the resolution limit of the x-ray diffractometer and the line shape typically reflects the rocking curve of the Ta (110). The same results were obtained for TbFe_2 (110) samples, and is shown in Fig. 1(c). However, for TbFe_2 on Ta (110) the initial two-dimensional character of the film surface did not recover for films up to 1000 Å thick as evidenced by spot-like intensity enhancements superimposed on the observed RHEED streaks.

The crossover from the pseudomorphic two-dimensional to three-dimensional growth in the early nucleation stage most probably arises from the large lattice misfit (10%) between the Ta and Laves phase (110) surfaces, which causes

^{a)}Electronic mail: mhuth@uiuc.edu

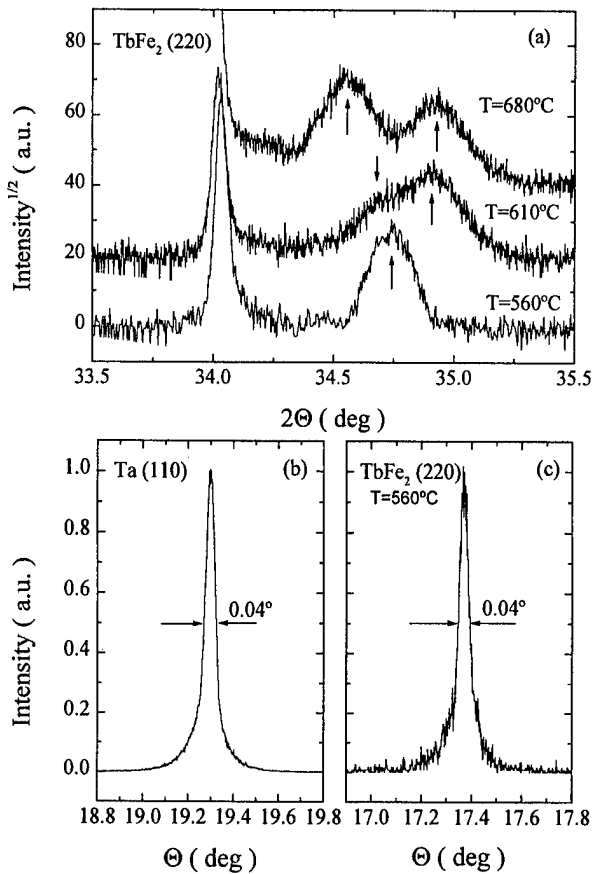


FIG. 1. (a) TbFe_2 (220) Bragg reflection for 850 Å thick films grown at various substrate temperatures indicated. The sharp peaks at 34° are caused by the $\text{Cu } K_{\beta_1}$ satellite of the sapphire (110) reflection. (b) Rocking curve of the Ta (110) reflection. (c) Rocking curve of the TbFe_2 (220) reflection. The TbFe_2 film was grown at 560°C .

the critical strain state to be exceeded after less than three monolayers. This growth behavior was insensitive to the substrate temperature during growth. However, x-ray analysis revealed a clear dependence at room temperature of the residual tensile strain in the film plane on the growth temperature. Two effects were observed. First, with increasing growth temperature at $T > 600^\circ\text{C}$ the (220) TbFe_2 reflection

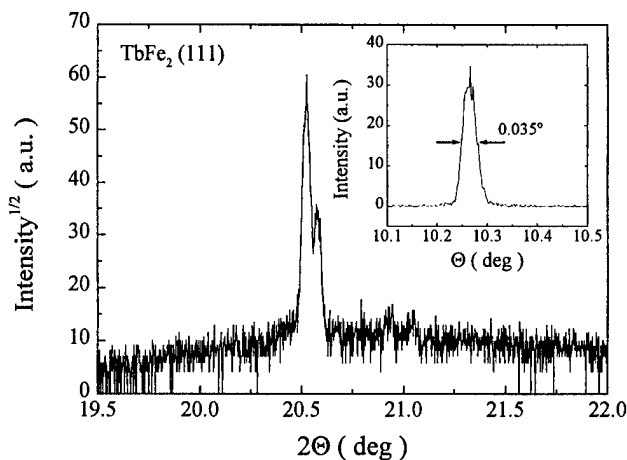


FIG. 2. (111) Bragg reflection and rocking curve (inset) of 400 Å thick TbFe_2 grown on Nb (111).

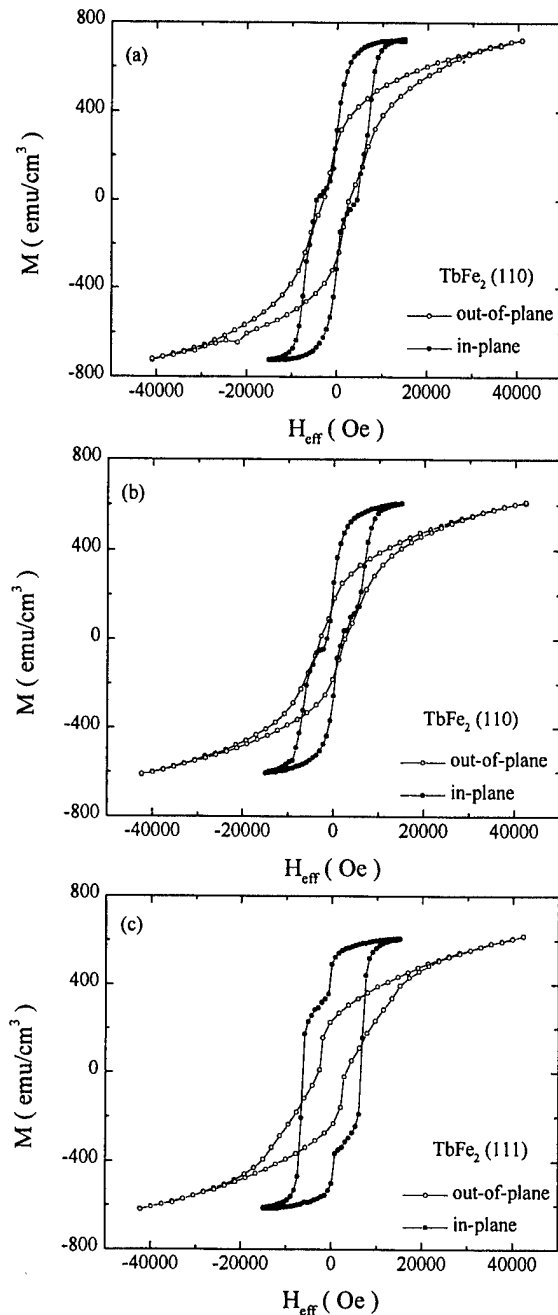


FIG. 3. Magnetic hysteresis of TbFe_2 films grown on (a) Ta (110) at 560°C , (b) Ta (110) at 680°C , and (c) Nb (111) at 520°C . All measurements were performed at room temperature.

splits into two components with a clear separation between two peaks for a film grown at 680°C [see Fig. 1(a)]. The low angle peak corresponds to a strain free film. The Ta (110) Bragg peak also suggests an essentially strain free template and the strong similarity of the rocking curves of the Ta (110) and TbFe_2 (220) reflection, both resolution limited, points clearly to the structural coherence between the buffer and the Laves phase epilayer. Second, the high angle component shifts towards increasing tensile strain in the film plane with higher growth temperature. The cause of the tensile strain may relate to the difference in the thermal expansion coefficients of sapphire and TbFe_2 since the large lattice misfit strain can be assumed to be compensated by disloca-

tion formation in the early stages of the film growth. The difference in thermal expansion can account for a tensile biaxial strain in the (110) plane of 0.5% at room temperature for a film grown at 680 °C.³ This is compatible with the observed 1% decrease of the d value for the (110) planes. The rocking curve width of this (220) component extends over several degrees. In order to create the observed strain-free Ta template and TbFe₂ epilayer at room temperature, the clamping effect of the substrate must be neutralized either by a compressive strain formed during growth or by a large increase of dislocations formed in the Ta buffer layer and part of the TbFe₂ film. In addition, the buffer layer partly alloyed with the Laves phase and RBS reveals a small interdiffusion in the interfacial region. This can also explain the observed saturation moment, which is only 70% of the expected magnetization of 800 emu/cm³ for TbFe₂ at room temperature,⁴ as evident in Fig. 3(b).

TbFe₂ (111) was grown on Nb (111). The very low surface free energy of the Nb (110) surface causes facets to form on the (111) Nb surface and results in a reduced structural quality of this template, compared to Ta (110) buffer layers. A strong tendency towards highly ordered TbFe₂ (111) phase formation was nevertheless observed. As shown in Fig. 2 the (111) reflection separates into a two-component line shape with a sharp Cu $K_{\alpha 1/\alpha 2}$ -split Bragg component on a broad background. The rocking curve of the sharp component is resolution-limited even though the Nb (222) rocking curve width is 0.41°. This suggests an intrinsic (111) growth preference for TbFe₂, which is corroborated by the fact that on Mo (110) and W (110), (111) growth was indeed observed.^{5,6}

Finally, we mention the results of magnetic measurements on these samples. Demagnetization effects were accounted for by calculating the effective field $H_{\text{eff}} = H - 4\pi N \cdot M$ with the demagnetization factor N equal to 0 and 1 for measurements with the applied field H in the plane and perpendicular to the plane of the films, respectively. As shown for TbFe₂ (110) and (111) in Fig. 3, the hysteresis curves suggest that the axis of easy magnetization lies in the film plane. Similar results were obtained for (110) DyFe₂ films on Ta (110). The qualitative characteristics of the hysteresis curves showed no temperature dependence in the range of 5 to 300 K. For an applied field in the film plane, the magnetization is reduced by coherent domain ro-

tation during reduction of the field from the saturated regime. At zero field the magnetization drops sharply followed by a step like feature. This magnetization characteristic probably arises from the magnetic anisotropy energy which favors the (111) axes of TbFe₂ bulk samples. Due to the form anisotropy the in-plane $[1\bar{1}1]$ direction of the TbFe₂ (110) plane or the $\langle 111 \rangle$ directions 20° off the film plane for TbFe₂ (111) are energetically preferred. Wang *et al.*,⁵ who observed a comparable magnetization drop for TbFe₂ (111) sputtered on W (110) buffer layers, suggest that the system has magnetic properties caused by interface reactions. They assumed a constant thickness of 10 nm for a soft magnetic material in the interfacial region causing a significant magnetization drop for thin films only. Our results do not support the same conclusion for films grown on Ta at low enough temperature to avoid interdiffusion. In these samples the saturation moments were close to the expected value of 800 emu/cm³ at room temperature and the magnetization drop occurred independent of the thickness of the films. Possible magnetic anisotropies in the film plane were not investigated.

ACKNOWLEDGMENTS

The synthesis was supported in part by the U. S. Department of Energy under Award No. DEFG02-96ER45439 and the magnetic measurements by the National Science Foundation Grant No. DMR-9424339. For early help with this research, the authors thank the Office of Naval Research through Grant No. ONR N 00014-94-I-0068. One of the authors (M. H.) thanks the *Deutsche Forschungsgemeinschaft* for additional support.

¹For example, H. Uchida, M. Wada, K. Koike, H. H. Uchida, V. Koeninger, Y. Matsumura, H. Kaneko, and T. Kurino, *J. Alloys Compd.* **211/212**, 576 (1994).

²V. Oderso, C. Dufour, K. Dumesnil, Ph. Mangin, and G. Marchal, *J. Cryst. Growth* **165**, 175 (1996); V. Oderso, C. Dufour, K. Dumesnil, Ph. Bauer, Ph. Mangin, and G. Marchal, *Phys. Rev. B* **54**, R17375 (1996).

³C. T. Wang, B. M. Clemens, and R. L. White, *IEEE Trans. Magn.* **32**, 4752 (1996).

⁴A. E. Clark, *Handbook of the Physics and Chemistry of Rare Earth*, Vol. 2, edited by K. A. Gschneidner and L. Eyring (North-Holland, Amsterdam, reprint 1982).

⁵C. T. Wang, R. M. Osgood, III, R. L. White, and B. M. Clemens, *Mater. Res. Soc. Symp. Proc.* **384**, 79 (1995).

⁶S. Jaren, E. du Trémolet de Lacheisserie, D. Givord, and C. Meyer, *J. Magn. Magn. Mater.* **165**, 172 (1997).

Magnetomechanical instability in FeTb/Fe multilayers

Manfred Wuttig, Quanmin Su, and Fabrice Masson^{a)}

Department of Materials Science and Engineering, University of Maryland, College Park, Maryland 20742-2115

Eckhard Quandt and Alfred Ludwig

Institut fuer Materialforschung I, Forschungszentrum Karlsruhe, Postfach 3640, 76021 Karlsruhe, Germany

Multilayers composed of alternate layers of iron-rare earth and Fe or FeCo alloys feature a high magnetostriction at low external fields and a coercive force as low as 5 mT. The coercive fields of as sputtered multilayers are significantly higher than that and the low values are attained after an anneal at 473 K. Since the hysteresis remaining after the heat treatment might be of magnetomechanical origin it is of interest to investigate the dynamic magnetomechanical characteristics of this class of multilayers. Experiments on multilayers of the composition (7 nm FeTb)/(8 nm/Fe) show a pronounced magnetomechanical damping maximum and an attendant decrease of Young's modulus upon annealing. Both occur in the vicinity of the coercive field. Their evolution as a function of the annealing and magnetic field will be described and it will be shown that they reflect an instability principally caused by the magnetomechanical interaction of the component layers of the multilayer. © 1998 American Institute of Physics.

[S0021-8979(98)40711-4]

INTRODUCTION

This article addresses instabilities in giant magnetostrictive, GMA, multilayers. GMA films have attracted attention in view of their potential applications as microactuators. Amorphous films of rare-earth metals can be prepared such that only the shape anisotropy remains.^{1,2} However, they display a low Curie temperature limiting their usefulness. Crystalline or microcrystalline GMA single-layer films have a higher Curie temperature but are characterized by a large coercive force which is equally detrimental. Nanocrystalline single layer GMA, finally, have a small coercive force but are to a large extent superparamagnetic.³ All desirable properties of GMA films, giant magnetostriction, high Curie temperature, large saturation magnetization, and low coercive force can be obtained by preparing suitable film composites and utilizing the multilayer concept developed in the late 1990s.⁴⁻⁷ The low coercive force may be understood to be a consequence of a rotational instability which might occur when, in response to an increasing external field the magnetically hard component of the multilayer, FeTb, suddenly adapts its orientation to the one of the magnetically soft components, Fe or FeCo. In GMA films a sizable strain accompanies the evolution of the magnetization. Therefore it must be expected that the magnetic instability is accompanied by an internal friction maximum. This article, then, reports on such an internal friction maximum which occurs at the steepest part of the magnetization curve and interprets it in terms of a magnetomechanical instability.

MODELING

It has been proposed that the large and sharp damping maximum at a critical field oriented perpendicularly to the

film surface occurring in amorphous Terfenol-D single-layer films is the signature of a magnetomechanical instability.⁸ The basis of the interpretation was a model free energy consisting of the sum of the magnetostatic, magnetoelastic, and elastic energies. A similar free energy may form the basis for the modeling of a magnetomechanical instability in a double layer, the elementary constituent of multilayers. Such a free energy will consist of three terms, the magnetoelastic, magnetostatic, and elastic energies. The magnetic properties of the multilayer can be understood in terms of the average magnetization and average magnetoelastic coupling constants of the component layers.⁷ Hence a model free energy, ϕ , is given by

$$\phi(\xi, \bar{\sigma}) = -(1 + \bar{\sigma})\cos^2(\xi) - h \sin(\xi) + \frac{1}{2}j\bar{\sigma}^2. \quad (1)$$

The energy ϕ , applied stress $\bar{\sigma}$, and the compliance j , are normalized as $\Phi/(\lambda\sigma_i)$, σ/σ_i , and $J\sigma_i/\lambda$. The normalized field is given by the parameter $h = M_s H/(\lambda\sigma_i)$. The quantities λ , σ_i , M_s , and J represent the average magnetostrictive strain, internal stress, saturation magnetization, and compliance. The quantity H is the external field. No demagnetization field has been included since only in-plane magnetization is considered.

The minimum of the energy (1) is located at $\xi_0, \bar{\sigma}_0$, which are solutions of $\partial\phi/\partial\xi = \partial\phi/\partial\bar{\sigma} = 0$. The quadratic expansion of the energy $\Delta\phi(\xi, \bar{\sigma}) = \phi(\xi, \bar{\sigma}) - \phi(\xi_0, \bar{\sigma}_0)$ around this minimum is given by

$$\begin{aligned} \Delta\phi(\xi, \bar{\sigma}) = & \frac{1}{2} \frac{\partial^2 \phi}{\partial \xi^2} (\xi - \xi_0)^2 + \frac{\partial^2 \phi}{\partial \xi \partial \bar{\sigma}} (\xi - \xi_0)(\bar{\sigma} - \bar{\sigma}_0) \\ & + \frac{1}{2} \frac{\partial^2 \phi}{\partial \bar{\sigma}^2} (\bar{\sigma} - \bar{\sigma}_0)^2. \end{aligned} \quad (2)$$

The cross term can be eliminated by the transformation

$$\Xi = (\xi - \xi_0)\cos(\theta) + (\bar{\sigma} - \bar{\sigma}_0)\sin(\theta),$$

^{a)}Summer intern from Ecole des Mines d'Als.

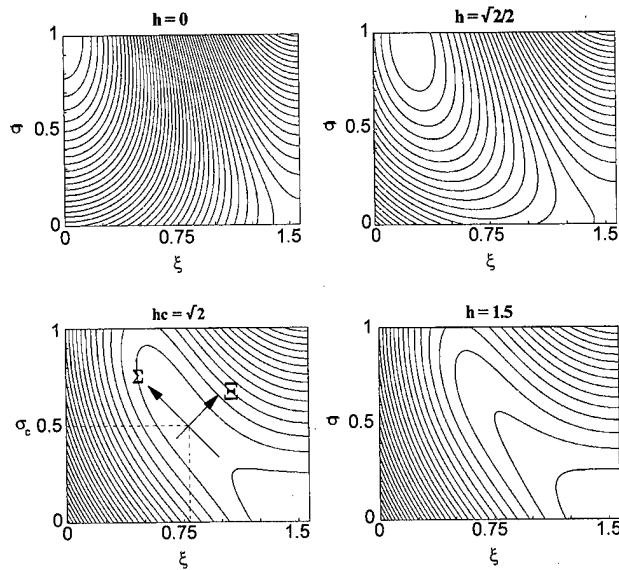


FIG. 1. Isopotential contours of the magnetomechanical potential (1) at four different values of the externally applied field h .

$$\Sigma = -(\xi - \xi_0)\sin(\theta) + (\bar{\sigma} - \bar{\sigma}_0)\cos(\theta),$$

where

$$\tan(2\theta) = \frac{2 \sin(2\xi_0)}{2(1 + \bar{\sigma}_0)\cos(2\xi_0) + h \sin(\xi_0) - j}.$$

The result of the transformation is the potential

$$\Delta\phi(\Xi, \Sigma) = \frac{\partial^2\phi}{\partial\Xi^2} \Xi^2 + \frac{\partial^2\phi}{\partial\Sigma^2} \Sigma^2, \quad (3)$$

in which the second derivatives $\partial^2\Delta\phi/\partial\Sigma^2$ and $\partial^2\Delta\phi/\partial\Xi^2$ represent the generalized magnetoelastic compliance and susceptibility. The generalized compliance becomes zero at a critical field h_c given by

$$h_c = \frac{\sin^2(2\xi_c) - 2j(1 + \bar{\sigma}_c)\cos(2\xi_c)}{j \sin(\xi_c)}, \quad (4)$$

in which equation the critical coordinates ξ_c and $\bar{\sigma}_c$ are

$$\sin(\xi_c) = \pm \sqrt{\frac{j+1}{3}}, \quad \bar{\sigma}_c = -\frac{j-2}{j},$$

$$h_c = \pm \frac{4(j+1)}{j} \sqrt{\frac{j+1}{3}}. \quad (5)$$

Isopotential lines for the potential (1) for $j=0.5$ are presented in Fig. 1 for various values of the field h . It can be seen from the figure that the two pairs ξ_0 , $\bar{\sigma}_0$ represent an extremum. At $h=h_c$ the potential displays a saddle point signaling an instability.

An expression for the internal friction as a function of the external field h can now be found. Physically, the internal friction, Q^{-1} , is the relative loss of mechanical energy, W , $\delta W/W$ per oscillatory cycle,⁹

$$2\pi Q^{-1} = \frac{\delta W}{W} = \frac{\oint \sigma d\epsilon}{1/2 J \sigma^2}. \quad (6)$$

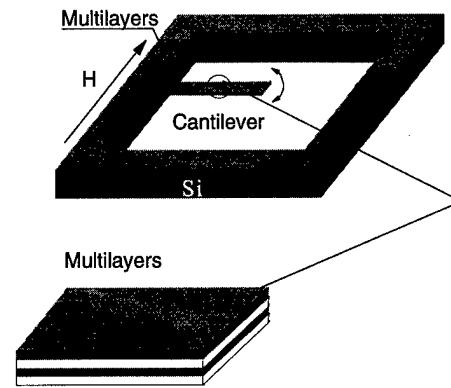


FIG. 2. Experimental schematic.

Thus in terms of the generalized magnetoelastic compliance it may be written as

$$Q^{-1}(h) \propto \left[\frac{\partial^2 \Delta\phi}{\partial \Sigma^2}(h) \right]^{-1}. \quad (7)$$

It follows that in the linear approximation of Eq. (2) $Q^{-1}(h_c) \rightarrow \infty$, i.e., a sharp maximum of the internal friction will occur as the magnetization becomes unstable with respect to the applied field.

EXPERIMENTAL RESULTS

Multilayers of the configuration (7 nm FeTb)/(8 nm Fe) were sputtered¹⁰ on micromachined Si cantilevers. The dynamic mechanical properties of the composite Si/(7 nm FeTb)/(8 nm Fe) cantilever were determined as described before.¹¹ The sample configuration is also sketched in Fig. 2. The magnetic data were taken with a vibrating sample magnetometer (VSM). All data are room-temperature data. Annealing of the cantilevers was performed in high purity argon. Figures 3 and 4 contain the key experimental results. They show that the damping displays a maximum at the field where the change of the magnetization is greatest, approxi-

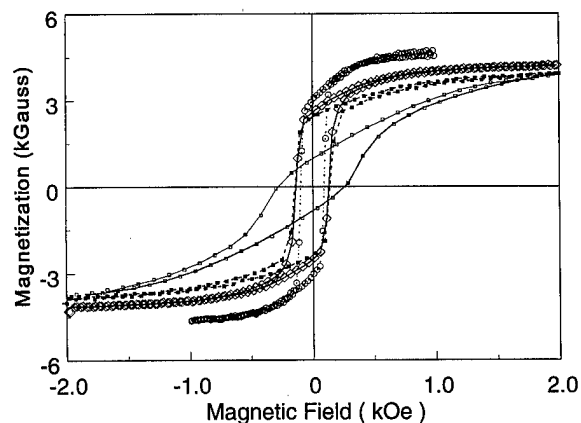


FIG. 3. Magnetization curves of the (7 nm FeTb)/(8 nm Fe) multilayers in different states of heat treatment, $\square\square\square$ as deposited, $\blacksquare\blacksquare\blacksquare$ 30 min at 171 °C, $\diamond\diamond\diamond$ additional 30 min at 220 °C, $\bullet\bullet\bullet$ additional 30 min at 270 °C.

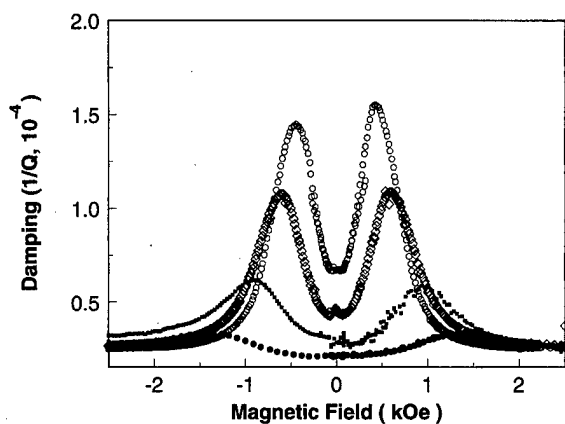


FIG. 4. Magnetomechanical damping of a Si/SiO₂/(7 nm/FeTb)/(8 nm/Fe) cantilever as a function of an externally applied field applied directed perpendicularly to the length of the cantilever and the direction of the flexural vibrations. The different states of heat treatment are, ●●● as deposited, ■■■ 30 min at 171 °C, ◇◇◇ additional 30 min at 220 °C, ○○○ additional 30 min at 270 °C.

mately the coercive field which decreases as the annealing temperature increases. The damping maximum is more pronounced in the annealed samples showing a steeper change of the magnetization. It is proposed that both phenomena are a consequence of the observed changes of the state of stress¹² upon annealing.

DISCUSSION

Generally, domain wall nucleation and motion precedes rotation of the magnetization as saturation is approached, i.e., the transition from one poled state to its opposite re-

sembles a first-order transition whereas the formalism presented above applies only to a second-order transition. This apparent difficulty can be resolved by noting that, contrary to experiments determining $m(h)$, the present internal friction experiment determines the stress-induced change of the magnetization as a function of an external biasing field. Observations of the evolution of the domain structure in the investigated multilayers as a function of the externally applied magnetic and stress fields will further clarify this point.

ACKNOWLEDGMENTS

This study was supported by the Office of Naval Research, Contract No. N00014-93-10506 and the National Science Foundation, Grant No. DMR-97-06815.

- ¹F. Schatz, M. Hirscher, M. Schnell, G. Flick, and H. Kronmüller, *J. Appl. Phys.* **76**, 189 (1994).
- ²M. Wuttig, H. Zheng, and Q. Su, *Mater. Res. Soc. Symp. Proc.* **360**, 195 (1995).
- ³C. Bailly, M.S. thesis, University of Maryland, 1997.
- ⁴J. Betz, Ph. D. thesis, Grenoble, 1997.
- ⁵E. Quandt and A. Ludwig, *Mater. Res. Soc. Symp. Proc.* **459**, 565 (1997).
- ⁶J. Betz, K. Mackay, and D. Givord, *Mater. Res. Soc. Symp. Proc.* **459**, 571 (1997).
- ⁷E. Quandt, A. Ludwig, J. Betz, K. Mackay, and D. Givord, *J. Appl. Phys.* **81**, 5420 (1997).
- ⁸M. Wuttig, Q. Su, Y. Zheng, and Y. Wen, *Appl. Phys. Lett.* **67**, 3641 (1995).
- ⁹A. S. Nowick and B. S. Berry, *An Elastic Relaxation in Crystalline Solids* (Academic, New York, 1972).
- ¹⁰E. Quandt, A. Ludwig, J. Mencik, and E. Nold, *J. Alloys Compd.* **258**, 133 (1997).
- ¹¹Q. Su, J. Morillo, Y. Wen, and Manfred Wuttig, *J. Appl. Phys.* **80**, 3604 (1996).
- ¹²E. Quandt, A. Ludwig, D. G. Lord, and C. A. Faunce, *J. Appl. Phys.* **83**, (1998), these proceedings.

Magnetic properties and microstructure of giant magnetostrictive TbFe/FeCo multilayers

E. Quandt and A. Ludwig

*Forschungszentrum Karlsruhe, Institute of Materials Research I, P.O. Box 3640,
D-76021 Karlsruhe, Germany*

D. G. Lord and C. A. Faunce

University of Salford, Department of Physics, Salford M5 4WT, United Kingdom

Magnetostrictive multilayer films which combine exchange coupled giant magnetostrictive materials (amorphous $\text{Tb}_{0.4}\text{Fe}_{0.6}$) and soft magnetic materials with large polarizations and considerable magnetostriction (crystalline $\text{Fe}_{0.5}\text{Co}_{0.5}$) were prepared by magnetron sputtering. The microstructure and the magnetic properties of these multilayers were investigated as a function of the annealing temperatures and the corresponding film stresses. Giant magnetoelastic coupling coefficients (or magnetostrictions) are achieved at low fields, due to the magnetic polarization enhancement in such multilayers, the optimized stress state, and a suitable microstructure. For these optimized $\text{Tb}_{0.4}\text{Fe}_{0.6}$ (7 nm)/ $\text{Fe}_{0.5}\text{Co}_{0.5}$ (9 nm) multilayers a saturation magnetoelastic coupling coefficient of 27.5 MPa at 20 mT and a coercive field of 2 mT has been achieved. © 1998 American Institute of Physics. [S0021-8979(98)40811-9]

I. INTRODUCTION

Interest in giant magnetostrictive thin films has rapidly grown over the past few years due to their potential as powerful transducers for microactuators. Special features of magnetostrictive thin films in comparison to other smart materials in thin film form based on piezoelectric or shape memory effects are their remote control operation, their simple actuator layout, and low temperatures during fabrication being compatible to batch fabrication processes in the field of microelectronics and microelectromechanical systems (MEMS).

Research on these magnetostrictive materials concentrates on reducing the necessary driving magnetic fields. The most prominent approaches to date have been based on amorphous films of the system Tb-Dy-Fe-Co with a total rare-earth content of 33–45 at. %.¹

An alternative, very promising approach uses the combination of these amorphous giant magnetostrictive films and a nanocrystalline soft magnetic material with very high magnetic polarization in a multilayer arrangement. Giant magnetostriction at very low driving magnetic fields has been obtained for these multilayer materials, provided that the layers are thinner than the magnetic exchange length in order to be magnetically coupled. In this case the enhanced magnetization and the reduced anisotropy due to the soft magnetic, high polarization material introduced in the multilayer structure results in a decrease of the magnetic saturation field which is proportional to the ratio of the anisotropy and the saturation magnetization.² Using this approach, magnetoelastic coupling coefficients of 20 MPa at 20 mT for TbFe/Fe and of 28 MPa at 20 mT for TbFe/FeCo multilayers are obtained.³

In this paper, the effects of annealing processes and the individual layer thicknesses of $\text{Tb}_{0.4}\text{Fe}_{0.6}/\text{Fe}_{0.5}\text{Co}_{0.5}$ multilayers on the microstructure and the film stress are discussed in view of the corresponding magnetic and magnetostrictive

properties. The TbFe/FeCo multilayer system has been chosen for this study as amorphous TbFe exhibits the highest magnetostriction in amorphous single-layer films⁴ and FeCo combines both very high magnetization and high magnetoelastic coupling coefficients due to a saturation magnetostriction of $\lambda_s = 100 \times 10^{-6}$ and an effective Young's modulus of $E/(1 + \nu) = 200$ GPa.

II. EXPERIMENTAL DETAILS

The TbFe/FeCo multilayers were magnetron sputtered onto Si {100} substrates using a modified Leybold Z 550 device with composite-type targets (75 mm \varnothing) and a rotary turntable technique in a stop- and go-mode with no intentional substrate heating. The base pressure was $< 5 \times 10^{-5}$ Pa, the Ar sputtering pressure in all experiments was 0.4 Pa. The TbFe layers were dc magnetron sputtered



FIG. 1. High-resolution TEM micrograph from an as-deposited multilayer showing the amorphous structure of the TbFe layers and the long-range lattice fringe contrast in the FeCo layers.

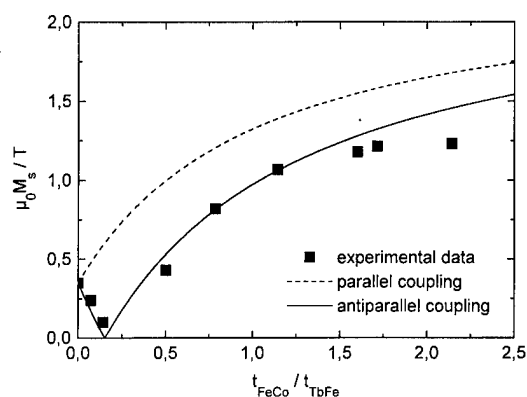


FIG. 2. Magnetic polarization of $\text{Tb}_{0.4}\text{Fe}_{0.6}/\text{Fe}_{0.5}\text{Co}_{0.5}$ multilayers as a function of the layer thickness ratio. The comparison to the theoretical behavior for spring-magnet type multilayers assuming both parallel and antiparallel coupling reveals the antiparallel coupling of the films.

with a power of 150 W and an rf bias voltage of 220 V resulting in a deposition rate of 1.8 nm/s, while the FeCo films were deposited by rf magnetron sputtering with a power of 200 W and a deposition rate of 0.3 nm/s. These sputtering conditions lead to single-layer materials with in-plane magnetic easy axes. The polarization of the amorphous TbFe and the crystalline FeCo single layers were 0.35 and 2.3 T, respectively. Within this investigation the TbFe and FeCo layer thicknesses were varied between 2–15 and 1–25 nm, respectively. The total layer number was kept constant at 141, the first and the last layer being of FeCo: Auger electron spectroscopy (AES) depth profiling has shown that the upper FeCo layer works as a protective layer against oxidation.⁵

The microstructure of the films has been investigated by transmission electron microscopy (TEM) observation using a Jeol 3010 instrument. Specimens have been prepared in cross-section geometry by a combination of mechanical dimpling and ion-beam thinning. The film stresses were calculated by measuring the difference of the curvature of uncoated and coated Si {100} substrates using a laser interferometer. Young's modulus values for the multilayers were calculated from nanoindentation measurements at different loads which have been extrapolated to zero indenta-

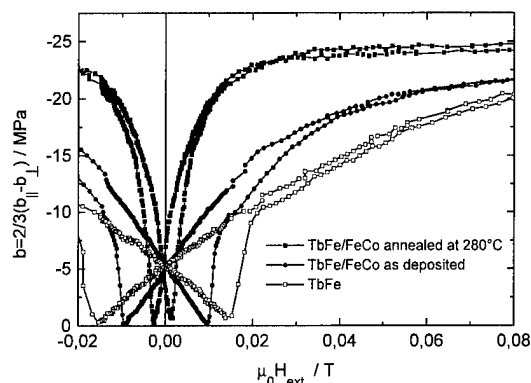


FIG. 3. Low-field magnetoelastic coupling coefficient for as-deposited and stress annealed (250 °C, 45 min) $\text{Tb}_{0.4}\text{Fe}_{0.6}$ (7 nm)/ $\text{Fe}_{0.5}\text{Co}_{0.5}$ (8 nm) multilayers in comparison to an amorphous, stress annealed (250 °C, 45 min) $\text{Tb}_{0.4}\text{Fe}_{0.6}$ single-layer film showing the significantly enhanced low-field magnetostriction especially for the stress annealed multilayer.

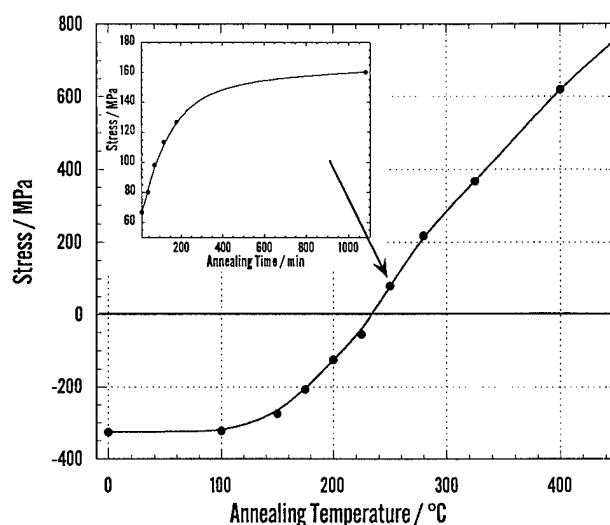


FIG. 4. Film stress for $\text{Tb}_{0.4}\text{Fe}_{0.6}$ (7 nm)/ $\text{Fe}_{0.5}\text{Co}_{0.5}$ (8 nm) multilayers as a function of the annealing temperature for an annealing time of 45 min and as a function of the annealing time for an annealing temperature of 250 °C (inset) showing the change of film stress from compressive to tensile state both with temperature and time.

tion depths in order to eliminate the substrate contribution.⁶ The magnetic properties were measured by vibrating sample magnetometry (VSM). The magnetostriction was characterized using the cantilevered substrate technique that allows the magnetoelastic coupling coefficient (b) to be determined from the bending of the substrate due to the magnetostriction (λ) in the film.⁷ The magnetoelastic coupling coefficient is defined by

$$b = \frac{-\lambda E_f}{1 + \nu_f},$$

with E_f and ν_f being the film's Young's modulus and Poisson ratio, respectively. The parameter b is, on one hand, a significant material-dependent parameter characterizing thin film bending actuators and, on the other hand, independent of the elastic data of the films.

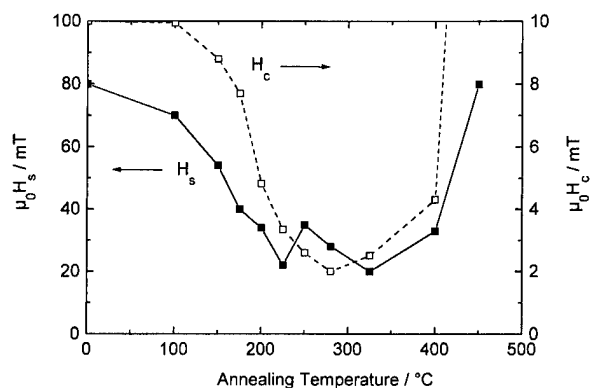


FIG. 5. Coercive ($\mu_0 H_c$) and saturation ($\mu_0 H_s$) fields for $\text{Tb}_{0.4}\text{Fe}_{0.6}$ (7 nm)/ $\text{Fe}_{0.5}\text{Co}_{0.5}$ (8 nm) multilayers as a function of the annealing temperature for an annealing time of 45 min indicating minimum values for the multilayer being annealed at 250 °C.



FIG. 6. High-resolution TEM micrograph from a multilayer being annealed at 250 °C showing the lattice fringe contrast in the FeCo layers and in some interfacial areas of the TbFe layers.

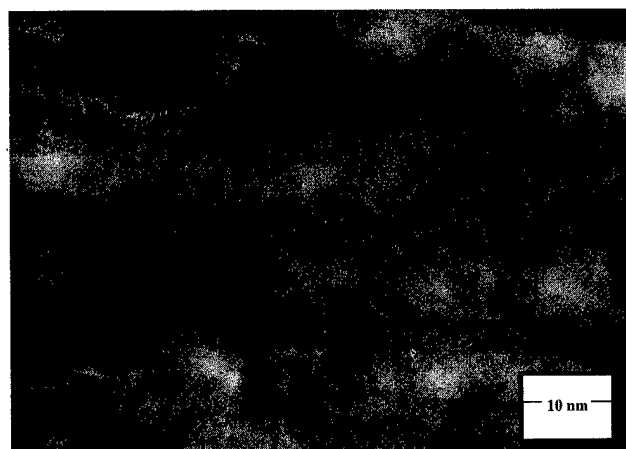


FIG. 7. High-resolution TEM micrograph from a multilayer being annealed at 450 °C showing the absence of any amorphous phase TbFe.

III. RESULTS AND DISCUSSION

The TEM micrographs of the as-deposited samples show clearly the high degree of layer periodicity and, at high magnification, contrast from lattice fringes is evident (Fig. 1). Such contrast from the FeCo layers shows that the orientations of the grains are not random but, surprisingly, exhibit only a small number of variations and some of the layers contain crystallites with a lateral extent exceeding 100 μm while the normal extent is limited by the layer thickness. The TbFe layers are mainly amorphous, though isolated areas throughout the multilayer show lattice fringe contrast suggesting nanocrystallization or local oxidation, possibly initiated during the specimen preparation. At other isolated areas there is some evidence of contrast variations associated with the interfaces between the layers, which is thought to arise from local thickness variations produced by specimen preparation.

The saturation magnetic polarization, measured as a function of the layer thicknesses, reveals the antiparallel coupling of the layers by comparison with the theoretical behavior for exchange-coupled multilayers assuming both parallel and antiparallel coupling (Fig. 2). This antiparallel coupling reflects the strong interaction and therefore parallel coupling of the transition metals in both layers, which leads to an overall antiparallel coupling due to the stronger Tb moments in the ferrimagnetic TbFe layer. Furthermore, the magnetic data show that for FeCo/TbFe layer thickness ratios higher than 0.5, the total magnetic saturation polarization can be significantly enhanced compared to the single layer film.

Figure 3 exhibits not only the enhanced low field magnetostriction of $\text{Tb}_{0.4}\text{Fe}_{0.6}$ (7 nm)/ $\text{Fe}_{0.5}\text{Co}_{0.5}$ (9 nm) multilayers in comparison to an amorphous $\text{Tb}_{0.4}\text{Fe}_{0.6}$ single-layer film but reveals also the further enhancement in low field magnetostriction of multilayers being annealed at 280 °C in order to release compressive stresses. This multilayer shows a saturation magnetoelastic coupling coefficient of 27.5 MPa with a saturation and a coercive field of 20 and 2 mT, respectively. Compared to these values the magnetoelastic

coupling coefficient of a state-of-the-art amorphous TbFe single-layer film approaches only 10 MPa in an external field of 20 mT with a coercivity of the same magnitude. The as-deposited multilayers were found to be under compressive stress (approximately -300 MPa) leading to a perpendicular anisotropy while stress annealing at approximately 240 °C results in almost stress-free films and films being annealed at higher temperatures show tensile stress up to 700 MPa (Fig. 4). As a result of the altered stress state, annealing leads to an in-plane magnetic easy axis with reduced values for the magnetic saturation and coercive fields (Fig. 5) which are both determined by field-dependent magnetostriction measurements with the external field being applied parallel or perpendicular to the long axis of the cantilever, but always parallel to the film plane. While annealing at approximately 250 °C results in an optimum in terms of low field magnetoelastic behavior, the multilayers being annealed at higher temperatures show again higher values for coercive and saturation fields. This result can be explained by the microstructure of films, which in the case of an annealing temperature not higher than 250 °C (Fig. 6) shows only small changes, indicative of the onset of crystallization in the TbFe, compared to the as-deposited sample, while a multilayer being annealed at 450 °C reveals significant interdiffusion and total absence of any amorphous phase (Fig. 7).

ACKNOWLEDGMENTS

This work was carried out as part of the E.C. funded "ECAMMA" project.

¹ See, for example, P. J. Grundy, D. G. Lord, and P. I. Williams, *J. Appl. Phys.* **76**, 7003 (1994); E. Quandt, B. Gerlach, and K. Seemann, *ibid.* **76**, 7000 (1994); N. H. Duc, K. Mackay, J. Betz, and D. Givord, *ibid.* **79**, 973 (1996).

² E. Quandt, A. Ludwig, J. Betz, K. Mackay, and D. Givord, *J. Appl. Phys.* **81**, 5420 (1997).

³ E. Quandt and A. Ludwig, *Mater. Res. Soc. Symp. Proc.* **459**, 565 (1997).

⁴ E. Quandt, *J. Alloys Compd.* **258**, 126 (1997).

⁵ E. Quandt, A. Ludwig, J. Mencik, and E. Nold, *J. Alloys Compd.* **258**, 133 (1997).

⁶ J. Mencik, E. Quandt, and D. Munz, *Thin Solid Films* **287**, 208 (1996).

⁷ E. du Trémolet de Lacheisserie and J. C. Peuzin, *J. Magn. Magn. Mater.* **136**, 189 (1994).

Magnetic properties of amorphous Sm-Fe and Sm-Fe-B thin films fabricated by radio-frequency magnetron sputtering

Y. S. Choi and S. R. Lee

Department of Materials Science and Engineering, Korea University, Seoul, Korea

S. H. Han, H. J. Kim, and S. H. Lim^{a)}

Thin Film Technology Research Center, Korea Institute of Science and Technology, Seoul, Korea

Magnetic properties of giant magnetostrictive Sm-Fe and Sm-Fe-B thin films are systematically investigated over a wide composition range from 14.1 to 71.7 at. % Sm. The amount of B added ranges from 0.3 to 0.8 at. %. The microstructure mainly consists of an amorphous phase in the intermediate Sm content range from 20 to 45 at. %. Together with an amorphous phase, crystalline phases of Fe and Sm also exist at low and high ends of the Sm content, respectively. Well-developed in-plane anisotropy is formed over the whole composition range, except for the low Sm content below 15 at. % and the high Sm content above 55 at. %. As the Sm content increases, the saturation magnetization decreases linearly and the coercive force tends to increase, with the exception of the low Sm content where very large magnitudes of the saturation magnetization and the coercive force are observed due to the existence of the crystalline α -Fe phase. The coercive force is affected rather substantially by the B addition, resulting in lower values of the coercive force in the practically important Sm content range of 30–40 at. %. © 1998 American Institute of Physics.

[S0021-8979(98)25511-3]

Magnetic properties of amorphous Sm-Fe based alloys were previously investigated by many workers: for example, by Miyazaki and co-workers for thin films prepared by an evaporation method¹ and for melt-spun ribbons;² by Honda *et al.* for thin films fabricated by rf magnetron sputtering;³ more recently, by Seqqat *et al.* for thin films of Sm-Fe and Sm-Fe-B alloys and also for melt-spun ribbons of Sm-Fe-B alloys.⁴ Except for the results of Honda *et al.*,³ however, the previous investigations are more concerned about basic magnetic properties of rare-earth-Fe alloys rather than the improvement of the magnetic softness pertinent to practical applications of giant magnetostrictive materials. The present work is performed in a way similar to that of Honda *et al.*,³ but the effects of B are additionally examined and a more systematic investigation is carried out. The effects of B on magnetic and magnetostrictive properties of Tb-Fe based thin films were recently investigated by the present authors^{5,6} and it was found that B affects magnetic properties substantially and also improves the magnetostrictive characteristics of the thin films. The effects of B on magnetostriction and other magnetic properties of Sm-Fe based alloys were previously investigated for melt-spun ribbons produced by rapid quenching⁷ and amorphous bulks fabricated by high-speed sputtering.^{8,9} However, no attempts were made so far for Sm-Fe based thin films with the magnetostrictive applications in mind. It is noted that Sm-Fe-B thin films were previously fabricated by Seqqat *et al.*,⁴ but the investigated films are not pertinent to magnetostrictive applications, since the amount of B is very high (20 at. %) and the Sm content is below 26 at. %, being below the optimum composition of 30 at. % Sm.^{3,10}

Sm-Fe and Sm-Fe-B thin films with a thickness of about 1 μm were coated by rf magnetron sputtering on Si (100) substrates. A composite target consisting of an Fe disk (4 in. in diameter) and Sm chips was used. A pure Fe disk and an Fe (99.0 at. %)-B (1.0 at. %) disk were used to fabricate Sm-Fe and Sm-Fe-B thin films, respectively. Argon was used as the sputtering gas. The sputtering pressure was varied from 1 to 10 mTorr. The other sputtering conditions used in this work were: the base pressure of below 7×10^{-7} Torr, the target-to-substrate distance of 60 mm, and the rf input power of 300 W. The film thickness was measured by using a stylus-type surface profiler. The film composition of Sm and Fe was determined by electron-probe microanalysis. The amount of B was analyzed by spectrophotometry. The degree of crystallinity was observed by x-ray diffraction with Cu $K\alpha$ radiation. Magnetic properties were measured by using a vibrating sample magnetometer with a maximum magnetic field of 15 kOe.

In our experiments, widely ranged compositions were obtained by varying both the area fraction of Sm chips and the Ar gas pressure. More specifically, several experimental runs at various Ar gas pressures were carried out at a fixed target configuration and thin films with varying compositions were then obtained. Similar experimental runs were again conducted at different target configurations, producing thin films with varying compositions. The Sm content in the thin films fabricated at a fixed target configuration is found to increase with the Ar pressure. The present Ar gas dependence of composition is similar to that observed for Tb-Fe based thin films⁵ and may be explained by the difference in the scattering of sputtered Fe and Sm particles.

All the fabricated films were checked by x-ray diffraction to examine the degree of crystallinity, and some of the diffraction results are shown in Fig. 1 for the Sm-Fe system

^{a)}Electronic mail: mmlshl@kistmail.kist.re.kr

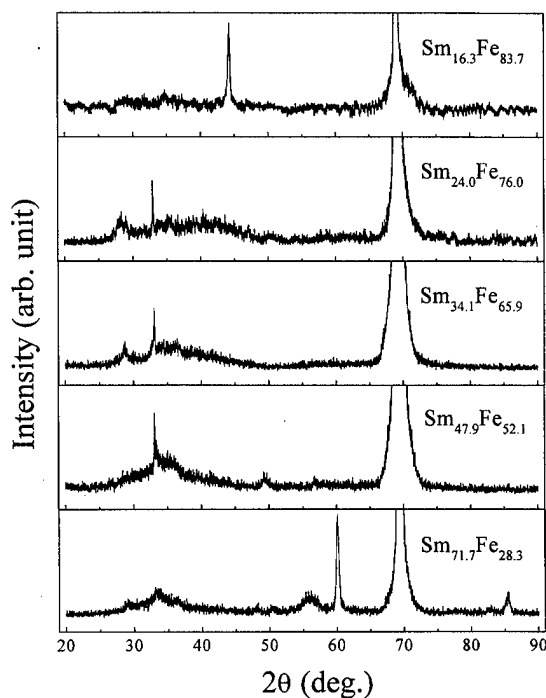


FIG. 1. The variation of x-ray diffraction patterns with Sm content for the Sm-Fe system.

over a wide composition range. The results for the Sm-Fe-B system are similar to those for the Sm-Fe system. The peaks at $2\theta = 33^\circ$ and 70° are from the Si substrate. Sharp crystalline peaks of α -Fe are clearly seen at low Sm content below ~ 20 at. %. The α -Fe peaks are slightly shifted toward a lower diffraction angle indicating a lattice expansion of the α -Fe phase. The α -Fe crystalline peaks disappear and a broad peak characteristic of an amorphous phase emerges as the Sm content exceeds ~ 20 at. %. It is of interest to note that the position of the broad maximum (in 2θ) shifts toward the lower diffraction angle as the Sm content increases. This is clearly seen for the films of $\text{Sm}_{24.0}\text{Fe}_{76.0}$ and $\text{Sm}_{34.1}\text{Fe}_{65.9}$ where broad maxima occur at $2\theta = 41^\circ$ and 35° , respectively. At a Sm content higher than 45 at. %, the microstructure consists of a mixture of an amorphous phase and the α -Sm phase. The relatively large peak below $2\theta = 30^\circ$ observed in some samples is thought to be related to a Sm oxide, possibly Sm_2O_3 .

The direction of easy magnetization is known to be an important factor for the magnetic softness of R-Fe thin films,^{5,6,11} and hence, the change in anisotropy is investigated as a function of the composition. The distribution of magnetic anisotropy is investigated by examining hysteresis loops measured in the in-plane and the direction perpendicular to the film plane. Some results for these hysteresis loops are shown in Figs. 2(a)–2(d). Corrections with regard to demagnetizing fields are not made, so the loops shown in the figures are more squared than the “true” ones and, due to a larger demagnetizing field for a perpendicular loop, the degree of squareness of a perpendicular loop is expected to be larger. For the films with a similar Sm content, no noticeable difference in the direction of easy magnetization is observed with the addition of B, except for the films with low Sm

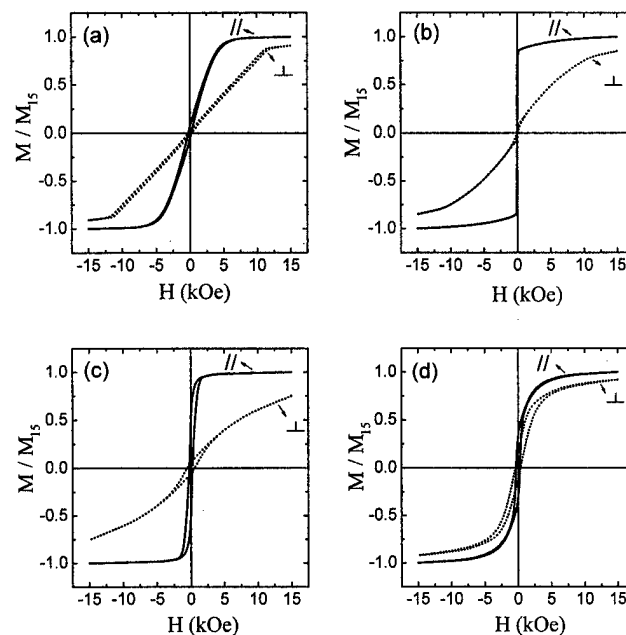


FIG. 2. The variation of the shape of M - H hysteresis with Sm content for alloys of (a) $\text{Sm}_{15.2}\text{Fe}_{84.0}\text{B}_{0.8}$, (b) $\text{Sm}_{25.8}\text{Fe}_{73.5}\text{B}_{0.7}$, (c) $\text{Sm}_{36.9}\text{Fe}_{62.5}\text{B}_{0.6}$, and (d) $\text{Sm}_{68.4}\text{Fe}_{31.3}\text{B}_{0.3}$. Two hysteresis loops are shown for each sample, one measured by applying magnetic fields in the in-plane direction and the other in the perpendicular direction.

content where the α -Fe phase exists. In this low Sm content range, both B-free and B containing films exhibit in-plane anisotropy but better in-plane anisotropy is observed for B added films. Also, at this low Sm content, the shape of hysteresis loops measured in the in-plane direction is inclined substantially. This is indicated by low magnitudes (below 0.1) of the remanence ratio, the results of which are shown in Fig. 3(a) as a function of the composition. The remanence ratio is defined as M_r/M_{15} , where M_r is the remanent magnetization and M_{15} the magnetization at 15 kOe. In the composition range from 20 to 55 at. % Sm, well-developed in-plane anisotropy is formed and hysteresis loops are highly squared with the remanence ratio of most thin films being greater than 0.6 [Fig. 3(a)]. No substantial anisotropy is observed at a Sm content higher than 55 at. %; no substantial difference being noted in the shape of hysteresis loops measured in the in-plane and perpendicular directions. Intermediate magnitudes of the remanence ratio (0.29–0.40) are seen at this high Sm content. Anisotropy is little affected by the B addition and this behavior is in contrast with that observed in Tb-Fe based thin films where anisotropy is greatly influenced by the presence of B.⁵ Ferromagnetic behavior is observed to exist in the present Sm content range (up to 71.7 at. %). This behavior is to be compared with that observed in Tb-Fe based thin films where superparamagnetic behavior appears as the rare-earth content exceeds ~ 66 at. %.⁵

The results for M_{15} and the coercive force are shown, respectively, in Figs. 3(b) and 3(c) as a function of the composition. Since most of the present thin films saturate at a magnetic field well below 15 kOe, M_{15} is practically identical to the saturation magnetization. The coercive force (H_c) is obtained by applying the maximum magnetic field of 15

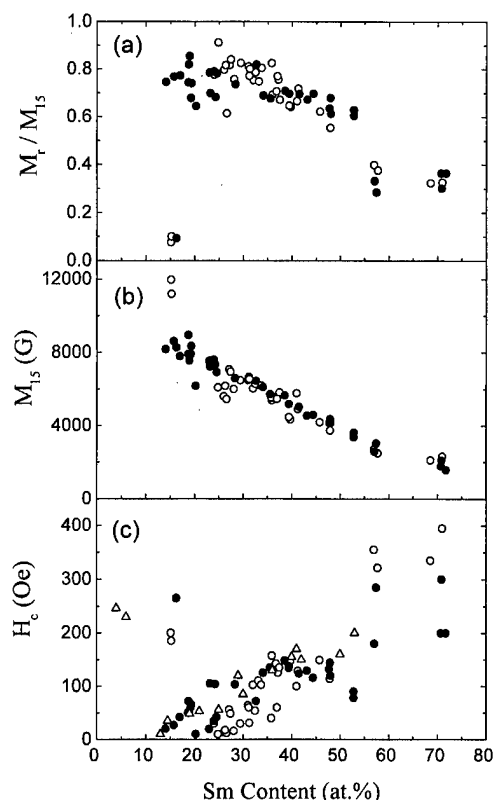


FIG. 3. The value of (a) the remanence ratio (M_r/M_{15}), (b) saturation magnetization (M_{15}), and (c) coercive force (H_c) as a function of Sm content. The results of Sm-Fe thin films are indicated by filled circles and those of Sm-Fe-B thin films by unfilled circles. In the case of H_c , the results of Honda *et al.* (Ref. 3) for Sm-Fe thin films (indicated by triangles) are also shown for comparison.

kOe. The results are obtained from the hysteresis loops measured in the in-plane direction. In the case of the coercive force, the results of Honda *et al.*³ obtained for Sm-Fe thin films are also shown in Fig. 3(c) for comparison.

Except for very low Sm content where the α -Fe phase exists, the saturation magnetization decreases nearly linearly from 8950 to 1580 G as the Sm content increases from 14.1 to 71.7 at. %. Again, no substantial difference in the saturation magnetization is seen with the B addition and this is compared with relatively large reduction in Tb-Fe based thin films by the B addition.⁵ As can be expected from the ferromagnetic coupling between Sm and Fe (note that Sm is a light rare-earth element), no compensation composition is observed. The linear dependence of the magnetization may indicate that the total magnetization of the alloy is simply an arithmetic sum of Fe and Sm elements, the magnetic moment of Fe being larger than that of Sm.⁴ Of course, the relation of the arithmetic sum will hold only in the composition range where no paramagnetic α -Sm precipitates exist. It is estimated from the extrapolation of the present data that the magnetization reaches zero at ~ 85 at. % Sm. The extraordinarily large magnitude of M_{15} at the low end of the Sm content is due to the formation of the α -Fe phase with a large magnetic moment.

The magnitude of H_c is large for the thin films with the α -Fe phase, but, with the disappearance of the crystalline phase, the value of H_c is reduced significantly to 10 Oe. This may be because intrinsic magnetocrystalline anisotropy is effectively reduced by the formation of an amorphous phase. The value of H_c tends to increase with increasing Sm content. This can be expected from the larger anisotropy of Sm than that of the Fe element. It may be noted, however that in the case of binary Sm-Fe thin films, a closer examination shows a tendency of a broad maximum in the H_c -Sm content plots at a Sm content of 40 at. % when the data of the thin films with well-developed in-plane anisotropy are taken into account. A similar result was previously reported by Miyazaki *et al.* for melt-spun Sm-Fe ribbons.² The coercive force of Sm-Fe thin films was also investigated by Honda *et al.*³ but with a paucity of data and a large data scattering at the Sm content of 50 at. %, the tendency of the coercive force as a function of the composition cannot be drawn. Unlike the other magnetic properties, the coercive force is affected rather substantially by the addition of B; the H_c -Sm content plot is shifted toward higher Sm content with the B addition. This results in lower values of the coercive force of B containing thin films in the practically important Sm content range of 30–40 at. % where optimum magnetostrictive characteristics are observed.^{3,10} Since the coercive force is closely related to magnetostrictive characteristics at low magnetic fields, low-field magnetostrictive characteristics are improved by the addition of B.¹⁰ As can be seen in Fig. 3(c), at a Sm content below 40 at. %, the present values of H_c of the Sm-Fe thin films are in fair agreement with those reported by Honda *et al.*³ At a Sm content higher than 40 at. %, however, our values are lower than the reported ones. Magnetostrictive properties of the present thin films are found to be very good, particularly at low magnetic fields, and these magnetostrictive results will be published elsewhere.¹⁰

¹T. Miyazaki, K. Hayashi, T. Otaki, M. Takahashi, and T. Shimamori, J. Magn. Magn. Mater. **71**, 83 (1987).

²T. Miyazaki, X. Yang, K. Takakura, and M. Takahashi, J. Magn. Magn. Mater. **60**, 211 (1986).

³T. Honda, Y. Hayashi, K. I. Arai, K. Ishiyama, and M. Yamaguchi, IEEE Trans. Magn. **29**, 3126 (1993).

⁴M. Seqqat, M. Nogues, O. Crisan, V. Kuncser, L. Cristea, A. Jianu, G. Filoti, J. L. Dormann, D. Sayah, and M. Godinho, J. Magn. Magn. Mater. **157/158**, 225 (1996).

⁵Y. S. Choi, S. R. Lee, S. H. Han, H. J. Kim, and S. H. Lim, J. Alloys Compd. **258**, 155 (1997).

⁶S. H. Lim, Y. S. Choi, S. H. Han, H. J. Kim, T. Shima, and H. Fujimori, IEEE Trans. Magn. **33**, 3940 (1997).

⁷S. R. Kim and S. H. Lim, J. Alloys Compd. **258**, 163 (1997).

⁸H. Fujimori, J. Y. Kim, S. Suzuki, H. Morita, and N. Kataoka, J. Magn. Magn. Mater. **124**, 115 (1993).

⁹J.-Y. Kim, J. Appl. Phys. **74**, 2701 (1993).

¹⁰S. H. Lim, Y. S. Choi, S. H. Han, H. J. Kim, T. Shima, and H. Fujimori (unpublished).

¹¹E. Quandt, J. Appl. Phys. **75**, 5653 (1994).

Application of the ratio $\Delta\lambda/\Delta M$ to giant magnetostrictive materials in the $\langle 110 \rangle$ easy regime

S. C. Busbridge and A. R. Piercy

Department of Mechanical and Manufacturing Engineering, University of Brighton, Brighton BN2 4GJ, United Kingdom

The parameter $\Delta\lambda/\Delta M$ is a useful tool for investigating the magnetization process in magnetostrictive materials. This work extends the use of this parameter from that previously explored in the $\langle 100 \rangle$ and $\langle 111 \rangle$ easy regimes to the $\langle 110 \rangle$ easy regime. Theoretical values of $\Delta\lambda/\Delta M$ are presented for all possible domain wall motions that produce an increase in magnetization. In the $\langle 110 \rangle$ easy regime, $\Delta\lambda/\Delta M$ has contributions from both λ_{100} and λ_{111} , but for practical purposes it is only necessary to consider the latter for the C15 phase giant magnetostrictive materials, because $\lambda_{111} \gg \lambda_{100}$. Under such conditions there are 61 different wall motions but only four (nonzero) values for $\Delta\lambda/\Delta M$. We have obtained the theoretically generated magnetostrain versus magnetization curve, derived from a model of distinct domain wall motions with successively higher values of $\Delta\lambda/\Delta M$. It is shown that this curve is a good fit to the experimental magnetostrain versus magnetization curve obtained for $\text{Tb}_{0.1}\text{Ho}_{0.9}\text{Fe}_{1.9}$, measured at intervals over the temperature range 213–373 K. Since it is known that equivalent theoretical curves in the $\langle 100 \rangle$ and $\langle 111 \rangle$ easy regimes model the magnetization process well, and that $\text{Tb}_x\text{Ho}_{1-x}\text{Fe}_{1.9}$ ($0 < x < 0.2$) undergoes a spin reorientation from $\langle 111 \rangle$ to $\langle 110 \rangle$ at approximately 260 K, and then to $\langle 100 \rangle$ as the temperature is reduced further, we conclude that $\Delta\lambda/\Delta M$ may be used in the $\langle 110 \rangle$ easy regime. However, the large number of wall motions makes it more difficult to identify any particular motion. © 1998 American Institute of Physics. [S0021-8979(98)40911-3]

INTRODUCTION

The ratio of the change in magnetostriction to the change in magnetization, $\Delta\lambda/\Delta M$ is a useful parameter with which to probe the magnetization process in magnetostrictive materials. An understanding of the magnetization process is important to the further improvement of device grade material.^{1,2} This article extends the use of this parameter from that previously explored in the $\langle 100 \rangle$ and $\langle 111 \rangle$ easy regimes³ to the $\langle 110 \rangle$ easy regime.

The $\langle 110 \rangle$ easy regime is relatively unusual, but it does occur under certain conditions in the $\text{Ra}_x\text{Rb}_{1-x}\text{Fe}_2$ (Ra, Rb=rare-earth elements) system.⁴ Under such conditions, the usual two-term anisotropy model is adequate provided that $-\frac{4}{9}K_1 < K_2 < 0$.

THEORETICAL BASIS FOR $\Delta\lambda/\Delta M$

A domain wall moving through a volume fraction f of the sample will give rise to a change in magnetization ΔM :

$$\Delta M = fM_s(\cos \theta_2 - \cos \theta_1), \quad (1)$$

where M_s is the saturation magnetization and θ_2 and θ_1 are the directions of the magnetization in each domain either side of the moving wall with respect to the measurement direction 0. Thus

$$\cos \theta_2 = (l_2 l_0 + m_2 m_0 + n_2 n_0) \quad (2)$$

and similarly for $\cos \theta_1$, where l , m , and n are the direction cosines. The change in strain $\Delta\lambda$ is given by

$$\Delta\lambda = f(\lambda_{2,0} - \lambda_{1,0}), \quad (3)$$

where $\lambda_{2,0}$ and $\lambda_{1,0}$ are the magnetostrains measured in direction 0 when the magnetization lies in directions 2 and 1, respectively. Hence

$$\lambda_{2,0} = \left(\frac{3\lambda_{100}}{2} \right) \left(l_2^2 l_0^2 + m_2^2 m_0^2 + n_2^2 n_0^2 - \frac{1}{3} \right) + 3\lambda_{111}(l_2 m_2 l_0 m_0 + m_2 n_2 m_0 n_0 + n_2 l_2 n_0 l_0) \quad (4)$$

and similarly for $\lambda_{1,0}$. The normalized value of $\Delta\lambda/\Delta M$ is therefore intrinsic to the magnetization process in that it is dependent only on the change of direction of the magnetization and the resultant change in strain. In the case of domain wall motion, $\Delta\lambda/\Delta M$ will take a unique value, for each type of wall motion, in terms of the ratios of the constants λ_{111}/M_s and λ_{100}/M_s . For the $\langle 111 \rangle$ easy regime the contribution of λ_{100}/M_s to $\Delta\lambda/\Delta M$ is always zero, and for the $\langle 100 \rangle$ regime the contribution of λ_{111}/M_s to $\Delta\lambda/\Delta M$ is always zero. In the $\langle 110 \rangle$ easy regime, the value of $\Delta\lambda/\Delta M$ will, in general, consist of contributions from both λ_{111}/M_s and λ_{100}/M_s . In the case of magnetic rotation, $\Delta\lambda/\Delta M$ will generally be a function of M and depend on the direction of rotation of M_s , again with contributions from both λ_{111}/M_s and λ_{100}/M_s . When considering dynamic changes in magnetization⁵ the equivalent parameter is d/χ , because $d = \Delta\lambda/\Delta H$ and $\chi = \Delta M/\Delta H$. We have previously shown that the quasistatic and dynamic magnetization processes are likely to be the same in the $\langle 111 \rangle$ and $\langle 100 \rangle$ regimes.⁶ A more detailed comparison of $\Delta\lambda/\Delta M$ and d/χ as functions of M/M_s suggests that this conclusion also holds true in the $\langle 110 \rangle$ easy regime.

TABLE I. Values of $\Delta\lambda/\Delta M = A(\lambda_{100}/M_s) + B(\lambda_{111}/M_s)$ for all possible wall motions in the $\langle 110 \rangle$ easy regime.

Wall type	$\theta_2 \rightarrow \theta_1$	No. of walls	Example	A	B
180°	125.3° → 55.7°	1	$[\bar{1}\bar{1}0] \rightarrow [110]$	0	0
	150.0° → 30.0°	2	$[\bar{1}0\bar{1}] \rightarrow [101]$	0	0
	106.8° → 73.2°	2	$[10\bar{1}] \rightarrow [\bar{1}01]$	0	0
120°	150.0° → 54.7°	2	$[\bar{1}0\bar{1}] \rightarrow [110]$	-0.260	-0.173
	73.2° → 54.7°	2	$[\bar{1}01] \rightarrow [110]$	-1.299	+2.598
	125.3° → 30.0°	2	$[\bar{1}\bar{1}0] \rightarrow [101]$	+0.260	+0.173
	150.0° → 30.0°	2	$[0\bar{1}\bar{1}] \rightarrow [101]$	0	0
	90.0° → 30.0°	2	$[\bar{1}10] \rightarrow [101]$	+0.433	+0.866
	106.8° → 30.0°	2	$[01\bar{1}] \rightarrow [101]$	0	+0.866
	150.0° → 90.0°	2	$[0\bar{1}\bar{1}] \rightarrow [\bar{1}10]$	-0.433	-0.866
	106.8° → 90.0°	2	$[10\bar{1}] \rightarrow [\bar{1}10]$	-1.299	+0.866
	150.0° → 73.2°	2	$[0\bar{1}\bar{1}] \rightarrow [\bar{1}01]$	0	-0.866
	90.0° → 73.2°	2	$[\bar{1}\bar{1}0] \rightarrow [\bar{1}01]$	+1.299	-0.866
	106.8° → 73.2°	2	$[01\bar{1}] \rightarrow [\bar{1}01]$	0	0
	125.3° → 106.8°	2	$[\bar{1}\bar{1}0] \rightarrow [10\bar{1}]$	+1.299	-2.598
90°	90.0° → 54.7°	2	$[\bar{1}\bar{1}0] \rightarrow [110]$	0	+0.866
	73.2° → 30.0°	2	$[\bar{1}01] \rightarrow [101]$	0	+1.732
	106.8° → 30.0°	2	$[10\bar{1}] \rightarrow [101]$	0	+0.866
	125.3° → 90.0°	2	$[\bar{1}\bar{1}0] \rightarrow [\bar{1}10]$	0	-0.866
	150.0° → 73.2°	2	$[\bar{1}01] \rightarrow [\bar{1}01]$	0	-0.866
	150.0° → 106.8°	2	$[\bar{1}01] \rightarrow [10\bar{1}]$	0	-1.732
60°	106.8° → 54.7°	2	$[10\bar{1}] \rightarrow [110]$	-0.433	+0.866
	90.0° → 30.0°	2	$[\bar{1}\bar{1}0] \rightarrow [101]$	+0.433	+0.866
	73.2° → 30.0°	2	$[0\bar{1}\bar{1}] \rightarrow [101]$	0	+1.732
	54.7° → 30.0°	2	$[110] \rightarrow [101]$	+1.299	+0.866
	150.0° → 90.0°	2	$[\bar{1}0\bar{1}] \rightarrow [\bar{1}10]$	-0.433	+0.866
	106.8° → 90.0°	2	$[01\bar{1}] \rightarrow [\bar{1}10]$	-1.299	+0.866
	125.3° → 73.2°	2	$[\bar{1}\bar{1}0] \rightarrow [\bar{1}01]$	+0.433	-0.866
	90.0° → 73.2°	2	$[\bar{1}\bar{1}0] \rightarrow [\bar{1}01]$	+1.299	-0.866
	150.0° → 106.8°	2	$[01\bar{1}] \rightarrow [10\bar{1}]$	0	-1.732
	150.0° → 125.3°	2	$[\bar{1}01] \rightarrow [\bar{1}10]$	-1.299	-0.866

When considering the possible values for $\Delta\lambda/\Delta M$, it is only necessary to consider those magnetization processes that give rise to a positive value for ΔM . Most of the values for $\Delta\lambda/\Delta M$ so generated are positive (for positive magnetostriction constants), although negative values are also generated. Experimental evidence suggests that negative values of $\Delta\lambda/\Delta M$ are not generally observed. A negative value of $\Delta\lambda/\Delta M$ would require a decrease in magnetostriction to accompany an increase in magnetization. Although this is possible (the magnetostriction is an even power function of the magnetization) it appears not to be energetically favorable. In essence the magnetization drives the magnetostriction with increases in the value of $\cos \phi$ (ϕ being the angle between M_s and H) being magnetostatically inefficient.

In the $\langle 100 \rangle$ easy regime the possible values for $\Delta\lambda/\Delta M$ are (in units of λ_{100}/M_s) 0, 0.612, and 1.837. A value of -0.612 is also possible. In the $\langle 111 \rangle$ easy regime the possible values are (in units of λ_{111}/M_s) 0, 0.707, 1.414, and 2.123. Negative values for each of these are also possible. In the $\langle 110 \rangle$ easy regime there is a total of 132 possible different wall motions (12 are 180°, 48 are 120°, 24 are 90°, and 48 are 60°) and of these, 61 give rise to a positive value for

ΔM . The corresponding different values for $\Delta\lambda/\Delta M = A(\lambda_{100}/M_s) + B(\lambda_{111}/M_s)$ are given in Table I, together with the type and equivalent number of wall motions. In all cases it is assumed that the measurement and magnetization directions are $[112]$.

Although there is a large number of different wall motions, for practical purposes it is only necessary to consider the values of B for the giant magnetostrictive rare-earth iron materials, since $\lambda_{111} \gg \lambda_{100}$ (even though this may be true, it is necessary to consider λ_{100} in the $\langle 100 \rangle$ easy regime, because the contribution to $\Delta\lambda/\Delta M$ from λ_{111}/M_s is always zero). There are therefore only five different non-negative values of $\delta\lambda/\Delta M$ (0, 0.173, 0.866, 1.732, and 2.598).

According to torque measurements made by Koon *et al.* on single crystals, $\text{Tb}_x\text{Ho}_{1-x}\text{Fe}_2$ ($0 < x < 0.20$) undergoes a spin re-orientation from $\langle 111 \rangle$ to $\langle 110 \rangle$ just below room temperature as the composition is made more Ho rich.⁷ When $x=0.1$ the spin reorientation is close to 260 K. Cooling below this temperature and/or a reduction in the value of x brings about a gradual shift in the easy direction of magnetization towards $\langle 100 \rangle$.

Figure 1 shows normalized magnetostrain versus magne-

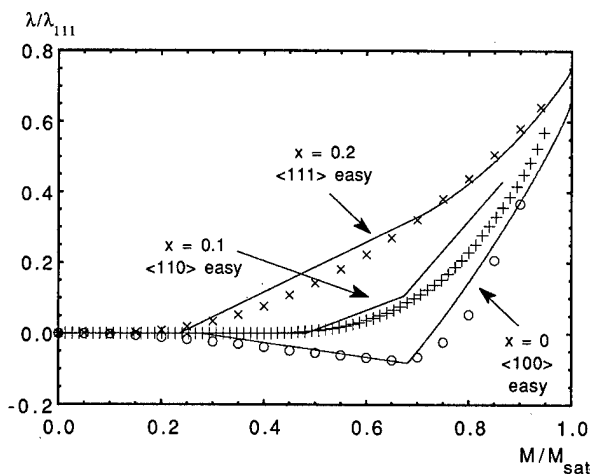


FIG. 1. Normalized strain versus normalized magnetization for $\text{Tb}_x\text{Ho}_{1-x}\text{Fe}_{1.9}$. The points are experimental data and the lines are theoretically derived from $\Delta\lambda/\Delta M$. For each easy axis regime the strain has been normalized to the appropriate value of λ_{111} .

tization measurements for $\text{Tb}_x\text{Ho}_{1-x}\text{Fe}_{1.9}$ ($x=0, 0.1$, and 0.2) obtained at a temperature of 260 K. The magnetostrain was measured with a strain gauge and the magnetization by a two-coil induction technique. Similar curves are obtained for $x=0.1$ over the temperature range 170–370 K. The solid lines represent possible theoretical magnetization processes for the $\langle 100 \rangle$, $\langle 110 \rangle$, and $\langle 111 \rangle$ easy regimes obtained from values of $\Delta\lambda/\Delta M$. In all three regimes the initial demagnetized state is assumed to be one in which all equivalent easy directions are equally populated. The magnetization is postulated to proceed by domain wall motions with the lowest possible values of $\Delta\lambda/\Delta M$, each process being completely exhausted before moving onto wall motions with successively higher values of $\Delta\lambda/\Delta M$. The total magnetization and total strain are treated as cumulative summations of the contributions from the individual wall motions. Rotation must be included to describe the final approach to saturation.

The theoretical curves follow the general change in shape of the experimental curves, as the direction of the easy axis is varied. This substantiates a correlation between the observed strain versus magnetization curve and the theoretical plot predicted from the values of $\Delta\lambda/\Delta M$ in each of the easy axis regimes. It should be noted, however, that the results from torque measurements and from Mossbauer studies do not entirely agree with each other in the transition region, and that the alternative transition from $\langle 111 \rangle$ to $\langle 100 \rangle$ via $\langle 1uu \rangle$ ($0 < u < 1$) proposed by Altzmony and Dariel⁸ is also well described by the theoretical magnetization processes shown in Fig. 1.

DISCUSSION

The parameter $\Delta\lambda/\Delta M$ is a useful tool for investigating the magnetization process in magnetostrictive materials, and gives a good fit to experimentally obtained data in the $\langle 100 \rangle$ and $\langle 111 \rangle$ easy regimes.

However, in the $\langle 110 \rangle$ easy regime the method has become insensitive to the precise direction of the easy axis, because the large number of possible wall motions permits a greater number of plausible theoretical magnetostriction versus magnetization curves to be postulated. Unless it is possible to identify a single domain wall motion process, it will always be possible to find more than one theoretical magnetization process to fit a given set of experimental data.

¹D. C. Jiles and J. B. Thoeke, *J. Magn. Magn. Mater.* **134**, 143 (1994).

²R. D. James and D. Kinderlehrer, *Philos. Mag. B* **68**, 237 (1993).

³A. R. Piercy, S. C. Busbridge, and D. Kendall, *J. Appl. Phys.* **76**, 7006 (1994).

⁴U. Atzmony and M. P. Dariel, *Phys. Rev. B* **13**, 4006 (1976).

⁵S. C. Busbridge and A. R. Piercy, *J. Magn. Magn. Mater.* **140–144**, 817 (1995).

⁶D. Kendall and A. R. Piercy, *IEEE Trans. Magn.* **26**, 1837 (1990).

⁷N. C. Koon, C. M. Williams, and B. N. Das, *J. Magn. Magn. Mater.* **100**, 173 (1991).

⁸U. Atzmony *et al.*, *Phys. Rev. Lett.* **28**, 244 (1972).

Magnetostriction and susceptibilities of twinned single crystals of Terfenol-D

X. G. Zhao^{a)} and D. G. Lord

Joule Laboratory, Department of Physics, University of Salford, Salford M5 4WT, United Kingdom

Measurements are presented of the dc magnetostriction, and both the ac and dc susceptibility along the three orthogonal axes of $[11\bar{2}]$, $[111]$, and $[1\bar{1}0]$ from twinned single crystals of Terfenol-D as a function of varying compressive stress and magnetic field mutually applied along the $[11\bar{2}]$ rod axis. The data are used in an attempt to analyze the magnetization processes occurring in such a specimen. The experimental results show clearly the two characteristics of the magnetization process corresponding to (i) the magnetostrictive “jump” effect, and (ii) the slow changes of magnetostriction occurring above the “jump.” It is estimated that in stage (i) of the magnetization process, the domains aligned along the $[111]$ axis by the applied stress rapidly and massively redistribute their moments both to the $[111]$ direction closest to the applied field as well as to the $[\bar{1}\bar{1}\bar{1}]$ and $[1\bar{1}\bar{1}]$ directions; and during stage (ii), the domains occupying the $[\bar{1}\bar{1}\bar{1}]$ and $[1\bar{1}\bar{1}]$ directions redistribute to the $[111]$ successively by non- 180° domain-wall motion. However, two fine magnetization processes are found in the field range of the jump effect indicating that some domains must redistribute from the $[111]$ to the $[\bar{1}\bar{1}\bar{1}]$ and $[1\bar{1}\bar{1}]$ initially, then to the $[111]$ even when the field is only increased in the initial stage (i). The nonzero susceptibilities measured along the $[111]$ and $[1\bar{1}0]$ suggest that both the volumes of parent and twin material as well as the probabilities for domain redistribution from one easy direction to the $[\bar{1}\bar{1}\bar{1}]$ and $[1\bar{1}\bar{1}]$ might be different. © 1998 American Institute of Physics. [S0021-8979(98)25611-8]

I. INTRODUCTION

Giant magnetostrictive $\text{Tb}_{0.3}\text{Dy}_{0.7}\text{Fe}_2$, known as Terfenol-D, is of significant interest technologically for actuator and transducer applications. Commercially available material, grown by a free-standing zone (FSZ) technique, is normally composed of dendritic plates which often contain single or multiple crystallographic twins with a common (111) plane. Such materials exhibit significant magnetoelastic strain,^{1,2} the evolution of which is characterized by discontinuous strain changes, known as “jump” or “burst” effects, which occur at particular values of applied field. It was initially thought such jumps were the result of magnetization rotation from other easy directions to that closest to the applied field. However, numerous experimental investigations by Teter *et al.*³ and other authors^{4–9} have shown the dendritic and twin structure of Terfenol-D make the magnetization process much more complicated, and infer that there must be various processes involved, including domain-wall movement, and not only the one domain rotation process.

In this paper, measurements of the dc magnetostriction, and both the ac and dc susceptibility along the three orthogonal axes of $[11\bar{2}]$, $[111]$, and $[1\bar{1}0]$ (as shown in Fig. 1) are presented from twinned single crystals of Terfenol-D as a function of varying compressive stress and magnetic field mutually applied along the $[11\bar{2}]$ rod axis. The data are used in an attempt to analyze the magnetization processes occurring in such a specimen.

II. EXPERIMENTAL DETAILS

Samples of 54 mm in length along the $[11\bar{2}]$ growth direction were obtained from 7.7 mm diam rods prepared by Edge Technologies, Inc. by a FSZ technique, and were metallographically checked to be twinned single crystals. Each rod was supported in an assembly containing three pairs of mutually orthogonal pick-up coils. Differential magnetic susceptibility data were obtained by subjecting the rod specimens to a dc and superimposed ac magnetic field directed along the $[11\bar{2}]$ rod axis. The ac ripple field, of frequency 77 Hz and of 4 Oe in amplitude, was held constant while a lock-in amplifier was used to detect the signals induced in the coils. The magnetization along the $[11\bar{2}]$ was determined by a flux meter. Magnetostriction measurements were made

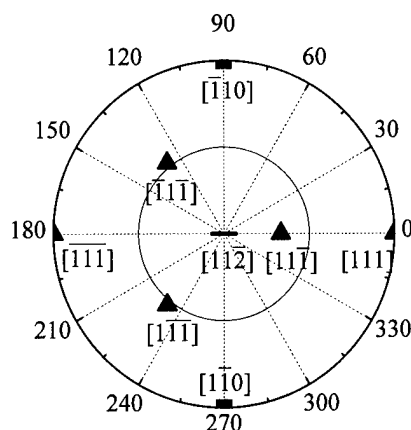


FIG. 1. The polar projection of principal crystallographic axes of Terfenol-D in the $(11\bar{2})$ plane.

^{a)}Electronic mail: x.zhao@physics.salford.ac.uk

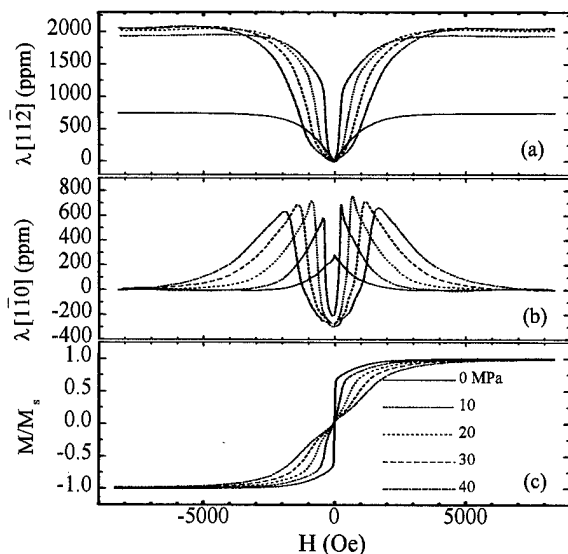


FIG. 2. The field dependencies of (a) $\lambda[112]$, (b) $\lambda[110]$, and (c) $M[112]$ for different values of applied stress.

using standard strain gauge techniques. The compressive stress was applied to the ends of the rod by a pair of modified electromagnet pole pieces, in one of which a piston could be driven by compressed air. All measurements were carried out at ambient temperature and with closed magnetic circuits. For all the data described here, the applied field was swept from +8000 to -8000 Oe.

III. RESULTS AND DISCUSSION

The field dependencies of magnetostrictions along the $[112]$ and $[110]$ directions and magnetization along the $[112]$, named $\lambda[112]$, $\lambda[110]$, and $M[112]$, respectively, are shown in Fig. 2 for different values of applied stress. With zero stress applied, the material shows a small saturation value of $\lambda[112]$ of about 750×10^{-6} . It is clear from considering $\lambda[112]$ and $M[112]$ that 180° domain-wall motions dominate the magnetization process near zero field. However, when a 10 MPa compressive stress is applied to the specimen, a "jump" effect occurs at a particular field, the "jump" field, of about 250 Oe. When this initial "jump" is completed, the measured magnetostrictions reach relatively high values of about 1100×10^{-6} for $\lambda[112]$ and 800×10^{-6} for $\lambda[110]$. Further increases in applied field result in the magnetostrictions changing slowly in a manner analogous to that pertaining to the zero stress situation. When the applied stress is increased further, there is only a small influence on the saturation value of $\lambda[112]$, but the "jump" field increases to higher values. The curves seem to be shifted to the higher fields as a whole, especially for the portion associated with the slow variations occurring above the "jump" field. This characteristic of the slow change in magnetostriction towards saturation has been observed in all available twinned crystals of Terfenol-D.

It is reasonable to suppose that the magnetization process can be simply divided into two stages which correspond to (i) the magnetostrictive "jump" effect, and to (ii) the slow changes of magnetostriction occurring above the "jump."

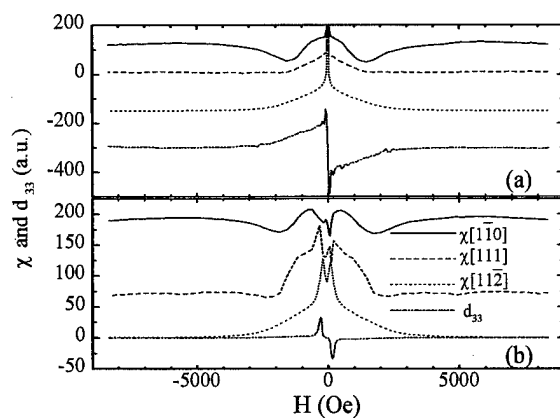


FIG. 3. The field dependency of the ac susceptibilities $\chi[112]$, $\chi[111]$, and $\chi[110]$ as well as that of quasistatic d_{33} , for different values of applied stress: (a) zero and (b) 10 MPa.

Referring to Fig. 1, the experimental results indicate that in stage (i) of the magnetization process, the domains aligned along the $[111]$ axis by the applied stress rapidly and massively redistribute their moments both to the $[111]$ direction that is closest to the applied field as well as to the $[1\bar{1}\bar{1}]$ and $[11\bar{1}]$ directions. During stage (ii), the domains having magnetizations occupying the $[11\bar{1}]$ and $[1\bar{1}\bar{1}]$ directions redistribute their moments to the $[111]$ successively by non- 180° domain-wall motion. The large demagnetization factor along the $[111]$ axis, resulting from the platelike microstructure of the twinned crystals, is thought to be responsible for the characteristic strain behavior exhibited in this second stage of the magnetization process.¹⁰

The field dependency of the ac susceptibilities $\chi[112]$, $\chi[111]$, and $\chi[110]$, as well as that of quasistatic d_{33} ($d\lambda[112]/dH$), are shown in Fig. 3(a) for the zero-stress situation. Consistent with the slow change of magnetostriction, d_{33} and $\chi[112]$ illustrate almost linear changes with applied field between zero and 2500 Oe. However, more complicated variations are exhibited in the field behavior of both $\chi[111]$ and $\chi[110]$. When the field is decreased from positive saturation to zero, $\chi[110]$ decreases from its saturation value, reaches a negative maximum at an applied field of 1500 Oe, then increases until zero field. At the same time, $\chi[111]$ keeps almost unchanged until the field reduces to 1500 Oe, then it linearly increases until the field reduces down to zero.

Figure 3(b) shows the influence of a 10 MPa applied stress on the change of d_{33} and the susceptibilities. Some peaks appear in the field range between ± 250 Oe that corresponds to stage (i) of the magnetization process. Beyond this field range, all the variations behave like those in the unstressed case. The peak maximum in $\chi[112]$ and the peak minima in $\chi[111]$ and $\chi[110]$ are located at the same field value, but this value is lower than that associated with the peak in d_{33} . This situation is found for both positive and negative applied fields and would suggest that, at these low fields, 180° domain-wall motion is occurring, which yields zero contribution to the magnetostriction.

With reference to Fig. 1 depicting the projections from, say, a parent crystal plate, it can be seen that $\chi[110]$ results

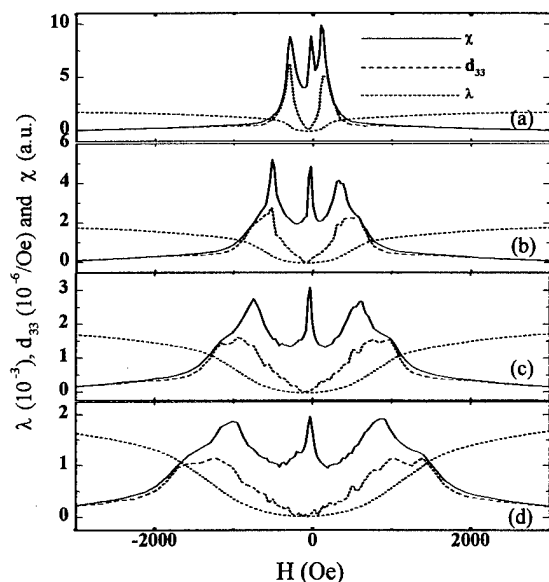


FIG. 4. The field dependencies of the quasistatic (dc) susceptibility and d_{33} along the $[11\bar{2}]$ direction for different values of applied stress: (a) 10, (b) 20, (c) 30, and (d) 40 MPa.

from the competition between the magnetization contributions from along the $[\bar{1}11]$ and $[11\bar{1}]$ axes. Similarly, $\chi[111]$ is from the competition between the magnetization contributions along the $[111]$ and the $[\bar{1}11]$, $[\bar{1}\bar{1}1]$, $[\bar{1}1\bar{1}]$, and $[11\bar{1}]$. If (a) the volumes of parent and twin plates in such a twinned single crystal were equal, and (b) the probabilities for a domain rotating its moment from $[111]$ to $[\bar{1}11]$ and $[11\bar{1}]$ were equal, too, no matter where this domain was located, then the $\chi[111]$ and $\chi[1\bar{1}0]$ should remain zero during both these two stages of the magnetization process. However, this has not been found to be the case in any of our susceptibility measurements and would suggest the existence of differences in both volume fraction and domain occupation probability.

The quasistatic (dc) susceptibility and d_{33} along the $[11\bar{2}]$ direction were obtained by differentiating the experimental data of magnetization and magnetostriction variations with field and are shown in Fig. 4. Two peaks can be distinguished in the field variations from both of these parameters in the field range of the stage (i) jump effect. The two peaks in d_{33} appear to be almost the same in amplitude whereas in the susceptibility, the higher-field peak appears as a shoulder on the more prominent lower-field peak. A sharp peak in dc susceptibility is also evident near zero field, even when the stress is applied, indicating the existence of 180° domain-wall motion in all cases. It is interesting to note that this peak is not evident from the nonzero stress data obtained from ac susceptibility measurements; this may be due to the higher magnetic hysteresis in this case.

In Fig. 5 the field variation of the ratio d_{33}/χ , experimentally determined from the quasistatic data, is shown for

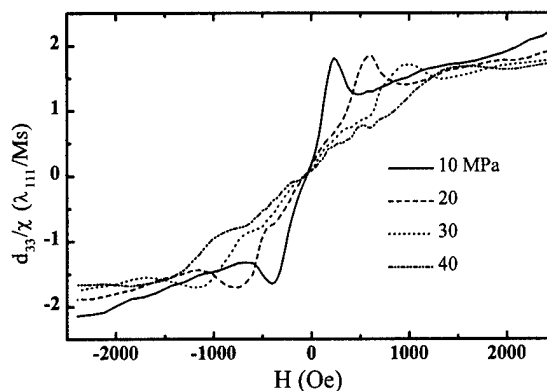


FIG. 5. The field variation of the ratio d_{33}/χ along the $[11\bar{2}]$, experimentally determined from the quasistatic data, for various applied stresses.

various applied stresses. A peak, with an amplitude of about 1.75 clearly appears in the stage (i) jump-field range: this corresponds to both the peak with a higher field as shown in Fig. 4, and to the peak of $\lambda[1\bar{1}0]$ in Fig. 1(b). It is known that the ratio (d_{33}/χ) , in units of λ_{111}/M_s , has values about 2.1, 1.4, and 0.7 when domains rotate from the $[\bar{1}11]$ to the $[\bar{1}\bar{1}1]$ or $[11\bar{1}]$, from the $[\bar{1}11]$ to the $[111]$ axis, and from the $[\bar{1}\bar{1}1]$ or $[11\bar{1}]$ to the $[111]$ axis, respectively.¹¹ It would appear, therefore, that the observed peak seems to result from the redistribution of domain magnetizations from the $[111]$ to the $[\bar{1}11]$ or the $[11\bar{1}]$ directions. The peak with the lower field value in Fig. 4 may be mainly due to the redistribution of domains from the $[111]$ to the $[11\bar{1}]$ axis.

The mechanisms responsible for the domain redistributions in different ways has not been observed clearly so far by experiment.

ACKNOWLEDGMENT

This work was supported by the EC Brite/Euram III Project under No. BE95-1372.

- ¹A. E. Clark, J. P. Teter, and O. D. McMasters, J. Appl. Phys. **63**, 3910 (1988).
- ²J. D. Verhoeven, J. E. Ostenson, E. D. Gibson, and O. D. McMasters, J. Appl. Phys. **66**, 772 (1989).
- ³J. P. Teter, M. Wun-Fogle, A. E. Clark, and K. Mahoney, J. Appl. Phys. **67**, 5004 (1990).
- ⁴D. C. Jiles, J. E. Ostenson, and C. V. Owen, J. Phys. (Paris), Colloq. **49**, C8, 1939 (1989).
- ⁵D. C. Jiles and S. Hariharan, J. Appl. Phys. **67**, 5013 (1990).
- ⁶M. Al-Jiboory, D. G. Lord, Y. J. Bi, J. S. Abell, and A. M. Hwang, J. Appl. Phys. **73**, 6168 (1993).
- ⁷A. P. Holden, D. G. Lord, and P. J. Grundy, J. Appl. Phys. **79**, 6070 (1996).
- ⁸D. G. Lord, A. P. Holden, and P. J. Grundy, J. Appl. Phys. **81**, 5728 (1997).
- ⁹D. G. Lord and D. Harvey, J. Appl. Phys. **76**, 7151 (1994).
- ¹⁰X. G. Zhao and D. G. Lord (unpublished).
- ¹¹A. R. Piercy, S. C. Busbridge, and D. Kendall, J. Appl. Phys. **76**, 7006 (1994).

Magnetization and magnetostriction of dendritic $[112]$ $\text{Tb}_x\text{Dy}_y\text{Ho}_z\text{Fe}_{1.95}$ ($x+y+z=1$) rods under compressive stress

M. Wun-Fogle^{a)} and J. B. Restorff

Carderock Division, Naval Surface Warfare Center, Code 684, West Bethesda, Maryland 20817-5700

A. E. Clark

Clark Associates, Adelphi, Maryland 20783-1225

J. F. Lindberg

Naval Undersea Warfare Center, Newport, Rhode Island 02841

The field dependencies of the magnetization and magnetostriction of the Laves phase pseudobinary $\text{Tb}_x\text{Dy}_y\text{Ho}_z\text{Fe}_{1.95}$ ($x+y+z=1$) compounds were measured as a function of compressive stress T ($10\text{ MPa} < |T| < 70\text{ MPa}$) and applied magnetic field H ($0 < H < 135\text{ kA/m}$). Values of x , y , and z were chosen to obtain minimum magnetic anisotropy and easy magnetization axis rotation near room temperature. At a compressive stress of 34 MPa , the addition of Ho to the binary $\text{Tb}_{1-x}\text{Dy}_x\text{Fe}_{1.95}$ compound reduced the width of the strain versus magnetic field hysteresis curves in $\text{Tb}_{0.28}\text{Dy}_{0.57}\text{Ho}_{0.15}\text{Fe}_{1.95}$ and $\text{Tb}_{0.26}\text{Dy}_{0.54}\text{Ho}_{0.2}\text{Fe}_{1.95}$ by 23% and 54%, respectively, compared to the original alloy, while the strains were reduced by only 7% and 10%. © 1998 American Institute of Physics. [S0021-8979(98)34411-4]

I. INTRODUCTION

The pseudobinary Laves phase $(R_x^1R_y^2\ldots)\text{Fe}_2$ compounds (R^i =rare earth, $x+y+\ldots=1$) are known to possess very large magnetostrictions, strong stress dependencies, and unusual ΔE effects.¹ The effects of crystalline anisotropy can be quite large in these materials, resulting in large hysteresis losses. Spin reorientation diagrams of the $\text{Tb}_{1-x}\text{Dy}_x\text{Fe}_2$ and $\text{Tb}_{1-x}\text{Ho}_x\text{Fe}_2$ ternary compounds show that the anisotropy can be minimized by a suitable combination of rare earths.² This kind of ternary alloy has one degree of freedom, x , which permits only the combined effects of all of the anisotropy constants to be minimized. In practice, this results in minimizing the largest anisotropy constant, K_1 .

By adding a third rare earth element, an additional degree of freedom is obtained and both of the two largest anisotropy constants, K_1 and K_2 can be minimized. Holmium is a good choice since, like Tb and Dy, it has a large, positive magnetostriction. This approach was followed by Williams and Koon³ who reported a very low anisotropy with the composition $\text{Tb}_{0.2}\text{Dy}_{0.22}\text{Ho}_{0.58}\text{Fe}_{1.95}$, but at the cost of substantially lowering the saturation magnetostriction. The reason for this lower magnetostriction is that Ho has only 1/3 of the intrinsic magnetostriction of Tb and Dy. In this article, we examine the reduction in the hysteresis losses and magnetostriction caused by substituting small amounts of Ho ($z \leq 0.2$) for Tb and Dy in the highly magnetostrictive $\text{Tb}_x\text{Dy}_{1-x}\text{Fe}_2$ pseudobinary.

II. EXPERIMENT

Five $\text{Tb}_x\text{Dy}_y\text{Ho}_z\text{Fe}_{1.95}$ ($x+y+z=1$) samples (0.48 cm diam \times 1.91 cm long) were prepared using a free standing zone melt method.⁴ A slightly iron deficient alloy

($\text{Fe}_{1.95}$ instead of Fe_2) is used in order to create a small amount of rare earth eutectic which thereby increases the mechanical robustness of the samples. The compositions examined in this study are shown in Table I along with the saturation magnetostriction S_{sat} . For a given Ho concentration, all of the samples except sample C lie on a linear minimum anisotropy line created by compounds of the form:

$$x(\text{Tb}_{0.15}\text{Ho}_{0.85}\text{Fe}_2) + (1-x)(\text{Tb}_{0.3}\text{Dy}_{0.7}\text{Fe}_2), \quad 0 \leq x \leq 1.$$

Sample A is the room temperature Terfenol-D composition and was used to provide a control for the experiment, while sample E is at the zero anisotropy composition found by Williams and Koon.³ Figure 1 shows these compositions on a ternary phase diagram. These relatively small diameter samples appear to be of very good quality since sample A (Terfenol-D) has a large magnetostriction and markedly lower hysteresis losses than larger size rods of the same composition. We believe this is due to good alignment of the $[112]$ platelets in these samples.

The magnetization and magnetostriction at compressive stresses T ($10\text{ MPa} < |T| < 70\text{ MPa}$) and fields H ($0 \leq H \leq 135\text{ kA/m}$) were measured at room temperature. The apparatus used a dead weight to apply the stress; length changes were measured by LVDTs, and the magnetization was measured by a small pickup coil wound around the

TABLE I. Composition and saturation magnetostriction S_{sat} of the $\text{Tb}_x\text{Dy}_y\text{Ho}_z\text{Fe}_{1.95}$ ($x+y+z=1$) samples reported in this study.

Sample	x	y	z	S_{sat} (ppm)
A	0.30	0.70	0.00	1850
B	0.28	0.57	0.15	1650
C	0.30	0.55	0.15	1600
D	0.26	0.54	0.20	1500
E	0.20	0.22	0.58	1000

^{a)}Electronic mail: wunfogle@oasys.dt.navy.mil

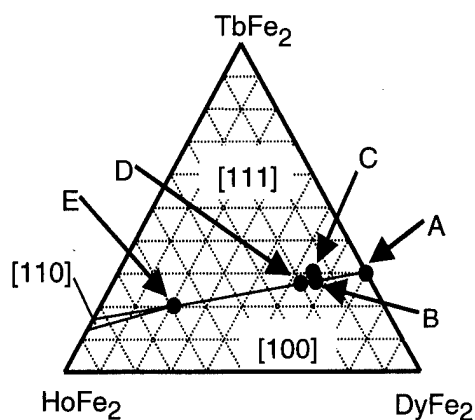


FIG. 1. Ternary phase diagram for the TbFe_2 - HoFe_2 - DyFe_2 system. The regions marked [100], [111], and [110] indicate the direction of the easy magnetization axis. The locations of the samples discussed in the article are indicated. The line of minimum anisotropy runs through samples A and E.

sample. Figure 2 shows the magnetostriction of a typical sample with Ho added (sample B). The primary objective of this work is to determine how the width of the hysteresis loop depends upon the Holmium concentration and compare this dependence with the decrease in magnetostriction as the Ho concentration was increased. For purposes of this comparison, we used application oriented measures of magnetostriction and hysteresis. The peak-to-peak magnetostriction S_{pp} is defined as the change in strain over a range of 71.6 kA/m (~ 900 Oe) centered around the field at which the piezomagnetic constant d has a maximum, subject to the restriction that the field is always positive, i.e., the center field is ≥ 35.8 kA/m. The hysteresis width W_h is defined as the average width of the magnetic field-strain curve at the field where d has a maximum.

Figure 3 shows S_{pp} as a function of Ho concentration and stress for samples A, B, D, and E, the samples that lie along the minimum anisotropy line. (Sample C, which lies on the Tb rich side of the minimum anisotropy line, has a

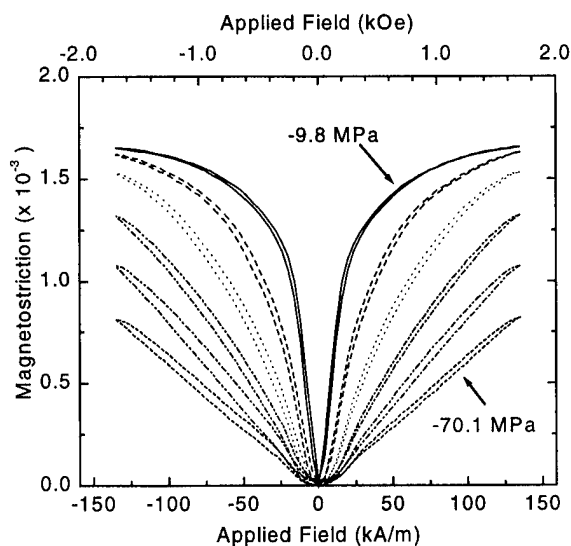


FIG. 2. Magnetostriction vs applied magnetic field for sample B, $\text{Tb}_{0.28}\text{Dy}_{0.57}\text{Ho}_{0.15}\text{Fe}_{1.95}$, for stresses of -9.8 , -21.9 , -33.9 , -46.0 , -58.1 , and -70.1 MPa.

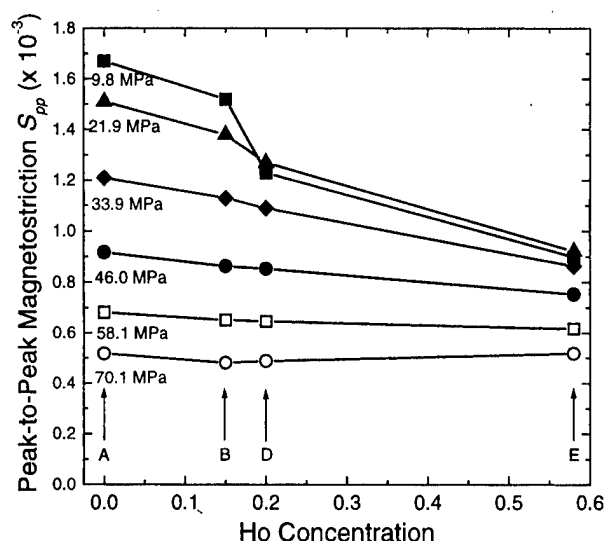


FIG. 3. Peak-to-peak magnetostriction S_{pp} vs holmium concentration as a function of applied stress for samples A, B, D, and E.

slightly higher magnetostriction.) Figure 4 shows W_h as a function of Ho concentration and stress for the same four samples. For sample D ($\text{Tb}_{0.26}\text{Dy}_{0.54}\text{Ho}_{0.2}\text{Fe}_{1.95}$), at $T = -9.8$ MPa, an artifact of our definition of the width gave meaningless results: Part of the 71.6 kA/m magnetic field range used to determine W_h is at fields where the magnetostriction is saturated.

III. DISCUSSION

Figure 3 shows the reduction in S_{pp} as the Ho concentration is increased. The effect is moderately large at low stresses and decreases as the stress is increased and the applied stress begins to dominate the magnetostrictive behavior. At the same time, Fig. 4 shows that W_h also decreases as the Ho concentration increases. The reduction in S_{pp} and W_h for several of the stresses are summarized in Table II.

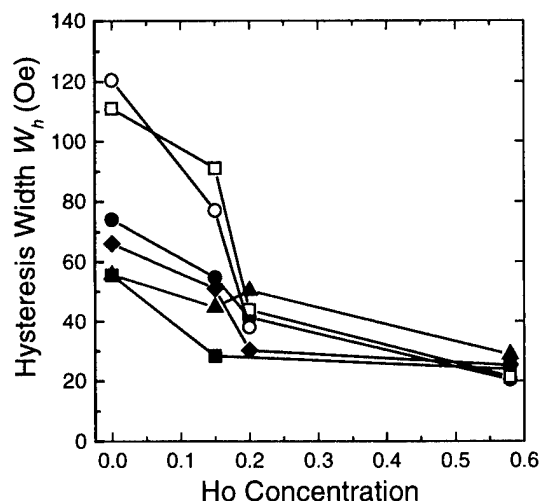


FIG. 4. Hysteresis width W_h vs Ho concentration for samples A, B, D, and E for applied stresses of -9.8 (filled square), -21.9 (filled triangle), -33.9 (filled diamond), -46.0 (filled circle), -58.1 (open square), and -70.1 MPa (open circle).

TABLE II. Fractional change in peak-to-peak magnetostriction $\Delta S = [S_{pp} - S_{pp}(A)]/S_{pp}(A)$ and fractional change in hysteresis width $\Delta W = [W_h - W_h(A)]/W_h(A)$ for samples B, C, D, and E as a function of applied stress. The reference values $S_{pp}(A)$ and $W_h(A)$ are the values for sample A.

$T(\text{MPa})$	Sample B		Sample C		Sample D		Sample E	
	ΔW	ΔS	ΔW	ΔS	ΔW	ΔS	ΔW	ΔS
-9.8	-49%	-9.4%	-3%	-16%	no data	-26%	-54%	-46%
-21.9	-20%	-8.5%	-10%	-12%	-10%	-16%	-48%	-39%
-33.9	-23%	-6.7%	-13%	-5.7%	-54%	-10%	-62%	-29%
-46.0	-26%	-5.9%	-15%	0.4%	-44%	-7.0%	-72%	-18%
-58.1	-18%	-4.2%	-33%	2.6%	-61%	-5.1%	-81%	-9.3%
-70.1	-36%	-7.2%	-21%	5.1%	-68%	-6.0%	-36%	-0.1%

In conclusion, small amounts of Ho (<20%) replacing Tb and Dy in the usual Terfenol-D formulation, while decreasing the magnetostriction, provide a much larger decrease in hysteresis losses. Such a tradeoff is very important for many device applications.

ACKNOWLEDGMENTS

This work was supported by the Materials S & T Division of the Office of Naval Research, the Defense Advanced Research Projects Agency, the Naval Undersea Warfare Center Detachment, New London, Active Source Technology

task, sponsored by the Office of Naval Research and the Independent Research Program at the Naval Surface Warfare Center, Carderock Division. We would like to thank Kitty Leung and Thu Van Thi Luu for their assistance with the measurements and data analysis.

¹See, for example, A. E. Clark, in *Ferromagnetic Materials Handbook*, edited by E. P. Wohlfarth (North Holland, Amsterdam, 1980), p. 531.

²U. Atzmony, M. P. Dariel, E. R. Bauminger, D. Ledenbaum, I. Nowik, and S. Ofer, *Phys. Rev. B* **7**, 4220 (1973).

³C. Williams, and N. Koon, *Physica B* **86-88**, 14 (1977).

⁴The samples were purchased from ETREMA Products, Ames, IA.

Development of Terfenol-D transducer material

E. A. Lindgren^{a)}

Industrial Quality, Inc., Gaithersburg, Maryland 20879

S. Haroush, J. C. Poret, A. D. Mazzatesta, and M. Rosen

Department of Materials Science and Engineering, Johns Hopkins University, Baltimore, Maryland 21218

M. Wun-Fogle and J. B. Restorff

Naval Surface Warfare Center, Carderock Division, Code 684, W. Bethesda, Maryland 20917

A. E. Clark

Clark Associates, Adelphi, Maryland 20783

J. F. Lindberg

Naval Undersea Warfare Center, Code 213, Newport, Rhode Island 02841

Terfenol-D, $\text{Tb}_{1-x}\text{Dy}_x\text{Fe}_2$ ($x \approx 0.7$), is successfully used as a magnetostrictive transducer material for low-frequency applications. To extend the frequency range of magnetostrictive transducers into the high kHz and MHz range, new materials processing techniques must be developed to minimize eddy current losses. The method that has demonstrated the greatest potential to date is based on rapid solidification by melt spinning to obtain thin strips of material. The objective of this program includes refining the casting procedure to yield ribbons with the [111] direction oriented along the length of the ribbon, with the (110) plane in the plane of the ribbon. The crystallographic orientation of the Terfenol-D ribbons have been controlled by varying the cooling rate of the melt-spinning process. The cooling rates were controlled by a number of parameters in the melt-spinning process and ribbons have been obtained with an enhancement of the (110) plane parallel to the surface of the ribbon. Magnetostrictive measurements under tensile stresses up to 3 MPa and magnetic fields up to 4 kOe yielded magnetostrictive displacements of 850×10^{-6} . © 1998 American Institute of Physics. [S0021-8979(98)25711-2]

INTRODUCTION

Terfenol-D, $\text{Tb}_{1-x}\text{Dy}_x\text{Fe}_2$ ($x \approx 0.7$), has one of the largest magnetostrictive displacements under ambient (room-temperature) operating conditions.¹ To date, the standard design for transducers that use Terfenol-D as the actuator incorporates a rod of the material cast under specific cooling conditions.² The cooling parameters are designed to generate a uniform crystallographic structure in the rod to obtain the largest possible magnetostrictive displacement. The large displacement increases the energy of the acoustic signal that is generated by the transducers.

One of the limits of this type of magnetostrictive transducer is the frequency range of the generated acoustic signal. The large size of the actuator rod limits the effectiveness of the transducer at higher frequencies due to eddy current losses.³ The optimal configuration for higher-frequency (ultrasonic) magnetostrictive transducers is to have thin layers of the material stacked to form the transducer rod. This maximizes the magnetostrictive behavior as it minimizes the eddy current losses that occur when the rod configuration is used, enabling generation of ultrasonic signals with frequencies in the low megahertz (MHz) range. This means that the alloy needs to be manufactured in thin strips with the appropriate crystallographic orientation. The method reported here for manufacturing thin strips of Terfenol-D is a modification of the melt-spinning rapid solidification technique.

The preferred direction of magnetization in Terfenol-D is [111] in the cubic Laves' phase.¹ For melt-spun ribbons, this means that this direction should be oriented along the length of the ribbon. To achieve this orientation, the (110) plane could lie in the plane of the ribbon, as the [111] direction is located in the (110) plane. The work that will be described here is an ongoing effort to develop methods to obtain this desired orientation in Terfenol-D ribbons by controlling the cooling rate of the melt-spinning process. The cooling rate is controlled by varying the velocity of the melt-spinning wheel and by changing the composition of the melt-spinning wheel, which yields different values for the thermal conductivity of the wheel.

EXPERIMENT

To generate ribbons of Terfenol-D, the melt-spinning technique commonly used for rapid solidification was used.⁴ A schematic of the melt spinner is shown in Fig. 1. The melt-spinning procedure was initiated by placing a 5 gm piece of nonoriented Terfenol-D in a quartz crucible, which, in turn, was placed inside an induction coil. The Terfenol-D was heated by induction heating just past the melt point, at which time it was ejected onto the spinning wheel through a 0.6 mm hole in the quartz crucible. The molten metal was ejected by applied argon gas. The melt-spinning process was performed inside an enclosed chamber under an argon atmosphere at ambient pressure to prevent oxidation. The velocity of the melt-spinning wheel was set by a controller and was

^{a)}Electronic mail: lindgren@indqual.com

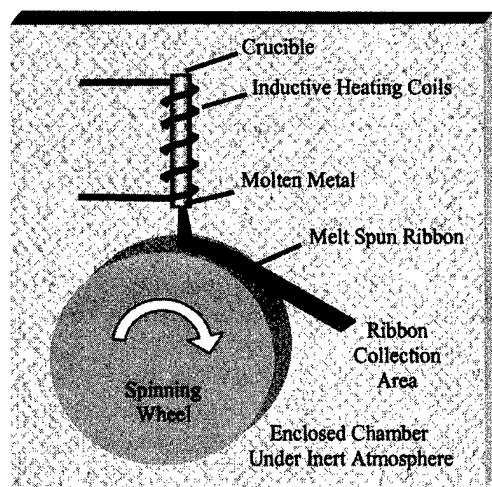


FIG. 1. Schematic of the melt spinner used to manufacture Terfenol-D ribbons.

measured using an optical tachometer. Changes in the wheel velocity were used to control the cooling rate of the solidification process. Five wheel compositions that had values for the thermal conductivity that ranged from 2.0 to 0.29 W cm/K were investigated in combination with the wheel velocities to obtain a broad range of cooling conditions.

Using the melt-spinning technique, sections of ribbon over 100 mm in length were obtained. The dimensions of the ribbon depended on the wheel velocity, with thicknesses that ranged from 60 to 450 μm and widths from 1 to 5 mm. The crystallographic orientation of the ribbons was determined by x-ray diffraction (XRD). The ribbons were mounted on amorphous glass slides with tape. The mounting tape was placed outside the x-ray beam to insure that it did not affect the diffraction pattern. The samples were scanned at 2° per minute in a computer controlled Diano XRD 8535 x-ray diffractometer. Each diffraction pattern was analyzed by subtracting the background radiation and normalizing the diffraction pattern to itself. This was followed by normalizing the pattern to a powder diffraction pattern of Terfenol-D. The powder sample was obtained by crushing a section of the as-received Terfenol-D rod.

The magnetostrictive performance of the ribbon was determined using a custom measurement system. Figure 2 shows a schematic of the experimental apparatus. The ribbons were mounted between the pole faces of an electromagnet in a loosely fitting channel made of glass slides to keep the ribbon from swinging. Measurements on bulk Terfenol-D commonly utilize compressive stresses. Since it is not practical to apply a compressive stress to ribbons, a tensile stress was used instead. The upper end of the ribbon was clamped to an aluminum support rod with a rubber-jawed clamp. A similar clamp attached a weight holder to the lower end of the ribbon. Weights of 50, 100, 200, and 500 gm were hung from the weight holder to apply the stress. This resulted in average stresses of 0.31, 0.72, 1.4, and 2.7 MPa. Because the width and thickness of the ribbon varied with position, the local stress varied somewhat throughout the sample. Based on the variations of the ribbon's width and thickness, the estimated standard deviation of the stress is 15%. An MTI

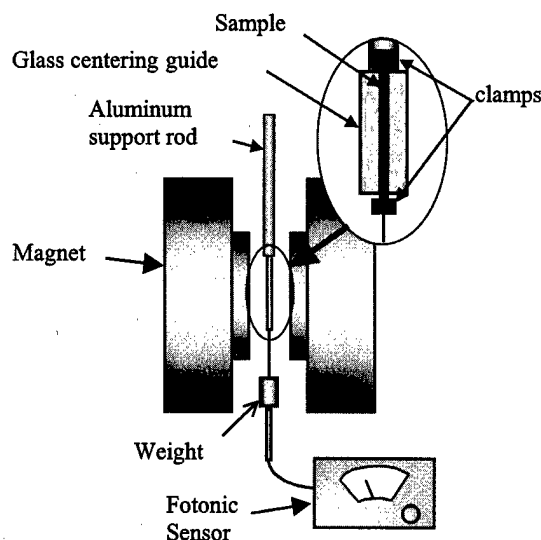


FIG. 2. Schematic of experimental apparatus for measuring magnetostriction of melt-spun ribbons as a function of magnetic field and tensile stress.

1000 Photonic sensor was used to measure the motion of the bottom of the weight and a Lakeshore Gaussmeter was used to measure the applied field. It was found that the ribbon's magnetostriction stabilized after maintaining tension on the ribbon overnight.

Terfenol-D has a positive magnetostriction, which means that tensile stress aligns the moments along the length of the ribbon. In order to rotate the moments to measure the magnetostriction, a magnetic field perpendicular to the ribbon length must be applied, in this case, across the width of the ribbon. Because of the large length-to-width ratio of the sample and the orientation of the applied field with respect to the ribbon, the demagnetizing effect is significant. The demagnetizing field parallel to the width at the center of sample was calculated to be 700 Oe.⁵

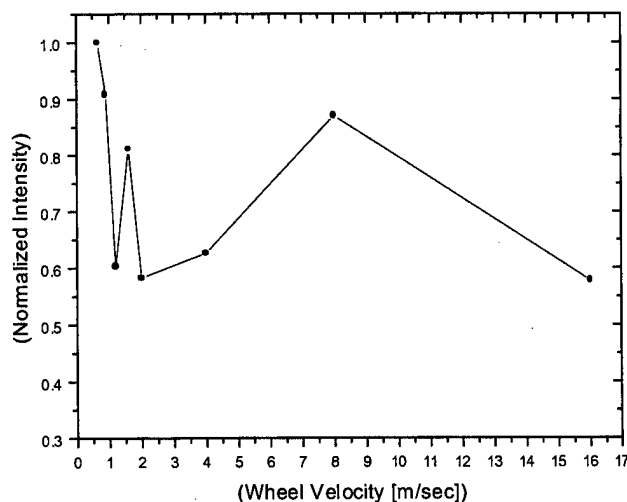


FIG. 3. Normalized intensity of the (220) diffraction peak as a function of wheel velocity for the wheel with a thermal conductivity of 2.0 W cm/K.

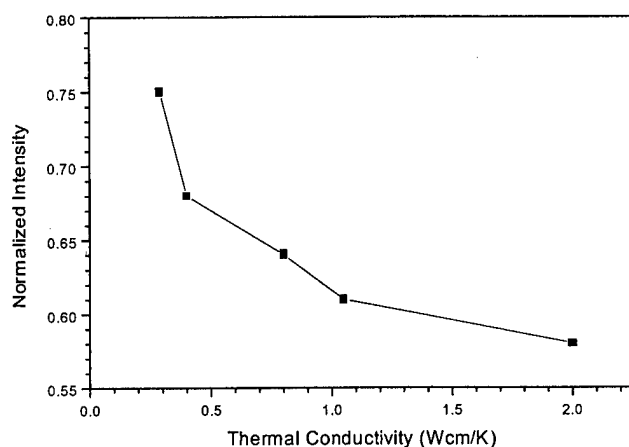


FIG. 4. Normalized intensity of the (220) diffraction peak as a function of thermal conductivity of the melt-spinning wheel.

RESULTS AND DISCUSSION

The ability to control the crystallographic orientation of the Terfenol-D ribbon is shown in Fig. 3, which is a plot of the amplitude of the (220) diffraction peak as a function of wheel velocity for the wheel with a thermal conductivity of 2.0 W cm/K. While there is scatter in the trend of the amplitude of the (220) peak, especially at a wheel velocity of 8 m/s, the data show that slower wheel velocities, and therefore, lower cooling rates, yields ribbon with a greater amount of the (220) plane in the plane of the ribbon. Recall that this is the desired result as the [111] direction, the direction of maximum magnetostrictive displacement, is in the (220) plane.

The systematic dependence of the crystallographic orientation on the cooling rate of the melt-spinning process is further shown in Fig. 4, which shows the amplitude of the (220) peak as a function of the thermal conductivity of the melt-spinning wheel. The amplitude for the diffraction peaks was taken for the melt spinning performed with a wheel velocity of 2 m/s, except for the wheel with the lowest thermal conductivity. To obtain continuous ribbons with this wheel, the velocity was set to 13 m/s. Figure 4 clearly demonstrates that lower values of the thermal conductivity of the melt-spinning wheel will result in a greater amount of the preferred crystalline orientation in the Terfenol-D ribbons. Therefore, as illustrated by Figs. 3 and 4, it has been demonstrated that the velocity and composition of the melt-spinning wheel can be used to control the crystalline orientation of Terfenol-D.

Figure 5 shows the magnetostriction of the ribbon melt spun at 2 m/s on the wheel composition with a thermal conductivity of 0.4 W cm/K for two different tensile stresses.

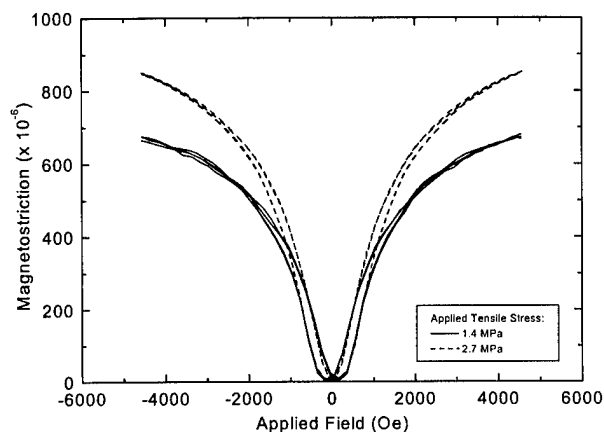


FIG. 5. Magnetostriction vs applied field for Terfenol ribbon melt spun on the wheel with a thermal conductivity of 0.4 W cm/K at 2 m/s.

Each curve shows two magnetic-field sweeps overlaid. The data are repeatable (within 10% from day to day and when the stresses are removed and replaced). The detailed shape of the curve is quite similar to bulk Terfenol-D. This can be seen in the region around zero field where the double well shape is observed. The maximum magnetostriction was measured to be 850×10^{-6} , about half that of high-quality bulk material.

SUMMARY AND CONCLUSIONS

The results that have been obtained demonstrate the ability to manufacture continuous ribbons of Terfenol-D by melt spinning. The cooling rate of the solidification process was controlled by varying the velocity and the composition of the melt-spinning wheel. X-ray diffraction of the ribbons determined that the greater amount of the desired crystalline orientation, with the (110) plane in the plane of the ribbon, was obtained for the slowest cooling rates of the melt-spinning process. Magnetostrictive measurements indicate that the ribbons are not fully in the optimal crystalline orientation. The maximum value for the magnetostriction is approximately 50% that of the high-quality bulk materials.

ACKNOWLEDGMENTS

This work was sponsored by an ONR SBIR Phase II contract administered by NUWC Newport. The ONR Acoustic Source Technology task supported the measurements and analysis by NSWC Carderock.

¹R. Abbundi and A. E. Clark, IEEE Trans. Magn. **13**, 1519 (1977).

²D. G. Lord, H. Savage, and R. G. Rosemeier, J. Magn. Magn. Mater. **29**, 137 (1982).

³J. F. Lindberg, Mater. Res. Soc. Symp. Proc. **459**, 509 (1997).

⁴R. B. Pond, Sr., U.S. Patent No. 2825108 (1958).

⁵R. I. Joseph and E. Schlomann, J. Appl. Phys. **36**, 1579 (1965).

Magnetostrictive properties of polymer-bonded amorphous Tb-Fe-B composites

S. R. Kim and S. Y. Kang

Thin Film Technology Research Center, Korea Institute of Science and Technology, Seoul, Korea

J. K. Park

Ceramic Processing Research Center, Korea Institute of Science and Technology, Seoul, Korea

J. T. Nam and Derac Son

Department of Physics, Hannam University, Taejeon, Korea

S. H. Lim^{a)}

Thin Film Technology Research Center, Korea Institute of Science and Technology, Seoul, Korea

Amorphous ribbons of an alloy with the composition $(\text{Tb}_{0.33}\text{Fe}_{0.67})_{0.98}\text{B}_{0.02}$, which exhibit good magnetostrictive properties at low magnetic fields, are bonded with a phenol-based binder to fabricate bulk composites. Efforts to determine optimum fabrication parameters are made by examining magnetic and mechanical properties of bulk compacts obtained at various fabrication conditions. From the binder content dependence of magnetostriction and compressive strength, the optimum binder content is estimated to be about 4.3 wt %, taking into account magnetostrictive and mechanical properties and the necessity of reducing nonmagnetic binder content. The two properties of magnetostriction and compressive strength vary nearly linearly with the compaction pressure; as the compaction pressure varies from 0.25 to 1.0 GPa, magnetostriction decreases but compressive strength increases, making it difficult to determine the optimum compaction pressure. A magnetostriction of 493 ppm (at 1.1 kOe) is achieved from the present bulk composites, together with a high $d\lambda/dH$ (sensitivity of magnetostriction with applied magnetic field) of 1 ppm/Oe.

© 1998 American Institute of Physics. [S0021-8979(98)25811-7]

Cubic Laves RFe_2 (R: rare-earth elements) compounds possess giant magnetostriction at room temperature.¹ However, since the magnetocrystalline anisotropy of the compounds is also very large, intrinsically large magnetostriction is usually not realized at a magnetic field applicable in device applications. Two methods have mainly been used: alloy design and microstructural modification. In line with the latter method, it has been demonstrated for Dy-Fe,² Tb-Fe,³ and Tb-Dy-Fe alloys⁴ that very good magnetostrictive properties are achieved at low magnetic fields by grain refinement or amorphization. Since grain refinement or amorphization can most conveniently be done by melt spinning, the samples with good low-field properties are ribbon type and usually very brittle, which limit applications in the as-spun ribbon form. In an effort to solve this problem, rod-shaped composites are fabricated by combining amorphous melt-spun ribbons with a polymer binder. Amorphous ribbons of a $(\text{Tb}_{0.33}\text{Fe}_{0.67})_{0.98}\text{B}_{0.02}$ alloy, which were melt spun at a wheel velocity of 50 m/s, were used in the composite fabrication, since from the previous study³ they were observed to exhibit good magnetostrictive properties at low magnetic fields. It is expected that with the inclusion of a polymer binder the frequency limit of the materials can be extended to high region due to high resistivity of composites. Furthermore, this way of producing R-Fe-based magnetostrictive bulk materials is simple and cost effective over the currently popular directional solidification process.

An alloy of $(\text{Tb}_{0.33}\text{Fe}_{0.67})_{0.98}\text{B}_{0.02}$ was induction melted

and then melt spun in an Ar atmosphere at a wheel velocity of 50 m/s. The resultant ribbons were crushed to powders with a size below 45 μm . The powders were then mixed with a phenol-type binder, the amount of which was varied from 3.1 to 6.7 wt %. The mixed powders were compacted at varying pressures ranging from 0.25 to 1 GPa. Composites with high mechanical strength were finally obtained by curing at 150 °C. The dimension of the present composites is 3.5 mm×3.5 mm×10 mm (length). The microstructure of melt-spun ribbons was examined by x-ray diffraction and also by transmission electron microscopy. The magnetostriction (λ) of the ribbons was measured by a three-terminal capacitance method at magnetic fields (H) up to 8 kOe, while that of bulk composites by using a linear variable differential transformer type apparatus with a maximum magnetic field of 1.1 kOe. In the case of bulk materials, compressive stress was applied to the specimen during the measurement. Magnetic properties of both melt-spun ribbons and composites were measured with a vibrating sample magnetometer at magnetic fields up to 15 kOe. A mechanical tester was used to measure the compressive strength of cured composites. All the measurements were done at room temperature.

The microstructure of the as-spun ribbons mainly consists of an amorphous phase with a trace of the crystalline TbFe_2 phase. The magnitude of H_c of these ribbons is relatively low, being about 0.5 kOe, and, as expected, magnetostrictive characteristics are observed to be good, particularly at low magnetic fields. In Fig. 1 are shown the results for $\lambda-H$ plots for the as-spun ribbons. The value of λ shown in

^{a)}Electronic mail: mmlshl@kistmail.kist.re.kr

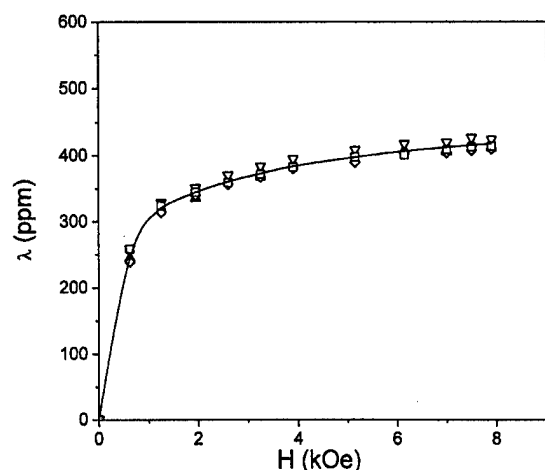


FIG. 1. λ - H plots for the amorphous ribbons of an alloy $(\text{Tb}_{0.33}\text{Fe}_{0.67})_{0.98}\text{B}_{0.02}$ in the as-spun state.

Fig. 1 is obtained by the relation $\lambda = \frac{2}{3}(\lambda_{\parallel} - \lambda_{\perp})$. Here, λ_{\parallel} and λ_{\perp} are, respectively, the values of magnetostriction measured in the parallel and the transverse directions in the ribbon plane. The difference $(\lambda_{\parallel} - \lambda_{\perp})$ corresponds to the peak-to-peak value when rotating in-plane magnetic fields are applied. The value of λ is therefore the *intrinsic* magnetostriction at a given field, being independent of the domain structure. The reliability of the present magnetostrictive results for the as-spun ribbons is found to be good, as can be judged from the small scatter in the measured data. The small magnitude of saturation magnetostriction, together with good low-field magnetostrictive properties, is characteristic of a material with an amorphous structure.

One of the most important tasks during the fabrication of bulk composites is to conserve, as much as possible, the good magnetic and magnetostrictive properties of the melt-spun ribbons. As the process proceeds, however, these properties steadily deteriorate; for example, the (average) value of H_c of final bulk composites is increased to 1.0 kOe from the initial (average) value of 0.5 kOe of the melt-spun ribbons, the largest increase of H_c being observed during the milling process. It is worth noting here that saturation magnetization (actually, magnetization at 15 kOe, M_{15}) remains nearly unchanged during the whole process; rather, a slight increase is observed from 53.4 to 56.5 emu/g during the compaction process to form green compacts. No deterioration of M_{15} indicates that all fabrication processes are well controlled. This is of particular importance, since some of the processes such as pressing were performed in air. This is made possible by the fact that each powder is completely coated by the binder, thus preventing powder/air contact. During the early stage of work when the fabrication conditions were not optimized, a very large reduction of M_{15} occurred during the fabrication processes involving air atmosphere, due to the incomplete coverage of powders with polymer binder.

Magnetostriction of bulk composites was measured only in the parallel (length) direction, since, with the present sample dimension, demagnetizing fields are very large in the transverse direction and, furthermore, an accurate estimation of them is not easy in this direction. It is noted that, from the

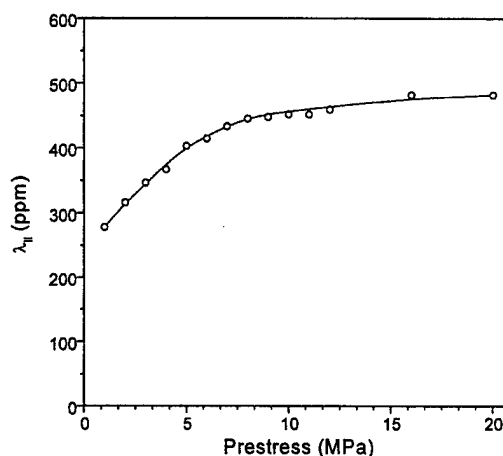


FIG. 2. The magnitude of λ_{\parallel} as a function of applied compressive stress during the measurement. The results are for the bulk composites fabricated at the compaction pressure of 0.5 GPa and the binder content of 6.7 wt %.

applications point of view, the magnitude of λ_{\parallel} is much more important than that of λ_{\perp} , since the applied magnetic field is usually in the length direction. Unlike λ , the magnitudes of λ_{\parallel} and λ_{\perp} depend on the domain structure, and therefore, they are expected to vary with applied (compressive) stress, the spin direction being affected via magnetoelastic interactions. The results for λ_{\parallel} are shown in Fig. 2 as a function of applied compressive stress during the magnetostriction measurement. The results are for the sample fabricated at a compaction pressure of 0.5 GPa and a binder content of 6.7 wt %. The value of λ_{\parallel} increases with increasing compressive stress. This is expected since more spins can be directed towards the transverse direction by the application of larger compressive stress. Saturation in the plot of λ_{\parallel} versus applied compressive stress is reached at about 16 MPa, indicating that at this stress spins are aligned nearly completely in the transverse direction. In later measurements, the applied compressive stress is fixed at 16 MPa.

Magnetic (including magnetostrictive) and mechanical properties of bulk composites with varying binder contents from 3.1 to 6.7 wt % were investigated and some results for λ_{\parallel} and compressive strength are shown in Figs. 3(a) and 3(b), respectively, for the samples fabricated at a fixed compaction pressure of 0.5 GPa. It is seen from the figures that the magnitude of λ_{\parallel} is increased substantially as the binder content is varied from 3.1 to 4.3 wt %, but is little affected by further increase of the binder content. The small magnetostriction at the low binder content may result from the fact that the strain produced in a particle does not transfer efficiently to neighboring particles due to the lack of binder. On the other hand, compressive strength increases continuously with increasing binder content. Although large mechanical strength is desirable in some applications, it is also important to reduce the amount of nonmagnetic binder content in order to have a material with a high performance/volume ratio. With this consideration, the optimum binder content is considered to be around 4.3 wt %, large magnetostriction being combined with relatively large compressive strength. However, in some applications where large compressive strength is required, composites with a high binder content may preferably be used.

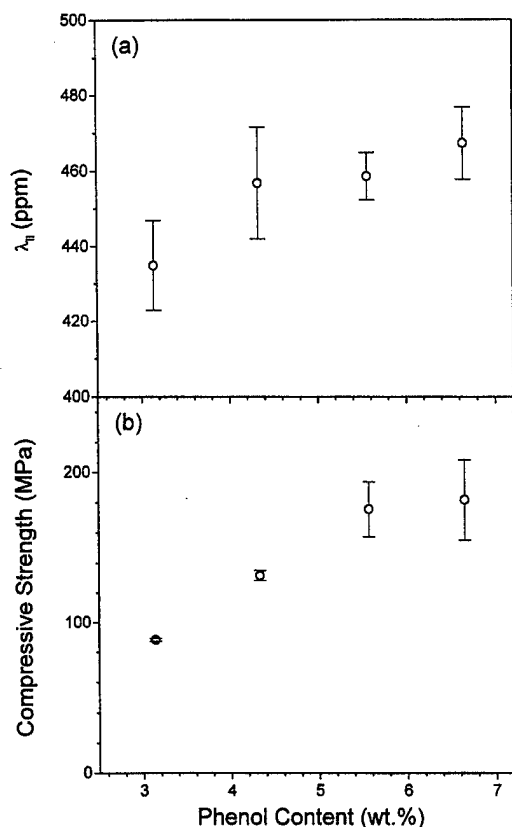


FIG. 3. The magnitude of (a) λ_{\parallel} (measured at a compressive stress of 16 MPa) and (b) compressive strength as functions of the binder content. The composites are fabricated at a fixed compaction pressure of 0.5 GPa.

In Figs. 4(a) and 4(b) are shown the results for λ_{\parallel} and compressive strength as functions of the compaction pressure. The compaction pressure is varied from 0.25 to 1.0 GPa and the results shown in Figs. 4(a) and 4(b) are for the compacts with a fixed binder content of 4.3 wt %. From these figures it is observed that, as the compaction pressure increases, the magnetic property of λ_{\parallel} deteriorates, while the mechanical property of compressive strength improves. Since the compaction pressure dependence of the two properties varies nearly linearly, it is hard to decide the optimum compaction pressure. Rather, the compaction pressure can be determined depending on particular applications; for example, in applications where large magnetostriction is required but mechanical strength is not of prime importance, bulk samples fabricated at low compaction pressure may be used.

The highest (average) magnitude of λ_{\parallel} obtained in this work is just below 500 ppm (493 ppm), which is equivalent to the value of 329 ppm for λ , with the assumption of complete spin alignment in the transverse direction via magnetoelastic interactions by the applied compressive stress during the measurement. The value of λ estimated from the bulk composites is higher than the value of 310 ppm obtained for the melt-spun ribbons. The increase of the "intrinsic" λ value for the bulk composites, though very small, is not clearly understood. One possibility is that a small portion of an amorphous phase is transformed into the crystalline phase

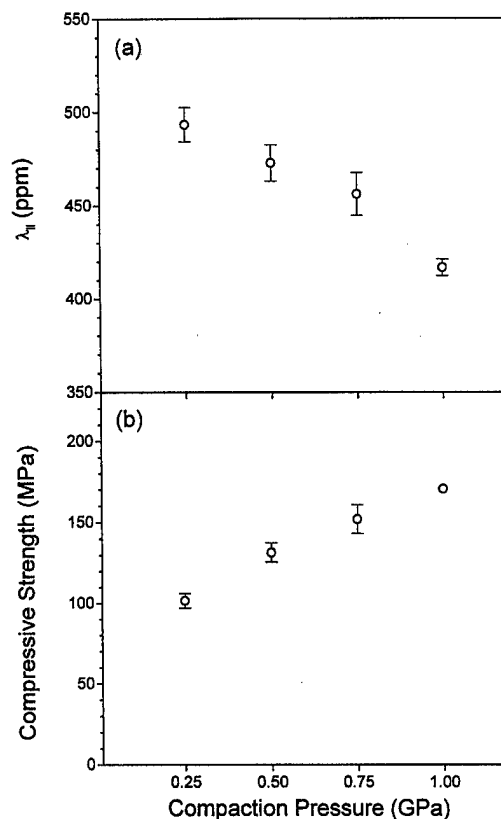


FIG. 4. The magnitude of (a) λ_{\parallel} (measured at a compressive stress of 16 MPa) and (b) compressive strength as functions of the compaction pressure. The composites are fabricated at a fixed binder content of 4.3 wt %.

in the course of the bulk fabrication. This may also explain a slight increase of M_{15} of bulk composites, compared with the initial melt-spun ribbons.

Equally good magnetostrictive properties are also obtained at intermediate magnetic fields. For example, at a magnetic field of 0.64 kOe (which is the smallest magnetic field applied to measure the melt-spun ribbons), the magnitude of λ_{\parallel} for bulk composites is 384 ppm (which is equivalent to the intrinsic value of 256 ppm). This value is nearly equal to the value of 260 ppm for the melt-spun ribbons. However, at magnetic fields below 0.2 kOe, the magnetostriction of the bulk composites is very small. This can be actually expected by the increase of H_c during the fabrication processes, since low-field magnetostrictive properties are sensitive to H_c .⁵ The problem of small low-field magnetostriction may be solved by the application of a bias magnetic field. In applications, the sensitivity of magnetostriction with magnetic field ($d\lambda/dH$) as well as the absolute magnitude of magnetostriction is considered to be an important property. In this work, a high sensitivity of over 1 ppm/Oe is also achieved in the present bulk composites.

¹ A. E. Clark, in *Ferromagnetic Materials*, Vol. 1, edited by E. P. Wohlfarth (North-Holland, Amsterdam, 1980), Chap. 7.

² S. H. Lim, T. H. Noh, I. K. Kang, S. R. Kim, and S. R. Lee, *J. Appl. Phys.* **76**, 7021 (1994).

³ S. H. Lim, S. R. Kim, and H. J. Kim, *IEEE Trans. Magn.* **32**, 4770 (1996).

⁴ S. H. Lim, S. Y. Kang, and S. R. Kim, *IEEE Trans. Magn.* **33**, 3943 (1997).

⁵ S. R. Kim, S. Y. Kang, and S. H. Lim, *J. Korean Inst. Metals Mater.* **35**, 1386 (1997).

Piezomagnetic properties, saturation magnetostriction, and ΔE effect in DyZn at 77 K

J. B. Restorff^{a)} and M. Wun-Fogle

Naval Surface Warfare Center, Code 684, Carderock Division, West Bethesda, Maryland 20817-5700

A. E. Clark

Clark Associates, Adelphi, Maryland 20783-1225

Young's modulus, magnetization, and magnetostriction measurements were made as a function of applied magnetic field ($0 < H < 160$ kA/m) and compressive stress ($8.5 \text{ MPa} < |T| < 57.3 \text{ MPa}$) in [100] single crystal DyZn at 77 K. Piezomagnetic d constants greater than 300 nm/A and changes in Young's modulus greater than 40 GPa were found. Pronounced features are abrupt changes in the elastic moduli, magnetostriction, and coupling factors arising from "jumps" in the magnetization occurring as the moment changes from one easy [100] axis to another. The characteristic magnetic fields at which this change occurs depend strongly upon the stress induced magnetic anisotropy. Magnetomechanical coupling factors reach 0.91. © 1998 American Institute of Physics. [S0021-8979(98)34511-9]

I. INTRODUCTION

Morin *et al.*¹ have shown that large values of magnetostriction exist in rare-earth-zinc compounds having the CsCl structure. These values are only slightly smaller than those found in the heavy rare earth elements themselves. Recently, measurements of the piezomagnetic properties were reported for single crystal $\text{Tb}_{1-x}\text{Dy}_x\text{Zn}$ for $x=0, 0.4$, and 0.5 .²⁻⁴ From these observations and more extensive magnetization and magnetomechanical measurements on polycrystals, a magnetic easy axis phase diagram for $\text{Tb}_{1-x}\text{Dy}_x\text{Zn}$ ($0 \leq x \leq 0.5$) was obtained.^{3,5} In this article, we report measurements of piezomagnetic properties of DyZn at 77 K that occur during the magnetization process and compare these measurements with those for TbZn, $\text{Tb}_{0.6}\text{Dy}_{0.4}\text{Zn}$, and $\text{Tb}_{0.5}\text{Dy}_{0.5}\text{Zn}$. In all the measured rare-earth-zinc compounds to date, the $\langle 100 \rangle$ axes are the easy magnetization axes at 77 K and huge magnetostrictive distortions occur as the magnetization changes from one easy direction to another. In the following sections, piezomagnetic d constants, permeabilities, and Young's moduli under constant magnetic field, Y^H , and magnetic induction, Y^B , are reported. From these measurements, magnetomechanical coupling factors were calculated.

II. EXPERIMENT

Single crystals of DyZn were prepared at the Materials Preparation Center, Ames Laboratory, Ames, IA by a Bridgman growth technique using sealed Ta crucibles.⁶ For this study a large cylindrical single crystal sample ($1.92 \text{ cm} \times 0.65 \text{ cm}$ diam) with its axis oriented along the easy [100] direction was selected. Compressive stresses $8.5 \text{ MPa} < |T| < 57.3 \text{ MPa}$ and magnetic fields $0 < H < 160$ kA/m were applied along the long dimension of the cylinder. Magnetostriction as a function of H was obtained by (1) conventional strain gage methods and (2) LVDT's po-

sitioned to measure overall sample length changes. The magnetization was determined simultaneously by integrating the voltage of a pickup coil wound around the center of the sample. The results are shown in Fig. 1. Compressive stresses lower the energies of the [010] and [001] easy directions perpendicular to the rod axis. (Only a small compressive stress is needed to rotate all of the magnetic moments toward the perpendicular easy axes.) The presence of a relatively strong magnetocrystalline anisotropy can be seen in the magnetization versus field and the magnetostriction versus field curves. As a magnetic field is applied, three distinct magnetic regions are observed: (1) a low field region con-

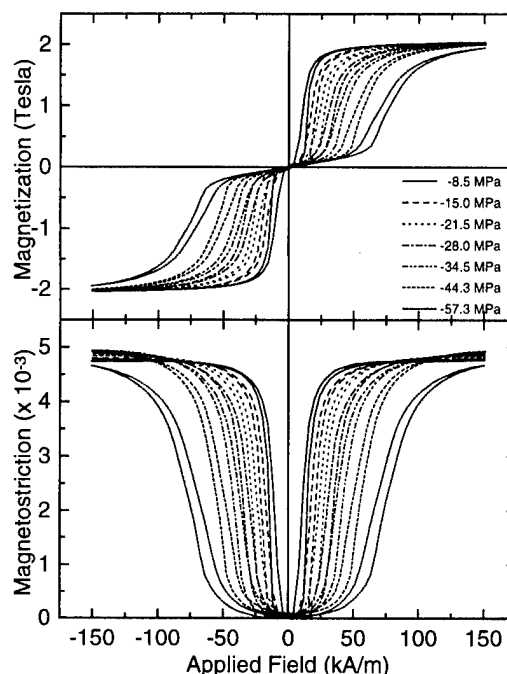


FIG. 1. Magnetization and magnetostriction vs magnetic field of single crystal DyZn along the easy [100] axis at 77 K for stresses from -8.5 to -57.3 MPa.

^{a)}Electronic mail: restorff@oasys.dt.navy.mil

sisting of a stress controlled magnetic moment rotation away from the perpendicular easy axes, (2) a region of high permeability and magnetostriction where the magnetic moments jump discontinuously from a direction near the perpendicular easy axes to the easy [100] axis along the rod, and (3) magnetic saturation. The region of high permeability and magnetization “jumping” broadens as the compressive stress is increased. We attribute this broadening to stress inhomogeneities within the sample giving rise to 90° domains which are mobile at fields below those required for magnetization rotation.

Young's moduli under constant magnetic field, Y^H , and under constant magnetic induction, Y^B , were measured as a function of magnetic field at fixed stresses, T , of -24.8 and -44 MPa. These moduli were obtained by changing the stress by ± 3.25 MPa and measuring the average strain registered by two strain gages attached on opposite sides of the sample for different values of the applied field.

III. THEORY

For a simple single domain magnetization rotation process in cubic compounds, which is applicable to DyZn in the low field magnetization region, the energy can be written as a sum of a Zeeman term, magnetocrystalline anisotropy terms, stress anisotropy terms, and an elastic term, as follows:

$$E_{\text{tot}} = -M_s \sum H_i \alpha_i + K_1 (\alpha_1^2 \alpha_2^2 + \alpha_2^2 \alpha_3^2 + \alpha_3^2 \alpha_1^2) \\ + K_2 \alpha_1^2 \alpha_2^2 \alpha_3^2 - (3/2) \lambda_{100} T (\sum (\alpha_i^2 \beta_i^2) - (1/3)) \\ - (3/2) \lambda_{111} T \sum_{i \neq j} \alpha_i \alpha_j \beta_i \beta_j + E_{\text{el}}.$$

Here M_s denotes the saturation magnetization in tesla; λ_{100} and λ_{111} are the cubic magnetostriction constants; K_1 and K_2 are the fourth order and sixth order cubic anisotropy constants, α_i and β_i are the direction cosines of the magnetization and stress direction, respectively; and E_{el} is the conventional elastic energy expression for cubic crystals. (Since K_1 is strongly positive and the magnetization remains in the (001) plane, the λ_{111} term can be neglected.)

Figure 2 illustrates the magnetic behavior for $(3/2)\lambda_{100} = 4.8 \times 10^{-3}$ and $M_s = 2.0$ T, using values of $K_1 = 1, 3, 5$ ($\times 10^5$ J/m³). Three regions, similar to the three observed in DyZn, are predicted for all values of $K_2 > -2 \times 10^6$ J/m³. In the low magnetic field region, the susceptibility, dM/dH , is given by $M_s^2/(2K_1 - 3\lambda_{100}T)$, and the piezomagnetic d constant, $d\lambda_{100}/dH$, is given by $3\lambda_{100}TM_s^2H/(2K_1 - 3\lambda_{100}T)$. As K_1 is increased, the susceptibility decreases and the jumping region moves to lower fields. For $K_1 \rightarrow \infty$, $H_{\text{sat}} \rightarrow -(3/2)\lambda_{100}T/M_s$. From these expressions values of K_1 can be obtained. In the magnetization jumping region, the susceptibility is given by $1/N$ and the piezomagnetic constant is given by $(3/2)\lambda_{100}/NM_s$, where N is the demagnetization factor. For very large negative values of K_2 , the magnetization jumps out of the (100) plane toward a $\langle 111 \rangle$ direction and back into the (100) plane, yielding two discontinuities in the magnetization and magnetostriction curves as seen in Fig. 2(b). This is not observed in DyZn.

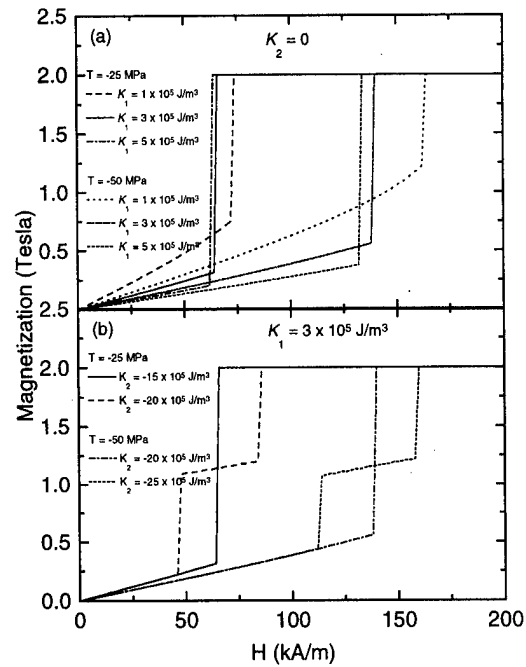


FIG. 2. Magnetization vs magnetic field for the single domain rotation model in cubic single crystals with field parallel to [100], $\lambda_{100} = 3.2 \times 10^{-3}$ and $M_s = 2.0$ T.

It is important to note that the total lowest order anisotropy constant, K_1^{TOT} , in magnetostrictive materials has two sources: (1) an intrinsic source, K_1 , and (2) a contribution which arises from the magnetostriction through the elastic energy term, ΔK_1 . When a cubic material is free to strain under magnetization rotation (constant external stress), the presence of magnetostriction gives rise to a contribution to the anisotropy not included in the K_1 term above. (For a clamped lattice, there is no magnetostrictive contribution to the anisotropy.) Substituting equilibrium strains into the elastic energy term above yields the total value of K_1 (at constant stress) to be:

$$K_1^{\text{TOT}} = K_1 + (9/4)[(c_{11} - c_{12})\lambda_{100}^2 - 2c_{44}\lambda_{111}^2].$$

IV. DISCUSSION

From the low field region of Fig. 1, the value of K_1^{TOT} for DyZn is found to be 2.9×10^5 J/m³. In Table I are compared the values of K_1^{TOT} calculated for DyZn, Tb_{0.5}Dy_{0.5}Zn, Tb_{0.5}Dy_{0.5}Zn, and TbZn. Also, in the table, calculated values of ΔK_1 , using elastic constants reported by Morin and Schmitt⁷ are listed for DyZn and TbZn. The calculated contributions to K_1^{TOT} from the magnetostriction are substantially larger than those observed in the DyZn and TbZn com-

TABLE I. Measured values of K_1^{TOT} and calculated values of $\Delta K_1 = (9/4)(c_{11} - c_{12})\lambda_{100}^2$ at 77 K.

	DyZn ($\times 10^5$ J/m ³)	Tb _{0.5} Dy _{0.5} Zn ($\times 10^5$ J/m ³)	Tb _{0.6} Dy _{0.4} Zn ($\times 10^5$ J/m ³)	TbZn ($\times 10^5$ J/m ³)
K_1^{TOT}	2.9	0.5	1.9	3.1
ΔK_1	8.3	10.0

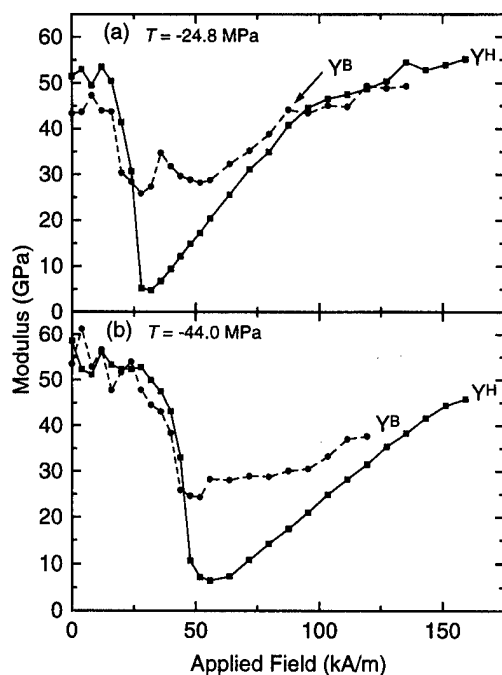


FIG. 3. Young's Moduli, Y^H and Y^B , of single crystal DyZn along the easy [100] axis at 77 K for stresses of (a) -24.8 and (b) -44.0 MPa.

pounds. Thus we conclude that the major source of K_1^{TOT} is not the intrinsic anisotropy, but the contribution arising from the change in anisotropy with strain, i.e., the magnetostriction.

For technical purposes, it is often important to know the modulus of the magnetostrictive material. In the region of magnetization jumping, where the material is most useful, the modulus is substantially lowered (ΔE Effect) due to easy domain wall motion. As a stress is applied in this region, the sample changes length by the softer magnetization process rather than by the much stiffer interatomic elasticity. Thus in a magnetically free sample, a dip is observed in the elastic modulus (Y^H) as a function of magnetic field. This dip is always reduced when the induction B is kept fixed as the stress is applied. In a material containing a single domain, the dip in Y^B disappears completely because the length change occurs only by the compression of atomic distances between the atoms. In a multidomain sample, 90° domain walls are often redistributed by the stress, resulting in a soft-

TABLE II. Relative permeability, μ_R , piezomagnetic d constant, d , Young's moduli, Y^H and Y^B , and magnetomechanical coupling factor, k , of DyZn at 77 K. $k = (1 - Y^H/Y^B)^{1/2}$.

T (MPa)	H (kA/m)	μ_R	d (nm/A)	Y^H (GPa)	Y^B (GPa)	k
-11.8	30	110	360
-24.8	31	54	295	5.0	30	0.91
-44.0	54	30	140	6.6	28	0.87

ening of the sample even though the total induction B is kept constant. The extent of the Y^B dip depends upon the ease of antiparallel 90° domains moving with respect to antiparallel 180° walls.

In Fig. 3 are plotted Young's moduli Y^H and Y^B for compressive stresses of -24.8 and -44 MPa. Note the large ΔE effect. A maximum of $Y^B/Y^H \approx 6$ is reached during the magnetization process. Since the magnetomechanical coupling $k = (1 - Y^H/Y^B)^{1/2}$, these results imply highly efficient transduction. Table II lists values of the piezomagnetic d constants, permeabilities, Young's moduli, and magnetomechanical coupling factors for stresses of -13.3 , -31.1 , and -44.0 MPa. The high coupling factors, high saturation magnetostriction, and high magnetization make the $\text{Tb}_{1-x}\text{Dy}_x\text{Zn}$ compounds attractive materials for low temperature actuators, valves, and transducers.

ACKNOWLEDGMENTS

The authors wish to acknowledge the support of the Independent Research Program of the Carderock Division of NSWC and the Materials Division of the Office of Naval Research.

- ¹P. Morin, J. Rouchy, and E. du Tremolet de Lacheisserie, *Phys. Rev. B* **16**, 3182 (1977).
- ²A. E. Clark, J. B. Restorff, M. Wun-Fogle, and J. F. Lindberg, *J. Magn. Magn. Mater.* **140-144**, 1151 (1995).
- ³J. B. Restorff, M. Wun-Fogle, J. P. Teter, J. R. Cullen, and A. E. Clark, *IEEE Trans. Magn.* **32**, 4782 (1996).
- ⁴J. R. Cullen, J. P. Teter, M. Wun-Fogle, J. B. Restorff, and A. E. Clark, *IEEE Trans. Magn.* **33**, 3949 (1997).
- ⁵J. R. Cullen, M. Wun-Fogle, J. B. Restorff, J. P. Teter, and A. E. Clark, *J. Appl. Phys.* **79**, 6216 (1996).
- ⁶Prepared by T. Lograsso at the Materials Preparation Center, Ames Lab., Ames, IA 50011.
- ⁷P. Morin and D. Schmitt, in *Ferromagnetic Materials* (North-Holland, Amsterdam, 1990), Vol. 5, Chap. 1, p. 1.

Experimental evidence of pressure-induced magnetic phase transition in $\text{Fe}_{72}\text{Pt}_{28}$ Invar alloy

S. Odin and F. Baudalet

Laboratoire pour l'Utilisation du Rayonnement Electromagnétique, Orsay, France

J. P. Itié and A. Polian

Laboratoire des Milieux Condensés, Université Paris VI, France

S. Pizzini and A. Fontaine

Laboratoire de Magnétisme Louis Néel, Grenoble, France

Ch. Giorgetti and E. Dartyge

Laboratoire pour l'Utilisation du Rayonnement Electromagnétique, Orsay, France

J. P. Kappler

Institut de Physique et Chimie des Matériaux de Strasbourg, Strasbourg, France

X-ray magnetic circular dichroism (XMCD) measurements have been performed under high pressure and used to study the disordered $\text{Fe}_{72}\text{Pt}_{28}$ Invar alloy in conjunction with x-ray diffraction. The high spin to low spin state transition is observed by both techniques and is compared with previous work. Furthermore, XMCD gives the first evidence of the complete disappearance of the magnetic moment at high pressure in this alloy. It also proves the existence of an hysteresis cycle due to the pressure-dependent magnetic moment. © 1998 American Institute of Physics. [S0021-8979(98)41011-9]

INTRODUCTION

Many transition metal alloys have been found to present magnetic volume instabilities. In certain composition range, binary and ternary alloy systems show Invar behavior.¹ In such systems, the thermal expansion is invariant in a large temperature range about the room temperature. Theoretical calculations² have shown the coexistence of two magnetic states energetically closed (about 1.5 mRy) in these systems: a high spin state (HS) centered at high volume with a large magnetic moment and a low spin state (LS) centered at low volume with a small magnetic moment. At low temperature, the HS state is totally occupied. With increasing temperature, population of the LS state is expected leading to an equal occupation of the two states at high temperature. Thus the Invar anomaly is explained with the compensation of the lattice expansion by the occupation of this low spin and low volume state. The $\text{Fe}_{72}\text{Pt}_{28}$ compound is known to be a strong ferromagnet showing an Invar anomaly. In the special case of the ordered Fe_3Pt ,³ calculations have predicted a pressure-induced transition from the HS to the LS state, i.e., a collapse of the magnetic moment. Mössbauer-effect spectroscopy experiments⁴ have given experimental evidence of this transition.

X-ray magnetic circular dichroism⁵ (XMCD) appears to be a meaningful technique in probing the magnetic properties of matter because of its double selectivity (element and orbital). In this paper, we will present the first high-pressure XMCD measurements which have been performed on the disordered $\text{Fe}_{72}\text{Pt}_{28}$ compound at the PtL_3 edge. High-pressure diffraction experiments have also been carried out and we will discuss the magnetic behavior of the compound in view to its structural properties.

HIGH-PRESSURE DIFFRACTION EXPERIMENTS

Figure 1 shows the evolution of the lattice constant with pressure for the disordered $\text{Fe}_{72}\text{Pt}_{28}$ alloy obtained by the high-pressure diffraction experiments. From the discontinuity of the lattice constant expansion rate corresponding to a change of the compressibility coefficient we have found that the transition from the mixture of HS and LS states to a pure LS one is complete at a critical pressure of about 4 GPa. Below 4 GPa, the lattice parameter decrease is due to the sample compression and the HS/LS transition. Above 4 GPa, the only contribution to the lattice parameter decrease is the sample compression in the LS state. The fact that no difference in the five fcc structure diffraction lines indexing were detected below and above the critical pressure shows that no structural phase transition occurs. In the whole pressure range, the fcc lattice remains stable.

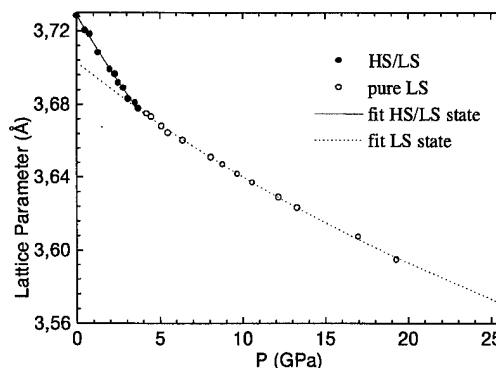


FIG. 1. Lattice parameter as a function of pressure for the $\text{Fe}_{72}\text{Pt}_{28}$ disordered compound.

In the pressure ranges below and above 4 GPa, the lattice constant pressure dependence can be well fitted with the Murnaghan equation at the first order:

$$a = a_0(1 + B'_0 P/B_0)^{-1/3B'_0},$$

where B_0 and B'_0 are, respectively, the bulk modulus and its first derivative at $P=0$. We find the bulk modulus values of 78 ± 8 and 167 ± 7 GPa, respectively, below and above 4 GPa.

Ultrasonic waves experiments⁶ (USW) have been made on the $\text{Fe}_{72}\text{Pt}_{28}$ disordered crystal. They have found at room pressure and room temperature a value of 114 GPa for the bulk modulus which is very much larger than the one we have found (78 GPa). The difference between the two values could be explained by the fact that ultrasonics measurements at room pressure do not provoke the HS/LS transition. The only contribution to the bulk modulus is the sample compression in the mixture of the HS and LS state. Therefore the bulk modulus deduced from ultrasonics has to be compared with that measured in a state where no magnetovolumic effect takes place, i.e., in the pure LS state. From the B_0 and B'_0 parameters values above 4 GPa, we have extrapolated the bulk modulus of the LS state with a lattice parameter corresponding to the room pressure one. We have found a value of 167 GPa; the sample in the mixture of the HS and LS state is more compressible than in the LS state. Since the compressibility is directly related to the number of bonding electrons, in a crude approximation, more electrons are involved in the LS state binding than in the HS one. Podgorny⁷ has calculated the electronic contribution in the bonding of Fe–Pt alloys. In strong ferromagnets such as $\text{Fe}_{72}\text{Pt}_{28}$ in the HS state, the majority Fe 3d band is full and has no bonding properties. He has shown that the electrons implied in the binding of Fe–Pt alloys are mainly from the Fe 3d minority band hybridized with the Pt 5d minority band. Under compression, the number of Fe minority electron increases leading to a magnetic moment decrease. This may support our view concerning the number of electrons implied in the bonding since the LS phase corresponds to the magnetic state at high pressure.

HIGH-PRESSURE XMCD EXPERIMENTS

The high-pressure XMCD experiments have been carried out on the energy dispersive x-ray absorption beamline D11 at DCI, Orsay. The polychromator was a bent silicon (111) crystal, focusing right at the sample position located between the poles of an electromagnet (0.3 T), where the high-pressure cell is placed. Right circularly polarized photons were selected by a slit set 0.3 mrad below the orbit plane of the storage ring and the magnetic field was reversed to make the XMCD measurements.

Figure 2(a) presents the XMCD spectra at 2.5 GPa of the disordered $\text{Fe}_{72}\text{Pt}_{28}$ at the PtL_{III} edge and the signal obtained is directly related to the magnetic moment of the Pt 5d band. Our results at room pressure are in good agreement with former works which have been made on this compound.⁸ The existence of the XMCD spectra shows a spin polarization of the Pt 5d band induced by the Fe 3d band. This

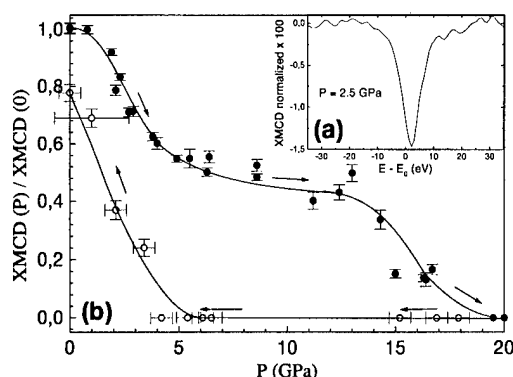


FIG. 2. (a) Normalized XMCD signal at the PtL_{III} edge of the disordered $\text{Fe}_{72}\text{Pt}_{28}$ compound at 2.5 GPa. (b) Evolution of the XMCD integral at increasing (full circle) and decreasing (empty circle) pressure.

polarization results from two factors: the Fe spin polarization, which depends on the Fe–Fe distance, and the Fe–Pt hybridization. The sign of the spectra indicates a ferromagnetic coupling between the Pt and the Fe moments.

Figure 2(b) shows the integral of the spectra of the disordered $\text{Fe}_{72}\text{Pt}_{28}$ at different pressures. For the disordered alloy, an increase of the pressure from 2 to 4 GPa decreases the XMCD signal and indicates a magnetic phase transition. From 4 GPa, the signal is stabilized with a lower intensity, and we attribute this first magnetic phase transition to the well-known transition from the mixture of the HS and the LS state to the pure LS state.

Around 13 GPa, the XMCD signal decreases drastically and vanishes totally above a critical pressure of 20 GPa. This is the first experimental evidence of a pressure-induced magnetic moment collapse in this compound. The disordered $\text{Fe}_{72}\text{Pt}_{28}$ undergoes a magnetic transition from the LS state to a nonmagnetic state (NM) as expected from theoretical calculations.³

The first transition from the HS to the LS state has already been observed at 4.2 K at about the same pressure by Abd-Elmeguid *et al.* using ^{57}Fe high-pressure Mössbauer spectroscopy (MS).⁴ In addition, MS follows the pressure dependence of the Curie temperature. At about 8.2 GPa, the T_c of the disordered phase is 40 K which is in contradiction with the existence of a XMCD signal above this pressure at room temperature. MS experiments have also been performed on the ordered phase of the $\text{Fe}_{72}\text{Pt}_{28}$ compound and the transition from the HS to the LS state has been observed at a critical pressure of 6 GPa. A pressure dependence of the Curie temperature has been observed and the value of T_c at 7.1 GPa is about 110 K.

We have also measured the pressure-dependent XMCD signal of the ordered phase of $\text{Fe}_{72}\text{Pt}_{28}$ at 300 K. The XMCD signal decreases before 6 GPa and at about 9 GPa the signal is already very small. The XMCD magnitude decreases because of the concomitant pressure dependence of the Curie temperature and the HS–LS transition. In the special case of the ordered phase, the transition from the HS to the LS state followed by XMCD seems to be hidden by the thermal decrease of the magnetization.

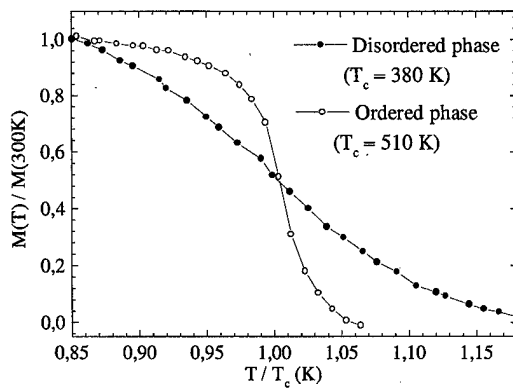


FIG. 3. Magnetization as a function of temperature for the ordered and disordered $\text{Fe}_{72}\text{Pt}_{28}$ compound.

The temperature dependence of magnetization has been investigated for the two phases (Fig. 3). Compared to the ordered phase, the decrease of magnetization of the disordered phase is very soft around the Curie temperature. In the disordered phase, the Pt and Fe atoms are randomly distributed over all the sites of the fcc structure which leads to local fluctuations of concentration. Spatial inhomogeneities can lead to variations of Curie temperature which broadens the distribution of the magnetization curve. Under compression, the difference of the Curie temperature between various domains may be enhanced leading to a broadening of the paramagnetic transition width: at high pressure the magnetization should still remain well above the Curie temperature.

In the disordered compound, the flat part of the XMCD curve in the pressure range above 4 GPa proves that the system is in the LS state. According to MS results, the Curie temperature is around room temperature in the pressure range of the HS/LS transition and the thermal decrease of the magnetization is an additional cause of the decreasing XMCD signal. In parallel, we have to consider the increase of Pt spin polarization due to the strengthening of hybridization with pressure which leads to the opposite trends, i.e., an

increase of the XMCD signal. At the Pt L edges, XMCD probes the 5d band of platinum and according to other studies⁹ the orbital moment of the 5d band is less than 10% of the total magnetic moment. Consequently, the XMCD signal is directly related to the spin polarization of the 5d. Because of the volumic compression, the overlap between the Fe 3d band and the Pt 5d band increases leading to a larger spin polarization of the platinum induced by the hybridization with the spin polarized 3d band of iron. This reinforcement of hybridization counterbalances part of the decrease of the spin polarization of platinum. This effect may fully counterbalance the decrease of the XMCD signal expected from thermal effects.

When the pressure is released, the XMCD signal of the disordered phase appears at about 5 GPa and finally the integral of the XMCD signal at room pressure is stabilized at a value which is lower than the initial HS state one. At the same time, diffraction experiments have shown that the volume of the sample after releasing the pressure is the same as the one obtained in the HS initial state. We have clearly shown that the $\text{Fe}_{72}\text{Pt}_{28}$ alloy undergoes directly the transition from the NM to the HS states when the pressure is released. The existence of such a cycle of hysteresis in the evolution of the magnetic moment is in good agreement with the calculations of Podgorny.³ This proves that such compounds can have different magnetic states with the same crystallographic structures, depending on the history of the system.

¹E. F. Wassermann, in *Ferromagnetic Materials*, edited by K. H. J. Buschow and E. P. Wohlfarth (North-Holland, Amsterdam, 1990), Vol. 5, p 238.

²V. L. Moruzzi, *Phys. Rev. B* **41**, 6939 (1990).

³M. Podgorny, *Physica B* **161**, 105 (1989).

⁴M. M. Abd-Elmeguid and H. Micklitz, *Phys. Rev. B* **40**, 7395 (1989).

⁵G. Schütz et al., *Phys. Rev. Lett.* **58**, 737 (1987).

⁶L. I. Manosa et al., *J. Phys.: Condens. Matter* **3**, 2273 (1991).

⁷M. Podgorny, *Phys. Rev. B* **43**, 11300 (1991).

⁸S. Stähler et al., *J. Appl. Phys.* **73**, 6063 (1993); H. Ebert et al., *Solid State Commun.* **69**, 485 (1989).

⁹W. Grange and J. P. Kappler (private communication).

Electrochemical deposition of amorphous FeB films with soft magnetic properties

Naoyuki Fujita

Department of Electrical Engineering and Computer Science, Osaka Prefectural College of Technology, Saiwai, Neyagawa 572, Japan

Mitsuteru Inoue and Ken'ichi Arai

Research Institute of Electrical Communication, Tohoku University, Sendai 980-77, Japan

Pang Boey Lim

Department of Functional Material Sciences, Faculty of Engineering, Saitama University, Shimo-Okubo, Urawa 338, Japan

Toshitaka Fujii

Department of Electrical and Electronic Engineering, Toyohashi University of Technology, Toyohashi 441, Japan

To obtain FeB amorphous plated films with soft magnetization and high magnetostriction, effects of three kinds of agents [sodium L-ascorbate ($C_6H_7NaO_6$), thiourea (NH_2CSNH_2), and ammonium sulfate ($(NH_4)_2SO_4$)] on magnetic and magnetoelastic properties of films were investigated systematically. The first two agents, $C_6H_7NaO_6$ and NH_2CSNH_2 were found to be ineffective for improving the soft magnetic properties of films. To the contrary, however, $(NH_4)_2SO_4$ is very effective for the magnetic softening: Amorphous FeB plated films with coercivity less than 4 Oe were obtained by employing the bath composition of $FeSO_4 \cdot 7H_2O$ (71.9 mM), KBH_4 (296.6 mM), NaOH (400 mM), $KNaC_4H_4O_6 \cdot 4H_2O$ (600 mM) and $(NH_4)_2SO_4$ (80 mM). These soft films exhibited a favorable large magnetostriction of 26×10^{-6} , being adequate for micromagnetoelastic devices. © 1998 American Institute of Physics. [S0021-8979(98)41111-3]

I. INTRODUCTION

Recently, we have demonstrated that amorphous FeB films are obtained by electroless plating.¹ The resultant film thickness was, however, very thin due to low catalytic activity of iron. To overcome this problem, we employed electroplating technique and showed that thick amorphous FeB films can be formed by carefully controlling the bath temperature and current density.² The plated films unfavorably exhibited hard magnetic properties (20–50 Oe coercivity) and small magnetostriction, although the alloy film prepared by physical means such as sputtering generally has very soft magnetization and large magnetostriction simultaneously. Thus, magnetic softening of the plated films has become indispensable for using the films in practical micromagnetoelastic devices.³

Certain agents for reducing the coercivity of plated alloy films exist with the choice depending on the alloy systems and the plating mechanism. For instance, Kim *et al.*⁴ showed that sodium L-ascorbate ($C_6H_7NaO_6$), acting as an oxidation prevention agent for ferrous ion, was effective for the magnetic softening of NiFe electroless plated films. For CoNiFe plated films, however, thiourea (NH_2CSNH_2) is useful, because NH_2CSNH_2 causes the reduction in CoNiFe grain sizes, yielding the reduction in coercivity of the alloy films.⁵ Appropriate choice of complexing agent can also lead to the magnetic softening, as is the case for the CoB electroless plated films of Osaka *et al.*,⁶ made with a combined complexing agent of sodium tartrate ($Na_2C_4H_4O_6 \cdot 2H_2O$) and ammonium sulfate ($(NH_4)_2SO_4$).

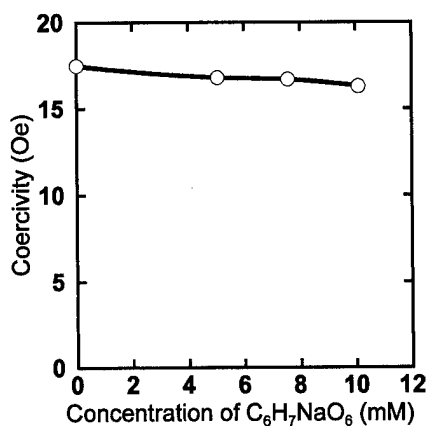
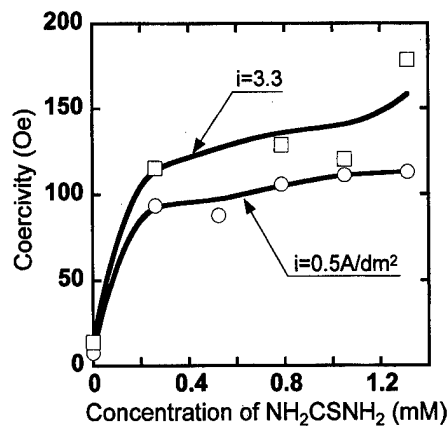
In this study, therefore, the effects of the above three kinds of agents ($C_6H_7NaO_6$, NH_2CSNH_2 , and $(NH_4)_2SO_4$) on magnetic and magnetoelastic properties of amorphous FeB plated films have been investigated, so as to obtain electrochemically an alloy film with soft magnetization and large magnetostriction which are comparable to those of sputtered films.

II. PLATING OF AMORPHOUS FeB FILMS

Let us briefly describe the plating conditions for obtaining amorphous FeB film, because the effects of all additional agents were studied based on the original conditions. Table I shows the composition of original plating bath; iron sulfate ($FeSO_4 \cdot 7H_2O$) and potassium borohydride (KBH_4) were used as the sources for iron and boron. Sodium hydroxide (NaOH) was used as a pH control agent, while potassium sodium tartrate ($KNaC_4H_4O_6 \cdot 4H_2O$) was used as a complexing agent. The plating bath was prepared, by first dissolving the $KNaC_4H_4O_6 \cdot 4H_2O$ in distilled water, whose temperature was about 25 °C. Then, the $FeSO_4 \cdot 7H_2O$ was added and dissolved. After dissolving $FeSO_4 \cdot 7H_2O$ completely, the NaOH solution and KBH_4 were added. The preparation procedure

TABLE I. The basic plating bath compositions.

Iron sulfate	$FeSO_4 \cdot 7H_2O$	71.9 mM
Potassium borohydride	KBH_4	296.6 mM
Sodium hydroxide	NaOH	400 mM
Potassium sodium tartrate	$KNaC_4H_4O_6 \cdot 4H_2O$	318.9 mM

FIG. 1. Coercivity vs $C_6H_7NaO_6$ concentration in bath.FIG. 2. Coercivity vs NH_2CSNH_2 concentration in bath.

of plating bath as well as the amount and the temperature of distilled water in which $KNaC_4H_4O_6 \cdot 4H_2O$ was dissolved are very important for preventing the precipitation of iron hydroxide. The bath temperature during the film deposition was kept below $35^\circ C$, because the alloy film with amorphous structure could not be obtained when the film was formed at above that temperature. With the current density of $1 A/dm^2$, amorphous $Fe_{80}B_{20}$ film with about $1 \mu m$ thickness was formed after 30 min. deposition.

III. EXPERIMENT

The effects of additional agents were studied by dissolving the individual agents into the bath solution (Table I). The bath with $C_6H_7NaO_6$ was obtained by dissolving $C_6H_7NaO_6$ (5.04–10.1 mM) prior to dissolving $KNaC_4H_4O_6 \cdot 4H_2O$. In this case, the concentration of $KNaC_4H_4O_6 \cdot 4H_2O$ was 600 mM. The bath with NH_2CSNH_2 was prepared by dissolving NH_2CSNH_2 (0.263–1.31 mM) into the base solution after all other ingredients were mixed without changing the original composition. As for the bath with $(NH_4)_2SO_4$, $(NH_4)_2SO_4$ (0–100 mM) was added into the base solution after dissolving $KNaC_4H_4O_6 \cdot 4H_2O$. In this case, however, the concentration of $KNaC_4H_4O_6 \cdot 4H_2O$ was changed, ranging from 200 to 600 mM. The reason is that $(NH_4)_2SO_4$ and $KNaC_4H_4O_6 \cdot 4H_2O$ form a combined complex agent, and the complexing effect of the combined agent is presumably governed by this ratio.

In all cases, bath temperature was maintained at $30 \pm 2^\circ C$ during the film formation by using automatic thermostat mechanism equipped for the bath. The film substrates were copper foils and glass plates covered with Cu ($100 \mu m$ thick)/Cr ($50 \mu m$ thick) double layers. The Cr underlayers, which were directly deposited on the glass plates, were used to prevent the exfoliation of the top Cu layers during plating.

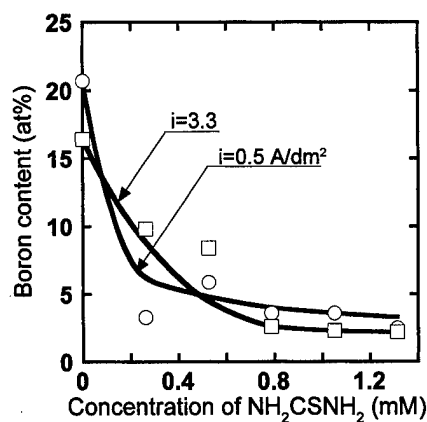
IV. RESULT AND DISCUSSION

Figure 1 shows the change in coercivity of films versus the concentration of $C_6H_7NaO_6$. Although $C_6H_7NaO_6$ was expected to be effective for magnetic softening by decreasing the dissolved oxygen and preventing oxidation of ferrous ion in the bath, no apparent change in the coercivity of amorphous FeB plated film was observed. This indicates that the

hard magnetic properties of films are not caused by the dissolved oxygen in the bath. The amount of dissolved oxygen in the bath is unclear, but is considered to be negligible. This is because KBH_4 as the boron supplier also acts as a reducing agent whose reducing power is presumably sufficient for reducing the dissolved oxygen without $C_6H_7NaO_6$.

Figure 2 shows the change in coercivity of films versus the concentration of NH_2CHNH_2 , where the current intensity i is taken as a parameter. The coercivity of films unfavorably increased by the addition of NH_2CHNH_2 to about 100 Oe, suggesting the existence of crystal phase in films. In fact, x-ray diffraction peaks corresponding to α -Fe phase were observed for these films. This situation is well explained from Fig. 3, showing that the boron content of these films is markedly reduced by the addition of NH_2CHNH_2 , which results in the change in crystallographic structure of films from amorphous to polycrystalline. Then, in our plating system, NH_2CHNH_2 is less attractive agent for magnetic softening of amorphous FeB films.

Contrary to the above two cases, addition of $(NH_4)_2SO_4$ was found to be very effective for reducing the coercivity of plated films. Figure 4 shows a coercivity map, in which coercivities of the films are plotted as a function of the concentrations of both $(NH_4)_2SO_4$ and $KNaC_4H_4O_6 \cdot 4H_2O$. The film coercivities vary depending strongly on the concentrations of $KNaC_4H_4O_6 \cdot 4H_2O$ and $(NH_4)_2SO_4$, but in general they be-

FIG. 3. Boron content vs NH_2CSNH_2 concentration in bath.

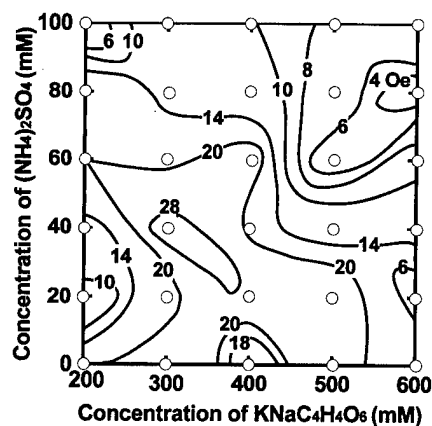


FIG. 4. Coercivity of the film vs $\text{KNaC}_4\text{H}_4\text{O}_6$ and $(\text{NH}_4)_2\text{SO}_4$ concentration in bath.

come smaller when the concentrations of these agents are increased simultaneously. Especially, for the combination of $\text{KNaC}_4\text{H}_4\text{O}_6 \cdot 4\text{H}_2\text{O}$ (600 mM) and $(\text{NH}_4)_2\text{SO}_4$ (80 mM), the film exhibited a coercivity less than 4 Oe, suggesting that the use of combined complex agents composed of $\text{KNaC}_4\text{H}_4\text{O}_6 \cdot 4\text{H}_2\text{O}$ and $(\text{NH}_4)_2\text{SO}_4$ is very effective for magnetic softening. Because of the wide variety of coercivities of films, the magnetic softening was considered due to the change in film compositions. Then, film compositions for all samples in Fig. 4 were evaluated. The results are summarized in Fig. 5 as a composition map with respect to the concentrations of complex agents. In comparison with Fig. 4, meaningful correlation between the coercivity and the composition of films is not seen: the composition of film with coercivity of 4 Oe is 30 at. % from Fig. 5, but the coercivity

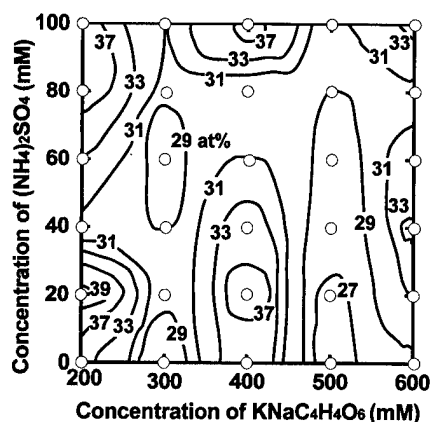


FIG. 5. Boron content of the film vs $\text{KNaC}_4\text{H}_4\text{O}_6$ and $(\text{NH}_4)_2\text{SO}_4$ concentration in bath.

of films with the same composition varies from sample to sample in Fig. 4. Therefore, the change in film composition is not responsible for the magnetic softening.

Apart from the mechanism of magnetic softening with the combined complex agent, the plated FeB films exhibiting such a small coercivity are very attractive for micromagnetoelastic devices. In this case, films are required to exhibit large magnetostriction as well as the soft magnetic properties. The plated film with soft magnetic properties showed a considerably large magnetostriction of 26×10^{-6} . Since the magnetostriction of plated films which have been formed without using $(\text{NH}_4)_2\text{SO}_4$ is as small as 1×10^{-6} , the use of a combined complex agent is thus also useful for improving the magnetoelastic properties of films through magnetic softening.

V. CONCLUSION

It is concluded that the use of combined complex agent composed of $\text{KNaC}_4\text{H}_4\text{O}_6 \cdot 4\text{H}_2\text{O}$ and $(\text{NH}_4)_2\text{SO}_4$ is useful for obtaining amorphous FeB plated films with small coercivity and large magnetostriction. The use of $\text{C}_6\text{H}_7\text{NaO}_6$ or NH_2CSNH_2 is, however, less effective for magnetic softening of the FeB plated films contrary to other alloy systems such as NiFe^4 and CoNiFe films.⁵

The mechanism of magnetic softening by the combined complex agent is still unclear, although the changes in grain sizes and/or crystallographic structures of films are likely to be responsible. To clarify this, further investigations are now under progress, together with the determination of optimum plating conditions for obtaining amorphous FeB films with soft magnetization and large magnetostriction.

ACKNOWLEDGMENTS

This work was supported in part by IKETANI Science and Technology Foundation. Part of this work was also carried out under the Cooperative Research Project Program of the Research Institute of Electrical Communication, Tohoku University.

¹N. Fujita, A. Tanaka, P. T. Squire, P. B. Lim, M. Inoue, and T. Fujii, *Appl. Surf. Sci.* **113/114**, 61 (1997).

²P. B. Lim, N. Fujita, P. T. Squire, M. Inoue, and T. Fujii, *Mater. Res. Soc. Symp. Proc.* **451**, 495 (1997).

³cf., M. Inoue, S. Tanaka, T. Yoshimine, and T. Fujii, *Elsevier Studies in Applied Electromagnetic in Materials* **4**, 127 (1993).

⁴D. H. Kim, K. Aoki, and O. Takano, *J. Surf. Finsh. Soc. Jpn.* **46**, 567 (1995), in Japanese.

⁵M. Takai, K. Hayashi, M. Aoyagi, and T. Osaka, Abstract of 95th conference of J. Surf. Finsh. Soc. Jpn. 24 (1997), in Japanese.

⁶T. Osaka, T. Honma, N. Masubuchi, K. Saito, M. Yoshino, Y. Yamazaki, and T. Namikawa, *J. Magn. Soc. Jpn.* **14**, 309 (1990), in Japanese.

Field-induced strain under load in Ni–Mn–Ga magnetic shape memory materials

S. J. Murray, M. Farinelli, C. Kantner, J. K. Huang, S. M. Allen, and R. C. O'Handley
Massachusetts Institute of Technology, Cambridge, Massachusetts 02139

Single-crystal Ni_2MnGa shows a nearly 0.2% strain under a magnetic field of 8 kOe at -8°C . Polycrystalline samples have been prepared near stoichiometry to study the composition dependence of the magnetic and elastic properties. A narrow band of compositions has been found having a range of Curie and martensitic transformation temperatures, T_C and T_0 , extending to above room temperature. The compressive stress-strain characteristics in variable transverse field were studied in samples selected to have T_0 just below room temperature. Stress-induced martensite was observed as expected and the magnetic field was applied under fixed load for various stresses. A transverse field of 3200 Oe caused the sample to strain under load doing work that increased up to 1.3 J/kg with increasing volume fraction of stress-induced martensite. © 1998 American Institute of Physics. [S0021-8979(98)41211-8]

I. INTRODUCTION

Very large magnetic-field-induced free strains (no load) have been observed in the low-temperature phase of certain magnetic alloys that show a martensitic transformation and exhibit the associated shape-memory effect.¹ A field-induced, free strain of 0.2% was reported^{2,3} in single crystals of Ni_2MnGa at -8°C . James and Wuttig⁴ reported a free strain 0.5% in single crystals of FePd at -17°C . Further, James and Wuttig have observed⁵ that a stress-cooled, off-stoichiometry, single crystal of Ni_2MnGa shows a field-induced, free strain of 1.3% below 0°C . Clearly, these magnetic martensitic materials already surpass piezoelectric materials and magnetostrictive materials such as Terfenol-D, in their ability to generate free strain. They can be expected to have potential in a variety of actuation devices and smart materials.

There is new science to be uncovered as we understand better how the twin boundaries in these shape memory materials respond to the application of a magnetic field as well as to stress. Progress is already being made in this direction.^{4,6,7} The observations of this magnetic shape memory effect reported so far indicate some of the major challenges faced in advancing these materials toward application:

- (1) The operating temperature of these materials must be increased.
- (2) Their performance under significant loads must be characterized.
- (3) These characteristics should be sought in more robust, and (probably) polycrystalline materials.

This paper describes results that begin to address each of these issues. Polycrystalline samples of Ni–Mn–Ga alloys have been made that show martensitic transformation temperatures in excess of 40°C and that are ferromagnetic to higher temperatures. So far these samples show only relatively small magnetic-field-induced strains, possibly because

they are untextured. Further, the strain under loads up to 110 MPa has been measured in NiMnGa polycrystals at room temperature.

II. EXPERIMENT

Several samples weighing approximately 50 g each were induction melted and some were vacuum cast. Pieces were cut from these samples for magnetometry, field-induced strain and mechanical testing. Magnetometry was done in fields up to 10 kOe at temperatures from 200 to 400 K. Field-induced strain was measured using metal foil strain gauges and a bridge circuit. The field range accessible here was ± 5 kOe over temperatures of 200 to 400 K. Field-induced strain under load was measured using an Instron machine fitted with a hybrid electro-permanent magnet capable of fields up to 3.2 kOe.

III. RESULTS

A. Composition dependence

The polycrystalline samples were characterized by three fundamental parameters that are believed to be critical to observing magnetic-field-induced strains in shape memory alloys. These are saturation magnetization, M_s , Curie temperature, T_C , and martensitic temperature, T_{mart} . M_s is important because the magnetic pressure driving twin boundary motion is given by $2M_sH$. Further, the material should be in the martensitic state at the operating temperature, $T < T_{\text{mart}}$, and operation at or above room temperature is an immediate goal. The variation of M_s , T_C , and T_{mart} are given in Table I for some of the polycrystalline samples made.

These results are shown graphically in a ternary phase diagram, Fig. 1, which defines the field of $M_s > 45$ emu/g, $T_C > 70$ and 80°C , as well as $T_{\text{mart}} > 20$ and 40°C . Samples having appreciable magnetization and T_{mart} in the ferromagnetic phase at or above room temperature are found in a band of compositions stretching roughly from $\text{Ni}_{50}\text{Mn}_{29}\text{Ga}_{21}$ toward $\text{Ni}_{44}\text{Mn}_{34}\text{Ga}_{22}$. While these samples are of importance for further development, in this paper we focus on the inter-

TABLE I. Saturation magnetization, M_s , Curie temperature, T_C , and martensitic transformation temperature, T_{mart} , of some polycrystalline Ni-Mn-Ga alloys.

Composition			M_s (emu/gm)	T_C (Centigrade)	T_{mart} (Centigrade)
Ni	Ga	Mn			
50.7	20.0	20.3	50.3	70	12
48.6	32.6	18.8	16.8	51	42
47.1	35.1	17.8	9.0	47	-
52.0	33.1	14.9	0.6	-	-
41.7	34.1	24.2	24.3	80	< -80
50.0	27.2	22.8	45.4	66	-80
51.1	30.5	18.4	20.2	45	-
53.7	29.7	16.6	0.7	-	-
44.2	32.3	23.5	43.8	75	< -80
44.2	31.1	24.7	32.8	70	< -80
42.9	32.8	24.3	27.0	75	< -80
50.2	30.0	19.8	47.9	53	29
50.1	30.7	19.2	32.9	60	1
46.6	34.1	19.3	38.8	70	43

esting behavior of $\text{Ni}_{50}\text{Mn}_{28}\text{Ga}_{22}$ alloy which is austenitic at room temperature and martensitic below 12 °C.

B. Temperature dependence

The field induced strain of single crystal Ni_2MnGa has been reported above and below the transformation temperature.^{2,3} It is of interest to know the details of the temperature dependence of the strain associated with twin boundary motion. The top part of Fig. 2 shows the temperature dependence of the magnetization measured in $H = 100$ Oe. The magnetization step at T_{mart} is a reflection of the stronger magnetic anisotropy in the tetragonal martensitic phase. The saturation magnetization is fairly continuous through the transformation. The lower part of Fig. 2 shows the variation of the strain, e_0 , with increasing and decreasing temperature about T_{mart} . e_0 is measured in a saturating field parallel to the strain gauge and is negative.

Note that the strain in the martensitic phase ($T < 12$ °C) is more than an order of magnitude smaller than

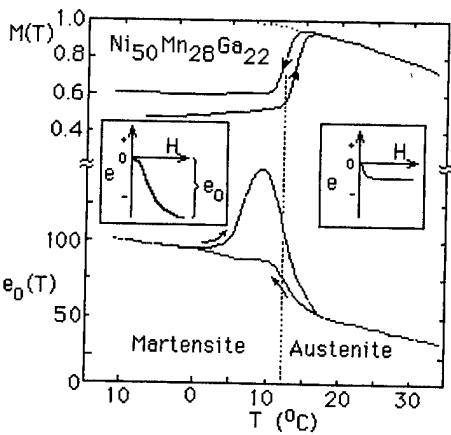


FIG. 2. Above, temperature dependence of magnetization in $H = 100$ Oe on cycling polycrystalline $\text{Ni}_{50}\text{Mn}_{28}\text{Ga}_{22}$ through its martensitic transformation temperature. Below, temperature variation of field-induced strain in a saturating field. Inserts show the field dependence of the strain above and below T_{mart} as well as the definition of e_0 .

that reported in single crystals of the stoichiometric compound.^{2,3} The reasons for this are not yet clear but it may be due to the polycrystalline nature of the material or to the presence in this sample of impurities that impede twin boundary motion. The strain increases on cooling from the austenitic phase, making an abrupt increase with the appearance of twinning below 12 °C. On heating from the low-temperature phase there is a clear peak in field-induced strain just below the transformation temperature. This may be a manifestation of lattice softening near the transformation. This peak is less pronounced on cooling than on heating from deep in the martensitic phase because in the latter case the material is more fully transformed and more twinning would have occurred than on first cooling through T_{mart} .

C. Strain under load

Polycrystalline $\text{Ni}_{50}\text{Mn}_{28}\text{Ga}_{22}$ is interesting from another point of view that exploits its austenitic state at room temperature. Figure 3 shows that this material exhibits what is commonly referred to as stress-induced martensite when the

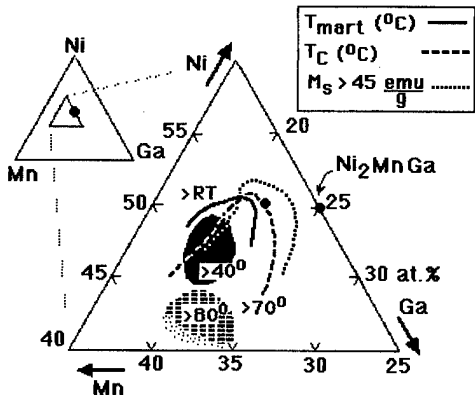


FIG. 1. Partial ternary phase diagram for polycrystalline Ni-Mn-Ga alloys showing M_s , T_C , and T_{mart} fields of interest. The solid dots show the stoichiometric composition, Ni_2MnGa and the location of $\text{Ni}_{50}\text{Mn}_{28}\text{Ga}_{22}$ which is focused on in this paper.

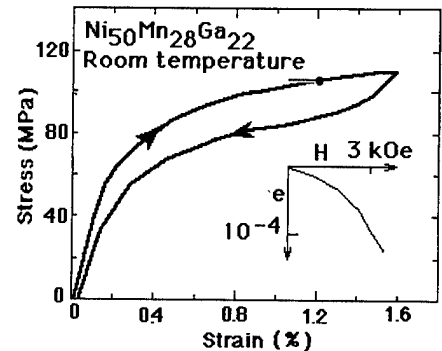


FIG. 3. Stress-strain curve taken on polycrystalline $\text{Ni}_{50}\text{Mn}_{28}\text{Ga}_{22}$ at room temperature (austenitic) using an Instron machine. The nonlinearity is evidence of stress-induced martensite. The insert, lower right, shows the field induced strain under constant load from the starting point indicated by the solid dot on the σ - e curve.

austenitic phase is loaded at temperatures not too far above T_{mart} . On first loading the material, it shows a stiffness characteristic of the high-temperature phase. However, at higher loads, some regions transform to martensite and twins form with a preferred orientation that effectively accommodates the applied load. On reducing the load, the stress-induced martensite reverts to austenite and the large strain is returned, hence the name superelasticity.

It is interesting for several reasons to use this stress-induced martensite as a starting material for measuring field-induced strain. First, the twins formed are preferentially aligned by the applied load. Second, observation of significant field-induced strain above the transformation temperature would extend the temperature range over which these materials would be useful. Third, such measurements provide strain-under-load data that are not yet available on these magnetic shape memory materials.

The insert in Fig. 3 shows the strain achieved in an applied field of 3.2 kOe transverse to the load axis, at a constant load of 108 MPa, (600 lbs over a 0.25 cm^2 area). The solid dot on the stress strain curve locates the starting condition. The solid line extending to the left of the dot indicates the nature of the experiment, i.e., the applied field causes the material to reverse the strain induced by the load which is held constant. The strains measured here in 3.2 kOe are considerably larger than those shown in Fig. 2 in the austenitic phase (taken in 6 kOe); they are comparable in magnitude to those measured in the martensitic phase. The sign of the field-induced strain is consistent with a free-energy model for martensite-austenite phase boundary motion⁷ and with the observed destabilization of the martensitic phase in a magnetic field.²

The work done by the sample on the Instron machine during field actuations is 11 kJ/m^3 (or 1.3 J/kg). This is comparable to the work output of Terfenol-D actuators (10 to 20 kJ/m^3) reported by Clark *et al.*⁸ Perhaps more importantly, if one connects the greatest free strain yet measured on single crystal NiMnGa⁵, namely 1.3% , with the load bearing ability of the polycrystalline samples, in excess of 110 MPa , the potential for mechanical work output can be inferred to be of order 715 kJ/m^3 (90 J/kg). This estimate of the potential of magnetic shape memory materials to do work compares very favorably with the comparable quality factor for Terfenol-D, namely $0.24\% \times 100 \text{ MPa}/2 \approx 120 \text{ kJ/m}^3$.

ACKNOWLEDGMENT

This work was supported by a grant from the Technology Development Center of Finland through Data City Center and from the Academy of Finland.

¹M. Cohen and C. M. Wayman, in *Metallurgical Treatises*, edited by J. K. Tien and J. F. Elliott (The Metallurgical Society of AIME, New York, 1981), p. 445; C. M. Wayman, MRS Bull. April, 49 (1993).

²K. Ullakko, J. K. Huang, C. Kantner, R. C. O'Handley, and V. V. Kokorin, Appl. Phys. Lett. **69**, 1966 (1996).

³K. Ullakko, J. K. Huang, V. V. Kokorin, and R. C. O'Handley, Scr. Mater. **36**, 1133 (1997).

⁴R. D. James and M. Wuttig, Philos. Mag. A **77**, 1273 (1998).

⁵R. D. James and M. Wuttig (personal communication).

⁶R. D. James and D. Kinderlehrer, Philos. Mag. B **68**, 237 (1993).

⁷R. C. O'Handley, J. Appl. Phys. **83**, 3263 (1998).

⁸A. E. Clark, J. P. Teter, and O. D. McMasters, J. Appl. Phys. **63**, 3910 (1988).

Magnetoelastic behavior of the Heusler Ni_2MnGa alloy

Eduard Obradó,^{a)} Alfons González-Comas, Lluís Mañosa, and Antoni Planes

Departament d'Estructura i Constituents de la Matèria, Facultat de Física, Universitat de Barcelona, Av. Diagonal 647, E-08028 Barcelona, Spain

In this work the effect of the interplay between magnetic and structural degrees of freedom in the structural transitions undergone by Ni_2MnGa alloy is investigated. Elastic constant and magnetic susceptibility measurements in a magnetic field are presented. A simple phenomenological model is proposed to account for the experimental observations. © 1998 American Institute of Physics. [S0021-8979(98)25911-1]

I. INTRODUCTION

The Ni_2MnGa alloy is the only known ferromagnetic material exhibiting a martensitic transition from a high temperature Heusler structure towards a close-packed phase.^{1,2} Associated with this phase transition, this material exhibits shape memory properties.³ These properties are related to the ability of the system to reverse large deformations in the martensitic phase by heating the alloy up to the high temperature phase. The interest of ferromagnetic compounds compared with other shape memory alloys is the possibility of magnetic field control of the shape memory properties. The potentiality of the Ni_2MnGa alloy for such a purpose has been recently proved by Ullakko and co-workers.⁴ They have shown that the application of a magnetic field provokes a tendency of the martensitic variants to be aligned with the field. As a consequence, the field modifies the induced transformation strain.

More fundamental is the fact that, in this material, the martensitic transition is preceded by the appearance of a micromodulated structure which is accompanied by the condensation of a $q=0.33\text{ TA}_2$ phonon.⁵ Recently, we have shown^{6,7} that this premartensitic structure develops via a weakly first order transition. Since such a premartensitic transition is not observed in other nonferromagnetic materials, it seems reasonable to believe that it is a consequence of a magnetoelastic interaction.

In this paper we show the existence of magnetoelastic effects in this material, from elastic constant and magnetic susceptibility measurements in an applied magnetic field. The relevance that the magnetoelastic interplay between structural and magnetic degrees of freedom has on the premartensitic transition is finally discussed in the framework of a Landau model.

II. EXPERIMENTAL RESULTS

A single crystal grown by the Bridgman method with composition very close to stoichiometric Ni_2MnGa was investigated. From the original rod two samples were cut using a low-speed diamond saw. The smaller sample ($3.1 \times 1.0 \times 1.4\text{ mm}^3$) was used in ac susceptibility measurements. The

larger one ($6.75 \times 4.8 \times 11.45\text{ mm}^3$), which had its faces parallel to the (110), ($\bar{1}\bar{1}0$), and (001) planes, was used in ultrasonic measurements.

Magnetic susceptibility measurements were conducted on an ac susceptometer. The elastic constants were obtained from ultrasonic measurements (pulsed-echo technique). In these ultrasonic measurements, a magnetic field up to 1 T was applied.

The Ni_2MnGa sample investigated displays a bcc structure with an $L2_1$ atomic order (space group $Fm\bar{3}m$) at high temperature. It orders ferromagnetically below $T_c=381\text{ K}$, and it transforms martensitically to a modulated tetragonal structure at $T_M=175\text{ K}$. The premartensitic transition occurs at $T_I=230\text{ K}$.

Clear evidence of the existence of a magnetoelastic interaction is the dependence of the elastic properties on the magnetic structure of the solid. To show this for Ni_2MnGa , we have measured its elastic constants under different magnetic fields, at room temperature. Prior to each measurement, the sample was subjected to a thermal treatment to ensure that the measured dependence of each elastic constant corresponded to the first magnetization process. A typical example of the behavior found is presented in Fig. 1, which shows the evolution of the three independent elastic constants as functions of a magnetic field applied along the

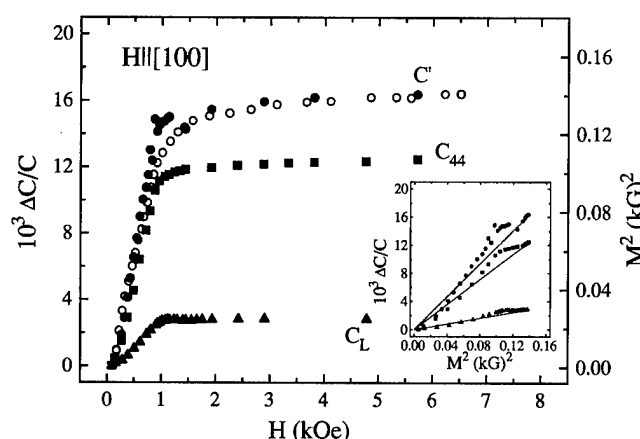


FIG. 1. Relative changes of the elastic constants (solid symbols) as functions of a magnetic field applied along the [100] direction. Open symbols correspond to the square of the magnetization extracted from Ref. 4. The inset shows the relative changes of the elastic constants as functions of the square of the magnetization.

^{a)}Electronic mail: eol@clyde.ecm.ub.es

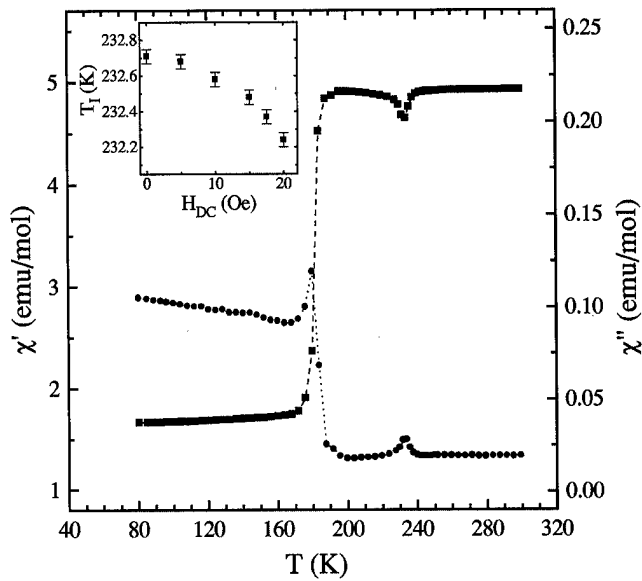


FIG. 2. Real (χ' , squares) and imaginary (χ'' , circles) parts of the magnetic susceptibility as functions of temperature measured for $H_{dc}=10$ Oe and $f=66$ Hz. The inset shows the dependence of the temperature of the intermediate transition with a magnetic field applied along the [100] direction.

[100] direction. As the magnetic field is increased, all the elastic constants slightly increase up to a saturation value. Similar behavior is obtained with the magnetic field applied along the $[\bar{1}10]$ direction: the same saturation values are obtained (within experimental error) but at a larger value of the magnetic field. In order to prove that the measured change in the elastic constants is due to a change in the value of the magnetization, and is not due to rotation of the equilibrium magnetization, we have plotted the square of the magnetization (M) measured by Ullakko and co-workers in a similar sample.⁴ A good correlation exists between the change in the elastic constants and that of M . In the inset we have plotted the relative change of the elastic constants as functions of M^2 . It is interesting to note that, within the experimental errors, the same linear behavior is observed for low and high values of M^2 . At intermediate values, the data points deviate from this linear behavior. Such a deviation can be ascribed to the fact that ultrasonic and magnetic measurements have been conducted on different specimens and also to minor misalignments of the magnetic field in both sets of measurements which can result in slightly different values for the saturation field.

The interplay between the magnetic and structural degrees of freedom is also apparent in the change of the magnetic properties of the alloy as it goes through the structural phase transitions. This behavior is illustrated in Fig. 2, which shows an example of the evolution of the real (χ') and imaginary (χ'') parts of the magnetic susceptibility as functions of temperature. χ' has a significant change at around 175 K associated with the martensitic transition, and it displays a small anomaly at around 230 K. Such an anomaly is located at the temperature where a peak in the specific heat curve has been measured,⁶ and it is related to the condensation of the $q=0.33$ TA_2 phonon. At the temperatures of the structural transitions, χ'' increases; this is an indication of a

dissipative effect which, in each case, is due to the motion of domain boundaries.⁶ This phenomenon is in agreement with a measured increase in the internal friction at these phase transitions.⁸ Another manifestation of the magnetoelastic interplay is a dependence of the temperature of the premartensitic transition upon the magnetic field. In particular, for a first order phase transition the Clausius–Clapeyron law must hold. We have explored such a possibility by applying a low dc magnetic field along the [100] direction during the measurement of the ac susceptibility. We have found that T_I decreases with increasing magnetic field as shown in the inset of Fig. 2. These low magnetic fields do not modify the martensitic transition temperature and do not affect the characteristics of this transition. Fields in the range of several kOe are needed to induce significant changes in the characteristics of the martensitic transition.

III. DISCUSSION AND CONCLUSIONS

The results presented above give clear evidence for the existence of magnetoelastic coupling in Ni_2MnGa . In this section we would like to discuss the relevance of this coupling to the features of the premartensitic and martensitic transitions undergone by the studied alloy. We first introduce a Landau model suitable to describe the phase transitions of this system. The primary order parameter is taken to be the amplitude of the $q=0.33$ TA_2 phonon (related to the micro-modulation at the premartensitic transition), and we consider two secondary order parameters: ϵ , a (110)[$\bar{1}10$] homogeneous shear adequate to describe a cubic to tetragonal change of symmetry, and the magnetization M (considered to be a scalar). We assume the following general form of the Landau free energy:

$$\mathcal{F}(\eta, \epsilon, M) = F_{str}(\eta, \epsilon) + F_{mag}(M) + F_{me}(\eta, \epsilon, M), \quad (1)$$

where F_{str} is a purely structural term, F_{mag} is the magnetic term, and F_{me} is the contribution accounting for the magnetoelastic coupling. The explicit free energy expansion takes into consideration the symmetries of the system and the fact that the two structural transitions take place well below the Curie point, resulting in a breaking of the $\pm M$ invariance in the free energy. For the premartensitic transition, minimization of \mathcal{F} with respect to ϵ and M [which yields a path $\epsilon=0$, $M=M(\eta)$], leads to the following effective free energy:⁷

$$\mathcal{F}_{eff} = \frac{1}{2} A \eta^2 + \frac{1}{4} B \eta^4 + \frac{1}{6} C \eta^6, \quad (2)$$

where A is a linear function of temperature and of the high temperature phase magnetization M_0 ; B and C are temperature-independent functions of M_0 . It is interesting to point out that for large enough magnetoelastic coupling, B can be negative, and in this case the system can show a first order transition before becoming dynamically unstable ($A \rightarrow 0$). Within this picture, the softening of the characteristic phonon is expected to be incomplete at the transition, in accord with experimental observations.⁵ From this model the dependence of T_I on an externally applied magnetic field can be obtained. It is given by (Clausius–Clapeyron equation):

$(dT_I/dH) = -\alpha M_0/(1 + \alpha|\Delta S|)$, where α is a parameter related to the magnetoelastic coupling and ΔS is the entropy change at the premartensitic transition. From calorimetric measurements $\Delta S = -0.04$ J/K mol has been determined in the absence of magnetic field. The decrease of T_I with H (inset in Fig. 2) appears to be in agreement with the above equation.⁹ Even more, the above expression provides a justification for the nonlinear dependence shown in the figure: as the phase transition moves towards lower values, the stability limit of the high temperature phase is approached and the absolute values of ΔS are expected to decrease.

In nonferromagnetic alloys, the martensitic transition has been related to an anharmonic coupling between the TA_2 phonon and the homogeneous strain ϵ .¹⁰ In our model, this term is supposed to be negligible in comparison with the magnetoelastic coupling term. Nevertheless, it is worth noting that the magnetoelastic interaction indirectly couples η and ϵ . At the martensitic transition, ϵ becomes different from zero and a close-packed tetragonal phase is obtained. Such a symmetry change is accompanied by a change in the wave vector of the transverse modulation. In order to account for such a change in the Landau model, an explicit wavevector dependence of the Landau free energy should be considered.

Up to now, the microscopic origin of the magnetoelastic coupling in Ni_2MnGa has not yet been established. Short wavelength anomalies preceding the martensitic transition have also been observed in Ni-Al alloys.¹¹ They have been related to specific nesting properties of the multiply connected Fermi surfaces.¹² Nevertheless, Ni-Al is not ferromagnetic and no premartensitic transition has been observed in this alloy. In addition, in Ni-Mn-Ga alloys close to stoichiometric Ni_2MnGa but with less Mn content, the premartensitic transition is not observed although a magnetoelastic coupling has been proven to exist.¹³ We suggest that this different behavior could be due to the fact that the substitution of Mn by Ni atoms causes an increase in the martensitic transition temperature,¹⁴ and the magnetoelastic coupling is likely to be weaker. These two features imply that the bcc phase transforms to a close-packed one (martensitic transition) at a temperature higher than the temperature at

which the intermediate transition would occur (which is essentially controlled by the magnetoelastic coupling), and therefore, the micromodulated phase cannot develop independently of the martensitic transition in alloys with low Mn content.

To conclude, we have experimentally proven the existence of a magnetoelastic coupling in Ni_2MnGa . By means of a simple Landau-type model, it has also been shown that such a coupling leads to a first order phase transition that occurs as a lock-in of a soft phonon in the TA_2 branch. A knowledge of the microscopic origin of such a coupling and its relationship to the martensitic transition is still lacking.

ACKNOWLEDGMENTS

This work has received financial support from the CICyT (Spain), Project No. MAT95-504 and CIRIT (Catalonia), Project No. SGR00119. The single crystal was kindly provided by V. A. Chernenko. E.O. and A.G. acknowledge financial support from DGICYT (Spain).

- ¹P. J. Webster, K. R. A. Ziebeck, S. L. Town, and M. S. Peak, *Philos. Mag. B* **49**, 295 (1984).
- ²V. V. Martynov, *J. Phys. IV* **5**, C8-91 (1995).
- ³L. Delaey, *Materials Science and Technology*, edited by P. Haasen (VCH, Weinheim, 1991), Vol. 5, p. 339.
- ⁴K. Ullakko, J. K. Huang, C. Kantner, R. C. O'Handley, and V. V. Kokorin, *Appl. Phys. Lett.* **69**, 1966 (1996).
- ⁵A. Zheludev, S. M. Shapiro, P. Wochner, A. Schwarz, M. Wall, and L. E. Tanner, *Phys. Rev. B* **51**, 11 319 (1995).
- ⁶L. Mañosa, A. González-Comas, E. Obradó, A. Planes, V. A. Chernenko, V. V. Kokorin, and E. Cesari, *Phys. Rev. B* **55**, 11 068 (1997).
- ⁷A. Planes, E. Obradó, A. González-Comas, and L. Mañosa, *Phys. Rev. Lett.* **79**, 3926 (1997).
- ⁸V. V. Kokorin, V. A. Chernenko, E. Cesari, J. Pons, and C. Seguí, *J. Phys.: Condens. Matter* **8**, 6457 (1996).
- ⁹This point will be discussed in detail in E. Obradó, A. González-Comas, L. Mañosa, A. Planes, V. A. Chernenko, and A. Labarta (to be published).
- ¹⁰P. A. Lindgård and O. G. Mouritsen, *Phys. Rev. Lett.* **57**, 2458 (1986); J. A. Krumhansl, *Solid State Commun.* **84**, 251 (1992).
- ¹¹S. M. Shapiro, B. X. Yang, Y. Noda, L. E. Tanner, and D. Schryvers, *Phys. Rev. B* **44**, 9301 (1991).
- ¹²G. L. Zhao and B. N. Harmon, *Phys. Rev. B* **45**, 2818 (1992).
- ¹³U. Stühr, P. Vorderwisch, V. V. Kokorin, and P. A. Lindgård, *Phys. Rev. B* **56**, 14 360 (1997).
- ¹⁴V. A. Chernenko, E. Cesari, V. V. Kokorin, and I. N. Vitenko, *Sov. Metall. Mater.* **33**, 1239 (1995).

Trial on-silicon micromagnetoelastic devices

M. Takezawa, M. Yamaguchi, K. Ishiyama, and K. I. Arai

Research Institute of Electrical Communication, Tohoku University, 2-1-1 Katahira, Aoba-ku, Sendai 980-8577, Japan

This paper discusses two new kinds of micromagnetoelastic devices made on silicon wafer whose function is to control the permeability of magnetostrictive soft magnetic thin films by voltage-controlled elastic strain. One is piezoelectric type and the other is electrostatic type. Structure, fabrication process, characteristics, and maximum possible output are discussed. The feasibility of these devices has been clarified although the rate of obtained permeability change was less than 1%. These device characteristics could be improved to 11% for piezoelectric type and to 80% for electrostatic type by the optimization of device dimensions and reduction of process damage to the magnetic film. © 1998 American Institute of Physics. [S0021-8979(98)41311-2]

I. INTRODUCTION

Magnetostrictive thin-film materials are of current interest for microfabricated sensors,¹ actuators,^{2,3} magnetosurface acoustic wave (MSAW) devices,⁴ etc. A potential benefit of these devices is the capability of silicon integrated intelligent systems. However, little work has been reported on the combination of magnetostrictive films and silicon.³

Therefore, this paper discusses two new kinds of micromagnetoelastic devices made on a silicon wafer whose function is to control the permeability of magnetostrictive soft magnetic thin film by voltage-controlled elastic strain. One is piezoelectric type and the other is electrostatic type.

The piezoelectric type is the extension of our previous work¹ that used FeSiB film and bulk PZT. In this work we microfabricated a FeSiB/ZnO double layer film structure on a silicon membrane. The electrostatic type utilizes bending of FeSiB film-substrate beam caused by electrostatic force. The space to bend is formed by anisotropic etching of silicon. Feasibility of these devices is demonstrated in this paper.

II. FILM MATERIALS

A. Magnetostrictive FeSiB film

The 0.5 μm thick $\text{Fe}_{77}\text{Si}_{11}\text{B}_{12}$ amorphous film was rf-sputter deposited onto a surface oxidized (100) orientated silicon wafers. The Ar gas pressure was 3.3 Pa and the rf power was 100 W ($5.7 \times 10^2 \text{ W/m}^2$). The as-deposited film had saturation magnetostriction of 33×10^{-6} , Curie temperature of 703 K, and a crystallization temperature of 743 K. These are similar to the published values.⁵

The stress release annealing without magnetic field was applied up to 673 K at below 2.7×10^{-4} Pa, which resulted in a remarkable coercive force decrease from 1990 A/m to 32 A/m and a permeability increase from 90 to 2300, as shown in Fig. 1. Then the films were annealed again in a static magnetic field of 39.8 kA/m at below 8.0×10^{-4} Pa for 2 h in order to stabilize the uniaxial anisotropy. The anisotropy field was increased from 200 to 280 A/m, and the squareness ratio, M_r/M_s along easy axis of magnetization was improved from 0.9 to nearly unity.

B. ZnO piezoelectric film

A 1 μm thick ZnO film was rf-sputter deposited on a surface oxidized (100) orientated silicon wafer using Ar: $\text{O}_2 = 8:2$ mixture gas. The total gas pressure was 4.0 Pa. The rf power was 100 W ($5.7 \times 10^2 \text{ W/m}^2$) and the substrate temperature was 473 K. The x-ray diffraction pattern of the film showed that the c axis was perpendicular to the film plane and its dispersion was 4 degrees. Since the threshold c -axis dispersion to degrade the piezoelectric properties is 6 degrees,⁶ crystal orientation of the fabricated ZnO film is adequate for the proposed sensors. The resistivity was $4 \times 10^9 \Omega\text{cm}$, which is similar to the published values.^{7,8}

The piezoelectric constant d_{31} was measured using a $\text{Au}(0.4 \mu\text{m})/\text{ZnO}(3 \mu\text{m})/\text{Cr}(0.5 \mu\text{m})$ multilayer film rf-sputtered on (100) orientated silicon wafer. The Cr and Au films were used as electrodes. The measured strain was almost proportional to the applied dc voltage of $\pm 2 \text{ V}$ as shown in Fig. 2. The readout of d_{31} was $-5 \times 10^{-12} \text{ m/V}$, which is similar to the published values.⁶

C. FeSiB/ZnO double layer film

Figure 3 shows the annealing temperature dependence of initial permeability of FeSiB film deposited on the 1 μm thick ZnO film substrate. The as-deposited FeSiB film on ZnO film had permeability higher than single layer FeSiB

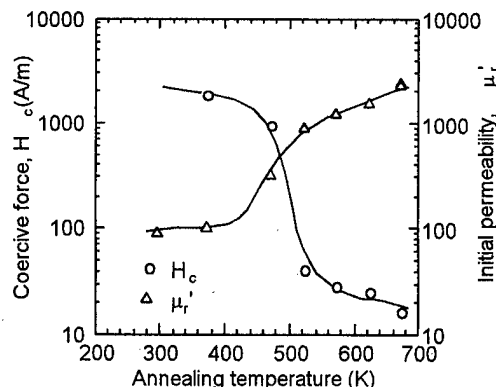


FIG. 1. Annealing temperature dependence of coercive force and permeability.

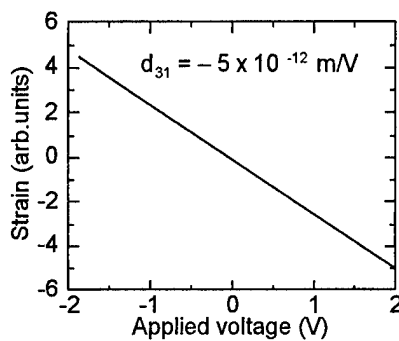


FIG. 2. Applied voltage dependence of ZnO strain.

film because of tensile stress given by the ZnO under layer. With raising the annealing temperature, the permeability reached 1000 at 673 K and was further enhanced to 1500 by static magnetic field annealing of 39.8 kA/m at below 8.0×10^{-4} Pa for 2 h. The value obtained is slightly degraded compared to the single layer FeSiB film but still compatible to that.

III. PIEZOELECTRIC TYPE DEVICE

Figure 4 shows the schematic view of the magnetostrictive-piezoelectric type microdevice. A $0.5 \mu\text{m}$ thick SiO_2 under layer, $0.5 \mu\text{m}$ thick FeSiB film, $0.5 \mu\text{m}$ thick Cr electrode layer, $6.5 \mu\text{m}$ thick ZnO piezoelectric film, $3 \mu\text{m}$ thick SiO_2 over layer and $2 \mu\text{m}$ thick Cr electrode layer were rf-sputter deposited in turn onto the (100) oriented silicon wafer. The main parts are FeSiB/ZnO double layers of $12 \text{ mm} \times 13 \text{ mm}$ rectangle area. Then the wafer was anisotropically etched from the back side in tetramethyl ammonium hydroxide (TMAH) to form a $15 \mu\text{m}$ thick membrane.

Applying a voltage between the top and the bottom Cr electrode layers, a strain is produced in the ZnO film perpendicular to the film plane by inverse piezoelectric effect. The in-plane component of the strain causes in-plane strain to the FeSiB film, which controls the permeability of FeSiB film by the inverse magnetoelastic effect. The neutral plane of elastic strain is in the Si membrane. Positive applied voltage yields permeability decrease and negative voltage results in perme-

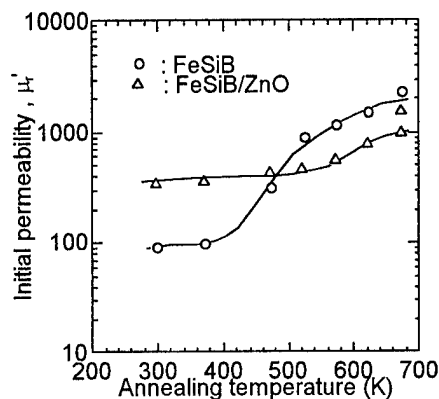


FIG. 3. Annealing temperature dependence of permeability of FeSiB/ZnO double layer film.

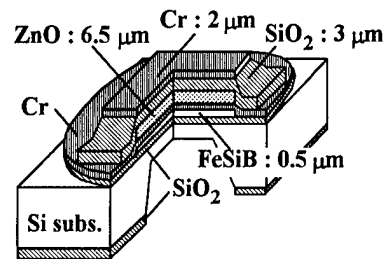


FIG. 4. Structure of micromagnetorestrictive-piezoelectric device.

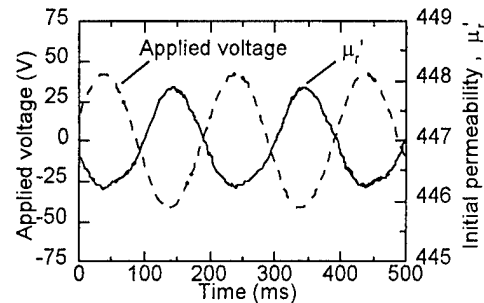


FIG. 5. Time variation of permeability for piezoelectric type device.

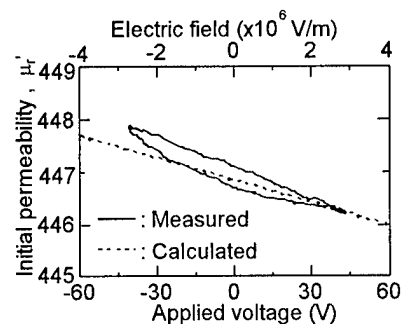


FIG. 6. Permeability vs applied voltage relationship for piezoelectric type device.

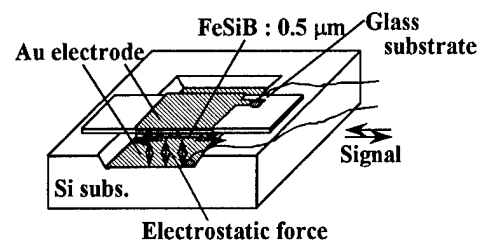


FIG. 7. Structure of micromagnetorestrictive-electrostatic type device.

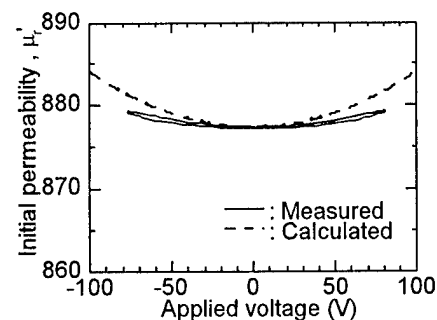


FIG. 8. Permeability vs applied voltage relationship for electrostatic type device.

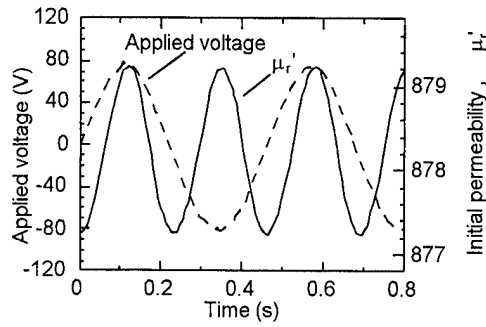


FIG. 9. Time variation of permeability for electrostatic type device.

ability increase because the sign of piezoelectric constant, d_{31} , is negative as showed in Fig. 2. Figure 5 is the experimental verification that a 5 Hz, ± 30 V_{rms} ($\pm 2 \times 10^6$ V/m) sinusoidal voltage yielded the in-phase permeability change.

Theoretical permeability change is given by the following equation:

$$\mu_r' = M_s^2 / [\mu_0 \{2K_u - 3\lambda_s E(\Delta l/l)\}], \quad (1)$$

$$\Delta l/l = z/R, \quad (2)$$

where M_s is the saturation magnetization, K_u the anisotropy constant, E the Young's modulus, λ_s the saturation magnetostriction, z the distance from the neutral plane of elastic strain, and R the radius of film curvature. The film curvature and the position of neutral plane are determined by the thickness and Young's modulus of each of seven stacked film layer and the d_{31} of ZnO film.

Figure 6 shows the calculated permeability agrees with measured values but the rate of change was only 0.35%. This is because the permeability in micro structure is degraded from 1500 to 447 and the silicon membrane was as thick as 15 μ m. The rate of permeability change can be enhanced to 11% by removing the 15 μ m thick silicon membrane and also by improving the permeability from 450 to 1500.

IV. ELECTROSTATIC TYPE DEVICE

Figure 7 shows the schematic view of the magnetoelastic-electrostatic type microdevice. The 0.5 μ m thick FeSiB film was rf-sputter deposited onto a 50 μ m thick soda glass substrate and 0.4 μ m thick Au film for electrode was also deposited onto the opposite surface. This film-substrate was fixed over a grooved silicon wafer having a Au film electrode at the bottom of the groove. The groove is 40 μ m deep and formed by the 10% TMAH anisotropic wet-etching process. With applying a voltage between the two Au electrodes, attractive electrostatic force is generated and the FeSiB film feels tensile stress. Therefore, the permeability always increases regardless of the polarity of the applied voltage.

The generated electrostatic force f operates as a uniformly distributed load, w , and is proportional to the square of the applied voltage V ,

$$w = (f/l) = -(\epsilon_0 b/2)(V/d)^2. \quad (3)$$

When ϵ_0 is the permittivity of vacuum, b the beam width and d the beam thickness. Let the beam length be l , then the deflection y of the beam is given as follows.

$$y = -(w/24EI)x^2(l-x)^2, \quad (4)$$

where I is the geometrical moment of inertia and x the distance from the end of the beam along length direction. Then the radius R of beam curvature is given as $1/R = d^2y/dx^2$. Substituting R into (1) and (2), we obtain the permeability change.

The observed permeability change was in phase as the applied ac voltage and it roughly agreed with theory as shown in Fig. 8. The observed permeability change was 0.23% when 2 Hz, ± 77.5 V ($\pm 0.7 \times 10^6$ V/m) sinusoidal electric field was applied. The calculation above predicted that the permeability change can be improved to 80% if both the groove depth and the glass substrate are as thin as 20 μ m, respectively.

Time domain observation of the initial permeability was done using a figure-8 coil and a two-phase lock-in amplifier. Figure 9 shows the ac component of the initial permeability when a 2 Hz sinusoidal electric field is applied. The permeability varied at double the frequency of applied field because the strain due to the static field was always unidirectional.

V. CONCLUSION

A magnetostrictive-piezoelectric type micro device has been microfabricated using sputter deposited FeSiB amorphous magnetostrictive film with soft magnetic property and the ZnO piezoelectric film. Micromagnetostrictive-electrostatic type is also possible using the FeSiB film. The feasibility of these devices has been clarified although the rate of obtained permeability change was less than 1%. These device characteristics could be improved to 11% for piezoelectric type and to 80% for electrostatic type by the optimization of device dimensions and reduction of process damage to the magnetic film.

¹ K. I. Arai, C. S. Muranaka, and M. Yamaguchi, IEEE Trans. Magn. **30**, 916 (1994).

² T. Honda, K. I. Arai, and M. Yamaguchi, J. Appl. Phys. **76**, 6994 (1994).

³ E. Quandt and K. Seemann, Proc. IEEE Micro Electro Mechanical Systems (MEMS 95), p. 273 (1995).

⁴ M. Inoue, Y. Tuboi, N. Yokokawa, and T. Fujii, IEEE Trans. Magn. **26**, 1465 (1990).

⁵ M. Naoe, H. Yamamoto, and S. Yamanaka, J. Appl. Phys. **50**, 7606 (1979).

⁶ N. Chubachi, M. Minakata, and Y. Kikuchi, Jpn. J. Appl. Phys., Suppl. **2**, Pt. 1, 737 (1974).

⁷ N. F. Foster, Proc. IEEE **53**, 1400 (1965).

⁸ G. A. Rozgonyi and W. J. Ploito, Appl. Phys. Lett. **8**, 220 (1996).

⁹ M. D. Mermelstein and A. Drandridge, Appl. Phys. Lett. **51**, 545 (1987).

Nonlinear self-localized magnetoelastic surface waves in antiferromagnetic media

Igor E. Dikshtein^{a)}

Institute of Radioengineering and Electronics, RAS, Mokhovaya Street, 11, Moscow 103907, Russia

Sung-Ho Suck Salk

Department of Physics, Pohang University of Science and Technology, Pohang 790-784, Korea

Types of self-localized, magnetoelastic (ME) surface waves in antiferromagnets (AFs) are predicted, the existence of which is determined entirely by the nonlinear properties of the AFs. The frequency spectrum of the self-localized ME surface waves is shown to lie in a gap between the upper quasimagnon and lower quasiphonon branches of the harmonic ME spectrum. A nonlinear Schrödinger equation for the envelope of ME waves is derived and its solitonic solutions are obtained. When spin pinning or capillary effects on the surface of the crystal exist, we find that the nonlinear surface ME wave excites the volume ME wave at fundamental harmonics carrying energy into the interior of a crystal. © 1998 American Institute of Physics. [S0021-8979(98)52111-1]

Nonlinear magnetoelastic (ME) waves in an antiferromagnet (AF) possess a variety of distinguishing features that can be of great importance for magnetoacoustics.¹ Strong ME interaction is responsible for the giant effective anharmonicity of the elastic system ($\Delta C_3 \sim 10^3 - 10^4 C_2$ where $\Delta C_3 \sim C_3^{\text{eff}} - C_3$, C_2 , and C_3 are the second and third order elastic moduli, respectively).¹ The dispersion of ME waves increases considerably in the region of the magnetoacoustic resonance.²

It is easy to stimulate large amplitudes of surface ME waves at an AF surface. In such a case, nonlinear effects are especially important for surface ME wave propagation. The problem of the second ME harmonic generation³ and the effects of acoustic convolution in the nonlinear interaction of the Rayleigh surface ME waves^{4,5} was studied experimentally.

For the study of surface waves understanding of the interaction of a wave with other degrees of freedom in a system is essential. New types of linear surface waves can arise from such interaction. For example, the shear volume elastic wave in a ferromagnet transforms into a surface wave if ME coupling and dipole-dipole interaction are taken into account.⁶ The linear surface Rayleigh,⁷ Love,⁸ and Stonely⁹ waves can be damped out due to spin wave radiation into the interior of crystal.

In the present study we consider a new type of nonlinear surface ME waves in an AF that have no analogs to the case of linear waves and become delocalized with a zero amplitude. Nowadays the nonlinear self-localized surface waves of various kinds are well known in solids, e.g., the nonlinear surface acoustic waves,¹⁰ the nonlinear surface exchange spin waves,¹¹ and three-dimensional surface precession solitons.¹²

The system of present interest is a two-sublattice AF with weak ferromagnetism and an easy-plane-type anisotropy, occupying the half-space $z < 0$, in an external magnetic

field \mathbf{H} parallel to the surface ($\mathbf{H} \parallel \mathbf{x}$). The crystal axis perpendicular to the easy plane is directed along the z axis. In this case the free energy density of an AF is given by

$$F = F_m + F_{me} + F_e, \quad (1)$$

where

$$F_m = M_0 [H_E m^2 + H_A l_z^2 - 2H_D(\mathbf{m} \times \mathbf{l}) + \alpha M_0 (\partial V / \partial x_i)^2],$$

$$F_{me} = b M_0^2 l_i l_k u_{ik}, \quad F_e = (1/2) c_{iklm} u_{ik} u_{lm}$$

are the magnetic, ME, and elastic energy densities, respectively; H_E , H_A , and H_D are the exchange, anisotropy, and Moriya-Dzyaloshinsky fields; α , \hat{c} , and b are the nonuniform exchange, elastic, and ME constants; \hat{u} is the deformation tensor; $\mathbf{M}_{1,2}$ are the sublattice magnetizations ($|\mathbf{M}_1| = |\mathbf{M}_2| = M_0$); $\mathbf{L} = \mathbf{M}_1 - \mathbf{M}_2 = 2M_0 \mathbf{l}$ and $\mathbf{M} = \mathbf{M}_1 + \mathbf{M}_2 = 2M_0 \mathbf{m}$ are the ferromagnetic and AF vectors. For simplicity the AF is assumed to be ME and elastically isotropic. The inherent anharmonicity of the elastic lattice is neglected since it is not as important compared to the effective anharmonicity associated with ME coupling.¹ In an AF of a sufficient high Néel temperature $H_E \gg H_A$, H_D .¹ For the case of $H \ll H_E$, we note $m \ll l$ and $l^2 = 1 - m^2 \approx 1$.

The energy (1) is minimized for the ground state with $\mathbf{m}_0 \parallel \mathbf{x}$ and $\mathbf{l}_0 \parallel \mathbf{y}$ and $m_{0x} = (H_D + H)/H_E \ll l_{y0}$.

The nonlinear AF dynamics is described by the equations of motion²

$$\partial \mathbf{M}_n / \partial t = -g(\mathbf{M}_n \times \mathbf{H}_n^{(e)}), \quad \dot{\rho} \partial^2 u_i / \partial t^2 = \partial \sigma_{ik} / \partial x_k, \quad (2)$$

where $\mathbf{H}_n^{(e)} = -\partial F / \partial \mathbf{M}_n$ is the effective magnetic field, $\sigma_{ik} = \partial F / \partial u_{ik}$ is the tensor of the mechanical stresses, u_{ik} is the deformation tensor, g is the gyromagnetic ratio, and $n = 1, 2$ are the magnetic sublattice indexes.

The boundary conditions at the stress-free AF surface are

$$\sigma_{iz} = 0 \quad (i = x, y, z), \quad \mathbf{l} \times (\partial V / \partial \mathbf{z} + \beta_s \mathbf{l}) = 0, \quad (3)$$

with β_s the surface anisotropy constant.

^{a)}Electronic mail: diksh@mail.cplire.ru

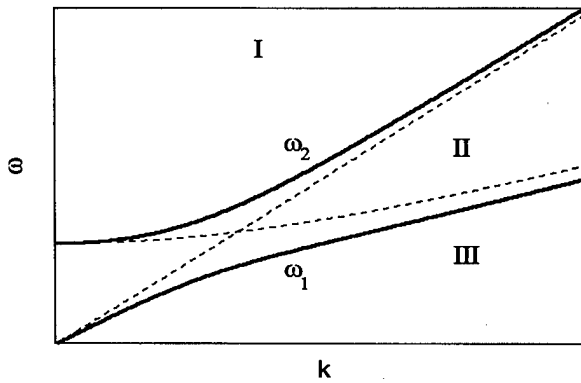


FIG. 1. Classification of the roots characteristic of the characteristic equation (4). The noninteracting magnons and phonons are shown by dashed lines.

For a surface ME wave the decay conditions for \mathbf{l} and \mathbf{u} at $z \rightarrow -\infty$ are $|\mathbf{l}_x| \rightarrow 0$, $|\mathbf{u}| \rightarrow 0$.

It is easy to show that for an AF with sufficiently large easy-plane anisotropy [$H_A \gg H_{me} = b^2 M_0^2 / (2c_{44})$] $l_z \ll l_x$. Therefore, we assume $l_z = 0$ everywhere and do not take into account the high-frequency branch corresponding to vibrations involving a departure of \mathbf{l} from the basis plane.

Using the linear approximation of $\exp[i(ky - \omega t) + qz]$ for l_x and u_x , the characteristic equation for the ME waves is

$$(\omega^2 - \omega_{sk}^2 + V_m^2 q^2)(\omega^2 - \omega_{ik}^2 + S_t^2 q^2) - \omega_{me} \omega_E \omega_{ik}^2 = 0, \quad (4)$$

with V_m and S_t , the velocities of spin waves and the transverse sound,

$$\omega_{sk} = \sqrt{V_m^2 k^2 + \omega_H(\omega_H + \omega_D) + \omega_E \omega_{me}}, \quad \omega_{ik} = S_t k,$$

$$S_t = \sqrt{c_{44}/\rho},$$

$$\omega_E = gH_E, \quad \omega_H = gH, \quad \omega_D = gH_D, \quad \omega_{me} = gH_{me}.$$

Equation (4) has four roots q vanishing along curves $\omega = \omega_1(k)$ and $\omega = \omega_2(k)$, respectively,

$$\omega_{1,2}(k) = [\omega_{sk}^2 + \omega_{ik}^2 \mp \sqrt{(\omega_{sk}^2 - \omega_{ik}^2)^2 + 4\omega_E \omega_{me} \omega_{ik}^2}]^{1/2} / \sqrt{2}.$$

Figure 1 shows the behavior of the solutions of (4) on the plane (ω, k) for the low-temperature AF (MnCO_3 , CoCO_3 , CsMnF_3) with $T_N < T_D$ (T_N and T_D are the Néel and Debye temperatures, respectively) and $S_t > V_m$. The plane is divided into three regions. In region I [$\omega > \omega_2(k)$], and Eq. (4) has four imaginary roots. Volume ME waves correspond to region I. In region II [$\omega_1(k) < \omega < \omega_2(k)$], it has two real and two imaginary roots. In region III [$\omega < \omega_1(k)$], it has four real roots. The linear surface ME waves in region III and the linear leaky ME waves in region II can exist only when spin pinning and capillary effects on an AF surface are available.

The solutions of nonlinear equations (2) for the main harmonics of the upper branch of the ME waves have the form

$$l_x = (1/2)A(y, z, t) \exp i(ky - \omega_2 t) + c.c.; \quad (5)$$

$$u_x = (1/2)B(y, z, t) \exp i(ky - \omega_2 t) + c.c. \quad (6)$$

Here amplitudes A and B are the slowly varying envelopes to the rapid oscillations of the carrier waves,

$$\left| \frac{\partial G}{\partial t} \right| \ll \omega_2 |G|, \quad \left| \frac{\partial G}{\partial z} \right| \ll k |G|, \quad \left| \frac{\partial G}{\partial y} \right| \ll k |G|,$$

$$G = (A, B).$$

For weakly localized nonlinear surface ME waves of small amplitude the substitution of solutions (5) and (6) into (2) yields

$$i \left(\frac{\partial A}{\partial t} + v_{g2} \frac{\partial A}{\partial y} \right) + (1/2) D_2 \frac{\partial^2 A}{\partial z^2} + N_2 |A|^2 A = 0, \quad (7)$$

$$B = \gamma A [\gamma = -ikb\rho^{-1} M_0^2 / (\omega_{2k}^2 - \omega_{ik}^2)], \quad (8)$$

with the boundary conditions $\partial A / \partial z = \partial B / \partial z = 0$ for $\beta_s = 0$, where

$$v_{g2} = \Omega_2 k [S_t^2 (\Omega_{s2} + \omega_E \omega_{me}) + V_m^2 \Omega_{t2}], \quad D_2 = v_{g2} / k, \quad (9)$$

$$N_2 = \Omega_2 [\omega_E \omega_{me} \omega_{ik}^2 + \Omega_{t2} (4\omega_H^2 + 4\omega_E \omega_{me} + \omega_H \omega_D) / 16], \quad (10)$$

$\Omega_2 = [\omega_{2k}(\omega_{2k}^2 - \omega_{1k}^2)]^{-1}$, $\Omega_{s2} = \omega_{2k}^2 - \omega_{sk}^2$, and $\Omega_{t2} = \omega_{2k}^2 - \omega_{ik}^2$. In the present case of interest an AF is found to possess nonlinearity of the self-focusing type ($D_2 > 0$ and $N_2 > 0$).

From Eqs. (7) and (8) we get the nonlinear surface waves

$$l_x = (1/2)A_0 \text{sech}(z/z_0) \exp i[ky - (\omega_2 - 1/2T)t] + c.c.; \quad (11)$$

$$u_x = \gamma l_x, \quad T^{-1} = N_2 A_0^2, \quad z_0^{-1} = A_0 \sqrt{N_2 / D_2}, \quad (12)$$

where A_0 is the maximum envelope amplitude. A dispersion relation for nonlinear surface ME waves is then

$$\omega = \omega_2(k) - N_2 A_0^2 / 2. \quad (13)$$

The penetration depth of the surface ME wave is $z_0 \approx A_0^{-1}$ and tends to reach infinity as its amplitude decreases. When the frequency and the amplitude of waves are fixed, a wavelength of the nonlinear ME wave is smaller than that of the linear one.

According to the Lighthill criterion the nonlinear ME wave is modulationally unstable to create a train of solitary waves in the direction of propagation. It can give rise to formation of three-dimensional (3D) surface ME solitons. Such 3D surface solitons for spin waves were considered in Ref. 12.

A dispersion relation for a nonlinear volume surface ME wave that is uniform over the thickness of a crystal has the form

$$\omega = \omega_2(k) - N_2 A_0^2. \quad (14)$$

We now investigate the influence of surface spin pinning on the propagation of the nonlinear surface ME wave. In this case the boundary conditions (3) have the form

$$\partial u_x / \partial z = 0, \quad l_x (\partial l_y / \partial z + \beta_s l_y) - l_y \partial l_x / \partial z = 0. \quad (15)$$

In the present case solutions (11) and (12) from the nonlinear equations (2) do not satisfy the boundary conditions (15), owing to radiation of the energy of volume ME waves into the interior of the crystal.

For the purposes of illustration of the radiation effects we will consider the ME waves close to the upper quasimagnon branch ($\omega \leq \omega_{2k}$) in the range of small wave numbers k . In this limit the interaction between spin and elastic waves is weak. Substitution of Eqs. (11) and (12) (where the envelope amplitudes are the functions of z and index $2k$ is omitted for ω) into (2) yields

$$\frac{D_2}{2} \frac{\partial^2 A}{\partial z^2} + \frac{(\omega^2 - \omega_{sk}^2)A}{2\omega_{2k}} + N_2 A |A|^2 = \epsilon B, \quad (16)$$

$$\partial^2 B / \partial z^2 + Q^2 B = \epsilon_1 A. \quad (17)$$

Here $\epsilon = ikbgM_0\omega_E/(4\omega_{2k})$ and $\epsilon_1 = -ikbM_0^2/c_{44}$ are small values, $\omega_{2k} \approx \omega_{sk}$, $D_2 \approx V_m^2/\omega_{sk}$, $Q^2 = (\omega_{sk}^2 - \omega_{ik}^2)/S_i^2$, and the nonlinear term is ignored in (17). Inserting the unperturbed ($\epsilon = 0$) solution of (16): $A = A_0 \operatorname{sech}(z+Z)/z_0$ into (17), we can get

$$B = B_1 \exp(-iQz) - \frac{ikbAM_0^2}{Q^2 c_{44}} \operatorname{sech} \frac{z+Z}{z_0}, \quad (18)$$

where $A_0 = \sqrt{2(\omega_{sk} - \omega)/N_2}$ and $z_0 = \sqrt{D_2/[2(\omega_{sk} - \omega)]}$. A shift Z is obtained from the first boundary condition (15) as $Z = -z_0 \tanh^{-1}(\beta_s z_0)$. The amplitude of the outgoing ME wave $B_1 \propto \beta_s b A_0$ is determined from the second boundary condition (15).

It follows from (18) that the nonlinear surface ME wave excites volume ME waves at the frequency of the fundamental wave carrying energy into the interior of a crystal. Therefore, there is no energy localization of nonlinear surface ME waves, and they are, in fact, quasisurface waves. The effect results solely from the ME interaction. For $b = 0$ there is no radiation of energy from the surface ($B_1 = 0$).

In the case $\beta_s < 0$, the amplitude maximum of the nonlinear surface ME wave, is shifted into the interior of the crystal. In this case the "repulsion" of the surface ME wave from the surface is compensated for by nonlinear "attraction." Such a wave can be detached from the surface to become a volume soliton. For $\beta_s > 0$ the amplitude is maximal on the AF surface.

The characteristic damping time of the surface ME wave can be evaluated from

$$T_d \approx E/(\partial E/\partial t) \propto \beta_s^{-2} A_0^{-1}, \quad (19)$$

where $E = \int_{-\infty}^0 F dz \propto A_0$ is the energy density and $\partial E/\partial t = -c_{44}(\partial u_x/\partial t)(\partial u_x/\partial z) \propto \beta_s^2 A_0^2$ is the energy flux density of the nonlinear surface ME wave per unit surface area. Therefore, the characteristic distance $L_d = V_{g2} T_d$ for the propagation of surface ME waves during $T_d \propto \beta_s^{-2} A_0^{-1}$ is large for the small amplitude wave.

It is easy to show that close to the lower quasiphonon branch of a ME spectrum an AF possesses nonlinearity of the defocusing type ($N_1 < 0$, $D_1 > 0$) and nonlinear, self-localized surface ME waves do not exist for the free boundary conditions ($\beta_s = 0$).

In conclusion, we have demonstrated that ME waves in an AF can be localized near the surface due to nonlinearity of the crystal. In contrast to the linear case nonlinear quasisurface waves can exist for both positive and negative signs of surface anisotropy constants. Nonlinear surface and quasisurface waves are expected to occur in other interacting systems involving different kinds of waves, e.g., the acoustic and optic waves in ferroelectrics and the spin and electromagnetic waves in ferromagnets.

This work was supported by the Basic Science Research Center of Pohang University of Science and Technology and by Russian Foundation Basic Research Grant No. 96-02-16082a.

¹ V. I. Ozhogin and V. L. Preobrazhenskii, J. Magn. Magn. Mater. **100**, 544 (1991).

² A. I. Akhiezer, V. G. Bar'yakhtar, and S. V. Peletminskii, *Spin Waves* (North-Holland, Amsterdam, 1968).

³ V. A. Krasil'nikov, T. A. Mamatova, and V. G. Prokhorov, Sov. Tech. Phys. Lett. **10**, 506 (1984).

⁴ M. K. Gubkin, T. A. Mamatova, and V. G. Prokhorov, Sov. Phys. Acoust. **31**, 410 (1985).

⁵ V. A. Ermolov, A. I. Alekseev, and V. G. Pankratov, Sov. Tech. Phys. Lett. **11**, 156 (1985).

⁶ J. P. Parekh, Electron. Lett. **5**, 322 (1969); **5**, 540 (1969).

⁷ B. N. Filippov and L. G. Onoprienko, Fiz. Met. Metalloved. **30**, 1121 (1970).

⁸ H. Mattheus and H. Van De Vaart, Appl. Phys. Lett. **15**, 373 (1969).

⁹ R. E. Camley and A. A. Maradudin, Appl. Phys. Lett. **38**, 610 (1981).

¹⁰ V. G. Mozhaev, Phys. Lett. A **139**, 333 (1989).

¹¹ Yu. I. Bespyatykh and I. E. Dikhshtein, Sov. Phys. Solid State **38**, 1175 (1993).

¹² Yu. I. Bespyatykh, I. E. Dikhshtein, and S. A. Nikitov, Phys. Lett. A **184**, 198 (1994).

Superconductivity II

Mike Osofsky, Chairman

The Re-doped high T_c superconductor $\text{HgBa}_2\text{Ca}_2\text{Cu}_3\text{O}_x$: Magnetic irreversibility versus anisotropy

L. Fàbrega, B. Martínez, J. Fontcuberta, A. Sin, S. Piñol, and X. Obradors
Institut de Ciència de Materials (CSIC), Campus de la U.A.B., 08193 Bellaterra, Spain

We report on magnetization measurements on grain-aligned Re-doped Hg-1223 superconductor ($T_c \approx 133$ K). We analyze the anisotropic magnetic hysteresis M_{irr} as a function of temperature and magnetic field, and determine the irreversibility line $H_{\text{irr}}(T)$ for magnetic fields applied parallel and perpendicular to the c axis of the structure. The similar values of both M_{irr} and $H_{\text{irr}}(T)$ along the two main crystallographic directions reveal a marked decrease of the superconducting anisotropy, due to the Re substitution. This anisotropy reduction might be at the origin of the rise of the magnetic irreversibility already reported in these compounds, as compared to those without Re. © 1998 American Institute of Physics. [S0021-8979(98)42511-8]

I. INTRODUCTION

The copper oxide $\text{HgBa}_2\text{Ca}_2\text{Cu}_3\text{O}_x$ is the superconductor with the highest T_c (≈ 134 K) reported to the date.¹ However, it has been rather poorly characterized, because of its difficult synthesis (requiring high pressure) and its reported high anisotropy. It is well known that superconducting copper oxides with extreme anisotropy have important disadvantages for their use in applications, because magnetic flux moves very easily in them, and therefore they are unable to carry high electrical currents, without dissipation, in most of their H - T phase diagram.

An important step forward was realized when it was shown² that the partial substitution of Hg by Re stabilizes the phase, allowing its synthesis without application of high pressure. Furthermore, this substitution does not lower T_c and rises the irreversibility line of the superconductor,²⁻⁵ i.e., broadens the nondissipative region of its H - T phase diagram.

These important issues—particularly the last result, which was soon attributed to a decrease of the anisotropy^{5,6}—have awakened the interest for this material. Indeed, from the above considerations, the relevance of having a superconductor with very high critical temperature and reduced anisotropy may be clearly presumed. Therefore, to determine the anisotropic irreversibility line of this superconductor and establish the effect of the Re have become a matter of the greatest interest, and are the object of this article.

We report on magnetic hysteresis measurements of grain-aligned $\text{Hg}_{0.82}\text{Re}_{0.18}\text{Ba}_2\text{Ca}_2\text{Cu}_3\text{O}_{8+\delta}$ for both $H//ab$ and $H//c$. These data were analyzed in order to extract the anisotropic magnetic irreversibility, as well as the irreversibility line along the two main crystal directions, and therefore get an insight into the effective anisotropy of these Re-doped superconductors. The results reveal a huge anisotropy decrease, which should modify both the bulk pinning and surface barrier effects of the superconductor. We discuss this

feature and try to correlate it to the already reported enhancement of magnetic irreversibility due to the Re substitution.

II. EXPERIMENT

Ceramic $\text{Hg}_{0.82}\text{Re}_{0.18}\text{Ba}_2\text{Ca}_2\text{Cu}_3\text{O}_{8+\delta}$ was synthesized following the procedure described in Ref. 7. The as-prepared material, with $T_c \approx 133$ K, was powdered, dispersed in an insulating epoxy down to a volume concentration of 3%, and oriented by using a high magnetic field. The superconducting grains, which may be considered as isolated, are platelets of average width 3 μm and thickness 0.5 μm .

The x-ray diffractograms (Fig. 1) confirmed the good orientation of the superconducting grains, showing mainly the (0 0 1) peaks; only some traces of other reflections could be detected. The c -axis spread is $\Delta\theta \approx 3.5^\circ$ [full width at half maximum of the rocking curve of the (0 0 6) peak].

DC magnetization was measured for $H//c$ and $H//ab$ with a Quantum Design superconducting quantum interference device magnetometer, as a function of temperature and magnetic field ($H < 55$ kOe). The samples used in these measurements are bars with typical dimensions $2 \times 2 \times 5$ mm³, the longest one being either parallel or perpendicular to the c -axis direction.

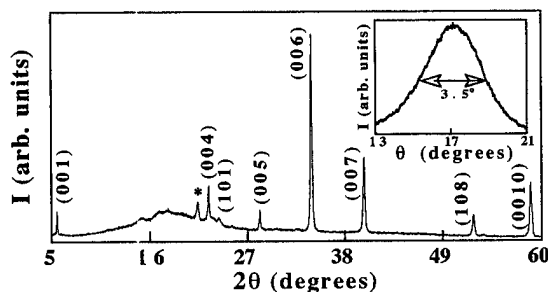
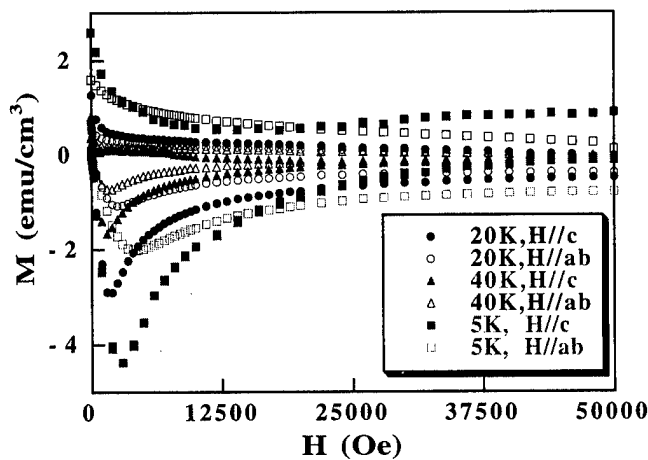


FIG. 1. θ - 2θ diffractogram of a grain-oriented sample. Inset: rocking curve of the (006) peak.

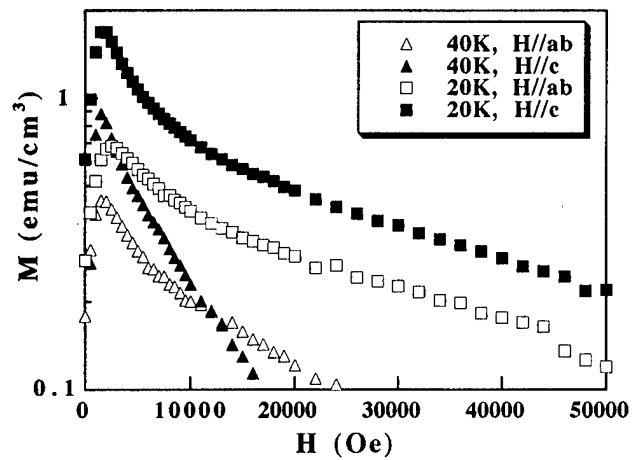
FIG. 2. Hysteresis cycles measured at 5, 20, and 40 K, for $H//ab$ and $H//c$.

III. RESULTS AND DISCUSSION

Figure 2 shows the hysteresis cycles for the field applied along the two main crystal directions, at $T=5, 20$, and 40 K. The different slopes of the overall $M(H)$ at high fields are due to the background contribution of the epoxy used to orient the samples. A strong decrease of the superconductor hysteresis width with temperature is appreciated. Also, at the lower temperatures the ascending and descending field branches are quite symmetric, indicating that bulk pinning is responsible for the observed magnetic irreversibility. As temperature increases and approaches 40 K, the hysteresis cycles lose their symmetric character, denoting a strong reduction of bulk pinning. Surface barriers then become the main contribution to the magnetic irreversibility of these superconductors, as revealed by the field return branch becoming increasingly flat, with magnetization values close to zero.⁸ The crossover from bulk pinning to surface barrier irreversibility for $H//c$ has been carefully analyzed in Ref. 9, where it was shown that bulk pinning remains observable up to 40 K.

Dominant contributions of surface barriers to the magnetic irreversibility have been earlier reported for several Hg-based compounds, with and without Re.^{6,10} Our results, however, reveal an important difference. For the Hg phases without Re, surface barriers seem to dominate in most of the $H-T$ phase diagram; bulk pinning is almost unobservable in these materials at temperatures above 15 K.¹⁰ Yamasaki *et al.* also report surface barrier irreversibility down to 30 K for a grain aligned sample with 10% Re. In our samples, with 18% Re, bulk pinning is still observable at 40 K. Comparison of the aforementioned results suggests thus an enhancement of the low temperature flux pinning as the Re content increases.

Figure 3 shows the field dependence of the irreversible magnetization $M_{irr} = |M_{\uparrow} - M_{\downarrow}|/2$ for $H//c$ and $H//ab$, at 20 and 40 K. We appreciate that, in agreement with the above arguments, the hysteresis width at 20 K is about a factor of 5 larger than that observed in Ref. 10 at 15 K, for a sample without Re. The critical currents extracted from our M_{irr} data by using the critical state model displays in fact quite high values; the critical current along the planes $J_c^{ab;H//c}$ lies

FIG. 3. $M_{irr}(H)$ at $T=20$ and 40 K, for $H//ab$ and $H//c$.

above 10^6 A/cm² at 5 K and 3 T. However, bulk pinning displays a strong decay with temperature and field, which is responsible for the dominant contribution of surface barriers to M_{irr} at $T > 40$ K.⁹ The same feature is observed for the unsubstituted samples, although at much lower temperatures. Therefore, the improvement of bulk pinning by Re, though significant, is not as yet sufficient to make these materials interesting for applications at high temperatures or fields.

We move now to another remarkable feature revealed by Figs. 2 and 3; this is the similarity of the magnetic irreversibility values—as well as their temperature and field dependences—for the field applied along the two main crystal directions of the superconductor. At low temperatures, $M_{irr}^{H//c}$ is at most a factor of 3 larger than $M_{irr}^{H//ab}$. As H increases, this difference is even lower, due to the stronger decay of $M_{irr}^{H//c}$ with field. In fact, the $M_{irr}(H)$ curves cross each other at high enough temperatures, as clearly appreciated in Fig. 3 for $T=40$ K.

The close values of $M_{irr}^{H//c}$ and $M_{irr}^{H//ab}$ point to a very moderate value of the anisotropy in these materials. In fact, analyses of the high field reversible magnetization performed on the same grain-aligned samples,¹¹ reveal a very low anisotropy ratio $\gamma = m_c/m_{ab} \approx 5$. Yamasaki *et al.*⁶ have also reported $\gamma \approx 8$ from equivalent analyses on samples with 10% Re. Such low values are to be compared with $\gamma \approx 50$, reported for a Hg-1223 single crystal.¹² These recent works reveal therefore a huge anisotropy reduction induced by the Re; such a huge effect is outstanding, even though it had already been pointed out, as a consequence of the metallization of the interlayers. Evidences for this metallization, which would be due to the metallic character of ReO_3 , have been claimed to exist upon comparison of μSR data for these and other high temperature superconductors.⁵

We would like to stress that a misorientation of the applied field with regard to the main crystal directions cannot account for the similarity of the data for $H//c$ and $H//ab$, shown in Figs. 2 and 3. Indeed, unrealistic misorientation angles of about 45° should be considered in order to accommodate the $M(H)$ data to the picture of a highly anisotropic superconductor in which only $H//c$ contributes to M . Note, for instance, that the magnetization minima, denoting the full

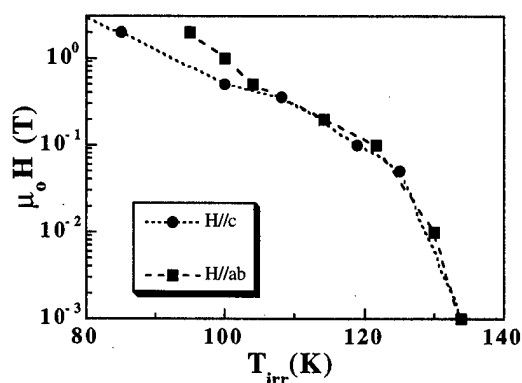


FIG. 4. Irreversibility line extracted from Zero Field Cooling/Field Cooling $M(T)$ data, for $H//ab$ and $H//c$.

penetration of the sample by the applied field, occur at similar values for both field orientations, at any temperature.

On the other hand, we have verified that demagnetization effects are not important by performing $M(H)$ measurements for both orientations of the external field using samples with the long dimension parallel and perpendicular to the field; these measurements, which turn out to depend only on the orientation of H regarding the crystal axes, have allowed to rule out any sample shape effect.

The low anisotropy of this material is further confirmed by the irreversibility lines for $H//ab$ and $H//c$, which are shown in Fig. 4, for $\mu_0 H < 2$ T. They have been obtained from the merging point of the Zero Field Cooling and Field Cooling $M(T)$ curves; at higher fields, both branches of the $M(T)$ data approach each other asymptotically and it becomes extremely difficult to define T_{irr} . We see in Fig. 4 that, for the low field/high temperature range explored, both irreversibility lines are almost coincident. Similar conclusions may be drawn from preliminary AC susceptibility data analyses. We would like to remind here that, in this region of the H - T phase diagram, magnetic irreversibility is governed by surface barriers.⁹ The likeliness of both $H_{irr}(T)$ lines points, therefore, to a quite isotropic surface barrier contribution, giving further support to the already discussed low anisotropy of these compounds.

The Re substitution appears thus to influence both bulk pinning and surface barriers. The observed effects seem to be mainly related to the induced anisotropy reduction, which would imply a change of the superconductor dimensionality, from two-dimensional to three-dimensional. As already discussed, a reduction of the anisotropy γ would result in an increase of the vortex lines stiffness, which would lead to an enhancement of flux pinning, as observed at low temperatures. At the same time, lower γ values would result in an

increase of the full penetration and irreversibility fields due to surface barriers, as shown in Ref. 9. However, other contributions to the irreversibility, as Re originated microstructural changes, might also be relevant.

In conclusion, we have shown that the magnetic irreversibility of Re-substituted Hg-1223 superconductors is larger than that of the unsubstituted compounds. We have presented evidence that at low temperatures this increase is due to a significant improvement of bulk pinning, which overcomes the surface barrier contribution up to 40 K. At higher temperatures, surface barriers dominate the irreversible magnetization, as it happens in the unsubstituted samples. The anisotropic magnetic hysteresis, determined from the hysteresis cycles at low temperatures, reveals a very moderate value of the anisotropy. Such a surprising effect of the Re-substitution is likely due to the reduction of the distance between superconducting Cu-O planes and the metallization of the interlayers because of the presence of ReO_3 . Both effects might lead to the existence of proximity induced superconductivity in the interlayers, and therefore account for the low γ value, which in fact is the lowest reported for high- T_c ($T_c > 77$ K) superconducting cuprates. Further studies of the anisotropy and pinning in these materials become thus compelling, since they might be extraordinary interesting for applications.

ACKNOWLEDGMENTS

We would like to acknowledge financial support by the CICYT (MAT96-1052 and MAT 94-1924) and the Generalitat de Catalunya (GRQ95-8029).

- ¹A. Schilling, M. Cantoni, J. D. Guo, and H. R. Ott, *Nature (London)* **363**, 56 (1993).
- ²J. Shimoyama, S. Hahakura, K. Kitazawa, K. Yamafuji, and K. Kishio, *Physica C* **224**, 1 (1994); K. Yamaura, J. Shimoyama, S. Hahakura, Z. Hiroi, M. Takano, and K. Kishio, *Physica C* **246**, 351 (1995).
- ³O. Chmaissem, J. D. Jorgensen, K. Yamaura, Z. Hiroi, M. Takano, J. Shimoyama, and K. Kishio, *Phys. Rev. B* **53**, 14 647 (1996).
- ⁴K. Kishio, J. Shimoyama, A. Yoshikawa, K. Kitazawa, O. Chmaissem, and J. D. Jorgensen, *J. Low Temp. Phys.* **105**, 1359 (1996).
- ⁵J. L. Tallon, C. Bernhard, Ch. Niedermayer, J. Shimoyama, S. Hahakura, K. Yamaura, Z. Hiroi, M. Takano, and K. Kishio, *J. Low Temp. Phys.* **105**, 1379 (1996).
- ⁶H. Yamasaki, Y. Nakagawa, Y. Mawatari, and B. Cao, *Physica C* **274**, 213 (1997).
- ⁷S. Piñol, A. Sin, A. Calleja, J. Fontcuberta, X. Obradors, and F. Espiell, *J. Supercond.* (in press).
- ⁸N. Chikumoto, M. Konczykowski, N. Motohira, and A. P. Malozemoff, *Phys. Rev. Lett.* **69**, 1260 (1992).
- ⁹L. Fàbrega et al., *Physica C* February, 296 (1998).
- ¹⁰Y. C. Kim, J. R. Thompson, D. K. Christen, Y. R. Sun, M. Paranthaman, and E. D. Specht, *Phys. Rev. B* **52**, 4438 (1995).
- ¹¹L. Fàbrega et al. (unpublished).
- ¹²G. Le Bras, J. Hamman, A. Bertinotti, D. Colson, A. Forget, J. F. Maruco, and V. Viallet, *Czech. J. Phys.* **46**, 1769 (1996).

Structural and magnetic properties of $\text{RSr}_2\text{Fe}_3\text{O}_9$ ($\text{R}=\text{La}$, Y , Pr , and Gd)

V. P. S. Awana^{a)} and S. X. Dou

Centre for Superconducting and Electronic Materials, University of Wollongong, NSW 2522, Australia

I. Felner and I. Nowik

Racah Institute of Physics, The Hebrew University, Jerusalem 91904, Israel

S. K. Malik

Tata Institute of Fundamental Research, Homi Bhabha Road, Bombay 400005, India

Apurva Mehta

SSRL/SLAC, Stanford, California 94309

Rajvir Singh and A. V. Narlikar

National Physical Laboratory, K. S. Krishnan Marg, New Delhi 110012, India

W. B. Yelon

Research Reactor Facility, University of Missouri, Columbia, Missouri 65211

We have investigated the $\text{RSr}_2\text{Fe}_3\text{O}_9$ ($\text{R}=\text{La}$, Y , Pr , and Gd) materials by several experimental techniques, including x-ray and neutron diffraction, magnetic susceptibility, and Mossbauer spectroscopy measurements. All materials studied are single phase and crystallize in the hexagonal perovskite structure. Magnetic susceptibility studies reveal that, for $\text{R}=\text{La}$ and Pr , the Fe ions order antiferromagnetically at about $T_N=190$ K. Short range magnetic correlations are observed up to 250 K. For $\text{R}=\text{La}$ and Pr , ^{57}Fe Mossbauer studies reveal two inequivalent magnetic sextets below 190 K, with the area ratio 2:1. Above T_N , one singlet is observed with an isomer shift value typical to Fe^{4+} . For $\text{R}=\text{Y}$ and Gd , the magnetization curves do not lend themselves to easy determination of the magnetic transition due to an extra magnetic phase which exists up to 350 K. This phase is a result of deficiency of oxygen. The ^{57}Fe Mossbauer spectra at 300 K indicate two superimposed singlet lines, and contain a small magnetic sextet. There is no indication that the R sublattice in $\text{RSr}_2\text{Fe}_3\text{O}_9$ ($\text{R}=\text{Pr}$ and Gd) orders magnetically down to 1.5 K. © 1998 American Institute of Physics. [S0021-8979(98)49511-2]

I. INTRODUCTION

Discovery of high T_c superconductivity (HTSc), above 90 K in (rare earth) R based oxygen deficient perovskite cuprates $\text{RBa}_2\text{Cu}_3\text{O}_7$ ($\text{R}:\text{123}$) has provoked considerable interest in superconductivity and magnetism of various R based perovskites.^{1,2} In principle, R:123 type compounds can be obtained with Ba replaced by Sr and Cu replaced by Fe.^{3,4} Fe based oxides ($\text{RBa}_2\text{Fe}_3\text{O}_8$ and $\text{RSr}_2\text{Fe}_3\text{O}_8$) are not superconducting.³⁻⁵ There are reports of structural magnetic and thermal measurements on some members of the series $\text{RBa}_2\text{Fe}_3\text{O}_8$ (RBFO).³⁻⁷ Also a unique behavior of $\text{PrBa}_2\text{Fe}_3\text{O}_8$ (PBFO), in terms of magnetic and thermal properties was observed in comparison to other R counter parts of the same formula.^{8,9} RBFO compounds are more or less widely explored until now.³⁻⁹ On the other hand for $\text{RSr}_2\text{Fe}_3\text{O}_9$ (RSFO), while the structural details are available for most of R members,¹⁰ detailed magnetic measurements were reported recently only for $\text{LaSr}_2\text{Fe}_3\text{O}_9$ (LSFO).¹¹

In present the article we report details of the structural and magnetic properties of RSFO compounds with $\text{R}=\text{Y}$, La , Pr , and Gd . Details of neutron diffraction, magnetic measurements, and Mossbauer spectroscopy are to be presented.

II. EXPERIMENT

The samples of RSFO with $\text{R}=\text{Y}$, La , Pr , and Gd were synthesized through a solid state reaction route with ingredients of Y_2O_3 , La_2O_3 , Pr_6O_{11} , Gd_2O_3 , SrCO_3 , and Fe_3O_4 . The samples were calcined and reground several times at temperatures of 950, 1000, 1050, 1100, 1150, 1200, 1250, 1300, 1350, and 1400 °C, for 24 h at each temperature, to ensure the formation of single phase compounds. The samples were further annealed at 1000 °C for 48 h in flowing oxygen and were subsequently cooled to room temperature in the same gas atmosphere over a span of 10 h. Neutron diffraction patterns were obtained at room temperature on the powder diffractometer at the Missouri University Research Reactor Centre, with neutrons of wavelength 1.7675 Å. The dc magnetic measurements on solid ceramic pieces in the range of 2–300 K were performed in a commercial (Quantum Design) superconducting quantum interface device (SQUID) magnetometer. The magnetization was measured by two different procedures. (a) The sample was zero field cooled (ZFC) to 5 K, a field was applied and the magnetization was measured as a function of temperature. (b) The sample was field cooled (FC) from above 300 to 5 K and the magnetization was measured. The Mossbauer spectroscopic studies (MS) were carried out using a conventional

^{a)}Electronic mail: awana@uow.edu.au

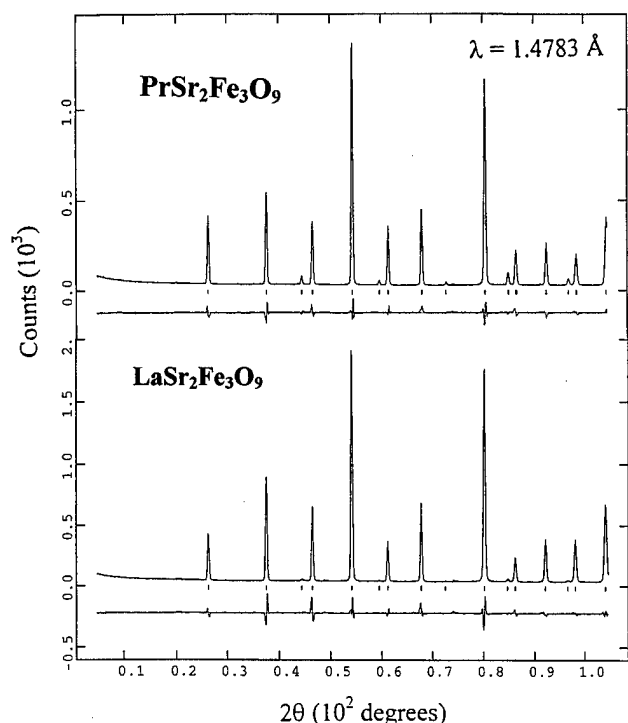


FIG. 1. Observed and fitted neutron diffraction patterns for $\text{LaSr}_2\text{Fe}_3\text{O}_9$ and $\text{PrSr}_2\text{Fe}_3\text{O}_9$ samples, shown one over the other, and taken at room temperature.

constant acceleration spectrometer. The ^{57}Fe MS were measured with a 50 mCi $^{57}\text{Co}:\text{Rh}$ source and the isomer shift (IS) are reported with respect to metallic Fe.

III. RESULTS AND DISCUSSION

A. Neutron diffraction

Figure 1, depicts the observed and fitted neutron diffraction patterns for RSFO samples with $\text{R}=\text{La}$ and Pr . As evident from this figure, the samples are single phase with no impurity lines in the neutron patterns. All the samples of series RSFO with $\text{R}=\text{Y}$, La , Pr , and Gd crystallize in the Rhombohedral structure ($a=b\neq c$, $\alpha=90^\circ$, $\beta=90^\circ$, and $\gamma=120^\circ$) with space group $R3c$. Earlier a cubic structure was proposed for the LSFO compound,^{4,5} but later it was observed that nearly all R with formula RSFO are better fitted in a hexagonal structure.¹⁰ The same is true for our samples also, where we observed a very good fit to the observed patterns with a $R3c$ hexagonal structure, see Fig. 1. The a , b , and c lattice parameters for various samples of RSFO series are as follows:

$\text{YSr}_2\text{Fe}_3\text{O}_9$

$$a=b=5.4664(7) \text{ \AA}, \quad c=13.3793(34) \text{ \AA},$$

$\text{LaSr}_2\text{Fe}_3\text{O}_9$

$$a=b=5.4883(7) \text{ \AA}, \quad c=13.4331(31) \text{ \AA},$$

$\text{PrSr}_2\text{Fe}_3\text{O}_9$

$$a=b=5.47601(15) \text{ \AA}, \quad c=13.3819(7) \text{ \AA},$$

and $\text{GdSr}_2\text{Fe}_3\text{O}_9$

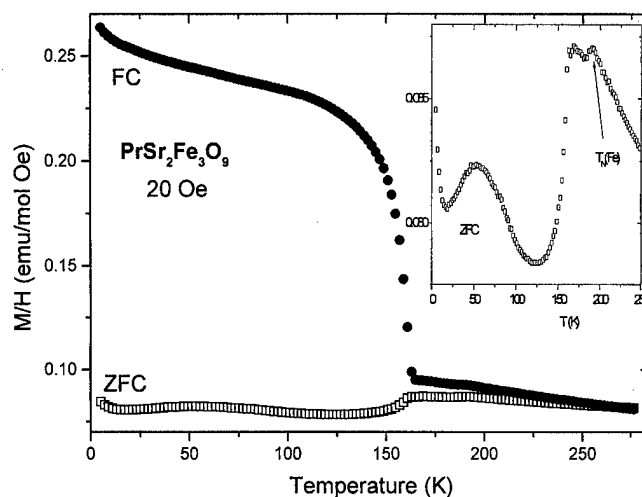


FIG. 2. Temperature dependence of the susceptibility for $\text{PrSr}_2\text{Fe}_3\text{O}_9$ measured at 20 Oe, and the ZFC branch in inset. Note that the ZFC and FC branches merge at 260 K.

$$a=b=5.4668(9) \text{ \AA}, \quad c=13.3798(19) \text{ \AA}.$$

Our values of a , b , and c -lattice parameters for various samples, studied presently are comparable to those reported earlier.¹⁰ These values of lattice parameters also follow the ionic radius difference of the Y, La, Pr, and Gd. Lowest ionic size Y and Gd, are followed by relatively bigger ions La and Pr with increasing c -lattice parameters.

B. Magnetic behavior

The ZFC and FC magnetic susceptibility, measured at 20 Oe of $\text{PrSr}_2\text{Fe}_3\text{O}_9$ (PSFO) is shown in Fig. 2. Generally speaking, in both branches, only one distinct anomaly is observed. In analogy to $\text{PrBa}_2\text{Cu}_3\text{O}_7$,¹² it is possible that the Pr sublattice is magnetically ordered at low temperatures, but this ordering is not visible in the curves. We tend to believe that the anomalies in these branches are related to the Fe sites. The Neel temperature, $T_N(\text{Fe})$ is 195(1) K and is defined as the peak in the ZFC branch (Fig. 2 inset), which is above the sharp decrease position of the FC branch. Within the limit of uncertainty the same $T_N(\text{Fe})$ is obtained for La containing compound. It appears that T_N of Fe is about 200 K for all R, apparently independent of whether the trivalent R ions are magnetic (Pr, Fe) or not (Y, La). It is worth mentioning here that in RBFO compounds, the PBFO showed a unique behavior in terms of Fe ordering temperature.^{8,9} Particularly Fe moment orders around 700 K for all studied RBFO compounds, except PBFO, for which the same happens at around 290 K. The nearly linear (at high applied field) field dependence of the magnetization at 5 K (not shown), suggests that Fe sublattice order antiferromagnetically (AFM). The irreversibility probably arises from this AFM alignment of the Fe sublattice. It is assumed that in the FC process the external field causes the spins to cant slightly out of their original direction. This canting abruptly aligns a component of the moments with the direction of the field, and the FC branch is obtained. The effect of field strength on the irreversibility is significant. At low applied fields, the

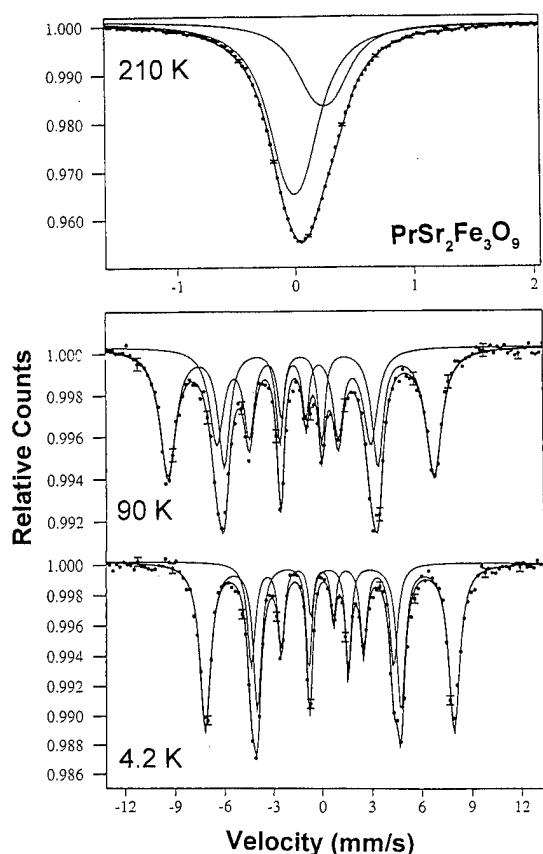


FIG. 3. Mossbauer spectra of $\text{PrSr}_2\text{Fe}_3\text{O}_9$ in the paramagnetic state (210 K) and below $T_N(\text{Fe})$. The solid curves are theoretical least square fits in terms of 2 subspectra corresponding to inequivalent Fe sites.

field dependence of the magnetization is not linear, and the fact that the ZFC and FC curves merge at 260 K [above $T_N(\text{Fe})$], indicated the existence of an internal magnetic field at low temperatures, which vanishes at 260 K. The magnetic results, shown in Fig. 2, confirm our Mossbauer (MS) studies, which are displayed and discussed in the next section.

C. Mossbauer spectroscopy

Mossbauer spectrum of ^{57}Fe in $\text{PrSr}_2\text{Fe}_3\text{O}_9$ (PSFO) at 210 K [above $T_N(\text{Fe})$] is shown in Fig. 3. The main information obtained from visual and computer analysis is the presence of two subspectra corresponding to inequivalent Fe sites, which are immediately identified from their hyperfine parameters: the isomer shift (IS) and quadrupole splitting ($\Delta = 1/4e^2qQ$) values, with a common line width of 0.40(2) mm/s. The *dominant* line which accounts for 66% of the spectra area, has a small IS = -0.11 mm/s and a Δ of 0.06(1) mm/s and can be assigned as Fe^{4+} in the low spin state. Both, the IS = 0.17 and $\Delta = 0.07$ mm/s of the *minor* doublet (33%), are typical to Fe^{3+} . For $\text{R}=\text{La}$, the MS measured at various temperatures (not shown) are very similar to the spectra shown in Fig. 3, proving the Pr ions are trivalent.

In fitting the experimental parameters below $T_N(\text{Fe})$, the iron in $\text{PrSr}_2\text{Fe}_3\text{O}_9$ (and for $\text{R}=\text{La}$), is composed of *predomi-*

nantly Fe^{3+} (66% at 4.2 K), Fe^{5+} (33% at 4.2 K), and an increasing fraction with temperature of Fe^{4+} (zero at 4.2 K). The 4.2 K spectrum (Fig. 3) is composed of two magnetic subspectra with IS = 0.37 and -0.03 , an effective magnetic hyperfine field: $H_{\text{eff}} = 469(3)$ and $269(2)$ kOe (the effective quadrupole splitting is zero for both sites), corresponding to Fe^{3+} and Fe^{6+} , respectively. These hyperfine parameters are consistent with this assignment. The spectrum at 90 K (Fig. 3) is fitted in the same manner. It thus assumed, that the nonmagnetic Fe^{4+} ions fraction increases with temperature and dilutes the magnetic Fe^{3+} and Fe^{5+} ions. At $T_N(\text{Fe})$, (the Fe^{4+} fraction becomes 66%) the magnetic order disappears.

IV. CONCLUSIONS

In conclusion we assume below $T_N(\text{Fe})$, the presence of Fe^{5+} (33% at 4.2 K, lowest IS and small H_{eff}) and Fe^{3+} (66% at 4.2 K, highest IS and large H_{eff}), and Fe^{4+} (0% at 4.2 K, intermediate IS and no H_{eff}). Whereas, at high temperatures [above $T_N(\text{Fe})$], most of the Fe ions are in nonmagnetic Fe^{4+} state. The valance fluctuations occur only as a single electron process: $\text{Fe}^{5+} \rightarrow \text{Fe}^{4+}$ and $\text{Fe}^{3+} \rightarrow \text{Fe}^{4+}$.

In summary all the samples of series $\text{RSr}_2\text{Fe}_3\text{O}_9$ with $\text{R}=\text{Y}$, La, Pr, and Gd crystallize in hexagonal $\text{R}\bar{3}c$ structure. Also their magnetic properties are very similar to each other. $\text{PrSr}_2\text{Fe}_3\text{O}_9$ behaves magnetically in a similar way as other $\text{RSr}_2\text{Fe}_3\text{O}_9$ compounds, unlike the case of $\text{PrBa}_2\text{Cu}_3\text{O}_7$ and $\text{PrBa}_2\text{Fe}_3\text{O}_8$, which are reported to have unique behavior.^{8,9,12}

ACKNOWLEDGMENTS

The authors at the University of Wollongong thank the Australian Research Council (ARC) for financial support. The research at Racah Institute Jerusalem is sponsored by the Israel Academy of Science and Technology and by the Klachky Foundation for Superconductivity. Part of the work at MURR was supported by US Department of Energy Grant No. DE-FG02-90ER4527 through the Midwest Superconductivity Consortium.

- ¹P. Hor, R. L. Meng, Y. Q. Wang, L. Gao, Z. J. Huang, J. Bechtold, K. Forster, and C. W. Chu, *Phys. Rev. Lett.* **58**, 1891 (1987).
- ²P. D. Battle, T. C. Gibb, and S. Nixon, *J. Solid State Chem.* **77**, 124 (1988).
- ³I. Felner, I. Nowik, U. Yaron, O. Cohen, E. R. Bauminger, T. Kroener, and C. Czjzek, *Phys. Rev. B* **48**, 16 040 (1993).
- ⁴P. D. Battle, T. C. Gibb, and S. Nixon, *J. Solid State Chem.* **79**, 75 (1989).
- ⁵P. D. Battle, T. C. Gibb, and S. Nixon, *J. Solid State Chem.* **79**, 86 (1989).
- ⁶J. T. Wang, C. L. Lin, and T. Mihalisin, *J. Appl. Phys.* **79**, 6608 (1996).
- ⁷Q. Huang, P. Karen, A. Kjekshus, J. W. Lynn, A. D. Mighell, N. Rosov, and A. Santoro, *Phys. Rev. B* **45**, 9611 (1992).
- ⁸M. Almassalami, A. Elzubair, H. M. Ibrahim, and M. A. Rizgalla, *Physica C* **183**, 143 (1991).
- ⁹V. P. S. Awana, Latika Menon, S. K. Malik, Apurva Mehta, Sanjay Mishra, and W. B. Yelon, *Physica B* **223&224**, 558 (1996).
- ¹⁰I. Felner, G. Hilscher, M. Michor, B. Wortmann, J. Dumschat, V. P. S. Awana, and S. K. Malik, *Phys. Rev. B* **54**, 11 999 (1996).
- ¹¹P. D. Battle, T. C. Gibb, and S. Nixon, *J. Solid State Chem.* **79**, 86 (1989).
- ¹²H. B. Radousky, *J. Mater. Res.* **7**, 1917 (1992).

Magnetic and superconducting properties of Pr in $\text{La}_{1-x}\text{Pr}_x\text{BaCaCu}_3\text{O}_7$ system with $0.0 \leq x \leq 1.0$

V. P. S. Awana and S. X. Dou

*Institute for Superconducting and Electronic Materials, University of Wollongong,
New South Wales 2522, Australia*

Rajvir Singh and A. V. Narlikar

National Physical Laboratory, Krishnan Marg, New Delhi 110012, India

S. K. Malik

Tata Institute of Fundamental Research, Homi Bhabha Road, Bombay 400005, India

W. B. Yelon

Research Reactor Facility, University of Missouri, Columbia, Missouri 65211

We report the results on structural aspects, magnetic, and superconducting properties of the $\text{La}_{1-x}\text{Pr}_x\text{BaCaCu}_3\text{O}_7$ system. Both x-ray and neutron diffraction studies reveal that Pr substitutes isostructurally in the tetragonal $\text{LaBaCaCu}_3\text{O}_7$ (La:1113) system until the complete replacement of La by Pr. The superconducting transition temperature, T_c , determined from ac susceptibility measurements decreases, with increasing x . The relative T_c depression due to Pr in the $\text{LaBaCaCu}_3\text{O}_7$ superconductor is less in comparison to that found for La-site Pr substituted $\text{LaBa}_2\text{Cu}_3\text{O}_7$ (La:123). While the critical Pr concentration (x_{cr}) to completely suppress the superconductivity in the former is around 70 at. % of Pr at La site, the same is reported as only 30 at. % for the latter. For nonsuperconducting samples, i.e., for $x=0.70$ and 1.0, possible antiferromagnetic ordering with Neel temperatures, T_N , of 4 and 8 K, respectively, are observed from both dc magnetic and heat capacity measurements. Interestingly in the $\text{La}_{1-x}\text{Pr}_x$:1113 system the x_{cr} of Pr is 0.70, and T_N of Pr:1113 is 8 K, while for the $\text{La}_{1-x}\text{Pr}_x$:123 system x_{cr} is 0.30 and T_N of Pr:123 is 17 K. The results are explained on the basis of distribution of Pr at both RE and Ba sites in the RE:1113 structure. This leads to a lower T_N and a less deleterious effect of Pr on superconductivity of La:1113 compared to La:123. © 1998 American Institute of Physics. [S0021-8979(98)17411-X]

I. INTRODUCTION

High temperature superconductivity (HTSc) above 90 K is observed in nearly all RE (rare earth) based $\text{REBa}_2\text{Cu}_3\text{O}_7$ (RE:123) compounds, except Ce, Pr, and Tb.¹ The structure of RE based 123 perovskite compound consists of two dimensional Cu–O planes and one dimensional Cu–O chains embedded between Ba and RE layers.² Both Ce and Tb based RE:123 compounds do not crystallize in the required structure: instead they form a multiphase system.³ The situation is more interesting in the case of Pr:123 ($\text{PrBa}_2\text{Cu}_3\text{O}_7$). This compound crystallizes in ideal orthorhombic RE:123 structure, similar to that of other superconducting compounds of this family, yet with no superconductivity.^{4–15} In fact, $\text{PrBa}_2\text{Cu}_3\text{O}_7$ is an antiferromagnetic insulator, with Cu spins in CuO_2 planes ordered near room temperature and Pr moments ordered at nearly 17 K.¹⁵ However, as far as we know, three reports exist in literature which claim superconductivity of Pr:123: one on laser ablated $\text{Pr}_{0.5}\text{Ca}_{0.5}\text{Ba}_2\text{Cu}_3\text{O}_7$ thin film,⁶ another on bulk $\text{Pr}_{1-x}\text{Ca}_x\text{Sr}_2\text{Cu}_{2.7}\text{Mo}_{0.3}\text{O}_7$ and one on recently reported $\text{PrBa}_2\text{Cu}_3\text{O}_7$ single crystals.⁸ Unfortunately, none of these results have been confirmed till now. The most promising one is the latest⁸ by Zou *et al.* [Jpn. J. Appl. Phys., Part 2 36, L18 (1997)]. These authors show bulk superconductivity of 80 K for $\text{PrBa}_2\text{Cu}_3\text{O}_7$ single crystals. These results have been greeted with considerable criti-

cism since the structure of superconducting Pr:123 compound reveals an anomalously long c axis questioning whether this material is truly isostructural with the superconducting RE:123 materials. Moreover, like other reports on superconducting Pr:123 compounds,^{6,7} the latest one,⁸ also lacks the universal reproduction of the same by other groups.

There are several models in the literature which try to explain the nonobservation of superconductivity in $\text{PrBa}_2\text{Cu}_3\text{O}_7$. The most widely discussed are the hole filling model,^{4,9,10} and pair breaking mediated by the hybridization of Pr 4*f* with O 2*p* states.^{11,12} The hole filling model is based on the existence of Pr in a valence state of more than +3, and whereby the extra electrons from Pr neutralizes mobile holes and brings the compound to near insulating regime. This model also accounts for the restoration of superconductivity in $\text{Pr}_{0.5}\text{Ca}_{0.5}\text{Ba}_2\text{Cu}_3\text{O}_7$, where the holes are restored by lower valence Ca substitution at Pr site in the compound.⁶ The main drawback of this model is that a valence state of more than 3+ could never be detected in the $\text{PrBa}_2\text{Cu}_3\text{O}_7$ compound. In fact the detailed magnetic susceptibility,^{13,14} photoemission spectroscopy,¹⁵ x-ray absorption,¹⁶ and electron energy loss spectroscopy¹⁷ results altogether favor a +3 valence state of Pr in $\text{PrBa}_2\text{Cu}_3\text{O}_7$.

While the pair breaking model appeared to be promising, in that it could explain the suppression of superconductivity

in $\text{RE}_{1-x}\text{Pr}_x:123$ systems,^{11,12} pair breaking itself could not account for the insulating behavior of the $\text{PrBa}_2\text{Cu}_3\text{O}_7$ compound.

Two more recent and better understood models are given by Fehrenbacher and Rice (FR) and Liechtenstein and Mazin (LM).^{18,19} Both models involve the transfer of holes from superconducting $p d \sigma$ state to the $p d \pi$ state. In the FR model, the $p \pi$ orbitals of the planar oxygens neighboring a Pr ion, form a hybrid with the $\text{Pr-}f_{z(x^2-y^2)}$ orbital, which is strongly localized.¹⁸ Further in this model, the $p \pi$ holes are predominantly planar (p_{xy}), according to LM,¹⁹ the same have comparable amounts of $p_{x,y}$ and p_z character. The FR and LM models could also gain credence from recent x-ray absorption spectroscopy results on the $\text{Y}_{1-x}\text{Pr}_x\text{Ba}_2\text{Cu}_3\text{O}_7$ system.²⁰ Although both the FR and LM models explain the insulating behavior of $\text{PrBa}_2\text{Cu}_3\text{O}_7$, they do not successfully account for the T_N of nearly 17 K for Pr moments in this compound.

With more and more experimental results appearing in the literature the mystery of nonsuperconducting $\text{PrBa}_2\text{Cu}_3\text{O}_7$ is becoming increasingly complicated. In the present study we report an interesting result on two different types of Pr doped RE:123 compounds, with the same rare earth, La. These results suggest that both T_c suppression and the antiferromagnetic ordering of Pr moments are closely related to each other. We study the compound $\text{La}_{1-x}\text{Pr}_x\text{BaCaCu}_3\text{O}_7$ with several x values and compare the same with reported data²¹ on $\text{La}_{1-x}\text{Pr}_x\text{Ba}_2\text{Cu}_3\text{O}_7$. Our structural, magnetic and thermal measurements on this system show that the critical concentration of Pr (x_{cr}) to quench superconductivity in this system is 0.70 which is double of that found earlier for $\text{La}_{1-x}\text{Pr}_x\text{Ba}_2\text{Cu}_3\text{O}_7$ ($x_{cr}=0.30$).

II. EXPERIMENT

Samples of the series $\text{La}_{1-x}\text{Pr}_x\text{BaCaCu}_3\text{O}_7$, with $x=0.0, 0.10, 0.20, 0.30, 0.40, 0.50, 0.60$, and 1.0, were prepared by a solid state reaction from La_2O_3 , BaCO_3 , CaCO_3 , Pr_6O_{11} , and CuO each of 4N purity with the procedure, as reported in Ref. 22. The samples were characterized for their phase purity by x-ray diffraction (XRD) measurements. Alternating current magnetic susceptibility measurements were carried out on a Quantum Design SQUID magnetometer, in an applied r.m.s. field of 0.01 mT and 31 Hz. Neutron diffraction patterns at room temperature were obtained for the samples with $x=0.0$ and 1.0 using the research reactor facility of the University of Missouri. The experimental details are similar to those reported earlier for RE:123 ceramic samples.²³

III. RESULTS AND DISCUSSION

X-ray diffraction studies show that $\text{La}_{1-x}\text{Pr}_x\text{BaCaCu}_3\text{O}_7$ samples are nearly single phase materials. All the samples crystallize in a P4/mmm tetragonal RE:123 phase with a decrease in the c parameter with increasing x .²² The $\text{LaBaCaCu}_3\text{O}_7$ compound is known to crystallize in the tetragonal RE:123 structure, despite having an oxygen content close to 7.0, due to the intermixing of La, Ba, and Ca sites which gives rise to equally occupied O(1) and O(5) sites in CuO chains, resulting in $a=b$.^{24,25}

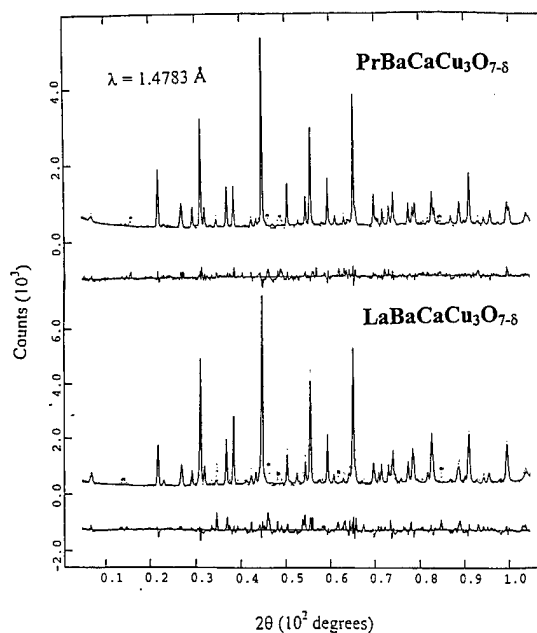


FIG. 1. Fitted and observed Neutron diffraction patterns for $\text{LaBaCaCu}_3\text{O}_7$ and $\text{PrBaCaCu}_3\text{O}_7$ samples, taken at room temperature.

Room temperature observed and fitted neutron diffractions patterns for $\text{PrBaCaCu}_3\text{O}_7$ and $\text{LaBaCaCu}_3\text{O}_7$ compounds are shown in Fig. 1. In addition to the lines from main phase, both the samples show a few diffraction lines from unreacted species in their respective spectra, similar to those observed earlier in x-ray diffraction patterns of these compounds.^{22,26} The results of the Rietveld refinement procedure using the Generalized Structural Analysis System (GSAS) for $\text{LaBaCaCu}_3\text{O}_7$ sample reveal that part of La occupies Ba site with a corresponding amount of Ca occupying the nominal RE site. Quantitatively 46% of Ca atoms occupy the usual La site, and the remaining 54% are at the Ba site. It is presumed that a similar situation occurs when Pr is substituted at La site, i.e., part of Pr occupies the Ba site. Unfortunately, the neutron scattering cross sections of Pr and Ba are very similar preventing accurate determination of their occupancies. The oxygen contents of the two samples were found to be 7.01 and 6.86, respectively, for $x=0.0$ and 1.0.

In Fig. 2 are shown the real and imaginary parts of ac susceptibility versus temperature plots for the $\text{La}_{1-x}\text{Pr}_x\text{BaCaCu}_3\text{O}_7$ system with various x values. The inset shows the T_c vs x behavior for the presently studied system and that reported in $\text{La}_{1-x}\text{Pr}_x\text{Ba}_2\text{Cu}_3\text{O}_7$ system.²¹ The superconducting transition temperature, T_c , is defined as the onset of the diamagnetic transition, which is around 70 K for the unsubstituted sample. T_c decreases with increasing x in both $\text{La}_{1-x}\text{Pr}_x\text{BaCaCu}_3\text{O}_7$ and $\text{La}_{1-x}\text{Pr}_x\text{Ba}_2\text{Cu}_3\text{O}_7$ systems. In $\text{RE}_{1-x}\text{Pr}_x:123$, the depression of T_c depends strongly on the ionic radius of the host rare earth. Hence a comparison of the $\text{La}_{1-x}\text{Pr}_x\text{BaCaCu}_3\text{O}_7$ system can be made with the Pr substituted La:123 system only. As seen from inset of Fig. 2, the critical Pr concentration (x_{cr}) for destroying superconductivity is 0.70 in the $\text{La}_{1-x}\text{Pr}_x\text{BaCaCu}_3\text{O}_7$ system, while the same is nearly 0.30 for the $\text{La}_{1-x}\text{Pr}_x\text{Ba}_2\text{Cu}_3\text{O}_7$ system. This shows that Pr is less effective in destroying the superconduc-

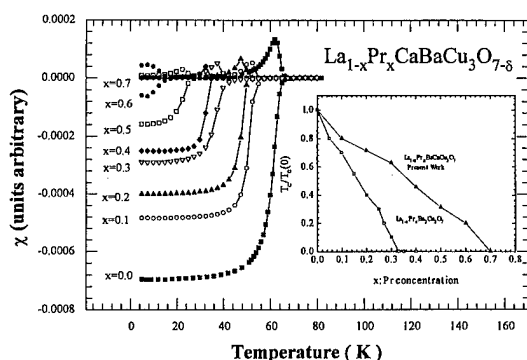


FIG. 2. ac susceptibility (both real and imaginary parts) vs temperature plots for $\text{La}_{1-x}\text{Pr}_x\text{BaCaCu}_3\text{O}_7$ system with various x values, the inset shows the T_c vs x behavior for presently studied and reported (Ref. 21) $\text{La}_{1-x}\text{Pr}_x\text{Ba}_2\text{Cu}_3\text{O}_7$ systems.

tivity of $\text{La}_{1-x}\text{Pr}_x\text{BaCaCu}_3\text{O}_7$ than that of $\text{La}_{1-x}\text{Pr}_x\text{Ba}_2\text{Cu}_3\text{O}_7$.

The susceptibility (χ) of both $x=0.70$ and 1.0 samples showed deviations from the standard Curie-Weiss behavior at 4 and 8 K, respectively. Heat capacity measurements²² also show humps at these temperatures. These results indicate the possibility of magnetic ordering of Pr moments at these temperatures in the two compounds. Incidentally, similar deviation in dc magnetic susceptibility measurements and a broad hump in C_p occurs at 17 K for the $\text{PrBa}_2\text{Cu}_3\text{O}_7$ compound (see, for instance, Ref. 5). Interestingly, while the x_{cr} is higher, the T_N of Pr is lower for the presently studied system than for $\text{La}_{1-x}\text{Pr}_x\text{:123}$. The lower T_N of Pr in the $\text{La}_{1-x}\text{Pr}_x\text{BaCaCu}_3\text{O}_7$ system, perhaps explains the less deleterious effect of the Pr on superconductivity.

The high T_N of Pr in Pr:123 type compounds is presumed to arise from the strong hybridization of Pr 4f orbital with the neighboring Cu-O conduction band.⁵ Decreased oxygen content in Pr:123 compounds, decreases the number of charge carriers in the Cu-O conduction band and increases the Pr to Cu-O distance, which results in a decreased T_N . For example, a T_N of 12 K is reported for $\text{PrBa}_2\text{Cu}_3\text{O}_{6.4}$.²⁷ This shows that the small decrease of oxygen content in our sample of composition $\text{PrBaCaCu}_3\text{O}_{6.86}$ cannot explain solely the lowering of T_N to 8 K. Another possible and more viable reason for the decreased T_N may be the distribution of Pr at both the usual Pr site (sandwiched between two Cu-O planes) and the Ba site. This may result in a lower T_N and a less destructive effect of Pr on superconductivity in the present system.²⁸

In conclusion our study indicates that superconductivity can be induced in $\text{RE}_{1-x}\text{Pr}_x\text{:123}$ compounds for higher x values by separating the Pr from Cu-O conduction band. In this way one can decrease the magnetic interaction of Pr 4f with the Cu-O conduction band and induce superconductivity in Pr:123 type compounds.

ACKNOWLEDGMENTS

The authors at the University of Wollongong, would like to thank Australian Research Council (ARC) for financial support. Part of this work at MURR was supported by U. S. Department of Energy Grant No. DE-FG02-90ER45427 through the Midwest Superconductivity Consortium.

- ¹ Z. Fisk, J. D. Thompson, E. Zirngiebl, J. L. Smith, and S.-W. Cheong, *Solid State Commun.* **62**, 743 (1987).
- ² P. K. Gallagher, *Mater. Res. Bull.* **22**, 995 (1987).
- ³ P. Hor, R. L. Meng, Y. Q. Wang, L. Gao, Z. J. Huang, J. Bechtold, K. Forster, and C. W. Chu, *Phys. Rev. Lett.* **58**, 1891 (1987).
- ⁴ A. Matsuda, K. Kinoshita, T. Ishii, H. Shibata, T. Watanabe, and T. Yamada, *Phys. Rev. B* **38**, 2910 (1988).
- ⁵ H. B. Radousky, *J. Mater. Res.* **7**, 1917 (1992).
- ⁶ D. P. Norton, D. H. Lowndes, B. C. Sales, J. D. Budai, B. C. Chakoumakos, and H. R. Krechner, *Phys. Rev. Lett.* **66**, 1537 (1991).
- ⁷ H. D. Yang, H. L. Tsay, C. R. Shih, and Y. C. Chen, *Phys. Rev. B* **51**, 8543 (1995); H. L. Tsay, Y. C. Chen, F. L. Juang, W. M. Wang, and H. D. Yang, *ibid.* **53**, 11340 (1996).
- ⁸ Z. Zou, K. Oka, T. Ito, and Y. Nishihara, *Jpn. J. Appl. Phys., Part 2* **36**, L18 (1997).
- ⁹ Z. Qiu, Z. H. Zhenhui, Z. Han, X. Jiansheng, W. Shenxi, and F. Minghu, *Physica C* **162-164**, 963 (1989).
- ¹⁰ B. Fisher, J. Genossar, L. Patlagan, and J. Ashkenazi, *Phys. Rev. B* **43**, 2821 (1991).
- ¹¹ A. Kebede, C. S. Jee, J. Schwegler, J. E. Crow, T. Mihailisin, G. H. Myer, R. E. Salomon, P. Schlottmann, M. V. Kuric, S. H. Bloom, and R. P. Guertin, *Phys. Rev. B* **40**, 4517 (1989).
- ¹² S. K. Malik, Parag Bhargava, and C. V. Tomy, *Phys. Rev. B* **44**, 7042 (1991).
- ¹³ L. Soderholm, C.-K. Loong, G. I. Goodman, and B. D. Dabrowski, *Phys. Rev. B* **43**, 7923 (1991).
- ¹⁴ G. Hilscher, E. Holland-Moritz, T. Holubar, H.-D. Jostardt, V. Nekvasil, G. Schaudy, U. Walter, and G. Fillion, *Phys. Rev. B* **49**, 535 (1994).
- ¹⁵ J. S. Kang, J. W. Allen, Z.-X. Shen, W. P. Ellis, J. J. Yeh, B. W. Lee, M. B. Maple, W. E. Spicer, and I. Lindau, *J. Less-Common Met.* **148**, 121 (1989).
- ¹⁶ U. Neukrich, C. T. Simmons, D. Sladeczek, C. Laubschat, O. Strebel, G. Kaindl, and D. D. Sarma, *Europhys. Lett.* **5**, 567 (1988).
- ¹⁷ J. Fink, N. Nucker, H. Romberg, M. Alexander, M. B. Maple, J. J. Neumeier, and J. W. Allen, *Phys. Rev. B* **42**, 4823 (1990).
- ¹⁸ R. Fehrenbacher and T. M. Rice, *Phys. Rev. Lett.* **70**, 3471 (1993).
- ¹⁹ A. I. Liechtenstein and I. I. Mazin, *Phys. Rev. Lett.* **74**, 1000 (1995).
- ²⁰ M. Mertz, N. Nucker, E. Pellegrin, P. Schweiss, S. Schupler, M. Kielwein, M. Knupfer, M. S. Golden, J. Fink, C. T. Chen, V. Chakarian, Y. U. Idzerda, and A. Erb, *Phys. Rev. B* **55**, 9160 (1997).
- ²¹ K. Sekizawa, Y. Takano, K. Kanno, H. Ikuta, H. Ozaki, and H. Enomoto, *Physica B* **194-196**, 1937 (1994).
- ²² V. P. S. Awana, Rajvir Singh, D.A. Landinez Tellez, J. M. Ferreira, J. Albino Aguiar, S. Uma, E. Gmelin, and A. V. Narlikar, *Mod. Phys. Lett. B* **11**, 323 (1997).
- ²³ V. P. S. Awana, S. K. Malik, and W. B. Yelon, *Physica C* **262**, 272 (1996).
- ²⁴ W. T. Fu, H. W. Zandbergen, C. J. van der Beek, and L. J. de Jongh, *Physica C* **156**, 133 (1988).
- ²⁵ T. Yagi, M. Domon, Y. Okajima, and K. Yamaya, *Physica C* **173**, 453 (1991).
- ²⁶ R. A. Gunasekaran, I. K. Gopalakrishnan, P. V. P. S. Sastry, J. V. Yakhmi, and R. M. Iyer, *Physica C* **199**, 240 (1992).
- ²⁷ S. K. Malik, W. B. Yelon, J. J. Rhyne, W. J. James, Ram Prasad, K. Adhikary, and N. C. Soni, *Solid State Commun.* **89**, 383 (1994).
- ²⁸ S. K. Malik, S. M. Patalwar, C. V. Tomy, Ram Prasad, N. C. Soni, and K. Adhikary, *Phys. Rev. B* **46**, 544 (1992).

Magnetic properties of $\text{Pb}_2\text{Sr}_2\text{PrCu}_3\text{O}_8$ studied by ac susceptibility

S. Y. Wu, Y. C. Chang, K. C. Lee, and W.-H. Li

Department of Physics, National Central University, Chung-Li, Taiwan 32054, Republic of China

The magnetic responses of vacuum annealed polycrystalline $\text{Pb}_2\text{Sr}_2\text{PrCu}_3\text{O}_8$ to a magnetic field have been studied by ac magnetic susceptibility measurements, where both the in-phase component χ' and the out-of-phase component χ'' were measured. Diamagnetic responses in $\chi'(T)$ below 60 K were clearly seen, showing the occurrence of superconductivity, but it is filamentary. This filamentary superconductivity was also evident in the $\chi''(T)$. Under an applied dc field, both the $\chi'(T)$ and $\chi''(T)$ behave as what are expected for a superconducting system. At lower temperatures, a well-defined peak associated with the Pr spin ordering is also clearly revealed at 5 K. Correspondingly, an anomaly is also seen in the specific heat data. © 1998 American Institute of Physics. [S0021-8979(98)22911-2]

Since the discovery of high- T_c oxides, intensive studies have been made on this class of material, especially on their superconducting and magnetic properties. Yet, many physical phenomena are still not well understood. In the Pb-based 2213 systems, $\text{Pb}_2\text{Sr}_2\text{RCu}_3\text{O}_{8+x}$ (R=rare earth), superconductivity around 70 K has been observed in the alkaline earth metal doped compounds.^{1,2} For the alkaline earth metal free compounds, filamentary superconductivity and superconducting-like resistivity drop around 70 K have been reported.^{3,4} The crystal structure of the $\text{Pb}_2\text{Sr}_2\text{RCu}_3\text{O}_{8+x}$ compound can be obtained from the well-known $\text{RBa}_2\text{Cu}_3\text{O}_{6+x}$ structure by replacing the CuO-chain layer in the latter with two PbO and one Cu layers for the former. In this paper, we report the observations of superconductivity and magnetic order of the Pr spins in a polycrystalline $\text{Pb}_2\text{Sr}_2\text{PrCu}_3\text{O}_8$ compound by using ac magnetic susceptibility and specific heat measurements.

A vacuum annealed polycrystalline sample of $\text{Pb}_2\text{Sr}_2\text{PrCu}_3\text{O}_8$ was prepared by the two-stage solid state reaction techniques. High purity powders of SrCO_3 , Pr_2O_3 , and CuO with a ratio of Sr:Pr:Cu=2:1:3 were well mixed and calcined at 930 °C in air for 12 h with two intermediate grinding. The obtained precursor $\text{Sr}_2\text{PrCu}_3\text{O}_x$ powders was then mixed with an appropriate amount of high purity PbO powder, followed by a heating in air at 750 °C for 12 h with three intermediate grinding. The reacted powders were then pressed into pellets and annealed at 870 °C in vacuum of pressure 10^{-2} Torr for 24 h, followed by furnace cooling to room temperature. The sample fabricated was characterized by a complete structural analysis using x-ray diffraction and Rietveld analysis.⁵ High resolution diffraction pattern taken at room temperature was analyzed using the General Structure Analysis System (GSAS) program of Larson and von Dreele.⁶ The diffraction pattern obtained may be well described using the structure reported⁷ for $\text{Pb}_2\text{Sr}_2\text{YCu}_3\text{O}_8$. The refinement was carried out assuming the symmetry of space group $P2_1/m$. In the refining process, all structural parameters were allowed to vary simultaneously unit R_w , the weighted R factor,⁶ differed by less than one part in a thousand in two successive cycles. Only a few additional very weak peaks were present, showing the compound is practi-

cally of single phase. We estimated that the impurity phases should be less than 3%. Careful analysis of the occupancy factor of the oxygen atoms showed that the O sites were almost fully occupied. The compound crystallizes into a monoclinic phase with lattice constants $a=5.3901(4)\text{Å}$, $b=5.4302(4)\text{Å}$, $c=15.655(1)\text{Å}$, and the angle between the a and b axes $\beta=89.69(4)^\circ$ at room temperature.

The ac susceptibility measurements were performed using a Lake Shore 7221 ac susceptometer, with which both the in-phase component χ' and the out-of-phase component χ'' can be measured simultaneously. Shown in Fig. 1 are the low temperature portions of $\chi'(T)$ measured using driving fields of rms strength 1 Oe and at three frequencies. Above 60 K, $\chi'(T)$ is essentially independent of the driving frequency used, and it follows the Curie—Weiss law. The solid curve shown in Fig. 1 is an extrapolation of a fit to $\chi'(T)$ data obtained between 80 and 320 K (not shown) to the expression $\chi'_0 + C/(T - \theta)$, where χ'_0 is a temperature independent constant represents the contribution from the conduction electrons. Using the fitted value for the Curie—Weiss constant C , we obtained a value of $2.90\mu_B$ for the effective moment. The value obtained for μ_{eff} is about 20% smaller

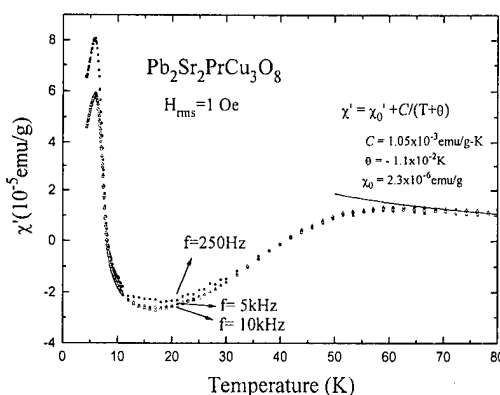


FIG. 1. Temperature dependence of χ' measured at three driving frequencies. Diamagnetic responses below 60 K and a well-defined peak at 5 K are clearly seen.

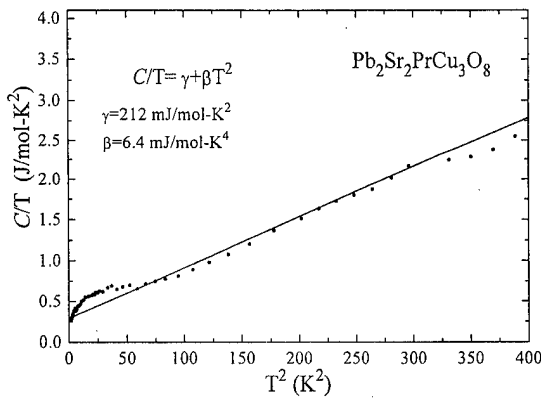


FIG. 2. Temperature dependence of the specific heat measured using the time constant techniques (Ref. 8). The anomaly seen at low temperatures is associated with the ordering of the Pr spins. The solid curve shown is a fit of the data obtained between 15 K $\leq T \leq$ 40 K (not shown) to the expression $C/T = \gamma + \beta T^2$, with $\gamma = 212$ mJ/mol K² for the contribution from electrons and $\beta = 6.4$ mJ/mol K⁴ from phonons.

than the value of $3.58 \mu_B$ expected for the free Pr ions. This discrepancy likely originates from the crystalline electric field effects.

The main features seen in Fig. 1 are the diamagnetic responses occur below ~ 60 K and the well-defined peak at 5 K. The diamagnetic responses, which are essentially independent of the driving frequency used, signifies the occurrence of superconductivity. Although negative values for χ' were obtained at temperatures below 40 K, it is obvious that the screening effect is never complete. By fitting the $\chi'(T)$ data obtained between 20 and 60 K to the Meissner diamagnetic screening function, it shows that only about 2% of the sample volume shows a superconducting phase. The superconductivity observed is only filamentary. It is possible that the observed superconductivity is of impurity-origin, since a 2% impurity volume can usually not be identified by x-ray diffraction technique. The other possible explanation, however, is that oxygen is unevenly distributed in the sample, that is likely to happen for high- T_c oxides, and superconductivity occurs only in the portion that contains "correct" oxygen concentration.

At lower temperatures, χ' begins to show an upturn around 15 K. A peak in $\chi'(T)$ is clearly seen at 5 K. Correspondingly, an anomaly is also seen in the specific heat data shown in Fig. 2, where the low temperature portion of C/T vs T^2 is plotted. Both anomalies are associated with the ordering of the Pr spins, and it has an antiferromagnetic character as a cusp is present in $\chi'(T)$. The correlated Pr spins respond "better" to lower driving frequencies, as the peak in $\chi'(T)$ goes higher when lower frequencies were used. This frequency-dependent behavior becomes less pronounced in the higher frequency regime. Beyond 5000 Hz, $\chi'(T)$ becomes essentially frequency independent. It, nevertheless, still indicates that the relaxation rate of the correlated Pr spins is relatively slow. We note that no frequency dependence was found for the paramagnetic Pr spins. Showing their relaxation rate is far beyond the driving frequency used.

In Fig. 3(a) we show the effects of the strength of the driving field on $\chi'(T)$. As the strength of the driving field

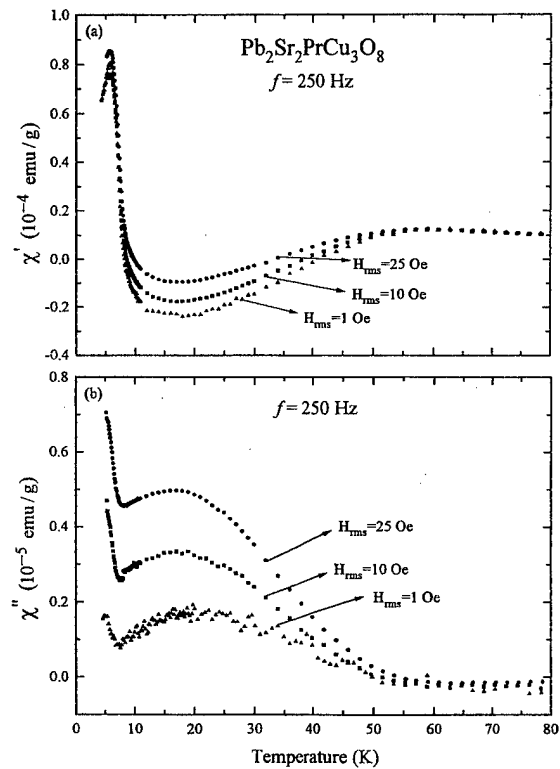


FIG. 3. Effects of the strength of driving field on (a) $\chi'(T)$ and (b) $\chi''(T)$.

was raised, the diamagnetic responses become weaker while it places no obvious effects on the paramagnetic and spin ordered states. These behaviors are understandable, since superconductivity is expected to be weakened by a magnetic field and a field of strength several Oe is not strong enough to alter Pr spins. The Pr ordering and the occurrence of superconductivity are also evident in $\chi''(T)$ shown in Fig. 3(b), where two dissipation peaks at 5 and 18 K are clearly seen. The former is associated with the losses occurring as the Pr spins order, and the latter shows the losses to the superconducting grains. The temperature at which $\chi'(T)$ reaches its minimum value matches to the temperature at which $\chi''(T)$ peaks. This phenomenon may be understood easier if we first consider a superconducting system to be at a low temperature, at which the flux is fully excluded from the polycrystalline grains. The contribution to χ'' is then small. As the field begins to penetrate into the grains at a higher temperature, the loss increases. It peaks when the field penetrates into the grains completely. Above this temperature, less and less of the grain volume remains superconducting, and the diamagnetic response become weaker while the loss relaxed.

The effects of an applied dc magnetic field on the magnetic responses at two representative temperatures are shown in Fig. 4. At 20 K, the main contribution to χ' is from the intragranular screening current, the diamagnetic response was found to be weakened by the applied dc field, as expected. Figure 4(a) shows that the diamagnetic response is mostly suppressed by an applied field of strength 2 kOe, beyond that it is gradually smeared, and is still evident at 10 kOe. At 4.5 K, χ' first increasing and then decreasing with increasing strength of the applied field, as seen in Fig. 4(b). Neutron diffraction measurements⁹ have confirmed that the Pr spin

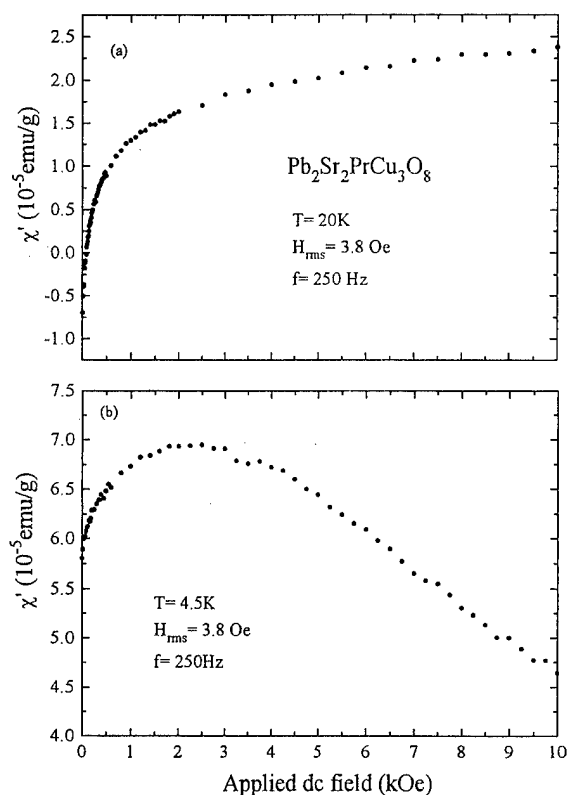


FIG. 4. Effects of an applied dc magnetic field on χ' at two representative temperatures.

ordering is antiferromagnetic in nature. An applied field is expected to reduce the magnetic response from ordered Pr spins. The enhancing of χ' by a low applied field than originates from the suppression of the diamagnetic response, that

indicates the superconductivity remains as the Pr spins order. Beyond 2 kOe, this suppression effect is much reduced, as seen in Fig. 4(a), the contribution to χ' from ordered Pr spins becomes dominating and a decreasing χ' with increasing strength of the applied field is then observed.

In summary, we have observed filamentary superconductivity and Pr spin ordering in a vacuum annealed polycrystalline $\text{Pb}_2\text{Sr}_2\text{PrCu}_3\text{O}_8$ using ac susceptibility and specific heat measurements. Competition between superconductivity and magnetic order was seen as an applied magnetic field is present. An applied field of strength 2 kOe suppresses about 80% of the diamagnetic response, it, however, is still evident at a strength of 10 kOe.

The research at the NCU was supported by the National Science Council of the Republic of China under Grant No. NSC 87-2112-M-008-017.

¹R. J. Cava, B. Bratlogg, J. J. Krajewski, L. W. Rupp, Jr., L. F. Schneemeyer, T. Siegrist, R. B. von Dover, P. Marsh, W. W. Peck, Jr., P. K. Gallagher, S. H. Glarum, J. H. Marshall, R. C. Farrow, J. V. Waszczak, R. Hull, and P. Trevor, *Nature (London)* **336**, 211 (1988).

²M. A. Subramanian, J. Gopalakrishnan, C. C. Torardi, P. L. Gai, E. D. Boyes, T. R. Askew, R. B. Flippen, W. E. Farneth, and A. W. Sleight, *Physica C* **157**, 124 (1989).

³R. Prasad, N. C. Soni, K. Adhikary, S. K. Malik, and C. V. Tomy, *Solid State Commun.* **76**, 667 (1990).

⁴H. C. Ku, C. C. Lai, J. H. Shieh, J. W. Liou, C. Y. Wu, and J. C. Ho, *Physica B* **194-196**, 213 (1994).

⁵H. M. Rietveld, *J. Appl. Crystallogr.* **2**, 65 (1969).

⁶A. C. Larson and R. B. Von Dreele, *General Structure Analysis System*, Report LA-UR-86-748, Los Alamos National Laboratory, Los Alamos, NM 87545 (1990).

⁷H. Fujishita, M. Sato, Y. Morii, and S. Funahashi, *Physica C* **210**, 529 (1993).

⁸G. R. Stewart, *Rev. Sci. Instrum.* **54**, 1 (1983).

⁹W. T. Hsieh, W.-H. Li, K. C. Lee, J. W. Lynn, J. H. Shieh, and H. C. Ku, *J. Appl. Phys.* **76**, 7124 (1994).

Specific heat, magnetization and C-isotope effect of $\text{Y}_2\text{C}_2(\text{Br},\text{I})_2$ superconductors

W. Schnelle, R. W. Henn, Th. Gulden, R. K. Kremer, and A. Simon

Max-Planck-Institut für Festkörperforschung, Heisenbergstraße 1, 70569 Stuttgart, Germany

The specific heat $c_p(T)$ and the magnetization $M(B,T)$ of the layered superconductors $\text{Y}_2\text{C}_2\text{I}_2$, $\text{Y}_2^{13}\text{C}_2\text{I}_2$ ($T_c \approx 10$ K), $\text{Y}_2\text{C}_2\text{Br}_2$ ($T_c \approx 5$ K), and of $\text{Y}_2\text{C}_2\text{Br}_{0.5}\text{I}_{1.5}$ ($T_c \approx 11.6$ K) were measured from 2–80 K in magnetic fields up to 10 T. All samples exhibit sharp phase transitions in zero field. The jump Δc_p at T_c is drastically reduced in amplitude and broadens significantly with increasing field. The temperature dependence of $\Delta c_p(T)$ and of $B_c(T)$ is analyzed and is consistent with strong electron–phonon coupling. The $^{13}\text{C}/^{12}\text{C}$ isotope effect of $\text{Y}_2\text{C}_2\text{X}_2$ is found to be nearly zero. In contrast to this finding the 3-dimensional parent compound YC_2 shows weak-coupling BCS behavior. The anisotropic thermodynamic parameters of the materials are evaluated and discussed.

© 1998 American Institute of Physics. [S0021-8979(98)18711-X]

I. INTRODUCTION

Materials with layered crystal structure display a wealth of unusual electronic effects. Well known recent examples are the exceptionally high transition temperatures of the cuprate high T_c superconductors and the manganates. In the Bi, Tl, and Hg based cuprate systems the anisotropic superconducting parameters are strongly modified by the thickness and character of the rocksalt-type building blocks between the Cu–O units which essentially contain the carriers of the superconductivity.¹ In addition the Bi, Tl, or Hg–O units provide a charge reservoir for the doping of the Cu–O layers. However, other superconducting materials with quasi-two-dimensional layered structure were studied intensively since the 1970s. Among them are the layered Ta and Nb dichalcogenides and their intercalated derivatives² and intercalated graphites which display less spectacular transition temperatures. In these materials the interlayer distance can be varied by intercalation and the transition from three-dimensional to quasi-two-dimensional superconductivity could be studied favorably. The variation of the interlayer coupling has a tremendous effect on the superconducting properties, e.g., T_c and the critical fields. It is widely believed that low-dimensional and especially layered structures provide optimum conditions for superconductivity with high T_c .^{3,4}

In this contribution we report on thermodynamic measurements on superconducting metal-rich rare-earth carbide halides $\text{RE}_2\text{C}_2\text{X}_2$ with RE either Y or La, and the halide X being Cl, Br, or I. These compounds were found to be superconducting^{5,6} with a maximum T_c up to 11.6 K. They adopt a layered crystal structure (monoclinic $\text{Gd}_2\text{C}_2\text{Cl}_2$ type, space group $\text{C2/m}^{7,8}$) with units of bilayers of close-packed RE metal atoms which are sandwiched between layers of halogen atoms X (see Fig. 1). The thick and strongly electronegative halogen atom double layers lead to ionic bonds between X and RE atoms and to a van der Waals gap resulting in very weak bonds between adjacent RE_2C_2 building blocks (distance 6.85 Å in $\text{Y}_2\text{C}_2\text{Br}_2$). In the RE atom bilayers (Y–Y distance 3.76 Å) the octahedral voids are filled with dimeric C–C dumbbells. Depending on the mean radius of the halogen composition $\text{X}=(\text{Cl},\text{Br},\text{I})$ the stacking se-

quence of the layers, the lattice constants, and the T_c varies.⁶ T_c reaches a maximum of 11.6 K at a composition of $\text{Y}_2\text{C}_2\text{Br}_{0.5}\text{I}_{1.5}$.^{6,9} The layered compounds $\text{Y}_2\text{C}_2\text{X}_2$ are closely related to the three-dimensional superconducting dicarbide YC_2 .¹⁰ This compound is a textbook example for a weak coupling BCS superconductor with $\kappa_{\text{GL}} \approx 1/\sqrt{2}$ and with a clear $^{13}\text{C}/^{12}\text{C}$ isotope effect of $-0.51(7)$ demonstrating that the vibrations of the C–C dumbbells are important for the pairing mechanism.⁹

II. RESULTS AND DISCUSSION

The samples were prepared by heating Y metal chips, YX_3 , and graphite powder to 1320 K in sealed tantalum crucibles.⁷ The <50 μm sized crystallites were single phase as characterized by x-ray and neutron diffraction.⁹ The compounds are very sensitive to moisture. All handling and measurements were done in a glove box with dried argon atmosphere or in specially fabricated quartz or Duran glass ampoules. For cryogenic measurements the ampoules were filled with He exchange gas. Specific heat was measured

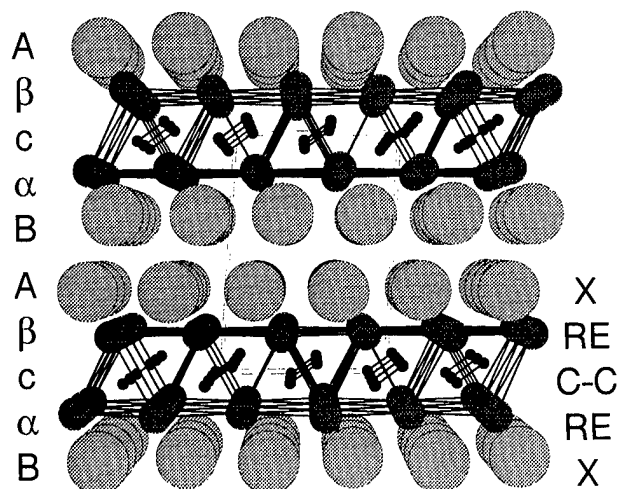


FIG. 1. Perspective view of the crystal structure of $3s\text{-Y}_2\text{C}_2\text{Br}_2$ along [010]. The monoclinic unit cell is indicated by the dashed line.

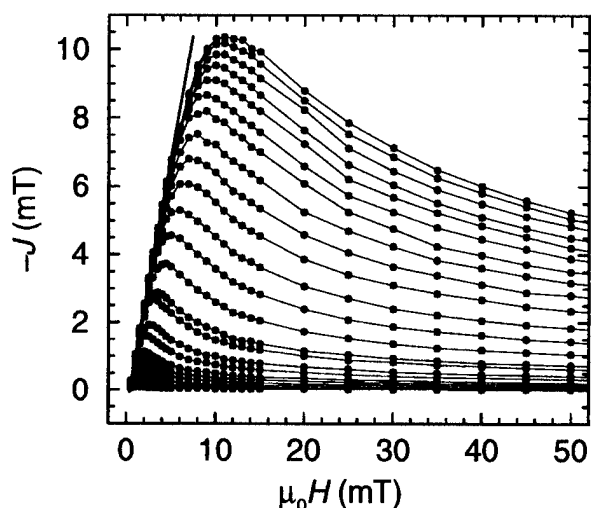


FIG. 2. Low field part of the isothermal magnetic polarization of $\text{Y}_2\text{C}_2\text{I}_2$ for $2.0 \text{ K} < T < 9.9 \text{ K}$.

with the quasiadiabatic step-heating method in an improved version of a calorimeter as described in Ref. 11. Magnetic fields up to 10 T were applied. The shift of the Cernox thermometer temperature calibration curve with field $\Delta T(R, B)$ was calibrated *in-situ* and corrected for in the $c_p(T)$ measurements.

Isothermal dc-magnetization measurements of the $\text{Y}_2\text{C}_2\text{I}_2$ sample (Fig. 2) were recorded in a SQUID-magnetometer. The curves are typical for a type-II superconductor with a large Ginzburg-Landau (GL) parameter ($\kappa_{\text{GL}} \approx 60$). An upper estimate for the first critical field $B_{c1}(0) = 6 \text{ mT}$ is gained from the deviation of the isotherms from their initial linear rise. The interceptions of the isotherms with $B = 0$ were used for the determination of the upper critical field $B_{c2}(0) = 11.8(2) \text{ T}$. The corresponding values for $\text{Y}_2\text{C}_2\text{Br}_2$ are $B_{c1} < 1.5 \text{ mT}$, $B_{c2} = 3.0(2) \text{ T}$, and $\kappa_{\text{GL}} \approx 50$.⁹

The temperature dependence of the critical fields and of the electronic specific heat $\Delta c_p(T)$ of a superconductor is given by its gap, i.e., determined by the electron-phonon coupling strength $\alpha = \Delta(0)/k_B T_c$. A phenomenological model describing the thermodynamics at arbitrary coupling strength is given by the α -model by Padamsee *et al.*¹² This model is fitted to the data of the thermodynamic critical field $B_{\text{cth}}(T)$ obtained by integration of the isotherms. The result for $\text{Y}_2\text{C}_2\text{I}_2$ is $\alpha = 2.15 \pm 0.10$ which is in the range of intermediate strong coupling. The deviation of $B_{\text{cth}}(T)$ from the parabolic law is quite small and therefore the thermodynamics of $\text{Y}_2\text{C}_2\text{I}_2$ is described well by the two fluid (2fl) model.

The specific heat of the four $\text{Y}_2\text{C}_2\text{X}_2$ compounds is plotted in Fig. 3. As expected the bromine compound has the lowest lattice specific heat, i.e., the highest Debye temperature ($\Theta_D(0) \propto 1/\sqrt{M}$; M = molar mass). We roughly estimate $\theta_D = 240 \pm 10 \text{ K}$ for the $\text{Y}_2\text{C}_2\text{Br}_2$ and $210 \pm 10 \text{ K}$ for $\text{Y}_2\text{C}_2\text{I}_2$, taking into consideration the $\gamma_{2\text{fl}}$ -values as determined below.

Powder samples sealed in Duran glass ampoules with ^4He contact gas ($\approx 1 \text{ bar}$) is a technique utilized successfully in c_p measurements for many years in our laboratory. However, in measurements on $\text{Y}_2\text{C}_2\text{X}_2$ samples we detected an

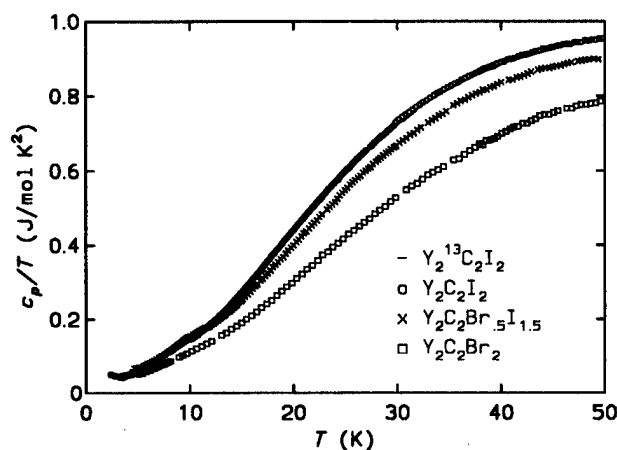


FIG. 3. Specific heat $c_p(T)/T$ of $\text{Y}_2\text{C}_2\text{X}_2$ samples. The data for $\text{Y}_2^{13}\text{C}_2\text{I}_2$ and $\text{Y}_2\text{C}_2\text{I}_2$ are identical within error bars.

upturn in c_p/T at temperatures below 4.4 K ¹³ and broad peaks at ≈ 3.7 and $\approx 2.0 \text{ K}$. These peaks we assign to the desorption and to the λ transition of ^4He adsorbed on the (large) internal surface of the layered $\text{Y}_2\text{C}_2\text{X}_2$ crystallites. ^3He offers the advantage of a substantially higher vapor pressure below 5 K . We therefore resealed the $\text{Y}_2\text{C}_2\text{X}_2$ samples under $\approx 0.5 \text{ bar}$ of ^3He gas at ambient temperature.

In Fig. 4 the specific heat of $\text{Y}_2\text{C}_2\text{I}_2$ (sample from Ref. 13 with ^3He contact gas) is given in a c_p/T vs T^2 representation for various magnetic fields. The results above 6 K are identical to the previous data¹³ and there are no peaks below 4.2 K . However, even with this precautions an upturn in c_p/T below 3.2 K remains. This may originate from ^3He desorption and/or $\approx 0.5\%$ of $S = \frac{1}{2}$ paramagnetic impurities found by high field susceptibility measurements.^{9,13} A clear phase transition, a sharp step in $c_p(T)$, can be seen at 9.94 K (calorimetric midpoint) for $B = 0 \text{ T}$, indicating bulk superconductivity.¹³ Closer inspection of the data in 6 and 10 T shows that the step at $T_c(B)$ is depressed to temperatures below 4 K for a field of 10 T . The 10 T data extrapolate to an intercept $\gamma^* \approx 35(5) \text{ mJ/mol K}^2$.

The midpoint of the transition of the iodine sample with ^{13}C is at 9.76 K which would correspond to an $^{13}\text{C}/^{12}\text{C}$ isotope effect of -0.23 . However, the T_c of our samples of

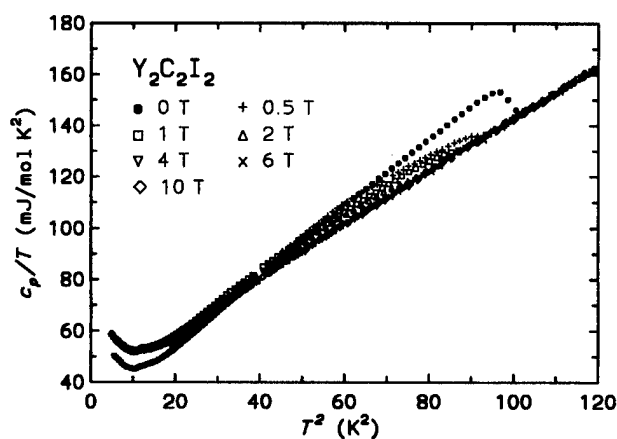


FIG. 4. Specific heat $c_p(T, B)/T$ vs T^2 of the $\text{Y}_2\text{C}_2\text{I}_2$ sample in magnetic fields up to 10 T .

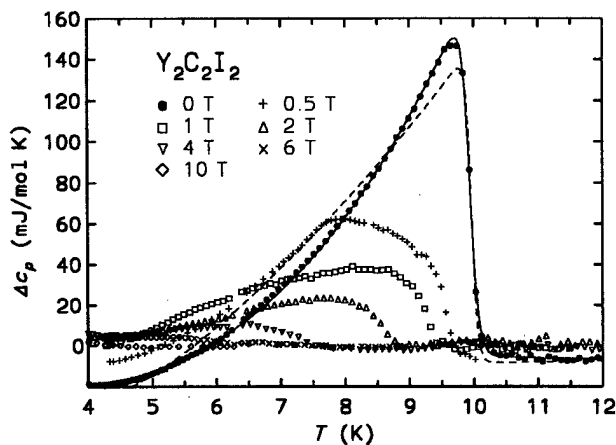


FIG. 5. Difference $\Delta c_p(T, B)/T = [c_p(T, B) - c_p(T, 10 \text{ T})]/T$ of the specific heat of the $\text{Y}_2\text{C}_2\text{I}_2$ sample. The full line is a fit with the two fluid model, the dashed line a fit with the weak coupling BCS theory (see the text).

$\text{Y}_2\text{C}_2\text{I}_2$ show some scatter and the result should be taken more as an upper limit for this isotope effect. In an earlier determination of the $^{13}\text{C}/^{12}\text{C}$ isotope effect of the bromine compound, which has a very good reproducibility of T_c , we found 0.00 ± 0.05 by susceptibility measurements.^{6,9}

Figure 5 displays the difference $\Delta c_p(T, B)$ between $c_p(T, B)$ and $c_p(T, 10 \text{ T})$, i.e., the purely electronic specific heat difference between superconducting and normal state. In this representation it can be clearly seen that the superconducting transition in magnetic fields broadens strongly and two characteristic temperatures becomes discernable. For example, in the curve for $B = 0.5 \text{ T}$ a clear kink at 7.74 K and a first deviation from the expected straight step at 9.45 K are visible. The sample consists of small crystallites with c axes enclosing a random angle ϕ to the direction of the magnetic field B . This results in a distribution of the critical field $B_c(T, \phi)$ limited by the values for $B \parallel c$ and $B \perp c$. The lower temperature kinks in the $\Delta c_p(T, B)$ curves have therefore to be assigned to $T_c(B)$ with B perpendicular to the layers and the higher characteristic temperature to $T_c(B)$ for B parallel to the layer structure, i.e., B perpendicular to the c axis. An evaluation of the temperatures of the kinks and of the first

deviation from the idealized steps for all measured fields yields $B_{c2\parallel}(0) \geq 7 \text{ T}$ ($B \perp c$) and $B_{c2\perp}(0) \geq 1.5 \text{ T}$. The anisotropy factor is about $4.7(3)$, consistent with values of ≈ 5 from determinations on larger single crystals of $\text{Y}_2\text{C}_2\text{I}_2$ with magnetization measurements.⁹ This value is similar to that of fully oxygenated $\text{YBa}_2\text{Cu}_3\text{O}_7$.¹

An analysis of the electronic specific heat difference $\Delta c_p(T, 0)$ of $\text{Y}_2\text{C}_2\text{I}_2$ between 0 and 10 T was carried out within the weak coupling BCS theory¹⁴ (Fig. 5 dashed line) and the two fluid (2fl) model (Fig. 5 full line). The excellent agreement of the data with the latter model is also rendered from the interception of the $c_p(T)$ curves in 0 and 10 T at $0.58T_c$ in agreement with the 2fl model result. The fitted parameters are the electronic coefficient $\gamma_{2fl} = 9.01(6) \text{ mJ/mol K}^2$ and $T_c = 9.94(1) \text{ K}$. These values are very near to those determined in Ref. 13. The narrow transition width of about $0.01 T_c$ proves the sample's homogeneity.

In conclusion, the layered $\text{Y}_2\text{C}_2\text{X}_2$ compounds are intermediate strong coupling, extreme type-II bulk superconductors with T_c upto 11.6 K at present. These findings differ markedly from that for the structurally closely related carbide YC_2 which has a three-dimensional structure.^{13,10}

¹ D. R. Harshman and A. P. Mills, Jr., Phys. Rev. B **45**, 10 684 (1992).

² L. N. Bulaevskii, Sov. Phys. Usp. **18**, 514 (1975).

³ V. L. Ginzburg and D. A. Kirzhnits, *High-Temperature Superconductivity* [Consultants Bureau (Plenum), New York, 1982].

⁴ T. H. Geballe, in *Physics of High-Temperature Superconductors*, No. 106, in Springer Series in Solid-State Sciences, edited by S. Maekawa and M. Sato (Springer, Berlin, 1992), p. 339; Science **259**, 1550 (1993).

⁵ A. Simon, H. Mattausch, R. Eger, and R. K. Kremer, Angew. Chem. Int. Ed. Engl. **30**, 1188 (1991).

⁶ A. Simon et al., Z. Anorg. Allg. Chem. **622**, 123 (1996).

⁷ U. Schwanitz-Schüller and A. Simon, Z. Naturforsch. B **40**, 710 (1985).

⁸ H. Mattausch, R. K. Kremer, R. Eger, and A. Simon, Z. Anorg. Allg. Chem. **609**, 7 (1992).

⁹ R. W. Henn, Ph.D. thesis, Universität Karlsruhe, 1996.

¹⁰ Th. Gulden et al., Phys. Rev. B **56**, 9021 (1997).

¹¹ E. Gmelin, Thermochim. Acta **110**, 183 (1987).

¹² H. Padamsee, J. E. Neighbor, and C. A. Shiffman, J. Low Temp. Phys. **12**, 387 (1973).

¹³ R. W. Henn, W. Schnelle, R. K. Kremer, and A. Simon, Phys. Rev. Lett. **77**, 374 (1996).

¹⁴ B. Mühlischlegel, Z. Phys. **155**, 313 (1959).

***H*-*T* phase diagram for the giant magnetic flux jumps in low temperature superconductors and high temperature superconductors**

V. V. Chabanenko,^{a)} A. I. D'yachenko, and A. V. Chabanenko

Donetsk Physico-Technical Institute, Academy of Sciences, Ulitsa R. Luxembour, 72, 340114 Donetsk, Ukraine

H. Szymczak, S. Piechota, A. Nabialek, and N. D. Dung

Institute of Physics, Polish Academy of Science, Al. Lotnikow 32/46, 02-668 Warsaw, Poland

We have studied magnetothermal instabilities both theoretically and experimentally. Magnetostriction and magnetization hysteresis loops with flux jumps were calculated over a wide range of experimental parameters employing three critical state models: the original Bean model, the Kim-Anderson model, and the exponential model. The influence of the magnetic prehistory on the flux jumps, magnetostriction, and the magnetization was investigated for the LaSrCuO crystal. *H*-*T* diagrams of flux instabilities were constructed from calculation and from experimental results. One can see good qualitative agreement between these two diagrams. © 1998 American Institute of Physics. [S0021-8979(98)30111-5]

I. INTRODUCTION

When the magnetic field is ramping, the appearance of a small increase temperature leads to decrease of the value of the critical current density of hard type II superconductors. In adiabatic conditions this increases dissipation and can lead to a "thermomagnetic catastrophe." As a result, giant flux jumps appear and the sample goes to the resistive or normal state. The investigation of flux instabilities in high temperature superconductors (HTSCs) is interesting because of their potential applications as well as the importance of gaining a fundamental understanding of the phenomenon. We have studied magnetothermal instabilities both theoretically and experimentally in LaSrCuO.

II. *H*-*T* DIAGRAM OF FLUX INSTABILITIES: THEORY AND EXPERIMENT

The influence of the magnetic prehistory on the flux jumps was investigated in the LaSrCuO crystal. Magnetostriction and magnetization hysteresis loops with flux jumps were calculated employing three critical state models: the original Bean model, the Kim-Anderson model, and the exponential model.

A. Critical state

Let us consider the pinning induced magnetization and magnetostriction loops with flux jumps for a specimen having a slab geometry with thickness of $L = 2d$ ($-d \leq x \leq d$). Suppose that the external magnetic field H_e is applied parallel to the slab face. The magnetic field profile $H(x)$ inside the slab is given by the solutions of the critical state equation,

$$dB/dx = -\mu_0 J(x), \quad (1)$$

where current density $|J(x)| \leq |J_c(x)|\mu_0$, the permeability of vacuum. This critical-state equation can be used to determine

the magnetization and the magnetostriction when $H \gg H_{c1}$ (for YBCO the lower critical field H is of the order of several hundred gauss at $T=0$ while the flux jumps are observed at the fields $\mu_0 H$ of the order of several tesla). According to the Kim-Anderson model¹

$$J_c(B) = \pm J_0(T) B_0 / (B_0 + |B|); \quad (2)$$

here B_0 is a phenomenological parameter and J_0 is the critical current density at zero magnetic field B in HTS materials $J_0(T) \approx J_0(0)(1 - T/T_c)$. Integration of Eqs. (1) and (2) gives

$$B_{\pm}(x) = B_0 - [(B_0 - B^*)^2 \pm 2\mu_0 J_0(x - x^*) B_0]^{1/2}, \quad (3)$$

$$B(x) < 0,$$

$$B_{\pm}(x) = -B_0 + [(B_0 + B^*)^2 \pm 2\mu_0 J_0(x - x^*) B_0]^{1/2},$$

$$B(x) > 0.$$

The sign $+$ ($-$) corresponds to domains of vortices where $dB/dx > 0$ ($dB/dx < 0$) and the field $B^* = B(x^*)$. In the exponential model² the critical current density is expressed as follows:

$$J_c(B) = \pm J_0 \exp(-B/B_0), \quad (4)$$

and the sign shows the flow direction of the current. Integration of Eqs. (1) and (4) provides the local field distribution,

$$B_{\pm}(x) = B_0 \ln[\exp(B^*/B_0) \pm \mu_0 J_0(x - x^*)/B_0],$$

$$B(x) > 0,$$

$$B_{\pm}(x) = B_0 \ln[\exp(-B^*/B_0) \pm \mu_0 J_0(x - x^*)/B_0],$$

$$B(x) < 0. \quad (5)$$

Here the sign $+$ ($-$) again corresponds to the local field distribution where $dB/dx > 0$ (or $dB/dx < 0$) and the boundary field $B^* = B(x^*)$. The full magnetic field profile in the sample is given by a combination of solutions (3) and (5). The parameters x^* and B^* are chosen so that the condition $\mu_0 H_e = B(x=0)$ holds and the field $B(x)$ distribution is con-

^{a)}Electronic mail: chaban@host.dipt.donetsk.ua

tinuous. Comparison of solutions (3) and (5) shows that they are close to each other if $B^*/B_0 \ll 1$. From the four solutions [those in (3) and (5)], all the necessary magnetic field profiles can be constructed.^{3,4} When the value of the magnetic field $B(x)$ is known, the magnetization M and magnetostriction $\Delta L/L_0$ can be calculated by simple integration

$$\Delta L(B)/L_0 = -1/(\mu_0 E L_0) \int_0^d [B_e^2 - B^2(x)] dx, \quad (6)$$

$$M(B) = 1/(\mu_0 d) \int_0^d B(x) dx - H_e; \quad (7)$$

here E is the elastic constant of the material along the x axis, $L = 2d$.

B. Flux jumps, instability criterion, magnetization, and magnetostriction loops

The instability criterion (under adiabatic conditions) in the case of the Kim–Anderson type critical current density $J_c(B)$ can be derived analytically.³ For the exponential model (4) it is not possible and we have used in this case the calculations based on the adiabatic flux- B jump instability criterion. Let the applied field H_e increases (decreases) by a small amount ΔH_e ($|\Delta H_e| \ll |H_e|$). Due to the moving of flux lines, the magnetic field, $B(x)$, in the sample, increases by $\Delta B(x)$. The $\Delta B(x)$ value has to be calculated from Eq. (1) in the following way. Let x_i be the points at which the $B(x_i) = B_i$ values are calculated with the index $1 \leq i \leq n$, $x_1 = 0$, $x_n = d$ and $B^0(x)$ as the initial local field. We put $\Delta B = B_{i+1}^0 - B_i$, where $i > 1$, $B_i = B(x=0) = \mu_0 H_e$. The critical state Eq. (1) gives the conditions one

$$B(x_{i+1}) = \begin{cases} B(x_i) + \Delta B & |\Delta B| < \mu_0 J_c(B_i) \\ B(x_i) + \text{sign}(\Delta B) \mu_0 J_c(B_i) dx, & |\Delta B| > \mu_0 J_c(B_i) \end{cases} \quad (8)$$

where $dx = x_{i+1} - x_i$.

Due to exchange of the magnetic field, $B(x)$, the energy per unit volume, Q , is dissipated in the vicinity of x where

$$Q(x) = J_c(x) \int_x^d [B(x') - B^0(x')] dx'. \quad (9)$$

Under local adiabatic conditions one obtains

$$\Delta T(x) = Q(x)/C_V, \quad (10)$$

where C_V is the specific heat of the superconductor. For YBCO,⁵ C_V (1–26 K) (J cm^{-3}) = $2.68 \times 10^{-4} T^{-2} + 1.01 \times 10^{-4} T + 2.53 \times 10^{-6} T^3 + 7.17 \times 10^{-9} T^5$ and C_V (26–100 K) (J cm^{-3}) = $2.02 \times 10^{-4} T^2 - 7.82 \times 10^{-9} T^4$. The rise of temperature ΔT reduces the critical current J_c ,

$$\Delta J_c(x) = \partial J_c / \partial T \Delta T(x). \quad (11)$$

According to the critical state Eqs. (8), the reduction in J_c leads to a decrease in the shielding ability of the superconductor by ΔH_s , where

$$\Delta H_s = - \int_x^d \Delta J_c(x') dx'. \quad (12)$$

The magnetic configuration is unstable with respect to a flux jump if $\Delta H_s > \Delta H_e$.^{6,7}

During a flux jump, the temperature inside the sample increases and reaches a maximum value $T^* < T_c$, which is assumed to be independent of the position x inside the sample. The critical current density at T^* is $J_c(T^*) < J_c(T_0)$, where T_0 is the temperature of the sample before the flux jump. Therefore, according to the critical state conditions, the magnetic field configuration is given by the solution of Eqs. (8) for $J_c = J_c(T^*)$. After the flux jump the temperature inside the sample returns to the starting value T_0 , but the magnetic field profiles in the slab are unchanged, i.e., they are the same as for $T = T^*$. An increase (decrease) of the external field, H_e , leads to the new magnetic field distributions. It is assumed that the maximum temperature, T^* , reached during a jump, which is less than T_c , is the same for all jumps. Generally speaking the T^* value is unknown because it depends on the microstructure of the sample, the sweep rate, and the adiabatic conditions of the sample. The critical state conditions (8) for a type II superconductor allow one to calculate magnetic field profiles in a slab and for any number of the flux jumps independent of the magnetic prehistory.

These results and experimental data^{3,4} are used for computer simulations. Magnetostriction and magnetization loops are constructed over a wide range of experimental parameters. In Fig. 1, one can see an example of theoretically calculated magnetostriction and magnetization hysteresis loops with magnetostriction and magnetization jumps on the basis of the Kim–Anderson model. ΔH_{rj} is the flux instability range of the magnetic field. Similar calculations were per-

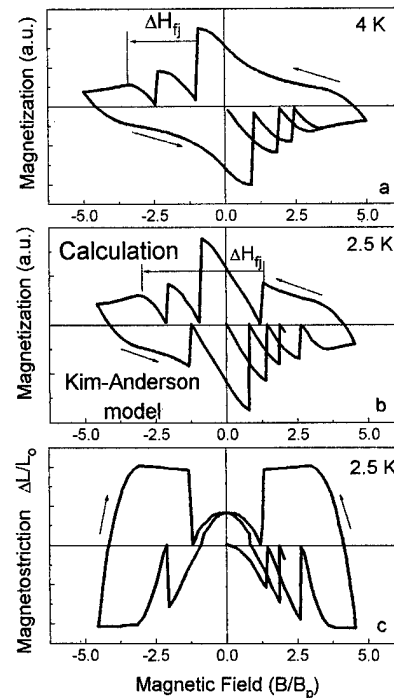


FIG. 1. Magnetization and magnetostriction loops with flux jumps, calculated by the Kim–Anderson model.

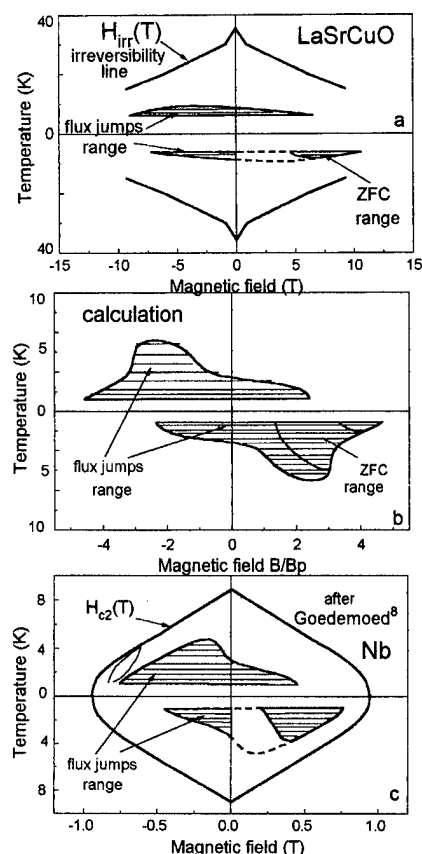


FIG. 2. H - T ranges of the flux instability from (a) experiment on the LaSrCuO and from (b) calculation, $d=5$ mm, $j_c=10^9$ A/m², $B_0=2$ T, B_p full penetration field, and (c) experiment on the Nb from (Ref. 8).

formed for different temperatures and were used for the construction of the H - T phase diagram of flux instability [Fig. 2(b)].

The experiments reported here have been performed on a La_{1.85}Sr_{0.15}CuO₄ single crystal with its fields oriented along the c axis. The sample had dimensions of $2.15 \times 2.24 \times 5.42$ mm³, with the c axis the shortest test axis. The change of length ΔL of the sample was measured in the ab plane along the longest dimension using a strain gauge technique. The resistance change of strain gauges is measured by an ac bridge. The magnetic field was swept at a constant cyclic rate of 0.5 T/min after the sample was zero-field cooled to the measuring temperature. An onset temperature of superconductivity of 35.5 K was observed in a field of 10 G. Figure 3 shows evidence of flux jump instabilities in the virgin magnetization curve for the LaSrCuO single crystal. H_{irr} is the field where M becomes irreversible.

As can be seen from Figs. 2(a) and 2(c) the overall picture of the H - T ranges of flux instability are similar in shape for Nb (Ref. 8) and LaSrCuO. One can also see good qualitative agreement between the experimental and the calculated phase diagrams. That is to say, the Kim-Anderson

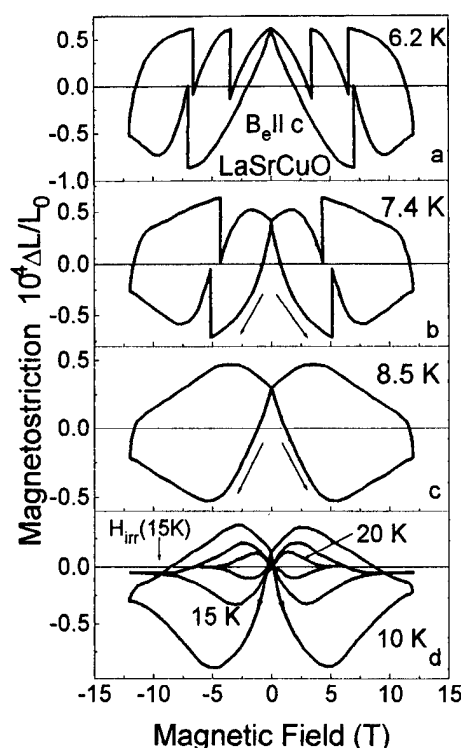


FIG. 3. Magnetostriction loops for different temperatures of LaSrCuO.

model is applicable at large distances from the irreversibility line for HTSC materials whereas the exponential model is applicable in the vicinity of the irreversibility line.

As is clear from both calculation and experiment, the first and third quadrants have significantly fewer flux jumps than the second and fourth quadrants. For example, for the $T=4$ K curve [Fig. 1(a)] and experiment,⁹ flux jumps are completely absent in the first and third quadrants. According to our calculation, the difference in the frequency of occurrence of the flux jumps in the different quadrants is related to the shape of the flux profiles in the various quadrants.

¹Y. B. Kim, C. F. Hempstead, and A. R. Strnad, Phys. Rev. Lett. **9**, 306 (1962).

²V. R. Karasik, N. G. Vasil'ev, and V. G. Ershov, Zh. Eksp. Teor. Fiz. **59**, 790 (1970) [Zh. Eksp. Teor. Fiz. **32**, 433 (1971)]; S. Senoussi, M. Oussena, G. Collin, and I. A. Campbell, Phys. Rev. B **37**, 9792 (1988); P. Chaddah, K. V. Bhagwat, and G. Ravikumar, Physica C **159**, 570 (1989).

³K.-H. Müller and C. Andrikidis, Phys. Rev. B **49**, 1294 (1994).

⁴H. Ikuta, K. Kishio, and K. Kitazawa, J. Appl. Phys. **76**, 4776 (1994).

⁵E. W. Collings, in *Advances in Superconductivity II, Proceedings of the ISS 89*, edited by T. Ishiguro and K. K. Kajimura (Springer, Tokyo, 1990), p. 327.

⁶S. L. Wipf, Phys. Rev. **161**, 404 (1967); P. S. Swartz and C. P. Bean, J. Appl. Phys. **39**, 4991 (1968).

⁷R. G. Mints and A. L. Rakhmanov, Rev. Mod. Phys. **53**, 551 (1981).

⁸S. H. Goedemoed, C. Van Kolmeschate, J. W. Metselaar, and D. De Klerk, Physica (Amsterdam) **31**, 573 (1965).

⁹M. E. McHenry, H. S. Lessure, M. P. Maley, J. Y. Coulter, I. Tanaka, and H. Kojima, Physica C **190**, 403 (1992).

Magnetic memory effect in $\text{YBa}_2\text{Cu}_3\text{O}_{7-x}/(\text{BiDy})_3(\text{FeGa})_5\text{O}_{12}$ heterostructures

D. Mou, A. M. Grishin,^{a)} and K. V. Rao^{b)}

Department of Condensed Matter Physics, Royal Institute of Technology, S-100 44 Stockholm, Sweden

$\text{YBa}_2\text{Cu}_3\text{O}_{7-x}/(\text{YBCO})(\text{BiDy})_3(\text{FeGa})_5\text{O}_{12}$ heterostructures have been prepared on ceramic glass substrates by Nd-yttrium–aluminum–garnet pulsed laser ablation. Both YBCO and BiDy-IG garnet layers are found to be polycrystalline without any preferential crystallite orientation. Magnetic hysteresis loop measurements made before and after YBCO deposition reveal perpendicular magnetic anisotropy in the garnet film. The resistance versus temperature measurements indicate that the YBCO layer contains both superconducting and semiconducting phases and exhibits a broad superconducting transition with $T_{C|R=0} = 22$ K. The resistivity of the fabricated heterostructures was found to be very sensitive to external magnetic field and the remnant magnetization of the garnet layer. At 18 K, in a magnetic field of 0.5 T applied perpendicular to the surface of the sample, the magnetoresistance figure of merit $\Delta R/\Delta H$ reaches the value of $0.26 \text{ } \Omega/\text{Oe}$ and the absolute resistance value of the YBCO channel changes from the m Ω range up to k Ω . In the wide fluctuation temperature range (from 22 to 80 K), the $R(T)$ curve of the YBCO layer is strongly modulated by the remnant magnetization of the garnet layer, clearly exhibiting a magnetic memory effect. A reduction of as much as 9 K in $T_{C|R=0}$ is observed when the garnet layer has remnant magnetization after having been magnetized. At a measuring current of 1 A/cm^2 , the output voltage obtainable is in the mV range, which is adequate for use in nonvolatile memory applications. © 1998 American Institute of Physics. [S0021-8979(98)49611-7]

I. INTRODUCTION

The discovery of high- T_c oxide superconductors stimulated widely study of their electronic applications. Many studies on high- T_c superconducting electric field effect transistors (SuFET)^{1–5} and high- T_c superconducting flux flow transistors (SFFT)^{6,7} have been carried out. However, high- T_c superconductor (HTSC)/magnetic layer-type heterostructures for memory device applications have not yet been discussed. Also, most of the basic studies, as well as proposed applications, have been focused on superconducting state of the high- T_c oxides. Only recently, the properties of semiconducting $\text{YBa}_2\text{Cu}_3\text{O}_{7-x}$ (YBCO) films are being investigated and the potential application as bolometer has been proposed.^{8–10} The performance of such bolometers and SFTTs can be achieved at levels as high as the temperature sensitivity of the resistivity of YBCO thin film containing superconducting and semiconducting mixed phases and the corresponding magnetic field.

Another area of great potential for nanoelectronics is *in situ* pulsed laser deposited complex oxide heterostructures, with *competing interactions* (ferroelectric, magnetic, and HTSC), which is as yet rarely explored. In this study, we have investigated the magnetic field and magnetic memory effects in pulsed laser deposited YBCO/BiDy-IG heterostructures containing superconducting and semiconducting mixed phases to the corresponding oxygen nonstoichiometric YBCO.

II. EXPERIMENTAL RESULTS AND DISCUSSIONS

A Nd-yttrium–aluminum–garnet (YAG) pulsed laser ablation system was used to fabricate the $\text{YBa}_2\text{Cu}_3\text{O}_{7-x}$ (YBCO) and $(\text{BiDy})_3(\text{FeGa})_5\text{O}_{12}$ (BiDy-IG) thin film heterostructures on commercial ceramic glass substrates. The wavelength, repetition frequency, and the pulsed width of the laser were 355 nm, 10 Hz, and 10 ns, respectively. The focused laser beam with energy density of 3 to 4 J/cm² was directed on the rotating ceramic YBCO or BiDy-IG target with the incident angle of 45° in order to make the laser plume perpendicular to the substrate surface (on-axis deposition). The distance between the targets and the substrates was 55 mm. The vacuum chamber was evacuated to base pressure $<10^{-5}$ Torr before introducing pure oxygen gas. The BiDy-IG films were deposited at room temperature with the oxygen pressure of 40 mTorr and then postannealed in the range of 650–760 °C for 2 to 3 min. X-ray diffraction (XRD) indicated the BiDy-IG films were polycrystalline without a preferred orientation of the crystallites.

After depositing the BiDy-IG layer the YBCO layer is deposited, at 760 °C in a oxygen pressure of 200 mTorr, on the garnet covered ceramic glass substrates, and then the heterostructure is cooled down to 450 °C to anneal it in oxygen pressure of 600 Torr for one hour. XRD patterns indicated that both YBCO and garnet layers in the heterostructure were polycrystalline with random orientation of the crystallites. The thickness of the YBCO and BiDy-IG layers was about 2000 and 4000 Å, respectively, as determined using an atomic force microscope (AFM). Magnetic hysteresis loop measurements and magneto-optic Faraday-rotation technique have been used to determine the orientation of the magnetization in the fabricated thin films.¹¹ A perpendicular

^{a)}Visiting at: Dept. of Elec. and Computer Eng, Kumamoto University, Kumamoto 860, Japan

^{b)}Electronic mail: rao@cmp.kth.se

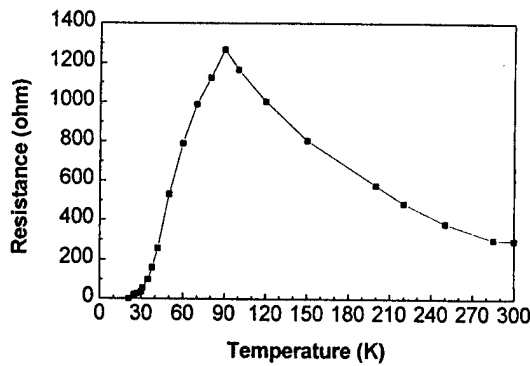


FIG. 1. The resistance of the YBCO/BiDy-IG heterostructure vs temperature measured in demagnetized state in zero magnetic field.

magnetic anisotropy is observed both in the single garnet layers as well as in YBCO/garnet bilayers.

A. dc transport properties of YBCO layer at zero magnetic field

The transport properties of the YBCO layer were characterized by a standard four probe method. Figure 1 shows the dc resistance of the YBCO layer versus temperature at zero magnetic field. The resistance increases with temperature decrease in the interval from 300 down to 90 K, exhibiting typical semiconductor temperature dependence behavior. There is a superconductivity onset around $T_{c \text{ onset}} = 90$ K. Below the $T_{c \text{ onset}}$ point, the resistance falls with decreasing temperatures and finally vanishes at $T_{C|R=0} = 22$ K. This confirms that the YBCO layer experiences the transition (percolation) to the macroscopic superconducting state.

B. Magnetic field effect in the YBCO/BiDy-IG heterostructure

After zero field (FZ) resistance versus temperature measurements, the magnetic field effect measurements were carried out. In these measurements after applying magnetic field for each measurement, the sample has been demagnetized at room temperature, and then zero field cooled to the desirable temperature for the next measurement. At 18 K, when a magnetic field of 0.5 T is applied perpendicular to the surface of the sample, the resistance of the YBCO layer increases from the mΩ range up to 1288 Ω, and the magnetoresistance figure of merit $\Delta R/\Delta H$ (1288 Ω/5000 Oe) reaches the value of 0.26 Ω/Oe. In the wide fluctuation range above $T_{C|R=0}$, the resistance increment $\Delta R = R(T, H) - R(T, 0)$ becomes smaller with the temperature increase. Nevertheless, the magnetic field needed to modulate the superconductivity in YBCO layer becomes smaller as well. Thus, the relatively high figure of merit $\Delta R/\Delta H$ is kept constant over the fluctuation region. For instance, at 77 K, the $\Delta R/\Delta H$ value is still about 0.1 Ω/Oe at applied field of $\Delta H = 2000$ Oe.

A qualitative explanation for the above data would be as follows: The existence both superconducting and semiconducting mixed phases implies there is a Josephson weak link network in the YBCO layer. A dc current passing through

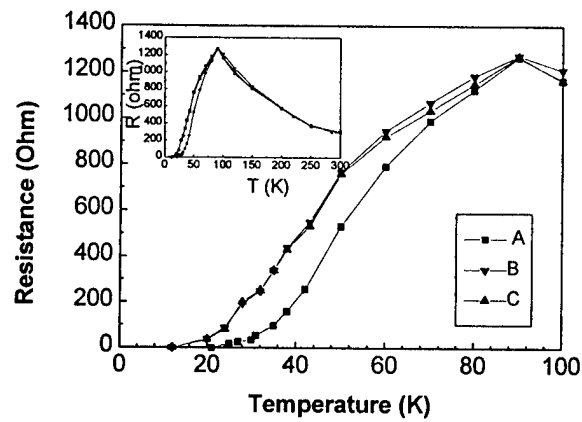


FIG. 2. (a) The inset shows the dc resistance vs temperature with and without remnant magnetization in the BiDy-IG layer. (b) Curve A was measured in the demagnetized state, curve B with the remnant magnetization pointing away from the YBCO layer, curve C with remnant magnetization pointing towards the YBCO layer.

the weak link drives the vortices along the link, which results in energy dissipation and thus a voltage appears across the link.

Vortices start to penetrate into the Josephson junction at the critical field $H_{c1} = (32\phi_0 j_c / \pi^2 c d)^{1/2}$. For granular films with a large intergranular spacing d and a low intergranular critical current density j_c this critical field turns out to be much lower than in the continuous metallic YBCO film. Hence, a relatively small magnetic field can change the film resistance greatly. As j_c is decreasing monotonously with the temperature increase, a weaker magnetic field is needed to modulate the intergranular superconducting state of the YBCO at higher temperatures. Therefore, we arrive to the conclusion that even at temperatures over 77 K, considerable figure of merit $\Delta R/\Delta H$ is still available, which is of great importance for weak magnetic field sensors and SFFT-like device applications.

C. Magnetic memory effect

After demagnetizing, the sample was zero field (FZ) cooled down to 18 K, a 0.5 T magnetic field was applied perpendicular to the sample surface to magnetize the BiDy-IG layer. Then the field was taken away, and the R vs T (curve B) is measured (shown in Fig. 2) to find that $T_{C|R=0}$ is shifted down to 12 K, and below 90 K a distinct shift of the R - T curve is found towards lower temperatures. This implies a *magnetic after-action effect*.

The sample was then demagnetized at room temperature and cooled down to 18 K at zero field. The measured R vs T curve is found to almost coincide with the previous zero field curve A. At 18 K, an opposite 0.5 T magnetic field was applied to change the direction of the remnant moment in BiDy-IG layer and then taken away. In the Fig. 2, it is clearly seen from curve C, that the opposite polarization has almost the same effect as obtained in curve B. This is consistent with the Onsager theorem, but different from the SuFET results, where the opposite direction of the electrical polarization of the ferroelectric layer resulted in up and down shifts of the curves. The effects described above clearly exhibits

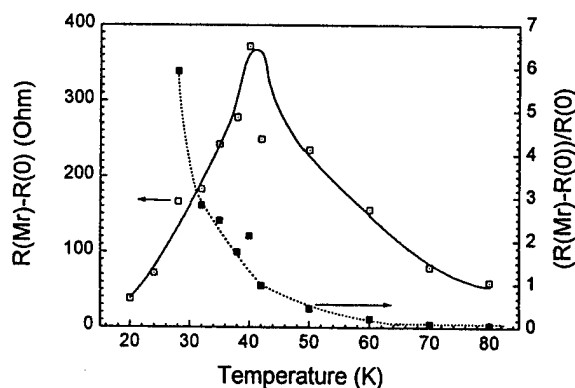


FIG. 3. The resistance increment due to the magnetized layer in the YBCO/BiDy-IG heterostructure in the temperature range 20–80 K. $R(M_r)$ and $R(0)$ are the resistances in the remnant and demagnetized states of the BiDy-IG layer, respectively.

magnetic memory, and demonstrates that the remnant moment in BiDy-IG layer can modulate the transport properties of the YBCO layer.

The measured absolute $R(M_r) - R(0)$ and normalized $[R(M_r) - R(0)]/R(0)$ resistance increments versus temperature are shown in Fig. 3. There $R(M_r)$ and $R(0)$ are resistances in the remnant and demagnetized states of the garnet layer, respectively. From the figure, it is easy to see that over a wide temperature range the output voltage increment $\Delta V = V(M_r) - V(0)$ can be achieved from 0.5 to 3.7 mV for a constant current of 10 μ A through the film. Also, the relative voltage increment $\Delta V/V(0)$ is larger than 10%, which is adequate for detection. In order to get large modulation of resistance in high- T_c superconductor/magnetic layer heterostructure, one of the key points is to prepare a oxygen non-stoichiometric YBCO layer to produce a mixture of superconducting and semiconducting phases.

III. CONCLUSIONS

In summary, magnetic field and magnetic memory effects have been observed in the YBCO/BiDy-IG heterostruc-

ture for the first time. The two state behavior, remnant and demagnetized garnet layer, can be easily distinguished by measuring the resistance of the YBCO layer. The observed effect is promising for use in nonvolatile memory applications. In order to achieve significant magnetic after-action effect in high- T_c superconducting layer at relatively weak magnetic fields, a suitable mixture of semi- and superconducting phases is essential. Existence of the semiconducting phase simplifies greatly the device fabrication processing, and various large area and cheap substrates, such as glass become suitable. The operating temperature range of this type of devices is expected to move to much higher temperatures on using Bi- and Hg-based materials with higher T_c .

ACKNOWLEDGMENT

This research has been supported by the Swedish funding Agency NUTEK.

- ¹Mannhart, D. G. Schlom, J. G. Bednorz, and K. A. Muller, Phys. Rev. Lett. **67**, 2099 (1991).
- ²X. Xi, Qi Li, C. Doughty, C. Kown, S. Bhattacharya, A. T. Findikoglu, and T. Venkatesan, Appl. Phys. Lett. **59**, 3470 (1991).
- ³Gim, G. Doughty, X. X. Xi, A. Amar, T. Venkatesan, and F. C. Wellstood, Appl. Phys. Lett. **62**, 3198 (1993).
- ⁴Lin, N. J. Wu, K. Xie, X. Y. Li, and A. Ignatiev, Appl. Phys. Lett. **65**, 953 (1994).
- ⁵Mannhart, J. Ströbel, J. G. Bednorz, and Ch. Gerber, Appl. Phys. Lett. **62**, 630 (1993).
- ⁶K. G. Hohenwarter, J. S. Martens, J. H. Thompson, J. B. Beyer, J. E. Nordman, and D. S. Ginley, IEEE Trans. Magn. **27**, 3297 (1991).
- ⁷S. Martens, D. S. Ginley, J. B. Beyer, J. E. Nordman, and G. K. G. Hohenwarter, IEEE Trans. Magn. **1**, 95 (1991).
- ⁸P. C. Shan, Z. Celik-Butler, D. P. Butler, and A. Jahanzeb, J. Appl. Phys. **78**, 7334 (1995).
- ⁹P. C. Shan, Z. Celik-Butler, D. P. Butler, A. Jahanzeb, and C. M. Travers, J. Appl. Phys. **80**, 7118 (1996).
- ¹⁰P. C. Shan, A. Jahanzeb, D. P. Butler, Z. Cerlik-Butler, W. Kula, and Roman Sobolewski, J. Appl. Phys. **81**, 6866 (1997).
- ¹¹M. Duan, A. M. Grishin, K. V. Rao, and T. Suzuki, IEEE Trans. Magn. **31**, 3245 (1995).
- ¹²Tinkham, *Introduction to Superconductivity* (McGraw-Hill, New York, 1975), p. 181.

Spin wave scattering and intermode transitions induced by the magnetic vortex lattice in the ferrite–high-temperature superconductor film structure

L. V. Lutsev^{a)} and S. V. Yakovlev

Research Institute "Domen," Chernigovskaya, 8, St. Petersburg 196084, Russia

A model of dipole-exchange spin wave scattering induced by the periodic magnetic vortex lattice in the in-plane magnetized ferrite–high-temperature superconductor film structure is considered. The vortex magnetic field action leads to spin wave intermode transitions occurring in the ferrite film. It is found that an admixture of the higher mode in the crossing region of the surface spin wave mode with the higher mode (hybrid state) increases the direct intermode transition probability significantly. It is shown that mixing of modes and the formation of hybrid spin wave states depend on the magnetic inhomogeneity over the ferrite film thickness. The theoretical model is verified for a YIG–YBa₂Cu₃O_{7+δ} structure. © 1998 American Institute of Physics. [S0021-8979(98)18811-4]

I. INTRODUCTION

The experimental study of the spin wave propagation in the film structure of a YIG–high-temperature superconductor (HTSC) showed the influence of the magnetic vortex lattice (MVL) on spin wave (SW) scattering.¹ This influence leads to the appearance of absorption peaks on the long-wavelength excitation region of the SW spectrum (SWS). For magnetic fields in the interval $H_{C1} < 10^2$ Oe $\leq H \leq 10^3$ Oe $< H_{C2}$ a type II superconductor (the group to which HTSCs belong) is found in a mixed state.² In this interval the period of the two-dimensional MVL λ is given by the magnetic field and the magnetic flux quantum and is equal to 0.14–0.46 μ m. The wavelength of the spin waves, which was scattered by the MVL, was greater than the vortex lattice period ($> 10 \mu$ m). The appearance of absorption peaks on the SWS cannot be explained by Bragg scattering. The theoretical model of the resonant interaction^{3,4} between long-wavelength spin waves and short-wavelength ones due to the presence of a vortex lattice cannot explain this experimental fact either. The probability of this interaction in homogeneous ferrite films is very small. In the present paper we consider the theory of SW scattering based on intermode transitions. This theoretical model explains the above-mentioned experimental fact. Computer calculations show that the SW-scattering probability is increased significantly when the ferromagnetic film has a specific magnetic inhomogeneity profile through thickness. As a result of this the SW-scattering method can be a very sensitive tool for investigation of the MVL structure.

II. SW-SCATTERING EQUATIONS

We consider a structure consisting of an in-plane magnetized inhomogeneous ferromagnetic film of thickness $2d$ and a HTSC film (Fig. 1). The MVL in the HTSC film is assumed to be composed of interplanar vortices parallel to the y axis and to create a periodic magnetic field $\mathbf{h}_L(x, z, t) \propto \exp(iqx)$, where q is determined by the MVL period: q

$= 2\pi/\lambda$. The spin wave dynamics is governed by the Landau–Lifshitz and the magnetostatic equations,

$$\frac{\partial \mathbf{M}}{\partial t} = \gamma [\mathbf{M} \times (\mathbf{H} - \nabla \varphi + \alpha \Delta \mathbf{M})], \quad (1)$$

$$\Delta \varphi - 4\pi \operatorname{div} \mathbf{m} = 0, \quad (2)$$

where γ is the gyromagnetic ratio, $\mathbf{H} = \mathbf{H}_0 + \mathbf{h}_L$, $\mathbf{M}(t) = \mathbf{M}_0 + \mathbf{m}(t)$, $\mathbf{H}_0 \parallel \mathbf{M}_0 \parallel$ the y axis, φ is the magnetostatic potential of the spin wave, and α is the exchange interaction constant. We write M_0 as the sum of homogeneous and inhomogeneous terms: $M_0(z) = M_0^{(hom)} + \delta M(z)$.

Dropping the derivatives with respect to y and retaining in Eq. (1) the terms linear in $\mathbf{m}(t)$, we obtain

$$B_{\pm} m_{\pm} = \pm i \gamma M_0 D_{\pm} \varphi, \quad (3)$$

where $m_{\pm} = m_x \pm i m_z$, $B_{\pm} = \partial/\partial t \mp i \gamma (H - \alpha M_0 \Delta)$, $D_{\pm} = \partial/\partial x \pm i \partial/\partial z$, and $\Delta = D_+ D_- = \partial^2/\partial x^2 + \partial^2/\partial z^2$.

The requirement that there does not exist a spin wave with $m_{\pm}(x, z, t) \neq 0$ and $\varphi(x, z, t) \equiv 0$ is equivalent to the restriction of the functional space $m_{\pm}(x, z, t) \in C^2((-\infty, \infty), [-d, d], (-\infty, \infty)) \setminus \operatorname{Ker} B_{\pm}$, on which the operators B_{\pm} have inverse operators.⁵ In other words, the functions $m_{\pm}(x, z, t)$ must be orthogonal to the kernel functional space $\operatorname{Ker} B_{\pm}$.

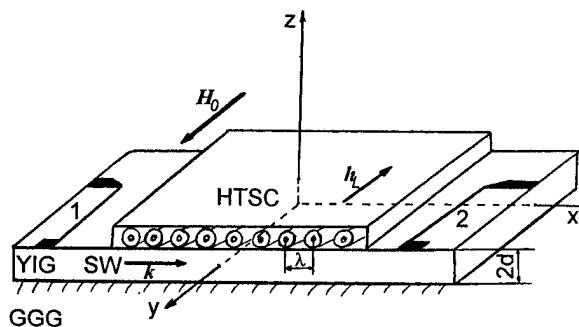


FIG. 1. Ferrite–HTSC film structure. (1), (2)—generator and receiver antennae.

^{a)}Electronic mail: chvv@energo.ru

The use of exchange boundary conditions (spin pinning)^{6,7} is incorrect, since it admits the existence of waves only with a change in the magnetic moment $\mathbf{m}(x, z, t)$.

Substituting m_{\pm} into (2) and assuming the invertibility of B_{\pm} , we obtain the equation for the magnetostatic potential of the spin wave,

$$\Delta\varphi - 2\pi i \sum_{\pm} (\pm D_{\pm} B_{\pm}^{-1} \gamma M_0 D_{\pm}) \varphi = 0. \quad (4)$$

For a homogeneous ferromagnetic film with the magnetic moment density $M_0^{(hom)}$ and without the HTSC film the solutions of Eq. (4) are the wave functions: A. the surface mode $|s\rangle$, for which $D_+|s\rangle=0$ (or $D_-|s\rangle=0$); B. the volume modes,

$$|n\rangle = d^{-1/2} \exp(ik_n x + i\omega_n t) \times \begin{cases} \sin(k_z^{(n)} z + \pi n/2) & z \in [-d, d], \\ 0 & z \notin [-d, d], \end{cases} \quad (5)$$

with the dispersion relation

$$\omega_n = \gamma[(H_0 + \alpha M_0^{(hom)} k_0^{(n)2})(H_0 + 4\pi M_0^{(hom)} + \alpha M_0^{(hom)} k_0^{(n)2})]^{1/2}, \quad (6)$$

where $k_z^{(n)} = \pi n/2d$, $k_0^{(n)2} = k_n^2 + k_z^{(n)2}$, $n=1, 2, 3, \dots$. The set of functions $\{|s\rangle, |n\rangle\}$ is a complete system on $[-d, d]$.

In the case of an inhomogeneous ferromagnetic film with the HTSC film for the SW-scattering analysis it is convenient to single out the proper small terms and to rewrite Eq. (4) in the form

$$\frac{\partial^2 \varphi}{\partial z^2} + A(A + 4\pi\gamma M_0^{(hom)})\varphi + (V_M + V_h)\varphi = 0, \quad (7)$$

where

$$A = \gamma(H_0 - \alpha M_0^{(hom)} \Delta),$$

$$V_M = -2\pi i \gamma \sum_{\pm} [\pm D_{\pm}^{-1} B_{\pm}^{(hom)} \delta M(z) D_{\pm}],$$

$$V_h = 2\pi\gamma^2 M_0^{(hom)} \sum_{\pm} D_{\pm}^{-1} B_{\pm}^{(hom)} h_L(z, x, t) B_{\pm}^{(hom)-1} D_{\pm}.$$

The use of the linear approximation of V_M , V_h in Eq. (7) is justified when $h_L \ll H_0$ and a dispersion curve shift $\delta\omega_n$, induced by V_M , is much less than ω_n in Eq. (6). The perturbation operator V_M leads to the formation of hybrid states, the dispersion curve repulsion at the crossing point and determines the exchange "gaps" observed in the SWS. The perturbation operator V_h governs SW scattering and determines intermode transitions.

III. INTERMODE TRANSITIONS

Let us consider the intermode transition occurring from the hybrid state $|f\rangle = a_s|s\rangle + a_n|n\rangle$ near the crossing point of the dispersion curves of the surface and the volume modes in an inhomogeneous ferromagnetic film (Fig. 2). The perturbation V_h couples modes $|f\rangle$ and $|p\rangle$ having frequencies and wave vectors obeying the conditions

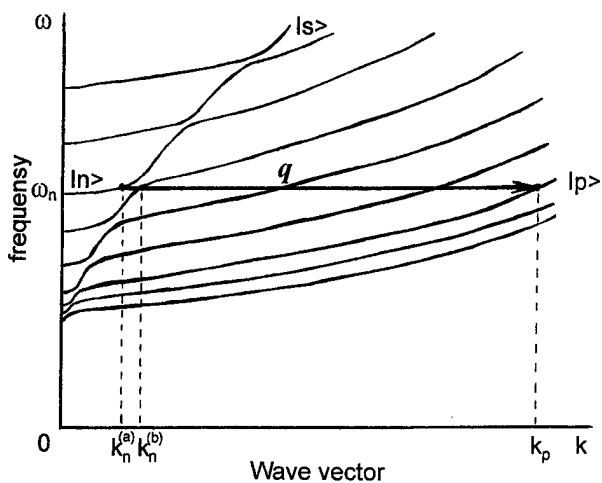


FIG. 2. Direct intermode transitions occurring from the hybrid spin wave states $a_s^{(a,b)}|s\rangle + a_n^{(a,b)}|n\rangle$ near the crossing point of the dispersion curves.

$$\omega_p = \omega_n, \quad k_p = k_n \pm q. \quad (8)$$

To derive the coupling equations we seek a solution in the form

$$\varphi = C(t)|f\rangle + F(t)|p\rangle. \quad (9)$$

Substituting (9) into (7) and keeping terms of first order, we obtain coupling equations for slowly varying amplitudes $C(t)$, $F(t)$,

$$\begin{aligned} \frac{\partial C(t)}{\partial t} &= \frac{i}{2\omega_n} \langle n|V_h|p\rangle F(t), \\ \frac{\partial F(t)}{\partial t} &= \frac{i}{2\omega_p} \langle p|V_h|n\rangle C(t). \end{aligned} \quad (10)$$

For $F(t) \ll C(t)$ the probability of an intermode transition over a time τ is found from Eq. (10)

$$\begin{aligned} P_{pf} &= \frac{F^2(t)}{C^2(t)} = \left| \frac{1}{2\omega_p} \int_0^\tau \langle p|V_h|f\rangle dt \right|^2 \\ &= \left| \frac{\pi\gamma^2 M_0^{(hom)}}{\omega_p k_0^{(p)2}} \sum_{\pm} \int_0^\tau \left[B_{\pm}^{(p,hom)} \right. \right. \\ &\quad \times \langle p|D_{\pm} h_L D_{\pm}(|s\rangle a_s B_{\pm}^{(s,hom)-1} \\ &\quad \left. \left. + |n\rangle a_n B_{\pm}^{(n,hom)-1}) \right] d\tau \right|^2, \end{aligned} \quad (11)$$

where $B_{\pm}^{(l,hom)} = i\omega_l \mp i\gamma(H_0 + \alpha M_0^{(hom)} k_0^{(l)2} \delta_l)$, $\delta_l=0$ for $|s\rangle$ and $\delta_l=1$ for $|n\rangle$, and the integration in $\langle p|V_h|f\rangle$ is over x, z of the film volume.

The existence of the second summand in Eq. (11) with $B_{\pm}^{(n,hom)-1} \gg B_{\pm}^{(s,hom)-1}$ leads to a sharp increase in the probability of the intermode transition from hybrid states. Conversely, the presence of hybrid states depends on the inhomogeneity of the ferromagnetic film.

IV. CALCULATIONS AND EXPERIMENT

We define the spin wave spectrum SWS as the frequency dependence of the square of the ratio of currents in the receiver and generator antennae: $W = (J_{rec}/J_{gen})^2$. J_{rec} is proportional to the sum E_{rec} of the induced electromagnetic signal E_e and two signals of spin waves (Fig. 2) with amplitudes $C^{(a,b)}(\tau_l)$

$$E_{rec} = \{E_e + [C^{(a)}(\tau_l)\exp(ik_n^{(a)}l) + C^{(b)}(\tau_l)\exp(ik_n^{(b)}l)] \times \exp(-\gamma\Delta H\tau_l)\}\exp(i\omega_n t), \quad (12)$$

where $C^{(a,b)}$ should be found from Eq. (10), l is the space between the antennae, $\tau_l = l(\partial\omega/\partial k)^{-1}$ is the spin wave propagation time between the antennae, and ΔH is the relaxation parameter. We have calculated SWS using Eqs. (7) and (11) for a YIG film (for $2d = 14\mu\text{m}$) and taking into account three assumptions:

A. The YIG film has the linear variation of M_0 from $M_0^{(hom)}$ to 0 over the sublayer of thickness $0.5\mu\text{m}$ near the substrate. This assumption gives operator V_M in Eq. (7) and determines the dispersion curve repulsion.

B. $h_L(z, x, t) = H_0 \exp[iqx + q(z - d - \lambda/2)]$. It gives the form of the SW scattering.

C. The MVL period $\lambda \propto H_0^{-1/2}$.

We have obtained the following results.

1. Absorption peaks are observed only in the region of the crossing point of the dispersion curves of the surface $|s\rangle$ and the volume $|n\rangle$ modes. Conditions (8) must be realized.

2. A greater value of H_0 leads to the observation of peaks with greater n .

3. If n is fixed, the transition $|f\rangle = a_s|s\rangle + a_n|n\rangle \rightarrow |p\rangle$ with $p=1$ gives the absorption peak with the maximal H_0 .

4. The MVL period can be found by $\lambda = 4d/\sqrt{n^2 - p^2}$.

These dependences have been observed in the experiment. The experiment has been undertaken in the heterostructure of a YIG film of thickness $14\mu\text{m}$ and a monocrystal HTSC film $\text{YBa}_2\text{Cu}_3\text{O}_{7+\delta}$ of thickness $0.5\mu\text{m}$ on a MgO substrate (Fig. 1). l is equal to 7.8 mm . Figure 3 shows the absorption peak on the SWS at 3.17 GHz ($H_0 = 363\text{ Oe}$) with

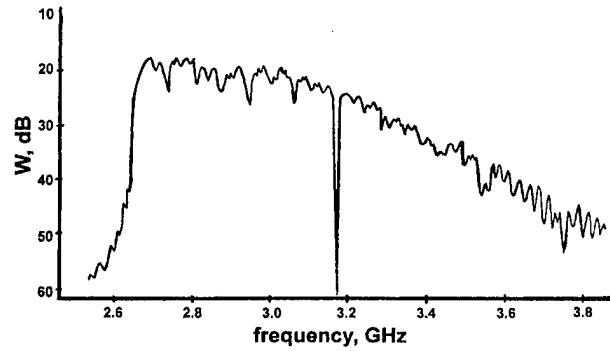


FIG. 3. Spin wave spectrum of the ferrite-HTSC film structure at $H_0 = 363\text{ Oe}$.

$n=66$, $p=1$. The MVL period λ is equal to $0.42\mu\text{m}$. This value is a little greater than the lattice constant in volume samples defined by the quantum of the magnetic flux $\psi = 2.07 \times 10^{-7}\text{ Oe cm}^2$: $\lambda_0 = \sqrt{\psi/H_0} = 0.239\mu\text{m}$. The increase of the lattice parameter may be explained by the influence of the surfaces of the films.² In the next paper we intend to consider in more detail experiment verification of the present theoretical model.

ACKNOWLEDGMENT

This work was supported in part by the Russian Foundation for Basic Research.

¹B. M. Lebed', A. V. Nikiforov, S. V. Yakovlev, and I. A. Yakovlev, *Fiz. Tverd. Tela* (Leningrad) **34**, 656 (1992) [*Sov. Phys. Solid State* **34**, 351 (1992)].

²R. P. Huebener, *Magnetic Flux Structures in Superconductors* (Springer, Berlin, 1979).

³N. I. Polsikova, *Pis'ma Zh. Tekh. Fiz.* **19**, 28 (1993) [*Sov. Tech. Phys. Lett.* **19**, 712 (1993)].

⁴N. I. Polsikova and A. O. Raevskii, *J. Adv. Sci.* **4**, 197 (1992).

⁵L. V. Lutsev, *Zh. Tekh. Fiz.* **65**, 41 (1995) [*J. Tech. Phys.* **40**, 139 (1995)].

⁶B. A. Kalinikos and A. N. Slavin, *J. Phys. C* **19**, 7013 (1986).

⁷A. G. Gurevich and G. A. Melkov, *Magnetic Oscillations and Waves* (CRC, New York, 1996).

Magnetic dissipation force microscopy studies of magnetic materials (invited)

Y. Liu and P. Grütter^{a)}

Centre for the Physics of Materials, Department of Physics, McGill University, Montréal, Québec, H3A 2T8 Canada

We describe the principles of dissipation measurements, discuss various eddy current damping mechanisms, give a brief review of a model for magnetoelastic dissipation due to domain-wall width oscillations, and present some applications of magnetic dissipation force microscopy to magnetic materials. Energy dissipation is measured by simultaneous monitoring of the damping of an oscillating cantilever and the shift in resonant frequency in a magnetic force microscope. Magnetoelastic dissipation is caused by tip-field-induced domain-wall width oscillations through magnetostriction effects. Magnetoelastic damping is strongly correlated with micromagnetic structures and allows different domain walls (such as Bloch and Néel walls) to be distinguished.

© 1998 American Institute of Physics. [S0021-8979(98)48611-0]

Magnetic dissipation force microscopy¹⁻⁴ is a working mode of an ac magnetic force microscope (MFM). In this mode, the magnetic tip oscillating at resonance serves as both force gradient and dissipation sensor. Energy dissipation causes damping of the oscillating tip and is measured by monitoring the oscillation amplitude.

This new working mode of the ac MFM directly measures the local magnetic energy dissipation with lateral resolution at least as good as the normal MFM. We do this by measuring the damping of the oscillating tip in a MFM simultaneously with the usual frequency shifts associated with tip-sample force gradient variations. A change in damping of the MFM probe is the result of energy transferred between the tip and the sample and is detected as a difference in cantilever oscillation amplitude. Damping due to Joule dissipation in semiconductors has previously been measured with a different detection scheme by Denk and Pohl.⁵

In the ac MFM, a magnetic tip is vibrated above a sample surface and creates a local alternating magnetic field at the sample, resulting in energy dissipation in the sample. The thin-film tip stray field, which contains a dc part and an ac part, is concentrated on a region of the sample 50–500 nm in diameter, depending on the tip shape and tip-sample separation.² By using this highly localized tip field and measuring the resulting energy dissipation, we can quantitatively determine the local effect of the tip field on the micromagnetic structure of the sample.

We measure the damping γ or equivalent quality factor Q change of the cantilever, which can be described by a driven damped harmonic oscillator ($\gamma = k_l / \omega_0 Q$). Here, k_l is the cantilever spring constant and ω_0 is the resonant frequency of the cantilever. At resonance, the vibration amplitude is $A = (F_0 / \omega_0) Q_0$, where F_0 is the driving amplitude

(proportional to the ac voltage applied to the piezoelectric bimorph) and Q_0 is the quality factor of the cantilever. Magnetic dissipation in the sample causes an energy loss in the cantilever and so reduces the Q factor. A larger driving force is thus needed to keep the vibration amplitude constant. The extra force is given by

$$\Delta F = -(F_0 / Q_0) \Delta Q. \quad (1)$$

The energy loss (dissipation) in one cycle is then

$$\Delta E = -(E_k / Q_0^2) \Delta Q. \quad (2)$$

Here, $E_k = (1/2) k_l A^2$ is the vibration energy of the cantilever with k_l the spring constant of the cantilever.

We can thus measure the energy loss (dissipation) by measuring the driving force change while keeping the cantilever vibrating at resonance with a constant amplitude if we ensure that any phase shifts are negligible. By recording the driving signal changes simultaneously with the usual frequency shifts associated with tip-sample force gradient variations, a normal MFM image and a dissipation image can be acquired simultaneously. This allows the study of correlations between magnetic dissipation and domain structure. In the following, we will use ΔQ in our discussion. ΔQ can easily be transformed to ΔE or $\Delta \gamma$.

We employ the same phase-locked loop (PLL) demodulator⁶ to track both the resonant frequency and the driving force of the cantilever. When the PLL is locked to the cantilever resonance, it will always keep the cantilever vibrating on resonance and at a constant vibration amplitude by adjusting the driving amplitude to compensate for any damping. This is achieved with an additional feedback circuit to keep the cantilever's vibration amplitude constant at a preset value. A dc voltage proportional to the cantilever's vibration amplitude is compared with a set value and the difference signal is integrated. The output signal of the inte-

^{a)}Electronic mail address: grutter@physics.mcgill.ca

grator will determine the driving signal amplitude to a piezoelectric bimorph, which excites the cantilever. The integrator output serves as the signal for dissipation images.

The fundamental limit for the detection of a Q -factor change δQ , assuming that the displacement measurement is limited only by the cantilever's thermal motion, is given by

$$\delta Q_{\text{thermal}} = \frac{1}{A} \sqrt{\frac{2k_B T Q^3 B_W}{k_l \omega_0}}, \quad (3)$$

with k_B being the Boltzmann's constant, T being the temperature, and B_W being the measurement bandwidth. For our cantilevers ($k_l = 0.1$ N/m, $f_0 = 30$ kHz, and $Q = 1000$ in vacuum) $\delta Q_{\text{thermal}} = 5.3$ (which corresponds to a $\delta \gamma_{\text{thermal}} = 2.8$ pNs/m or $\Delta E = 1.0 \times 10^{-3}$ eV, respectively) with $B_W = 35$ Hz and $A = 25$ nm. All our dissipation data are thermally limited. A better signal-to-noise ratio is predicted, and indeed, observed by measuring dissipation in vacuum. All of the data presented here were obtained at 5×10^{-5} mbar.

Minimizing the phase error between the cantilever oscillation and its drive signal is crucial to obtaining a meaningful damping measurement. Phase errors (e.g., due to filters) will drive the cantilever off-resonance. A larger drive amplitude F' would then be necessary to maintain a constant amplitude, which would falsely be interpreted as a change in cantilever damping. The Q -factor error δQ , due to phase error $\delta \phi$, is given by

$$\delta Q_{\text{Phase}} \approx \frac{1}{2} Q (\delta \phi)^2. \quad (4)$$

Our carefully optimized electronics maintain a phase error of less than 0.003 rad for frequencies between 10 kHz and 2 MHz. This amounts to an error of $\delta Q < 0.005$ for $Q_0 = 1000$, substantially smaller than the thermal limit. A second source of phase shifts is frequency feedback errors, e.g., as a result of varying force gradients between tip and sample. The influence of frequency error on the drive output can directly be measured by modulating the PLL reference frequency. We determined $\delta Q < 0.004$ for a 10 Hz modulation in vacuum. In our experiments, the frequency feedback errors are kept smaller than 2 Hz, resulting in $\delta Q < 0.001$. A further potential phase error is particular to our fiber-optic interferometric deflection sensing technique. Dc deflection Δz as a result of forces acting on the cantilever will result in an optical path-length difference, and thus, a phase-shift $\Delta \phi = (2\Delta z/\lambda)2\pi$. In our experiments we monitor this deflection simultaneously with the damping and the force gradient signal. The maximum total deflection is always smaller than 1 nm, and thus, introduces a phase error of 0.01, resulting in an error of $\delta Q < 0.05$.

A further potential error in damping measurements is due to the tip-sample separation dependence of the hydrodynamic cantilever damping observed in air.⁷ Typically, Q changes larger than the thermal limit are observed for tip-sample separation changes of a few nm if the average separation is 50 nm or less. To avoid the potential convolution of the regular MFM (acquired at variable tip-sample separation as $F' = \text{const.}$) and dissipation data, we always acquire our dissipation data in vacuum, where a separation-dependent Q factor is not observed for tip-sample separations larger than several nm.

In conclusion, by carefully designing and characterizing our PLL, keeping feedback errors to 2 Hz, and controlling phase errors due to optical path-length changes and vacuum operation, we are confident that all measured drive amplitude changes are only due to changes in the magnetic damping of the cantilever.

The following loss mechanisms due to eddy and induced currents can be identified:

- (1) Eddy currents in the sample due to oscillations of the domain-wall position. An ac magnetic field may lead to domain-wall oscillations around the wall equilibrium position, generating eddy currents around the oscillating domain walls.
- (2) Eddy currents in the MFM tip due to the stray field from the sample. When the tip is oscillating, the sample stray field generates eddy currents in the tip.
- (3) Eddy currents in the tip due to tip magnetization changes. When the tip is oscillating, the gradient of the sample stray field may induce tip magnetization change dM/dt , which generates eddy currents in the tip.
- (4) Eddy currents in the sample due to tip field. An oscillating tip creates an alternating magnetic field at the sample, thus leading to magnetic-flux changes in the sample. For a conducting sample, eddy currents are induced in the sample.
- (5) Eddy currents in the sample due to domain-wall jumps.
- (6) Induced currents in the sample due to capacitance changes between the tip and sample. The capacitance of the tip-sample system oscillates as a result of the tip oscillation. If a constant voltage is applied between the tip and the sample (as in our instrument for servopurpose⁸), the oscillating capacitance leads to an alternating current as a result of alternating charge redistribution. Variations in magnetoresistance could thus lead to magnetic contrast. This source of damping is not related to eddy currents.

We have theoretically calculated and experimentally tested the contributions of eddy current losses (1), (2), and (3) to the damping of a Si cantilever (coated with 20 nm CoNi film) and a Si_3N_4 cantilever (coated with 90 nm CoPtCr film) on several samples (30 nm thick patterned $\text{Ni}_{80}\text{Fe}_{20}$ film, 4 nm thick Co film, and 40 nm thick CoPtCr film) and found that these contributions are far too small (by 4–6 orders of magnitude) to explain the observed damping signal.^{2,3} The damping signals due to losses (4) and (6) depend on the resistivity of the sample. The dissipation due to induced currents (6) is proportional to the sample's resistivity and can be used to determine dopant concentration in semiconductors.⁵ The resistivity of the metallic samples is low (for cobalt it is $9.8 \times 10^{-8} \Omega \text{ m}$), which leads to a dissipation signal that is below the thermal limited minimum detectable resistivity change of about $4 \times 10^{-3} \Omega \text{ m}$.⁵ The small variations of resistivity due to magnetoresistive effects (typically, $\Delta R/R < 1\%$) do not lead to a measurable dissipation contrast. The dissipation due to eddy current (4) is an inverse measure of resistivity. However, a dissipation measurement on a patterned permalloy film on a Si substrate¹ shows that the background dissipation signal on the permal-

loy area (with a resistivity on the order of $10^{-7} \Omega \text{ m}$) is smaller than in the Si area (with a much higher resistivity). The permalloy background signal corresponds to the thermal limit, in contrast to the observed resistive dissipation on Si. We conclude that the effect of the induced current (6) is larger than that of the eddy current (4) in this sample. Due to the very short time scales involved in domain-wall jumps, eddy currents (5) might lead to some dissipation contrast.³ In wall jumps (induced by the tip field), the wall speed can be extremely high, resulting in substantial, but difficult to quantify, eddy current losses.

In conclusion, all eddy current related processes, with the exception of tip-induced domain-wall jumps, lead to dissipation values not measurable in vacuum with our standard MFM tips.

A magnetoelastic model for dissipation, which bases the dissipation on domain-wall width oscillations and the resulting phonon emission through the magnetostriction effect, has given quantitative agreement with experiments on samples investigated in detail.^{2,4} The domain-wall width oscillations $W(t)$ can be treated as a simple harmonic oscillator described by an equation, which contains an inertia term $m\ddot{W}$, a stiffness force $\alpha(\Delta W)$, a damping term,⁹ and an external alternating driving force term related to the external ac tip field. Here, m is the effective mass of the domain wall for width oscillations and α is the wall stiffness of the domain wall for width oscillations. In most problems, damping terms are considered to be viscous in nature (i.e., the damping force is proportional to velocity). However, for magnetoelastic loss, the damping of wall width oscillations appears to be frictional in nature since the elastic energy changes associated with the wall width change only depend on the magnitude of the wall width change and not on the rate of the width change. Hence, the damping term can be written as $-\beta\dot{W}/|\dot{W}|$. The equation of motion for wall width oscillations is then

$$m\ddot{W} + \beta \frac{\dot{W}}{|\dot{W}|} + \alpha(W - W_0) = F, \quad (5)$$

where W_0 is the equilibrium width of the domain wall and $F = F_0 \exp(i2\pi ft)$ is the force trying to oscillate the wall width.

The parameters m , α , β , and W_0 have been derived and expressed in basic magnetic properties of magnetic materials⁴ with $m = \pi\mu_0/48\gamma^2 W_0$, $\alpha = K_1/W_0$, $\beta = \frac{1}{2}c\lambda^2$, and $W_0 = \sqrt{2JS^2\pi^2/K_1\alpha}$, assuming that the demagnetization energy of the wall can be neglected. Here, K_1 is the anisotropy constant; c is Young's modulus; λ is the magnetostriction constant; J is the exchange integral; S is the spin; a is the unit cell length; and γ is the gyromagnetic ratio. The driving force for wall width oscillations F was found to be strongly dependent on the relative orientation of the mean-magnetization direction inside a domain wall and the external magnetic field. For a Bloch wall $F = \pm(2\mu_0 M_s H_z/\pi)$, depending only on the out-of-plane component of the external tip field, while for a Néel wall F is related to the in-plane component of the external tip field. In magnetic dissipation force microscopy, the external field is created by an oscillat-

ing magnetic tip and is highly localized. Thus, different micromagnetic structures in a domain wall will result in dissipation contrast for a given tip. Letting $F = F_0 \exp(i2\pi ft)$ and $W = W_0 + W_1 \exp[i(2\pi ft + \delta)]$ (f is the oscillation frequency of the tip), we can obtain the energy dissipation in one oscillation cycle as

$$P = 4f\beta W_1 = 4f\beta \frac{\sqrt{F_0^2 - \beta^2}}{\alpha - (2\pi f)^2 m}. \quad (6)$$

Quantitative agreement between this equation and experiments for a Co film sample and a Co/Ni multilayer sample was previously obtained.^{2,4} Furthermore, by comparing permalloy and Terfenol-D (which has a much higher λ than permalloy), we observed the expected relative dissipation increase in the Terfenol-D sample. In addition to this agreement, the model predicts a wall width resonance. The resonant frequency for the Co sample was calculated to be on the order of 10^{10} Hz .⁴ Hence, the wall width resonance might influence the high-frequency properties of magnetic materials.

An interesting consequence of Eq. (6) is that a minimum driving force is necessary to observe dissipation. By engineering suitable tips (e.g., by selecting a thin, low moment coating), a small F_0 can be created, thus inhibiting energy loss due to domain-wall width oscillations. The absence or presence of nonconservative tip-sample interactions (at least above the thermal limit) can thus be monitored by dissipation force microscopy.

Magnetic dissipation force microscopy has been used to study the magnetic domain structures of several samples, including a patterned permalloy film,^{1,4} and transitions in a CoPtCr magnetic recording medium,¹ Co/Ni multilayer,² and Terfenol-D.^{1,4} The experimental dissipation showed discontinuous change along domain walls in the patterned permalloy film.¹ This suggests that there are different micromagnetic structures in the domain walls. Figure 1 shows a high-resolution MFM image and the simultaneously acquired magnetic dissipation image on a part of one permalloy square. It can be seen from Fig. 1(a) that the magnetic domain walls in this permalloy are not pure Néel or pure Bloch walls. They contain complicated micromagnetic structures, possibly Bloch points and Bloch lines. We observe that on the same sample but for different squares, domain walls have different micromagnetic structures. In Fig. 1(b) the long micromagnetic features (indicated by the arrows), which cross the main wall and connect the two adjacent magnetic domains, are formed by finer identical spots. Black and white spots are observed. They show opposite signs of magnetic tip-sample interactions. Other domain walls even on the same square show less magnetic substructure [top left of Fig. 1(a)].

Figure 2(a) gives another example of a domain-wall structure observed on the permalloy film. Here, there are fewer internal micromagnetic features inside the main domain wall, which shows up as a bold dark line from the lower-left corner to the upper-right corner (the bold white line on the left side of the image is the edge of the permalloy square). However, one observes a lot of ripplelike magnetic features, which are perpendicular to and terminated at the

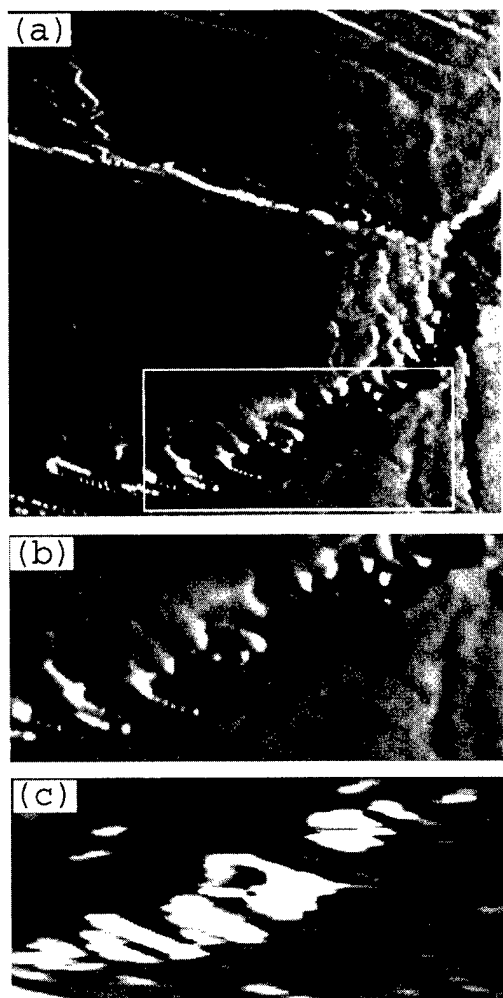


FIG. 1. High-resolution MFM and magnetic dissipation images on a permalloy square with a 20 nm CoNi film coated Si tip. The MFM image is differentiated along the fast scan direction to enhance the contrast. (a) is the $12\ \mu\text{m} \times 12\ \mu\text{m}$ MFM image, (b) is the enlarged area shown by the rectangle in (a), and (c) is the magnetic dissipation image of the same area as (b).

main wall position. Ripples in permalloy films are commonly observed¹⁰ and have been observed by MFM.¹¹ Figure 2(b) is the simultaneously acquired dissipation image, which shows again that the dissipation signal is associated with some of the magnetic wall features. There is a magnetic feature (indicated by an arrow), which leads to a pronounced dissipation signal (about 0.03 eV in one oscillation cycle), and is not part of the main wall. A reproducible jump of this magnetic feature is observed as a highly localized change in dissipation on several scan lines indicated by an arrow in Fig. 2(b). By applying a field of only 2 Oe with an *in situ* electromagnet, this feature disappears while the main wall is displaced by less than $1\ \mu\text{m}$, confirming that the feature is magnetic in origin.

The existence of different micromagnetic domain-wall structures of the permalloy film suggest that there are many wall configurations which have very similar energy minima. In order to advance our understanding of the micromagnetic wall structures and the associated magnetic dissipation in patterned permalloy films, micromagnetic calculations are needed. Such calculations are not presently feasible for sys-

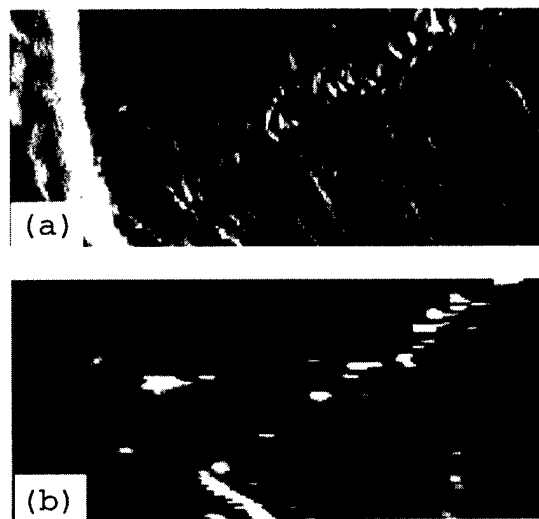


FIG. 2. Ripplelike magnetic features intersect with this main wall in a permalloy film. The image area is $8\ \mu\text{m} \times 4\ \mu\text{m}$. (a) differentiated MFM image. The domain wall is the black structure running diagonally across the image. The white vertical line to the left of the image is the edge of the permalloy square. (b) Magnetic dissipation image.

tems as large as the $20\ \mu\text{m}$ squares. Clearly, however, dissipation imaging opens the possibility of characterizing a variety of micromagnetic structures.

For this study, we used our home-built high-resolution magnetic dissipation force microscope (MDM) with an *in situ* magnetizing stage. The magnetizing stage is also home-built¹² and the field (in the sample plane) can be changed continuously from -1 to $+1$ kOe. The MFM and MDM images are taken simultaneously as a function of this external magnetic field. Prior to experiments, the sample is saturated and then ac demagnetized. The procedure for changing the field follows the macroscopic $M-H$ hysteresis loop. We first increase the field from zero to saturation and then decrease it to zero. An opposite field is then applied to the opposite saturation value and decreased to zero again. The procedure is then finished by again changing the sign of the field and increasing it to the first saturation value. The field is changed in small steps. After each of these steps, a MFM and a MDM image are taken simultaneously. For each experimental run, typically, 20–30 images are taken and assembled as a video to allow easier observation of changes between field steps.

Figure 3 shows the evolution of the domain configuration with decreasing magnetic field after saturating along one edge of the permalloy square. Figure 4 gives the simultaneously acquired dissipation images. The image of the permalloy is not square due to uncorrected piezo-nonlinearity.

The saturation field is 90 Oe for the patterned permalloy film, at which no contrast is observed in either MFM or dissipation images. This saturation field here is much higher than for a film of the same thickness, but infinite extent in the plane of the film (which has a coercivity of around 2 Oe). The higher saturation field in the patterned film is due to demagnetization effects, since for an external field larger than 10 Oe the domain walls are concentrated at the edge area of the squares. A much higher external field is needed to

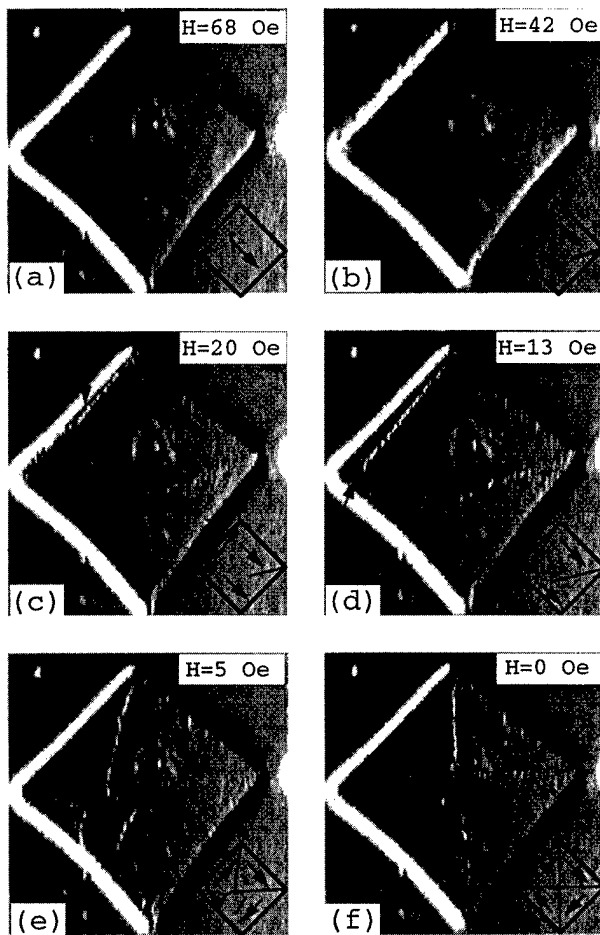


FIG. 3. Evolution of the domain configuration with decreasing magnetic field after saturating along one edge of the permalloy square. The field direction is indicated in (a). (a)–(f) are taken consecutively with the *in situ* applied field shown in the individual images. The inset in each individual image depicts the proposed domain structure.

remove these domain walls. On decreasing the field, magnetization reversal takes place first by reverse-domain nucleation at one edge at a field of 68 Oe [Figs. 3(a) and 4(a)]. Note that although nucleation is not seen in the regular MFM image, it is clearly seen in the dissipation image. Hence, dissipation imaging allows the observation of early stage domain nucleation especially at sample edges, where other magnetic imaging techniques have major problems. On decreasing the field further, the reverse domain grows [as indicated by a solid arrow in Fig. 3(c)] with its magnetization direction probably perpendicular to the external field (parallel to the edge). At $H = 13$ Oe, a new domain with a magnetization direction antiparallel to the external field (parallel to one edge of the sample) is formed. Figures 3(b), 3(c), and 3(d) also show a long magnetic structure (indicated by a dashed arrow) starting from the right corner of the square. This structure, becoming longer with decreasing external field, is believed to be a 360° wall (simulations of the expected MFM response of a 360° wall are comparable with experimental results).³ At $H = 5$ Oe, all the four domains with parallel, antiparallel, and perpendicular magnetization with respect to the external field are present. For this configuration to be achieved, a domain rotation from the exter-

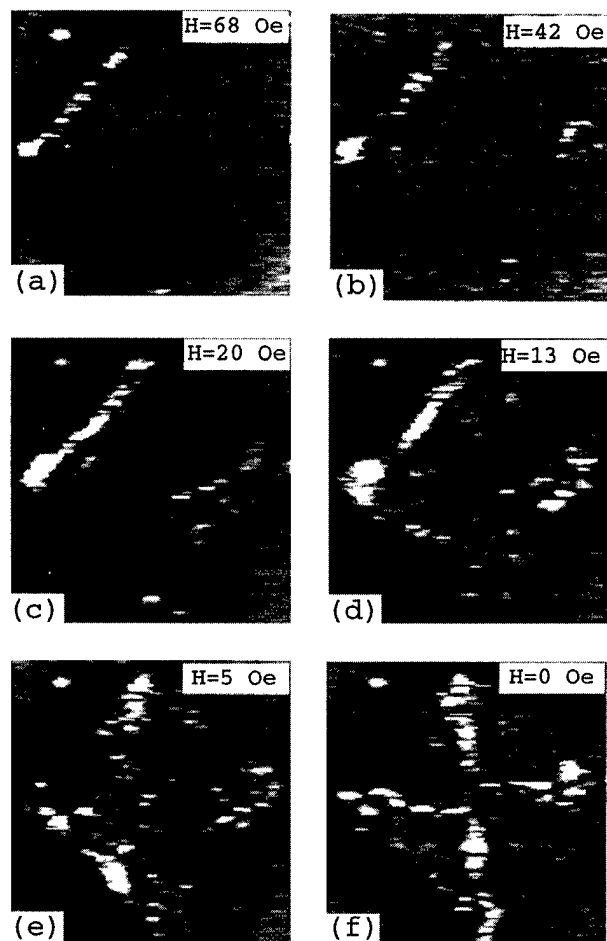


FIG. 4. Evolution of the dissipation configuration with decreasing magnetic field after saturation along one edge of the permalloy square. (a)–(f) are simultaneously acquired with (a)–(f) of Fig. 3, respectively.

nal field direction to a direction perpendicular to the field (parallel to the edge) must have occurred when the long magnetic structure meets other domain walls. The exact field at which this happens could not be determined. Possibly, this might be due to the limited time resolution of our nonoptimized imaging (each image takes 10–20 min). The rotated domain is indicated in Fig. 4(e) by an arrow. Inside this rotated domain, another long magnetic structure is seen, which disappears when the external field is reduced to zero. At this point, the four domains become equal in size and the edge effect driven closure domain configuration is formed. The magnetic domain structure in Fig. 4(f) differs from the ac demagnetized sample in that the magnetic ripples appear only on two edges of the sample instead of on all the four edges.¹ The magnetization direction of the two domains, which shows magnetic ripples, is either parallel or antiparallel to the previously applied field.

The magnetic dissipation signals (Fig. 4) show maxima always associated with domain-wall positions during the reversal.

Applying an external magnetic field does not move some structures [e.g., the “crater” in the middle of the square and the bright spots outside the square in Fig. 4(a)]. This indicates that they are topography that was not served out and

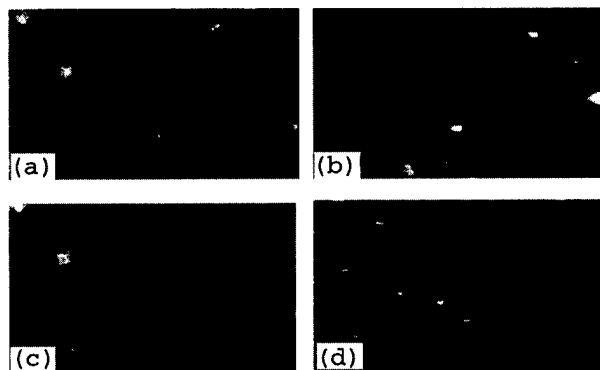


FIG. 5. Constant force gradient and magnetic dissipation images of an Fe/Cu multilayer (GMR) sample. Image size is $5\ \mu\text{m}$ by $2.9\ \mu\text{m}$. The average tip-sample separation is 60 nm. (a) and (b) are the constant force gradient and the simultaneously acquired dissipation images in the absence of an external field. (c) and (d) are the constant force gradient and the simultaneously acquired dissipation images in the presence of an external field of 30 Oe on the same area as (a). Maximum z variations in both (a) and (c) are all 1 nm. The variation of driving amplitude in (b) is 70 mV (corresponding to an energy loss of 0.019 eV in one oscillation cycle, $Q_0 = 10\ 000$ for this experiment), while in (d) it is 18 mV (thermal noise level). The average driving amplitude for (b) and (d) is 3000 mV. No image processing except for a plane subtraction was performed for the constant force gradient images. The dissipation images are raw data.

provided convenient markers that were independent of the magnetic structures.

In multilayer GMR samples (consisting of alternative nonmagnetic and magnetic layers), the adjacent magnetic layers are antiferromagnetically coupled through a Ruderman-Kittel-Kasuya-Yosida interaction.¹³ A single nonmagnetic or magnetic layer has a typical thickness of only several angstroms. As a result, the sample stray field at positions thousands of angstroms above the sample surface is virtually zero since the fields from the adjacent magnetic layers cancel each other. This raises a challenge to image the magnetic domain structure in these samples by normal magnetic force microscopy, which relies on the interaction between the tip magnetization and sample stray field. Figures 5(a) and (b) show the experimental results on a (Cu 25 Å/Fe 11 Å)×36 multilayer GMR sample at $z = 60$ nm. The contrast in Fig. 5(a) comes from the sample surface topography while the contrast in Fig. 5(b) is a result of tip stray field influencing the sample magnetic structure. We verify this by imaging with an external field. At a field of 30 Oe parallel to the sample surface (the sample's coercivity is 3 Oe), the contrast in the dissipation image [Fig. 5(d)] disappears while the constant force gradient image [Fig. 5(c)] is unchanged. The signal observed in Fig. 5(d) corresponds quantitatively to the thermal noise limited dissipation measurements. Magnetic dissipation microscopy can thus detect magnetic structures not observable by magnetic force microscopy. This might have future applications in investigating antiferromagnets, spin glasses, and patterned magnetic media as well as in high-density storage if data rates and reliability issues can be solved.

Further studies on the origin of the dissipation in the GMR samples might help to determine the interlayer coupling strength and micromagnetic structure in these samples.

In conclusion, the nonconservative interaction of the tip stray field with micromagnetic structures can be deduced by measuring dissipation in an ac MFM. We find that the major contribution to magnetic dissipation originates in magnetoelastic losses as a result of the tip-field coupling to the sample magnetization. Dissipation measurements are thermally limited. We have achieved a sensitivity of better than 2.0×10^{-4} eV/ \sqrt{Hz} per oscillation cycle of the tip in a vacuum MFM. Lateral resolution in dissipation imaging is at least as good as standard MFM imaging. Quantitative dissipation measurements in combination with micromagnetic simulations should allow an upper boundary to be put on the influence of the tip stray field on the switching behaviors of small magnetic particles. Dissipation measurements allow us to determine the onset of tip influences on the micromagnetic structures long before they are observable in regular MFM. Dissipation also allows us to distinguish between different micromagnetic wall structures such as Néel and Bloch walls, Bloch lines, etc. Furthermore, the presence of domain walls can be deduced with dissipation measurements when standard MFM fails, such as at the edges of permalloy samples (large topography variations) or when the sample stray field is very weak (e.g., in antiferromagnetically coupled multilayer thin-film structures). Quantitative dissipation imaging on a suitable reference sample can also be used as a relative calibration of tip stray fields, an important parameter in qualitative and quantitative interpretation of MFM data.

The authors acknowledge initial help with the PLL electronic by U. Dürig (IBM Research Division) and F. Battistoni. The GMR sample was kindly provided by Dok Won Lee (McGill). We appreciate D. Ryan's critical comments on the manuscript. This work was supported by grants from the National Science and Engineering Research Council of Canada and Le Fonds pour la Formation des Chercheurs et l'Aide à la Recherche de la Province de Québec.

¹P. Grütter, Y. Liu, P. LeBlanc, and U. Dürig, *Appl. Phys. Lett.* **71**, 279 (1997).

²Y. Liu, B. Ellman, and P. Grütter, *Appl. Phys. Lett.* **71**, 1418 (1997).

³Y. Liu, Ph.D. thesis, McGill University, 1997.

⁴Y. Liu and P. Grütter, *J. Appl. Phys.* **83**, 5922 (1998).

⁵W. Denk and D. W. Pohl, *Appl. Phys. Lett.* **59**, 2171 (1991).

⁶U. Dürig, H. R. Steinauer, and N. Blanc, *J. Appl. Phys.* **82**, 3641 (1997).

⁷G. Lévêque, P. Girard, S. Belaidi, and G. Cohen Solal, *Rev. Sci. Instrum.* **68**, 4137 (1997).

⁸D. Rugar, H. L. Mamin, P. Guethner, S. E. Lambert, J. E. Stern, I. McFadyen, and T. Yogi, *J. Appl. Phys.* **68**, 1169 (1990).

⁹H. J. Williams, W. Shockley, and C. Kittle, *Phys. Rev.* **80**, 1090 (1950).

¹⁰H. W. Fuller and M. E. Hale, *J. Appl. Phys.* **31**, 238 (1960).

¹¹H. J. Mamin, D. Rugar, J. E. Stern, R. E. Fontana, Jr., and P. Kasiraj, *Appl. Phys. Lett.* **55**, 318 (1989).

¹²P. LeBlanc, Master thesis, McGill University, 1996.

¹³P. Bruno and C. Chappert, *Phys. Rev. Lett.* **67**, 1602 (1991).

Long wavelength spin dynamics in $\text{La}_{0.53}\text{Ca}_{0.47}\text{MnO}_3$

J. J. Rhyne,^{a)} H. Kaiser, and H. Luo

University of Missouri, Columbia, Missouri 65211

Gang Xiao and M. L. Gardel

Brown University, Providence, Rhode Island 02912

The magnetic structure and dynamics in the colossal magnetoresistance (CMR) class perovskite $\text{La}_{0.53}\text{Ca}_{0.47}\text{MnO}_3$ have been studied by elastic and inelastic neutron scattering. This composition is near the 0.5 Ca transition from a metallic ferromagnet to an insulating antiferromagnet. Powder neutron diffraction on these samples showed coexisting ferromagnetic and antiferromagnetic phases at low temperature and a splitting of the lattice parameters of the antiferromagnetic phase near T_N , reflecting the onset of the charge ordered state. Inelastic scattering measurements of the ferromagnetic excitations exhibited well-defined spin waves of resolution width below T_c . The spin waves exhibited conventional Heisenberg behavior with dispersion of the form $E = Dq^2 + \Delta$ with spin stiffness $D(T=0\text{ K}) \approx 135\text{ meV \AA}^2$ and an energy gap $\Delta \approx 0.1\text{ meV}$. The value of the spin wave stiffness D is similar to that found for other ferromagnetic perovskite materials, and it renormalized with temperature in a manner consistent with the magnetization. © 1998 American Institute of Physics. [S0021-8979(98)27211-2]

I. INTRODUCTION

The discovery in the early 1990s of a colossal magnetoresistance effect¹ (CMR) in perovskite manganite compounds and their potential technological applications has sparked an intense revival of interest in the magnetic properties of these materials, for which the basic magnetic and crystal structure data date back to 1955.² Key to the understanding of the magneto and transport properties of the compounds is the relationship of Mn^{+3} – Mn^{+4} double exchange interactions, Jahn–Teller distortions, polarons, and charge ordering. Inelastic neutron scattering provides a mechanism to study these mechanisms via their influence on the spin wave excitations, including anomalous dispersion effects, spin diffusion central modes, and unusual spin wave lifetimes.

The $\text{La}_{1-x}\text{Ca}_x\text{MnO}_3$ system exhibits metallic ferromagnetism above a threshold value of $x \approx 0.2$ and above $x \approx 0.5$ becomes an insulating antiferromagnet. Previous magnetization and transport results have indicated³ that compositions between $x=0.47$ and $x=0.50$ exhibit concomitant ferro and antiferromagnetic states with the ferromagnetic transition temperature approximately 40 K higher than the antiferromagnetic transition temperature for $x=0.48$. The onset of the antiferromagnetic state is accompanied by charge ordering of the Mn^{+3} and Mn^{+4} on distinct lattice sites and is reflected in a splitting of the lattice parameters ascribed to Jahn–Teller distortions of the Mn^{+4}O_6 octahedra.⁴ In this article we present neutron results on the magnetic structure and spin dynamics measured in a polycrystalline sample of

$\text{La}_{0.53}\text{Ca}_{0.47}\text{MnO}_3$. This composition was chosen to examine the nature of the coexistence of ferro and antiferro order and the effect of this coexistence on the ferromagnetic spin excitations.

The crystal structure, confirmed by neutron powder diffraction, was indexed as a slightly orthorhombic $Pnma$ space group at room temperature with an additional monoclinic $P2_1/m$ structure at low temperature amounting to a 40% volume fraction. The magnetic refinement confirmed the coexistence of both ferromagnetic and antiferromagnetic phases below T_N that persisted down to 10 K, the lowest temperature measured. The low T values of the Mn moment were $2.8\mu_B$ for the ferromagnetic phase derived from the orthorhombic crystal phase, and $3.7\mu_B$ for the Mn^{+3} and $2.8\mu_B$ for the Mn^{+4} site of the monoclinic phase. The latter phase exhibited a change in lattice parameters near T_N reflecting the onset of charge ordering.

II. MAGNETIC INELASTIC SCATTERING

Lynn *et al.*^{5,6} have studied the spin dynamics in the CMR optimally doped composition $\text{La}_{0.66}\text{Ca}_{0.33}\text{MnO}_3$ and have found marked departures from conventional Heisenberg spin wave behavior. They observed a quadratic dependence of the spin wave energy on wave vector transfer ($E_{\text{sw}} = Dq^2 + \Delta$) as expected with no measurable energy gap Δ at $E=0$. However, the spin stiffness D , which usually mimics the magnetization, showed only a relatively weak renormalization with temperature of approximately 50% up to T_c . Spin waves were not observed above T_c ; however, an anomalous large central (elastic) mode developed above about 80% of T_c that persisted to temperatures well in excess

^{a)}Electronic mail: jrhyne@showme.missouri.edu

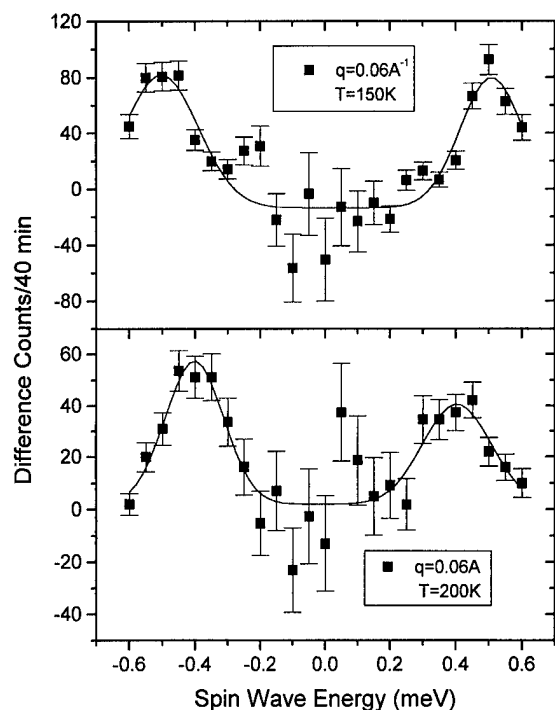


FIG. 1. Spin wave spectra for $q=0.06 \text{ \AA}^{-1}$ at 150 and 200 K. Data taken at 10 K have been subtracted to remove parasitic scattering near $E=0$.

of T_c . This central mode was observed to exchange spectral weight with the spin wave excitations, and to have a width varying with q^2 indicative of spin diffusion.

In the present work, inelastic scattering data were taken on a powder sample of $\text{La}_{0.53}\text{Ca}_{0.47}\text{MnO}_3$ from 240 K ($T_c \approx 237 \text{ K}$) down to 10 K using a triple axis spectrometer at the University of Missouri Research Reactor. The incident neutrons derived from a focused (002) pyrolytic graphite monochromator had energy of 14.2 meV. A pyrolytic graphite analyzer was used with Soller slit collimations of $10' - 10' - S - 10' - 10'$ before and after the monochromator and analyzer. Due to the polycrystalline form of the sample, inelastic data could only be taken in the first Brillouin zone about the (000) reflection. At these low scattering angles, the range of energy transfers that could be measured for each q is significantly restricted by kinematic considerations, and in general only the longer wavelength spin waves can be examined, which must be assumed to be isotropic in q . The spectrometer configuration gave a resolution for elastic scattering of 0.2 meV, and due to focusing conditions that are nearly identical for neutron energy gain and loss peaks at low q , the intrinsic spin wave widths are somewhat narrower.

Constant q -mode inelastic scattering data were taken at a number of q s in the range $0.04 \text{ \AA}^{-1} \leq q \leq 0.1 \text{ \AA}^{-1}$ at each temperature and over both positive (neutron energy loss) and negative (neutron energy gain) maximum energy ranges dictated by the kinematic restrictions. Figure 1 shows the results of constant $q=0.06 \text{ \AA}^{-1}$ inelastic scans at 150 and 200 K (the ferromagnetic $T_c=237 \text{ K}$). The increased statistical error near $E=0$ results from the subtraction of data taken below 10 K, which effectively suppresses the parasitic incoherent elastic scattering from the cryostat and from the sample.

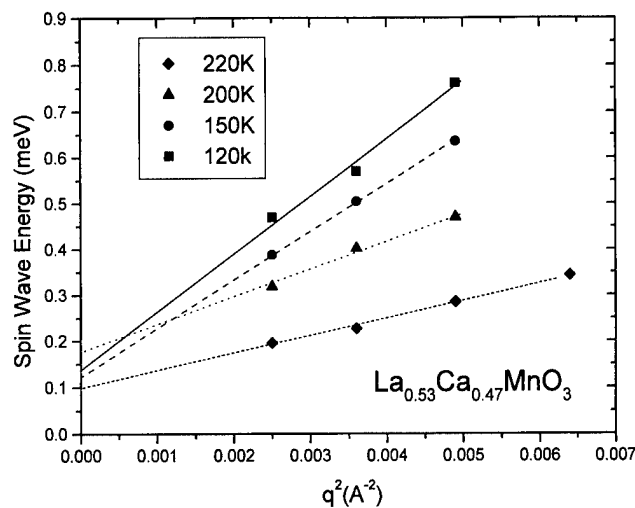


FIG. 2. Plot of the spin wave energies vs q^2 showing the quadratic dispersion and the existence of a small $q=0$ energy gap.

At 10 K, thermal population effects produce negligible spin wave scattering. (It is noted that the $E=0$ parasitic scattering in this sample was quite large relative to the ferromagnet spin wave scattering due to the spurious extra contributions from the coexistent antiferromagnetic phase that may indeed contain almost half the atoms.) The data of Fig. 1 also confirm that the spin wave energies reduce with increasing temperature as expected.

The spin waves measured at different q values show a quadratic dispersion as illustrated in Fig. 2 for the temperatures studied between 220 K ($0.93 T_c$) and 120 K ($0.51 T_c$) again reflecting conventional Heisenberg behavior. Lower temperatures could not be fully measured because of the above-mentioned restrictions on the energy range of the spectrometer. A small $q=0$ energy gap $\Delta \approx 0.1 \text{ meV}$ is evident and presumably originates from crystal field anisotropy. This is in contrast to the gapless behavior seen for the $x=0.33$ compound.⁵ It should be noted that the quadratic dispersion of Fig. 2, combined with the (0,0,0) origin for q ,

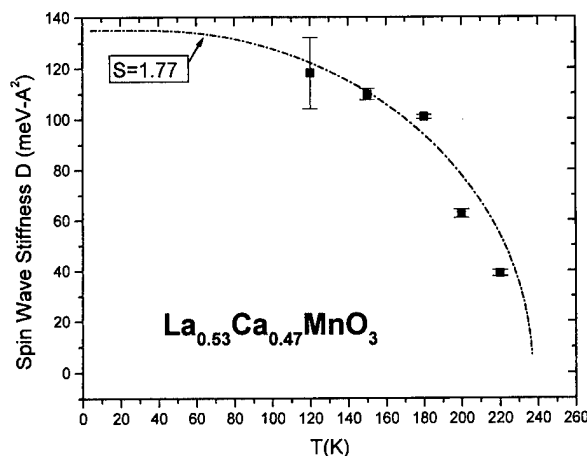


FIG. 3. Temperature dependence of the spin wave stiffness parameter D as a function of temperature. The solid line is the Brillouin function for $S=1.77$ that represents the magnetization.

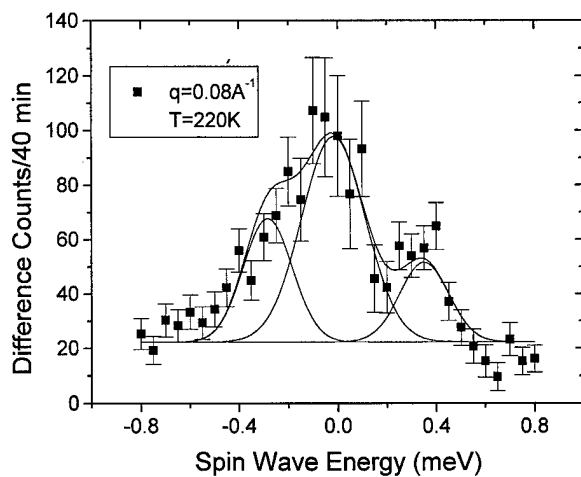


FIG. 4. Scattering data at 220 K ($0.93 T_c$) for $q=0.08 \text{ \AA}^{-1}$ showing the central ($E=0$) mode intensity that is significantly smaller than that observed previously in an $x=0.33$ compound (see Ref. 5).

definitively confirms the existence of long wavelength *ferromagnetic* spin waves existing in a compound that also shows antiferromagnetic spin order.

Figure 3 shows the temperature dependence of the spin wave stiffness parameter D over the above temperature range. The stiffness exhibits significant renormalization with temperature again in contrast to the results for the $x=0.33$ sample.⁵ The figure also shows a curve of the Brillouin function for $S=1.77$ (effective Mn spin for this composition) normalized to $T_c=237$ K. This curve represents the temperature dependence of the Mn order parameter and also represents the approximate higher temperature dependence of D in a conventional ferromagnet. The extrapolated $T=0$ K value of the spin stiffness is 135 meV \AA^2 that gives a value of $D/T_c=0.57$ characteristic of an itinerant system.

The large $E=0$ parasitic scattering in this sample makes the determination problematical of the magnitude and q dependence of any central mode that appears as the spin waves merge into the elastic position on approach to T_c . Figure 4

shows the inelastic scattering (10 K data have been subtracted) at 220 K ($0.93 T_c$) and $q=0.08 \text{ \AA}^{-1}$. The solid lines are Gaussian fits to the expected spin waves and the central $E=0$ peak. Although within experimental uncertainty the central peak is not negligible, its intensity certainly does not exceed the spin waves by a factor of three as observed in the $x=0.33$ material at this same fraction of T_c ; nor is there much evidence of an exchange of spectral weight between the spin wave peaks and the central mode starting below $0.9 T_c$. It was suggested the large central mode is related to the formation of a magnetic polaron and is consequently found to be very sensitive to applied magnetic fields.⁶ The observed weakening or absence of these effects in other compositions would support this concept.

In summary our neutron results on $\text{La}_{0.53}\text{Ca}_{0.47}\text{MnO}_3$ show definitely coexisting phases of ferromagnetic and antiferromagnetic bulk spin ordering. The spin dynamics representative of the ferromagnetic phase were strongly characteristic of a conventional ferromagnet and did not show the anomalies found for the optimally doped $x=0.33$ compounds.⁵ While the antiferromagnetic spin waves could not be observed at the $q=0$ origin, their assumed presence did not destroy the ferromagnetic spin waves nor perturb them from conventional behavior.

ACKNOWLEDGMENT

The research work at Brown University was supported by NSF Grant No. DMR94-14160.

¹For example, R. von Helmlot, B. Holzapfel, L. Schultz, and K. Samwer, *Phys. Rev. Lett.* **63**, 1990 (1993); Y. Tokura, A. Urushibara, Y. Morimoto, T. Arima, A. Asamitsu, G. Kido, and N. Furukawa, *J. Phys. Soc. Jpn.* **63**, 3931 (1994).

²E. O. Wollan and W. C. Koehler, *Phys. Rev.* **100**, 545 (1955).

³P. Schiffer, A. P. Ramirez, W. Bao, and S. W. Cheong, *Phys. Rev. Lett.* **75**, 3336 (1995).

⁴P. G. Radaeli, M. Marezzio, H. Y. Hwang, S.-W. Cheong, and B. Batlogg, *Phys. Rev. B* **54**, 8992 (1996).

⁵J. W. Lynn, R. W. Erwin, J. A. Borchers, Q. Huang, and A. Santoro, *Phys. Rev. Lett.* **76**, 4046 (1996).

⁶J. W. Lynn, R. W. Erwin, J. A. Borchers, A. Santoro, Q. Huang, J.-L. Peng, and R. L. Greene, *J. Appl. Phys.* **81**, 5488 (1997).

Spin dynamics of strongly doped $\text{La}_{1-x}\text{Sr}_x\text{MnO}_3$

L. Vasiliu-Doloc^{a)} and J. W. Lynn

NIST Center for Neutron Research, National Institute of Standards and Technology, Gaithersburg, Maryland 20899 and Center for Superconductivity Research, University of Maryland, College Park, Maryland 20742

Y. M. Mukovskii, A. A. Arsenov, and D. A. Shulyatev

Moscow Steel and Alloys Institute, Moscow 117936, Russia

Cold neutron triple-axis measurements have been used to investigate the nature of the long-wavelength spin dynamics in strongly doped $\text{La}_{1-x}\text{Sr}_x\text{MnO}_3$ single crystals with $x=0.2$ and 0.3 . Both systems behave like isotropic ferromagnets at low T , with a gapless ($E_0 < 0.02$ meV) quadratic dispersion relation $E = E_0 + Dq^2$. The values of the spin-wave stiffness constant D are large ($D_{T=0} = 167$ meV \AA^2 for $x=0.2$ and $D_{T=0} = 176$ meV \AA^2 for $x=0.3$), which directly shows that the electron transfer energy for the d band is large. D exhibits a power law behavior as a function of temperature, and appears to collapse as $T \rightarrow T_C$. Nevertheless, an anomalously strong quasielastic central component develops and dominates the fluctuation spectrum as $T \rightarrow T_C$. Bragg scattering indicates that the magnetization near T_C exhibits power law behavior, with $\beta \approx 0.30$ for both systems, as expected for a three-dimensional ferromagnet. © 1998 American Institute of Physics. [S0021-8979(98)27311-7]

Since the recent discovery of unusually large magnetoresistive effects in perovskite manganites, the doped LaMnO_3 class of materials¹ has generated continued interest and has motivated experimental and theoretical work devoted to understanding of the origin of this colossal magnetoresistance (CMR) phenomenon. The large variation in the carrier mobility originates from an insulator-metal transition that is closely associated with the magnetic ordering. The on-site exchange interaction between the spins on the manganese ions is believed to be strong enough to completely polarize the (e_g) conduction electrons in the ground state, forming a "half-metallic" ferromagnet. However, hopping, and hence conduction, may only occur if the Mn core spins (formed by the d electrons in a t_{2g} orbital) on adjacent sites are parallel, which then directly couples ferromagnetic order with the electrical conductivity at elevated temperatures. This mechanism, known as the double exchange mechanism,² was first proposed in the 1950s, and has provided a good description of the evolution of the magnetic properties with band filling. However, in order to fully explain all the properties of the CMR materials, strong electron correlations,³ and/or a strong electron-lattice coupling⁴ in different polaronic approaches are invoked. This unique class of half-metallic ferromagnets provides an excellent opportunity to elucidate the influence of such correlations on the lattice and spin dynamics, which can best be probed by inelastic neutron scattering.

In the optimally doped regime with $x \sim 0.3$ it has been shown that the ground state spin dynamics is essentially that expected for a conventional metallic ferromagnet described by an isotropic Heisenberg model.⁵⁻⁷ For the Ca-doped system, however, results obtained on polycrystalline samples⁸ have indicated a possible coexistence of spin-wave excitations and spin diffusion in the ferromagnetic phase. In par-

ticular, it was suggested that it is this spin diffusion that drives the ferromagnetic phase transition rather than the thermal population of conventional spin waves. In the present publication we report diffraction and inelastic measurements of the spin dynamics in the metallic ferromagnets $\text{La}_{0.8}\text{Sr}_{0.2}\text{MnO}_3$ and $\text{La}_{0.7}\text{Sr}_{0.3}\text{MnO}_3$.

The single crystals used in the present neutron scattering experiments were grown at the Steel and Alloys Institute in Moscow, using the floating zone method. The crystals weighed 2.25 and 4.25 g, respectively. The samples were oriented such that the $[100]$ and $[010]$ axes of the rhombohedral $R\bar{3}c$ cell lie in the scattering plane. The neutron scattering measurements have been carried out on the NG-5 (SPINS) cold neutron triple-axis spectrometer at the NIST research reactor. The (002) reflection of pyrolytic graphite (PG) was used as monochromator and analyzer for measuring the low-energy part of the spin-wave spectrum. We have used a flat analyzer with a fixed final energy $E_f = 3.7$ meV, a cold Be filter on the incident beam, and collimations $40' - S - 40' - 130'$ in sequence from the neutron guide to detector. This configuration offered an energy resolution of ~ 0.15 meV, together with good q resolution. Each sample was placed in a helium-filled aluminum cell in a displax refrigerator. The sample temperature ranged from 15 to 325 K for $\text{La}_{0.8}\text{Sr}_{0.2}\text{MnO}_3$, and from 30 to 375 K for $\text{La}_{0.7}\text{Sr}_{0.3}\text{MnO}_3$, and was controlled to within 0.1° .

The crystal structure of both systems at room temperature and below is rhombohedral ($R\bar{3}c$), with $a_0 \approx b_0 \approx c_0 \approx 3.892$ \AA for $x=0.2$ and $a_0 \approx b_0 \approx c_0 \approx 3.884$ \AA for $x=0.3$.

Figure 1 shows the integrated intensity of the (100) Bragg reflection as a function of temperature for both samples. This reflection has a finite nuclear structure factor, and therefore the intensity in the paramagnetic phase is non-zero. The increase in intensity below T_C is due to magnetic scattering produced by the ferromagnetism of spins aligning

^{a)}Electronic mail: lida@rddstrad.nist.gov

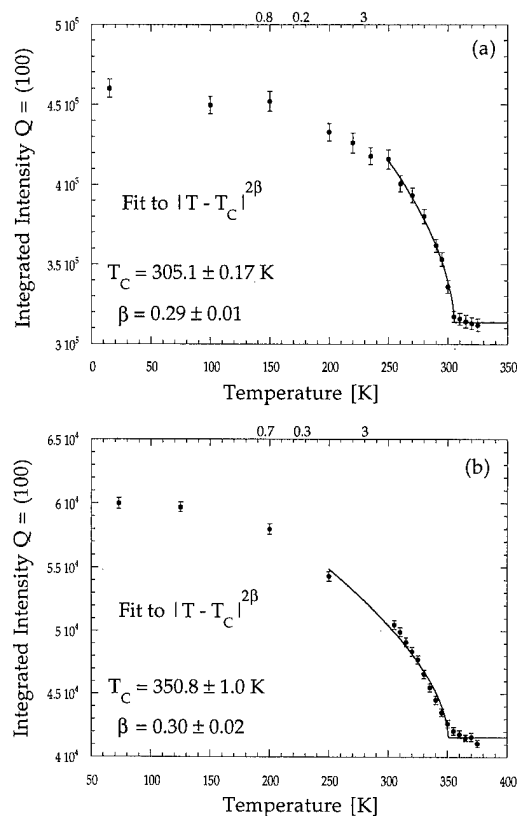


FIG. 1. Temperature dependence of the integrated intensity of the (100) Bragg peak for (a) $\text{La}_{0.8}\text{Sr}_{0.2}\text{MnO}_3$ and (b) $\text{La}_{0.7}\text{Sr}_{0.3}\text{MnO}_3$. There is a nuclear contribution to this peak, and the additional temperature-dependent intensity originates from the onset of the ferromagnetic order at $T_C = 305$ K for the $x=0.2$ system, and $T_C = 350.8$ K for $x=0.3$. The solid curves are fits of the points near T_C to a power law.

on the manganese ions and yielding a magnetic structure factor. The solid curve is a fit of the points near T_C to a power law. The best fits give $T_C = 305.1$ K and a critical exponent $\beta = 0.29 \pm 0.01$ for $\text{La}_{0.8}\text{Sr}_{0.2}\text{MnO}_3$, and $T_C = 350.8$ K and $\beta = 0.30 \pm 0.02$ for $\text{La}_{0.7}\text{Sr}_{0.3}\text{MnO}_3$. Both values of the critical exponent are slightly below, but rather close to, the well known three-dimensional Heisenberg ferromagnet model value of $\sim 1/3$.

We have investigated the spin dynamics in the (1,0,0) high-symmetry direction in both samples. The ground state spin dynamics for a half-metallic ferromagnet was not expected to differ much from the conventional picture of well defined spin waves, and we found that the long-wavelength magnetic excitations were in fact the usual spin waves, with a dispersion relation given by $E = E_0 + Dq^2$, where E_0 represents the spin-wave energy gap and the spin stiffness coefficient is directly related to the exchange interactions. The spin-wave gap E_0 was too small to be measured directly in energy scans at the zone center, but very high-resolution measurements on the NG-5 (SPINS) cold-neutron triple-axis spectrometer have allowed us to determine that $E_0 < 0.02$ meV for both systems, which demonstrates that these are "soft" isotropic ferromagnets. A previously reported value of $E_0 = 0.75$ meV for the $x=0.3$ system⁶ was obtained from an extrapolation of higher q data, not from direct high-resolution measurements as in the present case. The low-

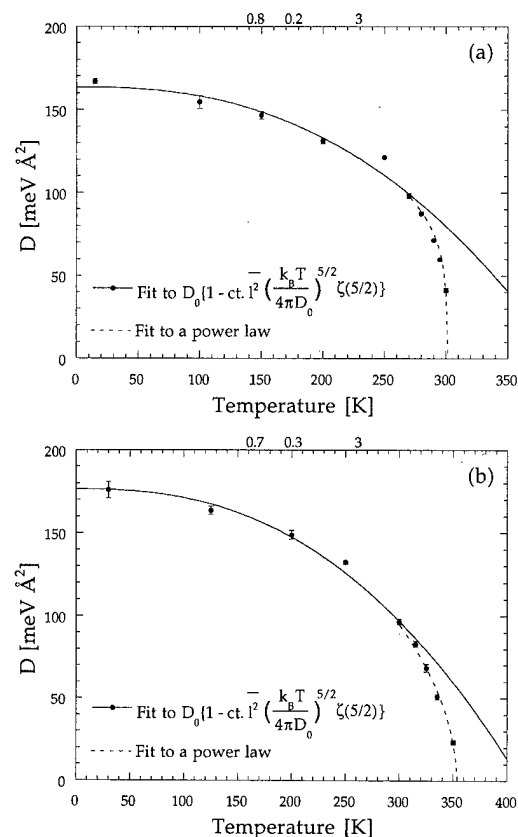


FIG. 2. Spin-wave stiffness coefficient D in $E = E_0 + Dq^2$ as a function of temperature for (a) $\text{La}_{0.8}\text{Sr}_{0.2}\text{MnO}_3$ and (b) $\text{La}_{0.7}\text{Sr}_{0.3}\text{MnO}_3$. The solid curves are fits to Eq. (1). D appears to vanish at the ferromagnetic transition temperature, as expected for a conventional ferromagnet. The dashed curves are fits to a power law.

temperature values of the spin-wave stiffness constant D are large: $D_{T=0} = (166.8 \pm 1.51)$ meV \AA^2 for $x=0.2$ and $D_{T=0} = (176 \pm 5.00)$ meV \AA^2 for $x=0.3$, and give a ratio $D/k_B T_C \sim 6.34$ \AA^2 and 5.82 \AA^2 for the $x=0.2$ and 0.3 systems, respectively. Both values are quite large, as might be expected for an itinerant electron system.

Figure 2 plots the temperature dependence of the spin-wave stiffness D . The data have been analyzed in terms of two-spin-wave interactions in a Heisenberg ferromagnet within the Dyson formalism,¹⁰ which predicts that the dynamical interaction between the spin waves gives, to leading order, a temperature dependence:

$$D(T) = D_0 \left\{ 1 - \frac{v_0 \bar{l}^2 \pi}{S} \left(\frac{k_B T}{4\pi D_0} \right)^{5/2} \zeta\left(\frac{5}{2}\right) \right\}, \quad (1)$$

where v_0 is the volume of the unit cell, S is the average value of the manganese spin, and $\zeta(5/2)$ is the Riemann zeta integral. \bar{l}^2 is the moment defined by $\bar{l}^2 = S/3D \{ \sum J(\mathbf{r}) \}$ and which, compared to the square of the lattice parameter a^2 , gives information about the range of the exchange interaction. The solid curves in Fig. 2 are fits to Eq. (1), and are in good agreement with the experimental data for reduced temperatures $t = (T - T_C)/T_C$ up to $t_1 \approx -0.1$ for $\text{La}_{0.8}\text{Sr}_{0.2}\text{MnO}_3$ and -0.14 for $\text{La}_{0.7}\text{Sr}_{0.3}\text{MnO}_3$. The fitted values of \bar{l}^2 give $\sqrt{\bar{l}^2} = (3.92 \pm 1.04)a_0$ for $x=0.2$, and $\sqrt{\bar{l}^2} = (3.84 \pm 1.22)a_0$ for $x=0.3$, which indicates that the exchange interaction extends beyond nearest neighbors in both

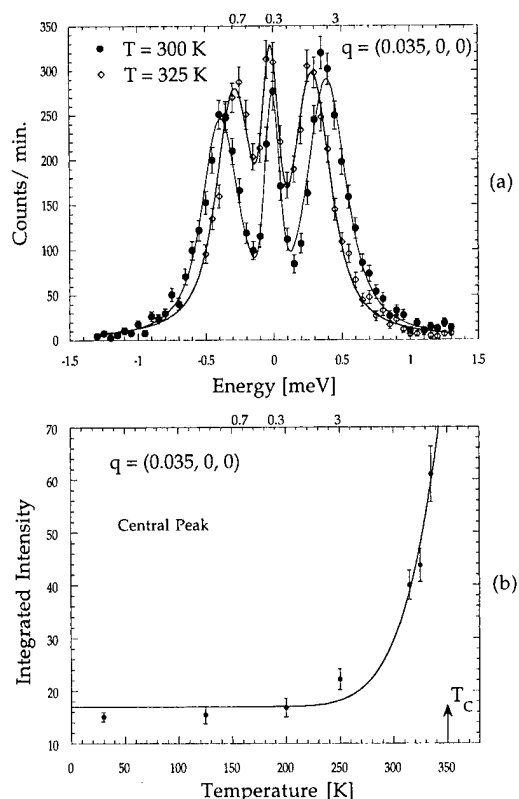


FIG. 3. (a) Constant- q magnetic inelastic spectra collected at 300 and 325 K and a reduced wave vector $q = (0, 0, 0.035)$ for $\text{La}_{0.7}\text{Sr}_{0.3}\text{MnO}_3$ ($T_C = 350.8$ K), and (b) temperature dependence of the integrated intensity of the quasielastic central component. The dominant effect is the development of a strong quasielastic component in the spectrum. Above T_C , all the scattering in this range of q is quasielastic.

systems. For $t > t_1$, the experimentally measured values of D depart from the $T^{5/2}$ dependence, having rather a power law behavior and appearing to collapse as $T \rightarrow T_C$. The dashed lines in Fig. 2 are fits to a power law $[1 - (T/T_C)]^{\nu' - \beta}$, where ν' is the critical exponent for a three-dimensional ferromagnet.

In the course of our measurements we have noticed that the central peak has a strong temperature dependence on approaching T_C , while typically the central peak originates from weak temperature-independent nuclear incoherent scattering. Figure 3(a) shows two magnetic inelastic spectra collected at 300 and 325 K, and reduced wave vector $q = 0.035$ away from the (100) reciprocal point in $\text{La}_{0.7}\text{Sr}_{0.3}\text{MnO}_3$ ($T_C = 351$ K). A flat background of 4.9 counts plus an elastic incoherent nuclear peak of 110 counts, measured at 30 K, have been subtracted from these data. We can clearly see the development of the quasielastic component, comparable in intensity to the spin waves, and the temperature dependence of the strength of this scattering is

shown in Fig. 3(b) as a function of temperature. We observe a significant intensity starting at 250 K (~ 100 K below T_C), and the scattering peaks at T_C . At and above T_C all the scattering is quasielastic. For typical isotropic ferromagnets, such as Ni, Co, Fe, any quasielastic scattering below T_C is too weak and broad to be observed directly in the data, and can only be distinguished by the use of polarized neutron techniques. In Fig. 3(a) we can nevertheless see that the spectrum starts to be dominated by this quasielastic component at temperatures well below T_C . The appearance in the ferromagnetic phase of a quasielastic component was first observed on Ca-doped polycrystalline samples,⁸ and it has been suggested that it is associated with the localization of the e_g electrons on the $\text{Mn}^{3+}/\text{Mn}^{4+}$ lattice, and may be related to the formation of spin polarons in the system.⁹ We have observed a similar anomalous behavior of the central peak in the more lightly doped system $\text{La}_{0.85}\text{Sr}_{0.15}\text{MnO}_3$,¹¹ but for that doping we find that the central component becomes evident only much closer (~ 25 K) to the Curie temperature. It thus appears that the coexistence of spin-wave excitations and spin diffusion is a common characteristic for many perovskite manganites, and that it may be relevant for the giant magnetoresistance property of these systems. It is therefore important to pursue the study of this aspect with polarized neutron techniques, in order to determine the nature of the fluctuations involved in this new quasielastic component to the fluctuation spectrum.

Research at the University of Maryland is supported by the NSF under Grant No. DMR-97-01339 and by the NSF-MRSEC, DMR-96-32521. Experiments on the NG-5 spectrometer at the NIST Research Reactor are supported by the NSF under Agreement No. DMR-94-23101. Work at Moscow Steel Institute is supported by the ISTC Grant No. 636.

¹G. H. Jonker and J. H. van Santen, *Physica (Utrecht)* **16**, 337 (1950); E. O. Wollan and W. C. Koehler, *Phys. Rev.* **100**, 545 (1955); G. H. Jonker, *Physica (Utrecht)* **22**, 707 (1956).

²C. Zener, *Phys. Rev.* **82**, 403 (1951); P. W. Anderson and H. Hasegawa, *ibid.* **100**, 675 (1955); P. G. de Gennes, *ibid.* **100**, 564 (1955).

³Y. Tokura, A. Urushibara, Y. Moritomo, T. Arima, A. Asamitsu, G. Kido, and N. Furukawa, *J. Phys. Soc. Jpn.* **63**, 3931 (1994).

⁴A. J. Millis, P. B. Littlewood, and B. I. Shraiman, *Phys. Rev. Lett.* **74**, 5144 (1995); A. J. Millis, *Phys. Rev. B* **55**, 6405 (1997).

⁵T. G. Perring, G. Aeppli, S. M. Hayden, S. A. Carter, J. P. Remeika, and S.-W. Cheong, *Phys. Rev. Lett.* **77**, 711 (1996).

⁶M. C. Martin, G. Shirane, Y. Endoh, K. Hirota, Y. Moritomo, and Y. Tokura, *Phys. Rev. B* **53**, 14285 (1996).

⁷A. H. Moudden, L. Pinsard, L. Vasiliu-Doloc, and A. Revcolevschi, *Czech. J. Phys.* **46**, 2163 (1996).

⁸J. W. Lynn, R. W. Erwin, J. A. Borchers, Q. Huang, and A. Santoro, *Phys. Rev. Lett.* **76**, 4046 (1996).

⁹J. W. Lynn, R. W. Erwin, J. A. Borchers, A. Santoro, Q. Huang, J.-L. Peng, and R. L. Greene, *J. Appl. Phys.* **81**, 5488 (1997).

¹⁰D. C. Mattis, *The Theory of Magnetism* (Springer, Heidelberg, 1981).

¹¹L. Vasiliu-Doloc, J. W. Lynn, A. H. Moudden, A. M. de Leon-Guevara, and A. Revcolevschi, *J. Appl. Phys.* **81**, 5491 (1997).

Tilted antiferromagnetic ordering of Mn in $\text{Nd}_{0.62}\text{Ca}_{0.38}\text{MnO}_3$

S. Y. Wu, W.-H. Li,^{a)} and K. C. Lee

Department of Physics, National Central University, Chung-Li, Taiwan 32054, Republic of China

J. W. Lynn

NIST Center for Neutron Research, NIST, Gaithersburg, Maryland 20899

R. S. Liu and J. B. Wu

Department of Chemistry, National Taiwan University, Taipei, Taiwan 106, Republic of China

C. Y. Huang

Center for Condensed Matter Sciences and Department of Physics, National Taiwan University, Taipei, Taiwan 106, Republic of China

The magnetic ordering of the Mn spins in polycrystalline $\text{Nd}_{0.62}\text{Ca}_{0.38}\text{MnO}_3$ has been investigated by means of neutron diffraction and ac magnetic susceptibility measurements. Three peaks around 230, 90, and 40 K were observed in the temperature dependence of the in-phase component of the ac susceptibility, $\chi'(T)$. Neutron diffraction measurements show that the peak at 90 K is associated with the ordering of the Mn spins, and that at 40 K is due to the reorientation of the Mn spins. Both ferromagnetic and antiferromagnetic coupling between the Mn spins were observed. The spins order at $T_N \approx 130$ K, with a spin structure consisting of ferromagnetically coupled, tilted antiferromagnetic sheets. No evidence was found from the neutron diffraction data to indicate that the peak around 230 K in $\chi'(T)$ is of magnetic origin, which suggests that it is associated with charge ordering. © 1998 American Institute of Physics. [S0021-8979(98)27411-1]

The discovery of colossal magnetoresistance (CMR) in distorted rare-earth containing manganites has sparked renewed interest in this class of materials.^{1,2} CMR as large as ten thousand fold has been observed in many systems. This phenomenon is now known to arise from the occurrence of a ferromagnetic transition accompanied by a insulator-metal transition, in which the double exchange (DE) interaction involving charge and spin exchanges is the main mechanism believed to be operating.^{3,4} The ferromagnetic metallic state is achieved by partially substituting trivalent rare-earth ions with divalent alkaline-earth ions. So far, the La-based compounds have been intensely investigated, whereas fewer studies have concentrated on the Nd-based systems. In this article, we present studies made on a Ca-doped Nd-based compound using neutron diffraction and ac magnetic susceptibility measurements. Charge ordering, tilted antiferromagnetic ordering of the Mn spins, and spin reorientation were observed.

Polycrystalline sample was prepared by the standard solid-state reaction techniques. Detailed sample fabrication procedures can be found elsewhere.⁵ The sample fabricated was characterized by a complete structural analysis using neutron powder diffraction and Rietveld analysis.⁶ High-resolution neutron diffraction patterns taken at eight temperatures were collected on BT-1, the 32-detector powder diffractometer at the U.S. NIST Research Reactor. A conventional setup of Cu(311) monochromator, pyrolytic graphite (PG) filter, and collimations of 15'-20'-7' full width at half maximum (FWHM) acceptance was employed. The high-resolution diffraction patterns were analyzed using the

General Structure Analysis System (GSAS) program.⁷ The refinements were carried out assuming the symmetry of space group $Pbnm$. There are essentially no unexpected peaks present, showing that the sample is practically single phase. We estimated the impurity level to be less than 1%. Careful analysis of the occupancy factors shows that 38% of the Nd sites are occupied by Ca atoms, while the O sites are almost fully occupied. Hence a chemical formula of $\text{Nd}_{0.62}\text{Ca}_{0.38}\text{MnO}_3$ is obtained. The compound crystallizes into an orthorhombic phase, with a crystal structure that may be viewed as a stacking of $\text{MnO}_2-(\text{Nd}/\text{Ca})\text{O}$ layers ($a-b$ planes) along the c axis direction. Lattice constants that we obtained at $T = 180$ K are $a = 5.4041(2)$, $b = 5.4526(2)$, and $c = 7.6274(4)$ Å.

The ac susceptibility measurements were performed on a conventional susceptometer, with which both the in-phase component χ' and the out-of-phase component χ'' can be measured. The temperature dependence of the ac susceptibility data were collected using a driving field of frequency 100 Hz and rms strength 1 Oe. Shown in Fig. 1 is the variation of χ' with temperature. Three peaks are seen over the temperature range studied. Using an expanded y scale, shown as an inset of Fig. 1, a small but definitive peak is clearly revealed around 230 K. This peak is *not* of magnetic origin (see below), and we believe it originates from charge ordering.⁸ The main feature seen in Fig. 1 is of course the huge but broad peak around 90 K. This peak is associated with the ordering of the Mn spins (see below), and it has an antiferromagnetic character as a cusp is present. At 40 K another peak is clearly seen in $\chi'(T)$, which is due to the change of the moment direction of the Mn spins (see below). This behavior is much

^{a)}Electronic mail: whli@joule.phy.ncu.edu.tw

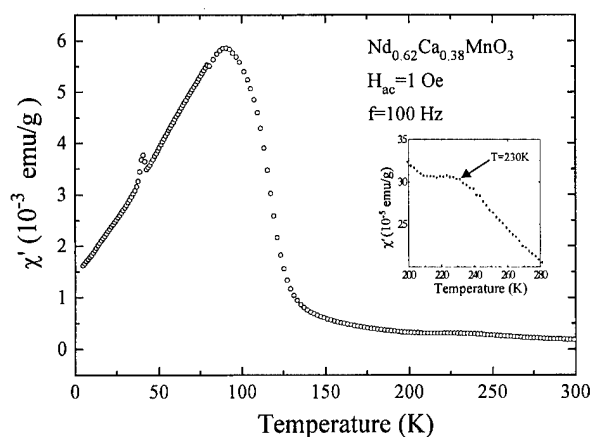


FIG. 1. Temperature dependence of χ' measured using a driving field of frequency 100 Hz and rms strength 1 Oe. Three definite peaks at 230, 90, and 40 K are clearly seen.

reduced as a dc field is applied. No ac losses were detected, as essentially zero values were obtained for χ'' at all temperatures studied.

Neutron magnetic diffraction was performed also at the NIST Research Reactor. Data were collected on the BT-9 triple-axis spectrometer operated in double-axis mode, using a conventional setup with PG monochromator and filter. Neutrons of wavelength $\lambda = 2.351$ Å and angular collimations of 40'-48'-48' FWHM acceptance were used. A pumped ^4He cryostat was used to cool the sample. Diffraction patterns covering a range in scattering angle 2θ from 10° to 65° were taken at several temperatures ranging from 1.8 to 325 K. No structural changes were observed over the temperature range studied. Detectable nuclear peaks appear at 2θ greater than 30° , while the main magnetic peaks occur below 20° . Figure 2 shows the low scattering-angle portions of the diffraction patterns collected at four temperatures. At 160 K, which is above the temperature at which the most pronounced peak in $\chi'(T)$ appears, only background intensities are present in this 2θ range. At lower temperatures, several new peaks develop, while the background intensities become lower as the magnetic scattering evolve into Bragg peaks.

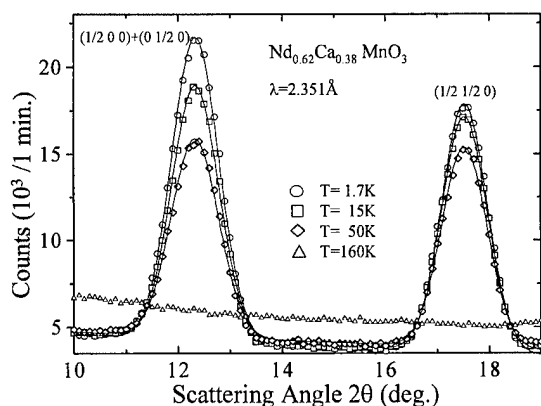


FIG. 2. Portions of the diffraction patterns taken at four temperatures. Only background intensities are present at 160 K. At lower temperatures, two magnetic peaks develop while the background intensities become lower. The intensities of these two peaks vary differently with temperature. The indices shown are based on the nuclear unit cell.

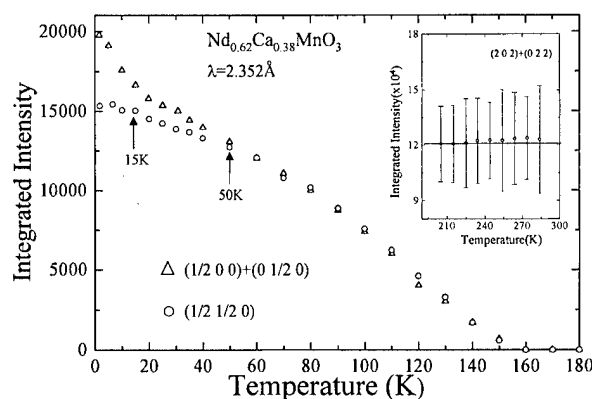


FIG. 3. Temperature dependence of the integrated intensities of the $\{\frac{1}{2}00\} + \{0\frac{1}{2}0\}$ and $\{\frac{1}{2}\frac{1}{2}0\}$ reflections, showing a $T_N \approx 130$ K for the Mn spins. The two curves shown separate at 50 K. The inset shows the integrated intensity of the $\{202\} + \{022\}$ peak measured at high temperatures. No intensity variation is seen.

Based on the nuclear unit cell, the two peaks shown in Fig. 2 may be indexed as the $\{\frac{1}{2}00\} + \{0\frac{1}{2}0\}$ and $\{\frac{1}{2}\frac{1}{2}0\}$ Bragg reflections, that originate from the ordering of the Mn spins. Clearly, the intensities of the $\{\frac{1}{2}00\} + \{0\frac{1}{2}0\}$ and $\{\frac{1}{2}\frac{1}{2}0\}$ reflections vary differently with temperature, especially at temperatures below 15 K. The ratio between the $\{\frac{1}{2}00\} + \{0\frac{1}{2}0\}$ and $\{\frac{1}{2}\frac{1}{2}0\}$ integrated intensities changes from being equal to 1.09 at 50 K, to 1.28 at 15 K, then to 1.40 at 1.7 K. These data indicate that the moment directions of the Mn spins vary with temperature. Besides the two peaks shown in Fig. 2, additional magnetic peaks that may be indexed as the $\{\frac{1}{2}10\} + \{1\frac{1}{2}0\}$, $\{\frac{1}{2}01\} + \{0\frac{3}{2}1\} + \{0\frac{1}{2}0\}$, and $\{\frac{1}{2}\frac{1}{2}1\}$ reflections were also observed (not shown).

The temperature dependence of the $\{\frac{1}{2}00\} + \{0\frac{1}{2}0\}$ and $\{\frac{1}{2}\frac{1}{2}0\}$ integrated intensities are shown in Fig. 3. Both peaks begin to develop around 150 K. The ordering temperature of the Mn spins, as determined by the inflection point, is $T_N \approx 130$ K. Above 50 K, these two peaks follow essentially the same temperature-dependent curve, showing that the spin direction does not change over this temperature regime. Below 50 K, the intensity of the $\{\frac{1}{2}00\} + \{0\frac{1}{2}0\}$ peaks increase faster than that of the $\{\frac{1}{2}\frac{1}{2}0\}$ peak, implying that the spin directions are changing with temperature. We note that a corresponding peak, which may be completely smeared by an applied dc field of 1 kOe, appears in the $\chi'(T)$ data. The intensity of the $\{\frac{1}{2}\frac{1}{2}0\}$ peak saturates at 15 K. This is the temperature at which the Mn moment is essentially saturated. However, the intensity of the $\{\frac{1}{2}00\} + \{0\frac{1}{2}0\}$ peak continues to increase as the temperature decreases further. This intensity is still not saturated even at 1.7 K, the lowest temperature studied. If this further increase of the $\{\frac{1}{2}00\} + \{0\frac{1}{2}0\}$ intensity is due to the reorientation of the Mn spins, it must be accompanied by decreases of the intensities of other magnetic peaks. However, no such evidence was found. Instead, the intensity of the $\{\frac{1}{2}01\} + \{0\frac{3}{2}1\} + \{0\frac{1}{2}0\}$ peak was found to increase with reducing temperature as well. Another possible origin is the ordering of the Nd spins, and the observed data indeed may be explained quite well if one assumes the Nd spins are ordered with a simple antiferromagnetic arrangement. However, Nd spins usually order at quite low temperatures, lead-

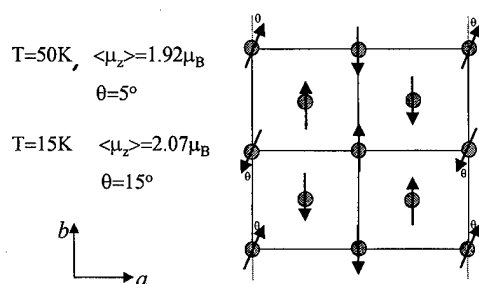


FIG. 4. Schematic of the spin configuration in the a - b plane. The moment directions are arbitrarily chosen to be along the b axis for clarity.

ing us to propose that the moments on the Nd are induced by the ordered Mn moments. More data taken at lower temperatures are needed to make this argument conclusive.

At high temperatures, on the other hand, the intensity ratios did not vary significantly. Shown as an inset in Fig. 3 is the $\{202\} + \{022\}$ integrated intensity measured at high temperatures. No evidence was found to support the argument⁵ that the peak observed in $\chi'(T)$ around 230 K is due to a ferromagnetic transition induced by the Ca substitution.

Based on the data presented above, we propose the following magnetic structure and its variation with temperature for the Mn spins in $\text{Nd}_{0.62}\text{Ca}_{0.38}\text{MnO}_3$: The coupling of the Mn spins in the a - b plane is basically antiferromagnetic, while the interlayer coupling is ferromagnetic. Figure 4 shows the arrangement of the Mn spins in the a - b plane. It consists of antiferromagnetic chains along the b axis, with

the moment directions of every fourth chain tilted by a small angle with respect to that of other chains. The tilting is necessary to explain the appearance of the $\{\frac{1}{2}ll\}$ -type (l =integer) reflections that accompany the $\{\frac{1}{2}\frac{1}{2}l\}$ -type reflections, which we believe is caused by the Ca substitution. Our powder neutron data *cannot* resolve the a axis from the b axis due to their similarity. The specific moment directions in the a - b plane hence *cannot* be determined from our data. For clarity, in Fig. 4 we choose the moments to be basically along the b axis. Above 50 K the tilt angle is about 5° . Below 50 K this tilt angle increases with decreasing temperature, and reaches 15° as the Mn moments saturated at $T \approx 15$ K, with $\langle \mu_z \rangle = 2.07(3)\mu_B$.

The research at the NCU was supported by the National Science Council of the Republic of China under Grant No. NSC-87-2112-M-008-017.

¹ K. Chabara, T. Ohno, M. Kasai, and Y. Kozono, Appl. Phys. Lett. **63**, 1990 (1993).

² R. von Helmolt, J. Wecker, B. Holzapfel, L. Schultz, and K. Samwer, Phys. Rev. Lett. **71**, 2331 (1993).

³ P. Schiffer, A. P. Ramirez, W. Bao, and S.-W. Cheong, Phys. Rev. Lett. **75**, 3336 (1995).

⁴ J. M. Coey, M. Viret, L. Ramno, and K. Ounadjela, Phys. Rev. Lett. **75**, 3910 (1995).

⁵ R. S. Liu, J. B. Wu, C. Y. Chang, J. G. Lin, C. Y. Huang, J. M. Chen, and R. G. Liu, Solid State Chem. **125**, 112 (1996).

⁶ H. M. Rietveld, J. Appl. Crystallogr. **2**, 65 (1969).

⁷ A. C. Larson and R. B. Von Dreele, General Structure Analysis System, Report LA-UR-86-748, Los Alamos National Laboratory, Los Alamos, NM 87545, 1990.

⁸ A. I. Millis, P. B. Littlewood, and B. I. Shraiman, Phys. Rev. Lett. **74**, 5144 (1995).

Magnetic correlations in the bilayer manganite $\text{La}_{1.2}\text{Sr}_{1.8}\text{Mn}_2\text{O}_7$

S. Rosenkranz,^{a)} R. Osborn, and J. F. Mitchell

Materials Science Division, Argonne National Laboratory, Argonne, Illinois 60439

L. Vasiliiu-Doloc^{b)} and J. W. Lynn^{b)}

NIST Center for Neutron Research, National Institute for Standards and Technology, Gaithersburg, Maryland 20899

S. K. Sinha

Advanced Photon Source, Argonne National Laboratory, Argonne, Illinois 60439

D. N. Argyriou

Los Alamos Neutron Science Center, Los Alamos National Laboratory, Los Alamos, New Mexico 87545

Neutron scattering has been used to study the magnetic correlations in the double-layer manganite $\text{La}_{1.2}\text{Sr}_{1.8}\text{Mn}_2\text{O}_7$, which exhibits colossal magnetoresistance in the vicinity of the ferromagnetic transition at $T_c = 112$ K. Over a large temperature range above T_c , there is evidence for two-dimensional magnetic correlations which peak in intensity at the transition. Although the in-plane correlations are predominantly ferromagnetic, a strong canting of spins in neighboring planes within the bilayers, at an angle that is dependent on both the temperature and magnetic field, is observed. There are indications of a crossover to three-dimensional critical scattering very close to T_c , but the nature of the phase transition has yet to be determined. © 1998 American Institute of Physics. [S0021-8979(98)45411-2]

I. INTRODUCTION

Colossal magnetoresistance can be strongly enhanced in systems with reduced dimensionality and so there has been considerable interest in the two-layer Ruddlesdon-Popper compounds, $\text{La}_{2-2x}\text{Sr}_{1+2x}\text{Mn}_2\text{O}_7$, where x is the hole doping in the MnO_2 planes.¹⁻³ In zero field, these systems undergo a ferromagnetic phase transition at around 100 K with a concomitant metal-insulator transition. Although this transition temperature is much lower than in the three-dimensional Perovskite manganites, the reduced dimensionality leads to a significant extension of the temperature range over which magnetic correlations are important, and thereby allows a detailed examination of the link between local spin correlations and the resulting transport properties.

The origin of colossal magnetoresistance (CMR) was first explained by double-exchange interactions,⁴⁻⁶ but recently it has been proposed that electron-phonon interactions play an important role in enhancing the CMR.⁷ However, in the two-layer compounds, it was found that the influence of antiferromagnetic interactions competing with the ferromagnetic double exchange is of equal importance.^{3,8} This aspect was first considered nearly 40 years ago by de Gennes,⁶ but is only now being investigated further theoretically.⁹ As part of a general study to investigate the link between the magnetic and transport properties of naturally layered manganites, we have been measuring the magnetic correlations using neutron diffraction and spectroscopy.

II. EXPERIMENTAL RESULTS

A single crystal of the double-layer compound $\text{La}_{1.2}\text{Sr}_{1.8}\text{Mn}_2\text{O}_7$ with dimensions $2 \times 4 \times 6$ mm³ was grown using the floating-zone technique. Bulk measurements showed a ferromagnetic transition at $T_c \approx 112$ K in correspondence with the metal-insulator transition observed in resistivity measurements, both parallel and perpendicular to the MnO_2 planes. The lattice parameters are $a = 3.862$ Å and $c = 20.032$ Å at 125 K in agreement with earlier measurements for this composition.² More details on the preparation and characterization of this sample are given by Mitchell *et al.*² Neutron scattering experiments were performed on the triple-axis spectrometers BT2 and BT9 at the National Institute for Standards and Technology (NIST), Gaithersburg. Scans were taken in the $(0k0)$ scattering plane with incident neutron energies of 13.7 and 14.7 meV, without analyzing the energy of the scattered neutrons. A superconducting solenoid which provided vertical magnetic fields up to 7 T was employed in the measurements on BT9.

Diffuse scattering studies^{10,11} show clear evidence of spin correlations above T_c which have much longer correlation lengths within the MnO_2 planes than perpendicular to them. The two-dimensional character of these correlations is manifest in scattering in the form of rods perpendicular to the bilayer planes, i.e., parallel to $[00l]$ for all integer h in the scattering geometry used. Figure 1 shows the temperature dependence of this rod-scattering measured on BT2 at $\mathbf{Q} = [1, 0, 1.833]$. At this particular value of momentum transfer (for the given incident energy), the wavevector \mathbf{k}_f of the scattered neutrons is parallel to the c axis, leading to an optimal energy integration. The diffuse scattering is strongly

^{a)}Electronic mail: srosenkranz@anl.gov

^{b)}Also at: The University of Maryland, College Park, MD 20742.

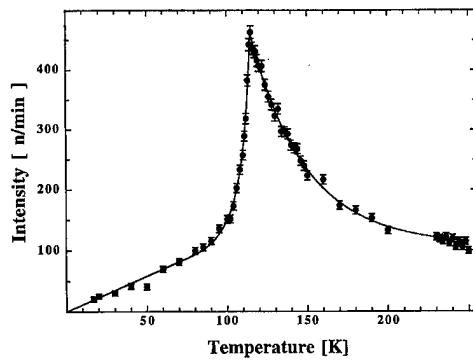


FIG. 1. Temperature dependence of the diffuse scattering measured at $Q = [1,0,1.833]$. A constant background, determined from a scan along $[h,0,1.833]$ at 4 K has been subtracted from the data. The solid line is a guide to the eye.

temperature dependent, becoming stronger in amplitude as the transition temperature $T_c = 112$ K is approached and peaking sharply at T_c . Below T_c , the scattering arises from inelastic spin wave excitations and therefore rapidly decreases with decreasing temperature.

Because of the large separation between different bilayers, we can expect the exchange interaction along the c axis to be small and the dispersion of the spin waves along this direction to be much weaker than in the plane. Recent spin wave measurements carried out on the cold triple-axis spectrometer SPINS at NIST indicated that the spin-wave energy at the zone boundary along the c direction is only ~ 0.5 meV, nearly two orders of magnitude smaller than the in-plane zone boundary energy. For our experiments ($T > 10$ K), the intensity is proportional to the magnon population, which is given by $n_q \sim k_B T / \hbar \omega_q$ when $k_B T \gg \hbar \omega_q$,¹² where ω_q is the spin wave energy along the c axis with momentum q . The observed diffuse scattering (Fig. 1) follows this linear dependence up to $T \sim 80$ K where the scattering increases more rapidly. This is evidence of a softening of the spin wave energies as T_c is approached.

The temperature and magnetic field dependence of the rods was studied by measuring both parallel and perpendicular to the rods at $[00l]$ and $[10l]$. Because of the large separation between different bilayers, the modulation of the diffuse scattering along the rods is determined by the spin correlations of Mn spins in neighboring layers within each bilayer, i.e., at $\mathbf{r}_i = \pm z\mathbf{c}$. The energy-integrated magnetic neutron scattering cross section for wavevector transfer \mathbf{Q} is then proportional to¹⁰

$$S(\mathbf{Q}) \approx S^2(1 + \langle \cos \theta \rangle \cos 4\pi z l). \quad (1)$$

Here θ is the in-plane cant angle of the two Mn spins. Since $z = 0.0965$ in the 40% compound,² the rod scattering due to ferromagnetic correlations ($\theta = 0$) would peak at $l = 0$ and fall to zero at $l = 2.59$. In-plane spin correlations produce a broadening of the rods along the $[h00]$ direction with the half-width equal to the inverse correlation length.

Figure 2 shows scans along $[0.95, 0, l]$, displaced from the $[1, 0, l]$ rod in order to avoid the nuclear Bragg peaks. For comparison, we have included data from Ref. 10 (upper part of Fig. 2). Clearly, the observed modulation along the rod is

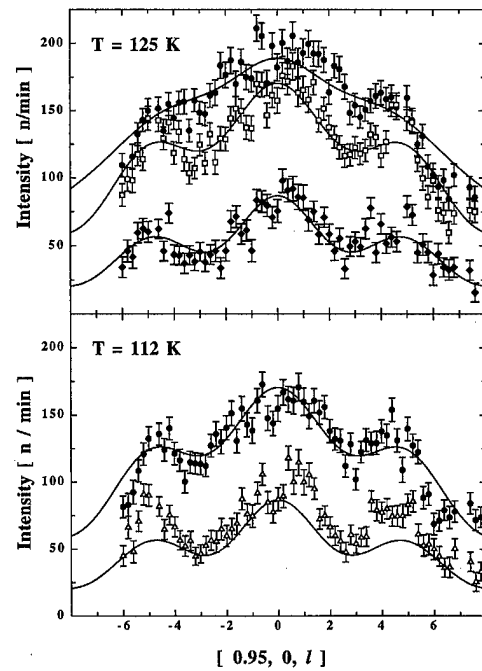


FIG. 2. Diffuse scattering along the $Q = [0.95, 0, l]$ direction in a vertical magnetic field of 0 (circles), 0.5 (triangles), 1 (squares), and 2 T (diamonds). The solid lines are fits of Eq. (1) to the $T = 125$ K data with $\theta = 86.6^\circ$, 74.1° , and 53° , respectively. The upper part of the figure is taken from Osborn et al. (Ref. 10).

not very strong, even close to T_c , showing that $\langle \cos \theta \rangle \ll 1$. Either the magnetic correlations between the neighboring planes are extremely weak, or the spins are strongly canted with respect to each other. The first possibility seems unlikely since the nearest neighbor distance between the planes is nearly identical to the distance within the planes. The ferromagnetic in-plane correlation length is already 9.7 \AA at 125 K,¹⁰ which would give $\langle \cos \theta \rangle \approx 0.67$ for nearest neighbors, whereas the weak modulation is consistent with a value of $\langle \cos \theta \rangle = 0.06$. Such a difference would require the interaction between planes to be nearly two orders of magnitude weaker than within the planes. On the other hand, canting is predicted to occur when there is a competition between double exchange and superexchange interactions, as discussed below.

A magnetic field applied vertically along the b axis should lead to a decrease of the cant angle and to a stronger modulation, in agreement with our observation. From least-squares fits of Eq. (1), we determined an average in-plane cant angle of 86.6° at $T = 125$ K. This cant angle is reduced to 74.1° at $H = 1$ T and 53° at $H = 2$ T. Since, at this field strength, the diffuse scattering has become more inelastic and a substantial part of the scattering has been transferred to three-dimensional (3D) Bragg scattering, the diffuse signal has decreased strongly.

Reducing the temperature towards T_c leads again to an increase in the modulation so that the zero field and 0.5 T data at 112 K are very similar to the 1 and 2 T data, respectively, at 125 K. This similarity is seen in the lower part of Fig. 2, where the data measured at 112 K are shown together with the best fits obtained for the 125 K data.

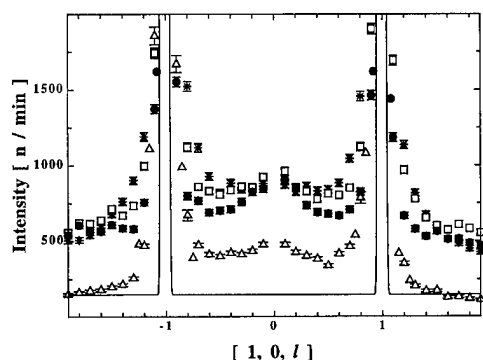


FIG. 3. Diffuse magnetic and nuclear scattering along the $Q=[10l]$ direction at $T=120$ (circles), 116 (squares), 112 (stars), and 4 K (triangles). The solid line gives an indication of the Bragg peaks widths at $[10\pm 1]$.

Below 120 K, we observe an increase in the magnetic scattering around the $[10\pm 1]$ Bragg peaks along the $[10l]$ rod, which disappears again below T_C (Fig. 3). Since the in-plane correlations have no influence on the modulation along the rod, this scattering is due to the build-up of correlations between different bilayers. In other words, 3D correlations are developing as the transition is approached. However, because of the strength of the nuclear Bragg peaks, it has not been possible to derive out-of-plane correlation lengths.

III. DISCUSSION

Although measurements of spin wave dispersions, e.g., in LaMnO_3 ,¹³ have provided evidence of competing ferromagnetic and antiferromagnetic exchange interactions of the usual Heisenberg form, the observation of canted spin correlations is clear evidence of a competition between double exchange and superexchange. Nearest-neighbor Heisenberg exchange will only produce collinear ferro- or antiferromagnetic ordering. However, because the energy of double exchange interactions for a pair of spins depends on $\cos(\theta/2)$,⁵ rather than $\cos \theta$ as in the case of Heisenberg exchange, a minimum energy at $\theta \neq 0$ or π can result from a competition between the two.⁶ The large cant angles observed in our experiments imply that the double exchange and superexchange interactions are of the same order of magnitude in this compound.

Evidently, lowering the temperature towards T_C is equivalent to applying an in-plane magnetic field since both have the effect of reducing the cant angle. This is due to the growth of correlations between different bilayers, seen in Fig. 3, which produce an in-plane molecular field stabilizing ferromagnetic order and eventually lead to the 3D ordering at T_C . However, the nature of the transition is still uncertain. Earlier measurements of the in-plane correlation length indicate that it does not diverge at T_C ¹⁰ and so far no evidence of

a crossover to 3D scaling was found. From the strong anisotropy in the spin wave dispersion below T_C we estimate that the correlations between different bilayers are at least two orders of magnitude weaker than the correlations within the plane. Therefore, if there is a crossover to true 3D scaling, it would only occur within a narrow temperature range of about 1 K above T_C and could be smeared by sample inhomogeneity.

A nondivergent correlation length on the other hand would indicate that the transition is first order, although the evidence of spin wave softening below T_C (Fig. 1) and the absence of any hysteresis in this compound¹⁴ show that, if the transition is first order, it is only weakly so. In the case of the three-dimensional CMR perovskites, it was found that the transition in $\text{La}_{2/3}\text{Ca}_{1/3}\text{MnO}_3$ is not a continuous second-order phase transition¹⁵ and it was argued that the nondivergence of the correlation length is related to the formation of magnetic polarons above T_C .¹⁶ However, it has not yet been established that this is a universal feature of CMR compounds, and from our present data, we cannot draw such a conclusion on the nature or the mechanism of the phase transition in the layered manganites.

This work was supported by the U.S. Department of Energy, Basic Energy Sciences, Division of Materials Science, under Contract Nos. W-31-109-ENG-38 and W-7405-ENG-36. Research at the University of Maryland was supported by the NSF-MRSEC, DMR 96-32521.

¹Y. Moritomo, A. Asamitsu, H. Kuwahara, and Y. Tokura, *Nature (London)* **380**, 141 (1996).

²J. F. Mitchell, D. N. Argyriou, J. D. Jorgensen, D. G. Hinks, C. D. Potter, and S. D. Bader, *Phys. Rev. B* **55**, 63 (1997).

³T. G. Perring, G. Aeppli, Y. Moritomo, and Y. Tokura, *Phys. Rev. Lett.* **78**, 3197 (1997).

⁴C. Zener, *Phys. Rev.* **82**, 403 (1951).

⁵P. W. Anderson and H. Hasegawa, *Phys. Rev.* **100**, 675 (1955).

⁶P.-G. de Gennes, *Phys. Rev.* **118**, 141 (1960).

⁷A. J. Millis, P. B. Littlewood, and B. I. Shraiman, *Phys. Rev. Lett.* **74**, 5144 (1995).

⁸D. N. Argyriou, J. F. Mitchell, J. B. Goodenough, O. Chmaissem, S. Short, and J. D. Jorgensen, *Phys. Rev. Lett.* **78**, 1568 (1997).

⁹D. Golosov, M. R. Norman, and K. Levin (unpublished).

¹⁰R. Osborn, S. Rosenkranz, D. N. Argyriou, L. Vasiliu-Doloc, J. W. Lynn, S. K. Sinha, J. F. Mitchell, K. E. Gray, and S. D. Bader (unpublished).

¹¹D. N. Argyriou, T. Kelley, J. F. Mitchell, R. A. Robinson, R. Osborn, S. Rosenkranz, R. I. Sheldon, and J. D. Jorgensen, *J. Appl. Phys.* **83** (1998), these proceedings.

¹²K. Hirakawa and H. Yoshizawa, *J. Phys. Soc. Jpn.* **47**, 368 (1979).

¹³F. Moussa, M. Hennion, J. Rodriguez-Carvajal, and H. Moudden, *Phys. Rev. B* **54**, 15 149 (1996).

¹⁴C. D. Potter, M. Swiatek, S. D. Bader, D. N. Argyriou, J. F. Mitchell, D. J. Miller, D. G. Hinks, and J. D. Jorgensen, *Phys. Rev. B* **57**, 72 (1998).

¹⁵J. W. Lynn, R. W. Erwin, J. A. Borchers, Q. Huang, A. Santoro, J.-L. Peng, and Z. Y. Li, *Phys. Rev. Lett.* **76**, 4046 (1996).

¹⁶J. M. De Teresa, M. R. Ibarra, P. A. Algarabel, C. Ritter, C. Marquina, J. Blasco, J. Garcia, A. del Moral, and Z. Arnold, *Nature (London)* **386**, 256 (1997).

The complex magnetic behavior and the role of dynamic structural fluctuations in $\text{La}_{1.2}\text{Sr}_{1.8}\text{Mn}_2\text{O}_7$ crystals

R. P. Sharma,^{a)} P. Fournier, R. L. Greene, and T. Venkatesan

Center for Superconductivity Research, Physics Department, University of Maryland, College Park, Maryland 20742

J. F. Mitchell and D. Miller

Materials Science Division, Argonne National Laboratory, Argonne, Illinois 60439

The presence of dynamic structural distortions at the magnetic phase transitions in layered perovskite $\text{La}_{1.2}\text{Sr}_{1.8}\text{Mn}_2\text{O}_7$ crystals is found by ion channeling. Their amplitude is ~ 1.5 picometer between 70 and 150 K, twice as that expected due to the thermal vibrations and static changes seen by neutron diffraction. Over the range 150 to 320 K a total change of ~ 2.3 picometer is observed with discontinuities, which correlate well with the anomalous features seen in magnetic studies. In this material a small ferromagnetic component persists in the region 120 to 320 K, and it is fully paramagnetic above 320 K. © 1998 American Institute of Physics. [S0021-8979(98)45511-7]

Recent observation of colossal magnetoresistance effect¹⁻³ in doped perovskite-type manganites, like $\text{La}_{1-x}\text{Sr}_x\text{MnO}_3$, has generated great interest in these materials. A prominent feature of these materials is the observation of several orders of magnitude change in electrical resistance in response to the applied magnetic field at the ferromagnetic transition temperature (T_c). Efforts are being made to make them technologically viable, by improving their field sensitivity and magnetoresistance (MR) temperature dependence behavior. New materials are being searched. Even the perovskite-type structure has been modified recently into a layered-type structure by inserting a rock-salt-type $[(\text{La}, \text{Sr})_2\text{O}_2]$ block layer,⁴ for every n MnO_2 sheets, i.e., the compound $(\text{La}, \text{Sr})_{n+1}\text{Mn}_n\text{O}_{3n+1}$. In this system the double sheet, $n=2$ compound $\text{La}_{1.2}\text{Sr}_{1.8}\text{Mn}_2\text{O}_7$, has been found to be a ferromagnetic metal below $T_c = 120$ K with large MR. It shows an unconventional magnetic response at temperatures well above T_c , and the transport properties are highly anisotropic.

There are different models which try to explain the transport properties of these manganites in terms of magnetic polarons, Zener double exchange, and Jahn-Teller distortions⁵ of the lattice. In the double exchange mechanism there is a simultaneous transfer of an electron from Mn^{3+} to O^{2-} and from O^{2-} to Mn^{4+} . In this mechanism, the travelling electrons tend to retain their spin orientation. If the orientation of the magnetic moments of the Mn^{3+} and Mn^{4+} ions is the same, there is an enhanced hopping probability. Hence any intrinsic alignment of the spins (e.g., onset of ferromagnetic order) or extrinsic alignment (e.g., application of an external magnetic field) could cause an increase in the conductivity. It has been also argued that the strength of the magnetic exchange interaction depends on the lattice distortions, (for example, in perovskite-type structure with orthorhombic distortions resulting from cooperative Jahn-Teller effect). A phase transition from a structurally distorted paramagnetic lattice with hopping-type conductivity to a ferromagnetic state will be accompanied by a dramatic reduction

in resistivity. However the magnitude of the observed effect cannot be totally accounted for by this picture.

The present investigations are performed on single crystals of the layered perovskite, double sheet, $\text{La}_{1.2}\text{Sr}_{1.8}\text{Mn}_2\text{O}_7$ crystals described above. Main stress is laid on the role of static and dynamic structural variations in this material. In order to remove any ambiguity, both the magnetization and ion channeling experiments have been made on the same specimen.

The ion channeling technique, which provides a direct real space probe of small atomic displacements from their regular lattice sites, even smaller than 1 picometer, is used to investigate the static and/or dynamic incoherent distortions in the above material. Ion channeling occurs when energetic ions, incident along a major crystallographic direction, are steered by the atomic rows and planes of a single crystal, through a series of correlated, gentle, small angle collisions.⁶ This phenomena causes one to two orders of magnitude reduction in a small impact parameter event such as Rutherford back scattering (RBS). The full width at half maximum (FWHM) of the channeling angular scan is directly related to any displacements (dynamic or static) of the atoms from their regular lattice sites. It is important to note that neutron and x-ray diffraction are relatively insensitive to local uncorrelated atomic displacements in the sample due to the fact that the diffraction data are analyzed within the constraints of a particular model based on the symmetry of the crystal space group. Random displacements from the ideal atom positions, whether static or thermal, contribute only to diffuse scattering, which is not included in the model.

The $\langle 100 \rangle$ crystals of $\text{La}_{1.2}\text{Sr}_{1.8}\text{Mn}_2\text{O}_7$ were melt grown in a flowing mixture of 20% O_2 and Ar as described elsewhere.⁷ These crystals were of dimensions $\sim 5 \text{ mm} \times 4 \text{ mm}$ and thickness about 1 mm. Both magnetization and channeling measurements were made on the same crystal and three sets of data were collected using three separate crystals. In these crystals the value of the resistivity ρ_{ab} at 300 K was found to be 120 m Ω cm which rose to about 3500 m Ω cm at $T \sim 133$ K, then dropped to ~ 60 m Ω cm at 108 K.

The dc magnetization measurements were carried out us-

^{a)}Electronic mail: rps@squid.umd.edu

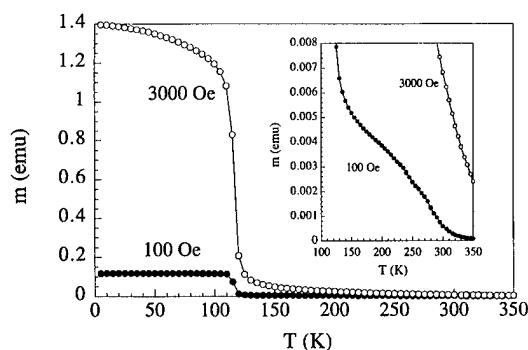


FIG. 1. The magnetization m plotted as a function of temperature in 100 and 3000 Oe. The inset shows the low field measurement in an expanded scale to bring out small changes in magnetization.

ing a quantum design superconducting quantum interference device (SQUID) magnetometer both in a low field (100 Oe) and a high field (3 kOe). A transition to the ferromagnetic state was seen around 120 K which is in agreement with earlier measurements.⁴ In addition, a gradual rise in the magnetic moment is seen in the low field measurements (Fig. 1 inset) as the sample temperature is decreased from 300 to 120 K. The 77 K magnetic isotherms (Fig. 2) were measured with the field directions along a , b , and c , respectively, as defined in Fig. 2 ($a > b > c$). Saturation was reached at ~ 300 Oe when the magnetic field was along a and at about 800 Oe when it was along b as expected when considering static demagnetizing fields. The saturation value for $4\pi M(77\text{ K})$ is 4.4 kOe and is in good agreement with Ref. 4. However, when the field is along c , the magnetization does not saturate until $H \sim 20$ kOe. This is an indication of a large magnetocrystalline anisotropy with the hard axis along the c direction. Thus, the ab plane is the easy plane, as also indicated by Moritomo *et al.*⁴

The 140 K isotherms (Fig. 3) can be analyzed to provide evidence of a small ferromagnetic contribution. The high field magnetization gives a nonzero intercept at $H=0$, and the out-of-plane anisotropy is nonzero. There are no in plane shape effects; the hysteresis loops almost coincide when the magnetic field is applied along the a and b directions. For H applied along c , demagnetization and possible magnetocrystalline effects are seen. The 140 K measurements suggest that the geometry of the ferromagnetic regions is layered (thickness/area is very small) and that they lie in the ab

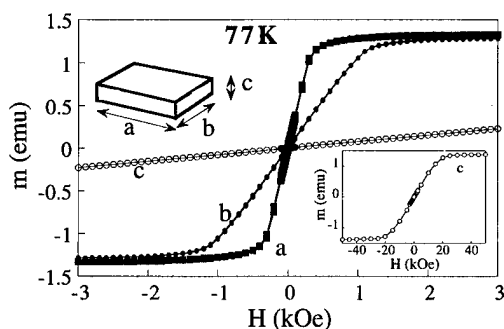


FIG. 2. The magnetization m vs H at 77 K with the magnetic field applied in the a , b , and c directions, respectively. The inset shows the data for a larger H scale in the c direction to indicate saturation of m .

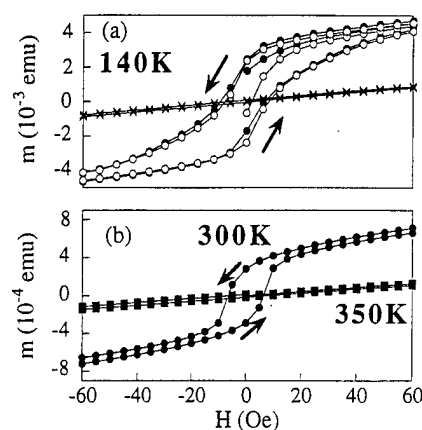


FIG. 3. The magnetization m vs H at (a) 140, (b) 300, and 350 K. In (a) magnetic field is applied along a (\circ), along b (\bullet), and c (\times) directions. In (b) the field is applied along b direction.

plane. Even at 300 K the “ferromagnetic” response persists (Fig. 3), though with decreased magnitude. All signs of ferromagnetic response disappear at 350 K and only the paramagnetic response remains (Fig. 3), consistent with the T dependence shown in Fig. 1.

Ion channeling measurements have been carried out using a very well collimated beam (0.5 mm diameter and $<0.01^\circ$ divergence) of 1.5 MeV He ions obtained from a 1.7 MeV tandem pelletron accelerator. The sample was mounted with a thermally conducting paste on a precision four-axis goniometer having an angular resolution of 0.01° . The target holder was thermally insulated from the goniometer and could be cooled down to 35 K by a closed cycle refrigeration system. The effective pressure of condensable gases was reduced to a negligible level at the target surface by cryogenic shielding. The sample temperature was varied by a small 25 W heater, and could be maintained within ± 2 K at any desired temperature between 40 and 400 K.

The 1.5 MeV He⁺ beam was incident on the sample and the backscattered particles were detected in an annular surface barrier detector of 300 mm² active area with a 4-mm-diam central hole and mounted along the beam axis at a distance of 7 cm from the target. This arrangement gave RBS signals with good statistics at a nominal dose of incident He ions, thus minimizing the radiation damage effects. The channeling angular scans were made about the [001] axis of the crystal with the RBS gate which included the signals from La, Sr, and Mn. A minimum RBS yield of about 2% in these scans demonstrated a very high quality single crystal.

The FWHM of the channeling angular scans measured at different temperatures showed a clear enhanced variation of $\sim 12\%$ in FWHM in the region of T_c (70–150 K) and a few smaller variations in the wide region 150–320 K. Similar measurements were made on three specimens and a standard deviation of $<1\%$ was determined. The larger change is seen a little below T_c i.e., in the region of 90 K.

The FWHM of the channeling angular scans is directly related to small atomic displacements (static or dynamic), from their regular lattice sites, normal to the channeling direction. We extract the magnitude of the atomic displacement u , from the measured FWHM using the continuum

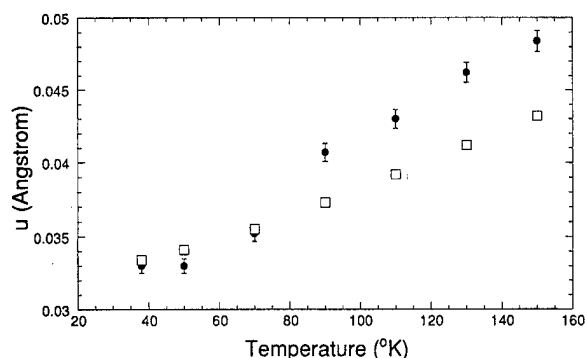


FIG. 4. The atomic displacement u as obtained from the measured FWHM of the channeling angular scans (●) and the calculated value of u (□) for normal thermal behavior vs T (30–160 K) in $\text{La}_{1.2}\text{Sr}_{1.8}\text{Mn}_2\text{O}_7$ crystals.

model⁶ for channeling, with corrections based upon the Monte Carlo computer simulation of Barrett⁷ and using average atomic numbers and lattice spacings. The results are shown in Figs. 4 and 5 as closed circles.

The decrease in thermal vibrational amplitude as a function of temperature is shown by the calculated values using the Debye relation in Figs. 4 and 5 (open squares). The measured variation in u is much larger than the expected thermal behavior. Between 70 and 150 K the total change was ~ 1.5 picometer, two times larger than the thermal change. This increase was not due to any abrupt change in thermal vibrations, but appears to be related to structural distortions (dynamic and/or static incoherent) in the specimen in the region of the transition to the ferromagnetic state.

There are a few smaller anomalies spread in the region 120–320 K. The change due to thermal vibrations in this region are of the order of 0.3 to 0.4 picometers. The deviation from normal thermal behavior is clearly seen and seems to be related with the para to ferromagnetic phase transition in certain regions in the material as indicated by low field magnetization measurements. It is clear that there are dynamic and/or static-incoherent structural changes associated with the phase transitions in the material.

As shown above, the $\text{La}_{1.2}\text{Sr}_{1.8}\text{Mn}_2\text{O}_7$ system is a complex inhomogeneous system, in which below 120 K, ferromagnetism dominates. Earlier in the spin resonance studies⁸ a multiline spectrum is seen at 115 K, which merges into a broad line below 80 K, indicating the possibility of different spin networks, i.e., a nonuniform ferromagnetic behavior. A

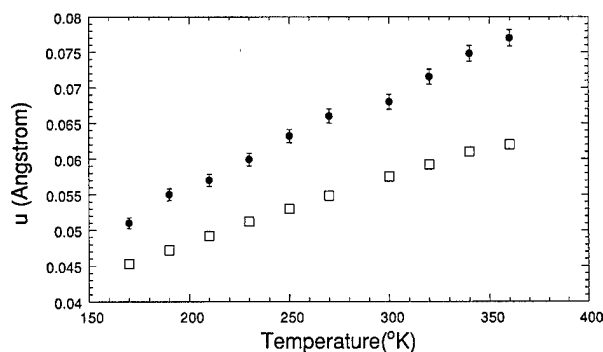


FIG. 5. Same as Fig. 4, but in the temperature region 150–360 K.

large MR is also seen in this region. In ion channeling, the maximum variation in the atomic displacement u is also spread in the region of 150–70 K. The transport properties, could be due to the double exchange mechanism and formation of polarons⁵ driven by Jahn–Teller distortion of the MnO_6 octahedra. Such distortions in terms of elongation along c and contraction in a axis in the region of 120 K are seen by neutron diffraction.⁹ This static change in a and c axes will not appreciably affect the FWHM of the channeling angular scans. Thus, there seems to be dynamic incoherent fluctuations in these octahedra, spread in the region 150–70 K before a long range magnetic order is reached, as seen by ion channeling (Fig. 4).

The small magnetic moment and corresponding transitions in the region 120–320 K could also arise from ferromagnetic intergrowths of $\text{La}_{1.2}\text{Sr}_{1.8}\text{Mn}_2\text{O}_7$ (LSMO) layers with different Sr/La concentration and a distribution of T_c . Although the ion channeling data cannot rule out the possible role of intergrowths, the magnitude of observed large variation in u between 150 and 320 K (Fig. 5) cannot be fully explained by such an intergrowth model. The channeling results represent the observed structural change from a thickness of ~ 3000 Å in the near surface region of the sample and ~ 2 intergrowths, each covering ~ 10 Å in this depth (seen in TEM). Thus it is unlikely that the intergrowths will affect the channeling to a measurable extent. It is possible that small locally correlated ferromagnetic (FM) spin networks, aligned parallel to the ab plane do exist in the system even at 300 K. In this double sheet material where every two magnetic layers (two dimensional networks of MnO_6 octahedra) are separated by an insulating layer, there seems to be two dimensional spin correlation. As the temperature is lowered below 300 K, the magnetic order increases slowly and incoherently (Fig. 1 inset). The existence of correlation between channeling anomalies and the magnetic behavior from 120 to 320 K could be intrinsic in origin. The possibility of two-dimensional magnetic order has been suggested by Potter *et al.*¹⁰ and the existence of antiferromagnetic clusters along with the ferromagnetic fluctuations is reported by Perring *et al.*¹¹ in the temperature region above 120 K in this material. The presence of antiferromagnetic clusters seems consistent with the above behavior. It hinders long range order in the c direction, thus supporting two-dimensional magnetic order. Below 120 K the fluctuations are much larger and are spread in a wider region since the whole system is passing through a nonuniform ferromagnetic state at the phase transition.

This work is supported by NSF MRSEC Grant No. DMR96-32521.

¹H. Kuwahara *et al.*, Science **270**, 961 (1995).

²Y. Tomiyoka *et al.*, Phys. Rev. Lett. **74**, 5108 (1995).

³H. L. Ju *et al.*, Appl. Phys. Lett. **65**, 2108 (1994).

⁴Y. Moritomo *et al.*, Nature (London) **380**, 141 (1996).

⁵A. J. Millis *et al.*, Phys. Rev. Lett. **77**, 175 (1996).

⁶J. Lindhard, Mat. Fys. Medd. K. Dan. Vidensk. Selsk. **34**, No. 14 (1965).

⁷J. F. Mitchell *et al.*, Phys. Rev. B **55**, 63 (1997).

⁸J. H. Barrett, Phys. Rev. B **3**, 1527 (1971).

⁹R. P. Sharma *et al.* (unpublished).

¹⁰C. D. Potter *et al.* (to be published).

¹¹T. G. Perring *et al.*, Phys. Rev. Lett. **78**, 3197 (1997).

Lattice effects in ferromagnetic manganite perovskites

D. J. Singh

Complex Systems Theory Branch, Naval Research Laboratory, Washington, DC 20375-5320

W. E. Pickett

Department of Physics, University of California, Davis, California 95616

Density functional calculations are used to investigate the relationships among lattice distortions, magnetic ordering, and electronic properties in manganite perovskites. Distortions open narrow pseudogaps at the middle of the majority e_g manifold. The effect on transport is very dependent on doping and falls off as divalent ions replace La in LaMnO_3 . Distortions in the ferromagnetic ordered colossal magnetoresistance regime are weakly coupled to electronic properties relative to pure LaMnO_3 . © 1998 American Institute of Physics. [S0021-8979(98)32111-8]

Understanding colossal magnetoresistance (CMR) in manganites depends on elucidating the metal-insulator transition at the Curie temperature, T_C . As noted early on,¹⁻³ there are strong couplings among doping level, lattice distortions, magnetic order and electronic properties. LaMnO_3 occurs in distorted Pnma orthorhombic or similar structures^{1,4} and is an A-type antiferromagnetic (AFM) insulator. The distortions, relative to cubic, are rotations of octahedra and Jahn-Teller (JT) effects that change Mn-O bond lengths (from 1.97 to 1.91, 1.96, and 2.18 Å). We use the term JT loosely for the nonrotational component. They are understood qualitatively via ion size and electron counting: La^{3+} and Mn^{3+} ionic radii yield a large misfit parameter, $\sqrt{2}(R_O + R_{\text{Mn}})/(R_O + R_{\text{La}})$, favoring rotations, while the high spin Mn^{3+} ion has a half occupied majority spin e_g orbital favoring JT distortions. Doping LaMnO_3 by substituting La^{3+} with divalent ions, the order becomes FM, lattice distortions are more purely rotational^{1,5,6} and CMR occurs. Several experimental and theoretical studies have suggested that lattice effects may be needed to understand CMR⁵⁻¹⁰ but, while clearly there are lattice anomalies at T_C , the extent of their direct influence on transport is still not established. Further, a CMR like effect has been discovered in a pyrochlore, $\text{Ti}_2\text{Mn}_2\text{O}_7$ that has neither lattice distortions nor nonintegral valence needed for a double exchange picture.¹¹⁻¹³

Local spin density approximation (LSDA) studies have been reported for the end-point compounds and some alloy compositions.¹⁴⁻²⁰ Besides verifying that known properties are reproduced, they have elucidated the electronic and magnetic structure. Well hybridized bands derived from majority spin Mn e_g states and O p states dominate the electronic structure near the Fermi energy, E_F in the metallic FM materials, while the minority spin channel is effectively insulating leading to half metallic properties.²⁰ This combined with the local moment behavior may be compatible with high resistivities in the spin disordered state above T_C even before consideration of lattice effects. The calculations also show strong couplings between lattice distortions, magnetic order and electronic properties at least in undoped LaMnO_3 . In particular, it is found that without lattice distortions LaMnO_3 would have a FM metallic ground state, and even if forced to be AFM, it would still be metallic.¹⁸ With the lattice distortion,

the ground state becomes A-type AFM, and is found insulating in agreement with experiment. The present article reports further calculations aimed at better understanding the role of lattice distortions in the CMR alloys $\text{La}_{1-x}\text{D}_x\text{MnO}_3$ near $x = 1/3$.

We used the linearized augmented planewave (LAPW) method²¹ as in our previous work.¹⁸ Calculations were done for 20 atom Pnma and 5 atom perovskite cells with well converged basis sets and zone samplings. Lattice parameters were fixed in relaxations since effects of homogeneous strains produced by anomalies measured at T_C ^{8,9} will be small compared to the bond length and angle changes due to JT and rotational distortions. Pnma symmetry was enforced, so that lower symmetry structures cannot occur.

Undistorted AFM LaMnO_3 is unstable against distortion, and this changes the electronic structure from metallic to insulating. This distortion has both a strong JT component and a rotation that changes the Mn-O-Mn bond angles from 180° to $\approx 160^\circ$. However, the CMR compositions are FM, and the question of the extent to which lattice distortion affects the electronic properties remains. A structural relaxation was performed for FM LaMnO_3 within the Pnma unit cell. The $x = 1/3$ composition range was studied with virtual crystal approximation calculations for $\text{La}_{2/3}\text{Ba}_{1/3}\text{MnO}_3$. These were for a structure approximating that of $\text{La}_{0.65}\text{Ca}_{0.35}\text{MnO}_3$ as determined by Dai *et al.*⁵ This had pseudocubic lattice parameters corresponding to the volume measured by Dai *et al.*⁵ and an average A-site cation charge $Z_{\text{VC}} = 56\frac{2}{3}$. The calculated electronic structure near and below E_F , should be representative of Sr or Ca substitution of La as well, since these are isovalent with Ba and the A-site cations are fully ionized. However, since Ba^{2+} ions are considerably larger than Ca^{2+} , the lattice will be under compressive strain which may alter the magnitude of lattice distortions in relaxations. The virtual crystal approach allows self-consistent treatment of the change in charge density and carrier density. Scattering due to the random occupation of the A site is not included. This has little effect on the broad bands characteristic of the FM majority spin channel, but localizes the minority spin carriers.²⁰ The relationship of virtual crystal and supercell calculations and reliability is discussed elsewhere.²⁰ Here we find that lattice distortions bring

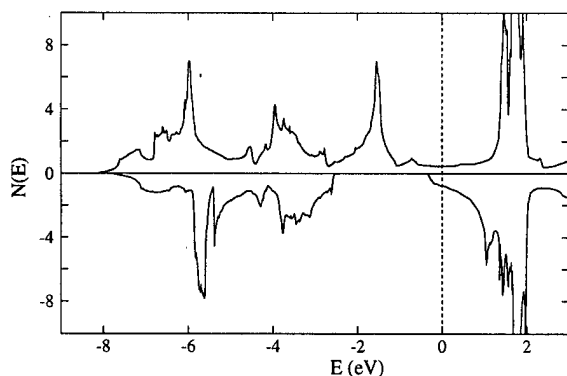
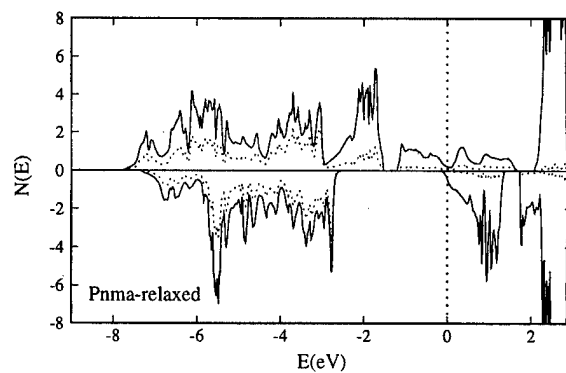
TABLE I. Relaxed structure of FM Pnma LaMnO_3 . The pseudocubic lattice parameter is 3.936 Å.

	x	y	z
La	0.535	0.250	0.007
Mn	0.000	0.000	0.000
O1	0.013	0.750	0.071
O2	0.283	0.038	0.219

the minority spin band edge closer to E_F , further increasing the tendency towards minority spin localization, and as such transport is discussed in terms of the majority spin carriers only.

Relaxing Pnma FM LaMnO_3 a large rotational instability is found with final Mn–O–Mn bond angles of 165° , but the structure, as given in Table I, has almost no JT component. The Mn–O distances are all between 2.00, and 2.01 Å. The JT distortion occurs for AFM but not for FM order! This is another indication of large magnetostructural coupling in LaMnO_3 ; other evidence is the quite different crystal structures of FM and AFM modifications of LaMnO_3 ,⁴ the fact that magnetic order changes from FM to A-type AFM as the lattice is distorted,¹⁸ and that the structure changes from strongly orthorhombic in LaMnO_3 to more nearly cubic around the AFM to FM transition when doped with divalent A-site cations.¹

The electronic density of states (DOS) of undistorted cubic FM LaMnO_3 is shown in Fig. 1. The spin magnetization is $3.61 \mu_B$ per formula unit. The majority spin and minority spin DOS at E_F , $N(E_F)$ are comparable, and conduction in both spin channels is expected. Since we are interested in the CMR materials, where the minority carriers are localized, we focus on the majority channel. Calculations in the perovskite structure yield $N_\uparrow(E_F) = 0.45 \text{ eV}^{-1}$ and majority spin Fermi velocity, $v_{F\uparrow x} = 4.2 \times 10^7 \text{ cm/s}$. In Fig. 2, we show the DOS of FM LaMnO_3 in the relaxed structure. New gaps are opened between the hybridized t_{2g} and e_g manifolds in both the majority and minority channels, reflecting band narrowing due to less favorable hopping when the Mn–O–Mn bonds are bent. The distortion empties the minority states and thereby increases the magnetization to $4.00 \mu_B$ and lowers the energy by 0.24 eV, both on a per formula unit basis. Besides making FM LaMnO_3 essentially

FIG. 1. DOS of FM LaMnO_3 in the cubic perovskite structure. Majority spin is shown as positive and minority spin as negative. $E_F = 0$.FIG. 2. DOS of FM LaMnO_3 in the relaxed Pnma structure. The dotted line is the O contribution as defined by the weight inside the O LAPW spheres. The DOS is on a per formula unit.

half metallic, the distortion strongly reduces the majority spin conductivity. $N_\uparrow(E_F)$ becomes 0.21 eV^{-1} , while $v_{F\uparrow x} = 2.2 \times 10^7 \text{ cm/s}$ (although the symmetry is orthorhombic there is very little anisotropy in $v_{F\uparrow}$). If changes in scattering rate due to the distortion are neglected, as may be reasonable, an eightfold reduction in majority spin conductivity, σ due to the lattice distortion results within kinetic transport theory, where $\sigma \propto N(E_F)v_F^2$. This strong suppression of the conductivity with the lattice distortion is due to a pseudogap that opens in the majority channel at E_F . This occurs at the center of the roughly 3 eV wide e_g (hybridized with O $p\sigma$) derived manifold.

The DOS for virtual crystal $(\text{La}_{2/3}\text{Ba}_{1/3})\text{MnO}_3$ with the undistorted cubic perovskite structure shows near half metallic behavior with a smooth featureless majority spin component around E_F . The spin magnetization is $3.40 \mu_B$, with majority spin $N_\uparrow(E_F) = 0.53 \text{ eV}^{-1}$ and $v_{F\uparrow x} = 4.2 \times 10^7 \text{ cm/s}$. These values are similar to those obtained for perovskite structure FM LaMnO_3 .

Dai *et al.*⁵ reported neutron refinements of lattice parameters and some bond lengths and angles for FM Pnma $\text{La}_{0.65}\text{Ca}_{0.35}\text{MnO}_3$ at 300 and 40 K. The lattice parameters are very nearly pseudocubic (to about 0.2%), and the Mn–O bond lengths are all equal (to within 0.004 Å) showing a rotational component but no JT component to the distortion. The Mn–O–Mn bond angles are $160^\circ \pm 1^\circ$. We performed virtual crystal calculations using a Pnma structure derived from this one by making all bond lengths and Mn–O–Mn bond angles equal. The DOS is shown in Fig. 3. As in FM LaMnO_3 the distortion brings the minority spin band edge closer to E_F . The spin magnetization increases to $3.56 \mu_B$. Like undoped LaMnO_3 , a pseudogap opens at the center of the majority spin e_g manifold. At $x = 1/3$, the majority e_g manifold is far from half full, so the pseudogap is not near E_F . Rather, $N_\uparrow(E_F) = 0.68 \text{ eV}^{-1}$: somewhat larger than for the cubic structure. The velocity, $v_{F\uparrow x} = 3.1 \times 10^7 \text{ cm/s}$, is nearly isotropic and is reduced relative to cubic. The net result is that the distorted structure has a value $N_\uparrow(E_F)v_{F\uparrow x}^2$ that is reduced to 70% of the undistorted value, showing a relatively small effect from lattice distortions on the conductivity, particularly considering the large distortion that occurs. Thus there are couplings of lattice distortions and magnetic order to electronic properties in CMR alloys near

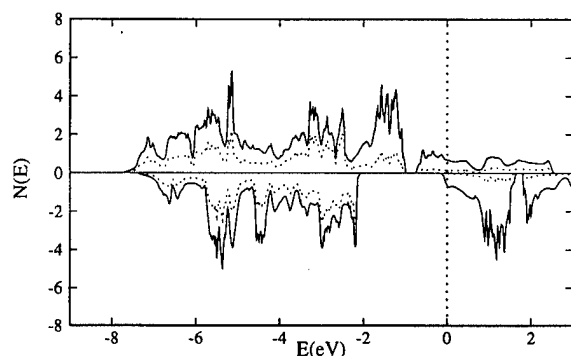


FIG. 3. DOS of virtual crystal $(\text{La}_{2/3}\text{Ba}_{1/3})\text{MnO}_3$ in the Pnma structure. Note the shift of the Fermi level in the majority bands compared to Fig. 2.

$x=1/3$, but these are weak, compared to those in pure LaMnO_3 . This is due to the narrowness of the e_g pseudogap that opens as the octahedra rotate in these materials. The calculations address the effects of static lattice distortions in fully ordered FM phases. They imply that the electron lattice coupling decreases strongly as LaMnO_3 is hole doped, a trend that is consistent with the high conductivities observed in some samples at low temperature. On the other hand, they do not address the metal insulator transition at T_C , which occurs simultaneously with a change in magnetic order. Observations of anomalies in Debye–Waller factors and lattice parameters near T_C imply significant coupling to the lattice. It has been observed by several authors that the properties above T_C are consistent with a polaronic state with strong charge carrier lattice interactions. Combined with the present results it would seem then that electron lattice interactions are stronger in the spin disordered paramagnetic state than the FM state. Previous calculations have shown that these local moment alloys are effectively half metallic when ordered and it is conjectured that this character persists locally for disordered states (strong Hund's rule). Carriers on Mn ions with moments rotated with respect to neighbors will be substantially localized and thus less strongly hybridized with O, as hopping is suppressed. These carriers occupy the JT active e_g orbital. This could lead to a local JT distortion,

providing a mechanism for strongly enhanced electron lattice interaction as spin disorder increases. This picture, related to that of Millis and co-workers,⁷ is consistent with a good metallic ground state, rapid onset of resistivity at T_C and a highly resistive paramagnetic state.

This work is supported by ONR and DoD HPCMO facilities at NAVO and ASC.

- ¹E. O. Wollan and W. C. Koehler, Phys. Rev. **100**, 545 (1955).
- ²G. H. Jonker and J. H. van Santen, Physica (Utrecht) **16**, 337 (1950); J. H. van Santen and G. H. Jonker, *ibid.* **16**, 599 (1950).
- ³C. W. Searle and S. T. Wang, Can. J. Phys. **48**, 2023 (1970).
- ⁴Q. Huang, A. Santoro, J. W. Lynn, R. W. Erwin, J. A. Borchers, J. L. Peng, and R. L. Greene, Phys. Rev. B **55**, 14987 (1997).
- ⁵P. Dai, J. Zhang, H. A. Mook, S. H. Liou, P. A. Dowben, and E. W. Plummer, Phys. Rev. B **54**, R3694 (1996).
- ⁶P. G. Radaelli, D. E. Cox, M. Marezio, S. W. Cheong, P. E. Schiffer, and A. P. Ramirez, Phys. Rev. Lett. **75**, 4488 (1995).
- ⁷A. J. Millis, P. B. Littlewood, and B. I. Shraiman, Phys. Rev. Lett. **74**, 5144 (1995).
- ⁸M. R. Ibarra, P. A. Algarabel, C. Marquina, J. Blasco, and J. Garcia, Phys. Rev. Lett. **75**, 3541 (1995).
- ⁹J. M. De Teresa, M. R. Ibarra, P. A. Algarabel, C. Ritter, C. Marquina, J. Blasco, J. Garcia, A. del Moral, and Z. Arnold, Nature (London) **386**, 256 (1997).
- ¹⁰A. P. Ramirez, P. Schiffer, S. W. Cheong, C. H. Chen, W. Bao, T. T. M. Palstra, P. L. Gammel, D. J. Bishop, and B. Zegarski, Phys. Rev. Lett. **76**, 3188 (1996).
- ¹¹Y. Shimakawa, Y. Kubo, and T. Manako, Nature (London) **379**, 53 (1996).
- ¹²M. A. Subramanian, B. H. Toby, A. P. Ramirez, W. J. Marshall, A. W. Sleight, and G. H. Kwei, Science **273**, 81 (1996).
- ¹³D. J. Singh, Phys. Rev. B **55**, 313 (1997).
- ¹⁴D. D. Sarma, N. Shanthi, S. R. Barman, N. Hamada, H. Sawada, and K. Terakura, Phys. Rev. Lett. **75**, 1126 (1995).
- ¹⁵I. Solovyev, N. Hamada, and K. Terakura, Phys. Rev. Lett. **76**, 4825 (1996).
- ¹⁶S. Satpathy, Z. S. Popovic, and F. R. Vukajlovic, Phys. Rev. Lett. **76**, 960 (1996).
- ¹⁷W. H. Butler, X.-G. Zhang, and J. M. MacLaren, in *Magnetic Ultrathin Films and Multilayers and Surfaces*, MRS Symp. Proc. No. 384, edited by E. E. Marinero *et al.* (Materials Research Society, Pittsburgh, 1995), pp. 439–443.
- ¹⁸W. E. Pickett and D. J. Singh, Phys. Rev. B **53**, 1146 (1996).
- ¹⁹W. E. Pickett and D. J. Singh, Europhys. Lett. **32**, 759 (1995).
- ²⁰W. E. Pickett and D. J. Singh, Phys. Rev. B **55**, R8642 (1997).
- ²¹D. J. Singh, *Planewaves Pseudopotentials and the LAPW Method* (Kluwer, Boston, 1994).

Isotope effect and T_c in manganites and high T_c oxides

Vladimir Z. Kresin

Lawrence Berkeley Laboratory, University of California, Berkeley, California 94720

Stuart A. Wolf

Naval Research Laboratory, Washington, DC 20375

Oxygen isotope effect in manganites (cuprates) is caused by the dynamic Jahn–Teller effect on the bridging oxygen ion (e.g., the ion between Mn^{3+} and Mn^{4+} in manganites). This effect leads also to the vibronic reduction and effective decrease of the ferromagnetic transition temperature.

© 1998 American Institute of Physics. [S0021-8979(98)32211-2]

I. INTRODUCTION

The oxides, cuprates, and manganites have attracted a lot of attention. The cuprates display a remarkable property, high-temperature superconductivity,¹ whereas the manganites are characterized by a number of unusual properties, inducing a very large magnetoresistance in the vicinity of the ferromagnetic transition.^{2–6} Needless to say that it is of definite interest to carry out the comparison of these two classes of materials. The nonadiabatic isotope effect in the cuprates was described by us in Ref. 7. As is shown in this article, one can also explain a large oxygen isotope effect observed in Ref. 5. It turns out that a similar scenario based on the dynamic Jahn–Teller (JT) effect determines the dependence of the transition temperature on oxygen substitution ($\text{O}^{16} \rightarrow \text{O}^{18}$) for the manganites. As is known, the transition to the ferromagnetic state (at $T = T_c$) has been described by the double exchange picture.^{8–10}

Both types of oxides have a similar structure. In both cases the doping plays a key role. In addition, one can observe the oxygen isotope effect. The isotope coefficient is very large for manganites, although it is not small in the underdoped cuprates.

Cuprates as well as manganites contain the Jahn–Teller (JT) ions, e.g., Cu^{++} , Mn^{+++} . This common feature is very important and, along with hybridization with oxygen orbitals, leads to unusual, non-adiabatic dynamics for the oxygen motion. For both systems one can observe a double-well structure of the potential. Below we are going to focus on this property of the materials.

II. MANGANESE OXIDES

Oxygen isotope substitution ($\text{O}^{16} \rightarrow \text{O}^{18}$) leads to a large effect on T_c . According to Ref. 5, the isotope coefficient $\alpha(T_c \propto M^{-\alpha})$ is equal to 0.85 for $\text{La}_{0.8}\text{Ca}_{0.2}\text{MnO}_{3+y}$ and 0.70 for $\text{La}_{0.9}\text{Ca}_{0.1}\text{MnO}_{3+y}$. In addition, the band structure analysis^{6,11} leads to a T_c about 2000 K which greatly exceeds the experimental value which is about of order of magnitude less (≈ 200 K).

These phenomena can be understood as a manifestation of the dynamic Jahn–Teller (JT) effect for oxygen. The key ingredient of our analysis is that the oxygen position is characterized by two close minima (double-well structure). This structure drastically affects the oxygen dynamics and is

caused by proximity to the crossing of two electronic terms (JT degeneracy). The JT splitting of the Mn ions, along with the manganese d -oxygen p hybridization³ leads to the JT behavior of the Mn–O–Mn unit. We focus on the vibrational motion of the oxygen ion which is the lightest member of the unit. Such a dynamic picture (two close minima) has been recently observed by a novel ion channeling technique in Ref. 12.

Our goal is to describe the charge transfer between two Mn ions; it is very important to take into consideration the peculiar oxygen dynamics. In this case the charge transfer is accompanied by transition between two electronic terms. It is very convenient to employ the method based on the diabatic representation (see, e.g., Ref. 13).

Because of the JT crossing, the total wave function $\psi(\mathbf{r}, \mathbf{R})$ (\mathbf{r} and \mathbf{R} are the electronic and nuclear coordinates, correspondingly) can be written in the form:

$$\psi(\mathbf{r}, \mathbf{R}) = C_\alpha \varphi_\alpha(\mathbf{r}, \mathbf{R}) \phi_\alpha(\mathbf{R}) + C_\beta \varphi_\beta(\mathbf{r}, \mathbf{R}) \phi_\beta(\mathbf{R}). \quad (1)$$

Here φ_i and ϕ_i ($i \equiv \alpha, \beta$) are the electronic and nuclear wave functions, corresponding to the α and β terms. Therefore, the total wave function is a superposition of two configurations α and β : $\alpha) \text{A}^+ \text{O}_\alpha \text{A}$, $\beta) \text{A} - \text{O}_\beta \text{A}^+$. In our case $\text{A} \equiv \text{Mn}^{3+}$, $\text{A}^+ \equiv \text{Mn}^{4+}$, $\text{O}_{\alpha(\beta)}$ is located near the left (right) minimum. In the diabatic representation the wave function $\Psi_\alpha = \varphi_\alpha \phi_\alpha$ coincides with the eigenfunction of the total electronic Hamiltonian $H_e = T_r + V(\mathbf{r}, \mathbf{R})$ in the region α and it is not an eigenfunction of H_e in the region β ; analogous behavior is true for ϕ_β (cf. Refs. 13 and 14; T_r is the electronic kinetic energy operator, V is the total potential energy). Substituting Eq. (1) into the stationary Schrödinger equation, one can evaluate the energy splitting ΔE between the symmetric and asymmetric terms. After a long, but straightforward calculation we obtain: $\Delta E = \int L(\mathbf{R}) \phi_\alpha(\mathbf{R}) \phi_\beta(\mathbf{R}) d\mathbf{R}$; here $L(\mathbf{R}) = \int \varphi_\alpha^*(\mathbf{r}, \mathbf{R}) H_e \varphi_\beta(\mathbf{r}, \mathbf{R}) d\mathbf{r}$ is the electronic factor. It is important to stress that this factor is an off-diagonal matrix element which is finite in the diabatic representation.¹³

The integrand in this factor differs from zero in the region a , a is the amplitude of the vibrations. The electronic factor has a scale l , l is the length of the bond. Since $l \gg a$, one can put $L(\mathbf{R}) \equiv L_0 \equiv L(\mathbf{R}_0)$ (\mathbf{R}_0 corresponds to the frozen lattice). We obtain: $\Delta E \equiv L_0 F$, where L_0 is the electronic factor, and

$$F = \int \phi_\alpha(\mathbf{R}) \phi_\beta(\mathbf{R}) d\mathbf{R} \quad (2)$$

is the Franck–Condon (FC) factor. It is essential that one can factorize the splitting into the electronic and FC terms.

The energy splitting corresponds to the time t for the jump between two Mn ions (see Ref. 8), that is to the period of oscillations between the configurations. Therefore, the splitting determines the critical temperature of the ferromagnetic ordering ($T_c \propto t^{-1}$, see Refs. 8, 11, 15), so that $T_c \propto \Delta E$. The electronic factor L [see Eqs. (2) and (3)] determines T_c for the usual double exchange model (see, e.g., Ref. 8). One can see that the JT dynamic instability of the O ion leads to an appearance of the additional FC factor. The inequality, $F < 1$, leads to a decrease in the value of T_c relative to the conventional result. Qualitatively, the charge transfer for the extra electron can be visualized as a multistep process; first the electron makes a transition from the Mn^{4+} site to the oxygen, then the oxygen transfers to another term, and this is finally followed by the transition of the electron to the other Mn ion. Therefore, the charge transfer contains an important additional step, namely, the oxygen transition between two terms. This additional step caused by the JT effect, leads to a drastic increase in the characteristic time for the jump between two Mn ions, and thus to a decrease in the strength of the ferromagnetic coupling, and, consequently, T_c . It is important, that the presence of the FC factor leads to the oxygen isotope effect (see below).

In order to estimate the FC factor, we are using harmonic oscillator wave functions. The factor is affected by the shift $\Delta\rho$ between the equilibrium positions. For simplicity, we consider a one-dimensional model. Simple calculation leads to the expression: $F = \exp(-\kappa^2)$; $\kappa = (\Delta\rho/2a)$, where $a^2 = (\hbar/m\Omega)$ is the amplitude of vibration. If we take the value $\kappa \approx 1.25$ –1.5 (this is consistent with the data¹²), we obtain $F \approx 0.18$ –0.2. If $L \approx 0.2$ (which alone would predict a T_{c0} between 1000 to 2000 K for La–Ca–Mn–O) (see Refs. 6 and 11), we obtain the value $T_c \approx 200$ –400 K, in an agreement with the experimental values. Note that the importance of the FC factor for the shift in the electronic excitation spectra for the intermediate valence systems was stressed in Ref. 16.

Let us now discuss the isotopic dependence observed in Ref. 5. This dependence is a direct consequence of the appearance of the FC factor [see Eq. (2)]. Indeed, this factor contains the nuclear wave functions and, therefore, depends on the nuclear mass M . The value of the isotope coefficient appears to be in good agreement with the data.⁵ Indeed, the isotope coefficient $\alpha(T_c \propto M^{-\alpha})$ is equal to $-(M/\Delta M) \times (\Delta T_c/T_c)$, where $\Delta M = M - M^*$ (we make the isotope substitution $M \rightarrow M^*$). Since $T_c \propto \Delta E \approx L_0 F$ (see above), we obtain $\alpha = -(M/\Delta M)(\Delta F/F)$. Based on the expression for the FC factor (see above), we obtain $\alpha = 0.5\kappa^2$. Using the value $\kappa \approx 1.25$ –1.5 for LaCaMnO (see above), we obtain the values in the range of 0.8–1.1, in an agreement with the value obtained in Ref. 5. Note that the values of κ and α depend on the sample and its preparation.

A more detailed quantitative evaluation using normal modes for the lattice configuration will be described else-

where. In this article, we describe the underlying physics and present the analysis that demonstrates that our model is in agreement with experimental data.

III. HIGH T_c OXIDES

Let us discuss the isotope effect in the cuprates. This problem was described by us in Ref. 7. As is known, the small value of the isotope coefficient α was considered as an argument against the phonon contribution to the pairing. However, it turns out that α strongly depends on the carrier concentration n and might exceed the BCS value $\alpha = 0.5$ (see, e.g., Refs. 17–19). It has been established that the minimum value of α corresponds to $T_c = T_{c,\max}$.

The oxygen dynamics in cuprates is also affected by presence of two minima. This has been observed in Ref. 12 by ion channeling and in Ref. 20 by x-ray (XANEX) measurements.

In order to describe the isotope effect in the cuprates, one can employ a method similar to that for the manganites. In accord with this, we are using the diabatic representation. In this case we focus on the charge redistribution between the reservoir (chains) and the CuO planes. Such redistribution requires an asymmetric positions of the minima (such a requirement is not needed for the manganites). In order to evaluate the carrier concentration, it is more convenient to use the quantum transition theory, that is to use a time-dependent picture. As in the case of manganites, the presence of the Franck–Condon factor is a key ingredient of our analysis. Its value strongly depends on the ionic mass and, therefore is affected by the isotope substitution. We obtain the following expression for the isotope coefficient (see Ref. 7):

$$\alpha_2 = \gamma \frac{n}{T_c} \frac{\partial T_c}{\partial n}, \quad (3)$$

where γ is a constant. Expression (3) allows us to compare directly with experimental data. Equation (3) contains the derivative $\partial T_c / \partial n$. Since T_c has a maximum at some value $n = n_{\max}$, the isotope coefficient α_2 is equal to zero if $T_c = T_{c,\max}$ (the small value of α actually observed is due to a small contribution from α_1). Therefore, the maximum value of T_c corresponds to a minimum in isotope coefficient.

Note that the dependence $n(M)$ is manifested not only in the isotopic dependence of the critical temperature. One can observe the isotope effect for the penetration depth,²¹ transport coefficients, etc., since they are affected by the value of the carrier concentration.

The cuprates contain different oxygen ions. If we are dealing with oxygen depletion from the chains, then the charge transfer is affected by nonadiabaticity of the apical oxygen. If we study the Pr substitution, then the charge transfer between the Pr ion and the CuO plane is modified by the JT dynamics of the in-plane oxygen (see Ref. 22).

IV. CONCLUSION

The isotopic dependence of the critical temperature for the transition to the superconducting (ferromagnetic) state is

caused by a nonadiabatic behavior of the oxygen ions. Oxygen dynamics for both types of oxides is characterized by presence of two close minima; their presence was observed experimentally in Refs. 12 and 20. The appearance of such double-well structure is due to the crossing of the electronic terms; this factor drastically affects the charge transfer, which is a key ingredient underlying many properties of the materials.

It is important to note that the double-well structure for the oxygen corresponds an unusual anharmonic picture. Indeed, according to such a picture the electronic and nuclear degrees of freedom are separated, but the potential for the nuclear motion is not harmonic. In our case we are dealing with a nonseparability of the motions, and the minima correspond to different terms.

It is essential to stress the difference between the nature of the phase transitions and isotopic dependencies for these two types of oxides. In both cases we are dealing with a dynamic Jahn–Teller instability of the oxygen ion. As for the superconducting transition in the cuprates, it is caused by a pairing interaction in the Cu–O plane, and the JT instability affects the doping level, that is, the carrier concentration in the plane n . The dependence $n(M)$ affects the value of the critical temperature. In the manganites the phase transition into the ferromagnetic state is due to the motion of the extra electron between Mn ions, and the JT dynamics of the O ion significantly affects the time scale, and therefore, the resulting value of T_c .

ACKNOWLEDGMENT

The research of VZK was supported by the US Office of Naval Research under Contract No. N00014-97-F0006.

- ¹G. Bednorz and K. A. Mueller, Z. Phys. B **64**, 189 (1986).
- ²G. Jonker and J. van Santen, Physica (Utrecht) **16**, 337 (1950).
- ³J. Goodenough, Phys. Rev. **100**, 564 (1955); in *Progress in Solid State Chemistry*, edited by H. Reiss (Pergamon, New York, 1971), Vol. 5, p. 145.
- ⁴S. Jin *et al.*, Science **264**, 413 (1994).
- ⁵G. Zhao *et al.*, Nature (London) **381**, 676 (1996).
- ⁶W. Pickett and D. Singh, Phys. Rev. B **53**, 1146 (1996).
- ⁷V. Kresin and S. Wolf, Phys. Rev. B **49**, 3652 (1994).
- ⁸C. Zener, Phys. Rev. **82**, 403 (1951).
- ⁹P. Anderson and H. Hasegawa, Phys. Rev. **100**, 675 (1955).
- ¹⁰P. de Gennes, Phys. Rev. **118**, 141 (1960).
- ¹¹A. Millis, P. Littlewood, and B. Shraiman, Phys. Rev. Lett. **74**, 5144 (1995); A. J. Millis, B. Shraiman, and R. Mueller, *ibid.* **77**, 175 (1996).
- ¹²R. Sharma *et al.*, Phys. Rev. B **54**, 10014 (1996); Phys. Rev. Lett. **77**, 4624 (1997).
- ¹³T. O'Malley, Phys. Rev. **152**, 98 (1967); in *Advances in Atomic and Molecular Physics*, edited by D. Bates and I. Esterman (1971), Vol. 7, p. 223; F. Smith, Phys. Rev. **179**, 111 (1969); V. Kresin and W. Lester, Jr., Chem. Phys. **90**, 935 (1984); D. Dateo *et al.*, J. Chem. Phys. **86**, 2639 (1987).
- ¹⁴J. Bardeen, Phys. Rev. Lett. **6**, 57 (1961); E. Kane, in *Tunneling Phenomena in Solids*, edited by E. Burstein and S. Lundqvist (Plenum, New York, 1969), Chap. 1.
- ¹⁵G. Rushbrooke, G. Baker, and P. Wood, in *Phase Transitions and Critical Phenomena*, edited by C. Domb and M. Green (Academic, New York, 1974).
- ¹⁶D. Sherrington and S. von Molnar, Solid State Commun. **16**, 1347 (1975).
- ¹⁷J. P. Franck *et al.*, Phys. Rev. B **44**, 5318 (1991); in *High T_c Superconductivity, Physical Properties, Microscopic Theory and Mechanisms*, edited by J. Ashkenazi *et al.* (Plenum, New York, 1992), p. 411.
- ¹⁸H. Bornemann *et al.*, Physica C **182**, 132 (1991).
- ¹⁹D. Zech *et al.*, Nature (London) **371**, 681 (1994); *Anharmonic Properties of High T_c Cuprates*, edited by D. Mihailovic, G. Ruani, E. Kaldos, and K. A. Mueller (World Science, Singapore, 1995); Physica B **219**, 136 (1996).
- ²⁰D. Haskel *et al.*, Phys. Rev. B **56**, R521 (1997).
- ²¹V. Kresin and S. Wolf, p. 7; A. Bill, S. Wolf, and V. Kresin, Phys. Rev. B (to be published).
- ²²V. Kresin, A. Bill, S. Wolf, and Yu. Ovchinnikov, Phys. Rev. B **56**, 107 (1997).

A mean field theory of magnets with competing double exchange and superexchange interactions

D. I. Golosov^{a)}

The James Franck Institute, The University of Chicago, 5640 S. Ellis Avenue, Chicago, Illinois 60637 and Materials Science Division, Argonne National Laboratory, 9700 S. Cass Avenue, Argonne, Illinois 60439

M. R. Norman

Materials Science Division, Argonne National Laboratory, 9700 S. Cass Avenue, Argonne, Illinois 60439

K. Levin

The James Franck Institute, The University of Chicago, 5640 S. Ellis Avenue, Chicago, Illinois 60637

We study the competition between ferromagnetic double exchange (DE) and direct nearest-neighbor antiferromagnetic exchange J_{AF} in two-dimensional colossal magnetoresistance materials. Towards this end, a single site mean field theory is proposed which incorporates the hopping-mediated nature of the DE contribution. The canted state appears only under highly restricted conditions. Instead, in the regime where the antiferromagnetic and DE ferromagnetic interactions are of comparable scale (and in the classical limit), the system exhibits ferro- or antiferromagnetic order with incomplete saturation of the lattice or sublattice magnetization. We interpret these results as an indication that spin fluctuations remain strong even at low temperatures and discuss the associated experimental implications. © 1998 American Institute of Physics. [S0021-8979(98)45611-1]

The colossal magnetoresistance (CMR) manganese oxides have received considerable attention recently both theoretically and experimentally.¹ In the CMR regime, these materials exhibit ferromagnetism which is generally believed to result from a conduction electron-mediated double exchange (DE) mechanism.² There is, in addition, considerable evidence^{3,4} for antiferromagnetic exchange interactions of comparable scale, resulting from a superexchange mechanism. Thus, a full understanding of the magnetic order in the CMR materials requires a treatment of the competition between ferro- and antiferromagnetic interactions. The aim of the present article is to address this competition and by doing so, revisit earlier claims in the literature⁵ which suggest that spin canting may be the most natural means of accommodating these two opposing exchange interactions. Here in view of the considerable interest in the layered systems $\text{SrO}(\text{La}_{1-x}\text{Sr}_x\text{MnO}_3)_2$, we consider the two dimensional CMR compounds.

Our theoretical approach is based on a single site mean field theory which emphasizes the hopping-mediated nature of the DE contribution. In this way, we are led to consider the problem of off-diagonal (i.e., hopping) disorder associated with a single impurity atom in an otherwise uniform host material. This is to be contrasted with alternative approaches in the literature^{5,6} which implicitly introduce an exchange interaction to represent these DE effects. Our starting point is the standard Hamiltonian^{5,7} derived for the case of infinite Hund's rule coupling:

$$\mathcal{H} = -\frac{t_0}{2} \sum_{\langle i,j \rangle} \cos \frac{\theta_{ij}}{2} (c_i^\dagger c_j + c_j^\dagger c_i) + \frac{J_{AF}}{S^2} \sum_{\langle i,j \rangle} \mathbf{S}_i \mathbf{S}_j - \frac{H}{S} \sum_i S_i^z - \mu \sum_i c_i^\dagger c_i. \quad (1)$$

Here operator c_j annihilates a fermion on site j , \mathbf{S}_i represents a classical core (localized) spin ($S \gg 1$), J_{AF} is the nearest-neighbor antiferromagnetic exchange integral, H -external field, μ -chemical potential. Throughout this article, we use units in which the bare hopping t_0 , \hbar , κ_B , μ_B , and the lattice period are all equal to unity. In the first term of Eq. (1), we have omitted Berry phase effects which are insignificant for a single-site mean field treatment.

The Hamiltonian of Eq. (1) represents, at $T > 0$, a highly disordered electronic hopping problem, deriving from the random distribution of localized spins. In our mean field approach we focus on a central site characterized by hopping b to the surrounding sites. This site is embedded in a medium with average hopping t . These hopping matrix elements are the counterparts of the central spin and spin background encountered in standard mean field theories of magnetism and are associated with appropriate spin configurations. These parameters are indicated schematically in Fig. 1. Here $t \leq 1$, and $t \neq b$.⁸ To arrive at appropriate self-consistency conditions for b and t , we compute the change in thermodynamical potential Ω associated with the change in hopping matrix elements $t \rightarrow b$. Because of the locality of the perturbation this contribution to Ω can be evaluated exactly.⁹ For simplicity, we first present our results in the limit of small perturbations, $|t - b| \ll t$. To leading order in T/t

^{a)}Electronic mail: golosov@control.uchicago.edu

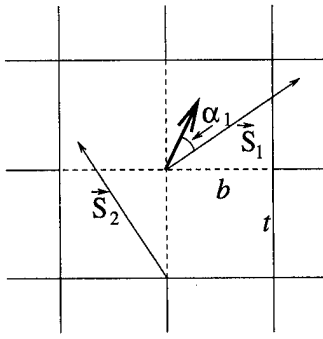


FIG. 1. Single-spin fluctuation in the ferromagnetic phase. The bold arrow represents average magnetization, and the dashed lines correspond to the hopping amplitude b , which differs from the background hopping value t (solid lines).

$$\delta\Omega_{\text{DE}}(b, t, T) \approx -2 \frac{t-b}{t} \int \epsilon f(\epsilon) \nu(\epsilon) d\epsilon \approx 2(t-b)|E_0|, \quad (2)$$

where E_0 is the kinetic energy of conduction electrons for $t=1$.

In the ferromagnetic case, which will be addressed first, this change in Ω is combined with terms arising from the superexchange and magnetic field components, so that the net contribution is

$$\delta\Omega_1 = \delta\Omega_{\text{DE}}(b_1, t, T) + 4J_{\text{AF}} \langle \cos \theta_{12} \rangle_2 - H \cos \alpha_1. \quad (3)$$

Here, θ_{12} is the angle formed by the spin \mathbf{S}_1 with a neighboring spin \mathbf{S}_2 and α_1 is the angle formed by the fluctuating spin \mathbf{S}_1 with the direction of average magnetization. We use the notation $\langle \dots \rangle_1$ to represent averaging over the Boltzmann probability distribution of spin \mathbf{S}_1 , $w_1 \propto \exp(-\delta\Omega_1/T)$. We find $\langle \cos \theta_{12} \rangle_2 = M \cos \alpha_1$, and

$$b_1^2 = \langle \cos^2(\theta_{12}/2) \rangle_2 = (1 + M \cos \alpha_1)/2, \quad (4)$$

$$t^2 = \langle b_1^2 \rangle_1 = (1 + M^2)/2.$$

The central mean field equation is given by $M = \langle \cos \alpha_1 \rangle_1$.

In the limit of small fluctuations of $\cos \alpha_1$ around its average value M , Eq. (2) can be used to deduce an effective exchange interaction for the ferromagnetic phase. For the 2D case this exchange constant is given by

$$J_{\text{eff}}(M) = J_{\text{DE}}(M) + J_{\text{AF}}, \quad (5)$$

$$J_{\text{DE}}(ME) \approx -\frac{1}{8} |E_0| \cdot \sqrt{\frac{2}{1+M^2}},$$

Here the DE contribution increases as M decreases, and is similar to that which is implicitly contained in alternative mean field schemes.^{6,10}

For moderately strong antiferromagnetic exchange interactions ($|E_0| + 2H < 8J_{\text{AF}} < \sqrt{2}|E_0| + 2H$), $J_{\text{eff}}(M)$ changes sign as M varies from 0 to 1. In Fig. 2 we plot the temperature dependence of the magnetization for this situation. Here the solid line corresponds to the fully self-consistent calculation, while the dashed line is obtained using Eq. (5). For comparison we plot (dotted line) the behavior obtained for a conventional Heisenberg magnet with the same T_c . The lack

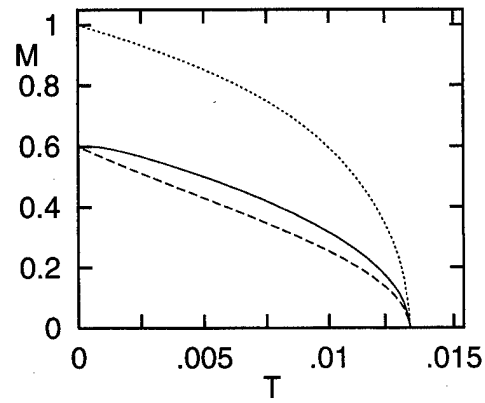


FIG. 2. Magnetization vs temperature in the ferromagnetic phase at $H=0$, $x=0.4$, and $J_{\text{AF}}=0.06$. The solid, dashed, and dotted lines correspond to the 2D DE-superexchange magnet, effective exchange approximation, and usual Heisenberg ferromagnet (with the same value of T_c), respectively.

of saturation of the magnetization at low temperatures (in the classical limit) is a consequence of the competition between ferromagnetic and antiferromagnetic terms. As T decreases, the magnitude of single spin fluctuations also decreases. This leads to an increase of M , which in turn implies a decrease in $|J_{\text{eff}}|$ (and thereby a tendency to decrease M). Thus, through this self-adjustment of the effective exchange interaction (which never becomes large in comparison with T), the magnetization fails to saturate. Rather, the limiting value of the zero field, zero temperature magnetization is given by $M_0 = \{2[J_{\text{DE}}(1)/J_{\text{AF}}]^2 - 1\}^{1/2} < 1$. It can be seen from Fig. 2 that there are important differences, primarily at low temperatures, between the full calculation of M and that derived from the effective exchange approximation. This reflects the inadequacies of Eq. (2).

It should be noted that stability considerations indicate that other spin arrangements (such as the antiferromagnetic one) have higher energy at low T than the undersaturated ferromagnetic phase. However, the Néel phase is stabilized for $J_{\text{AF}} > 2^{-5/2}|E_0|$ in zero field, and, moreover, it always exhibits undersaturation of the sublattice magnetization.

DeGennes⁵ has argued that competition between DE and superexchange will result in spin canting. It should be stressed that his calculations were appropriate to a strongly anisotropic model (chosen to fit the known magnetic behavior of the undoped perovskite LaMnO_3). In this case the spins of entire lattice layers are locked together by a ferromagnetic exchange. Here we examine the stability of the canted state for an isotropic situation. For these purposes the nonperturbative expression for the change in thermodynamical potential $\delta\Omega_{\text{DE}}$ is required. Thus, other theoretical approaches^{6,10} based on Hartree-Fock-like approximation cannot address the canted phase. This phase is characterized by two ordered sublattices with equal sublattice magnetizations m , which form an angle 2γ between them. For the present Hamiltonian (within a mean field scheme), it can be seen that spin canting always requires the presence of non-zero magnetic field and low temperatures. The former is a consequence of the high degree of degeneracy of the zero field canted state. In zero field, the energy of the system

depends solely on the cosine of the angle which the spin S_1 (of sublattice I) forms with its nearest neighbors belonging to sublattice II. This energy does not change as the spin S_1 moves along any cone around the average direction of spins of sublattice II. Thus, on the average the spin S_1 will be aligned with sublattice II, rather than I. Thus, this degeneracy destabilizes the canted state. Moreover, these results are robust with respect to small perturbations (caused by anisotropy effects, quantum corrections, and small external fields) that may lift the degeneracy described above. Since this degeneracy is site local, its effects will be suppressed only when the energy scale of a perturbation per individual spin is comparable with that of the thermal motion of a single spin, that is, with the temperature T .

The canted phase is stable for $H > 0$, sufficiently strong antiferromagnetism ($8J_{AF} > |E_0| + H$), and at low temperatures. To characterize the canted state, one has to solve two coupled equations, one for the component of $\langle S_1 \rangle$ parallel to the magnetization of sublattice I,

$$-\sin 2\gamma \langle \sin \alpha_1 \cos \beta_1 \rangle_1 + \cos 2\gamma \langle \cos \alpha_1 \rangle_1 = m, \quad (6)$$

and another for the perpendicular component,

$$\cos 2\gamma \langle \sin \alpha_1 \cos \beta_1 \rangle_1 + \sin 2\gamma \langle \cos \alpha_1 \rangle_1 = 0, \quad (7)$$

where α_1 and β_1 are polar and azimuthal angles of the spin S_1 measured with respect to the coordinate system that has, as its polar axis, the average direction of the spins of sublattice II. We choose $\beta_1 = 0$ for the spin S_1 lying within the plane containing the two sublattice magnetizations.

In order to solve Eqs. (6) and (7), the full expression for $\delta\Omega_{DE}$ is needed. Following Ref. 9, it can be shown that

$$\delta\Omega_{DE}(b, t, T) = \int f(\epsilon) \xi(\epsilon) d\epsilon + \theta(b-t) \cdot [\varphi(z_0) - \varphi(-Dt)], \quad (8)$$

where the spectral shift function $\xi(\epsilon)$ is given by

$$\pi \text{ctg} \pi \xi(\epsilon) = -\frac{1}{\epsilon \nu(\epsilon)} \frac{b^2}{t^2 - b^2} - \frac{1}{\nu(\epsilon)} \text{V.P.} \int \frac{\nu(\eta) d\eta}{\epsilon - \eta}, \quad (9)$$

the bound state energy z_0 is the root of equation

$$1 + \frac{t^2 - b^2}{t^2} \left\{ -1 + z \int \frac{\nu(\eta) d\eta}{z - \eta} \right\} = 0, \quad (10)$$

$\nu(\epsilon)$ is the density of states, $\varphi(z) = -T \ln\{1 + \exp[(\mu - z)/T]\}$, and $f(z) = \{\exp[(z - \mu)/T] + 1\}^{-1}$. Equations (8)–(10) are valid for a square (cubic) lattice in any dimensionality D from 1 to 3; the energy integrations are performed over the entire conduction band, extending from $-Dt$ to Dt . In the canted state, Eqs. (3) and (4) have to be modified appropriately.¹¹

An analysis of these equations reveals an important feature of the canted state. As $T \rightarrow 0$, m approaches its proper saturation value $m=1$. This reflects the fact that at finite field, the canted state is associated with a nondegenerate energy minimum. Moreover, at temperature $T_1 \sim H$, the undersaturated ferromagnetic state undergoes a continuous phase transition into the low temperature canted state. This lends

support to the notion that undersaturation is characteristic of the generic low temperature regime.¹² Thus, the canted state does not appear in the $H=0$ phase diagram, which consists of antiferro- (low T , small x), ferro- (low T , larger x), and paramagnetic (high T) regions.

These calculations have made a number of predictions which can be tested experimentally. The layered materials $\text{La}_{2-2x}\text{Sr}_{1+2x}\text{Mn}_2\text{O}_7$, with $x=0.4$, presumably lie either within the region where the system should display undersaturated ferromagnetic behavior at low T , or on the brink of this region, where thermal fluctuations should still be stronger than in a conventional magnet. Direct verification of the presence of undersaturation at low T should be possible via Rietveld measurements. The presently available results for the absolute value of magnetization in $x=0.4$ systems^{13,14} indicate that the low-temperature limiting value of the magnetization is lower than expected, but further experiments in a broader H, T range would be desirable.

It is natural to expect that the relative strength of the superexchange interaction is even higher in $x=0.3$ compounds, so that this compound may be suitable for observing canting under the proper field and temperature conditions: $T \lesssim H$, although experiments have not yet been performed in this regime. There have been no observations of the canted phase in the layered compounds to date, which is consistent with our results.

This work has benefitted from enlightening discussions that we had with many theorists and experimentalists. We are grateful to all of them, especially to A. G. Abanov, A. Auerbach, A. V. Chubukov, M. I. Kaganov, R. Osborn, R. Osgood, and A. E. Ruckenstein. We acknowledge the support of the University of Chicago/Argonne National Laboratory collaborative Grant, U.S. DOE, Basic Energy Sciences, Contract No. W-31-109-ENG-38, and the MRSEC program of the NSF under Award No. DMR 9400379.

¹For a review, see A. P. Ramirez, J. Phys.: Condens. Matter **9**, 8171 (1997).

²C. Zener, Phys. Rev. **82**, 403 (1951).

³T. G. Perring *et al.*, Phys. Rev. Lett. **78**, 3197 (1997).

⁴R. Osborn *et al.* (unpublished).

⁵P.-G. De Gennes, Phys. Rev. **118**, 141 (1960).

⁶A. J. Millis, P. B. Littlewood, and B. I. Shraiman, Phys. Rev. Lett. **74**, 5144 (1995).

⁷P. W. Anderson and H. Hasegawa, Phys. Rev. **100**, 675 (1955).

⁸We are, in effect, using the so-called "virtual crystal approximation," which is expected to be adequate for computing thermodynamic quantities of a system with sufficiently large carrier concentration.

⁹I. M. Lifshits, Usp. Mat. Nauk **7**, 171 (1952) and Zh. Eksp. Teor. Fiz. **17**, 1076 (1947) (in Russian); I. M. Lifshits, S. A. Gredeskul, and L. A. Pastur, *Introduction to the Theory of Disordered Systems* (Wiley, New York, 1988); M. G. Krein, *Topics in Differential Equations and Operator Theory* (Birkhäuser, Basel, 1983).

¹⁰N. Furukawa, J. Phys. Soc. Jpn. **64**, 3164 (1995), and references therein.

¹¹Namely, $\delta\Omega_1 = \delta\Omega_{DE}(b_1, t, T) + 4J_{AFm} \cos \alpha_1 - H(-\sin \gamma \sin \alpha_1 \cos \beta_1 + \cos \gamma \cos \alpha_1)$, $b_1^2 = (1 + m \cos \alpha_1)/2$, and $t^2 = (1 + m^2 \cos 2\gamma)/2$.

¹²Quantum $T \rightarrow 0$ undersaturation is consistent with results reported earlier for quantum ferrimagnets (see: A. V. Chubukov *et al.* J. Phys.: Condens. Matter **3**, 2665 (1991)). We also note that at low T and low concentrations (in 2D, $x < 0.215$), the canted and undersaturated ferro- and antiferromagnetic states become thermodynamically unstable, signalling either the onset of more complicated spin arrangement or phase separation.

¹³J. F. Mitchell *et al.*, Phys. Rev. B **55**, 63 (1997).

¹⁴R. Seshadri *et al.*, Chem. Mater. **9**, 1778 (1997).

Composite polaron mechanism for colossal magnetoresistance in perovskite manganites

Liang-Jian Zou^{a)}

Institute of Solid State Physics, Academia Sinica, Post Office Box 1129, Hefei 230031, People's Republic of China and CCAST (World Laboratory), Post Office BOX 8730, Beijing, 100083, People's Republic of China

H. Q. Lin

Department of Physics, the Chinese University of Hong Kong, Shatin, N. T. Hong Kong

Q.-Q. Zheng

Institute of Solid State Physics, Academia Sinica, Post Office Box 1129, Hefei 230031, People's Republic of China

The mechanism of carriers accompanied by spin-wave cloud and Jahn-Teller phononic cloud, called composite polaron, is proposed to explain the unusual transport and thermodynamic properties in perovskite manganites over all the temperature and magnetic field range. It is shown that the energy bandwidth of composite polarons is strongly renormalized with the increases of temperature and magnetic field, the bandwidth narrows with elevated temperature, while it broadens with increasing magnetic field. The resistivity of composite polarons increases with elevated temperature strongly, reaches a maximum near the Curie temperature T_C , and decreases with the increase of magnetic field. The specific heat of composite polarons also exhibits a maximum near T_C . These results agree with experiments in a broad temperature and magnetic field range, suggesting that composite polarons contribute to the unusual properties in manganites. © 1998 American Institute of Physics. [S0021-8979(98)45711-6]

I. INTRODUCTION

Huge resistance change under magnetic field found in ferromagnetic perovskite manganites has been under extensive theoretical and experimental studies in order to elucidate the mechanism of such a colossal change in resistance, and to explore its potential applications. The magnetic structure and the electronic states of $A_{1-x}R_x\text{MnO}_3$ (where $A=\text{La, Nd, Pr, ...}$ and $R=\text{Co, Sr, Pb, ...}$) were extensively studied since 1950's.¹ It is known that in manganites, three $d-t_{2g}$ electrons in Mn^{3+} and Mn^{4+} ions form localized core spins with $S=\frac{3}{2}$ via a strong intra-atomic Hund's coupling; the extra $d-e_g$ electron in Mn^{3+} , about 1.5 eV above the $d-t_{2g}$ level,² interacts with the core spins through strong Hund's coupling. The localized spins tend to align paralleled through the oxygen bridges among Mn^{3+} and Mn^{4+} ions and form ferromagnetic background.³ Electrons in the $d-e_g$ band hop between Mn ions as itinerant ones and are responsible for the electric conduction in these systems. This picture describes the essential process of the double exchange model.³⁻⁵

Several models⁶⁻¹⁰ have been proposed to explain the unusual transport properties observed in $A_{1-x}R_x\text{MnO}_3$ compounds. Early experiments⁶⁻⁸ had suggested that the anomalous magnetoresistance behavior could be understood in terms of the magnetic polaron mechanism. However, because of the Jahn-Teller distortion of MnO_6 octahedron,^{11,12} electrons moving together with the distorted crystalline field (dynamic Jahn-Teller distortion) will be damped or trapped by the distorted lattice potential and form phononic polaron.¹³ Recently many experiments¹⁴⁻¹⁶ confirm the exis-

tence of lattice distortion and the formation of polaron in doped lanthanum manganites. Millis *et al.*⁹ and Zang *et al.*¹⁰ suggested that the dynamic Jahn-Teller effect plays an important role in the doped manganites. However, their models only explained some of experimental facts. To fully understand the static and transport properties of manganites over all temperature and magnetic field range, further studies are still needed.

A moving electron in ferromagnetic (or antiferromagnetic) background disturbs its nearby local spin field and excites spin waves, so the moving electron at e_g level in lanthanum manganites is surrounded by spin-wave clouds and can form a magnetic polaron.¹⁷ On the other hand, in the presence of strong electron-lattice interaction, the magnetic polaron clouded by phonons can simultaneously form a kind of new quasiparticle, which we call the composite polaron (CP). In this article, we propose that the composite polaron is responsible for some unusual physical properties in manganites. The current work is different from our previous work¹⁸ where we did not discuss transport properties and specific heat. Approximation was made here in the low doping limit in order to calculate correlation functions.

II. FORMALISM OF COMPOSITE POLARONS

In $A_{1-x}B_x\text{MnO}_3$, it is believed that the essential interactions come from two parts, double exchange and Jahn-Teller lattice distortion. The double exchange interaction comes from the hopping of the e_g electrons between Mn^{3+} and Mn^{4+} ions via oxygen anion, which gives rise to the long-range ferromagnetic ordering among core spins. The dynamic Jahn-Teller electron-lattice coupling, originating from the degeneracy of e_g orbitals, is thought to play an

^{a)}Electronic mail: zou@isp.hfcas.ac.cn

important role for the transport properties⁹ and the magnetic properties.¹⁹ Considering these two interactions, the model Hamiltonian for the doped $R_{1-x}A_x\text{MnO}_3$ reads

$$H = \sum_{i\sigma} \epsilon_{d\sigma} d_{i\sigma}^\dagger d_{i\sigma} + t \sum_{\langle ij \rangle \sigma} d_{i\sigma}^\dagger d_{j\sigma} - J_H \sum_{i\mu\nu} \mathbf{S}_i \cdot d_{i\mu}^\dagger \sigma_{\mu\nu} d_{i\nu} - g\mu_B B \sum_i S_i^z + \alpha \hbar \omega \sum_i n_i [b_i^\dagger + b_i] + \sum_i \hbar \omega b_i^\dagger b_i, \quad (1)$$

where $d_{i\sigma}^\dagger$ creates an e_g electron at site \mathbf{R}_i with site energy ϵ_d and spin σ , t denotes the hopping integral of the e_g electrons from one site to its nearest-neighbor; b_i^\dagger creates a Jahn-Teller phonon at site \mathbf{R}_i with mode $\hbar\omega$, α represents the relative electron-phonon coupling constant. These parameters are chosen as $t \approx 1.8$, $J_H \approx 2.0$, and $\hbar\omega \approx 0.05$ eV, respectively; the relative electron-phonon interaction is about $\alpha \approx 1.5$.

Since the strong Hund's coupling between the conduction electron and the localized spin is confined to the same site, and since the strong Jahn-Teller coupling between the conduction electrons and the distorted lattice is extended only several lattice constant distance, the small polaron picture is more suitable for describing the motion of electrons in $\text{La}_{1-x}\text{Ca}_x\text{MnO}_3$. Therefore our treatment to Eq. (1) is in the framework of small polaron theory. The concept of the CP is supported by recent small-angle neutron scattering experiments by De Teresa *et al.*²⁰ After applying a unitary transformation²¹ to the model Hamiltonian Eq. (1) to eliminate the linear term of the phonon operators, $H' = e^{-S} H e^S$, where $S = \alpha \sum_i n_i [b_i^\dagger - b_i]$, one gets an effective Hamiltonian

$$H' = \sum_{i\sigma} \epsilon_{i\sigma} d_{i\sigma}^\dagger d_{i\sigma} + t \sum_{\langle ij \rangle \sigma} d_{i\sigma}^\dagger d_{j\sigma} \hat{X}_i^\dagger \hat{X}_j - J_H \sum_{i\mu\nu} \mathbf{S}_i \cdot d_{i\mu}^\dagger \sigma_{\mu\nu} d_{i\nu} \quad (2)$$

where $\epsilon_{d\sigma} = \epsilon_d - \mu - \sigma\mu_B B$, and $\hat{X}_{ia}^\dagger = \exp[\alpha(b_i - b_i^\dagger)]$. A constant term, $-\sum_{ij} \alpha n_i n_j$, is dropped off for simplicity.

The wave function of the composite polaron, $|\Phi\rangle$, can be constructed in terms of the basis functions, $|\phi_i(S_0^z)\rangle$,¹⁸

$$|\Phi\rangle = \sum_i a_i |\phi_i(S_0^z)\rangle \quad (3)$$

with

$$|\psi_i(S_0^z)\rangle = \sqrt{\frac{S+S_{0i}^z+1}{2S+1}} \left[d_{i\uparrow}^\dagger + \frac{d_{i\downarrow}^\dagger S_i^+}{S+S_{0i}^z+1} \right] |0\rangle_e,$$

where a_i^\dagger creates a CP and $|0\rangle_e$ denotes the fermion vacuum state. In the CP representation, the Hamiltonian Eq. (2) is rewritten

$$\tilde{H} = \sum_i \tilde{\epsilon}_0 a_i^\dagger a_i + \frac{t}{2S+1} \sum_{\langle ij \rangle} \left[\sqrt{(S+S_{0i}^z+1)(S+S_{0j}^z+1)} + \frac{1}{\sqrt{S+S_{0i}^z+1}} S_i^- S_j^+ \frac{1}{\sqrt{S+S_{0j}^z+1}} \right] X_i^\dagger X_j a_i^\dagger a_j. \quad (4)$$

In Eq. (4), the first term is diagonal, $\tilde{\epsilon}_0 = \epsilon_d - \alpha \hbar \omega - J_H S - 2S/(2S+1)(\mu_B B + g/2S \mu_B B)$, denoting the spin-dependent and the phonon-dependent site energy of the CP and describing the central position of energy band of the CP, which is almost not shifted by temperature and applied magnetic field; the second term, the nondiagonal part, describes the hopping process and the energy band of the CP, which contributes to the transport properties. After the thermal average over phononic states and spin configurations, the energy band of the CP can be obtained:

$$\epsilon_k = \tilde{\epsilon}_0 + \frac{zt\gamma(k)}{2S+1} e^{-\alpha(\langle n_B \rangle + 1/2)} \times \left[\langle \sqrt{(S+S_{0i}^z+1)(S+S_{0\delta}^z+1)} \rangle + \left\langle \frac{1}{\sqrt{S+S_{0i}^z+1}} S_i^- S_{i+\delta}^+ \frac{1}{\sqrt{S+S_{0i+\delta}^z+1}} \right\rangle \right]. \quad (5)$$

It is interesting to compare the above dispersion with the bare energy spectrum of conduction electrons, $zt\gamma(k)$. It is found that the energy band of the CP is renormalized by a phononic part depending only on temperature and a magnetic part depending both on temperature and magnetic field. The increases of electron-phonon interaction and temperature narrow the energy band of the CP, while the increase of magnetic field broadens it. It can be shown that when temperature varies from 50 to 250 K, the CP bandwidth in $\text{La}_{0.67}\text{Co}_{0.33}\text{MnO}_3$ decreases by about one order in magnitude.¹⁸ With the increase of temperature from $T < T_C$ to $T > T_C$, the spin-dependent correlation function exhibits a minimum near T_C , so the bandwidth of the CP has a minimum. Thus the CP energy band is controlled by both temperature and magnetic field, in agreement with the experimental observation.²²

III. TRANSPORT PROPERTIES OF COMPOSITE POLARONS

According to the preceding analysis, the CP formed in doped LaMnO_3 is a type of small polaron and its transport properties can be obtained from the small polaron theory. The direct-current conductivity is deduced from the Kubo formula²³ in terms of the nondiagonal transition process

$$\sigma = \frac{\beta}{6} \left(\frac{t}{2S+1} \right)^2 \sum_{ij\delta\delta'} \delta \cdot \delta' \int_{-\infty}^{\infty} dt \langle a_i^\dagger(t) a_{i+\delta}(t) a_{j+\delta'}^\dagger a_j \rangle \times \langle X_i^\dagger(t) X_{i+\delta}(t) X_{j+\delta'}^\dagger X_j \rangle F_{ij}(\delta, \delta', t). \quad (6)$$

Here $F_{ij}(t)$ is a spin-dependent correlation function. The conductivity is measured in the units of e^2/\hbar and it can be calculated so long as these correlation functions are known in the presence of magnetic field at temperature of T .

Assuming that the leading contribution of the CP to the direct-current conductivity comes from the self-correlation part, i.e., $j=i$, $\delta=\delta'$, to the zero-order approximation of the expansion of S matrix in the interaction representation, the correlation function for the CP becomes of the product of the occupied number of the CP in one site and the unoccupied

number in the nearest neighbor site, $n_i(1 - n_{i+\delta}) \approx c(1 - c)$, where c is the concentration of the CP per site. The thermal average of the Jahn–Teller phononic correlation function gives rise to $\exp\{-2\alpha^2(\langle n_B \rangle + 1/2)[1 - 2\cos(\omega t) + \cos(2\omega t)]\}$, where $\langle n_B \rangle$ is the thermal averaged occupation of the phonon. The spin-dependent correlation function in Eq. (5) is that of the double exchange ferromagnet and the expression of $F_{ij}(B, T)$ is rather complicated. Detailed calculation will be given in a further article.²⁴

Temperature dependence of the resistivity of the CP is obtained numerically and it agrees with the experiments well.^{6–8} The temperature and the field behavior of the CP could be understood as follows: at temperatures below the Curie temperature T_C , there exists both ferromagnetic long-range order and dynamic electron-phonon coupling, more and more spin waves and phonons are excited with the increase of temperature, the CP becomes more and more heavy and is trapped, so the electric resistivity of the CP increases. Above T_C , only the short-range magnetic order and the Jahn–Teller effect play roles, the hopping probability of the CP increases with the elevating temperature, so the resistance declines. The resistivity maximum in CMR compounds near T_C originates from the crossover of the magnetic contribution for the CP from the long-range order to the short-range order of double exchange ferromagnet.

The application of external magnetic field to system suppresses the spin excitation and reduces the effective mass of the CP, so the resistivity decreases with the increase of magnetic field. These behaviors agree with experiments very well.

One important result of the present model is that the magnetic scattering contribution to the resistivity comes from both the two-point spin-correlation function of the short-range ($T > T_C$) or the long range ($T < T_C$) magnetic fluctuations, and the four point spin correlation function¹² if high order approximation is adopted. Therefore the CP mechanism may be a more suitable description for the unusual properties of lanthanum manganites than either the magnetic polaron or the Jahn–Teller polaron mechanism.

IV. SPECIFIC HEAT OF COMPOSITE POLARONS

The thermodynamic properties of lanthanum manganites also can be deduced from the properties of the CP. The specific heat can be obtained from the total energy of the CP in the system,

$$C_v = \frac{\beta^2}{4} \sum_k \epsilon_k (\epsilon_k - \mu) Ch^{-2} [\beta(\epsilon_k - \mu)/2], \quad (7)$$

where the specific heat is in the units of k_B , ϵ_k denotes the energy band of the CP. Also we need the spin-dependent correlation function to calculate the specific heat of the CP. Since it is hard to obtain analytic results from such a complicated polaron energy band, the numerical result of the temperature dependence of the specific heat is obtained. It is

found that the specific heat of the CP increases gradually with the increasing of temperature, and exhibits a maximum near the Curie temperature. This maximum is related to the crossover of the leading contribution to the CP from the magnetic scattering character ($T < T_C$) to phononic scattering character ($T > T_C$). This behavior also agrees with recent experiments.²⁵

V. CONCLUSION

To summarize, a new kind of quasiparticle, the composite polaron, can form in the doped lanthanum manganites. The unusual transport and thermodynamic properties in manganites could be understood in the framework of the composite polaron theory.

ACKNOWLEDGMENTS

L.-J. Zou thanks Z. Zeng and M.-Z. Li for their help. This work is supported by the Grant of the NSFC and of the CAS, and by the Direct Grant for Research from the Research Grants Council (RGC) of the Hong Kong Government.

¹For an example see Goodenough, *Phys. Rev.* **29**, 111 (1957); *J. Appl. Phys.* **81**, 5330 (1997).

²J. M. D. Coey, M. Viret, and L. Ranno, *Phys. Rev. Lett.* **75**, 3910 (1995).

³C. Zener, *Phys. Rev.* **81**, 440 (1951); **82**, 403 (1951).

⁴P. W. Anderson and H. Hasegawa, *Phys. Rev.* **100**, 675 (1955).

⁵P. G. De Gennes, *Phys. Rev.* **100**, 564 (1955); **118**, 141 (1960).

⁶R. M. Kusters, J. Singleton, D. A. Keen, R. McGreevy, and W. Hayes, *Physica B* **155**, 362 (1989).

⁷R. Von Helmolt, J. Wecker, B. Holzapfel, L. Schultz, and K. Samwer, *Phys. Rev. Lett.* **71**, 2331 (1993); *J. Appl. Phys.* **76**, 6925 (1994).

⁸S. Jin, T. H. Tiefel, M. McCormack, R. A. Fastnacht, R. Ramesh, and L. H. Chen, *Science* **264**, 413 (1994).

⁹A. J. Millis, P. B. Littlewood, and B. I. Shraiman, *Phys. Rev. Lett.* **74**, 3407 (1995).

¹⁰Jun Zang, A. R. Bishop, and H. Roder, *Phys. Rev. B* **53**, R8 840 (1996).

¹¹H. A. Jahn, *Proc. R. Soc. London* **164**, 117 (1938).

¹²Y. E. Perlin and M. Wagner, *The Dynamic Jahn–Teller Effect in Localized Systems* (North-Holland, Amsterdam, 1984).

¹³S. I. Pekar, *Zh. Eksp. Teor. Fiz.* **16**, 341 (1946).

¹⁴S. J. L. Billinge, R. G. DiFrancesco, G. H. Kwei, J. J. Neumeier, and J. D. Thompson, *Phys. Rev. Lett.* **77**, 715 (1996).

¹⁵M. C. Martin, G. Shirane, Y. Endoh, K. Hirota, Y. Moritomo, and Y. Tokura, *Phys. Rev. B* **53**, 14 285 (1996).

¹⁶T. A. Tyson, J. Mustre de Leon, S. D. Conradson, A. R. Bishop, J. J. Neumeier, H. Roder, and J. Zang, *Phys. Rev. B* **53**, 13 985 (1996).

¹⁷E. L. Nagaev, *Sov. Phys. JETP* **29**, 545 (1969); **31**, 682 (1969).

¹⁸L.-J. Zou, H. Q. Lin, and Q. Q. Zheng, *J. Phys.: Condens. Matter* **9**, 8623 (1997).

¹⁹G.-M. Zhao, K. Conder, H. Keller, and K. A. Muller, *Nature (London)* **381**, 676 (1996).

²⁰J. M. De Teresa, M. R. Ibarra, P. A. Algarabel, C. Ritter, C. Marquina, J. Blasco, J. Garcia, A. del Moral, and Z. Arnold, *Nature (London)* **386**, 256 (1997).

²¹I. G. Lang and Yu A. Firsov, *Sov. Phys. JETP* **16**, 1301 (1961).

²²J. Fontcuberta, B. Martinez, A. Seffar, S. Pinol, J. L. Garciamunoz, and X. Obradors, *Phys. Rev. Lett.* **76**, 1122 (1996).

²³G. D. Mahan, *Many Body Physics* (Plenum, New York, 1981).

²⁴L.-J. Zou, *et al.* (unpublished).

²⁵S. H. Park, Y.-H. Jeong, K.-B. Lee, and S. J. Kwon, *Phys. Rev. B* **56**, 67 (1997).

Tunneling evidence of half-metallicity in epitaxial films of ferromagnetic perovskite manganites and ferrimagnetic magnetite

J. Y. T. Wei^{a)} and N.-C. Yeh

Department of Physics, California Institute of Technology, Pasadena, California 91125

R. P. Vasquez

Center for Space Microelectronics Technology, Jet Propulsion Laboratory, California Institute of Technology, Pasadena, California 91109

A. Gupta

IBM, Thomas J. Watson Research Center, Yorktown Heights, New York 10598

Direct evidence of half-metallic density of states is observed by scanning tunneling spectroscopy of ferromagnetic $\text{La}_{0.7}\text{Ca}_{0.3}\text{MnO}_3$ and $\text{La}_{1-x}\text{Sr}_x\text{MnO}_3$ ($x=0.3, 0.33$) epitaxial films which exhibit colossal magnetoresistance (CMR). At 77 K, well below the Curie temperatures, the normalized tunneling conductance $(dI/dV)/\langle I/V \rangle$ for all samples exhibits similar pronounced peak structures, consistent with the spin-split density of states spectra for the itinerant bands in the ferromagnetic state. The exchange energy splitting between the majority and minority spins, as well as an apparent energy gap near the Fermi level, show variations with the chemical composition and the temperature. For comparison, the tunneling spectrum of a half-metallic ferrimagnet Fe_3O_4 is also studied. The characteristic spin-split density of states spectrum is observed, and the similarities and differences of Fe_3O_4 compared with the perovskite manganites are discussed. © 1998 American Institute of Physics. [S0021-8979(98)45811-0]

Half-metallic ferromagnetic materials, characterized by the presence of an energy gap for one of the spin orientations at the Fermi level and continuous bands for the other, have been a subject of interest for more than a decade.¹⁻⁴ An important consequence of the half-metallicity is the complete spin polarization in the ferromagnetic state of these materials,^{1,2} giving rise to novel physical properties, such as very large magneto-optical Kerr effects⁵ in the Heusler alloys (e.g., PtMnSb).⁶ Recently, the intensively studied phenomenon of negative colossal magnetoresistance (CMR) in the perovskite manganites, $\text{Ln}_{1-x}\text{M}_x\text{MnO}_3$ (Ln: trivalent rare earth ions, M: divalent alkaline earth ions), has been attributed to the half-metallic characteristics of these materials based on electronic band structure calculations⁷ and on various supportive though indirect experiments.^{8,9} In this work, we provide temperature-dependent tunneling spectroscopy data as direct experimental evidence for the half-metallicity of various perovskite manganites. In addition, we compare these results with the first temperature-dependent tunneling spectroscopy data ever taken on a ferrimagnetic half-metal, Fe_3O_4 .¹⁰⁻¹² The similarities and differences in the spectral behavior of these half-metallic ferromagnets and ferrimagnets (HMF) are discussed.

The perovskite manganites studied in this work are 200-nm-thick epitaxial films of $\text{La}_{0.7}\text{Ca}_{0.3}\text{MnO}_3$ and $\text{La}_{0.7}\text{Sr}_{0.3}\text{MnO}_3$ grown on single crystalline LaAlO_3 substrates,¹³⁻¹⁶ and 150-nm-thick $\text{La}_{0.67}\text{Sr}_{0.33}\text{MnO}_3$ on single crystalline SrTiO_3 substrates, using pulsed laser deposition.¹⁷ The Curie temperatures (T_C) for these samples are 260, 320, and 360 K, respectively. Details of the deposition procedure

and the characterizations of the structural and physical properties (including the electronic, electrical transport, magnetic, and optical properties) of the manganite epitaxial films have been reported elsewhere.¹³⁻¹⁷ The Fe_3O_4 sample is an epitaxial film grown on a (001)-oriented MgO substrate, also using the pulsed laser deposition technique.¹²

To investigate the HMF characteristics of these ferromagnetic films, we employ tunneling spectroscopy on these samples using a variable-temperature scanning tunneling microscope (STM). Tunneling spectroscopy is known to be a sensitive probe for studying the density of states of material,¹⁸ particularly if the tunneling is into a many-body system characterized by a renormalized quasiparticle dispersion.¹⁹ In this work, we study the tunneling spectroscopy of the magnetic epitaxial films by measuring the tunneling current as a function of the sample bias voltage. All measured spectra are highly reproducible, and the characteristics are essentially independent of the junction impedance, ranging from high impedance $\sim 100 \text{ M}\Omega$ to low impedance $\sim 1 \text{ M}\Omega$. We use paramagnetic Pt for the tunneling tip to prevent possible complications in revealing the magnetic properties of the samples.

The main panels of Figs. 1(a)–1(c) illustrate the differential conductance, $(dI/dV)/\langle I/V \rangle$, normalized with the standard formalism given in Ref. 18, as a function of the bias voltage (V) for $\text{La}_{0.7}\text{Ca}_{0.3}\text{MnO}_3$ (LCMO), $\text{La}_{0.67}\text{Sr}_{0.33}\text{MnO}_3$ (LSMO), and Fe_3O_4 films at $T=77 \text{ K}$, respectively. The insets depict the corresponding data taken at $T=300 \text{ K}$. Similar measurements have also been conducted on the $\text{La}_{0.7}\text{Sr}_{0.3}\text{MnO}_3$ sample, and the results are qualitatively similar to those obtained on the $\text{La}_{0.67}\text{Sr}_{0.33}\text{MnO}_3$ sample, although small quantitative differences exist. These quantitative variations are given in Table I.

^{a)}Electronic mail: jytwei@cco.caltech.edu

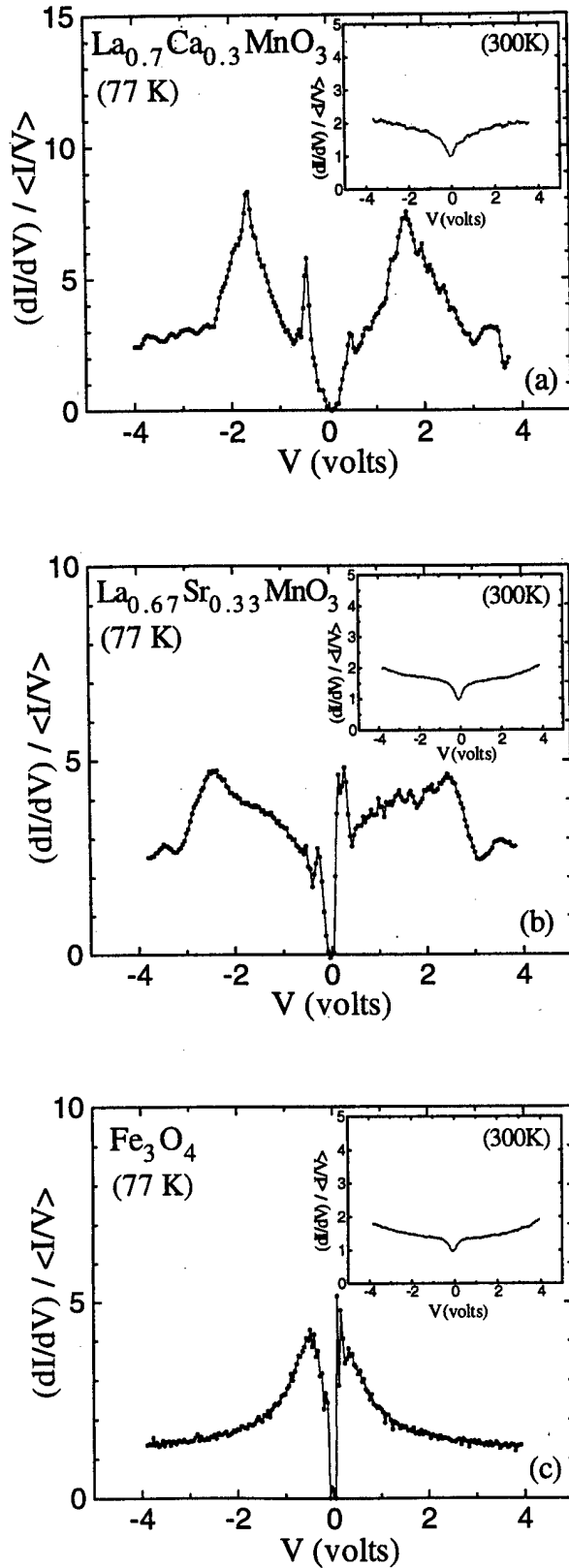


FIG. 1. The normalized differential conductance, $(dI/dV)/\langle I \rangle$, of (a) $\text{La}_{0.7}\text{Ca}_{0.3}\text{MnO}_3$, (b) $\text{La}_{0.67}\text{Sr}_{0.33}\text{MnO}_3$, and (c) Fe_3O_4 , as a function of the bias voltage V at $T=77$ K. The insets show the corresponding tunneling spectroscopy data at 300 K. The exchange energy splitting ΔE_{ex} and the energy gap ΔE_G values determined from the low-temperature data are given in Table I.

TABLE I. Summary of the tunneling spectroscopy measurements on the manganite and magnetite epitaxial films. The uncertainties in the energies come from spectral variations, and T_v is the Verwey temperature for Fe_3O_4 .

Material	T_C [K]	ΔE_{ex} [eV]	ΔE_G [eV]
$\text{La}_{0.7}\text{Ca}_{0.3}\text{MnO}_3$	260	3.3 ± 0.2	0.9 ± 0.1
$\text{La}_{0.7}\text{Sr}_{0.3}\text{MnO}_3$	320	4.0 ± 0.2	0.7 ± 0.1
$\text{La}_{0.67}\text{Sr}_{0.33}\text{MnO}_3$	360	5.0 ± 0.2	0.6 ± 0.1
Fe_3O_4	850 ($T_v = 120$ K)	0.8 ± 0.2	0.2 ± 0.1

Several important features of the data are noteworthy. First, two large peaks, which correspond to the density of states of the majority and minority carriers energetically separated by the on-site exchange energy, are clearly visible in each sample at 77 K. These features disappear at room temperature. Second, near zero bias voltage, the normalized differential conductivity appears to be zero for each sample at 77 K, suggesting the existence of a small energy gap ΔE_G near the Fermi level, attributable to either a density-of-states gap in the minority band or a mobility gap in the majority band.⁴ Furthermore, ΔE_G is the largest in LCMO and the smallest in Fe_3O_4 . Third, in the case of perovskite manganites, the exchange energy splitting ΔE_{ex} for the same alkaline earth doping level $x=0.3$ is larger in $\text{La}_{0.7}\text{Sr}_{0.3}\text{MnO}_3$ ($\Delta E_{\text{ex}} = 4.0 \pm 0.2$ eV) than in $\text{La}_{0.7}\text{Ca}_{0.3}\text{MnO}_3$ ($\Delta E_{\text{ex}} = 3.3 \pm 0.2$ eV), as shown in Table I. We note that the observed exchange energy in $\text{La}_{0.7}\text{Sr}_{0.3}\text{MnO}_3$ is in good agreement with that ($\Delta E_{\text{ex}} \approx 3.5$ eV) obtained from band-structure calculations using the local spin-density approximation.⁶ For the Sr-doped manganites, on the other hand, the exchange energy splitting is larger in $\text{La}_{0.67}\text{Sr}_{0.33}\text{MnO}_3$ ($\Delta E_{\text{ex}} = 5.0 \pm 0.2$ eV) than that in $\text{La}_{0.7}\text{Sr}_{0.3}\text{MnO}_3$. Fourth, we note that the bandwidths of the majority and minority bands are significantly narrower in the LCMO system than those in the LSMO system. Finally, the exchange energies ΔE_{ex} in the perovskite manganites are significantly larger than that in the magnetite Fe_3O_4 ($\Delta E_{\text{ex}} = 0.8 \pm 0.2$ eV), as summarized in Table I.

Next, we consider the physical implications of our tunneling data taken on these HMF epitaxial films. On the issue of increasing ΔE_{ex} with the increasing alkaline doping level in the ferromagnetic state of perovskite manganites, we note that the ratio of Mn^{4+} ions ($e_g^0 t_{2g}^3$) to Mn^{3+} ions ($e_g^1 t_{2g}^3$) increases with increasing x , and that the crystal-field energy splitting between the e_g - and t_{2g} -orbitals results in a larger on-site exchange energy for the Mn^{4+} ions than for the Mn^{3+} ions. Hence, we would expect ΔE_{ex} to increase with increasing x , which is also consistent with the increase of T_C observed for these two LSMO films. However, the magnitude of increase in ΔE_{ex} with increasing x cannot be estimated easily; spin-dependent band-structure calculations will be necessary to obtain theoretical values of ΔE_{ex} for LSMO and to compare those values with our experimental results.

Regarding the enhanced ΔE_{ex} and reduced ΔE_G of the Sr-doped manganites relative to the Ca-doped manganites, we note that the smaller ionic size of Ca^{2+} results in a larger degree of lattice distortion from the ideal cubic structure.²⁰ There are two important consequences of the larger degree of

lattice distortion. First, stronger electron localization occurs near the Ca^{2+} site, thereby increasing the density of localized minority carriers and reducing the density of mobile majority carriers. Hence, the conductivity of LCMO is smaller relative to that of LSMO, and the double exchange interaction between the neighboring Mn^{3+} and Mn^{4+} ions,^{21,22} which is responsible for the ferromagnetism of these doped manganites,^{20–22} is also weakened in the case of LCMO. Both the Curie temperature T_C and the exchange energy ΔE_{ex} therefore decrease with the decreasing alkaline earth ion size, consistent with our experimental observation. Second, a larger deviation from the cubic structure also results in stronger hybridization of the Mn t_{2g} orbital and the oxygen p orbital. The stronger p – d hybridization is believed to enhance the half-metallicity of the manganites,^{4,6} yielding a larger energy gap in the minority bands. This argument would be consistent with the larger ΔE_G observed in LCMO relative to that in LSMO.

Comparing the exchange energy splitting of the perovskite manganites with that of magnetite Fe_3O_4 , we note that the ferromagnetic exchange interaction for $\text{Fe}^{2+}(e_g^2 t_{2g}^4)$ and $\text{Fe}^{3+}(e_g^2 t_{2g}^3)$ at the B site of the spinel lattice⁵ is compensated by the antiferromagnetic exchange interaction between the A and B -site Fe^{3+} ions.⁵ Hence, the resulting exchange energy splitting between the minority (associated with the A -site ions) and majority (at the B site) carriers is significantly reduced, consistent with our experimental observation of a much smaller ΔE_{ex} in Fe_3O_4 than in the manganites.

The above discussion suggests that the tunneling spectra in Figs. 1(a)–1(c) can be well understood in the context of ferro- and ferrimagnetic half-metallicity. Next, we consider the temperature dependence of the tunneling spectra. In the case of $\text{La}_{0.7}\text{Ca}_{0.3}\text{MnO}_3$, it is easily understood that the energy splitting between the majority and minority bands disappears in the paramagnetic state at room temperature, because $T_C \approx 260$ K. Regarding the absence of room temperature half-metallicity in Fe_3O_4 , we note that magnetite Fe_3O_4 is known to exhibit a sharp Verwey order-disorder transition involving Fe^{3+} and Fe^{2+} ions¹⁰ below the ferrimagnetic-to-paramagnetic transition at $T_C = 850$ K. An energy gap ~ 0.76 eV in the minority bands has been predicted from the band-structure calculations.^{3,5} However, the presence of disorder above the Verwey transition temperature $T_V \sim 120$ K may result in smearing of the energy gap in the minority subbands, and hence the loss of half-metallic characteristics. This scenario is consistent with the NMR measurements of the longitudinal spin relaxation rate $(1/T_1)$,¹¹ where anomalous temperature dependence of $(1/T_1) \sim T^{5/2}$ for the HMF disappears and a typical metallic dependence of $(1/T_1) \sim T$ is recovered at $T_V < T \ll T_C$. Recent magnetization and magnetoresistance measurements of Fe_3O_4 epitaxial films also indicate the occurrence of the Verwey transition T_V at about 120 K.¹²

On the other hand, the disappearance of room-temperature (below T_C) energy splitting between the majority and minority bands in both Sr-doped manganites is not easily comprehensible. This observation is nonetheless consistent with a recent finding of temperature-dependent spin-

resolved photoemission spectroscopy on $\text{La}_{0.7}\text{Sr}_{0.3}\text{MnO}_3$,²³ where the difference between the spin density of states of the majority and minority bands decreases linearly with increasing temperature, even at temperatures well below T_C . The rapidly vanishing half-metallic ferromagnetism with increasing temperature from the surface-sensitive photoemission measurements has been attributed to the existence of surface magnetization in LSMO, which may be significantly different from the bulk magnetization. Since STM measurements are also surface sensitive, our results may also be representative of the surface magnetization, and therefore not inconsistent with the bulk half-metallic properties. This issue awaits further quantitative investigation as a function of temperature.

The research at Caltech is supported by the Packard Foundation and the National Aeronautics and Space Administration, Office of Space Science (NASA/OSS). Part of the research was performed by the Center for Space Microelectronics Technology, Jet Propulsion Laboratory, Caltech, and was sponsored by NASA/OSS.

- ¹R. A. de Groot, F. M. Mueller, P. G. van Engen, and K. H. J. Buschow, *Phys. Rev. Lett.* **50**, 2024 (1983).
- ²P. G. van Engen, K. H. J. Buschow, R. Jongebreur, and M. Erman, *Appl. Phys. Lett.* **42**, 202 (1983).
- ³R. A. de Groot and K. H. J. Buschow, *J. Magn. Magn. Mater.* **54–57**, 1377 (1986).
- ⁴V. Yu. Irkhin and M. I. Katsnel'son, *Phys. Usp.* **37**, 659 (1994).
- ⁵A. Yanase and K. Siratori, *J. Phys. Soc. Jpn.* **53**, 312 (1984).
- ⁶W. E. Pickett and D. J. Singh, *Phys. Rev. B* **53**, 1146 (1996).
- ⁷F. Heusler, *Verh. Dtsch. Phys. Ges.* **5**, 219 (1903).
- ⁸H. Y. Hwang, S.-W. Cheong, N. P. Ong, and B. Batlogg, *Phys. Rev. Lett.* **77**, 2041 (1996).
- ⁹J. Z. Sun, W. J. Gallagher, P. R. Duncombe, L. Krusin-Elbaum, and R. A. Altman, *Appl. Phys. Lett.* **69**, 3266 (1996).
- ¹⁰E. J. Verywey, P. W. Haayman, and F. C. Romeijn, *J. Chem. Phys.* **15**, 458 (1947).
- ¹¹T. Mizoguchi and M. Inoue, *J. Phys. Soc. Jpn.* **21**, 310 (1966).
- ¹²G. Q. Gong, A. Gupta, G. Xiao, W. Qian, and V. P. Dravid, *Phys. Rev. B* **56**, 5096 (1997).
- ¹³N.-C. Yeh, R. P. Vasquez, D. A. Beam, C. C. Fu, J. Huynh, and G. Beach, *J. Phys.: Condens. Matter* **9**, 3713 (1997); N.-C. Yeh et al., *J. Appl. Phys.* **81**, 5499 (1997); *Mater. Res. Soc. Symp. Proc.* **474**, 145 (1997).
- ¹⁴J. Y. T. Wei, N.-C. Yeh, and R. P. Vasquez, *Phys. Rev. Lett.* **79**, 5150 (1998).
- ¹⁵R. P. Vasquez, *Phys. Rev. B* **54**, 14 938 (1996).
- ¹⁶A. V. Boris, N. N. Kovaleva, A. V. Bazhenov, A. V. Samoilov, N.-C. Yeh, and R. P. Vasquez, *J. Appl. Phys.* **81**, 5756 (1997).
- ¹⁷A. Gupta, G. Q. Gong, G. Xiao, P. R. Duncombe, P. Lecoer, P. Trouiloud, Y. Y. Wang, V. P. Dravid, and J. Z. Sun, *Phys. Rev. B* **54**, R15 629 (1997); *Appl. Phys. Lett.* **67**, 3494 (1995).
- ¹⁸For a review, see, for example, R. M. Feenstra, *Surf. Sci.* **299/300**, 965 (1994); R. J. Hamers, *Annu. Rev. Phys. Chem.* **40**, 531 (1989).
- ¹⁹G. D. Mahan, *Many Particle Physics* (Plenum, New York, 1990); E. L. Wolf, *Principles of Electron Tunnel Spectroscopy* (Oxford University Press, Oxford, 1985).
- ²⁰J. B. Goodenough, A. Wold, R. J. Arnett, and N. Menyuk, *Phys. Rev.* **124**, 373 (1961); J. B. Goodenough, *Progress in Solid State Chemistry*, Vol. 5, edited by H. Reiss (Pergamon, Oxford, 1971).
- ²¹G. H. Jonker and J. H. van Santen, *Physica* **16**, 337 (1950); J. H. van Santen and G. H. Jonker, *ibid.* **16**, 599 (1950).
- ²²C. Zener, *Phys. Rev.* **82**, 403 (1951); E. O. Wollan and W. C. Koehler, *ibid.* **100**, 545 (1955).
- ²³J. H. Park, E. Vescovo, H.-J. Kim, C. Kwon, R. Ramesh, and T. Venkatesan, *Nature (London)* (in press); *Phys. Rev. Lett.* (submitted).

Metal-insulator transition induced by ^{16}O – ^{18}O oxygen isotope exchange in colossal negative magnetoresistance manganites

N. A. Babushkina, L. M. Belova,^{a)} and V. I. Ozhgin

Russian Research Center Kurchatov Institute, Kurchatov Square 1, Moscow 123182, Russia

O. Yu. Gorbenko, A. R. Kaul, and A. A. Bosak

Chemistry Department, Moscow State University, Vorobievsky Gory, Moscow 119899, Russia

D. I. Khomskii

Materials Science Center, University of Groningen, Nijenborgh 4, 9747 AG Groningen, The Netherlands and Lebedev Physics Institute, Leninskii Prospekt 53, Moscow 117924, Russia

K. I. Kugel

Scientific Center for Applied Problems in Electrodynamics, Izhorskaya Street 13/19, Moscow 127412, Russia

The effect of ^{16}O – ^{18}O isotope exchange on the electric resistivity was studied for $(\text{La}_{1-y}\text{Pr}_y)_{0.7}\text{Ca}_{0.3}\text{MnO}_3$ ceramic samples. It was found that at $y=0.75$, the substitution of ^{16}O by ^{18}O results in the reversible transition from a ferromagnetic metal (FM) to charge ordered (CO) insulator at zero magnetic field. The applied magnetic field ($H \geq 2$ T) transformed the sample with ^{18}O again to the metallic state and caused the increase in the FM transition temperature T_C of the ^{16}O sample. As a result, the isotope shift of T_C at $H=2$ T was as high as 63 K. Such unique sensitivity of the system to oxygen isotope exchange, giving rise even to the metal-insulator transition, is discussed in terms of the isotope dependence of the effective electron bandwidth which shifts the balance between the CO and FM phases. © 1998 American Institute of Physics. [S0021-8979(98)27511-6]

INTRODUCTION

The perovskite manganites $\text{R}_{1-x}\text{M}_x\text{MnO}_3$ (Ref. 1), (R^{3+} is a rare earth cation, M is a doubly charged cation with a large ionic radius, attract considerable current interest owing to the recent discovery of colossal negative magnetoresistance (CMR). These materials are characterized by a strong interplay of structural, orbital, and spin degrees of freedom dramatically affecting their transport properties. The important role of the electron-lattice interaction was pointed out in Ref. 3. There are a number of factors contributing to these interactions, including the Jahn-Teller nature of Mn^{3+} ions, the strong dependence of electron transfer on the Mn-O-Mn bond angle,^{4,5} trapping of charge carriers due to the optical breathing mode, and different polaronic effects.

Another feature of the perovskite manganites is the possible formation of the charge ordered (CO) state, manifesting itself in localization of charge carriers accompanied by the regular arrangement of Mn^{3+} and Mn^{4+} ions.⁶⁻⁸ The CO state is usually characterized by semiconductorlike and antiferromagnetic behavior and is accompanied by lattice distortions. Such an ordering, characteristic of $\text{Pr}_{1-x}\text{Ca}_x\text{MnO}_3$ ($x=0.2-0.5$), was actively studied recently.^{7,8}

The significant role of electron-lattice interactions in manganites is confirmed by a pronounced isotope effect on the electrical and magnetic properties: in $\text{La}_{0.8}\text{Ca}_{0.2}\text{MnO}_3$ the isotope shift of the Curie temperature was as large as 21 K.^{9,10} The isotope effect should be even more pronounced in the vicinity of lattice instability related to the charge ordering. Bearing this in mind, we studied the effect of oxygen isotope substitution on the electrical resistivity of a mixed

compound $(\text{La}_{1-y}\text{Pr}_y)_{0.7}\text{Ca}_{0.3}\text{MnO}_3$. By varying the relative contents of Pr and La (i.e., changing the average radius of the rare earth ion) it is possible to obtain the different types of low-temperature behavior [from the ferromagnetic metal (FM) $\text{La}_{0.7}\text{Ca}_{0.3}\text{MnO}_3$ to the charge-ordered antiferromagnetic (AF) insulator $\text{Pr}_{0.7}\text{Ca}_{0.3}\text{MnO}_3$].^{4,11}

The isotope effect in electrical resistivity which we observed for $\text{La}_{0.175}\text{Pr}_{0.525}\text{Ca}_{0.3}\text{MnO}_3$ ($y=0.75$) samples appeared to be far in the excess of our expectations since the ^{16}O – ^{18}O exchange resulted not only in the significant lowering of the Curie temperature, but also in the metal-insulator transition.

EXPERIMENT

The preparation of the ceramic samples is described in Ref. 2. X-ray diffraction (XRD) showed that the $\text{La}_{0.175}\text{Pr}_{0.525}\text{Ca}_{0.3}\text{MnO}_3$ ceramic samples produced were of single phase with an orthorhombic structure [lattice parameters $a=0.5436(2)$ nm, $b=0.5461(2)$ nm, $c=0.7686(3)$ nm at 300 K].

The $(\text{La}_{1-y}\text{Pr}_y)_{0.7}\text{Ca}_{0.3}\text{MnO}_3$ system appeared to be convenient for oxygen isotope substitution since its oxygen stoichiometry depends only slightly on variations in the thermal treatment conditions (temperature and partial pressure of O_2). The method used for oxygen isotope substitution ^{16}O – ^{18}O in the selected manganite was similar to that utilized for high-temperature superconductor ceramics.¹³ Two $1 \times 1 \times 8$ mm³ bars were cut from the sintered pellet of $\text{La}_{0.175}\text{Pr}_{0.525}\text{Ca}_{0.3}\text{MnO}_3$. Both samples were treated simultaneously: one sample was heated in $^{16}\text{O}_2$ atmosphere, the other sample was heated in $^{18}\text{O}_2$ (the molar fraction of $^{18}\text{O}_2$ was 85%) for 48 h at 950 °C under oxygen pressure of 1 bar. The ^{18}O content in the samples was determined by measure-

^{a)}Electronic mail: belova@imp.kiae.ru

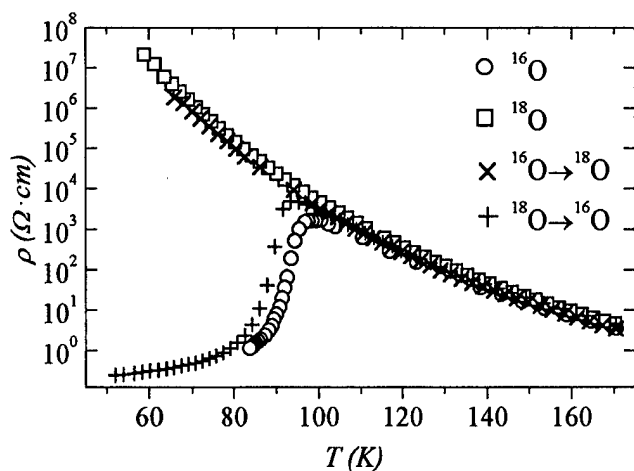


FIG. 1. Temperature dependence of resistivity for ^{16}O and ^{18}O samples of $\text{La}_{0.175}\text{Pr}_{0.525}\text{Ca}_{0.3}\text{MnO}_3$ before and after oxygen backexchange.

ment of the weight change of the samples after the isotope enrichment. As a result, the completeness of the isotope exchange was verified.

The electric resistivity was measured by the standard four-probe technique at temperatures down to 4.2 K. The highest resistance that could be measured with the experimental setup was 1 GΩ. The resistivity measurements in the magnetic field applied along the bar sample were performed only during the cooling stages. The magnetic properties were not measured in the current study, thus the assignment of the magnetic states was qualitative and based on experimental data for similar compounds published earlier.^{6-8,13}

RESULTS

The temperature dependence of resistivity $\rho(T)$ in zero magnetic field for the $\text{La}_{0.175}\text{Pr}_{0.525}\text{Ca}_{0.3}\text{MnO}_3$ samples is shown in Fig. 1. The resistivity curves for samples treated in $^{16}\text{O}_2$ and $^{18}\text{O}_2$ differ drastically. The ^{16}O sample exhibits a clearly pronounced resistivity peak at $T_C = 95$ K associated with transition to the FM state. This value of T_C is in good agreement with Ref. 4. For the ^{18}O sample the resistivity increases monotonically with decreasing temperature and attains about $10^8 \Omega \text{ cm}$ at 50 K, below which the $\rho(T)$ value is so large that it exceeds our measuring limit. This behavior can be attributed to the charge-ordered state which is usually responsible for such an increase in the resistivity.¹³

To make sure that the effect is due precisely to the isotope exchange, we carried out an isotope backexchange. The completeness of the exchange was proved again by changing the sample weight. The sample, which had been first saturated by ^{18}O and was insulating thereafter, became metallic below 95 K after subsequent annealing in $^{16}\text{O}_2$. Correspondingly, the sample that had been first treated in $^{16}\text{O}_2$ and was metallic below 95 K thereafter became an insulator after the subsequent treatment in $^{18}\text{O}_2$ (Fig. 1).

Application of the magnetic field is known to provide melting of the CO state in $(\text{La}_{1-y}\text{Pr}_y)_{0.7}\text{Ca}_{0.3}\text{MnO}_3$, resulting in a metamagnetic phase transition with a drastic decrease of the electric resistivity.^{4,11} This is a magnetic transition of the first order, exhibiting a pronounced temperature hysteresis.

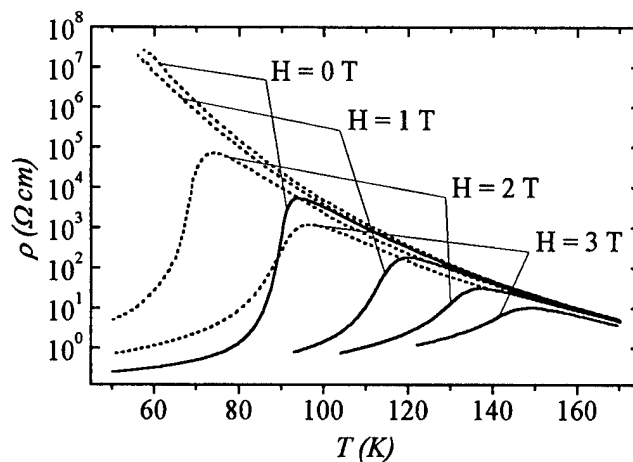


FIG. 2. Temperature dependence of resistivity for ^{16}O and ^{18}O samples of $\text{La}_{0.175}\text{Pr}_{0.525}\text{Ca}_{0.3}\text{MnO}_3$ in different magnetic fields. The solid line is for the ^{16}O sample; the dashed line is for the ^{18}O sample.

To avoid hysteresis the samples were heated above 150 K, then cooled in the applied magnetic field.

Temperature dependencies of resistivity $\rho(T)$ in the magnetic field are shown in Fig. 2. We found that a magnetic field of 1 T was not enough to suppress the CO state in $\text{La}_{0.175}\text{Pr}_{0.525}\text{Ca}_{0.3}\text{Mn}(\text{}^{18}\text{O}_{0.85}\text{}^{16}\text{O}_{0.15})_3$ in spite of the more than 30 K upward shift of T_C in the case of $\text{La}_{0.175}\text{Pr}_{0.525}\text{Ca}_{0.3}\text{Mn}(\text{}^{16}\text{O})_3$. Nevertheless, in a field of 2 T melting of the charge-ordered state was clearly demonstrated (Fig. 2).

The isotope shift of T_C was as large as 63 K in a field of 2 T and 54 K in a field of 3 T, which is considerably larger than isotope effects ever reported for $\text{R}_{1-x}\text{M}_x\text{MnO}_3$. It is of note that T_C grows significantly with the increase of the applied magnetic field for both samples. The $\rho(T)$ curves at higher temperature are nearly independent of the isotope exchange (Fig. 2).

Under an external field of 2 T, the resistivity drops by more than seven orders of magnitude to $\rho_{2\text{T}} = 1.5 \Omega \text{ cm}$ at 50 K, exhibiting one of the largest magnitudes of CMR (10^7). For the ^{18}O sample the large decrease in ρ , and thus CMR, can be related to the field-induced melting of the CO state. For the ^{16}O sample the magnitude of the CMR is much less (10^4 for $H = 2$ T).

Note the striking difference between the results for CMR in the ^{16}O and ^{18}O samples. In the ^{16}O sample metallic conduction and ferromagnetism occur spontaneously below the Curie temperature T_C . CMR arises from the abrupt increase in electron hopping via DE at the onset of the spontaneous FM ordering. Sizable CMR exists in the vicinity of T_C . In the ^{18}O sample neither metallic conduction nor ferromagnetism is observed in zero field. CMR originates from the field-induced simultaneous semiconductor-metal and AF-FM transitions.

DISCUSSION

The samples studied in current research lie close to the FM-CO phase boundary and a relatively small influence can in principle transform one state into another, this can be achieved even by isotope substitution.

The relative stability of different phases is determined

mainly by the electron bandwidth or the effective hopping integral t_{eff} . The CO state is favored in the situation when t_{eff} is small enough.^{4,5} One can show this for a simple case of one electron per two sites using the model initially formulated for magnetite,^{14,15} which takes into account the Coulomb repulsion V of electrons at neighboring lattice sites. Its Hamiltonian has the form

$$H = t \sum_{\langle i,j \rangle} a_i^+ a_j + \frac{V}{2} \sum_{\langle i,j \rangle} n_i n_j, \quad (1)$$

where a_i^+ and a_i are creation and annihilation operators for an electron at the i th site, $n = a^+ a$, and $\langle \dots \rangle$ means the summation over the nearest neighbors. On-site Coulomb interaction U is assumed to be the largest parameter, $U \rightarrow \infty$.

The standard mean-field treatment shows¹⁵ that the CO state occurs if the hopping integral t is less than a certain critical value, $t < t_c = Vz/2$ (z is the number of nearest neighbors). The CO critical temperature is given by the expression

$$T_{\text{CO}} \approx Vz \sqrt{1 - (t/t_c)^2} \quad (2)$$

and is reduced with the increase of t , especially strongly for $t \approx t_c$. Thus, the increase of the hopping integral t destabilizes the CO phase.

The t_{eff} value is determined by averaging t over corresponding lattice vibrations that, in turn, depend on the isotope composition of the material. In the simplest case: $t(r) \propto \exp(-\alpha r)$ and

$$t_{\text{eff}} = \langle t \rangle = t_0 \left(1 + \frac{1}{2} \alpha^2 \langle u^2 \rangle \right), \quad (3)$$

where the interatomic distance $r = r_0 + u$, $t_0 = t(r_0)$, and $\alpha \propto 1/r_0$. The mean-square displacement $\langle u^2 \rangle$, and hence t_{eff} , depend on the ionic mass M (even at $T=0$ due to the zero-point vibrations). In case of dominant contribution of zero-point vibrations, we have

$$\langle u^2 \rangle = \hbar / (2M \Theta_D) = \hbar / [2(BM)^{1/2}]$$

where B is the bulk modulus. Thus

$$\delta t_{\text{eff}} \approx -t_0 (\langle u^2 \rangle / r_0^2) (\delta M / M). \quad (4)$$

The corresponding change in t_{eff} is generally not large, especially taking into account that we have to use the reduced mass instead of the pure ionic mass. But this change may still be sufficient to shift our system from one state to another if we are close to the phase boundary at the phase diagram, which is apparently the case in our system. In this situation $t \approx t_c$ and, as follows from Eq. (2),

$$\delta T_{\text{CO}} \propto \delta t / \sqrt{1 - (t/t_c)^2}. \quad (5)$$

Note that in Eq. (2) the typical values of the intersite Coulomb repulsion $Vz \approx 1$ eV (10^4 K), while $T_{\text{CO}} \sim 10^2$ K; hence the square roots in (2) and (5) are of the order of 10^{-2} . Thus, $\delta T_{\text{CO}} \propto \delta t \times 10^2$, and it is not surprising $\delta T_{\text{CO}} \propto \delta t \times 10^2$ that even a relatively small variation of t_{eff} caused by isotope substitution leads to such a drastic change in properties.

The effect discussed above may be strongly enhanced if the charge carriers have polaronic nature. In this case the polaronic band narrowing gives

$$t_{\text{eff}} = t_0 \exp(-E_{\text{pol}}/\omega) \propto t_0 \exp(-\text{const}/\sqrt{M}) \quad (6)$$

and in the specific case considered here it is the oxygen mass that enters Eq. (6).¹⁶

Another factor which may play a role in this effect is possible change of the Mn–O–Nm angle which can also influence t_{eff} .

CONCLUSIONS

The electric resistivity of $(\text{La}_{1-y}\text{Pr}_y)_{0.7}\text{Ca}_{0.3}\text{MnO}_3$ ceramics demonstrates very high sensitivity to the oxygen isotope exchange. At $y=0.75$, the samples with ^{16}O are metallic at low temperatures, while substitution of ^{16}O by ^{18}O results in the insulatorlike behavior. The magnetic field exceeding 1 T restores the metallicity, but the isotope shift of the resistivity peak is very large, 63 and 54 K at $H=2$ and 3 T, respectively.

We argue that this effect is caused by modification of the effective hopping integrals and the resulting electron bandwidth due to isotope substitution, which shifts the relative stability of the CO versus FM states and leads to a transition between these phases. Simple model considerations suggest a significant enhancement of the isotope effect near the onset of the charge-ordered state and the corresponding lattice instability. To analyze this problem quantitatively we must take into account a whole set of competing mechanisms: electron–phonon interaction, polaronic band narrowing, the Jahn–Teller effect, double exchange, intersite Coulomb repulsion of electrons, etc. Nonetheless, we think that our simple arguments correctly describe the main physics of the phenomenon observed.

ACKNOWLEDGMENTS

The authors are grateful to A. N. Taldenkov and A. V. Inyushkin for help in the work. The work has partially supported by the Russian Foundation for Basic Research, Project No. 97-03-32979a. One of the authors (D.I.K.) acknowledges The Netherlands Foundation for the Fundamental Research of Matter (FOM) for support.

- ¹C. N. R. Rao, A. K. Cheetham, and R. Mahesh, *Chem. Mater.* **8**, 2421 (1996).
- ²N. A. Babushkina, L. M. Belova, O. Yu. Gorbenco, A. R. Kaul, A. A. Bosak, V. I. Ozhogin, and K. I. Kugel, *Nature* **391**, 159 (1998).
- ³A. J. Millis, P. B. Littlewood, and B. I. Shraiman, *Phys. Rev. Lett.* **74**, 5144 (1995).
- ⁴H. Y. Hwang, S.-W. Cheong, P. G. Radaelli, M. Marezio, and B. Batlogg, *Phys. Rev. Lett.* **75**, 914 (1995).
- ⁵J. Fontcuberta, B. Martinez, A. Seffar, S. Pinol, J. L. Garcia-Muñoz, and X. Obradors, *Phys. Rev. Lett.* **76**, 1122 (1996).
- ⁶Z. Jirak, S. Krupicka, Z. Simsa, M. Dlouha, and S. Vratislav, *J. Magn. Magn. Mater.* **53**, 153 (1985).
- ⁷H. Yoshizawa, H. Kawano, Y. Tomioka, and Y. Tokura, *J. Phys. Soc. Jpn.* **65**, 1043 (1996).
- ⁸M. R. Lees, J. Baratt, G. Balakrishnan, and D. McK. Paul, *Phys. Rev. B* **52**, 14 303 (1995).
- ⁹G.-M. Zhao, K. Conder, H. Keller, and K. A. Müller, *Nature (London)* **381**, 676 (1996).
- ¹⁰G.-M. Zhao, M. B. Hunt, and H. Keller, *Phys. Rev. Lett.* **78**, 955 (1997).
- ¹¹O. Yu. Gorbenco, A. R. Kaul, N. A. Babushkina, and L. M. Belova, *J. Mater. Chem.* **7**, 747 (1997).
- ¹²N. A. Babushkina, A. P. Zhernov, A. V. Inyushkin, T. N. Kulagina, V. I. Ozhogin, and L. V. Molchanova, *Physica C* **272**, 257 (1996).
- ¹³M. Kasai, H. Kuwahara, Y. Tomioka, and Y. Tokura, *J. Appl. Phys.* **80**, 6894 (1996).
- ¹⁴J. R. Cullen and E. Callen, *J. Appl. Phys.* **41**, 879 (1969).
- ¹⁵D. I. Khomskii, Preprint No. 105, Lebedev Physics Institute, 1969.
- ¹⁶V. Z. Kresin and S. A. Wolf, *Philos. Mag. B* **76**, 241 (1997).

Magnetic susceptibility of Fe/Cu multilayers: Ferromagnetic, antiferromagnetic, and spin-glass phases

A. J. A. de Oliveira and W. A. Ortiz^{a)}

Departamento de Física-UFSCar, C.P. 676, 13565-905, São Carlos, SP Brazil

D. H. Mosca, N. Mattoso, and W. H. Schreiner

Departamento de Física-UFPR, C.P. 19081, 81531-990, Curitiba, PR Brazil

S. R. Teixeira

Instituto de Física-UFRGS, C.P. 15051, 91501-970, Porto Alegre, RS Brazil

In this work we present low-field magnetic measurements on multilayers of Fe 1.5 nm and Cu 1.5 nm layers, repeated 10 times, grown on Si(111) and Fe 5 nm/CaF₂ 40 nm/Si(111) substrates. Magnetic characteristics of a spin-glass phase are exhibited by samples directly grown on Si(111), for which the glass temperatures (T_G) depend strongly on the magnetic field. Above T_G those samples exhibit a ferromagnetic behavior. In contrast, samples grown on Fe/CaF₂ buffer structure also show the spin-glass characteristics, but are antiferromagnetic above T_G . This work deals with the fundamental role played by the interface between Fe and Cu for these effects, which is clearly emphasized by the experimental results. © 1998 American Institute of Physics. [S0021-8979(98)46011-0]

Research and development of metallic magnetic multilayers is an area of increasing interest, not only for the fundamental physics involved with films and layers, but especially due to its great potential for a variety of applications. Fe/Cu multilayers are very interesting systems exhibiting a strong correlation between magnetic and structural properties. For example, it is well known that face centered cubic (fcc) γ -Fe and body centered cubic (bcc) Cu metastable phases can be obtained in epitaxial or highly textured films.¹⁻¹⁰ Experimental results and first-principle magnetic structure calculations confirmed that a rich variety of magnetic configurations can be stabilized in fcc γ -Fe with a lattice constant range near that of fcc Cu.¹¹⁻¹⁵ It has also been shown that the magnetic anisotropy energies are rather different for the ferromagnetic and various antiferromagnetic configurations in fcc Fe.^{11,12} Fe/Cu multilayers also present antiferromagnetic exchange coupling which is accompanied by moderate magnetoresistive and magneto-optic effects for chemical modulation periods in the nanometer length scale.¹⁶ Despite of the great interest on magnetic properties of Fe/Cu multilayers, its low-field magnetic susceptibility behavior has not been thoroughly explored in the literature.

The present article reports on the irreversible behavior exhibited by zero-field-cooled (ZFC) and field-cooled (FC) magnetization curves of highly oriented Fe/Cu multilayers. Our experimental results are discussed assuming that a magnetic metastable phase occurs at the interfaces due to the existence of some interdiffusion between Fe and Cu.

Previous studies¹⁷⁻¹⁹ have shown that highly oriented Fe(110)/Cu(111) multilayers consisting of successive depo-

sition of Cu 1.5 nm and Fe 1.5 nm layers repeated 10 times can be grown directly either on Si(111) or on Fe 5 nm/CaF₂ 40 nm/Si(111) substrates. X-ray diffraction and electron diffraction analyses confirmed that the Fe/Cu multilayers grown on Fe/CaF₂ buffer structure have a better structural quality than those grown on Si(111) surfaces. Besides, x-ray reflectivity data reveal that each of these multilayers exhibits rather different interfacial roughness. The samples investigated in this study belong to a series widely explored so far. Despite the wide range of layer thicknesses in the series, we found no meaningful way to explain the very low magnetoresistance in these multilayer systems.

The dc magnetic susceptibility (χ_{dc}) measurements, performed in the temperature range 5–400 K and fields up to 1 kOe, were taken with a superconducting quantum interference device (SQUID) magnetometer (MPMS-5S, Quantum Design). Each measurement resulted from two sample scans over a length of 4 cm, with 40 point readings per scan. Low-field susceptibility measurements as a function of the temperature for different values of the applied field, were carried out using a routine combining a ZFC warming run followed by a FC experiment. To start the procedure, the sample was first heated up to 400 K and then cooled down to 5 K in the absence of magnetic field. Magnetization loops were also measured for many temperatures in between 5 and 400 K. Remnant demagnetization cycles were done at 400 K to prevent spurious irreversible effects associated with magnetic history of the sample in the ZFC measurements. Real and imaginary parts of the low-field ac susceptibility ($\chi_{ac} = \chi' + j\chi''$) of the samples were also measured using the SQUID

^{a)}Electronic mail: adilson@power.ufscar.br

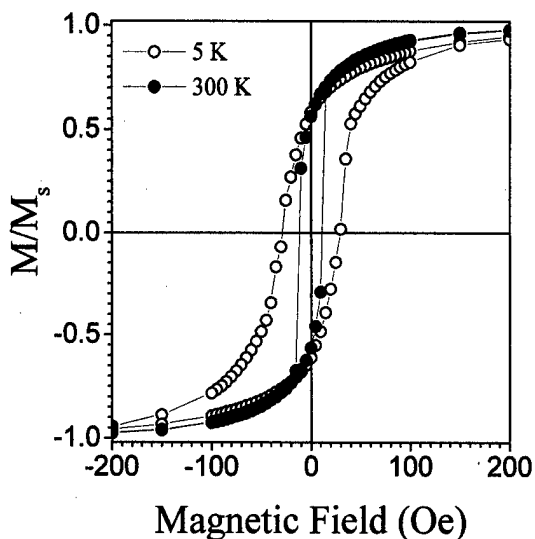


FIG. 1. Hysteresis loops measured for sample 2, at temperatures (○) 5 and (●) 300 K.

magnetometer with an excitation field $h_{ac} = 3.0$ Oe. The temperature dependence χ_{ac} at different frequencies was measured while heating the samples.

Figure 1 shows the central portion of hysteresis loops, measured at 5 and 300 K, for one of the Fe/Cu multilayers investigated, grown on a Fe/CaF₂ buffer structure (sample 2). Notice that, at 200 Oe, the relative magnetization is about 95% of its saturation value. Hysteresis loops for the other multilayer studied here, grown on a Si(111) surface (sample 1), are similar and will appear in another publication.¹⁷ Both samples exhibit typical ferromagnetic behavior, saturating at

relatively low magnetic fields. It is worth mentioning that the remnant magnetization values measured at 5 and 300 K for sample 2 are smaller than those observed for sample 1.

Figure 2 shows measurements of χ_{dc} for those two multilayers. One can see that both exhibit a spin-glasslike behavior at low magnetic fields, manifested by several typical signatures, including a field-dependent irreversible magnetization, a frequency dependent χ_{ac} , and the occurrence of metastable states characterized by a logarithmic time relaxation upon application or suppression of external fields of low magnitude.

The irreversible behavior is relatively weak, being more pronounced for sample 2. Besides, the irreversibility temperature associated with the bifurcation in the ZFC/FC curves is quite high and strongly dependent on the applied magnetic field. A glass temperature T_G , associated with a hump in the ZFC curve, is also observed for low fields. Another important feature when comparing these multilayers is that the FC curves for low fields are clearly different. While the FC response for sample 1 resembles those of a ferromagnet, sample 2 exhibits a more complex behavior, including antiferromagnetism for higher temperatures, bounded by a local maximum of χ_{dc} on the vicinity of 380 K. Since the crystal structure of both multilayers is similar, exhibiting identical orientation along the film growth axis, one would conclude that irreversibility comes from the occurrence of dissimilar interfaces in different samples. This magnetic behavior seems to be related to a certain roughness at the Fe/Cu interfaces, which manifests itself as a local intermixing of adjacent layers. Our results suggest that the width of the

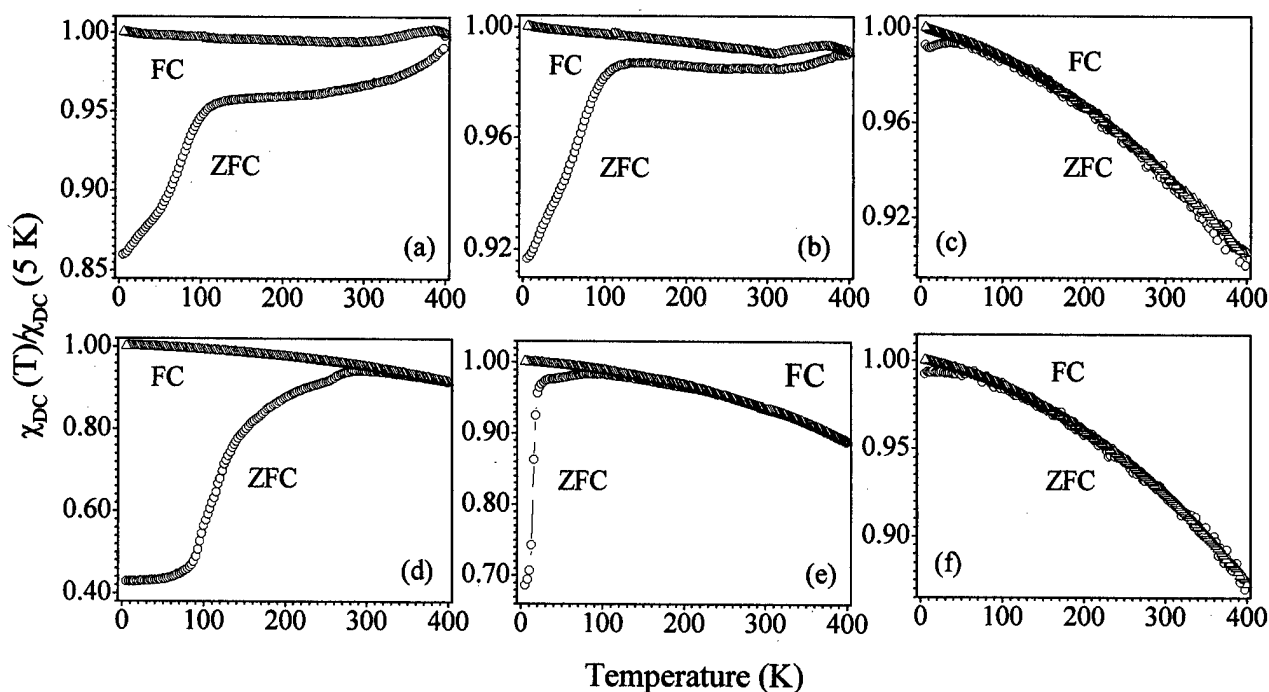


FIG. 2. Temperature dependence of χ_{dc} for sample 2 at fields: (a) 10, (b) 50, and (c) 1000 Oe; and for sample 1: (d) 10, (e) 50, and (f) 1000 Oe. Two curves are shown for each value of the field: the lower (○) is for the multilayer zero-field cooled to 5 K while the upper (△) is for the film cooled in the measuring field. Irreversibility temperatures associated with a bifurcation in ZFC/FC curves are observed.

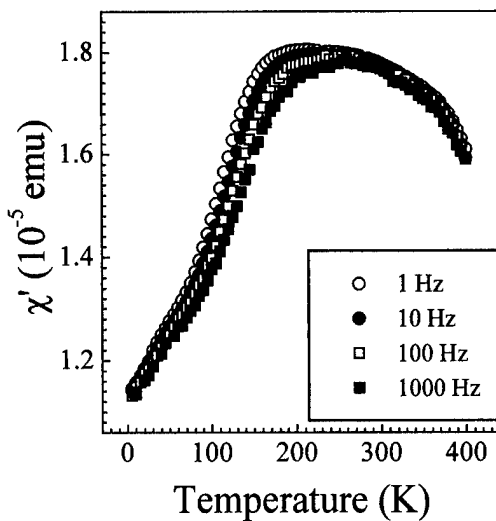


FIG. 3. Temperature dependence of χ' for sample 2. A small memory effect, dependent on the frequency, is present.

mixed interfacial region should be small, involving only a few number of monolayers. Otherwise, one could not explain the ferromagnetic and antiferromagnetic behavior of FC curves.^{20,21}

Figure 3 shows $\chi'(T)$ for sample 2, whereas $\chi''(T)$ appears in Fig. 4. Both exhibit the expected frequency dependence for a spin-glass system.²² χ' shows a typical frequency shift, while χ'' has a maximum which also shifts towards high temperatures. An interesting feature of Fig. 3 is the flatness of χ' between 200 and 350 K which might be evidencing a possible overlapping of spin-glass and antiferromagnetic phases. Also noticeable is the increase in χ'' dispersion for higher frequencies, which could be attributed to an enhanced activity of magnetic domains induced by the rapidly varying excitation field.

In summing up, we have reported clear experimental evidences of a spin-glass behavior overlapping with ferro- and antiferromagnetism in Fe/Cu multilayers. As a matter of fact, a detailed investigation of the microscopic character of the interfaces in the samples of interest is a crucial task in the study of the mechanisms leading to the behavior reported here. In the past we have employed x-ray reflectivity with a double-crystal setup and also conventional θ - 2θ low-angle diffraction, in an attempt to clarify those questions. Other powerful techniques, like *in situ* transmission, tunneling, and atomic force microscopy, could represent an expressive step forward in this subject, but neither is available at the moment. We are now conducting an alternative study, to appear soon elsewhere, in which we change the number of interfaces and the surface/volume ratio.

Furthermore, there is an still unpublished work resulting from near-edge extended x-ray absorption fine structure experiments conducted at LURE (Orsay, France) on these multilayers, which indicates the existence of highly disordered Cu sites at the interfaces, corroborating the proposed scenario of local intermixing and roughness at adjacent layers.

As we see, a considerable amount of information on the structure of these systems has been collected in this and in previous work, indicating that the Fe/Cu interface peculiari-

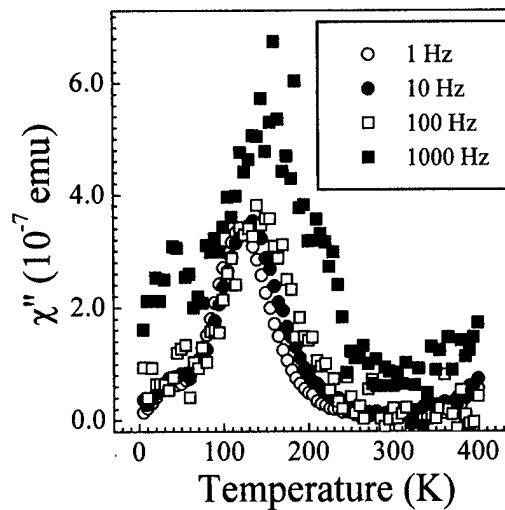


FIG. 4. Temperature dependence of χ'' for sample 2. Typical frequency shifts of χ'' peaks are observed.

ties are to be responsible for the presently reported behavior, as well as for the absence of significant giant magnetoresistance effects in these multilayers.¹⁹

Financial support from FAPESP, FAPERGS, CNPq, and FINEP/PRONEX is acknowledged.

- ¹D. Li, M. Freitag, J. Pearson, Z. Q. Qiu, and S. D. Bader, J. Appl. Phys. **76**, 6425 (1994).
- ²O. Durand, J. M. George, J. R. Childress, S. Lequien, A. Schuhl, and A. Fert, J. Magn. Magn. Mater. **121**, 140 (1993).
- ³S. F. Cheng, A. N. Mansur, J. P. Teter, K. B. Hathaway, and L. Kabacoff, Phys. Rev. B **47**, 206 (1993).
- ⁴G. J. Mankey, R. F. Willis, and F. J. Himpsel, Phys. Rev. B **48**, 10 284 (1993).
- ⁵D. Tian, F. Jona, and P. M. Marcus, Phys. Rev. B **45**, 11 216 (1992).
- ⁶H. Magnan, D. Chandesris, B. Villet, O. Heckmann, and J. Lecante, Phys. Rev. Lett. **67**, 859 (1991).
- ⁷F. J. Himpsel, Phys. Rev. Lett. **67**, 2363 (1991).
- ⁸B. Heinrich, Z. Celinski, J. F. Cochrane, W. B. Muir, J. Rudd, Q. M. Zhong, A. S. Arott, K. Myrtle, and J. Kirschner, Phys. Rev. Lett. **64**, 673 (1990).
- ⁹F. Pontkees and H. Neddermeyer, Physica B **161**, 276 (1989).
- ¹⁰D. Pescia, M. Stapanony, G. L. Bone, A. Vaterlaus, R. F. Willis, and F. Meier, Phys. Rev. Lett. **58**, 2126 (1987).
- ¹¹L. Szunyogh, B. Ujfalussy, and P. Weinberger, Phys. Rev. B **55**, 14 392 (1997).
- ¹²Y.-M. Zhou, W.-Q. Zhang, L.-P. Zhong, and D.-S. Wang, J. Magn. Magn. Mater. **145**, L273 (1995).
- ¹³F. Baudalet, M. T. Lin, W. Kuch, K. Meinel, B. Choi, C. M. Schneider, and J. Kirschner, Phys. Rev. B **51**, 12 563 (1995).
- ¹⁴T. Detzel, M. Vonbank, M. Donath, and V. Dose, J. Magn. Magn. Mater. **147**, L1 (1995).
- ¹⁵T. Kraft, P. M. Marcus, and Scheffler, Phys. Rev. B **49**, 11 511 (1994).
- ¹⁶See, for example, *Ultrathin Magnetic Structures I and II*, edited by B. Heinrich and J. A. C. Bland (Springer, New York, 1994).
- ¹⁷A. J. A. de Oliveira, W. A. Ortiz, D. H. Mosca, N. Mattoso, I. Mazzaro, W. H. Schreiner, and S. R. Teixeira, J. Phys. Condens. Matter (submitted).
- ¹⁸W. H. Schreiner, D. H. Mosca, S. R. Teixeira, and N. Mattoso, J. Appl. Phys. **72**, 5682 (1992).
- ¹⁹J. F. M. Borges, G. Tosin, L. F. Schelp, N. Mattoso, S. R. Teixeira, D. H. Mosca, and W. H. Schreiner, J. Magn. Magn. Mater. **121**, 53 (1993).
- ²⁰D. H. Mosca, N. Mattoso, E. M. Kakuno, W. H. Schreiner, I. Mazzaro, and S. R. Teixeira, J. Magn. Magn. Mater. **156**, 391 (1996).
- ²¹A. Brodde, K. Dreps, J. Binder, C. Lunau, and H. Neddermeyer, Phys. Rev. B **47**, 6609 (1993).
- ²²J. A. Mydosh, in *Spin Glasses: An Experimental Introduction* (Taylor and Francis, London, 1993), p. 68.

Origin of magnetic anomalies in the spin glass system, $\text{La}_{0.85}\text{Sr}_{0.15}\text{CoO}_3$

P. S. Anil Kumar

Centre for Advanced Studies in Material Science and Solid State Physics, Department of Physics,
University of Pune, Pune 411007, India

P. A. Joy^{a)} and S. K. Date

Physical and Materials Chemistry Division, National Chemical Laboratory, Pune 411008, India

The composition with $x=0.15$ in the spin glass regime ($0 \leq x \leq 0.18$) of the perovskite system, $\text{La}_{1-x}\text{Sr}_x\text{CoO}_3$, is investigated in detail to understand the unusual magnetic properties reported in the literature. AC susceptibility and field-cooled and zero-field-cooled magnetization measurements give sufficient evidence for compositional inhomogeneity as the origin of the magnetic anomalies. A well-defined spin glass behavior is obtained only for a highly homogeneous sample. © 1998 American Institute of Physics. [S0021-8979(98)32311-7]

I. INTRODUCTION

The perovskite system, $\text{La}_{1-x}\text{Sr}_x\text{CoO}_3$, has been studied extensively in the recent past to understand the evolution of its unusual electronic properties. Jonker and van Santen¹ first reported that the paramagnetic Curie temperature increases from negative to positive value for $x > 0.1$ and the onset of ferromagnetism is caused by the $\text{Co}^{3+}-\text{O}-\text{Co}^{4+}$ double exchange interaction as proposed by Zener.² From detailed studies on the magnetic properties, Itoh *et al.*³ have reported that there is no true long range ferromagnetic ordering as reported previously and there exists spin glass for $0 \leq x \leq 0.18$ and cluster glass for $0.18 \leq x \leq 0.5$ regions in $\text{La}_{1-x}\text{Sr}_x\text{CoO}_3$. Senaris-Rodriguez and Goodenough⁴ recently reported the superparamagnetic blocking model to explain the unusual magnetic behavior of their low Sr-doped samples.

Most of the unusual behavior observed for the $\text{La}_{1-x}\text{Sr}_x\text{CoO}_3$ system is in the spin glass composition regime. For example, a spin glass freezing temperature of 65 K with a well-defined cusp-like magnetization behavior is reported by Itoh *et al.*³ for $\text{La}_{0.85}\text{Sr}_{0.15}\text{CoO}_3$ whereas recent investigations^{4,5} on the same composition showed multiple magnetic transitions; (i) a Curie temperature of ~ 240 K due to ferromagnetic ordering within large magnetic clusters, (ii) a shoulder-like transition at ~ 170 K due to blocking of these larger clusters below which the field cooled and zero field cooled magnetization shows irreversible behavior, and (iii) a spin glass freezing at ~ 70 K which is due to the final collective blocking of small clusters. Though blocking of large clusters takes place at ~ 170 K, there was no cusp in the ac susceptibility observed at this temperature.

We have investigated the origin of this unusual magnetic behavior of the spin glass composition $\text{La}_{0.85}\text{Sr}_{0.15}\text{CoO}_3$ using ac magnetic susceptibility and dc magnetization studies. Our studies are based on the fact that the above interesting results are obtained from measurements on samples processed at different heat treatment conditions.

II. EXPERIMENT

$\text{La}_{0.85}\text{Sr}_{0.15}\text{CoO}_3$ samples were prepared by the high-temperature ceramic (solid-state reaction) and by the low-temperature coprecipitation methods. In the ceramic method, molar ratios of La_2O_3 (preheated at 1000°C), SrCO_3 and $\text{CoC}_2\text{O}_4 \cdot 2\text{H}_2\text{O}$, are mixed together and calcined at 950°C . The calcined sample was heated at 1000°C for 72 h with six intermediate grindings. The bulk sample was then pressed into pellets and annealed at different temperatures in the range 1000 – 1300°C . Low-temperature synthesis by the coprecipitation method was performed following the reported method.^{4,5} The mixed hydroxide precipitate was initially decomposed at 750°C and then annealed at different temperatures. The oxygen stoichiometry of all the samples were determined by oxidation-reduction titrations using potassium permanganate and ferrous sulfate solutions and were stoichiometric ($\text{La}_{0.85}\text{Sr}_{0.15}\text{CoO}_{3 \pm 0.01}$). The microstructural features were obtained using a Leica-Cambridge 440 Scanning Electron Microscope (SEM). AC magnetic susceptibility (27 Hz, 10 Oe) was measured by the mutual inductance method in an APD close-cycle helium cryostat (15 – 300 K). Field-cooled (FC) and zero-field-cooled (ZFC) dc magnetization ($H_A = 100$ Oe) studies were done on a EG&G PAR VSM model 4500 fitted with a Janis liquid nitrogen cryostat (80 – 300 K).

III. RESULTS AND DISCUSSION

Figure 1 shows the ac susceptibility curves of the sample prepared by the ceramic method and annealed at different temperatures. The sample annealed at 1000°C for 72 h shows a magnetic transition at $T_c \approx 250$ K and this transition temperature shifts to lower temperatures as the annealing temperature is increased. All the curves show a second magnetic transition immediately below the first transition and a maximum in the susceptibility is observed at $T = T_{\chi_{\text{max}}}$, which also decreases continuously with increasing annealing temperature. As T_c is decreased, the magnitude of susceptibility at T_c is also decreased and finally a cusp-shaped magnetic susceptibility curve is obtained at $T_g = 75$ K.

^{a)}Electronic mail: joy@dalton.ncl.res.in

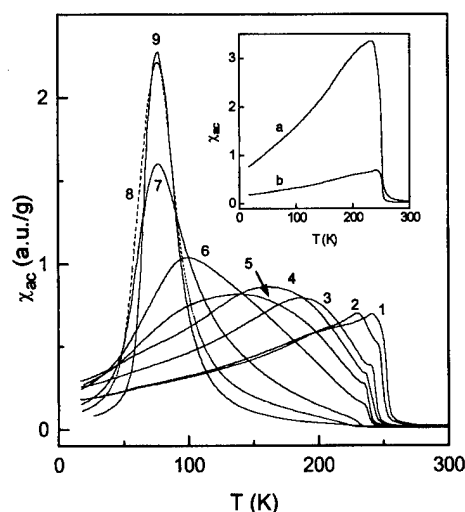


FIG. 1. AC susceptibility curves of $\text{La}_{0.85}\text{Sr}_{0.15}\text{CoO}_3$ synthesized by the ceramic method and annealed at different temperatures. (1) 1000 °C/72 h, (2) 1050 °C/12 h, (3) 1100 °C/12 h, (4) 1100 °C/24 h, (5) 1100 °C/48 h, (6) 1150 °C/12 h, (7) 1200 °C/12 h, (8) 1250 °C/12 h, (9) 1300 °C/12 h. Inset: ac susceptibility curves of (a) $\text{La}_{0.5}\text{Sr}_{0.5}\text{CoO}_3$ and (b) $\text{La}_{0.85}\text{Sr}_{0.15}\text{CoO}_3$ samples prepared by the ceramic method annealed at 1000 °C/72 h.

In the inset of Fig. 1, the ac susceptibility curve of $\text{La}_{0.85}\text{Sr}_{0.15}\text{CoO}_3$ annealed at 1000 °C (curve 1 in Fig. 1) is compared with that of $\text{La}_{0.5}\text{Sr}_{0.5}\text{CoO}_3$ processed under identical conditions. In $\text{La}_{1-x}\text{Sr}_x\text{CoO}_3$ system, maximum ferromagnetic Curie temperature is observed for $x=0.5$.¹ Both these curves are identical, showing a sharp transition at ~250 K, with the maximum value of susceptibility for the $\text{La}_{0.85}\text{Sr}_{0.15}\text{CoO}_3$ composition approximately 1/5th of that of the $\text{La}_{0.5}\text{Sr}_{0.5}\text{CoO}_3$ sample. It appears that the $x=0.15$ composition annealed at 1000 °C contains a minimum of ~20% of the $x=0.5$ composition. This implies that the low temperature annealed $x=0.15$ sample is highly compositionally inhomogeneous. This sample may contain various phases of $\text{La}_{1-x}\text{Sr}_x\text{CoO}_3$ having different x values. On further annealing of the sample at higher temperatures, the sharp magnetic transition is shifted to lower temperatures indicating narrowing down of the compositional range and finally a well-defined magnetic transition is obtained for the high temperature annealed sample.

The FC and ZFC curves of two samples prepared by the ceramic method are shown in Fig. 2. The nature of the FC and ZFC curves of both the 1000 and 1100 °C annealed samples are similar to that reported for the sample prepared by coprecipitation method.⁵ The ferromagnetic composition $\text{La}_{0.5}\text{Sr}_{0.5}\text{CoO}_3$ also shows similar behavior which is assigned to the cluster-glass nature of the compound.^{3,6} Inset in Fig. 2 compares the identical nature of the ZFC and ac susceptibility curves of the sample annealed at 1100 °C. The ac susceptibility curve of the sample annealed at 1300 °C is similarly identical to that of the ZFC curve reported by Itoh *et al.*³

Figure 3 shows the FC and ZFC curves of the sample prepared by the coprecipitation method. The sample heated to 750 °C shows behavior similar to that of the ceramic sample annealed at 1000 °C showing a magnetic transition below ~250 K. The ZFC curves of the ceramic sample an-

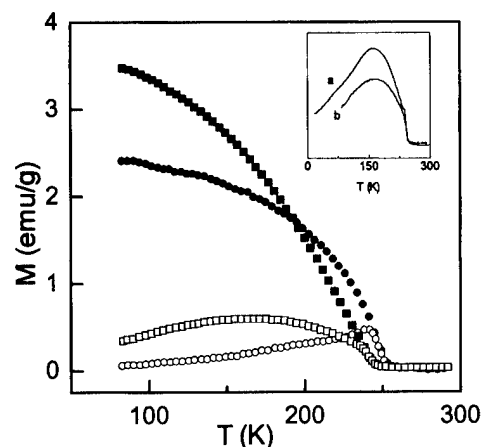


FIG. 2. FC (solid symbols) and ZFC (open symbols) curves of $\text{La}_{0.85}\text{Sr}_{0.15}\text{CoO}_3$ ceramic samples annealed at 1000 °C/72 h (squares) and 1100 °C/24 h (circles). Inset: (a) ac susceptibility and (b) ZFC curves of the 1100 °C/24 h annealed sample showing identical nature of the curves.

nealed at 1100 °C/24 h and the coprecipitated sample annealed at 1000 °C are compared in the inset. Both the curves show an initial magnetic transition below ~240 K and a maximum in the magnetization below ~200 K. The particle sizes obtained from SEM for the above samples were ~1000 and ~200 nm, respectively. However, the T_c and the magnitude of the magnetization at T_c of the coprecipitated sample is lower than that of the ceramic sample indicating that the contribution due to the Sr-rich phase is less in the coprecipitated sample. This sample also shows an increase in magnetization below ~100 K which marks the formation of the required composition at this processing temperature. ZFC curves of the coprecipitated sample annealed at different temperatures are compared in Fig. 4. As in the case of the ceramic samples, the increase in annealing temperature decreases the contribution due to the Sr-rich phase as well as narrow down the compositional range. The behavior of this

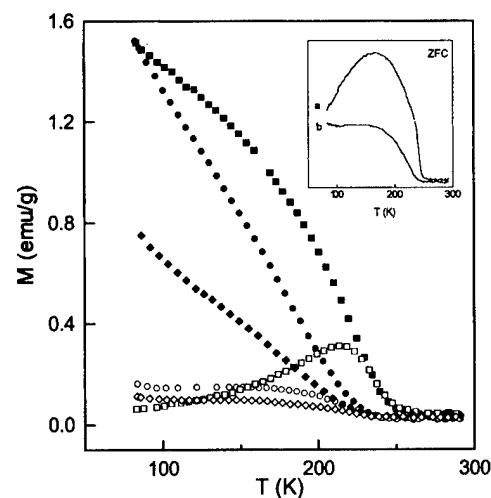


FIG. 3. FC (solid symbols) and ZFC (open symbols) curves of $\text{La}_{0.85}\text{Sr}_{0.15}\text{CoO}_3$ sample prepared by the coprecipitation method and annealed at different temperatures, 750 °C/16 h (squares), 1000 °C/12 h (diamonds), and 1100 °C/12 h (circles). Inset: ZFC curves of the composition prepared by (a) ceramic method 1100 °C/24 h and (b) coprecipitation method, 1000 °C/12 h.

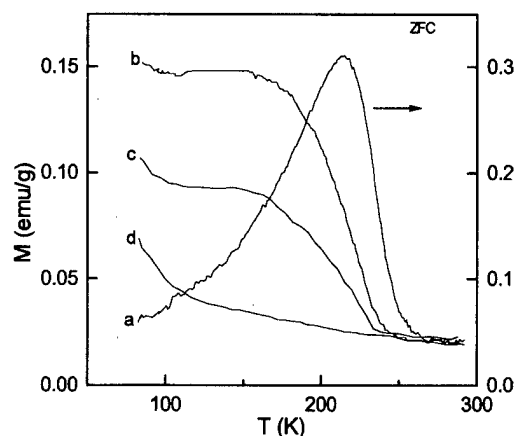


FIG. 4. Comparison of the ZFC curves of the $\text{La}_{0.85}\text{Sr}_{0.15}\text{CoO}_3$ sample prepared by the coprecipitation method, (a) 750 °C/16 h, (b) 1000 °C/12 h, (c) 1100 °C/12 h, and (d) 1200 °C/12 h. Curve (a) refers to the right vertical axis.

sample annealed at 1200 °C is better than that of the ceramic sample annealed at 1300 °C, with no other magnetic transition apart from the slow increase in the magnetization below ~100 K which is due to the contribution from the spin glass phase alone. This implies that the low-temperature synthesized sample if processed at sufficiently higher temperature ensures compositional homogeneity and will show similar spin glass behavior obtained for the sample prepared by the ceramic method and annealed at very high temperatures (Fig. 1). The particle size of the coprecipitated sample annealed at 1200 °C was less than 1000 nm. This shows that the observed differences in the magnetic behavior is not particle size dependent.

The unusual results of Mira *et al.*⁵ and Senaris-Rodriguez and Goodenough⁴ showing multiple magnetic

transitions for the $\text{La}_{0.85}\text{Sr}_{0.15}\text{CoO}_3$ composition is thus due to compositional inhomogeneity rather than due to the cluster size dependence. The transition at ~240 K and the shoulder below ~200 K indicate that the compound contains sufficient amount of phases with composition close to $x=0.5$ ($T_c \approx 245$ K) and $x=0.2$ ($T_c \approx 180$ K). These results may be compared with the ZFC magnetization curves reported by Itoh *et al.*³ and Golovanov *et al.*⁷ for $\text{La}_{0.85}\text{Sr}_{0.15}\text{CoO}_3$ which show only a cusp at the spin glass freezing temperature. It has been shown earlier from energy-dispersive analysis by x-ray by Baythoun and Sale⁸ and Chick *et al.*⁹ that perovskites with similar compositions synthesized by the sol-gel method are highly compositionally inhomogeneous when processed at low temperatures. It appears that processing conditions are extremely important in determining the true magnetic behavior of perovskite type $\text{La}_{1-x}\text{Sr}_x\text{CoO}_3$ compounds.

ACKNOWLEDGMENT

One of the authors (P.S.A.K.) is grateful to UGC, India for financial assistance.

- ¹G. H. Jonker and J. H. Van Santen, *Physica (Utrecht)* **19**, 120 (1953).
- ²C. Zener, *Phys. Rev.* **82**, 403 (1951).
- ³M. Itoh, I. Natori, S. Kubota, and K. Motoya, *J. Phys. Soc. Jpn.* **63**, 1486 (1994).
- ⁴M. A. Senaris-Rodriguez and J. B. Goodenough, *J. Solid State Chem.* **118**, 323 (1995).
- ⁵J. Mira, J. Rivas, R. D. Sanchez, M. A. Senaris-Rodriguez, D. Fiorani, D. Rinaldi, and R. Caciuffo, *J. Appl. Phys.* **81**, 5753 (1997).
- ⁶S. Mukherjee, R. Ranganathan, P. S. Anil Kumar, and P. A. Joy, *Phys. Rev. B* **54**, 9267 (1996).
- ⁷V. Golovanov, L. Mihaly, and A. R. Moodenbaugh, *Phys. Rev. B* **53**, 8207 (1996).
- ⁸M. S. G. Baythoun and F. R. Sale, *J. Mater. Sci.* **17**, 2757 (1982).
- ⁹L. A. Chick, L. R. Pederson, G. D. Moupin, J. L. Bates, L. E. Thomas, and G. J. Exarhos, *Mater. Lett.* **10**, 6 (1990).

Canted antiferromagnetism and spin glasslike behavior in a family of two-dimensional organic/inorganic nanocomposites

M. A. Girtu^{a)} and C. M. Wynn

Department of Physics, The Ohio State University, Columbus, Ohio 43210-1106

W. Fujita and K. Awaga

Department of Basic Sciences, The University of Tokyo, Komaba, Meguro-ku, Tokyo 153, Japan

A. J. Epstein

Department of Physics, The Ohio State University, Columbus, Ohio 43210-1106 and

Department of Chemistry, The Ohio State University, Columbus, Ohio 43210

We report magnetic properties of a new class of hybrid organic/inorganic layered materials, $\text{Cu}_2(\text{OH})_3(\text{C}_m\text{H}_{2m+1}\text{COO})$, $m=7, 9$, and 11 . The frequency dependence of the linear ac susceptibility and the irreversibility in the field-cooled/zero-field-cooled magnetization show that the geometrical frustration of the triangular lattice is strong enough to cause glassiness. The strong peak in the second harmonic of the nonlinear ac susceptibility indicates that frustration is not sufficient to prevent the system from developing a spontaneous moment. We propose that the interplay of Heisenberg antiferromagnetic exchange and Dzyaloshinskii–Moriya interaction leads to the unusual coexistence of glassiness and canted antiferromagnetism. © 1998 American Institute of Physics. [S0021-8979(98)46111-5]

I. INTRODUCTION

The question whether geometrical frustration alone, as opposed to random exchange, is strong enough to destroy magnetic order has preoccupied not just the theoretical community¹ but the experimental one as well. Traditionally, spin glass behavior was thought to require both disorder and frustration.^{2,3} It has been argued that frustration alone can lead to large ground-states degeneracies, accompanied by extensive ground-state entropies, but cannot produce a sufficiently “rough” free energy landscape necessary for the development of glassiness.⁴ Since the effects of frustration are more pronounced in lower dimensions, the best candidates for disorder-free glassiness are two-dimensional antiferromagnets on triangular or kagomé lattices.^{1,4} Such systems have been intensely studied in recent years, glassiness being found in kagomé systems⁵ as well as in other materials,^{6,7} all having continuous symmetry spins and sharing the same basic building block—the triangular plaquette—for their lattices.

We recently reported the first evidence for hybrid organic/inorganic triangular quantum Heisenberg antiferromagnets (TQHAF) with weak additional Dzyaloshinskii–Moriya (DM) interaction, $\text{Cu}_2(\text{OH})_3(\text{C}_m\text{H}_{2m+1}\text{COO})$, $m=7, 9$, and 11 .⁸ Based on dc magnetization and magnetic irreversibility studies, and on linear and nonlinear ac susceptibility data we showed that these compounds have an unusual magnetic behavior, inconsistent with both the resonant valence bond (RVB)⁹ and the noncollinear Néel ground state.¹⁰ We suggested that the DM antisymmetric exchange is responsible for the spontaneous moment and Ising-like ordering. We present here further evidence to support our claim that the interplay between the Heisenberg antiferro-

magnetic exchange causing geometrical frustration and the DM interaction leading to spin canting allows these systems to evolve into a new unusual state with both canted antiferromagnetic and glassy characteristics.

II. EXPERIMENT

The samples we have studied are compounds obtained by intercalation of saturated organic chains between inorganic layers of copper hydroxides.¹¹ The copper hydroxy salts $\text{Cu}_2(\text{OH})_3\text{X}$ ($\text{X}=\text{NO}_3$, $\text{C}_m\text{H}_{2m+1}\text{COO}$, $m\geq 0$, etc.) exhibit a botallackite-type structure,¹² in which two-crystallographically distinct copper atoms lie in different octahedral environments.¹¹ X-ray powder diffraction studies revealed layered structures with interlayer distances of 24.1, 29.4, and 34.4 Å for $m=7, 9$, and 11 , respectively.¹¹ Extended x-ray absorption fine structure (EXAFS) measurements showed¹³ that the polycrystalline powder samples of the intercalation compounds maintain the basic framework of the crystalline inorganic layer $\text{Cu}_2(\text{OH})_3\text{NO}_3$, with slight distortions of the local octahedral symmetry. Though it is difficult to put an upper limit to any structural disorder present, transmission electron microscopy photographs of the polycrystalline powders revealed interference patterns usually observed in structurally well ordered materials,¹⁴ and the x-ray diffraction studies indicate crystallites of ~ 300 Å diameter.

The Cu^{2+} ions (no single ion anisotropy) are $S=1/2$ Heisenberg spins located on nonequilateral triangular magnetic lattices.¹¹ The most important interactions consistent with this structure are the Heisenberg (symmetric) superexchange through oxygen atoms and then the DM (antisymmetric) exchange¹⁵ caused by the spin-orbit interactions and the different local environments of adjacent copper sites.¹³ DM interaction recently was shown to be responsible for canted antiferromagnetic behavior in other two-dimensional

^{a)}Electronic mail: girtu@mps.ohio-stae.edu

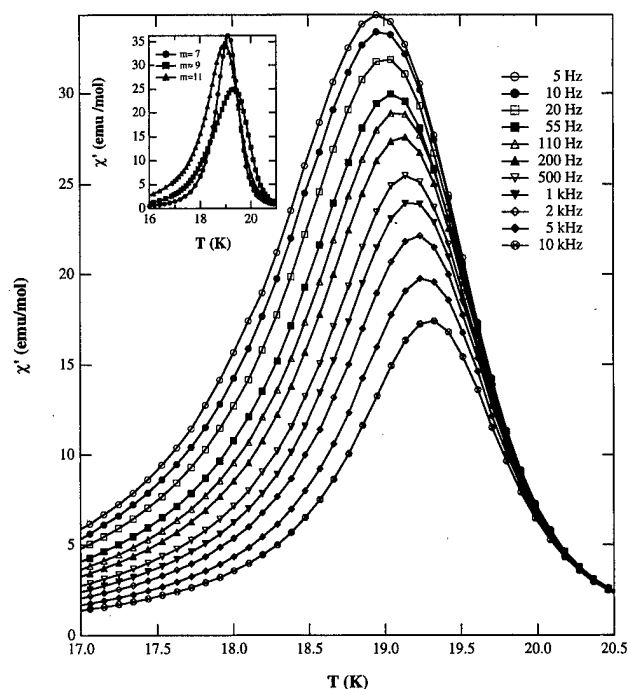


FIG. 1. χ'_1 of $\text{Cu}_2(\text{OH})_3(\text{C}_{11}\text{H}_{23}\text{COO})$, in $H_{ac}=1$ Oe (zero applied dc field) at frequencies $5 \leq f \leq 10\,000$ Hz. Inset: χ'_1 of $\text{Cu}_2(\text{OH})_3(\text{C}_m\text{H}_{2m+1}\text{COO})$, $m=7, 9$, and 11 , in $H_{ac}=1$ Oe (zero applied dc field) at $f=5$ Hz.

(2D) oxygen bridged copper systems, the parent compounds for high temperature superconductors.¹⁶

The ac magnetic susceptibility was measured with a Lake Shore 7225 ac susceptometer dc magnetometer in zero dc applied field and in the temperature range $5 \leq T \leq 30$ K, on warming. Both the in-phase (χ'_1) and out-of-phase (χ''_1) linear susceptibilities, $\chi_1 = \chi'_1 + i\chi''_1$, were measured under an ac field $H_{ac}=1$ Oe and a wide range of frequencies ($5 \leq f \leq 10\,000$ Hz). The second and third harmonics of the magnetic susceptibility χ_2 and χ_3 were obtained by reading the $2f$ and $3f$ lock-in responses, respectively, to an ac field with frequency f . The harmonics were measured on warming, in zero applied magnetic field, at fixed ac field amplitude (1.3 Oe) and frequencies between 10 and 3330 Hz. The magnetization was measured with a Quantum Design MPMS 5 superconducting quantum interference device (SQUID) magnetometer for $5 \leq T \leq 350$ K and $0 \leq H_{dc} \leq 55\,000$ Oe.

III. RESULTS AND DISCUSSION

The lowest frequency (5 Hz) χ'_1 data for the three compounds is displayed in the inset of Fig. 1. The independence of the peak temperatures ($T_p=19.1, 19.3$, and 19.0 K, for $m=7, 9$, and 11 , respectively) on the interlayer distances indicates that the magnetic behavior is governed by the intralayer interactions and, therefore, that these compounds are true 2D systems. Also, the relatively sharp peaks of the ac susceptibility suggest divergencies and, therefore, true magnetic transitions.

The peak temperature of χ'_1 increases and the peak height decreases with increasing frequency, Fig. 1, indicative of slow relaxation processes that characterize the glassy behavior.³ The values of the relative variation of the peak

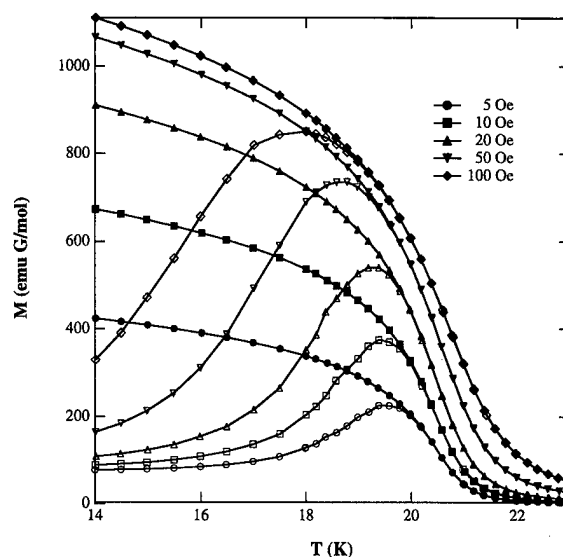


FIG. 2. FC (filled symbols) and ZFC (empty symbols) magnetization of $\text{Cu}_2(\text{OH})_3(\text{C}_{11}\text{H}_{23}\text{COO})$ in dc applied fields of $5 \leq H_{dc} \leq 100$ Oe.

temperature per decade of frequency, $(\Delta T_p/T_p)/\Delta(\log f) = 0.003, 0.008$, and 0.008 , for $m=7, 9$, and 11 , respectively) place these compounds in the range of canonical spin glasses.³ The strength of frustration in these geometrically frustrated systems, estimated from the ratio between the Curie-Weiss mean field ordering temperature Θ_{CW} and the true critical temperature T_c , $f_R = \Theta_{CW}/T_c$,⁷ was found to be 7, 6.5, and 6 for the three compounds, respectively.⁸ These values suggest moderate strength frustration,⁷ however they appear to be enough to cause the slow relaxation processes characteristic for glassy systems.

The field-cooled (FC) and zero-field-cooled (ZFC) magnetization curves for the $m=11$ compound ($m=7$ and 9 compounds have almost identical behavior),^{8,17} Fig. 2, show a rapid rise with decreasing T just above 20 K. At lower T the ZFC magnetization deviates below the FC magnetization indicating history dependence of the magnetization processes in the T range where χ'_1 shows frequency dependence. The field dependence of the bifurcation point T_b between the FC and ZFC curves (T_b decreases with increasing the applied dc field) reinforces the glassy behavior description.³

Even harmonics can be observed only if a system exhibits a spontaneous magnetization, due to the lack of inversion symmetry with respect to the applied field.¹⁸ Only odd harmonics are expected for a spin glass while for ferromagnets both even and odd harmonics should be present.¹⁹ Both second and third harmonics ($2f$ and $3f$ responses, respectively), for the $m=11$ compound, Fig. 3, (the $m=7$ and 9 compounds have almost identical behavior),^{8,17} have sharp peaks suggesting divergencies of both these quantities and, therefore, true magnetic transitions. The peak in the second harmonic indicates that a spontaneous moment is formed at that transition while the frequency dependence of both components of the nonlinear susceptibility suggests slow relaxation processes and glassiness.

Thus, all three systems show very similar magnetic properties. The high temperature TQHAF behavior was pre-

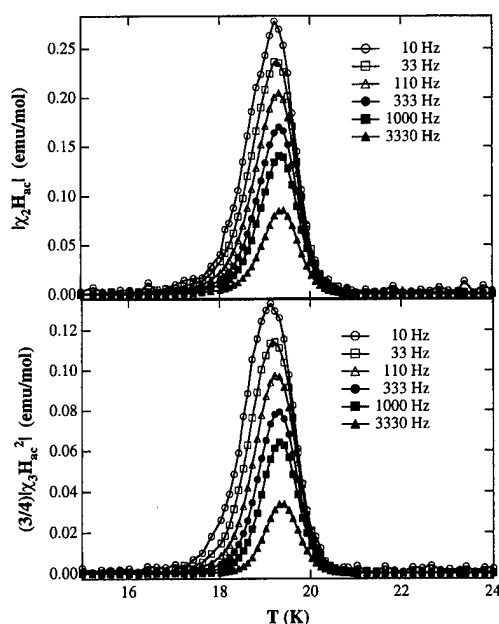


FIG. 3. Nonlinear susceptibilities $|\chi_{2,\text{exp}} H_{\text{ac}}|$ and $|3/4 \chi_{3,\text{exp}} H_{\text{ac}}^2|$ of $\text{Cu}_2(\text{OH})_3(\text{C}_{11}\text{H}_{23}\text{COO})$ measured at $2f$ and $3f$, respectively, in $H_{\text{ac}} = 1.3$ Oe (zero applied dc field) at frequencies $10 \leq f \leq 3330$ Hz.

viously shown by the fit of the static susceptibility to high temperature series expansions. At low temperatures the frequency dependence of the linear ac susceptibility and the field dependence of the bifurcation point of the field-cooled/zero-field-cooled magnetization data suggest slow relaxation and glassiness. The second harmonic of the nonlinear ac susceptibility indicates that geometrical frustration is not strong enough to prevent the system from canted antiferromagnetic type of ordering. Hence, we propose that these are three TQHAF systems with weak additional DM interaction whose unusual behavior is determined by the interplay between the

Heisenberg exchange, causing frustration and glassiness, and the DM exchange, causing spin canting and 2D Ising-like behavior.

ACKNOWLEDGMENT

The support of the Department of Energy Division of Materials Science (DE-FG02-86BR45271) is gratefully acknowledged.

- ¹G. Aeppli and P. Chandra, *Science* **275**, 177 (1997).
- ²K. Binder and A. P. Young, *Rev. Mod. Phys.* **58**, 801 (1986).
- ³J. A. Mydosh, *Spin Glasses: An Experimental Introduction* (Taylor and Francis, London, 1993).
- ⁴P. Chandra *et al.*, *J. Phys. I* **3**, 591 (1993).
- ⁵A. P. Ramirez *et al.*, *Phys. Rev. Lett.* **64**, 2070 (1990); C. Broholm *et al.*, *Phys. Rev. Lett.* **65**, 3173 (1990).
- ⁶B. D. Gaulin *et al.*, *Phys. Rev. Lett.* **69**, 3244 (1992); P. Schiffer *et al.*, *Phys. Rev. Lett.* **74**, 2379 (1995); P. Schiffer and A. P. Ramirez, *Comments Condens. Matter Phys.* **18**, 21 (1996); *Magnetic Systems with Competing Interactions-Frustrated Spin Systems*, edited by H. T. Diep (World Scientific, Singapore, 1994).
- ⁷A. P. Ramirez, *Annu. Rev. Mater. Sci.* **24**, 453 (1994).
- ⁸M. A. Gîrțu, C. M. Wynn, W. Fujita, K. Awaga, and A. J. Epstein (unpublished).
- ⁹P. W. Anderson, *Mater. Res. Bull.* **8**, 153 (1973); P. Fazekas and P. W. Anderson, *Philos. Mag.* **30**, 423 (1974).
- ¹⁰N. Elstner, R. R. P. Singh, and A. P. Young, *Phys. Rev. Lett.* **71**, 1629 (1993).
- ¹¹W. Fujita and K. Awaga, *Inorg. Chem.* **35**, 1915 (1996).
- ¹²S. Yamanaka *et al.*, *Chem. Lett.*, 1869 (1989).
- ¹³W. Fujita, K. Awaga, and T. Yokoyama, *Inorg. Chem.* **36**, 196 (1997).
- ¹⁴W. Fujita, Doctoral Thesis, The University of Tokyo, 1997.
- ¹⁵T. Moriya, *Phys. Rev.* **120**, 91 (1960); I. Dzyaloshinskii, *J. Phys. Chem. Solids* **4**, 241 (1958).
- ¹⁶T. Yildirim *et al.*, *Phys. Rev. B* **52**, 10 239 (1995).
- ¹⁷M. A. Gîrțu, C. M. Wynn, W. Fujita, K. Awaga, and A. J. Epstein (unpublished).
- ¹⁸T. Hashimoto *et al.*, *J. Phys. Soc. Jpn.* **35**, 81 (1973).
- ¹⁹T. Sato and Y. Miyako, *J. Phys. Soc. Jpn.* **51**, 1394 (1981); S. Mukherjee *et al.*, *Phys. Rev. B* **50**, 1084 (1994). Note that we use the usual harmonic labelling convention, see Mukherjee *et al.*

Magnetic and structural properties of $\text{PrCo}_{3-x}\text{Si}_x$ compounds

T. Matsui, R. D. Stevenson, R. D. Kirby,^{a)} and D. J. Sellmyer

Behlen Laboratory of Physics and Center for Materials Research and Analysis, University of Nebraska, Lincoln, Nebraska 68588-0111

We have systematically investigated the magnetic properties of the rare-earth compounds PrCo_8Si and $\text{PrCo}_{3-x}\text{Si}_x$, the crystal structures of which are hexagonal CeNi_3 -type and rhombohedral Be_3Nb -type, respectively. Sharp cusps were observed in the real and imaginary parts of the ac susceptibility at temperatures between 282 ($x=0.08$) and 209 K ($x=0.23$). Also observed were bifurcations of the zero-field-cooled and field-cooled magnetization curves at the same temperatures, showing that the magnetization was irreversible below these temperatures. The effect of Si substitution for Co in this system is to decrease the average ferromagnetic exchange interaction, thus decreasing the Curie temperature, without introducing significant random magnetism effects due to exchange fluctuations or random magnetic anisotropy. © 1998 American Institute of Physics. [S0021-8979(98)46211-X]

I. INTRODUCTION

Considerable effort has been devoted to understanding disordered magnetic systems which can result from exchange fluctuations or random anisotropy.¹⁻³ Letting \mathbf{S}_i be the spin vector at site i and \mathbf{n}_i be a random unit vector whose direction varies independently from site to site, the Hamiltonian describing the system can be written

$$H = -\sum (J_0 + \Delta J_{ij}) \mathbf{S}_i \cdot \mathbf{S}_j - D \sum (\mathbf{n}_i \cdot \mathbf{S}_i)^2, \quad (1)$$

where J_0 is an average exchange interaction, ΔJ_{ij} is the fluctuations in the exchange interactions, and D is a measure of the strength of the random anisotropy.⁴ For real materials, both exchange fluctuations and random anisotropy should be taken into consideration. In the case of $D \approx 0$, for example materials containing isotropic rare-earth elements, there is a possibility for a spin-glass phase (SG) or a re-entrant spin glass phase (RSG) as a disordered state. However, if ΔJ_{ij} is negligible compared to D , a random magnetic anisotropy (RMA) glass phase may appear. In such a case the above equation becomes the Harris-Plischke-Zuckermann Hamiltonian on which much of the theory of the RMA problem is based.⁵ Almost all of the materials studied previously can be classified as either SG or RMA, which avoids difficulties in separating an exchange-fluctuation effect and a random-anisotropy effect.

In this study we have sought to investigate the above effects in an intermetallic compound system, $\text{PrCo}_{3-x}\text{Si}_x$, in which one expects strong single-ion anisotropy from the Pr, and a weakening average exchange (J_0) from the Si doping. The presence of any randomness is anisotropy or significant exchange fluctuation was also a subject for study.

II. EXPERIMENTAL PROCEDURE

Bulk samples of $\text{PrCo}_{3-x}\text{Si}_x$ ($x=0.0-0.23$) were prepared by arc melting in purified argon gas. The starting elements all had purity higher than 99.9%. The compositions of

the samples were determined from the initial weights of the component elements and checked by weighing after melting. The alloys were subsequently homogenized for 100 h at 800 °C in vacuum. The crystal structures were determined by x-ray diffraction using $\text{Cu } K\alpha$ radiation and a graphite monochromator. The magnetization was measured by a Faraday balance and a superconducting quantum interference device (SQUID) magnetometer over the temperature range from 5 to 500 K. Powdered samples were used for SQUID measurements so that individual grains could rotate freely along the direction of the applied magnetic field. The ac susceptibility measurements for the bulk samples were performed with a driving frequency between 10 and 1600 Hz and a driving field of 1 Oe.

III. RESULTS AND DISCUSSION

Figure 1 shows the x-ray diffraction scans for the $\text{PrCo}_{3-x}\text{Si}_x$ samples with various x values. It is found that the pattern for the $x=0.0$ sample was almost entirely single phase PrCo_3 . Upon adding silicon up to $x=0.23$ the diffraction patterns did not change basically except for that a very small peak around $2\theta=44.5^\circ$ (indicated by lower triangle) appeared in some of the alloys. This peak is likely due to ferromagnetic Pr_2Co_7 . However, the effect of this small amount of Pr_2Co_7 on the magnetic properties discussed here could be accounted for easily.

The temperature dependence of magnetization for the $x=0.17$ sample is shown in Fig. 2. After initial zero-field cooling, the magnetization was measured in a 50 Oe applied field as the temperature was raised to 300 K [solid circles in Fig. 2(a)]. A peak at a temperature around 225 K was found. In subsequent cooling in the same applied field, the magnetization followed the same curve until it reached the peak. Below that temperature, it followed another path, showing a thermal hysteresis. The temperature at which the bifurcation of the zero-field-cooled (ZFC) and the field-cooled (FC) magnetization curves appears, decreases with an increasing applied magnetic field, as shown for the case of $H=1000$ Oe in Fig. 2(b).

^{a)}Electronic mail: rdk@unlinfo.und.edu

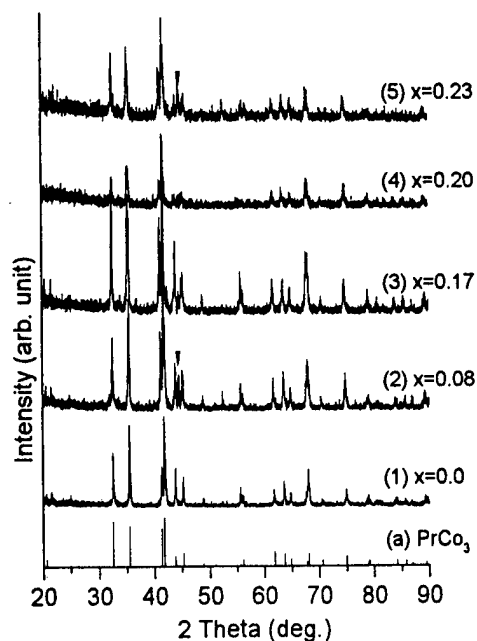


FIG. 1. X-ray diffraction scans for the $\text{PrCo}_{3-x}\text{Si}_x$ samples: (1) $x=0.08$, (2) 0.17, (3) 0.20, and (4) 0.23, and (a) peak intensities for PrCo_3 from (JCPDS) database.

Figure 3 shows the in-phase (χ') and out-of-phase (χ'') components of the ac susceptibility for the $x=0.17$ sample. Sharp cusps are found in both the χ' and χ'' curves in the same temperature region where the bifurcation appears on the FC and ZFC magnetization curves. It should be noticed that the peak in χ' shifts towards a higher temperature with increasing frequency, suggesting that thermally activated

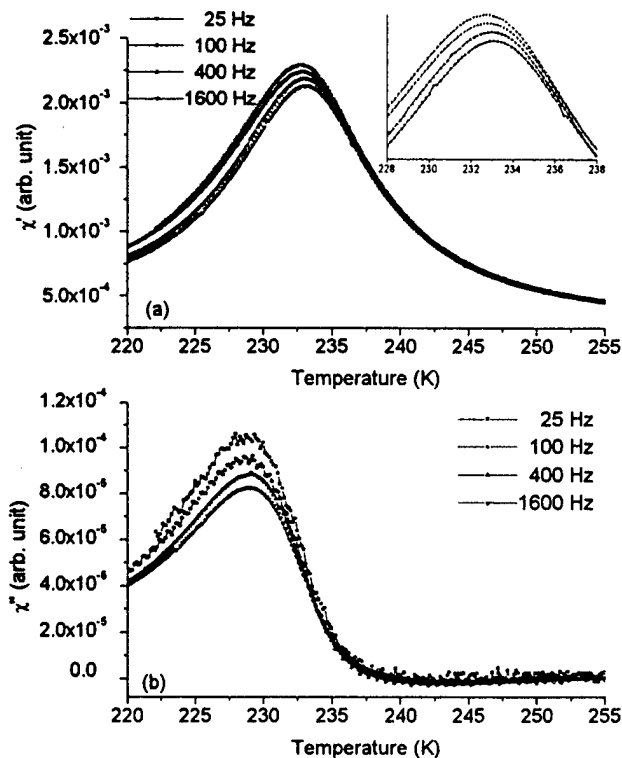


FIG. 3. Frequency dependence of in-phase (a) and out-of-phase (b) ac susceptibility of $\text{PrCo}_{3-x}\text{Si}_x$ for $x=0.17$ and $\nu=25, 100, 400$, and 1600 Hz. The inset shows the cusps in more detail.

processes are significant. In addition, the peak in $\chi'(T)$ corresponds to the maximum slope in $\chi''(T)$, $(d\chi''/dT)_{\text{max}}$.

In order to get an insight into the effect of the Si substitution on the interaction parameters of Eq. (1), the Si content

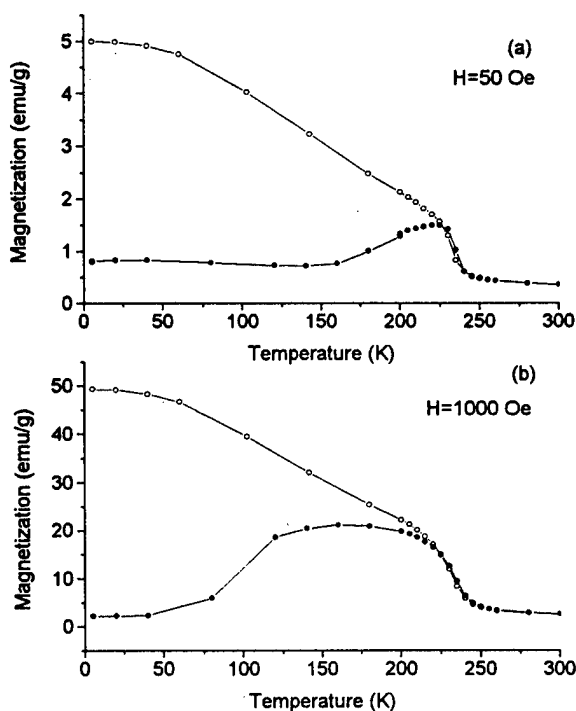


FIG. 2. Zero-field-cooled (solid) and field-cooled (open) magnetization vs temperature of $\text{PrCo}_{3-x}\text{Si}_x$ for $x=0.17$, measured at applied field of 50 Oe (a) and 1000 Oe (b).

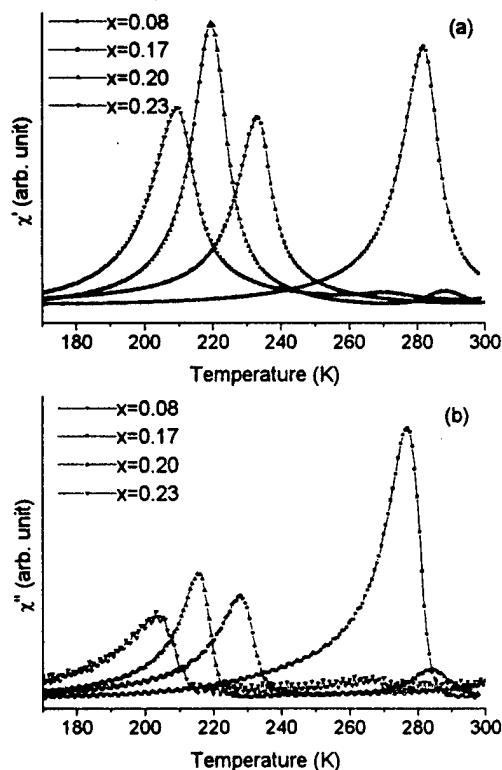


FIG. 4. In-phase (a) and out-of-phase (b) ac susceptibility vs temperature of $\text{PrCo}_{3-x}\text{Si}_x$ for $x=0.08, 0.17, 0.20$, and 0.23.

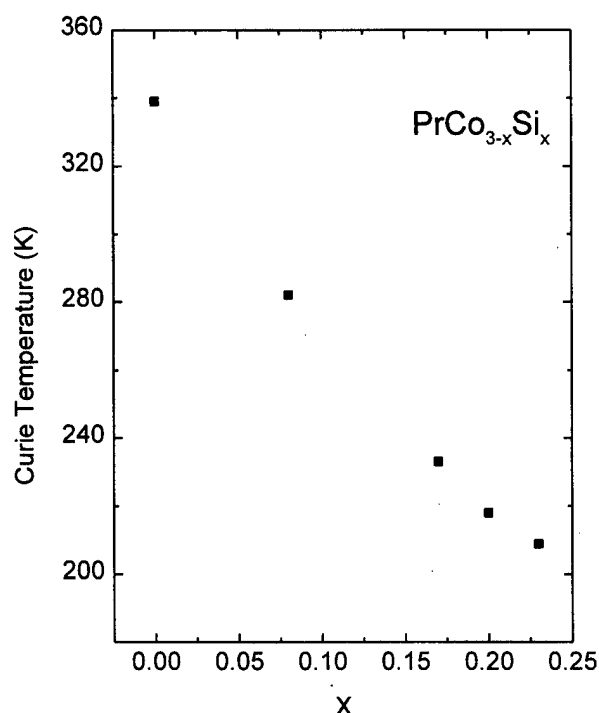


FIG. 5. Estimated Curie temperature of $\text{PrCo}_{3-x}\text{Si}_x$ as a function of x .

dependence of ac susceptibility was investigated. Figure 4 shows the χ' and χ'' versus temperature curves for the $x = 0.08, 0.17, 0.20$, and 0.23 samples. Sharp cusps appear in both χ' and χ'' curves for all the samples at temperatures between 282 K ($x = 0.08$) and 209 K ($x = 0.23$). Although these measurements could not be extended above 300 K, χ' for the $x = 0.0$ sample increases with temperature up to 300 K, suggesting that it will also exhibit a sharp cusp near the Curie temperature of 339 K. It was also found from the SQUID measurement that the magnetization becomes irreversible below each cusp temperature. The additional small peaks appearing on the high temperature side of the ac susceptibility peak for the $x = 0.20$ and 0.23 samples may be due to the presence of a small amount of the Pr_2Co_7 phase. Magnetization measurements in the $x = 0.0$ sample show an abrupt drop in the magnetization as the temperature increases above 339 K, suggesting the presence of a ferromagneticlike transition at that temperature.

The binary compound PrCo_3 was reported by Yakinthos *et al.*⁶ and Buschow *et al.*⁷ to be ferromagnetic with the easy direction along c axis below the Curie temperature of $T_c = 349$ and 339.5 K, respectively, and our temperature dependent magnetization measurements are consistent with this.

Figure 5 shows the Si-concentration dependence of the Curie temperature as measured by the temperature of the peak in χ' . It can be seen that the decrease with x is clearly

nonlinear in x . In a simple mean-field model $T_c \propto zJ_0$, where z is the number of nearest-neighbor magnetic ions and J_0 is the average exchange of Eq. (1). However, this model is not realistic for $\text{PrCo}_{3-x}\text{Si}_x$ alloys because the exchange interactions are quite sensitive to local environments. (It should be noted that YCo_2 , for example, is not magnetic.⁸) A spin-fluctuation model for which $T_c \propto M_s^2/\chi_0$, where χ_0 is the exchange-enhanced susceptibility, is likely to be more appropriate.⁹ For example, if χ_0 is assumed to be constant and M_s to vary linearly in x , then $T_c(x)$ would change in a nonlinear way as seen in Fig. 5.

The relatively sharp peaks in χ' and χ'' are of interest because they are reminiscent of spin-glasslike freezing due either to random anisotropy or exchange fluctuations. However, in this series of alloys, with relatively small Si doping levels, it seems likely that any such effects are small perturbations on a basically ferromagneticlike system whose positive exchange interactions are weakened by Si addition. The sharp susceptibility peaks can be understood in terms of a model developed by Buschow and Brouha¹⁰ for rare earth-cobalt alloys based on RCo_5 . In such compounds, where there is large single-ion anisotropy due to the rare earths, domain walls can be pinned by the lattice but thermal irreversibilities such as observed in Fig. 2, can be caused by thermally assisted domain-wall motion. This also could lead to the sharp cusps in susceptibility at T_c .

IV. CONCLUSIONS

In summary, $\text{PrCo}_{3-x}\text{Si}_x$ represents a diluted ferromagnetic system with a decreasing exchange and Curie temperature with an increasing Si concentration. The sharp ac susceptibility peaks and nonlinear variation of T_c can be rationalized on the basis of an itinerant spin-fluctuation model and thermally activated pinning of domain walls.

ACKNOWLEDGMENTS

The authors gratefully acknowledge the financial support of the U.S. National Science Foundation under Grant No. DMR-9623992, and support from the Center for Materials Research and Analysis of the University of Nebraska.

¹C. Y. Huang, J. Magn. Magn. Mater. **51**, 1 (1985).

²*Recent Progress in Random Magnets*, edited by D. H. Ryan (World Scientific, Singapore, 1992).

³*Spin Glasses: An Experimental Introduction*, edited by J. A. Mydosh (Taylor and Francis, London, 1993).

⁴D. J. Sellmyer and S. Nafis, J. Appl. Phys. **57**, 3584 (1985).

⁵R. Harris, M. Plischke, and M. J. Zuckermann, Phys. Rev. Lett. **31**, 160 (1973).

⁶J. Yakinthos and J. Rossat-Mignod, Phys. Status Solidi **50**, 747 (1972).

⁷K. H. J. Buschow, Rep. Prog. Phys. **40**, 1179 (1977).

⁸K. H. J. Buschow, Phys. Status Solidi **7**, 199 (1971).

⁹P. Mohn and E. P. Wohlfarth, J. Phys. F **17**, 2421 (1987).

¹⁰K. H. J. Buschow and M. Brouha, J. Appl. Phys. **47**, 1653 (1976).

Frustration in the paramagnetic phase of spin-density-wave CrFeV alloys

V. Yu. Galkin

I. P. Bardin Central Research Institute for Ferrous Metallurgy, Moscow, Russia and Departamento de Fisica, Universidade Federal de São Carlos, Brazil

W. A. Ortiz

Departamento de Fisica, Universidade Federal de São Carlos, Brazil

E. Fawcett

Department of Physics, University of Toronto, Toronto, Canada

The magnetic susceptibility $\chi(T)$ of the spin-density-wave (SDW) alloys $(\text{Cr}+2.7\% \text{Fe})_{1-x}\text{V}_x$ ($x=0.07, 0.29, 0.61, 0.9, 1.28$, and 2.0% V) and of the paramagnetic alloys ($x=5$ and 10% V) measured in a field, $H=100$ Oe, in the temperature range, $T=5-400$ K, was found to exhibit hysteresis between the field-cooled and zero-field-cooled states, starting at an irreversibility limiting temperature T_i well above the Néel temperature T_N in the SDW alloys, and also in the paramagnetic alloy $(\text{Cr}+2.7\% \text{Fe})_{95}\text{V}_5$. This behavior is attributed to the frustration of moments on the Cr atoms associated with the formation of a local-SDW phase above the bulk Néel transition. © 1998 American Institute of Physics. [S0021-8979(98)32411-1]

Following the observation¹ of hysteresis with respect to field cooling in the temperature dependence of the magnetic susceptibility $\chi(T)$, measured in a field, $H=100$ Oe, in the spin-density-wave (SDW) alloys $(\text{Cr}+3.2\% \text{Co})_{1-x}\text{V}_x$ ($x \leq 1\%$) at an irreversibility limiting temperature well above the Néel temperature T_N , we have found similar behavior in the corresponding system of CrFeV alloys containing the magnetic impurity Fe.

We note first that the behavior of Fe impurity in Cr and Cr alloys is unique in that the temperature dependence of $\chi(T)$ obeys a Curie–Weiss law, indicating that the Fe atom carries a moment, in the SDW phase as well as in the paramagnetic phase.² SDW CrCoV alloys exhibit a Curie–Weiss paramagnetism only in the paramagnetic phase, and the moment is believed to be frozen in the SDW state.² This difference from the behavior of the CrFeV alloys is however not relevant to the present work, since the onset of irreversibility occurs in the paramagnetic phase. We note also that irreversibility was not observed in other recent work on these CrFeV alloys,³ since the measurements were performed in a relatively high measuring field, $H \geq 1$ kOe, and only in the zero-field-cooled state.

We report here the temperature dependence of $\chi(T) = M(T)/H$, M being the magnetization measured with a SQUID magnetometer MPMS-5S from Quantum Design, of $(\text{Cr}+2.7\% \text{Fe})_{1-x}\text{V}_x$ ($x=0, 0.07, 0.29, 0.61, 0.9, 1.28, 2, 5$, and 10% V; all percentages are atomic) with a measuring field of 100 Oe over the temperature range from 5 to 400 K in the field-cooled (FC) and zero-field-cooled (ZFC) states. The FC measurements were performed after applying the measuring field at $T=400$ K, while cooling (FCC) and then warming (FCW). The experimental procedure and methods of sample preparation and characterization were the same as those followed in Refs. 3 and 4.

No temperature hysteresis of $\chi(T)$ was found between the FCC and FCW states, but all the ternary alloys except $(\text{Cr}+2.7\% \text{Fe})_{90}\text{V}_{10}$ show strong hysteresis between the FC

and ZFC states, as shown in Fig. 1. A distinct anomaly occurs in both the FCC and FCW curves at the temperature where they begin to diverge from the ZFC curve, which is taken to define the irreversibility limiting temperature T_i .

Alloys containing $x \geq 0.29\%$ V show no anomaly in $\chi(T)$ at the Néel temperature T_N [see Fig. 1(c)] perhaps because the SDW becomes commensurate at higher concentrations of V in CrFeV alloys.⁵ We have therefore used the anomaly in the temperature dependence of the resistivity $\rho(T)$ to define $T_N(x)$.⁶

In the CrFeV alloys, just as in CrCoV,¹ $T_i(x)$ decreases like $T_N(x)$ as the concentration x of V increases, but rather less rapidly, as seen in Fig. 2. It is especially interesting to see that there is still strong irreversibility in the paramagnetic alloy $(\text{Cr}+2.7\% \text{Fe})_{95}\text{V}_5$ starting at a high temperature, $T_i=210$ K [see Fig. 1(g)]. For $x=10\%$ V, there is no irreversibility [see Fig. 1(h)] so $T_i(x)$ must vanish somewhere between $x=5$ and 10% V.

It should be noted that, while the difference between the susceptibility in the FC and ZFC states increases in rough proportionality with the V concentration between $x=0.3$ and 2% V, the very small concentration, $x=0.07\%$ V, produces a disproportionately large effect, as illustrated in Fig. 3. A trace of V produces a remarkably large effect also in the CrCoV system.¹

We believe that the well-defined anomaly in the FCC and FCW curves of $\chi(T)$ and the onset of irreversibility at T_i in both the CrFeV and CrCoV systems corresponds to the new magnetic phase transition, which occurs in the paramagnetic phase well above the bulk Néel transition at T_N .¹ The rapid divergence between the FC and ZFC curves of $\chi(T)$ is similar to that seen in SDW Cr alloys containing Mn.^{4,7} In the latter case, however, the irreversibility appears at the so-called pinning temperature in the SDW phase well below T_N , and has been attributed to the frustration of Cr moments at the boundaries of polarization domains of the SDW centered on the Mn moments.⁴

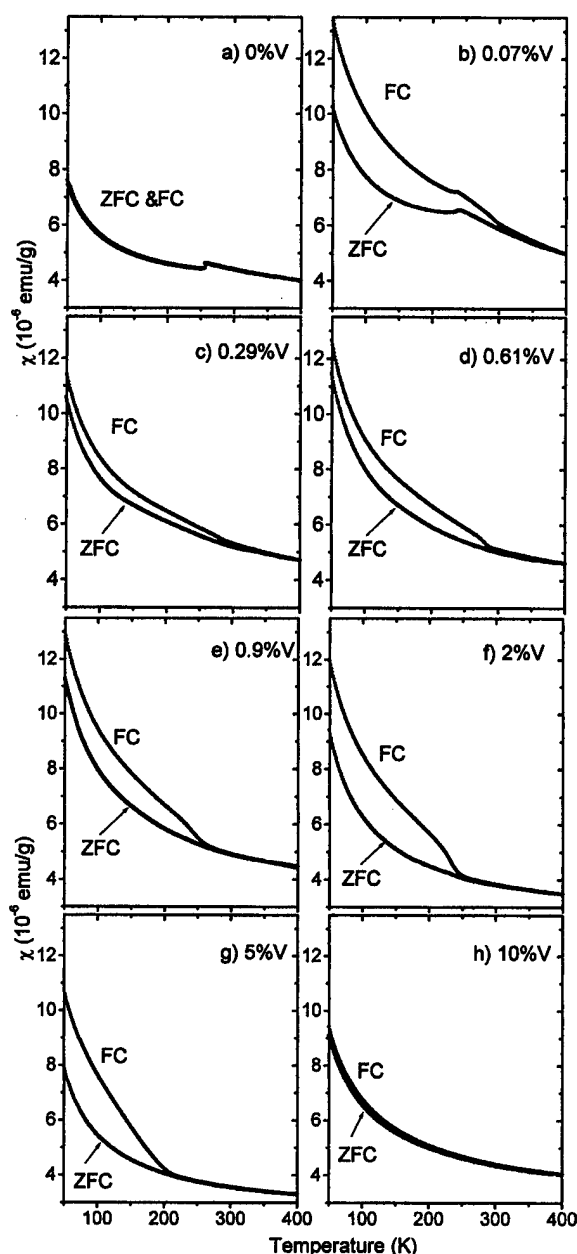


FIG. 1. Temperature dependence of the magnetic susceptibility $\chi(T)$ of $(\text{Cr}+2.7\% \text{Fe})_{1-x}\text{V}_x$ alloys, the concentration of V being shown in each panel. ZFC and FC indicate the zero-field-cooled and field-cooled state, respectively, measured and field-cooled in a field, $H=100$ Oe.

We propose that the anomaly seen in FC $\chi(T)$ curves in both CrFeV and CrCoV alloy corresponds to the onset of a local-SDW phase. Tugushev⁸ has predicted that regions of short-range SDW order will develop around a defect or impurity in a SDW host at a temperature above the bulk Néel transition to the SDW phase. We attribute the irreversibility to frustration of Cr moments that lie at the boundaries between these local-SDW regions centered on Fe moments.

The irreversibility in the paramagnetic alloy $(\text{Cr}+2.7\% \text{Fe})_{0.95}\text{V}_5$ is presumably due to its proximity to the SDW phase, though long-range order never develops in this alloy. There is negligible hysteresis in the binary alloy Cr+2.7% Fe, but the addition of only 0.07% V produces strong irreversibility [compare Figs. 1(a) and 1(b)]. The

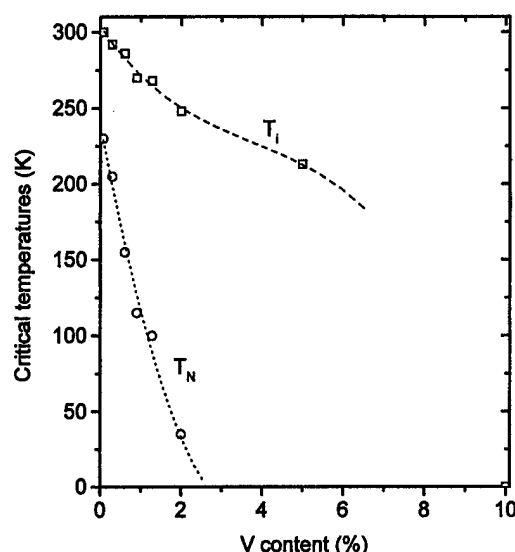


FIG. 2. Phase diagram for $(\text{Cr}+2.7\% \text{Fe})_{1-x}\text{V}_x$ alloys showing the irreversibility limiting temperature $T_i(x)$ and the Néel temperature $T_N(x)$. The $\chi(T)$ curves for $x=1.28\%$ V are not shown in Fig. 1. The experimental data point, $T_i=0$ K, $x=10\%$ V signifies that no irreversibility (and no Néel transition) was observed in this sample down to temperature 5 K. No data point is shown for the binary alloy, Cr+2.7% Fe ($x=0\%$ V), which does not exhibit irreversibility, its Néel temperature is, $T_N=257$ K.

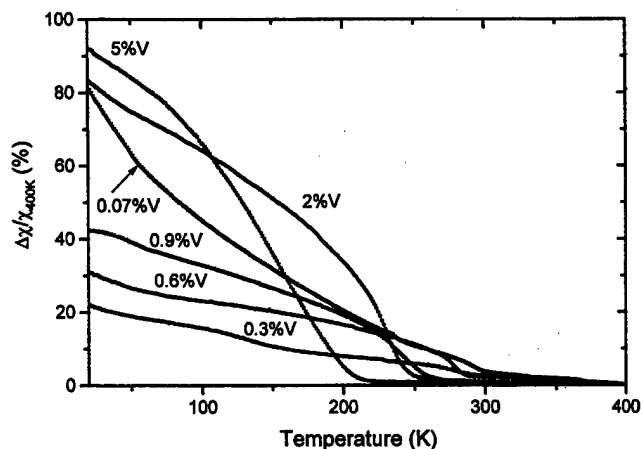


FIG. 3. Temperature dependence of the difference $\Delta\chi(T)$ between the FC and ZFC susceptibility relative to the value at temperature 400 K.

weak irreversibility in the binary alloy Cr+3.2% Co is also greatly enhanced by adding only 0.1% V.¹ This interesting effect, which we do not understand, is not however peculiar to V, and we see similar behavior in preliminary work on ternary alloys of Cr+2.7% Fe doped with Mo, Si, or Al.

ACKNOWLEDGMENTS

This work was performed with partial support from the Brazilian agencies CNPq and FAPESP (V. Yu. G. and W. A. O.) and by the Natural Sciences and Engineering Research Council, Canada (E. F.).

- ¹V. Yu Galkin, W. A. Ortiz, and E. Fawcett, *J. Phys.: Condens. Matter* **9**, L577 (1997).
- ²E. Fawcett, H. L. Alberts, V. Yu Galkin, D. R. Noakes, and J. V. Yakhmi, *Rev. Mod. Phys.* **66**, 25 (1994).
- ³V. Yu Galkin, N. Ali, E. Fawcett, and P. C. de Camargo, *J. Phys.: Condens. Matter* (in press).
- ⁴V. Yu Galkin, P. C. de Camargo, N. Ali, J. Schaf, and E. Fawcett, *J. Phys.: Condens. Matter* **7**, L649 (1995); **8**, 7925 (1996).
- ⁵E. Fawcett and V. Yu Galkin, *J. Magn. Magn. Mater.* **119**, 329 (1993).
- ⁶V. Yu Galkin and E. Fawcett, *J. Magn. Magn. Mater.* **119**, 321 (1993).
- ⁷V. Yu Galkin, P. C. de Camargo, N. Ali, and E. Fawcett, *Physica C* **237-238** (1997).
- ⁸V. V. Tugushev, in *Electronic Phase Transitions*, edited by X. Hanke and Yu. V. Kopaeu (Elsevier Science, Amsterdam, 1992), p. 237.

A new paradigm for two-dimensional spin liquids

R. R. P. Singh

Department of Physics, University of California, Davis, California 95616

O. A. Starykh

Department of Physics, University of Florida, Gainesville, Florida 32611

P. J. Freitas

Department of Physics, University of California, Davis, California 95616

Motivated by the geometry of the materials $\text{Na}_2\text{Ti}_2\text{As}_2\text{O}$ and $\text{Na}_2\text{Ti}_2\text{Sb}_2\text{O}$, we study a square-lattice Heisenberg antiferromagnet, with spins located at the bond centers. The largest exchange constant J couples neighboring spins in a given row or column. This leads to a mesh of isolated spin chains running along the X and Y axes. A weaker exchange constant J' couples the nearest-neighbor spins on the lattice. Classically, J' fails to fix the relative spin orientation for different chains and hence the ground state is highly degenerate. Quantum order by disorder effect is studied by spin-wave theory and numerical methods. It is shown that a four-sublattice order is favored by quantum fluctuations. However, several arguments are presented that suggest that the ground state of the system remains disordered, thus providing us with a paradigm for a two-dimensional spin liquid.

© 1998 American Institute of Physics. [S0021-8979(98)32511-6]

In recent years many new materials have been discovered which exhibit novel magnetic behavior. Various aspects of quantum magnetism, including quantum critical phenomena and existence of spin-disordered ground states with spin gaps have been observed in a variety of Cuprates, Germanates, Vanadates and other low-dimensional materials. One interesting fact that has come to light in these studies is that the geometrical arrangement of the transition metal and oxygen ions can have a dramatic impact on the underlying microscopic spin Hamiltonian and hence on the macroscopic magnetic properties of the system. For example in various cuprates, the Cu–O–Cu bond angle is crucial for determining the effective exchange constant between copper spins. Thus, strontium cuprates with certain stoichiometry behave as virtually decoupled spin ladders,¹ even though the separation of the copper spins between neighboring ladders may be smaller than their separation within a given ladder. In the CuGeO_3 (Ref. 2) and $\text{CaV}_n\text{O}_{2n+1}$,³ it is also believed that superexchange between the transition metal ions is mediated by oxygen and because of the geometry of various bond angles and occupied orbitals the second neighbor interactions are substantial compared to nearest neighbor ones.

Here, we consider a Heisenberg Hamiltonian:

$$\mathcal{H} = J \sum_{\langle i,j \rangle} \mathbf{S}_i \cdot \mathbf{S}_j + J' \sum_{\langle i,j \rangle} \mathbf{S}_i \cdot \mathbf{S}_j, \quad (1)$$

with $J' \ll J$. The interactions are shown in Fig. 1. The exchange J couples neighboring spins in a given row or column, whereas J' is the nearest neighbor coupling between rows and columns. In the absence of J' the system consists of a square mesh of decoupled spin chains running along the X and Y axes. The motivation for studying such a model comes from the materials $\text{Na}_2\text{Ti}_2\text{Sb}_2\text{O}$ (and also $\text{Na}_2\text{Ti}_2\text{As}_2\text{O}$).^{4,5} These layered titanates consist of planes of $(\text{Ti}_2\text{Sb}_2\text{O})^{2-}$, where the oxygen atoms form a square lattice and the titanium atoms sit at the bond centers of the lattice.

The antimony atoms sit above and below the centers of the elementary squares. The titanium atoms carry spin half. It is evident from the geometry that if the dominant exchange interaction is provided by a direct overlap between the titanium orbitals, this material would behave as a nearest-neighbor Heisenberg model. If, on the other hand, the dominant interaction is mediated by oxygen orbitals, it would result in the largest interaction between neighboring spins in a given row or column, thus leading to our Eq. (1).⁶ Finally, if the dominant exchange is mediated by the p orbitals of antimony, the Hamiltonian in Eq. (1) could still be appropriate, the lattice being dual to the one shown.

We begin by studying this model in the linear spin-wave approximation. As finding the correct local spin configuration is based on energetic considerations, we expect the spin-wave theory to be at least qualitatively correct. Notice that the problem at hand has “double” degeneracy in the classical limit: it is evidently degenerate with respect to relative angle θ between quantization axes on vertical and horizontal chains, as well as with respect to relative orientation ϕ of quantization axes on the neighboring *parallel* chains. Based on the fact that Hamiltonian (1) classically has no spiral ordering, and on insight from a somewhat analogous problem of coupled planes,⁷ we restrict variation in ϕ to two possible values: $\phi=0$ (ferromagnetic ordering of neighboring parallel chains) and $\phi=\pi$ (antiferromagnetic one). This degree of freedom is then naturally represented by Ising-type discrete variable $\tau_{i,i+1}=1$ ($\phi=0$) or $\tau_{i,i+1}=0$ ($\phi=\pi$), defined for each pair of chains $(i,i+1)$. The calculations are simplified greatly by choosing quantization axes on all sites such that the ordering is ferromagnetic. This is achieved by a unitary transformation parametrized by an angle θ and a set of $(\tau_{i,i+1})$.

We now integrate out spins on the horizontal chains to find an effective Hamiltonian for the remaining spins. This is achieved by representing spins on vertical (horizontal) chains

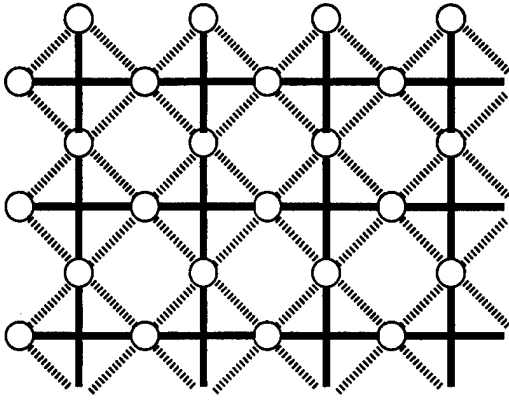


FIG. 1. The exchange interactions J and J' in our model, shown by solid lines and broken lines, respectively.

in terms of Holstein–Primakoff bosons $a(b)$, and doing perturbation expansion in J'/J . First, nonzero contribution is of the type $J'^2 \sum_{e,e'} S_{i+e}^\alpha(a) S_{j+e'}^\beta(a) \langle S_i^\alpha(b) S_j^\beta(b) \rangle_b$, where averaging is with respect to the bare Hamiltonian of horizontal chains and S_{i+e} spins belong to vertical chains, i.e., J' acts along the $\langle i, i+e \rangle$ links. The average is nonzero when i and j belong to the same horizontal chain and $\alpha = \beta$. It is seen that effective interaction between spins on vertical chains is time-dependent, but strongest contribution comes from static ($\omega_n = 0$) part of the average. Denoting $J_\perp^\alpha(i-j) = J'^2 \langle S_i^\alpha(b) S_j^\beta(b) \rangle_b$ and $\hat{J}_\perp^\alpha(r) = J_\perp^\alpha(r-1) + J_\perp^\alpha(r)$, we find that geometry dictates the following coupling between remaining parallel chains n and m ,

$$H_{nm}^\perp = \sum_{i\alpha} \hat{J}_\perp^\alpha(n-m) S_{n,i}^\alpha (2S_{m,i}^\alpha + S_{m,i+1}^\alpha + S_{m,i-1}^\alpha). \quad (2)$$

Notice that long-range-ordered part of $\langle S_i^\alpha(b) S_j^\beta(b) \rangle_b$, if any, cancels out due to antiferromagnetic (AFM) correlations along the chains, and the effective interaction decays at least as $(n-m)^{-2}$. It is also important to realize that \hat{J}_\perp^α is anisotropic in spin space, in particular $\hat{J}_\perp^{x(z)} \sim \cos^2 \theta$. Notice that classically the system remains degenerate because $\langle 2S_{m,i}^\alpha + S_{m,i+1}^\alpha + S_{m,i-1}^\alpha \rangle = 0$. Given the fast decay of the induced interchain interaction with the distance we restrict ourselves to the strongest interaction, $\hat{J}_\perp^\alpha(1)$, between nearest chains. To find corrections to ground state energy due to this coupling, we next treat \hat{J}_\perp as a perturbation (see Ref. 7 for description of the procedure). After long algebra one finds quantum correction to the ground state energy (per chain) of M parallel chains of length N :

$$\delta E_{GS} = -\frac{1}{M} \sum_{q_y} \epsilon(q_y) C (J'/J)^4 \cos^2 \theta \sum_{i=1}^M (1 - 2\tau_{i,i+1}), \quad (3)$$

where $\epsilon(q) = 2JS|\sin q|$ is the single AFM chain dispersion in spin-wave theory, $C = (\langle S_0^x S_0^x \rangle + \langle S_0^y S_0^y \rangle)^2 / 64$, and explicit form of \hat{J}_\perp was used. Note that correction is down by $1/S$ factor, showing its quantum origin. Thus the energy is minimized by choosing all $\tau_{i,i+1} = 0$ (AFM configuration) and $\cos^2 \theta = 1$. This result agrees with well-known tendency of quantum fluctuations to favor collinear structures.^{8,9}

Having found the ground state configuration of spins, we can determine the spin-wave dispersion and calculate the reduction in sublattice magnetization due to quantum fluctuations. This reduction turns out to be divergent due to a remaining artificial degeneracy of the spin-wave spectra. Similar divergency arises in a quantum order by disorder calculations on other systems and is known to be removed by the higher-order quantum corrections to the spin-wave spectra.¹⁰ This technically difficult calculation has not been done. We would like to stress that the ground state structure found in Eq. (3) is determined by short-range spin correlations (i.e., by the correlations within the correlation length range) for which spin-wave approximation should work even if the sublattice magnetization vanishes.

Let us now take a closer look at the elementary excitations of the single chain. It is convenient to perform “staggering” of the spin configuration so that Néel ordering along the chain corresponds to the ferromagnetic one in the new representation. In this representation an elementary excitation of the chain is a domain wall (spinon) separating ferromagnetic domains of different orientation. The energy of a single domain wall is J_z . Consider now unfrustrated coupling J_\perp between nearest spins on neighboring parallel chains: however, small J_\perp is, it immediately leads to the suppression of spinons because the energy costs is proportional to $J_\perp \times (\text{length of domain})$ and diverges in the thermodynamic limit. This is an intuitive reason for the stabilization of LRO in the system of unfrustrated coupled chains.¹¹ But this is not true for our Hamiltonian (2), where each spin is coupled to the zero-spin combination of spins on the neighboring chains. Thus domain wall excitations of the single chain seems to survive in the presence of nonzero J' , hinting to the possibility of the absence of LRO.

The effect of the “mixing” interchain coupling J' can also be taken into account in the disordered phase, where the interspin interaction is isotropic. We write the partition function of the Hamiltonian (1) in the interaction representation, where independent chains are considered as unperturbed system and interchain coupling J' as a perturbation.¹² Performing trace over the horizontal chains first one finds effective interaction between spins on the vertical chains proportional to $(J'(\mathbf{k}))^2 G^{(0)}(k_x, \omega_n) S^\alpha(\mathbf{k}, \omega_n) S^\alpha(\mathbf{k}, \omega_n)$, similar to our previous spin-wave calculations. Here $G^{(0)}(k_x, \omega_n)$ is the rotationally-invariant one-dimensional spins Green’s function in Matsubara representation, and $J'(\mathbf{k}) = J' \cos(k_x/2) \cos(k_y/2)$. Decoupling spins on different chains via a Hubbard–Stratonovich transformation,¹² the 2D Green’s function of the spins on vertical chains becomes

$$G(k_x, k_y, \omega_n) = \frac{G^{(0)}(k_y, \omega_n)}{1 - (J'(\mathbf{k}))^2 G^{(0)}(k_x, \omega_n) G^{(0)}(k_y, \omega_n)}. \quad (4)$$

The known form of $G^{(0)}(k_x, \omega_n)$ ¹³ implies that (i) the singularity at $\mathbf{k}_0 = (\pi, \pi)$ remains unchanged because $J'(\mathbf{k}_0) = 0$, (ii) the uniform susceptibility is $\chi = \chi_0 / [1 - (\chi_0 J')^2]$, where $\chi_0 = 1/(\pi^2 J)$ is susceptibility of single chain, and (iii) interchain coupling comes into play below $T^* \sim J'$. Within this approximation, the two-dimensional system remains in the disordered critical state at $T = 0$, and in the quantum-critical

one at finite temperatures. This result should also be viewed with some caution due to the large degeneracies in the underlying problem.

We now turn to numerical studies. Because of multiple energy scales, the development of short-range order at high temperatures is not necessarily indicative of the order for $T \sim J' \ll J$. Thus we need to study the ordering tendency directly at low temperatures. As $J'/J \ll 1$, the coupling between the local order parameters on the neighboring parallel chains can be gotten by perturbation theory. We study the following correlation function between neighboring vertical chains:

$$c_{12} = \left\langle \sum_i (-1)^i \mathbf{S}_{1,i} \cdot \sum_j (-1)^j \mathbf{S}_{2,j} \right\rangle, \quad (5)$$

here $\mathbf{S}_{1,i}$ represents spins on first vertical chain and $\mathbf{S}_{2,i}$ represents spins on second vertical chain. A value of $c_{12} > 0$ would imply ferromagnetic ordering whereas $c_{12} < 0$ would imply antiferromagnetic ordering. The leading order contribution to c_{12} requires the interactions to be mediated by at least two horizontal chains. To make the perturbation theory numerically tractable, we confine ourselves to finite chains along vertical and horizontal directions (with periodic boundary conditions). For four spins in each of the chains, we can carry out perturbation theory using series expansion methods.¹⁴ We find that $c_{12} \approx -9 \times 10^{-6} (J'/J)^6$, which is negative confirming the tendency of the parallel chains to align antiferromagnetically. We have also used Lanczos methods to calculate this correlation function with up to 6 spins in each chain for $|J'/J| \leq 0.3$. In all cases the coupling remains antiferromagnetic and very weak. For the six-spin system, c_{12} appears to scale as $(J'/J)^4$ as expected from general arguments and spin-wave theory presented earlier. Diagonalization of a 32-site system is in progress.

Assuming the local ordering pattern obtained in spin-wave theory, we can now investigate the question of long-range order by an Ising expansion for our original Hamiltonian. We write the Hamiltonian as $\mathcal{H}(\lambda) = H_0 + \lambda H_1$, where H_0 consists of an Ising Hamiltonian, whose two ground states are ordered in the four-sublattice pattern and $H_1 = \mathcal{H} - H_0$, with \mathcal{H} being the full Hamiltonian in Eq. (1). We develop expansions for the sublattice magnetization in terms of the expansion parameter λ . If the system has long-range order, the expansion should converge up to $\lambda = 1$, whereas if it is disordered there should be a critical point at $\lambda < 1$. Without explicit calculations, we can make the following observation: because of the cancellation of the effective field from one chain to another, the purely one-dimensional graphs remain unaffected by the coupling between the chains. We know that these add up to zero sublattice magnetization at the Heisenberg point. The effects of the other graphs is to further reduce order, thus moving the Heisenberg system into a quantum disordered phase. We have carried out these expansions to order λ^8 for a range of J'/J values. The analysis suggests critical values less than unity, implying a disordered ground state for the Heisenberg limit.

Additional insight can be gained by studying the $J' \gg J$ limit of the model, where the Néel state on 45° rotated lattice is stabilized by the J' interaction. As J increases from zero, quantum fluctuations grow stronger and at $(J/J')_{\text{crit}} = 0.76$ (within linear spin-wave approximation) finally destroy long-range order, analogous to $J_1 - J_2$ model.⁸ That these two systems are very similar is also supported by the fact that the critical value of frustrating interaction J quoted above is exactly twice the corresponding critical value of $J_1 - J_2$ model. Given this analogy, we speculate that disordered phase at $J/J' \geq 0.76$ is a spontaneously dimerized one,^{14,15} with vertical and horizontal chains formed by the exchange J being in the valence-bond-type state. However, extensions of these results to $J/J' > 1$ is problematic as at $J = J'$ this system classically has a finite ground state entropy¹⁶ and may change character at that point. Clearly, more work is needed to understand the nature of the disordered phase. It is interesting to ask what will happen upon introducing of a mobile charge carriers into the chains. There are apparent similarities of this problem with a recent study of a square mesh of conducting horizontal and vertical stripes.¹⁷

In conclusion, we have identified a new frustrated layered Heisenberg model, which could have a two-dimensional spin-liquid ground state. The magnetic properties of the materials $\text{Na}_2\text{Ti}_2\text{As}_2\text{O}$ and $\text{Na}_2\text{Ti}_2\text{Sb}_2\text{O}$ maybe represented by such a model.

The authors thank S. Kauzlarich and A. Axtell for bringing these materials to our attention, and I. Affleck, A. Chubukov, S. Sachdev, and M. Zhitomirsky for discussions. This work is supported in part by the NSF Grant No. DMR-9616574, the Campus Laboratory Collaboration of the University of California, and NHMFL.

¹E. Dagotto and T. M. Rice, *Science* **271**, 618 (1996).

²G. Castilla, V. Emery, and S. Chakravarty, *Phys. Rev. Lett.* **75**, 1823 (1995); W. Geertsma and D. Khomskii, *Phys. Rev. B* **54**, 3011 (1996).

³K. Ueda, H. Kontani, M. Sigrist, and P. A. Lee, *Phys. Rev. Lett.* **76**, 1932 (1996).

⁴A. Adam and H. U. Schuster, *Z. Anorg. Allg. Chem.* **584**, 150 (1990).

⁵E. A. Axtell III, T. Ozawa, S. M. Kauzlarich, and R. R. P. Singh, *J. Solid State Chem.* **134**, 423 (1997).

⁶J. B. Goodenough, *Magnetism and the Chemical Bond* (Interscience, New York, 1963).

⁷T. Yildirim, A. B. Harris, and E. F. Shender, *Phys. Rev. B* **53**, 6455 (1996).

⁸A. Moreo, E. Dagotto, T. Jolicoeur, and J. Riera, *Phys. Rev. B* **42**, 6283 (1990).

⁹P. Chandra, P. Coleman, and A. I. Larkin, *Phys. Rev. Lett.* **64**, 88 (1990).

¹⁰A. V. Chubukov, *Phys. Rev. B* **44**, 392 (1991).

¹¹H. J. Schulz, *Phys. Rev. Lett.* **77**, 2790 (1996).

¹²D. Boies, C. Bourbonnais, and A. M. S. Tremblay, *Phys. Rev. Lett.* **74**, 968 (1995).

¹³S. Sachdev, *Phys. Rev. B* **50**, 13006 (1994).

¹⁴M. P. Gelfand, R. R. P. Singh, and D. A. Huse, *J. Stat. Phys.* **59**, 1093 (1990); H. X. He, C. J. Hamer, and J. Oitmaa, *J. Phys. A* **23**, 1775 (1990).

¹⁵I. Affleck and J. B. Marston, *Phys. Rev. B* **37**, 3774 (1988); N. Read and S. Sachdev, *Phys. Rev. Lett.* **62**, 1694 (1989); S. Sachdev and N. Read, *ibid.* **77**, 4800 (1996).

¹⁶C. L. Henley (private communication).

¹⁷A. H. Castro Neto and F. Guinea, cond-mat/9709324.

Calculation of the energy barriers in strongly interacting many-particle systems

D. V. Berkov

INNOVENT e.V., Göschwitzer str. 22, D-07745, Jena, Germany

A numerical method which allows the evaluation of the energy barrier height between any two metastable states in a many-particle system with continuous degrees of freedom and arbitrary interparticle interaction is presented. The method uses the minimization of the Onsager–Machlup action corresponding to the given path between the two states. The path which minimizes this action is supposed to be the optimal path between the states under consideration and the height of the energy barrier separating these states is determined as the energy barrier along this optimal path. Test results for a simple two-dimensional potential (where the optimal path can easily be visualized) and for a dipolar glass are presented. © 1998 American Institute of Physics.
[S0021-8979(98)32611-0]

Evaluation of the energy (and free energy) barriers between metastable states in interacting many-particle systems is one of the most challenging problems in various areas of physics,¹ in particular, in the condensed matter physics of disordered systems with frustration like spin glasses.^{2,3}

At the present time we lack general methods for the evaluation of these barrier heights, except, maybe, direct Monte Carlo simulations of the system escape over such barriers which are based on the Langevin equations^{1,4,5} and can be applied only if the barrier height ΔE is comparable with the temperature T . In this contribution we would like to propose a numerical method which in its initial form is suitable for the energy barrier evaluation of arbitrary height in any classical interacting many particle system with continuous degrees of freedom, e.g., systems of “usual” classical particles, dipolar and RKKI spin glasses, Heisenberg (but not Ising!) models.

Main idea. Since the work of Onsager and Machlup,⁶ it is well known (see also Ref. 7) that for a system of N classical particles which motion can be described by coordinates $\mathbf{x}=(x_1, \dots, x_N)$ and velocities $\dot{\mathbf{x}}$ and which interaction energy $V(\mathbf{x})$ depends on their coordinates only the probability to observe a given trajectory $\mathbf{x}(t)$ for the transition between the two states A and B during the time t_f [$\mathbf{x}_A(0) \rightarrow \mathbf{x}_B(t_f)$] is given by

$$P[\mathbf{x}(t)] \approx J[\mathbf{x}] \exp \left[-\frac{S[\mathbf{x}(t)]}{4D} \right], \quad (1)$$

where the action $S[\mathbf{x}(t)]$ is defined as

$$S[\mathbf{x}(t), t_f] = \int_0^{t_f} dt \sum_i \left(\frac{dx_i}{dt} + \frac{\partial V(\mathbf{x})}{\partial x_i} \right)^2. \quad (2)$$

The form of the action (2) is the direct consequence of (i) the Langevin equations of the particle motion under the influence of the deterministic and random thermal forces (neglecting inertial terms) and (ii) the assumption that these thermal forces can be considered as independent Gaussian random quantities with zero correlation time. The Jacobian $J[\mathbf{x}]$ accounts for the variable transformation from the system coordinates to the thermal forces and the coefficient D in

the exponent of (1) characterizes the thermal noise power and hence is proportional to the system temperature: $D \sim T$.

In principle, the statement (1) solves any problem related to the transition between A and B , because the total transition probability $P_{\text{tot}}(A \rightarrow B)$ is then given by the integral of (1) over all paths $\mathbf{x}(t)$ and transition times t_f . Unfortunately, the evaluation of the corresponding path integral is not possible for any interacting system of real interest, which is probably the reason why the idea outlined above was not used in real calculations except some one-dimensional (1D) problems.^{8,9}

However, it can be seen from (1) that in the low temperature limit ($D \rightarrow 0$ and hence $T \rightarrow 0$) the only significant contribution to $P[\mathbf{x}(t)]$ comes from the paths near the trajectory which minimizes the action $S[\mathbf{x}(t)]$; it is called an “optimal” path $\mathbf{x}_{\text{opt}}(t)$. In this case the energy barrier for the transition $A \rightarrow B$ can be found as the barrier along this trajectory: $\Delta E(A \rightarrow B) = E_{\text{max}}(\mathbf{x}_{\text{opt}}) - E_A$. So the “only” problem left is the minimization of the action functional $S(\mathbf{x})$.

The easiest way to perform this minimization is the approximation of the integral (2) by some numerical quadrature formula and the subsequent minimization of the many-variable function obtained this way. Approximating (2) by the simplest quadrature, we obtain

$$S_d(\mathbf{x}) = \Delta t \sum_{i,k} \left[\frac{x_i^{k+1} - x_i^k}{\Delta t} + \frac{1}{2} \left(\frac{\partial V(\mathbf{x})}{\partial x_i^{k+1}} + \frac{\partial V(\mathbf{x})}{\partial x_i^k} \right) \right]^2, \quad (3)$$

where $\Delta t = t_f/K$, K is the number of time slices used, x_i^k is the coordinate of the i th particle at the time $t_k = k\Delta t$. The problem of the determination of the time slice number will be addressed elsewhere.¹⁰ Minimization of $S_d(\mathbf{x})$ as a function of $N \cdot K$ variables x_i^k provides a discrete representation of the optimal path which can be used to calculate the corresponding energy barrier.

A simple test example. The result of the simplest possible test of the method, calculation of an optimal trajectory for a transition of a particle in a 2D space (x_1, x_2) between the two local minima of the potential

$$V(\mathbf{x}) = \sum_j U_j \left[1 + \left(\frac{\mathbf{x} - \mathbf{r}_j}{\Delta_j} \right)^2 \right]^{-1} \quad (4)$$

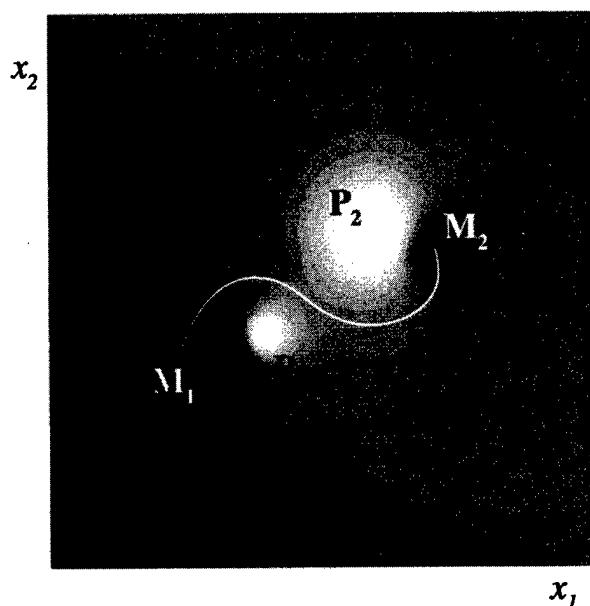


FIG. 1. Optimal trajectory (white line) for the particle transition between the two minima M_1 and M_2 .

is shown in Fig. 1. The energy surface used possesses two peaks P_1 and P_2 ($U_j > 0$) and two holes M_1 and M_2 ($U_j < 0$). The starting trajectory for the minimization process was a straight line $M_1 - M_2$. The final trajectory shown in Fig. 1 clearly passes through a saddle point providing the correct value of the energy barrier separating the minima M_1 and M_2 (a "true" optimal trajectory).

In this test case the optimal trajectory could be easily found due to a simple energy landscape. For a many-particle system, the search for a true optimal path between the two energy minima by the minimization of the action (2) [or (3)] is much more difficult, because this action has many local minima. Namely, any trajectory which proceeds along the gradient lines of the energy surface (i.e., for which $\dot{x}_i = \pm \partial V\{x\}/\partial x_i$) provides a local extremum to the action (2), see Ref. 9 for the proof in the 1D case.

For the energy surface presented in Fig. 1, this means, e.g., that the trajectory climbing along the gradient lines from M_1 up to P_1 and then going downhill from P_1 to M_2 also provides a local minimum to the action (2), and obviously gives a wrong value of the energy barrier (a "false" optimal trajectory). It is easy to construct an example where even the values of the action corresponding to the true and false optimal paths would be the same (just consider a system of two noninteracting particles each moving in a 1D double-well potential). For this reason, an additional analysis of the found optimal trajectories is necessary, so we developed an algorithm to distinguish between the true and false action minima (trajectories passing through the saddle points and climbing over the local maxima); due to the lack of space details of this algorithm will be described elsewhere.¹⁰ Here we would like to present only its main idea: for many-particle systems with complicate energy landscape, we expect that *many different* local energy minima can be achieved when we minimize the system energy starting from any en-

ergy maximum and moving in different directions (in contrast to Fig. 1 where only two minima exist). For this reason, we have tried to find out which local energy minima can be found starting from various points scattered randomly in the vicinity of the trajectory point P_E with the largest energy. For a true optimal trajectory, P_E is a saddle point for the transition $M_1 \rightarrow M_2$ and the energy minimization starting P_E (or sufficiently close points) would bring us either to M_1 or to M_2 . For a false optimal trajectory, P_E represents an energy maximum so that minimizing the system energy starting from P_E we would (with the probability rapidly growing with the particle number) discover other local minima different from both M_1 and M_2 . This would indicate that P_E is a maximum rather than a saddle point and that the corresponding optimal trajectory is a false one.

Implementation of the method for a system of magnetic particles. Let us consider, e.g., a system of small identical single-domain ferromagnetic particles (fixed in a nonmagnetic matrix) each having the volume V and the saturation magnetization M_s and carrying the magnetic moment \mathbf{m}_i of a constant magnitude $m_i = VM_s$. The magnetization state of such a system can be defined most conveniently using the spherical angles (θ_i, ϕ_i) characterizing the orientation of the i th magnetic moment. Below we denote the set of these spherical coordinates for all particles as Ω .

The action $S[\Omega(t)]$ corresponding to the transition $\Omega_A \rightarrow \Omega_B$ between the two given metastable states A and B of the system can be derived from the Landau-Lifshitz-Gilbert equations of motion for magnetic moments in the presence of thermal fluctuations¹¹ exactly as the action (2) is derived from the Langevin equations of motion for usual particles.^{6,9} The result is (if the precession term can be neglected)

$$S[\Omega(t)] = \int_0^{t_f} dt \sum_i \left[\left(\frac{d\theta_i}{dt} + \frac{\partial E\{\Omega\}}{\partial \theta_i} \right)^2 + \left(\sin \theta_i \frac{d\phi_i}{dt} + \frac{1}{\sin \theta_i} \frac{\partial E\{\Omega\}}{\partial \phi_i} \right)^2 \right]. \quad (5)$$

Minimization of this functional in the Ω space gives the "optimal" path which can provide information about the energy barrier between the states Ω_A and Ω_B exactly as explained above.

The method was applied to a system of magnetic particles having the "easy axis" magnetic anisotropy with the energy $E_{an} = 0.5\beta M_s^2 V \sin^2 \psi$, where $\beta(>0)$ is the reduced anisotropy constant and ψ is the angle between \mathbf{m} and the easy axis direction \mathbf{n} . Without the external field (this was always the case for the results reported below) a single such particle has two equivalent equilibrium magnetization states (along the two opposite directions of the anisotropy axis) separated by the reduced energy barrier $\epsilon \equiv E/(M_s^2 V) = \beta/2$. The barrier found by our algorithm for a single such particle or for a system of noninteracting particles with different anisotropy constants agreed with this value within the numerical accuracy. The test on a system of noninteracting particles was necessary to ensure that the algorithm discriminating between the false and true local minima of the action works properly.

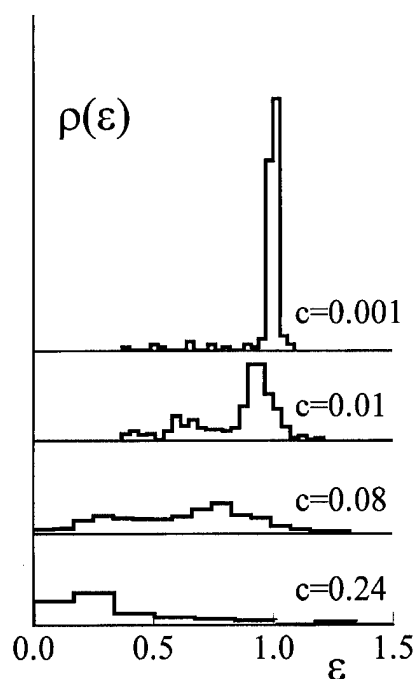


FIG. 2. Energy barrier distributions found by our algorithm for the system of $N=128$ dipolarly interacting magnetic particles with the uniaxial anisotropy ($\beta=2.0$) for various particle volume fractions c as shown in the figure.

Next we considered a system of $N=128$ dipolarly interacting particles with equal anisotropies $\beta_0=2.0$ which were placed randomly (but nonoverlapping) in the cubic volume; periodic boundary conditions were assumed. The dependence of the energy barrier distribution on the particle volume concentration c was studied. To obtain the distribution density of energy barriers we have generated a number of (meta)stable states starting from various initial moment orientations and then minimized the actions (5) corresponding to the transitions between various pairs of these states. Typically for each histogram shown in Fig. 2 and Fig. 3 several hundred energy barriers were calculated.

Results of our simulations are shown in Fig. 2. As it should be, for the lowest concentration ($\eta=0.001$) almost all barriers are nearly equal to the single-particle barrier $\epsilon = \beta_0/2 = 1.0$ because for this concentration the interaction effects are almost negligible. Note, however, a few barriers well below this value which occur due to a strong interaction of particles positioned by chance very close to each other. Already for the next (still quite low) volume concentration $\eta=0.01$, a considerable amount of barriers with another (mostly lower) values occur, because a fraction of closely positioned particles increased. For the system with the moderate ($c=0.08$) and high ($c=0.24$) concentrations, the collective interaction effects lead to a qualitatively different energy barrier distribution strongly shifted to the lower energies.

Another example of such a transition from the single particle to the collective behaviour is presented in Fig. 3, where results of our simulations for a system of $N=128$ particles with the particle volume concentration $c=0.04$ and different single-particle anisotropy constants are shown (note

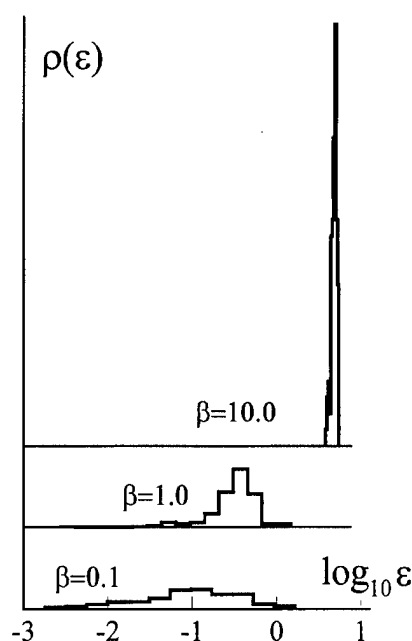


FIG. 3. The same as in Fig. 2 for systems of particles with the concentration $c=0.04$ and various anisotropy constants β as shown in the figure.

the logarithmic scale of the energy axis). It can be seen that for the smallest anisotropy considered ($\beta=0.1$) collective effects clearly dominate, whereby all barriers found in the system with the largest anisotropy value ($\beta=10.0$) lie in the vicinity of the single-particle energy barrier $\epsilon = \beta/2 = 5.0$.

Due to the limited paper length we cannot discuss the relation between our results and experimental data, e.g., for magnetic viscosity^{12,13} or ac susceptibility of ferrofluids.¹⁴ We only mention that care should be taken by establishing such a relation because (i) all experiments were performed at finite (and even not at low) temperatures so that the density of free energy barriers is required for their interpretation, (ii) transitions over different barriers lead to different moment changes which is essential for the calculation of both magnetic susceptibility and magnetic viscosity. Clearly further investigations are necessary.

¹P. Hoenggi, P. Talkner, and M. Borkovec, Rev. Mod. Phys. **62**, 251 (1990).

²K. Binder and A. P. Young, Rev. Mod. Phys. **58**, 801 (1986).

³V. S. Dotsenko, Sov. Phys. Usp. (USA) **36**, 455 (1993).

⁴J. M. Gonzalez, R. Ramirez, R. Smirnov-Rueda, and J. Gonzalez, Phys. Rev. B **52**, 16034 (1995).

⁵J. M. Sancho, A. M. Lacasta, M. C. Torrent, J. Garcia-Ojalvo, and J. Tejada, Phys. Lett. A **181**, 335 (1993).

⁶L. Onsager and S. Machlup, Phys. Rev. **91**, 1505 (1953).

⁷R. Graham, in *Fluctuations, Instabilities and Phase Transitions*, edited by T. Riste (Plenum, New York, 1975).

⁸A. J. McKane, H. C. Luckock, and A. J. Bray, Phys. Rev. A **41**, 644 (1990).

⁹A. J. Bray and A. J. McKane, Phys. Rev. Lett. **62**, 493 (1989).

¹⁰D. V. Berkov, J. Magn. Magn. Mater. (accepted).

¹¹W. F. Brown, Jr., Phys. Rev. **130**, 1677 (1963).

¹²X. Battle, M. Garcia del Muro, and A. Labarta, Phys. Rev. B **55**, 6440 (1997).

¹³D. Fiorani, A. M. Testa, E. Tronc, P. Prene, J. P. Jolivet, R. Cherkaoui, J. L. Dormann, and M. Nogues, J. Magn. Magn. Mater. **140-144**, 395 (1995).

¹⁴J. Zhang, C. Boyd, and W. Luo, Phys. Rev. Lett. **77**, 390 (1996).

Influence of the configurational degeneracy on the hysteretic behavior of a system of magnetostatically coupled magnetic moments

J. M. González and O. A. Chubykalo

Instituto de Ciencia de Materiales de Madrid—CSIC, Cantoblanco, 28049 Madrid, Spain

A. Hernando and M. Vázquez

Instituto de Magnetismo Aplicado—RENFE/UCM, Apartado de Correos 155, 28230 Las Rozas, (Madrid) Spain

The dynamics of dipolarly coupled magnetic moment systems representing sets of microwires has been simulated in the cases of (i) moments coupled through first-neighbors dipolar interactions and in that of (ii) moments coupled through exact many-body dipolar ones. Our results show that, in the case of the small size systems and independently from their parity, the dynamics is based either on localized excitations (of the antiferromagnetic domain wall-like type) or in collective modes depending on the occurrence of either short- or long-range dipolar interactions, respectively. When large size systems are considered the dynamics is based on localized interactions independently of the parity and the type of the present interactions. © 1998 American Institute of Physics. [S0021-8979(98)32711-5]

It has been shown that sets of glass-coated microwires, produced by the Taylor technique,¹ have an interesting dynamics characterized by the occurrence of multistable behavior² which makes them especially interesting in order to develop magnetic field sensors.³ Our purpose here is to analyze, in terms of a simple model, the dynamics of the magnetization reversal of sets of microwires having different size, parity, and range of dipolar coupling. Our model system corresponds to equally spaced individual microwires disposed in a ring. In real microwires, the field-induced magnetic moment reversal proceeds through a nucleation-propagation sequence with associated local moment structures involving only a small part of the total volume of the wire.¹ Therefore, a fine microwire discretization would be necessary in order to describe that reversal in a rigorous manner. Nevertheless, and since the propagation of the initially reversed nucleus is very rapid¹ and considering the fact that the wires have a length-to-diameter ratio of the order 10^3 , in what follows we will represent their magnetic state by that of a single magnetic moment with only two possible orientations. We will also assume that those magnetic moments (as the applied magnetic field) always point perpendicularly to the ring plane. To allow that thermal fluctuations could play a significant role in the demagnetization process, we have chosen a magnitude for the magnetic moments forming the system of 10^{-14} A m². The total system energy includes dipolar and Zeeman terms and is written as

$$E = \mu_0 M_s^2 \sum_{i,j=1}^N \frac{1}{d_{ij}^3} (\vec{m}_i \vec{m}_j) - \mu_0 M_s \sum_{i=1}^N \vec{m}_i (\vec{H} - \vec{H}_c),$$

where $m_i = \pm 1$, d_{ij} is the intermoment distance corresponding to the i th and j th sites (the distance between neighboring microwires is $d = 2 \times 10^{-5}$ m), $\mu_0 H$ is the applied magnetic field and $\mu_0 H_c = 5 \times 10^{-6}$ T represents the microwire coercivity which we phenomenologically introduce as a field parallel to the applied one for the demagnetizing branch of the hysteresis loop and antiparallel to it for the remagnetizing

one. We have considered two different interactions schemes: (i) nearest-neighbors interactions (in this case $j = i \pm 1$, $d_{ij} = d$ and the model coincided with the antiferromagnetic Ising) and (ii) exact, long-range, many-body interactions. When the external applied field was varied in small steps ($\mu_0 \Delta h = 5 \times 10^{-8}$ T), the dynamics of the system was followed by means of a Monte Carlo algorithm implemented with Metropolis dynamics in a canonical ensemble. The temperature fluctuations were introduced as random moment reversals. These reversals were accepted either in the case when they resulted in system internal energy decrease or when a system energy increase was consistent with the Boltzmann distribution function. Figures 1(a) and 1(b) show the hysteresis loops evaluated in two small size systems having first-neighbors interactions and even (8) and odd number (9) of moments, respectively. In the case of the 8 moments system, a state of zero component (measured along the applied field direction) of the total magnetic moment, corresponding to the (antiferromagnetic) ground state of the dipolar interactions, can be achieved. In contrast with this, in the case of

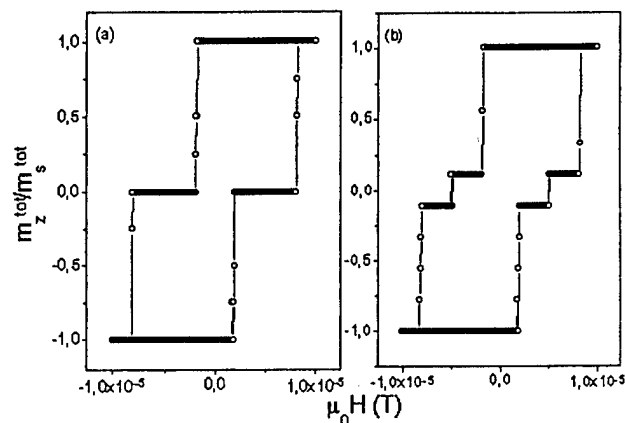


FIG. 1. (a) Hysteresis loop evaluated in (a) 8 moment and (b) 9 moment systems (first-neighbors coupling, $T = 50$ K).

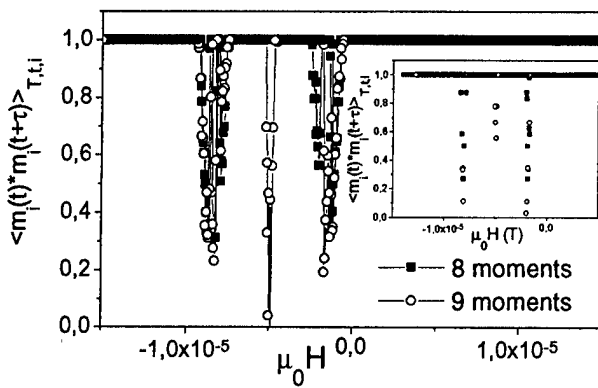


FIG. 2. Field dependence of the temporal correlations in systems having 8 and 9 moments coupled by many-body and first-neighbors interactions (inset) ($T=100$ K, $\tau=20$ MCS measured after a thermalization stage of 20 MCS).

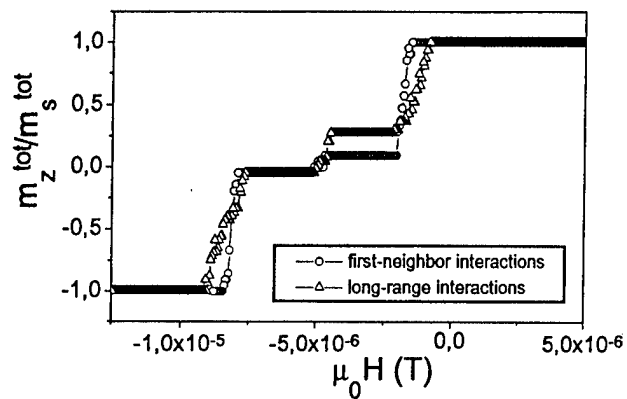


FIG. 3. Demagnetization branches of the hysteresis loops corresponding to systems formed by 21 moments coupled through first-neighbors and long-range interactions ($T=100$ K, average over 10^3 temperature realizations).

the 9 moments system that zero component state cannot be achieved due to the topological frustration of one of the moments in the system. That frustration is associated to the twofold total moment degeneracy of the ground state of the dipolar interactions and is made evident by the four different states that can be stabilized, in different field ranges, in this case. The dynamics of small size systems with only first-neighbors interactions is illustrated as inset in Fig. 2, where we present data corresponding to the applied field dependence of the quantity $\langle m_i(t)m_i(t+\tau) \rangle_{i,t,T}$ giving the configurational, thermal and time (measured in number of MCS) average of the system correlations after a time. As it is clear from the figure both systems are perfectly autocorrelated at all the field values with the only exception of those corresponding to the transitions between the stable states. This result suggests that these transitions involve localized excitations which should correspond to the creation or annihilation of pairs of antiparallel local moments (the exception to this should be the reversal of the frustrated moment in the case of the odd number of moments systems, which could involve three moments). Evaluation of $\langle m_i(t)m_i(t+\tau) \rangle_{i,t,T}$ in systems having 8 and 9 moments and many-body dipolar interactions (see Fig. 2) revealed that in this case the system was more frustrated than when only the first-neighbor interactions are present. In a larger size system with many-body dipolar interactions, the dynamics is of the collective type. To discuss that point let us assume that the system is saturated upwards and submitted to a demagnetizing applied field slightly lower than that corresponding (in systems with only first-neighbors interactions) to the transition from the saturated state to the ground state of the dipolar coupling. If, due to the thermal fluctuations the i th moment reverses, its reversal induces changes in the local field of the $(i \pm 1)$ th moments. If the acting dipolar interactions are of the nearest-neighbors type, the dipolar field at the $(i \pm 1)$ th moments will be zero since the $(i \pm 2)$ th and the i th moments are antiparallel. Differently, if the moments are coupled through long-range interactions the dipolar field at the $(i \pm 1)$ th moments reinforces the applied one: the first-neighbors contribution to the local field is still zero but the second neighbors one (which dominates the total dipolar field) is of the demag-

netizing type (both second neighbors still point along the initial saturation direction). Thus, the reversal of the $(i \pm 1)$ th moments is favored in the case of the long-range interactions with respect to that of first neighbors ones. Once the reversal of the $(i \pm 1)$ th moments is accomplished the antiparallel alignment with the field of the i th moment is, for similar reasons, favored, which allows to achieve locally the antiferromagnetic magnetic moment configuration. Also, and more generally, in a system with many-body interactions, the first-neighbor moments of those limiting a region with antiparallel moment configuration will always tend to flip due to the demagnetizing dipolar field created by their second neighbors. In conclusion, the presence of long-range dipolar interactions favors a system size large avalanche-like reversal process. Our point is clearly illustrated in Fig. 3 where we compare the demagnetizing branches of the hysteresis loops evaluated in two 21-moment systems having first-neighbors and many-body interactions, respectively. From these results, it is clear that the nucleation of the antiferromagnetic state takes place at a measurably smaller field in the case of the system undergoing many-body interactions. Figure 4 shows the variation of the demagnetization branch of the hysteresis loop with the number of moments integrating the system.

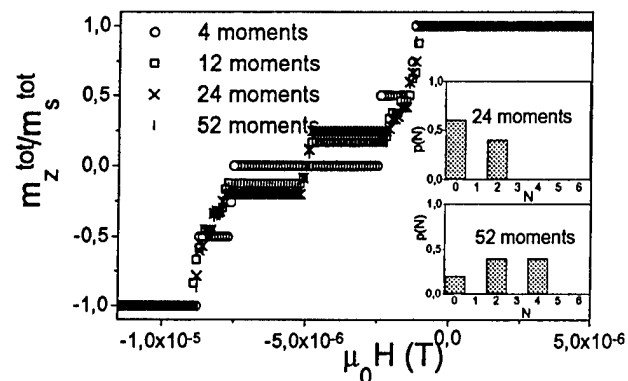


FIG. 4. Demagnetization branches of the hysteresis loops corresponding to systems formed by different (even) number of moments coupled through long-range interactions ($T=10$ K, average over 200 temperature realizations). The insets show the probability of occurrence (in two different systems) of spinons of different sizes.

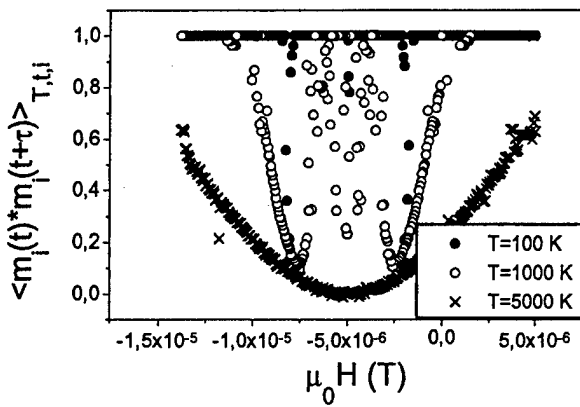


FIG. 5. Field dependence of the temporal correlations in a system having 52 moments coupled by first neighbors ($\tau=10$ MCS measured after a thermalization stage of 20 MCS).

Our data show the occurrence, for sufficiently large system sizes, of intermediate states in the moment reversal process as those observed in the case of the odd number of moments systems. These states are characterized by the presence of uncompensated moments (antiferromagnetic domain wall-like structures or spinons).⁴ The insets in the figure present, for the case of the systems having 24 and 52 moments, histograms showing the probability of occurrence of a given number of antiferromagnetic domain wall structures at a field of -4.5×10^{-6} T. In Fig. 5 we have plotted the temperature and field dependence of the $\langle m_i(t) m_i(t+\tau) \rangle_{i,t,T}$ correlations evaluated for a system having 52 moments (first-neighbors interactions). Our results (indistinguishable from those obtained in a system with 51 moments) clearly evidence that the dynamics of these large systems is linked to localized excitations. Finally, in Fig. 6 we show the time evolution of the $\langle m_i(t) m_i(t+\tau) \rangle_{i,t,T}$ correlations of two systems formed by 51 moments and having first-neighbors (inset) and many-body interactions, respectively. If the moments are coupled through many-body interactions it is possible to observe, at an intermediate temperature range, that the correlations oscillate. These oscillations are related to the site degeneracy, since they are produced by the continuous displacement of the spinons present in the system. Comparison of the behavior of the two considered systems reveals that at sufficiently low temperatures both systems are perfectly time autocorrelated.

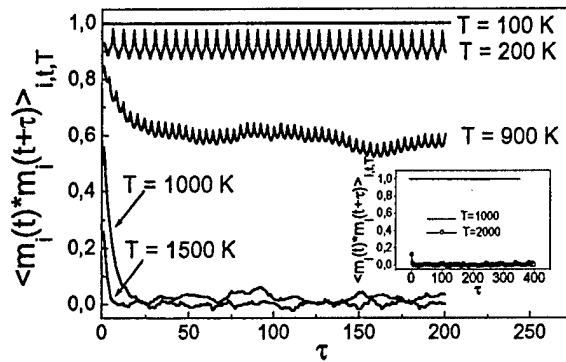


FIG. 6. Constant field (-4.8×10^{-6} T) time dependence of the temporal correlations evaluated in a system having 51 moments coupled through long-range interactions. The inset shows the time dependence of the same quantity in a system of 51 moments coupled through first-neighbor interactions.

lated. Nevertheless, the increase of the temperature produce different effects on the correlation depending on the type of interactions. For instance, at 1000 K, the system with first-neighbors interactions is still perfectly time autocorrelated whereas that having many-body interactions evidences that the correlation is lost after a short time. This result clearly indicates that, upon the introduction of the long-range dipolar coupling, it is much easier to achieve excited states of the dipolar interactions. To conclude we should say that, independently from the parity of the system (and therefore from the occurrence of frustration and from that of topological degeneracy), in the case of small size systems, the dynamics seems to be collective if many-body dipolar interactions are present and related to localized excitations if the moments are coupled through short-range dipolar fields. The dynamics of the larger system is always linked to localized excitations since, for the considered geometry, the increase of the total number of magnetic moments results in the increase of the distance between different regions of the system (the increase in size is thus associated to a decrease of the magnitude of the long-range interactions).

¹A. Zhukov, M. Vázquez, J. Velázquez, A. Hernando, and V. Larin, *J. Magn. Magn. Mater.* **170**, 323 (1997).

²J. Velázquez, M. Vázquez, D.-X. Chen, and A. Hernando, *Phys. Rev. B* **50**, 16737 (1994).

³R. Valenzuela, J. J. Freijo, A. Salcedo, M. Vázquez, and A. Hernando, *J. Appl. Phys.* **81**, 4301 (1997).

⁴R. Singh, *Phys. Rev. B* **53**, 11582 (1996).

Domain models for aging in spin glasses

Derek Walton

Department of Physics and Astronomy, McMaster University, Hamilton, Ontario, Canada

A simple domain growth model is shown to account for aging in spin glasses. It accounts quantitatively for the change in glass temperature with frequency. It is shown that percolation clusters present in disordered systems are responsible for the peak in $\partial M / \partial \ln t$, where M is the magnetization, and t is the time. © 1998 American Institute of Physics. [S0021-8979(98)27611-0]

INTRODUCTION

The magnetization of a spin-glass which has been cooled in zero field displays aging effects below the glass temperature, i.e. it depends on the time elapsed before application of the magnetic field. The derivative of the magnetization with respect to $\ln t$, divided by the field, called S , shows a similar structure in all systems investigated.^{1,2} Characteristics are a peak at a time close to the waiting time, t_w , and a difference in the initial value of S which depends on the waiting time, with longer waiting times resulting in lower initial values of S . Longer waiting times also result in lower initial values of the magnetization.

At present two seemingly quite different explanations are advanced: The Parisi³ solution of the Sherrington-Kirkpatrick Hamiltonian⁴ has inspired a model in which metastable states are hierarchically organized in phase space. Aging is the result of the system overcoming barriers and populating additional states.⁵ The other considers aging to result from the growth of droplets⁶ or domains of correlated spins.^{7,8} Both approaches lead to spin relaxation times which slow as $\ln t$; so the differences between them may be more conceptual than real.

Qualitative agreement with experiment, in the sense that calculated curves are more or less similar to measured data, has been demonstrated by many authors, but quantitative agreement is another matter. The hierarchical model has been shown⁵ to yield a substantially correct position for the peak in S , but a relatively large initial value of S , on the order of half the peak value, which depends on the waiting time, is not reproduced. It will be shown that a domain model gives not only the correct peak position, but the other details as well.

Following Fisher and Huse,⁶ FH, consider an Ising spin glass with nearest neighbor interactions on a d dimensional lattice. The Hamiltonian is

$$\mathcal{H} = - \sum_{\langle i,j \rangle} J S_i S_j - H \sum_i S_i, \quad (1)$$

where the spins, $S_i = \pm 1$, J is the nearest neighbor exchange, and H is a uniform magnetic field.

In FH the characteristic length scale of domains grows as

$$R \sim \left[\frac{T \ln(t/\tau)}{\Delta(T)} \right]^{1/\psi} \quad (2)$$

where τ is a microscopic time, and ψ is the barrier exponent, $1 \geq \psi > \frac{1}{2}$. Δ sets the overall free energy scale of the barriers; for $T \ll T_g$ it is $\sim J$.

If the microscopic nature of the spin relaxation is considered it is clear that the relaxation of a spin reduces its constraint on its neighbors one of which can then relax, reducing the constraint on its neighbors, and so on along a sequence of spins. It is clear that the domain size cannot exceed the size of such a sequence. If the domain size is proportional to the distance between the first and last spins in the sequence Walton,⁸ W , derives

$$R \sim \left[\frac{\ln(t/\tau)}{\ln p} \right]^\beta, \quad (3)$$

where p is the number of equilibrium positions for S , in the Ising model $p=2$ (the Ising model will be used in the remainder of this paper), and β relates the number of spins in a sequence of relaxed spins,

$$n = \frac{\ln(t/\tau)}{\ln p},$$

to R , the average distance between the first and last spins in the sequence, i.e., $R \sim n^\beta$. If \hat{d} is the spreading dimension,⁹ and D the fractal dimension, the number of spins in the domain is R^D , and $\beta \sim \hat{d}/D$. In 3 dimensions $\hat{d}=1.83$, and $D=2.5$,⁹ yielding $\beta=0.732$. On the other hand, numerical simulations give $\beta \approx 0.88$.¹⁰

Making an effective medium approximation¹⁰ for the energy barrier to spin reversal, $\tau \sim \omega_0 e^{-(E/T)}$, where ω_0 is a fundamental attempt frequency, and E is the effective medium energy barrier in temperature units.

Both expressions are of the form

$$R = A [\ln(t/\tau)]^a = A \ln^a(t/\tau), \quad (4)$$

where a is now a parameter, and A is temperature dependent in FH, but not in W . FH require $1 \leq a < 2$, and in $W a < 1$.

It is clear that if t is measured from the end of a waiting time t_w

$$R \propto \ln^a \left(\frac{t_w + t}{\tau} \right) \equiv \ln^a(g + k). \quad (5)$$

THE GLASS TRANSITION TEMPERATURE, T_g

If after cooling to a low temperature a small field is applied, an increase in moment occurs because domains are able to grow, and R is able to increase. An increase in tem-

perature allows R to increase faster, and the moment increases as the temperature is raised. Eventually nucleation of new domains in the interior of existing domains limits their size. After a time $t_l < \tau_n$ the domain volume is $R^D = A^D \ln^b(t_l/\tau)$, where $b = aD$. If there N spins, and the difference in energy between the two spin orientations is V , $n_\tau = Ne^{-(V/T)}$ spins will be reversed, and can nucleate new domains. Using the criterion that the maximum domain size is one that contains one reversed spin. The maximum susceptibility will occur when $R^D e^{(-V/T)} \sim 1$, leading to

$$T_g = \frac{V}{D \ln A + b \ln(\ln \omega_0 t_l - (E_l/T_g))}. \quad (6)$$

T_g can be obtained from this rather inconvenient expression.

THE PEAK IN $S = \partial M / H \partial \ln t$

Domain boundary motion takes place by relaxation of spins on the boundary. This will occur preferentially at spins with equal numbers of neighbors on both sides of the boundary so that the constraint imposed by the interaction with the neighbors is removed. Thus relaxation of spins on the boundary can be considered to be a process of continual nucleation of new domains at spins. Therefore, the boundary of a domain of scale R can be viewed as consisting of smaller domains of scale $\ln^a(t'/\tau)$, where $t' < (t + t_w)$, resulting in a self-similar fractal surface for the domain boundary, and the area of the boundary will be R^{d_s} , where $d_s > d - 1$.⁶ Thus after a time t has elapsed it should be possible to identify volumes on the boundary on all scales $\ln^a(t')$ where $t' \leq t$. In zero field this picture becomes somewhat academic since growth proceeds at equal rates for both spin orientations. However, in a magnetic field this is no longer the case, and the volumes of domains nucleated after the field is applied is different for the two spin orientations.

In a magnetic field H , $\tau \sim \omega_0 e^{-(Q \pm \mu H)/(T)} = \tau_0 e^{\pm h}$, where $h = (\mu H)/(T)$. If t is measured from the time the field was first applied

$$R^\pm \propto \ln^a(g + ke^{\pm h}) \quad (7)$$

and the new domain volumes are different.

The spins can be expected to lie on a percolation structure which can be viewed as a collection of clusters.¹¹ Below the percolation limit the clusters are isolated from each other. Above it the infinite cluster can be viewed as an assembly of clusters, some of which are connected, this is the "blobs" and "links" model.¹² For concentrations above the percolation threshold the cluster size distribution can be approximated by $s^\theta e^{-Cs^\nu}$,¹¹ where s is the number of spins in the cluster, and C is a constant on the order of the number of spins in the average cluster. In 3d, above the percolation threshold $\theta \sim \frac{1}{3}$, and $\nu = \frac{2}{3}$, below, $\theta \sim -\frac{3}{2}$ and $\nu = 1$.

Clusters smaller than $\ln^a g$ will be single domain. After the field is applied domain growth will take place in the larger clusters at different rates for the two spin orientations. As a consequence clusters with $\ln^a g < R^\pm \leq \ln^a(g + ke^{\pm h})$ will become single domain. The difference between their vol-

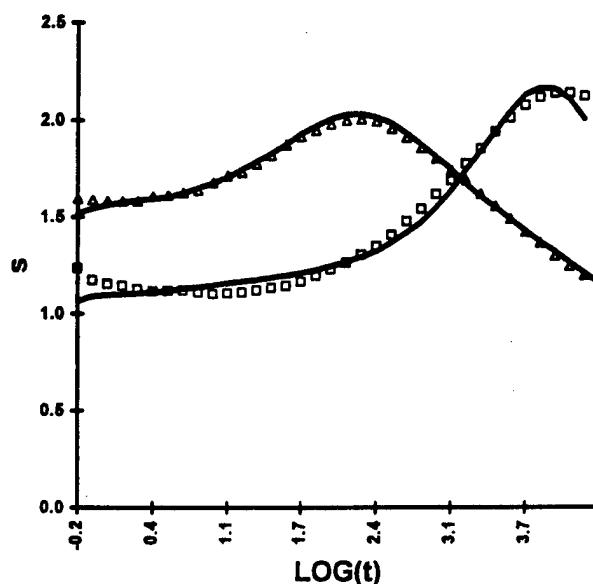


FIG. 1. The points are experimental values of $S = (1/H)(\partial M / \partial \ln t)$ in units of $0.01M/H$ for $\text{Fe}_{0.5}\text{Mn}_{0.5}\text{TiO}_2$ for two different waiting times, 10^2 s, and 10^4 s from Svedlindh *et al.*¹³ The solid lines are calculated.

umes will contribute to the moment. The number of spins in the domain is $\sim R^D$ and this contribution to the moment is

$$\delta M_d \propto \int_{[\ln^a g]^D}^{[\ln^a(g+ke^h)]^D} s^{1+\theta} e^{-Cs^\nu} - \int_{[\ln^a g]^D}^{[\ln^a(g+ke^{-h})]^D} s^{1+\theta} e^{-Cs^\nu}. \quad (8)$$

Clusters smaller than $[\ln^a g]^D$ will have become single domain during the waiting period before the field was applied. Their moments cancel since the temperature is below T_g , and nucleation of new domains in the interior of clusters can be neglected.

A second contribution will come from nucleation of new domains after the field is applied. The moment produced will just be proportional to the difference in volume of the new domains. Domains will nucleate most easily on the domain boundary. Nucleation in the interior of existing domains will be unimportant at temperatures below T_g , and will be neglected, thus, with $b = aD$

$$\delta m_n \propto \ln^b(ke^h) - \ln^b(ke^{-h}) = 2hb \ln^{b-1} k. \quad (9)$$

This contribution to the sample moment will be proportional to the total domain boundary area: If the domain contains $n^b = \ln^b(g+k)$ spins, and has area R^{d_s} or n^c , where $c = ad_s$, a cluster of s spins will contain $\sim s/n^b$ domains, whose total area can be roughly estimated as $\sim (s/n^b)n^c$, and

$$\begin{aligned} \delta M_n &\propto h \ln^{b-1} k \left[\int_{n^b}^{\infty} \frac{s^{1+\theta}}{n^{b-c}} e^{-Cs^\nu} \right] \\ &= h \frac{\ln^{b-1} k}{\Gamma(\alpha) \ln^{b-c}(g+k)} \Gamma(\alpha, Cn^{\nu b}), \end{aligned} \quad (10)$$

where $\alpha = (2 + \theta)/(\nu)$, $\Gamma(\alpha, x)$ is the incomplete gamma function, and $\Gamma(\alpha)$ is the gamma function.

We wish to calculate $S = S_d + S_n = \partial / h \partial \ln t (\delta M_d + \delta M_n)$.

Differentiating the integrals in Eq. (8), expanding, and only retaining terms in h

$$S_d \propto \frac{kg}{(g+k)^2} \left\{ 1 + \frac{k}{g \ln(g+k)} [(2+\theta)b-1 - C\nu b \times \ln^{\nu b}(g+k)] \right\} \frac{\ln^{(2+\theta)b-1}(g+k)}{e^{C \ln^{\nu b}(g+k)}}. \quad (11)$$

Differentiating (10), and neglecting terms in h^2 ,

$$S_n \propto \frac{\ln^{b-2} k}{\ln^{b-c}(g+k)} \left\{ \Gamma(\alpha, Cn^{\nu b}) \left[b-1 - \frac{k(b-c) \ln k}{(g+k) \ln(g+k)} \right] - \frac{k \ln k C^{\alpha} \nu b \ln^{\alpha \nu b-1}(g+k)}{(g+k) e^{C \ln^{\nu b}(g+k)}} \right\}$$

and if $Cn^{\nu b} < 1$,

$$S_n \propto \frac{\ln^{b-2} k}{\ln^{b-c}(g+k)} \left[b-1 - \frac{k(b-c) \ln k}{(g+k) \ln(g+k)} \right]. \quad (12)$$

Because $\ln k = \ln t + \ln \tau$ is appreciable, initially the initial change in M is given by Eq. (12), which yields the initial values of S . If $\ln \tau \gg \ln t$, it will be linear in $\ln t$, and if $b \sim 2$, S will be roughly constant initially, which appears to be the case for many spin glasses. n^{b-c} determines the difference between the initial values of S .

The factor $k/(g+k)^2$ in Eq. (11) ensures that initially it makes no contribution to S . On the other hand, it is responsible for the peak in S , and it is easy to see why this maximum occurs when $k \sim g$. It should be noted that this contribution depends on the existence of percolation clusters, and should disappear if the sample is not disordered.

COMPARISON WITH EXPERIMENT

Experimental data for S for $\text{Fe}_{0.5}\text{Mn}_{0.5}\text{TiO}_2$ obtained by Svedlindh *et al.*¹³ were compared with the predictions of the model. The fits are shown in Fig. 1. It was not possible to fit the data with the assumption that the system was below the percolation limit. The fits were scaled so that the single value calculated for $t_w = 10^3$ s, and $t = 10$ s agreed with experiment. The fraction of sites on the boundary where domain growth could start was left as an adjustable parameter. The other parameters were $d_s = 2.06$, $1/\tau = e^{6.5}$, $C = 0.0145$, and $b = 2.2$ which, if D is equal to 2.5, yields $a = 0.88$.

The value of a seems to favor Walton's model, but since the parameters are not completely independent this conclusion can only be tentative.

The change in T_g with frequency has been measured by Gunnarsson *et al.*¹⁴ for the same material. The values have been calculated from Eq. (6)

Frequency, Hz	0.005	0.05	0.5	5.1	55	510	5100	51000
T_g -measured, K	21.7	22	22.3	22.6	23	23.5	24.2	25
T_g -calculated, K	21.8	22.0	22.3	22.6	23.0	23.4	24.0	24.9

The parameters are $E = 390$ K, $V = 616$ K, $\ln \omega_0 = 30$, and $b = 2.2$. Note that these values yield the value for $1/\tau$ from the fit to S .

It is important to note that, according to the model, the peak in S is due to percolation clusters. Thus a non-disordered spin glass in which such a structure is absent should not display a peak in S . Such a system is provided by the fully frustrated pyrochlore, $\text{Y}_2\text{Mo}_2\text{O}_7$, and indeed no peak has been observed.¹⁵ However, when about 1/4 to 1/3 of the Mo is replaced by nonmagnetic Ti the peak reappears.

In conclusion, it has been shown that a simple domain growth model combined with the disordered structure of a spin glass can account for T_g and S .

ACKNOWLEDGMENT

This research was supported by a grant from the Natural Sciences and Engineering Council of Canada.

¹L. Lundgren, P. Svedlindh, P. Nordblad, and O. Beckman, Phys. Rev. Lett. **51**, 911 (1983).

²P. Granberg, L. Sandlund, P. Nordblad, P. Svedlindh, and L. Lundgren, Phys. Rev. B **38**, 7097 (1988).

³G. Parisi, Phys. Lett. **73A**, 203 (1979); Phys. Rev. Lett. **43**, 1574 (1979); J. Phys. A **13**, L115 (1980); Phys. Rev. Lett. **50**, 1946 (1983).

⁴D. Sherrington and S. Kirkpatrick, Phys. Rev. B **17**, 4384 (1978).

⁵Y. G. Joh, R. Orbach, and J. Hammann, Phys. Rev. Lett. **77**, 4648 (1996).

⁶D. S. Fisher and D. A. Huse, Phys. Rev. B **38**, 373,386 (1988).

⁷G. J. M. Koper and H. J. Hilhorst, J. Phys. **49**, 429 (1988).

⁸D. Walton, Phys. Rev. B **53**, 14980 (1996).

⁹J. Vannimenus, *The Art of Walking on Fractal Spaces and Random Media*, in Physics of Finely Divided Matter, edited by F. Boccara and M. Daoud (Springer, Berlin, 1985).

¹⁰S. Havlin and D. Ben-Avraham, Adv. Phys. **36**, 718 (1987).

¹¹D. Stauffer and A. Aharony, *Introduction to Percolation Theory* (Taylor and Francis, London, 1994).

¹²H. E. Stanley, J. Phys. A **10**, L211 (1977).

¹³P. Svedlindh *et al.*, J. Magn. Magn. Mater. **71**, 22 (1987).

¹⁴K. Gunnarsson, P. Svedlindh, P. Nordblad, and L. Lundgren, Phys. Rev. Lett. **61**, 754 (1988).

¹⁵D. Walton *et al.* (to be published).

AUTHOR INDEX

All authors published in these Proceedings of the Seventh Joint Magnetism and Magnetic Materials-Intermag Conference are listed alphabetically with the issue and page numbers following the dash.

- Abarra, E. N.-(11) 6527
 Abe, Masanori-(11) 6768
 Acharya, B. Ramamurthy-(11) 6879
 Adachi, Yoshiya-(11) 6961
 Ahlers, D.-(11) 7082, 7085
 Ajan, Antony-(11) 6879, 7169
 Akyl, C.-(11) 6563
 Alascio, B.-(11) 7201
 Albuquerque, E. L.-(11) 6955
 Alders, D.-(11) 6855
 Algarabel, P. A.-(11) 7154
 Ali, Naushad-(11) 6299, 6974
 Al-Khafaji, M.-(11) 6411
 Allen, L. H.-(11) 7067
 Allen, S. M.-(11) 7297
 Altman, R. A.-(11) 6515
 Al-Wazzan, R.-(11) 6858
 Amado, M. M.-(11) 6852
 Amaral, V. S.-(11) 7154
 Ambrose, T.-(11) 6822, 7222
 Amin, Nurul-(11) 6807
 An, Sung Yong-(11) 6929
 Anderson, A. J.-(11) 6226
 Andersson, Y.-(11) 6980
 Ando, K.-(11) 6545, 6548, 6551
 Andreev, A. V.-(11) 6435, 6986
 Andrei, P.-(11) 6359
 Andrieu, S.-(11) 6293
 Anil Kumar, P. S.-(11) 6536, 6864, 7375
 Ankudinov, A.-(11) 7025
 Anselmo, D. H. A. L.-(11) 6955
 Anthony, T. C.-(11) 6840
 Anthony, Thomas C.-(11) 6816
 Antonenko, A. N.-(11) 6587
 Araghi, M. S.-(11) 6670
 Arai, K. I.-(11) 7303
 Arai, Ken'ichi-(11) 6768, 7294
 Aranda, G. R.-(11) 6341
 Araújo, J. P.-(11) 7154
 Araujo, R. C.-(11) 6932
 Archambault, P.-(11) 7234
 Argyriou, D. N.-(11) 6374, 7348
 Arnold, Z.-(11) 6964, 7204
 Arora, S. K.-(11) 7174
 Arsenov, A. A.-(11) 7342
 Arvanitis, D.-(11) 7025
 Asamitsu, A.-(11) 7064
 Atherton, D. L.-(11) 7106
 Atkinson, D.-(11) 6569
 Atkinson, R.-(11) 6670, 6750, 6858
 Attenkofer, K.-(11) 7085
 Auyeung, R. C. Y.-(11) 6774, 7189
 Awaga, K.-(11) 7378
 Awana, V. P. S.-(11) 7312, 7315
 Babcock, K. L.-(11) 7127
 Baberschke, K.-(11) 7025, 7028
 Babushkina, N. A.-(11) 7369
 Bader, S. D.-(11) 6238, 6385
 Baek, Jong-Sung-(11) 6646
 Bahaj, A. S.-(11) 6444
 Bakhr, H.-(11) 6759
 Balakrishnan, G.-(11) 7151
 Balbashov, A. M.-(11) 7160, 7180
 Balcells, L.-(11) 7058
 Barandiarán, J. M.-(11) 7171
 Barbara-Dechelette, A.-(11) 6293
 Bardou, F.-(11) 6703
 Bärner, K.-(11) 6977, 7148
 Barratt, J.-(11) 7151
 Barrett, T. A.-(11) 6235
 Barry, A.-(11) 7166
 Bartashevich, Michael-(11) 6961
 Barthel, J.-(11) 7019
 Bartolomé, F.-(11) 6293, 7091
 Bartolomé, J.-(11) 6934, 6940, 7091
 Basso, V.-(11) 6497
 Bathe, Ravi-(11) 7174
 Battle, P. D.-(11) 6379
 Baudelet, F.-(11) 7291
 Bauer, E.-(11) 6423
 Bayreuther, G.-(11) 7088
 Beach, G.-(11) 6998
 Béal, C.-(11) 6703
 Beaupaire, E.-(11) 7043
 Beech, Russell S.-(11) 6688
 Belova, L. M.-(11) 7369
 Beltrán, D.-(11) 6542
 Bentzon, M.-(11) 6798
 Berkov, D. V.-(11) 6350, 7390
 Berkowitz, A. E.-(11) 6888, 7219
 Bernardi, J.-(11) 6396
 Bertotti, G.-(11) 6497
 Bertram, H. Neal-(11) 6344
 Bertrand, P.-(11) 6834
 Bessho, K.-(11) 6685
 Bhatt, R. N.-(11) 7231
 Bi, Y.-(11) 6497
 Bibicu, I.-(11) 6852
 Bishop, J. E. L.-(11) 6411
 Bitoh, T.-(11) 6332
 Blamire, M. G.-(11) 6697, 7157
 Blanco, J. J.-(11) 7171
 Blanco, J. M.-(11) 6338
 Blundell, S. J.-(11) 6379
 Bobo, J. F.-(11) 6685
 Bodin, P.-(11) 6798
 Boekema, C.-(11) 6795
 Boeve, H.-(11) 6700
 Borchers, J. A.-(11) 6882, 7219
 Bordallo, H. N.-(11) 6986
 Borghs, G.-(11) 6700
 Borsia, F.-(11) 6946
 Bosak, A. A.-(11) 7369
 Boumaiz, E.-(11) 6679
 Bounds, C. O.-(11) 6271, 6709, 6712
 Bramwell, S. T.-(11) 6314, 7234
 Branagan, D. J.-(11) 6631
 Bratsberg, H.-(11) 6798
 Brewer, E. G.-(11) 7252
 Britel, M.-(11) 6563
 Brodbeck, A.-(11) 6980
 Brookes, N. B.-(11) 6617
 Broussard, P. R.-(11) 7067
 Brown, G. W.-(11) 7010
 Browning, V. M.-(11) 6783, 6867, 7070
 Brück, E.-(11) 6727, 7136
 Brug, J. A.-(11) 6840
 Brugna, C.-(11) 6605
 Bruno, E.-(11) 7097
 Bryant, R. G.-(11) 6474
 Bubendorff, J. L.-(11) 7043
 Bucher, J. P.-(11) 6703, 7043
 Buchman, A.-(11) 6474
 Bularzik, J. H.-(11) 6477
 Burke, E. R.-(11) 6226
 Busbridge, S. C.-(11) 7255, 7273
 Buschow, K. H. J.-(11) 6727, 6736, 7136
 Bussmann, K.-(11) 6290, 7034
 Butera, A.-(11) 7201
 Butler, W. H.-(11) 6521, 7225
 Byeon, Soon Cheon-(11) 6873
 Byers, J. M.-(11) 6774, 7070
 Cabral, F. A. O.-(11) 6932
 Cadieu, C. F.-(11) 7195
 Cadieu, F. J.-(11) 6247, 7195
 Caltun, O.-(11) 6359
 Camley, R. E.-(11) 6280
 Canepa, F.-(11) 6438
 Canfield, P.-(11) 6843
 Cao, G.-(11) 6989, 6992
 Cao, W.-(11) 6888
 Capehart, T. W.-(11) 7252
 Capsoni, D.-(11) 6605
 Carey, R.-(11) 6739
 Carretta, P.-(11) 6602
 Caspi, El'ad N.-(11) 6733
 Causa, M. T.-(11) 7201
 Cavanaugh, A.-(11) 6780
 Cebollada, F.-(11) 6277
 Chabanenko, A. V.-(11) 7324
 Chabanenko, V. V.-(11) 7324
 Chaboy, J.-(11) 7091
 Chai, K. H.-(11) 6480
 Chaiken, A.-(11) 6828
 Chakalov, R. A.-(11) 7079
 Chakalova, R. I.-(11) 7079
 Chakarian, V.-(11) 6290, 6293, 7028
 Chan, J. Y.-(11) 7192
 Chang, Ching-Ray-(11) 6593
 Chang, S. S.-(11) 6643
 Chang, W. C.-(11) 6271, 6914
 Chang, Y. C.-(11) 7318
 Chari, M. V. K.-(11) 6347
 Charpentier, J. F.-(11) 7121
 Chauvistré, R.-(11) 7025
 Chen, C. H.-(11) 6706, 6712
 Chen, Feng-(11) 6429
 Chen, Li-(11) 6247, 7195
 Chen, M.-(11) 6914
 Chen, P. J.-(11) 7037
 Chen, Q.-(11) 6271, 6471, 6718
 Chen, S. K.-(11) 6241
 Chen, X.-(11) 7139
 Chen, Y. Y.-(11) 6426
 Chen, Z. Y.-(11) 6780
 Cheng, Benpei-(11) 6640
 Cheng, C. W.-(11) 6417
 Cheng, F. T.-(11) 6417
 Cheng, Shufan-(11) 6819
 Cheong, S-W.-(11) 7064, 7201
 Chiang, H. C.-(11) 6789
 Chiba, A.-(11) 6545
 Chien, C. L.-(11) 6822, 7222
 Chin, T. S.-(11) 6241
 Chiou, D. Y.-(11) 6271
 Chiriac, H.-(11) 6566, 6584, 6628
 Cho, W. S.-(11) 6575
 Choe, Sug-Bong-(11) 6952
 Choi, Y. S.-(11) 7270
 Chouteau, G.-(11) 6899
 Chrisey, D. B.-(11) 6774, 7070, 7189
 Chubykalo, O. A.-(11) 6509, 7228, 7393
 Chudnovsky, E. M.-(11) 6934
 Cibin, G.-(11) 7091
 Ciureanu, P.-(11) 6563, 6566
 Clark, A. E.-(11) 7279, 7282, 7288
 Clemens, B. M.-(11) 6685
 Clinton, T. W.-(11) 6774, 6777
 Cochran, J. F.-(11) 6296
 Cochran, R. W.-(11) 6563, 6566
 Coehoorn, R.-(11) 6855
 Coey, J. M. D.-(11) 6447, 6902, 6983, 7145, 7166
 Cohen, R.-(11) 7192
 Cohenca, C. H.-(11) 7058
 Conin, L.-(11) 6834
 Constantinides, S.-(11) 7127
 Continenza, A.-(11) 6438
 Cooke, D. W.-(11) 6795
 Cooley, J. C.-(11) 6542
 Cooper, B. R.-(11) 6432
 Cornejo, D. R.-(11) 6268, 6637
 Cornia, A.-(11) 6946
 Corti, M.-(11) 6602, 6605
 Cottam, M. G.-(11) 6955
 Coutinho-Filho, M. D.-(11) 6311
 Coyle, S. T.-(11) 7040
 Crocker, B. C.-(11) 6557
 Crow, J.-(11) 6786
 Crow, J. E.-(11) 6989, 6992
 Crow, M. L.-(11) 7076
 Cullen, J.-(11) 6983
 Cullen, J. R.-(11) 6500
 Cuong, T. D.-(11) 6964
 Czauszejko, T.-(11) 6371
 Da Costa, V.-(11) 6703
 da Cunha, S. F.-(11) 6969
 Dahlberg, E. Dan-(11) 6893
 Dahlgren, M.-(11) 6268
 Dahmen, K. H.-(11) 7055
 Dai, S.-(11) 7198
 Daly, G. M.-(11) 6774
 Damay, F.-(11) 7204
 Dartyge, E.-(11) 7291
 Date, S. K.-(11) 6536, 6864, 7174, 7375
 Daughton, J. M.-(11) 7034
 Daughton, James M.-(11) 6688
 David, S.-(11) 6506
 Davies, H. A.-(11) 6335, 6411, 6634
 Dawson, F. P.-(11) 7103
 de Araujo, J. H.-(11) 6932
 De Boeck, J.-(11) 6700

- de Boer, F. R.-(11) 6408, 6727, 6899
 Dedukh, L. M.-(11) 6828
 De Graef, Marc-(11) 6837
 de Jonge, W. J. M.-(11) 7207
 del Barco, E.-(11) 6934
 DeLong, L. E.-(11) 6435
 Demangeat, C.-(11) 7013
 Dempsey, N. M.-(11) 6902
 Dennis, K. W.-(11) 6631
 de Oliveira, A. J. A.-(11) 7372
 de Oliveira, A. L.-(11) 6971
 de Oliveira, N. A.-(11) 6967, 6971
 De Raedt, H.-(11) 6937
 Deshpande, C. E.-(11) 6864
 Devasahayam, A. J.-(11) 7216
 DeVries, Michael J.-(11) 6747
 Diep, H. T.-(11) 6317
 Dikshstein, Igor E.-(11) 7306
 Ding, J.-(11) 6256
 Ding, Y.-(11) 6926
 Dobrovitski, V. V.-(11) 6599
 Dodd, P. M.-(11) 6670, 6750
 Donahue, M. J.-(11) 6491
 Dong, Shengzhi-(11) 6626
 Dong, Z. W.-(11) 6780
 Dooley, Jennifer-(11) 6837
 Dörr, K.-(11) 7079
 dos Santos, H.-(11) 6969
 Dou, S. X.-(11) 7177, 7312, 7315
 Dowben, P. A.-(11) 6284, 7246
 Drulis, H.-(11) 6986
 Duncombe, P. R.-(11) 7076
 Dung, N. D.-(11) 7324
 Dutta, B.-(11) 6700
 D'yachenko, A. I.-(11) 7324
- Ebert, H.-(11) 7082
 Echer, C. J.-(11) 6810
 Echigoya, J.-(11) 7213
 Eckert, D.-(11) 7240
 Eckert, J.-(11) 6986
 Eddy, C. R.-(11) 6774, 7189
 Egelhoff, W. F., Jr.-(11) 7037
 Ellouze, M.-(11) 6911
 Elmouhssine, O.-(11) 7013
 Emura, M.-(11) 7127
 Endo, Masato-(11) 6961
 Enokizono, Masato-(11) 6486
 Eom, C. B.-(11) 6539, 6995
 Epstein, A. J.-(11) 7378
 Erwin, R. W.-(11) 6882
 Ettegui, Hanania-(11) 6733
 Evetts, J. E.-(11) 6697, 7157
 Ezekwenna, P. C.-(11) 6736, 6911
- Fàbrega, L.-(11) 7309
 Falco, C. M.-(11) 6232
 Fan, Y.-(11) 7052
 Fanelisa, A.-(11) 7094
 Farinelli, M.-(11) 7297
 Farrow, R. F. C.-(11) 6810
 Fatemi, D. J.-(11) 6783, 6867, 6920
 Faunce, C. A.-(11) 7267
 Faust, A.-(11) 7094
 Fawcett, E.-(11) 7384
 Feiven, S. A.-(11) 6280
 Felcher, G. P.-(11) 6801, 7219
 Felner, I.-(11) 7312
 Felner, Israel-(11) 6733
 Fernández, J. F.-(11) 6940
 Ferrari, E. F.-(11) 7007
 Fetisov, V. B.-(11) 6876
 Fidler, J.-(11) 6396
 Fidler, Josef-(11) 6262
 Fiebig, M.-(11) 6560
 Finazzi, M.-(11) 6617
 Fink, Anita-(11) 6688
 Fischer, H.-(11) 6293
- Fischer, P.-(11) 7088
 Fischer, R.-(11) 7148
 Fishman, A. Ya.-(11) 6876
 Fitzsimmons, M. R.-(11) 7010
 Flynn, C. P.-(11) 7261
 Fontaine, A.-(11) 6617, 7291
 Fontcuberta, J.-(11) 7058, 7309
 Fontijn, W. F. J.-(11) 6765
 Forasini, M. L.-(11) 6438
 Fortin, J.-Y.-(11) 7234
 Fournier, P.-(11) 7351
 Frankland, D.-(11) 6566
 Freeland, J. W.-(11) 6290, 7028
 Freeman, A. J.-(11) 7016, 7022, 7258
 Freeman, M. R.-(11) 6217
 Freitas, P. J.-(11) 7387
 Freitas, P. P.-(11) 6694
 Freltoft, T.-(11) 6798
 Fröhlich, D.-(11) 6560
 From, M.-(11) 6296
 Fruchart, O.-(11) 6293
 Fu, C. C.-(11) 6998
 Fujii, Toshitaka-(11) 6768, 7294
 Fujikata, Junichi-(11) 7210
 Fujimori, H.-(11) 6524
 Fujisaki, Keisuke-(11) 6356
 Fujita, A.-(11) 6320
 Fujita, M.-(11) 6390
 Fujita, Naoyuki-(11) 7294
 Fujita, W.-(11) 7378
 Fukamichi, K.-(11) 6320, 7213
 Fukunaga, H.-(11) 6623
 Fukuno, A.-(11) 6917
 Fukuoka, K.-(11) 6390
 Fuller-Mora, W. W.-(11) 7070
 Fullerton, E. E.-(11) 6801
 Fullerton, Eric E.-(11) 6238
 Furdyna, J. K.-(11) 6554
- Galatanu, A.-(11) 6423
 Galkin, A.-(11) 6798
 Galkin, V. Yu.-(11) 7384
 Gallagher, W. J.-(11) 6515
 Galli, M.-(11) 6438
 Galvão, T. T. P.-(11) 6694
 Gama, S.-(11) 6932
 Gambino, R. J.-(11) 6676
 Gamble, H. S.-(11) 6670
 Gan, Q.-(11) 6539
 Gao, Xiang-(11) 6747
 Gao, Xingyu-(11) 7019
 Garcia, F.-(11) 6969
 García, L. M.-(11) 7091
 García, N.-(11) 6937
 García-Beneytez, J. M.-(11) 6578, 6581
 García-Pablos, D.-(11) 6937
 García Tello, P.-(11) 6338
 Gardel, M. L.-(11) 7339
 Gatteschi, D.-(11) 6946
 Gebhardt, Jeffrey R.-(11) 6299
 Gehringer, Peter-(11) 7177
 Gervais, B.-(11) 6902
 Geshev, J.-(11) 7007
 Gewinner, G.-(11) 7013
 Ghidini, M.-(11) 6902
 Ghigna, P.-(11) 6602
 Gibbs, M. R. J.-(11) 6335, 6411
 Giebutowicz, T. M.-(11) 6554
 Gill, H. S.-(11) 7061
 Gillies, M. F.-(11) 6855
 Gillman, E. S.-(11) 7055
 Ginatempo, B.-(11) 7097
 Giorgetti, Ch.-(11) 7291
 Girju, M. A.-(11) 7378
 Givord, D.-(11) 6506
 Gmulin, E.-(11) 6977, 7148
 Goerigk, G.-(11) 7088
- Goldman, A. I.-(11) 7243
 Golosov, D. I.-(11) 7360
 Gomes, A. M.-(11) 6943
 Gomez, R. D.-(11) 6226
 Gommert, E.-(11) 7148
 Gong, G. Q.-(11) 7049, 7076
 Gong, W.-(11) 6709, 6712
 Gong, X. G.-(11) 7100
 González, J.-(11) 6338, 6341, 6509
 González, J. M.-(11) 6277, 6338, 6509, 7228, 7249, 7393
 González-Comas, Alfons-(11) 7300
 Gorbenco, O. Yu.-(11) 7369
 Gorn, N. L.-(11) 6350
 Gornakov, V. S.-(11) 6828
 Goto, K.-(11) 6465
 Goto, Tsuneaki-(11) 6961
 Goulon, J.-(11) 6617
 Grabowski, K. S.-(11) 7070
 Granberg, P.-(11) 6980
 Grandjean, F.-(11) 6736
 Grange, W.-(11) 6617
 Greene, R. L.-(11) 6780, 7351
 Grigorov, Ilya L.-(11) 7010
 Grimsditch, M.-(11) 6238
 Grishin, A. M.-(11) 7327
 Grössinger, R.-(11) 6268
 Grundy, P. J.-(11) 6750
 Grüter, P.-(11) 7333
 Gu, T.-(11) 7243
 Guarisco, D.-(11) 6685
 Guertin, R. P.-(11) 6992
 Guillot, M.-(11) 6730, 6756, 6762, 7237
 Guimaraes, L.-(11) 6852
 Gulden, Th.-(11) 7321
 Gupta, A.-(11) 7049, 7061, 7076, 7366
 Guruswamy, S.-(11) 6393
 Gutfleisch, O.-(11) 6905
 Gutiérrez, J.-(11) 7171
- Haack, N.-(11) 7025
 Hadjipanayis, G.-(11) 7124, 7139
 Hadjipanayis, G. C.-(11) 6253
 Hagiwara, T.-(11) 6420
 Hagmusa, I. H.-(11) 7136
 Han, S. H.-(11) 6652, 7270
 Handstein, A.-(11) 7079
 Hanf, M. C.-(11) 7013
 Harmon, B. N.-(11) 6599
 Haroush, S.-(11) 7282
 Harris, I. R.-(11) 6905
 Harris, K. D. M.-(11) 6314
 Harris, V. G.-(11) 6783, 6867, 6920
 Hartman, A.-(11) 6362
 Hatanai, T.-(11) 6332, 6658
 Hathaway, Kristl B.-(11) 7067
 Haubold, H.-G.-(11) 7088
 Haupt, L.-(11) 7148
 Hauser, R.-(11) 6423
 Hautot, Dimitri-(11) 6736
 Havela, L.-(11) 6435, 6964, 6986
 Hawley, M. E.-(11) 7010
 Hayashi, Kazuhiko-(11) 7210
 Hayashi, T.-(11) 6548, 6551
 Hayes, W.-(11) 6379
 Heinrich, B.-(11) 6296
 Hejtmánek, J.-(11) 7204
 Helmolt, R. v.-(11) 7148
 Henn, R. W.-(11) 7321
 Henning, P. F.-(11) 6989
 Henry, Y.-(11) 6703
 Heo, N. H.-(11) 6480, 6483
 Herbst, J. F.-(11) 7252
 Heremans, J. J.-(11) 7055
 Hermann, C.-(11) 6834
 Hermann, R.-(11) 6399
- Hernandez, J. M.-(11) 6934
 Hernando, A.-(11) 6277, 7393
 Hidaka, T.-(11) 6917
 Hiebert, W. K.-(11) 6217
 Hill, Bradford-(11) 6893
 Hillebrecht, F. U.-(11) 7094
 Hilscher, G.-(11) 6423, 7163
 Hinds, G.-(11) 6447
 Hiramoto, M.-(11) 6655
 Hirosawa, S.-(11) 6265
 Hirose, Y.-(11) 6396
 Holdsworth, P. C. W.-(11) 7234
 Holzapfel, B.-(11) 7079
 Honda, N.-(11) 6533
 Honda, T.-(11) 7115
 Hong, B.-(11) 6465
 Hong, Chin-Yih-(11) 6771
 Hong, Kug Sun-(11) 6873
 Hong, Soon C.-(11) 7016
 Honig, J. M.-(11) 7243
 Horng, H. E.-(11) 6771
 Horwitz, J. S.-(11) 6774, 7070, 7189
 Hoshi, Y.-(11) 6250
 Howe, D.-(11) 7112
 Hsu, Y. Y.-(11) 6789
 Hu, Y. M.-(11) 7046
 Huang, C. Y.-(11) 7345
 Huang, E. Y.-(11) 6241
 Huang, H. L.-(11) 6643
 Huang, J. C. A.-(11) 7046
 Huang, J. K.-(11) 7297
 Huang, M. Q.-(11) 6468, 6471, 6718
 Huber, D. L.-(11) 6949
 Hudson, J.-(11) 7255
 Hundley, M. F.-(11) 7052
 Hunter-Dunn, J.-(11) 7025
 Hurley, R. E.-(11) 6670
 Huth, M.-(11) 7261
 Hwang, H. Y.-(11) 7064
- Ibañez, G.-(11) 7201
 Ichihara, Takayuki-(11) 6673
 Ichikawa, Y.-(11) 6655
 Ido, H.-(11) 7133
 Idzerda, Y. U.-(11) 6290, 7028
 Ijima, K.-(11) 6655
 Ijiri, Y.-(11) 6882, 7219
 Ikarashi, K.-(11) 7213
 Inoue, A.-(11) 6329, 6332
 Inoue, Akihisa-(11) 6326
 Inoue, Mitsuteru-(11) 6768, 7294
 Insausti, M.-(11) 7171
 Ionov, A. M.-(11) 7163
 Iqbal, Z.-(11) 6542
 Iraha, T.-(11) 6365
 Iramina, K.-(11) 6465
 Iriguchi, N.-(11) 6450
 Isaac, S. P.-(11) 7157
 Ishikawa, Masayasu-(11) 6792
 Ishiyama, K.-(11) 7303
 Isnard, O.-(11) 6730
 Itié, J. P.-(11) 7291
 Itoh, Y.-(11) 6753
 Ivanov, V. Yu.-(11) 7160, 7180
 Iwahara, M.-(11) 7103
 Iwaki, Sunao-(11) 6441
 Iwasaka, M.-(11) 6453, 6456, 6459
 Iwasieczko, W.-(11) 6986
 Iwatsubo, S.-(11) 6667
- Jahnes, C.-(11) 6676
 James, P. A. B.-(11) 6444
 James, W. J.-(11) 6911
 Jang, I. J.-(11) 6771
 Jang, P. W.-(11) 6614
 Jang, Z. H.-(11) 6946
 Jansen, R.-(11) 6682
 Januszewski, D.-(11) 6634

- Jardim, R. F.-(11) 7058
 Jaswal, S. S.-(11) 6745
 Jensen, M. R. F.-(11) 6280
 Jensen, P. J.-(11) 6542
 Jeung, W. Y.-(11) 6405
 Jewell, G. W.-(11) 7112
 Jezierska, E.-(11) 6634
 Jia, Q. X.-(11) 7052
 Jiang, J. S.-(11) 6238, 6385
 Jiang, X. L.-(11) 6780
 Jiles, D. C.-(11) 6353, 6497
 Jing, X. N.-(11) 6530
 Jiráček, Z.-(11) 7204
 Jirsa, M.-(11) 6798
 Johansen, T. H.-(11) 6798
 Johnson, Mark-(11) 6774, 6777, 6780
 Jones, B.-(11) 6489
 Jonsson, B. J.-(11) 6893
 Jorgensen, J. D.-(11) 6374
 Joy, P. A.-(11) 6536, 7375
 Ju, H. L.-(11) 7073, 7183
 Judy, Jack H.-(11) 6825
- Kabanov, Yu. P.-(11) 6828
 Kacedon, D. B.-(11) 6539, 6995
 Kadomtseva, A. M.-(11) 7160
 Kaiser, H.-(11) 7339
 Kakuno, K.-(11) 6533
 Kamarád, J.-(11) 6964
 Kanai, Y.-(11) 6623
 Kanekiyo, H.-(11) 6265
 Kang, H.-(11) 6977, 7148
 Kang, Jong Seog-(11) 6620
 Kang, S. J.-(11) 7130
 Kang, S. Y.-(11) 7285
 Kantner, C.-(11) 7297
 Kao, C. C.-(11) 6293
 Kao, C.-C.-(11) 6290
 Kao, C.-C.-(11) 7091
 Kappler, J. P.-(11) 7291
 Kappler, J.-P.-(11) 6617
 Kapusta, Cz.-(11) 7151
 Kariuki, B. M.-(11) 6314
 Kasimir, N.-(11) 6379
 Kaszuwara, W.-(11) 6634
 Katayama, T.-(11) 6742, 6813, 7031
 Katter, M.-(11) 6721
 Kaufman, J. H.-(11) 6489
 Kaul, A. R.-(11) 7369
 Kauzlarich, S. M.-(11) 7192
 Kayzel, F. E.-(11) 7136
 Kelley, T. M.-(11) 6374
 Kellock, A. J.-(11) 6810
 Kennedy, S. J.-(11) 7177
 Kevorkian, B.-(11) 6506
 Khapikov, A. F.-(11) 6828
 Khomskii, D. I.-(11) 7369
 Kikitsu, A.-(11) 6232
 Kikuchi, H.-(11) 6691
 Kim, A.-(11) 7139
 Kim, A. S.-(11) 6715
 Kim, C. O.-(11) 6575
 Kim, C. S.-(11) 6929
 Kim, Chong-Oh-(11) 6646
 Kim, Chul Sung-(11) 6929
 Kim, Chul-Sung-(11) 6646
 Kim, D.-(11) 7243
 Kim, D. H.-(11) 7124
 Kim, D. W.-(11) 6614
 Kim, H. J.-(11) 6649, 6652, 7270
 Kim, In-Tae-(11) 6873
 Kim, J.-(11) 6483, 6652, 6774, 7070, 7189
 Kim, K. S.-(11) 7142
 Kim, K. Y.-(11) 6649
 Kim, Miyoung-(11) 7016
 Kim, S. R.-(11) 7142, 7285
 Kim, SangWon-(11) 6620
- Kim, T. K.-(11) 6575
 Kim, T. W.-(11) 6676
 Kim, Taek-Soo-(11) 6646
 Kim, Y. B.-(11) 6929
 Kim, Y. K.-(11) 6575
 Kim, Yoon B.-(11) 6405
 Kioussis, Nicholas-(11) 6429
 Kirby, R. D.-(11) 7381
 Kirchmayr, H.-(11) 6423
 Kirkland, J. P.-(11) 6867
 Kirschner, J.-(11) 7019
 Kirtley, J. R.-(11) 7061
 Kisker, E.-(11) 7094
 Kitajima, N.-(11) 6623
 Kitakami, O.-(11) 6661, 7213
 Klaua, M.-(11) 7019
 Klavins, P.-(11) 7192
 Klehe, A. K.-(11) 6379
 Knies, D. L.-(11) 7070
 Kobayashi, K.-(11) 6691
 Kobayashi, Koichiro-(11) 6462
 Koblishka, M. R.-(11) 6798
 Kodama, Hiroyoshi-(11) 6831
 Kodama, R. H.-(11) 6888, 7219
 Koehler, T.-(11) 6489
 Kokal, H. R.-(11) 6477
 Kolenbrander, M.-(11) 6870
 Koller, D.-(11) 7070, 7189
 Koller, Daniel-(11) 6774
 Kolomiets, A. V.-(11) 6435, 6986
 Kong, F.-(11) 6795
 Kools, J. C. S.-(11) 7207
 Koshiba, Hisato-(11) 6326
 Kou, X. C.-(11) 6408, 6727, 6899
 Kozhina, G. A.-(11) 6876
 Krabbes, G.-(11) 7240
 Kramer, M. J.-(11) 6631
 Krause, R. F.-(11) 6477
 Krebs, J. J.-(11) 6819
 Krembel, C.-(11) 7013
 Kremer, R. K.-(11) 7321
 Kresin, Vladimir Z.-(11) 7357
 Krill, G.-(11) 6617
 Krisch, M.-(11) 7091
 Krishnan, Kannan M.-(11) 6810, 7073, 7183
 Krommüller, H.-(11) 6408, 6908
 Krupicka, S.-(11) 7204
 Krusin-Elbaum, L.-(11) 7061
 Kryder, M. H.-(11) 7216
 Ku, H. C.-(11) 6789
 Kubis, M.-(11) 6905
 Kubota, Takeshi-(11) 6486
 Kuch, W.-(11) 7019
 Kugel, K. I.-(11) 7369
 Kuhl, E.-(11) 6706
 Kuji, T.-(11) 6390
 Kulakowski, K.-(11) 6341
 Kulkarni, S. D.-(11) 6864
 Kuma, J.-(11) 6623
 Kumar, A.-(11) 6759
 Kumar, Ravi-(11) 7174
 Kuno, S.-(11) 6533
 Kuo, C. M.-(11) 6643
 Kuo, P. C.-(11) 6643
 Kurenykh, T. E.-(11) 6876
 Kurlyandskaya, G. V.-(11) 6581
 Kuznietz, Moshe-(11) 6733
 Kwon, C.-(11) 7052
 Kwon, H. W.-(11) 7130
- Labitzke, H.-(11) 6908
 Labroo, Sunil-(11) 6974
 Lai, Chih-Huang-(11) 6816
 Lampel, G.-(11) 6834
 Landau, D. P.-(11) 6305
 Lang, Wolfgang-(11) 7177
 Larin, V. S.-(11) 6587
- Lascialfari, A.-(11) 6602, 6605, 6946
 Lebedev, S. P.-(11) 7180
 Lederman, D.-(11) 7073
 Ledue, D.-(11) 6305
 Lee, C. S.-(11) 6483
 Lee, Ching-Ming-(11) 6593
 Lee, Heebok-(11) 6575
 Lee, J. J.-(11) 6652
 Lee, K. C.-(11) 6426, 7318, 7345
 Lee, S. H.-(11) 6882, 7219
 Lee, S. L.-(11) 6771
 Lee, S. R.-(11) 6483, 6614, 7270
 Lee, Seung Wha-(11) 6929
 Lees, M. R.-(11) 7151
 Lemarquand, G.-(11) 7118, 7121
 Lemarquand, V.-(11) 7118
 Lemke, L.-(11) 7025, 7028
 Leonowicz, M.-(11) 6634
 Leute, S.-(11) 6560
 Levin, K.-(11) 7360
 Levy, M.-(11) 6759
 Lewis, L. H.-(11) 6274, 6631, 6843
 Leyendecker, A. J.-(11) 6226
 Lezama, L.-(11) 7171
 l'Héritier, Ph.-(11) 6911
 Li, C. P.-(11) 6631
 Li, Fashen-(11) 6923
 Li, Lin-(11) 6578
 Li, M.-(11) 6287
 Li, M. Z.-(11) 6596
 Li, W. D.-(11) 6661
 Li, W. H.-(11) 6426, 7318, 7345
 Li, X. W.-(11) 6515, 7049, 7076
 Li, Z. W.-(11) 7198
 Liebe, J.-(11) 6977, 7148
 Liechtenstein, A. I.-(11) 7022
 Lieu, D. K.-(11) 6362
 Lim, Pang Boey-(11) 7294
 Lim, S. H.-(11) 7142, 7270, 7285
 Lim, Woo-Young-(11) 6646
 Lin, H. Q.-(11) 7100, 7363
 Lin, J.-(11) 6554, 6926
 Lin, Xiangdong-(11) 6223
 Lin, Y.-C.-(11) 6426
 Lin, Y.-L.-(11) 6432
 Lindbaum, A.-(11) 6423
 Lindberg, J. F.-(11) 7279, 7282
 Lindgren, E. A.-(11) 7282
 Liorzou, F.-(11) 7106
 Liou, S. H.-(11) 6244, 6611
 Lisiansky, A. A.-(11) 6308
 Liu, H. K.-(11) 7177
 Liu, Haiying-(11) 6846, 6849
 Liu, Hui-ping-(11) 6980
 Liu, J. F.-(11) 7139
 Liu, J. P.-(11) 6608
 Liu, R. S.-(11) 7345
 Liu, S.-(11) 6706
 Liu, Y.-(11) 6244, 6608, 6611, 7333
 Loidl, A.-(11) 7180
 Long, Gary J.-(11) 6736
 Loong, C.-K.-(11) 6926
 Lopes dos Santos, J. M. B.-(11) 7154
 Lord, D. G.-(11) 7267, 7276
 Lorenzo, J. E.-(11) 7091
 Lorimer, W. L.-(11) 6362
 Löser, W.-(11) 6399
 Lourenço, A. A. C. S.-(11) 7154
 Lu, Qing Feng-(11) 6961
 Lu, Ying-(11) 6961
 Lu, Yu-(11) 6515
 Lubitz, P.-(11) 6819
 Ludwig, A.-(11) 7267
 Ludwig, Alfred-(11) 7264
 Luis, F.-(11) 6934, 6940
 Lukshina, V. A.-(11) 6581
 Luo, H.-(11) 6911, 6914, 7339
 Luo, Yansheng-(11) 6223
- Lutsev, L. V.-(11) 7330
 Lütt, M.-(11) 7010
 Lynn, J. W.-(11) 6426, 7342, 7345, 7348
 Lyons, M. E. G.-(11) 6447
- Ma, B. M.-(11) 6271, 6471, 6709, 6712, 6718
 Maas, T. F. M. M.-(11) 7207
 MacLaren, J. M.-(11) 6521
 Majetich, S. A.-(11) 6468
 Majkrzak, C. F.-(11) 7219
 Major, R. V.-(11) 6335
 Makino, A.-(11) 6329, 6332, 6658, 6861, 7213
 Makino, Akihiro-(11) 6326
 Malhotra, S. S.-(11) 6244
 Malik, S. K.-(11) 7312, 7315
 Man, H. C.-(11) 6417
 Mancoff, F. B.-(11) 6685
 Mandal, P.-(11) 6977, 7148
 Manoharan, S. Sundar-(11) 7183
 Mañosa, Lluís-(11) 7300
 Manov, V.-(11) 6587
 Mansuripur, M.-(11) 6232
 Mao, Sining-(11) 6807
 Mao, Weihua-(11) 6640, 6923
 Marabelli, F.-(11) 6438
 Marasinghe, G. K.-(11) 6911
 Marcelli, A.-(11) 7091
 Maret, M.-(11) 6617
 Marinescu, C. S.-(11) 6584
 Marinescu, M.-(11) 6628
 Markert, J. T.-(11) 6235
 Marks, R. F.-(11) 6810
 Marley, A.-(11) 6515
 Mårtensson, N.-(11) 7025
 Martin, C.-(11) 7204
 Martínez, B.-(11) 7058, 7309
 Martins, C. S.-(11) 7001
 Maryško, M.-(11) 6798, 7204
 Massarotti, V.-(11) 6605
 Masson, Fabrice-(11) 7264
 Mathur, N. D.-(11) 7157
 Matsui, T.-(11) 7381
 Matsukawa, N.-(11) 6655
 Matsumura, Hiroaki-(11) 6673
 Matsumura, S.-(11) 6658
 Mattoso, N.-(11) 7372
 Mayergoyz, I. D.-(11) 6226, 6347
 Mazzatesta, A. D.-(11) 7282
 McAvoy, T.-(11) 6284, 7246
 McCall, S.-(11) 6992
 McCallum, R. W.-(11) 6631
 McCartney, M. R.-(11) 6414
 McCormick, P. G.-(11) 6256
 McGuire, T. R.-(11) 7076
 McHenry, M.-(11) 6718
 McHenry, Michael E.-(11) 6837
 McIlroy, D. N.-(11) 6284
 McMichael, R. D.-(11) 7037
 Medvedeva, I. V.-(11) 6977, 7148
 Mehta, Apurva-(11) 7312
 Mehta, G. K.-(11) 7174
 Melamud, Mordechai-(11) 6733
 Ménard, D.-(11) 6563, 6566
 Mendoza, G.-(11) 6634
 Mendoza, W.-(11) 7195
 Mény, C.-(11) 7043
 Mercey, B.-(11) 7186
 Metselaar, R.-(11) 6765
 Miao, W. F.-(11) 6256
 Michel, R. P.-(11) 6828
 Michor, H.-(11) 7163
 Middleton, D. P.-(11) 6736
 Miers, C. R.-(11) 6235
 Mihut, A.-(11) 6379

- Mikamoto, T.-(11) 6402
 Millburn, J. E.-(11) 6379
 Miller, Brad.-(11) 6893
 Miller, D.-(11) 7351
 Miller, D. J.-(11) 6385
 Miller, M. M.-(11) 6819
 Miller, Michael M.-(11) 7067
 Millev, Y. T.-(11) 6500
 Min, H.-G.-(11) 6287
 Miotkowski, I.-(11) 6557
 Missell, F. P.-(11) 6268, 6637, 7001, 7127
 Mitani, S.-(11) 6524
 Mitchell, J. F.-(11) 6374, 6385, 7348, 7351
 Miura, Y.-(11) 6658
 Miyatani, Kazuo-(11) 6302, 6792
 Mizushima, T.-(11) 6329
 Mochizuki, K.-(11) 6235
 Moeschler, F. D.-(11) 6444
 Mohan, Ch. V.-(11) 7019
 Monachesi, P.-(11) 6438
 Montero, M. I.-(11) 6277
 Moodera, J. S.-(11) 6682, 6700
 Moraitis, G.-(11) 7013
 Morales, M. P.-(11) 6277
 Morikawa, Takeshi-(11) 6664
 Morita, S.-(11) 6658
 Morrish, A. H.-(11) 7198
 Morrow, T.-(11) 6858
 Mosca, D. H.-(11) 7372
 Moser, A.-(11) 6489
 Mou, D.-(11) 7327
 Mozhaev, A. V.-(11) 7180
 Mukasa, Kōichi-(11) 6831
 Mukhin, A. A.-(11) 7160, 7180
 Mukhopadhyay, S. C.-(11) 6368
 Mukovskii, Y. M.-(11) 7163, 7342
 Müller, K.-H.-(11) 6905, 7079, 7240
 Murdock, Ed.-(11) 6807
 Murillo, N.-(11) 6338
 Murphy, C. B.-(11) 7252
 Murray, S. J.-(11) 7297
 Muruguraj, P.-(11) 7148
- Na, J. G.-(11) 6480, 6483, 6614
 Nabialek, A.-(11) 7324
 Nafalski, A.-(11) 6371
 Naitoh, Y.-(11) 6332
 Nakada, Masafumi-(11) 7210
 Nakagawa, Shigeki-(11) 6673
 Nakajima, N.-(11) 6742
 Nakamae, S. C.-(11) 6786
 Nakamura, H.-(11) 6917
 Nakatani, I.-(11) 6323
 Nakayama, S.-(11) 6465
 Nakotte, H.-(11) 6986
 Nálevka, P.-(11) 6798
 Nam, J. T.-(11) 7285
 Namkung, M.-(11) 6474
 Naoo, M.-(11) 6250, 6667
 Naoo, Masahiko-(11) 6673
 Narlikar, A. V.-(11) 7312, 7315
 Neiva, A. C.-(11) 7127
 Nelson, C.-(11) 6810
 Nenkov, K. A.-(11) 7079
 Netto, Paulo R. S.-(11) 6958
 Newman, D. M.-(11) 6739
 Ni, C.-(11) 7139
 Nicolaidis, D.-(11) 6308
 Nigam, A. K.-(11) 7169
 Nikitenko, V. I.-(11) 6828
 Nishinaga, T.-(11) 6551
 Nixon, L.-(11) 6314
 Noguees, Josep-(11) 6893
 Noh, T. H.-(11) 6649
 Nordblad, P.-(11) 6980
 Norman, M. R.-(11) 7360
- Novak, M. A.-(11) 6943
 Novikov, D. L.-(11) 7258
 Novotny, M. A.-(11) 6494
 Nowik, I.-(11) 7312
 Nozières, J. P.-(11) 6902
 Nývlt, M.-(11) 6813, 7031
- Obradó, Eduard-(11) 7300
 Obradors, X.-(11) 7058, 7201, 7309
 Odin, S.-(11) 7291
 Oepen, H. P.-(11) 6500
 Ogale, S.-(11) 6780
 Ogale, S. B.-(11) 7174
 O'Handley, R. C.-(11) 7297
 Okuyama, Kentaro-(11) 7004
 O'Neill, M. C.-(11) 6858
 Onuki, T.-(11) 6365
 Ooba, Makoto-(11) 7004
 Ormerod, J.-(11) 7127
 Ortega, R. J.-(11) 6542
 Ortiz, W. A.-(11) 7372, 7384
 Osborn, R.-(11) 6374, 7348
 Oseroff, S. B.-(11) 7201
 Osgood, R. M., II-(11) 6801
 Osgood, R. M., III-(11) 6385
 Osgood, R. M., Jr.-(11) 6759
 Oshiki, Mitsumasa-(11) 6831
 Osofsky, M. S.-(11) 6774, 6783, 7070, 7189
 Ostoréro, J.-(11) 6756
 Otani, Y.-(11) 7213
 Ounadjela, K.-(11) 6703, 7166
 Quyang, C.-(11) 6676
 Óvári, T. A.-(11) 6566, 6584
 Ozhogin, V. I.-(11) 7369
- Pai, S. P.-(11) 6780
 Pak, A. O.-(11) 6226
 Pal, S. K.-(11) 6368
 Palmer, S. B.-(11) 6852
 Panchanathan, V.-(11) 6274, 6393
 Papakonstantinou, P.-(11) 6858
 Park, C. H.-(11) 6483, 6614
 Park, J. K.-(11) 7285
 Park, J. Y.-(11) 6649
 Parker, T. J.-(11) 6280
 Parkin, I. P.-(11) 6314
 Parkin, S.-(11) 6515
 Parlebas, J. C.-(11) 7013
 Parmar, B. S.-(11) 6335
 Pasquale, M.-(11) 6497
 Paszula, J.-(11) 6634
 Patel, R. T.-(11) 6379
 Patil, S. I.-(11) 7174
 Paul, D. McK.-(11) 7151
 Pearson, J.-(11) 6572
 Pekarek, T. M.-(11) 6557, 7243
 Peña, A.-(11) 7171
 Peng, J. C.-(11) 6426
 Peretti, J.-(11) 6834
 Pérez Alcázar, G. A.-(11) 7249
 Pettford-Long, A. K.-(11) 6840
 Pétróff, F.-(11) 6617
 Petrov, D. K.-(11) 7061
 Petukhov, A. V.-(11) 6742
 Peysson, S.-(11) 7234
 Pickart, S. J.-(11) 7076
 Pickett, W. E.-(11) 7354
 Piechota, S.-(11) 7324
 Piercy, A. R.-(11) 7255, 7273
 Pimenov, A.-(11) 7180
 Pinettes, C.-(11) 6317
 Pinkerton, F. E.-(11) 7252
 Piñol, S.-(11) 7201, 7309
 Pinski, F. J.-(11) 7097
 Pinto, Haim-(11) 6733
 Pinto, R.-(11) 7169
 Pinton, J.-F.-(11) 7234
- Pisarev, R. V.-(11) 6560
 Piskun, N. Y.-(11) 6590
 Pizzini, S.-(11) 7291
 Plaks, Alexander-(11) 6344
 Planes, Antoni-(11) 7300
 Plaskett, T. S.-(11) 6694
 Pobre, Z. C.-(11) 6795
 Poddar, A.-(11) 6977, 7148
 Pogorelov, Yu. G.-(11) 7154
 Polian, A.-(11) 7291
 Popescu, V.-(11) 7082
 Popov, Yu. F.-(11) 7160
 Poret, J. C.-(11) 7282
 Portier, X.-(11) 6840
 Potapov, A. P.-(11) 6581
 Prados, C.-(11) 6253
 Prasad, Shiva-(11) 6879, 7169
 Prellier, W.-(11) 7186
 Prinz, G. A.-(11) 7034
 Pruegl, K.-(11) 7088
 Punjabi, S. R.-(11) 6795
 Püst, L.-(11) 6798
- Qian, X. R.-(11) 6247, 7195
 Qian, Zhenghong-(11) 6825
 Quandt, E.-(11) 7267
 Quandt, Eckhard-(11) 7264
 Quellec, L.-(11) 7118
- Rainforth, W. M.-(11) 6411
 Rama Rao, K. V. S.-(11) 6920
 Ramdas, A. K.-(11) 6557
 Ramesh, R.-(11) 6780
 Ramos, C. A.-(11) 7201
 Ramunni, V. P.-(11) 6971
 Rani, R.-(11) 6247, 7195
 Ranno, L.-(11) 7166
 Rao, G. H.-(11) 6977, 7148
 Rao, K. V.-(11) 6542, 6893, 7327
 Rao, R. A.-(11) 6539, 6995
 Rao, X. L.-(11) 6902
 Rao, Xiao-lei-(11) 6983, 7145
 Raoux, D.-(11) 6293, 7091
 Raposo, E. P.-(11) 6311
 Rapp, R. E.-(11) 6943
 Rasing, Th.-(11) 6742
 Razee, S. S. A.-(11) 7097
 Reagor, D. W.-(11) 7052
 Rechenberg, H. R.-(11) 7001
 Rehr, J. J.-(11) 7025
 Rekveldt, M. Th.-(11) 6870
 Restorff, J. B.-(11) 7279, 7282, 7288
 Restrepo, J.-(11) 7249
 Rhyne, J. J.-(11) 6554, 7339
 Riedi, P. C.-(11) 7151
 Rigamonti, A.-(11) 6605
 Rikvold, P. A.-(11) 6494
 Riley, C. D.-(11) 7112
 Ritter, C.-(11) 6314
 Rivadulla, F.-(11) 7201
 Robinson, R. A.-(11) 6374
 Roche, K.-(11) 6515
 Rogalev, A.-(11) 6617, 7091
 Rogalski, M. S.-(11) 6852
 Rogl, P.-(11) 6423
 Rojo, T.-(11) 7171
 Roozeboom, F.-(11) 7207
 Rosen, M.-(11) 7282
 Rosenkranz, S.-(11) 6374, 7348
 Rosseinsky, M. J.-(11) 6379
 Rouabhi, M.-(11) 6563, 6566
 Rubinstein, Mark-(11) 7067
 Rubshtein, A.-(11) 6587
 Ruck, K.-(11) 7240
 Rudkowski, P.-(11) 6563
 Ruiz, E. J.-(11) 6795
- Sabiryanov, R. F.-(11) 6745
 Safarov, V. I.-(11) 6834
 Sagawa, M.-(11) 6396
 Saha, Shibaji-(11) 6974
 Sainkar, S. R.-(11) 6864
 Saito, K.-(11) 6533
 Saito, T.-(11) 6390
 Sakaguchi, K.-(11) 7109
 Sakakima, H.-(11) 6655
 Salk, Sung-Ho Suck-(11) 7306
 Salon, S.-(11) 6347
 Salter, I. W.-(11) 6750, 6858
 Salvietti, M.-(11) 7019
 Samoilov, A. V.-(11) 6998
 Saotome, H.-(11) 6420, 7109
 Sapina, F.-(11) 6542
 Saraf, L. V.-(11) 7174
 Sarrao, J.-(11) 6786
 Sasada, I.-(11) 6861
 Sasaki, Y.-(11) 6658
 Sassik, H.-(11) 6423
 Sato, Kiyoo-(11) 6961
 Sato, M.-(11) 6691
 Sato, T.-(11) 6658
 Sato, Y.-(11) 6420
 Scheinfein, M. R.-(11) 7040
 Schellenberg, R.-(11) 7094
 Schieffer, P.-(11) 7013
 Schmidt, J. E.-(11) 7007
 Schmiedel, T.-(11) 6762
 Schnelle, W.-(11) 7321
 Schrefl, Thomas-(11) 6262
 Schreiner, W. H.-(11) 7372
 Schuller, Ivan K.-(11) 6893
 Schulthess, T. C.-(11) 7225
 Schultz, L.-(11) 7079
 Schultz, S.-(11) 6229
 Schütz, G.-(11) 7082, 7085, 7088
 Schutz, L.-(11) 6905
 Schwartz, J.-(11) 6786
 Scott, J. H.-(11) 6468
 Sechovský, V.-(11) 6435, 6964
 Seeger, M.-(11) 6908
 Sellers, C. H.-(11) 6631
 Sellmyer, D. J.-(11) 6244, 6608, 6611, 7381
 Sereni, J. G.-(11) 6423
 Serimaa, R.-(11) 7091
 Serrano-González, H.-(11) 6314
 Seto, K.-(11) 6551
 Sève, L.-(11) 6293, 7091
 Shaheen, S. A.-(11) 7195
 Shaked, Hagai-(11) 6733
 Shan, Z. S.-(11) 6244
 Shapiro, A. J.-(11) 6828
 Sharma, M.-(11) 6685
 Sharma, R. P.-(11) 6780, 7351
 Sheldon, R. I.-(11) 6374
 Shelton, R. N.-(11) 7192
 Sheludko, N.-(11) 7145
 Shepard, M.-(11) 6989
 Shi, Rick C.-(11) 6223
 Shi, Y.-(11) 6353
 Shick, A. B.-(11) 7022, 7258
 Shimada, H.-(11) 6551
 Shimada, Y.-(11) 6661, 7213
 Shin, Sung-Chul-(11) 6952
 Shinde, S. R.-(11) 7174
 Short, S. M.-(11) 6926
 Shringi, S. N.-(11) 6879, 7169
 Shrotri, J. J.-(11) 6864
 Shull, R. D.-(11) 6828
 Shulyatev, D. A.-(11) 7342
 Sides, P. J.-(11) 7216
 Sides, S. W.-(11) 6494
 Siegrist, T.-(11) 7064
 Simon, A.-(11) 7321

- Simon, Ch.-(11) 7186
 Simon, G.-(11) 6706
 Sin, A.-(11) 7309
 Sin, K.-(11) 6685
 Singh, D. J.-(11) 7354
 Singh, R. R. P.-(11) 7387
 Singh, Rajvir-(11) 7312, 7315
 Singleton, J.-(11) 6379
 Sinha, S. K.-(11) 7348
 Sinnecker, J. P.-(11) 6578, 6581
 Sivasubramaniam, K.-(11) 6347
 Sivertsen, John M.-(11) 6825
 Skomski, R.-(11) 6896
 Skomski, Ralph-(11) 6503, 6724
 Skumryev, V.-(11) 6983, 7145
 Slawska-Waniewska, A.-(11) 6338
 Smirnov-Rueda, R.-(11) 6509
 Smith, J. L.-(11) 6542
 Smith, P. A. I.-(11) 6256
 Soares, M. R.-(11) 6969
 Soares, V.-(11) 6694
 Somasundaram, P.-(11) 7243
 Sommer, H. A.-(11) 6235
 Son, Derac-(11) 7285
 Song, J. Y.-(11) 6652
 Sorkine, E.-(11) 6587
 Soulen, R. J., Jr.-(11) 6774, 7189
 Sousa, J. B.-(11) 6852, 7154
 Sousa, R. C.-(11) 6694
 Sowers, C. H.-(11) 6238
 Spring, L. E.-(11) 6379
 Squire, P. T.-(11) 6569, 6572
 Srivastava, P.-(11) 7025
 Stancu, Al.-(11) 6359
 Stankiewicz, A.-(11) 6217
 Starykh, O. A.-(11) 7387
 Staunton, J. B.-(11) 7097
 Stevenson, R. D.-(11) 7381
 Stiles, M. D.-(11) 7037
 Street, R.-(11) 6256
 Strom, Valter-(11) 6893
 Ström-Olsen, J. O.-(11) 6563
 Stroud, R. M.-(11) 6774, 7070, 7189
 Su, Quanmin-(11) 7264
 Sueoka, Kazuhisa-(11) 6831
 Suh, S. J.-(11) 6649
 Sun, J. J.-(11) 6694
 Sun, Jonathan Z.-(11) 7067
 Suran, G.-(11) 6679
 Suresh, K. G.-(11) 6920
 Sutani, T.-(11) 6371
 Suzuki, E.-(11) 6250
 Suzuki, Motofumi-(11) 6664
 Suzuki, T.-(11) 6527, 6753, 7133
 Suzuki, Y.-(11) 6742, 6813, 7031, 7064, 7133
 Syono, Y.-(11) 6390
 Szymczak, H.-(11) 7324
- Taga, Yasunori-(11) 6664
 Takadate, K.-(11) 6861
 Takahashi, M.-(11) 6402
 Takahashi, Migaku-(11) 7004
 Takahashi, T.-(11) 6533, 6667
 Takanashi, K.-(11) 6524
 Takano, K.-(11) 7219
 Takano, Kentaro-(11) 6888
 Takemura, Y.-(11) 6533
- Takeuchi, A. Y.-(11) 6969
 Takeuchi, M.-(11) 6453
 Takezawa, M.-(11) 7303
 Tanabe, Ikuo-(11) 6486
 Tanaka, M.-(11) 6548, 6551
 Tanaka, Toshiro-(11) 6302, 6792
 Taniguchi, F.-(11) 6402
 Taniyama, T.-(11) 6323
 Tanoue, H.-(11) 6545
 Tate, B. J.-(11) 6335
 Tatamatsu, K.-(11) 6365
 Tillet, C. J.-(11) 6305
 Tavares, P. B.-(11) 7154
 Taylor, John A.-(11) 6688
 Tedoldi, F.-(11) 6605
 Teillet, J.-(11) 6305
 Teixeira, S. R.-(11) 7372
 Tejada, J.-(11) 6934
 Teo, B. S.-(11) 7157
 Thomas, G.-(11) 6888
 Thomas, J.-(11) 6908
 Thomas, Richard A.-(11) 6244
 Thompson, Daniel W.-(11) 6747
 Tobola, J.-(11) 7237
 Todd, I.-(11) 6335
 Todorovic, M.-(11) 6229
 Tokura, Y.-(11) 7064
 Tomka, G. J.-(11) 7151
 Tondra, Mark-(11) 6688
 Tonnerre, J. M.-(11) 6293, 7091
 Toussaint, J. C.-(11) 6506
 Tovar, M.-(11) 7201
 Tovar Costa, M. V.-(11) 6971
 Travkin, V. D.-(11) 7180
 Troper, A.-(11) 6971
 Tsai, J. L.-(11) 6241
 Tsai, S. H.-(11) 6914
 Tsuda, H.-(11) 6453
 Tsukerman, Igor-(11) 6344
 Tsunoda, Masakiyo-(11) 7004
 Turgut, Z.-(11) 6468
 Twardowski, A.-(11) 6548
- Uchida, K.-(11) 6402
 Uchida, S.-(11) 6465
 Uchikawa, Yoshinori-(11) 6462
 Ueno, S.-(11) 6450, 6453, 6456, 6459, 6465
 Ueno, Shoogo-(11) 6441
 Ueyama, Takatsugu-(11) 6356
 Uhm, Young Rang-(11) 6929
 Umehara, Izuru-(11) 6961
 Uyama, H.-(11) 7213
 Uzumaki, Takuya-(11) 6831
- Valls, Oriol T.-(11) 6804
 Vanderah, T. A.-(11) 6783
 van der Heijden, P. A. A.-(11) 7207
 van der Zaag, P. J.-(11) 6765, 6870, 6882, 7207
 van de Veerdonk, R. J. M.-(11) 6700
 van Dover, R. B.-(11) 7064
 Van Drent, W. P.-(11) 6527, 6753
 van Lier, J.-(11) 6908
 van Zon, J. B. A.-(11) 6855
 Vase, P.-(11) 6798
 Vasiliu-Doloc, L.-(11) 7342, 7348
- Vasquez, R. P.-(11) 6998, 7366
 Vázquez, M.-(11) 6578, 6581, 7393
 Venegas, Pablo A.-(11) 6958
 Venkataramani, N.-(11) 6879, 7169
 Venkatesan, T.-(11) 6780, 7351
 Vente, J. F.-(11) 6379
 Vera, O.-(11) 6795
 Vescovo, E.-(11) 6284, 7246
 Viegas, A. D. C.-(11) 7007
 Vieira, J. M.-(11) 7154
 Villas-Boas, V.-(11) 6637
 Vlachov, E. S.-(11) 7079
 Vogel, J.-(11) 6617
 Volkov, A. A.-(11) 7180
 Von Dreelle, R. B.-(11) 6911
 von Molnár, S.-(11) 7055
 von Ranke, P. J.-(11) 6967
 Vorob'ev, G. P.-(11) 7160
 Vykhodets, V. B.-(11) 6876
- Wakao, S.-(11) 6365
 Waldfried, C.-(11) 6284, 7246
 Walker, J. C.-(11) 7010
 Wallace, W. E.-(11) 6471, 6718
 Walmer, M. H.-(11) 6706
 Walmer, M. S.-(11) 6706, 6712
 Walton, Derek-(11) 7396
 Wang, Connie P.-(11) 6816
 Wang, D.-(11) 7034
 Wang, Dexin-(11) 6688
 Wang, G. C.-(11) 6287
 Wang, J. P.-(11) 6362
 Wang, J. Y.-(11) 6631
 Wang, J. Y.-(11) 6274, 6843
 Wang, Run-(11) 6626
 Wang, S. X.-(11) 6685
 Wang, S. Y.-(11) 7100
 Wang, X. L.-(11) 7177
 Wang, Xindong-(11) 6518
 Wang, Y. R.-(11) 6393
 Watkins, D. B.-(11) 6435
 Watts, S.-(11) 7055
 Wears, M. L.-(11) 6739
 Webb, D. J.-(11) 7192
 Wecker, J.-(11) 7148
 Wei, J. Y. T.-(11) 7366
 Welch, D. O.-(11) 6274
 Welch, R. G.-(11) 6852
 Welipitiya, D.-(11) 6284, 7246
 Weller, D.-(11) 6489
 Wende, H.-(11) 6290, 7025, 7028
 White, R. M.-(11) 6512
 White, Robert L.-(11) 6816
 Wigen, P. E.-(11) 6590
 Wincheski, B.-(11) 6474
 Wirth, S.-(11) 6896, 7055
 Wolf, M.-(11) 7240
 Wolf, R. M.-(11) 6882
 Wolf, Stuart A.-(11) 7357
 Wolfman, J.-(11) 7186
 Wong, P. K.-(11) 6697
 Woo, J. S.-(11) 6480, 6483
 Woodfield, B. F.-(11) 6774
 Woollam, John A.-(11) 6747
 Wu, J. B.-(11) 7345
 Wu, J. M.-(11) 6771
 Wu, S. H.-(11) 6271
 Wu, S. Y.-(11) 7318, 7345
- Wun-Fogle, M.-(11) 7279, 7282, 7288
 Wuttig, Manfred-(11) 7264
 Wynn, C. M.-(11) 7378
- Xiao, Gang-(11) 6515, 7049, 7339
 Xiao, Yiaofu-(11) 6626
 Xu, You-(11) 6762
- Yakovlev, S. V.-(11) 7330
 Yakushiji, K.-(11) 6524
 Yamada, S.-(11) 7103
 Yamada, Y.-(11) 6527
 Yamaguchi, M.-(11) 7303
 Yamaguchi, T.-(11) 6861
 Yamamoto, Hidefumi-(11) 7210
 Yamamoto, T.-(11) 6917
 Yamamoto, Y.-(11) 6861
 Yamasaki, J.-(11) 7115
 Yamasawa, K.-(11) 6658
 Yan, X.-(11) 6530
 Yang, Choongjin-(11) 6620
 Yang, H. C.-(11) 6771
 Yang, Jinbo-(11) 6640, 6923
 Yang, Kun-(11) 7231
 Yang, Yingchang-(11) 6640, 6923
 Yao, Y. D.-(11) 6643
 Yeh, N. C.-(11) 6998, 7366
 Yelon, A.-(11) 6563, 6566
 Yelon, W. B.-(11) 6911, 6914, 7312, 7315
 Yeung, Wai Bong-(11) 6771
 Yori, T.-(11) 7031
 Young, S.-(11) 7103
 Yu, C. C.-(11) 7046
 Yu, M.-(11) 6611
 Yu, S. C.-(11) 7142
 Yu, Seong-Cho-(11) 6646
 Yu, X.-(11) 7055
 Yu, Y.-(11) 7106
 Yuasa, S.-(11) 6813, 7031
 Yusuf, S. M.-(11) 6801
- Zach, R.-(11) 7237
 Zeller, R.-(11) 7088
 Zeng, Qi-(11) 6626
 Zern, A.-(11) 6908
 Zhang, C.-(11) 6727
 Zhang, J.-(11) 6512
 Zhang, Tao-(11) 6326
 Zhang, X. G.-(11) 6521
 Zhang, X. X.-(11) 6934
 Zhao, X. G.-(11) 7276
 Zhao, Y.-(11) 6911
 Zhao, Y. G.-(11) 6780
 Zhao, Y. P.-(11) 6287
 Zhao, Z. G.-(11) 6727
 Zhao, Zhenjie-(11) 6923
 Zheng, Q. Q.-(11) 6596, 7100
 Zheng, Q. Q.-(11) 7363
 Zhou, X. Z.-(11) 7198
 Zhu, Jian-Gang-(11) 6223
 Zhu, Yimei-(11) 6414
 Zou, Liang-Jian-(11) 6596, 7100, 7363
 Zuberak, R.-(11) 6338
 Žutić, Igor-(11) 6804
 Zvezdin, A. K.-(11) 7160
 Zych, Dale-(11) 6974

AIP

Conference Proceedings from the American Institute of Physics are timely accounts of the important meetings in physics. To keep abreast of new developments, be sure to recommend them to your institution's librarian.

BRINGS THE CONFERENCE

TO YOU

394 NREL/SNL PHOTOVOLTAICS PROGRAM

REVIEW, Lakewood, CO, 18-22 November 1996 • Edited by C. E. Witt and M. Al-Jassim, *National Renewable Energy Laboratory*, and J. M. Gee, *Sandia National Laboratory* • June 1997, 1-56396-687-5, 957 pages, illustrated, cloth, 6x9, \$225.00

395 NONLINEAR AND COLLECTIVE PHENOMENA IN

BEAM PHYSICS - ICFA, Arcidosso, Italy, 2-6 September 1996 • Edited by S. Chattopadhyay, *Lawrence Berkeley National Laboratory*, M. Cornacchia, *Stanford Linear Accelerator Center*, and C. Pellegrini, *University of California, Los Angeles* • July 1997, 1-56396-668-9, 459 pages, illustrated, cloth, 6x9, \$115.00

396 NEW MODES OF PARTICLE ACCELERATION -

TECHNIQUES AND SOURCES, Santa Barbara, CA, 19-23 August 1996 • Edited by Z. Parsa, *Brookhaven National Laboratory* • August 1997, 1-56396-728-6, 208 pages, illustrated, cloth, 6x9, \$70.00

397 FUTURE HIGH ENERGY COLLIDERS

, Santa Barbara, CA, 21-25 October 1996 • Edited by Z. Parsa, *Brookhaven National Laboratory* • August 1997, 1-56396-729-4, 384 pages, illustrated, cloth, 6x9, \$110.00

398 ADVANCED ACCELERATOR CONCEPTS

, Lake Tahoe, CA, 12-18 October 1996 • Edited by S. Chattopadhyay, J. McCullough, and P. Dahl, *Lawrence Berkeley National Laboratory* • August 1997, 1-56396-697-2, 992 pages, illustrated, cloth, 6x9, \$220.00 • Book and CD-ROM packaged together.

399 THE CHANGING ROLE OF PHYSICS

DEPARTMENTS IN MODERN UNIVERSITIES:ICUPE, 31 July-2 August 1996 • Edited by E. F. Redish, *University of Maryland*, and J. S. Rigden, *American Institute of Physics* • October 1997, 1-56396-698-0, 1200 pages (2 vols.), illustrated, cloth, 6x9, \$165.00

400 FIRST LATIN AMERICAN SYMPOSIUM ON

HIGH ENERGY PHYSICS AND VII MEXICAN SCHOOL OF PARTICLES AND FIELDS, Yucatan, Mexico, 30 October-6 November 1996 • Edited by Juan Carlos D'Olivo, *ICN-UNAM*, M. Klein-Kreisler, *IF-UNAM*, and H. Mendez, *CINVESTAV* • September 1997, 1-56396-686-7, 608 pages, illustrated, cloth, 6x9, \$135.00

401 THERMOPHOTOVOLTAIC GENERATION OF

ELECTRICITY, Colorado Springs, CO, 18-21 May 1997 • Edited by J. P. Benner, and T. J. Coutts, *National Renewable Energy Laboratory* • September 1997, 1-56396-734-0, 608 pages, illustrated, cloth, 6x9, \$140.00

402 ASTROPHYSICAL IMPLICATIONS OF THE

LABORATORY STUDY OF PRESOLAR MATERIALS, 31 October-2 November 1996 • Edited by E. K. Zinner and T. J. Bernatowicz, *Washington University, St. Louis, MO* • October 1997, 1-56396-664-6, 768 pages, illustrated, cloth, 6x9, \$165.00

403 RADIO FREQUENCY POWER IN PLASMAS

, Savannah, GA, 1-3 April 1997 • Edited by P. M. Ryan, *Oak Ridge National Laboratory* and *Lockheed-Martin Energy Research Corp.*, and T. Intrator, *University of Wisconsin* • September 1997, 1-56396-709-X, 512 pages, illustrated, cloth, 6x9, \$120.00

404 FUTURE GENERATION PHOTOVOLTAIC

TECHNOLOGIES, Denver, CO 1997 • Edited by R. D. McConnell, *National Renewable Energy Laboratory* • October 1997, 1-56396-704-9, 464 pages, illustrated, cloth, 6x9, \$115.00

405 BEAM STABILITY AND NONLINEAR

DYNAMICS, Santa Barbara, CA, 3-5 December 1996 • Edited by Z. Parsa, *Brookhaven National Laboratory* • October 1997, 1-56396-731-6, 240 pages, illustrated, cloth, 6x9, \$80.00

406 LASER INTERACTION AND RELATED PLASMA

PHENOMENA • Edited by G. Miley, *University of Illinois* and E. M. Campbell, *Lawrence Livermore National Lab* • November 1997, 1-56396-696-4, 800 pages, illustrated, cloth, 6x9, \$185.00

407 DEEP INELASTIC SCATTERING AND QCD

, Chicago, Illinois, 14-18 April 1997 • Edited by J. Repond and D. Krakauer, *Argonne National Laboratory* • November 1997, 1-56396-716-2, 1088 pages, illustrated, cloth, 6x9, \$210.00

408 THE ULTRAVIOLET UNIVERSE AT LOW AND

HIGH REDSHIFT, College Park, MD, 2-4 May 1997 • Edited by W. H. Waller, M. N. Fanelli, J. E. Hollis, and A. C. Danks, *Hughes STX Corporation* and *NASA Goddard Space Flight Center, Greenbelt, MD* • November 1997, 1-56396-708-1, 544 pages, illustrated (color plates), cloth, 6x9, \$145.00

409 DENSE Z-PINCHES

, Vancouver, Canada, 28-31 May 1997 • Edited by N. Pereira, *Berkeley Research Associates*, J. Davis and P. Pulsifer, *Naval Research Lab* • December 1997, 1-56396-610-7, 656 pages, illustrated, cloth, 6x9, \$145.00

410 PROCEEDINGS OF THE FOURTH COMPTON

SYMPOSIUM: Part One: The Compton Observatory in Review - Part Two: Papers and Presentations, Williamsburg, Virginia, 27-30 April 1997 • Edited by C. D. Dermer, M. S. Strickman, and J. D. Kurfess, *Naval Research Laboratory* • December 1997, illustrated, 1760 pages (2-vol. set), cloth, 6x9 • **Part 1**: 1-56396-772-3, 592 pages, \$120.00; **Set**: 1-56396-659-X, \$300 **Note**: You may purchase the 2-vol. set or you may purchase only Part One separately.

411 APPLIED NONLINEAR DYNAMICS AND

STOCHASTIC SYSTEMS NEAR THE MILLENNIUM, University of California, San Diego, 7-11 July 1997 • Edited by J. B. Kadtko, *University of California, San Diego* and A. Bulsara, *Naval Command, Control, and Ocean Surveillance Center, San Diego* • November 1997, 1-56396-736-7, 384 pages, illustrated, cloth, 6x9, \$85.00

412 INTERSECTIONS BETWEEN PARTICLE AND

NUCLEAR PHYSICS, Big Sky Ski and Summer Resort, Big Sky, Montana, 27 May-2 June 1997 • Edited by T. W. Donnelly, *Massachusetts Institute of Technology* • December 1997, 1-56396-712-X, 1056 pages, illustrated, cloth, 6x9, \$225.00

413 TOWARDS X-RAY FREE ELECTRON LASERS

, Palazzo Feltrinelli, Gargnano, Garda Lake, Italy, 1-7 June 1997 • Edited by R. Bonifacio, *University of Milan* and W. A. Barletta, *Lawrence Berkeley National Lab* • December 1997, 1-56396-744-8, 352 pages, illustrated, cloth, 6x9, \$90.00

414 RESEARCH WORKSHOP ON TWO-DIMENSIONAL

TURBULENCE IN PLASMAS AND FLUIDS, The Australian National University (ANU), Canberra, Australia, 16 June-11 July 1997 • Edited by R. L. Dewar and R. W. Griffiths, *The Australian National University* • December 1997, 1-56396-764-2, 320 pages, illustrated, cloth, 6x9, \$90.00

415 BEYOND THE STANDARD MODEL V

, Balholm, Norway, 29 April-4 May 1997 • Edited by G. Eigen, P. Osland, and B. Stugu, *University of Bergen, Norway* • December 1997, 1-56396-735-9, 560 pages, illustrated, cloth, 6x9, \$145.00

416 SIMILARITIES AND DIFFERENCES BETWEEN

ATOMIC NUCLEI AND CLUSTERS, Tsukuba, Japan, 1-4 July 1997 • Edited by Y. Abe, *Kyoto University*, I. Arai and S. M. Lee, *University of Tsukuba*, and K. Yabana, *Niigata University* • January 1998 • 1-56396-714-6, 524 pages, illustrated, cloth, 6x9, \$124.00 (tent.)

417 SYNCHROTRON RADIATION INSTRUMENTATION

, Cornell University, Ithaca, NY, 17-20 June 1997 • Edited by E. Fontes, *Cornell University* • December 1997, 1-56396-742-1, 288 pages, illustrated, cloth, 8 1/2 x 11, \$95.00

418 STRESS INDUCED PHENOMENA IN

METALLIZATION, Tokyo, Japan, 4-6 June, 1997 • Edited by H. Okabayashi, *NEC Corporation*, S. Shingubara, *Hiroshima University*, and P. S. Ho, *University of Texas, Austin* • January 1998, 1-56396-682-4, 480 pages, illustrated, cloth, 6x9, \$130.00 (tent.)

419 TRENDS IN THEORETICAL PHYSICS

, La Plata, Argentina, 28 April-6 May 1997 • Edited by H. Falomir, R. E. Gamboa Saravi, and F. A. Schaposnik, *Universidad Nacional de la Plata* • January 1998, 1-56396-743-X, 464 pages, illustrated, cloth, 6x9, \$150.00

AMERICAN
INSTITUTE
OF PHYSICS

To order call 516-576-2411 or write: American Institute of Physics, Marketing Department, 500 Sunnyside Boulevard, Woodbury, NY 11797. Members of AIP Member Societies are entitled to a 20% discount.



"A PHYSICIST'S OFFICE ON THE WEB"



With **PINET Plus**, you have the world of physics—and the scientists behind it—all within arm's reach. It's a research library, news center, and conference hall all in one convenient site on the World Wide Web.

**Free two-week trial—
visit today!**
<http://www.aip.org/pinet>

**e-mail: pinet@aip.org
tel.: 800-874-6383
fax: 516-349-9704**

**AMERICAN
INSTITUTE
OF PHYSICS**

PINET Plus gives you:

- **SPIN** (Searchable Physics Information Notices)—this fully searchable, browsable database is your direct link to over 750,000 abstracts from more than 80 journals, from 1985 to the present; forty-five thousand new records are added annually, and SPIN offers online ordering for full-text articles of all entries
- **Advance SPIN**—available only on **PINET Plus**, this database lets you search or browse abstracts of articles in AIP, APS, OSA and other Society journals before publication
- **Early Alert Tables of Contents**—**PINET Plus** subscribers receive exclusive, automatic early notice of the contents of AIP journals of their choice, up to four weeks in advance of publication
- **News Center**—this up-to-the-minute information service posts the latest physics-related news from research centers worldwide. It also keeps track of science-related decisions made by the U.S. Congress and other policy-making institutions
- **Membership Directories**—this online Rolodex® contains over 150,000 names and addresses from seven member societies, as well as AIP's Directory of Physics and Astronomy Staff
- **Conference Hall**—**PINET Plus** offers special-interest discussion areas. Choose from hypermail environments devoted to Applications and Industry; Astronomy, Earth, and Space Science; Funding and Grants; Employment Issues; and others

SAVE TIME AND MONEY ON CORE RESEARCH

from *The Journal of Chemical Physics* &
the Journal of Applied Physics

JCP & JAP on the Web

For decades *The Journal of Chemical Physics* and *Journal of Applied Physics* have been among the leading publications reporting vital new research in the physical sciences. Now they are also available in powerful, convenient electronic formats that can save you time and money. *JCP* and *JAP* online editions are free with a print subscription, and their CD-ROM versions can save you as much as 60% off the regular print rate.

AIP's new Online Journal Service (OJS) brings print subscribers *free* access to highly enhanced, full-text electronic versions via the World Wide Web. Available 24 hours a day, seven days a week, *JCP* Online and *JAP* Online are posted more than three weeks before their print editions. Features include: fast searches, access to the SPIN database with abstracts from over 80 physics journals, and much more.

JCP & JAP on CD

On CD-ROM these indispensable journals offer you the speed and power of electronic searching, plus a comprehensive and compact archive—imagine holding 20,000 pages of *JCP* in the palm of your hand! "CD only" subscribers can also enjoy very substantial subscription savings—see details below.

Journal of Applied Physics—1998 Rates*

24 issues, quarterly CDs ISSN 0021-8979	U.S. & Possessions	Canada, Mexico, Cent. & S. America, Caribbean	Europe, Asia, Middle East, Africa, Oceania
print †	\$240	\$325	\$510
CD-ROM	205	205	205
CD-ROM & online	240	240	240
print, CD-ROM & online	290	375	560

Journal of Chemical Physics—1998 Rates*

48 issues, quarterly CDs ISSN 0021-9606	U.S. & Possessions	Canada, Mexico, Cent. & S. America, Caribbean	Europe, Asia, Middle East, Africa, Oceania
print †	\$270	\$380	\$530
CD-ROM	230	230	230
CD-ROM & online	270	270	270
print, CD-ROM & online	320	430	580

* Rates apply to Members of AIP Member and Affiliated Societies. Call for institutional rates.

† Print includes free online access.

If you are involved in chemical or applied research in the physical sciences, you'll want to subscribe to one or both of these premier journals. The only question is, which format? For more information, call 800-344-6902 or e-mail: subs@aip.org.

www.aip.org

**AMERICAN
INSTITUTE
OF PHYSICS**

500 Sunnyside Boulevard
Woodbury, NY 11797, USA

SIGN UP NOW! FREE with print in '98.

AIP's Online Journal Service — Creating a Whole New Research Environment

Subscribe to any AIP print journal in 1998 and you'll get access to a powerful online edition of that journal, at no additional charge. It's that easy. With the **Online Journal Service (OJS)**, you'll receive your Web version up to three weeks prior to receipt of your print copy. It's that fast.

Here are some exciting new features you'll enjoy in 1998:

- ▶ **Reference linking** — Now available on all AIP journals. Just click on an article citation and link to the referenced article's abstract in SPIN, INSPEC, and additional databases including LANL and SPIRES.
- ▶ **Online document delivery** — For journals to which you do not subscribe, download a PDF file by purchasing the article through our secure, online ordering system.
- ▶ **Full-Text HTML** — Available now for *Applied Physics Letters*. In addition to PDF and PostScript formats, you can now view articles in HTML and link to equations, tables, figures, and references. Print and download separately figures, tables, and sections of articles.
- ▶ **Article Collection** — Create your own "personal library" by storing articles of interest in a new virtual filing cabinet.

In addition, your 1998 Online Journal Service access includes — at no extra cost — a subscription to PINET Plus, your gateway to SPIN and to Advance SPIN, which give you cross-journal searching of over 80 physical science journals. PINET Plus also brings you news from national labs, searchable directories from leading science organizations, and much more.

AIP JOURNALS

- ▶ **Applied Physics Letters**
- ▶ **Chaos**
- ▶ **Computers in Physics**
(Archival Papers)
- ▶ **Journal of Applied Physics**
- ▶ **The Journal of Chemical Physics**
- ▶ **Journal of Mathematical Physics**
- ▶ **Physics of Fluids**
- ▶ **Physics of Plasmas**
- ▶ **Review of Scientific Instruments**

AIP TRANSLATION JOURNALS

- ▶ **JETP Letters**
- ▶ **Journal of Experimental and Theoretical Physics**
- ▶ **Low Temperature Physics**
- ▶ **Physics of Particles and Nuclei**
- ▶ **Semiconductors**
- ▶ **Technical Physics**
- ▶ **Technical Physics Letters**

For sign-up details and more information about the AIP Online Journal Service, visit our Web site at:
www.aip.org/ojs.
You can also call 800-344-6902 or 516-576-2270, or e-mail online@aip.org.